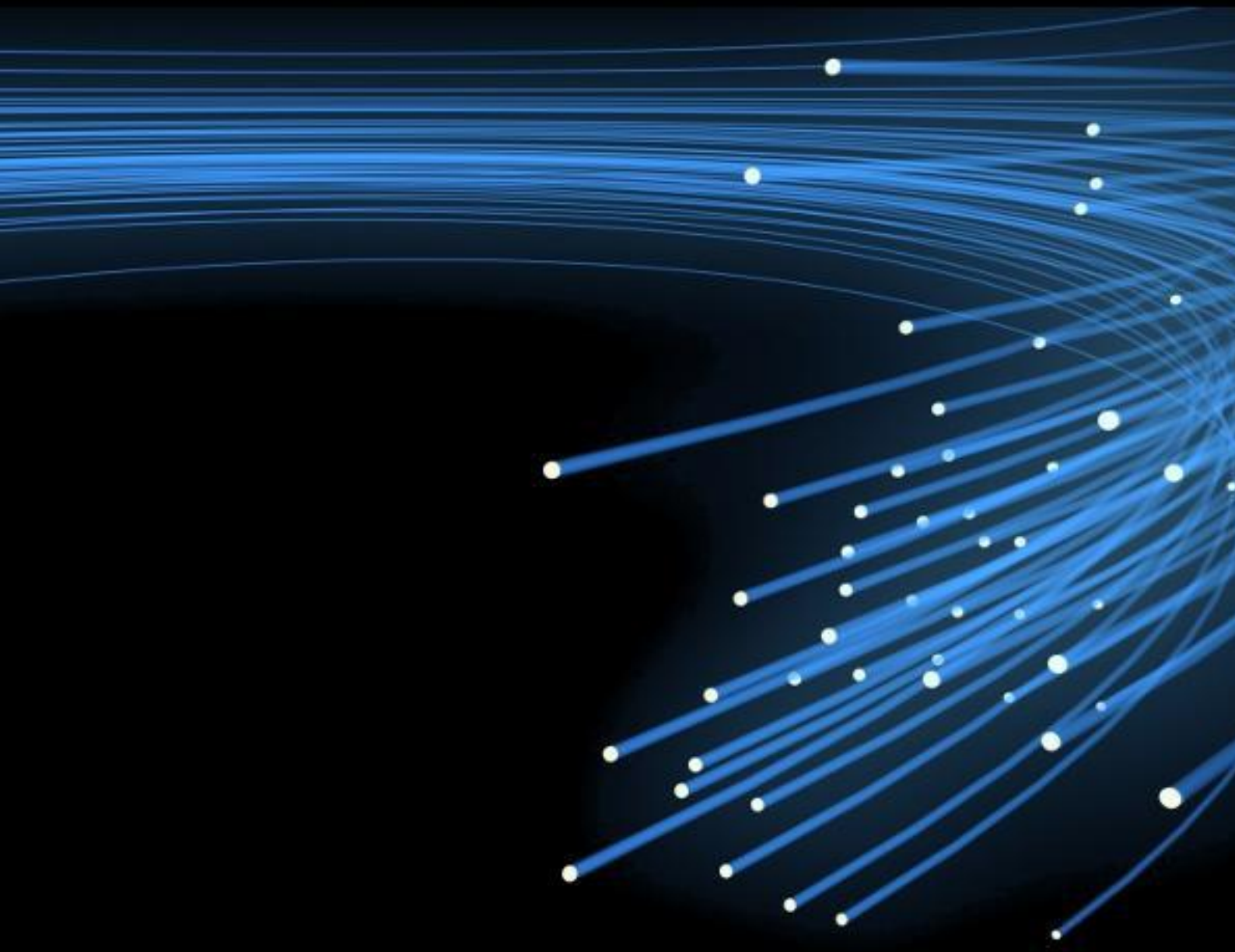
# META'16 Malaga - Spain

**The 7th International Conference on Metamaterials, Photonic Crystals and Plasmonics**



## Proceedings

**ISSN 2429-1390**

**metaconferences.org**


CSIC
CONSEJO SUPERIOR
DE INVESTIGACIONES
CIENTÍFICAS
UNIVERSITÉ
PARIS
SUD
CentraleSupélec
GeePS
Génie électrique et électronique de Paris
icmm
epl
A Letters Journal
Exploring the
Frontiers of Physics
NT-MDT
STS
ELIONIX
ACS
Photonics
Smart
Force
Technologies
Nanotechnology on your desk
CST
WITec
focus innovations
nea
see the nanoworld
spec
Photon
Design
ACS
OMEGA
Materials
Horizons
symmetry
an open access journal by

# META'16 Malaga - Spain

**The 7th International Conference on Metamaterials, Photonic Crystals and Plasmonics**

**Please share your comments, photos & videos !**




**www.facebook.com/metaconference**




**@metaconference ; #meta16malaga**

Edited by

Said Zouhdi | Paris-Sud University, France
Manuel Nieto-Vesperinas | CSIC, Spain

# CONTENTS

**META'16 ORGANIZATION** . . . . . 1
**SPONSORS AND SUPPORTERS** . . . . . 3
**PLENARY SPEAKERS** . . . . . 5
**KEYNOTE SPEAKERS** . . . . . 8
**META'16 VENUE** . . . . . 11
**TABLE OF CONTENTS** . . . . . 13

# META'16 ORGANIZATION



Said Zouhdi, General Chair
Paris–Sud University, France



Manuel Nieto-Vesperinas, General Co-Chair
CSIC, Spain

## ORGANIZING COMMITTEE



Inigo Molina Fernandez, Chair
Universidad de Malaga, Spain

Laurent Daniel, CentraleSupelec, France

Laurent Santandrea, GeePs–CNRS, France

## INTERNATIONAL ADVISORY COMMITTEE

Harry Atwater, USA
Federico Capasso, USA
Andre de Lustrac, France
Nader Engheta, USA
Tatsuo Itoh, USA
Yuri Kivshar, Australia
Graeme W. Milton, USA
Raj Mittra, USA
Susumu Noda, Japan
Masaya Notomi, Japan
Yahya Rahmat-Samii, USA
Vladimir Shalaev, USA
Ari Sihvola, Finland
David R. Smith, USA
J(Yiannis) Vardaxoglou, UK
Alexey Vinogradov, Russia
Martin Wegener, Germany
Nikolay Zheludev, UK

## TECHNICAL PROGRAM COMMITTEE

Javier Aizpurua, Spain
Tahsin Akalin, France
Xavier Begaud, France
Svetlana V. Boriskina, USA
Kurt Busch, Germany
Che Ting Chan, Hong Kong
Arkadi Chipouline, Germany
Johan Christensen, Spain
David T. Crouse, USA
Alexander Dmitriev, Sweden
Didier Felbacq, France
Michael A. Fiddy, USA
Monika Fleischer, Germany
Wolfgang Fritzsche, Germany
Francisco Garcia-Vidal, Spain
Alexander Govorov, USA
Ortwin Hess, United Kingdom
Rainer Hillenbrand, Spain
Zubin Jacob, Canada
Dai-Sik Kim, Korea
Joachim Krenn, Austria
Kristjan Leosson, Iceland
Jensen Li, Hong Kong
Ferran Martin, Spain
Martin McCall, UK
Fernando Moreno, Spain
Teri Odom, USA
Peter Nordlander, USA
Elyas Palantei, Indonesia
Dorota Pawlak, Poland
Cheng-Wei Qiu, Singapore
Min Qiu, China
Michael Stuke, Germany
Mohamed Swillam, Egypt
Takuo Tanaka, Japan
Giorgos P. Tsironis, Greece
Augustine Urbas, USA Joel K. W. Yang, Singapore
Anatoly V Zayats, UK
Xiang Zhang, USA
Lei Zhou, China

## SPECIAL SYMPOSIA ORGANIZERS



Alexander Govorov, USA



Xing Yi Ling, Singapore



Jerome Plain, France

## SPECIAL SESSIONS ORGANIZERS

Redha Abdeddaim, France
Pierre-Michel Adam, France
Hatice Altug, Switzerland
David Andrews, UK
Christos Argyropoulos, USA
Serkan Ates, Turkey
Pavel Belov, Russia
Henri Benisty, France
Mohamed Boutchich, France
Alberto Bramati, France
Jorge Bravo-Abad, Spain
Pierre-Francois Brevet, France
Humeyra Caglayan, Turkey
Alessandro Casaburi, UK
Bernard Casse, USA
Giulio Cerullo , Italy
Pavel Cheben, Canada
Pai-Yen Chen, USA
Xianzhong Chen, UK
Aristide Dogariu, USA
Ramy El-Ganainy, USA
Mohamed Farhat, Saudi Arabia
Liang Feng, USA
Roberto Fernandez-Garcia, UK
Bruno Gallas, France
Ruben Gerardo Barrera, Mexico
Vincent Ginis, USA
Francisco Gonzalez, Spain
Sebastien Guenneau, France
Robert Halir, Spain
Fumin Huang, UK
Yeon Sik Jung, Korea
Eugene Kamenetskii, Israel
Themos Kallos, Canada
Mikhail Kats, USA
Panagiotis Kosmas, UK
Laura M. Lechuga, Spain
Howard Lee, USA
Jensen Li, UK
Haitao Liu, China
Anatole Lupu, France
Renmin Ma, China
Boris Malomed, Israel
Fernando Moreno, Spain
Manuel Nieto-Vesperinas, Spain
Wounjhang (Won) Park, USA
Dorota Pawlak, Poland
Junsuk Rho, Korea
Juan J. Saenz, Spain
Jose A. Sanchez-Gil, Spain
Luca Sapienza, UK
Frank Scheffold, Switzerland
Wei-Chuan Shih, USA
Giuseppe Strangi, USA
Mohamed Swillam, Egypt
Philippe Tassin, Sweden
Vasily Temnov, France
Raa'nan Tobey, The Netherlands
Augusto G. Valenzuela, Mexico
Alexandre Vignaud, France
Silvia Vignolini, UK
Jian Wang, China
Hong Wei, China
Fangwei Ye, China
Shuang Zhang, UK

# SPONSORS AND SUPPORTERS

META'16 gratefully acknowledges the support of these institutions and companies for their contribution to the success of this conference :

## SUPPORTERS

CSIC

UNIVERSITÉ PARIS SUD

CentraleSupélec

icmm

GeePS
Génie électrique et électronique de Paris

## GOLD SPONSORS

epl A Letters Journal Exploring the Frontiers of Physics

**EPL**
**www.epljournal.org**

NT-MDT

**NT-MDT Co.**
**www.ntmdt.com**

STS ELIONIX

**STS-Elionix**
**www.sts-elionix.com**

ACS Photonics

**ACS Photonics**
**pubs.acs.org/photonics**

CST

**CST**
**www.cst.com**

**Smart Force Technologies**
**www.smartforcetechnologies.com**

## SILVER SPONSORS

**WITec**
**www.witec.de**

**Neaspec**
**www.neaspec.com**

**Photon Design**
**www.photond.com**

## BEST POSTER AWARD SPONSOR

**ACS Omega**
**pubs.acs.org/journal/acsodf**

**Materials Horizons**
**pubs.rsc.org**

## CONFERENCE SUPPORT PROGRAM SPONSOR

**Symmetry**
**www.mdpi.com/journal/symmetry**

# PLENARY SPEAKERS



## Andrea Alu

*University of Texas at Austin, USA*

### Breaking reciprocity and time-reversal symmetry with metamaterials

Andrea Alu is an Associate Professor and the Cockrell Family Dean's Chair in Engineering Excellence Fellow at the University of Texas at Austin. He received his PhD from the University of Roma Tre, Italy, in 2007 and, after a postdoc at the University of Pennsylvania, he joined the faculty of the University of Texas at Austin in 2009. His current research interests span over a broad range of areas, including metamaterials and plasmonics, electromagnetics, nano-optics, photonics and acoustics. Dr. Alu has authored and co-authored over 300 journal papers, he is a Fellow of IEEE, OSA, and APS, and has received several scientific awards, including the NSF Alan T. Waterman award (2015), the OSA Adolph Lomb Medal (2013), the URSI Issac Koga Gold Medal (2011), and the Edith and Peter O'Donnell Award in Engineering (2016).



## Harry Atwater

*California Institute of Technology, USA*

Harry Atwater is currently Howard Hughes Professor and Professor of Applied Physics and Materials Science at the California Institute of Technology. His research interests center around two interwoven research themes : photovoltaics and solar energy ; and plasmonics and optical metamaterials. Atwater and his group have been active in photovoltaics research for more than 20 years. Recently they have created new photovoltaic devices, including silicon wire array solar cells, and transferred-layer designs for III-V semiconductor and multijunction cells. They are making exciting advances in plasmonic light absorber structures for III-V compound and silicon thin films. Atwater is an early pioneer in surface plasmon photonics ; he gave the name to the field of plasmonics in 2001. He has authored or co-authored over 200 publications, and his group's developments in the solar and plasmonics field have been featured in Scientific American and in research papers in Science, Nature Materials, Nature Photonics and Advanced Materials.



## Stephen M. Barnett

*University of Glasgow, UK*

### Optical forces on exotic materials

Stephen Barnett studied for both his Bachelors and Doctoral degrees at Imperial College London, receiving his PhD in 1985. He is currently the Cargill Chair of Natural Philosophy at the University of Glasgow. His principal field of expertise is in quantum theory, most especially quantum optics and quantum information, but he has very wide research interests including atomic physics, optics, relativity, low temperature physics and aspects of chiral chemistry. He is best known for his discovery with David Pegg of the correct form of the quantum phase operator, his resolution of the long-standing Abraham-Minkowski dilemma concerning he momentum of light in a medium, and his extensive work with Miles Padgett on the angular momentum of light. His contributions have been recognised through the awards of the Maxwell Medal (1994) and the Dirac Prize (2013).



## Nader Engheta

*University of Pennsylvania, USA*

### Near-Zero Photonics

Nader Engheta, is the H. Nedwill Ramsey Professor at the University of Pennsylvania in Philadelphia, with affiliations in the Departments of Electrical and Systems Engineering, Materials Science and Engineering, Physics and Astronomy, and Bioengineering. He received his B.S. degree from the University of Tehran, and his M.S and Ph.D. degrees from Caltech. He has received several awards for his research including the 2015 Fellow of US National Academy of Inventors (NAI), the 2015 Gold Medal from SPIE (the international society for optics and photonics), the 2015 National Security Science and Engineering Faculty Fellowship (NSSEFF) Award from US Department of Defense, the 2015 IEEE Antennas and Propagation Society Distinguished Achievement Award, the 2015 Wheatstone Lecture in King's College London, the 2014 Balthasar van der Pol Gold Medal from the International Union of Radio Science (URSI), the 2013 Inaugural SINA Award in Engineering, the 2013 Benjamin Franklin Key Award, the 2012 IEEE Electromagnetics Award, the 2008 George H. Heilmeier Award for Excellence in Research, the Fulbright Naples Chair Award, NSF Presidential Young Investigator award, the UPS Foundation Distinguished Educator term Chair, 2006 Scientific American Magazine 50 Leaders in Science and Technology, Guggenheim Fellowship, and IEEE Third Millennium Medal. He is a Fellow of six international scientific and technical societies, i.e., IEEE, APS, OSA, MRS, SPIE, and American Association for the Advancement of Science (AAAS). His current research activities span a broad range of areas including nanophotonics, metamaterials, nano-scale optics, graphene optics, imaging and sensing inspired by eyes of animal species, optical nanoengineering, microwave and optical antennas, and engineering and physics of fields and waves. He has co-edited (with R. W. Ziolkowski) the book entitled "Metamaterials : Physics and Engineering Explorations" by Wiley-IEEE Press, 2006. He was the Chair of the Gordon Research Conference on Plasmonics in June 2012.



## Demetrios Christodoulides

*University of Central Florida, USA*

Demetrios Christodoulides is the Cobb Family Endowed Chair and Pegasus Professor of Optics at CREOL-the College of Optics and Photonics of the University of Central Florida. He received his Ph.D. degree from Johns Hopkins University in 1986 and he subsequently joined Bellcore as a postdoctoral fellow at Murray Hill. Between 1988 and 2002 he was with the faculty of the Department of Electrical Engineering at Lehigh University. His research interests include linear and nonlinear optical beam interactions, synthetic optical materials, optical solitons, and quantum electronics. He has authored and co-authored more than 250 papers. He is a Fellow of the Optical Society of America and the American Physical Society. In 2011 he received the R.W. Wood Prize of OSA.

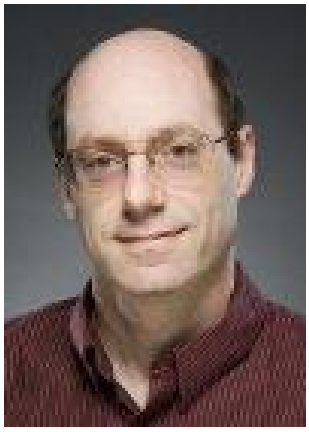


## Sir John Brian Pendry

*Imperial College London, UK*

### Transformation optics, surface plasmons, and metasurfaces

Sir John B. Pendry is an English theoretical physicist educated at Downing College, Cambridge, UK, graduating with a Master of Arts degree in Natural Sciences and a PhD in 1969. He is a professor of theoretical solid - state physics at Imperial College London where he was Head of the Department of Physics (1998 - 2001) and Principal of the Faculty of Physical Sciences (2001 - 2002). John Pendry has made seminal contributions to surface science, disordered systems and photonics. His most famous work has introduced a new class of materials, metamaterials, whose electromagnetic properties depend on their internal structure rather than their chemical constitution. He discovered that a perfect lens manufactured from negatively refracting material would circumvent AbbeÊijs diffraction limit to spatial resolution, which has stood for more than a century. His most recent innovation of transformation optics gives the metamaterial specifications required torearrange electromagnetic field configurations at will, by representing the field distortions as a warping of the space in which they exist. In its simplest form the theory shows how we can direct field lines around a given obstacle and thus provide a cloak of invisibility. John Pendry's outstanding contributions have been awarded by many prizes, among which the Dirac Prize(1996), the Knight Bachelor (2004), the Royal Medal (2006), the Isaac Newton Medal (2013) and the Kavli Prize (2014).



## David R. Smith

*Duke University, USA*

### Translational Metamaterials Research : Taking Metamaterials from the Laboratory to the Marketplace

David R. Smith is currently the James B. Duke Distinguished Professor of Electrical and Computer Engineering Department at Duke University and Director of the Center for Metamaterial and Integrated Plasmonics. He also holds the positions of Adjunct Associate Professor in the Physics Department at the University of California, San Diego, and Visiting Professor of Physics at Imperial College, London. Dr. Smith received his Ph.D. in 1994 in Physics from the University of California, San Diego (UCSD). Dr. Smith's research interests include the theory, simulation and characterization of unique electromagnetic structures, including photonic crystals and metamaterials.
Smith and his colleagues at UCSD demonstrated the first left-handed (or negative index) metamaterial at microwave frequencies in 2000–a material that had been predicted theoretically more than thirty years prior by Russian physicist Victor Veselago. No naturally occurring material or compound with a negative index-of-refraction had ever been reported until this experiment. In 2001, Smith and colleagues followed up with a second experiment confirming one of Veselago's key conjectures : the 'reversal' of Snell's law. These two papers–the first published in Physical Review Letters and the second in Science–generated enormous interest throughout the community in the possibility of metamaterials to extend and augment the properties of conventional materials. Both papers have now been cited nearly 4,000 times each.

# KEYNOTE SPEAKERS



## David Andrews

*University of East Anglia, UK*

**Exploring nanoscale chirality : issues of parity, scale and measurement**



## Federico Capasso

*Harvard University, USA*

**High Performance Visible Wavelength Dielectric Metasurfaces for Planar Photonic Components**



## Benoit Deveaud

*EPFL, Switzerland*

**Microcavity polaritons : fundamental physics and devices**



## Nicholas X. Fang

*MIT, USA*



## Mathias Fink

*Institut Langevin, France*

**Wave Control with space-time transformations**



## Javier Garcia de Abajo

*ICFO-The Institute of Photonic Sciences, Spain*

**Nanoplasmonics in 2D and atomic-scale materials**



## Alexander Govorov

*Ohio University, USA*

**Quantum Phenomena in Hybrid Nanostructures : Exciton-Plasmon Interactions and the Quantum Structure of the Plasmon Excitations**



## Laura M. Lechuga

*Catalan Institute of Nanoscience and Nanotechnology (CSIC), Spain*

**Nanoplasmonic biosensors for real applications : trends and challenges**



## Boris Luk'yanchuk

*Data Storage Institute (A*STAR), Singapore*

**Selected problems of light scattering by dielectric nanostructures**



## Teri W. Odom

*Northwestern University, USA*

**Real-time Tunable Nanoparticle Lasing Spasers**



## Omar Ramahi

*University of Waterloo, Canada*

**Metamaterial Elements as Huygens Radiators**



## Juan Jose Saenz

*Donostia International Physics Center (DIPC), Spain*

**Casimir-like forces between particles under fluctuating optical fields**



## Vladimir Shalaev

*Purdue University, USA*

**Nanophotonics with Plasmonic Ceramics**



## Ari Sihvola

*Aalto University, Finland*

**Anisotropy makes the difference : systropic, bulbic, and porcupic metamaterials**



## Marin Soljacic

*MIT, USA*

**Topologically Non-Trivial States in Photonic Crystals**

# META'16 VENUE

META'16 will be held at the **Palacio de Congresos y Exposiciones de la Costa del Sol** (Torremolinos Congress Center), 3 Calle Mexico, 29620 **Torremolinos**, Spain, from **25 to 28 July 2016**.




## GETTING TO VENUE

### Address

**Palacio de Congresos y Exposiciones de la Costa del Sol**, 3 Calle Mexico, 29620 **Torremolinos**, Spain.

### Getting to Torremolinos from Malaga Airport

Torremolinos is around 8km away from Malaga international airport. You can go from the airport to the city center by taxi, by train or by bus.

### By Taxi

The airport has a well-signposted taxi rank outside the arrivals area of Terminal T3. Make sure that the taxi driver has started the taximeter at the beginning of the journey (minimum fare). We recommend requesting a receipt for any complaint or claim. The cost of a taxi from the airport into Torremolinos City Centre will cost between €15-20 depending on your time of travel.

### By Train

The new suburban train station in the new Terminal T3 building links the airport with Torremolinos city centre and other cities like Benalmadena and Fuengirola in one direction, and it links Malaga city center in the other direction.

The new train station is situated underground and accessed via escalators. It is well signposted and can be reached via the square outside arrivals or outside departures. Before the station entry barriers you will see several self-service tickets machines on your right where you can buy your tickets.

The first train to Torremolinos leaves the airport at 05 :32, leaving every 20-30 minutes until the last train at 23.42. Line : C1. Estimated travel time : 10 minutes. The single fare for this journey is €1.80.

### By Bus

You will find the bus stop straight in front of you outside the arrivals area of Terminal T3 on the side of the road where there are a couple of shelters with seats.

You will also see a ticket office in the left hand corner of the arrivals forecourt where you should purchase your tickets for the journey. Line : Torremolinos-Benalmadena-Airport. Estimated travel time : 30

minutes. The single fare for this journey is €3.80.

### Getting to Torremolinos from Malaga train station

There are two train stations in the centre of Malaga : Maria Zambrano and Centro Alameda. Maria Zambrano station provides high-speed (AVE) and long-distance links to many Spanish cities like Barcelona, Cordoba, Madrid, Santiago de Compostela, Seville..., as well as local and regional routes.

You can take Line C1 from any of the two stations to reach Torremolinos. Estimated travel time : 20 minutes. The single fare for this journey is âĆň1.80. You can check the timetables on the website of the national rail company RENFE (http ://www.renfe.com/viajeros/cercanias/malaga/).

### Getting to Torremolinos from Malaga bus station

Malaga bus station is located at the street "Paseo de los Tilos" very near Maria Zambrano train station. So it will be very easy to take a bus or a train from this station. You can take bus line Malaga-Torremolinos. Estimated travel time : 20 minutes. The single fare for this journey is €1.42.

# TABLE OF CONTENTS

## Plenary Presentation

**Transformation optics, surface plasmons, and metasurfaces (pp. 89)**
*John B. Pendry,*

**Breaking reciprocity and time-reversal symmetry with metamaterials (pp. 90)**
*Andrea Alu,*

**Photonic design of nanoscale energy converters (pp. 91)**
*Harry Atwater,*

**Optical forces on exotic materials (pp. 92)**
*Stephen Barnett,*

**Near-Zero Photonics (pp. 93)**
*Nader Engheta,*

**Non-Hermitian photonics: PT symmetry and beyond (pp. 94)**
*Demetrios N. Christodoulides,*

**Translational Metamaterials Research: Taking Metamaterials from the Laboratory to the Marketplace (pp. 95)**
*David R. Smith,*

## Keynote Presentation

**Anisotropy makes the difference: systropic, bulbic, and porcupic metamaterials (pp. 97)**
*Ari Sihvola, Tommi Rimpilainen, Henrik Wallen,*

**Selected problems of light scattering by dielectric nanostructures (pp. 99)**
*Boris Luk'yanchuk, Ramon Paniagua-Dominguez, A. Kuznetsov,*

**Exploring nanoscale chirality: issues of parity, scale and measurement (pp. 101)**
*David L. Andrews,*

**Real-time Tunable Nanoparticle Lasing Spasers (pp. 103)**
*Teri W. Odom,*

**High Performance Visible Wavelength Dielectric Metasurfaces for Planar Photonic Components (pp. 105)**
*Federico Capasso,*

**Quantum Phenomena in Hybrid Nanostructures: Exciton-Plasmon Interactions and the Quantum Structure of the Plasmon Excitations (pp. 107)**
*Alexander Govorov,*

**Casimir-like forces between particles under fluctuating optical fields (pp. 108)**
*Juan Jose Saenz,*

**Tunable Light-matter Interaction With Quantum Spillover and Super-radiance in Two Dimensional Molecular Aggregates (pp. 110)**

*Nicholas X. Fang,*

**Wave Control with space-time transformations (pp. 111)**
*Mathias Fink,*

**Nanoplasmonic biosensors for real applications: trends and challenges (pp. 112)**
*Laura M. Lechuga,*

**Metamaterial Elements as Huygens Radiators (pp. 113)**
*Omar Ramahi,*

## PT-symmetry in photonics, metamaterials and plasmonic systems

**Parity-Time Symmetry in Organic Thin Films and Waveguides (pp. 116)**
*Noel C. Giebink,*

**Conserved Quantities and Phase Locking in PT-symmetric Lattices (pp. 118)**
*A. K. Harter, F. A. Onanga, Yogesh N. Joglekar,*

**Linear and Nonlinear Light Propagation in PT-Symmetric Fiber Networks (pp. 119)**
*Martin Wimmer, Mohammad-Ali Miri, Alois Regensburger, Christoph Bersch, Demetrios N. Christodoulides, Ulf Peschel,*

**Side-coupled resonators with parity-time symmetry for broadband unidirectional invisibility (pp. 121)**
*Nicolas Rivolta, Bjorn Maes,*

**Revival of bistable state near the exceptional point of a non-Hermitian photonic molecule (pp. 123)**
*Ke-jia Zhu, Yong Sun, Jie Ren, Haitao Jiang, Hong Chen,*

**The Lorentz group and PT-symmetric waveguide couplers. (pp. 125)**
*Blas Manuel Rodriguez-Lara, Julio Guerrero,*

**Graphene-based PT-symmetric structures (pp. 127)**
*Yuliy Bludov,*

**Parity-time symmetric analogy of relativistic electrodynamics (pp. 129)**
*Sunkyu Yu, Xianji Piao, Namkyoo Park,*

**Parity-Time Symmetric Chain Resonators (pp. 131)**
*Sendy Phang, Ana Vukovic, Stephen C. Creagh, Gabriele Gradoni, Phillip D. Sewell, Trevor Benson,*

**Constant-Intensity waves in Media with Gain and Loss (pp. 133)**
*Konstantinos Makris, Andre Brandstotter, Philipp Ambichl, Ziad Musslimani, Demetrios Christodoulides, Stefan Rotter,*

**Parity-time symmetry and nonreciprocal light transmission in high-Q microcavity systems (pp. 134)**
*Min Xiao, Xiaoshun Jiang, Long Chang, Jianming Wen, Liang Jiang,*

**Unidirectional Reflectivity in Quarter Stacks with Balanced Losses/Gains (pp. 136)**
*Josue Ramirez-Hernandez, Felix Izrailev, Nykolay Makarov, Demetrios Christodoulides,*

**Field concentration by local PT-symmetry and global P-symmetry (pp. 138)**
*Waqas Wasseem Ahmed, Muriel Botey, Ramon Herrero, Kestutis Staliunas,*

**PT-symmetry control with spatial and temporal modulations (pp. 140)**
*Andrey A. Sukhorukov,*

**Control of Power in Parity-Time Symmetric Lattices (pp. 141)**
*Maksim Kozlov, Georgios Tsironis,*

**Origin of folded bands in metamaterial crystals (pp. 143)**
*Peter Markos, Richard Hlubina,*

**Non-Hermitian Acoustics (pp. 145)**
*Hamidreza Ramezani, Chengzhi Shi, Marc Dubois, Yuan Wang, Xiang Zhang,*

**Rings of Exceptional Points (pp. 147)**
*Marin Soljacic,*

**Tailoring spectral properties of local Parity-Time symmetry grating devices for integrated optics (pp. 148)**
*Anatole Lupu, Henri Benisty, Andrei V. Lavrinenko,*

## Plasmonics and Nanophotonics Based on Graphene and Related 2D Materials

**Hybrid Graphene Metasurfaces to Control Electromagnetic Radiation (pp. 151)**
*Christos Argyropoulos,*

**Controlling the tunability of graphene in bridged and unbridged nano-disk dimers (pp. 153)**
*Gilles Rosolen, Bjorn Maes,*

**Light Manipulation in Cylindrical Graphene-Covered Gyrotropic Structures (pp. 155)**
*Dmitry Kuzmin, Igor Bychkov, Vladimir Shavrov,*

**Ultrafast Plasmon Emission and Hot Carrier Dynamics in Photoexcited Graphene (pp. 157)**
*Joachim Michael Hamm, A. F. Page, J. Bravo-Abad, F. J. Garcia-Vidal, O. Hess,*

**Electrical Detection of Graphene Plasmons (pp. 159)**
*Renwen Yu, Javier Garcia de Abajo,*

**Plasmon-assisted complete optical absorption of ultrashort pulses in nanostructured graphene (pp. 161)**
*Jose Ramon Martinez-Saavedra, Giulio Cerullo, Valerio Pruneri, Simon Wall, Javier Garcia de Abajo,*

**Classical and quantum plasmonics in nanostructured graphene (pp. 162)**
*Martijn Wubs, Thomas Christensen, Weihua Wang, Antti-Pekka Jauho, N. Asger Mortensen,*

**Surface acoustic wave-assisted plasmonics in graphene (pp. 164)**
*Jorge Pedros, Jurgen Schiefele, Alberto Bosca, Javier Martinez, Fernando Sols, Francisco Guinea, Fernando Calle,*

**Nanoplasmonics in 2D and atomic-scale materials (pp. 166)**
*Javier Garcia de Abajo,*

**Experimental Demonstration of Unidirectional Terahertz Waves Propagation Using Graphene (pp. 168)**
*Michele Tamagnone, Clara Fausta Moldovan, Jean-Marie Poumirol, Alexey B. Kuzmenko, Adrian Mihai Ionescu, Juan Ramon Mosig,*

**Long-range Tamm surface plasmons in graphene metamaterials (pp. 170)**
*Hodjat Hajian, Humeyra Caglayan, Ekmel Ozbay,*

**Graphene Plasmonics for Controlled Manipulation of Sub 2 nm Nanoparticles (pp. 172)**
*Mohammad Danesh, Zhengtong Liu, Cheng-Wei Qiu,*

**Ultrasensitive PT-Symmetric Graphene Quantum-Capacitance Sensors (pp. 174)**
*Pai-Yen Chen,*

**Graphene-based van-der-Waals heterostructure plasmonic metamaterials for terahertz device applications (pp. 175)**
*Taiichi Otsuji, Dmitry Svintsov, Alexander Dubinov, Deepika Yadav, Stephane Boubanga Tombet, Takayuki Watanabe, Akira Satou, Victor Ryzhii, Vladimir Mitin, Michael Shur,*

## Industrial Applications of Metamaterials

**Additive manufacturing of dielectric lenses for electromagnetic beam control (pp. 178)**
*Jianjia Yi, Andre de Lustrac, Gerard-Pascal Piau, Shah Nawaz Burokur,*

**Modeling and design of metasurfaces for beam scanning (pp. 180)**
*Badreddine Ratni, Andre de Lustrac, Gerard-Pascal Piau, Shah Nawaz Burokur,*

**Accelerating Metamaterial Design (pp. 182)**
*Tryfon Antonakakis, Mehul Makwana,*

**Investigation of deformation on microstructures in shape memory Cu69.95Zn26.04Al4.01 Alloy (pp. 184)**
*Emine Aldirmaz, Harun Celik, Meryem Evecen, Y. O. Ciftci,*

**Refractory plasmonic materials for high temperature plasmonic devices (pp. 185)**
*Urcan Guler, Ernesto Marinero, Alexandra Boltasseva, Vladimir Shalaev,*

**Study of Phase formation in rapidly and slowly quenched Cu-13.81 percent Mn-3.7 percent Al Alloy (pp. 187)**
*Emine Aldirmaz, Meryem Evecen, Hasan Tanak,*

**Nanoantenna-Enhanced Infrared Detectors for Improved Performance and Spectral Tunability (pp. 188)**
*David W. Peters, J. K. Kim, A. Tauke-Pedretti, T. E. Beechem, J. F. Ihlefeld, P. Davids, M. B. Sinclair, J. R. Wendt,*

**Surface wave-based field confinement device for UHF-RFID readers (pp. 190)**
*Jordi Bonache, Gerard Zamora, Ferran Paredes, Simone Zuffanelli, Pau Aguila, Ferran Martin,*

**Metamaterial Structures Applied to Wireless RF Front-End Distributed PA, BAW Filters, and Antennas (pp. 192)**
*Maha Achour,*

**ISM (Industry Scientific and Medical standard) band flex fuel sensor using electrical metamaterial device (pp. 193)**
*V. Rawat, Vihang Nadkarni, Sangeeta Narendra Kale,*

**Metamaterials Research at PARC (pp. 197)**

*Bernard D. Casse,*

**Commercializing Metamaterials Through the Lens of the Mythical Man Month (pp. 198)**
*Themos Kallos,*

## Quantum plasmonics and metamaterials

**Quantum metamaterials as active lasing medium: Effects of disorder (pp. 200)**
*Michael Marthaler, Martin Koppenhofer, Gerd Schon,*

**Single solid-state quantum emitters for plasmonics (pp. 202)**
*X. Wu, P. Jiang, H. Zhang, M. Pfeiffer, K. Lindfors, A. Rastelli, O. G. Schmidt, M. Lippitz,*

**Quantum Metamaterials with quantum dots (pp. 203)**
*Emmanuel Rousseau, Felbacq Didier,*

**Photonic Integrated Circuits with On-Chip Single-Photon Emitters (pp. 205)**
*Peter Michler,*

**Hybrid nanophotonics and light-matter interaction (pp. 207)**
*Femius Koenderink,*

**Quantum Many-Body Theory of Nonlocal Electromagnetic Response at Metallo-Dielectric Interfaces (pp. 208)**
*Fouad Ballout, Joachim Hamm, Ortwin Hess,*

**Exploring nm-scale plasmonic cavities through light (pp. 210)**
*Jeremy J. Baumberg, Anna Lombardi,*

**Coupling of quantum emitters and single plasmonic particles for quantum non-linear elements (pp. 211)**
*Gunter Kewes, Alexander Kuhlicke, Andreas W. Schell, Oliver Benson,*

**Light Emission in Nanogap Emitting Devices: efficiency issues (pp. 213)**
*R. Faggiani, J. Yang, P. Lalanne,*

**Broadband Purcell enhancement in highly efficient photonic nanowire-based single-photon sources (pp. 214)**
*Niels Gregersen, Dara P. S. McCutcheon, Jesper Mork, Julien Claudon, Jean-Michel Gerard,*

**Controlling quantum states of light with plasmonic metamaterials (pp. 216)**
*Mark Tame,*

**Quantum Optics with One-Dimensional Artificial Atoms (pp. 218)**
*Niccolo Somaschi, V. Giesz, L. De Santis, G. Hornecker, T. Grange, B. Reznychenko, J. Demory, C. Gomez, I. Sagnes, A. Lemaitre,*

**Noise induced narrowing of metamolecule fluorescence spectral line (pp. 220)**
*Evgeny Andrianov, Nikolay Chtchelkatchev, Alexander Pukhov,*

**The role of spontaneous emission in the plasmon distribute feedback laser (pp. 222)**
*Alexander Andreevich Zyablovsky, Igor Alexandrovich Nechepurenko, Eugeny Sergeevich Andrianov, Alexander Victorovich*

*Dorofeenko, Alexey Petrovich Vinogradov, Alexander Alexandrovich Pukhov, Alexander Abramovich Lisyansky,*

**Quantum Dot Microlenses: Building Blocks for Quantum Communication Networks (pp. 224)**
*A. Thoma, M. Gschrey, P. Schnauber, A. Kaganskiy, S. Fischbach, R. Schmidt, B. Wohlfeil, M. Seifried, J.-H. Schulze, S. Burger,*

**Quasinormal mode approach to modelling light-matter interactions in quantum-dot plasmonic resonator systems (pp. 226)**
*Stephen Hughes,*

**Quantum Photonics (pp. 228)**
*David Zueco, Eduardo Sanchez-Burillo, Juanjo Garcia-Ripoll, Luis Martin-Moreno,*

## Current Advances in Electromagnetics of Metal and HRI dielectric nanostructures

**Optical spectroscopy of individual nano-objects in correlation with electron microscopy imaging: plasmon interferences in strongly coupled systems (pp. 230)**
*Emmanuel Cottancin,*

**Spherical silicon photonic microcavities: Looking inside (pp. 232)**
*Roberto Fenollosa, Moises Garin, Francisco Meseguer,*

**The magnetic response in high-index nanophotonics: from magnetic hot-spots to Huygens' sources and generalized Brewster's effect (pp. 234)**
*Ramon Paniagua-Dominguez, Y. F. Yu, R. M. Bakker, Y. H. Fu, B. Luk'yanchuk, A. I. Kuznetsov,*

**Dielectric nanoantennas as a new way to enhance and direct scattered light with minimal losses (pp. 236)**
*Pablo Albella, Toshihiko Shibanuma, Stefan A. Maier,*

**Localized magnetic plasmons in all-dielectric structures (pp. 238)**
*Ramon Paniagua-Dominguez, Luis S. Froufe-Perez, J. J. Saenz, J. A. Sanchez-Gil,*

**Analysis of directionality effects in magnetodielectric core-shell nanoparticles by means of polarimetric techniques (pp. 240)**
*Angela Inmaculada Barreda, Yael Gutierrez Vela, Juan Marcos Sanz, Francisco Gonzalez, Fernando Moreno,*

**Studying Individual Nanostructures using Light Tailored at the Nanoscale (pp. 242)**
*Peter Banzer, Gerd Leuchs,*

**Broadband Enhancement or Inhibition of Spontaneous Photon Emission in the Vicinity of Nanometer-Sized Silicon Resonators (pp. 244)**
*Dorian Bouchet, Mathieu Mivelle, Julien Proust, Bruno Gallas, Igor Ozerov, Maria F. Garcia-Parajo, Yannick De Wilde, Nicolas Bonod, Valentina Krachmalnicoff, Sebastien Bidault,*

**Subwavelength flat-lensing of hybrid nanowire metamaterial with low-loss, isotropic optical negative-index behavior (pp. 246)**
*Diego R. Abujetas, Ramon Paniagua-Dominguez, Manuel Nieto-Vesperinas, Jose Antonio Sanchez-Gil,*

**Magneto-optical activity in high-index dielectric materials (pp. 248)**
*Nuno de Sousa, Juan Jose Saenz, Antonio Garcia-Martin,*

**Integration of metallic and dielectric nanostructures in silicon waveguides: properties and applications (pp. 250)**
*Alejandro Martinez,*

**Effect of the oxide shell thickness on the UV plasmonic performance of Ga, Mg and Al nanoparticles (pp. 252)**
*Yael Gutierrez, Dolores Oritz, Juan Marcos Sanz, Francisco Gonzalez, Jose Maria Saiz, Henry. O. Everitt, Fernando Moreno,*

**Quantum plasmons on topological particle surface (pp. 254)**
*Vincenzo Giannini,*

**Precise Nanoparticle Localization using Complex Spatial Modes of Light (pp. 255)**
*Ankan Bag, Martin Neugebauer, Pawel Wozniak, Gerd Leuchs, Peter Banzer,*

**Controllable excitation of a high refractive-index dielectric nanoparticle using a tightly focused vector beam (pp. 257)**
*Pawel Wozniak, Gerd Leuchs, Peter Banzer,*

**Active Semiconductor THz metasurfaces (pp. 259)**
*Jaime Gomez Rivas, A. Batthacharya, G. Georgiou, A. Halpin,*

**Metallo-dielectric sensor: toward zeptogram-scale colorimetric sensing (pp. 260)**
*Julien Proust, Jerome Martin, Davy Gerard, Jean-Louis Bijeon, Jerome Plain,*

**Studying light concentration in a dimer of semiconductor nanoparticles for all-optical devices (pp. 262)**
*Ricardo Vergaz, Francisco Algorri, Alexander Cuadrado, Virginia Urruchi, Jose Manuel Sanchez-Pena, Braulio Garcia-Camara,*

**Magnetic properties of a mixture of a Liquid Crystal doped with Semiconductor Nanoparticles (pp. 264)**
*Vicente Marzal, Braulio Garcia-Camara, Isabel Perez, Jose Manuel Sanchez-Pena,*

**Full-solution process approach for tailoring light-matter interaction at the nanoscale (pp. 266)**
*Juan F. Galisteo-Lopez, Alberto Jimenez-Solano, Hernan Miguez,*

**Graphene as a tunable plasmonic metasurface with transformation optics (pp. 268)**
*Paloma Arroyo Huidobro, Matthias Kraft, Stefan A. Maier, John B. Pendry,*

**Self-assembled disorder in photonic materials (pp. 270)**
*Alvaro Blanco, Denise Montesdeoca, Cefe Lopez, Jose Angel Pariente, Carlos Pecharroman,*

**Towards the Polarization Control of the Directional Scattering of Semiconductor Nanodisks (pp. 271)**
*Ricardo Vergaz, Francisco Algorri, Alexander Cuadrado, Jose Manuel Sanchez-Pena, Braulio Garcia-Camara,*

**Tunable Negative Nano Composites for Low Frequency Metamaterials (pp. 273)**
*Carlos Pecharroman, Lucia Fernandez, Miguel Morales, Celia Mallada, Jose Luis Menendez,*

**Controlling harmonic generation in plasmonic systems (pp. 275)**
*Ruben Esteban, Garikoitz Aguirregabiria, Dana-Codruta Marinica, Andrey K. Kazansky, Javier Aizpurua, Andrei Borisov,*

**Metasurface Generation of Accelerating Light (pp. 277)**
*Meredith A. Henstridge, Carl Pfeiffer, Di Wang, Alexandra Boltasseva, Vladimir Shalaev, Anthony Grbic, Roberto Merlin,*

**Quenching, Plasmonic, and Radiative Decays in Nanogap-based Antennas (pp. 279)**
*Remi Faggiani, Philippe Lalanne,*

**Multipolar decomposition of the field scattered by nonspherical and noncylindrical particles (pp. 281)**

*Miguel Angel Gonzalez, Eugenio Rafael Mendez,*

**Tuning the plasmonic resonances of metallic nanoparticles for thermal applications (pp. 282)**
*Juana Gabriela Calvillo Vazquez, Eugenio Mendez,*

**Modelling of phase change material based tunable meta-materials (pp. 284)**
*Dmitry N. Chigrin,*

**Discontinuous Galerkin Methods in Nano-Photonics (pp. 285)**
*Kurt Busch,*

**Plasmonic and all-dielectric nanoantennas for wavelength-controlled directional scattering of visible lightÂ (pp. 286)**
*Pol Van Dorpe, Jiaqi Li, Dries Vercruysse, Niels Verellen,*

**Polarization singularities on high index nanoparticles (pp. 287)**
*Aitzol Garcia-Etxarri,*

**Towards large-scale highly sensitive substrates for surface enhanced spectroscopies (pp. 289)**
*Pierre Michel Adam,*

**Hybrid optoplasmonic platforms for sensing, spectroscopy, energy transfer, and radiative cooling (pp. 291)**
*Svetlana V. Boriskina, Jonathan K. Tong, Gang Chen, Wonmi Ahn, Yan Hong, Xin Zhao, Bjoern Reinhard,*

**Electrically-Small Dielectric Resonator Elements for Electromagnetic Energy Harvestin (pp. 292)**
*Ahmed Ashoor, Omar Ramahi,*

## Metasurface and its application in optical devices

**Flexible Coherent Control of Plasmonic Spin-Hall Effect (pp. 295)**
*Shiyi Xiao, Fan Zhong, Hui Liu, Shining Zhu, Jensen Li,*

**High-performance metasurfaces based on extraordinary optical diffraction (pp. 297)**
*Zi-Lan Deng, Shuang Zhang, Guo Ping Wang,*

**Phase manipulation of nonlinear harmonic generation with plasmonic metasurfaces (pp. 299)**
*Thomas Zentgraf, Guixin Li, Shumei Chen, Franziska Zeuner, Nitipat Pholchai, Bernhard Reineke, Kok-Wai Cheah, Shuang Zhang,*

**Terahertz Metasurface-based Devices (pp. 301)**
*Jingwen He, Xinke Wang, Yan Zhang,*

**Metasurfaces for engineering of reflected light (pp. 303)**
*Anders Pors, Sergey I. Bozhevolnyi,*

**Highly efficient decoupling-free surface plasmon meta-couplers (pp. 305)**
*Wujiong Sun, Qiong He, Shulin Sun, Lei Zhou,*

**Metasurface for helicity multiplexed broadband holograms (pp. 306)**
*Xianzhong Chen, Dandan Wen, Fuyong Yue, Guixin Li, Guoxing Zheng, Kinlong Chan, Shumei Chen, Ming Chen, King Fai Li,*

*Polis Wing Han Wong,*

**High-Eciency Metasurface Flat Lenses (pp. 308)**
*Chun-Chieh Chang, Beibei Zeng, Abul K. Azad, Anatoly Efimov, Daniel Headland, Withawat Withayachumnankul, Derek Abbott, Antoinette J. Taylor, Hou-Tong Chen,*

**Reflective metasurface and metadevice (pp. 309)**
*Wei-Yi Tsai, Wei Ting Chen, Yao-Wei Huang, Pin Chieh Wu, Chun Yen Liao, Kuang-Yu Yang, Hao-Tsun Lin, Vassili Fedotov, Greg Sun, Shulin Sun,*

**Active Photonic Devices Based on Metasurfaces Integrated with Phase-Transition Correlated Perovskites (pp. 311)**
*Zhaoyi Li, You Zhou, Hao Qi, Qiwei Pan, Norman Nan Shi, Ming Lu, Aaron Stein, Christopher Y. Li, Shriram Ramanathan, Nanfang Yu,*

## Non-Hermitian engineering in photonics, plasmonics and metamaterial

**Scattering in PT and RT Symmetric Multimode Waveguides: Generalized Conservation Laws beyond One Dimension (pp. 314)**
*Li Ge, Konstantinos G. Makris, Demetrios N. Christodoulides, Liang Feng,*

**PT-symmetry breaking in the steady state of coupled phonon lasers (pp. 316)**
*Kosmas Kepesidis, Thomas Milburn, Konstantinos Makris, Stefan Rotter, Peter Rabl,*

**Extreme Wave Manipulation with Parity-Time Symmetric Metasurfaces (pp. 317)**
*Romain Fleury, Dimitrios Sounas, Andrea Alu,*

**Non-Hermitian topological photonics (pp. 319)**
*Steffen Weimann, Julia M. Zeuner, Mark Kremer, Mikael Rechtsman, Konstantinos Makris, Yonatan Plotnik, Yakov Lumer, Mark Rudner, Moti Segev, Alexander Szameit,*

**Optomechanical interactions in coupled resonators with unbalanced gain and loss (pp. 321)**
*David Schoenleber, Ramy El-Ganainy, Alexander Eisfeld,*

**Observation of optically induced transparency in a micro-cavity (pp. 323)**
*Yuanlin Zheng, Xianfeng Chen, Li Ge, Wenjie Wan,*

**Perfect compensation of absorption in metamaterials for diffraction-unlimited imaging (pp. 325)**
*Wyatt Adams, Durdu Guney,*

**Investigation of light transport for Non-Hermitian photonics in the silicon platform (pp. 327)**
*Minghui Lu, Ye-Long Xu, Xue-Yi Zhu, Li Liu, Yi Zou, Xiao-Ping Liu, Yan-Feng Chen,*

**Selective amplification of semi-chiral defect states (pp. 329)**
*Henning Schomerus,*

**Non-Hermitian phase matching in atomic scattering (pp. 331)**
*Sebastian Wuester, Ramy El-Ganainy,*

**Symmetry approach to non-Hermitian waveguide arrays (pp. 332)**

*Julio Guerrero, Blas Manuel Rodriguez-Lara,*

**Dynamically encircling exceptional points in a waveguide: asymmetric mode switching from the breakdown of adiabaticity (pp. 334)**
*Jorg Doppler, Alexei Mailybaev, Julian Bohm, Ulrich Kuhl, Adrian Girschik, Florian Libisch, Thomas Milburn, Peter Rabl, Nimrod Moiseyev, Stefan Rotter,*

**Parametric instability of non-Hermitian systems near the exceptional point (pp. 336)**
*Alexander Andreevich Zyablovsky, Eugeny Sergeevich Andrianov, Alexander Alexandrovich Pukhov,*

**Non-Hermitian Modulation Instability (pp. 338)**
*Konstantinos Makris, Justin Cole, Ziad Musslimani, Demetrios Christodoulides, Stefan Rotter,*

**lasing characteristics in parity-time symmetric microcavities (pp. 340)**
*Mercedeh Khajavikhan, H. Hodaei, M.-A. Miri, M. Heinrich, W. Hayenga, A. U. Hassan, J. Ren, D. N. Christodoulides,*

**Reversing phase transitions in a nonlinear PT-symmetric dimer laser (pp. 342)**
*Absar Hassan, Hossein Hodaei, M.-A Miri, Mercedeh Khajavikhan, Demetrios N. Christodoulides,*

**Non-Hermitian Photonic Structures (pp. 344)**
*Tsampikos Kottos,*

**Photonic topological insulators in PT-symmetric systems (pp. 345)**
*Miguel A. Bandres, Gal Harari, Mordechai Segev,*

**Nanoscale Engineering Optical Nonlinearities and Nanoemitters (pp. 347)**
*Yeshaiahu Fainman, M. Puckett, R. Sharma, J. Smalley, A. Pang, Q. Gu, A. El Amili, F. Vallini,*

**Optical and Electrical Control of NonHermition Silicon Nanophotonics (pp. 349)**
*Mohamed Swillam,*

**Spontaneous symmetry breaking and switching in coupled photonic crystal nanolasers (pp. 351)**
*Alejandro Yacomotti, Philippe Hamel, Mathias Marconi, Fabrice Raineri, Ariel Levenson,*

**Controlling optical whispering galleries at exceptional points (pp. 353)**
*Sahin Kaya Ozdemir, Lan Yang,*

**Parity-time-symmetric photonic hypercrystals (pp. 355)**
*Oksana Shramkova, G. P. Tsironis,*

**Parity-time symmetry synthetic metamaterials on silicon photonic chips (pp. 357)**
*Yanfeng Chen, Minghui Lu, Liang Feng, Xiao-Ping Liu, Yelong Xu, William S. Fegadolli, Lin Gan, Axel Scherer, Zhi-Yuan Li,*

## Nanophotonics using Hybrid and New Plasmonic Materials

**Strong Coupling between Silver nanoshells and semiconductor quantum dots (pp. 360)**
*Ning Zhou, Dongsheng Li, Deren Yang,*

**Breaking the Space Charge Limit in Organic Semiconductors by Novel Plasmon-Electrical Concept (pp. 362)**

*Wallace Choy, W. E. I Sha, X. Li, L. Zhu,*

**Subwavelength grating engineered metamaterial waveguide structures for silicon photonic integrated circuits (pp. 366)**
*Pavel Cheben, J. H. Schmid, D. -X. Xu, S. Janz, J. Lapointe, M. Rahim, S. Wang, M. Vachon, R. Halir, A. Ortega-Monux,*

**Semiconductors for infrared plasmonics and metamaterials (pp. 368)**
*Stephanie Law,*

**Nonlinear organic plasmonics: Bistability of exciton polaritons and applications to optical control of Coulomb blocking in nanojunctions (pp. 370)**
*Boris Fainberg, Guangqi Li,*

**Biomimetic gyroid photonic crystals (pp. 372)**
*Min Gu,*

**Plasmonic and thermal properties of TiN/Au core-shell nanoparticles (pp. 374)**
*Stacey Drakeley, William Hendren, Robert Bowman, Fumin Huang,*

**THz lattice vibrations for active plasmonics with light: Ultrafast optical response in gold/telluride hybrid plasmonic crystals (pp. 376)**
*Lars Erik Kreilkamp, I. A. Akimov, V. I. Belotelov, B. A. Glavin, L. Litvin, A. Rudzinski, M. Kahl, R. Jede, M. Wiater, T. Wojtowicz,*

**Characterizing Selection Rules of Nonlinear Plasmonics by Maxwell-Hydrodynamic Equations (pp. 378)**
*Ming Fang, Xiaoyan Y. Z. Xiong, Wei E. I. Sha, Li Jun Jiang, Zhixiang Huang,*

**Designing efficient hybrid plasmonics based durable nanolenses for ultrafast laser induced nanocavitation (pp. 380)**
*Michel Meunier, Remi Lachaine, Christos Boutopoulos, Etienne Boulais,*

**Plasmonic electric field enhancement on a graphene surface (pp. 382)**
*Lin Chen, Xun Li,*

**Designing broadband silicon devices using subwavelength structures (pp. 384)**
*Robert Halir, Jose Manuel Luque-Gonzalez, Shurui Wang, Alejandro Sanchez-Postigo, Juan Wanguemert-Perez, Pavel Cheben, Jens Schmid, Dan-Xia Xu, Siegfried Janz, Jean Lapointe,*

**Transfer printing approach to fabricate adaptable, self-standing and high efficiency polymer solar cells (pp. 386)**
*Silvia Colodrero, Pablo Romero-Gomez, Paola Mantilla-Perez, Jordi Martorell,*

**Annealing Studies of Gold Plasmonic Nanostructured Arrays (pp. 388)**
*Matthew Nicholson, Robert Bowman, Antony Murphy, Robert Pollard,*

**Active modulation of visible light with graphene-loaded ultrathin metal plasmonic antennas (pp. 390)**
*Renwen Yu, Valerio Pruneri, Javier Garcia de Abajo,*

**Highly-responsive subwavelength plasmonic photodetector for silicon nanophotonics (pp. 392)**
*Igor A. Khramtsov, Dmitry Yu. Fedyanin,*

**Plasmonic materials for hot carrier devices (pp. 394)**

*Jeremy Munday,*

**Enhanced optical nonlinearities in periodic photonic nanostructures containing patterned graphene and other 2D materials (pp. 395)**
*Nicolae Panoiu, Martin Weismann,*

**Quantum efficiency gains by metal nanostructures in organic and quantum dot solar cells (pp. 396)**
*Jung-Yong Lee, Doh Chang Lee,*

**Interactions between organic excitons and plasmonic metasurfaces (pp. 398)**
*Deirdre M. O'Carroll, Zeqing Shen, Christopher Petoukhoff, Katsuya Noji, Ankur Dalsania,*

**Plasmonic resonances in gold nanorod-film coupled system (pp. 399)**
*Xingxing Chen, Richard Blaikie, Boyang Ding, Min Qiu,*

**Selecting a Plasmonic Material Using a Two-Dimensional Analysis of Confinement and Propagation Length (pp. 401)**
*Babak Dastmalchi, Thomas Koschny, Costas M. Soukoulis, Philippe Tassin,*

**Non-Hermitian Wave Mixing (pp. 402)**
*Ramy El-Ganainy, J. I. Dadap, R. M. Osgood Jr.,*

**Multiphysics simulation of tunable and frequency selective metamaterial absorbers (pp. 404)**
*Amy Liu, Ahsan Alam, Jens Niegemann, James Pond,*

**Observation of topologically protected edge states in arrays of evanescently coupled plasmonic waveguides (pp. 406)**
*Stefan Linden, Felix Bleckmann, Andrea Alberti,*

**New Trends in Computational Photonics (pp. 407)**
*Salah Sabry Obayya,*

**Hybrid Single Mode Nanophotonic-Plasmonic Waveguides for On-Chip Surface Enhanced Raman Spectroscopy (pp. 409)**
*Frederic Peyskens, Ashim Dhakal, Pol Van Dorpe, Nicolas Le Thomas, Roel Baets,*

**High Performance Nano-Plasmonic MIM-Based Lab-on-Chip Sensor (pp. 411)**
*Ahmad Bassam Ayoub, Mohamed Swillam,*

**Controlling fluorescence emission by surface plasmon resonance in multilayer core-shell metallic nanoparticles (pp. 413)**
*Monica Focsan, Andreea Campu, Ana Craciun, Sorina Suarasan, Cristian Tira, Adriana Lazar, Simion Astilean,*

**Long-Range Surface Plasmon-Polariton Waveguide Biosensors for Disease Detection (pp. 414)**
*Oleksiy Krupin, Wei Ru Wong, Paul Beland, Rafik Adikan, Pierre Berini,*

**Hybrid plasmonic structures for wave mixing at the nanoscale (pp. 416)**
*Guillaume Laurent, M. Ethis De Corny, N. Chauvet, G. Nogues, M. Jeannin, A. Drezet, S. Huant, G. Dantelle, T. Gacoin, G. Bachelier,*

**All-Dielectric Metasurfaces for Structured Light Manipulation (pp. 417)**
*Natalia Litchinitser, Mikhail I. Shalaev, Jingbo Sun, Alexander Tsukernik, Apra Pandey,*

**Hybrid plasmonic add-drop filter based on novel micro-ring-disk resonators with fJ switching energy (pp. 419)**
*Dimitrios C. Zografopoulos, Mohamed A. Swillam, Romeo Beccherelli,*

**Strong Light-matter Interaction in Two-dimensional Transition Metal Dichalcogenides Through Integration with Plasmonic Nanoantenna Arrays (pp. 420)**
*Syed Hamed Shams Mousavi, Hossein Taghinejad, Mohammad Taghinejad, Ali A. Eftekhar, Ali Adibi,*

**Plasmonic Mach-Zehnder Modulator with Direct Coupling Silicon Waveguides (pp. 421)**
*Abdalrahman Mohamed, Mohamed Swillam,*

**Long Range Plasmonic Waveguide Using Doped Silicon in Mid-Infrared (pp. 423)**
*Raghi El Shamy, Hany Mossad, Mohamed Swillam,*

**Hybrid silicon organic directional coupler based modulator (pp. 425)**
*Mohamed Youssef Abdelatty, Aya Zaki, Mohamed Swillam,*

**Semiconductor Plasmonic Gas Sensor Using On-Chip Infrared Spectroscopy (pp. 428)**
*Mohamed Yousef Elsayed, Yehea Ismail, Mohamed A. Swillam,*

**Directional Coupler Modulator based on Silicon Nanowires Platform (pp. 430)**
*Sherif Mohamed, Lamees Shahada, Mohamed Swillam,*

**Silicon Organic Hybrid Plasmonic Modulator (pp. 433)**
*Sherif Mohamed, Aya Zaki, Lamees Shahada, Mohamed Swillam,*

**Resonance based hybrid plasmonic on-chip sensor (pp. 436)**
*Aya Zaki, Khaled Kirah, Mohamed Swillam,*

## Hyperbolic metamaterials: Theory, Experiments and Applications

**Dielectric singularity in hyperbolic metamaterials: the inversion point of coexisting anisotropies (pp. 439)**
*Vincenzo Caligiuri, Rakesh Dhama, Kandammathe Valiyaveedu Sreekanth, Giuseppe Strangi, Antonio De Luca,*

**Block-copolymer based self-assembled hyperbolic metamaterials in the visible range (pp. 441)**
*Xuan Wang, Kevin Ehrhardt, Morten Kildemo, Alexandre Baron, Valeria Lotito, Philippe Barois, Ashod Aradian, Virginie Ponsinet,*

**Purcell effect in multiperiodic multilayered metal-dielectric metamaterials (pp. 443)**
*Alexandr V. Chebykin, Victoria Babicheva, Ivan V. Iorsh, Alexey A. Orlov, Pavel Belov, Sergei Zhukovsky,*

**Strongly subwavelength cavities in multilayer hyperbolic metamaterials based on nanometric steps (pp. 444)**
*Fabio Vaianella, Bjorn Maes,*

**Thermal Radiation from Semiconductor Hyperbolic Metamaterials (pp. 446)**
*Salvatore Campione, Francois Marquier, Jean-Paul Hugonin, A. Robert Ellis, John Klem, Michael Sinclair, Ting Luk,*

**Controlling quantum photonics with metamaterials (pp. 448)**
*Mikhail Y. Shalaginov, Simeon Bogdanov, Vadim V. Vorobyov, Jing Liu, Alexei Lagutchev, Alexander Kildishev, Joseph Irudayaraj, Alexandra Boltasseva, Alexey Akimov, Vladimir M. Shalaev,*

**Metamaterial Behavior of Hyperbolic Bimetallic Nanostructures (pp. 450)**
*Silvia Cortes-Lopez, Felipe Perez-Rodriguez,*

**Optical signal dispersion in hyperbolic metamaterials (pp. 452)**
*Tomasz Stefaniuk, Anatoly Zayats,*

**Hyperbolic Metamaterials with Complex Geometry (pp. 454)**
*Andrei V. Lavrinenko, Andrei Andryieuski, Sergei Zhukovsky, Osamu Takayama, Evgeniy Skhondin, Mohammad Aryaee Panah, Radu Malureanu, Flemming Jensen,*

**Advanced plasmonic metamaterials for ultrasensitive biosensing (pp. 456)**
*Andrei V. Kabashin,*

**Hyperbolic Magnetic Media as Tunable Slab Lenses (pp. 458)**
*Rair Macedo, Robert L. Stamps, Thomas Dumelow,*

**Imaging of anomalous internal reflections of hyperbolic phonon-polaritons in hexagonal boron nitride nanocones (pp. 460)**
*Alexander J. Giles, Siyuan Dai, Orest J. Glembocki, Andrey V. Kretinin, Zhiyuan Sun, Chase T. Ellis, Joseph G. Tischler, Takashi Tanaguchi, Kenji Watanabe, Michael M. Fogler,*

**THz wire medium operating as a ultra-broadband imaging device (pp. 461)**
*Korbinian Julius Kaltenecker, Alessandro Tuinz, Simon C. Fleming, Alexander Argyros, Boris T. Kuhlmey, Markus Walther, Bernd M. Fischer,*

**Microscopic Calculations of Dielectric Properties for Hyperbolic Metamaterials (pp. 463)**
*Maxim Anokhin, Alexey Tishchenko, Mikhail Strikhanov,*

## Active and passive optical metasurfaces

**Dynamics of Non-Linear Hybrid ITO-Plasmonic Metasurfaces (pp. 468)**
*Miguel Navarro-Cia, Heykel Aouani, Mohsen Rahmani, Stefan A. Maier,*

**Metasurfaces based on defect-engineered phase transition materials (pp. 470)**
*Jura Rensberg, Shuyan Zhang, Alexander S. McLeod, Christian Schwarz, Michael Goldflam, Ronny Nawrodt, Mengkun Liu, Jochen Kerbusch, You Zhou, Shriram Ramanathan,*

**Metasurface for the creation of surface plasmon vortex and towards multi-functional optofluidics (pp. 472)**
*C.-Y. Lin, C.-F. Chen, C.-T. Ku, C.-B. Huang,*

**Conformal Boundary Optics (pp. 474)**
*Jonathon Yi Han Teo, Liang Jie Wong, Carlo Molardi, Patrice Genevet,*

**Atomic metasurface for control single photons (pp. 476)**
*Ming Zhou, Jingfeng Liu, Mikhail Kats, Zongfu Yu,*

**Electrochemically Programmable Plasmonic Antennas (pp. 478)**
*Shi Dong, Kai Zhang, Zhiping Yu, Jonathan A. Fan,*

**A metasurface designed for adaptive optical near-field routing (pp. 480)**

*Chung-Ying Lin, C. -B Huang,*

**Graded Metasurfaces for Advanced Wave Control (pp. 482)**
*Nasim Mohammadi Estakhri, Mykhailo Tymchenko, Yakir Hadad, Juan Sebastian Gomez-Diaz, Dimitrios Sounas, Andrea Alu,*

**Frequency comb generation in a time-dependent graphene ribbon lattice (pp. 483)**
*Galaad Altares Menendez, Bjorn Maes,*

**Plasmonic Metasurfaces for the Near-Field Directional Control of Light Emission (pp. 485)**
*Roberto Paiella, Leonard Kogos, Jeff DiMaria,*

**Lossy and gain metasurfaces for applications of antireflection coatings and parity-time-symmetric systems (pp. 487)**
*Jie Luo, Jensen Li, Yun Lai,*

**High speed optical modulators with tunable metasurface absorber (pp. 488)**
*Yu Yao, Ali Basiri,*

**Novel dielectric nanophotonic structures with unusual nonlinear and spectral properties (pp. 490)**
*Zin Lin, Yang Li, Eric Mazur, Marco Loncar, Alejandro Rodriguez,*

**Dielectric Nanostructures with High Laser Damage Threshold (pp. 492)**
*Andrew Chun Yong Ngo, Liying Hong, Jie Deng, Eng Huat Khoo, Zhengtong Liu, Rui Fen Wu, Jing Hua Teng,*

**Metasurfaces becoming real: a new class of polarimeters (pp. 494)**
*Anders Pors, Sergey I. Bozhevolnyi,*

**Durable plasmonic metal nitrides and transparent conducting oxides for flat photonics (pp. 496)**
*Krishnakali Chaudhuri, Jongbum Kim, Amr M. Shaltout, Nathaniel G. Kinsey, Sajid Choudhury, Vladimir M. Shalaev, Alexandra Boltasseva,*

**Holographic Nonlinear Metamaterials (pp. 498)**
*Euclides Almeida, Y. Prior,*

**Nonlinear Beam Shaping with Plasmonic Metasurfaces (pp. 500)**
*Shay Keren-Zur, Ori Avayu, Lior Michaeli, Tal Ellenbogen,*

**Electrically Tunable Metasurface Absorber (pp. 502)**
*Juhyung Kang, Junghyun Park, Mark L. Brongersma,*

**Tunable metasurfaces for active manipulations of electromagnetic waves (pp. 504)**
*Ziqi Miao, Che Qu, Shaojie Ma, Shulin Sun, Qiong He, Lei Zhou,*

**Tunneling rectification in an infrared nanoantenna coupled MOS diode (pp. 506)**
*Paul S. Davids, E. A. Kadlec, S. W. Howell, D. W. Peters,*

**3D plasmonic resonators for sensing and metadevice (pp. 508)**
*Wei-Yi Tsai, Ching-Fu Chen, Mu-Ku Chen, Pei Ru Wu, Yi-Hao Chen, Ting-Yu Chen, Jia-Wern Chen, Cheng Hung Chu, Wei Ting Chen, Ming Lun Tseng,*

**Network metamaterials: An alternative platform for optical materials (pp. 510)**
*Henning Galinski Galinski, Andrea Fratalocchi, Federico Capasso,*

**Reconfigurable Metasurfaces Based on Graphene and Indium Tin Oxide Materials (pp. 512)**
*Ali Forouzmand, Jierong Cheng, Hossein Mosallaei,*

**Widely Tunable Optical Antennas for Reconfigurable Metasurfaces (pp. 514)**
*T. Lewi, P. P. Iyer, N. A. Butakov, Jon A. Schuller,*

**Device Applications of Metafilms (pp. 515)**
*M. L. Brongersma,*

**Topological darkness of Tamm plasmons for high-sensitivity singular-phase optical detection and tunable thermal emission (pp. 516)**
*Svetlana V. Boriskina, Jonathan K. Tong, Yoichiro Tsurimaki, Bolin Liao, Yi Huang, Victor Boriskin, Alexander Semenov, Mykola I. Ayzatskiy, Gang Chen,*

**Electrostatically Tunable Graphene Metasurfaces for Control of Thermal Radiation (pp. 517)**
*V. W. Brar, L. Kim, M. C. Sherrott, M. S. Jang, S. Kim, W.-H. Lin, M. Choi, L. A. Sweatlock, H. A. Atwater,*

**Active conducting oxide plasmonics and metasurfaces (pp. 519)**
*Howard (Ho Wai) Lee, Harry Atwater,*

**Tunable mid-infrared photonics with phase transition materials (pp. 521)**
*Mikhail Kats,*

**Natural and Biomimetic Radiative Cooling Nano-Photonic Structures (pp. 523)**
*Norman Nan Shi, Cheng-Chia Tsai, Fernando Camino, Gary D. Bernard, Rudiger Wehner, Nanfang Yu,*

**Polarization tunable monolithic semiconductor lasers with metasurfaces (pp. 525)**
*Guozhen Liang, Yongquan Zeng, Xiaonan Hu, Hao Yu, Houkun Liang, Ying Zhang, Lianhe Li, Alexander Giles Davies, Edmund H. Linfield, Qijie Wang,*

## Disordered photonics

**Anomalous light tunneling through two interlaced 3D metallic wire meshes (pp. 528)**
*Hafssaa Latioui, Mario Silveirinha,*

**Wide-field ultrafast imaging of light diffusion in structured soft matter (pp. 530)**
*Simone Zanotto, Lorenzo Pattelli, Dmitry Nuzhdin, Sara Nocentini, Hao Zeng, Daniele Martella, Camilla Parmeggiani, Diederik Wiersma,*

**Optical Reflectance of Plasmonic Nanoparticles forming a Disordered Monolayer (pp. 532)**
*Alejandro Reyes-Coronado, Gesuri Morales-Luna, Omar Vazquez-Estrada, Augusto Garcia-Valenzuela, Arturo Rodriguez-Gomez, Ruben Barrera,*

**Thermo-optical response of nanoparticles embedded in a glass matrix (pp. 534)**
*Emmanuel Haro-Poniatowski, M. Jimenez de Castro, I. Camarillo, G. Munoz, J. Toudert, R. Serna,*

**Graphene-based random meta-laser (pp. 536)**
*Andrea Marini, Javier F. Garcia de Abajo,*

**Reflection amplitudes for turbid colloidal suspensions: Theory and experiment (pp. 538)**
*Gesuri Morales-Luna, Humberto Contreras-Tello, Augusto Garcia-Valenzuela, Ruben Gerardo Barrera,*

**Landau Damping in the Nonlocal Response of Metal-Dielectric Metamaterials (pp. 541)**
*Felipe Perez-Rodriguez,*

**Metallic Nanocolloids: Theoretical Modeling and Characterization Techniques (pp. 542)**
*Ana Lilia Gonzalez, Enrique Sanchez Mora,*

**Polarization statistics in disordered media:Modelization and measurements (pp. 544)**
*Myriam Zerrad, Ayman Ghabbach, Gabriel Soriano, Quentin Ailloud, Claude Amra,*

**Controlling light-scattering losses in dense nanocolloids (pp. 546)**
*Augusto Garcia-Valenzuela, Roberto Marquez-Islas, Ruben G. Barrera,*

## Nano and Mesoscopic Optics in Colloidal and Granular Systems

**Optical tweezers unveil new physics: Nonadditivity of critical Casimir forces and failure of Jarzynski equality in active baths (pp. 553)**
*Giovanni Volpe,*

**Controlling and probing weak colloidal interactions with complex laser light fields (pp. 555)**
*Frank Scheffold,*

**Controlling Active Crowds with Random Light Fields (pp. 557)**
*E. Pince, S. K. P. Velu, A. Callegari, P. Elahi, S. Gigan, Giorgio Volpe,*

**Transport and emission in in colloidal and granular systems (pp. 558)**
*Cefe Lopez,*

**Spatial structure of transmission eigenchannels and densities of states of random media (pp. 560)**
*Matthieu Davy, Z. Shi, C. Tian, A. Z. Genack,*

**Light Emission Statistics as a Local Probe for Structural Phase Switching (pp. 562)**
*Nuno de Sousa, Juan Jose Saenz, Frank Scheffold, Antonio Garcia-Martin, Luis Froufe-Perez,*

**Coherent Control of Light in Disordered Media Assisted by Long-range Correlations (pp. 564)**
*Chia Wei Hsu, Seng Fatt Liew, Arthur Goetschy, Yaron Bromberg, A. Douglas Stone, Hui Cao,*

**Colloids manipulation with optical radiation (pp. 566)**
*Sergey Sukhov, Colin Constant, Veerachart Kajorndejnukul, Aristide Dogariu,*

**Polarization revival through scattering media (pp. 568)**
*Hilton B. de Aguiar, Sylvain Gigan, Sophie Brasselet,*

**Launching optical energy into the fundamental diffusion mode of a complex nanophotonic medium (pp. 570)**

*Femi Ojambati, Hasan Yilmaz, Ad Lagendijk, Allard P. Mosk, Willem L. Vos,*

**Theory for the diffusion of light polarization in disordered media with short-range structural correlations (pp. 572)**
*Kevin Vynck, Romain Pierrat, Remi Carminati,*

**Light propagation and optical response in two-dimensional silicon nanowire random fractal arrays (pp. 574)**
*Barbara Fazio, Pietro Artoni, Maria Antonia Iati, Cristiano D'Andrea, Stefano Pirotta, Maria Jose Lo Faro, Salvatore Del Sorbo, Pietro Giuseppe Gucciardi, Rosalba Saija, Paolo Musumeci,*

**Experimental verification of mean path length invariance in multiple light scattering (pp. 576)**
*Romolo Savo, Romain Pierrat, Remi Carminati, Stefan Rotter, Sylvain Gigan,*

**Brownian motion of self-assembled colloid structures in optical fields (pp. 578)**
*Philip Jones, Kiran Govind, Nicholas Tidy, Xiang Han,*

**Diffussion of an electric dipole in a fluctuating random electromagnetic field (pp. 580)**
*Manuel I. Marques,*

**Eigenchannels in scattering media: from manipulation to inverse design (pp. 582)**
*Alexey Yamilov, Sasha Petrenko, Milan Koirala, Raktim Sarma, Hui Cao,*

**Chiral Light-Matter Interaction (pp. 584)**
*Peter Lodhal,*

**Intensity fluctuations of light emitted by two classical or quantum sources in a structured environment (pp. 585)**
*Remi Carminati, Juan Jose Saenz, Antoine Canaguier-Durand,*

**Coherent spatiotemporal control of a femtosecond pulse through an opaque medium (pp. 586)**
*Mickael Mounaix, Daria Andreoli, Hugo Defienne, Giorgio Volpe, Ori Katz, Samuel Gresillon, Sylvain Gigan,*

**Everything is connected with everything: Can the study and tools of complex network theory tell us something about mesoscopic physics? (pp. 588)**
*Gabriel A. Cwilich,*

**Hybridization of Optical Forces (pp. 590)**
*Onofrio M. Marago,*

**Light trapping and extinction in large random aggregates of particles. An investigation through the Transition matrix method (pp. 592)**
*Maria Antonia Iati, Rosalba Saija, Cristiano D'Andrea, Maria Jose Lo Faro, Pietro Giuseppe Gucciardi, Alessia Irrera, Barbara Fazio,*

**The effective medium in disordered waveguides: the role of evanescent modes (pp. 594)**
*Miztli Yepez, Juan Jose Saenz,*

**A spectral model for the speckle temporal coherence (pp. 596)**
*Gabriel Soriano, Myriam Zerrad, Claude Amra,*

**Cellulose bio-inspired hierarchical structures (pp. 598)**

*Silvia Vignolini,*

**Light generation and scattering in a photonic network of sub-wavelength nanofibres (pp. 599)**
*Riccardo Sapienza,*

## Non-linear and ultra-fast spectroscopy of nano- and meta-materials

**Observation of plasmon wave packet motions with ultrafast near-field microscopy (pp. 601)**
*Hiromi Okamoto, Yoshio Nishiyama, Kohei Imura,*

**Optical properties of supported size-selected metal clusters (pp. 603)**
*Aras Kartouzian, M. Thamer, T. Lunskens, P. Heister, A. Von Weber, U. Heiz,*

**Shaping the nonlinear near-field: the plasmonic analogue of Young's double slit experiment (pp. 605)**
*D. Wolf, T. Schumacher, Markus Lippitz,*

**Linear and nonlinear plasmonics with single gold nanorods (pp. 607)**
*Martin Caldarola, W. Zhang, M. Orrit,*

**Ultrafast Hot Plasmonic Electrons in Nanostructures with Hot Spots (pp. 610)**
*Alexander O. Govorov, Lucas V. Besteiro, Larousse Khorashad, Gary P. Wiederrecht,*

**Extreme light confinement in plasmonic taper (pp. 611)**
*Stefan Dilhaire, olga lozan, Buntha Ea Kim, Philippe Lalanne,*

**Nonlinear plasmonics: confinement effect, delocalization and ultrafast responses (pp. 613)**
*Sviatlana Viarbitskaya, Olivier Demichel, Upkar Kumar, Regis Mejard, Aurelien Cuche, Gerard Colas des Francs, Christian Girard, Benoit Cluzel, Erik Dujardin, Alexandre Bouhelier,*

**Quantitative optical spectroscopy of single metal nano-objects (pp. 615)**
*Aurelien Crut, Anna Lombardi, Etienne Pertreux, Paolo Maioli, Fabrice Vallee, Natalia Del Fatti,*

**Vector Field Nonlinear Optical Microscopy of Nanoparticles (pp. 617)**
*Martti Kauranen, Leo Turquet, Abdallah Slablab, Godofredo Bautista,*

**Quantum nonlinear graphene plasmonics (pp. 618)**
*Joel Douglas Cox, Javier Garcia de Abajo,*

**Two photon luminescence microscopy maps the plasmonic density of state and plasmon propagation in 2D gold crystals (pp. 620)**
*Upkar Kumar, Universite Federale de Toulouse Viarbitskaya, Aurelien Cuche, Gerard Colas des Francs, Rafaelle Mezzenga, Christian Girard, Alexandre Bouhelier, Erik Dujardin,*

**Nonlinear Optical Effects in Nanoantennas (pp. 622)**
*Anke Horneber, Jiyong Wang, Jeremy Butet, Anne-Laure Baudrion, Andreas Horrer, Olivier J. F. Martin, Monika Fleischer, Alfred J. Meixner, Pierre-Michel Adam, Dai Zhang,*

**Optical Control of Electron Tunneling in Plasmonic Nanoantennas via Single-Cycle Pulses (pp. 624)**
*Daniele Brida, Tobias Rybka, Alfred Leitenstorfer,*

**Ultrafast relaxation of optically excited hot electrons in plasmonic structures (pp. 626)**
*Felix Spitzer, Boris Glavin, Vladimir I. Belotelov, Jonas Vondran, Ilya A. Akimov, Sachin Kasture, Arvind S. Vengurlekar, Achanta V. Gopal, Dmitri R. Yakovlev, Manfred Bayer,*

**Spatial Dependence of the Electron-hole correlation in Hybrid Perovskite Crystals (pp. 628)**
*Giulia Grancini, Daniele Viola, Marina Gandini, Davide Altamura, Cinzia Giannini, Giulio Cerullo, Annamaria Petrozza,*

**Plasmon-Mediated Nonlinear Optical-Detected Circular Dichroism (pp. 630)**
*Kenneth L. Knappenberger, Jeremy W. Jarrett,*

**Impact of analyte molecule distribution on the SERS efficiency of nanoplasmonic assemblies: a full-wave simulation study (pp. 632)**
*Diego M. Solis, Jose M. Taboada, Fernando Obelleiro, Luis M. Liz-Marzan, Francisco J Garcia de Abajo,*

**Mode-matched multiresonant plasmonic antennas for enhanced wave mixing at the nanoscale (pp. 634)**
*Michele Celebrano, Xiaofei Wu, Milena Luisa Baselli, Swen Grossmann, Paolo Biagioni, Lavinia Ghirardini, Giovanni Pellegrini, Andrea Locatelli, Costantino De Angelis, Giulio Cerullo,*

**Ultrafast all-optical control of the coherent nonlinear emission of multi-resonant plasmonic metasurfaces (pp. 636)**
*Giovanni Sartorello, Nicolas Olivier, Jingjing Zhang, Weisheng Yue, David J. Gosztola, Gary P. Wiederrecht, Gregory Wurtz, Anatoly V. Zayats,*

**Nonlinear Optical Properties of Atomically Defined Thiolate Protected Gold Clusters (pp. 639)**
*Stefan Knoppe, Thierry Verbiest,*

**Monitoring of core-shell particles freely diffusing in solution (pp. 641)**
*Matteo Martini, Meriem Stamboul, Anne Debarre,*

**MultiPhoton chiroptical effects in nanospirals and in chirally coupled plasmonic nanostructures (pp. 643)**
*Ventsislav K. Valev,*

**Femtosecond Exciton and Charge Dynamics and unusual Stark Effect in Mono- and Few-layer Transition Metal Dichalcogenides (pp. 645)**
*Christoph Gadermaier, Tetiana Borzda, Victor Vega-Mayoral, Daniele Vella, Peter Topolovsek, Matej Prijatelj, Tomaz Mertelj, Natasa Vujicic, Dmitry Ovchinnikov, Dumitru Dumcenco,*

**Cesium Lead Halide Perovskite Nanorcystals as a New Optoelectronic Material (pp. 647)**
*Handong Sun,*

## Hyperuniformity and structural correlation in bio-inspired photonics

**Designing hyperuniform structures for efficient light harvesting (pp. 649)**
*Georgios Gkantzounis, Marian Florescu,*

**Hyperuniformity and local self-uniformity: Photonics band gaps in disordered materials (pp. 651)**
*Marian Florescu, Timothy Amoah, Steven Sellers,*

**Locally Self-uniform Photonic Networks (pp. 653)**
*Steven Sellers, Weining Man, Marian Florescu,*

**Transparency of dense hyperuniform systems (pp. 655)**
*Romain Pierrat, Olivier Leseur, Remi Carminati,*

**Isotropically Polarized Speckle Patterns (pp. 656)**
*Mikolaj K. Schmidt, Javier Aizpurua, Xavier Zambrana-Puyalto, Xavi Vidal, Gabriel Molina-Terriza, Juan Jose Saenz,*

**Photonic structures in nature: on order and disorder (pp. 657)**
*Bodo D. Wilts,*

**Disorder to enhance and tailor the light-matter interaction (pp. 659)**
*Pedro David Garcia Fernandez,*

**The Role of Short-Range Order and Hyperuniformity in the Formation of Band Gaps in Disordered Photonic Materials (pp. 661)**
*Luis S. Froufe-Perez, Michael Engel, Pablo F. Damasceno, Nicolas Muller, Jakub Haberko, Sharon C. Glotzer, Frank Scheffold,*

**A deterministic aperiodic approach to three-dimensionally photonic structures with tailored disorder (pp. 663)**
*Michael Renner, Marie-Christine Angermann, Georg von Freymann,*

**Photonic structures in plants (pp. 665)**
*Ullrich Steiner,*

**Biotechnological routes to photonic nanostructures from diatoms microalgae and light emitting molecules (pp. 666)**
*Roberta Ragni, Danilo Vona, Marco Lo Presti, Gabriella Leone, Luca Moretti, Francesco Scotognella, Guglielmo Lanzani, Stefania Roberta Cicco, Gianluca Maria Farinola,*

**Chiro-optical effects in disordered photonics : Harmonic distortions enhance circular dichroism of Gyroids, and stochastic noise does not destroy it (pp. 668)**
*Gerd Elmar Schroeder-Turk, Johannes Hielscher, Caroline Pouya, Peter Vukusic,*

**Bio-inspired Surfaces with Nano-scale Structural Randomness: From Analysis to Fabrication and Applications (pp. 670)**
*R. H. Siddique, Y. Donie, G. Gomard, Hendrik Hoelscher,*

**Robustness and fragility of photonic bandgap in photonic amorphous diamond structures (pp. 672)**
*Shigeki Imagawa, Keiichi Edagawa,*

## Metamaterials for Magnetic Resonance Imaging

**Metamaterial-based Resonators for Magnetic Resonance Imaging (pp. 681)**
*Alexey Slobozhanyuk,*

**Parallel Transceive for 7T MRI with Mushroom Electromagnetic Bandgap Structures (pp. 684)**
*A. A. Hurshkainen, T. A. Derzhavskaya, Stanislav B. Glybovski, I. J. Voogt, I. V. Melchakova, C. A. T. van den Berg, A. J. E. Raaijmakers,*

**An Anthropomorphic head phantom including both electromagnetic and NMR relaxation properties for ultra-high field MRI Applications: Preliminary results (pp. 686)**
*Ana Luisa Neves, Nicolas Cochinaire, Alexandre Vignaud, Pierre Sabouroux,*

**Passive decoupling of dipoles for a transmit-array MRI antenna at 7T with stacked magnetic resonators (pp. 689)**
*Elodie Georget, Michel Luong, Alexandre Vignaud, Eric Giacomini, Edouard Chazel, Guillaume Ferrand, Alexis Amadon, Stefan Enoch, Gerard Tayeb, Cyril Poupon,*

**Alternative antenna designs for ultra-high field MRI (pp. 691)**
*Bart R. Steensma, Anna Hurshkainen, Stanislav Glybovski, Irina Melchakova, Peter R. Luijten, J. M. Hoogduin, Dennis W. Klomp, C. A. T. Van den Berg, Alexander J. E. Raaijmakers,*

**Realization of a Magnetic Coil Based on Mode Hybridization and Application to Magnetic Resonance Imaging (pp. 693)**
*Camille Jouvaud, Redha Abdeddaim, Benoit Larrat, Julien de Rosny,*

**Dielectric shimming optimization (pp. 694)**
*Tryfon Antonakakis,*

**Flexible and compact metamaterials for high field in vivo magnetic resonance imaging (pp. 696)**
*Rita Schmidt, A. G. Webb,*

## A bottom-up approach towards metamaterials and plasmonics

**Hierarchical Oriented Assembly of Gold Nanorods (pp. 699)**
*Luis M. Liz-Marzan,*

**Optical magnetism in a self-assembled 3D isotropic metamaterial (pp. 700)**
*Sergio Gomez-Grana, Mona Treguer-Delapierre, Etienne Duguet, Vasyl Kravets, Alexander Grigorenko, Jacques Leng, Jean-Baptiste Salmon, Alexandre Baron, Daniel Torrent, Philippe Richetti,*

**Semiconductor Nanowire antennas (pp. 702)**
*Jaime Gomez Rivas, D. van Dam, J. E. M. Haverkort, E. P. A. M Bakkers, D. Romero Abujetas, J. A. Sanchez Gil,*

**Bulk rigid terahertz metamaterials based on dielectric microspheres (pp. 703)**
*Christelle Kadlec, Michal Sindler, Filip Dominec, Petr Kuzel, Catherine Elissalde, U-Chan Chung, Patrick Mounaix, Hynek Nemec,*

**Assembling plasmonic nanoparticles through supramolecules (pp. 705)**
*Andres Guerrero-Martinez,*

**Self-collapsed meta-structures of alumina and TiO2 nanowires for energy harvesting applications (pp. 707)**
*Kyuyoung Bae, Gumin Kang, Yunha Ryu, Kyoungsik Kim,*

**Photocatalysis through anisotropic plasmonic nanoparticles with hot spots in Au-TiO2 nanoarchitectures (pp. 708)**
*Miguel Comesana-Hermo, Ana Sousa-Castillo, Benito Rodriguez-Gonzalez, Moises Perez-Lorenzo, Xiang-Tian Kong, Zhiming Wang, Alexander O. Govorov, Miguel ingel Correa-Duarte,*

**Comparing the Potential of Gallium and Bismuth Nanostructures for Switchable Optical Filtering (pp. 710)**
*Alexander Cuadrado, Johann Toudert, Rosalia Serna,*

**Optical Metamaterials based on p-block Elements for Switchable Nanophotonics (pp. 711)**
*Johann Toudert, Alexander Cuadrado, Rosalia Serna,*

**Plasmon Enhanced Luminescence Upconversion in Self-Assembled Nanostructures (pp. 712)**
*Dawei Lu, Chenchen Mao, Suehyun Cho, Won Park,*

**Optical and Opto-electronic Properties of Self-Assembled Meta Systems (pp. 714)**
*Augustine Urbas,*

**Band-edge photonics: a promising approach for next-generation light emitters (pp. 715)**
*Kyungtaek Min, Heonsu Jeon,*

**Ultra-confined acoustic THz graphene plasmons revealed by photocurrent nanoscopy (pp. 716)**
*Pablo Alonso-Gonzalez, Alexey Y. Nikitin, Yuanda Gao, Achim Woessner, Mark B. Lundeberg, Alessandro Principi, Nicolo Forcellini, Wenjing Yan, Saul Velez, Andreas. J. Huber,*

## Nanophotonics, optical forces and the momentum of light

**Manipulation of optical gradient forces for reconfigurable and selective assembly of gold nanoplates (pp. 718)**
*Delphine Coursault, Ying Bao, Patrick Figliozzi, Zijie Yan, Norbert F. Scherer,*

**Significance of the electromagnetic spin and orbital-angular-momentum conservation: The optical torque (pp. 720)**
*Manuel Nieto-Vesperinas,*

**Optical negative forces on particles near plasmonic interfaces (pp. 721)**
*Sergey Sukhov, Mihail Petrov, Andrey Bogdanov, Alexander Shalin, Aristide Dogariu,*

**Boundary optical stress: pressure or tension? (pp. 723)**
*Shubo Wang, C. T. Chan,*

**THz polarization control with chiral metamaterials (pp. 725)**
*M. Kafesaki, G. Kenanakis, A. Xomalis, M. Farsari, G. Konstantinidis, E. N. Economou, C. M. Soukoulis,*

**Strong coupling between waveguide-modes of opposite directionality: nearly-frozen light modes (pp. 727)**
*S. Foteinopoulou,*

**Measurement of Sub-femtonewton forces at the thermal limit in fluid (pp. 729)**
*Lulu Liu, Simon Kheifets, Vincent Ginis, Federico Capasso,*

**General Design Approaches in Geometrical Optics, Graded-Index Lenses, and Tracing of Optical Force (pp. 730)**
*Aaron J. Danner, Alireza Akbarzadeh, Tomas Tyc,*

**Polarization Engineering in Photonic Crystal Waveguides for Spin-Photon Entanglers (pp. 732)**
*Andrew Young, Arthur Thijssen, Daryl Beggs, Petros Androvitsaneas, Kobus L Kuipers, John Rarity, Stephen Hughes, Ruth Oulton,*

**Tunable and nonlinear metamaterials made of superconducting thin films (pp. 734)**
*Cihan Kurter, S. M. Anlage,*

**Enhancing optical forces between coupled waveguides using complex effective gauge fields (pp. 736)**
*Lana Descheemaeker, Vincent Ginis, Sophie Viaene, Jan Danckaert, Philippe Tassin,*

**Van der Waals forces at surfaces (pp. 737)**

*J. Pendry, K. Sasihithlu,*

## Chiral Optics and Chiral Materials: Interplaying Structures

**Electromagnetic Duality Symmetry in Optical Activity (pp. 739)**
*Ivan Fernandez-Corbaton, Martin Fruhnert, Carsten Rockstuhl,*

**Chiral Rotational Spectroscopy (pp. 741)**
*Robert. P. Cameron, J. B. Gotte, S. M. Barnett,*

**Chirality in evanescent near fields (pp. 743)**
*Euan Hendry,*

**Chirality of microwave fields (pp. 744)**
*Eugene Kamenetskii, Maksim Berezin, Elad Hollander, Reuven Shavit,*

**Helicity transfer between particles (pp. 746)**
*Manuel Nieto-Vesperinas,*

**Chiral Tips and Nanoparticles for Visible and Ultraviolet Plasmonics (pp. 747)**
*David J. Norris,*

**Formation of chiral nanostructures by optical angular momentum transfer effects (pp. 749)**
*Takashige Omatsu,*

**Helicity of Structured Light (pp. 751)**
*Alison Yao, Robert Cameron, Christopher Gibson, Stephen Barnett, Gian-Luca Oppo,*

**One-way waveguide by self-collimation in photonic crystals (pp. 753)**
*Rui-Xin Wu, Qing-Bo Li, Yin Poo,*

**Chirality control at the nanoscale (pp. 755)**
*Xavier Zambrana-Puyalto, N. Bonod,*

**Classical electromagnetic scattering response of topological insulators (pp. 757)**
*Tom Mackay, Akhlesh Lakhtakia,*

**Manipulating the hybridisation of chiral plasmonic metamaterials using molecular and macromolecular stereostructure (pp. 759)**
*Calum Jack, Affar S. Karimullah, Ryan Tullius, Vincent M. Rotello, Graeme Cooke, Nikolaj Gadegaard, Laurence D. Barron, Malcolm Kadodwala,*

**Selectively Driving Optical Matter (pp. 760)**
*Uttam Manna, Jung-Hoon Lee, John A. Parker, Nolan Shepherd, Tiansong Deng, Youssef Weizmann, Norbert F. Scherer,*

**Probing chirality of molecule in the presence of nanoparticles (pp. 762)**
*Tong Wu, Xiangdong Zhang,*

**Optical and acoustical radiation torque and forces: overview, applications, and selected recent developments (pp. 764)**

*Philip Marston, Likun Zhang,*

**Directionality in coherent dipole-dipole interactions (pp. 766)**
*Joerg Bernhard Goette, Gaoyong Sun, Koen Corstiaan van Kruining, Thomas Pohl,*

**Mechanical effects of highly twisted light interacting with two-level atoms (pp. 767)**
*Vasileios E. Lembessis, Mohamed Babiker, Demosthenes Ellinas,*

**Cold atoms and optical vortex beams (pp. 769)**
*Sonja Franke-Arnold,*

## Plasmonics and propagation of electromagnetic radiations in low-dimensional materials

**Plasmonic excitations in thin topological insulators (pp. 771)**
*Tobias Stauber,*

**Effect of Remote Impurity Layer on THz gain in Graphene Bilayers with Population Inversion (pp. 772)**
*Maxim Ryzhii, Taiichi Otsuji, Victor Ryzhii, Vladimir Mitin, Michael Shur,*

**Enhanced Sensing and PT-Symmetry in Photoexcited Graphene Nanostructures (pp. 774)**
*Pai-Yen Chen,*

**Terahertz Photogalvanics and Opto-Electronic Characterization of Topological Insulators (pp. 776)**
*Sergey Ganichev,*

**Atomic scale meta-surfaces based on graphene and hexagonal boron nitride (pp. 778)**
*Dmitri Basov,*

**Surface Electromagnetic Waves on Metamaterial Absorbers (pp. 779)**
*Willie Padilla, Andrew Cardin,*

**Controlled signal propagation in a metamaterial analogue of tripod EIT medium (pp. 781)**
*Sylwia Zielinska - Raczynska, David Ziemkiewicz,*

## Microcavity Polaritons: fundamental physics and devices

**Spin selective filtering and spin textures in quasi-one-dimensional polariton condensates (pp. 783)**
*C. Anton, T. Gao, S. Morina, T. C. H. Liew, M. D. Martin, Z. Hatzopoulos, P. S. Eldridge, P. G. Savvidis, Luis Vina,*

**Instabilities of polariton condensates in patterned microcavities (pp. 785)**
*Michiel Wouters, V. N. Gladilin, D. De Bernardis,*

**Exciton-polariton lasers based on biologically produced fluorescent proteins (pp. 786)**
*Sven Hoefling, C. P. Dietrich, A. Steude, L. Tropf, M. Schubert, N. M. Kronenberg, K. Ostermann, M. C. Gather,*

**Towards strongly confined exciton-polariton Bose-Einstein condensates with a polymer at ambient conditions (pp. 788)**
*Darius Urbonas, Fabio Scafirimuto, Lijian Mai, Rainer F. Mahrt, Thilo Stoeferle,*

**Unitary dynamics of a propagating quantum fluid of light in a cavityless nonlinear optical medium (pp. 790)**
*P.- E. Larre, Iacopo Carusotto,*

**Quantum Statistics of Bosonic Cascades (pp. 792)**
*Timothy C. H. Liew, Y. G. Rubo, A. S. Sheremet, S. De Liberato, I. A. Shelykh, F. P. Laussy, A. V. Kavokin,*

**Nonlocal Fluids of Light (pp. 793)**
*Daniele Faccio, David Vocke, Kali Wilson, Thomas Roger, Francesco Marino, Calum Maitland, Iacopo Carusotto, Brian P. Anderson, Ewan M. Wright,*

**Dynamic Control of Polariton States in Spin-Orbit Poincare Spheres using Ultrafast Stark Pulses (pp. 795)**
*Emiliano Cancellieri, F. Li, G. Buonaiuto, D. N. Krizhanovskii, M. S. Skolnick, D. M. Whittaker,*

**Microcavity polaritons: fundamental physics and devices (pp. 797)**
*Benoit Deveaud,*

**Transport properties of electromagnetically dressed graphene (pp. 798)**
*Ivan A. Shelykh, Skender Morina, Kristinn Kristinsson, Kevin Dini, Oleg Kibis,*

**Polariton lasing in hybrid organic-inorganic microcavity (pp. 800)**
*G. Paschos, N. Somaschi, G. Christmann, D. Coles, D. G. Lidzey, Z. Hatzopoulos, S. I. Tsintzos, P. G. Lagoudakis, Pavlos Savvidis,*

**Polariton condensation phase diagram in a ZnO microcavity: what else besides room-temperature? (pp. 801)**
*Jesus Zuniga-Perez, Omar Jamadi, Francois Reveret, Rereao Hahe, Feng Li, Mathieu Leroux, Fabrice Semond, Joel Leymarie, Pierre Disseix, Francois Medard,*

**Spatio-temporal polariton phenomena in GaAs-based slab waveguides with giant optical nonlinearity (pp. 803)**
*P. M. Walker, C. Whittaker, L. Tinkler, M. Sich, E. Cancelliery, D. V. Skryabin, A. Yulin, B. Royall, I. Farrer, D. A. Ritchie,*

**Spin-orbit coupling in photonic systems: from Optical Spin Hall Effect to Z topological insulator (pp. 805)**
*Guillaume Malpuech,*

**Manipulating and controlling polariton superfluid vortices (pp. 806)**
*Simon Pigeon,*

**Discrete vortex solitons in polariton lattices (pp. 808)**
*Natalia Berloff,*

**Control of the generation and propagation of polariton condensates at 300K in ZnO microcavities (pp. 810)**
*Rereao Hahe, Hamis Gargoubi, Christelle Brimont, Brahim Guizal, Sihem Jaziri, Sophie Bouchoule, Xavier Lafosse, Feng Li, Mathieu Leroux, Fabrice Semond,*

**Quantum Spin Hall phase and topologically protected edge states in the polariton rings lattices (pp. 812)**
*Mehedi Hasan, Ivan Iorsh, Ivan Shelykh,*

**Nonequilibrium thermodynamics of quantum fluids of polaritons (pp. 814)**
*Sebastian Klembt, Thorsten Klein, Anna Minguzzi, Maxime Richard,*

**Fractal and topological properties of Fibonacci quasi-crystals for polaritons (pp. 816)**
*Florent Baboux, D. Tanese, T. Jacqmin, A. Lemaitre, E. Galopin, I. Sagnes, A. Amo, J. Bloch, E. Levy, E. Gurevich,*

**Exciton-polariton condensates in non-Hermitian potentials (pp. 818)**
*Elena Ostrovskaya,*

**Exploring the potential of microcavity polariton physics for photonic devices (pp. 820)**
*O. Lafont, P. Lewandowski, M. H. Luk, N. H. Kwong, K. P. Chan, P. T. Leung, E. Galopin, A. Lemaitre, P. Roussignol, S. Schumacher,*

**Exciting polaritons with quantum light (pp. 822)**
*Juan Camilo Lopez Carreno, Carlos Sanchez Munoz, Elena del Valle, Fabrice P. Laussy,*

**Advances on strongly correlated photonic systems (pp. 824)**
*Cristiano Ciuti,*

**Collective Scattering of an Incoherently Driven Exciton-Polariton Condensate in Disordered Environment (pp. 825)**
*Maciej Pieczarka, Marcin Syperek, Lukasz Dusanowski, Jan Misiewicz, Fabian Langer, Martin Kamp, Christian Schneider, Sven Hoefling, Alexey Kavokin, Grzegorz Sek,*

**Ultra-strong coupling with the free space: the superradiance (pp. 827)**
*Carlo Sirtori, A. Vasanelli, Y. Todorov,*

**Polariton Stirring and Storage of Quantized Vortices (pp. 829)**
*Nicolas D. Sangouard, Thomas Boulier, Emiliano Cancellieri, Quentin Glorieux, David M. Whittaker, Alexey V. Kavokin, Elisabeth Giacobino, Alberto Bramati,*

**Quantum Simulations with Polariton Graphs (pp. 831)**
*Pavlos Lagoudakis,*

## Subwavelength grating structures and metamaterials for integrated photonics

**Spatial Heterodyne Fourier-transform Spectroscopy: from fundamentals to array waveguide interferometers (pp. 834)**
*Maria L. Calvo, A. V. Velasco, P. Cheben, M. Florjanczyk,*

**On-chip Bragg gratings for Bloch surface waves (pp. 836)**
*Leonid L. Doskolovich, Evgeni A. Bezus, Dmitry A. Bykov,*

**Dielectric on-chip diffraction gratings for surface plasmon polaritons (pp. 838)**
*Evgeni A. Bezus, Leonid L. Doskolovich, Victor A. Soifer,*

**Effect of jitter in subwavelength grating waveguides and devices (pp. 840)**
*Jiri Ctyroky,*

**Directing OLED emission via subwavelength aluminium grating (pp. 842)**
*Veronika Tretnak, Manuel Auer-Berger, Joachim R. Krenn,*

**Optimization of Subwavelength Structures for Efficient Couplers and Hyperuniform Disordered Integrated Polarizers (pp. 843)**

*Hon Ki Tsang, Wen Zhou, Bing Qing Zhu, Linghai Liu,*

**Transmitting and reflective subwavelength azimuthal micropolarizers (pp. 845)**
*Sergey S. Stafeev, Anton G. Nalimov, Liam O'Faolain, Maria V. Kotlyar, Victor Kotlyar,*

**Subwavelength-engineered interferometer arrays for Fourier-transform spectrometry (pp. 847)**
*Aitor V. Velasco, Pavel Cheben, Jens Schmid, Andre Delage, Jean Lapointe, Dan-Xia Xu, Martin Vachon, Siegried Janz, Maria Calvo, Alaine Herrero-Bermello,*

**Inverse dispersion engineering in integrated waveguides (pp. 849)**
*David Castello-Lurbe, Victor Torres-Company, Enrique Silvestre,*

**Photonic crystal slot cavities, high-sensitivity nanotweezers (pp. 851)**
*S. Hamed Mirsadeghi, Jonathan Massey-Allard, Jeff F. Young,*

**High-efficiency single etch step surface grating couplers engineered by subwavelength structured metamaterials (pp. 853)**
*Daniel Benedikovic, Carlos Alonso-Ramos, Laurent Vivien, Pavel Cheben, Jens H. Schmid, Shurui Wang, Dan-Xia Xu, Boris Lamontagne, Jean Lapointe, Siegfried Janz,*

**On leakage losses in subwavelength grating devices (pp. 855)**
*J. Dario Sarmiento-Merenguel, Alejandro Ortega-Monux, Jean-Marc Fedeli, J. Gonzalo Wanguemert-Perez, Carlos Alonso-Ramos, Elena Duran-Valdeiglesias, Pavel Cheben, Inigo Molina-Fernandez, Robert Halir,*

**Sub-wavelength engineered high directionality fiber-to-chip blazed grating couplers (pp. 857)**
*Carlos Alonso Ramos, Daniel Benedikovic, Pavel Cheben, Diego Perez-Galacho, Jens H. Schmid, Shurui Wang, Dan-Xia Xu, Boris Lamontagne, Jean Lapointe, Siegfried Janz,*

**Sub-wavelength cladded suspended silicon photonic components for the mid-infrared: fabrication and experiments (pp. 859)**
*Milos Nedeljkovic, Alejandro Ortega-Monux, Jordi Soler Penades, Gonzalo Wanguemert-Perez, Ali Z. Khokhar, Robert Halir, Zhibo Qu, Wei Cao, Colin Mitchell, Stevan Stankovic,*

**Sub-wavelength Grating Components for the Silicon-on-insulator Platform (pp. 861)**
*Yun Wang, Jonas Flueckiger, Zeqin Lu, Han Yun, Minglei Ma, Fan Zhang, Valentina Donzella, Nicolas A. F. Jaeger, Lukas Chrostowski,*

**High efficiency, ultra-broadband fiber-to-chip coupler based on subwavelength gratings (pp. 863)**
*Alejandro Sanchez-Postigo, Alejandro Ortega-Monux, Jose Manuel Luque-Gonzalez, Carlos Alonso-Ramos, Robert Halir, Jens Schmid, Pavel Cheben, Juan Gonzalo Wanguemert-Perez, Inigo Molina-Fernandez,*

**Recent advancements towards all-optical signal processing (pp. 864)**
*Ivan Glesk, J. Wang, L. Chen,*

**Subwavelength structures in silicon-on-insulator waveguides for efficient and broadband fiber-chip coupling (pp. 866)**
*Jens H. Schmid, Pavel Cheben, Dan-Xia Xu, Siegfried Janz, Jean Lapointe, Mohamed Rahim, Shurui Wang, Martin Vachon, Robert Halir, Alejandro Ortega-Monux,*

**Design of integrated photonic devices based on subwavelength structures for Near and Mid-Infrared applications (pp. 868)**
*Alejandro Ortega-Monux, J. Gonzalo Wanguemert-Perez, Robert Halir, Inigo Molina-Fernandez, Jordi Soler-Penades, Milos Nedeljkovic, Ali Z. Khokhar, Zhibo Qu, Wei Cao, Colin Mitchell,*

**Homogenisation of sub-wavelength grating waveguides (pp. 870)**
*Trevor James Hall, Hamdam Nikkhah,*

**Efficient optimization of subwavelength gratings for photonic integrated circuits (pp. 872)**
*James Pond, Amy Liu, Jens Niegemann, Xu Wang, Pavel Cheben,*

**Dielectric metasurfaces for beam shaping, mode matching and polarization selection (pp. 874)**
*Meir Grajower, Boris Desiatov, David Ohana, Jonathan Bar David, Noa Mazurski, Uriel Levy,*

**Silicon Nitride for Integrated Photonic Applications (pp. 875)**
*Thalia Dominguez Bucio, Abdelrahman Zaher Al-Attili, Kapil Debnath, Shinichi Saito, Goran Mashanovich, Alejandro Sanchez-Postigo, Gonzalo Waguemert-Perez, Alejandro Ortega-Monux, Robert Halir, Pavel Cheben,*

**Photonic crystal member lasers with integrated beam routing gratings and metasurfaces (pp. 876)**
*Weidong Zhou, Shichia Liu, Deyin Zhao, Hongjun Yang, Zhenqiang Ma,*

**Monolithic Subwavelength High-index Contrast Surface Gratings for ultra-thin VCSELs (pp. 877)**
*M. Gebski, E. Haglund, P. Moser, M. Riaziat, M. Dems, A. Larsson, T. Czyszanowski, J. A. Lott,*

## Nanophotonics and plasmonics for information applications

**Photonic spin Hall effect in waveguides composed of two kinds of single-negative metamaterials (pp. 880)**
*Z. W. Guo, K. Yu, Haitao Jiang, H. Chen,*

**Efficient spectral and spatial manipulation of optical field hot spots via plasmonic mode hybridization in hierarchical nanostructures (pp. 882)**
*Benfeng Bai, Zhendong Zhu,*

**Efficient generation of prominent and robust plasmonic Fano resonances in a 3D metamaterial (pp. 884)**
*Jiafang Li, Zhiguang Liu, Zhi-Yuan Li,*

**Surface plasmon model for the radiation enhancement by resonant optical dipole antennas (pp. 885)**
*Haitao Liu, Hongwei Jia, Ying Zhong,*

**3D optical nanofabrication in glass (pp. 887)**
*Yang Liao, Jielei Ni, Ya Cheng,*

**Dynamic plasmonic tweezers for nanoparticles and nanowires (pp. 888)**
*Xiujie Dou, Changjun Min, Lichao Zhang, Yuquan Zhang, Xiaocong Yuan,*

**Lithium-niobate-based micro-resonators (pp. 890)**
*Guoquan Zhang, Fang Bo, Jie Wang, Jiao Cui, Yongfa Kong, Jingjun Xu,*

**Quasi-normal mode formalism for the radiation properties of nanoparticles in optical stacks (pp. 892)**
*Kevin Vynck, Remi Faggiani, Jianji Yang, Philippe Lalanne,*

**Spatiotemporal 3D pulse shaping using phase-shifted Bragg gratings (pp. 894)**
*Nikita V. Golovastikov, Dmitry A. Bykov, Leonid L. Doskolovich,*

**The Exceptional Point in Plasmonic Waveguide Arrays (pp. 896)**
*Shaolin Ke, Bing Wang, Peixiang Lu,*

**Surface Plasmon Polariton Manipulation in Graphene Sheet Arrays (pp. 898)**
*Bing Wang,*

**Overcoming Quenching in Plasmonic Nanoantennas (pp. 900)**
*Christophe Sauvan,*

**Plasmonic and Dielectric Nanoantennas for Integrated Photonic Circuitry (pp. 902)**
*Yuanqing Yang, Jingyi Tian, Hang Zhao, Qiang Li, Min Qiu,*

## Topological photonics

**Weyl Points and Topological Notions in Electromagnetic Waves (pp. 905)**
*Wenjie Chen, Meng Xiao, Wen-Yu He, Z. Q. Zhang, C. T. Chan,*

**Synthetic dimensions in multi-mode ring-resonator arrays (pp. 907)**
*Tomoki Ozawa, Hannah M. Price, Nathan Goldman, Oded Zilberberg, Iacopo Carusotto,*

**Topological effects based on spin-orbit coupling of cavity polaritons (pp. 908)**
*Dmitry Solnyshkov, A. V. Nalitov, G. Malpuech,*

**Topological Properties of Quasicrystals: A Scattering Analysis (pp. 910)**
*Eli Eliyahu Levy, Assaf Barak, Amnon Fisher, Eric Akkermans,*

**Metamaterial structures to realize real-space gauge-field (pp. 912)**
*Fu Liu, Jensen Li,*

**Metasurface laser (pp. 914)**
*Boubacar Kante,*

**Nonlinear topological states of interacting photons (pp. 917)**
*Alexander N. Poddubny,*

**Topological Transport in Photonic Quasicrystals (pp. 918)**
*Miguel A. Bandres, Mikael C. Rechtsman, Mordechai Segev,*

**Two-dimensional topological photonic crystals (pp. 920)**
*S. Barik, H. Miyake, W. DeGottardi, E. Waks, Mohammad Hafezi,*

**Pseudospin-mediated phenomena in photonic graphene (pp. 923)**
*Zhigang Chen,*

**Z2 Topological Photonics derived from Crystal Symmetry (pp. 924)**
*Xiao Hu,*

**Topologically Non-Trivial States in Photonic Crystals (pp. 926)**
*Marin Soljacic,*

**Anomalous Topological Phases and Unpaired Dirac Cones in Photonic Lattices (pp. 927)**
*Yidong Chong, Daniel Leykam, Mikael C. Rechtsman,*

**Reconfigurable and all-dielectric photonic topological insulators in two and three dimensions (pp. 929)**
*Alexander Khanikaev,*

**Topological excitons, plexcitons, and polaritons in organic materials (pp. 931)**
*Joel Yuen-Zhou,*

## Advances in plasmonic and metamaterial devices

**Scalable Nanoarchitecturing for Commercially-feasible Applications in Electronics, Photonics, and Metastructures (pp. 934)**
*Jong G. Ok,*

**Versatile and controllable excitation of SPPs by a metasurface composed of triangular nanoantennas (pp. 935)**
*Benfeng Bai, Oubo You,*

**Wavefront shaping through emulated curved space (pp. 937)**
*Chong Sheng, Rivka Bekenstein, Hui Liu, Shining Zhu, Mordechai Segev,*

**Metasurfaces for refractomatric sensing and advanced functionalities (pp. 939)**
*Ruggero Verre, M. Svedendahl, T. Antosiewicz, M. Kall,*

**Hybrid graphene-plasmonic antenna arrays for the fast detection of terahertz quantum cascade lasers (pp. 941)**
*Riccardo Degl'Innocenti, David Jessop, Long Xiao, Stephen Kindness, Yuan Ren, Hungyen Lin, Axel Zeitler, Philipp Braeuninger-Weimer, Stephan Hofmann, Harvey Beere,*

**KERR Effect in Hybrid Plasmonic Waveguides (pp. 943)**
*Stefano Palomba, F. J. Diaz, G. Li, C. Martijn de Sterke, B. T. Kuhlmey,*

**Coplanar isolator based on gap plasmon resonators (pp. 944)**
*E. Djekounyom, E. Verney, D. Pietroy, J. P. Chatelon,*

**Backward spoof surface plasmonic wave propagation and waveguide devices utilizing structured ultra-thin metallic films (pp. 946)**
*Yijun Feng, Xiaoyong Liu, Junming Zhao, Bo Zhu, Tian Jiang,*

**Quantum plasmons in nanoscale waveguides (pp. 948)**
*Xi-Feng Ren, Yong-Jing Cai, Ming Li, Chang-Ling Zou, Xiao Xiong, Hua-Lin Lei, Bi-Heng Liu, Guo-Ping Guo, Guang-Can Guo,*

**Optimal and reproducible surface-enhanced Raman scattering with precisely-controlled nanometer-scale gaps (pp. 950)**
*Joel M. Katzen, Antony Murphy, Robert Pollard, Fumin Huang,*

**Disposable Plasmonics: Plastic Templated Plasmonic Metamaterials with Tunable Chirality (pp. 952)**
*Affar S. Karimullah, Calum Jack, Ryan Tullius, Vincent M. Rotello, Graeme Cooke, Nikolaj Gadegaard, Laurence D. Barron, Malcolm Kadodwala,*

**Ultra narrow resonances, giant field enhancement and sensitivity by low-loss waveguide modes for sensing applications (pp. 953)**

*Dmitry V. Nesterenko, Shinji Hayashi, Zouheir Sekkat,*

**Hot spot engineering in 3D Multibranched Nanostructures: realization of ultrasensitive platforms for Raman spectroscopy (pp. 955)**
*Manohar Chirumamilla, Anisha Gopalakrishnan, Alexander S. Roberts, Remo Proietti Zaccaria, Francesco De Angelis, Peter Kjaer Kristensen, Roman Krahne, Sergey I. Bozhevolnyi, Kjeld Pedersen, Andrea Toma,*

**The applications of propagating surface plasmon waves in the SERS (pp. 957)**
*Lierong Yuan, Lei Zhang, Qianjin Wang, Yongyuan Zhu, Yanqing Lu, Xuejin Zhang,*

**Integrated Photonics Engineered Around Exceptional Points (pp. 958)**
*Liang Feng,*

**A flexible THz random reflector by 1 bit coding metamaterial (pp. 960)**
*Biaobing Jin, Weiwei Liu, Tiejun Cui,*

**An MOS platform for sub-wavelength focusing and shaping of visible light (pp. 962)**
*Guy Bartal,*

**Plasmon Lasers for Sensing (pp. 963)**
*Renmin Ma,*

**Physical Scaling Laws of Nanophotonics (pp. 964)**
*Ke Liu, Arka Majumdar, Volker J. Sorger,*

**PT symmetric Bragg gratings operating with long-range surface plasmons (pp. 966)**
*Elham Karami Keshmarzi, R. Niall Tait, Pierre Berini,*

**CMOS THz On-chip Surface-wave Resonator and Oscillator (pp. 967)**
*Yuan Liang, Hao Yu, Xiaojian Fu,*

## Magnetic Surface Polaritons: interactions between the magnetic, plasmonic, acoustic surface waves

**Switching of the Magnetic Moment by Mechanical Motion (pp. 970)**
*Eugene M. Chudnovsky,*

**Tunable magneto-acoustic crystals (pp. 971)**
*Florian Allein, Vincent Tournat, Vitali Gusev, Georgios Theocharis,*

**Inverse Magneto-Optical Effects in Cylindrical Graphene-Coated Nanowires (pp. 973)**
*Dmitry Kuzmin, Igor Bychkov, Vladimir Shavrov, Vasily Temnov, Hyong-In Lee, Jinsik Mok,*

**Nonlinear surface photonics in hybrid magnetic structures (pp. 975)**
*Ilya Razdolski, Denys Makarov, Alexander Paarmann, Martin Wolf, Vasily Temnov,*

**Propagating magnons with sub-100 nm wavelength excited by microwaves in nanostructured metal/insulator thin-film magnets (pp. 977)**
*H. Yu, O. d'Allivy Kelly, V. Cros, R. Bernard, P. Bortolotti, A. Anane, F. Brandl, F. Heimbach, Dirk Grundler,*

**Ultrafast Surface Magnetoelastic Waves (pp. 979)**
*J. Janusonis, C. L. Chang, A. M. Lomonosov, V. Shalagatskyi, V. S. Vlasov, V. V. Temnov, Raa'nan Itzhak Tobey,*

**Tunable plasmonic heterostructures: magnetic and optical-pump ultrafast control (pp. 981)**
*Vladimir Belotelov,*

**Localized Surface Plasmons and Magnetooptical Activity Enhancement (pp. 983)**
*Gaspar Armelles,*

**Curvilinear magnetism (pp. 984)**
*Denys Makarov,*

**Spin transport and manipulation in GaAs quantum wells by surface acoustic waves (pp. 986)**
*Alberto Hernandez-Minguez, Klaus Biermann, Rudolf Hey, Paulo Ventura Santos,*

**Enhanced Magneto-optical Effect in Magnetoplasmonic Ring-Split ring structures (pp. 988)**
*Hua Yu Feng, Feng Luo, Raul Arenal, Fernando Garcia, Gaspar Armelles, Alfonso Cebollada,*

**Ultrafast spin-lattice coupling investigation in magnetostrictive Terfenol films by picosecond shear acoustic pulses (pp. 990)**
*Tymur Parpiiev, Arnaud Hillion, Vladimir Vlasov, Vincent Polewczyk, Vasily Temnov, Karine Dumesnil, Stephane Andrieu, Abdelmadjid Anane, Vitalyi Gusev, Thomas Pezeril,*

**Magneto-elastic Symmetry Breaking with Surface Acoustic Waves (pp. 992)**
*Alexey Lomonosov, Vladimir Vlasov, Julius Janusonis, Chia-Lin Chang, Raanan Tobey, Thomas Pezeril, Vasily Temnov,*

**Harnessing magnetoplasmons to induce topological excitations (pp. 994)**
*Joel Yuen-Zhou,*

**Static and dynamic properties of hybrid magnetoplasmonic structures (pp. 996)**
*Minh Ngoc Tran, Tom Seifert, Tymur Parpiiev, Gwenaelle Vaudel, Thomas Pezeril, D. Makarov, T. Kampfrath, Vasily Temnov,*

## On-chip Integrated Quantum Photonics

**A heterogeneous III-V / Si3N4 quantum photonic integration platform (pp. 1000)**
*Marcelo Davanco, Jin Liu, Chen-Zhao Zhang, Liu Liu, Kartik Srinivasan,*

**Resonant laser spectroscopy of localized bright and dark excitons in monolayer WSe2 (pp. 1002)**
*S. Kumar, M. Brotons-Gisbert, R. Al-Khuzheyri, A. Kaczmarczyk, G. Ballesteros-Garcia, J. F. Sanchez-Royo, B. D. Gerardot,*

**Quantum nanophotonics: controlling spins with single photons on-a-chip (pp. 1004)**
*Edo Waks, Shuo Sun, Tao Cai, Ranojoy Bose, Hyochul Kim, Glenn S. Solomon,*

**Integrated Quantum Frequency Comb Source of Entangled Qubits (pp. 1006)**
*Michael Kues, Christian Reimer, Piotr Roztocki, Benjamin Wetzel, Yaron Bromberg, Brent E. Little, Sai T. Chu, David J. Moss, Lucia Caspani, Roberto Morandotti,*

**Fully-tuneable, cavity-enhanced waveguide single-photon sources (pp. 1008)**
*Andrea Fiore, Maurangelo Petruzzella, Simone Birindelli, Francesco Pagliano, Zarko Zobenica, Lianhe Li, Edmund Linfield,*

**Comparison of four computational methods for computing Q factors and resonance wavelengths in photonic crystal membrane cavities (pp. 1010)**
*Jakob Rosenkrantz de Lasson, Lars Hagedorn Frandsen, Sven Burger, Philipp Gutsche, Oleksiy Kim, Olav Breinbjerg, Ole Sigmund, Jesper Mork, Niels Gregersen,*

**Fundamental limitations to the coherence of single-photon sources due to phonon scattering (pp. 1012)**
*Jesper Mork, Dara McCutcheon, Jake Iles-Smith, Niels Gregersen,*

**A modal approach to light emission and propagation in coupled cavity waveguide systems (pp. 1014)**
*Philip T. Kristensen, Jakob Rosenkrantz de Lasson, Niels Gregersen, Jesper Mork,*

**Photonic Crystal-Based Single Photon Infrared Detectors and Sources in Silicon-on-Inuslator Photonic Circuits (pp. 1016)**
*Mohsen Akhlaghi, Ellen Schelew, Jeff Young,*

**Quantum-dot-based on-chip functionality in III-V circuits (pp. 1018)**
*Maurice Skolnick,*

**Quantum correlations of light and matter through environmental transitions (pp. 1019)**
*Ahsan Nazir, Jake Iles-Smith,*

**New approaches in the design of quantum sources (pp. 1020)**
*Carlos Sanchez Munoz, Juan Camilo Lopez Carreno, Fabrice P. Laussy, Elena del Valle,*

**Site-controlled quantum dots coupled to photonic crystal waveguides (pp. 1022)**
*Bruno Rigal, Jakob Rosenkrantz de Lasson, Clement Jarlov, Benjamin Dwir, Alok Rudra, Alexey Lyasota, Irina Kulkova, Niels Gregersen, Jesper Mork, Elyahou Kapon,*

**Polarization Engineering in Photonic Crystal Waveguides for Spin-Photon Entanglers (pp. 1024)**
*A.?B. Young, A.?C.?T. Thijssen, D.?M. Beggs, P. Androvitsaneas, L. Kuipers, J.?G. Rarity, Stephen Hughes, Ruth Oulton,*

**Quantum dots in monolayered WSe2 : A new class of high purity solid state single photon sources (pp. 1026)**
*Yu-Ming He, Oliver Iff, Nils Lundt, Sven Hoefling, Christian Schneider,*

**Quantum entanglement between distant quantum dot spins (pp. 1027)**
*Emre Togan, Jan Klaers, Aymeric Delteil, Zhe Sun, Atac Imamoglu,*

**Heterogeneous integration and trimming of complex silicon photonic circuits (pp. 1028)**
*Graham J. Sharp, Laura Meriggi, Charalambos Klitis, Barry M. Holmes, Ying Ding, Stuart May, Giuseppe Cantarella, Michael J. Strain, Marc Sorel,*

**Efficient parametric interactions in Photonic Crystals Waveguides and Resonators (pp. 1030)**
*A. Martin, G. Moille, T. Debuisschert, A. P. Mosk, G. Eisenstein, S. Combrie, A. De Rossi,*

**Quantum photonics with quantum dots in photonic wires (pp. 1032)**
*Mathieu Munsch, Andreas Kuhlmann, Davide Cadeddu, Jean Teissier, Martino Poggio, Niels Gregersen, Jean-Michel Gerard, Julien Claudon, Richard J. Warburton,*

**Quantum photonic circuits using single photons from a quantum dot. (pp. 1034)**
*Anthony J. Bennett, J. P. Lee, D. J. P. Ellis, E. Murray, F. Floether, J. Griffiths, T. Meany, I. Farrer, D. A. Ritchie, A. J. Shields,*

**Silica on silicon planar photonic circuits for Quantum Information Processing (pp. 1036)**
*Peter G.R. Smith, James C. Gates, Corin B. E. Gawith, Christopher Holmes, Lewis G. Carpenter, Samuel A. Berry, Teresa I. Ferreiro, Paolo L. Mennea, Matthew T. Posner, Peter A. Cooper,*

**Superconducting Nanowire Single Photon Detectors Integrated with GaAs Waveguide Circuits (pp. 1037)**
*Robert Kirkwood, Chandra M. Natarajan, Alessandro Casaburi, Mike Tanner, Robert Hadfield,*

## Nonlinear photonic crystals and metamaterials

**High-efficiency Ultra-Broadband Supercontinuum High-Harmonic Generation from a Single Nonlinear Crystal (pp. 1039)**
*Chen-Yang Hu, Bao-Qin Chen, Jiafang Li, Zhi-Yuan Li,*

**Topological Description and Nonlinearity Enhancement for Optical Mirrors (pp. 1040)**
*Hong Chen,*

**Self-accelerating Pulses and Their Nonlinear Dynamics (pp. 1041)**
*Yi Hu, Zhigang Chen, Jingjun Xu,*

**Optical control of patterns and polariton flow in semiconductor microcavities (pp. 1042)**
*Stefan Schumacher,*

**Shaping optical absorption in disorder gold nanorod assemblies (pp. 1043)**
*Yi Xu, Jin-Xiang Li, Qiao-Feng Dai, Shao-Long Tie, Sheng Lan,*

**Third harmonic emission from self-organized dielectric meta-surfaces (pp. 1045)**
*S. V. Makarov, T. Voitova, A. Tsypkin, V. A. Milichko, I. S. Mukhin, Alexey Yulin, E. Putilin, M. Baranov, A. E. Krasnok, P. A. Belov,*

**Improved nonlinear plasmonic slot waveguides (pp. 1047)**
*Mahmoud Mohamed Reda Elsawy, Gilles Renversez,*

**Still azimuthal doughnuts in near-zero-index media (pp. 1049)**
*Andrea Marini, Javier F. Garcia de Abajo,*

**Structured Light in Nonlinear Colloidal Media (pp. 1051)**
*Salih Silahli, Wiktor Walasik, Natalia Litchinitser,*

**All-optical light storage in nonlinear Fabry-Perot resonator and release by demand (pp. 1053)**
*Konstantin Pichugin, Almas Sadreev,*

## Plasmonics and metamaterials beyond pure noble metals

**Advances in Nano-aperture Optics and Ultrathin Overcoats for Heat-assisted Magnetic Recording (pp. 1062)**
*Reuben J. Yeo, Sajid Hussain, Neeraj Dwivedi, Shreya Kundu, Hyunsoo Yang, Aaron J. Danner, Charanjit Singh Bhatia,*

**Alternative Materials for Plasmonic Applications (pp. 1065)**
*Peter K. Petrov, Andrei Mihai, Bin Zou, Laurentiu Braic, Nikolaos Vasilantonakis, Stefan Maier, Neil Alford, Anatoly Zayats,*

**Hot carrier excitation in transition metal nitrides (pp. 1067)**

*Satoshi Ishii, Satish Laxman Shinde, Mukesh Kumar, Ramu Pasupathi Sugavaneshwar, Thang Duy Dao, Takahiro Yokoyama, Naoto Umezawa, Tadaaki Nagao,*

**Plasmonic and thermal properties of transition metal nitride/noble metal core-shell nanoparticles (pp. 1069)**
*Fumin Huang, Stacey Drakeley, Muigahid Ali, William Hendren, Robert M. Bowman,*

**Comparing the efficiency of plasmonic materials The case of metal nitrides (pp. 1071)**
*Adrien Lalisse, Gilles Tessier, Jerome Plain, Guillaume Baffou,*

**Fully-integrated Light Delivery System for Heat Assisted Magnetic Recording (pp. 1073)**
*Qian Wang, Kim Peng Lim, Vivek Krishnamurthy, Jing Pu,*

**HAMR and the Future of Hard Drives (pp. 1075)**
*Roberto F. Garcia, Mark Gubbins,*

**All-dielectric light concentrator for heat assisted magnetic recording (pp. 1076)**
*Andrey K. Sarychev, Sergey S. Vergeles, Gennady Tartakovsky,*

**Antenna-assisted picosecond control of the vanadium dioxide phase transition through resonant near-field excitation (pp. 1078)**
*Otto L. Muskens, Yudong Wang, Kees de Groot, Luca Bergamini, Nerea Zabala, Javier Aizpurua, Jeff Gaskell, David Sheel,*

**Refractory Plasmonic Materials for Heat Assisted Magnetic Recording (pp. 1080)**
*Alexandra Boltasseva, Urcan Guler, Alexander V. Kildishev, Ernesto E. Marinero, Vladimir M. Shalaev,*

**Metal alloys for plasmonics applications (pp. 1081)**
*Marina S. Leite,*

**Physics, Signal, and Noise in Heat-Assisted Magnetic Recording (pp. 1083)**
*Jian-Gang Zhu, Hai Li,*

## Plasmonic Nanocircuits: Fundamentals and Devices

**Plasmonic vector near-field for composite interference, SPP switches and optical simulators (pp. 1086)**
*Tao Li, Yulin Wang, Qingqing Cheng, Shining Zhu,*

**Mechanisms of plasmon-mediated light emission in biased nanoscale constrictions (pp. 1087)**
*A. V. Uskov, I. V. Smetanin, I. E. Protsenko, J. B. Khurgin, M. Buret, A. Bouhelier,*

**Composite interference based plasmonic switches and logical gates (pp. 1089)**
*Yulin Wang, Tao Li, Shining Zhu,*

**Room temperature lasers at subwavelength scale by top-down fabrication (pp. 1091)**
*Ning Liu, Brian Corbett,*

**Localized surface plasmon enhanced and modulated nonlinear optical processes: second harmonic generation and upconversion emissions (pp. 1092)**
*Dang Yuan Lei,*

**Taming single solid-state quantum systems and mesoscopic objectives at the nanoscale (pp. 1093)**

*Xuewen Chen,*

**Nanometric imaging of the few-cycle plasmonic near-field within single nanoobjects (pp. 1094)**
*Arthur Losquin, Erik Marsell, Eleonora Lorek, Robin Svard, Chen Guo, Anne Harth, Miguel Miranda, Cord Arnold, Hongxin Xu, Anne L'Huillier,*

**Plasmonic metasurfaces for polarization and phase sensing (pp. 1096)**
*Evgeniy Panchenko, Jasper Cadusch, Panji Achmari, Kalpana Singh, Timothy James, Daniel Gomez, Timothy Davis, Ann Roberts,*

**Optical Stark-effect in J-aggregate-metal hybrid nanostructures (pp. 1098)**
*Parinda Vasa,*

**Interaction of quantum dots and plasmonic nanoparticle dimers (pp. 1100)**
*Marija Gasparic, Andreas Hohenau, Ulrich Hohenester, Joachim R. Krenn,*

**Strong plasmon-exciton coupling on individual nanoantenna level (pp. 1101)**
*G. Zengin, M. Wersall, T. J. Antosiewicz, M. Kall, Timur Shegai,*

**Multimodal plasmonics devices in crystalline colloidal systems (pp. 1103)**
*Sviatlana Viarbitskaya, Alexandre Teulle, Upkar Kumar, Jadab Sharma, Kargal Gurunatha, Aurelien Cuche, Michel Bosman, Alexandre Bouhelier, Gerard Colas des Francs, Arnaud Arbouet,*

**Strong Plasmon-Emitter Coupling: Beyond the Jaynes-Cummings Model (pp. 1105)**
*Benjamin Lawrie, Roderick B. Davidson II, Pavel Lougovski,*

**Plasmon-mediated generation of continuum emission in metal nanoparticle hot spots (pp. 1107)**
*Sebastian Bange, Tobias Haug, Philippe Klemm, John M. Lupton,*

**CMOS copper plasmonic nanocircuitry (pp. 1109)**
*Dmitry Yu. Fedyanin, Dmitry I. Yakubovsky, Roman V. Kirtaev, Valentyn S Volkov,*

**Optical nanoantenna excitation through the dissipative instability of DC current in a quantum well near a metal surface (pp. 1111)**
*Igor Valentinovich Smetanin, Alexander Bouhelier, Igor Protsenko, Alexander Uskov,*

**Surface plasmon enabled fast LED, compact waveguide device and OAM demultiplexor (pp. 1113)**
*Jinghua Teng,*

**Control of Gap Plasmon Resonance in a Suspended Nanowire By Electrostatic Force (pp. 1115)**
*Junichi Takahara, Akira Kaijima, Yusuke Nagasaki, Masashi Miyata,*

**New Building Blocks for Quantum Technologies: Doped Carbon Nanotubes and Plasmonically Coupled Quantum Dots Molecules (pp. 1116)**
*Han Htoon,*

**Revealing Optical Properties of Two-Dimensional Semiconductors at Relevant Length Scales (pp. 1118)**
*P. James Schuck,*

**Quantum Yield of Single Surface Plasmons Generated by a Quantum Dot Coupled with a Silver Nanowire (pp. 1119)**

*Hong Wei, Qiang Li, Hongxing Xu,*

**VO2-driven switchable-beam directional antenna for micro/nano scale optical communications (pp. 1121)**
*Eesa Rahimi,*

## Novel photonic and plasmonic structures: theory and applications

**Optoelectronic applications of graphene-integrated silica nanowires (pp. 1124)**
*Fei Xu,*

**Light-trapping in perovskite solar cells (pp. 1126)**
*Qingguo Du, Ching Eng Png,*

**Optical Periodic Structures with Double Spatial Resonance (pp. 1128)**
*Alagappan Gandhi , C. E. Png,*

**Manipulating polarization of radially polarized beams by anisotropic Kerr media (pp. 1130)**
*Bing Gu, Bo Wen, Guanghao Rui, Yuxiong Xue, Qiwen Zhan, Yiping Cui,*

**Plasmonic design for enhanced light emission and detection (pp. 1132)**
*Fang-Fang Ren, Guo-Gang Zhang, Meng Yang, Wei-Zong Xu, Jiandong Ye, Hai Lu, Rong Zhang, Yi Shi, Hark Hoe Tan, Chennupati Jagadish,*

**The applications of macro-optical elements in micro/nano scale (pp. 1134)**
*Haitao Dai, M. X. Run,*

**Refractory metal based broadband, omnidirectional and polarization-insensitive light absorber for high-temperature applications (pp. 1136)**
*Manohar Chirumamilla, Alexander S. Roberts, Fei Ding, Deyong Wang, Sergey I. Bozhevolnyi, Kjeld Pedersen,*

**Whispering Bloch modes (pp. 1138)**
*Ben John Maling, Richard Craster,*

**Sub-THz Optical antenna in a Standard CMOS Technology (pp. 1140)**
*Xiaoli Ji, Yiming Liao, Qun Lou, Reixin Wu, Feng Yan,*

**Broadband absorption enhancement in ZnTe nanowire intermediate solar cells with plasmonic bowtie antennas (pp. 1141)**
*Kuiying Nie, Fangfang Ren, Jing Li, Jiandong Ye, Kun Tang, Shulin Gu, Rong Zhang, Youdou Zheng,*

**Optical and mechanical properties of chitosan-based interpenetrating polymer networks (pp. 1142)**
*Catherine Claire Ryan, Maria Bardosova, Martyn Pemble,*

**Towards Single Antenna On-Chip Surface Enhanced Raman Spectroscopy: Arch Dipole Antenna (pp. 1144)**
*Ali Raza, Frederic Peyskens, Stephane Clemmen, Roel Baets,*

**Synthesis of ZnO Nanoparticles and their Application in Quantum Dot Light Emitting Diodes (pp. 1146)**
*Jiangyong Pan, Jing Chen, Yuning Zhang, Qianqian Huang, Yan Tu, Chao Lei, Kaifeng Zhou, Wei Lei,*

**Incorporation of graphene as the hole transfer layer for quantum dot light emitting diode (pp. 1149)**

*Qianqian Huang, Jing Chen, Yuning Zhang, Jiangyong Pan, Wei Lei, Chao Lei, Kaifeng Zhou,*

## Metamaterial structures for healthcare applications

**Microwave Devices for Theranostic Applications (pp. 1154)**
*Margarita Puentes, Carolin Reimann, Martin Schubler, Rolf Jakoby,*

**Large-Scale Metamaterial Anti-Reflection Coating for Biological Tissues at 60 GHz (pp. 1156)**
*Helena Cano Garcia, Shimul Saha, Panagiotis Kosmas, Efthymios Kallos,*

**A novel microwave image slices (MIS) technique for Early Breast Tumors Detection based on Metalenses (pp. 1158)**
*Mazhar B. Tayel, Mohamed Ismail Badawi, Heba Tallah A. Hasan,*

## Fano resonances in optics and microwaves: Physics and application

**Demonstration of true electromagnetically induced transparency in a metamaterial (pp. 1169)**
*Toshihiro Nakanishi, Masao Kitano,*

**The nanofabrication and unusual Fano resonances of 3D metamaterials (pp. 1171)**
*Changzhi Z. Gu, Z. Liu, A. J. Cui, W. X. Li, J. J. Li,*

**Explicit demonstration of how path interference can enhance plasmonic nonlinearity (pp. 1172)**
*Mehmet Emre Tasgin,*

**Highly contrasted structural colors for industrial applications using the Fano lineshape (pp. 1174)**
*Benjamin Gallinet,*

**Fano resonances, their relation to exceptional points, and applications (pp. 1176)**
*Holger Cartarius, L. Schwarz, G. Wunner, W. D. Heiss, J. Main,*

**Interference of nano-vortex fields formed by plasmonic cavities (pp. 1178)**
*Keiji Sasaki,*

**Exploring Fano-Resonance Phenomenology with Quantum Point Contacts (pp. 1179)**
*Jonas Fransson, J. P. Bird,*

**Multivariable Fano line shape in guided-mode resonant gratings (pp. 1181)**
*Dmitry A. Bykov, Leonid L. Doskolovich, Nikita V. Golovastikov,*

**Fano effects in hybrid nanostructures (pp. 1183)**
*Wei Zhang,*

**Sharp Fano resonances arising from coupling between surface plasmon polariton and waveguide modes (pp. 1184)**
*Shinji Hayashi, Dmitry V. Nesterenko, Anouar Rahmouni, Zouheir Sekkat,*

**Utilizing Fano resonances in chiral and dielectric nanoparticle oligomers (pp. 1186)**
*Ben Hopkins, Francesco Monticone, Andrey E. Miroshnichenko, Andrea Alu, Yuri Kivshar,*

**Lineshape inheritance and coherent absorption at the boundary between weak and strong critical coupling in lossy coupled**

**oscillators (pp. 1188)**
*Simone Zanotto, Alessandro Tredicucci,*

**Ultra-High Q Fano Resonances and its Figure of Merit in metasurfaces (pp. 1190)**
*Manukumara Manjappa, Longqing Cong, Yogesh Kumar Srivastava, Ningning Xu, Ibraheem Al-Naib, Weili Zhang, Ranjan Singh,*

**Broken Symmetry Dielectric Resonators for Scalable, High Quality-Factor Fano Metasurfaces (pp. 1192)**
*Michael B. Sinclair, Salvatore Campione, Sheng Liu, Lorena Basilio, Larry Warne, William Langston, Ting Luk, Joel Wendt, John Reno, Gordon Keeler,*

**Photonic crystal Fano structure for all-optical switching (pp. 1194)**
*Yi Yu, Weiqi Xue, Hao Hu, Leif Katsuo Oxenlowe, Kresten Yvind, Jesper Mork,*

**High-Q perfect absorption based on coherent Fano resonances (pp. 1196)**
*Xianji Piao, Sunkyu Yu, Namkyoo Park,*

**Optical spin-dependent Fano resonances (pp. 1198)**
*Xianji Piao, Sunkyu Yu, Namkyoo Park,*

**Modal Fano resonances and off-diagonal photonic Lamb shift in reactively coupled waveguide-resonator systems (pp. 1200)**
*Mher Ghulinyan, M. Bernard, F. Ramiro Manzano, G. Pucker, L. Pavesi, I. Carusotto,*

**Degenerate Fano resonance between multipole surface plasmons in a metallic nanohole array (pp. 1202)**
*Munehiro Nishida, Noriyuki Hatakenaka, Yutaka Kadoya,*

**Electromagnetically Induced Transparency and Absorption (pp. 1204)**
*Philippe Tassin,*

**Excitation of non-radiating anapole mode with focused radially polarized beams (pp. 1205)**
*Lei Wei, Zheng Xi, Nandini Bhattacharya, H. Paul Urbach,*

**Fano resonances and band structure of two-dimensional photonic structures (pp. 1206)**
*Peter Markos,*

**Microwave magnetoelectric fields and Fano resonances (pp. 1208)**
*Eugene Kamenetskii,*

**Trapping of light with angular orbital momentum above the light cone in a periodic array of dielectric spheres (pp. 1210)**
*Evgeny Bulgakov, Almas Sadreev,*

**A wideband resonant cavity antenna based on Fano resonance effect in a two-layer patch array superstrate (pp. 1219)**
*K. Kanjanasit, C. H. Wang, P. Record,*

**Multiple electric and magnetic Fano resonances in single-layered core-shell particles (pp. 1226)**
*Tiago Jose Arruda, Alexandre Souto Martinez, Felipe Arruda de Araujo Pinheiro,*

## (Nano)Plasmonic Biosensors

**Selective detection of elevated IgG in human blood serum using surface modified chiral plasmonic metamaterials (pp. 1229)**

*Ryan Tullius, A. S. Karimullah, C. Jack, M. Rodier, G. Cooke, V. M. Rotello, M. Kadodwala,*

**3D Flexible and Tunable Plasmonic Platforms for Optical Biosensing (pp. 1231)**
*Monica Focsan, Monica Potara, Cosmin Leordean, Ana Maria Craciun, Dana Maniu, Simion Astilean,*

**Plasmonic (Nano)biosensors for Clinical Chemistry (pp. 1233)**
*Jean-Francois Masson,*

**Detecting Variations in Serum Composition through Chiral Plasmonic Metafilms (pp. 1234)**
*Affar Shahid Karimullah, R. Tullius, C. Jack, M. Rodier, G. Cooke, V. M. Rotello, M. Kadodwala,*

**Graphene plasmonics for tunable mid-infrared biosensors (pp. 1236)**
*Daniel Rodrigo, Odeta Limaj, Davide Janner, Dordaneh Etezadi, F. Javier Garcia-de-Abajo, Valerio Pruneri, Hatice Altug,*

**Biological and chemical sensing within plasmonic nano-gaps (pp. 1238)**
*Anna Lombardi, Bart de Nijs, Setu Kasera, Daniel Sigle, Felix Benz, Rohit Chikkaraddy, Cloudy Carnegie, Jeremy Baumberg,*

**Quantitative Reflection Imaging for Morphology and Dynamics of Live Aplysia Californica Pedal Ganglion Neurons on Nanostructured Plasmonic Crystals (pp. 1239)**
*S. Kang, A. Badea, S. S. Rubakhin, J. V. Sweedler, J. A. Rogers, Ralph Nuzzo,*

**Responsive hydrogel-metallic nanostructures for plasmonic biosensing (pp. 1241)**
*Nestor Gisbert Quilis, Peter Kogler, Christian Petri, Ulrich Jonas, Wolfgang Knoll, Jakub Dostalek,*

**Lattice localized plasmons for fluorescence immunosensing (pp. 1243)**
*Stefan Fossati, Simone Hageneder, Martin Bauch, Wolfgang Knoll, Jakub Dostalek,*

**Plasmonically amplified fluorescence for biomarker analysis (pp. 1244)**
*Jakub Dostalek,*

**Bioanalytics using single plasmonic nanostructures (pp. 1246)**
*T. Schneider, J. Jatschka, N. Jahr, D. Zopf, A. Dathe, J. Wirth, F. Garwe, A. Csaki, O. Stranik, W. Fritzsche,*

**Towards Sensitive, Selective Point-Of -Care Plasmonic Diagnostic Devices (pp. 1248)**
*Debrina Jana, Jie He, Ian Bruzas, Sarah Unser, Laura Sagle,*

**Plasmonic Biosensors and Their Bioanalytical Applications (pp. 1250)**
*Jiri Homola,*

**Ultrasensitive plasmonic biosensors platforms-from conception to controllable biofunctionalization and detection of target (bio)molecules (pp. 1252)**
*Rodica Elena Ionescu, Pierre-Michel Adam, Jean-Louis Bijeon,*

**Nanoplasmonic Sensor Arrays for Rapid Detection of Biomolecules and Nanoparticles (pp. 1253)**
*Avijit Barik, Shailabh Kumar, Daehan Yoo, Yong-Sang Ryu, Xiaoshu Chen, Daniel A. Mohr, Daniel J. Klemme, Christopher Ertsgaard, Nathan J. Wittenberg, Sang-Hyun Oh,*

## Plasmonic sensing, imaging, and other active functions in biology and medicine

**Surface Plasmon Resonance Behaviors of Gold Nanoring and Their Application to Photothermal and Photodynamic Therapies (pp. 1256)**
*Chih-Ken Chu, Che-Kuan Chu, Yi-Chou Tu, Jen-Hung Hsiao, Jian-He Yu, Yean-Woei Kiang, Chih-Chung Yang,*

**Recent progress in chirality-based biomolecular sensing and hyperlens-based biological imaging (pp. 1257)**
*Minkyung Kim, Jungho Mun, Inki Kim, Dasol Lee, Junsuk Rho,*

**Metamaterial Integrated Microfluidic Terahertz Sensors (pp. 1258)**
*Xin Hu, Gaiqi Xu, Yaxin Zhang, David Cumming, Qin Chen,*

**Plasmon-Enhanced Raman Spectroelectrochemistry (pp. 1260)**
*Kyohei Okubo, Loan Le Thi Ngoc, Edwin Carlen,*

**Three-dimensional plasmonic metastructures for sensing and imaging (pp. 1262)**
*Jonghwa Shin, Nayeun Lee, Reehyang Kim, Taeyong Chang, J. Young Kim, Hyowook Kim,*

**Reduced Graphene Oxide (RGO) Sensor for Confocal Microwave Imaging Technique in Detecting Human Brain Tumor (pp. 1264)**
*Mohd Aminudin Bin Jamlos, Abdul Hafiizh Ismail, Mubaraq Von Schleusingen,*

**Sensing the surface plasmon resonance at the quantum noise limit (pp. 1266)**
*Karsten Pufahl, Jan Heckmann, Ulrike Woggon, Nicolai B. Grosse,*

**Ordered Arrays of Au NP on Nanopipettes for SERS Sensing (pp. 1268)**
*Hu Zhu, J. P. Spatz, J.-F. Masson, C. G. Bazuin,*

**Multiplexed molecular imaging with targeted SERS nanoparticles for intraoperative guidance of tumor resection (pp. 1270)**
*Yu Winston Wang, Soyoung Kang, Jonathan Liu,*

**Vertical dimer antennas for microfluidic biosensing (pp. 1272)**
*Andreas Horrer, Katrin Krieg, Kathrin Freudenberger, Sabrina Rau, Lothar Leidner, Gunter Gauglitz, Dieter Kern, Monika Fleischer,*

**The longitudinal magnetophotonic effect in a magnetoplasmonic crystal for magnetic field sensing (pp. 1274)**
*Aleksandr Rogachev, Mikhail Kozhaev, Petr Vetoshko, Sarkis Dagesian, Andrey Kalish, Anatoly Zvezdin, Vladimir Belotelov,*

**Miniaturized Motor-Sensor Unibody Devices for Tunable Biochemical Release, DNA Removal, and Microfluidic Manipulation (pp. 1276)**
*Donglei (Emma) Fan, K. Kim, J. H. Guo, X. B. Xu,*

**Nanoparticle mediated photo-protection and - therapy (pp. 1277)**
*Valery Victorovich Tuchin,*

**Plasmon-enhanced molecular sensing and imaging on nanoporous gold disks (pp. 1279)**
*Fusheng Zhao, Greggy Santos, Md Masud Arnob, Wei-Chuan Shih,*

**Multiplex Detection and Imaging of Tumor Cells using Gold-based SERS platforms (pp. 1281)**
*Gustavo Bodelon, Veronica Montes-Garcia, Cristina Fernandez-Lopez, Jorge Perez-Juste, Luis M. Liz-Marzan, Isabel Pastoriza-Santos,*

**3 Dimensionally Stacked Surface Enhanced Raman Scattering (SERS) Substrates with pico-Molar Sensitivity (pp. 1283)**
*Daejong Yang, Hyunjun Cho, Sukmo Koo, Sagar Vaidyanathan, Kelly Woo, Hyuck Choo,*

**Biocompatible, Liposome-Based Surface Enhanced Raman Spectroscopy (SERS) Substrates (pp. 1284)**
*Ian Bruzas, William Lum, Sarah Unser, Laura Sagle,*

## Manipulating Light using Integrated Nanophotonic Devices

**Signal storage in tripod structure metamaterial (pp. 1287)**
*Sylwia Zielinska - Raczynska, David Ziemkiewicz,*

**Silicon-graphene hybrid devices for signal modulations (pp. 1288)**
*Ciyuan Qiu, Yong Zhang, Ruili Liu, Yikai Su,*

**Nonlinear applications in the mid-infrared regime based on germanium on silicon platform (pp. 1290)**
*Li Shen, Noel Healy, Colin Mitchell, Jordi Soler Penades, Milos Nedeljkovic, Goran Mashanovich, Anna Peacock,*

**Approach total absorption in critically coupled photonic crystal structures with monolayer 2D materials (pp. 1291)**
*Weidong Zhou, Yonghao Liu, Xiaochen Ge, Xiuling Li, Shanhui Fan,*

**Recent advances in light manipulation using plasmonic and dielectric metasurfaces (pp. 1292)**
*Jian Wang,*

**Reconfigurable Integrated Optical Signal Processing (pp. 1294)**
*Ming Li,*

**Photonic integrated devices for the emission and detection of optical vortex beams (pp. 1295)**
*Laura Meriggi, Charalambos Klitis, Xinlun Cai, Shimao Li, Jiangbo Zhu, Siyuan Yu, Michael Strain, Marc Sorel,*

## Hybrid Plasmonics and Functional Nanomaterials

**Hyperlensing at NIR Frequencies Using a Hemi-spherical Metallic Nanowire Lens in Sea-urchin Geometry (pp. 1298)**
*Ankit Bisht, Wei He, Xiaotian Wang, Linda Y. L. Wu, Xiaodong Chen, Shuzhou Li,*

**Nanoscale surface chemistry directs the tunable assembly of silver octahedra into three two-dimensional plasmonic superlattices (pp. 1300)**
*Yih Hong Lee, Wenxiong Shi, Ruibin Jiang, Jianfang Wang, Shuzhou Li, Xing Yi Ling,*

**3D DNA Plasmonics (pp. 1301)**
*Maximilian Julius Urban, Na Liu,*

**Optically active nanomaterials (pp. 1302)**
*Yurii K. Gun'ko, Finn-Purcell Milton, Joseph E. Govan, Alexander Loudon, Olan Cleary, Maria Mukhina, Alexander Baranov, Anatoly Fedorov,*

**Single-Particle Absorption Spectroscopy of Plasmonic Nanostructures (pp. 1304)**
*Stephan Link,*

**Colloidal Plasmonic Metasurfaces for Nonlinear Optics (pp. 1305)**

*Shangjr Gwo, Chun-Yuan Wang, Hung-Ying Chen, Liuyang Sun, Xiaoqin Li, Wei-Liang Chen, Yu-Ming Chang, Hyeyoung Ahn,*

**Significant enhancement of the chiral correlation length in nematic liquid crystals by gold nanoparticles capped with axially chiral binaphthyl ligands (pp. 1306)**
*Torsten Mori, A. Sharma, T. Hegmann,*

**Recent advances and perspectives of magnetoplasmonic metamaterials (pp. 1308)**
*Paolo Vavassori,*

**Assembling Plasmonic Nanoantennas on DNA (pp. 1310)**
*Sebastien Bidault,*

**The Active Plasmonics Paradigm (pp. 1312)**
*Roberto Caputo, Luciano De Sio, Ugo Cataldi, Thomas Maurer, Renaud Bachelot,*

**Biocompatible Liquid Crystal Elastomers with Unique Properties for Cell Scaffolds (pp. 1314)**
*Taizo Mori, Anshul Sharma, Yunxiang Gao, Robert Clements, Ernest Freeman, Christopher Malcuit, Jennifer McDonough, LaShanda Worley, Torsten Hegmann, Elda Hegmann,*

**Optical Activity in Organic-Silver Hybrid Nanoparticles (pp. 1316)**
*Cecilia Noguez, Francisco Hidalgo,*

**Plasmonics of Dielectric-Metallic Hybrid Nanostructures (pp. 1318)**
*Huanjun Chen, Hao Wang, Zhang-Kai Zhou,*

**Magneto-chiral Effect in Hybrid Plasmonic Nanostructures (pp. 1320)**
*Marion Rodier, Christopher Kelly, Affar Karimullah, Calum Jack, Ryan Tullius, Malcolm Kadodwala,*

**Electrochemical control of plasmonic nanomaterial surface chemistry (pp. 1322)**
*Christy Landes,*

**Enhancing Solar Cells and Photocatalysis via Plasmonic Nanostructures (pp. 1323)**
*Dongling Ma,*

**Plasmon-enhanced heteronanostructures for photocatalysis (pp. 1325)**
*Shah M. Bahauddin, Hossein Robatjazi, Chloe Doiron, Xuejun Liu, Thejaswi Tumkur, Parker Wray, Wei-Ren Wang, Bo Jiang, Isabell Thomann,*

**Spatial Control of Chemical Processes on Nanostructures through Nano-Localised Water Heating (pp. 1326)**
*Calum Jack, Affar S. Karimullah, Ryan Tullius, Larousse Khosravi Khorashad, Marion Rodier, Brian Fitzpatrick, Laurence D. Barron, Nikolaj Gadegaard, Adrian J. Lapthorn, Vincent M. Rotello,*

**Engineering the Electromagnetic Properties of Plasmonic Nanohybrids for Solar Water Splitting (pp. 1327)**
*Luca Razzari, Jianming Zhang, Xin Jin, Pablo I. Morales-Guzman, Jerome Claverie,*

**Plasmon-induced photoenergy conversion systems (pp. 1329)**
*Hiroaki Misawa,*

**Optical Liquid Biopsy in microfluidic devices (pp. 1330)**

*Ramon Puebla,*

**Modal engineering in plasmonic crystalline colloidal systems (pp. 1331)**
*Upkar Kumar, Sviatlana Viarbitskaya, Aurelien Cuche, Alexandre Bouhelier, Gerard Francs, Jadab Sharma, Christian Girard, Erik Dujardin,*

**Preparation of Au-Ag Alloy Nanoparticles via Ionic Liquid/Metal Sputter Deposition and Their Application to Plasmon-induced Photosensitization (pp. 1333)**
*Tatsuya Kameyama, Eisaku Kumazawa, Susumu Kuwabata, Tsukasa Torimoto,*

**Plexitonic QED: Strong coupling effect in absorption and photoluminescence spectra of hybrid systems of gold nanorods and J-aggregates (pp. 1335)**
*Dzmitry Melnikau, Ruben Esteban, Diana Savateeva, Ana Sanchez-Iglesias, Marek Grzelczak, Mikolaj Schmidt, Luis Liz-Marzan, Javier Aizpurua, Yury P. Rakovich,*

**Nanophotonic Designs for Photovoltaics and Luminescent Solar Concentrators (pp. 1337)**
*Vivian Ferry,*

**On the use of hybrid modal properties to design enhanced nonlinear and ultrafast optical properties (pp. 1339)**
*Cillian McPollin, Silvia Peruch, David J. Gosztola, Gary P. Wiederrecht, Gregory Wurtz, Anatoly V Zayats,*

**Manipulation of Molecules adsorbed on Metal Nanostructures under Plasmon Excitation (pp. 1341)**
*Kei Murakoshi,*

**Self-aligned fabrication and spectroscopy of coupled hybrid antenna-nanoemitter-structures (pp. 1343)**
*Annika Brauer, Regina Jager, Julia Fulmes, Kerstin Scherzinger, Sebastian Jager, Sven zur Oven-Krockhaus, Dominik Gollmer, Alfred Meixner, Dieter Kern, Monika Fleischer,*

**High Resolution Technique for Simultaneous Proteins and Nanoparticles Patterning (pp. 1345)**
*Lourdes Basabe-Desmonts,*

**Fano resonance in self-organized embedded metallic nanoparticle gratings and application as optical security features (pp. 1347)**
*Said Bakhti, Giorgio Baraldi, Zeming Liu, Nathalie Destouches,*

**Scalable Fabrication of 2 nm-Wide Plasmonic Nanotrench Arrays For Strong Field Enhancements (pp. 1349)**
*Joel K. W. Yang,*

**Ultrafast hot electrons spice up localized plasmons (pp. 1351)**
*Bruno Palpant, T. Labouret, J. F. Audibert, R. Pansu,*

**Infrared and THz plasmonics using nano-engineered gold structures (pp. 1353)**
*Kosei Ueno,*

**Colloidal Nano-Assemblies for DNA Detection and Label-Free SERS Tagging (pp. 1355)**
*Jessica Rodriguez-Fernandez,*

**Hierarchical Plasmonic Nanostructured Materials: Synthesis and Applications (pp. 1357)**
*Miguel A. Correa-Duarte,*

**Spatial localization of plasmonic hot spots as probed by molecular nanomotors and atomic force microscopy (pp. 1358)**
*Yinping Zhang, Jerome Plain, Davy Gerard, Guillaume Demesy, Nicolas Bonod, Renaud Bachelot,*

**SERS inside Au@Ag nanocuboids and Au@Gap@Au nanomatryoshkas (pp. 1360)**
*Nikolai Khlebtsov, B. N. Khlebtsov,*

**Nano-optical Chemical and Structural Classification of Nucleic Acids via Label-free Surface-enhanced Raman Scattering Analysis (pp. 1362)**
*Judit Morla-Folch, P. Gisbert-Quilis, A. Torres, R. A. Alvarez-Puebla, Luca Guerrini,*

## Plasmonics and nanophotonics

**Fano and Induced Transparency in Plasmon Based Optical Sensors (pp. 1365)**
*Zouheir Sekkat, Shinji Hayashi,*

**Additive nano- and micro-structures towards perfect anti-refector surfaces (pp. 1366)**
*Yoshiaki Nishijima, Ryosuke Komatsu, Shunsuke Ohta, Gediminas Seniutinas, Armandas Balcytis, Saulius Juodkazis,*

**Full-spectrum solar light absorbtion and photothermal conversion with Ge-Sn on black silicon (pp. 1368)**
*Yoshiaki Nishijima, Ryosuke Komatsu, Takuya Yamamura, Gediminas Seniutinas, Armandas Balcytis, Saulius Juodkazis,*

**Leakage imaging and tracking of ultrafast surface plasmon pulses (pp. 1370)**
*Yuri Gorodetski, Thibault Chervy, Shaojun Wang, James Andel Hutchison, Aurelien Drezet, Cyriaque Genet, Thomas Ebbesen,*

**Unravelling the optomechanical nature of plasmonic trapping (pp. 1372)**
*Pau Mestres, Johann Berthelot, Srdjan S. Acimovic, Romain Quidant,*

**Fabrication of Hyperuniform Disordered Photonic Bandgap Materials (pp. 1374)**
*Nicolas Muller, J. Haberko, C. Marichy, F. Scheffold,*

**Multipolar behavior of hollow plasmonic nanospheres: obvious or mysterious? (pp. 1376)**
*Ari Sihvola, Dimitrios C. Tzarouchis, Pasi Yla-Oijala,*

**Spatial non-locality and Landau damping in the dynamics of a quantum dot coupled to surface plasmons (pp. 1378)**
*Alexei Vagov, I. A. Larkin, M. D. Croitoru, K. Keil, V. M. Axt,*

**Hybrid surface plasmon modes in metallic nanostructures: Complete numerical analysis and application to bio-sensing (pp. 1380)**
*Mitradeep Sarkar, Jean-Francois Bryche, Raymond Gillibert, Julien Moreau, Mondher Besbes, Aurore Olivero, Gregory Barbillon, Bernard Bartenlian, Marc Lamy de la Chapelle, Michael Canva,*

**Enhanced light emission in organic materials caused by constructive surface plasmon generation and scattering (pp. 1382)**
*Takahiro Inui, Yuhta Mizoguchi, Takuya Yoneda, Taichi Ishiguro, Kenichi Kasahara, Naoki Ikeda, Yoshimasa Sugimoto,*

**Plasmonic color printing combining conjugate twin phase modulation with plasmonic broadband absorption (pp. 1384)**
*Jiancai Xue, Zhang-Kai Zhou, Xue-Hua Wang,*

**Optical properties of nanoparticle chains (Ag, Au, Ag-Au) embedded in a dielectric matrix (pp. 1386)**
*Alexandre Fafin, Senda Yazidi, Sophie Camelio, David Babonneau,*

**UV Circular Polarization Selection using Aluminum Nano-Spirals (pp. 1388)**
*Matthew S. Davis, J. Strait, J. K. Lee, S. Blair, A. Agrawal, H. J. Lezec,*

**3D toroidal metamaterial on suspended SiN film (pp. 1390)**
*Z. Liu, Shuo Du, Z. C. Li, S. Q. Chen, Junjie Li, Changzhi Gu,*

**Ag and Au nanoparticles synthesis with pulsed laser ablation in monomer solution (pp. 1392)**
*Igor Denisyuk, Natalia Zulina, Il'ya Pavlovets,*

**Dark chameleon nanomaterials for lasing and energy harvesting (pp. 1394)**
*Andrea Fratalocchi,*

**Shape and phase of surface plasmon lasers on active metasurfaces (pp. 1395)**
*V. T. Tenner, M. J. A. de Dood, M. P. van Exter,*

**Stokes Polarimetry using Silicon Nanoantennas (pp. 1397)**
*Alba Espinosa-Soria, Francisco Jose Rodriguez-Fortuno, Amadeu Griol, Alejandro Martinez,*

**Tailoring Resonances in Hybridized Plasmonic Systems (pp. 1399)**
*Ashok Kodigala, Thomas Lepetit, Boubacar Kante,*

**Optical Properties of Strained Metal Thin-Films (pp. 1401)**
*J. Kenji Clark, N. P. Kherani,*

**Metal-Dielectric Flexible Films for Ultrahigh Transmission (pp. 1403)**
*Jin-Young Na, Yoon-Jong Moon, Da-Som Kim, Sun-Kyung Kim,*

**High-Index-Contrast Bubble Patterns for High-Efficiency Light Emitting Devices (pp. 1405)**
*Yoon-Jong Moon, Jin-Young Na, Da-Som Kim, Dae-Woong Hwang, Dukkyu Bae, Euijoon Yoon, Sun-Kyung Kim,*

**Optically-controlled local plasmonic nanosoldering of silver nanowires (pp. 1407)**
*Qiang Li, Guoping Liu, Hangbo Yang, Wei Wang, Si Luo, Shuowei Dai, Min Qiu,*

**Dynamic Plasmonics with Aluminum-Doped Zinc Oxide (pp. 1409)**
*Marcello Ferrera, Matteo Clerici, Nathaniel Kinsey, Amr Shaltout, Clayton DeVault, Lucia Caspani, Jongbum Kim, Rishad Kaipurath, Thomas Roger, Enrico Giuseppe Carnemolla,*

**Applying the Otto geometry to access the intrinsic nonlinearity of propagating surface plasmon modes (pp. 1411)**
*Jan Heckmann, Karsten Pufahl, Nicolai B. Grosse, John E. Sipe, Ulrike Woggon,*

**Hole arrays in metal film as distributed feedback plasmonic laser and its dynamics (pp. 1413)**
*Andrey Pavlov, I. V. Zabkov, V. V. Klimov,*

**Probing the radiative and full electromagnetic local densities of states through electron energy loss spectroscopy and cathodoluminescence spectroscopy (pp. 1415)**
*Arthur Losquin, Mathieu Kociak,*

**Surface plasmon generation by light scattering in terminated metallic slabs: interference effects between diffracted light and surface waves (pp. 1417)**

*Luis Angel Mayoral-Astorga, Jorge Alberto Gaspar-Armenta, Felipe Ramos-Mendieta,*

**Theory and Experiment on Coherent Nanoscopic Light-sources: Spasers vs. Nano-Lasers (pp. 1419)**
*Gunter Kewes, Kathrin Herrmann, Andreas Ott, Rogelio Rodriguez-Oliveros, Alexander Kuhlicke, Yan Lu, Matthias Ballauff, Kurt Busch, Oliver Benson,*

**Exploring scattering phenomena at the nano-scale by angle- and polarization-resolved cathodoluminescence spectroscopy and imaging (pp. 1421)**
*Viktor Myroshnychenko, Natsuki Nishio, Jens Forstner, Naoki Yamamoto,*

**Metal-insulator-metal plasmonic sensor for high sensing sensitivity (pp. 1423)**
*Siham Refki, Shinji Hayashi, Zouheir Sekkat, Hidekazu Ishitobi, Yasushi Inouye,*

**Metallic nanocylinder metasurfaces for filtering and reflecting properties in the visible spectrum (pp. 1424)**
*Herve Bertin, Yoann Brule, Guillaume Demesy, Anne-Laure Fehrembach, Boris Gralak, Evgueni Popov, Gerard Tayeb, David Barat, Philippe Gogol, Vi Yam,*

**Spin-controlled switching of near field excitation of optical nanoantennas (pp. 1426)**
*Yannick Lefier, U. Fischer, R. Salut, M. Suarez, T. Grosjean,*

**Tunable optomagnets in diamagnetic thin metal layers and plasmonic nano-antennas (pp. 1428)**
*Yannick Lefier, U. Fischer, T. Grosjean,*

**Smith-Purcell radiation emission by non-periodic array nanostructures (pp. 1430)**
*Jose Ramon Martinez-Saavedra, David Castells, Javier Garcia de Abajo,*

**Foerster resonance energy transfer in inhomogeneous non-dispersive nanophotonic environments (pp. 1431)**
*Martijn Wubs, Willem L. Vos,*

**Optical Multiple Bistability in Metal-Insulator-Metal Plasmonic Waveguides Side-coupled with Twin Resonators (pp. 1433)**
*Ruei-Cheng Shiu, Yung-Chiang Lan, Guang-Yu Guo,*

**Plasmonic magneto-optical light modulator with the domain wall manipulation via giant magneto-electric effect (pp. 1435)**
*Nikolai Evgen'evich Khokhlov, Anastasiya Khramova, Elena Nikolaeva, Tatiana Kosykh, Alexey Nikolaev, Alexander Pyatakov, Vladimir Belotelov,*

**Resonant nanophotonics with dielectric particles (pp. 1437)**
*A. Devilez, X. Zambrana-Puyalto, B. Stout, Nicolas Bonod,*

**Induced modulation instability of surface plasmon polaritons in an ultra-thin metal film (pp. 1439)**
*Sergey Moiseev, D. Korobko, I. Zolotovskii, S. Sukhov,*

**Excitation of quantum dot by femtosecond plasmon-polariton pulse focused by conducting cone (pp. 1440)**
*Pavel A. Golovinski, Valeri A. Astapenko, Egor S. Manuylovich,*

**Plasmonic hybridization investigated in non-local response regime (pp. 1441)**
*Simone Panaro, Stefania D'Agostino, Cristian Ciraci,*

**Direct coupling of InAs quantum dot excitons with surface plasmon polaritons (pp. 1443)**

*Fernando Wellysson de Alencar Sobreira, Yuriy Mazur, A. Xian Hu, Gregory Joseph Salamo, Euclydes Marega Junior,*

**Plasmonic properties of metal-doped ZnO transparent conductive oxides for energy conversion (pp. 1445)**
*Alessandra Catellani, Alice Ruini, Arrigo Calzolari,*

**Luminescence upconversion of Er3+ doped tellurite glass through subwavelengh metallic nanostructures (pp. 1447)**
*Otavio Brito Silva, Victor Antony Garcia Riveira, Sebastiao Pratavieira, Euclydes Marega Junior,*

**Coherent and non-coherent interactions between quantum emitters induced by plasmonic hot spots (pp. 1449)**
*Jun Ren, Xiangdong Zhang,*

**Study of Surface Plasmons in 1D and 2D Structured Metallic Surfaces (pp. 1450)**
*Raul Garcia-Llamas, Sandra Luz Gastelum-Acuna, Damasio Morales-Cruz, Aldo Santiago Ramirez-Duverger,*

**Towards a quantitative description of the plasmonic character of optical excitations in nanostructures (pp. 1452)**
*Luca Bursi, Arrigo Calzolari, Stefano Corni, Elisa Molinari,*

**Optical spin-orbit interaction in plasmonic structures (pp. 1454)**
*Feng Lin,*

**The on and off of optical waves in planar multilayer stacks (pp. 1455)**
*Yikuan Wang,*

**Resonance Coupling between Excitons and Magnetic Dipole Resonances in Hybrid Nanostructure Composed of J-Aggregate and Dielectric Nanoparticle (pp. 1457)**
*Hao Wang, Huanjun Chen,*

**Extension of standard transfer-matrix method for three-wavemixing for plasmonic structures (pp. 1459)**
*Ardi Loot, Vladimir Hizhnyakov,*

**Tuning the optical response of dewetted silver lms through nanopatterning (pp. 1461)**
*Paul Jacquet, Iryna Gozhyk, Jeremie Teisseire, Jacques Jupille, Remi Lazzari,*

**Chiral Au-crescents fabricated by angled hole-mask colloidal lithography for plasmon-enhanced CD measurements (pp. 1463)**
*Gunnar Klos, Duncan Stewart Sutherland,*

**Optical Nanofilters Based on Plasmonics Waveguide with Archimedes Spiral Nanostructure (pp. 1465)**
*Youwen Liu, Yuncai Feng, Daxing Dong, Xiaohua Wang,*

**Minimum Forward Light Scattering by Silicon nanopillars (pp. 1467)**
*Jose Francisco Algorri, R. Vergaz, A. Cuadrado, J. M. Sanchez-Pena, B. Garcia-Camara,*

**Large Radiative Decay Rate Enhancement of Single Quantum Dots by a Gold Nanocone Antenna (pp. 1469)**
*Korenobu Matsuzaki, Hsuan-Wei Liu, Bjorn Hoffmann, Anke Dutschke, Silke Christiansen, Stephan Gotzinger, Vahid Sandoghdar,*

**Out-of-Plane Optical Interactions of Nanohole Trimers Milled in Stacked Gold Films (pp. 1471)**
*Mohsen Janipour, Kursat Sendur,*

**Far-field control of hot-spots on random metal-dielectric networks (pp. 1473)**

*Pierre Bondareff, Giorgio Volpe, Sylvain Gigan, Samuel Gresillon,*

**Double Hot-Spot Dual-Polarization Elliptical Crescent Nanoantenna for Near-Infrared Detection Applications (pp. 1475)**
*Ahmed Elsharabasy, Mohamed Bakr, M. Jamal Deen,*

**Hybrid plasmonic directional coupler switches and modulators (pp. 1477)**
*Dimitrios C. Zografopoulos, Mohamed Swillam, Lamees Shahada, Romeo Beccherelli,*

**Ultrafast dynamics of plasmonic vortices (pp. 1478)**
*Deirdre Kilbane, G. Spektor, A. K. Mahro, B. Frank, L. Gal, H. Giessen, F.-J. Meyer zu Heringdorf, M. Orenstein, M. Aeschlimann,*

**Propagation of nolinear surface waves through metamaterial waveguide structure (pp. 1479)**
*Bouchra Mokhtari, N. Hissi, Mohammed M. Shabat, N. Cherkaoui Eddeqaqi, S. Bahsine, J. Atangana ,*

**Nanoparticle multilayers and colloidal solutions of silver nanoparticles synthesized by femtosecond pulsed laser ablation (pp. 1480)**
*Ovidio Pena Rodriguez, Pablo Diaz Nunez, Jesus Gonzalez Izquierdo, Guillermo Gonzalez Rubio, Gabriel Balabanian, Andres Guerrero Martinez, Antonio Rivera, Jose Olivares, Jose Manuel Perlado, Luis Banares,*

**Quantum Plasmonics with Finite Carbon Nanotubes (pp. 1482)**
*Sandra de Vega Esteban, Joel Douglas Cox, Javier Garcia de Abajo,*

**Near infrared distributed feedback surface plasmon lasers (pp. 1483)**
*Elham Karami Keshmarzi, R. Niall Tait, Pierre Berini,*

**Plasmonic nanoparticles fabricated on a wave shape flexible substrate (pp. 1484)**
*Di Feng, Ningfang Song, Hui Fang, Hui Zhang, Dewei Yang, Yue Zheng, Haowei Li, Shaobo Zhang,*

**Focusing of EM Wave through Square-microhole Aperture (pp. 1489)**
*Santosh Kumar Maurya, Suyog Rajendra Hawal, Raghvendra Pratap Chaudhary, Shobha Shukla, Sumit Saxena,*

**Complete Picture of Dispersion Relation for Surface Plasmon Polaritons in Layered Media (pp. 1490)**
*Huseyin Serhat Tetikol, M. Irsadi Aksun,*

**Refractive index sensitivity characteristics of dual-resonant plasmonic perfect absorber (pp. 1492)**
*Mustafa Turkmen, Sabri Kaya, Semih Korkmaz, Ekin Aslan,*

**Utilization of hybrid plasmonic modes to investigate surface interactions between nanocubes and polymer substrates (pp. 1494)**
*Adam Bottomley, Mike Bushell, Daniel Prezgot, Jason P. Coyle, Anatoli Ianoul,*

**Disordered plasmonic nanoholes in Ag thin films (pp. 1499)**
*Kumar R. M. Piragash, Alagesan Venkatesh, V. H. S. Moorthy,*

**Plasmonic Induced Transparency in a MIM Waveguide with Two Side Coupled Cavities (pp. 1502)**
*Adnane Noual, Ossama El Abouti, El Houssaine El Boudouti, Abdellatif Akjouj, Yan Pennec, Bahram Djafari-Rouhani,*

**Enhanced subwavelength focusing properties of Ag-Au hybrid plasmonic lens with outer slit design (pp. 1509)**
*Kai Hao Chang, Min Hsiu Cheng, Po Tsung Lee,*

# Metamaterials and negative index materials

**Soliton-induced transparency in one-dimensional non linear Kerr/metamaterial heterostructures (pp. 1513)**
*Ernesto Reyes Gomez, Solange Bessa Cavalcanti, Luiz Eduardo Oliveira,*

**Absorption effects and non-Bragg gap solitons in quasiperiodic Fibonacci and disordered Kerr-metamaterial heterostructures (pp. 1515)**
*Ernesto Reyes Gomez, Solange Bessa Cavalcanti, Luiz Eduardo Oliveira,*

**Recent experimental progress of reversed Cherenkov radiation in left-handed metamaterial (pp. 1517)**
*Zhaoyun Duan, Xianfeng Tang, Zhanliang Wang, Yabin Zhang, Xiaodong Chen, Min Chen, Yubin Gong,*

**Magnetic Uniaxial Wire Medium (pp. 1519)**
*Tiago Morgado, Joao Costa, Mario Silveirinha,*

**Reconfigurable holographic generation of non-Hermitian and parity-time symmetric photonic lattices (pp. 1521)**
*Choloong Hahn, Youngsun Choi, Jae Woong Yoon, Cha Hwan Oh, Seok Ho Song,*

**Transparent conductive oxide-based hyperbolic metamaterials for telecommunication wavelengths (pp. 1523)**
*Evgenij Travkin, Laura Orphal, Oliver Benson, Sergey Sadofev, Sascha Kalusniak,*

**The natural way of obtaining metamaterial by thermoradiation treatment of iron oxide doped potassium-aluminum-Boron glass (pp. 1525)**
*Amriddin Nuritdinovich Salakhitdinov, Maysara Kamolidinovna Salakhitdinova, N. S. Saydirasulov, Aminjon Abdurashidovich Yusupov, Elvira Memetovna Ibragimova,*

**Metal-Dielectric-Semiconductor Hyperbolic Metamaterial for selectable canalization wavelength (pp. 1527)**
*Vincenzo Caligiuri, Antonio De Luca,*

**Optical response of periodic/quasiperiodic structures containing a left-handed material (pp. 1529)**
*Miller Toledo-Solano, Martha Palomino, Isabel Paredes-Perez,*

**Optical metamaterial slabs based on hexagonal arrays of metallic nano-resonators with three-fold rotational symmetry (pp. 1531)**
*Mircea Giloan, Robert Gutt, Gavril Saplacan,*

**Simulation of graphene-negative index waveguide structure model for solar cell (pp. 1532)**
*Nour El Houda Hissi, Saida Bahsine, Noureddine Cherkaoui Eddeqaqi, Mohammed Musa Shabat, Jacques Atangana,*

**Coupled-Mode Equations for Third-Harmonic Generation in A One-Dimensional PIM/NIM Structure (pp. 1534)**
*Surawut Wicharn, Prathan Buranasiri, Witoon Yindeesuk,*

**High-speed Detection of Microorganisms in Ambient and Aqueous Environments Using Metamaterials (pp. 1536)**
*Sae-June Park, Yeong-Hwan Ahn,*

**Coupling effects between three dimensional split ring resonators (pp. 1538)**
*Che-Chin Chen, M. H. Shiao, Y. H. Lin, C. N. Hsiao,*

**Refraction at a flat interface of an optically anisotropic metamaterial (pp. 1540)**

*Anja Bregar, Miha Ravnik,*

**All-optical phase-change tuning in hybrid dielectric EIT-like metamaterials (pp. 1542)**
*Emilija Petronijevic, Roberto Li Voti, Alessandro Belardini, Grigore Leahu, Gianmario Cesarini, Concita Sibilia,*

**Developing a FETD method for modeling of the optical black hole in metamaterials (pp. 1543)**
*Wei Yang, Jichun Li, Yunqing Huang,*

**Optical diode based on unidirectional state exchange around an exceptional point (pp. 1545)**
*Youngsun Choi, Choloong Hahn, Jae Woong Yoon, Seok Ho Song,*

**Zero index metamaterial for enhanced transmission and beaming (pp. 1548)**
*H. Hajian, E. Ozbay, Humeyra Caglayan,*

**Dual Band Metamaterial Perfect Absorber with Nearly Polarization-Independent (pp. 1550)**
*Osman Bin Ayop, M. K. A. Rahim, N. A. Murad, N. A. Samsuri, F. Zubir, H. A. Majid,*

**Metafilm consisting of spherical silica glass particles (pp. 1552)**
*Zhanna Dombrovskaya, Anton Zhuravlev,*

**Wideband Metamaterial Absorber with Polarization-dependent Operation (pp. 1553)**
*Osman bin Ayop, M. K. A. Rahim, N. A. Murad, N. A. Samsuri, F. Zubir, H. A. Majid,*

**Transmission properties of electromagnetic waves incident to moire superlattices exhibiting quasiperiodic interference patterns (pp. 1555)**
*Jung-Wan Ryu, Jae-Hyung Han, Inbo Kim, Muhan Choi,*

**Modeling of 1D Dc-SQUID Metamaterials (pp. 1556)**
*Oksana Shramkova, N. Lazarides, A. V. Ustinov, G. P. Tsironis,*

**Second-harmonic generation from toroidal moments of all-dielectric metasurfaces (pp. 1558)**
*Daniel Timbrell, Nicolae Coriolan Panoiu,*

**Simultaneous Phase-Matching in Dirac-Cone-Based Zero-Index Metamaterials (pp. 1560)**
*Orad Reshef, Yang Li, Mei Yin, Lysander Christakis, Daryl Inna Vulis, Philip Camayd-Munoz, Shota Kita, Marko Loncar, Eric Mazur,*

**RF Energy Harvesting Study Using Variable Metamaterial Structure (pp. 1562)**
*M. K. A Rahim, N. A. Samsuri, M. S. Zainudin,*

**Analysis of TM surface plasmons at Graphene-MTM interface (pp. 1564)**
*Rifa Jarallah El-Khozondar, Hala Jarallah El-Khozondar, Mohammed M Shabat,*

**A New Wideband Negative Refractive Index Metamaterial for Dual-band Operation (pp. 1568)**
*Sikder S. Islam, M. R. I. Faruque, M. T. Islam,*

**Metamaterial Absorber Insensitive To Polarization and Incidence Angle Based on Multi-Layer Structure (pp. 1574)**
*Leila Belaid, Rachid Oussaid,*

**Design and analysis of a new double C-shaped miniaturized metamaterial for multiband applications (pp. 1578)**
*Mohammad Jakir Hossain, Mohammad Rashed Iqbal Faruque, Sikder Sunbeam Islam, M. F. Jamlos,*

**A Complementary Chiral Metamaterial with Giant Electromagnetic Activity and Low Losses (pp. 1585)**
*Ismael Barba, Ana Grande, Ana Cristina Lopez-Cabeceira, Jose Represa, Gregorio J. Molina-Cuberos, Oscar Fernandez, Alvaro Gomez,*

**A New Metasurface based on Meta-atom Cluster for Terahertz Applications (pp. 1589)**
*Md. Moinul Islam, M. F. Mansor, Mohammad Rashed Iqbal Faruque, Mohammad Tariqul Islam,*

**Left-Handed Compact MIMO Antenna Array Based on Wire Spiral Resonator for 5 GHz Wireless Applications (pp. 1595)**
*Abdulrahman Shueai Mohsen Alqadami, Mohd Faizal Jamlos, Ping Jack Soh, S. K. A. Rahim,*

**Miniaturized Dual Band Antenna Array with Double Negative (DNG) Metamaterial for Wireless Applications (pp. 1597)**
*Abdulrahman Shueai Mohsen Alqadami, Mohd Faizal Jamlos, Ping Jack Soh, S. K. A. Rahim,*

**Permeability tensor for a metamaterial adjacent to a metal (pp. 1599)**
*Olga Porvatkina, Alexey Alexandrovich Tishchenko, Mikhail Nikolayevich Strikhanov,*

## Photonic crystals and cavities

**2D photonic crystal-based double switch-divider (pp. 1605)**
*Victor Dmitriev, Leno Martins,*

**Spectral Scalability and Optical Spectra of Fractal Multilayer Structures: FDTD analysis (pp. 1607)**
*Sevket Simsek, Selami Palaz, Amirullah Mamedov, Ekmel Ozbay,*

**Temporally resolved fourwave mixing in a photonic crystal switch (pp. 1608)**
*Per Lunnemann, Pierre Colman, Yi Yu, Jesper Mork,*

**Magnetic collinear holograms with magnetophotonic crystals (pp. 1610)**
*Yuichi Nakamura, Ryosuke Isogai, Hiroyuki Takagi, Taichi Goto, Pang Boey Lim, Mitsuteru Inoue,*

**Full-k-space flat bands in photonic crystals beyond the tight-binding picture (pp. 1612)**
*ChangQing Xu, Yun Lai,*

**Nitride nanophotonics from the deep ultra-violet to the near infrared: non-linear optics and microlasers (pp. 1614)**
*Julien Selles, Christelle Brimont, Brahim Guizal, Bruno Gayral, Meletios Mexis, Fabrice Semond, Iannis Roland, Yijia Zeng, Xavier Checoury, Philippe Boucaud,*

**Out-of-plane photonic band structures of two-dimensional photonic crystals: a study of the complete band gap (pp. 1616)**
*Jesus D. Valenzuela-Sau, Raul Garcia-Llamas,*

**Optical correlations in 2D and 3D photonic crystals with weak and strong disorder (pp. 1618)**
*Femi Ojambati, E. Yeganegi, Allard P. Mosk, Willem L. Vos,*

**Active control of the vacuum field in nanomechanical photonic crystal structures (pp. 1620)**
*Michele Cotrufo, L. Midolo, M. Petruzzella, Z. Zobenica, F. W. M. van Otten, A. Fiore,*

**High-Emissivity Thermal Emitters on Patterned Dielectric Substrates for Thermophotovoltaics (pp. 1622)**
*Da-Som Kim, Jin-Young Na, Yoon-Jong Moon, Young-Seok Kim, Sun-Kyung Kim,*

**Fully optically built tunable photonic crystal (pp. 1624)**
*Oto Brzobohaty, L. Chvatal, P. Zemanek,*

**Optimization of silicon slot waveguide micro-ring resonator cavities (pp. 1626)**
*Weiwei Zhang, Samuel Serna, Xavier Le Roux, Carlos Alonso-Ramos, Laurent Vivien, Eric Cassan,*

**Magneto-optical nonreciprocity of the waveguide modes in one-dimensional magnetophotonic crystals (pp. 1628)**
*Dariya Sylgacheva, Nikolai Evgen'evich Khokhlov, Andrey Kalish, Anatoliy Prokopov, Alexander Shaposhnikov, Vladimir Berzhansky, Mohammad Nur-E-Alam, Mikhail Vasiliev, Kamal Alameh, Sarkis Dagesyan,*

**All-dielectric Zero-Index Metamaterial (pp. 1630)**
*Daryl Inna Vulis, Yang Li, Orad Reshef, Mei Yin, Philip Camayd-Munoz, Shota Kita, Marko Loncar, Eric Mazur,*

**Wave transmission and photonic frequency bands in graphene superlattices with sequentially modulated doping (pp. 1632)**
*Ivan Fuentecilla-Carcamo, Martha Alicia Palomino-Ovando, Felipe Ramos-Mendieta,*

**Influence of microscale and nanoscale size effects on optoelectronic properties of metallic patterned structures (pp. 1634)**
*Mikita Marus, Aliaksandr Hubarevich, Aliaksandr Smirnov, Xiao Wei Sun, Huang Hui, Weijun Fan,*

**Highly efficient high-speed thermal emitters based on quantum wells and photonic crystals (pp. 1637)**
*Takuya Inoue, Takashi Asano, Menaka D. Zoysa, Susumu Noda,*

**Chiral photonic crystals to control the circular polarization of quantum dots' light emission (pp. 1639)**
*Sergei G. Tikhodeev, S. V. Lobanov, N. A. Gippius, T. Weiss, C. Schneider, J. Gebler, M. Kamp, S. Hofling, A. A. Maksimov, E. V. Filatov,*

**Coupling between Guided Spoof Surface Plasmon Polaritons (pp. 1641)**
*Seong-Han Kim, Kap-Joong Kim, Chul-Sik Kee,*

**Dielectric metamaterial fabricated from silicon pyramid grating as an effective optical sensor (pp. 1643)**
*Andrey K. Sarychev, Konstantin Afanasev, Irina Boginskaya, Igor Budashov, Ilya Kurochkin, Ilya Ryzhikov, Andrey Ivanov, Marina Sedova, Andrey Lagarkov,*

**Temperature tunable waveguide modes in a semiconductor quaternary alloy hexagonal photonic-crystal hole slab (pp. 1645)**
*Robert Sanchez Cano, Nelson Porras Montenegro,*

**Nanophotonic devices with integrated color centers in diamond and silicon carbide (pp. 1648)**
*David O. Bracher, Evelyn L. Hu,*

**Coupling to Photonic Crystal Waveguide by Polarization Tailored Free Space Beam (pp. 1650)**
*Ali Mahdavi, P. Banzer, F. Vollmer,*

**Electromagnetic Mode Profile Shaping in Waveguides (pp. 1652)**
*Jonathan Gratus, Paul Kinsler, Rosa Letizia, William Taylor Boyd,*

## Acoustic metamaterials

**Experimental demonstration of anomalous Floquet topological insulators for sound (pp. 1659)**
*Yu-Gui Peng, Xue-Feng Zhu,*

**Coherent perfect absorption induced by the nonlinearity of coupled Helmholtz resonators (pp. 1660)**
*Vassos Achilleos, Olivier Richoux, Georgios Theocharis,*

**Tunable waveguide and cavity in a phononic crystal/acoustic metamaterial plate by controlling whispering-gallery modes (pp. 1662)**
*Yabin Jin, Yan Pennec, Yongdong Pan, Bahram Djafari-Rouhani,*

**Simultaneous Full Control of Elastic Waves in Plates by Gradient Index Devices (pp. 1664)**
*Yabin Jin, Daniel Torrent, Yan Pennec, Yongdong Pan, Bahram Djafari-Rouhani,*

**Reconfigurable Acoustic Metasurface for Dynamic Steering of Sound Waves (pp. 1666)**
*Po-Han Fu, Tsung-Yu Chiang, Ding-Wei Huang,*

**Hybridization of multi-mode waves in thin plates (pp. 1668)**
*Matthieu Rupin, P. Roux, G. Lerosey, F. Lemoult,*

**Annular Hole Phononic Crystals for Surface Acoustic Waves (pp. 1670)**
*Benjamin James Ash, S. R. Worsfold, Peter Vukusic, Geoffrey R. Nash,*

**Zero-frequency and extremely slow edge states in mechanical granular graphene (pp. 1672)**
*Li-Yang Zheng, Vincent Tournat, Georgios Theocharis, Vitalyi Gusev,*

**Multi-particle trapping and patterning using phononic crystal plates (pp. 1674)**
*Tian Wang, Manzhu Ke, Zhengyou Liu,*

**Effect of Material Parameters on Band Gap of Sonic Crystals (BaTiO3/Polar Liquids) (pp. 1676)**
*Oral Oltulu, Amirullah Mamedov, Ekmel Ozbay,*

**Wave Propagation and Acoustic Band Gaps of Two-Dimensional Liquid Crystal/Solid Phononic Crystals (pp. 1681)**
*Oral Oltulu, A. M. Mamedov, E. Ozbay,*

## Materials for photonics (Graphene, MoS2, WS2, etc)

**Correlative Microscopy for 2D Material Characterization (pp. 1688)**
*Ute Schmidt, Elena Bailo, David Steinmetz, Thomas Dieing,*

**Resonance Raman scattering studies of tungsten diselenide (WSe2) (pp. 1690)**
*Hankyoul Moon, Ja-Yeong Kim, Seokhyun Yoon,*

**Electro-modulation spectroscopy of electronic band structure for MoS2, MoSe2, WS2, and WSe2 crystals and single layers (pp. 1692)**
*Robert Kudrawiec, J. Kopaczek, M. Welna, M. Baranowski, M. Polak, P. Scharoch, K. Wu, B. Chen, S. Tongay,*

**Raman scattering studies of tungsten disulfide (WS2) (pp. 1694)**
*Jayeong Kim, Hankyoul Moon, Seokhyun Yoon,*

**Linear enhancement of the Kerr nonlinear index in the epsilon-near-zero regime (pp. 1696)**
*Lucia Caspani, Rishad Kaipurath, Matteo Clerici, Marcello Ferrera, Thomas Roger, Andrea Di Falco, Jongbum Kim, Nathaniel Kinsey, Vladimir Shalaev, Alexandra Boltasseva,*

**Numerical simulations of nonlinear optical properties of carbon quantum dots embedded in a polymeric matrix (pp. 1698)**
*Cristian Kusko, Roxana Tomescu, Mihai Kusko,*

**Non-Volatile Optoelectronic Phase-Change Meta-Displays (pp. 1700)**
*Santiago Garcia-Cuevas Carrillo, Christopher David Wright, Peiman Hosseini, Harish Bhaskaran,*

**Characterisation and Dynamic Control of Graphene-Liquid Crystal Composite Microfluidic Systems (pp. 1702)**
*Benjamin Thomas Hogan, Salma Younesy, Lorcan Brennan, Tatiana Perova, Yuri Gun'ko, Sergey Dyakov, Monica Craciun, Anna Baldycheva,*

**Photoconductivity of few layer MoTe2 (pp. 1705)**
*Toby Octon, Karthik Nagareddy, Monica Craciun, David Wright,*

**Sensitivity of Graphene-Nonlinear Waveguide Sensors (pp. 1708)**
*Hala Jarallah El-Khozondar, Mohammed M. Shabat, Rana Khalefa,*

**Plasmon Characteristics of Chemically-Doped Graphene Revealed by Near-Field Optical Nanoscopy (pp. 1710)**
*Zebo Zheng, Huanjun Chen,*

**Dynamic Metamaterial based on the Graphene Split Ring High-Q Fano-resonnator for Terahertz Sensing Applications (pp. 1712)**
*Lin Wang, Xiaoshuang Chen, Wei Lu,*

**Tungsten disulfide nanotubes decorated with gold nanoparticles as electrochemical electrodes with improved response (pp. 1714)**
*Filip Ligmajer, Lukas Kejik, Ales Danhel, Miroslav Kolibal, Miroslav Fojta, Tomas Sikola,*

**Improvement of Metal-Based THz Patch Antenna Parameters Using Monolayer Graphene (pp. 1716)**
*Mohammed Taih Gatte, Ping Jack Soh, Mohd Faizal Jamlos, R. B. Ahmad, Mohamed Fareq AbdulMalek, Hasliza A. Rahim,*

**Graphene three-port circulator (pp. 1720)**
*Victor Dmitriev, Wagner Castro, Clerisson Nascimento,*

**Graphene-Based Multi-Resonant Metamaterial Absorber in the Terahertz Regime (pp. 1724)**
*Reza Parvaz, Hamidreza Karami,*

## Photonics based on 2D materials

**Mageto-transport study in GaAs/Al0.3Ga0.7As nanostructure superlattice at very low temperature (pp. 1731)**
*Driss Barkissy, Abdelhakim Nafidi, Abderrazak Boutramine, Ali Khalal, Thami El Gouti, Mustapha Massaq,*

**Topological transition in anisotropic plasmonic metasurface (pp. 1733)**
*Andrey Bogdanov, O. Y. Yermakov, A. I. Ovcharenko, M. Song, D. A. Baranov, I. S. Sinev, I. S. Mukhin, A. K. Samusev, I. V. Iorsh, A. V. Lavrinenko,*

**Terahertz Electron-Beam Radiation in Graphene (pp. 1735)**
*Khwanchai Tantiwanichapan, Xuanye Wang, Anna Swan, Roberto Paiella,*

**A subcell technique for numerical analysis of optical properties of graphene metamaterials with the finite-difference time-domain method (pp. 1737)**
*Ilya Valuev, Sergei Belousov, Maria Bogdanova, Oleg Kotov, Yuri Lozovik,*

**Resonant Visible Light Modulation with Graphene (pp. 1739)**
*Renwen Yu, Valerio Pruneri, Javier Garcia de Abajo,*

**Investigation in band structure and gap engineering of GaAs/AlxGa1-xAs nanostructures superlattices at high magnetic field and low temperature (pp. 1741)**
*Driss Barkissy, Abdelhakim Nafidi, Abderrazak Boutramine, Nassima Benchtaber, Ali Khalal, Thami El Gouti,*

## Chiral and bianisotropic materials

**The Electromagnetic Chirality of an Object (pp. 1748)**
*Ivan Fernandez-Corbaton, Carsten Rockstuhl,*

**Concentration and redirection of light in in metal nanoparticle/polymer nanocomposites waveguides (pp. 1750)**
*Mattia Signoretto, I. Suarez, R. Abargues, P. Rodriguez-Canto, V. Chirvony, J. Martinez-Pastor,*

**Controllable Large Circular Dichroism of a Chiral Metasurface Induced by Coupling Localized and Propagating Modes (pp. 1752)**
*Zeng Wang, Yue Wang, Giorgio Adamo, Bing Hong Teh, Qing Yang Steve Wu, Jinghua Teng, Handong Sun,*

**Asymmetric Transmission with Chiral Photonic Crystals (pp. 1754)**
*Nikhil Parappurath, Filippo Alpeggiani, Kobus Kuipers, Ewold Verhagen,*

**Single-particle plasmonic structures reveal extrinsic chirality (pp. 1756)**
*Vladimir E. Bochenkov, D. S. Sutherland,*

**Chiral Metamaterial Structure With High Optical Activity Based On Conjugated Omega Particles (pp. 1757)**
*Oscar Fernandez, Alvaro Gomez, Angel J. Garcia-Collado, Gregorio J. Molina-Cuberos, Angel Vegas,*

**Optical characterization of U-shaped resonators : from array to single scattererTransmission measurements have been performed on arrays and single U-shaped resonators. We show that optical activity can be evidenced in arrays of resonators and that this activity, associated with the magnetic modes, is already present in single resonators. (pp. 1759)**
*Julien Proust, Johan Grand, Geraldine Guida, Nicolas Bonod, Bruno Gallas,*

**Design of Planar Chiral Metamaterials for Near Infrared Regime (pp. 1761)**
*Sabri Kaya, Mustafa Turkmen, Omer Topaktas,*

## Metamaterial-based devices and antennas

**Design by using equivalent circuits of reflective FSS's converting (pp. 1767)**
*Juan E. Page,*

**Printed Monopole Single Notch UWB Antenna using Low loss Glass-Polytetra?uoroethylene Composite Material (pp. 1769)**

*M. Z. Mahmud, M. T. Islam, M. Samsuzzaman,*

**Design of plasmonic structures in CMOS technology for low-cost, enhanced infra-red gas sensors (pp. 1771)**
*Julian Gardner, Yuxin Xing, Barbara Urasinska-Wojcik, Andrea de Luca, Florin Udrea,*

**Wood zone plate lens based on fishnet metamaterial (pp. 1773)**
*Bakhtiyar Orazbayev, Miguel Navarro-Cia, Miguel Beruete,*

**Bandwidth Enhancement of Multilayer Polymeric Comb Array Antenna for Millimeter Wave Applications (pp. 1775)**
*Wan Asilah Wan Muhamad, Razali Ngah, Mohd Faizal Jamlos, Ping Jack Soh,*

**Tunable EIT-like effect in wire/ring structure metamaterial (pp. 1777)**
*Quanhong Fu, Fuli Zhang, Yuancheng Fan,*

**Magnonic-crystal-based magnon transistor (pp. 1779)**
*Alexander A. Serga, Andrii V. Chumak, Burkard Hillebrands,*

**Gold nanotube metamaterial for plasmonic cavity resonator (pp. 1780)**
*Junxi Zhang, Junfeng Wang, Cheng Zhang, Haojie Song, Pei Wang, Yonghua Lu, Guangtao Fei, Lide Zhang, Lin Zhang,*

**Compensating wave packet distortion with active anomalously dispersive media or devices (pp. 1782)**
*Chun Wang, Anjie Zhu, Shan Qiao, Yongzhi Sun, Dexin Ye, Lixin Ran,*

**Active dispersion compensation for metamateirals and devices based on the wideband frequency response of non-Foster elements (pp. 1784)**
*Anjie Zhu, Chun Wang, Shan Qiao, Yongzhi Sun, Dexin Ye, Lixin Ran,*

**Tuning of the lattice mode in 2D array of split-ring resonators (pp. 1786)**
*Dalius Seliuta, Gediminas Slekas, Rimas Simniskis, Ignas Grigelionis, Andrius Vaitkunas, Zilvinas Kancleris,*

**Conformal Dual Band Textile Antenna with Metasurface for WBAN Applications (pp. 1788)**
*Fatin Nabilah Giman, Ping Jack Soh, Mohd Faizal Jamlos, Herwanshah Lago, Azremi Abdullah Al-Hadi,*

**Effect of the material thicknesses on the transmission spectra of multi-resonant metamaterials (pp. 1792)**
*Sabri Kaya, Mustafa Turkmen, Halis Karakaya,*

**Optical Focusing via Epsilon-Near-Zero Plasmonic Metalens (pp. 1794)**
*Victor Manuel Pacheco Pena, Miguel Navarro-Cia, Miguel Beruete,*

**Perfect Absorbers for Microwave Energy Harvesting (pp. 1796)**
*Thamer Almoneef, Omar Ramahi,*

**Pattern Reconfigurable Antenna using Electromagnetic Band Gap Structure (pp. 1798)**
*Muhammad Faizal Ismail, Mohamad Kamal A. Rahim, Huda A. Majid, Mohamad Rijal Hamid,*

**A Microwave Planar Near-Field Sensor based on Metamaterial Unit Cells for Sensitivity Enhancement (pp. 1800)**
*Ali M. Albishi, Mohamed K. El Badawe, Omar M. Ramahi,*

**Flexible Ultra-Wideband Antenna with Incorporated Metamaterial Structures-Multiple Notches for Data Encoding of Chipless**

**RFID Application (pp. 1802)**
*Mohd Ezwan Bin Jalil, Mohamad Kamal Bin A. Rahim, Nor Asmawati Samsuri, Raimi Bin Dewan, Kamilia Kamardin,*

**Positions of Dual-band Textile Diamond Dipole Antenna with Dual-band Textile Artificial Magnetic Conductor Waveguide Sheet for Body Centric Communication (pp. 1804)**
*Muhammad Azfar Bin Abdullah, Mohamad Kamal Bin A. Rahim, Noor Asmawati Samsuri, Huda Bin Abdul Majid,*

**Improved Single Layer Microwave Absorber Performance of Rice Husk with CNT Composite (pp. 1806)**
*Yeng Seng Lee, F. H. Wee, F. Malek, Y. K. You, Z. Liyana, H. A. Rahim, A. A. M. Ezanuddin,*

**Feed interactions in metamaterial diplexers and radomes (pp. 1809)**
*Yiannis Vardaxoglou,*

**Artificial Dielectric Metamaterials for Antenna Applications (pp. 1810)**
*Shiyu Zhang, Yiannis Vardaxoglou, Will Whittow, Raj Mittra,*

**High efficient wireless power transfer system based on dielectric resonators (pp. 1811)**
*Polina Kapitanova, Minghzao Song, Pavel Belov,*

**Electrical control of circular dichroism and optical activity in graphene chiral metamaterials (pp. 1813)**
*Sang Soon Oh, Teun-Teun Kim, Hyeon-Don Kim, H. S. Park, Ortwin Hess, Bumki Min, Shuang Zhang,*

**Design, Fabrication and Testing of Negative Index Metamaterials for X, Ku, and K Microwave bands (pp. 1815)**
*David Lee, James Vedral, Randall L. Musselman, Anatoliy Pinchuk,*

**Excitation, Verification and Exploitation of Prohibited Modes of Dielectric Resonators (pp. 1817)**
*Amin Kianinejad, Zhi Ning Chen, Cheng-Wei Qiu,*

**Plasmon based three-layer antireflection coating for infrared photodetectors (pp. 1819)**
*Jun Oh Kim, Jiyeon Jeon, Khagendra Bhattarai, Jiangfeng Zhou, Augustine Urbas, Zahyun Ku, Sang Jun Lee,*

**Voltage Controlled Unidirectional Propagation of Microwaves in Metastructures Ferrite/Conductive Elements with Varactors (pp. 1821)**
*Valery Butylkin, Yury Kazantsev, Galina Kraftmakher, Valery Mal'tsev,*

**EBG-based transmission lines with slow-wave characteristics and application to miniaturization of microwave components (pp. 1829)**
*Jordi Selga, Paris Velez, Jordi Bonache, Ferran Martin,*

**Multi-Band CRLH Loaded Patch Antenna (pp. 1835)**
*Sally I. El-Henawy, Ahmed Abdelmottaleb Omar, Amr M. E. Safwat, Hadia Said El-Hennawy,*

**Bandwidth Enhancement using Polymeric PDMS-Grid Array Antenna (pp. 1839)**
*Wan Asilah Wan Muhamad, Razali Ngah, Mohd Faizal Jamlos, Ping Jack Soh, Mohd Tarmizi Ali,*

**High Gain Polydimethylsiloxane-Glass Microsphere (PDMS-GM) Antenna for 5G Applications (pp. 1841)**
*Wan Asilah Wan Muhamad, Razali Ngah, Mohd Faizal Jamlos, Ping Jack Soh, Mohd Tarmizi Ali,*

**Bandwidth Enhancement of Array Antenna using Double Positive Artificial Magnetic Conductor (pp. 1843)**

*H. Lago, M. F. Jamlos, P. J. Soh, M. H. Muslim,*

**Metasurface for Low Profile X-Band Antenna Application with High Permeability and Low Permittivity Substrate (pp. 1845)**
*H. Lago, M. F. Jamlos, P. J. Soh, M. H. Muslim,*

**Complex permittivity of Sugarcane Bagasse and Rubber Tire Dust Within 1 to 18 GHz Frequency Range (pp. 1847)**
*Liyana Zahid, Muzammil Jusoh, Muhammad Ramlee Kamarudin, Sharul Kamal A. Rahim, Yeng Seng Lee, Hasliza A. Rahim, M. K. A. Rahim, T. Sabapathy,*

**Branch-Line Coupler Using PDMS and SHIELDIT Super Fabric Conductor (pp. 1853)**
*Suleiman Aliyu Babale, Sharul Kamal Abdul Rahim, Muzammil Jusoh,*

**A Wideband Corner-Notched Artificial Magnetic Conductor (AMC) Integrated With a Rectangular Ring Antenna (pp. 1857)**
*N. F. M. Aun, P. J. Soh, M. F. Jamlos, H. Lago, A. A. Al-Hadi,*

**Circularly split ring resonator based frequency reconfigurable antenna (pp. 1860)**
*Md. Atiqur Rahman, Mohammad Rashed Iqbal Faruque, Mohammad Tariqul Islam,*

**Wideband Textile Antenna with AMC Plane (pp. 1866)**
*Ezzaty Faridah Nor Mohd Hussin, Ping Jack Soh, Mohd Faizal Jamlos, H. Lago,*

**Design of Multiple layer microwave absorbing structure based on rice husk and carbon nanotubes (pp. 1870)**
*Yeng Seng Lee, F. H. Wee, H. A. Rahim, Y. K. You, Z. Liyana, F. Malek, A. A. M. Ezanuddin,*

**Multi resonance perfect absorber based on graphene micro ribbons (pp. 1876)**
*Majid Roshanaei, Erfan Dezhband, Hamid Reza Karami, Reza Parvaz,*

**Electronically tunable band-stop plasmonic filter based on spoof surface plasmon polaritons (pp. 1880)**
*Qian Xun Xiao, Yong Jin Zhou, Liu Yang, Chong Tan,*

**Absorption Modulation of FSS-Polymer nanocomposites through Incorporation of Graded Conductive nano-fillers (pp. 1885)**
*Rajkumar Jaiswar , Yann Danlee, Henok Mesfin, Arnaud Delcorte, Sophie Hermans, Christian Bailly, Isabelle Huynen,*

**Compact and Broadband Antenna using Double Negative Transmission line Metamaterial (pp. 1891)**
*Md. Moinul Islam, Mohammad Rashed Iqbal Faruque, Mohammad Tariqul Islam, M. F. Mansor,*

**A Double-Layer Metamaterial-Based Technique for Interference Mitigation and Shielding of Planar Microwave Structures (pp. 1897)**
*Athanasios N. Papadimopoulos, Theodosios D. Karamanos, Nikolaos L. Tsitsas, Constantinos A. Valagiannopoulos, Nikolaos V. Kantartzis, Theodoros D. Tsiboukis,*

**Dual band Wearable Fluidic Antenna with Metasurface Embedded in a PDMS substrate (pp. 1899)**
*Muhammad Nazrin Ramli, Ping Jack Soh, Mohd Faizal Jamlos, Herwansyah Lago, Nor Azizan Aziz,*

**A triangular coupled-resonator antenna for ultra-wideband applications (pp. 1902)**
*Md. Zulfiker Mahmud, Touhidul Alam, Mohammad Tariqul Islam,*

**Textile Antenna Integrated with an AMC Plane for WBAN (pp. 1906)**
*Herwansyah Lago, Ping Jack Soh, Mohd Faizal Jamlos, Norsuriati Shohaimi, Sen Yan, Guy A. E. Vandenbosch,*

**Double Negative Metamaterial for Mobile Phone Application (pp. 1908)**
*Md Ikbal Hossain, M. R. I. Faruque, M. T. Islam,*

**Low SAR Metamaterial inspired Printed Monopole Antenna (pp. 1915)**
*Md Ikbal Hossain, M. R. I. Faruque, M. T. Islam, M. T. Ali,*

**Response of ZnAl2O4 Ceramics to Ultra Wideband Antenna (pp. 1921)**
*Ashiqur Rahman, Mohd. Termizi Ali, Mohammad Tariqul Islam, Mandeep Jit Singh, Norbahiah Misran,*

**Microstrip Antenna Gain Enhancement by Metamaterial Radome for millimiter wave applications (pp. 1927)**
*Mouloud Bouzouad , Sidali Attachi , Shaker Mohsen Saleh,*

**Agile Radiation Pattern Control of Metamaterial Microstrip antenna (pp. 1931)**
*Djalaleddine Bensafieddine, S. Attachi, S. M. Chaker, M. Laamari, M. Bouzouad,*

**EM absorption reduction of wireless mobile antenna using printed paper based metamaterial (pp. 1936)**
*Touhidul Alam, Mohammad Tariqul Islam, Salehin Kibria, Mohammad Rashed Iqbal Faruque,*

## Metasurfaces and optical antennas

**Coherent control of the optical absorption and fluorescence enhancement in a plasmonic lattice coupled to a luminescent layer (pp. 1941)**
*Giuseppe Pirruccio, Mohammad Ramezani, Said Rahimzadeh-Kalaleh Rodriguez, Jaime Gomez Rivas,*

**Single metasurface for hybrid functions realization (pp. 1943)**
*Dandan Wen, Shumei Chen, Fuyong Yue, Kinlong Chan, Ming Chen, Marcus Ardron, King Fai Li, Polis Wing HanWong, KokWai Cheah, Edwin Yue Bun Pun,*

**Tunable Metasurfaces in Control of Beam Steering and Surface State Resonance with Liquid Crystals (pp. 1945)**
*Kuo-Ping Chen, Mong-Yin Lin, Shi-Cheng Ye, Mao-Guo Sun, Chi-Yin Yang,*

**Observation of magneto-optic terahertz effects in a hybrid graphene-embedding metasurface (pp. 1947)**
*Simone Zanotto, Christoph Lange, Thomas Maag, Alessandro Pitanti, Vaidotas Miseikis, Camilla Coletti, Riccardo Degl'Innocenti, Lorenzo Baldacci, Rupert Huber, Alessandro Tredicucci,*

**Full cloaks based on metasurfaces (pp. 1949)**
*HongChen Chu, Jie Luo, Yun Lai,*

**Broadband polarization conversion in plasmonic metasurfaces with symmetry breaking (pp. 1951)**
*Shengyan Yang, Zhe Liu, Xiaoxiang Xia, Junjie Li, Changzhi Gu,*

**Extrinsic orbital Hall effect in cyclic group symmetric metamaterial (pp. 1953)**
*Yeon Ui Lee, Igor Ozerov, Frederic Bedu, Ji Su Kim, Frederic Fages, Jeong Weon Wu,*

**Angle-resolved far-field scattering/extinction characteristics of single Ag nanowire (pp. 1955)**
*Jinhyung Kim, Ho-Seok Ee, Min-Soo Hwang, Kwang-Yong Jeong, Juhyung Kang, Hong-Gyu Park, Min-Kyo Seo,*

**Reshaping Electromagnetic Emissions with Meta-substrate based on Spoof Plasmons (pp. 1957)**
*Yao Gao, Agnes Maurel, Abdel Ourir,*

**Orthogonally polarised modes sharing a single metasurface for dual-pol antennas (pp. 1962)**
*Amagoia Tellechea, Francesco Caminita, Enrica Martini, I. Ederra, Juan Carlos Iriarte, Ramon Gonzalo, Stefano Maci,*

**Wideband Metasurface Energy Harvester (pp. 1964)**
*Mohamed El Badawe, Ali Albishi, Omar Ramahi,*

**High-performance planar holographic structures for complex focusing of terahertz beams (pp. 1966)**
*Sergei A. Kuznetsov, Mikhail A. Astafev, Alexandr N. Gentselev, Miguel Navarro-Cia, Miguel Beruete, Andrey V. Arzhannikov,*

**Novel Photonic Devices with Spatiotemporally Engineered Metasurfaces (pp. 1968)**
*Amr Shaltout, Alexander Kildishev, Vladimir Shalaev,*

**Resonances in metasurfaces and their applications in SPR sensing (pp. 1970)**
*Ivan Richter, Jakub Lelek, Pavel Kwiecien, Jan Fiala,*

**Far field dark modes excitation and electromagnetically induced transparency (pp. 1972)**
*Elena Bochkova, Shah Nawaz Burokur, Andre de Lustrac, Anatole Lupu,*

**Periodic arrays of film-coupled nanoparticles as tunable all-dielectric metasurfaces (pp. 1974)**
*Evangelos Almpanis, Nikolaos Papanikolaou, Vassilios Yannopapas, Nikoalos Stefanou,*

**Nanoantennas for controlled enhancement and interference of higher-multipole molecular transitions (pp. 1976)**
*Karolina Slowik, Evgenia Rusak, Mirko Goeddel, Jakob Straubel, Michael Kuehn, Florian Weigend, Carsten Rockstuhl,*

**Multimodal nanoantennas for engineering quantum light (pp. 1978)**
*Karolina Slowik, Jakob Straubel, Rafal Sarniak, Robert Filter, Carsten Rockstuhl,*

**Band stop filters for THz waves based on dielectric metasurfaces (pp. 1980)**
*Jose Francisco Algorri, R. Vergaz, V. Urruchi, J. M. Sanchez-Pena, B. Garcia-Camara,*

**All-dielectric bianisotropic metasurface for microwave applications (pp. 1982)**
*Mikhail Aleksandrovich Odit, Polina Kapitanova, Yuri Kivshar, Pavel Belov,*

**Highly Sensitive Room Temperature Graphene-based Sub-terahertz Photoconductor via Electromagnetic Gating Effect (pp. 1984)**
*Lin Wang, Xiaoshuang Chen, Changlong Liu, Weiwei Tang, Wei Lu,*

**Quantitative characterization of a plasmonic zone plate using coherence-controlled holographic microscopy (pp. 1987)**
*Jiri Babocky, Filip Ligmajer, Radek Kalousek, Aneta Krizova, Lukas Kejik, Martin Hrton, Petr Dvorak, Vlastimil Krapek, Matej Tyc, Radim Chmelik,*

**Blackbody Metamaterial Composite film of Nanoparticle and Polymer (pp. 1989)**
*Kotaro Kajikawa, Hisashi Karube,*

**Gradient phase Metasurface lens to focus electromagnetic waves (pp. 1991)**
*Akram Boubakri, Fethi Choubeni, Tan Hoa Vuong, Jacques David,*

## Plasmon-enhanced photovoltaics, photocatalysis, and solar fuels

**Silver as Terbium-Yterbium sensitizer in glass and glass-ceramic thin films for photovoltaic efficiency enhancement (pp. 1996)**
*Saloua Belmokhtar, Adel Bouajaj, M. R. Britel, J. Heminej, F. Enrichi, C. Armellini, G. Battaglin, F. Belluomo, E. Cattaruzza, M. Ferrari,*

**Plasmonic improvement of low cost anatase nanoparticles for dye sensitized solar cells (pp. 1997)**
*Mohamed M. Rashad, M. S. Sanad, A. E. Shalan,*

**Metamaterials for Solar Cell Applications (pp. 1998)**
*Nicholas Sharac, R. Flynn, H. Kim, A. Makinen, L. Hirst, C. Ellis, J. Tischler, P. Jenkins, P. Campbell, J. Owrutsky,*

## Topological photonics

**Photonic Analog of Chern Insulators (pp. 2000)**
*Hsun-Chi Chan, Ta-Chun Lin, Guang-Yu Guo,*

**Topological properties of nearly flat bands in two-dimensional photonic crystals (pp. 2001)**
*Bing Yang, Tong Wu, Xiangdong Zhang,*

## Quantum photonics

**Optimal Ultra-wide Spatial-Spectral Windows for Hyperentangled Two-photon Emission (pp. 2004)**
*Salem F. Hegazy, Jala El-Azab, Y. A. Badr, Salah Sabry Obayya,*

**Modeling of optical gain in Ge-based two dimensional structures (pp. 2006)**
*Marta Gladysiewicz, Herbert Maczko, Robert Kudrawiec,*

**Integrated Photonics Platform for Single Quantum Dots at Telecom Wavelengths (pp. 2008)**
*Khaled Mnaymneh, D. Dalacu, S. Haffouz, J. Lapointe, P. J. Poole, R. L. Williams,*

## Nanobiophotonics

**Single bacteria identification with an optical silicon microcavity (pp. 2010)**
*Manon Tardif, Jean-Baptiste Jager, Christophe Pin, Emmanuel Picard, Emmanuel Hadji, David Peyrade,*

**Plasmonics enhanced ultrafast laser nanosurgery: Fundamentals and applications in nanomedecine (pp. 2012)**
*Michel Meunier,*

**Octupolar Metastructures for a sensitive detection of bacteriophages by surfaced enhanced Raman spectroscopy (pp. 2014)**
*Massimo Rippa, Riccardo Castagna, Marianna Pannico, Pellegrino Musto, Rubina Paradiso, Giorgia Borriello, Jun Zhou, Joseph Zyss, Lucia Petti,*

**Enhanced molecular overtone absorption by light-on-a-chip (pp. 2016)**
*Alina Karabchevsky, Alexey Kavokin,*

**Electrical Detection of miRNA using Photoconductance in Plasmonic Nanowire (pp. 2018)**
*Jihye Lee, Jeong Hyeon Kim, Jong-Souk Yeo,*

**Fabrication of random optical diffusers with prescribed scattering properties using three-dimensional printers (pp. 2020)**
*Alma Karen Gonzalez-Alcalde, Eugenio Rafael Mendez,*

## Near-field optics and nano-optics

**Near-field dichroism of azo-polymers for optical switching and image storage (pp. 2023)**
*Sergey Kharintsev, A. V. Kharitonov, M. D. Dmitrieva, A. I. Fishman, S. G. Kazarian,*

**Study of Near and Far Fields of a Super-Gaussian Beam on a Step Discontinues Interface using FFT-BPM (pp. 2025)**
*Adel Shaaban, Lotfi R. Gomaa, Mohamed Farhat O. Hameed, Salah Sabry Obayya,*

**Analysis of Lorentz Beam Propagation at Critical Angle Using Accelerated Beam Propagation Method (pp. 2027)**
*Adel Shaaban, Mohamed Farhat O. Hameed, Mahmoud Sayed, Hassan Saleh, Lotfi Gomaa, Salah Sabry Obayya,*

**Enhancement of light emission from an optically pumped bias driven tunneling junction (pp. 2029)**
*Xiao Wang, Kai Braun, Dai Zhang, Heiko Peisert, Hilmar Adler, Thomas Chasse, Alfred J. Meixner,*

**Near-field optical response of gold gap nanoantennas (pp. 2031)**
*Michele Celebrano, Milena Baselli, Giovanni Pellegrini, Xiaofei Wu, Bert Hecht, Lamberto Duo, Marco Finazzi, Paolo Biagioni,*

**Anomalous spectral shift of near- and far-field plasmonic resonances in nano-gaps (pp. 2033)**
*Anna Lombardi, Angela Demetriadou, Lee Weller, Felix Benz, Rohit Chikkaraddy, Patrick Andrae, Javier Aizpurua, Jeremy Baumberg,*

**The Spectral Phase and Temporal Shape of Femtosecond Laser Pulses in the Nearfield of Plasmonic Nanostructures (pp. 2034)**
*Richard Ciesielski, Tobia Mancabelli, Jurgen Kraus, Alberto Comin, Sebastian Gunther, Achim Hartschuh,*

**Plasmonic Pickup Head with Dual Wavelength Operations (pp. 2036)**
*Kai Hao Chang, Po Tsung Lee,*

**Introducing nano-FTIR: Imaging and Spectroscopy at 10nm spatial resolution (pp. 2038)**
*Adrian Cernescu,*

**Numerical simulations of signal acquisition in aperture SNOM (pp. 2039)**
*Martin Hrton, Petr Dvorak, Tomas Samoril, Filip Ligmajer, Tomas Sikola,*

**Spectroscopic measurements of near-field interference patterns by a-SNOM (pp. 2041)**
*Zoltan Edes, Petr Dvorak, Michal Kvapil, Tomas Samoril, Filip Ligmajer, Martin Hrton, Vlastimil Krapek, Radek Kalousek, Petr Dub, Peter Varga,*

## Transformational electromagnetics, cloaking

**Ultrathin metasurface carpet cloak (pp. 2044)**
*Bakhtiyar Orazbayev, Nasim Mohammadi Estakhri, Miguel Beruete, Andrea Alu,*

**Wave Propagation in Complex Coordinates, Reflectionless Media and Localization (pp. 2046)**
*Christopher G. King, Simon Horsley, Thomas Philbin,*

**Random Transformation Optics (pp. 2048)**
*Gael Favraud, Juan Sebastian Totero Gongora, Andrea Fratalocchi,*

**Implementation of Remote Mach-Zehnder Switch by Illusion Optics (pp. 2050)**

*Hamed Reza Shoorian, Reza Rezapour, David Margousi,*

**Low Profile Superstrate using Transformation Optics to modify Radiation Pattern of Antenna (pp. 2052)**
*Chetan Joshi, Anne Claire Lepage, Xavier Begaud,*

**Numerical modeling of time-domain cloaking with metamaterials (pp. 2054)**
*Yunqing Huang, Jichun Li, Wei Yang,*

**A level-set based topology optimisation of cloaking devices with the boundary element method (pp. 2056)**
*Kenta Nakamoto, Hiroshi Isakari, Toru Takahashi, Toshiro Matsumoto,*

**Multi-physics simulations for 3D isotropic transformation optics (pp. 2058)**
*Dongheok Shin, Kyoungsik Kim,*

**Identifying Microwave Magnetic Resonance in Chiral Elements for Creation of Controlled Matched Absorbing Metastructures (pp. 2060)**
*Galina Kraftmakher, Valery Butylkin, Yuri Kazantsev, Valery Mal'tsev, Yuri Temirov,*

**A New Metamaterial-based C-band Electromagnetic Cloak (pp. 2067)**
*Sikder Sunbeam Islam, Mohammad Rashed Iqbal Faruque, Mohammad Tariqul Islam,*

## FSS, HIS and Extraordinary transmission

**Design of a THz-MEMS Frequency Selective Surface for Structural Health Monitoring (pp. 2073)**
*Joao Pedro Pavia, W. J. Otter, S. Lucyszyn, M. A. Ribeiro,*

**THz sensing with FSS at oblique incidence (pp. 2075)**
*Pablo Rodriguez-Ulibarri, Sergei Alexandrovich Kuznetsov, Miguel Beruete,*

**Off-Axis Beaming 3D-Printed Bull's-Eye Antenna (pp. 2077)**
*Unai Beaskoetxea Gartzia, Stefano Maci, Miguel Navarro-Cia, Miguel Beruete,*

**New compact AMC structure for low profile antenna (pp. 2079)**
*Nebil Kristou, Jean-Francois Pintos, Kourosh Mahjoubi,*

**Frequency Selective Surfaces to improve the performance of systems with dual-band antennas (pp. 2081)**
*Elidiane Mirella Farias Fernandes, Mauricio Weber Benjo da Silva, Leni Joaquim de Matos, Andres Pablo Lopez Barbero,*

**Frequency Reconfigurable Antenna with Metamaterial Electromagnetic Band Gap (EBG) structures (pp. 2083)**
*Raimi Dewan, Mohamad Kamal A. Rahim, Mohamad Rijal Hamid, Mohd Ezwan Jalil, Huda A. Majid,*

**10.7 GHz Switchable Metamaterial Absorber/ Reflector for X-band Applications (pp. 2085)**
*Mohammed M. Gajibo, Mohamad Kamal A. Rahim, Noor Asniza Murad, Osman Ayop, Mohamad Rijal Hamid, Huda A. Majid,*

**Alternative Approach to Miniaturize an AMC Structure (pp. 2087)**
*Nebil Kristou, Jean-FrranÃ§ois Pintos, Kourosh Mahjoubi,*

**Two Equivalent Circuit Models for Double Concentric Squares AMC (pp. 2089)**
*Mohamad Mantash, Anne-Claude Tarot,*

## Modeling, Computational Techniques and Verification of Theory

**Discontinuous Galerkin Time Domain Methods for Nonlocal Dispersion Models and Electron Beam Modeling in the Context of Nanoplasmonics (pp. 2095)**
*S. Lanteri, C. Scheid, Nikolai Schmitt, J. Viquerat,*

**Modeling of periodically-structured fiber-reinforced laminates with multiple fibers absent (pp. 2097)**
*Zicheng Liu, Changyou Li, Dominique Lesselier, Yu Zhong,*

**Disordered metamaterials achieve broadband enhancement of quantum effciency of photoelectrochemical devices for water splitting (pp. 2099)**
*Marcella Bonifazi, Hui-Chun Fu, Jr Hau He, Andrea Fratalocchi,*

**Symmetry Analysis for Metamaterials with Periodic Microstructure (pp. 2101)**
*Pu Zhang,*

**First-order perturbation theory with analytical mode normalization for plasmonic nanoantenna arrays applied to refractive index sensing (pp. 2102)**
*Thomas Weiss, Martin Mesch, Martin Schaferling, Harald Giessen, Wolfgang Langbein, Egor Muljarov,*

**The structural, elastic, electronic and dynamical properties of chalcopyrite semiconductor BeGeAs2 from first principles calculations (pp. 2104)**
*Yasemin O. Ciftci, Meryem Evecen, Emine Aldirmaz,*

**Density functional modeling studies of (E)-4-Bromo-N-(2-chlorobenzylidene)-aniline (pp. 2105)**
*Hasan Tanak, Meryem Evecen, Emine Aldirmaz,*

**Quantum chemical computational studies of (E)-N-(1-Benzothiophen-3-ylmethylidene)-2,6-dimethylaniline (pp. 2106)**
*Hasan Tanak,*

**Accelerating Performances of a Waveguide Mode Solver Based on Boundary Integral Equations (pp. 2107)**
*Julien Vincent, Priscillia Daquin, Ronan Perrussel, Jean-Rene Poirier, Han-Cheng Seat,*

**Microwave Permeability of Hollow Iron Spheres (pp. 2109)**
*Conor John McKeever, Mustafa Aziz, Feodor Ogrin,*

**Vortices and orbital angular momentum of naturally occurring patterns (pp. 2112)**
*Mohamed Babiker, Jun Yuan, Yuanjie Yang, G. Thirunavukkarasu,*

**Scattering Calculation of Bianisotropic Particle Slabs for Normal Incidence via Retrieved Polarizabilities (pp. 2113)**
*Theodosios D. Karamanos, Athanasios N. Papadimopoulos, Nikolaos V. Kantartzis, Theodoros D. Tsiboukis,*

## Emerging applications

**Energy Tunneling Behavior in Geometrically Separated Wave Guides (pp. 2117)**
*Muhammad Omar, Rashad Ramzan, Omar Farooq Siddiqui,*

**Plasmonic Color Filters for Industrial Applications (pp. 2119)**
*Luc Duempelmann, Angelique Luu-Dinh, Benjamin Gallinet, Lukas Novotny,*

**An electromechanically tunable photonic crystal nanocavity with integrated photodetector for wavelength and displacement sensing (pp. 2121)**
*Zarko Zobenica, Rob van der Heijden, Maurangelo Petruzella, Francesco Pagliano, Rick Leijssen, Tian Xia, Leonardo Midolo, Michele Cotrufo, Yongjin Cho, Frank van Otten,*

**Tuning the Propagation of Spoof Surface-Plasmon Polaritons (pp. 2123)**
*Mario F. Pantoja, Zhihao Jiang, Pingjuan L. Werner, Douglas H. Werner,*

**Hybrid Graphene-Copper UWB Array Sensor for Brain Tumor Detection via Scattering Parameters in Microwave Detection System (pp. 2125)**
*Mohd Aminudin Bin Jamlos, Abdul Hafiizh Ismail,*

**Plasmonic waveguide based mid-infrared lab-on-a-chip (pp. 2127)**
*Benedikt Schwarz, Daniela Ristanic, Peter Reininger, Hermann Detz, Aaron Andrews, Werner Schrenk, Gottfried Strasser,*

**Design of Monopole Graphene Antenna for 5G Applications (pp. 2128)**
*Siti Nor Hafizah Sa'don, Muhammad Ramlee Kamarudin, Fauzan Ahmad,*

**Electric field induced visually observable change in light scattering and absorption in doped ZnO nanowire colloidal suspensions (pp. 2130)**
*Martin Timusk, Andris Sutka, Maris Knite,*

**Enhancement of an Ultra-Wide Band Antenna System for Breast Cancer Detection using Metamaterials (pp. 2132)**
*Asma Mohamed Boudellioua, Mohammed Bait-Suwailam,*

**Plasmonic Sensing Below the Quantum Noise Limit with Intensity Squeezed Light (pp. 2134)**
*Benjamin Lawrie, Raphael Pooser,*

**Nano-optomechanics with subwavelength light fields (pp. 2136)**
*Juha Muhonen, Rick Leijssen, Freek Ruesink, Lars Freisem, Giada La Gala, Randy Meijer, Rutger Thijssen, Ewold Verhagen,*

**Graphene Array Antenna for 5G Applications (pp. 2138)**
*Siti Nor Hafizah Sa'don, Muhammad Ramlee Kamarudin, Fauzan Ahmad, Muzammil Jusoh,*

**Tunable assembly of plasmonic nanoparticles for use as reversible mirrors and sensors (pp. 2140)**
*Leonora Velleman, Debabrata Sikdar, Yunuen Montelongo, Ye Ma, Yi Huang, James Million, William Pitchford, Vlad Turek, Steve Roser, Anthony Kucernak,*

**Evaluation of Broadband Textile Monopole Antenna Performance for Subject-Specific On-body Applications (pp. 2141)**
*Hasliza A. Rahim, Mohamed Fareq AbdulMalek, Ping Jack Soh, Guy A. E. Vandenbosch,*

## Nanofabrication Technology

**High-Precision Fabrication Technology for Gold Nanoparticle Assemblies with Sub-10 nm Nanogaps (pp. 2151)**
*Yusuke Niimura, Naoto Oonishi, Kyohei Okubo, Edwin Carlen,*

**Q-factor Tuning of Gold Nanoresonators by Thermal Annealing (pp. 2153)**
*Naoto Oonishi, Yusuke Niimura, Kyohei Okubo, Edwin Carlen,*

**Plasmonic nanorod array: novel fabrication methods and applications (pp. 2155)**
*Zhang-Kai Zhou, J. Xue, J. Li, X. H. Wang,*

**Fine tuning of submicron pattern dimensions in Displacement Talbot Lithography (pp. 2157)**
*Emmanuel Damien Le Boulbar, Philip Adam Shields,*

**3D chiral plasmonic metamaterials fabricated by direct laser writing: The twisted omega particle (pp. 2159)**
*Ioanna Sakellari, Xinghui Yin, Maxim Nesterov, Konstantina Terzaki, Aggelos Xomalis, Maria Farsari,*

**Tunable optical properties of some rare earth elements doped mayenite Ca12Al14O33 nanopowders elaborated by oxalate precursor route (pp. 2161)**
*Mohamed M. Rashad, A. G. Mostafa, D. A. Rayan,*

**Optical Properties of Metal-Dielectric Nanocomposite Coatings Obtained by Gas Phase Condensation (GPC) and PECVD processes (pp. 2162)**
*Harry Nizard, M. Maicu, D. Hecker, D. Gloess, P. Frach, G. Gerlach,*

**Soft-glass scalable metamaterials: fiber drawn split ring resonators (pp. 2164)**
*Alessio Stefani, Juliano Grigoleto Hayashi, Xiaoli Tang, Alexander Argyros,*

**Template transfer for fabrication of freestanding gold nanohole membrane (pp. 2166)**
*Peipei Jia, Heike Ebendorff-Heidepriem,*

## Active, Nonlinear and Reconfigurable Plasmonics and Metamaterials

**Nanophotonics with Plasmonic Ceramics (pp. 2169)**
*Nathaniel Kinsey, Clayton DeVault, Marcello Ferrera, Urcan Guler, Amr Shaltout, Aveek Dutta, Soham Saha, Alexandra Boltasseva, Vladimir Shalaev,*

**Wavelength dependence of longitudinal photo-induced voltage in nano-porous gold thin film in visible frequencies (pp. 2171)**
*Marjan Akbari, K. Iwata, Teruya Ishihara,*

**Hyperbolic-Metamaterial Integrated Devices for Efficient Infrared Rectification (pp. 2173)**
*Pai-Yen Chen,*

**Anomalous spectral shifts in plasmonic nano-cavities (pp. 2175)**
*Angela Demetriadou, Anna Lombardi, Jan Mertens, Ortwin Hess, Jeremy J. Baumberg, Javier Aizpurua,*

**Nonlocal phenomena in metastructures with near-zero parameters (pp. 2177)**
*Inigo Liberal, Yue Li, Nader Engheta,*

**Nonlinear Reconfigurable All-Dielectric and Hybrid Nanoantennae (pp. 2179)**
*S. V. Makarov, A. E. Krasnok, D. A. Zuev, V. A. Milichko, I. S. Mukhin, Pavel A. Belov,*

**Experimental Time-Varying Light Reflection in an Epsilon-Near-Zero Active Medium (pp. 2181)**
*Amr Shaltout, Matteo Clerici, Nathaniel Kinsey, Rishad Kaipurath, Jongbum Kim, Enrico Carnemolla, Daniele Faccio, Alexandra Boltasseva, Vladimir Shalaev, Marcello Ferrera,*

**Quantum Hydrodynamic Theory of Second-Harmonic Generation (pp. 2183)**

*Cristian Ciraci,*

**Silver grain nonlinear metamaterial (pp. 2185)**
*Tomasz Stefaniuk, Nicolas Olivier, Alessandro Belardini, Concita Sibilia, Aleksandra Wronkowska, Andrzej Wronkowski, Tomasz Szoplik, Anatoly Zayats,*

**Reconfigurable THz metamaterials based on nematic liquid crystals (pp. 2187)**
*Dimitrios C. Zografopoulos, Goran Isic, Borislav Vasic, Rados Gajic, Romeo Beccherelli,*

**Tunable Generation of Graphene Surface Plasmon Polaritons (pp. 2189)**
*Mohamed Farhat, Hakan Bagci, Pai-Yen Chen, Sebastien Guenneau,*

**Plasmonic Launchers for Quantitative Nonlinear and Quantum Plasmonics (pp. 2191)**
*Alexandre Baron, David R. Smith, Philippe Lalanne,*

**Inherently Nonrecirocal: Nonlinear Metamaterials (pp. 2193)**
*Ekaterina Poutrina, Augustine Urbas,*

**Laser light generation in plasmonic crystals and metallic nanoparticles (pp. 2195)**
*J. Cuerda, F. Ruting, F. J. Garcia-Vidal, Jorge Bravo-Abad,*

**Antenna-enhanced third-order nonlinear response of an epsilon-near-zero medium (pp. 2197)**
*Mohammad Z. Alam, S. A. Schulz, J. Upham, I. De Leon, R. W. Boyd,*

**Switchable and reconfigurable nanophotonics: from single antennas to complex systems (pp. 2199)**
*Otto L. Muskens, Roman Bruck, Yudong Wang, Kees de Groot, Kevin Vynck, Philippe Lalanne, Goran Mashanovic, Graham Reed,*

**Second Harmonic Generation from Sub-Wavelength Triangular Hole Array in Au Thin Film (pp. 2201)**
*Mizuki Saikawa, Yuta Hachiya, Kengo Iwata, Masakazu Matsubara, Teruya Ishihara,*

## Acoustic, Mechanical and Thermal Metamaterials

**Theory and experimental realization of the emergence, coalescence and topological properties of multiple exceptional points (pp. 2205)**
*Kun Ding, Guancong Ma, Meng Xiao, Z. Q. Zhang, C. T. Chan,*

**Parity-time synthetic phononic media (pp. 2206)**
*Johan Christensen,*

**Total transmission super-resolution imaging with a hyperbolic elastic metamaterial (pp. 2207)**
*Hyuk Lee, Joo Hwan Oh, Hong Min Seung, Seung Hyun Cho, Yoon Young Kim,*

**Rainbow trapping in mechanical vibrations (pp. 2209)**
*Rafael A. Mendez-Sanchez, Arturo Arreola-Lucas, Gabriela Baez, Francisco Cervera, Alfonso Climente, Jose Sanchez-Dehesa,*

**Three-dimensional Resonant Elastic Metamaterials with Fluid-like Property (pp. 2211)**
*Guancong Ma, Caixing Fu, Guanghao Wang, Philipp del-Hougne, Johan Christensen, Yun Lai, Ping Sheng,*

**Dynamic elastic anisotropy and homogenisation (pp. 2213)**

*Richard Craster, D. Colquitt, Tryfon Antonakakis,*

**Locally resonant acoustic metamaterials beyond homogenization: subwavelength control of waves, slow waves, negative index and other exotic phenomena (pp. 2215)**
*Nadege Kaina, Fabrice Lemoult, Mathias Fink, Geoffroy Lerosey,*

**Total hyperelastic invariance - stretching the truth? (pp. 2216)**
*William J. Parnell, Pu Zhang, Vincent Pagneux,*

**Homogenisation of acoustic and elastic metamaterials (pp. 2218)**
*Mehul Makwana, B. Maling, S. Guenneau, R. V. Craster,*

**Bio-inspired seismic metamaterials (pp. 2220)**
*Ronald Aznavourian, Tania Puvirajesinghe, Stephane Brule, Stefan Enoch, Sebastien Guenneau,*

**Applications of Local Resonances in Civil Engineering Seismic Protection (pp. 2222)**
*Bogdan Ungureanu, Younes Achaoui, Stephane Brule, Stefan Enoch, Sebastien Guenneau,*

**Acoustic resonator systems with topological semimetal phases (pp. 2224)**
*Zhaoju Yang, Baile Zhang,*

**Heat mimicking of given objects (pp. 2226)**
*Ahmed Alwakil, Myriam Zerrad, Michel Bellieud, Claude Amra,*

**Double Zero Index Acoustic Metamaterial (pp. 2228)**
*Marc Dubois, Chengzhi Shi, Yuan Wang, Xiang Zhang,*

**Low frequency sound screening using an acoustic metamaterial made of space-coiled resonant cavities (pp. 2230)**
*A. Elayouch, M. Addouche, Y. Tejda, A. Khelif,*

**Wave propagation in periodic structures and focusing of the ultrasound waves (pp. 2232)**
*Piotr Fiborek, Pawel Kudela, Maciej Radzienski, Wieslaw Mieczyslaw Ostachowicz,*

**Plenary Presentation**

# Transformation optics, surface plasmons, and metasurfaces

John B. Pendry
Imperial College London, United Kingdom
E-mail: j.pendry@imperial.ac.uk

Metallic surfaces support surface plasmon excitations whose properties are intimately connected to the surface geometry. For example a flat silver surface is an excellent mirror, but the same material with a rough surface is black, reflecting hardly any light. Here we use transformation optics to relate many complex surface structures to a single mother structure. In this way we can classify the spectra of these complex surfaces. Examples will be given of singular structures that harvest light, electron energy loss, van der Waals forces and other properties that are related to the surface plasmon spectrum.

# Breaking reciprocity and time-reversal symmetry with metamaterials

**Andrea Alu**
*The University of Texas at Austin, USA*
*E-mail address: alu@mail.utexas.edu*

**Abstract**- I will discuss our recent work in the area of non-reciprocal devices, from acoustics to nanophotonics, with the overall goal of largely breaking Lorentz reciprocity and realize isolation in practical devices without using magnetic bias. Our approaches are based on using suitably tailored mechanical motion, spatio-temporal modulation, and large nonlinearities in coupled resonator systems. In the talk, I will discuss the impact of these concepts from basic science, to integrated technology, and how this platform may be at the basis of topological insulators for light and sound.

# Photonic design of nanoscale energy converters

**Harry Atwater**
California Institute of Technology, USA

# Optical forces on exotic materials

**Stephen Barnett**
*University of Glasgow, United Kingdom*
*E-mail address: Stephen.Barnett@glasgow.ac.uk*

**Abstract**- Light has mechanical properties and it can transfer these to the material bodies with which it interacts. Radiation pressure and dipole forces on dielectrics are familiar, but this talk will concentrate on the subtleties that appear with more exotic objects including magneto-dielectrics, negative-index materials and chiral molecules.

***Near-Zero Photonics***

*Nader Engheta*

*University of Pennsylvania*
*Philadelphia, PA 19104, USA*
*Email: engheta@ee.upenn.edu*
*Web: www.seas.upenn.edu/~engheta/*

In this talk, I will present an overview of our ongoing efforts in exploring various aspects of light-matter interaction in platforms and structures with effective near-zero parameters. We have found exciting phenomena in classical and quantum aspects of wave interaction with such media that may show new roads towards novel devices with unprecedented functionalities, and fundamental features in quantum optics and wave physics. I will discuss some of our most recent results and forecast future directions and potentials.

# Non-Hermitian photonics: PT symmetry and beyond

**Demetrios Christodoulides**
University of Central Florida, USA

# Translational Metamaterials Research: Taking Metamaterials from the Laboratory to the Marketplace

**David. R. Smith**
Duke University, USA

**Keynote Presentation**

# Anisotropy makes the difference: systropic, bulbic, and porcupic metamaterials

**Ari Sihvola, Tommi Rimpiläinen, and Henrik Wallén**

Department of Radio Science and Engineering,
Aalto University School of Electrical Engineering, Espoo, Finland
E-mail: ari.sihvola@aalto.fi

**Abstract**— This presentation focuses on the additional dimensions in material response that particular type of anisotropies bring into the electromagnetic behavior of nanoparticles and metamaterial inclusions. The particles under discussion are spherical or spheroidal, and the anisotropy to be treated is radial (in the spheroidal configuration, radiality is understood in a generalized sense). The concepts of bulbic and porcupic anisotropies bring forth a distinction which has interesting repercussions in the global response of the particle. Furthermore, the generalization of radial anisotropy into systropic material response will be discussed.

The desired properties of metamaterials result often from the structure of microgeometry. Chirality and artificial magnetism due to helix- and loop-shaped inclusions are examples of such emergent effects in complex media response. One further important domain of a similar type of effects created by homogenization is anisotropy.

While the concept of radial anisotropy (RA) has appeared in the electromagnetics literature already more than thirty years ago [1, 2], it seems that its meaning and impact in the context of metamaterials have not been given sufficient attention.

Scattering by radially anisotropic spheres has been shown to be a fascinating electromagnetic problem which leads to many unintuitive effects [3, 4]. In this presentation, some of these are discussed. The classification of RA scatterers, introduced in [5], distinguishes between *bulbic* ($\varepsilon_{\rm rad} < \varepsilon_{\rm tan}$) and *porcupic* ($\varepsilon_{\rm rad} > \varepsilon_{\rm tan}$) anisotropies where the permittivity components of the medium in the radial ($\varepsilon_{\rm rad}$) and tangential ($\varepsilon_{\rm tan}$) directions are different. The denotation comes from the observations that a layered (onion-type bulb) displays a tangential permittivity component stronger than the radial one, while a configuration of radial needles (a "porcupine") emphasizes the radial response more than the tangential one. Figure 1 sketches the structures.

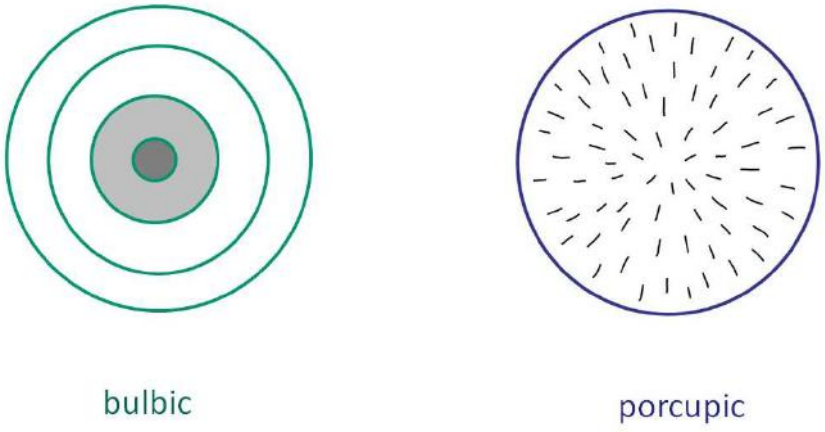



Figure 1: A bulbic anisotropy is a result of a layered structure, and the porcupic one comes from a radially pronounced geometry.

A further class of anisotropies is systropy which is a generalization of the locally uniaxial anisotropy of RA spheres into a locally biaxial domain [6, 7], in such a way that the eigenaxes of the permittivity dyadic are always aligned with the spherical coordinate system. Due to this additional dimension, systropic spheres have a richer electromagnetic response than ordinary RA inclusions. These effects will be discussed in the presentation.

**REFERENCES**


1. Schulgasser, K., "Sphere assemblage model for polycrystals and symmetric materials," *J. Appl. Phys.*, Vol. 54, No. 2, 1380–1382, 1983.
2. Sten, J. C.-E., "DC fields and analytical image solutions for a radially anisotropic spherical conductor," *IEEE Trans. Dielectr. Eletr. Insul.*, Vol. 2, No. 3, 360–367, 1995.
3. Qiu, C.-W., L.-W. Li, T.-S. Yeo, and S. Zouhdi, "Scattering by rotationally symmetric anisotropic spheres: Potential formulation and parametric studies," *Phys. Rev. E.*, Vol. 75, No. 2, 026609, 2007.
4. Wallén, H., H. Kettunen, and A. Sihvola, "Anomalous absorption, plasmonic resonances, and invisibility of radially anisotropic spheres," *Radio Sci.*, Vol. 50, 18–28, 2015.
5. Rimpiläinen, T., H. Wallén, and A. Sihvola, "Radial anisotropy in spheroidal scatterers," *IEEE Trans. Antennas Propag.*, Vol. 63, No. 7, 3127–3135, 2015.
6. Rimpiläinen, T., H. Wallén, H. Kettunen, and A. Sihvola, "Electrocal response of systropic sphere," *IEEE Trans. Antennas Propag.*, Vol. 60, No. 11, 5348–5355, 2012.
7. Rimpiläinen, T., M. Pitkonen, H. Wallén, H. Kettunen, and A. Sihvola, "General systropy in spherical scatterers," *IEEE Trans. Antennas Propag.*, Vol. 62, No. 1, 327–333, 2014.

# Selected problems of light scattering by dielectric nanostructures

B. Luk`yanchuk*, R. Paniagua-Dominguez, A. Kuznetsov

*Data Storage Institute, A*STAR (Agency for Science, Technology and Research), 138634 Singapore*

*corresponding author: Boris_L@dsi.a-star.edu.sg

**Abstract**- Light scattering from structures with high refractive index may produce strong, optically-induced electric and magnetic resonances. This allows controlling many characteristics of the scattered light, including its scattering diagram, intensity distribution and light polarization. As a consequence, it is possible to realize interference effects such as Kerker and Fano resonances, formation of optical vortices and excitation of anapole modes. In this presentation we illustrate some of these effects with the help of exact solutions in the Mie theory.

Scattering of light by dielectrics have attracted interest of people since ancient times. Archimedes, Ptolemy and apparently all antique physics knew the effect of light refraction. Pliny the Elder reported on incendiary action of glass spheres. Seneca wrote about the magnifying action of such spheres if one looks through it at small letters. General understanding of such effects can be achieved on the level of geometrical optics. As one can see e.g. from this approximation, a spherical transparent particle works as a focusing lens with focal point situated out of the particle when its refractive index is $1<n<2$ and inside the particle when $n>2$. On the other hand, this problem can be exactly analyzed with the help of the Mie theory. It shows that even with a mere refractive index $n\approx(1.5-1.6)$ (glass, $SiO_2$, polystyrene in visible range, etc.) and particle radius of the order of radiation wavelength, $a\approx(2-5)\lambda$, field enhancements of one-two orders of magnitude[1-7] are reached near the particle, as shown in Fig. 1. Similar effects were found later for cylindrical[8,9], spheroidal[10], cubic[11] and other structures[12]. Authors of Ref. [5] named this effect the "photonic nanojet". Over the past few years an increasing interest has grown in the study of high-refractive index nanoparticles. These particles exhibit both strong electric and magnetic resonances[13-15]. This permits the creation of huge electric and magnetic hotspots inside the particle[16], see e.g. Fig. 2. Moreover, the combination of these electric and magnetic resonances open the possibility to control the scattering diagram and create directional scattering[17-19]. Periodical structures of such resonant elements allows the realization of effective negative permeability[13], external and internal Fano resonances[20], metasurfaces with 2π phase control at visible wavelengths[21], generalized Brewster effect[22], etc.

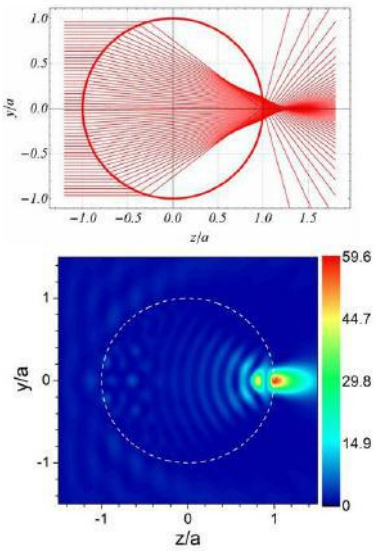



Fig. 1. Rays tracing according to approximation of geometrical optics and distribution of field intensity calculated from the Mie theory for a particle with $n=1.6$, $a=500$ nm, and $\lambda=248$ nm.

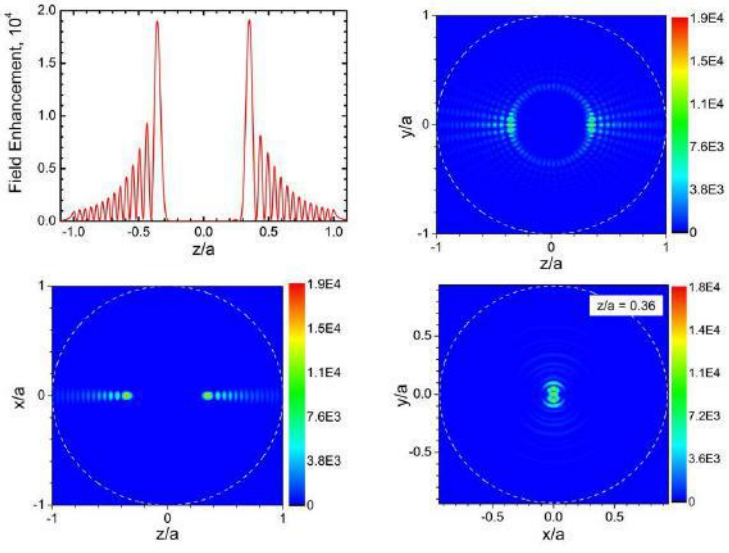



Fig. 2. Distribution of the field intensity along the central axes and within different planes for a particle with refractive index $n=4$ and size parameter $q=2\pi a/\lambda=19.415275$. A similar intensity can be reach at internal resonances and smaller size parameters, e.g. $q\approx1.7$.

Here, we will analyze the internal resonances in high refractive index particles and their ability to create magnetic hot spots[23] with extremely high values of magnetic intensity, as depicted in Fig. 3 and Fig. 4.

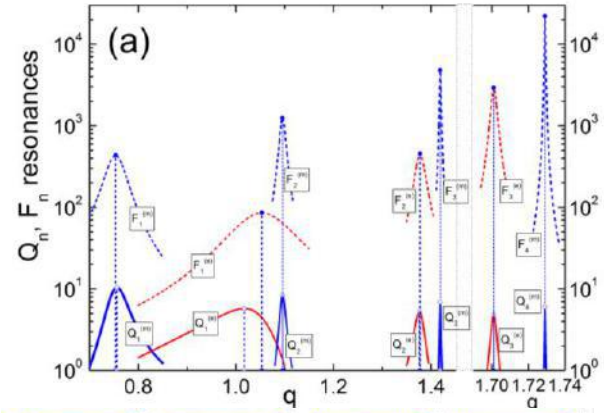



Fig. 3. Partial electrical and magnetic scattering efficiencies outside the particle, $Q_\ell^{(e)}$ and $Q_\ell^{(m)}$, and inside the particle, $F_\ell^{(e)}$ and $F_\ell^{(m)}$, for the particle with refractive index $n=4$. Electric efficiencies are red and magnetic are blue. Solid lines refer to the efficiencies outside the particle and dashed lines refer to the efficiencies inside the particle.

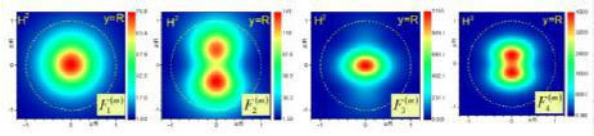


Fig. 4. Field distributions for different magnetic resonances within the side $x-z$ plane at $y/R=1$.

## References


1. Luk'yanchuk, B. S. et al., "Laser cleaning of solid surface: Optical resonance and near-field effects", Proc. SPIE **4065**, 576 (2000).
2. Lu, Y. F. et al., "Laser writing of a subwavelength structure on silicon (100) surfaces with particle enhanced optical irradiation", JETP Lett. **72**, 457 (2000).
3. Mosbacher, M. et al, "Optical field enhancement effects in laser-assisted particle removal", Appl. Phys. A **72**, 41 (2001).
4. Huang, S. M. et al., "Pulsed laser-assisted surface structuring with optical near-field enhanced effects", J. Appl. Phys. **92**, 2495 (2002).
5. Luk'yanchuk, B. S., "Laser Cleaning", (World Scientific, Singapore 2002).
6. Luk`yanchuk B. S. et al., "Three-dimensional effects in dry laser cleaning", Appl. Phys. A **77**, 209 (2003).
7. Geints, Yu. E., Panina, E.K., Zemlyanov, A.A., "Control over parameters of photonic nanojets of dielectric microspheres", Opt. Communications **283**, 4775 (2010).
8. Chen, Z., Taflove, A, Backman, V., "Photonic nanojet enhancement of backscattering of light by nanoparticles: a potential novel visible-light ultramicroscopy technique", Opt. Express **12**, 1214 (2004).
9. Heifetz, A. et al., "Photonic Nanojets", J. Comput. Theor. Nanosci. **6**, 1979 (2009).
10. Mendes, M. J. et al., "Near-field scattering by dielectric spheroidal particles with sizes on the order of the illuminating wavelength," J. Opt. Soc. Am. B **27**, 1221 (2010).
11. Minin, I. V., Minin, O. V., Geints, Y. E., "Localized EM and photonic jets from non-spherical and non-symmetrical dielectric mesoscale objects: Brief review", Ann. Phys. (Berlin) **527**, 491 (2015).
12. Geints, Yu. E., Zemlyanov, A.A., Panina, E. K., "Microaxicon-generated photonic nanojets", J. Opt. Soc. Am. B **32**, 1570 (2015).
13. Evlyukhin, A. B. et al., "Optical response features of Si-nanoparticle arrays", Phys. Rev. B **82**, 045404 (2010).
14. Kuznetsov, A. I. et al., "Magnetic Light", Sci. Rep. 2, 492 (2012).
15. Evlyukhin, A. B. et al., "Demonstration of magnetic dipole resonances of dielectric nanospheres in the visible region", Nano Lett. **12**, 3749 (2012).
16. Wang, Z. B., Yi Z., Luk'yanchuk, B., "Near-field focusing of dielectric microspheres: Super-resolution and field-invariant parameter scaling", arXiv:1304.4139v2 [physics, optics], 23 Apr 2013
17. Geffrin, J. M. et al, "Magnetic and electric coherence in forward- and back-scattered electromagnetic waves by a single dielectric sub*wavelength* sphere", Nat. Commun. **3**, 1171 (2012).
18. Fu, Y. H. et al, "Directional visible light scattering by silicon nanoparticles", Nat. Commun. **4**, 1527 (2013).
19. Person, S. et al, "Demonstration of Zero Optical Backscattering from Single Nanoparticles", Nano Letters **13**, 1806 (2013).
20. Tribelsky, M. I., Miroshnichenko A. E., "Giant In-Particle Field Concentration and Fano Resonances at Light Scattering by High-Refractive Index Particles", arXiv:1511.0293v1 [physics, optics], 9 Nov 2015.
21. Yu, Y. F. et al, "High-transmission dielectric metasurface with 2π phase control at visible wavelengths", Laser and Photonics Reviews **9**, 412 (2015).
22. Paniagua-Dominguez, R. et al, "Generalized Brewster effect in dielectric metasurfaces", Nat. Commun. **7**, 10362 (2016).
23. Bakker, R. et al, "Magnetic and Electric Hotspots with Silicon Nanodimers", Nano Letters **15**, 2137 (2015).

# Exploring nanoscale chirality: issues of parity, scale and measurement

**D. L. Andrews**
School of Chemistry, University of East Anglia, Norwich Research Park, Norwich NR4 7TJ, United Kingdom

**Abstract** The development of light beams with a vortex character in wave-front or polarization structure has brought a new focus upon the fundamental science of chiral interactions. To understand the interplay and coupling of optical and material chirality on the nanoscale generally invites recognition of quantum facets to the light-matter interaction. This presentation identifies some of the key issues associated with spatial and temporal parity, scale and measurement.

Since the turn of the century, advances in the science and technology of structured light and plasmonics have brought a renewed focus upon the mechanisms and principles of chiral interaction over nanoscale dimensions.[1-4] Given that the quantum nature of matter is most obviously manifest at sub-wavelength scales, and that photons are usually few and far between even within the span of an optical wavelength – unless very high pulsed laser intensities are involved – it is surprising to find that many of the newly emergent phenomena are nonetheless very often being described in terms of essentially classical frames of representation. In fact a strong case can be made that, in order to understand the interplay and coupling of optical and material chirality on the nanoscale, it is crucial to account for the quantum aspects of light-matter interaction. In this account, a quantum electrodynamical description is developed to spotlight and address some of the key issues.

First, by focusing attention upon the general symmetry features of a closed system state evolving under a complete Hamiltonian, it is shown how parity rules determine the interplay of optical and material chirality, with specific regard to the possibility of chirally selective interactions.[5,6] This confronts one of the main motivations for many of the recent studies in this area: the prospect of achieving, by optical means, a separation of particles with opposite handedness (which, for molecules, are known as enantiomers).[7-9] In considering spatial and temporal parity there are several traps for the unwary, with scope to deliver misleading conclusions. It is salutary to recall, for example, that any individual enantiomer – even in its ground state – necessarily has a wavefunction of lower symmetry than the corresponding Hamiltonian.[10] Similarly, there is no requirement for any specific optical field to satisfy the constraints of parity that are demanded of the quantum field operators.

Issues of measurability also lie at the heart of the quantum treatment. The theory to be presented clarifies a distinction between processes for which there is a directly identifiable evolution of the system state vector, such that an intrinsic rate can be determined, and other kinds of interaction responsible for energy shifts. The former are generally associated with detectable transitions between electronic states of the material, and/or changes in the state of the radiation field. Energy shifts can only give rise to subsidiary processes: for example, when an optically induced energy shift has a well-defined spatial, orientational or temporal variation it will often lead to measurable rates of response to the resultant force fields.[11] However the latter kinds of mechanical effect are necessarily dependent on bulk properties of the local media, e.g. dielectric constant, viscosity and temperature.

Lastly, attention is drawn to the significance of scale, in terms of material complexity, particle size and any long-range order. In the case of molecular enantiomers, for example, it is not only necessary to account for the multiplicity of vibrational modes that rise in tiers within every electronic state: the physical dimensions of the individual molecules also prove to play a role that is often overlooked. The significance is indeed trivial in the case of incoherent or colligative processes, but it assumes a much greater importance for many processes of an optically parametric or coherent character. Equally, it is important to recognize the scale of any system order of either translational or orientational form. Once again, these factors have to be taken into serious consideration in realistically assessing the viability of any optical scheme for enantiomer distinction and separation.[I2-15]

**REFERENCES**


1. Andrews, D. L., Dávila Romero, L. C. and Babiker, M., "On optical vortex interactions with chiral matter," *Opt. Commun.*, Vol. 237, 133-139, 2004.
2. Valev, V. K., Baumberg, J. J., Sibilia, C. and Verbiest, T., "Chirality and chiroptical effects in plasmonic nanostructures: fundamentals, recent progress, and outlook," *Adv. Mater.*, Vol. 25, 2517–2534, 2013.
3. Wang, Y., Xu, J., Wang, Y. and Chen. H., "Emerging chirality in nanoscience," *Chem. Soc. Rev.*, Vol. 42, 2930–2962, 2013.
4. Bradshaw, D. S., Forbes, K. A., Leeder, J. M. and Andrews, D. L., "Chirality in optical trapping and optical binding," *Photonics*, Vol. 2, No. 2, 483–497, 2015.
5. Churcher, C. D. and Stedman, G. E., "Symmetry restrictions for natural and induced circular dichroism and optical activity for all point groups," *J. Phys. C: Solid State Phys*., Vol. 15, No. 26, 5507, 1982.
6. Bradshaw, D. S., Leeder, J. M., Coles, M. M. and Andrews, D. L., "Signatures of optical and material chirality: Origins and measures," *Chem. Phys. Lett.*, Vol. 626, 106-110, 2015.
7. Salam, A. and Meath, W.J., "On enantiomeric excesses obtained from racemic mixtures by using circularly polarized pulsed lasers of varying durations," *Chem. Phys.*, Vol. 228, 115–129, 1998.
8. Li, X. and Shapiro, M., "Theory of the optical spatial separation of racemic mixtures of chiral molecules," *J. Chem. Phys.*, Vol. 132, 194315, 2010.
9. Bradshaw, D. S. and Andrews, D. L., "Laser optical separation of chiral molecules," *Opt. Lett.*, Vol. 40, 677–680, 2015.
10. Woolley, R. G., "Reply to 'Fundamental symmetry aspects of optical activity'," *Chem. Phys. Lett.*, Vol.79, No. 2, 395–398, 1981.
11. Bradshaw, D. S. and Andrews, D. L., "Chiral discrimination in optical trapping and manipulation," *New J. Phys.*, Vol. 16, 103021, 2014.
12. Král, P., Thanopulos, I., Shapiro, M. and Cohen, D., "Two-step enantio-selective optical switch," *Phys. Rev. Lett.*, Vol. 90, 033001, 2003.
13. Salam, A., "On the effect of a radiation field in modifying the intermolecular interaction between two chiral molecules," *J. Chem. Phys.*, Vol. 124, 014302, 2006.
14. Canaguier-Durand, A., Hutchison, J. A., Genet, C. and Ebbesen, T. W., "Mechanical separation of chiral dipoles by chiral light," *New J. Phys.*, Vol. 15, 123037, 2013.
15. Tkachenko, G. and Brasselet, E., "Helicity-dependent three-dimensional optical trapping of chiral nanoparticles," *Nature Commun*., Vol. 5, 4491, 2014.

# Real-time Tunable Nanoparticle Lasing Spasers

**T. W. Odom**[1*]
[1]Northwestern University, Evanston, IL USA
[*]corresponding author: todom@northwestern.edu

**Abstract**. This talk will discuss cavity architectures based on nanoparticle arrays that can achieve tunable lasing at room temperature. We will also describe competing and unique loss mechanisms in nanoparticle cavity arrays and design principles for an optimized lasing devices by comparing different plasmonic materials, unit cell shapes, and gain materials.

Plasmon nanolasers—or spasers (surface plasmon amplification by stimulated emission of radiation)—are devices based on plasmonic cavities and gain media that can compensate loss and achieve amplification of nano-localized electromagnetic fields. Several nanocavity architectures have been reported for spasers, such as a metal film-dielectric spacer-semiconductor nanowire configuration or arrays of plasmonic cavities, where unit cells are nanoparticles or nanoholes. We will describe different platforms based on metal nanoparticle arrays that support lattice plasmons, show far-field directional emission, and can exhibit lasing at room temperature that can be tuned in real time. Also, we will discuss competing and unique loss mechanisms in nanoparticle cavity arrays as well as the design rules for an optimized lasing devices. Finally, we will discuss the distinct ultra-fast energy processes that underlie lattice plasmon lasing.

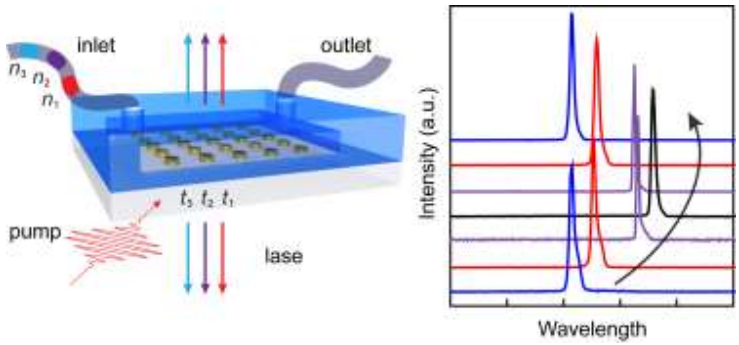



**Figure 1.** Scheme of nanoparticle lattice plasmon lasing device and spectra of tunable lasing emission from changing the refractive index of the gain media.

**Acknowledgements.** This work was supported by the National Science Foundation under DMR-1306514 and DMR-1121262.

**REFERENCES**

1. A. Yang, T.B. Hoang, M. Dridi, C. Deeb, M.H. Mikkelsen, G.C. Schatz, and T.W. Odom. “Real-time Tunable Lasing from Plasmonic Nanocavity Arrays.” *Nature Comm*. **6**, 1–7 (2015).
2. N.I. Zheludev, S.L. Prosvirnin, N. Papasimakis, and V.A. Fedotov. “Lasing Spaser,” *Nature Phot.* **2**,

351-354 (2008).
3. W. Zhou, M. Dridi, J.Y. Suh, C.H. Kim, D.T. Co, M.R. Wasielewski, G.C. Schatz, and T.W. Odom. "Lasing Action in Strongly Coupled Plasmonic Nanocavity Arrays," *Nature Nanotech.* **8**, 506–511 (2013).
4. A. Yang, Z. Li, M.P. Knudson, A.J. Hryn, W. Wang, K. Aydin, and T.W. Odom. "Unidirectional Lasing from Template-stripped Two-dimensional Plasmonic Crystals," *ACS Nano* **9**, 11582–11588 (2015).

# High Performance Visible Wavelength Dielectric Metasurfaces for Planar Photonic Components

**Federico Capasso**
*Harvard John A. Paulson School of Engineering and Applied Sciences, Harvard University, Cambridge, Massachussetts 02138, USA*

*Author e-mail address: capasso@seas.harvard.edu*

Conventional refractive optical components, such as lenses, rely on volumetric propagation distance to impart the desired phase profile onto an incident lightwave. Recently a new class of device, the metasurface, has emerged that breaks this propagation dependence and allows one to achieve a variety of optical components with nanometer thickness. Originally designed as plasmonic nanoantennas[1], researchers have now moved to all-dielectric silicon metasurfaces[2-4] to eliminate optical loss and achieve high transmission efficiency at infrared wavelengths.

While the current demonstrations have shown the versatility of these transmissive metasurfaces the base material, silicon, has high absorption loss at visible wavelengths. It is thus critical that new materials and techniques be explored to create high efficiency dielectric metasurfaces (DM) at visible wavelength. We demonstrate the use of nanostructured $TiO_2$, which is transparent throughout the visible spectrum ($\lambda$ = 400 – 750 nm), as a general platform to achieve DMs at visible wavelengths. We show efficiencies of 61%, 82% and 81% at design wavelengths of 480 nm, 532 nm, and 660 nm. We choose amorphous $TiO_2$, deposited by atomic layer deposition (ALD) as the base material for our DM. Specifically $TiO_2$ is transparent ($k \approx 0$) for wavelengths longer than ~350 nm and the index of refraction ($n$) is sufficiently large to provide strong light-material interaction required to have full control over the wavefront. Additionally the amorphous $TiO_2$ is atomically smooth, with surface roughness of 0.738 nm. This low roughness ensures that our fabricated DMs have minimal scattering loss.

To create a metasurface from the $TiO_2$ we pattern the material into anisotropic and birefringent nanostructures (Fig. 1). The nanostructures have subwavelength dimensions and sidewall slopes approaching 90$^o$, as seen from the cross section SEM (Fig 1b). The ability to create these structures with high aspect ratios and high anisotropy at nanoscale dimensions is key to implementing a variety of high efficiency DMs.

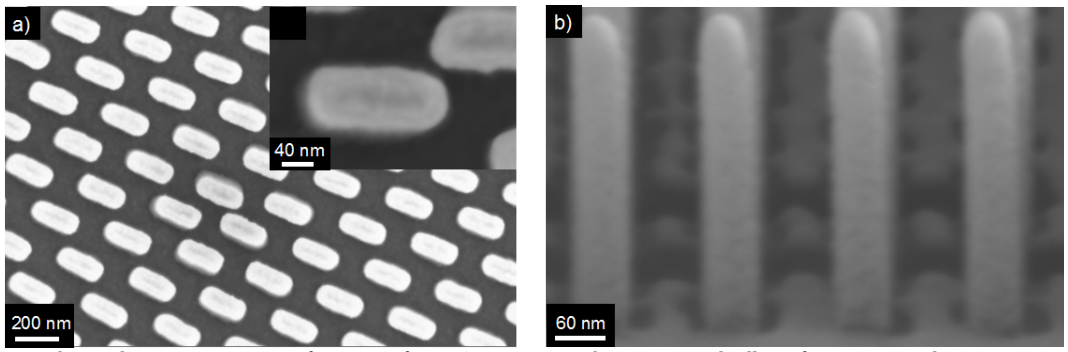



Figure 1. Fabricated $TiO_2$ nanostructures for metasurfaces. a) SEM image showing arrayed pillars of 60 x 170 nm dimensions. Inset shows spacing of 10nm between individual pillars. b) Cross section SEM showing anisotropy of the fabricated nanopillars

We have demonstrated planar lenses based on high quality grown titanium dioxide in the visible range ($\lambda$= 405nm, 532nm, and 660nm) with superior performance over a commercially-available objectives. Our lenses have focusing efficiencies as high as 86% with a numerical aperture of 0.8.We also compare the performance of these planar lenses with a Nikon objective (100× Nikon CFI 60, NA=0.8). They have focal spots 1.5 times smaller than their refractive optics counterpart. These properties show that planar lenses can substitute conventional objectives in laser-based imaging/spectroscopy systems while delivering superior performance at a fraction of the cost.

In addition we have also produced a variety of other DMs at visible wavelengths such q-plates to generate optical vortices, broadband metagratings and holograms. This work enables important technological and scientific developments that require flat, transmissive optical elements at visible wavelengths.

*Acknowledgements*. It is a pleasure to acknowledge collaborations with R. C. Devlin1, M. Khorasaninejad, Wei-Ting Chen, A. Ambrosio, J. Oh1, A. Y. Zhu . This work was supported in part by the Air Force Office of Scientific Research (MURI, FA9550-14-1-0389), and Thorlabs Inc.

## References

[1] Yu, N.F., et al., *Light Propagation with Phase Discontinuities: Generalized Laws of Reflection and Refraction.* Science, 2011. **334**(6054): p. 333-337.
[2] Lin, D.M., et al., *Dielectric gradient metasurface optical elements.* Science, 2014. **345**(6194): p. 298-302
[3] Arbabi, A., et al., *Dielectric metasurfaces for complete control of phase and polarization with subwavelength spatial resolution and high transmission.* Nat. Nanotech., 2015. **10**: p. 937-943.
[4] Yang, Y.M., et al., *Dielectric Meta-Reflectarray for Broadband Linear Polarization Conversion and Optical Vortex Generation.* Nano Letters, 2014. **14**(3): p. 1394-1399

# Quantum Phenomena in Hybrid Nanostructures: Exciton-Plasmon Interactions and the Quantum Structure of the Plasmon Excitations


## Alexander Govorov

*Department of Physics and Astronomy, Ohio University, Athens, OH, 45701*
Govorov@ohiou.edu


The talk will review quantum effects predicted and observed in hybrid nanostructures composed of metal and semiconductor components. Strong interactions between excitons, plasmons and phonons in hybrid geometries lead to the Fano interference effect [1], which was observed experimentally as an appearance of an optical transparency window [2,3]. In purely plasmonic structures, the quantum effects in confined geometries lead to the peculiar structure of the wave function of a plasmon [4,5]. The plasmonic wave function includes both low-energy Drude electrons and high-energy hot electrons [4,5]. Hot plasmonic electrons were revealed in a number of recent experiments on ultra-fast spectroscopy, photo-currents and photo-chemistry [6,7,8].


[1] W. Zhang, G. W. Bryant, A. O. Govorov, *Semiconductor-metal nanoparticle molecules: hybrid excitons and non-linear Fano effect*. Phys. Rev. Lett. 97, 146804 (2006).
[2] M. Kroner, A. O. Govorov, S. Remi, B. Biedermann, S. Seidl, A. Badolato, P.M.Petroff, W. Zhang, R. Barbour, B. D. Gerardot, R. J. Warburton, and K. Karrai, *The nonlinear Fano effect*. Nature 451, 311 (2008).
[3] M. L. Kerfoot, A.O. Govorov, D. Lu, R. J. O. Babaoye, Y. N. Gad, C. Czarnocki, M. Tsukamoto, A. S. Bracker, D. Gammon, and M. Scheibner, *Optophononics with Coupled Quantum Dots.* Nature Communications 5, 3299 (2014).
[4] A.O. Govorov, H. Zhang, V. Demir, and Y.K. Gun'ko, *Photogeneration of Hot Plasmonic Electrons with Metal Nanocrystals: Quantum Description and Potential Applications.* Nano Today 9, 85–101 (2014).
[5] A.O. Govorov and H. Zhang, *Kinetic Density Functional Theory for Plasmonic Nanostructures: Breaking of the Plasmon Peak in the Quantum Regime and Generation of Hot Electrons.* The Journal of Physical Chemistry C *119*, 6181–6194 (2015).
[6] H. Harutyunyan, A. B. F. Martinson, D. Rosenmann, L. Khosravi Khorashad, L. V. Besteiro, A.O.Govorov, and G.P. Wiederrecht, *Anomalous ultrafast dynamics of hot plasmonic electrons in nanostructures with hot spots.* Nature Nanotechnology 10, 770-774 (2015).
[7] W. Li, Z. J. Coppens, L. Vázquez, W. Wang, A. O. Govorov, and J. Valentine, *Circularly polarized light detection with hot electrons in chiral plasmonic metamaterials.* Nature Communications 6, 8379 (2015).
[8] L. Weng, H. Zhang, A. O. Govorov, and M. Ouyang, *Hierarchical Synthesis of Non-Centrosymmetric Hybrid Nanooligomers and Enabled Plasmon-Driven Hot Electron Photocatalysis.* Nature Communications 5, 4792 (2014).

# Casimir-like forces between particles under fluctuating optical fields

**J.J. Sáenz**[1,2]

[1] Donostia International Physics Center (DIPC),
Paseo Manuel de Lardizabal 4, Donostia-San Sebastian 20018, Spain.
[2]IKERBASQUE, Basque Foundation for Science, 48013 Bilbao, Spain.
[*]corresponding author: juanjo.saenz@dipc.org

**Abstract**- We review some basic concepts related to the optical forces on small (subwavelength) particles, focusing on the interplay between scattering asymmetry and momentum transfer. We show that artificially created random fluctuating light fields can be used to induce and control isotropic Casimir-like forces between small colloidal particles.

Appropriate combinations of laser beams can be used to trap and manipulate small particles with "optical tweezers" as well as to induce significant "optical binding" forces between particles. Here we review some basic concepts related to the optical forces on small (subwavelength) particles, focusing on the interplay between scattering asymmetry and momentum transfer. These forces are, in general, non-conservative (curl forces) [1,2] which lead to a number of intriguing predictions regarding the dynamics of nanoparticles [3].

Optical forces between small particles are usually strongly anisotropic depending on the interference landscape of the external fields. This is in contrast with the familiar isotropic van der Waals and, in general, Casimir-Lifshitz interactions between neutral bodies arising from random electromagnetic waves generated by equilibrium quantum and thermal fluctuations. As we will see, artificially created random fluctuating light fields can be used to induce and control isotropic dispersion forces between small colloidal particles [4]. Using optical tweezers as a gauge (see Fig.1), we present experimental evidence for the predicted isotropic attractive interactions between dielectric microspheres induced by laser-generated, random light fields. The external control of isotropic interaction forces between particles can influence dramatically the macroscopic properties of colloidal suspensions and is of key importance not only for Biological or Materials Science applications but also to address fundamental questions about the nature of liquids, crystals, and glasses.

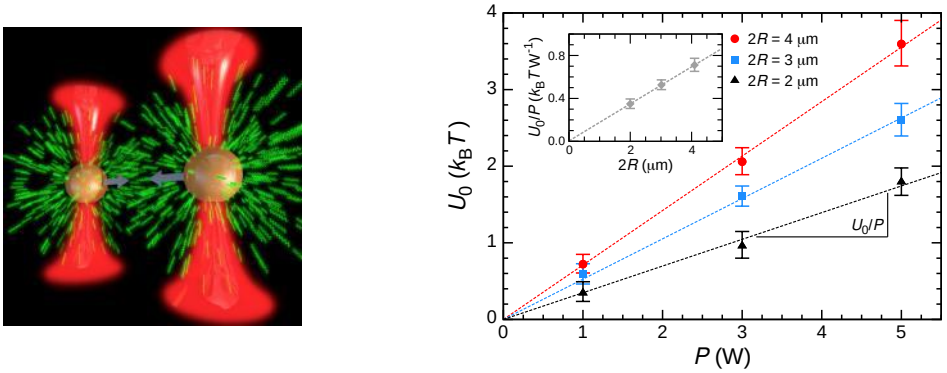



Fig. 1 ***Tunable interparticle dispersion forces induced by fluctuating, random light fields***. Experimental attractive contact potential $U_0$ versus laser power P for dielectric melamine (n=1.68) particles of different size [After Ref. 4].

Interestingly, for relatively high refractive index semiconductor nanoparticles like Silicon, the interactions can be tuned from attractive to strongly repulsive when the frequency of the external fluctuating field is tuned near the first magnetic Mie-resonance [5]. Interactions induced by randomly fluctuating light fields open a path towards the control of translational invariant interactions with tuneable strength and range in colloidal systems.

**Acknowledgements**, Work on random light forces was done in collaboration with Scheffold's group in Fribourg (G. Brügger, L. Froufe-Pérez and F. Scheffold). I would like to acknowledge the contributions and discussions with M. Nieto-Vesperinas at ICMM-CSIC as well as those of N. de Sousa, J. Luis-Hita and M. I. Marqués at UAM.

**REFERENCES**

1. Albaladejo, S. et al., "Scattering forces from the curl of the spin angular momentum of a light field," *Phys. Rev. Lett.*, Vol. 102, No. 11, 113602, 2009.
2. Nieto-Vesperinas, M. et al. "Optical forces on small magneto-dielectric particles," *Opt. Express*, Vol. 18, No. 11, 11428-11443, 2010.
3. Albaladejo, S. et al., "Giant enhanced diffusion of gold nanoparticles in optical vortex fields.", *Nano Lett.*, Vol. 9, No. 10, 3527-3531, 2009.
4. Brügger, G., et al. "Controlling dispersion forces between small particles with artificially created random light fields," *Nat. Commun.*, Vol. 6, 7460, DOI: 10.1038/ncomms8460, 2015.
5. García-Etxarri, A. et al., "Strong magnetic response of submicron silicon particles in the infrared." *Opt. Express*, Vol. 19, No. 6, 4815-4826, 2011.

# Tunable Light-matter Interaction With Quantum Spillover and Super-radiance in Two Dimensional Molecular Aggregates

**Nicholas X. Fang**
MIT, USA

# Wave Control with space-time transformations

**Mathias Fink**
*Institut Langevin, France*
*E-mail address: mathias.fink@espci.fr*

**Abstract**- Because time and space play a similar role in wave propagation, wave control in complex media can be achieved or by manipulating spatial boundaries or by manipulating time boundaries. Here we first emphasize the role of time boundaries manipulation. We show that sudden changes of the medium properties generate instant wave sources that emerge instantaneously from the entire wavefield and can be used to control this wavefield. We will also discussed a dual approach to control a wavefield in reverberating medium by introducing tunable metasurfaces as controllable spatial boundaries.

# Nanoplasmonic biosensors for real applications: trends and challenges

**Laura M. Lechuga**
*NanoBiosensors and Bioanalytical Applications Group*
*Catalan Institute of Nanoscience and Nanotechnology (ICN2),*
*CSIC, The Barcelona Institute of Science and Technology and CIBER-BBN, Spain*
*E-mail address: laura.lechuga@icn2.cat*

Nanoplasmonic biosensors have profiled themselves as competitive alternative to traditional analytical techniques. But one main challenge is their applicability in real scenarios by directly analysing minimum amounts of body fluids or environmental samples. We will show our main achievements able to surpass this challenge, rendering our plasmonic sensors in a valuable tool for fast diagnostics, prognosis and follow-up of diseases or environmental outbreaks.

# Metamaterial Elements as Huygens Radiators

**Omar M. Ramahi**

University of Waterloo, Canada
oramahi@uwaterloo.ca

**Abstract**— Metamaterial particles are essentially electrically-small radiators with polarization dependency. Previous works on metamaterials was concerned primarily with using such particles to achieve homogeneous media that enabled unconventional propagation. The fact that the particles are radiators suggests that they can be used as antennas. In antennas, not only radiation but radiation efficiency is critical. In fact, because of their electrically-small size, metamaterial elements can be considered as Huygens radiators. With this perspective, a systematic procedure for designing directional and efficient antennas can be developed as we demonstrate here.

Practically everything that can hold accelerating charges can radiate. To design effective radiators for communication purposes, however, one needs to excite accelerating charges with information content but also to ensure efficient radiation in a specific direction and specific polarization. Throughout the past 100 years, antennas evolved from the most simple dipoles and loops to highly complex structures with intricate feeding circuitry. Some well-known antennas were designed with the help of empirical findings such as the Yagi-Uda antenna while others were designed based on circuit resonance principles such as the microstrip and cavity-backed antennas. In fact, why certain antennas radiate was not clear when they were first used but became known with time. Overall, antennas can be grouped into three different categories based on their electrical size: small, comparable to the wavelength (CWL) which have largest dimension typically between 0.5 and 1.5 wavelength and large. The performance of electrically-small antennas is inherently limited in many respects as they are used whenever size is the most pressing constraint. Electrically-large antennas are made of arrays of CWL type antennas (or elements) that collectively and predictably can achieve very high gain in specific direction. CWL antennas don't have the severe constraints of electrically-small antennas but are limited to specific designs such as dipoles, patches, inverted F, ...etc. which put constraints on their radiation pattern and gain.

In this work, we introduce a concept for a systematic design of antennas and especially conformal low-profile antennas. These new type of antennas will be composed of electrically-small radiators resembling Huygens point sources. The radiation of each element will be quasi-isotropic rather than fully isotropic because of the presence of the platform on which the antenna is placed, the geometry of the element which affects polarization and because of coupling to adjacent radiating elements. Fig. 1 shows a schematic of Huygens radiators placed on a conformal surface. Each radiator emits radiation in all directions not hindered by the surface of the structure. Under this assumption, the rays emanating from all radiators can add either constructively or destructively to create the radiation pattern of the entire ensemble of radiators. Of course, each radiator will result in near- and far-field components (evanescent and traveling waves), but the far-field components are based on traveling waves that are near and far to the radiator. Under this Huygens-based model, considering that each radiator produces rays in all directions where radiation can take place, the design principle will be based on tailoring the phase of each radiator to provide a uniform phase front that is orthogonal to the direction where maximum radiation is desired as illustrated in Fig. 2. To achieve maximum radiation in a specific direction, say the direction indicated in Fig. 2 by the angle $\theta$, the phase of each element is set such that the electrical lengths $k_0 l_i$ for all elements are equal ($k_0$ is the wavenumber in free space and $l_i$ is the physical distance between each element and uniform phase front as shown in 2). To change to direction of maximum radiation to a different angle, the phase for each element is set accordingly. This design procedure gives flexibility, and in essence provides a systematic procedure for designing low-profile antennas in general instead of optimization that is typically not based on physical principles.

The design procedure is simple requiring algebraic calculations only. In principle, any electrically-small radiator can be used as the Huygens element, however, optimal impedance matching between

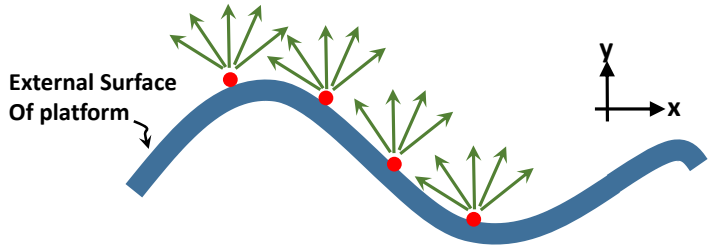



Figure 1: A schematic diagram showing Huygens radiators placed on a non-planer surface. Because each element is electrically small, it radiates in all directions not hindered by the surface.

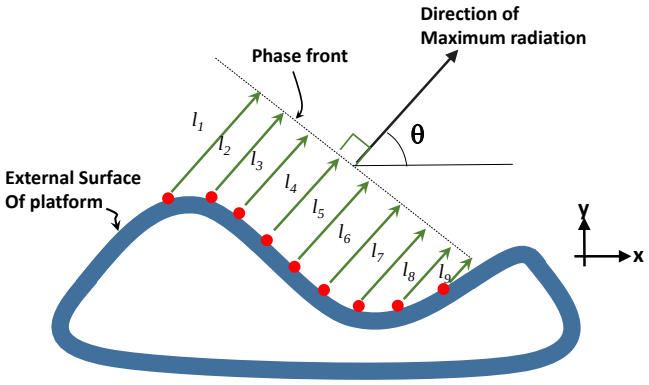



Figure 2: Schematic showing the design principle used to design Huygens antennas with maximum direction as shown.

the source and each radiator is needed to enable efficient overall antenna performance. Therefore, careful study of any proposed Huygens radiator while in the presence of a periodic ensemble of radiators is needed. Since any chosen Huygens radiators cannot be extremely small electrically, fine adjustment of the radiation pattern might be needed through phase optimization. In this presentation, we present several examples that show how antennas can be designed using elementary (Huygens) building blocks. Additionally, we demonstrate the design flexibility when designing antennas that need to conform to non-Cartesian surfaces while maintaining low profile.

# PT-symmetry in photonics, metamaterials and plasmonic systems

# Parity-Time Symmetry in Organic Thin Films and Waveguides

**N. C. Giebink**
The Pennsylvania State University, University Park, PA, 16802, USA
ncg2@psu.edu

**Abstract** - We demonstrate organic thin films and waveguides that exhibit passive parity-time (PT) symmetry by modulating their refractive index in the form of a complex exponential function. The resulting films and waveguides exhibit strong asymmetry in their reflectivity that maximizes when the real and imaginary components of the index modulation are balanced, marking an exceptional point transition to the broken PT phase. Progress toward active PT symmetry incorporating laser dyes to achieve balanced gain and loss will be discussed.

Rapid theoretical progress in non-Hermitian optics has stimulated a growing desire to realize experimental material systems with unconventional spatial distributions of the real and imaginary refractive index components. In particular, the complex exponential index distribution, $\tilde{n}(x) \sim e^{iqx}$, provides a simple periodic system in which wave propagation can exhibit parity-time (PT) symmetry and has been pursued in the context of applications such as asymmetric mode conversion and unidirectional invisibility. Organic small molecules and polymers provide a unique materials platform to experimentally realize such distributions because they feature strong optical responses and can be mixed in arbitrary proportions on the nanoscale to form high optical quality films. Figure 1 overviews one route to create an evanescently-coupled thin film waveguide with a complex exponential modulation in the effective index of its fundamental mode.

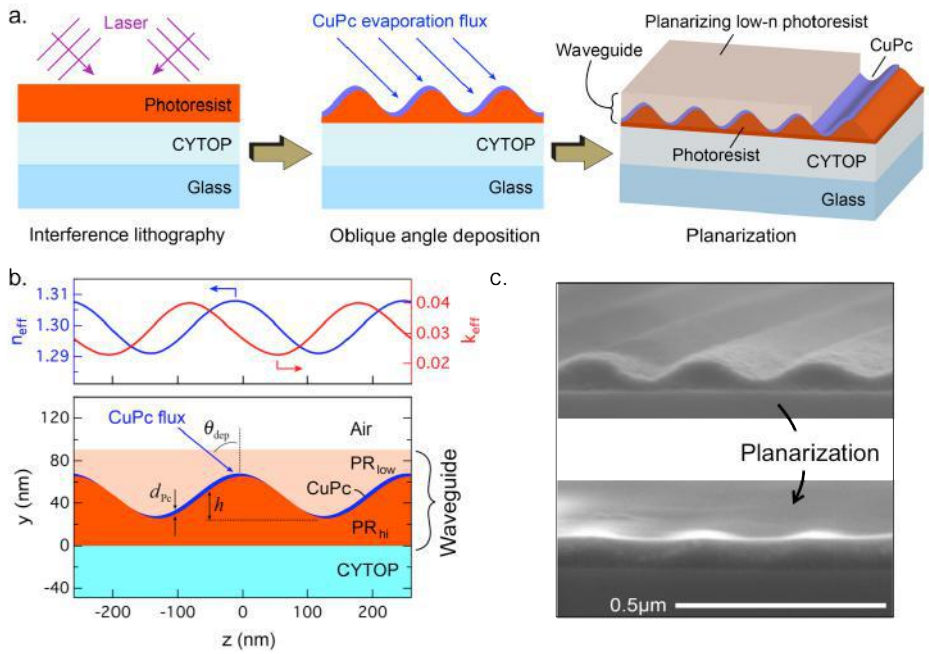



**Figure 1. (a)** Process used to create a thin film waveguide in which the real and imaginary components of the effective index modulation are phase-shifted by $\pi/2$ as calculated in (b) and displayed in the SEM images of (c). Figure adapted and reprinted with permission of Ref. [1].

There, a sinusoidal photoresist grating is selectively coated on one side by oblique angle thermal evaporation of a strongly absorbing dye followed by planarization with a spin-coated top layer of photoresist that has a slightly lower refractive index than the underlying grating layer. By separating the resulting waveguide from its glass substrate with a thin (~λ/2), low refractive index layer, light can be evanescently coupled in and out of the guide in a Kretschmann configuration as shown in Fig. 2(a) to probe its reflectivity via the -1 Littrow diffracted order. Because the complex exponential index modulation represents a one-side scattering vector, the mode is expected to be reflectionless in one propagation direction but not in the other as shown schematically in Fig. 2(b).

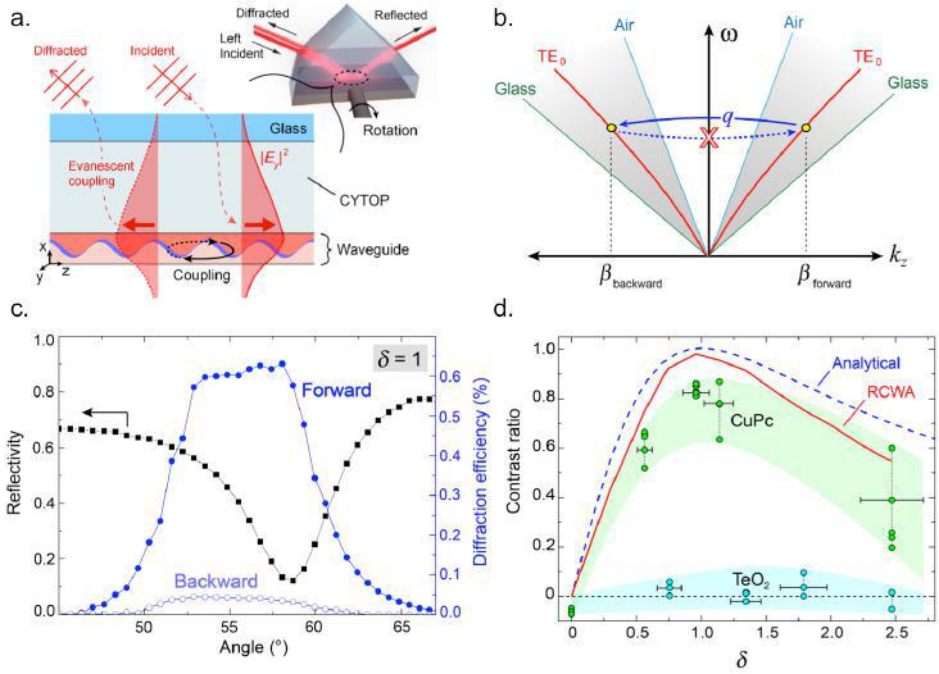



**Figure 2. (a)** Schematic showing the measurement configuration. **(b)** Dispersion diagram illustrating unidirectional scattering between the forward and backward-going modes. **(c)** Diffraction efficiencies measured for a sample demonstrating strong asymmetry for forward and backward directions. The forward-backward contrast for many different samples is summarized in (d). Figure adapted and reprinted with permission of Ref. [1].

Figure 2(c) presents the diffraction efficiency measured for the -1 Littrow diffracted order, demonstrating a strong asymmetry between forward and backward propagating directions at the in-coupling resonance angle of ~55°. Figure 2(d) plots the contrast ratio between forward and backward diffraction efficiencies, $[D_F - D_B]/[D_F + D_B]$, as a function of the absorbing dye thickness, demonstrating a peak when the real and imaginary index modulation amplitudes are equal and marking an exceptional point transition from the exact to the broken passive PT phase. By doping the planarization layer with an organic dye that can provide gain under optical pumping, it is possible to achieve a structure with balanced gain and loss that reaches the active PT regime; preliminary observations toward this goal will be discussed.

**Acknowledgements**. This work was supported by the Air Force Office of Scientific Research Young Investigator Program.

## REFERENCES

1. Y. Jia, Y. Yan, S.V. Kesava, E.D. Gomez, and N.C. Giebink. “Passive parity-time symmetry breaking in organic thin film waveguides,” *ACS Photonics*, Vol. 2, No. 2, 319–325, 2015.

# Conserved Quantities and Phase Locking in PT-symmetric Lattices

**A. K. Harter[1], F.A. Onanga[1], and Y. N. Joglekar[1]**

[1]Indiana University Purdue University Indianapolis (IUPUI), Indianapolis, Indiana, USA

[*]corresponding author: yojoglek@iupui.edu

**Abstract:** Non-Hermitian Hamiltonians that are invariant under combined operations of parity and time-reversal (PT) faithfully described propagation of light in the presence of balanced gain and loss. Due to the non-unitary nature of such time evolution, the net intensity of light in such a system is not constant with time. Motivated by the early attempts to develop a unitary theory for such Hamiltonians, we present conserved quantities in PT-symmetric systems that are determined by the wave-function or electric field amplitudes and phases. We show that in the PT-broken region, these constants of motion imply observable phase-relationships between electric field amplitudes in adjacent waveguides. We also validate these findings, based on a tight-binding lattice model, through continuum beam-propagation analysis.

**Acknowledgements**: This work was supported by NSF-DMR 1054020.

# Linear and Nonlinear Light Propagation in $\mathcal{PT}$-Symmetric Fiber Networks

**M. Wimmer[1,2,3], M.-A. Miri[4], A. Regensburger[1], C. Bersch[1], D. N. Christodoulides[4] and U. Peschel[3,*]**

[1]Institute for Optics, Information and Photonics, Friedrich-Alexander-Universität Erlangen-Nürnberg, Haberstraße 9a, 91058 Erlangen

[2]Erlangen Graduate School in Advanced Optical Technologies (SAOT), Friedrich-Alexander-Universität Erlangen-Nürnberg, Paul-Gordan-Str. 6 91052 Erlangen

[3]Institute of Solid State Theory and Optics, Friedrich Schiller University Jena, Max-Wien-Platz 1, 07743 Jena

[4]CREOL, College of Optics and Photonics, University of Central Florida, Orlando, Florida 32816-2700, USA

[*]Corresponding author: Ulf.Peschel@uni-jena.de

**Abstract**-In our experimental work, we create a Parity-Time ($\mathcal{PT}$) symmetric material by coupling two fiber loops of different length. Applying an additional external phase gradient to the system leads to Bloch oscillations, which show the intriguing behavior of exceptional points as well as the existence of phase gradients, for which a pseudo-Hermitian propagation is reestablished. Furthermore, we experimentally investigate the nonlinear regime and the formation of $\mathcal{PT}$ solitons.

Since the last years, tremendous interest is drawn towards the physics of Parity-Time ($\mathcal{PT}$) symmetric systems [1]. In the optical domain, $\mathcal{PT}$ symmetry can be established by a balanced gain and loss distribution in combination with a symmetric phase potential [2]. While the fabrication of such $\mathcal{PT}$ materials is still an enormous challenge, optical fiber loops consisting of telecommunication equipment can provide a versatile experimental platform [3].

In the experiment, we use two coupled fiber loops of different lengths (see Fig. 1a), which are equivalent to the lattice shown in Fig. 1b. In this picture, each path on the lattice going from North West (East) to South East (West) corresponds in the temporal scheme of coupled fiber loops to a round trip in the long (short) loop.

The evolution of pulses in this system is described by a set of two coupled equations

$$u_n^{m+1} = \frac{G_\mathrm{u}}{\sqrt{2}}(u_{n+1}^m + iv_{n+1}^m)e^{\frac{i\Gamma}{2}|u_{n+1}^m + iv_{n+1}^m|^2}e^{i\varphi_n^m} \tag{1.1}$$

$$v_n^{m+1} = \frac{G_\mathrm{v}}{\sqrt{2}}(v_{n-1}^m + iu_{n-1}^m)e^{\frac{i\Gamma}{2}|v_{n-1}^m + iu_{n-1}^m|^2}, \tag{1.2}$$

where $u_n^m$ and $v_n^m$ stand for the pulses propagating in the shorter and longer loop. Additionally, gain and loss $G_{\mathrm{u,v}}$ is implemented by changing the transmission of acousto-optical modulators (AOM) in each fiber loop. A phase modulator (PM) in the shorter loop allows for arbitrary phase shifts $\varphi_n^m$ of the pulses. Finally, by choosing dispersion compensated fibers, nonlinear effects can be investigated which are included by a nonlinear phase shift.

By alternating gain and loss in both fiber loops $G = G_u = G_v^{-1}$ after every round trip and implementing a symmetric phase modulation, a full $\mathcal{PT}$-symmetric mesh lattice is created (see Fig. 1c). In such a $\mathcal{PT}$-symmetric lattice, the beam propagation shows a wide spectrum of novel phenomena, where e.g. Bloch oscillations clearly depict the behavior near exceptional points leading to a splitting of wave packets (see Fig. 1d) [4]. Furthermore, in the regime of high peak powers, we observe the formation of $\mathcal{PT}$ solitons (see Fig. 1e) [5].

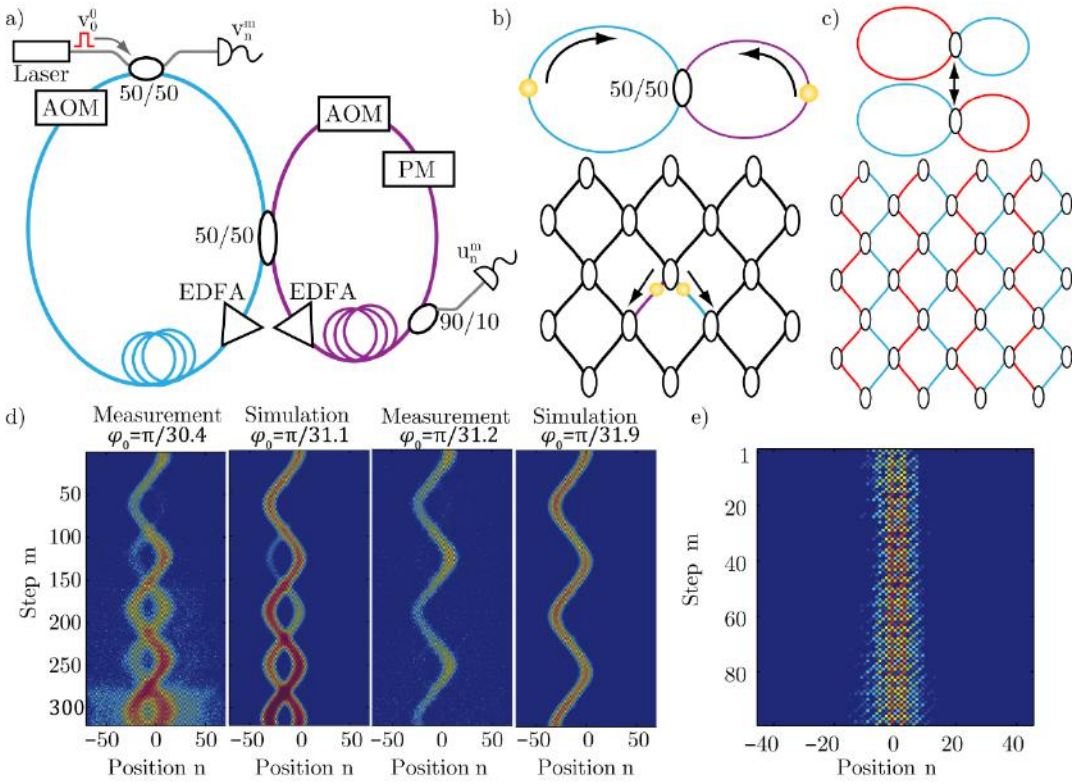



**Figure 1:** (a) In experiment, a single pulse is inserted into the longer fiber loop. Erbium-doped fiber amplifiers (EDFA) are used to compensate losses, acousto-optical modulators (AOM) allow for a variable loss and a phase modulator (PM) is utilized to generate arbitrary phase shifts. In the analogue spatial picture, pulses propagate on a mesh lattice either to the right (long loop) or to the left (short loop) (b). By amplifying one loop and attenuating the other in an alternating way and in combination with a phase potential, $\mathcal{PT}$ symmetry is stablished (c). (d) Bloch oscillations in such materials show a pseudo-Hermitian propagation for magic Bloch gradients $\varphi_0$. At high powers, $\mathcal{PT}$ solitons can be excited in the experiment, which propagate for stable about 100 roundtrips (e).

**Acknowledgements**, M. Wimmer would like to thank the School of Advanced Optical Technologies (SAOT) for financial support.

## REFERENCES

1. Bender, C. M. and Boettcher, S. "Real Spectra in Non-Hermitian Hamiltonians Having PT Symmetry," *Phys. Rev. Lett.*, Vol. 80, No. 24, 5243–5246, 1998.
2. Rüter, C. E. et al. "Observation of parity–time symmetry in optics," *Nat. Phys*, Vol. 6, No. 3, 192–195, 2010.
3. Regensburger, A. *et al.* "Parity-time synthetic photonic lattices," *Nature*, Vol. 488, No. 7410, 167–71, 2012.
4. Klaiman, S., Günther, U. and Moiseyev, N. "Visualization of Branch Points in PT-Symmetric Waveguides," *Phys. Rev. Lett*, Vol. 101, No. 8, 080402, 2008, Longhi, S. "Bloch Oscillations in Complex Crystals with PT Symmetry," *Phys. Rev. Lett*, Vol. 103, No. 12, 123601, 2009, Wimmer, M., Miri, M.-A., Christodoulides, D. and Peschel, U. "Observation of Bloch oscillations in complex PT-symmetric photonic lattices," *Sci. Rep*, Vol. 5, 17760, 2015.
5. Wimmer, M. et al. "Observation of optical solitons in PT-symmetric lattices," *Nat. Commun*, Vol. 6, 7782, 2015.

# Side-coupled resonators with parity-time symmetry for broadband unidirectional invisibility

**Nicolas Rivolta[1*], and Bjorn Maes**[1]

[1]Micro- and Nanophotonic Materials Group, Faculty of Science, University of Mons, 20, place du Parc, B-7000 Mons, Belgium

[*]corresponding author: nicolas.rivolta@umons.ac.be

**Abstract**-We analyze the scattering properties of a PT-structure made of a waveguide and a finite chain of side-coupled resonators. Typical 1D PT-structures exhibit unidirectional invisibility (also called anisotropic transmission resonances), meaning unit-transmission and zero-reflection for incidence from one direction. The side-coupled nature of our structure provides different features than the traditional tight-binding chain, which we explore rigorously. For example, we can achieve a broadband unidirectional invisibility with only two resonators, and we observe rich dispersions for ATRs with four resonators.

Originating from fundamental studies of parity-time (PT) symmetric Hamiltonians in quantum mechanics [1], PT symmetric photonic structures have now been investigated for a decade, exploiting the combination of balanced gain and loss to achieve particular properties. Usually in optics loss is an unwanted feature that limits many applications. But in the framework of PT-symmetry, it becomes a key element.

Here we focus on 1D PT symmetric structures that exhibit what is called anisotropic transmission resonances (ATRs) [2] or unidirectional invisibility [3]. It means that, for a particular frequency and for incidence from one side, one obtains unit transmission and zero reflection. We study the effects of PT symmetry applied to a finite chain of resonators next to a waveguide (Figure 1), using analytical approaches with coupled-mode-theory and the transfer-matrix approach. Because our geometry is side coupled, the behavior is very different from typical tight-binding or Bragg structures. For example, for two resonators, with the correct parameters, we can achieve either broadband or narrow ATRs. In addition, we address the stability of this kind of system, as the presence of gain can readily make them unstable. Moreover, study of the scattering matrix provides us detailed info on lasing states, and on exceptional points.

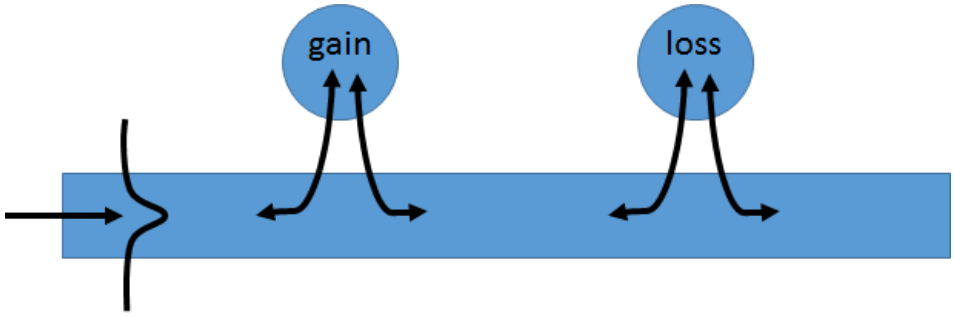



**Figure 1 Scheme of a two resonator chain.**

For a chain of four resonators the possible configurations are numerous, as we can choose between a Gain-Gain-Loss-Loss or Gain-Loss-Gain-Loss profile, and we can even symmetrically modify the frequencies of the resonators and the amount of gain and loss. Each of these configurations gives rise to a unidirectional invisibility scheme with complex behavior as a function of the frequencies (Figure 2): a rich, tunable dispersion with multiple, crossing ATRs (the dark blue lines) is obtained, offering possibilities for "ATR engineering".

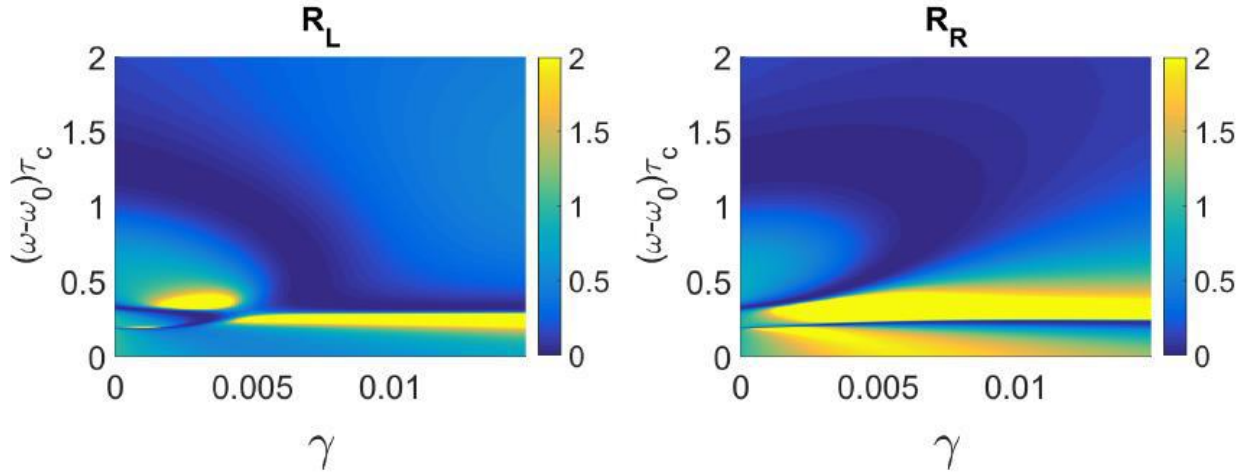



**Figure 2 : Left reflection (left figure) and right reflection (right figure) as a function of the gain/loss amount γ and the detuning for a four resonator structure. Graphs are saturated to two. The dark blue zones indicate the ATRs.**

**Acknowledgements**: this work is supported by the Belgian Science Policy Office under the project ``Photonics@be" (P7-35) and by the Fonds National de Recherche Scientifique (FNRS) in Belgium.

**REFERENCES**

1. C. M. Bender and S. Boettcher, "Real spectra in non-Hermitian Hamiltonians having PT symmetry," *Phys. Rev. Lett.*, Vol. 20, No. 24, 5243–5246, 1998.
2. L. Ge, Y. D. Chong and A. D. Stone, "Conservation relations and anisotropic transmission resonances in one-dimensional PT-symmetric photonic heterostructures," *Phys. Rev. A*, Vol. 34, No. 85, 023802, 2012.
3. Z. Lin, H. Ramezani, T. Eichelkraut, T. Kottos, H. Cao and D. N. Christodoulides, "Unidirectional invisibility induced by PT-symmetric periodic structures," *Phys. Rev. Lett*, Vol. 106, 213901, 2011.

# Revival of bistable state near the exceptional point of a non-Hermitian photonic molecule.

**Ke-jia Zhu**[1], **Yong Sun**[1], **Jie Ren**[1], **Haitao Jiang**[1] **and Hong Chen**[1]

[1]Tongji University, China 200092
1510042_zhu@tongji.edu.cn

**Abstract**— Dissipation always wasting energy, reducing field intensity or increasing threshold in conventional system, however which can turn losses into gain in no-Hermitian systems. Here, we investigate bistable state by manufacturing such a no-Hermitian photonic molecule which own an exceptional point (EP). The observation show bistable state of this system from suppression to revival only by adding loss while in the vicinity of the EP.

Non-Hermitian systems[1] with an exceptional point have attracted enormous attention cause of its non-trivial effects such as coherent perfect absorption[2], dephasing-induced control of interference nature[3], lasing revival[4] and chiral modes[5]. Our system is based on transmission lines and split ring resonators which can offer effective gain and loss. By steering the loss of resistor, this system may emerge an exceptional point where the eigenfrequencies coalesce. As shown in Figure.1, we measured the transmissions $T_{1\to2}$, $T_{1\to4}$ and observed bistable state with adding loss continuously. In Figure.1.(a)and(b), case(i) is weak resistance regime, case(ii) is middle resistance regime which is near the EP and case(iii) is strong resistance regime. We can see the low intensity distribution, eigenfrequencies coalesce and bistable state suppression in case(ii) clearly.

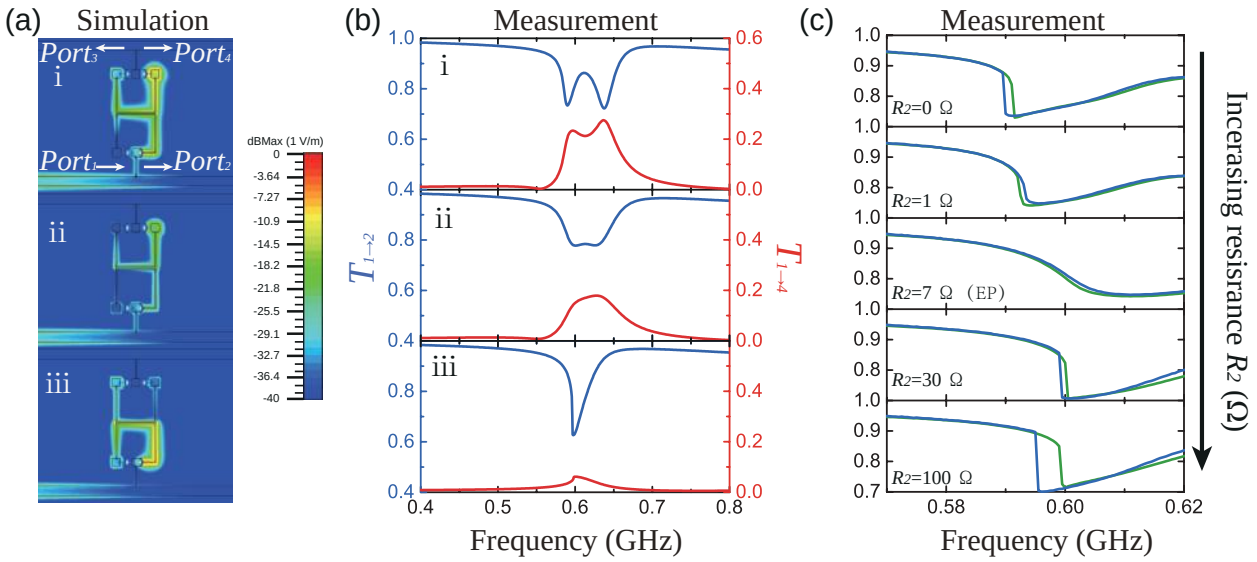



Figure 1: (a) simulated intensity distribution (b) measured tensmission case (ii) is near the EP (c) observation of bistable state with increasing loss

The Hamiltonian of this system is describe as,

$$H = \begin{pmatrix} \omega_0 - i\left(\gamma_1 - \Gamma_1\right) & \kappa \\ \kappa & \omega_0 + i\left(\gamma_2 + \Gamma_2\right) \end{pmatrix} \tag{1}$$

While the eigenfrequencies is given as,

$$\omega_\pm = \omega_0 - i\frac{\gamma_1 - \Gamma_1 - \gamma_2 - \Gamma_2}{2} \pm \sqrt{\kappa^2 - \left(\frac{\gamma_1 - \Gamma_1 + \gamma_2 + \Gamma_2}{2}\right)^2} \tag{2}$$

Here, we figured some further results in Figure.2. In Figure.2.(a), we can see the calculated and measured results of eigenfrequencies match very well. Figure.2.(c) express the threshold back to low condition with revival of corresponding normalized intensity.

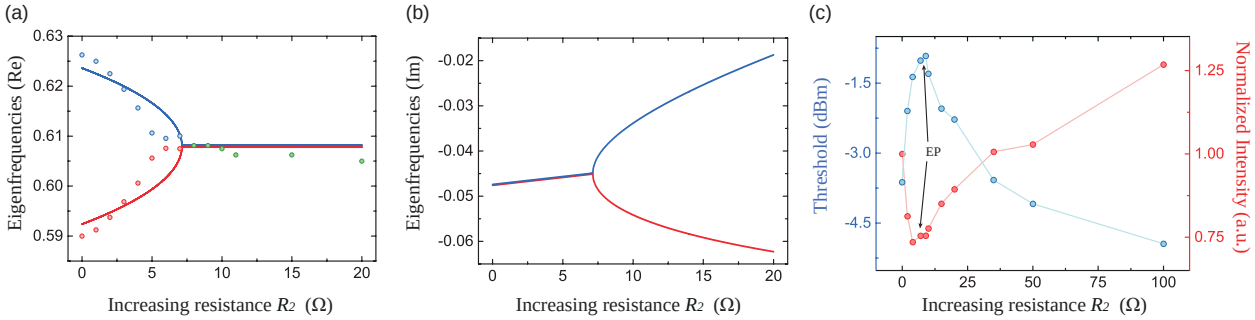



Figure 2: (a) calculated and measured results of real part of eigenfrequencies (b) measured tensmission case (ii) calculated results of imaginary part of eigenfrequencies (c) measured threshold and normalized intensity

In this work, we demonstrated a non-Hermitian photonic molecule with an exceptional point when increasing loss. We also observed the revival of bistable state when system near the exceptional point.

## ACKNOWLEDGMENT

This research was supported CNSF (Grants No. 11234010)

## REFERENCES

1. Heiss, W. D., "The physics of exceptional points," *Journal of Physics A: Mathematical and Theoretical*, Vol. 45, No. 44, 1607–1653, 2012.
2. Yong Sun et al., "Experimental Demonstration of a Coherent Perfect Absorber with PT Phase Transition," *Physical Review Letters*, Vol. 112, No. 14, 143903–143903, 2014.
3. Yong Sun et al., "Dephasing-Induced Control of Interference Nature in ThreeLevel Electromagnetically Induced Tansparency Systems," *Scientific Reports*, Vol. 5, 2015.
4. Peng Bo et al., "Loss-induced suppression and revival of lasin," *Science*, Vol. 346, No. 6207, 328–332, 2014.
5. Dembowski, C., "Observation of a chiral state in a microwave cavity," in *Physical Review Letters*, Vol. 90, No. 3, 034101, 2003.

# The Lorentz group and $PT$-symmetric waveguide couplers.

**B. M. Rodíguez-Lara**[1], **and J. Guerrero**[2]

[1]Instituto Nacional de Astrofísica, Óptica y Electrónica, Calle Luis Enrique Erro No. 1, Sta. Ma. Tonantzintla, Pue. CP 72840, México

[2]Departamento de Matemática Aplicada, Facultad de Informática, Campus Espinardo, Universidad de Murcia, 30100 Murcia, Spain

bmlara@inaoep.mx

**Abstract**— We show that finite-dimensional optical implementations of the 2+1D Lorentz group in arrays of coupled waveguides can be used as a platform for $PT$-symmetric all-optical devices. In particular, we explore the linear $PT$-symmetric dimer and planar three-waveguide coupler, where directional coupling and conversion of amplitude to phase modulation can be demonstrated.

Optical waveguide couplers offer an opportunity for compact and robust photonic integrated circuit design [1]. We want to show that underlying symmetries are an important factor to explore in the design of waveguide couplers. For this, we will focus on the so-called $PT$-symmetric $J_x$ waveguide coupler [2],

$$-i\frac{d}{dz}\vec{\mathcal{E}}(z) = \left[i\omega\hat{J}_z + g\hat{J}_x\right]\vec{\mathcal{E}}(z), \tag{1}$$

where the amplitude vector $\vec{\mathcal{E}}(z)$ collects all the localized field mode amplitudes at each waveguide, the parameters $\omega$ and $g$ are the constant effective refractive index and couplings, in that order, and the matrices for an array of $2N+1$ waveguides are,

$$\hat{J}_z = \begin{pmatrix} -N & 0 & \dots & \dots \\ 0 & -N+1 & \dots & \dots \\ \dots & \dots & \dots & \dots \\ \dots & \dots & N-1 & 0 \\ \dots & \dots & 0 & N \end{pmatrix}, \quad \hat{J}_x = \begin{pmatrix} 0 & \gamma_1 & \dots & \dots \\ \gamma_1 & 0 & \gamma_2 & \dots \\ \dots & \dots & \dots & \dots \\ \dots & \dots & 0 & \gamma_{2N-1} \\ \dots & \dots & \gamma_{2N-1} & 0 \end{pmatrix}, \tag{2}$$

with $\gamma_j = \sqrt{(N+j)(N-j+1)}$. This photonic integrated circuit balancing gain and losses at each waveguide belongs to a class of waveguide couplers with underlying $PT$-symmetry provided by the $2D+1$ Lorentz group [3]. Thus, their eigenvalues which may be real, $\omega < 2g$, or purely imaginary, $\omega \geq 2g$, are simple to calculate,

$$\Omega(m) = \sqrt{4g^2-\omega^2}(m-N) \tag{3}$$

as well as the propagation of any given initial field superposition,

$$\vec{\mathcal{E}}(z) = \hat{U}(z)\vec{\mathcal{E}}(z), \tag{4}$$

with the elements of the propagator matrix given by,

$$\begin{aligned}\hat{U}_{m,n}(z) &= \sqrt{\binom{2N}{m}\binom{2N}{n}}\frac{\left(2ig\sin\frac{\sqrt{4g^2-\omega^2}}{2}z\right)^{m+n}}{(4g^2-\omega^2)^N} K_m\left(n; \frac{4g^2}{\sqrt{4g^2-\omega^2}^2}\sin^2\frac{\sqrt{4g^2-\omega^2}}{2}z, 2N\right) \\ &\left(\sqrt{4g^2-\omega^2}\cos\frac{\sqrt{4g^2-\omega^2}}{2}z + \omega\sin\frac{\sqrt{4g^2-\omega^2}}{2}z\right)^{2N-m-n},\end{aligned} \tag{5}$$

where we have used binomial coefficients and Krawtchouk polynomials.

We will use these results to revisit the linear $PT$-symmetric dimer,

$$-i\frac{d}{dz}\mathcal{E}_0(z) = -i\omega\mathcal{E}_0(z) + g\mathcal{E}_1(z), \tag{6}$$

$$-i\frac{d}{dz}\mathcal{E}_1(z) = i\omega\mathcal{E}_1(z) + g\mathcal{E}_0(z), \tag{7}$$

and the linear $PT$-symmetric planar three-waveguide coupler,

$$-i\frac{d}{dz}\mathcal{E}_0(z) = -i\omega\mathcal{E}_0(z) + g\mathcal{E}_1(z), \tag{8}$$

$$-i\frac{d}{dz}\mathcal{E}_1(z) = g\left[\mathcal{E}_0(z) + \mathcal{E}_2(z)\right], \tag{9}$$

$$-i\frac{d}{dz}\mathcal{E}_2(z) = i\omega\mathcal{E}_2(z) + g\mathcal{E}_1(z), \tag{10}$$

and show how the Lorenz $PT$-symmetric class can be used to design valuable all-optical integrated photonic devices [4].

**REFERENCES**


1. Yu, X. et al., "Monolithically integrated self-rolled-up microtube-based vertical coupler for threedimensional photonic integration," *Appl. Phys. Lett.*, Vol. 107, 031102, 2015.
2. Teimourpour, M. H. et al., "Light transport in $PT$-invariant photonic structures with hidden symmetries," *Phys. Rev. A*, Vol. 90, 053817, 2014.
3. Rodríguez-Lara, B. M. and J. Guerrero, "Optical finite representation of the Lorentz group," *Optics Lett.*, Vol. 40, No. 23, 5682–5685, 2015.
4. Zaragoza Gutiérrez, O. I. et al., "All-optical $PT$-symmetric conversion of amplitude (phase) modulation to phase (amplitude) modulation," Accepted in *Optics Express*, 2016.

# Graphene-based PT-symmetric structures.

**Yu. V. Bludov**

Centro de física, Universidade do Minho, Campus de Gualtar, Braga, 4710-057, Portugal
bludov@fisica.uminho.pt

**Abstract**— The PT-symmetric graphene-based linear and nonlinear periodic structures are considered theoretically. We show, that possibility of variation of graphene's conductivity by electrostatic gating allows to make the parameters of such structures (like exceptional point positions, reflectivity, spectrum, etc.) to be dynamically tunable.

A two-dimensional carbon material graphene is characterized by the series of fascinating and unique properties, like enhanced mobility of charge carriers, and possibility to dynamically tune the charge-carrier density through the electrostatic gating [1]. These properties are crucial for the nowadays rapidly growing area – graphene plasmonics [2], where tunability of graphene's conductivity implies the possibility to control dynamically the dispersion properties of surface polaritons [3]. Besides the single-layer graphene structures, a lot of attention was paid to the multi-layer graphene. For example, using graphene in photonic crystals [4] results in the possibility to vary both the positions and widths of stop-bands by changing the applied gate voltage.

In the present paper we consider the variety of linear and nonlinear PT-symmetric graphene-based structures. We show, that it is possible to make the parameters of such structures (like exceptional points, reflectivity, spectrum, etc.) dynamically tunable. An example of such a structure is a multilayer graphene stack, composed of an infinite number of single graphene layers with equal Fermi energy $E_F$. We suppose that graphene layers are arranged at equal distance $d$ from each other at planes $z = md$, $m \in (-\infty, \infty)$ and are embedded into the PT-symmetric dielectric medium with complex dielectric constant $\varepsilon = \varepsilon' + i\varepsilon''$ (at $(2m-1)d < z < 2md$) and $\varepsilon^* = \varepsilon' - i\varepsilon''$ (at $2md < z < (2m+1)d$). The spectrum of this structure is depicted in Fig.1 and consists of the plasmonic band (red lines) and photonic bands (green, orange and blue lines). As it follows from the comparison of Figs.1(a)–1(c), an increase of the dielectric constant's imaginary part results in gradual disappearance of high-frequency bands, where the exceptional point takes place at certain value of in-plane wavevector $k_x$ [this phenomenon can also be seen more evidently from Fig.1(e)]. At the same time from comparison of Figs.1(a) and 1(d) [as well as from comparison of Figs.1(e)

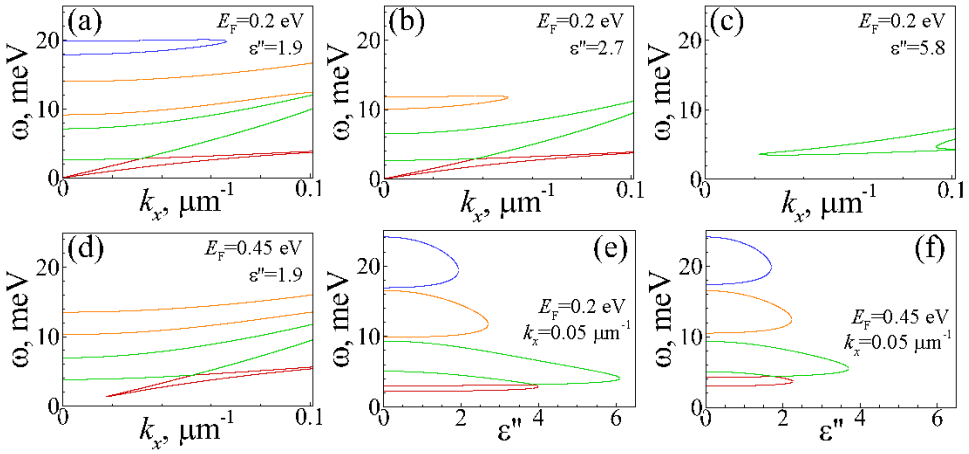



Figure 1: (a)–(d) Dispersion curves (frequency $\omega$ *versus* component of wavevector $k_x$ along graphene layers) of graphene multilayer photonic crystal; (e),(f) Dependence of frequency $\omega$ upon the imaginary part of dielectric constant $\varepsilon''$ for fixed value of $k_x$. In all panels $\epsilon' = 3.9$, $d = 40\,\mu$m. Other parameters are depicted in corresponding panels.

and 1(f)] it follows, that variation of the Fermi energy $E_F$ (through electrostatic gating) changes the position of exceptional points. We demonstrate that both plasmonic and photonic modes of such a photonic crystal can be excited by bulk electromagnetic wave falling on lateral surface of such a structure.

As it was shown theoretically [5], owing to the Dirac-cone shape of charge-carrier spectrum, graphene is strongly nonlinear material with high third-order (cubic) Kerr nonlinearity. We show that due to this fact the graphene-based crystal can support PT-symmetric nonlinear periodic patterns as well as localized structures in form of solitons.


## ACKNOWLEDGMENT

We acknowledge support from the EC under the Graphene Flagship (Contract No. CNECT-ICT-604391).


## REFERENCES


1. Li, Z. Q., *et al.,* "Dirac charge dynamics in graphene by infrared spectroscopy," *Nat. Phys.*, Vol. 4, No. 7, 532–535, 2008.
2. García de Abajo, F. J., "Graphene Plasmonics: Challenges and Opportunities," *ACS Photonics*, Vol. 1, No. 3, 135–140, 2014.
3. Chen, J.,*et al.,* "Optical nano-imaging of gate-tunable graphene plasmons," *Nature*, Vol. 487, No. 7405, 77–81, 2012.
4. Bludov, Y. V., N. M. R. Peres, and M. I. Vasilevskiy, "Unusual reflection of electromagnetic radiation from a stack of graphene layers at oblique incidence," *J. Opt.*, Vol. 15, No. 11, 114004 (2013).
5. Mikhailov, S.,and K. Ziegler, "Nonlinear electromagnetic response of graphene: frequency multiplication and the self-consistent-field effects," *J. Phys.: Cond. Mat.*, Vol. 20, No. 38, 384204 (2008).

# Parity-time symmetric analogy of relativistic electrodynamics

**Sunkyu Yu*, Xianji Piao, and Namkyoo Park**
Photonic Systems Laboratory, School of ECE, Seoul National University, Seoul 08826, Korea
**E-mail*: sk8513e@gmail.com

**Abstract** We prove that there exists a strong correspondence between optical PT symmetry and relativistic electrodynamics; in the frame of 'pseudo'-particle defined as the state of polarization (SOP) and Lorentz-like pseudo-force defined as the distribution of optical material parameters. We show that the SOP evolution on the Poincare sphere in the slowly-varying optical potential directly follows the relativistic motion of the electric charge governed by electric, magnetic, and nonlinear Lorentz force terms, and then interpret the phases of PT symmetry in terms of electric- or magnetic-force dominant regimes.

The motion of charged particles accelerated by electromagnetic fields plays a critical role in plasma physics. For example, the relativistic Lorentz force exerted from electric, magnetic field and nonlinear term in $\partial_t \boldsymbol{\beta} \sim \mathbf{E} + \boldsymbol{\beta}\times\mathbf{B} - (\boldsymbol{\beta}\cdot\mathbf{E})\boldsymbol{\beta}$ results in the intriguing motion of charged particles, the relativistic EB acceleration[1] of drifted gyro-motions. Due to the change of $\boldsymbol{\beta}\cdot\mathbf{E}$ originating from the time component of 4-vector momentum which is dependent on the particle velocity, the governing Lorentz force equation is nonlinear, and exhibits fundamental difference from linear Maxwell's equations.

In this presentation, we show that there exists direct analogy between the relativistic EB acceleration of charge and the movement of optical SOP on the Poincare sphere in the slowly-varying optical potential. We demonstrate that the change of SOP in PT-symmetric optical materials can be interpreted as the acceleration of 'charged pseudo-particles' under the Lorentz pseudo-forces[2] (Fig. 1), which follow the nonlinear equation of

$$\partial_z \vec{S} \sim \vec{\mathcal{E}} + \vec{S}\times\vec{\mathcal{B}} - \mathcal{W}_J \vec{S} \tag{1}$$

where $\boldsymbol{S}$ is the pseudo-velocity corresponding to the SOP of propagating wave, $\boldsymbol{\mathcal{E}}$ and $\boldsymbol{\mathcal{B}}$ are electric and magnetic orthogonal pseudo-fields corresponding to linear dichroism and birefringence, and $\mathcal{W}_J = \mathbf{S}\cdot\boldsymbol{\mathcal{E}}$ is the Joule heating of pseudo-particles corresponding to the non-Hermiticity of optical materials. It is found that the phases of PT symmetry classified by the PT symmetry breaking can then be understood as **B**-dominant and **E**-dominant regimes of relativistic Lorentz motion, divided by **B** = **E** stable point.




Figure 1. Optical analogy of relativistic electrodynamics: the force induced by electric- ($\boldsymbol{\mathcal{E}}$), magnetic- ($\boldsymbol{\mathcal{B}}$) pseudo-fields, and relativistic non-Hermiticity ( $\mathcal{W}_J$) in complex anisotropic optical materials, which is applied to pseudo-particles with the pseudo-velocity $\boldsymbol{S}$.

From this viewpoint, in the talk we will interpret the origin of strong chiral interactions of light with PT-symmetrically polarized materials[3,4], which allow the collection of optical SOP to one of the spin states (LCP or RCP, Fig. 2). We will also discuss on the modification of the Lorentz pseudo-force equation in the presence of 3D optical chirality, and the application on the SOP convergence to an 'achiral' state.

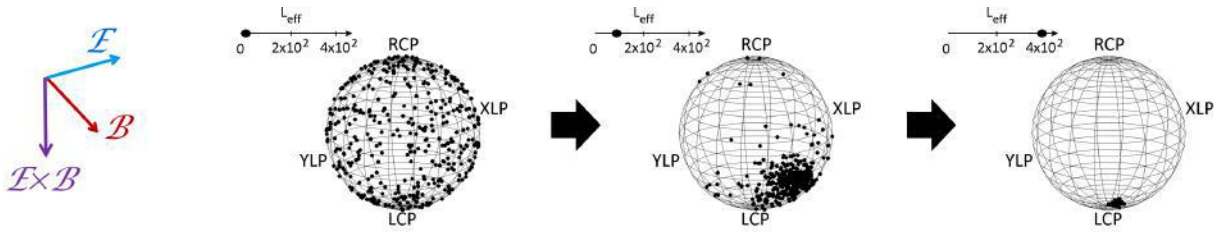



Figure 2. The evolution of optical SOP through the EB acceleration on the Poincare sphere.

**REFERENCES**


1. Takeuchi, S., "Relativistic E×B acceleration," *Phys. Rev. E* Vol. **66**, 037402, 2002.
2. Yu, S., Piao, X. and Park, N., "Relativistic E×B polarization drift of light," *arXiv preprint* arXiv:1602.01281, 2016.
3. Lawrence, M. *et al.* "Manifestation of P T Symmetry Breaking in Polarization Space with Terahertz Metasurfaces," *Phys. Rev. Lett.* Vol. **113**, 093901, 2014.
4. Yu, S., Park, H. S., Piao, X., Min, B. and Park, N., "Low-dimensional optical chirality in complex potentials," *arXiv preprint* arXiv:1409.0180, 2014.

# Parity-Time Symmetric Chain Resonators

**S. Phang[1,2], A. Vukovic[1], S. C. Creagh[2], G. Gradoni[2], P. Sewell[1] and T. M. Benson[1]**
[1]George Green Institute for Electromagnetics Research, University of Nottingham, UK
[2]School of Mathematical Sciences, University of Nottingham, UK
[*]corresponding author: sendy.phang@nottingham.ac.uk

**Abstract-** A simple tight-binding model to study the band-structure of an infinite length Parity-time (PT) symmetric chain of resonators is presented in this paper. In the talk, we will investigate the impact of having a structure of finite length and consider the effect of a modulation of the real part of the refractive index on the complete band-structure of the PT-chain system. For a finite PT-chain structure under certain modulation, we observe the existence of a localised mode which is either lasing or dissipating.

Photonic structures with combined gain and loss, known as Parity-Time (PT) symmetric structures, have been shown to exhibit unique properties [1,2]. Within the context of PT-resonator structures, we have reported an analytical approach for calculating the threshold point of such structures using a Boundary Integral Equation method[1]. Furthermore we also analysed the impact of unbalancing gain/loss in the PT-resonator structure in which we observed a laser operation in a loss dominated structure [1]. In this contribution, we report our recent study of a PT-symmetric chain of resonator structures (see Fig. 1).

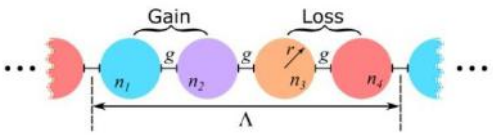



Figure 1. Schematic illustration of the PT-chain resonator structure.

The PT-chain considered is schematically illustrated in Fig. 1; each cell is comprised of 4 cylindrical resonators of the same radius $r$ and separated by a fixed gap $g$. The refractive index within a unit cell is given by:

$$\begin{cases} n_1 = n_0 + \Delta n' + jn'' \\ n_2 = n_0 - \Delta n' + jn'' \\ n_3 = n_0 - \Delta n' - jn'' \\ n_4 = n_0 + \Delta n' - jn'' \end{cases} \tag{1}$$

where, $n_0$, $\Delta n'$ and $n''$ are the average refractive index, modulation of the real part of the refractive index and modulation of the imaginary part of the refractive index (gain/loss), respectively.

In this work, we investigate the impact of having a structure of finite length and consider the effect of a modulation of the real part of the refractive index on the complete band-structure of the PT-chain system. A simple tight-binding model of the *infinite* chain for the case of no real modulation, i.e. $\Delta n' = 0$ is given by,

$$H = \begin{pmatrix} \omega_0 & \kappa & & e^{j\beta\Lambda}\kappa \\ \kappa & \omega_0 & \kappa & \\ & \kappa & {\omega_0}^* & \kappa \\ e^{-j\beta\Lambda}\kappa & & \kappa & {\omega_0}^* \end{pmatrix} \tag{2}$$

where $\omega_0$ is the complex resonant frequency of the resonator, $\kappa$ is the coupling strength between resonators

and $\beta\Lambda$ is the Bloch phase. The Hamiltonian $H$ has multiple degeneracies even when the non-Hermitian parameter, $\gamma = \Im(\omega_0)/\kappa$ is zero, see Fig. 2(a); thus a PT-chain structure without modulation $\Delta n' = 0$ will spontaneously break the PT-symmetry for a non-zero $\gamma$, i.e. $n'' > 0$, as shown in Fig. 2(b).

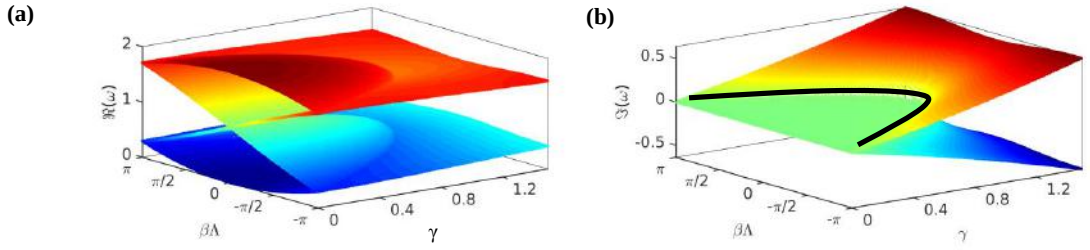



Figure 2. Band-structure of an infinitely long PT-chain with no real part modulation $\Delta n' = 0$

Meanwhile, by introducing a small real part modulation $\Delta n' \neq 0$, the resonant frequencies of the resonator are shifted, i.e. they decrease if $\Delta n' < 0$ and increase if $\Delta n' > 0$; now the Hamiltonian is given by,

$$H = \begin{pmatrix} \omega_1 & \kappa & & e^{j\beta\Lambda}\kappa \\ \kappa & \omega_2 & \kappa & \\ & \kappa & \omega_2^* & \kappa \\ e^{-j\beta\Lambda}\kappa & & \kappa & \omega_1^* \end{pmatrix} \tag{3}$$

where $\omega_1 - \omega_2 = 2\delta$ and $\omega_0 = (\omega_1 + \omega_2)/2$. The real part and the imaginary part of the eigenfrequencies of (3) are plotted in Fig. 3(a,b) respectively for $\delta = 0.25\omega_0$. It can be seen in Fig. 3(a) that by introducing real modulation $\Delta n'$, the eigenfrequencies at the edge of the Brillouin zone are no longer degenerate. As such there exists a minimum threshold of the $\gamma$ parameter which causes PT-symmetry breaking.

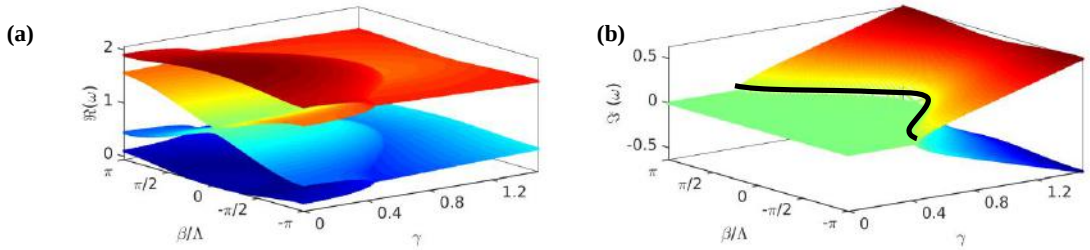



Figure3. Band-structure of an infinitely long PT-chain with real modulation

In the talk, we will discuss the effect of having a finite length of chain in which we observed the presence of localised broken-PT-symmetry mode, which has a characteristic of either lasing or decaying and is localised at either end of the chain structure.

**REFERENCES**


1. Sendy Phang, Ana Vukovic, Stephen C. Creagh, Trevor M. Benson, Phillip D. Sewell, and Gabriele Gradoni, "Parity-time symmetric coupled microresonators with a dispersive gain/loss," Opt. Express 23, 11493-11507 (2015).
2. Sendy Phang, Ana Vukovic, Stephen C. Creagh, Trevor M. Benson, Phillip D. Sewell, and Gabriele Gradoni, " Localized Single Frequency Lasing States in a Finite Parity-Time Symmetric Resonator Chain," Scientific Reports 6, 20499 (2016).

# Constant-Intensity waves in Media with Gain and Loss

**K.G. Makris[1], A. Brandstötter[2], P. Ambichl[2], Z. H. Musslimani[3], D. N. Christodoulides[4], and S. Rotter[2,*]**

[1]Crete Center for Quantum Complexity and Nanotechnology, Department of Physics, University of Crete, 71003, Heraklion, Greece, EU

[2]Institute for Theoretical Physics, Vienna University of Technology (TU Wien), Vienna, A-1040, Austria, EU

[3]Department of Mathematics, Florida State University, Tallahassee, Florida 32306, USA

[4]CREOL, College of Optics & Photonics, University of Central Florida, Orlando, Florida 32816, USA

[*]corresponding author: stefan.rotter@tuwien.ac.at

**Abstract** When impinging on a non-uniform potential landscape, waves typically scatter and diffract, resulting in a highly complex interference pattern in the waves' intensity. In my talk I will introduce a special class of waves that defy this common picture by maintaining a constant-intensity even in the presence of strong variations of the potential, provided that a suitable combination of gain and loss is added to it.

In all of the diverse areas of science where waves play an important role, one of the most fundamental solutions of the corresponding wave equation is a stationary wave with constant intensity. The most familiar example is that of a plane wave propagating in free space. In the presence of any Hermitian potential, a wave's constant intensity is, however, immediately destroyed due to scattering. I will show that this fundamental restriction is conveniently lifted when working with non-Hermitian potentials. In particular, a whole class of waves can be identified that have constant intensity in the presence of inhomogeneous media with gain and loss. It turns out that the systems that give rise to this special property may be, but don't necessarily have to be PT-symmetric.

I will demonstrate that this new concept can also be applied to strongly fluctuating potentials, such as in disordered media. In this case we identify a corresponding gain-loss profile that allows for these constant-intensity waves to propagate through the disorder without any back-reflection or interference fringes that usually occur in this context. An experimental demonstration of these unique wave states is envisioned based on spatially modulated pump beams that can flexibly control the gain and loss components in an active medium.

**Acknowledgements**. This work has been supported by the Austrian Science Fund (FWF), the European Union (FP7), and the American National Science Foundation (NSF).

**REFERENCES**

1. K. G. Makris, Z. H. Musslimani, D. N. Christodoulides, and S. Rotter, Nature Commun. 6, 7257 (2015).
2. K. G. Makris, A. Brandstötter, P. Ambichl, Z. H. Musslimani, and S. Rotter (in preparation).

# Parity-time symmetry and nonreciprocal light transmission in high-Q microcavity systems

**Min Xiao[1,2*], Xiaoshun Jiang[1], Long Chang[1], Jianming Wen[3] and Liang Jiang[3]**

[1]National Laboratory of Solid State Microstructures, College of Engineering and Applied Sciences, and School of Physics, Nanjing University, Nanjing 210093, China

[2]Department of Physics, University of Arkansas, Fayetteville, Arkansas 72701, USA

[3]Department of Physics, Yale University, New Haven, Connecticut 06511, USA

[*]corresponding author: mxiao@uark.edu

**Abstract**-We have realized parity-time symmetry in a coupled active-passive microcavity system with balanced gain and loss. On-chip nonreciprocal light transmission and circulation due to gain-saturation nonlinearity are experimentally demonstrated in coupled active-passive, as well as in single active high-Q, microcavity systems. There are certain advantages by using a single active microcavity with gain saturation for achieving nonreciprocal light transmission and circulation, such as simplicity in the structure, easy to control, low insertion loss and superior isolation performance.

A coupled gain-loss waveguide pair with balanced gain and loss can mimic the parity-time (PT) symmetric Hamiltonian constructed in quantum mechanics [1], which has started an active research field of PT-symmetric optics in the past few years. On-chip nonreciprocal light propagation is highly desired in constructing integrated photonic circuits [2], but hard to achieve due to the required optical nonlinearity and proper designs to break the time-reversal symmetry [3]. Achieving efficient on-chip optical isolator and circulator will be very useful for implementing practical integrated optical information processing circuits and networks.

Using a system with coupled active-passive microtoroid cavities, we have demonstrated clear PT-symmetry behaviors. With the carefully balanced gain and loss in the active and passive microtoroids, an exceptional point appears in the output spectral splitting plot as the distance between the two microtoroids increases (i.e. decreasing the coupling strength) indicating a PT-symmetry breaking phenomenon. Two frequency peaks exist when the PT symmetry (gain equals to loss) is upheld, while the two frequency peaks collapse into one when the PT symmetry breaks down (i.e. the loss equals to gain in the microtoroids, and is larger than the coupling strength between the two microtoroids). It is crucial to precisely balance the gain and loss in the two microtoroid cavities to satisfy the true PT-symmetry condition during the experiment [4].

When the gain-saturation nonlinearity in the active microtoroid is taken into account in this coupled microcavity system, nonreciprocal light propagation can be realized. By carefully designing and implementing an experimental measurement system, we have demonstrated ultrasensitive nonreciprocal light transmission in this coupled microtoroid system [4]. By optimizing the system parameters, nonreciprocal light propagation can be achieved for the input signal powers ranging from

about 10 nW up to 10 μW with good isolation ratio [4].

Considering it further, on-chip nonreciprocal light propagation and optical circulation [5] can actually be realized simultaneously in a much simpler system with only one active microcavity [6,7]. We have experimentally shown that, by exploring the gain-saturation nonlinearity, on-chip optical nonreciprocity with excellent isolation performance at telecommunication wavelength can be achieved using a system of one active microtoroid cavity [7]. The performances of such single microtoroid system for optical isolation and circulation versus various experimental parameters have been carefully evaluated experimentally. The advantages of using such one active microcavity system for nonreciprocal light propagation and optical circulation include simplicity of the system for controlling and tuning, its compatibility with the current metal-oxide-semiconductor process, relatively low insertion loss in one-way light transport, and good isolation/circulation ratios at a broad input power range. These superior features could make the demonstrated device serve as a promising fundamental building block for future integrated photonic networks. Very recently, by exploring momentum conservation we have for the first time demonstrated an on-chip nonlinear optical isolator by injecting light simultaneously in both forward and backward directions, with use of only one microcavity.

In summary, parity-time symmetry and its breaking, as well as nonreciprocal light propagation, have been experimentally demonstrated in a coupled active-passive microtoroid system [4]. The on-chip nonreciprocal light propagation is caused by the gain-saturation nonlinearity in the active microtoroid and therefore can work for both balanced and unbalanced gain/loss conditions, as well as under both PT-symmetry and broken PT-symmetry cases [4]. The on-chip nonreciprocal light propagation and optical circulation have also been experimentally demonstrated in a single active microcavity system with gain saturation [6,7], which can have practical applications in integrated photonic circuits and networks.

**Acknowledgements**: We acknowledge funding support from NBRPC (no. 2012CB921804) and NSFC (nos. 61435007 and 11574144). J.W. and L.J. acknowledge funding support from the ARO, the AFSOR MURI, the DARPA QUINESS program.

**REFERENCES**

[1] El-Ganainy, R., K. G. Makris, D. N. Christodoulides, and Z. H. Musslimani, “Theory of coupled optical PT-symmetric structures,” *Opt. Lett.*, vol. 32, pp. 2632-2634, 2007.

[2] Bi, L., J. Hu, P. Jiang, D. H. Kim, G. F. Dionne, L. C. Kimerling and C. A. Ross, “On-chip optical isolation in monolithically integrated non-reciprocal optical resonators,” *Nature Photonics*, vol. 5, pp. 758-762, 2011.

[3] Jalas, D. *et al*, "What is and what is not an optical isolator", *Nature Photonics*, vol. 7, pp. 579, 2013.

[4] Chang, L., X. S. Jiang, S. Hua, C. Yang, J. Wen, L. Jiang, G. Li, G. Wang, and M. Xiao, “Parity-time symmetry and variable optical isolation in active-passive-coupled microresonators,” *Nature Photonics*, vol. 8, pp. 524-528, 2014.

[5] Jalas, D., A. Y. Petrov, M. Eich, “Optical three-port circulators made with ring resonators,” *Opt. Lett.*, Vol. 39, pp. 1425-1428, 2014.

[6] Wen, J., X. S. Jiang, M. Zhang, L. Jiang, S. Hua, H. Wu, C. Yang, and M. Xiao, “Modeling of on-chip optical nonreciprocity with an active microcavity”, *Photonics*, vol. **2**, pp. 498-508, 2015.

[7] Jiang, X. S., C. Yang, H. Wu, S. Hua, J. Wen, L. Jiang, L. Chang, Y. Ding, M. Zhang, Q. Hua, and M. Xiao, “On-chip optical nonreciprocity using an active microcavity”, submitted for publication, 2015.

# Unidirectional Reflectivity in Quarter Stacks with Balanced Losses/Gains

**J. Ramirez-Hernandez**[1], **F. M. Izrailev**[1], **N. M. Makarov**[2] **and D. N. Christodoulides**[3]

[1]Instituto de Física, Benemérita Universidad Autónoma de Puebla,
Apartado Postal J-48, Puebla, Pue., 72570, México
[2]Instituto de Ciencias, Universidad Autónoma de Puebla,
Priv. 17 Norte No. 3417, Col. San Miguel Hueyotlipan, Puebla, Pue., 72050, México
[3]College of Optics and Photonics-CREOL, University of Central Florida, 32816, USA
felix.izrailev@gmail.com

**Abstract**— We study transport properties of a periodic 1D array of bi-layers focusing on the unidirectional reflectivity that emerges as a result of the balanced losses/gains incorporated into the arrays. Our analysis is based on the transfer matrix method according to which we derive analytical expressions for both spectral and transport characteristics of the model. We have unexpectedly found that the $\mathcal{PT}$-symmetric transport can emerge even when the system itself is not $\mathcal{PT}$-symmetric.

We consider the perpendicular propagation of an electromagnetic wave of frequency $\omega$ through an array of $N$ unit $(a, b)$ cells embedded in a homogeneous medium. Each unit cell consists of two dielectric $a$ and $b$ layers with thicknesses $d_a$ and $d_b$ such as $d = d_a + d_b$ is the unit-cell size. The $a$ layers absorb the energy and the $b$ layers are composed of the amplifying material. The losses and gains in the layers are incorporated via corresponding complex dielectric functions, while the magnetic permeabilities $\mu_{a,b}$ are assumed to be real and positive constants. The main optic parameters (refractive indices $n_{a,b}$, impedances $Z_{a,b}$ and wave phase shifts $\varphi_{a,b}$) of two constitutive layers, $a$ and $b$, are defined as follows,

$$n_a = n_a^{(0)}(1 + i\gamma), \qquad Z_a = Z(1 + i\gamma)^{-1}, \qquad \varphi_a = \frac{\varphi}{2}(1 + i\gamma)\,; \tag{1a}$$

$$n_b = n_b^{(0)}(1 - i\gamma), \qquad Z_b = Z(1 - i\gamma)^{-1}, \qquad \varphi_b = \frac{\varphi}{2}(1 - i\gamma)\,, \tag{1b}$$

where $Z = \mu_a/n_a^{(0)} = \mu_b/n_b^{(0)}$ and $\varphi = 2\omega n_a^{(0)} d_a/c = 2\omega n_b^{(0)} d_b/c$. Above, the key parameter $\gamma$ stands for the strength of losses and gains. In the case of no losses/gains ($\gamma = 0$) this setup is known as *matched quarter stack*. In this case basic $a$ and $b$ layers are perfectly matched (their impedances are the same) and, in addition, they have the same length of optic path ($n_a^{(0)} d_a = n_b^{(0)} d_b$), therefore, the same phase shift $\varphi/2$.

With the use of the transfer matrix method one can get the dispersion relation,

$$\cos\varphi_B = \frac{\cos\varphi + \gamma^2 \cosh(\gamma\varphi)}{1 + \gamma^2}\,. \tag{2}$$

that determines the band-structure as the dependence of the Bloch phase $\varphi_B = \kappa d$ on the wave frequency $\omega$. One of the important consequences of non-zero value of $\gamma$ in Eq. (2) is an emergence of *finite* number $N_{band}$ of *spectral bands* defined by the condition $|\cos\mu_B| < 1$. This number $N_{band}$ depends on the parameter $\gamma$ only, and for $\gamma \ll 1$ can be estimated as

$$N_{band} \approx (1/\pi\gamma)\ln(1/\gamma). \tag{3}$$

Within the spectral bands the Bloch index $\mu_B$ is real in spite of the presence of loss and gain. The analysis shows that every spectral band consists of the central region with $T_N \geqslant 1$ and those with $T_N \leqslant 1$. At the borders between these regions the transmission is perfect, $T_N = 1$, and this happens at specific points $\varphi = \varphi_s(\gamma)$ at which, however, the Bloch index $\mu_B(\gamma, \varphi_s)$ does not vanish.

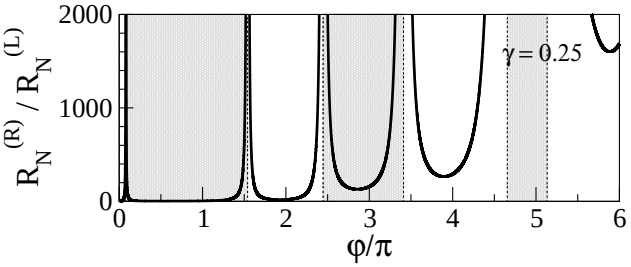



Figure 1: Ratio right-to-left reflectances (full curve) versus $\varphi$ for $\gamma = 0.25$. Dashed regions are those where $\mu_B$ is real and $T_N > 1$.

The key point of our approach is to analyze the dispersion relation together with the expressions for the transmittance $T_N$ and left/right reflectances $R_N^{(L)}$ and $R_N^{(R)}$. In the presence of gain/loss terms, the relation between the above quantities is known to have the form,

$$|1 - T_N| = \sqrt{R_N^{(L)} R_N^{(R)}}. \tag{4}$$

The analysis shows that at the specific points $\varphi = \varphi_s(\gamma)$ the left reflectance vanishes, however, the right one remains finite. This effect is known as the *unidirectional reflectivity*. It is one of the most important properties of scattering in the $\mathcal{PT}$-symmetric systems. For $\gamma \ll 1$ and $\gamma \exp(\gamma\varphi) \gg 1$ one can obtain the estimate,

$$R_N^{(R)} \approx 16\, \gamma^{-4} \sin^2 (N\mu_B)\,. \tag{5}$$

The ratio between right and left reflectances,

$$R_N^{(R)}/R_N^{(L)} = \mathcal{F}^2(-\gamma, \varphi)/\mathcal{F}^2(\gamma, \varphi), \tag{6}$$

is shown in Fig. 1 in dependence on $\varphi$ for $\gamma = 0.25$. Here, the functions are defined as

$$\mathcal{F}(\gamma, \varphi) = \gamma^2 \sinh(\gamma\varphi) - \gamma \sin\varphi + 2(\cos\varphi - \mathrm{e}^{-\gamma\varphi}). \tag{7}$$

Remarkably, the ratio $R_N^{(R)}/R_N^{(L)}$ turns out to be $N$-independent. Note that at the *Fabry-Perot resonances* for which $\sin(N\mu_B)/\sin\mu_B = 0$, and, therefore, $T_N = 1$, both reflectances expectedly vanish, $R_N^{(L)} = R_N^{(R)} = 0$.

Apart from the set of specific points $\varphi_s$ there is a set of *exceptional points* $\varphi_{sp}$ for which both $T_N = 1$ and $\mu_B(\gamma_{sp}, \varphi_{sp}) = 0$. Here the left reflectance vanishes, $R_N^{(L)} = 0$, while the right one is very large,

$$R_N^{(R)} = \frac{4\gamma^2 N^2}{(1+\gamma^2)^2} \left[\cosh(\gamma\varphi) - \cos\varphi\right]^2 \approx \gamma^2 N^2 \mathrm{e}^{2\gamma\varphi}. \tag{8}$$

The estimate is given for $\gamma_{sp} \ll 1$ and, hence, $\gamma_{sp}\varphi_{sp} \gg 1$.

It is worthwhile to stress that our analysis is general and valid also for the case when the thicknesses of $a$ and $b$ layers are not equal, $d_a \neq d_b$, therefore, the Hamiltonian of the model is *non-$\mathcal{PT}$-symmetric*. However, the scattering properties through finite samples are similar to those previously found for the $\mathcal{PT}$-symmetric models. This happens since the optical paths in $a, b$ layers are equal, however, the matching remains perfect. Note that in the case of equal thicknesses, $d_a = d_b$, the model is $\mathcal{PT}$-symmetric on definition.

**ACKNOWLEDGMENT**

This work was supported by the SEP-CONACYT (México) grant No. CB-2011-01-166382.

# Field concentration by local PT-symmetry and global P-symmetry

**Waqas W. Ahmed[1], Muriel Botey[1], Ramon Herrero[1], and Kestutis Staliunas[2]**

[1] Departament de Física, Universitat Politècnica de Catalunya, Spain

[2] Institució Catalana de Reserca i Estudis Avançats (ICREA), Spain

[*]corresponding author: muriel.botey@upc.edu

**Abstract**- We propose a new class of systems holding *PT*-symmetry only locally; the potential fulfills: $U(\mathbf{r}-\mathbf{r_0})=U^*(-\mathbf{r}+\mathbf{r_0})$ in a small neighborhood of any point $\mathbf{r_0}$ being $\mathbf{r_0}\neq\mathbf{0}$, whereas on a global scale the system is only Parity symmetric: $U(\mathbf{r}-\mathbf{r_0})=U(-\mathbf{r}+\mathbf{r_0})$ for all $\mathbf{r}$. We show that such systems lead to a strong field localization at $\mathbf{r}=0$, arising from the merge of the two different symmetries. We explore these new potentials in one- and two- dimensional complex nanophotonic structures, combining gain/loss and index modulations, which we expect to have direct applications as turning broad aperture lasers into bright and narrow output beam sources.

Initially introduced as a curiosity in quantum mechanics [1], Parity-Time (*PT*-) symmetric systems have recently found realizations in optics such as asymmetric reflections, transmissions, asymmetric chirality [2-5]. The general requirement for an optic PT-symmetric system is that the optical potential (complex refractive index including index and gain/loss modulations) fulfills $n(\mathbf{r}) = n^*(-\mathbf{r})$. In the simplest one-dimension (1D) realization: $n(x)= n_0 \exp(iqx)$, which at resonance, $k=q/2$ (PT-transition) asymmetrically couples the left-propagating mode, $\exp(-ikx)$, to the right-propagating mode $\exp(ikx)$, but not vice versa. However, what happens if such PT-symmetry condition is not imposed globally, over the whole space, but only locally? Let's consider the situation depicted on Fig.1.a, a complex symmetric potentials, locally PT-symmetric except for x=0. The optical complex potential imposes unidirectional coupling "to the right" on the left half-plane, while the coupling is "to the left" on the right half-plane. As a consequence, a strong filed localization may be intuitively expected around $x=0$. The same idea applies to 2D (or 3D), where radial (or coaxial) dephased modulations of the index and gain/loss may lead to asymmetric coupling between incoming and outgoing waves, see Figs.1.b and 1.c




***Figure 1.*** *Local unidirectional coupling: (a) 1D complex optical potential, where $n_{Re}$ is the real index modulation, and $n_{Im}$ the gain/loss modulation. (b) 2D analogous axisymmetric configuration, (c) 3D coaxial index and gail/loss modulations, analogous for fields propagating along z. The arrows indicate the direction of the asymmetric mode coupling, at resonance.*

Indeed, we explore the field dynamics in spatial and temporal domains within a 1D optical potential in the form: $n(x) = n_{Re}\cos(|x|)$-i $n_{Im}\sin(|x|)$ as well the 2D axisymmetric case: $n(r) = n_{Re}\cos(|r|)$-i $n_{Im}\sin(|r|)$. Both systems show equivalent localization regimes, depending upon the real and imaginary modulation amplitudes. Strong field localizations always occur close to the *PT*-transition point, see Fig.2 which summarizes the effect.

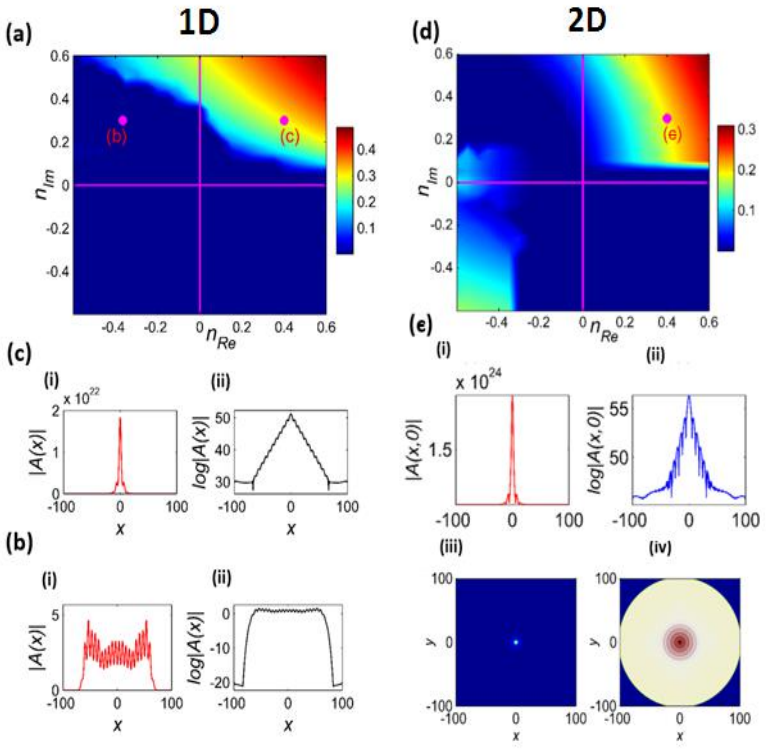



***Figure 2 1D:*** *(a) Map of the spatial growth exponent calculated after a sufficient long time (t>300 units) in the parameter space ($n_{Im}$, $n_{Re}$). Spatial field profiles for representative cases (b,c) in linear and in logarithmic scales, (i)/(ii). (d)* ***2D:*** *(d) Axial field localization exponent in parameter space($n_{Im}$, $n_{Re}$). (e) Axial/total cross-sectional field distribution in real (i)/(iii) and logarithmic scales (ii)/(iv).*

We show that the proposed systems simultaneously localize and enhance the field due to the asymmetric radial coupling of inward and outward waves. Since the physical realizations of the above discussed arrangements in 1D and 2D are nowadays available, we expect this light-matter interaction phenomena to find remarkable applications in many linear and nonlinear devices where high degree of localization is desirable such as: beam focusing, narrow beam enhancement, laser emission, switching in nanostructures,…

**REFERENCES**


1. C. M. Bender, and S. Boettcher, "Real spectra in non-Hermitian Hamiltonian having PT symmetry," Phys. Rev. Lett. 80, 5243–5246 (1998).
2. A. Guo, et al. "Observation of PT-symmetry breaking in complex optical potentials" Phys. Rev. Lett. 103, 93902 (2009).
3. C. E. Ruter, K. G. Makris, R. El-Ganainy, D. N. Christodoulides, M. Segev, and D. Kip, "Observation of parity–time symmetry in optics", Nat. Phys. 6, 192–195 (2010).
4. L. Feng, Y.-L. Xu, W. S. Fegadolli, M.-H. Lu, J. E. Oliveira, V. R. Almeida, Y.-F. Chen, and A. Scherer, "Experimental demonstration of a unidirectional reflectionless parity-time metamaterial at optical frequencies," Nat. Mater. 12, 108–113 ( 2012).
5. M. Turduev, M. Botey, I.H. Giden, R. Herrero, H. Kurt, E Ozbay, and K. Staliunas, “Two-dimensional complex parity-time-symmetric photonic structures“ Phy. Rev. A, 91(2), 023825 (2015).

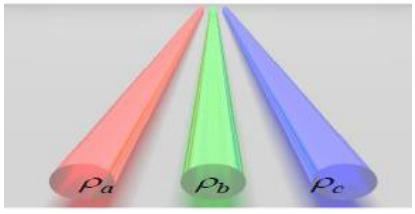
# PT-symmetry control with spatial and temporal modulations

**Andrey A. Sukhorukov**
Nonlinear Physics Centre, Research School of Physics and Engineering, Australian National University, Canberra, ACT 2601, Australia
*corresponding author: Andrey.Sukhorukov@anu.edu.au

**Abstract**- We present an overview of results on the effects of spatial and temporal modulations in coupled waveguides and fiber loop resonator structures with gain and loss, which demonstrate features of parity-time symmetry with real spectrum and transition to amplification and lasing.

One of the challenges of the modern photonics is to develop all-optical devices enabling increased speed and energy efficiency for transmitting and processing information on an optical chip. Parity-Time (PT) symmetric photonic systems with alternating regions of gain and loss can bring novel functionalities [1]. In such systems, losses are as important as gain and, depending on the structural parameters, gain compensates losses, which can be employed for signal filtering and switching, opening new prospects for active control of light (see a review paper [2], and references therein).

Here, we overview our recent results on spatial and temporal modulation in structures with gain and loss for controlling transition between gain-loss compensation to amplification and lasing [3,4]. First, we consider a structure composed of three coupled waveguides [3], see Fig. 1(a). We demonstrate that three waveguides with different strengths of dissipation and gain might demonstrate PT-like spectral behavior if the couplings between the waveguides are specially chosen, despite the fact that such systems have no PT spatial symmetry. We further find that the scattering properties and lasing threshold of such structures embedded in a waveguide array critically depend on internal structure. Second, we suggest a realization of PT fiber laser, based on cross-coupled loop resonators [4], see Fig. 1(b). We further show that PT breaking in such resonators can be flexibly controlled by temporal modulation of gain and phase shifts.

(a) 

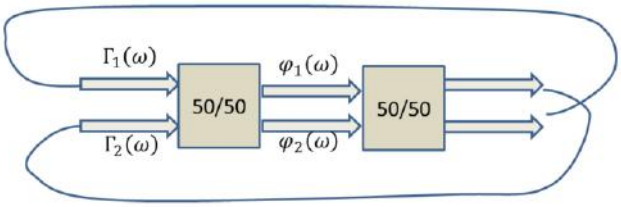
(b) 


**Figure 1**. (a) Sketch of a three-waveguide coupler with gain and loss, with no spatial PT symmetry [3]. (b) Schematic diagram of PT fiber loop structure [4].

**REFERENCES**

1. C. E. Ruter, K. G. Makris, R. El Ganainy, D. N. Christodoulides, M. Segev, and D. Kip, Observation of parity-time symmetry in optics, Nature Physics 6, 192 (2010).
2. S. V. Suchkov, A. A. Sukhorukov, J. Huang, S. V. Dmitriev, C. Lee, and Yu. S. Kivshar, "Nonlinear switching and solitons in PT-symmetric photonic systems," Laser Photonics Reviews, in press (2016),
3. S. V. Suchkov, A. A. Sukhorukov, F. Fotsa-Ngaffo, A. D. Tikeng, A. Kenfack-Jiotsa, T. C. Kofane, and Yu. S. Kivshar, "Dissipative trimer: PT-symmetry vs Pseudo-Hermisity," submitted.
4. I. D. Vatnik, S. V. Smirnov, A. M. Tikan, D. V. Churkin, and A. A. Sukhorukov, to be submitted.

# Control of Power in Parity-Time Symmetric Lattices.

**Maksim Kozlov[1] and G. P. Tsironis[2,3,4]**

[1]NUFYP, Nazarbayev University, Astana, 010000, Republic of Kazakhstan

[2]Department of Physics, University of Crete, Heraklion, 71003, Greece

[3]IESL, Foundation for Research and Technology-Hellas, P. O. Box 1527, Heraklion, 71110, Greece

[4]National University of Science and Technology MISiS, Leninsky prosp. 4, Moscow, 119049, Russia

[*]corresponding author: maksim.kozlov@nu.edu.kz

**Abstract** We demonstrate that in the longitudinally modulated Parity-Time symmetric lattices the light wave power can be controlled through overlap of gain-loss distribution with intensity pattern formed by interference of Rabi-coupled Floquet-Bloch modes.

Entirely real eigenvalue spectrum of Parity-Time symmetrical (PTS) non-Hermitian Hamiltonians was first predicted in the context of quantum mechanics[1]. In optics, complex PTS refractive index can support stable wave propagation[2]. Similarly, Rabi oscillations (RO) were first predicted[3] and demonstrated[4] as electrons transitions from conduction to valence band induced by external optical field. Optical RO, i.e., resonant transitions between different light modes originally proposed[5,6] and observed[7] in longitudinally modulated Hermitian waveguides and waveguide arrays, and recently predicted in PTS waveguides[8]. We investigate paraxial beam propagation approximated by the normalized Schrodinger equation $i\partial\psi/\partial z+\partial^2\psi/\partial^2 z+U[1+\varepsilon\cos(\beta_0 z)]\psi=0$ in PTS lattice $U=V\cos(2\pi x/D)+iW\sin(2\pi x/D)$ modulated along direction of propagation with frequency $\beta_0$ and amplitude $\varepsilon<<1(\varepsilon=0.05)$ and show that in the PTS phase ($W\leq V$) when all separate Flouqet-Bloch (FB) modes remain stable their interference gives rise to either controlled power oscillations or unlimited linear amplification occurring exactly at the phase transition point (PTP). The propagation constants of the first 3 bands ($\beta_1$, $\beta_2$ and $\beta_3$) are shown in Fig. 1(a-b) for the under-critical regime (UCR) $W/V=0.8$ and at the PTP ($W/V=1$) respectively. We consider resonant transitions between $1^{st}$ and $2^{nd}$ mode ($\beta_0=\beta_2-\beta_1$) in the UCR [green arrows in Fig. 1(a)] and at the PTP [green arrow in Fig. 1(b)]. The coupling between $m^{th}$ and $n^{th}$ FB modes depends on the transition matrix elements $M_{mn}=<\psi^*_m|U|\psi_n>$ defined through biorthogonality condition[2]. $M_{21}$ and $M_{12}$ for UCR and at the PTP are shown in Fig. 1(c-d) respectively. In contrast with Hermitian Hamiltonians $M_{mn}$ are asymmetrical with respect to Bloch wave-number $k$ and index interchange. At the PTP $M_{12}=0\,\forall\, k\leq 0$ and $M_{21}=0\,\forall\, k\geq 0$. The propagation in the UCR with single $k_0$ $1^{st}$ mode at the input is depicted in Figs. 1(e-h). The evolution of the $1^{st}$ (blue curves) and $2^{nd}$ (green curves) mode populations ($A_1$ and $A_2$) are shown in Fig. 1(e-f) for the left tilted incidence (LTI) and right tilted incidence (RTI) respectively ($k_0D/\pi=\pm 0.15$). In contrast with Hermitian lattices amplitudes of mode population oscillations in PTS lattices are not equal since the exchange of energy between the two modes is augmented by their amplification (damping) due to the positive (negative) overlap of intensity pattern with the gain-loss distribution, which results in the periodically oscillating total power shown in Fig. 1(g-h) for the LTI and RTI respectively. Numerically obtained power (blue curves) exhibits fast oscillations around coupled mode theory (CMT) solution (red curves) due to the beating of non-orthogonal modes[2] that were omitted in the CMT solution. For the LTI ($M_{21}>M_{12}$) the amplitude of the $2^{nd}$ mode population is higher and total power increases whereas for the RTI ($M_{21}<M_{12}$) the amplitude of the $2^{nd}$ mode is lower and total power decreases.

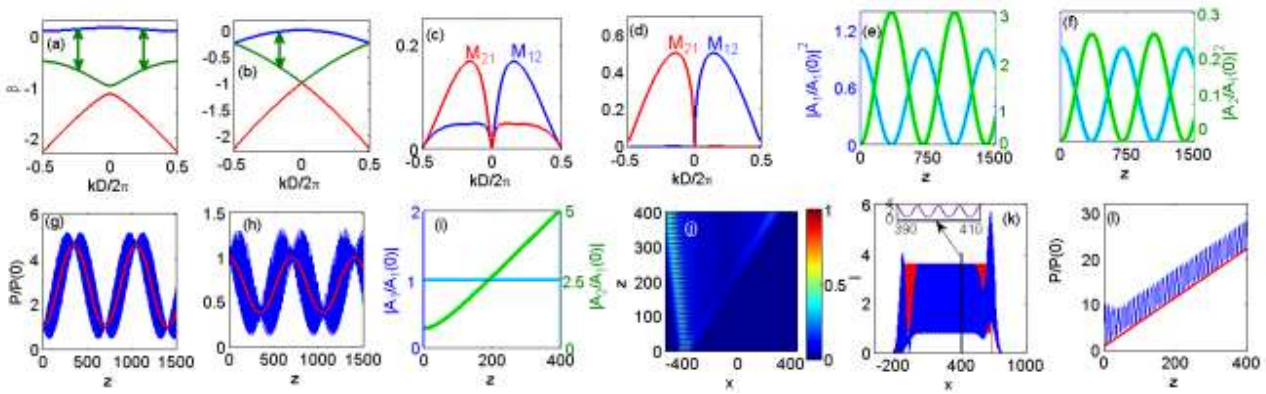



**Figure 1.** Transmission properties of PTS lattices. Transmission spectra and transition matrix elements $M_{21}$ and $M_{12}$ for $W/V$=0.8 [(a) and (c)] and for $W/V$=1 [(b) and (d)]. (e-h) - propagation dynamics for $W/V$=0.8 and *1*st FB mode with single $k_0$ at the input. Evolution of the relative populations of the 1st (blue curves) and 2nd (green curves) modes for the left $k_0D/\pi$=-0.15 (e) and right $k_0D/\pi$=0.15 (f) tilted incidence; power evolution for the left (g) and right (h) tilted incidences. (i-l) - propagation dynamics for $W/V$=1 and the left tilted Gaussian beam at the input. Evolution of the relative populations of the 1st (blue curves) and 2nd (green curves) modes (i); intensity pattern (j); intensity at $z$=400 (k); power evolution (l); dark-colored thin lines in figs. (e, f, i) and blue lines in fig. 1 (g, h, k, l) represent numerical results while light-colored thick lines in fig. 1 (e, f, i) and red lines in figs. (g, h, k, l) represent CMT results.

The propagation dynamics of the LTI beam $\psi(x, z=0)=\exp[-(x+\delta)^2/\sigma^2]\exp(ik_0x)$ ($\sigma$=60, $\delta$ =*400*, $k_0D/\pi$ = -0.15) at the PTP is shown in Fig. 1 (i-l). The evolution of $A_1$ (blue curves) and $A_2$ (green curves) at $k=k_0$ are depicted in Fig. 1(i). $A_1$ remains constant upon propagation ($M_{12}=0 \forall k \leq 0$), which results in the almost linear growth of $A_2$ (small deviation of linear growth is due to the phase-shifted initial population of the *2*nd mode). The numerically obtained intensity pattern is shown in Fig. 1(j). In addition to the double refraction[2] the intensity pattern exhibits an intensity-locked region between the two diverging beams, which develops due to the positive overlap of intensity pattern with gain-loss distribution. Intensity oscillations in this region conform to the periodicity of the lattice while the amplitude of oscillations remains constant between the two diverging beams, which can be seen in Fig. 1(k) showing cross-section of intensity at $z$=400. The amplitude of the intensity in this region remains constant upon propagation whereas its width growth linearly as distance between diverging beams increases corresponding to the linear growth of power shown in Fig. 1(l). Using the angular dependence of $M_{21}$ and $M_{12}$ one can control the power response of the system by changing the angle of incidence and corresponding adjustment of longitudinal frequency modulations to satisfy the resonance condition. In the UCR one can manipulate both sign and magnitude of power oscillations whereas at the PTP only the rate of the linear power amplification can be adjusted.

The power control technique introduced here should pave the road for new discoveries and applications in PTS optics and gain-loss metamaterials. In addition we are working on a similar power control technique based on Landau-Zener tunnelling induced by applying AC field to PTS lattices (investigation is currently in progress).

## REFERENCES


1. Bender, C. M. and C. Boettcher, *Phys. Rev. Lett.*, Vol. 80, 5243-5246, 1998.
2. Makris K. G., R. El-Ganainy, and D. N. Christodoulides, *Phys. Rev. Lett.* Vol. 100, 103904, 2008.
3. Zhao X., G. A. Georgakis, and Q. Niu, *Phys. Rev. B* Vol. 54, R5235-R5238, 1996.
4. Fischer M. C., K. W. Madison, Q. Niu, and M. G. Raizen, *Phys. Rev. A* Vol. 58, R2648-R2651, 1998.
5. Kartashov Y. V., V. A. Vysloukh, and L. Torner, *Phys. Rev. Lett.* Vol. 99, 233903, 2007.
6. Makris K. G., D. N. Christodoulides, O. Peleg, M. Segev, and D. Kip, *Opt. Exp.* Vol. 16, 10309, 2008.
7. Shandarova K., et. al., *Phys. Rev. Lett.* Vol. 102, 123905, 2009.
8. Vysloukh1 V. A. and Y. V. Kartashov, *Opt. Lett.* Vol. 39, 5933-5936, 2014.

# Origin of folded bands in metamaterial crystals

**Peter Markoš** and **Richard Hlubina**

Department of Experimental Physics, Faculty of Mathematics, Physics and Informatics,
Comenius University in Bratislava, Slovakia
peter.markos@fmph.uniba.sk

**Abstract**— Spectra of metamaterial photonic crystals may contain frequency bands which disappear inside the Brillouin zone (folded bands). We observe that the wave equations for such systems are essentially non-Hermitian, but $\mathcal{PT}$ -symmetric. We show that the real-frequency spectra correspond to $\mathcal{PT}$-symmetric solutions of the wave equation. At those momenta in the Brillouin zone where no real solutions exist, there appear pairs of complex-frequency solutions with spontaneously broken $\mathcal{PT}$ symmetry.

Recently, it has been found [1] that two dimensional array of cylinders made from the left-handed material with simultaneously negative permittivity and permeability exhibits unusual frequency spectrum. In particular, the spectrum contains so-called folded bands which disappear in certain region of the Brillouin zone.

We calculate numerically the transmission of plane electromagnetic wave through two dimensional array of left handed cylinders, find the band structure and study how folded bands arises in the frequency spectrum when the radius $R$ of metamaterial cylinders increases (Figure 1). The existence of folded bands indicates that the wave equation for the electromagnetic field in a metamaterial photonic crystal is non-Hermitian. We indeed show [2] that the operator $\mathcal{M}$ which enters the wave equation for the propagating wave

$$\mathcal{M}\vec{H} \equiv \frac{1}{\mu}\mathrm{rot}\left[\frac{1}{\varepsilon}\mathrm{rot}\right]\vec{H} = \omega^2\vec{H} \tag{1}$$

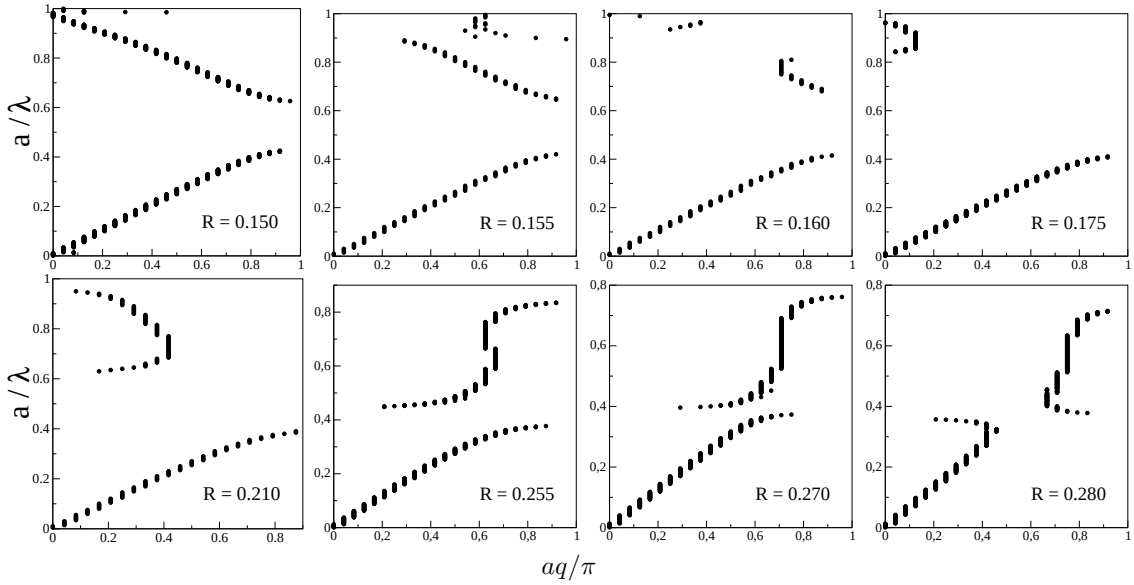



Figure 1: Low frequency ($a/\lambda < 1$) band structure of two dimensional periodic array of left-handed cylinders with permittivity $\epsilon = -1.8$ and permeability $\mu = -5$ and various cylinder radius $R$ (measured in lattice period $a$). The wave vector $q$ is parallel to the ΓX direction. Various folded bands appears when the cylinder radius $R$ increases. Note two folded bands which arise when the radius $R$ increases from 0.270 to 0.280.

is essentially non-Hermitian when both permittivity $\varepsilon$ and the permeability $\mu$ are negative inside cylinders. The essential non-Hermiticity means that, in contrast to dielectric photonic crystals [3], it cannot be avoided by any reformulation of the problem.

In spite of this non-Hermiticity, the operator $\mathcal{M}$ has real frequency spectra, $\omega^2 > 0$, if it possesses additional symmetry – the $\mathcal{PT}$ symmetry in the present case. Folded bands appear in the spectrum if this symmetry is broken [4]. This can be explicitly verified for the simplest one-dimensional case where the eigenfunctions, which correspond to complex frequencies, lost the $\mathcal{PT}$ symmetry [2].

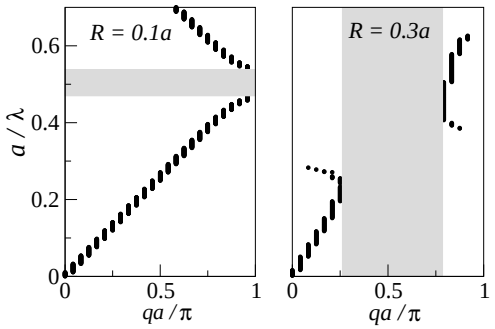



Figure 2: Dispersion relations along the ΓX direction for the two-dimensional model with cylinder radii $R = 0.1a$ and $R = 0.3a$. Shaded regions highlight the frequency gap (with complex momentum solutions inside) and the momentum gap (with complex frequency solutions inside) in the left and right panels, respectively.

Folded bands are closely related to the frequency gap in periodic systems. In fact, it is well known that within the frequency gap, there exist only solutions with a complex wave-vector. On the other hand, folded bands imply the existence of a momentum gap, inside which there appear only states with a complex frequency. Thus the momentum gap is a space-time dual of the frequency gap (Figure 2).

We have explained the origin of the recently discovered folded bands in spectra of metamaterial photonic crystals. They could be observed if (1) the boundary-value problem is essentially non-Hermitian and (2) the possible reality of its spectrum has to be guaranteed by additional symmetry, such as the $\mathcal{PT}$ symmetry in the metamaterial case. In systems fulfilling these assumptions, folded bands should be commonplace.

## ACKNOWLEDGMENT

This work was supported by the Slovak Research and Development Agency under Contract No. APVV-0108-11 and by Agency VEGA under Contract No. 1/0372/13.

## REFERENCES

1. Chen, P. Y., C.G. Poulton, A. A. Asatryan, M. J. Steel, L. C. Botten, C. Martin de Sterke and R. C. McPhedran, "Folded bands in metamaterial photonic crystals," *New J. Phys.* Vol. 13, 053007, 2011.
2. Markoš, P. and R. Hlubina, "Origin of folded bands in metamaterial crystals," *Phys. Lett. A* Vol. 380, 811, 2016.
3. Sakoda, K., "Optical Properties of Photonic Crystals", Springer, 2005.
4. Bender, C. M., "Introduction to PT symmetric quantum theory," *Contemp. Phys.* Vol. 46, 277, 2005.

# Non-Hermitian Acoustics

**H. Ramezani[1,2], C. Shi[2], M. Dubois[2], Y. Wang[2], and X. Zhang[2]**

[1]Department of Physics, University of Texas Rio Grande Valley, Brownsville, TX, USA
[2]NSF Nano-scale Science and Engineering Center, University of California, Berkeley, USA
hamidreza.ramezani@utrgv.edu

**Abstract**— We introduce the concept of non-Hermitian parity-time (PT) symmetric acoustics. We show that the PT symmetric acoustic structure becomes transparent from one side at the exceptional point with perfect transmission and zero reflection from one side. We demonstrate a method to obtain simultaneous control of complex-valued potentials and multiple interference inside the structure to accomplish the exceptional point at any given frequency. Moreover, we propose a mechanism for directional excitation based on impedance matched PT symmetric potential.

Controlling acoustic transport at will is a long-sought-after goal in modern physics and applications. On the other hand, parity and time symmetric structures show extraordinary transport properties. Thus, realizing PT symmetric acoustic structure is highly desirable. The common physical feature of any parity and time symmetric structure is the existence of a deliberate non-Hermiticity. Namely, a carefully and delicately balanced amplification and absorption mechanism. Starting from Helmholtz equation and using the symmetries in the system, we can show that only at specific frequencies called exceptional point, the PT symmetric acoustic structure becomes transparent [1]. More specifically transmission becomes perfect and reflection from one side tends to zero. Exceptional points occur only for specific values of the gain and loss parameter. Unidirectional transparency is a consequence of destructive interference generated by the gain and loss layers.

In acoustics, one can find materials with inherent damping. On the other hand until now, nobody claimed the observation of the acoustic gain material in the nature. Fortunately, we can realize gain materials effectively by delicate feed-back systems using the active sound controlling apparatus. However, as mentioned earlier, PT symmetry requires an exact balance of loss and gain in the medium, and the dispersive behavior of the most loss and gain materials (if any exists) prevents this condition to be fulfilled over a broad frequency range. Hence, it is challenging to access the exceptional points in practice.

By designing the spacing between the gain and loss layers, in an Experiment, we show that one can control the scattering process in any PT symmetric acoustic structure. The gap corresponds to a phase delay between the gain and loss cells. We can scan the response of the structure as a function of spacing and frequency using the transfer-matrix formalism. Thus, we can access an exceptional point where the reflection from the loss side vanishes; the transmission becomes unity and the reflection from the gain side gets nonzero values, making the system to be unidirectional transparent [2].

Unidirectional transparency at the exceptional point of a PT symmetric acoustic structure can be combined with transformation optics to result in a one-way cloak. This is possible since the acoustic wave equation is invariant under coordinate transformation. Our proposed PT symmetric cloak protects its inner information from being detected only along one side and not another [1].

We mentioned that the existence of the exceptional point is a consequence of the interferences. By eliminating the interferences using impedance matching, we can remove all the scattering events in the 1D PT symmetric acoustic structure and have a perfect transmission without refection from both side. However, the field amplitude distribution within the gain and loss regions is strongly influenced by the direction of the incoming field. This suggest that by embedding an impedance matched PT symmetric potential in a three-port system we can achieve directional excitation without breaking reciprocity. Specifically, the excitation of the third port is contingent on the direction of incidence while transmission in the main channel is immune [3].

In conclusion, we introduce the notion of PT symmetry in acoustics. We show how one can obtain the exceptional point at will and have unidirectional transparency in the desire direction. We demonstrate one-way PT symmetric cloak. Finally, we proposed a unique approach to obtain unidirectional excitation. Our approach broadens the scope of applications for PT symmetric devices in different fields including optics, microwaves, electronics, which are crucial for sensing, imaging, cloaking, lasing, and absorbing.

**REFERENCES**


1. Zhu, X., Ramezani, H., Shi, C., Zhu, J. and Zhang, X. "PT Symmetric Acoustics," *PRX*, Vol. 4, 031042, 2014.
2. Shi, C., Dubois, M.,Chen, Y., Cheng, L., Ramezani, H.,Wang, Y. and Zhang, X., "Accessing the Exceptional Points of Parity-Time Symmetric Acoustics," *Nat. Com.*, In press, 2016.
3. Ramezani, H., Dubois, M., Wang, Y. and Zhang, X., "Directional Excitation Without Breaking Reciprocity," Under review, 2016.

# Rings of Exceptional Points

**M. Soljačić**[1*]
[1] Department of Physics, MIT; USA
[*]corresponding author: soljacic@mit.edu

**Abstract** – We present our recent work on exceptional points in 2D periodic photonic crystal slabs. Since these are 2D systems, the resulting system has not only one exceptional point (like is typical in 1D), but rather a ring of exceptional points. Its properties and potential applications will be discussed.

In recent years, 3 quite different novel photonic phenomena have been drawing a lot of attention: accidental Dirac points, Bound States in Continuum, and Exceptional Points (in non-Hermitian systems). It turns out that at the boundary of these 3 systems, an interesting new phenomenon emerges: a ring of Exceptional Points. We present our recent results on this topic [1], as well as some potential applications.

**REFERENCES**

1. "Spawning rings of exceptional points out of Dirac cones" B. Zhen, C. W. Hsu, Y. Igarashi, L. Lu, I. Kaminer, A. Pick, S-L Chua, J.D. Joannopoulos, and M. Soljacic. *Nature*, **525**, 354 (2015).

# Tailoring spectral properties of local Parity-Time symmetry grating devices for integrated optics

**Anatole Lupu [1*], Henri Benisty[2], Andrei V Lavrinenko[3]**

[1] IEF, CNRS, Univ Paris Sud, Université Paris-Saclay, 91405 Orsay, France

[2] Laboratoire Charles Fabry, Institut d'Optique Graduate School, CNRS, Univ Paris Sud, Université Paris-Saclay, 2 Avenue Augustin Fresnel, 91127 Palaiseau, France

[3] DTU Fotonik – Department of Photonics Engineering, Technical University of Denmark, Oersteds Plads 343, DK-2800 Kgs. Lyngby, Denmark

[*]corresponding author: anatole.lupu@u-psud.fr

**Abstract-**

We explore the functionalities of nonuniform Parity-Time -symmetric structures with engineered complex-index-modulation profiles. The use of nonuniform coupling or gain-loss modulation profiles brings a number of advantages as compared to the uniform PT-symmetric structures. The intention of the undertaken approach is to show that many conventional techniques previously developed for passive-type grating-assisted or coupled-waveguide devices for integrated optics can be transposed and adapted to a PT-symmetric case, fostering thus a new generation of active and functional photonic devices.

## 1. Introduction

In our recent work [1] we considered the example of nonuniform PT-symmetric Bragg gratings with a complex index profile modulated by a slowly varying envelope function, with the aim of combining the apodization techniques of classical Bragg gratings with the advantages of PT-symmetry such as unidirectionality. We demonstrated in these two-port devices the possibility to achieve an efficient apodization of the PT-symmetric Bragg grating spectral response with a standard Hamming window function. To ease implementation of the apodization in real structures with local binary nature of the real and imaginary index contributions, this approach was extended to the duty-cycle modulated periodic or deterministic aperiodic binary PT-symmetric gratings. It appears that many conventional techniques previously developed for passive type Bragg gratings or related devices can be transposed and adapted to a PT-symmetric case, provided the constraints of real and imaginary part modulation are properly combined. In the current contribution we further extend this concept to explore the functionalities that can be achieved in the case of four-ports Bragg grating assisted directional couplers with a nonuniform complex PT-symmetric profile.

## 2. Nonuniform local PT-symmetric Bragg grating assisted directional coupler switch

Add-drop multiplexers combining operation of a directional coupler with a Bragg reflector (BR) are known for years. An important feature of these devices is the very versatile operation that can be achieved by slightly changing their design. Single [2] or dual band transmission operation [3], frustration of co-directional coupling [4] are only a few examples of functional possibilities. The implementation in such structures PT-symmetric gain-loss variations brings the additional and highly desirable tunability and switching functionalities.

A sketch of a PT symmetric Bragg grating waveguide (PTSBG) based vertical coupler is shown in Fig. 1(a). The operation principle is based on the modification of the PTSBG dispersion properties used for controlling

phase matching between two waveguides [5]. A practical realization can be envisioned, for example, by means of hybrid integration technology of III-V/SOI semiconductors. The use of PTSBG assisted directional couplers in WDM applications requires the control of the spectral profile, related namely to the reduction of the secondary sidelobes level to avoid impairment on adjacent WDM channel cross-talk.

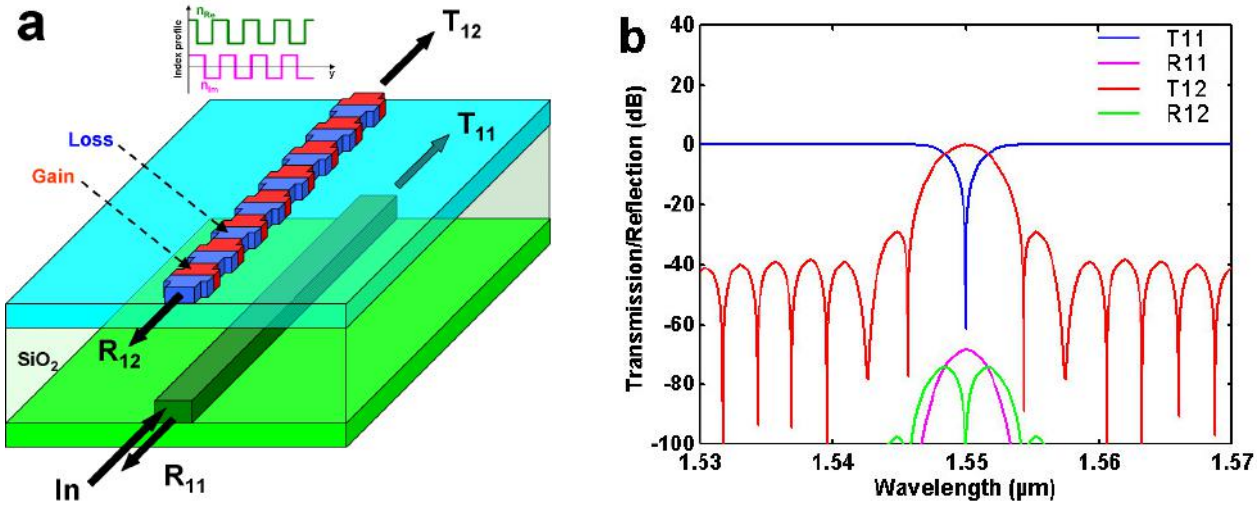



**Fig. 1: (a) Sketch of a PTSBG assisted directional coupler with rectangular grating profile. Gain and loss grating sections are indicated by red and blue colors, respectively; (b) Phase-matching-allowed apodized spectral response.**

The stamp down of secondary sidelobes for the considered example of PTSBG-assisted directional couplers can be achieved by tapering/apodizing the coupling profile. As appears in Fig. 1(b), the application of a Hamming function suppresses by more than 30dB the sidelobes level (vs. ~15 dB for a uniform PSTBG). Moreover, the reflection level remains very low, indicating that the core PT-symmetric properties of PTSBG are fully preserved.

As a further prospect to master linear and nonlinear operation of such devices, it would be interesting to bridge our current approach exploiting PT-symmetric and apodization techniques with the additional degree of freedom that can be achieved by the longitudinal offset in the periodic index modulation [6,7].

## REFERENCES


[1] A. Lupu, H. Benisty and A.V. Lavrinenko, “Tailoring spectral properties of binary PT-symmetric gratings by duty-cycle methods,” IEEE J. Sel. Top. Quant Electron. (2016); http://dx.doi.org/10.1109/JSTQE.2016.2542791.

[2] K. Muhieddine, A. Lupu, E. Cassan, J-M. Lourtioz, “Proposal and analysis of narrow band transmission asymmetric directional couplers with Bragg grating induced phase matching,” Opt. Express 18, 23183-23195 (2010).

[3] A. Lupu, K. Muhieddine, E. Cassan, J-M. Lourtioz, “Dual transmission band Bragg grating assisted asymmetric directional couplers,” Opt. Express 19, 1246-1259 (2011).

[4] J.-L. Archambault, P.St.J. Russell, S. Barcelos, P. Hua, L. Reekie, “Grating-frustrated coupler: a novel channel-dropping filter in single-mode optical fiber,” Opt. Lett. 19,180–182 (1994).

[5] A. Lupu, H. Benisty, and A. Degiron, “Using optical PT-symmetry for switching applications,” Photonics Nanostruct. Fundam. Appl. 12, 305-311 (2014).

[6] A. A. Sukhorukov, A. V. Lavrinenko, D. N. Chigrin, D. E. Pelinovsky, and Y. S. Kivshar, "Slow-light dispersion in coupled periodic waveguides," J. Opt. Soc. Am. B 25, C65-C74 (2008).

S. Ha, A.A. Sukhorukov, A.V. Lavrinenko, I.V. Shadrivov, D.A. Powell, and Y.S. Kivshar, “Observation of tunneling of slow and fast electromagnetic modes in coupled periodic waveguides,” Appl. Phys. Lett. 98, 061909 (2011).

# Plasmonics and Nanophotonics Based on Graphene and Related 2D Materials

# Hybrid Graphene Metasurfaces to Control Electromagnetic Radiation

**Christos Argyropoulos**
Department of Electrical and Computer Engineering, University of Nebraska-Lincoln, Lincoln, Nebraska, 68588, USA
corresponding author: christos.argyropoulos@unl.edu

**Abstract**-Graphene cannot efficiently interact with light due to its extremely thin nature. We will demonstrate ways to hybridize graphene with all-dielectric metasurfaces in order to increase the coupling between the far-field radiation and graphene. In addition, we will introduce metasurfaces with resonating elements made only of graphene, designed based on the appropriate patterning of the graphene monolayer's shape. The proposed hybrid graphene metasurfaces can lead to the design of electro-optical modulators and THz non-reciprocal devices, operating as magnetic-free isolators.

The recently discovered graphene is a two-dimensional—one-atom-thick— conductive material with zero-bandgap and linear dispersion. Its properties can be tuned in the entire infrared and optical frequency range by varying its doping level with chemical, electrostatic and optical ways. However, it cannot efficiently interact with light due to its extremely thin (one-atom-thick) nature. Towards this goal, we will present ways to hybridize graphene with special metasurfaces in order to increase the coupling and interaction between the far-field radiation and graphene at the nanoscale. These metasurfaces are designed to possess very high in-plane fields to strongly interact with the surface conductivity properties of graphene. It will be demonstrated that all-dielectric metasurfaces are more appropriate compared to metallic metasurfaces to produce strong in-plane fields along their geometry.

In general, all-dielectric silicon-based metasurfaces are powerful platforms to enhance light-matter interactions at nanoscale regions. Their low-loss nature, CMOS processing compatibility, and increased damage threshold from heating promise to outperform the functionalities of the recently established plasmonic metallic metasurfaces, which exhibit high Ohmic losses and broader scattering or transmission responses. The low-loss properties of all-dielectric metasurfaces can lead to very high quality factor (Q-factor) Fano [1] and electromagnetically induced transparency (EIT) resonances [2]. These type of metasurfaces can provide fine control over the amplitude, phase and polarization of light, with the possibility to fabricate a number of compact subwavelength optical components and with the additional advantage of being ultrathin and CMOS-compatible.

In our talk, we will present all-dielectric semiconductor-based metasurfaces hybridized with graphene in order to obtain new electro-optical modulators at telecom wavelengths. As an example, a hybrid graphene/dielectric metasurface design is presented in Fig. 1(a) to achieve tunable and modulated transmission at near-IR frequencies [3]. The all-dielectric hybrid metasurface is composed of periodically arranged pairs of asymmetric silicon (Si) nanobars with graphene placed on top of this configuration. This dielectric metasurface can sustain trapped magnetic resonances with a sharp Fano-type transmission or reflection signature [4]. The strong in-plane electric field distribution at the resonance is computed and shown in the inset of Fig. 1(b). One-atom-thick graphene is placed over this dielectric metasurface and very strong transmission modulation is

obtained at near-IR telecom wavelengths when the doping level of graphene is increased, as it can be seen in Fig. 1(b). The enhanced in-plane fields along the all-dielectric metasurface strongly interact with the tunable properties of graphene. This leads to strong coupling between the incoming radiation and graphene. Several new integrated nanophotonic components are envisioned based on the proposed devices, such as efficient electro-optical transmission modulators and new sensitive biosensors.

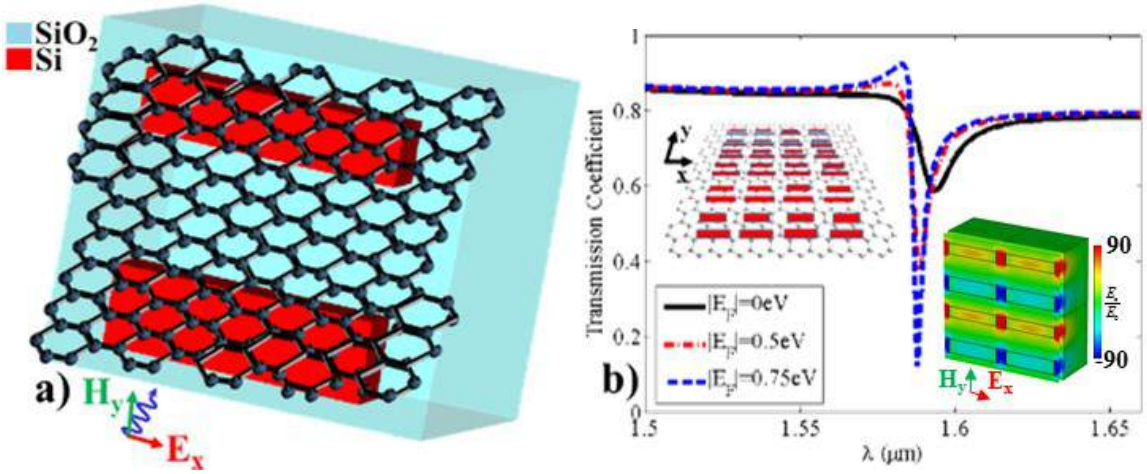



Figure 1 (a) Unit cell of the hybrid graphene/dielectric metasurface configuration. (b) Enhanced transmission modulation. The sharp Fano resonance transmission signature rapidly varies as we increase the doping levels in graphene from $|E_F|$=0eV to $|E_F|$=0.75eV. The insets show the periodic geometry and the strong in-plane fields induced at the resonant frequency.

Graphene can also be patterned to circular or rectangular patches and can be used by itself as the building element of metasurfaces. Highly confined surface plasmons are formed at the surface of graphene at low THz frequencies. It effectively behaves as metal at this frequency range. Hence, graphene THz metasurfaces can be designed when we appropriately decorate the shape of a graphene monolayer. Towards this end, graphene offers unique opportunities, considering the unusually strong interaction of this material with THz waves and its unique field effect, which allows efficient control of its electromagnetic properties via electrical signals and chemical doping. During our talk, we will present magnetic devices, ultrathin waveplates and polarizers, and magnetic-free isolators operating at THz frequencies based on different patterned graphene metasurface designs.

**Acknowledgements:** This work was partially supported by the Office of Research and Economic Development at University of Nebraska-Lincoln.

## REFERENCES

1. Wu, C., *et al.*, "Spectrally selective chiral silicon metasurfaces based on infrared Fano resonances," *Nat. Commun.*, Vol. 5, 3892, 2014.
2. Yang, Y., *et al.*, "All-dielectric metasurface analogue of electromagnetically induced transparency," *Nat. Commun.*, Vol. 5, 5753, 2014.
3. Argyropoulos, C., "Enhanced transmission modulation based on dielectric metasurfaces loaded with graphene," Opt. Express, Vol. 23, 23787-23797, 2015.
4. Zhang, J., MacDonald, K. F., and Zheludev, N. I., "Near-infrared trapped mode magnetic resonance in an all-dielectric metamaterial," *Opt. Express*, Vol. 21, 26721–26728, 2013.

# Controlling the tunability of graphene in bridged and unbridged nano-disk dimers

**G. Rosolen[1*] and B. Maes[1]**

[1]Micro- and Nanophotonic Materials Group, University of Mons, Place du Parc, 20, 7000, Mons, Belgium

[*]corresponding author: gilles.rosolen@umons.ac.be

**Abstract**-Graphene is a promising material for sensor applications thanks to its strong light-matter interaction and its high tunability by doping. We investigate varyingly doped graphene nano-disks in a dimer configuration and demonstrate a complex absorption response arising from hybridization of dark modes. The resonances can be further enhanced and sharpened when a graphene ribbon links the two dimers, with a tunable resonance wavelength enabled by the junction doping.

The resonant properties of metallic nanoparticles are actively explored nowadays for a wide range of applications[1]: biosensing, nonlinear optics, nanocircuits, optoelectronics, transparent displays etc. However, they suffer from a limited tunability, only possible by varying size, geometry or constitutive metals, while graphene flakes offer resonances strongly adjustable by doping[2]. Here, this property is judiciously exploited in graphene nano-disk dimers with strong absorption resonances and complex modes coupling[3], as shown in Figure 1(a) and (c). Furthermore, an enhanced and narrower resonance is obtained when connecting the dimer with a graphene ribbon bridge: the charge transfer plasmon (not shown here). All these excitations are tunable with graphene doping, paving the way for new optoelectronic devices.

Graphene single disk resonances have already been investigated[4], but here we extend the study to higher order modes. Although various resonances are dark under normal incidence (they do not couple with the incident field), we show that they become bright (they resonate) when we consider graphene nano-disk dimers[3]. The absorption spectrum and the graphene disk modes are obtained with three-dimensional COMSOL simulations, corroborated with an analytical model. Figure 1(b) shows the considered dimer of 60 nm diameter graphene disks separated by a 5 nm distance. One of the disks is 0.4 eV doped and the second one has a doping varying from 0 to 1 eV. Their absorption efficiency under normal incidence (electric field in the x-direction) is represented in logarithmic scale in Figure 1(c) and shows an intricate absorption pattern, explained in the following.

There are two main patterns: one curved (with stronger absorption for the curved line at the top) and one vertical. The straight vertical resonances are from the fixed 0.4 eV doped graphene disk, with the first dipolar mode resonating at 6.3 μm and the higher order modes appearing at smaller wavelengths. The curved pattern comes from the disk with varying doping. The continuous (dashed) black lines represent the theoretical 6 first modes of the varying (0.4 eV) doping graphene disk.

When the resonance patterns (curved and straight) interact, the modes hybridize and give rise to two anti-crossing resonances. For example, this is observed in points 1 and 2 or in points 3 and 4 in Figure 1(c). The corresponding enhanced electric field of point 4 is represented in Figure 1(a) and shows that the single disk dark quadrupolar mode becomes bright when it hybridizes with a dipolar mode in a dimer configuration.

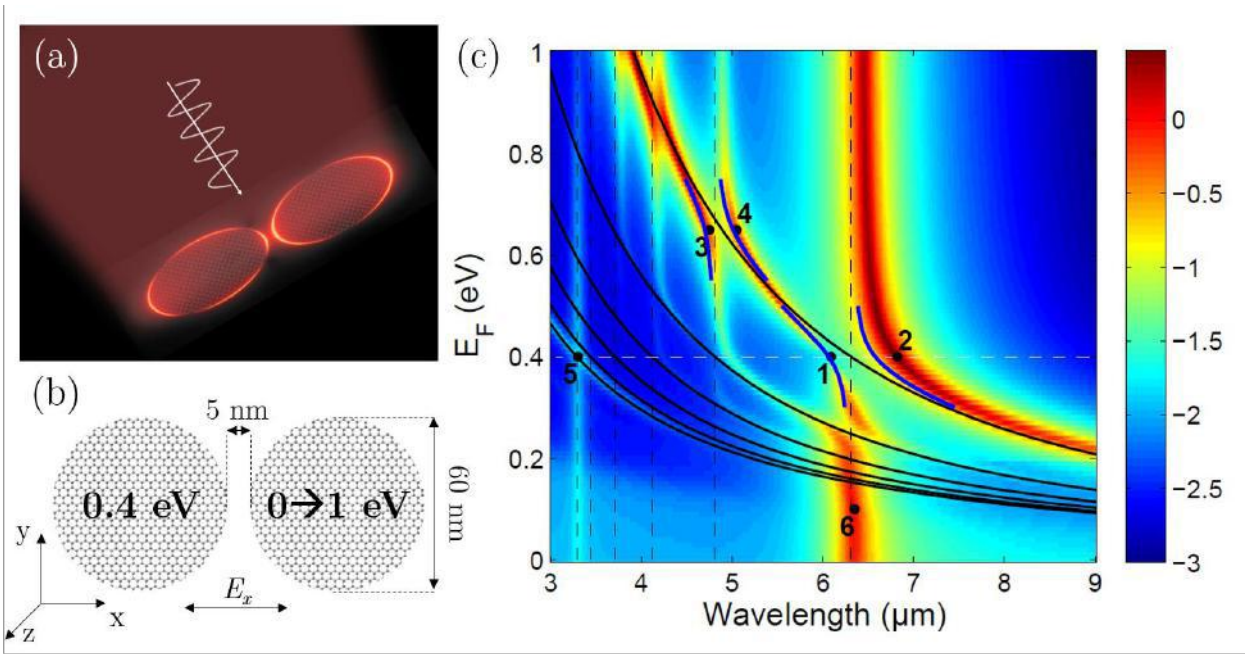



**Figure 1 : (a) Incident electric field exciting a hybridized graphene dimer mode. (b) Top view of the asymmetrically doped graphene nano-disk dimer. The incident field is propagating along z. (c) Absorption efficiency in logarithmic scale of the graphene dimer represented in (b) for the x-polarization. The modes hybridize when the modes of the single 0.4 eV doped disk (dashed lines) cross the modes of the variously doped single disk (solid lines).**

Another part of the work is devoted to bridged dimers, demonstrating a red-shifted resonance, stronger and narrower than the unbridged dimer resonance. Furthermore, that resonance is adjustable by doping the graphene junction connecting the nano-disks. Graphene-based components thus offer new exciting possibilities compared to conventional metals for their ease of tunability.

**Acknowledgements**

This work is supported by the Belgian Science Policy Office under the project Photonics@be (P7-35) and by the Fonds National de Recherche Scientifique (FNRS) in Belgium.

**REFERENCES**

1. Pelton, M. *et al.* "Metal-nanoparticle plasmonics," *Laser & Photon. Rev.*, Vol. 2, No. 3, 136-159, 2008.
2. Fang, Z. *et al.* "Gated Tunability and Hybridization of Localized Plasmons in Nanostructured Graphene," *ACS Nano*, Vol. 7, No. 3, 2388-2395, 2013.
3. Rosolen, G. and B. Maes, "Asymmetric and connected graphene dimers for a tunable plasmonic response," *Phys. Rev. B*, Vol. 92, No. 20, 205405, 2015.
4. García de Abajo, F.J. *et al.*, "Graphene plasmonic: Challenge and opportunities," *ACS Phot.*, Vol. 80, No. 24, 245435, 2009.

# Light Manipulation in Cylindrical Graphene-Covered Gyrotropic Structures.

**D. A. Kuzmin[1*], I. V. Bychkov[1], and V. G. Shavrov[2]**
[1]Chelyabinsk State University, Chelyabinsk, Russian Federation
[2]Kotel'nikov Institute of Radio Engineering and Electronics of RAS, Moscow, Russian Federation
[*]corresponding author: kuzminda89@gmail.com

**Abstract**-In this work we summarize results of our previous investigation on speckle-pattern rotation of light propagating in gyrotropic graphene-covered optical fiber and present our new study on plasmon-polariton manipulation in gyrotropic graphene-covered nanowire. Investigation shows that in both cases light energy distribution rotates moving along propagation axis. Rotation angle may be controlled by both gyrotropy of the core and chemical potential of graphene. Results may be used for development optics and plasmonic devices as well as for sensing applications.

It is well known that magnetic field (or magnetization) may lead to rotation of speckle-pattern of light propagating in gyrotropic optical fiber[1-3]. Recently, we have shown that in case of graphene-coated optical fiber, one may control rotation angle by both magnetic field and chemical potential of graphene layer[4]. Rotation angle may reach about 20 degrees at wavelength of light 0.633 μm, fiber core radius 4.5 μm, graphene chemical potential 1 eV, fiber length about some centimeters, and magnetic fields about some Teslas. Taking into account the possibility of magnetooptics effects enhancement in magnetoplasmonic structures, it is of interest to investigate the possibility of realization the similar effect for cylindrical plasmonic waveguides.

Investigation shows, for example, that rotational angle may reach up to 45 degrees at gyration parameter $\varepsilon_a$ = ±0.5 (antisimmetric part of permittivity), radius of nanowire $R$ = 50 nm, frequency $f$ = 100 THz, and graphene chemical potential 1 eV. Plasmon-polaritons distribution rotates at scale of 100 nm. Variation of chemical potential of graphene may be used for rotation angle manipulation as well. Example distributions of longitudinal electric field component $E_z$ for mode with azimuthal index $m$ = 4 are shown on Fig. 1.

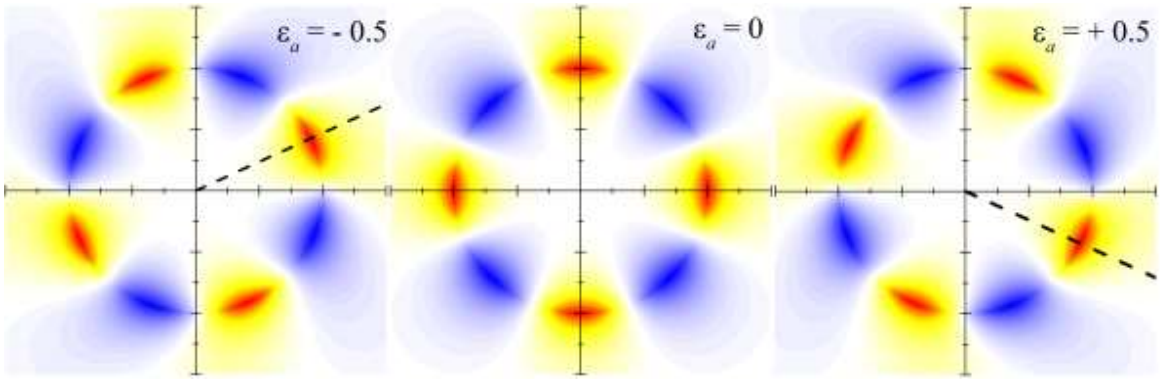



Figure 1. Distribution of longitudinal electric field component for plasmonic mode with azimuthal index $m$ = 4, graphene chemical potential 1 eV. Dashed line shows the position of maximum. Angles of rotation are ±25 degrees at gyration parameter $\varepsilon_a$ = ±0.5, respectively.

Rotation angle reaches a maximum when plasmonic mode become non-propagating one, i.e. when propagation length became comparable with wavelength of plasmon-polariton. Thus, manipulation is more effective for evanescent modes.

Results of the investigation may be used for numerous plasmonic applications as well, as for magnetic sensing.

The work was supported by RFBR grants ## 16-37-00023, 16-07-00751. Numerical calculations were supported by RScF grant # 14-22-00279.

**REFERENCES**

1. Baranova, N. B., and B. Y. Zel'dovich, “Rotation of a ray by a magnetic field,” *JETP Letters*, Vol. 59, No. 10, 681-684, 1994.
2. Darsht, M. Y., I. V. Zhirgalova, B. Y. Zel'dovich and N. D. Kundikova, “Observation of a" magnetic" rotation of the speckle of light passed through an optical fiber,” *JETP Letters*, Vol. 59, No. 11, 763-763, 1994.
3. Ardasheva, L. I., N. D. Kundikova, M. O. Sadykova, N. R. Sadykov and V. E. Chernyakov, “Speckle-pattern rotation in a few-mode optical fiber in a longitudinal magnetic field,” *Optics and Spectroscopy*, Vol. 95, No. 4, 645–651, 2003.
4. Kuzmin, D. A., I. V. Bychkov and V. G. Shavrov, “Influence of graphene coating on speckle-pattern rotation of light in gyrotropic optical fiber,” *Optics Letters*, Vol. 40, No. 6, 890-893, 2015.

# Ultrafast Plasmon Emission and Hot Carrier Dynamics in Photoexcited Graphene

**J. M. Hamm**[1], **A. F. Page**[1], **J. Bravo-Abad**[2], **F. J. Garcia-Vidal**[2],**and O. Hess**[1]

[1]Imperial College London, UK
[2]Universidad Autonoma de Madrid, Spain
j.hamm@imperial.ac.uk

**Abstract**— Owing to the overlap of plasmon and pair excitations in energy/momentum space plasmons in photoexcited graphene can become amplified or spontaneously emitted via the decay of electron/hole excitations. Based on Boltzmann equations for the carrier, plasmon and phonon populations we investigate the nonequilibrium relaxation dynamics after femtosecond excitation and show that plasmon emission drives the decay of population inversion on 100-fs scales.

Graphene owes its extraordinary optical properties to the presence of Dirac points in its bandstructure. The particular combination of a 2D plasmon dispersion and a gapless bandstructure allows plasmons to couple strongly to the particle/hole plasma via interband absorption (Landau-damping) and emission processes. It was recently established that nonequilibrium plasmon emission, similar to Auger recombination [1], provides a mechanism for the ultrafast decay of population inversion (see Fig. 1) [2, 3, 4].

We here study the transient nonequilibrium relaxation dynamics of the coupled carrier, plasmon and phonon system in suspended graphene after photoexcitation. Our analysis is based on Boltzmann equations, the random-phase approximation, and the assumption of a two-component particle/hole plasma in quasi-equilibrium. We calculate the inter- and intraband emission rates in dependence on the momentary nonequilibrium distribution functions of the carriers, plasmons and phonons and solve the coupled system of nonlinear dynamic equations in time. To identify the role of plasmon and phonon channels during the relaxation dynamics, we first consider these channels in isolation and find that the intraband emission of optical phonons provide efficient channels for plasma cooling once the chemical potential has dropped below the optical phonon energies. In contrast, interband plasmon emission facilitates a fast decay of population inversion, but heats up the plasma, as plasmons are dominatly emitted above the Fermi edge. A main finding of our work is that the combination of plasmon and phonon emission removes bottlenecks present in the phonon and plasmon channels enabling the rapid cooling of the plasma and decay of inversion in photoexcited graphene (see Fig. 2). Our results are in qualitative agreement with experimental observations and suggest that plasmon emission might be the driving mechanism for the decay of population inversion on 100-fs scales [5, 6].

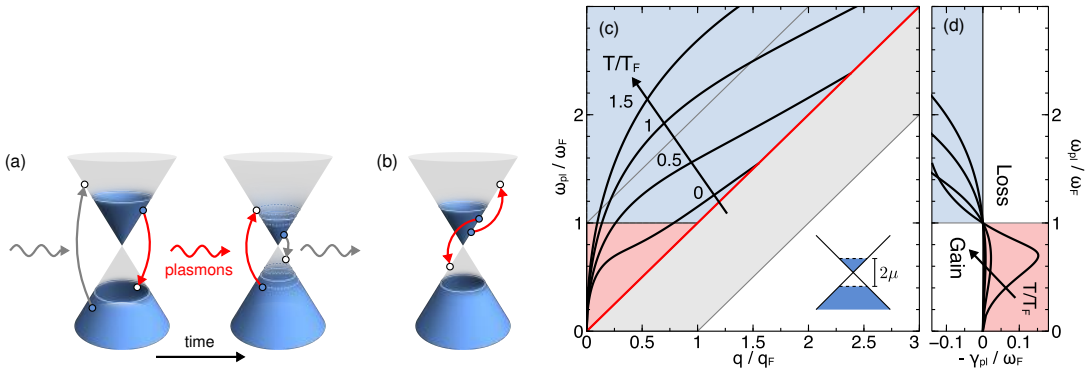



Figure 1: (a) Nonequilibrium plasmon emission in comparison to (b) Auger recombination. cb) Plasmon dispersion $\omega_{\rm pl}(q)$ and (d) plasmon loss/gain spectrum $\gamma_{\rm pl}(\omega)$ of photo-excited (intrinsic) graphene for varying temperature $T/T_F$. The dispersion crosses through regimes of interband gain (red area) and absorption (blue area); quantities scaled with $E_F = 2\mu = \hbar\omega_F = \hbar v_F q_F = k_B T_F$.

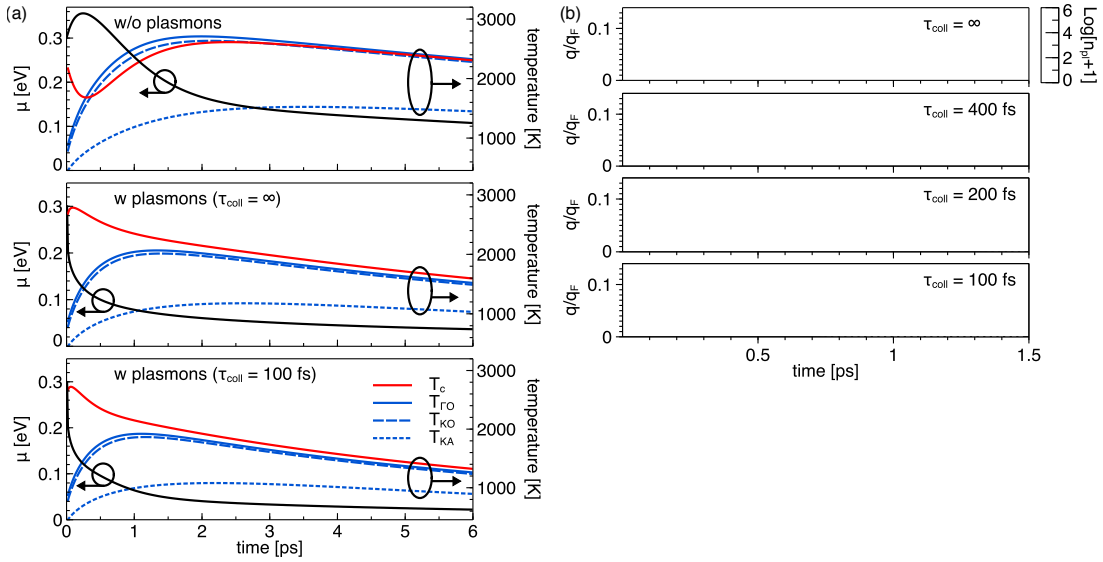



Figure 2: Relaxation dynamics of coupled nonequilibrium electron/hole, plasmon, and phonon systems. (a) shown are chemical potential (black line), carrier temperature (red line) and phonon temperatures without plasmon emission, with plasmon emission and for the collision-free case; (b) dynamical evolution of the nonequilibrium plasmon distribution within the first 1.5 ps.

**REFERENCES**


1. A. Tomadin, D. Brida, G. Cerullo, A. C. Ferrari, and M. Polini, "Nonequilibrium dynamics of photoexcited electrons in graphene: Collinear scattering, Auger processes, and the impact of screening," *Phys. Rev. B* , Vol. 88, 035430, 2013.
2. J. M. Hamm, A. F. Page, J. Bravo-Abad, F. J. Garcia-Vidal , and O. Hess, and "Nonequilibrium plasmon emission drives ultrafast carrier relaxation dynamics in photoexcited graphene," *Phys. Rev. B*, Vol. 93, 041408(R), 2016.
3. A. F. Page, F. Ballout, O. Hess, and J. M. Hamm, "Nonequilibrium plasmons with gain in graphene," *Phys. Rev. B*, Vol. 91, 075404, 2015.
4. F. Rana, J. H. Strait, H. Wang, and C. Manolatou "Ultrafast carrier recombination and generation rates for plasmon emission and absorption in graphene," *Phys. Rev. B* , Vol 84, 045437, 2011.
5. T. Li, L. Luo, M. Hupalo, J. Zhang, M. C. Tringides, J. Schmalian, and J. Wang "Femtosecond Population Inversion and Stimulated Emission of Dense Dirac Fermions in Graphene," Phys. Rev. Lett., Vol. 108, 167401, 2012.
6. I. Gierz, J. C. Petersen, M. Mitrano, C. Cacho, I. C. E. Turcu, E. Springate, A. Stohr, A. Kohler, U. Starke, and A. Cavalleri, "Snapshots of non-equilibrium Dirac carrier distributions in graphene," Nat. Mater., Vol. 12, 1119, 2013.

# Electrical Detection of Graphene Plasmons

**Renwen. Yu[1*], and F. Javier García de Abajo[1,2]**

[1] ICFO-Institut de Ciències Fotòniques, The Barcelona Institute of Science and Technology, 08860 Castelldefels (Barcelona), Spain

[2] ICREA-Institució Catalana de Recerca i Estudis Avançats, Passeig Lluís Companys 23, 08010 Barcelona, Spain

[*]corresponding author: renwen.yu@icfo.es

**Abstract**- Plasmons, the collective oscillations of electrons in conducting materials, have the potential to interface electronic and photonic devices, and thus are widely studied in nanophotonics. Graphene, which has extraordinary optoelectronic properties due to its peculiar band structure, has proven to be an excellent plasmonic material, offering extremely strong, sub-wavelength electric field concentration with low loss. Here we predict extremely compact on-chip electrical detection of single plasmons supported by nanostructured graphene.

Our findings show great promise for the development of integrated plasmonic circuitry, as well as basic components for quantum information processors. Specifically, we calculate a ~16-fold increase in electrical signal across a graphene nanostructure junction when one of its plasmon resonance is excited. By either doping the whole junction or varying the size of the graphene nanostructure, a broad spectral range can be covered, suggesting that this graphene plasmon-meter can find application in future on-chip photonic detectors or sensors.

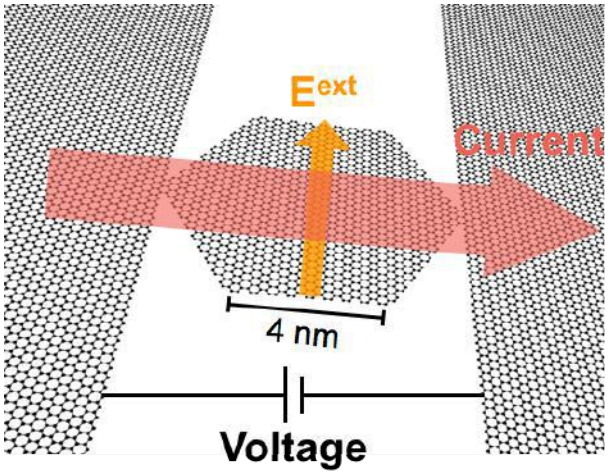



**Figure 1:** Schematics of a plasmon-meter base on nanostructured graphene. A graphene hexagon nanostructure is connected two infinitely extended graphene sheets working as two electrodes.

**REFERENCES**

1. F. Bonaccorso, *et al*., "Graphene photonics and optoelectronics," *Nature Photonics*, Vol. 4, 611, 2010.

2. R. W. Heeres, *et al.*, “On-chip single plasmon detection,” *Nano Letters*, Vol. 10, 661, 2009.
3. K. M. Goodfellow, “Direct on-chip optical plasmon detection with an atomically thin semiconductor,” *Nano Letters*, Vol. 15, 5477, 2015.

# Plasmon-assisted complete optical absorption of ultrashort pulses in nanostructured graphene

**J.R.M. Saavedra[1]**, J. Cerullo[2], V. Pruneri[1,3], S. Wall[1], and F. Javier García de Abajo[1,3]

[1] ICFO Institut de Ciencies Fotoniques, The Barcelona Institute of Science and Technology, 08860 Castelldefels (Barcelona), Spain
[2]Politecnico di Milano, Milano, Italy
[3]ICREA-Institució Catalana de Recerca i Estudis Avançats, Passeig Lluís Companys 23, 08010 Barcelona, Spain
jose.martinez@icfo.es , javier.garciadeabajo@icfo.es

## Abstract

The peculiar electronic structure of graphene results in a large optoelectronic response that holds great potential for technology. For example, this material exhibits a nearly constant absorption ~2.3% over a broad spectral range [1], which can be electrically modulated in the mid-IR by injecting attainable densities of charge carriers. When doped, graphene can sustain plasmons that radically modify its optical response, enabling complete optical absorption for suitably designed patterns [2]. Graphene nanoribbons constitute one of the simplest geometrical patterns that one can produce. They have been extensively studied and their plasmons accurately explained with simple models [3]. When heated to a large electronic temperature, graphene behaves nearly as if is was highly doped, also giving rise to plasmon modes [4].

In this work, we study the possibility of using ultrashort light pulses together with the natural electronic relaxation mechanisms in graphene nanoribbons as a way to tune their optical response. We first discuss the optically induced plasmons of individual nanoribbons when illuminated with ultrashort pulses and then analyze the evolution of the plasmon frequency as a function of the delay between pump and probe. We study the redshift of these plasmons with increasing delay due to electron relaxation. We also investigate the optical response of the ribbon exposed to a train of optical pulses. We further discuss ribbon arrays illuminated from the substrate under total internal reflection conditions, for which we predict complete absorption for a suitable choice of geometrical and illumination parameters (see Fig. 1).

## References

[1] F. H. L. Koppens, D. E. Chang, and F. J. García de Abajo, *Nano Letters* **11**, 3370-3377 (2011)
[2] S. Thongrattanasiri, F. H. L. Koppens, and F. J. García de Abajo, *Phys. Rev. Lett.* **108**, 047401 (2012)
[3] I. Silveiro, J. M. Plaza Ortega, and F. J. García de Abajo, *Light: Science & Applications* **4**, e241 (2015)
[4] F. J. García de Abajo, *ACS Photon.* **1**, 135 (2014).

## Figures

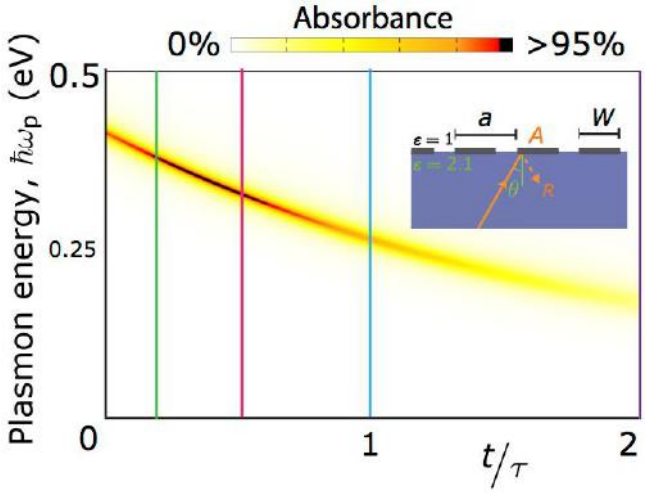



**Fig. 1.** Complete optical absorption experienced by a probe pulse after a time *t* following an optical pump illuminating a nanoribbon array under total internal reflection conditions (see inset).

# Classical and quantum plasmonics in nanostructured graphene

**M. Wubs[1,2*], T. Christensen[1,2], W. Wang[1,2], A.-P. Jauho[2,3], and N. A. Mortensen[2]**

[1]Department of Photonics Engineering, Technical University of Denmark

[2]Center for Nanostructured Graphene, Technical University of Denmark

[3]Department of Micro- and Nanotechnology, Technical University of Denmark

[*]corresponding author: mwubs@fotonik.dtu.dk

**Abstract**- In graphene plasmonics, the classical description of graphene as a sheet with bulk conductivity breaks down for nanostructured pieces of graphene, because finite-size effects emerge, resonance shifts for example. Unlike for noble metals where this size dependence is well captured by a hydrodynamical model for the free-electron response, in graphene additional competing size-dependent effects due to edge states can occur which are even the dominant effects.

For small metal nanoparticles classical electrodynamics breaks down as size-dependent shifts of plasmonic resonances are observed. For metal nanoparticles these effects can be explained as due to nonlocal response, as captured in Bloch's hydrodynamic Drude model and its modern extensions [1,2].

The classical description of graphene is that of an infinitely thin sheet with bulk conductivity. We recently used it to predict the plasmonic resonances of dielectric and conducting graphene-coated nanospheres [3]. In the former case the graphene coating introduces the plasmons in this hybrid structure, while in the latter case (graphene coating on a conductor) it modifies in interesting ways the existing plasmons. Our study is directly relevant to experiments.

Also in nanostructured graphene the classical theory will break down as size-dependent effects emerge [4,5,6]. The important role of edge states enriches the picture. For graphene structures with arm-chair termination, there are no edge states and a hydrodynamic description agrees well with more microscopic RPA calculations and predicts resonance blueshifts for smaller structures. On the other hand, graphene flakes with zig-zag termination do have edge states and we find an overall redshift, because a redshift associated with the edge states even dominates the hydrodynamic blueshift.

We present detailed calculations for graphene disks [5] and for nanotriangles and bow-tie structures of two such triangles [6]. Our various results illustrate a surprising phenomenon: even 20 nm large graphene structures clearly exhibit quantum plasmonic features due to atomic-scale details in the edge termination.

**Acknowledgements** We thank Wei Yan, Xiaolong Zhu, and Nicolas Stenger for stimulating discussions. The Center for Nanostructured Graphene is sponsored by the Danish National Research Foundation, Project DNRF58. This work was also supported by the Danish Council for Independent Research, Project 1323-00087.

## REFERENCES

1. T. Christensen, W. Yan, S. Raza, A.-P. Jauho, N. A. Mortensen, and M. Wubs, "Nonlocal response of metallic nanospheres probed by light, electrons, and atoms", *ACS Nano,* Vol. 8, 1745-1758, 2014.

2. S. Raza, S. I. Bozhevolnyi, M. Wubs, and N. A. Mortensen, "Nonlocal optical response in metallic nanostructures," *J. Phys.: Condens. Matter,* Vol. 27, 183204, 2015.
3. T. Christensen, A.-P. Jauho, M. Wubs, and N. A. Mortensen, "Localized plasmons in graphene-coated nanospheres," *Phys. Rev. B*, Vol. 91, 125414, 2015.
4. S. Thongrattanasiri, A. Manjavacas, and F. J. Garcia de Abajo, "Quantum finite-size effects in graphene plasmons," *ACS Nano,* Vol. 6, 1766-1775, 2012.
5. T. Christensen, W. Wang, A.-P. Jauho, M. Wubs, and N. A. Mortensen, "Classical and Quantum Plasmonics in Graphene Nanodisks: Role of Edge States," *Phys. Rev. B*, Vol. 90, 241414(R), 2014.
6. W. Wang, T. Christensen, A.-P. Jauho, K.S. Thygesen, M. Wubs, and N. A. Mortensen, "Plasmonic eigenmodes in individual and bow-tie graphene nanotriangles," *Sci. Rep.*, Vol. 5, 9535, 2015.

# Surface acoustic wave-assisted plasmonics in graphene

**J. Pedrós[1,2*], J. Schiefele[3], A. Boscá[1,2], J. Martínez[1,4], F. Sols[5], F. Guinea[6,7], and F. Calle[1,2]**

[1]Instituto de Sistemas Optoelectrónicos y Microtecnología, Universidad Politécnica de Madrid, Spain

[2]Departamento de Ingeniería Electrónica, Universidad Politécnica de Madrid, Spain

[3]Instituto de Ciencia de Materiales de Madrid, CSIC, Spain

[4]Departamento de Ciencia de Materiales, Universidad Politécnica de Madrid, Spain

[5]Departamento de Física de Materiales, Universidad Complutense de Madrid, Spain

[6]IMDEA Nanociencia, Spain

[7]Department of Physics and Astronomy, University of Manchester, UK

[*]corresponding author: j.pedros@upm.es

**Abstract**- A novel scheme for the far-field generation of propagating plasmons in unpatterned graphene structures mediated by a surface acoustic wave (SAW) has been demonstrated. The SAW-induced dynamic modulation of the graphene surface creates a diffraction grating which allows to excite the long-lived phonon-like branch of the hybridized graphene/piezoelectric plasmon-phonon dispersion with infrared laser light.

In comparison to conventional plasmonics, the tunability of graphene plasmons offers unique possibilities for applications in metamaterials, quantum optics control, biosensing, and light harvesting. However, in the experiments realized so far, laser coupling into graphene plasmons required either complex near-field techniques [1,2] or the patterning of micro- or nanoscale graphene arrays for far-field coupling [3,4], where edge scattering reduces the localized plasmon lifetime. This patterning can be also be performed in the supporting substrate in order to generate propagating plasmons, though this leads to fragile suspended graphene structures [5]. These technological limitations are hindering the potential of the plasmonic applications of graphene. Therefore, a simple and efficient method to excite propagating plasmons in unpatterned graphene structures is needed for the development of integrated and scalable graphene plasmonic devices and circuits.

We have recently demonstrated a method to couple far-field radiation into propagating graphene plasmons by periodically deforming a continuous graphene sheet with an electrically generated surface acoustic wave (SAW) [6]. This mechanism allows to create a tunable optical grating without the need of any patterning in either the graphene layer or the substrate, thus eliminating edge scattering and fragility issues. An interdigital transducer (IDT) on a piezoelectric film is used to launch the SAW across the graphene sheet, as shown in Fig. 1. By diffraction at the grating, incident laser light can overcome the momentum mismatch and excite propagating plasmons in the graphene sheet. Independently, another research group arrived at a similar proposal using an external mechanical vibrator [7]. However, the use of integrated IDTs enables the fabrication of graphene plasmonic devices by the microelectronics industry. Moreover, this approach permits to efficiently control the graphene plasmons both temporally and spatially. Thus, the propagating plasmons can be switched electrically via the high-frequency signal at the IDT and the generated plasmon wavefronts can be shaped by tailoring the IDT design. For example, curved IDTs creating interfering SAWs can be used for plasmon focusing.

In this talk, we will briefly review the different methods used so far for the generation of graphene plasmons, before presenting the details of our novel SAW-assisted approach. We will present the hybridized graphene plasmon-phonon dispersion in the graphene/piezoelectric structures, as well as the design and fabrication technology of the plasmonic devices, including the transfer of graphene [8] to various piezoelectric materials. We will finally discuss different SAW-mediated plasmon functionalities based on several engineered device geometries.

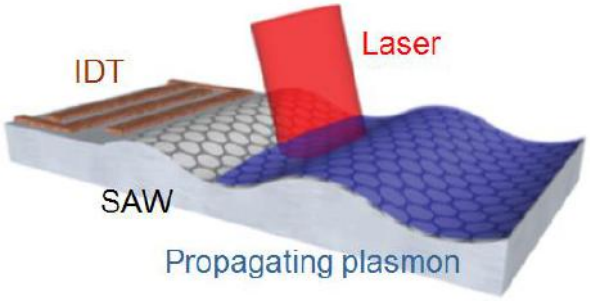



**Figure 1.** Sketch of a SAW-assisted graphene plasmon launcher using an IDT on a piezoelectric substrate.

**Acknowledgements:** Financial support from the Spanish MINECO project GRAFAGEN (ENE2013-47904-C3-1-R) and the EU project SAWTrain (H2020-MSCA-ITN-2014-642688).

**REFERENCES**

1. Chen J., Badioli M., Alonso-González P., Thongrattanasiri S., Huth F., Osmond J., Spasenović M., Centeno A., Pesquera A., Godignon P., Zurutuza Elorza A., Camara N., García de Abajo F.J., Hillenbrand R., and Koppens F.H.L., "Optical nano-imaging of gate-tunable graphene plasmons", *Nature* Vol. 487, 77–81, 2012.
2. Fei Z., Rodin A. S., Andreev G. O, Bao W., McLeod A. S.,Wagner M., Zhang L. M., Zhao Z., Thiemens M., Dominguez G., Fogler M.M., Castro Neto A. H., Lau C. N., Keilmann F., and Basov D.N., "Gate-tuning of graphene plasmons revealed by infrared nano-imaging" *Nature* Vol. 487, 82–85, 2012.
3. Ju L., Geng B., Horng J., Girit C., Martin M., Hao Z., Bechtel H.A., Liang X., Zettl A., Shen Y.R., and Wang F., "Graphene plasmonics for tunable terahertz metamaterials", *Nat. Nanotechnol.* Vol. 6, 630−634, 2011.
4. Yan H., Low T., Zhu W., Wu Y., Freitag M., Li X., Guinea F., Avouris P., and Xia F., "Damping pathways of mid-infrared plasmons in graphene nanostructures", *Nat. Photon.* Vol. 7, 394−399, 2013.
5. Gao W., Shi G., Jin Z., Shu J., Zhang Q., Vajtai R., Ajayan P.M., Kono J., and Xu Q., "Excitation and Active Control of Propagating Surface Plasmon Polaritons in Graphene", *Nano Lett*. Vol. 13, 3698−3702, 2013.
6. Schiefele J., Pedrós J., Sols F., Calle F., and Guinea F., "Coupling Light into Graphene Plasmons through Surface Acoustic Waves", *Phys. Rev. Lett.*, Vol. 111, 237405 (1-5), 2013.
7. Farhat M., Guenneau S., and Bagcı H., "Exciting Graphene Surface Plasmon Polaritons through Light and Sound Interplay", *Phys. Rev. Lett*., Vol. 111, 237404 (1-5), 2013.
8. Boscá A., Pedrós J., Martínez J., Palacios T., and Calle F., "Automatic graphene transfer system for improved material and efficiency" *Sci. Rep*. Vol. 6, 21676 (1–8), 2016.

# Nanoplasmonics in 2D and atomic-scale materials

**F. J. García de Abajo**[1,2,*]

[1]ICFO, The Barcelona Institute of Science and Technology, Castelldefels, 08860 Barcelona, Spain

[2]ICREA-Institució Catalana de Recerca i Estudis Avançats, Passeig Lluís Companys 23, 08010 Barcelona, Spain

[*]javier.garciadeabajo@icfo.es

**Abstract**-In this talk we will review recent advances in the study and applications of plasmons in 2D crystals, including graphene, and other atomic-scale materials.

Recent experimental [1-5] and theoretical [6-10] advances in the study of graphene plasmons have triggered the search for similar phenomena in other materials that are structured down to the atomic scale, and in particular, alternative 2D crystals [11], noble-metal monolayers [12], and polycyclic aromatic hydrocarbons, which can be regarded as molecular versions of graphene [13]. The number of valence electrons that are engaged in the plasmon excitations of these materials is small compared with those of conventional 3D metallic nanostructures, and consequently, the addition or removal of a comparatively small number of electrons produces sizeable changes in their frequencies and near-field distributions. Graphene in particular has been shown to exhibit a large degree of electrical modulation due to its peculiar electronic band structure, which is characterized by a linear dispersion relation and vanishing of the electron density of states at the Fermi level; few electrons are needed to considerably change the Fermi energy. However, plasmons in graphene have only been observed at mid-infrared and lower frequencies [1-5], and therefore, small molecular structures [13] and atomically thin metals [12] constitute attractive alternatives to achieve fast electro-optical modulation in the visible and near-infrared (vis-NIR) parts of the spectrum. In this presentation, we review different strategies and recent advances in the achievement of strong optical tunability in the vis-NIR using plasmons of atomic-scale materials, as well as their potential application for quantum optics, light manipulation, and sensing.

Acknowledgements: This work has been supported in part by the Spanish MINECO (MAT2014-59096-P and SEV-2015-0522) and the European Commission (Graphene Flagship CNECT-ICT-604391 and FP7-ICT-2013-613024-GRASP).

## REFERENCES

[1] J. Chen *et al*., "Optical nano-imaging of gate-tunable graphene plasmons," *Nature* **487**, 77 (2012).

[2] Fei *et al*., "Gate-tuning of graphene plasmons revealed by infrared nano- imaging," *Nature* **487**, 82 (2012).

[3] Fang *et al*., "Gated tunability and hybridization of localized plasmons in nanostructured graphene," *ACS Nano* **7**, 2388 (2013).

[4] Brar *et al*., "Highly confined tunable mid-infrared plasmonics in graphene nanoresonators," *Nano Lett*. **13**, 2541 (2013).

[5] Fang *et al*., "Active tunable absorption enhancement with graphene nanodisk arrays," *Nano Lett*. **14**, 299 (2014).

[6] A. Vakil and N. Engheta, "Transformation optics using graphene," *Science* **332**, 1291 (2011).
[7] F. H. L. Koppens, D. E. Chang and García de Abajo, "Graphene plasmonics: A platform for strong light-matter interactions," *Nano Lett*. **11**, 3370 (2011).
[8] A. Y. Nikitin, F. Guinea, F. J. García-Vidal and L. Martín-Moreno, "Edge and waveguide terahertz surface plasmon modes in graphene microribbons," *Phys. Rev. B* **84**, 161407 (2011).
[9] S. Thongrattanasiri, A. Manjavacas and F. J. García de Abajo, "Quantum finite-size effects in graphene plasmons," *ACS Nano* **6**, 1766 (2012).
[10] F. J. García de Abajo, "Graphene plasmonics: Challenges and opportunities", *ACS Photonics* **1**, 135 (2014).
[11] A. Scholz, T. Stauber and J. Schliemann, "Plasmons and screening in monolayer $MoS_2$," *Phys. Rev. B* **88**, 035135 (2013).
[12] A. Manjacacas and F. J. García de Abajo, "Tunable plasmons in atomically thin gold nanodisks,", *Nat. Commun*. **5**, 3548 (2014).
[13] A. Manjavacas *et al*., "Tunable molecular plasmons in polycyclic aromatic hydrocarbons," *ACS Nano* **7**, 3635 (2013).

# Experimental Demonstration of Unidirectional Terahertz Waves Propagation Using Graphene

**M. Tamagnone[1*†], C. Moldovan[2†], J.-M. Poumirol[3†], A. B. Kuzmenko[3], A. M. Ionescu[2], J. R. Mosig[1]**

[1] Laboratory of ElectroMagnetics and Antennas, École Polytechnique Fédérale de Lausanne, Switzerland

[2] Nanoelectronic Devices Laboratory, École Polytechnique Fédérale de Lausanne, Switzerland

[3] Department of Quantum Matter Physics (DQMP), Université de Genève, Switzerland

[†] Equal contributions. [*]Corresponding author: michele.tamagnone@epfl.ch

**Abstract**- We present the experimental demonstration of the first terahertz isolator (working frequency larger than 1 THz), obtained using the non-reciprocal electromagnetic properties of graphene under magnetostatic bias. The presentation will cover in detail the design, fabrication and measurement of the device. The isolator exhibits unidirectional terahertz propagation in reflection for circularly polarized waves, showing two bands at 2.9 and 7.6 terahertz respectively. In spite of the simplicity of design and fabrication, the proposed device geometry achieves near-optimal performances.

The potential applications of graphene for terahertz passive and active devices have received a considerable attention in recent scientific literature [1-4]. One of the most promising research directions is the possibility of breaking the time-reversal symmetry in photonic devices based on magnetostatically biased graphene. The clearest evidence of such non-reciprocal effects is the experimental demonstration of Faraday rotation in graphene for terahertz frequencies [3, 4]. Several theoretical works have proposed devices based on magnetostatically biased graphene including non-reciprocal isolators (also known as optical diodes), i.e. photonic devices that support unidirectional light propagation. In addition, a narrowband graphene isolator was recently measured at 20 GHz [4]. Exploring the potential of graphene for terahertz isolation is important being currently available ferrite isolators useful only up 500 GHz and showing, beyond this frequency, prohibitive insertion losses in the order of tens of dB [5].

We present here the first experimental terahertz isolator (frequency > 1THz), obtained using magnetically biased graphene [1]. The proposed isolator is illustrated in Figure 1. A number N of graphene sheets are placed on a back-metallized thin silicon layer of thickness 10 μm (for our device N=3). The sheets are separated by thin PMMA layers (approximately 60 nm), while the thickness of the metallization (chromium and platinum) is 200 nm. The whole structure is bonded to a Pyrex wafer which has solely the function of mechanical support. A magnetostatic field B is applied orthogonally to graphene. The device operation is based on reflecting incident LHCP (left hand circularly polarized) plane waves as RHCP (right hand circularly polarized) ones, while absorbing RHCP incident waves. The device thus achieves non-reciprocal unidirectional propagation and isolation for circularly polarized waves. Our device exploits Fabry-Perot resonances in the silicon layer to increase light-matter interaction in graphene. As a result, three monolayers of graphene are sufficient to obtain near perfect isolation. The device has two working bands, namely 2.9 THz and 7.6 THz. In both bands the isolation reaches almost 20 dB (18.8 dB and 18.5 dB respectively) and the insertion loss is approximatively 7.5 dB. The measurements have been fit with the presented layered model, reaching a very good agreement.

Operation can be extended to linearly polarized waves using quarter wave plates.

We believe these results to be of great importance, and performance can be sensibly improved using last-generation graphene on boron nitride, bringing forth the creation of commercial isolators with less than 3 dB of insertion loss for low magnetostatic fields.

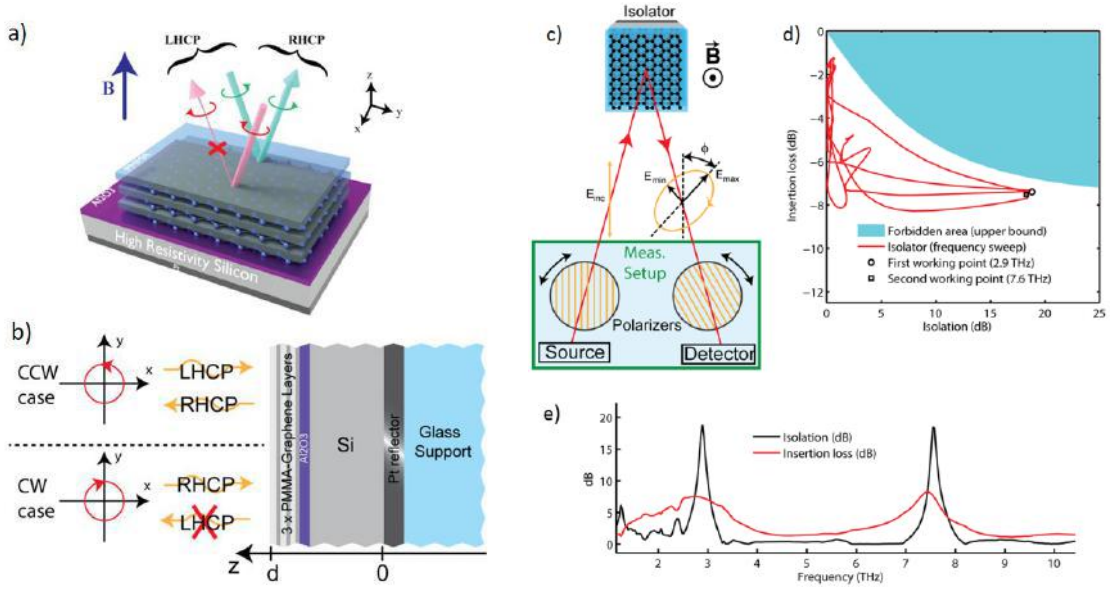



**Figure 1**: Isolator structure and characterization a) 3D view of the isolator stack, b) working principle, c) measurement setup for isolation characterization, d-e) measured performances of the fabricated device.

**Acknowledgements** This work was supported by the Hasler Foundation (Project 11149), by the Swiss National Science Foundation (SNSF) under grant 133583, by the EU Graphene Flagship (contract no. CNECT-ICT-604391) and by the FP7 European project "Grafol" (grant number 133583). The authors would like to dedicate this paper to the memory of Prof. Julien Perruisseau-Carrier.

**REFERENCES**

1. Tamagnone, M., Moldovan, C., Poumirol, J.-M., Kuzmenko, A. B., Ionescu, A. M., Mosig, J. R., Perruisseau-Carrier, J., "Near optimal graphene terahertz non-reciprocal isolator", Accepted in *Nature Communications*, 2016
2. Tamagnone, M., Fallahi, A., Mosig, J. R., and Perruisseau-Carrier, J., "Fundamental limits and near-optimal design of graphene modulators and non-reciprocal devices," *Nature Photonics*, vol. 8, pp. 556-563, 2014.
3. Crassee, I., Levallois, J., Walter, A. L., Ostler, M., Bostwick, A., Rotenberg, E., Seyller, T., van der Marel, D., and Kuzmenko, A. B., "Giant Faraday rotation in single- and multilayer graphene," *Nature Physics*, vol. 7, pp. 48-51, 2011.
4. Sounas, D. L., Skulason, H. S., Nguyen, H. V., Guermoune, A., Siaj, M., Szkopek, T., and Caloz, C., "Faraday rotation in magnetically biased graphene at microwave frequencies," *Applied Physics Letters*, vol. 102, pp. 191901-4, 2013.
5. Shalaby, M., Peccianti, M., Ozturk, Y. & Morandotti, R., "A magnetic non-reciprocal isolator for broadband terahertz operation". *Nature Communications* 4, 1558, 2013.

# Long-range Tamm surface plasmons in graphene metamaterials

**H. Hajian[1*], H. Caglayan[1,2], and E. Ozbay[1,3,4]**

[1]Nanotechnology Research Center, Bilkent University, 06800 Ankara, Turkey

[2]Department of Electrical and Electronics Engineering, Abdullah Gul University, 38080 Kayseri, Turkey

[3]Department of Physics, Bilkent University, 06800 Ankara, Turkey

[4]Department of Electrical and Electronics Engineering, Bilkent University, 06800 Ankara, Turkey

[*]corresponding author: hodjat.hajian@bilkent.edu.tr

**Abstract-** Considering the Ohmic losses of graphene, we study linear Tamm surface plasmons supported by air-terminated graphene metamaterials composed of alternating layers of graphene and dielectric. We theoretically prove that with sufficiently large thickness of the dielectric layers, i.e. 100 nm, the Tamm surface plasmons have considerably large (small) propagation (localization) length, comparable with those of a single layer of graphene.

Neglecting the Ohmic losses of graphene, it has been demonstrated that similar to the metal-dielectric systems [1], multilayer graphene hyperbolic metamaterials [2-5] are also capable of supporting long- and short-range surface plasmons (SPs) and also bulk modes, for transverse magnetic (TM) polarization of light. These systems are created by alternating graphene sheets separated by layers of dielectric with subwavelength-thickness (*d*). Moreover, TM Tamm surface plasmons localized at the surface of the system can also be realized in terminated graphene metamaterials [6].

In realistic graphene-based plasmonic devices, the losses of the system can considerably affect the SPs propagation and localization characteristics. Therefore, in this abstract, considering the Ohmic losses of the graphene sheets, we investigate the normalized propagation length ($PL/\lambda_{SP}$) and localization length (*LL*) of the Tamm SPs in the graphene-dielectric ($\varepsilon=4$) metamaterials terminated with air, where $PL=1/2\beta''$, $\lambda_{SP}=2\pi/\beta'$ and $LL=1/Re(q)$ with $q=(\beta^2-\varepsilon\omega^2/c^2)^{1/2}$. When the losses are included in the calculations, allowed and forbidden regions in the band diagram of the metamaterial (depicted in Fig. 2 of [3] as well as that of Ref. 6) lose their concepts and the Bloch wave vector is always complex. In this metamaterial, for *d=10 nm*, first the Tamm SPs are supported in a narrower range of frequency and, second, there is a considerable decrease (increase) in their PL (LL), as compared with those of a single layer graphene bounded with air and material with $\varepsilon=4$. Moreover, by increasing *d* to *100 nm*, *PL* (*LL*) of the modes and the frequency range of their appearance will be increased (decreased) while there is still a large length of localization for Tamm SPs at lower frequencies ($f<20$ *THz*).

In conclusion, we have examined the propagation and localization characteristics of low-loss Tamm surface plasmons supported by graphene metamaterials. We have demonstrated that by taking the subwavelength thickness of the dielectric layers as *100 nm*, Tamm SPs with long propagation and small localization lengths can be supported by the air-truncated graphene metamaterial at frequencies larger than *20 THz*.

**Acknowledgements**

This work is supported by the projects DPT-HAMIT, NATO-SET-193 and TUBITAK under Project Nos.,

113E331, 114E374. E.O. and H.C. also acknowledges partial support from the Turkish Academy of Sciences.

**REFERENCES**

1. Avrutsky, I., I. Salakhutdinov, J. Elser, and V. Podolskiy, "Highly confined optical modes in nanoscale metal-dielectric multilayers," *Phys. Rev. B*, Vol. 75, No. **24**, 241402-1-4, 2007.
2. Iorsh, I. V., I. S. Mukhin, I. V. Shadrivov, P. A. Belov, and Y. S. Kivshar, "Hyperbolic metamaterials based on multilayer graphene structures," *Phys. Rev. B.*, Vol. **87**, No. 7, 075416-1-6, 2013.
3. Hajian, H., A. Soltani-Vala, and M. Kalafi, "Characteristics of band structure and surface plasmons supported by a one-dimensional graphene-dielectric photonic crystal," *Opt. Commun.*, Vol. **292**, No. 7, 149-157, 2013.
4. Smirnova, D. A., I. V. Iorsh, I. V. Shadrivov, Y. S. Kivshar, "Multilayer graphene waveguide," *JETP Lett.* Vol. **99**, No. 8, 456-460, 2014.
5. Zhang, L., Z. Zhang, C. Kang, B. Cheng, L. Chen, X. Yang, J. Wang, W. Li, and B. Wang, "Tunable bulk polaritons of graphene-based hyperbolic metamaterials," *Opt. Express*, Vol. **22**, No. 11, 14022-14030, 2014.
6. Smirnova, D., P. Buslaev, I. Iorsh, I. V. Shadrivov, P. A. Belov, and Y. S. Kivshar, "Deeply subwavelength electromagnetic Tamm states in graphene metamaterials," *Phys. Rev. B*, Vol. **89**, No. 24, 245414-1-4, 2014.

# Graphene Plasmonics for Controlled Manipulation of Sub 2 nm Nanoparticles

**M. Danesh**[1, 2*], **Z. Liu**[1], **and C.-W. Qiu**[2]
[1]Electronics and Photonics Department, Institute of High Performance Computing, Singapore
[2]Electrical and Computer Engineering Department, National University of Singapore, Singapore
[*]corresponding author: danesh@u.nus.edu

**Abstract-** Accurate control over the position of nanoparticles is of great interest in future nanotechnology and nano science related applications. However, exact control over the position of sub 2 nm particles is particularly difficult and faces many challenges. In this work we propose a novel and electrically controllable method to overcome this challenge by taking advantage of the Dirac plasmons in a graphene sheet. In our design we produce an optical potential which is electrically tunable and apply Langevin dynamics to study the nanoparticle dynamics in real time to see how tuning the electrical and optical properties can result in effective control of the dynamics of the nanoparticle.

Many efforts have been made to manipulate nanoparticles for advanced biomedical applications such as futuristic lab on chips. Amongst various methods used to reach this goal, many have used highly localized electromagnetic near fields created by surface plasmons [1-5]. A major challenge in this field is the accurate positioning and control of sub 2 nm particles. This is mainly due to random Brownian motions taking over the transport dynamics [6]. In this work we propose an enhanced method to overcome the many limitations associated with accurate positioning of these nanoparticles using the unique properties of the Dirac plasmons in graphene.

In summary in this work we propose applying a back gated tuning mechanism to a graphene sheet with a nanostructured substrate [7] . The nanostructured substrate and back gate induce a variable doping profile on the graphene sheet creating tunable resonances using Graphene's Dirac plasmons [8, 9]. This mechanism allows us to tune the position of the localized plasmonic resonances in an electrical manner. In this structure we show that we can create a tunable optical potential and by changing the position of the dip of the optical potential we can induce varying forms of optical forces on the the nanoparticles placed within the vicinity of the structure and thereby control its position.

A major challenge that effects trapping of very small particles is random heat fluctuations. In order to accurately address this issue in our analysis we have carefully considered the effects of heating and random Brownian motions using Langevin dynamics. In addition we have also taken into account intermolecular forces that exist between the nanoparticle and the graphene sheet. Using the Langevin dynamics we calculate the propagation path of our nanoparticle in real time by varying the gate voltage in a step like manner which results in changing the total Fermi level of the graphene sheet in 0.01 eV steps. We calculate the changes in the position of the nanoparticle for each step showing how this method can be used to potentially achieve effective control over a

nanoparticle position. We believe this novel design can potentially help in achieving high performance single molecule position control for future lab on chip applications.

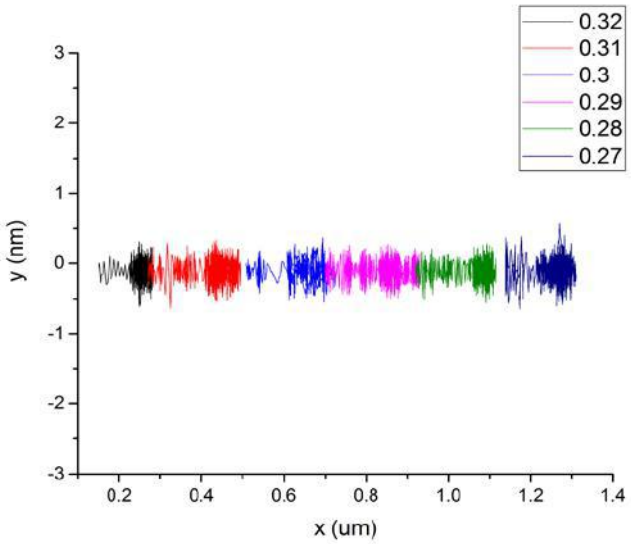



Figure 1. Showing the propagation dynamics of a nanoparticle moving along the x dimension. In this structure the electric gating applied on the graphene is changed in a step like fashion resulting in the Fermi level to shift in 0.01 eV steps from 0.32 to 0.27 eV. As it can be seen in the results the particle is firmly trapped within the y dimension. In the x direction however the voltage dictates the effective location of the particle allowing a transport mechanism to be realized.

**REFERENCES**


1. Grigorenko, A.N., et al., *Nanometric optical tweezers based on nanostructured substrates.* Nature Photon., 2008. **2**: p. 365-370.
2. Juan, M.L., et al., *Self-induced back-action optical trapping of dielectric nanoparticles.* Nature Physics, 2009. **5**(12): p. 915-919.
3. Righini, M., et al., *Nano-optical trapping of rayleigh particles and Escherichia coli bacteria with resonant optical antennas.* Nano Letters, 2009. **9**(10): p. 3387-3391.
4. Righini, M., et al., *Parallel and selective trapping in a patterned plasmonic landscape.* Nature Physics, 2007. **3**(7): p. 477-480.
5. Zhang, W., et al., *Trapping and sensing 10 nm metal nanoparticles using plasmonic dipole antennas.* Nano Lett., 2010. **10**: p. 1006-1011.
6. Juan, M.L., M. Righini, and R. Quidant, *Plasmon nano-optical tweezers.* Nature Photonics, 2011. **5**(6): p. 349-356.
7. Vakil, A. and N. Engheta, *Transformation optics using graphene.* Science, 2011. **332**(6035): p. 1291-1294.
8. Ju, L., et al., *Graphene plasmonics for tunable terahertz metamaterials.* Nature Nanotechnology, 2011. **6**(10): p. 630-634.
9. Thongrattanasiri, S., I. Silveiro, and F. Javier García De Abajo, *Plasmons in electrostatically doped graphene*. Applied Physics Letters, 2012. **100**(20).

# Ultrasensitive $\mathcal{PT}$-Symmetric Graphene Quantum-Capacitance Sensors

**Pai-Yen Chen**
[1]Department of Electrical and Computer Engineering,
Wayne State University, Detroit, Michigan 48202, USA
[*]corresponding author: userid@institution.edu

**Abstract**- In this talk, we introduce a new concept of parity-time ($\mathcal{PT}$) symmetric radio-frequency (RF) circuit capable of sensing tiny variations in reactive power caused by changes in physical, biological, and environmental events. An ultrahigh sensitivity is enabled by the spectral singularity arising from the spontaneous $\mathcal{PT}$-symmetry breaking point (exceptional point). We theoretically show that for $\mathcal{PT}$-sensors with a fixed inductance, the critical frequency of exception point is proportional to the fractional change in capacitance $\varepsilon$ by $\sqrt{1/\varepsilon - 1/\varepsilon^2}$, instead of $\sqrt{1/\varepsilon}$ for a typical *LC* resonant circuit. We demonstrate with a practical quantum-capacitance sensor that a $\mathcal{PT}$–symmetric circuit topology may offer significantly enhanced sensitivity compared to conventional passive RF sensors. The proposed $\mathcal{PT}$-sensors may impact not only extraordinary manipulation of radio-frequency signals, but also practical wireless sensing and detection applications.

# Graphene-based van-der-Waals heterostructure plasmonic metamaterials for terahertz device applications

**T. Otsuji[1*], D. Svintsov[2], A. Dubinov[3], D. Yadav[1], S. Boubanga Tombet[1], T. Watanabe[1], A. Satou[1], V. Ryzhii[1], V. Mitin[4], and M.S. Shur[5]**

[1] Research Inst. of Electrical Communication, Tohoku University, Japan

[2] Moscow Inst. of Physics and Technology, RAS, Russia

[3] Inst. of Microstructure Physics, RAS, Russia

[4] Dept. of Electrical Eng., University at Buffalo, SUNY, USA

[5] Dept. of Electrical, Electron., and System Eng., Rensselaer Polytechnic Institute, USA

[*]Corresponding author: otsuji@riec.tohoku.ac.jp

**Abstract**- This paper reviews recent advances in the research of graphene-based van der Waals heterostructure plasmonic metamaterials for terahertz device applications. A double graphene layer heterostructure consisting of an atomically thin tunnel barrier layer sandwiched between two graphene electrodes works for active metamaterials in the terahertz electromagnetic frequency range.

Massless Dirac Fermions of electrons and holes in gapless and linear symmetric band structures in graphene support the emergence of carrier population inversion and resultant negative dynamic conductivity in a wide THz frequency range under optical or electrical pumping [1]. Experimental observations of THz frequency amplification [2] support the concept of graphene-based THz amplifiers and THz lasers (yet to be realized), which has been one of the hottest research topics [3, 4]. Their full-scale realization, however, faces a number of challenges. First, the coefficient of the interband amplification by a single layer of pumped graphene cannot exceed 2.3% [1], which is directly linked with the universal optical conductivity of graphene [5]. Second, the radiation amplification associated with the direct interband electron transitions competes with the intraband Drude absorption [1]. The slow-wave nature of the graphene surface plasmon polaritons (SPPs) can dramatically enhance the interaction between THz photons and graphene [6], resulting in a giant enhancement of the THz gain and super-radiant plasmonic lasing in the population-inverted graphene meta-surface structures [7, 8].

The graphene-based van der Waals heterostructures have recently attracted considerable attention [9]. A gated double-graphene-layer (G-DGL) nano-capacitor structure (Fig. 1) exhibits quantum mechanical resonant tunneling (RT) and the resultant nonlinear negative differential conductivity (NDC) when the band offset between the two GLs is properly aligned [10]. When the band offset is aligned to the TM-mode THz photon energy, the DGL structure can mediate the photon-assisted RT, resulting in the resonant emission or detection of the TM-mode THz radiation (Fig. 1) [11, 12]. The excitation of the graphene plasmons in the GLs strongly modulates the inter-GL RT [13] and dramatically enhances the quantum efficiency of the THz lasing as well as that of the THz detection [13, 14].The in-plane electric field components in TE modes or TM modes of photons can directly excite the GL SPPs. The DGL supports optical and acoustic SPP modes having symmetric and anti-symmetric distributions of the electric potential, respectively (Fig. 2(a)) [15]. The dispersion of the symmetric (optical) mode is proportional to the square-root of the plasmon wave vector, while the dispersion of the anti-symmetric (acoustic) mode is sound-like in the long-wavelength limit [15, 16]. Its velocity $s$ approaches the Fermi velocity $v_F$ as the interlayer distance $d$ decreases. In the realistic tunnel-coupled double layers ($d \approx 3$ nm, $\varepsilon_F \approx 100$ meV), $s \approx 1.15 v_F$, so that it could survive the Landau damping ( Fig. 2(b)).

Figure 2(c) plots the wave vector- and energy dependence of the real part of the effective conductivities at 300K for a typical G-DGL having the 2.5-nm thick $WS_2$ tunnel barrier and a inter-GL voltage $V = V_{DGL} = 0.2$ V. The two sets of singularities are clearly present (shown with blue dotted lines) in the conductivity spectra: the

absorption singularity at $\omega = qv_F$ coming from the in-plane conductivity and the gain singularity at $\omega = \mathrm{e}V_{DGL} \pm qv_F$ coming from the enhanced tunneling between the collinear states in the GLs [16]. The gain factor of the plasmon assisted RT that traces on the acoustic SPP dispersion line is reproduced in Fig. 2(b).

**Acknowledgements** The authors thank S. Arnold, V. Ya. Aleshkin, V. Vyurkov, and M. Ryzhii for their contributions and valuable discussion. This work is financially supported by JSPS GA-SPR (23000008), JSPS-RFBR, Japan, the Dynasty Foundation, Russia, Russian Foundation for Basic Research (14-02-92102), Russia, AFOSR Award (FA9550-10-1-0391), USA, and US Army Cooperative Research Agreement, USA.

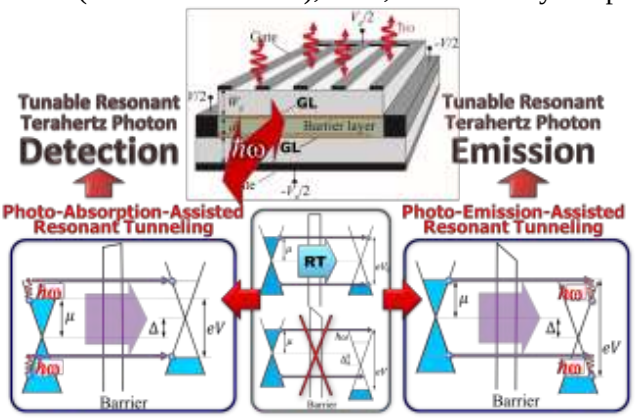



Fig. 1. Photon-assisted RT for tunable emission and detection of THz radiation in a G-DGL metamaterial structure.

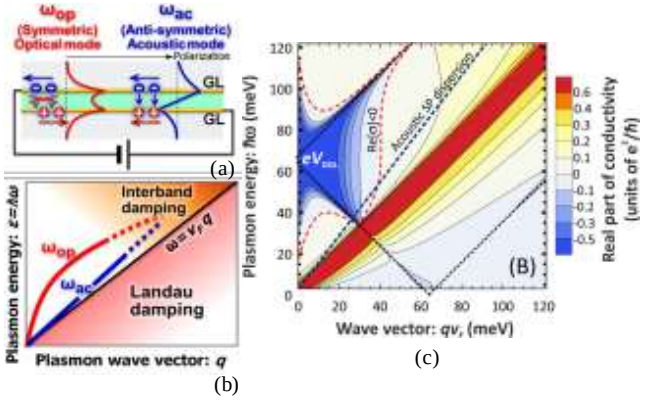



Fig. 2. The modes (a), dispersions (b), and gains (c) of SPPs in DGLs.

## REFERENCES

1. Ryzhii V, Ryzhii M, Otsuji T, "Negative dynamic conductivity of graphene with optical pumping," *J. Appl. Phys.* 2007; 101: 083114.
2. Boubanga-Tombet S, Chan S, Watanabe T, Satou A, Ryzhii V, and Otsuji T, *Phys. Rev. B* 2012; **85**: 035443.
3. Otsuji T, Boubanga-Tombet SA, Satou A, Fukidome H, Suemitsu M, Sano E, Popov V, Ryzhii M, and Ryzhii V, "Graphene-based devices in terahertz science and technology," *J. Phys. D: Appl. Phys.* 2012; 45: 303001.
4. Tredicucci A, and Vitiello MS, "Device concepts for graphene-based terahertz photonics," *IEEE J. Sel. Top. Quantum Electron*. 2014; 20: 8500109.
5. Nair RR, Blake P, AN Grigorenko, Novoselov KS, Booth TJ, Stauber T, Peres NMR, and Geim AK, "Fine Structure Constant Defines Visual Transparency of Graphene," *Science* 2008; 320: 1308.
6. Dubinov AA, Aleshkin VY, Mitin V, Otsuji T, and Ryzhii V, "Terahertz surface plasmons in optically pumped graphene structures," *J. Phys. Condens. Matter* 2011; 23: 145302.
7. Watanabe T, Fukushima T, Yabe Y, Boubanga Tombet SA, Satou A, Dubinov AA, Aleshkin VY, Mitin V, Ryzhii V, and Otsuji T, "The gain enhancement effect of surface plasmon polaritons on terahertz stimulated emission in optically pumped monolayer graphene," *New J. Phys.* 2013; 15: 075003.
8. Popov VV, Polischuk OV, Davoyan AR, Ryzhii V, Otsuji T, and Shur MS, "Plasmonic terahertz lasing in an array of graphene nanocavities," *Phys. Rev. B* 2012; 86: 195437.
9. Britnell L, Gorbachev RV, Jalil R, Belle BD, Shedin F, Mishenko A, Georgiou T, Katsnelson MI, Eaves L, Morozov SV, Peres NMR, Leist J, Geim AK Novoselov KS, and Ponomarenko LA, "Field-effect tunneling transistor based on vertical graphene heterostructures," *Science* 2012; 335: 947-950.
10. Britnell L, Gorbachev RV, Geim AK, Ponomarenko LA, Mishenko A, Greenaway MT, Fromhold TM, Novoselov KS, and Eaves L, "Resonant tunneling and negative differential conductance in graphene transistors," *Nature Comm.* 2013; 4: 1794-1799.
11. Ryzhii V, Dubinov AA, Otsuji T, Aleshkin VY. Ryzhii M, and Shur M, "Double-graphene-layer terahertz laser: concept, characteristics, and comparison," *Opt. Exp.* 2013; 21: 31569-31579.
12. Ryzhii V, Otsuji T, Aleshkin VY, Dubinov AA, Ryzhii M, Mitin V, and Shur MS, "Voltage-tunable terahertz and infrared photodetectors based on double-graphene-layer structures," *Appl. Phys. Lett.* 2014; 104: 163505.
13. Ryzhii V, Satou A, Otsuji T, Ryzhii M, Mitin V, and Shur MS, "Dynamic effects in double graphene-layer structures with inter-layer resonant-tunneling negative conductivity," *J. Phys. D: Appl. Phys.* 2013; 46: 315107.
14. Dubinov AA, Aleshkin VY, Ryzhii V, Shur MS, and Otsuji T, "Surface-plasmons lasing in double-graphene-layer structures," *J. Appl. Phys.* 2014; 115: 044511.
15. Hwang EH, and Das Sarma S, "Plasmon modes of spatially separated double-layer graphene," *Phys. Rev. B* 2009; 80: 205405.
16. Svintsov D, Devizorova X, Otsuji T, and Ryzhii V, "Emission and amplification of surface plasmons in resonant - tunneling van der Waals heterostructures," arXiv: 1509.03776v1 (2015).

# Industrial Applications of Metamaterials

# Additive manufacturing of dielectric lenses for electromagnetic beam control

**J. Yi[1], A. de Lustrac[1,2], G.-P. Piau[3], and S. N. Burokur[4*]**

[1]IEF, CNRS, UMR 8622, Univ Paris Sud, Université Paris-Saclay, 91405 Orsay cedex, France

[2]Université Paris Ouest, 92410 Ville d'Avray, France

[3]AIRBUS Group Innovations, 92150 Suresnes, France

[4]LEME, EA 4416, Université Paris Ouest, 92410 Ville d'Avray, France

[*]corresponding author: sburokur@u-paris10.fr

**Abstract**-Dielectric lenses are designed using Quasi-Conformal Transformation Optics (QCTO) concept and fabricated by additive manufacturing for the control of wave propagation direction. Three lenses are studied; the first one is used to compensate for the curvature of a non-planar antenna array, the second one to steer an electromagnetic beam and the last one to concentrate an electromagnetic field.

Transformation Optics (TO) is a powerful tool that enables to control electromagnetic (EM) fields in unprecedented and unbelievable ways through the use of judiciously engineered materials with parameters that vary spatially [1, 2]. The TO formalism is based on the invariance of Maxwell's equations over space-time coordinate transformations. Such flexibility in controlling EM waves appears to be convenient in the design of innovative devices with performances or special properties difficult to achieve from classical methods and has therefore inspired considerable research interests in wave propagation. The electromagnetic cloak is one of the most striking deices realized with TO concept [3].

In order to avoid anisotropy in material parameters that arises during coordinate transformation, an equivalence between coordinate transformation and spatial deformation by using Laplace's equation to determine the deformation of coordinate grids during the transformation has been proposed [4]. So the transformed material parameters are determined by the solutions of the Laplace's equation under proper boundary conditions. Such mapping known as quasi-conformal transformation optics (QCTO) has been proposed to simplify the electromagnetic distributions in the new transformed coordinate space. QCTO helps to minimize the anisotropy of the constitutive materials, giving the possibility to implement all-dielectric materials in the transformed medium. As a result, nearly-isotropic gradient index (GRIN) materials with broad frequency bandwidth and low losses can be employed, opening the way to broadband devices.

Here, QCTO is applied to design two broadband lenses; the first one capable of restoring in-phase emissions from an array of radiators fixed on a non-planar ground plane and the second one capable of steering the radiated beam of an antenna to an off-normal direction.

Firstly, we study the enhancement of directivity through the use of a QCTO-based lens conformed on a non-planar array of radiating elements that follows a cylindrical shape. The lens is capable of restoring in-phase emissions from a conformal array of antennas so as to obtain performances similar to that of a linear one. Calculations have shown that the effective permittivity varies from 1 to 2.76 in the lens [5]. The design of the conformal lens-antenna and its performances are presented in Fig. 1. Secondly, we design a lens able to steer an

antenna's radiated beam to an off-normal direction. The lens-antenna structure and the associated performances are shown in Fig. 2. The permittivity ranges from 1 to 2.8 [6-7]. The prototypes are realized using 3D printing additive fabrication technique. The polymer used in the printing process presents a relative permittivity $\varepsilon_d = 2.8$.

This work was supported in part by the French-UK project MIMiCRA No. B0883 GEM1 ERG.

## REFERENCES


1. Leonhardt U. "Optical conformal mapping," *Science*, Vol. 312, No. 5781, 1777-1780, 2006.
2. Pendry J. B., D. Schurig and D. R. Smith, "Controlling electromagnetic fields," *Science*, Vol. 312, No. 5781, 1780-1782, 2006.
3. Schurig D., J. J. Mock, B. J. Justice, S. A. Cummer, J. B. Pendry, A. F. Starr, D. R. Smith, "Metamaterial electromagnetic cloak at microwave frequencies," *Science*, Vol. 314, No. 5801, 977-980, 2006.
4. Hu J., X. Zhou, G. Hu, "Design method for electromagnetic cloak with arbitrary shapes based on Laplace's equation," *Opt. Express*, Vol. 17, No. 3, 1308-1320, 2009.
5. Yi J., S. N. Burokur, G.-P. Piau, A. de Lustrac, "Restoring in-phase emissions from non-planar radiating elements using a transformation optics based lens," *Appl. Phys. Lett.*, Vol. 107, No. 2, 024101, 2015.
6. Yi J., S. N. Burokur, A. de Lustrac, "Conceptual design of a beam steering lens through transformation electromagnetics," *Opt. Express*, Vol. 23, No. 10, 12942-12951, 2015.
7. Yi J., S. N. Burokur, G.-P. Piau, A. de Lustrac, "Coherent beam control with an all-dielectric transformation optics based lens," *Scientific Reports*, Vol. 6, 18819, 2016.

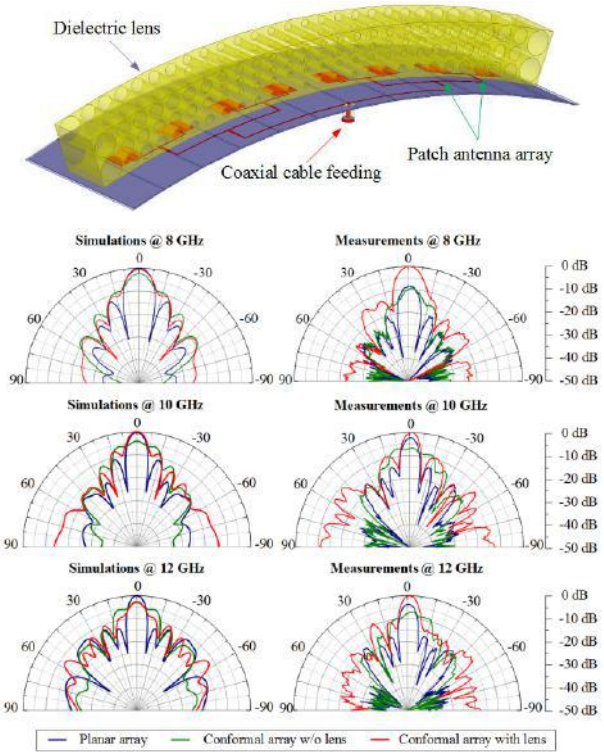




**Fig. 1. Design of the conformal lens-antenna system and the associated performances.**

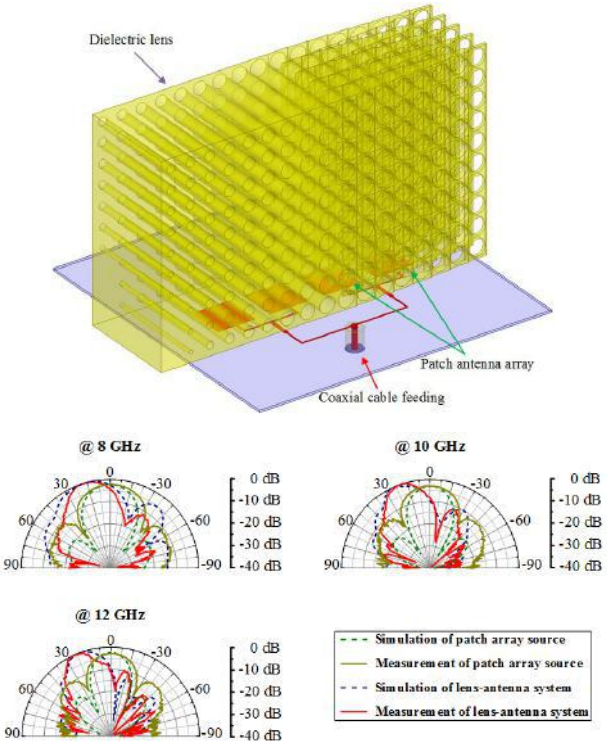



**Fig. 2. Design of the beam steering lens-antenna system and the associated performances.**

# Modeling and design of metasurfaces for beam scanning

**B. Ratni**[1], **A. de Lustrac**[1,2], **G.-P. Piau**[3], **and S. N. Burokur**[4*]

[1]IEF, CNRS, UMR 8622, Univ Paris Sud, Université Paris-Saclay, 91405 Orsay cedex, France

[2]Université Paris Ouest, 92410 Ville d'Avray, France

[3]AIRBUS Group Innovations, 92150 Suresnes, France

[4]LEME, EA 4416, Université Paris Ouest, 92410 Ville d'Avray, France

[*]corresponding author: sburokur@u-paris10.fr

**Abstract**-We present the modeling and engineering of phase-modulated metasurfaces so as to control the direction of an antenna's radiated beam. The phase modulation on the metasurface is derived from the ray optics analysis. Such a non-uniform metasurface is utilized as a partially reflective surface in Fabry-Perot cavity antenna. Beam scanning is obtained and depending on the phase modulation applied, the scan angle can be controlled.

The interesting features of partial reflection has contributed to the design of metasurfaces to be used as superstrate layers so as to significantly enhance the directivity of radiating sources at boresight [1-2]. The designed structure is based on a parallel-plate configuration, enclosing a resonant Fabry-Perot (FP) cavity. In a conventional FP leaky-wave antenna (LWA), the Partially Reflecting Surface (PRS) is placed half a wavelength above the Perfect Electric Conductor (PEC) ground plane of the primary radiating source. The use of an *LC*-resonant metasurface allows reducing the antenna profile [3]. Beam-steering performances from such FP antennas have attracted lots of interests recently [4-5].

In this paper, we propose to design phase-modulated metasurfaces by using an analytical model based on a simple ray optics analysis as previously used in ref. [1]. For a desired angle of beam scanning, the model allows to calculate the transmission phase of the *LC*-resonant cells composing the metasurface, which is used as PRS in Fabry-Perot leaky wave antennas. Full-wave simulations are performed on different configurations of FP LWA to validate the model and the designed phase-modulated metasurfaces.

The unit cell of the metasurface consists of simultaneously a capacitive and an inductive grid on the two faces of a Rogers TMM4 ($\varepsilon_r$ = 4.5 and tan $\delta$ = 0.002) dielectric substrate of thickness $t$ = 2.54 mm, as presented in Fig. 1(a). The capacitive grid is formed by a row of metallic patches with width $w$ = 27.2 mm and period $p$ = 30 mm, whereas the mesh strips of the inductive grid have similar period $p$ and width $l$. The PRS is composed of 20 by 20 cells, where each cell has each an elementary capacitance and inductance. The phase modulation, as presented in Fig. 1(b), is achieved by manipulating the line width $l$, which will allow engineering the desired gradient for beam steering.

Two PRS configurations are studied numerically in the Fabry-Perot cavity antennas operating around 2.15 GHz. A cavity with $h$ = 15 mm ($\approx \lambda/9$) is therefore designed to operate near 2.15 GHz. In both cases, the primary source is a 31.2 mm x 31.2 mm microstrip patch antenna with a 4 mm offset coaxial feed. The simulated three dimensional (3D) radiation patterns are presented in Figs. 1(c)-(d). Steered beams at 30° and 60° are observed thanks to the phase-modulated PRS.

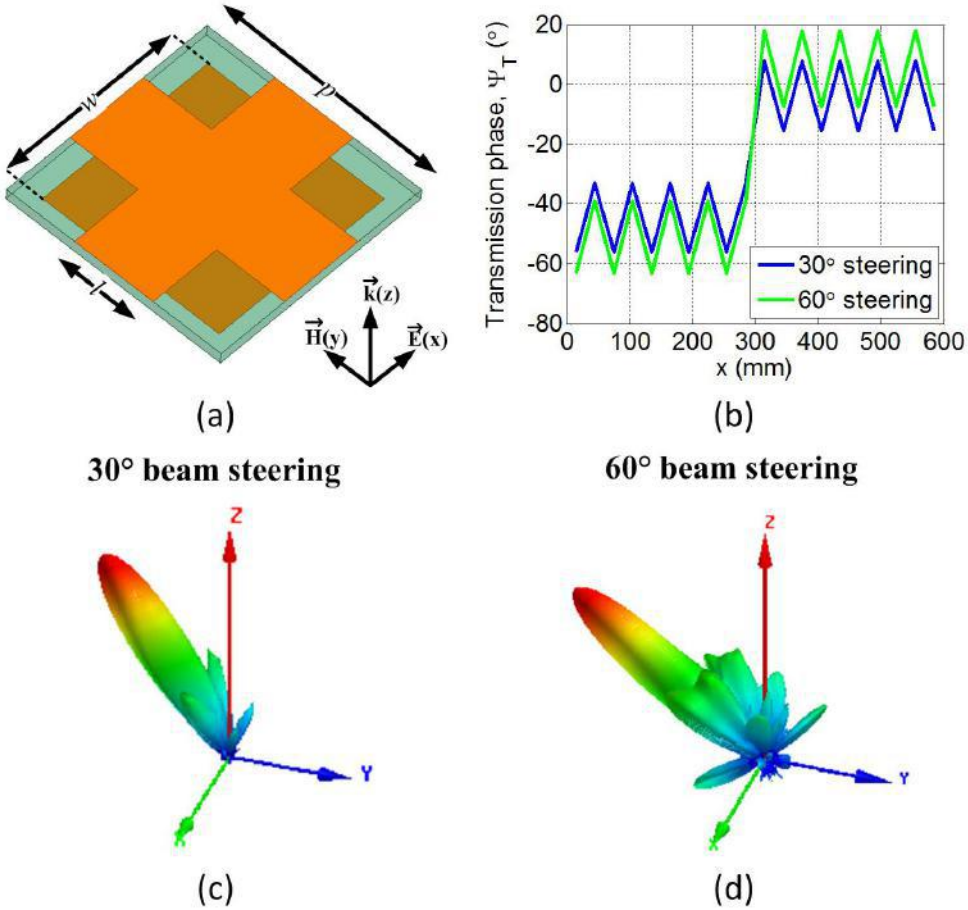



**Fig. 1. (a) Unit cell of the metasurface. (b)Engineered transmission phase of the metasurface. (c) 30° beam steering antenna. (d) 60° beam steering antenna.**

## REFERENCES


1. Trentini G. V., "Partially reflecting sheet arrays," *IRE Trans. Antennas Propag*., Vol. 4, No.4, 666-671, 1956.
2. Feresidis A. P. and J. C. Vardaxoglou, "High gain planar antenna using optimized partially reflective surfaces," *Proc. Inst. Elect. Eng. Microw. Antennas Propag*., Vol. 148, No. 6, 345-350, 2001.
3. Ourir A., A. de Lustrac and J.-M. Lourtioz, "All-metamaterial-based sub-wavelength cavities (λ/60) for ultrathin directive antennas," *Appl. Phys. Lett.*, Vol. 88, No. 8, 084103, 2006.
4. Ghasemi A., S. N. Burokur, A. Dhouibi and A. de Lustrac, "High beam steering in Fabry-Pérot leaky-wave antennas," *IEEE Antennas Wireless Propag. Lett*., Vol. 12, 261-264, 2013.
5. Ghasemi A., S. N. Burokur, A. Dhouibi and A. de Lustrac, "Inductive-varying grid for highly beam-steerable cavity antennas," *Electron. Lett*., Vol. 49, No. 5, 319-321, 2013.

# Multiwave Technologies AG
## Accelerating Metamaterial Design

**T. Antonakakis**[1], **M. Makwana**[1]

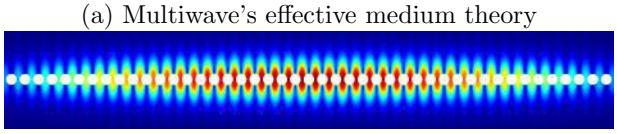
[1]Multiwave Technologies AG, Switzerland
tryfon@multiwave.ch

**Abstract**— Metamaterial design is hindered by lengthy computational time and a plethora of possible microstructures. Modeling a structured material is expensive in terms of computing memory, time and cost. One needs to have the right structure or topology combined with the adequate materials responding to engineering requirements of permittivity, permeability, or elastic wave velocities. Multiwaves' proprietary software has the ability to compute these effective parameters and as a result we are able to design structured media with desired properties. We have developed algorithms in the fields of homogenization reducing metamaterial analysis to a single cell. Our algorithms are integrated with software and run on super- computers allowing for extremely fast optimization in terms of topology and material. The entire design process is accelerated by several orders of magnitude and is abstract enough to be applied to the discovery of novel photonic, phononic and elastic crystals or metamaterials.

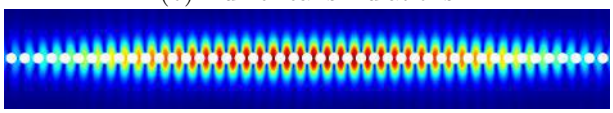
To demonstrate the capabilities of our algorithms we elucidate the homogenization procedure that forms a crucial component of one of our post-processing algorithms, by examining two case studies applicable to elasticity and electromagnetism [1, 2]. For the former case we examine waves guided along surfaces by periodic corrugations, more commonly known as gratings. Gratings are present in photonic circuits where they serve to transmit light from an optical fiber onto a plane as the light couples with the micro-structure of the grating. Despite their pseudo one-dimensional identity, which could suggest that they are relatively easy to compute without requiring much RAM, they pose several challenges to scientists, which in turn impacts their design processes. Results using classical software yield many junk modes together with the good one(s) and a filtering process needs to be put in place that is highly specific to each geometry. Our proprietary solver overcomes this issue by solving directly for the modes of interest.

Secondly we examine Maxwell's equations of electromagnetism; like the equations of elasticity,

(a) Multiwave's effective medium theory



(b) Numerical simulations



Maxwell's equations are vector equations and are therefore cumbersome to solve via brute-force numerical methods. Hence it is natural that we should seek to obtain effective media equations that encompass all the desired information of comparable numerical methods but at a fraction of the time. For example it was demonstrated in [2] that the computational cost of calculating an anisotropic mode of oscillation required approximately 11.5 hours on a dedicated machine using 77GB of RAM and 16 processor cores running at 2.5GHz. In comparison, the homogenization scheme used around 3.7GB of RAM and required 2.7 minutes to solve on a laptop with 2 cores running at 2.5GHz and yield similar results.

Naturally, these are only two applications of a single post-processing algorithm that we have within our proprietary software. More applications include detection of band-gaps and localized defect-modes, high transmission, unidirective propagation and more.

**REFERENCES**


1. D. J. Colquitt, R. V. Craster, T. Antonakakis, S. Guenneau, "Rayleigh Bloch waves along elastic diffraction gratings," *Proceedings of the Royal Society A*, Vol. 471, No. 2173, 2014.

2. B. J. Maling, D. J. Colquitt, R. V. Craster, "The homogenisation of Maxwells equations with applications to photonic crystals and localised waveforms on metafilms," *arXiv:1506.02292* , 2015

# Investigation of deformation on microstructures in shape memory $Cu_{69.95}Zn_{26.04}Al_{4.01}$ Alloy

**E. Aldirmaz[1*], H. Celik[2], M. Evecen[1] and Y. Ö. Çiftci[3]**

[1]Department of Physics, Faculty of Science and Arts, Amasya University, Ipekkoy, Amasya, Turkey
[2]Department of Elementary Education, Education Faculty, Kırıkkale University, Yahsihan, Kırıkkale, Turkey
[3]Department of Physics, Faculty of Sciences, Gazi University Teknikokullar, 06500, Ankara, TURKEY
ealdirmaz@gmail.com

**Abstract**- The effect of deformation on phase transformation temperatures and microstructures of Cu-Zn-Al SMA were investigated. For Cu-Zn-Al SMAs, two martensite structures are typically produced, 2H and18R. Stress-strain curves obtained from the tensile test performed at the room temperature are determined the ultimate yield strength, compressive strength and the ductility. The differential scanning calorimetry experimental results show that the transformation temperatures are raised by an increase in stress.

Shape-memory alloys (SMAs) are used as sensors and actuators in most engineering and medical applications and are optimized to exhibit either high stress recovery or high strain recovery. The Cu-Zn-AI alloy is one of the most popular shape memory alloys. The Cu–Al–Zn system is interesting to researchers, because Cu-based alloys, among other SMAs, have been extensively used many technological applications [1, 2]. The martensite structures in Cu-based alloys (Cu-Zn-Al and Cu-Al-Ni) possess 9R (or 18R), 3R (or 6R) and 2H structure depending on the alloy composition, heat treatment and the stress-induced condition [3]. The rare earth elements are often used as alloying element to purify the grain boundary, refine the grains and improve the mechanical properties. [4]. In this work purpose of the microstructural changes and mechanical properties resulting from the quenching treatments have also been studied.

**Acknowledgment,** this study was supported financially by the Research Centre of Amasya University (Project No: FMB-BAP 16-0174).

**REFERENCES**

1. Van Humbeeck J., "Non-medical applications of shape memory Alloys", Mat. Sci. Eng. A 273–275, 134–148, 1999.

2. Morgan, NB., "Medical shape memory alloy applications the market and its products", Mater. Sci. Eng. A *378*, 16–23, 2004.

3. Tadaki T., Tokoro M., Shimizu K., "Thermoelastic nature and crystal structure of the Cu-Zn martensite related to the shape memory", Transact of the Japan Institute of Metals. 16, 5285-296, 1975.

4. Adiguzel O., "Observation of ageing effects in a shape memory CuZnAl alloy", Turkish J Phys. 13, 71–179, 1989.

# Refractory plasmonic materials for high temperature plasmonic devices

**U. Guler[1*], E. Marinero[1, 2], A. Boltasseva[1, 2], and V. M. Shalaev[1,2]**

[1]Nano-Meta Technologies, Inc., West Lafayette, USA

[2] School of Electrical & Computer Engineering and Birck Nanotechnology Center, Purdue University, West Lafayette, USA

[*]corresponding author: uguler@nanometatech.com

**Abstract**- Transition metal nitrides exhibit plasmonic properties in the visible and infrared regions of the electromagnetic spectrum together with refractory properties that makes them uniquely viable as plasmonic components for applications that require harsh operational conditions. In this talk, we will discuss metamaterials designed for a variety of applications, such as thermophotovoltaics and sensors for extreme environments, where high temperature durability and chemical stability are essential for proper functioning.

Intensive research in the fields of plasmonics and metamaterials over the last two decades has led to a large number of demonstrations in a wide range of application areas [1]. While enhanced capability to control and manipulate light has been found very useful, several challenges due to material limitations were identified as roadblocks on the way to successful technology transfer in general. We believe, investigation of alternative plasmonic materials and therefore their improvement in accordance with the application-specific requirements will help realization of devices utilizing plasmonic components [2].

Transition metal nitrides, more specifically titanium nitride (TiN) and zirconium nitride (ZrN), are widely used in different industries due to their refractory properties. The frequent use of these materials resulted in a good understanding of fabrication process and led to the optimization of different deposition techniques [3]. Over the last decade, TiN and ZrN have been studied as plasmonic components in the visible and infrared regions where their optical properties were found comparable with existing plasmonic metals [4]. Single crystalline thin films of TiN offer enhanced interaction with light together with high temperature durability, wear resistance, as well as CMOS and bio-compatibility.

Metamaterials based on transition metal nitrides are promising as spectrally selective surfaces over a wide range covering visible and infrared regions. Thermophotovoltaics (TPV), and by extension solar/TPV, is one technology that can benefit from high efficiency spectrally selective components with refractory properties [5]. Improved control over the blackbody spectrum combined with the enhanced peak intensities arising from higher operation temperatures can solve the long-standing durability and efficiency problems in the field [6]. Refractory metamaterial broadband perfect absorbers in the visible [7] and narrowband emitters in the near-infrared regions will be presented with an emphasis on high temperature applications. The discussion will be extended to plasmonic sensor systems in harsh environments.

**Acknowledgements**: The authors acknowledge generous support from NSF SBIR grant IIP-1416232.

**REFERENCES**


1. Schuller, J. A., E. S. Bernard, W. Cai, Y. C. Jun, J. S. White, and M. L. Brongersma, "Plasmonics for extreme light concentration and manipulation", Nat. Mater., Vol. 9, 193-204, 2010.
2. Guler, U., A. V. Kildishev, A. Boltasseva, and V. M. Shalaev, "Plasmonics on the slope of enlightenment: the role of transition metal nitrides," Faraday Discuss., Vol. 178, 71-86, 2015.
3. Pierson, H., Handbook of Refractory Carbides & Nitrides: Properties, Characteristics, Processing and Applications, William Andrew, Incorporated, 1996.
4. Naik, G., V. M. Shalaev, and A. Boltasseva, "Alternative plasmonic materials: beyond gold and silver," Adv. Mater., Vol. 25, 3264-3294, 2013.
5. Guler, U., V. M. Shalaev, and A. Boltasseva, "Nanoparticle plasmonics: going practical with transition metal nitrides," Mater. Today, Vol. 18, 227-237, 2015.
6. Guler, U., A. Boltasseva, and V. M. Shalaev, "Refractory Plasmonics," Science, Vol. 344, 263-264, 2014.
7. Li, W. U. Guler, N. Kinsey, G. V. Naik, A. Boltasseva, J. Guan, V. M. Shalaev, and A. V. Kildishev, "Refractory Plasmonics with Titanium Nitride: Broadband Metamaterial Absorber," Adv. Mater., Vol. 26, 7959-7965, 2014.

# Study of Phase formation in rapidly and slowly quenched Cu-13.81%Mn-3.7%Al Alloy

**E. Aldirmaz[1], M. Evecen[1] and H. Tanak[1]**

[1]Department of Physics, Faculty of Arts and Sciences, Amasya University, 05100 Amasya, TURKEY

ealdirmaz@gmail.com

**Abstract-** This paper reports the morphological and mechanical properties of Cu-13.81%Mn-3.78%Al (wt.%) alloy was investigated. SEM observations of Cu-13.81%Mn-3.78%Al (wt.%) alloy precipitates formed in the slowly-cooling sample while austenite phase was occured in rapidly quenched sample. Compression stress was applied on the alloy in order to investigate the deformation effect on the phase transformations. The structural and mechanicals features of the phase transformations have been determined.

The microstructure of Cu-Mn-Al alloys is almost similar to that of high-tensile brass and aluminum bronze; it consists of α, β and a dispersion of intermetallic precipitates [1]. In previous study reported that both the morphology of the β-Mn precipitates and the orientation relationship between the β-Mn and $L2_1$ matrix would vary with the aging temperature. Moreover, at lower temperature, the concentrations of both Al and Mn plays important an role for the formation of the β-Mn precipitates [2, 3]. The influence of the heat treatment solid-state reactions depending on homogenization periods, diffusion-strengthening effect, grain size and cooling rates on the phase structure of alloys. In this study investigated the effects of composition, heat treatments and deformation on different cooling rates, occurrence phases in each Cu-13.81%Mn-3.78%Al (wt.%) alloy.

**Acknowledgment,** this study was supported financially by the Research Centre of Amasya University (Project No: FMB-BAP 16-0174).

**REFERENCES**

1. Iqbal J, Hasan F, Ahmad F., "Characterization of phases in an as-cast copper-manganese-aluminum alloy", J. Mater. Sci. Tech. 22 (6), 779-784, 2006

2. S.Y. Yang, Liu T.F., "Phase transformations in a Cu–35 at.% Mn–25 at.% Al alloy", J. Alloys Comp. 417, 63-68, 2006

3. Kozubski R., Soltys J., Dutkiewicz J., Morgiel J., "TEM study of the decomposition of the Heusler alloy $Cu_2MnAl$", J. of Mater. Sci. 22, 3843-3846, 1987

# Nanoantenna-Enhanced Infrared Detectors for Improved Performance and Spectral Tunability

**D. W. Peters[1*], J. K. Kim[1], A. Tauke-Pedretti[1], T. E. Beechem[1], J. F. Ihlefeld[1], P. Davids[1], M. B. Sinclair[1], J. R. Wendt[1]**

[1]Sandia National Laboratories, U.S.A.

[*]corresponding author: dwpeter@sandia.gov

**Abstract**- Incorporating nanoantennas onto infrared focal plane arrays (FPAs) may offer significant performance improvements and enhanced functionality over today's state-of-the-art MWIR and LWIR FPAs. We are using nanoantennas to concentrate light in a small volume, thereby allowing us to use less active material than in current infrared detectors and thus lower the dark current. In the limiting case, we can envision using atomically thin detector layers such as graphene. We are using this architecture to incorporate real-time spectral tunability.

Infrared detectors used in focal plane arrays (FPAs) have been made for decades of alloys of mercury cadmium telluride. These infrared detectors are nearing the believed limit of their sensitivity at a given cooled temperature. This limit, known in the infrared detector community as Rule 07, dictates the sensitivity floor for mercury cadmium telluride (MCT) detectors in their traditional architecture. [1,2] There are paths around Rule 07, with many in the infrared community working on detector compounds other than MCT. We are looking at changing the material and also the basic architecture of the individual pixels. Our architecture relies on a nanoantenna array to couple the incoming radiation to a surface wave which is tightly confined to the nanoantenna surface.[3,4] This confinement of the incident energy in a thin layer allows us to greatly reduce the volume of the absorbing layer, with a corresponding reduction in dark current from spontaneously generated electron-hole pairs in the absorber material.

A schematic of the basic structure and an SEM of the fabricated detector are shown in Figure 1. The nanoantenna array is fabricated directly on the detector material to maximize absorption of the surface waves in the active layer. Below the detector material is a continuous metal layer which acts as a back reflector to make the entire structure optically resonant, and also serves as a bottom electrical contact. We are currently using epitaxial InAsSb as the detector material which leads to many challenges in the fabrication of the detector shown in Figure 1. We will discuss the fabrication processes that we have developed to overcome these difficulties.

This nanoantenna-based architecture also allows us to explore some new possibilities for adding functionality to infrared detectors. We would like to have the ability to tune the spectral window over which our resonant device absorbs light. Changing the resonance condition requires a change in the optical properties of some component in the stack or physically altering the topology of the nanoantenna.

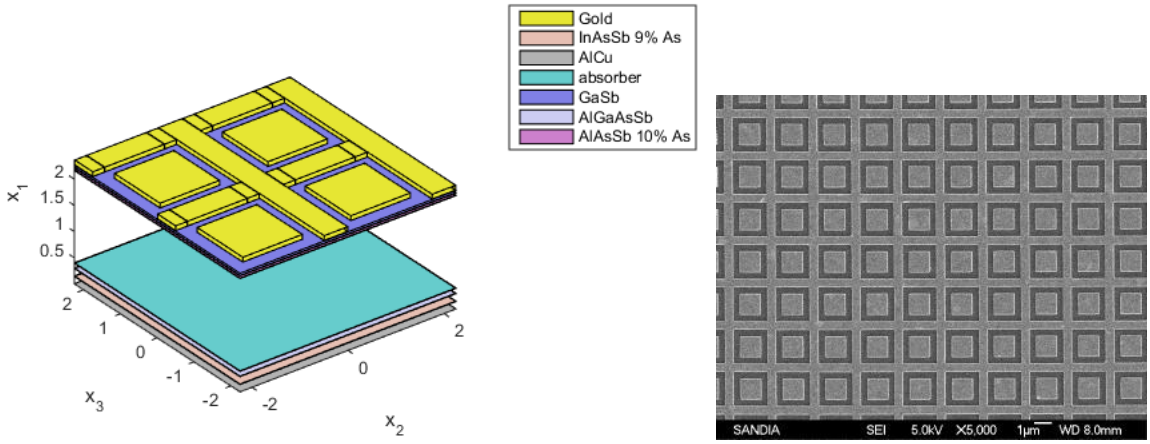



**Figure 1.** (left) Four unit cells of a nanoantenna-enabled long-wave infrared detector using a 1.7μm thick absorber layer. Figure units are in microns. (right) SEM of fabricated detector.

Changing the optical cavity resonance may be achieved by using one of several optical materials whose optical properties change with an applied voltage. While well-known materials such as $VO_2$ change properties with temperature, this is not a practical path for cooled infrared detectors. Luckily, there are several types of semiconductors, oxides, and other materials such as graphene whose optical properties can be altered with an applied voltage.

We will present results from nanoantenna-enabled detectors and also the current state of our tunable materials synthesis and tunable devices.

**Acknowledgements**: Sandia National Laboratories is a multi-program laboratory managed and operated by Sandia Corporation, a wholly owned subsidiary of Lockheed Martin Corporation, for the U.S. Department of Energy's National Nuclear Security Administration under contract DE-AC04-94AL85000.

**REFERENCES**

1. Tennant, W., D. Lee, M. Zandian, E. Piquette, and M. Carmody, “MBE HgCdTe technology: a very general solution to IR detection, described by ‘Rule 07’, a very convenient heuristic.” *J. of Electronic Materials*, Vol. 37, 1406-1410, 2008.
2. Tennant, W., “’Rule 07’ Revisited: Still a Good Heuristic Predictor of p/n HgCdTe Photodiode Performance?,” *J. of Electronic Materials*, Vol. 39, 1030-1035, 2010.
3. Peters, D.W., P. Davids, J.R. Wendt, A.A. Cruz-Cabrera, S.A. Kemme, S. Samora, “Metamaterial-inspired high-absorption surfaces for thermal infrared applications,” *Proc. of SPIE*, vol. 7609, 2010.
4. Peters, D.W., P. S. Davids, J. K. Kim, T. E. Beechem, S. W. Howell, D. Leonhardt, T. Ohta, J. R. Wendt, J. A. Montoya, “Plasmonic nanoantennas for enhanced midwave and longwave infrared imaging,” *Proc. SPIE*, Vol. 9467, 946729, May 22, 2015.

# Surface wave-based field confinement device for UHF-RFID readers

**J. Bonache [1*], G. Zamora[1], F.Paredes[1], S. Zuffanelli[1], P. Aguila[1], F. Martin[1]**
[1]Author Affiliation, Country
[*]corresponding author: Jordi.Bonache@uab.es

**Abstract**-In this work, we study the use of metamaterials for the generation of surface waves with controllable levels of confinement for applications in near field UHF-RFID readers. This solution overcomes the limitation of conventional nearfield RFID readers, which are unable to define an accurate detection zone due to the presence of significant levels of radiation leakage. We analyze the field distribution and polarization of several structures to determine the most suitable configuration for different applications.

Far field readers based on antennas are very suitable for carrying inventory without having to approach to the product, so that a complete inventory of every store can be made within seconds [1]. Therefore, in some scenarios, as in payment applications or inventory at small distances, these devices are not appropriate since the definition of a clear coverage zone is troublesome and hence it is impossible to ensure that only the desired tags are detected. Some solutions based on current loops are used in UHF-RFID near field applications [2]. However, with these types of devices it is difficult to achieve a good trade-off between low radiation gain and large near field coverage. This is because the near field region is always of the same order of the loop size [3], whereas the radiation gain of a current loop increases strongly with its radius. As a result, when the required coverage zone is comparable to the wavelength of the UHF-RFID signal in free space, excessive values of radiation gain arise. To overcome these issues, a new strategy to control the field confinement based on the generation of a surface wave by means of a metamaterial structure is presented in [4]. These types of waves induce an exponential decay of the field versus distance and are unable to radiate [5]. Thanks to the possibility to simultaneously and accurately tailor the phase velocity and Bloch impedance at wish with these structures, the generation of evanescent waves with the desired level of confinement is possible. In this work, we study different configurations of structures and unit cells based on the concept presented in [4] to achieve an adequate field distribution and polarization depending on the application.

Given a surface wave propagating between two media in the *x*-direction, the electromagnetic fields at the interface can be expressed in terms of the phase constant of the propagating mode ($\beta$) and the phase constant of the signal in the medium surrounding the propagating structure ($k_0$). Considering a mode that has no *z* variation ($k_z = 0$), the *i* component of the field can be expressed as:

$$A_i(x,y,t) = A_{0i}e^{-j\vec{k}\cdot\vec{r}}e^{j\omega t} = A_{0i}e^{-j\beta x}e^{-\alpha y}e^{j\omega t} \quad (1)$$

where $\alpha = \sqrt{\beta^2 - k_0^2}$ is a positive real number, which determines the level of confinement of the fields around the structure. Since metamaterials allows controlling the value of $\beta$, $\alpha$ can be tailored to adjust the desired coverage zone without introducing radiation leakage. Figure 1 shows an example of application of this technique using a left-handed metamaterial transmission line, where the field confinement can be clearly observed. Depending on the structure design the field distribution can be modified according to the requirements of the

application. Figure 2 shows an example of the field distribution for the case of a metamaterial transmission line with reduced dimensions of the ground plane (a) and with extended ground plane (b). In the conference, a comparison between different structures and an analysis of which field distribution is more suitable depending on the application will be shown.

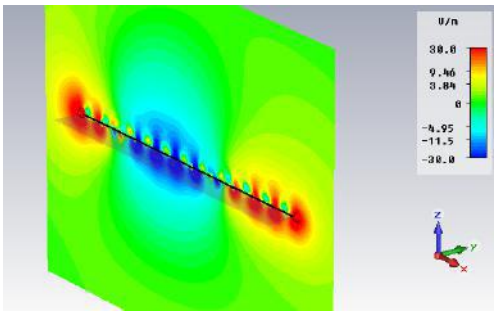


**Figure 1:** Electric field around a left handed metamaterial transmission line

**(a)**

**(b)**

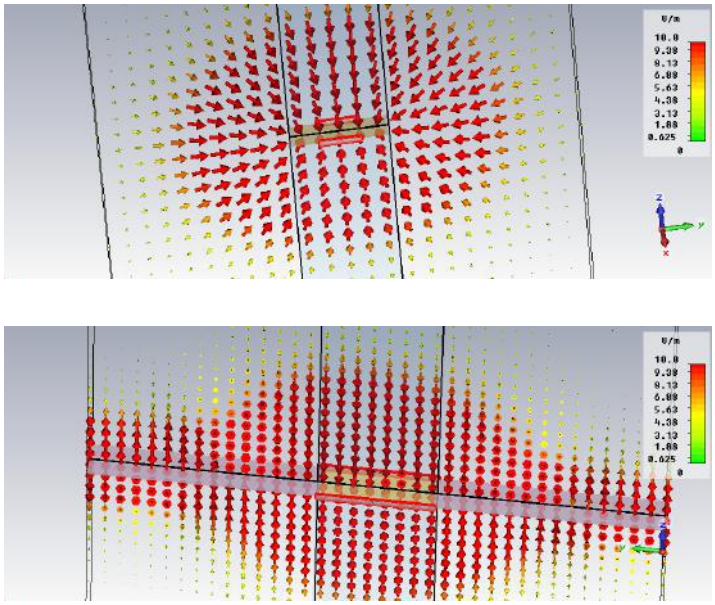


**Figure 2:** Electric field lines for a metamaterial with reduced ground plane (a) and extended ground plane (b).

**Acknowledgements**, This work has been supported by MINECO-Spain (project TEC2013-40600-R COM-SEN-RFID, project RTC-2015-4385-7 META-ACCESS, project RTC-2015-3709-7 META-STOCK), by FEDER funds, and by Generalitat de Catalunya (project 2014SGR-157, project 2014 PROD 00042). F. Martin is in debt to ICREA for supporting his work and by awarding him with an ICREA Academia Award.

## REFERENCES

[1] P. V. Nikitin, K. V. S. Rao, S. Lazar, "An Overview of Near Field UHF" RFID. IEEE International Conference on RFID, Grapevine, TX, 26-28 March 2007.
[2] Dobkin , D. M., Weigand, S. M., Iyer, N. Segmented magnetic antennas for near-field UHF RFID. Microwave J. 50, 96–102 (2007).
[3] C. A. Balanis, "Antenna Theory: Analysis and Design" (New Jersey: John Wiley & Sons, ed. 3, 2005).
[4] J. Bonache et. al., "Controlling the Electromagnetic Field Confinement with Metamaterials," unpublished.
[5] F. J. Zucker "Surface-wave antennas" in Antenna Engineering Handbook (ed. Johnson, R.C) Ch. 12 (McGraw-Hill, NY, ed. 3, 1993).

# Metamaterial Structures Applied to Wireless RF Front-End Distributed PA, BAW Filters, and Antennas

Recent growth in the use of wireless wide-area networks (WWAN), the adoption of broadband wireless local-area networks (WLAN), and consumer demand for seamless global access has pushed the wireless industry to support multi-band, multimode, and broadband standards in mobile devices, access points, automobile, and home automations. This has pushed RF front-end design beyond the capabilities of current technologies, opening the door for creative solutions that are 1) Integrated, 2) low profile, 3) small, 4) higher isolation, 5) faster time to market, 6) low cost, and 7) easy to adapt to high peak-to-average modulations. In this presentation, we apply metamaterial-based structures to a multi-band / multi-antenna RF front-end while illustrating the key benefits of metamaterial-based RF design. Pentaband antennas directly printed on PCB, novel and simple distributed power amplifier architecture using GaAs fabrication for improving efficiency, bandwidth and linearity at backed-off RF power is presented, BAW filters designs, and integrated directional coupler for increased antenna isolation and MIMO channel de-correlation.

## About Dr. Achour

**Science**

- Focus on fundamental science that solves key industry challenges
- Universities: Worked closely with top university professors
  - UCLA Metamaterial: licensed IP, funded research, and commercialized technologies
  - Solar energy conversion: Interacted with leading professors at EPFL and UC Boulder
- 20+ journal/conference publications

**Novel Devices and IP**

- 40 issued patents and 100+ pending applications
  - Metamaterial structures and applications
  - Smart Material
  - Optical antennas
  - Wireless devices, communication, and network
  - Most are licensed and used in products

**Industry & Commercialization**

- Founder & CEO: Polyceed Inc. self-powered and user controlled dynamic smart material
- Co-founded and led two startups focused on Metamaterial (Rayspan), RF/microwave, and optical technologies development and commercialization (LightPointe); held CTO position.
- Built companies with R&D focus and raised capital from Sequoia Capital and Khosla venture
- Built Rayspan's 120+ patents portfolio from scratch in less than 5 years.

**Education**

- Ph.D. in Elementary Particle Physics from MIT

# ISM (Industry Scientific and Medical standard) band flex fuel sensor using electrical metamaterial device

**Vaishali Rawat, Vihang Nadkarni and Sangeeta Kale***
Depatment of Applied Physics, Defence Institute of Advanced Technology, Pune, India
*Corresponding author, E-mail: sangeetakale@diat.ac.in sangeetakale2004@gmail.com

## Abstract

A stand-alone device working on the electrical metamaterial concept, operating at 2.47 GHz (ISM band), using merely 10 μL sample is proposed to detect petrol:ethanol ratio in given hybrid fuel. Systematic shifts in the transmission frequency as well as magnitude are observed, upto a maximum of ~160 MHz and 12 dBm with the hybrid fuels. The sensing was fast with instantaneous recovery; promising an accurate and sensitive device of detection of flex fuel.

## 1. Introduction

Metamaterials in general consists of artificially engineered structures made from conventional materials which exhibit very unique and intriguing sets of properties by manupilating the electromagnetic waves and therefore have enormous potential applications in imaging (superlenses)[1,2], miniaturized antennae/devices[3,4] and other high end appplications[5,6] Sensors is also one of the recent domain, in which metamaterials have made exponential progress in current decade[7-9]. The reason being metamaterial based sensors offer high miniaturization and large values of Q-factor which makes them highly sensitive to environmental changes hence, very suitable for sensing applications. Metamaterials have been explored for various sensing applications like displacement[10,11], rotation[12], strain sensing[13,14] level sensing[15] and material sensing which include solid dielectrics[16], liquids[17,18], hazardous chemicals[19], and bio-molecules[20,21].

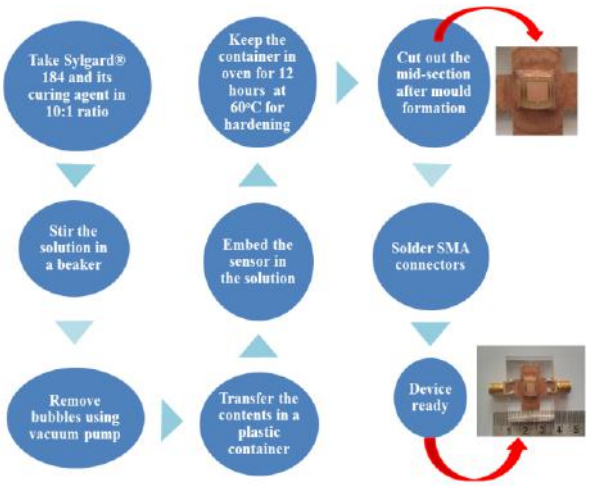
From applications perspective, a flexible fuel vehicle (FFV) is an alternative fuel vehicle with an engine designed to run on more than one fuel, usually gasoline (petrol) blended with either ethanol or methanol fuel. Modern flex fuel engines are capable of burning any proportion of the resulting blend in the combustion chamber as fuel injection and spark timing are adjusted automatically according to the actual blend detected by a fuel composition sensor. Very few studies have been done to develop a sensor which can sense the individual percentages of petrol and ethanol in a flex fuel system, basically because the property-range of these liquids are very close. A combination of a lambda and capacitive sensor is considered to be the best option in the current market[22]. However, the probability of false values is reasonably high resulting in damage of the engine. Hence, the opportunity of an efficient, selective and recoverable sensor is much on the anvil. In this work, a practical implementable metamaterial device is designed and developed in the standard ISM (Industry Scientific and Medical standard) band, hence proposed and calibrated to detect petrol:ethanol ratio in given flex fuel (from 5 to 85% ethanol in petrol). The device requires only 10 microliter (μL) of hybrid fuel samples. Petrol samples were obtained from the Company operated Company owned (CoCo) petrol pump (gas stations). The variation in the petrol:ethanol ratios was decided on the Government norms (5% and 20% ethanol in petrol) and standards for E50 and E85 ( 50% and 85% ethanol in petrol) flex fuels. The sensor is a Complementary split ring resonator (CSRR), excited by a microstrip line, which exhibit negative permittivity, was designed and simulated using CST Microwave Studio to operate at 2.51GHz, thereafter fabricated on general Cu-clad on FR-4 epoxy substrate using photolithography technique,. The device is further developed using polydimethylsiloxane (PDMS) for precise micro-quantity sensing. The sensing measurements were done on vector network analyzer (VNA, (Agilent PNA N5222A)). The sensor exhibits corresponding shifts in transmission frequency as well as magnitude for various concentration of hybrid fuels. Extreme miniaturization and high sensitivity due to the metamaterial approach, being sub-wavelength in nature (resonance at λ/18 in this case) is the prominent advantage of the envisaged device.

## 2. Theory, Design and Device Development

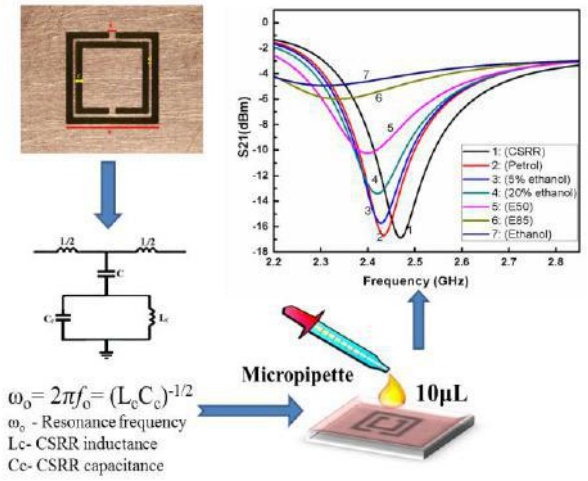
Complementary Split Ring Resonator CSRR is in general known as a dual of a Split Ring Resonator, based on Babinet's principle[23]. CSRR is basically an electrical metamaterial which resonates at sub-wavelength dimensions thereby exhibiting negative permittivity. The structure inherently behaves as an electric dipole when excited by an axial electric field, applied perpendicular to the CSRR plane [24]. CSRRs have been used for various applications like filters, antennas and planar characterization[16,25,26]. The easiest way of excitation for CSRR is accomplished by using a microstrip transmission line. The sensor was fabricated on a commercially available FR4 epoxy (εr= 4.4 thickness h=1.6 mm) substrate. Detailed explaination of the CSRR unit cell and experimental set up has been mentioned in ref [18].

Further, for precise and uniform fuel sensing a Polydimethylsiloxane (PDMS) layer was grown around the CSRR. Figure1(a) explains the device development procedure. Sylgard® 184 silicone elastomer base along with its curing agent were used for cavity devolopment. The silicon base and its curing agent were mixed in 10:1 ratio.

The solution was placed under vacuum till all the air bubbles from the solution were absent. The solution was poured in an empty container and the CSRR sensor was embedded inside the solution. Finally, the container with the solution and sensor was kept in an oven at 60°C for 12 hours which led to hardening of the PDMS mold around the sensor. The mold was cut off above the active area of the CSRR sensor to make a cavity. The PDMS cavity designed confines the fuel sample strictly over the active area of CSRR. The resonating frequency of the device after development shifts at 2.47GHz. Figure 1(b) depicts the active area of CSRR along with its dimensions, the equivalent circuit of microstrip based CSRR, equations involved in the sensing procedure and experimental results. Thereafter, the sample fuel was drop-cast using a micropipette in the cavity on the active area of CSRR. The measurements were carried out for 5%, 20%, 50% and 85% of hybrid fuels along with 100% petrol and 100% ethanol. The over-all dimensions of the device are 26mm x 20mm.




(a)

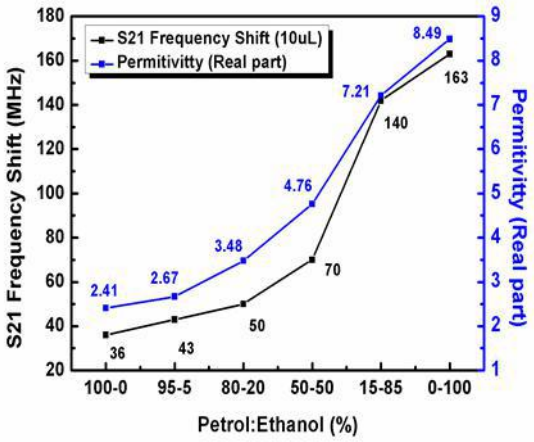



(b)

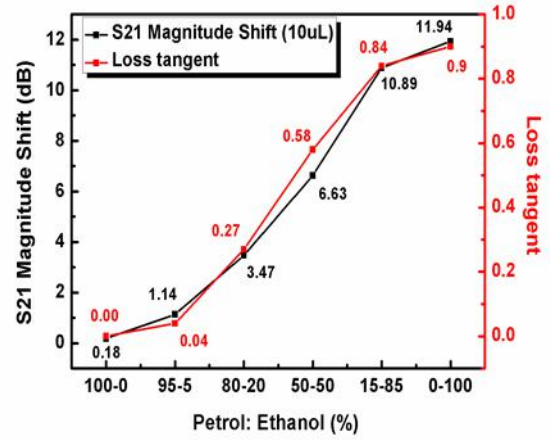
Figure1. (a) depicts the schematic of device development. (b) shows the CSRR Sensor with dimensions a = 6.6 mm, c =0.42 mm, d = 0.16 mm and g = 0.3 mm, equivalent circuit of microstripline based CSRR, relevant equations, and plot of the frequency and magnitude shifts w.r.t. standard compositions of flex fuels.

## 3. Results and Discussion

The simulation of CSRR design (with and without PDMS cavity) was carried out using CST Microwave Studio. The simulation was run on Transient Solver. Systematic shifts in transmission frequency as well as magnitude were observed, with the varied standard concentration of hybrid fuels as shown in Fig. 1(b). From the equations in Figure 1(b), it can be inferred that change in the permittivity of the sample material reflects the change in the capacitance of the CSRR ($C_C$) of the sensor which shifts the resonance frequency of the device [16].




(a)




(b)

**Figure2(a).** shows the variation in $S_{21}$ with respect to the frequency to various petrol: ethanol ratios and their corresponding real part of permitivitty at 2.47GHz (b) shows the variation in $S_{21}$ with respect to the magnitiude to various petrol: ethanol ratios and their loss tangent values at 2.47GHz

Figure 2(a) shows the S21 resonant frequency response of the sensor for different flex fuel combinations. It was found that the resonant frequency of the empty cavity was at 2.47

GHz, which shifted by 36 MHz, with 10 μL of petrol to 2.434 GHz. This further shifted to lower values with the addition of ethanol, going maximum to 2.330 GHz with E85 fuel (140 MHz shift). Pure ethanol showed its signature at 2.307 GHz (163 MHz shift).The corresponding resonance frequency shifts are well complied with the real permittivity($\varepsilon_r$) values of flex fuels also shown in Figure 2(a) as $\varepsilon_r$ is directly proportional to Cc i.e. capacitance value of the CSRR. The permittivity values of the samples were measured using Agilent Dielectric Probe Kit (85070E) [27]. Further, frequency shift was also accompanied by systematic gain in $S_{21}$ magnitude of ~12 dBm for 100% ethanol; 0.18 dBm for 100% petrol. Figure 2(b) depicts variation in $S_{21}$ magnitude i.e. insertion loss with different concentration of flex fuels and corresponding loss tangents variation which aptly correlates. Change in $S_{21}$ magnitude has been attributed to the loss tangent and imaginary part of the permittivity of the sample. A low value of loss tangent signifies less transmission because of low dissipative loss and conductivity and visa-versa [28]. Therefore, transmission is lowest in case of 100% petrol and highest for 100% ethanol as they have lowest and highest value of loss tangent respectively.

## 4. Conclusions

In conclusion, a microstrip based electrical metamaterial sensor has been designed which provide good and stable sensitivity in detecting a micro-quantity of hybrid fuel samples. The proposed device overcomes the drawbacks of the conventional existing flex fuel sensor along with several advantages like extreme miniaturization, micro-quantity sensing, high sensitivity, ISM band applicability for ease in manufacturing, hence ensures its practical applicability to check the quality of fuel, reduce cost and enhance the life of the automobile engines.

## Acknowledgements

Authors acknowledge the Vice-Chancellor DIAT, for support, KPIT Technologies for providing standard hybrid fuels data and Dr. Harsh Rajesh, SAMEER Mumbai for dielectric measurements.

## References

[1] J. B. Pendry, Negative Refraction Makes a Perfect Lens, *Phys. Rev. Lett.* 85: 3966–3969, 2000.

[2] N. Fang, H. Lee, C. Sun, X. Zhang, Sub-Diffraction-Limited Optical Imaging with a Silver Superlens, *Science* 308: 534–537, 2005.

[3] Y. Dong, T. Itoh, Metamaterial-Based Antennas, *Proc. IEEE* 100: 2271–2285, 2012.

[4] Y. Dong, T.Itoh, Promising Future of Metamaterials. *IEEE Microw. Mag.* 13: 39–56, 2012.

[5] J.B. Pendry, Photonics: Metamaterials in the Sunshine, Nat. Mater 5: 599–600, 2006.

[6] J. B. Pendry, D. Schurig, D.R. Smith, Controlling Electromagnetic Fields, Science, 312: 1780–1782, 2006.

[7] M. Schüßler, C. Mandel, M. Puentes, R. Jakoby, Metamaterial Inspired Microwave Sensors, *IEEE Microw. Mag.* 13: 57–68, 2012.

[8] M. Huang, J. Yang, *Microwave sensor using Metamaterials*, in Wave Propagation, In-tech Press: Vienna, Austria: 13–36, 2011.

[9] T. Chen, S. Li, H. Sun, Metamaterials application in sensing, *Sensors*, 12: 2742–2765, 2012.

[10] A.K. Horestani, C. Fumeaux, S.F. Al-Sarawi, D. Abbott, Displacement Sensor Based on Diamond-Shaped Tapered Split Ring Resonator, *IEEE Sens. J* 13: 1153–1160, 2013.

[11] J. Naqui, M. Durán-Sindreu, F.Martín, Novel Sensors Based on the Symmetry Properties of Split Ring Resonators (SRRs). *Sensors (Basel).*11: 7545–7553, 2011.

[12] A. K. Horestani, D. Abbott, C. Fumeaux, Rotation Sensor Based on Horn-Shaped Split Ring Resonator, *IEEE Sens. J* 13: 3014–3015, 2013.

[13] R. Melik, E. Unal, N. K. Perkgoz, C. Puttlitz, H. Demir, H. V. Metamaterial-Based Wireless RF-MEMS Strain Sensors, *In 2010 IEEE Sensors* : pp.2173–2176, 2010.

[14] J. Li, C. M. Shah, W. Withayachumnankul, B. S-Y. Ung, A. Mitchell, S. Sriram, M. Bhaskaran, S. Chang, D. Abbott, Flexible Terahertz Metamaterials for Dual-Axis Strain Sensing. *Opt. Lett.* 38: 2104–2106, 2013.

[15] M. Schussler, C. Mandel, M. Puentes, R. Jakoby, Capacitive Level Monitoring of Layered Fillings in Vessels Using Composite Right/left-Handed Transmission Lines, *In 2011 IEEE MTT-S International Microwave Symposium; IEEE:* pp.1–4, 2011.

[16] M. Boybay, O.M. Ramahi, Material Characterization Using Complementary Split-Ring Resonators, *IEEE Trans. Instrum. Meas.* 61: 3039–3046, 2012.

[17] A. Ebrahimi, W. Withayachumnankul, S. Al-Sarawi, D.Abbott, High-Sensitivity Metamaterial-Inspired Sensor for Microfluidic Dielectric Characterization, *IEEE Sens. J.* 14: 1345–1351, 2014.

[18] V. Rawat, S. Dhobale, S.N.Kale, Ultra-Fast Selective Sensing of Ethanol and Petrol Using Microwave-Range Metamaterial Complementary Split-Ring Resonators, *J. Appl. Phys.* 116: 164106, 2014.

[19] V. Rawat, R. Kitture, D. Kumari, H. Rajesh, S. Banerjee, S.N. Kale, Hazardous Materials Sensing: An Electrical Metamaterial Approach. *J. Magn. Magn. Mater.* 2015. doi:10.1016/j.jmmm.2015.11.023

[20] H.-J. Lee, J.-H. Lee, H.-S.Moon, I.-S.Jang, J.-S. Choi, J.-G. Yook, H.-I. Jung, A Planar Split-Ring Resonator-Based Microwave Biosensor for Label-Free Detection of Biomolecules, *Sensors Actuators B Chem.*, 169: 26–31, 2012.

[21] A.W. Clark, A. Glidle, D.R.S. Cumming, J.M. Cooper, Plasmonic Split-Ring Resonators as Dichroic Nanophotonic DNA Biosensors, *J. Am. Chem. Soc.* 131: 17615–17619, 2009.

[22] J. Bachmann, A. Fahrenbruch, Ethanol Sensors for Flex Fuel operations, *MTZ Worldwide* 69: 46–49, 2008.
[23] F. Falcone, T. Lopetegi, M. A. G. Laso, J. D. Baena, J. Bonache, M. Beruete, F. Martın, Babinet principle applied of the design of metasurfaces and metamaterials, *Phys.Rev.Lett* .93: 1974011, 2004.
[24] F. Falcone, T. Lopetegi, J.D. Baena, R. Marqués, F. Martín, M. Sorolla, Effective Negative-ϵ Stopband Microstrip Lines Based on Complementary Split Ring Resonators, *in: Proceedings of the IEEE Microw. Wirel. Components Lett.* 14: 280-282, 2004.
[25] J. D. Baena, J. Bonache, F. Martın, R. M. Sillero, F. Falcone, T. Lopetegi, M. A. G. Laso, J. Garcıa–Garcıa, I. Gil, M. F. Portillo, and M. Sorolla, Equivalent-circuit models for split-ring resonators and complementary split-ring resonators coupled to planar transmission lines, *IEEE Trans. Microwave Theory Tech.* 53: 1451-1461, 2005.
[26] Y. D. Dong, T. Yang, and T. Itoh, Substrate Integrated Waveguide Loaded by Complementary Split-Ring Resonators and Its Applications to Miniaturized Waveguide Filters, *IEEE Trans. Microwave Theory Tech.* 57: 2211-2223, 2009.
[27] A. Technologies, Agilent 85070E Dielectric Probe Kit 200 MHz to 50 GHz Swept High-Frequency Dielectric Measurements,-*http://cp.literature.agilent.com/litweb/pdf/5989-0222EN.pdf*
[28] C.A. Balanis, *Advanced Engineering Electromagnetics*, Second Edi. John Wiley & Sons Inc., New York, pp.78, 2012.

# Metamaterials Research at PARC

**Bernard D. Casse**
PARC, a Xerox company, USA

**Abstract**- PARC, a Xerox company, is an applied R&D powerhouse with a world-class team of experts, a long-standing culture of innovation, and unprecedented resources for applied research. This strong value proposition uniquely positions PARC to bring to market exciting and disruptive metamaterials technology platforms across multiple market segments from consumer electronics, cleantech/energy, healthcare, to the defense sector. For the past 3 years, PARC has been developing exciting and impactful metamaterial technologies for Fortune 500 companies and Government clients. Some of these technologies include passive radiative cooling (self-cooling films) for building and power plant cooling; electronically scanned array platform for drones self-driving cars; metamaterial antennas for 5G networks and satellites; metasurfaces for wireless communications; thermal barriers for single-pane windows; battery-free wireless platform for IoT; peripheral nerves/brain focused magnetic stimulation (FMS) technologies; thermophotovoltaics devices, and state-of-the-art EM computing platform. In my talk, I will give an overview of our innovation agenda.

# Commercializing Metamaterials Through the Lens of the Mythical Man Month

**Themos Kallos**
Metamaterial Technologies Inc., Canada

**Abstract**- As is the case with many early stage technologies, the commercialization of metamaterials requires significant resources in both money and collective human effort. In this work we investigate whether optical metamaterials in particular may require more than the typical resources to lead to successful commercialization. We also compare the estimated efforts with other technology commercialization projects of the recent past. The recent developments of MTI to develop optical laser filters for aircraft and aerospace applications will also be presented.

# Quantum plasmonics and metamaterials

# Quantum metamaterials as active lasing medium: Effects of disorder

**M. Marthaler**[1], **M. Koppenhöfer**[1], **and G. Schön**[1]

[1]Karlsruher Institue für Technologie, Germany

**Abstract**— A metamaterial formed by superconducting circuits or quantum dots can serve as active lasing medium when coupled to a cavity. In contrast to real atoms, for artifical atoms variations in their parameters cannot be avoided. We examine the influence of disorder on such a multi-atom lasing setup. We find that the lasing process evolves into a self-organized stationary state that is quite robust against disorder. We present relations how the allowed disorder scales with the atom number and confirm it by a numerical analysis.

Solid-state systems representing several artificial atoms invariably suffer from disorder [1, 2], either due to the variations in the fabrication process or in the environment. As a result, the level-splitting $\epsilon_j$ $(j = 1, \dots M)$ and hence the detuning from a cavity frequency $\Delta_j = \epsilon_j/\hbar - \omega$ varies. Other parameters such as the coupling strength to the cavity or the local driving can vary similarly. We examine the influence of disorder in various parameters on multi-atom lasing. Here, only static disorder is considered. We show that the lasing process is rather robust against disorder over a wide range of disorder variances. This perhaps surprising effect can be understood as follows: Those atoms which are in or close to resonance start emitting photons into the cavity. These photons enhance the process of stimulated emission, which is proportional to their number $\langle n \rangle$, also for more detuned atoms. Hence these atoms start participating in the lasing process, and $\langle n \rangle$ increases further, as well as the range of allowed detuning.

We will study the effects of disorder in detuning, coupling strength of the individual atoms, and the pumping strength. Results are presented for a Gaussian and a box distribution with similar results. Since probably most experiments in the near future will be carried out with not too large number of atoms ($M \lesssim 100$) one should expect significant sample-specific deviations from the average behavior. We therefore study also these statistical properties.

In the stationary state, the multi-atom laser can be described by a fixed point equation for the quantum statistical average photon number $\langle n \rangle = \langle a^\dagger a \rangle$,

$$\langle n \rangle = \sum_{j=1}^{M} \beta_j \frac{D_{0,j}\left(\langle n \rangle + \frac{1}{2}\right) + \frac{1}{2}}{\Gamma_{\kappa,j}^2 + \Delta_j^2 + \alpha_j \left(\langle n \rangle + \frac{1}{2}\right)} \ . \tag{1}$$

We introduced the parameters

$$\alpha_j = 4g_j^2 \frac{\Gamma_{\kappa,j}}{\Gamma_{1,j}} \ , \quad \text{and} \quad \beta_j = 2g_j^2 \frac{\Gamma_{\kappa,j}}{\kappa} \ .$$

We defined the relaxation rate $\Gamma_{1,j} = \Gamma_{\uparrow,j} + \Gamma_{\downarrow,j}$ and the total dephasing rate $\Gamma_{\varphi,j} = \Gamma_{1,j}/2 + \Gamma_{\varphi,j}^*$. We also use the abbreviation $\Gamma_{\kappa,j} = \Gamma_{\varphi,j} + \kappa/2$. Here $\Gamma_{\uparrow,j}$ and $\Gamma_{\downarrow,j}$ are the effective excitation and relaxation rates of atom $j$, $\Gamma_{\varphi,j}^*$ is its pure dephasing rate, and $\kappa$ the decay rate of the cavity and $g_j$ the coupling strength between atom an cavity.

The term $\langle n \rangle$ on the right-hand side of Eq. (1) accounts for the stimulated emission. The average total photon number $\overline{\langle n \rangle}_M$ of the setup can be calculated by performing the averages implied by the fixed point equation (1).

These stationary fixpoint equations can be solved numerically for $\overline{\langle n \rangle}_M(\sigma_\Delta)$. Results for $M = 100$ atoms are shown by the thick upper curves in Fig. 1 for three values of $g$ and the two types of distribution $p_{G/B}(\Delta)$. We note that disorder in the detuning decreases $\overline{\langle n \rangle}_{100}(\sigma_\Delta)$ only weakly over a broad range of the variance $\sigma_\Delta$. This behavior cannot be explained as an average of the single-atom laser resonances, $\langle n \rangle_1(\Delta)$. The single atoms results are displayed in the inset. Averaging

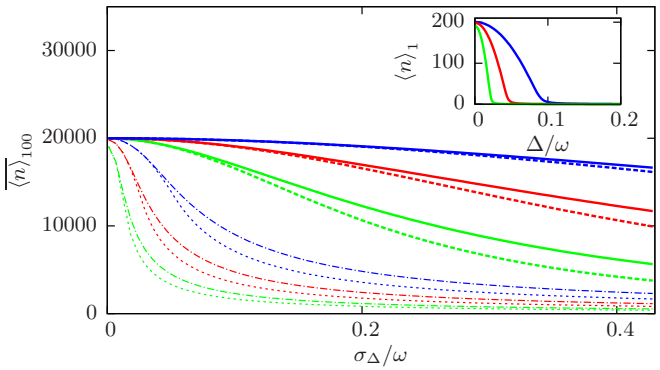



Figure 1: Influence of disorder in the detuning $\Delta$ on the quantum statistical average photon number $\overline{\langle n\rangle}_{100}$ in the resonator. Solid lines are calculated for a Gaussian distribution with mean $\overline{\Delta} = 0$ and standard deviation $\sigma_\Delta$, dashed lines represent a box distribution with the same parameters. The average photon number decreases remarkably slowly with increasing disorder. This cannot be explained by averaging the single-atom resonance curves $\langle n\rangle_1(\Delta)$, examples of which are shown in the inset, over the same distribution of detuning. Averaging of the single-atom results would lead to the curves plotted with thin lines. Plot parameters are $M = 100$, $\Gamma_\uparrow = 0.006$, $\Gamma_\downarrow = 0.002$, $\Gamma_\varphi = 0.001$ and $\kappa = 0.00001$; blue curves $g = 0.004$, red curves $g = 0.002$ and green curves $g = 0.001$. All rates and couplings are measured in units of $\omega$.

them over the distributions $p_{G/B}(\Delta)$ leads to the thin lower curves in Fig. 1, which obviously are much narrower in the disorder variance than the collective behavior of the $M$ atoms. We conclude that for disorder in the detuning, the setup with $M$ atoms shows lasing in a much broader range of detunings than what we obtain from the single-atom results $\langle n\rangle_1$ averaged over the same probability distribution.

The conclusion form our analysis is that imperfections in the control of material parameters do not prohibit the construction of multi-atom lasing setups. This will help the construction of miniaturized on-chip radiation sources for low-temperature microwave experiments.

**REFERENCES**

1. P. Macha, G. Oelsner, J. Reiner, M. Marthaler, S. Andre, G. Schön, U. Hübner, H.-G. Meyer, E. Ilichev and A. V. Ustinov, Nature Communications 5, 5146 (2014)
2. M. Koppenhöfer, M. Marthaler and G. Schön, arXiv:1602.01367

# Single solid-state quantum emitters for plasmonics.

**X. Wu[1,2], P. Jiang[1], H. Zhang[2,4], M. Pfeiffer[2,3], K. Lindfors[2,3], A. Rastelli[4], O. G. Schmidt[4], and M. Lippitz[1,2,*]**

[1] Experimental Physics III, University of Bayreuth, Germany

[2] Max Planck Institute for Solid State Research, Stuttgart, Germany

[3] Physical Chemistry, University of Cologne, Germany

[4] Institute for Integrative Nanosciences, IFW Dresden, Germany

[*]corresponding author: markus.lippitz@uni-bayreuth.de

**Abstract**- Plasmonics promises to enable sub-wavelength photonics and quantum optics. Quantum emitters have to be integrated to provide single photons and ultimate optical nonlinearites. We present our recent work on coupling GaAs quantum dots to localized and propagating plasmon modes.

Plasmonics offers the opportunity of tailoring the interaction of light with single quantum emitters. However, the strong field localization of plasmons requires spatial fabrication accuracy far beyond what is required for other nanophotonic technologies. Furthermore, this accuracy has to be achieved across different fabrication processes to combine quantum emitters and plasmonics. We demonstrate [1] a solution to this critical problem by controlled positioning of plasmonic nanoantennas with an accuracy of 11 nm next to single self-assembled GaAs semiconductor quantum dots, whose position can be determined with nanometer precision. These dots do not suffer from blinking or bleaching or from random orientation of the transition dipole moment as colloidal nanocrystals do. Our method introduces flexible fabrication of arbitrary nanostructures coupled to single-photon sources in a controllable and scalable fashion.

We also demonstrate [2] efficient coupling of excitons in near-surface GaAs quantum dots (QDs) to surface-plasmon polaritons. We observe distinct changes in the photoluminescence of the emitters as the distance between the QDs and the gold interface decreases. Based on an electric point-dipole model, we identify the surface plasmon launching rates for different QD-surface distances. While in conventional far-field experiments only a few percent of the emitted photons can be collected due to the high refractive index semiconductor substrate, already for distances around 30 nm the plasmon launching-rate becomes comparable to the emission rate into bulk photon modes, thus much larger than the photon collection rate. For even smaller distances, the degrading optical properties of the emitter counterweight the increasing coupling efficiency to plasmonic modes

Finally, we will present a hybrid approach combining a dielectric and a plasmonic waveguide to optimize coupling of a quantum dot to a propagating plasmonic mode.

**REFERENCES**

1. Pfeiffer, M. et al., “Eleven Nanometer Alignment Precision of a Plasmonic Nanoantenna with a Self-Assembled GaAs Quantum Dot”, *Nano Letters*, Vol. 14, 197, 2014.
2. Zhang, H. et al., “Narrow-line self-assembled GaAs quantum dots for plasmonics“, *Applied Physics Letters*, Vol. 16, 101110, 2015.

# Quantum Metamaterials with quantum dots

**E. Rousseau and D. Felbacq**

Laboratoire Charles Coulomb - Université de Montpellier - CNRS -UMR5221, France
emmanuel.rousseau@umontpellier.fr

**Abstract**— This paper adresses the question of the correct hamiltonian to describe a quantum metamaterials in the optical frequency range. A quantum metamaterials is a metamaterial structure inside which quantum degrees of freedom have been inserted. We consider a dielectric metamaterials made of dielectrics rods in a periodic configuration. Such a structure exhibits homogeneous optical properties including negative refraction. The quantum degree of freedom are quantum dots.

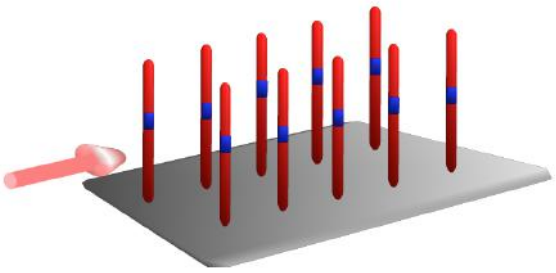


Figure 1: Geometry considered in this paper. Dielectric cylinders are sketch up in red and the quantum dots are in blue. The arrow represents an incoming light beam.

Introducing quantum degrees of freedom into metamaterials structures opens the way to an external control of the effective electromagnetic properties of the metamaterial[1]. New phenomena are expected as the modulation of a probe beam through the quantum state of the quantum degrees of freedom[2]. Recent calculations predict the existence of oscillating band-gaps [3].
Periodic arrangements of dielectric cylinders, as sketched up in figure 1, are interesting to make metamaterials from both an experimental and a theoretical point of view. Indeed the simplicity of the geometry makes it ideal to be realized with present days nanotechnology tools. Nevertheless this geometry exhibits many properties of metamaterials as negative refraction or artificial magnetism [4, 5]. Moreover in such a geometry a complete theory of homogenization can be achieved [6]. In this study, a quantum dot is inserted inside each dielectric cylinder.
Although simple this geometry raises questions when treated at the quantum level. Concerning the description of the electromagnetic field, because the metamaterials structure is an open-system scatterer, its description in term of electromagnetic modes is not effective and well-suited. The modeling of the quantum dots is not simpler since they can demonstrate experimental behavior that deviates either from the point-dipole description[7] and/or from the two-level approximation model[8]. So the usually used minimal-coupling hamiltonian in the Coulomb gauge may not be the appropriate or the most convienient starting point for modeling quantum metamaterials in the visible range. As a matter of fact, it treats matter as moving charges coupled to the electromagnetic field through the potential vector and not through the physical field (electric and magnetic fields). A usual approximation of this hamiltonian (*i.e.* through the Göpper-Meyer transformation) leads to an hamiltonian that describes quantum dots as dipoles which is not accurate enough for our studies.
It has been shown in the past that a gauge transformation can be applied to the minimal-coupling hamiltonian to describe matter globally through the knowledge of its energy levels. The coupling with the electromagnetic arises through the physical field at any order of the multipolar development. This hamiltonian is known as the Power-Zienau-Woolley hamiltonian. In this paper we discuss the relevance of the Power-Zienau-Woolley hamiltonian to describe quantum metamaterials.

**REFERENCES**


1. A. Zagoskin, D. Felbacq and E. Rousseau, "Quantum metamaterials in the microwave and optical ranges," *arXiv:1601.06587*, Accepted for publication in *EPJ Quantum Technology* .
2. D. Felbacq and M. Antezza, "Quantum metamaterials: a brave new world," *SPIE Newsroom*, doi: 10.1117/2.1201206.004296
3. Rakhmanov et al., "Quantum metamaterials: Electromagnetic waves in a Josephson qubit line," *Phy. Rev. B*, Vol. 77, 144507, 2008.
4. D. Felbacq et al., "Homogenization of a set of parallel fibres," *Waves in random media*, Vol. 7, 245-256, 1997.
5. D. Felbacq et al., "Homogenization near resonance and artificial magnetism," *Comptes Rendus Mathmatiques*, Vol. 339, 377-382, 2004.
6. G. Bouchitté et al., "Homogenization of the 3D Maxwell system near resonance and artificial magnetism," *Comptes Rendus Mathmatiques*, Vol. 347, 571-576, 2006.
7. Tighineanu et al., "Unraveling the Mesoscopic Character of Quantum Dots in Nanophotonics," *Phys. Rev. Lett.*, Vol. 114, 247401, 2015.
8. Q. Le-Van et al., "Temperature dependence of quantum dot fluorescence assisted by plasmonic nanoantennas," *Phys. Rev. B*, Vol. 91, 085412, 2015.
9. E. A. Power and S. Zienau, "Coulomb gauge in non-relativistic quantum electrodynamics and the shape of spectral lines," *Trans. R Soc. London Ser. A*, Vol. 251, 427, 1959.
10. R. G. Woolley, "Molecular quantum electrodynamics," *Trans. R Soc. London Ser. A*, Vol. 321, 557-572, 1971.

# Photonic Integrated Circuits with On-Chip Single-Photon Emitters

**P. Michler**[1]

[1]Institute of Semiconductor Optics and Functional Interfaces and Center for Integrated Quantum Science and Technology (IQ$^{ST}$), University of Stuttgart, Germany

[*]corresponding author: p.michler@ihfg.uni-stuttgart.de

**Abstract**-In quantum photonics the full on-chip integration of major optical components, like beamsplitters, single-photon sources and detectors are currently one of the main goals. Here, we present our progress on the implementation of In(Ga)As quantum dots as single-photon sources in on-chip GaAs/AlGaAs waveguide structures. Photon cross-correlation measurements between the two output arms of an on-chip beamsplitter demonstrate the generation, guiding and splitting of triggered single photons under resonant excitation in an on-chip device.

The future use of linear optics quantum computation depends on a miniaturization and therefore a full integration of single-photon sources, beamsplitters and detectors on single chips. III-V semiconductors are promising candidates of the realization of such devices due to the simple implementation of quantum dots (QDs) as single-photon sources.

We present the integration of QDs in rib-waveguides together with directional evanescent field couplers to realize a well-defined coupling between the propagating modes. The layer structure of the waveguides was grown by metal-organic vapor-phase epitaxy (MOVPE) using exactly oriented (100)-GaAs substrates. It consists of a 2 µm $Al_{0.39}Ga_{0.61}As$ cladding layer at the bottom and a 380 nm thick GaAs core layer on top. A layer of InGaAs QDs with an emission wavelength around 890 to 910 nm was used as integrated single photon emitters and grown 135 nm above the $Al_{0.39}Ga_{0.61}As$ layer to enhance the coupling efficiency into the guided mode. The waveguides were created with electron beam lithography using a negative tone resist and a subsequent dry etching step using an inductively coupled plasma reactive ion etcher with chlorine-based chemistry. Figure 1 shows an angular scanning electron microscopy (SEM) image of the finalized waveguide structure with an evanescent field coupler.

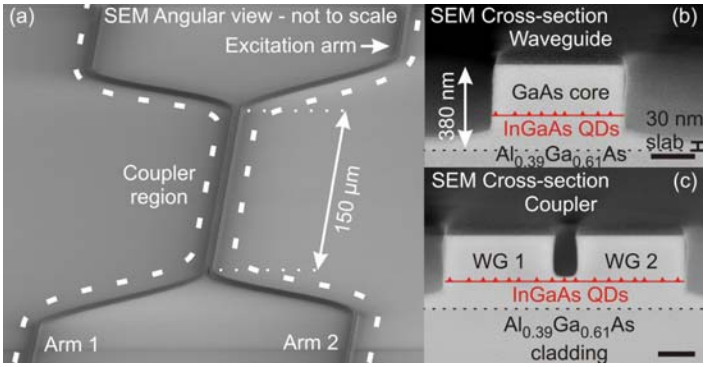



**Figure 1:** SEM measurements of a waveguide structure similar to the one used for optical characterization. a) Angular view of the coupler. b) Cross-section of the waveguide. The QD layer is marked. c) Cross-section of a coupler. The waveguides are separated by a small gap (scale bars = 200 nm)

For the optical characterization, the sample was cleaved perpendicular to the waveguides and placed on a motorized stage inside a He-flow cryostat and cooled to 5 K. The excitation was carried out from the top, whereas the emission from the waveguides was detected to the side through a microscope objective with a NA of 0.45. The optical setup allows for the simultaneously observation of both output arms of a beamsplitter.

The purity of single photon emission is verified under quasi-resonant and resonant continuous wave excitation, by directly measuring the photon correlations at the output arms of the on-chip beamsplitter [1]. Especially for pulsed resonant excitation, we demonstrate that the hurdle of strong laser stray light can be overcome by carefully adjusted laser excitation pulses enabling nearly background free, triggered single-photon emission [2]. This manifests in the observation of clear Rabi oscillations over two periods of the quantum dot emission as a function of laser excitation power. The present results open exciting new perspectives for fully integrated quantum circuits.

**Acknowledgements**, The author acknowledge the Deutsche Forschungsgemeinschaft for financial support via the project MI 500/29-1

**REFERENCES**

1. Rengstl, U., Schwartz, M., Herzog, T., Hargart, F., Paul, M., Portalupi, S. L., Jetter, M., and Michler P., Appl. Phys. Lett., *"On-chip beamsplitter operation on single photons from quasi-resonantly excited quantum dots embedded in GaAs rib waveguides"*, Vol 107, 021101 (2015)
2. Schwartz, M., Rengstl, U., Herzog, T., Paul, M., Kettler, J., Portalupi S. L., Jetter, M., and Michler, P., Optics Express "*Generation, guiding and splitting of triggered single photons from a resonantly excited quantum dot in a photonic circuit*" Vol. 24, No. 3, 3089 (2016)

# Hybrid nanophotonics and light-matter interaction

**A. Femius Koenderink**

[1]Center for Nanophotonics, FOM Institute AMOLF, Science Park 102, NL-1098XG, Amsterdam, The Netherlands

[*]corresponding author: f.koenderink@amolf.nl

**Abstract**-Plasmonic antennas and modest-Q dielectric cavities can be combined into hybrid nanophotonic structures with very high Purcell factors, essentially providing plasmonic mode volumes at cavity Q's up to $10^3$. I discuss the subtle underlying hybridization physics both in context of this proposal for quantum optics, and in context of our experiments on microtoroid cavities coupled to antenna arrays that probe both cavity shifts and antenna polarizability changes. Furthermore I present progress in scatterometry measurement methods on single nanophotonic systems.

Hybrid nanophotonic structures integrate different nanoscale platforms to attain unique figures of merit light-matter interaction. We propose that hybridization of appropriately chosen plasmonic antennas with modest-Q microcavities can lead to very high Purcell factors, yielding plasmonic mode volumes at essentially cavity quality factors. The underlying hybridization mechanisms are nontrivial:, how plasmon antennas with large polarizability either spoil or improve microcavities and vice versa, contains physics beyond perturbation theory, and is an interplay of back-action, and interference. For example, we predict that the local density of states of hybrid systems shows Fano interferences. I will discuss recent experiments in which toroidal microcavities were coupled to plasmon particle arrays, and we probed both cavity resonance shifts and particle polarizability changes. Furthermore I will also discuss our recently developed techniques to probe single plasmon antennas coupled to emitters and complex environments. In particular, we developed the method of `k-space polarimetry', a technique to completely determine the intensity and polarization state of light radiated by a single nano-object into any emission direction that is based on high-NA back focal plane imaging and Stokes polarimetry. I show benchmarks results for scattering, fluorescence, and cathodoluminescence of directional surface plasmon polariton antennas.

**Acknowledgements** This work is part of the research program of the Foundation for Fundamental Research on Matter (FOM), which is part of the Netherlands Organisation for Scientific Research (NWO). I acknowledge an NWI-Vici personal grant.

**REFERENCES**

1. Ruesink, F., H. M. Doeleman, R. Hendrikx, A. F. Koenderink and E. Verhagen, "Perturbing open cavities: Anomalous resonance frequency shifts in a hybrid cavity-nanoantenna system," *Phys. Rev. Lett.* Vol. 115 , 203904:1-5, 2015.
2. Mohtashami, A., C. I. Osorio, and A. F. Koenderink, "Angle-resolved polarimetry of antenna-mediated fluorescence," *Phys. Rev. Appl.* Vol. 4, 054014:1-7, 2015.
3. Osorio, C. I., A. Mohtashami and A. F. Koenderink, "K-space polarimetry of bullseye plasmon antennas," *Sci. Rep.* Vol. 5, 9966:1-7, 2015.
4. Osorio, C. I., T. Coenen, B. C. Brenny, A. Polman, and A. F. Koenderink, "Angle-resolved catholdoluminescence imaging polarimetry," *ACS Photonics* Vol. 3, 147-154, 2016.

# Quantum Many-Body Theory of Nonlocal Electromagnetic Response at Metallo-Dielectric Interfaces

**F. Ballout**[1], **J. M. Hamm**[1], **and O. Hess**[1]

[1]Blackett Laboratory, Department of Physics, Imperial College London, London SW7 2AZ, United Kingdom
f.ballout@imperial.ac.uk, o.hess@imperial.ac.uk

**Abstract**— We present on the basis of the jellium model a quantum field theory of surface-plasmon polaritons (SPPs) in which they emerge as extended objects as a result of an inhomogeneous condensation of bosons around a topological singularity describing the surface. The benefit of this approach lies in relating the electromagnetic fields belonging to such a macroscopic quantum state with the surface topology and nonlocal response function (i.e. the retarded photon self-energy) of the delimited electron gas sustaining that state.

In recent years plasmonics has advanced to ever decreasing length scales reaching dimensions comparable to the de Broglie wavelength of an electron, which has a significant influence on the plasmon dispersion [1]. The associated phenomenology lies beyond the reach of the classical Drude free electron theory or its nonlocal extension and adequate models are needed to address the quantum matter aspects of light-matter interaction that are responsible for plasmonic quantum size effects. This calls for a condensed matter field theory of SPPs, which relates the macroscopic phenomena appearing at the surface of a plasmonic material with the elementary matter degrees of freedom participating into the build-up of this collective excitation. To this end, we formulate a quantum electrodynamic Lagrangian in the framework of canonical quantization and apply the concepts of dynamical mapping and boson transformation as presented in Ref. [2] to implement the surface boundary as a topological singularity, which breaks the translation symmetry and leads to an inhomogeneous condensation of bosons around that singularity. The latter give rise to a macroscopic, ordered state obeying the following field equation in momentum space

$$\left\{k^2 g_\mu^\lambda - k^\lambda k_\mu + \frac{4\pi}{c^2}\Pi_\mu^\lambda(k)\right\} a_\lambda(k) = \frac{4\pi\hbar}{ec}\Pi_\mu^\lambda(k) F_\lambda(k) \tag{1}$$

where $k \equiv k^\mu = \left(\frac{\omega}{c}, \vec{k}\right)$ is the four momentum, $g_{\mu\nu} = \mathrm{diag}(-1,1,1,1)$ the metric tensor, $\Pi^{\mu\nu}$ the retarded photon self-energy, i.e. the polarization operator of the in-medium photon, which has transverse and longitudinal components, $a_\lambda(k)$ the four potential of the macroscopic field and $F_\lambda(k)$ the Fourier transform of the singularity defining function. We use the solution of Eq. 1 to calculate the electric and magnetic field components parallel to the interface in order to determine the surface impedance through which we obtain the dispersion relation of the macroscopic field by boundary matching. In local response approximation ($\vec{k} \to 0$) and for a planar metallo-dielectric interface [3] this gives the well-known SPP dispersion with the classical nondispersive surface plasmon frequency, $\omega_{SP} = \omega_P/\sqrt{2}$, in the nonretarded limit, i.e. at short wavelengths, where $\omega_P$ is the bulk plasmon frequency. As we consider a nonlocal response, our preliminary results suggest that the asymptotic frequency of the nonlocal SPP dispersion approaches $\omega_P$, whereas the hydrodynamic approaches [4, 5] found the asymptotic frequency not to be bounded for large momenta at all. It should be noted that the hydrodynamic approach only considers a spatial dispersion in the longitudinal component of the electric field, while our approach incorporates a spatial dispersion for the longitudinal as well the transverse field components. However, the advantage of this approach is that it describes surfaces or gaps as topological singularities and thus could be in principle applied to study light-matter interaction in cavity gaps of atomic length scales where quantum tunneling effects [6, 7] give rise to new plasmonic modes, which so far has been modelled using either computational demanding or semiclassical approaches such as density-functional theory [9] or the quantum corrected model [10], respectively. Such an ambition is not far fetched as our approach has been used to successfully reproduce the quantum tunneling across the gap between two superconductors (Josephson effect) [8].

**ACKNOWLEDGMENT**

F. Ballout acknowledges the financial support provided by the Postdoctoral Research Fellowship of the Deutsche Forschungsgemeinschaft under BA 5155/1-1.

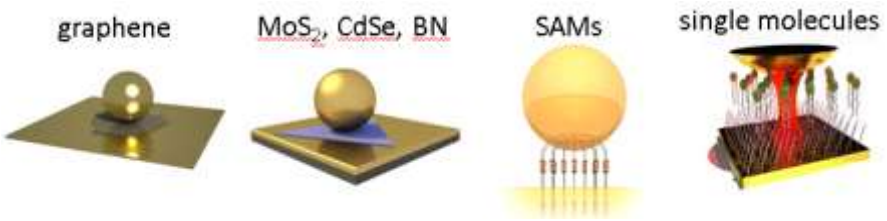
**REFERENCES**

1. Tame, M. S., McEnery, K. R., Oezdemir, . K., Lee, J., Maier, S. A. and Kim, M. S., "Quantum Plasmonics," *Nature Physics*, Vol. 9, 329, 2013
2. Matsumoto, H., Semenoff, G., Umezawa, H. and Tachiki, M., "Quantum Electrodynamics in Solids," *Fortschritte d. Phys.*, Vol. 28, 67, 1980
3. Kleiner, P., "A Quantum Field Theoretical View on the Surface Plasmon," *Phys. Status Solidi B*, Vol. 138, 599, 1986
4. Boardman, A. D., Paranjape, B. V. and Nakamura, Y. O., "Surface Plasmon-Polaritons in a Spatially Dispersive Inhomogeneous Medium," *Phys. Status Solidi B*, Vol. 75, 347, 1976
5. Raza, S., Christensen, T., Wubs, M., Bozhevolnyi, S. I. and Mortensen, N. A., "Nonlocal response in thin-film waveguides: Loss versus nonlocality and breaking of complementarity," *Phys. Rev. B*, Vol. 88, 115401, 2013.
6. Savage, K. J., Hawkeye, M. M., Esteban, R., Borisov, A. G., Aizpurua, J. and Baumberg, J. J.,"Revealing the quantum regime in tunnelling plasmonics," *Nature*, Vol. 491, 574, 2012.
7. Scholl, J., Garcia-Etxarri, A., Koh, A. L. and Dionne, J. A., "Observation of quantum tunneling between two plasmonic nanoparticles," *Nano Lett.*, Vol. 13, 564, 2013.
8. Mancini, F., Matsumoto, H., Umezawa, H. and Wadati, M., "The Macroscopic Surface Phenomena and Topological Singularities in the Superconductivity," *Progr. Theoret. Phys.*, Vol. 62, 12, 1979
9. Zhang, P., Feist, J., Rubio, A., Garcia-Gonzalez, P. and Garcia-Vidal, F. J., "Ab initio nanoplasmonics: The impact of atomic structure," *Phys. Rev. B*, Vol. 90, 161407, 2014
10. Esteban, R., Borisov, A. G., Nordlander, P. and Aizpurua, J., "Bridging quantum and classical plasmonics with a quantum-corrected model," *Nature Commun.*, Vol. 3, 825, 2012.

**Exploring nm-scale plasmonic cavities through light**

Prof Jeremy J. Baumberg, Dr Anna Lombardi
NanoPhotonics Centre, Cavendish Laboratory, University of Cambridge, UK
*jjb12@cam.ac.uk, al716@cam.ac.uk*

Plasmonic nanostructures continue to draw much interest in the scientific community due to their ability to both strongly confine light at the nanoscale and to create intense localized electromagnetic fields. In particular, coupling between nano-components allows direct observation of few molecules as well as excitations in semiconductors.
We deeply explore plasmonic coupling through reliable bottom-up self-assembly, namely nanoparticles deposited on a metal mirror with different spacers in bewteen, and DNA-origami-based dimers. The investigation of these systems, extremely sensitive to the physical properties of the separation gap, give new insights into plasmonic and quantum plasmonic properties at the nanoscale.[1-2]
By exploiting the nanoparticle on mirror geometry, we show how the new generation of 2D semiconductors can couple to such nano-scale gaps.[3-4] We find that changing just a single atom on each molecule of a self-assembled monolayer can shift the plasmon by over 50nm, and produce surprising vibrational signatures.[5-8]
More recently, we have demonstrated strong coupling with single molecules in appropriately designed nano-structures. We have also probed, by developing a widely tuneable optical technique, the near-field resonances within individual plasmonic nanostructures, directly comparing them with the corresponding far-field response.[9] All these results are encouraging for future applications in (bio)molecular sensing as well as fundamental science.[10-14]




[1] *Nature* **491**, 574 (2012); Revealing the quantum regime in tunnelling plasmonics
[2] *ACS Nano* **5**, 3878 (2011); Precise sub-nm plasmonic junctions within Au NP assemblies
[3] *Nano Lett* **13**, 5033 (2013); Controlling sub-nm plasmonic gaps using graphene
[4] *ACS Nano* **9**, 825 (2014); Monitoring Morphological Changes in 2D Monolayer Semiconductors …
[5] *Nano Letters* **15**, 669 (2015); Nano-optics of molecular-shunted plasmonic nanojunctions
[6] *Science Reports* **4**, 5490 (2014); Watching individual molecules flex within lipid membranes using SERS
[7] *Nature Comm*. **5**, 4568 (2014); Threading plasmonic nanoparticle strings with light
[8] *Nature Comm*. **5**, 3448 (2014); DNA origami based assembly of gold nanoparticle dimers for SERS detection
[9] *ACS Photonics, just accepted* (2016); Anomalous spectral shift of near- and far-field…
[10] *Scientific Reports* **4**, 6785 (2014); Quantitative multiplexing with nano-self-assemblies in SERS
[11] *Nano Lett* **13**, 5985 (2013); In-situ SERS monitoring of photochemistry within a nano-junction reactor
[12] *Opt.Exp* **23**, 33255 (2015); A generalized circuit model for coupled plasmonic systems
[13] *Nano Lett* **15**, 2600 (2015); Demonstrating PL from Au is Electronic Inelastic Light Scattering …
[14] *Phys.Rev.A* **92**, 053811 (2015); Hybridization of plasmonic antenna and cavity modes: Extreme optics…

# Coupling of quantum emitters and single plasmonic particles for quantum non-linear elements

**G. Kewes[1], A. Kuhlicke[1], A. W. Schell[2] and O. Benson[1*]**

[1]Nano-Optik, Institut für Physik, Humboldt-Universität zu Berlin, Newtonstr. 15, D-12489 Berlin, Germany

[2]Dep. of Electronic Science & Engineering, Kyoto Univ., Kyoto daigaku-katsura, Nishikyo-ku, Kyoto, Japan

[*]corresponding author: oliver.benson@physik.hu-berlin.de

**Abstract** – We introduce realistic structures for non-linear quantum plasmonic elements. The structures consist of grating coupler, dielectric and plasmonic waveguides coupled to single organic molecules. Fabrication, numerical simulation and optimization strategies are discussed. Additionally, we demonstrate a novel approach for detailed investigation of chemically synthesized plasmonic nanoparticles or nanowires.

Surface plasmon polaritons, or in brief 'plasmons', can confine the electromagnetic field much more tightly than it is possible with purely dielectric structures. Thereby, a very strong coupling of the electromagnetic field and matter can be realized. On the fundamental level even single emitters such as atoms, molecules or quantum dots can control the transmission of light rendering quantum non-linear elements [1] possible. Critical dimensions of architectures for such elements are in the nanometer range [2]. In addition, plasmonic structures will inevitably introduce loss, which has to be minimized or compensated. For this reason precise fabrication, assembly, and characterization of the emitters as well as of the plasmonic structure is crucial for predicting the performance of plasmonic elements.

We first discuss a plasmonic-dielectric structure where a single emitter, in our case a single organic DBT molecule, shall be coupled to a plasmonic waveguide. The structure, resembling the single photon transistor according to the design by Chang et al. [1], also includes a grating coupler and a dielectric-plasmonic transducer. In this way an efficient coupling of free-space light to plasmons is possible. We precisely describe fabrication and characterization of the fabricated chip (Fig. 1). We find very good agreement with rigorous numerical simulations [3]. Based on these findings we perform a numerical optimization and calculate concrete numbers for the performance of a realistic structure.

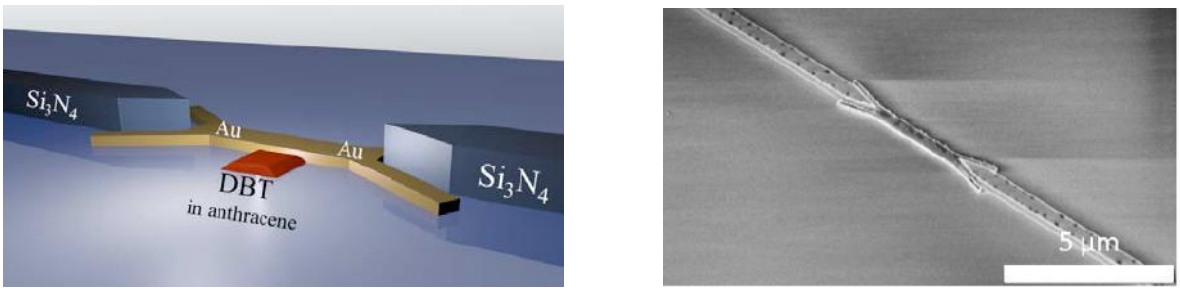



**Figure 1:** Left: Schematic of a single photon non-linear device consisting of single molecules coupled to a plasmonic waveguide. Right: Scanning electron micrographs of a fabricated structure.

Compared to top-down structures fabricated by optical and electron beam lithographically chemically synthesized plasmonic particles or wires show excellent properties with respect to losses. This is crucial, e.g., when studying single plasmonic excitations [4]. We introduce a unique approach to investigate single plasmonic nanostructures, i.e. silver nanowires, which are completely isolated from any substrate. In order to achieve this we levitate single wires in a linear AC Paul trap [5]. Plasmons can be excited directly with focused laser light. In a levitated wire also weakly confined plasmonic modes, which would otherwise be damped by coupling to the substrate can be studied in detail. The approach is also useful when releasing pre-characterized isolated plasmonic particles or wires on fragile integrated structures.

**Acknowledgements** The authors acknowledge financial support by the Deutsche Forschungsgemeinschaft in the frame of SFB 951 and the Einstein Stiftung, Berlin.

## REFERENCES

1. Chang, D. E., Sørensen, A. S., Demler, E. A. & Lukin, M. D. „A single-photon transistor using nanoscale surface plasmons“, *Nature Physics* 3, 807–812 (2007).
2. Benson, O. “Assembly of hybrid photonic architectures from nanophotonic constituents“, *Nature* 480, 193–199 (2011).
3. Kewes, G., Schell, A.W., Henze, R., Schönfeld, R.S., Burger, S., Busch, K., and Benson, O., „Design and numerical optimization of an easy-to-fabricate photon-to-plasmon coupler for quantum plasmonics“, *Appl. Phys. Lett.* 102, 051104 (2013).
4. Wolters, J., Kewes, G., Schell, A.W., Nüsse, N., Schoengen, M., Löchel, B., Hanke, T., Bratschitsch, R., Leitenstorfer, A., Aichele, T., and Benson, O., „Coupling of single nitrogen-vacancy defect centers in diamond nanocrystals to optical antennas and photonic crystal cavities“, *Phys. Status Solidi* B 249, 918-924 (2012).
5. Kuhlicke, A., Rylke, A., and Benson, O., „On-Demand Electrostatic Coupling of Individual Precharacterized Nano- and Microparticles in a Segmented Paul Trap“, *Nano Letters* 15, 1993-2000 (2015).

# Light Emission in Nanogap Emitting Devices: efficiency issues

Rémi Faggiani, Jianji Yang, Philippe Lalanne

Laboratoire Photonique, Numérique et Nanosciences (LP2N), UMR 5298, CNRS-IOGS-University of Bordeaux, 33400 Talence, France

Very large spontaneous-emission-rate enhancements (~1000) are obtained for quantum emitters coupled with tiny plasmonic resonance, especially when emitters are placed in the mouth of nanogaps formed by metal nanoparticles that are nearly in contact [1]. This fundamental effect of light emission at subwavelength scales is well documented and understood as resulting from the smallness of nanogap modes. In contrasts, it is much less obvious to figure out whether the radiation efficiency is high in these gaps, or if the emission is quenched by metal absorption especially for tiny gaps a few nanometers wide; the whole literature only contains scattered electromagnetic calculations on the subject, which suggest that absorption and quenching can be kept at a small level despite the emitter proximity to metal. A deep understanding of the emission processes involved in such systems is central in the design of modern plasmonic nanoantennas and yet is still missing.

In this contribution, we clarify through analytical derivations in the limit of small gap thickness why quenching is not necessarily dominant, why quantum emitters in nanogap antennas may offer good efficiencies, what are the circumstances in which high efficiency is obtained, and whether there exists an upper bound for the maximum efficiency achievable [2,3].

In particular, we will show that the nanogap-based antenna efficiency $\varepsilon$ can be written as the product of two terms : $\varepsilon = \varepsilon_e \varepsilon_i$ where the first term refers to extrinsic properties and is dominantly driven by the antenna capability to convert the energy mediated by gap plasmons into photons. It directly depends on our ability to design and engineer antenna geometries. The second term refers to intrinsic properties and only depends on the nature of the nanogap, irrespectively of the precise shape of the antenna. In addition, we will show that due to the fact that the decay rate into gap plasmons and quenching obey the same scaling with the nanogap thickness *d* , $\propto (k_0 d)^{-3}$, the intrinsic efficiency becomes independent of *d* and only depends on the material dielectric constants [3]. Therefore by properly selecting dielectric and metallic materials, quenching can be overcome in tiny gaps offering new opportunities to optimize the performance of nanogap emitting devices.

[1] Jun, Y. C.; Kekatpure, R. D.; White, J. S.; Brongersma, M. L. Nonresonant enhancement of spontaneous emission in metal dielectric metal plasmon waveguide structures. Phys. Rev. B **78**, 153111 (2008).
[2] J. Yang, R. Faggiani, P. Lalanne, "Light emission in nanogaps: overcoming quenching", Nanoscale Horizons, **1**, 11-13 (2016).
[3] R. Faggiani, J. Yang, P. Lalanne, "Quenching, Plasmonic, and Radiative Decays in Nanogap Emitting Devices", ACS Photonics, **2**, 1739-1744 (2015).

# Broadband Purcell enhancement in highly efficient photonic nanowire-based single-photon sources

**Niels Gregersen[1*], Dara P. S. McCutcheon[1], Jesper Mørk[1], Julien Claudon[2] and Jean-Michel Gérard[2]**
[1]DTU Fotonik, Department of Photonics Engineering, Technical University of Denmark
[2]CEA-CNRS-UJF Group "Nanophysique et Semiconducteurs", CEA, INAC, SP2M, Grenoble, France
[*]corresponding author: ngre@fotonik.dtu.dk

**Abstract** – The photonic nanowire single-photon source design approach allows for efficient broadband coupling between a quantum dot and a 1D photonic environment. In this work, we introduce weak cavity effects to the design by implementing a distributed Bragg reflector in the inverted taper. This leads to broadband enhancement of the photon emission rate with a Purcell factor of 6 over a full-width half-maximum range of 20 nm while maintaining a total outcoupling efficiency of 0.8 to a Gaussian profile.

A current challenge within the emerging field of optical quantum information processing is to construct an efficient single-photon source (SPS) capable of emitting single indistinguishable photons on demand. An attractive platform for such a source is a quantum light emitter, e.g. a nitrogen-vacancy center or a semiconductor quantum dot (QD), embedded in a solid-state semiconductor host material[1]. For a QD in bulk material, the large index contrast at the semiconductor-air interface leads to a collection efficiency of only 1-2 %, and efficient light extraction thus poses a major challenge in SPS engineering. An approach based on an InAs QD in a photonic nanowire[2] to control the light emission was recently proposed. A second generation device based on the "trumpet" design[3] featuring an inverted taper recently resulted in a measured efficiency of 0.75 under optical excitation. These SPS designs do not employ a cavity meaning that efficient coupling from the QD to the guided mode is obtained over a broad spectral range above 100 nm.

However, so far indistinguishable photon emission from the photonic nanowire SPS with spectral linewidth limited only by the radiative lifetime has not yet been observed. A possible source of decoherence during photon

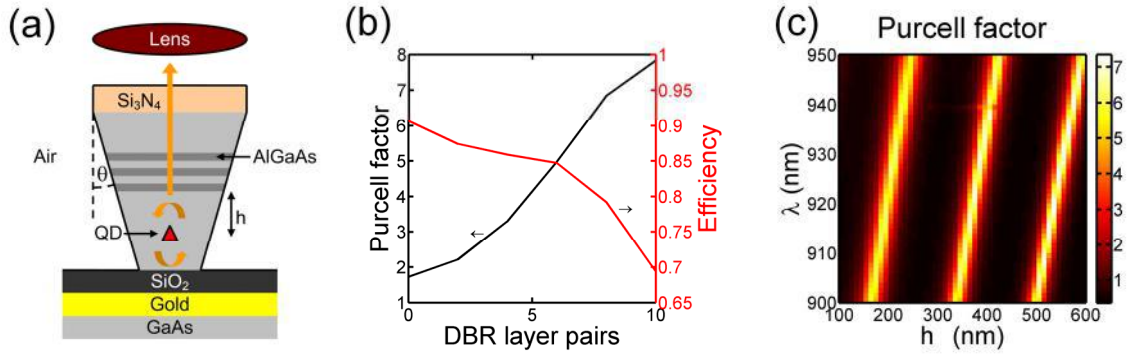



**Fig. 1:** (a) The photonic trumpet design featuring a DBR a distance h above the QD. (b) Purcell factor and single-photon source efficiency as function of number of DBR layer pairs. (c) Purcell factor as function of QD emission wavelength $\lambda$ and QD-DBR distance $h$ for 6 DBR layer pairs.

emission is interaction with vibrations in the solid-state environment[4], and this detrimental influence can in the weak coupling regime be reduced by increasing the spontaneous emission rate. A strategy to improve the coherence of the emitted photons is thus to accelerate the photon emission rate using weak cavity effects, while taking care to preserve a reasonable tolerance towards spectral misalignment of the emitter and the cavity resonance.

In this work, we extend the photonic trumpet design by implementing weak cavity QED effects with the purpose of increasing the rate of emission via the Purcell effect. This is achieved by implementing a distributed Bragg reflector (DBR) in the inverted conical taper as illustrated in Fig. 1(a). The introduction of the weak cavity leads to a relative increase in the Purcell factor by a factor of 3 (Fig. 1b) at only a 5 % reduction in the efficiency in the case of 6 DBR layer pairs. The resulting accelerated photon emission rate lowers the relative influence of decoherence due to phonon interaction and spectral diffusion and therefore improves the indistinguishability of the emitted photons. The resonant cavity QED effect introduced in this work is identical to that used for the micropillar SPS, however since the Purcell factor is proportional to Q/V and since the nanowire area is two orders of magnitude smaller than that of a typical micropillar, significant Purcell enhancement is obtained for modest Q factors.

Indeed, we will show that a Purcell factor of 6 for a remarkable 20 nm full-width half-maximum (Fig. 1c) of the resonance is achievable[5] combined with an efficiency of 0.8. This large bandwidth greatly relaxes the requirements for the fine structure splitting for entangled photon generation using the exciton-biexciton cascade and additionally enables tuning of the QD emission line over a broad range. Broadband Purcell enhancement from SPSs, typically exploiting plasmonic effects to decrease the mode volume, has been proposed previously[6], however so far at the cost of significantly reduced efficiency compared to our photonic trumpet design approach.

**Acknowledgements**. Support from the Danish Research Council for Technology and Production via the Sapere Aude project LOQIT (DFF - 4005-00370) is gratefully acknowledged.

**REFERENCES**

1. Gregersen, N., P. Kaer, and J. Mørk, "Modeling and Design of High-Efficiency Single-Photon Sources," *IEEE J. Sel. Top. Quantum Electron.*, Vol. 19, No. 5, 9000516, 2013.
2. Claudon, J., J. Bleuse, N. S. Malik, M. Bazin, P. Jaffrennou, N. Gregersen, C. Sauvan, P. Lalanne, and J.-M. Gerard, "A highly efficient single-photon source based on a quantum dot in a photonic nanowire," *Nat. Photonics*, Vol. 4, No. 3, 174–177, 2010.
3. Munsch, M., N. S. Malik, E. Dupuy, A. Delga, J. Bleuse, J.-M. Gérard, J. Claudon, N. Gregersen, and J. Mørk, "Dielectric GaAs antenna ensuring an efficient broadband coupling between an InAs quantum dot and a Gaussian optical beam," *Phys. Rev. Lett.*, Vol. 110, No. 17, 177402, 2013.
4. Kaer, P., N. Gregersen, and J. Mørk, "The role of phonon scattering in the indistinguishability of photons emitted from semiconductor cavity QED systems," *New J. Phys.*, Vol. 15, 035027, 2013.
5. Gregersen, N., D. P. S. McCutcheon, J. Mørk, J. Claudon and J.-M. Gérard, "A Hybrid Photonic Nanowire-Cavity Design for a Source of Indistinguishable Single Photons and Entangled Photon Pairs," *Opt. Express*, in preparation.
6. Maksymov, I. S., M. Besbes, J. P. Hugonin, J. Yang, A. Beveratos, I. Sagnes, I. Robert-Philip, and P. Lalanne, "Metal-coated nanocylinder cavity for broadband nonclassical light emission," *Phys. Rev. Lett.*, Vol. 105, No. 18, 180502, 2010.

# Controlling quantum states of light with plasmonic metamaterials

**M. S. Tame**[1,2*]

[1]School of Chemistry and Physics, University of KwaZulu-Natal, Durban 4001, South Africa

[2]National Institute for Theoretical Physics, University of KwaZulu-Natal, Durban 4001, South Africa

[*]corresponding author: markstame@gmail.com

**Abstract**- Plasmonics is a promising platform for quantum state engineering with the potential for building ultra-compact and hybrid optoelectronic devices. Recent experiments have shown that despite the presence of decoherence and loss, photon statistics and entanglement can be preserved in single plasmonic systems. This preserving ability should carry over to plasmonic metamaterials, whose properties are the result of many individual plasmonic systems acting collectively, and can be used to engineer optical states of light. I will present recent work on an experimental demonstration of quantum state filtering, also known as entanglement distillation, using a passive metamaterial. The metamaterial can be used to distill highly entangled states from less entangled states. I will also discuss the embedding of emitters into metamaterials in order to enhance functionality and provide dynamic nonlinear control. As metamaterials can be integrated with other optical components, such as waveguides, there is the intriguing possibility of incorporating plasmonic metamaterials in on-chip quantum state engineering tasks.

Entanglement plays a vital role in a wide variety of quantum information processing tasks, enabling quantum communication protocols such as quantum key distribution and quantum computing algorithms providing computational speedup compared to conventional computers. The task of carrying out filtering operations to improve the amount of entanglement in non-ideal generated states is therefore of great importance in quantum information processing. Previous work on photonic entanglement filtering, also called entanglement distillation, used standard bulk optical components. I will discuss recent experimental work exploring the possibility of using metamaterials for this important task [1].

The study builds upon previous work on the classical characterization of the collective response of nanostructured arrays, and in the quantum regime on the assisted-transmission of entanglement in periodic plasmonic nano-hole arrays and related work [2]. However, different to these works, this study goes beyond a simple transmission scenario in the quantum regime and shows that plasmonic nanostructured arrays can be used not only for basic transfer of quantum information, but also for the manipulation of quantum information in the form of quantum state engineering. Furthermore, the integration of quantum emitters into metamaterials [3] shows that they can introduce tunability as well as nonlinear behaviour in the quantum regime.

**REFERENCES**

1. Asano, M. et al., Distillation of photon entanglement using a plasmonic metamaterial, *Scientific Reports*, Vol. 5, 18313, 2015.
2. Tame, M. S. et al., Quantum Plasmonics, *Nature Physics*, 9, 329, 2013.
3. McEnery, K. R. et al., Tunable negative permeability in a quantum plasmonic metamaterial, *Physical*

*Review A*, 89, 013822, 2014.

# Quantum Optics with One-Dimensional Artificial Atoms

**N. Somaschi[1*], V. Giesz[1], L. De Santis[1], G. Hornecker[2], T. Grange[2], B. Reznychenko[2], J. Demory[1], C. Gomez[1], I. Sagnes[1], A. Lemaître[1], L. Lanco[1,3], A. Auffeves[2], and P. Senellart[1,4]**

[1]Laboratoire de Photonique et de Nanostructures, 91460 Marcoussis, France

[2]Université Grenoble Alpes, 38000 Grenoble, France

[3]Université Paris Diderot - Paris 7, 75205 Paris, France

[4]Physics Department, Ecole Polytechnique, 91128 Palaiseau, France

[*]corresponding author: niccolo.somaschi@lpn.cnrs.fr

**Abstract**-In a quantum network the quantum information is coherently transferred between material nodes and photonic channels. One of the main challenges to implement such a network is to control the light-matter interaction at the single photon level. Ideally, one atom acting as a stationary quantum bit should deterministically control the state of a photon, and vice versa. This can be obtained in a so-called one-dimensional atom system, where a single atom interacts with only a single and well-defined mode of the electromagnetic field.

We have recently fabricated near 1D-atom systems by deterministically [1] coupling a semiconductor quantum dot (QD) in an electrically controlled pillar microcavity [2]. Reflectivity measurements allow extracting the QD-cavity coupling parameters as well as the cavity characteristics. From this, we conclude that every photon sent on the device enters the cavity with probability > 0.95 and interacts with the exciton. The exciton emits a photon back into the cavity mode with probability 0.96 that escapes through the top mirror with a probability $0.7 \pm 0.05$.

In such device, we show that it is possible to coherently manipulate the exciton quantum bit with only few photon pulses. By monitoring the exciton population through resonant fluorescence spectroscopy, we demonstrate Rabi oscillations with a $\pi$-pulse obtained for coherent pulses with only 3.8 photons on average [3]. The same device operated with true single photon Fock states would allow flipping the exciton quantum bit with 0.55 probability.

Finally, we study the devices as single photon sources. Under non-resonant excitation we report on a brightness as large as 0.65 and a photon indistinguishability in the 0.7-0.8 range. Data gathered on several devices and emission lifetime analysis suggest that the indistinguishability is limited by the non-resonant carrier creation, resulting in a time jitter for the emission process, commensurable to the radiative recombination time ($\approx$130ps). This hypothesis is confirmed by using strictly resonant excitation: in this case, indistinguishability of $M=0.9956\pm0.0045$ is measured with $g^2(0)=0.0028\pm0.0012$. Furthermore measured brightness of $0.16\pm0.02$ makes this source more than one order of magnitude brighter than a parametric down conversion based single photon source of the same quality [4].

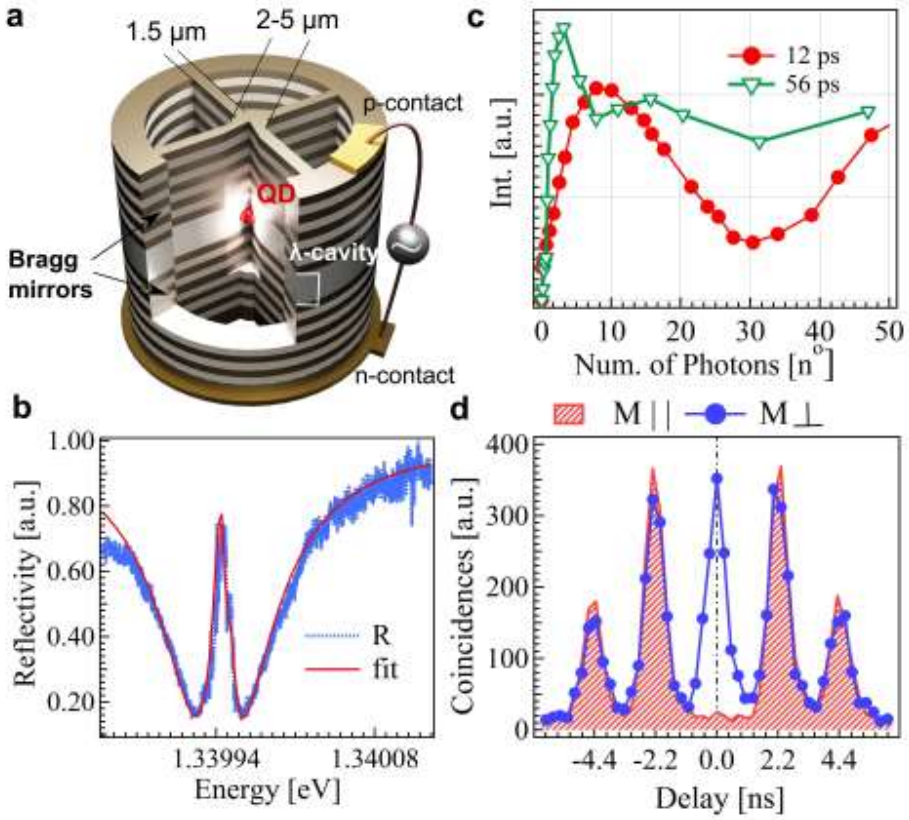



**Figure 1: a.** Sketch of the device under study: a single QD is deterministically placed at the center of a micropillar cavity, connected through 1.5 µm wide ridges to a circular frame where the electrical contact is defined **b.** Reflectivity spectrum obtained scanning a monomode laser through the cavity resonance. The central peak is the coherent reflection from the QD exciton transition. The device cooperativity is C=13. **c.** Intensity of the exciton resonant fluorescence as a function of the average number of photons in the excitation pulse, for two pulse durations. **d.** HOM measurement for photons successively generated by the same source, with parallel (filled curve) or cross polarized (dotted curve) photons. The fluorescence is obtained under strictly resonant excitation with 12 ps pulses.

**REFERENCES**


1. A. Dousse, L. Lanco, J. Suffczyński, E. Semenova, A. Miard, A. Lemaître, I. Sagnes, C. Roblin, J. Bloch, and P. Senellart in: Phys. Rev. Lett. 101, 267404 (2008).
2. A. K. Nowak, S. L. Portalupi, V. Giesz, O. Gazzano, C. Dal Savio, P.-F. Braun, K. Karrai, C. Arnold, L. Lanco, I. Sagnes, A. Lemaître and P. Senellart in: Nature Communications 5, 3240 (2014).
3. V. Giesz, N. Somaschi, G. Hornecker, T. Grange, B. Reznychenko, L. De Santis, J. Demory, C. Gomez, I. Sagnes, A. Lemaitre, O. Krebs, N. D. Lanzillotti-Kimura, L. Lanco, A. Auffeves, P. Senellart in Arxiv 1512.04725 (2015).
4. N. Somaschi, V. Giesz, L. De Santis, J. C. Loredo, M. P. Almeida, G. Hornecker, S. L. Portalupi, T. Grange, C. Anton, J. Demory, C. Gomez, I. Sagnes, N. D. Lanzillotti Kimura, A. Lemaitre, A. Auffeves, A. G. White, L. Lanco, P. Senellart in: Arxiv 1510.06499 (2015).

# Noise induced narrowing of metamolecule fluorescence spectral line

**E. S. Andrianov**[1,2,*], **N. M. Chtchelkatchev**[2,3,4], **and A. A. Pukhov**[1,2,5]

[1]All-Russia Research Institute of Automatics, 22 Sushchevskaya, Moscow 127055, Russia
[2]Moscow Institute of Physics and Technology, Moscow 141700, Russia
[3]Institute for High Pressure Physics, Russian Academy of Science, Troitsk 142190, Russia
[4]L.D. Landau Institute for Theoretical Physics, Russian Academy of Sciences,117940 Moscow, Russia
[5]Institute for Theoretical and Applied Electromagnetics, 13 Izhorskaya, Moscow 125412, Russia
*corresponding author: andrianov.es@mipt.ru

**Abstract**— We consider metamolecule consisting of plasmonic nanoparticle correlated with the atoms and driven by external electromagnetic field. Quantum Monte-Carlo simulations show splitting of the Wigner function of metamolecule near-field and a strong (by the order of magnitude) narrowing of spectral line of metamolecule fluorescence which take place at finite domain over the coherent drive with sharp threshold. Such narrow line fluorescence may find wide applications in plasmonics where high losses is unavoidable problem.

Correlated plasmonic structures and molecules attract much attention last time. They bind together quantum optics [1], chemistry and biology [3], nanophysics [2] that includes nanolasers [4, 5], qubits and quantum plasmonic nanoprobes and biosensors [6]. One of the main problem of such structures is high losses in metal which accompanied by noise according fluctuation-dissipation theorem. Losses and noise lead to fast destroying of coherent properties of such systems.

However, there are a number of known cases when losses and noise may effectively increase coherence: this is the stochastic resonance [7]. It is well understood in classical systems where it shows itself due to some nonlinearity [7]. In quantum systems quantum stochastic resonance is the field of intense research [8]. In most cases it manifests itself in one component systems like oscillator or spins in a bath.

Here we consider the system consisting of plasmonic nanoparticle which interacts with atoms and driven by external electromagnetic field. Such plasmonic nanosystems are often referred to as "metamolecules" [9]. Our system is multicomponent and strongly correlated. In this system the dynamics is complicated and it is not clear in advance what noise and losses may do. Usually there is no well defined small or large interaction parameter in such systems, there is high level of dissipation and there are large fluctuations and so advanced computational efforts are required [10].

We consider within Jaynes-Cummings model dynamics of such metamolecule. Dynamics of interacting near-field of plasmonic structure and two-level atom driven by an external electromagnetic wave is described by the following Hamiltonian

$$\hat{H} = \hat{H}_b + \hat{H}_a + \hat{V}_{a-w} + \hat{V}_{b-w} + \hat{V}_{a-b} \tag{1}$$

Here $\hat{H}_b = \hbar\omega_b \hat{a}^+\hat{a}$ is the Hamiltonian of the near-field of plasmonic structure after second quantization procedure ($\hat{a}$ is annihilation operator), $\hat{H}_a = \hbar\omega_a \hat{\sigma}^+\hat{\sigma}$ is a two-level atom Hamiltonian ($\hat{\sigma} = |g\rangle\langle e|$ is operator of transition from the excited state $|e\rangle$ to the ground one $|g\rangle$), $\hat{V}_{b-a} = \hbar\Omega_R(\hat{a}^+\hat{\sigma} + \hat{\sigma}^+\hat{a})$ is the interaction between the near-field and the two-level atom where $\Omega_R$ is the Rabi frequency. The coherent pumping of two-level atom and plasmonic near-field is described by $\hat{V}_{a-w} = \hbar\Omega_a(\hat{\sigma} + \hat{\sigma}^+)$ and $\hat{V}_{b-w} = \hbar\Omega_b(\hat{a}^+ + \hat{a})$.

The dynamics of the system in Markov approximation is governed by the Lindblad equation [11]:

$$d\hat{\rho}/dt = -i\left[\hat{H}, \hat{\rho}\right] + \frac{\gamma_b}{2}\left(2\hat{a}\hat{\rho}\hat{a}^+ - \hat{\rho}\hat{a}^+\hat{a} - \hat{a}^+\hat{a}\hat{\rho}\right) + \frac{\gamma_a}{2}\left(2\hat{\sigma}\hat{\rho}\hat{\sigma}^+ - \hat{\rho}\hat{\sigma}^+\hat{\sigma} - \hat{\sigma}^+\hat{\sigma}\hat{\rho}\right) \tag{2}$$

where $\gamma_a$ and $\gamma_b$ are the dissipation rates of the two-level atom and plasmonic near-field, respectively. We use the quantum Monte Carlo algorithm where the Lindblad equation reduces to the piecewise deterministic process on quantum trajectories [11].

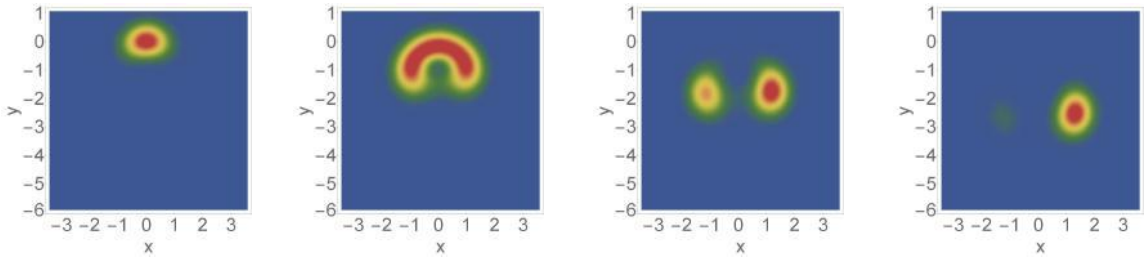



Figure 1: The Wigner function for different values of amplitude $\Omega$ of coherent drive, $\Omega = 0.03, 0.05, 0.07, 0.09$. $\Omega$ increases from left to right.

The Wigner function evolution obtained from Eq. 2 is presented in Fig. 1. At very small driving fields the Wigner function has only one peak located near the state with zero quanta of bosonic mode. Above the threshold, it has the "atoll" form. Then we see new behavior: the Wigner function first splits up into two narrow peaks, but going to larger field amplitudes we observe that the left peak of the Wigner function disappears and only the right one survives.

Finally we consider the spectra of the plasmonic near-field correlators, $\langle \hat{a}^+(t+\tau)\hat{a}(t)\rangle$ that describe coherence and spectral properties of irradiation. It turns out that splitting of Wigner function is accompanied by narrowing of spectral line by the order of magnitude.

To conclude, we have demonstrated by quantum Monte-Carlo simulations of metamolecule which consists of the plasmonic nanoparticle interacting with the atom a narrowing of the spectral line of metamolecule fluorescence by the order of magnitude and splitting of the Wigner function of plasmonic near-field. Noise induced narrow line fluorescence may find wide applications in plasmonic systems where strong noise due to high losses is unavoidable problem.

**REFERENCES**


1. Carmichael, H. and L. A. Orozco, "Quantum optics: Single atom lases orderly light," *Nature*, Vol. 425, No. 6955, 246–247, 2003.
2. Astafiev, O. V. et. al., "Coherent quantum phase slip," *Nature*, Vol. 484, No. 7394, 355–358, 2012.
3. Jain, P. K. et. al., "Noble metals on the nanoscale: optical and photothermal properties and some applications in imaging, sensing, biology, and medicine," *Acc. Chem. Res.*, Vol. 41, No. 12, 1578–1586, 2008.
4. Bergman, D. J. and M. I. Stockman, "Surface Plasmon Amplification by Stimulated Emission of Radiation: Quantum Generation of Coherent Surface Plasmons in Nanosystems," *Phys. Rev. Lett.*, Vol. 90, No. 2, 027402, 2003.
5. Noginov, M. A. et. al., "Demonstration of a spaser-based nanolaser," *Nature*, Vol. 460, No. 7259, 1110–1112, 2009.
6. Maier, S. A., *Plasmonics: fundamentals and applications*, Springer, Berlin, 2007.
7. Gammaitoni, L. et. al., "Stochastic resonance," *Rev. Mod. Phys.*, Vol. 70, No. 1, 223–287, 1998.
8. Wellens, T., V. Shatokhin and A. Buchleitner, "Stochastic resonance," *Rep. Prog. Phys.*, Vol. 67, No. 1, 45–105, 2004.
9. Ridolfo, A. et.al., "Quantum Plasmonics with Quantum Dot-Metal Nanoparticle Molecules: Influence of the Fano Effect on Photon Statistics," *Phys. Rev. Lett.*, Vol. 105, No. 26, 263601, 2010.
10. Hughes, S. and H. Carmichael, "Stationary Inversion of a Two Level System Coupled to an Off-Resonant Cavity with Strong Dissipation," *Phys. Rev. Lett.*, Vol. 107, No. 19, 193601, 2011.
11. Breuer, H.-P. and F. Petruccione, *The theory of open quantum systems*, Oxford Univ. Press, New York, 2002.

# The role of spontaneous emission in the plasmon distribute feedback laser

**A. A. Zyablovsky[1,2*], I. A. Nechepurenko[1,3], E. S. Andrianov[1,2], A. V. Dorofeenko[1,2,3], A. P. Vinogradov[1,2,3], A. A. Pukhov[1,2,3] and A. A. Lisyansky[4]**

[1]The Federal State Unitary Enterprise All-Russia Research Institute of Automatics, Moscow, Russia

[2]Moscow Institute of Physics and Technology, Moscow, Russia

[3]Institute for Theoretical and Applied Electromagnetics RAS, Moscow, Russia

[4]Department of Physics of the Division of Mathematics and Natural Sciences, Queens College of the City University of New York, New York, USA

[*]corresponding author: zyablovskiy@mail.ru

**Abstract**-We investigate lasing in the plasmon distributed feedback laser. For this we derive equations of DFB laser which take into account the process of spontaneous emission in the gain medium and modes competition. We find dependence number of photons in the laser modes of lasing on the intensity of pumping and on the gain coefficient. We show that intensity of lasing nonmonotonically depends on gain coefficient of amplifying medium.

In this paper, we investigate plasmon distributed feedback (DFB) laser [1-4] which consist of nanoparticles array which is placed in layer of quantum dots. For the aim we calculated eigenmodes of the DFB laser. Due to the small quality factor of plasmon lasers the spontaneous emission play significant role in lasing ones. We derive equations of DFB laser which take into account the process of spontaneous emission in the gain medium and modes competition

$$\frac{dn_i}{dt} = -\gamma_i n_i + \sum_n I \tag{1}$$

$$\frac{dD_n}{dt} = -\gamma_d \left( D_n - D_n^0 \right) - 2\sum_i I \tag{2}$$

$$\frac{dI_{in}}{dt} = -\gamma_\sigma I_{in} + \left( \omega_i - \omega_\sigma \right) V_{in} + \left| \Omega_{in} \right|^2 \left( 2n_i + 1 \right) D_n + \left| \Omega_{in} \right|^2 \tag{3}$$

$$\frac{dV_{in}}{dt} = -\gamma_\sigma V_{in} + \left( \omega_n - \omega_i \right) I_{in} \tag{4}$$

Here $n_i$ is a number of photons in the mode with number $i$, $D_n$ is population inversion of atom with number $n$, $I_{in}$ is a energy fluid from atom with number $n$ at the mode with number $i$, $V_{in}$ is a energy of interaction between atom with number $n$ and the mode with number $i$. $\gamma_{ia}$, $\gamma_d$, $\gamma_\sigma$ are widthlines of

modes resonator and quantum dots. $\omega_i$ is a eigenfrequency of mode with number $i$, $\omega_\sigma$ is a transition frequency of quantum dot. The term $\gamma_d D_n^0$ describe pumping.

By equations (1)-(4) we find dependence number of photons in the laser modes on the intensity of pumping and on the gain coefficient (Fig. 1).

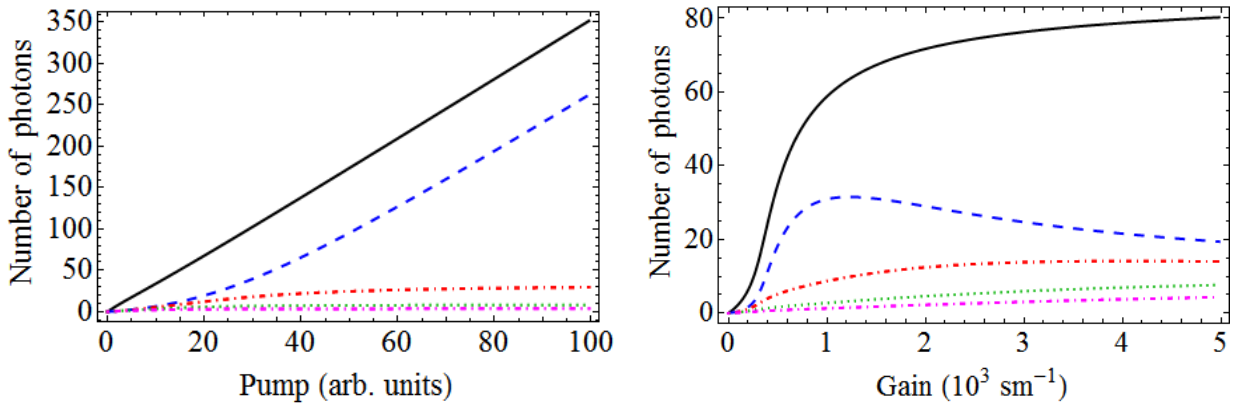



Fig. 1. The dependence number of photons on (left) the intensity of pumping, (right) the gain coefficient. Black solid line: sum number of photons in all modes, blue dashed line: number of photons in the mode for which $\omega_i = \omega_\sigma$, other lines: number of photons in other modes.

Our numerical simulation of equations (1)-(4) demonstrates that number of photons at the mode for which $\omega_i = \omega_\sigma$ nonmonotonically depends on gain coefficient. The nonmonotonic behavior of number of photons occurs because of spontaneous emission and it does not observe without them.

To verify the results of the numerical simulation, we have constructed an approximate theory of lasing in plasmon DFB laser. As a result, we demonstrate that the theoretical curve for the laser threshold practically coincides with the curve obtained by numerical simulation.

**Acknowledgements**, this work was supported in part by RFBR grant nos. 12-02-010193 and 13-02-00407, as well as by the ”Dynasty” foundation.

**REFERENCES**

1. Beijnum F., P. J. Veldhoven, E. J. Geluk, M. J. A. Dood, G. W. Hooft and M. P. van Exter, “Surface Plasmon Lasing Observed in Metal Hole Arrays,” *Phys. Rev. Lett.*, Vol. 110, 206802, 2013.
2. Zhou W., M. Dridi, J. Y. Suh, C. H. Kim, D. T. Co, M. R. Wasielewski, G. C. Schatz and T. W. Odom, “Lasing action in strongly coupled plasmonic nanocavity arrays,” *Nature Nanotech.*, Vol. 8, 506-511, 2013.
3. Meng X., J. Liu, A. V. Kildishev and V. M. Shalaev, “Highly directional spaser array for the red wavelength region,” *Laser & Phot. Rev.*, Vol. 8, 896-903, 2014.
4. Schokker A. H. and A. F. Koenderink, “Lasing at the band edge of plasmonic lattices,” *Phys. Rev. B*, Vol. 90, 155452, 2014.

# Quantum Dot Microlenses:

# Building Blocks for Quantum Communication Networks

**A. Thoma[1], M. Gschrey[1], P. Schnauber[1], A. Kaganskiy[1], S. Fischbach[1], R. Schmidt[1], B. Wohlfeil[2], M. Seifried[1], J.-H. Schulze[1], S. Burger[2], F. Schmidt[2], A. Carmele[3], A. Knorr[3], A. Strittmatter[1], T. Heindel[1], S. Rodt[1], and S. Reitzenstein[1, *]**

[1]Institute of Solid State Physics, Technische Universität Berlin, Berlin, Germany

[2]Zuse-Institut Berlin (ZIB), Berlin, Germany

[3]Institute for Theoretical Physics, Technische Universität Berlin, Germany

[*]corresponding author: stephan.reitzenstein@physik.tu-berlin.de

**Abstract** Bright quantum light sources based on single semiconductor quantum dots (QDs) integrated into photonic microstructures are key building blocks for the realization of advanced quantum communication schemes. Here, we report on the deterministic fabrication of QD-microlenses with excellent optical and quantum-optical properties in terms of the photon extraction efficiency ($\eta_{ext}$~30%), the single photon purity ($g^{(2)}(0)<0.01$) and the photon indistinguishability (V up to 96 %). Moreover, we explore limitations of the indistinguishability by spectral diffusion and decoherence on the nanosecond timescale.

The realization of building blocks for quantum networks has become one of the driving forces for the development of advanced nanophotonic device concepts and nanofabrication technologies [1]. Within this field, significant progress has been achieved regarding for instance the fabrication of efficient quantum dot (QD) based single-photon sources. This work has almost elusively been performed on self-assembled QDs, which is explained by their superb optical and quantum optical properties. However, due to the self-assembled growth, neither the position nor the emission energy of individual QDs is controlled which leads to a very low yield of usable optical devices when standard nano-processing schemes are used. This issue strongly limits the applicability upscaling of single QD based photon sources in practical systems such as multi-partite quantum networks.

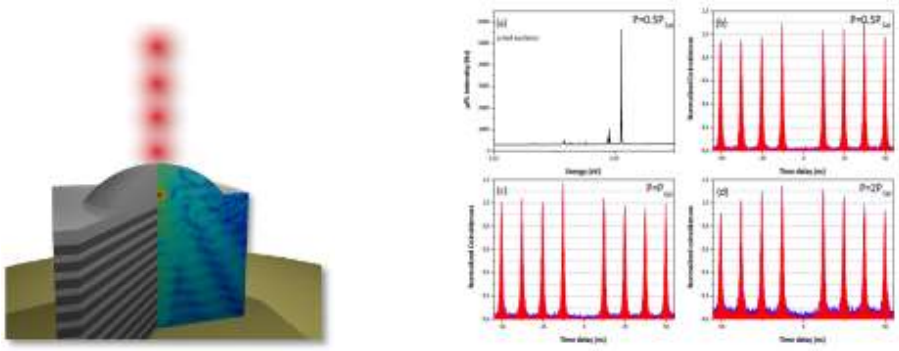


Fig. 1: Schematic view of a microlens with a deterministically integrated single QD (left). Micro-photoluminescence spectrum obtained by pulsed p-shell excitation (a), and corresponding auto-correlation functions at for different excitation powers P (b-d).

In this contribution I will present a nanotechnology platform for the deterministic fabrication of high quality quantum light sources based on self-assembled QDs. Our technique is based on in-situ electron-beam lithography which allows us to integrate pre-selected quantum dots into photonic devices with nm-accuracy and flexible device design [2, 3]. In this way we realize deterministic QD microlenses (see Fig. 1, left) which can act as non-classical light sources with superb optical and quantum-optical properties in terms of the photon extraction efficiency, the single photon purity (see Fig. 1 right) and the degree of photon indistinguishability [4]. I will also discuss effects limiting the photon indistinguishability and show how they can be explored by delay-time and temperature dependent Hong-Ou-Mandel experiments [5]. To this end I will present Hong-Ou-Mandel measurements on single photons emitted by spatially separated QD-microlenses – a key experiment towards advanced quantum communication schemes such as the quantum repeater.

**Acknowledgements** The research leading to these results has received funding from the German Research Foundation via the SFB787, and the European Research Council under the European Union's Seventh Framework ERC Grant Agreement No. 615613.

**REFERENCES**

1. Gisin, N. et al. "Quantum communication," *Nat. Photonics* 1, 165, 2007
2. Gschrey, M. et al. "In situ electron-beam lithography of deterministic single-quantum-dot mesa-structures using low-temperature cathodoluminescence spectroscopy," *Appl. Phys. Lett.* 102, 251113, 2013
3. Gschrey, M. et al. "Resolution and alignment accuracy of low-temperature in situ electron beam lithography for nanophotonic device fabrication," *J. Vac. Sci. Technol. B* 33, 021603, 2015
4. Gschrey, M. et al. "Highly indistinguishable photons from deterministic quantum-dot microlenses utilizing three-dimensional in situ electron-beam lithography," *Nat. Comms.* 6, 7662, 2015
5. Thoma, A. et al. "Exploring Dephasing of a Solid-State Quantum Emitter via Time- and Temperature-Dependent Hong-Ou-Mandel Experiments," *Phys. Rev. Lett.* 116, 033601, 2016

# Quasinormal mode approach to modelling light-matter interactions in quantum-dot plasmonic resonator systems

**S. Hughes**[1]

Department of Physics, Queen's University, Kingston, Ontario, Canada K7L 3N6

**Abstract**— We present an intuitive and efficient quasinormal mode (QNMs) approach to modelling quantum light-matter interactions in hybrid systems of quantum-dots (or artificial atoms) and plasmonic resonators. We first explore the semiclassical regime of enhanced spontaneous emission and radiative quenching for a selection of plasmonic resonators including metal nanorods, nanorod dimers, and hyperbolic metamaterial structures. Second, we study the quantum dynamics using a time-local master equation, and study regimes of single photon emission, two quantum-dot entanglement and nonlinear photoluminescence.

Various open cavity structures have been designed and fabricated to manipulate the interaction between single quantum dipole emitters and local electric fields, where the fields can be enhanced by tailoring the local density of optical states (LDOS), typically through some discrete cavity resonance [1, 2]. For emitter coupling to electric fields below the diffraction limit, metallic nanoparticles (MNPs) and nanoresonators have been shown to yield an unprecedented confinement of light at the nm-scale due to the unique spatial structure of localized surface plasmons (LSPs). As a consequence of the extreme spatial confinement of the LSP, the corresponding effective mode volume of the electric field is much smaller and richer than more traditional dielectric cavity structures, which leads to a strong enhancement of the spontaneous emission rate in the weak-to-intermediate coupling regime [4–6]. For quantum dot (QD) emitters or artificial atoms placed sufficiently close to a MNP, the strong coupling regime has also been shown to be experimentally accessible [3, 7–9].

Recently, it has been shown that LSPs can be effectively described as the quasinormal modes (QNMs) of the MNP [11, 12], similar to open cavity dielectric resonators [12, 13], which are defined as the eigenfunctions of the wave equation with open boundary conditions [14]. A generalized QNM mode expansion technique of the photon Green function can then work extremely well for various shaped MNPs, and the spontaneous emission enhancement of an electric dipole located near the MNP given by the QNM Green function calculation shows excellent agreement with full numerical calculations over a broad range of frequencies [15, 16]. The combination of an insightful QNM approach and a rigorous Green function approach to quantum optics is now highly desired, as MNPs facilitate a rich coupling regime, well beyond a dissipative Jaynes-Cumming model. Recently we have introduced such an approach [10], which allows one to explore semiclassical and fully quantum regimes of QD metal resonator systems.

The QNM Green function is remarkably simple. Consider any two spatial points near the MNP, but outside the regime of Ohmic heating; in a single mode coupling regime, the transverse Green function is accurately described through [15, 16]

$$\mathbf{G}_{\rm c}(\mathbf{r}_1,\mathbf{r}_2;\omega) = \frac{\omega^2}{2\tilde{\omega}_{\rm c}(\tilde{\omega}_{\rm c}-\omega)}\tilde{\mathbf{f}}_{\rm c}(\mathbf{r}_1)\tilde{\mathbf{f}}_{\rm c}(\mathbf{r}_2), \tag{1}$$

where $\tilde{\mathbf{f}}_{\rm c}(\mathbf{r})$ and $\tilde{\omega}_{\rm c}$ are the QNM and the complex eigenfrequency of interest, respectively.

By way of an example, consider a metal nanorod with length $L = 100$ nm and radius $r_c = 15$ nm (see Fig. 1(a)), described by the Drude model for the dielectric constant, $\varepsilon(\omega) = 1 - \omega_{\rm p}^2/(\omega^2 + {\rm i}\omega\gamma)$, where $\omega_{\rm p} = 1.26 \times 10^{16}$ rad/s (bulk plasmon frequency) and $\gamma = 1.41 \times 10^{14}$ rad/s (collision rate), similar to the parameters for gold; the background refractive index is $n_B = 1.5$. In our quantum models, we will also consider the possibility of an incoherent or coherent pump field. For this MNP resonator, the resonance of the dominant LSP is calculated to be $\tilde{\omega}_{\rm c}/(2\pi) = \omega_{\rm c}/2\pi + {\rm i}\gamma_{\rm c}/2\pi = 324.981 - {\rm i}16.584$ THz (1.344 - i0.0684 eV) [16] with a quality factor $Q = \omega_{\rm c}/2\gamma_{\rm c} \approx 9.8$. To obtain the QNM numerically, we use FDTD techniques [15], and the spatial dependence of the mode profile, $|\tilde{\mathbf{f}}(x, y, z = 0)|$, is shown around the nanorod in Fig. 1(a). Using the analytic QNM Green

[1]Work done in partial collabaration with R.-C. Ge, S. Axelrod, M. Kamandar Dezfouli, J.F. Young and P. T. Kristensen

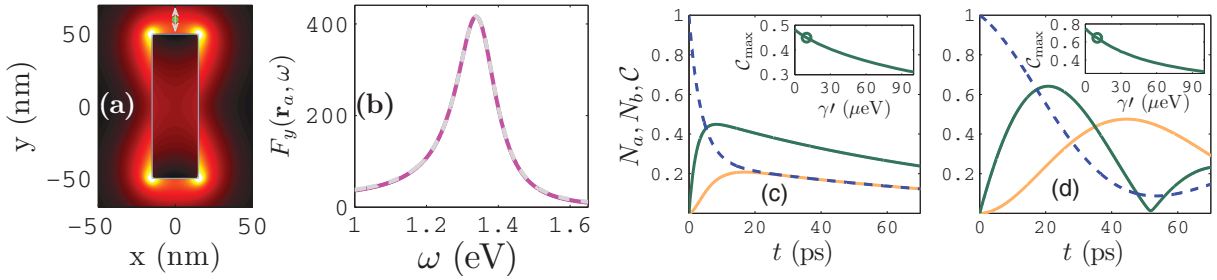



Figure 1: (a) Surface plot of an example QNM spatial profile near a gold nanorod. (b) Enhanced emission factor ($F_y$) for a dipole emitter at 10 nm from the end of the nanorod as shown in (a); the solid line of the analytical QNM calculation and the dashed is a full-dipole simulation using FDTD methods. (c) Quantum dynamics of two spatially separated QDs with $y$-polarized excited QD$a$ and unexcited QD$b$, with dots at 10 nm from the top and bottom of the rod, respectively; we show the exciton population of QD$a$/QD$b$, $N_{a/b}$ (blue dashed/orange solid), and entanglement $\mathcal{C}$ (dark green solid) with a pure dephasing rate $\gamma' = 10$ $\mu$eV for $\omega_a = \omega_b = \omega_p$ (i.e., on resonance with the LSP). The inset shows $\mathcal{C}_{\max}$ as a function of pure dephasing rate, $\gamma'$, and the circle shows the position at which the dynamics is studied. (d) Same as (c) except for $\omega_a = \omega_b = \omega_p - 220$ meV.

function, it is easy to compute the enhanced emission factor or Purcell factor, and in Fig. 1(b) we show the enhanced emission factor of a $y$-polarized dipole, 10 nm from the rod top surface, on-axis; the solid and dashed curves show the analytical QNM calculation and a full numerical dipole result, respectively, demonstrating excellent agreement over broadband frequencies. The former calculation is not only orders of magnitude faster but also allows one to compute such emission factors over various spatial positions without doing any more numerical calculations of the mode.

By deriving a quantum master equation for QDs or two-level atoms in a MNP environment [10], we can also explore a wide range of quantum light-matter interactions using the same analytical Green function as the photon bath function. Figure 1(c-d) shows two examples of the quantum dynamics of two QDs placed symmetrically at the top and bottom of the nanorod, with one of the QDs initially excited; we see that the two QDs become entangled with each other, through the LSP, and the amount of entanglement depends on the QD spatial positions, emitter frequency, and pure dephasing rates of the excitons. The QNM approach allows us to investigate a wide range of such coupling scenarios to optimize such a configuration, e.g., for entanglement applications, and we will show several examples in the talk.

In summary, we will present a QNM approach to modelling light-matter interactions in QD metal resonator systems. The approach is efficient and intuitive, and can be applied to a wide range of problems in classical and quantum plasmonics.

## ACKNOWLEDGMENT

This work was supported by the Natural Sciences and Engineering Research Council of Canada and Queen's University.

## REFERENCES

1. K. J. Vahala, Nature **424**, 839 (2003).
2. M. S. Tame *et al.*, Nat. Phys. **9**, 329 (2013).
3. A. Delga, J. Feist, J. Bravo-Abad, and F. J. Garcia-Vidal, Phys. Rev. Lett. **112**, 253601 (2014).
4. P. Anger, P. Bharadwaj, and L. Novotny, Phys. Rev. Lett. **96**, 113002 (2006).
5. M. Frimmer and A. F. Koenderink, Phys. Rev. Lett. **110**, 217405 (2013).
6. C. Belacel *et al.*, Nano Lett. **13**, 1516 (2013).
7. C. Van Vlack, P. T. Kristensen, and S. Hughes, Phys. Rev. B **85**, 075303 (2012).
8. A. Trügler and U. Hohenester, Phys. Rev. B **77**, 115403 (2008).
9. F. Alpeggiani, S. D'Agostino, and L. C. Andreani, Phys. Rev. B **86**, 035421 (2012).
10. R. Ge and S. Hughes, Phys. Rev. B **92**, 205420 (2015).
11. C. Sauvan, J. P. Hugonin, I. S. Maksymov, P. Lalanne, Phys. Rev. Lett. **110**, 237401 (2013).
12. P. T. Kristensen and S. Hughes, ACS Photonics **1**, 2 (2014).
13. P. T. Kristensen, C. Van Vlack, and S. Hughes, Opt. Lett. **37**, 1649 (2012).
14. K. M. Lee, P. T. Leung, and K. M. Pang, J. Opt. Soc. Am. B **16**, 1409 (1999).
15. R.-C. Ge and S. Hughes, Opt. Lett. **39**, 4235 (2014).
16. R.-C. Ge, P. T. Kristensen, Jeff. F. Young, and S. Hughes, New J. Phys. **16**, 113048 (2014).

# Quantum photonics

**D Zueco**[1], **E. Sánchez-Burillo**[1], **J. García-Ripoll**[2] **and L Martín-Moreno**[1]

[1] Instituto de Ciencia de Materiales de Aragon and Departamento de Fisica de la Materia Condensada, CSIC-Universidad de Zaragoza, E-50012 Zaragoza, Spain

[2] Instituto de Fisica Fundamental, IFF-CSIC, Calle Serrano 113b, Madrid E-28006, Spain dzueco@unizar.es

**Abstract**— We discuss our approach for describing few photons and few scatterers at the quantum level, both analytically and numerically. Our tools are applied to Raman, downconversion, entanglement generation and nonlinear phases gates at the single photon level. We also discuss how to implement our ideas in circuit QED.

In waveguide QED travelling photons are strongly coupled to natural or artificial atoms for doing photonics at the few photon level. It is a emerging field since it promises new advances in quantum information and provides a natural platform for generating photon-photon interactions [1]. Both photons and atoms must be treated quantum mechanically making this optics setup a many body problem. A natural technique for solving many body in one dimension is Matrix Product States [2]. We adapt this technique for solving problems in few photon photonics. We apply it to several problems as Raman, downconversion, entanglement generation and nonlinear phase gates [3, 4, 5]. These applications are used to emphasize the necessity of importing many body problem techniques in quantum optics.

**REFERENCES**

1. D Roy, CM Wilson and O Firstenberg. arXiv:1603.06590
2. E. Sánchez-Burillo, D. Zueco, J García-Ripoll, L. Martín-Moreno, *Phys. Rev. Lett* 113, 263604 (2014)
3. E. Sánchez-Burillo, J García-Ripoll, L. Martín-Moreno, D. Zueco, *Faraday Discussions* 178, 335 (2015)
4. E. Sánchez-Burillo, J García-Ripoll, L. Martín-Moreno, D. Zueco, arXiv:1602:05603
5. E. Sánchez-Burillo, L. Martín-Moreno, D. Zueco, J García-Ripoll, arXiv:1602:05603

# Current Advances in Electromagnetics of Metal and HRI dielectric nanostructures

# Optical spectroscopy of individual nano-objects in correlation with electron microscopy imaging: plasmon interferences in strongly coupled systems

**E. Cottancin**[1*]

[1]*Institut Lumière-Matière (iLM) , CNRS & University Lyon 1, UMR 5306, Bât A. Kastler, 43, bd du 11 Novembre 1918, 69622 Villeurbanne cedex, France*

[*]corresponding author: emmanuel.cottancin@univ-lyon1.fr

Metallic nanoparticles (NPs) have long been known for their peculiar optical properties exhibiting a giant resonance corresponding to an electromagnetic (EM) field enhancement, and known as Localized Surface Plasmon Resonance (LSPR). The near- and far-field optical response of such systems (which can be viewed as nano-antennas (NAs) is closely dependent on their morphology and chemical composition. In order to understand the relation between the optical response and the morphology of the NPs, we have developed ultra-sensitive spectrophotometers based on the spatial modulation spectroscopy (SMS) technique [1]. This allows the measurement of the absolute extinction (or quantitative scattering) of light by a single nano-object over a broad spectral range (from the near UV to the near infrared). Moreover, this optical technique can be coupled with electron microscopy (classical or 3D TEM, SEM, AFM), to correlate the exact morphology of nanoparticles with their optical response [2, 3].

The LSPR is also strongly sensitive to the presence of other nearby particles. Mutual coupling induces complex collective excitations within these nanoantennas and can be used to tailor the LSPR shape over a wide spectral range. Simple pairs of nanoparticles are the most basic systems for understanding mechanisms of plasmon hybridization and interference. First, the optical response is drastically modified for very low interparticle distances for a longitudinal excitation. The most striking effect is a red-shift of the LSPR with decreasing interparticle distance, following a scaling law known as “Plasmon ruler” opening innovating perspectives in the field of bio-sensing. Besides the distance, the gap morphology becomes of crucial importance for very short interparticle distances (strong coupling regime) for which the “Plasmon ruler” is no longer valid. Thanks to the combining of optical measurements and electron microscopy, very thin interspacing distances (< 1 nm) and morphological effects have been explored for pairs of spherical and cubic NPs made of gold or silver. In the case of nanocubes, besides the redshift of the resonance with decreasing interparticle distance, we observed a clear anti-resonance dip in the main dipolar LSPR [4] which can be viewed as a Fano resonance due to the coupling between the broad dipolar resonance of the dimer with gap plasmon modes confined in the interparticle zone (see Figure 1).

On the other hand, we will see that the plasmonic coupling is also a powerful tool to involve LSPRs in NAs made of most of the transition metals [5]. This opens up the range of applications in the field of photo-catalysis, nano-sensing or magneto-plasmonics.

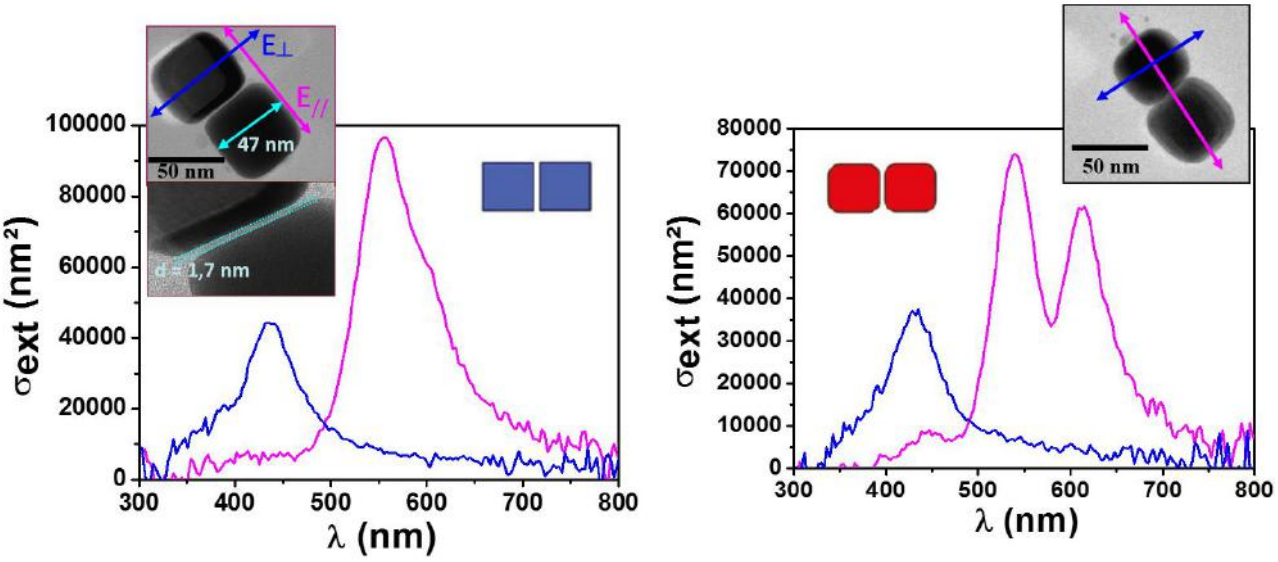



Figure 1 : absolute extinction spectra of single silver nanocube dimers for an incident electric field polarized along (magenta) or perpendicular (blue) to the interparticle axis. The insets show the TEM images of the optically investigated dimers. For almost perfect cubes with an interparticle distance of a few nanometers, the main resonance for longitudinal excitations is simply red-shifted as compared to the resonance obtained for perpendicular excitations (left). On the other hand, an anti-resonance dip clearly appears for sufficiently low interparticle distances, and as soon as edges and corners are rounded (right).

**REFERENCES**


1. P. Billaud, S. Marhaba, N. Grillet, E. Cottancin, C. Bonnet, J. Lermé, J.-L. Vialle, M. Broyer and M. Pellarin, *Review of Scientific Instruments*, Vol. 81, 043101, 2010.
2. P. Billaud, S. Marhaba, E. Cottancin, L. Arnaud, G. Bachelier, C. Bonnet, N. Del Fatti, J. Lermé, F. Vallée, J.-L. Vialle, M. Broyer and M. Pellarin, *J. Phys. Chem. C*, Vol. 112, 978-982, 2008.
3. J. R. G. Navarro, D. Manchon, F. Lerouge, E. Cottancin, J. Lerme, C. Bonnet, F. Chaput, A. Mosset, M. Pellarin and S. Parola, *Nanotechnology*, Vol. 23, 145707-1/145707-8, 2012.
4. N. Grillet, D. Manchon, F. Bertorelle, C. Bonnet, M. Broyer, E. Cottancin, J. Lermé, M. Hillenkamp and M. Pellarin, *ACSNano*, Vol. 5, 9450-9462, 2011.
5. D. Manchon, J. Lermé, T. Zhang, A. Mosset, C. Jamois, C. Bonnet, J.-M. Rye, A. Belarouci, M. Broyer, M. Pellarin and E. Cottancin, *Nanoscale*, Vol. 7, 1181-1192, 2015.

# Spherical silicon photonic microcavities: Looking inside.

**R. Fenollosa[1*], M. Garín[2], and F. Meseguer[1]**
[1]Instituto de Tecnología Química (CSIC-UPV), Spain
[2]Universitat Politècnica de Catalunya, Dep. d'Enginyeria Electrònica, Spain
[*]corresponding author: rfenollo@ter.upv.es

**Abstract**-Silicon microspheres yield a rich electronic response in the near infrared via Mie resonance optical absorption. The investigation of the internal structure and the optical properties of the microspheres has revealed that they posses a richly structured core, surrounded by a non-porous shell. While such a porous core kills those resonances whose electromagnetic field is well distributed in the porous region, high-*Q* modes should occur at the non-porous shell.

Silicon microspheres constitute a promising platform for developing applications in different fields of technology such as photonics, optoelectronics, and medicine.[1] Their possibilities stem from their ability to sustain optical resonances and the fact that they are made of silicon, which is the material basis for the current microelectronics industry. So far, the applications based on this material have relied on bare quality particles. The study of magnetic light is an example[2] where low number resonant modes are used. These modes are wide, i.e. with low *Q* factor, and therefore they are little influenced by any defects of the particle constituting the microcavity. However, other recent developments like that of the spherical-Mie-resonator photodiode[3] [Fig 1. (a)], combining photonic and electronic applications, require higher *Q* resonances. The spectral electronic response of such devices [Fig.1. (b)] shows plenty of sharp peaks that correspond to Mie resonances. This demonstrates the capability of the microspheres for absorbing light below the band gap of the material and, at the same time it proves that the technique of optical absorption via the electronic response is a very sensitive approach for measuring high-*Q* resonant modes. However, a precise fitting of such resonances to Mie theory has not been achieved yet. For that purpose, it is necessary to investigate the structural properties of the microspheres, focusing not only on their external aspects, such as sphericity and surface smoothness, but also on their internal structure, and to perform a more in deep optical characterization.

We have found that poly-crystalline microspheres have a richly structured porous core surrounded by a non-porous shell. Such pores kill those resonant modes whose electromagnetic field is well distributed inside the sphere volume. Fig. 2 corresponds to a HRTEM image of the inside area of a carved poly-crystalline silicon microsphere showing the pores at the sphere center. The electromagnetic field intensity distribution of mode $b_{13,5}$ has been superimposed, as an example of a mode overlapping the porous region. Optical scattering spectroscopy at 90º confirmed the suppression of this type of modes. Therefore we hypothesize that the high-*Q* resonant modes, which are responsible of the electronic response [Fig. 1 (b)], occur mainly at the non-porous shell of the microspheres.

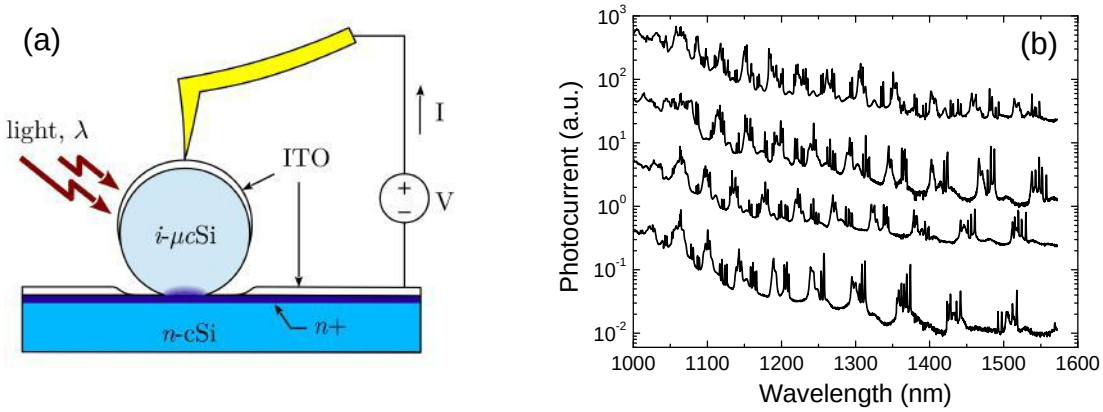



**Fig 1:** (a) Scheme of a photodiode based on a silicon microsphere, (b) measured spectral response (short circuit current) of several devices corresponding to different sphere diameters. The sharp peaks correspond to Mie resonances.

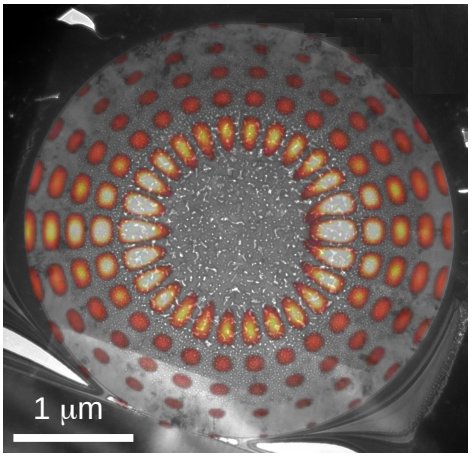



**Fig 2:** (a) HRTEM image of the internal surface of a poly-crystalline silicon microsphere showing the porous structure at the core. The electric field intensity distribution of mode $b_{13,5}$ has been superimposed.

**Acknowledgements**, This work was supported by projects ENE2013-49984--EXP (Spanish Ministry of Economy and Competitiveness, MINECO), MAT2012-35040, and PROMETEOII/2014/026.

**REFERENCES**

1. F. Meseguer, R. Fenollosa, I. Rodríguez, E. Xifré-Pérez, F. Ramiro-Manzano, M. Garín, M. Tymczenko, " Silicon colloids: A new enabling nanomaterial", *J. Appl. Phys*., 102424, 2011.
2. A. I. Kuznetsov, A. E. Miroshnichenko, Y. H. Fu, J. Zhang, B. Luk'yanchuk, "Magnetic light", *Sci. Rep*. 2, 492, 2012.
3. M. Garín, R. Fenollosa, R. Alcubilla, L. Shi, L.F. Marsal, F. Meseguer, " All-silicon spherical-Mie-resonator photodiode with spectral response in the infrared region", *Nat. Comm*., 5, 3440, 2014.

# The magnetic response in high-index nanophotonics: from magnetic hot-spots to Huygens' sources and generalized Brewster's effect.

**R. Paniagua-Dominguez[1*], Y. F. Yu[1], R. M. Bakker[1], Y. H. Fu[1], B. Luk'yanchuk[1] and A. I. Kuznetsov[1]**
[1]Data Storage Institute (A*STAR), Singapore
[*]corresponding author: ramon-paniag@dsi.a-star.edu.sg

**Abstract**- All dielectric nanophotonics based on high-refractive index (HRI) particles has emerged as an alternative to plasmonics for those cases in which losses are an important concern. They also offer new possibilities due to magnetic resonances naturally excited in HRI nanoparticles. Here we review some of these in connection with electromagnetic hotspots in HRI dimers and electric and magnetic dipole interference effects, with focus on metasurfaces.

Over the past few years an increasing interest has grown in the study of high-refractive index (HRI) nanoparticles. In many ways similar to their plasmonics counterparts, HRI sub-wavelength structures may resonantly interact with incident light [1-3]. However, in the case of HRI particles resonances are driven by polarization currents, and that strongly mitigates absorption losses. In addition, HRI particles have a unique feature as compared to metallic particles; on top of the family of multipolar electric resonances supported by the latter they support additional multipolar magnetic resonances [1-3]. Due to their distinct near-field distributions and radiation characteristics, new optical phenomena have been described recently associated to these magnetic resonances and their interaction with the family of electric ones.

Here, it is shown that HRI dimers, unlike plasmonics ones, exhibit hotspots in the gap between the particles both when the electric or when the magnetic field is aligned with the axis of the dimer [4]. A qualitative explanation of the mechanism is shown in Fig.1(a). When the field is directed along the axis of the dimers, polarization charges generate an index-dependent field enhancement, reaching ~8-fold for a dimer of silicon (Si) disks. When the magnetic field is oriented along the axis, induced magnetic dipoles interact and part of the field is localized in the gap, with ~8-fold enhancement observed. The effect is experimentally measured through Near-field Scanning Optical Microscope, as shown in Fig.1(b).

Another property that follows from the excitation of magnetic resonances is the angle-suppressed radiation caused by directional interference between these and electric resonances. This lead to nanoantennas with suppressed backscattering [5, 6] that can be used in high-transmission metasurfaces for phase control [7, 8], as that shown in Fig.2(a). This metasurface, composed by Si disks and designed to bend transmitting light at ~10° shows a total efficiency of ~45%. It is shown that the angle suppressed scattering may lead to another intriguing phenomenon, namely, that a HRI-based metasurface may exhibit Brewster's effect, potentially, for any polarization and angle of incidence. This property, intimately related with the interference between the dipoles induced in the particles forming the metasurface, is theoretically and experimentally investigated [9]. Figs.2(b) and (c) show the simulated reflection for square arrays of Si spheres with diameter 180 nm and period 300 nm as a function of the angle of incidence for different wavelengths showing, respectively, that Brewster's angle can be observed for p- and s-polarizations in this system.

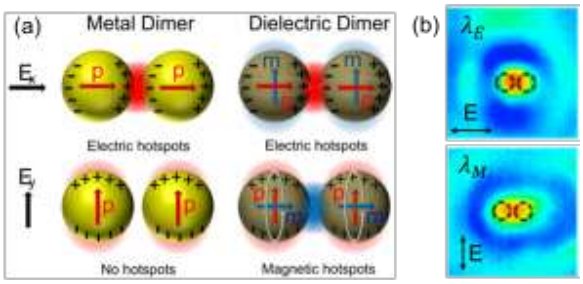



**Figure 1:** (a) Schematic of the mechanism of electric and magnetic hotspot generation in dielectric dimers compared to plasmonic ones. (b) NSOM measurements at electric (top) and magnetic (bottom) resonance excited the indicated polarization.

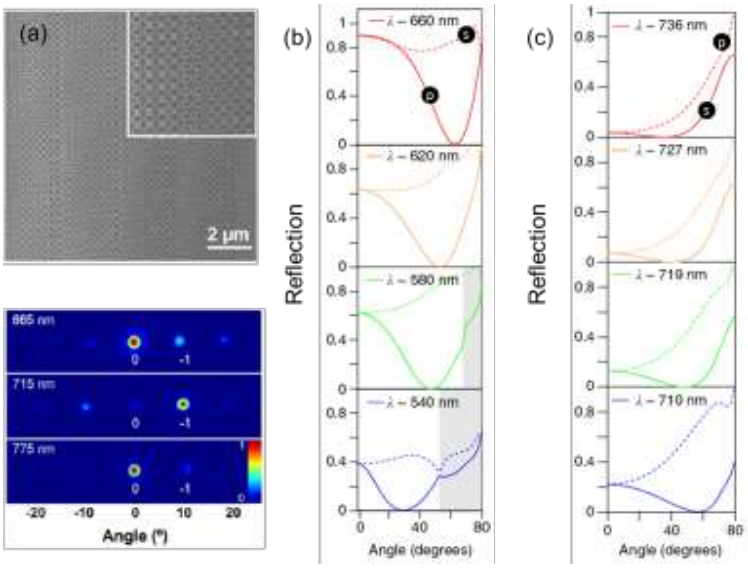



**Figure 2:** (a) SEM of the beam-bending metasurface (top) and back-focal plane image at the operating wavelength (715 nm) and out of it (bottom). (b) and (c), respectively, reflection versus angle of incidence at different wavelengths from a metasurface designed to exhibit Brewster angle for p- and s-polarized light.

**REFERENCES**


1. Evlyukhin, A. "Optical response features of Si-nanoparticle arrays", *Phys.Rev.B*, Vol.82, No.4,045404, 2010
2. Garcia-Etxarri, A. et al. "Strong magnetic response of submicron silicon particles in the infrared," *Opt. Express*, Vol. 19, No. 6, 4815-4826, 2011.
3. Kuznetsov, A. I. et al. "Magnetic Light," *Sci. Reports*, Vol. 2, 492, 2012.
4. Bakker, R. M. et al., "Magnetic and Electric Hotspots with Silicon Dimers," *Nano. Lett.*, Vol.15, No. 3, 2137-2142, 2015.
5. Geffrin, J. M., "Magnetic and electric coherence in forward-and back-scattered electromagnetic waves by a single dielectric subwavelength sphere," *Nat. Comm.*, Vol. 3, 1171, 2012.
6. Fu, Y.H. et al. "Directional visible light scattering by silicon nanoparticles", *Nat. Comm.*, Vol. 4, 1527, 2012
7. Yu, Y. F. et al. "High-transmission dielectric metasurface with 2π phase control at visible wavelengths", *Laser & Phot. Rev.*, Vol. 9, No. 4, 412-418, 2015.
8. Decker, M. "High-Efficiency Dielectric Huygens' Surfaces", *Adv. Mater.* Vol. 3, No.6, 813-820, 2015.
9. Paniagua-Dominguez, R. et al. "Generalized Brewster's effect in all-dielectric metasurfaces", *Nat. Comm.* Vol. 7, 10362, 2016.

# Dielectric nanoantennas as a new way to enhance and direct scattered light with minimal losses.

**P. Albella**[1,*]**, T. Shibanuma**[1]**, and S. A. Maier**[1]

[1] The Blackett Laboratory, Department of Physics, Imperial College London, London SW7 2AZ, UK.

[*]presenting author: p.albella@imperial.ac.uk

**Abstract-** Plasmonic nanostructures enable control of light at subwavelength scales. However, substantial losses are inevitable, especially at optical wavelengths. High-refractive index dielectrics show strong promise as a complementary nanophotonics platform. Dielectric nanostructures are able to show not only electric but also magnetic resonances, both with low-losses. Here, we present asymmetric-dimers of dielectric nanoparticles that exploit the interaction of those resonances to show tunable directional scattering. We also explore its application as tuneable routing element at nanoscale, suggesting applications like optical nanocircuitry.

Over the past several years plasmonics has been employed to obtain strong light-matter interactions at deep subwavelength size scales. In particular, plasmonic nanoantennas have been used to enhance and control the emission from quantum dot and molecular emitters, offering the possibility to develop more efficient light emitting devices for integrated photonics[1]. More recently, several groups have begun to explore the use of high-index dielectric nanostructures for their ability to manipulate electromagnetic fields[2-6].In addition to low optical losses, such structures exhibit resonances with both the electric and magnetic fields due to the oscillation and rotation of displacement current caused by incident field penetration[7-9]. This type of interaction opens up new pathways for manipulating.

In this work, we show that a dielectric nanodimer consisting of nanoparticles with different dimensions can scatter light directionally to either the right or left direction by tuning the incident wavelength. The underlying reason is that amplitude and phase differences of electric and magnetic resonances in dielectric nanoparticles can be tuned by changing geometrical dimensions. By carefully designing the dimer configuration, therefore, the direction of the scattered light becomes tuneable due to the interference between the dipoles excited in each particle. Full theoretical calculations using an analytical dipole-dipole model help to determine a favourable configuration for highly directional scattering tuneable via the incident wavelength[9]. We will also discuss a practical configuration of asymmetric dimers as a nanoscale routing element for electromagnetic radiation. Directional control of the scattered light combined with low energy losses presented here can facilitate the development of efficient sensors, waveguides and optical circuits at the nanometer scale.

Figure 1a shows the angle of maximum scattering intensity of the radiation pattern in the y-z projection plane. Here the scattering angle of 90º corresponds to the forward scattering, and the two quadrants (0–90º and 90–180º) correspond to the scattering hemisphere of the larger and smaller particles, respectively. The direction of the scattered light bends left (108°) or right (38°) at λ~500 nm and λ~630 nm, respectively (inset shows the radiation pattern on the y-z plane). At λ ~500 nm, the scattered light was directed to the smaller sphere but suppressed in the direction of the larger sphere. Meanwhile, a completely opposite result was achieved at λ ~ 630 nm; the light

scattered to the smaller sphere was suppressed but the light to the larger sphere was intensified. This means that the direction of the scattered field can be tuned by changing incident wavelength. To understand the basic mechanism of this directional scattering, a phase difference of the magnetic dipoles which are excited perpendicular to the scattering plane and, hence, responsible for the directional scattering was analysed. Exciting the dimer with polarization perpendicular to the dimer axis, also result in a switchable directional scattering, but this time at blue-shifted wavelengths due to the phase difference of excited electric dipoles. We also explore the possibility of using this directional scattering to excite selective positions in a practical configuration with asymmetric silicon nanodisk dimers on a silica substrate (Fig. 1b). Light illumination of the first dimer results in the selective excitation of another dimer placed either in the left or right direction, depending on the excitation wavelength and/or polarization. Switchable control of the scattering direction could facilitate the development of sensitive spectroscopic technique with selective excitation or tuneable optical nanocircuit.

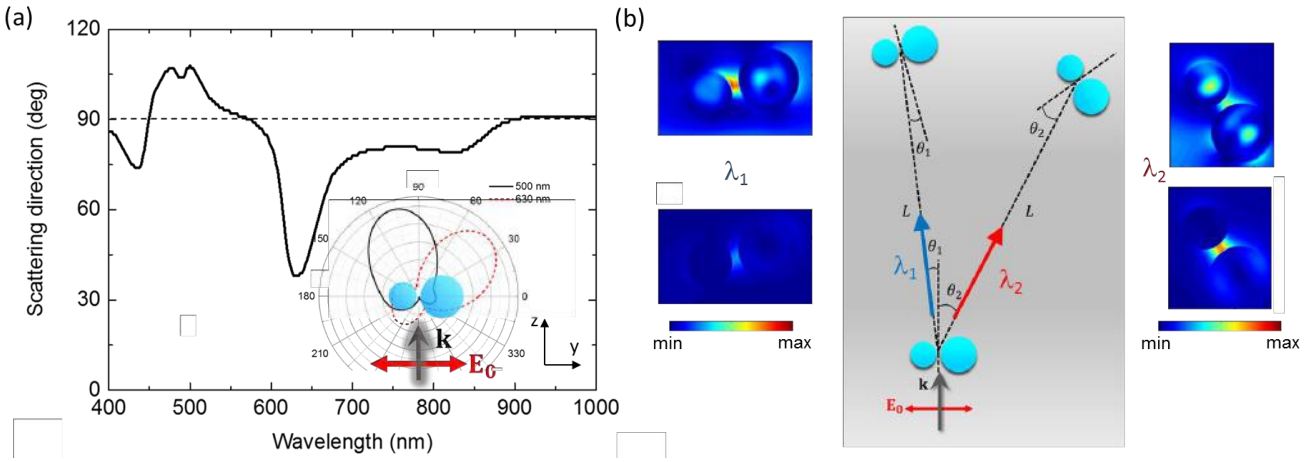



**Figure 1:** (a) Maximum angle of scattered intensity. Inset shows the Far field radiation patterns of the scattered light at λ ~ 500 nm and λ ~ 630 nm. (b) Schematic illustration of tunable optical guide. The first dimer was illuminated by the incident light parallel to the substrate with polarization along the dimer axis. The second was placed at either left ($\theta_1$=7.2°) or right ($\theta_2$=27°) from the first one, at a distance of 1.2 μm.

**Acknowledgements**, The authors acknowledge funding provided by grants the EPSRC Active Plasmonics Programme (UK), the Leverhulme Trust (UK), ONR Global, and the US Army Transatlantic Research Office.

**REFERENCES**

1. Giannini, V. et al. *Chemical Reviews* **111**, 3888-3912, (2011).
2. Geffrin, J. M. et al. *Nature Communications* **3**, 8, (2012).
3. Albella, P. et al. *Journal of Physical Chemistry C* **117**, 13573-13584 (2013).
4. Bakker, R. M. et al. *Nano Letters* **15**, 2137-2142, (2015).
5. Caldarola, M. et al. *Nature Communications* **6**, 7915, (2015).
6. Yan, J. H. et al. *Nature Communications* 6, 7042, (2015).
7. Garcia-Etxarri, A. et al. *Optics Express* **19**, 4815-4826, (2011).
8. Schmidt, M. K. et al. *Optics Express* **20**, 13636-13650, (2012).
9. Albella, P., Shibanuma, T. & Maier, S. A. *Scientific Reports* **5**:18832, (2015).

# Localized magnetic plasmons in all-dielectric structures.

**R. Paniagua-Domínguez[1], L. S. Froufe-Pérez[2*], J. J. Sáenz[3], and J. A. Sánchez-Gil[4]**

[1] Data Storage Institute, Agency for Science, Technology and Research, Singapore.

[2] Physics Department, University of Fribourg, Fribourg, Switzerland.

[3] Donostia International Physics Center (DIPC), Donostia-San Sebastián. Spain.

[4] Instituto de Estructura de la Materia, Consejo Superior de Investigaciones Científicas, Spain.

[*]corresponding author: luis.froufe@unifr.ch

**Abstract**- We theoretically show how an assembly of all-dielectric nonmagnetic scatterers can effectively support a strong localized magnetic plasmon resonance. We consider collections of disordered but correlated monodisperse high refractive index spheres exhibiting a strong magnetic dipole resonance. The effective magnetic permeability of such an ensemble is negative in a given fequency range, while the effective dielectric permittivity is possitive and small. We show that localized magnetic plasmon resonances can be excited in a metasphere made of such metamaterial.

The natural magnetic response is negligible for the majority of materials at high frequencies, i.e. its effective permeability is $\mu \approx 1$. However, it is well known that materials exhibiting prescribed permeability and permittivity would open routes towards extraordinary applications. Probably, one of the best known such materials are negative refractive index (NRI) ones, first studied by Veselago [1], where simultaneous $\varepsilon=-1$ and $\mu=-1$ lead to a refactive index $n=-1$. As a consequence of this NRI and impedance matching, it would be possible to build flat perfectly converging lenses breaking Abbe's diffraction limit.

Proposals for actual realizations of such materials [2, 3] can be considered as the origin of modern electromagnetic (EM) metamaterials science and technology. One of the main goals is designing structures presenting an effective magnetic response $\mu_{eff} \neq 1$ with all $\mu=1$ blocks. Many of the practical implementations and theoretical designs are based on resonant metal structures [4]. Such structures are suitable for producing strong magnetic resonances at the expense of presenting also a strong absorption. Nevertheless, it has been pointed out that single scatterers as simple as a high refractive index (HRI) nonmagnetic homogeneous sphere can give support to strong magnetic resonances [5], under certain conditions, the coherent superposition of scattered EM waves by dipole electric and magnetic resonances by a single object leads to a strong inhibition or enhancement of either backward or forward scattering by a single scatterer. These conditions, first discovered by Kerker and coworkers [6] for dielectric spheres with $\mu \neq 1$ , can be achieved also with nonmagnetic HRI when size, refactive index and frequency are chosen appropriately [7].

When the effective EM response of a medium comprised of scatterers with electric and magnetic dipole resonances is considered, in principle not only the electric permittivity is different from the host medium but also the effective magnetic permeability even if none of the microscopic constituents present magnetic response. In this regard, we propose and theoretically study in this paper [8] a metamaterial made of nonmagnetic HRI scatterers whose effective magnetic permeability is negative while its effective electrical permittivity is comparable to that of the host medium.

Our system is a collection of monodisperse homogeneous nonmagnetic HRI spheres. The size, refractive

index and density of scatterers is chosen in such a way that the effective permeability $\mu_{eff} \neq 1$, derived from Clusius-Mosotti formula applied to the magnetic polarizability, can be prescribed to tailor the magnetic response of the system.

Due to the symmetry of the Maxwell equations, if electric and magnetic variables are adequately transformed, the electric plasmon resonances are transformed into magnetic plasmon resonances. In particular, localized plasmon resonances encountered in metallic spheres with $\varepsilon \approx -2$ and $\mu \approx 1$, have a magnetic counterpart in spheres with $\mu \approx -2$ and $\varepsilon \approx 1$. In this work we design a metamaterial such that, when carved in a spherical shape with the appropriate radius, a "metasphere", it clearly supports a localized magnetic plasmon resonance that can be identified with the magnetic dipole scattering channel of the Mie theory for a sphere of the same radius as the metasphere and $\mu \approx -2$, $\varepsilon \approx 1$. In this way, our metamaterial effectively behaves as a "magnetic metal" supporting localized magnetic plasmons.

We derive approximate, though universal, conditions for the occurrence of such magnetic plasmon phenomena, revealing that available materials and geometrical parameters enable it for a wide spectral regime from microwave to near infrared and even visible for geometries other than the spherical. This effective medium together with our design rules paves the way towards realistic plasmonic $\mu<0$ structures, unlocking a whole new quadrant of the $\varepsilon$–$\mu$ plane.

**Acknowledgements**, We are grateful to M. Nieto-Vesperinas and F. Moreno for fruitful discussions. This work was supported by the Spanish MINECO (FIS2012-31070 and FIS2012-36113) and Consolider-Ingenio EMET (CSD2008-00066). L.S.F.P. was supported by the Swiss National Science Foundation through the National Centre of Competence in Research Bio-Inspired Materials.

## REFERENCES

1. V. G. Veselago, "The electrodynamics of substances with simultaneously negative values of ε and μ," *Sov. Phys. Usp. (Engl. Transl.)*, Vol. 10, 509-514, 1968.
2. J. B. Pendry, "Negative Refraction Makes a Perfect Lens, "*Phys. Rev. Lett.*, Vol. 85, 3966-3969, 2000.
3. D. R. Smith, W. J. Padilla, D. C. Vier, S. C. Nemat-Nasser, and S. Schultz, "Composite Medium with Simultaneously Negative Permeability and Permittivity," *Phys. Rev. Lett.*, Vol. 84, 4184-4187, 2000.
4. R. Paniagua-Domínguez, F. López-Tejeira, R. Marqués, and J. A. Sánchez-Gil, "Metallo-dielectric core–shell nanospheres as building blocks for optical three-dimensional isotropic negative-index metamaterials," *New J. Phys.*, Vol. 13, 123017, 2011.
5. A. García-Etxarri, R. Gómez-Medina, L. S. Froufe-Pérez, C. López, L. Chantada, F. Scheffold, J. Aizpurua, M. Nieto-Vesperinas, and J. J. Sáenz, "Strong magnetic response of submicron Silicon particles in the infrared," *Opt. Express*, Vol. 19, 4815-4826 ,2011.
6. M. Kerker, D.S. Wang, and L. Giles, "Electromagnetic scattering by magnetic spheres," J. *Opt. Soc. Am.* Vol. 73, 765–767, 1983.
7. J. M. Geffrin, B. García-Cámara, R. Gómez-Medina, P. Albella, L. S. Froufe-Pérez, C. Eyraud, A. Litman, R. Vaillon, F. González, M. Nieto-Vesperinas, J. J. Sáenz, and F. Moreno, "Magnetic and electric coherence in forward- and back-scattered electromagnetic waves by a single dielectric subwavelength sphere," *Nat. Commun.*, Vol. 3, 1171, 2012.
8. R. Paniagua-Domínguez, L. S. Froufe-Pérez, J. J. Sáenz, and J. A. Sánchez-Gil, "Localized magnetic plasmons in all-dielectric μ<0 metastructures," *Phys. Rev. B*, Vol. 91, 235120, 2015.

# Analysis of directionality effects in magnetodielectric core-shell nanoparticles by means of polarimetric techniques.

**A. I. Barreda[1*], Y. G. Vela[1], J. M. Sanz[1,2], F. González[1] and F. Moreno[1]**

[1]Grupo de óptica, Departamento de Física Aplicada, Universidad de Cantabria, Facultad de Ciencias, Avda. Los Castros s/n, 39005 Santander, Spain

[2]Departamento de I+D, Textil Santanderina, S.A., Avenida Textil Santanderina, s/n 39500 Cabezón de la Sal, Spain

[*]corresponding author: barredaai@unican.es

**Abstract**-The influence of increasing the core size of a Ag-Si core-shell nanoparticle has been investigated by using the values of the linear polarization degree at right angle scattering configuration, $P_L(90º)$. Changes in dipolar resonances and Scattering Directionality Conditions as a function of the core radius ($R_{int}$) for a fixed shell size ($R_{ext}$ = 230 nm) have been analyzed. An empirical formula to obtain the ratio $R_{int}/R_{ext}$ by monitoring the influence of the magnetic dipolar resonance in $P_L(90º)$ has been found.

In spite of the good response of metallic nanoparticles (NPs) in visible and infrared ranges, their inherent ohmic losses make them useless in many practical applications. High Refractive Index (HRI) dielectric NPs have been proposed to address this issue. Some of their most important advantages are that light can travel through them without being absorbed and that they can present magnetic effects even for non-magnetic ($\mu = 1$) NPs, [1]. This magneto-dielectric behavior is responsible for interesting directionality properties. Under certain conditions of the electric permittivity $\varepsilon$ and magnetic permeability $\mu$, proposed by Kerker et al [2, 3], the forward and backward scattered intensity is almost null or null respectively. Those conditions are also known as either Kerker's conditions or Scattering Directionality Conditions. Metal-dielectric core-shell HRI NPs have been proposed during last years for controlling the direction of the scattered radiation because they support tunable electric and magnetic resonances [4]. In this work, using the linear polarization degree at right angle scattering configuration $P_L(90º)$, we have analyzed the influence of increasing the core size of an Ag-Si core-shell NP on both its dipolar resonances and the SDCs. Furthermore, we have obtained an empiric formula to reckon either the core radius $R_{int}$ or the ratio $R_{int}/R_{ext}$ by means of the footprint of the magnetic dipolar resonance in the $P_L(90º)$ spectra.

In Fig. 1 it is represented the spectral location of the dipolar magnetic resonance in $P_L(90º)$ as a function of the ratio $R_{int}/R_{ext}$, while $R_{ext}$ was fixed to 230 nm. The theoretical data have been fitted to a cubic function ($\lambda(\min[P_L(90º)]) = A\,(R_{int}/R_{ext})^3 + B$, where A = −1686 nm and B = 1676 nm). The shadowed region represents $R_{int}/R_{ext}$ in the interval 0.25 to 0.45, where $a_1$ and $b_1$ overlap. In this region $P_L(90º) \sim 0$ and the magnetic dipole resonance cannot be identified using $P_L(90º)$.

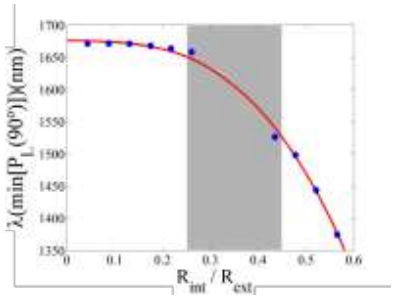



**Figure 1.** Location of $P_L(90^o)$ minimum (corresponding to the dipolar magnetic resonance) as a function of $R_{int}/R_{ext}$.

In Fig. 2 we show the scattering diagrams for the first (blue) and second (red) SDCs. Core radii $R_{int}$ correspond to a) 10 nm, b) 50 nm, c) 70 nm, d) 80 nm, e) 90 nm, and f) 130 nm.

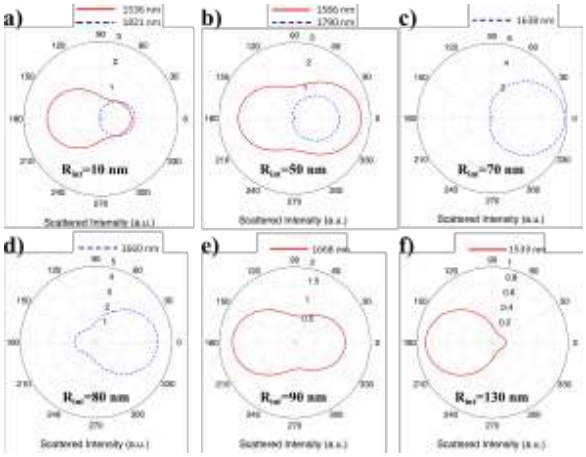



**Figure 2.** Scattering diagrams for the first (blue) and second (red) SDCs for different core radii.

As shown in Fig. 2, low ratios $R_{int}/R_{ext}$ lead to good performance for the near zero-forward intensity SDC, whereas $R_{int}/R_{ext} > 0.4$ produce more directional scattering patterns, but with lower efficiencies. On the contrary, in the zero-backward SDC, low ratios give good scattering patterns but medium ratios (i.e. $R_{int}/R_{ext} \sim 0.3$) lead to an improved efficiency. Therefore, the performance of the SDCs can be tailored (optimized and spectrally tuned) by changing the core-shell ratio $R_{int}/R_{ext}$.

**Acknowledgements**, This research was supported by MICINN (FIS2013-45854-P). Ángela I. Barreda and Y. Gutiérrez want to express their gratitude to the University of Cantabria for their FPU grant.

## REFERENCES

1. García-Etxarri, A., et al., "Strong magnetic response of submicron silicon particles in the infrared," *Opt. Express*, Vol. 19, No. 6, 4815-4826, 2011.
2. Kerker, M., Wang D. S. and Giles, C. L., "Electromagnetic scattering by magnetic spheres," *J. Opt. Soc. Am.*, Vol. 73, No. 6, 765-767, 1983.
3. Geffrin, J. M., et al., "Magnetic and electric coherence in forward-and back-scattered electromagnetic waves by a single dielectric subwavelength sphere," *Nat. Commun.*, Vol. 3, No. 1171, 2012.
4. Liu, W., Miroshnichenko, A. E., Neshev, D. N. and Kivshar, Y. S., "Broadband Unidirectional Scattering by Magneto-Electric Core–Shell Nanoparticles," *ACS Nano*, Vol. 6, No. 6, 5489-5497, 2012.

# Studying Individual Nanostructures using Light Tailored at the Nanoscale.

**P. Banzer**[1,2,3] **and G. Leuchs**[1,2,3]

[1]Max Planck Institute for the Science of Light, Erlangen, Germany

[2]Department of Physics, Friedrich-Alexander-University Erlangen-Nuremberg, Erlangen, Germany

[3]Max Planck – University of Ottawa Centre for Extreme and Quantum Photonics, Ottawa, Canada

[*]corresponding author: peter.banzer@mpl.mpg.de

**Abstract**-We review recent work aimed at the utilization of complex electromagnetic field landscapes as versatile tools for the experimental study of the optical properties of individual dielectric and metallic nanostructures.

Light beams may carry a spatially inhomogeneous intensity, phase and polarization distributions. Structured light is of great interest in the research fields of photonics, plasmonics and imaging. Tight focusing of such spatial modes of light enables the controllable generation of complex three-dimensional electromagnetic field distributions. It was shown that tailored field distributions exhibiting nanoscale features may serve as excellent tools for studying the properties of nanoscopic systems or of individual nanostructures (see for instance [1-3] and reference therein). If the nanostructure under investigation is smaller than the wavelength of the aforementioned highly confined light beam used for excitation, its interaction with the light beam will sensitively depend on the position relative to the field distribution (see Fig. 1). By laterally displacing the nanostructure with respect to the excitation field, a variety of different coupling scenarios can be realized by tailoring the input beam accordingly. The detailed analysis of the position-dependent scattering enables the retrieval of the nanostructure's geometrical and optical properties.

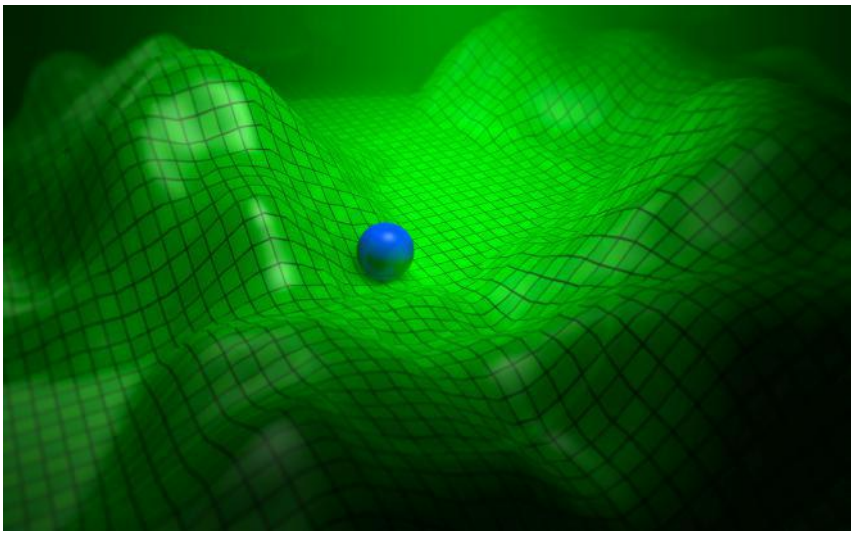


Figure 1. Artist's impression of a nanoparticle of sub-wavelength dimensions scanned through a complex 3D electromagnetic field distribution.

Based on this idea, the waveguide properties of sub-wavelength apertures [1,2], the selective excitation and addressing of resonances [3,4] supported by individual nanostructures or of dark modes in nanoparticle clusters [5] as well as the geometrical properties of sub-wavelength nanostructures [6.7] have been investigated using tailored light beams.

In this presentation, we will discuss the optical investigation of individual nanostructures using tailored electromagnetic fields.

**Acknowledgements-**P.B. acknowledges financial support by the Alexander von Humboldt Foundation and the Canada Excellence Research Chair in Quantum Nonlinear Optics.

**REFERENCES**

1. J. Müller, P. Banzer, S. Quabis, U. Peschel and G. Leuchs, ”Waveguide properties of single subwavelength holes demonstrated with radially and azimuthally polarized light,” *Appl. Phys. B*, Vol. 89, 517-520, 2007.
2. P. Banzer, J. Kindler, S. Quabis, U. Peschel and G. Leuchs, ”Extraordinary transmission through a single coaxial aperture in a thin metal film,” *Opt. Express*, Vol. 18, 10, 10896-10904, 2010.
3. P. Banzer, U. Peschel, S. Quabis and G. Leuchs, ”On the experimental investigation of the electric and magnetic response of a single nano-structure,” *Opt. Express*, Vol. 18, 10905–10923, 2010.
4. P. Wozniak, P. Banzer and G. Leuchs, ”Selective switching of individual multipole resonances in single dielectric nanoparticles,” *Laser Photon. Rev.*, Vol. 9, 231-240, 2015.
5. J. Sancho-Parramon and S. Bosch, “Dark Modes and Fano Resonances in Plasmonic Clusters Excited by Cylindrical Vector Beams,” *ACS Nano*, Vol. **6**, 8415–8423, 2012.
6. T. Züchner, A. V. Failla, A. Hartschuh, and A. J. Meixner, “A novel approach to detect and characterize the scattering patterns of single Au nanoparticles using confocal microscopy,” *J. Microscopy*, Vol. 229, 337–343, 2008.
7. T. Bauer, S. Orlov, G. Leuchs and P. Banzer, “Towards an optical far-field measurement of higher-order multipole contributions to the scattering response of nanoparticles,” *Appl. Phys. Lett.*, Vol. 106, 091108, 2015.

# Broadband Enhancement or Inhibition of Spontaneous Photon Emission in the Vicinity of Nanometer-Sized Silicon Resonators

**Dorian Bouchet,[1] Mathieu Mivelle,[1,2] Julien Proust,[3] Bruno Gallas,[4] Igor Ozerov,[5] Maria F. Garcia-Parajo,[2,6] Yannick De Wilde,[1] Nicolas Bonod,[3] Valentina Krachmalnicoff[1] and Sébastien Bidault[1*]**

[1]ESPCI ParisTech, PSL Research University, CNRS, Institut Langevin, Paris, France

[2]ICFO-Institut de Ciencies Fotoniques, Mediterranean Technology Park, 08860 Castelldefels (Barcelona), Spain

[3]CNRS, Aix-Marseille Université, Centrale Marseille, Institut Fresnel, Marseille, France

[4]Sorbonne Universités, UPMC Univ Paris 06, CNRS UMR 7588, Institut des Nanosciences de Paris, 75005 Paris, France

[5]Aix-Marseille Université, CNRS, CINAM, UMR 7325, 13288 Marseille, France

[6]ICREA-Institució Catalana de Recerca i Estudis Avançats, 08010 Barcelona, Spain

[*]corresponding author: sebastien.bidault@espci.fr

**Abstract**- Substituting noble metals for high-index dielectrics has recently been proposed as an alternative strategy to design optical nanoantennas while circumventing the ohmic losses of plasmonic materials. In this report, we experimentally demonstrate that silicon resonators can enhance or inhibit the photon emission dynamics of fluorescent molecules. Using scanning probe microscopy, we analyze the near-field interaction between a fluorescent nanosphere and silicon nanoparticles, and highlight how dielectric nanoantennas increase the far-field collection of emitted photons, in excellent agreement with numerical simulations.

High-index dielectric nanoparticles, featuring broadband low-order Mie resonances, have recently been proposed to design optical nanoantennas with weak ohmic losses and strong magnetic modes [1,2] in order to accelerate spontaneous decay processes from isolated emitters [3] and control emission directivity [4]. In this work, we demonstrate that silicon nanoantennas can indeed be used to resonantly enhance but also to inhibit spontaneous photon emission in fluorescent molecules at room temperature thanks to their low non-radiative losses. In practice, to fully characterize the spatial dependence of the interaction between solid-state light sources and a silicon nanoantenna, an atomic force microscope (AFM) tip featuring a fluorescent polystyrene sphere is scanned with nanometer precision in the vicinity of the resonator (Fig. 1a). By monitoring continuously the excited-state lifetime and intensity of the luminescent molecules, such near-field optical microscopy measurements provide a three-dimensional map of the local density of optical states in complex photonic environments [5,6].

The use of two different silicon particle diameters, fabricated by e-beam lithography and reactive ion etching [7], allows us to tune the molecular fluorescence spectrum in and out of resonance with the dipolar modes of the antenna. A silicon resonator that matches the emission wavelength of the sphere leads to an increased luminescence decay rate and measured photon count, in excellent agreement with numerical simulations (Fig. 1b-c). Inversely, an "off resonance" dielectric antenna leads to a longer fluorescence lifetime and a reduced intensity. This modulation of the fluorescence lifetime of solid-state emitters occurs at the nanoscale in three dimensions as observed when scanning the AFM tip in the sample plane (Fig. 1d-e). Furthermore, by controlling in 3D the position of the emitter with respect to the resonator, we show that nanoantennas built with a single silicon particle

provide a gain in fluorescence signal mainly by increasing the photon collection efficiency and not by changing the excited-state decay dynamics. By showing experimentally how sub-wavelength sized silicon resonators manipulate and engineer spontaneous light emission with low ohmic losses, this study highlights the potential of dielectric antennas for nanoscale photon management.

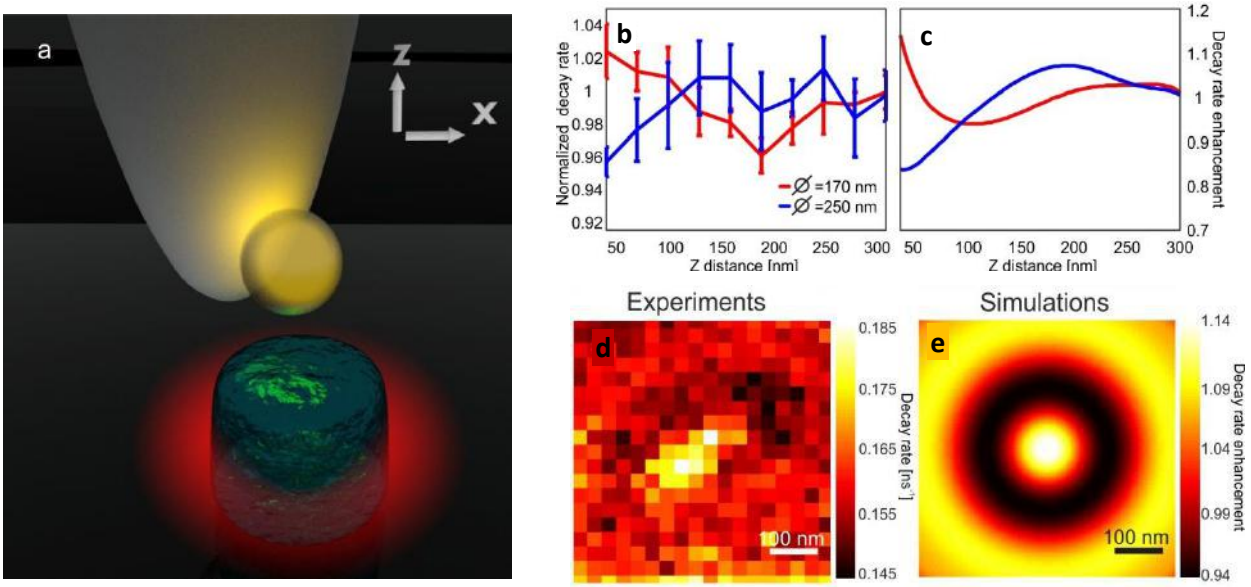



**Figure 1.** (a) Schematic representation of a fluorescent sphere being scanned, at the nanoscale, next to a silicon disk. Experimental (b) and simulated (c) evolution of the fluorescence decay rate when increasing the height of the sphere with respect to an "on resonance" 170 nm diameter disk (red data) or an "off resonance" 250 nm silicon antenna. Experimental (d) and simulated (e) 2D map of the decay rate when scanning the fluorescent sphere at 35 nm above a 170 nm diameter silicon resonator.

**Acknowledgements**, This work received funding from LABEX WIFI under references ANR-10-LABX-24 and ANR-10-IDEX-0001-02 PSL*, and by Region Ile-de-France in the framework of DIM Nano-K. Work at Institut Fresnel was carried out with the support of the A*MIDEX project (No. ANR-11-IDEX-0001-02) funded by the Investissements d'Avenir French Government program and managed by the French National Research Agency (ANR). Nanofabrication processes were performed in the PLANETE cleanroom facility.

**REFERENCES**

1. A. B. Evlyukhin, et al., *Phys. Rev. B* 82, 045404, 2010.
2. A. Garcia-Etxarri, et al., *Opt. Express* 19, 4815, 2011.
3. B. Rolly, B. Bebey, S. Bidault, B. Stout, N. Bonod, *Phys. Rev. B* 85, 245432, 2012.
4. B. Rolly, B. Stout, N. Bonod, *Opt. Express* 20, 20376, 2012.
5. V. Krachmalnicoff, D. Cao, A. Caze, E. Castanie, R. Pierrat, N. Bardou, S. Collin, R. Carminati, Y. De Wilde, *Opt. Express* 21, 11536, 2013.
6. D. Cao, A. Cazé, M. Calabrese, R. Pierrat, N. Bardou, S. Collin, R. Carminati, V. Krachmalnicoff, Y. De Wilde, *ACS Photonics* 2, 189, 2015.
7. J. Proust, F. Bedu, S. Chenot, I. Soumahoro, I. Ozerov, B. Gallas, R. Abdeddaim, N. Bonod, *Adv. Opt. Mater.* 3, 1280, 2015.

# Subwavelength flat-lensing of hybrid nanowire metamaterial with low-loss, isotropic optical negative-index behavior.

**D. R. Abujetas**[1], **R. Paniagua–Domínguez**[2], **M. Nieto–Vesperinas**[3], **and J. A. Sánchez–Gil**[1]

[1]Instituto de Estructura de la Materia (IEM-CSIC), Consejo Superior de Investigaciones Científicas, Serrano 121, E-28006 Madrid, Spain

[2]Data Storage Institute, Agency for Science, Technology and Research, 117608, Singapore

[3]Instituto de Ciencia de Materiales de Madrid (ICMM-CSIC), Consejo Superior de Investigaciones Cientfícas, Campus de Cantoblanco, E-28049 Madrid, Spain

diego.romero@iem.cfmac.csic.es

**Abstract**—

We investigate theoretically and numerically the optical properties of metamaterials based on metallo-dielectric core-shell nanowires. Single nanowires exhibit negative electric and magnetic responses stemming from the spectral overlap of the lowest magnetic resonance of the dielectric shell with the plasmon resonance of the metal core. Properties extracted from photonic band structure confirm the structure behaves as a low-loss, isotropic (2D) and bulk, optical negative index metamaterial; this is further demonstrated through numerical simulations of flat-lense focusing.

Artificial materials showing electromagnetic properties not attainable in naturally occurring media, the so called metamaterials, are among the most active fields of research in optical and material physics. One of the major challenges found is to obtain truly bulk isotropic negative index metamaterials (NIM) at optical frequencies [1]. Recently, we reported [2] the possibility to use a certain class of Ag@Si core-shell (CS) nanowires (NWs) as building blocks of 2D isotropic NIMs, operating in the near infrared. These CS-NWs, made of a metallic core and a high permittivity shell, are doubly-resonant, allowing for a spectral overlap of their first electric and magnetic dipolar resonances. Since the responses do not depend on the interaction between constituents, no particular arrangement is needed to build the metamaterial, which is, moreover, broadly isotropic for TE-polarization waves. We show that, for certain geometrical parameters and filling fractions, metamaterials composed by such CS-NWs can have simultaneously negative permittivity and permeability between 1.2-1.5 $\mu$m [2]. The resulting metamaterial then behaves as a 2D isotropic NIM with extremely low losses [2] ($f.o.m. \equiv -\Re(n_{\text{eff}})/\Im(n_{\text{eff}}) \sim 200$, about one order of magnitude better than previously proposed designs).

However, it has been pointed out in [3] that the constitutive parameters retrieved through effective medium theories in other dielectric-rod ordered arrays do not reproduce the negative refraction observations in those composites, being mostly due to photonic crystal diffraction effects. For this reason, we have studied the 2D potonic band structure [4], identifying the second photonic band with negative-index properties that stem from the resonant character of the basic constituents. The resulting equifrequency surfaces (EFSs) in the first Brillouin zone are circular for most of this band as is shown in Fig. 1a), thus indicating the full (2D) isotropic character. In addition, such isotropic NIM behavior is very clearly evidenced through numerical simulations in canonical examples for finite geometries, as point dipole transmission through a slab, in which different positions of the dipole with respect to the slab were tested, showing in all the cases a flat lensing behavior with subwavelength resolution [4]. These numerical simulations are compared to equivalent (ideal) slabs characterized by homogeneous dielectric permittivity and magnetic permeability exactly given by the effective parameter retrieval (from S-parameters), in very good agreement (see Fig. 1b)), confirming the isotropic, low-loss NIM behavior [4].

In conclusion, we have carried out a full description of the photonic band structure of doubly resonant core-shell metallo-dielectric NW arrays, in order to demonstrate their behavior as low-loss, isotropic bulk optical NIMs. In this manner, we have rigorously demonstrated (and improved) [4] the highly isotropic and ultra low-loss ($f.o.m. \sim 200$) character of Ag@Si NW arrays, exhibiting indeed robust flat lensing with subwavelength resolution and dipole position independence, in good agreement with the expected behavior for a negative-index homogeneous slab.

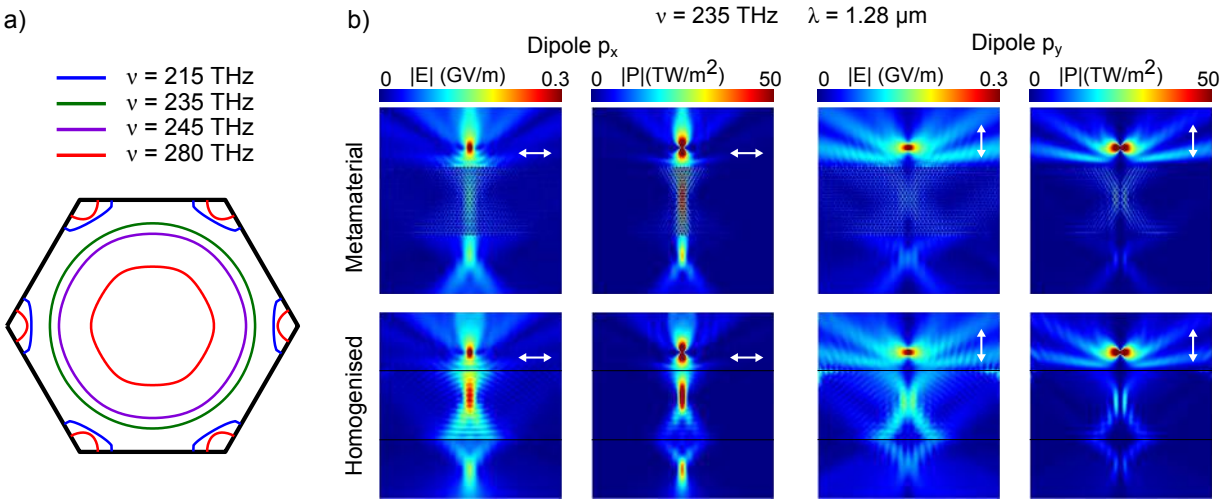



Figure 1: a) EFSs of Ag@Si core-shell nanowires with inner and outer radius $R_{in} = 90$ nm and $R_{out} = 170$ nm, respectively, arranged in a hexagonal lattice with lattice parameter $a = 350$ nm. b) Norm of the in-plane electromagnetic field and of the Poynting vector for in-plane point dipole sources at $\nu = 235$ THz ($\lambda = 1.28$ $\mu$m) located at 1.8 $\mu$m above a slab made of the metamaterial described in a), with the slab surface along the ΓK direction. Parallel ($p_x$, left) and perpendicular ($p_y$, right) dipoles to the surface are shown. The results for a homogeneous slab are also shown, with $\varepsilon_{eff} = -0.734 - i0.157$ and $\mu_{eff} = -2.094 + i0.532$, so that $n_{eff} = -1.264 + i0.0069$ ($f.o.m. \sim 180$).


## ACKNOWLEDGMENT

The authors acknowledge the Spanish Ministerio de Economía y Competitividad for financial support through NANOPLAS+(FIS2012-31070), MINIELPHO (FIS201236113-C03-03) and LENSBEAM (FIS2015-69295).


## REFERENCES


1. Soukoulis, C. and Wegener, M., "Optical metamaterials–more bulky and less lossy," *Science*, Vol. 330, 1633–1634, 2010.
2. Paniagua–Domínguez, R., Abujetas, D. R and Sánchez–Gil, J. A., "Ultra low-loss, isotropic 2D optical negative-index metamaterial based on hybrid metal-semiconductor nanowires," *Sci. Rep.*, Vol. 3, 1507, 2013.
3. Valdivia–Valero, F. J. and Nieto–Vesperinas, M., "Composites of resonant dielectric rods: a test of their behavior as metamaterial refractive element," *Phot. Nano. Fund. Appl.*, Vol. 10, 423–434, 2012.
4. Abujetas, D. R., Paniagua–Domínguez, R., Nieto–Vesperinas, M. and Sánchez–Gil, J. A., "Photonic band structure and effective medium properties of doubly-resonant core-shell metallodielectric nanowire arrays: low-loss, isotropic optical negative-index behavior," *J. Opt.*, Vol. 17, 125104, 2015.

# Magneto-optical activity in high-index dielectric materials

**N. de Sousa[1], J.J. Sáenz[1,2,3] A. Garcia-Martin[4]**

[1] Departamento de Física de la Materia Condensada, Universidad Autónoma de Madrid, 28049, Madrid, SPAIN

[2] Condensed Matter Physics Center (IFIMAC) and Instituto "Nicolás Cabrera", Universidad Autónoma de Madrid, 28049, Madrid, SPAIN

[3] Donostia International Physics Center (DIPC), Paseo Manuel de Lardizabal, 5, Donostia - San Sebastián 20018, SPAIN

[4] IMM-Instituto de Microelectrónica de Madrid (CNM-CSIC), Isaac Newton 8, PTM, Tres Cantos, E-28760 Madrid, SPAIN

[*]corresponding author: a.garcia.martin@csic.es

**Abstract**-The magneto-optical response of high-index, non-absorbing dielectric nanospheres is theoretically analyzed. We will show that in these systems the magneto-optical response is fully governed by the magnetic resonances with little effect of the electric ones.

The control of light propagation in the visible and near-infrared domain using resonant systems such as optical nanoantennas has been a matter of intense research during the last decades. The possibility to create and manipulate nanostructured materials encouraged the exploration of new strategies to control the electromagnetic properties with an external agent. A possible approach is combining magnetic and plasmonic materials, where it is feasible to control the optical properties with magnetic fields in connection to the excitation of plasmon resonances [1].

These nanoantennas have been traditionally made of metallic entities, which have the important drawback of a sizeable absorption. In the case of magnetic resonances based on Babinet inverted magnetoplasmonic structures, it has already been demonstrated that the magneto-optical effect has the ability to manipulate magnetic dipole-like resonances [2].

In the last years, there has been a quest for the so-called magnetic resonances in the visible domain [3]. Linked to it, there has been an increasing interest in the use of high index dielectric nanospheres as optical antennas, in particular for their ability to sustain magnetic resonances and the absence of absorption [4-6].

In this work we introduce the magneto-optical effect in the context of those high index dielectric nanospheres, i.e. a silicon nanosphere with a non-negligible of diagonal element in the dielectric tensor. We will show how the magneto-optical effect is controlled by the internal resonances of the nanosphere, and that the magnetic resonances dominate the spectral dependence of the magneto-optical response, having the electric dipolar resonance a very weak effect. We will establish a clear correlation of the spectral magneto-optical response with the spatial field profile at the interior of the nanosphere that is, in turn, linked to each type of resonance [7].

**REFERENCES**

1. Armelles, G., Cebollada, A., García-Martín, A. and González, M. U. "Magnetoplasmonics: combining magnetic and plasmonic functionalities". *Adv. Opt. Materials*, Vol. 1, 10–35, 2013.
2. Armelles, G., Caballero, B., Cebollada, A., Garcia-Martin, A. and Meneses-Rodríguez, D., "Magnetic field

modification of optical magnetic dipoles" *Nano Lett.*, Vol. 15, 2045–2049, 2015.
3. Alu, A. and Engheta, N., "The quest for magnetic plasmons at optical frequencies", *Opt. Express*, Vol. 17, 5723–5730, 2009.
4. García-Etxarri, A. et al. "Strong magnetic response of submicron silicon particles in the infrared", *Opt. Express*, Vol. 19, 4815–4826, 2011.
5. Schmidt, M. K., Esteban, R., Sáenz, J. J., Suárez-Lacalle, I., Mackowski, S., and Aizpurua, J., "Dielectric antennas - a suitable platform for controlling magnetic dipolar emission," in *Opt. Express*, Vol. 19, 13636-13650, 2012.
6. Person, S., et al., "Demonstration of Zero Optical Backscattering from Single Nanoparticles", Nano. Lett. 13, 1806-1809, 2013.
7. de Sousa, N., Sáenz, J.J., and Garcia-Martin, A., *submitted*, 2016

# Integration of metallic and dielectric nanostructures in silicon waveguides: properties and applications

**A. Martínez**[1*]
[1]Nanophotonics Technology Center, Universitat Politècnica de València, Spain
[*]corresponding author: amartinez@ntc.upv.es

**Abstract**-In this work, we show recent advances related to the integration of metallic and dielectric scatterers into dielectric waveguides created on a silicon chip at telecom wavelengths. We show that dielectric scatterers placed in the waveguide proximity can be employed as polarization-sensitive nanoantennas. We also show that subwavelength metallic elements can be efficiently coupled to silicon waveguides by inserting them in a gap etched in the waveguide.

Silicon photonics is a technological platform enabling low-cost, mass-manufacturing of photonic integrated circuits using tools and processes that are standard in CMOS microelectronics industry. Nowadays, silicon photonics is a mature technology and silicon PICs fabricated on silicon-on-insulator (SOI) wafers are currently being exploited for and label-free biosensors and data communications even with commercial products. In order to exploit the full potential of plasmonics science and related concepts (namely, nanoantennas and metamaterials), it would make sense to integrate plasmonics elements into silicon photonics, which could pave the way for the near-term commercialization of plasmonics devices (1). This approach would also benefit current silicon photonic devices, first because of the additional miniaturization that plasmonics can provide and second because of new functionalities that can be incorporated into a silicon chip, including imaging via nanoantennas or sensing via plasmonic nanoresonators (2).

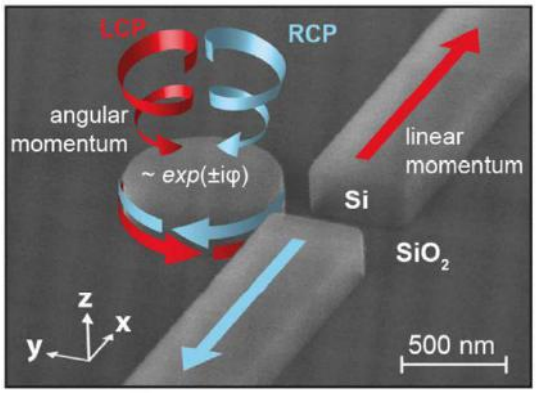
In silicon PICs, light propagates along silicon waveguides at near-infrared wavelengths. In order to ensure a maximum confinement of the light inside the waveguide, strip and slot geometries for the waveguide core are typically considered. Subwavelength-size dielectric and metallic elements could be placed in the proximities of such waveguides to be excited by the guided light. In addition, the element response should be coupled to the waveguide mode so that we can detect its properties by measuring the power at the output of the waveguide. In this approach, we need to consider that the guided mode properties are quite different from those observed in a free-space beam. Remarkably, the strong field confinement in the silicon waveguide will lead to a huge longitudinal component of the electric field (3). This means that the guided modes display transverse spin, mainly in the evanescent region, which has to be properly considered when the guided mode interacts with subwavelength elements.

Making use of this property my group has recently shown that a silicon scatterer attached to a silicon waveguide can act as a polarization-sensitive nanoantenna. By properly shaping the scatterer, the scatterer-waveguide system is able to sort linearly- (4) as well as circularly-polarized (5) incoming photons (see Fig. 1(a)). Moreover, in transmission the scatterer-waveguide system can act as a nanoantennas radiating a polarization state that can be tailored on the whole Poincaré sphere by properly selecting the optical signals feeding the scatterer (6).

If the scatterer is metallic, it can have subwavelength dimensions via localization of surface plasmons.

Recent experiments have shown that localized plasmonic resonances of metallic nanostructures can be excited by placing them on top of a dielectric waveguide (2,7). However, excitation efficiencies remain low (< 20%) because the plasmonielement is excited by the evanescent tails of the guided field. A full excitation of the plasmonic element can be achieved by embedding it in a subwavelength gap created in the waveguide (Fig. 1(b)), as my team has recently shown (8).

This plasmonics-on-silicon field, merging the best of two worlds (the maturity of silicon photonics technology and the light manipulation abilities of plasmonics, metamaterials and nanoantennas), holds the promises for novel hybrid PICs for application in disciplines such as lab-on-a-chip or all-optical processing.

(a) 

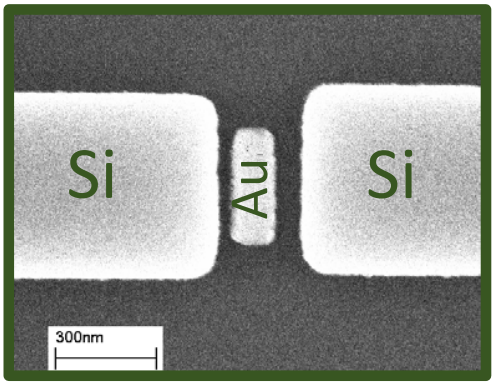

(b) 


Figure 1. SEM images of (a) a silicon disk nanonantenna that separates circularly polarized photons into opposite guided directions and (b) a gold nanostrip in a gap created in a silicon waveguide.

**Acknowledgements:** This work was supported in part by the Spanish Ministry of Economy and Competiveness (MINECO) through grant TEC2014-51902-C2-1-R.

**REFERENCES**

1. Editorial, “Commercializing plasmonics,” *Nature Photon.* Vol. 9, p. 477, 2015.
2. Chamanzar, M., Z. Xia, S. Yegnanarayanan, A. Adibi, “Hybrid integrated plasmonic-photonic waveguides for on-chip localized surface plasmon resonance (LSPR) sensing and spectroscopy,” *Opt. Express*, Vol. 21, No. 26, 32086-32098, 2013.
3. Espinosa-Soria, A. and A. Martinez, “Transverse spin and spin-orbit coupling in silicon waveguides,” submitted, http://arxiv.org/abs/1507.04859
4. Rodríguez-Fortuño, F. J., D. Puerto, A. Griol, L. Bellieres, J. Martí, and A. Martínez, “Sorting linearly polarized photons with a single scatterer,” *Opt. Lett.*, Vol. 39, No. 6, 1394-1397, 2014.
5. Rodríguez-Fortuño, F. J., I. Barber-Sanz, D. Puerto, A. Griol, A. Martinez, “Resolving light handedness with an on-chip silicon microdisk”, *ACS Photon.*, Vol. 1, No. 9, pp. 762–767, 2014.
6. Rodríguez-Fortuño, F. J. et al., “Universal method for the synthesis of arbitrary polarization states radiated by a nanoantennas,” *Laser Photonics Rev.*, Vol. 8, No. 3, pp. L27–L31, 2014.
7. Peyskens, F. et al., “Bright and dark plasmon resonances of nanoplasmonic antennas evanescently coupled with a silicon nitride waveguide,” *Opt. Express*, Vol. 23, No. 3, pp. 3088-3101, 2015.
8. Espinosa-Soria, A., A. Griol, A. Martínez, “Experimental measurement of plasmonic nanostructures embedded in silicon waveguide gaps,” submitted.

# Effect of the oxide shell thickness on the UV plasmonic performance of Ga, Mg and Al nanoparticles.

**Y. Gutiérrez[1], D. Ortiz[1], J. M Sanz[1,2], J. M. Saiz[1], F. González[1], H. O. Everitt[3,4] and F. Moreno[1]**

[1] Group of Optics, Department of Applied Physics, University of Cantabria, Avda. Los Castros s/n. 39509 - Santander (Spain)

[2] R & D Deparment, Textil Santanderina S.A. Avda. Textil Santanderina, s/n. 39500 - Cabezón de la Sal (Spain)

[3] Deparment of Physics, Duke University, Durham, North Carolina 27708, United States

[4] U.S. Army Aviation and Missile RD& E Center, Redstone Arsenal, Alabama 35898, United States

morenof@unican.es

**Abstract**— A recent interest in UV-plasmonics has appeared due to its increasing potential in many applications ranging from biology, spectroscopy or engineering. Magnesium, Aluminum and Gallium have been pointed out as promising materials for this purpose. However, these metals form an oxide layer, several nanometers thick, that may affect the formation of localized plasmons. In this work we analyze how the oxide shell thickness affect the plasmonic performance of nanostructures made from these metals.

Plasmonics in the UV regime has awakened recent interest in fields such as biology, spectroscopy or nanosensing [1, 2, 3]. The plasmonic performance of various metals in the UV regime has been previously studied in order to find those more promising for UV plasmonics [4]. From this study those which were found to be more promising were Magnesium (Mg), Aluminum (Al), Gallium (Ga) and Rhodium (Rh). Although Rh does not oxidise, Mg, Al and Ga suffer from the formation of a several nanometer thick layer of oxide. The change in the surrounding properties affect the plasmonic behavior of the metal inside [5].

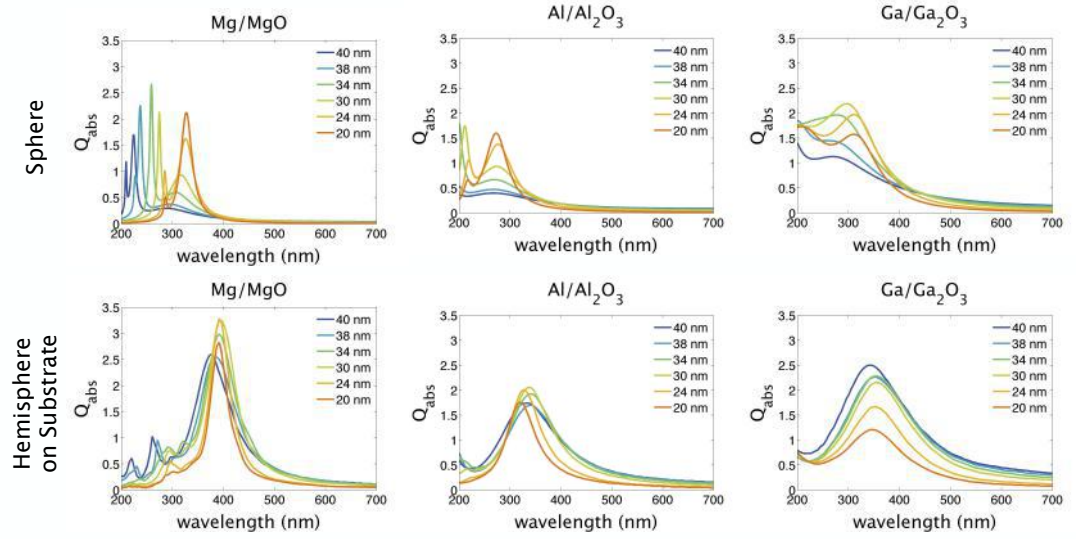



Figure 1: Absorption efficiency, $Q_{abs}(\lambda)$, of an isolated sphere (top) and hemisphere on substrate (bottom) NPs made of Mg, Al and Ga, all with radius $R = 40$ nm, as function of the core radius, $R_{core} = 20 - 40$ nm.

Two geometries have been studied: the isolated sphere and the hemispherical nanoparticle (NP) on a sapphire substrate, which represents the common experimental conditions for Mg and Ga [6]. Both near-field (intensity of the local field averaged over the NP surface $I(\lambda) =< |E/E_{inc}|^2 >$) and far-field (absorption efficiency $Q_{abs}(\lambda)$) magnitudes have been analysed through this work.

From the results, it can be concluded that either a red-shift or a blue-shift of the resonance peak is produced depending on the material and the oxide layer thickness (see Fig. 1). The absorption efficiency of Mg and Al spheres increases as the oxide shell thickness increases. However, for the Ga sphere, the absorption efficiency maximum is produced for intermediate values of the oxide thickness, as for Mg and Al hemispheres. On the contrary, the Ga hemisphere increases its absorption efficiency as the oxide layer thickness decreases. In addition, the characteristic red-shift of the near-field, $I(\lambda) =< |E/E_{inc}|^2 >$, with respect to the far-field, $Q_{abs}(\lambda)$, has been also observed. Further analysis will be introduced to give more insight on the subject. These results show both the importance of controlling the oxide contamination, and the possibility of tuning UV-resonances by means of oxide, or other non-metal coatings.

**ACKNOWLEDGMENT**

This research has been supported by MICINN (Spanish Ministry of Science and Innovation, project FIS2013-45854P). Y. G thanks the University of Cantabria for her FPU grant.

**REFERENCES**

1. J. N. Anker, W. Hall, O. Lyandres, N. C. Shah, J. Zhao, R. P. V. Duyne ,"Biosensing with plasmonics nanosensors", *Nat. Mater.* , Vol. 7, 442–453, 2008.
2. M. H. Chowdhury, K. Ray, S. K. Gray, J. Pond, J. Lakowicz ,"Aluminum Nanoparticles as Substrates for Metal-Enhanced Fluorescence in the Ultraviolet for the Label-Free Detection of Biomolecules", *Anal. Chem.* , Vol. 81, 1397–1403, 2009.
3. A. Taguchi,N. Hayazawa, K. Furusawa, H. Ishitobi, S. Kawata ,"Deep-UV tip-enhanced Raman scattering ", *J. Raman Spectrosc* , Vol. 40, 1324–1330, 2009.
4. J. M. Sanz, D. Ortiz, R. Alcaraz de la Osa , J. M. Saiz, F. González, A. S. Brown, M. Losurdo, H. O. Everitt and F. Moreno, "UV Plasmonic Behavior of Various Metal Nanoparticles in the Near- and Far-Field Regimes: Geometry and Substrate Effects", *JPCC* , Vol. 117, 19606–19615, 2013.
5. M. W. Knight, N. S. King, L. Liu, H. O. Everitt, P. Nordlander and N. J. Halas, "Aluminum for Plasmonics", *Nano Lett.* , Vol. 8, 834–840, 2014.
6. Y. Yang, N. Akozbek, T. Kim, J. M. Sanz, F. Moreno, M. Losurdo, A. S. Brown and H. O. Everitt,"UltravioletVisible Plasmonic Properties of Gallium Nanoparticles Investigated by Variable-Angle Spectroscopic and Mueller Matrix Ellipsometry", *ACS Photonics* , Vol. 1, 582–589, 2014.

# Quantum plasmons on topological particle surface.

**Vincenzo Giannini**

Imperial College London, UK
v.giannini@imperial.ac.uk

**Abstract**— A key feature of topological insulators is the presence of surface states immune to disorder and impurities due to topological protection. These states modify the optical properties of topological insulators compared to their ordinary counterparts.

We show that topological insulators nanoparticles sustain a new kind of excitation when interacting with light. This is a topological localized surface plasmon polariton obtained perturbing the nanoparticle surface electron state with light.

Quantum phenomena are usually restricted to the nanoscale (atoms, molecules), low temperatures (superfluids, superconductors) or both. Here we demonstrate a phenomenon which may pave the way for quantum behaviour to be observed at the mesoscale and room temperature.

The key role is played by topological insulators materials that have surface states protected by time-reversal symmetry. Such states are delocalised over the surface and are immune to its imperfections in contrast to ordinary insulators. For topological insulators the effects of these surface states will be more strongly pronounced in the case of nanoparticles.

Here we study the interaction of such nanoparticles with light. We report a previously unknown light-matter mode that was not revealed in earlier studies, which focused on bulk samples and thin films of topological insulators. In the nanoparticles the topologically protected surface states efficiently couple phonons and light giving rise to the topological particle polariton mode. In addition, the surface states can act as a screening layer which suppresses absorption inside the particle. These effects may be useful in the areas of plasmonics, cavity electrodynamics and quantum information.

## ACKNOWLEDGMENT

This work was supported by the Leverhulme Trust.

## REFERENCES

1. G. Siroki, D. K. K. Lee, P. D. Haynes, V. Giannini, "Quantum plasmons on topological particle surface," *Submitted* .

# Precise Nanoparticle Localization using Complex Spatial Modes of Light

**A. Bag**[1,2], **M. Neugebauer**[1,2], **P. Woźniak**[1,2], **G. Leuchs**[1,2], **and P. Banzer**[1,2]

[1]Max Planck Institute for the Science of Light, Germany
[2]Institute of Optics, Information and Photonics, Department of Physics,
Friedrich-Alexander-University Erlangen-Nuremberg, Germany
ankan.bag@mpl.mpg.de

**Abstract**— High refractive index materials such as silicon are of paramount importance due to their rich spectral properties and their application in directional coupling of electromagnetic wave. This directionality can be enhanced remarkably by taking advantage of the interference of electric and magnetic resonances of the scatterer. Based on this strong directional light emission, we now present a novel position sensing technique, enabling Ångström localization accuracy (lateral), which can find applications in nanometrology and super-resolution microscopy techniques.

Precise position sensing of a nanoparticle or biomolecule is an essential prerequisite for the fields of nanometrology and in photonics, medicine and biophysics. It constitutes one of the fundamental steps in several super-resolution imaging techniques, such as fluorescence based photoactivated localization microscopy (PALM) [1]. In the last decade, a localization precision down to few nanometers or even Ångström has been achieved, using different nonlinear or linear techniques [2].

Here, we present a new concept for position sensing enabling Ångström accuracy (lateral), based on strongly laterally directional light emission of a single subwavelength dielectric scatterer.

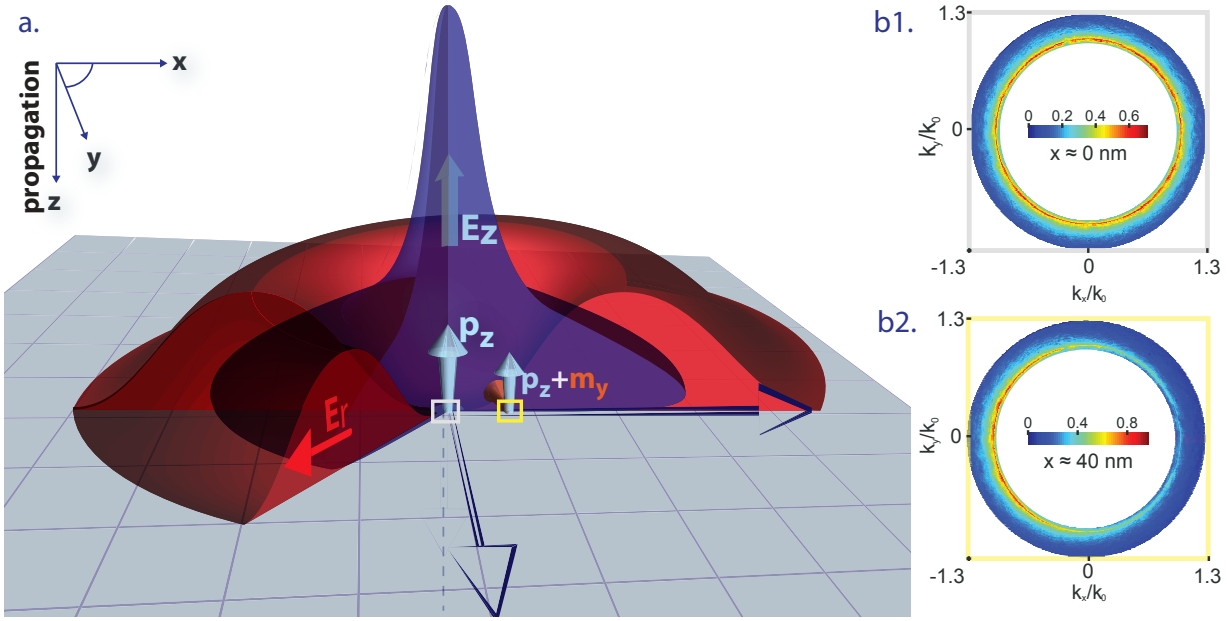



Figure 1: a. Complex 3-D electric field distribution in the focal plane of a tightly focused radially polarized vector beam comprising a strong longitudinal component at the center (blue) and transverse field components (red). On the optical axis, only a longitudinal electric dipole will be excited in the silicon particle (sitting on a glass substrate), and thus a symmetric emission pattern will be observed in the far-field (see b1). Whereas, for the particle placed off-axis, the symmetry will be broken. In this scheme both electric and magnetic dipole moments can be excited, and interference of which will result in an asymmetric far-field distribution (see b2). These far-field distributions are recorded by imaging the back-focal plane of a collection lens, representing the angular spectrum. Only values above an effective numerical aperture of 1 are shown, containing scattered field only.

We take advantage of the rich electromagnetic spectra of a high refractive index dielectric silicon nanosphere. The silicon nanoparticles support both electric as well as magnetic resonances in the visible spectral range [3, 4, 5, 6]. By taking advantage of the simultaneous excitation of multiple particle modes and the interference of their emission, strong lateral directivity of the emitted signal can be observed [6]. As a probe beam, we use a radially polarized vector beam, which upon tight focusing provides an inhomogeneous three-dimensional field distribution, with a strong on-axis longitudinal electric field component [7] (see Fig. 1a). The transverse electric field components vanish on-axis, but increase linearly with radial distance (linearity holds in close vicinity (50 nm radius) to the optical axis). Thus, for each position in the focal plane of the probe beam there is a different field distribution resulting in a different coupling scenario. This directly influences the scattering pattern in the far-field where we achieve a very strong position-dependent directivity. With proper calibration, it is possible without further optimization to measure displacements of 5 nm. With further statistical analysis, it is possible to resolve even smaller particle displacements with a localization uncertainty of 2 Ångström [6].

This fast, easy-to-calibrate, linear technique can be very useful for single-shot lateral position sensing with Ångström resolution and can find various applications in modern metrology and biosensing. A thorough study of several parameters such as size, structure of the scatterer along with wavelength of the excitation beam allows for optimizing the lateral directivity of the far-field scattered light resulting in an even higher accuracy.

**REFERENCES**


1. Betzig, E., G. H. Patterson, R. Sougrat, O. W. Lindwasser, S. Olenych, J. S. Bonifacino, M. W. Davidson, J. Lippincott-Schwartz and H. F. Hess, "Imaging intracellular fluorescent proteins at nanometer resolution," *Science*, Vol. 313, No. 5793, 1642–1645, 2006.
2. Nugent-Glandorf, L. and T. T. Perkins, "Measuring 0.1-nm motion in 1 ms in an optical microscope with differential back-focal-plane detection," *Opt. Lett.*, Vol. 29, No. 22, 2611–2613, 2004.
3. Kerker, M., D. S. Wang and C. L. Giles, "Electromagnetic scattering by magnetic spheres," *J. Opt. Soc. Am.*, Vol. 73, No. 6, 765–767, 2015.
4. Staude, I., A. E. Miroshnichenko, M. Decker, N. T. Fofang, S. Liu, E. Gonzales, J. Dominguez, T. S. Luk, D. N. Neshev, I. Brener and Y. Kivshar, "Tailoring directional scattering through magnetic and electric resonances in subwavelength silicon nanodisks," *J. Opt. Soc. Am.*, Vol. 7, No. 9, 7824–7832, 2013.
5. Woźniak, P., P. Banzer and G. Leuchs, "Selective switching of individual multipole resonances in single dielectric nanoparticles," *Laser Photon. Rev.*, Vol. 9, No. 2, 231–240, 2015.
6. Neugebauer, M., P. Woźniak, A. Bag, G. Leuchs and P. Banzer, "Polarization Controlled Directional Scattering for Nanoscopic Position Sensing," arXiv:1511.02066v2 [physics.optics].
7. Quabis, S., R. Dorn, M. Eberler, O. Glöckl and G. Leuchs, "Focusing light to a tighter spot," *Opt. Commun.*, Vol. 179, No. 1–6, 1–7, 2000.

# Controllable excitation of a high refractive-index dielectric nanoparticle using a tightly focused vector beam

**P. Woźniak**[1,2], **G. Leuchs**[1,2,3], **P. Banzer**[1,2,3]

[1]Max Planck Institute for the Science of Light, Germany
[2]Institute of Optics, Information and Photonics, Department of Physics, Friedrich-Alexander-University Erlangen-Nuremberg, Germany
[3]Max Planck–University of Ottawa Centre for Extreme and Quantum Photonics, Canada
pawel.wozniak@mpl.mpg.de

**Abstract**— Non-paraxial propagation of a laser beam allows for creating highly confined non–uniform fields. In this context, tightly focused cylindrical vector beams are experimentally examined as versatile tools for the realization of multiple excitation schemes used to study a single high refractive–index dielectric nanosphere.

## 1. INTRODUCTION

According to Mie theory, a high refractive-index dielectric sphere supports strong magnetic and electric resonances [1]. Recent experiments showed that under plane-wave-like excitation, particles made of materials such as silicon support both resonance types [2, 3, 4]. If a particle is excited, however, with an appropriately tailored field, either the magnetic or the electric resonances can be addressed selectively [5]. Tightly focused azimuthally and radially polarized vector beams are perfectly suited for this purpose. The focal field distributions of such beams resemble, for instance, the emission patterns of point-like magnetic and electric dipoles and, hence, allow for their selective excitation, if the particle is placed on-axis in the focal plane. Here we now discuss the extension of this idea, using tightly focused vector beams for the realization of multiple excitation schemes within a single beam scenario.

## 2. CONTROLLABLE POLARIZATION-DEPENDENT EXCITATION

Tight focusing of light beams, results in highly confined non-uniform focal fields. Consequently, a sub-wavelength-sized nanostructure will experience different excitation scenarios at different positions in such a field distribution [6, 7]. Here, this versatile polarization–controlled excitation is now demonstrated by measuring the resonance spectra of an individual silicon sphere ($n \sim 4$; 185 nm in diameter; placed on a glass substrate). It was shown recently that nanoparticles made from a high refractive-index dielectric, such as silicon, exhibit very rich resonance spectra [2, 3, 4, 5]. As an exemplary case, we choose tightly focused azimuthally polarized light as excitation field.
Accordingly, a tightly focused azimuthally polarized vector-beam, in a simplified form, can be decomposed into a transverse electric field, which stays azimuthally polarized and a linear oscillation of the magnetic field along the optical axis (Fig. 1a). The particle spectra are measured as a function of particle positions with respect to the optical axis. Due to the cylindrical symmetry of the chosen excitaion field, only the excitation of magnetic resonance is possible, if the nanoparticle is centered on the optical axis [5] (blue curve in Fig. 1b). In contrast, if the particle is placed 400 nm away from the optical axis, the excitation field symmetry is broken. For this case, the strength of the longitudinal magnetic field is minimal, while the transverse electric field is very strong. Therefore, the situation is similar to the excitation with a linearly polarized field and, hence, allows both resonance types to be excited. Consequently, off-axis excitation of the particle results in a spectrum with clear signatures of magnetic and electric resonances (red curve in Fig. 1b).

## 3. CONCLUSIONS

In summary, we discussed the excitation of individual silicon nanoparticles taking advantage of the complex spatial field distributions of tightly focused light beams. Depending on the particle position within the beam, multiple excitation schemes can be achieved within a single beam scenario. By further tailoring the spatial field distribution used for excitation, more complex coupling scenarios

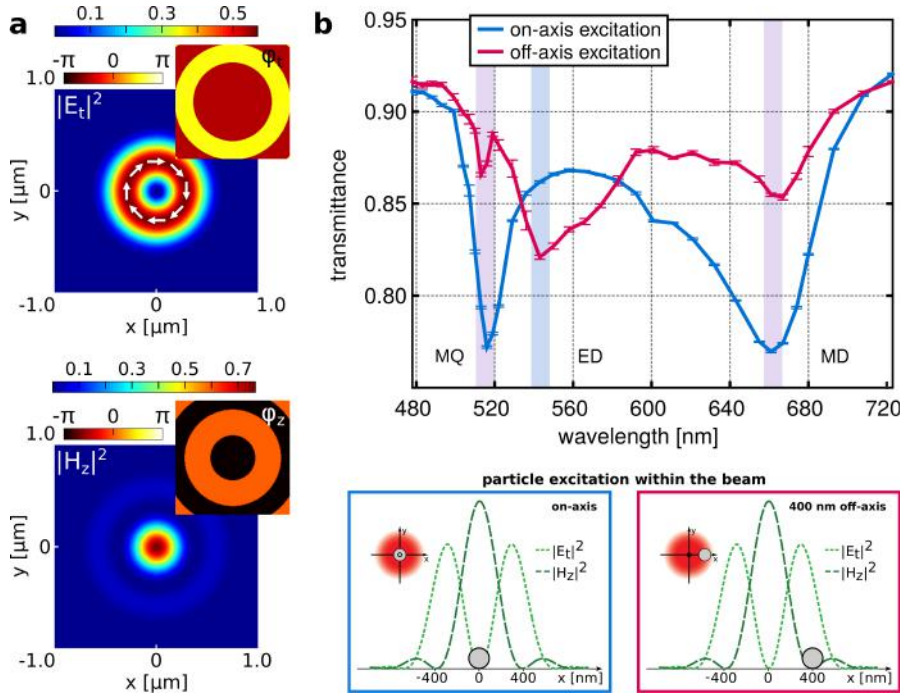



Figure 1: a) Distributions of the focal transverse electric and longitudinal magnetic energy densities (and relative phases) of a tightly focused azimuthally polarized vector beam in air for $\lambda = 661$ nm and a numerical aperture (NA) of 0.9, calculated using vectorial diffraction theory [8]. Both distributions are normalized to the maximum of the total energy density. b) Experimentally recorded transmittance spectra of a Si particle (185 nm in diameter) placed on a glass substrate excited with a tightly focused azimuthally polarized vector beam (on-axis — blue curve and 400 nm off-axis — red curve; MD — magnetic dipole, ED — electric dipole, MQ — magnetic quadrupole).

can be realized, enabling a more detailed study and the selective addressing of particle resonances. In fact, also the controlled simultaneous excitation of multiple modes for controlling the emission of the particle is conceivable [9].

**REFERENCES**


[1] van de Hulst, H. C., *Light Scattering by Small Particles*, Wiley, New York, 1957.

[2] Kuznetsov, A. I., A. E. Miroshnichenko, Y. H. Fu, J. Zhang, B. Luk'yanchuk, "Magnetic light," *Sci. Rep.*, Vol. 2, 492, 2012.

[3] Evlyukhin, A. B., S. M. Novikov, U. Zywietz, R. L. Eriksen, C. Reinhardt, S. I. Bozhevolnyi, B. N. Chichkov, "Demonstration of magnetic dipole resonances of dielectric nanospheres in the visible region," *Nano Lett.*, Vol. 12, No. 7, 3749–3755, 2012.

[4] Staude, I., A. E. Miroshnichenko, M. Decker, N. T. Fofang, S. Liu, E. Gonzales, J. Dominguez, T. S. Luk, D. N. Neshev, I. Brener, Y. S. Kivshar, "Demonstration of magnetic dipole resonances of dielectric nanospheres in the visible region," *ACS Nano*, Vol. 7, No. 9, 7824–7832, 2013.

[5] Woźniak, P., P. Banzer, G. Leuchs, "Selective switching of individual multipole resonances in single dielectric nanoparticles," *Laser Photon. Rev.*, Vol. 9, No. 2, 231–240, 2015.

[6] Banzer, P., U. Peschel, S. Quabis, G. Leuchs, "On the experimental investigation of the electric and magnetic response of a single nano-structure," *Opt. Express*, Vol. 18, No. 10, 10905–10923, 2010.

[7] Bauer, T., S. Orlov, G. Leuchs, P. Banzer, "Towards an optical far-field measurement of higher-order multipole contributions to the scattering response of nanoparticles," *Appl. Phys. Lett.*, Vol. 106, 091108, 2015.

[8] Richards, B., E. Wolf, "Electromagnetic Diffraction in Optical Systems. II. Structure of the Image Field in an Aplanatic System," *Proc. R. Soc. A*, Vol. 253, No. 1274, 358–379, 1959.

[9] Neugebauer, M., P. Woźniak, A. Bag, G. Leuchs, P. Banzer, "Polarization Controlled Directional Scattering for Nanoscopic Position Sensing," arXiv: 1511.02066, 2015.

# Active Semiconductor THz metasurfaces

**J. Gómez Rivas[1,2], A. Batthacharya[1], G. Georgiou[1], and A. Halpin[1]**

[1]Dutch Institute for Fundamental Energy Research, DIFFER, P.O. Box 6336, 5600 HH Eindhoven, The Netherlands

[2]Eindhoven University of Technology, P.O. Box 513, 5600 MB Eindhoven, The Netherlands

j.gomezrivas@differ.nl

The resonant interaction of electromagnetic waves with structured surfaces can lead to a fascinating phenomena, such as excitation of surface waves with large electromagnetic field enhancements, anomalous refraction due to interference of the coherently scattered partial waves [1], and electromagnetically induced transparency with large group velocity reduction [2]. These and other phenomena can profit tremendously if they can be actively controlled.

In this contribution we demonstrate an all-optical active control of the excitation of THz resonant structures and surface waves on flat semiconductor surfaces. This control is achieved by the photo-generation of resonant conducting structures on the semiconductor with the illumination of an optical pump beam. This pump beam is spatially structured with the shape of the resonant structures by means of a spatial light modulator (SLM). In this way we achieve full control of the dimensions and location of the structures onto the surface and gives unprecedented possibilities for actively tuning the response of photo-excited materials to THz radiation [3,4]. We also show how and inhomogeneous optical illumination of a semiconductor can be used for THz beaming in certain direction in analogy to metasurfaces [5].

We also probe the near field associated to THz resonators, demonstrating a large shift with respect to the far-field resonant response that cannot be explained with the oscillator model extensively used in the literature [6].

**Acknowledgements**, This research was financed by the ERC projects THz plasmon and MicroMap.

**REFERENCES**

1. Yu, N. *et al.,* "Light Propagation with Phase Discontinuities: Generalized Laws of Reflection and Refraction", *Science* 334, 333 (2011).
2. Zhang, *et al.*, "Plasmon-Induced Transparency in Metamaterials," Phys. Rev. Lett. **101**, 047401 (2008).
3. G. Georgiou, *et al.*, "Photo-generated THz antennas", Sci. Rep. 4, 3584 (2014).
4. G. Georgiou, *et al.*, "Active loaded plasmonic antennas at terahertz frequencies: Optical control of their capacitive-inductive coupling", Phys. Rev. B **91**, 125443 (2015).
5. T.P. Steinbusch,, *et al.*, "Active terahertz beam steering by photo-generated graded index gratings in thin semiconductor films", Opt. Express **22**, 26559 (2014).
6. A. Bhattacharya, G. Georgiou, S. Sawallich, C. Matheisen, M. Nagel, and J. Gómez Rivas, "Large near-to-far field spectral shifts for terahertz resonances", Phys. Rev. B 93, 035438 (2016).

# Metallo-dielectric sensor: toward zeptogram-scale colorimetric sensing.

**J. Proust, J. Martin, D. Gérard, J-L. Bijeon, and J. Plain***

[1]*LNIO/ICD, Université de technologie de Troyes, France*

[*]corresponding author: Jerome.plain@utt.fr

**Abstract**-We report on the fabrication of plasmonic hybrid sensors made of a micro-axicon dielectric lens and a single metallic nanoparticle. The dielectric lens produces a Bessel-like beam of light at its apex under plane wave excitation confining light in a narrow and intense beam with a low divergence. This Bessel-like beam can be used to optimize efficiently the excitation of a plasmonic nano-object and the collection of its far-field collected signal. This hybrid structure using the optical properties of a single metallic nanoparticle can act as a highly sensitive nanosensor.

Due to the Localized Surface Plasmon Resonance (LSPR), light is intensively absorbed and scattered by metal nanoparticles. LSPR phenomenon confers to MNPs extremely attractive nano-optical properties and the subsequent technological applications are various. As it is well known, LSPR is extremely sensitive to the dielectric environment of the MNPs paving the way to highly sensitive sensors. Consequently, any optical change in the environment will induce a measurable shift of the plasmon resonance. This property is widely used to develop plasmon-based nanosensors[1]. In general, plasmon-based nanosensors are developed as an array of nanoparticles in order to get an easily measurable signal[2]. Unfortunately, the quality factor of the LSPR of such an array is strongly reduced due to various phenomena. Such damping can be partially limited by using a single nanoparticle in place of an array as nanosensor. Using single MNP as an active nano-optical device relies in the development of efficient techniques to measure their optical properties with a good signal-to-noise ratio. In order to significantly optimize our signal, our single MNP-based nanosensor is integrated into a system shown figure 1a[3]. It allows to efficiently couple the far field excitation to the single particle and then to efficiently collect the transmitted light. Our approach is based on the integration of the MNP-based nanosensor onto an axicon lens (see figure 1b)[4]. We report a limit of detection of about some tens of zeptograms as shown figure 1c. As a conclusion, we clearly show the ability to measure a signal variation induced by some tens of zeptogram of organic material absorbed onto a single metal nanoparticule-based nanosensor.

**Acknowledgements**, Financial supports from the ANR "grant NATO", the European community (FEDER funds), the « conseil général de l'Aube » and the « Conseil Régional Champagne-Ardenne », grant NANO'MAT (www.nanomat.eu) are highly acknowledged.

**REFERENCES**

1. Anker, J. N.; Hall, W. P.; Lyandres, O.; Shah, N. C.; Zhao, J.; Van Duyne, R. P. *Nature Materials* 7 **(2008)** 442–453.
2. Barbillon, G.; Bijeon, J.-L.; Plain, J.; Lamy De La Chapelle, M.; Adam, P.-M.; Royer, P. *Gold Bull* 40, **(2007)** 240–244.
3. Barbillon, G.; Bijeon, J.; Lerondel, G.; Plain, J.; Royer, P. *Surface Science* 602, **(2008)** L119–L122.
4. Martin, J.; Proust, J.; Gerard, D.; Bijeon, J.-L.; Plain, J. *Opt Lett* 37, (**2012**) 1274–1276.

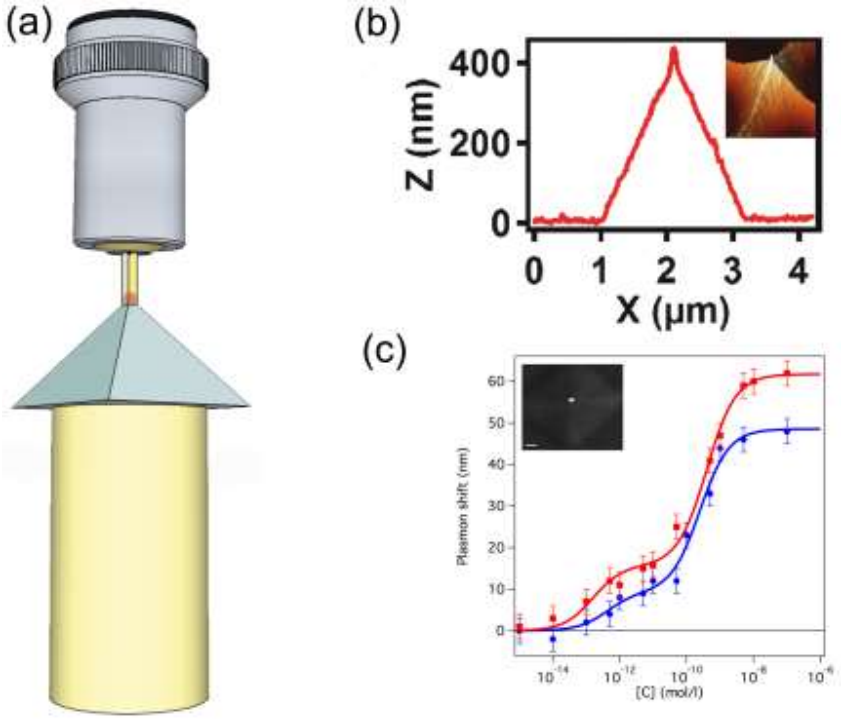



Figure 1: (a) Schematic representation of the developed system. (b) AFM image showing one axicon lens functionalized with a single gold nanoparticle. (c) Limit of detection measured onto a dimer for both polarizations (longitudinal in red and transverse in blue).

# Studying light concentration in a dimer of semiconductor nanoparticles for all-optical devices

**R. Vergaz[1*], J. F. Algorri[1], A. Cuadrado[2], V. Urruchi[1], J. M. Sánchez-Pena[1], and B. García-Cámara[1]**

[1] Group of Displays and Photonic Applications (GDAF-UC3M), Carlos III University of Madrid, Spain.

[2] Laser Processing Group, Instituto de Óptica, CSIC, C/Serrano 121, 28006 Madrid, Spain

[*]corresponding author: rvergaz@ing.uc3m.es

**Abstract**. Scattering by subwavelength dielectric nanospheres can have interesting directional effects in the case of accomplishing Kerker's conditions. We have taken advantage of these conditions to design a dimer of semiconductor nanoparticles where an important contrast can be achieved in their gap, due to the directionality and the interferential interaction of the scattered fields.

Light scattering in subwavelength spheres ($R/\lambda<<1$) is described by Mie theory. In the case of dipole-like particles, it is enough to use the first two Mie coefficients ($a_1$ and $b_1$, regarding dipolar electric and magnetic effects respectively). Starting from that point, Kerker and co-workers [1] reported that particles can present a lack of scattering in the forward or the backward directions, if the scattering coefficients accomplish certain conditions, known as minimum-forward (MF) and zero-backward (ZB) conditions or Kerker's conditions:

$$\begin{aligned} &\mathrm{Re}(a_1) = -\mathrm{Re}(b_1);\ \mathrm{Im}(a_1) = \mathrm{Im}(b_1) \\ &a_1 = b_1 \end{aligned} \tag{1}$$

Kerker's conditions can be satisfied in nanoparticles made of several usual semiconductor materials, such as Silicon, Germanium, $TiO_2$, GaAs, etc., in the visible range [2, 3]. Using two different nanoparticles with different sizes, we are able to accomplish each Kerker's condition at each nanoparticle at the same wavelength. Then, we have proposed a dimer of silicon nanoparticles [4] presenting such a combination of directional scattering in the visible range. This anisotropic scattering, as well as the interferential effects between the scattered fields, can produce an intense maximum or a deep minimum of the light intensity in the gap region. As Kerker's conditions are very dependent on the wavelength, a slight shift of the incident wavelength can perturb the satisfaction of the conditions producing a drastic change of the light intensity in the gap (Fig. 1).

This effect has been explored considering several semiconductor materials, sweeping sizes and distance between nanoparticles, in order to optimize the contrast between the states fulfilling or not the Kerker's conditions. Figure 2 shows the example of $TiO_2$ nanoparticles illuminated with a light beam of 543 nm. As it can be seen, for a light impinging first on a nanoparticle satisfying the ZB and then on MF nanoparticle (case 180º), strong interferential effects appear. The anisotropic scattering distribution of the nanoparticles enables this strong interaction, even producing that the scattered fields null each other. Sweeping wavelength in the vicinity of the target one, the Kerker's conditions do not apply anymore, and a strong contrast can be achieved with a small change in wavelength.

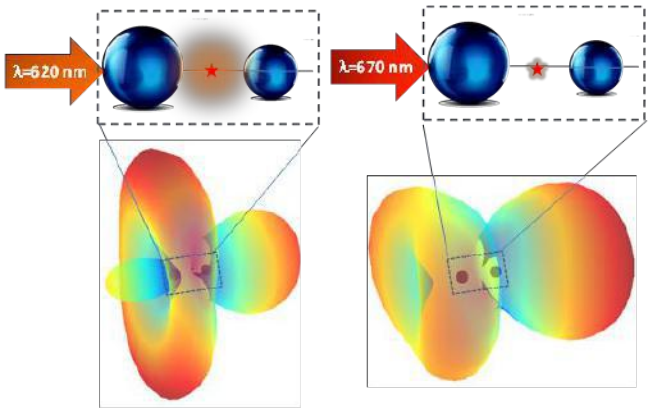



**Figure 1.** Up: Scheme of the configuration of a silicon dimer with nanoparticles of radius 96 and 82 nm and a gap distance of 360 nm. Down: spatial distribution of the scattered fields in the far-field region in each case.

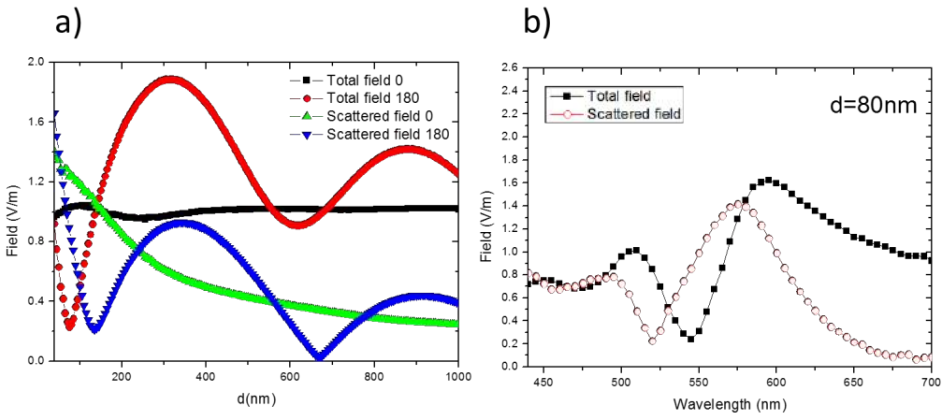



**Figure 2.** a) Scattered and total field of a dimer of $TiO_2$ nanoparticles ($R_1$=78 and $R_2$=93 nm) at 543 nm as a function of the gap distance, considering the two possible impinging directions. b) Scattered and total field of a dimer of $TiO_2$ nanoparticles at the middle point of the gap for a distance of 80nm as a function of the wavelength and considering the 180º configuration (as in Figure 1). Interferential effects lead to a remarkable 20% to 160% of incident field contrast around 550 nm.

New studies regarding polarization effects are currently on the way.

**Acknowledgements**: This work has been supported by Ministerio de Economía y Competitividad of Spain (grant no. TEC2013-50138-EXP) and the R&D Program SINFOTON S2013/MIT-2790 of the Comunidad de Madrid.

**REFERENCES**

1. Kerker, M., D. S. Wang and C. L. Giles, *J. Opt. Soc. Am.*, Vol. 73, 765-767, 1983.
2. Luk`yanchuk, B.S., et al., *ACS Photonics*, Vol. 2¸ 993-999, 2015.
3. Garcia-Cámara, B., et al., *IEEE Photonic Technol. L.*, Vol. 27, No. 19, 2059-2062, 2015.
4. García-Cámara, B., et al, *J. Phys. Chem. C.*, Vol. 119, No. 33, 19558-19564, 2015.

# Magnetic properties of a mixture of a Liquid Crystal doped with Semiconductor Nanoparticles

**V. Marzal*, B. García-Cámara, I. Pérez and J.M. Sánchez-Pena**
Group of Displays and Photonic Applications (GDAF-UC3M), Carlos III University of Madrid, Spain
*corresponding author: vmarzal@ing.uc3m.es

**Abstract**- Currently there are many efforts to improve the electro-optical properties of liquid crystals by means of doping them with different nanoparticle types. In this work we present simulation results of the magnetic properties of several liquid crystals with inclusions of spherical resonant semiconductor nanoparticles. Effective magnetic permeability was obtained through three effective medium theories. Furthermore, the permeability variations with size of the nanoparticle, its concentration in the liquid crystal and the magnetic anisotropy have been studied.

The calculation of the effective permeability $\mu_{eff}$ of mixtures composed of a liquid crystal (LC) doped with resonant nanoparticles (NPs) can be made with several effective medium approximations, e.g. Maxwell-Garnett's model [1]. This theory establishes that the effective dielectric function $\varepsilon_{eff}$ of a composite of a matrix with spherical and homogeneous inclusions can be expressed in terms of the optical properties of each component and the volume fraction of the dopants (*f*). Due to the symmetric nature of the electromagnetic field, an analogue expression can be derived for the magnetic permeability $\mu_{eff}$ [2]:

$$\mu_{eff} = \mu_h \left[ 1 + \frac{3f\left(\frac{\mu_s - \mu_h}{\mu_s + 2\mu_h}\right)}{1 - f\left(\frac{\mu_s - \mu_h}{\mu_s + 2\mu_h}\right)} \right] \quad (1)$$

where $\mu_h$ and $\mu_s$ are the magnetic permeability of the host medium and the inclusion, respectively.

In our particular case, we consider a LC as host medium while the inclusions are semiconductor nanoparticles presenting both electric and magnetic resonances. These NPs present magnetic response although they are composed of non-magnetic materials in the visible range, e.g. silicon, germanium, etc. [3]. Thus, effective optical constants can also be derived for the individual particles: the effective magnetic permeability of these nanoparticles have been obtained through the Mie theory [1]. Due to the dominant dipolar response of these NPs, the complex expressions of the Mie coefficients have been simplified under the Rayleigh approximation and the following Mie coefficient $b_1$ has been used to derive the permeability $\mu_s$ of the nanoparticles:

$$b_1 = -i\frac{2x^3}{3}\frac{\mu_s - 1}{\mu_s + 2} \quad (2)$$

The magnitude of the effective permeability ($\mu_s$) of AlSb nanoparticles (R=66 nm) is shown in Figure 1 as a function of the incident wavelength. In the optical properties of surrounding medium both the ordinary and the extraordinary refractive indexes of LC E44 have been considered.

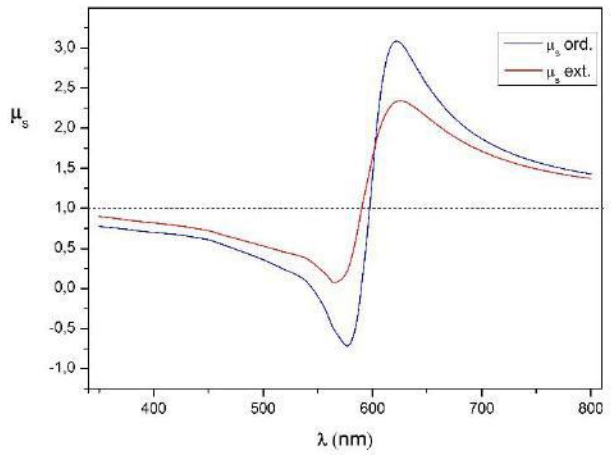



**Figure 1. Effective permeability $\mu_s$ of a AlSb nanoparticle (R=66 nm) as a function of the wavelength when the surrounding medium is LC E44**

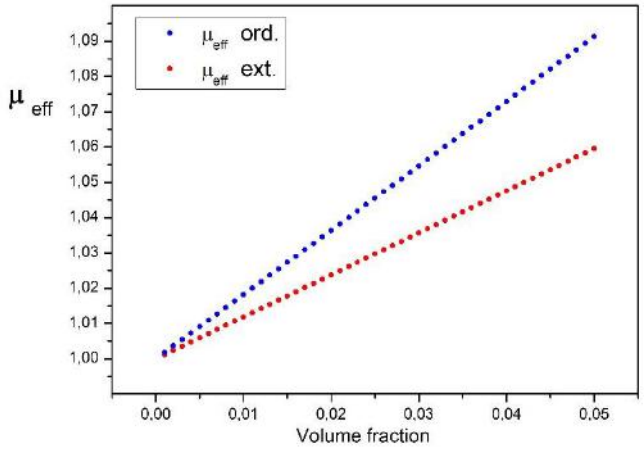



**Figure 2: Effective permeability ($\mu_{eff}$) of the mixture NP+LC as function of the volume fraction of AlSb nanoparticle (R=66 nm).**

Once this permeability is deduced, we can use it to obtain the effective permeability ($\mu_{eff}$) of the mixture. We have made simulations with several LCs of high birefringence and different types of semiconductor materials as dopants. The main goal of this work has been the maximization of the $\mu_{eff}$ optimizing the NP's size and concentration for each mixture. We found an optimum value of the NP radius that maximize the $\mu_{eff}$. In addition, we observed that $\mu_{eff}$ linearly increases with the volume fraction of NPs (see Fig. 2). Although the values of $\mu_{eff}$ are not very high, a remarkable magnetic anisotropy have been obtained, as can be seen in the example of Figure 2.

**Acknowledgements**: This work has been supported by Ministry of Economy and Competitiveness (Grants n. TEC2013-47342-C2-2-R and TEC2013-50138-EXP) and the I+D program SINFOTON S2013/MIT-2790 of the Madrid community.

**REFERENCES**

1. Bohren, C. F., and Huffman D. R. *Absorption and Scattering of Light by Small Particles*, Wiley-Interscience, New York, 1983.
2. Ruppin, R., "Evaluation of extended Maxwell-Garnett theories", Optics Communications, vol. 182, no. 4, 273–279, 2000.
3. Gómez-Medina, R., B. García-Cámara, I. Suárez-Lacalle, F. González, F. Moreno, M. Nieto-Vesperinas, and J.J. Sáenz, "Electric and magnetic dipolar response of germanium nanospheres: Interference effects, scattering anisotropy and optical forces" J. Nanophoton, vol. 5, 053512:1–053512:10, 2011.

# Full-solution process approach for tailoring light-matter interaction at the nanoscale

**J. F. Galisteo-López*, A. Jiménez-Solano, and H. Míguez**
Instituto de Ciencia de Materiales de Sevilla (CSIC-US)
c/Américo Vespucio 49, 41092 Sevilla (Spain)
*corresponding author: juan.galisteo@csic.es

**Abstract**- One dimensional nano-porous Photonic Crystals can be used as efficient emissive optical coatings by placing nano-emitters at deterministically controlled positions where the local density of states is known. Combining full solution-process techniques we can introduce nano-sized emitters at well-known positions which allow us to probe the local photonic environment of the emitters. Further, a proper design of the photonic structure allows us to optimize intensity, directionality and polarization of the coating's emission.

One dimensional (1D) nanoporous Photonic Crystals (PhC) offer a large potential to tailor light-matter interaction at the nanoscale. [1] Such control is achieved via the two levels of structuration present in these systems, comprising the few nanometers (within each layer) and hundreds of nanometers range (layer to layer). While the former allows infiltrating the structure with different materials (thus increasing its functionality) the latter introduces a modulation in the refractive index on a spatial scale which permits tailoring light-matter interaction within each layer.

The potential of these photonic structures regarding enhanced light-matter interaction has been widely exploited from the point of view of light absorption allowing i.e. enhanced photovoltaic operation of dye-sensitized solar cells [2] as well as modified absorption of metal nanoparticles coupled to optical cavities. [3] Infiltrating these materials with luminescent species permits creating photonic coatings with tunable emission [4] and even the possibility to achieve lasing. [5]

To achieve an optimized control on the emission of nanosized light sources, their position should be deterministically chosen within the structure in order to control their local photonic environment via the local density of states (LDOS). We can profit from the layer-by-layer procedure used to fabricate these structures to incorporate monolayers of nano-emitters at well-defined positions. In particular, combining dip and spin coating techniques we can deposit monolayers of dye-doped nanospheres at planes of constant LDOS. In this manner we have mapped the LDOS across an optical resonator incorporated within a 1D PhC with a spatial resolution given by the size of the emitters used (30 nm in this case). [6]

Beyond using the nanoemitters as a probe for LDOS in 1D PhC one can combine these systems with metals in order to enhance light-matter interaction. In this sense we have optimized designs for emissive coatings where light intensity, directionality and polarization can be controlled. The possibility of improving the functionality of these coatings by making them flexible is also discussed.

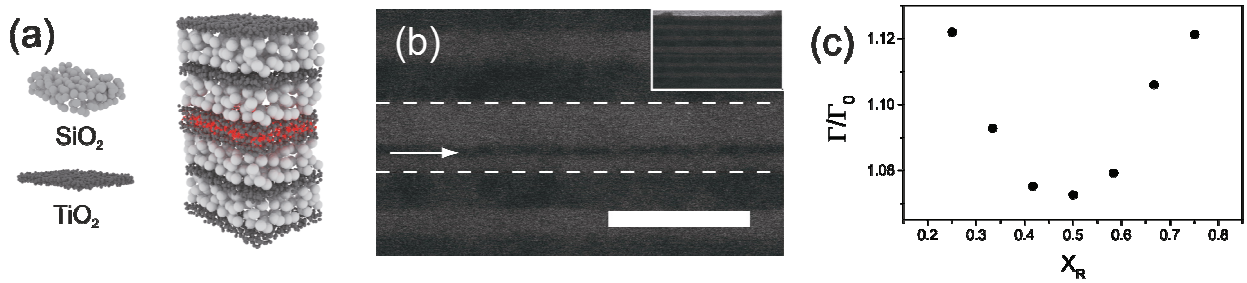



**Figure 1.** (a) Diagram of a 1D nanoporous PhC with a cavity containing nanoemiters. (b) SEM image of a fabricated sample. Dashed lines highlight the cavity and arrow points the position of a monolayer of nanoemitters. (Scale bar is 300 nm) (c) Variation of the decay rate of the monolayer of emitters as their relative position within the cavity ($X_R$) is modified.

**Acknowledgements**, The research leading to these results has received funding from the European Research Council under the European Union's Seventh Framework Programme (FP7/2007–2013)/ERC Grant Agreement No. 307081 (POLIGHT) and the Spanish Ministry of Economy and Competitiveness under Grant No. MAT2011-23593.

**REFERENCES**

1. Calvo, M. E., S. Colodrero, N. Hidalgo, G. Lozano, C. López-López, O. Sánchez-Sobrado and H. Míguez, "Poroous one dimensional photonic crystals: novel multifunctional materials for environmental and energy applications," *Energy. Environ. Sci.*, Vol. 4, 4800–4812, 2011.
2. Colodrero, S., A. Fornelli, C. López-López, L. Pelleja, H. Míguez and E. Palomares, "Efficient Transparent Thin Dye Solar Cells Based on Highly Porous 1D Photonic Crystals," *Adv. Funct. Mater.*, Vol. 22, No. 6, 1303–1310, 2012.
3. Jiménez-Solano, A., C. López-López, O. Sánchez-Sobrado, J. M. Luque, M. E. Calvo, C. Fernández-López, A. Sánchez.-Iglesias, L. Liz-Marzán and H. Míguez, "Integration of Gold Nanoparticles in Optical Resonators," *Langmuir*, Vol. 28, No. 24, 9161–6167, 2012.
4. Calvo, M. E.., N. Hidalgo, R. Schierholz, A. Kovács, A. Fernández, M. G. Bellino, G. J. A. A. Soler-Illia and H. Míguez, "Full solution processed mesostructured optical resonators integrating colloidal semiconductor quantum dots," *Nanoscale*, Vol. 7, 16583–16589, 2015.
5. Scotognella, F., D. P. Puzzo, A. Monguzzi, D. W. Wiersma, D. Maschke, R. Tubino and G. A. Ozin, "Nanoparticle One-Dimensional Photonic-Crystal Dye Laser," *Small*, Vol. 5, No. 18, 2048–2052, 2009.
6. Jiménez-Solano, A., J. F. Galisteo-López and H. Míguez, "Fine Tuning the Emission Properties of Nanoemitters in Multilayered Structures by Deterministic Control of their Local Photonic Environment," *Small*, Vol. 11, No. 23, 2727–2732, 2015.

# Graphene as a tunable plasmonic metasurface with transformation optics

**Paloma A. Huidobro**[1], **M. Kraft**[1], **S. A. Maier**[1], **and J. B. Pendry**[2]

[1]Imperial College London, UK
p.arroyo-huidobro@imperial.ac.uk

**Abstract**— We demonstrate a tunable plasmonic metasurface by considering a graphene sheet subject to a periodically patterned doping level. By extracting the effective conductivity of the sheet we characterize metasurfaces periodically modulated along one or two directions. In the first case, and making use of the analytical insight provided by transformation optics, we show an efficient control of THz radiation for one polarization. In the second case, we demonstrate a metasurface with an isotropic response that is independent of wave polarization and orientation.

Graphene can be biased by electrical gating or by chemical doping, which modifies its Fermi level and enables the existence of surface plasmons propagating along graphene. These surface plasmons, because of the two-dimensional (2D) nature of this material, have very short wavelengths and extreme lateral. Graphene plasmons feature in the THz regime with relatively low losses, where the plasmonic response of metals is weak. These facts, added to the important ingredient of tunability with external bias, make graphene a very suitable platform for the design of plasmonic metasurfaces in the THz regime. Metasurfaces, which are the 2D counterpart of metamaterials, consist of a planar arrangement of resonant subwavelength-size building blocks. By appropriately them, metasurfaces provide an ultra-thin platform for manipulating electromagnetic waves, and they have shown novel phenomena and applications as from broadband light bending and anomalous reflection and refraction.

In this contribution we demonstrate a tunable meta-surface by inducing a periodic conductivity modulation in a graphene sheet. The conductivity modulation acts as a subwavelength grating

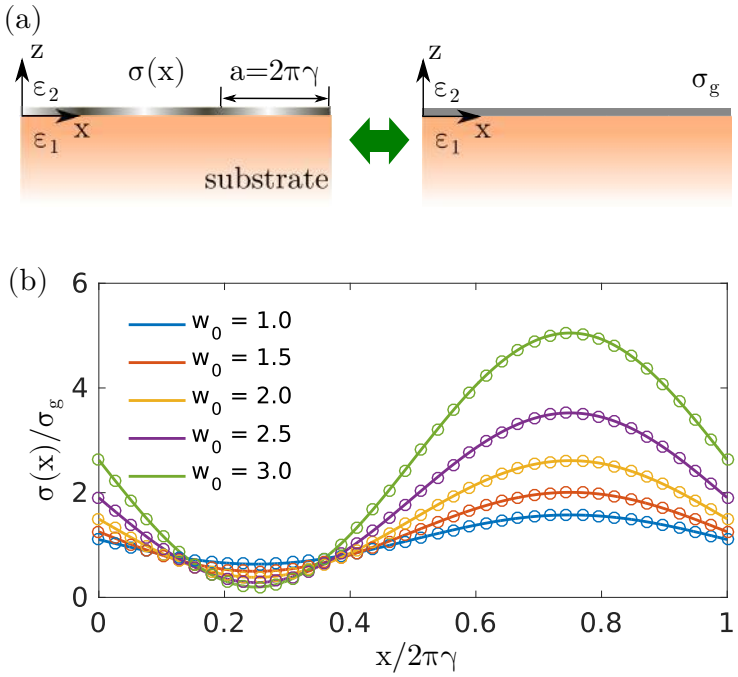



Figure 1: Transformation optics applied to graphene. (a) A flat graphene sheet between two dielectric media transforms to a graphene sheet of periodically modulated thickness while it keeps the same permittivity, $\epsilon_g$. This is equivalent to a periodic modulation of the sheet's conductivity, $\sigma(v)$, which can be achieved by means of a 1D modulated bias. (b) The conductivity profile has a sinusoidal shape and modulation strength $w_0$.

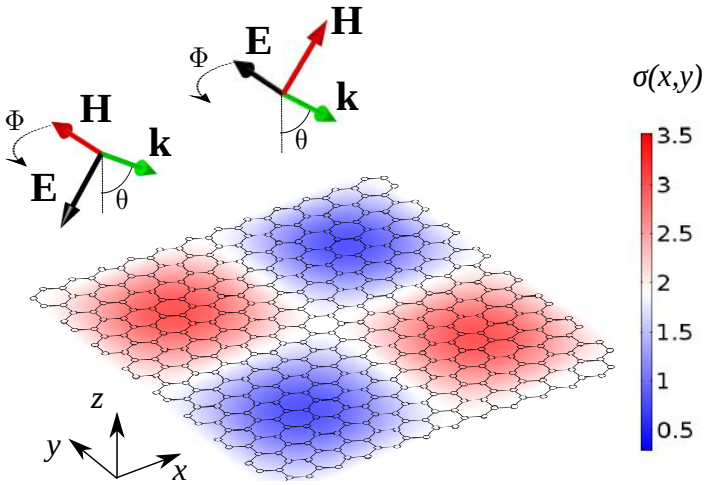



Figure 2: Metasurface with periodically modulated graphene. For radiation of relevant wavelengths, the graphene appears as a ho- mogeneous sheet with effective conductivity $\sigma_{\text{eff}}$.

that allows for external terahertz radiation to couple into the surface plasmons supported by the graphene layer. The coupling to highly confined plasmons provides a dramatic enhancement of the interaction of electromagnetic radiation with graphene. Making use of transformation optics see Fig. 1, we derive analytical expressions for the optical response of the system, and find the optimal configuration for coupling into plasmons.

These graphene conductivity gratings are tunable plasmonic metasurfaces characterized by an effective surface conductivity, which is derived from a sheet retrieval method. In addition, for the case of conductivity modulations along two directions, see Fig. 2, we find that the graphene metasurface responds isotropically under electromagnetic fields incident at any angle. Thus, the modulated graphene can be used for fast switching and tuning of THz radiation of arbitrary polarisation and orientation.

**REFERENCES**

1. Huidobro, P. A., Matthias, K., Kun, R., Maier, S. A. and Pendry, J. B., "Graphene, plasmons and transformation optics," *Journal Of Optics*, accepted, 2015.
2. Huidobro, P. A., Matthias, K., Maier, S. A. and Pendry, J. B., " Graphene as a tunable and isotropic plasmonic metasurface," *in preparation* , 2016.

# Self-assembled disorder in photonic materials

**A. Blanco*, D. Montesdeoca, J.A. Partiente, C. Pecharromán, and C. López**
Instituto de Ciencia de Materiales de Madrid – ICMM-CSIC, Sor Juana Inés de la Cruz 3, 28049 Madrid Spain
*corresponding author: a.blanco@csic.es

**Abstract**- Complex material structures are inherently interesting for the curious scientific mind due to the challenge their in depth understanding constitutes. Periodicity greatly simplifies their understanding and adds interesting new properties. Self-assembled nanostructures usually develop ordered patterns in three dimensions [1]. When disorder is dominant, some interesting new phenomena may appear, as random lasing [2]. Artificial opals are one of such possible arrangements usually forming *fcc* structures with promising photonic properties. Often, and undesirably, unwanted defects are present spoiling the optical properties of such nanostructures [3]. On the other hand, and contrary to intuition, the introduction of arbitrarily high amounts of disorder is, in some cases, an equally difficult task but the resulting material presents intriguing new optical properties. We have grown novel nanophotonic materials, *photonic glasses*, which are solid, disordered assembly of monodisperse dielectric spheres [4], in which novel devices such as resonant random lasing may be observed [5].

In this talk, I will summarize our latest results regarding self-assembled photonic materials and, in particular, a new method to prepare photonic glasses from different colloidal suspensions ($SiO_2$, Polystyrene, or PMMA) in a very fast fashion will be presented. Starting from raw materials in the form of powder (as synthesized or purchased) we demonstrate high quality photonic glasses prepared in minutes by simple pressure [6]. In addition, our studies on how monodisperse powder is packed open a new window to understand light behaviour in complex optical media and might find application to gain general knowledge on random granular media in the nanoscale [7].

**REFERENCES**

1. J.F. Galisteo-López, M. Ibisate, R. Sapienza, L. Froufe-Pérez, A. Blanco, and C. López, *Adv. Mater.* **23**, 30-69 (2011).
2. M. Leonetti, C. Conti, C. López, *Nat. Photonics* **5,** 615 (2011).
3. X. Checoury, S. Enoch, C. López, and A. Blanco, *Appl. Phys. Lett*. **90**, 161131 (2007)
4. P. D. García, R. Sapienza, A. Blanco, and C. López, *Adv. Mater.* **19**, 2597, (2007)
5. S. Gottardo, R. Sapienza, P. D. García, A. Blanco, D. S. Wiersma, C. López, *Nat. Photonics* **2008**, *2*, 429.
6. D. Montesdeoca et al. submitted (2016).
7. Y. Kallus, S. Torquato, Ph. Rev. E, 90, 022114 (2014).

# Towards the Polarization Control of the Directional Scattering of Semiconductor Nanodisks

**R. Vergaz[1*], J. F. Algorri[1], A. Cuadrado[2], J. M. Sánchez-Pena[1], and B. García-Cámara[1]**
[1] Group of Displays and Photonic Applications (GDAF-UC3M), Carlos III University of Madrid, Spain.
[2] Laser Processing Group, Instituto de Óptica, CSIC, C/Serrano 121, 28006 Madrid, Spain
[*]corresponding author: rvergaz@ing.uc3m.es

**Abstract**- In this work we analyze the sensitivity of the directional scattering conditions in semiconductor nanodisks with the polarization of the incident light. The possibility to reach or not this directional scattering as a function of the polarization of the incident beam could be very interesting for the design of new all-optical devices for optical communications and computing.

In the last years, light scattering of semiconductor nanoparticles becomes an attractive field due to the appearance of both electric and magnetic resonances, as well as the satisfaction of the Kerker's conditions [1, 2]. These effects are currently the base of a new research line devoted to the analysis and design of new dieletric devices, like all-optical switches [3]. Kerker's conditions were established in the last century, but they are intensely studied in the last few years [4, 5]. They were proposed considering spherical dipole-like particles. However, these effects can also be observed in other geometrical structures, like disks [6]. In addition, while the zero-forward condition is strongly sensitive to any change, the zero-backward condition is more stable.

In this work, we have considered nanodisks made of different high-refractive index semiconductor materials on a substrate and illuminated with a linear-polarized small-incident-angle beam (see Fig. 1). By means of FEM simulations (®Comsol), we observed the directional conditions at an incident wavelength of 632.8 nm (He-Ne laser) and considering a TE polarization. As the incident polarization changes (TM mode) the directional conditions are not satisfied anymore and the spatial distribution of the electric field in the surroundings of the nanodisk strongly changes. Both the radius and the height of the disk were optimized to obtain a maximum contrast between both polarizations.

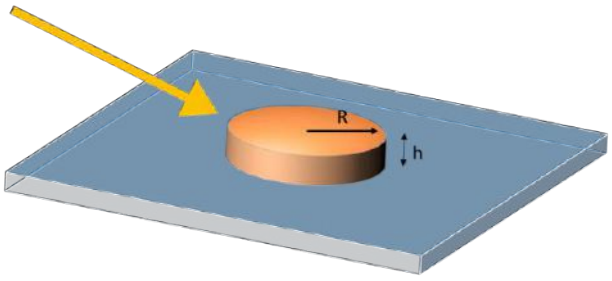



Figure 1. Scheme of the considered geometry. Light impinges at 10º with respect to the substrate plane.

This polarization sensitivity is now applied to design a polarization-driven switch based on two nanodisks, producing a strong concentration of light if the directional conditions are satisfied, and a poor light intensity in any other case.

**Acknowledgements.** This work has been supported by Ministerio de Economía y Competitividad of Spain (grant no. TEC2013-50138-EXP) and the R&D Program SINFOTON S2013/MIT-2790 of the Comunidad de Madrid.

**REFERENCES**

1. Geffrin, J.M., et al., "Magnetic and electric coherence in forward- and back-scattered electromagnetic waves by a single dielectric subwavelength sphere", Nature Commun., Vol. 3, 1171, 2012.
2. Fu, Y. H., A. I. Kuznetsov, A. E. Miroshnichenko, Y. F. Yu and B. Luk'yanchuk, "Directional visible light scattering by silicon nanoparticles", *Nature Commun.*, Vol . 4, 1527, 2013.
3. García-Cámara B., J.F. Algorri, A. Cuadrado, V. Urruchi, J.M. Sánchez-Pena, R. Serna and R. Vergaz, "All-Optical Nanometric Switch Based on the Directional Scattering of Semiconductor Nanoparticles" *J. Phys. Chem. C.*, Vol. 119, No. 33, 19558-19564, 2015.
4. Kerker, M., D. S. Wang and C. L. Giles, "Electromagnetic scattering by magnetic spheres" *J. Opt. Soc. Am.*, Vol. 73, 765-767, 1983.
5. Garcia-Camara, B., R. Alcaraz de la Osa, J.M. Saiz, F. González and F. Moreno, "Directionality in scattering by nanoparticles: Kerker's null-scattering conditions revisited" *Opt. Lett.*, Vol. 36, No. 5, 728-730, 2011.
6. Staude, I et al., "Tailoring Directional Scattering through Magnetic and Electric Resonances in Subwavelength Silicon Nanodisks", *ACS Nano*, vol 7, No. 9, 7824-7832, 2013.

# Tunable Negative Nano Composites for Low Frequency Metamaterials.

**Carlos Pecharromán[*] [1], Lucía Fernández [2], and Miguel Morales[1], Celia Mallada[2], José Luis Menéndez [2]**

[1] Instituto de Ciencia de Materiales de Madrid-CSIC, C/ Sor Juana Inés de la Cruz, Madrid, 28049 Spain

[2] Centro de Investigación en Nanomateriales y Nanotecnología-CSIC, Avda. Vega 4, S. Martín del Rey Aurelio, Asturias, 33940 Spain

[*]corresponding author: cpg@icmm.csic.es

**Abstract**-Negative and zero permittivity nanostructure composites have been obtained on a broad frequency domain. Additionally, it has been found that the effective dielectric constant can be modified by the application of a magnetic field. At low frequencies, these materials present a close resemblance to plasmonics. Additionally, effective dielectric losses can be suppressed by the introduction of some passive electric elements. In this regard, this kind of devices can be used in applications such as new electric passive elements.

During the last years, nanometer size FET's (Field-Electric Transistors) in IC's, present a serious limitations due to the generated heat under. This effect, which hinders the size reduction required for larger levels of nanointegration, is known as "Bolztmann Tyranny". Basically, this limitation states that, at room temperature, changing the current by a factor of 10 requires at least 60 mV which generates excessive heating. In order to lower the required voltage, several authors have proposed connecting the FET gate to a "negative capacity capacitor" to dramatically reduce the voltage and therefore the heating[1,2,3]. In that sense, it has been recently detected some examples of negative capacitance in ferroelectric thin films[3,4].

In this regard, we have chosen a different approximation: magnetic-conductor nanocomposites. For this kind of metamaterial nanocomposites, made by combining an insulating ferromagnetic matrix with conductive graphene-like inclusions, the capacity can be tailored, from negative to positive values by changing the conductive phase concentration around the percolation threshold[5]. However, the more striking property is that this value can be modified in real time by the effect of a static magnetic field ($H$<2000 Oe), and even it can be set to zero for a very wide range of frequencies.

Experimental results can be seen in figure 1a. In this plot, the apparent capacity of a nearly percolated sample shows a continuous variation of the permittivity as a function of an external applied field from negative ($B$~ 0 Oe) to positive ($B$~2000 Oe).

We attribute this tunable permeability (negative to positive) to the effect of the magnetically induced current (inductance). It should be remarked the similitude of the role of the magnetic field in this system with the dispersion of dielectric constant and depolarization electric field in the Surface Plasmon Resonances (SPR) at optical frequencies. Actually, in these composites, the applied current generates an a.c. magnetic field and consequently an electric field opposed to the external field in a similar way as the depolarization field does it in SPR (see figure 1b). Because the composite has a ferromagnetic phase, its self-inductance depends on the permeability and consequently the effect of a magnetic field is enough to notably modify this value, so that, the magneto-electric depolarization field and its apparent permittivity can be tuned by the effect of a static magnetic field. Following the similitude with plasmonic materials, it is well known than a SPR verifies when a metal (with

negative value of the real part of dielectric constant) is embedded into a dielectric matrix. In the case of negative capacitance composites, the resonance is easily reached by connecting this material in serial with an ordinary capacitor. Without losses, the equivalent capacity whould be: $C_{eq}=C^{-}C^{+}/(C^{+}+C^{-})$ (where $C^{-}$ and $C^{+}$ are respectively the capacity of the negative and positive capacitors), so that, $C_{eq}$ tends to infinity when $C^{+}=-C^{-}$. The possibility to modify the value of $C^{-}$ by the application of a static magnetic field allows us to reach this resonant condition.

In many others metamaterials it has been found that negative values of permittivity are associated to large dielectric losses. This is an undesired property, and it has prevented the development of a large number of practical applications. However, in the case of the low frequency regime, several electric circuits, containing only passive (resistor and capacitors) can be designed to modify and even suppress the effect of dielectric losses. In this regard, several designs as well as their electrical characterization will be presented showing how a negative or zero permittivity metamaterial would operate without dielectric losses.

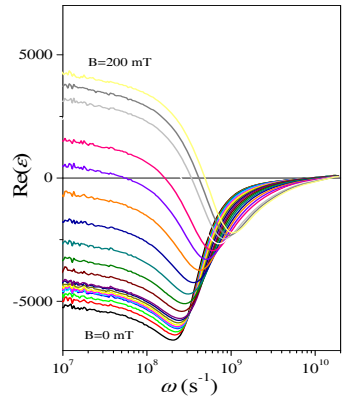



Fig.1*a* Field distribution in a cylindrical capacitor.

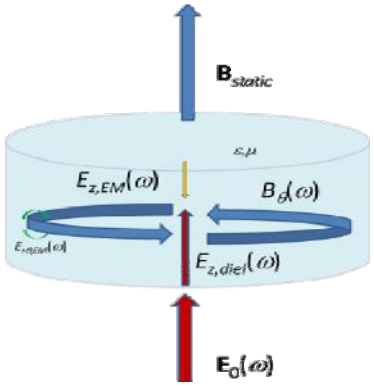



Fig.1*b* Apparent permittivity of composites under different static magnetic fields.

**Acknowledgements**, The authors acknowledge funding through the Projects MAT2011-29174-C02-01, TEC2014-53088-C3-2-R and ….

**REFERENCES**

1. Victor V. Zhirnov* and Ralph K. Cavin. "Nanoelectronics: Negative capacitance to the rescue?" *Nature Nanotech.*, Vol. 3, 77–78, 2008.
2. Sayeef Salahuddin and Supriyo Datta, "Use of Negative Capacitance to Provide Voltage Amplification for Low Power" Nano Lett. Vol. 8, 405-410, 2008
3. Asif Islam Khan, Korok Chatterjee et al. "Negative capacitance in a ferroelectric capacitor", Nature Mat. Vol 14 182-186. 2015,
4. Gustau Catalan, David Jiménez and Alexei Gruverman, "Negative capacitance detected", Nature Mat. Vol 14, 137-139, 2015
5. Carlos Pecharroman, Fatima Esteban-Betegon, Josef F Bartolome, Sonia Lopez-Esteban, Jose S Moya, "New Percolative BaTiO3–Ni Composites with a High and Frequency‐Independent Dielectric Constant (ϵr ≈ 80000)", Adv. Mat. Vol. 13, 1541-1544, 2001

# Controlling harmonic generation in plasmonic systems

**R. Esteban[1*], G. Aguirregabiria[1], D.C. Marinica[2], A.K. Kazansky[1,3], J. Aizpurua[1] and A. Borisov[2]**
[1]Donostia International Physics Center (DIPC) and Material Physics Center (Centro Mixto CSIC-UPV), Spain
[2]Institut des Sciences Moléculaires d'Orsay-UMR 8214, CNRS-Université Paris Sud, France
[3]IKERBASQUE, Basque Foundation for Science, E-48011 Bilbao, Spain
[*]corresponding author: ruben_esteban@ehu.eus

**Abstract** Plasmonic resonances can be strongly affected by quantum effects. We extend here previous work on quantum phenomena that can be observed on the linear optical response of these systems to non-linear processes. We demonstrate that polarizing metallic particles by an external static field allows modifying their non-linear optical response at optical frequencies, as desired for active control of plasmonic resonances.

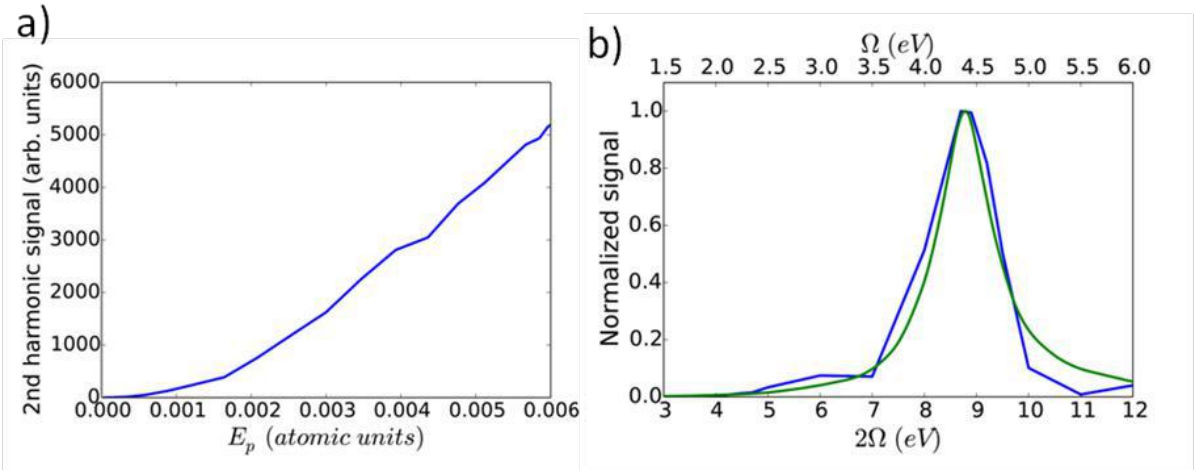
The interest of pushing plasmonics to its ultimate limits has motivated considerable recent research on the understanding and control of quantum effects in the optical response that are not captured by the classical electromagnetic framework [1,2]. These effects can completely change the plasmonic response, modifying or suppressing some modes and establishing new ones.

Large effects can be observed, for example, in the linear response of two particles separated by a subnanometer distance, due to the emergence of electron tunneling across the gap. In the first part of this contribution, we describe the optoelectronic phenomena characterizing these systems [3] and show how to model them using either (i) a Quantum corrected model (QCM) that allows treating large systems or (ii) more rigorous TDDFT simulations [4-6]. We also present recent experimental demonstrations of these effects [7-9].

We consider next the non-linear response [10] of metallic nanostructures, namely the generation of light at frequencies that are a multiple of the laser frequency used for excitation. We are particularly interested in the phenomena emerging after applying an external polarization to the system. For practical optoelectronic applications, a particularly promising possibility is to introduce the polarization by using an external electric bias voltage.

We observe a strong dependence of the optical response of the system on the external static field. Notably, we consider systems where, due to symmetry, the even harmonics are not generated if no static field is used to polarize the system. The addition of the polarizing field, however, breaks the symmetry, and even harmonics clearly emerge in the resulting spectra. We analyze how the signal evolves as a function of the different parameters, with a considerable increase of the strength of the even harmonic when both the intensity of the excitation laser and the applied bias (Figure 1a) are large. Furthermore, we show a strong plasmonic enhancement when the frequency of a given high-order harmonic is resonant with a plasmon resonance, as illustrated in Figure 1b, where the second harmonic for a laser illuminating at energy $\Omega$ and the resonant absorption spectra for a laser energy $2\Omega$ are very similar.

In summary, we demonstrate that quantum effects can have a strong influence on plasmonic systems. The possibility to engineer the optical response of the metallic nanostructures by applying an external bias, as demonstrated here for non-linear generation of light, is a key step for active control of plasmonic systems.




**Figures 1: Figures 1: Second harmonic generation when illuminating an aluminum sphere resonant near 9 eV. (a) The strength of the second harmonic increases approximately quadratically as the static polarizing field becomes larger. (b) When the frequency of the second harmonic 2Ω coincides with the plasmonic resonance, the efficiency of the process is strongly enhanced (blue line). The plasmonic nature of the enhancement is emphasized by plotting the elastic absorption at 2Ω (green line).**

**Acknowledgements** We acknowledge the project FIS2013-41184P from the MINECO. R. E. acknowledges the Fellowship Gipuzkoa of the Gipuzkoako Foru Aldundia through FEDER Funds "Una manera de hacer Europa"

**REFERENCES**

1. M. S. Tame et al, "Quantum Plasmonics", Nat. Phys. 9, 329–340, 2013
2. Zhu, W. et al, "Quantum mechanical effects in plasmonic structures with subnanometre gaps" Accepted
3. Zuloaga, J. et al. "Quantum Description of the Plasmon Resonances of a Nanoparticle Dimer" *Nano Lett.* 9, 887-891, 2009
4. R. Esteban et al., "Bridging quantum and classical plasmonics with a quantum-corrected model" *Nat. Comm.* 3, 825, 2012
5. Barbry, M. et al, "Atomistic Near-Field Nanoplasmonics: Reaching Atomic-Scale Resolution in Nanooptics" *Nano Lett.* 15, 3410−3419, 2015
6. Zhang, P. et al. "Ab initio nanoplasmonics: The impact of atomic structure" *Phys. Rev B* 90, 161407(R), 2014
7. K. J. Savage et al, "Revealing the quantum regime in tunnelling plasmonics" *Nature* 491, 574, 2012
8. Scholl, J. A. et al, "Observation of Quantum Tunneling between Two Plasmonic Nanoparticles" *Nano Lett.* 13, 564−569, 2013
9. Scholl, J. A. et al, "Evolution of Plasmonic Metamolecule Modes in the Quantum Tunneling Regime" *ACS Nano* 10, 1346−1354, 2016
10. Marinica, D. C. et al. "Active quantum plasmonics" *Sci. Adv.*1:e1501095, 2015

# Metasurface Generation of Accelerating Light

**M. Henstridge**[1,2], **C. Pfeiffer**[1,3], **D. Wang**[1,4], **A. Boltasseva**[1,4], **V. Shalaev**[1,4], **A. Grbic**[1,3], and **R. Merlin**[1,2]

[1]Center for Photonics and Multi-Scale Nanomaterials, University of Michigan, Ann Arbor, 48109, USA

[2] Department of Physics, University of Michigan, Ann Arbor, 48109-1040, USA

[3]Department of Electrical Engineering and Computer Science, University of Michigan, Ann Arbor, 48109-2122, USA

[4]School of Electrical and Computer Engineering and Birck Nanotechnology Center, Purdue University, West Lafayette, IN, 47907, USA

[*]corresponding author: mhenst@umich.edu

**Abstract**: We demonstrate a compact, planar-optic approach for the generation of accelerating near-IR laser pulses by illuminating metasurfaces consisting of plasmonic nanoantennas patterned onto a glass substrate. Two accelerating beam trajectories were generated within the glass and imaged onto a CCD; close agreement is shown with theory. The simplicity and compactness of the proposed planar-optics approach to generating accelerating beams opens new opportunities in the realization of accelerating beams and related devices for advanced manipulation of light.

Solutions to the Helmholtz equation that self-accelerate belong to a novel class of non-diffracting solutions to Maxwell's equations. Their application to curved plasma channels [1], microparticle manipulation [2] and nonlinear optics [3] has been reported. Typically, accelerating beams are generated using spatial light modulators [4], a method that cannot generate highly non-paraxial beams in high index materials, since free space optical systems cannot produce transverse wavenumbers greater than $k = \omega c$; $c$ is the speed of light and ω is the light frequency. Alternatively, accelerating beams can be generated without this constraint by illuminating a metasurface. The use of a metasurface reduces the optical setup to a single element, thus introducing new opportunities for implementing beams that curve into compact integrated systems. Here, we report the first implementation of a metasurface to generate an accelerating beam.

We demonstrate the generation of accelerating optical laser pulses inside a glass substrate patterned with a metasurface consisting of V-shaped plasmonic nanoantennas [5]. Tuning the nanoantenna's geometry allows the phase of the cross-polarized scattered field to vary between $0^o$ and $360^o$. The metasurface was designed to generate a half-Bessel beam [4] that accelerates along a portion of a circular trajectory inside the glass when illuminated with a Gaussian beam of wavelength 800 nm at an incident angle of $45^o$. The V-shaped plasmonic nanoantennas can only redirect ~ 5% of the incident power to the desired direction, whereas ~ 50% passes through the metasurface unperturbed. Using this "off-axis" illumination of the metasurface allows the accelerating beam to be spatially separated from the unperturbed beam; see Figure 1.

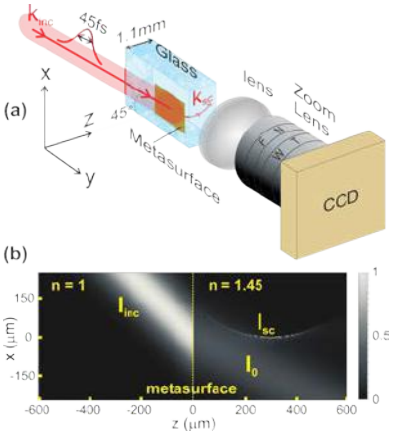



**Figure 1:** (a) Experimental set-up used to illuminate the metasurface and image the resulting accelerating beam. (b) Calculated intensity plot describing the off-axis illumination of the metasurface.

The nanoantennas were fabricated using standard electron-beam lithography on ITO-coated glass, followed by electron-beam evaporation of 3 nm Ti / 30 nm Au and lift-off processes. To facilitate the imaging of the accelerating beam inside the glass, one of the edges of the ITO-coated glass slide was polished to optical quality prior to fabrication; the leading edge of the metasurface was fabricated within 500 μm from the edge of the slide

The metasurface was illuminated with a mode-locked Ti:Sapphire oscillator, which produced pulses of central wavelength 800 nm and bandwidth of 30 nm at full-width half-maximum (FWHM) at a 78 MHz repetition rate. As shown in Fig. 1(a), a standard imaging setup with a resolution of 3 μm was used to image the intensity of the accelerating beam by collecting Rayleigh-scattered light from the beam trajectory.

Figure 2 shows images of accelerating beams of 400μm and 100μm radii of curvature along with results of intensity calculation. The features of the experimental trajectories resolved by the imaging system agree very well with those from the simulations.

In summary, we demonstrated a simple, planar-optics approach for generating broadband accelerating optical pulses in a glass substrate. Our results hold promise for the integration of curved trajectory beams into a wide range of photonic systems.

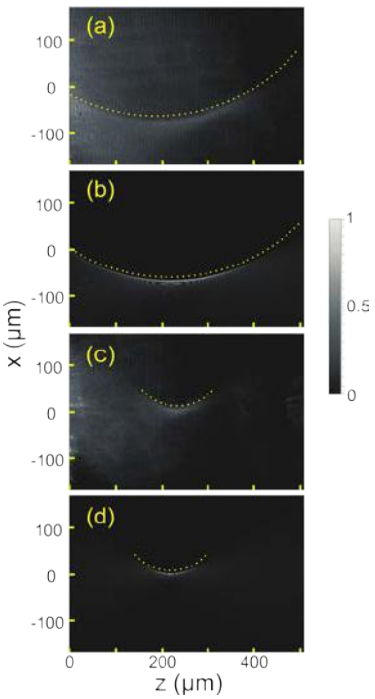



**Figure 2:** Experimental (a), (c) and calculated (b), (d) intensity plots for the metasurfaces with radius of curvature 400 μm and 100 μm, respectively. Dotted lines are guides to the eye, tracing a partial circular trajectory.

**Acknowledgement**: This work was supported by the U.S. National Science Foundation under the Materials Research Science and Engineering Center program DMR-1120923.

**REFERENCES**

1. Polynkin, P., Kolesik, M., Moloney, J.V., G. A. Siviloglou, and D. N. Christodoulides, "Curved plasma channel generation using ultraintense Airy beams," *Science* Vol. 324, 229–232, 2009.
2. Zhang, P., Prakash, J., Mills, M.S., Efremidis, N.K., D.N. Christodoulides, and Z. Chen, "Trapping and guiding microparticles with morphing autofocusing Airy beams," *Opt. Lett.* Vol. 36, No.15, 2883–2885, 2011.
3. Dolev, I., Kaminer, I., Shapira, A., M. Segev, and A. Arie, "Experimental observation of self-accelerating beams in quadratic nonlinear media," *Phys. Rev. Lett.* Vol. 108, 113903, 2012.
4. Zhang, P., Hu, Y., Cannan, D., Salandrino, A., Li, T., Morandotti, R., X. Zhang, and Z. Chen, "Generation of linear and nonlinear nonparaxial accelerating beams," *Opt. Lett.* Vol. 37, No.14, 2820-2822, 2012.
5. Yu, N., Genevet, P., Kats, M.A., Aieta, F., Tetienne, J., F. Capasso, and Z. Gaburro, "Light Propagation with Phase Discontinuities: Generalized Laws of Reflection and Refraction," *Science*, Vol. 334, 333–337, 2011.

# Quenching, Plasmonic, and Radiative Decays in Nanogap-based Antennas

**R. Faggiani*, P. Lalanne**

Laboratoire Photonique, Numérique et Nanosciences (LP2N), UMR 5298, CNRS-IOGS-University of Bordeaux, 33400 Talence, France
*remi.faggiani@institutoptique.fr

**Abstract -** In this contribution, we show that nanogap-based antennas can provide large spontaneous emission rate enhancement and good extraction efficiency despite the close proximity between quantum emitters and metallic objects. We argue thanks to accurate closed-form expressions that quenching can be overcome by the strong decay into slow gap-plasmons modes supported by nanogaps. To support these theoretical predictions and help future designs, we provide a numerical analysis of nanocube-type antennas and propose a classification of nanoantennas based on two important figures of merit, the emission rate and the extraction efficiency.

It is generally accepted that sub-wavelength geometries increase the spontaneous emission rate of quantum emitters by orders of magnitude by concentrating light. As shown by numerical calculations and experimental measurements, it is also accepted that this enhancement can be achieved with relatively good efficiencies, ~ 10-60% depending on the geometry [1]. However the precise physical mechanisms that drive the emission of quantum emitters placed very close to metal surfaces in tiny gaps are not well understood. In particular, it is unclear from the literature why a good efficiency is achieved despite the proximity to the metal, where quenching should dominate. So far, it has been discussed only with scattered numerical calculations performed for specific gap thicknesses and metal dielectric constants [2,3].

In order to better engineer optical nanoantennas, it is important to first understand the different physical mechanisms at play when quantum emitters in nanogaps emit light in the immediate vicinity of metal surfaces and then draw a relationship between this basic situation and more complex problems of light emission and coupling with subwavelength architectures.

This is exactly the approach that is adopted here. With accurate and simple closed-form expressions for the quenching rate and the decay rate into gap plasmons, we disclose that the total spontaneous emission rate of quantum emitters in nanometer-thin gaps can largely overcome quenching, for specifically selected metallic and insulator materials, regardless of the gap size. Furthermore, to help further designs, we propose a classification of nanogap emitting devices based on two important figures of merit, the emission rate acceleration and the extraction efficiency, and further position a whole family of state-of-the-art devices based on nanogaps formed by nanocubes laying on metallic substrates in the classification [4].

**Acknowledgmen**t. R. F. acknowledges financial support from the French "Direction Générale de l'Armement" (DGA).

**REFERENCES**

[1] Akselrod, G. M.; Argyropoulos, C.; Hoang, T. B.; Ciracì, C.; Fang, C.; Huang, J.; Smith, D. R.; Mikkelsen, M. H. Probing the mechanisms of large Purcell enhancement in plasmonic nanoantennas. Nature Photon., **8**, 835-840 (2014)

[2] Russell, K. J.; Liu, T.-L.; Cui, S.; Hu, E. L. Large spontaneous emission enhancement in plasmonic nanocavities. Nature Photon., **6**, 459-462 (2012).

[3] Jun, Y. C.; Kekatpure, R. D.; White, J. S.;Brongersma, M. L. Nonresonant enhancement of spontaneous emission in metal-dielectric-metal plasmon waveguide structures. Phys. Rev. B, **78**, 153111 (2008).

[4] R. Faggiani, J. Yang, P. Lalanne, "Quenching, Plasmonic, and Radiative Decays in Nanogap Emitting Devices", ACS Photonics, **2**, 1739-1744 (2015).

# Multipolar decomposition of the field scattered by nonspherical and noncylindrical particles

**M. G. Mandujano**[1], and **E. R. Méndez**[1]

[1] Centro de Investigación Científica y de Educación Superior de Ensenada, Mexico.
gmanduja@cicese.edu.mx

**Abstract**— Employing a surface integral equation method we study the scattering of light by dielectric particles of various shapes, and decompose the numerically calculated scattered field to determine the strength of the multipolar fields excited in the particle.

Optical metamaterials are composite artificial materials that owe their properties to the size and shape of their subwavelength constituents. The excitation of different kinds of optical resonances in the inclusions is of crucial importance for the design of novel optical metamaterials, and the optical properties that may be obtained in the presence of electric and magnetic resonances can be rather unusual.

Mie type solutions exist for simple geometries like that of a sphere or a cylinder. In such cases, the basis functions, and the strength of the coefficients that appear in the series, provide a fairly clear interpretation of the nature of the excitation in the particle. With such tools, for instance, it can be shown that it is possible to excite strong magnetic dipolar resonances in dielectric particles of high refractive index [1].

Several numerical technique have been developed to study the scattering of light by particles of non-spherical and non-cylindrical shapes. Unfortunately, in most cases, the solution provides little insight into the physical processes that give rise to the results. It is thus important to develop tools that may be of help in the visualization of the physical processes involved.

In this work, we present results for the angular scattering of dielectric particles of high refractive index obtained with a method based on surface integral equations and the method of moments. The calculated scattered field is then decomposed into the appropriate multipolar basis functions to obtain information about the multipoles excited in the particle. The results obtained may be relevant for the design of optical metamaterials with a magnetic response.

**REFERENCES**

1. A. García-Etxarri, R. Gómez-Medina, L. S. Froufe-Pérez, C. López, L. Chantada, F. Scheffold, J. Aizpurua, M. Nieto-Vesperinas, and J. J. Sáenz, "Strong magnetic response of submicron Silicon particles in the infrared," Opt. Expr. **19**, 4815-4826 (2011).

# Tuning the plasmonic resonances of metallic nanoparticles for thermal applications.

**J. Gabriela Calvillo**[1] and **Eugenio R. Méndez**[1]

[1] Centro de Investigaciión Científica y de Educación Superior de Ensenada (CICESE), Baja California, México
jcalvill@cicese.edu.mx

**Abstract**— The resonant absorption of light in metallic nanoparticles can be used to transform them into switchable nanosources of heat. Modifications of the shape of the nanoparticle permit also the tuning of the resonance to a specific wavelength. In this work, we study the evolution of the absorption peaks as the dimensions of a rectangular prism nanoparticle made of gold are changed.

The phenomenon of selective optical absorption by metallic nanoparticles has been used in architectonic applications for several centuries. Much has been learned about these plasmonic effects since those days, and the development of nanoscale fabrication techniques has opened novel possibilities for applications. Also of interest, are the thermal aspects associated with this absorption. When illuminated by a light source with the appropriate wavelength, the nanoparticles can be viewed as controllable sources of heat, a fact has been used in methods to selectively kill cancer cells.

The temperature change induced by the absorption of light in the particle is proportional to its absorption cross section [1]. Depending on the application, it might be necessary to tune the absorption peak to a particular wavelength and there might also be some requirements on the spectral width of the resonance. The spectral position and strength of these resonances depend on the size, shape and dielectric constant of the nanoparticles, as well as the medium in which they are embedded. Modification of the particle shape permit the tuning of the resonance over a fairly large spectral range.

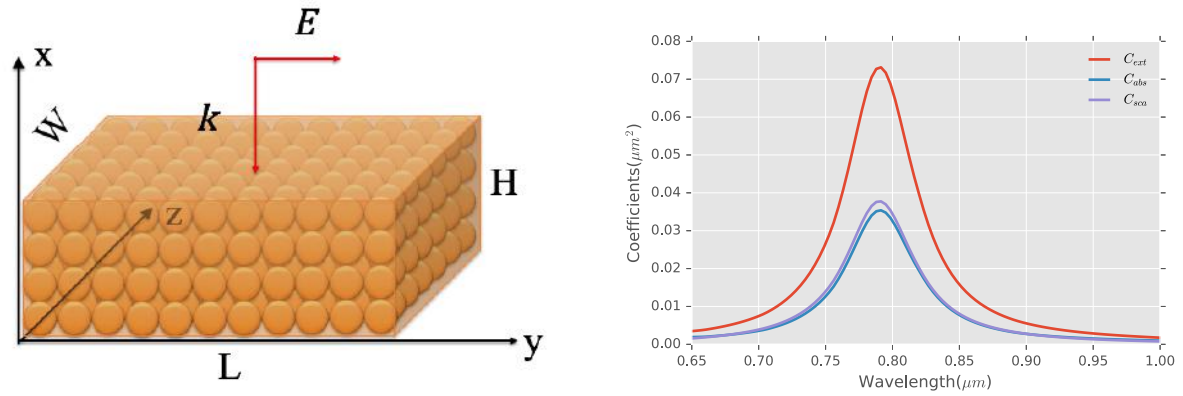
For many thermal applications that require the tuning of the plasmonic resonance, it is important to consider questions like the optimum shape for a particle of a given material and the consequences of modifying its shape on the heating properties. In this work, we present a systematic study of the behavior of the absorption peak of gold nanoparticles using different strategies for tuning the resonance to different spectral regions.

In particular, we consider rectangular prisms (cuboids) of gold immersed in water, whose nanometric dimensions (length $L$, width $W$ and thickness $H$) are used as the tuning parameters. The geometry considered is illustrated in Fig. 1(a). Our calculations are based on the discrete-dipole approximation (DDA) method [2], which constitutes a flexible and powerful technique for computing scattering and absorption by particles of arbitrary shape. We search for resonances that lie within the first biological window, 700-950nm [3]. Some illustrative results for the cross sections are shown in Fig. 1(b).

We study the evolution of the maxima of the absorption cross section peaks, as we change the geometrical parameters of the gold nanoprisms. With reference to the illumination conditions illustrated in Fig. 1(a), the results presented in Fig. 2(a) show that the maximum of the absorption cross section increases as the resonance is tuned to longer wavelengths by reducing $W$ and $H$. On the other hand, the results presented in Fig. 2(b) show that changing the length $L$ of the nanoparticle (dimension along the direction of vibration of the electric field) permits the tuning of the resonance with very little effect on the maximum of the absorption cross section.

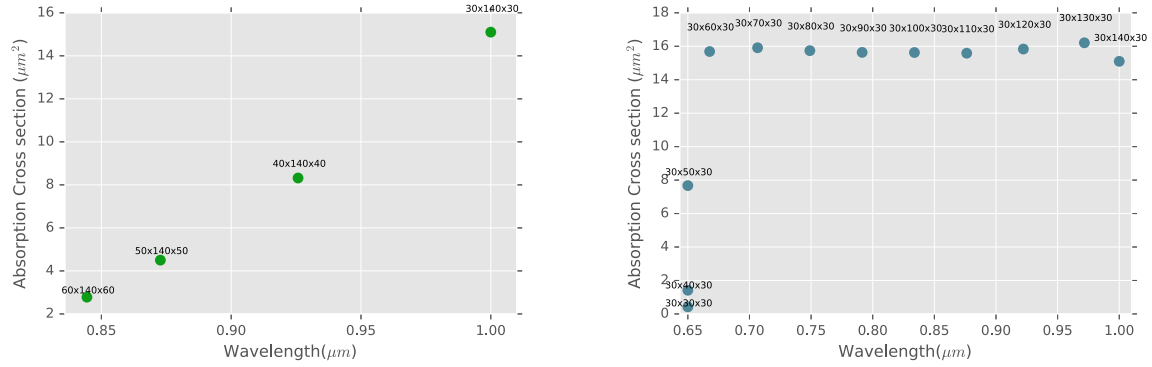
## REFERENCES

1. Baffou, G. and Quidant, R., "Thermo-plasmonics: using metallic nanostructures as nanosources of heat" *Laser Photonics Rev*, **7**, 171–187 (2013).
2. Draine, B. T. and Flatau, P. J., "Discrete-dipole approximation for scattering calculations", *J. Opt. Soc. Am.*, **11**, 1491–1499 (1994).
3. Martínez Maestro, L. *et. al.*, "Gold nanorods for optimized photothermal therapy: the influence of irradiating in the first and second biological window", *RSC Adv.*, **4**, 54122 (2014).




(a) (b)

Figure 1: (a) Illustration of the geometry considered and the dimensions of the nanoparticle: $W$–width, $H$–height, and $L$–length. (b) Absorption, scattering and extinction cross sections versus wavelength for a nanoparticle with dimensions $30 \times 90 \times 30$ nm.




(a) (b)

Figure 2: (a) Maximum of absorption coefficients increasing the $W$ and $H$ parameters, fixing $L$; (b) and increasing only $L$, with $W$ and $H$ fixed.

# Modelling of phase change material based tunable meta-materials

**D. N. Chigrin**[1*]

[1]Institute of Physics (IA), RWTH Aachen University, Aachen, Germany

[*]corresponding author: chigrin@physik.rwth-aachen.de

Today it is possible to engineer the building blocks (meta-atoms) of artificial materials (meta-materials) with feature sizes smaller than the wavelength of light. The ability to design meta-atoms in a largely arbitrary fashion adds a new degree of freedom in material engineering, allowing to create artificial materials with unusual electromagnetic properties rare or absent in nature. Achieving tunable, switchable and non-linear functionalities of meta-materials at individual meta-atom level could potentially lead to additional flexibility in designing active photonic devices. Active tunability, switching or non-linearity of meta-material properties can be achieved by electro-optical, electromagnetic or micro-electromechanical altering of the meta-atom materials. These include among others, meta-materials based on phase-change materials, whose properties could be altered by thermal or photo-thermal means. In this presentation, our recent results on design and modeling of active meta-materials based on plasmonic and phononic materials and incorporating phase-change materials as active elements will be discussed.

# Discontinuous Galerkin Methods in Nano-Photonics

**Kurt Busch**[1]
[1]Humboldt-Universität zu Berlin, AG Theoretische Optik & Photonik, 12489 Berlin
and
Max-Born-Institut, 12489 Berlin, Germany
[*]corresponding author: kurt.busch@physik.hu-berlin.de

**Abstract**-An overview of the recent progress in applying the Discontinuous Galerkin Finite-Element Time-Domain approach to nano-plasmonic systems including the development of advanced material models is provided.

Discontinuous Galerkin (DG) methods facilitate efficient computations of nano-photonic systems [1] by combining the flexibility of finite element approaches with efficient time-stepping capabilities. While the former allows for an accurate representation of complex geometries, the latter requires material models that are amenable to auxiliary differential equations techniques. This latter aspect specifically includes material models for magneto- [2] and/or nonlinear-optical properties.

In this talk, the present state of Discontinuous Galerkin Time-Domain (DGTD) approaches to nano photonic systems is presented. This includes (i) methodic aspects such as convergence properties of DGTD computations with regards to the above-mentioned material models as well as (ii) selected applications such as the computation electron energy loss spectra [3,4] and modified emission dynamics [5], and the nonlinear-optical properties of plasmonic nanostructures [6,7].

**REFERENCES**

1. K. Busch et al. “Discontinuous Galerkin methods in nanophotonics,” *Laser Photon. Rev.*, Vol. 5, 773–808, 2011.
2. C. Wolff et al., “Simple magneto–optic transition metal models for time–domain simulations,” *Opt. Express*, Vol. 21, 12022–12037, 2013.
3. F. von Cube et al., “From Isolated Metaatoms to Photonic Metamaterials: Evolution of the Plasmonic Near-Field,” *Nano Lett.*, Vol. 13, 703–708, 2013.
4. B. Schröder et al., “Real-space imaging of nanotip plasmons using electron energy loss spectroscopy,” Phys. Rev. B, Vol. 92, 085411/1–7, 2015.
5. A.W. Schell et al., “Scanning Single Quantum Emitter Fluorescence Lifetime Imaging: Quantitative Analysis of the Local Density of Photonic States,” Nano Lett., Vol. 14, 2623–2627, 2014.
6. A. Hille et al., “Second Harmonic Generation from Metal Nano-Particle Resonators: Numerical Analysis On the Basis of the Hydrodynamic Drude Model,” J. Phys. Chem. C, Vol. 120, 1163–1169, 2016.
7. D. Huynh et al., “Ultrafast Three-Wave-Mixing in Plasmonic Nanostructures,” Appl. Phys. B, in press

# Plasmonic and all-dielectric nanoantennas for wavelength-controlled directional scattering of visible light

**P. Van Dorpe**[1,2]**, J. Li**[1,2]**, D. Vercruysse and N. Verellen**[2,1]
[1]Imec, Kapeldreef 75, 3001 Heverlee, Belgium
[2]KULeuven, Department of physics, Celestynenlaan 200D, 3001 Heverlee, Belgium
[*]corresponding author: pvandorp@imec.be

**Abstract**- We will review our recent work on dielectric scattering using both metal and dielectric nano-antennas.

Optical antennas have the prospect to redirect light rays into engineered directions at the subwavelength scale. They offer new options for photodetection, color routing, fluorescence emission and sensing applications. Previously, metallic nanoantennas based on localized surface plasmon resonance (LSPR) have commonly been exploited to fulfill this purpose, e.g. the gold Yagi-Uda array and split-ring resonator. However, the intrinsic ohmic losses of metals are large especially in the visible range, hindering further efficiency improvement for practical applications. In addition, the interaction of the metallic nanoantennas with the magnetic component of light is relatively weak, adding to their lack of highly tunable scattering directionality. In this presentation, we will demonstrate our recent experimental progress on plasmonic, Au, nano-antennas[1,2] and all-dielectric nanoantennas made of amorphous silicon with tunable scattering directionality. Our nanoantennas are designed as V-shaped single element and fabricated using electron-beam lithography followed by dry reactive ion etching. It is illustrated that the scattering cross section of the silicon nanoantenna can be considerably higher than that of comparable Au antennas. In addition, the extinction coefficient of amorphous silicon is adequately low in the considered wavelength range, resulting in minimal absorption losses and an enhanced scattering efficiency. More interestingly, compared to Au nanoantennas that exhibit light scattering in a single particular direction, by carefully engineering the geometry of the silicon nano-antennas, their scattering can be effectively tuned into two opposite directions within the visible range. Over a spectral range of less than 100 nm, the scattering directionality gradually shifts from the leftward to the rightward. More simulation results based on the finite difference time domain (FDTD) methods are available to perfectly match and corroborate our experimental measurement. Such unique optical properties make the silicon nanoantenna promising candidates for novel low-loss optical devices that can enable unprecedented control over the scattering directionality.

## REFERENCES

1. D. Vercruysse, Y. Sonnefraud, N. Verellen, F. B. Fuchs, G. Di Martino, L. Lagae, V. V. Moshchalkov, S. A. Maier, and P. Van Dorpe, *Nano Letters* **2013** *13* (8), 3843-3849.
2. D. Vercruysse, X. Zheng, Y. Sonnefraud, N. Verellen, G. Di Martino, L. Lagae, G. A. E. Vandenbosch, V. V. Moshchalkov, S. A. Maier, and P. Van Dorpe, *ACS Nano* **2014** *8* (8), 8232-8241

# Polarization singularities on high index nanoparticles

**Aitzol Garcia-Etxarri**[1]

[1] Donostia International Physics Center (DIPC), Donostia - San Sebastian 20018, Spain

[*]corresponding author: aitzolgarcia@dipc.org

**Abstract**- In this contribution, we study the emergence of polarization singularities in the scattered fields of optical resonators excited by linearly polarized plane waves. First, we prove analytically that combinations of isotropic electric and magnetic dipoles can sustain L surfaces, and C lines that propagate from the near-field to the far field. Moreover, based on these analytical results, we derive anomalous scattering Kerker conditions trough singular optics arguments. Secondly, through exact full-field calculations, we demonstrate that high refractive index spherical resonators present such topologically protected features. Furthermore, we calculate the polarization structure of light around the generated C lines, unveiling a Möbius strip structure in the main axis of the polarization ellipse. These results prove that high-index nanoparticles are excellent candidates for the generation and control of polarization singularities and that they may lead to new platforms for the experimental study of the topology of light fields around optical antennas [1].

We prove that high index nanoparticles support polarization singularities that propagate from the near-field to the far-field. In particular, C lines arise from the interference of the fields scattered by electric and magnetic isotropic dipolar excitations. The study of polarization singularities is a rapidly growing field of research, on one hand due to the intrinsic theoretical interest of the topology of light fields and on the other hand because of the upcoming applications on quantum information systems. This theoretical contribution proves that combinations of electric and magnetic dipoles supported by high index nanoparticles create such topologically protected features and may facilitate new experimental platforms to study polarization singularities

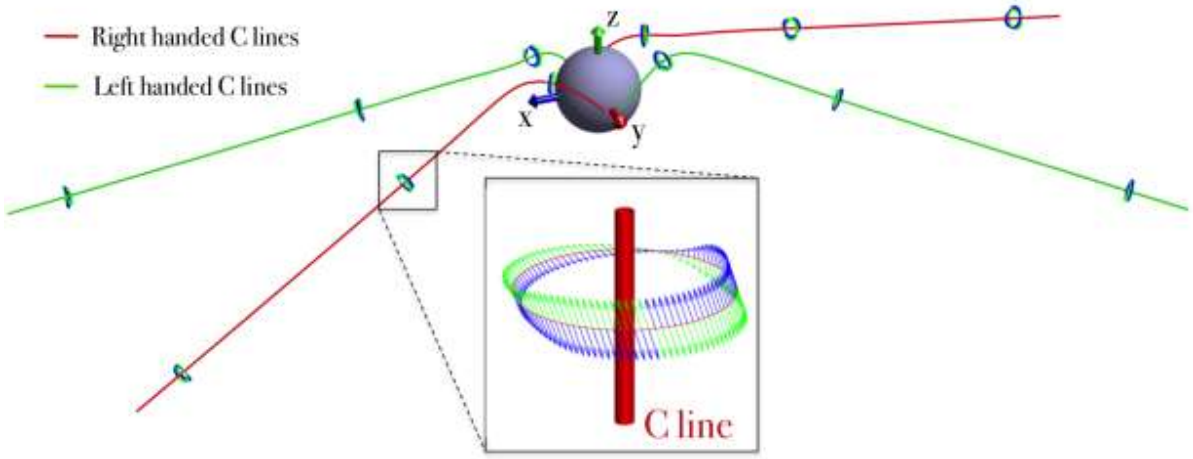



**Figure 1:** C lines around a Si nanoparticle for lambda=1110nm in all the radiation regions. The blue sphere represents the silicon nanoparticle. Green and red lines are the left and right-handed C lines respectively. The main axis of the polarization ellipse forms a single twist Möbius strip in any curve enclosing a C line. The inset is a zoom of this polarization structure around one particular $C$ line.

**Acknowledgements**: A. G.-E. received funding from the Fellows Gipuzkoa fellowship of the Gipuzkoako Foru Aldundia through FEDER "Una Manera de hacer Europa".

**REFERENCES**

1. A. Garcia-Etxarri “Polarization singularities on high index nanoparticles“, arXiv:1601.04365 (2016)

# Towards large-scale highly sensitive substrates for surface enhanced spectroscopies

**P. M. ADAM**[1]

[1]Laboratoire de Nanotechnologie et d'Instrumentation Optique, ICD, CNRS UMR 6281, Université de Technologie de Troyes, 12 Rue Marie Curie, CS42060, 10004 Troyes Cedex, France

[*]corresponding author: adam@utt.fr

**Abstract-** Nanoplasmonics concerns the excitation, manipulation and detection of the surface plasmons at the nanometric scale. It has highly potential applications for ultrasensitive biochemical sensing. Surface enhanced spectroscopies are the ultimate sensor tools as they can reach single molecule sensitivity. We will present in this paper our latest results towards the realization of highly controllable and reproducible nanoplasmonics substrates.

Plasmonics is a now well-established field finding numerous applications in pharmacology, biology, optoelectronics and metamaterials among others. For the sensitive detection of molecules or markers Surface Enhanced Spectroscopies, such as Surface Enhanced Raman Spectroscopy (SERS) and Surface Enhanced Fluorescence (SEF), are widespread and the most used for applications. Both these enhanced spectroscopies rely on local field enhancements in the near vicinity of resonant metallic nanoparticles when Surface Plasmon oscillations are driven for a specific optical wavelength. SERS can achieve single molecule detection when two or more metallic nanoparticles are coupled through their near-fields, resulting in enhancements usually ranging from 4 up to 10 orders of magnitude, even if the way to evaluate such an absolute magnitude of enhancement is still a subject of debate. A drawback is that these highly sensitive SERS substrates are difficult to reproduce and to control.

Less enhancement is obtained with SEF but usually the intrinsic fluorescence cross section of a molecule is more than 10 orders of magnitude more important than that of its non-resonant Raman cross-section. In SEF one has to take into account the finite lifetime of the excited levels of the molecule of interest, which results in quantum yield modifications in the presence of the metallic nanoparticles. Quantum yield can be enhanced or even reduced, leading in the latter case to a competition with local field excitation enhancement and thus the possibility of quenched fluorescence from the emitters.

This contribution will show our recent progress towards the realization of large-scale and highly sensitive substrates for surface enhanced spectroscopies [1-3].

**Acknowledgements**: The authors would like to acknowledge COST Action MP1302 Nanospectroscopy.

**REFERENCES**

1. Yehia Khaywah, M., S. Jradi, G. Louarn, Y. Lacroute, J. Toufaily, Tayssir Hamieh and P.-M. Adam, "Ultra Stable, Uniform, Reproducible and Highly Sensitive Random Arrays of Bimetallic Nanoparticles as Reliable Large Scale SERS Substrates, *The Journal of Physical Chemistry C*., 119 (46), 26091–26100, 2015

2. Muravitskaya, A., A. Rumyantseva, S. Kostcheev, V. Dzhagan, O. Stroyuk and P.-M. Adam, “Enhanced Raman scattering of ZnO nanocrystals in the vicinity of gold and silver nanostructured surfaces“, *Optics Express*, 24 (2), A168-A173, 2016
3. Ashraf, S., M. Skandary, M. Y. Khaywah, M. Metzger, A. J. Meixner, P.-M. Adam and M. Brecht, “Effects of irregular Bi-metallic nanostructures on fluorescence emission of Photosystem I from Thermosynechococcus elongatus“, *Photonics*, 2, 838-854, 2015

# Hybrid optoplasmonic platforms for sensing, spectroscopy, energy transfer, and radiative cooling

**Svetlana V. Boriskina[1,*], Jonathan K. Tong[1], and Gang Chen[1]**
**Wonmi Ahn[2], Yan Hong[2], Xin Zhao[2], and Bjoern Reinhard[2]**
[1] Department of Mechanical Engineering, Massachusetts Institute of Technology, Cambridge, MA, USA
[2] Department of Chemistry, Boston University, Boston, MA, USA
[*]corresponding author: sborisk@mit.edu

**Abstract**- I will discuss our efforts in developing hybrid optoplasmonic architectures to tailor resonant energy transfer between photons, plasmons, quantum emitters and elementary heat carriers. Near- and far-field electromagnetic coupling between plasmonic and photonics elements can be tailored to trigger new physical effects, which add new functionalities to optoplasmonic platforms. Among the emergent properties of optoplasmonic structures is their ability to simultaneously achieve extreme spectral and spatial localization of light, making possible ultrasensitive schemes for optical detection, spectroscopy, and imaging. Counter-intuitively, the enhanced light focusing in optoplasmonic structures may be accompanied by reduced absorption in their metal constituents. Furthermore, hybrid systems can be designed to provide passive cooling via radiative heat extraction. A combination of the strong light localization and spectral selectivity achievable under lower operating temperatures in optoplasmonic devices yields many applications in ultrasensitive detection, spectroscopy, imaging, thermal emission manipulation and radiative cooling.

**Acknowledgements**. This work was supported by the U.S. Department of Energy, Office of Basic Energy Sciences, Division of Materials Science and Engineering Award No. DE-FG02-02ER45977 (for the near-field energy transfer and far-field thermal emission manipulation) and Award No. DE-SC0010679 (for light focusing and resonant energy transfer).

**REFERENCES**

1. Boriskina, S. V., Reinhard, B. M., *Proc. Natl. Acad. Sci. U. S. A.* Vol. 108, No. 8, 3147–3151, 2011.
2. Ahn, W., Boriskina, S. V., Hong, Y.., Reinhard, B. M., *ACS Nano*, Vol. 6, no. 1, 951–960, 2012.
3. Santiago-Cordoba, M. A., Cetinkaya, M., Boriskina, S. V., Vollmer, F.., Demirel, M. C., *J. Biophotonics*, Vol. 638, No. 8, 629–638, 2012.
4. Santiago-Cordoba, M.A., Boriskina, S.V., Vollmer, F., Demirel, M.C., *Appl. Phys. Lett.*, Vol. 99, No 7, 073701, 2011.
5. Boriskina, S. V., Reinhard, B. M., Opt. Express, Vol. 19, No. 22, 22305, 2011.
6. Boriskina, S. V., Weinstein, L. A., Hsu, W.-C., Tong, J., Chen, G., "Hybrid optical-thermal nanoantennas for enhanced light focusing and radiative cooling," submitted, 2016.
7. Ahn, W., Hong, Y., Boriskina, S.V., Zhao X., Reinhard, B.M., *Nanophotonics*, Vol. 4, No. 1, 250–260, 2015.
8. Hong, Y., Ahn, W., Boriskina, S.V., Zhao, X., Reinhard, B.M., *J. Phys. Chem. Lett*. Vol. 6, 2056–2064, 2015.
9. Boriskina, S.V., H. Ghasemi, and G. Chen, *Mater. Today*, vol. 16, pp. 379–390, 2013.

# Electrically-Small Dielectric Resonator Elements for Electromagnetic Energy Harvesting

**Ahmed Z. Ashoor and** [1] and **Omar M. Ramahi**[1]

[1]University of Waterloo, Canada
aashoor@uwaterloo.ca

**Abstract**— This summary presents electrically-small resonator elements as efficient energy harvesters in the microwave regime. The study examined different array factors that affect the efficiency of the harvested power. The coupling between adjacent elements and the self-coupling within each unit were studied to highlight their effects on the overall harvesting efficiency.

Several researchers have studied rectifying antenna systems (rectennas) to provide power for low-power devices. Commonly used rectennas consist of a microwave harvester to deliver AC power and rectifying circuitry that would then convert the AC power to usable DC [1, 2]. Those metallic harvesters suffer from the metallic losses when operating in high frequencies [3]. In this summery we present a study for electrically small none-metallic DR elements as an efficient microwaves to AC energy harvester. We showed using an aperture feeding a way to control the coupling in the array configuration as the spacing between electrically-small resonators is critical.

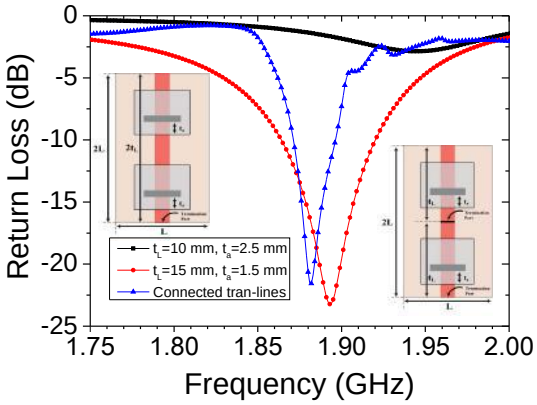



Figure 1: The return loss of to three different configurations of a single cell DRA (refer to Fig. **??** for the aperture position and transmission line length). The two schematics attached to the figure show how the two configurations when $t_a = 1.5\ mm$ and $t_L = 15\ mm$ were set, each cells was terminated (right) and vertical cells were connected with single transmission line (left). Note: here we only showed an example of $2 \times 1$ elements.

Initially and for the purpose of validating the concept, an electrically-small DR element operating at frequency of $2GHz$ was considered. Our aim is to build a large array energy harvester (e.g., $20 \times 20$ elements) using the electrically small DRA cell that was established in previous section. Once the DRA cells became part of an array, the self-coupling (i.e. the energy coupled from the aperture to the DR) within each DRA cell was affected by any neighboring adjacent cell. It was noticed from the return loss of the infinite array configured using the dimensions of the single DRA cell that most of the power was reflected as shown in Fig. 1. To regain an efficient self-coupling for the array cells, different aperture positions and transmission line lengths were studied. Here, the dimensions of the unite cell of the infinite array has to be kept electrically-small and unchanged, and only the aperture position and the length of transmission line were modified to minimize the return loss reflection. Two configurations are reported here. The first case was when having $t_a = 1.5\ mm$ and $t_L = 15\ mm$. In this case, the transmission line became of the same length as the single cell where $L = 15\ mm$ (refer to the right schematic attach to Fig. 1). The second case was to study the first mentioned configuration without having the terminated loads between the array

cells (only the front load was kept) while keeping other specifications unchanged. For this setup, a $10 \times 1$ cells has been considered as a unit cell fed by a single transmission line terminated with $50\Omega$ (refer to the left schematic attach to Fig. 1). The return loss of the two cases is shown in Fig. 1.

Now we consider studying the infinite array for the above mentioned configurations as an energy harvester. A normally incident to plane wave was used as a source of the incident field. The overall harvesting efficiency of the array $\eta_{eff}$ was defined as the ratio of the total time-average power $P_{out}$ to the microwave power $P_{in}$ available at the entire footprint area and dependent only on the incident plane wave, its propagation direction and polarization. This efficiency is given by [1]:

$$\eta_{eff} = P_{out}/P_{in} \tag{1}$$

The harvesting efficiency of the normally incident microwave power based on the above efficiency definition for the three configurations are shown in Fig. 2. The case with connected transmission line that was terminated only in the front (the $10 \times 1$ unit cell for the infinite array) gave the highest efficiency among the cases with a harvesting efficiency close to 85%. The study shows a suitable and configuration for an efficient DR array elements that can be efficiently matched and integrated to a full-efficient rectenna system for microwave energy harvesting.

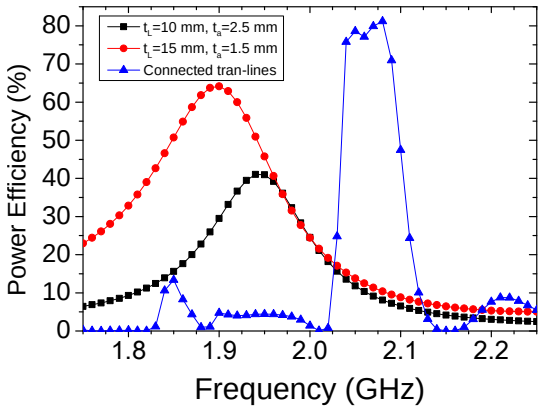



Figure 2: The energy harvesting efficiency for the three studied infinite array configurations.

The connected-line array configuration of electrically-small DR elements show microwave to AC conversion efficiency close to 85%. Exciting the $10 \times 1$ electrically-small cells by a single transmission line connected without any termination except at the feeding points was further improve the harvesting efficiency and has increase it to 85%. The case of having connected transmission line array configuration is suggested to achieve a highly efficient rectenna system as it can be easily integrated with a rectification circuit.

## ACKNOWLEDGMENT

The authors acknowledge the Saudi Arabian Ministry of Education. We also acknowledge CMC Microsystems for the provision of products and services that facilitated this research, including CAD tools and test support.

## REFERENCES

1. O. M. Ramahi, T. S. Almoneef, M. Alshareef, and M. S. Boybay, "Metamaterial particles for electromagnetic energy harvesting," *Applied Physics Letters*, vol. 101, no. 17, pp. 173 903–173 903–5, Oct. 2012.
2. J. Hagerty, F. Helmbrecht, W. McCalpin, R. Zane, and Z. Popovic, "Recycling ambient microwave energy with broad-band rectenna arrays," *Microwave Theory and Techniques, IEEE Transactions on*, vol. 52, no. 3, pp. 1014–1024, 2004.
3. Q. Lai, G. Almpanis, C. Fumeaux, H. Benedickter, and R. Vahldieck, "Comparison of the radiation efficiency for the dielectric resonator antenna and the microstrip antenna at ka band," *Antennas and Propagation, IEEE Transactions on*, vol. 56, no. 11, pp. 3589–3592, Nov. 2008.

# Metasurface and its application in optical devices

# Flexible Coherent Control of Plasmonic Spin-Hall Effect

**Shiyi Xiao[1], Fan Zhong[2], Hui Liu[2,*], Shining Zhu[2], and Jensen Li[1]**

[1] National Laboratory of solid State Microstructures & Department and Physics, National Center of Microstructures and Quantum Manipulation, Nanjing University 210093, China

[2] School of Physics and Astronomy, University of Birmingham, Birmingham, United Kingdom, B15 2TT

[*]corresponding author: liuhui@nju.edu.cn

**Abstract**- We demonstrate coherent and independent control of SPP orbitals for the two opposite spins using multiple rings of nano-slots with properly designed orientations on a metasurface. This scheme provides us to achieve arbitrary optical spin-Hall effect. This is a form of spin-enabled coherent control and provides a unique way in achieving tunable orbital motions in plasmonics.

In recent years, many attentions have been paid to the spin-orbit interaction (SOI) of light using geometric-phase enabled optical and plasmonic systems. Together with the recent developments of resonator-based and geometric-phase-enabled metasurfaces [1-5], it offers an alternative route to excite SPPs through SOI with opposite geometric phases for the two spins. The associated spin-dependent phenomena can be regarded as the optical spin-Hall effect (OSHE) in a more general context about spin-splitting of orbitals [6-8]. However, the time-reversely related SPP profiles, from the opposite geometric phases, generated with the two normal incident spins in these cases have so far only demonstrated simple and symmetric splitting of the two spins, known as optical spin Hall effect. Without a proper geometric phase design scheme, the generated SPP profiles are far from arbitrary and independent for the two spins. It refrains us to fully exploit the potential of OSHE and to allow the two spins to work cooperatively in a flexible manner.

Here we demonstrate coherent and independent control of SPP orbitals for the two opposite spins using multiple rings of nano-slots with properly designed orientations on a metasurface [9]. Figure 1 shows our metasurface platform. It consists of two silver films separated by a dielectric spacer. An array of nano-slots on the upper film is etched with specific orientation profile $\alpha(x,y)$ (inset of Fig. 1a). A semiconductor laser at 1064 nm is normally shined on the metasurface to generate a target SPP profile on the air-metal interface. The simulated and experimental SPP profiles for LCP/RCP incidence are shown in Fig. 2 (c-f) which faithfully realize the local SPP profiles within the target region, and indicate the two orbitals (LCP and RCP incidence) can be arbitrarily designed and are not necessarily bounded to beam displacement splitting comparable to a wavelength in real space or bounded to opposite k-space splitting relation between the two spins. Apart from the simple focusing, our current scheme can actually be used to construct far more complicated SPP profiles. In figure 2 (g), we generate a triangle for LCP incidence and a cross-shape for RCP incidence. Fig. 2 (i-l) present the simulated and experimentally achieved SPP profiles, and both clearly show the targeted triangle and cross SPP profile with LCP and RCP incidence.

**REFERENCES**

1. N. Shitrit, I. Yulevich, E. Maguid, D. Ozeri, D.Veksler,V. Kleiner, and E. Hasman, Science 340, 724 (2013)
2. J. Lin, J.B. Mueller, Q. Wang, G. Yuan, N. Antoniou, X. C. Yuan, and F. Capasso, Science 340, 331 (2013)
3. X. Yin, Z. Ye, J. Rho, Y. Wang, and X. Zhang, Science 339, 1405 (2013)

4. L. Huang, X. Chen, B. Bai, Q. Tan, G. Jin, T. Zentgraf, S. Zhang, Light: Sci. Appl. 2, e70 (2013)
5. G. Li, M. Kang, S. Chen, S. Zhang, E. Y. B. Pun, K. W. Cheah, and J. Li, Nano Lett. 13, 4148 (2013)
6. K. Y. Bliokh, A. Niv, V. Kleiner, and E. Hasman, Nature Photonics 2, 748 (2008)
7. O. Hosten, and P. Kwiat, Science 319, 787 (2008)
8. K. Y. Bliokh , F. J. Rodríguez-Fortuño, F. Nori and A. V. Zayats, Nature Photonics 9,796 (2015)
9. S.Y. Xiao, F. Zhong, H. Liu, S. N. Zhu, and J. Li, Nature Communications 6:8360 (2015)

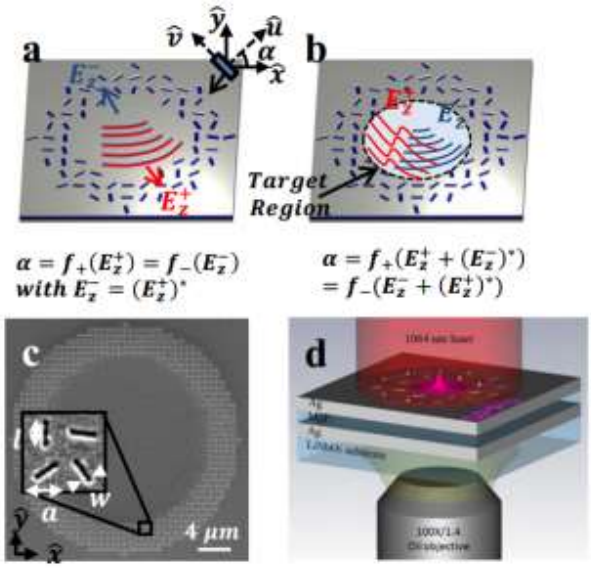



Figure 1 Arbitrary optical spin-Hall effect of SPP. (a-b), Identical nano-slots with orientation profile α(x,y) on the x-y plane. (c) Top-view SEM image of experiment sample. (d) Schematics of the experimental set-up.

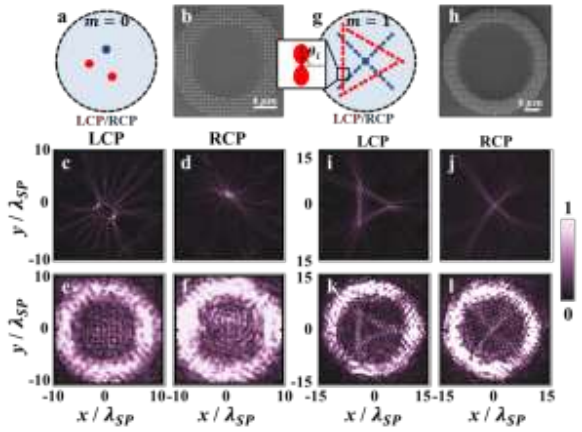



Figure 2 Arbitrary spin-Hall effect. (a) Arbitrary spin-splitting: LCP orbital to focus to two spots (red) while RCP orbital to focus a single spot (blue). (b) Top-view SEM image of the fabricated sample. (c-f) are simulated and experimental intensity profiles for LCP and RCP incidence. (g) Arbitrary spin-dependent SPP profiles with more complicated pattern: shining LCP generating a triangle pattern (red) and shining RCP generating a cross pattern (blue). h, Top-view SEM image of the fabricated sample. (i-l) simulated and experimental intensity profiles for LCP and RCP incidence.

# High-performance metasurfaces based on extraordinary optical diffraction

**Zi-Lan Deng,[1] Shuang Zhang[2] and Guo Ping Wang[1]**

[1.]College of Electronic Science and Technology and Key Laboratory of Optoelectronic Devices and Systems of Ministry of Education and Guangdong Province, Shenzhen University, Shenzhen 518060, China.

[2.]School of Physics & Astronomy, University of Birmingham, Birmingham B15 2TT, UK.

**Abstract**- We show that the incident light can be near-completely reflected in the -1th diffraction order in a planar thin metallic grating due to the excitation of localized cavity mode. Such extraordinary optical diffraction exists for a wide-angle, broadband regime and a large modulation range of the grating period, allowing for a high-performance wavefront-shaping approach based on binary holography techniques. Our findings provide a facile approach to build arbitrary wavefront-shaping metasurfaces with wide-angle, broadband, and high efficiency performance.

Metasurfaces, consisting of a single layer of periodic subwavelength antenna array [1] or nanostructured holographic interferogram [2], have been widely studied in recent years due to their powerful ability to control electromagnetic wave at will with ultrathin thickness. Here, we consider a metallic groove grating as shown in Fig. 1(a) with period comparable to the wavelength, allowing for $0^{th}$ and $-1^{st}$ diffraction orders. We find that, the excitation of localized cavity mode (CM) can completely suppress the ordinary $0^{th}$ reflection while enhance extraordinarily the $-1^{st}$ reflection with near-unity efficiency, which is achieved just by thin binary metallic gratings with simple rectangular cross sections instead of blazed gratings. By the mode expansion theory, we obtained the $-1^{st}$ diffraction efficiencies ($|R_{-1}|^2$) for varying incident angles and wavenumbers (Fig. 1(b)). In the area bounded by $-2^{nd}$, $-1^{st}$, and $1^{st}$ Rayleigh Anomalies (RAs), where only the $0^{th}$ and $-1^{st}$ diffraction orders are allowed to propagate, $|R_{-1}|^2$ exhibit unity peaks, which is coincident with the maxima of the cavity mode amplitude (upright panel of Fig. 1(b)). Because the excitation of the localized cavity mode is independent of the incident angles, the peak of $|R_{-1}|^2$ exists for a wide range of incident angles (upper panel of Fig. 1(b)). Increment of the groove width of the grating can reduce the quality factor of the cavity mode and thus broaden the linewidth of $|R_{-1}|^2$. When the groove width is half of the period (lower panel of Fig. 1(b)), the high efficiency of $|R_{-1}|^2$ expands to nearly the whole area bounded by the $-2^{nd}$, $-1^{st}$ and $1^{st}$ RAs, exhibiting a simultaneous wide-angle and broadband performance. The EOD survives even if the period is varied in a large range, and hence it can be used to mold the phase of an arbitrary wavefront with high efficiency by modulating the grating period based on binary computer-generated hologram (CGH) techniques [3, 4]. Based on this approach, we construct various holographic metasurfaces with different phase profiles for achieving near-unity conversion from a Gaussian beam into a focused beam (Fig. 1(c)), Bessel beam, and vortex beam, respectively, with complete suppression of the undesired $0^{th}$ diffraction [5]. Our finding therefore provides a facile approach towards various practical applications such as imaging, beam-shaping and holographic display with wide-angle, broadband, and high efficiency performance.

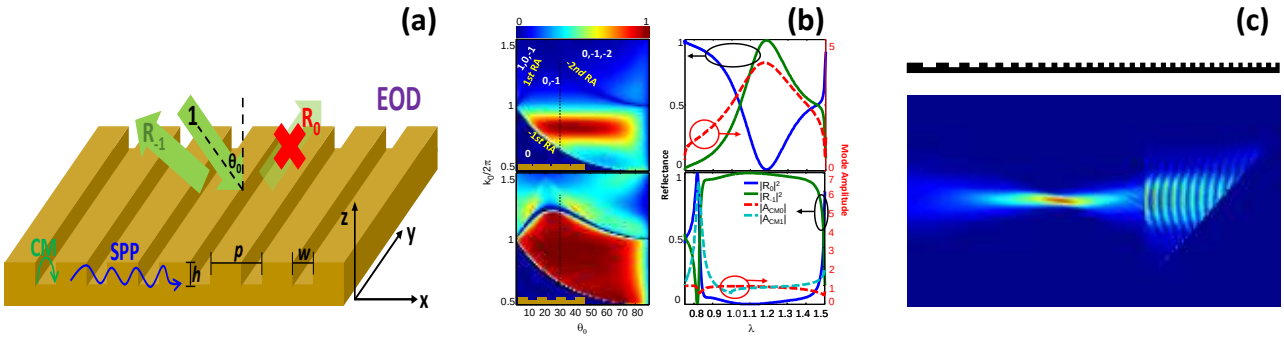



Fig. 1. (a) Schematic of extraordinary optical diffraction by excitation of cavity mode or SPP in a metallic reflection grating. (b) The analytically obtained diffraction efficiency in -1$^{st}$ order for (upper panel) broad groove gratings and (lower panel) narrow gratings. (c) The gradient grating modulated a quadratic phase for a high-efficiency focusing metasurface.

**Acknowledgements**, This work is supported by National Natural Science Foundation of China (NSFC) (Grant 11274247, 11574218, 11504243), Natural Science Foundation of Guangdong Province, China (Grant 2015A030310400).

## REFERENCES

1. N. Yu, and F. Capasso, "Flat optics with designer metasurfaces," Nat. Mater. **13**, 139-150 (2014).
2. P. Genevet, and F. Capasso, "Holographic optical metasurfaces: a review of current progress," Rep. Prog. Phys. **78**, 024401 (2015).
3. W.-H. Lee, "Binary computer-generated holograms," Appl. Opt. **18**, 3661-3669 (1979).
4. G. P. Wang, T. Sugiura, and S. Kawata, "Holography with surface-plasmon-coupled waveguide modes," Appl. Opt. **40**, 3649-3653 (2001).
5. Z.-L. Deng, S. Zhang, and G. P. Wang, "A facile grating approach towards broadband, wide-angle and high-efficiency holographic metasurfaces," Nanoscale **8**, 1588-1594 (2016).

# Phase manipulation of nonlinear harmonic generation with plasmonic metasurfaces

**T. Zentgraf[1*], G. Li[2], S. Chen[2], F. Zeuner[1], N. Pholchai[3], B. Reineke[1], P. W. H. Wong[4], E. Y. Pun[4], K.-W. Cheah[5], and S. Zhang[2]**

[1]Department of Physics, University of Paderborn, D-33098 Paderborn, Germany

[2]School of Physics & Astronomy, University of Birmingham, Birmingham, B15 2TT, UK

[3]King Mongkut's University of Technology North Bangkok, Bangkok, Thailand

[4]Department of Electronic Engineering, City University of Hong Kong

[5]Department of Physics, Hong Kong Baptist University, Hong Kong

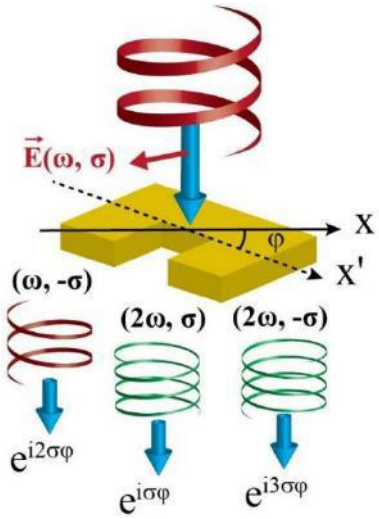
[*]corresponding author: thomas.zentgraf@uni-paderborn.de

**Abstract**- Tailoring nonlinear optical properties is crucial in nonlinear optics. Here we will demonstrate a nonlinear metamaterial with homogeneous linear properties but continuously controllable phase of the local effective nonlinear polarizability. Such a continuous phase engineering of the effective nonlinear polarizability enables complete control of the propagation of nonlinear signals and seamlessly combines the generation and manipulation of harmonic waves. We will show how the symmetry of meta-atoms influences the nonlinear phase and how versatile second harmonic processes can be controlled on a sub-wavelength scale.

For efficient nonlinear processes it is important to engineering the nonlinear optical properties of media. In particular the phase relation between the fundamental and the nonlinear waves plays here an important role. The most well-known technique for spatially engineering the nonlinear properties is quasi-phase matching for second-order processes like SHG [1]. The quasi-phase matching leads to efficient frequency conversion compared to a homogeneous nonlinear medium by providing the extra momentum to compensate the phase mismatch between the fundamental and harmonic waves. The so-called 'poling' is the most widely employed technique for achieving quasi-phase matching. By periodically reversing the crystalline orientation of ferroelectric materials, the sign of the $\chi^{(2)}$ nonlinear susceptibility can be spatially modulated along the propagation direction. However, such a poling only leads to a binary state for the nonlinear material polarization, which is equivalent to a discrete phase change of $\pi$ of the nonlinear polarization.

Here we will demonstrate a novel nonlinear metamaterial with homogeneous linear optical properties but continuously controllable phase of the local effective nonlinear polarizability. For the demonstration we use plasmonic metasurfaces with various designs for the meta-atom geometry and circular polarized light states [2]. The controllable nonlinearity phase results from the phase accumulation due to the polarization change along the polarization path on the Poincare Sphere (Pancharatnam-Berry phase [3,4]) and depends therefore only on the spatial geometry of the metasurface. In contrast to the quasi-phase matching the continuous phase engineering of the effective nonlinear polarizability enables complete control of the propagation of harmonic generation signals, and therefore, it seamlessly combines the generation and manipulation of the harmonic waves for highly compact

nonlinear nanophotonic devices. We will demonstrate the concept of phase engineering for the manipulation of the SHG and THG from metasurfaces and the restriction on the symmetry properties of the geometry [5].




**Figures 1.** Pancharatnam-Berry phase for linear and nonlinear scattered light from a split-ring resonator. The fundamental incident wave of circular polarization state σ leads to SHG signals with different polarization state and phase. The phase of the SHG is hereby related to the orientation of the split-ring resonator.

**Acknowledgements.** This work was financial support by EPSRC and the Deutsche Forschungsgemeinschaft (Grant Nos. TRR142/A05 and ZE953/7-1). The authors would like to acknowledge support from Cedrik Meier by providing his electron beam lithography system.

**REFERENCES**

[1] Armstrong, J. A., Bloembergen, N., Ducuing, J. & Pershan, P. S. Interactions between light waves in a nonlinear dielectric. *Phys. Rev.* ***127****, 1918–1939 (1962).*

[2] Li, G. X. et al. Spin-enabled plasmonic metasurfaces for manipulating orbital angular momentum of light. *Nano Lett.* ***13****, 4148–4151 (2013).*

[3] Berry, M. V. Quantal phase factors accompanying adiabatic changes. *Proc. R. Soc. Lond.* ***392****, 45–57 (1984).*

[4] Bomzon, Z., Kleiner, V. & Hasman, E. Pancharatnam-Berry phase in space-variant polarization state manipulations with subwavelength gratings. *Opt. Lett.* ***26****, 1424–1426 (2001).*

[5] Li, G., Chen, S., Pholchai, N., Reineke, B., Wong, P. W. H., Pun, E. Y. B., Cheah, K. W., Zentgraf, T. & Zhang, S. Continuous control of the nonlinearity phase for harmonic generations. *Nature Materials* ***14****, 607-612 (2015)*

# Terahertz Metasurface-based Devices

**J. W. He, X. K. Wang, and Y. Zhang***

Department of Physics, Capital Normal University, Beijing Key Laboratory of Metamaterials and Devices, and Key Laboratory of Terahertz Optoelectronics, Ministry of Education, Beijing 100048, P.R. China

*corresponding author: yzhang@cnu.edu.cn

**Abstract**-Traditional terahertz (THz) devices have relatively large size due to the long wavelength nature of the THz radiation. Several metasurface-based THz devices, including lens, computer generated holograms, spin selected focusing lens, as well as wavelength selected diffractive elements, have been demonstrated. The thickness of these device is only 1/4000 of the working wavelength. A THz focusing plane imaging system is employed to characterize the function devices. Experimental results verified the theoretical expectations.

Due to the longer wavelength of the terahertz (THz) radiation, the traditional THz devices are relatively larger which blocks the integration of the THz system. The traditional devices employ the phase accumulation during the light propagation. Although the diffractive optical element can remove the thickness which corresponds to multiple of wavelength, this technology cannot be used to reduce the thickness of the devices further.

Alternatively, the phase changes can also be introduced by an optical resonator. The subwavelength antennas can modulate both the amplitude and phase of the reradiated light. Based on this new idea, a lot of THz devices, such as THz waveplate, THz ultrathin lens, THz hologram plate, and THz vortex plate, are being designed and fabricated. These devices are fabricated on 100 nm thick gold film, which is only 1/4000 of the working wavelength. A THz focal plane imaging system is built up to characterize the functions of the fabricated devices. The amplitude, phase, frequency and polarization of the THz wavefront can be measured with this system. Experiment results agree with the theoretical expectation quite well.

For designing the ultrathin planar devices, a series of antennas are designed as the phase modulation units. Each unit could provide the desired phase changes (from 0 to 2 $\pi$ in $\pi$ /4 intervals) and equal intensity modulation. The Yang-Gu algorithm is adopted to design the phase distribution of desired elements, then the corresponding modulation units are selected to compose the devices. Several THz devices are fabricated, including computer generated holograms, long focal length lens, THz vortex plate, wavelength selected CGH, and spin selected lens. Figure 1 presents an experiment result of a spin selected lens. This lens can image an object on the different position according to the polarization of the input light. It can be found that the object is imaged on the left side of the image plane if the illuminating light is left circularly polarized while it is imaged on the right if the illuminating light is right circularly polarized. If the illuminating light is linearly polarized, two images are displayed on the image plane.

The similar technology can also be used to modulate the amplitude and polarization of the THz light. Therefore, all of parameters of a wavefront, including frequency, amplitude, phase and polarization, can be modulated by a single thin metasurface, which provide a new method to control the wavefront. This research is a significant step towards the reduction of the THz elements size and, therefore, to the development of micro-integrated THz systems and to other applications where the compaction is necessary.

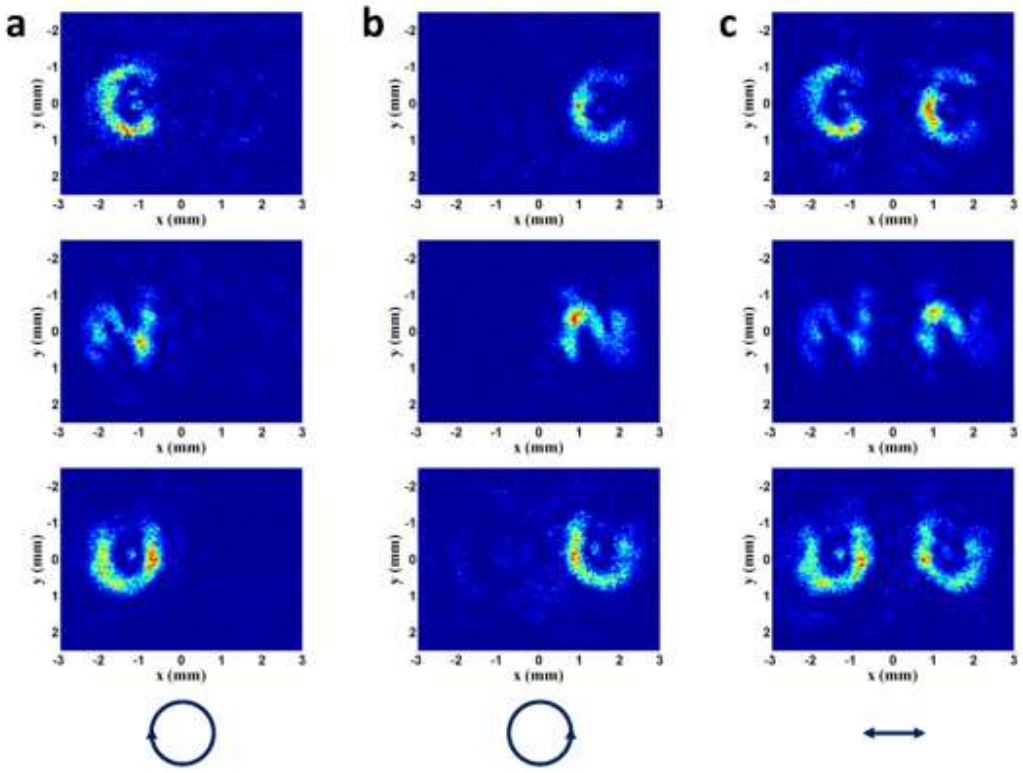



Fig. 1 Experiment results of a spin selected lens. (a) When the lens is illuminated with a left circularly polarized light, the object is imaged on the left. (b) When the lens is illuminated with a right circularly polarized light, the object is imaged on the right. (c) When the lens is illuminated with a linearly polarized light, the object is imaged doubly on both left and right.

This work was supported by the 973 Program of China (No. 2013CBA01702), the National Natural Science Foundation of China (Nos. 11474206, 91233202, 11374216, and 11404224), the Program for New Century Excellent Talents in University (NCET-12-0607), the Scientific Research Project of Beijing Education Commission (KM201310028005), the Specialized Research Fund for the Doctoral Program of Higher Education (20121108120009) and the Scientific Research Base Development Program of the Beijing Municipal Commission of Education.

**REFERENCES**

1. N. Yu, F. Aieta, P. Genevet, M. A. Kats, Z. Gaburro, and F. Capasso, "A broadband, background-free quarterwave plate based on plasmonic metasurfaces," *Nano Lett.* 12(12), 6328–6333 (2012).
2. L. L. Huang, X. Z. Chen, H. Muhlenbernd, H. Zhang, S. M. Chen, B. F. Bai, Q. F. Tan, G. F. Jin, K. W. Cheah, C. W. Qiu, J. S. Li, T. Zentgraf, and S. Zhang, "Three-dimensional optical holography using a plasmonic metasurface," *Nat. Commun.* 4, 2808 (2013).
3. D. Hu, X. Wang, S. Feng, J. Ye, W. Sun, Q. Kan, P. J. Klar, and Y. Zhang, "Ultrathin terahertz planar elements," *Adv. Opt. Mater.* 1(2), 186–191 (2013).

# Metasurfaces for engineering of reflected light

**A. Pors*** and **S. I. Bozhevolnyi**

Centre for Nano Optics, University of Southern Denmark, Campusvej 55, DK-5230 Odense M, Denmark
*corresponding author: alp@iti.sdu.dk

**Abstract**— Gap surface plasmon-based metasurfaces, consisting of a subwavelength thin dielectric spacer sandwiched between an optically thick metal film and an array of metal nanobricks, feature the crucial property of being easy to fabricate, yet with the possibility to fully control the reflected light. In this talk we discuss the peculiar optical properties of these metasurfaces, while demonstrating their great utility in a broad range of applications.

Metasurfaces, being the two-dimensional analog of conventional metamaterials, are typically characterized as interface discontinuities, since they impose a change in the wave front of the incident light on a scale considerably smaller than the wavelength of operation [1]. The majority of metasurfaces consist of metallic or high-permittivity inclusions that are arranged in a two-dimensional array with a period much smaller than the wavelength, hereby ensuring that the incident light does not diffract but merely feels an effective surface response originating from the tailored inclusions. One configuration that, due to its ease of fabrication, has attracted considerable attention in practically any frequency regime is based on the generalization of the reflectarray concept from the antenna community [2], and it consists of an optically thick metal film overlaid by a subwavelength thin dielectric spacer and an array of metal nanobricks (also known as nanopatches), as sketched in Fig. 1. This type of metasurface is in the visible and infrared regimes known as meta-reflectarrays [3], film-coupled nanoantenna metasurfaces [4] or, as used here, gap plasmon-based metasurfaces [5], thus highlighting the crucial role of gap surface plasmon (GSP) resonances in achieving the control of reflected light.

In this talk, we will discuss the fundamentals of GSP-based metasurfaces, particularly highlighting the possibility to either simultaneously control the amplitude and phase of reflected light for one polarization, or to independently engineer the reflection phases of two orthogonal polarizations simultaneously [5]. In the second part of the talk, we will utilize the peculiar properties of GSP-based metasurfaces in various applications, ranging from polarization-controlled unidirectional excitation of surface plasmon polaritons [6], via optical processing [7], to the detection of light's state of polarization [8].

## ACKNOWLEDGMENT

We acknowledge financial support for this work from the European Research Council (the PLAQNAP project, grant 341054) and the University of Southern Denmark (SDU2020 funding).

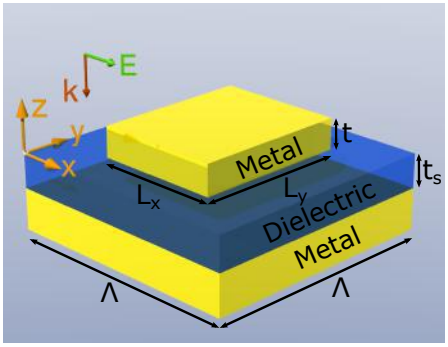



Figure 1: Sketch of the unit cell in GSP-based metasurfaces, consisting of an optically thick metal film overlaid by a dielectric spacer of thickness $t_s$ and an array of metal nanobricks of height $t$ and widths $(L_x, L_y)$ separated by the distance $\Lambda$.

**REFERENCES**


1. Yu, N. and Capasso, F., "Flat optics with designer metasurfaces," *Nat. Mater.*, Vol. 13, 139–150, 2014.
2. Pozar, D. M., Targonski, S. D. and Syrigos, H., "Design of millimeter wave microstrip reflectarrays," *IEEE Trans. Antennas Propag.*, Vol. 45, 287–296, 1997.
3. Yang, Y., Wang, W., Moitra, P., Kravchenko, I. I., Briggs, D. P. and Valentine, J., "Dielectric meta-reflectarray for broadband linear polarization conversion and optical vortex generation," *Nano Lett.*, Vol. 14, 1394–1399, 2014.
4. Moreau, A., Cirací, C., Mock, J. J., Hill, R. T., Wang, O., Wiley, B. J., Chilkoti, A. and Smith, D. R., "Controlled-reflectance surfaces with film-coupled colloidal nanoantennas," *Nature*, Vol. 493, 86–89, 2012.
5. Pors, A., Albrektsen, O., Radko, I. P. and Bozhevolnyi, S. I., "Gap plasmon-based metasurfaces for total control of reflected light," *Sci. Rep.*, Vol. 3, 2155, 2013.
6. Pors, A., Nielsen, M. G., Bernardin, T., Weeber, J.-C. and Bozhevolnyi, S. I., "Efficient unidirectional polarization-controlled excitation of surface plasmon polaritons," *Light: Sci. Appl.*, Vol. 3, e197, 2014.
7. Pors, A., Nielsen, M. G. and Bozhevolnyi, S. I., "Analog computing using reflective plasmonic metasurfaces," *Nano Lett.*, Vol. 15, 791–797, 2015.
8. Pors, A., Nielsen, M. G. and Bozhevolnyi, S. I., "Plasmonic metagratings for simultaneous determination of Stokes parameters," *Optica*, Vol. 2, 716–723, 2015.

# Highly efficient decoupling-free surface plasmon meta-couplers

**Wujiong Sun[1], Qiong He[1], Shulin Sun[2,*] and Lei Zhou[1,*]**

[1] Depatement of Physics, Fudan University, Shanghai 200433, China

[2] Department of Optical Science and Engineering, Fudan University, Shanghai 200433, China

[*]corresponding author: phzhou@fudan.edu.cn; sls@fudan.edu.cn

Surface plasmon polaritons (SPPs) have recently found numerous applications in photonics, but traditional devices to excite them (such as grating and prism couplers) all suffer inherent low-efficiency issues, since the generated SPPs can decouple back to free space and the reflection at the device surface can never be avoided.

Metasurfaces, ultrathin metamaterials composed by array of planar "meta-atoms" with pre-designed electromagnetic (EM) properties, have attracted extensive attention recently [1-3], due to their new degree of freedom to control the EM wave.

Here, based on a transparent gradient metasurface, we propose a new SPP-excitation scheme and numerically demonstrate that it exhibits inherently high efficiency ( 94%), since the designed meta-coupler kills both the decoupling and the reflection at its surface[4]. As a proof of concept, we fabricate a meta-coupler in the microwave regime, and combine near- and far-field experiments to demonstrate that the achieved SPP-excitation efficiency reaches 75%, which is several times higher than all other available devices. Our findings can inspire the designs and realizations of high-performance plasmonic devices to harvest light-matter interactions.

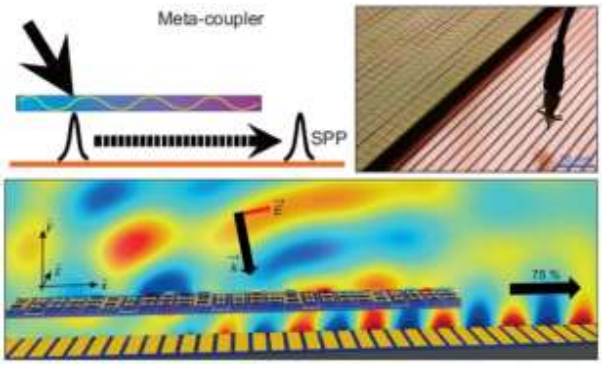



Fig1. Scheme of high efficient SPP Meta-coupler and microwave realization

**REFERENCES**

1. Shulin Sun, et al., "Gradient-index meta-surfaces as a bridge linking propagating waves and surface waves", Nature Materials 11, 426-431 (2012).
2. Shulin Sun, et al., "High-Efficiency Broadband Anomalous Reflection by Gradient Meta-Surfaces", Nano Lett. 12, 6223−6229 (2012).
3. Nanfang Yu & Federico Capasso, "Flat optics with designer metasurfaces", Nature Materials 13,139–150(2014)
4. Wujiong Sun, et al., "High-efficiency Surface Plasmon Meta-couplers: Concept and Microwave-regime realizations ", Light: Science & Applications 5, 16003 (2016).

# Metasurface for helicity multiplexed broadband holograms

**X. Chen[1*], D. Wen[1], F. Yue[1], G. Li[2, 3], G. Zheng[2, 4], K. Chan[3], S. Chen[3], M. Chen[1,5], K. F. Li[3], P. W. H. Wong[6], K. W. Cheah[3], E. Y. B. Pun[6,7], S. Zhang[2]**

1. Institute of Photonics and Quantum Sciences, School of Engineering and Physical Sciences, Heriot-Watt University, Edinburgh, EH14 4AS, UK
2. School of Physics & Astronomy, University of Birmingham, Birmingham, B15 2TT, UK
3. Department of Physics, Hong Kong Baptist University, Hong Kong
4. School of Electronic Information, Wuhan University, Wuhan, 430072, China
5. Guangxi Experiment Center of Information Science, Guilin 541004, China
6. Department of Electronic Engineering, City University of Hong Kong, 83 Tat Chee Avenue, Hong Kong.
7. State Key Laboratory of Millimeter Waves, City University of Hong Kong, 83 Tat Chee Avenue, Hong Kong.

[*]corresponding author: x.chen@hw.ac.uk

**Abstract**-Practical application of metasurface holograms for achieving polarization-multiplexed functionalities has been limited by their capability for achieving high efficiency and high image quality. We experimentally demonstrate helicity multiplexed metasurface holograms with high efficiency and good image fidelity over a broad range of frequencies. The metasurface hologram features the combination of two sets of hologram patterns operating with opposite incident helicities. The demonstrated helicity multiplexed metasurface hologram with its high performance opens avenues for future applications with functionality-switchable

With the rapid development in metasurfaces [1] and the unprecedented capabilities of manipulating light in a desirable manner by imparting local and space-variant abrupt phase change, the conventional concept of what constitutes an optical hologram device continues to evolve [2]. To date, all the demonstrated polarization multiplexed hologram based on metasurfaces suffer from either low efficiency or poor image quality. There are numerous technological or fundamental challenges. For example, although multi-level phase CGHs can improve the image fidelity, they require delicately controlled geometry to achieve a desired phase profile while maintaining uniform amplitude. The experimental demonstration of visible frequency metasurface holograms with broadband optical response has been a significant challenge due to the high plasmonic loss and difficulties in high-uniformity nanofabrication.

To address these challenges, we propose and experimentally demonstrate a helicity multiplexed metasurface hologram capable of achieving high image quality and high efficiency in the visible and near infrared spectrum [3]. The metasurface hologram features the combination of two sets of hologram patterns operating with opposite incident helicities. A 16-level phase metasurface in the reflection mode is realized by patterning sub-wavelength metallic nanorods with spatially varying orientation on the $SiO_2$ interlayer and the ground gold plane**.** The metasurface is designed to display two symmetrically distributed off-axis images with high fidelity and a $64.7^{\circ}$ field of view that are interchangeable by controlling the helicity of the input light. The

demonstrated switchable metasurface hologram with its high performance in image quality, efficiency and bandwidth, represent a major advance in performance compared with previously demonstrated devices with polarization multiplexed functionalities. Our work broadens the general applicability and opens avenues for future applications with functionality-switchable optical devices.

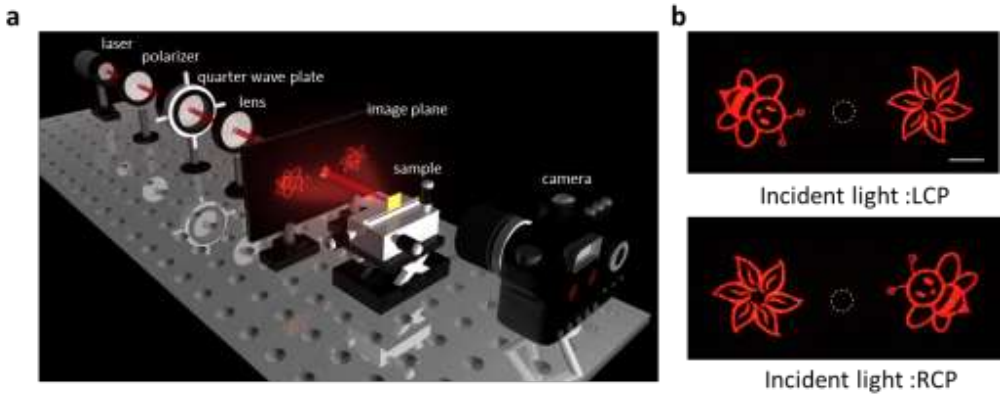



**Figure 1** Illustration of the experiment setup and the dependence of experimental results on the helicity of the incident light. (a) The incident light with various polarization states is obtained by controlling the angle $\theta$ between the polarization axis of the polarizer and the fast axis of the quarter wave plate. The incident light impinges normally onto the metasurface and the reconstructed images are projected onto the image plane. The screen is a white paper board with an opening (diameter 6 mm) in the middle, which allows the incident light and zero order reflected light passing through. (b) The experimentally obtained images for the incident light with LCP (top) and RCP (bottom). The wavelength of the incident light is 633 nm. The dashed circles mark the edge of the opening. The scale bar is 1 cm.

**Acknowledgements**, X.C. acknowledges the Engineering and Physical Sciences Research Council of the United Kingdom (Grant Ref: EP/M003175/1). E.Y.B.P. would like to thank the support from Research Grant Council of Hong Kong under CUHK1/CRF/12G.

**REFERENCES**

1. Yu, N., *et al.,* "Light Propagation with phase discontinuities: Generalized laws of reflection and refraction", *Science,* Vol. **334**, 333-337, 2011.
2. Zheng, G., et al., "Metasurface holograms reaching 80% efficiency", *Nat. Nano.*, Vol. **10**, 308-312, 2015.
3. Wen, D., et al., "Helicity multiplexed broadband metasurface holograms", *Nat. Commun.*, No. 8241, 2015.

# High-Efficiency Metasurface Flat Lenses

**C.-C. Chang**[1], **B. B. Zeng**[1], **A. K. Azad**[1], **A. Efimov**[1], **D. Headland**[2], **W. Withayachumnankul**[2], **D. Abbott**[2], **A. J. Taylor**[1], **and H.-T. Chen**[1]

[1]Center for Integrated Nanotechnologies, Los Alamos National Laboratory, USA
[2]School of Electrical & Electronic Engineering, The University of Adelaide, Australia
chenht@lanl.gov

**Abstract**— Metasurfaces provide unprecedented opportunities in creating novel optical devices in manipulating amplitude, phase, and polarization states. It has been shown that few-layer metasurfaces can dramatically improve the device performance in efficiency and bandwidth. Here we present the design, fabrication, and characterization of metasurface flat lenses based on three-layer metasurfaces in the microwave and terahertz frequency ranges, achieving outstanding performance toward real world applications.

Optical devices control and manipulate light by altering its amplitude, phase, and polarization states in a desired manner, which result in steering the beam propagation direction, shaping the wavefront (e.g., focusing), and imparting information for applications such as sensing, imaging and communication. In contrast to relying on properties of natural materials and their geometric shapes, these functionalities have been now accomplished using metasurfaces, consisting of single-layer or few-layer planar metal/dielectric subwavelength resonator arrays. Tailoring the geometry and arrangement of the structures yields a complete control of the reflection/transmission amplitude, phase, and polarization states. The ultrathin thickness in the wave propagation direction can greatly suppress the undesirable losses by using appropriately chosen materials and metasurface structures. The planar nature of the structures can be readily fabricated using existing technologies such as lithography and nanoprinting methods, which makes them more accessible particularly in the optical regime.

The performance of metasurface devices made of single-layer metasurface is yet unsatisfying in real world applications because of the limited light-matter interaction strength. Few-layer metasurfaces can circumvent this issue and even obtain functionalities beyond the individual layers. Recently, we have developed a three-layer metasurface structure that is capable of rotating the incident linear polarization by 90° with a very high efficiency over a bandwidth of two octaves. More importantly, the phase of the output light can be tuned over the entire $2\pi$ range with subwavelength resolution through simply tailoring the structure geometry of the basic building blocks. This creates an important opportunity in designing highly efficient optical devices for wavefront engineering, such as flat lenses working in the microwave, terahertz, and infrared frequency ranges.

Here we will present the design, fabrication, and characterization metasurface flat lenses based on this concept. Our initial results have shown excellent focusing can be accomplished. In the microwave frequency range the losses are negligible, and in the terahertz frequency range the efficiency is up to 80%, limited by the dielectric loss in the spacer materials being used.

## ACKNOWLEDGMENT

We acknowledge support in part from the Los Alamos National Laboratory LDRD Program. This work was performed, in part, at the Center for Integrated Nanotechnologies, a U.S. Department of Energy, Office of Basic Energy Sciences Nanoscale Science Research Center operated jointly by Los Alamos and Sandia National Laboratories. Los Alamos National Laboratory, an affirmative action/equal opportunity employer, is operated by Los Alamos National Security, LLC, for the National Nuclear Security Administration of the U.S. Department of Energy under Contract No. DE-AC52-06NA25396.

## REFERENCES

1. Grady, N. K., J. E. Heyes, D. Roy Chowdhury, Y. Zeng, M. T. Reiten, A. K. Azad, A. J. Taylor, D. A. R. Dalvit, and H.-T. Chen, "Terahertz metamaterials for linear polarization conversion and anomalous refraction," *Science* **340**, 1304–1307 (2013).

# Reflective metasurface and metadevice

**Wei-Yi Tsai[1], Wei Ting Chen[1], Yao-Wei Huang[1], Pin Chieh Wu[1], Chun Yen Liao[1], Kuang-Yu Yang[2], Hao-Tsun Lin[1], Vassili Fedotov[3], Greg Sun[4], Shulin Sun[5], Lei Zhou[5], Ai Qun Liu[6], Nikolay I. Zheludev[3,6], and Din Ping Tsai[1,2*]**

[1]Department of Physics, National Taiwan University, Taipei 10617, Taiwan

[2]Research Center for Applied Sciences, Academia Sinica, Taipei 11529, Taiwan

[3]Optoelectronics Research Centre and Centre for Photonic Metamaterials, University of Southampton, Southampton SO17 1BJ, UK

[4]Department of Physics, University of Massachusetts Boston, Boston, Massachusetts 02125, USA

[5]Department of Optical Science and Engineering, Fudan University, Shanghai 200433, China

[6]School of Electrical and Electronic Engineering, Nanyang Technological University, Singapore 639798, Singapore

**Abstract**- Metamaterial and Metasurface, as artificial nanostructure, have recently been studied for the electromagnetic manipulation and observation of unusual optical phenomena in arbitrary frequency regions. In this paper, we demonstrate the reflective-type and high efficiency metasurface in visible region and a polarization controllable meta-hologram by adequately designing. The full color meta-hologram can also be achieved based on aluminum metasurface. Furthermore, we exhibit meta-device of circular polarization generator based on the concept of previous work. Our works provide potentials to develop novel devices which are not limited by material composition.

**Summary**-The manipulation of light is highly desired in nanophonics research to overcome the limitation of natural materials. Restricted by the permittivity of material, the conventional phonics elements need thicker spacer layer for the phase modulation to realize the capability of manipulating light. Metamaterials are composed of sub-wavelength local resonance structure of electric or magnetic type with novel optical properties, such as negative refraction and perfect lens, etc. [1, 2]. Recently, an ultra-thin structure called metasurface with strong optical responses provided by metallic nanostructure has been demonstrated the ability of broadband light manipulation [3]. We introduce a reflective type gradient metasurface [4], shown in Fig. 1(a). The reflective type structure can cancel transmitted light and enhanced the anomalous reflection beam so that the efficiency of light manipulation is significantly improved around wavelength 850 nm [5]. Based on the reflective type metasurface, the high-efficiency polarization controllable meta-hologram working in visible is further achieved. Utilizing the inherent material properties, the functionality of color multiplexing can be demonstrated and shown in fig.1 (c) by aluminum metasurface [6]. To develop a practical optical device in terms of polarization optics, the multifuntional metasurface is proposed, which can accurately generate circular polarization, shown in fig.1 (d). In summary, we have demonstrated a reflective and high-efficiency meta-surface using quasistatic phase elements, polarization controllable meta-hologram, multi-color meta-hologram, and multifuntional metasurface. These works provide the possibilities to achieve optical devices in arbitrary frequency regions.

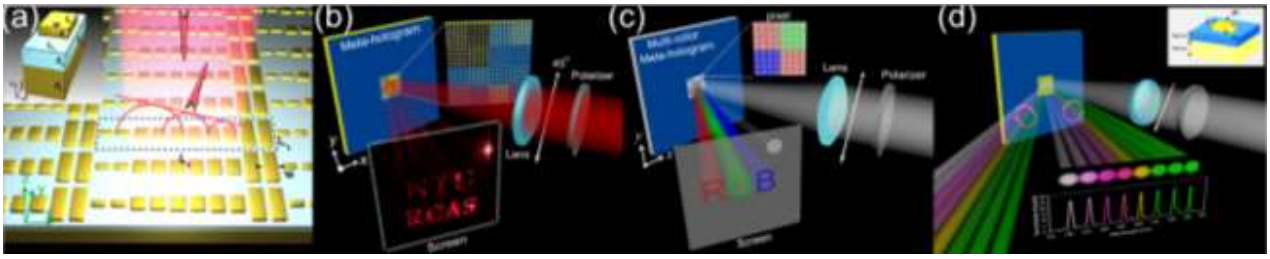



Figure 1 (a-d). Show the schematic of reflective type gradient metasurface, polarization controller able meta-hologram, mutil-color meta-hologram, and mutifunctional metasurface.

**Acknowledgements**, the authors acknowledge financial support from Ministry of Science and Technology, Taiwan (Grant Nos.104-2745-M-002-003-ASP) and Academia Sinica (Grant No. AS-103-TP-A06). They are also grateful to National Center for Theoretical Sciences, Molecular Imaging Center of National Taiwan University, National Center for High-Performance Computing, Taiwan, and Research Center for Applied Sciences, Academia Sinica, Taiwan for their supports.

**REFERENCES**

1. R. A. Shelby, D. R. Smith, S. Schultz, "Experimental verification of a negative index of refraction," *Science* 292, pp. 77-79, 2001.
2. J. B. Pendry, "Negative refraction makes a perfect lens," *Phys. Rev. Lett.* 85, pp. 3966-3969, 2000.
3. N. Yu, P. Genevet, M. A. Kats, F. Aieta, J.-P. Tetienne, F. Capasso, Z. Gaburro, "Light propagation with phase discontinuities: generalized laws of reflection and refraction," *Science* 334, pp. 333-337, 2011.
4. S. Sun, K.-Y. Yang, C.-M. Wang, T.-K. Juan, W. T. Chen, C. Y. Liao, Q. He, S. Xiao, W.-T. Kung, G.-Y. Guo, L. Zhou, D. P. Tsai, "High-efficiency broadband anomalous reflection by gradient meta-surfaces," *Nano Letters* 12(12), 6223-6229, 2012.
5. W. T. Chen, K.-Y. Yang, C.-M. Wang, Y.-W. Huang, G. Sun, I.-D. Chiang, C. Y. Liao, W.-L. Hsu, H. T. Lin, S. Sun, L. Zhou, A.-Q. Liu, D. P. Tsai, "High-efficiency broadband meta-hologram with polarization-controlled dual images," *Nano Letters* 14 (1), 225-230, 2014.
6. Y.-W. Huang, W. T. Chen, W.-Y. Tsai, P. C. Wu, C.-M. Wang, G. Sun, D. P. Tsai, "Aluminum Plasmonic Multicolor Meta-Hologram," *Nano Letters* 15(5), 3122-3127, 2015.

# Active Photonic Devices Based on Metasurfaces Integrated with Phase-Transition Correlated Perovskites

Zhaoyi Li[1], You Zhou[2], Hao Qi[3], Qiwei Pan[3], Norman Nan Shi[1], Ming Lu[5], Aaron Stein[5], Christopher Y. Li[3], Shriram Ramanathan[2,4], and Nanfang Yu[1]*

[1]Department of Applied Physics and Applied Mathematics, Columbia University, New York, NY 10027, USA
[2]John A. Paulson School of Engineering and Applied Sciences, Harvard University, Cambridge, MA 02138, USA
[3]Department of Materials Science and Engineering, Drexel University, Philadelphia, PA 19104, USA
[4]School of Materials Engineering, Purdue University, West Lafayette, IN 47907, USA
[5]Center for Functional Nanomaterials, Brookhaven National Laboratory, Upton, NY 11973, USA
*corresponding author: ny2214@columbia.edu

**Abstract**-We report strong and non-volatile optical modulation utilizing electron-doping induced phase change of a perovskite, $SmNiO_3$. Broadband modulation (λ=400nm-17μm) is demonstrated using thin-film $SmNiO_3$, and narrowband modulation is realized with metasurfaces integrated with $SmNiO_3$.

In this talk I will report experimental results showing that samarium nickelate ($SmNiO_3$), a prototypical phase-change perovskite nickelate, exhibits reversible large refractive index changes over an ultra-broad spectral range, from the visible to the long-wavelength mid-infrared (λ= 400 nm - 17 μm) [1]. The super broadband performance is due to strong electron correlation effects that allow extraordinarily large bandgap tuning of the order of 3 eV, and this new mechanism can be exploited to create active photonic devices.

In pristine $SmNiO_3$, $Ni^{3+}$ has an electron configuration of $t_{2g}^6 e_g^1$ and the single $e_g$ electron causes strong optical losses through free carrier absorption. Therefore, pristine $SmNiO_3$ is optically lossy. By acquiring an extra electron, the four-fold degenerate (including spin) $e_g$ manifold is occupied by two electrons. The strong intra-orbital Coulomb repulsion between $e_g$ electrons opens a bandgap of ~3 eV and almost completely suppresses the free carrier absorption. Thus, $SmNiO_3$ is transformed into an optically transparent dielectric with $n$ ~ 2.2 and $k$ close to zero throughout the visible, near-infrared, and mid-infrared. The switching between the two states can occur at room temperature in a non-volatile fashion, and the two states have no obvious differences in their crystalline symmetry (within the detection limits of electron diffraction) [1]. These desirable properties open up opportunities to realize electrically tunable and non-volatile planar photonic devices at any desired wavelength from the visible to the mid-infrared.

We demonstrated large, super broadband and reversible changes of optical transmission through thin-film $SmNiO_3$ (**Figs. 1(a)-(c)**). The $SmNiO_3$ thin film was deposited on a suspended 1-μm-thick $Si_3N_4$ membrane through sputtering, followed by high temperature annealing to form the perovskite phase. Lithium intercalation (de-intercalation) was used to facilitate the incorporation (extraction) of electrons into (from) $SmNiO_3$. **Figure 1(b)** shows that pristine un-doped $SmNiO_3$ is lossy and transmission is below 5% in the near-infrared (λ=1-2.5 μm) and below 17% in the mid-infrared (λ=2.5-17 μm), while in the electron-doped state $SmNiO_3$ becomes transparent with transmissivity around 70%, except for a pronounced dip around $\nu$ = 1000 $cm^{-1}$ or λ = 10 μm, which is due to optical absorption as a result of the phonon resonance in $Si_3N_4$. By switching $SmNiO_3$ between its opaque and transparent state, we were able to modulate optical transmissivity by a factor as large as ~270 at $\nu$ = 9,000 $cm^{-1}$ or λ ≅ 1.1 μm and by a factor larger than 10 for $\nu$ > 2,000 $cm^{-1}$ or λ < 5 μm (**Fig. 1(c)**).

We realized a solid-state modulator based on thin-film $SmNiO_3$ and a solid polymer electrolyte (SPE) (**Figs. 1(d)-(f)**). The SPE transports lithium ions between a $LiCoO_2$ electrode and a $SmNiO_3$ film to induce phase change of the latter. We demonstrated modulation of light reflected from the solid-state device of ~5.5% at λ=1.55 μm by switching the gate voltage between +3.8V and -5V for multiple cycles. The device response time is on the order of a few seconds (**Figs. 1(e)-(f)**).

By integrating plasmonic metasurface structures with $SmNiO_3$, modulation of a narrow band of light that resonantly interacts with the metasurfaces was realized (**Fig. 2**). The device consists of platinum (Pt) aperture antennas separated from a back mirror by $SmNiO_3$ and $SiO_2$ thin films (**Figs. 2(a)(b)**). The phase transition of $SmNiO_3$ was induced by hydrogenation/de-hydrogenation, which was achieved by annealing the device in $H_2/O_3$

gas.

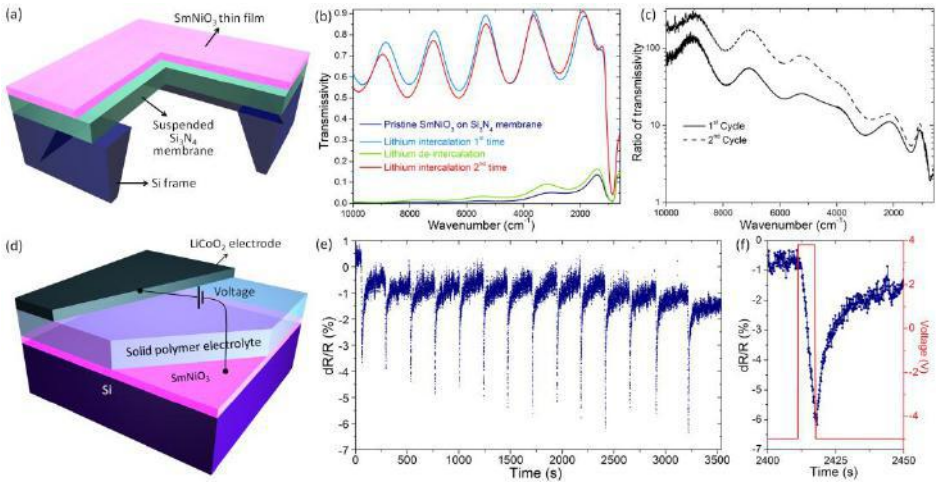



**Fig. 1** (a) Schematic of a device consisting of a $SmNiO_3$ film deposited on a $Si_3N_4$ membrane. (b) Measured transmission spectra when $SmNiO_3$ is switched between its two states. (c) On-off ratio of transmission during two cycles of phase transition of $SmNiO_3$. (d) Schematic of a solid-state device based on thin-film $SmNiO_3$ and a solid polymer electrolyte. (e) Temporal response of reflectivity during repeated phase-transition cycles of $SmNiO_3$. (f) Zoom-in of (e) showing one cycle of modulation.

When $SmNiO_3$ is at its optically transparent state, incident infrared light generates strong plasmonic resonance in the aperture antennas, which leads to significant absorption of optical power, which results in a dip in the reflection spectra (**Fig. 2(c)**). The spectral location of the dip is controlled by the size of the aperture antennas: longer apertures resonantly interact with light with proportionally longer wavelengths. When $SmNiO_3$ is at its pristine state, however, strong optical losses in the material will completely damp the plasmonic resonance so that the reflection spectra will be featurelessly flat (**Fig. 2(d)**). The experimental results were in good agreement with full-wave simulations (**Figs. 2(e)(f)**).

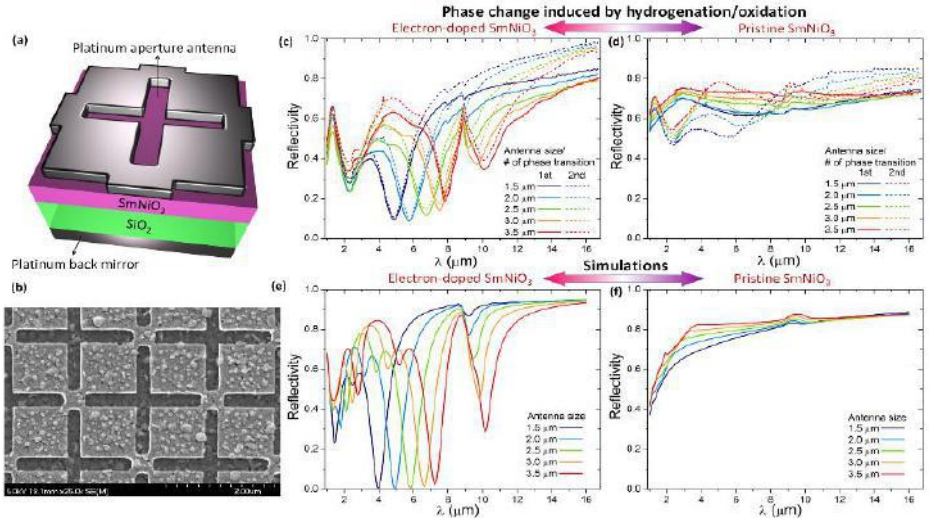



**Fig. 2** (a) Schematic of the unit cell of a device consisting of a Pt aperture antenna separated from a Pt mirror by thin films of $SmNiO_3$ and $SiO_2$. (b) SEM image of a region of a device consisting of cross apertures 2 μm×2μm in size patterned on $SmNiO_3$. (c) and (d) Measured reflection spectra of the device when $SmNiO_3$ is switched between its two states. (e) and (f) Simulated reflection spectra of the device when $SmNiO_3$ is switched between its two states.

In summary, the correlated perovskite nickelate $SmNiO_3$ has great potential for active photonic device applications. The phase transition of $SmNiO_3$ is induced by strong electron correlation effects and there is no crystalline structure change during the phase transition. This quite unusual feature implies that fast switching between the two phases of $SmNiO_3$ is possible. The non-volatile, multi-level optical states of $SmNiO_3$ could be exploited to create reconfigurable, planar photonic devices, such as programmable holograms and optical memories. The super broadband performance of $SmNiO_3$ and its second-to-minute level phase transition time demonstrated so far could be exploited for applications in smart windows and variable emissivity coatings.

**Acknowledgements** The work was supported by AFOSR MURI (grant No. FA9550-14-1-0389), DARPA YFA (grant No. D15AP00111), and NSF (grant No. ECCS-1307948).

**REFERENCES**

1. J. Shi, Y. Zhou, and S. Ramanathan, "Colossal resistance switching and band gap modulation in a perovskite nickelate by electron doping," *Nature Commun.* **5**, 4860 (2014).

# Non-Hermitian engineering in photonics, plasmonics and metamaterial

# Scattering in PT and RT Symmetric Multimode Waveguides: Generalized Conservation Laws beyond One Dimension

**Li Ge**[1], **Konstantinos G. Makris**[2], **Demetrios N. Christodoulides**[3], **and Liang Feng**[4]

[1]Department of Engineering Science and Physics, College of Staten Island, CUNY, Staten Island, NY 10314, USA and The Graduate Center, CUNY, New York, NY 10016, USA

[2]Crete Center for Quantum Complexity and Nanotechnology, Department of Physics, University of Crete, P.O. Box 2208, 71003, Heraklion, Greece

[3] College of Optics and Photonics – CREOL, University of Central Florida, Orlando, Florida 32816, USA

[4] Department of Electrical Engineering, The State University of New York at Buffalo, Buffalo, NY 14260, USA

li.ge@csi.cuny.edu

**Abstract**— We extend the generalized conservation law of light propagating in a one-dimensional PT-symmetric system to a multimode system with either PT or RT symmetry, in which higher dimensional investigations are necessary. These conservation laws exist not only in a matrix form for the transmission and reflection matrices; they also exist in a scalar form for generalized transmittance and reflectance.

Recently it was found that the scattering eigenstates of a $\mathcal{PT}$-symmetric system display a spontaneous symmetry breaking [1], independent of its shape and dimension: the eigenvalues of the scattering ($\boldsymbol{S}$) matrix can remain on the unit circle in the complex plane, conserving optical flux despite the non-hermiticity; the symmetry breaking results in pairs of scattering eigenvalues with inverse moduli [1, 2, 3]. Using the symmetry property of the $\boldsymbol{S}$ matrix or equivalently that of the transfer matrix, one can derive a generalized conservation law in one dimension (1D) [2], i.e.,

$$|T-1| = \sqrt{R_L R_R}, \tag{1}$$

in contrast to the usual conservation relation $T + R_{L(R)} = 1$ when the system is hermitian. Here $T$ is the transmittance from either the left or right side (they are identical due to optical reciprocity) and $R_{L,R}$ are the reflectance from the two sides, respectively. At an accidental reflection degeneracy where $R_L = R_R \equiv R$, the generalized conservation law above indicates two possible scenarios, where either $T + R = 1$ or $T - R = 1$. The former is identical to the hermitian conservation law even though the system is non-hermitian, and the transmittance in the latter is clearly super-unitary.

In this talk we discuss the extension of the generalized conservation law above in 1D to higher dimensions, i.e., in a multimode waveguide with either $\mathcal{PT}$ or Rotation-Time ($\mathcal{RT}$) symmetry [4], where $\mathcal{R}$ is rotation by $\pi$ about a given axis. Using the matrix representation of $\mathcal{P}$ and $\mathcal{R}$ in block form, we show that a similar expression exists for the transmission and reflection matrices, which holds independent of the details of the channels, i.e., whether they are sinusoidal waves in a ridge waveguide or cylindrical waves in an optical fiber. By further defining the generalized transmittance and reflectance suitable for $\mathcal{PT}$- and $\mathcal{RT}$-symmetric systems, we also reduce these conservation laws to their scalar forms with only real-valued quantities. For example, with the constituent transmission and reflection matrices $\boldsymbol{t}, \boldsymbol{r}_{L,R}$ of the $\boldsymbol{S}$ matrix, a Hermitian system satisfies

$$T + R_L = T + R_L = N, \tag{2}$$

where $N$ is the number of channels and $T \equiv Tr(\boldsymbol{t}\boldsymbol{t}^\dagger), R_{L,R} \equiv Tr(\boldsymbol{r}_{L,R}\boldsymbol{r}_{L,R}^\dagger)$ are the *real-valued* transmittance and reflectances. For a $\mathcal{PT}$-symmetric system, however, the left and right channels are inseparable in the derivation of a conservation relation similar to Eq. (2), just like in the 1D case given by Eq. (1). More specifically, a $N$-channel $\mathcal{PT}$-symmetric system features

$$\overline{T} + \overline{R} = N, \tag{3}$$

where $\overline{T} \equiv Tr(\boldsymbol{t}\boldsymbol{t}^*), \overline{R} \equiv Tr(\boldsymbol{r}_L\boldsymbol{r}_R^*)$ are the modified transmittance and reflectance, and they are *also* real. In the case of a $\mathcal{RT}$-symmetric system, the conservation relation is $\tilde{T} + \tilde{R} = \delta_{N,2M+1}$, or

equivalently

$$\mathrm{Re}[\tilde{T}] + \mathrm{Re}[\tilde{R}] = \begin{cases} 0, & N \text{ even} \\ 1, & N \text{ odd} \end{cases} \tag{4}$$

$$\mathrm{Im}[\tilde{T}] + \mathrm{Im}[\tilde{R}] = 0. \tag{5}$$

Here $\tilde{T} \equiv Tr(\tilde{\mathbf{1}}_N \boldsymbol{t}^* \boldsymbol{t})$, $\tilde{R} \equiv Tr(\tilde{\mathbf{1}}_N \boldsymbol{r}_R^* \boldsymbol{r}_L)$ are the generalized transmittance and reflectance for $\mathcal{RT}$-symmetric systems, and they are *no longer* real in general but their sum *is*. $\tilde{\mathbf{1}}_N$ is a diagonal matrix with the element $(-1)^{n+1}$ in row $n$, and $\delta_{N,2M+1}$ is the Kronecker delta where $M$ represents any positive integer. Due to the phase of $\boldsymbol{t}, \boldsymbol{r}_{L,R}$, it would be challenging to verify these generalized conservation relations in optics, which however, should be straightforward in the microwave regime and acoustics.


## ACKNOWLEDGMENT

We thank Douglas Stone for helpful discussions. L.G. acknowledges support by NSF under grant No. DMR-1506987. L.F. acknowledges support by NSF under grant No. DMR-1506884 and by US Army Research Office under grant No. W911NF-15-1-0152. K.G.M. is supported by the People Programme (Marie Curie Actions) of the European Union's Seventh Framework Programme (FP7/2007-2013) under REA grant agreement number PIOF-GA-2011- 303228 (project NOLACOME) and by the European Union's Seventh Framework Programme (FP7-REGPOT-2012-2013-1) under grant agreement 316165.


## REFERENCES


1. Y. D. Chong, L. Ge, and A. D. Stone, *$\mathcal{PT}$-Symmetry Breaking and Laser-Absorber Modes in Optical Scattering systems*, Phys. Rev. Lett. **106**, 093902 (2011).
2. L. Ge, Y. D. Chong, and A. D. Stone, *Conservation Relations and Anisotropic Transmission Resonances in One-Dimensional $\mathcal{PT}$-Symmetric Photonic Heterostructures*, Phys. Rev. A **85**, 023802 (2012).
3. P. Ambichl, K. G. Makris, L.Ge, Y. Chong, A. D. Stone, and S. Rotter, *Breaking of PT Symmetry in Bounded and Unbounded Scattering Systems*, Phys. Rev. X **3**, 041030 (2013).
4. L. Ge and A. D. Stone, *Parity-time symmetry breaking beyond one dimension: the role of degeneracy*, Phys. Rev. X **4**, 031011 (2014).

# PT-symmetry breaking in the steady state of coupled phonon lasers

**K.V. Kepesidis[1], T. J. Milburn[1], K. G. Makris[2], S. Rotter[2], and P. Rabl[1*]**

[1]Institute of Atomic and Subatomic Physics, TU Wien, Stadionallee 2, 1020 Vienna, Austria

[2]Institute for Theoretical Physics, TU Wien, 1040 Vienna, Austria

[*]corresponding author: peter.rabl@ati.ac.at

**Abstract**- We discuss the phenomenon of PT-symmetric breaking in the steady state distribution of noisy systems with balanced gain and loss. By considering a system of two coupled mechanical resonators with optically-induced loss and gain, we show that the combination of nonlinear saturation effects and thermal noise results in a unexpected steady-state behavior that differs significantly from the usual dynamical picture of PT-symmetry breaking.

The breaking of a combined PT (parity- and time-reversal) symmetry in non-Hermitian systems with gain and loss is conventionally associated with a transition from a purely oscillatory to an exponentially amplified dynamical regime [1]. Here [2] we address a still open question in this field, namely: What are the steady states of real physical systems with an underlying PT symmetry? This question becomes particularly relevant for microscopic systems and for systems operated close to the quantum regime, where the effect of strong intrinsic nonlinearities and thermal or quantum fluctuation plays a dominant role. By focusing on the setup of two coupled mechanical resonators with optically-induced loss and gain as a relevant example, we show that PT-symmetry breaking in the steady state exhibits various unexpected features and in general occurs via additional intermediate phases with retained or `weakly' broken PT symmetry. Most importantly, we identify an unconventional transition from a high-noise thermal state to a low-amplitude lasing state, which generalizes the PT-symmetry breaking - hitherto defined only for eigenstates - to steady-state distributions of noisy systems.

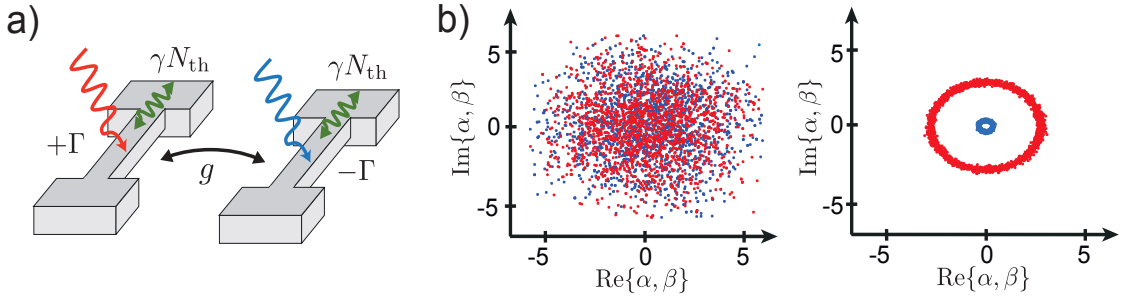



**Figure 1: a)** Setup of to coupled mechanical beams with laser-induced gain and loss [3]. **b)** Steady-state distribution of the two resonator amplitudes below and above the PT-symmetry breaking transition [2].

**REFERENCES**

1. Bender, C.M., "Making sense of non-Hermitian Hamiltonians," Rep. Prog. Phys., Vol. 70, 947, 2007.
2. Kepesidis, K.V., T. J. Milburn, K. Makris, S. Rotter, and P. Rabl. "PT-symmetry breaking in the steady state," *arXiv:1508.00594*, 2015.
3. Kepesidis, K.V., S. D. Bennett, S. Portolan, M. D. Lukin, and P. Rabl. "Phonon cooling and lasing with nitrogen-vacancy centers in diamond," *Phys. Rev. B*, Vol. 88, 064105, 2013.

# Extreme Wave Manipulation with Parity-Time Symmetric Metasurfaces

**R. Fleury**[1,2]**, D. Sounas**[3] **and A. Alù**[3]
[1]Institut Langevin, ESPCI Paris Tech, France,
[2]Ecole Polytechnique Fédérale de Lausanne (EPFL), Switzerland
[3]The University of Texas at Austin, USA
[*]corresponding author: romain.fleury@epfl.ch

**Abstract**- We study the unique wave manipulation capabilities of Parity-Time symmetric pairs of metasurfaces operated at exceptional point conditions. We demonstrate theoretically and experimentally the relevance of these systems to induce wave phenomena typically observed with bulk metamaterials, including negative refraction, planar focusing, or cloaking, while avoiding their typical drawbacks, such as sensitivity to losses, imperfect isotropy, and fabrication complexity. We discuss the relations between bandwidth and stability, demonstrating the practical potential of these systems for controlling waves in unprecedented ways.

Non-Hermitian systems with Parity-Time (PT) symmetry have attracted a lot of attention over the past decades [1], due to their unique spectral and scattering properties. In wave physics, these systems are typically obtained from a balanced distribution of gain and loss that obeys PT symmetry. One of the most attractive features of PT symmetric systems is that, albeit non-Hermitian, they can exhibit an entirely real spectrum, and undergo distinctive spectral phase transitions that lends them exceptional scattering and wave manipulation properties, including novel beam dynamics, laser-absorber modes, anisotropic transmission resonances, and unidirectional invisibility.

In this paper, we explore the largely uncharted scattering properties of PT symmetric systems that are composed of a PT symmetric pair of lumped elements, one with loss, and one with gain, separated by free-space. Such association of lumped impedances separated by a portion of lossless transmission-line define a one-dimensional two-port electrical network (Fig. 1a) that can be used to model a pair of distant, parallel metasurfaces. We consider the simplest case where the two impedances are resistors of opposite values, as in Fig. 1a: on the left, we have a passive resistor of value $R>0$, whereas on the right, we have its time reversed-image, an active source of value $R<0$. In this scenario, we show [2] that if the value of $R$ is equal to *half* of the characteristic impedance of the line separating the two resistors, the system is operated at an exceptional point condition associated with unitary transmission from both sides, and no reflection from the left. More importantly, transmission is accompanied by a phase *advance* that is exactly opposite of the phase *delay* that the wave would acquire in the transmission line in the absence of the resistors. At this exceptional point, the system supports a transmission associated to a *negative phase velocity* between the resistors, in perfect analogy to a double negative metamaterial slab. We demonstrate the potential of PT symmetric metasurfaces for inducing negative refraction in free-space, not only for plane wave at normal incidence (Fig. 1b), but also for Gaussian beams at arbitrary incidence (Fig. 1c). Such a property leads to negative refraction with only two lumped elements, and without resorting to bulk metamaterials, avoiding their principal drawbacks, including sensitivity to losses,

imperfect isotropy, granularity and complexity of fabrication. In addition, we present and discuss a variant of this scenario that can be exploited to cloak large objects from a given incidence direction (Fig. 1.d) [3].

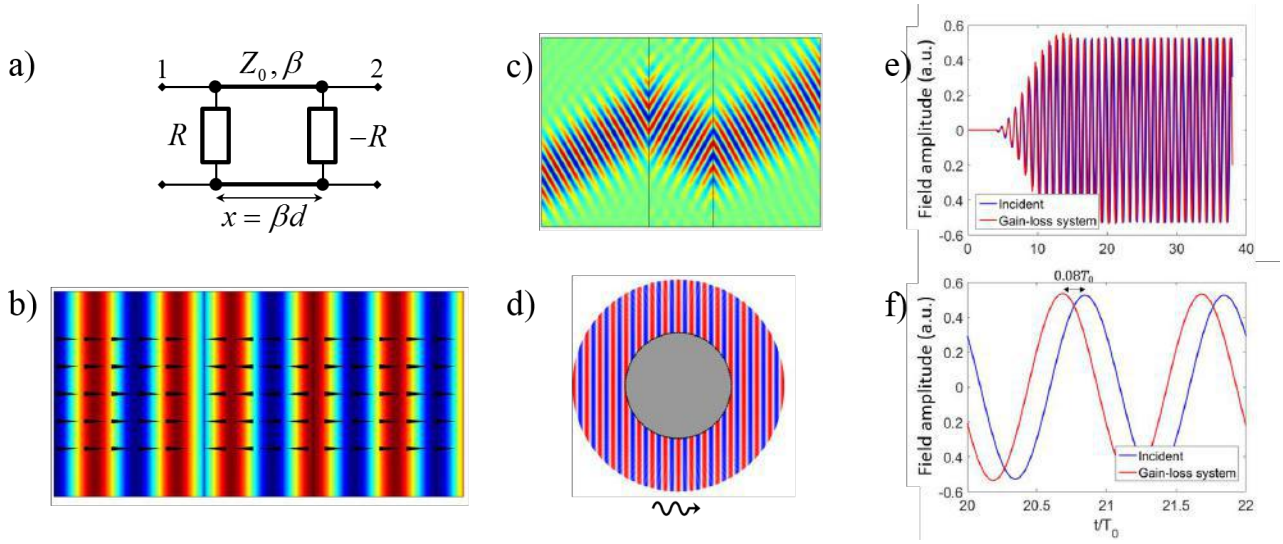



Figure 1: (a) We study a PT symmetric 2-port network composed of two resistors of opposite sign separated by a portion of transmission line. (b) Negative refraction for a plane wave at normal incidence. The color shows the wave amplitude, and the arrows the power flow. (c) PT-induced negative refraction of a Gaussian beam using two metasurfaces. (d) Unidirectional cloaking of large objects with PT-symmetric metasurfaces. (e) Time-domain response for the system in (b), designed to be stable by dispersion engineering. (f) Steady state field amplitude corresponding to the scenario in e), demonstrating the phase advance of the output wave.

Finally, we will present and analyze the time-domain response of these systems using numerical experiments based on the FDTD method. We show that, in general, stability is a crucial problem in the practical design of PT symmetric devices. However, by carefully engineering the dispersion of the gain elements, it is possible to guarantee their stability (Fig. 1e-f). We will explore the link between stability, bandwidth and size, which will enable us to design fully-stable PT symmetric systems. Finally, we present the results of a proof-of-concept experiment demonstrating PT-induced negative refraction in free-space for audible acoustic waves [4], establishing the practical relevance of PT symmetric metasurfaces for manipulating waves in unprecedented ways.

**REFERENCES**


1. Bender, C. M. and S. Boettcher, "Real spectra in non-Hermitian Hamiltonians having PT symmetry. *Phys. Rev. Lett.*, Vol. 80, 5243, 1998.
2. Fleury, R., Sounas, D. and A. Alù, "Negative refraction and planar focusing based on parity-time symmetric metasurfaces," *Phys. Rev. Lett.*, Vol. 113, 023903, 2014.
3. Sounas, D., Fleury, R. and A. Alù,, "Unidirectional cloaking based on metasurfaces with balanced gain and loss," *Phys. Rev. Appl.*, Vol. 4, 014005, 2015.
4. Fleury, R., Sounas, D. and A. Alù, "An invisible acoustic sensor based on parity-time symmetry," *Nat. Commun.*, Vol. 6, 5905, 2015.

# Non-Hermitian topological photonics

**S. Weimann**[1], **J. Zeuner**[1], **M. Kremer**[1], **M. Rechtsman**[2], **K. G. Makris**[3,4], **Y. Plotnik**[5], **Y. Lumer**[5], **M. S. Rudner**[6], **M. Segev**[5], **A. Szameit**[1*]

[1]Institut für Angewandte Physik, Abbe School of Photonics, Friedrich-Schiller-Universität Jena, Max-Wien Platz 1, 07743 Jena, Germany

[2]Department of Physics, the Pennsylvania State University, University Park, PA 16801, USA

[3] Institute for Theoretical Physics, Vienna University of Technology, A–1040 Vienna, Austria, EU

[4] Department of Electrical Engineering, Princeton University, Princeton, 08544 NJ USA

[5]Department of Physics, Technion – Israel Institute of Technology, Haifa 32000, Israel

[6]The Niels Bohr International Academy, Niels Bohr Institute, 2100 Copenhagen, Denmark

[*]corresponding author: alexander.szameit@uni-jena.de

**Abstract** We present the first experimental observation of a topological transition in a non-Hermitian system. We monitor the topological transition by employing bulk dynamics only. Moreover, we demonstrate, theoretically and experimentally, topological interface states in a PT-symmetric system. The PT-symmetric structure has unbroken PT symmetry, i.e., all eigenvalues in the spectrum are real, despite the system's non-Hermiticity. The non-Hermitian behavior is engineered by inducing bending loss by spatially "wiggling" every second waveguide.

The recent development of topological insulator states for photons[1–3] has led to an exciting new field of "topological photonics," which has as a central goal the development of extremely robust photonic devices[4]. Topological insulator physics has been studied extensively in condensed matter[5] and cold atoms[6], but photonics facilitates introducing non-Hermitian effects through the engineering of optical gain and loss. In this talk, we will present two results demonstrating non-Hermitian topological systems for the first time, as described below. Our systems are realized in an array of laser-written waveguides. Losses in the waveguides are engineered by oscillating waveguide trajectories (Fig. 1(b)). Although in the experiment there are only passive components, this maps directly onto the problem with gain and loss (modulo an overall exponential decay).

(1) The first experiment concerns a one-dimensional dimer model (lattice part S in Fig. 1(b)) in which the non-Hermitian character of the system can be used to extract topological information purely from the bulk dynamics of the system[7]. Since the diffraction of light through the waveguides maps to the Schrödinger equation, its topological character carries over into the optical domain. We show that, as predicted in[7], the 'mean displacement' $\langle \Delta m \rangle$ of the optical wavepacket on the B sites undergoes a transition as a function of the 'dimerization' $[d_1\text{-}d_2]/2$ of the lattice (Fig.1 (a)). This transition measures the 'winding number' of the lattice, a topological number that must be either zero or one in our case.

(2) The second is the proposal of the first non-Hermitian, PT-symmetric topological system, and its experimental realization in the 'passive-PT' framework. It had been previously thought that PT-symmetric topological states were impossible[8]. Here we provide an example of such a state. The model comprises a topological defect state in a one-dimensional system (shown in Fig.1(b)). Due to the global PT symmetry, both the bulk and defect states have real eigenvalues. The defect state is observed in Fig. 1(c).

In conclusion, these two experiments constitute the first realization of non-Hermitian topological states in any system in nature.

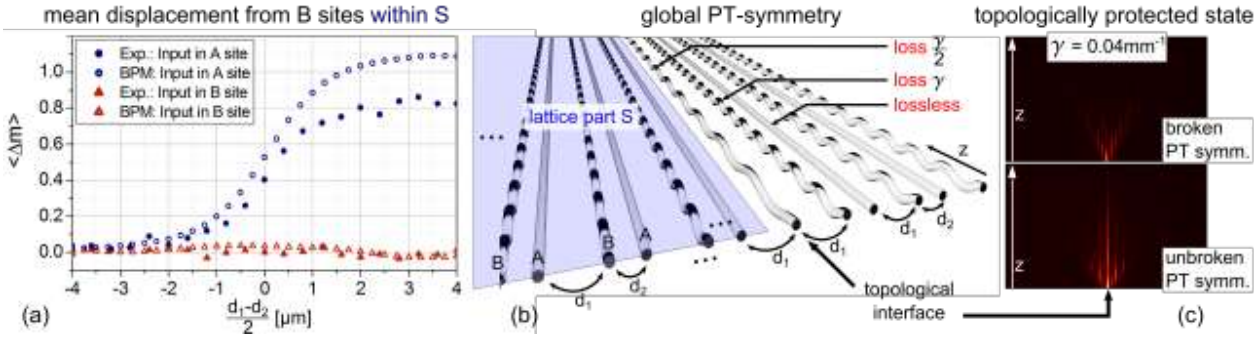



**Fig. 1:** (left) Simulation and experiment showing the topological transition in the non-Hermitian dimer model; (center) Schematic showing the experimental setup with global PT symmetry; (right) experiment showing no topological state (above), and with topological state (below).

**Acknowledgements** The authors gratefully acknowledge financial support by the German Ministry of Education and Research (Center for Innovation Competence programme, grant no. 03Z1HN31) and the Deutsche Forschungsgemeinschaft (grant no. NO462/6-1 and SFB 652). K.G.M. is supported by the People Programme (Marie Curie Actions) of the European Union's Seventh Framework Programme (FP7/2007-2013) under REA grant agreement number PIOF-GA-2011- 303228 (project NOLACOME), and by the European Union Seventh Framework Programme (FP7-REGPOT-2012-2013-1) under grant agreement 316165.

**REFERENCES**

1. Haldane, F. D. M. and S. Raghu, "Possible Realization of Directional Optical Waveguides in Photonic Crystals with Broken Time-Reversal Symmetry," *Phys. Rev. Lett.*, Vol. 100, 013904, 2008.
2. Wang, Z., Y. Chong, J. D. Joannopoulos and M. Soljacic, "Obersvation of unidirectional backscattering-immune topological electromagnetic states," *Nature*, Vol. 461, 772–775, 2009.
3. Rechtsmann, M. C., J. M. Zeuner, Y. Plotnik, Y. Lumer, D. Podolsky, F. Dreisow, S. Nolte, M. Segev and A. Szameit, "Photonic Floquet topological insulators," *Nature*, Vol. 496, 196–200, 2013.
4. Hafezi, M., E. A. Demler, M. D. Lukin, and J. M. Taylor, "Robust optical delay lines with topological protection," *Nature Physics*, Vol. 7, 907–912, 2011.
5. Hasan, M. Z. and C. L. Kane, "Colloquium: Topological insulators," *Rev. Mod. Phys.*, Vol. 82, 3045, 2010.
6. Jotzu, G., M. Messer, M. Desbuquois, M. Lebrat, T. Uehlinger, D. Greif and T. Esslinger, "Experimental realization of the topological Haldane model with ultracold Fermions," *Nature*, Vol. 515, 237-240, 2014.
7. Rudner, M. S. and L. S. Levitov, "Topological Transition in a Non-Hermitian Quantum Walk," *Phys. Rev. Lett.*, Vol. 102, 065703, 2009.
8. Hu, Y. C. and T. L. Hughes, "Absence of topological insulator phases in non-Hermitian PT-symmetric Hamiltonians," *Phys. Rev. B*, Vol. 84, 153101, 2011.

# Optomechanical interactions in coupled resonators with unbalanced gain and loss.

**D.W. Schönleber[1], R. El-Ganainy[1,2] and A. Eisfeld[1]**

[1]Max Planck Institute for the Physics of Complex Systems, Nöthnitzer Strasse 38, 01187 Dresden, Germany

[2]Department of Physics and Henes Center for Quantum Phenomena, Michigan Technological University, Houghton, Michigan 49931, USA

[*]corresponding author: eisfeld@pks.mpg.de

**Abstract**—We show that in non-Hermitian photonic molecules the maximum enhancement of optomechanical coupling for stable steady-state solutions is achieved for unbalanced gain and loss profiles away from exceptional points. Including the effect of gain saturation, we find regimes of self-sustained oscillations in the mechanical displacement.

Cavity optomechanics have attracted considerable attention over the past decade with several potential applications in sensing, quantum information and gravitational wave detection, to mention a few [1]. Recently, optomechanical interaction in two coupled passive resonators was investigated and saser action (acoustic analog of laser) was experimentally demonstrated [2]. Later, it was predicted that the interaction strength in this setup can be significantly enhanced if the two coupled resonators exhibit balanced gain/loss profile and operate near the so called exceptional point [3]. However, in this important study in which this novel concept was introduced, stability landscapes and dynamic evolution of this system were not investigated in detail.

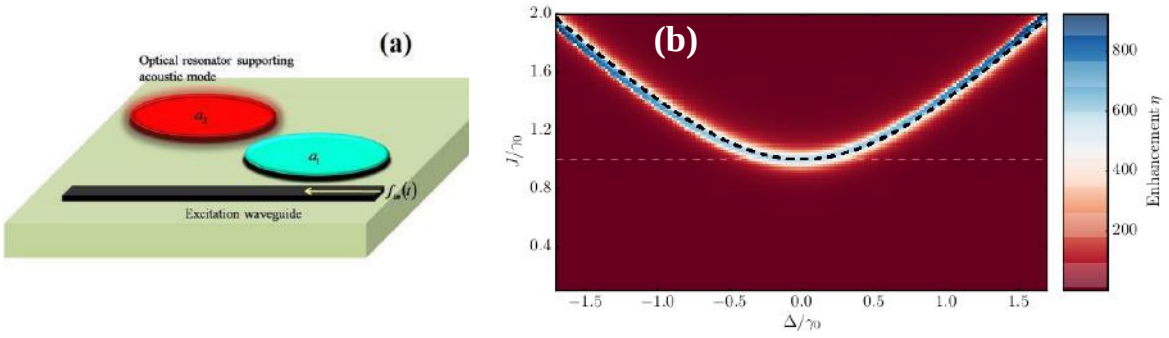



*Figure 1 (a) Schematic of the investigated system. The two non-Hermitian optical resonators are driven by an external laser and support two optical and one acoustic mode. (b) Enhancement landscape as a function of the intercavity coupling and the laser detuning for balanced gain and loss.*

The setup is displayed in Figure 1(a). The resonators $a_{1,2}$ have identical resonant frequency and exhibit optical gain and loss, respectively while $a_2$ also supports an acoustic mode. The external optical excitation of the system is provided

through the waveguide coupling to $a_1$. Figure 1 (b) depicts the enhancement in this system when tuning the intercavity coupling $J$, for a set of parameters similar to that considered in [3]. Here, $\gamma_o$ is the total loss in $a_2$ and it is equal in magnitude to the optical coupling between the two cavities $J$, $\gamma_1$ is the total gain in cavity $a_1$ and $\Delta$ is the detuning between the pump laser frequency and the eigenfrequencies of the individual resonators in isolation. Figure 1 (b) indicates that the maximal enhancement is not found at the exceptional point $J=\gamma_0$, but rather if the laser detuning $\Delta$ is tuned on a resonance of the eigenfrequencies of the coupled system [black line in Figure 1 (b)]. However, many of the steady-state values are not stable according to linear stability analysis if unbounded gain is used in the calculations rather than gain saturation.

Including the effect of gain saturation, i.e., replacing the gain term $\gamma_1$ by $\gamma_1/(1+|a_1|^2/a_s^2)$, with $a_s$ being the saturation threshold, we find that the formerly unstable regimes now display either stable or oscillatory behavior. This is shown in Figure 2 where in (i) both unstable and stable dynamics is shown for the case of unbounded gain. Conversely, in Figure 2 (ii) stable as well as self-sustained oscillatory solutions are shown for different values of the gain saturation threshold $a_s$. Hence, gain saturation is needed to ensure non-divergent solutions for balanced gain and loss, and for self-sustained oscillatory solutions to exist.

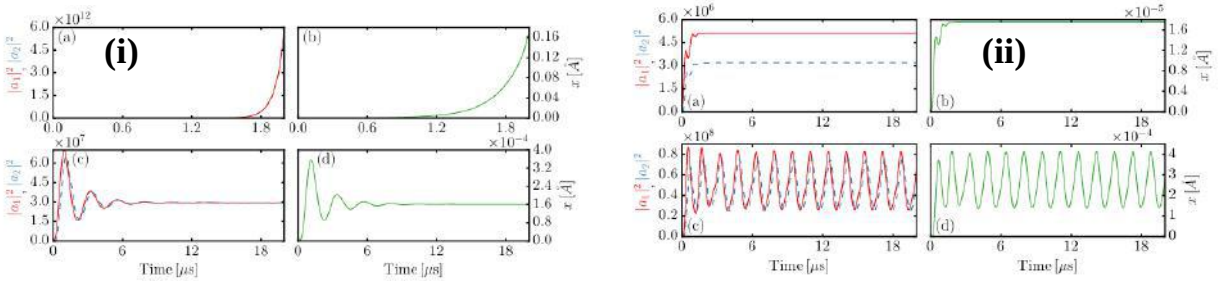



*Figure 2: Examples of different dynamical regimes. In (i) examples for divergent and stable dynamics are shown for the case of unbounded gain. In (ii), examples of the two regimes that exist upon introducing gain saturation are shown, namely stable and self-sustained oscillatory dynamics.*

**REFERENCES**


1. M.Aspelmeyer, T.J.Kippenberg, F.Marquardt, "Cavity Optomechanics: Nano- and Micromechanical Resonators Interacting with Light", Springer (2014)
2. I. S. Grudinin, H. Lee, O. Painter, and K. J. Vahala, "Phonon Laser Action in a Tunable Two-Level System", *Phys. Rev. Lett.* 104, 083901 (2010)
3. H. Jing, S.K. Ozdemir, X.Y. Lu, J. Zhang, L. Yang and F. Nori, "PT-Symmetric Phonon Laser", *Phys Rev. Lett*. 113, 053604 (2014)

# Observation of optically induced transparency in a micro-cavity

**Yuanlin Zheng[1], Xianfeng Chen[1], Li Ge[2], and Wenjie Wan[1,3*]**

[1]MOE Key Laboratory for Laser Plasmas and Collaborative Innovation Center of IFSA,
Department of Physics and Astronomy, Shanghai Jiao Tong University, Shanghai 200240, China

[2]Department of Engineering Science and Physics, College of Staten Island, New York, USA

[3]The University of Michigan-Shanghai Jiao Tong University Joint Institute,
The State Key Laboratory of Advanced Optical Communication Systems and Networks,
Shanghai Jiao Tong University, Shanghai 200240, China

[*]*email: wenjie.wan@sjtu.edu.cn*

**Abstract**-We report on the observation of optically induced transparency (OIT) in a compact microresonator in an ambient environment by introducing a four-wave mixing (FWM) gain to nonlinearly couple two separated resonances of the micro-cavity. Its optical-controlling capacity and non-reciprocity characteristics at the transparency windows are also demonstrated. The FWM in microcavities can be described by an effective Hamiltonian whose square root singularity at an exceptional point enables a pseudo-Hermitian transition similar to that in Parity-Time symmetry systems.

Electromagnetically induced transparency (EIT) allows for the flipping of an optical opaque transmission window to a transparent one under illumination of a second coherent light beam even at the few-photon limit[1]. This provides tremendous opportunities for quantum physics and information science. However, atomic gas systems requires optical cooling or vapor heating techniques combined with vacuum isolation in most circumstances, making it difficult for chip-scale integrations, which are the major proposed applications. Alternatively, classical analogies that mimic the EIT effect are under active pursuit in various physical systems, including coupled resonators [2], photonic crystals, and plasmonic meta-materials. However, most of them rely on linear coupling between the resonances, which can only exhibit EIT-like spectra but lack of active-controlled transparency. Until recently, successful attempts [3-6] have cloned the idea of EIT in an opto-mechanical micro-cavity to induce a narrow transparency with the aid of mechanical oscillations excited through Brillouin scattering (BS), which provide enough phonons to couple some hybrid optical-mechanical resonances. However, most of these attempts still require cooling and vacuum systems to preserve high-quality mechanical modes; furthermore, careful designs must be addressed to both the mechanical and optical modes.

We report an optically induced transparency (OIT) scheme in a compact micro-cavity in an ambient environment by exploring cavity-enhanced four-wave mixing (FWM) gain to introduce a transparency window in an opaque resonance dip. The dip directly results from the interference between two resonances that are coupled nonlinearly through the FWM process. Active-controlling of the OIT can be achieved by varying a strong pump beam, and small frequency detuning of the pump can lead to a Fano-like asymmetric resonance to justify the interference nature of the OIT. The OIT observed here is a non-reciprocal one, since the FWM gain is unidirectional owing to the conservation law of momentum. Furthermore, we also show that degenerate four-wave mixing (FWM) in nonlinear optics can be described by an effective Hamiltonian that is pseudo-hermitian, which enables a transition similar to that in Parity-Time (PT) symmetry systems. Both processes are due to a square root singularity at an exceptional point.

A relative strong pump beam is injected to one resonance of a micro-cavity with third-order nonlinearity, enabling degenerated FWMs enhanced by the cavity resonance. A second signal beam scans through one of the resonances. The parametric gain is a narrow-linewidth one owing to the cavity resonance's enhancement; hence, its linewidth is imprinted by the resonances'. Effectively, two resonances near the signal and idler waves' frequencies are nonlinearly coupled together via the FWM process. The observed OIT rises from the interference of the signal and idler resonances through nonlinear coupling during FWMs, where the gain induced near the signal resonance is a narrow one enhanced by two other resonances at the pump and idler. The FWM gain near the signal resonance purely imprint the idler resonance's linewidth through nonlinear coupling, effectively creating a virtual resonance peak near the signal resonance. Likewise, a similar narrow gain is initiated simultaneously at the idler resonance. This hump-in-dip spectrum around the signal resonance results from the interference between this virtual gain peak and the original signal resonance dip. This cross-coupling can also be verified by the generation of idler wave as shown, which grows with increasing coupling strength. Note that, a broad-spectrum gain/loss like scattering loss and absorption cannot lead to this OIT transmission, and it only affects the quality factor (Q-factor) of the resonance.

The measured forward transmission is featured with the OIT window, which is absent in the backward transmission. This is because of the unidirectional gain nature of FWM, which strictly follows the phase matching conditions. The forward momentum carried by the pump only enables the FWM gain in the same direction while inhibiting the gain in reverse. Our novel approach utilizes unidirectional FWM gain in a micro-cavity, which features with non-reciprocal gain arising from the strong pump.

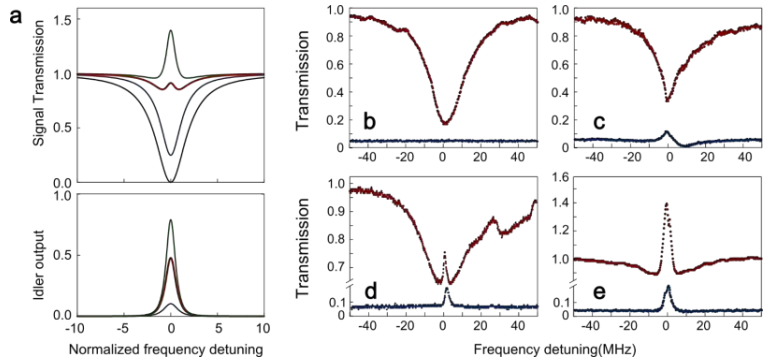



Figure 1 | Theoretical and experimental transmission spectra of optically induced transparency

## REFERENCES


1. Boller, K. J., Imamoglu, A., and Harris, S. E., "Observation of electromagnetically induced transparency," Phys. Rev. Lett., Vol. 66, 2593-2596, 1991.
2. Xu, Q., et al., "Experimental realization of an on-chip all-optical analogue to electromagnetically induced transparency," Phys. Rev. Lett. , Vol. 96, 123901, 2006.
3. Weis, S., et al., "Optomechanically induced transparency," Science, Vol. 330, 1520-1523, 2010.
4. Safavi-Naeini, A. H., et al., "Electromagnetically induced transparency and slow light with optomechanics," Nature, Vol. 472, 69-73, 2011.
5. Dong, C. H., Fiore, V., Kuzyk, M. C., and Wang, H. L., "Optomechanical dark mode," Science, Vol. 338, 1609-1613, 2012.
6. Kim, J., Kuzyk, M. C., Han, K., Wang, H., and Bahl, G., "Non-reciprocal Brillouin scattering induced transparency," Nat. Physics, Vol. 11, 275-280, 2015.

# Perfect compensation of absorption in metamaterials for diffraction-unlimited imaging

**W. Adams**[1], **and D. Ö. Güney**[1*]
[1]Department of Electrical & Computer Engineering, Michigan Technological University, 1400 Townsend Dr., Houghton, MI 49931-1295, USA
[*]dguney@mtu.edu

**Abstract**-To overcome the resolution limit of conventional optics, near field imaging techniques using a negative index flat lens (NIFL) have been previously developed that amplify the evanescent components of the incident field. Here, a technique is developed and demonstrated to compensate for losses in a non-ideal NIFL by determining the transfer function of the lens and subsequently applying the inverse to the unresolved raw image. The result is a compensated image with sub-diffraction-limited resolution.

In conventional imaging systems, the field components with spatial frequency greater than $\omega/c$, where $\omega$ is angular frequency of the wave and $c$ is the speed of light in the medium, become evanescent and decay rapidly. Typically, the image sensor is located far from the source such that all the evanescent components are decayed beyond the sensitivity of the sensor. Therefore, the largest spatial frequency components a conventional imaging system can detect is theoretically limited to $\omega/c$; the so-called diffraction limit. In order to capture higher spatial frequency components and increase the resolution of imaging systems beyond this limit, Pendry proposed a near field imaging technique with a slab of negative index material [1]. In this work, a new near field imaging technique is presented using a lossy negative index flat lens (NIFL) in conjunction with the post-processing loss compensation technique inspired by plasmon injection scheme [2] and described in Fig. 1. The process begins with an image produced by a NIFL. A compensation filter is then applied to the image in order to amplify the high spatial frequency components which have been attenuated. The compensation filter is the inverse of the transfer function of the NIFL, which can be obtained analytically or from numerical simulation.

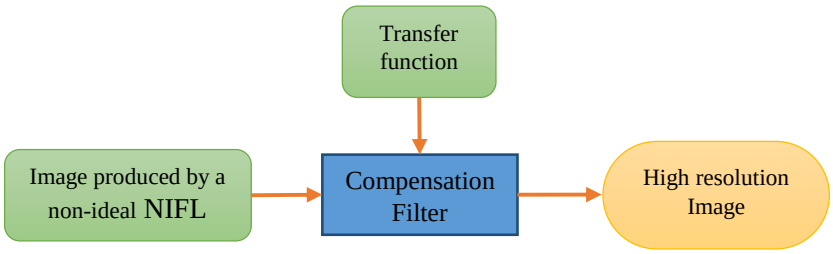



**Figure 1** Block diagram of the proposed near field imaging technique.

Unlike the previous near field imaging methods, this technique does not benefit from a lossless NIFL. The technique developed here is based on a non-ideal NIFL with a practically achievable figure-of-merit (FOM) for loss, defined by the ratio of the real and imaginary parts of the refractive index [3-5].

The optical properties of the NIFL are defined in terms of complex relative permittivity $\varepsilon_r = -1 + j\varepsilon''$ and complex relative permeability $\mu_r = -1 + j\mu''$ with $\varepsilon'' = \mu'' = 0.1$, resulting in a FOM of about 10 and an impedance match with free space. In this work, the transfer function for the NIFL was obtained by numerical simulation in COMSOL. The incident wavelength $\lambda_0$ was chosen to be 1μm, and the thickness $2d$ of the NIFL was chosen to be 0.5μm. $d$ was chosen as thin enough to minimize the loss experienced by high spatial frequency components of the incident field while still providing sufficient

amplification, in addition to considering practical concerns such as the unit cell size of possible constitutive negative index metamaterials, mechanical strength of the lens, and challenges with optical alignment of submicron imaging systems since the thickness of the lens determines the distance from the object and image planes.

In order to perform imaging with the NIFL, a simulation was configured with an arbitrary "object" electric field defined at the object plane with sub-diffraction feature size ($\lambda_0/4$). A raw image was then recorded at the image plane that is subsequently compensated with the technique in Fig. 1. The result is a sub-diffraction compensated image as seen in Fig. 2. It can clearly be seen that while the raw image does not provide a resolved image, the compensated image results in a near-perfect reconstruction of the object.

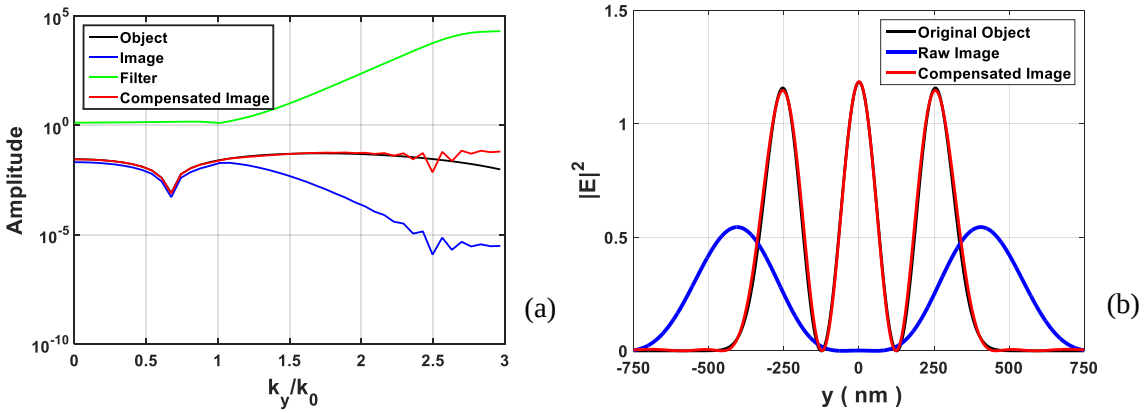



**Figure 2** (a) Fourier transform of the object and image demonstrating compensation of high $k_y$ attenuation and (b) calculated intensity of the object, raw image, and compensated image. ($\lambda_0 = 1\mu m$)

Previously, near field imaging techniques have been proposed using a NIFL to achieve image resolution beyond the diffraction limit. However, compensation of losses in a non-ideal NIFL has been largely ignored. Here, the transfer function of a lossy NIFL is determined by simulation, and the inverse is used as a filter to recover lost high spatial frequency components of the raw image that is produced. In Fig. 2(b), it can be seen that the resulting raw image from the lossy NIFL does not resolve the original object containing sub-diffraction feature size. After application of the compensation filter in Fig. 2(a), many of the lost high spatial frequency components are recovered, resulting in the compensated image shown in Fig. 2(b). The compensated image displays sub-diffraction-limited resolution.

This work was supported by Office of Naval Research (award N00014-15-1-2684) and the National Science Foundation under Grant No. ECCS-1202443.

**REFERENCES**

1. Pendry, J. B. "Negative refraction makes a perfect lens," *Phys. Rev. Lett.*, Vol. 85, No. 18, 3966–3969, 2000.
2. Sadatgol, M, S. K. Ozdemir, L. Yang, and D. O. Guney, "Plasmon injection to compensate and control losses in negative index metamaterials," *Phys. Rev. Lett.*, Vol. 115, No. 3, 035502 (2015).
3. Fang, N. and X. Zhang, "Imaging properties of a metamaterial superlens," *Appl. Phys. Lett.*, Vol. 82, No. 2, 161–163, 2003.
4. Fang, N., H. Lee, C. Sun, and X. Zhang, "Sub-diffraction-limited optical imaging with a silver superlens," *Science*, Vol. 308, No. 5721, 534–537, 2005.
5. Lee, H. Y. Xiong N. Fang, W. Srituravanich, S. Durant, M. Ambati, C. Sun, X. Zhang, "Realization of optical superlens imaging below the diffraction limit," *New J. Phys.*, Vol. 7, No. 1, 255, 2005.

# Investigation of light transport for Non-Hermitian photonics in the silicon platform

**Ming-Hui Lu[1,2*], Ye-Long Xu[1], Xue-Yi Zhu[1], Li Liu[1], Yi Zou[1], Xiao-Ping Liu[1], Yan-Feng Chen[1]**

[1] *National Laboratory of Solid State Microstructures and Department of Materials Science and Engineering, Nanjing University, Nanjing, Jiangsu 210093, China*

[2]*Collaborative Innovation Center of Advanced Microstructures, Nanjing University, Nanjing, 210093, China.*

**Recently rapid progress in integrated plasmonic/photonic circuits demands all the optical components for high speed processing of light signals. To break the reciprocity of optical and plasmonic signal propagation, much research effort relies on non-Hermitian, PT symmetric optical potentials instead of using bulky elements in the presence of static magnetic fields and paramagnetic materials. In contrast to Hermitian system, wave propagation in non-Hermitian system show numerous novel phenomena such as asymmetric diffraction, power oscillations, unidirectional invisibility, double refraction and many more. PT symmetric non-Hermitian systems with real energies are very exciting because one can have fully consistent quantum theory by restoring the Hermiticity and by upholding unitary time evolution for such systems in a modified Hilbert Space. In optics, PT symmetry potentials can easily be realized by spatially modulating the refractive index with properly placed gain and loss in a balanced manner. From an experimental point of view, such structures require two main components: one with absorption and another that is optically or electrically pumped (active PT-symmetry) or lossless (passive PT- symmetry). In this talk, firstly we would like to demonstrate the polarization dependent asymmetry diffraction phenomena using a passive 1-D and 2-D PT symmetry grating structure. Secondly, our experiment demonstrating the realization of Bloch oscillations in integrated passive photonic circuits open a way exploring the unprecedented transport phenomena on a chip in non-Hermitian physics. Thirdly, by using PT symmetry concept onto some active devices such as an optical laser system, we can study the quantum physical phenomena of light from a wider prospect view of design parameters, symmetry and material choices using which we could find a novel physical phenomenon and design a series of photo-devices. We can improve the performance of a PT laser based on erbium doped alumina waveguide by improving the gain by strategically using the optical loss and controlling the coupling strength between the gain and loss regions making it possible for phase transitions. Our insights in using non-Hermitian PT symmetric optical potientals for both active and passive devices provide new methods for manipulating light transportation and open a door towards fabricating**

**many novel photonic structures for potential applications in optics, on-chip light control and optical communications.**

**REFERENCES (SIZE 10, BOLD)**


[1] Ruter, C. E. et.al. Observation of parity-time symmetry in optics, Nature Phys. 6, 192-195 (2010).
[2] Regensburger, A. et.al. Parity-time synthetic photonic lattices, Nature 488, 167-171 (2012).
[3] Guo, A. et.al. Observation of PT-symmetry breaking in complex optical potenstials, Phys. Rev. Lett. 103, 093902 (2009).
[4] Bloch, F. Quantum mechanics of electrons in crystal lattices. Zeitschrift fur Physik 52, 555-600 (1928).
[5] Longhi, S. Bloch Oscillations in Complex Crystals with PT Symmetry. Phys. Rev. Lett. 103, 123601 (2009).
[6] Feng, L. et al. Experimental demonstration of a unidirectional reflectionless parity-time metamaterial at optical frequencies. Nat. Mater. 12, 108-113 (2013).
[7] Kulishov, M. et.al. Analysis of Pt-symmetric volume gratings beyond the paraxial approximation, Opt. Express 23, 9347-62 (2015).
[8] Yan, Y. and Giebink, N.C., Passive PT symmetry in organic composite films via complex refractive index modulation, Adv. Opt. Mater. 2, 423-27 (2014).
[9] Peng, B. et.al. Parity-time-symmetric whispering-gallery microcavities, Nature Phys. 10, 394-98 (2014).


.

# Selective amplification of semi-chiral defect states

**H. Schomerus**

Department of Physics, Lancaster University, Lancaster, LA1 4YB, United Kingdom
h.schomerus@lancaster.ac.uk

**Abstract**— In systems with suitable symmetries, topologically protected states can arise that are immune to perturbations. We discuss how the appearance of such states can be tailored by modifying the chiral symmetry, which is one of the most common symmetries exploited in artificially engineered systems. We also discuss how the properties of the topologically protected states can be enriched by the non-hermitian effects of amplification and absorption.

One of the main goals of present research in electronic and photonic systems is the realisation of topologically protected states. The existence of such states relies on symmetries, with the present focus set on the roles of time-reversal symmetry, chiral symmetry and charge-conjugation symmetry. In combination with considerations of dimensionality, a classification of robust protected states can then be achieved [1, 2], which guides the design of theoretical models and experimental realizations [3].

In the photonic setting, the most interesting symmetry classes are difficult to realise - e.g., magneto-optical effects to break Time-reversal symmetry and induce quantum-hall like phases are typically too weak. The chiral symmetry is most easily realised, but instead of being desirable some of the symmetry-induced effects can be more of an obstacle. In particular, point-defect states are vulnerable to hybridization with states from flat bands, which occur in many interesting models [4, 5, 6, 7, 8, 9, 10, 11].

In this talk I discuss the results of [12], which shows theoretically as well as experimentally that this obstacle can be overcome by modifying the chiral symmetry in a very natural way. This exploits that chiral symmetry relies on settings with two subsystems, with the flat bands supported by the larger of the two [13, 14]. We generate point-defect states in the complementary subsystem, and then induce terms that remove the flat band. This has a precise and general mathematical meaning, which leads to the notion of a semichiral symmetry [12]. We implement this program for a prototypical example, the Lieb lattice [14], which has seen much recent activity [10, 11]. We not only demonstrate the robustness of point-defect states in the semichiral setting, but also show that the states can be manipulated via judiciously introduced absorption. This extends our previous work on selective amplification of topological states [15, 16, 17].

Our findings introduce a whole new element into considerations of topology and symmetry, which is both of fundamental importance as well as of practical value.

**ACKNOWLEDGMENT**

This talk is based on joint work with C. Poli (Lancaster), as well as M. Bellec, U. Kuhl, and F. Mortessagne (Université Nice Sophia Antipolis, Nice) [12]. The underlying research was supported by EPSRC via Grant No. EP/J019585/1.

**REFERENCES**

1. S. Ryu, A. P. Schnyder, A. Furusaki, and A. W. W. Ludwig, New J. Phys. **12**, 065010 (2010).
2. J. C. Y. Teo and C. L. Kane, Phys. Rev. B **82**, 115120 (2010).
3. L. Lu, J. D. Joannopoulos, and M. Soljačić, Nat. Photon. **8**, 821 (2014).
4. D. L. Bergman, C. Wu, and L. Balents, Phys. Rev. B **78**, 125104 (2008).
5. D. Green, L. Santos, and C. Chamon, Phys. Rev. B **82**, 075104 (2010).
6. J. Mur-Petit and R. A. Molina, Phys. Rev. B **90**, 035434 (2014).
7. D. Leykam, O. Bahat-Treidel, and A. S. Desyatnikov, Phys. Rev. A **86**, 031805(R) (2012).
8. J. D. Bodyfelt, D. Leykam, C. Danieli, X. Yu, and S. Flach, Phys. Rev. Lett. **113**, 236403 (2014).
9. D. Guzmán-Silva, C. Mejía-Cortés, M. A. Bandres, M. C. Rechtsman, S. Weimann, S. Nolte, M. Segev, A. Szameit, and R. A. Vicencio, New J. Phys. **16**, 063061 (2014).
10. R. A. Vicencio, C. Cantillano, L. Morales-Inostroza, B. Real, C. Mejía-Cortés, St. Weimann, A. Szameit, and M. I. Molina, Phys. Rev. Lett. **114**, 245503 (2015).
11. S. Mukherjee, A. Spracklen, D. Choudhury, N. Goldman, P. Öhberg, E. Andersson, and R. R. Thomson, Phys. Rev. Lett. **114**, 245504 (2015).

12. C. Poli, H. Schomerus, M. Bellec, U. Kuhl, and F. Mortessagne, arXiv:1512.02284 (2015).
13. B. Sutherland, Phys. Rev. B **34**, 5208 (1986).
14. E. H. Lieb, Phys. Rev. Lett. **62**, 1201 (1989).
15. H. Schomerus and N. Y. Halpern, Phys. Rev. Lett. **110**, 013903 (2013).
16. H. Schomerus, Opt. Lett. **38**, 1912 (2013).
17. C. Poli, M. Bellec, U. Kuhl, F. Mortessagne, and H. Schomerus, Nat. Commun. **6** (2015).

# Non-Hermitian phase matching in atomic scattering

**S. Wüster**[1] and **R. El-Ganainy**[2]

[1]Department of Physics, Bilkent University, Ankara 06800, Turkey
[2]Department of Physics and Henes Center for Quantum Phenomena, Michigan Technological University, Houghton, Michigan 49931, USA
sebastian.wuster@bilkent.edu.tr

**Abstract**— We consider the effect of velocity dependent loss processes on the scattering of ultracold matter-waves. Due to the loss, the entire process can be viewed as non-Hermitean four-wave-mixing of matter waves. We find that suitable loss can actually strengthen certain scattering processes that would otherwise be suppressed by energy and momentum conservation and explore to what extend this effect can be put to use for atom optical applications.

It is now firmly established in the context of PT-symmetric theory, that the effect of loss or dissipation, for example in non-linear optical setups, is not always detrimental but can in fact be highly beneficial. In the context of ultracold atomic gases, where a variety of one-, two- and three-body loss processes are always present, it was realized that these can be exploited, for example in dissipative system engineering [1].

Recent studies of non-Hermitian optical parametric amplifiers (OPA) show a variety of interesting consequences of loss [2, 3, 4]. Particularly it has been shown that it can facilitate phase-matching in a one dimensional OPA, leading to the counter-intuitive effect of an amplification of the signal beam, facilitated by the introduction of a loss process for the idler beam [2]. Here we explore the ramifications of this fundamental result for atomic scattering processes, which exhibit strong similarities with optical four-wave mixing.

As in optics, matter wave four wave mixing processes are strongly constrained by energy and momentum conservation (phase-matching) in free-space. Experiments on four-wave mixing in condensate have thus so far introduced additional features, such as an optical lattice [5] or multiple atomic spin states [6] as additional handles to satisfy conservation laws. By exploiting non-Hermiticity due to engineered, velocity dependent, atomic losses, we show that phase-matching is eased also in free-space, promising some new flexibility for matter wave manipulations driven by the non-linear inter-atomic interactions themselves.

We numerically model BEC four-wave mixing in the presence of losses using the time-dependent Gross-Pitaevskii equation and propose practical implementations of the required spectrally dependent loss processes.

**REFERENCES**

1. A. J. Daley, J. M. Taylor, S. Diehl, M. Baranov and P. Zoller, "Atomic Three-Body Loss as a Dynamical Three-Body Interaction" *Phys. Rev. Lett.*, Vol. 102, 040402, 2009.
2. R. El-Ganainy, J. I. Dadap and R. M. Osgood, Jr., , "Optical parametric amplification via non-Hermitian phase matching," *Opt. Lett.*, Vol. 40, 5086, 2015.
3. D. A. Antonosyan, A. S. Solntsev and A. A. Sukhorukov, "Parity-time anti-symmetric parametric amplifier" *Opt. Lett.*, Vol. 40, 4575, 2015.
4. T. Wasak, P. Szańkowski, V. V. Konotop and M. Trippenbach, "Four-wave mixing in a parity-time (PT)-symmetric coupler" *Opt. Lett.*, Vol. 40, 5291, 2015.
5. G. K. Campbell, J. Mun, M. Boyd, E. W. Streed, W. Ketterle, and D. E. Pritchard, "Parametric Amplification of Scattered Atom Pairs" *Phys. Rev. Lett.*, Vol. 96, 020406, 2006.
6. R. Bücker, J. Grond, S. Manz, T. Berrada, T. Betz, C. Koller, U. Hohenester, T. Schumm, A. Perrin and J. Schmiedmayer "Twin-atom beams" *Nat. Phys.*, Vol. 7, 608, 2011.

# Symmetry approach to non-Hermitian waveguide arrays

**J. Guerrero**[1], **B.M. Rodríguez-Lara**[2]

[1]Dpt. Matemática Aplicada, Facultad de Informática, Campus de Espinardo, Universidad de Murcia, Murcia 30100, Spain

[2] Instituto Nacional de Astrofísica, Óptica y Electrónica, Calle Luis Enrique Erro No. 1, Sta. Ma. Tonantzintla, Pue. CP 72840, México

juguerre@um.es

**Abstract**— We show that a wide class of non-Hermitian finite waveguide couplers, those with non-balanced gain and losses and complex couplings, possess an underlying $SO(3,1)$ symmetry realized in a non-unitary way; i.e., they are finite, non-unitary, optical realizations of the Lorentz group in 3+1D. We give analytic solutions for the mode-coupling equations of the simplest array of the class: the non-hermitian dimer.

Symmetry has shown to be an important tool in the design of photonic devices [1, 2]. Even in the case of $PT$-symmetric optical waveguide arrays [3, 4], symmetry groups have been shown to play an important role [5, 6]. For example, the linear $PT$-symmetric dimer and $J_x$ array belong to the optical, finite, non-unitary representation of $SO(2,1)$ where the non-unitarity accounts for the balanced gains and losses in these systems.

Here, we show that even in the non-Hermitian and non-PT symmetric case, i.e. unbalanced gain/loss or complex couplings, optical waveguide arrays possessing an underlying $SO(3,1)$ symmetry can be designed using, again, a non-unitary representation that accounts for the unbalanced gain/loss. As a practical example, we consider the simplest case of the non-Hermitian dimer satisfying the coupled mode equation,

$$-i\partial_z \begin{pmatrix} E_0 \\ E_1 \end{pmatrix} = \begin{pmatrix} \alpha_0 & \gamma_0 \\ \gamma_1 & \alpha_1 \end{pmatrix} \begin{pmatrix} E_0 \\ E_1 \end{pmatrix}, \tag{1}$$

where $E_j$ represents the localized field mode amplitude at the $j$th waveguide, for $j = 0, 1$, with $\alpha_0, \alpha_1, \gamma_0, \gamma_1 \in \mathbb{C}$. Defining $\alpha_\pm = \frac{1}{2}(\alpha_0 \pm \alpha_1)$, we can perform the non-unitary transformation,

$$E_j = e^{i\alpha_+ z} A_j, \quad j = 0, 1, \tag{2}$$

The new field amplitudes $A_j\,, j = 0, 1$ satisfy:

$$-i\partial_z \begin{pmatrix} A_0 \\ A_1 \end{pmatrix} = \begin{pmatrix} \alpha & \gamma_0 \\ \gamma_1 & -\alpha \end{pmatrix} \begin{pmatrix} A_0 \\ A_1 \end{pmatrix}. \tag{3}$$

where we have denoted $\alpha = \alpha_-$. Now, the traceless matrix can be expressed as a linear combination, with real coefficients, of the matrices $\hat{\sigma}_z = \hat{\sigma}_3$, $\hat{\sigma}_\pm = \frac{1}{2}(\hat{\sigma}_1 \pm i\hat{\sigma}_2)$, $\hat{\rho}_z = i\hat{\sigma}_3$, $\hat{\rho}_\pm = i\hat{\sigma}_\pm$, where $\hat{\sigma}_j$, $j = 1, 2, 3$ are Pauli matrices, generating the so(3,1) algebra under commutation, c.f. [5],

$$\begin{pmatrix} \alpha & \gamma_0 \\ \gamma_1 & -\alpha \end{pmatrix} = \alpha_r \hat{\sigma}_z + \gamma_{0r}\hat{\sigma}_+ + \gamma_{1r}\hat{\sigma}_- + \alpha_i \hat{\rho}_z + \gamma_{0i}\hat{\rho}_+ + \gamma_{1i}\hat{\rho}_-. \tag{4}$$

The notation $x_r$ and $x_i$ has been used to indicate real and imaginary parts, respectively. Equation (1) can be solved analytically, even for propagation dependent parameters $\alpha_j(z)$, $\gamma_j(z)\,, j = 0, 1$ (in this case the transformation (2) changes to $E_j = e^{i\int^z \alpha_+(z)dz} A_j$, $j = 0, 1$) using the Wei-Norman method [7], which requires solving a pair of Riccati equations. It is interesting to note that the renormalized field amplitudes,

$$\mathcal{A}_j = \frac{A_j}{\sqrt{A_0^2 + A_1^2}}, \quad j = 0, 1, \tag{5}$$

satisfy non-linear equations [5, 3].

Our study can be extended to larger non-hermitian optical waveguide arrays, as far the non-Hermitian matrix in the coupled mode equation can be transformed into a traceless matrix that can be expanded as a sum with real coefficients similar to Eq.(4), where $\hat{\sigma}_z, \hat{\sigma}_\pm, \hat{\rho}_z, \hat{\rho}_\pm$ are now the matrices corresponding to a higher finite-dimensional, non-unitary representation of the $so(3,1)$ algebra.

**REFERENCES**


1. Rodríguez-Lara, B. M., F. Soto-Eguibar, and D. N. Christodoulides, "Quantum optics as a tool for photonic lattice design," *Phys. Scr.*, Vol. 90, 068014, 2015.
2. Villanueva Vergara, L. and B. M. Rodríguez-Lara, "Gilmore-Perelomov symmetry based approach to photonic lattices," *Opt. Express* , Vol. 23, 22836 – 22846, 2015.
3. Rüter, C. E. et al., "Observation of parity-time symmetry in optics," *Nature Phys.*, Vol. 6, 192 – 195, 2010.
4. Teimourpour, M. H. et al., "Light transport in PT-invariant photonic structures with hidden symmetries," *Phys. Rev. A*, Vol. 90, 053817, 2014.
5. Rodríguez-Lara, B. M. and J. Guerrero, "Optical finite representation of the Lorentz group," *Optics Lett.* , Vol. 40, No. 23, 56825685, 2015.
6. Zaragoza Gutiérrez, O. I. et al., "All-optical PT-symmetric conversion of amplitude (phase) modulation to phase (amplitude) modulation," Accepted in *Optics Express* , 2016.
7. Wei, J. and E. Norman, "Lie Algebraic Solution of Linear Differential Equations," *J. Math. Phys.*, Vol. 4, 575, 1963.

# Dynamically encircling exceptional points in a waveguide: asymmetric mode switching from the breakdown of adiabaticity

**J. Doppler[1], A. A. Mailybaev[2], J. Böhm[3], U. Kuhl[3], A. Girschik[1], F. Libisch[1], T. J. Milburn[4], P. Rabl[4], N. Moiseyev[5], and S. Rotter[1,*]**

[1]Institute for Theoretical Physics, Vienna University of Technology (TU Wien), Vienna, A-1040, Austria, EU

[2]Instituto Nacional de Matemática Pura e Aplicada - IMPA, 22460-320 Rio de Janeiro, RJ, Brazil

[3]Laboratoire de Physique de la Matière Condensée, CNRS UMR 7336, Université Nice Sophia Antipolis, 06108 Nice, France, EU

[4]Institute of Atomic and Subatomic Physics, Vienna University of Technology (TU Wien), Vienna, A-1040, Austria, EU

[5]Schulich Faculty of Chemistry and Faculty of Physics, Technion - Israel Institute of Technology, Haifa, 32000, Israel

[*]corresponding author: stefan.rotter@tuwien.ac.at

**Abstract** In my talk I will present our recent work on encircling so-called "exceptional points". In particular, I will show that a fully dynamical rather than a parametric encircling of these non-Hermitian degeneracies leads to an asymmetric mode switching. Mapping this feature onto the transmission through two-mode waveguides allows us to access this phenomenon for the first time in the experiment.

Systems with loss or gain give rise to resonant modes that are decaying or growing exponentially with time. Whenever two such modes coalesce both in their resonant frequency and their width, a so-called "exceptional point" occurs, in the vicinity of which many fascinating phenomena have recently been reported to occur. Particularly interesting phenomena are predicted to appear when encircling an exceptional point sufficiently slowly[1,2], like a state-flip or the accumulation of a geometric phase[3,4]. Corresponding experiments were already able to explore the topological structure of exceptional points[5-7], but a full dynamical encircling and the breakdown of adiabaticity associated with it[8-14] could not be measured so far.

In my talk I will show how a dynamical encircling of an exceptional point can be mapped onto the wave transmission through a two-mode waveguide, which permits us for the first time to get access to the elusive effects occurring in such a situation. In particular, I will present experimental data from a boundary-modulated waveguide that steers incoming waves around an exceptional point during the transmission from one end of the waveguide to the other. The resulting asymmetric mode transitions that are induced in this way make this waveguide structure ideally suited as a broad-band switch between different waveguide modes. This work opens up novel and interesting ways to study exceptional point physics at the intersection between basic research and practical applications.

**Acknowledgements**. This work has been supported by the Austrian Science Fund (FWF), the Brazilian National Council for Scientific and Technological Development (CNPq), the French Agence Nationale de la Recherche (ANR), the Vienna Science Fund (WWTF), and the Israel Science Foundation (ISF).

**REFERENCES**

1. Lefebvre, R., Atabek, O., Šindelka, M. & Moiseyev, N. Resonance Coalescence in Molecular Photodissociation. Phys. Rev. Lett. 103, 123003 (2009).
2. Atabek, O. et al. Proposal for a Laser Control of Vibrational Cooling in Na2 Using Resonance Coalescence. Phys. Rev. Lett. 106, 173002 (2011).
3. Latinne, O. et al. Laser-Induced Degeneracies Involving Autoionizing States in Complex Atoms. Phys. Rev. Lett. 74, 46–49 (1995).
4. Mailybaev, A. A., Kirillov, O. N. & Seyranian, A. P. Geometric phase around exceptional points. Phys. Rev. A 72, 014104 (2005).
5. Dembowski, C. et al. Experimental Observation of the Topological Structure of Exceptional Points. Phys. Rev. Lett. 86, 787–790 (2001).
6. Lee, S. B. et al. Observation of an Exceptional Point in a Chaotic Optical Microcavity. Phys Rev Lett 103, 134101 (2009).
7. Gao, T. et al. Observation of non-Hermitian degeneracies in a chaotic exciton-polariton billiard. Nature 526, 554–558 (2015).
8. Uzdin, R., Mailybaev, A. & Moiseyev, N. On the observability and asymmetry of adiabatic state flips generated by exceptional points. J. Phys. Math. Theor. 44, 435302 (2011).
9. Berry, M. V. Optical polarization evolution near a non-Hermitian degeneracy. J. Opt. 13, 115701 (2011).
10. Berry, M. V. & Uzdin, R. Slow non-Hermitian cycling: exact solutions and the Stokes phenomenon. J. Phys. Math. Theor. 44, 435303 (2011).
11. Gilary, I., Mailybaev, A. A. & Moiseyev, N. Time-asymmetric quantum-state-exchange mechanism. Phys. Rev. A 88, 010102 (2013).
12. Graefe, E.-M., Mailybaev, A. A. & Moiseyev, N. Breakdown of adiabatic transfer of light in waveguides in the presence of absorption. Phys. Rev. A 88, 033842 (2013).
13. Kaprálová-Žďánská, P. R. & Moiseyev, N. Helium in chirped laser fields as a time-asymmetric atomic switch. J. Chem. Phys. 141, 014307 (2014).
14. Milburn, T. J. et al. General description of quasiadiabatic dynamical phenomena near exceptional points. Phys. Rev. A 92, 052124 (2015).

# Parametric instability of non-Hermitian systems near the exceptional point

**A. A. Zyablovsky**[1,2*], **E. S. Andrianov**[1,2], **and A. A. Pukhov**[1,2,3]

[1]The Federal State Unitary Enterprise All-Russia Research Institute of Automatics, Moscow, Russia

[2]Moscow Institute of Physics and Technology, Moscow, Russia

[3]Institute for Theoretical and Applied Electromagnetics RAS, Moscow, Russia

[*]corresponding author: zyablovskiy@mail.ru

**Abstract**-In contrast to Hermitian systems, modes of non-Hermitian ones are nonorthogonal. As a result, system energy depends not only on mode amplitudes but also on phase shift between them. In this work we show that it is possible to increase amplitudes of the modes without increasing of system energy. Moreover, we demonstrate that when system is in exceptional point any infinitesimally small changing of the system parameters leads to increasing of mode amplitudes.

Non-Hermitian systems attract attention due to their specific properties which do not take place in Hermitian ones. In general cases, the eigenstates of non-Hermitian systems are not orthogonal [1-3], unlike those of Hermitian ones. The maximal degree of non-orthogonality is reached at the exceptional point, where some of the eigenstates become linearly dependent [3]. Non-orthogonality of eigenstates leads to energy oscillations when the total energy in the system oscillates in time [1, 2].

Also, due to the non-orthogonality of eigenstates, non-Hermitian systems may exhibit non-exponential behavior [4] when all the eigenstates are decaying. In this case at the first stage the field amplitude increases compared with the initial value and decreases exponentially at the second stage [4].

In this work we investigate the behavior of a non-Hermitian system with periodic perturbation of system parameters. We consider only the case when all eigenmodes are decaing at anytime. We show that even in this case change of parameters of non-Hermitian system may result in increase of eigenmodes amplitudes without simultaneously increasing of energy of the system during change. Increase of amplitudes of the eigenmodes leads to increasing of amplitude of energy oscillations. If such perturbations are repeated with energy oscillation period then amplitudes of eigenmodes and energy of system growth infinitely.

In general case, not all perturbation of parameters results in increasing of amplitudes of eigenmodes. However, we demonstrate that when system is in exceptional point any infinitesimally small changing of the system parameters leads to increasing of amplitudes of eigenmodes. As a result, system becomes unstable with respect to such perturbation. So new effect in the non-Hermitian systems- parametric instability near the exceptional point - occurs. We illustrate the phenomenon of parametric instability near the exceptional point in the case of two coupling waveguides with gain and loss when the loss in one waveguide is more than the gain in the other. In this system, total energy may increase indefinitely even when all waveguide modes are always decaying. This phenomenon opens a wide range of applications in optics, plasmonics, and optoelectronics, where loss is an inevitable problem and plays a crucial role.

**Acknowledgements**, This work was supported in part by RFBR grant nos. 12-02-010193 and 13-02-00407, as well as by the ”Dynasty” foundation.

**REFERENCES**

1. Bagchi, B., C. Quesne and M. Znojil, “Generalized continuity equation and modified normalization in PT-symmetric quantum mechanics,” *Mod. Phys. Lett. A*, Vol. 16, 2047–2057, 2001.
2. Makris, K., R. El-Ganainy, D. Christodoulides and Z. H. Musslimani, “Beam dynamics in p t symmetric optical lattices, ” *Phys. Rev. Lett.* Vol. 100, 103904, 2008.
3. Klaiman, S., U. Gunther and N. Moiseyev, “Visualization of branch points in PT-symmetric waveguides,” *Phys. Rev. Lett.*, Vol. 101, 080402, 2008.
4. Makris, K., L. Ge and H. Tureci, “Anomalous transient amplification of waves in non-normal photonic media,” *Phys. Rev. X*, Vol. 4, 041044, 2014.

# Non-Hermitian Modulation Instability

**K. G. Makris[1*], J. Cole[2], Z. H. Musslimani[2], D. N. Christodoulides[3], and S. Rotter[4]**

[1]Crete Center for Quantum Complexity and Nanotechnology,
Physics Department, University of Crete, 71003, Heraklion, Greece

[2]Mathematics Department, Florida State University, Tallahassee, Florida, 32306-4510, USA

[3]College of Optics–CREOL, University of Central Florida, Orlando, Florida 32816, USA

[4]Institute for Theoretical Physics, Vienna University of Technology, 1040, Vienna, Austria

[*]corresponding author: makris@physics.uoc.gr

**Abstract**-We introduce a new type of nonlinear waves in inhomogeneous photonic systems. Such waves have *constant intensity* in all space and exist only in complex potentials with gain and loss. Based on these exact solutions of nonlinear Schrodinger equation, we examine theoretically their modulation instability on parity-time symmetric potentials with cubic nonlinearities. We also investigate the stability and dynamics of vector constant-intensity waves as solutions of a two-component nonlinear Schrodinger equation.

Plane wave solutions play a fundamental role in diverse areas of science. In particular, plane waves are also exact solutions of the well known nonlinear Schrodinger equation (NLSE). For this reason are crucial for the fundamental phenomenon of modulation instability. Here we present a whole new class of nonlinear waves that feature a constant intensity (CI-waves) in the presence of a nonlinear inhomogeneous media with gain and loss [1-4]. These "generalized plane waves", allow us to study for the first time, modulation instability [5] in an inhomogeneous environment. Our starting point is the normalized-NLSE, $i\psi_z + \psi_{xx} + V(x)\psi + \sigma|\psi|^2\psi = 0$, with a non-Hermitian potential V(x), and $\sigma$ the Kerr coefficient. The complex function $\psi(x,z)$ describes the electric field envelope along the propagation distance *z*. In this general framework, we investigate a whole family of complex potentials V(x), which are determined by the following relation,

$$V(x) = W^2(x) - i\,dW/dx \qquad (1)$$

where W(x) is a given real function that is directly related to the transverse power flow. For the entire non-Hermitian family of these potentials V(x) (PT-symmetric or not) we can prove, that the following constant-intensity wave is an exact solution of NLSE,

$$\psi(x,z) = A\exp\left[i\sigma A^2 z + i\int W(x)dx\right] \qquad (2)$$

with a real constant amplitude A [5]. These constant-intensity waves also exist in two spatial dimensions as well as in Kerr media. Composite systems of vector NLSE's (Manakov type) are considered. In this case vector CI-waves can be derived for the following set of coupled NLSE's:

$$\begin{aligned} &i\psi_z + \psi_{xx} + V(x)\psi + \left[\sigma|\psi|^2 + \beta|\phi|^2\right]\psi = 0 \\ &i\phi_z + \phi_{xx} + V(x)\phi + \left[\sigma|\phi|^2 + \beta|\psi|^2\right]\phi = 0 \end{aligned} \quad (3)$$

where $\beta$ is the cross-phase modulation term. The linear stability analysis of such vector CI-waves is investigated in detail.

**Acknowledgements**, K.G.M. is supported by the People Programme} (Marie Curie Actions) of the European Union's Seventh Framework Programme (FP7/2007-2013) under REA grant agreement number PIOF-GA-2011-303228 (project NOLACOME), and by the European Union Seventh Framework Programme (FP7-REGPOT-2012-2013-1) under grant agreement No. 316165.

**REFERENCES**

1. K. G. Makris, R. El-Ganainy, D. N. Christodoulides and Z. H. Musslimani, *Phys. Rev. Lett*. **100**, 103904 (2008).
2. Z. H. Musslimani, K. G. Makris, R. El-Ganainy, D. N. Christodoulides, *Phys. Rev. Lett.* **100**, 030402 (2008).
3. A. Guo *et al.*, *Phys. Rev. Lett.* **103**, 093902 (2009).
4. C. E. Ruter, K. G. Makris, R. El-Ganainy, D. N. Christodoulides, M. Segev, and D. Kip, *Nat. Phys*. **6**, 192 (2010).
5. K. G. Makris, Z. H. Musslimani, D. N. Christodoulides, and S. Rotter, *Nat. Comm.* **6**, 7257 (2015).

# Lasing characteristics in parity-time-symmetric microcavities

**M. Khajavikhan[1*], H. Hodaei[1], M.-A. Miri[1], M. Heinrich[1], W. Hayenga[1], A. U. Hassan[1], J. Ren[1], D. N. Christodoulides[1]**

[1]CREOL, The College of Optics and Photonics, University of Central Florida, Orlando, FL 32816-2700, USA

[*]corresponding author: mercedeh@creol.ucf.edu

**Abstract**- Parity-time (PT) symmetry has been recently utilized as a new means of mode selection in micro-cavity lasers. Single-mode lasing is demonstrated in PT-symmetric micro-ring resonators that support several longitudinal and transverse modes.

Mode selection is of fundamental importance in laser science and engineering. In general, the presence of multiple oscillating modes can be detrimental to beam quality and spectral purity of lasers. This will lead to spatial as well as temporal fluctuations in the emitted radiation. Several schemes have been proposed in the literature to control the modal content of laser cavities, for example, employing intra-cavity apertures for manipulating spatial modes or external cavity dispersive elements to suppress longitudinal modes. However, each of these solutions requires complicated fabrication techniques and also can only be applied to specific class of lasers. Microrings are an example of such laser cavities for which enforcing single mode operation is not trivial. They can support highly confined modes that exhibit both high quality factors and small footprints due to their high refractive index contrast, thus making them excellent candidates to use in integrated photonic devices. Nevertheless, their inherent multimode operation, specially within the inhomogenously broaden gain bandwidths, drastically hinders the prospects of such semiconductor resonators as on-chip light sources.

Recently, the selective breaking of parity-time (PT) symmetry has been proposed as a new methodology to achieve single mode operation [1]. In this approach, an active resonator/waveguide is coupled to an identical but lossy counterpart to enforce single-mode performance even in the presence of strong mode competition in laser/amplifier configurations. In general, a structure respects PT-symmetry if it is invariant under the simultaneous action of the P (parity) and T (time) inversion operations. While first developed in the context of quantum mechanics [2], this notion has lately attracted considerable attention in the field of optics and photonics [3-6]. In optical settings, a structure is considered to be PT-symmetric if the real part of the refractive index is an even function of position, whereas the imaginary component (representing gain and loss) follows an odd profile. Such a system can support an entirely real range of eigenfrequencies despite having a non-Hermitian representation.

In this work, we experimentally demonstrate how the notion of PT symmetry can be used to obtain single *longitudinal* and *transverse* mode operation in multi-moded microring laser systems. Moreover, this can be done without compromising the output power. In such system, spontaneous breaking of PT symmetry serves as a virtual lasing threshold and enforces single mode operation at pump powers way above threshold. The PT-symmetry is established in our double coupled microring system by withholding the pump power from one of the resonators. In this case, the net differential gain associated with the spectral curvature of the lineshape function is systematically enhanced resulting in considerable longitudinal mode discrimination- a direct byproduct of the presence of a non-Hermitian exceptional point. Furthermore, the coupling constant $\kappa$ between the pumped and the lossy rings

provides an additional degree of freedom in the system to reach the exceptional point (g/ $\kappa=1$). This spatial coupling constant $\kappa$, is a function of the evanescent overlap of the respective modes and it is different for spatial modes [7]. As it is well known, higher order spatial modes exhibit stronger coupling coefficients due to their lower degree of confinement. Consequently, in a PT symmetric arrangement, the fundamental mode is the first in line to break its symmetry as the gain increases (when $g > \kappa$), thus experiencing a net amplification. On the other hand, for this same gain level, for the rest of the modes PT-symmetry is maintained and therefore they remain entirely neutral. Our approach provides a new path to globally enforce single-mode behavior both in the spatial and spectral domains.

**Acknowledgements**, We acknowledge the support from NSF (ECCS-1454531, ECCS-1128520), ARO (W911NF-16-1-0013), and AFOSR (FA9550-12-1-0148, FA9550-14-1-0037).

**REFERENCES**

1. Hodaei, H., M. A., Miri, M., Heinrich, D. N. Christodoulides and M. Khajavikhan, "Parity-time–symmetric microring lasers," *Science*, Vol. 346, No. 6212, 975–978, 2014.
2. Bender, C. M. and S. Boettcher, "Real spectra in non-Hermitian Hamiltonians having P T symmetry," *Phys. Rev. Lett*, Vol. 80, No. 24, 5243, 1998.
3. Makris, K. G., R. El-Ganainy, D. N. Christodoulides and Z. Musslimani, "Beam dynamics in P T symmetric optical lattices," *Phys. Rev. Lett*, Vol. 100, No. 10, 103904, 2008.
4. Guo, A., G. J. Salamo, D. Duchesne, R. Morandotti, M. Volatier-Ravat, V. Aimez, G. A. Siviloglou and D. N. Christodoulides, "Observation of P T-symmetry breaking in complex optical potentials," *Phys. Rev. Lett*, Vol. 103, No. 9, 093902, 2009.
5. Rüter, C. E., K. G. Makris, R. El-Ganainy, D. N. Christodoulides, M. Segev and D. Kip, "Observation of parity–time symmetry in optics," *Nat. Phys*, Vol. 6, No. 3, 192–195, 2010.
6. Regensburger, A., C. Bersch, M. A. Miri, G. Onishchukov, D. N. Christodoulides and U. Peschel, "Parity-time synthetic photonic lattices," *Nature*, Vol. 488, No. 7410, 167–171, 2012.
7. Miri, M. A., P. LiKamWa and D. N. Christodoulides, "Large area single-mode parity–time-symmetric laser amplifiers," *Opt. Lett*, Vol. 37, No. 5, 764–766, 2012.

# Reversing phase transitions in a nonlinear PT-symmetric dimer laser

**Absar U. Hassan[1], Hossein Hodaei[1], Mohammad-Ali Miri[2], Mercedeh Khajavikhan[1], and Demetrios N. Christodoulides[1]**

[1]*CREOL/College of Optics and Photonics, University of Central Florida, Orlando, Florida 32816, USA*
[2]*The University of Texas at Austin, 1616 Guadalupe Street, Austin, Texas 78701, USA*

**Abstract:** It is demonstrated that in the presence of gain and loss saturation effects, a PT-symmetric coupled arrangement is able to undergo a transition in reverse order to that expected from a linear model. This process was observed in a set of semiconductor microring resonators by optically pumping one of the rings while keeping the other in the dark. As the pumping level increased, the laser modes gradually moved from a broken phase to the PT-symmetric regime, in accord with theoretical predictions.

A system described by a parity-time (PT) symmetric Hamiltonian can in principle support entirely real eigenvalues in spite of the fact that it is inherently dissipative or amplifying. Mathematically, this translates to a class of non-Hermitian Hamiltonians that are known to commute with the anti-linear PT operator [1]. Yet, once a system parameter exceeds a critical threshold, this property is no longer observed and the spectrum ceases to be entirely real-thus entering the so-called broken symmetry phase. This transition from an unbroken to a broken regime is marked by the presence of an exceptional point where not only the eigenvalues but also the eigenvectors converge [2]. As recently indicated in several studies, optics provides a viable avenue where such concepts can be observed and tested. What makes this possible is the isomorphism between the quantum Schrödinger and the optical wave equation, where the gain-loss parameters are responsible for introducing non-Hermiticity. Indeed, a number of intriguing results theoretically predicted in PT-symmetric configurations have recently been observed in photonic platforms [2-4]. The majority of them were based on linear PT-symmetric models, suggesting that upon an increase in the gain-loss contrast, an optical system will always move from an unbroken to a broken-symmetry phase [1-3]. Here, we reexamine this transition behavior in light of the fact that nonlinearity, in its various manifestations, is often capable of totally altering the dynamical response a system.

In this work we experimentally demonstrate for the first time a reversed phase transition in a coupled pair of semiconductor micro-ring PT-symmetric InP lasers-similar to that employed in Ref. [5]. The quantum wells in the structure provide saturation in both the gain and the loss when being optically pumped and un-pumped respectively. A schematic and the fabricated structure of our design is shown in Fig. 1 (a) and (b) respectively. Considering the steady state field characteristics in these micro-cavities, it was found that the intensity ($I_1$) in the micro-ring with gain remains above that in its coupled lossy counterpart ($I_2$) when the gain level is below a certain critical value. This is characteristic of a broken (B) PT-phase as shown in Fig. 1(c). On the other hand, once the gain-loss contrast exceeds this threshold, the solutions assume an unbroken PT-symmetric form (U), having equal intensities in both micro-ring cavities of the dimer. This transition behavior is depicted in Fig. 1(c).




Fig. 1. (a) A PT-symmetric coupled arrangement of two micro-rings where one of them is optically pumped. (b) An SEM image of the micro-ring lasers used. (c) Steady-state field intensities in the ring with gain ($I_1$) and ring with loss ($I_2$) are shown as a function of the gain parameter, $g$. The loss values are chosen to be $\gamma = 0.1$ and $f = 2$. B-represents broken (purple) and U-unbroken symmetry (yellow). Before the critical value of $g_c = 2.4$ is crossed, the solutions are in the broken-PT phase with unequal intensities and afterwards, light is equally distributed in an unbroken PT-symmetric fashion.

These effects can be examined using the following dimensionless dynamical model,

$$\dot{\psi}_1 = -\gamma\psi_1 + \left(\frac{g}{1+|\psi_1|^2}\right)\psi_1 + i\psi_2 \qquad (1)$$

$$\dot{\psi}_2 = -\gamma\psi_2 - \left(\frac{f}{1+|\psi_2|^2}\right)\psi_2 + i\psi_1. \qquad (2)$$

In the above equations, $\psi_1$ and $\psi_2$ represent the modal field amplitudes in the cavities with gain and loss respectively and $\dot{\psi} = d\psi/dt$ etc. Note that a PT-configuration is established here by simply subjecting one micro-ring to optical pumping while keeping the other un-pumped. Scattering losses are denoted by $\gamma$, and $g$ and $f$ respectively represent the small-signal values of gain and loss due to the quantum wells in the semiconductor structure. In our set-up we vary the gain in a dynamical manner while keeping the loss and coupling fixed. The ratio between the total loss and coupling (i.e. $\gamma + f$) determines whether the reversed phase transition takes place or not. In this case, one can show that if $(\gamma + f) > 1$, not only does lasing start in the broken symmetry domain, but also the mode profiles assume symmetric steady-state values, equally occupying both cavities as the gain is increased beyond a critical point. However, if the total loss to coupling ratio is less than unity, the solutions always remain in the nonlinear unbroken symmetry form and no transition is observable. A high value of $f$ due to the quantum wells ensured that the experiment took place in the regime of interest.

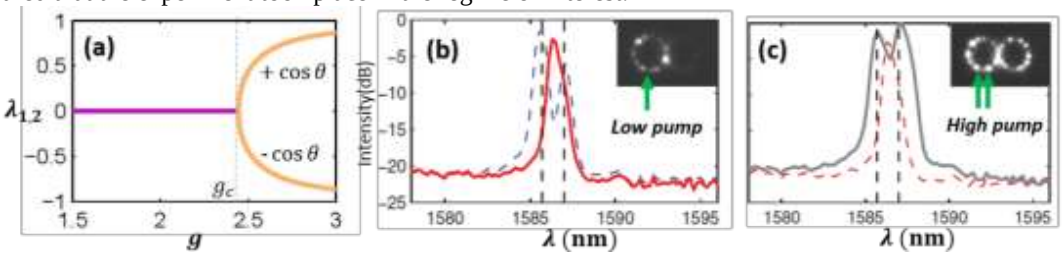



Fig. 2. (a) Square root PT-bifurcation at a nonlinear phase transition point. (b) Experimental observation of the broken PT-phase at a pump power of 0.4 mW. Upon doubling of the pump power, the steady state acquires a PT-symmetric form, as in (c) with equivalent intensities

Solutions in both domains of PT-symmetry can be obtained using a steady-state eigenmode analysis of Eqs. (1) and (2). The nonlinear modes in the symmetric phase are found to be, $\sqrt{(g-f)/(2\gamma)-1}\left(1, \pm e^{\pm i\theta}\right)$, where $\sin\theta = \gamma(g+f)/(g-f)$, and the nonlinear phase transition shown in Fig. 1(c) occurs at the critical gain value of $g_c = f(1+\gamma)/(1-\gamma)$. It is interesting to note the formal equivalence of these modes with their linear PT-symmetric counterparts [3]. Another relevant aspect is the behavior of the eigenvalues around the nonlinear exceptional point, involving a characteristic square-root bifurcation when entering the nonlinear unbroken regime, as shown in Fig. 2(a). From the emission spectrum, the nonlinear broken regime is characterized by the appearance of a single longitudinal mode. If the pumping level is increased, the eigenmodes are expected to transition into a set of unbroken PT-symmetric states exhibiting two real eigenvalues, thus resulting into a pair of longitudinal lasing modes in the spectrum.

A set of coupled micro-rings having an outer radius of 10 μm, a width of 500 nm and comprising six InGaAsP quantum wells were fabricated for the experiment. The separation between the micro-rings was 50 nm , establishing a strong coupling ($\kappa \sim 1 \times 10^{11} s^{-1}$) which ensures that detuning has negligible effects on the field dynamics. When the pump power is small (but still above threshold) lasing is shown to occur in the broken phase – red curve in Fig. 2(b) where for comparison, the dashed line in the backdrop shows coupling induced degeneracy splitting. A single line appears upon blocking the pump beam from one ring – broken phase. When the pump power over the exposed micro-ring is doubled, the system goes into the unbroken PT-symmetric phase with both rings lit-up, as depicted in Fig. 2(c). Here the two lines correspond to the two real eigenvalues $\lambda_{1,2}$. This observation indicates that nonlinear saturation effects can indeed reverse the order in which symmetry breaking occurs.

**References**


[1]. C. M. Bender and S. Boettcher, 'Real Spectra in Non-Hermitian Hamiltonians Having PT Symmetry,' Phys. Rev. Lett. **80**, 5243 (1998).

[2]. A. Guo, G. J. Salamo, D. Duchesne, R. Morandotti, M. Volatier-Ravat, V. Aimez, G. A. Siviloglou, and D. N. Christodoulides, 'Observation of PT-Symmetry Breaking in Complex Optical Potentials,' Phys. Rev. Lett. **103**, 093902 (2009).

[3] C. E. Ruter, K. G. Makris, R. El-Ganainy, D. N. Christodoulides, M. Segev, and D. Kip, 'Observation of parity–time symmetry in optics,' Nat. Phys. **6**, 192 (2010).

[4]. H. Hodaei, M.-A. Miri, M. Heinrich, D. N. Christodoulides, and M. Khajavikhan, 'Parity-time–symmetric microring lasers,' Science **346**, 975 (2014).

**Non-Hermitian Photonic Structures**

Tsampikos Kottos
Department of Physics, Wesleyan University, Middletown CT-06459, USA

In recent years non-hermitian photonics has attracted a lot of attention. One of the goals of this subfield is to introduce and tailor losses in microwave and optical structures in order to come up with designs that show novel transport features like asymmetric transport, switching, invisibility etc. We will discuss some of these set-ups and illuminate on the dual role of loss as a source of absorption and enhanced reflection due to impedance mismatching. Applications along these lines will be discussed.

# Photonic topological insulators in PT-symmetric systems

**Miguel A. Bandres, Gal Harari, and Mordechai Segev**
Physics Department and Solid State Institute, Technion, Haifa 32000, Israel

**Abstract**- We present the first PT-symmetric topological insulator systems. We find that transport in this photonic lattices is unidirectional and completely robust to PT-conserving defects. By combining topological systems with non-Hermitian systems we found a new phenomenon: sources and sinks of topological protected edge states.

Topological insulators are materials that insulate in their bulk, but allow extremely robust flow of current on their surfaces. A topological insulator is characterized by a bulk bandgap where topological gapless unidirectional edge states reside. These edge states are robust to any perturbation that does not close the bandgap. In this way, deformations of the system like disorder, strain, or imperfections have little effect on the transport of such topological edge modes. Due to this robust transport, topological physics is now at the forefront of research in multiple fields, such as condensed matter, cold atoms, exciton-polariton condensates, acoustics, and photonics [1-3]. In photonics, the first topological insulators were demonstrated using strong magnetic fields in microwave frequencies [1], and more recently at optical frequencies in a modulated photonic lattice [2] and silicon ring resonators arrays [3]. Introducing topological protection into photonics provides an excellent platform for probing novel phenomena that would be extremely difficult or impossible to access in the solid state.

In 1998, Bender has shown that a wide class of non-Hermitian Hamiltonians can still show entirely real spectra, if they respect parity-time (PT) symmetry [4]. Ten years later, Christodouldies and his team have introduced the concept of PT-symmetry into the realm of electromagnetic waves [5], which had a huge impact – because the concepts of PT-symmetry and non-Hermitian Hamiltonians have entered into very many classical waves systems, by properly engineered gain and loss, as is now done in optics [5,6], electronics, and acoustics. In particular, optics has been the most successful platform to implement and experimentally investigated PT-symmetry [5,6]. In optics, non-Hermitian systems naturally arise due to the use of optical amplification (gain) and absorption (loss). In PT-symmetric optical systems the complex interplay between gain and loss give rise to unique physical phenomena, which are otherwise unattainable in standard configurations.

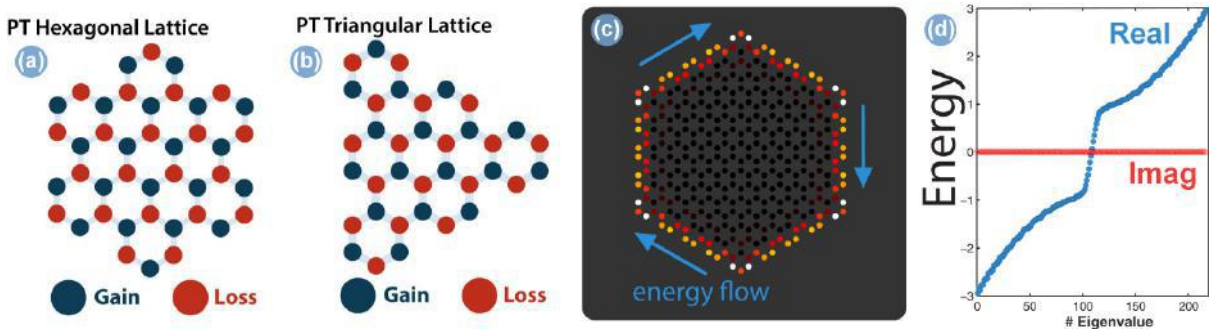



Figure 1. (a)-(b) PT-symmetric topological finite lattices. (c) Topological one-way edge state of the PT-symmetric lattice. (d) Spectrum of the lattice in the full-PT regime.

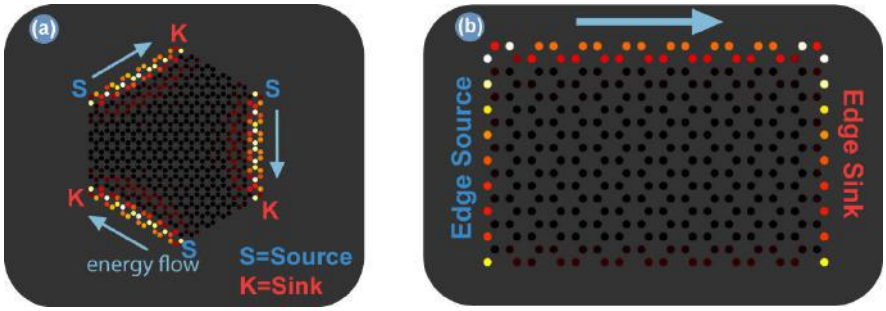



Figure 2. (a) Single lattice sites on the vertices of our PT photonic topological insulator act as sources and sinks of topological edge states. Since the transport is unidirectional, the edge states are present just between a source and a sink. (b) A whole edge of the lattice acts as a sink/source.

The major progress in photonic topological insulators and photonic PT systems raises a natural question: can topological insulators exist in PT-symmetric systems? The present literature suggests that this may be impossible. However, we found that these theories fail to describe the relevant physical effects because they are premised on the low-energy limit of infinite size systems.

Here we show that it is possible to have 2D non-Hermitian PT-symmetric lattices that display the behavior of a topological insulator: unidirectional and topological protected transport. An example of such a system is shown in Fig. 1a-b: a hexagonal or triangular lattice (of helical waveguides) where the sites have alternating gain and loss. We find that the edge states in this lattice has purely-real energies (Fig. 1d), and that transport in this lattice is unidirectional and completely robust to PT-conserving defects (Fig. 1c) (without scattering backwards or into the bulk). We find that these non-Hermitian topological insulators can have either a completely real spectrum (full PT-symmetry) or a complex spectrum (broken PT-symmetry), depending on the amount of gain/loss. In the broken PT-symmetry regime, we find that the topological states are more resilient to breakup and develop complex energies. Moreover, we find that this "merging of non-Hermiticity and topological insulators" gives rise to many new interesting physical phenomena: for example, the existence of "sources and sinks" for the unidirectional protected edge states. As shown in Fig. 2a, the corners of the lattice act as sources or sinks (depending if they end on a site with gain or with loss), and because the edge states are unidirectional, they are present just between a source and a sink (but never between a sink and a source). Interestedly, we also found that some types of edge can act as edge-sinks or edge-sources of topological edge-modes, as depicted in Fig 2(b). Moreover, these topological edge states of the non-Hermitian lattice exhibit some other features that make them distinct from ordinary topological insulators. Our results open the door to new conceptual ideas involving topological phases in non-Hermitian systems.

The research leading to these results has received funding from the European Union's – Seventh Framework Programme (FP7/2007-2013) under grant agreement n◦ 629114 MC–Structured Light.

## REFERENCES

1. Z. Wang, et al., Nature 461, 772 (2009).
2. M. C. Rechtsman, et al., "Photonic Floquet topological insulators," Nature 496, (2013).
3. M. Hafezi, et al., "Imaging topological edge states in silicon photonics," Nature Photonics 7, (2013).
4. C. M. Bender and S. Boettcher, Phys. Rev. Lett. 80, 5243 (1998).
5. R. El-Ganainy, et al., "Theory of coupled optical PT-symmetric structures," Opt. Lett. 32, 2632 (2007).
6. C. E. Rüter, et al., "Observation of parity–time symmetry in optics," Nat. Phys. 6, 192–195 (2010).

# Nanoscale Engineering Optical Nonlinearities and Nanoemitters

**Y. Fainman, M. Puckett, R. Sharma, J. Smalley, A. Pang, Q. Gu, A. El Amili, F. Vallini**
Department of Electrical and Computer Engineering, University of California, San Diego
9500 Gilman Drive, La Jolla, California, 92093-0407
*corresponding author: fainman@ece.ucsd.edu

**Abstract**-The integration of a photonic information processing system onto a single chip requires great research effort toward engineering metamaterials for miniaturization of the optical devices and circuits. We discuss nanoscale engineered optical nonlinearities for modulation and wave mixing of optical fields, and metal-dielectric-semiconductor nanostructures and compositions to construct nanoemitters for chip-scale integration.

The integration of photonic systems requires miniaturization of the optical components, similar to the effort that has led to the extensive miniaturization in electronics. For applications involving a photonics layer between different components on the same chip, the photonic components must be comparable in size to the electronic components, and minimally interfer with each other when densely packed. Such future systems, further require the discovery of new technologies that can operate not only at ultrafast rates (<1 ps), but also at extremely low energies, and with low levels of insertion loss. Additionally, future technologies will need to be highly compact, as well as resilient to temperature change. Moreover, the device designs should provide scalability with respect to the operating wavelength, and the optical carrier should be allowed to range in a broad spectral range to support the necessary aggregate information bandwidth. As specific examples of our most recent work towards these goals, we present nanoscale engineered second order nonlinearities and various composite metal-dielectric-semiconductor gain geometries used to create new types of nanolasers and nanoemitters for chip-scale integration of optical information systems.

The strain-induced second order optical nonlinear effects were demonstrated, but despite recent accomplishments, the physical mechanisms behind strained silicon's characteristics remain poorly understood. Therefore, the calculations of scaling coefficients which relate the nonlinearity to the local strain gradient are critical to the design of future devices implementing strained silicon. To this end, we have theoretically analyzed the breaking of symmetry which occurs in silicon as a result of asymmetric strain which was validated experimentally. We fabricated and characterized Fabry-Perot waveguide resonators strained by a compressively stressed silicon nitride cladding. By applying a voltage of either positive or negative 25 volts vertically across the waveguides, we induced and measured shifts in the resonances exhibited by the transmission spectra. However, we also observed effect of the cladding on the nonlinear response that led us recently to study effects of free carriers in fully-etched, dielectric-clad silicon waveguides. We theoretically characterized the free-carrier plasma dispersion effect in fully-etched silicon waveguides, with various dielectric material claddings, due to fixed interface charges and trap states at the silicon-dielectric interfaces. The values used for these charges are obtained from the measured capacitance-voltage (C-V) characteristics of SiO2, SiNx, and Al2O3 thin films deposited on silicon substrates. Our results show that, in addition to being a critical factor in the analysis of such active devices as capacitively-driven silicon modulators, this effect should also be taken into account when considering the propagation losses of passive silicon waveguides. Most rcently, we fabricated silicon waveguides in silicon-on-insulator (SOI) wafers clad with either silicon dioxide, silicon nitride, or aluminum

oxide, and by measuring the electro-optic behavior of ring resonators, we characterize the cladding-dependent and capacitively-induced free-carrier effects in each of these waveguides. By comparing our measured data with simulation results, we confirm that the observed voltage dependences of the transmission spectra are due to changes in the concentrations of holes and electrons within the semiconductor waveguide, and we show for the first time how strongly these effects depend on the cladding material which comes into contact with the silicon waveguide. Additionally, the waveguide loss is found to have a particularly high sensitivity to the applied voltage, suggesting that these effects may find use in a wide range of applications which require low- or high-loss propagation. These phenomena, which are present in all semiconductor waveguides, may be incorporated into more complex waveguide designs in the future to create high-efficiency electro-optic modulators and wavemixers.

The research towards building light emitters with most compact footprint is a challenge that we also have been investigating. One approach for making compact light emitters is to incorporate metals into their design, since metals can effectively confine leaky optical modes while isolating the lasers from their neighboring environment. We incorporate metals to reduce the size of the light emitter resonator in all 3-D. In this type of cavity it is possible to achieve higher Q factors and lower lasing gain thresholds, albeit at the expense of reduced mode confinement. Specifically, we describe two types of metal-dielectric 3-D resonators: (a) a composite metal-dielectric-semiconductor cavity where the low index dielectric acts as a shield to reduce the loss into the metal and (b) a coaxial resonator that supports a TEM-like mode which has no cut-off and the physical size of the cavity can be infinitely scaled down in lateral dimensions. The modes in such 3-D cavities can be grouped into two main categories: (i) surface bound (that is, surface plasmon polariton (SPP)) resonant modes and (ii) conventional resonant modes within the metal cavity. Although highly confined, the plasmonic modes are lossy and the lasing gain threshold for such cavities can be very large. However, the negative permittivity of metals enables them to act as efficient mirrors, leading to the second class of metallo-dielectric cavity modes, which can be viewed as lossy approximations of the modes in a perfectly conducting metal resonator.

Recently, we also initiated a study of transmission and emission properties of lossy and gain-compensated near-infrared hyperbolic metamaterials. We demonstrate luminescent hyperbolic metasurfaces (LuHMS), in which semiconductor quantum heterostructures simultaneously function as light-emitters and the constituent dielectric. The unique design of the LuHMS enables verification of broadband hyperbolic dispersion by extreme polarization anisotropy of photoluminescence. LuHMS open the door to “meta-gain” media, with gain spectra dependent upon co-optimization of pump properties and the metamaterial’s optical and electronic densities of states. The findings have broad implications in the field of active metamaterials, with applications ranging from enhanced nonlinear interactions to improved hyper-lenses and asymmetric transmission devices.

# Optical and Electrical Control of NonHermition Silicon Nanophotonics

**Mohamed A. Swillam**
Department of Physics, School of Mathematics and Physics, The American University in Cairo, New Cairo, Egypt, 11835
*corresponding author: m.swillam@aucegypt.edu.

**Abstract**-We propose novel techniques for introducing controlling the loss mechanism in nanophotonic systems. Different configurations have been exploited to electrically and optically control the loss mechanism in silicon nanostructures at the Near and Mid infra red region.

Silicon photonics and nanophotonics attracts great attention in the last decade due to its ease of fabrication and high tolerance and fabrication yield which. The ability to control the loss and gain for such systems opens new directions of signal control and manipulation to achieve novel on chip functionalities. For this purpose, we discuses two novel systems in both the near and MIR range with electrical and optical control of the loss mechanisms in these systems. This fast control allow for optical modulation of the output signal using the control pulse.

The first system utilizes ITO plasmonic configuration to control the loss in a long range silicon plasmonic system. In this system, the low loss long range plasmonic mode is excited in a silicon hybrid symmetric structure. For this system, the field is localized in in the ITO/ SiO2 layer. Thus, by controlling the optical characteristics of the ITO layer, the behavior of the systems changes dramatically. This mainly due the change in the real part of the refractive index of ITO layer [1]. This change create asymmetry in the system and hence the long range symmetric mode which was originally excited in the systems exhibit fast radiation due to the mismatch introduced in its momentum.

For the second system, highly doped silicon is exploited as a plasmonic like material in the mid infrared (MIR) range. For this system, controlling the number of free career in the doped silicon should allow the system to move from dielectric like to plasmonic like material [2]. Optical and electrical carrier excitation mechanisms are exploited for such purpose. Using this career control machoism the localized field inside silicon insulator silicon (SIS) can be easily manipulated. Various plasmonic waveguides configuration are studies to demonstrate such control. This novel control mechanism opens the door to wide range of applications including for example, optical switching, optical control and modulation, optical routing, optical gates, and optical transistors.

**Acknowledgements** This work was made possible by a NPRP award [NPRP7456-1-085] from the Qatar National Research Fund (member of the Qatar Foundation). The statements made herein are solely the responsibility of the authors.

## REFERENCES

1. A, O. Zaki, K. Kirah, and M. A. Swillam, “Hybrid electro-optic plasmonic modulators based on directional coupler switches, ” Applied Physics A, 2016, in Press
2. R. Gamal, Y Ismail, M. A. Swillam,” Silicon Waveguides at the Mid-Infrared Range,” J. Lightwave Technology 33, Aug. 2015.

# Spontaneous symmetry breaking and switching in coupled photonic crystal nanolasers.

**A. M. Yacomotti[1*], P. Hamel[1], M. Marconi[1], F. Raineri and J. A. Levenson[1]**

[1]LPN CNRS, Laboratoire de Photonique et de Nanostructures (CNRS UPR 20), Route de Nozay, Marcoussis, 91460, France

[*]corresponding author: alejandro.giacomotti@lpn.cnrs.fr

**Abstract**- We show spontaneous mirror-symmetry breaking in two coupled photonic crystal nanolasers. This is the first experimental demonstration of such transition in micro/nanophotonics. A pitchfork bifurcation exhibits two localized states, whose coexistence has been shown by optical switching with short pulses. This opens exciting avenues for integrated optical flip-flop memories. In addition, the symmetry breaking bifurcation has been observed with only ~100 intracavity photons, which makes this system promising to investigate non-classical photon correlations.

The interplay between photon tunneling and light-matter interactions in multi-well optical potentials –or photonic molecules (PMs)– is at the heart of many recent developments in quantum and nonlinear optics (see e.g. [1]). A key phenomenon taking place in double well potentials is the spontaneous breaking of the inversion symmetry: a bifurcation from delocalized to localized states in the wells, which are mirror images of each other. Although few theoretical studies have addressed mirror-symmetry breaking in micro and nanophotonic systems [2], experimental evidence has been elusive so far, having been reported for the first time only recently [3].

Here we show the spontaneous symmetry breaking (SSB) of the inversion symmetry in two coupled semiconductor photonic crystal (PhC) nanocavities in a laser regime. In order to achieve this goal we have designed and fabricated a PhC molecule formed by two evanescently coupled PhC L3 cavities in an InP freestanding membrane containing four InGaAs/InGaAsP quantum wells (period $a$ = 425 nm, hole radius r = 0.266$a$ see Ref. [3] for further details). The key ingredient in order to achieve SSB in this system is that the nonlinear frequency shift (given by the α factor in the QWs) must overcome the evanescent intercavity coupling –or photon tunneling–. Hence we implemented a barrier engineering technique in order to control the potential barrier between the cavities by design [4].

Thanks to this technique, the strong cavity-to-cavity coupling has been lowered such that the mode splitting is reduced to $\Delta\lambda$~1.5 nm (middle row-hole radius in the barrier= r - 20%), equal to ~3 times the mode linewidth, which fulfills the requirements for the occurrence of SSB. Light coming out from the cavities was spatially filtered using single mode fibers as pinholes, coupled to low noise APD detectors. As a result, photons emitted from the individual nanolasers were independently and simultaneously measured. This technique allowed us to show spontaneous light localization in either the left (L1R0 state) or the right (L0R1) cavities. The observed bifurcation diagram exhibits a pitchfork bifurcation leading to two broken parity states [3].

In order to demonstrate SSB, coexistence of these states has to be proven. With this aim we injected 100 ps pulses @ $\lambda$=800 nm in each cavity. As a result, the L1R0 state is switched to the L0R1 state as long as the excitation pulse impinged the left cavity (Fig. 1 left, middle frame), whereas L0R1 switching to L1R0 was observed provided the pulse perturbed the right cavity (Fig. 1 left, bottom frame). The experimental results are well reproduced using coupled mode theory in semiconductor media (Fig. 1 right). Switching off a cavity by an

extra pump pulse can be explained as follows: since carrier density in the high intensity cavity is lower because of gain saturation, only a carrier excess arriving to the high intensity cavity is able to go towards the low intensity state. Indeed, it can be observed from Fig. 1 (right) that a kick pulse on the R cavity when the R cavity is in the low intensity state does not induce any switching.

Our bistable switchable PM nanolaser opens exciting prospects for the realization of ultra-compact, scalable optical flip-flop memories based on SSB without any resonant driving beam. In addition, since the tunneling rate can be finely adjusted using the potential barrier engineering implemented here, we can predict SSB transitions with few intracavity photons for future nanolaser devices with strong quantum correlations.

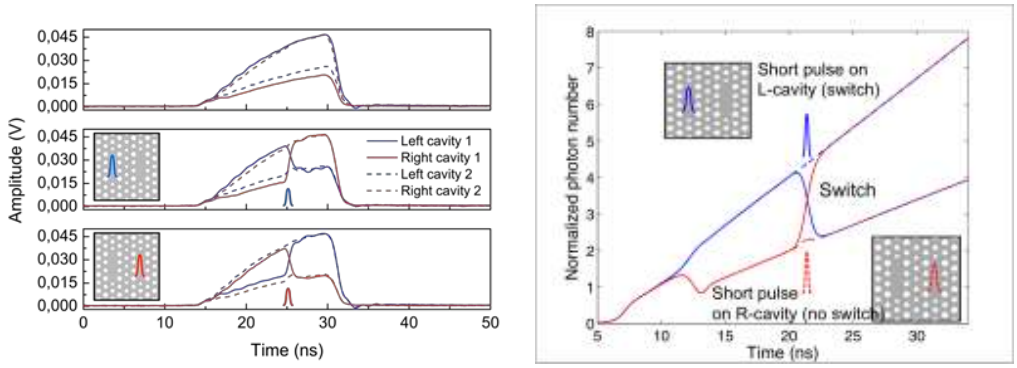



**Figure 1**: a) Coexistence of parity broken states, experimental results: cavity switching is triggered by a short (100 ps) pulse. Top: non-perturbed spontaneous switching. Center: the pulse is applied to the L cavity (sketched as a blue peak). Bottom: the perturbation is applied to the R cavity (sketched as a red peak). b) Numerical simulations of switching broken parity states. A short pulse arrives to the L-cavity at t = 21.3 ns. Switching is observed pulse energies overcoming a threshold.

**Acknowledgements** The authors acknowledge the financial support of Centre National de la Recherche Scientifique (CNRS), the Agence Nationale de la Recherche (ANR, ANR-12-BS04-0011), the Labex « NanoSaclay » and the RENATECH network.

## REFERENCES

1. M. Abbarchi, A. Amo, V. G. Sala, D. D. Solnyshkov, H. Flayac, L. Ferrier, I. Sagnes, E. Galopin, A. Lemaitre, G. Malpuech, and J. Bloch, "Macroscopic quantum self-trapping and Josephson oscillations of exciton polaritons", Nat Phys **9**, 275 (2013).
2. B. Maes, M. Soljacic, J. D. Joannopoulos, P. Bienstman, R. Baets, S.-P. Gorza, and M. Haelterman, "Switching through symmetry breaking in coupled nonlinear micro-cavities", Opt. Express **14**, 10678 (2006).
3. P. Hamel, S. Haddadi, F. Raineri, P. Monnier, G. Beaudoin, I. Sagnes, A. Levenson, and A. M. Yacomotti, "Spontaneous symmetry breaking in coupled photonic crystal nanolasers", Nature Photonics **9**, 311–315 (2015)
4. S. Haddadi, P. Hamel, G. Beaudoin, I. Sagnes, C. Sauvan, P. Lalanne, J. A. Levenson, and A. M. Yacomotti, "Photonic molecules: tailoring the coupling strength and sign", Opt. Express **22**, 12359 (2014).

# Controlling optical whispering galleries at exceptional points

**Ş. K. Özdemir[1*], and L. Yang[1]**

[1]Department of Electrical and Systems Engineering, Washington University in St. Louis, USA
[*]corresponding author: ozdemir@wustl.edu

**Abstract**- We will report our experiments on controlling the flow of light in high-quality whispering-gallery-mode (WGM) resonators by bringing them to the vicinity of their exceptional points (EPs), which are characterized by the coalescence of the eigenvalues and eigenstates of the system. We have shown that in the vicinity of an EP, the effect of loss can be reversed, chirality of the light in WGMs can be controlled, and the emission direction of a WGM microlaser can be selected at will.

Whispering-Gallery-Mode (WGM) microresonators, with their high quality factors and highly-confined optical modes, have emerged as excellent platforms for exploring basic science and for fabricating functional devices. They have been used for sensing, cavity-QED, optomechanics, optical filtering, low threshold lasing, and most recently for the realization of parity-time symmetry in optics. Waveguide coupled WGM microresonators (stand alone or coupled) are ideal model systems for the studies of non-Hermitian physics. The WGM resonators are open systems due to optical losses originating from absorption, coupling and radiation. As is the case for any non-Hermitian system, if the system parameters are steered, the WGM-microresonator system can be brought to an EP, which is a non-Hermitian degeneracy at which complex eigenvalues and the corresponding eigenstates of a physical system coalesce. The presence of an EP affects the system significantly, leading to nontrivial physics with interesting counterintuitive features.

In this talk, we will report and discuss how to control optical processes and the flow of light in WGM microresonators by operating them in the vicinity of EPs. In particular, we will present techniques and methods on how to bring a system of waveguide-coupled WGM resonators to the vicinity of EPs, and report on our experimental studies where we have showed reversing the effect of loss in optical systems and controlling the propagation properties of light in WGM microresonators in the vicinity of EPs. First, in a system of two coupled WGM microresonators, we will show loss-induced suppression and revival of optical nonlinearities and Raman lasing at an EP of the system: An existing Raman laser is annihilated when additional loss is introduced into the system. However, the laser revives back if the amount of loss exceeds a critical value [1]. Second, in a waveguide coupled WGM microresonator, we will show how to dynamically control the chirality of resonator modes and the emission direction of a WGM microlaser in the vicinity of EPs where strong asymmetric backscattering takes place. When the system is far from the EPs, it is nonchiral and laser emission is bidirectional (both clockwise and counterclockwise). However, when it is brought to the EPs, the modes become chiral and lead to unidirectional emission such that the emission is in the clockwise direction at one of the EPs and in the counter-clockwise direction at a different EP of the system [2].

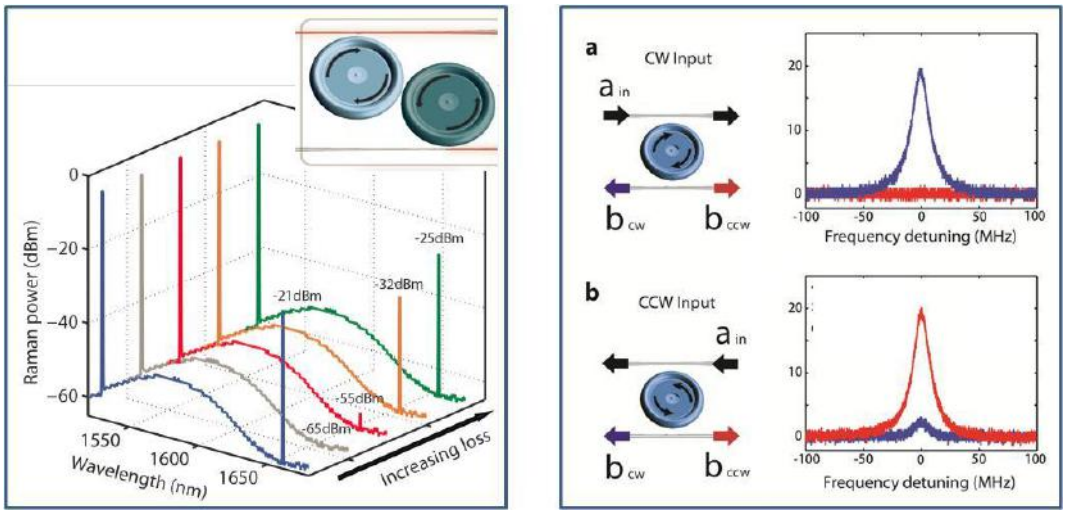



**Figure 1. Controlling light at exceptional points.** (Left) Loss-induced suppression and revival of Raman lasing in the vicinity of an EP in a coupled system of two WGM microresonator where additional loss is introduced to the resonator on the right. (Right) Asymmetric backscattering at an EP when two scatterers are placed within the mode volume of a WGM microresonator. When the input is in clockwise (CW) direction from left (upper panel), no light is scattered into the counter-clockwise (CCW) direction (red spectrum) whereas when the input is in the CCW direction from right (lower panel), back-scattering into CW takes place (blue spectrum).

**Acknowledgements**. This work was performed in collaboration with the groups of C. Bender (Washington University in St. Louis, USA), Franco Nori (Riken, Japan), Stefan Rotter (Vienna University of Technology, Austria), and Jan Wiersig (Otto-von-Guericke University, Magdeburg, Germany). This work was supported by ARO grant No. W911NF-12-1-0026.

**REFERENCES**

1. Peng, B. *et al.* "Loss-induced suppression and revival of lasing," *Science*, Vol. 346**,** 328–332, 2014.
2. Peng, B. *et al.* "Chiral modes at exceptional points," *submitted.*

# Parity-time-symmetric photonic hypercrystals

**O.V. Shramkova*, G.P. Tsironis**
Crete Center for Quantum Complexity and Nanotechnology, Department of Physics, University of Crete
P.O. Box 2208, 71003 Heraklion, Greece
*corresponding author: oksana@physics.uoc.gr

**Abstract**-In this work we investigate the electromagnetic wave propagation in a *PT*-symmetric hypercrystal composed of hyperbolic metamaterial layers separated by dielectric media with balanced loss and gain. The effect of the loss/gain level on the evolution of dispersion curves is considered. It is shown that the scattering properties of the stack and spontaneous symmetry breaking are strongly influenced by the constitutive and geometrical parameters of the layers and wave angles of incidence.

The dispersion properties of multilayered structures formed by hyperbolic media have been investigated mainly for the photonic crystal regime avoiding the hypercrystal limit [1]. Such materials exhibit unusual properties that can find many applications in nanophotonics. The discovery of parity-time ($PT$)-symmetric media [2] has shown significant potential for advancing toward the goal of new metamaterial design. In this work we explore the optical properties of the *PT*-symmetric hyperbolic semiconductor metamaterial formed by periodic variation of uniaxial metamaterial layer placed between two dielectric slabs of identical thickness, with complex-conjugate dielectric permittivities $\varepsilon_d = \varepsilon' - i\varepsilon''$ and $\varepsilon_d^* = \varepsilon' + i\varepsilon''$ (Fig.1a). We assume that the metamaterial medium is a periodic multilayer stack of alternating layers of two lossless semiconductors.

The dispersion relation and characteristic frequencies for dispersion dependencies of the eigenwaves of *PT*-symmetric hypercrystal were determined. Using the exact transfer-matrix approach and an effective medium theory, we have analysed the scattering properties of *PT*-symmetric hypercrystal stack of total thickness *L*. It was obtained that the effective medium approach does not adequately describe the propagating waves in the *PT*-symmetric stacks. We have shown that the unidirectional

invisibility can be observed at frequencies corresponding to hyperbolic regimes. The amplification of reflected waves was obtained for a case of left incidence. The spontaneous symmetry breaking phenomenon is observed at frequencies corresponding to first hyperbolic regime (blue shaded area, $\varepsilon_{xx} < 0, \varepsilon_{zz} > 0$ , where $\varepsilon_{xx,zz}$ are the components of an effective permittivity tensor), where $|\lambda_1| = 1/|\lambda_2| > 1$ (Fig.1b).

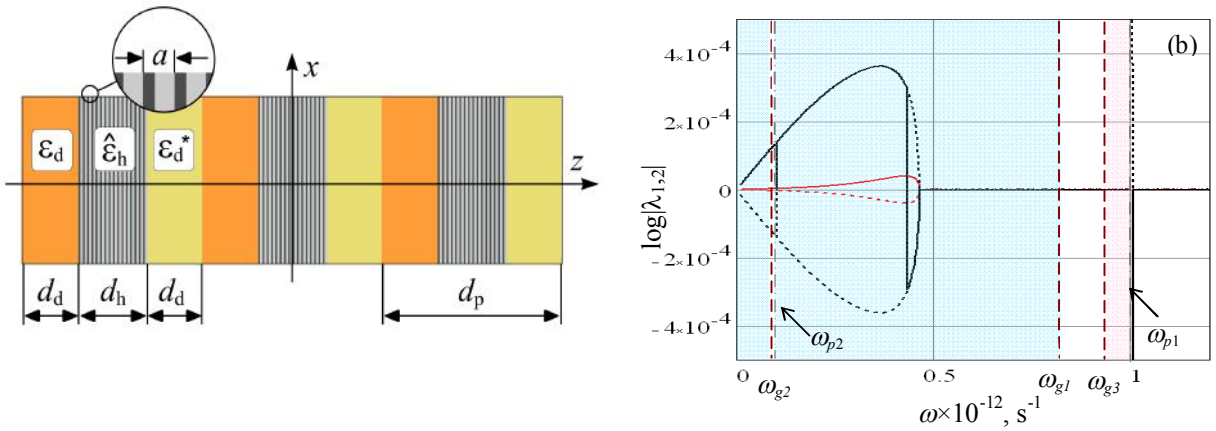



Fig.1. (a) – Geometry of the problem; (b) – $\log|\lambda_{1,2}|$ as a function of frequency at $\varepsilon' = 2.1$ , $\varepsilon'' = 0.1$ , $L$=1.2 mm; red lines - $\theta_i$ = 15°, black lines - $\theta_i$ = 75°; solid and dashed curves of the same colour correspond to the different eigenvalues of the same scattering matrix.

**Acknowledgements** - The research work was partially supported by the European Union Seventh Framework Program (FP7-REGPOT-2012-2013-1) under grant agreement No. 316165.

## REFERENCES

1. Narimanov E. E., “Photonic Hypercrystals,” *Phys. Rev. X*, Vol. 4, No. 4, 041014, 2014.
2. C. M. Bender and S. Boettcher, “Real Spectra in Non-Hermitian Hamiltonians having PT symmetry,” Phys. Rev. Lett., Vol. 80, 5243-5246, 1998.

# Parity-time symmetry synthetic metamaterials on silicon photonic chips

Yan-Feng Chen[1], Ming-Hui Lu[1], Liang Feng[2], Xiao-Ping Liu[1], Ye-Long Xu[1], William S. Fegadolli[3], Lin Gan[4], Axel Scherer[3] and Zhi-Yuan Li[4]

[1]National Laboratory of Solid State Microstructures, Nanjing University, Nanjing, Jiangsu 210093, China

[2]Department of Electrical Engineering, The State University of New York at Buffalo, Buffalo, NY 14260, USA

[3]Department of Physics and Kavli Nanoscience Institute, California Institute of Technology, Pasadena, CA91125, USA

[4]Laboratory of Optical Physics, Institute of Physics, Chinese Academy of Sciences, Beijing 100190, China

**Abstract:** Recently, parity-time (PT) symmetric optics has become an emerging field which allows a controlled interplay between real and imaginary parts of refractive index. Here by exploiting the concept of PT symmetry, we experimentally synthesize one kind of unidirectional reflectionless optical metamaterial on a silicon chip where reflection from one side is significantly suppressed near the spontaneous PT phase transition point. In addition, on the same platform, we experimentally realize passive PT photonic lattices where we observe complex Bloch oscillations that have no counterpart in Hermitian lattices. This PT-synthetic silicon photonic platform can be used to measure dynamics in non-Hermitian quantum mechanics which may pave the way to novel optical effects and a new generation of optical devices.

The past 20 years have witnessed great progress of artificial microstructures like photonic crystals, plasmonics and metamaterials which provide people new ideas and materials to manipulate light in demand. However, most of such structures and devices have been based on delicately control of real refractive index. The ubiquitous loss in these systems is typically considered a problem. Recently, notion of parity-time (PT) symmetry has been developed in optics[1,2] from previous quantum theory. This emerging field provides a new way to utilize material loss to realize novel optical effects and devices. In this work, we propose a passive PT metamaterial[3] which share similar phase transition process with balanced PT metamaterial[4,5] despite some background absorption, both of which have unidirectional reflectionless phenomenon at the exceptional point. This passive optical metamaterial is designed by engineering profile and thickness of optical materials on a silicon-on-insulator (SOI) platform. Numerical simulations and experimental verification of the designed metamaterial consistently show asymmetric reflection with high contrast ratios in a broadband communication wavelength. The observed unidirectional scattering characteristics have clearly demonstrated the exceptional point as well as its associated spontaneous breaking of PT symmetry. On the other hand, inspired by the concept of photonic simulation[6] of condensed matter physics, we experimentally investigate PT Bloch oscillations (BO) in non-Hermitian silicon photonic lattices consisting of an array of bent dissipative silicon waveguides[7]. By using

scanning near-field optical microscope (SNOM), we are able to directly observe continuous wave dynamics responsible for complex BO in real space[8]. The spatial wave dynamics recorded by the SNOM reveal a prominent secondary emission around the BO recovery point that is related to the PT symmetry breaking in contrast to the classical picture of BO in a Hermitian system. Further engineering of the complex optical potentials is expected to create novel PT metamaterials with more counterintuitive phenomena in the field of quantum mechanics and condensed matter physics. This fully integrated non-Hermitian silicon photonic platform provides a major step forward in expanding the application scope of on-chip photonics in quantum simulation and studying unprecedented non-Hermitian transport phenomena as well.

**References**


[1] Rüter, C.E. et al. Observation of parity–time symmetry in optics. *Nat. Phys.* **6,** 192-195 (2010).

[2] Guo, A. et al. Observation of PT-Symmetry Breaking in Complex Optical Potentials. *Phys. Rev. Lett.* **103**, 093902 (2009).

[3] Feng, L. et al. Experimental demonstration of a unidirectional reflectionless parity-time metamaterial at optical frequencies. *Nat. Mater.* **12**, 108-113 (2013).

[4] Lin, Z. et al. Unidirectional Invisibility Induced by PT-Symmetric Periodic Structures. *Phys. Rev. Lett.* **106**, 213901 (2011).

[5] Regensburger, A. et al. Parity–time synthetic photonic lattices. *Nature* **488**, 167-171 (2012).

[6] Longhi, S. Quantum-optical analogies using photonic structures. *Laser Photon. Rev.* **3**, 243-261 (2009).

[7] Xu, Y-L. et al. Experimental realization of Bloch oscillations in a Parity-Time synthetic silicon photonic lattice. *Nat. Commun.* (2016) (in press)

[8] Longhi, S. Bloch Oscillations in Complex Crystals with PT Symmetry. *Phys. Rev. Lett.* **103**, 123601 (2009).

# Nanophotonics using Hybrid and New Plasmonic Materials

# Strong Coupling between Silver nanoshells and semiconductor quantum dots

**Ning Zhou, Dongsheng Li*, and Deren Yang**
State Key Laboratory of Silicon Materials and School of Materials Science and Engineering, Zhejiang University, Hangzhou 310027, P.R. China
*corresponding author: mselds@zju.edu.cn

**Abstract**- We report on the observation of Rabi splitting of approximately 123 meV in photoluminescence spectra as an indication of strong coupling between excited states of CdSe/ZnS quantum dots (QDs) and localized surface plasmon modes of silver nanoshells under nonresonant nanosecond pulsed laser excitation at room temperature. The strong coupling manifests itself as an anticrossing-like behavior of the two newly formed polaritons when tuning the silver nanoshell plasmon energies across the exciton line of the QDs.

Combining metal and semiconductor nanostructures being resonant with each other opens up unique possibilities for the coupled excitations that can act differently than the optical excitations of the individual components and potentially lead to synergistic properties caused by interactions between the constituents [1]. Such exciton-plasmon interactions allow manipulation of absorption and emission properties, control of energy-transfer processes, creation of new polaritons in the strong coupling regime, and enhancement of optical nonlinearities. Strong coupling regime has been realized between emitter and cavity exciton–photon interaction, when their interaction becomes larger than the dipole emitter decay rate and the cavity field decay rate [2-3]. However, the diffraction-limited optical cavities place a lower bound on the size of these systems [4]. Surface plasmons (SPs) of metal nanoparticles (NPs) are regarded as promising candidates for the investigation of strong coupling effects. Since the first observation of strong coupling between a SP mode and excitons in J-aggregates [5], great progress has been made and Rabi splitting even in the ultrastrong coupling regime has been achieved [6-7]. However, there are few reports about strong coupling between QDs and SPs except the works made by D. E. Gómez group utilizing prism coupling and attenuated total reflection technique [8, 9]. Moreover, systematic study concerning how the emission from the plexciton state is modified by SPs at the strong coupling regime is necessary and meaningful for quantum information processing. In this paper, we integrate CdSe/ZnS QDs and silver nanoshells together, and, for the first time, Rabi splitting approximately as large as 123 meV in PL spectra is realized under the nonresonant excitation of nanosecond pulsed laser at room temperature.

Figure 1a illustrates the excitation-detection scheme for the studies on strong coupling between localized surface plasmon (LSP) of Ag nanoshells and exciton of CdSe/ZnS QDs. The evolution of emission spectra of QDs_565, QDs_585 and QDs_605 (the number denotes the emission center wavelength of QDs) together with Ag nanoshells as a function of pump energy are depicted in Figure 2a-c, respectively. Under low pump energy, the spectral features resemble that of pure QDs. For pure QDs, only broad spontaneous emission of QDs was identified when excited up to the maximum pump energy and the emission intensity increases to a peak value due to gain saturation. As the pump energy exceeds a threshold, the emission spectra of the mixture systems begin to manifest distinctive characteristics and show a doublet of peaks around the exciton resonance frequency which is the direct evidence of Rabi splitting. The higher energy mode on the blue side of the exciton is referred to as the UP branch and the lower energy mode on the red side is referred to as the lower polariton (LP) branch. After analyzing the spectra by fitting with two or three Lorentzian peaks, it is apparent that the UP and LP shift

to higher or lower energy with the increase of the pump energy as depicted in Figure 2d-f, meaning that the Rabi splitting energy increases with the pump energy. As for 220 $SiO_2$@30 Ag/QDs_585 systems displayed in Figure 2b and 2e, remarkable splitting value up to 103 meV has been achieved when the pump energy is 179.6 μJ, the maximum pump energy limited by our laser instrument. When the exciton energy of QDs is close to the pump energy like QDs_565, even at lower pump energy (130.5 μJ), Rabi splitting value up to 123 meV could be achieved (Figure 2a and 2d)，perhaps owing to pump and emission energy matching resultant higher pump efficiency. On the other hand, because the emission wavelength of QDs_605 match the extinction peak of 220 $SiO_2$ @30 Ag, the better overlap contributes to easily realized strong coupling compared to QDs_585 (Figure 2c and 2f).

The Rabi splitting energy is found to increase linearly with the excitation density. By tuning the silver nanoshell plasmon energies across the exciton line of the QDs, the dispersion lines present an anticrossing-like behavior, which is the signature of strong plasmon-exciton coupling. High pump energy and collective strong coupling of many QDs with the radiative dipole mode of Ag nanoshell are believed vital to the realization of strong coupling in our system.

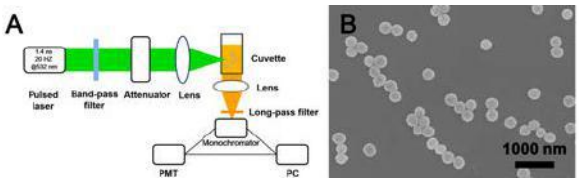



Figure 1. (a) Schematic of the excitation-detection configuration. (b) SEM image of the 220 SiO2@30 Ag standing for Ag nanosells with SiO2 core (diameter: 220 nm) – Ag shell (thickness: 30 nm).

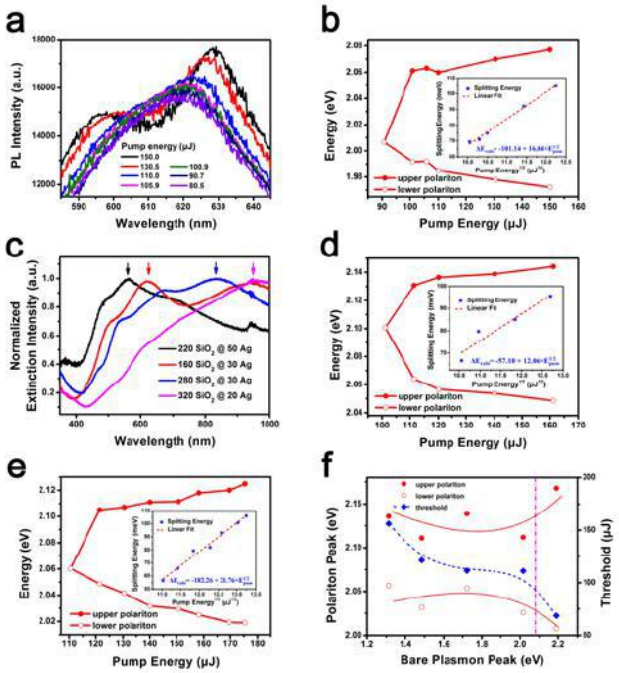



Figure 2. Evolution of emission spectra as a function of pump energy for 220 SiO2@ 30Ag mixed with QDs with different emission centers (a) 565 nm, (b) 585 nm, (c) 605 nm. (d-f) Evolution of UP and LP resonance energies as a function of pump energy deduced from (a-c), respectively. The insets in d-f are fits of splitting energy of polariton emission as a function of pump energy.

**Acknowledgements:** This work is supported by the National Basic Research Program of China (Grant No. 2013CB632102) and the National Natural Science Foundation of China (No.61176117).

# Breaking the Space Charge Limit in Organic Semiconductors by Novel Plasmon-Electrical Concept

**Wallace C. H. Choy*, W.E.I. Sha, X. Li, and L. Zhu**

[1] Department of Electrical and Electronic Engineering, The University of Hong Kong, Pokfulam Road, Hong Kong.

*corresponding author: chchoy@eee.hku.hk

**Abstract**- As a fundamental electrostatic limit, the space charge limit (SCL) for photocurrent is a universal feature and of paramount importance in organic semiconductors with unbalanced electron/hole mobility and high exciton generation. Here, we propose a new concept of plasmonic-electrical effect to manipulate the electrical properties (photocarrier generation, recombination, transport, and collection) of semiconductor devices with the help of plasmonically induced light redistribution. As a proof-of-concept, organic solar cells (OSCs) incorporating metallic planar and grating anodes are systematically investigated for normal and inverted device structures. Interestingly, although strong plasmonic resonances induce abnormally dense photocarriers around a grating anode, the grating-inverted OSC is exempt from space charge accumulation (limit) and degradation of electrical properties in contrast to the planar-inverted and planar-normal ones. It is because abnormally redistributed holes by the plasmonic-electrical effect, despite of the typically low mobility of holes, shorten hopping path of low mobility holes to reach the grating anode. Consequently, the work contributes to the evolution of device architecture to break the SCL with detailed multiphysics explanations. Moreover, the proposed plasmonic-electrical concept will open up a novel way to manipulate both optical and electrical properties of organic semiconductor devices for optoelectronic applications.

The space charge limit (SCL) effect is a universal phenomenon in semiconductor devices involving light emitting diodes, solar cells, and photodetectors. Typically, the SCL will exist in the condition of (1) unbalanced hole and electron mobility; (2) thick active layer; (3) high light intensity or dense photocarriers (electrons and holes) generation; and (4) moderate reverse bias. A low mobility of hole as compared to that of electron can be occurred in organic semiconductor devices dependent on device fabrication procedures, for instance, the thermal annealing, solvent annealing, etc. In the planar-inverted organic solar cells (OSCs), photocarriers will be generated at the region close to the transparent cathode, such as indium tin oxide (ITO), where incident light will first penetrate. The photogenerated holes with a low mobility will have to transport through the whole active layer, and then reach to the anode. If the length of the active layer is longer than the mean drift length of holes, the incurred SCL can be easily observed due to the severely unbalanced mobility of electron and hole and the accumulated holes (i.e. space charges) inside the device. As a consequence, the short circuit current and fill factor of OSCs will drop significantly due to both bulk recombination and space charge formations.

In this work, through the study of plasmonic OSCs, we will show metallic nanostructures go beyond their optical functions to control recombination, transport, and collection of photocarriers generated from active organic materials. Through spatially redistributing light absorption at the active layer, the proposed plasmonic-electrical concept is fundamentally different from the hot carrier effect where photocarriers are generated from metallic nanostructures. The eliminated SCL in OSCs has been demonstrated through incorporating metallic (Ag or Au) nanostructures and then the

improved efficiency is achieved [1]. Consequently, the investigation of plasmonic-electrical [2-4] and plasmonic-optical [5-9] effects can enhance device performances such as improving the light absorption of solar cells, increasing emission efficiency of light emitting devices, reducing dark current and enhancing sensitivity of photodetector as well as intensifying the surface enhanced Raman scattering for biosensor applications.

The commonly polymer blend of poly(3-hexylthiophene):[6,6]-phenyl-C61-butyric acid methyl ester (P3HT:PCBM) is used. To demonstrate the SCL effect, three structural and material configurations were fabricated to intuitively show the plasmonic-electrical effects. 1. Annealed P3HT:PCBM active layer at non-optimized annealing temperature (robust and well-recognized) for unbalanced electron/ hole mobility and low hole mobility (to favor SCL effects). 2. Inverted OSC structures for a long hole transport path (to favor SCL effects). 3. Metallic nanograting as an anode shown in Figure 1(b) for demonstrating the plasmonically modified SCL effect. The planar and grating OSCs are inverted device structures of ITO/$TiO_2$ (20 nm)/active layer (220 nm)/$MoO_3$ (10 nm)/Ag (with or without grating) (100 nm) (See Figure 1). For comparative and systematic study, the planar and grating OSCs with normal device structures of ITO/ PEDOT:PSS (30 nm)/active layer (220 nm)/Ca (10 nm)/Ag (with or without grating) (100 nm) are also fabricated. All the active layer thicknesses are about 220 nm.

According to the Mott-Gurney law states photocurrent ($J_{ph}$) in the SCL regime can be described as following using negligible number of deep localized states and field independent mobility.

$$J_{ph} = \left( \frac{9\varepsilon_0 \varepsilon_r \mu_h}{8} \right)^{1/4} (qG)^{3/4} V_e^{1/2} \qquad (1)$$

where $G$, $V_e$, $\mu_h$, $q$, $\varepsilon_0\varepsilon_r$ are the averaged generation rate, the effective voltage drop across the active layer or hole accumulation region, the hole mobility, the electron charge and the dielectric permittivity of the active layer respectively. The compensation voltage $V_0$, which is almost equal to the built-in potential of OSCs, is defined as $J_{ph}(V_0)=0$. The effective applied voltage $V_e$ is given as $V_0$-$V$, where $V$ is the applied bias voltage. Differently, under a sufficiently large reverse bias (ignorable recombination), $J_{ph}$ is approximated as

$$J_{ph} = qGL \qquad (2)$$

where $L$ is the active layer's thickness.

SCL characteristics in Ag-planar-inverted and Ag-grating-inverted OSCs have been studied by measuring $J_{ph}$ under various incident light intensity and effective applied voltage ($V_0$-$V$l) conditions at room temperature and the results are shown in Figure 2**.** For the Ag-planar-inverted device, when $V_0$-$V$<0.2 V (i.e. a low internal electrostatic field, see Figure 2(a)), the approximately linear proportion of $J_{ph}$ to $V_0$-$V$ is mainly governed by the diffusion and drift currents effect. As internal field increases, $J_{ph}$ shows a square-root dependence on $V_0$-$V$. When the internal field further increases, under sufficiently high reverse voltage, photocurrent becomes saturated (internal-field independent) with no occurrence of recombination, indicating the mean distance ($w$) of free charge carriers becomes equal to or larger than the active layer thickness ($L$). The $J_{ph}$'s dependence on $V_0$-$V$ reveal the current transition from diffusion and drift current, to SCL limited current and finally saturated current with no occurrence of recombination. The $J_{ph}$ versus light intensity at three different effective applied voltages (at $V_0$-$V$ =0.2 V, 0.5 V, 1 V in the square-root regime, and $V_0$-$V$ =10 V in the saturation regime) is extracted as shown in Figure 3 and further verify the SCL occurrence in the Ag-planar-inverted OSC. From the results for planar inverted OSCs (see Figure 3(a)), $J_{ph}$ is approximately proportional to $I^{3/4}$ at the SCL region (1/2 power dependence of $J_{ph}$ on $V_0$-$V$) and proportional to $I^{0.93}$ at the saturation region for sufficiently high $V_0$-$V$. According to Equation (1) and (2), we conclude that the space charge effect occurs and dominates electrical properties of the Ag-planar-inverted device.

Regarding the Ag-grating-inverted OSCs, $J_{ph}$ versus $V_0$-$V$ at different incident light intensities is shown in Figure 3(b).

Amazingly, the SCL characteristics disappear when a metallic grating anode is incorporated. When $V_0$-$V$ <0.2 V, $J_{ph}$ is almost linearly proportional to $V_0$-$V$, which is the same as the Ag-planarinverted device. However, at higher voltages, $J_{ph}$ becomes saturated and shows no square-root dependence on $V_0$-$V$. Furthermore, extracting the curve of $J_{ph}$ versus the light intensity at different $V_0$-$V$, $J_{ph}$ shows a linear dependence on the light intensity. This suggests the eliminated SCL and reduced bulk recombination.

Electrical characteristic parameters of OSCs with four different device structures are listed in Table 1. For the Ag-normal OSCs, the characteristic parameters including shortcircuit current ($J_{SC}$) and fill factor (FF) show no significant distinction for both planar and grating devices. After introducing the nanostructured cathode, the increased $J_{SC}$ and reduced FF are respectively due to the metallic grating enhanced optical absorption and elongated hole (shortened electron) transport path. However, for the Ag-inverted OSCs, the characteristic parameters of the planar and grating devices show considerable differences. For example, FF of the Ag-planar-inverted device drops drastically compared to that of Ag-grating-inverted one. The maximum possible FF at the SCL regime is about 42%.

FF of the Ag-planar-inverted and Ag-grating-inverted devices are respectively lower and higher than 42%. The OSCs, which achieve a FF significantly larger than 42%, will be exempt from the SCL. The FF of the Ag-planar-inverted device is noticeably smaller than 42% due to the SCL effect with a large recombination loss. Furthermore, $J_{SC}$ of the Ag-grating-inverted device is improved by 75% in comparison with the Ag planar-inverted one. On one hand, surface plasmons excited in the metallic grating enhance the optical absorption of OSCs. On other hand, low-mobility holes, abnormally generated around the grating anode, are collected fast and easily leading to the reduced recombination loss. Hence, the Ag-grating-inverted device improves $J_{SC}$ much more significantly than the Ag-grating-normal one, although the same optical enhancement can be achieved by the Ag-grating-normal device. Considering the improved FF together with the boosted short-circuit current, the PCE of the Ag-gratinginverted device is remarkably increased by 137%.

In conclusion, the work demonstrated the plasmonic-electrical effect breaks the SCL in inverted OSCs through introducing a metallic nanostructured anode. The linear dependence of photocurrent on light intensity and significantly improved FF are clear proofs for the eliminated SCL characteristics. Plasmonically induced light absorption redistribution shortens the transport path of low-mobility holes; and thus reduces bulk recombination and space charge accumulation. Consequently, exploiting both plasmonic-optical and plasmonic-electrical effects via metallic nanostructures will open up a more flexible and integrated way to design high-performance optoelectronic nanodevices.

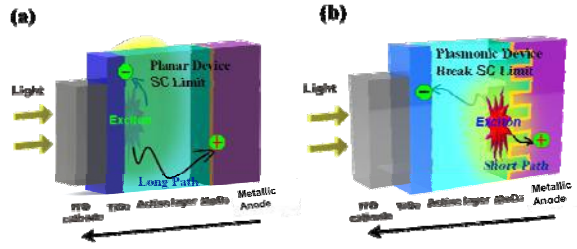



Figure 1. A schematic pattern of inverted OSC devices. (a) inverted OSCs with a planar metallic anode; (b) inverted OSCs with a grating metallic anode. 'SC' denotes the space charge. A long transport path of holes in the planar-inverted OSC induces the SCL characteristics. A short transport path of holes manipulated by the plasmonic-electrical effect in the grating-inverted OSC breaks the SCL.

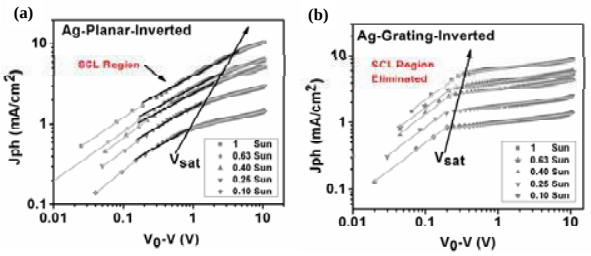



Figure 2. SCL characteristics for Ag-inverted OSCs. photocurrents versus effective applied voltage at different incident light intensities. (a) Ag-planar-inverted OSCs, and (b) Ag-grating-inverted OSCs. Light intensity is varied from 100, 63, 40, 25, to 10 mW cm$^{-2}$ by using neutral density filters. The black solid lines in (a) represent the square-root dependence of

photocurrent on effective applied voltage (SCL region).

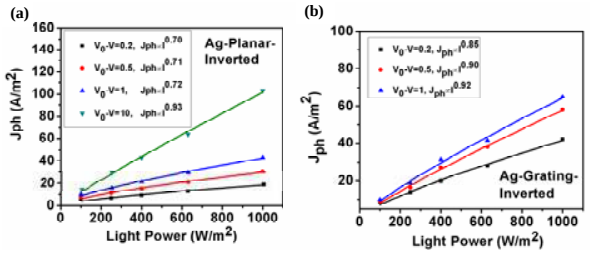



Figure 3. Photocurrents versus incident light intensity at different effective applied voltages. (a) Ag-planar-inverted OSCs, and (b) Ag-grating-inverted OSCs.

**Acknowledgements** The work is supported by the General Research Fund (grants HKU711813 and HKU711612E), the Collaborative Research Fund (grant C7045-14E) and RGC-NSFC grant (N_HKU709/12) from the Research Grants Council of Hong Kong Special Administrative Region, China, and grant CAS14601 from CAS-Croucher Funding Scheme for Joint Laboratories and the Collaborative Research grant from the research grant council of Hong Kong (CUHK1/CRF/12G).

**REFERENCES**

1. W.E.I. Sha, X. Li, W.C.H. Choy, "Breaking the Space Charge Limit in Organic Solar Cells by a Novel Plasmonic-Electrical Concept", Sci. Rep., vol. 4, p. 6236 (10pp), 2014.
2. F.X. Xie, W.C.H. Choy, W.E.I. Sha, D. Zhang, S. Zhang, X. Li, C.W. Leung, J. Hou, “Enhanced Charge Extraction in Organic Solar Cells through Electron Accumulation Effects Induced by Metal Nanoparticles”, Energy Environ. Sci., vol. 6, pp.3372 – 3379, 2013.
3. D. Zhang, W.C.H. Choy, F. Xie, W.E.I. Sha, X. Li, “Plasmonic-electrically Functionalized TiO2 for High Performance Organic Solar Cells”, Adv. Funct. Mat., vol. 23, pp.4255–4261, 2013.
4. D.D.S. Fung, L. Qiao, W.C.H. Choy, C.C.D. Wang, W.E.I. Sha, F. Xie, S. He, "Optical and Electrical Properties of Efficiency Enhanced Polymer Solar Cells with Au Nanoparticles in PEDOT-PSS Layer", J. Mat. Chem., vol. 21, pp. 16349 – 16356, 2011.
5. X.H. Li, W.C. H. Choy, X. Ren, D. Zhang, H.F. Lu, "Highly Intensified Surface Enhanced Raman Scattering by Using Monolayer Graphene as the Nanospacer of Metal Film- Metal Nanoparticle Coupling System", Adv. Funct. Mat., vol. 24, pp.3114–3122, 2014.
6. X.H.Li, W.C.H.Choy, H.F. Lu, W.E.I. Sha, H. P. Ho, "Efficiency Enhancement of Organic Solar Cells by Using Shape Dependent Broadband Plasmonic Absorption in Metallic Nanoparticles", Adv. Funct. Mat., vol.23, pp.2728–2735, 2013.
7. X.H. Li, W. C.H. Choy, L Huo, F.X. Xie, W.E.I. Sha, B. Ding, X. Guo, Y. Li, J. Hou, Y. Yang, "Dual Plasmonic Nanostructures for High Performance Inverted Organic Solar Cells", Adv. Mat. vol. 24, pp.3046-3052, 2012.
8. X.H. Li, W. E.I. Sha, W.C.H. Choy, D.D.S. Fung, F. X. Xie, "Efficient Inverted Polymer Solar Cells with Directly Patterned Active Layer and Silver Back Grating", J. Phys. Chem. C, vol. 116, pp.7200-7206, 2012.
9. C.C.D. Wang, W. C. H. Choy, C. Duan, D.D.S. Fung, W.E.I. Sha, F.X. Xie, F. Huang, and Y. Cao, "Optical and Electrical Effects of Gold Nanoparticles in the active layer of Polymer Solar Cells", J. Mat. Chem., vol. 22, pp.1206–1211, 2012.

# Subwavelength grating engineered metamaterial waveguide structures for silicon photonic integrated circuits

**P. Cheben[1], J.H. Schmid[1], D.-X. Xu[1], S. Janz[1], J. Lapointe[1], M. Rahim[1], S. Wang[1], M. Vachon[1], R. Halir[2], A. Ortega-Moñux[2], G. Wangüemert-Pérez[2], I. Molina-Fernández[2], J. Pond[3], D. Benedikovic[4], C. Alonso-Ramos[4], J. Soler Penadés[5], M. Nedeljkovic[5], G.Z. Mashanovich[5], A.V. Velasco[6], M.L. Calvo[6], Y. Painchaud[7], M.-J. Picard[7], M. Poulin[7], M. Dado[8], J. Müllerová[8], W.N. Ye[9], M. Pápeš[10] and V. Vašinek[10]**

[1] National Research Council, Ottawa, Canada

[2] ETSI Telecomunicación, Universidad de Málaga, Spain

[3] Lumerical, Inc., Vancouver, Canada

[4] University of Paris Sud and CNRS, Paris, France

[5] University of Southampton, United Kingdom

[6] CSIC and Universidad Complutense, Madrid, Spain

[7] Ciena, Québec, Canada

[8] University of Žilina, Slovak Republic

[9] Carleton University, Canada

[10] VSB – Technical University of Ostrava, Czech Republic

E-mail: pavel.cheben@nrc.ca

**Abstract**- We report our advances in development of subwavelength engineered metamaterial structures for silicon photonics. This unique technology allows synthesis of an effective photonic medium with an unprecedented control of material properties, constituting a powerful tool for a designer of photonic integrated circuits. We present an overview of different implementations of these nanophotonic structures in silicon photonic integrated circuits, such as high-efficiency fiber-chip couplers, wavelength multiplexers and microspectrometers, waveguide crossovers, ultra-broadband splitters and mid-infrared waveguide components, to name a few.

By locally engineering the refractive index of silicon by forming a pattern of holes at the subwavelength scale it is possible to manipulate the flow of light in silicon photonic waveguides [1-6]. We have demonstrated a number of subwavelength engineered devices operating at telecom wavelengths, including fibre-chip couplers, waveguide crossings, WDM multiplexers, ultra-fast optical switches, athermal waveguides, evanescent field sensors, polarization rotators, transceiver hybrids and colorless interference couplers [6]. The subwavelength metamaterial concept has been adopted by industry (IBM) for fibre-chip coupling [7] and subwavelength structures are likely to become key building blocks for the next generation of integrated photonic circuits. We have demonstrated an unprecedented control over the light coupling between optical fibers and silicon chips by constructing several types of subwavelength index engineered couplers [1,3,4,8-10] operating at telecom (1.55 μm) and datacom (1.3 μm) wavelengts with a coupling efficiency exceeding 90%. We also developed dispersion engineered colorless splitters operating over an ultra-broad wavelength range 1260 nm - 1675 nm, exceeding the O, E, S, C, L and U optical communication bands. Implementations of subwavelength grating engineered structures for evanescent field sensing [11] and mid-infrared silicon photonic circuits [12] with waveguide

propagation losses <0.9 dB/cm at 3.8 μm will also be discussed.

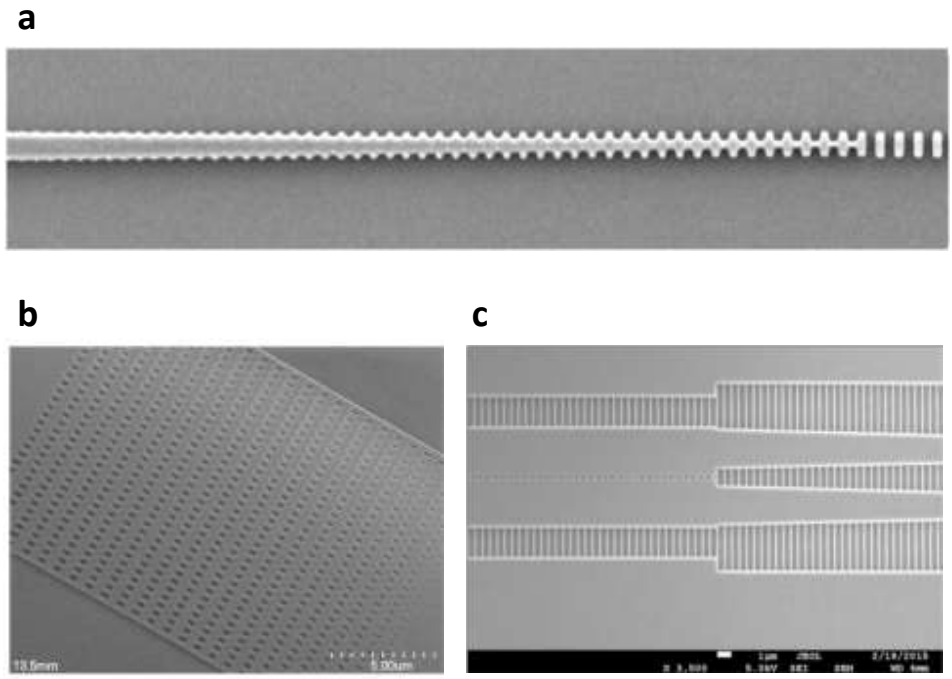



**Figure 1:** Subwavelength grating metamaterial structures in silicon waveguides. a) Broadband polarization independent fiber-chip edge coupler, b) high-efficiency surface grating coupler, and c) multimode interference coupler for mid-infrared applications.

**REFERENCES**


1. P. Cheben et al., US patent 7,376,308 B2 (2008).
2. P. Cheben et al., US patent 8,503,839 B2 (2013).
3. P. Cheben et al., *Optics Express,* Vol. 14, 4695-4702 (2006).
4. P. Cheben et al., *Optics Letters,* Vol. 35, 2526-2528 (2010).
5. J. H. Schmid et al., *IEEE Photon. J.*, Vol. 3, 597-607 (2011).
6. R. Halir et al., *Laser and Photonics Reviews,* Vol. 9, 25-49 (2015).
7. T. Barwicz et al., Optical Fiber Communication Conference, paper Th3F.3 (2015).
8. P. Cheben et al., *Optics Express,* Vol. 23, 22553-22563 (2015).
9. D. Benedikovic et al., *Optics Express,* Vol. 23, 22628-22635 (2015).
10. M. Papes et al., *Optics Express,* submitted (2016).
11. G. Wangüemert-Pérez et al., *Optics Letters,* Vol. 39, 4442-4445 (2014).
12. J. S. Penades et al., IEEE Group IV Photonics Conference (2015).

# Semiconductors for Infrared Plasmonics and Metamaterials

**S. Law**

University of Delaware, USA
slaw@udel.edu

**Abstract**— This paper discusses the use of heavily-doped III/V semiconductors as the building blocks for infrared plasmonic and metamaterial devices. We begin by demonstrating the ability to tune the optical properties of our materials by changing the electron doping density, leading to designer low-loss infrared plasmonic materials with plasma wavelengths spanning the mid-infrared. We then describe plasmonic devices created with these materials, including plasmonic nanoantennas and perfect absorbers. Finally, we describe recent work using doped semiconductors for infrared metamaterials.

Much plasmonics research to date has been performed in the visible spectral range using traditional metals, such as gold and silver. This work has been quite successful, producing significant advances and a variety of visible-wavelength devices. There are many applications for plasmonic materials in the infrared, including gas sensing, control of thermal emission, and enhanced infrared imaging capabilities. However, in order for plasmonic devices to function, the permittivity of the metallic components needs to be of the same order of magnitude as the corresponding dielectrics. Functionally, this requires metallic components with small negative permittivities. Traditional metals have very large negative permittivities in the mid-infrared, making it impossible to find a suitable matching dielectric. Instead, we must turn to new materials.

Doped semiconductors offer a solution. The optical properties of these materials can be accurately modeled using the Drude formalism, giving the frequency-dependent permittivity as

$$\varepsilon(\omega) = \varepsilon_s \left(1 - \frac{\omega_p^2}{\omega^2 + i\omega\Gamma}\right) \quad \text{with} \quad \omega_p^2 = \frac{ne^2}{\varepsilon_s \varepsilon_0 m^*} \tag{1}$$

where $\varepsilon_s$ is the permittivity of the undoped semiconductor, $\omega_p$ is the plasma frequency, $\Gamma$ is the scattering rate for carriers in the semiconductor, $n$ is the carrier density in the semiconductor, $\varepsilon_0$ is the permittivity of free space, and $m^*$ is the effective mass of the carriers in the semiconductor. By adjusting the doping density in the material, the plasma frequency can be tuned across the infrared. III/V semiconductors can be grown using molecular beam epitaxy, resulting in crystalline films with precise control over the doping density and material thickness. For InAs, the combination of high maximum doping density and a small electron effective mass results in plasma wavelengths tunable across the mid-infrared, from 5.5$\mu$m to longer than 15$\mu$m[1, 2]. InSb has demonstrated plasma wavelengths as short as 6.9$\mu$m, shorter than the room-temperature bandgap[3]. Other semiconductor materials have also been shown to work in the infrared[4, 5, 6].

These plasmonic materials have been used to create a variety of infrared devices, including perfect absorbers, which concentrate light within a layered semiconductor structure, and nanoantennas, which exhibit a large electric field around the subwavelength feature. There are a variety of applications for these plasmonic structures, including the creation of more sensitive detectors and better gas monitoring systems. Since the plasmonic structures are based on doped semiconductors, it is easy to incorporate existing semiconductor optoelectronic devices, including detector and emitter structures.

Finally, doped semiconductor materials can be used to create layered hyperbolic metamaterials (HMMs). The first realization of this idea used doped InGaAs as the metal layer and undoped InAlAs as the dielectric layer[7]. By tuning the doping density, the onset and bandwidth of the HMM behavior can be tuned. Our recent efforts builds on this work, demonstrating HMMs made using a single semiconductor material system, comprising doped InAs as the metal layer and undoped InAs as the dielectric. We are able to obtain HMM onset wavelengths as short as 5.8$\mu$m. By adjusting the ratio of the metal:dielectric layer thicknesses, we can obtain multiple optical behaviors in a single system, including metal, dielectric and HMM. Finally, we use a geometric optics experiment inspired by [7] to show that our materials exhibit negative refraction, a hallmark of HMM behavior.

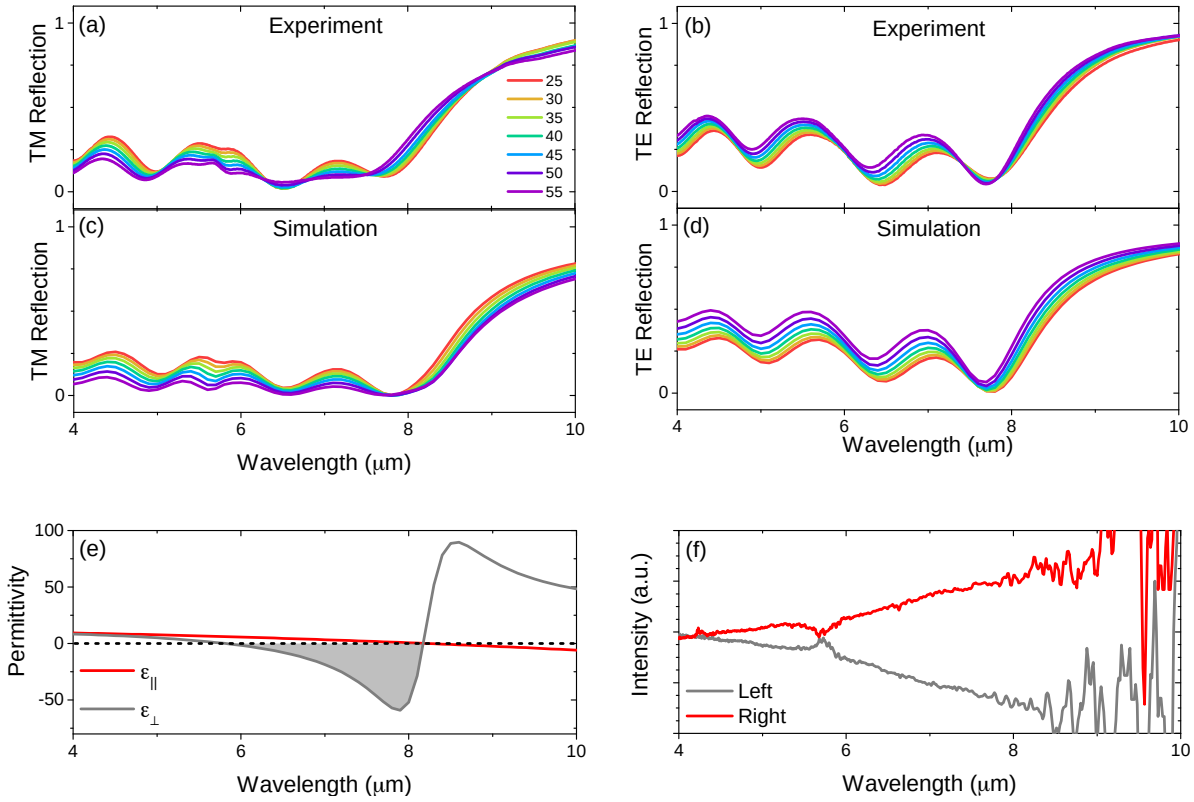



Figure 1: Experimental TM (a) and TE (b) polarized reflection for a metamaterial sample with fill factor 0.5 and plasma wavelength 5.8$\mu$m. Simulated TM (c) and TE (d) reflection using effective medium theory. (e) Parallel and perpendicular permittivity determined using effective medium theory. (f) Negative refraction data for razor blocking half the transmitted light on the left and right of the sample.

In conclusion, we have shown that doped semiconductors act as tunable, low-loss infrared metals, and can be used an applications as varied as nanoantennas, perfect absorbers, and hyperbolic metamaterials. Since these materials are grown using molecular beam epitaxy, they can easily be integrated with existing semiconductor optoelectronic devices. These alternative plasmonic materials show great promise for moving plasmonics to the infrared frequency range.

**REFERENCES**


1. Law, S., Adams, D. C., Taylor, A. M., and Wasserman, D. "Mid-infrared designer metals," *Opt. Express*, Vol. 20, No. 11, 12155–12165, 2012.
2. Law, S., Yu, L., and Wasserman, D. "Epitaxial growth of engineered metals for mid-infrared plasmonics," *J. Vac. Sci. Technol. B*, Vol. 31, No. 3, 03C121, 2013.
3. Law, S., Liu, R., and Wasserman, D. "Doped semiconductors with band-edge plasma frequencies," *J. Vac. Sci. Technol. B*, Vol. 32, No. 5, 052601, 2014.
4. Ginn, J. C., Jarecki, R. L., Shaner, E. A., and Davids, P. S. "Infrared plasmons on heavily-doped silicon," *J. Appl. Phys.*, Vol. 110, 043110, 2011.
5. Shahzad, M., Madhi, G., Peale, R. E., Buchwald, W. R., Cleary, J. W., Soref, R., Boreman, G. D., and Edwards, O. "Infrared surface plasmons on heavily doped silicon," *J. Appl. Phys.*, Vol. 110, 123105, 2011.
6. Rosenberg, A., Surya, J., Liu, R., Streyer, W., Law, S., Leslie, L. S., Bhargava, R., and Wasserman, D. "Flat mid-infrared composite plasmonic materials using lateral doping-patterned semiconductors," *J. Opt.*, Vol. 16, 094102, 2014.
7. Hoffman, A. J., Alekseyev, L., Howard, S. S., Franz, K. J., Wasserman, D., Podolskiy, V. A., Narimanov, E. E., Sicvo, D. L., and Gmachl, C. "Negative refraction in semiconductor metamaterials," *Nat. Mat.*, Vol. 6, No. 12, 946-950, 2007.

# Nonlinear organic "plasmonics": Bistability of exciton polaritons and applications to optical control of Coulomb blocking in nanojunctions.

**B. D. Fainberg**[1,2*], **and G. Li**[3]
[1]Faculty of Sciences, Holon Institute of Technology, Holon, Israel
[2]School of Chemistry, Tel Aviv University, Tel Aviv, Israel
[3]Department of Chemistry, Northwestern University, Evanston, IL, USA
[*]corresponding author: fainberg@hit.ac.il

**Abstract**-We develop a theory of nonlinear organic "plasmonics" with strong laser pulses. The bistability response of the electron-vibrational model of organic materials in the condensed phase has been demonstrated that results in bistability of the surface localized polaritons. We propose the exciton control of Coulomb blocking in the quantum dot wire based on non-steady-state nonlinear organic "plasmonics" that enable us to obtain near-zero dielectric permittivity during a short time.

Purely organic materials characterized by low losses with negative, near-zero, and smaller than unity dielectric permittivities can be easily fabricated. Here we develop a theory of non-steady-state organic "plasmonics" with strong short laser pulses that enable us to obtain near-zero dielectric permittivity during a short time [1]. We have proposed to use non-steady-state organic "plasmonics" for the enhancement of intersite dipolar energy-transfer interaction in the quantum dot wire that influences on electron transport through nanojunctions. Such interactions can compensate Coulomb repulsions for particular relationships between their values. We propose the exciton control of Coulomb blocking in the quantum dot wire based on the non-steady-state near-zero dielectric permittivity of the organic host medium using chirped laser pulses [1].

If one does not use suitably chirped pulses that compensate for a change of frequency of the optical transition in time induced by the pulses themselves (see above), equations for populations become nonlinear and can demonstrate a bistable behavior. The bistability response of the electron-vibrational model of organic materials in the condensed phase has been demonstrated [2]. Fig.1 shows steady-state solutions for the populations of the excited electronic state $n_2$ as a function of the power density of the exciting radiation $R$ at different detunings $y = \omega_{21} - \omega$. One can see that each value of $R$ within the corresponding interval produces three different solutions of the equation for the populations of the excited electronic state at dimensionless detunings y=0, 0.25 and 0.5, however, only lower and upper branches are stable. Such detunings correspond to the excitation at the short-wave part of the equilibrium absorption spectrum (see the Inset to Fig.1). As the excited state population increases, the spectrum exhibits the blue shift that should essentially contribute to the absorption. As a matter of fact, the bistable behavior of the population arises from the dependence of the resonance frequency of the molecules in dense medium on the number of excited molecules. The bistable behavior of the population results in the bistability of the surface localized

polaritons that is also the subject of the present work.

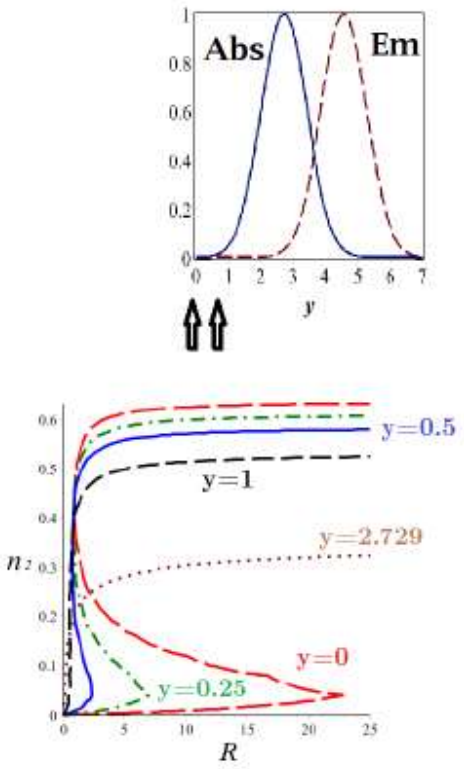



**Figure 1.** Dependence of excited state population on power density of the exciting radiation at different detunings.

**REFERENCES**


1. Fainberg, B. D. and Li G., "Nonlinear organic plasmonics: Applications to optical control of Coulomb blocking in nanojunctions," *Applied Phys. Lett.*, Vol. 107, 053302 and 109902, 2015.
2. Fainberg, B. D. and Li G., "Nonlinear organic plasmonics," *arXiv:* 1510.00205, 2015.

# Biomimetic gyroid photonic crystals

Min Gu[1,2]

[1]Artificial-Intelligence Nanophotonics Laboratory, School of Science,
RMIT University, Melbourne, Victoria 3001, Australia
[2]Centre for Micro-Photonics and CUDOS, Faculty of Science, Engineering and Technology
Swinburne University of Technology, Hawthorn, Victoria 3122, Australia

Biomimetic photonics is inspired by nature's ability to self-assemble complex nanostructured materials with superior properties to that of conventional materials. Here we demonstrate the fabrication of a novel class of 3D gyroid photonic microstructures inspired by a recent finding in butterfly wing-scales and show that these 3D gyroid structures have the ability to redirect circularly polarized light as a chiral beamsplitter. We will present the first experimental evidence that 8 srs single gyroid nets possess the strong optical activity without circular dichroism due to their four-fold rotational symmetry. More intriguingly, we will show these nano-engineered gyroid structures can support the topologic state of light if the parity symmetry is broken.

**Brief CV:**



Professor Gu is a Laureate Fellow of the Australian Research Council as well as is Pro Vice-Chancellor (Research Capacity), Director of the Centre for Micro-Photonics and University Distinguished Professor at Swinburne University of Technology. He is a sole author of two standard reference books and has over 800 publications in nano/biophotonics. He is an elected Fellow of the Australian Academy of Science as well as the Australian Academy of Technological Sciences and Engineering. He is also an elected fellow of the Australian Institute of Physics, the Optical Society of America, the International Society for Optical Engineering, the Institute of Physics (UK), and the International Institute of Electric and Electronic Engineers. He was President of the International Society of Optics within Life Sciences and Vice President of the Bureau of the International Commission for Optics (ICO) (Chair of the ICO Prize Committee, Galileo Galilei Award Committee). He served on the Young Scientist Prize Committee in Optics of the International Union of Pure and Applied Physics. He is a Director of the Board of the Optical Society of America. He was awarded the Einstein Professorship (Chinese Academy of Science, 2010) and the W. H. (Beattie) Steel Medal of the Australian Optical Society (2011). He was a Finalist of The 2013 Australian Innovation Challenge Competition and the recipient of the 2014 Ian Wark Medal and Lecture of the Australian Academy of Science.

# Plasmonic and thermal properties of TiN/Au core-shell nanoparticles

**S. Drakeley*, W. Hendren, R. Bowman and F. Huang**

[1]School of Mathematics and Physics, Queen's University Belfast, Belfast, BT7 1NN, United Kingdom,

*corresponding author: sdrakeley01@qub.ac.uk

**Abstract** We report a systematic experimental investigation on the optical and thermal properties of TiN/Au core shell nanoparticles. Coating Au nanoparticles with TiN creates hybrid core-shell structures, which show strong surface plasmon resonance effects. The plasmonic resonance of such nanoparticles is found to be tunable with TiN thickness. The thermal properties of such hybrid nanoparticles were also systematically investigated and compared to bare Au nanoparticles. The results will be significant for key applications such as heat-assisted magnetic recording.

Key plasmonic applications such as heat assisted magnetic recording (HAMR) [1] requires plasmonic materials able to withstand temperatures up to several hundred degrees Celsius. Noble metals, such as gold and silver, though exhibiting superior plasmonic properties, are unstable at elevated temperatures of a few hundred degrees Celsius. Recently there is increasing interest in the search of alternative plasmonic materials that can work at extreme conditions, such as high pressure, high temperature and long lifespan.

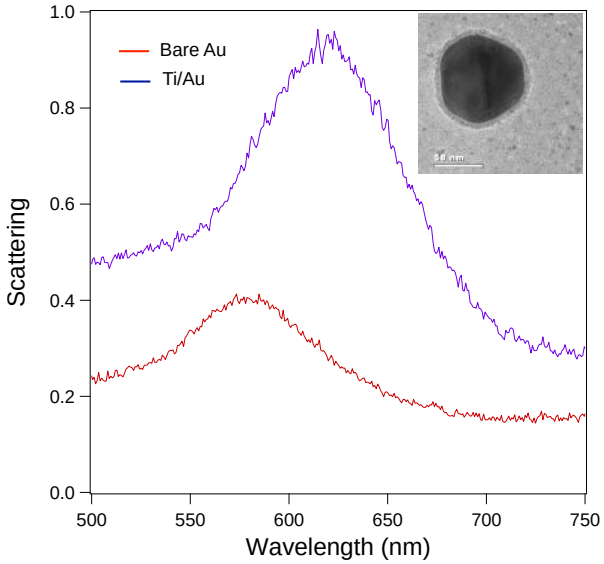



Figure 1 Comparison of the scattering spectra of bare Au nanoparticle (red curve) and TiN-coated Au nanoparticle (purple curve). Inset: TEM image of a TiN-coated Au nanoparticle.

Conducting oxides, metallic nitrides and even 2D materials like graphene have shown to be promising alternative plasmonic materials [2]. In particular, metallic nitrides, such as TiN and ZrN, have been demonstrated to exhibit plasmonic properties similar to those of gold at visible and near-infrared (NIR) frequencies, whereas having much higher melting temperatures and significantly stronger hardness. These outstanding properties make them attractive candidates for HAMR and other plasmonic and metamaterials applications. Here we report a systematic investigation of hybrid plasmonic nanoparticles composed of Au nanoparticles coated with TiN. The idea is to combine the superior plasmonic properties of Au nanoparticles with the robust thermal stability of TiN .

Core-shell nanoparticles were prepared by depositing TiN onto Au nanoparticles by reactive magnetron sputtering from a Ti target (a TEM image of one such nanoparticle is shown in inset, Fig.1). The TiN is shown to be able to significantly shift the plasmonic resonance to longer wavelengths, as indicated by measured dark-field optical scattering spectroscopy (Fig.1). The plasmonic resonance may be tuned across a broad spectral range from visible to NIR through the size and shape of Au nanoparticles, and the thickness of TiN. We also systematically investigate the thermal properties of such hybrid core-shell nanoparticles. The evolution of nanoparticle morphology and their plasmonic properties are investigated at a variety of temperatures. The robustness of such core-shell nanoparticles is compared to that of bare Au nanoparticles. Results from the investigation are relevant to the search for alternative plasmonic materials and structures for HAMR, and other important applications that require operation under harsh conditions, such as high temperature, high pressure and long-durance.

**REFERENCES**


1. Challener, W. A., C. Peng, A. V. Itagi, D. Karns, W. Peng, Y. Peng, X. Yang, X. Zhu, N. J. Gokemeijer, Y. -T. Hsia, G. Ju, R. E. Rottmayer, M. A. Seigler and E. C. Gage, “Heat-assisted magnetic recording by near-field transducer with efficient optical energy transfer,” *Nature Photonics*, Vol. 3, 220-224, 2009.
2. G. V. Naik, V. M. Shalaev, and A. Boltasseva, Adv. Mater. 25, 3264 (2013).

# THz lattice vibrations for active plasmonics with light: Ultrafast optical response in gold/telluride hybrid plasmonic crystals

**L. E. Kreilkamp[1,*], I. A. Akimov[1,2], V. I. Belotelov[3,4], B. A. Glavin[5],L. Litvin[6], A. Rudzinski[6], M. Kahl[6], R. Jede[6], M. Wiater[7], T. Wojtowicz[7], G. Karczewski[7], D. R. Yakovlev[1,2], and M. Bayer[1,2]**

[1]Experimentelle Physik 2, Technische Universität Dortmund, D-44221 Dortmund, Germany
[2]Ioffe Institute, Russian Academy of Sciences, 194021 St. Petersburg, Russia
[3]Lomonosov Moscow State University, 119991 Moscow, Russia
[4]Russian Quantum Center, 143025 Skolkovo, Moscow Region, Russia
[5]Lashkaryov Institute of Semiconductor Physics, 03028 Kyiv, Ukraine
[6]Raith GmbH, Konrad-Adenauer-Allee 8, 44263 Dortmund, Germany
[7]Institute of Physics, Polish Academy of Sciences, PL-02668 Warsaw, Poland
*email: lars.kreilkamp@tu-dortmund.de

**Abstract**— The excitation of coherent optical phonons in solids provides a pathway for ultrafast modulation of light on a sub-ps timescale. Here, we report on efficient 3.6 THz modulation of light reflected from hybrid metal-semiconductor plasmonic crystals caused by lattice vibrations in a few nm thick layer of elemental tellurium. Two effects mediated by plasmonic field enhancement are studied via time-resolved pump-probe spectroscopy: photoinduced formation of Te at the gold-semiconductor interface and enhancement of the optical response.

Ultrafast laser pulses with pulse durations considerably smaller than the period of an ionic vibration can be used to impulsively excite coherent lattice vibrations in solid state crystals [1]. As such a coherent phonon periodically modulates the dielectric function of the material at hand, the phase and amplitude of reflected light pulses can be significantly altered in their presence allowing to follow the time evolution of the lattice motion.

Here, we study the time-resolved pump-probe transients of hybrid plasmonic crystals consisting of an epilayer of the semiconductor CdMgTe and a gold film which is unidirectionally perforated with slits of 100 nm width. A schematic sketch of such a sample can be found in Fig.1(a). In the case of p-polarized light incidence, the reflectivity spectrum presents asymmetrically shaped resonances [see Fig. 1(b)] whose spectral position depends on the incidence angle. These dispersive resonance features are caused by the excitation of surface plasmon polaritons (SPP), collective oscillations of the metal electrons coupling to the electromagnetic field, which can propagate on the two opposite interfaces of the gold film and lead to locally enhanced fields at the interface. A selection of pump-probe transients gathered in the p-polarized excitation configuration are summarized in Fig. 1(c). For long time exposure to laser pulses having a pump fluence of $140\,\mu\mathrm{J/cm^2}$ (e.g. $\tau_{\mathbf{exp}} = 50\,\mathrm{min}$), pronounced oscillations can be observed in the differential reflectivity at room temperature with a characteristic frequency of 3.6 THz. While not compatible to eigenfrequencies of lattice vibrations in CdMgTe itself, the observed oscillation frequency coincides well with the symmetric $A_1$ breathing mode reported for bulk tellurium. A gradual build-up of the oscillation amplitude suggests that the elemental tellurium detected in the experiment is formed under laser illumination. Such an optically induced tellurium segregation has been observed via CW micro-Raman experiments in several other II-VI compounds [2]. An initial frequency shift to higher energies observed in the transients, which can be interpreted as caused by confinement of lattice motion during the formation of interfacial Te, is further supporting this explanation.

When no gold grating is patterned onto the semiconductor, the oscillatory signal is barely visible for the laser fluences used in this experiment and its elevated frequency suggests that only a thin layer of segregated Te forms under the laser spot. The added gold layer thus leads to a considerable increase in the efficiency of the segregation process. The lack of dependence on the ambient temperature of both the signal amplitude and the speed of the segregation process strongly suggest that electronic effects rather than thermal effects are responsible for the Te segregation mechanism in hybrid CdTe/Au structures. Here, both injection of hot electrons from the metal into the interface or hot electrons generated optically within the semiconductor may play an important role.

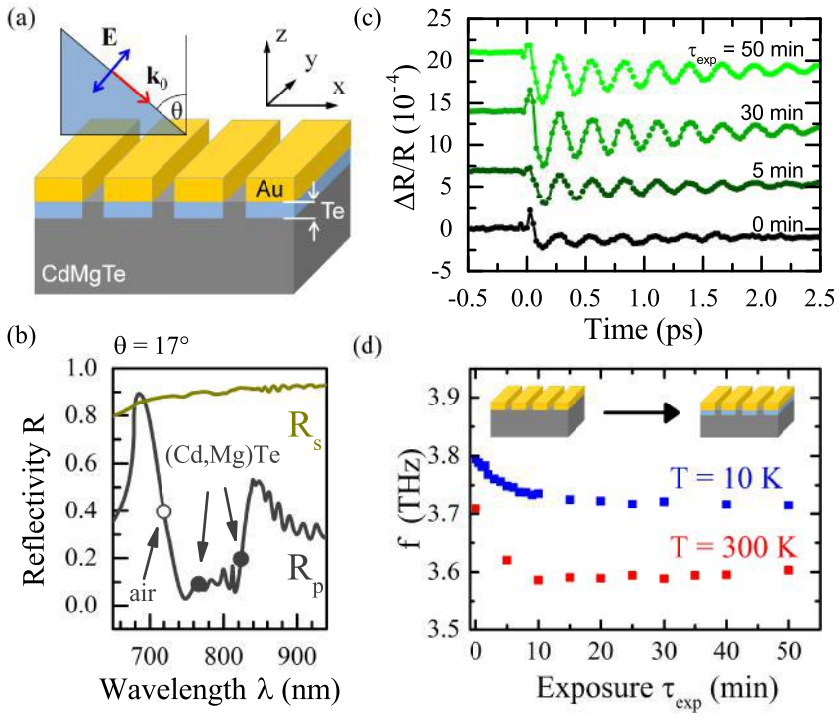



Figure 1: (a) Schematic sketch of the investigated hybrid structure after Te segregation has taken place (b) p- and s-polarized whitelight reflectivity spectra modeled with the Rigorous Coupled Wave Analysis. Resonance energies of the SPP modes were found via the transfer matrix formalism. (c) Time evolution of the pump-probe transients ($T = 300\,\mathrm{K}$) for different exposure times to a pump beam having a fluence of $140\,\mu\mathrm{J/cm^2}$ (d) Oscillation frequencies at two different ambient temperatures extracted from the pump-probe transients.

The plasmonic crystal not only helps to build-up the interfacial Te layer responsible for modulation but also allows a higher sensitivity of the reflected light intensity to lattice vibrations leading to a stronger optical response. Polarization and energy resolved measurements allow us to identify the impact that SPP have on the signal enhancement [3]. Comparison of the experimental results with model calculations using the Rigorous Coupled Wave Analysis technique allow us to attribute the transient reflectivity changes to variations of the plasmon linewidth.

In conclusion, we demonstrate that the presence of propagating surface plasmon polaritons at the interface between a noble metal grating and a II-VI semiconductor enhances the tellurium segregation under sub-bandgap illumination. The formation of elemental tellurium takes place under the metal stripes. Next, a significant enhancement of the excitation and detection of coherent optical phonons observed by pump-probe transients is manifested in the THz modulation of the SPP spectral width (quality factor). The overall sensitivity to lattice vibrations is increased by more than one order of magnitude. This allows measuring the coherent phonon dynamics in a very thin Te layer (1 nm) and resolving the confinement of the $A_1$ symmetry optical phonon mode. The modulation of surface plasmon resonances at THz frequencies with the help of optical phonons holds promise for application in ultrafast active plasmonics. In this respect, the use of optical phonons is appealing because the amplitude of lattice motion can be coherently controlled by a train of optical pulses.

**REFERENCES**

1. T. Dekorsy, G. C. Cho and H. Kurz, "Coherent phonons in condensed media" in *Light Scattering in Solids VIII*, Springer, Berlin Heidelberg, 2000, 169–209.
2. V. G. Wiedemeier, G. Berth, A. Zrenner, E. M. Larramendi, U. Woggon, K. Lischka and D. Schikora, *Semicond. Sci. Technol.* Vol. 26, No. 10, 105023, 2011.
3. L. E. Kreilkamp, I. A. Akimov, V. I. Belotelov, B. A. Glavin, L. Litvin, A. Rudzinski, M. Kahl, R. Jede, M. Wiater, T. Wojtowicz, G. Karczewski, D. R. Yakovlev and M. Bayer, "Terahertz dynamics of lattice vibrations in Au/CdTe plasmonic crystals: Photoinduced segregation of Te and enhancement of optical response," *Phys. Rev. B*, to be published.

# Characterizing Selection Rules of Nonlinear Plasmonics by Maxwell-Hydrodynamic Equations

**Ming Fang[1,2], Xiaoyan Y.Z. Xiong[1], Wei E.I. Sha[1*], Li Jun Jiang[1], and Zhixiang Huang[2]**

[1]Department of Electrical and Electronic Engineering, University of Hong Kong, Pokfulam Road, Hong Kong
[2]Key Laboratory of Intelligent Computing and Signal Processing, Anhui University, Hefei 230039, China
[*]corresponding author: wsha@eee.hku.hk

**Abstract**- When electromagnetic waves strongly interact with metallic nanostructures, it can couple to free electrons near the metal surface resulting in complex linear and nonlinear responses with fundamental and high-order harmonic generation. Interestingly, the complex motion of electrons in metallic nanostructures resembles that of fluids governed by the same hydrodynamic equation. In this work, the nonlinear response from metallic nanostructures governed by the special selection rules is understood by a finite-difference time-domain solution to the Maxwell-hydrodynamic equations.

In this work, the nonlinear response from metallic nanostructures is characterized by a finite-difference time-domain solution to the Maxwell-hydrodynamic equations. When studying second harmonic generation from subwavelength nanostructures, not only the symmetry of the bulk atomic structure of the nonlinear material should be considered but also the symmetry of the nanostructure itself. Regarding centrosymmetric metals, the local-bulk source is absent. Thus, the second harmonic radiation from metallic nanostructures shows a complex surface-induced multipolar interaction, which arises a great challenge to control its radiation pattern and intensity. Understanding symmetry dependent selection rules that govern the second harmonic radiation will offer an important route to nonlinear plasmonic sensing, detection, and signal manipulation. The selection rules for second harmonic radiation from metallic nanostructures include: (i) parity conservation, i.e. second harmonic radiation from an object is strictly zero along the incident direction (z axis), if the projection of the object onto the xoy plane is centrosymmetric. (ii) total angular momentum conservation. (iii) symmetry breaking, i.e. radiation intensity can be enhanced by reducing the symmetric degree of freedom. Here, we show that Maxwell-hydrodynamic equations capture the selection rules well if a proper numerical discretization is implemented. Through exploring the selection rules, a novel nonlinear Yagi-Uda nanoantenna is proposed to direct second harmonic radiation from a centrosymmetric nanoparticle. By tuning the spacing and dimensions of two lossless dielectric elements, which function respectively as a compact director and reflector, the second harmonic radiation is deflected 90 degrees with reference to the incident pump direction. This abnormal light-bending phenomenon is due to the constructive and destructive interference between the second harmonic radiation governed by the selection rule and the induced electric dipolar and magnetic quadrupolar radiation from the two dielectric antenna elements. Simultaneous spectral and spatial isolations of scattered second harmonic waves from incident fundamental waves pave a new way towards nonlinear signal detection and sensing.

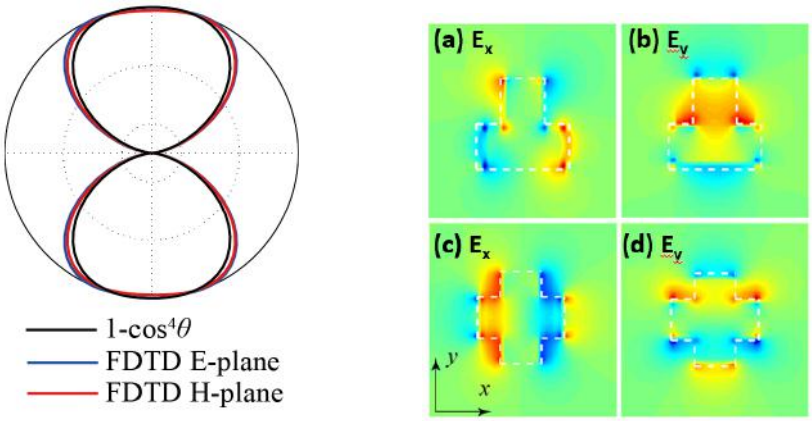
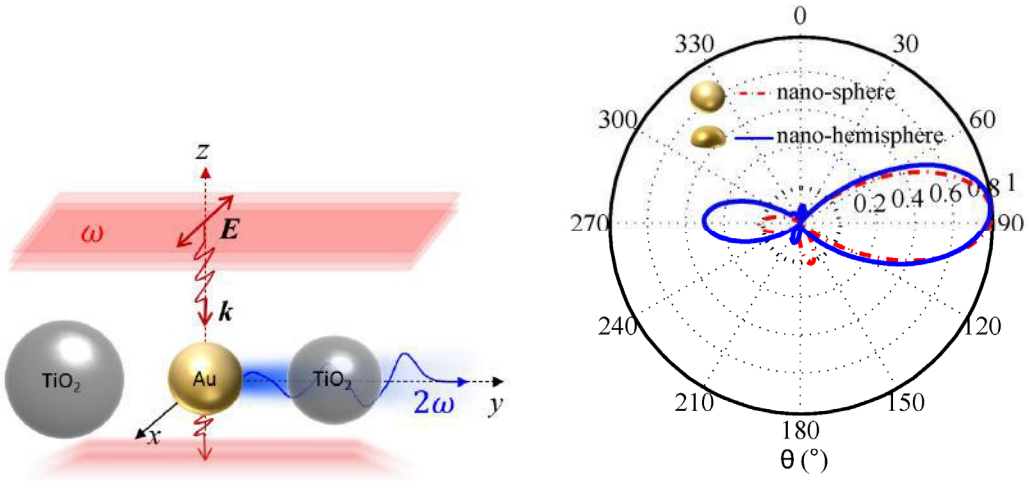



**Fig. 1**. FDTD method for characterizing selection rules of second harmonic radiation. Left diagram shows the radiation pattern of a metallic sphere with a radius of 50 nm. The incident wave is a circularly polarized plane wave. Right diagram shows the near-field distributions at the second harmonic frequency for the axially symmetric T shape and the centrosymmetric cross shape. The incident wave is an *x* polarized plane wave.




**(a)** **(b)**

**Fig. 2**. (a) The schematic pattern of a unidirectional, compact and nonlinear Yagi-Uda nanoantenna. The incident pump (with a red wavefront) is an *x* polarized plane wave propagating along the *–z* direction. A metallic (Au) nanosphere radiating SH waves (denoted by blue color) can be regarded as a dipole-like feed. The left and right dielectric ($TiO_2$) spheres, working respectively as the reflector and the director, realize the unidirectional radiation of SH waves. The SH radiation is bent at 90 degrees with reference to the incident pump direction. (b) Radiation patterns of the nonlinear spherical and hemispherical nanoantennas at the *yoz* plane.

**REFERENCES**

Xiaoyan Y.Z. Xiong, Li Jun Jiang, Wei E.I. Sha, Yat Hei Lo, and Weng Cho Chew, "Compact Nonlinear Yagi-Uda Nanoantennas," *Scientific Reports*, vol. 6, pp. 18872, Jan. 2016.

# Designing efficient hybrid plasmonics based durable nanolenses for ultrafast laser induced nanocavitation.

**M. Meunier, R. Lachaine, C. Boutopoulos and E. Boulais**
Laser Processing and Plasmonics Laboratory, Department of Engineering Physics, Polytechnique Montreal, Montreal, Canada H3C 3A7
*corresponding author: michel.meunier@polymtl.ca

**Abstract**- Irradiating plasmonics nanostructures in liquids with an ultrafast laser may lead to various highly localized phenomena, including nanocavitation. This paper describes an *in-silico* rational design approach based on theoretical modeling that optimizes cavitation without breaking the nanostructure. As an example, we optimize the core radius and the shell layer thickness of Au-$SiO_2$ nanoshell nanostructures (AuNS) to minimize the laser fluence needed for nanocavitation, without altering the nanolens integrity. Our design approach is confirmed by a thorough nanocharacterization of (AuNS) and in situ bubble spectroscopy and imaging.

Plasmonic nanoantennas are capable of absorbing and converting photon energy with sub-wavelength resolution. Irradiating plasmonics nanostructures in liquids with an ultrafast laser may lead to various highly localized phenomena, including heating, plasma production due to optical breakdown, pressure wave and nanocavitation (1,2,3). All these phenomena can be exploited for instance in nanomedecine applications to image, damage or destroy targeted cells and sub-cellular structures with unprecedented precision (4,5,6). While a large library of plasmonics nanostructures exists with a variety of shapes and composition, identifying and tailoring the morphology of nanoparticles to specific applications remain challenging and limit the development of efficient nanoplasmonic technologies. In this paper, we report a strategy for the *in-silico* rational design of hybrid plasmonic nanostructure for the efficient ultrafast laser-based nanoscale bubble generation and cell membrane perforation, which constitute one of the most crucial challenges towards the development of effective gene therapy treatments.

Our computational approach can reliably predicts the morphology-dependent irradiation conditions that lead to cavitation or structural damage. In our model, nanocavitation is triggered by the near-field induced optical breakdown, while nanostructure deformation occurs when the nanostructure reach the gold melting temperature. As an example of hybrid plasmonic nanostructure, we tuned the morphology of Au-$SiO_2$ nanoshell nanostructures (AuNS) to simultaneously optimize for the reduction of the cavitation threshold and preservation of the particle structural integrity when irradiated with a 800 nm, 70 fs laser. Our optimization procedure yields optimal AuNS that are slightly detuned compared to their plasmonic resonance conditions, with an optical breakdown threshold 34 % lower than randomly picked AuNS, and 14 % lower compared to similarly optimized gold nanoparticles (AuNP). This design strategy is validated using time-resolved bubble spectroscopy, shadowgraphy imaging (7,8) and electron microscopy, confirming that the particle structural integrity is preserved and that the cavitation threshold is reduced by 51 % compared to optimal AuNP. Rationally designed AuNS are finally used to perforate cancer cells with an efficiency of 61 %, using 33 % less energy than with AuNP, which demonstrate that our rational design framework is readily transferable to a cell environment. The

methodology developed here thus provides a general strategy for the systematic design of nanoparticles for nanomedical applications and should be broadly applicable to bio-imaging and cell nanosurgery.

**REFERENCES**


1. E. Boulais, R. Lachaine, M. Meunier "Plasma Mediated Off-resonance Plasmonic Enhanced Ultrafast Laser Induced Nanocavitation" Nanoletters, 12, 4763-4769 (2012)
2. E. Boulais, R. Lachaine, A. Hatef, M. Meunier "Plasmonics for Pulsed-laser Cell Nanosurgery: Fundamentals and Applications" Journal of Photochemistry and Photobiology C: Photochemistry Reviews, 17, 26-49 (2013)
3. R. Lachaine, E. Boulais, M. Meunier "From Thermo- to Plasma-Mediated Ultrafast Laser Induced Plasmonic Nanobubbles" ACS Photonics 1, 331-336 (2014)
4. J. Baumgart, L. Humbert, E. Boulais, R. Lachaine, J.-J. Lebrun, M. Meunier, "Off-resonance Plasmonic Enhanced Femtosecond Laser Optoporation and Transfection of Cancer Cells" Biomaterials, 33, 2345-2350 (2012).
5. W. Ding, E. Bergeron, R. Lachaine, M. Meunier "Nanomaterial-Assisted Light-induced Poration and Transfection of Mammalian Cells" Applications of Nanoscience in Photomedicine, 331, (2015)
6. E. Bergeron, C. Boutopoulos, R. Martel, A. Torres, C. Rodriguez, J. Niskanen, J.-J. Lebrun, F. M. Winnik, P. Sapieha, M. Meunier "Cell-specific optoporation with near-infrared ultrafast laser and functionalized gold nanoparticles" Nanoscale, 7, 17836-17847 (2015)
7. C. Boutopoulos, E. Bergeron, M. Meunier "Cell perforation mediated by plasmonic bubbles generated by a single near infrared femtosecond laser pulse" Journal of biophotonics, 1-6 (2015)
8. C. Boutopoulos, A. Hatef, M. Fortin-Deschênes, M. Meunier "Dynamic Imaging of a Single Gold Nanoparticle in Liquid Irradiated by Off-resonance Femtosecond Laser" Nanoscale 7 (27), 11758-11765 (2015)

# Plasmonic electric field enhancement on a graphene surface

**Lin Chen**[1,*]**, and Xun Li**[2]

[1]Wuhan National Laboratory for Optoelectronics, Huazhong University of Science and Technology, Wuhan 430074, China

[2]Department of Electrical and Computer Engineering, McMaster University, 1280 Main Street West, Hamilton, Ontario, L8S 4L8, Canada

[*]corresponding author: chen.lin@mail.hust.edu.cn

**Abstract**-Surface plasmon polaritons (SPPs) provides the capability of guiding light signal within ultra-small volume. Here we will present our recent work on guiding, slowing down, and exciting plasmonic mode on a graphene surface based on various nanostructures. Our results show that plasmonic wave localization in graphene is also followed by a strong optical field enhancement due to the significant reduction of the group velocity of the graphene plasmonic mode.

Firstly, we have proposed and investigated a graphene-based hybrid plasmonic waveguide at terahertz frequency, which is analogous to the concept of hybrid plasmonic waveguide based on a metal surface [1]. By utilizing the strong coupling between the dielectric waveguide and plasmonic modes, the proposed hybrid plasmonic terahertz waveguides [see Fig. 1] that not only significantly suppress the mode field confinement, but also maintain a compact size.

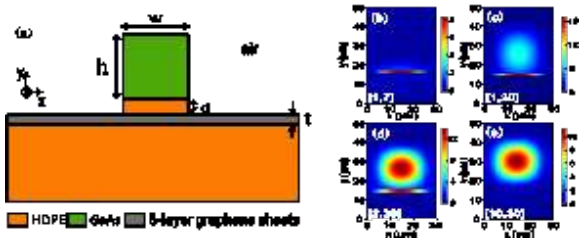



Fig. 1. (a) Cross section of a hybrid plasmonic terahertz waveguide. The excitation wavelength is 100 um (3 THz). (b-e) Electromagnetic energy density distributions for (b) [ $d$ , $h$ ]=[0.5, 7] um, (c) [ $d$ , $h$ ]=[0.5, 30] um, (d) [ $d$ , $h$ ]=[5, 21] um, and (e) [ $d$ , $h$ ]=[10, 30] um.

We then investigate how to slow down the group velocity of the plasmonic mode on a graphene surface. We found the dispersion curve of graphene plasmon mode can be tuned by using a slope substrate beneath the graphene surface or a dielectric grating substrate [Fig. 2]. Both of the theoretical and numerical simulation results demonstrate that the group velocity of graphene plasmon mode can be significantly reduced. Furthermore, such a slow light system is capable of operating with a broad spectral band by flexibly tuning the chemical potential of graphene via gate voltage. More interestingly, we also predict the capability of completely releasing the trapped SPPs by dynamically tuning the chemical potential of graphene by means of gate voltage. In addition, giant local field enhancement can be formed on the graphene surface since light energy is accumulated due to the reduction of propagation velocity of graphene plasmonic mode.

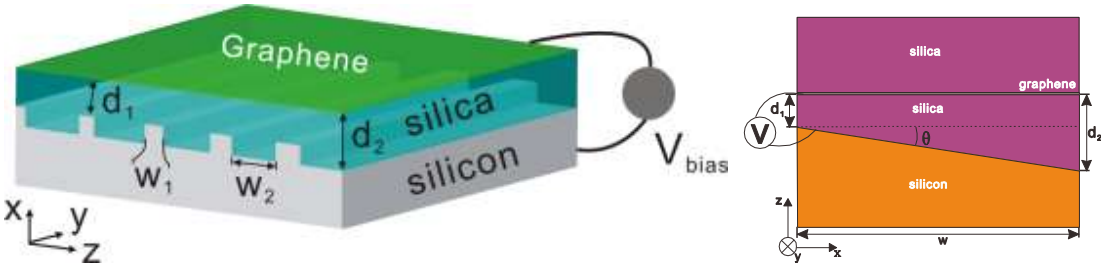



Fig. 2. Schematic of a graphene sheet on a dielectric grating substrate (left) and a sloping-silicon substrate (right).

The remaining issue after guiding and slowing down of plasmon mode on a graphene surface is how to efficiently couple radiation waves into graphene plasmonic mode [2]. We propose to excite the plasmonic mode by illuminating a normal-incidence plane wave on the dielectric gratings due to guided-mode resonance. The gratings of varying period enable the excitation of the plasmonic mode with a very high field enhancement factor (to the order of magnitude of 1000) within a wide spectral band, which leads to the frequency dependent spatially separated localization of the infrared spectrum modes [Fig. 3]. We also demonstrate that the excitation position of the plasmonic mode can be freely tuned by varying the thickness of the interlayer as well as the chemical potential of the graphene monolayer.

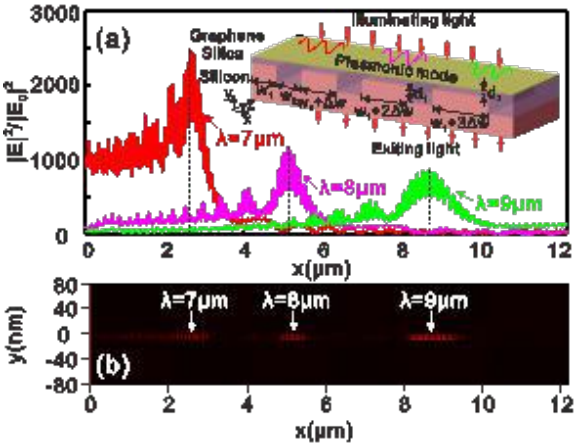



Fig. 3. Electric field enhancement on the graphene surface of the structure with μc=0.65 eV, d2=5 nm for three different incident wavelengths

**Acknowledgements** This work was supported by National Natural Science Foundation of China (Grant Nos. 11104093 and 11474116), and Fundamental Research Funds for the Central Universities, China (No. 2015TS074)

**REFERENCES**

1. R. F. Oulton, V. J. Sorger, D. A. Genov, D. F. P. Pile, and X. Zhang, "A hybrid plasmonic waveguide for subwavelength confinement and long-range propagation," *Nature photon.*, Vol. 2, No. 8, 496–500, 2008.
2. Gao, W.; Shu, J.; Qiu, C.; Xu, Q., Excitation of plasmonic waves in graphene by guided-mode resonances. ACS nano 2012, 6 (9), 7806-7813.

# Designing broadband silicon devices using subwavelength structures

**R. Halir,[1] J. M. Luque-González,[1] S. Wang,[2] A. Sánchez-Postigo,[1]**
**J. G. Wangüemert-Pérez,[1] P. Cheben,[2] J. Schmid,[2] D.-X. Xu,[2]**
**S. Janz,[2] J. Lapointe,[2] I. Molina-Fernández,[1] and A. Ortega-Moñux[1]**

[1)]Universidad de Málaga, ETSI Telecomunicación, Spain
[2)]National Research Council, Ottawa, Canada
E-mail: robert.halir@ic.uma.es

**Abstract**- Photonic structures with a sub-wavelength pitch, small enough to suppress diffraction, can behave as equivalent homogenous materials that can be engineered to exhibit a specific refractive index and dispersion. Here we discuss the design of directional couplers and multi-mode interference couplers with an unprecedented bandwidth in both the near-infrared and mid-infrared bands using such sub-wavelength structures. First experimental results indicate virtually perfect device performance in a bandwidth beyond 200nm at telecom wavelengths.

When integrated photonic waveguides are patterned at the sub-wavelength scale, their optical properties can change significantly, enabling the concepts of refractive index and dispersion engineering [1-3]. These sub-wavelength gratings (SWG) have given rise to myriad applications, including efficient fiber-to-chip couplers [4], enhanced waveguide sensing [5] and suspended waveguides for mid-infrared applications [6].

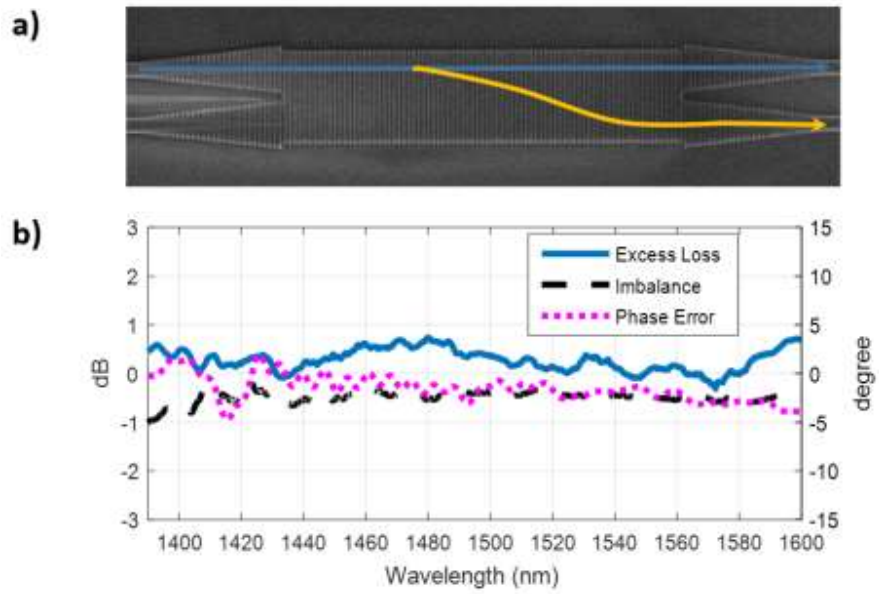



**Figure 1:** a) Subwavelength engineered, ultra-broadband multimode interference coupler. b) Measured performance of the device indicating virtually perfect performance in a bandwidth of more than 200nm.

SWG structures have also been proposed to extend the operational bandwidth of directional couplers and multimode interference couplers, both in the near-infrared and the mid-infrared wavelength bands [7-9]. Such couplers divide the lightwave in the input waveguide with a 50/50 ratio between the output waveguide waveguides, additionally introducing a 90º phase shift [see illustration in Fig. 1a)]. In these devices the sub-wavelength structure is used to simultaneously control the equivalent refractive index and the dispersion characteristics of the waveguide. Full 3D finite-difference-time-domain (FDTD) simulations have shown that multimode interference couplers based on these structures can potentially achieve bandwidths exceeding 400nm, thereby covering all major telecommunication bands simultaneously with a single, passive device. Fig. 1a) shows a scanning electron microscope of a SWG engineered multimode interference couplers. The input and output waveguides are gradually tapered from conventional strip waveguides to wider, sub-wavelength segmented waveguides, ensuring index matching with the central multimode region. The pitch and duty-cycle of the central region is designed to provide a virtually wavelength independent interference of the propagating higher order modes. Fig. 1b) shows first measurements of the device. The splitting ratio (imbalance between the two outputs) is virtually flat and close to the ideal value of 0dB (indicating 50/50 splitting) over a bandwidth in excess of 200nm. Furthermore, the phase between the outputs deviates from the ideal 90º by less than 5º over that same bandwidth, while excess losses are kept below 1dB.

We believe that the outstanding performance afforded by such ultra-broadband devices will give rise to a wide range of novel applications in communications in the near-infrared and in sensing in the mid-infrared.

**ACKNOWLEDGMENTS**

Ministerio de Economía y Competitividad, "Programa Estatal de Investigación, Desarrollo e Innovación Orientada a los Retos de la Sociedad (cofinanciado FEDER)", Proyecto TEC2013-46917-C2-1-R.

**REFERENCES**

1. P. Cheben et al., *Optics Letters,* Vol. 35, 2526-2528 (2010).
2. J. H. Schmid et al., *IEEE Photon. J.,* Vol. 3, 597-607 (2011).
3. R. Halir et al., *Laser and Photonics Reviews,* Vol. 9, 25-49 (2015).
4. D. Benedikovic et al., *Optics Express,* Vol. 23, 22628-22635 (2015).
5. G. Wangüemert-Pérez et al., *Optics Letters,* Vol. 39, 4442-4445 (2014).
6. J. S. Penades et al., IEEE Group IV Photonics Conference (2015).
7. R. Halir et al., *Optics Express*, Vol. 20, 13470-13477 (2012)
8. A. Maese-Novo, et al., *Optics Express*, Vol. 21, 7033-7040 (2013).
9. A. Sánchez-Postigo et al., *SPIE Optics Optoelectronics Conference* (2015)

# Transfer printing approach to fabricate adaptable, self-standing and high efficiency polymer solar cells

**S. Colodrero[1*], P. Romero-Gomez[1], P. Mantilla-Perez[1], J. Martorell[1,2]**
[1]ICFO-Institut de Ciencies Fotoniques, Mediterranean Technology Park, Castelldefels, Spain
[2]Departament de Física, Universitat Politecnica de Catalunya, Terrassa, Spain
[*]corresponding author: silvia.colodrero@icfo.es

**Abstract**-A significant step towards a low cost printable electronics with the potential to be incorporated in wearable flexible devices may be achieved once such devices can be fabricated on any kind of material surface. Herein, we present a new method based on a transfer printing approach to successfully detach from their original substrate efficient polymer solar cells (PSCs). The ulterior incorporation of plasmonic nano-structures to the cell architecture will be discussed, too.

For several years it has been noted that the incorporation of plasmonic nano-particles in the active layer of organic solar cells, composed of a donor and acceptor bulk hetero-junction blend, may significantly enhance the light harvesting capacity of such devices [1,2]. However, an optimal nano-morphology during the cell fabrication must be ensured for such blend to reach high efficiency cells. So, any nanometric disturbance in the fabrication procedure or inappropriate substrate surface roughness values can lead to dramatic losses in the final performance [3].

In this article, we propose a new route to fabricate high efficiency PSCs that can be transferred to any kind of surface regardless its roughness, composition, stability, etc (cf. Figure 1a). This may largely facilitate an ulterior incorporation of plasmonic nanoparticles or other kinds of plasmonic nano-structuration. Fabricating photovoltaic devices on top of high quality smooth surfaces and subsequently transferring them onto the desired final surface has been applied successfully for cells based on inorganic materials [4,5]. However, the delicate nature of the organic materials makes the approaches used for thin film inorganic cells impracticable for polymer ones.

We implemented an alternative route applicable to organics which makes use of a transfer printing technique incorporating a nanoparticle sacrificial layer (cf. Figure 1b) in between the flat glass substrate and the semi-transparent electrode of the cell. The role of the nanoparticles is to reduce the adhesion properties of the complete set of cell layers to the glass substrate, so that it can be mechanically detached. An optimization of the underneath layers by introducing a large to small nanoparticle size gradient helps to have a minimal impact on the blend morphology. By doing so, transferred and free standing PSCs, with efficiencies as high as 8.17% and 7.12% respectively, were obtained when using PTB7:PC71BM blend based active layers. Comparatively, the performance of an ITO reference cell of the same characteristics but deposited on a flat substrate was 7.67%.

In summary the methodology presented may facilitate the incorporation of a large variety of metal

nanoparticles or plasmonic nano-structures within the device architecture to obtain an enhanced light absorption while avoiding the deleterious impact on the blend morphology. In addition, transferring such solar cells to a large variety of flexible substrates to, for instance, incorporate them as power sources for any kind of portable or wearable devices will be feasible, too.

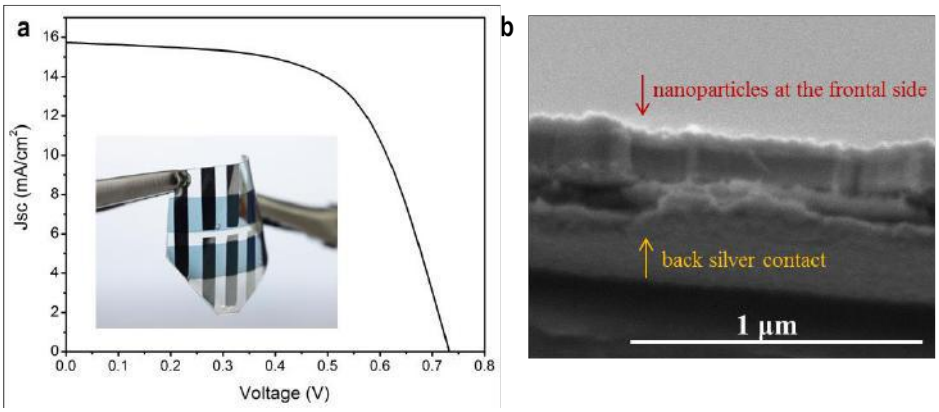



**Figure 1.** a) J-V characteristic curve for the free standing PSC developed in this paper. Inset picture shows the appearance of the cell. b) SEM cross section image of the cell architecture.

**Acknowledgements** We acknowledge financial support from MINECO and the "Fondo Europeo de Desarrollo Regional" (FEDER) through grant MAT2014-52985-R and from the EC under the project Solprocel with grant number no. 604506.

**REFERENCES**

1. Gan, Q. Q.; Bartoli, F. J.; Kafafi, Z. H., "Plasmonic-Enhanced Organic Photovoltaics: Breaking the 10% Efficiency Barrier", *Adv. Mater.*, 25, 17, 2385-2396, 2013.
2. Pastorelli, F et al., "Self-Assembled Plasmonic Oligomers for Organic Photovoltaics", *Adv. Optical Mater.* 2, 171-175, 2014.
3. Tumbleston, J. R. et al., "Modifications in Morphology Resulting from Nanoimprinting Bulk Heterojunction Blends for Light Trapping Organic Solar Cell Designs", *ACS Appl. Mater. Interfaces*, 5, 16, 8225-8230, 2013.
4. Lee C. H. et al., "Peel-and-Stick: Fabricating Thin Film Solar Cell on Universal Substrates", *Scientific Reports*, 2, 1000, 2012.
5. Lee C. H.; Kim, D. R.; Zheng, X. L., "Transfer Printing Methods for Flexible Thin Film Solar Cells: Basic Concepts and Working Principles", *ACS Nano*, 8, 9, 8746-8756, 2014.

# Annealing Studies of Gold Plasmonic Nanostructured Arrays

**M. Nicholson[1], R. J. Pollard[1*], R. M. Bowman[1] and A. Murphy[1]**
[1]School of Mathematics and Physics, Queen's University Belfast, United Kingdom
[*]corresponding author: R.Pollard@qub.ac.uk

**Abstract**-We investigate the plasmonic and physical properties of gold plasmonic nanostructured arrays when annealed at various temperatures. The annealing of the gold nanorods yielded destruction of the array, however this was avoided when embedded in an alumina template or encased with a nickel shell. The plasmonic resonance of the gold was also enhanced in the alumina template.

The applications in the field of plasmonics have significantly grown due to the increasing availability of fabrication and characterization of nanostructured materials. One such application is a near-field transducer (NFT) for use in heat-assisted magnetic recording (HAMR), a promising alternative technology to improve the areal densities of hard disk drives to beyond 1 Tb/in$^2$. Gold has been determined as suitable for the NFT as a plasmonic material at wavelengths longer than 700nm, and is also chemically inert and has a relatively high melting point[1]. However, one significant issue with gold is its low thermal stability. It has a low Tammann temperature, and so gold nanostructures tend to sinter when heated[2]. This is problematic in the field of plasmonics, as the plasmonic resonance of a material is dependent on the size and shape of the nanostructure. Therefore, it is imperative to maintain their intended structure.

The work conducted focused on fabricating arrays of gold nanorods, and observing their plasmonic and mechanical behaviour. Samples were fabricated by employing a novel fabrication process of gold nanorods that is cheap and rapid to produce[3]. The gold nanorods arrays were electrodeposited in an anodised aluminium oxide (AAO) porous template on a glass substrate. The samples were then annealed in a vacuum oven at various temperatures, mainly 300$^O$C and 600$^O$C, and then characterized via far-field optical metrology and near-field metrology.

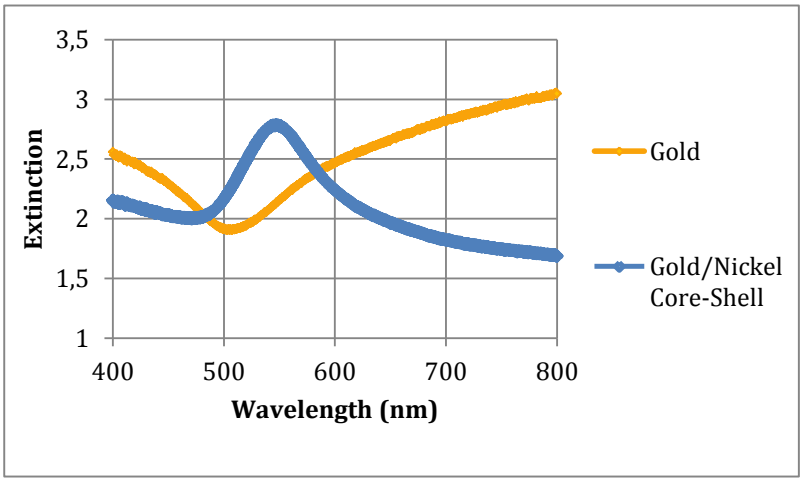



Figure 1: Optical Extinction Behaviour of gold nanorods and gold/nickel core-shells annealed at 300$^O$C

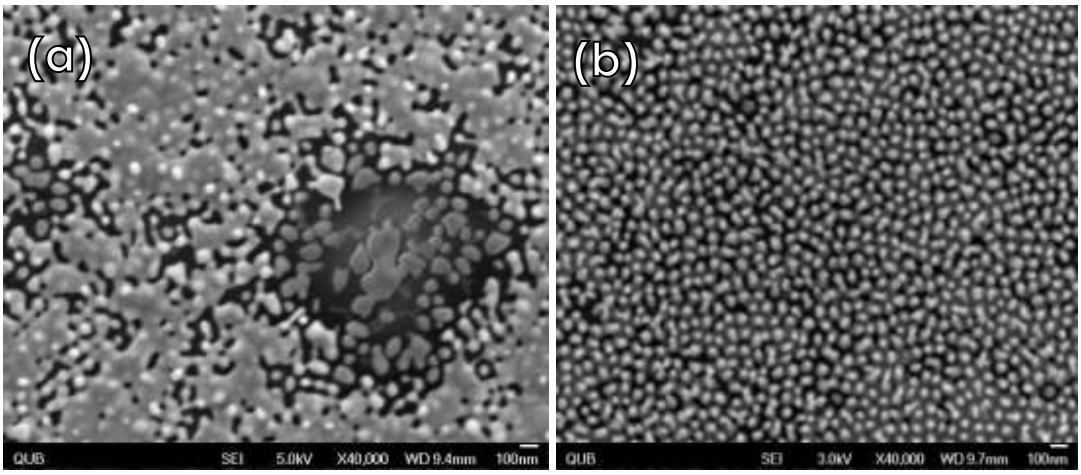



Figure 2: SEM Images of (a) gold nanorods (b) gold/nickel core-shells annealed at $300^{O}C$

Various parameters of the gold arrays were tested in the annealing experiments, with the two largest factors contributing towards a change of morphology being the annealing temperature and whether or not the gold rods were embedded or encased with another material. Destruction of the nanostructures was visibly seen after annealing of $300^{O}C$ for 6 hours (figure 1 and 2a), forming a film-like structure. The introduction of the alumina template or nickel shell (figure 2b) restricted the gold's mobility during annealing, maintaining the original rod structure, although at the expense of dampening the rod's plasmonic resonance (figure 1).

While gold is a strong candidate for the choice of material of the NFT in HAMR technologies, especially due to its plasmonic properties, its thermal mobility proves a hindrance. While nickel provided an adequate shell in maintaining the structure's morphology, its poor plasmonic respnsivity makes it a poor candidate for use in an NFT, and further investigation into more suitable plasmonic materials would be required.

**Acknowledgements** The authors would like to thank Seagate Technology for their financial support

## REFERENCES

1. Rottmayer, R. E., Batra, and S., Buechel, D., "Heat-Assisted Magnetic Recording", *Nature Photon.*, Vol. 3, 220-224, 2009.
2. Veith, G. M., Lupini, A. R., and Rashkeev, S., "Thermal Stability and catalytic activity of gold nanoparticles supported on silica", *J. Catal*, Vol. 262, 92-101, 2009
3. Evans, P., Hendren, W. R., and Atkinson, R., "Growth and properties of gold and nickel nanorods in thin film alumina", *Nanotechnology*, Vol. 17, 5746-5753, 2006

# Active modulation of visible light with graphene-loaded ultrathin metal plasmonic antennas

**Renwen. Yu[1*], Valerio Pruneri[1,2], and F. Javier García de Abajo[1,2]**

[1] ICFO-Institut de Ciències Fotòniques, The Barcelona Institute of Science and Technology, 08860 Castelldefels (Barcelona), Spain

[2] ICREA-Institució Catalana de Recerca i Estudis Avançats, Passeig Lluís Companys 23, 08010 Barcelona, Spain

[*]corresponding author: renwen.yu@icfo.es

**Abstract**- Electro-optical modulation of visible and near-infrared light is important for a wide variety of applications, ranging from communications to sensing and smart windows. However, currently available approaches result in rather bulky devices, suffer from low integrability, and can hardly operate at the low power consumption and fast switching rates of microelectronic drivers. Here we show that planar nanostructures patterned in ultrathin metal-graphene hybrid films sustain highly tunable plasmons in the visible and near-infrared spectral regions.

We have shown that planar nanostructures patterned in ultrathin metal-graphene hybrid films sustain highly tunable plasmons in the visible and near-infrared spectral regions. Strong variations in the reflection and absorption of incident light take place when the plasmons are tuned on- and off-resonance with respect to externally incident light. As a result, a remarkable modulation depth exceeding 90% in transmission and even more dramatic in reflection (>600%) is predicted for graphene-loaded silver film of 1-5 nm thickness and currently attainable lateral dimensions. These new structures hold great potential for fast low-power electro-optical modulation.

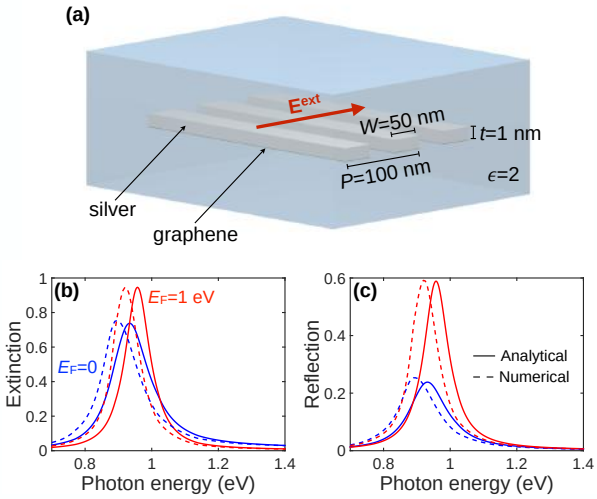



**Figure 1:** Optical switch based upon a periodic array of ultrathin silver/graphene ribbons. (a) Scheme of the

structure under consideration. (b,c) Extinction and reflection spectra for either doped (red curves) or undoped (blue curves) graphene. Full numerical simulations (dashed curves) are in good agreement with analytical theory (solid curves).

**REFERENCES**


1. R. Yu, *et al*., "Resonant visible light modulation with graphene," *ACS Photonics*, Vol. 2, 550, 2015.
2. F. J. García de Abajo, "Graphene plasmonics: challenges and opportunities," *ACS Photonics*, Vol. 1, 135, 2014.

# Highly-responsive subwavelength plasmonic photodetector for silicon nanophotonics

**I. A. Khramtcov*, and D. Yu. Fedyanin**
Laboratory of Nanooptics and Plasmonics, Moscow Institute of Physics and Technology,
Russian Federation
*corresponding author: khramtsov@phystech.edu

**Abstract**-We demonstrate a deep-subwavelength integrated copper/germanium/copper plasmonic photodetector, which can be directly integrated in silicon-photonic nanocircuitry operating at telecom wavelengths. In spite of the low Schottky barrier height, we show for the first time how to use this drawback to increase the responsivity of the nanoscale photodetector. The resulting output voltage exceeds 100 meV and the photocurrent-to-dark-current ratio is of about 1000 for typical values of the optical signal power in on-chip optical interconnects.

Silicon photonics emerged in the early 2000s as a solution to replace electrical interconnects in integrated circuits with optical links. To realize optical communication on an electronic chip, optoelectronic components are needed to transform digital electrical signals into optical pulses, transmit and convert them back into the initial bit sequences. An integrated photodetector is a key element for optical interconnects along with an integrated light source and a modulator. Energy consumption of the photodetector and receiver (which is required to amplify the electrical signal from the photodetector) plays a crucial role in on-chip optical communication, while its sensitivity determines the limiting parameters for other optoelectronic components (integrated lasers and modulators). Miniaturization is one of the essential approaches to improve the photodetector performance. As the size decreases, the capacitance also decreases and therefore the output voltage increases. Consequently, one can avoid using amplifiers, which consume a lot of energy [1], in the receiver. In addition, miniaturization increases the integration density and operating speed of the device. However, conventional photodetector designs [2] are not suitable for scaling down to the size smaller than the light wavelength.

One can go beyond the diffraction limit of light using plasmonic nanostructures based on the metal/semiconductor/metal (MSM) configuration (Figure 1). However, in that case, a significant part of the plasmonic mode is absorbed in the metal, which results in a low responsivity of the photodetector. For this reason, we have to use only so-called plasmonic metals. Unfortunately, they form Schottky contact to germanium with very low Schottky barrier heights and the dark current is typically very high [3] for practical applications.

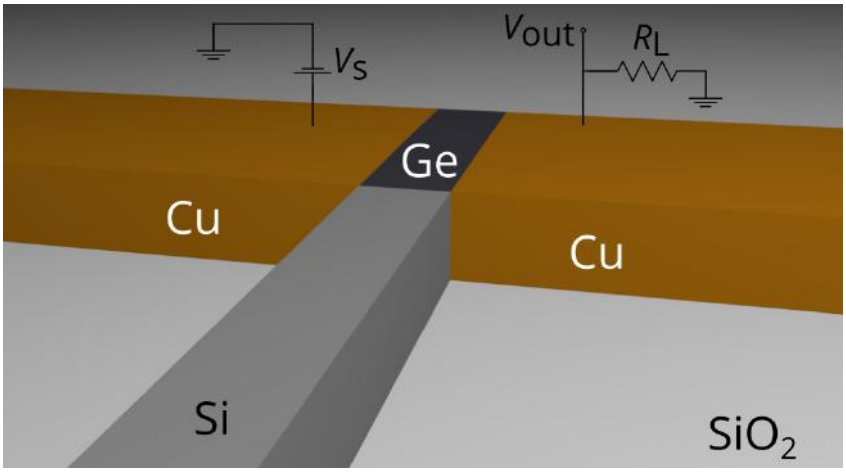



**Figure 1.** Illustration of the Cu/Ge/Cu MSM photodetector coupled to a silicon nanophotonic waveguide. The electronic circuit is also shown schematically, $V_s$ is the supply voltage, $V_{out}$ is the output voltage and $R_L$ is the load resistance.

In this work we show that the operation of the plasmonic MSM photodetector can be significantly improved by reducing its size down to several hundred nanometers. Using this size effect, we can use the dark current to enhance the signal current in spite of the low Schottky barrier height at the metal/semiconductor interface. The output voltages can be as high as 100 meV and the photocurrent-to-dark-current ratio approaches 1000 at an average optical power of 10 μW for the pseudo-random bit sequence. These values are high enough to remove amplifiers from the receiver and drastically reduce the photodetector power consumption. At the same time, the device footprint is very small and the operation speed allows to operate in all silicon-photonic integrated circuits.

## REFERENCES

1. Assefa, S. et al., "CMOS-integrated Optical Receivers for On-Chip Interconnects," *IEEE J. Sel. Top. Quantum Electron.*, Vol. 16, No. 5, 1376–1385, 2010.
2. Chen, L., and Lipson, M., "Ultra-low capacitance and high speed germanium photodetectors on silicon," *Opt. Express*, Vol. 17, No. 10, 7901–7906, 2009.
3. Balram, K. C., Audet, R. M., and Miller, D. A. B., "Nanoscale resonant-cavity-enhanced germanium photodetectors with lithographically defined spectral response for improved performance at telecommunications wavelengths," *Opt.Express*, Vol. 21, No. 8, 10228–10233, 2013.

# Plasmonic materials for hot carrier devices

**Jeremy N. Munday**[1,2*]

[1] Department of Electrical and Computer Engineering, University of Maryland, College Park, MD, 20742, USA

[2] Institute for Research in Electronics and Applied Physics, University of Maryland, College Park, MD, 20742, USA

[*]corresponding author: jnmunday@umd.edu

**Abstract**- When high-energy photons are absorbed within a metal, they generate a distribution of carriers at a significantly higher effective temperature than the surrounding lattice, so-called 'hot carriers.' Before cooling, these carriers can traverse distances of tens of nanometers, enabling nanoscale plasmonic devices that take advantage of this phenomenon. Here, I discuss our recent work using non-traditional metals for hot carrier generation and the fabrication of detectors and energy converters that exploit this phenomenon.

The field of plasmonics has thrived over the past decade, leading to the development of many optical devices and the discovery of novel phenomenon based on light-matter interactions. One hindrance to the further development of plasmonic devices is optical loss. Several techniques have been suggested to circumvent this issue by finding low-loss materials over an appropriate spectral range or through the addition of a gain material. Alternatively, one could embrace this loss and try to exploit it.

In this talk, I will discuss our efforts to recover the energy that is usually lost to thermalization, by collecting hot carriers before they cool. I will discuss a variety of devices including both planar [1] and nanostructured systems that cover a wide-spectral range. In addition, I will discuss how alternatives to traditional noble metals can be used and advantages that can be obtained by engineering the electron density of states of materials [2]. Finally, I will discuss our recent work in IR detection based on sub-bandgap photon absorption, and the possibility of a hybrid device that could enable high efficiency solar energy conversion [3].

**Acknowledgements**: this work is partially funded by an NSF CAREER Award #1554503.

**REFERENCES**

1. Tao Gong and Jeremy N. Munday, "Angle-Independent Hot Carrier Generation and Collection Using Transparent Conducting Oxides," *Nano Lett.*, Vol. 15, 147–152, 2015.
2. Tao Gong and Jeremy N. Munday, "Materials for hot carrier plasmonics [Invited]," *Opt. Mat. Express.*, Vol. 5, 2501-2512, 2015.
3. Tao Gong, Lisa Krayer, and Jeremy N. Munday, in review.

# Enhanced optical nonlinearities in periodic photonic nanostructures containing patterned graphene and other 2D materials

**Nicolae C. Panoiu*** **and Martin Weismann**
Department of Electronic and Electrical Engineering, University College London, Torrington Place, London WC1E 7JE, UK
*corresponding author: n.panoiu@ucl.ac.uk

**Abstract**-We present a rigorous numerical method to analyze optical higher harmonic generation in one- and two-dimensional (1D, 2D) periodically patterned structures containing different 2D materials, such as graphene, $MoS_2$, and $WSe_2$, and investigate resonantly enhanced nonlinear interactions in such devices.

We have developed a new approach [1,2] based on the rigorous coupled-wave analysis (RCWA) method to describe the interaction of light with periodic structures containing 2D-3D heteromaterials. Our method employs a set of modified boundary conditions [2] for conductive interfaces: tangent components of the magnetic field at interfaces are discontinuous. Their variation across the 2D material at is given by a surface current, $\boldsymbol{j}_t = \sigma_s \boldsymbol{E}_t + \boldsymbol{j}_t^{\mathrm{NL}}(\boldsymbol{E}^s)$, where $\boldsymbol{E}_t^s$ denotes the tangential component of the electric field at the interface, $\sigma_s$ is the conductivity of the 2D material, and $\boldsymbol{j}_t^{\mathrm{NL}}(\boldsymbol{E}^s)$ is the surface current associated to the nonlinear optical process in the 2D material. A key feature of this approach is that it only depends on the sheet conductance of a 2D material, and not on the effective thickness of the 2D material under consideration. This modified boundary condition is incorporated in our improved RCWA formalism, in which the electromagnetic fields are described by their modal coefficients, which are determined using a novel, inhomogeneous *S*-matrix approach accounting for the modified, inhomogeneous boundary condition and its optical nonlinearity. The specific form of the nonlinear surface current is determined by the symmetry properties of a material: graphene, as member of the symmetry group $\mathcal{O}_{6h}$, is centrosymmetric, hence even-order nonlinear processes like second-harmonic generation (SHG) are forbidden. However, it allows strong third harmonic generation. This enters the algorithm as $\boldsymbol{j}_t^{\mathrm{NL}}(\boldsymbol{E}^S) = \hat{\sigma}^{(3)} \vdots \boldsymbol{E}^S \boldsymbol{E}^S \boldsymbol{E}^S$, where $\hat{\sigma}^{(3)}$ is the nonlinear surface conductivity tensor of graphene.

We use this method to analyze the linear and nonlinear optics of periodically patterned 2D materials, and find distinct differences between graphene and other 2D materials, in particular the transition metal dichalcogenides (TMDC)-monolayers ($MoS_2$, $WSe_2$). Whereas graphene supports surface plasmons due to its metallic nature, the dielectric TMDCs do not support plasmon- or intrinsic geometric resonances. We also design a resonant waveguide and combine it with 2D materials to obtain enhanced absorption and increased optical harmonic generation, and investigate tuneable Fano resonances observed in this photonic device.

**Acknowledgements**, This work was supported by European Research Council / ERC Grant Agreement no. ERC-2014-CoG-648328.

**REFERENCES**

1. M. Weismann, D. F. G. Gallagher, and N. C. Panoiu, *J. Opt.* **17**, 125612 (2015).
2. M. Weismann and N. C. Panoiu, *Phys. Rev. B* (in preparation).

# Quantum efficiency gains by metal nanostructures in organic and quantum dot solar cells

**Jung-Yong Lee**[1*] **and Doh Chang Lee**[2]

[1] Graduate School of Energy, Environment, Water, and Sustainability (EEWS), Graphene Research Center, Korea Advanced Institute of Science and Technology (KAIST), Daejeon 34141, Republic of Korea

[2] Department of Chemical and Biomolecular Engineering, Korea Advanced Institute of Science and Technology (KAIST), Daejeon 34141, Republic of Korea

[*]corresponding author: jungyong.lee@kaist.ac.kr

**Abstract**-We discuss the effect of metal nanoparticles on the quantum efficiency of organic and quantum dot solar cells. Both optical and electrical gains can be obtained when the metal nanoparticles are incorporated into the solar cells appropriately. Optical gains can be maximized when the scattering power of the metal nanoparticles dominates the absorption power. The nano-funneling effect of the metal nanoparticles improves the electrical performance of the solar cells.

First, we investigate the dependence of metal nanoparticles' size on the power conversion efficiency of organic solar cells (OSCs) [1]. Also, as an advanced plasmonic material for highly efficient OSCs, we propose a metal-metal core-shell nanocube (NC), which shows stronger scattering efficiency than pristine Au nanoparticles (AuNPs) throughout the visible range. Highly efficient plasmonic organic solar cells are fabricated by embedding Au@Ag NCs into an anodic buffer layer, PEDOT:PSS [2, 3]. Second, we demonstrate that the metal nanoparticles can improve the performance of OSCs by boosting the internal quantum efficiency (IQE) of the devices even without a notable plasmonic optical gain [4]. As shown in Figure 1, A hybrid layer platform in combination of silver nanoparticles (AgNPs) and polyethylenimine-ethoxylated (PEIE) layer maximizes the IQE of the OSCs to nearly 100 %, yielding a PCE of 10.1 % in the OSCs. 2D surface characterization confirms the AgNPs provide the short path and funnel charge carriers to a cathode, which would effectively raise the carrier mobility. Lastly, we utilize Au@Ag core-shell nanocubes (NCs) by embedding them in a low temperature-processed anatase $TiO_2$ layer to form a resonance-shifting hybrid n-layer (Au@Ag NCs-HL) for efficient PbS-based solar cells [5]. We show that the Au@Ag NCs-HL broadly enhances the absorption of the device via the near-infrared plasmonic scattering effect.

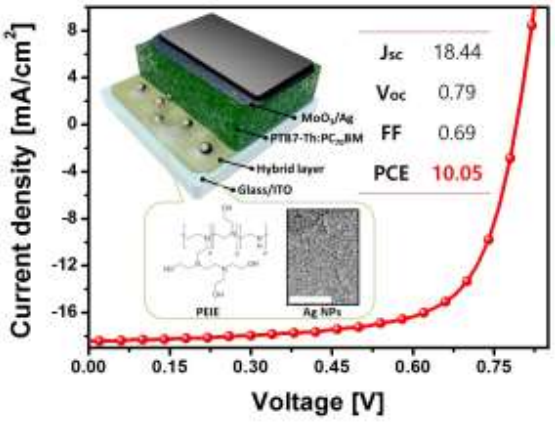



**Figure 1** The internal quantum efficiency of organic solar cells is enhanced *via* metallic nano-funnels

**REFERENCES**


1. J.-Y. Lee *et al.* "Plasmonic Forward Scattering Effect in Organic Solar Cells: A Powerful Optical Engineering Method," *Scientific Reports*, 3, 1726, 2013.
2. J.-Y. Lee *et al.* "Au@Ag Core-Shell Nanocubes for Efficient Plasmonic Light Scattering Effect in Low Bandgap Organic Solar Cells," *ACS Nano*, 8, 3302, 2014.
3. J.-Y. Lee *et al.* "Nanoimprinting-induced nanomorphological transition in polymer solar cells: enhanced electrical and optical performance," *ACS Nano* 9, 2773, 2015.
4. J.-Y. Lee *et al.* "Enhancing the internal quantum efficiency and stability of organic solar cells *via* metallic nano-funnels," *Advanced Energy Materials*, 2015 (*Online published*).
5. J.-Y. Lee *et al.* "Resonance-shifting hybrid n-layer for boosting near infrared response in highly efficient colloidal quantum dots solar cells," *Advanced Materials*, 27, 8102, 2015.

# Interactions between organic excitons and plasmonic metasurfaces

**Deirdre O'Carroll[1,2,3*], Zeqing Shen[2], Christopher Petoukhoff[1], Katsuya Noji[1,4], and Ankur Dalsania[2]**

[1]Rutgers University, Department of Materials Science and Engineering, Piscataway, NJ, USA

[2]Rutgers University, Department of Chemistry and Chemical Biology, Piscataway, NJ, USA

[3]Rutgers University, Institute for Advanced Materials, Devices and Nanotechnology, Piscataway, NJ USA

[4]Tokyo Institute of Technology, Iyoda Group, Tokyo, Japan

[*]corresponding author: ocarroll@rutgers.edu

**Abstract**-To improve energy conversion efficiency in thin-film organic optoelectronics, light management using nanophotonic structures is necessary. Here, our recent work on improving light trapping and light extraction in organic semiconductor thin films using nanostructured silver plasmonic metasurfaces will be presented. Numerous optical phenomena, such as absorption induced scattering, out-of-plane waveguiding and morphology-dependent surface plasmon outcoupling, are identified due to exciton-plasmon coupling between the organic semiconductor and the metasurface.

Thin-film organic semiconductor materials are emerging as energy-efficient, versatile alternatives to inorganic semiconductors for display and solid-state lighting applications. Additionally, thin-film organic laser and photovoltaic technologies, while not yet competitive with inorganic semiconductor-based analogues, can exhibit small device embodied energies (due to comparatively low temperature and low energy-use fabrication processes) which is of interest for reducing overall device cost. To improve energy conversion efficiency in thin-film organic optoelectronics, light management using nanophotonic structures is necessary. Here, our recent work on improving light trapping and light extraction in organic semiconductor thin films using nanostructured silver plasmonic metasurfaces will be presented [1,2]. Numerous optical phenomena, such as absorption induced scattering, out-of-plane waveguiding and morphology-dependent surface plasmon outcoupling, are identified due to exciton-plasmon coupling between the organic semiconductor and the metasurface. Interactions between localized and propagating surface plasmon polaritons and the excitonic transitions of a variety of organic conjugated polymer materials will be discussed and ways in which these interactions may be optimized for particular optoelectronic applications will be presented.

## REFERENCES

1. Petoukhoff, C. E. and O'Carroll, D. M. "Absorption-Induced Scattering and Surface Plasmon Out-Coupling from Absorber-Coated Plasmonic Metasurfaces," *Nat. Commun.* 6, 7899-1-13, 2015.
2. Shen, Z. and O'Carroll, D. M. "Nanoporous Silver Thin Films: Multifunctional Platforms for Influencing Chain Morphology and Optical Properties of Conjugated Polymers." *Adv. Funct. Mater.* 25, 3302-3313 (2015).

# Plasmonic resonances in gold nanorod-film coupled system

**Xingxing Chen[1], Richard J. Blaikie[2], Boyang Ding[2], and Min Qiu[1]**

[1]State Key Laboratory of Modern Optical Instrumentation, Department of Optical Engineering, Zhejiang University, Hangzhou 310027, Zhejiang, China

[2]MacDiarmid Institute for Advanced Materials and Nanotechnology, Department of Physics, University of Otago, P.O. Box 56, Dunedin 9016, New Zealand

[*]corresponding author: minqiu@zju.edu.cn boyang.ding@otago.ac.nz

**Abstract**-Plasmonic resonances in individual gold nanorod-film coupled system have been investigated. The spectral shapes are significantly modified by the gap distance. These modifications arise from the hybridization of several dipolar and multipolar plasmon modes that are strongly localized at the gap in sub-20nm domain. When the gap distance is increased further, scattering characteristics of such nanorod-film coupled system are highly dependent on illumination conditions due to interference. Finally we propose an application of the studied system in facilitating photo-thermal conversion.

Here we present a comprehensive study of the tightly confined plasmonic gap resonances (gap thickness is less than 20nm) between individual AuNRs and a metallic film substrate, revealing the transition of gap modes with gap spacing and their influence on far-field scattering properties[1].

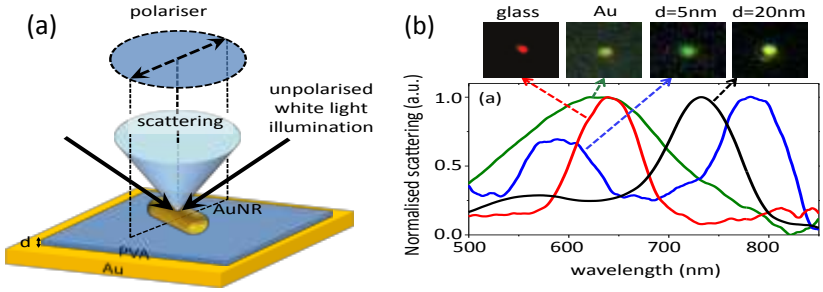



Fig.1 Schematic: dark-field scattering measurement of a single gold nanorod (AuNR) deposited on a PVA film with a thickness d coated on an Au substrate.

The schematic in Figure 1 shows the measurement setup of scattering spectra for a single AuNR on top of a poly(vinylalcohol) (PVA) film coated on an Au substrate using a reflected dark-field microscope. As the gap spacing increases, the scattering spectra of AuNRs vary significantly, but a blue-shift trend is observed for resonances at long wavelengths. The resonances at short wavelengths exhibit random shifts (see in Figure 1(b)). We also find the optical polarizability of different resonances in scattering spectra of AuNRs varies with substrates as shown in Figure 2. Simulations agree with the measured results.

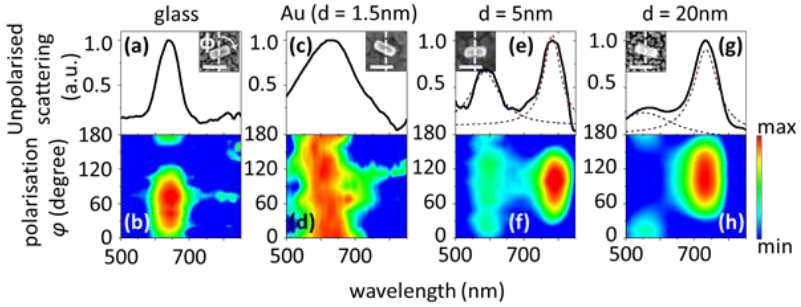



Fig.2 Un/polarized scattering spectra of same AuNRs shown in Fig.1b on (a)/(b) a glass substrate (reference sample), or (c)/(d) 1.5 nm, (e)/(f) 5 nm, and (g)/(h) 20 nm above a Au substrate.

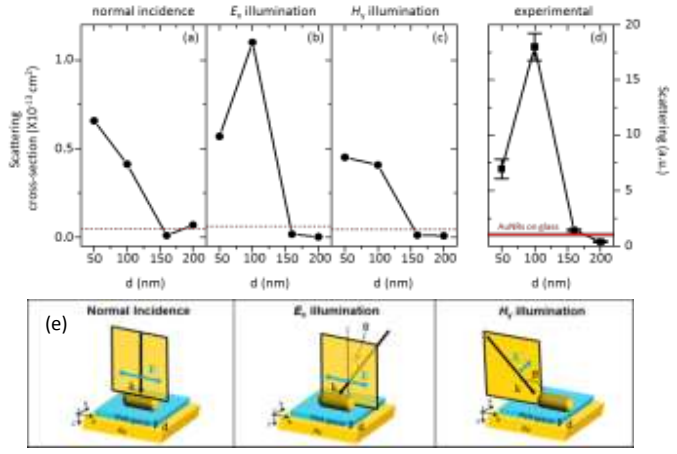



Figure 3. Magnitudes of scattering maxima for AuNRs at varied distances above a Au substrate under different illumination condition (a-c) and in the experiment (d). (e) Schematics that show configurations for each illumination conditions. Dashed line (thick red line) in each panel indicates the scattering magnitude of AuNRs on a glass substrate under the same illumination conditions.

When the gap distance is increased further, it is found that optical characteristics of such nanorod-system can be greatly modified by altering illumination conditions[2]. Figures 2a–c demonstrate that the magnitude variation of scattering maxima for AuNRs at different distances above a Au film under normal incidence, *Ex* and *Hy* illumination, respectively. The variation of scattering magnitudes with NR-film distance has also been observed in our experiment, as shown in Figure 3(d).

It is worth mentioning that optimizing the NR-film distance can greatly enhance the scattering intensity up to ~20 times for certain illumination conditions. So we propose an application of the studied structure in photothermal conversion, illustrating that the NR-cavity system acquires much better capability to facilitate the heating or annealing of metallic NPs than the traditional MIM absorbers[3-4].

| Sample | Illumination | | |
|---|---|---|---|
| | Normal | $E_x$ | $H_y$ |
| d = 10 nm | 16.57 fJ | 1.17 fJ | 0.99 fJ |
| d = 50 nm | 13.33 fJ | 11.36 fJ | 9.25 fJ |
| d =100 nm | 9.99 fJ | 24.07 fJ | 9.48 fJ |
| Glass | 3.73 fJ | 3.71 fJ | 2.96 fJ |

Table 1 Relative energy transfer ΔE in AuNRs placed at different distances above a Au film and a glass substrate under different illumination conditions. $\Delta E=E_{tot}-E_{exch}$ refers to the energy transfer in a AuNR to achieve thermal equilibrium with surroundings under optical illumination, while the NR cavity system was initially placed at room temperature (T= 300 K); where $E_{tot}$ is the total energy the AuNR absorbs from the illumination and $E_{exch}$ refers to the heat exchange between the AuNR and surroundings (air, the PVA spacer and Au film) during the heating process.

**Acknowledgements**, This work was financially supported by the National Natural Science Foundation of China (grants 61275030, 61205030, and 61235007), New Zealand's Marsden Fund through contract UOO-1214, and the Priming Partnership Pilot Funding (University of Otago).

**REFERENCES**

1. Chen, X. X., Yang, Y.Q., Chen, Y-H., Qiu, M., Blaikie, R. J. and Ding, B. Y., *J Phys Chem C* 119, 18627–18634, 2015.
2. Chen X. X., Qiu, M., Blaikie, R. J. and Ding, B. Y., *Plasmonics*, published online :08 December 2015..
3. Chen, X., Chen, Y. T., Yan, M. and Qiu, M., *ACS Nano*, 6, 2550−2557, 2012.
4. Chen, X., Chen, Y. T., Dai, J., Yan, M., Zhao, D., Li, Q. and Qiu, M., *Nanoscale*, 6, 1756−1762, 2014.

# Selecting a Plasmonic Material Using a Two-Dimensional Analysis of Confinement and Propagation Length

**B. Dastmalchi[1,2], T. Koschny[1], C. M. Soukoulis[1,2] and P. Tassin[3]**

[1]Ames Laboratory, U.S. DOE, and Department of Physics and Astronomy, Iowa State University, USA

[2]Institute of Electronic Structure and Lasers (IESL), FORTH, Greece

[3]Department of Physics, Chalmers University, Sweden

**Abstract**-We show that the properties of plasmonic materials (and also different plasmonic waveguide geometries) have to be understood using a two-dimensional graph combining two figures-of-merit: the propagation length and the confinement strength. In this way, one can naturally account for the trade-off between propagation length and confinement that is typically observed for plasmonic materials. I will first discuss the method and then apply it to different materials and waveguide geometries. For example, I will compare the properties of noble metals, aluminum, silicon carbide, doped semiconductors, graphene, etc. I will also compare single-interface structure with thin films and metal-dielectric-metal structures. Our analysis provides guidance on how to improve the performance of any particular plasmonic application and substantially eases the selection of the plasmonic material.

**Acknowledgements**: Work at Ames Laboratory was partially supported by the U.S. Department of Energy, Office of Basic Energy Science, Division of Materials Science and Engineering (Ames Laboratory is operated for the U.S. Department of Energy by Iowa State University under contract No. DE-AC02-07CH11358), by the U.S. Office of Naval Research, award No. N00014-14-1-0474 (simulations). The European Research Council under the ERC Advanced Grant No. 320081 (PHOTOMETA) supported work (theory) at FORTH. Work at Chalmers was partially supported by the Area of Advance Nano.

**REFERENCES**

Dastmalchi, B., P. Tassin, T. Koschny and C. M. Soukoulis, "A New Perspective on Plasmonics: Confinement and Propagation Length of Surface Plasmons for Different Materials and Geometries," *Adv. Optical Mater.*, Vol. 4, 177–184, 2015.

# Non-Hermitian Wave Mixing

**R. El-Ganainy[1], J.I. Dadap,[2] and R.M. Osgood, Jr.[2]**

[1]*Department of Physics and Henes Center for Quantum Phenomena, Michigan Technological University, Houghton, Michigan 49931, USA*

[2]*Microelectronics Sciences Laboratories, Columbia University, New York, New York 10027, USA*

**Abstract:**
We introduce the notion of non-Hermitian wave mixing and show that it can be utilized to achieve efficient nonlinear energy transfer between different optical modes even in the absence of the usual phase matching condition. We discuss the optical implementation of this concept in waveguide platforms and plasmonic structures. This work may enable the realization of semiconductor-based long wavelength light sources and parametric amplifiers which are otherwise difficult to build due to the stringent Hermitian phase matching requirements.

Nonlinear optics (NLO) is currently one of the main cornerstones of optical science [1] with a wide range of applications from optical communications and quantum optics to bio-imaging and sensing. In particular, nonlinear wave mixing processes have enabled the realization of novel light sources that can emit at frequencies that are not attainable using conventional lasers. In this regard, nonlinear devices such as optical parametric amplifiers (OPA) and oscillators (OPO) have become indispensable tools in optical physics and engineering [1,2]. Despite the tremendous success of these light sources, their proper operation require stringent phase-matching conditions between the different frequency components. Traditionally, this constraint is usually achieved for example by using periodically poled structures or by using birefringent crystals [1-3]. These techniques, however, are difficult to implement in chip-scale semiconductor platforms. While several ideas to overcome this problem have been proposed, they often tend to pose tight geometric constraints on the device geometry [4,5].

Here we explore an altogether new direction for achieving efficient nonlinear wave mixing by engineering the non-Hermiticity of the nonlinear process. As an example, we consider the process of optical parametric amplification which requires second order nonlinearity and is described by the set of equations:

$$\begin{aligned} \frac{dE_S}{dz} &= i\kappa'_S E_P E_I^* \exp(i\Delta\beta z) - \gamma_S E_S \\ \frac{dE_I}{dz} &= i\kappa'_I E_P E_S^* \exp(i\Delta\beta z) - \gamma_I E_I \\ \frac{dE_P}{dz} &= i\kappa'_P E_I E_S \exp(-i\Delta\beta z) \end{aligned} \quad , \quad (1)$$

where $E_{S,I,P}$ are the signal, idler and pump field amplitudes respectively and $\Delta\beta = \beta_P - (\beta_S + \beta_I)$ is the propagation constant mismatch between the three different waves [1]. Also in Eq.(1), $\kappa'_{S,I,P}$ are the coupling coefficients, which are functions of the second order nonlinearity as well as the optical frequencies $\omega_{S,I,P}$ .Finally, $\gamma_{S,I}$ are the signal and idler linear loss coefficients, $z$ is the propagation distance, and asterisks denote complex conjugation. In the absence of any optical losses, optical amplification of the signal component occurs only when the phase matching condition $\Delta\beta/2 < \sqrt{\kappa_S \kappa_I}$ is satisfied.

Interestingly, our simulations predict that by engineering the optical losses of the idler beam, optical amplification can be achieved even outside the phase matching regime, i.e. $\Delta\beta/2 > \sqrt{\kappa_S \kappa_I}$ . This is illustrated in Fig.1 where the normalized optical intensities for the signal and idler beams are plotted against the normalized propagation distance for different values of normalized idler loss coefficients (see Ref.[6] for details of normalization scheme). In all simulations, the systems properties were chosen to ensure that the Hermitian phase matching requirement is not satisfied. Evidently, by engineering the non-Hermitian spectral features of system to add optical losses to the idler can lead to the amplification of the signal wave. While the results obtained in Fig.1

neglect pump depletion, out studies show that similar behavior persist even when pump depletion is accounted for [6].

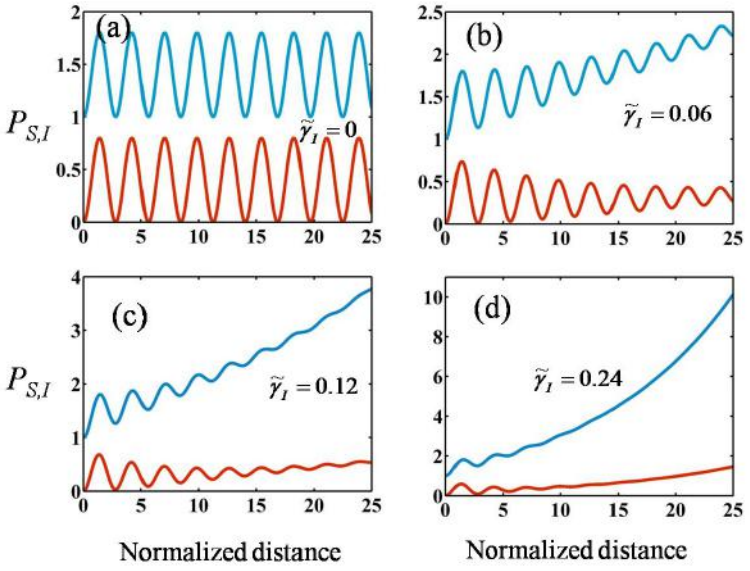



Fig. 1. Evolution of normalized power of signal and idler beams as a function of the normalized distance when $\Delta\tilde{\beta} = 3$ under the following different idler loss coefficients: (a) $\tilde{\gamma}_I = 0$ , (b) $\tilde{\gamma}_I = 0.06$, (c) $\tilde{\gamma}_I = 0.12$ and (d) $\tilde{\gamma}_I = 1.2$ . In all cases, the initial conditions for the normalized field amplitudes were taken to be $a_S(\xi = 0) = 1$ and $a_I(\xi = 0) = 0$. See ref. [6] for the details of normalization scheme.

A nonlinear device that exhibit these non-Hermitian features can be implemented by using several different platforms. For instance, PT symmetric waveguides that selectively introduce losses for certain frequencies can be used. Alternatively, one can introduce optical losses to the idler beam through a frequency selective radiation losses by using Bragg gratings. Another option is to use plasmonic structures having dispersive loss profile that is tailored to selectively target the idler component.

In conclusion, we introduced a new concept for achieving efficient energy transfer between different components in nonlinear wave mixing processes by using non-Hermitian engineering of the spectral properties of the interacting waves. We demonstrated by using numerical simulations that this novel concept can be utilized to build on-chip optical parametric amplifiers.

References


1. R.W. Boyd, *Nonlinear Optics*, Academic Press (2008)
2. A. Yariv, Quantum Electronics, Wiley (1989).
3. G.I. Stegeman and R.I. Stegeman, Nonlinear Optics: Phenomena, Materials and Devices, Wiley (2012).
4. P. Abolghasem, A. S. Helmy, "Single-sided Bragg reflection waveguides with multilayer core for monolithic semiconductor parametric devices," JOSA B, **29**, 1367(2012).
5. A.S. Helmy, P. Abolghasem, J. S. Aitchison[1], B.J. Bijlan, J. Han, B.M. Holmes, D.C. Hutchings, U. Younisand S.J. Wagner, "Recent advances in phase matching of second-order nonlinearities in monolithic semiconductor waveguides," Laser and Photonics Reviews, **5**, 272 (2011).
6. R El-Ganainy, JI Dadap, RM Osgood, "Optical parametric amplification via non-Hermitian phase matching," Opt. Lett. **40**, 5086 (2015)

# Multiphysics simulation of tunable and frequency selective metamaterial absorbers

**A. Liu[1*], A. Alam[1], J. Niegemann[1], and J. Pond[1]**
[1]Lumerical Solutions, Inc., Canada
[*]corresponding author: aliu@lumerical.com

**Abstract-**We consider microbolometer applications of metamaterial absorbers where multiphysics simulations are necessary to optimize the device performance. We present a workflow where optical simulations are used to provide insight into the absorption mechanism, followed by electro-thermal transport simulations to assess the subsequent thermal effects. Finally, we extend the methodology to include tunable graphene metamaterial absorbers, where an additional electrical simulation is used to determine the change in the chemical potential of the graphene prior to the optical simulation.

In recent years, metamaterial-based optical absorbers have attracted significant interest as a way of achieving spectral selectivity [1-3] as well as active tuning [4]. Optical simulations are very useful for providing insight into the absorption mechanism of these complex nanostructures [4-5]. However, for many applications such as thermal imaging and detection, optical simulation alone is insufficient to fully characterize the device, and multiphysics simulations are necessary to optimize the device performance. For microbolometers, where the thermal transport effects after optical absorption need to be considered, we present an optimization workflow that includes both optical and electro-thermal transport simulations. For the optical simulations, it is often useful to simulate the angular dependence of the absorber over a broad spectrum since the ideal design will absorb light only in the desired wavelength range and over a wide range of angles. Here, we employ a broadband fixed-angle source technique (BFAST) to obtain broadband spectra for each angle of incidence using a finite-difference time-domain (FDTD) simulation. The optical absorption is then used in a subsequent electro-thermal transport simulation to calculate the temperature in the thermistor and the change in the electrical resistance as a function of time. Finally, we extend the methodology to include more exotic absorbers such as graphene based metamaterials, where active tuning can be achieved by applying a bias voltage to modify the Fermi level of the graphene layers. We show how charge transport drift-diffusion simulations can first be used to calculate the carrier density and, therefore, chemical potential of graphene, followed by optical simulations of the graphene metamaterial absorber.

Some example applications are shown in Figures 1-3. Figure 1 shows absorption of light by plasmonic metamaterials [5] for high performance, narrow band and wide angle absorption. Figure 2 shows the temperature response of a metamaterial microbolometer [6]. The optical response of a graphene metamaterial absorber [4] for different chemical potentials is shown in Figure 3.

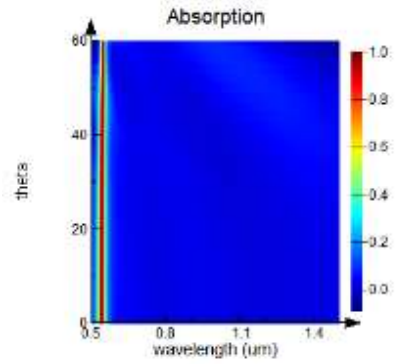



**Figure 1.** Absorption spectrum for plasmonic metamaterial absorber shows little dependence of resonance wavelength on incident angle.

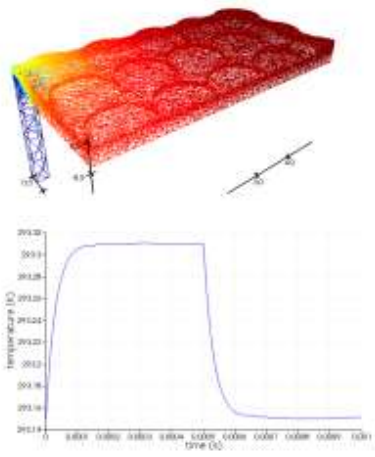


**Figure 2**. Temperature distribution (top) and time-domain temperature response (bottom) of a metamaterial-based microbolometer.

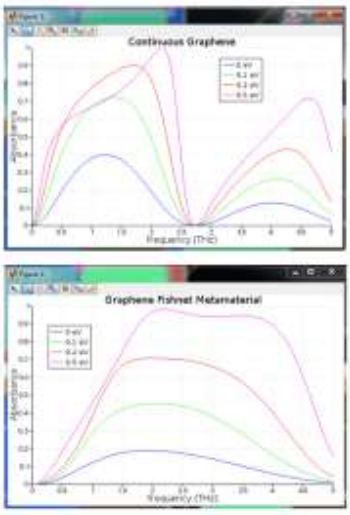



**Figure 3.** Absorption spectrum for continuous graphene (top) and graphene fishnet metamaterial (bottom) under different chemical potentials.

**REFERENCES**


1. Liu, X., Starr, T. and Padilla, W. J., "Infrared spatial and frequency selective metamaterials with near-unity absorbance," Phys. Rev. Lett., Vol. 104, 207403, 2010
2. Hao, J., et al., "High performance optical absorber based on a plasmonic metamaterial," Appl. Phys. Lett., Vol. 96, 251104, 2010
3. Tao, H., et al., "Highly flexible wide angle of incidence terahertz metamaterial absorber: Design, fabrication, and characterization," Phys. Rev. B, Vol. 78, 241103, 2008
4. Andryieuski, A. and Lavrinenko, A. V., "Graphene metamaterials based tunable terahertz absorber: effective surface conductivity approach," Opt. Express Vol. 21, 9144-9155, 2013
5. Hao, J., Zhou, L. and Qiu, M., "Nearly total absorption of light and heat generation by plasmonic metamaterials," Physical Review B, Vol. 83, 165107, 2011
6. Du. K., et al., "Wavelength and thermal distribution selectable microbolometers based on metamaterial absorbers,", IEEE Photonics Journal, Vol. 7, 6800908, 2015

# Observation of topologically protected edge states in arrays of evanescently coupled plasmonic waveguides

**S. Linden**[1*]**, F. Bleckmann**[1]**, and A. Alberti**[2]
[1]Physikalisches Institut, Universität Bonn, Germany
[2]Institut für Angewandte Physik, Universität Bonn, Germany
[*]corresponding author: linden@physik.uni-bonn.de

**Abstract**- Arrays of evanescently coupled dielectric-loaded SPP waveguides were used to implement the Su-Schrieffer-Heeger (SSH) model in a plasmonic system. The waveguide arrays were fabricated by negative-tone grey-scale electron beam lithography. Excitation of a single waveguide in the bulk of the array resulted in discrete diffraction. In contrast, topological edge states were observed at the boundaries between two topologically distinct domains.

Coupled arrays of optical waveguides can be used as an experimental platform to simulate the evolution of quantum mechanical systems in a classical wave environment [1]. The basis for this is the mathematical equivalence between the time dependent Schrödinger equation and the coupled mode equation that describes the propagation of light in the waveguide arrays. Examples include the observation of discrete diffraction, Bloch oscillations, Zener tunneling, and Anderson localization in dielectric waveguide arrays.

Here, we implement the Su-Schrieffer-Heeger (SSH) model [2], i.e., the prototypical system of a 1D topological insulator, in arrays of evanescently coupled dielectric-loaded surface plasmon polariton waveguides (DLSPPWs). The waveguide arrays were fabricated by negative-tone grey-scale electron beam lithography [3], whereby alternating strong and weak bonds were realized by choosing two different separations between neighboring plasmonic waveguides. The evolution of the surface plasmon polaritons was monitored in real and Fourier space by leakage radiation microscopy. Excitation of a single waveguide in the bulk of the array resulted in discrete diffraction. In contrast, a localized topological edge states was observed upon excitation of the array at the boundary between two topologically distinct domains. The experimental findings are in excellent agreement with numerical calculations based on the finite element method.

**REFERENCES**

1. Longhi, S. "Quantum-optical analogies using photonic structures," *Laser & Photon. Rev*, Vol. 3, 243–261, 2009.
2. Su, W. P., J. R. Schrieffer and A. J. Heeger, "Soliton excitations in polyacetylene," *Phys. Rev. B*, Vol. 22, 2099–2111, 1983.
3. Block, A., C. Etrich, T. Limboeck, F. Bleckmann, E. Soergel, C. Rockstuhl, S. Linden, "Bloch oscillations in plasmonic waveguide arrays," *Nat. Commun*. 5:3843 (**2014**), http://dx.doi.org/10.1038/ncomms4843.

# New Trends in Computational Photonics

**S. S. Obayya**[1*]
[1]Center for Photonics and Smart Materials, Zewail City of Science and Technology, Egypt
[*]corresponding author: sobayya@zewailcity.edu.eg

**Abstract**-For any photonic device simulation, the accuracy of the numerical solution not only depends on the methods being used but also on the discretization parameters used in that numerical method. The analysis of optical waveguides with strong longitudinal and transverse discontinuities remains a defiance facing numerical techniques. In this work, three innovative methods will be presented to overcome some of the problems facing the traditional methods of modeling photonic devices, especially plasmonics. A new smoothed finite element method (SFEM) is proposed to analyse time domain wave propagation in photonic devices. Moreover, to accurately analyze plasmonic structures with strong discontinuities, a stable Bidirectional Beam Propagation Method (BiBPM) based on Blocked Schur (BS) algorithm is introduced. Finally, an accurate and computationally efficient rational Chebyshev multi-domain pseudo-spectral method (RC-MDPSM) for modal analysis of Photonic devices is presented. The efficiency of the suggested technique stems from using rational Chebyshev basis functions to accurately represent the semi-infinite computational domain; thus, eliminating the use of PML like absorbing boundary conditions.

The propagation of light through optical guided wave devices can be characterized by using various modeling techniques. These techniques can be classified into analytical methods and numerical methods [1]. Analytical methods, if possible, a solution may be obtained by solving the basic electromagnetic equations. In contrast, numerical methods are computational schemes or models that can be applied to a spectrum of problems by modifying the basic model to fit the problem.

Finite difference method (FDM) is one of the most widely used numerical tools for optical circuits analysis. Although simple and efficient, FDM suffers from the insufficient discretization of irregularly-shaped geometries (staircasing problem). Alternatively, the finite element method (FEM) is able to divide the computational domain into triangular elements and to accurately model complex geometries. Several FEM analyses rely on the second order triangular element (T6) due to the poor accuracy of the first order triangular element (T3). However, for the conventional T6 element, the additional nodes located midway the distance between the pairs of triangle vertexes cannot be adjusted to set on the boundary of a curved structure. This problem was solved by using curvilinear elements. Compared with conventional elements, curvilinear element approach converges faster for curved structures. However, the T3 element is often preferable because of its computational simplicity and easiness for adaptive mesh refinement. Moreover, most of mesh generation software's rely on first order triangular elements [2].

As a consequence, several research efforts have been dedicated to increase the accuracy of the T3 element. Recently, a new technique termed "smoothed Galerkin" has been introduced [3]. This new technique relies on weakening the weak form ($W^2$) as in meshfree methods. Beside approximating the field, $W^2$ form approximates also the field derivatives via the gradient smoothing technique. The high accuracy and the less sensitivity to mesh distortion are the most important features of $W^2$ form. The accuracy of any method relies on

Galerkin form can be improved by using the smoothed Galekrin form. Based on the smoothed Galerkin technique, a novel class of so-called smoothed finite element method (SFEM) has been introduced for various mechanics problems. The shape function derivatives at element boundaries, in the conventional FEM, are numerically discontinuous which causes FEM poor performance. This disadvantage in FEM has been smartly overcome in SFEM by approximating the derivatives at the element boundaries to be continuous. Dissimilar to conventional FEM, efficient ”inter-element” matrices are accurately formed through smoothing the field derivatives across element boundaries. In this sense, the new approach is termed ”smoothed FEM” (SFETD).

Recently plasmonics is expected to play a vital role in achieving high density integrated photonic circuits. However, the efficient analysis of such plasmonic based devices is still a challenge facing numerical modeling techniques. Beam propagation methods (BPM), which are well known for their simplicity and numerical speed in analyzing photonic devices, sustain serious stability problem when treating high-index-contrast structures and completely fail in handling such plasmonic based devices. Alternatively, we developed a new type of bidirectional BPM able to overcome all shortages in plasmonics modeling techniques. Besides increasing computational speed through our suggested method, it could efficiently treat all the very-wide spectrum of radiation, evanescent, guided modes excited in such plasmonic based devices with excellent numerical stability [4].

Pseudospectral methods have recently emerged as efficient and accurate tools in the field of optical waveguides analysis. Unlike the finite difference and finite element methods, spectral methods provide very high convergence rates in addition to the higher efficiency and accuracy. Since spectral methods require the solution to be smooth enough to achieve a high convergence rate, we should employ also a domain decomposition technique in case of problems with discontinuities. Most of the waveguiding structures have discontinuities due to different materials with different refractive indices used in fabricating the waveguide [5].

An important problem that should be treated carefully is the semi-infinite extension of the computational domains denoted as open waveguides. Perfectly-matched layers (PMLs) proved to be a good solution to the problem leading to domain truncation. However, there are still serious simulation problems in which PMLs collapse, confront inevitable reflections or even exponential growth. Other major drawbacks are the high sensitivity to the selection of the PML parameters such as conductivity profile, thickness of the layer, permittivity, and the distance to the structure. Moreover, non-physical Berenger PML modes appear in the numerical solution that cannot be wiped out. Another approach we have proposed is using rational Chebyshev functions in semi-infinite subdomains. The rational basis functions are constructed by composing cardinal Chebyshev functions with a carefully selected conformal map. The proposed approach renders itself to have advantages such as achieving a high convergence rate and the convergence is independent of any prior estimates.

**REFERENCES**

[1] Obayya, S. S. A., “Computational Photonics,”. *John Wiley & Sons, Ltd*, 2010.

[2] Liu, G. R., N. T. Trung, “Smoothed Finite Element Methods,” *CRC Press*, 2010

[3] Atia K. S. R., A. M. Heikal, and S. S. A. Obayya. “Efficient smoothed finite element time domain analysis for photonic devices, ” *Optics express*, Vol. 23, No. 17, 22199-22213, 2015.

[4] Obayya, S. S. A., “Novel finite element analysis of optical waveguide discontinuity problems,” *Lightwave Technology, Journal of*, Vol. 22, No. 5, 1420–1425, 2004.

[5] Huang, C. C., C. C. Huang, and J. Y. Yang, “A full-vectorial pseudospectral modal analysis of dielectric optical waveguides with stepped refractive index profiles,” *IEEE J. Sel. Top. Quantum Electron.*, Vol. 11, 457–465, 2005.

# Hybrid Single Mode Nanophotonic-Plasmonic Waveguides for On-Chip Surface Enhanced Raman Spectroscopy

**F. Peyskens**[1], **A. Dhakal**[1], **P. Van Dorpe**[2], **N. Le Thomas**[1], **and R. Baets**[1],

[1]Photonics Research Group, INTEC-department, Ghent University-imec; Center for Nano-and BioPhotonics, Ghent University, Technologiepark-Zwijnaarde 15, 9052 Ghent, Belgium
[2]imec, Kapeldreef 75, 3001 Heverlee, Belgium; Department of Physics, KULeuven, Celestijnenlaan 200D, 3001 Leuven, Belgium
frederic.peyskens@ugent.be

**Abstract**— We introduce a hybrid nanophotonic-plasmonic platform capable of generating Surface Enhanced Raman Spectroscopy signals from integrated bowtie antennas, excited and collected by a single mode silicon nitride waveguide. Moreover we discuss the relevant figure of merit, which represents the total Stokes power coupled into the fundamental waveguide mode for a given pump power, and outline strategies to optimize the Signal-to-Noise Ratio.

## 1. INTRODUCTION

Surface Enhanced Raman Spectroscopy (SERS) is a well-known technique to enhance Raman spectra by placing a resonant metallic nanostructure near the analyte under study. [1, 2] SERS signals are however mainly generated and collected by bulky and expensive microscopy systems. The development of photonic integrated circuits functionalized with dedicated nanoplasmonic structures would hence present a major step towards the realization of dense SERS probes, allowing multiplexed detection of extremely weak Raman signals. We have demonstrated for the first time such a hybrid platform where the SERS signal from integrated bowtie antennas, coated with a self-assembled monolayer of 4-nitrothiophenol (NTP), is excited and collected by a single mode silicon nitride waveguide (Fig. 1(a)). Due to the fully integrated nature of this single mode SERS-probe, one can rigorously quantify the complete enhancement and coupling process. [3] Below we will discuss the relevant figure of merit ($FOM$) of this new on-chip SERS platform and outline strategies to optimize the Signal-to-Noise Ratio ($SNR$).

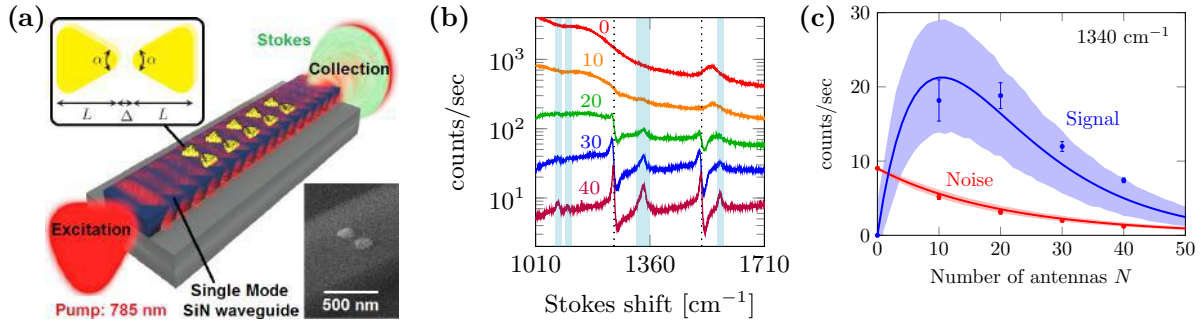



Figure 1: **(a)** Silicon nitride (SiN) waveguide functionalized with an array of $N$ bowtie antennas. The bottom inset shows a SEM image of an integrated bowtie antenna. [3] **(b)** SERS spectra of waveguides functionalized with a varying number of $N$ ($N = 0, 10, 20, 30, 40$) bowtie antennas with $\alpha \approx 60°$, $L \approx 106 \pm 8$ nm and $\Delta \approx 48 \pm 13$ nm. [3] **(c)** Signal (blue) and shot noise (red) strength of the 1340 cm$^{-1}$ peak as a function of $N$. The solid curve represents a fit of the experimental data to a theoretical model describing the on-chip SERS effects, developed in [3], while the shaded areas incorporate the theoretical impact of disorder in the system [3].

## 2. SIGNAL ENHANCEMENT AND NOISE REDUCTION

Figure 1(b) shows the Raman spectra obtained from waveguides functionalized with a different number of antennas $N$. The cyan shaded areas mark the spectral positions where an NTP Stokes peak is expected. The peaks denoted by the black dashed lines result from interference effects generated by the Au array. [3] While the non-functionalized ($N = 0$) reference waveguide does not generate any NTP SERS signal, it does have a large Raman background originating from the SiN core. The shot noise associated to this background will limit the detection of the smallest NTP features, but can be reduced by the attenuation caused by the nanoantennas if the waveguides are functionalized with a sufficiently large $N$ (see Fig. 1(b)). While the dominant 1340

cm$^{-1}$ peak is visible in all cases, the smallest 1110 cm$^{-1}$ peak only appears for a sufficiently low background. In that respect the $N = 40$ waveguide exhibits a better performance as compared to the $N = 10$ case. However, the absolute signal strength of all the $N = 40$ peaks is lower than the $N = 10$ peaks as exemplified in Fig. 1(c) for the 1340 cm$^{-1}$ peak. [3] Hence, there is a trade-off between signal enhancement and noise reduction, which in turn affects the $SNR$. In order to investigate this trade-off we developed an on-chip SERS model. Each antenna generates $\eta_A P_{pump}$ guided Stokes power, in both forward and backward direction, for a given pump power $P_{pump}$. The single antenna conversion efficiency $\eta_A$ is an antenna dependent factor incorporating the integrated field enhancement profile near the metal surface. The total forward propagating Stokes power generated by an array of $N$ coated antennas was shown to be proportional to $FOM_F = \eta_A e_S^{(1-N)} \left(1 - (e_S/e_P)^N\right) (1 - e_S/e_P)^{-1}$. The additional array factor results from the combined extinction of pump ($e_P$) and Stokes ($e_S$) light due to all the antennas. The background on the other hand is proportional to $FOM_{bg} = \eta_{bg} L_1 \left(e_P^{-N} + e_S^{-N}\right)$ in which $\eta_{bg}$ is a waveguide dependent factor incorporating the specific modal field profile and $2L_1$ is the total length of the waveguide. Finally, the $SNR$ is then proportional to $SNR \propto FOM_F / \sqrt{FOM_F + FOM_{bg}}$. [3]

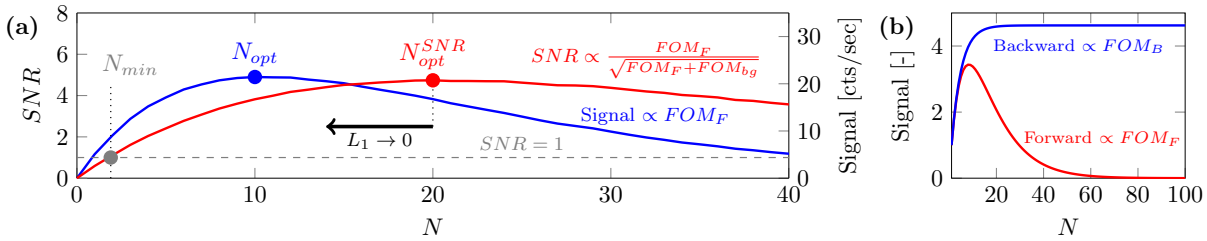



Figure 2: **(a)** Signal and $SNR$ as a function of $N$ for the 1340 cm$^{-1}$ peak of Fig. 1(c). **(b)** Comparison between Forward and Backward on-chip SERS scattering for $e_P = 1.16$ and $e_S = 1.10$.

The experimental signal strength and corresponding $SNR$ of the 1340 cm$^{-1}$ peak are shown in Fig. 2(a). One can see that if $N < N_{min}$, detection is not possible because $SNR < 1$. The signal is maximal for $N = N_{opt}$ while the $SNR$ is maximal for $N_{opt}^{SNR} > N_{opt}$. This exemplifies the trade-off between signal enhancement and noise reduction. It should be noted however that the SERS signal originates from a relatively short section (which can be made as short as $\approx 10$ $\mu m$ for a single antenna) as compared to the total length $2L_1$ ($\approx 10000$ $\mu$m in our experiment) which is responsible for the large background. By sufficiently reducing $L_1$ ($L_1 \to 0$), the trade-off relaxes because one maintains the possibility to select an antenna number which maximizes $FOM_F$ while achieving the maximum $SNR$ at the same time (i.e. $N_{opt}^{SNR} \to N_{opt}$). Furthermore, one can gain in absolute signal strength by collecting the backward propagating SERS light because the backscattered signal from the first antenna, which is the strongest, is still fully available at the output. The signal from subsequent antennas then experiences an ever increasing attenuation by the previous antennas, such that the signal eventually saturates for a sufficiently large number of antennas (see Fig. 2(b)). By applying similar reasonings as in [3], one can show that the backward propagating SERS signal is proportional to $FOM_B = \eta_A \left(1 - (e_P e_S)^{-N}\right) \left(1 - (e_P e_S)^{-1}\right)^{-1}$. The highest SERS signal $S_{max}$ that can be collected from this hybrid platform is hence given by $S_{max} = \eta_A \left(1 - 1/(e_P e_S)\right)^{-1}$ for a given antenna geometry. When one eventually is limited to the shot noise of the SERS signal (i.e. $FOM_B >> FOM_{bg}$), the highest possible $SNR$ is proportional to $SNR_{max} \propto \sqrt{\eta_A \left(1 - 1/(e_P e_S)\right)^{-1}}$. Currently we are working on dedicated on-chip Y-splitters which decouple the pump beam from the waveguide carrying the SERS signal in order to reduce the background signal. Moreover, the backscattered light is collected in such a Y-splitter configuration to improve on the absolute signal strength. Initial experiments show that the background can be reduced by a factor 100 (shot noise reduction by 10) compared to the background of simple straight waveguides (for the same pump power). So the $SNR$ is expected to increase by at least 10.

Improved chip designs are expected to push towards the $N_{min} = 1$ limit, such that signals from a single antenna can be detected, and could ultimately enable quantitative and multiplexed detection of several biological and chemical substances, such as viruses or DNA, on a fully integrated platform.

## REFERENCES


1. Anker, J. N., et al. "Biosensing with plasmonic nanosensors," *Nat. Mater.*, Vol. 7, 442–453, 2008.
2. Halas, N. J., et al. "Plasmons in strongly coupled metallic nanostructures," *Chem. Rev.*, Vol. 111, 3913–3961, 2011.
3. Peyskens, F., et al. "Surface Enhanced Raman Spectroscopy Using a Single Mode Nanophotonic-Plasmonic Platform," *ACS Photonics*, Vol. 3(1), 102–108, 2016.

# High Performance Nano-Plasmonic MIM-Based Lab-on-Chip Sensor

**Ahmad B. Ayoub**[1], **and Mohamed A. Swillam**[1*]
[1]American University in Cairo, Egypt
[*]corresponding author: m.swillam@aucegypt.edu

**Abstract**-We propose a novel structure for a plasmonic gas sensor. The idea of operation is based on Metal-Insulator-Metal approach. The plasmonic slot mode enables high confinement in the insulator gap which is the gas being sensed leading to high sensitivity. High sensitivity and small foot print is achieved through this plasmonic design. Optimization processes yield high sensitivity as high as 1,521 nm/RIU, FWHM down to 9 nm and FOM of 169 which is the greatest FOM to our knowledge.

***Keywords—surface plasmon polariton; full width half maximum; lab-on-chip, silicon-coupled***

## INTRODUCTION

The focus on gas detection has been exponentially increasing due to their strong impact on a lot of industrial and environmental applications. The use of highly sensitive gas detectors in industry has been wide spreading and has a lot of potentials and promising applications [1]. Our sensing technique is based on having air as the background (reference) index. Changing gas type will affect the effective index of the medium, and hence results in a phase or wavelength shift. Surface Plasmon Wave is originated through the coherent oscillations of the excited charges at the metal-dielectric interface. This attractive property of SPs is the basis for surface plasmon resonance (SPR) bio-medical, chemical, and environmental sensing [1]. In the recent years, a lot of architectures have been proposed, however, they lack the either small foot print, which is the case for most of photonic based sensors, or high sensitivity for plasmonic based sensors. Plasmonic slot mode is of promising applications because of the high mode confinement in the gap between the two metal surfaces [2]. Some analytical approaches have been used to estimate the transmission patterns in complex configurations like the x junctions for example that can also be utilized in our design [3]. In this paper, we propose a novel architecture which merges between high sensitivity and small foot print.

## DESIGN

The design is based on a resonant cavity where the gas being sensed is inside the cavity etched in silver which results in a Metal-Insulator-Metal (MIM) structure. Changing the design parameters helped us in choosing a desired resonant frequency of about 1550 nm for our design. Also, changing the dimensions will affect the full width half maximum (FWHM) of the output normalized transmission, which will counts into the figure of merit (FOM) which represent the overall performance of the sensor. The FOM is determined by dividing the sensitivity by the FWHM, so better FOM which is interpreted as better performance can be achieved by having higher sensitivity and narrower FWHM. As shown in the figure, the FWHM of the transmitted signal was about 9 nm which helped in having high FOM of 169 which is the greatest among other sensors to our knowledge. This will enable for high performance lab-on-chip sensors which can be coupled to electronic chips through silicon waveguide coupling ports.

## CONCLUSION

We demonstrated a gas sensor that is characterized by its high sensitivity of 1521 nm/RIU, narrow FWHM of the transmitted signal of 9 nm, and also high figure of merit (FOM) of 169 which is the best sensor's performance reported till now.

## ACKNOWLEDGMENT

The research has been partially funded from the American University in Cairo (AUC) internal grants.

## REFERENCES

1. Homola, Jiri, S. S. Yee, and G. Gauglitz, "Surface plasmon resonance sensors: review," Sens. Actuators, B 54, 3–15, 1999.
2. Azzazi, Abdulilah, Ahmad B. Ayoub and Mohamed A. Swillam, "Nanoscale highly selective plasmonic multi-channnel demultiplexer," Proc. SPIE 9756, Photonic and Phononic Properties of Engineered Nanostructures VI, San Francisco, California, United States, 2016.
3. Swillam, M. A., A. S. Helmy, "Feedback Effects in Plasmonic Slot Waveguides Examined Using a Closed Form Model," in IEEE Photonics Technology Letters, vol. 24, 6, 497-499, 2012.

# Controlling fluorescence emission by surface plasmon resonance in multilayer „core-shell" metallic nanoparticles.

**M. Focsan[1*], A. Campu[1], A. M. Craciun[1], S. Suarasan[1], C. Tira[1], A. Lazar[1] and S. Astilean[1,2]**

Nanobiophotonics and Laser Microspectroscopy Center, Interdisciplinary Research Institute on Bio-Nano-Sciences, Babes-Bolyai University, Treboniu Laurean Str. 42, Cluj-Napoca 400271, Romania

[2]Biomolecular Physics Department, Faculty of Physics, Babes-Bolyai University, M. Kogalniceanu Str. 1, Cluj-Napoca 400084, Romania

[*]corresponding author: monica.iosin@phys.ubbcluj.ro

**Abstract**- There is still the need of not only controlling and understanding of fluorescent molecules-nanoparticles interactions but also of designing new types of fluorescent hybrid nanostructures with substantially improved brightness and photo-stability [1].

Here we develop a novel strategy for designing a model of multilayer core-shell gold nanoparticles (AuNPs) with optimized photophysical properties, consisting of a Au core and surrounding FRET pairs (i.e. fluorescent molecules and quantum dots). Specifically, we employed polyelectrolyte multilayers fabricated using layer-by-layer assembly as dielectric spacers for precisely tuning the Au core/acceptor/donor distances and to modulate FRET enhancement. Then, the experimental measured photophysical parameters were compared to numerical simulations. In particular, the electromagnetic response was simulated by finite-difference time-domain (FDTD) method in order to ensure theoretical description of the coupling between metallic AuNPs and emitters.

We consider that the integration of AuNPs with fluorescent molecules into composite nanostructures where the emitters are precisely positioned relative to the plasmonic surface enables the use of these multilayer core-shell AuNPs as ideal efficient nanoscopic light sources.

**Acknowledgements**. This work was supported by CNCS - UEFISCDI Romania, under the project number PN-II-RU-TE-2014-4-2102.

**REFERENCES**

1. Kochuveedu S. T., S. Taehwang, L. Youmin, L. Minyung, K. Donghyun and D. H Kim, "Revolutionizing the FRET-Based Light Emission in Core-Shell Nanostructures via Comprehensive Activity of Surface Plasmons", *Scientific Reports,* Vol. 4, 4735, 2014.

# Long-Range Surface Plasmon-Polariton Waveguide Biosensors for Disease Detection

**Oleksiy Krupin,[1] Wei Ru Wong,[2] Paul Béland,[1] Faisal Rafiq Mahamd Adikan,[2] and Pierre Berini[1,3,4*]**

[1] School of Electrical Engineering and Computer Science, University of Ottawa, Ottawa, Canada

[2] Department of Electrical Engineering, University of Malaya, Kuala Lumpur, Malaysia

[3] Department of Physics, University of Ottawa, Ottawa, Canada

[4] Centre for Research in Photonics, University of Ottawa, Ottawa, Canada

[*]corresponding author: berini@eecs.uottawa.ca

**Abstract**- We review recent progress on the application of long-range surface plasmon-polariton waveguide biosensors for disease detection. The biosensors are constructed from metal stripe waveguides cladded in Cytop with etched microfluidic channels to expose the stripe surface to the sensing fluid. Application of straight waveguide biosensors to the detection of leukemia in patient blood serum, dengue infection in patient blood plasma and bacteria in urine is reviewed.

Conventional clinical detection methods such as ELISA (enzyme-linked immunosorbent assay) and flow cytometry use fluorescence detection which requires well-trained personnel to label biomolecules and run test protocols, often requiring hours to carry out. Alternatively, optical biosensors are label-free and provide a real-time response. The field of optical biosensing is dominated by Surface Plasmon Resonance (SPR) in the Kretschmann-Raether configuration, which involves a thin Au film on a prism integrated with microfluidics and interrogation optoelectronics [1-3]. Despite the success of this technique, miniaturization, multiplexing and sensitivity remain challenges.

Long-range surface plasmon polaritons (LRSPPs) are transverse magnetic (TM) surface waves that propagate on a thin metal slab or stripe cladded by dielectrics of similar refractive index [4]. LRSPPs can propagate up to centimeters along stripes in the infrared, which is significantly further than the propagation of single-interface SPPs. The LRSPP's increased propagation length is due to reduced confinement to the metal which leads to reduced modal sensitivity, but the longer propagation length enables a longer optical interaction length with the sensing medium, leading to a higher overall sensitivity [5]. LRSPP waveguide biosensors are compact and mass manufacturable using semiconductor fabrication tools and processes.

In this paper we review recent work carried out with LRSPP straight waveguide biosensors [6] for the detection of diseases in complex fluids. Specifically, we review work carried out on the detection of leukemia in patient blood sera [7], on the detection of dengue infection in patient blood plasma [8,9], and on the detection of bacteria in urine [10]. We discuss prospects for the detection of other diseases, including HIV, malaria and cardiac infarction.

**REFERENCES**

1. M. A. Cooper, "Optical biosensors in drug discovery," *Nat. Rev. Drug Discov.*, vol. 1, pp. 515-528, 2002.
2. J. Homola, "Surface plasmon resonance sensors for detection of chemical and biological species," *Chem. Rev.*, vol. 108, pp. 462-493, 2008.

3. S. Löfås, "Optimizing the hit-to-lead process using SPR analysis," *Assay Drug Dev. Technol*., vol. 2, pp. 407-416, 2004.
4. P. Berini, "Long-range surface plasmon polaritons," *Adv. Opt. Photonics*, vol. 1, pp. 484-588, 2009.
5. P. Berini, "Bulk and surface sensitivities of surface plasmon waveguides," *New J. Phys*., vol. 10, p. 105010, 2008.
6. O. Krupin, H. Asiri, C. Wang, R. N. Tait, and P. Berini, "Biosensing using straight long-range surface plasmon waveguides," *Opt. Express*, vol. 21, pp. 698-709, 2013
7. O. Krupin, C. Wang, P. Berini, "Detection of leukemia markers using long-range surface plasmon waveguides functionalized with protein G," *Lab on a Chip*, Vol. 15, pp. 4156-4165, 2015
8. W. R. Wong, O. Krupin, S. D. Sekaran, F. R. Mahamd Adikan, and P. Berini, "Serological diagnosis of dengue infection in blood plasma using long-range surface plasmon waveguides," *Anal. Chem*., vol. 86, p. 1735−1743, 2014.
9. W. R. Wong, S. D. Sekaran, F. R. Mahamd Adikan, and P. Berini, "Detection of dengue NS1 antigen using long-range surface plasmon waveguides," *Biosens. Bioelectron*., vol. 78, p. 132−139, 2016.
10. P. Béland, O. Krupin, P. Berini, "Selective detection of bacteria in urine with a long-range surface plasmon waveguide biosensor," *Biomedical Optics Express*, Vol. 6, pp. 2908-2922, 2015.

# Hybrid plasmonic structures for wave mixing at the nanoscale

**G. Laurent**[1], **M. Ethis De Corny**[1], **N. Chauvet**[1], **G. Nogues**[1], **M. Jeannin**[1], **A. Drezet**[1], **S. Huant**[1], **G. Dantelle**[1], **T. Gacoin**[2], **and G. Bachelier**[1]

[1]Neel Institute, CNRS-Université Grenoble Alpes, France
[1]Laboratoire Charles Fabry de lInstitut dOptique, CNRS, Orsay, France
guillaume.laurent@neel.cnrs.fr

**Abstract**— Our work focuses on the optical response of hybride nano-particles composed of metal particles coupled with non-linear crystal. Electromagnetic field enhancement due to plasmonic resonance is expected to enhance the non-linear response of nano-sized KTP like crystals. Here, we present our results on the modelling and the experimental study of the Second Harmonic Generation (SHG) in nonlinear cristals coupled or not with metal particles.

## 1. INTRODUCTION

Scalability of optical devices is a major challenge for quantum optics and quantum cryptography fields. However, non-linear optical processes such as second harmonic generation and parametric down conversion become very inefficient when the active medium is reduced to the nanoscale. Enhancement strategies are therefore mandatory. Here, we investigate the SHG response of a nano-crystal of KTP and its modification by the proximity of a plasmonics antenna.

## 2. METHOD AND RESULTS

By Finite Element Method simulation of SHG [1,2], we investigate the non linear response of several structures: i) non-linear crystal, ii) metallic antenna and also iii) hybrid structures. Comparing quantitatively simulated and experimental data on metallic particles allows to infer the origin of SHG response in metallic antennas, and to design doubly resonant structures in the visible range with aluminium antennas.

To further enhance the nonlinear response, hybrid structures are envisionned by coupling a KTP crystal to the plasmonic structure. The efficiency of individual building blocks are first compared in terms of collected counts of photons/s, allowing to establish the net gain offered by the hybrid structure. Figure 1 shows that these structures can exhibit a largely enhanced SHG signal. It raises the question of the best strategy to optimize this phenomenon. Using hybrid structures realized with monocrystalline KTP [4], experiments show that parameters such as the antenna size or the crystalline orientation are crucial.

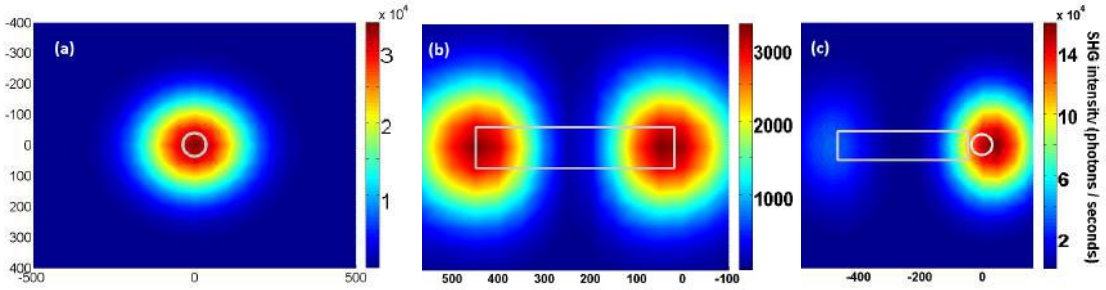



Figure 1: Simulated SHG map obtained by scanning a single nonlinear crystal (a), a single plasmonic antenna (b) and the corresponding hybrid structure (c) with nonlinear efficiencies taken from the litterature.

## REFERENCES

1. Bachelier, G. *et al*, *J. Opt. Soc. Am. B*, Vol. 25, 955, 2008.
2. Bachelier, G. *et al*, *PRB*, Vol. 82, 2010.
3. Gloppe, A. *et al*, *Nature Nanotechnology*, Vol. 9, 920-926, 2014.
4. Mayer, L *et al*, *Nanoscale*, Vol. 5, 8466, 2013.

# All-Dielectric Metasurfaces for Structured Light Manipulation

**Natalia M. Litchinitser,[1] Mikhail I. Shalaev,[1] Jingbo Sun,[1] Alexander Tsukernik,[2] and Apra Pandey[3]**

[1] University at Buffalo, The State University of New York, Buffalo, New York 14260, United States

[2]Toronto Nanofabrication Centre, University of Toronto, Toronto, ON M5S 3G4, Canada

[3]CST, Inc., San Mateo, California 94404, United States

*corresponding author: natashal@buffalo.edu

**Abstract**- We experimentally demonstrate an all-dielectric resonant metasurface with full 0-to-2π phase control at near infrared wavelengths. We design and fabricate dielectric nanoblocks-based metasurfaces for various functionalities, including high-efficiency beam deflector and light converter for generating optical vortex beams, carrying an orbital angular momentum.

Metasurfaces (MS) are two-dimensional artificial materials with thicknesses much smaller than incident light wavelength, allowing complete control of the phase, amplitude, and polarization of light beams [1,2]. Compared to conventional optical elements, which rely on long propagation distances, these devices facilitate strong light-matter interaction in subwavelength-width material layers, allowing abrupt changes of beam parameters. Dielectric MS, unlike their three-dimensional analogues, metamaterials, do not require complicated fabrication techniques and can be produced in one lithographical step. A majority of the recent studies have focused on metal-dielectric structures, which have relatively low efficiency due to orthogonal polarizations coupling and nonradiative Ohmic losses in metals [3,4].

Dielectric MS, unlike their three-dimensional analogues, metamaterials, do not require complicated fabrication techniques and can be produced in one lithographical step [5-9]. In our initial studies, we theoretically investigated and experimentally demonstrated an all-dielectric resonant metasurface with full 0-to-2π phase control at near-infrared wavelength as shown in Fig. 1. We designed and fabricated a high-efficiency beam deflector and a light converter for generating an optical vortex beam, carrying an orbital angular momentum. In addition to 0 to π phase control enabled by a single magnetic or electric resonance, overlapping of magnetic and electric resonances in the frequency domain enabled an additional phase control with optical impedance matching and, as a result, high efficiency in transmission mode with full 2π phase manipulation. These particular functionalities can serve as specific examples of vast possibilities offered by the planar Mie-resonance-based metasurface approach. In this talk, we will discuss linear and nonlinear dielectric metasurfaces made of silicon and chalcogenide glasses.

All-dielectric-based metasurfaces can be used for fabrication of miniaturized high-efficiency optical components for near infra-red photonics, such as flat lenses, beam deflectors, antireflection coatings, and phase modulators. Elimination of metals and, as a result, no ohmic losses, compared to plasmonic counterparts and not requiring cross-polarized field interaction to cover full phase, makes them well-suited for integration on optical chip and for large-scale production.

**Acknowledgements**

This work was supported by the U.S. Army Research Office Award No. W911NF-11-1-0333.

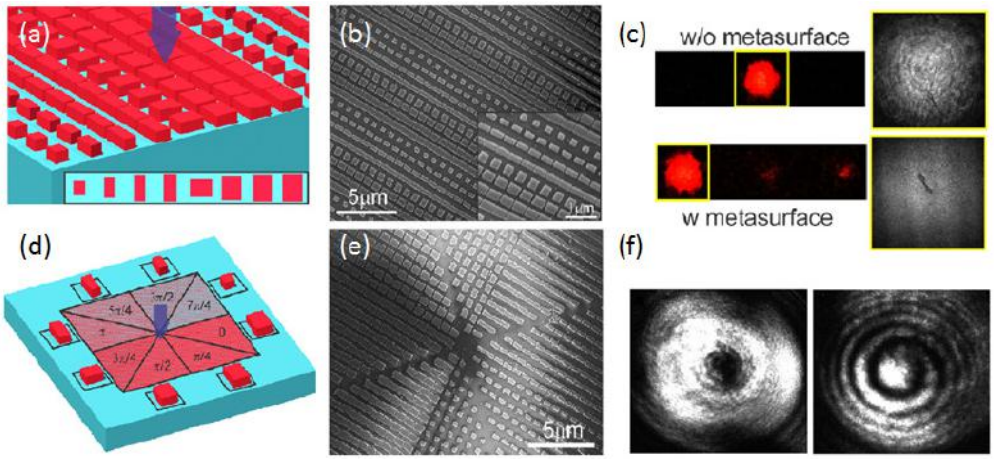



**Figure 1.** (a) Schematics of the proposed beam deflector with the unit cell (shown in the inset) containing eight nanoblocks, each responsible for the phase shift from 0 to 2π with π/4 increments. (b) Scanning electron microscopy image of fabricated metasurfaces with 96 × 96 μm total size; zoomed-in picture is shown in the inset. (c) Beam position without (left top) and with (left bottom) metasurface; the beam power is refracted to the left side with deflection angle 13.1° and transmission of ~36%. Input and output beam photographs are also shown in the inset (right). (d) Schematics and (e) scanning electron microscopy image for optical vortex beam converter with eight sectors with different unit cells for each sector of metasurface. Each sector introduces an additional π/4 phase shift, thus covering 0 to 2π phase change. (e) Intensity distribution for measured output vortex beam in form of donut shape. (f) Vortex and Gaussian beams interference experiment results showing spiral-shaped intensity distribution.

## REFERENCES


1. Bomzon, Z., Biener, G., Kleiner, V., and Hasman, E., "Space-variant Pancharatnam–Berry phase optical elements with computer-generated subwavelength gratings ," Opt. Lett. 27, 1141–1143, 2002.
2. Bomzon, Z., Kleiner, V., and Hasman, E., "Formation of radially and azimuthally polarized light using spacevariant subwavelength metal strip grating," Appl. Phys. Lett. 79, 1587–1589, 2001.
3. Yu, N. and Capasso, F., "Flat optics with designer metasurfaces," Nat. Mater. 13, 139–150, 2014).
4. Yu, N. F., Genevet, P., Kats, M. A., Aieta, F., Tetienne, J. P., Capasso, F., and Gaburro, Z., "Light propagation with phase discontinuities: Generalized laws of reflection and refraction," Science 334, 333–337, 2011.
5. Yu, Y. F., Zhu, A. Y., Paniagua-Domınguez, R., Fu, Y. H., Luk'yanchuk, B., and Kuznetsov, A. I., "High transmission dielectric metasurface with 2π phase control at visible wavelengths," Laser Photonics Rev. 9, 412–418, 2015.
6. Chong, K. E., Staude, I., James, A., Dominguez, J., Liu, S., Campione, S., Subramania, G. S.,
7. Luk, T. S., Decker, M., Neshev, D. N., Brener, I., Kivshar, Y. S., "Polarization-independent silicon metadevices for efficient optical wavefront control," Nano Lett. 15, 5369–5374, 2015.
8. Lin, D. M., Fan, P. Y., Hasman, E., and Brongersma, M. L., "Dielectric gradient metasurface optical elements," Science 345, 298–302, 2014.
9. Shalaev, M. I., Sun, J., Tsukernik, A., Pandey, A., Nikolskiy, K., Litchinitser, N. M., High-efficiency all-dielectric metasurfaces for ultracompact beam manipulation in transmission mode," Nano Lett. 15, 6261–6266, 2015.

# Hybrid plasmonic add-drop filter based on novel micro-ring-disk resonators with fJ switching energy

**D. C. Zografopoulos[1], M. A. Swillam[2], and R. Beccherelli[1*]**

[1]Consiglio Nazionale delle Ricerche, Istituto per la Microelettronica e Microsistemi (CNR-IMM), Roma 00133, Italy

[2] Department of Physics, School of Science and Engineering, The American University in Cairo, New Cairo, 11835, Egypt

[*]corresponding author: romeo.beccherelli@artov.imm.cnr.it

**Abstract**- We present a hybrid plasmonic add-drop filter based on a micro-ring-disk with submicron dimensions. The device is based on the conductor-gap-silicon hybrid plasmonic platform and utilizes an embedded electro-optical polymer to control the wavelength-selective coupling between two bus lines. The novel micro-ring-disk resonator combines the easier fabrication of a microdisk resonator with the lower capacitance of a microring resonator and provides high modulation depths, low insertion losses, and power consumption around 1 fJ/bit.

Electro-optic polymers (EOP) have been widely used in the fabrication of silicon-on-insulator (SOI) modulators in the so-called the silicon-organic hybrid (SOH) platform, owing to their high operation speed and low power consumption [1]. Recently, we have combined the advantages of EOP modulators with the compact sizes of hybrid plasmonic circuits based on conductor-gap-silicon (CGS) waveguides in both resonating [2,3] and directional coupling configurations [4]. In this work, we extend our previous design to add-drop filter circuits, where the resonating element is a silicon microdisk on top of which a ring structure is patterned for the EOP and the metal cap. The proposed structure features high modulation depths, low insertion losses and low switching power.

**Acknowledgements**. This work was made possible by a NPRP award [NPRP 7456-1-085] from the Qatar National Research Fund (member of the Qatar Foundation). The statements made herein are solely the responsibility of the authors.

**REFERENCES**

1. D. Korn *et al.*, "Silicon-organic hybrid (SOH) IQ modulator using the linear electro-optic effect for transmitting 16QAM at 112 Gbit/s," *Opt. Express*, vol. 21, pp. 13219-13227 (2013).
2. D. C. Zografopoulos, M. A. Swillam, and R. Beccherelli, "Electro-optic hybrid plasmonic modulator based on electromagnetically induced transparency" *IEEE Photon. Technol. Lett.*, Vol. 28, Issue 7, pp. 818-821 (2016).
3. A. O. Zaki, N. H. Fouad, D. C. Zografopoulos, R. Beccherelli, and M. A. Swillam, "Low power, compact hybrid plasmonic double microring electro-optical modulator" (submitted).
4. D. C. Zografopoulos, M. A. Swillam, L. A. Shahada, and R. Beccherelli, "Hybrid electro-optic plasmonic modulators based on directional coupler switches", *Appl. Phys. A*, Vol. 12, art. no. 344 (2016).

**Strong Light-matter Interaction in Two-dimensional Transition Metal Dichalcogenides Through Integration with Plasmonic Nanoantenna Arrays**

Syed Hamed Shams Mousavi, Hossein Taghinejad, Mohammad Taghinejad, Ali A. Eftekhar, and Ali Adibi

School of Electrical and Computer Engineering

Georgia Institute of Technology

Two-dimensional metal dichalcogenides (2D TMDCs) have been of great interest lately due to their unique potentials for forming new optoelectronic devices. On the other hand, plasmonic nanostructures have been considered as a powerful platform for strong-light-matter interaction in optoelectronic devices. In this talk, a hybrid material platform based on careful integration of these two powerful material structures is presented, and its use for optoelectronic applications (especially light generation) is presented. We show that by combining lattice plasmon modes with local surface plasmon polaritons in plasmonic nanoantenna arrays, new modes with Fano-type resonances for enhancing light –matter interaction at desired wavelengths can be engineered. These modes can be used to enhance light emission from 2D TMDCs when they are integrated with such plasmonic nanostructures. This effect will be experimentally presented, and its prospects for forming new light-emitting devices (especially lasers) will be discussed.

# Plasmonic Mach-Zehnder Modulator with Direct Coupling Silicon Waveguides

**Abdalrahman Mohamed, Mohamed Swillam**

School of Science and Engineering, American University in Cairo, Cairo, Egypt
corresponding author, E-mail: m.swillam@aucegypt.edu

## Abstract

Optical interconnects as a solution for electrical interconnects speed problem is in need for optical modulators, that can overcome the power and size constrains. An organic mach-zehnder modulator was used, whose arms are made of metal-polymer-metal waveguides, and the 90 degree plasmonic to silicon waveguide coupling scheme was exploited. An extinction ratio of 15.8 dB, insertion loss of 3.38 dB was reached under 10 V bias, with a device length of 4.7 µm. Smaller polymer slot size, and higher nonlinear coefficient can further enhance this design.

## 1. Introduction

Electrical interconnects is a bottle neck for today's processors. The delay of communicating data in and between processors is comparable or longer than the gate delays. One of the competing technologies to solve this problem is optical interconnects. Optical modulators with low power consumption and small footprint in comparison with the electrical interconnects is needed.

Many trials has been made to achieve this goal. Different silicon photonic modulators, including ring resonators, electro absorption and mach-zehnder have failed in general to fulfill the footprint and the power specifications [1]. Plasmonics can solve these problems due to its ability to confine light in nano-scale dimensions. Plasmonic mach-zehnder modulator has been presented before, and showed a promising results [2].

In our work, we used the advantages of the plasmonic mach-zehnder modulator, and exploited the 90 degree coupling between the silicon wave guides and the plasmonic arms of the modulator [3]. This combination eliminates the need for tapers or any special junction, so the dimensions of the modulator was halved.

The design is presented in the next section followed by a results section, then a conclusion.

## 2. Modulator Design

The modulator is shown in figure(1). It consists of an input silicon waveguide, fed from a laser source, then the 90 degree coupler to the metal-polymer-metal waveguides, that forms the mach-zehnder arms. The polymer refractive index in each arm varies on applying voltage, cause a delay between the two waves, that creates destructive interference at the combiner. lastly, the output is fed to output silicon waveguide, which will communicate data through processor.

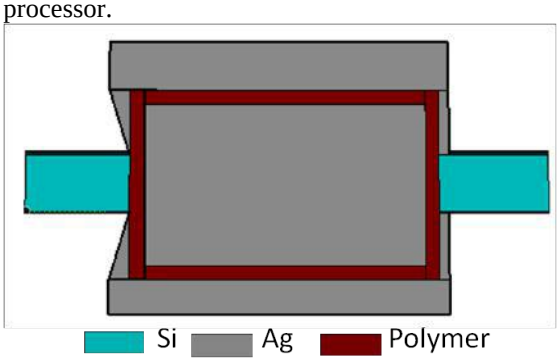



Figure 1: The mach-zehnder modulator formed of the two metal insulator metal waveguides, with input and output silicon waveguides.

FDTD tool was used to simulate the 3D structure. constant refractive indices was used for the silicon and the silicon dioxide, that forms the substrate. Wavelength dependant refractive index was used for the silver. The refractive index variation of the polymer was calculated using Pockel's effect nonlinear dependence between the electric field and refractive index, and it was changed manually.

## 3. Results

In the on state, at no bias, insertion loss of 3.38 dB was reached. In the off state, at 10 V bias, 15.8 dB extinction ratio was reached. The device footprint is 5 µm * 1.3 µm. The maximum reflection from the modulator was less than 15%.

## 4. Conclusions

Mach-Zehnder plasmonic modulator can fulfill the footprint requirement for on chip integration. The use of materials with stronger nonlinear properties, and smaller polymer slot sizes can enhance the footprint more, and in turns enhance the insertion loss, and decrease the power consumption significantly through decreasing the capacitance.

## Acknowledgements

This work was made possible by a NPRP award [NPRP7456-1-085] from the Qatar National Research Fund (member of the Qatar Foundation). The statements made herein are solely the responsibility of the authors.

## References


[1] G. T. Reed, G. Mashanovich, F. Y. Gardes, and D. J. Thomson, “Silicon optical modulators,” *Nat. Photonics*, vol. 4, no. 8, pp. 518–526, Aug. 2010.

[2] HaffnerC., HeniW., FedoryshynY., NiegemannJ., MelikyanA., ElderD. L., BaeuerleB., SalaminY., JostenA., KochU., HoessbacherC., DucryF., JuchliL., EmborasA., HillerkussD., KohlM., DaltonL. R., HafnerC., and LeutholdJ., “All-plasmonic Mach–Zehnder modulator enabling optical high-speed communication at the microscale,” *Nat Photon*, vol. 9, no. 8, pp. 525–528, Aug. 2015.

[3] C. Lin, H. M. Wong, B. Lau, M. A. Swillam, and A. S. Helmy, “Efficient broadband energy transfer via momentum matching at hybrid junctions of guided-waves,” *Appl. Phys. Lett.*, vol. 101, no. 12, p. 123115, 2012.

# Long Range Plasmonic Waveguide Using Doped Silicon in Mid-Infrared

**Raghi S. El Shamy[1], Hany Mossad[1], and Mohamed A. Swillam[1]**

[1]Department of Physics, the American University in Cairo (AUC), Cairo, Egypt
*corresponding author, E-mail: m.swillam@aucegypt.edu

## Abstract

The modal analysis of CMOS compatible hybrid plasmonic waveguide in the mid-infrared region (4-6μm) using doped silicon is introduced. Manipulating the design parameters of the waveguide such as the thickness of the doped silicon layer and the nearby sapphire layers can effectively change the propagation length and the mode confinement. The simulation results show that a propagation length of 220μm can be achieved at wavelength 6μm.

## 1. Introduction

Mid infrared is a promising range with lots of applications such as infrared spectroscopy and chemical detection [1] which have impact in many fields such as medicine, astronomy and other [2,3], due to the absorption peaks of many biological and chemical molecules that lay in this range.

Insulator Metal Insulator (IMI) plasmonic waveguide with low refractive index have long propagation length but large modal area. On the other hand, IMI plasmonic waveguide with high refractive index have small modal area but short propagation length [4]. Hybrid plasmonic waveguides [4,5] which consist from metal layer sandwiched with low then high index layers is compromise of these two structures. The modes of this structure can be interpreted as coupled mode between the plasmonic waveguide mode and the dielectric waveguide mode which are separated by the low index layer [5].

This paper present the modal analysis of Complementary Metal Oxide Semiconductor (CMOS) compatible hybrid waveguides in the mid infrared region from 4-6μm where the metal layer is replace by highly doped silicon. The dependence of the mode effective index and propagation length on the different waveguide parameters are studied. To allow for both the successful waveguiding in the wavelength range between 4 and 6 μm, and CMOS compatibility of the structure, the high index and low index materials were chosen as silicon and sapphire, respectively [6].

This structure achieve 220μm propagation length at wavelength 6μm. Our analysis showed also, that our structures exhibit anomalous dispersion (i.e. negative group velocity) for wavelengths around 3μm and can support slow and fast light.

## 2. Modal Analysis

The modal analysis of the hybrid waveguide (Fig. 1-(a)) has been carried on using Finite Element Method (FEM) solver [7] for various wavelengths in the mid-infrared region λ=4-6μm. The wavelength range is chosen to be far away from the resonance wavelength (2.63μm) of the doped silicon and at the same time far from the sapphire absorption region (λ>6μm). The $5\times10^{20}$ $cm^3$ doped silicon layer is modeled using Drude model.

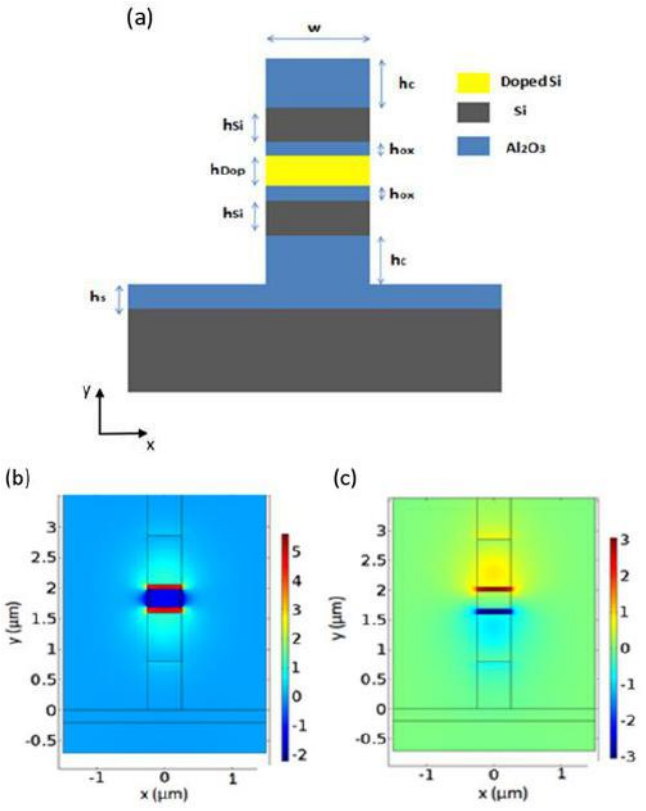



Figure 1: (a) Hybrid waveguide. Ey component of the: (b) symmetric mode with $h_{ox}$=80nm and $h_{Dop}$=300nm, (c) anti-symmetric mode with $h_{ox}$=80nm and $h_{Dop}$=300nm.

The width (w) of the hybrid waveguide is chosen such that it supports only fundamental modes. The thickness of the silicon doped layer ($h_{Dop}$) is spanned from 60nm to 500nm. Also the thickness of the sapphire ($h_{ox}$) is spanned from 20nm to 120nm.

The hybrid waveguide supports both the fundamental symmetric (Fig-1(b)) and anti-symmetric modes (Fig. 1-(c)). By increasing the doped silicon layer $h_{Dop}$ the symmetric mode effective index increase while the anti-symmetric mode effective index decreases. In addition, as the sapphire thickness ($h_{ox}$) decreases, the effective index of both modes increases due to stronger coupling between the plasmonic and the dielectric mode [5] as mentioned above. As the effective index of the mode increase as the mode becomes more confined and hence the losses increase. Figure 2 show the mode effective index and the propagation length of both symmetric and anti-symmetric mode at 5.5μm wavelength.

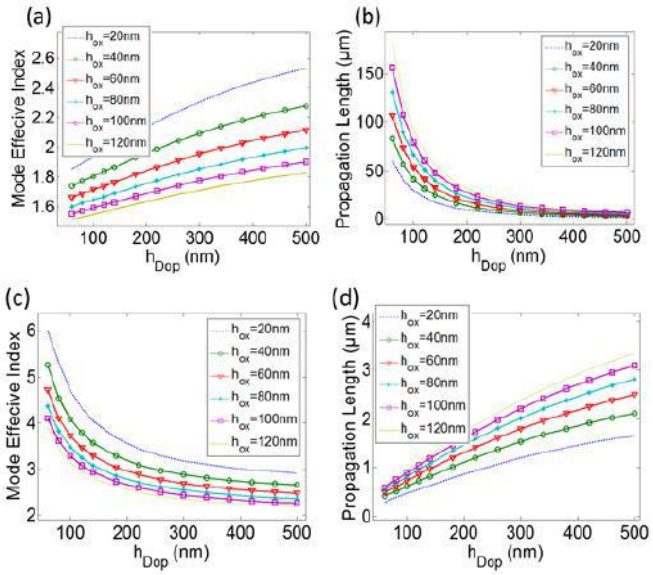



Figure 2: (a) Mode effective index and (b) Propagation length of the symmetric mode at wavelength=5.5μm. (c) Mode effective index and (d) Propagation length of the anti-symmetric mode at wavelength=5.5μm.

## 3. Conclusions

In this work we present the modal analysis of hybrid waveguides using doped silicon in the mid infrared range from 4μm to 6μm. The propagation distance and the normalized modal area of the fundamental modes are calculated. In this modal analysis the dependence of the mode parameters on the wavelength, doped layer thickness and nearby sapphire layer thicknesses was investigated.

## Acknowledgements

This work was supported by Information Technology Industry Development Agency (ITIDA) under the ITAC Program CFP#70.

## References

[1] Richard Soref. “Mid-infrared photonics in silicon and germanium”. NATURE PHOTONICS| VOL 4 | AUGUST 2010.

[2] Labadie L. and Wallner O. “Mid-infrared guided optics: a perspective for astronomical instruments,” Opt. Express 2009.

[3] G. C. Holst and S. W. McHugh, “Review of thermal imaging system performance,” Proc. SPIE 1689, 78–84 (1992).

[4] Lin Chen, Xun Li, Guoping Wang, Wei Li, Sihai Chen, Long Xiao, and Dingshan Gao. “A Silicon-Based 3-D Hybrid Long-Range Plasmonic Waveguide for Nanophotonic Integration”. Journal of Lightwave Technology, vol. 30, pp. 163 – 168, 2012.

[5] R. F. Oulton, V. J. Sorger, D. A. Genov, D. F. P. Pile, and X. Zhang. “A hybrid plasmonic waveguide for subwavelength confinement and long-range propagation,” Nature Photon., vol. 2, pp. 496–500, 2008.

[6] Tom Baehr-Jones, Alexander Spott, Rob Ilic, Andrew Spott, Boyan Penkov, William Asher and Michael Hochberg. “Silicon-on-sapphire integrated waveguides for the mid-infrared“. 24 May 2010 / Vol. 18, No. 12 / OPTICS EXPRESS.

[7] FEM Solver: http://www.comsol.com/.

# Hybrid silicon organic directional coupler based modulator

**M. Y. Abdelatty[1,2], A. O. Zaki[2,3], and M. A. Swillam[*1]**

[1]Dept. of Physics, School of Science and Engineering, American University in Cairo, New Cairo, 11835
[2]Basic Sciences Dept., Faculty of Engineering, The British University in Egypt, Cairo, Egypt
[3]Engineering Physics Dept., Faculty of Engineering, Ain Shams University, Abassia, Cairo, 11517
*corresponding author: m.swillam@aucegypt.edu

**Abstract**

An optical directional coupler (ODC) based on silicon-on-insulator waveguide is designed and demonstrated, with a power-splitting mechanism that can be tuned with applying the external electric field. The tuning mechanism takes the advantage of changing the refractive index of polymer when applying external electric field. The ODC operates under 1550 nm telecommunication wavelength. A finite difference time domain method with perfect matching layer (PML) absorbing boundary condition is taken up to simulate and analyze the ODC.

## 1. Introduction

Switching and modulating are the main operations in digital computing signal processing. The growing demand for high capacity systems to process optical signals has concerned a lot of research [1, 2]. Optical directional coupler is one of the fundamental components in optical systems; it can be used as switch, modulator, and power splitter. Directional coupler's structure involves two adjacent wave guides creating a coupling environment [3]. Conventional directional couplers are silica-based, lithium niobate-based, or made of optical fibers waveguides [4]. The length of these directional couplers ranges from several hundred micrometers to several millimeters [5].

Polymer electro-optic directional couplers are becoming popular due to the polymer advantages over other optical materials [6]. Polymers have low dispersion profile in the range of telecommunication wavelength and large electro-optic coefficient; polymers are flexible for integration with electronic circuits. Switching time and frequency depends on many factors, such as response time of the electro-optic polymer materials [7]. Since the response time of almost all polymers as fast as femtosecond, we can consider that there is no delay between the the change of the electric signal and that of the refractive index of the electro-optic polymer [8].

## 2. Design

The proposed directional coupler is based on silicon-on-insulator waveguide topped with polymer and metal is shown in figure 1. The optical wave is guided in the polymer between the silicon and metal. The refractive index of polymer changes with the applied electric field; that results in changes in the mode profile in the two ports which affects the power-splitting ratio between them. In other words, the change in polymer refractive index changes significantly the effective refractive index of the modes due to the high confinement in the polymer.

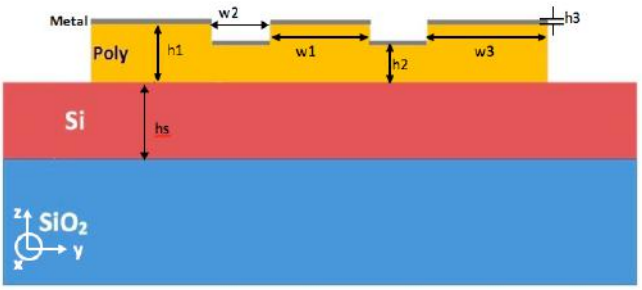



Figure 1: Cross section view of the direct coupler based modulator.

## 3. Modal analysis

The proposed structure is composed of 2 channels. We excite the input optical wave through one of them. The optical wave is guided mainly in the polymer layer of this channel. At the coupling length most of the power is coupled into the other channel.

### 3.1. Single channel waveguide

Electric field intensity profile of a single channel is shown in fig.2. The light is confined in the polymer region of smaller thickness (h1). The regions of larger thickness(h2) are of lower effective index so they act as waveguide cladding in the horizontal direction. Mode analysis held using Lumerical Mode solution show that the real part of the effective index of the mode in fig.2 is 2.47 and the propagation losses are estimated to be 0.15 dB/μm.

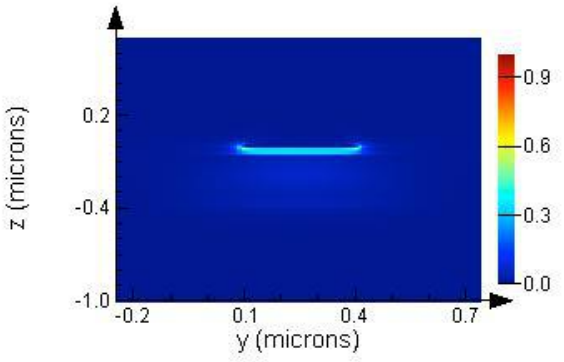



Figure 2: The single channel electric field intensity mode profile.

### 3.2. Two channel waveguide

#### *3.2.1. Off-state*

With no potential difference applied across the polymer regions, the refractive index of the polymer is the same everywhere. The mode excited at the input of one channel would be resolved into 2 modes of different propagation constants. Figure 3 shows the electric intensity profiles of those two modes, namely, the even and the odd modes. The interaction between these modes results in the power being fully coupled to the other channel after a specific distance defined as the beating length ($L_B$).

$$L_B = \frac{\lambda}{2(n_e - n_o)}$$

Equation 1: beating length equation.

where $n_e$ and $n_o$ are the effective indices of the even and the odd mode, respectively.

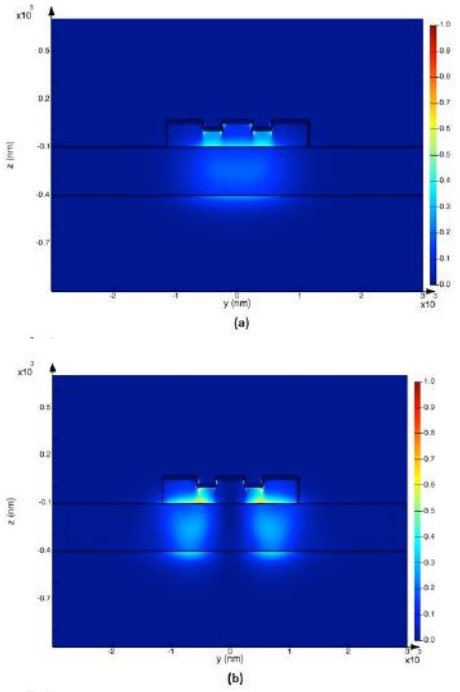



Figure 3: (a) the even mode in the off state, (b) the odd mode in the off state

#### *3.2.2. On-state*

When the voltage is applied, the polymer refractive index changes and changes the effective index of the even and odd modes. According to (1), the value of beating length is changed. This, in turn, changes the power splitting ratio between the 2 channels. This way the output power is modulated by the applied potential difference. Figure 4 shows the symmetric and the anti-symmetric mode profiles in the on-state.

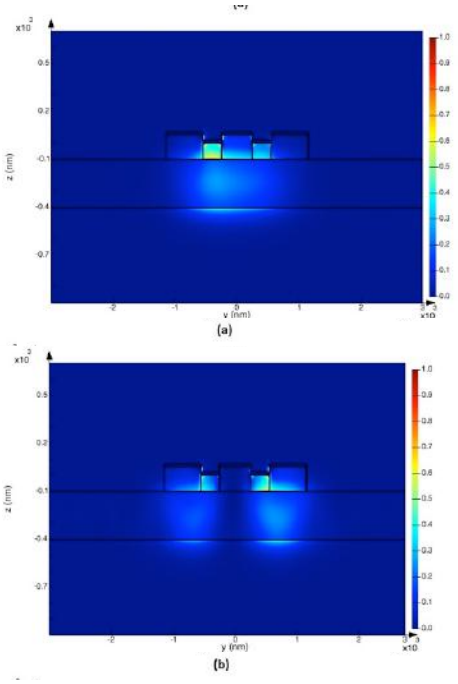


Figure 4: (a) the even mode in the on state, and (b) the odd mode in the on state.

## 4. Conclusions

We have proposed an optical directional coupler based on polymer electro-optic characteristics. The structure and principles are described. Modal analysis is used to verify the design and to calculate the coupling ratio between the two channels of the directional coupler.

## Acknowledgements

This work was made possible by a NPRP award [NPRP7-456- 1- 085] from the Qatar National Research Fund (member of the Qatar Foundation). The statements made herein are solely the responsibility of the authors.

## References

[1] Zhao, H., X. G. Guang and J. Huang, “Novel optical directional coupler based on surface plasmon polaritons,” *Physica E Low Dimens Syst Nanostruct*, Vol. 40, No. 10, 1386-9477, 2008.

[2] Zaki, Aya O., Khaled Kirah, and Mohamed A. Swillam. "Hybrid plasmonic electro-optical modulator." Applied Physics A 122.4 (2016): 1-7.

[3] Zheng, C. T., C. S. Ma and X. Yan, “Design of a polymer directional coupler electro-optic switch using two-section reversed electrodes,” *Appl Phys B*, Vol. 96, No. 1, 0946-2171, 2009.

[4] Yamada, H., Chu, T., Ishida, S., and Arakawa, Y., “Optical Directional Coupler Based on Si-Wire Waveguides,” *IEEE Photon. Technol. Lett.*, VOL. 17, NO. 3, MARCH 2005

[5] Zhang, X., B. Lee and C. Lin, “Highly Linear Broadband Optical Modulator Based on Electro-Optic Polymer,” *JPHOT*, Vol. 4, No. 6, 1943-0655, 2012.

[6] Fan, G., Y. Li and B. Han, “Study of an Electro-Optic Polymer Modulator,” *J. Lightwave Technol.*, Vol. 30, No. 15, 0733-8724, 2012.

[7] Zografopoulos ,D.,C., Swillam, M., A., Shahada, L. A. , Beccherelli, R., “Hybrid electro-optic plasmonic modulators based on directional coupler switches” *Appl Phys A*, Vol 122, No. 344 (2016).

[8] Zheng, C., Ma, C., Yan, X., and Wang, X. D., “Analysis of response characteristics for polymer directional coupler electro-optic switches,” *Opt. Commun.*, Vol 281, No. 24 (2008).

# SEMICONDUCTOR PLASMONIC GAS SENSOR USING ON-CHIP INFRARED SPECTROSCOPY

**Mohamed Y. Elsayed[1], Yehea Ismail[1], Mohamed A. Swillam[2]**

[1]Center for Nanoelectronics and Devices AUC / Zewail City of Science and Technology, Egypt
[2]Department of Physics, American University in Cairo (AUC), Egypt
*corresponding author, E-mail: m.swillam@aucegypt.edu

## Abstract

We designed a plasmonic slot waveguide that works in the mid infrared range using Indium Arsenide. By operating in the fingerprint region of IR spectroscopy, the waveguide acted as a selective sensor, with peaks in the transmission spectrum corresponding to the characteristic IR absorption spectrum. The sensor was demonstrated using finite different time domain simulations with a couple of gases. This constitutes a label-free sensing method that can be used for a variety of IR-active analytes.

## 1. Introduction

Guiding mid-infrared waves is important for on chip sensing applications. In particular, plasmonic modes couple well to the dielectric media to be sensed. Semiconductors are very promising as plasmonic materials due to the ability to engineer the material for certain responses, unlike metals[1, 2]. However, in silicon, very high carrier concentrations – on the order of $10^{21}$ $cm^{-3}$ – are required to achieve plasma frequency in the MIR [3]. Indium Arsenide has been identified as an excellent candidate for MIR plasmonics and has also been used for sensing applications using local surface plasmon resonance (LSPR) [4]. By using InAs, we designed a gas sensor based on propagating surface plasmon polaritons (SPPs) at much lower carrier concentrations. Gas sensing typically requires very high sensitivity which can result in complex designs [5, 6]. Because it is based on SPPs instead of LSPR, simple integration with InAs-based source and detector is feasible.

## 2. Simulations

Our sensor design is based on the plasmonic slot waveguide in figure 1. We modeled highly doped InAs using a Drude empirical model, verified with the experimental data in [2]. Dispersion analysis was performed using the finite element method using COMSOL to study the effect of geometry and carrier concentrations. The dispersion analysis confirmed that carrier concentrations around $10^{19}$ $cm^{-3}$ to $10^{20}$ $cm^{-3}$ only were required to operate in the mid infrared. We optimized the gas sensor's dopant concentration and geometry to operate in the fingerprint region of IR spectroscopy yielding an ultracompact design with a 200 nm gap and length of only 1 µm. Finite-difference time-domain simulations were used to simulate the transmission spectrum, first based on air (n=1).

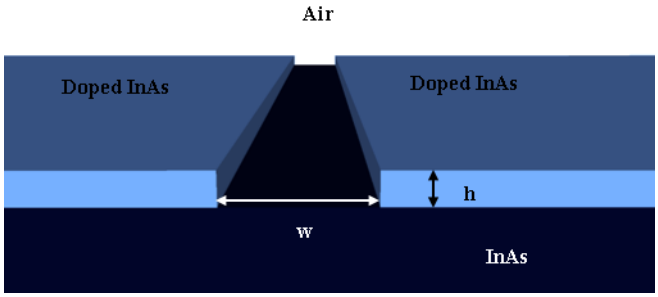



Figure 1. InAs plasmonic slot waveguide used as a gas sensor. Optimized cross sectional area was 200nm x 200nm. Simulation was performed for 1µm long waveguide.

Infrared absorption data from the NIST database [7] was used to develop models for refractive index and extinction coefficient of octane vapor. The extinction coefficient, k, was obtained from absorption, α, through the relation in equation (1).

$$\alpha(\lambda) = \frac{4\pi k(\lambda)}{\lambda}. \quad (1)$$

Then, the refractive index was estimated using Kramers-Kronig relations in equation (2) following the approach in [8].

$$n(\lambda_0) = n(\lambda_1) + P\left[\frac{2(\lambda_1^2 - \lambda_0^2)}{\pi}\int_0^\infty \frac{\lambda k(\lambda)\, d\lambda}{(\lambda_0^2 - \lambda^2)(\lambda_1^2 - \lambda^2)}\right], \quad (2)$$

where $n(\lambda_1)$ is a known refractive index of the analyte at wavelength $\lambda_1$ and P is the Cauchy principal value of the integral.

The fingerprint region for this gas was in the range 6 µm to 10 µm, and a carrier concentration of $2.2\times10^{20}$ $cm^{-3}$ was found to give a response covering all this range. Air was replaced by the octane vapor in the simulation by changing the refractive index to the material model obtained. The refractive index has peaks corresponding to the characteristic absorption peaks.

## 3. Results and Discussion

Figure 2 shows that when simulating the transmission of the plasmonic slot waveguide using these models, the transmission spectrum also contained the peaks

corresponding to the characteristic IR absorption peaks. The peaks can be more pronounced if higher light-matter interaction is available, either with a longer structure or by introducing a structure that traps the light for some time such as a ring or cavity.

For different types of materials where the characteristic peaks are in a different region of mid infrared, different carrier concentrations can yield a sensor with a transmission window in a different wavelength range. This can even be done "on-line" using the same device where carriers are injected using an applied electric field.

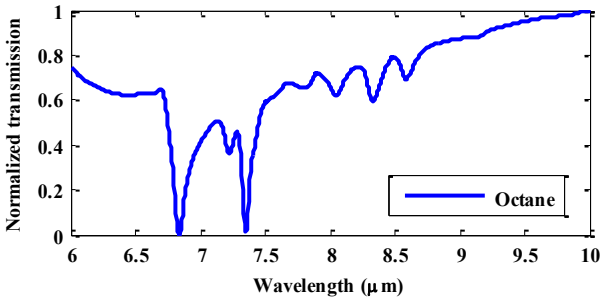



Figure 2. Transmission spectra of Octane vapor after normalization. Normalization was doneby subtracting the transmission spectrum from air and stretching the spectrum such that the minimum transmission is 0 and maximum is 1.

In particular, a lower carrier concentration of, say $10^{19}$ $cm^{-3}$ will give a transmission window beyond 10 μm, which is suitable for a variety of organic materials including amino acids, aromatic compounds and unsaturated hydrocarbons. A higher carrier concentration, closer to $10^{21}$ $cm^{-3}$, will give a transmission window from 3 to 5 μm. While far from the fingerprint region, this mode of operation enables identifying the functional groups in the analyte to determine the type of material instead of actual identification of the material. This is useful in case we don't have a reference spectrum for the material being sensed, some information can still be gathered. Thus, we have a sensor with tunable transmission window in the mid-infrared to suit different sensing media and different modes of operation.

## 4. Conclusions

While we simulated the sensor with a couple of gases, this constitutes a general label-free detection mechanism that makes on-chip IR spectroscopy ubiquitous whether in gases for environmental and quality assurance applications or lab on chip applications.

## Acknowledgements

Research partially funded by Zewail City of Science and Technology, AUC, the STDF, Intel, Mentor Graphics, ITIDA, SRC, ASRT and MCIT.

## References

[1] S. Law, L. Yu, and D. Wasserman, "Epitaxial growth of engineered metals for mid-infrared plasmonics," *Journal of Vacuum Science & Technology B: Microelectronics and Nanometer Structures,* vol. 31, p. 03C121, 2013.

[2] S. Law, D. C. Adams, A. M. Taylor, and D. Wasserman, "Mid-infrared designer metals," *Opt Express,* vol. 20, pp. 12155-65, May 21 2012.

[3] R. Gamal, Y. Ismail, and M. A. Swillam, "Silicon Waveguides at the Mid-Infrared Range," *Lightwave Technology, Journal of,* vol. 33, pp. 3207 - 3214, 2015.

[4] S. Law, L. Yu, A. Rosenberg, and D. Wasserman, "All-Semiconductor Plasmonic Nanoantennas for Infrared Sensing," *Nano Letters,* vol. 13, pp. 4569-4574, 2013/09/11 2013.

[5] R. Kotb, Y. Ismail, and M. A. Swillam, "Integrated coupled multi-stage plasmonic resonator for on-chip sensing," in *Proc. SPIE 9126, Nanophotonics V*, 2014, p. 91263M.

[6] R. Gamal, Y. Ismail, and M. A. Swillam, "Optical biosensor based on a silicon nanowire ridge waveguide for lab on chip applications," *Journal of Optics,* vol. 17, p. 045802, 2015.

[7] I. Coblentz Society, "Evaluated Infrared Reference Spectra," in *NIST Chemistry WebBook, NIST Standard Reference Database Number 69*, P. J. L. a. W. G. Mallard, Ed., ed Gaithersburg MD, 20899: National Institute of Standards and Technology.

[8] J. J. S. V. Lucarini, K.-E. Peiponen, E.M. Vartiainen, *Kramers-Kronig Relations in Optical Materials Research* vol. 110. Berlin, Germany: Springer, 2005.

# Directional Coupler Modulator based on Silicon Nanowires Platform

**Sherif Mohamed[1], Lamees Shahada[1], Mohamed Swillam[2]**

[1]Department of Chemistry and Earth Sciences, College of Arts and Sciences, Qatar University, P.O. Box 2713, Doha, Qatar
[2]Department of Physics, School of Science and Engineering, The American University in Cairo, New Cairo 11835, Egypt
*corresponding author, E-mail: m.swillam@aucegypt.edu

## Abstract

All CMOS compatible optical modulator based on directional coupler configuration is presented, simulated, and analyzed. The device structure utilizes the silicon-organic hybrid platform. The waveguides are made of arrays of silicon nanowires on a buried oxide layer. While the cladding and the voids between the silicon nanowires are filled with an electro-optic polymer. When a voltage is applied across the electro-optic polymer layer, the polymer will have its refractive index value changed, leading to a change in the effective index of the guided mode. Thus, there will be a change in the level of optical power coupled and exchanged between the two arms of the directional coupler. Utilizing Finite Difference Time Domain simulations tools, we design and simulate the operation of the modulator at the telecommunication wavelength, with promising extinction ratios and losses.

## 1. Introduction

There is an increasing demand for fast, low power optical modulators as required for modern telecommunications systems and data networks. While silicon represents the most established and reliable platform for optical waveguides, there are some challenges concerning the use of silicon for optical modulation, but also great efforts have been done on silicon modulators [1].

The centro-symmetric structure of silicon prevents it from exhibiting the linear electro-optic effect (Pockels effect), while the second order electro-optic effect (Kerr effect) is rather weak in silicon [2]. So, the integration of organics that possess strong electro-optic effects with silicon photonics can be very useful for low power and fast optical modulation. Indeed, silicon organic hybrid (SOH) platform adds strong linear electro-optic effect and a variety of other optical properties to silicon photonics [3]. Also, hybrid plasmonic platforms have been investigated for realizing low power and fast modulators [4-6]. Moreover, directional coupler based modulators have recently shown low power, large bandwidth and moderate insertion losses in their operation [7]. The SOH structures make use of the mature CMOS technology [8], which adds the advantage of utilizing already existing manufacturing technologies, without the need for developing new costly fabrication methods.

Hereby, we propose a directional coupler modulator, which is based on SOH platform. The modulator is an all CMOS compatible structure. The modulator is a directional coupler formed of an array of silicon nanowires (SiNWs) [9] on bulk $SiO_2$, while the SiNWs forms the two arms of the directional coupler, and the cladding of the silicon nanowires is the electro-optic organic. When there is no electrical signal applied (OFF state) to the organic, the device operates as a conventional directional coupler where the optical power is exchanged periodically between its two arms. However, when an electrical signal is applied (ON state) to the cladding (electro-optic organic), the refractive index of the organic changes, causing a change in the effective index of the guided mode propagating through the silicon nanowires. This causes a difference in the level of optical power coupled between the two arms compared to the OFF state. So, at the 1.55μm wavelength, we can observe the power difference coupled between the directional coupler arms for the ON and OFF states, i.e. modulation at 1.55μm wavelength.

A commercial-grade simulator based on the finite-difference time-domain (FDTD) method was used to perform the calculations [10]. FDTD simulation methods have shown accurate and efficient sensitivity measurements for different structures including guided wave [11], complex [12], and lossy [13] structures, as well as for dielectric discontinuities [14].

## 2. Device Structure

The modulator utilizes the directional coupler operation where optical power is coupled and exchanged periodically between its two arms. The layout of the directional coupler based modulator is shown in figure 1.

The two arms of the directional coupler are formed of arrays of SiNWs on a buried oxide $SiO_2$ layer. While the electro-optic polymer (EOP) forms the cladding, and fills the voids between the silicon nanowires.

The use of SiNWs instead of bulk Si waveguides has the advantage of introducing voids to the structure, which maximizes the overlap between the optical mode and the cladding [15]. The cladding can be a material under test for sensing purposes or an electro-optical material for modulation purposes as in our case.

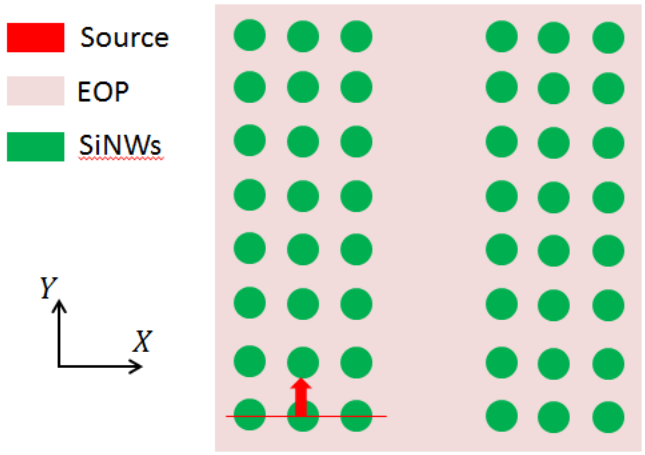



Figure 1: Layout of the SiNW directional coupler modulator.

## 3. Results and Discussion

The excited mode profile is shown in figure 2, where it can be observed that the electric field is strongly confined within the SiNWs waveguides and the EOP cladding filling the voids.

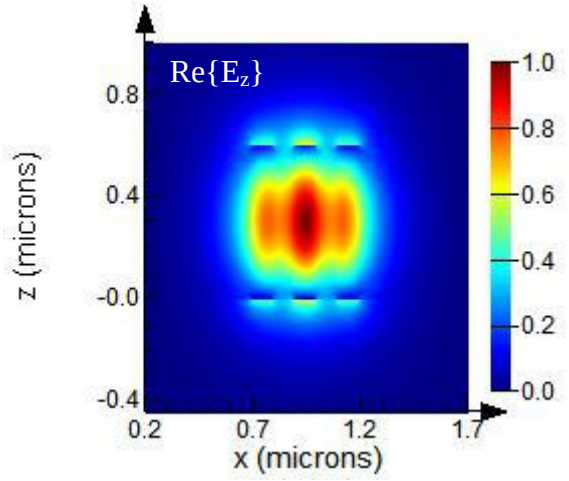



Figure 2: Excited electric field (Re{ $E_z$ }) distribution in the bar waveguide at λ=1.55μm.

So, the SiNWs serve for light guiding, while the field concentrated in the EOP will be more sensitive to refractive index changes in the EOP.

Thus, on applying voltages to the metal contacts (across the EOP), the guided mode will be strongly affected by the change of the EOP index, which leads to changes in the levels of optical power exchanged between the directional coupler two arms. Thus, the device can be optimized for detecting such optical power level change at the specific propagation distance.

In our device, the maximum difference in the level of power exchanged between the directional coupler arms can be pronounced at a propagating distance of 24μm. The extinction ratio defined as:

$$ER = 10\log(\frac{P_{on}}{P_{off}}), \quad (1)$$

Where, ER is the extinction ratio in dB, while $P_{on}$ , and $P_{off}$ are the power levels in the excited waveguide at the ON, and OFF voltage states, respectively.

The extinction ratio calculated for our device reaches 24dB, with insertion losses of 1.4dB at a propagation distance of 24μm, and at the 1.55μm telecom wavelength.

## 4. Conclusions

A CMOS compatible optical modulator has been presented, the device is based on directional coupler operation. Modulation was achieved through the change of power levels exchanged between the directional coupler arms. An extinction ratio of 24 dB has been achieved with insertion losses of 1.4 dB at the 1.55μm telecom wavelength.

## Acknowledgements

"This work was made possible by NPRP grant # NPRP 7-456-1-085 from the Qatar National Research Fund (a member of Qatar Foundation, Doha, Qatar). The statements made herein are solely the responsibility of the author(s)."

## References

[1] G.T. Reed, G. Mashanovich, F.Y. Gardes, and D.J. Thomson, "Silicon optical modulators," *Nat. photonics*, 4(8), pp.518-526, 2010.

[2] G.T. Reed, *"Silicon photonics the state of the art,"* John Wiley & Sons, 2008.

[3] J. Leuthold, C. Koos, W. Freude, L. Alloatti, R. Palmer, D. Korn, J. Pfeifle, M. Lauermann, R. Dinu, S. Wehrli, and M. Jazbinsek, "Silicon-organic hybrid electro-optical devices," *IEEE J. Sel. Top. Quantum Electron*, 19(6), 114-126, 2013.

[4] A.O. Zaki, K. Kirah, and M.A. Swillam, "Hybrid plasmonic electro-optical modulator," *Appl. Phys. A*, 122(4), 1-7, 2016.

[5] D. C. Zografopoulos, M. Swillam, and R. Beccherelli, "Hybrid Plasmonic Modulators and Filters Based on Electromagnetically Induced Transparency," in *IEEE Photon. Technol. Lett.*, 28(7), 818-821, 2016.

[6] D. C. Zografopoulos, M.A. Swillam, L.A. Shahada, and R. Beccherelli, "Hybrid electro-optic plasmonic modulators based on directional coupler switches," *Appl. Phys. A*, 122(4), 1-6, 2016.

[7] A. Melikyan, L. Alloatti, A. Muslija, D. Hillerkuss, P.C. Schindler, J. Li, R. Palmer, D. Korn, S. Muehlbrandt, D. Van Thourhout, B. Chen, R. Dinu, M. Sommer, C. Koos, M. Kohl, W. Freude, and J. Leuthold, "High-speed plasmonic phase modulators," *Nat. Photonics*, 8(3), 229-233, 2014.

[8] W. Bogaerts, R. Baets, P. Dumon, V. Wiaux, S. Beckx, D. Taillaert, B. Luyssaert, J. Van Campenhout, P. Bienstman, and D. Van Thourhout, "Nanophotonic waveguides in silicon-on-insulator fabricated with CMOS technology," *J. Lightwave Technol.*, 23(1), 401-412, 2005.

[9] M. Khorasaninejad, M.A. Swillam, K. Pillai, and S.S. Saini, S.S., "Silicon nanowire arrays with enhanced optical properties," *Opt. lett.*, *37*(20), 4194-4196, 2012.
[10] Lumerical Solutions, Inc. http://www.lumerical.com/tcad-products/fdtd/
[11] M.A. Swillam, M.H. Bakr, and X. Li, "Full wave sensitivity analysis of guided wave structures using FDTD," *J. Electromagnet. Wave*, 22(16), 2135-2145, 2008.
[12] M.A. Swillam, M.H. Bakr, and X. Li, X., "Accurate and efficient sensitivity extraction of complex structures using FDTD," In Photonics North, International Society for Optics and Photonics, 67963A-67963A, 2007.
[13] M.A. Swillam, R.H. Gohary, M.H. Bakr, and X. Li, "Efficient sensitivity analysis of modal parameters of lossy structure using FDTD," In IEEE/Antenna and propagation international symposium, Toronto, 2010.
[14] M.A. Swillam, M.H. Bakr, N.K. Nikolova, and X. Li, "Adjoint sensitivity analysis of dielectric discontinuities using FDTD. *Electromagnetics*," 27(2-3), 123-140, 2007.
[15] R. Gamal, Y. Ismail, and M.A. Swillam, "Optical biosensor based on a silicon nanowire ridge waveguide for lab on chip applications," *J. Opt.*, 17(4), 045802, 2015.

# Silicon Organic Hybrid Plasmonic Modulator

**Sherif Mohamed[1], Aya Zaki[2], Lamees Shahada[1], Mohamed Swillam[2]**

[1]Department of Chemistry and Earth Sciences, College of Arts and Sciences, Qatar University, P.O. Box 2713, Doha, Qatar
[2]Department of Physics, School of Science and Engineering, The American University in Cairo, New Cairo 11835, Egypt
*corresponding author, E-mail: m.swillam@aucegypt.edu

## Abstract

Optical modulators are key components in the telecommunication technology. Ongoing research aims at achieving high modulation depths, low power consumption and compact designs of the optical modulator. Modulators based on plasmonic structures integrated with electro-optic polymers provide such interesting properties. We demonstrate a novel on-chip modulator for telecommunication applications. The modulator is based on the ring resonator mechanism, while utilizing the hybrid plasmonic platform. The proposed device is characterized by its small footprint, high extinction ratio, and low insertion losses. 3D Finite Difference Time Domain simulation tools were employed for designing and simulating the operation of the modulator at the telecommunication wavelength, while observing the device performance.

## 1. Introduction

The optical modulator is one of the main building blocks of modern communication systems. There are several modulation mechanisms in silicon, such as the thermo-optic effect, and the electro-optic effect. The thermo-optic effect (change of optical parameters with temperature) is still challenging due to speed limitations associated with heat dissipation issues [1], while the electro-optic effect has an almost instantaneous response with the applied electric signal. However, silicon does not exhibit the linear electro-optic (Pockel's effects) due to its centro-symmetric structure, while its second-order (Kerr effect) is relatively weak [2]. So, organics with strong electro-optic effects were studied for potential use for modulation purposes. Such organics when integrated with the silicon platform produce the silicon organic hybrid structures [3].

The miniaturization of photonic devise to reach ultra-compact photonic devices of 100's nm devices is limited by the classic diffraction limit in silicon photonics [4]. Thereby, the ability of surface plasmon polaritons propagating at a metal/dielectric interface to be confined to sub-wavelength scales can be very useful for producing such ultra-compact devices. Therefore, attention has been given to modulators with hybrid plasmonic structures, combining the advantages of the high speed operation, low insertion losses, low operation voltages, and the very compact designs [5-8].

In this work, we propose a hybrid silicon plasmonic modulator, with a small footprint and compact design. The modulator is based on the ring resonator configuration. Resonant modulators can have very compact designs due to the large quality factor of the resonant cavity which enhances the nonlinear interaction with several orders of magnitude [5]. The structure of the ring resonator is formed of a stack of layers, silicon-insulator-metal-insulator-silicon. The refractive index of the insulator layer EOP (electro-optic polymer) changes in response to an applied electrical signal. This causes a change in the resonant wavelength of the ring resonator. So, the resonant wavelength shift directly causes variation in the intensity of the specific wavelength of operation, in particular the 1.55μm telecom wavelength. A commercial-grade simulator based on the finite-difference time-domain (FDTD) method was used to perform the calculations [9]. Numerical calculations utilizing FDTD simulation methods have shown accurate and efficient sensitivity measurements for various structures including guided wave [10], complex [11], and lossy [12] structures, as well as for dielectric discontinuities [13].

## 2. Operation Mechanism

We demonstrate a highly compact hybrid plasmonic modulator with low loss operation suitable for integration on photonic chips with other electronic or photonics components. The layout of the ring resonator based modulator is shown in figure 1.

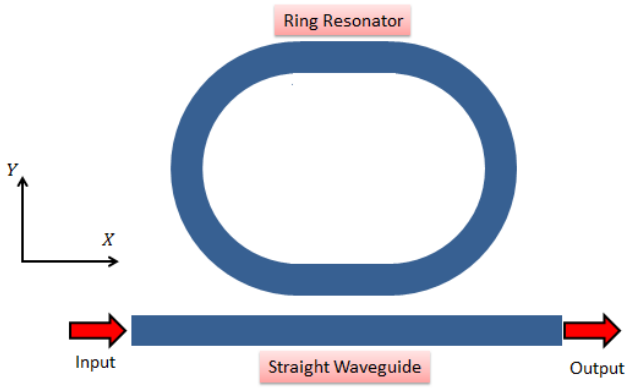



Figure 1: Layout of the proposed ring resonator modulator.

The device is composed of a straight waveguide and a ring resonator. The straight waveguide delivers the input power to be coupled to the ring resonator, and also delivers the output power of the device. The device structure is formed of a stack of layers arranged as silicon-EOP-silver-EOP-silicon layers, all on a buried oxide $SiO_2$ as shown in figure 2 for the cross-section of the device. Such structure provides the confinement of the hybrid plasmonic mode in the EOP layers, with low propagation losses and compact design.

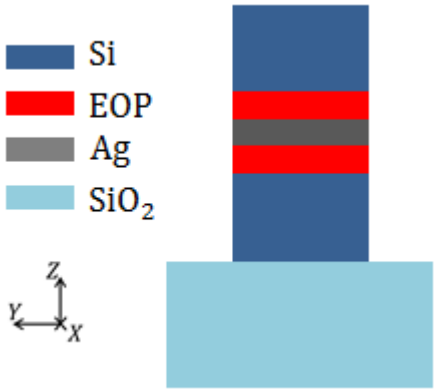



Figure 2: Cross-section of the straight waveguide.

Where the EOP refractive index is dependent on the applied fields as:

$$\Delta n_p = \frac{1}{2} n_p^3 r_{33} E \qquad (1),$$

The EOP refractive index $n_p$=1.6, and the electro-optic coefficient $r_{33}$=300pm/V [2,3], while E is the applied electric field in (V/pm).

## 3. Results and Discussion

The excited electric field profile is shown in figure 3, where it can be observed that the electric field is strongly confined in the EOP layers and symmetric about the metal layer.

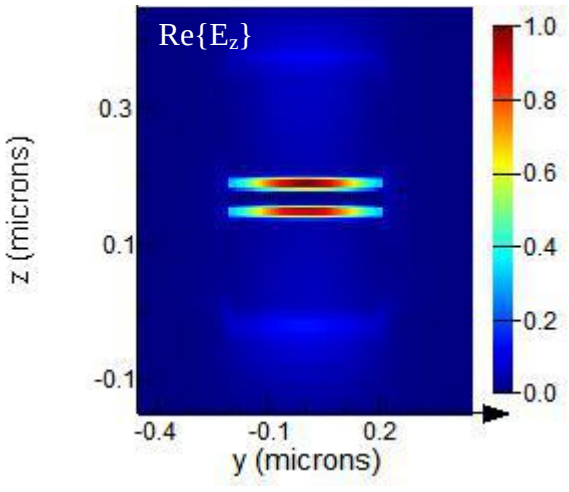



Figure 3: Excited electric field (Re{ $E_z$ }) distribution in the straight waveguide at λ=1.55μm.

The confinement and concentration of the electric field in the EOP layers lead to maximum response of the EOP refractive index change to small variations in the applied electric field, which is very useful for achieving low operation voltages.

When a small voltage is applied across the EOP layer, its refractive index is changed according to (1). The effective index of the hybrid plasmonic mode changes accordingly. This in turns results in shifting the resonant wavelength of the ring resonator as can be observed from figure 4.

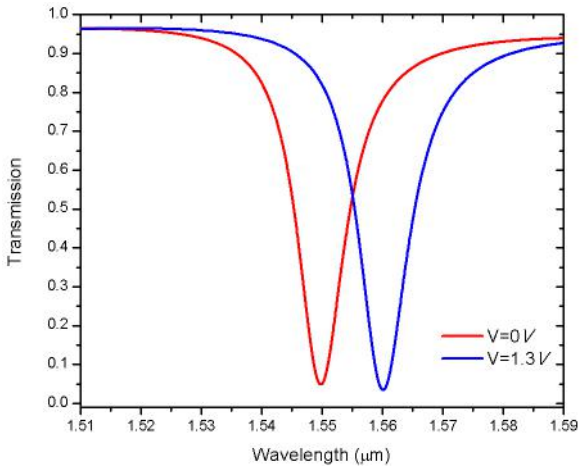



Figure 4: Resonant wavelength shift due to voltage application across the EOP layer.

As can be deduced from figure 4, upon applying a small voltage of only 1.3V, the resonant wavelength at λ=1.55μm gets red-shifted, resulting in an extinction ratio of 12dB, while the insertion losses were as low as 1dB at wavelength of 1.55 μm.

## 4. Conclusion

The proposed modulator based on the hybrid silicon plasmonic platform was studied and optimized to be operational at the 1.55 μm wavelength. 3D FDTD tools were used for the design and simulation of the device operation. The extinction ratio of the modulator is calculated to be 12dB, and the insertion loss is of 1dB.


## Acknowledgements

This work was made possible by NPRP grant # NPRP 7-456-1-085 from the Qatar National Research Fund (a member of Qatar Foundation, Doha, Qatar). The statements made herein are solely the responsibility of the author(s).


## References


[1] V. E. Babicheva, A. Boltasseva, and A. V. Lavrinenko, "Transparent conducting oxides for electro-optical plasmonic modulators," *Nanophotonics*, 4(1), 165-185, 2015.

[2] G.T. Reed, *"Silicon photonics the state of the art,"* John Wiley & Sons, 2008.

[3] J. Leuthold, C. Koos, W. Freude, L. Alloatti, R. Palmer, D. Korn, J. Pfeifle, M. Lauermann, R. Dinu, S. Wehrli, and M. Jazbinsek, "Silicon-organic hybrid electro-optical devices," *IEEE J. Sel. Top. Quantum Electron*, 19(6), 114-126, 2013.

[4] S. A. Maier, and H. A. Atwater, "Plasmonics: Localization and guiding of electromagnetic energy in metal/dielectric structures," *J. Appl. Phys*., 98(1), 2005.

[5] A. Melikyan, L. Alloatti, A. Muslija, D. Hillerkuss, P.C. Schindler, J. Li, R. Palmer, D. Korn, S. Muehlbrandt, D. Van Thourhout, B. Chen, R. Dinu, M. Sommer, C. Koos, M. Kohl, W. Freude, and J. Leuthold, "High-speed plasmonic phase modulators," *Nat. Photonics*, 8(3), 229-233, 2014.

[6] A.O. Zaki, K. Kirah, and M.A. Swillam, "Hybrid plasmonic electro-optical modulator," *Appl. Phys. A*, 122(4), 1-7, 2016.

[7] D. C. Zografopoulos, M. Swillam, and R. Beccherelli, "Hybrid Plasmonic Modulators and Filters Based on Electromagnetically Induced Transparency," in *IEEE Photon. Technol. Lett.*, 28(7), 818-821, 2016.

[8] D. C. Zografopoulos, M.A. Swillam, L.A. Shahada, and R. Beccherelli, "Hybrid electro-optic plasmonic modulators based on directional coupler switches," *Appl. Phys. A*, 122(4), 1-6, 2016.

[9] Lumerical Solutions, Inc. http://www.lumerical.com/tcad-products/fdtd/

[10] M.A. Swillam, M.H. Bakr, and X. Li, "Full wave sensitivity analysis of guided wave structures using FDTD," *J. Electromagnet. Wave*, 22(16), 2135-2145, 2008.

[11] M.A. Swillam, M.H. Bakr, and X. Li, X., "Accurate and efficient sensitivity extraction of complex structures using FDTD," In Photonics North, International Society for Optics and Photonics, 67963A-67963A, 2007.

[12] M.A. Swillam, R.H. Gohary, M.H. Bakr, and X. Li, "Efficient sensitivity analysis of modal parameters of lossy structure using FDTD," In IEEE/Antenna and propagation international symposium, Toronto, 2010.

[13] M.A. Swillam, M.H. Bakr, N.K. Nikolova, and X. Li, "Adjoint sensitivity analysis of dielectric discontinuities using FDTD. *Electromagnetics*," 27(2-3), 123-140, 2007.

# Resonance based hybrid plasmonic on-chip sensor

**Aya O Zaki[1, 2], Khaled A. Kirah[2], Mohamed Swillam[1]**

[1]Department of Physics, School of Science and Engineering, The American University in Cairo, New Cairo 11835, Egypt
[2]Department of Engineering Physics, Faculty of Engineering, Ain Shams University, Abassia, Cairo, 11517, Egypt
*corresponding author, E-mail: m.swillam@aucegypt.edu

## Abstract

We introduce a highly sensitive ultra-compact plasmonics sensor based on resonance. The plasmonic nature of the cavity allows the light to bend over its sharp edges resulting in more light confinement at the edges. We provide a novel mechanism of coupling that enhances the light matter interaction inside the cavity. Sensitivity of 1500 nm/RIU is reached for a cavity of ultra-small area of 0.21 μm² at wavelength around 1.55 μm.

## 1. Introduction

On-chip label-free biochemical sensors have attracted much research interest in recent years due to their small footprint and high sensitivity. The miniaturization of sensors is of great importance for lab-on-chip sensing applications, as only a small amount of analyte is needed to accomplish the analysis.

Sensors play a significant role in on chip integrated systems. Photonic sensors have shown significant advantages over their electric counterparts such as CMOS, electrochemical, RF and mechanical sensors, in view of their immunity to electromagnetic interference, wide dynamic range, multiplexing capabilities and greater sensitivity [1].

A lot of research work has been introduced based on the utilization of plasmonic metal cavities in sensing applications [2-5]. These cavities offer high light matter interaction due to the capability of plasmonic modes to confine the light into ultra-small regions.

A plasmonic resonator based on a rectangular cavity coupled to a metal-insulator-metal waveguide is introduced. A new coupling mechanism through a hybrid plasmonic waveguide section is proposed. Investigation of the transmission spectrum of the system is performed using 2D finite difference time domain method. Numerical simulations results show that high sensitivity sensors can be created by the proposed structure. This is due to the strong overlap of the hybrid plasmonic mode with the sensed gas in the cavity. Through optimization of the cavity dimensions and other design parameters, sensitivity of 1500 nm/RIU is reached at wavelength around 1.55 μm. The fabrication of this compact hybrid plasmonic sensor is reliable and cost efficient. The proposed plasmonic structure offers potential applications in integrated on-chip sensors.

## 2. Operation Mechanism

In a rectangular air cavity inside the metal, the light interaction with the air is enhanced due to high confinement at the rectangle corners. Thus, the resonant wavelength is highly sensitive to the refractive index of the air inside the cavity. We demonstrate a novel way to couple the light to such cavity. As with all resonators, the coupling coefficient is critical for its performance. To achieve a high quality resonator, the coupling coefficient should be decreased while keeping an acceptable extinction ratio. Conventionally, the light is coupled into plasmonic cavities from a metal-insulator-metal (MIM) waveguide through a thin metal gap [2, 4]. For efficient coupling, the thickness of the gap must be kept less than skin depth of the metal which is in the range of 20 nm [5]. The small dimensions of the metal gap introduce many fabrication complexities. In our proposal, the light is coupled to the cavity through a silicon strip of thickness *s*, as shown in figure 1.

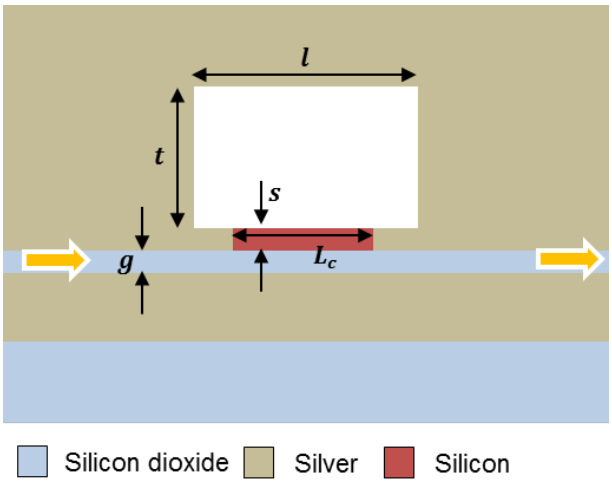



Figure 1: 2D schematic of the proposed rectangular sensor.

The optical wave is excited at input of the MIM access waveguide. When it reaches the silicon strip, MIM mode is coupled into a hybrid plasmonic mode along the coupling length $L_c$. The hybrid mode allows the power to get coupled to the cavity through a relatively thick silicon layer of 100 nm. The coupling length is designed to be less than the total side length *l*. This allows the modes inside the cavity to be pure plasmonic around the corners so that the light can bend with less radiation losses. In addition, the

coupling length is an additional design parameter to control the coupling coefficient and avoid over-coupling.

We propose that this structure be fabricated vertically where all layers are deposited on the buffer oxide in order. Then, the cavity is etched inside a metal bulk, flipped and adhered to the lower part.

## 3. Results and Discussion

The transmission spectra of a sub-micron cavity of $l$ = 700 nm and $t$ = 300 nm are shown in figure 2. The coupling length $L_c$ is set to half the length of the cavity, i.e. 350 nm, while the silicon layer thickness is 100 nm. When the refractive index of the air inside the cavity is increased by 0.01, the resonance dip is red shifted from 1585 nm to 1600 nm. Thus, the design offers a sensitivity of 1500 nm/RIU and a figure-of-merit of about 128.

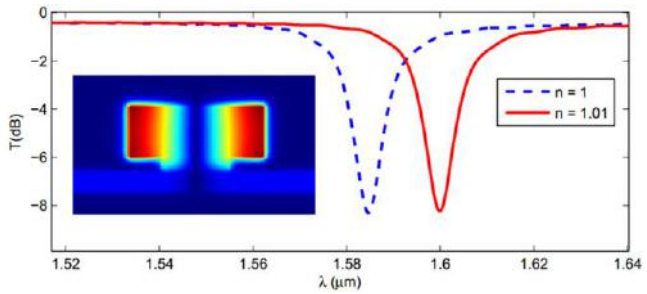



Figure 2: Transmission spectra of a sub-micron cavity of dimensions $l$ = 700 nm and $t$ = 300 nm and coupling distance $L_c$ = 0.5$l$. Inset shows the H field of the resonance mode.

A key advantage to the proposed sensor is its fabrication feasibility. Considering a 248 nm or 193 nm deep UV photolithography fabrication process, dimensional variations can be few tens of nanometers [6, 7]. This shows the robustness of the proposed sensor since the minimum feature size is 350 nm.

## 4. Conclusion

A new coupling mechanism to plasmonic cavities is proposed. A sub-micron highly sensitive plasmonic sensor is introduced based on the new hybrid plasmonic coupling. The sensitivity reaches 1500 nm/RIU for a 210 $nm^2$ rectangular cavity at 1550 nm operating wavelength. The sensor is suitable for lab-on-chip applications and can be integrated with electronic photonic circuits.

## Acknowledgements

This work was made possible by the internal AUC grant.

## References

[1] Kim GD, Lee HS, Park CH, Lee SS, Lim BT, Bae HK, et al. Silicon photonic temperature sensor employing a ring resonator manufactured using a standard CMOS process. Optics express. 2010; 18(21):22215–22221.

[2] Xie YY, Huang YX, Zhao WL, Xu WH, He C. A Novel Plasmonic Sensor Based on Metal Insulator Metal Waveguide with Side-Coupled Hexagonal Cavity. IEEE Photonics Journal. 2015 Apr; 7(2):1–12.

[3] Zou S, Wang F, Liang R, Xiao L, Hu M. A nanoscale refractive index sensor based on asymmetric plasmonic waveguide with a ring resonator: a review. Sensors Journal, IEEE. 2015; 15(2):646– 650.

[4] Xie Y, Huang Y, Che H, Zhao W, Xu W, Li X, et al. Theoretical investigation of a plasmonic sensor based on a metal insulator metal waveguide with a side-coupled nanodisk resonator. Journal of Nanophotonics. 2015 Jan;9(1):093099

[5] El-Zohary SE, Azzazi A, Okamoto H, Okamoto T, Haraguchi M, Swillam Ma. Resonance-based integrated plasmonic nanosensor for lab-on-chip applications. Journal of Nanophotonics. 2013 Nov;7(1):073077

[6] Mikkelsen JC, Sacher WD, Poon JK. Dimensional variation tolerant silicon-on-insulator directional couplers. Optics express. 2014 Feb 10;22(3):3145-50.

[7] Selvaraja SK, Bogaerts W, Dumon P, Van Thourhout D, Baets R. Subnanometer linewidth uniformity in silicon nanophotonic waveguide devices using CMOS fabrication technology. Selected Topics in Quantum Electronics, IEEE Journal of. 2010 Jan;16(1):316-24

# Hyperbolic metamaterials: Theory, Experiments and Applications

# Dielectric singularity in hyperbolic metamaterials: the inversion point of coexisting anisotropies

**V. Caligiuri**[1], **R. Dhama**[1], **K. V. Sreekanth**[2], **G. Strangi**[2,1] **and A. De Luca**[1,*]

[1]Dept. of Physics and CNR UOS CS - University of Calabria - 87036 - Rende (Italy)
[2]Nanoplasm Laboratory, Department of Physics - Case Western Reserve University - 44106 Cleveland (USA)
*antonio.deluca@fis.unical.it

**Abstract**— We report on the realization and characterization of an extreme hyperbolic metamaterial in which coexisting type I/type II anisotropies completely reverse at the so called "canalization wavelength", lying in the visible range. Spectroscopic ellipsometry confirms the simultaneous type I/type II response of the obtained structure. Confocal microscopy experiments, conducted at the canalization wavelength, confirm the supercollimation effect and the perfect lens behaviour. Numerical simulations are found to be in very good agreement with experiments. In the end, it is demonstrated how a three-material configuration is capable to overcome the lack of band selectivity typical of simple two-material HMMs, opening the way to real applications.

Since Veselago seminal work made its advent in the scientific panorama, metamaterials and perfect lenses have constituted a sort of inseparable binomial.[1, 2, 3] The possibility of resolving objects in the extreme proximity of a lens, fascinated scientists for fifty years. Unfortunately, following the original idea of Veselago, in the framework of conventional optics, realizing such a perfect lens would require a negative refractive index medium. More recently, S. A. Ramakrishna et. al. [4] demonstrated the possibility of using extremely anisotropic media, such as hyperbolic metamaterials (HMMs), to reach the so called "canalization regime", a condition we renamed $\varepsilon_{NZP}$ under which the medium shows $\varepsilon_x = \varepsilon_y = 0$ and $\varepsilon_z = \infty$ simultaneously.

These materials present a uniaxial form of the dielectric tensor $\bar{\bar{\varepsilon}}(\vec{r}) = diag(\varepsilon_{xx}, \varepsilon_{yy}, \varepsilon_{zz})$, where $\varepsilon_{xx} = \varepsilon_{yy} = \varepsilon_{\parallel}$ and $\varepsilon_{zz} = \varepsilon_{\perp}$. The iso-frequency surface for the extraordinary (TM-polarized) waves propagating in such an HMM is given by

$$\frac{k_x^2 + k_y^2}{\varepsilon_{\perp}} + \frac{k_z^2}{\varepsilon_{\parallel}} = \frac{\omega^2}{c^2} \tag{1}$$

where: $\varepsilon_{\parallel} = \varepsilon_d L_d + \varepsilon_m L_m / L_d + L_m$ and $\varepsilon_{\perp} = \varepsilon_d \varepsilon_m (L_d + L_m) / L_d \varepsilon_m + L_m \varepsilon_d$. Here $\varepsilon_m$ and $\varepsilon_d$ are the permittivities of the two materials chosen as building blocks ($m$ for metal and $d$ for dielectric). The simultaneous condition of $\varepsilon_{\parallel} \approx 0$ and $\varepsilon_{\perp} \approx \infty$ can be fulfilled if $L_d = L_m$ and, contemporarily, $\varepsilon_m = -\varepsilon_d$.

In this work we show the experimental realization and characterization of a particular HMM showing the aforementioned condition we called epsilon near zero and pole ($\varepsilon_{NZP}$), in the visible range. Spectroscopic ellipsometry confirms the presence of both the type I and type II behaviour, whereas their inversion at a specific wavelenth revelas the presence of Ferrel-Berreman modes and confirms their hyperbolic nature. The supercollimation effect at the transition wavelength, together with the possibility to use this system as a near field perfect lens with a resolution down to $\lambda/10$, has been experimentally demonstrated by means of confocal microscopy experiments. A strong spontaneous emission rate enhancement has been experimentally demonstrated. Results we got are well confirmed by simulations.[5]

As a first step we engineered the metamaterial by means of the Effective Medium Theory (EMT). The optical constants used in the design process have been extracted directly from a spectroscopic ellipsometrical analysis of each of the deposited layer (fig.1a). Then, the final multilayer structure has been realized by means of a PVD technique, by alternating 5 bilayers, each of which made of a transparent oxide and a metal. In particular a 20 nm thick layer of Indium Tin Oxide (ITO) has been deposited on a glass substrate by means of a DC Magnetron sputtering system (Edwards Auto 306), with a power of 40W for 2 minutes at a distance of 7.2cm between the substrate and the ITO target. Then, an Ag layer (20 nm thick) has been deposited on the ITO using 10W of power for 3 minutes. This constitutes the bilayer. For each deposition session a control sample has been placed side by side with the main one, allowing to check the optical properties of each sputtered layer, as well as its thickness and uniformity, at the end of each deposition. Spectroscopic ellipsometry has been used to perform this analysis by means of a V-VASE Ellipsometer (Woollam Co.). By setting up a multistep deposition procedure we were able to realize the complete multilayered metamaterial (see fig. 1a, inset). Its good morphology has been investigated by means of the

scanning electron microscopy analysis (SEM). Indeed, ellipsometry has been used as a powerful tool to perform angular transmission and reflection characterizations, as well as the Brewster angle evaluation. Transmission and reflection responses of the structure have been simulated by means of a classic transfer

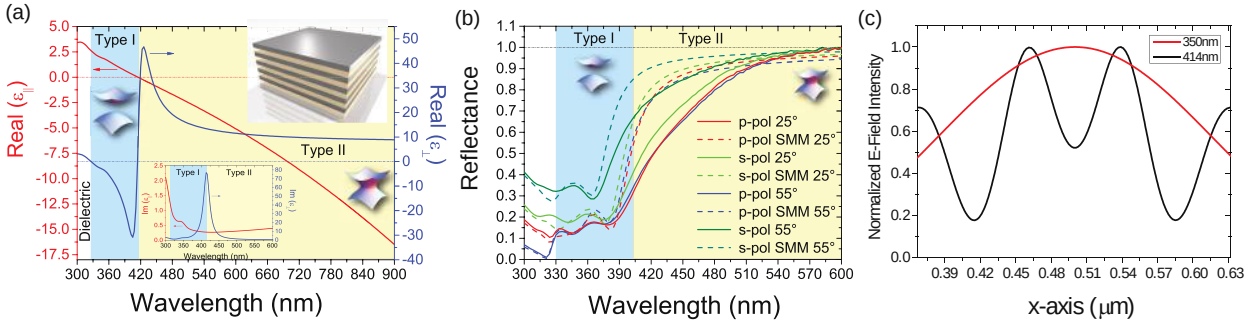



Figure 1: (a) Real parts of effective dielectric permittivities ($\varepsilon_{\parallel}$ and $\varepsilon_{\perp}$) determined by means of effective medium theory and ellipsometry measurements. Inset: Imaginary parts of $\varepsilon_{\parallel}$ and $\varepsilon_{\perp}$ and schematic of the fabricated HMM, (b) Comparison between experimental reflectance measured by ellipsometry and SMM simulations at different angles for p- and s- polarized incident beams. (c) Transversal cuts of a FEM analysis of a plane wave propagating from a slit of 500nm at the top of a three PMMA nanometric elements through the HMM at two different wavelengths 355nm and 414nm. It is evident the superesolution obtained at the transition of type I/type II region (414nm).

and scattering matrix method (TMM and SMM) code, which takes into account the contribution of air as the incoming medium and glass as the outgoing one, as well as all the imaginary parts. Ellipsometrical measurements made at different angles have been compared with simulations, obtaining very good agreement (see fig.1b). It is well evident the almost complete reflective behavior of the system above 414nm, whereas the appearing of a trasmissive window in the type I region (below 414nm). Supercollimation and perfect lens simulation have been performed by means of a Finite Element Method (FEM) based software. We investigated the possibility to use our $\varepsilon_{NZP}$ HMM as a supercollimator and a perfect lens. Confocal microscopy experiments conducted over a subwavelength 1D grating lithographied on the top of the $\varepsilon_{NZP}$ together with FEM simulation analysis, experimentally and theoretically confirms the possibility of confining light at the canalization wavelength through the bulk of the structure within a distance comparable to the step of the HMM.

In conclusion we have realized and characterized a HMM made of five Ag/ITO bilayers with same thickness. Due to the relative dielectric response of the two materials, we have fulfilled the condition of $\varepsilon_{NZP}$ that translates into a simultaneous type I/type II HMM. The obtained system has been analyzed by means of spectroscopic ellissometry, from which transmission and reflection spectra at different angles have been acquired and compared with a complete TMM and SMM simulation. A confocal microscope analysis with an external laser beam at two impinging wavelengths permitted to demonstrate the "canalization regime", the supercollimation effect and the perfect lens behaviour. A FEM analysis has been used to show how this system can be used as a perfect lens and obtain a superesolution down to $\lambda/10$.

## ACKNOWLEDGMENT

The research leading to these results has received support and funding from the Italian Project "NanoLase" - PRIN 2012, protocol number 2012JHFYMC, and from the Ohio Third Frontier Project Research Cluster on Surfaces in Advanced Materials (RC-SAM).

## REFERENCES

1. V. G. Veselago, "The electrodynamics of substances with simultaneously negative values of eps and mu," *Sov. Phys. Usp.*, vol. 10, p. 509, 1968.
2. J. B. Pendry, "Negative Refraction Makes a Perfect Lens," *Phys. Rev. Lett.*, vol. 85, pp. 3966–3969, 2000.
3. Z. Liu, H. Lee, Y. Xiong, C. Sun, and X. Zhang, "Far-field optical hyperlens magnifying sub-diffraction-limited objects," *Science*, vol. 315, no. 5819, p. 1686, 2007.
4. S. Anantha Ramakrishna, J. B. Pendry, W. C. K. Wiltshire, and W. J. Stewart, "Imaging the near field," *Journal of Modern Optics*, vol. 50, no. 9, pp. 1419–1430, 2003.
5. V. Caligiuri, R. Dhama, K. V. Sreekanth, G. Strangi, and A. De Luca, "Dielectric singularity in hyperbolic metamaterials: the inversion point of coexisting anisotropies," *Scientific Reports*, vol. 6, p. 20002, Feb. 2016.

# Block-copolymer based self-assembled hyperbolic metamaterials in the visible range.

**X. Wang[1], K. Ehrhardt[1], M. Kildemo[2], A. Baron[1], V. Lotito[1], P. Barois[1], A. Aradian[1], V. Ponsinet[1*]**

[1]Univ. Bordeaux - CNRS, Centre de Recherche Paul Pascal, UPR 8641, Pessac, France

[2]Physics Department, NTNU, Trondheim, Norway

[*]corresponding author: ponsinet@crpp-bordeaux.cnrs.fr

**Abstract** (limited to 80 words max) - Hyperbolic metamaterials use the concept of controlling the propagative modes through the engineering of the dispersion relation, and are considered highly promising to reach different meta-properties. However, robust, simple and large scale fabrication technologies allowing controlled final optical properties at chosen frequency ranges (including the visible one) are still needed. Here we present the fabrication and optical study using spectroscopic ellipsometry, of nanocomposites based on metal nanoparticles embedded in a self-assembled anisotropic polymer host, presenting a strong spectrally selective optical anisotropy.

Diblock copolymer thin film engineering[1] offers a genuine technological platform for the generation of nanostructured thin films with different morphologies. Two thin film morphologies are particularly attractive, presenting high degree of order and uniaxial symmetry: the lamellar phase with layers parallel to the substrate and the phase of hexagonally-packed cylinders with cylinders perpendicular to the substrate. Here, we use a lamellar poly(styrene)-b-poly(2-vinyl pyridine) (PS-P2VP) copolymer. We spin-cast flat and homogeneous films, of controlled thickness between 200 and 700 nm and of large lateral dimensions, which spontaneously develop a multilayered structurally uniaxial thin film of alternate poly(styrene) and poly(2-vinyl pyridine) layers, each of size $d_o$ /216 nm. This step provides both the **uniaxial symmetry** and the **subwavelength characteristic size** ($d_o << \lambda$), which are required for hyperbolic metamaterials. In order to obtain a large **contrast of dielectric permittivity** along orthogonal directions, which constitutes the third requirement to obtain a hyperbolic medium[2], we introduce Au nanoparticles selectively within the P2VP layers, thus producing a structure of alternating pure polymer (P) and Au nanoparticles:P2VP nanocomposite (NC) layers. This is achieved by dipping successively the film-bearing wafer into an Au salt solution and then into a reducing agent solution. This infiltration procedure is repeated N times, and N controls the volume fraction of nanoparticles in the (NC) layers.

As can be seen on an example shown in Figure 1, the films are structurally uniaxial and homogeneous and we can define their dielectric permittivity tensor with the ordinary (parallel to the substrate) and extraordinary (normal to the substrate) components. Variable angle spectroscopic ellipsometry (VASE) was performed in reflection with a phase-modulated ellipsometer (from Horiba Scientific), using the UVISEL II (P=45; M=0) and III (P=45; M=45) configurations. We measured $Is = \sin 2\Psi \sin\Delta$, $Ic = \sin 2\Psi \cos\Delta$ and $Ic' = \cos 2\Psi$, with $\Psi$ and $\Delta$ the two ellipsometric angles, for three values of the incident angle 55°, 65° and 75°. Each multilayer film was measured as a function of the number (N) of gold loading cycles. The VASE data were on the one hand analyzed with a superlattice model, using the layer thicknesses, appropriate interface layers and number of bi-layer repetitions inferred from the SEM images. Then, the optical properties of the Au loaded polymer layers were accurately determined and used in a layered effective medium model to provide the effective uniaxial dielectric

function. The latter result was on the other hand confirmed experimentally through direct inversion of the VASE data using a uniaxial effective medium model. The analysis was performed using both the DeltaPsi2 software from Horiba Scientific and exploring the B-spline feature of the Complete Ease software (JA Woolam company). Both models lead to the extraction of the components $\varepsilon_o$ and $\varepsilon_e$, both presenting a resonance close to 2.3 eV, with a significantly stronger amplitude for $\varepsilon_o$. For N>20, the values of $\varepsilon_o$ become negative close to the resonance, demonstrating the hyperbolic nature of the material.

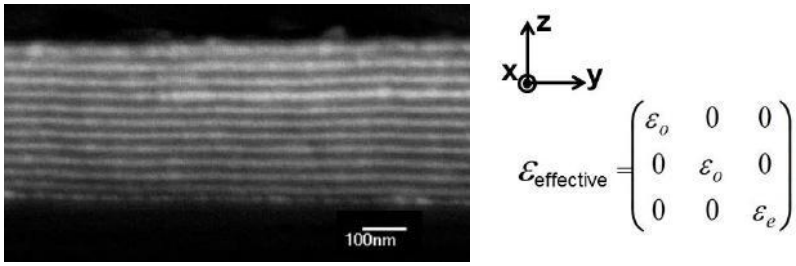



**Figure 1.** **(left)** Scanning electron microscopy side-view image (SEM) of a 370 nm-thick film of alternating pure polymer (appearing black) and Au nanoparticles:P2VP nanocomposite (appearing white) layers. The lower and upper black domains of the micrograph stand for the substrate and the air, respectively. **(right)** Tensorial form of the anisotropic dielectric permittivity with ordinary $\varepsilon_o$ and extraordinary $\varepsilon_e$ components.

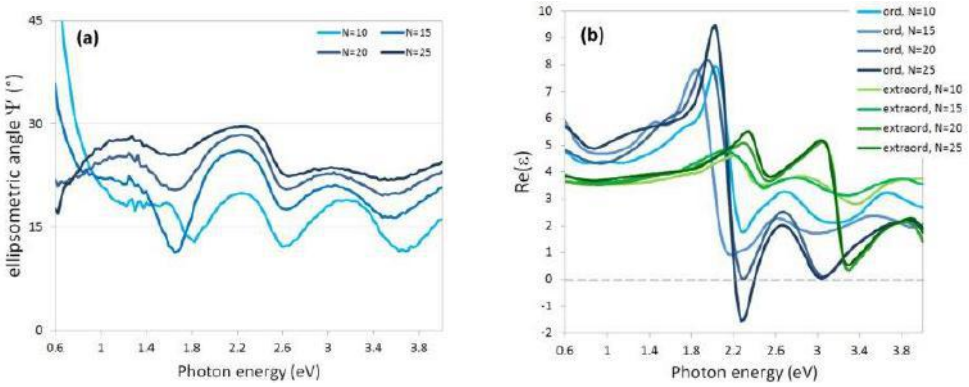



**Figure 2.** **(a)** Ellipsometric angle Ψ as a function of the energy of the incident light, for different loading in gold, as given by the number N. We see the deformation of the initial interference pattern as the gold loading affects both the index and the absorption of the film. **(b)** Real part of the ordinary (blue) and extraordinary (green) components of the dielectric permittivity, showing the strong optical anisotropy of the film, and demonstrating the hyperbolic nature for N>20.

**Acknowledgements.** This work was supported by the LabEx AMADEus (ANR-10-LABX-42) in the framework of IdEx Bordeaux (ANR-10-IDEX-03-02), France.

## REFERENCES

[1] Ponsinet, V., in *Polymer Surfaces in Motion - Unconventional Patterning Methods*, J. Rodríguez-Hernández, C. Drummond, Eds., Springer International Publishing, 2015.

[2] Ferrari, L., C. Wu, D. Lepage, X. Zhang and Z. Liu, "Hyperbolic metamaterials and their applications," *Progr. Quant. Electr.*, Vol. 40, 1–40, 2015.

# Purcell effect in multiperiodic multilayered metal-dielectric metamaterials

**A. V. Chebykin[1], V. E. Babicheva[2,1], I. V. Iorsh[1], A. A. Orlov[1], P. A. Belov[1], and S. V. Zhukovsky[1,3]**

[1] ITMO University, St. Petersburg 197101, Russia

[2] Center for Nano-Optics, Georgia State University, P.O. Box 3965, Atlanta, GA 30302, USA

[3] DTU Fotonik – Department of Photonics Engineering,
Technical University of Denmark, Ørsteds Plads 343, DK-2800 Kgs. Lyngby, Denmark

[*]corresponding author: chebykin.alexandr@gmail.com

**Abstract**- Purcell effect in multiperiodic metal-dielectric metamaterials was studied theoretically. We have demonstrated that one can use multiperiodicity to obtain greater values of Purcell factor than in ordinary periodic metamaterials. Further enhancement of spontaneous emission was reached by including a cavity layer in multiperiodic structure. We have analyzed the dependency of Purcell factor on the emitter location for structures both with and without cavity. Our results can be useful for more efficient manipulation of spontaneous emission in metamaterials.

In this work we have investigated the effect of multiperiodicity [1] in multilayered metal-dielectric metamaterials on the spontaneous emission of an embedded emitting center. Emission enhancement (Purcell) factor was calculated numerically based on the method of impedances [2]. We show that along with the expected increase of the Purcell factor, primarily caused by surface plasmon excitation at the nearest metal-dielectric boundary, there exists an enhancement of spontaneous emission specific to multiperiodicity, i.e., the values of Purcell factor in multiperiodic metamaterials can exceed these values in ordinary periodic metamaterials. This increase can be explained by the presence of more than one type of elementary surface plasmon excitations in the metamaterial's unit cell consisting of more than two distinct layers. Therefore, a larger portion of the wavevector space becomes populated by propagating states that the embedded emitter can couple with.

We have also demonstrated that further enhancement of Purcell factor may be obtained by introducing cavity (defect) layer into the multiperiodic lattice. In this case the additional Purcell enhancement is achieved due to interplay between surface plasmon excitations at the two metal-dielectric interfaces closest to the emitter.

Our calculations fully take into account the internal structure of the material and are thus more accurate than the effective medium approximation, which in this case strongly underestimates the value of Purcell factor. Our results are useful for understanding the physics of light-matter interaction in plasmonic metamaterials. We have clearly shown that making the topology of plasmonic multilayered metamaterials more complex than simply periodic may be used for a more flexible tuning of effects such as spontaneous emission of atoms.

**REFERENCES**

1. Orlov A. A, Krylova A. K., Zhukovsky S. V., Babicheva V. E., and Belov P. A., "Multiperiodicity in plasmonic multilayers: General description and diversity of topologies," *Phys. Rev. A*, Vol. 90, 013812, 2014.
2. Krasnok A. E., Filonov D. S., Simovski C. R., Kivshar Y. S., and Belov P. A. "Experimental demonstration of superdirective dielectric antenna," *Appl. Phys. Lett.*, Vol. 104, 133502, 2014.

# Strongly subwavelength cavities in multilayer hyperbolic metamaterials based on nanometric steps

**F. Vaianella[1*] and B. Maes[1]**

[1]Micro- and Nanophotonic Materials Group, Faculty of Science, University of Mons, 20 place du Parc, B-7000 Mons, Belgium

[*]corresponding author: Fabio.Vaianella@umons.ac.be

**Abstract**- Using well-known hyperbolic multilayer metamaterials, we show a new and very simple design of deeply subwavelength cavities based on nanoscale steps between the layers. We demonstrate that the transmission in these structures is similar to a waveguide side-coupled with a classical cavity. Subsequently, by judiciously tuning the distance between two of these nanosteps one can create very tight transmission resonances.

Hyperbolic metamaterials are a class of engineered materials that are interesting for many applications thanks to the large density of states and the extreme confinement of light [1]. Typical hyperbolic metamaterials are a periodic metal-dielectric multilayer structure and an array of cylindrical metallic nanorods in a dielectric host. We study the propagation of light in a multilayer made of silver (Ag) (thickness $d_{Ag}$ = 10 nm) and $TiO_2$ (thickness $d_{Tio2}$ = 20 nm) when light encounters a nanoscale step in the layers. Because of the transverse periodic nature of the system, no radiation occurs. In addition to the wavelength, we found that two other parameters strongly determine the reflection and transmission of light: the vertical offset A and the horizontal shift B of the step (Figure 1, left). We establish with rigorous numerics that a narrow combination of the parameters A and B gives rise to a strong reflection (up to 100%) of the mode at the step (Figure 1, right). This resonance effect is similar to the one obtained for a waveguide coupled to an adjacent cavity (Figure 2, right, red solid curve). [2]

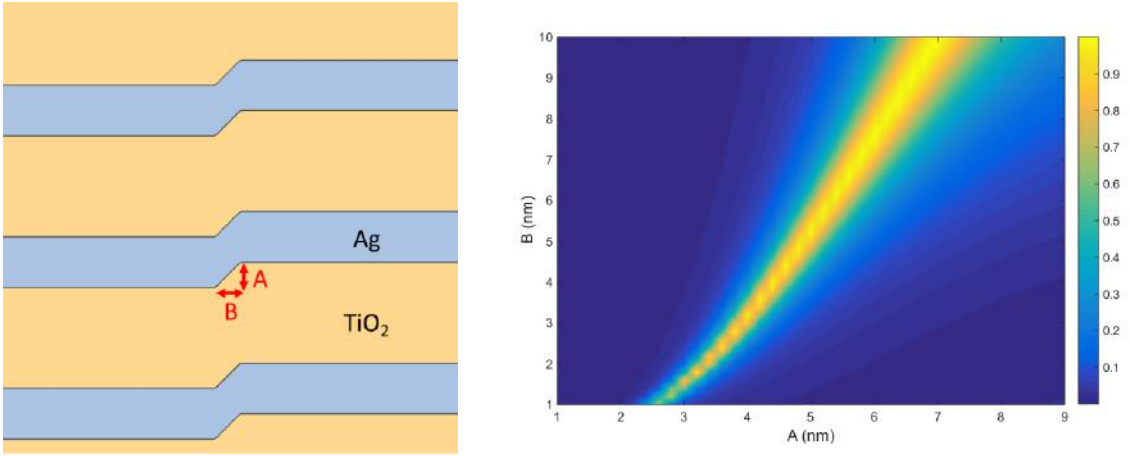



**Figure 1: Left, structure under study: nanometric step in the Ag/$TiO_2$ multilayer structure. The parameter A represents the vertical offset and B the horizontal shift. Right, reflection of light as a function of the geometric parameters A and B for a wavelength λ = 700 nm.**

We also study a symmetric structure made of two nanosteps with a distance L between them (Figure 2, left). We choose the vertical offset of the step to be A = 5 nm and the horizontal shift B = 5 nm in order to have the resonance (no transmission) at a wavelength of 700 nm (Figure 2, right, red solid curve). As in the case of a waveguide side-coupled with two cavities, according to the distance between the steps it is possible to tune the frequency at which the transmission is total (while it was quasi zero with only one step). For instance, as shown on the right side of Figure 2, the transmission at 700 nm changes from 2% with only one step to 100% with two steps with interdistance L = 86.8 nm, and the transmission at 705 nm changes from 7% to 100% for an interdistance L = 100 nm. It should be noted that the width of the peak of transmission is larger the more distant one operates from the single-cavity resonance.

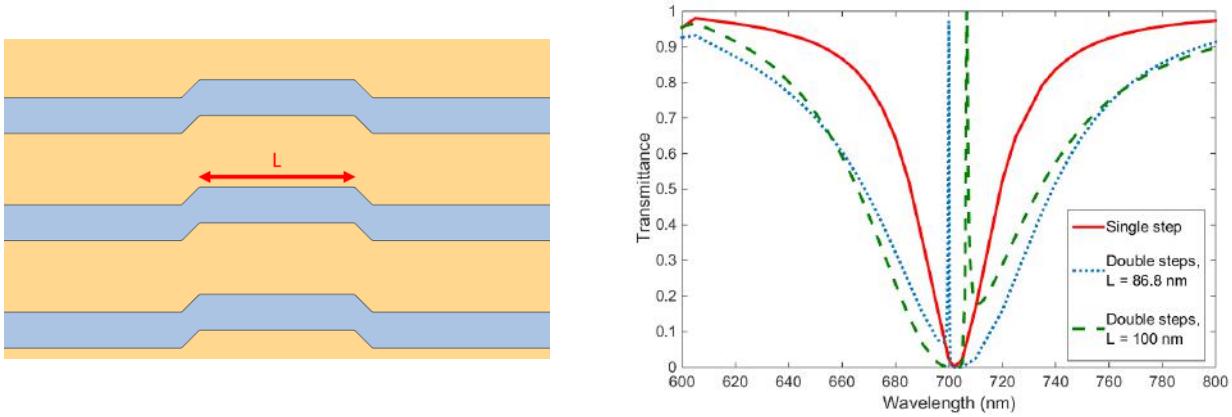



**Figure 2 : Left, symmetric structure made of two nanoscale steps. L is the distance between the two steps. Right, transmittance of light when passing through a single step (red solid curve), through the structure with two steps and L = 86.8 nm (blue dotted curve) and L = 100 nm (green dashed curve). For all three curves, A =5 nm and B = 5 nm.**

This work reports the first case, to our knowledge, of strong reflection by nanometric metallic edges and allows for a great control of light propagation in metamaterials.

**Acknowledgements**

This work was supported by the Belgian Science Policy Office under the project "Photonics@be" (P7-35) and by the Fonds pour la Formation à la Recherche dans l'Industrie et dans l'Agriculture (FRIA) in Belgium.

**REFERENCES**

1. L. Ferrari, C. Wu, D. Lepage, X. Zhang and Z. Liu, "Hyperbolic metamaterials and their applications," *Progress in Quantum Electronics*, Vol. 40, 1–40, 2015.
2. B. Maes, P. Bienstman and R. Baets, "Switching in coupled nonlinear photonic-crystal resonators," *J. Opt. Soc. Am. B*, Vol. 22, No. 8, 1778, 2005.

# Thermal Radiation from Semiconductor Hyperbolic Metamaterials

**S. Campione[1,2,*], F. Marquier[3], J.-P. Hugonin[3], A. R. Ellis[1], J. F. Klem[1], M. B. Sinclair[1], and T. S. Luk[1,2]**

[1]Sandia National Laboratories, Albuquerque NM 87185 USA

[2]Center for Integrated Nanotechnologies, Sandia National Laboratories, Albuquerque NM 87185 USA

[3]Laboratoire Charles Fabry, Institut d Optique, CNRS–Univ Paris-Sud, 91127 Palaiseau Cedex, France

[*]corresponding author: sncampi@sandia.gov

**Abstract**-We investigate the thermal radiation properties of semiconductor hyperbolic metamaterials. We show that, in proximity of epsilon-near-zero conditions, directional and monochromatic thermal radiation is achieved. Different properties are observed for *s* and *p* polarizations, following the characteristics of the strong anisotropy of hyperbolic metamaterials.

In the mid-infrared region of the electromagnetic spectrum, only a few kinds of sources are available, mainly quantum cascade lasers and thermal sources (blackbodies). In the last few years however, research on thermal radiation has led to the achievement of 1) *spatially coherent (i.e. directional)* [1] or 2) *temporally coherent* [2] thermal sources by using wavelength-scale optical structures [3]. A few recent papers even succeeded to combine both properties of directionality and monochromaticity using diffraction order engineering in periodic structures [4, 5]. Very recently, high-speed modulation of thermal emission has been demonstrated using a quantum well stack and a photonic crystal [6].

In this work, we show that simple multilayer structures without any periodic corrugation behave as *directive and monochromatic* thermal sources in the infrared. For this purpose, we take advantage of an absorption resonance in a semiconductor hyperbolic metamaterial (SHM). This kind of structure can be realized at mid-infrared frequencies where highly doped semiconductor materials behave like metals so that SHMs can be fabricated using alternating layers of doped and undoped semiconductor materials [7-9]. The absorption resonance is fundamentally related to an epsilon-near-zero effect in the doped layers [10-12]: due to the vanishing dielectric constant in these layers, the electric field and the absorption are resonantly enhanced.

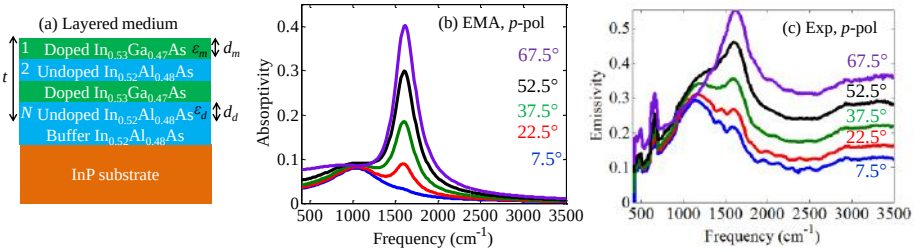



Fig. 1. (a) A schematic of the fabricated SHM. (b) Theoretical *p*-polarized absorptivity and (c) experimental *p*-polarized thermal emissivity.

A schematic of the fabricated SHM sample is depicted in Fig. 1(a). The sample was grown by molecular beam epitaxy on a 0.65-mm-thick InP substrate with a 200-nm-thick buffer layer of $In_{0.52}Al_{0.48}As$, as shown in Fig. 1(a). The $In_{0.53}Ga_{0.47}As$ and $Al_{0.48}In_{0.52}As$ layers are lattice matched to the InP substrate.

The sample is mounted on a heater in order to characterize its thermal emission properties. The measured *p*-polarized emissivity, along with the absorptivity simulated from effective medium theory, is shown in Fig. 1(b-c). The resonance location (~1600 $cm^{-1}$), as well as the behavior for increasing angle observed in the experiment, are well recovered by our absorptivity simulations.

In conclusion, we have experimentally analyzed the thermal radiation properties of SHMs and found strong directive and monochromatic emission features in proximity of epsilon-near-zero conditions that may open up new avenues of fast modulation of thermal radiation.

**Acknowledgements**. This work was supported by the U.S. Department of Energy, Office of Basic Energy Sciences, Division of Materials Sciences and Engineering and performed, in part, at the Center for Integrated Nanotechnologies, an Office of Science User Facility operated for the U.S. Department of Energy Office of Science. Sandia National Laboratories is a multi-program laboratory managed and operated by Sandia Corporation, a wholly owned subsidiary of Lockheed Martin Corporation, for the U.S. Department of Energy's National Nuclear Security Administration under contract DE-AC04-94AL85000. F. M. acknowledges financial support from the French Ministry of Defense, grant ERE 2014.60.0082 from the Direction Générale de l'Armement.

## REFERENCES

1. Greffet, J.-J., et al. "Coherent emission of light by thermal sources," *Nature*, Vol. 416, No. 6876, 61-64, 2002.
2. Bouchon, P., et al. "Wideband omnidirectional infrared absorber with a patchwork of plasmonic nanoantennas," *Opt. Lett.*, Vol. 37, No. 6, 1038-1040, 2012.
3. Vassant, S., et al. "Electrical modulation of emissivity," *Appl. Phys. Lett.*, Vol. 102, No. 8, 081125, 2013.
4. De Zoysa, M., et al. "Conversion of broadband to narrowband thermal emission through energy recycling," *Nat. Photon.*, Vol. 6, No. 8, 535-539, 2012.
5. Costantini, D., et al. "Plasmonic Metasurface for Directional and Frequency-Selective Thermal Emission," *Phys. Rev. Appl.*, Vol. 4, No. 1, 014023, 2015.
6. Inoue, T., et al. "Realization of dynamic thermal emission control," *Nat. Mater.*, Vol. 13, No. 10, 928-931, 2014.
7. Campione, S., et al. "Optical properties of transiently-excited semiconductor hyperbolic metamaterials," *Opt. Mater. Express*, Vol. 5, No. 11, 2385-2394, 2015.
8. Hoffman, A.J., et al. "Negative refraction in semiconductor metamaterials," *Nat. Mater.*, Vol. 6, No. 12, 946-950, 2007.
9. Campione, S., et al. "Realizing high-quality, ultralarge momentum states and ultrafast topological transitions using semiconductor hyperbolic metamaterials," *J. Opt. Soc. Am. B*, Vol. 32, No. 9, 1809-1815, 2015.
10. Vassant, S., et al. "Berreman mode and epsilon near zero mode," *Opt. Express*, Vol. 20, No. 21, 23971-23977, 2012.
11. Campione, S., et al. "Theory of epsilon-near-zero modes in ultrathin films," *Phys. Rev. B*, Vol. 91, No. 12, 121408, 2015.
12. Jun, Y.C., et al. "Doping-tunable thermal emission from plasmon polaritons in semiconductor epsilon-near-zero thin films," *Appl. Phys. Lett.*, Vol. 104, No. 13, 131109, 2014.

# Controlling quantum photonics with metamaterials

**M. Y. Shalaginov [1], S. Bogdanov [1], V. Vorobyov [2,3,4], J. Liu [5], A. S. Lagutchev [1], A. V. Kildishev [1], J. Irudayaraj [6], A. Boltasseva [1], A. V. Akimov [2,7,8], and V. M. Shalaev [1,*]**

[1]School of Electrical and Computer Engineering & Birck Nanotechnology Center, Purdue University, West Lafayette, IN 47907, USA

[2]Russian Quantum Center, 143025 Moscow, Russia

[3]Moscow Institute of Physics and Technology, 141700 Moscow Region, Russia

[4]Photonic Nano-Meta Technologies LLC, 141009 Moscow Region, Russia

[5]South Dakota School of Mines & Technology, Rapid City, SD 57701, USA

[6]Agricultural and Biological Engineering, Purdue University, West Lafayette, IN 47907, USA

[7]P.N. Lebedev Physical Institute of RAS, 119991 Moscow, Russia

[8]Texas A & M University, College Station, TX 77843, USA

[*]corresponding author: shalaev@purdue.edu

**Abstract**-Building a robust light-matter interface is a challenging task in the field of quantum photonics. In this talk, we present our advances in controlling the emission of nitrogen-vacancy (NV) centers in nanodiamonds. The broadband emission enhancement has been implemented by coupling NV centers to hyperbolic metamaterials composed of novel CMOS-compatible plasmonic materials. Further, we discuss how Purcell enhancement of the optical transition affects the optical readout of the NV center spin-state. These findings could be helpful for engineering integrated quantum registers.

## I. Introduction

Nitrogen-vacancy (NV) centers are atom-like defects in the diamond crystal lattice, which possess attractive characteristics, such as a long room-temperature electron-spin coherence time as well as optical spin state readout and initialization [1]. These unique properties could lead to room-temperature integrated implementation of qubits, quantum gates, and nanoscale sensors [2,3]. These applications could substantially benefit from coupling the NV centers to nanophotonic structures such as plasmonic antennae or waveguides.

## II. Enhancing atom-like emitters with hyperbolic metamaterials

We suggest a CMOS compatible approach for engineering the photonic environment of NV centers by using hyperbolic metamaterials formed by an epitaxial TiN/(Al,Sc)N superlattice [4]. The high-k plasmonic modes supported by the hyperbolic medium ensure a faster decay rate, an increased collected count rate, and an improved emission directionality. One of the key remaining challenges is the controlled outcoupling of the radiation from the high-k modes to free space, which was in our case realized by scattering on random superlattice structural defects located on the sample surface.

## III. Effect of nanophotonic structures on spin-readout properties of nitrogen-vacancy centers in diamond

As a result of a plasmonic enhancement of the optical transition, both of the NVs spin subsystems (1 and 0)

experience a significant increase in direct decay rate, which affects the optical readout of the spin state. In this work, we experimentally studied the influence of spontaneous emission lifetime on spin-induced fluorescence contrast in nanodiamond NV center ensembles and obtained a good agreement with a simple analytical model.

## IV. Conclusions

Plasmonic metamaterials can enhance the transition rates of quantum systems in a non-resonant manner achieving a fast, on-demand, broadband single-photon response without major fabrication difficulties. We have shown that the influence of the plasmonic environment on the spin contrast of the optically detected electron spin resonance should still allow for successful spin-state readout under moderate (< 4) Purcell factor. The obtained findings will assist the engineering of nanophotonic quantum registers based on color centers or similar type of atomic systems.

**Acknowledgements**: This work was supported by AFOSR-MURI grant (FA9550-10-1-0264), NSF-MRSEC grant (DMR 1120923). The authors would like to thank Nathaniel Kinsey for his help with the paper preparation.

## REFERENCES

1. A. Gruber et al., “Scanning Confocal Optical Microscopy and Magnetic Resonance on Single Defect Centers”, Science, vol. 276, pp. 2012-2014, 1997.
2. N. Gisin, R. Thew, “Quantum communication”, Nat. Photon., vol. 1, pp. 165-171, 2007.
3. S. Hong et al., “Nanoscale magnetometry with NV centers in diamond”, MRS Bulletin, vol. 38, pp. 155- 161, 2013.
4. M. Y. Shalaginov et al., “Enhancement of single-photon emission from nitrogen-vacancy centers with TiN/(Al,Sc)N hyperbolic metamaterial”, Laser Photon. Rev., vol. 9, p. 120, 2015.

# Metamaterial Behavior of Hyperbolic Bimetallic Nanostructures.

**S. Cortés-López and F. Pérez-Rodríguez**

Instituto de Física, Benemérita Universidad Autónoma de Puebla, Mexico
scortesl@ifuap.buap.mx

**Abstract**— The $s$- and $p$-polarization reflectivity spectra for a nanostructure composed of alternating Ag and Al layers have been calculated by using an average permittivity tensor in the long wavelength limit. A pass band of negative refraction in the $p$-polarization reflectivity for the bimetallic hyperbolic metamaterial, just above the lower plasma frequency, was found.

The negative refraction can be observed in the double-negative metamaterials, whose effective permittivity and permeability are simultaneously negative. Such a phenomenon can also be observed in anisotropic media without requiring negative permeability. For instance, a metal-dielectric superlattice possesses negative index of refraction in the frequency interval where the effective permittivity principal values, corresponding to the directions parallel and perpendicular to the plane of the layers, have opposite signs. These inherently anisotropic structures are known as hyperbolic metamaterials and their optical properties have been widely studied in recent years. In order to apply hyperbolic metal-dielectric metamaterials in the visible range, it is necessary to construct periodic nanostructures, having a lattice constant of the order or even much smaller than the typical wavelength (390–750 nm).

In the present work, we study the optical properties of a nanostructure composed of two alternating metallic layers. The permittivities of the metallic components are here described by Drude model:

$$\epsilon_1 = 1 - \frac{\omega_{p_1}^2}{(\omega^2 + i\nu_1\omega)}, \qquad \epsilon_2 = 1 - \frac{\omega_{p_2}^2}{(\omega^2 + i\nu_2\omega)}. \tag{1}$$

where $\omega_{p_1}$ and $\omega_{p_2}$ are the plasma frequencies of the two metal layers, $\nu_1$ and $\nu_2$ are the corresponding damping parameters. Using Eq. (1), we have calculated the components of the average permittivity tensor in the long wavelength limit [1]:

$$\epsilon_x = \epsilon_y = \epsilon_1 f + \epsilon_2(1-f), \quad \frac{1}{\epsilon_z} = \frac{1}{\epsilon_1} f + \frac{1}{\epsilon_2}(1-f). \tag{2}$$

Here, the $z$-axis is a assumed to be parallel to the growth direction of the bimetallic nanostructure, and $f$ is the volume filling fraction of the metal 1. Fig. 1 exhibits the calculated frequency dependence of the average permittivity principal values (2) for a nanostructured Ag-Al multilayer stack with $f = 0.5$. The dispersion relation $k_z(\omega)$ for $s$- and $p$-polarized electromagnetic modes are, respectively, given by:

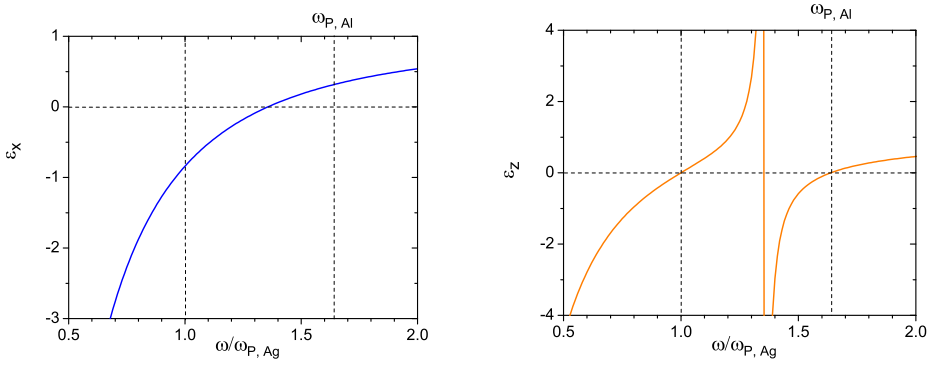



Figure 1: Frequency dependence of the average permittivity principal values.

$$k_z^{(s)} = \sqrt{\epsilon_y \frac{\omega^2}{c^2} - k_x^2}, \qquad k_z^{(p)} = \sqrt{\epsilon_x \left( \frac{\omega^2}{c^2} - \frac{k_x^2}{\epsilon_z} \right)}, \tag{3}$$

where $k_x = (\omega/c)\sin\theta$, and $\theta$ is the incidence angle. Fig. 2 shows the dispersion relation for the $s$- and $p$-polarized modes in the homogenized Ag-Al multilayer stack with $\theta = 45°$. As is seen, there is a frequency interval just above the plasma frequency for silver ($\omega_{p,Ag}$) where the vector $k_z^{(p)}$ for the $p$-polarized modes is real and negative, but the derivative $d\omega/dk_z$ has a positive sign. Therefore, this frequency interval corresponds to a pass band of negative refraction. There, the average permittivity components $\epsilon_x$ and $\epsilon_z$ have different signs (see Fig. 1). At higher pass bands the effective refractive index turns out to be positive.

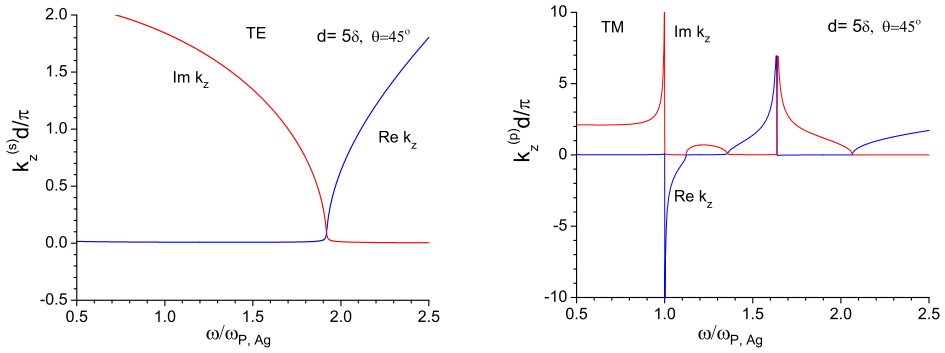



Figure 2: Dispersion curves of $s$- and $p$-polarized modes for a Ag-Al hyperbolic metamaterial.

We have also calculated $s$- and $p$-polarization reflectivity spectra for the Ag-Al hyperbolic metamaterial with thickness $d = 5\delta$, where $\delta = c/\omega_{p,Al}$ (Fig. 3). The pass bands for both $s$- and $p$-polarized modes are well observed in the $R_s$ and $R_p$ spectra, having Fabry-Perot resonances at frequencies satisfying $k_z^{(s)} d = n\pi$, $k_z^{(p)} d = m\pi$ ($n, m = 1, 2, \dots$). The first Fabry-Perot resonance in a pass band of negative (positive) refraction is that at the highest (lowest) frequency.

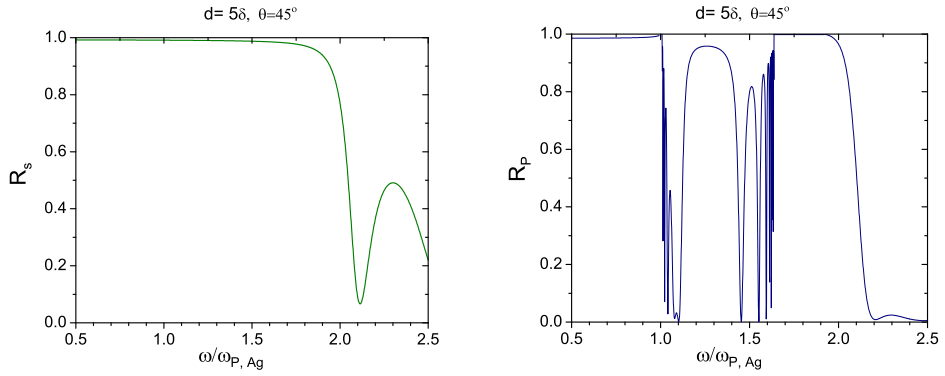



Figure 3: $s$- and $p$-polarization reflectivity for a Ag-Al hyperbolic metamaterial at $d = 5\delta$ and $\theta = 45°$.

In conclusion, a pass band of negative dispersion in the spectra of $p$-polarization reflectivity for the bimetallic hyperbolic metamaterial was found just above the lower plasma frequency.


## ACKNOWLEDGMENT

This work was partially supported by VIEP-BUAP, PIFCA, and PROFOCIE.


## REFERENCES


1. Rytov, S.M., "Electromagnetic properties of a finely stratified medium", *Sov. Phys. JETP*, Vol. 2, 466-475, 1956.

# Optical signal dispersion in hyperbolic metamaterials

**T. Stefaniuk**[1*], **A. Zayats**[1]
[1]King's College London, UK

[*]corresponding author: tomasz.stefaniuk@kcl.ac.uk

**Abstract**- We present the study of ultrashort pulse dynamics in hyperbolic plasmonic metamaterial. The transient Kerr-type nonlinear response of metamaterials is simulated by introducing the nonlinearity of Au using the two temperature model. In the nanorod metamaterial the nonlinearity is not limited by the optical properties of the constituents, but it can be designed to be stronger than in uniform materials at a given spectral range. We demonstrate that this effect can be used for dispersion management of ultrashort pulses.

The nano-engineered metamaterials exhibit optical properties beyond natural materials. In particular, metamaterials have shown promise in varied applications including imaging [1], sensing [2] or waveguiding [3]. One class of metamaterials is highly anisotropic media that have hyperbolic isofrequency surfaces [4]. This kind of dispersion gives the unprecedented ability to sustain and enhance waves of infinitely high wavenumber. In the recent years, the focus of metamaterial research has shifted towards the nonlinear properties. It has been demonstrated that the optical pulses can be used to controllably modulate the material losses at the picosecond timescale [5]. It has been also shown that the nonlinearity of Au nanorod-based metamaterial can exhibit strong nonlinearity at the wavelengths where negligible nonlinearity of the consistent materials exist [6], and the effective plasma frequency determining this behavior can be tuned to telecom wavelengths [7].

In this talk, we present the Finite Difference Time Domain analysis of the ultrafast nonlinear response of gold-nanorods-based metamaterial. The metamaterial is excited with a 20-100 fs Gaussian-shaped optical pulse with the central frequency in the IR region. The evolution of electrons and phonons temperatures in the nanorods is described by the two-temperature model. Kerr-type optical nonlinearity of gold is modelled within the random phase approximation, which includes the dependence of intraband and interband components of permittivities on both electron and phonon temperatures. During the excitation and relaxation of the system, we are monitoring several quantities like electron and lattice temperature at each point inside the gold nanorods and the changes in the real and imaginary parts of permittivities.

We used the developed model to study the possibility of dispersion management in nanorod metamaterial in linear and nonlinear regimes. We demonstrate the correlation between the nonlinear transient response of the metamaterial and the possibility of shaping the optical pulses in both time and frequency domain. Furthermore, we prove that our approach not only provides freedom in designing the nonlinearities at any frequency of interest, but also enables ultrafast self-modulation, stronger that in classical semiconducting materials.

**Acknowledgements.** This work was supported, in part, by EPSRC (UK) and the ERC iPLASMM project (321268). A.Z. acknowledges support from the Royal Society and the Wolfson Foundation.

**REFERENCES**

1. Kotyński, R., Stefaniuk, T. "Multiscale analysis of subwavelength imaging with metal-dielectric multilayers," *Opt. Lett.*, Vol. 35, 1133-1135, 2010.
2. Nasir, M.E., Dickson, W., Wurtz, G.A., Wardley, W.P., Zayats, A.V., "Hydrogen detected by the naked eye: Optical hydrogen gas sensors based on core/shell plasmonic nanorod metamaterials," *Adv. Mater.*, Vol. 26, 3532-3537, 2014.
3. Vasilantonakis, N., Nasir, M.E., Dickson, W., Wurtz, G.A., Zayats, A.V., "Bulk plasmon-polaritons in hyperbolic nanorod metamaterial waveguides," *Laser Photon. Rev.*, Vol. 9, 345-353, 2015.
4. Dickson, W., Beckett, S., McClatchey, C., Murphy, A., O'Connor, D., Wurtz, G.A., Pollard, R., Zayats, A.V. "Hyperbolic Polaritonic Crystals Based on Nanostructured Nanorod Metamaterials," *Adv. Mater.*, Vol. 27, 5974-5980, 2015.
5. Neira, A.D., Wurtz, G.A., Ginzburg, P., Zayats, A.V., "Ultrafast all-optical modulation with hyperbolic metamaterial integrated in Si photonic circuitry," *Opt. Express*, Vol. 22, 10987-10994, 2014.
6. Neira, A.D., Olivier, N., Nasir, M.E., Dickson, W., Wurtz, G.A., Zayats, A.V., "Eliminating material constraints for nonlinearity with plasmonic metamaterials," *Nat. Commun.*, Vol. 6, No. 7757, 1–8, 2015.
7. Nasir, M.E., Peruch, S., Vasilantonakis, N., Wardley, W.P., Dickson, W., Wurtz, G.A., Zayats, A.V., "Tuning the effective plasma frequency of nanorod metamaterials from visible to telecom wavelengths," *Appl. Phys. Lett.*, Vol. 107, No. 121110, 2015.

# Hyperbolic Metamaterials with Complex Geometry

**Andrei V. Lavrinenko [*], Andrei Andryieuski , Sergei V. Zhukovsky, Osamu Takayama, Evgeniy Shkondin, Mohammad E. Aryaee Panah, Radu Malureanu, and Flemming Jensen**

DTU Fotonik, Technical University of Denmark, Oersteds pl. 343, 2800 Kongens Lyngby, Denmark

[*]corresponding author: alav@fotonik.dtu.dk

**Abstract** We investigate new geometries of hyperbolic metamaterials such as highly corrugated structures, nanoparticle monolayer assemblies, super-structured or vertically arranged multilayers and nanopillars. All structures retain basic properties of hyperbolic metamaterials, but have functionality improved on particular purpose: increased absorption, radiative rate engineering, and selective control over volume plasmon-polaritons or directional surface waves.

The recent decade in modern physics has featured the concept of metamaterials. The central idea of this concept is to ensure that structural issues – how normal material constituents are arranged – can impose strikingly different physical properties beyond the frames erected with conventional natural nomenclature. A prominent example of such artificial materials are hyperbolic metamaterials (HMMs), in which anisotropy is pushed to extreme case when the medium reacts on light like metal in one direction and like dielectric in other [1]. One of the main reasons that HMMs have attracted much interest is the discovery that hyperbolic dispersion can be achieved with relatively simple geometries, e.g. metal-dielectric multilayers [2]. Such simplicity makes it tempting to explore whether their functionality can be essentially broadened by more sophisticated geometries.

We report on few cases of hyperbolic metamaterials (HMMs) with geometries more complex than metal-dielectric multilayers deposited by planar technologies. First, we examined a multilayer HMM with imperfections represented by fluctuations of the layers thickness that is accumulated from layer to layer, mimicking realistic evaporation or sputtering process of material deposition [3]. As shown [4], the increased surface roughness leads to enhanced absorption compared to smooth-layered HMMs. Moreover, keeping the outer surface smooth and increasing only the internal layer roughness also leads to enhanced absorption, making the effect distinct from the already observed super-absorption in HMMs with a rough surface [5].

An interesting way to fabricate a multilayer structure is to use building blocks of self-assembled monolayers that can be deposited from colloidal solutions of nanoparticles. Polyelectrolyte coatings can be used both as support, to stack several monolayers in a multilayer structure, and as nanometer-thick spacers, to separate individual monolayers in a controlled manner. This way, a HMM can be realized by alternating monolayers of metal nanoparticles with dielectric spacers. As the latter we consider layers of semiconductor quantum dots, which serve both as effective dielectric layers and as emitting centers. By varying the spacer thickness between nanoparticle and quantum dot layers, we can fine-tune the structure, transforming it from a conventional multilater to a HMM and vice versa [6]. In the HMM regime, the existence of a volume plasmon-polaritons band can cause an increase of measured luminescence, thus interpretation of the observable effect [7] can be given.

One more extension of the simple metal-dielectric multilayer geometry is super-structuring of the multilayer [8,9], modulating its properties, such as the thickness ratio between metal and dielectric layers, Fig. 1, Left. The substructure with a period of the basic multilayer stack possesses hyperbolic dispersion, making the HMM support propagating volume plasmon-polaritons. The superstructure serves to transmit some of

plasmon-polaritons and to reflect others by virtue of the same photonic band gap effects that underlie the physics of photonic crystals.

We report about efforts towards experimental realization of HMMs structures in the IR range by employing new fabrication methods hitherto untried for HMM fabrication, such as atomic layer deposition. This way we demonstrate HMMs with vertically arranged layers or two-dimensional arrays of nanopillars, Fig.1, Right.

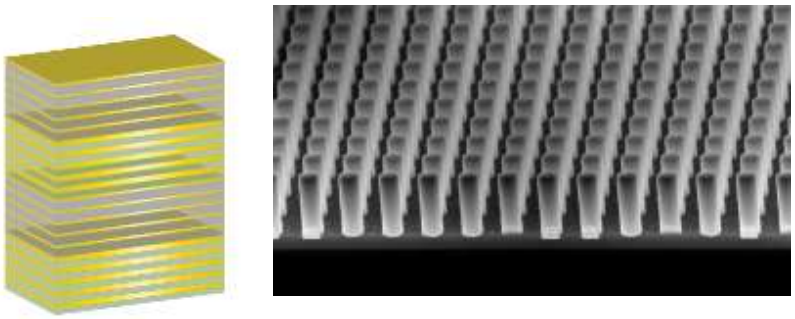


Figure 1. Left: superstructured HMM; Right: array of AZO nanopillars with height 1μm, pitch 500 nm, diameter 250 nm.

**Acknowledgements.** This work is partially supported by the project HyPHONE (Marie Curie Action FP7-PEOPLE-2011-IIF 302009), the Villum Fonden and the Directør Ib Henriksens Fond.

**REFERENCES**

1. Cai, W. and V. M. Shalaev, *Optical Metamaterials: Fundamentals and Applications*, Springer, New York, 2009.
2. Poddubny, A., I. Iorsh, P. Belov, and Y. Kivshar, "Hyperbolic metamaterials," *Nat. Photon*., Vol. 7, No. 12, 948–957, 2013.
3. Leandro, L, R. Malureanu, N. Rozlosnik, and A. Lavrinenko, "Ultrathin, ultrasmooth gold layer on dielectrics without the use of additional metallic adhesion layers." *ACS Appl. Mater. Interfaces*, Vol.7, 5797–5802, 2015.
4. Andryieuski, A., S. V. Zhukovsky, and A. V. Lavrinenko, "Rough metal and dielectric layers make an even better hyperbolic metamaterial absorber," *Opt. Express*, Vol.22, No.12, 14975–14980, 2014.
5. Narimanov, E. E., H. Li, Y. A. Barnakov, T. U. Tumkur, and M. A. Noginov, "Reduced reflection from roughened hyperbolic metamaterial," *Opt. Express*, Vol.21, No.12, 14956–14961, 2013.
6. Zhukovsky, S. V. , T. Ozel, E. Mutlugun, N. Gaponik, A. Eychmuller, A. V. Lavrinenko, H. V. Demir, and S. V. Gaponenko, "Hyperbolic metamaterials based on quantum-dot plasmon-resonator nanocomposites," *Opt. Express*, Vol. 22, No.15, 18290–18298, 2014.
7. Ozel, T., S. Nizamoglu, M. A. Sefunc, O. Samarskaya, I. O. Ozel, E. Mutlugun, V. Lesnyak, N. Gaponik, A. Eychmuller, S. V. Gaponenko, and H. V. Demir, "Anisotropic emission from multilayered plasmon resonator nanocomposites of isotropic semiconductor quantum dots," *ACS Nano*, Vol.5, No.2, 1328–1334, 2011.
8. Zhukovsky S., A. V. Orlov, V. E. Babicheva, A. V. Lavrinenko, J. E. Sipe, "Photonic-band-gap engineering for volume plasmon polaritons in multiscale multilayer hyperbolic metamaterials," *Phys. Rev. A*, Vol.90, 013801, 2014.
9. Narimanov E, "Photonic hypercrystals," *Phys. Rev. X*, Vol.4, 041014, 2014.

# Advanced plasmonic metamaterials for ultrasensitive biosensing

**A. V. Kabashin**
Aix Marseille University, CNRS, LP3 UMR 7341, Campus de Luminy - Case 917, 13288, Marseille, France
kabashin@lp3.univ-mrs.fr

**Abstract**- This presentation will overview our on-going activities on the improvement of physical sensitivity of plasmonic biosensors. Our approach is based on the employment of designed plasmonic metamaterials, which could provide a much improved sensing response over conventional Surface Plasmon Resonance (SPR) sensor configurations and offer novel attractive functionalities for biological sensing/recognition.

Over last 15 years plasmonic biosensing has become a technology of choice for label-free detection and studies of biological binding events on the surface [1,2]. Plasmonic sensing methods avoid expensive, time-consuming and precision-interfering labelling steps to mark analytes. Instead, they register the attachment of a ligand to its receptor via refractive index (RI) monitoring, which enables a real-time control of binding/recognition events. Surface plasmon resonance (SPR) forms the core of label-free optical transduction technology offering much superior sensitivity due to the strong electric field probing the target molecules under conditions of resonant excitation of plasmons over a thin Au film [1]. An extension of SPR called localized plasmon resonance (LPR) employs metallic nanostructures and thus makes possible an excellent compatibility of the sensor transducer with modern bio-molecular nano-architectures, although this approach manifests a lower sensitivity to RI variations [3]. The detection limit of SPR and LPR in terms of resolvable surface coverage of biomaterial is of the order of 1 pg/mm$^2$ and 1 ng/mm$^2$, respectively, which makes possible label-free studies of many interactions, but still inferior to labeling methods by more than 2 orders of magnitude.

We have recently introduced a series of sensor-oriented artificial plasmonic materials (metamaterials), which promise a breakthrough in the solution of the sensitivity problem of plasmonic biosensors. Our original approach addresses to the employment of phase properties of light instead of amplitude ones in order to improve the performance of plasmonic biosensing technology [4,5]. As it was confirmed in numerous studies and commercial implementations, such approach makes possible at least 2 orders of gain of sensor sensitivity in classical thin film geometry of plasmon excitation [6]. The concept of phase-sensitive plasmonic biosensing is now extended to a variety of new nanoscale architectures, including ones involving metamaterials, which are better adapted for modern requirements of bio-nanotechnology and offer new functionalities. The presentation will describe several novel promising nanoscale designs and architectures, including: (i) periodically arrayed gold nanodots, which support diffractive-coupled plasmon modes yielding to a drastic improvement of plasmon resonance quality and, as a consequence, to the amplification of sensing response [7,8]; (ii) gold nanorod metamaterials, which are capable of supporting new guided modes, which are more sensitive to refractive index changes compared to localized plasmon counterparts [9]; Gold-graphene metasurface architectures, which can profit from a combination of high phase sensitivity and new graphene-based functionalization strategies based on many aromatic structure biomolecules (helical peptides, proteins, ssDNA, etc.) [10]. Depending on a concrete biosensing task, the metamaterials can be designed either to record several binding events (a way toward ultimate label-free single molecular detection) or to enable large surface coverage in order to improve integral

sensitivity. Combined with tuneable spectral response and strong local field enhancement, the designed biosensors outperform conventional plasmonics-based counterparts and open up new opportunities for the advancement of current state-of-the-art biosensing technology.

**REFERENCES**


1. Liedberg, B., Nylander, C., Lundstrom, I. "Biosensing with surface plasmon resonance - how it all started," *Biosens. Bioelectron*. Vol. 10, i-ix, 1995.
2. Schasfoort, M., Tudos, A. J. (Eds), *Handbook of Surface Plasmon Resonance*, Royal Society of Chemistry, 2008.
3. Anker, J. N., Hall, W. P., Lyandres, O., Shah, N. C., Zhao, J., Van Duyne, R. P. "Biosensing with plasmonic nanosensors," *Nature Mater*. Vol. 7, 442-453, 2008.
4. Kabashin, A.V., Nikitin, P. I., "Interferometer based on a surface-plasmon resonance for sensor applications," *Quant. Electron*. Vol. 27, 653-654, 1997.
5. Kabashin, A. V., Patskovsky, S., Grigorenko, A. N. "Phase and amplitude sensitivities in Surface Plasmon Resonance bio- and chemical sensing," *Opt. Express*, Vol. 17, 21191-21204, 2009.
6. Huang, Y., Ho, H. P., Kong, S. K., Kabashin, A. V. "Phase-sensitive surface plasmon resonance biosensors: methodology, instrumentation and applications," *Annalen Der Physik*, Vol. 524, 637-662, 2012.
7. Kravets, V. G., Schedin, F., Jalil, R., Britnell, L., Gorbachev, R. V., Ansell, D., Thackray, B., Novoselov, K. S., Geim, A. K., Kabashin, A. V., Grigorenko, A. N. "Singular-phase nanooptics in plasmonic metamaterials for single molecular detection," *Nature Mater*., Vol. 12, 304-309, 2013.
8. Aristov, A., Zywietz, U., Evlyukhin, A., Reinhardt, C., Chichkov, B., Kabashin, A. V. "Laser-ablative engineering of phase singularities in plasmonic metamat. arrays for biosensing applications," *Appl. Phys. Lett*. 104, 071101, 2014).
9. Kabashin, A. V., Evans, P., Patskovsky, S., Wurtz, G., Hendren, W., Dickson, W., Pollard, R. J., Podolsky, V., Zayats, A. V. "Plasmonic nanorod metamaterials for biosensing," *Nature Mater*., Vol. 8, 867-871, 2009.
10. Zeng, S., Sreekanth, K. V., Shang, J., Yu T., Chen, C.-K., Yin, F., Baillargeat, D., Coquet, P., Ho, H.-P., Kabashin, A. V., Yong, K.-T., "Graphene-Gold Metasurface Architectures for Ultrasensitive Plasmonic Biosensing", *Adv. Mater.*, 27, 6163–6169, 2015.

# Hyperbolic Magnetic Media as Tunable Slab Lenses

**R. Macêdo**[1], **R. L. Stamps**[1], **and T. Dumelow**[2]

[1]SUPA School of Physics and Astronomy, University of Glasgow, Glasgow G12 8QQ, United Kingdom
[2]Departamento de F'isica, Universidade do Estado do Rio Grande do Norte, Costa e Silva, 59625-620 Mossor'o RN, Brazil
RairMacedo@gmail.com

**Abstract**— We investigate a class of hyperbolic materials that not only display negative refraction and focusing in a lens with parallel sides but also allow one to modify the focal length of a slab lens with an externally applied magnetic field. This is possible because antiferromagnets are gyrotropic and support magnetic polaritons whose frequencies are sensitive to magnetic fields. In addition, a rich caustic structure emerges at low temperatures, when damping should be small.

Magnon-polaritons in antiferromagnets have field tunable resonances that make them of interest for possible use as THz optical materials. Field tunability arises because of how applied magnetic fields affect permeabilities and the magnetic resonant response [3]. Magnon-polaritons in these materials can exist in the terahertz region. [4].

Magnetic field dependent optical properties in antiferromagnets can be described with gyrotropic susceptibilites. In this class of materials it is possible to induce negative refraction by operating at wavelengths and fields such that the principal components of the permeability tensor have opposite sign. What is perhaps most appealing about this effect is that the position of an image formed by a lens made of such material can be tuned. This is possible near an antiferromagnetic resonance, and the resonance can be very sensitive to externally applied magnetic fields. Up to now, the majority of works on tunability in slab lensing have considered such tuning in man-made structures, either using external applied electric fields [1] or by controlling the structural parame-ters [2]. Here we propose a simpler manner to achieve tunable slab lenses. We use hyperbolic dispersion in an antiferromagnetic crystal ($MnF_2$).

Here we study an antiferromagnet in a geometry which the principal axes of the crystal lie along the Cartesian axes $x$, $y$, and $z$. $xz$ is the plane of incidence and $z$ is normal to the slab surface. The antiferromanget spins are aligned along the $x$ direction. We consider the incident radiation to be s-polarized (**H** field in the plane of incidence $xz$). We also consider an external field $\mathbf{B}_0$ applied along $y$. In this case the permeability tensor is [5]

$$\mu = \begin{pmatrix} \mu_{xx} & 0 & \mu_{xz} \\ 0 & \mu_{yy} & 0 \\ -\mu_{xz} & 0 & \mu_{zz} \end{pmatrix}. \tag{1}$$

Hyperbolic media derive their name from the topology of their isofrequency curves, which are calculated from the dispersion relation between the frequency $\omega$ and the wave vector $\mathbf{k}$. Within the antiferromagnet, where the permeability is a tensor $\overleftrightarrow{\mu}(\omega)$ with frequency dependent components in the form shown by Equation (1), waves with transverse electric (TE) polarization have a behaviour described by a dispersion relation in the form

$$k_{z2}^2\mu_{zz} + k_x^2\mu_{xx} = \frac{\omega^2}{c^2}\varepsilon(\mu_{xx}\mu_{zz} + \mu_{xz}^2). \tag{2}$$

In these materials, all-angle negative refraction can happen when the condition $\mu_{xx} > 0$ and $\mu_{zz} < 0$ is satisfied since the isofrequency plot obtained from Eq. (2) is hyperbolic [5]. As a result, it is possible to obtain focusing inside an antiferromagnetic flat lens with parallel sides. In order to illustrate this, we consider a line point source at a distance $l_1$ above an $MnF_2$ slab of thickness $l$, as depicted in Figure 1(a). The ray diagram shows the path of the beams through the slab, being focused inside and outside the slab. In such a configuration, however, not all beams are focused at the paraxial focus. Marginal rays are focused after the paraxial focus within the slab, and before the paraxial focus outside the slab. This leads to an envelope of interfering refracted rays, i.e. caustics.

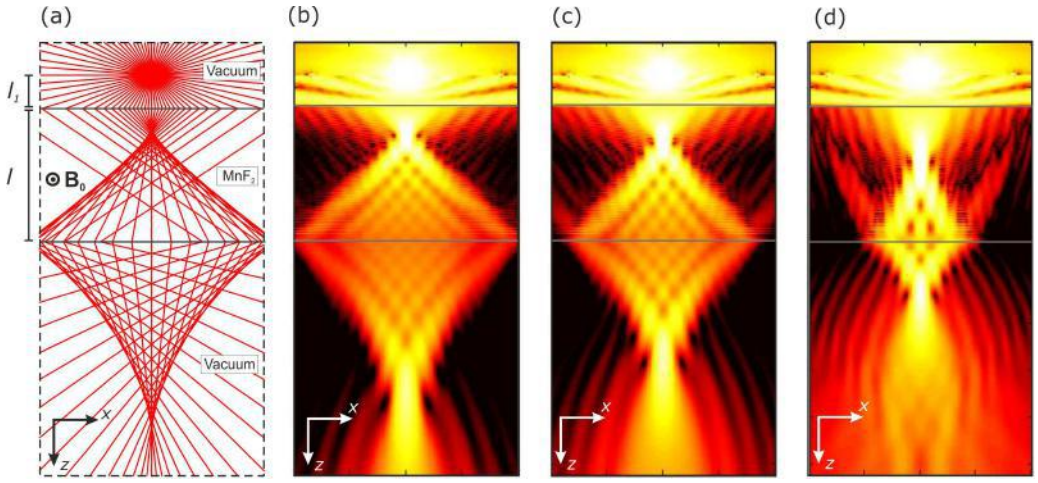



Figure 1: Image formation and caustics: s-polarization image formation at T = 0.06 $T_N$ due to a line source placed above an $MnF_2$ slab. The distance $l$ is $20\lambda$', where $\lambda$' represents the wavelength within the antiferromagnet at normal incidence (about half the free-space wavelength). The distance $l_1$ is equal to $l/4$. The extraordinary axis is directed along $x$ and the frequency of the incident radiation is $\omega/\omega_0 = 1.005$. (a) Schematic showing the path of multiple rays passing through an $MnF_2$ slab for $B_0 = 0.0$. (b) Power flow intensity for the setup shown in (a). Effect of a magnetic field on the intensity profile for (c) $B_0 = 0.2$ T and (d) $B_0 = 0.4$ T.

In Figure 1(b) we show how the behaviour of the power flow, given by the time-average Poynting vector $\langle \mathbf{S}_2 \rangle$ of each ray, emanating from the line source across the slab, at a frequency $\omega/\omega_0 = 1.005$ in the absence of an externally applied field. Due to high levels of transmission for all incident angles, intersecting rays produces a network of constructive and destructive interference within the caustic envelope, both inside and outside the slab. This is most visible when damping is extremely low (as would be expected at low temperatures for good crystals). Nevertheless, despite the complications of the caustics due to imperfect focusing at high angles, there is a high intensity sharp focus at the cusp.

The angle of refraction decreases as the magnetic field increases (given a chosen frequency $\omega/\omega_0 = 1.005$), which means that the paraxial focus, and hence image position, can be moved closer to the lens by simply changing the magnitude of the external field (See Figures 1(c)-(d)).

The key point here is that for hyperbolic magnetic media, not only can a caustic structure be seen, but focusing can also be achieved in a slab lens. Natural magnetic media are field reliant which allows tunable image formation at a single frequency without changing the crystal structure or the physical shape of the lens. Finally, we stress that the analysis and general principles presented in this letter apply equally well to other types of hyperbolic media, both natural or artificial.

## ACKNOWLEDGMENT

The authors would like to thank to R. E. Camley for helpful discussions. This work was supported by EPSRC EP/M024423/1 and the Brazilian research agency CNPq.

## REFERENCES

1. Shi, L. et. al., "Tunable negative refraction and subwavelength imaging in the metal-dielectric composites of nonspherical particles," *IEEE*, 463–466, 2006.
2. Forouzmand, A. and Yakovlev, A.B., "Tunable dual-band subwavelength imaging with a wire medium slab loaded with nanostructured graphene metasurfaces," *AIP Advances*, Vol. 5, No. 7, 077108, 2015.
3. R. E. Camley and D. L. Mills, "Surface polaritons on uniaxial antiferromagnets," *Physical Review B,* vol. 26, p. 1280, 1982.
4. N. S. Almeida and D. L. Mills, "Dynamical response of antiferromagnets in an oblique magnetic field: application to surface magnons, *Physical Review B,* vol. 37, p. 3626, 1988.
5. R. Macêdo and T. Dumelow, "Tunable all-angle negative refraction using antiferromagnets," *Physical Review B,* vol. 89, p. 035135, 2014.

# Imaging of anomalous internal reflections of hyperbolic phonon-polaritons in hexagonal boron nitride nanocones

**Alexander J. Giles,[†] Siyuan Dai,[‡] Orest J. Glembocki,[♯] Andrey V. Kretinin,[¶] Zhiyuan Sun,[‡] Chase T. Ellis,[†] Joseph G. Tischler,[♯] Takashi Tanaguchi,[§] Kenji Watanabe,[§] Michael M. Fogler,[‡] Kostya S. Novoselov,[¶] Dimitri. N. Basov,[‡,ǁ] and Joshua D. Caldwell[*,♯]**

[†]NRC Postdoctoral Fellow at U.S. Naval Research Laboratory, Washington, D.C., USA
[♯]U.S. Naval Research Laboratory, Washington, D.C., USA
[‡]Department of Physics, University of California San Diego, La Jolla, California 92093, USA
[¶]School of Physics and Astronomy, University of Manchester, Oxford Rd, Manchester, UK
[§]National Institute for Materials Science, 1-1 Namiki Tsukuba, Ibaraki, Japan
[ǁ]Department of Physics, Columbia University, 538 West 120th Street, New York, New York 10027

E-mail: alexander.giles@gmail.com

We use scanning near-field optical microscopy to study the response of hexagonal boron nitride nanocones at infrared frequencies, where this material behaves as a hyperbolic medium. The obtained images are dominated by a series of "hot" rings that occur on the sloped sidewalls of the nanocones. The ring positions depend on the incident laser frequency and the nanocone shape. Both dependences are consistent with directional propagation of hyperbolic phonon-polariton (HPhP) rays that are launched at the edges and zigzag through the interior of the nanocones, sustaining multiple internal reflections off the sidewalls. Additionally, we observe a strong overall enhancement of the near-field signal at discrete resonance frequencies. These resonances attest to low dielectric losses that permit coherent standing waves of the subdiffractional polaritons to form. We also discuss potential applications of such shape-dependent resonances and the field concentration at the hot rings.

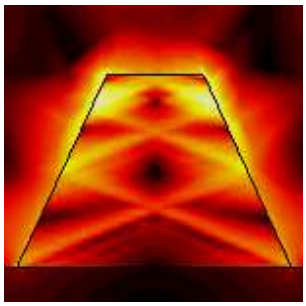


**Figure 1**: Numerically calculated distribution of tangential electric field in the *x*–*z* cross section of the nanocone (side view). The calculation was done for the $^{U}TM_{13}$ resonant frequency. The hot rings arise at the sidewall reflection points of the HPhP trajectories launched at the nanocone base.

# THz wire medium operating as a ultra-broadband imaging device

**K. J. Kaltenecker[1,2,3], A. Tuniz[4,5], S. C. Fleming[4], A. Argyros[4], B. T. Kuhlmey[4], M. Walther[2], and B. M. Fischer[1]**

[1]French-German Research Institute of Saint-Louis, France
[2]University of Freiburg, Institute of Physics, Germany
[3]Technical University of Denmark, Department of Photonics Engineering, Denmark
[4]University of Sydney, Institute of Photonics and Optical Science, Australia
[5]Leibniz Institute of Photonic Technology, Germany
Korbinian.Kaltenecker@isl.eu

**Abstract**— Wire media can be used for non-diffractive, sub-diffraction-limited image transmission over several wavelength. A perfect reconstruction of transmitted field distribution, however, has been limited to narrow frequency windows defined by the Fabry-Perot resonance condition. Away from these resonances, the image is distorted due to formation of harmful surface wave supported by the wire medium. We propose and demonstrate that this effect can be overcome by using ultra short THz pulses and measuring the electric field in the time domain. This allows to separate the initial pulse from subsequent back-reflections. Using a THz near-field microscope, we demonstrate ultra-broadband perfect transmission of complex field distributions over the entire frequency band of the source.

## 1. INTRODUCTION

The resolution of common imaging systems is restricted to approximately half the wavelength as a result of the diffraction limit. A promising device to overcome this restriction is the wire medium (WM) which is composed of an array of subwavelength scaled metal wires [1]. Wire media provide an opportunity to transmit the near-field with super-resolution [2]. By using electric fields that are polarized orthogonal towards the front interface of the WM, perfect imaging can be achieved. The excited electromagnetic modes are constituted exclusively by extraordinary waves, filtering out all ordinary waves. However, so far it has been accepted that tuning the length of the WM to the Fabry-Perot resonance condition is crucial for obtaining distortion-free images [3]. Otherwise back-reflections perturb the image formation at the image plane, amplifying the evanescent modes supported by the WM, and severely distorting the image [3, 4]. As we will demonstrate by our THz time-domain measurements, in the case of experiments with pulsed light sources, obeying the Fabry-Perot condition is not necessarily required. Reflected pulses are usually well-separated from the main pulse and the pulses are typically short enough to prohibit the formation of resonant slab modes. Thus, using pulsed sources allows to remove detrimental back-reflections through simple post-processing. As a result perfect, ultra-broadband terahertz imaging is realized.

## 2. EXPERIMENTAL DETAILS AND RESULTS

The WM are fabricated by a fibre draw technique [5]. They contain 453 hexagonally arranged indium wires of nominally 10 µm diameter and 50 µm pitch and different length. As one example, we show that it is possible to transport the field distribution formed on top of a plasmonic lens (PL) through the WM when illuminated by linearly polarized THz pulses. For this purpose we measured the electric field distribution with a terahertz near-field microscope [6, 7]. By using an electro-optical detection scheme with a ZnTe crystal cut in (100)-direction in order to measure the longitudinal field component, we directly map the field in close vicinity to the samples and are able to reconstruct the field pattern in the time and the frequency domain. The PL, consisting of a metal disc with 350 µm diameter surrounded by a 90 µm-wide annular gap has been fabricated by etching the circular gap through a 500 nm thick aluminium layer which was deposited on a 300 µm thick quartz wafer (Fig. 1(b)). If $x$-polarized light is normally incident from the bottom side of the annular slit the light is diffractively coupled into surface plasmon polaritons (SPPs), which counter-propagate with opposite phase toward the centre of the disc. As a result of the cylindrical symmetry of the structure, interference leads to the dominant electric field $z$-component of the SPPs being proportional to the first-order Bessel function. We scanned spatial distribution of the

electric near-field close to both the PL and the WM placed on top of the PL, and compared the resulting field patterns.

The THz time-domain approach provides imaging data over a broad frequency range by Fourier-transforming the time dependent signal. Figure 1(c) shows the frequency-dependent intensity profile along a line through the centre of the plasmonic lens (red line in (a)). For better representation the scan along the $x$-axis has been normalized to the field maximum at the respective frequency. The dashed white lines indicate the extend of the metal structure. The corresponding intensity profile measured with the WM on top of the PL is shown in Fig. 1(d). The periodic distortions ($\Delta\nu \approx 75GHz$) are a result of reflected pulses inside the WM. Only at frequencies close to the Fabry-Perot resonance condition undistorted images are obtained. By windowing the transients such that the reflected pulses are suppressed undistorted images are obtained over the entire frequency band covered by the experiment.

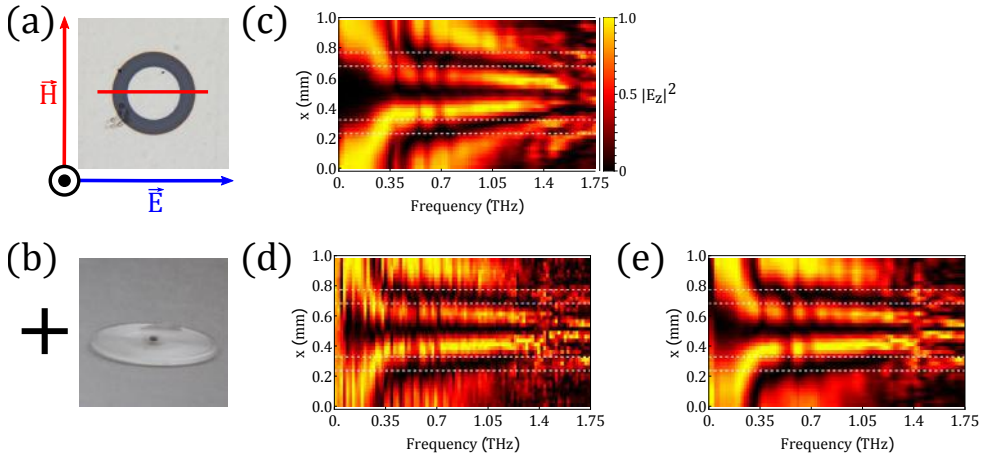



Figure 1: (a) Plasmonic lens, (b) short WM fixed in transparent sample mount. The red line indicate the position of the frequency dependent intensity profile (c) without WM, (d) with WM, and (e) with WM after post processing.

## 3. CONCLUSION

In summary, we have studied the impact of internal reflections within the WM on the image quality, which cause severe artefacts, unless the WM length is tuned to the Fabry-Perot resonance condition. We have shown that such a criterion is not required in time-domain measurements using short light pulses, if the main pulse can be temporally separated from subsequent internal reflections. As a result ultra-broadband operation with a single WM length can be realized.

## REFERENCES


1. R. Simovski, P. A. Belov, A. Atraschenko, and Y. S. Kivshar, ,Advanced Materials, vol. 24, no. 31, pp. 4229-4248, 2012.
2. A. Tuniz, K. J. Kaltenecker, B. M. Fischer, M. Walther, S. C. Fleming, A. Argyros, and B. T. Kuhlmey, , Nature Communications, vol. 4, no. 2706, 2013.
3. A. Rahman, P. A. Belov, M. G. Silveirinha, C. R. Simovski, Y. Hao, and C. Parini, , Applied Physics Letters, 94(3), 2009.
4. A. Tuniz, D. Ireland, L. Poladian, A. Argyros, C. M. de Sterke, and B. T. Kuhlmey,, Opt. Lett., 39(11):32863289, 2014.
5. A. Tuniz, R. Lwin, A. Argyros, S. C. Fleming, and B. T. Kuhlmey, , J. Vis. Exp., vol. 68, no. e4299, 2012.
6. A. Bitzer, A. Ortner, and M. Walther, , Appl. Opt., vol. 49, no. 19, pp. E1-E6, 2010.
7. S. Waselikowski, J. Wallauer, C. Fischer, and M. Walther, , New Journal of Physics, 15(7), 2013.

# Microscopic Calculations of Dielectric Properties for Hyperbolic Metamaterials

**Maxim Anokhin*, Alexey Tishchenko, and Mikhail Strikhanov**

National Research Nuclear University MEPhI, Moscow, Russia
*E-mail: MNAnokhin@mephi.ru

## Abstract

We theoretically study macroscopic dielectric properties of hyperbolic metamaterials proceeding from microscopic description. The theory constructed gives the answer to the question "what properties should microscopic elements have in order to macroscopic system consisting of these elements would be a hyperbolic metamaterial". Generalized Clausius-Mossotti relation as well as existence conditions for such metamaterials are obtained with help of the local field theory. The perpendicular and parallel components of the dielectric permittivity are found as functions of microscopic parameters of a single particle and a dielectric matrix.

## 1. Introduction

Metamaterials are artificial composite media with unique optical properties which allow one to manipulate light propagation [1-3]. One of the most interesting classes of metamaterials is the so-called "double-negative metamaterials": they have both negative permittivity and permeability. They held much promise because of their negative refraction. As was mentioned in [4], it is considerably easier to produce hyperbolic structures than double-negative media, as the only essential criterion for hyperbolic structures is that the motion of free electrons be constrained in one or two spatial directions.

Here we study hyperbolic metamaterials, i.e. metamaterials which show a hyperbolic dispersion. They were firstly called indefinite materials [5]. In such media an isofrequency surface in space $\left(k_x, k_y, k_z\right)$ has a form of a hyperboloid. The perpendicular and parallel components of the dielectric permittivity and / or permeability have opposite signs.

$$\hat{\varepsilon}\left(\omega\right)=\begin{pmatrix}\varepsilon_{\perp}\left(\omega\right) & 0 & 0\\ 0 & \varepsilon_{\perp}\left(\omega\right) & 0\\ 0 & 0 & \varepsilon_{\parallel}\left(\omega\right)\end{pmatrix};$$
$$\hat{\mu}\left(\omega\right)=\begin{pmatrix}\mu_{\perp}\left(\omega\right) & 0 & 0\\ 0 & \mu_{\perp}\left(\omega\right) & 0\\ 0 & 0 & \mu_{\parallel}\left(\omega\right)\end{pmatrix}. \quad (1)$$

Hyperbolic metamaterials have the potential for use in fluorescence engineering, nanoimaging, subsurface sensing, Dyakonov plasmons and super-Planckian thermal emission [6].

We consider electric hyperbolic structure where

$$\begin{cases}\mu_{\perp}\left(\omega\right)=\mu_{\parallel}\left(\omega\right)>0;\\ \varepsilon_{\perp}\left(\omega\right)>0;\\ \varepsilon_{\parallel}\left(\omega\right)<0.\end{cases}, \quad (2)$$

or

$$\begin{cases}\mu_{\perp}\left(\omega\right)=\mu_{\parallel}\left(\omega\right)>0;\\ \varepsilon_{\perp}\left(\omega\right)<0;\\ \varepsilon_{\parallel}\left(\omega\right)>0.\end{cases}. \quad (3)$$

In this work we develop the method used in our previous article [7] for calculating dielectric function of a periodical structure from the first principles, proceeding from microscopic Maxwell's equations and two procedures of averaging, with taking into account the local field effects [8-11] and spatial dispersion.

## 2. Microscopic calculations of dielectric permittivity

Let us consider the hyperbolic metamaterial as an infinite periodic structure affected by the external field $\mathbf{E}^{ext}$ and composed of $N$ anisotropic particles characterized by a polarizability $\alpha_s\left(\omega\right)$ in a dielectric matrix consisting of particles with polarizability $\alpha_m\left(\omega\right)$.

The solution of Maxwell's equations in a medium can be written in form of a system of $N$ equations for the field acting on the $a$-th particle:

$$E_i^{mic}\left(\mathbf{R}_a,\omega\right)=E_i^{ext}\left(\mathbf{R}_a,\omega\right)+E_{si}^{\sec}\left(\mathbf{R}_a,\omega\right)+E_{mi}^{\sec}\left(\mathbf{R}_a,\omega\right), \quad (4)$$

where $E_{si}^{\sec}$ and $E_{mi}^{\sec}$ are the secondary fields are created by the rest particles of matter and the dielectric matrix, respectively:

$$E_{si}^{\sec}\left(\mathbf{R}_a,\omega\right)=\frac{1}{2\pi^2}\alpha_s\left(\omega\right)\int d^3l S_{ij}\left(\mathbf{l},\omega\right)\times \\ \times\sum_b E_j^{mic}\left(\mathbf{R}_b,\omega\right)\exp\left\{-i\mathbf{l}\left(\mathbf{R}_b-\mathbf{R}_a\right)\right\}; \quad (5)$$

$$E_{mi}^{\text{sec}}(\mathbf{R}_a,\omega)=\frac{1}{2\pi^2}\alpha_m(\omega)\int d^3l S_{ij}(\mathbf{l},\omega)\times \\ \times\sum_c E_j^{mic}(\mathbf{R}_c,\omega)\exp\{-i\mathbf{l}(\mathbf{R}_c-\mathbf{R}_a)\}, \quad (6)$$

where index $b$ corresponds to all the other particles of this structure with the exception of $a$-th particle, index $c$ corresponds to all the dielectric matrix;

$$S_{ij}(\mathbf{l},\omega)=\frac{k^2\delta_{ij}-l_i l_j}{l^2-k^2-i0}; \quad (7)$$

$$k=\frac{\omega}{c}\sqrt{\varepsilon_0}, \quad (8)$$

where $\varepsilon_0$ is widely known Clausius-Mossotti relation:

$$\varepsilon_0=\frac{1+\frac{8\pi}{3}n\alpha_m}{1-\frac{4\pi}{3}n\alpha_m} \quad (9)$$

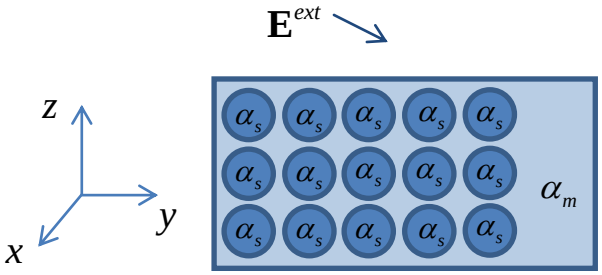



Figure 1: Schematic illustration of considered matter.

From the Eqs. (5) and (6) one can see that the contribution of any particle depends on its position relative to the $a$-th particle. It determines the dependence of the effective field on the mutual arrangement of the particles, i.e. in fact the structure of matter.

Let $w(\mathbf{R}_{ba})$ be the probability density of finding the $b$-th particle at the distance $\mathbf{R}_{ba}=\mathbf{R}_b-\mathbf{R}_a$ from the $a$-th one:

$$w(\mathbf{R}_{ba})=\frac{1}{N}\sum_{m=1}^{N}\delta(\mathbf{R}_{ba}-\mathbf{R}_m). \quad (10)$$

The system given by Eq. (4), due to the condition $N\gg 1$, can be solved only approximately. By averaging Eqs. (5) and (6) over the coordinates of all the rest particles, the material consists of, one can find the local and the macroscopic fields, correspondingly [5]:

$$E_i^{loc}(\mathbf{R}_a,\omega)=E_i^{ext}(\mathbf{R}_a,\omega)+\frac{1}{2\pi^2}N\alpha(\omega)\int d^3l S_{ij}(\mathbf{l},\omega)\times \\ \times\int d^3R_{ba}\, w(\mathbf{R}_{ba})E_j^{loc}(\mathbf{R}_a+\mathbf{R}_{ba},\omega)\exp\{-i\mathbf{l}\mathbf{R}_{ba}\}; \quad (11)$$

$$E_i(\mathbf{R},\omega)=E_i^{ext}(\mathbf{R},\omega)+4\pi n\alpha(\omega)S_{ij}(\mathbf{R},\omega)E_j^{loc}(\mathbf{R},\omega), \quad (12)$$

where

$$\alpha(\omega)=\alpha_s(\omega)+\alpha_m(\omega); \quad (13)$$

$$S_{ij}(\mathbf{R},\omega)=\int d^3l S_{ij}(\mathbf{l},\omega)\exp\{i\mathbf{l}\mathbf{R}\}. \quad (14)$$

Using Eq. (11) and (12) one can express the macroscopic field $\mathbf{E}$ trough the local field $\mathbf{E}^{loc}$:

$$E_i(\mathbf{R},\omega)=E_i^{loc}(\mathbf{R},\omega)+ \\ +4\pi n\alpha(\omega)S_{ij}(\mathbf{R},\omega)E_j^{loc}(\mathbf{R},\omega)- \\ -\frac{1}{2\pi^2}\alpha(\omega)\sum_{m=1}^{N}S_{ij}(-\mathbf{R}_m,\omega)E_j^{loc}(\mathbf{R}+\mathbf{R}_m,\omega). \quad (15)$$

From obtained expressions we write the equation for the corresponding Fourier images in variables $(\mathbf{q},\omega)$:

$$t_{ij}(\mathbf{q},\omega)E_j^{loc}(\mathbf{q},\omega)=E_i(\mathbf{q},\omega), \quad (16)$$

where

$$t_{ij}(\mathbf{q},\omega)=\delta_{ij}+4\pi n\alpha(\omega)S_{ij}(\mathbf{q},\omega)- \\ -\frac{1}{2\pi^2}\alpha(\omega)\sum_{m=1}^{N}\exp\{i\mathbf{q}\mathbf{R}_m\}S_{ij}(-\mathbf{R}_m,\omega). \quad (17)$$

Let us make some auxiliary manipulations:

$$S_{ij}(-\mathbf{R},\omega)=f_1(R)\delta_{ij}+f_2(R)\frac{R_i R_j}{R^2}. \quad (18)$$

Functions $f_1(R)$ and $f_2(R)$ can be obtained by multiplying Eq. (18) by $\delta_{ji}$ and $\frac{R_j R_i}{R^2}$:

$$f_1(R)=-2\frac{\pi^2 k}{R^2}\sin(kR)-2\frac{\pi^2}{R^3}\cos(kR); \\ f_2(R)=4\frac{\pi^2 k^2}{R}\cos(kR)+6\frac{\pi^2 k}{R^2}\sin(kR)+6\frac{\pi^2}{R^3}\cos(kR). \quad (19)$$

Thus, tensor $t_{ik}(\mathbf{q},\omega)$ has the form:

$$t_{ik}(\mathbf{q},\omega)=\delta_{ik}+4\pi n\alpha(\omega)\frac{k^2\delta_{ik}-q_i q_k}{q^2-k^2-i0}- \\ -\frac{\alpha(\omega)}{2\pi^2}\sum_{m=1}^{N}\left[f_1(R_m)\delta_{ik}+f_2(R_m)\frac{R_{mi}R_{mk}}{R_m^2}\right]\exp\{i\mathbf{q}\mathbf{R}_m\}. \quad (20)$$

Thus, the dielectric permittivity is expressed through the reciprocal tensor $t_{jk}^{-1}(\mathbf{q},\omega)$:

$$\varepsilon_{ik}(\mathbf{q},\omega)=\delta_{ik}+4\pi n\alpha_{ij}(\omega)t_{jk}^{-1}(\mathbf{q},\omega). \quad (21)$$

Let us present tensor $t_{ij}(\mathbf{q},\omega)$ in the form:

$$t_{ij}(\mathbf{q},\omega)=\left(\delta_{ij}-\frac{q_i q_j}{q^2}\right)a(q,\omega)+\frac{q_i q_j}{q^2}b(q,\omega). \quad (22)$$

Coefficients $a(q,\omega)$ and $b(q,\omega)$ can be found from Eqs. (18) and (20):

$$a(q,\omega)=c_1(\mathrm{q},\omega)k^2+c_2(\mathrm{q},\omega); \quad (23)$$

$$b(q,\omega)=c_3(\mathrm{q},\omega)-4\pi n\alpha(\omega), \quad (24)$$

where the coefficients $c_1(\mathrm{q},\omega)$, $c_2(\mathrm{q},\omega)$ and $c_3(\mathrm{q},\omega)$ are determined by the expressions ($\theta$ is an angle between vectors $\mathbf{q}$ and $\mathbf{R}$):

$$c_1(\mathrm{q},\omega)=\frac{4\pi n\alpha(\omega)}{q^2-k^2};$$

$$c_2(\mathrm{q},\omega)=1-$$

$$-\frac{\alpha(\omega)}{2\pi^2}\sum_{m=1}^{N}\left[f_1(R_m)+\frac{f_2(R_m)}{2}\sin^2\theta\right]\exp\{iqR_m\cos\theta\}. \quad (25)$$

$$c_3(\mathrm{q},\omega)=1-$$

$$-\frac{\alpha(\omega)}{2\pi^2}\sum_{m=1}^{N}\left[f_1(R_m)+f_2(R_m)\cos^2\theta\right]\exp\{iqR_m\cos\theta\}$$

Tensor $t_{ij}^{-1}(\mathbf{q},\omega)$ has the same structure as $t_{ij}(\mathbf{q},\omega)$ in Eq. *(22)* and therefore it is easy to show that:

$$t_{ij}^{-1}(\mathbf{q},\omega)=\left(\delta_{ij}-\frac{q_iq_j}{q^2}\right)\frac{1}{a(q,\omega)}+\frac{q_iq_j}{q^2}\frac{1}{b(q,\omega)}. \quad (26)$$

From Eqs. (26) and (21) we obtain the dielectric permittivity tensor:

$$\varepsilon_{ij}(\mathbf{q},\omega)=\varepsilon_{\perp}(\mathrm{q},\omega)\left(\delta_{ik}-\frac{q_iq_j}{q^2}\right)+\varepsilon_{\parallel}(\mathrm{q},\omega)\frac{q_iq_j}{q^2}, \quad (27)$$

where the perpendicular $\varepsilon_{\perp}(\mathrm{q},\omega)$ and parallel $\varepsilon_{\parallel}(\mathrm{q},\omega)$ components expressed through the microscopic parameters have form:

$$\varepsilon_{\perp}(\mathrm{q},\omega)=\frac{c_1(\mathrm{q},\omega)q^2-c_2(\mathrm{q},\omega)}{c_1(\mathrm{q},\omega)k^2-c_2(\mathrm{q},\omega)}; \quad (28)$$

$$\varepsilon_{\parallel}(\mathrm{q},\omega)=\frac{c_3(\mathrm{q},\omega)}{c_3(\mathrm{q},\omega)-4\pi n\alpha(\omega)}. \quad (29)$$

Eq. (27) is the generalized Clausius-Mossotti relation for hyperbolic metamaterial considered as an infinite periodic structure. This expression connects values at different level of consideration: the macroscopic dielectric permittivity $\varepsilon_{ij}(\mathbf{q},\omega)$ is presented as function of the microscopic polarizability $\alpha(\omega)$ of the single particles. Eqs. (27) - (29) describe dielectric properties of the media.

## 3. Discussion

In this work we have theoretically studied the dielectric properties of the hyperbolic metamaterial.

All results are obtained by the direct solving Maxwell's equations. In the dipole approximation we find connection between the macroscopic field **E** and the local field – Eq. (16). We obtained the dielectric function of the hyperbolic material – Eq. (27). The effects of spatial dispersion are taken into account.

The poles of the tensor $t_{ij}(\mathbf{q},\omega)$ and the dielectric permittivity $\varepsilon_{ij}(\mathbf{q},\omega)$ demonstrate the local field effects.

Using obtained expressions (28) and (29) for $\varepsilon_{\perp}(\mathrm{q},\omega)$ and $\varepsilon_{\parallel}(\mathrm{q},\omega)$ and according to Eqs. (2) and (3) we can find existence conditions for hyperbolic metamaterials.

For conditions determined by Eqs. (2):

$$\begin{cases}\mu_{\perp}(\omega)=\mu_{\parallel}(\omega)>0;\\ q^2>\dfrac{c_2(\mathrm{q},\omega)}{c_1(\mathrm{q},\omega)};\\ k^2>\dfrac{c_2(\mathrm{q},\omega)}{c_1(\mathrm{q},\omega)};\\ c_3(\mathrm{q},\omega)>0;\\ c_3(\mathrm{q},\omega)<4\pi n\alpha(\omega);\end{cases} \quad \text{or} \quad \begin{cases}\mu_{\perp}(\omega)=\mu_{\parallel}(\omega)>0;\\ q^2<\dfrac{c_2(\mathrm{q},\omega)}{c_1(\mathrm{q},\omega)};\\ k^2<\dfrac{c_2(\mathrm{q},\omega)}{c_1(\mathrm{q},\omega)};\\ c_3(\mathrm{q},\omega)<0;\\ c_3(\mathrm{q},\omega)>4\pi n\alpha(\omega).\end{cases} \quad (30)$$

For conditions determined by Eqs. (3):

$$\begin{cases}\mu_{\perp}(\omega)=\mu_{\parallel}(\omega)>0;\\ q^2>\dfrac{c_2(\mathrm{q},\omega)}{c_1(\mathrm{q},\omega)};\\ k^2<\dfrac{c_2(\mathrm{q},\omega)}{c_1(\mathrm{q},\omega)};\\ c_3(\mathrm{q},\omega)>0;\\ c_3(\mathrm{q},\omega)>4\pi n\alpha(\omega);\end{cases} \quad \text{or} \quad \begin{cases}\mu_{\perp}(\omega)=\mu_{\parallel}(\omega)>0;\\ q^2<\dfrac{c_2(\mathrm{q},\omega)}{c_1(\mathrm{q},\omega)};\\ k^2>\dfrac{c_2(\mathrm{q},\omega)}{c_1(\mathrm{q},\omega)};\\ c_3(\mathrm{q},\omega)<0;\\ c_3(\mathrm{q},\omega)<4\pi n\alpha(\omega).\end{cases} \quad (31)$$

where the coefficients C1, C2, C3 are defined by the Eqs. (25).

## 4. Conclusions

Hyperbolic metamaterials is rather new but rapidly developing direction in modern science , which is caused by the relative ease of nanofabrication, broadband nonresonant response, wavelength tunability, bulk three-dimensional response, and high figure of merit [12].

The results obtained in this work give the relation between microscopic and macroscopic properties, and therefore can be important for engineering of metamaterials with required electromagnetic properties.


## Acknowledgements

This work was supported by the Ministry of Education and Science of the Russian Federation, the project 3.1110.2014/K and by Competitiveness Growth Program of the Federal Autonomous Educational Institution of Higher Education National Research Nuclear University MEPhI (Moscow Engineering Physics Institute).


## References


[1] O.V. Porvatkina, A.A. Tishchenko, M.I. Ryazanov, M.N. Strikhanov, Local field effects in anisotropic metamaterials, *IOP Conference Series* 541: 012024, 2014.

[2] V.M. Shalaev, Optical negative-index metamaterials, *Nature Photonics* 1: 41–48, 2007.

[3] W. Cai, V.M. Shalaev, *Optical Metamaterials: Fundamentals and Applications*, Springer, New York, 2010.

[4] A. Poddubny, I. Iorsh, P. Belov, Y. Kivshar, Hyperbolic metamaterials, *Nature Photonics* 7: 948–957, 2013.

[5] D.R. Smith, D. Schuring, Electromagnetic wave propagation in media with indefinite permittivity and permeability tensors, *Physical Review Letters* 90 (7): 077405/1-077405/4, 2003.
[6] Y. Guo, W. Newman, C. L. Cortes, Z. Jacob, Applications of hyperbolic metamaterial substrates, *Advances in OptoElectronics* 2012: 452502, 2012.
[7] M. N. Anokhin, A. A. Tishchenko, M. N. Strikhanov, Dielectric permittivity of artificial periodic structure and local field effects, *Journal of Physics: Conference Series* 643: 012066, 2015.
[8] M. I. Ryazanov, A. A. Tishchenko, Clausius-Mossotti-type relation for planar monolayers, *JETP* 103: 539-545, 2006.
[9] M. N. Anokhin, A. A. Tishchenko, M. N. Strikhanov, Permittivity of thin quantum dot film with local field effects, *PIERS Proceedings*: 1370-1372, 2015.
[10] O.V. Porvatkina, A.A. Tishchenko, M.N. Strikhanov, Local field effects in periodic metamaterials , *IOP Conference Series* (in print), 2016.
[11] M. N. Anokhin, A. A. Tishchenko, M. N. Strikhanov, Permittivity of anisotropic dielectric near surface with local field effects, *Journal of Physics: Conference Series* 541: 012023, 2014.
[12] A. J. Hoffman, L. Alekseyev, S. S. Howard et al., Negative refraction in semiconductormetamaterials, *NatureMaterials* 6 (12): 946–950, 2007

# Active and passive optical metasurfaces

# Dynamics of Non-Linear Hybrid ITO-Plasmonic Metasurfaces

**M. Navarro-Cía[1*], H. Aouani[2], M. Rahmani[2,3], and S. A. Maier[2]**

[1]School of Physics and Astronomy, University of Birmingham, Birmingham B15 2TT, UK

[2]The Blackett Laboratory, Department of Physics, Imperial College London, London SW7 2AZ, UK

[3]Nonlinear Physics Centre, Research School of Physics and Engineering, The Australian National University, Canberra, ACT 0200, Australia

[*]corresponding author: m.navarro-cia@bham.ac.uk

**Abstract-** Optical nonlinearities are intrinsically weak, but can be strengthened in scenarios that provide field enhancement mechanisms. Hybrid structures combining the high inherent material nonlinearity of semiconductors along with plasmonic-induced strong fields are promising platforms for on-chip nonlinear optics. However, due to their complexity, understanding the mechanisms involved is sometimes challenging. Here, the spectral response of metal dimers loaded with an ITO nanoparticle at their gap is investigated numerically and experimentally to provide an understanding and design rules.

Nonlinear metasurfaces is a thriving research field, which creates transformative opportunities for manipulating light in a very compact way [1]-[4]. Since the length scales are short, nonlinear interactions are enhanced by exploiting materials with large nonlinearity in combination with plasmonic strong fields [3], [5]-[8]. Realizing experimentally this hybrid approach has been made possible thanks to advances in nanofabrication.

Unfortunately, the recently proposed hybrid structures are relatively complex and a full understanding of the mechanisms involve in the high nonlinear efficiency observed is yet to be provided. To address this, we investigate here different metal dimers loaded with an ITO nanoparticle at their gap (see Fig. 1(a,b)) with a systematic combined approach involving numerical and experimental spectral analysis. The methodology shown here allows us to trace the origin of the nonlinear signal to the semiconductor or metal.

All dimers (with and without ITO nanoparticle) investigated were fabricated by a combination of etch-down and lift-of methods. They were modelled with a full-wave finite-difference time-domain technique and their linear and nonlinear responses were studied by Fourier-transform infrared spectroscopy and a custom nonlinear inverted microscope, respectively.

Figure 1(c) shows the experimental third harmonic intensity for a nano-dipole with and without the ITO nanoparticle at its gap. Remarkably, the hybrid metasurface shows a six-fold intensity. The origin of this enhancement could be either a favorable change in the resonant condition of the nano-dipole or the boost of the ITO nonlinearity by the strong field expected at the gap of the nano-dipole. To resolve this, we compare the experimental normalized spectra to the numerically-computed ones (see Fig. 1(d)). The nonlinear simulations allow us to switch on and off the third order susceptibility of the metal and ITO independently, which proves to be a very powerful tool. Both measurements and simulation results show that the third harmonic linewidth of the bare plasmonic configuration is larger than that of the hybrid nanostructure when considering the ITO

nanoparticle nonlinear. Meanwhile, the simulations reveal that the hybrid and bare nanostructures exhibit identical spectra when ITO is considered linear. This clearly indicates that the third harmonic signal is generated in our system from the ITO nanoparticle.

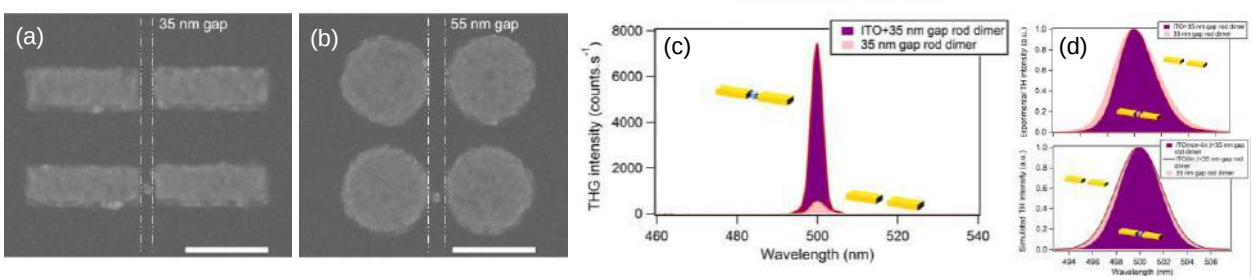



Figure 1. (a) SEM image of a 35 nm gap nanorod dimer without (top) / with (bottom) a ~25 nm ITO nanoparticle at its gap; scale bar: 200 nm. (b) SEM image of a 55 nm gap nanocylinder dimer without (top) / with (bottom) a ~25 nm ITO nanoparticle at its gap; scale bar: 200 nm. (c) Experimental THG spectra from the nano-dipoles (a,b) under parallel polarized excitation. (d) Experimental, top, and simulated, bottom, normalized THG spectra from a 35 nm gap nanorod dimer with and without the ITO nanoparticle at its gap under parallel polarized excitation.

**Acknowledgements.** This work was funded by the Engineering and Physical Sciences Research Council (EPSRC) through the Active Plasmonics programme, the Leverhulme Trust, the US Army International Technology Centre Atlantic (USAITC-A) and the Office of Naval Research (ONR and ONR Global). M.N-C. is supported by a Birmingham Fellowship.

**REFERENCES**

1. Zhang, Y., N. K. Grady, C. Ayala-Orozco, and N. J. Halas, "Three-Dimensional Nanostructures as Highly Efficient Generators of Second Harmonic Light," *Nano Lett.*, Vol. 11, No. 12, 5519-5523, 2011.
2. Schumacher, T., K. Kratzer, D. Molnar, M. Hentschel, H. Giessen, and M. Lippitz, "Nanoantenna-enhanced ultrafast nonlinear spectroscopy of a single gold nanoparticle," *Nature Comm.*, Vol. 2, 333, 2011.
3. Navarro-Cía, M. and S.A. Maier, "Broad-Band Near-Infrared Plasmonic Nanoantennas for Higher Harmonic Generation," *ACS Nano*, Vol. 6, No. 4, 3537–3544, 2012.
4. Aouani, H., M. Navarro-Cia, M. Rahmani, T. P. H. Sidiropoulos, M. Hong, R. F. Oulton, and S. A. Maier, "Multiresonant Broadband Optical Antennas As Efficient Tunable Nanosources of Second Harmonic Light," *Nano Lett.*, Vol. 12, No. 9, 4997-5002, 2012.
5. Harutyunyan, H., G. Volpe, R. Quidant, and L. Novotny, "Enhancing the Nonlinear Optical Response Using Multifrequency Gold-Nanowire Antennas," *Phys. Rev. Lett.*, Vol. 108, No. 21, 217403, 2012.
6. Aouani, H., M. Rahmani, M. Navarro-Cía, and S. A. Maier, "Third-harmonic-upconversion enhancement from a single semiconductor nanoparticle coupled to a plasmonic antenna," *Nature Nanotech.*, Vol. 9, 290-294, 2014.
7. Metzger, B., M. Hentschel, T. Schumacher, M. Lippitz, X. Ye, C. B. Murray, B. Knabe, K. Buse, and H. Giessen, "Doubling the Efficiency of Third Harmonic Generation by Positioning ITO Nanocrystals into the Hot-Spot of Plasmonic Gap-Antennas," *Nano Lett.*, Vol. 14, NO. 5, 2867-2872, 2014.
8. Aouani, H., M. Navarro-Cía, M. Rahmani, and S. A. Maier, "Unveiling the Origin of Third Harmonic Generation in Hybrid ITO–Plasmonic Crystals," *Adv. Opt. Mat.*, Vol. 3, 1059-1065, 2015.

# Metasurfaces based on defect-engineered phase transition materials

**Jura Rensberg[1], Shuyan Zhang[2], Alexander S. McLeod[3], Christian Schwarz[1], Michael Goldflam[3] Ronny Nawrodt[1], Mengkun Liu[3,4], Jochen Kerbusch[5], You Zhou[2], Shriram Ramanathan[2], D. N. Basov[3], Federico Capasso[2], Carsten Ronning[1,*], Mikhail A. Kats[2,6]**

[1]Institute for Solid State Physics, Friedrich-Schiller-Universität Jena, 07743 Jena, Germany
[2]School of Engineering and Applied Sciences, Harvard University, Cambridge, Massachusetts 02138, USA
[3]Department of Physics, University of California - San Diego, La Jolla, California 92093, USA
[4]Department of Physics, Stony Brook University, Stony Brook, New York 11794, USA
[5]Institute of Ion Beam Physics and Materials Research, Helmholtz-Zentrum Dresden-Rossendorf, 01328 Dresden, Germany
[6]Department of Electrical and Computer Engineering, University of Wisconsin, Madison, Wisconsin 53706, USA

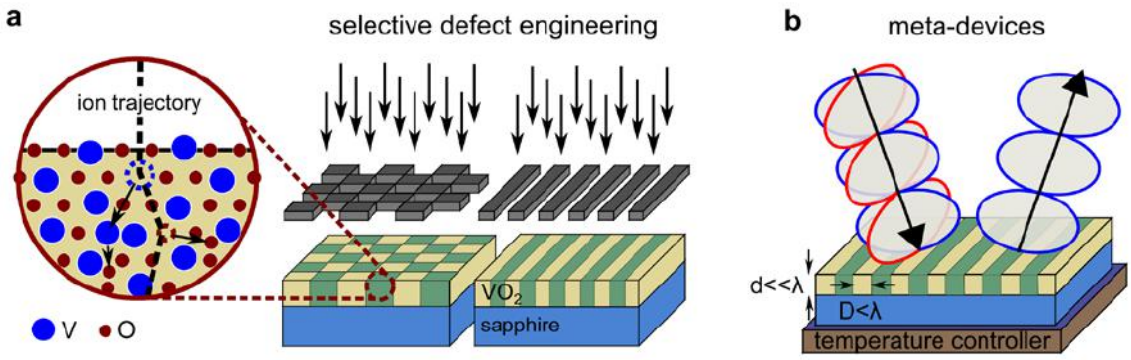
[*]corresponding author: Carsten.ronning@uni-jena.de

**Abstract** Metamaterials and metasurfaces enable unprecedented flexibility in manipulating electromagnetic waves. The optical response of most metamaterials is static, modified only by adjusting the geometric parameters of the constituent building blocks. Many functionalities of metamaterials and metasurfaces may be greatly enhanced by hybridizing these materials with functional matter, like phase-change materials, where the dielectric properties can be controlled in real-time by an external stimulus such as an applied electric field, light, mechanical stress or temperature.

We demonstrate a new type of temperature-tunable metasurfaces based on ultra-thin films of phase change materials [Ref. 1]. One of the most widely studied phase change materials is vanadium dioxide ($VO_2$), which exhibits a reversible insulator to metal transition (IMT) as the temperature is increased above a critical temperature TC ~ 68°C. At high temperatures, $VO_2$ is in a metallic rutile phase, while the low-temperature insulating state is monoclinic. The transition temperature is very sensitive to structural defects and strain. In thin epitaxial $VO_2$ films the IMT occurs gradually because of the strain distribution imposed from lattice mismatch with the substrate. Therefore, in the vicinity of the IMT, nanoscale islands of the metallic phase start to nucleate surrounded by insulating $VO_2$, which then grow and connect in a percolation process. Because of this naturally occurring coexistence of sub-wavelength domains of metallic and insulating phase, $VO_2$ can already be thought of as a natural disordered metamaterial during its phase transition.

In this contribution, we demonstrate that phase coexistence can also be artificially introduced in $VO_2$ by patterned local ion beam irradiation with spatial resolution much smaller than the wavelength of light, as shown in figure 1. The presence of a small amount of structural defects caused by ion irradiation significantly decreases the transition temperature – even below room temperature – of the irradiated regions. Thus, the metal and insulating phase of $VO_2$ coexist in a regular pattern in the temperature range between the IMT of irradiated and intrinsic $VO_2$. This results in a metasurface with effective optical properties that can be predicted applying an appropriate effective medium theory.

These thin film structures are promising for dynamic polarization control, reconfigurable absorbers and emitters, and the tuning of plasmonic and dielectric resonant nanostructures for adaptive optics applications.




**Figurea 1:** Optical meta-devices based on defect engineering of phase-transition materials. (A) The thermally driven insulator-to-metal phase transition of vanadium dioxide ($VO_2$) can be modified by deliberately introducing structural defects into the lattice (defect engineering). Spatially selective defect engineering is achieved by ion beam irradiation through a mask. The enlarged area shows the primary displacement of both vanadium and oxygen lattice atoms by an incoming energetic ion and the subsequent damage cascade. The complex refractive indices of the insulating and metallic states are similar for the intrinsic and irradiated $VO_2$, but the phase transition of the irradiated regions occurs at a much lower temperature. (B) The irradiated features can be made much smaller than the wavelength of light, so the resulting film becomes a metasurface with effective optical properties. One example is a tunable polarizer comprising stripes of irradiated and intrinsic $VO_2$, creating a metasurface with a variable degree of optical anisotropy.

**Acknowledgements.** We thank A. Kildishev for helpful comments. This work has been partially financed by the Initiative and Networking Fund of German Helmholtz Association, Helmholtz Virtual Institute VH-VI-422 MEMRIOX, DAAD program 57051746, ARO through grant W911NF-14-1-0669, AFOSR through grant FA9550-12-1-0289, and by Draper Laboratory. S. Zhang acknowledges support from the Singapore A*STAR National Science Graduate Scholarship. The fabrication and some of the measurements were performed at the Center for Nanoscale Systems (CNS) at Harvard University, a member of the National Nanotechnology Infrastructure Network (NNIN). Work at UCSD is supported through a grant ARO w911NF-13-1-0210. The authors declare no competing financial interest.

**REFERENCES**

1. Rensberg, J., et al. “Active Optical Metasurfaces Based on Defect-Engineered Phase-Transition Materials” *Nano Letters* 16, (2016), in press, **DOI:** 10.1021/acs.nanolett.5b04122

# Metasurface for the creation of surface plasmon vortex and towards multi-functional optofluidics

**C.-Y. Lin, C.-F. Chen, C.-T. Ku, and C.-B. Huang***
Institute of Photonics Technologies, National Tsing Hua University, Taiwan

*corresponding author: robin@ee.nthu.edu.tw

**Abstract**-The generation of optical vortices using plasmonics has drawn immense recent research attentions. However, in the past, these near-field vortices carrying orbital angular momentum were excited by waves that carry spin angular momentum, i.e., circularly polarized waves. In this talk, we will introduce the advantage of a designed metasurface, in which vortices could be created under linearly polarized excitations. We will also illustrate the applications of such novel device for multiple selective controls to micro-particles.

Optical vortices are waves carrying orbital angular momentum and exhibit helical phase fronts. Helical phase front leads to discontinuous azimuthal phase jumps and the number of phase discontinuities (abrupt phase jumps from $-\pi$ to $\pi$) within a $2\pi$ range is referred to as the topological charge of an optical vortex. Optical vortices have been applied in trapping and spinning of micro-particles, and recently in free-space data transmission. Generation of optical beams carrying orbital angular momentum has received increasing attentions recently, both in the far-field and in the near-field. Near-field vortices are typically generated through the excitation of surface plasmons (SPs) [1-3]. However in the past, SP vortices were generated using circularly polarized optical excitations that carry spin angular momentum (SAM). The functionality of the plasmonic spiral/slot can thus be understood as the conversion from far-field optical SAM to near-field orbital angular momentum (OAM) given by the chirality of the device.

In the first part of this presentation, a nanocavity embedded in a gold thin film is carefully designed and arranged to form a metasurface. For the first time to our best knowledge, we demonstrated numerically and experimentally the ability to generate SP vortex carrying OAM in our designed metasurface under linearly polarized optical excitation that carries absolutely no angular momentum [4]. Figure 1(a) shows the schematics of our design. Our numerical studies are performed using three-dimensional finite-difference time-domain (FDTD) method simulations. A single nanocavity is formed by embedding a crossed air-slit onto a gold thin film of 200 nm thick over a silica substrate. The arm lengths of the air-slits are 500 nm in the x- and 780 nm in the y-directions, respectively. When a normally incident laser source illuminates the nanocavity, SPPs polarized in the z-direction with distinct spatial and phase characteristics can be selectively excited depending on the input laser polarization. In our current design, the difference in the arm lengths is optimized to provide a $\pi/2$ ($-\pi/2$) phase difference in the resulting SPP when the laser with vacuum wavelength of 1545 nm is 45° (-45°) linearly polarized, as shown in Fig. 1(b) (Fig. 1(c)), respectively. The resulting local SPP vortex fields are beneficial in the later generation of near-field optical OAM. The near-field experimental results will also be presented.

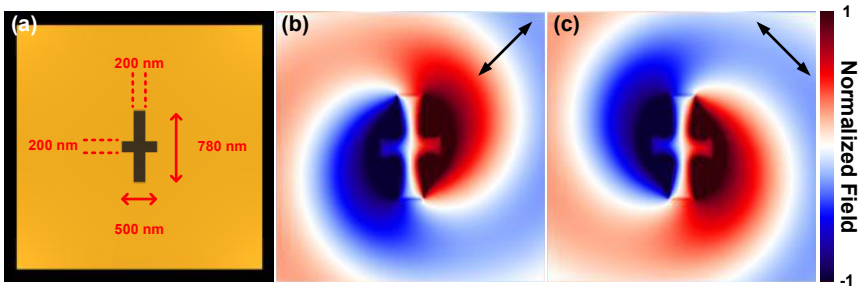



Figure 1. (a) Schematics of a single nanocavity. Instantaneous $E_z$ field when the laser input is linearly (b) 45°-polarized, (c) -45°-polarized, respectively.

In the second part of this presentation, we will focus on the application of surface plasmon vortex for particle trapping and rotation. We recently demonstrated the first controllable trapping or rotation of micro-particles using such spiral device [3]. The working principle was based on coherent control of angular momenta carried by optical near-fields in a plasmonic Archimedes spiral. Depending on the handedness of the input circularly polarized light, we showed that the surface plasmon focusing field provides stable optical potential at the spiral origin and can be used to trap micro-particles. On the other hand, the primary ring of the surface plasmon vortex provided a stable track to rotate the micro-particles. However, we were limited by two main factors: (1) the generation SP vortices or subwavelength focusing requires circularly polarized excitations of different handedness; and (2) It would not be possible to control the rotational direction of the SP vortex (and therefore the micro-particles when driven by the SP field) in a given plasmonic spiral. To alleviate the first limitation, the plasmonic metasurface addressed in the first part could be used to dynamically create SP vortex or subwavelength focusing, purely through linearly polarized optical excitations. We will also show that the metasurface could be used to alleviate the second limitation after a minor modification. We numerically demonstrate the ability not only to create SP subwavelength focusing, but also bi-directionally tunable SP vortices in a designed metasurface under linearly polarized optical excitations that carry absolutely no angular momenta. We envision major impacts in selectable motional control of nanoparticles and opto-fluidics.

These works were supported by the Ministry of Science and Technology of Taiwan under Grant MoST 103-2112-M-007-017-MY3.

**REFERENCES**

1. H. Kim, J. Park, S.-W. Cho, S.-Y. Lee, M. Kang, and B. Lee, "Synthesis and dynamic switching of surface plasmon vortices with plasmonic vortex lens", *Nano Lett.***10**, 529 (2010).
2. C.-T. Ku, H.-N. Lin, and C.-B. Huang*, "Direct observation of surface plasmon vortex and subwavelength focusing with arbitrarily-tailored intensity patterns," *Appl. Phys. Lett.* **106**, 053112 (2015).
3. W.-Y. Tsai, J.-S. Huang, and C.-B. Huang, "Selective trapping or rotation of isotropic dielectric microparticles by optical near field in a plasmonic Archimedes spiral", *Nano Lett.* **14**, 547 (2014).
4. C.-F. Chen, C.-T. Ku, Y.-H. Tai, P.-K. Wei, H.-N. Lin, and C.-B. Huang, "Creating optical near-field orbital angular momentum in a gold metasurface," *Nano Lett.* **15**, 2746 (2015).

# Conformal Boundary Optics

**Jonathon Yi Han Teo[1], Liang Jie Wong[1], Carlo Molardi[1], and Patrice Genevet[2,*]**

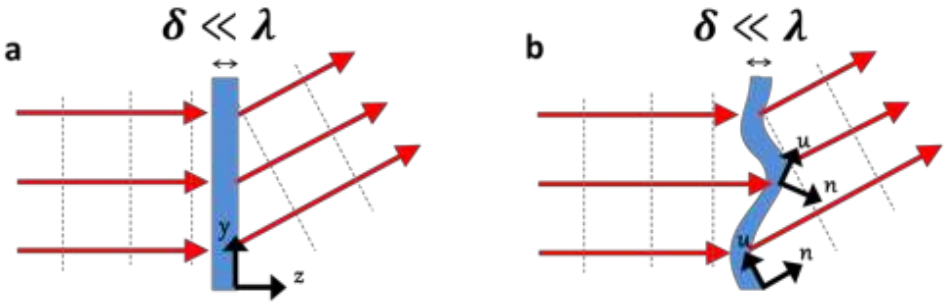
[1] Singapore Institute of Manufacturing Technology, Agency for Science, Technology and Research (A*STAR), 71 Nanyang Drive, Singapore, 638075, Singapore

[2]Centre de Recherche sur l'Hétéro-Epitaxie et ses Application (CRHEA, UPR 10), CNRS, Rue Bernard Gregory, Sophia-Antipolis, 06560 Valbonne, France.

[*]corresponding author: pg@crhea.cnrs.fr

**Abstract**-Rapid developments in the emerging field of stretchable and conformable photonics necessitate analytical expressions for boundary conditions at metasurfaces of arbitrary geometries. We will discuss the idea of ''conformal boundary optics'': a design theory that determines the optical response for designer input and output fields at interfaces of arbitrary shapes. Given any object, one can now realise coatings to achieve exotic effects like optical illusions and anomalous diffraction behavior [1].

To date, a rigorous expression of the electromagnetic boundary conditions at designer interfaces --also called métasurfaces-- has been proposed only for planar interfaces where the electromagnetic fields are defined using a Cartesian coordinate system [2-6]. These equations are known as the generalized sheet transition conditions (GSTCs). From a physical point of view, discontinuities in electromagnetic fields across any regular surface depend upon the constitutive parameters of the interface: namely, surface charge density ρ , the current density j, the induced dipole moments at the interface and the optical response of the surrounding media. This requires (ρ, j) and the fields **E**,**H**,**p** and **m** in the Maxwell's equations to be expressed in the sense of distributions, where **E,H** are respectively the electric and magnetic fields, and **p** and **m** respectively represent the surface electric and magnetic induced currents derived by averaging the local fields of the electric and magnetic induced dipole moments in the plane z=0. In a planar configuration, writing each variable as a discontinuous function at z=0, it is possible to derive a set of generalized sheet transition conditions (GSTCs) for the electromagnetic fields [2,3]. However, this derivation is possible only because the ambient coordinate system is chosen to conform to the interface, a method that becomes very restrictive when the interface contains arbitrary contours (Fig. 1).




**Figures 1: . a), a 2D planar metasurface of sub-wavelength thickness δ≪λ, can transmit any incident optical field at a specific angle by imposing a gradient of phase discontinuity. For planar interfaces, GSTC boundary conditions readily apply and the surface susceptibility tensors can be calculated. b, The local coordinate system of the surface follows its local curvature, and therefore it changes with the position**

**along the interface. Boundary conditions of the fields are obtained in the coordinate system of the interface, and are therefore position dependent. To produce an effect equivalent to that in b, the surface susceptibilities of the optical interface have to be engineered to account for the effect of the physical distortion. The dashed blue lines denote the equiphase fronts of the electromagnetic fields.**

Here, we introduce the concept of conformal boundary optics, an analytical method – based on novel, first-principle derivations – that allows us to engineer transmission and reflection at will for any interface geometry and any given incident wave.

Whereas transformation optics determines bulk optical properties by exploiting the relationship between a given coordinate system and the coordinate system that conforms to the travel of light [7], the proposed concept determines the optical properties of a metasurface of arbitrary geometry by exploiting the relationship between a given ambient coordinate system and the coordinate system that conforms to the geometry of the boundary [1]. While a powerful concept in itself, the mathematical derivation associated with its analytical formulation is highly non-trivial since it cannot be generalized from existing boundary conditions for generic surface geometries. This concept provides a wide range of new design opportunities, for example, to hide objects behind an "optical curtain", to create optical illusions by reflecting virtual images, or to suppress the diffraction generally occurring during light scattering at corrugated interfaces.

**Acknowledgements**, we gratefully acknowledge financial supports from the European Research Council under grant no. 639109.

**REFERENCES**

1. Han, J. T. H., Wong, L.J., Molardi C. & Genevet P., Controlling Electromagnetic Fields at Boundaries of Arbitrary Geometries, submitted (2016).
2. Kuester, E. F., Mohamed, M. A., Piket-May, M., & Holloway, C. L. (2003). Averaged transition conditions for electromagnetic fields at a metafilm. Antennas and Propagation, IEEE Transactions on, 51(10), 2641-2651.
3. Kuester, E. F., Holloway, C. L., & Mohamed, M. A. (2010, July). A generalized sheet transition condition model for a metafilm partially embedded in an interface. In Antennas and Propagation Society International Symposium (APSURSI), 2010 IEEE (pp. 1-4). IEEE.
4. Idemen, M. (1990). Universal boundary relations of the electromagnetic field. Journal of the Physical Society of Japan, 59(1), 71-80.
5. Zhao, Y., Liu, X. X., & Alu, A. (2014). Recent advances on optical metasurfaces. Journal of Optics, 16(12), 123001.
6. Achouri, K., Salem, M. A., & Caloz, C. (2014). General metasurface synthesis based on susceptibility tensors. Antennas and Propagation, IEEE Transactions on, Vol. 63, 2977 - 2991 (2015).
7. Pendry, J. B., Schurig, D., & Smith, D. R. (2006). Controlling electromagnetic fields. science, 312(5781), 1780-1782.

# Atomic metasurface for control single photons

**Ming Zhou, Jingfeng Liu, Mikhail Kats, Zongfu Yu***

1. Department of Electrical and Computer Engineering, University of Wisconsin – Madison, 53706, U.S.A.
*corresponding author: zyu54@wisc.edu

**Abstract**- An atom with a resonant transition can capture the energy of a single photon and store it in the excited energy level for a brief moment, before it is re-emitted. During this process, a phase is acquired. By exploiting this resonant scattering phase in electronic transitions, here we show that atomic metasurface can be realized to control non-classical light such as Fock states.

Classical metasurfaces [1] have seen explosive development in the past few years. These optically functionalized surfaces offer completely new ways of control light, and have enabled new phenomena such as anomalous reflection, extreme nonlinearity, and the spin hall effect, as well as applications such as flat lenses and cloaking. Figure 1a shows the general operation principle of classical metasurfaces. A subwavelength optical resonator, for example a nano-rod made from a high-index material, imparts a phase on the incident plane wave. For a single resonance, the phase of the scattered light ranges from 0 to $\pi$ and is determined by the frequency detuning between the incident light and the resonance. Rods with different radii have different resonant frequencies, thereby creating different scattering phases (Fig. 1b). With arrays of spatially-variant micro-resonators, one can steer, focus, or reshape a light beam, all in a surface thinner than the wavelength.

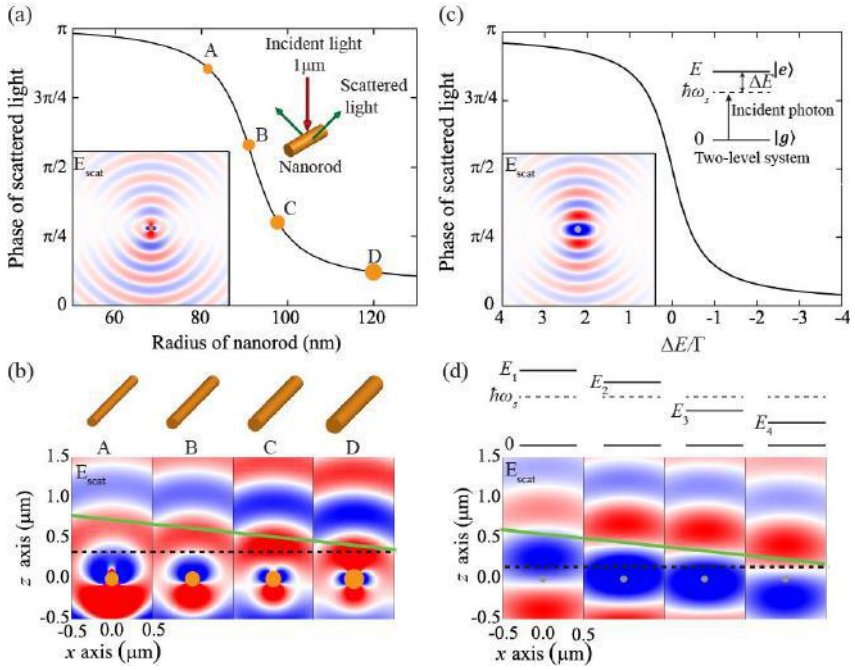



Figure (a) Phase of scattered light versus the radius of nanorod. We use finite-difference frequency-domain (FDFD) method to solve the Maxwell's equations. Light is normally incident (red arrow) onto the nanorod from the top and is scattered to all directions (green arrows). The inset shows a

typical scattering field of the nanorod. As the radius of the nanorod increases, the phase of scattered light varies from π to 0. (B) Tilted phase front of an array of spatially variant nanorods. (c) Phase of scattered light versus the energy detuning of TLS, normalized to the resonance linewidth Γ. Light is also normally incident onto the TLS. The inset shows the scattering field of the TLS. As the detuning energy varies, the phase of scattered light also varies from π to 0. (d) Phase front of an array of spatially variant TLSs with different detuning energies. Similar to nanorods, the reflected phase front is tilted.

Similar to optical micro-resonators, resonant electronic transitions in two-level systems (TLSs) also impart a scattering phase on incident photons. TLSs are most-commonly found in the electronic transitions of atoms and molecules. Solid-state TLSs such as quantum dots, nitrogen-vacancy centers in diamond, and Josephson junctions are also rapidly emerging. The field of a single photon scattered by a TLS in the center is shown in the inset of Fig. 1c. The phase ranges from 0 to π depending on the relative energy detuning $\Delta E/\Gamma=(E-\hbar\omega)/\Gamma$, where E and Γ is the transition energy and the energy bandwidth of the TLS, respectively. $\hbar\omega$ is the photon's energy. Figure 1c shows the relation between the scattering phase and the energy detuning $\Delta E/\Gamma$, which closely resembles that in the classical micro-resonators (Fig. 1a). An array of TLSs with varying transition energies create different scattering phases as shown in Fig. 1d. Similar to the classical resonator array (Fig. 1b), the TLS array can tilt the phase front and tailor the directions of reflection and refraction (Fig. 1d).

Compared to classical metasurfaces, atomic metasurfaces can realize unique features that are extremely challenging for micro-resonators. First, atomic metasurfaces are naturally reconfigurable, even in the challenging visible wavelength range. The energy level of TLSs could be rapidly tuned using laser illumination, or external electric or magnetic fields. In contrast, micro-resonators are fixed after their fabrication and cannot be easily tuned through index modulation. Second, the scattering elements in atomic metasurfaces can be extremely small, lossless, and highly efficient. The optical cross section of TLS is fairly large (~λ^2) but their physical sizes are often many orders of magnitude smaller than the wavelength λ. Their scattering efficiency, measured by the ratio between the optical and physical cross section, can be extremely large (>1000). This scattering efficiency is normally typically than 10 for micro resonators. This feature is particularly attractive for synthesizing metasurfaces for advanced functionalities such as multi-band operation. Also because of the small physical sizes and large optical cross section of the TLS, we do not necessarily need to precisely position them on a surface. In terms of optical loss, the quantum efficiency of TLS can easily reach above 99%. They can scatter light more efficient than metals and yet have nearly zero optical absorption. Lastly, atomic metasurface can tap into the quantum degrees of freedom such as entanglement and photon-photon interactions, they could be useful for quantum information networks and simulations of many-body physics.

**References:**

[1] Yu, N., Genevet, P., Kats, M. A., Aieta, F., Tetienne, J. P., Capasso, F., & Gaburro, Z. (2011). Light propagation with phase discontinuities: generalized laws of reflection and refraction. *Science*, *334*(6054), 333-337.

# Electrochemically Programmable Plasmonic Antennas

**Shi Dong[1], Kai Zhang[2], Zhiping Yu[1], and Jonathan A. Fan[2*]**

[1] Institute of Microelectronics, Tsinghua University, Beijing, China 100084

[2]Department of Electrical Engineering, Stanford University, Stanford, CA USA 94305

[*]corresponding author: jonfan@stanford.edu

**Abstract.** We propose a scalable, fast, and energy efficient implementation to programming the optical properties of individual dipole antennas using an electrochemical approach. The concepts are inspired by conductive-bridge random access memory and enable plasmonic modes to be programmed "on" or "off."

Plasmonic antennas are building blocks in advanced nano-optical systems due to their ability to tailor optical response based on their geometry. We propose a scalable, fast, and energy efficient implementation to programming the optical properties of dipole antennas using an electrochemical approach. These antennas comprise two arms, one serving as an anode and the other a cathode, separated by a solid electrolyte. As a voltage is applied between the antenna arms, a conductive filament either grows or dissolves within the electrolyte, modifying the antenna load. This programming modality is inspired by conductive bridge random access memory[1] and introduces a new level of optical tuning control that enables not only fine shifts in mode frequency, but also the creation of new optical modes.

These optical tuning regimes are described in Figure 1. If there is no filament, the lowest order antenna mode is the capacitively-coupled bonding dipole (BDP) mode, which supports a dipolar charge distribution in each antenna arm. As a filamentary bridge forms, a charge transfer plasmon (CTP) mode emerges at a frequency red-shifted relative to the BDP mode.[2] We can clearly see here that the growth and dissolution of a bridging filament can cause the CTP mode to modulate between the "on" and "off" states. Further filament thickening leads to the gradual and controllable blue-shifting of the CTP mode.

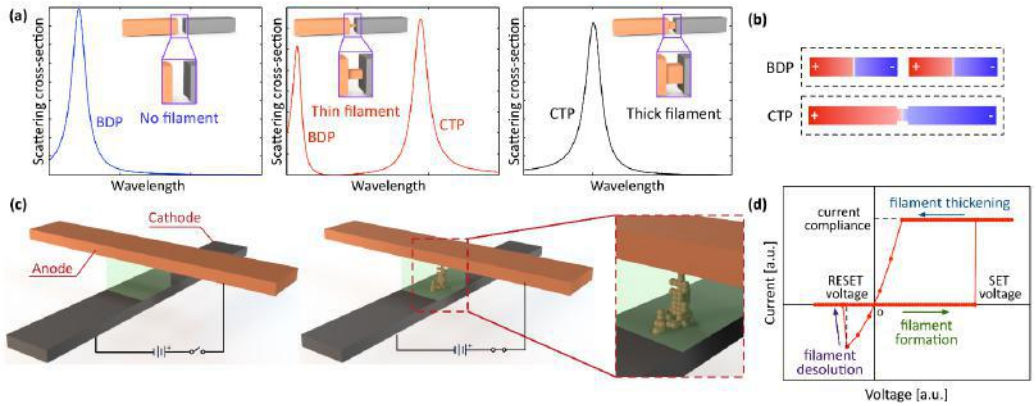



**Figure 1. Overview of programmable plasmonic antennas. a)** Schematic and scattering spectra of a dipole antenna loaded with no filament (left), a narrow filament (middle), and a thick filament (right). **b)** Surface charge distributions of the BDP and CTP modes. c) Schematic of stochastic filament growth in a CBRAM memory cell. d) Typical current-voltage plot of a CBRAM cell.

We probe the dynamics of stochastic filament formation and their effects on plasmonic mode programming using a combination of three-dimensional optical and electronic simulations. We characterize optical response using finite-difference time-domain (FDTD) simulations, which is an established tool in the precise characterization of nano-plasmonic systems. We model the process of electrochemical filament growth and dissolution using three-dimensional kinetic Monte Carlo (3D KMC) simulations.[3] Filament dissolution and growth are highly stochastic processes yielding unpredictable branch-like filament morphologies, and the KMC method can capture these filament growth dynamics over time. By coupling together FDTD and KMC simulations in our analysis, we quantified device regimes in which the CTP mode could be shifted and modulated. In addition, we identified a strong correlation between filament resistance and charge transfer plasmon mode frequency that is insensitive to the detailed filament morphology.

These concepts in programmable nano-optics can generalize to complex antenna layouts with multiple electrochemical cells, enabling a multitude of antenna configurations with a broad range of magnitude and phase responses. We envision that the scalability of these programmable electrochemical junctions, which currently scale to millions of devices in CBRAM memory chips, will enable macroscopic programmable metamaterials and metasurfaces with optical responses that can tune across the infrared and terahertz frequency ranges.

**Acknowledgements.** This work was supported by the U.S. Air Force under Award Number FA9550-15-1-0161. We acknowledge B. Magyari-Kope and P. Wong for useful discussions and Y. Wang for help with the figures.

**REFERENCES**

1. Ilia, V., Rainer, W., John, R. J. & Michael, N. K. “Electrochemical metallization memories—fundamentals, applications, prospects.” Nanotechnology 22, 254003 (2011).
2. Esteban, R., Borisov, A. G., Nordlander, P. & Aizpurua, J. “Bridging quantum and classical plasmonics with a quantum-corrected model.” Nature Communications 3, 825 (2012).
3. Pan, F. and Subramanian, V. "Kinetic Monte Carlo simulation of resistive switching and filament growth in electrochemical RRAMs," in Device Research Conference (DRC), 2010, vol., no., pp.255-256, 21-23 June 2010

# A metasurface designed for adaptive optical near-field routing

**C.-Y. Lin and C.-B. Huang***
Institute of Photonics Technologies, National Tsing Hua University, Hsinchu 30013, Taiwan
*corresponding author: robin@ee.nthu.edu.tw

**Abstract:** A metasurface comprised of v-grooves etched into a gold thin film is presented. We numerically demonstrate that multi-functional near-field optical routing could be achieved in our metasurface through simple polarization control to the excitation plane wave.

Adaptive control to the optical near-fields has attracted immense research attentions [1-4]. Quite recently, a metasurface formed by v-grooves arrange in circular geometry has been used to control the excitation direction of surface plasmon polaritons (SPP) [5]. In another study, a metasurface has been used to create either SPP focusing or vortex fields, depending on the polarization of the excitation plane wave [6]. However, up to now, adaptive control of SPP are limited to two possible states [1,4,5,6]. In Ref. [3], we proposed a novel scheme where a cluster of 7 metallic spheres could be used to achieve up to 10 adaptive states to the localized surface plasmons. However, such multi-selectivity could only be obtained through the combination of a quantum emitter.

In this presentation, v-grooves etched in a gold thin film is carefully designed and arranged to form a metasurface. We numerically demonstrate the ability to achieve multiple near-field routing possibilities using plane wave excitations. By changing the polarizations of the optical excitation, adaptive routing paths in the near-field are realized and are observed in the far-field via scattering through a circular groove. We anticipate such adaptive routing of SPP a step closer to the widely envisioned optical circuit in the near future.

Our numerical studies are performed using three-dimensional finite-difference time-domain (FDTD) method simulations. Figure 1(a) shows a column of identical v-grooves forming a metasurface. The v-grooves are etched into a 200 nm thick gold film on top of a silica substrate. The length of the two arms is 780 nm, the width is 200 nm, and the angle between the two arms is 90°. As shown in the Fig. 1(b), when the metasurface is excited by a 1560 nm left-hand circularly-polarized (LHCP) plane wave, SPP propagate to the left. On the other hand, in Fig. 1(c), SPP propagate to the right when the excitation polarization is changed right-hand circularly-polarized (RHCP). Up to this point the working principle is identical to that illustrated in Ref. [5].

In our design, four identical v-grooves with dimensions as described in Fig. 1(a) are sequentially rotated by 90° to form the metasurface, as depicted in Fig. 2(a). The grey dashed circle represents a half-etched groove that serves to scatter the excited SPP into the far-field for observations. Along the circle, various possible routing locations are labeled from 1 to 8. Figures 2(b)-(g) show the far-field intensity patterns as a result of adaptive routing to the SPP under different input polarizations. In Figs. 2(b) and 2(c), correspondingly under RHCP and LHCP plane wave excitations, SPPs generated from the metasurface propagate onto routing locations of {1,3,5,7} and {2,4,6,8}, respectively. On the other hand, Figs. 2(d-g) show adaptive routing under different linearly-polarized excitations where the excited SPPs can be routed to two locations. In Fig. 2(d), SPPs are routed onto locations between {1, 8} and {4, 5} when excited by 45° linear polarization. When the linear polarization is rotated to −45°, SPPs are routed to locations between {2,3} and {6,7}, as shown in Fig. 2(e). In Figs. 2(f) and 2(g), under 0° or 90° linearly-polarized illuminations, SPPs are routed onto locations {3,4,7,8} and {1,2,5,6}, respectively. We note here when adequate plasmonic waveguides are connected to the routing locations, our design will facilitate controllable optical nanocircuit [7].

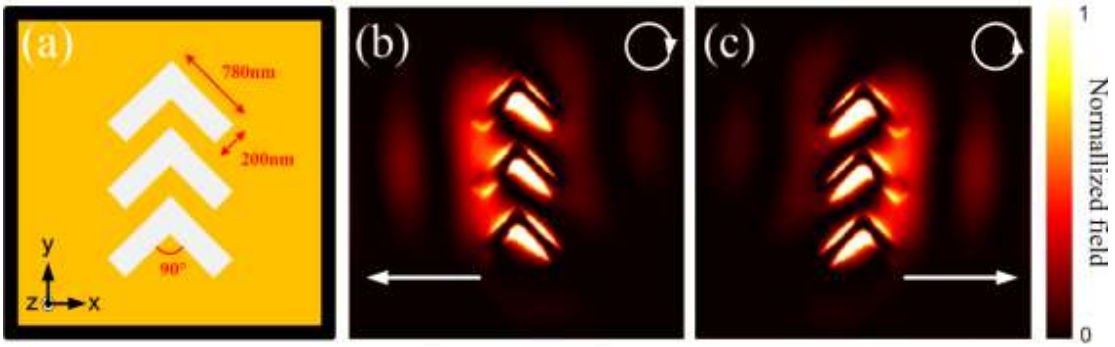



Figure 1. (a) Schematics of the v-groove metasurface. The SPP propagations are selectively excited (b) to the left by left-hand circular-polarization and (c) to the right by right-hand circular-polarization, respectively.

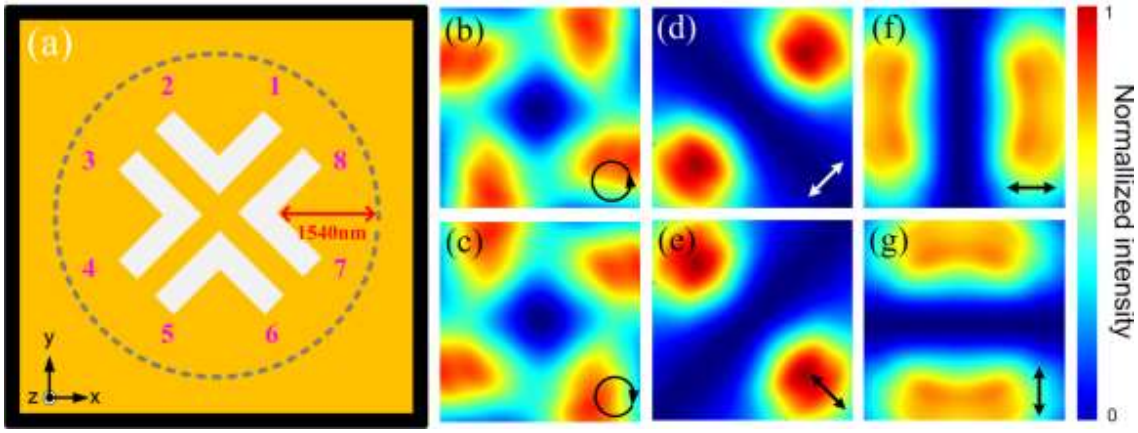



Figure 2. (a) Schematics of the our design. The grey line depicted a half-etched groove to scatter the SPP into the far-field. The far-field intensity pattern under (b) right-hand circularly-polarized, (c) left-hand circularly-polarized, (d) 45° linear, (e) -45° linear, (f) 0° linear , and (g) 90°-linear polarizations.

In summary, a gold metasurface comprised of v-grooves is designed. We numerically demonstrate the ability in achieving multi-selectable polarization-dependent routing to the SPPs. This work was supported by the Ministry of Science and Technology of Taiwan under grant MoST 103-2112-M-007-017-MY3.

**References**

1. Asechlimann, M., M. Bauer, D. Bayer, T. Brixner, F. Javier Garcia de Abajo, and W. Pfeifer, "Adaptive subwavelength control of nano-optical fields," Nature, Vol 446, No. 15, 301-304, 2007.
2. Asechlimann, M. et.al, "Spatiotemporal control of nanooptical excitations," Proc. Nat. Acad. Science, Vol 107, No. 12, 5329-5333, 2010
3. Li, P.-N., H.-H. Tsao, J.-S. Huang, and C.-B. Huang, "Subwavelength localization of near fields in coupled metallic spheres for single-emitter polarization analysis," Opt. Lett., Vol 36, No. 12, 2339-2341, 2011.
4. Rewitz, C. et.al, "Coherent control of plasmon propagation in a nanocircuit," Phys. Rev. Appl., Vol 1, No. 1, 014007, 2014.
5. Lin, J., J. P. B. Mueller, Q. Wang, G. Yuan, N. Antoniou, X.-C. Yuan, and F. Capasso, "Polarization-controlled tunable directional coupling of surface plasmon polaritons," Science, Vol. 340, No. 6130, 331-334, 2013.
6. Chen, C.-F., C.-T. Ku, Y.-H. Tai, P.-K. Wei, H.-N. Lin, and C.-B. Huang, "Creating optical near-field orbital angular momentum in a gold metasurface," Nano Lett., Vol. 15, No. 4, 2746-2750, 2015.
7. Dai, W.-H., F.-C. Lin, C.-B. Huang, and J.-S. Huang, "Mode conversion in high-definition plasmonic optical nanocircuits," Nano Lett., Vol. 14, No. 7, 3881-3886, 2014.

# Graded Metasurfaces for Advanced Wave Control

**N. Mohammadi Estakhri, M. Tymchenko, Y. Hadad, J. S. Gomez-Diaz, D. L. Sounas, and A. Alù**
Department of Electrical and Computer Engineering, The University of Texas at Austin, Austin, TX 78701, USA
*corresponding author: alu@mail.utexas.edu

**Abstract** – In this contribution, we review our recent work on passive and active graded metasurfaces, highlighting the relevant new physics unveiled by introducing spatial and possibly temporal gradients of the impedance along a thin surface with subwavelength resolution. We present the principles behind our designs, and a number of applications of these concepts, with special emphasis on optics and nanophotonics.

In the past few years, our group has put forward a variety of exciting opportunities offered by gradient metsurfaces [1-5], offering detailed modeling principles and design procedures to efficiently mold the impinging wavefront at will with subwavelength resolution. These approaches pave the ground to interesting applications in nanophotonics, which we will described and outline during our talk. In addition, we have recently explored the possibility of introducing temporal gradients [6] and large nonlinearities into this picture [7], offering additional knobs that allow overcoming some of the fundamental constraints of passive metasurfaces, including temporal and geometrical symmetries. These possibilities open a plethora of possibilities for applications in nanophotonics radio-frequencies and thermo-photovoltaics. We will discuss our vision of the future of this field during our presentation.

**REFERENCES**

1. N. Mohammadi Estakhri, and A. Alù, "Recent Progress in Gradient Metasurfaces," Journal of the Optical Society of America B, Vol. 33, No. 2, pp. A21-A30, December 16, 2015.
2. N. Mohammadi Estakhri, C. Argyropoulos, and A. Alù, "Graded Metascreens to Enable a New Degree of Nanoscale Light Management," Philosophical Transactions A, Special Issue on Spatial Transformations: from Fundamentals to Applications, Vol. 373, No. 2049, 20140351 (15 pages), July 27, 2015.
3. N. Mohammadi Estakhri, and A. Alù, "Ultra-Thin Unidirectional Carpet Cloak and Wavefront Reconstruction with Graded Metasurfaces," IEEE Antennas and Wireless Propagation Letters, Special Cluster on Transformation Electromagnetics, Vol. 13, pp. 1775-1778, January 28, 2015.
4. N. Mohammadi Estakhri, and A. Alù, "Manipulating Optical Reflections Using Engineered Nanoscale Metasurfaces," Physical Review B, Vol. 89, No. 23, 235419 (8 pages), June 16, 2014.
5. F. Monticone, N. Mohammadi Estakhri, and A. Alù, "Full Control of Nanoscale Optical Transmission with a Composite Metascreen," Physical Review Letters, Vol. 110, No. 20, 203903 (5 pages), May 14, 2013.
6. Y. Hadad, D. L. Sounas, and A. Alù, "Space-Time Gradient Metasurfaces," Physical Review B, Rapid Communications, Vol. 92, No. 10, 100304R (6 pages), September 22, 2015.
7. M. Tymchenko, J. S. Gomez-Diaz, J. Lee, M. A. Belkin, and A. Alù, "Gradient Nonlinear Pancharatnam-Berry Metasurfaces," Physical Review Letters, Vol. 115, No. 20, 207403 (5 pages), November 10, 2015.

# Frequency comb generation in a time-dependent graphene ribbon lattice

**G. Altares Menendez**[1] **and B. Maes**[1]

[1] Micro- and Nanophotonic Materials Group, Faculty of Science, University of Mons, Place du Parc 20, B-7000 Mons, Belgium.
Galaad.AltaresMenendez@umons.ac.be

**Abstract**— Recently, frequency comb generation using modulated planar graphene sheets was introduced [1]. Here we show that this process is more efficient in a graphene ribbon lattice than in a planar structure. To do so we exploit the plasmonic resonances of the lattice, which are very sensitive to the graphene doping level. By dynamically changing this doping the transmission becomes time-dependent and allows for effective frequency comb generation in the infrared range.

## 1. INTRODUCTION

Graphene is a 2D hexagonal lattice of carbon atoms with remarkable optical properties. At infrared frequencies, graphene sheets support plasmonic modes that have already been observed [2]. A recent paper [1] reported that if the conductivity of a graphene sheet is modulated in time, a monochromatic incident plane wave can generate a frequency comb in transmission. The frequency separation between the peaks of this frequency comb is given by the modulation frequency applied to the graphene sheet. In this work we investigate 2D graphene ribbon lattices to enhance this process. These lattices support plasmonic resonances that are widely tunable [3] and of high quality for sufficiently large relaxation times (Figure 1).

## 2. RESULTS

The graphene lattice resonances are very sensitive to the doping level, thus by slightly changing this doping one can significantly change the transmission of the lattice (Figure 2). Therefore, to instigate frequency comb generation in lattices we can employ a time-dependant doping that is small, compared to the conductivity change required for planar sheets in [1].

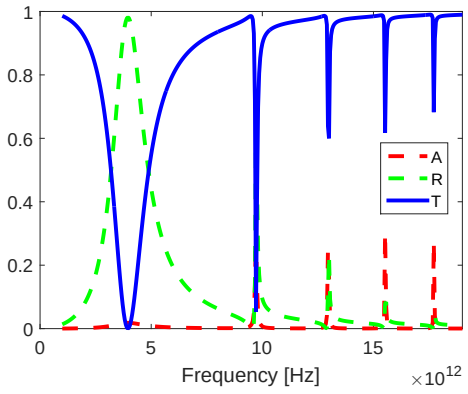



Figure 1: Transmission $T$, absorption $A$ and reflexion $R$ of a typical graphene ribbon lattice used for frequency comb generation.

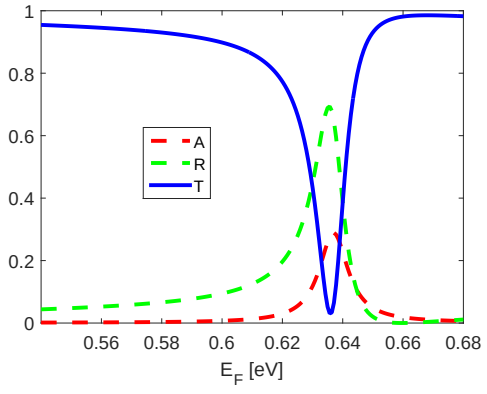



Figure 2: Transmission $T$, absorption $A$ and reflexion $R$ as a function of graphene doping for a given frequency (10 THz).

With this alternative technique the comb generation process is more efficient than for a planar graphene sheet, even if the lattice covers a smaller area (Figures 3 and 4). These results are obtained with rigorous finite-element simulations. A theoretical model is currently under development.

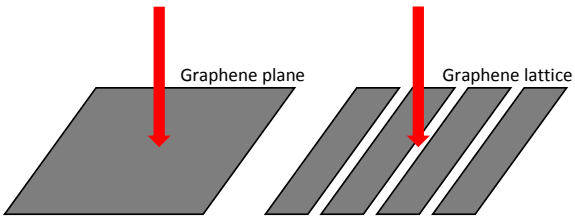



Figure 3: Geometries used for the frequency comb generation with a graphene plane and a graphene lattice.

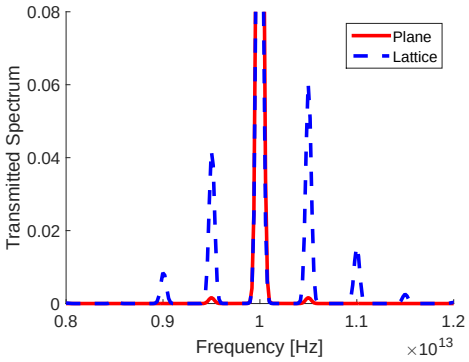



Figure 4: Comparison between a frequency comb generated by a plane and a lattice. All the parameters used in the simulations are the same, except for the geometry.

## 3. CONCLUSION

We show that frequency comb generation using time-dependent graphene ribbon lattices is possible and more efficient than in a planar structure. Furthermore, this effect is widely tunable as the resonance frequency of plasmonic modes in graphene lattices scales with the ribbon width. This generation process can then be used for a very wide range of frequencies in the THz range.

## ACKNOWLEDGMENT

This work was supported by the Belgian Science Policy Office under the project "Photonics@be" (P7-35) and by the Fonds pour la Formation à la Recherche dans l'Industrie et dans l'Agriculture (FRIA) in Belgium.

## REFERENCES

1. V. Ginis, P. Tassin, T. Koschny, and C. M. Soukoulis. Tunable Terahertz frequency comb generation using time-dependent graphene sheets. *Phys. Rev. B*, 91:161403, 2015.
2. J. Chen, M. Badioli, P. Alonso-Gonzalez, S. Thongrattanasiri, F. Huth, J. Osmond, M. Spasenovic, A. Centeno, A. Pesquera, P. Godignon, A. Zurutuza Elorza, N. Camara, F. J. Garcia de Abajo, R. Hillenbrand, and F. H. L. Koppens. Optical nano-imaging of gate-tunable graphene plasmons. *Nature*, 487(7405):77–81, 2012.
3. A. Yu. Nikitin, F. Guinea, F. J. Garcia-Vidal, and L. Martin-Moreno. Surface plasmon enhanced absorption and suppressed transmission in periodic arrays of graphene ribbons. *Phys. Rev. B*, 85:081405, 2012.

# Plasmonic Metasurfaces for the Near-Field Directional Control of Light Emission

**R. Paiella*, L. C. Kogos, and J. DiMaria**
Department of Electrical and Computer Engineering, Boston University, Boston (MA) USA
*corresponding author: rpaiella@bu.edu

**Abstract**-The use of plasmonic metasurfaces to control the radiation properties of nearby emitters is investigated with two related approaches. First, off-axis unidirectional beaming is demonstrated using an array of asymmetric metallic nanoparticles coupled to an ultrathin metal film. Second, light emission near a gradient metasurface is studied numerically, showing that geometrically tunable directional radiation patterns can be obtained at highly enhanced emission rates.

Research in nanophotonics is generally aimed at the continued miniaturization of optical components, to enable ever increasing levels of system integration and device functionality. In this context, a goal of key importance is the ability to efficiently extract light from an active source, and either radiate it in a desired direction or couple it into a guided mode of a photonic integrated circuit, without the need to use bulky external optical elements. Here we investigate the use of planar arrays of metallic nanoantennas to achieve this goal based on two related approaches. Our results show that these systems have significant technological potential for future applications in, e.g., solid-state smart lighting, integrated nanophotonics, and highly multiplexed fluorescence sensing.

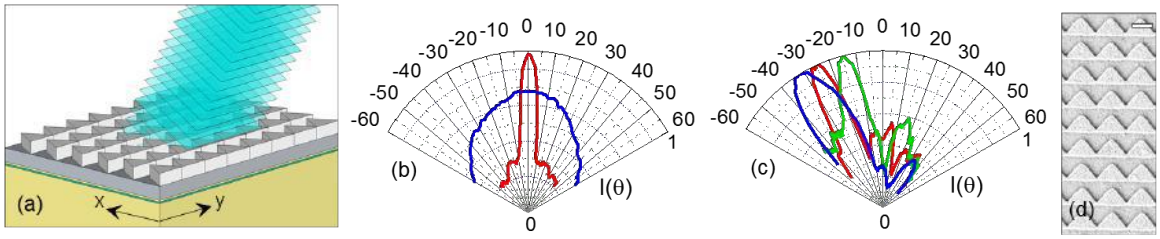



Figure 1. (a) Schematic illustration of the sample geometry used to demonstrate plasmonic beaming. (b), (c) Experimental far-field radiation patterns. (d) SEM image of a fabricated device (the scale bar is 500 nm).

In the first study [1], we have demonstrated plasmonic unidirectional beaming based on the device geometry of Fig. 1(a), where an ultrathin Ag film is deposited over a light-emitting active layer (InGaN/GaN quantum wells) and then coated with a periodic array of Ag nanoparticles (NPs). In this geometry, light can be emitted across the Ag film through a two-step process, where surface plasmon polaritons (SPPs) are first excited on the Ag film and then diffractively scattered by the overlaying NPs. As a result, the far-field pattern of the emitted light can be tailored by controlling the NP shape and spatial distribution. In particular, if the NP array consists of a simple 1D grating of rectangular ridges with period equal to the SPP wavelength, beam collimation along the sample surface normal is obtained via first-order diffraction of the excited SPPs [red trace in Fig. 1(b)]. By comparison, a much broader Lambertian profile is measured from the same samples without any metallic coating [blue trace]. Unidirectional beaming along arbitrary off-axis angles can then be obtained by replacing the rectangular ridges with lines of triangular NPs, as shown in Fig. 1(a) and in the top-view SEM image of Fig. 1(d). In this geometry, diffractive scattering of backward traveling SPPs can be suppressed in favor of forward

diffraction (or vice versa), leading to single-beam emission at geometrically tunable oblique angles [Fig. 1(c)].

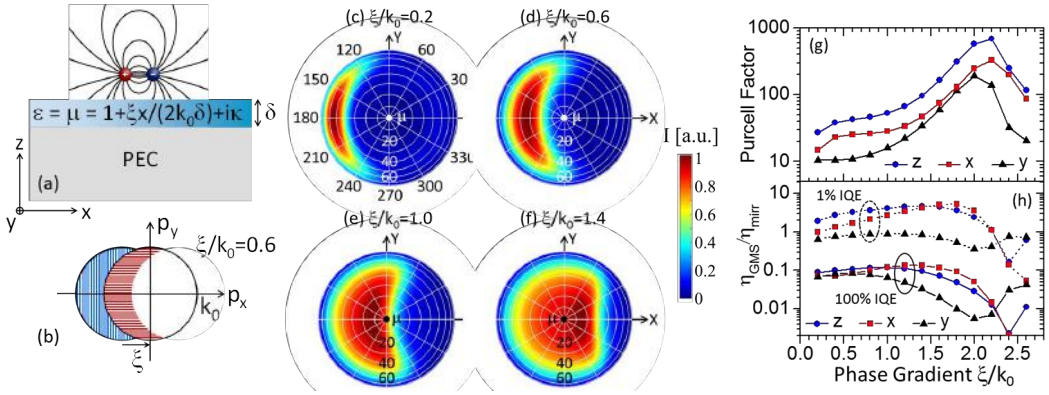



Figure 2. (a) Schematic cross-sectional view of the GMS model used in this work. (b) Distribution of the plane-wave components of the dipole field involved in the main radiation process. (c)-(f) Calculated far-field radiation patterns for different values of $\xi/k_0$. (e) Purcell enhancement factor for all three possible dipole orientations, versus $\xi/k_0$. (f) Radiative efficiency ratio between a dipole near a GMS and in front of a perfect mirror, plotted as a function of $\xi/k_0$ for two different values of the dipole internal quantum efficiency (IQE).

In a recent theoretical study [2] we have investigated a related approach, where a gradient metasurface (GMS) is used to control the radiation properties of light emitters located in its near field [Fig. 2(a)]. The resulting behavior can be understood by first decomposing the optical field emitted by the source (modeled as a dipole) in a superposition of plane waves with all possible in-plane wavevectors **p**, including evanescent terms. At the GMS, each such wave produces a reflected wave of in-plane wavevector $\mathbf{p}+\mathbf{u}\xi$, where **u** and $\xi$ are the direction and magnitude of the phase gradient. As a result, some of the evanescent components of the dipole field [from the blue region of Fig. 2(b)] can be diffracted by the GMS into propagating waves (red region), and thus contribute to the radiation output. Since this mechanism involves near-field interactions with highly confined evanescent fields, it can be expected to occur with high probability and thus dominate the dipole emission.

These expectations are confirmed by the far-field radiation patterns shown in Figs. 2(c)-2(f), which were computed via FDTD simulations for different values of the normalized phase gradient $\xi/k_0$. Highly asymmetric directional emission is observed, with the angle of peak emission and the width of the radiation pattern depending on $\xi/k_0$ consistent with the qualitative picture just presented. At the same time, the spontaneous emission decay of the dipole is greatly accelerated by the GMS, again through the diffractive scattering of evanescent components of the dipole field. The resulting Purcell enhancement factor can be as large as several 100s, depending on $\xi/k_0$ and on the dipole orientation as shown in Fig. 2(g). Finally, our simulations also show that the total output radiation power can be increased by the GMS in the case of low-efficiency emitters [Fig. 2(h)], or quenched in favor of directional excitation of surface waves for $\xi/k_0 > 2$ [2].

**Acknowledgements**. This work was supported by DOE under Grant DE-FG02-06ER46332.

## REFERENCES

1. DiMaria J., E. Dimakis, T. D. Moustakas and R. Paiella, "Plasmonic off-axis unidirectional beaming of quantum-well luminescence," *Appl. Phys. Lett.*, Vol. 103, Art. No. 251108, 2013.
2. Kogos L. C. and R. Paiella, "Light emission near a gradient metasurface," *ACS Photon.*, Vol. 3, 243–248, 2016.

# Lossy and gain metasurfaces for applications of antireflection coatings and parity-time-symmetric systems

**Jie Luo**[1], **Jensen Li**[2], **and Yun Lai**[1*]

[1]College of Physics, Optoelectronics and Energy & Collaborative Innovation Center of Suzhou Nano Science and Technology, Soochow University, Suzhou 215006, China

[2]School of Physics and Astronomy, University of Birmingham, Birmingham B15 2TT, United Kingdom

[*]corresponding author: laiyun@suda.edu.cn

**Abstract**-We investigate lossy and gain metasurfaces with pure imaginary permittivity or permeability in detail. In such particular metasurfaces, either electric or magnetic field is almost constant. Based on such a unique characteristic, we find out some applications in antireflection coatings and parity-time-symmetric systems. For instance, it is found that both lossy and gain metasurfaces can operate as ultrathin antireflection coatings. In addition, some unique properties are found in the parity-time-symmetric systems composed of the lossy and gain metasurfaces.

We consider wave incident from dielectric medium with relative permittivity of $\varepsilon_1$ into dielectric medium with relative permittivity of $\varepsilon_2$. Generally, reflections exist at the interface of the two dielectric media due to the impedance mismatch. To eliminate the reflections, we place an ultrathin metasurface between the two dielectric media. And under normal incidence, we find that the relative permittivity of the metasurface ($\mu = 1$) is required to be,

$$\varepsilon = i\frac{\sqrt{\varepsilon_1} - \sqrt{\varepsilon_2}}{k_0 d} \qquad (1)$$

Equation (1) indicates that the required permittivity is pure imaginary, and both lossy and gain media can operate as the antireflection coatings.

**REFERENCES**

1. Luo, J., Li, S., Hou, B., Lai, Y. "Unified theory for perfect absorption in ultrathin absorptive films with constant tangential electric or magnetic fields," *Phys. Rev. B* Vol. 90, 165128, 2014.
2. Fleury, R., Sounas, D. L., Alù, A. "Negative refraction and planar focusing based on parity-time symmetric metasurfaces," *Phys. Rev. Lett.* Vol. 113, 023903, 2014.
3. Sounas, D. L., Fleury, R., Alù, A. "Unidirectional cloaking based on metasurfaces with balanced loss and gain," *Phys. Rev. Applied* Vol. 4, 014005, 2015.
4. Monticone, F., Valagiannopoulos, C. A., Alù, A. "Aberration-free imaging based on parity-time symmetric nonlocal metasurfaces," http://arxiv.org/abs/1509.07300, 2015.

# High speed optical modulators with tunable metasurface absorber

**Yu Yao*** **and Ali Basiri**
School of Electrical, Computer & Energy Engineering, Arizona State University, USA
*corresponding author: yuyao@asu.edu

**Abstract**- We show that graphene can be integrated into the metasurface absorbers to realize high speed strong optical modulation in the mid-infrared (MIR) wavelength. Our device design is featured with a maximum modulation depth up to 100% and an insertion loss of <1.5 dB. A rigorous device model including full wave simulation and microscopic carrier dynamics in graphene is developed to investigate the ultimate limit of the modulator response time and it is estimated to be <1 ps.

There has been lack of high speed optical modulators in the MIR wavelength region. Conventional electro-optic crystals cannot be used for wavelength longer than 4 or 5 μm due to material absorption. Graphene, a monolayer of hexagonally-arranged carbon atoms[1], exhibits gate-voltage dependent optical conductivity and ultrafast carrier dynamics, which make it a great candidate for optical modulators [2-4].

The origin of gate-voltage dependent optical properties in graphene lies in the fact that its carrier density and Fermi level can be controlled by the gate voltage, or in other words, electrostatic doping. However, it has been a great challenge to achieve high performance graphene detector with large modulation depth due to the limited absorption in graphene. We have investigated strategies to enhance light graphene interaction in various plasmonic structures [5-7] and demonstrated a high speed broadband optical modulator with modulation depth up to 95% in the mid-infrared wavelength based on electrically tunable graphene-metasurface perfect absorber (Fig. 1a) [8].

Despite of the ultra-fast carrier dynamics in graphene, the electrically controlled modulators are limited by the RC constant [8]. To achieve the ultimate limit of modulation speed, we demonstrate all-optical modulators based on graphene metasurface hybrid structures, which can be structurally designed for any wavelength in the MIR region. When the pump light is incident on the graphene metasurface, the absorbed photons in graphene result in photo-generated carriers *(*$\Delta n$ *and* $\Delta p$), which lead to a transient change in graphene optical conductivity and permittivity. Thus the optical response of the graphene-metasurface hybrid structures will be changed due to the photo-generated carries. Meanwhile, ultra-fast carrier dynamics are exploited to achieve the high speed all-optical modulators with sub-picosecond response times. We will integrate full wave simulation and microscopic carrier dynamics in graphene to gain insight into the transient behavior and reveal the fundamental limit of the modulation speed.

[1] K. S. Novoselov, A. K. Geim, S. V. Morozov, D. Jiang, M. I. Katsnelson, I. V. Grigorieva*, et al.*, "Two-dimensional gas of massless Dirac fermions in graphene," *Nature,* vol. 438, pp. 197-200, Nov 10 2005.

[2] M. Liu, X. Yin, E. Ulin-Avila, B. Geng, T. Zentgraf, L. Ju*, et al.*, "A graphene-based broadband optical modulator," *Nature,* vol. 474, pp. 64-67, 2011.

[3] K. Kim, J.-Y. Choi, T. Kim, S.-H. Cho, and H.-J. Chung, "A role for graphene in silicon-based semiconductor devices," *Nature,* vol. 479, pp. 338-344, 2011.

[4] S. H. Lee, M. Choi, T.-T. Kim, S. Lee, M. Liu, X. Yin*, et al.*, "Switching terahertz waves with gate-controlled

active graphene metamaterials," *Nature materials,* vol. 11, pp. 936-941, 2012.

[5] R. Shankar, Y. Yao, J. Frish, I. Frank, Y. Song, J. Kong*, et al.*, "Electro-Optic tuning of mid-infrared photonic crystal cavities using graphene," in *CLEO: Science and Innovations*, 2013, p. CTu1F. 5.

[6] Y. Yao, M. Kats, P. Genevet, N. Yu, Y. Song, J. Kong*, et al.*, "Broad electrical tuning of graphene-loaded plasmonic antennas," *Nano letters,* 2013.

[7] Y. Yao, M. A. Kats, R. Shankar, Y. Song, J. Kong, M. Loncar*, et al.*, "Wide wavelength tuning of optical antennas on graphene with nanosecond response time," *Nano letters,* vol. 14, pp. 214-219, 2013.

[8] Y. Yao, R. Shankar, M. A. Kats, Y. Song, J. Kong, M. Loncar*, et al.*, "Electrically Tunable Metasurface Perfect Absorbers for Ultrathin Mid-Infrared Optical Modulators," *Nano letters,* vol. 14, pp. 6526-6532, 2014.

[9] Ali Basiri, Yu Yao, "Ultrafast all-optical modulators based on graphene-metasurface absorber", in preparation.

# Novel dielectric nanophotonic structures with unusual nonlinear and spectral properties

**Zin Lin**[1], **Yang Li**[1], **Eric Mazur**[1], **Marko Loncar**[1], **and Alejandro W. Rodriguez**[2*]

[1]Harvard University School of Engineering and Applied Sciences, USA
[2]Princeton University Department of Electrical Engineering, USA
*arod@princeton.edu

We describe novel nanophotonic structures—new kinds of optical micropillars, slabs, and waveguides—consisting of aperiodic or complicated arrangements of subwavelength dielectrics designed to exhibit unusual nonlinear and spectral properties [Figs. 1,2]. In contrast to conventional, hand-designed nanostructures relying on well-known and intuitive design principles such as Bragg scattering (band gaps) or index guiding, our structures arise from the application of brute-force adjoint optimization techniques. Such a framework allows automatic discovery of structures specifically tailored and optimized for specific applications, leading for instance to orders of magnitude enhancements in nonlinear interactions, e.g. high-effiency frequency conversion from visible to telecom wavelengths, and unusual/exotic spectral features, e.g. doubly and even triply degenerate Dirac cones that yield novel types of zero-index metamaterials and exceptional points (EP).

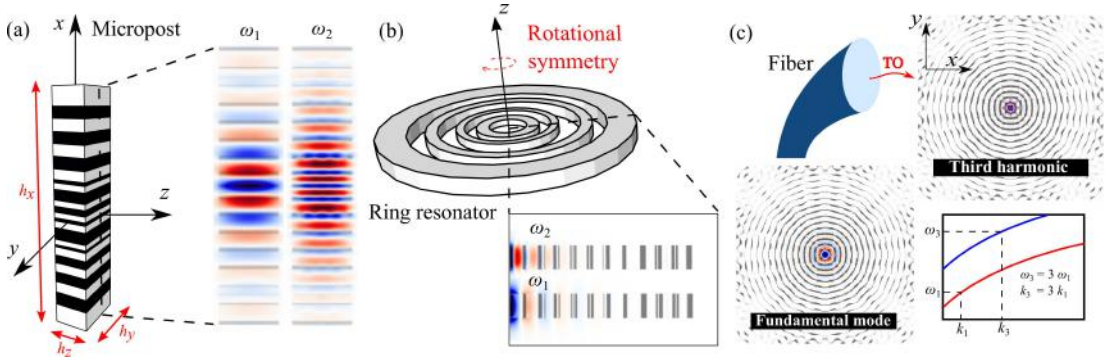



Figure 1: (a) Schematic of a micropost cavity consisting of aperiodically alternating AlGaAs/$AlO_x$ layers of dimension $h_x \times h_y \times h_z = 8.4 \times 3.5 \times 0.84$ ($\lambda_1^3$), designed to enhance the efficiency of SHG processes. Shown are $x$-$z$ cross-sections of the $E_y$ components of two localized modes at $\lambda_1 = 1.5$ $\mu$m and $\lambda_2 = 0.75$ $\mu$m exhibiting radiative lifetimes $Q_1^{\rm rad} = 1.4 \times 10^5$, $Q_2^{\rm rad} = 1.3 \times 10^5$, respectively, and an ultra-large nonlinear spatial overlap $\bar{\beta} = 0.018$. (b) Schematic of GaAs ($0.39\lambda_1$ thick) concentric-ring cavity exhibiting tightly localized TM modes at $\lambda_1 = 1.8$ $\mu$m and $\lambda_2 = 0.9$ $\mu$m with $Q_1^{\rm rad} = 10^5$, $Q_2^{\rm rad} = 3 \times 10^4$, and $\bar{\beta} = 0.041$. (c) Cross section and mode profiles of an $As_2Se_3$/PES nanostructured fiber designed to enhance THG processes, showing huge modal confinements and nonlinear overlaps, and exhibiting perfect phase- and frequency-matching.

The efficiency of nonlinear frequency conversion processes is well known to be greatly enhanced in nanostructures supporting confined modes exhibiting (i) tightly localized fields, (ii) long lifetimes, (iii) exactly matched resonant frequencies, and (iv) strong nonlinear modal overlaps (selection rules that generalize the well-known concept of quasiphase matching of waveguides modes to wavelength-scale cavities). Thus far, these requirements have not been met by common micro- and nano-photonic structures, including PhC cavities and micro-ring resonators, but are manifested in our optimized, *aperiodic* photonic designs. For example, Fig. 1 shows schematics of structures optimized to enhance second harmonic generation (SHG) and third harmonic generation (THG) in the smallest modal volumes possible. Figure 1(a) reveals a doubly-resonant rectangular micropost cavity with alternating AlGaAs/$AlO_x$ layers in an aperiodic sequence that supports modes exactly an octave apart ($\lambda_1 = 1.5$ $\mu$m and $\lambda_2 = \lambda_1/2$) with large radiative $Q^{\rm rad} \gtrsim 10^5$ and small $V \sim (\lambda_1/n)^3$, and whose spatial profiles exhibit ultra-large nonlinear overlaps, $\bar{\beta} = \int d\mathbf{r}\bar{\epsilon}(\mathbf{r})E_2^* E_1^2 / \left(\int d\mathbf{r}\epsilon_1|\mathbf{E}_1|^2\right)\left(\sqrt{\int d\mathbf{r}\epsilon_2|\mathbf{E}_2|^2}\right)\sqrt{\lambda_1^3} \sim 0.02$ [1]. Figure 1(b) shows a thin-film GaAs cavity comprising aperiodic arrangements of planar concentric rings, in which both fundamental (1.8 $\mu$m)

and second harmonic modes (0.9 $\mu$m) are tightly localized in the cavity, with $Q^{\text{rad}} \gtrsim 10^4$ and $\bar{\beta} \sim 0.04$. Such giant $\bar{\beta}$ greatly exceed those of existing, hand-designed structures, including for instance recently proposed nanobeam cavities [2] and nanoring resonators [3], leading to orders of magnitude enhancement in SHG efficiencies $\sim \left(Q_1^{\text{rad}}\right)^2 Q_2^{\text{rad}} |\bar{\beta}|^2$. Yet another powerful application of our optimization techniques can be found in the area of fiber design, where novel cross-sectional nanostructures provide fertile ground for dispersion engineering and nonlinear enhancements, as exemplified by the chalcogenide/polymer fiber of Fig. 1(c).

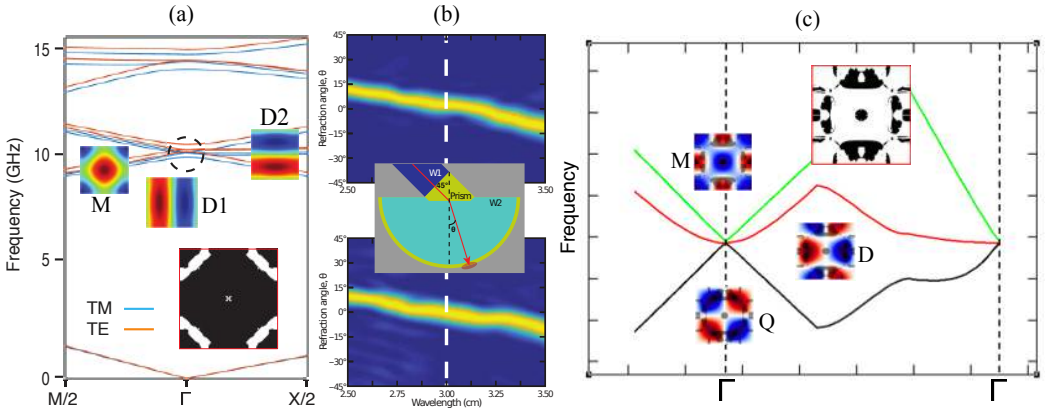



Figure 2: (a) Band structure of a PhC metamaterial exhibiting dual-polarization (TE and TM) Dirac cone (inset). Two overlapping Dirac cones form at the Γ point (circled), one for each polarization of light. Insets also show the three different modes (one monopole, M, and two dipoles, D1 and D2) that form each Dirac cone. (b) Demonstration of prism test (inset) for both polarizations, illustrating the angle of refraction as a function of wavelength. Dashed white line indicates the designed wavelength, for which the angle of refraction is nearly zero. (c) Band structure of PhC metamaterial exhibiting a tri-modal Dirac cone (inset) induced by a degeneracy of monopolar (M), dipolar (D), and quadrupolar (Q) eigenmodes.

Recent works have shown that the presence of linear dispersion at the center of the Brillouin zone of a PhC can lead to effectively vanishing permittivity and permeability [4, 5]. Such materials, known as Dirac-cone zero-index metamaterials (ZIMs), are usually designed via a tedious tria-and-error approach that can only handle a small number of simple design parameters. Here, going beyond such design methodologies, we demonstrate new flavors of Dirac cones and ZIMs arising from complex geometries, whose spectrum exhibit high-order degeneracies among modes of differing symmetries and polarizations. For instance, we demonstrate a novel class of 2d PhCs exhibiting dual-polarization Dirac cones, i.e. a linear Dirac dispersion with (approximately) degenerate TE and TM polarizations [Fig. 2(a)]. The resulting zero-index behavior is tested via FDTD simulations of incident light refracting from a prism composed of multiple unit cells [Fig. 2(b)], leading to output beams emerging perpendicular to the prism facet independently of the incident polarization. Finally, we describe a structure exhibiting a Dirac cone induced by an "accidental" degeneracy of monopolar, dipolar and quadrupolar modes [Fig. 2(c)] that can lead to so-called third-order EP whereby three eigenmodes coalesce (becoming self orthogonal to one another). Such EPs are difficult to hand-engineer but are useful for many applications, from loss-induced transparency, to unidirectional transmission or reflection, to enhanced emission from quantum/active emitters.

**REFERENCES**


1. Zin Lin, Xiangdong Liang, Steven G. Johnson, Marko Lončar and Alejandro W. Rodriguez. "Cavity-enhanced second harmonic generation via nonlinear overlap optimization" ArXiv:1505.02880 (2015)
2. Sonia Buckley, Marina Radulaski, Jingyuan Linda Zhang, Jan Petykiewicz, Klaus Biermann and Jelena Vučković. "Multimode nanobeam cavities for nonlinear optics: high quality resonances separated by an octave" Opt. Express **22**, 26498–26509 (2014).
3. Zhuan-Fang Bi, Alejandro W. Rodriguez, Hila Hashemi, David Duchesne, Marko Lončar, Ke-Ming Wang, and Steven G. Johnson. "High-efficiency second-harmonic generation in doubly-resonant $\chi(2)$ microring resonators" Opt. Express **20**, 7526–7543 (2012).
4. Xueqin Huang, Yun Lai, Zhi Hong Hang, Huihuo Zheng, and C. T. Chan. Dirac cones induced by accidental degeneracy in photonic crystals and zero-refractive-index materials, 2011.
5. Yang Li, Shota Kita, Philip Munoz, Orad Reshef, Daryl I. Vulis, Mei Yin, Marko Loncar, and Eric Mazur. On-chip zero-index metamaterials. *Nature Photonics*, 9:738 – 742, 2015.

# Dielectric Nanostructures with High Laser Damage Threshold

**C. Y. Ngo[1*], L. Y. Hong[2], J. Deng[1], E. H. Khoo[3], Z. Liu[3], R. F. Wu[4], J. H. Teng[1*]**

[1]Institute of Materials Research and Engineering, Singapore

[2]Nanyang Technological University, Singapore

[3]Institute of High Performance Computing, Singapore

[4]DSO National Laboratories, Singapore

[*]ngocya@imre.a-star.edu.sg; jh-teng@imre.a-star.edu.sg

**Abstract**- Dielectric-based metamaterials are proposed to be the ideal candidates for low-loss, high efficiency devices. However, to employ dielectric nanostructures for high power applications, the dielectric material must have a high laser induced damaged threshold (LIDT) value. In this work, we investigated the LIDT values of dielectric materials for high power fiber laser applications. Consequently, we found that the fabricated $SiO_2$ nano-structures can withstand laser fluence exceeding 100 J/cm$^2$.

Dielectric-based metamaterials are proposed to be the ideal candidate for low-loss, high efficiency devices [1]. Our preliminary laser induced damaged threshold (LIDT) measurement suggested that $SiO_2$ was the most promising dielectric material that can withstand high laser fluence before breakdown [2]. In this work, we characterized the $SiO_2$ nanostructures "lens" that we designed with traditional geometrical optical methods, using energy conservation and optical coordinate transformation algorithms [3].

We measured high transmittance for the $SiO_2$ nanostructures, and observed that the result is position independent in the wavelength range of 500 nm and above. These results agree well with our FDTD simulations. Detailed LIDT measurements were performed on both $SiO_2$ film and nanostructures, and we found that the fabricated nano-structures can withstand laser fluence exceeding 100 J/cm$^2$. This value is 45% higher than that of bulk $SiO_2$ film. All these findings will be beneficial for researchers working on dielectric materials for high power applications.

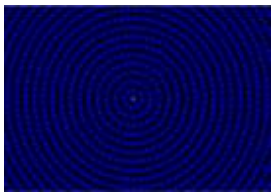
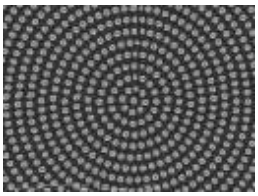
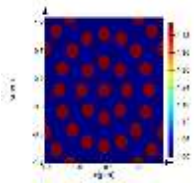
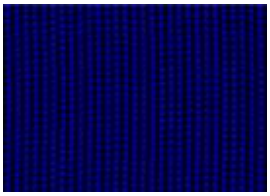
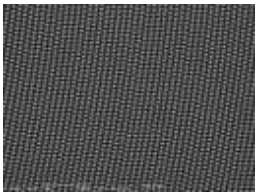
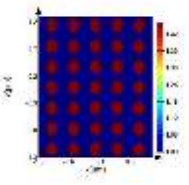
| GDS Image | SEM Image | FDTD Image |
|---|---|---|
|  |  |  |
|  |  |  |

Figure 1. GDS, SEM and FDTD images at the centre (top row) and outer circle (bottom row) of the $SiO_2$ nanostructures.

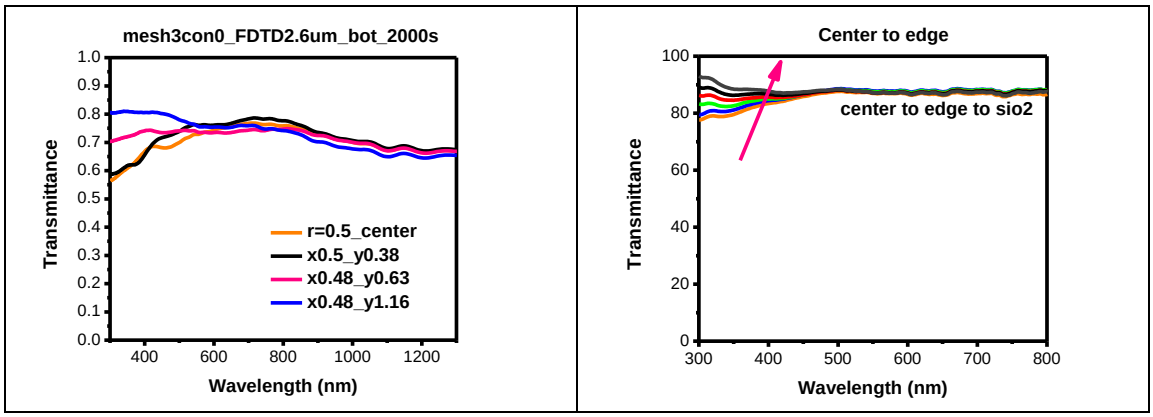
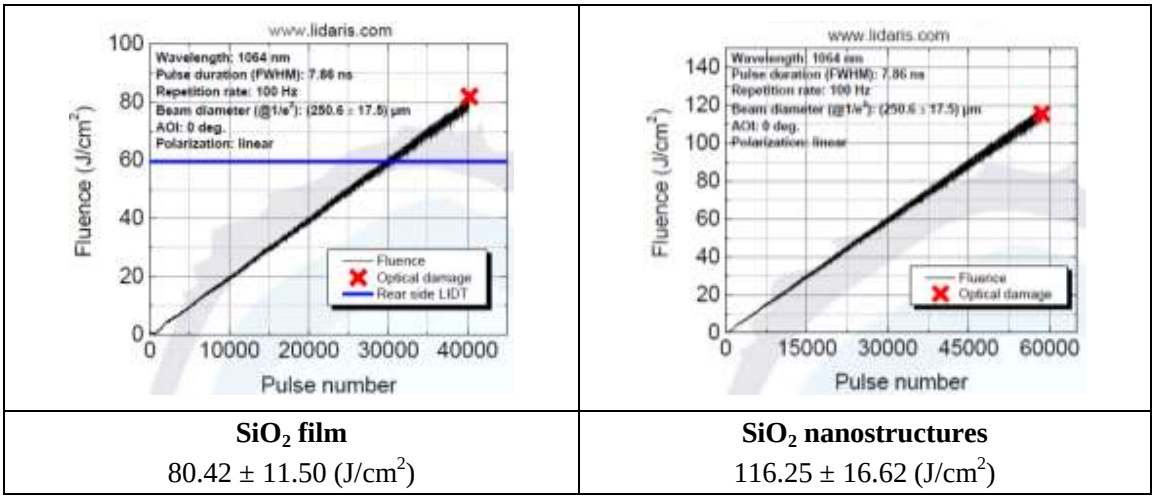



Figure 2. FDTD simulation and transmission measurements of the $SiO_2$ nanostructures at various positions from the centre. Note that the result is position independent for wavelength range of 500 nm and above.

LIDT measurement was performed by irradiating one site on the sample with 100 pulses of a particular laser energy level, before increasing the fluence by 0.1 J/cm$^2$ and irradiating with another 100 pulses, repeating this until damage occurs. The results show that the LIDT value of $SiO_2$ nanostructures is significantly (45%) higher than that of the bulk $SiO_2$ film.




| **$SiO_2$ film** | **$SiO_2$ nanostructures** |
|---|---|
| 80.42 ± 11.50 (J/cm$^2$) | 116.25 ± 16.62 (J/cm$^2$) |

Figure 3. Measured peak fluence of $SiO_2$ film (left) and $SiO_2$ nanostructures (right).

**Acknowledgements** The authors greatly acknowledge Dr. Eunice S. P. Leong for the FDTD simulation work. This project is partially supported by A*STAR-MINDEF Science & Technology Joint Funding Programme (Grant No. 102-174-0172).

**REFERENCES**

1. Jahani, S. and Z. Jacob, "All-dielectric metamaterials," *Nature Nanotechnology*, Vol. 11, 23-36, 2016.
2. Ngo, C. Y. , L. Y. Hong, Z. Liu, R. F. Wu, E. H. Khoo and J. H. Teng, "Nano-structures for high intensity fiber laser applications," *Proceedings of SPIE*, Vol. 9172, San Diego, USA, Aug. 2014, 917207.
3. Z. Liu, E. H. Khoo, C. Y. Ngo, L. Y. Hong, R. F. Wu, J. H. Teng, "Laser beam shaping with nano-structured lens", *Proceedings of SPIE*, Vol. 9149, San Diego, USA, Aug. 2014, 91940L.

# Metasurfaces becoming real: a new class of polarimeters

**A. Pors*** and **S. I. Bozhevolnyi**

Centre for Nano Optics, University of Southern Denmark, Campusvej 55, DK-5230 Odense M, Denmark
*corresponding author: alp@iti.sdu.dk

**Abstract**— Based on appropriately designed phase-gradient birefringent metasurfaces, we introduce a new type of compact polarimeter that, unlike conventional approaches, allows one to easily analyze an arbitrary state of light polarization by conducting simultaneous (i.e., parallel) measurements of the corresponding diffraction intensities. We experimentally demonstrate the functionality of the proposed device at a wavelength of 800 nm, while also addressing extensions of the design concept to in-plane polarimeters and spectrally-resolved measurements.

A monochromatic electromagnetic wave is typically characterized by its intensity, frequency, and state of polarization (SOP). Here, the first two characteristics are quite easily measured by the use of suitable photodetectors and spectrometers. The SOP, on the other hand, is inherently difficult to probe experimentally, which stems from the fact that conventional detection schemes are only sensitive to the intensity of light, hence any phase information between orthogonal polarization states are lost in the detection process. For this reason, the determination of SOP typically necessitates a (time-consuming) series of measurements with properly arranged polarizers placed consecutively in front of the detector, allowing one to eventually obtain the Stokes parameters that, similarly to the ellipsometric parameters, fully describe the SOP [1]. We would like to note that the series of measurements for the determination of SOP can be parallelized or automated, though at the expense of a more complex optical system. Despite the inconvenience in determining SOP, we emphasize that polarimetric measurements are of crucial importance in a wide range of applications, ranging from thin-film characterization [2], optical network monitoring [3], biology [4], camouflage technology [5], and astronomy [6].

In this talk, we discuss a certain type of phase-gradient plasmonic metasurfaces, consisting of a subwavelength-thin dielectric spacer sandwiched between an optically thick metal film and an array of carefully designed metal nanobricks (also known as nanopatches), which allow us to fully control the phase of the reflected light for two orthogonal polarizations simultaneously [7]. Moreover, we bring to the fore the equivalence between normalized Stokes parameters and diffraction contrasts in properly designed birefringent metasurfaces, which allow us to design a polarimeter, consisting of three interweaved metasurfaces, from which a simultaneous measurement (i.e., parallel) of the corresponding six diffraction intensities (see sketch in Fig. 1) immediately reveal, without the need of any calibration, the Stokes parameters of the SOP under examination [8, 9]. The polarimeter is realized at an operation wavelength of 800 nm, and experimental characterization convincingly demonstrates the expected functionalities. In the talk, we also demonstrate how the same design principle can be extended to achieve spectrally-resolved polarimetric measurements, and novel in-plane polarimeters where part of the free-space incident light couples to waveguide modes.

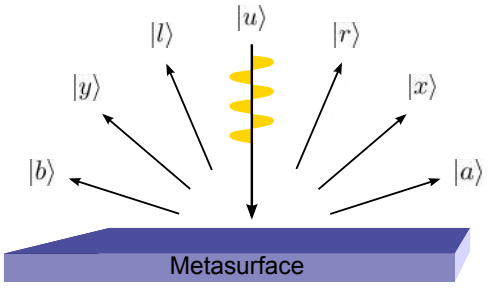



Figure 1: Sketch of the functionality of the metasurface-based polarimeter. An incident wave with polarization $|u\rangle$ is upon reflection split into three pairs of orthogonal polarizations [($|x\rangle$,$|y\rangle$), ($|a\rangle$,$|b\rangle$), and ($|r\rangle$,$|l\rangle$)], which allows one to immediately obtain the associated Stokes parameters.

**ACKNOWLEDGMENT**

We acknowledge financial support for this work from the European Research Council (the PLAQNAP project, grant 341054) and the University of Southern Denmark (SDU2020 funding).

**REFERENCES**

1. Bohren, C. F and Huffman, D. R., *Absorption and scattering of light by small particles*, Wiley-VCH, 2004.
2. Rzhanov, A. and Svitashev, K., "Ellipsometric techniques to study surfaces and thin films," *Adv. Electron. Electron Phys.*, Vol. 49, 1–84, 1979.
3. Damask, J. N., *Polarization optics in telecommunications*, Springer, 2004.
4. Collings, A. F. and Caruso, F., "Biosensors: recent advances," *Rep. Prog. Phys.*, Vol. 60, 1397–1445, 1997.
5. Tyo, J. S., Goldstein, D. L., Chenault, D. B. and Shaw, J. A., "Review of passive imaging polarimetry for remote sensing applications," *Appl. Opt.*, Vol. 45, 5453–5469, 2006.
6. Tinbergen, J., *Astronomical polarimetry,* Cambridge University, 1996.
7. Pors, A., Albrektsen, O., Radko, I. P. and Bozhevolnyi, S. I., "Gap plasmon-based metasurfaces for total control of reflected light," *Sci. Rep.*, Vol. 3, 2155, 2013.
8. Pors, A., Nielsen, M. G. and Bozhevolnyi, S. I., "Plasmonic metagratings for simultaneous determination of Stokes parameters," *Optica*, Vol. 2, 716–723, 2015.
9. Lepetit, T. and Kanté, B., "Metasurfaces: simultaneous Stokes parameters," *Nat. Photon.*, Vol. 9, 709–710, 2015.

# Durable plasmonic metal nitrides and transparent conducting oxides for flat photonics

**K. Chaudhuri[1], J. Kim[1], A. M. Shaltout[1], N. Kinsey[1], S. Choudhuri[1], V. M. Shalaev[1] and A. Boltasseva[1]***

*[1]School of Electrical & Computer Engineering and Birck Nanotechnology Center, Purdue University, 1205 West State St., West Lafayette, IN 47907, USA.*

*corresponding author: aeb@purdue.edu

**Abstract**- Transition metal nitrides and transparent conducting oxides are utilized as metallic components in the design of plasmonic metasurfaces. A phase-gradient metasurface with zirconium nitride and a quarter waveplate metasurface with gallium doped zinc oxide have been developed for the realization of practical plasmonic devices with CMOS-compatible materials.

Flat photonics is an emerging field in optics that utilizes the concept of metasurfaces capable of controlling the phase and/or the amplitude of the reflected/transmitted light by employing plasmonic nanoantennas [1]. Noble metals such as gold (Au) or silver (Ag) have been employed to demonstrate numerous extraordinary metasurfaces including lenses, wave plates, holograms, and polarization selective elements. However, these metals have several drawbacks such as the difficulty to fabricate continuous ultrathin films (<10 nm), their incompatibility with the well-established processes for silicon-based products, high temperature instability and the lack of tunability in linear permittivity. Recent works have shown that transparent conducting oxides (TCOs) and refractory plasmonic materials such as transition metal nitrides can be alternatives to overcome several of the drawback of noble metals [2]. In this work, we will discuss these two candidates as metallic components in plasmonic metasurfaces, which have already been demonstrated using gold or silver, and compare the performance to the noble metal counterpart.

Zirconium nitride (ZrN) is a refractory plasmonic material which can sustain its optical properties at high temperatures (up to 1100 °C in the atmosphere). Using the empirical optical properties of ZrN, we have designed a phase gradient metasurface that exhibits the photonic Spin Hall Effect (PSHE). The design is based on unit cell structures containing arrays of rectangular brick antennas (ZrN) on a metal/dielectric stack of ZrN/AlScN (Aluminium scandium nitride) (Fig.1a). The metasurface design concept is adapted from (and compared to) our previous work studying Au based metasurface which separates the two circular polarizations, right (RCP) and left (LCP), of the incident light by reflecting them in opposite directions[3]. In our design, we have replaced the Au with ZrN, and through optimization, have reached a working efficiency as large as the Au based design as shown in Fig.1b and 1c. Our ZrN device is able to achieve transfer ~60% of the input power to the anomalous mode within a broad wavelength range around 1.4um.

In addition to refractory plasmonic nitrides, transparent conducting oxides (TCOs) are another leading alternative plasmonic material in the near infrared range. An Ag based metasurface converting linear polarization into circular polarization was well-demonstrated theoretically and experimentally in the visible range [4]. The design of the metasurface is based on the two orthogonal patterned nanorods which provide a phase shift of $\pi/2$ between two orthogonal polarizations at the operating wavelength. In this work, we realize a TCO-based metasurface that functions as a quarter waveplate (QWP) based on the design parameters depicted in Fig. 1e. The scanning electron microscope (SEM) images in Fig. 1f and 1g show the 500nm tall GZO structures of the fabricated metasurface.

From the phase difference (Δ) measurement between the reflected s and p polarizations for light incident at an angle of $18^0$, we observe that the TCO based metasurface operates as a quarter-wave-plate in reflection mode with a 500nm bandwidth (1.7 μm to 2.2 μm) highlighted by the gray area on the plot.

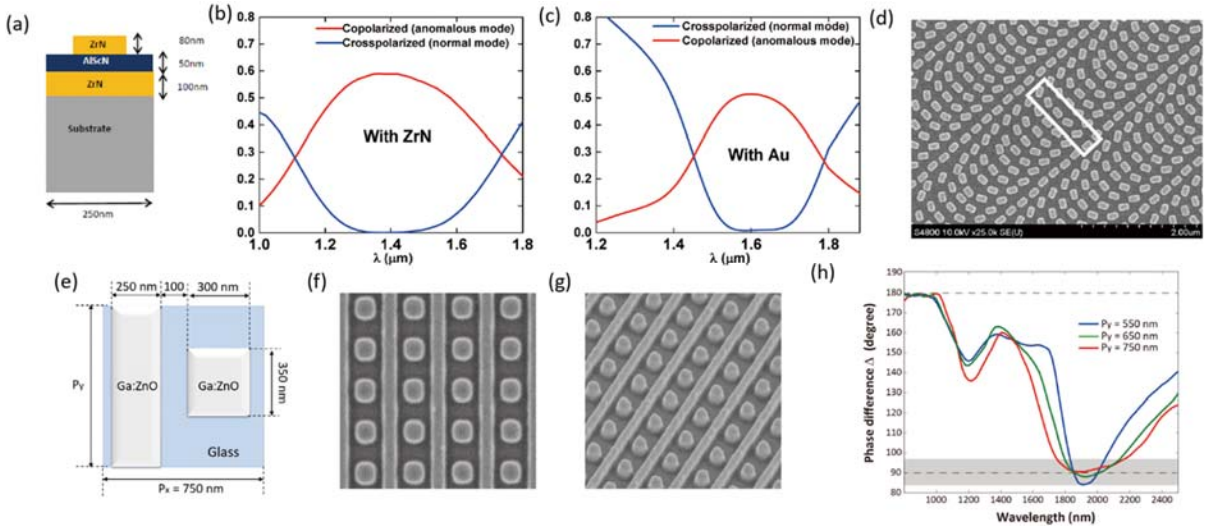



**Fig. 1.** (a) Schematic of a gap surface plasmon unit cell of the metasurface. (b) and (c) Reflected power distribution between circular co-polarized (red) and cross-polarized (blue) components as obtained in simulations for Au (b) and ZrN (c). (d) Field emission scanning electron microscopy (FE SEM) image of the fabricated metasurface. (e) Unit cells of two different nanorod of QWP metasurfaces and the corresponding geometrical parameters. Top view (f) and $30^0$ tilted view (g) of SEM image of patterned nanorod plasmonic metasurface. (f) Phase difference (Δ) of the reflected light between two orthogonal polarizations (s and p) at $18^0$ tilted incident light.

In conclusion, transition metal nitrides and TCOs are successfully employed to form metasurfaces that manipulate the phase and the amplitude of reflected light. These alternative materials can open the possibility of integration with nanophotonic devices which require tight light confinement, high-temperature operational conditions, silicon compatibility, and special incoming polarization states.

**Acknowledgements** This work is partly supported by AFOSR MURI Grant FA9550-12-1-0389, ARO grant W911NF-13-1-0226, NSF grant DMR-1120923

## REFERENCES

1 Yu, N. *et al.* Light propagation with phase discontinuities: generalized laws of reflection and refraction. *science* **334**, 333-337 (2011).

2 Naik, G. V., Shalaev, V. M. & Boltasseva, A. Alternative plasmonic materials: beyond gold and silver. *Adv. Mater.* **25**, 3264-3294 (2013).

3 Shaltout, A., Liu, J., Kildishev, A. & Shalaev, V. Photonic spin Hall effect in gap–plasmon metasurfaces for on-chip chiroptical spectroscopy. *Optica* **2**, 860-863 (2015).

4 Zhao, Y. & Alù, A. Tailoring the dispersion of plasmonic nanorods to realize broadband optical meta-waveplates. *Nano letters* **13**, 1086-1091 (2013).

# Holographic nonlinear metamaterials

**E. Almeida* and Y. Prior**
Department of Chemical Physics, Weizmann Institute of Science, Rehovot, Israel
*corresponding author: euclides.almeida@weizmann.ac.il

**Abstract**-We fabricated and demonstrated three-dimensional computer generated nonlinear metamaterial holograms based on third harmonic generation. Using plasmonic antennas, we built phase holograms that generate holographic images in the visible when pumped by an infrared beam. Other polarization-multiplexed optical elements, such as nonlinear lenses and blazed gratings, were also demonstrated.

Recently, a novel class of nonlinear metasurfaces has emerged in which the phase of the nonlinear susceptibility can be controlled in the subwavelength regime, enabling the realization of functional optical elements that can both generate and shape coherent light beams [1]. So far, these elements are mostly confined to metasurfaces, which are essentially two-dimensional metamaterials. Here we demonstrate polarization multiplexed three-dimensional metamaterial holograms which are capable of generating holographic images at the third harmonic frequency of the input beam [2]. In our holograms, plasmonic V-shaped gold nanoatennas are used as the local source of the nonlinear radiation (Fig.1). By controlling the geometry of the nanoantennas, the plasmonic resonances are tuned around the frequency of the fundamental beam and a phase shift of up to $2\pi$ radians can be imparted on the third harmonic signal. In Figs. 1c-e we show examples of computer generated nonlinear hologram, where the phase profile of the virtual object on the hologram is recorded by each antenna. Due to frequency conversion, these holograms are capable of generating background-free images.

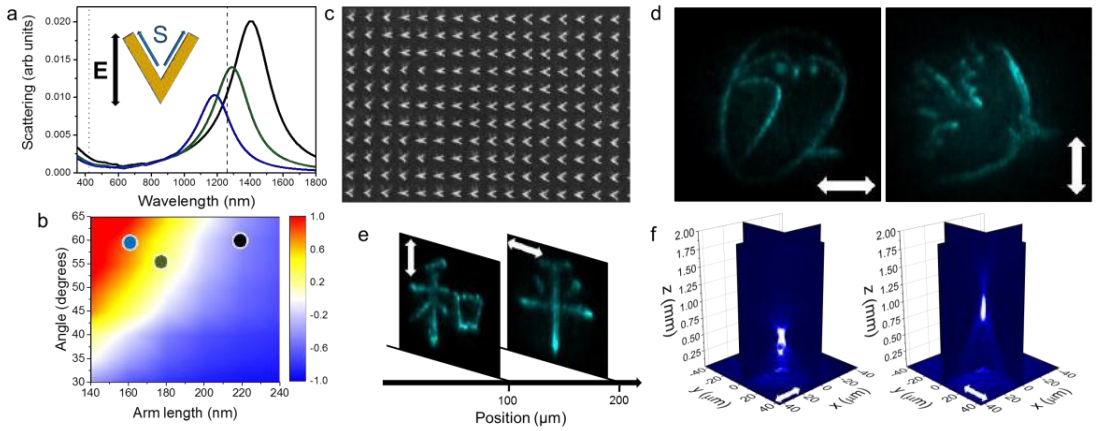



Figure 1. Examples of holographic nonlinear metamaterials. A) Scattering spectra of individual V-shaped gold antennas. By controlling the length of the arms and the angle between them, the symmetric resonance (S) is tuned around the frequency of the pump beam ($\lambda_F$ = 1266 nm). b) phase map of the third harmonic signal at $\lambda_{TH}$ = 422 nm. c) SEM image of a two-layer device. d) Holographic reconstruction of famous line drawings by Spanish artist Pablo Picasso. When illuminated by an horizontally polarized infrared beam at 1266 nm, the device reconstructs the Owl at 422 nm. For vertical input, the Dove of Peace is generated. e) Hologram with 3D displaying the Chinese characters for “peace and harmony”. f) An analytic type, dual foci nonlinear lens.

Other polarization dependent, analytic type diffractive optical elements such as nonlinear lenses were also demonstrated, in which the focal position of the beam can be controlled by the polarization state of the input beam (Fig. 1f). Holographic nonlinear metamaterials may find application as functional optical elements where the coherent radiation is generated *in situ*. Other possible applications include holographic displays based on nonlinear phenomena such as lasing and gain.

**REFERENCES**


1. Almeida, E. and Y. Prior. "Subwavelength nonlinear phase control and anomalous phase matching in plasmonic metasurfaces," *Nat. Comm.*, Vol. 7, 10367, 2016.
2. Almeida, E., O. Bitton and Y. Prior, "Nonlinear metamaterials for holography," *submitted and Arxiv:1512.07899*.

# Nonlinear Beam Shaping with Plasmonic Metasurfaces

**Shay Keren-Zur[1], Ori Avayu[1], Lior Michaeli[2], and Tal Ellenbogen[1]**

[1]*Department of Physical Electronics, Faculty of Engineering, Tel-Aviv University, Tel-Aviv 69978, Israel*

[2]*Raymond and Beverly Sackler School of Physics & Astronomy, Tel Aviv University, Tel Aviv 69978, Israel*

tellenbogen@tauex.tau.ac.il

**Abstract**- We demonstrate how to engineer the nonlinear interaction in plasmonic metasurfaces and shape the nonlinear emission by tailoring the spatial distribution of the metasurface nonlinearity. This enables perfect nonlinear beam shaping, unmatched by conventional nonlinear materials.

Recent years have taught us that metasurfaces provide a powerful tool to control and shape light. Various demonstrations of the functionality of metasurfaces were reported, including artificial refraction, light focusing, polarization conversion, and even multicolor holography [1]. Moreover, several works have demonstrated that metasurfaces exhibit also enhanced intrinsic quadratic optical nonlinearities [2]. These enhanced nonlinearities origin from multiple effects including symmetry breaking at the surface of the inclusions that form the building blocks of the metasurfaces, local field confinement, and coupling of the nonlinear currents to bright radiating modes of the subwavelength inclusions. In addition it was demonstrated that hybrid metasurfaces on top of quantum-well structures lead to giant nonlinear quadratic coefficients that are up to four orders of magnitude larger than conventional nonlinear quadratic materials [3]. Leveraging the ability of metasurfaces to manipulate light, in order to control also the nonlinear optical interactions, paves the way to create active light shaping metasurfaces, and to tailor the interaction between light and matter in exotic frequency regimes and in compact integrated platforms.

In this work we demonstrate different methods to control the quadratic nonlinear interactions in metasurfaces and specifically to construct nonlinear metasurfaces for light control and wavefront shaping applications. We discuss the benefits of metasurfaces allowing engineering of the local nonlinearity at the level of the single subwavelength inclusion to provide local amplitude and phase control, and in addition we explore effects of designing the collective interaction of many subwavelength inclusions to shape the far field beam profile. We use metallic split ring resonators (SRRs) to construct the metasurfaces [4]. Controlling the orientation, size, and location of each single SRR provides several independent knobs to set the phase and amplitude of the locally generated second harmonic (SH). We first use orientation flipping of the SRRs, that lead to binary SH phase manipulations, in order to demonstrate the construction of nonlinear metamaterial based photonic crystals (NLMPC) [5]. These are metamaterials that have a uniform effective linear susceptibility and a periodically or quasi-periodically modulated quadratic nonlinear susceptibility. The simplest form of an NLMPC can be described by a 1D periodic binary modulation of the nonlinear coefficient of a metasurface $\chi^{(2)}(x,y) \propto sign[\cos(2\pi x/\Lambda)]$, where $\Lambda$ is the modulation period. The nonlinear interaction in such a metasurface experiences the presence of a nonlinear lattice which leads to nonlinear Raman-Nath diffraction. In the case of second harmonic generation (SHG) the resulting nonlinear diffraction can be described by $k_2 \sin\theta_{2,m} = 2k_1 \sin\theta_1 + mK_\Lambda$, where $k_1$, $k_2$ and $K_\Lambda$ are the wave vectors of the FH, SH, and the reciprocal lattice vector (RLV) respectively, $m$ is an integer, $\theta_1$ is the incident angle of the FH wave with respect to the surface normal in the plane defined by the $x$ axis and surface normal, $\theta_{2,m}$ is the angle of $m^{th}$ order emission. This enables several new functionalities including ultra-wide angular scanning of the nonlinear output from the metamaterial [5]. The extension to 2D allows also constructing 2D nonlinear photonic crystals, new types of

flat nonlinear lenses and also to use different methods in holography to control the nonlinear output [5,6].

The concept of 2D nonlinear beam shaping by nonlinear computer generated holograms (NL-CGH) in poled ferroelectric crystals was recently introduced by Shapira et al. [7]. To encode a desired beam at the output of the nonlinear process in a metasurface, the modulation described above for a 1D NLMPC is extended in the following form $\chi^{(2)}(x,y) \propto sign\{cos[2\pi x/\Lambda - \varphi(x,y)] - cos[\pi q(x,y)]\}$, where $\varphi(x,y)$ encodes the phase of the Fourier transform of the desired wavefront, and $q(x,y)$ encodes its amplitude, $A$, according to the relation $A(x,y) = sign[\pi q(x,y)]$. The SH field emanating from the metasurface will have the form $E_{SH}(x,y) \propto \chi^{(2)}(x,y) E_{FH}(x,y)^2$ and the desired waveform will appear in the optical Fourier plane. We used this method to demonstrate nonlinear beam shaping by metasurface based NL-CGH and specifically to generate Airy and vortex beams [6].

While binary phase manipulations of the nonlinear coefficient can be achieved also with poled ferroelectric crystals, one of the greatest advantages of nonlinear metasurfaces is their ability to completely define the effective nonlinear tensors. This adds flexibility to freely design the nonlinear interaction and specifically it can facilitate perfect nonlinear beam shaping that cannot be achieved with natural nonlinear optical materials [8]. We demonstrate this concept for perfect generation of a first order Hermite-Gaussian ($HG_{01}$) beam, that follows the form $E_{SH}(x,y) \propto x exp[-(x^2+y^2)/w_0^2]$, in the near optical field of the metasurface, using a Gaussian pump beam. Whereas the Gaussian envelop of the $HG_{01}$ SH beam can be transferred from the pump Gaussian beam, for perfect beam shaping in the near optical field, the linear spatial dependence of the amplitude has to be encoded in the metasurface, $\chi^{(2)}(x,y) \propto x$. With the ability to control also the spatial phase of the nonlinear output from the metasurface this method can be extended to create any desired wavefront in the near-optical field of the nonlinear metasurface.

**Acknowledgements**, This research was supported by the Israeli Science Foundation (grant no. 1331/13) and by the European Commission Marie Curie Career Integration Grant (grant no. 333821). S.K. acknowledges support from the Tel-Aviv University Center for Renewable Energy President Scholarship for Outstanding PhD Students.

**REFERENCES**

1. N. Yu and F. Capasso, "Flat optics with designer metasurfaces," Nat. Mater. **13**, 139–150 (2014).
2. A. E. Minovich, A. E. Miroshnichenko, A. Y. Bykov, T. V. Murzina, D. N. Neshev, and Y. S. Kivshar, "Functional and nonlinear optical metasurfaces," Laser Photon. Rev. **9**, 195–213 (2015).
3. J. Lee, M. Tymchenko, C. Argyropoulos, P. Y. Chen, F. Lu, F. Demmerle, G. Boehm, M. C. Amann, A. Alù, and M. A. Belkin, "Giant nonlinear response from plasmonic metasurfaces coupled to intersubband transitions.," Nature **511**, 65–9 (2014).
4. M. W. Klein, C. Enkrich, M. Wegener, and S. Linden, "Second-harmonic generation from magnetic metamaterials.," Science **313**, 502–4 (2006).
5. N. Segal, S. Keren-Zur, N. Hendler, and T. Ellenbogen, "Controlling light with metamaterial-based nonlinear photonic crystals," Nat. Photonics **9**, 180–184 (2015).
6. S. Keren-Zur, O. Avayu, L. Michaeli, and T. Ellenbogen, "Nonlinear beam shaping with plasmonic metasurfaces," ACS Photonics **3**, 117–123 (2016).
7. A. Shapira, R. Shiloh, I. Juwiler, and A. Arie, "Two-dimensional nonlinear beam shaping," Opt. Lett. **37**, 2136 (2012).
8. T. Ellenbogen, I. Dolev, and A. Arie, "Mode conversion in quadratic nonlinear crystals.," Opt. Lett. **33**, 1207–9 (2008).

# Electrically Tunable Metasurface Absorber

**Ju-Hyung Kang[1*], Junghyun Park[1], and Mark L. Brongersma[1]**

[1]Geballe Laboratory for Advanced Materials, Stanford University, Stanford, California 94305, USA

[*]corresponding author: kangjuhy@stanford.edu

**Abstract**- We propose an electrically tunable optical absorber in the infrared regime by using the indium-tin-oxide (ITO) as the electrically tunable material in the metal-insulator-metal cavities which support localized surface plasmons. The depletion and accumulation operations at the epsilon-near-zero (ENZ) wavelength regime of the ITO give rise to dramatic changes in the carrier concentration in the ITO, which in turn lead to unprecedentedly substantial changes in the optical absorption. Our proposed configuration presents the immense potential of a number of important applications such as photodetectors, optical sensors, tuning of thermal emission, and active metasurface devices.

Novel concept of plasmonic absorbers has attracted significant interest due to their unprecedented strong absorption with insensitivity on incident angle and polarization state[1]. As a next logical step, there have been tremendous efforts to implement actively controllable plasmonic absorbers[2]. Although considerable research has been devoted to development of tunable absorbers, it still remains difficult to realize highly efficient ability of electrical tuning. In this study, we present an electrically tunable optical absorber in the infrared regime.

Figures 1a–c show the configuration of the electrically tunable optical absorber. Electrically tunable layer (ITO) and the dielectric spacer ($HfO_2$) are sandwiched between the top metallic gratings and the bottom metallic planar layer which support gap plasmon[3]. Electrical voltage is applied between the bottom Au and the ITO (Fig. 1b). By using standard e-beam lithography and lift-off process, the top Au gratings are fabricated on a regime where the ITO layer and the bottom Au are overlapped (Fig. 1c). The cross-sectional view of the structure is schematically depicted in Fig. 1d. The incident light is coupled to the metal-insulator-metal (MIM) gap plasmons when it suffices the resonance condition. The gap plasmons run back and forth to form the localized surface plasmon resonance of which electromagnetic energy is strongly confined in deep subwavelength gap and thus the light in the active layer can be efficiently modulated due to high confinement factor (Fig. 1e). The coupled optical energy is absorbed and dissipated in top and bottom metals so that the reflection spectrum exhibits dips at the resonance wavelength (Fig. 1f). By tuning the optical property of the active layer under electric gating, the resonance condition can be significantly changed, which in turn results in substantial changes in reflection signals.

The reflection spectra are measured by using the Fourier Transform infrared (FT-IR) microscopy (Fig. 1f). The red curve corresponds to a case without any bias. As we apply the positive bias to the ITO layer from 0 V to +5 V with 1 V step size, the carriers in the ITO are depleted and the reflection spectrum gradually changes to the green curve. For the negative bias at ITO from 0 V to -5 V, the electrons are accumulated at the interface between the ITO and $HfO_2$ layers and we also observe changes in the reflection spectrum to the blue curve. It is noteworthy that the devised structure shows unprecedentedly significant modulation; at the wavelength at 3.7 μm the reflection signal switches between 45% and 59%.

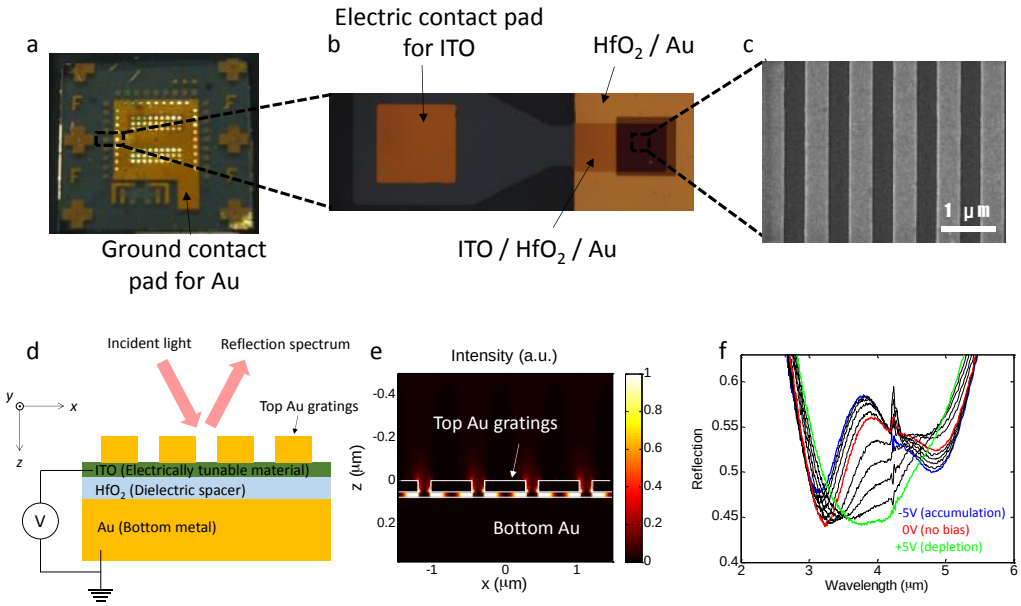



Figure 1. Optical image of a. the fabricated sample, b. electric contact pad for ITO and the Au grating area on the ITO/$HfO_2$/Au region. c. Scanning electron microscopy (SEM) image of the Au gratings. The size of the grating region is 100 μm. d. Schematic diagram of the tunable optical absorber. The $HfO_2$ layer plays roles of the dielectric spacer and the electrical insulating layer. The bottom Au is grounded with the ITO layer being connected with an external voltage source. The top Au grating and the bottom Au layer support the gap plasmons. e. Intensity distribution of the gap plasmons with the first-order Fabry-Pérot resonance. The significantly enhanced electric field has a strong overlap with the active layer, allowing for efficient modulation. f. Reflection spectra measured by FT-IR microscope. The red, blue, and green curves denote the reflection spectra under no bias, -5 V for accumulation, and +5 V for depletion, respectively, whereas the black curves represent those under the intermediate voltage with incremental step size of 1 V.

These innovative strategies allow for hitherto inaccessible efficiency and establish momentous milestones for other active plasmonics applications such as modulators and switches in the plasmonic nano-circuits, optical sensors, and thermal emitters. In addition, the conductivity of the ITO empowers us to further envisage more complex nano-structures with higher degree of freedom, facilitating the realization of various tunable metasurfaces for synthesis of light field, beam phase manipulation, and on-demand local heat generation.

## REFERENCES


1. Liu, N., M. Mesch, T. Weiss, M. Hentschel, and H. Giessen, “Infrared perfect absorber and its application as plasmonic sensor,” *Nano Lett.* Vol. 10, 2342–2348, 2010.
2. Yao, Y., R. Shankar, M. A. Kats, Y. Song, J. Kong, M. Loncar and F. Capasso, “Electrically tunable metasurface perfect absorbers for ultrathin mid-infrared optical modulators,” *Nano Lett.*, Vol. 14, 6526–6532, 2014.
3. Park, J., J.-H. Kang, X. Liu, and M. L. Brongersma "Electrically tunable epsilon-near-zero (ENZ) metafilm absorbers," Scientific Reports , Vol. 5, 15754, 2015.

# Tunable metasurfaces for active manipulations of electromagnetic waves

**Ziqi Miao [1], Che Qu [1], Shaojie Ma[1], Shulin Sun[2], Qiong He[1] and Lei Zhou[1*]**

[1] Physics Department, Fudan University, Shanghai 200433, China

[2]Department of Optical Science and Engineering, Fudan University, Shanghai 200433

[*]corresponding author: phzhou@fudan.edu.cn

Metasurfaces, ultrathin metamaterials composed by array of planar "meta-atoms" with pre-designed electromagnetic (EM) properties, have attracted extensive attention recently [1-3]. However, so far the realized metasurfaces are mostly passive systems [1-3], which cannot be used to dynamically control EM waves.

In this talk, we briefly summarize our recent efforts in making tunable metasurfaces to actively control EM waves. We first present a complete phase diagram that can describe the functionalities of diversified meta/insulator/metal (MIM) metasurfaces in a unified framework [4]. Inspired by such a complete phase diagram, we show that a wide-range dynamical phase modulation in the THz regime can be achieved by combining gate-controlled graphene with MIM metasurfaces, where graphene plays as a tunable loss to drive an underdamped to overdamped resonator transition [5]. Finally, we present our latest experimental efforts in making tunable metasurfaces to overcome several key restrictions that are inherent to their passive counterparts, and a practical way to realize surface plasmon coupler with very high efficiency.

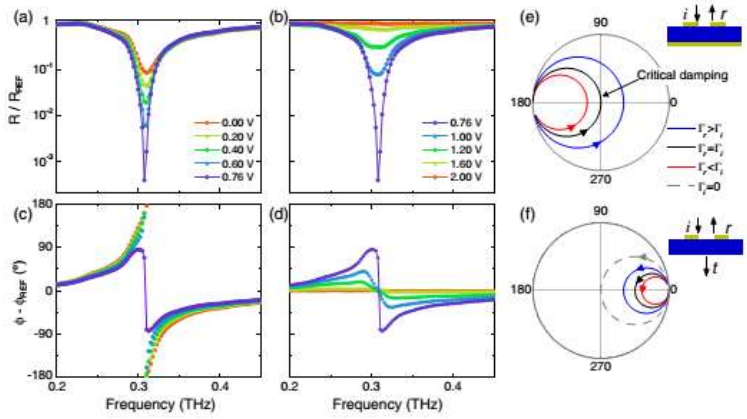



Figure 1. Reflection amplitude/phase modulation in a gate-controlled graphene metasurface, and a coupled-mode model to interpret the critical transition.

## REFERENCES

1. Shulin Sun, et al.,"Gradient-index meta-surfaces as a bridge linking propagating waves and surface waves", Nature Materials 11, 426-431 (2012).
2. Shulin Sun, *et al.*, "High-Efficiency Broadband Anomalous Reflection by Gradient Meta-Surfaces", Nano Lett. 12, 6223−6229 (2012).
3. Nanfang Yu & Federico Capasso, "Flat optics with designer metasurfaces", Nature Materials 13,139–150(2014)

4. Che Qu, *et al*., “Tailor the functionalities of metasurfaces based on a complete phase diagram”, Phys. Rev. Lett. 115, 235503 (2015)
5. Ziqi Miao, *et al*., “Widely Tunable Terahertz Phase Modulation with Gate-controlled Graphene Metasurfaces”, Phys. Rev. X 5, 041027 (2015).

# Tunneling rectification in an infrared nanoantenna coupled MOS diode

**P. S. Davids**[1], **E. A. Kadlec**[1], **S. W. Howell**[1],**and D. W. Peters**[1]

[1]Sandia National Labs, Albuquerque, NM, USA
pdavids@sandia.gov

**Abstract**— We present experimental results that demonstrate direct tunneling rectification of infrared light in a large area nanoantenna coupled tunnel diode. This represents a new thermo-electric conversion mechanism for transformation of waste heat in the form of infrared radiation into electrical current.

The interplay of strong infrared photon-phonon coupling and electromagnetic (EM) confinement in nanoscale devices is demonstrated to have a large impact on ultrafast electronic tunneling in metal oxide semiconductor (MOS) structures[1]. An integrated nanoantenna structure on a distributed large area MOS tunnel diode rectifier designed to efficiently couple infrared radiation into the tunnel diode is shown to effectively channel infrared radiation into nanometer scale gaps in these MOS devices. lnfrared active optical phonon modes in oxides lead to strong dispersion and enhanced EM fields at material interfaces [2]. We find that the infrared dispersion of $SiO_2$ near a longitudinal optical (LO) phonon mode gives large transverse field confinement in a nanometer scale oxide tunnel gap as the wavelength-dependent permittivity changes from 1 to 0. The strong epsilon-near zero (ENZ) mode [3] concentrates the transverse field in the oxide tunnel diode gap. This enhanced gap transverse field results in a rectified displacement current[4] and enhanced direct conversion of infrared radiation. The spectral and electrical signatures of the nanoantenna coupled tunnel diodes are examined.

Figure 1 shows schematically and cross-sectional SEM cuts of the large area nanoantenna coupled diode that is designed to work with blackbody illumination that corresponds to the ENZ mode in the thin oxide tunnel barrier. Fogure 1(e) show the impact of enhanced tunneling current under incoherent blackbody illumination with and without a long-pass infrared filter. Figure 1 (f) shows the polarization response of the photocurrent under quantum cascade laser illumination in band where ENZ mode enhancement is strongest.

In this talk, we will present new 2D structures that further increase the field confinement in the tunnel oxide. The increased ENZ mode enhancement shows large tunnel currents in the large area structures. We will also present new results illustrating the tunneling nature of the rectification and advanced microradiometric measurement of the infrared photocurrent in energy harvesting configurations.

## ACKNOWLEDGMENT

Funding for this work was provided by Sandia's Laboratory Directed Research and Development (LDRD) program and the Department of Defense. Sandia is a multiprogram laboratory operated by Sandia Corporation, a Lockheed Martin Company, for the United States Department of Energy's National Nuclear Security Administration under contract DE-AC04-94AL85000.

## REFERENCES

1. P. S. Davids, R. L. Jarecki, A. Starbuck, D. B. Burckel, E. A. Kadlec, T. Ribaudo, E. A. Shaner, and D. W. Peters., Infrared rectification in a nanoantenna-coupled metal-oxide-semiconductor tunnel diode, *Nat Nanotechnol*, 10(12):10331038, 2015.
2. B. Song, Y. Ganjeh, S. Sadat, D. Thompson, A. Fiorino, V. Fern andez-Hurtado, J. Feist, F. J. Garcia- Vidal, J. C. Cuevas, P. Reddy, Enhancement of near-field radiative heat transfer using polar dielectric thin films. *Nature nanotechnol*, 10(3):253258, 2015.
3. B. Edwards, A. Alu', M. Young, M. Silveirinha, and N. Engheta, Experimental Verification of Epsilon- Near-Zero Metamaterial Coupling and Energy Squeezing Using a Microwave Waveguide, *Physical Review Letters*, 100(3):14, Jan. 2008.
4. A. Stolz, J. Berthelot, M. M. Mennemanteuil, G. Colas Des Francs, L. Markey, V. Meunier, and A. Bouhelier, Nonlinear photon-assisted tunneling transport in optical gap antennaa, *Nano Letters*, 14(5):2330 2338, 2014.

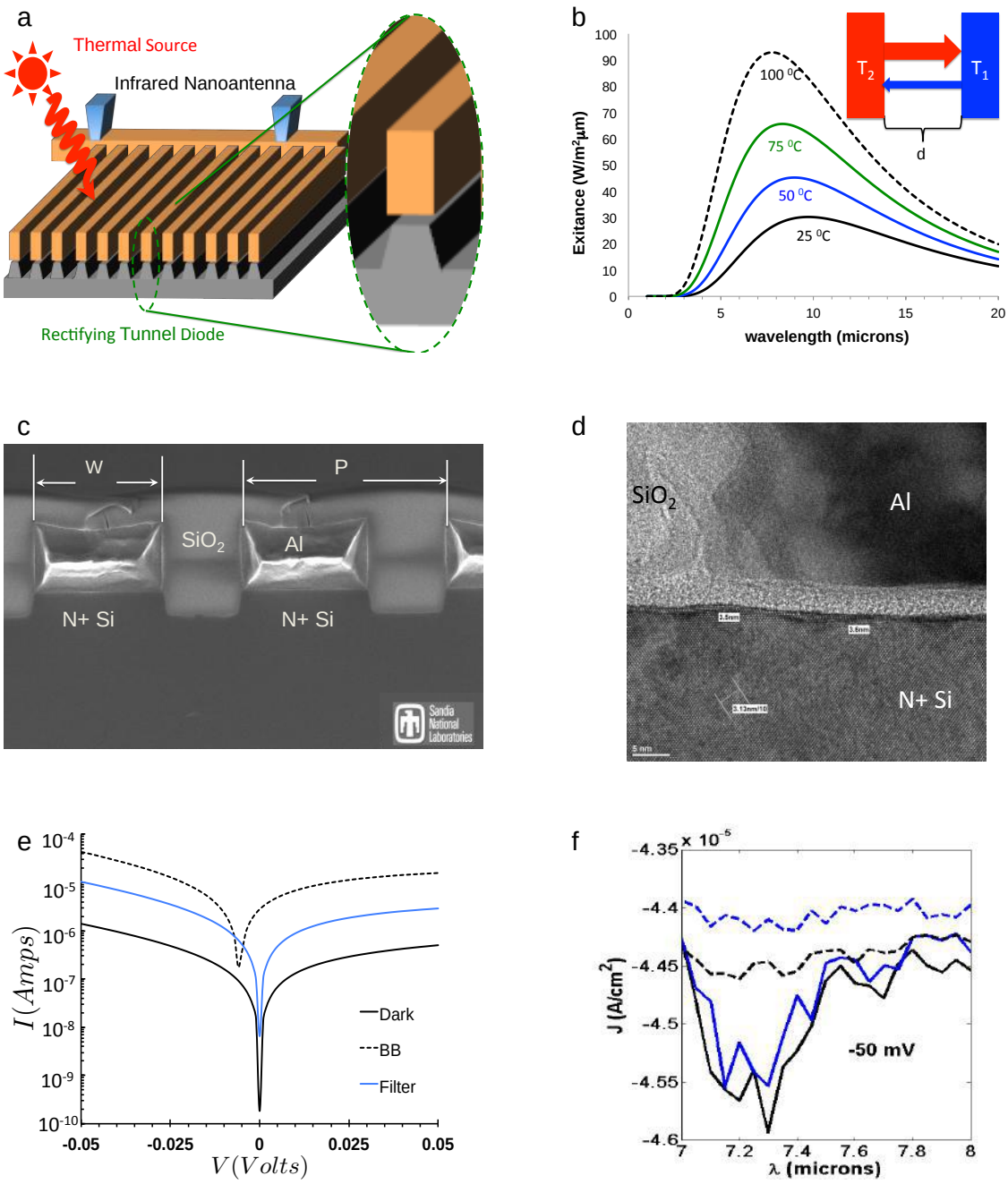



Figure 1: Nanoantenna coupled n-type MOS tunnel diode. (a) The schematic in the left panel shows the large area nanoantenna coupled diode illuminated by a thermal source. The inset shows an enlarged cross-section of the tunnel diode that consists of a thick Al top contact, a 3-5 nm thick thermal oxide on a heavily doped n-type Si substrate encased in HDP oxide. (b) Black-body exitance in power per unit area ($m^2$) per micron of bandwidth for various temperatures (25 C, 50 C,75 C, 100 C). The inset shows a schematic planar geometry with thermal source $T_2$ and cooler rectenna at $T_1$. (c) A cross-sectional SEM of the actual nanoantenna structure. The period (P=3.0$\mu$m) and the width (W=1.8$\mu$m) are illustrated. The metal antenna is covered in oxide and polished flat with the oxide approximately 200 nm over the Al contact and the Si is over-etched by approximately 200 nm. (d) Transmission electron micrograph showing the thin oxide tunnel barrier on the n-type Si substrate. (e) Current voltage sweeps under blackbody, infrared only and dark illumination. (f) Quantum cascade laser scans through infrared for TE (dashed) and TM (solid) polarization.

# 3D plasmonic resonators for sensing and metadevice

**Wei-Yi Tsai[1], Ching-Fu Chen[2], Mu-Ku Chen[1], Pei Ru Wu[1], Yi-Hao Chen[1], Ting-Yu Chen[1], Jia-Wern Chen[1], Cheng Hung Chu[2], Wei Ting Chen[1], Ming Lun Tseng[2], Yao-Wei Huang[2], Pin Chieh Wu[2], Chun Yen Liao[1], Huijun Wu[2], Wen Ting Hsieh[2], Shiang-Jiu Wang[2], Hung-I Lin[2], Greg Sun[3], Ai Qun Liu[4], and Nikolay I. Zheludev[5], Din Ping Tsai[1,2*]**

[1]Department of Physics, National Taiwan University, Taipei 10617, Taiwan

[2]Research Center for Applied Sciences, Academia Sinica, Taipei 11529, Taiwan

[3]Department of Physics, University of Massachusetts Boston, Boston, Massachusetts 02125, USA

[4]School of Electrical and Electronic Engineering, Nanyang Technological University, Singapore 639798, Singapore

[5]Optoelectronics Research Centre, University of Southampton, Southampton SO17 1BJ, UK

*corresponding author, E-mail: dptsai@phys.ntu.edu.tw

**Abstract**- Plasmonic metamaterials composed of artificial structures in subwavelength scale exhibit many novel properties for light manipulation and photonic device. Split-ring resonator (SRR), one kind of building block of metamaterials, has attracted wide attentions due to the resonance excitation of electric and magnetic dipolar response. Fundamental plasmon properties and potential applications in novel three dimensional vertical split-ring resonators (VSRRs) are designed and investigated. The resonant properties arose from the electric and magnetic interactions between the VSRR and light are theoretically and experimentally studied. Tuning the configuration of VSRR unit cells is able to generate various novel coupling phenomena in VSRRs, such as plasmon hybridization and Fano resonance. The magnetic resonance plays a key role in plasmon coupling in VSRRs. The VSRR-based refractive-index sensor will be demonstrated, as shown in Figs. 1. Due to the unique structural configuration, the enhanced plasmon fields localized in VSRR gaps can be lifted off from the dielectric substrate, allowing for the increase of sensing volume and enhancing the sensitivity. We perform a VSRR based metasurface for light manipulation in optical communication frequency, as shown in Fig. 1 as well. By varying the prong heights, the 2π phase modulation can be achieved in VSRR for the design of metasurface. Because the phase shift is changed via the upright configuration rather than the one parallel to the substrate, it can be used for high areal density integration of metal nanostructures and opto-electronic devices. Fabrication of three dimensional VSRR by stress-driven assembly method for uniaxial-isotropic metamaterials are demonstrated as well.

**Acknowledgements** The authors acknowledge financial support from Ministry of Science and Technology, Taiwan (Grant Nos.104-2745-M-002-003-ASP) and Academia Sinica (Grant No. AS-103-TP-A06). They are also grateful to National Center for Theoretical Sciences, Molecular Imaging Center of National Taiwan University, National Center for High-Performance Computing, Taiwan, and Research Center for Applied Sciences, Academia Sinica, Taiwan for their supports.

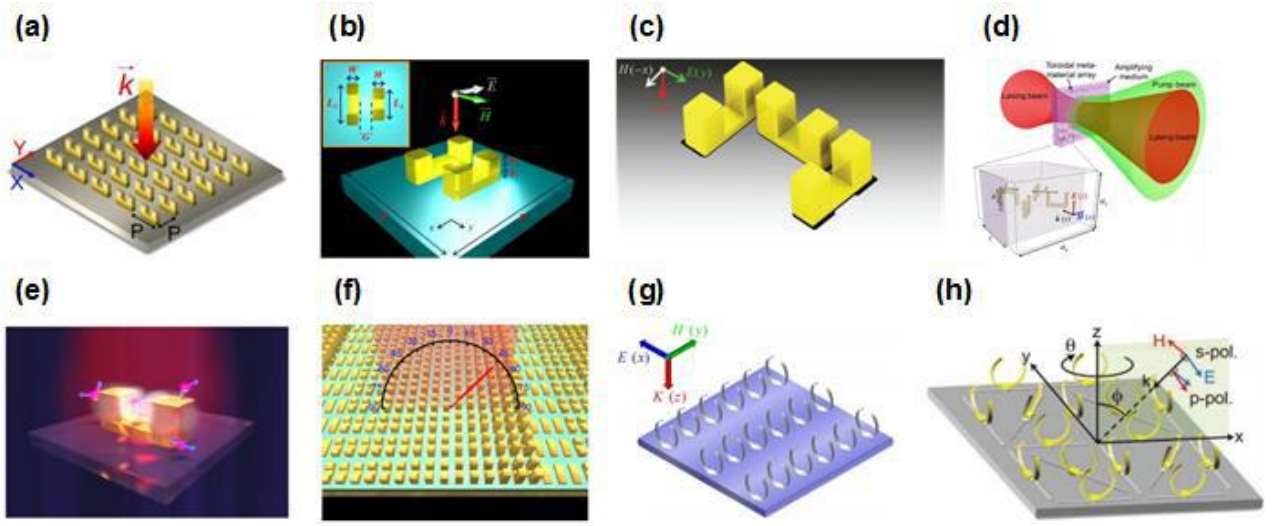



**Fig. 1.** Schematic diagrams for (a) VSRR (b) VSRR based plasmon coupling, (c) Fano resonance, (d) toroidal metamaterial, (e) nanoplasmonic sensor, (f) metasurface, (g) tunable VSRR and (h) uniaxial-isotropic metamaterials.

**REFERENCES**


1. Y.-W. Huang, W. T. Chen, P. C. Wu, V. Fedotov, V. Savinov, Y. Z. Ho, Y.-F. Chau, N. I. Zheludev, and D. P. Tsai, F. M. "Design of plasmonic toroidal metamaterials at optical frequencies," *Opt. Express* 20, 1760–1768, 2012.
2. Y.-W. Huang, W. T. Chen, P. C. Wu, V. A. Fedotov, N. I. Zheludev, D. P. Tsai, "Toroidal lasing spaser," *Sci. Rep.* 34, 1237, 2013.
3. S. Sun, K.-Y. Yang, C.-M. Wang, T.-K. Juan, W. T. Chen, C. Y. Liao, Q. He, S. Xiao, W.-T. Kung, G.-Y. Guo, L. Zhou, D. P. Tsai, "High-efficiency broadband anomalous reflection by gradient meta-surfaces," *Nano Lett.* 12, 6223–6229, 2012.
4. W. T. Chen, K.-Y. Yang, C.-M. Wang, Y.-W. Huang, G. Sun, I-Da Chiang, C. Y. Liao, W.-L. Hsu, H. T. Lin, S. Sun, L. Zhou, A. Q. Liu, D. P. Tsai, "High-efficiency broadband meta-hologram with polarization-controlled dual images," *Nano Lett.* 14, 225, 2014.
5. P. C. Wu, W.-L. Hsu, W. T. Chen, Y.-W. Huang, C. Y. Liao, A. Q. Liu, N. I. Zheludev, G. Sun, and D. P. Tsai, " Plasmon coupling in vertical split-ring resonator metamolecules," Sci. Rep. 5, 9726, 2015.
6. P. C. Wu, W. T. Chen, K.-Y. Yang, C. T. Hsiao, G. Sun, A. Q. Liu, N. I. Zheludev, D. P. Tsai, "Magnetic plasmon induced transparency in three-dimensional metamolecules," Nanophotonics 1, 131-138, 2012.
7. P. C. Wu, G. Sun, W. T. Chen, K.-Y. Yang, Y.-W. Huang, Y.-H. Chen, H. L. Huang, W.-L. Hsu, H. P. Chiang, D. P. Tsai, "Vertical split-ring resonator based nanoplasmonic sensor," *Appl. Phys. Lett.* 105, 033105, 2014.
8. W.-L. Hsu, P. C. Wu, J.-W. Chen, T.-Y. Chen, B. H. Cheng, W. T. Chen, Y.-W. Huang, C. Y. Liao, G. Sun, and D. P. Tsai, "Vertical split-ring resonator based anomalous beam steering with high extinction ratio," *Sci. Rep.* 5, 11226, 2015.
9. C. C. Chen, C. T. Hsiao, S. L. Sun, K.-Y. Yang, P. C. Wu, W. T. Chen, Y. H. Tang, Y.-F. Chau, E. Plum, G.-Y. Guo, N. I. Zheludev, D. P. Tsai, "Fabrication of three dimensional split ring resonators by stress-driven assembly method," *Opt. Express* 20, 115-120, 2012.
10. C.-C. Chen, A. Ishikawa, Y.-H. Tang, M.-H. Shiao, D. P. Tsai, T. Tanaka, "Uniaxial-isotropic metamaterials by three-dimensional split-ring resonators," *Adv. Opt. Mater.* 3, 44-48, 2015.

# Network metamaterials: An alternative platform for optical materials

**H. Galinski**[1], **A. Fratalocchi**[2], **and F. Capasso**[3]

[1]Laboratory for Nanometallurgy, Department of Materials, ETH Zürich, Zurich, Switzerland
[2]PRIMALIGHT, Faculty of Electrical Engineering, Applied Mathematics and Computational Science, KAUST, Thuwal, Kingdom of Saudi Arabia
[3]Harvard John A. Paulson School of Engineering and Applied Sciences, Harvard University, Cambridge, USA
henning.galinski@mat.ethz.ch

**Abstract**—

The massive exploitation of metamaterials caused a leap in controlling light at the nanoscale, bringing forward a manifold of entirely new functionalities. Traditionally the design of metamaterials has been inspired by the assembly of periodically spaced building blocks, which control their optical properties.

Here, I will discuss a new class of optical materials, dubbed network metamaterials. The key design principle is a sub-wavelength network with functional connectivity in analogy to other robust networks, such as the internet. Using experiments and theory, we demonstrate that network metamaterials harbor unexpected optical properties, such as structural color. We discuss the physical origin of these optical properties and point out several strategies to deterministically control them.

Metamaterials are engineered subwavelength structures designed to control electromagnetic fields. State-of-the-art metamaterials are highly influenced by microelectronic circuits design, which manifests in the systematic assembly of well defined and understood elements in periodic arrays [1, 2]. In this paper we endeavor to leave this path and focus on the use of metallic nanoscale networks, sustaining plasmonic resonances. At variance with classical metasurface, which are mostly lattice-based structures, the key element of network architecture is the local connectivity between different elements. Figure 1 illustrates this idea. Complex networks arise in many different fields, a prominent example of optical network metamaterials in nature are the blue fearther barbs of the *Cotayna Mayanana* [3]. The non-iridescent blue color of these feathers is produced by an aperiodic nanoporous keratin network with a typical feature size smaller 200 nm [3].

Inspired by these structures, we here use this network design principle to fabricate nano-photonic structures based on metallic nanoscale networks by dealloying. Dealloying is a versatile wet-echting technique [4], that allows to structure large areas in a fast and cost-effective fashion. In a series of experiments and Finite-Difference Time-Domain (FDTD) and Finite Element (FE) simulations, we investigate the light-matter interactions in Pt-based nanoscale networks. We demonstrate that the optical response of our complex structures is driven by the average connectivity of the metallic network. In combination with an ultra-thin "lossless" dielectric coating, a wide range of vibrant and highly saturated structural colors can be generated in these network metamaterials. These colors cannot be explained by thin-film interference effects, but are result of the selective coupling of light to a broad spectrum of resonant plasmonic modes in a non-uniform nano-cavity medium.

Furthermore, I will discuss our ongoing efforts to use network metamaterials as versatile platform to engineer new passive and active metamaterials.

The network metamaterials introduced in this work open up new possibilities to extend the application of metamaterials to areas where large active regions are mandatory. The possible applications include efficient light trapping layers in photovoltaics and pigment free automotive paints.

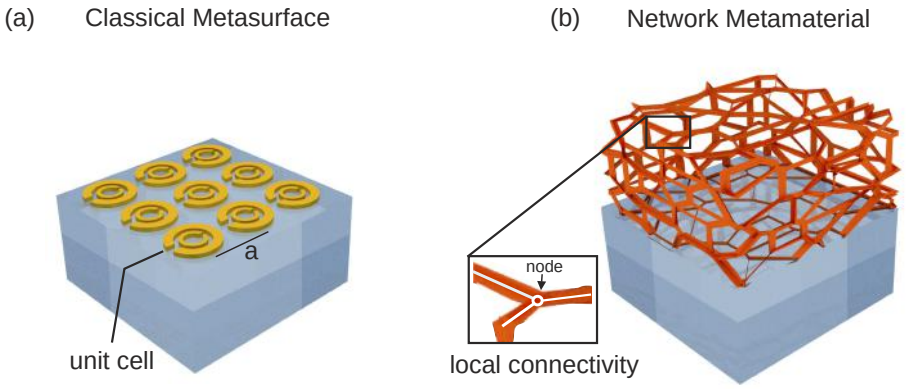



Figure 1: Network metamaterials versus classical metasurfaces: design principles. Panel (a) shows the design scheme of a classical metasurface, composed by the periodic patterning of identical units, here split ring resonators (SRR). Here each unit and their separation $a$ is significantly smaller than the design wavelength. In this architectural scheme, the material homogenizes the array of unit cells into a response that depends solely on the electromagnetic properties of the basic component. Panel (b) shows the working scheme of a network metamaterial. This system does not encompass unit cells, but conversely a network defined by its connectivity. The response of the system is a complex interaction among all the components of the network.

## ACKNOWLEDGMENT

H. Galinski gratefully acknowledges financial support from the "Size Matters! project" (TDA Capital, London, UK).
H. Galinski and F. Capasso acknowledge funding from AFOSR contract FA9550-14-0389 (MURI).
A. Fratalocchi and F. Capasso acknowledge funding from KAUST (Award No. CRG-1-2012-FRA-005).

## REFERENCES

1. Engheta, N., "Circuits with Light at Nanoscales: Optical Nanocircuits Inspired by Metamaterials," *Science*, Vol. 317, 1698–1702, 2007.
2. Yu, N., and Capasso, F., "Flat optics with designer metasurfaces," *Nature Materials*, Vol. 13, 139–150, 2014.
3. Prum, R. O. and Torres, R. H. and Williamson, S., and Dyck, J., "Coherent light scattering by blue feather barbs," *Nature* Vol. 396, 28-29, 1998.
4. Galinski, H. *et al.*, "Platinum-Based Nanowire Networks with Enhanced Oxygen-Reduction Activity," *Phys. Rev. Applied*, Vol. 2, No. 5, 054015, 2014.

# Reconfigurable Metasurfaces Based on Graphene and Indium Tin Oxide Materials

**A. Forouzmand[1], J. Cheng[1], and H. Mosallaei[1*]**
[1]Computational EM and Physics Laboratory, Electrical and Computer Engineering Department,
Northeastern University, Boston, Massachusetts 02115, USA
[*] hosseinm@ece.neu.edu

**Abstract**- Here, a leaky wave antenna is designed capable of full control over beam-width and beam steering direction in both elevation and azimuth planes operating at low-terahertz frequencies. In addition, a tunable dual-band reflectarray antenna is proposed by integration of a thin layer of indium tin oxide into a plasmonic double metal/insulator/metal ribbons unit-cell. An array of unit-cells with one-dimensional voltage biasing distribution creates a reconfigurable meta-lens with functionalities as bending, focusing, and beam shaping at two distinct near-infrared frequencies.

In recent years, electrically tunable metasurfaces have evolved as an attractive candidate for applications such as beam steering and shaping, holography, reflectarrays, and absorbers. In general, the physical mechanism behind these techniques is control over the surface impedance. Consequently, the reflection/transmission phase characteristics, surface-wave propagation, and leaky wave radiation of the structure can be tailored based on the requirements in desired applications. The characteristics of conventional antennas cannot be tuned after fabrication. Recently, the advent of gate-tunable materials (particularly, graphene and indium tin oxide) provides interesting material platforms for reconfigurable metasurfaces from terahertz to infrared. Graphene has versatile tunability by the change of electrochemical potential via chemical doping, magnetic field, and electrostatic gating. In addition, the integration of transparent conducting oxide materials like indium tin oxide (ITO) into a metasurface could add the significant advantage of reconfigurable functionality even after fabrication.

First, we propose a leaky wave antenna which offers dynamic beam scanning in both elevation and azimuth planes by simply applying two groups of one-dimensional (1D) gate biasing on the sides of a layer of graphene as a gate tunable material. The configuration of leaky wave antenna is depicted in Fig. 1(a). A large-scale pristine graphene is placed on top of the gate biasing vertical and horizontal strips with a thin layer of silicon dioxide ($SiO_2$) in-between. The direction of the surface wave propagation ($\alpha$) in *x*-*y* plane can be controlled by biasing pad group A. Pad group B provides sinusoidal impedance modulation which is necessary for the generation of leaky wave radiation. In other words, the radiation in $\varphi$ direction is mainly adjusted by pad group A and in $\theta$ by pad group B. The two groups of orthogonal and decoupled biasing allow for dynamic control of the beam radiation toward any desired two-dimensional (2D) direction, where the voltages can be simply applied on the two sides of the structure. The analysis is carried out using holographic design technique [1, 2] in which the relation between the radiation direction [$\theta$, $\varphi$], surface wave direction, and the impedance modulation is addressed. In this design, beam direction and beam-width can be reconfigurable by simple variation of the voltage combinations. In the presentation, several designs with variant beam-widths and radiation directions will be given along with the numerical results.

Second, an electrically tunable reflectarray capable of operating at two distinct frequencies in near-infrared regime is designed. The integration of a thin layer of ITO into a double metal/insulator/metal ribbons (bi-MIM) as building block of plasmonic reflectarray antenna leads to the design of a reconfigurable meta-lens with variant functionalities at two distinct frequencies. The control over phase and amplitude of the reflected beam is achieved via the tunable gate biasing of ITO. The desired functionality (bending, focusing, and beam shaping) can be attained by the proper distribution of applied bias voltages to an array of unit-cells. The design has been carried out in such a way that the compactness of the unit-cell remains promising although includes two nano-ribbons. The schematic of the electrically tunable plasmonic reflectarray is shown in Fig. 1(b). As depicted, the unit-cell is made of the combination of two MIM ribbons infinite along the $z$-axis. The double-resonance nature of the unit-cell is exploited to achieve two distinct operating frequencies. The strength and position of each resonance can be tailored independently by changing the width of the corresponding nano-ribbon [3]. By increasing the bias between the gold nano-ribbon and the back mirror, the carrier concentration in ITO (at the $Al_2O_3$-ITO interface) increases and creates an accumulation layer [4]. The significant phase change of the reflected beam occurs due to the zero-crossing of permittivity of active layer of ITO [5]. Here, an array of bi-MIMs is utilized in order to realize a dual-band bending lens. The angle of bending ($\theta_b$) can be controlled by adjusting the 1D voltage biasing distribution as shown in Fig. 1(b).

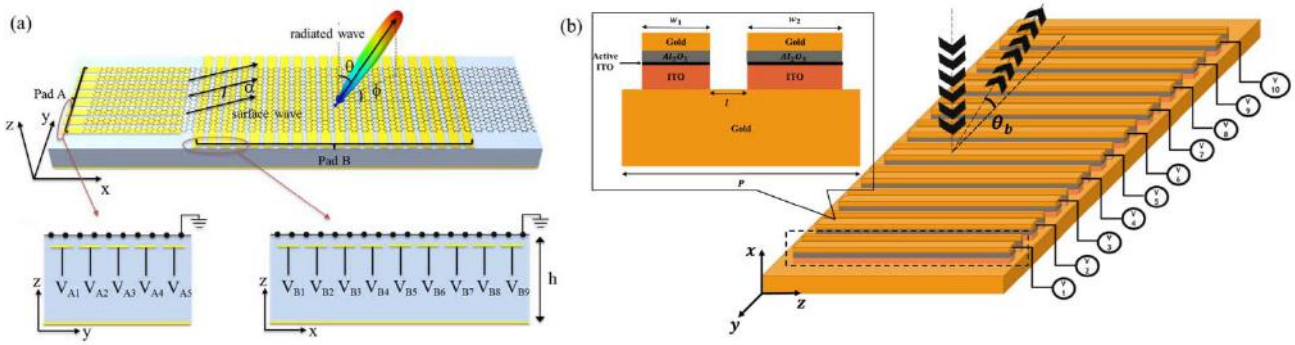



Figure 1. Reconfigurable metasurfaces, (a) a graphene leaky wave antenna for dynamic beam scanning towards any spatial 2-D direction [$\theta$, $\varphi$] and (b) the ITO plasmonic reflectarray metasurface for tunable dual-band beam manipulation.

**Acknowledgements**, This work was supported by the Air Force Office of Scientific Research (AFOSR) with grant No. #FA9550-14-1-0349.

**REFERENCES**

1. Fong, B. H., J. S. Colburn, J. J. Ottusch, J. L. Visher, and D. F. Sievenpiper, "Scalar and tensor holographic artificial impedance surfaces," *IEEE Trans. Antennas and Propag.*, Vol. 58, No. 10, 3212-3221, 2010.
2. Farmahini-Farahani, M. and H. Mosallaei, "Functional-graded index metasurfaces for infrared radiation and guiding," *IEEE Trans. Nanotechnol.*, Vol. 14, No. 1, 75-81, 2015.
3. Koechlin, C., P. Bouchon, F. Pardo, J.-L. Pelouard, and R. Haïdar, "Analytical description of subwavelength plasmonic MIM resonators and of their combination," *Opt. Express*, Vol. 21, No. 6, 7025-7032, 2013.
4. Yi, F., E. Shim, A. Y. Zhu, H. Zhu, J. C. Reed, and E. Cubukcu, "Voltage tuning of plasmonic absorbers by indium tin oxide," *Appl. Phys. Lett.*, Vol. 102, No. 22, 221102, 2013.
5. Huang, Y. W., H. W. Lee, R. Sokhoyan, R. Pala, K. Thyagarajan, S. Han, D. P. Tsai, and H. A. Atwater, "Gate-tunable conducting oxide metasurfaces," *arXiv preprint arXiv*: 1511.09380, 2015.

# Widely Tunable Optical Antennas for Reconfigurable Metasurfaces

**T. Lewi[1], P. P. Iyer[1], N.A. Butakov[1], and J. A. Schuller[1*]**
Electrical and Computer Engineering Department, UC Santa Barbara, CA, USA
[*]corresponding author: jonschuller@ucsb.edu

**Abstract**-The ability to engineer the optical phase at subwavelength dimensions has led to metasurfaces that provide unprecedented control of electromagnetic waves. To reach their ultimate potential, metasurfaces must incorporate reconfigurable functions. The central challenge is achieving large tunability in subwavelength elements. Here, we describe three different approaches for achieving order-unity index: free-carrier refraction, thermo-optic tuning, and metal-insulator transitions. We demonstrate wide tuning of single-particle infrared Mie resonances, and describe ongoing efforts to achieve tuning via electrical or optical gating.

The ability to engineer the scattering *phase* of subwavelength metamaterial constituents offers tremendous potential for constructing new classes of beam steering, shaping, and focusing technologies. Current methods for engineering phase rely on static geometry-based effects. In this talk we describe methods to *dynamically* tune the scattering phase of infrared semiconductor nanoantennas.

Mie resonances in high refractive dielectrics and semiconductors provide an alternative to metals for making metamaterials and metasurfaces. We fabricate Mie resonators via two approaches. In a top-down approach we use photolithography to define resonant nano-disks. In a bottom-up approach we fabricate spherical semiconductor nanoparticles via femtosecond laser ablation. We measure size dependent Mie resonances of individual structures throughout the mid-infrared. We demonstrate large shifts in Mie resonance wavelengths corresponding to order-unity refractive index tuning in three different material classes. In semiconductors, we see large shifts due to free-carrier refraction that agree with simple Drude models [1]. In chalcogenides and complex oxides we demonstrate large shifts due to thermo-optic effects and metal-insulator transitions respectively. Using a combination of theoretical and analytical calculations we show how such effects can enable reconfigurable optical antennas and metasurfaces. In particular, we demonstrate metasurface design where electrical pumping can tune the transmission or reflection phase by $2\pi$ while maintaining near-unity amplitude [2]. Such dynamic tuning will enable reconfigurable photonic devices based on optical antenna and metamaterial concepts.

**Acknowledgments:** This work was supported by the Air Force Office of Scientific Research Young Investigator Program (FA9550-13-1-0182) and by the UC Office of the President Multicampus Research Programs and Initiatives (MR-15-328528).

**REFERENCES**

1. Lewki, T., Iyer, P. P., Butakov, N.A., Mikhailovsky, A.A., and Schuller, J.A. "Widely Tunable Infrared Antennas Using Free Carrier Refraction," *Nano Lett.*, Vol. 15, 8188, 2015.
2. Iyer, P.P, Butakov, N.A., and Schuller,J.A. "Reconfigurable Semiconductor Phased Array Metasurfaces," *ACS Photon.*, Vol. 2, 1077, 2015.

# Device Applications of Metafilms

**M. L. Brongersma**
Geballe Laboratory for Advanced Materials, Stanford University, Stanford CA 94305, USA
*corresponding author: brongersma@stanford.edu

**Abstract**-Device applications of metafilms are discussed. Metafilms are thin films of semiconductor or metal material that are patterned at a subwavelength scale. The patterning is performed to modify the effective optical properties from those of bulk materials. This can be utilized to realize improved device performance or entirely new optical functions.

Many conventional optoelectronic devices consist of thin, stacked films of metals and semiconductors. In this presentation, I will demonstrate how one can improve the performance of such devices by nano-structuring the constituent layers at length scales below the wavelength of light. The resulting metafilms and metasurfaces offer opportunities to dramatically modify the optical transmission, absorption, reflection, and refraction properties of device layers. This is accomplished by encoding the optical response of nanoscale resonant building blocks into the effective properties of the films and surfaces. To illustrate these points, I will show how nanopatterned metal and semiconductor layers may be used to enhance the performance of solar cells, photodetectors, and enable new imaging technologies. I will also demonstrate how the use of active nanoscale building blocks can facilitate the creation of active metafilm devices.

**REFERENCES**

1. Linyou Cao, Pengyu Fan, Edward S. Barnard, Ana M. Brown and Mark L. Brongersma, "Tuning the Color of Silicon Nanostructures," *Nano Lett.*, 10, 2649–2654. 2010.
2. Linyou Cao, Pengyu Fan, and Mark L. Brongersma "Optical Coupling of Deep-Subwavelength Semiconductor Nanowires,", *Nano Letters* 11, 1463-1468, 2011.
3. Majid Esfandyarpour, Erik C. Garnett, Yi Cui, Michael D. McGehee, and Mark L. Brongersma "Metamaterial mirrors in optoelectronic devices,", *Nature Nanotechnology*, 9, 542-547 (2014).
4. Dianmin Lin, Pengyu Fan, Erez Hasman, and Mark L. Brongersma "Dielectric Gradient Metasurface Optical Elements," *Science*, 345, 298-302, 2014.
5. Junghyun Park,, Ju-hyung Kang, Soo Jin Kim, Erez Hasman, and Mark L Brongersma. "Tuning Optical Absorption in an Ultrathin Lossy Film by Use of a Metallic Metamaterial Mirror." *IEEE Photonics Technology Letters* 27, 1617–1620, 2015.
6. Ho-Seok Ee, Ju-Hyung Kang, Mark L. Brongersma, Min-Kyo Seo, "Shape-Dependent Light Scattering Properties of Subwavelength Silicon Nanoblocks," *Nano Letters*, 15, 1759-1765, 2015.
7. Soo Jin Kim, Pengyu Fan, Ju-Hyung Kang, and Mark L. Brongersma. "Creating Semiconductor Metafilms with Designer Absorption Spectra." *Nature Communications* 6, 7591 (2015).

# Topological darkness of Tamm plasmons for high-sensitivity singular-phase optical detection and tunable thermal emission

**Svetlana V. Boriskina[1,*], Jonathan K. Tong[1], Yoichiro Tsurimaki[1], Bolin Liao[1], Yi Huang[1], Victor N. Boriskin[2], Alexander Semenov[3], Mykola I. Ayzatskiy[2], and Gang Chen[1]**

[1] Department of Mechanical Engineering, Massachusetts Institute of Technology, Cambridge, MA, USA

[2] National Scientific Center 'Kharkiv Institute of Physics and Technology', Kharkiv, Ukraine

[3] Institute for Single Crystals, National Academy of Sciences of Ukraine, Kharkiv, 61001, Ukraine

[*]corresponding author: sborisk@mit.edu

**Abstract**- I will discuss our theoretical and experimental efforts in developing thin multilayered photonic-plasmonic structures that exhibit topologically protected zero reflection if designed to support Tamm plasmon modes. I will demonstrate that light interference within Tamm structures that is accompanied by zero reflection and fast phase variations can be used to improve the sensitivity of bio(chemical) sensors with optical transduction [1,2]. I will show how sharp phase changes associated with the Tamm state excitation can be used to dramatically improve sensitivity of temperature and bio(chemical) sensors. Furthermore, I will discuss the use of the Tamm plasmon structures for spectral tailoring of thermal emission, including dynamic spectral tunability via the use of the phase-change materials [3].

**Acknowledgements**. This work has been supported by the DOE BES Award no. DE-SC0001299 / DE-FG02-09ER46577.

**REFERENCES**

1. Boriskina, S.V., Tong, J.K., Boriskin, V.N., Semenov, A., Aizatsky, N.I., and Chen, G., "Topological darkness of Tamm plasmons for high-sensitivity singular-phase optical detection," submitted, 2016.
2. Boriskin, V.N., Aizatsky, N.I., Boriskina, S.V., Machehin, Y.P., and Semenov, A., "Theoretical and experimental study of temperature-dependent spectral properties of multilayer metal-dielectric nano-film structures," in *Proceedings of ICTON International Conference*, Rome, Italy, July 2007.
3. Boriskina, S.V., Tong, J.K., Hsu, W.-C., Liao, B., Huang, Y., Chiloyan, V., and Chen, G., "Heat meets light on the nanoscale," *Nanophotonics*, 2016, DOI: 10.1515/nanoph-2016-0010.

# Electrostatically Tunable Graphene Metasurfaces for Control of Thermal Radiation

**V. W. Brar[1,2*], L. Kim[1], M. C. Sherrott[1,3], M. S. Jang[4], S. Kim[1], W.-H. Lin[1], M. Choi[4], L. A. Sweatlock[5] and H. A. Atwater[1]**

[1] Thomas J. Watson Laboratory of Applied Physics, California Institute of Technology, Pasadena, California 91125, USA

[2] Physics Department, University of Wisconsin – Madison, Madison, Wisconsin 53706, USA

[3] Resnick Sustainability Institute, California Institute of Technology, Pasadena, California 91125, USA

[4] Global Frontier Center for Multiscale Energy Systems, Seoul National University, Seoul 151-747, Republic of Korea

[5] Nanophotonics and Metamaterials Laboratory, Northrop Grumman Aerospace Systems, Redondo Beach, California 90250, USA

[*]corresponding authors: vbrar@wisc.edu, haa@caltech.edu

**Abstract**- We experimentally demonstrate tunable electronic control of blackbody emission from a graphene metasurface. It is shown that graphene plasmonic resonators produce antenna-coupled thermal emission that can be varied in terms of spectral shape and intensity, and that incandescent devices with Khz response times can be created in this way. We analyze our results in terms of loss mechanisms of graphene electrons and substrate phonons, and we describe how device geometry can be optimized to create larger signals with faster response times.[1]

Thermal radiation is commonly viewed to be broadband, unpolarized, incoherent and isotropic, with a spectral profile and intensity that are dependent on the emissivity of a material, and that vary only with changes in temperature. Recent studies investigating thermal emission from metasurfaces, however, have shown that thermal emission can be highly directional and polarized,[2] with narrow spectral features.[3] By incorporating materials with electrostatically variable optical properties into metasurface structures, thermal emission can also be made dynamic, with spectra that can be dynamically tuned without changing the actual temperature of the surface.

In the present work, we experimentally demonstrate the dynamic tuning of blackbody emission through electronic control of 20 – 60 nm graphene plasmonic nanoresonators on a silicon nitride substrate at temperatures up to 250 C. Our device is based on field effect tuning of the carrier density in nanoresonators, which act as antennas to effectively outcouple thermal energy within the resonator mode volume. We show that through this mechanism the thermal radiation generated by substrate phonons and inelastic electron scattering in graphene can be tuned on and off. By varying the charge carrier density of the graphene from 0 to $1.2*10^{13}$ $cm^{-2}$, we show that a narrow bandwidth emission feature may be tuned in intensity and varied in frequency across the mid-IR, from 1,200–1,600 $cm^{-1}$. The large Purcell factors predicted for graphene plasmonic resonances suggest that devices operating in this way could potentially control thermal radiation at timescales much faster than the spontaneous emission rate for conventional light emitting diodes and classical blackbody emission sources.

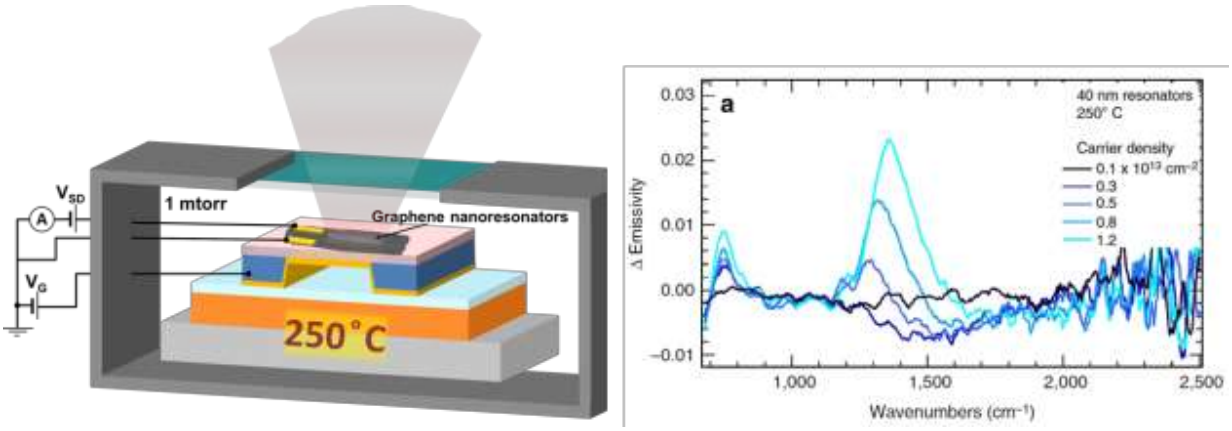



**Figure 1 –** (left) Schematic of electrostatically tunable incandescent light source. Graphene nanoresonators are patterned on a 1-um thick $SiN_x$ dielectric with a gold backreflector. The sample is held at constant temperature as the graphene sheet carrier density is varied with an applied gate voltage. (right) Carrier density dependent thermal emission from 40nm wide graphene nanoresonators at 250° C.

**Acknowledgements**, The experimental design, fabrication and characterization of tunable emission structures was supported by the 'Light-Material Interactions in Energy Conversion' Energy Frontier Research Center funded by the U.S. Department of Energy, Office of Science, Office of Basic Energy Sciences under Award Number DE-SC0001293. M.S.J. and M.C. acknowledge support for modelling and simulation from the Global Frontier R&D Program on Center for Multiscale Energy Systems funded by the National Research Foundation under the Ministry of Science, ITC & Future Planning, Korea (2011-0031561, 2014M3A6A7060584). M.C.S. acknowledges support from a Resnick Institute Graduate Fellowship. M.S.J. acknowledges a post-doctoral fellowship from the POSCO TJ Park Foundation. V.W.B. acknowledges support from a Kavli Nanoscience Postdoctoral Fellowship and use of facilities of the Kavli Nanoscience Institute.

## REFERENCES

1. Brar, V. W.; Sherrott, M. C.; Jang, M. S.; Kim, S.; Kim, L.; Choi, M.; Sweatlock, L. A.; Atwater, H. A., Electronic modulation of infrared radiation in graphene plasmonic resonators. *Nat Commun* **2015,** *6*.

2. Greffet, J.; Carminati, R.; Joulain, K.; Mulet, J.; Mainguy, S.; Chen, Y., Coherent emission of light by thermal sources. *Nature* **2002,** *416* (6876), 61-64.

3. Liu, X.; Tyler, T.; Starr, T.; Starr, A. F.; Jokerst, N. M.; Padilla, W. J., Taming the Blackbody with Infrared Metamaterials as Selective Thermal Emitters. *Physical Review Letters* **2011,** *107* (4), 045901.

# *Active conducting oxide plasmonics and metasurfaces*

**Howard Ho Wai Lee[1,2,*] and Harry A. Atwater[3]**

[1] *Department of Physics and Baylor Research & Innovation Collaborative, Baylor University, Waco TX, USA*

[2] *The Institute for Quantum Science and Engineering, Texas A&M University, College Station TX, USA*

[3] *Thomas J. Watson Laboratories of Applied Physics, California Institute of Technology, Pasadena, CA 91125, USA*

[*]corresponding author: Howard_Lee@Baylor.edu

**Abstract**- Metasurfaces composed of planar arrays of sub-wavelength artificial structures show promise for light manipulation, and have yielded novel ultrathin optical components such as flat lenses, holographic surfaces and orbital angular momentum manipulation. Here we experimentally demonstrate a gate- tunable metasurface that enables dynamic electrical control of the phase and amplitude of the plane wave reflected from the metasurface. Tunability arises from field-effect modulation of the complex refractive index of conducting oxide layers incorporated into metasurface antenna elements which are configured in a reflectarray geometry.

Metasurfaces composed of planar arrays of sub-wavelength artificial structures show promise for light manipulation, and have yielded novel ultrathin optical components such as flat lenses, wave plates, holographic surfaces and orbital angular momentum manipulation and detection over a broad range of electromagnetic spectrum [1]. However the optical properties of metasurfaces developed to date do not allow for versatile tunability of reflected or transmitted wave amplitude and phase after fabrication, thus limiting their use in a wide range of applications.

In this talk, I will discuss the use of alternative plasmonic materials, i.e., transparent conducting oxides (TCOs)[2], to actively electrical control the optical properties of plasmonic and metasurface structures for studying new optical physics and advanced applications. This approach combines the advantages of i) the large optical tunability of conducting oxide materials, ii) the field-effect dynamics of metal-oxide-semiconductor (MOS) transistor, and iii) the high field confinement of the plasmonic/metasurface structures to achieve strong control on the electron carrier density of the active conducting oxide layers for the realization of tunable plasmonics and metasurfaces.

I will present an experimental demonstration of an ultracompact PlasMOStor, a plasmon slot waveguide field-effect modulator based on a transparent conducting oxide active region that can modulate plasmonic signal with high dynamic range (2.71 dB/μm) and low waveguide loss (~0.45 dB/μm) [3]. In addition, I will present our recent experimental results on gate-tunable metasurface that enables dynamic electrical control of the phase and amplitude of the plane wave reflected from the metasurface.4 A phase shift of π and ~ 30% change in the reflectance are achieved by applying 2.5 V gate bias, a basic requirement for electrically tunable beam-steering phased array metasurfaces [4].

**REFERENCES**

1. N. Yu *et al.*, “Light Propagation with Phase Discontinuities: Generalized Laws of Reflection and Refraction,” *Science* **334**, 333 (2011)
2. E. Feigenbaum, K. Diest, and H. A. Atwater, “Unity-Order Index Change in Transparent Conducting Oxides

at Visible Frequencies," *Nano Lett.* **10**, 2111-2116 (2010).
3. H. W. Lee, G. Papadakis, S. P. Burgos, K. Chander, A. Kriesch, R. Pala, U. Peschel and H. A. Atwater, "Nanoscale Conducting Oxide PlasMOStor," *Nano Lett.* **14**, 6463 (2014).
4. Y. W. Huang*, H. W. Lee*, R. Sokhoyan, R. Pala, K. Thyagarajan, S. Han, D. P. Tsai, and H. A. Atwater, "Gate-tunable conducting oxide metasurfaces," submitted (2016).

# Tunable mid-infrared photonics with phase transition materials

**M. A. Kats**[1]

[1]Electrical and Computer Engineering and Materials Science and Engineering, University of Wisconsin – Madison, USA

mkats@wisc.edu

**Abstract**

The mid-infrared (mid-IR) spectral range (wavelengths from ~ 2 μm to ~20 μm) has recently become more important for both applications and fundamental science. However, compared to their counterparts in the visible, optical components in the mid-IR are still significantly under-developed. We create tunable optical components for the mid-IR by incorporating phase transition materials that respond to temperature, current, or light into photonic structures such as interference coatings, optical metasurfaces, and thermal emitters.

This talk will review our efforts to utilize phase transition materials in optical structures. Materials like vanadium dioxide ($VO_2$) and rare earth nickelates undergo structural and electronic phase transitions that can be driven via thermal, electrical, and optical means. These phase transitions result in dramatic changes in electronic properties, and correspond to large changes in optical properties, especially in the mid-infrared spectral range where the Drude response dominates. Previously we have demonstrated that $VO_2$ integrated into thin film structures enable temperature- and current-tunable absorbers and reflectors [1,2] and plasmonic antennas [3], as well as thermal emitters with anomalous temperature dependence [4].

More recently, we looked to expand the palette of tunable optical materials by defect engineering $VO_2$ to alter its properties [5], as by using less-studied phase transition materials such as samarium nickelate (SNO). By combining these approaches, thermally driven phase transitions can be found over a range of critical temperatures from below room temperature to above 100 degrees. We are currently demonstrating anomalous thermal emitters using SNO, which can mask the temperatures of objects from thermal imagers, and $VO_2$-based metasurfaces with new functionalities using nanoscale defect engineering with ion irradiation.

Many thanks to the contributions of numerous colleagues and collaborators, including Chenghao Wan, Patrick Roney, Jad Salman, Jura Rensberg, Carsten Ronning, You Zhou, Zhen Zhang, Shriram Ramanathan, Shuyan Zhang, and Federico Capasso.

**REFERENCES**

1. M. A. Kats, D. Sharma, J. Lin, P. Genevet, R. Blanchard, Z. Yang, M. M. Qazilbash, D. Basov, S. Ramanathan, and F. Capasso, "Ultra-thin perfect absorber using a tunable phase change material", *Applied Physics Letters* 101, 221101 (2012)
2. S. Zhang, M. A. Kats, Y. Cui, Y. Zhou, Y. Yao, S. Ramanathan, and F. Capasso, "Current-modulated optical properties of vanadium dioxide thin films in the phase transition region", Applied Physics Letters 105, 211104 (2014)

3. M. A. Kats, R. Blanchard, P. Genevet, J. Lin, D. Sharma, Z. Yang, M. M. Qazilbash, D. Basov, S. Ramanathan, and F. Capasso, "Thermal tuning of mid-infrared plasmonic antenna arrays using a phase change material", *Optics Letters* 38, 368 (2013)
4. M. A. Kats, R. Blanchard, S. Zhang, P. Genevet, C. Ko, S. Ramanathan, and F. Capasso, "Vanadium dioxide as a natural disordered metamaterial: perfect thermal emission and large broadband negative differential thermal emittance", *Physical Review X* 3, 041004 (2013)
5. J. Rensberg, S. Zhang, Y. Zhou, A. S. McLeod, C. Schwarz, M. Goldflam, M. Liu, J. Kerbusch, R. Nawrodt, S. Ramanathan, D. N. Basov, F. Capasso, C. Ronning, M. A. Kats, "Defect-engineered optical meta-devices in phase change materials", *Nano Letters* 16, 1050 (2016)

# Natural and Biomimetic Radiative Cooling Nano-Photonic Structures

**Norman Nan Shi[1], Cheng-Chia Tsai[1], Fernando Camino[2], Gary D. Bernard[3], Rüdiger Wehner[4], Nanfang Yu[1*]**

[1]*Department of Applied Physics & Applied Mathematics, Columbia University, USA*

[2]*Center for Functional Nanomaterials, Brookhaven National Laboratory, USA*

[3]*Department of Electrical Engineering, University of Washington, USA*

[4]*Brain Research Institute, University of Zürich, Switzerland*

[*]corresponding author: *ny2214@columbia.edu*

**Abstract** – I will talk about how Saharan silver ants utilize a uniquely shaped hair coating to substantially enhance reflectivity in the solar spectrum and emissivity in the mid-infrared. I will also talk about biomimetic metasurfaces with such radiative-cooling properties.

Saharan silver ants (*Cataglyphis bombycina*) are known to forage in the Sahara Desert under the full midday sun when surface temperatures can reach up to 70°C (158°F) [1]. Through a series of optical and thermodynamic measurements, we show how the ants utilize a layer of hairs with triangular shaped cross-sections that cover the top and sides of their bodies to keep their body temperature below their critical thermal maximum of 53.6°C (128.48°F). This unique hair coating keeps them cool in two ways: (i) The hairs enhance reflection in the visible and near-infrared of the electromagnetic spectrum, i.e., in the region of maximal solar radiation; (ii) The hairs are also highly emissive in the mid-infrared spectral range, where they enhance the ants' ability to offload excess heat via thermal radiation, which is emitted from the hot body of the ants to the cold sky. In these ants, the dorsal and the lateral sides of the ant body exhibit a silvery glare (**Fig. 1(a)**). These regions are covered by a dense array of hairs. As shown by SEM images, the hairs, which gradually taper off at the tip, are locally aligned in the same direction (**Figs. 1(b)(c)**). One significant structural feature is the triangular cross-section of the hairs, composed of two corrugated top facets and a flat bottom facet that faces the ant's body. Focused ion beam milling shows that the cross-section dimensions of the hair vary due to the tapering of the hairs, and there's a gap between the bottom hair facet and the cuticular surface (**Figs. 1(c)(d)**).

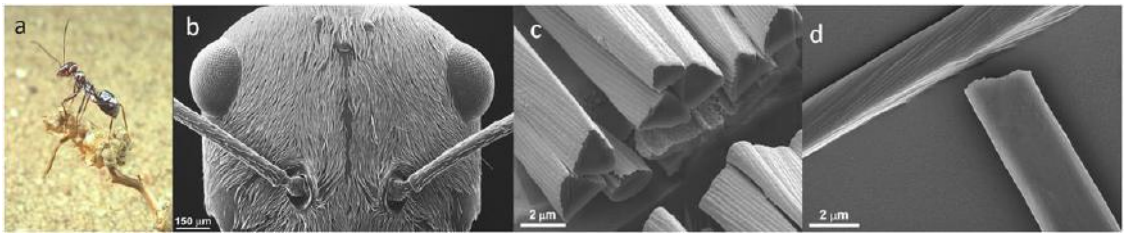



**Figure 1** Saharan silver ant and its radiative cooling hair structures.

At normal incidence, measured hemispherical reflectivity shows that regions with intact hair coverage reflect 67% of incoming solar radiations, while regions with hair removed only reflect 41% (**Fig. 2(a)**). This enhancement in reflectivity is due to optical Mie resonances inside the hair structures, which lead to enhanced backscattering of light [3]. The enhancement in reflectivity becomes larger at higher incidence angles when comparing regions with intact hair coverage to regions where hairs have been removed. This enhancement in reflectivity at large incident angles is the result of total internal reflection at the bottom facets of the triangular shaped hairs. The enhanced emissivity (**Fig. 2(b)**) in the mid-infrared is due to the fact that the triangular shaped

hairs form an effective anti-reflective coating that reduce reflection of thermal radiation as it propagates from the hot ant body to outside. Full wave simulations were used to confirm the optical measurement results, where **Fig. 2(c)** shows the simulated and measured results of hair reflectivity as a function of incidence angle.

Thermodynamic experiments (**Fig. 2(d)**) show that the hairs have the ability to lower the steady-state temperature of the ant by a few degrees Celsius when an ant body with the hairs intact is compared to the ant body with hairs removed. The enhanced emissivity also reduces the time constant associated with heating and cooling, allowing the ant to cool down to its equilibrium temperature faster. This passive cooling effect works under the full sun whenever the ants are exposed to the clear sky.

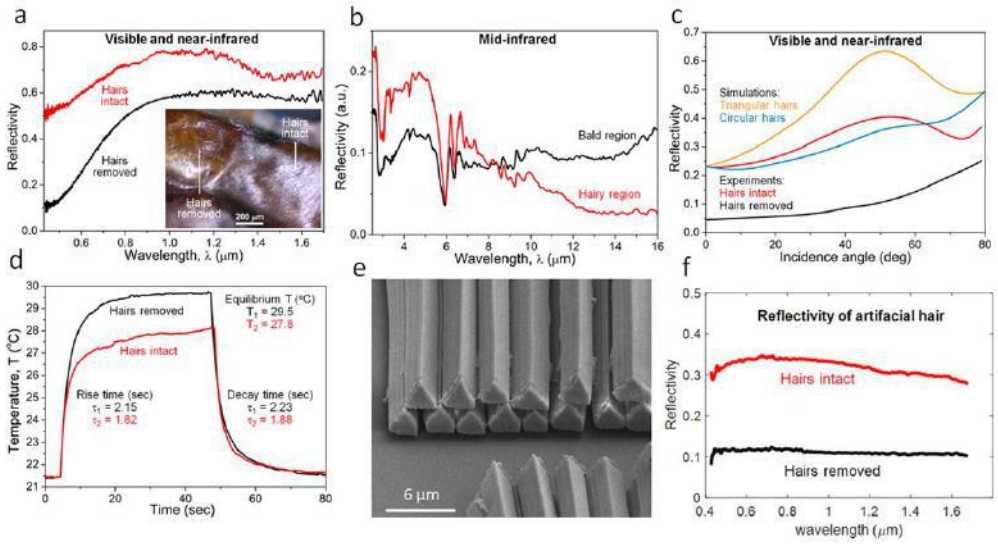



**Figure 2** Optical and thermodynamic characterization of the hair coatings of Saharan silver ants and biomimetic radiative cooling nanophotonic structures created using 3D printing.

Inspired by the hair coating of the Saharan silver ants, we are developing fabrication methods to create biomimetic metasurfaces for passive radiative cooling of objects. The structure shown in **Fig. 2(e)** is fabricated using a commercially available nano-3D lithography tool based on two-photon polymerization. Initial results (**Fig. 2(f)**) show that the fabricated structure was able to substantially enhance the hemispherical reflectivity of the surface in the visible and near-infrared. The talk will also cover radiative cooling coatings based on thin-film polymers embedded with nanoparticles.

**Acknowledgements** The work was supported by NSF (grants PHY-1411445 and ECCS-1307948) and the Air Force Office of Scientific Research, Multidisciplinary University Research Initiative program (grant FA9550-14-1-0389).

**REFERENCES**

1. R. Wehner, S. Wehner, "Parallel evolution of thermophilia: daily and seasonal foraging patterns of heat‐adapted desert ants: Cataglyphis and Ocymyrmex species," *Physiol. Entomol.* **36**, 271 (2011)
2. N. Shi, C. Tsai, F. Camino, G. Bernard, N. Yu, R. Wehner, "Keeping cool: Enhanced optical reflection and radiative heat dissipation in Saharan silver ants," *Science* **349,** 6245 (2015)
3. C. F. Bohren, D. R. Huffman, *Absorption and Scattering of Light by Small Particles* (John Wiley & Sons, 1998).

# Polarization tunable monolithic semiconductor lasers with metasurfaces

Guozhen Liang,[1] Yongquan Zeng,[1] Xiaonan Hu,[1] Hao Yu,[1] Houkun Liang[2], Ying Zhang[2], Lianhe Li,[3] Alexander Giles Davies,[3] Edmund H. Linfield,[3] Qi Jie Wang[1,*]

[1] *Center for OptoElectronics and Biophotonics, School of Electrical and Electronic Engineering & The Photonics Institute, Nanyang Technological University, 50 Nanyang Avenue, 639798 Singapore.*

[2]*Singapore Institute of Manufacturing Technology, 71 Nanyang Drive, 638075 Singapore.*

[3]*School of Electronic and Electrical Engineering, University of Leeds, Leeds LS2 9JT, UK.*

*Email: qjwang@ntu.edu.sg*

**Abstract**: In this paper, we demonstrate that the polarization of terahertz (THz) frequency radiation can be continuously tuned electronically from linear to circular polarization by monolithically integrating in-plane metasurfaces with two phase-locked semiconductor-based THz quantum cascade lasers (QCLs).

The ability to manipulate the polarization states of radiation has a breadth of applications across the electromagnetic spectrum， such as optical communication[1], optical holography[2], spectroscopy and sensing[3]. Manipulation of the polarization state of light usually relies on external optical components, e.g. wave plates and polarizers, which are bulky and sometimes lossy. Therefore, there is an essential need to develop low loss, monolithic devices with controllable polarization. In this work, we designed metallic subwavelength scattering antenna array integrated onto the SP waveguide to control the polarization of the beam emitted from phased coupled terahertz (THz) quantum cascade lasers (QCLs).

As shown in Fig. 1(a), series of antenna structures are fabricated, fed by phase-locked THz QCLs. The tapered QCLs are designed to collimate the emitted beam in the lateral direction, whilst simultaneously amplifying the power. The two sets of antennas (left and right) are cross oriented, and vertically shifted by 21 μm (see Fig. 1(a)), around one quarter of the SP wavelength (85 μm). This introduces a ~π/2 phase difference in the excitation of the two antenna arrays, which are also cross polarized. If the emission direction of the device is normal to the surface (as it is), no additional phase difference will be accumulated during free-space propagation of THz waves, the phase difference in the excitation of the two antenna arrays will be mirrored in their emissions in the far field.

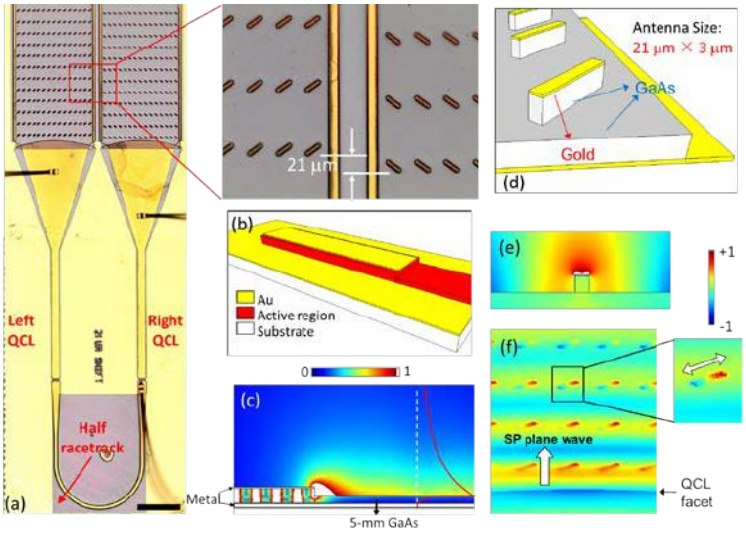



Figure 1 (a) Optical microscope image of a fabricated device. The two sets of antennas are cross oriented and vertically offset by 21 μm, corresponding to a ~π/2 phase shift. The left and right tapered QCLs are phase-locked by a half racetrack structure to ensure coherent interference of the radiation from the two antenna arrays. (b) Schematic geometry of the THz QCL with an integrated dielectric-loaded surface plasmon (DLSP) waveguide. (c) Cross-sectional electric field (amplitude) distribution of the device in (b), showing that the THz radiation is coupled from the QCL into the integrated DLSP waveguide, with a coupling efficiency of 55% for a 5 μm thick GaAs layer. The electric field profile along the white dashed line is illustrated by the red curve, and it can be seen that the THz wave is strongly confined to the GaAs surface. (d) Schematic illustration of the antenna structure. The antennas are placed on 5-μm-high GaAs pedestals, formed from the QCL active region. (e) Calculated electric field distribution on a plane 2 μm above the antennas. The antennas are excited by the propagating SP wave coupled from a THz QCL, resulting in electric dipoles oscillating along the antenna lengths. (f) The scattering effect of the antennas when placed at a 5-μm -high GaAs pedestal.

A dielectric-loaded surface plasmon (DLSP) waveguide is incorporated for the confinement and propagation of THz waves on a flat surface. This is much simpler, in both design and fabrication, than using a structured metal surface, as it comprises simply a GaAs coated metal layer (Fig. 1(b)). By correct choice of the thickness of the GaAs layer, the THz electric field can then be confined at the GaAs-air interface, with little field residing in the GaAs layer (Fig. 1(c)), leading to a low propagation loss in the waveguide being achieved. In the design, we chose a GaAs thickness of 5 μm to maintain a high coupling efficiency (55%) while simultaneously allowing a reasonable propagation length (3.3 mm). Note that the THz wave is strongly confined to the GaAs surface with an evanescent

tail of only ~30 μm penetrating into the air, with the electric field profile along the white dashed line depicted by the red curve.

Subwavelength metallic antennas are incorporated into the DLSP waveguide, as illustrated in Figs. 1(d). Each antenna is excited by an SP plane wave generated from a THz QCL, and will have electrons oscillating along the antenna length. The resultant oscillating electric dipoles will emit THz radiation polarized in the same direction (Fig. 1(f)). In contrast to the cases in Ref. [4]and [5], where slot antennas drilled on a metal film were used as a polarization-sensitive element, our strip-type antenna responds to, and re-emits, the electric field component parallel to its elongation. To produce a narrow directional THz beam from a set of antennas, they are arranged into an array and form a second-order grating with a period of 80 μm. The constructive interference of the THz radiation from each antenna leads to a collimated beam pointing normal to the surface.

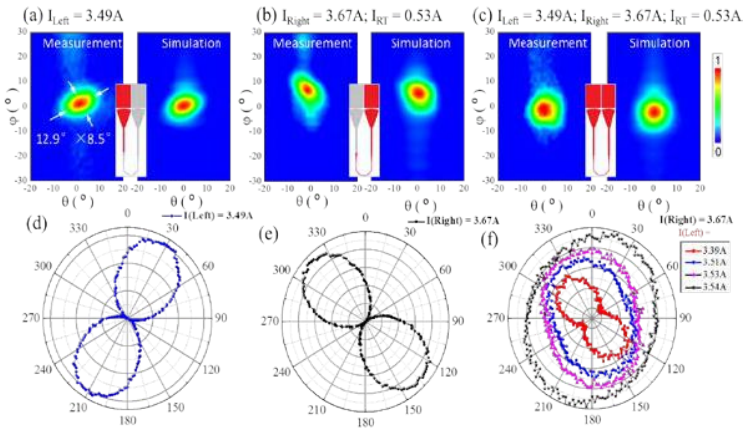



Figure 2 Measured and simulated far-field patterns of the device with (a) only the left hand QCL, (b) only the right QCL and the half racetrack, (c) all three parts of the structure are electrically pumped. Far-field emission patterns were measured by scanning a pyroelectric detector on a spherical surface 15 cm away from the emission area. The (0, 0) point in the far-field pattern corresponds to the direction normal to the device surface. The simulations are the calculated by a commercial simulation package Lumerical FDTD. (d), (e) and (f) measured polarization state with pump condition corresponding to (a), (b) and (c), respectively. The polarization states of the emission were measured by rotating a wire-grid polarizer in front of the detector, placed at the intensity maximum of the far-field distribution.

The device was operated at 10 K under pulse excitation with 10 kHz, 500 ns electric pulses. The far-field and polarization at different pump conditions have been measured. As shown in Fig. 2(a) and (b), when only the one QCL is biased (the red part in the inset), the far-field pattern exhibits a small (~13°×9° FWHM) elliptical spot. Therefore, the antenna structure is functioning as a highly efficient collimator. Another point is that the far-field patterns are slightly tilted in the orientation of the antennas. This is because an electric dipole radiates strongest along the perpendicular bisector of its length. The polarization state of the emission has been measured. When either laser is on, the radiation in the collected region is excellently linearly-polarized at a predetermined direction in Fig. 2(d) and (e), which is consistent with that of the antenna and the far-field patterns.

When the whole device is electrically pumped, the emission spectrum has a different main peak and the far-field pattern appears as not simply a superposition of the patterns of the left and right devices individually (Fig. 2(c)). This indicates that the left and right devices are phase-locked by the half racetrack structure, and their combined emission is coherent – the basis for demonstrating a polarization tunable device. Elliptical polarization is observed due to the coherent overlap of the two beams. Fig. 2(f) shows the evolution of the polarization state with the variation of the left pumping current while fixing the right pumping current at 3.67 A. For the black curve in Fig. 2(f), $I_{\max} : I_{\min} = 56 : 44$. According to the definition of DOCP in Ref. [5], which is DOCP $= 2 \cdot I_{\max}^{1/2} \cdot I_{\min}^{1/2} / (I_{\max} + I_{\min})$, a DOCP value as high as 99% is obtained.

In conclusion, we have developed an integrated metasurface antenna structure, which scatter and collimate the SP wave into the direction perpendicular to the waveguide surface. When two sets of cross-oriented metasurface antenna arrays with a quarter-wavelength shift are phase-locked, the polarization of the beam in the overlapping region can be dynamically tuned from linear to near-circular polarization, reaching a DOCP as high as 99%.

## References


[1] K. Roberts, M. O'Sullivan, K. T. Wu, H. Sun, A. Awadalla, D. J. Krause, *et al.*, "Performance of Dual-Polarization QPSK for Optical Transport Systems," *Journal of Lightwave Technology*, vol. 27, pp. 3546-3559, Aug 15 2009.

[2] G. X. Zheng, H. Muhlenbernd, M. Kenney, G. X. Li, T. Zentgraf, and S. Zhang, "Metasurface holograms reaching 80% efficiency," *Nature Nanotechnology*, vol. 10, pp. 308-312, Apr 2015.

[3] L. Whitmore and B. A. Wallace, "Protein secondary structure analyses from circular dichroism spectroscopy: Methods and reference databases," *Biopolymers*, vol. 89, pp. 392-400, May 2008

[4] J. Lin, J. P. B. Mueller, Q. Wang, G. H. Yuan, N. Antoniou, X. C. Yuan, *et al.*, "Polarization-Controlled Tunable Directional Coupling of Surface Plasmon Polaritons," *Science*, vol. 340, pp. 331-334, Apr 19 2013.

[5] P. Rauter, J. Lin, P. Genevet, S. P. Khanna, M. Lachab, A. G. Davies, *et al.*, "Electrically pumped semiconductor laser with monolithic control of circular polarization," *Proceedings of the National Academy of Sciences of the United States of America*, vol. 111, pp. E5623-E5632, Dec 30 2014.

# Disordered photonics

# Anomalous light tunneling through two interlaced 3D metallic wire meshes

**Hafssaa Latioui**[1], **Mário G. Silveirinha**[1,2*]

[1]University of Coimbra, Department of Electrical Engineering – Instituto de Telecomunicações, 3030-290, Coimbra, Portugal, hlatioui@co.it.pt

[2]University of Lisbon, Instituto Superior Técnico, Avenida Rovisco Pais, 1, 1049-001 Lisboa, Portugal

[*]corresponding author: mario.silveirinha@co.it.pt

**Abstract**- Three-dimensional connected metallic wire meshes are impenetrable by light in the long wavelength limit and have an electromagnetic response similar to that of an electron gas below the plasma frequency. Surprisingly, here we show when two of such meshes are spatially-interlaced the structure enables an anomalous light tunneling in the long wavelength regime.

Metallic grids block the propagation of light when the electric field is aligned with the grid. This property has been explored in many applications, such as light polarizers and frequency selective surfaces. In particular, when the wire grid spans the three directions of space − the so-called three-dimensional (3D) connected wire medium [1-5] − the corresponding photonic crystal does not support light states in the long wavelength regime. Indeed, a 3D connected wire metamaterial is completely opaque to light propagation and has an electromagnetic response analogous to that of free-electron gas [1-5].

In this article, we are interested in a metamaterial formed by two spatially-interlaced wire meshes (figure **1**a). Common sense suggests that the effects of the individual wire meshes should be "additive" in the sense that the interlaced wire meshes should scatter light more strongly and hence block the light propagation more effectively. However, we found out with full wave simulations that while each individual mesh exhibits an almost zero transmission in the low frequency limit, when the two 3D meshes are combined it is possible to have a large transmission (figure **1**b). To explain this rather surprising effect, we rely on an effective medium model. It was shown in Ref. [6] that, under the assumption that the two wire meshes interact with one another as effective media and supposing that the metal is a perfect conductor and the host material is air, the dielectric function of the metamaterial is given by:

$$\frac{\bar{\boldsymbol{\varepsilon}}}{\varepsilon_0} = \varepsilon_t(\omega)\left(1-\frac{1}{k^2}\mathbf{k}\otimes\mathbf{k}\right)+\varepsilon_l(\omega,k)\frac{1}{k^2}\mathbf{k}\otimes\mathbf{k}\,, \tag{1a}$$

$$\varepsilon_t(\omega)=1-\frac{k_{p,A}^2+k_{p,B}^2}{\omega^2/c^2} \quad \text{and} \quad \varepsilon_l(\omega,k)=1+\frac{k_{p,A}^2}{k^2/l_{0A}-\omega^2/c^2}+\frac{k_{p,B}^2}{k^2/l_{0B}-\omega^2/c^2} \tag{1b}$$

The metamaterial response is nonlocal as the effective permittivity depends strongly on the wave vector $\mathbf{k}=-i\nabla$. In the above, $k_{p,i}$ ($i=A,B$) is the plasma wave number of the $i$-th individual wire mesh component, and $l_{0,i}$ are dimensionless constants of the order of ~2 [3]. The effective medium supports transverse plane waves described by the permittivity $\varepsilon_t$, and longitudinal waves described by the permittivity $\varepsilon_l$. The longitudinal waves have a vanishing magnetic field and electric field directed along the wave vector. The dispersion of the longitudinal modes is determined by $\varepsilon_l=0$ and the dispersion of the transverse modes is determined by $k^2=\varepsilon_t\,\omega^2/c^2$. Notably, the interlaced wire medium supports two distinct longitudinal modes, and crucially one of the modes can

propagate at arbitrarily low frequencies (figure **1**c) [6-7]. We developed an analytical method to calculate the transmission coefficient when a finite thickness metamaterial slab is illuminated by a transverse magnetic polarized plane wave. Figure **1**b depicts the transmission coefficient (solid blue line) as function of the normalized thickness *L/a* for a fixed frequency well below the effective plasma frequency, being *a* the lattice constant. The radii of the wires are $r_A=0.001a$ and $r_B=0.05a$. As seen, the solid line follows closely the discrete symbols calculated using CST Microwave Studio, and predicts an anomalous light tunneling due to the excitation of the longitudinal-type light mode. At the conference we will discuss in detail the physics of this anomalous tunneling effect and highlight its possible applications.

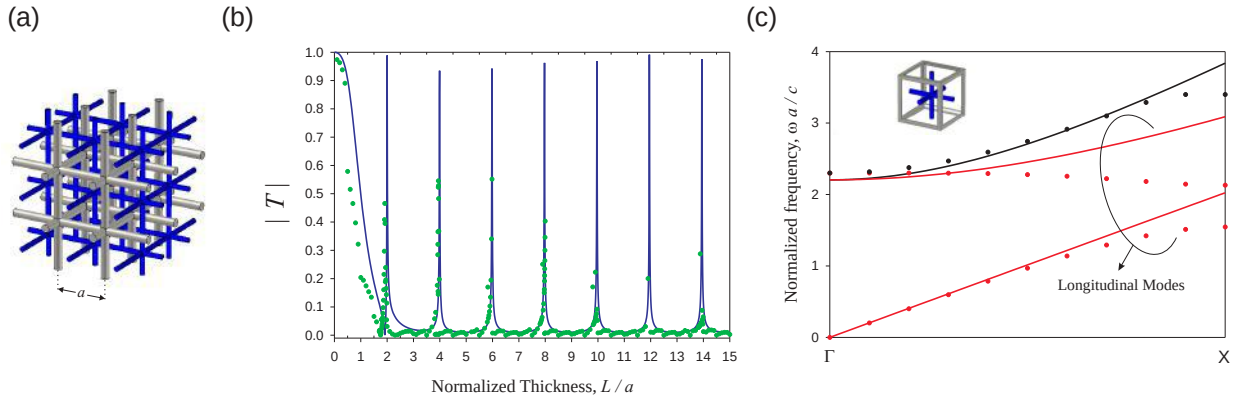



Figure 1: (a) Geometry of the interlaced wire meshes. The distance between the two non-connected networks is *a/2*. (b) Transmission coefficient as function of the normalized thickness for $\omega a/c$=1.32 and an incident angle of 80º (solid line: theory; discrete symbols: full wave simulations). (c) Dispersion characteristic of the electromagnetic modes along $\Gamma X$. The inset shows the cubic unit cell of the structure. (solid lines: theory; discrete symbols: full wave simulations).

**Acknowledgements**: This work is supported in part by Fundação para a Ciência e a Tecnologia with the grants PTDC/EEITEL/4543/2014 and UID/EEA/50008/2013. Hafssaa Latioui acknowledges financial support by the Erasmus Mundus programme of the European Union - Al-Idrisi II.

## REFERENCES

1. J. B. Pendry, A. J. Holden, W. J. Stewart and I. Youngs, "Extremely Low Frequency Plasmons in Metallic Mesostructures," *Phys. Rev Letters,* Vol. 76, No. 25, 4773–4776, 1996.
2. D. F. Sievenpiper, M. E. Sickmiller and E. Yablonovitch, "3D Wire Mesh Photonic Crystals," *Phys. Rev Letters,* Vol. 76, No. 14, 2480–2483, 1996.
3. M. G. Silveirinha and C. A. Fernandes, "Homogenization of 3-D-Connected and Nonconnected Wire Metamaterials," *IEEE Trans. on Microw. Theory and Techn.*, Vol. 53, No. 4, 1418–1430, 2005.
4. M. G. Silveirinha, "Artificial plasma formed by connected metallic wires at infrared frequencies," *Phys. Rev B*, Vol. 34, No. 79, 035118, (1–15), 2009.
5. A. Demetriadou and J. B. Pendry, "Taming spatial dispersion in wire metamaterial," *J. Phys.: Condens. Matter*, 295222, (1–11), 2008.
6. G. W. Hanson, E. Forati, M. G. Silveirinha, "Modeling of Spatially-Dispersive Wire Media: Transport Representation, Comparison With Natural Materials, and Additional Boundary Conditions," *IEEE Trans. on Antennas and Propag.*, Vol. 60, No. 9, 4219–4232, 2012.
7. J. Shin, J.-T. Shen and S. Fan, "Three-dimensional electromagnetic metamaterials that homogenize to uniform non-Maxwellian media," *Phys. Rev B*, Vol. 76, 113101, (1–4), 2007.

# Wide-field ultrafast imaging of light diffusion in structured soft matter

**S. Zanotto**[1,2*], **L. Pattelli**[1], **D. Nuzhdin**[1], **S. Nocentini**[1], **H. Zeng**[1], **D. Martella**[1], **C. Parmeggiani**[1,2], **and D. S. Wiersma**[1,3]

[1]LENS- Laboratorio Europeo di Spettroscopia Non-Lineare, Via Nello Carrara 1, 50019 Sesto Fiorentino (FI), Italy

[2]Istituto Nazionale di Ottica – CNR, and LENS, Via Nello Carrara 1, 50019 Sesto Fiorentino (FI), Italy

[3]Dipartimento di Fisica e Astronomia, Università di Firenze, Via Sansone, 50019 Sesto Fiorentino (FI), Italy

[*]corresponding author: simone.zanotto@ino.it

**Abstract**- Following light motion in real-time is an enabling tool which allows to understand a number of details about the interaction between a light beam and the environment which drives its propagation. We report a new developed time-resolved wide-field imaging system which allows to follow the light propagation on a millimeter scale and sub-picosecond temporal resolution. The potentials of this method for the study of optically thin and anomalously structured soft matter samples, such as fruit skins or patterned films fabricated out of responsive polymers, will be highlighted.

Whereas light transport in diffusive and disordered systems is a mature research topic, many new features still keep on emerging, mainly thanks to the increasing technological potential. For instance, the advent of nanotechnology opened up a new world of possibilities to structure on-demand patterns otherwise not obtainable in natural ways. However, also other kind of structures, and most of all those concerning the biological world, deserve an amazing richness in terms of structure and functionality. Here, a technological advance in the optical characterization technique would instead prove to be fruitful to get more insights into the light transport mechanisms.

The advance we would like to discuss is that of wide-field ultrafast imaging. To date, established fast imaging techniques mostly rely on electronics, hence limiting the minimum accessible temporal scale. This limitation can be overcome employing an all-optical gating technique [1], whose principle is sketched in Fig. 1 (a). It is based on the up-conversion of the optical field exiting from the diffusive sample by means of a non-linear crystal; the resulting time-resolved image is finally recorded through a CCD.

By means of this setup we were able to collect a sequence of images, at a frame rate of 100 trillion frames per second, of the diffused light exiting from several disordered samples [2]. When moving away from ordinary turbid media, we observed diffusion dynamics different from those predicted by ordinary diffusion theory. A striking example is that presented in Fig. 1 (b). Here we report a sequence of frames (which correspond to an overall time of about 5 picoseconds after pulse injection) recorded from a grapefruit skin sample (Fig. 1 (c)). The departure from the ordinary spot-shaped intensity distribution is a clear evidence that the light transport regime is well different from that of diffusion in an isotropic medium.

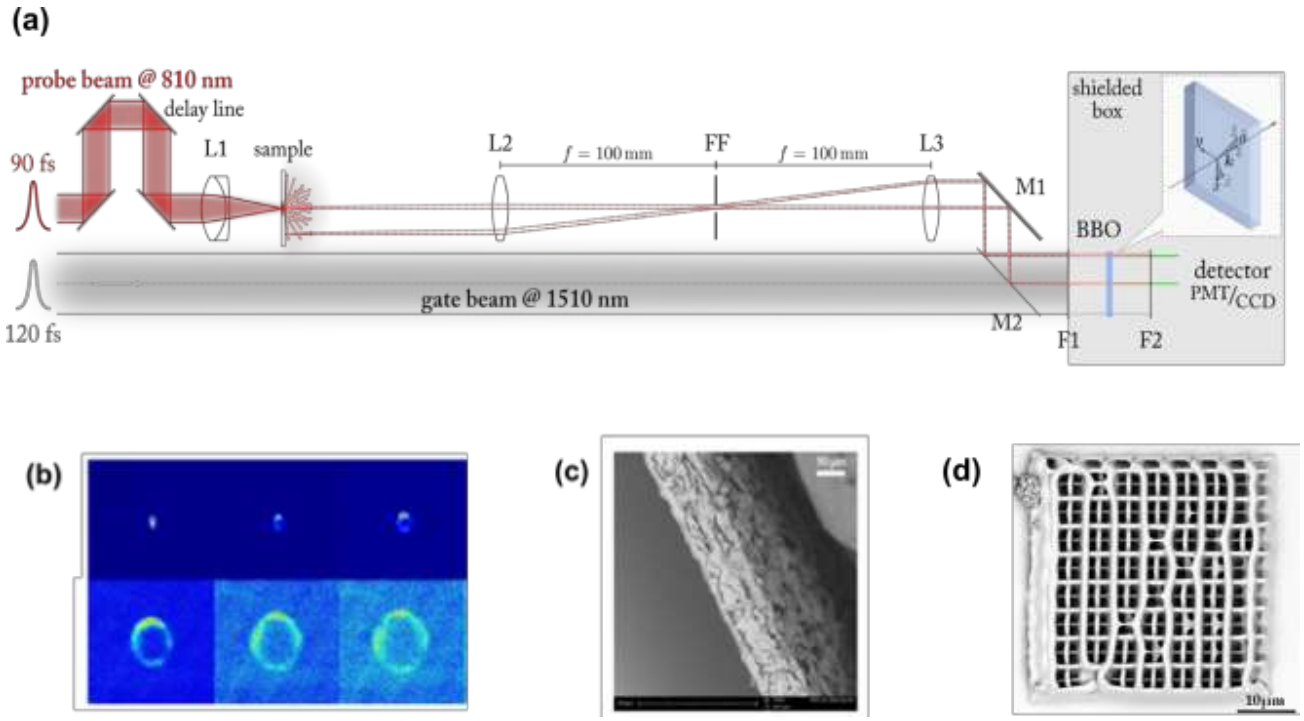



**Fig. 1.** Panel (a): Sketch of the optical set-up. The probe beam incident on the sample surface and diffused by the sample itself is imaged on a BBO crystal, where the up-conversion process takes place. Panel (b): Diffusion of light from a grapefruit skin sample (SEM picture in panel (c)). Due to the peculiar interplay between structural anisotropy and small optical thickness, light diffuses in the sample with a unique annular-shaped pattern. The technique can prove useful to analyze structures like that reported in panel (d): partially disordered photonic component fabricated from a responsive polymer [3].

What reported above is a single example, while the method can prove to be effective for retrieving invaluable information from other kind of disordered media, such as patterned responsive polymers (Fig. 1 (d)). We hence believe that the present technique will find applications in the diverse fields where disordered materials are commonly found, like biomedical imaging, coating technology, and in general micro- and nanotechnology.

**Acknowledgements.** Financial support from the European Research Council through the Advanced Grant "PHOTBOTS" is acknowledged.

## REFERENCES

1. Shah J. *Ultrafast luminescence spectroscopy using sum frequency generation*. IEEE J Quant Electron 1988; 24: 276-288.
2. Pattelli L, Savo R, Burresi M and Wiersma DS. *Spatio-temporal visualization of light transport in complex photonic structures.* Light: Science & Applications, accepted article preview, 5 February 2016
3. Zeng H, Martella D, Wasylczyk P, Cerretti G, Gomez Lavocat J-C, Ho C-H, Parmeggiani C, and Wiersma DS. "High-Resolution 3D Direct Laser Writing for Liquid-Crystalline Elastomer Microstructures." Advanced Materials 26 (15): 2319–22. (2014)

# Optical Reflectance of Plasmonic Nanoparticles forming a Disordered Monolayer

**A. Reyes-Coronado[1*], G. Morales-Luna[2], O. Vázquez-Estrada[2], A. García-Valenzuela[2], A. Rodríguez-Gómez[3], R. G. Barrera[3]**

[1]Facultad de Ciencias, Universidad Nacional Autónoma de México, Ciudad Universitaria, Av. Universidad 3000, Coyoacán, C.P. 04510, Mexico City, Mexico.

[2]Centro de Ciencias Aplicadas y Desarrollo Tecnológico, Universidad Nacional Autónoma de México, Apartado Postal 70-186, C.P. 04510, Mexico City, Mexico.

Instituto de Física, Universidad Nacional Autónoma de México, Apartado Postal 70-186, C.P. 04510, Mexico City, Mexico.

[*]corresponding author: coronado@ciencias.unam.mx

**Abstract**-In this work we present theoretical predictions for the reflectance of a disordered monolayer of plasmonic nanoparticles supported onto a glass substrate, in an internal reflection configuration, by using a recently derived multiple-scattering model for the coherent reflectance. To validate the theory, we compare the predictions with experimental reflectance data, both around the critical angle at a fixed wavelength of the incident radiation, as well as measuring spectroscopic reflectance at fixed angle of incidence, using monolayers of gold nanoparticles with mean radius of 3.5nm and moderately high surface coverage fraction, fabricated by sputtering technique.

The deposition or growing of metallic nanoparticles onto a substrate, forming a monolayer of particles, has great impact in several technological applications, ranging from biological to electronic devices, mainly used as ultrasensitive detectors. We propose the use of reflected visible light to monitor and characterize the fabrication of such systems, which can be performed in situ and in real time providing valuable information to experimentalists. We study the reflectance of a disordered monolayer of metallic nanoparticles by using a recently derived multiple-scattering model (MSM) [1], and explore its validity as an inspection tool during the deposition of monolayers [2]. We have tested experimentally the theory for the case of large and highly scattering particles forming the monolayer [3] and very recently we explored theoretically the sensitivity to all the relevant parameters [4], such as, particle radius and material of the nanoparticles, index of refraction of the embedded medium as well as the substrate, wavelength, polarization and angle of incidence of the incoming radiation, and the surface coverage fraction of the monolayer, finding a very high sensitivity to gold and silver monolayers, for several particle radii.

In this work we present the theoretical predictions of the MSM for the reflectance of a disordered monolayer of plasmonic nanoparticles supported onto a glass substrate, using an internal reflection configuration. In this configuration, for angles of incidence above the critical angle the nanoparticles are illuminated with an evanescent wave. We compare the predictions with experimental measurements of the reflectance coming from monolayers of gold nanoparticles, with mean radius of 3.5nm and moderately high surface coverage fraction (over 10%), fabricated by sputtering technique. The experiments were performed fixing the wavelength of the incident radiation and measuring the reflectance around the critical angle (before and after), as well as fixing the

angle of incidence and performing spectroscopic measurements, for both polarizations. Just after the critical angle appears a peak of high sensitivity but interestingly there is another region of interest at low angles of incidence (below the critical angle), which could be suitable to implement in any moderately equipped laboratory. We analyze and discuss possible measurements at low angles of incidence and their use to characterize plasmonic monolayers.

The coherent reflectance, $R_{coh}$, of the monolayer system is calculated as

$$R_{coh}(\theta_1) = r(\theta_1) r^*(\theta_1) = \left| r(\theta_1) \right|^2, \tag{1}$$

where $\theta_1$ is the angle of incidence and

$$r(\theta_1) = \frac{r_{12}(\theta_1) + r_{coh}(\theta_2) e^{\beta}}{1 + r_{12}(\theta_1) r_{coh}(\theta_2) e^{\beta}}, \tag{2}$$

with $\beta = 2ik_m a \cos(\theta_2)$, where $k_m$ is the wavenumber evaluated in the embedded medium, called the matrix, $a$ is the particle radius, $\theta_2$ is the transmitted angle that reaches the monolayer of particles, $r_{12}$ is the standard Fresnel reflection coefficient of the interface between the substrate and the matrix, and $r_{coh}$ is the coherent reflection coefficient of the free-standing monolayer with particles embedded in the matrix, obtained with the MSM and given by

$$r_{coh} = \frac{-\alpha S_j(\pi - 2\theta_1)}{1 + \alpha S(0) + \frac{\alpha^2}{4}\left[ S^2(0) - S_j^2(\pi - 2\theta_1) \right]}, \tag{3}$$

with $\alpha = (2\Theta)/x_m^2 \cos\theta_i$, where $\Theta$ is the surface coverage fraction by the particles, $x_m = k_m a$ is the size parameter and the function $S_j(\theta)$ is an element of the amplitude scattering matrix of an isolated spherical particle of radius $a$, where $j$=1,2 stands for TE or TM polarization of the incident light, respectively, and $S(\theta=0)=S(0)$ is the forward scattering amplitude of an isolated sphere.

**Acknowledgements**, We acknowledge financial support through grants PAPIIT IN-100615 and PAPIIT IN-113815.

**REFERENCES**

1. A. García-Valenzuela, E. Gutiérrez-Reyes and R. G. Barrera, "Multiple-scattering model for the coherent reflection and transmission of light from a disordered monolayer of particles," *J. Opt. Soc. Am. A*, Vol. 29, 1161–1179, 2012.
2. O. Vázquez-Estrada, G. Morales-Luna, A. Calles-Martínez, A. Reyes-Coronado and A. García-Valenzuela, "Optical reflectivity as an inspection tool for metallic nanoparticles deposited randomly on a flat substrate," *Proc. SPIE 9556, Nanoengineering: Fabrication, Properties, Optics, and Devices XII*, 2015, San Diego, USA, September 2015.
3. O. Vázquez-Estrada and A. García-Valenzuela, "Optical reflectivity of a disordered monolayer of highly scattring particles: coherent scattering model versus experiment," *J. Opt. Soc. Am. B*, Vol. 13, 745–754, 2014.
4. O. Vázquez-Estrada, G. Morales-Luna, A. Reyes-Coronado, A. Calles-Martínez, and A. García-Valenzuela, "Sensitivity of optical reflectance to the deposition of plasmonic nanoparticles and limits of detection", under review in *J. Nanophotonics.*

# Thermo-optical response of nanoparticles embedded in a glass matrix

**E. Haro-Poniatowski[1,2], M. Jiménez de Castro[2], I. Camarillo[1], G. Muñoz[1], J. Toudert[2,3], R. Serna[2]**

[1] Departamento de Física Universidad Autónoma Metropolitana, Apartado Postal 55-534, México 09340, DF, México

[2] Instituto de Óptica, CSIC,Serrano 121, 28006 Madrid, Spain

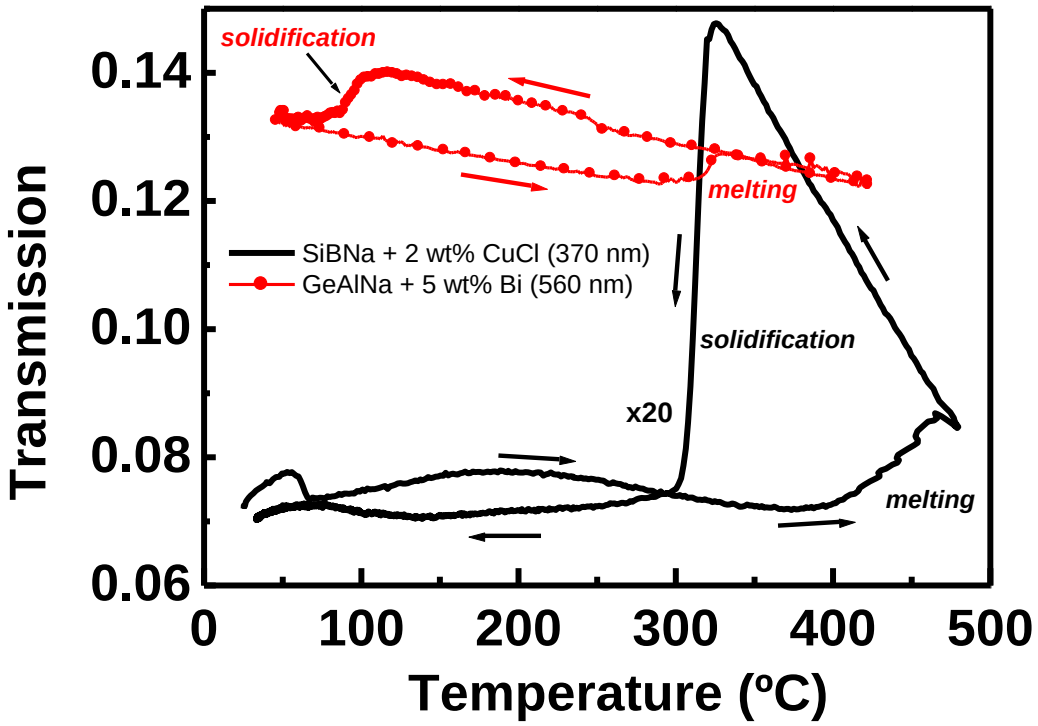
[3] Present address: ICFO - The Institute of Photonic Sciences, Castelldefels (Barcelona), Spain

**Abstract** Nanoparticles can be immersed in various materials and in particular in glasses, modifying their physical properties. In the present work we investigate the cases of Bi and CuCl nanocrystals embedded in two different glasses. The thermo-optical properties of these materials are described in detail.

When nanoparticles of materials having a low melting point are embedded in high melting point glass matrices, interesting reversible thermo-optical effects occur upon heating and cooling cycles. These effects are mainly due to the melting and solidification of the nanoparticles that can happen at very different temperatures giving rise to hysteresis effects [1-3]. These effects have been evidenced in a variety of experimental situations by X-rays, Raman, optical transmission measurements among others. In the figure below we show what is obtained when optical transmission through the material is measured as a function of temperature in the case of Bi NP's (upper graph) and CuCl NP's (lower graph) embedded in different glass matrices.

In the present work we give an overview of some previous investigations related to these effects. We also present our recent results concerning Bi (semimetal) and CuCl (semiconductor) nanoparticles embedded in different matrices [4,5]. The optical contrast and width (hysteresis) of these cycles depend on the NP's size and concentration. From the modeling of the optical properties of the NPs-doped glasses, it is proposed that the observed material thermo-optical response arises from the change in the dielectric function of the NPs upon melting [3,4]. Finally we discuss some possible applications for these systems in the design of spectral-selective thermo-optical devices.

.




**REFERENCES**


1. Valov P. M., Leiman V. I. "Size effects in the excitation energy and first-order phase transitions in CuCl nanocrystals in glass", *Phys. solid state*, Vol. 41, No. 2, 278–285, 1999.
2. Yoon Y. K., "Temperature dependent optical resonances of quantum confined CuCl nanocrystals in borosilicate glasses", *J. Appl. Phys.*, Vol. 51, No. 8, 2584–2589, 1997.
3. Jimenez de Castro M., Cabello F., Toudert J., Serna R., Haro-Poniatowski E. "Potential of bismuth nanoparticles embedded in a glass matrix for spectral-selective thermo-optical devices", *Applied Physics Letters*, Vol. 105, 113102, 2014.
4. Jimenez de Castro M., Serna R., Toudert J., Fernández Navarro J. M., Haro-Poniatowski E. "Thermo-optical properties of Bi nanoparticles embedded in germanate glasses and alumina thin films", *Ceram. Int.*, Vol. 41, No. 6, 8216–8222, 2015.
5. Haro-Poniatowski E., Suárez-García A., Serna R., Afonso C. N. "Thermally driven optical switching in Bi nanostructures", *Nanotechnology*, Vol. 16, 3142–3145, 2005.

# Graphene-based random meta-laser

**A. Marini**[1,*] **and F. J. García de Abajo**[2]
[1]ICFO-Institut de Ciencies Fotoniques, The Barcelona Institute of Science and Technology,
08860 Castelldefels (Barcelona), Spain
[2]ICREA-Institució Catalana de Recerca i Estudis Avançats,
Passeig Lluís Companys 23, 08010 Barcelona, Spain

[*]corresponding author: andrea.marini@icfo.es

**Abstract** - Controlling the optical energy flow inside random media is a research frontier of photonics. In spite of their success, random lasers still lack external tunability, reproducibility, and control over the beam spatial pattern, thus hindering their application in practical devices. Here we show that a graphene random metamaterial provides the means to overcome these limitations through its extraordinarily-low threshold for saturable absorption leading to efficient self-organization of the emitted light.

Laser operation is usually achieved through three basic elements: an amplifying medium, an external pumping setup, and an optical cavity that confines and shapes the emitted light in well-determined modes and directions. However, several modern approaches are extending this traditional laser paradigm into new avenues. Cavity-free stimulated emission of radiation has been widely studied in random lasers (RLs) [1], where the optical cavity modes of traditional lasers are replaced with multiple scattering in disordered media, while the interplay between gain and scattering determines the lasing properties. The physics behind RLs is rich and involved, as multiple scattering of light in disordered media leads to very complex electromagnetic mode structures. Indeed, RL emission is typically highly multi-mode owing to the co-existence of narrowly confined modes ensuing from Anderson localization [2] and extended modes [3]. In spite of their striking potential applications, RLs lack external tunability, reproducibility, and control over the spatial pattern of the output beam. Overcoming these limitations is central for the development and application of cost-effective cavity-free lasers.

Inspired by the aforementioned challenges, here we investigate the optical properties of randomly-oriented undoped graphene flakes embedded in externally pumped amplifying media. Conversely to traditional RLs, where sizes and separations of the random inclusions are larger than the optical wavelength in order to maximize scattering, here we focus in the opposite quasi-static regime where the medium behaves as an active random metamaterial (see Figs. 1a,b). We demonstrate a novel mechanism leading to stable and tunable single-mode cavity-free lasing characterized by a well-determined and highly coherent spatial pattern (see Figs. 2c). We find that the transverse size of the localized output beam, ranging from a few to several hundreds microns, can be accurately manipulated through the external pumping and through the volume density of graphene flakes (see Figs. 2d). This cavity-free lasing mechanism profoundly relies on the extraordinary optical properties of graphene, and particularly on its highly-saturated absorption at rather modest light intensities, a remarkable property which enables self-organization of light into a well determined spatial mode profile.

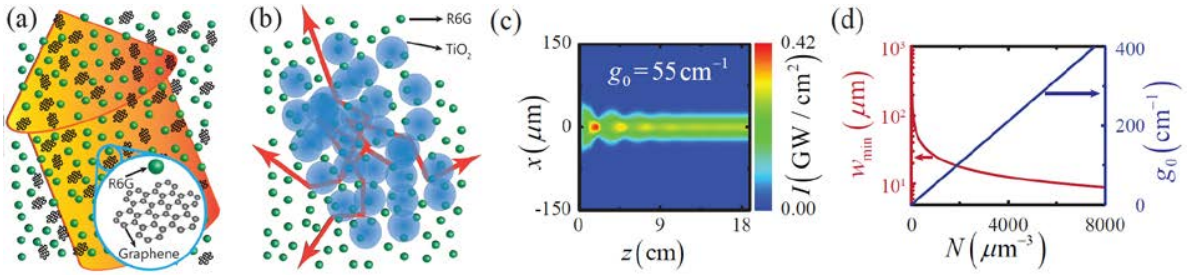



**Figure 1:** Meta-lasers versus traditional random lasers. (a) Our proposed graphene cavity-free laser consists of a mixture of sub-wavelength graphene flakes and dispersed Rhodamine 6G molecules embedded in PMMA. We envision graphene flakes of 10's nm in size, much smaller than the wavelength of light, which thus propagates in an effective medium with an exotic optical response. (b) In contrast, a traditional random laser uses dielectric particles instead of graphene, with sizes and separations that are comparable with the light wavelength in order to efficiently produce multiple scattering. (c) Propagation of an input Gaussian seed with peak intensity $I_0$ = 70 MW/cm$^2$ and width w = 70 μm naturally evolving into a stable mode with width w = 30 μm and peak intensity $I_{max}$ = 0.3 GW/cm$^2$ [operating wavelength λ = 593 μm, effective gain coefficient $g_0$ = 55 cm$^{-1}$ and graphene flake density N = 1000 μm$^{-3}$]. (d) Stable single-mode minimum width $w_{min}$ (red curve) and corresponding gain coefficient $g_0$ (blue curve) plotted against the graphene flake density N. In all plots graphene flakes are assumed to be disks with diameter D = 30 nm.

In conclusion, the extremely low-threshold saturable absorpion of graphene allows us to design an active random metamaterial capable of sustaining single-mode size/shape-controlled laser beams. The external pump intensity and the density of graphene flakes determine the regime of operation, which can be varied from chaotic to stable single-mode. Because the proposed random medium is a disordered mixture of currently available materials, it is promising as an inexpensive and versatile platform for the design of cavity-free light amplifiers and lasers.

**Acknowledgements**

This work has been partially supported by the Spanish MINECO (MAT2014-59096-P and SEV-2015-0522) and the European Commission (Graphene Flagship CNECT-ICT-604391 and FP7-ICT-2013-613024-GRASP). A.M. is supported by an ICFOnest+ Postdoctoral Fellowship (Marie Curie COFUND program). A.M. acknowledges useful discussions with Joel Cox and Valerio Pruneri.

**REFERENCES**

1. D. S. Wiersma, “The physics and applications of random lasers,” *Nat. Phys.*, Vol. 4, 359–367, 2008.
2. Segev, M., Y. Silberberg and D. N. Christodoulides, “Anderson localization of light,” *Nat. Photon.*, Vol. 7, 197–204, 2013.
3. J. Fallert, R. J. B. Dietz, J. Sartor, D. Schneider, C. Klingshirn and H. Kalt, “Co-existence of strongly and weakly localized random laser modes,” *Nat. Photon.*, Vol. 3, 279–282, 2009.

# Reflection amplitudes for turbid colloidal suspensions: Theory and experiment

**G. Morales-Luna[1], H. Contreras-Tello[1], A. García-Valenzuela[1], and R. G. Barrera[2]***

[1]Centro de Ciencias Aplicadas y Desarrollo Tecnológico, Universidad Nacional Autónoma de México, Apartado Postal 70-186, Distrito Federal 04510, México

[2]Instituto de Física, Universidad Nacional Autónoma de México, Apartado Postal 20-364, Distrito Federal 01000, México

*corresponding author: rbarrera@fisica.unam.mx

**Abstract**- First we present a brief review of recently derived formulas for the reflection-amplitude of turbid colloidal suspensions, pointing out the problems found when the effective-medium approach tries to be extended, unsuccessfully, to the calculation of the reflectance in turbid media. Then we report measurements of the reflectance, in an internal-reflection configuration, of turbid suspensions and their comparison with the results obtained with the above-mentioned formulas. Finally, we addressed different options of future work.

A colloidal suspension is a system composed by a collection of small particles dispersed within a homogeneous medium. One refers to the particles as colloidal particles or simply particles, and to the homogeneous medium as the matrix, usually a liquid. Since long, the optical properties of this kind of systems has attracted the attention of many researchers. The roots of this interest are twofold, first the challenge of being able to describe theoretically the propagation of electromagnetic waves through a multiple-scattering system, and second, how to use this knowledge as a practical tool for getting information about the optical and geometrical properties of the collection of colloidal particles, by analyzing the scattered light. The main advantage of an optical tool versus something like electronic microscopy is, that in order to put the samples in the vacuum chamber of an electronic microscope, samples are usually altered while, with an optical tool samples can be analyzed *in situ*. In addition, in many applications one requires to know the average properties of the whole collection of particles, rather than the detailed image of few of them.

A colloidal suspension is turbid when besides light traveling along a definite direction (collimated beam) there is light traveling in all-different directions (diffuse field). The physical origin of turbidity is the scattering of light by the colloidal particles. When the size of the particles is small in relation to the wavelength of the incident radiation, scattering can be neglected, there is only the coherent beam, and the suspension looks transparent. In this case, the optical properties of the suspension are usually described by using an effective-medium approach. In this approach, it is possible to define "effective" optical parameters, like, for example, an effective index of refraction, and then use Snell's law and Fresnel's formulas to describe the refraction, reflection and transmission of light, like in an ordinary material. The problem relies then in finding the effective properties of the suspension in terms of the optical, geometrical and statistical properties of the collection of particles.

Attempts to extend the effective-medium approach to the case of turbid colloids, have found that although it

is possible to define an effective index of refraction for the coherent beam, it is not possible to use it in Fresnel's formulas [1]. The reason is that the suspension has an effective magnetic response even if the particles are non-magnetic, thus an effective index of refraction is not enough for the calculation of the reflection amplitudes using Fresnel's formulas; both the electric permittivity $\varepsilon$ and the magnetic permeability $\mu$ are now necessary. Furthermore, it has been also found that both $\varepsilon$ and $\mu$ are spatially dispersive [1], this means that they depend not only on frequency but also on the wave-vector of the incident radiation. Consequently, it is not possible to obtain the fields by using boundary conditions at the interface and the coherent reflected and transmitted fields have to be calculated going back to Maxwell's equations along with a multiple-scattering formalism. This has been already done for a model of identical spheres randomly located [2, 3], and the formulas derived are given in terms of the diagonal elements of the scattering matrix, among other parameters.

We have also performed reflectance measurements of turbid colloidal suspension using an internal reflectance configuration [4]. We have used a cell containing a water suspension with particles of different materials and particle sizes, attached to the bottom of a cylindrical prism. Laser light enters the suspension through the prism and the angular distribution of the intensity of the reflected light, around the critical angle of the glass-water interface, is measured with a CCD camera. The experimental results are compared with the ones obtained with the above-mentioned formulas and this comparison is then used to discuss the validity of the model and the theoretical formalism.

Finally, we comment on a future project consisting in performing measurements at low angles on a suspension of particles immersed in an index-matching liquid. These measurements can provide a more detailed information about the constitution of the colloidal system, because according to the theoretical predictions, under these conditions the dependence of the reflectance with the angle of incidence has a richer structure. The problem is that at these angles of incidence, the reflectance is so small that improvements on the detection accuracy will be needed.

**Acknowledgements**: Funding of this research is by Dirección General de Asuntos del Personal Académico from Universidad Nacional Autónoma de México through grant PAPIIT IN-100615.

**REFERENCES**

1. R. G. Barrera, A. Reyes Coronado and A. García-Valenzuela, "Nonlocal nature of the electrodynamic response of colloidal systems", *Physical Review B*, Vol, 75, 184202, 2007.
2. R. G. Barrera and A. García-Valenzuela, "Coherent reflectance in a system of random Mie scatterers and its relation to the effective-medium approach," *Journal of the Optical Society of America A*, Vol. 20, 296, 2003.
3. E. Gutierrez-Reyes, A. García-Valenzuela and R. G. Barrera "Extension of Fresnel's Formulas for Turbid Colloidal Suspensions: A Rigorous Treatment", *Journal of Physical Chemistry B*, Vol. 118, 6015, 2014.
4. G. Morales-Luna, H. Contreras-Tello, A. García-Valenzuela, and R. G. Barrera, "Experimental Test of Reflectivity Formulas for Turbid Colloids: Beyond the Fresnel Reflection Amplitudes", *Journal of Physical Chemistry B*, Vol. 120, 583, 2015.

# Landau Damping in the Nonlocal Response of Metal-Dielectric Metamaterials.

**F. Pérez-Rodríguez**

Instituto de Física, Benemérita Universidad Autónoma de Puebla, Mexico
fperez@ifuap.buap.mx

**Abstract**— The propagation of electromagnetic waves through a one-dimensional periodic heterostructure of bilayers with nonlocal metal inclusions is studied. It is shown that the nonlocality of metal conductivity leads to the emergence of the fundamental collisionless Landau damping, which considerably alters the photonic transmission of the metal-dielectric metamaterial within the THz and near-infrared frequency range.

The optical properties of periodic metal-dielectric heterostructures are commonly described within the Drude model, which is based on the assumption of a local relation between the electrical current density and the electric field. However, because of the high mobility of conduction electrons and inhomogeneity of the electromagnetic field in metals, the constitutive equation actually has an integral form and, consequently, is nonlocal. It is well established that such a nonlocality (spatial dispersion) is responsible for the anomalous skin effect. Evidently, the simple Drude model absolutely ignores nonlocal effects. In addition, when the size of the metallic layers is comparable with the skin depth of the electromagnetic field penetration, as it occurs in modern micro- and nanostructures, it is necessary to consider the size effect. In the talk, the spatial-dispersion and size effects upon the photonic band structure of one-dimensional periodic metallodielectric systems are discussed. The nonlocal relation between the electric current density and the electric field inside the metal layers is calculated within the formalism of the Boltzmann kinetic equation in the case of arbitrary (either specular or diffuse) reflection of electrons from metal surface. Because of the nonlocality, the collisionless Landau damping emerges. It is caused by a direct absorption of electromagnetic energy by conduction electrons with large mean-free-path, whose velocity $\mathbf{v}$ coincides with the phase velocity of the wave of frequency $\omega$ and wave vector $\mathbf{k}_m$ inside the electron medium,

$$\omega = \mathbf{k}_m \cdot \mathbf{v}. \tag{1}$$

In the past, the Landau damping has been studied in bulk spatially distributed systems (see, for example, [1]). In the present work, this phenomenon is shown to be essential in the electromagnetic response of metal-dielectric metamaterials. Specifically, a one-dimensional periodic heterostructure composed of alternating nonlocal-metal and dielectric layers is considered. It is shown that if the metallic layers are thin enough, the photonic band structure for a metal-dielectric multilayer stack exhibits narrow pass bands due to the very strong contrast between the impedances of the metal and the dielectric. The narrow pass bands are associated to Fabry-Perot resonances occurring inside the relatively-thick dielectric layer. Besides, the emergence of the collisionless Landau damping considerably alters the photonic band structure of the metal-dielectric metamaterial and its transmission within the THz and infrared frequency range. In particular, the frequency dependence of the Landau damping, which strongly depends on the type of electron reflection from metal-dielectric interfaces, alters the form of the Fabry-Perot resonance structure in the transmission spectra.

**ACKNOWLEDGMENT**

This work was partially supported by VIEP-BUAP, PIFCA, and PROFOCIE.

**REFERENCES**

1. Kaner E. A., A. A. Krokhin, N. M. Makarov, "Spatial dispersion and surface electromagnetic absorption in metals", in the book *Spatial Dispersion in Solids and Plasmas*, Edited by P. Halevi, Elsevier, Amsterdam, Vol. 1, Chap. 2, 161-214, 1992.

# Metallic Nanocolloids: Theoretical Modeling and characterization techniques

**A. L. González**
Instituto de Física, Benemérita Universidad Autónoma de Puebla, Mexico
*corresponding author: anagr@ifuap.buap.mx

**Abstract**- Experimental techniques such as microscopy and spectroscopy (mainly in the range of ultraviolet-visible) offer information of a colloidal sample of metallic nanoparticles about its concentration, size and shape distribution. On the other hand, some theoretical models such as the Discrete Dipole Approximation allows estimate the position, intensity and number of surface plasmon resonances of a metallic nanoparticle with specific size and shape[1]. We present some cases where theorerical and experimental results can be complemented one each other to give a precise description of the size and shape of the nanoparticles that constitutes a colloidal solution.

A colloidal solution of metallic nanoparticles is usually sinthesized by chemical methods, in it the nanoparticles are randomly oriented and the sample presents size and shape distribution. People seek to control the syntesis process to reach one goal: a narrow size and shape distribution. But, then a question arises, how important is to obtain a sample with a very narrow distribution of size and shape? The response seems not to unique, specially if we think in the possible applications, for some of them it could be important but maybe not for others.

Metallic nanoparticles are important because they offer a wide range of applications due to the collective motion of its conduction electrons (surface plasmons) when an electromagnetic field is applied[2]. Particularly, medicine is one of the sciences that seem to be beneffit with the plasmonic properties of the nanoparticles, because with their help it is possible to make earlier detection, a better diagnosis, and hopefully a less painful treatment of some illnesses, such as cancer or diabetes.

From the basic science point of view it is important to identify if the average size and shape that describes a sample is enough to represent its physical properties. In this context, we present some cases about silver and gold nanoparticles colloids where the average size and shape have been considered in theoretical models to complement information obtained from experimental techniques such as spectroscopy UV-Vis and Transmission electron microscopy[2,3].

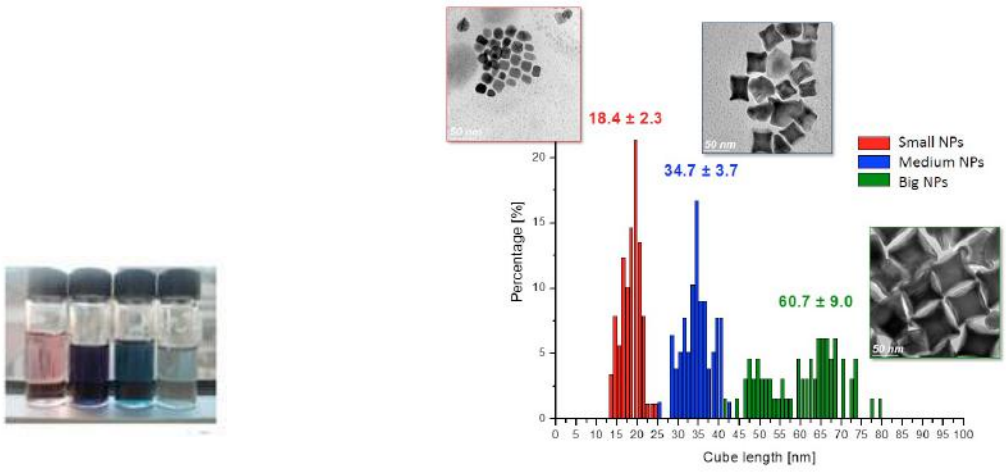



**Figure 1.** To the left, a picture of gold nanoparticles colloids with different sizes and shapes. To the right, the size distribution of each sample.

## REFERENCES


1. González, A. L., Noguez C., Ortiz G. P. and G. Rodríguez-Gattorno, "Optical Absorbance of Colloidal Suspensions of Silver Polyhedral Nanoparticles", *Journal of Physical Chemistry B*, 109, 17512-17517, 2005.
2. González, A. L. And C. Noguez, "Influence of Morphology on the Optical Properties of Metal Nanoparticles", *Journal of Computational and Theoretical Nanoscience*, 4, 231-238, 2007.
3. Romo Herrera J. M., González A. L., Guerrini L., Castiello F. R., Alonso-Nuñez G., Contreras O. E. and Alvarez-Puebla R. A.," Study of deph and size of Au concave cube nanoparticles as highly sensitive SERS probes", *submitted to Nanoscale*, 2016.

# Polarization statistics in disordered media:

# Modelization and measurements

**Myriam ZERRAD, Ayman GHABBACH, Gabriel SORIANO, Quentin AILLOUD, and Claude AMRA**

Aix-Marseille Université, CNRS, Ecole Centrale Marseille, Institut FRESNEL
Domaine universitaire de Saint Jérôme 13013 Marseille, France
corresponding author: myriam.zerrad@fresnel.fr

**Abstract**: A statistical study of polarimetric parameters of the speckle scattered by a disordered media under coherent illumination is presented. A dedicated metrology was developed to measure accurate histograms of the polarization degree. Recorded data are compared to modelization and structural signatures are extracted to analyze complex media.

Huge improvements were achieved in the field of imaging in complex media, with applications dedicated to living and space ... Most techniques involve near field or far field data, polarization and coherence, shaping or correction of wave fronts, tomography, structured illumination, forced depletion, multi-photonic and non-linear processes... However most often these techniques are deterministic, in the sense that we analyze an output signal resulting from a controlled input, even that input would sweep a large number of parameters (wavelength, polarization, incidence ...).

Within this framework, a statistical scan would provide an alternative technique, and this is made possible through the temporal statistics of light which characterize partial polarization. In other words, an incident partially polarized beam carries a temporal disorder whose statistics are modified by the spatial disorder of the illuminated sample. Here we analyze the detail of these modifications versus the structural parameters of the media, with a special attention to the histograms of state and polarization degree that can be predicted and measured within each speckle area of the scattering pattern. Such investigation provides complementary signatures specific of surface roughness and bulk heterogeneities. The formalism brings together statistical optics and electromagnetic optics. Measurements are provided by a specific facility on the support of ellipsometric techniques developed for each speckle area. A series of samples are compared and show how the dop histograms are modified with absorption, roughness and inhomogeneity.

**Acknowledgements**

This work was supported by the French National Research Agency (ANR – TraMEL Project)

**Mis en forme :** Retrait : Première ligne : 1,63 ca

**REFERENCES**

1. M. Zerrad, G. Soriano, A. Ghabbach, and C. Amra, "Light enpolarization by disordered media under partial

polarized illumination: The role of cross-scattering coefficients," Opt. Express 21, 2787-2794 (2013).
2. G. Soriano, M. Zerrad, and C. Amra, "Enpolarization and depolarization of light scattered from chromatic complex media," Opt. Express 22, 12603-12613 (2014)
3. A. Ghabbach, M. Zerrad, G. Soriano, and C. Amra, "Accurate metrology of polarization curves measured at the speckle size of visible light scattering," Opt. Express 22, 14594-14609 (2014)
4. A. Ghabbach, M. Zerrad, G. Soriano, S. Liukaityte, and C. Amra, "Depolarization and enpolarization DOP histograms measured for surface and bulk speckle patterns", Optics Express, Vol. 22, Iss. 18, p. 21427 (2014)
5. J. Dupont, X.r Orlik, A. Ghabbach, M. Zerrad, G. Soriano, and C. Amra, "Polarization analysis of speckle field below its transverse correlation width : application to surface and bulk scattering," Opt. Express 22, 24133-24141 (2014)
6. J. Sorrentini, M. Zerrad, G. Soriano, and C. Amra, "Enpolarization of light by scattering media," Optics Express 19, 21313-21320 (2011).
7. M. Zerrad, J. Sorrentini, G. Soriano, and C. Amra, "Gradual loss of polarization in light scattered from rough surfaces: Electromagnetic prediction," Optics Express 18, 15832-15843 (2010).

# Controlling light-scattering losses in dense nanocolloids

**Augusto Garcia-Valenzuela[1], Roberto Marquez-Islas[1], Rubén G. Barrera[2],**

[1]Centro de Ciencias Aplicadas y Desarrollo Tecnológico, Universidad Nacional Autónoma de México, Apartado Postal 70-186, Ciudad de México, 04510, México
[2] Instituto de Física, Universidad Nacional Autónoma de México, Apartado Postal 20-364, Ciudad de México, 01000, México
*corresponding author, E-mail: augusto.garcia@ccadet.unam.mx

## Abstract

First, we present a brief review of the two most common approximations available today to calculate the complex effective refractive index of a disordered suspension of nanoparticles that take into account the effects of scattering by the particles. We study theoretically the dependence of the scattering losses in nanocolloids with the concentration of non-absorbing and weakly-absorbing nanoparticles. Then, we explore a way to reduce scattering losses in non-absorbing nanoparticles, providing new physical insight into the dependence of scattering losses with the particle concentration and its possible control.

## 1. Introduction

Metamaterials based on metallic resonating structures have losses that undermine their performance in many interesting applications [1]. All-dielectric metamaterials are being investigated as a possible way to avoid absorption losses while still offering the possibility of exotic optical-properties such as optical magnetism [1,2]. Disordered systems of photonic elements are of particular interest, since in many cases, they are much simpler to fabricate than ordered ones. Colloidal suspensions or solid composite materials consisting of small particles embedded in a transparent matrix are some possible candidates for disordered metamaterials. In particular, nanocolloids of particles with a refractive index significantly different from that of the matrix are being looked at [2]. However, a large refractive index (RI) mismatch between the particles and the matrix causes an increase in scattering losses.

The attenuation of an electromagnetic wave propagating through a suspension of particles is $\exp(-\alpha l)$ where $\alpha$ is called the extinction coefficient. In general, the extinction coefficient can be related to an effective refractive index of the suspension of particle. This effective refractive index describes the propagation of the configurational-average electromagnetic field. Thus we can write,

$$\alpha = 2k_0 \mathrm{Im}\left(n_{eff}\right). \quad (1)$$

In general, $\alpha$ has contributions from scattering and absorption by the particles. From measurements of only the extinction coefficient of a nanocolloid, scattering losses are indistinguishable from absorption losses.

In non-absorbing suspensions of small particles, losses arise from scattering. Scattering losses are unavoidable and their magnitude depends non-trivially on the particles' size, shape, refractive index. For very dilute suspensions of particles the extinction coefficient is proportional to the particles' concentration. When this holds some researchers refer to being within the "independent-scattering" regime. However, it is well known that the extinction coefficient has a non-linear relationship with the particles' volume-concentration at moderate densities [3-7]. Such non-linearity is often referred to as "dependent-scattering". At low particle concentrations a quadratic dependence on the particle's concentration of the extinction coefficient is observed [4-6]. For particles very small compared to the wavelength of light, this quadratic dependence reduces the scattering losses compared to those predicted by the independent scattering approximation.

To date the general dependence and physical origin of dependent-scattering effects has remained somewhat obscure. For particles with low RI contrast with the surroundings, interference between the scattered fields by nearby particles may be held responsible for dependent scattering effects [7]. However, for highly scattering particles dependent scattering effects may have a qualitatively different origin and the interference explanation is no longer suitable [3-6]. When particles are small enough compared to the wavelength of light they can be regarded as radiating dipoles, either electric or magnetic, and if one ignores scattering losses, one can use Maxwell Garnett's type formulas to obtain an effective refractive index [3]. These formulas can be used at moderate particles' density and for absorbing particles with a complex refractive index, one obtains an effective RI with a nonlinear dependence with particles' concentration. Scattering effects can be introduced simply by including radiation corrections to the polarizability of particles [3,8]. However, these corrections are not enough to take into account properly scattering effects at moderately small particles' concentration and denser systems. Outside the very dilute regime and when the imaginary part of the effective RI is dominated by scattering losses we can use instead the small particle limit of the so-called Quasi-Crystalline Approximation (QCA) [3], which include "dependent scattering" effects.

Although the physical nature of the so-called "dependent scattering" is an interesting and relevant question, we will not address it now. Here, we will limit our attention to investigate a possible mechanism to reduce the light-scattering losses in a disordered system of nanoparticles. However, in order to obtain some insight into the dependence of scattering losses in moderately dense nanocolloids we need to consider both, the independent- and dependent-scattering regimes. For simplicity, we will consider a system of identical non-magnetic spherical particles of radius *a* and refractive index $n_p$ embedded in a non-magnetic transparent matrix of RI $n_m$, and for the independent- and dependent-scattering approximations we will consider the formulas for the effective refractive index obtained from the so-called van de Hulst approximation and the small-particle limit of the Quasi-Crystalline Approximation (QCA), respectively.

## 2. Van de Hulst's approximation

A widely used approximation for calculating the effective propagation constant in a dilute and random system of particles is the so called Effective-Field Approximation (EFA). This approximation assumes that the field exciting any given particle is the average field. The effective propagation constant obtained within the EFA is also referred to as the Foldy-Lax effective propagation constant [9,10] and is given by,

$$k_{eff} = k_m \sqrt{1 + i3f \frac{\mathrm{S}(0)}{x_m^3}} \qquad (2)$$

where *S*(0) is the forward scattering amplitude of an isolated particle embedded in the matrix, $x_m = k_m a$ is the size parameter, $k_m$ is the wave number in the medium surrounding the particle, called the matrix, and *a* is the radius of the particles. An effective refractive index can be obtained by dividing $k_{eff}$ by the wavenumber in vacuum, $k_0 = 2\pi/\lambda$. The EFA is valid only when the contribution of the particles to the effective propagation constant is small and thus we may expand the square root in Eq. (1) and keep only the first two terms. The resulting effective refractive index is that referred to as the van de Hulst effective refractive index given by [10],

$$n_{eff} = n_m \left(1 + i\frac{3}{2} f \frac{\mathrm{S}(0)}{x_m^3}\right). \qquad (3)$$

Let us denote then the extinction coefficient under the "independent-scattering" approximation as $\alpha_{ind}$. It is given by,

$$\alpha_{ind} = 2k_0 \mathrm{Im}\left(n_{eff}\right) = 3k_m f \frac{\mathrm{Re}[\mathrm{S}(0)]}{x_m^3} \qquad (4)$$

Using $f = \rho\,(4\pi/3)a^3$ , where $\rho$ is the number-density of particles and $(4\pi/3)a^3$ is the volume of one particle. We can rewrite the latter equations as

$$\alpha_{ind} = \frac{4\pi\rho}{k_m^2} \mathrm{Re}[\mathrm{S}(0)] = \rho C_{ext} \qquad (5)$$

where $C_{ext} = \frac{4\pi}{k_m^2}\mathrm{Re}[\mathrm{S}(0)]$ is the extinction cross section of the particles.

In the van de Hulst approximation the extinction coefficient grows linearly with the density of particles, and the attenuation of intensity follows Beer-Lambert's Law in the form, $I(l) = I_0 \exp(-\rho C_{ext} l)$ . However, as already mentioned in the introduction, when the density of particles is not small, and depending on the size and refractive index of the particles, the extinction coefficient has a non-linear dependence on the density of the particles. This non-linear dependence is also referred to as "dependent-scattering" effects, implying that the particles do not scatter light as isolated particles, but that their scattering efficiency is affected by the presence of the surrounding particles. In fact, the deviation of the scattering efficiency of particles from a linear relationship arises from the fact that the field exciting any of the particles is not really equal to the average field, but to the so called local-field. The average local-field for a given particle differs from the average field at a given position in space in that it does not include the field scattered by the particle itself. The first correction to the EFA is the so called Quasi-Crystalline Approximation (QCA) which we will briefly review in the next section.

## 3. The Quasi-Crystalline Approximation

The so called Quasi-Crystalline Approximation (QCA) consists on formulating and solving a self-consistent integral equation for the average exciting-field to any of the particles, and then using this exciting field to calculate the average field scattered by all the particles [11,12]. A correlation function for the position of any two particles appears when the average dipolar interaction between two particles is calculated.

The small particle limit of the QCA was calculated by Tsang and Kong some time ago [11,12]. They obtained,

$$n_{eff}^2 = n_m^2 +$$

$$+3f n_m^2 \Gamma \left\{1 + i\frac{2}{3} x_m^3 \Gamma \left[1 + 4\pi\rho \int_0^\infty r^2 (g(r) - 1) dr\right]\right\} \qquad (6)$$

where $n_m$ is the refractive index of the medium surrounding the particles (the matrix), $f$ is the volume fraction occupied by the particles, $\rho$ is the number volume-density of particles, $g(r)$ is the two-particle correlation function and

$$\Gamma = \frac{\chi}{1 - f\chi},$$

where $\chi$ is the normalized polarizability of a particle, and for spherical particles it is given by $\chi = (n_p^2/n_m^2 - 1)/(n_p^2/n_m^2 + 2)$ . For simplicity we will approximate the two-particle correlation function by the so-called "hole correction". That is, we assume that for any two given particles, the probability of finding their centers a distance *r* apart from each other is constant whenever they are separated by more than one diameter and zero otherwise. In other words, we suppose that the position of any given particle is completely random except that it cannot penetrate any other particle. This approximation is known to be good

for particles' volume concentration up to about 10% [13]. We have,

$$g(r) = \begin{cases} 1 & if \quad r \geq 2a \\ 0 & if \quad r < 2a' \end{cases} \qquad (7)$$

where $a$ is the radius of the particles. In this case the integral in Eq. (1) can be easily performed. We get,

$$\int_0^{2a} r^2(-1)dr = -\frac{8a^3}{3}$$

Then Eq. (6) yields,

$$n_{eff}^2 = n_m^2 + 3f n_m^2 \Gamma\left\{1 + i\frac{2}{3}x_m^3\Gamma[1-8f]\right\} \qquad (8)$$

where we used, $f = \rho\,(4\pi/3)a^3$. Since $\alpha = 2k_0 \mathrm{Im}\left(n_{eff}\right)$ one gets,

$$\alpha_{QCA} = 2k_0 \mathrm{Im}\left(\sqrt{n_m^2 + 3f n_m^2 \Gamma\left\{1 + i\frac{2}{3}x_m^3\Gamma[1-8f]\right\}}\right) \qquad (9)$$

In Fig. 1 we plot the imaginary part of $n_{eff}$ for a vacuum wavelength of 420 nm in the independent and quasi-crystalline approximations as a function of the particles' volume fraction $f$ for a nanocolloid of non-absorbing particles of radius $a$ = 5 nm and refractive index $n_p = 1.6$ dispersed in a medium of RI $n_m = 1.33$.

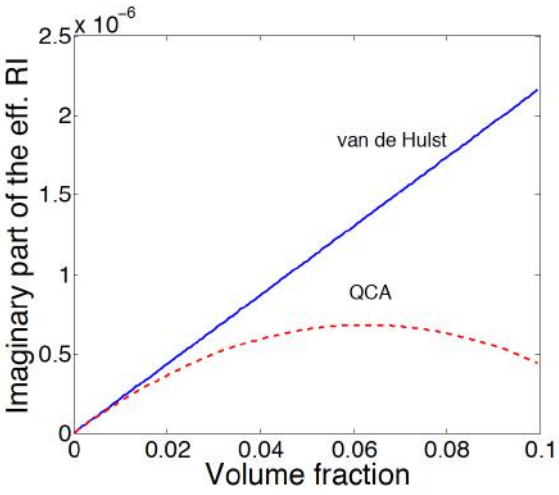



Figure 1: Plot of the Imaginary part of the effective refractive index of a nanocolloid of particles of 5 nm radius dispersed in a medium of RI $n_m$ = 1.33 at a wavelength of 420 nm in the van de Hulst approximation (full blue line) and in the Quasi-Crystalline approximation (dashed red line) for $n_p$ = 1.6.

We can see in Fig. 1 that the curve of the imaginary part of the effective refractive index in the QCA bends away from the independent scattering approximation to smaller values. In this example the imaginary part of $n_{eff}$ has a maximum for $f$ of about 6.5% and is somewhat less than half of the value for the independent scattering approximation. This means that as the the particles' volume fraction increases beyond 6.5% there is a decrease of the scattering losses.

## 4. The effective extinction factor

It is useful to define an Effective Extinction Factor (EEF) as the ratio between the actual extinction coefficient and the independent scattering approximation [6]. We will denote it as $\gamma$. The EEF under the QCA is given by,

$$\gamma_{QCA} = \frac{\alpha_{QCA}}{\alpha_{ind}}. \qquad (10)$$

When particles are small compared to the wavelength the EEF in the QCA is always less than one. In Fig. 2 we plot the EEF in the independent scattering approximation (van de Hulst) and the QCA versus $f$ for a nanocolloid of particles of radius $a$ = 5 nm and refractive index of $n_p = 1.6$ dispersed in a medium of refractive index $n_m = 1.33$ and a vacuum wavelength of 420nm. We have found that the EEF is rather insensitive to particle radius. For $a$ between 1 nm and 10 nm the EEF curves shown are practically indistinguishable for $n_p = 1.6$ and $n_m = 1.33$.

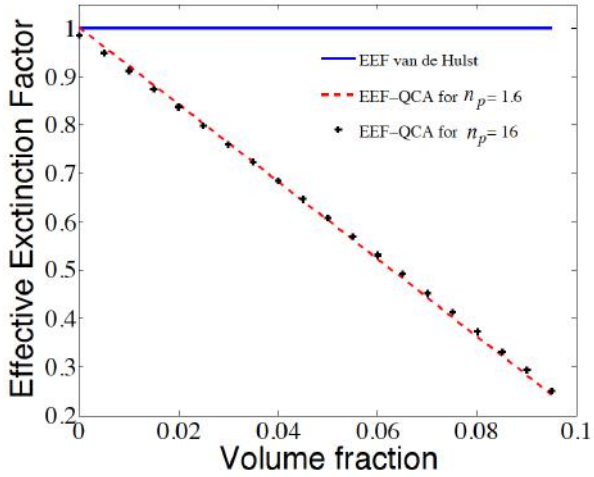



Figure 2: Plots of the EEF for a nanocolloid of particles of 5 nm radius dispersed in a medium of RI $n_m$ = 1.33 at a wavelength of 420 nm in the van de Hulst approximation (full blue line), Quasi-Crystalline approximation (dashed red line) for $n_p$ = 1.6 and Quasi-Crystalline approximation (black symbols) for $n_p$ = 16.

Also, the EEF is a rather insensitive function of the particle's refractive index. To illustrate this, we also plot in Fig. 2 the EEF in the QCA for particles of refractive index 10 times larger, that is for $n_p = 16$. A refractive index with such a large value and without an imaginary part may be unrealistic at optical frequencies. However, at smaller frequencies it may be possible. We can appreciate that the difference of the EFFs for particles of RI of 1.6 and 16 is very small. In fact, for particles of the same radius and of RI of unity (e.g. nanobubbles) the EEF is practically undistinguishable from that for particles with RI up to about 5. Of course, even

though the EEF is not very sensitive to neither $n_p$ nor $a$, the effective RI, $n_{eff}$, do depend noticeably on the particles' RI.

## 5. Effect of the nanoparticles' absorption on the extinction coefficient and the EEF

Up to this point we have assumed the nanoparticles are non-absorbing and have a real RI. When the particle's RI has an imaginary component the extinction will be due to scattering and absorption as well. In the next two figures, Figs. 3 and 4, we plot the Imaginary part of $n_{eff}$ and the corresponding EEF versus the particles volume fraction $f$ for particles of radii of $a$ = 10 nm and complex RI given by $n_{eff} = 1.6 + iy$. We show plots for values of $y$ of $1\times10^{-6}$, $1\times10^{-5}$, $5\times10^{-5}$, $1\times10^{-4}$ and $5\times10^{-4}$

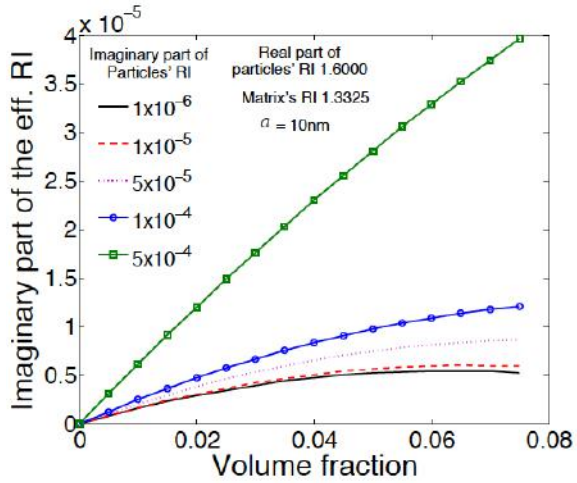



Figure 3: Plots of Im ($n_{eff}$) for a nanocolloid of particles of 10 nm radius and $n_p$ = 1.6 + $iy$, dispersed in a medium of RI $n_m$ = 1.33 at a wavelength of 420 nm for a few values of the imaginary part of the particles' RI, $y$ (values indicated in the legends).

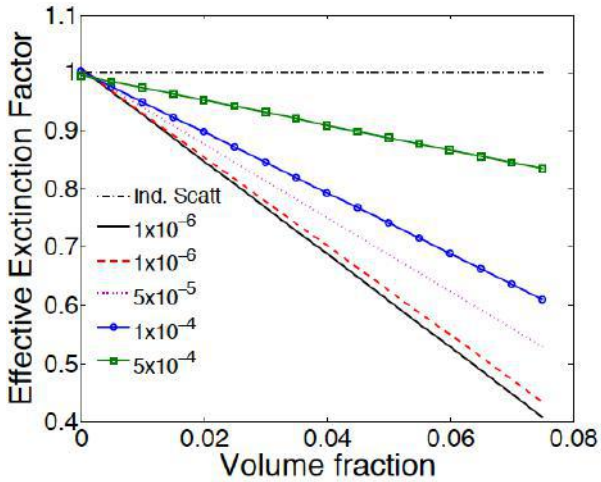



Figure 4: Plots of the EEF verus the particles' volume fraction for the corresponding curves shown in Fig. 5. In addition, here the independent scattering approximation curve is included (horizontal dashed curve).

We can appreciate in Fig. 3 that as the imaginary part of the particles' RI increases the curve for the imaginary part of $n_{eff}$ versus $f$ is steeper, meaning that the absorption rapidly dominates over the scattering losses. The curves also get straighter, meaning that the independent scattering approximation becomes more appropriate as the extinction of light is dominated by absorption instead of scattering. As a consequence, the EEF versus $f$ curves move towards a horizontal line as it can be seen in Fig. 4.

## 6. Controlled reduction of scattering losses in disordered nanoparticle suspensions

Here we will consider again only non-absorbing nanocolloids. As already mentioned in the introduction, it is of interest to modify the real part of the effective RI of a medium but without introducing appreciable turbidity. From Fig. 1 it is clear that for a random system of non-absorbing particles small compared to the wavelength of light, the so-called "dependent scattering" lessens the scattering losses below what it would be if every particle scatters independently (of the presence of others). This effect can be improved noticeably if the particles are not allowed to approach each other to the point where their surfaces touch each other. Let us suppose the centers of any two particles can approach each other a distance $2b > 2a$, where $a$ is the radii of the nanoparticles. In practice, this could be achieved by covering the particles with a material of the same RI of the matrix. For instance, by encapsulating the particles within a larger spherical particle or radius $b$ in such a way that their centers are concentric. To keep things simple, let us assume that the hole correction is still a valid approximation to the pair correlation function. Thus, we have,

$$g(r) = \begin{cases} 1 & if \quad r \geq 2b \\ 0 & if \quad r < 2b' \end{cases} \qquad (11)$$

In this case, Eq. (4) yields,

$$n_{eff}^2 = n_m^2 + 3f n_m^2 \Gamma \left\{ 1 + i\frac{2}{3}x_m^3 \Gamma \left[ 1 - 8f\frac{b^3}{a^3} \right] \right\}. \qquad (12)$$

It is clear from Eq. (12) that the increase in "effective-contact" radius will result in a reduction of the imaginary part of the square of the effective RI.

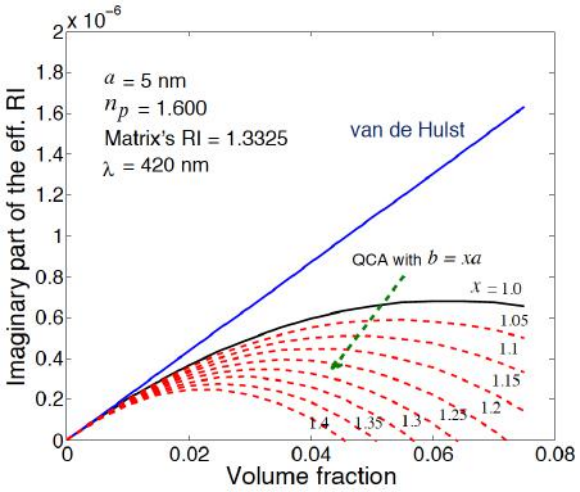



Figure 5: Graphs of Im ($n_{eff}$) for a nanocolloid of particles of 5 nm radius and $n_p$ = 1.6, dispersed in a medium of RI $n_m$ = 1.33 at a wavelength of 420 nm in the independent scattering approximation (van de Hulst approximation, full blue line) and the Quasi-Crystalline approximation with different values of the contact radius *b*.

In Fig. 5 we plot the imaginary part of the effective RI versus the particle's volume concentration, *f*, for a nanocolloid of particles of 5 nm radius and RI $n_p = 1.6$ dispersed in a medium of RI $n_m$ = 1.33 and a vacuum wavelength of 420 nm. We plot curves for the independent scattering approximation and for the QCA with a contact radius given by $b = xa$ with *x* varying from 1.0 (nude particles) to 1.4 in steps of 0.05 (covered particles). In Fig. 6 we plot the EEF for the curves shown in Fig. 5, but we only plot the EEF for values of *x* varying from 1.0 to 1.4 in steps of 0.1.

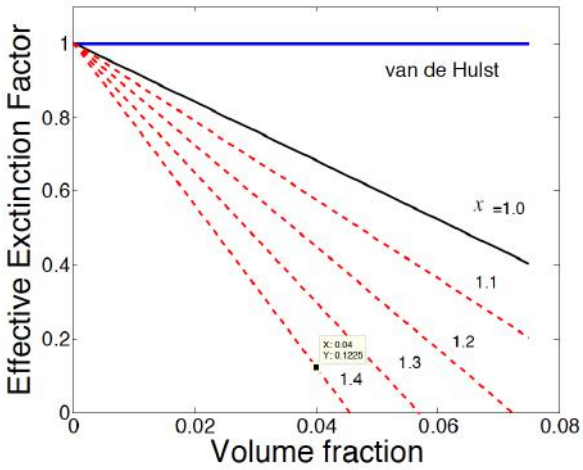



Figure 6: Plots of the EEF for a nanocolloid of particles of 5 nm radius and $n_p$ = 1.6 dispersed in medium of RI $n_m$ = 1.33 at a wavelength of 420 nm in the independent scattering approximation (van de Hulst approximation, full blue line) and Quasi-Crystalline approximation for different values of the contact radius *b*.

We can appreciate from Figs. 5 and 6 that the imaginary part of the effective RI, and thus, the extinction coefficient decreases noticeably as the effective contact radius *b* increases. In Fig. 3 we also see that the maximum of turbidity shifts to smaller values of the particles' volume fraction *f* as *b* increases. For instance, for a value of $b = 1.4a$ the turbidity predicted by the QCA at $f$ = 2% is about 60% less than that predicted by the independent scattering approximation whereas at $f$ = 4% it is 88% less. Of course the QCA must loose accuracy as the predicted value of the imaginary part of $n_{eff}$ approaches zero and is, of course, mistaken when it predicts negative values. Clearly $\mathrm{Im}(n_{eff})$ cannot take negative values in the current scenario. A more complete theory for the extinction of nanocolloids able to deal with higher densities is still to be developed.

## 7. Summary and conclusions

We studied theoretically the dependence of $n_{eff}$ with *f* in a disordered system of very small particles compared to the wavelength of radiation. The examples chosen in this work correspond to non-absorbing and weakly absorbing nanocolloids at visible wavelengths with the concentration of particles up to 10%. Our conclusions can be relevant on other analogous systems at other wavelengths for particles of similar size parameters and RI. We used two well known approximations. The so-called van de Hulst approximation and the Quasi-Crystalline Approximation in the limit of small particles. For simplicity, we considered the QCA with a pair correlation function consisting of a "hole correction" of radius equal to particles' radius.

We concentrated on the case of non-absorbing particles suspended in a transparent matrix. The van de Hulst approximation yields a contribution of the particles to the effective RI proportional to the particles' volume concentration, *f*. Thus, in this approximation, the extinction coefficient, which is proportional to Im($n_{eff}$) varies linearly with *f*. The QCA includes nonlinear terms on the dependence of $n_{eff}$ on *f*. Some researchers refer to the range of values of *f* where there is a linear dependence of Im($n_{eff}$) with *f*, as the "independent-scattering" regime. Outside the linear range one may refer to a "dependent-scattering" regime.

Both approximations considered, predict a linear dependence of the real part of the effective RI with *f* up to 10%. However, for the imaginary part of $n_{eff}$, the QCA yields a quadratic dependence on *f*, and Im($n_{eff}$) bends away from the independent scattering approximation towards smaller values. The effective extinction factor, EEF, defined as the ratio of the extinction coefficient divided by that one calculated with the independent scattering approximation, predicted by the QCA is basically a straight line up to $f$ =10% and insensitive to the particles' RI, $n_p$ when this is a real quantity.

Next we explored a simple idea to reduce the scattering losses (that is, reduce the extinction coefficient). Basically we proposed to increase the minimum distance that any two particles can approach each other. This can be achieved by, for example, encapsulating the particles within a spherical particle of larger radius and a RI that matches that of the matrix. We showed that the imaginary part of $n_{eff}$ bends faster

as the minimum distance between particles is increased. A noticeable reduction of the maximum turbidity of the system can achieved in this way. Then, we briefly considered a system of absorbing particles, showing that as the imaginary part of the particle's RI increases, the curve of Im($n_{eff}$) versus $f$ straightens, meaning that as absorption by the particles dominates over scattering, the independent scattering regime widens noticeably.

## Acknowledgements

We acknowledge financial support from Dirección General de Asuntos del Personal Académico from Universidad Nacional Autónoma de México through grant PAPIIT IN-100615.

## References

[1] Jahani Samani and Jacob Zubin, "All-dielectric metamaterials", *Nature Nanotechnology* 11: 23-36, 2016.

[2] Zhao Qian, Zhou Ji, Zhang Fuli, Lippens Didier, "Mie resonance-based dielectric metamaterials," *Materials Today* 12 (12): 60–69, 2009.

[3] Sihvola A., *Electromagnetic mixing formulas and applications*, The Institution of Engineering and Technology, London UK, 1999.

[4] L. Hespel, S. Mainguy, J-J Greffet, "Theoretical and experimental investigation of the extinction in a dense distribution of particles: nonlocal effects" *J. Opt. Soc. Am* 18 (12): 3072-3076, 2001.

[5] S. Durant, O. Calvo-Perez, N Vukadinovik, J-J Greffet, "Light scattering by a random distribution of particles embedded in absorbing media: full-wave Monte Carlo solutions of the extinction coefficient", *J. Opt. Soc. Am. A* 24 (9): 2953-2961, 2007.

[6] A. García-Valenzuela, H. Contreras-Tello, F. L. S. Cuppo, J. A. Olivares, Insights into the dependent scattering contributions to the extinction coefficient in highly scattering suspensions, *J. Opt. Soc. Am. A* 30 (7): 1328-1334, 2013.

[7] Y. Huang and E. M. Sevick-Muraca, Validating the assumption to the interference approximation by use of measurements of absorption efficiency and hindered scattering in dense suspensions, *Appl. Opt.* 43 (4): 814-819, 2004.

[8] Mallet Pierre, Guérin C. A. and Sentenac Anne, "Maxwell-Garnett mixing rule in the presence of multiple scattering: Derivation and accuracy", *Physical Review B* 72: 014205, 2005.

[9] L. L. Foldy, The Multiple Scattering of Waves. I. General Theory of Isotropic Scattering by Randomly Distributed Scatterers *Phys. Rev.* 67: 107-119 1945; M. Lax, Multiple Scattering of Waves, *Rev. Mod. Phys.* 23 (4): 287-310, 1951

[10] R. G. Barrera, A. Reyes-Coronado and A. García-Valenzuela, Nonlocal nature of the electrodynamic response of colloidal systems, *Physical Review B* 75: 184202, 2007.

[11] L. Tsang, J. A. Kong, Theory of microwave remote sensing, Wiley series in remote sensing, Wiley, New York, 1985.

[12] L. Tsang and J. A. Kong, *Scattering of Electromagnetic Waves; Advanced Topics*, John Wiley and Sons, Inc., New York, 2001

[13] A. Ishimaru and Y. Kuga, Attenuation constant of coherent field in a dense distribution of particles, *J. Opt. Soc. Am.* 72: 1317–1320, 1982.

[14] Ana Domínguez, Aurora Fernández, Noemí González, Emilia Iglesias, and Luis Montenegro, Determination of Critical Micelle Concentration of Some Surfactants by Three Techniques, *J. Chem Ed.* 74 (10): 1227-1231, 1997.

[15] Meggan King and Andrew M. Bowen, *The Microscope* 60 (1): 11-15, 2012.

# Nano and Mesoscopic Optics in Colloidal and Granular Systems

# Optical tweezers unveil new physics: Nonadditivity of critical Casimir forces and failure of Jarzynski equality in active baths

**Giovanni Volpe**[1]

[1] Soft Matter Lab, Physics Department, Bilkent University, Ankara, Turkey

[2] UNAM – National Nanotechnology Research Center Bilkent University, Ankara, Turkey

giovanni.volpe@fen.bilkent.edu.tr

**Abstract**-Since their invention, optical tweezers have been employed to uncover new physics. Here, I will discuss two recent experiments: (1) the experimental demonstration of the failure of Jerzynski equality in active baths; and (2) the experimental demonstration of the existence of many-body effects in critical Casimir forces.

Optical manipulation has been successfully applied to study a broad range of physical, chemical, and biological phenomena [1,2], often leading to the discovery of new physics. Here I will discuss (1) the experimental demonstration of the failure of Jerzynski equality in active baths; and (2) the experimental demonstration of the existence of many-body effects in critical Casimir forces.

## FAILURE OF JARZYNSKI EQUALITY IN ACTIVE BATHS

Understanding phenomena far from equilibrium, such as living matter, is the new frontier of physics. Important advances have been made in the last decades, introducing some mathematical relations capable of linking nonequilibrium and equilibrium phenomena. The Jarzynski equality, for example, has been verified experimentally in several systems all but always coupled to a thermal bath. However, these works have not considered the case where the environment is itself far from equilibrium. Our experiments with an optically trapped particle in a bacterial bath demonstrate that in such conditions, i.e. in an active bath, the JE fails because of the presence of non-Boltzmann statistics [3]. Our results point the study of nonequilibrium statistical physics towards a new direction, where also the environment is far from equilibrium.

## NONADDITIVITY OF CRITICAL CASIMIR FORCES

Recently, critical Casimir forces proved to be a paradigmatic tool for controlling the self-assembly and complex behavior of micro- and nanoparticles. They are central for these phenomena and entail many-particle interactions. Thus it is crucial to understand whether and to what extent many-body forces are in action. Despite available theoretical studies, their experimental demonstration has been lacking. Employing holographic optical tweezers, we provided the first experimental demonstration of the nonadditivity of critical Casimir forces [4]. The summary should describe the approach and the article's major contributions, emphasizing the importance and significance of the results with proper cited reference to be listed in the reference section at the end of the article. The paper length should not exceed 2 pages. Equations, figures, tables and references should follow a

sequential numerical scheme in order to ensure a logical development of subject matter.

**REFERENCES**


1. Maragò, O. M., P. H. Jones, P. Gucciardi, G. Volpe & A. Ferrari, "Optical trapping and manipulation of nano structures," *Nature Nanotech.* **8**, 807–819, 2013.
2. Jones, O. H., O. M. Maragò, and G. Volpe. *Optical Tweezers: Principles and Applications*, Cambridge University Press, 2015
3. Argun, A., A.-R. Moradi, E. Pince, G. B. Baris, and G. Volpe, "Experimental evidence of the failure of Jarzynski equality in active baths," *Arxiv*, 1601.01123 (2016).
4. Paladugu, A., A. Callegari, Y. Tuna, L. Barth, S. Dietrich, A. Gambassi, and G. Volpe, "Nonadditivity of Critical Casimir Forces," *Arxiv*, 1511.02613 (2015).

# Controlling and probing weak colloidal interactions with complex laser light fields

**F. Scheffold**[1]

[1]Department of Physics, University of Fribourg, Chemin du musée 3, CH-1700 Fribourg, Switzerland
Frank.Scheffold@unifr.ch

**Abstract**— I will discuss a several examples how we can manipulate and probe soft interactions between small, submicron colloidal spheres using optical means such as lasers, fluorescence and scattering.

The control and understanding of interactions between colloidal particles is of fundamental interest in condensed matter physics but also of great importance for the design of new materials. Here I will focus on three types of colloidal systems: charge stabilized polymer beads, emulsion droplets and microgels. These three popular model systems are rather well defined and the properties can be analyzed and tuned by different means. I will first speak about strongly screened charge stabilized polymer beads with a solid polymer core. In the absence of other forces these systems essentially behave as hard spheres. I will present an experiment on a pair of particles where we demonstrate that the interaction potential can be tuned externally by inducing artifical van-der Waals attractive forces when embedding the particles in a very intense diffuse light cloud [1]. I will then proceed to discuss two colloidal systems where the particles are deformable. First I will discuss the popular microgel particles where the swelling can be tuned by changing the solvent properties. These smart colloids with tunable size and elasticity have attracted much attention because of their potential use as drug delivery agent or for tuning the flow properties of complex fluids. Here I will present a novel experiment where we have used STORM superresolution microscopy (nanoscopy) to study the swelling of individual and jammed microgel particles on the nanoscale [2]. I will conclude by briefly presenting closely related results on dense suspensions of nano- and micron sized emulsion droplets where we study the glass and the jamming transition from the fluid to the highly compressed regime using a combination of confocal microscopy, low-coherence light scattering and diffusing wave spectroscopy [3, 4].

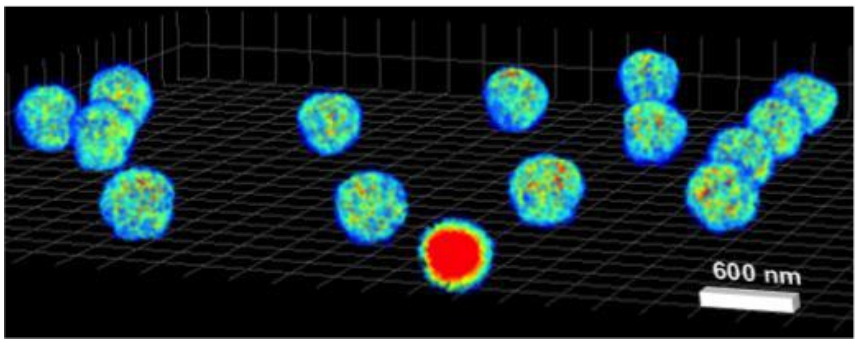



Figure 1: 3D superresolution image of pNIPAM microgels with a 30nm lateral optical resolution. Particle diameter ca. 500nm.

## ACKNOWLEDGMENT

I would like to acknowledge the contribution of coworkers and international collaborators listed in the respective publications.

## REFERENCES

1. Brügger, G., Froufe-Pérez, L.S., Scheffold, F. and Saenz, J. J., "Controlling dispersion forces between small particles with artificially created random light fields", *Nat. Comm.*, Vol. 6, 7460 (2015).

2. Conley, G. M., Nöjd, S., Braibanti, M., Schurtenberger, P. and Scheffold, F., "Three-dimensional nanoscopy of thermosensitive Poly(N- isopropylacrylamide) microgel particles ," *submitted*.
3. Mason, T. G. and Scheffold, F., "Crossover between entropic and interfacial elasticity and osmotic pressure in uniform disordered emulsions," *Soft Matter*, Vol. 10, 7109-7116, 2014.
4. Braibanti, M., Mason, T. G. and Scheffold, F., 'Experimentally disentangling the glass and the jamming transition in charge stabilized nanoemulsions," *in preparation*.

# Controlling Active Crowds with Random Light Fields

**E. Pinçe[1], S. K. P. Velu[1], A. Callegari[1], P. Elahi[1], S. Gigan[2], G. Volpe[1,3] and G. Volpe[4*]**

[1]Department of Physics, Bilkent University, Çankaya, 06800 Ankara, Turkey

[2]Laboratoire Kastler Brossel, Université Pierre et Marie Curie, École Normale Supérieure, CNRS, College de France, 24 rue Lhomond, 75005 Paris, France

[3]UNAM-National Nanotechnology Research Center, Bilkent University, Çankaya, 06800 Ankara, Turkey

[4]Department of Chemistry, University College London, 20 Gordon Street, London WC1H 0AJ, UK

[*]corresponding author: g.volpe@ucl.ac.uk

**Abstract**-Many living active-matter systems, such as schools of fish, flocking birds and bacterial colonies, exhibit collective and dynamic behaviors that are sensitive to changes in their environmental conditions. Here, we show that an active matter system of colloids in a bacterial bath switches between two long-term behaviors, i.e. gathering and dispersal of individuals, in response to the statistical properties of the underlying optical potential.

In recent years, active Brownian systems have attracted a lot of interest from the biology and physics communities. While the motion of passive Brownian particles is driven by equilibrium thermal fluctuations, active Brownian particles, often referred to as microswimmers, are able to propel themselves, exhibiting an interplay between random fluctuations and active swimming that drives them into a far-from-equilibrium state. Thanks to this property, they feature a series of novel behaviors that are not attainable by their counterpart, i.e. matter at thermal equilibrium, including, for example, self-assembly, swarming, and the emergence of other collective properties. In this talk, I will present some recent experimental results where we show that a colloidal active matter system switches between gathering and dispersal of individuals in response to a disordered potential. Interestingly, the statistical properties of the disorder potential allow us to dynamically control the long-term collective behaviour of the active matter system. Finally, I will discuss implications of this result on the design of artificial micro- and nano-swimmers, i.e. particles that can self-propel in response to an external stimulus, as autonomous agents to localize, pick up, and deliver nanoscopic objects, e.g., in catalysis, bioremediation, chemical sensing, and drug delivery.

**REFERENCES**

1. Ebbens, S. J. and J. R. Howse, "In pursuit of propulsion at the nanoscale," *Soft Matter* 6, 726-738, 2010.
2. Bechinger, C., R. di Leonardo, H. Löwen, C. Reichhardt, G. Volpe and G. Volpe, “Active Brownian particles in complex and crowded environments,” *arXiv*:1602.00081, 2016.
3. Volpe, G., G. Volpe, and S. Gigan, “Brownian Motion in a Speckle Light Field: Tunable Anomalous Diffusion and Selective Optical Manipulation,” *Sci. Rep.* **4**, 3936, 2014.

# Transport and emission in in colloidal and granular systems

**Cefe López**
Instituto de Ciencia de Materiales de Madrid–ICMM (CSIC)
Sor Juana Inés de la Cruz 3, 28049 Madrid, Spain
http://luxrerum.org

**Abstract**- Self-assembling *monodisperse* colloidal particles has served to random lasers resonant but the scattering properties of the passive part of the systems were hard to account for. Further complication is brought about if, in addition, disorder is manipulated introducing correlations. When *polydisperse* granular systems are used instead it is possible to separate the gain and feedback functions by physically separating the responsible materials.

Creating structured materials from the bottom up is a widely used method owing to the easy and inexpensive techniques it involves. Self-assembly entails allowing or inducing small particles to arrange themselves into photonic structures like photonic crystals and photonic glasses. Novel techniques dispensing with the liquid are nowadays being explored.[1] In this way we demonstrate monodisperse disordered structures in minutes and without the hassle associated with colloidal sedimentation. Alternative colloidal techniques [2] offer a tight control over the amount of disorder and may lead to correlated structures that present very intriguing properties preserving resonance even for very high levels of disorder.[3]

Non-spherical particles are less prone to control but still offer great possibilities related to disorder. Using these kinds of materials we design new random laser schemes that separate gain and feedback functions by placing scattering materials physically separated from the dye where amplification occurs.[4] This architecture is implemented by enclosing a dye solution between two agglomerations of randomly positioned titanium dioxide nanoparticles. The same spectral signature, consisting of sharp spikes with random spectral positions, is detected emerging from both ensembles of titanium dioxide nanoparticles. We interpret this newly observed behavior as due to the optical feedback given by back-scattered light from the scattering agglomerations, which also act as output couplers. This strategy allows to produce large area film-based random lasing even without added scattering material.[5] Scattering elements are either titanium dioxide nanoparticles or random defects at the interface between

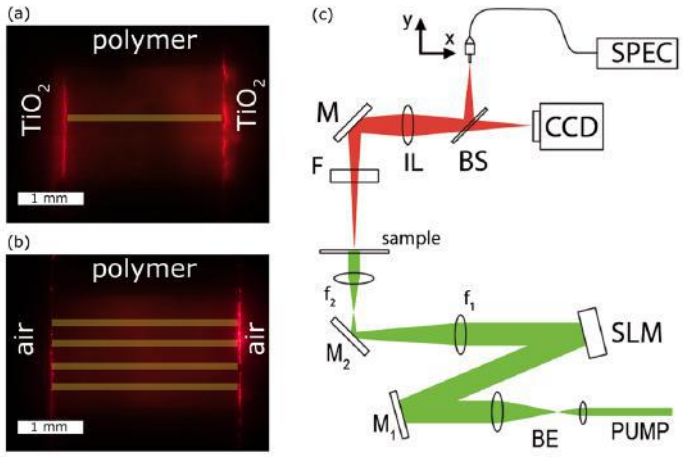



Fig. 1. Image of the sample with (a) and without (b) $TiO_2$ particles when illuminated at low pump flux with full SLM screen. Rectangular regions are highlighted in yellow, corresponding to the excited regions in lasing experiments. (c) Experimental set-up.

active polymer and air. Different emission spectra are observed, depending on the geometry of the excited area. A single random resonator with dimensions of 2.6 mm×0.65 mm is fabricated and random emission with resonant feedback is obtained by uniformly pumping the full device.

**REFERENCES**


[1] Montesdeoca, D. *et al*. to be published

[2] García, P. D., Sapienza, R., Blanco, Á. & López, C. Photonic Glass: A Novel Random Material for Light. *Adv. Mater.* **19,** 2597–2602 (2007).

[3] Pariente, J.A. et al. to be published

[4] Consoli, A; López, C; Decoupling gain and feedback in coherent random lasers: experiments and simulations; *Sci. Reports* **5**, 16848 (2015)

[5] Consoli, A, da Silva, DM, Wetter, NU; López, C, Large area resonant feedback random lasers based on dye-doped biopolymer films*; Opt. Express*, 23, 29954 (2015).

# Spatial structure of transmission eigenchannels and densities of states of random media

**M. Davy[1*], Z. Shi[2,3], C. Tian[4] and A.Z. Genack[2,3]**

[1] Institut d'Electronique et de Télécommunications de Rennes, University of Rennes 1, Rennes 35042, France.

[2] Department of Physics, Queens College of the City University of New York, Flushing, NY 11367, USA

[3] The Graduate Center, CUNY, 365 Fifth Avenue, New York, NY 10016, USA

[4] Institute for Advanced Study, Tsinghua University, Beijing 100084, China

[*]corresponding author: matthieu.davy@univ-rennes1.fr

**Abstract**- We explore the spatial structure of the energy density of eigenchannels of the transmission matrix within random media. Using a connection with the generalized diffusion equation, we provide an expression of its ensemble average for any transmission eigenvalue. We further show that the contribution of each eigenchannel to the density of states can be determined from measurements of spectra of the transmission matrix. This contribution is equal to the stored energy density in each eigenchannel.

The statistics of transmission and the degree of control that may be exerted over the transmitted wave by manipulating the incident wavefront may be fully described by the properties of the transmission matrix (TM). However, the TM does not provide any information regarding the spatial distribution of energy in different transmission eigenchannels. Only the average of the energy distribution over all *N* eigenchannels is known. For diffusive samples this is a linear decay of the energy density governed by Fick's law for particle diffusion. The variation of the distribution of the energy density for transmission eigenchannels with transmission eigenvalue has recently been explored in homogeneously disordered samples. Simulations (1-3) and measurements (4) in single realizations of random samples show that the intensity is enhanced in the middle of the sample as the transmission eigenvalue $\tau$ increases. The peak of the energy density profile moves towards the center of the sample for higher transmission eigenchannels.

Numerical simulations based on the recursive Green's function method in 2D make it possible to find not only the TM but also the profile with depth x of the eigenchannels. The ensemble average of the square of the field integrated across the cross section at this depth for transmission eigenchannels with transmission $\tau$ gives the profiles $W_\tau(x)$. We find that the average of the energy density profile within the sample of an individual eigenchannel with transmission $\tau$ is closely related to the generalized diffusion equation. Specifically, we find that (5):

- The energy density of the transmitting eigenchannel with $\tau = 1$ is the sum of a spatially uniform background and the probability density that a multiply scattered wave will arrive at and return to the cross section at given depth within the sample. This probability density is found from the generalized diffusion equation.

- The energy density profile of an eigenchannel with incomplete transmission $\tau$ can be factorized as, $W_\tau(x) = S_\tau(x)W_{\tau=1}(x)$, where $S_\tau(x)$ is a function which is independent of $L/\xi$ and $L/\ell$ in the diffusive limit. We find an

expression of $S_\tau(x)$ that involves only the auxiliary localization lengths previously used to parameterize the corresponding transmission eigenvalues (6). The expression of $W_{\tau=1}(x)$ and $S_\tau(x)$ are in excellent agreement with the profiles found in simulations for diffusive waves.

These results extend the knowledge of the average disposition of energy from the boundary into the bulk of the sample. It is in general difficult to probe the energy density within the medium. Integrating $W_\tau(x)$ over the depth gives the contribution of the eigenchannel to the density of states (DOS) of the sample, the eigenchannel density of states (EDOS) (7). The sum of the EDOS over the *N* eigenchannels gives the DOS. The EDOS can also be found from measurements of spectra of the TM. It is given by the composite phase derivative of transmission eigenchannels (7, 8). This composite phase derivative is equal to the delay time of pulsed excitation of an eigenchannel in the limit of vanishing bandwidth. The relation between the delay time for the $n^{th}$ transmission eigenchannel and the DOS is an extension to multichannel systems of the equality between the DOS and the transmission delay time in 1D systems (9).

**REFERENCES**


1. Choi W, Mosk AP, Park QH, & Choi W (2011) Transmission eigenchannels in a disordered medium. *Phys. Rev. B* 83(13):134207.
2. Liew SF, Popoff SM, Mosk AP, Vos WL, & Cao H (2014) Transmission channels for light in absorbing random media: From diffusive to ballistic-like transport. *Phys. Rev. B* 89(22):224202.
3. Peña A, Girschik A, Libisch F, Rotter S, & Chabanov A (2014) The single-channel regime of transport through random media. *Nature Commun.* 5.
4. Gérardin B, Laurent J, Derode A, Prada C, & Aubry A (2014) Full Transmission and Reflection of Waves Propagating through a Maze of Disorder. *Phys. Rev. Lett.* 113(17):173901.
5. Davy M, Shi Z, Park J, Tian C, & Genack AZ (2015) Universal structure of transmission eigenchannels inside opaque media. *Nat. Commun.* 6.
6. Dorokhov ON (1982) Transmission coefficient and the localization length of an electron in N bound disordered chains. *Pis'ma Zh. Eksp. Teor. Fiz.* 36(7):259.
7. Davy M, Shi Z, Wang J, Cheng X, & Genack AZ (2015) Transmission Eigenchannels and the Densities of States of Random Media. *Phys. Rev. Lett.* 114(3):033901.
8. Brandbyge M & Tsukada M (1998) Local density of states from transmission amplitudes in multichannel systems. *Phys. Rev. B* 57(24):R15088-R15091.
9. Avishai Y & Band YB (1985) One-dimensional density of states and the phase of the transmission amplitude. *Phys. Rev. B* 32(4):2674-2676.

# Light Emission Statistics as a Local Probe for Structural Phase Switching

**N. de Sousa**[1], **J.J. Sáenz**[2], **F. Scheffold**[3], **A. García-Martín**[4], **L.S. Froufe-Pérez**[3]

[1]Departamento de Física de la Materia Condensada, Universidad Autónoma de Madrid, 28049 Madrid, Spain.

[2]Donostia International Physics Center (DIPC), Paseo Manuel de Lardizabal 4, Donostia - San Sebastián 20018, Spain.

[3]Physics Department, University of Fribourg, Chemin du Musée 3 CH-1700 Fribourg, Switzerland.

[4]Instituto de Microelectrónica de Madrid, CSIC, Isaac Newton 8, Tres Cantos, 28760 Madrid, Spain.

nuno.teixeira@uam.es

**Abstract**— In this work we show that the statistics of emission rates in correlated disordered media is extremely sensitive to the details of the radial distribution function around the emitter. We analyze the emission statistics for single emitter embedded in a finite cluster of resonant particles during a solid-liquid phase transition. At the melting temperature, the total scattering cross section of the system does not present significant differences between the two phases while the emission rate jumps following the system dynamics.

The sensitivity of the spontaneous emission rate of an excited dipolar emitter to the local environment makes single-molecule spectroscopy a unique tool to sense optical and structural properties in its surrounding on the nanoscale. Modification of the emission rate has been reported in literature using well-defined structures, such as metal surfaces [1] or photonic crystals [2]. The increasing interest in the statistical properties of the spontaneous emission rates in complex media [3-6] is justified by their importance for many applications, such as molecular imaging or solar cells. From a fundamental point of view, the emission rate is proportional to the number of available optical modes at the position of the emitter, i.e. proportional to the electromagnetic local density of states (LDOS)[7]. In random uncorrelated media, the LDOS fluctuations can be explained to some extent by a single scattering statistical model and are dominated by the near-field interaction with the nearest scatterer at the scale of the excluded volume [4]. Temporal lifetime fluctuations can then be correlated to fluctuations in the position of the nearest scatterer and provide a suitable probe for the dynamics of the structure around the emitter. The observed variance of experimental spatial fluctuations of LDOS in random photonic media and lifetime measurements in dense colloidal suspensions of weak scattering particles seem to be consistent with this single-scattering regime. However, the experimental distributions of emission rates in disordered highly scattering dielectrics can present disparate results ranging from non-Gaussian long-tailed statistics with very large decay rates [5], to nearly Gaussian distributions [6]. It can be argued that the differences in the experimentally retrieved decay rate distributions are attributed to effect of multiple scattering between nearby scatterers or long-range spatial correlations between scatterers.

In this work we show that the statistics of emission rates in correlated disordered media is extremely sensitive to the details of the radial distribution function around the emitter. We analyze the emission statistics for single emitter embedded in a finite cluster of resonant particles. However, instead of generate random configurations of scatterers, we compute the emission rates as the system evolves with time under equilibrium conditions. Assuming a standard Lennard-Jones (L-J) interaction between particles, this system is known to present a peculiar solid-liquid-like phase transition at finite temperature: Due to finite-size effects, the two phases cannot coexist at the melting temperature and the whole cluster presents an interesting dynamical behavior, switching between an amorphous solid-like phase and liquid-like phases [8] This makes it an ideal model system to analyze the effects of local order on the emission rates. In the solid phase at low temperatures, the equilibrium positions are close to those corresponding to a face-centred-cubic (FCC) lattice, and the spectrum of emission rates present a strong chromatic dispersion reminiscent of the band structure of an infinite crystal of resonant dipoles, including spectral windows where the emission is enhanced and pseudo-gaps where it is dramatically inhibited. At the melting temperature, the total scattering cross section of the system does not present significant differences between the two phases while the emission rate jumps following the dynamics of the system. While light scattering

measurements would be blind to such dynamical changes, the lifetime statistics would then provide a direct signature of a phase switching behavior.

**REFERENCES**


1. R. Chance, et al. Adv. Chem. Phys 37, 65 (1978).
2. P. Lodahl, et al. Nature 430, 654 (2004).
3. J. Martorell et al. Phys. Rev. Lett. 65, 1877 (1990); L. Sapienza et al. Science 327, 1352 (2010).
4. L.S. Froufe-Pérez, et al. physica status solidi (a) 205 (2008).
5. R. Sapienza, et al. Phys. Rev. Lett. 106, 163902 (2011).
6. M. D. Birowosuto, et al. Phys. Rev. Lett. 105, 013904 (2010).
7. R. Carminati, et al. Surf. Sci. Rep. 70, 1 (2015).
8. N. de Sousa et al., *accepted*. Journal of Physics: Condensed Matter (2016).

# Coherent Control of Light in Disordered Media Assisted by Long-range Correlations

**C. W. Hsu[1*], S. F. Liew[1], A. Goetschy[2], Y. Bromberg[1], A. D. Stone[1], and H. Cao[1]**
[1]Yale University, USA
[2]ESPCI ParisTech, PSL Research University, CNRS, Institut Langevin, France
[*]corresponding author: chiawei.hsu@yale.edu

**Abstract**- In recent years, wavefront shaping has become a powerful tool for manipulating the transport of light in disordered media. We show that long-range correlations in the coherent diffusion allow more control on non-local properties than one could in uncorrelated systems. Spatially, moving from controlling a single speckle grain (local) to controlling a large area (global), the effects of long-range correlations become prominent. Spectrally, long-range correlations reduce the spectral degrees of freedom and enable the broadband control of light.

## 1. Introduction

Light scattering in disordered media poses a severe limitation for biomedical imaging and telecommunication. It has been shown that by shaping the incident wavefront with spatial light modulators (SLMs), one can focus light onto a single speckle behind or within a disordered medium [1]. More recently there has been progress in the control of non-local properties of the fields such as total transmission [2,3] and absorption [4]. Controlling the non-local properties is challenging as it requires the simultaneous control of a large number of speckles. But such non-local controls can benefit from long-range correlations that are negligible in local controls.

## 2. Increased range of control in multi-speckle focusing [5]

For some applications, it is desirable to concentrate energy within a target area that is larger than the size of a speckle. The possible range of control with wavefront shaping is the range of transmission eigenvalues of the partial transmission matrix corresponding to the target area. If the elements of the transmission matrix were to be uncorrelated, that range would be given by the Marcenko-Pastur (MP) distribution; meanwhile, experimentally measured transmission matrices reveal a wider range, with the brightest wavefront being brighter than MP, the darkest wavefront being darker than MP. This enhanced range comes from long-range correlations, and the enhancement increases with the target size, becoming dominant when the number of speckles in the target area approaches or exceeds the effective dimensionless conductance $g$ of the disordered medium. The experimental distributions of transmission eigenvalue are well described by the filtered random matrix formalism [6], which correctly accounts for correlations.

## 3. Broadband enhancement of total transmission and absorption [7]

As the coherent control through wavefront shaping is based on interference, these effects would seem to be intrinsically narrowband, limiting their applications in contexts such as power delivery, communications, or energy conversion. The expected bandwidth is limited by the frequency correlation scale, $\delta\omega$. For a broadband signal with bandwidth $\Delta\omega >> \delta\omega$, a natural hypothesis is that the effective number of independent frequencies

would be $M_{\text{eff}} \sim 1 + \Delta\omega/\delta\omega$, and that the maximal achievable enhancement decreases as $1/M_{\text{eff}}$. While this is indeed the behavior for broadband single-speckle focusing, it is not the case for total transmission or absorption due to the long-range correlations. We show analytically and numerically that these correlations dramatically reduce the effective number of independent degrees of freedom. Instead of a linear scaling, we find a square-root scaling with bandwidth, namely $M_{\text{eff}} \sim \sqrt{\Delta\omega/\delta\omega}$. This allows substantial coherent control of the total transmission and absorption across bandwidths that are orders of magnitude broader than the spectral correlation width of the medium.

**ACKNOWLEDGEMENTS**

This work is supported by the National Science Foundation under Grants No. DMR-1307632, No. DMR-1205307, and No. ECCS-1068642, and by the U.S. Office of Naval Research under Grant No. N00014-13-1-0649.

**REFERENCES**

1. Mosk, A. P., A. Lagendijk, G. Lerosey and M. Fink "Controlling waves in space and time for imaging and focusing in complex media," *Nature Photon.*, Vol. 6, 283-292, 2012.
2. Kim, M., Y. *et al*, "Maximal energy transport through disordered media with the implementation of transmission eigenchannels," *Nature Photon.*, Vol. 6, 581, 2012.
3. Popoff, S. M., A. Goetschy, S. F. Liew, A. D. Stone and H. Cao, "Coherent Control of Total Transmission of Light through Disordered Media," *Phys. Rev. Lett.*, Vol. 112, 100601, 2014.
4. Liew, S. F. *et al*, "Coherent control of photocurrent in a strongly scattering photoelectrochemical system," *ACS Photonics*, doi:10.1021/acsphotonics.5b00642, 2016.
5. Hsu, C. W. *et al*, unpublished.
6. Goetschy, A. and A. D. Stone, "Filtering Random Matrices: The Effect of Incomplete Channel Control in Multiple Scattering," *Phys. Rev. Lett.*, Vol. 111, 063901, 2013.
7. Hsu, C. W., A. Goetschy, Y. Bromberg, A. D. Stone and H. Cao, "Broadband Coherent Enhancement of Transmission and Absorption in Disordered Media," *Phys. Rev. Lett.*, Vol. 115, 223901, 2015.

# Colloids manipulation with optical radiation

**S. Sukhov*, C. Constant, V. Kajorndejnukul, and A. Dogariu**
CREOL, The College of Optics and Photonics, University of Central Florida, Orlando, Florida, USA
*corresponding author: ssukhov@creol.ucf.edu

**Abstract**-We explore the nature of forces induced by electromagnetic fields on colloidal systems. Particle-field coupling and particle-particle interactions are employed for manipulation of multiple interacting particles. Experiments for controlling diffusive and transport properties of disordered systems are discussed.

Most particle trapping and steering schemes rely on deterministic, engineered beams to manipulate a countable number of particles. However, new approaches have demonstrated that spatially random electromagnetic fields (known as speckle) are capable of exerting many degrees of control over the systems containing large number of particles. It was shown previously that speckles can be used as a size-selective, multi-particle trap for airborne particles or ultracold atoms [1,2]. Here we consider several situations when, instead of being trapped, colloidal particles demonstrate unusual dynamics in external electromagnetic fields.

At micron scales, the motion of small objects is heavily dominated by Brownian forces. When additional forces act on the objects, their diffusion could become anomalous with its mean squared displacement (MSD) growing nonlinearly in time $\left\langle |\Delta \mathbf{r}|^2 \right\rangle \propto t^{\alpha}$ with the case $\alpha > 1$ corresponding to super-diffusion and $\alpha < 1$ being sub-diffusion. We demonstrate that diffusion properties of colloidal particles can be optically-controlled through time and space varying speckles or through a dynamic coupling between colloidal particles.

Let us first consider stochastic motion of small spherical particle influenced by a force field $\mathbf{F}_{opt}(\mathbf{r},t)$ created by random electromagnetic field. For a dilute colloidal system, the particle motion can be described using the Langevin equation in an overdamped regime

$$\mu d\mathbf{r} = \mathbf{F}_{opt}(\mathbf{r},t)dt + \sqrt{2k_B T \mu} d\mathbf{W}\,, \tag{1}$$

where $\mu$ is the particle friction coefficient, $\mathbf{W}$ is a Wiener process, $k_B$ is the Boltzmann constant, and $T$ is the absolute temperature. It has been previously shown that time-invariant potential energy landscape diminish diffusion, while time-varying potentials can enhance it [3,4]. To explore diffusive properties of the system to greater extent, we increased the parameter space of the potential landscape by changing the degree of invariance $\rho$ of speckle patterns. We conducted systematic numerical simulations for different external potentials and, from the recorded particle trajectories, we evaluated the value of exponents $\alpha$ in a particle's time dependent MSD (Figure 1). Under this condition $\rho$ is unity for a time-invariant potential and it is zero for a fully dynamic field. From Figure 1, the diffusion is generally slower than normal for $\rho > 0.5$ independently of speckles modulation time $\tau$. Conversely, diffusion may be enhanced at particular correlation times when $\rho < 0.4$.

To test the possibility of controlling diffusion anomaly experimentally, we examined the behavior of micrometer-size colloidal particles placed in an optical speckle field. By imposing proper $\rho$ and $\tau$, we generated conditions corresponding to the points A, B, and C in theoretical Fig. 1. Under these conditions, the measured type of diffusion (super- or sub-) were corresponding to the one found theoretically.

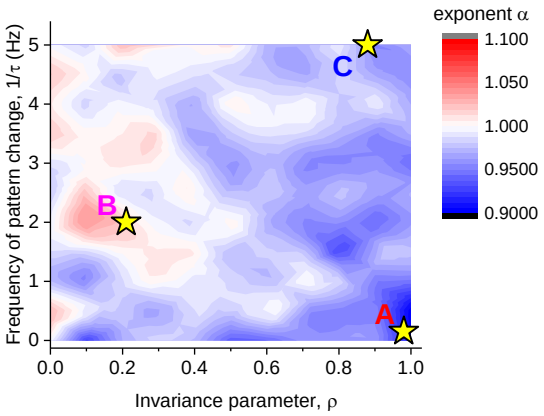



**Figure 1**. Exponent of temporal evolution of diffusion plotted as a function of frequency of random potential change ($1/\tau$) and the invariance parameter $\rho$ of random potential. Stars indicate the set of parameters for which experiments were also performed.

For a dense system of particles, hydrodynamic interaction (HI) should be also taken into account. HI is determined by mutual locations and velocities of particles [5,6] and is known to be long range. Thus, if the external force field maintains its directionality over significant volumes, the cumulative effect of HI can reach very large values. In this way HI can be harnessed to collectively enhance particles' velocities. In situation discussed here, we experimentally created the force field by optical radiation and detected fast motion of nanosize colloidal particles. The observed Péclet number Pe = 2 for the system of small colloidal particles was $10^5$ times larger than for a single particle demonstrating high efficiency of induced mass transport.

In conclusion, we demonstrate that diffusion can be controlled throughout the normal and anomalous regimes. For micron scale particles, the diffusion can be slowed down or speeded up by imposing optical potentials that vary both in time and space. Also, a new advection mechanism that can be controlled optically is proposed and demonstrated. The proposed optofluidic techniques permit to effectively regulate the mass transport in a remote, noninvasive, and power efficient manner, which should be of interest for microfluidic lab-on-chip platforms.

## REFERENCES

1. Shvedov, V. G., et al., "Selective trapping of multiple particles by volume speckle field," *Opt. Express*, Vol.18, No.3, 3137-3142, 2010.
2. J. Billy, et al. "Direct observation of Anderson localization of matter waves in controlled disorder," *Nature*, Vol.453, 891-94, 2008.
3. Volpe, G., G. Volpe and S. Gigan, "Brownian Motion in a Speckle Light Field: Tunable Anomalous Diffusion and Selective Optical Manipulation," *Sci. Rep*., Vol.4, Article number: 3936, 2014.
4. K. M. Douglass, S. Sukhov, and A. Dogariu, "Superdiffusion in Optically Controlled Active Media," *Nature Photon*. Vol.6, No.12, 833-836, 2012.
5. Happel J. and H. Brenner, *Low Reynolds number hydrodynamics: with special applications to particulate media*, Martinus Nijhoff, The Hague, 1983.
6. Kajorndejnukul, V., S. Sukhov, A. Dogariu, "Efficient mass transport by optical advection," *Sci. Rep*., Vol.5, Article number: 14861, 2015.

# Polarization revival through scattering media

**H. B. de Aguiar**[1], **S. Gigan**[2], **and S. Brasselet**[1]

[1]Aix-Marseille Université, CNRS, Centrale Marseille, Institut Fresnel UMR 7249, 13013 Marseille, France
[2]Laboratoire Kastler Brossel, UMR 8552 of CNRS and Université Pierre et Marie Curie, 24 rue Lhomond, 75005 Paris, France
h.aguiar@fresnel.fr

**Abstract**— Recently, microscopy in scattering media has been enabled by impressive developments of wavefront shaping techniques. However, current demonstrations only allow retrieving information at a microscopic level. In this contribution, we demonstrate an unprecedented phenomenon with which deep molecular-level imaging may be enabled: polarization revival *via* wavefront shaping.

Polarization-resolved (PR) microscopies are able to provide molecular-level structural insights beyond the diffraction-limited scale [1]. Unfortunately, structural imaging by PR approaches in scattering media is notoriously superficial because of the inherent mixing of both polarization and spatial degrees of freedom: after even a few scattering events the polarization state is scrambled thus generating a random elliptically polarized state, and the wavefront concomitantly distorted thus leading to a speckle. Under these circumstances, performing molecular-level structural imaging is currently impossible at depth in biological media.

Despite many demonstrations using wavefront shaping to refocus scattered light [1, 2], therefore enabling sub-cellular resolution microscopy, wavefront shaping is not compatible yet with PR microscopy: to obtain a controlled polarization state, one needs to generate and control the polarization state deterministically [4, 5, 6], a situation not possible to be achieved when focusing *inside* a scattering medium.

Here, we show that wavefront shaping is able to recover the injected polarization state without using any polarization selection at the detection [7]. This counter-intuitive effect occurs up to several transport mean free path thick samples, which exhibit a speckle with a scrambled polarization state. Most remarkably, an arbitrary rotation of the input polarization is transferred at the focus, without significant degradation of its refocusing intensity. This polarization revival — out of an scrambled polarization state — paves the way for PR microscopy at unprecedented depths in scattering media. We demonstrate how the observation of this phenomenon solves the issue of molecular-level structural imaging of collageneous biological tissues in scattering environments using second harmonic generation imaging.

**REFERENCES**

1. Brasselet, S., "Polarization-resolved nonlinear microscopy: application to structural molecular and biological imaging," *Adv. Opt. Photon.*, Vol. 3, 205–271, 2011.
2. Vellekoop, I. M. and A. P. Mosk, "Focusing coherent light through opaque strongly scattering media," *Opt. Lett.*, Vol. 32, 2309–2311, 2007.
3. Popoff, S. M., G. Lerosey, R. Carminati, M. Fink, A. C. Boccara and S. Gigan, "Measuring the Transmission Matrix in Optics: An Approach to the Study and Control of Light Propagation in Disordered Media," *Phys. Rev. Lett.*, Vol. 104, 100601, 2010.
4. Tripathi, S., R. Paxman, T. Bifano and K. C. Toussaint, "Vector transmission matrix for the polarization behavior of light propagation in highly scattering media." *Opt. Express* , Vol. 20, 16067–16076, 2012.
5. Guan, Y., O. Katz, E. Small, J. Zhou and Y. Silberberg, "Polarization control of multiply scattered light through random media by wavefront shaping." *Opt. Lett.* , Vol. 37, 4663–4665, 2012.
6. Park, J.-H., C. Park, H. Yu, Y.-H. Cho and Y.-K. Park. "Dynamic active wave plate using random nanoparticles." *Opt. Express* , Vol. 20, 17010–17016, 2012.
7. de Aguiar, H. B., S. Gigan and S. Brasselet. "Polarization-resolved microscopy through scattering media via wavefront shaping." *arXiv:1511.02347*, 2015.

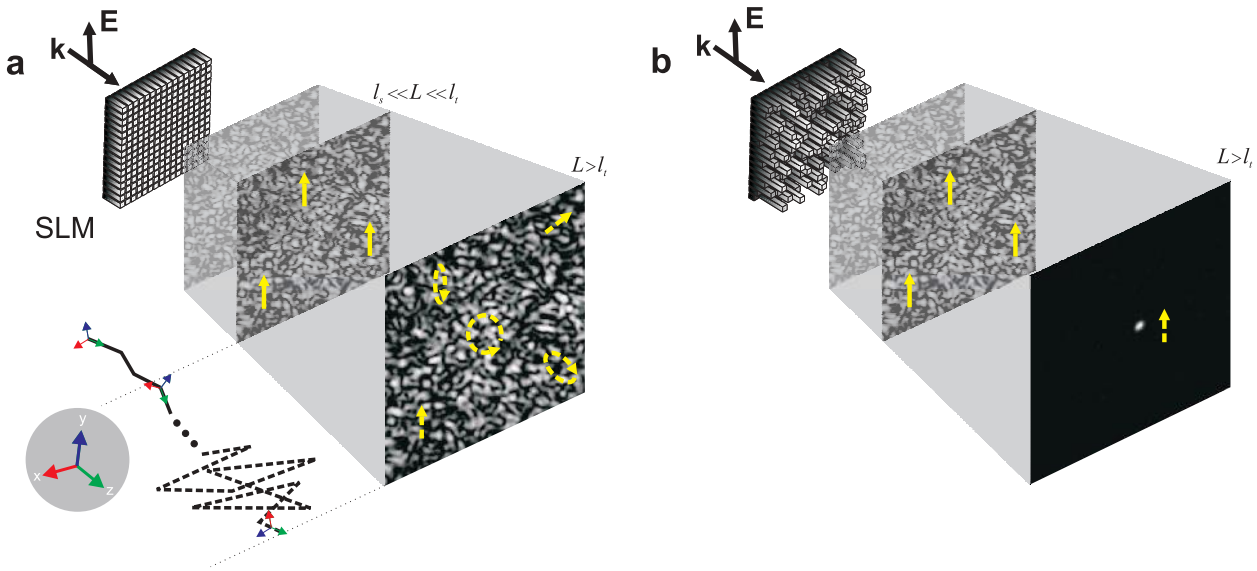



Figure 1: (a) An unshaped wavefront propagating through scattering media generates a speckle pattern. When the thickness $L$ is comparable to the transport mean free path $l_t$, the output speckle polarization has no correlation with the input one. (b) After wavefront shaping the beam, a polarized focus emerges with the same state as the input one. We stress that no polarization selection was performed during the acquisition procedure of the optimal wavefront to refocus.

# Launching optical energy into the fundamental diffusion mode of a complex nanophotonic medium

**Oluwafemi S. Ojambati*, Hasan Yilmaz, Ad Lagendijk, Allard P. Mosk, and Willem L. Vos**

*Complex Photonic Systems (COPS)*

*MESA+ Institute for Nanotechnology*

*University of Twente, P.O. Box 217, 7500 AE Enschede*

*The Netherlands.*

*corresponding author: o.s.ojambati@utwente.nl

**Abstract**- We demonstrate experimentally that optical wavefront shaping increases light coupling into the fundamental diffusion mode of a scattering medium. The total energy density inside a scattering medium of zinc oxide (ZnO) nanoparticles was probed by exciting fluorescent spheres that were randomly positioned in the medium. We observe that the total fluorescent power is enhanced when the incident wavefront is optimized. Our model, which is based on the fundamental diffusion eigensolution agrees well with experimental data.

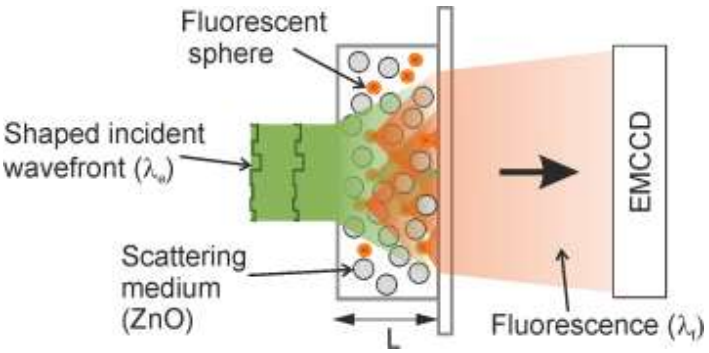



*Figure 1: (Color outline) A schematic drawing of the method of probing the total energy density inside a scattering medium. The scattering medium is an ensemble of disordered ZnO particles. The medium is illuminated with a shaped incident wavefront such that the incident light (green intensity) is optimized on a diffraction-limited spot at the back of the sample. The scattering medium is lightly doped with fluorescent spheres randomly positioned inside the medium. The fluorescent spheres probe the energy density inside the sample. The total fluorescent intensity emitted from the fluorescent spheres (red intensity) is measured by an electron multiplying charged-coupled device (EMCCD).*

It is well known that light transport through scattering media is described by the diffusion equation [1]. The fundamental question that we address here is whether it is feasible to send light into the fundamental diffusion eigensolution of the diffusion equation. Such a feasibility offers the opportunity to increase the total optical energy density stored inside the scattering sample. Enhanced total energy density is crucial to increase the efficiency of white LEDs, solar cells, and of random lasers, as well as to realize controlled illumination in biomedical optics.

As a tool to couple light into the fundamental diffusion eigensolution, we use optical wavefront shaping, which involves shaping the incident wavefront on the sample to obtain a bright focus at the back surface of the sample [2]. The total energy density inside a scattering medium of zinc oxide (ZnO) nanoparticles was probed by exciting fluorescent spheres that were randomly positioned in the medium (see Figure 1). We measured the total fluorescent intensity exiting the back surface of the sample and prove that the

total fluorescent power is proportional to the total energy density inside the sample. We found that the concomitant fluorescent power is enhanced compared to a non-optimized incident wavefront. The observed enhancement increases with sample thickness as shown in Figure 2. Based on diffusion theory, we derive a model wherein the distribution of the energy density of wavefront-shaped light is dominated by the fundamental diffusion mode [3,4]. Our model agrees remarkably well with our experiments, notably since the model has no freely adjustable parameters.

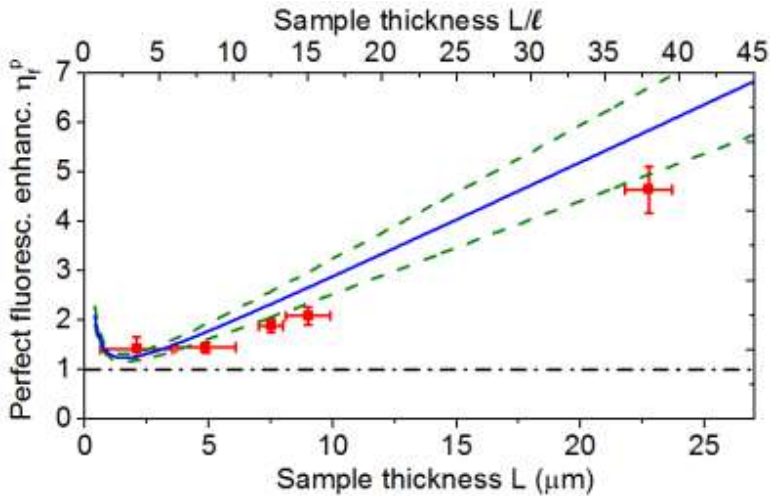



*Figure 2: Experimentally derived data and model curve of the fluorescent intensity enhancement in ZnO scattering sample versus sample thickness. The red squares are the results of the fluorescent intensity enhancement extrapolated to unity intensity control. The blue solid line is the calculated fluorescent intensity enhancement and the blue dashed curves are the upper and lower limit of the model as determined by the sample uncertainty.*

**REFERENCES**


1. A. Ishimaru, *Wave propagation and scattering in random media*, New York, Academic (1978)
2. I.M. Vellekoop and A.P. Mosk, "*Universal Optimal Transmission of Light through Disordered Materials*," Phys. Rev. Lett. **101**, 120601 (2008)
3. O.S. Ojambati, H. Yilmaz, A. Lagendijk, A.P. Mosk, and W.L. Vos, "*Selective coupling of optical energy into the fundamental diffusion mode of a scattering medium*", arXiv:1505.08103 (2015)
4. O.S. Ojambati, A.P. Mosk, I.M. Vellekoop, A. Lagendijk, and W.L. Vos, "*Energy density distribution of shaped waves inside scattering media mapped onto a complete set of diffusion modes*", arXiv:1602.03921 (2016)

# Theory for the diffusion of light polarization in disordered media with short-range structural correlations

**K. Vynck**[1], **R. Pierrat**[2] **and R. Carminati**[2]

[1]LP2N, CNRS - Institut d'Optique Graduate School - Univ. Bordeaux, F-33400 Talence, France
[2]Institut Langevin, ESPCI ParisTech - PSL Research University - CNRS, F-75005, Paris, France
kevin.vynck@institutoptique.fr

**Abstract**— We develop a model based on multiple scattering theory to describe the diffusion of light polarization in a disordered medium exhibiting structural correlations. A radiative transfer equation for the polarization-resolved specific intensity is derived and solved analytically in the diffusion approximation. Our study reveals the intricate relation between light polarization and short-range structural correlations.

Disordered media are the host for a large variety of optical phenomena, from light depolarization to speckle correlations to localization, the study of which is not only relevant to the optical spectroscopy of complex media (biological tissues, inorganic materials, planetary atmospheres) but also to the design of optical materials exhibiting new, exotic properties. The past few years have witnessed a strengthening of efforts to understand how the vector nature of light and structural correlations impact optical phenomena in disordered media. For instance, polarization was shown to play a critical role in the spontaneous emission of light sources in disordered media [1] and to hinder the Anderson localization of light [2]. Concurrently, short-range structural correlations in disordered media were found to enable the opening of a photonic gap, wherein light emission and propagation is inhibited, and to facilitate the formation of localized modes [3]. Theoretically describing the transport of polarized light in correlated disorder is however a difficult task, which has been tackled so far using a transfer matrix approach on scattering sequences [4, 5] or starting from a vector radiative transfer equation [6]. Multiple scattering theory, which constitutes the basis to describe mesoscopic optical phenomena, has been developed either by neglecting the light polarization or for uncorrelated disorder.

Here, we present a model based on multiple scattering theory that describes how the diffusion of polarized light is affected by short-range structural correlations [7], thereby generalizing previous models limited to uncorrelated disorders [8, 9]. Starting from a Bethe-Salpeter equation, which describes the spatial correlation of the electric field $\langle E_i(\mathbf{r})E_j^\star(\mathbf{r}')\rangle$ in a disordered medium, where $i$ and $j$ are the field components, we first derive a new version of the radiative transfer equation for the polarization-resolved specific intensity. We then apply the so-called $P_1$ approximation to reach the diffusion limit, wherein structural correlation is described via the standard anisotropy parameter $g$, i.e. the average cosine of the scattering phase function. The polarized version of the energy density $U_{ijkl}$ is finally written as a sum of modes on "polarization eigenchannels", which relate pairs of input field components $(i, j)$ to pairs of output field components $(k, l)$ (e.g., the scalar mode corresponds to $\delta_{ij}\delta_{kl}$).

Our main result is the finding that the diffusion constants and effective attenuation lengths describing the diffusion of the energy density in the individual eigenchannels do not exhibit a single, trivial dependence on $g$ (by contrast, the diffusion constant of the scalar mode simply scales as $(1-g)^{-1}$). We believe that the development of a rigorous model for the propagation of polarized light in correlated disorder and the formal demonstration of the intricate relation between light depolarization and structural correlations constitute an important advance in theoretical mesoscopic optics.

## ACKNOWLEDGMENT

This work was supported by LABEX WIFI (Laboratory of Excellence within the French Program "Investments for the Future") under references ANR-10-LABX-24 and ANR-10-IDEX-0001-02 PSL$^\star$ and by the PEPS program of CNRS through project LILAS.

**REFERENCES**


1. Cazé, A., R. Pierrat and R. Carminati, "Near-field interactions and nonuniversality in speckle patterns produced by a point source in a disordered medium," *Phys. Rev. A*, Vol. 82, No. 4, 043823, 2010.
2. Skipetrov, S. E. and I. M. Sokolov, "Absence of Anderson Localization of Light in a Random Ensemble of Point Scatterers," *Phys. Rev. Lett.*, Vol. 112, No. 2, 023905, 2014.
3. Imagawa, S., K. Edagawa, K. Morita, T. Niino, Y. Kagawa and M. Notomi, "Photonic band-gap formation, light diffusion, and localization in photonic amorphous diamond structures," *Phys. Rev. B*, Vol. 82, No. 11, 115116, 2010.
4. Rojas-Ochoa, L. F., D. Lacoste, R. Lenke, P. Schurtenberger and F. Scheffold, "Depolarization of backscattered linearly polarized light," *J. Opt. Soc. Am. A*, Vol. 21, No. 9, 1799-1804, 2004.
5. Xu, M. and R. R. Alfano, "Random Walk of Polarized Light in Turbid Media," *Phys. Rev. Lett.*, Vol. 95, No. 21, 213901, 2005.
6. Gorodnichev, E. E., A. I. Kuzovlev and D. B. Rogozkin, "Depolarization coefficients of light in multiply scattering media," *Phys. Rev. E*, Vol. 90, No. 4, 043205, 2014.
7. Vynck, K., R. Pierrat and R. Carminati, *in preparation*.
8. Stephen, M. J. and G. Cwilich, "Rayleigh scattering and weak localization," *Phys. Rev. B*, Vol. 34, No. 11, 7564-7572, 1986.
9. Vynck, K., R. Pierrat and R. Carminati, "Polarization and spatial coherence of electromagnetic waves in uncorrelated disordered media," *Phys. Rev. A*, Vol. 89, No. 1, 013842, 2014.

# Light propagation and optical response in two-dimensional silicon nanowire random fractal arrays

**B. Fazio[1*], P. Artoni [2], M. A. Iatì [1], C. D'Andrea [3], S. Pirotta [4], M. J. Lo Faro[1,2], S. Del Sorbo [4], P.G. Gucciardi [1], R. Saija [5], P. Musumeci [2,3], C. S. Vasi [1], D. S. Wiersma[6,7], F. Priolo [2,3], M. Galli [4] and A. Irrera[1]**

[1] IPCF-CNR, viale F. Stagno d'Alcontres 37, Faro Superiore, 98158 Messina, Italy.

[2] Dipartimento di Fisica e Astronomia, Università di Catania, via S. Sofia, 64, 95123 Catania, Italy.

[3] MATIS IMM-CNR, via S. Sofia, 64, 95123 Catania, Italy.

[4] Dipartimento di Fisica, Università degli Studi di Pavia, via Bassi 6, 27100 Pavia, Italy.

[5] Dipartimento di Fisica e di Scienze della Terra, Università di Messina, I-98166 Messina, Italy

[6] LENS, Università di Firenze, via Nello Carrara 1, 50019 Sesto Fiorentino, Firenze, Italy

[7] Dipartimento di Fisica e Astronomia, Largo Enrico Fermi, 2 , 50125 Firenze, Italy.

[*]corresponding author: : fazio@ipcf.cnr.it

**Abstract**-We report on the unusual optical properties of a forest of very thin silicon nanowires arranged in two-dimensional random fractal geometry. We show that the extreme light scattering properties of these novel nanostructured materials lead to strongly enhanced Raman and photoluminescence emission, which are driven by multiple light scattering phenomena and are correlated on all length scales, according to the refractive index fluctuations.

Novel concepts of disorder with short and long range correlations in array of nanostructures, can play a key role on the light transport inside the systems and, as a direct consequence, on their optical response, which may strongly differ from those of bulk materials [1,2]. The occurrence of striking optical performances based on multiple scattering lays the foundations of new photonics applications improving the absorption and emission of light. In this context, the production of a fractal pattern of nanostructures represents the opportunity of achieving a complex disorder with strong structural heterogeneities correlated on all length scales. Recently, we realized a two-dimensional array of vertically aligned thin silicon nanowires (SiNWs) arranged in random fractal geometry (figure 1.a,b) and fabricated by using an inexpensive, fast and maskless process compatible with Si technology[3-6].

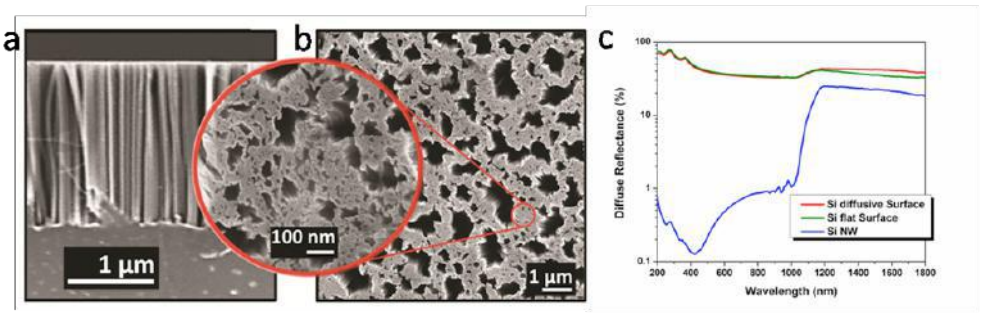



**Figure 1.** Cross section (**a)** and plan view (**b)** SEM images of Si NW fractal array; in the inset a high magnification of the plan view image. Diffuse (hemispherical) reflectance of Si NW sample (blue lines) and of a bulk *c*-Si flat (front) and diffusive rough (back) surface (green and red lines, respectively).

The fractal SiNW array promotes a very high light-trapping efficiency across the entire visible and near infrared range, converted in a notable light absorption in UV-VIS (figure 1.c) driven by multiple scattering processes. The latter are very intense inside the fractal array, thus leading to 1) a bright photoluminescence, due to quantum confinement effects, visible by naked eyes, and 2) to a greatly enhanced Raman scattering (figure 2a), correlated on all length scales according to the refractive index fluctuations. We demonstrate as a morphological property such as *lacunarity*, defined as the measure of alternation of full and empty space, is the main actor in the light scattering phenomena for this material, since it is strongly related to the fluctuations of refractive index.

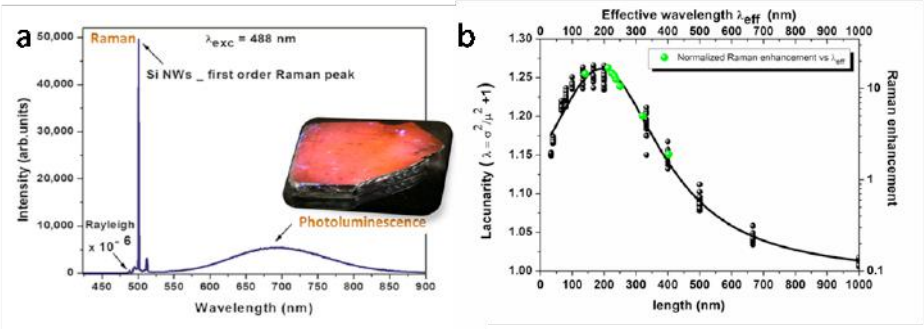



**Figure 2. (a)** Raman backscattered radiation and PL emission from the Si NW sample. **(b)** Comparison between lacunarity and Raman enhancement. The Raman enhancement values (green dots) are plotted as a function of the effective incident laser wavelength propagating in the medium $\lambda_{eff}$ and compared to the lacunarity curve plotted versus length (black line).

In particular, the enhancement of the Raman signal, with respect of that one of bare crystalline silicon used to obtain the NWs material, is shown to depend on the effective excitation wavelength that resonantly matches the heterogeneity sizes of the Si NW 2D fractal arrangement [6] (figure 2b).

Finally, a further issue concerns interference effects in Si NWs arrays and how these affect light transport and the material optical response. We show how the random organization and the strong scattering performances allow for the observation of novel unexpected and counterintuitive phenomena also in the inelastic scattering regime.

**REFERENCES**


1. Vynck, K., Burresi, M., Riboli, F., Wiersma, D.S., “Photon management in two-dimensional disordered media,” *Nature Mater.*, Vol. 11, 1017–1022, 2012.
2. Brongersma, M.L., Cui, Y., Fan S.H., “Light management for photovoltaics using high-index nanostructures,” *Nature Mater.*, Vol. 13, 451–460, 2014.
3. Irrera, A., et al. “Quantum confinement and electroluminescence in ultrathin silicon nanowires fabricated by a maskless etching technique” *Nanotechnology*, Vol. 23, 075204 , 2012.
4. Lo Faro, M.J., et al. “Silicon nanowire and carbon nanotube hybrid for room temperature multiwavelength light source”, *Sci. Rep.* Vol. 5, 16753, 2015.
5. Priolo, F ., Gregorkiewicz, T., Galli, M., Krauss, T.F. ,“ Silicon nanostructures for photonics and photovoltaics”, *Nature Nanotech*. Vol. 9, 19-32, 2014.
6. Fazio, B., et al. “Strongly Enhanced Light Trapping in a Two-dimensional Silicon Nanowire Random Fractal Array”, *Light Sci Appl*, doi: 10.1038/lsa.2016.62, 2016. (in press).

# Experimental verification of mean path length invariance in multiple light scattering

**R. Savo[1*], R. Pierrat[2], R. Carminati[2], S. Rotter[3] and S. Gigan[1]**
[1]Laboratoire Kastler Brossel, École Normale Supérieure, CNRS, UPMC, College de France, 24 Rue Lhomond 75005, Paris, France
[2] École Supérieure de Physique et de Chimie Industrielle ParisTech, CNRS, Institut Langevin, F-75005 Paris, France
[2] Institute for Theoretical Physics, Vienna University of Technology, A-1040 Vienna, Austria
[*]corresponding author: romolo.savo@lkb.ens.fr

**Abstract**-A surprising invariance property in transport phenomena has recently been discovered, according to which the mean trajectory length inside a disordered medium is entirely independent of the medium's mean free path. In spite of the general applicability of this result - ranging from the scattering of particles to that of waves and from weakly to very strongly disordered systems - no observation of this invariance has been reported so far. Here we present measurements for light propagating in multiple scattering media by which we experimentally verify the invariance of the mean path length for wave propagation for the first time.

Common experience with disordered systems shows that any variation in the concentration of scattering centers inevitably affects the transport properties of these systems such as, e.g., the transmission across the system, the corresponding traversal time and the return probability. Along these lines it would be natural to expect that a variation of a disordered medium's scattering strength also affects the mean length of trajectories that scatter through this medium. As was shown recently, however, this mean trajectory length between entering and exiting a certain spatial region does not depend on the typical scattering length (i.e., the mean free path), but is determined solely by the geometry of this bounded domain [1].

A natural setting for studying this curious property is wave scattering, for which this invariance has recently been extended theoretically [2], by showing its validity even in the presence of interferences, resonances and localization. Quite remarkably, the key insight for this extension is the connection to the density of state (DOS), which is the central quantity that stays invariant when changing the mean free path [2]. In spite of these fundamental aspects and widespread applicability, no observation of this invariance property has been reported so far.

Here we present measurements for light propagating in multiple scattering media by which we experimentally verify the invariance of the mean path length for light waves. We investigate light scattering in a simple colloidal solution and show how the mean trajectory length can be measured by monitoring in time the decorrelation of the speckle pattern generated by the Brownian motion of the scatterers. By controlling the concentration of the colloids we vary the transport mean free path and unambiguously observe an invariance of the mean path length [3]. Our measurements cover two orders of magnitude in the scattering strength, from weak scattering to deep multiple scattering, for which no significant change in the mean trajectory length is observed. We expect that our measurements can also be extended to more complex media such as biological tissues and foams.

REFERENCES

[1] Blanco, S. and R. Fournier, “An invariance property of diffusive random walks”, *Europhys. Lett.* 61, 168 (2003).

[2] Pierrat, R., P. Ambichl, S. Gigan, A. Haber, R. Carminati and S. Rotter, “Invariance property of wave scattering through disordered media", *PNAS* 111, 17765 (2014).
[3] Savo, R., R. Pierrat, R. Carminati, S. Rotter end S. Gigan, in preparation

# Brownian motion of self-assembled colloid structures in optical fields

**P. H. Jones**[1], **K. Govind**[1], **N. J. Tidy**[1], **and Xiang Han**[2]

[1]Department of Physics and Astronomy, University College London, Gower Street, London WC1E 6BT, United Kingdom

[2]College of Opto-Electric Science and Engineering, National University of Defense Technology, Changsha 410073, China

philip.jones@ucl.ac.uk

**Abstract**— We present a study of particle structures that are formed by optical binding interactions in counter-propagating beam optical traps, and their subsequent Brownian dynamics. By means of digital video microscopy we are able to track particle motion and measure the correlations in position fluctuations. The particle dynamics can be explained by considering the normal modes of a system of masses connected by linear springs and subject to thermal noise, and an analogy is made with the motion of extended polymer chains.

'Optical binding' [1, 2] describes the optically-induced association of potentially large numbers of colloidal particles as a result of their mutual light scattering interaction [3]. Such optically-ordered matter has been demonstrated in a variety of experimental configurations including an optical fiber trap [4], in evanescent fields on the surface of a prism [5], and in random (speckle) light fields [6], and for a variety of particle types, including microscopic dielectric spheres [7] and non-spherical carbon nanotube bundles [8].

Here we report the analysis of the Brownian dynamics of optically bound microparticle structures that spontaneously form in a number of different optical field configurations. Figure 1(a) shows an example of a chain of fourteen 1 $\mu$m diameter silica microparticles that has formed in perpendicularly polarized, counter-propagating evanescent optical fields above a dielectric interface. Digital video microscopy is used to track the Brownian motion of the particles in the chain, as shown in figure 1(b), and by treating the inter-particle optical binding interaction as analogous to a linear spring, the extent of the Brownian fluctuations is used to characterize the strength of optical binding between particles in the chain [9].

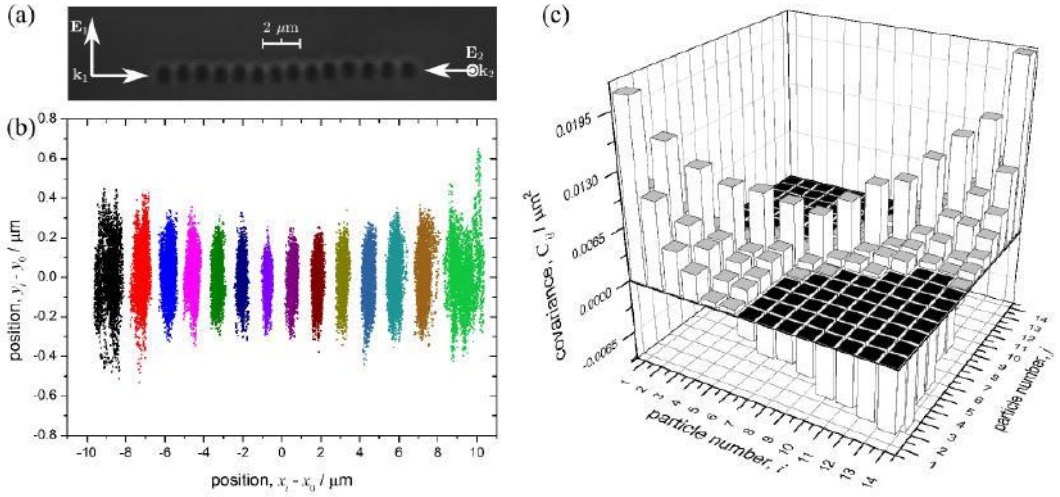



Figure 1: (a) Image of an optically bound chain showing directions of beam propagation and polarization; (b) Scatter plot of particle positions following subtraction of the center-of-mass motion of the chain; (c) Covariance of particle position fluctuations, $C_{ij}$, following subtraction of the center-of-mass motion of the chain.

We have previously observed the amplitude of the covariance, $C_{ij}$, of position fluctuations between two particles $i, j$ in the chain, as shown in figure 1(c) [10], demonstrating (anti-) correlations

in the particle position fluctuations. Here, with the benefit of increased temporal resolution, we are able to observe and measure the time-evolution (decay) of such correlations, and the factors which affect them, including optical power and the number of particles, both for one-dimensional chains as shown, and for more complex structures that occur in alternative field geometries. Our observations of the amplitude and time evolution of the covariance of particle positions are explained by considering the normal modes of a system of masses connected by linear springs, and subject to thermal noise. For the chains of particles we draw analogy between the dynamics of the optically bound microspheres and those of extended polymer molecules [11]. Our experimental results are complemented by Brownian motion simulations [12].

In conclusion, we study the Brownian dynamics of self-assembled structures of colloidal particles in an optical field that arise due to multiple scattering ("optical binding"). Our observations of the amplitude and rate of decay of correlations in the motion of optically bound particles can be explained by decomposing the motion into the normal modes of a system of particles connected by linear spring and subject to thermal fluctuations. The optical binding interaction provides a means for organizing a large number of micro- or nanoparticles over an extended area which could potentially be applied in, for example, the fabrication of photonic structures. Our results demonstrate the significance of fluctuations in particle positions and their short-time correlations during the formation of such structures.

## ACKNOWLEDGMENT

This work is supported by the Leverhulme Trust. Xiang Han thanks the China Scholarship Council for support.

## REFERENCES

1. Burns, M. M., Fournier, J.-M. and Golovchenko, J. A. "Optical binding," *Phys. Rev. Lett.* Vol. 63, No. 12, 1233-1236, 1989.
2. Burns, M. M., Fournier, J.-M. and Golovchenko, J. A. "Optical matter: crystallization and binding in intense optical fields," *Science* Vol. 249, No. 4970, 749-754, 1990.
3. Jones, P. H., Maragó, O. M., and Volpe, G. *Optical Tweezers: Principles and Applications*, Cambridge University Press, Cambridge, 2015.
4. Singer, W., Frick, M., Bernet, S. and Ritsch-Marte, M. "Self-organized array of regularly spaced microbeads in a fiber-optical trap", *J. Opt. Soc. Am. B* Vol. 20, No. 7, 1568-1574, 2003.
5. Garcés-Chávez, V., Dholakia, K. and Spalding, G. C. "Extended-area optically induced organization of microparticles on a surface," *Appl. Phys. Lett.* Vol. 86, No. 3, 031106, 2005.
6. Brügger, G. Froufe-Pérez, L. S., Scheffold, F. and Sáenz, J. J. "Controlling dispersion forces between small particles with artificially created random light fields," *Nat. Commun.* Vol. 6, 7460, 2015.
7. Tatarkova, S. A., Carruthers, A. E. and Dholakia, K. "One-dimensional optically bound arrays of microscopic particles," *Phys. Rev. Lett.* Vol. 89, 283901, 2002.
8. Maragó, O. M., Jones, P. H., Gucciardi, P. G., Volpe, G. and Ferrari, A. C. "Optical trapping and manipulation of nanostructures," *Nat. Nanotechnology* Vol. 8, No. 11, 807–819, 2013.
9. Han, X. and Jones, P. H. "Evanescent wave optical binding forces on spherical microparticles," *Opt. Lett.*, Vol. 40, No. 17, 4042–4045, 2015.
10. Smart, T. J., Richards, C. J., Han, X., Siwiak-Jaszek, S., and Jones, P. H. "Correlated fluctuations of optically trapped particles," in *Proceedings of SPIE 9548, Optical Trapping and Optical Micromanipulation XII*, San Diego, USA, August 2015, 954283.
11. Doi M. and Edwards, S. F. *The theory of polymer dynamics*, Clarendon Press, Oxford, 1988.
12. Volpe G. and Volpe G. "Simulation of a Brownian particle in an optical trap," *Am. J. Phys.* Vol. 81, No. 3, 224-230, 2013.

# Diffusion of an electric dipole in a fluctuating random electromagnetic field

**Manuel. I. Marqués**[1]

[1]Departamento de Física de Materiales, IFIMAC & Instituto "Nicolás Cabrera".
Universidad Autónoma de Madrid, Madrid, Spain
manuel.marques@uam.es

**Abstract**—

The dynamics of an electric dipole in a light field consisting on electromagnetic plane waves with polarizations randomly distributed and fluctuating phases is theoretically analyzed. The expression for the optical random force fluctuations, the optical drag force, the equilibrium kinetic energy and the diffusion constant are derived. Numerical simulations for the dynamics of a resonant dipole, initially at rest, show the crossover between the superdiffusive and the diffusive regimens theoretically predicted.

The dynamics of a particle under the influence of random forces with null average but with white noise fluctuations different from zero may be diffusive. In Brownian motion, force fluctuations $\Gamma$ and dissipation coming from the damping drag force $F = -\gamma v$ induce a diffusive behavior.

In this work we consider a monochromatic electromagnetic field ($\boldsymbol{E}e^{-i\omega t}$ and $\boldsymbol{B}e^{-i\omega t}$) and an electric dipole, with size much smaller than the wavelength. The polarization of the particle is given by $\boldsymbol{P} = \epsilon_0 \alpha \boldsymbol{E}$, being $\alpha$ the polarizability and $\epsilon_0$ the vacuum permittivity. The electromagnetic field consists of linearly polarized plane waves with random polarization, random wave-vector and a phase $\phi$ that fluctuates randomly in time [1], remaining constant within an interval given by $\delta t >> 2\pi/\omega$.

The random force fluctuations are given by [2]

$$\Gamma = \pi(\frac{I}{\omega})^2 \sigma_S \tag{1}$$

being $\sigma_S = k^4|\alpha|^2/6\pi$ the scattering cross section, $I$ the intensity of the field and $k = \omega/c$ the wave vector. On the other hand, the drag force is given by

$$F = -\frac{5I\sigma_{ext}}{3c^2} v \tag{2}$$

being $\sigma_{ext}$ the extinction cross section $k\Im(\alpha)$

From these quantities, we can obtain the values of the equilibrium kinetic energy and the diffusion constant:

$$E_k = \frac{3\pi}{20}\frac{I}{k^2}\frac{\sigma_S}{\sigma_{ext}}\delta t \tag{3}$$

$$D = \frac{3}{50}(\frac{c}{k})^2 \pi \delta t \frac{\sigma_S}{\sigma_{ext}^2} \tag{4}$$

If the particle is initially at rest, damping is negligible and the random force fluctuations dominates resulting in a superdiffusive motion with a mean square displacement proportional to the cubic power of time. However, as velocity increases, the drag force induces a diffusive behavior with constant kinetic energy and a mean square displacement growing linearly with time. Both behaviors are given by equations 3 and 4 respectively. These predictions have been checked by molecular dynamics simulation on the particular case of a resonant electric dipole. Numerical results are shown in Figure 1.

**ACKNOWLEDGMENT**

Comments from J. J. Sáenz and financial support from Spanish Grant FIS2012-36113-C03 are gratefully acknowledged.

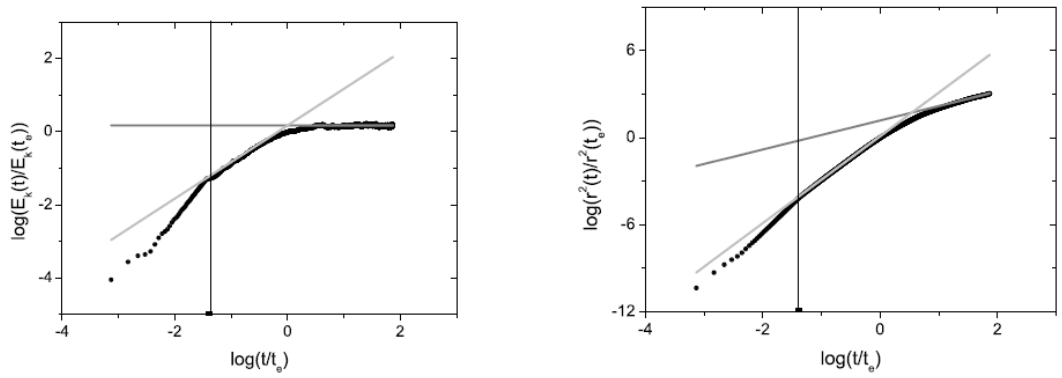



Figure 1: Log-Log plot of the molecular dynamics simulation results for the mean kinetic energy and the mean square displacement of a resonant electric dipole in a fluctuating random field (black dots). The dark gray line is the expected diffusive behavior. The gray line is the is the expected superdiffusive behavior. Time is normalized to the crossover time $t_e$. The mean kinetic energy is also normalized to the value at $t = t_e$. Vertical continuous line sets $t = \delta t$.

**REFERENCES**


1. G. Brügger, L. S. Froufe-Pérez, F. Scheffold and J. J. Sáenz, *Nat. Commun.*, Vol. 6, 7460-1–7460-7, 2015.
2. M. I. Marqués, *Opt. Lett.* Vol. 41, 796–799, 2016.

# Eigenchannels in scattering media: from manipulation to inverse design

**A. Yamilov[1], S. Petrenko[1], M. Koirala[1], R. Sarma[2], Hui Cao[2]**
[1*]Missouri University of Science and Technology, Missouri, USA
[2]Yale University, Connecticut, USA
[*]Corresponding author: yamilov@mst.edu

**Abstract***:* We demonstrate control of transport of light inside disordered waveguides by modifying the transmission eigenchannels. We obtain a relationship between the shape of the waveguide and the eigenchannel profile that opens the possibility of inverse design. Our approach allows one to control not only the transmitted but also reflected and absorbed light.

Diffusive transport of waves can be qualitatively different from that for particles due to the interference of scattered waves. One striking consequence of the interference effects is the creation of "open channels", which enables an optimally prepared coherent input beam transmitting through a lossless diffusive medium with order unity efficiency. The density of all transmission eigenvalues is given by the universal bimodal distribution, independent of both microscopic and macroscopic details of the system. The open channels (with transmission eigenvalues $\tau$ close to 1) have dominant contributions to the propagation of waves through random media, while the closed channels ($\tau \sim 0$) determine the reflected waves. Thus by modifying these channels, one would be able to control wave transport. The key question is, then, how to modify these channels.

In our work we demonstrate an effective approach to modify transmission eigenchannels of confined disordered media. Using shape of the waveguide, we can change the spatial profiles of the transmission channels significantly and deterministically from the universal one. It allows us to control the depth profile of the total energy as well as the energy density inside the random medium, thus controlling how much energy is concentrated inside the sample and where it is concentrated [1]. The ability to tailor the spatial distribution of energy density can be exploited to manipulate light-matter interactions in scattering media, which will be useful for numerous applications. By gradually increasing the cross-section, we can enhance the transmittance of all the transmission eigenchannels while keeping the number of input modes the same. Such geometries can be useful for applications related to enhancement of total transmission by shaping the input wavefront, as in such structures there will be more open channels due to larger conductance. Moreover, since the waveguide cross-section at the input end does not change, the number of input channels remains the same, and additional degree of control of the input field is not necessary for coupling into any one of the open channels. In addition, using geometry we can also convert evanescent channels to propagating channels and vice versa. In a waveguide with the output cross-section smaller than the input one, perfectly reflecting channels are created. The light injected to such a channel would penetrate inside the scattering media to a certain depth and then get fully reflected back to the input end. The penetration depth of such channels can be further tuned by geometry. Such channels have potential applications for probing deep inside turbid media. Since all the light exits from the input end, the collection efficiency of probe signal would be 100%.

We further design geometries with opposite taperings to have the same transmission eigenvalues but very different eigenchannel profiles. By breaking the reflection symmetry of confined geometry, the transmission

eigenchannels become asymmetric. In the presence of dissipation, the decay of energy flux inside the diffusive waveguide can be changed by modulating the cross-section of the waveguide along its axis. In a diffusive waveguide with nonmonotonic tapering boundary such as the lantern shape, energy can buildup inside the random medium, which will benefit the applications of energy harvesting and tailoring of optical excitations inside scattering media.

Since light in the perfect reflection channels can penetrate deep into the scattering system, such channels can be used for probing inside turbid media. Despite of the deeper penetration, all the light exits from the input end, making the collection efficiency of probe signal 100%, which is extremely useful for sensing or imaging applications. The penetration depth can be precisely tuned via tapering the boundary of a confined random system.

Optical absorption is ubiquitous and it often weakens the localization effects, but our approach of using geometry to control wave transport by manipulating the structure of eigenchannels proves to be effective and robust against strong absorption [1,2]. Therefore the confined geometries enable us to control not only the amount of light being transmitted or reflected, but also the amount of energy concentrated inside the random media. Although strong localization effects, absorption or asymmetric reflection from edges can modify the universal structure of transmission channels, but such effects also remove the open channels with perfect transmission. Unlike these effects, the approach of varying shape of confined geometries gives the significant advantage and freedom to alter the spatial structures of eigenchannels while retaining the open eigenchannels with perfect transmission.

We show that our approach is amenable to inverse design, i.e., to obtaining the waveguide shape based on the desired eigenchannel profiles. Our method is based on the previous studies on particle diffusion in confined geometries. A powerful theoretical method based on projection technique has been developed to model diffusion in 2D or 3D confined geometries as in 1D systems with an effective diffusion coefficient that varies spatially. In this work we show that such a technique can be applied to describe wave diffusion and include the absorption, which does not have a counterpart for particles.

**Acknowledgements**: The authors acknowledge support through National Science Foundation grants DMR-1205307 and DMR-1205223.

**REFERENCES**

1. Sarma, R., A. Yamilov, S. F. Liew, M. Guy, H. Cao, “Control of mesoscopic transport by modifying transmission channels in opaque media,” *Phys. Rev. B,* Vol. 92, 214206, 2015.
2. Yamilov, A., S. Petrenko, R. Sarma, H. Cao, “Shape-dependence of transmission, reflection and absorption eigenvalue densities in disordered waveguides with dissipation,” *Phys. Rev. B*(R) accepted, 2016, arXiv:1511.00958

# Chiral Light-Matter Interaction

**P. Lodahl**

[1]Niels Bohr Institute, University of Copenhagen, Blegdamsvej 17, DK-2100 Copenhagen, Denmark

[*]corresponding author: lodahl@nbi.ku.dk

**Abstract**-We review the physics of waveguide QED, notably recent progress on photonic-crystal waveguides containing single quantum emitters. It is found that chiral light-matter interaction can be engineered leading to new opportunities in quantum optics with applications for photonic quantum-information processing.

Quantum dots embedded in photonic-crystal waveguides [1] have proven to constitute an almost ideal platform for studying quantum electrodynamics (QED) in a 1D geometry, constituting a new paradigm often referred to as the "1D emitter". We show that single photons and single quantum emitters can be deterministically coupled as a basis of single-photon sources [2] and single-photon nonlinearity [3]. We furthermore discuss how chiral photon emission can be achieved an engineered in waveguides leading to new opportunities in quantum optics [4]. This includes the design of non-reciprocal integrated photonic devices and deterministic quantum gates. Finally, we discuss the prospects of scaling the platform to larger quantum architectures for applications in quantum-information processing, such as efficient photon sorting [5].

**REFERENCES**

1. P. Lodahl, S. Mahmoodian, and S. Stobbe, Reviews of Modern Physics 87, 347 (2015).
2. M. Arcari, I. Söllner, A. Javadi, S.L. Hansen, S. Mahmoodian, J. Liu, H. Thyrrestrup, E.H. Lee, J.D. Song, S. Stobbe, and P. Lodahl, Physical Review Letters 113, 093603 (2014).
3. A. Javadi, I. Sollner, M. Arcari, S.L. Hansen, L. Midolo, S. Mahmoodian, G. Kirsanske, T. Pregnolato, E. H. Lee, J. D. Song, S. Stobbe, and P. Lodahl, Nature Communications 6, 8655 (2015).
4. I. Söllner, S. Mahmoodian, S. Lindskov Hansen, L. Midolo, A. Javadi, G. Kiršanskė, T. Pregnolato, H. El-Ella, E.H. Lee, J.D. Song, S. Stobbe and P. Lodahl, Nature Nanotechnology 10, 775 (2015).
5. T.C. Ralph, I. Söllner, S. Mahmoodian, A.G. White, and P. Lodahl, Physical Review Letters 114, 173603 (2015).

# Intensity fluctuations of light emitted by two classical or quantum sources in a structured environment

**R. Carminati**[1], **J.J. Sáenz**[2], **and A. Canaguier-Durand**[3]

[1]Institut Langevin, ESPCI ParisTech, CNRS, PSL Research University, Paris, France
[2]Donostia International Physics Center (DIPC), Donostia-San Sebastian, Spain
[3]Laboratoire Kastler Brossel, UPMC Sorbonne Universités, CNRS, ENS, PSL Research University, Paris, France
remi.carminati@espci.fr

**Abstract**— We analyse theoretically intensity fluctuations of light emitted by two independent single-photon sources in an arbitrary environment. The theory shows that the interdistance between the sources is encoded in intensity fluctuations, and provides design rules for the control of the degree of quantum coherence of the emitted light. In particular, we derive generalized conditions to generate superradiant and subradiant states of the emitters. These results should find applications in quantum nanophotonics, and in sensing in complex media.

## 1. INTENSITY FLUCTUATIONS OF THE LIGHT EMITTED BY TWO INCOHERENT CLASSICAL SOURCES

In the first part of the talk, we discuss a method to capture the interaction between two identical dipole sources in a scattering environment, based only on the measurement of intensity fluctuations. This approach permits, in principle, to monitor the relative distance between the sources, with a precision that is not limited by diffraction, but by the microstructure of the medium. In a complex multiple scattering medium, the emitted intensity generates a speckle pattern. The result even suggests the intriguing possibility that intensity measurements at only one point in a speckle pattern produced by two incoherent sources can provide information about the relative distance between the sources. This information can in principle be extracted from the speckle contrast obtained after a proper time and configurational averaging process [1].

## 2. QUANTUM COHERENCE OF LIGHT EMITTED BY TWO SINGLE-PHOTON SOURCES

In the second part of the talk, we extend the approach to two quantum single-photon sources (as fluorescent molecules). We study the second-order quantum coherence of the emittted light in an arbitrary electromagnetic environment. We establish a general theoretical framework, in which design rules for the control of the degree of quantum coherence naturally emerge. As an important example, we derive the conditions for the observation of subradiant and superradiant states. In the case of a detection integrated over all output channels, the photodetection correlation functions are expressed in terms of the local and cross densities of states (LDOS and CDOS [2]) of the electromagnetic field, allowing a direct connection to classical quantities widely used in nanophotonics [3]. These general design rules should have broad applications in the emerging field of quantum nanophotonics, and could suggest new approaches for the sensing of fluorescent sources in complex media.

## ACKNOWLEDGMENT

This work was supported by LABEX WIFI (Laboratory of Excellence within the French Program "Investments for the Future") under references ANR-10-LABX-24 and ANR-10-IDEX-0001-02 PSL*.

## REFERENCES

1. Carminati, R., G. Cwilich, L.S. Froufe-Pérez, and J.J. Sáenz, *Phys. Rev. A* Vol. 91, 023807, 2015.
2. Cazé, A., R. Pierrat, and R. Carminati, *Phys. Rev. Lett.* Vol. 110, 063903, 2013.
3. Carminati, R., and A. Canaguier-Durand, submitted for publication, 2016.

# coherent spatiotemporal control of a femtosecond pulse through an opaque medium

**Mickael Mounaix**[1], **Daria Andreoli**[1,2], **Hugo Defienne**[1], **Giorgio Volpe**[1,3], **Ori Katz**[4], **Samuel Grésillon**[2], **Sylvain Gigan**[1]

[1] *Laboratoire Kastler Brossel, ENS-PSL Research University, CNRS, UPMC Paris Sorbonne, Collège de France, 24 rue Lhomond, 75005 Paris, France*

[2] *ESPCI ParisTech, PSL Research University, CNRS, Institut Langevin, 1 rue Jussieu, F-75005 Paris, France*

[3] *Department of Chemistry, University College London, 20 Gordon Street, London WC1H 0AJ, UK*

[4] *Department of Applied Physics, The Selim and Rachel Benin School of Computer Science and Engineering, The Hebrew University of Jerusalem, Jerusalem 9190401, Israel*

*sylvain.gigan@lkb.ens.fr*

**Abstract:** We report broadband characterization of the propagation of light through a multiply scattering medium by means of its Multi-Spectral Transmission Matrix. Using a spatial light modulator, we demonstrate full control of both spatial and spectral properties of an ultrashort pulse transmitted through the medium. We show spatiotemporal focusing of the pulse at any arbitrary position and time with any desired temporal shape. Our approach opens new perspectives for fundamental studies of light-matter interaction in disordered media, and has potential applications in coherent control and imaging.

**OCIS codes:** 070.6120 , 110.7348 , 070.4340

## 1. Introduction

Propagation of coherent light through a multiply scattering medium produces a speckle pattern at the output [1], due to multiple scattering events that scrambles the wavefront. Both phase and amplitude information of the light are spatially mixed, thus limiting resolution, depth and contrast of most optical imaging techniques. Over the last past years, wavefront shaping techniques have turned this paradigm around, and revolutionized the control of optical waves in disordered media. With more than a million degrees of freedom, spatial light modulators (SLMs) allow to manipulate the propagation of coherent light, using different techniques, from optimization, digital phase conjugation, or matricial methods [2, 3].

Due to the multiple scattering process, photons exit the scattering medium at different times, giving rise to a temporally broadened pulse at the output. Even in thin multiply scattering layers of paint can exhibit confinement times that can be order of magnitude longer than the initial time-width of the pulse. Therefore, applications that require an ultrashort pulse, such as multiphotonic imaging and non-linear physics are strongly impeded in a multiply scattering sample. With a single SLM, it has been shown that one can manipulate spatial degrees of freedom to adjust the delay between different optical paths. In this way, spatial and temporal distortions can be both compensated using wavefront shaping techniques, for example to perform spatiotemporal focusing [4–6].

In this work we explore the use of the Multi Spectral Transmission Matrix (MSTM), an extension of the Transmission Matrix approach in the spectral domain, to fully control, both spatially and spectrally, the propagation of an ultrashort pulse in a disordered medium. The MSTM coefficients include the relative phase relation between the different frequencies of the pulse, which is essential for the spectral control of the output pulse. We demonstrate deterministic spatiotemporal focusing and enhanced excitation of a non-linear process, as well as the deterministic realization of a variety of temporal profiles, that could not be directly reached with previous techniques [7].

## 2. Experimental results

The number of monochromatic transmission matrix to be measured to fully describe the propagation of the broadband signal is the number of spectral degrees of freedom, in essence the ratio between the spectral bandwidth of the ultrashort pulse and the spectral correlation bandwidth of the medium [8]. The latter is the inverse of the confinement time

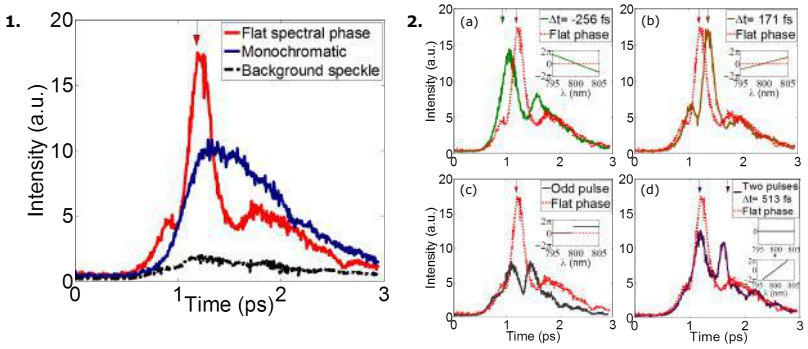



Fig. 1. Spatiotemporal control of an ultrashort pulse after propagation through the scattering sample. (1) Spatial and spatiotemporal focusing at a given time and at a given position are deterministically achievable. (2) Any spectral shape can be obtained. See main text.

of the medium. The MSTM is experimentally measured, using a Ti:Saph laser source producing either a wavelength-tunable continuous wave light, or broadband 110 fs ultrashort pulses. A phase-only SLM modulates the wavefront. The scattering sample is a thick layer of randomly distributed ZnO nanoparticles.

Two different methods are implemented to demonstrate spatiotemporal control of the output pulse. Firstly, we excite a non-linear process, two-photon fluorescence, that allows to discriminate the spatial from the spatiotemporal focusing. The second method is an interferometric cross correlation between an ultrashort pulse and the output pulse of the scattering medium, allowing a precise characterization of the spatiotemporal speckle at the output.

Fig 1 shows experimental results. We can deterministically temporally compress the pulse nearly to its initial time-width by imposing a flat phase relation between the different frequency component of the output pulse at any given position. Spatial focusing is achievable by focusing only one frequency of the output pulse. The MSTM gives also access to a more sophisticated spectral shape, as the spectral phase relation is known. For example, Fig 1 illustrates spectral shaping of the output pulse, by shifting with a controllable delay the arrival time of the pulse, creating a dip inside the pulse by adding a phase-jump in the spectral phase profile, or generating two pulses with a controlled delay.

As a conclusion, we demonstrate any temporal shape is achievable, with a resolution given by the temporal duration of the pulse, over a temporal interval related to the confinement time of the medium, using only spatial degrees of freedom of a single SLM. This full spatiotemporal control of the output pulse opens interesting perspectives for the study of light-matter interaction and for non-linear imaging in multiply scattering media.

## References


1. J. Goodman, "Some fundamental properties of speckle," J. Opt. Soc. Am. **66**, 1145-1150 (1976).
2. I. M. Vellekoop and A. P. Mosk, "Focusing coherent light through opaque strongly scattering media," Opt. Lett. **32**, 2309-2311 (2007)
3. Popoff, S. M., Lerosey, G., Carminati, R., Fink, M., Boccara, A. C., and Gigan, S. " Measuring the transmission matrix in optics: an approach to the study and control of light propagation in disordered media," Physical review letters, **104**, 100601 (2010)
4. Aulbach, J., Gjonaj, B., Johnson, P. M., Mosk, A. P., and Lagendijk, A. ."Control of light transmission through opaque scattering media in space and time," Physical review letters, **106**, 103901 (2011)
5. Ori Katz, Eran Small, Yaron Bromberg, and Yaron Silberberg, " Focusing and compression of ultrashort pulses through scattering media," Nature photonics, **5**, 372-377 (2011)
6. David J. McCabe, Ayhan Tajalli, Dane R. Austin, Pierre Bondareff, Ian A. Walmsley, Sylvain Gigan and Béatrice Chatel "Spatio-temporal focusing of an ultrafast pulse through a multiply scattering medium," Nature Communications, **2**, 447 (2011)
7. Mickael Mounaixet al. "Spatiotemporal coherent control of light through a multiply scattering medium with the Multi-Spectral Transmission Matrix," arXiv preprint arXiv:1512.07753 (2015)
8. Daria Andreoli, et al. "Deterministic control of broadband light through a multiply scattering medium via the multispectral transmission matrix," Scientific reports, **5** (2015)

# Everything is connected with everything: Can the study and tools of complex network theory tell us something about mesoscopic physics?

**Gabriel Cwilich**
Yeshiva University, USA
cwilich@yu.edu

**Abstract-** The mathematical framework and tools of complex network theory can be used to explore a variety of phenomena of diffusion and propagation in random systems and the resilience of structures under different percolation and decimation scenarios. Numerical and analytic results in a variety of models of single and interdependent networks will be reviewed.

Complex Network theory has been for a long time an area of intersection between mathematicians interested in graph theory and social scientists interested in modeling complex social phenomena[1]. As such it focused mainly in the structure and properties of networks at all scales, and the dynamics of their evolution and growth[2]. But in the last few years, with more physicists joining the field, increasing attention has been given to the function of networks: phenomena like percolation[3], resilience and collapse of networks on one hand, and transmission and propagation of processes and information on them on the other[4], have been discussed extensively.

This talk will illustrate some of the advances in these areas, particularly focusing on how networks and groups of interdependent networks behave after an initial attack or a random failure, or under targeted localized attacks, and how they disintegrate through a series of cascading failures.[5,6,7] The nature of the transition of the behavior of the system as a function of the size of the initial attack or region affected will be explored in a variety of different models, and the lessons that can be extracted to apply to artificially made or naturally occurring systems will be discussed.

**Acknowledgements**, Partial support for this work was received by the Gamson Computational Science Center at Yeshiva College.

**REFERENCES**

1. Newman, M. E. J., *Networks: An Introduction*, Oxford University Press, Oxford, 2010
2. Barabasi, A. L. and R. Albert , "Emerging of scaling in random networks," *Science*, Vol. 286, 509–512, 1999.
3. Gao, J., S. V. Buldyrev, H. E. Stanley, X. Xu and S. Havlin, "Percolation of a general network of networks," *Phys. Rev. E,* Vol 89, 062816, 2013.
4. Hethcote, H. W., "The mathematics of infectious diseases," *SIAM Rev.*, Vol 42, 599-653, 2000.

5. Motter. A. E. and Y. C. Lai, “Cascade-based attacks on complex networks”, *Phys. Rev. E*, Vol 66, 065202(R), 2002.
6. Buldyrev, S. V., R. Parshani, G. Paul, H. E. Stanley and S. Havlin, “Catastrophic cascade of failures in interdependent networks ,” *Science*, Vol. 464, 1025–1028, 2010.
7. Buldyrev, S. V., N. W. Shere and G. Cwilich, “Interdependent networks with identical degrees of mutually dependent nodes ,” *Phys. Rev. E*, Vol. 83, 16112–16116, 2011.

# Hybridization of Optical Forces

**Onofrio M. Maragò**[1*]
[1]CNR-IPCF, Istituto per i Processi Chimico-Fisici, V.le F. Stagno D'Alcontres 37, 98158, Messina, Italy
[*]corresponding author: marago@ipcf.cnr.it

**Abstract**-After an introduction to optical forces with a focus on the role of shape and aggregation, we present some experiments on optical trapping of core-shell nanoparticles and plasmonic mesocapsules. Thus, we discuss how material hybridization can promote accurate control of mechanical effects of light. In particular, we investigate models for laser cooling of hybrid plasmon-exciton systems and frequency-dependent optical forces on oligomers (meta-molecules).

Mechanical effects of light stem from momentum conservation in light scattering[1,2]. In the limiting cases of spherical particles either much smaller[3,4] (dipole approximation) or much larger[5,6] (ray optics) than the trapping wavelength, the force separates into different contributions: a conservative part proportional to the light intensity gradient responsible for trapping, and non-conservative scattering forces proportional to the light intensity that generally are detrimental for trapping, but fundamental for laser cooling. However, for non-spherical particles or at intermediate (meso)scale the situation is more complex and this traditional identification of intensity gradient and scattering forces is more elusive[7]. Moreover, shape and composition can have dramatic consequences for optically trapped particle dynamics.

Here, we present some experiments on optical trapping of core-shell nanoparticles[8] and plasmonic mesocapsules investigating the scaling properties of optical forces in these dielectric-plasmonic systems and their potential for SERS tweezers applications. Then we focus on the hybridization of optical forces by studying the control and engineering of mechanical effects of light in the presence of plasmon-exciton coupling. Optical forces on exemplar systems composed of plasmonic particles and quantum emitters (dimers[9], oligomers, linear chains[10]) are investigated theoretically by exploiting light scattering theory in the transition matrix (T-matrix) framework[7]. Results on laser cooling[9] and quantum-optical nanosailing[10] will be presented.

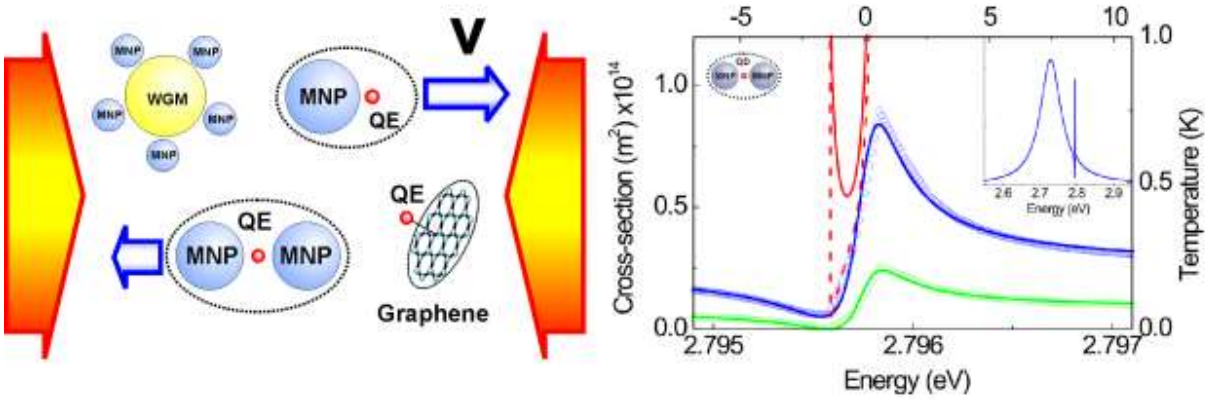



**Figure 1:** Fano-Doppler laser cooling[9] of hybrid nanostructures composed of plasmonic particles and a quantum emitter (left). The intrinsic Fano resonance typical of these systems enables laser cooling of the center-of-mass motion in the millikelvin range (right).

**REFERENCES**


1. Jones, P. H., Maragò, O. M., Volpe, G. *Optical Tweezers: Principles and Applications*, Cambridge University Press, Cambridge (UK), 2015.
2. Maragò, O. M., P. J. Jones P. G. Gucciardi, G. Volpe, A. C. Ferrari, "Optical trapping and manipulation of nanostructures". *Nature Nanotech.*, Vol. 8, 807, 2013.
3. Arias-González, J. R., and M. Nieto-Vesperinas. "Optical forces on small particles: attractive and repulsive nature and plasmon-resonance conditions." *JOSA A*, Vol. 20, No. 7, 1201-1209, 2003.
4. Albaladejo, S., et al. "Scattering forces from the curl of the spin angular momentum of a light field." *Physical Review Letters*, Vol. 102, No. 11, 113602, 2009.
5. Ashkin, A. "Forces of a single-beam gradient laser trap on a dielectric sphere in the ray optics regime." *Biophysical J.*, Vol. 61, No. 2, 569, 1992.
6. Callegari, A., et al. "Computational toolbox for optical tweezers in geometrical optics." JOSA B, Vol. 32, No. 5, B11-B19, 2015.
7. Borghese, F., P. Denti, R. Saija, M. A. Iatì, "Optical trapping of nonspherical particles in the T-matrix formalism", *Opt. Express* 15, 11984-11998, 2007.
8. Spadaro, D., et al. "Scaling of optical forces on Au–PEG core–shell nanoparticles." RSC Advances, Vol. 5, No. 113, 93139-93146, 2015.
9. Ridolfo, A., R. Saija, S. Savasta, P. H. Jones, M. A. Iatì, O. M. Maragò, "Fano-doppler laser cooling of hybrid nanostructures", *ACS Nano* Vol. 5, 7354, 2011.
10. Albaladejo, S., J. J. Sáenz, and M. I. Marqués. "Plasmonic nanoparticle chain in a light field: A resonant optical sail." *Nano Letters*, Vol. 11, No. 11, 4597-4600, 2011.

# Light trapping and extinction in large random aggregates of particles. An investigation through the Transition matrix method.

**M. A. Iatì**[1], **R. Saija**[2], **C. D'Andrea**[3], **M. J. Lo Faro**[1,3,4], **P. G. Gucciardi**[1], **A. Irrera**[1], **and B. Fazio**[1]

[1]CNR-Istituto per i Processi Chimico–Fisici, Messina, Italy
[2]Dipartimento di Scienze Matematiche e Informatiche, Scienze Fisiche e Scienze della Terra, Università di Messina, Italy [3]MATIS IMM-CNR, Catania, Italy [4]Dipartimento di Fisica e Astronomia, Università di Catania, Italy
iati@ipcf.cnr.it

**Abstract**— We study the optical behaviour of large random, fluffy or densely packed, aggregates of particles using a computational approach based on the Transition matrix technique. As a case study we apply this approach to the investigation of the outstanding optical properties, in terms of light trapping efficiency and light localization effects, of a two-dimensional random array of thin Si nanowires arranged in a fractal geometry.

The investigation of the optical properties of large aggregates of particles is a challenging topic with implications in many research and applicative fields, ranging from the optics of cosmic dust to nano-technology. Approximate solutions are often proposed in the literature, however in some situations there is the need for accurate and exact solutions to the problem [1]. Here we present an analytical and computational approach based on the Transition matrix (T-matrix) which has proved to be one of the most powerful methods for describing light scattering and absorption by aggregated particles, fully describing the multiple scattering processes among the constituent monomers [2, 3, 4]. This approach is based on the expansion of the electric fields in terms of spherical multipole fields with the T-matrix giving the relation between the multipole amplitudes of the incident and of the scattered fields.

As a case study here we discuss how the T-matrix approach allows the investigation of the optical properties of a two-dimensional array of thin Si nanowires arranged in a random fractal geometry [5]. In the visible region, incoming light remains mostly trapped in the nanowire forest due to strong multiple scattering processes. The nanowire array arrangement indeed, characterized by regions of tigthly spaced nanowires separated by air voids, introduces strong fluctuations in the material refractive index and consequentely causes strong in-plane multiple scattering processes [6]. Now, the fractal structure is characterized by a self-similarity so that the structural heterogeneities are correlated on all length scales. Whatever the effective wavelength propagating inside the medium, it will always be possible to match the length scale where the refractive index fluctuates thus generating a strong scattering.

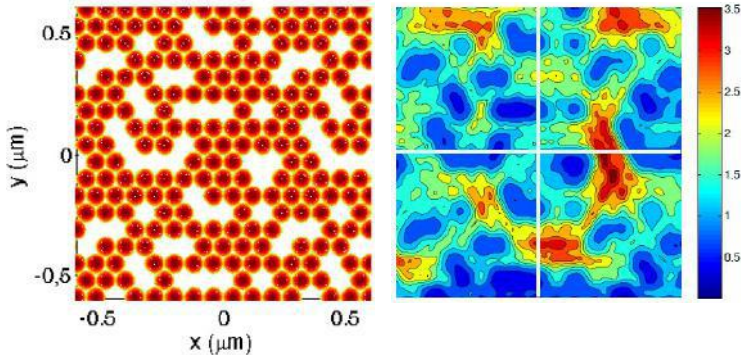



Figure 1: (left) Model random aggregated structure adopted in the computations. (right) Map of the normalized scattered field intensity for an exciting field with wavelength 633 nm.

We also simulate the near-field intensity distribution map of the light scattered by a random array of nanospheres, modelling the structure as an aggregate of 300 spheres, each with a radius

of 40 nm (left panel in figure 1) and with a refractive index given by a Bruggeman mixing rule, assuming a composition of 70% Si and 30% $SiO_2$. In figure 1 (right panel) we show the near field normalized intensity map distribution $|E_{sca}/E_{inc}|^2$, with $E_{sca}$ and $E_{inc}$ amplitudes of the scattered and of the incident electric field, respectively, at an exciting wavelength of 633 nm. We observe the formation of hot spot regions where the local fields is enhanced compared with the incident one [5]. Now, field localization effects occurring in random systems, appear even more strikingly in those with dilational symmetry, i.e. fractals [7, 8]. Thus, we can extend the results of this anaysis to fractal models.

Our investigation confirms how the optical properties of the system are strongly related to its random and fractal nature.

**REFERENCES**


1. Okada, Y., "Numerical simulations of light scattering and absorption characteristics of aggregates," in *Light scattering reviews 5*, Chapt 1. 4–36, A. Kokhanovsky ed. 2010.
2. Waterman, P. C., "Symmetry, unitarity, and geometry in electromagnetic scattering," *Physical review D*, Vol. 3, 825–839, 1971.
3. Borghese, F., Denti, P., Saija, R. *Scattering from model nonspherical particle*, Springer, 2007.
4. Mishchenko, M. I., Travis, L. D., Lacis, A. A. *Scattering, absorption, and emission of light by small particles*, Cambridge University Press, 2002.
5. Fazio, B., Artoni, P., Iatì, M. A. et al.,"Strongly enhanced light trapping in a two-dimensional silicon nanowire random fractal array," *Light Sci Appl*, doi: 10.1038/lsa.2016.62, 2016 (in press).
6. Vynck, K., Burresi, M., Riboli, F., and Wiersma, D. S., "Photon management in two-dimensional disordered media," *Nature Mater.*, Vol. 11, 1017–1022, 2012
7. Shalaev, V. M., Moskovits, M., Golubentsev, A. A., and John, S., "Scattering and localization of light on fractals," *Physica A*, Vol. 191, 352–357, 1992
8. Podolskiy, V. A., Shalaev, V. M., "Giant optical responses in microcavity-fractal composites," *Laser Phys*, Vol. 11, 26–30, 2001

# The effective medium in disordered waveguides: the role of evanescent modes

**M. Yépez[1] and J. J. Sáenz[2,3]**

[1]Departamento de Física, Universidad Autónoma Metropolitana-Iztapalapa, A. P. 55-534, 09340 México Distrito Federal, México.
ymmiztli@xanum.uam.mx
[2]Donostia International Physics Center (DIPC), Paseo Manuel Lardizabal 4, 20018 Donostia-San Sebastian, Spain.
[3]IKERBASQUE, Basque Foundation for Science, 48013 Bilbao, Spain.

**Abstract**— We study the wave propagation through a disordered slab inside a waveguide of finite width. In the dense weak-scattering limit, the statistics for the complex reflection and transmission coefficients of the coherent field depend on two characteristic lengths, leading to an effective refractive index, whose real part is quite sensitive to the evanescent modes. The theoretical predictions, derived within the Born series method, are in excellent agreement with numerical simulations.

The wave propagation through disordered systems has been studied extensively, in both electronic and electromagnetic systems, where scaling and universality are fundamental concepts. Different previous approaches have found some common features, showing notorious statistical regularities for the propagation of waves through complex media. Remarkable phenomena such a coherent enhanced backscattering, universal conductance fluctuations and the underlying correlations between transport coefficients or the shape of the conductance distributions in the diffusive and localized regimes were found to be independent of the microscopic details: statistical properties of *some macroscopic observables* are universal and only depend on the transport mean free path $\ell$.

In recent years, there has been a revival of interest in the impact of inhomogeneities and defects in the transmission properties in quasione-dimensional (Q1D) systems [1] and is the subject of intense research including the electronic conductance of nanowires, nanotubes and nanoribbons [2], the propagation of slow light through disordered photonic-crystal waveguides [3] or acoustic propagation [4]. A correct description of wave transport through inhomogeneous media involves not only propagating travelling modes (open channels) but it is also very sensitive to near-field evanescent modes (closed channels) [5]. However, the statistical properties of transport through disordered Q1D systems, obtained from numerical calculations, do not depend on the evanescent modes [6, 7] and they are in good agreement with theoretical scaling approaches [1, 6], which do not take into account explicitly evanescent modes [8, 9]. The effects of the evanescent modes on the statistical properties of wave transport through disordered waveguides, are studied in Ref. [7], where it is demonstrated that although accounting for evanescent channels manifests itself in the renormalization of the transport mean free path $\ell$, the distributions of angular transmission, total transmission and conductance remain universal.

In the present talk, we summarized the results found in Ref. [10], where it is studied the influence of the evanescent modes on the statistical properties of the complex reflection and transmission coefficients of the coherent field (scattering amplitudes) and the statistics of the transport coefficients. Figure 1 shows the numerical results for the statistical averages for the coherent field amplitudes $\langle t_{aa_0}\rangle$, $\langle r_{aa_0}\rangle$ and the transport coefficients $\langle T_{aa_0}\rangle$, $\langle R_{aa_0}\rangle$, as function of the length of the slab $L$ in units of the transport mean free path $\ell$. The statistical averages of (power) transmittances $\langle T_{aa_0}\rangle$ and reflectances $\langle R_{aa_0}\rangle$ are solely determined by the mean free paths (MFPs) (in agreement with the scaling theory), which do not depend drastically on the evanescent modes. In striking contrast, the statistical average of the scattered field amplitudes $\langle t_{aa_0}\rangle$, $\langle r_{aa_0}\rangle$ (coherent field) present a completely different behavior (which was not captured by previous scaling approaches). The propagation of the coherent wave field [11] is characterized by an effective refractive index, whose real part determines the speed of propagation, while its imaginary part represents the losses due to scattering (often known as waveguide extrinsic losses). The numerical simulations are analyzed theoretically with the perturbative Born series method: the agreement is excellent in the ballistic regime, where the length of the system $L$ is much smaller than the mean free path $\ell$. A more

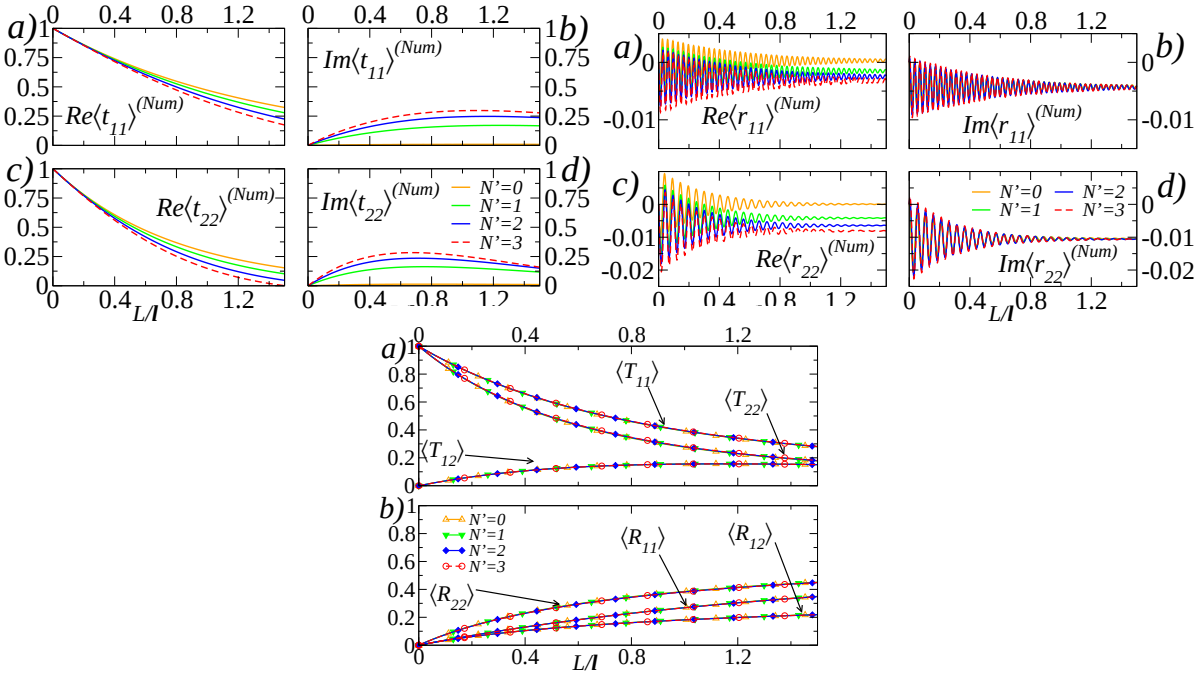



Figure 1: Top: Numerical results for $\langle t_{a_0a_0}\rangle$ and $\langle r_{a_0a_0}\rangle$ *vs* $L/\ell$. Bottom: Numerical results $\langle T_{aa_0}\rangle$ and $\langle R_{aa_0}\rangle$ *vs* $L/\ell$. Each simulation considers $N = 2$ propagating modes, several evanescent modes ($N' = 0, 1, 2, 3$) and $10^7$ realizations.

general method based on the transition matrix formalism [12], is in progress, which should give rise to a theoretical expression for $\langle t_{aa_0}\rangle$ and $\langle r_{aa_0}\rangle$ beyond the ballistic regime [13].

**REFERENCES**


1. Mello, P. A., and Kumar, N., Quantum Transport in Mesoscopic Systems (Oxford University Press, Oxford) 2010; Beenakker, C. W. J., *Rev. Mod. Phys.* **69**, 731 (1997).
2. Markussen, T., *et al.*, *Phys. Rev. Lett.* **99**, 076803 (2007); Lherbier A., *et al.*, *Phys. Rev. Lett.* **100**, 036803 (2008); López, B. A., *et al.*, *Nano Lett.* **9**, 940 (2009); Feilhauer, J., and Moško, M., *Phys. Rev. B* **83** 245328 (2011).
3. Patterson, M., *et al.*, *Phys. Rev. Lett.* **102**, 253903 (2009); Patterson, M. and Hughes S., *J. Opt.* **12**, 104013 (2010); Le Thomas N. *et al.*, *Phys. Rev. B* **80**, 125332 (2009); Mazoyer S., *et al.*, *Opt. Express* **18**, 14654 (2010); Baron A., *et al.*, *Phys. Rev. Lett.* **107**, 153901 (2011); Ott J., Mortensen N. and Lodahl P., Phys. Rev. Lett. **105**, 090501 (2010).
4. Derode A., Mamou V. and Tourin A., *Phys. Rev. E* **74**, 036606 (2006); Hegewisch K. C. and Tomsovic S., *Europhysics Letters (EPL)* **97**, 34002 (2012).
5. Carminati R., *et al.*, *Phys. Rev. A* **62**, 012712 (2000); Apostol A., and Dogariu A., *Phys. Rev. Lett* **91**, 093901 (2003); Miao F., *et al.*, *Science* **317**, 1530 (2007).
6. Froufe-Pérez, L. S., *et al.*, *Phys. Rev. E* **75**, 031113 (2007);
7. Payne, B., *et al.*, *Waves in Random and Complex Media* **23**, 43 (2013).
8. Mello, P. A., and Shapiro B., *Phys. Rev. B* **37**, 5860 (1988); Dorokhov O. N., *Pisma Zh. Eksp. Teor. Fiz.*, **36**, 259 (1982) (JETP Lett., **36**, 318 (1982)); Mello P. A., *et al.*, *Ann. Phys. (N.Y.)* **181**, 290 (1988)
9. Efetov K. B. and Larkin A. I., *Sov. Phys. JETP*, **58**, 444 (1983); Fyodorov Y. V. and Mirlin A. D., *Int. J. Mod. Phys. B* **8** 3795 (1994); Brouwer P. W. and Frahm K., *Phys. Rev. B* **53**, 1490 (1996).
10. Yépez, M., and Sáenz, J. J., *Europhysics Letters (EPL)* **108**, 17006 (2014).
11. Foldy L., *Phys. Rev.* **67**, 107 (1945); Lax M., *Phys. Rev.* **85**, 621 (1952).
12. Frisch U., *Ann. Astrophys.*, **30**, 565 (1967).
13. Yépez, M., and Sáenz, J. J., arXiv:1511.07931 [cond-mat.dis-nn].

# A spectral model for the speckle temporal coherence

**G. Soriano**[1], **M. Zerrad**[1], **and C. Amra**[1]

[1]Aix-Marseille Université, CNRS, Centrale Marseille,
Institut Fresnel UMR 7249, 13013 Marseille, France
gabriel.soriano@fresnel.fr

**Abstract**— We present a simple model for the spectrally-resolved (or multispectral) vector transmission matrix for the scattering of light from highly scattering media. It is used to numerically derive the spatial distribution of the coherence time in the speckle pattern for an incident light of given temporal coherence and state of polarization.

Light propagating through highly disordered media undergoes multiple scattering. This is turned into an advantage for several applications such as increasing the numerical aperture of imaging systems [1], and more generally paves a new way to control light [2]. The so-called transmission matrix of a thick disordered medium was recorded [3, 4, 5] for a single wavelength first. More recently, this measurement was made spectrally dependent for broadband light illumination [6, 7], leading to spatiospectral light shaping.

In [8], we numerically studied the coherence time variations in a speckle pattern. Incident light was partially polarized, with a given coherence time. The highly disordered medium was depicted by a vector transmission matrix with no spectral variation [9]. It was thus assumed that the incident light bandwidth was much narrower that the spectral variations of the medium response. In order to observe variations of the scattered light coherence time, the so-called spectral degree of coherence [10] of the incident light was made frequency-dependent.

In this paper, we focus on the effect of the spectral variations of the vector transmission matrix on the scattered light coherence time, with the incident light spectral degree of coherence a constant with respect to frequency. Our spectral model is very simple : the four elements of the transmission matrix have similar but independent frequency variations. They are four different realizations of the same Gaussian process with a given spectral width, to be compare to the incident light bandwidth [11]. This simplicity allows us to numerically derive the spatial distribution of the coherence time in the speckle pattern. Note that intensity and state of polarization distributions are also at hand.

We stress that this model gives insight about the impact of the incident light degree of polarization on the speckle coherence. This might prove useful for designing experimental setups with partially polarized illumination.

## REFERENCES

1. Y. Choi, T. D. Yang, C. Fang-Yen, P. Kang, K. J. Lee, R. R. Dasari, M. S. Feld, and W. Choi, "Overcoming the diffraction limit using multiple light scattering in a highly disordered medium," *Physical review letters*, vol. 107, no. 2, p. 023902, 2011.
2. A. P. Mosk, A. Lagendijk, G. Lerosey, and M. Fink, "Controlling waves in space and time for imaging and focusing in complex media," *Nature photonics*, vol. 6, no. 5, pp. 283–292, 2012.
3. T. Kohlgraf-Owens and A. Dogariu, "Finding the field transfer matrix of scattering media," *Optics express*, vol. 16, no. 17, pp. 13225–13232, 2008.
4. S. Popoff, G. Lerosey, R. Carminati, M. Fink, A. Boccara, and S. Gigan, "Measuring the transmission matrix in optics: an approach to the study and control of light propagation in disordered media," *Physical review letters*, vol. 104, no. 10, p. 100601, 2010.
5. S. Tripathi, R. Paxman, T. Bifano, and K. C. Toussaint, "Vector transmission matrix for the polarization behavior of light propagation in highly scattering media," *Optics express*, vol. 20, no. 14, pp. 16067–16076, 2012.
6. T. W. Kohlgraf-Owens and A. Dogariu, "Transmission matrices of random media: means for spectral polarimetric measurements," *Optics letters*, vol. 35, no. 13, pp. 2236–2238, 2010.
7. D. Andreoli, G. Volpe, S. Popoff, O. Katz, S. Grésillon, and S. Gigan, "Deterministic control of broadband light through a multiply scattering medium via the multispectral transmission matrix," *Scientific reports*, vol. 5, 2015.

8. G. Soriano, M. Zerrad, and C. Amra, "Mapping the coherence time of far-field speckle scattered by disordered media," *Optics express*, vol. 21, no. 20, pp. 24191–24200, 2013.
9. J. Sorrentini, M. Zerrad, G. Soriano, and C. Amra, "Enpolarization of light by scattering media," *Optics Express*, vol. 19, no. 22, pp. 21313–21320, 2011.
10. L. Mandel and E. Wolf, *Optical coherence and quantum optics*. Cambridge university press, 1995.
11. G. Soriano, M. Zerrad, and C. Amra, "Speckle intensity statistics for chromatic scattering media under partially polarized illumination," *Optics express*, vol. 23, no. 16, pp. 20796–20803, 2015.

# Cellulose bio-inspired hierarchical structures

**S. Vignolini**[1]

[1]Melville Laboratory for Polymer Synthesis, Department of Chemistry, University of Cambridge Lensfield Road, Cambridge CB2 1EW, UK

[*]corresponding author: sv319@cam.ac.uk

**Abstract**- Nature's strongest and vivid colours rely on the ability to produce complex and hierarchical photonic structures with lattice constants on the order of the wavelength of visible radiation [1]. A common strategy design that is found both in the animal and plant kingdoms for producing such effects is the helicoidal multilayers [2,3]. In such structures, a series of individual nano-fibers (made of natural polymers as cellulose and chitin) are arranged parallel to each other in stacked planes. When distance between such planes is comparable to the wavelength of light, a strong polarised, colour selective response can be obtained [4]. These helicoidal multilayers are generally structured on the micro-scale and macroscopic scale giving rise to complex hierarchical structures.

Biomimetic with cellulose-based architectures enables us to fabricate novel photonic structures using low cost materials in ambient conditions [2-4]. Importantly, it also allows us to understand the biological processes at work during the growth of these structures in plants.
In this talk the route for the fabrication of complex bio-mimetic cellulose-based photonic structures will be presented and the optical properties of artificial structures will be analyzed and compared with the natural ones.

**REFERENCES**

1. Kinoshita, S. et al. (2008). Physics of structural colors. *Rep. Prog. Phys*. 71(7), 076401.
2. Vignolini, S. et al. (2012). Pointillist structural color in Pollia fruit *PNAS* 109, 15712-15716.
3. Wilts, B. D, et al. (2014). Natural Helicoidal Structures: Morphology, Self-assembly and Optical Properties. *Materials Today: Proceedings*, 1, 177–185.
4. de Vries, H. (1951). Rotatory power and other optical properties of certain liquid crystals. *Acta Cryst.*, 4(3), 219–226.
5. Dumanli, A. G., et al. (2014). Controlled, Bio-inspired Self-Assembly of Cellulose-Based Chiral Reflectors. *Adv. Opt Mat*., 2(7), 646–650.
6. Arwin, H., et al. (2013). Cuticle structure of the scarab beetle Cetonia aurata analyzed by regression analysis of Mueller-matrix ellipsometric data. *Opt. Exp.*, 21(19), 22645.

# Light generation and scattering in a photonic network of sub-wavelength nanofibres

**Riccardo Sapienza**
Department of Physics, King's College London, Strand, London WC2R 2LS, United Kingdom
Riccardo.sapienza@kcl.ac.uk

**Abstract**-Nanoscale generation of individual photons in confined geometries is an exciting new research field aiming at exploiting localised electromagnetic fields for light manipulation. One of the outstanding challenges of photonic systems combining emitters with nanostructured media is the selective channelling of photons emitted by embedded sources into specific optical modes and their transport at distant locations in integrated systems. Here we discuss coupling experiments in plasmonic networks and electrospun nanofibres networks. While the former achieve large Purcell factors [1], the latter combine subwavelength field localisation and large broadband near-field coupling with low propagation losses [2]. By momentum spectroscopy, as in Figure, we quantify the modal coupling efficiency identifying the regime of single-mode coupling [2]. Moreover we identify an hybrid dielectric-plasmonic geometry as the most convenient for long-range energy transfer [3]. The hybrid dielectric networks do not rely on resonant interactions making them ideal for room-temperature operation, and offer a scalable platform for future quantum information technology.

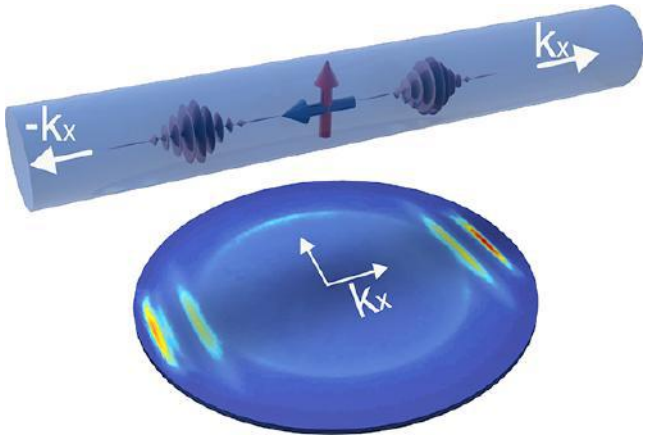



Figure: Sketch of the momentum spectroscopy measurement of the emitter-nanofibre coupling.

**REFERENCES**

1. M. Gaio, M. Castro-Lopez, J. Renger, N. van Hulst, and R. Sapienza, Percolating Plasmonic Networks for Light Emission Control, Faraday Discussions, 178, 237-252 (2015).
2. M. Gaio, M. Moffa, M. Castro-Lopez, D. Pisignano, A. Camposeo, and R. Sapienza "Modal coupling of single photon emitters within nanofibre waveguides" submitted.
3. P. M. de Roque, N. F. van Hulst and R. Sapienza, Nanophotonic boost of intermolecular energy transfer, New Journal of Physics 17, 113052 (2015).

# Non-linear and ultra-fast spectroscopy of nano- and meta-materials

# Observation of plasmon wave packet motions with ultrafast near-field microscopy

**H. Okamoto[1,2*], Y. Nishiyama[1], and K. Imura[3]**
[1]Institute for Molecular Science, Japan
[2]The Graduate University for Advanced Studies (Sokendai), Japan
[3]School of Advanced Science and Engineering, Waseda University Japan
[*]corresponding author: aho@ims.ac.jp

**Abstract** An aperture-type scanning near-field optical microscope was combined with ultrafast measurement system and achieved delivery of 15-fs optical pulses at the probe tip, which enables direct space-time domain observation of plasmon dynamics in gold nanostructures. With this apparatus, we studied plasmon wave packet dynamics in gold nanorods. On coherent multi-mode excitation with the ultrashort pulses, we found characteristic time-dependent features of near-field pump-probe images, which reflected wave packet propagation in the nanorod.

The unique optical characteristics of metal nanostructures are governed principally by interactions between surface plasmon resonance and electromagnetic fields. Characteristic spatial scale of plasmon resonance is essentially smaller than the diffraction limit of light resonant with the plasmon, and hence direct optical imaging of the spatial structure is difficult with conventional optical microscopy. We adopted aperture-type near-field optical microscopy to visualize optical field structures in the peripheries of metal nanostructures and plasmon waves. Local impulsive photoirradiation of metal nanostructures may generate plasmonic wave packets that propagate through the nanostructures and space, as a result of intra- and inter-particle interactions, which may yield a wide variety of unique optical characteristics. To visualize that directly and get basic information on plasmon dynamics, 10-fs level time resolution of near-field imaging is necessary because plasmons decay within 20 fs. In this study, we developed an ultrafast time-resolved near-field optical measurement system[1] and observed plasmon mode dephasing[2] and wave packet propagation[3] on gold nanorods.

Ultrashort pulses for optical excitation are seriously broadened in the near-field microscope due to dispersion effects of the optical components, particularly in the optical fiber of the probe. We compensated the dispersions effects by using a pulse-shaping device, in addition to passive devices (a grating pair and chirp mirrors), and achieved 15-fs FWHM pulse duration at the probe tip. The obtained pulses were used to observe plasmon dynamics at the probe tip position. The central wavelength of the pulses was around 840 nm. An equal pulse pump-probe correlation scheme was adopted to take the time-resolved data. The sample gold nanorods were fabricated either by chemical synthesis or by electron beam lithography lift-off method. When the incident photons are resonant with the plasmon resonance, the nanostructure is two-photon excited to emit photoluminescence, which was detected as the signal in this study. Pump-probe time-resolved signals were taken point by point on the rod, and the data were rearranged to obtain time-resolved pump-probe images.

For a relatively short (low aspect ratio) rod, the laser pulse excited one longitudinal plasmon mode, and the time-resolved signals basically showed single exponential decays reflecting the dephasing of the mode. The dephasing time was independent of the position on the rod. For a longer (higher aspect ratio) nanorod where two

longitudinal modes were simultaneously resonant with the pulse, the situation was different. The time-resolved signals at some specific positions showed beating features. In the time-resolved images, spatial features of the two modes excited appeared alternately in the time region around 20 fs (Figs. 1b,c). The line profile of the transient signal along the rod axis is mapped as a function of time as shown in Fig. 1d. This position-time profile of the signal was simulated based on a simple coherent two-mode model of plasmonic excitation. The simulated profile (Fig. 1e) well reproduced the qualitative features of the observed profile, indicating that the model successfully mimics the essential physical process of the dynamics of the plasmonic excitation in the nanorod. Then, using the same model of plasmonic excitation, we simulated dynamic behavior of plasmon waves after the pulsed photoexcitation of the nanorod at a specific position. Figure 1f shows a simulated plasmonic oscillation amplitude as a function of time after the excitation and position on the rod, when the rod is excited at the left end. Propagation of a plasmonic wave packet from the left end to right, up to ~20 fs after excitation, and reflection of the wave packet at the right end are clearly seen in the simulated profile. The result indicates that the characteristic feature observed in the time-resolved near-field image (Figs. 1a-d) mentioned above directly reflects the generation and propagation of a plasmonic wave packet in the gold nanorod.

The method demonstrated here allows not only fundamental researches on space-time characteristics of plasmonic excitations in metal nanostructures, but also applications to nano-precision optical manipulation of materials, basic design and instrumentation of information processing devices, and so forth. In the present study, double pulse experimental scheme was adopted, where two pulses were used as excitation and detection of plasmons. It leads seamlessly to a coherent control scheme where the two pulses are regarded as excitation and control pulses. Introduction of pulse-shape manipulation may further extend the control scheme in the future.

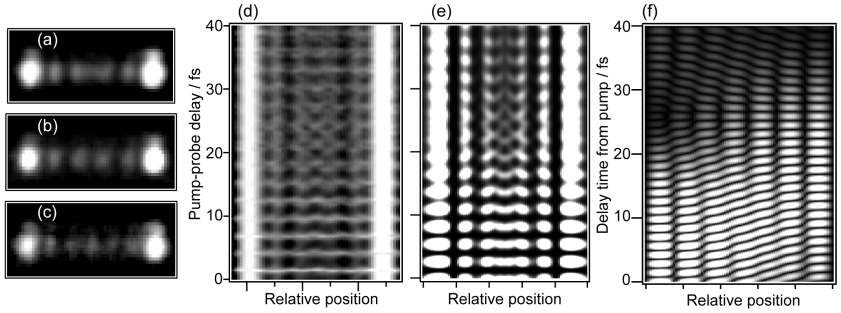



**Figure 1.** (a,b,c) Transient pump-probe near-field images of gold nanorod (1050 $nm^l$ × 70 $nm^w$ × 20 $nm^t$) at delay times of 0 fs, 22.5 fs, and 23.9 fs. (d) Experimental and (e) simulated time dependent line profiles of the pump-probe images along the rod axis, respectively. (f) Simulated plasmonic wave packet dynamics after photoexcitation at the left end of the rod.

**Acknowledgements** We thank Dr. T. Narushima, Mr. K. Imaeda, and Ms. A. Ishikawa for their help and discussion. The research was supported in part by Grants-in-Aid for Scientific Research (Nos. 22225002, 24350014, 25810013, 26107003 and 15H02161) from JSPS.

## REFERENCES

1. Wu, H. J., Nishiyama, Y., Narushima, T., Imura, K. and Okamoto, H., *Appl. Phys. Express*, 5, 062002, 2012.
2. Nishiyama, Y., Imaeda, K., Imura, K. and Okamoto, H., *J. Phys. Chem. C*, 119, 16215–16222, 2015.
3. Nishiyama, Y., Imura, K. and Okamoto, H., *Nano Lett.*, 15, 7657–7665, 2015.

# Optical properties of supported size-selected metal clusters.

**A. Kartouzian[1*], M. Thämer[2], T. Lünskens[1], P. Heister[1], A. Von Weber[1], and U.Heiz[1]**

[1]Technische Universität München, Lehrstuhl für Physikalische Chemie, Garching, Germany
[2]Fritz Haber Institute, Department of Physical Chemistry, Berlin, Germany
[*]corresponding author: aras.kartouzian@mytum.de

**Abstract**- By combining linear and nonlinear spectroscopic methods, we study the optical response of size-selected metal clusters supported on oxide materials. Such experiments could not be performed in the past due to extremely high sensitivities that are required to investigate truly monodispersed size-selected cluster samples with surface coverages as low as 0.1% of a monolayer. Our results on silver clusters ($Ag_n$, $9<n<55$) indicate a general trend in agreement with theoretical predictions and a nonscalable behavior characteristic of small clusters.

The main challenge in investigating size dependent properties of metal clusters is to fabricate a sample, dense enough to meet the sensitivity requirements of the method while keeping it dilute enough, to prevent agglomeration of clusters and thus loss of size specific information. Matrix isolation[1], or ligand stabilization[2] are common ways to resolve this issue. Although these approaches can lead to information on size dependent properties of clusters, they exclude further practical use of the clusters e.g. for catalytic purposes as the clusters are fully covered. Since the properties of metal clusters are generally influenced to a great extent by their surrounding medium, transferring the information obtained from such experiments to other conditions is not a reliable option. In turn, supported size-selected clusters provide the perfect case, where the size specific properties can be directly put to use. Unlike matrix-embedded and ligand stabilized clusters, where large number of clusters can be brought in close proximity without appreciable cluster-cluster interactions or agglomeration, supported samples require extremely low number densities in order to guarantee monodispersity[3]. This has been the reason for the scarcity/nonexistence of such experiments in the past.

In our lab we combined the linear absorption method of surface cavity ring-down spectroscopy (s-CRDS) and the nonlinear method of surface second harmonic generation spectroscopy (s-SHGS) to explore the optical properties of size-selected metal clusters[4, 5], which led to the first optical spectra of supported size-selected silver clusters to date[6]. Surface sensitivity of s-SHGS together with the high sensitivity of s-CRDS allows us to follow the size evolution of the optical properties of supported clusters and to investigate the third dimension of the periodic table.

Furthermore, the interaction of supported clusters with adsorbed molecules can also be considered and thus a better insight in mechanisms underlying catalytic behavior of size-selected metal clusters will be attainable.

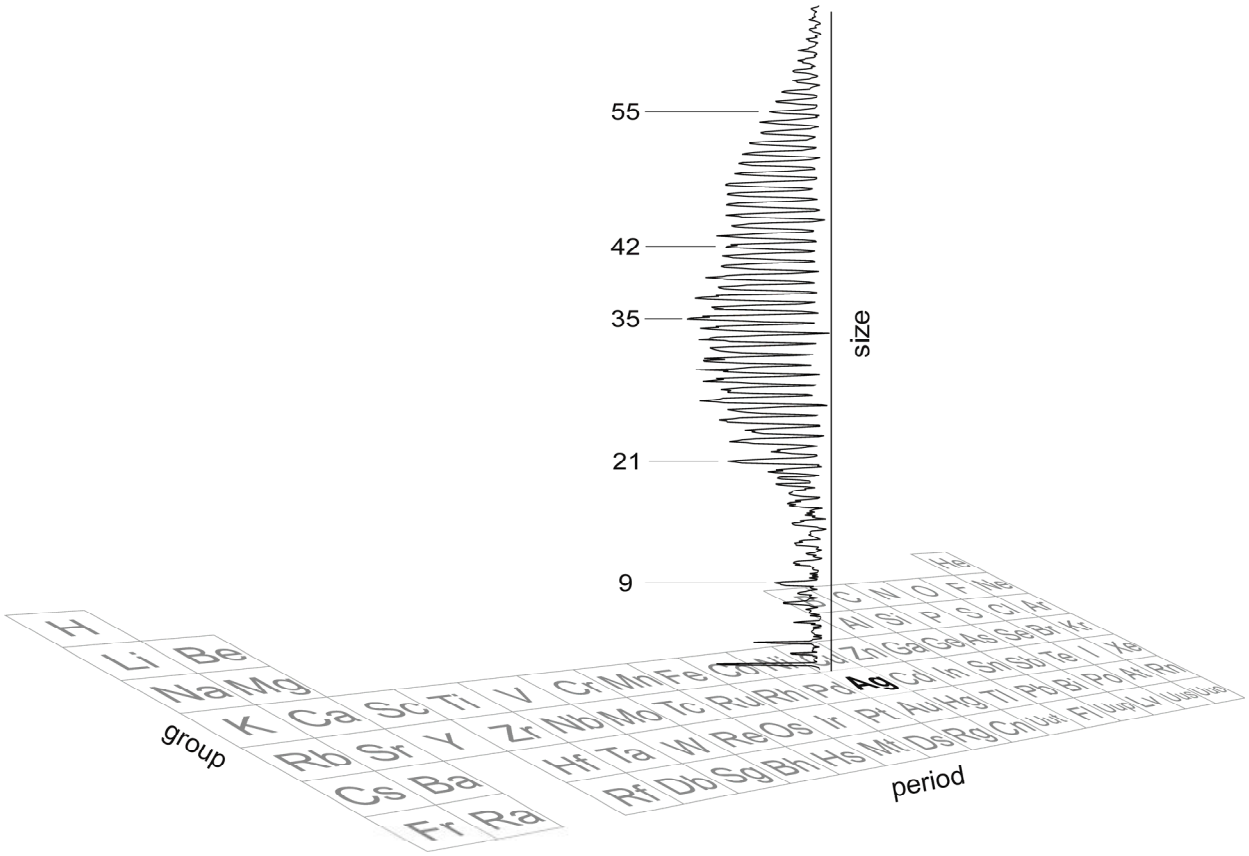



**Figure 1**: Clusters form the third dimension of the periodic table of elements, where the properties not only vary along the periods and groups, but also with the number of atoms constituting the clusters. A mass spectrum of silver clusters generated by a laser vaporization cluster source is shown.

**Acknowledgements**, This work was supported by the European Research Council through an Advanced Research Grant (246645-ASC3), and the DFG through the project (HE 3454/21-1)

**REFERENCES**

1. Harbich, W.; Fedrigo, S.; Buttet, J., *Chem. Phys. Lett.* **1992**, 195, 613-617.
2. Russier-Antoine, I.; Bertorelle, F.; Vojkovic, M.; Rayane, D.; Salmon, E.; Jonin, C.; Dugourd, P.; Antoine, R.; Brevet, P. F., *Nanoscale* **2014**, 6, 13572-13578.
3. Kartouzian, A.; Thämer, M.; Soini, T.; Peter, J.; Pitschi, P.; Heiz, U., *J. Appl. Phys.* **2008**, 104.
4. Thämer, M.; Kartouzian, A.; Heister, P.; Gerlach, S.; Tschurl, M.; Boesl, U.; Heiz, U., *J. Phys. Chem. C* **2012**, 116, 8642-8648.
5. Thämer, M.; Kartouzian, A.; Heister, P.; Lünskens, T.; Gerlach, S.; Heiz, U., *Small* **2014**, 10, 2340-2344.
6. Lünskens, T.; Heister, P.; Thämer, M.; Walenta, C. A.; Kartouzian, A.; Heiz, U., *Phys. Chem. Chem. Phys.***2015**, 17, 17541-17544.

# Shaping the nonlinear near-field: the plasmonic analogue of Young's double slit experiment

**D. Wolf[1,2], T. Schumacher[1], and M. Lippitz[1,*]**
[1] Experimental Physics III, University of Bayreuth, Germany
[2] Max Planck Institute for Solid State Research, Stuttgart, Germany

**Abstract**- Although shaping of fields around nanostructures is widely studied in plasmonics, the influence of the field inside the nanostructures is often overlooked. The linear field distribution inside the structure taken to the third power causes third-harmonic generation, a nonlinear optical response of matter. We demonstrate how this simple fact can be used to shape complex fields around a single particle alone. We employ this scheme to switch the emission from a single point to two spatially separated but coherent sources.

When metal nanostructures are excited by ultrafast laser pulses, nonlinear optical effects like higher harmonics generation or multiphoton induced luminescence can be observed. Most studies focus on the efficiency enhancement of non-linear processes and considerably less attention is paid to the spatial origin of the signals. It is the third power of the fundamental field inside the material that leads to the nonlinear response. Small variations in this field can have a large effect.

We image the emission of single gold nanostructures in the Fourier plane to obtain the emission direction and coherence. Tuning the fundamental wavelength over a third-order resonance of a gold nanorod, we observe [1] switching of the emission from one single emitting source to two spatially separated, but coherent sources. These two sources interfere in the optical far-field as expected from Young's double slit experiment. However, in our plasmonic analogue, we create the double slit not by shaping matter, but directly by shaping the nonlinear fields inside a continuous and homogeneous piece of matter. The nonlinearity of the signal generation amplifies smaller differences in amplitude and phase of the fundamental field, so that large differences in the resulting third-harmonic field can be obtained (Fig.1). We envision applications as diverse as coherently feeding antenna arrays and optical spectroscopy of spatially extended electronic states.

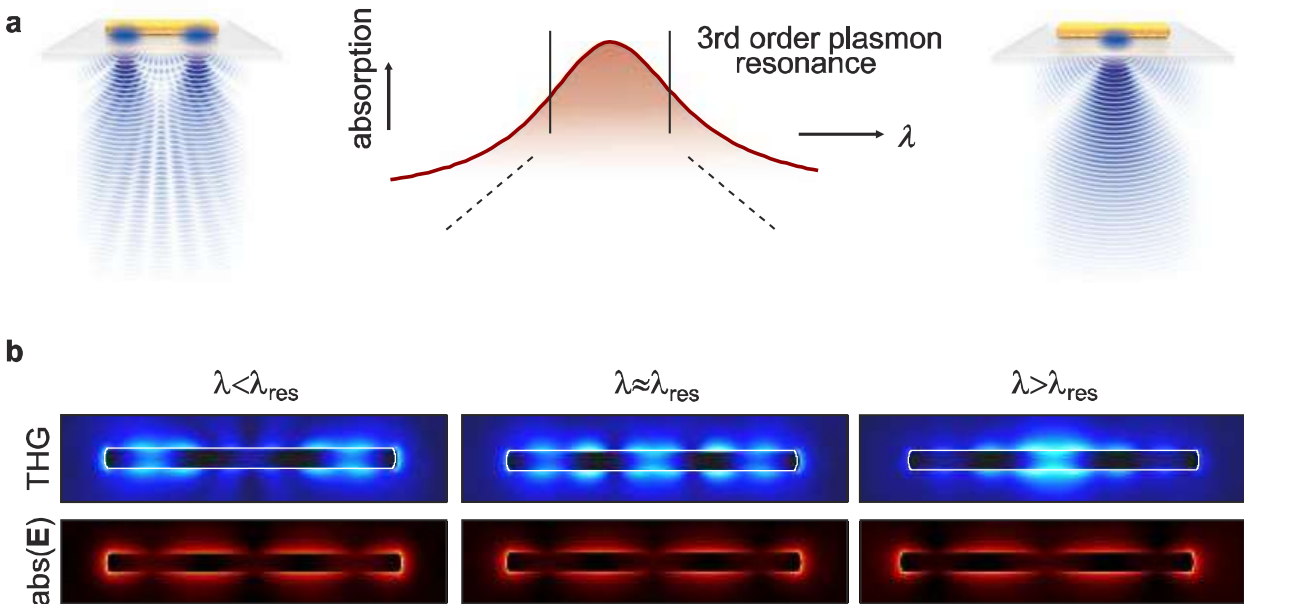



**Figure 1**. (a) Tuning the fundamental wavelength over a third-order resonance of a plasmonic nanorod (middle) changes the emission at the third harmonic from a single source (right) to two coherent sources, which interfere in the far-field (left). (b) This switching effect is caused by small variations in the fundamental field that only become observable when being taken to the third power.

**REFERENCES**

1. Wolf, D. et al. "Shaping the nonlinear near field", *Nature Communications*, Vol. 7, 10361, 2016

# Linear and nonlinear plasmonics with single gold nanorods.

**M. Caldarola, W. Zhang and M. Orrit***
Huygens-Kamerlingh Onnes Laboratory, Universiteit Leiden, The Netherlands

*corresponding author: orrit@physics.leidenuniv.nl

Plasmonics nanostructures have proven to be a tremendously useful tool for nanoscience due to their unique capability of controlling light confinement in sub-wavelength scales [1,2]. This confinement is based on the interaction between electromagnetic waves and the conduction electrons in the metallic nanostructure, which leads to resonances often at optical wavelengths [3].

Linear optical phenomena such as fluorescence enhancement using single nanostructures have been studied extensively [4,5] and many applications have risen, such as bio-sensing [6] or enhanced fluorescence correlation spectroscopy (EFCS)[7,8].

On the other hand, nonlinear phenomena such as optical harmonic generation or four-wave mixing (FWM) have a wide range of applications, from optical communications [9] to (bio)imaging [10, 11]. However, the observation of these effects requires high intensity optical fields [7], which is usually achieved with pulsed lasers.

The combination of these two areas, plasmonics and nonlinear optics has led to a very active research field, nonlinear plasmonics, due to the wide range of potential applications and because of the fundamental understanding of light-matter interaction it provides [1,13]. The notable advantage of these combinations relies on the giant enhancement of multiphoton processes by highly confined electromagnetic fields. In particular, third harmonic generation (THG) has been reported using gold nanoparticles [14], gold nanorods [15] and, more recently, the UV-light generation using a split hole resonator nanostructure [16].

I will review the recent work of our group using single gold nanorods for fluorescence enhancement as well as our current efforts to use higher harmonic generation in single nanorods for UV generation and its possible use as localized source for excitation of blue and near-UV fluorophores.

**REFERENCES**

1. Kauranen, Martti, and Anatoly V. Zayats. "Nonlinear plasmonics" *Nature Photonics*, Vol. 6 No. 11, 737-748, 2012.
2. Novotny, L., & van Hulst, N. "Antennas for light", *Nature Photonics*, 5(2), 83–90, 2011.
3. Maier, S. A., *Plasmonics: fundamentals and applications*. Springer Science & Business Media, 2007.
4. Khatua, S., Paulo, P. M. R., Yuan, H., Gupta, A., Zijlstra, P., & Orrit, M. "Resonant plasmonic enhancement of single-molecule fluorescence by individual gold nanorods", *ACS Nano*, 8(5), 4440–9, 2014.
5. Darvill, D., Centeno, A., & Xie, F, "Plasmonic fluorescence enhancement by metal nanostructures: shaping the future of bionanotechnology", *Phys. Chem. Chem. Phys.* Vol 15, 15709–15726, 2013.
6. Bauch, M., Toma, K., Toma, M., Zhang, Q., & Dostalek, J. "Plasmon-Enhanced Fluorescence Biosensors: a Review", *Plasmonics*, 1–19, 2013.
7. Khatua, S., Yuan, H., & Orrit, M. "Enhanced-fluorescence correlation spectroscopy at micro-molar dye concentration around a single gold nanorods". *Phys. Chem. Chem. Phys.*, *17*(33), 21127–21132, 2015.

8. Punj, Deep, et al. “A plasmonic ‘antenna-in-box’ platform for enhanced single-molecule analysis at micromolar concentrations”. *Nature nanotechnology* 8.7 (2013): 512-516.
9. Agrawal, Govind P. *Optical fiber communication systems*. A. Wiley, New York, 2003.
10. Débarre, D., et al. “Imaging lipid bodies in cells and tissues using third-harmonic generation microscopy”. *Nature methods* Vol.3 No.1 47-53, 2006.
11. Wang, Yong, et al. “Four-wave mixing microscopy of nanostructures”. *Advances in optics and photonics* Vol. 3 No. 1, 1-52, 2011.
12. Boyd, R. W. *Nonlinear optics*. Academic press, 2003.
13. Butet, J., Brevet, P. F., and Martin, O. J. "Optical Second Harmonic Generation in Plasmonic Nanostructures: From Fundamental Principles to Advanced Applications." *ACS nano* Vol. 9, No. 11, 10545-10562, 2015.
14. Lippitz, M., van Dijk, M. A., and Orrit, M. “Third-harmonic generation from single gold nanoparticles”. *Nano Letters*, Vol. 5, No.4, 799–802, 2005.
15. Schwartz, O., and Oron, D., “Background-free third harmonic imaging of gold nanorods”. *Nano Letters*, Vol. 9, No. 12, 4093–4097, 2009.
16. Melentiev, P. N., et. al. “Split Hole Resonator: A Nanoscale UV Light Source”. *Nano Letters*, Vol. 16. No.2, 1138–1142, 2016.

# SP15. "Non-linear and ultra-fast spectroscopy of nano- and meta-materials"

***Organizers:*** ***Pierre-Michel Adam*** *(University of Technology of Troyes, France),* ***Pierre-François Brevet*** *(University of Lyon, France),****Giulio Cerullo*** *(Politecnico di Milano, Italy)*

The session will focus on non-linear and ultra-fast spectroscopy of nano- and meta-materials. Special attention will be given to original spectroscopy approaches and new physical phenomena at the nanoscale or/and of metasurfaces. The session will also cover applications in condensed matter physics, nano-optics, metamaterials and physico-chemistry.

**Topics:**

1. Nanospectroscopy and physical processes at the nanoscale;
2. Surface Enhanced spectroscopies : SERS, SEIRA, MEF/SEF, SEHRS;
3. Tip–Enhanced spectroscopies : TERS, TEF;
4. Second-order non-linear processes : SHG, SFG, DFG;
5. Third-order non-linear processes : THG, FWM, TPL, Kerr effect;
6. Coherent Raman spectroscopies : CARS, SRS;
7. Pump-probe spectroscopy;
8. Multidimensional spectroscopy;
9. Metasurfaces;
10. New methods or instrumentation;
11. 2D materials : graphene, transition metal dichalcogenides;
12. Chiral nanomaterials and metamaterials;
13. Magnetic nanomaterials and metamaterials;
14. Exciton, Plasmons and Polaritons;
15. Conjugated Organic Materials : dyes, oligomers, polymers;
16. Liquid Crystals;
17. Metal based nano materials : nanoparticles, nanowires and their assemblies;
18. Inorganic Materials : dielectric and semiconducting nanostructures;
19. Photonics crystals;
20. Hybrid metal-organic systems : atomically defined clusters;
21. Supramolecular assemblies;
22. Bio-organic Materials : Light harvesting complexes, Proteins, DNA.

# Ultrafast Hot Plasmonic Electrons in Nanostructures with Hot Spots

**Alexander Govorov, Lucas V. Besteiro, Larousse Khosravi Khorashad,**

*Department of Physics and Astronomy, Ohio University, Athens, OH, 45701*
*Govorov@ohiou.edu*

**Gary P. Wiederrecht**

*Center for Nanoscale Materials, Argonne National Laboratory, Argonne, Illinois 60439, USA*

The efficiency of generation of energetic plasmonic carriers in metal nanostructures strongly depends on the optical design and material composition. By combining the lithographic technologies and theoretical predictions, we demonstrate the ability to generate large numbers of hot plasmonic carriers in specially-designed hybrid nanostructures [1,2,3]. The hot-electron generation becomes especially efficient in plasmonic nanostructures with electromagnetic hot spots [1,4]. Theoretically, the problem of generation of energetic plasmonic electrons is treated using the quantum mechanical approaches based on the kinetic DFT and the equation of motion of the density matrix [3,4,5]. The energy distributions of optically-excited plasmonic carriers are very different in metal nanocrystals with large and small sizes. In large nanocrystals, most excited carriers have very small excitation energies and the electron distribution resembles the case of the plasmon wave in bulk. For metal nanocrystals with smaller sizes (less than 10nm) or in nanostructures with hot spots, the excited state gets a large number of carriers with high energies [1,3-5]. Nanostructures with strong plasmonic enhancement generate unusually large numbers of energetic electrons that can be observed using the ultra-fast spectroscopy [1,4]. Overall, our investigations have shown that the resonant optical geometry of a metastructure is crucial for the hot-electron optics and photo-catalysis [6]. Finally, one can mention another related problem that is the generation of heat in a complex plasmonic nanostructure [7]. The latter process is relatively slow. The results obtained in this study can be used to design plasmonic hot-electron nanodevices for photo-catalysis, photo-detectors and solar-energy applications.

[1] H. Harutyunyan, A. B. F. Martinson, D. Rosenmann, L. Khosravi Khorashad, L.V. Besteiro, A.O.Govorov, and G.P. Wiederrecht, *Nature Nanotechnology* 10, 770–774 (2015).
[2] W. Li, Z. J. Coppens, L.V. Besteiro, W. Wang, A. O. Govorov, J. Valentine, *Nature Communications* 6, 8379 (2015).
[3] A.O. Govorov, H. Zhang, V. Demi, and Y. K. Gun'ko, *NanoToday* 9, 85 (2014).
[4] H. Zhang and A. O. Govorov, *J. Phys. Chem. C, 118*, 7606 (2014).
[5] A.O. Govorov and H. Zhang, *J. Phys. Chem. C, 119*, 6181 (2015).
[6] L. Weng, H. Zhang, A. O. Govorov, and M. Ouyang, *Nature Communications* 5, 4792 (2014).
[7] C. Jack, A. S. Karimullah, R. Tullius, L. Khosravi Khorashad, M. Rodier, B. Fitzpatrick, L. D. Barron, N. Gadegaard, A. Lapthorn, V. M. Rotello, G. Cooke, A.O. Govorov, M. Kadodwala, *Nature Communications* (2015), in press.

# Extreme light confinement in plasmonic taper

**Stefan Dilhaire[1*], Olga Lozan[1], Buntha Ea Kim[2], Philippe Lalanne[3]**

[1]Laboratoire Onde et Matière d'Aquitaine (LOMA) UMR 5798, CNRS-Université de Bordeaux, 33400 Talence, France
[2]Laboratoire Charles Fabry, UMR 5298, CNRS-IOGS-Université Paris XI, Institut d'Optique, 91120 Palaiseau, France
[3]Laboratoire Photonique, Numérique et Nanosciences (LP2N), UMR 5298, CNRS-IOGS-Université de Bordeaux, Institut d'Optique d'Aquitaine, 33400 Talence, France

[*]corresponding author: stefan.dilhaire@u-bordeaux.fr

**Abstract**-We introduce a Time Domain Thermoreflectance (TDTR) approach to reveal, understand and control energy confinement when going from macro- to nano-scale, i.e. including all conversion processes from incident photon, to plasmons, electrons, and phonons within space and time scales from micrometer to nanometer, and from tens of femtoseconds up to tens of picoseconds.

Recent advances in nano-photonics lead to extreme light confinement (ELC) and light manipulation. This progress has spawned a variety of new important technological possibilities for the efficient delivery, control and manipulation of optical radiation on the nanoscale. Although the physical principles of ELC with plasmons i.e. nano-focusing has been clearly demonstrated in several studies, further fundamental studies are needed to optimise these processes and control losses in plasmonic devices for viable technological applications.

The unprecedented ability of plasmonic structures to concentrate light in deep-subwavelength volumes has driven their use in numerous nanophotonics technologies [1]. In particular, the ability to concentrate large amounts of energy at nanometer and femtosecond scales has led to a recent emerging field based on plasmon-induced hot carriers (HC), as well as the emergence of new applications by stimulating complex electrical, thermal, mechanical, and chemical processes [1-3]. These recent advances have raised the demand for understanding and characterising the ELC on the nanometer and femtosecond scales. The generation of plasmon-induced HC in metals, i.e. carriers far from the equilibrium with energies significantly larger than the average thermal energy, can be achieved by appropriately concentrating the photon energy at the apex of a metal tip [4-9]. It has been shown that by using such a technique, HC can be extracted with an efficiency of about 30% and then be used as extremely localised sources [7], but the physical processes induced in such confinements are not yet understood. Many practical applications [10] also need a complete understanding of physical phenomena involved in ELC from the quantum aspect at nanometric and femtosecond scales up to the macroscopic behaviour.

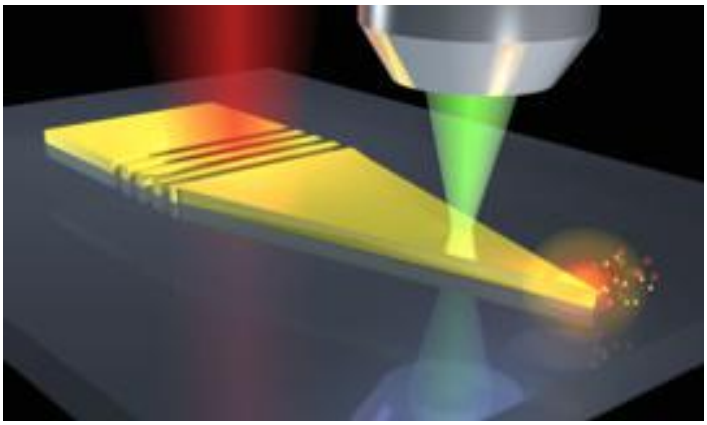


*Figure 1 : Schematic illustration of the experimental setup. The grating is shined by the red beam launches a plasmon focused at the tip apex producing hot carriers. The green laser probes the hot electrons during the focusing process.*

This work is devoted to the coupling of the ELC with the electron/hole and lattice dynamics in metals. In one of our recent works [11], we have demonstrated the capability to image and film plasmon propagation in a metallic film. We probed the hot electrons heated by the plasmon dissipation via a femtosecond pump-probe thermoreflectance approach.

Figure 1 describes an appropriated designed plasmonic device where plasmons can be concentrated in specific locations with a precision of about 10nm. TDTR offer a unique opportunity to reveal and study energy transport processes induced by extreme light confinement in nanometric devices that have not been explored so far in low-dimensional systems.

We have measured and characterised the hot carriers generated in the hot spot and exploited the mechanism of plasmon absorption in metals for the generation of hot carriers at femtosecond time scale, and this energy conversion was measured with femtosecond pump-probe technique. Femtosecond plasmon pulses will be launched and probed over hundreds of femtoseconds through the permittivity variations induced by the hot-carriers.

**Acknowledgements**, This study was carried out with financial support from “the Investments for the future” Programme IdEx Bordeaux–LAPHIA (ANR-10-IDEX-03-02).

**REFERENCES**

1. M. Moskovits, Nature Nanotechnology, 10 (2015), 6-8.
2. M. J. Kale et al, Science, 349 (2015), 587-88.
3. Brongersma, M. L., Halas, N. J. & Nordlander, P. Nat. Nanotechnol. 10, 25–34 (2015).
4. Chalabi, H. & Brongersma, M. L. Nat. Nanotechnol. 8, 229–230 (2013).
5. Clavero, C. Nat. Photonics 8, 95–103 (2014).
6. Tisdale, W. A. et al. Science 328, 1543–1547 (2010).
7. A. Giugni, et al, Nature Nanotechnology, 8 (2013), 845-52.
8. Mukherjee, S. et al. Nano Lett. 13, 240–247 (2012).
9. Linic, S., Christopher, P. & Ingram, D. B. Nat. Mater. 10, 911–921 (2011).
10. G. Baffou, and R. Quidant, Laser and Photonics Reviews, 7 (2013), 171-87.
11. O. Lozan, M. Perrin, B. Ea-Kim, J.M. Rampnoux, S. Dilhaire, and P. Lalanne, Phys. Rev. Lett. 112, 193903 (2014)

# Nonlinear plasmonics: confinement effect, delocalization and ultrafast responses.

**Sviatlana Viarbitskaya[1,2], Olivier Demichel[1], Upkar Kumar[2], Régis Méjard[1], Aurélien Cuche[2], Gérard Colas des Francs[1], Christian Girard[2], Benoit Cluzel[1], Erik Dujardin[2], Alexandre Bouhelier[1],**

[1] Laboratoire Interdisciplinaire Carnot de Bourgogne, CNRS UMR 6303, Université de Bourgogne Franche-Comté, 9 Avenue Alain Savary, Dijon, France.

Email: alexandre.bouhelier@u-bourgogne.fr

[2] CEMES CNRS UPR 8011 and Université Fédérale de Toulouse, 29 rue J. Marvig, 31055 Toulouse, France.

**Abstract**- In this presentation we address a series of fundamental issues that are emerging with the fast growing field of nonlinear plasmonics. Specifically, we will discuss the field sensitivities of $\chi^{(2)}$ and $\chi^{(3)}$ nonlinearities and address the ultrafast dynamics of photo-generated hot carriers. We will show that the nonlinearities are not restricted to the excitation spot but may be distributed through the plasmonic landscape. We will discuss possible applications and electrical control of the nonlinear mechanisms.

The large field enhancement generated at the surface of a resonant plasmonic nanoparticle, or optical antennas, is the key mechanism that eventually led to the development of nonlinear plasmonics [1-2]. While the resonance may boost the nonlinear yield of an adjacent structure or surrounding medium, it was soon realized that optical antennas possess nonlinear coefficients comparable or exceeding those of standard nonlinear optical materials [3]. Amplifying local electromagnetic fields by engineering optical interactions between individual constituents is considered fundamental for efficient wavelength conversion by nanometer-scale devices. In contrast to this general statement we show that high field enhancement does not necessarily lead to an optimized nonlinear activity [4]. We then investigate plasmon-assisted hot carrier nonlinear dynamics of the multiphoton luminescence emitted by optical antennas. We demonstrate that surface plasmons enable a nonlinear formation of hot carriers, providing thus a unique lever to optimize the energy distribution and generation efficiency of the photo-excited charges [5]. We will examine the ultrafast dynamics measured from single-crystal nanostructures fabricated by reactive ion etching and amorphous antennas produced by electron-beam lithography.

We further find that the nonlinear responses generated by focusing a pulsed laser on an extended structure are not locally emitted but are delocalized throughout the system [6] as illustrated in Fig. 1.

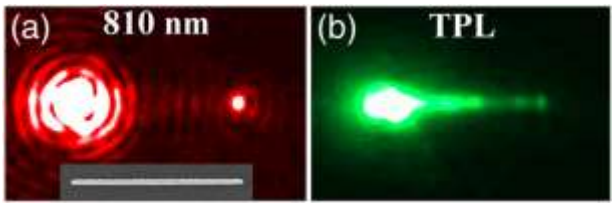



Figure 1: (a) optical micrograph of a focused laser exciting the left extremity of a nanowire. The weaker spot at the right is the out-of-plane scattering of surface plasmon launched at the distal end. Insert: SEM image of the 2 μm-long Ag nanowire. (b) Spectrally filtered image to record the nonlinear photoluminescence. The signal is not restricted to the excitation area but is emitted from the entire nanowire.

We show that these nonlinear radiations are emitted from the entire antenna and the measured far-field angular patterns bear the information regarding the nature and origins of the respective nonlinear

processes. We demonstrate that the nonlinear responses are locally induced by a surface plasmon propagating in the two-dimensional plasmonic LDOS at the excitation frequency, enabling thereby a polariton-mediated spatial tailoring and design of coherent and incoherent nonlinear responses. We will discuss the possibility to engineer the spatial distribution of the surface plasmon modes to implement advanced functionalities such as logical gates. We will conclude the presentation by showing how nonlinear responses can be controlled on-demand by a static electrical command.

**Acknowledgements**

The authors acknowledge funding from FP7/20072013 Grant Agreement No. 306772, the Agence Nationale de la Recherche through the projects PLACORE ANR-13-BS10-0007 and Labex ACTION ANR-11-LABX-0001-01, and the regional program PARI.

**References**

1. Martti Kauranen & Anatoly V. Zayats, Nonlinear Plasmonics, *Nature Photonics 6*, 737 (2012)
2. S. Bin Hasan, F. Lederer, C. Rockstuhl, Nonlinear plasmonic antennas, *Materials Today 14*, 478 (2014)
3. A. Baron, S. Larouche, D. J. Gauthier, & D. R. Smith, Scaling of the nonlinear response of the surface plasmon polariton at a metal/dielectric interface. *J. Opt. Soc. Am. B. 32*, 9 (2015).
4. J. Berthelot, G. Bachelier, M. Song, P. Rai, G. Colas ds Francs, A. Dereux & A. Bouhelier. Silencing second-harmonic generation is strongly-coupled optical gap antennas, *Optics Express 20*, 10498 (2012)
5. O. Demichel, M. Petit, S. Viarbitskaya, R. Mejard, F. de Fornel, E. Hertz, F. Billard, A. Bouhelier, & B. Cluzel. Dynamics, efficiency and energy distribution of nonlinear plasmon-assisted generation of hot carriers. *ArXiv 1601.02279*
6. S. Viarbitskaya, O. Demichel, B. Cluzel, G. Colas des Francs & A. Bouhelier, Delocalization of Nonlinear Optical Responses in Plasmonic Nanoantennas, *Phys. Rev. Lett. 115*, 197401 (2015)

# Quantitative optical spectroscopy of single metal nano-objects

**A. Crut*, A. Lombardi, E. Pertreux, P. Maioli, F. Vallée and N. Del Fatti**
FemtoNanoOptics group, Institut Lumière Matière UMR5306,
Université Lyon 1-CNRS, 69622 Villeurbanne, France
*corresponding author: aurelien.crut@univ-lyon1.fr

**Abstract:** We report quantitative investigations of the optical response of individual noble metal nano-objects, performed by coupling linear and nonlinear optical techniques (spatial modulation and time-resolved spectroscopies) with electron microscopy observations and numerical simulations. These studies reveal in particular how the surface plasmon resonances of metal nano-objects are affected by deposition on a substrate, nano-object 3D orientation and, in the case of nanodimers, by electromagnetic interactions.

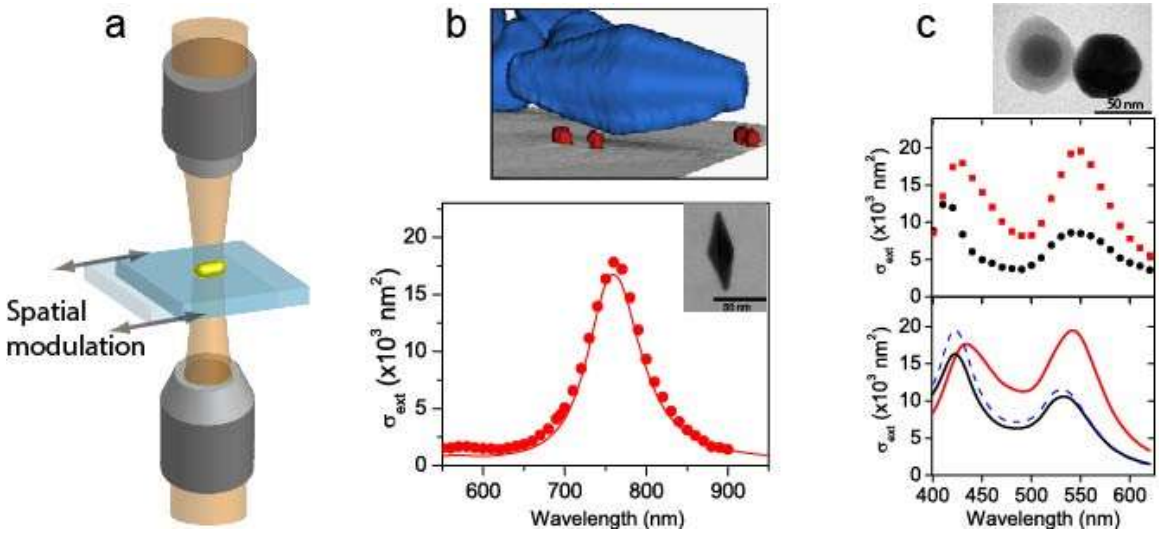



**Figure 1.** a) Principle of SMS. b) Electron tomography (top), measured (dots) and calculated (plain line) extinction of a gold bipyramid on a carbon substrate. c) Measured (dots) and calculated (plain lines) extinction of the gold-silver heterodimer shown on top for light parallel (red) or orthogonal (black) to dimer axis.

The localized surface plasmon resonances (SPRs) of metal nano-objects constitute the key feature of their optical response. Their detailed investigation in the last decade, in particular in view of biosensing applications, has greatly benefited from the development of experimental methods enabling optical spectroscopy of individual nanoparticles[1]. In particular, the polarization-resolved extinction spectrum of a single nano-object can be quantitatively measured by spatial modulation spectroscopy[2] (SMS, Fig. 1a) and compared to numerical simulations based on its actual morphology, determined by electron microscopy.

Such experiments typically involve nano-objects deposited on a solid substrate. While metal nano-objects encapsulated with a dielectric shell (e.g., silica-coated gold nanorods) are weakly sensitive to their

environment, deposition on transparent or absorbing substrates has a large impact for bare metal nano-objects, inducing a shift and, for absorbing substrates, broadening of SPR. In the first part of the talk, we will discuss these effects which have been investigated through SMS experiments, by comparing the optical responses of elongated gold nano-objects (nanorods or bipyramids) deposited on dielectric and absorbing substrates. Strong variations of absorbing substrate-induced SPR broadening with nano-object shape are observed. These observations are understood by performing numerical simulations highlighting the large importance of the particle-substrate distance and 3D nano-object orientation, and correlating the optical experiments with electron tomography, which provides direct access to these morphological parameters[3] (Fig. 1b).

Electromagnetic coupling between interacting metal nanoparticles also strongly affects their plasmonic response, offering many new possibilities for tailoring their properties. In the case of model systems formed by two interacting Au and Ag nanospheres, numerical simulations reveal two salient effects of electromagnetic interactions: (i) polarization-dependent red shifts and amplitude modification of gold and silver SPRs, and (ii) the appearance of a Fano resonance in gold absorption cross-section induced by interferences between the absorption channels associated to silver SPR and the continuum of interband transitions in gold[4]. These effects are investigated on electrostatically assembled dimers constituted by gold and silica-encapsulated silver nanoparticles (the silica shell acting as a spacer and protecting silver from spurious oxidation effects, Fig. 1c). Experiments demonstrate that the spectral signature of coupling (*i.e.*, red shift of SPRs for light polarized along the dimer axis as compared to perpendicular polarization) numerically predicted for nanosphere dimers is modified or even reversed when the constituent particles significantly deviate from sphericity, highlighting the importance of correlation between optical and morphological single particle characterizations[5]. Experimental unveiling of an absorption Fano effect is achieved for the first time using two-color nonlinear time-resolved spectroscopy, which provides a unique way to distinguish the optical response of each dimer component. Time-resolved measurements are found to be in excellent quantitative agreement with theoretical modeling taking into account the dimer morphology, confirming the presence of a strong light polarization-dependent Fano interference in the absorption of a gold nanosphere when interacting with a nearby silver nanoparticle.

**REFERENCES**


1. A. Crut, P. Maioli, N. Del Fatti and F. Vallée, "Optical absorption and scattering spectroscopies of single nano-objects", *Chem. Soc. Rev.*, Vol. 43, 3921-3956, 2014.

2. A. Arbouet, D. Christofilos, N. Del Fatti, F. Vallée, J.-R. Huntzinger, L. Arnaud, P. Billaud and M. Broyer, "Direct Measurement of the Single-Metal-Cluster Optical Absorption", *Phys. Rev. Lett.*, Vol. 93, 127401, 2004.

3. E. Pertreux, A. Lombardi, I. Florea, M. Spuch-Calvar, S. Gómez-Graña, D. Ihiawakrim, C. Hirlimann, O. Ersen, J. Majimel, M. Tréguer, M. Hettich, P. Maioli, A. Crut, F. Vallée and N. Del Fatti, "Surface Plasmon Resonance of an Individual Nano-object on an Absorbing Substrate: Quantitative Effects of Distance and 3D Orientation", *Adv. Opt. Mat.*, DOI: 10.1002/adom.201500548, 2015.

4. G. Bachelier, I. Russier-Antoine, E. Bénichou, C. Jonin, N. Del Fatti, F. Vallée and P.-F. Brevet, "Fano Profiles Induced by Near-Field Coupling in Heterogeneous Dimers of Gold and Silver Nanoparticles", *Phys. Rev. Lett.*, Vol. 101, 197401, 2008.

5. A. Lombardi, M. Grzelczak, A. Crut, P. Maioli, I. Pastoriza-Santos, L. M. Liz-Marzán, N. Del Fatti and F. Vallée, "Optical response of individual Au-Ag@$SiO_2$ heterodimers", *ACS Nano*, Vol. 7, 2522-2531, 2013.

# Vector Field Nonlinear Optical Microscopy of Nanoparticles

**M. Kauranen*, L. Turquet, A. Slablab, and G. Bautista**
Optics Laboratory, Department of Physics, Tampere University of Technology,
PO Box 692, FI-33101 Tampere, Finland
*corresponding author: martti.kauranen@tut.fi

**Abstract**-We review our work on the use of focused vector beams in nonlinear optical characterization of nanoparticles. We show that such beams, including radially and azimuthally polarized beams as well as more advanced high-order polarization beams, provide unique opportunities in the characterization of several types of nanostructures and in controlling the coupling of light into such structures.

Nonlinear optical processes provide new contrast mechanisms for microscopy. Focusing of polarized laser beams gives rise to three-dimensional vector fields in the focal volume. This idea can be taken even further through the use of high-order vector beams, where the prime examples are radially (RP) and azimuthally polarized (AP) beams. In particular, focusing of RP gives rise to a strong longitudinal field component at the geometrical focus, whereas focusing of AP maintains a strictly transverse field distribution in the focal volume. In this paper, we show that this provides completely new capabilities in the characterization of individual nano-objects at microscopic resolution.

Chiral objects have different response to left- and right-hand circular polarizations. In second-harmonic generation (SHG), this leads to different responses for the two circularly-polarized components of fundamental light. Under focusing, this can provide an unambiguous probe of surface chirality. For metal nano-objects, surface defects give rise to fluctuating SHG signals, but the normalized circular-difference response stays relatively constant, allowing the handedness of individual nano-objects to be recognized [1].

SHG with RP and AP provides even more exciting opportunities. We have shown that they provide sensitivity to the morphology of metal nanobumps and nanocones [2] as well as to orientation of nanorods. Coupling of light to nanotips is usually based on polarization component along the tip axis, which is often awkward. We have shown that lowering the particle symmetry makes possible more convenient geometries, but that efficient excitation requires that the focal field vector be tailored for the modes of the particle [3]. Finally, RP and AP beams allow the coupling of light to vertically-oriented semiconductor nanowires to be controlled [4], opening new opportunities for controlling and localizing the nonlinear response on the nanoscale.

**REFERENCES**

1. Huttunen, M. J. *et al.*, "Nonlinear chiral imaging of subwavelength-sized twisted-cross gold nanodimers", *Opt. Mat. Express*, Vol. 1, 46-56 (2011).
2. Bautista, G. *et al.*, "Second-harmonic generation imaging of metal nano-objects with cylindrical vector beams", *Nano Lett.*, Vol. 12, 3207-3212 (2012).
3. Huttunen, M. J. *et al.*, "Three-dimensional winged nanocone optical antennas", *Opt. Lett.*, Vol. 39, 3686-3689 (2014).
4. Bautista, G. *et al.*, "Second-harmonic generation imaging of semiconductor nanowires with focused vector beams", *Nano Lett.*, Vol. 15, 1564-1569 (2015).

# Quantum nonlinear graphene plasmonics

**J. D. Cox**[1*] **and F. J. García de Abajo**[1,2]

[1]ICFO-Institut de Ciencies Fotoniques, The Barcelona Institute of Science and Technology, Castelldefels, 08860 Barcelona, Spain

[2]ICREA-Institució Catalana de Recerca i Estudis Avançats, Passeig Lluís Companys 23, 08010 Barcelona, Spain

[*]corresponding author: joel.cox@icfo.es

**Abstract**-Based on realistic quantum-mechanical simulations of the nonlinear optical response for doped graphene nanostructures, we show that atomistic and nonlocal effects can increase the nonlinear response associated with plasmon resonances in these systems to significantly higher levels than previously thought. Motivated by this result, we explore various aspects of the plasmon-enhanced nonlinearity in doped nanographenes, such as saturable absorption and high-harmonic generation, and find further support for the exceptional potential of the atomically-thin material for nonlinear nanophotonic devices.

The intrinsically-high nonlinear optical response of graphene [1], combined with its ability to sustain long-lived, electrically tunable plasmons that couple strongly with light [2], has generated great expectations for application of the atomically-thin material to nanophotonic devices [3, 4]. However, many of these expectations are reinforced by classical analyses performed using the response derived from extended graphene, neglecting finite size and nonlocal effects that become important when the carbon layer is structured on the nanometer scale in actual device designs. Based on a realistic, quantum-mechanical (QM) description of nanostructured graphene, we show that finite-size and atomistic effects can produce large contributions that increase the nonlinear response associated with plasmon resonances in nanoislands and nanoribbons to significantly higher levels than previously thought, particularly in the case of Kerr-type optical nonlinearities. The discrepancy between classical and QM descriptions is at odds with the conclusions previously drawn by examining the linear response regime, where good agreement was found when either the plasmon energy is below the Fermi energy or when the size of the structure exceeds a few tens of nanometers. Motivated by this finding, we discuss and compare saturable absorption in extended and nanostructured graphene, with or without plasmonic enhancement, within the context of passive mode-locking for ultrafast lasers. We also explore the possibility of observing high-harmonic generation in doped nanographenes, where illumination by an infrared pulse of moderate intensity, tuned to a plasmon resonance, is predicted to generate light at frequencies extending to the visible or UV regimes. Our atomistic description of graphene's nonlinear optical response reveals its complex nature in both extended and nanostructured systems, while further supporting the exceptional potential of this material for nonlinear nanophotonic devices.

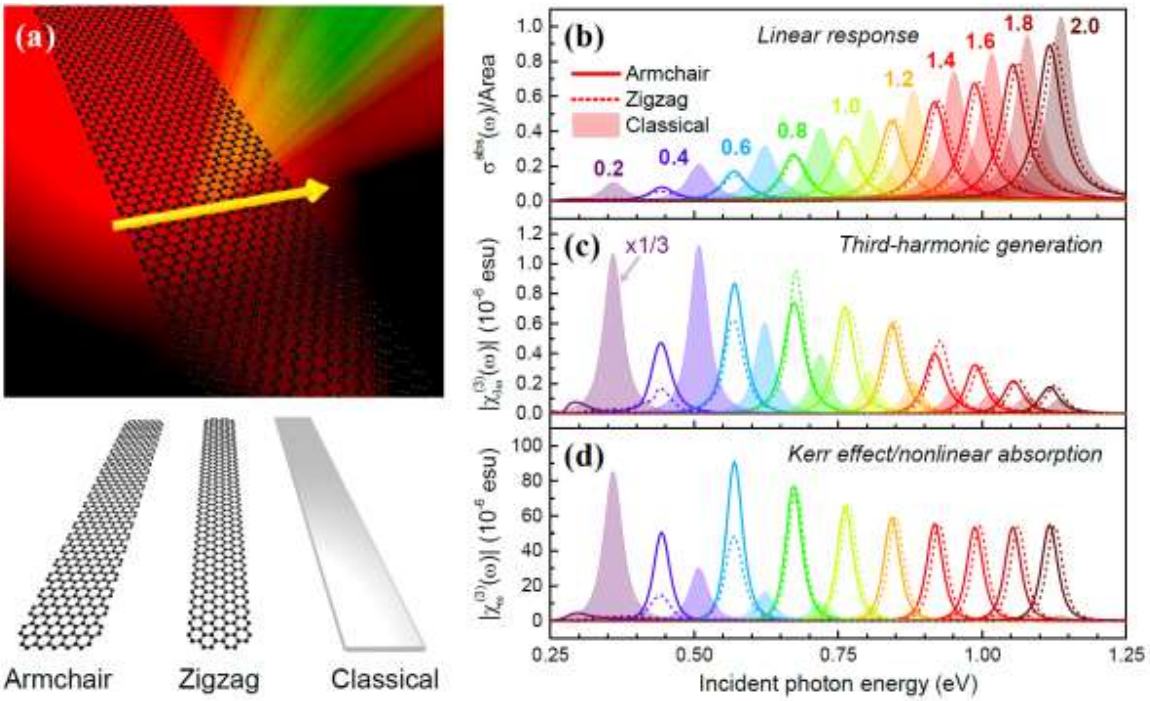



**Figure 1. Linear and nonlinear spectral response of graphene nanoribbons. (a)** We consider cw incident light linearly polarized across the ribbons (top) and present results derived from a quantum mechanical (QM) model (tight-binding and random-phase approximation) for structures with either armchair or zigzag edges, compared with classical electromagnetic simulations (local conductivity) for a homogeneous planar sheet. **(b-d)** Linear absorption cross-section **(b)**, and third-order susceptibilities for third-harmonic generation **(c)** and the Kerr nonlinearity **(d)**, as obtained from the QM model for armchair (solid curves) and zigzag (dashed curves) nanoribbons, compared with classical electrodynamic simulations (filled curves). Different Fermi energies (color-coded numerical values in **(b)**, eV) are considered, taking the ribbon width as approx. 10 nm and the damping $\hbar\tau^{-1}$ =50 meV in all cases.

**Acknowledgements:** This work has been supported in part by the Spanish MINECO (MAT2014-59096-P and SEV-2015-0522) and the European Commission (Graphene Flagship CNECT-ICT-604391 and FP7-ICT-2013-613024-GRASP).

## REFERENCES

1. Hendry, E. et al., "Coherent nonlinear optical response of graphene," *Phys. Rev. Lett.*, Vol. 105, No. 9, 097401, 2010.
2. Fang, Z. et al., "Gated tunabiltiy and hybridization of localized plasmons in nanostructured graphene,"*ACS Nano*, Vol. 7, No. 3, 2388–2395, 2013.
3. Grigorenko, A. N, M. Polini and K. S. Novoselov, "Graphene plasmonics," *Nat. Photon.*, Vol. 6, No. 11, 749–758, 2012.
4. García de Abajo, F. J., "Graphene plasmonics: Challenges and opportunities," *ACS Photon.*, Vol. 1, No. 3, 135–152, 2014.

# Two photon luminescence microscopy maps the plasmonic density of state and plasmon propagation in 2D gold crystals.

**Upkar Kumar[1]*, Sviatlana Viarbitskaya[1,2], Aurélien Cuche[1], Gérard Colas des Francs[2], Rafaelle Mezzenga,[3] Christian Girard[1], Alexandre Bouhelier[2]*, Erik Dujardin[1]***

[1] CEMES CNRS UPR 8011 and Université Fédérale de Toulouse, 29 rue J. Marvig, 31055 Toulouse, France.
[2] LICB, CNRS UMR 6303, Université de Bourgogne, 9 Av. A. Savary, Dijon, France.
[3] Lab.of Food & Soft Materials, IFNH, ETH Zurich, Schmelzbergstr. 9, LFO E22-23, 8092 Zürich, Switzerland
*corresponding authors: kumar@cemes.fr, bouhelier@u-bourgogne.fr, dujardin@cemes.fr

**Abstract**- We report on using two photon luminescence microscopy as an optical imaging technique for probing both the spatial distribution of Surface Plasmon Local Density of States (SP-LDOS) and the transmission efficiency inside chemically-grown crystalline gold platelets.

The last decade witnessed an enormous progress in fabrication and manipulation of nano-sized objects and a vast improvement in the crystallinity of the metallic nanostructures. It allowed to perform engineering of surface plasmon (SP) modes, which in turn has opened the prospect of optical information processing in plasmonic systems [1]. At the same time, various near and far field imaging techniques such as Cathodoluminescence (CL) [2], electron energy loss spectroscopy (EELS) [3], photoelectron emission microscopy (PEEM) [4,5] have been developed to probe optical near field produced by these SP modes. However, these techniques only probe specific components of SP-LDOS. For example, in CL, the power radiated is proportional to a partial SP-LDOS in the direction of the associated transient dipole at the impact point. Similarly, EELS intensity map can be related to integral over the electron path of z-component of the SPLDOS.

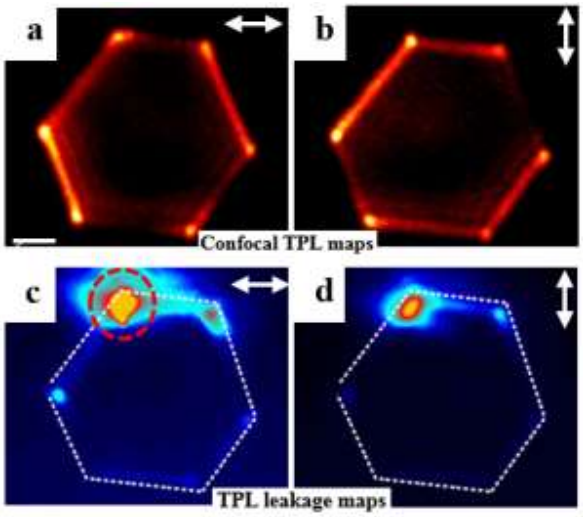



Figure1: (a,b) show confocal TPL images recorded with horizontally and vertically polarized excitation respectively at 810nm. (c,d) TPL images recorded on excitation at point 1 (shown by red dashed circle) showing transportation of TPL signal along the edges of the hexagon. Scale bar is 1 micron.

Here, we show that TPL microscopy can be used to produce direct maps of the squared SP-LDOS in confocal mode. We will demonstrate that TPL maps recorded on triangular and hexagonal nanoprisms exhibit a highly localized intensity distribution which depends both on incident wavelength and polarization.[6] Interestingly, we can also record images showing transfer of TPL signal inside nanostructures upon excitation at one fixed point in leakage mode.[7] The possible mechanisms will be exposed and experimental data will be compared to our simulations based on the Green Dyadic Method.

**Acknowledgements**

The authors acknowledge the financial support of the European Research Council (ERC) (contract number ERC-2 2007-StG Nr 203872 COMOSYEL), Agence Nationale de la Recherche (ANR) (Grant ANR-13-BS10-0007-PlaCoRe), and the computing center CALMIP in Toulouse.

**REFERENCES**

1. Brongersma, M. L., Hartman, J. W. & Atwater, H. A. Electromagnetic energy transfer and switching in nanoparticle chain arrays below the diffraction limit, *Phys. Rev. B 62*, R16356–R16359 (2000)
2. Vesseur, E. J. R., García de Abajo, F. J. & Polman, A. Modal decomposition of surface-plasmon whispering gallery resonators. *Nano Lett. 9*, 3147–3150 (2009).
3. A. Teulle, M. Bosman, C. Girard, K.L. Gurunatha, M. Li, S. Mann, E. Dujardin, Multimodal Plasmonics in fused colloidal networks, *Nature Materials 14, 8*7-94(2015)
4. Aeschlimann, M. et al. Adaptive subwavelength control of nano-optical fields. *Nature 446*, 301–304 (2007)
5. Douillard, L. et al. Short range plasmon resonators probed by photoemission electron microscopy. *Nano Lett. 8*, 935–940 (2008)
6. S. Viarbitskaya, A. Teulle, R. Marty, J. Sharma, C. Girard, A. Arbouet and E. Dujardin. Tailoring and imaging the plasmonic local density of states in crystalline nanoprisms. *Nature Materials* 12, 426 (2013)
7. S. Viarbitskaya, O. Demichel, B. Cluzel, G. Colas des Francs and A. Bouhelier, Delocalization of Nonlinear Optical Responses in Plasmonic Nanoantennas, *Phys. Rev. Lett. 115,* 197401 (2015)

# Nonlinear Optical Effects in Nanoantennas

**A. Horneber[1], J. Y. Wang[1,2] , J. Butet[3], A.-L. Baudrion[2], A. Horrer[4], O. J. F. Martin[3], M. Fleischer[4], A. J. Meixner[1], P.-M. Adam[2], D. Zhang[1]**

[1]Institute of Physical and Theoretical Chemistry and Center LISA$^+$, Eberhard Karls University of Tübingen, Germany

[2]Laboratoire de Nanotechnologie et d'Instrumentation Optique (LNIO)
Institut Charles Delaunay - UMR CNRS 6281, Université de Technologie Troyes, France

[3]Nanophotonics and Metrology Laboratory (NAM), Swiss Federal Institute of Technology, Lausanne (EPFL), 1015, Lausanne, Switzerland

[4]Institute for Applied Physics and Center LISA$^+$, Eberhard Karls University of Tübingen, Germany

[*]corresponding author: dai.zhang@uni-tuebingen.de

**Abstract**-The nonlinear optical effects in nanoantennas, such as the second harmonic generation and the two-photon photoluminescence, are investigated. Using lithographically fabricated homo- and hetero-dimers as model systems, we discuss the different intensity dependences of these two nonlinear processes on the particle size, material and gap distance. Furthermore, combining an ultrafast laser system with a scanning near-field optical microscope, we demonstrate that nonlinear effects can be used to image a single plasmonic nanostructure with an optical resolution better than thirty nm.

Metallic nanoantennas with sub-wavelength dimensions exhibit usually strong plasmon resonances, which influence their optical properties. The linear optical properties of dimer antennas consisting of two gold nanoparticles with a small gap in between have been extensively investigated. We have investigated the linear and non-linear optical effects from various plasmonic systems like nanoparticles [1,2], sharp tips and nanotriangles with either confocal optical microscopy [3,4] or scanning near-field optical microscopy (SNOM) [5,6].

In this contribution, we have chosen arrays of Au-Au, Al-Al and Au-Al dimers to study the influence of electromagnetic hot spots on the second harmonic generation (SHG) and the two photon photoluminescence (TPL). We show that the generation of both signals is differently influenced by the dimer gap distances, particle sizes and materials. We demonstrate that the strength of these nonlinear optical signals evolves differently with the near-field intensity around plasmonic nanostructures. To investigate nonlinear optical signals from a less than 5 nm gap, we have combined an ultrafast laser system with a SNOM. Based on the sensitive shear-force or tunneling current feedback, we are able to control the gap size between a sharp tip and a nanostructure accurately and study the nonlinear optical signals from such kind of extremely narrow gap that is difficult to be fabricated via conventional lithographical methods. Furthermore, using this combination the nonlinear optical signal generation from different positions of a plasmonic nanostructure can be resolved with an optical resolution of less than 30 nm [6].

**Acknowledgements**, The work reported in this talk is supported by the German Research Foundation DFG

priority program SPP 1391 and by the German Academic Exchange Service DAAD through the program PPP France/PROCOPE. J. Y. W. thanks the China Scholarship Council for supporting his research abroad. J. B. and O. J. F. M. acknowledge financial support from the Swiss National Science Foundation (SNSF, Project 200021_132694). A. Horneber thanks for the support of the Institutional Strategy of the University of Tübingen (DFG ZUK63). The authors acknowledge the Region Champagne-Ardennes, the Conseil general de l'Aube, and the FEDER funds through their support of the nanofabrication platform Nano'Mat. This work was performed in the context of the European COST Action MP1302 Nanospectroscopy.

**REFERENCES**

1. Butet, J.; Brevet, P.-F.; Martin, O. J. F. Optical Second Harmonic Generation in Plasmonic Nanostructures: From Fundamental Principles to Advanced Applications. *ACS Nano* Vol 9, 10545, 2015.
2. Butet, J.; Dutta-Gupta, S.; Martin, O. J. F. Surface second-harmonic generation from coupled spherical plasmonic nanoparticles: Eigenmode analysis and symmetry properties. *Phys. Rev. B* Vol 89, 245449, 2014.
3. Reichenbach, P.; Horneber, A.; Gollmer, D.A.; Hille, A.; Mihaljevic, J.; Schäfer, C.; Meixner, A.J.; Kern, D.P.; Zhang, D.; Fleischer, M.; Eng, L.M. Nonlinear optical point light sources through field enhancement at metallic nanocones. *Opt. Express* Vol 22, 15484, 2014.
4. Horneber, A.; Baudrion, A.-L.; Adam, P.-M.; Meixner, A. J.; Zhang, D. Compositional-asymmetry influenced non-linear optical processes of plasmonic nanoparticle dimers. *Phys. Chem. Chem. Phys*. Vol 15, 8031, 2013.
5. Wang, X.; Braun, K.; Zhang, D.; Peisert, H.; Adler, H.; Chassé, T.; Meixner, A. J. Enhancement of Radiative Plasmon Decay by Hot Electron Tunneling. *ACS Nano* Vol 9, 8176, 2015.
6. Horneber, A.; Braun, K.; Rogalski, J.; Leiderer, P.; Meixner, A.J.; Zhang, D. Nonlinear optical imaging of single plasmonic nanoparticles with 30 nm resolution. *Phys. Chem. Chem. Phys.* Vol 17, 21288, 2015.

# Optical Control of Electron Tunneling in Plasmonic Nanoantennas via Single-Cycle Pulses.

**D. Brida**[1*], **T. Rybka**[1], **and A. Leitenstorfer**[1]
[1]Department of Physics and Center of Applied Photonics, University of Konstanz, D-78457 Konstanz, Germany
[*]corresponding author: daniele.brida@uni-konstanz.de

**Abstract**- We exploit the electric field of near-infrared 1.4-cycle pulses with picojoule-level energy to drive tunneling of electrons across the 8 nm gap of a gold nanoantenna circuit at 80 MHz repetition rate. The control of the carrier-envelope phase of the pulses allows us to manipulate ultrafast single-electron currents in direction and amplitude at room temperature.

The electric field of ultrashort light pulses can be harnessed to establish and control charge transport on a subcycle timescale. In fact, the optical cycles contained in the transients can bias a gap between two metals and nonlinearly trigger the tunneling of electrons. Figure 1(left panel) sketches the effect of a few-cycle optical pulse (left) applied to a nanostructure with nonlinear and antisymmetric current-voltage characteristics (right). When the exciting electric field is cosine-shaped (green transient and dot in the I-V scheme) the symmetry break leads to a finite total current which is maximized by working in the single-cycle regime. Instead, with a sine-shaped pulse the effect of the adjacent maxima with precisely opposite polarity cancels out any cumulative effect (red transient and dot in the I-V graph). Consequently, the total current amplitude and direction may be set by varying the carrier-envelope phase (CEP) of the driving pulse, i.e., the phase difference between carrier wave and pulse envelope. In a nanoscale constriction, quantum tunneling currents may be driven with tiny optical pulse energies on the pJ level that are available from compact fiber laser systems based entirely on telecom technology. Such a source (bottom row of Fig. 1) produces phase-locked transients in the near-infrared with pulse duration of 1.4 optical cycles (the carrier wavelength is 1320 nm) at the repetition rate of 80 MHz [1,2]. CEP control is achieved by a pair of fused-silica wedges implemented before the last Er:fiber amplifier and the following synthesis of the ultrashort pulses. The material insertion $\Delta d$ of the wedges sets the CEP without affecting the temporal duration of the transients at the sample position.

An optical gold nanoantenna connected to a macroscopic circuit with lateral leads is used in the experiments. This bow-tie design ensures subcycle plasmon damping time due to strong radiation coupling [3] which is important to conserve the few-cycle character of the electric field applied to the gap region. Still, significant enhancement occurs due to the lightning-rod effect thus facilitating the tunneling process. The samples are fabricated by electron beam lithography and are fully characterized also in stationary condition to assess the nonlinear character of the I-V response. In our experiments we exposed the single nanoantenna with an 8 nm gap to the CEP-locked single-cycle pulses in a microscope equipped with an all-reflective objective. A mechanical chopper operating at 632 Hz modulates laser excitation and a femto-ampere amplifier performs electronic readout based on a lock-in detection scheme to minimize pickup noise. The current flowing in the nanogap is measured as a function of CEP and is reported in the right panel of Fig. 1. Biasing with 80 pJ of energy results in total currents up to 0.6 pA, equivalent to one electron tunneling every 25 pulses. Under those conditions, the peak electric field in free space amounts to 4 V/nm.

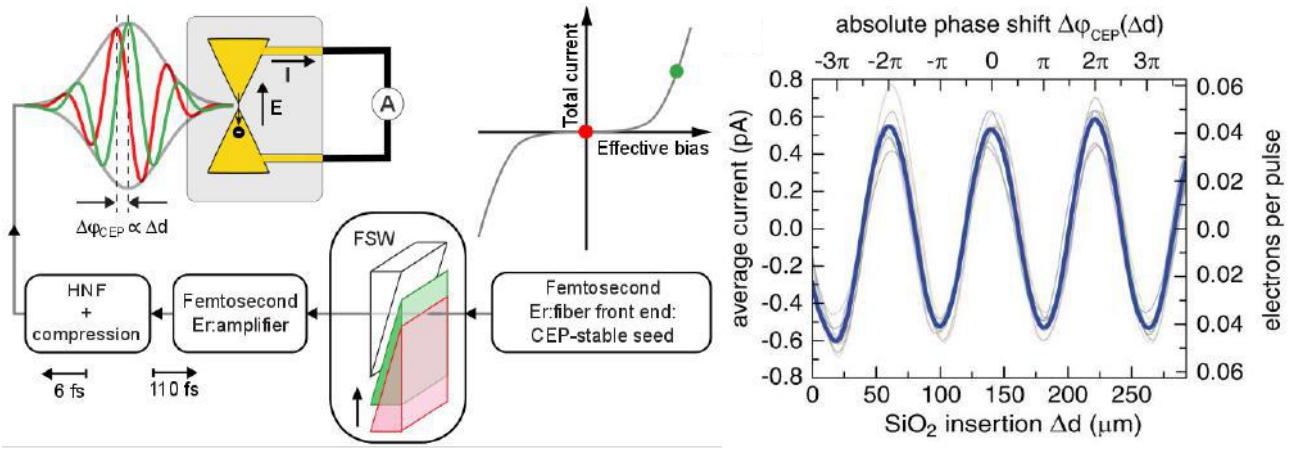



Figure 1 – (Left panel) Outline of the experimental setup and of the nonlinear characteristic of the gold nanocircuit based the optical antenna. The CEP-locked near-IR pulses are produced by a femtosecond Er:fiber laser. Spectral broadening in a highly nonlinear fiber (HNF) supports pulse compression to 6.3 fs. The current is controlled by the $\Delta\varphi_{CEP}$ that is tunable via the material insertion $\Delta d$ of fused-silica wedges (FSW). (Right panel) Carrier-envelope optical control of sub-cycle tunneling: current measured in the nanocircuit as a function of the FSW insertion $\Delta d$. The corresponding CEP slip is plot on the upper axis. The blue line represents an average over 8 scans (gray lines) acquired at the average optical power of 6.5 mW.

The Keldysh parameter is estimated to be well below 0.1 thus gauging the minimum contribution of multiphoton photoemission upon illumination. Under this extreme perturbation, the effective barrier of the energetic potential shrinks well below the size of the gap [4, 5] and the current dynamics contain phases of ballistic propagation. At pulse energy of 80 pJ, we estimate the tunneling of approximately 0.1 electrons over the central half-cycle. Peak current values up to tens of μA are detected, corresponding to subcycle current densities of several tens of MA/cm . These conditions establish a new regime of charge transport for operation at room temperature and with extreme temporal resolution.

The experiments demonstrate a robust class of nanoelectronic switches that are gated in the petahertz range by optical pulses with minute energy content. Our work lays the foundation for new studies of charge transport where Coulomb blockade or resonant tunneling may be exploited on subcycle optical timescales.

**REFERENCES**


1. Krauss, G., S. Lohss, T. Hanke, A. Sell, S. Eggert, R. Huber and A. Leitenstorfer "Synthesis of a single cycle of light with compact erbium-doped fibre technology," *Nature Photon.* Vol. 4, No. 1, 33-36, 2010.
2. Brida, D., G. Krauss, A. Sell and A. Leitenstorfer "Ultrabroadband Er:fiber lasers," *Laser Photon Rev.* Vol. 8, No. 3, 409-428, 2014.
3. Hanke, T., J. Cesar, V. Knittel, A. Trügler, U. Hohenester, A. Leitenstorfer and R. Bratschitsch "Tailoring Spatiotemporal Light Confinement in Single Plasmonic Nanoantennas," *Nano Lett.* Vol. 12, No. 2, 992-996, 2012.
4. Savage, K. J., M. M. Hawkeye, R. Esteban, A. G. Borisov, J. Aizpurua and J. J. Baumberg "Revealing the quantum regime in tunneling plasmonics," *Nature* Vol. 491, No. 7425, 574-577, 2012.
5. Wan, Y., M. Wubs and N. A. Mortensen "Projected Dipol Model for Quantum Plasmonics," *Phys. Rev. Lett.* Vol. 115, No. 13, 137403, 2015.

# Ultrafast relaxation of optically excited hot electrons in plasmonic structures

**F. Spitzer**[1], **B. Glavin**[2], **V. I. Belotelov**[3,4], **J. Vondran**[1], **I. A. Akimov**[1,5], **S. Kasture**[6], **A. S. Vengurlekar**[6], **A. V. Gopal**[6], **D. R. Yakovlev**[1,5] **and M. Bayer**[1,5]

[1]Experimentelle Physik 2, Technische Universität Dortmund, 44221 Dortmund, Germany
[2]Lashkaryov Institute of Semiconductor Physics, 03028 Kyiv, Ukraine
[3]Lomonosov Moscow State University, 119991 Moscow, Russia
[4]Russian Quantum Center, 143025 Skolkovo, Moscow Region, Russia
[5]Ioffe Institute, Russian Academy of Sciences, 194021 St. Petersburg, Russia
[6]Tata Institute of Fundamental Research, 400005, Mumbai, India
Contact: jonas.vondran@tu-dortmund.de

**Abstract**— Periodically perforated gold films are subject to femtosecond pump-probe transmission measurements which show relaxation dynamics of optically excited electrons. The transient data show two distinct exponential decays where the shorter decay switches sign depending if plasmonic or non-plasmonic excitation is used. We attribute this to the qualitatively different spatial distributions of the absorbed energy in these cases.

Current state-of-the-art criteria in telecommunications require plasmonics to be active. Modulation of the optical properties in plasmonic structures can be achieved via application of intense femtosecond laser pulses [1]. In our previous work we have shown that SPP resonances can be efficiently used to monitor the electron dynamics and demonstrated that dynamic changes in the real and imaginary part of the dielectric constant may alter significantly the optical response of the system [2]. However the role of SPPs for excitation was not discussed in the previous work. Here we demonstrate that dynamics of electron cooling may differ significantly in plasmonic crystals depending on which mechanism has been used to excite non-equilibrium high energy electrons.

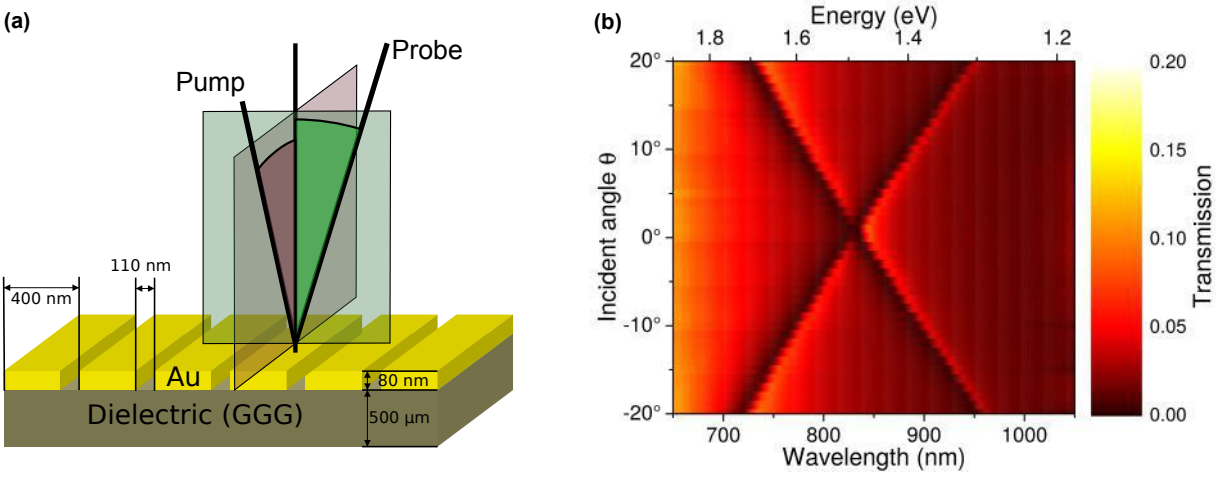



Figure 1: (a) Schematic of sample structure and incident geometry of pump (violet plane) and probe beam (green plane). (b) Transmission spectrum of the plasmonic structure.

As depicted in Figure 1(a), we study a structure which consists of a 500 $\mu$m thick dielectric layer (gadolinium gallium garnet) and a 80 nm thick periodic gold grating. The grating slabs are 290 nm wide and thermally and electronically isolated from each other by 110 nm wide air gaps. The periodic perforation enables coupling of far field radiation to propagating SPPs (and vice versa) whose resonances appear in the transmission spectrum in Figure 1(b).

We measure time resolved change of light transmission of plasmonic gratings using pump-probe technique with transform-limited 30 fs optical pulses at a center wavelength of 800 nm. The pump

and probe beams pass through the sample from different directions: While the pump is incident in a plane parallel to the grating slabs, the probe falls in a perpendicular plane on the grating (see Figure 1(a)). Both beams are tilted from the optical axis by 17 °.

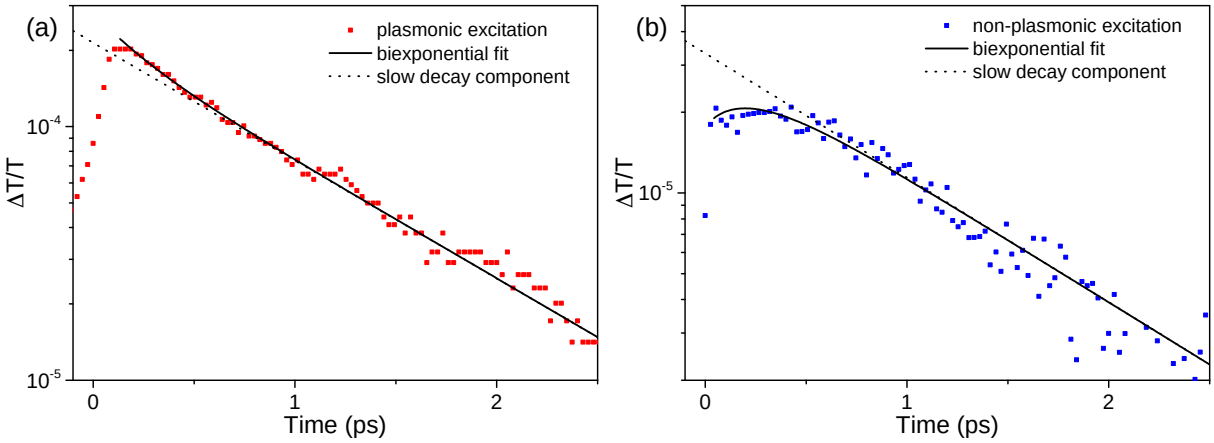



Figure 2: Time resolved differential transmission data for plasmonic and non-plasmonic excitation measured by pump-probe. $\Delta T/T$ axis is in logarithmic scale to facilitate distinction between different decays. The slow decay component with $\tau_1 = 940\,\text{fs}$ is shown as a guide to the eye (dotted line) to emphasize the sign of the faster decay.

Figure 2 shows two examples of measured transients which differ in the chosen polarisation of the pump laser beam: Whereas the plasmonic excitation features a corresponding polarisation to plasmon propagation (TM-polarised), the non-plasmonic polarisation does not support SPP excitation. It follows that in both cases the decay of the signal is biexponential with time constants of $\tau_1 = 940\,\text{fs}$ and $\tau_2 = 220\,\text{fs}$. Next, there is a change of the sign for the fast component when the polarisation of pump is changed from plamonic to non-plasmonic.

Experimental results can be explained in the following way: In case if surface plasmon polaritons are used to excite conduction band electrons in Au (TM-polarized pump), hot spots are formed and in addition to electron-phonon energy relaxation (longer time scale of 940 fs), thermal conductivity of electrons takes place. This leads to additional decay of energy from hot to cold spots which is manifested in pump-probe transients (see the shorter decay with 220 fs time constant). In case if non-plasmonic configuration is used to excite electrons in metal we notice the opposite sign which indicates that thermal distribution of cold and hot spots is opposite to plasmonic excitation. Our results demonstrate that thermal diffusion in plasmonic structures plays an important role in the relaxation processes of hot electrons on sub-picosecond timescales.

## ACKNOWLEDGMENT

The work was supported by the Deutsche Forschungsgemeinschaft (Project No. AK40/7-1), by the German Ministry of Education and Research (BMBF) (FKZ: 05K13PE1) and by the Russian Foundation for Basic Research (13-02-91334).

## REFERENCES

1. Vallée, F. and Del Fatti, N., "Ultrafast Nonlinear Plasmonics" in *Plasmonics: Theory and applications*, ed. by Shahbazyan, T.V. and Stockman, M.I., Springer, 2013.
2. Pohl, M., Belotelov, V. I., Akimov, I. A., Kasture, S., Vengurlekar, A. S., Gopal, A. V., Zvezdin, A. K., Yakovlev, D. R., and Bayer, M., "Plasmonic crystals for ultrafast nanophotonics: Optical switching of surface plasmon polaritons", *Phys. Rev. B* **85**, 081401(R), 2012.

# Spatial Dependence of the Electron-hole correlation in Hybrid Perovskite Crystals

**Giulia Grancini[1*], Daniele Viola[2], Marina Gandini[3], Davide Altamura[4], Cinzia Giannini[4], Giulio Cerullo[2], Annamaria Petrozza[3]**

[1] Group for Molecular Engineering of Functional Materials, Institute of Chemical Sciences and Engineering, Ecole polytechnique fédérale de Lausanne, Sion, Switzerland

[2]Dipartimento di Fisica, Politecnico di Milano, Milan, Italy

[3]Center for Nano Science and Technology @ Polimi, Istituto Italiano di Tecnologia, Milan, Italy

[4]Institute of Crystallography, National Research Council, Bari, Italy

[*]corresponding author: giulia.grancini@epfl.ch

**Abstract** Methylammonium-lead-iodide ($CH_3NH_3PbI_3$) perovskite are delivering impressive performances in photovoltaic field, creating much excitement in the research community. Monitoring the charge dynamics and revealing how they are influenced by the crystal order is of paramount importance to get a more fundamental insight into this fascinating material and a deeper understanding of the device operation. By combining state-of-the-art femtosecond microscopy with micro-Raman we image the photophysical scenario in $CH_3NH_3PbI_3$ micro-crystals determining the decisive role of the molecular disorder in screening the electron-hole correlation.

In recent years, perovskite materials have outperformed in the field of solar cells, with power conversion efficiencies beyond 20% in a short of five years.[1] However, behind device optimization, how to manipulate the perovskite crystallinity to get the desired optoelectronic properties still represents a critical issue. Perovskite structural characterization has been carried out applying several tools, however, they usually interrogate bulky portions of the material, averaging out over the intrinsic inhomogeneity at the sub-micron scale the film suffers.[2] Recently, to gain more insight into such problem, photoluminescence mapping has been applied monitoring the local distribution of trap density across the crystal grains.[3] Despite these preliminary results, a clear understanding of the entangled relationship between structural and physical properties of perovskites is still missing. With our work we demonstrate that the perovskite film morphology impacts on the electron-hole interaction, leading to a tunable electron-hole correlation resulting in free carrier or excitonic population. Ultrafast transient absorption (TA) experiments have been performed on macroscopic $CH_3NH_3PbI_3$ films with different mesoscale morphology.[4] We observed that in small crystals (<50 nm size), where the density of the grain boundaries is high, the dynamics are dominated by a population of free carriers, while larger crystals (~1um) sustained the formation of a stable exciton. These results have been interpreted in terms of the different lattice dielectric response which, through the organic cation dipoles, is responsible for tuning the electron-hole interaction. If the organic cations are frozen, a long-range order is established, leading to the formation of stable excitons. On the contrary, if the organic cations are free to rotate, the dipoles respond in a dielectric manner screening the exciton formation and leading to a predominance of free carriers. In order to verify that the two regimes are accessible even on a local scale within a single micrometer-large crystal, we performed ultrafast TA microscope, a state-of-the-art- tool to image on the sub-micrometer spatial scale the photoinduced dynamical

properties with 200 fs time- and 1um spatial- resolution.[5] In particular, we map the TA signal across a 4x5um$^2$ single $CH_3NH_3PbI_3$ crystals. Figure 1 shows the linear transmission (T) of the perovskite crystal and the TA spectra at 1 ps delay upon excitation at 630 nm probing at the central region (**1.**) and at the border (**2.**).

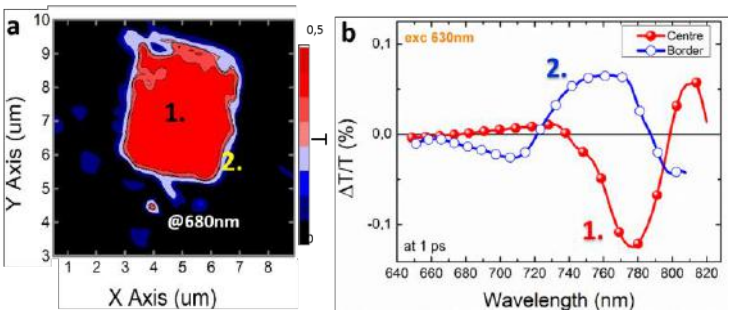



**Figure 1. a,** T map of the CH3NH3PbI3 crystal recorded at 680 nm wavelength. **b,** ΔT/T spectra at 1000 fs time delays upon excitation at 630 nm in the probed region corresponding to point 1. and 2. indicated in panel a.

The spectra registered look dramatically different: a "derivative-like" shape is observed in region 1., while a positive signal at 760 nm in region 2. According to literature[4] they are related to a modulation due to self-normalization of the exciton energy (blue-shift of the exciton absorption) upon strong exciton–exciton and exciton–carrier interactions and to free carrier bleaching, respectively. To understand the correlation to the local structure we performed micro-Raman monitoring the lattice vibrational spectra on the same points, i.e. 1. and 2. Results identify in point 2. *only* the presence of a defined peak at ~160 cm$^{-1}$, marker of the libration of the organic cation that is expected to be sharper when the organic cations have a reduced degree of freedom within the crystal unit cell.[6] This indicates that the motion of the organic cations, responsible for the dielectric response of the semiconductor, is playing a crucial role even on the sub-micron scale.

Thus, a different degree of order/disorder at the sub-micron scale is demonstrating to happen within micrometer large single $CH_3NH_3PbI_3$ crystals, affecting the ultrafast response of the material and the photoexcited electron-hole correlation. This can have dramatic impact on the perovskite active film where the tuning and the optimization of crystal size and crystal quality is essential for increasing the device performances.

**Acknowledgements** GG acknowledges the Laserlab Europe Proposal CUSBO002194 for funding.

1. Nazeeruddin, M. K. "A molecularly engineered hole-transporting material for efficient perovskite solar cells" *Nature Energy*, DOI: 10.1038/NENERGY.2015.1017, 2016
2. Snaith H. J. "Metal-halide perovskites for photovoltaic and light-emitting devices", *Nature Nanotechnology*, Vol. 10, 391–402, 2015.
3. Ginger D. S. "Impact of microstructure on local carrier lifetime in perovskite solar cells" *Science*, Vol. 348, No. 6235, 683–686, 2015.
4. Petrozza, A. "Role of microstructure in the electron–hole interaction of hybrid lead halide perovskites", *Nature Photonics* Vol.9, 695–701, 2015.
5. Lanzani, G. "Nanoscale Imaging of the Interface Dynamics in Polymer Blends by Femtosecond Pump-Probe Confocal Microscopy" *Adv. Mater*. Vol. 22, 3048–3051, 2010.
6. De Angelis, F. "The Raman Spectrum of the CH3NH3PbI3 Hybrid Perovskite: Interplay of Theory and Experiment", *J. Phys. Chem. Lett*., Vol. 5, Issue 2, 279–284, 2014.

# Plasmon-Mediated Nonlinear Optical-Detected Circular Dichroism

**K. L. Knappenberger, Jr.[1*] and J. W. Jarrett[1]**

[1]Department of Chemistry and Biochemistry, Florida State University, Tallahassee, Florida 32306-4390, USA

[*]corresponding author: kknappenberger@fsu.edu

**Abstract** – In this paper, we present results from studying the nonlinear circular dichroism response from colloidal metal nanoparticle assemblies. A pair of orthogonally polarized, phase-locked, temporally delayed laser pulses were used to create the excitation polarization state for circular dichroism (CD) microscopy. Analysis of the emission properties suggested that the CD responses were determined by properties of the one-photon-resonant mode excited by the laser. The methods used to generate phase-locked pulse sequences that modulate the excitation polarization are expected to simplify polarization-resolved microscopy.

Nonlinear optical (NLO) microscopy is a powerful tool capable of providing spatially resolved chemical- and material-specific information through the image contrast source. One common structure-specific probe, nonlinear differential circular dichroism (CD), can report on the chiro-optical activity of nanoparticle assemblies by comparing the magnitudes of absorption or scattering of left (LCP) and right (RCP) circularly polarized light. The information content generated by nonlinear CD has played a major role in recent emergence of chiro-optical photonic materials [1-2]. The precise arrangement of nanoparticles within a network is critical to the observed NLO response [2], which necessitates a method capable of measuring CD signals from single nanostructures.

Herein, we demonstrate a low-cost and straightforward method to create left- and right-handed circularly polarized ultrashort laser pulses for single-structure, nonlinear CD imaging using a pulse replica generator to create a pair of orthogonally polarized phase-locked laser pulses with a controllable inter-pulse time delay. We have used this method to perform CD imaging based on second harmonic generation (SHG), two-photon photoluminescence (TPPL), and one-photon photoluminescence (OPPL) from two different types of assemblies of solid gold nanospheres—homodimers (150-150 nm particles) and heterodimers (150-50 nm particles)—to investigate the source of the circular dichroism produced by these nanoparticle assemblies.

Incorporation of the PRG into our nonlinear microscope has been described previously [3, 4], and a schematic of the device is presented in Figure 1(a). Briefly, a laser pulse is split into phase-locked pulse replicas upon propagation through a series of a-BBO birefringent crystals cut and arranged into three different blocks (A, B, and C). This sequence of birefringent crystals generates a temporal delay between light polarized along the ordinary and extraordinary axes, which can be controlled with extremely high precision (down to 5.7 attoseconds) by transverse movement of the wedges in block B. Introducing inter-pulse delays of -0.667 and +0.667 femtoseconds generates left- and right-handed circularly polarized light, respectively, which can be used as the excitation source for NLO-CD imaging.

Differential CD is reported as the circular difference ratio, given by $|CDR| = |2(I_{LCP} - I_{RCP}) / (I_{LCP} + I_{RCP})|$, where $I$ is the integrated image contrast generated from a single nanostructure upon LCP or RCP excitation. Figure 1(b) illustrates the differential CD observed from a gold nanoparticle heterodimer. A notable difference in the SHG signal was observed upon excitation with LCP versus RCP, and the corresponding CDR value was 0.76 ± 0.07. A summary of the average CDR values for each dimer class and detection method is presented in Figure

1(c). The average CDR value for OPPL-detected CD was nearly zero for both sample types, indicating a lack of polarization specificity for the one-photon process. In contrast, both structure types displayed nonzero CDR values for TPPL- and SHG-detected CD, with close agreement between the CDR values obtained by the two detection methods, indicating that both NLO signals were dependent upon the one-photon resonant mode excited by the laser fundamental. Additionally, average heterodimer CDR values were higher than those determined for homodimer nanostructures. These data indicated that polarization-dependent SHG and TPPL measurements were sensitive probes of interparticle plasmon mode resonances and suggested that the larger, nonzero CDR values observed for heterodimeric structures likely arose from higher-order plasmon modes in the large nanosphere interfering with dipole modes from the small nanoparticle.

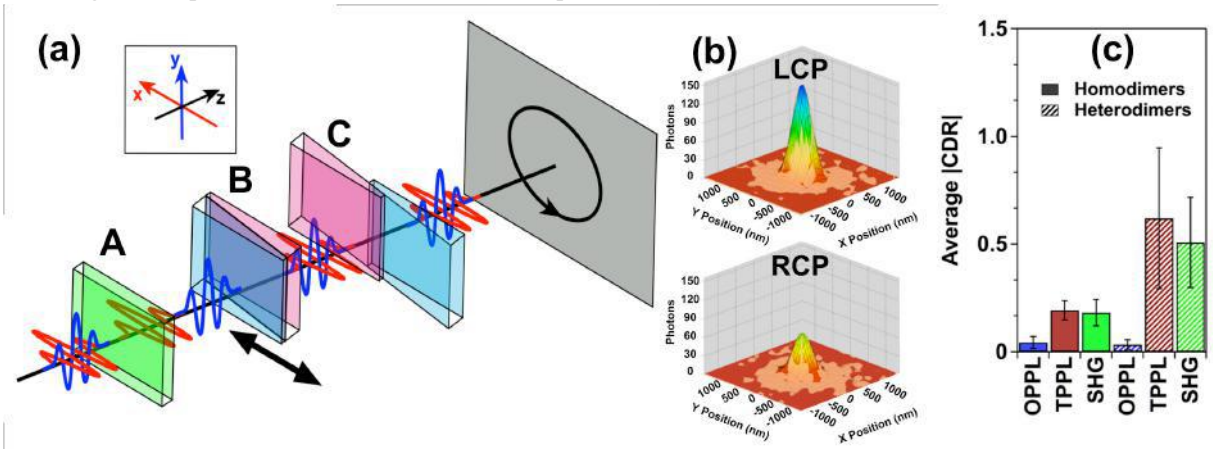



**Figure 1.** (a) Schematic depicting the PRG used for polarization manipulation. The “A,” “B,” and “C” labels designate the three blocks of birefringent materials. Block B is on a motorized translation stage which traverses the *x*-direction and induces time delays between two orthogonally polarized pulse replicas. The colors of the wedges designate the orientation of the optical axis of the birefringent crystal (green: *x*, cyan: *y*, magenta: *z*). (b) SHG imaging data upon LCP (top) and RCP (bottom) excitation. (c) Average |CDR| values across all homodimer (solid fill) and heterodimer (diagonal line fill) samples for OPPL, TPPL, and SHG detection.

**Acknowledgements**: This research was supported by a grant from the Air Force Office of Scientific Research, Grant Number FA9550-15-1-0114.

**REFERENCES**

1. Kauranen, M., T. Verbiest and A. Persoons. "Second-order nonlinear optical signatures of surface chirality," *J. Mod. Opt.*, Vol. 45, No. 2, 403-423, 1998.
2. Chandra, M., A.-M. Dowgiallo and K. L. Knappenberger. "Magnetic dipolar interactions in solid gold nanosphere dimers," *J. Am. Chem. Soc.*, Vol. 134, No. 10, 4477-4480, 2012.
3. Jarrett, J. W., X. Liu, P. F. Nealey, R. A. Vaia, G. Cerullo and K. L. Knappenberger. "Communication: SHG-detected circular dichroism imaging using orthogonal phase-locked laser pulses," *J. Chem. Phys.*, Vol. 142, No. 15, 151101, 2015.
4. Jarrett, J. W., T. Zhao, J. S. Johnson, X. Liu, P. F. Nealey, R. A. Vaia and K. L. Knappenberger. "Plasmon-mediated two-photon photoluminescence-detected circular dichroism in gold nanosphere assemblies," *The Journal of Physical Chemistry Letters*, Vol. 7, 765-770, 2016.

# Impact of analyte molecule distribution on the SERS efficiency of nanoplasmonic assemblies: a full-wave simulation study.

**D. M. Solís[1*], J. M. Taboada[2], F. Obelleiro[1], L M. Liz-Marzán[3, 4], and F. J. García de Abajo[5, 6]**

[1]Dept. Teoría do Sinal e Comunicacións, Universidade de Vigo, Vigo, Spain

[2]Dept. Tecnolog. de los Computadores y las Comunicaciones, Universidad de Extremadura, Cáceres, Spain

[3]Bionanoplasmonics Laboratory, CIC biomaGUNE, Donostia - San Sebastian, Spain

[4]Ikerbasque, Basque Foundation for Science, Bilbao, Spain

[5]ICFO—The Institute of Photonic Sciences, Castelldefels, Spain

[6]ICREA—Institució Catalana de Reserca i Estudis Avançats, Barcelona, Spain

[*]corresponding author: dmartinez@com.uvigo.es

**Abstract**-The SERS (surface-enhanced Raman spectroscopy) performance of plasmonic colloidal depositions is to a great extent determined by the distribution of the analyte molecules that attach to the nanoparticles' surface. We herein investigate this effect by considering a high-density monolayer of gold nanospheres (GNP's) and compare the SERS enhancement yielded by two different models of analyte distribution through full-wave numerical simulations. These are done with the aid of an accelerated surface integral equation method, extremely powerful for large-scale electromagnetic problems.

The way in which the analyte molecules deposit/penetrate onto/into a given plasmonic assembly gives rise to a specific distribution pattern of molecules adhered to the plasmonic surfaces, thereby playing a key role in the structure's SERS properties. In order to shed some light upon this matter, we consider a densely-compacted monolayer deposition of several hundreds of GNP's (minimum surface-to-surface separation of 1 nm) and, through intensive full-wave simulations, obtain its SERS performance (as a function of both wavelength and Raman shift) considering two different scenarios. In the first one, we assume that the molecules of the analyte solution, which fills up the plasmonic nanoparticle layer in its entirety, can move freely and hence completely penetrate into the colloid. Thus, prior to evaporation, the analyte molecules end up adhered to the nanoparticles' surface in an approximately uniform fashion. After evaporation, this results in a kind of skin of analyte molecules wrapping the nanoparticles. We will call it skin-type model. For the second scenario, we assume that the analyte molecules are uniformly dropped from above on the nanoparticle layer, resulting in a sort of sheet that covers the exposed surfaces of the nanoparticles and part of the substrate: sheet-type model. A distance of 1 nm from the molecules to the substrate and nanoparticles' surface is enforced in all cases, which is consistent with the usual sizes of the analyte molecules.

Regarding the simulation tool, capable of accurately modeling the interaction of light with such large-scale structures, the authors have shown in previous publications [1-2] that a method-of-moments (MoM) approach accelerated with the multilevel fast multipole algorithm (MLFMA) can address this sort of problems without the need of supercomputing resources.

**Acknowledgements.** D.M.S., J.M.T, and F.O acknowledge funding from the European Regional Development Fund (ERDF) and the Spanish Government, Ministerio de Economía y Competitividad, Dirección General de Investigación Científica y Técnica (Projects MAT2014-58201-C2-1-R, MAT2014-58201-C2-2-R), from the ERDF and the Galician Regional Government under agreement for funding the Atlantic Research Center for Information and Communication Technologies (AtlantTIC), and from the ERDF and the Extremadura Regional Government (Junta de Extremadura) under Project IB13185. L.M.L.-M. acknowledges funding from the European Research Council (ERC Advanced Grant #267867 Plasmaquo). F.J.G.A. acknowledges funding from the European Commission (Graphene Flagship CNECT-ICT-604391 and FP7-ICT-2013-613024-GRASP).

**REFERENCES**

1. Hamon, C., S. M. Novikov, L. Scarabelli, D. M. Solís, T. Altantzis, S. Bals, J. M. Taboada, F. Obelleiro and L. M. Liz-Marzán, "Collective Plasmonic Properties in Few-Layer Gold Nanorod Supercrystals," *ACS Photonics*, Vol. 2, No. 10, 1482–1488, 2015.
2. Solís, D. M., J. M. Taboada, F. Obelleiro, L. M. Liz-Marzán and F. J. García de Abajo, "Toward ultimate nanoplasmonics modeling," *ACS Nano*, Vol. 8, No. 8, 7559–7570, 2014.

# Mode-matched multiresonant plasmonic antennas for enhanced wave mixing at the nanoscale

**M. Celebrano[1], X. Wu[2,3], M. Baselli[1], S. Großmann[2], P. Biagioni[1], L. Ghirardini[1], G. Pellegrini[1], A. Locatelli[4], C. De Angelis[4], G. Cerullo[1,5], R. Osellame[5], B. Hecht[2], L. Duò[1], F. Ciccacci[1], & M. Finazzi1[1]**

[1]Physics Department, Politecnico Milano, P.zza Leonardo Da Vinci 32, 20133 Milano, Italy.

[2]Nano-Optics & Biophotonics Group - Department of Physics - Experimental Physics 5, University of Würzburg, Am Hubland, 97074 Würzburg, Germany.

[3]Present Address: Ultrafast Nanooptics Group – Department of Physics – Experimental Physics III, University of Bayreuth, Universitätsstraße 30, 95447 Bayreuth, Germany.

[4]Department of Information Engineering, University of Brescia, Via Branze 38, 25123 Brescia, Italy.

[5]IFN-CNR - Physics Department, Politecnico Milano, P.zza Leonardo Da Vinci 32, 20133 Milano, Italy.

*e-mail:* michele.celebrano@polimi.it

**Abstract** - We have developed a paradigm to optimize the second-order nonlinear emission in plasmonic nanoantennas. This approach is based on the design of broken-symmetry plasmonic nanostructures simultaneously displaying multiple resonances at both the excitation and emission wavelengths and spatial overlap between the local modes involved. We will describe the properties of the nonlinear emission from these structures and discuss possible implementations of the introduced paradigm to metasurfaces for applications to nonlinear sensing and quantum optics.

Second Harmonic Generation (SHG) is well known to be a powerful imaging tool for background-free and non-damaging living tissues investigation. Field enhancements in plasmonic nanostructures are often exploited to effectively compensate for the lack of phase-matching in confined volumes with the aim of obtaining brighter nanoscale nonlinear probes. Recently, a nanoantenna design featuring a double resonance at both the excitation and the emission wavelengths has been realized to improve SHG [1]. However, the high degree of symmetry in plasmonic materials at the atomic scale and in nanoantenna designs has so far limited SHG efficiency [2].

Here we report on especially engineered gold single-crystalline nanoantennas (see Figure inset) working in the near-infrared that show unprecedented SHG efficiency thanks to (i) a multi-resonant response occurring at both the excitation and SH wavelengths, (ii) a significant spatial overlap of the localized fields at the wavelengths of interest and (iii) a broken-symmetry geometry to achieve dipole-allowed SHG. The effective combination of these key features in a single plasmonic antenna, characterized by the absence of local defects,

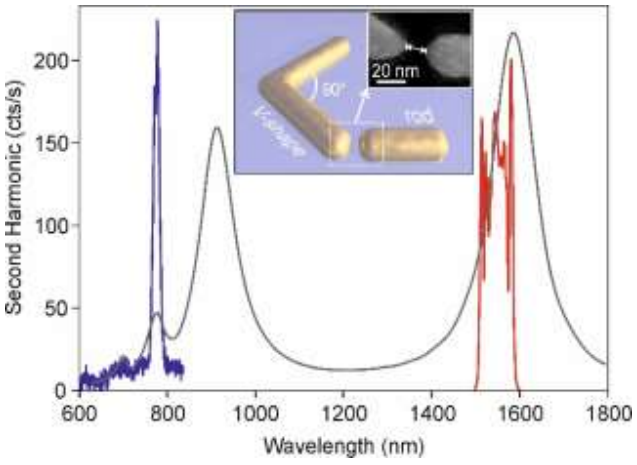



**Figure 1:** Superposition of the antenna modes with the SHG emission spectrum (blue line) and the excitation laser band (red line) shows excellent overlap with the doubly-resonant antenna calculated spectrum (light-grey line). Inset: sketch of the devised nanostructure. Sub-inset: SEM image of the gap-region revealing a gap-size of about 17 nm.

allows optimizing the SHG efficiency in a well-controlled fashion. Once the antenna geometry is properly tuned to display a double resonance matching simultaneously the laser excitation line (1560 nm, see red line in Fig. 1) and the SHG band (780 nm, see blue line in Fig. 1), it demonstrates a SHG nonlinear coefficient $\gamma_{SHG} = \hat{P}_{SH}/\hat{P}_{FW}^2 \approx 5 \times 10^{-10}$ $W^{-1}$, where $\hat{P}_{SH}$ and $\hat{P}_{FW}$ are the SH and excitation peak powers, respectively. This figure of merit is well above the ones retrieved by other SHG studies on broken-symmetry plasmonic structures [3, 4], thus achieving an extremely high conversion efficiency $\eta_{SHG} \sim 6.4 \times 10^{-9}$ [5].

We evaluated the sensing performances of our devices by theoretically estimating the figure of merit FOM* = ($\Delta I/I$)/$\Delta n$ of our nonlinear plasmonic devices, where $I$ is the SHG intensity and $n$ the refractive index of the environment. The nanostructure showing the best conversion efficiency features a FOM* = 40, which is about 4 times higher than the one of other individual plasmonic structures already applied to sensing [6]. The possibility to further optimize the second-order nonlinear response of nanoscale plasmonic structures paves the way to a new class of tunable molecular sensing devices and nanoscale coherent light sources based on nonlinear plasmonic platforms.

**Acknowledgements**, the authors acknowledge support from Fondazione Cariplo through the project SHAPES (2013-0736) and from the EC through the Graphene Flagship project (CNECT-ICT-604391). This work was performed in the context of the European COST Action MP1302 Nanospectroscopy.

**REFERENCES**

1. Thyagarajan, K., Rivier, S., Lovera, A. & Martin, O. J. F. "Enhanced second harmonic generation from double resonant plasmonic antennae," *Opt. Express*, Vol. 20, 12860–12865, 2012.
2. Finazzi, M., Biagioni, P., Celebrano, M. & Duò, L. "Selection rules for second harmonic generation in nanoparticles," *Phys. Rev. B*, Vol. 76, 125414, 2007.
3. Aouani, H. et al. "Multiresonant broadband optical antennas as efficient tunable nanosources of second harmonic light," *Nano Lett.*, Vol. 12, 4997–5002, 2012.
4. Zhang, Y., Grady, N. K., Ayala-Orozco, C. & Halas, N. J. Three-dimensional nanostructures as highly efficient generators of second harmonic light. *Nano Lett.*, Vol. 11, 5519–5523, 2011.
5. Celebrano M. et al., Mode matching in multiresonant plasmonic nanoantennas for enhanced second harmonic generation" *Nature Nanotech.*, Vol. 10, 412-417, 2015.
6. Ament, I., Prasad, J., Henkel, A., Schmachtel, S., and Sönnichsen, C. "Single unlabeled protein detection on individual plasmonic nanoparticles," *Nano Lett.*, Vol. 12, 1092–1095, (2012).

# Ultrafast all-optical control of the coherent nonlinear emission of multi-resonant plasmonic metasurfaces.

**Giovanni Sartorello[1], Nicolas A. H. Olivier[1], Jingjing Zhang[2], Weisheng Yue[3], David J. Gosztola[4], Gary P. Wiederrecht[4], Gregory Wurtz[1,5], and Anatoly V. Zayats** [1]

[1] Department of Physics, King's College London, Strand, London WC2R 2LS, United Kingdom

[2] School of Electrical and Electronic Engineering, Nanyang Technological University, Nanyang Avenue 639798, Singapore

[3] Advanced Nanofabrication, Imaging and Characterization Core Lab, King Abdullah University of Science and Technology, 4700 KAUST, Thuwal 23955-6900, Kingdom of Saudi Arabia

and

National Graphene Institute, University of Manchester, Oxford Road, Manchester M13 9PL, UK, United Kingdom

[4] Center for Nanoscale Materials, Argonne National Laboratory, 9700 South Cass Avenue, Argonne, IL 60439, United States of America

[5]Department of Physics, University of North Florida, 1 UNF Drive, Jacksonville, FL 32224, United States of America

[*]corresponding author: g.wurtz@unf.edu

**Abstract**- We demonstrate and rationalize the ultrafast modulation of the coherent nonlinear emission from plasmonic metasurfaces using all-optical means.

Optical metamaterials have stimulated an increasing interest from scientists over the past decade expanding our ability to manipulate electromagnetic fields in nanostructured systems in order to design selected functionalities with a degree of control never experienced before. The core of metamaterial design is in the crafting of their dispersion through careful geometrical nanostructuring. This has lead to the practical development of superlenses[1], sub-diffraction imaging systems[2], cloaking[3], and other enhanced optical nonlinearity design[4].

In this work we focus our attention on 2D metamaterials, metamaterials of sub-wavelength thickness, often referred to as metasurfaces, and which development provides both passive[5] and active optical functionalities.[6] In particular we studied the ultrafast transient response of a multi-resonant plasmonic metasurface made of cut-disk resonators acting as nonlinear coherent emitters. We demonstrate the ability to modulate both SHG and THG signals emitted by this type of metasurfaces at the sub-ps timescales (see figure 1) and rationalize the results on the basis of the temporal response of the electron density in the metal through both time-resolved transient extinction measurements and numerical simulations. Additionally, the effect of modal overlap between both the fundamental and coherent modes and the pump-induced position-sensitive transient permittivity changes is also found to play an important role in our observations and will be discussed in the context of the transient behavior of nanostructured systems.

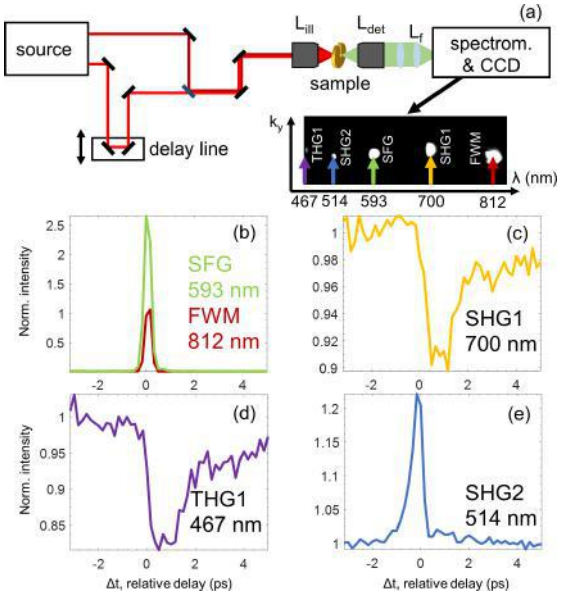



Figure 1. Ultrafast all-optical modulation of coherent nonlinear signals. (a) Schematic of the ultrafast pump-probe setup. The insert shows the spectrum of the nonlinear signals observed on the CCD chip for simultaneously overlapping pulses: $\lambda(2\omega_1)$=700 nm ($SHG_1$), $\lambda(2\omega_2)$=514 nm ($SHG_2$), $\lambda(\omega_1+\omega_2)$=593 nm (SFG), $\lambda(3\omega_1)$=467 nm ($THG_1$), and $\lambda(2\omega_2-\omega_1)$=812 nm (FWM). (b—e) Transient behavior of (b) SFG and FWM, (c) SHG1, (d) THG1, and (e) SHG2.

Our observations may contribute to the design of novel and efficient optical functionalities required for beam steering and directionality control of coherent signals under either multi-beam or single beam excitation.

**Acknowledgements**, This work was supported, in part, by EPSRC (UK). J. Z. was supported by the Royal Society Newton International Fellowship. A.Z. acknowledges support from the Royal Society and the Wolfson Foundation. G.W. acknowledges the support from the EC FP7 Project No. 304179 (Marie Curie Actions). Use of the Center for Nanoscale Materials, an Office of Science user facility, was supported by the U. S. Department of Energy, Office of Science, Office of Basic Energy Sciences, under Contract No. DE-AC02-06CH11357.

## REFERENCES

1. Pendry, J. B.; Ramakrishna, S. A., Focusing light using negative refraction. *Journal of Physics: Condensed Matter* **2003,** *15* (37), 6345-6364.

2. Fang, N.; Lee, H.; Sun, C.; Zhang, X., Sub-diffraction-limited optical imaging with a silver superlens. *Science* **2005,** *308* (5721), 534-7.

3. (a) Pendry, J. B.; Schurig, D.; Smith, D. R., Controlling electromagnetic fields. *Science (New York, N.Y.)* **2006,** *312* (5781), 1780-1782; (b) Cai, W.; Chettiar, U. K.; Kildishev, A. V.; Shalaev, V. M., Optical cloaking with metamaterials. *Nature photonics* **2007,** *1* (April), 224-224.

4. (a) Shadrivov, I. V.; Zharov, A. a.; Kivshar, Y. S., Second-harmonic generation in nonlinear left-handed metamaterials. *Journal of the Optical Society of America B* **2006,** *23* (3), 529-529; (b) Wurtz, G. A.; Pollard, R.; Hendren, W.; Wiederrecht, G. P.; Gosztola, D. J.; Podolskiy, V. A.; Zayats, A. V., Designed ultrafast optical nonlinearity in a plasmonic nanorod metamaterial enhanced by nonlocality. *Nature nanotechnology* **2011,** *6* (2), 107-11.

5. (a) Aieta, F.; Genevet, P.; Yu, N.; Kats, M. A.; Gaburro, Z.; Capasso, F., Out-of-Plane Reflection and Refraction of Light by Anisotropic Optical Antenna Metasurfaces with Phase Discontinuities. *Nano Letters* **2012,** *12* (3), 1702-1706; (b) Keren-Zur, S.; Avayu, O.; Michaeli, L.; Ellenbogen, T., Nonlinear Beam Shaping with Plasmonic Metasurfaces. *ACS Photonics* **2016,** *3* (1), 117-123; (c) Karimi, E.; Schulz, S. a.; De Leon, I.; Qassim, H.; Upham, J.; Boyd, R. W., Generating optical orbital angular momentum at visible wavelengths using a plasmonic metasurface. *Light: Science & Applications*

**2014,** *3* (5), e167-e167; (d) Yin, X.; Ye, Z.; Rho, J.; Wang, Y.; Zhang, X., Photonic Spin Hall Effect at Metasurfaces. *Science* **2013,** *339* (6126), 1405-1407.

6. (a) Sámson, Z. L.; MacDonald, K. F.; De Angelis, F.; Gholipour, B.; Knight, K.; Huang, C. C.; Di Fabrizio, E.; Hewak, D. W.; Zheludev, N. I., Metamaterial electro-optic switch of nanoscale thickness. *Applied Physics Letters* **2010,** *96* (14), 143105-143105; (b) Dani, K. M.; Ku, Z.; Upadhya, P. C.; Prasankumar, R. P.; Brueck, S. R. J.; Taylor, A. J., Subpicosecond optical switching with a negative index metamaterial. *Nano Letters* **2009,** *9* (10), 3565-3569.

# Nonlinear Optical Properties of Atomically Defined Thiolate Protected Gold Clusters

**S. Knoppe[1*], and T.Verbiest[1]**
[1]Author Department of Chemistry, KU Leuven, Belgium
[*]corresponding author: stefan.knoppe@chem.kuleuven.be

**Abstract**-Thiolate-protected gold clusters have become an intensely studied area of research in nanochemistry. Bridging the gap between true molecules and the metallic state, this class of compounds is characterized by highly size-dependent properties. Little is known about their nonlinear optical properties. We describe initial results on the first hyperpolarizabilities of a series of thiolate-protected gold clusters, supported by density functional theory calculations. Of note, the clusters are also efficient two photon absorbers.

Monolayer-protected metal clusters (MPCs) are composed of a defined number of metal atoms protected by a specific number of protecting ligands. Within this compound class, thiolate-protected gold clusters $[Au_m(SR)_n]^-$ are very prominent due to their exceptional stabilities. The stability can be explained by a combination of electronic and geometric shell closing. A series of single crystal structures has been solved for clusters of up to 133 gold atoms.[1,2,3,4] The properties of MPCs are strongly size-dependent and molecule-like, thus bridging the gap between molecular and metallic behavior.[5] The optical properties (linear absorption and fluorescence) of Au:thiolate clusters also vary with the composition of the cluster. Thus, one would expect that the second- and third-order nonlinear optical (NLO) properties are also drastically size-dependent.

However, the NLO properties of Au:thiolate clusters have not yet been unveiled in great detail. Goodson and co-workers demonstrated that $[Au_{25}(SR)_{18}]^-$ and $Au_{38}(SR)_{24}$ clusters are efficient two-photon absorbers.[6] Russier-Antoine et al. determined the first hyperpolarizability of $Au_{15}(SR)_{13}$ and $[Au_{25}(SR)_{18}]^-$ clusters by Hyper-Rayleigh Scattering (HRS).[7] We recently presented the first experiments on Second-Harmonic Generation (SHG) of $Au_{25}(SCH_2CH_2Ph)_{18}$ and $Au_{38}(SR)_{24}$ clusters.[8] While the prior is centrosymmetric – and therefore inactive in SHG – the latter is inherently chiral and active in SHG. This result is explained by the molecular symmetry of the clusters. We were able to show that protection of the $Au_{25}$ cluster with a chiral thiolate ligand (for this, we chose captopril) leads to emergence of SHG. This is a clear indication that the ligand plays a pivotal role in the NLO properties of MPCs. Both clusters are also active as two-photon excited fluorescence emitters.

On the basis of these findings, a density functional theory screening was performed, for which eight clusters in the range of 18-38 Au atoms were considered.[9] We chose clusters whose crystal structures are known. Using –SH model ligands, the polarizabilities $\alpha$ and first hyperpolarizabilities $\beta$ were calculated. While the polarizabilities scale linearly with the system size (number of gold atoms), no such trend was identified in the first hyperpolarizabilities. This is ascribed to the symmetry properties of the individual clusters, which vary greatly (between centrosymmetric and inherently chiral) between the clusters. We also demonstrate how substitution of the (achiral) –SH ligands by chiral ligands is able to generate

significant first hyperpolarizabilities in centrosymmetric clusters.

We also experimentally determined the first hyperpolarizabilities of a series of Au:thiolate clusters.[10] We identify the mechanisms that are responsible for second-harmonic scattering in the clusters. In metallic nanoparticles (> ca. 2 nm), SHG and HRS arise from local defects at the surface of the nanoparticles, which are enhanced by the localized surface plasmon resonance. In contrast, the behavior of Au:thiolate clusters is molecule-like, determined by the symmetry of the clusters and does not scale with the superatomic electron count.

**Acknowledgements**. We are grateful for financial support from KU Leuven, the Funds for Scientific Research – Flanders (FWO) and the German Academic Exchange Service (DAAD). The authors acknowledge assistance by their local co-workers and international collaborators (Hannu Häkkinen, University of Jyväskylä, and Amala Dass, University of Mississippi). All DFT calculations were carried out a 'CSC – The IT Center for Science' in Espoo (Finland).

**REFERENCES**

1. Heaven, M., Dass, A., White, P.S., Holt, K. M., Murray, R. W., "Crystal Structure of the gold nanoparticle $[N(C_8H_{17})_4][Au_{25}(SCH_2CH_2Ph)_{18}]$, *J. Am. Chem. Soc.*, Vol. 130, No. 12, 3754 – 3755.
2. Qian, H., Eckenhoff, W. T., Zhu, Y., Pintauer, T., Jin, R., "Total Structure Determination of Thiolate-Protected $Au_{38}$ Nanoparticles", *J. Am. Chem. Soc.*, Vol. 132, No. 24, 8280 – 8281.
3. Jadzinsky, P.D., Calero, G., Ackerson, C.J., Bushnell, D.A., Kornberg, R.D., "Structure of a thiol monolayer-protected gold nanoparticle at 1.1 A resolution", *Science*, Vol. 318, 5849, 430 - 433.
4. Zeng, C., Chen. Y., Kirschbaum, K., Appavoo, K., Sfeir, M.Y., Jin, R., "Structural patterns at all scales in a monometallic chiral $Au_{133}(SR)_{52}$ nanoparticle", *Sci. Adv.*, Vol. 1, 2, e1500045 – e1500045.
5. Jin, R., "Atomically precise metal nanoclusters: stable sizes and optical properties", *Nanoscale*, Vol. 7, 5, 1549 – 1565.
6. Ramakrishna, G., Varnavski, O., Kim, J., Lee, D., Goodson, T., "Quantum-Sized Gold Clusters as Efficient Two-Photon Absorbers", *J. Am. Chem. Soc.*, Vol. 130, 15, 5032 – 5033.
7. Russier-Antoine, I., Bertorelle, F., Vojkovic, M., Rayane, D., Salmon, E., Jonin, C., Dugourd, P., Antoine, R., Brevet, P.-F., "Non-linear Optical Properties of Gold Quantum Clusters: The Smaller The Better", *Nanoscale*, Vol. 6, 22, 13572 – 13578.
8. Knoppe, S., Vanbel, M., Van Cleuvenbergen, S., Vanpraet, L., Bürgi, T., Verbiest, T., "Nonlinear Optical Properties of Thiolate-Protected Gold Clusters", *J. Phys. Chem. C*, Vol. 119, 11, 6221 – 6226.
9. Knoppe, S., Häkkinen, H., Verbiest, T., ""Nonlinear Optical Properties of Thiolate-Protected Gold Clusters: A Theoretical Survey of the First Hyperpolarizabilities", *J. Phys. Chem. C*, Vol. 119, 11, 27676 – 27682.
10. Knoppe, S., Verbiest, T., et al., *submitted*.

# Monitoring of core-shell particles freely diffusing in solution.

**M. Martini[1], M. Stamboul[2], and A.Débarre[2,3*]**

[1]Institut Lumière Matière, Univ. Lyon 1, CNRS, 69622 Villeurbanne CEDEX, France

[2]Lab. Aimé Cotton, CNRS, Univ. Paris-Sud, ENS-Cachan, Université Paris-Saclay, 91405 Orsay Cedex, France

[3] Laboratoire PPSM, CNRS, ENS-Cachan, Université Paris-Saclay, 94235 Cachan cedex, France

[*]anne.debarre@lac.u-psud.fr

**Abstract**-We have developed a spectroscopic approach to study the optical properties of single nanoparticles in suspension. This approach includes the possibility of obtaining the emission spectrum of a particle diffusing during a few milliseconds in the excited volume of a microscope. To illustrate this multiparameter spectroscopy, we will discuss the case of the intrinsic photoluminescence of a mixture of gold monomers and gold dimers, and evoke the case of the spectrum evolution of (gold)core-(FITC doped)shell particles with increasing excitation power.

We will first report on the spectroscopic method that we have developed to record the spectrum of emission of a particle rapidly diffusing in solution. This method, named photon time-of-flight spectroscopy (PTOFS), exploits the time-frequency conversion principle [1]. This method is especially appropriate to monitor the intrinsic photoluminescence of individual metallic particles in solution. It can readily be associated with the simultaneous acquisition of other types of emission, such as light scattering, for example. PTOFS provides the spectral signature of the studied system whereas information on its diffusional and photo-physical dynamics are derived from fluctuation correlation spectroscopy (FCS). We will illustrate the advantage of PTOFS on the example of the intrinsic photoluminescence of a mixture of gold monomers and dimers [2].

We will then discuss some preliminary results obtained on the emission of core-shell particles in aqueous solution. The core is a gold sphere with a diameter of around 5 nm and the silica shell incorporates FITC molecules at high concentration. This system has similarities with the core-shell particles used to demonstrate the SPASER effect for the first time [3]. We will specifically focus our attention on the evolution of the spectrum of the emission when the power of the excitation tuned to the absorption band of the FITC molecules is increased.

**Acknowledgements**, This work has been supported by the Region Ile-de-France in the framework of C'Nano IdF, the nanoscience competence center of Paris Region. Financial support from the ANR-10-LABX-0035 (LabEx NanoSaclay) is also gratefully acknowledged.

**REFERENCES**

1. Loumaigne, M., P. Vasanthakumar, A. Richard, and A. Débarre, "Time-of-Flight Photon Spectroscopy: A Simple Scheme To Monitor Simultaneously Spectral and Temporal Fluctuations of Emission on Single Nanoparticles," *ACS Nano*, Vol. 6, No. 12, 10512–10523, 2012.
2. Loumaigne, M., Midelet, C., Doussineau, T., Dugourd, P., Antoine R., Stamboul, M., Débarre, A. and Werts, M. H. V., « Optical extinction and scattering cross sections of plasmonic nanoparticle dimers in aqueous suspension", *Nanoscale* , accepted DOI 10.1039/c6nr00918b, 2016.
3. Noginov, M. A., G. Zhu, G., M. Belgrave, R. Bakker, V. M. Shalaev, E. E. Narimanov, S. Stout, E. Herz, T. Suteewong, U. Wiesner, "Demonstration of a spaser-based nanolaser", *Nature*, Vol. 460, No. 7259, 1110-1112, 2009.

# MultiPhoton chiroptical effects in nanospirals and in chirally coupled plasmonic nanostructures

**V. K. Valev**
Centre for Photonics and Photonic Materials, Department of Physics, University of Bath, United Kingdom
*corresponding author: vkv23@bath.ac.uk

**Abstract**- Strong chiroptical effects in plasmonic nanostructures could find applications in chiral molecular sensing, separation and synthesis. Here we investigate a range of chiral plasmonic nanomaterials with voids in the centers, where molecules could benefit from a superchiral light enhancements. We show strong chiroptical responses in the second harmonic generation circular dichroism (CD) from a metasurfaces made with the smallest metal nanospirals studied so far. We also optimize the design and dimensions of chirally coupled planar nanostructures, probed through two-photon luminescence CD and linear CD in the diffraction pattern.

In recent years, plasmonic nanostructures with various chiral designs have been proposed and investigated.[1] Such nanostructures often draw attention due to their potential for achieving negative refractive index[2] and due to their ability to create superchiral light.[3] Because, for superchiral light, the pitch of the electric field of light is shorter than that of circularly polarized light, chiral plasmonic nanostructures can lead to enhanced chiroptical interactions with chiral molecules.[4] Additionally, recently, there has been an increasing interest in multiphoton chiroptical effects in chiral plasmonic nanostructures. Such multiphoton effects are strongly enhanced by the local field at the surface of plasmonic nanostructures as the intensity of multiphoton effects follows a power law of the electric field of light.[5,6]

To allow for strong interaction with molecules, our work concentrates on nanostructured geometries where a void is present at the chiral centers. Examples of such geometries are 3D spirals and chirally coupled plasmonic nanostructures.

The chirality of 3D nanospirals is often difficult to study because, on the one hand side, the structures can couple anisotropically to the substrate and because, on the other hand side, light can excite a dipole at the tip of the nanospirals. Further complications can arise from an anisotropic arrangement of the nanospirals themselves on the substrate. In our experiments, we measured the second harmonic generation (SHG) intensity as a function of the rotation of a quarter-wave-plate. This was done for 120 positions of rotation of the sample along the surface normal. The results were subsequently averaged in order to obtain the effective response of an isotropic chiral sample. We took great care to establish the robustness of our results by measuring quarter-wave-plate rotation dependences of the SHG intensity for the four main polariser-analyser configurations, by measuring a different batch of samples and by testing the repeatability of the results to eliminate any contribution from laser-induced damage on the nanospirals. The experimental data were subsequently fitted in order to extract values of the chiral nonlinear susceptibility tensor components. Furthermore, these were compared to a direct measurement of the SHG intensity attributable to chiral nonlinear susceptibility tensor components.

In our previous work, we have investigated the chiral coupling of plasmonic nanostructures with different shapes, including G-shaped, L-shaped, S-shaped, O-shaped and U-shaped.[6,7] We have thus established an

optimal separation distance between the nanostructures. Here we simplify considerably the design of the nanostructures to an I-shaped design and investigate the chiral coupling of four such nanostructures as a function of the width and length. Our study identifies optimum dimensions of the nanostructures and explores an efficient way of arranging them on a surface in order to maximize the chiroptical response per unit surface.

It has previously been demonstrated that, in diffracting chiral gratings, the CD measured in the first diffraction order is significantly larger than that in the zeroth order. We demonstrate an experimental chiroptical configuration, where the sensitivity to the handedness of the structures is additionally increased by 100%.

In the presented talk, we will conclude by highlighting a couple of cases where SHG-CD originates in achiral nanostructures and will discuss the origin of the effects for these cases.[8]

**REFERENCES**


1. Valev, V.K., Baumberg, J., Sibilia, C., Verbiest, T., "Chirality and Chiroptical Effects in Plasmonic Nanostructures: Fundamentals, Recent Progress, and Outlook," *Adv. Mater.*, Vol. 25, No. 18, 2508-2534, 2013.
2. Shelby, R.A., Smith, D.R., Schultz, S., "Experimental Verification of a Negative Index of Refraction," *Science*, Vol. 292, No. 5510, 77-79, 2010.
3. Tang, Y., Cohen, A.E., "Enhanced Enantioselectivity in Excitation of Chiral Molecules by Superchiral Light," *Science*, Vol. 332, 333-336, 2011.
4. Hendry, E., et al, "Ultrasensitive detection and characterization of biomolecules using superchiral fields," *Nat. Nano*., Vol. 5, 783-787, 2010.
5. Kauranen, M., Zayats, A.V., "Nonlinear plasmonics," *Nat. Photon.* Vol. 6, 737-748, 2012.
6. Valev, V.K., "Characterization of nanostructured plasmonic surfaces with second harmonic generation," *Langmuir*, Vol. 28, 15454–15471, 2012.
7. Valev, V.K., Baumberg, J.J., De Clercq, B., Braz, N., Zheng, X., Osley, E.J., Vandendriessche, S., Hojeij, M., Blejean, C., Mertens, J., Biris, C.G., Volskiy, V., Ameloot, M., Ekinci, Y., Vandenbosch, G. A. E., Warburton, P. A., Moshchalkov, V. V., Panoiu, N. C., Verbiest, T., "Nonlinear superchiral meta-surfaces: tuning chirality and disentangling non-reciprocity at the nanoscale," *Adv. Mater.* Vol. 26, 4074-4081, 2014.
8. Chen, S., Zeuner, F., Weismann, M., Reineke, B., Li, G., Valev, V. K., Cheah, K. W., Panoiu, N. C., Zentgraf, T. and Zhang, S., "Giant Nonlinear Optical Activity of Achiral Origin in Planar Metasurfaces with Quadratic and Cubic Nonlinearities". *Adv. Mater.*, 2016, doi:10.1002/adma.201505640.

# Femtosecond Exciton and Charge Dynamics and unusual Stark Effect in Mono- and Few-layer Transition Metal Dichalcogenides

**C.Gadermaier[1*], T. Borzda[1], V. Vega Mayoral[1], D. Vella[1], P. Topolovsek[1], M. Prijatelj[1], T. Mertelj[1], N. Vujicic[2], D. Ovchinnikov[3], D. Dumcenco[3], D. Viola[4], E. A. A. Pogna[4], C. Manzoni[4], S. Dal Conte[4], F. Scotognella[4], D. Brida[5], N. Martino[6], M. R. Antognazza[6], G. Lanzani[6], A. Kis[3], D. Mihailovic[1], and G. Cerullo[4]**

[1] Jozef Stefan Institute, Department of Complex Matter, Jamova 39, 1000 Ljubljana, Slovenia

[2] Institute of Physics, Bijenicka 46, 10000 Zagreb, Croatia

[3] Electrical Engineering Institute, Ecole Polytechnique Federale de Lausanne (EPFL), CH-1015 Lausanne, Switzerland

[4] IFN-CNR, Department of Physics, Politecnico di Milano, P. Leonardo da Vinci 32, 20133 Milan, Italy

[5] Department of Physics and Center of Applied Photonics, University of Konstanz, D-78457 Konstanz, Germany

[6] Center for Nano Science and Technology, Italian Institute of Technology, Via Pascoli 70/3, 20133 Milan, Italy

[*]corresponding author: christoph.gadermaier@ijs.si

**Abstract**-Despite the large exciton binding energy, mono- and few-layer transistion metal dichalcogenides (TMDCs) show strong photocurrents and photovoltaic effect. We report on the exciton dissociation into charges on the sub-ps scale and subsequent charge trapping in different TMDCs. An in-plane electric field further enhances the yield of exciton dissociation. Additionally, TMDCs show a strong Stark effect of unusual origin and field dependence, suggesting their use in extremely compact electroabsorption modulators for integrated photonics.

Recent progress in the exfoliation of layered materials and the nanofabrication of functional structures has revived the interest in two-dimensional materials with properties complementary to graphene, in particular transition metal dichalcogenides (TMDCs). Their potential for electronics has become evident by the realization of a field effect transistor and a logic circuit device based on a single flake of monolayer $MoS_2$. Despite their high exciton binding energy, mono- and few-layer semiconducting TMDCs show a strong photovoltaic effect and potential for high sensitivity photodetectors. Both these functionalities require efficient charge carrier photogeneration, either via direct excitation of mobile carriers or via exciton dissociation. We use continuous wave photomodulation and femtosecond pump-probe spectroscopy to identify the spectral features of photogenerated charges in an ensemble of few-layer $MoS_2$ and $WS_2$ dispersed in a transparent polymer and trace the dynamics of photogeneration and relaxation of both charges and excitons [1, 2]. We find that the primary photoexcitations are excitons which dissociate efficiently with a characteristic time several hundred fs. In $WS_2$, thanks to the larger separation of the two main excitonics resonances, we can also resolve the carrier trapping after exciton dissociation. While the yield of exciton dissociation into charges is close to unity in the few-layer case, in monolayers it is considerably lower, due to the higher exciton binding energy. We show that the exciton dissociation in monolayer $MoS_2$ can be enhanced via applying an electric field.

According to our findings, few-layer TMDCs display a behavior which is intermediate between conventional semiconductors on the one hand, and high exciton binding energy materials, such as organic semiconductors,

carbon nanotubes, and single-layer TMDCs on the other. High efficiency photodetectors and photovoltaic elements based on monolayers require additional measures to achieve efficient exciton dissociation, such as a strong built-in field using appropriate electrode materials, engineering a p-n junction, or a heterojunction device. In few-layers, which have the added benefit of absorbing a larger fraction of the incident light, such measures should not be necessary and simpler, more scalable device structures could be used.

To translate electrical into optical signals one uses either the modulation of the refractive index or the absorption of a material by an electric field. Contemporary electroabsorption modulators rely on the quantum confined Stark effect (QCSE), the field-induced red-shift and broadening of the strong excitonic absorption resonances characteristic of low-dimensional semiconductor structures. They require device lengths beyond 100 μm to achieve practical modulation depths of 10 dB. We show an unprecedentedly strong electro-absorption (EA) signal in a monolayer of the two-dimensional semiconductor $MoS_2$. The EA spectrum is dominated by linewidth broadening of almost 10% at a modulated transverse voltage $V_{pp}$ = 0.5 V. Contrary to the conventional QCSE, this effect increases linearly with the applied field strength and is due to an increase of the inhomogeneous rather that the homogeneous broadening. The signal magnitude corresponds to a length-specific modulation of up to 75 $dB\mu m^{-1}$. The extremely compact device design is the only technology to date that can enable on-chip photonic circuit integration.

**REFERENCES**


1. Borzda, T. et al., "Charge Photogeneration in FewLayer $MoS_2$," *Adv. Funct. Mater.*, Vol. 25, No. 22, 3351-3358, 2015.
2. Vega-Mayoral, V. et al., "Exciton and charge carrier dynamics in few-layer $WS_2$," *Nanoscale*, Vol. 8, No. 10, 5428-5434, 2016.

**Cesium Lead Halide Perovskite Nanorcystals as a New Optoelectronic Material**

*Handong SUN*

Division of Physics and Applied Physics, School of Physical and Mathematical Sciences, Nanyang Technological University, Singapore 637371, Singapore

Optical gain and lasing properties in a new class of emerging quantum materials, the colloidal all-inorganic cesium lead halide perovskite quantum dots (IPQDs) ($CsPbX_3$, X = Cl, Br, I) will be presented. Our result has indicated that such material system show combined merits of both colloidal quantum dots and halide perovskites. Low-threshold and ultrastable stimulated emission was demonstrated under atmospheric condition. The gain mechanism is attributed to biexcitonic recombination. The flexibility and superior optical gain properties of these $CsPbX_3$ IPQDs were manifested by demonstration of an optically pumped micro-laser. The nonlinear optical properties including the multi-photon absorption and resultant photoluminescence of the $CsPbX_3$ nanocrystals were investigated. A large two-photon absorption cross-section of up to ~$1.2\times10^5$ GM is determined from 9 nm-sized $CsPbBr_3$ nanocrystals. Moreover, low-threshold frequency-upconverted stimulated emission by multi-photon absorption was observed from the thin films of close-packed $CsPbBr_3$ nanocrystals.

# Hyperuniformity and structural correlation in bio-inspired photonics

# Designing hyperuniform structures for efficient light harvesting

**G. Gkantzounis[*] and M. Florescu**
Advanced Technology Institute and Department of Physics,
University of Surrey, Guildford, GU2 7XH, United Kingdom
[*]corresponding author: g.gkantzounis@surrey.ac.uk

**Abstract**-Photonic crystals have been proven very efficient for light manipulation. Lately, this has become even more efficient by the use of hyperuniform structures, which exhibit much richer Fourier spectra. We discuss a new approach to the design of hyperuniform structures for explicitly targeting a given Fourier spectrum. We were able to design large hyperuniform structures of different geometrical types and vanishing contribution to the radiative Fourier components. Consequently, we observe efficient light absorption in all cases considered.

Hyperuniform (HPU) structures can be very efficient in light trapping and absorption, due to their rich Fourier spectrum.[1,2] For an HPU structure of N points the structure factor[3,4] vanishes in a set Ω of the Fourier space, around $|\mathbf{k}|=0$.[3,4] A parameter descriptive of the Ω size is $\chi=M(K)/2N$, where M(K) is the number of independent collective coordinates within Ω.[3] Following a procedure similar to that described in Ref. 3, we calculate an HPU pattern by minimizing the sum of the structure factors in a certain set Ω of arbitrary shape. In most cases considered here this set involves all the Fourier components $|\mathbf{k}| < k_0$, for a given $k_0$.

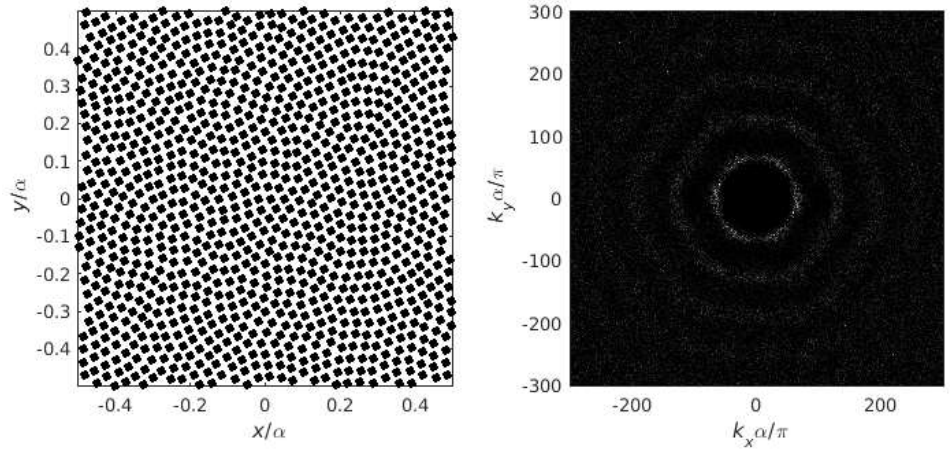



**Figure 1.** An HPU structure of 1000 particles, arranged in a periodic lattice of lattice constant *a*, and $\chi=0.60$ (left-hand diagram), together with the corresponding structure factor (right-hand diagram). Maximum values correspond to white.

As a first example, we consider a hyperuniform pattern of 1000 points and a very large parameter $\chi=0.60$, but before the regime referred as wavy crystalline[5]. According to our knowledge this is the largest parameter reported in the literature. The point structure together with the corresponding structure factor (ignoring forward scattering) is shown in Fig. 1. The area with of vanishing structure factor has a radius $k_0=50\pi/a$, where *a* is the

lattice constant of the supercell (periodic boundary conditions).

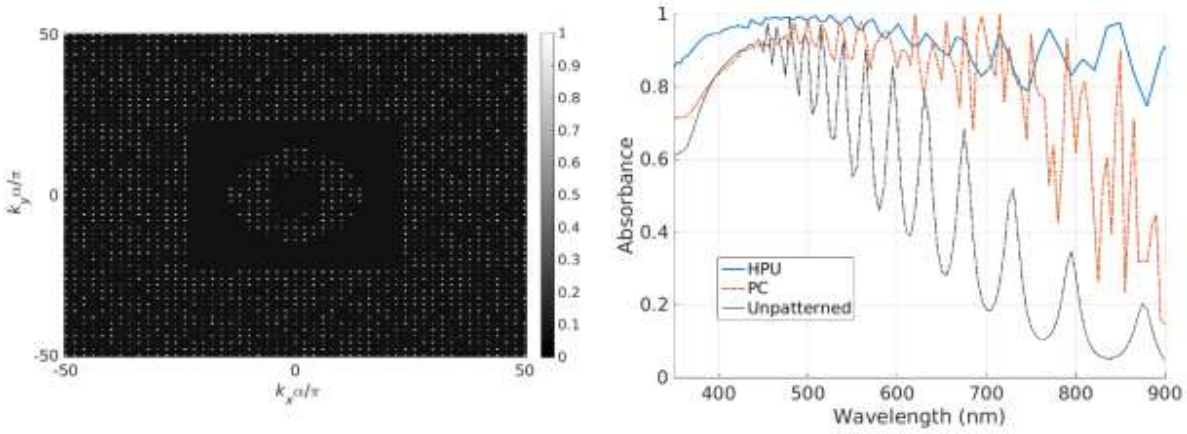



**Figure 2.** Optimized structure factor for an HPU-like structure of 200 particles and $\chi$=0.5 (left-hand diagram). The absorption spectrum for the unpatterned (thin black line), the optimized PC (red dotted line) and the HPU (blue solid line) are shown in the right-hand diagram.

We next consider a structure optimized for absorption. It consists of grooves of thickness 100nm on top of a 1μm thin Si film, covered with a 70nm thick anti-reflecting layer of refractive index 1.65.[6] The structure factor for the HPU-like structure of 200 cylindrical holes, similar to the one in Fig. 2(c) of Ref. 6, is shown in the left-hand diagram of Fig. 2. The absorption is shown in the right-hand diagram of Fig. 2. The parameters for the unpatterned and the optimized photonic crystal (PC) structure are taken from Ref. 6. Remarkably, our results demonstrate that it is possible to substantially increase the absorption in the long wavelength range and suggest that HPU structuring could provide a new avenue for efficient light harvesting.

**Acknowledgements**, This work was partially supported by the University of Surrey's FRSF and IAA awards to MF, EPSRC (United Kingdom) Strategic Equipment Grant No. EP/L02263X/1 (EP/M008576/1) and EPSRC (United Kingdom) Grant EP/M027791/1.

**REFERENCES**

1. Kelzenberg, M.D., S. W. Boettcher, J. A. Petykiewicz, D. B. Turner-Evans, M. C. Putnam, E. L. Warren, J. M. Spurgeon, R. M. Briggs, N. S. Lewis, and H. A. Atwater, "Enhanced absorption and carrier collection in Si wire arrays for photovoltaic applications," *Nature Mater.*, Vol. 9, No. 3, 239–244, 2010.
2. Wiersma, D. S, "Disordered photonics," *Nature Photon.*, Vol. 7, No. 3, 188–196, 2013.
3. Torquato, S., F. H. Stillinger, "Local density fluctuations, hyperuniformity, and order metrics." *Phys. Rev. E*, Vol. 68, No. 4, 041113/1–25, 2003.
4. Florescu, M., S. Torquato, and P. J. Steinhardta, "Designer disordered materials with large, complete photonic band gaps," in *Proc Nat I Sci*, USA, Month 2009,Vol 106, No. 49, 20658–20663.
5. Uche, O. U., F. H. Stillinger, and S. Torquato, "Constraints on collective density variables: Two dimensions," *Phys. Rev. E*, Vol. 70, 046122/1-9, 2004.
6. Martins, E. R.,J. Li, Y. K. Liu, V. Depauw, Z. Chen,J. Zhou, and T. F. Krauss, "Deterministic quasi-random nanostructures for photon control," *Nat. Commun.*, Vol. 4, No. 15, 155112/1-7, 2013.

# Hyperuniformity and local self-uniformity: Photonics band gaps in disordered materials

**M. Florescu*, T. Amoah and S. Sellers**
Advanced Technology Institute and Department of Physics,
University of Surrey, Guildford, GU2 7XH, United Kingdom
*corresponding author: m.florescu@surrey.ac.uk

**Abstract**-Hyperuniform disordered photonic structures are a new class of photonic solids with controlled correlations on a wide range of length scales. We explore the natural connection between hyperuniformity and photonic band gaps in structures with a variety of topologies. Furthermore, we introduce the concept of strong isotropy and local self-uniformity as a topological measure for connected disordered networks and demonstrate that all champion photonic band structures can be classified using the local self-uniformity metric.

Hyperuniform disordered (HUD) photonic structures are a new class of materials that harness structural disorder and control transport, emission and absorption of the electromagnetic radiation in unique ways, beyond the constraints imposed by conventional photonic architectures [1]. HUD materials are statistically isotropic and display constrained disorder such that density fluctuations on large scales are more similar to those of ordered structures, crystals or quasicrystals, rather than those of conventional disordered materials [2]. In HUD photonic structures, a wide range of novel phenomena are expected, due to the interplay between disorder, topological correlations and hyperuniformity. Hyperuniform or hyperuniform-like disordered structures have emerged as a contemporary research topic and have been recognized as an area that may lead to important technological advances: spatial bandgaps in correlated disordered structures with a low-dielectric contrast [3], increased absorption properties of nearly hyperuniform disordered photonic slabs [4], and fabrication of 3D hyperuniform structures for IR light [5]. Although photonic band gap (PBG) formation in disordered structures has recently attracted great interest, the physics behind the existence of a complete energy gap and the dramatic effects on photon transport and confinement are not yet fully understood and, to date, optical experimental work has been limited to passive structures in the microwave [6] and shortwave infrared [7] regimes.

Analogous to their periodic counter parts, HUD structures enable efficient confinement of both TM and TE-polarized radiation and the realization of high-Q optical cavities, and low-loss waveguides [8-9]. For 2D structures, quality factors exceeding $Q > 10^9$ are achieved, whilst here we report here 3D finite-height photonic slabs with high quality factors exceeding $Q > 30{,}000$. Moreover, a rich variety of cavity modes can be obtained and classified according to their approximate symmetry. We further introduce a novel design approach for planar freeform optical waveguides based on off-set curves. In contrast to traditional methods, where waveguides are designed based on the natural high-symmetry direction provided by a periodic or quasi-periodic template, we first design the waveguide channel and construct an optimized photonic band structure around it. We show that significant transmission can be achieved in the low-loss spectral range for several designs. Low loss waveguiding of light (13% of the maximal straight waveguide transmission) were identified around 1.6μm in a 220nm-thick suspended silicon membrane. The flexibility of the disordered sourroundings, makes further

optimization possible and puts to rest the conjecture that disorder would induce significant out of plane scattering in disordered structures. Our results directly demonstrate the ability of HUD PBG materials to provide a universal design platform for integrated optical micro-circuitry.

The fundamental connection between the geometrical/topological characteristics of photonic materials and the advanced optical functionalities they provide as epitomized by the HUD structuring deserves further scrutiny. To this end we introduce a new metric, local self-uniformity (LSU) as a measure of the structural order of photonic network architectures of predefined valency. The LSU metric is able to quantify the correlation between uniformity of the local environments and the overall photonic band gap properties and provides a new paradigm in the design of aperiodic media. LSU can be employed to uniquely classify photonic networks with a precisely defined upper limit reached for the only known strongly isotropic structures, the trivalent (SRS-gyroid) and tetravalent (diamond) networks. The lower end of the LSU metric describe an interesting class of structures displaying maximal self-dissimilarity. The LSU concept enables us to explore photonic band gap formation in a completely new architecture, the amorphous gyroid network and to show that very distinct photonic architectures presenting large photonic band gaps, be they periodic or aperiodic, all are characterized by high values levels of local self-uniformity. The LSU metric renders the exact nature of their underlying seed patterns, whether crystalline, quasicrystalline, or hyperuniform, irelevant.

**Acknowledgements**, This work was partially supported by the University of Surrey's FRSF and IAA awards to MF, the EPSRC (United Kingdom) DTG Grant No. EP/J500562/1, EPSRC (United Kingdom) Strategic Equipment Grant No. EP/L02263X/1 (EP/M008576/1) and EPSRC (United Kingdom) Grant EP/M027791/1.

**REFERENCES**

1. Florescu M., Torquato S. and Steinhardt P.J., "Designer disordered materials with large, complete photonic band gaps", *Proc. Natl. Acad. Sci. USA*, Vol. 106, No. 49, 20658-20663, 2009.
2. Torquato S. and Stillinger F.H., "Local density fluctuations, hyperuniformity, and order metrics", *Phys. Rev. E*, Vol. 68, 041113/1-25, 2003.
3. Man W., Florescu M., Williamson E.P., He Y.Q, Hashemizad S.R., Leung B.Y.C., Liner D. R., Torquato S., Chaikin P. M. and Steinhardt P. J. *Proc. Natl. Acad. Sci. USA*, Vol. 110, 15886–15891, 2013.
4. Vynck K., Burresi M., Riboli F. and Wiersma D. S., "Photon management in two-dimensional disordered media", *Nat. Mater.*, Vol. 11, 1017–1022, 2012.
5. Nicolas Muller N., Haberko J., Marichy C. and Scheffold, "Silicon Hyperuniform Disordered Photonic Materials with a Pronounced Gap in the Shortwave Infrared", *Adv. Optical Mater.*, Vol. 2, 115-119, 2014.
6. Man W., Florescu M., Matsuyama K., Yadak P., Nahal G., Hashemizad H., Williamson E., Steinhardt P., Torquato S., and Chaikin P., "Photonic band gap in isotropic hyperuniform disordered solids with low dielectric contrast", *Opt. Express*, Vol. 21, 19972-19981, 2013.
7. Florescu M., Man W., Mullen R.A, Milosevic M.M, Amoah T., Chaikin P.M., Torquato S., Steinhardt P., "Isotropic band gaps, optical cavities, and freeform waveguides in hyperuniform disordered photonic solids", *Proc. SPIE*, Vol. 9162, 91620G/1-5, 2014.
8. Florescu M., Steinhardt P. J. and Torquato S., "Optical cavities and waveguides in hyperuniform disordered photonic solids", *Phys. Rev. B*, Vol. 87, 165116/1-4, 2013.
9. Amoah T. and Florescu M., "High-Q optical cavities in hyperuniform disordered materials", *Phys. Rev. B*, Vol. 91, 020201(R)/1-4, 2015.

# Locally Self-uniform Photonic Networks

**S. R. Sellers**[1], **W. Man**[2], **and M. Florescu**[1]

[1]Advanced Technology Institute, University of Surrey, UK
[2]San Francisco State University, USA
steven.sellers@surrey.ac.uk

**Abstract**—

Connections between geometry and optical properties help us understand light's interaction with structured media. Here we introduce local self-uniformity to explore fundamental physics and unlock advanced optical control. Local self-uniformity measures the internal spatial similarities of a random network and unites the set of observed photonic band gap structures. We demonstrate its significance by generating novel band gap amorphous gyroid networks and we present a naturally-occurring network with amorphous gyroid character in the butterfly *Pseudolycaena marsyas*.

Intuitive frameworks that develop connections between a material's structure and its optical properties are highly desirable. They can illuminate the basic interaction of light with structured media and help solve outstanding problems in optics.

The question of the structural characteristics that render photonic band gap architectures 'champion' - i.e. possessing a particulary wide gap - is one such problem. The current champion structure is the diamond network, an FCC lattice with a 2-point motif. Indeed, initial proposals for photonic crystals focussed on FCC structures [1, 2], whose maximally spherical Brillouin zone is well suited to gap formation by Bragg scattering.

However, evidence suggests that a Bragg picture of band gap formation is incomplete. It has been shown that the diamond network remains champion under a reduction of its crystal symmetry [3]. Hyperuniform and photonic amorphous diamond networks [4, 5] exhibit weaker coherent scattering than photonic crystals but still possess large gaps. Topological optimisation suggests that network architectures of fixed coordination favour gap formation, regardless of crystal symmetry [6].

In this work we introduce a new geometrical measure, termed local self-uniformity (LSU), for analysing network architectures of fixed valency. This measure has a direct connection to the electromagnetic resonances the network supports and its band gap forming ability. LSU measures the internal geometrical similarity of the local environments about the vertices of a random network. We define an $n$-tree on a network as the set of vertices that can be accessed within $n$ edges of a given vertex point. Similarity is measured by the degree to which such trees, drawn from proximate vertices in the network, can be maximally overlapped (Fig.1A).

For any given CRN, it is possible to assemble a set of overlap statistics. This set - termed the local self-uniformity distribution - describes the spatial similarities of trees within the network. Certain crystals, such as diamond and the cubic scaffold, possess perfect local self-uniformity. CRNs with imperfect but strong local self-uniformity are epitomised by amorphous diamond - a globally aperiodic network whose geometries and topologies are comparable at a local level.

We unite the set of known band gap network architectures as structures which possess high levels of local self-uniformity. Such networks can be viewed as a connected collection of elementary scattering units which, in isolation, support a discretised set of electromagnetic resonances. The coupling of identical scatterers, as in photonic crystals, creates a gap between fundamental and first-type harmonic resonances. The spatial similarity of scatterers can be relaxed, as measured by local self-uniformity, breaking the degeneracy of the local resonances, but not perturbing them sufficiently to close the gap.

We test the significance of local self-uniformity as a determinant of band gaps by designing novel locally self-uniform amorphous gyroid networks. We find that large band gaps form in amorphous gyroid and observe a strong correlation between the local self-uniformities of our networks and their gap widths (Fig.1B). We fabricate high refractive index alumina prototypes of amorphous gyroid to illustrate our calculations and to probe the isotropy of the band gap (Fig.1C & D).

Finally we consider the variety of colour-producing microstructures in nature that appear locally self-uniform. In particular, we examine the butterfly *Pseudolycaena marsyas* (Theclinae, Fig.1E)

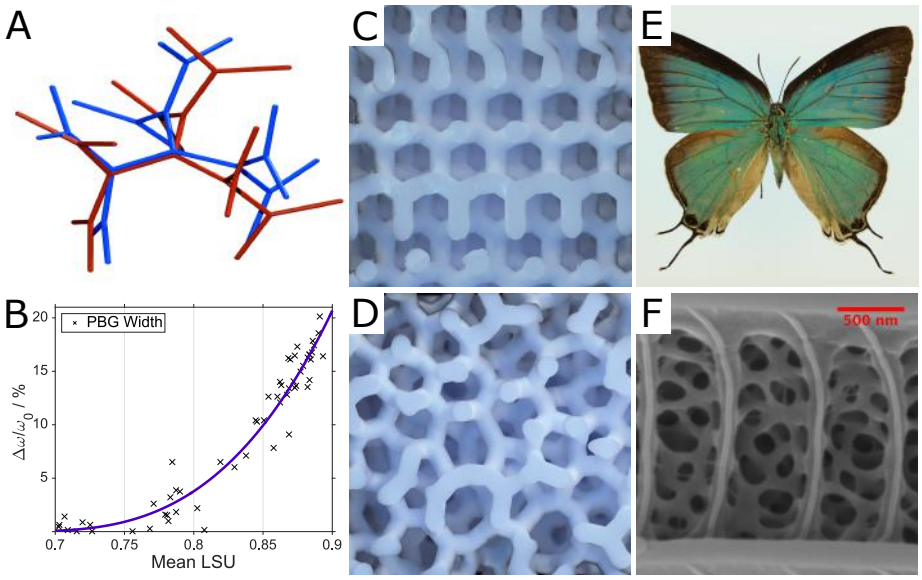



Figure 1: Two 3-trees drawn from an amorphous gyroid network, maximally aligned for calculation of overlap (A). Overlap statistics are assembled to form the local self-uniformity distribution, whose mean value is strongly correlated with band gap width (B). Alumina models of single network gyroid (C) and amorphous gyroid (D) with complete band gaps around 22GHz. A specimen of *Pseudolycaena marsyas* (E) whose scales contain a chitin network with significant amorphous gyroid character (F).

through microscopy and modelling and show that the chitin network in its scales possesses a substantial amorphous gyroid character (Fig.1F). The existence of a naturally-occurring amorphous gyroid requires that its self-assembly is possible, thus posing an interesting challenge to the field of block co-polymer self-assembly.

Local self-uniformity directly links a network's physical structure to its optical properties. In particular, it describes a fundamental mechanism of photonic band gap formation. Local self-uniformity, however, has significant relevance beyond this. It illuminates a subtlety in structural colouring architectures that has so far escaped detection. Further, an appreciation of a material's local electromagnetic resonances, and the control that local self-uniformity allows over the manner in which they couple, represents a new paradigm in complex optical material design.

## ACKNOWLEDGMENT

This work was partially supported by the University of Surrey's FRSF and IAA awards to MF, the EPSRC (United Kingdom) DTG Grant No. EP/L505092, EPSRC Strategic Equipment Grant No. EP/L02263X/1 (EP/M008576/1) and EPSRC Grant EP/M027791/1.

## REFERENCES

1. Yablonovitch, E., "Inhibited Spontaneous Emission in Solid-State Physics and Electronics," *PRL*, Vol. 58, No. 20, 2059–2062, 1987.
2. John, S., "Strong Localization of Photons in Certain Disordered Dielectric Superlattices," *PRL*, Vol. 58, No. 23, 2486–2489, 1987.
3. Maldovan, M. and E. Thomas, "Diamond-structured photonic crystals," *Nature Materials*, Vol. 3, No. 9, 593–600, 2004.
4. Florescu, M., S. Torquato and P. J. Steinhardt, "Designer disordered materials with large, complete photonic band gaps," *PNAS*, Vol. 106, No. 49, 20658–20663, 2009.
5. Edagawa, K., S. Kanoko and M. Notomi, "Photonic Amorphous Diamond Structure with a 3D Photonic Band Gap," *PRL*, Vol. 100, No. 1, 013901, 2008
6. Men, H. et al., "Robust topology optimization of three-dimensional photonic-crystal band-gap structures," *Optics Express*, Vol. 22, No. 19, 22632–22648, 2014

# Transparency of dense hyperuniform systems

**R. Pierrat**[1], **O. Leseur**[1], **and R. Carminati**[1]

[1]ESPCI ParisTech, PSL Research University, CNRS, Institut Langevin, 1 rue Jussieu, 75005 Paris, France
romain.pierrat@espci.fr

**Abstract**— We show that materials made of scatterers distributed on a hyperuniform point pattern can be transparent at densities for which an uncorrelated disordered material would be opaque due to multiple scattering. We give a simple criterion to predict the transparency property of such a system. This opens new perspectives in the control of waves in strongly disordered systems and for the design of photonic materials.

Correlated disordered materials can exhibit peculiar optical properties [1]. Recently, a new class of these materials has appeared. First designated by "superhomogeneous", and now called "hyperuniform", these systems ware first studied for their packing properties [2]. These last years, they are also seen as good candidates for the control of light-matter interaction in disordered systems. Indeed, they exhibit original optical properties such as photonic bandgaps [3, 4]. This has lead to the design and fabrication of hyperuniform structures at optical frequencies [5].

In this work, we show that hyperuniform systems can be transparent even in the multiple scattering regime. The standard theory to derive the average scattering respond of a disordered system is usually based on a perturbative approach. For a dilute system, the first order for the scattering mean-free path is given by the structure factor, a quantity vanishing for small wavevectors in the case of hyperuniform systems leading to their transparency. Going beyond the first order, we derive a criterion establishing a condition for which the transparency holds [6]:

$$b_B \ll k_0 \ell_B \tag{1}$$

where $b_B$ is the optical thickness of the fully uncorrelated system and $\ell_B = [\rho\sigma_s]^{-1}$, the Boltzmann scattering mean-free path. This expression is checked numerically using two-dimensional coupled dipoles simulations.

This result should be helpful in the engineering of disordered materials for the control of waves, with potential applications in many fields of wave physics.

**ACKNOWLEDGMENT**

This work was supported by LABEX WIFI (Laboratory of Excellence within the French Program "Investments for the Future") under references ANR-10-LABX-24 and ANR-10-IDEX-0001-02 PSL* and by the PEPS program of the French CNRS through project LILAS.

**REFERENCES**

1. Rojas-Ochoa, L. F., J. M. Mendez-Alcaraz, J.J. Senz, P. Schurtenberger and F. Scheffold, "Photonic Properties of Strongly Correlated Colloidal Liquids," *Phys. Rev. Lett.*, Vol. 93, No. 7, 073903, 2004.
2. Donev, A., F. Stillinger and S. Torquato, "Unexpected Density Fluctuations in Jammed Disordered Sphere Packings," *Phys. Rev. Lett.*, Vol. 95, No. 9, 1079–7114, 2005.
3. Florescu, M., S. Torquato and P. J. Steinhardt, "Designer disordered materials with large, complete photonic band gaps," *Proc. Natl. Acad. Sci. U.S.A.*, Vol. 106, No. 49, 20658–20663, 2009.
4. Froufe-Prez, L. S., M. Engel, P.F. Damasceno, N. Muller, J. Haberko, S. C. Glotzer and F. Scheffold, "The Role of Short-Range Order and Hyperuniformity in the Formation of Band Gaps in Disordered Photonic Materials," *arXiv:1602.01002*, 2016.
5. Haberko, J. and F. Scheffold, "Fabrication of mesoscale polymeric templates for three-dimensional disordered photonic materials," *Opt. Express*, Vol. 21, No. 1, 1057–1065, 2013.
6. Leseur, O., R. Pierrat and R. Carminati, "High-density hyperuniform materials can be transparent," *arXiv:1510.05807*, 2015.

# Isotropically Polarized Speckle Patterns

**M.K. Schmidt[1,2], J. Aizpurua[1,2], X. Zambrana-Puyalto[3,4], X. Vidal[3], G. Molina-Terriza[3,4] and J.J. Sáenz[2,5,*]**

[1] Materials Physics Center CSIC-UPV/EHU, Paseo Manuel de Lardizabal 5, 20018 Donostia-San Sebastián, Spain.

[2] Donostia International Physics Center (DIPC),
Paseo Manuel de Lardizabal 4, Donostia-San Sebastian 20018, Spain.

[3] Department of Physics and Astronomy, Macquarie University, North Ryde, New South Wales 2109, Australia

[4] ARC Center for Engineered Quantum Systems,
Macquarie University, North Ryde, New South Wales 2109, Australia

[5] IKERBASQUE, Basque Foundation for Science, 48013 Bilbao, Spain.

[*]corresponding author: juanjo.saenz@dipc.org

**Abstract**- We show that the multiple scattering of helical beams by a random dispersion of "dual" dipolar nanospheres leads to a speckle pattern exhibiting a perfect isotropic constant polarization, a situation that could be useful in coherent control of light as well as in lasing in random media.

The scattering of light by random media produces complex, irregular intensity distributions known as speckle patterns. It is generally assumed that multiple scattering of light in optically dense media randomizes the state of polarization of light. A wave propagating in such a medium becomes rapidly depolarized in a characteristic length scale that depends on the properties of both the scattering medium and the illuminating light. Here we discuss a peculiar combination of random samples and laser beams that lead to unusual "anomalously" polarized speckle patterns exhibiting isotropic constant polarization [1].

The polarization of the light scattered by an optically dense and random solution of dielectric nanoparticles shows peculiar properties when the scatterers exhibit strong electric and magnetic polarizabilities. While the distribution of the scattering intensity in these systems shows the typical irregular speckle patterns, the helicity of the incident light can be fully conserved when the electric and magnetic polarizabilities of the scatterers are equal. We show that the multiple scattering of helical beams by a random dispersion of "dual" dipolar nanospheres leads to a speckle pattern exhibiting a perfect isotropic constant polarization, a situation that could be useful in coherent control of light as well as in lasing in random media.

**REFERENCES**

1. Schmidt, M.K. et al., "Isotropically Polarized Speckle Patterns," *Phys. Rev. Lett.*, Vol. 114, No. 11, 113902 (2015).

# Photonic structures in nature: on order and disorder

**Bodo D. Wilts**[1,*]
[1]Adolphe Merkle Institute, University of Fribourg, Chemin des Verdiers 4, CH-1700 Fribourg, Switzerland
[*]corresponding author: bodo.wilts@unifr.ch

**Abstract** The striking colors of many animals are due to structural color that arises from light scattered from ordered, quasi-ordered and disordered material interfaces. Here, we will discuss various coloration mechanisms in nature, from ordered structures showing remarkable iridescence to disordered structures that feature brilliant whiteness due to optical scattering in randomly structured media.

The striking appearance of many animals is not obtained by pigments but rather by structuring transparent materials on the order of a few hundreds of nanometers [1,2]. The biological world has optimized such photonic structures in fish scales, bird feathers and insect wings [3-7], since the Cambrian explosion over 500 million years ago, with which an enormous diversification of insect coloration as well as visual systems started. By changing the dimensions of such nanostructures or the amount of order, quasi-order or disorder in these systems, these diverse nanostructures allow manipulation of incident electromagnetic radiation so to achieve colors that extend over the entire visible wavelength range and that are employed in courtship, to find prey or to escape predation risk by camouflage. A wealth of photonic systems with the most complicated and thoughtful structures can be found in animals, ranging from boomerang-like shapes in bird-of-paradise feathers [5] and complex amorphous, quasi-ordered nanostructures in parrot and king fisher feathers [3,6] to completely disordered chitin networks in beetle scales [7,8].



**Figure 1:** Various photonic structures in nature: an ordered bird-of-paradise feather barbule (left, ref. 5), a quasi-ordered Kingfisher barb (middle, ref. 6), and the disordered chitin network in white beetle scales (right, ref. 7).

Here, the optical properties of different topologies of biological photonics structures, from ordered structures in butterflies to quasi-ordered structures in birds and disordered structures in beetles will be presented and it will be discussed how such structures and topologies can be optically understood and serve as an inspiration to produce novel optical materials, e.g. by using these structures as templates for reconstruction into inorganic materials.

**Acknowledgements.** Collaborations with the groups of Drs. S. Vignolini, D. Stavenga, G. Schröder-Turk, D. Wiersma and F. Scheffold are greatly acknowledged. This research was partly supported through the National Centre of Competence in Research “Bio-Inspired Materials” and the Adolphe Merkle Foundation.

**REFERENCES**


1. Kinoshita, S. (2008) Structural colors in the realm of nature. World Scientific.
2. Dolan, J.A, et al. (2015) *Adv. Opt. Mater.*, 3, 12-32.
3. Saranathan, V., et al. (2012) *J. R. Soc. Interface*, 9, 2563-2580.
4. Saranathan, V., et al. (2015) *Nano. Lett.*, 15, 3735-3742.
5. Wilts, B. D., et al. (2014) *Proc. Natl. Acad. Sci. USA*, 111, 4363-4368.
6. Tinbergen, J., et al. (2013) *J. Exp. Biol.*, 216, 4358-4364.
7. Burresi, M., et al. (2014) *Sci. Rep.*, 4, 6075
8. Cortese, L., et al. (2015) *Adv. Opt. Mater.*, 3, 1337-1341.

# Disorder to enhance and tailor the light-matter interaction

**P. D. García**
Catalan Insitute of Nanoscience and Nanotechnology. Barcelona, Spain.
david.garcia@icn.cat

**Abstract**-Fabrication disorder is usually considered a nuisance in photonic nanostructures but it is essentially unavoidable. However, we can use it in our advantage to tailor the interaction between light and matter. Disorder can be exploited to enhance the spontaneous emission of light and to obtain efficient lasing at the nanoscale.

By harnessing the interaction between light and matter we gained new technologies raging from incandescent light emission to LEDs. How light is emitted (and absorbed) is at the forefront of modern photonics for energy harvesting, protocols for quantum security or the generation of light-matter entanglement for quantum information technology. For all these applications, precisely fabricated nanometer-scale devices are required. However, in such nanostructures, unavoidable fabrication imperfections impose severe performance limits and hamper their functionality. In this talk, I will show how disorder can also be used as a resource instead of being just a nuisance. Photonic glasses [1] are an example where the scattering properties of a structure can be tailored to control the interaction between light and matter. In these systems, the refractive index is modulated randomly but the building blocks are also equal in shape and size. A possible realization of this structure in three-dimensions consists of a self-assembled disordered arrangement of polymer spheres (see Fig. 1a). The equal shape and size of the spheres leads to resonant multiple scattering of light [2] and, when sufficient optical gain is embedded in the structure, the lasing wavelength emission is determined just by the sphere diameter [3] (see Fig. 1b). Also, deliberately introducing disorder in low-dimensional nanostructures like photonic crystal waveguides (PCWs) [4] or photonic crystals (PCs) [5] (see Fig. 1c) leads to Anderson localization where light is efficiently trapped by random multiple scattering with the lattice imperfections. These disorder-induced optical modes (Fig. 1d) have been demonstrated to be very promising for cavity-quantum electrodynamics (QED) experiments where the radiative emission rate of single quantum emitters can be controlled when tuned through resonance with one of these random cavities. Finally, increasing the optical gain in PCWs allows on-chip random nanolasing where the cavity feedback is provided by the intrinsic disorder which enables highly efficient, stable, and broadband tunable lasers with very small mode volumes [4]. The figure of merit of these disorder-induced cavities is their localization length, $\xi$, which determines to a large degree the coupling efficiency of a quantum emitter to a disorder-induced cavity as well as the efficiency of random lasing and reveals a strongly dispersive behavior and a non-trivial dependence on disorder in PCWs [7].

**Acknowledgements**, Villum fondet for the Villum young investigators program.

**REFERENCES**

1. Garcia, PD., Sapienza, R., López, C. Adv. Mater. Vol 22, 12, 2010.
2. Sapienza, R. García, P.D., Bertolotti, J., Martin, M.D., Blanco, A., Vina, L., López, C. and Wiersma, D.S. *Phys. Rev. Lett*. Vol. 99, 233902, 2007.
3. Gottardo, S., Sapienza, R., García, P.D., Blanco, A., Wiersma D.S. and López, C. *Nat. Photon*. Vol. 2, 429,

2008.
4. Sapienza, L., Thyrrestrup, H., Stobbe, S., Garcia, P.D., Smolka, S. and Lodahl, P. *Science* 327, 1352 (2010).
5. García, P.D., Stobbe, S., Soellner, I. and Lodahl, P. *Phys. Rev. Lett.* Vol. 109, 253902, 2012.
6. Liu, J., García, P.D., Ek, S., Gregersen, N., Suhr, T., Schubert, M., Mørk, J., Stobbe, S.and Lodahl, P. *Nat. Nanotech* Vol. 9, 285, 2014.
7. García, P.D., Javadi, A. and Lodahl, P. In preparation.

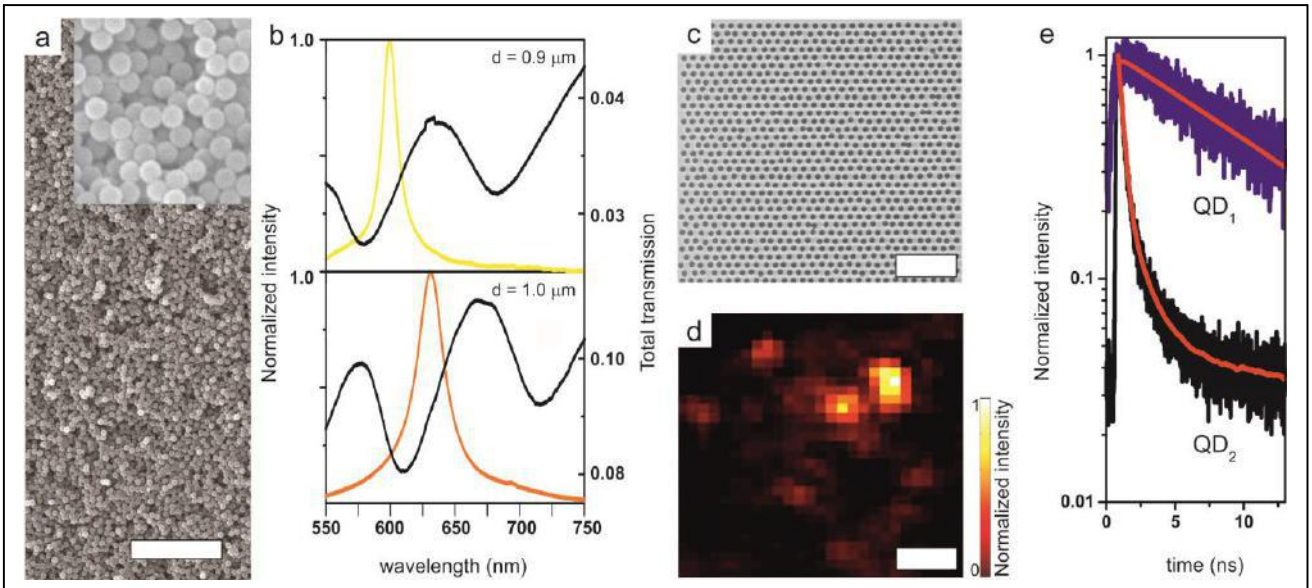



**Figure 1. Enhancement of light-matter interaction in disordered structures**. (a) SEM of a photonic glass made of polystyrene microspheres. The scale bar is 20 microns. (b) The diameter of the spheres determines the lasing wavelength emission of a photonic glass containing an organic dye. (c) Top view SEM of a disordered photonic crystal made by etching holes in a GaAs membrane. The scale bar is 1 micron. (d) Photoluminescence from InAs quantum dots embedded in the photonic crystal shown in (c), collected at a wavelength of (905 ± 1) nm under high-excitation power while scanning the structure. (e) Decay curves for two quantum dots at different positions in the photonic crystal with emission wavelength of 905 nm. The decay rate of QD2 is enhanced with respect to the decay rate of QD1 due to its spatial and spectral coupling to an Anderson-localized mode. The decay of QD2 is **114** times faster than the decay of QD1. Figures taken from Ref. [3] and [5].

# The Role of Short-Range Order and Hyperuniformity in the Formation of Band Gaps in Disordered Photonic Materials

**L. S. Froufe-Pérez[1], M. Engel[2,3*], P. F. Damasceno[2], N. Muller[1], J. Haberko[4], S. C. Glotzer[2], and F. Scheffold[1]**

[1]University of Fribourg, CH-1700 Fribourg, Switzerland

[2]University of Michigan, Ann Arbor, Michigan 48109, USA

[3]Friedrich-Alexander-University Erlangen-Nuremberg, 91052 Erlangen, Germany

[4]AGH University of Science and Technology, 30-059 Krakow, Poland

[*]corresponding author: michael.engel@fau.de

**Abstract**-We disentangle the role of short-range order and hyperuniformity in producing photonic band gaps. For this purpose we study two-dimensional high refractive index disordered materials. The dielectric structure is derived from packing disks in real and reciprocal space. Our findings suggest that the band gap width can be maximized by optimization of short-range order. Tailoring of Bragg scattering at the isotropic Brillouin zone is discussed.

Over the last decade disordered or amorphous photonic materials have gained growing attention [1,2]. Such materials should be less sensitive to fabrication errors and promise a robust design platform. Disordered dielectrics have an isotropic band gap while at the same time they offer better performance in wave guiding and design of non-iridescent stable pigments.

In 2009 the concept of hyperuniformity for photonic structures was introduced, which enforces a certain type of short-range order [3]. In particular so-called stealthy hyperuniform disordered patterns were reported to be fully transparent to incident long-wavelength radiation [4] and lead to strong isotropic band gaps at shorter wavelengths. In addition, numerical work showed that the amorphous diamond structure [5] and three-dimensional networks derived from systems of densely packed spheres [6] exhibit a full band gap in the absence of stealthiness. Thus, although the importance of appropriate order in disordered photonic materials has been discussed for some time, a strategy to maximize the photonic band gap width is lacking.

Here we compare the two strategies to achieve band gaps, stealthy hyperuniformity and hard disk packing. We generate hyperuniform patterns using simulated annealing and hard disk patterns using Monte Carlo equilibration as a function of the stealthiness parameter and packing density, respectively. Photonic densities of states are obtained using the open source MIT Photonic Bands code.

Our findings demonstrate that disordered packings in real and reciprocal space are equally suitable for generating isotropic photonic band gaps in two dimensions (Fig. 1). We present evidence that the optimization of short-range order and in particular the tailoring of Bragg scattering at the isotropic Brillouin zone are key aspects for designing photonic band gap materials. Suppression of scattering at small wave numbers and therefore the appearance of hyperuniformity (strictly or in approximation) are then natural consequences of the development of short-range order and vice versa.

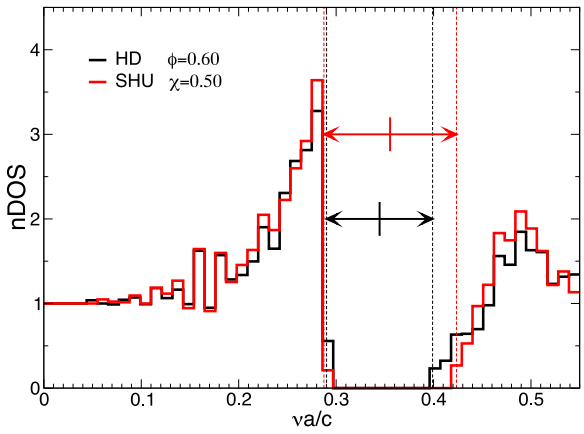



***Figure 1.*** *Photonic properties of a dielectric structure composed of a network of silicon rods. The figure shows the normalized density of state in TM polarization for patterns derive from hard disk (HD) systems at packing density 0.60 and the stealthy hyperuniform (SHU) systems at stealthiness parameter 0.50.*

**Acknowledgements.** We acknowledge support from the National Science Foundation USA, the Simons Foundation, the Swiss National Science Foundation, and the Luxembourg National Research fund.

**REFERENCES**

1. Rojas-Ochoa, L. F., J. M. Mendez-Alcaraz, J. J. Saénz, P. Schurtenberger and F. Scheffold, "Photonic properties of strongly correlated colloidal liquids", *Phys. Rev. Lett.*, Vol. 93, 073903, 2004.
2. Wiersma, D. S., "Disordered Photonics", *Nat. Photonics*, Vol. 7, 188-192, 2013.
3. Florescu, M., S. Torquato, and P. J. Steinhardt, "Designer disordered materials with large, complete photonic band gaps", *Proc. Natl. Acad. Sci. USA*, Vol. 106, 20658-20663, 2009.
4. Leseur, O., R. Pierrat, and R. Carminati, "High-density hyperuniform materials can be transparent", *preprint*, arXiv:1510.05807, 2015.
5. Edagawa, K., S. Kanoko, and M. Notomi, "Photonic amorphous diamond structure with a 3D photonic band gap", *Phys. Rev. Lett.*, Vol. 100, 013901, 2008.
6. Liew, S. F., J.-K. Yang, H. Noh, C. F. Schreck, E. R. Dufresne, C. S. OHern, and H. Cao, "Photonic band gaps in three-dimensional network structures with short-range order", *Phys. Rev. A*, Vol. 84, 063818, 2011.

# A deterministic aperiodic approach to three-dimensionally photonic structures with tailored disorder.

**M. Renner[1], M.-C. Angermann[1], and G. von Freymann[1,2*]**

[1]Physics Department and Research Center OPTIMAS, University of Kaiserslautern, 67663 Kaiserslautern, Germany

[2]Fraunhofer Institute for Physical Measurement Techniques IPM, 67663 Kaiserslautern, Germany

[*]corresponding author: georg.freymann@physik.uni-kl.de

**Abstract** Many structures in nature follow mathematical series to achieve distinct photonic effects. We tailor disorder in originally perfectly ordered samples by introducing deterministic aperiodic distortions following mathematical series, e.g., Fibonacci and Rudin-Shapiro. We investigate photonic transport properties and compare them to Monte-Carlo simulations finding almost isotropic scattering.

Recently, we observed distinct optical properties in direct-laser-written three-dimensional deterministic aperiodic samples following different mathematical series, i.e., Fibonacci, Thue-Morse, Rudin-Shapiro and compared them with randomly disordered samples [1,2]. For low-index dielectric materials characteristic mode patterns and transverse mode localization could be observed. Surprisingly, samples following the Rudin-Shapiro series showed stronger localization behavior than randomly disordered samples.

While characteristic spectral features of these samples are mainly dominated by the arrangement of sample planes along the propagation direction, we now realize for the first time aperiodic deterministic samples following an idealized Fibonacci tiling along all three spatial directions.

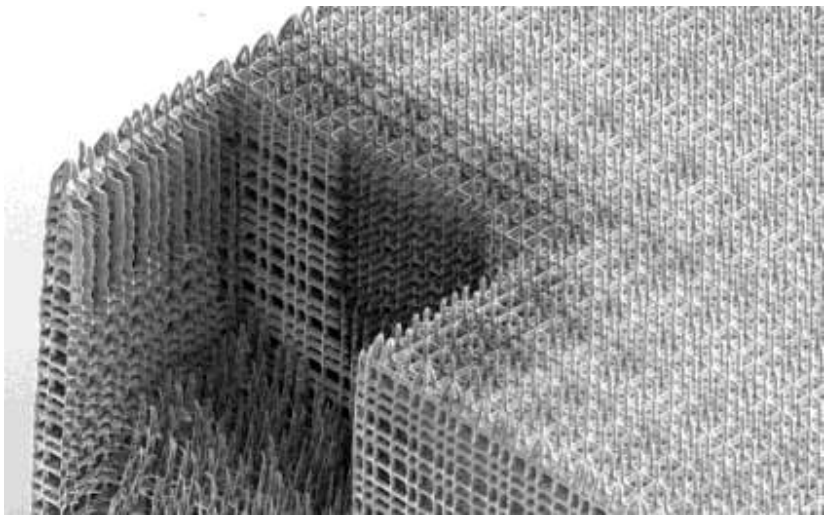


**Figure 1.** Scanning electron micrograph of a deterministic aperiodic structure following a three-dimensional ideal Fibonacci tiling. This tiling ensures almost isotropic characteristics along all three dimensions. The internal structure is revealed by a focused-ion-beam cut.

We characterize transport properties of corresponding samples by time-resolved upconversion spectroscopy for samples of varying lateral extensions and increasing refractive index contrast. Experimental results are in very good agreement with Monte-Carlo simulations. Characteristic differences between the different mathematical series cannot be identified any longer for larger sample dimensions even for low index contrast. This is due to the more isotropic structure and may point to a deterministic approach for strongly scattering materials.

**Acknowledgements:** We gratefully acknowledge financial support provided by the Deutsche Forschungsgemeinschaft (DFG) within projects FR 1672/9-1 and SPP 1839. We also thank the team of the Nano Structuring Center (NSC) at University of Kaiserslautern for their support with sputtering, focused-ion-beam cross sections and scanning electron microscopy.

**REFERENCES**

1. M. Renner and G. von Freymann "Transverse Mode Localization in Three-Dimensional Deterministic Aperiodic Structures", *Advanced Optical Materials*, Vol. 2(3), 226-230, 2014.
2. M. Renner and G. von Freymann "Spatial correlations and optical properties in three-dimensional deterministic aperiodic structures", *Scientific Reports*, Vol. 5, 13129, 2015.

# Photonic structures in plants

**Ullrich Steiner**
Adolphe Merkle Institute, Switzerland

**Abstract**- The study of structural colour in nature is a mature field, which invokes enduring interest. Most of the published work concentrates on the animal kingdom, where butterflies, beetles, weevils, birds and marine organisms are among the most studied. Plants are generally thought to employ mostly pigments, with only relatively few known examples of photonic structures. This talk will summarise recent activities on "photonics in plants" and present recent new results. It will also explore how some of these concepts can be employed in the biomimetic replication of structural colour.

# Biotechnological routes to photonic nanostructures from diatoms microalgae and light emitting molecules

**R. Ragni[1], D. Vona[1], M. Lo Presti[1], G. Leone [1], L. Moretti[2], F. Scotognella[2], G. Lanzani[2], S. R. Cicco[3] and G. M. Farinola[1]***

[1]Dipartimento di Chimica, Università degli Studi di Bari Aldo Moro, via Orabona 4, 70126 Bari, Italy
[2]Center for Nano Science and Technology (CNST) of the IIT, Via Pascoli 70/3, 20133 Milano, Italy
[3]CNR ICCOM Sezione di Bari, via Orabona 4, 70126 Bari, Italy

*corresponding author: gianlucamaria.farinola@uniba.it

**Abstract-** Biotechnological routes to luminescent nanostructured materials are presented, consisting in either *in vivo* or *in vitro* fluorochromation of diatoms microalgae biosilica shells (frustules) with tailored organic or organometallic light emitting molecules. This approach enables to combine the natural photonic behavior of diatom silica skeleton with the emissive properties of the molecular dyes, leading to new hybrid systems with attractive characteristics. The benefit of an easy and general protocol to produce photonic materials *via* living microorganisms are highlighted, together with the intriguing properties of the nanostructures obtained.

Diatoms are a prolific class of single cell photosynthetic algae living in both fresh and marine water ecosystems, which are characterized by having their cells encased in a three-dimensional amorphous silica shell (frustule) whose size and morphology are strictly dependent on the algal species. This shell looks like a micro pill-box composed of two valves (the epitheca and the hypotheca), connected by lateral rings (girdles) that confer flexibility to the structure. Frustules have a highly ordered “layer by layer” hierarchical architecture with periodic pore patterns [1].

These microorganisms can be regarded as low cost bio-factories able to produce a large amount of highly regular, symmetrically patterned 3-D biosilica nanostructures, with reproducible shape and micro- to nanoscale features. The highly regular and periodic nanostructure of diatoms biosilica shells explains their suitability for photonic applications. In fact, frustules act as natural photonic crystals in which very regular disposition of pores in a thin waveguiding layer is responsible for a periodic pattern of high and low refractive index. Due to their photonic crystal behavior, diatoms’ shells can be used as optical microlenses, filters, beam splitters and laser cavities [2, 3].

Chemical modification of diatoms’ biosilica paves the way to new generations of multifunctional materials for a variety of applications ranging from photonics to biosensing and drug delivery [4], which can be conveniently produced *via* biotechnological routes.

In particular, incorporation of organic emitters into diatom frustules exploiting the *in vivo* diatoms’ biomineralization process discloses new photonic materials whose properties result from the combination of the frustule hierarchical nanostructure with the luminescence of incorporated emitting molecules.

Here we report efficient protocols to chemically functionalize the frustules of two species of centric diatoms

(*Thalassiosira weissflogii* and *Coscinodiscus wailesii*) with tailored fluorescent organic molecules and organometallic phosphorescent complexes. The process can be performed following two possible protocols. The *in vitro* approach consists in covalently binding the organic molecules *via* condensation reactions on the activated biosilica which have been previously subjected to a chemical treatment to remove all the organic biological matter [5]. The *in vivo* fluorochromation protocols exploit the biological process of generation of the biosilica structures in the living cells to intimately embed properly functionalized luminescent molecules into the biosilica. The resulting luminescent nanostructures are finally isolated and purified from the organic protoplasm by an acid oxidative protocol retaining the natural frustules' morphology.

The photonic properties of the hybrid nanostructures obtained by both the methods will be comparatively discussed, also showing the possibility to combine the two approaches to obtain multifunctional nanomaterials.

Our approach discloses intriguing possibilities for the massive biotechnological production of photoactive nanostructured materials, whose features can be finely tailored by chemical design of the light emitting molecules and by selecting and modifying the characteristics of the microorganisms used.

**REFERENCES**


1. Cox, E.J., *In The Diatom World*, Springer, 21(4) (2011).
2. De Stefano, L., I. Rea, I. Rendina, M. De Stefano and L. Moretti "Lensless light focusing with the centric marine diatom Coscinodiscus walesii" *Optics Express*, Vol. 15, No. 26, 18082-18088, 2007.
3. Kieu, K., C. Li, Y. Fang, G. Cohoon, O. D. Herrera, M. Hildebrand, K. H. Sandhage and R. A. Norwood "Structure-based optical filtering by the silica microshell of the centric marine diatom Coscinodiscus wailesii" *Optics Express*, Vol. 22, No. 13, 15992-15999, 2014.
4. Cicco, S. R., D. Vona, E. De Giglio, S. Cometa, M. Mattioli-Belmonte, F. Palumbo, R. Ragni and G. M. Farinola "Chemically Modified Diatoms Biosilica for Bone Cell Growth with Combined Drug-Delivery and Antioxidant Properties" *Chem Plus Chem*, Vol. 80, 1104-1112, 2015.
5. Vona D., M. Lo Presti., S. R. Cicco, F. Palumbo, R. Ragni and G. M. Farinola "Light emitting silica nanostructures by surface functionalization of diatom algae shells with a triethoxysilane-functionalized π-conjugated fluorophore" *MRS Advances* 2015, DOI: 10.1557/adv.2015.21, Published online: 22 December 2015.

# Chiro-optical effects in disordered photonics : Harmonic distortions enhance circular dichroism of Gyroids, and stochastic noise does not destroy it.

**G.E. Schröder-Turk**[1], **J. Hielscher**[2], **C. Pouya**[3], **and P. Vukusic**[3]

[1] Murdoch University, School of Engineering and IT, Maths & Stats, Perth, Australia
[2] Friedrich-Alexander University Erlangen-Nuremberg, Theoretical Physics, Erlangen, Germany
[3] Exeter University, School of Physics, Exeter, UK
g.schroeder-turk@murdoch.edu.au

**Abstract**— The departure from strict periodic order in two-phase dielectric materials can offer properties that are otherwise inaccessible to perfectly ordered photonic crystals (PhC). Herewith, we investigate the circular dichroism of the single Gyroid PhC in the presence of spatial distortions. FDTD simulations and microwave transmission measurements on 3D-printed replicas show that harmonic long-wavelength spatial distortions ("sinusoidal chirp") manipulate the imbalance of the circular polarisation (CP) reflectances, as well as the polarisation-incoherent reflectance. The CP-resolved reflectance data are quantified by cumulative contrast. The observed changes are partially rationalised by comparison with simpler distortion models (linear chirp and tetragonal deformation) of the Gyroid.

When Yablonovitch, John and others proposed crystalline structured dielectrics as media tailored for photonics, the concept of these now-called "photonic crystals" (PhC) was based on exploiting their discrete translation symmetry, with lattice constants comparable to the electromagnetic wavelengths of concern. In this way, Rayleigh had covered simple 1D PhC already a century earlier.

Recent years have seen a surge in interest in disordered photonic materials, partially motivated by the strive for more isotropic (direction-independent) and partially by spectrally homogeneous/constant photonic signals. Amongst the former are isotropic band-gap materials in non-crystalline structures with constraints on density fluctuations, including materials with hyperuniform geometry. Amongst the latter are the brilliant whiteness of some beetles.

Here we study circular-polarisation effects in the single Gyroid, a photonic crystal which has attracted much attention due to its chirality [1, 2, 3, 4, 5]. We reduce the strictness of crystalline order by gradual changes of lattice constant along one direction. Reminiscent of deformations observed in some biophotonic crystals ("chirp"), these deformations allow some intuition into the mechanisms of the observed effects. As such they are stepping stones towards an understanding of polarisation effects in disordered photonic materials.

Here we show that a spatial long-wavelength deformation ("chirp") strengthens, to a surprising extent, the circular dichroism response of the single Gyroid photonic crystal, at a low (organic

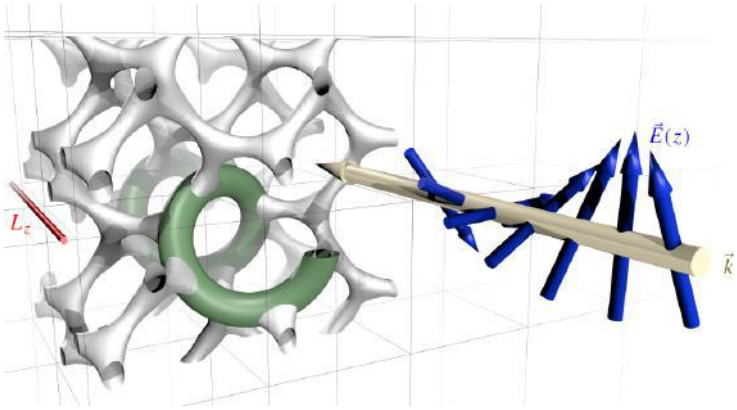



Figure 1: Setup of the FDTD simulations and microwave experiments: Irradiation of a [001]-inclined slab of a right-handed single Gyroid PhC with RCP circular-polarised light.

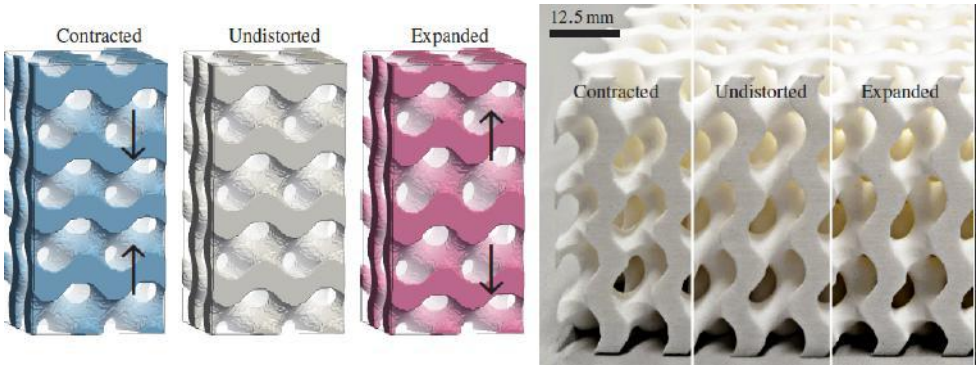



Figure 2: The Gyroid structured objects used in the simulations and experiments. Left: FDTD simulation boxes containing the chunks of the PhC slab. Photos, right: 3D-printed replicas, which have come to use in microwave transmission and reflectance experiments. The middle panel on both sides depicts the undistorted PhC, strictly periodic to translation by $a$ in $z$ direction; while the outer sides show PhCs with sinusoidal chirp introduced: Left contracted, i.e. normal (vertical) lattice constant shortest in the middle of the slab and longest at the surfaces (arrows indicate directions of decreasing lattice constant); the reverse (expanded) situation is depicted on the right sides. Note that the distortion amplitudes are to scale, and while the subtle differences are hardly visible to the naked eye, the impact on photonic properties proves substantial.

materials) dielectric contrast. Data, gathered from FDTD simulations and microwave transmission experiments, are in good agreement. The presence of modulations with low spatial frequency, namely longitudinal sinusoidal chirp, at an [0 0 1]-inclined Gyroid slab, manipulates coupling of light of the rotational sense opposite to the Gyroid, hence alters circular dichroism.

These observations are facilitated by a new analysis tool, cumulative circular contrast (CCR), the running balance of circular dichroism over a given frequency range, suitable for surveying arbitrary photonic structures.

We have shown that photonic performance (wide-band integral CD) can *improve* through distortion. While this "tailoring" relies on well-controlled displacement, stochastic disorder is tolerated to a certain degree. Indeed, the latter addresses the structural chirality of stochastic processes and the photonic response of systems with (or without) intrinsic handedness.

Sinusoidal chirp broadens the vocabulary of geometry-photonic materials. We suggest opening up photonic research to disorder of low spatial frequency, i.e. departure from strict periodicity, also under chiro-optical aspects. This study has restricted itself to a fixed parameter set; further studies may extend this, as well as apply more sophisticated models of distortion.

Moreover, it may prove worthwhile to look closely for low-frequency distortions (of any kind) in explaining the behaviour of complex natural PhC (beyond the most simple linear chirp layers found, e.g., in insect cuticles), or in enhancing the chiro-optical properties of designed PhC for technical applications.

## ACKNOWLEDGMENT

## REFERENCES

1. M. Saba, B. D. Wilts, J. Hielscher, and G. E. Schröder-Turk, Absence of circular polarisation in reflections of butterfly wing scales with chiral gyroid structure, Mater. Today: Proc. **1**, 193–208 (2014).
2. M. Saba, M. Thiel, M. D. Turner, S. T. Hyde, M. Gu, K. Große-Brauckmann, D. N. Neshev, K. Mecke, and G. E. Schröder-Turk, Circular dichroism in biological photonic crystals and cubic chiral nets, Phys. Rev. Lett. **106**, 103902 (2011).
3. S. Vignolini, N. A. Yufa, P. S. Cunha, S. Guldin, I. Rushkin, M. Stefik, K. Hur, U. Wiesner, J. J. Baumberg, and U. Steiner, A 3D optical metamaterial made by self-assembly, Adv. Mater. **24**, OP23–OP27 (2011).
4. K. Hur, Y. Francescato, V. Giannini, S. A. Maier, R. G. Hennig, and U. Wiesner, Three-dimensionally isotropic negative refractive index materials from block copolymer self-assembled chiral gyroid networks, Angew. Chem., Int. Ed. **50**, 11985–11989 (2011).
5. A. Demetriadou, S. S. Oh, S. Wuestner, and O. Hess, A tri-helical model for nanoplasmonic gyroid metamaterials, New J. Phys. **14**, 083032 (2012).

# Bio-inspired Surfaces with Nano-scale Structural Randomness: From Analysis to Fabrication and Applications.

**R. H. Siddique[1], Y. Donie[1], G. Gomard[1,2], and H. Hölscher[1,*]**

[1]Institute of Microstructure Technology (IMT), Karlsruhe Institute of Technology, Germany

[2]Light Technical Institute (LTI), Karlsruhe Institute of Technology (KIT), Germany

[*]corresponding author: Hendrik.Hoelscher@kit.edu

**Abstract**-Various nanostructured surfaces found in nature look random at first sight. A closer look, however, frequently reveals that randomness helps to improve useful properties ranging from self-cleaning to anti-reflection. Here, we present to two butterflies – a glasswing (*Greta oto*) and a black butterfly (*Pachliopta aristolochia*) serving as prototypes for nanostructured surfaces to improve the performance optical surfaces.

As its name suggests the glasswing butterfly (*Greta oto*) features transparent wings with remarkable low reflectance even for large view angles [1]. This omnidirectional anti-reflection behavior is caused by small nanopillars covering the transparent region of its wings. In difference to other anti-reflection coatings found in nature (moth eye, hawk moth wing, cicada wing) these pillars are not periodically arranged and feature a random height and width distribution. We analyze the specular and diffuse reflection of the surface and explain the concept of transparency by randomness. Angle-resolved spectroscopy reveal that the transparent parts of the Glasswing have a low reflection of 2% (two surfaces) in the visible regime for high radiation angles of 65° and almost 5% even at 85° of incidence angle. We simulate these omnidirectional anti-reflection properties by considering a Gaussian height distribution of the nanopillars as in the original glasswing. By varying size and distribution of the structures we demonstrate that the random distribution is the origin of the famous broadband omnidirectional anti-reflective property of *Greta oto*.

Such anti-reflective surfaces can be adapted to improve the light collection in solar cells or for efficient anti-reflection displays. The large-scale fabrication of the presented random height structures is feasible. In comparison to classical multi-layer broadband anti-reflection coatings which add up to at least 1 µm thickness to the surface, the glasswing structures are comparably thin as their mean height is only 500 nm and in addition they are hydrophobic.

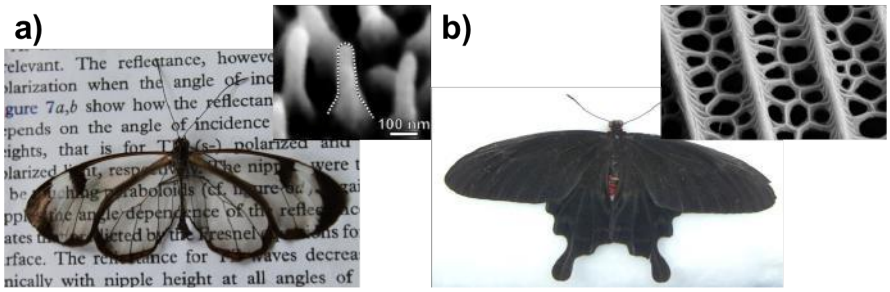



**Figure 1.** a) Photo of the glasswing butterfly *Greta oto* and the random nanopillars (inset) found on its wing membrane. b) The black butterfly *Pachliopta aristolochia* harvests light with its hierarchical structure (inset) of microridges and non-ordered nanoholes.

The hierarchical structures found in the scales of the black butterfly (*Pachliopta aristolochia*), consisting of disordered nano-holes assemblies surrounded by micrometer-spaced triangular ridges, are crucial for controlling light absorption and therefore the butterflies colors and thermoregulation properties. We studied numerically the light harvesting performance of these hierarchical structures. Those simulations, performed over the visible and near-infrared range, highlight broadband and omnidirectional anti-reflection properties mostly governed by light propagation within the nanoholes at short wavelengths, below the micro-ridges at large wavelengths, and through the whole structure at intermediate wavelengths. In addition, micro-reflectivity measurements demonstrate that light absorption increases in the wings parts where the nano-holes coverage is the highest, and can even exceed 95% over the whole visible range.

Based on these observations, efficient nano-patterned thin absorbers can be designed for photovoltaics applications. We show that using a lateral phase separation process enables to fabricate disordered nano-holes assemblies with tunable density and size distribution in a resist layer and onto large surfaces. This wet-processable and up-scalable technique was applied on a thin amorphous silicon layer, and the resulting pattern was transferred into the absorber by dry etching. The optical properties of the patterned absorbing layers will be discussed and compared to those derived from simulations in order to evaluate the potential of black butterfly inspired nanostructures for light collection and light trapping in thin film solar cells.

**REFERENCES**

1. Siddique, R. H., G. Gomard and H. Hölscher. “The role of random nanostructures for the omnidirectional anti-reflection properties of the glasswing butterfly”, *Nature Communications*, Vol. 6, 6909, 2015.

# Robustness and fragility of photonic bandgap in photonic amorphous diamond structures

**Shigeki Imagawa and Keiichi Edagawa***

Institute of Industrial Science, The University of Tokyo, Tokyo, Japan
*corresponding author, E-mail: edagawa@iis.u-tokyo.ac.jp

## Abstract

The robustness and fragility of the photonic bandgap (PBG) in disordered or modified photonic amorphous diamond (PAD) structures were investigated via numerical calculations. The original PAD has a rod-connected random network structure with a highly ordered local tetrahedral configuration, and it forms a sizable PBG. Our calculations indicated that the PBG of PAD is robust against the introduction of positional disorder that distorts the local tetrahedral configuration, but considerably fragile against the fragmentation of the network structure. PBG formation in a higher frequency region was found in a PAD structure of isolated dielectric spheres. Based on these findings, the physical origin of PBG formation in PADs has been discussed in light of the picture of dielectric and air bands.

## 1. Introduction

In 1987, Yablonovitch[1] and John [2] proposed the idea that a three-dimensional (3D) photonic band gap (PBG), in which electromagnetic wave propagation is forbidden in all directions, can be realized in artificial periodic dielectric structures, namely photonic crystals. A 3D PBG was predicted to enable 3D light confinement within a volume comparable to the wavelength without substantial loss, which is difficult to achieve with other media. Such strong light confinement is expected to lead to the development of novel types of efficient, minuscule optical devices [3].

Recently, photonic amorphous materials, i.e., artificial or natural amorphous structures of dielectrics, have gained growing attention [4-19] owing to their peculiar light transport properties and unique features related to isotropic PBG formation, noniridescent structural coloration, etc. With regard to PBG formation, Jin et al. [4] first reported the formation of a 2D PBG for transverse-magnetic (TM) polarization in a photonic amorphous structure consisting of dielectric cylinders in 2001. Since then, the formation of 2D TM PBGs have been reported in similar amorphous structures [5,6]. In general, the Bragg scattering of light due to lattice periodicity is believed to be the main origin of PBG formation in conventional photonic crystals; this should not be the case for photonic amorphous materials, which have no lattice periodicity. Instead, the evanescent coupling of Mie resonances of individual dielectric cylinders has been discussed as a plausible origin of the PBG formation in such photonic amorphous materials [5-7]. Recently, the formation of a sizable “complete” 2D PBG (PBG both for TM and TE polarizations) has been shown to be realizable in some 2D photonic amorphous structures [7].

The formation of a full 3D PBG has recently been demonstrated in a photonic amorphous structure via numerical calculations [16] as well as microwave and terahertz-wave transmission experiments [17,18]. This amorphous structure consists of a random network of dielectric rods with a diamond-like local tetrahedral configuration and is therefore named photonic amorphous diamond (PAD). It has been shown that the 3D PBG in PAD is clean with no trace of localized photonic states within it [17,19]. This indicates that strong light confinement is realizable in PAD as well as conventional photonic crystals, and it has actually been demonstrated numerically [19].

The physical origin of the PBG formation in PAD remains unclear. As described above, evanescent coupling of Mie resonances is a plausible explanation of the TM-gap formation in 2D photonic amorphous structures of isolated dielectric cylinders. However, such a mechanism appears not to work properly for the PBG formation in PAD that consists of a continuous network structure. In the present work, we modeled disordered or modified PAD structures and investigated the PBG formation in them to clarify the roles of the local order and connectivity of the network structure of PAD in the PBG formation.

## 2. Computational methods

The original PAD structure was constructed from a continuous random network (CRN) model that was originally developed to describe the atomic arrangement of amorphous Si or Ge [20-22]. The PAD structure was constructed by connecting tetrahedral bonds in the CRN structure with dielectric rods, as shown in Fig. 1. More specifically, the CRN structure constructed by Barkema and Mousseau [22] was used, which is characterized by a high degree of local regular-tetrahedron order and by the complete absence of lattice periodicity. This CRN

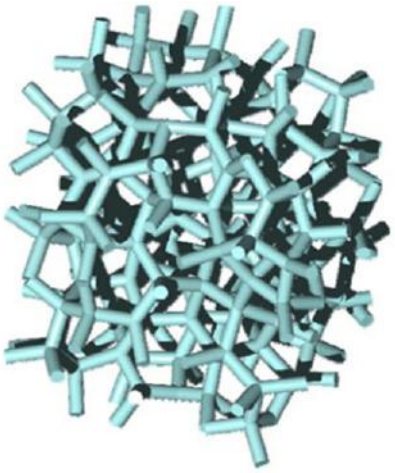


Figure 1: Computer graphics image of the original PAD.

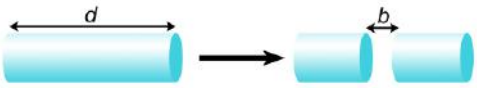



Figure 2: Schematic illustration of the construction of f-PADs. The central part with the length (*b*) has been removed from each rod having the length (d).

structure, and therefore the PAD structure, consists of a periodic arrangement of cubic supercells with a size of $(11.5d)^3$ (*d*: average bond length). The radius ($r_0$) of the rods was set as $r_0 / d = 0.26$, resulting in an air volume fraction of 78%. Detailed descriptions of the design of the original PAD structure have been given in our previous papers [16-18].

We constructed three types of disordered or modified PAD structures: positionally disordered (pd-), fragmented (f-), and dielectric-sphere (ds-) PADs. In pd-PADs, a random positional shift was given to each node of the network of the original PAD. The maximum distance (*s*) of the shift was set as *s*/*d*=0.1, 0.2, 0.3, and 0.4. That is, the distance of the shift was randomly chosen within the range [0, *s*], while the direction of the shift was randomly chosen from every $4\pi$ direction. Here, the network topology remains unchanged because *s*/*d*<0.5; fourfold connectivity is preserved at every node in the network structure. The radial distribution functions (RDFs) were calculated for the node points in pd-PADs. Here, the RDF is defined as the average point density in the spherical shell $(r, r+dr)$ around an arbitrarily selected node point. In f-PADs, we removed the central part with the length (*b*) from every rod, because of which the network was fragmented (Fig.2). Here, we set *b*/*d*=0.1 and 0.2.

Finally, in ds-PADs, we arranged dielectric spheres with the radius (*u*) at the node points of the network of the original PAD. Here, we set *u*/*d*=0.45 0.50, and 0.55, for which the spheres are isolated, in contact, and overlapped,

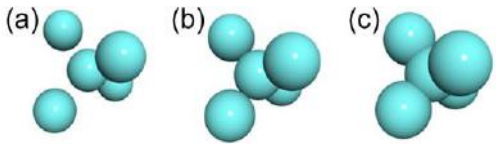



Figure 3: Local structures of ds-PADs with *u*/*d*=0.45 (a), 0.50 (b), and 0.55 (c), where the spheres are isolated, in contact, and overlapped, respectively.

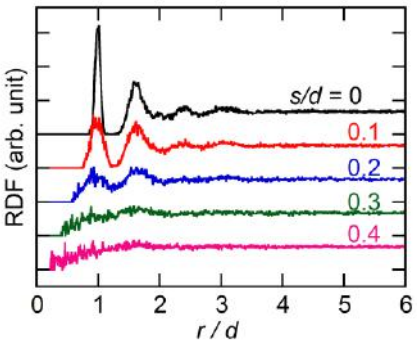



Figure 4: Radial distribution functions calculated for the original PAD (*s*/*d*=0), and pd-PADs (*s*/*d*=0.1, 0.2, 0.3 and 0.4).

respectively, as shown in Fig. 3. For comparison, crystalline counterparts of ds-PADs, i.e., dielectric-sphere (ds-) photonic crystalline diamonds (PCDs) were also constructed, where we arranged dielectric spheres at the lattice points in the crystalline diamond structure.

The spectral intensities, which represent the photonic density of states (PDOS), and the eigenmodes were calculated using a finite-difference time-domain (FDTD) spectral method originally developed by Chan et al. [23]. In this method, we start from a random electromagnetic field and calculate its time evolution. The time evolutions at each position is then Fourier transformed into the frequency domain to obtain the PDOS and eigemodes. For pd-, f-, and ds-PAD structures, the calculations were made for a periodic supercell structure of size $(11.5d)^3$. On the other hand, for ds-PCDs, we used a crystalline diamond structure with a fictitious supercell $(5a_0)^3 = (11.5d)^3$, where $a_0 = 4d/\sqrt{3}$ denotes the lattice constant of the crystalline diamond. The use of the fictitious supercell structure for ds-PCDs enables us to compare the results obtained under exactly the same conditions for ds-PADs and ds-PCDs. For the details of the calculation method, we followed Refs. 17 and 18. For ds-PCDs, the photonic band structure was also calculated via a plane-wave expansion method using "BandSOLVE" (RSoft Design Group, Inc.).

## 3. Results

### 3.1. Positionally disordered PADs

Figure 4 shows the RDFs calculated for the original PAD (*s*/*d*=0), and pd-PADs (*s*/*d*=0.1, 0.2, 0.3 and 0.4). In the RDF for *s*/*d* =0, the first peak at $r = d$ is very sharp with a full-

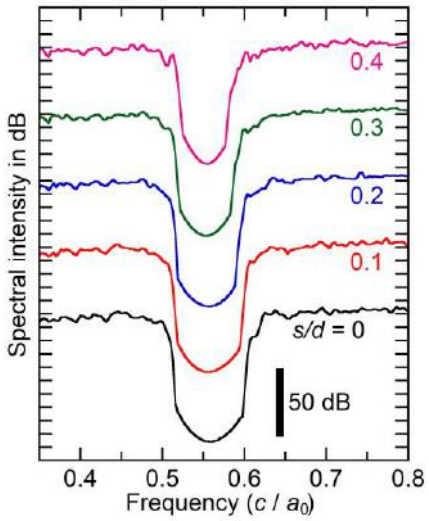



Figure 5: Spectral intensities calculated for the original PAD (*s*/*d*=0), and pd-PADs (*s*/*d*=0.1, 0.2, 0.3 and 0.4).

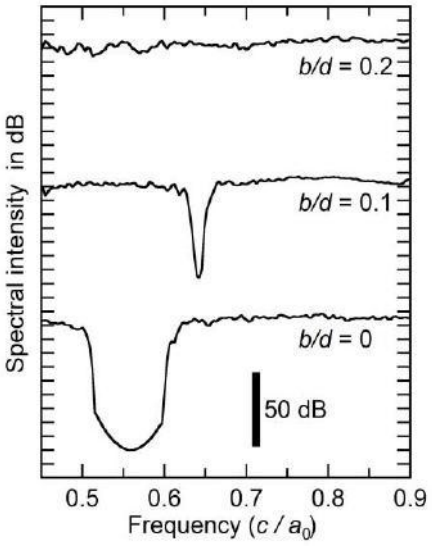



Figure 6: Spectral intensities calculated for the original PAD (*b*/*d*=0), and f- PADs (*b*/*d*=0.1 and 0.2).

width-at-half-maximum (FWHM) value of approximately $0.1d$. This peak represents the bond-length distribution, and its sharpness indicates the presence of a high local order with almost the same lengths for all the bonds. The second peak at $r \approx 1.7d$ is also relatively sharp but the subsequent peaks at $r \approx 2.4d$ and $3d$ are very broad and only marginally observed. Then, no peaks can be detected in the range $r > 3.5d$. This indicates that the original PAD has no order in the range beyond $r \approx 3.5d$. It should be noted that the range $r > 3.5d$ corresponds to $r > 1.5a_0$. This verifies the fact that the original PAD has no trace of the diamond-lattice periodicity.

In Fig. 4, as the value of *s* increases, i.e., as the degree of disorder increases, the first and second peaks become smaller and broader. For *s*/*d*=0.3 and 0.4, they disappear almost completely, indicating the loss of local order.

Figure 5 presents the spectral intensities calculated for the original PAD (*s*/*d*=0), and pd-PADs (*s*/*d*=0.1, 0.2, 0.3 and 0.4), where the frequency is in units of ($c / a_0$) (*c*: speed of light). In all the calculations, the refractive index of dielectric rods was set as *n*=3.6. In all the spectra, large decreases in intensity are clearly seen, corresponding to 3D PBGs. The ratios of PBG width ($\Delta f$) to the midgap frequency ($f_c$) were estimated to be $\Delta f / f_c \approx 18.9\%$, 16.7%, 16.2%, 15.2% and 13.7% for *s*/*d*=0, 0.1, 0.2, 0.3, and 0.4, respectively. It is noteworthy here that sizable 3D PBGs survive even in pd-PADs with *s*/*d*=0.3 and 0.4, in which the local order appears to be lost almost completely, as shown in the RDFs in Fig. 4. In addition, the PBG depths at $f_c$ for *s*/*d*=0.3 and 0.4 are approximately 80 dB, which is not significantly different from those for the original PAD with *s*/*d*=0. From these facts, we can conclude that the PBG is considerably robust against positional disorder that distorts the local tetrahedral configuration in the network PAD structure.

### 3.2. Fragmented PADs

Figure 6 shows the spectral intensities calculated for f-PADs with *b*/*d*=0.1 and 0.2, which are compared with that for the original PAD (*b*/*d*=0). Here, the refractive index of dielectric rods was set as *n*=3.6. In contrast to the results for pd-PADs in Fig. 5, the 3D PBG is drastically reduced in the spectra of f-PADs. In the spectrum for *b*/*d*=0.1, a small 3D PBG with $\Delta f / f_c \approx 4.8\%$ can be seen at $f_c \approx 0.64c / a_0$. Here, the upward shift of the PBG position from $f_c \approx 0.56c / a_0$ for the original PAD can be attributed to the decrease in the volume fraction of dielectric parts, which resulted in a decrease in the average refractive index of the structure. In the spectrum of *b*/*d*=0.2, no trace of PBG can be detected. These results indicate the considerable fragility of PBG against the fragmentation of the network structure of PAD.

### 3.3. Dielectric-sphere PADs and PCDs

Figure 7 shows the spectral intensities calculated for ds-PADs (black) and ds-PCDs (blue) with *u*/*d*=0.45, 0.50, and 0.55. Here, the refractive index of dielectric rods was set as *n*=4.0. In the spectra, decreases of intensity by >70dB are observed, indicating the formations of 3D PBGs. Here, we notice that the PBG positions in ds-PADs are in good agreement with those in the corresponding ds-PCDs. For *u*/*d*=0.45, we can observe a large PBG at $f_c \approx 0.72c / a_0$ in each spectrum of ds-PAD and PCD. For *u*/*d*=0.50, we have a large PBG at $f_c \approx 0.46c / a_0$, a relatively small one at $f_c \approx 0.65c / a_0$ for ds-PCD, and a small one at $f_c \approx 0.65c / a_0$ for ds-PAD. Finally, for *u*/*d*=0.55, a large

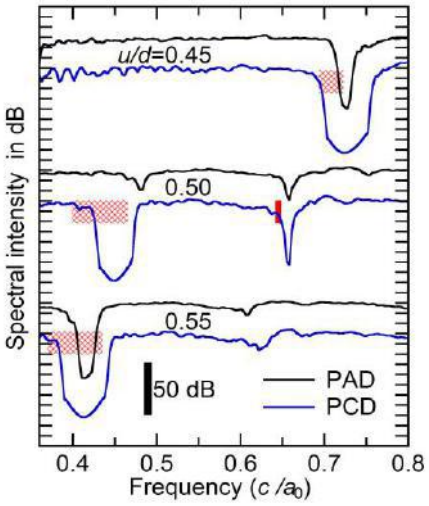



Figure 7: Spectral intensities calculated for ds-PADs (black) and ds-PCDs (blue) with $u/d$=0.45 0.50, and 0.55.

PBG is observed at $f_c \approx 0.41c/a_0$ for each of the two spectra.

In Figs 8(a)-(c), photonic band structures calculated for ds-PCDs with $u/d$=0.45, 0.50, and 0.55, respectively, are presented, where the red strips indicate the positions of complete 3D PBGs. These frequency ranges are also shown by the red strips in Fig. 7. Here, we have two different types of PBGs: the PBG between the second and third bands (2-3 gap) and that between the eighth and ninth bands (8-9 gap). For $u/d$=0.55 in Fig. 8(c), we have a large 2-3 gap at $f_c \approx 0.40c/a_0$. For $u/d$=0.50 in Fig. 8(b), a large 2-3 gap is again seen, but its position has shifted slightly upward. Here, an 8-9 gap is on the verge of opening (red broken line); the two bands are barely in contact at the point L. This frequency is indicated by a red vertical line in the corresponding spectrum in Fig. 7, which agrees with the position of the decrease in the spectral intensity. Finally for $u/d$=0.45 in Fig. 8(a), the 2-3 gap is closed, and the 8-9 gap is opened, where the position of the 8-9 gap has shifted slightly upward from the frequency at which the two bands are in contact in Fig.8 (b). Here, the slight upward shifts of the 2-3 (8-9) gap positions with decreasing $u/d$ value are attributable to the decrease in the volume fraction of dielectric parts in the structure, which has resulted in a decrease in the average refractive index of the structure.

## 4. Discussion

In previous papers [17,24], we have discussed the formation mechanism of PBG in PAD. In this section, we first review it.

The physical origin of PBG formation in conventional photonic crystals is often explained in terms of the picture of dielectric and air bands [25]. As an example, let us consider a simple one-dimensional photonic crystal consisting of alternately stacked dielectric and air layers. At the edge of

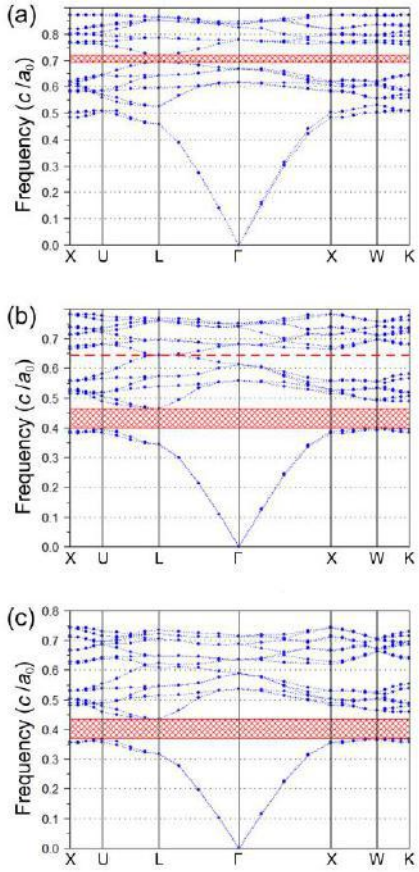



Figure 8: Photonic band structures calculated for ds-PCDs with $u/d$=0.45 (a), 0.50 (b), and 0.55 (c). The positions of complete 3D PBGs are indicated by red strips.

the Brillouin zone at $k = \pi/a$ ($a$: period), the eigenstates are stationary electromagnetic waves with a wavelength of $2a$. We have two ways to position such a wave to conform to the symmetry of the structure: in one way, the maximum points of the electric field intensity occur in dielectric layers, and in the other, they occur in air layers. The eigenfrequency of the former should be lower than that of the latter, leading to the formation of a PBG.

To examine whether this picture can also be applied to PAD, we previously evaluated the concentration factor (CF) of the electric field intensity $|\mathbf{E}(\mathbf{r})|^2$ in the air region for the eigenstates in the original PAD [17]. Here, CF is defined as

$$\mathrm{CF} \equiv \frac{\int_{V_{air}} |\mathbf{E}(\mathbf{r})|^2 \, d\mathbf{r}}{\int_{V_{tot}} |\mathbf{E}(\mathbf{r})|^2 \, d\mathbf{r}} \quad , \qquad (1)$$

where $V_{air}$ and $V_{tot}$ represent the air volume and total volume, respectively. For comparison, CF has also been evaluated for a rod-connected PCD, which was constructed

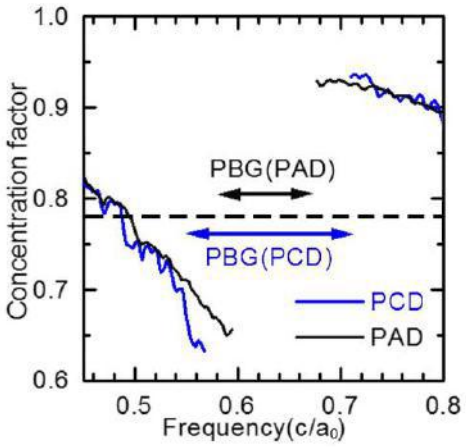



Figure 9: Frequency dependences of the concentration factor of the electric field for rod-connected PCD and PAD.

by connecting tetrahedral bonds in the crystalline structure of diamond with dielectric rods. We set the rod radius as $r_0 = 0.26d$ and the refractive index of rods as $n = 3.0$. The results are reproduced here in Fig. 9. If the electric field is distributed evenly for the dielectric and air regions, CF should equal the volume fraction of the air part, that is, 78%. In Fig. 9, at the lower-band top, CF is approximately 65% for both PAD and PCD. As the frequency decreases, CF increases and approaches the air-volume fraction of 78%. On the other hand, at the higher-band bottom, CF is approximately 93%, which is much higher than the volume fraction value. These results clearly show that the picture of dielectric and air bands can be applied not only to PCD but also to PAD, despite the complete absence of lattice periodicity.

In 3D photonic crystals, the structures in which both dielectric and air regions form connected and percolating networks are known to favor PBG formation [9,26-28]. The importance of the connected network structure for PBG fomation should be related to the vector nature of electromagnetic fields; in order for the field to be confined in the dielectric or air region to realize a dielectric or air band, a connected network should be favorable to accommodate the continuous field lines [24,25]. In fact, we have confirmed by examining the eigenstates at the lower-band top in our PCD that the continuous field lines are neatly accommodated in the rods connecting nodes in the dielectric network.

Our PAD has such a network structure, which should play a similar role in the realization of dielectric and air bands, leading to PBG formation. This is consistent with the considerable fragility of PBG against the fragmentation of the network structure of PAD shown in Sec. 3.2. When the dielectric network has been segmented, the field lines, which had been accommodated in the network before the segmentation, should be forced to penetrate the air regions. This should increase the eigenfrequency at the lower-band top, leading to the closing of the PBG.

The results for pd-PADs in Sec. 3.1 indicate that local structural order is much less important than network connectivity in PBG formation. With the introduction of positional disorder, the local tetrahdral configurations should be distorted. In particular, they should be severly distorted in pd-PADs with $s/d$=0.3 and 0.4, as evidenced by their RDFs in Fig. 4. Nevertheless, sizable 3D PBGs survive in these structures, exhibiting a high tolerance for the local distortion. This is advantageous for applications because a high precision is not necessary for fabricating a PAD to form a PBG. Here, it should be noted that such pd-PADs keep the fourfold connectivity of the network structure. In previous papers [16,19], we have shown that a localized state is formed when a rod has been removed from the PAD network structure. Here, the removal of a rod creates two threefold nodes in the network, and a localized state is formed in the space between them. The eigenfrequency of the localized state is located within the PBG. Therefore, such threefold nodes, when introduced in the fourfold network, should close the PBG, if their density is large.

It should be interesting to know what happens if the nodes in the network are entirely threefold or fivefold. Therefore, we constructed threefold and fivefold random network structures and investigated the PBG formation in them. Preliminary results have shown that they exhibit a signature of PBG formation, but the PBGs are much smaller and shallower than those in the PAD with a fourfold network structure. This result indicates the importance of the fourfold connectivity of the network structure in the formation of PBG.

In Sec. 3.3, we presented the results for ds-PADs and ds-PCDs. Here, let us first examine the results for ds-PCDs. In the ds-PCD with $u/d$=0.55, dielectric spheres are overlapped; dielectric regions are connected to form a network structure. Therefore, this structure resembles a rod-connected PCD, for which photonic band structure calculations have previously been made [17,26,28]. The calculations have indicated that the rod-connected PCD forms a large 3D PBG between the second and third bands, which agrees with our result for the ds-PCD with $u/d$=0.55. For ds-PCDs with $u/d \le 0.5$, where dielectric spheres are in contact or isolated, calculations have previously been performed by other groups [29-31]. Moroz [31] reported the results for $u/d$=0.50 and 0.40 with various refractive indices, $n$, of rods. Here, for $u/d$=0.50 with $n$=4.0, a 2-3 gap and an 8-9 gap are simultaneously formed, and for $u/d$=0.40 with n=4.0, where dielectric sphperes are isolated, the 2-3 gap gets closed while the 8-9 gap grows considerably. These results are in agreement with our calculations.

It was shown in Fig. 7 that the PBG positions in ds-PADs agree well with those in the corresponding ds-PCDs. This fact suggests that the origin of the formation of each PBG in ds-PADs should be the same as that of the corresponding PBG in ds-PCDs. That is, the PBG at

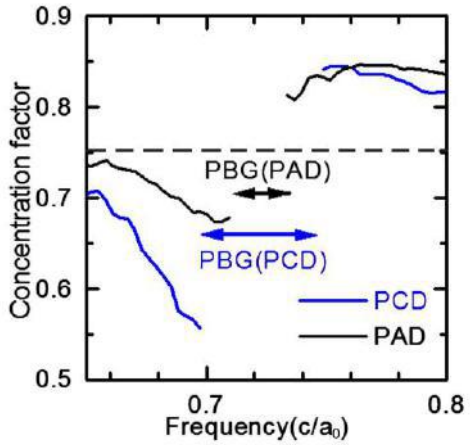



Figure 10: Frequency dependences of the concentration factor of the electric field for dielectric-sphere PCD and PAD.

$f_c \approx 0.41c/a_0$ for the ds-PAD with $u/d$=0.55 that corresponds to the 2-3 gap for the ds-PCD with $u/d$=0.55 should originate from the realization of dielectric and air bands due to the fourfold connected network structure. On the other hand, the PBG at $f_c \approx 0.72c/a_0$ for the ds-PAD with $u/d$=0.45 corresponds to the 8-9 gap for the ds-PCD with $u/d$=0.45, and the origin of the PBG formation should be different from that for the ds-PAD with $u/d$=0.55.

To investigate the formation mechanism of PBGs in a high-frequency region in the PAD and PCD structures of isolated dielectric spheres, we evaluated the CF for the ds-PAD and ds-PCD with $u/d$=0.45, and the results are shown in Fig. 10. For both structures, the tendency of dielectric and air bands is observed: CF values are smaller and larger than the average value of 75% at the lower band top and at the higher band bottom, respectively. In particular, for the PCD of isolated dielectric spheres, the difference between the CF values of the higher band bottom and the lower band top is almost the same as that for the rod-connected network PCD in Fig. 9.

Figures 11(a) and (b) show 2D sections of typical electric-field profiles at around an isolated dielectric sphere for the eigenstates at the lower band top and the higher band bottom, respectively, for the ds-PCD with $u/d$=0.45. At the lower band top, the electric-field intensity is well concentrated on the dielectric sphere. However, it is not on the entire sphere but only on the outside of the central part. Correspondingly, at the higher band bottom, the electric field is expelled from the region where the field intensity is high at the lower band top. In the high-field-intensity region at the lower band top in Fig. 11(a), the direction of **E** has been confirmed to be mostly perpendicular to the radial direction of the dielectric sphere. As a result, the field lines should be mostly closed within the dielectric sphere. This is the reason why the field intensity is well concentrated on the dielectric parts at the lower band top, even in a structure

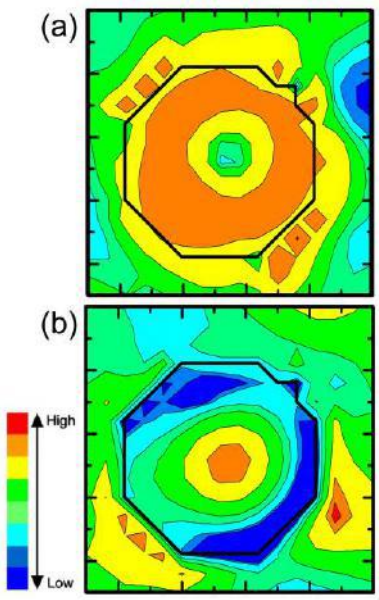



Figure 11: 2D sections of typical electric-field profiles around an isolated dielectric sphere for the eigenstates at the lower band top (a) and at the higher band bottom (b) for the ds-PCD with $u/d$=0.45.

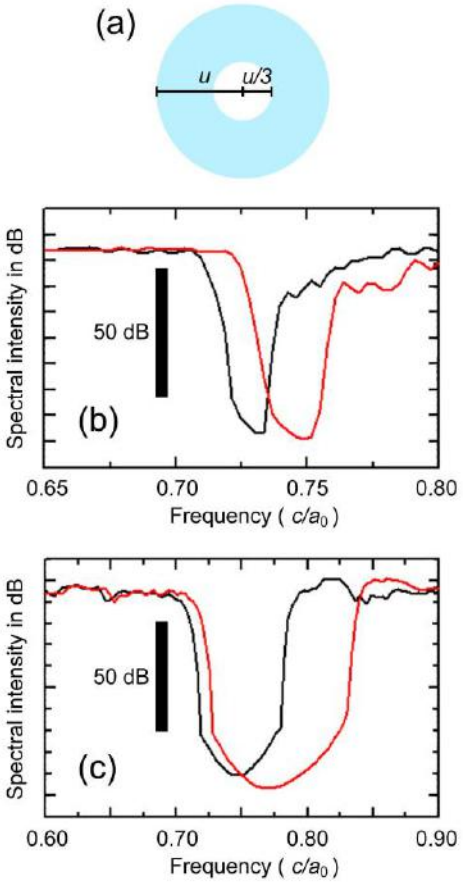



Figure 12: (a): Schematic illustration of the hollow dielectric sphere that constitutes hds-PAD and PCDs; (b): Spectral intensities calculated for ds-PAD (black) and hds-PAD (red); (c): those for ds-PCD (black) and hds-PCD (red). n=4.0 is used for all the calculations.

consisting of isolated dielectric parts. This is in sharp contrast to the field pattern at the lower band top in the rod-connected PCD or PAD network, in which the field lines pass along the rods and travel from node to node in the network. Such a difference in the field pattern between the rod-connected and isolated-dielectric-sphere structures should cause the difference in the PBG position. When the characteristic length of the spatial modulation in the field pattern is long (short), the corresponding frequency should be low (high).

The electric-field patterns in Figs. 11 (a) and (b) suggest that the CF contrast between the lower band top and the higher band bottom would be enhanced and the PBG would get widened, if the central part of the dielectric sphere is converted to air. To confirm this, we constructed PCD and PAD structures consisting of hollow dielectric spheres (hds-PCD and hds-PAD), and calculated their spectral intensities. Here, the hollow dielectric spheres have an outer radius of $u$=0.45$d$ and the inner radius of $u$/3, as shown in Fig. 12(a). The spectral intensities calculated for ds- and hds-PADs and those for ds- and hds-PCDs are shown in Figs. 12 (b) and (c), respectively. Here, $n$=4.0 is used for all the calculations. As expected, the PBG sizes have considerably increased: $\Delta f / f_c \approx 5.5$ and 4.7% for hds-PAD and ds-PAD, and $\Delta f / f_c \approx 16.2$ and 11.5% for hds-PCD and ds-PCD, respectively.

## 5. Conclusions

The robustness and fragility of PBG in disordered or modified PAD structures were investigated via numerical calculations. The original PAD has a rod-connected random network structure with a highly ordered local tetrahedral configuration, and it forms a sizable PBG. We constructed three types of disordered or modified PAD structures: positionally disordered (pd-), fragmented (f-), and dielectric-sphere (ds-) PADs. Photonic-density-of-states calculations for these structures indicated that the PBG of PAD is robust against the introduction of positional disorder that distorts the local tetrahedral configuration, but considerably fragile against the fragmentation of the network structure.

The picture of dielectric and air bands in conventional photonic crystals has been shown to be applicable to the PBG formation in the rod-connected original PAD as well. Here, in the electric-field pattern at the lower band top, the field lines pass along the rods and travel from node to node in the network. This can explain the considerable fragility of PBG against the fragmentation of the network. That is, when the dielectric network has been segmented, the electric-field lines, which had been accommodated in the network before the segmentation, should be forced to penetrate the air regions, increasing the eigenfrequency at the lower-band top to close the PBG.

PBG formation in a higher frequency region was observed in a PAD structure of isolated dielectric spheres. The picture of dielectric and air bands is applicable here as well. In this case, the electric field lines in the field pattern at the lower band top are mostly closed within the dielectric sphere. This is the reason why the field intensity is well concentrated on the dielectric parts at the lower band top, even in a structure consisting of isolated dielectric parts. The difference in the characteristic length of the spatial modulation in the field pattern between the rod-connected and isolated-dielectric-sphere structures should cause the difference in the PBG position. The PBG was shown to get widened by use of hollow dielectric spheres instead of solid ones.

## Acknowledgements

We thank M. Notomi of NTT Co., Ltd. for valuable comments and discussion. We acknowledge the help of Y. Kamimura in manuscript preparation. This work was supported by a Grant-in-Aid for Scientific Research (B) (24360024) from the Ministry of Education, Culture, Sports, Science and Technology (MEXT).

## References

[1] E. Yablonovitch, Phys. Rev. Lett. **58**, 2059 (1987).

[2] S. John, Phys. Rev. Lett. **58**, 2486 (1987).

[3] M. Notomi, Rep. Prog. Phys. **73**, 096501 (2010).

[4] C. Jin, X. Meng, B. Cheng, Z. Li and D. Zhang, Phys. Rev. B**63**, 195107 (2001).

[5] H. Miyazaki, M. Hase, H.T. Miyazaki, Y. Kurokawa and N. Shinya, Phys. Rev. B**67**, 235109 (2003).

[6] C. Rockstuhl, U. Peschel and F. Lederer, Opt. Lett. **31**, 1741 (2006).

[7] M. Florescu, S. Torquato and P.J. Steinhardt, PNAS, **106**, 20658 (2009).

[8] C. Rockstuhl and F. Lederer, Phys. Rev. B**79**, 132202 (2009).

[9] S.F. Liew, J.K. Yang, H. Noh, C.F. Schreck, E.R. Dufresne, C.S. O'Hern and H. Cao, Phys. Rev. A**84**, 063818 (2011).

[10] L.F. Rojas-Ochoa, J.M. Mendez-Alcaraz, J.J. Saenz, P. Shurtenberger and F. Scheffold, Phys. Rev. Lett. **93**, 073903 (2004).

[11] G.M. Conley, M. Burresi, F. Pratesi, K. Vynck and D.S. Wiersma, Phys. Rev. Lett. **112**, 143901 (2014).

[12] L.S. Froufe-Perez, M. Engel, P.F. Damasceno, N. Muller, J. Haberko, S.C. Glotzer and F. Scheffold, arXiv: 1602.01002v1.

[13] J. Sun, B. Bhushan and J. Tong, RSC Advances **3**, 14862 (2013).

[14] Y. Takeoka, J. Mater. Chem. **22**, 23299 (2012).

[15] H.W. Yin, B.Q. Dong, X.H. Liu, T.R. Zhan, L. Shi, J. Zi, and E. Yablonovitch, Proc. Natl. Acad. Sci. USA **109**, 10798 (2012).

[16] K. Edagawa, S. Kanoko and M. Notomi, Phys. Rev. Lett. **100**, 013901 (2008).

[17] S. Imagawa, K. Edagawa, K. Morita, T. Niino, Y. Kagawa and M. Notomi, Phys. Rev. B**82**, 115116 (2010).

[18] Y. Komiyama, H. Abe, Y. Kamimura and K. Edagawa, Appl. Phys. Lett. **108**, 191110 (2016).

[19] S. Imagawa, K. Edagawa and M. Notomi, Appl. Phys. Lett. **100**, 151103 (2012).

[20] D.E. Polk, J. Non-Cryst. Solids **5**, 365 (1971).

[21] F. Wooten, K. Winer and D. Weaire, Phys. Rev. Lett. **54**, 1392 (1985).

[22] G. T. Barkema and N. Mousseau, Phys. Rev. B**62**, 4985 (2000).

[23] C.T. Chan, Q.L. Yu, and K.M. Ho, Phys. Rev. B**51**, 16635 (1995).

[24] K. Edagawa, Sci. Technol. Adv. Mater. **15**, 034805 (2014).

[25] J.D. Joannopoulos, S.G. Johnson, J.N. Winn and R.D. Meade, *Photonic Crystals–Molding the Flow of Light (Princeton Univ. Press, 2008)*

[26] M. Maldovan and E. L. Thomas, Nature Mater. **3**, 593 (2004).

[27] E.N. Economou and M.M. Sigalas, Phys. Rev. B**48**, 13434 (1993).

[28] C.T. Chan, S. Datta, K. M. Ho and C.M. Soukoulis, Phys. Rev. B **50**, 1988 (1994).

[29] K.M. Ho, C.T. Chan, and C.M. Soukoulis, Phys. Rev. Lett. **65**, 3152–3155 (1990).

[30] H.S. Sozuer, J.W. Haus, and R. Inguva, Phys. Rev. B**45**, 13962–13972 (1992).

[31] A. Moroz, Phys. Rev. B**66**, 115109 (2002).

# Metamaterials for Magnetic Resonance Imaging

# Metamaterial-based Resonators for Magnetic Resonance Imaging

**A. P. Slobozhanyuk**[1,2,*]
[1]The Australian National University, Australia
[2]ITMO University, Russia
[*]corresponding author: aleksei.slobozhaniuk@anu.edu.au

**Abstract**-In this contribution, we will discuss potential applications of metamaterials resonators for magnetic resonance imaging (MRI). More concrete, we reveal that the unique properties of ultrathin metasurface resonators can substantially improve MRI characteristics. We place a metasurface formed by an array of metallic wires inside a scanner under the studied object and achieve a substantial enhancement of the radiofrequency magnetic field by means of subwavelength near-field manipulation with metasurface, also allowing to improve signal-to-noise ratio (SNR) and image resolution.

Metamaterials are artificial composite materials that exhibit electromagnetic properties, which cannot be found in naturally available materials [1]. The extensive fundamental research in the area of metamaterials in the past 16 years has created a foundation for the next stage of developing metamaterial applications. During recent years, metamaterials were successfully applied in many areas, e.g. as building blocks for creating invisibility cloaks [2], as a coating material for cooling buildings [3] and as highly efficient tunable satellite antennas [4]. The use of metamaterials for improving the performance of MRI has also been suggested [5-7]. In particular, it was shown that electromagnetic endoscopes formed by arrays of metallic wires can be employed in order to guide the signal emitted by an object from inside the MRI machine to the external detector [7]. This approach allows using simpler and cheaper detectors. Furthermore, it was shown that Swiss-roll arrays [5], and split-ring resonator arrays with negative magnetic permeability [6] can be used as matching devices between the patient and the receiving coils.

However, we believe that the full potential of the metamaterials for MRI applications is far from being uncovered. In contrast to previous works which considered the transmission of radio frequency fields [5-7], here we report a novel concept how to effectively use resonators based on metamaterials in order to manipulate, enhance and redistribute electromagnetic near fields [8]. In particular, we utilize metasurfaces, two-dimensional metamaterials which were studied in various contexts [9-11] and which have shown some spectacular effects in both linear [10] and nonlinear regimes [11]. We employ a metasurface created by an array of wires placed under an object inside a MRI scanner, and demonstrate a giant enhancement of the SNR by means of subwavelength manipulation with the metasurface resonances, thus strongly increasing the scanner sensitivity.

The enhancement of the signal with addition of metamaterial is due to the resonant coupling to electromagnetic modes of the metasurface. The length of each wire is tuned in order to match the half a wavelength at the operating frequency of 1.5 T MRI machine, which corresponds to the first eigenstate of metasurface resonator (or Fabry-Pérot regime). For the first Fabry-Pérot mode the highest magnetic field is localized in the middle part of the surface and the electric field is localized near the edges of the wires [13]. Hence, the SNR increase can be explained by the radiofrequency magnetic field enhancement on the wire metasurface. In particular, the SNR ratio is determined as a ratio of the radiofrequency magnetic field in the

scanned region (a signal) to the square root of the absorbed power (a noise) [12]. The resonance mode of the metasurface leads not only to the overall enhancement of both magnetic field and noise in the phantom, but it pins also the magnetic field to the scanned region suppressing the electric field and, hence, the absorbed power in this region. Such a relative redistribution of the spatial fields leads to a growth of SNR.

To summarized, we have realized a unique metamaterial resonator in the form of a wire metasurface [8]. The resonance mode of the wire array is spectrally tuned to the nuclear magnetic resonance. This allows us to observe a substantial enhancement of the signal-to-noise ratio enabling a reduction of the MRI scanning time and also obtain higher image resolutions. Also it provides an opportunity to locally control the electric and magnetic fields near the object. There exists quite a number of possible implementations of metasurfaces for medical examinations inspired by the concepts of smart clothes and wearable electronics. Our proposal bridges a gap between the fundamental ideas of metamaterials and applications spanning the research fields from electromagnetic engineering to medical diagnostics.

**Acknowledgements**, This work was supported by Russian Science Foundation (Project No. 15-19-20054) and the Australian Research Council..

**REFERENCES**

1. Engheta, N. and R. W. Ziolkowski, *Metamaterials: Physics and Engineering Explorations*, Wiley-IEEE Press, Piscataway, NJ, 2006.
2. Fleury, R., F. Monticone and A. Alù, "Invisibility and Cloaking: Origins, Present, and Future Perspectives", *Phys. Rev. Appl*., Vol. 4, 037001, 2015.
3. Raman, A. P., M. A. Anoma, L. Zhu, E. Rephaeli and S. Fan, "Passive radiative cooling below ambient air temperature under direct sunlight", *Nature*, Vol. 515, pp. 540–544, 2014.
4. Lier, E., D. H. Werner, C. P. Scarborough, Q. Wu and J. A. Bossard, "An octave-bandwidth negligible-loss radiofrequency metamaterial", *Nat. Mater*., Vol. 10, pp. 216–222, 2008.
5. Wiltshire, M. C. K., J. B. Pendry, I. R. Young, D. J. Larkman, D. J. Gilderdale, and J. V. Hajnal, "Microstructured magnetic materials for rf flux guides in magnetic resonance imaging", *Science*, Vol. 291, pp. 849-851, 2001.
6. Freire, M. J., L. Jelinek, R. Marques, and M. Lapine, "On the applications of metamaterial lenses for magnetic resonance imaging", *J. Magn. Reson.*, Vol. 203, pp. 81- 90, 2010.
7. Radu, X., D. Garray, and C. Craeye, "Toward a wire medium endoscope for MRI imaging", *Metamaterials*, Vol. 3, pp. 90- 99, 2009.
8. Slobozhanyuk, A. P., et al., "Enhancement of Magnetic Resonance Imaging with Metasurfaces", *Adv. Materials*, 10.1002/adma.201504270, 2016.
9. Holloway, C. L., E. F. Kuester, J. A. Gordon, J. O'Hara, J. Booth, and D. R. Smith, "An overview of the theory and applications of metasurfaces: The two dimensional equivalents of metamaterials" *IEEE Antennas and Propogat. Mag*., Vol. 54, pp. 10-35, 2012.
10. Yu, N., P. Genevet, M. A. Kats, F. Aieta, J.-P. Tetienne, F. Capasso and Z. Gaburro, "Light propagation with phase discontinuities: Generalized laws of reflection and refraction", *Science*, Vol. 334, pp. 333-337, 2011.
11. Lee, J., et al., "Giant Nonlinear Response from Plasmonic Metasurfaces Coupled to Intersubband Transitions", *Nature*, Vol. 511, pp. 65-69, 2014.
12. Haacke, E. M., R. W. Brown, M. R. Thompson, R. Venkatesan, *Magnetic Resonance Imaging: Principles*

*and Sequence Design*, Wiley, New York, 1999.

13. Lemoult, F., G. Lerosey, J. d. Rosny, M. Fink, "Resonant metalenses for breaking the diffraction barrier", *Phys. Rev. Lett*., Vol. 104, pp. 203901, 2010.

# Parallel Transceive for 7T MRI with Mushroom Electromagnetic Bandgap Structures

**A.A. Hurshkainen**[1], **T.A. Derzhavskaya**[1], **S.B. Glybovski**[1], **I.J. Voogt**[2], **I.V. Melchakova**[1], **C.A.T. van den Berg**[2], **and A.J.E. Raaijmakers**[2]

[1]ITMO University, 197101 St. Petersburg, Russia
[2]University Medical Center Utrecht, 3584 CX, Netherlands
s.glybovski@metalab.ifmo.ru

**Abstract**— We experimentally characterize performance of so-called mushroom-type electromagnetic bandgap structures in parallel transceive body array coils for 7T MRI. A sample structure is manufactured and used for suppression of mutual coupling between two neighboring closely-spaced dipole elements of a six-element array. By measurements on a research MRI machine we study the decoupling effect under the MRI bore conditions as well as $B_1^+$ field redistribution due to the sample. We show that the structure, though reducing inter-element coupling, does not negatively affect the $B_1^+$ level and the penetration depth.

## 1. INTRODUCTION

Multi-transmit coils driven with a number of independent channels allow radio frequency field optimization (RF shimming), which partially solves the problem of a destructive interference inherent to ultrahigh field MRI. The increased number of channels improves efficiency of parallel transmit, but reduces the inter-element separation, which raises mutual coupling of neighboring elements. For conventional antenna elements (e.g. magnetic loops or TEM microstrip coils) several efficient decoupling techniques have been developed [1, 2, 3]. However, it was recently demonstrated that also dipole antennas may be very suitable low SAR array elements for 7T MRI [4]. For this new type of coils decoupling techniques conventional for MRI become useless. Therefore, approaches suitable for dipole decoupling need to be tested for MRI applications. Meanwhile, in [5] it was proposed to improve 7T coils with so-called electromagnetic bandgap (EBG) metasurfaces, that are periodic two-dimensional arrays of structured inclusions with sub-wavelength dimensions and periodicity capable of near-field manipulation. EBG structures have been successfully employed in the microwave range to decouple antenna array elements [6, 7]. In this work we experimentally study decoupling of dipole elements of a parallel transceive body array coil for 7T MRI and $B_1^+$ field redistribution due to a manufactured EBG sample.

## 2. EXPERIMENT: RESULTS AND CONCLUSION

In order to decouple two of six fractionated dipole elements [4] of a body array coil we have manufactured a finite sample of the "mushroom" high-impedance metasurface, originally proposed in [6]. Metasurfaces of this type suppress propagation of all surface modes in a particular frequency range. This mechanism is responsible for decoupling capabilities. The manufactured sample was composed of $14 \times 3$ unit cells, arranged in a square lattice with a 19.5 mm period. The structure comprised two overlapping grids of square metal patches printed on the opposite sides of a 0.5 mm-thick substrate (Isola I-Tera laminate). All patches were connected to the common ground plate with metal wires of 37 mm length. The geometric parameters of the unit cells were optimized by numerical simulations to have the EBG range around 298 MHz (which is the Larmor frequency for MRI at 7T). A photograph of the top view of the sample is shown in inset of Figure 1(a). In MRI studies we used a homogeneous phantom filled with Ethylene-glycol-NaCl, 34 g/l with $\varepsilon_r = 45$ and $\sigma = 0.25$ S/m. The experimental setup is depicted in Figure 1(a). Each antenna was separated from the phantom by a foam spacer of thickness $d = 25$ mm. The EBG sample was installed in the vicinity of the two top antennas (the dipoles 1 and 2) $h = 45$ mm away from the antenna's plane. The distance between the axes of the dipoles was only $g = 30$ mm. Both the antennas were matched with lumped-element networks. The S-parameter magnitudes measured with and without the EBG sample by the vector network analyzer (VNA) Planar TR 1300/1 are shown in Figure 1(b). It is seen that the coupling coefficient $|S_{21}|$ of two matched dipoles was improved by -3.6 dB

at 298 MHz due to the sample, while the reflection loss $|S_{11}| \approx |S_{22}|$ held below -15 dB in both cases. Next, the setup was studied in a 7T MRI system (Achieva, Philips Healthcare, 8x2 kW RF power). The improvement of $|S_{21}|$ due to the sample measured by the scanner was -4.1 dB. The measured $B_1^+$ patterns created by the dipole 1 with and without the EBG sample in the central transverse plane are presented in Figure 1(c). It was observed that the sample had no negative effect on the magnitude and the penetration depth of the $B_1^+$ field inside the phantom.

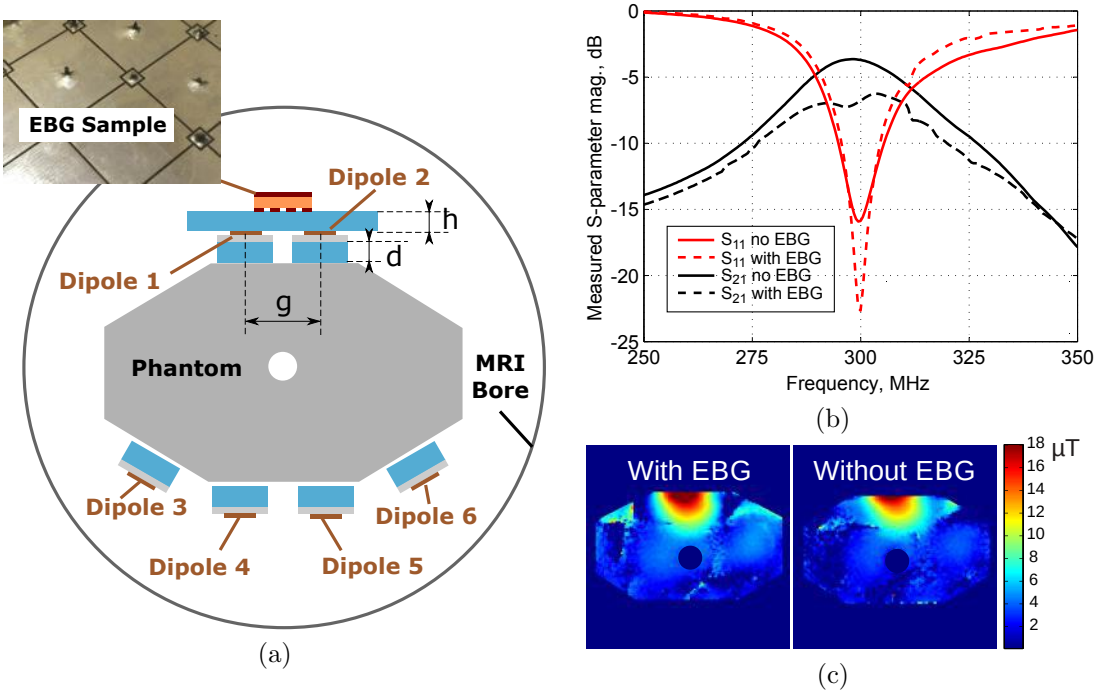



Figure 1: To the experiment with EBG: (a) MRI setup with body array coil having two of six decoupled dipoles (inset: manufactured sample); (b) S-parameter magnitudes of dipoles 1 and 2 measured by VNA outside of MRI bore; (c) measured $B_1^+$ patterns (with and without EBG sample).

In conclusion, a "mushroom" EBG structure has been tested as a passive decoupling element placed between two dipoles of a six-element body array coil for 7T MRI. By VNA and MRI measurements it was checked that the sample improves isolation between two dipoles having the separation of only 30 mm at least by -3.6 dB without any negative effect on the $B_1^+$ field. Therefore, it was confirmed that EBG metasurfaces can become building blocks of prospective 7T arrays of fractionated dipoles with reduced inter-element coupling, unprecedented element densities, increased degrees of freedom and reduction in maximum local SAR levels.

## ACKNOWLEDGMENT

This work was supported by the Russian Science Foundation (Project No. 15-19-20054).

## REFERENCES

1. P. B. Roemer et al., The NMR phased array. *Magn Reson Med*, 16, 192–225, 1990.
2. C. J. Snyder et al., Comparison between eight- and sixteen-channel TEM transceive arrays for body imaging at 7 T. *Magn Reson Med*, 67, 954–964, 2012
3. I.R.O. Connell et al., MRI RF Array Decoupling Method With Magnetic Wall Distributed Filters, *IEEE Trans. Med. Imag* , 34 (4), 825–835, 2015
4. A. J.E Raaijmakers et al., The fractionated dipole antenna: A new antenna for body imaging at 7 Tesla.*Magn Reson Med*, 75(3), 1366-1374, 2016
5. G. Saleh et al., EBG structure for low frequency applications, *in GeMiC 2012*, 1-4, 2012
6. D. Sievenpiper et al., High-impedance electromagnetic surfaces with a forbidden frequency band, *IEEE Trans. Microw. Theory Techn.*, 47(11), 2059–2074, 1999
7. Fan Yang and Rahmat-Samii, Y., Microstrip antennas integrated with electromagnetic band-gap (EBG) structures: a low mutual coupling design for array applications, *IEEE Trans. Antennas Propag.*, 51 (10), 2936–2946, 2003

# An Anthropomorphic head phantom including both electromagnetic and NMR relaxation properties for ultra-high field MRI Applications: Preliminary results

**A.L. Neves[1,2*], N. Cochinaire[1,2], A. Vignaud[3], and P. Sabouroux[1]**

[1]Aix Marseille Université, CNRS, Centrale Marseille, Institut Fresnel UMR 7249, 13013, Marseille, France

[2]Centre Commun de Ressources en Micro-ondes, IUSTI - Technopôle de Château-Gombert, 13453 Marseille, France

[3] CEA-Saclay, DRF/I2BM/Neurospin, 91191, Gif-sur-Yvette Cedex, France

[*]corresponding author: luisa.neves@fresnel.fr

**Abstract** – There is a crucial need in the MRI research field, on one hand for realistic distributed biological tissue electromagnetic property phantoms for RF coil designers to validate prototypes and to assess Specific Absorption Ratio (SAR) studies. On the other hand, there is also a need for phantoms with truthfully distributed biological tissue NMR relaxation properties such as longitudinal and transversal relaxation time, respectively called T1 (spin-lattice relaxation time) and T2 (spin-spin relaxation time) for MR pulse design and evaluation. With this project, we intended to develop an accurate head phantom able to answer both claims. Based on the reference values found in the literature, research was made to find the best materials to simulate brain properties; the latter were electromagnetically characterized with the multi-material permittivity and permeability measurement kit *EpsiMu*, and with MRI measurements, for relaxivities. Two phantom prototypes have been molded into an anthropomorphic skull and scanned in a 7T experimental MRI.

Due to its innumerous advantages, the static magnetic fields ($B_0$) of MRI scanners have increased considerably in the past few years, soon reaching 11.7 T [1]. At larger $B_0$, higher RF frequency is required for excitation. Unfortunately when the wavelength of the field is commensurable with the size of human body parts [2, 3] - as it is the case when $B_0$ reaches 7T - it leads to inhomogeneous energy deposition inside the patient. Depending on the coil architecture, patient anatomy and RF pulse design, so called "hot spots" can be produced if not watchful. In these conditions, water and gel-based phantoms are no longer viable, since their shape and electrical properties are not comparable to those of the human body [3-5].Therefore it has become pertinent to accurately reproduce the human brain/head in terms of permittivity, conductivity and the inherent MRI relaxation times, in a more detailed manner than what has been performed and described so far in the literature. In most cases, MRI phantoms are simply composed by a plastic cylindrical or elliptical shell filled with a NaCl doped homogeneous water solution, in addition with other molecules to manipulate the relaxation times, such as $NiCl_2$ or $CuSO_4$ [6-10]. To proceed to the electromagnetic characterization of several types of materials (solid, gels, liquids, granular) it was developed amidst *Institut Fresnel*, Marseille (France), a complex permittivity $\varepsilon^*$ and conductivity $\sigma$ measurement tool, *EpsiMu*®, used in this study. A few tissue-equivalent materials proposed in the literature [11-13] served as basis for the development of complex solutions able to recreate the electromagnetic properties of the human head. These were assessed with the *EpsiMu*® tool, as far as determining the correct proportions to have the complex permittivity $\varepsilon^*$ and conductivity $\sigma$ of three main parts of the brain

(white matter WM, Grey matter GM and Cerebrospinal fluid CSF) When reaching reproducible solutions in terms of ε* and σ, two phantom prototypes have been molded into a polymeric anthropomorphic skull (3bscientifique, ref. A20/T)The first phantom was a single-compartment phantom, filled with a high-sucrose concentration solution, having a dielectric permittivity and conductivity close to the brain WM, according to [14]. The second phantom, was produced a high flour/oil content solution, as seen in [9]. Both phantoms underwent 7T MRI scans (Siemens Healthcare, Elangen, Germany) using a Nova Medical 1Tx/32 Rx coil in Neurospin (CEA, Saclay, France) to confirm the RF distribution observed in CST simulations using Actual Flip Angle sequence (AFI) [15] and to measure the relaxation times T1, using Variable Flip Angle (VFA) method [16], and T2, using Multi Spin Echo technique [17, 18]. High resolution T1 weighted images were also acquired to carefully evaluate manufacturing flaws. After attentive evaluation of all parameters and comparison with the literature, the tissue-equivalent solutions of the second phantom fitted the best with both the electromagnetic properties and the NMR relaxation times targeted. As it can be seen in Table 1, contrary to the other parameters, T2 failed to reach biological tissue values. This might be due to one of the major problems, encountered when manufacturing the phantoms - the presence of microscopic air bubbles inside the solutions, which can be seen on HR T1w images. This can lead to a decrease in the transverse relaxation time and can lower the real part of permittivity. Further tests will be carried out to solve this problem, by taking advantage of a vacuum pump and a mixing machine. Additionally, the heat capacity of the mixtures serving as base for the phantoms is being taken into consideration. The knowledge of this characteristic is essential for hyperthermia assessment in the brain's tissue due to the "hot spots" emergence in an undergoing MRI examination. Long term study is also underway to assess the time stability of the chosen mixture. Of course, it is possible to influence the electromagnetic and NMR properties while playing with the component concentration. Therefore, since the texture of the mixture is very similar to pastry dough, it has the potential to be shaped in thin independent layers to mimic brain compartments and properties. Nonetheless, when working with multi-compartment structures, special attention has to be taken concerning the interaction between adjacent layers, since diffusion or deterioration of the contact surface can occur. In the case of two structures with high dielectric contrast, if diffusion shall occur, severe modification in terms of permittivity of the solutions can happen, leading to a loss in functionality of the phantom. As it was proven in our earlier experiences when manufacturing the first phantom, high sucrose concentration solutions form a thin hard outer coat when exposed to air and suffer osmosis when in contact with other sucrose solutions of lower concertation. In such case, a stabilizing film may be useful to prevent deterioration between layers. Thus, shortly, a third phantom prototype having a multi-compartment structure (physically distinguishable WM, GM, cerebellum, *etc*.) will be manufactured, tested and the evolution and stability of its many components will be followed over time.

| | **Literature values at 300 MHz** | **Phantom 1** | **Phantom 2** |
|---|---|---|---|
| | White matter | Sucrose solution | Flour & oil solution |
| **ε'** | 44 | 43 | 43 |
| **σ (S/m)** | 0.41 | 0.93 | 0.46 |
| **T1 (ms)** | 1400 | 550 | 1560 |
| **T2 (ms)** | 50 | [not measured] | 20.5 |

Table 1. The expected and obtained values for ε', σ, T1 and T2 for the two phantom prototypes at 7T/ 298 MHz.

**Acknowledgements** – The authors would like to sincerely thank the *Neurospin* team at the *CEA-Commissariat à l'Energie Atomique et aux Energies Alternatives* (Saclay, France), in particular to Dr. Elodie Georget and Lisa Leroi and their collaborator at *Institut Fresnel (*Marseille, France*),* Dr. Redha Abdeddaim, for their availability and large contribution to this project. The author would also like to acknowledge the *Centre Commum de Resources en Microondes (CCRM)* for the investment in this project.

## REFERENCES

1. Vedrine, P., G. Gilgrass, G. Aubert, J. Belorgey, C. Berriaud, A. Bourquard, P. Bredy, A. Donati, O. Dubois, F.P. Juster, H. Lannou, F. Molinié, M. Nusbaum, F. Nunio, A. Payn, L. Quettier, T. Schild, L. Scola, A. Sinanna, and V. Stepanov, "Iseult/INUMAC Whole Body 11.7 T MRI Magnet". *IEEE Trans Appl Supercond*, Vol. 25, 696-701, 2010.
2. Akca, I., O. Ferhanoglu, C. Yeung, S. Guney, T. Tasci, and E. Atalar, "Measuring Local RF Heating in MRI: Simulating Perfusion in a Perfusionless Phantom", *Magn Reson Med*, Vol. 26, 1228-1235, 2007.
3. Yang, Q., J. Wang, C. Collins, M. Smith, X. Zhang, K. Ugurbil and W. Chen, "Phantom Design Method for High-Field MRI Human Systems". *Magn Reson Med*, Vol. 52, 1016-1020, 2004.
4. Yang, QX., JH. Wang, CM. Collins, BM. Smith, X. Zhang, H. Liu, S. Michaeli, X.H. Zhu, G. Adriany, J.T. Vaughan, A. Anderson, K. Ugurbil and W. Chen, "Analysis of wave behavior in dielectric sample at high field", *Magn Reson Med*, vol. 47, 982–989, 2002.
5. Wang JH., Q.Z. Yang, C.M. Collins, M.B. Smith, X. Zhang, H. Liu, X.H. Zhu, G. Adriany, K. Ugurbil and W. Chen, "The polarization of the radiofrequency field in a human head at high field: a study with a quadrature surface coil at 7.0 Tesla". *Magn Reson Med*, vol. 48, 362–369, 2002.
6. Van Lier, A., A. Raaijmakers, T. Voigt, J. Lagendijk, P. Luijten, U. Katscher and C. Van den Berg, "Electrical properties tomography in the human brain at 1.5, 3 and 7T: A comparison study", *Magn Reson Med,* vol. 71, 354–363, 2014.
7. Graedel, N., J. Polimeni, B. Guerin, B. Gagoski and L. Wald, "An Anatomically Realistic Temperature Phantom for Radiofrequency Heating Measurements", *Magn Reson Med*, vol. 73, 442–450, 2015.
8. Kato, H., M. Kuroda, K. Yoshimura, A. Yoshida, K. Hanamoto, S. Kawasaki, K. Shibuya and S. Kanazawa, "Composition of MRI phantom equivalent to human tissues", *Med Phys*, vol. 32, 3199, 2005.
9. Tofts P., *Quantitative MRI of the Brain: Measuring Changes Caused by Disease,* Wiley, 2004.
10. Seifert, F. and H. Rinnenberg, "Adaptive coil control: SNR optimization of a TR volume coil for single voxel MRS at 3T", *Proc Intl Soc Mag Reson Med*, vol. 10, 2002.
11. Mobashsher, A.T., and A.M. Abbosh, "Three-Dimensional Human Head Phantom With Realistic Electrical Properties and Anatomy", *IEEE Antenn Wireless Propag Lett*, vol. 13, 1401-1404, 2014.
12. Mohammed, B.J. And A.M. Abbosh, "Realistic Head Phantom to test microwave systems for brain imaging", *Microw Opt Technol Lett*, Vol. 56, 979-982, 2013.
13. Bah, MH., J.S. Hong and D.A. Jamro, "Study of Breast Tissues Dielectric Properties in UWB Range for Microwave Breast Cancer Imaging"*, International Conference on Computer Information Systems and Industrial Applications (CISIA)*. Atlantic Press, 2015.
14. Gabriel, S., R.W. Lau and C. Gabriel, "The dielectric properties of biological tissues: II. Measurements in the frequency range 10 Hz to 20 GHz", *Phys Med Biol*, vol. 41, 2251-2269, 1996.
15. Yarnykh V.L. "Actual flip-angle imaging in the pulsed steady state: a method for rapid three-dimensional mapping of the transmitted radiofrequency field", *Magn Reson Med*, Vol. 57, 192-200, 2007.
16. Cheng H.L.M and G.A. Wright, "Rapid High resolution T1 mapping by variable flip angles: accurate and precise measurements in the presence of radiofrequency field inhomogeneity", *Magn Reson Med*, vol. 55, 566-574, 2006.
17. Young I.R., D.R. Bailes, M. Burl, A.G. Collins, D.T. Smith, M.J. McDonnell, J.S. Orr, L.M. Banks, G.M. Bydder, R.H. Greenspan and R.E Steiner, "Initial clinical evaluation of a whole body nuclear magnetic resonance (NMR) tomograph", *J Comput Assist Tomogr*, vol. 6, 1-18, 1982.
18. Duhamel G., M. Jubeau, M. Sdika, Y. Le Fur, S. Confort-Gouny, C. Vilmen, A. Vignaud, P.J. Cozzone, J. Gondin and D. Bendahan, "Transverse Relaxation Time (T2) Measurements of the Human Thigh Muscles at High Magnetic Field using Segmented Echo-Planar imaging", *Proc Intl Soc Mag Reson Med*, vol. 20, 449, 2012.

# Passive decoupling of dipoles for a transmit-array MRI antenna at 7T with stacked magnetic resonators

**E. Georget[1*], M. Luong[2], A. Vignaud[1], E. Giacomini[1], E. Chazel[1], G. Ferrand[2], A. Amadon[1], S. Enoch[3], G. Tayeb[3], C. Poupon[1], and R. Abdeddaim[3]**

[1]CEA-Saclay, DRF/I2BM/Neurospin/UNIRS, 91191 Gif-sur-Yvette Cedex, France

[2]CEA-Saclay, DRF/IRFU/SACM, 91191 Gif-sur-Yvette Cedex, France

[3]Aix Marseille Université, CNRS, Centrale Marseille, Institut Fresnel, UMR 7249, 13013 Marseille, France

[*]corresponding author: elodie.georget@cea.fr

**Abstract***:* In magnetic resonance imaging (MRI) at ultra-high field ($B_0 \geq$ 7 T), transmit-array RF coils (antennas) are preferred to homogenize the transmitted $B_1^+$ field. Strong coupling occurs between transmit array elements. A passive decoupling solution is proposed based on a metamaterial solution. This structure composed of stacked magnetic resonators was studied for the decoupling of two adjacent dipoles at a proton Larmor frequency of 297.2 MHz. The structure increased the decoupling of 13.3 dB, and increased the flip angle values in a 7 T MRI scanner.

**Introduction.** For magnetic resonance imaging (MRI), improvement of images is provided by increasing the magnetic field strength $B_0$ [1]. However, at ultra-high field ($B_0 \geq$ 7 T), the transmitted field $B_1^+$ features inhomogeneities in the human body at the proton Larmor frequency. Parallel transmission technology gives control of spatial and temporal RF pulses and has been successfully used to mitigate inhomogeneities of RF excitations [2]. To ensure maximum efficiency, several transmitters are located around the scanned sample. Thus, the higher the number of elements, the smaller the distance between them, and the higher the inter-element coupling. This coupling decreases significantly the efficiency of the transmit-array coil, and may increase the specific absorption rate and damage electronic materials (variable capacitors, RF amplifiers …). In this paper, a passive decoupling method based on Stacked Magnetic Resonators (SMR) is developed to decouple dipoles of a transmit-array coil.

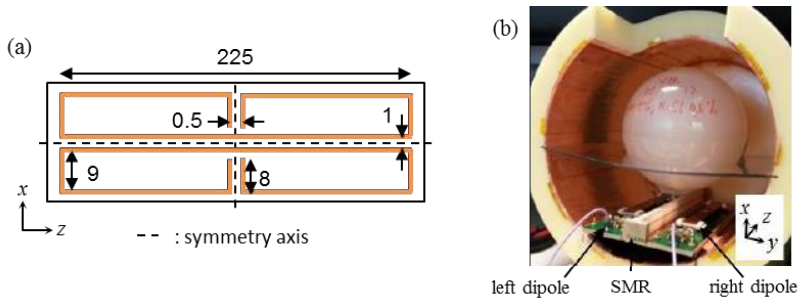



**Figure 1.** (a) Pattern of one layer of the SMR. Drawing is not to scale; dimensions are in mm. Copper path (0.4 mm width, in orange) on Rogers RO4004C substrate (white rectangle). (b) Experimental array coil with SMR.

**Materials and methods.** In order to reduce the mutual coupling between adjacent dipoles, SMR inspired by Artificial Magnetic Conductors (AMC) [3] were designed for 297.2 MHz, the Larmor frequency of our 7T scanner. Our structure is a Capacitive Loaded Loop (CLL) that exhibits a magnetic resonance. Two CLL are positioned on a Rogers RO4003C substrate with 0.813mm width (Fig. 1a). The SMR structure is made up of three AMC layers with 1.65 mm between each layer. In order to validate the decoupling efficiency of the SMR,

an experimental setup designed for 7 Tesla MRI was built. The setup was made up of two dipole antennas fixed to a copper plate in a shielded shell with a spherical phantom (Fig 1b). The SMR is oriented perpendicular to the y-axis (see Fig. 1b).

The experimental procedure is as follows. At first, each dipole was tuned and matched independently at the Larmor frequency, only one at a time in the shielded shell with the phantom (case (a): isolated). Then, the two dipoles are positioned at 7.6 cm from each other (case (b): without SMR). Finally, the SMR was positioned between the dipoles, 1 mm above the copper plate (case (c): with SMR). First, the scattering-parameters of the dipoles were measured. Then, to check the influence of SMR on MRI data, the setup was tested in a Siemens Magnetom 7 T MRI scanner. For cases (b-c), when the first dipole was emitting, the other one was loaded to 50Ω.

| | $\|S_{11}\|$ (dB) | $\|S_{21}\|$ (dB) | $\alpha_1$(°) | $\alpha_2$(°) |
|---|---|---|---|---|
| (a) Isolated | -34.2 | | 43 | 172 |
| (b) Without | -15.6 | -6.7 | 81 | 149 |
| (c) With | -33.6 | -20.0 | 39 | 165 |

**Table 1.** Measurement results on the entire phantom for the right dipole emitting. Flip angles $\alpha_1$ and $\alpha_2$ on Fig. 2(a)-(c).

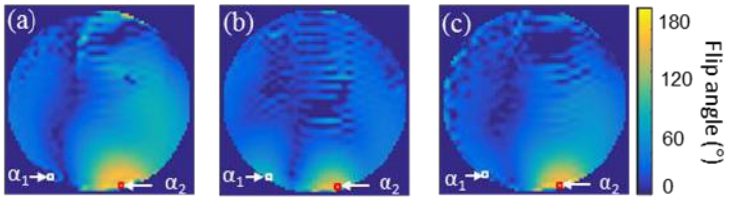



**Figure 2.** Central axial slices of the measured flip angle maps of the right dipole: isolated (a), with (c) and without (b) SMR.

**Results.** The scattering-parameters for the right dipole emitting are reported in Table 1. We note that the dipole is better matched with the SMR than without. With the SMR, the crosstalk between the dipoles is drastically reduced at the Larmor frequency. Moreover, the reflection coefficient $S_{11}$ of the dipole is similar to the one of the isolated case. The flip angle (FA) maps are shown on Fig. 2 for the three cases (a, b, c) when the right dipole is the transmitter. The FA $\alpha_1$ and $\alpha_2$ (white and red squares on Fig. 2) at the positions in the phantom the closest of the left and right dipole respectively are reported in Table 1. The SMR configuration yields a FA-map closer to the isolated case, and FA values at the left $\alpha_1$ and right $\alpha_2$ positions approximately match. The coupling is reduced at the position of the left dipole since the spot on the left on Fig. 2(b) is removed with the presence of SMR.

**Conclusion.** In this study, a new passive decoupling method for parallel imaging RF coils based on metamaterial solutions was investigated. The SMR structure was efficient in terms of transmission coefficient and transmitted field (FA). A considerable 13.3 dB decoupling improvement was obtained with this structure. The next step of our study is to implement a complete array coil with SMR structures between adjacent elements.

**Acknowledgements.** This project received financial support from Conseil Général de l'Essonne (ASTRE-2012), France Life Imaging, and Institut Carnot Star (CMRI).

**REFERENCES**

1. Vaughan, J. T., and M. Garwood, and C. M. Collins, et al., "7T vs. 4T: RF power, homogeneity, and signal-to-noise comparison in head images," *Magn Reson Med*, Vol. 46, No. 1, 24-30, 2001.
2. Cloos, M. A., and N. Boulant, and M. Luong, et al., "kT-points: Short three-dimensional tailored RF pulses for flip-angle homogenization over an extended volume," *Magn Reson Med*, Vol. 67, No. 1, 72-80, 2012.
3. Ferrer, P. J., and J. M. González-Arbesú, and J. Romeu, "Decorrelation of two closely spaced antennas with a metamaterial AMC surface," *Microw Opt Tech Letters*, Vol. 50, No. 5, 1414-1417, 2008.

# Alternative antenna designs for ultra-high field MRI.

**B. R. Steensma**[1], **A. A. Hurshkainen**[2], **S. B. Glybovski**[2], **I. V. Melchakova**[2], **P. R. Luijten**[1], **J. M. Hoogduin**[1], **D. W. Klomp**[1], **C. A. T. van den Berg**[1] **and A. J. E. Raaijmakers**[1*]

[1]University Medical Center Utrecht, The Netherlands

[2]ITMO University, St Petersburg, Russia

[*]corresponding author: a.raaijmakers@umcutrecht.nl

**Abstract**- MRI of the body at 7T or higher requires dedicated antenna arrays. This work is presenting two alternative antenna designs for this purpose. One design increases the space between the antenna and the patient resulting in enhanced, but still acceptable, coupling levels. The other design uses sinusoidally shaped antenna legs and is therefore called 'snake antenna'. Both designs have demonstrated good imaging performance and equal or better transmit efficiency while realizing up to 45% lower SAR levels.

**Introduction** In Magnetic Resonance Imaging (MRI), clinical 1.5 or 3T systems (64 or 128 MHz) use what is called a 'birdcage body coil' for transmitting the RF signals that excite the atomic nuclei. Starting from 7T systems (300 MHz), this concept is not feasible anymore for body imaging because the RF wavelength within tissue has decreased to become smaller than the transverse body dimensions [1]. Therefore, so-called multi-transmit imaging systems have been developed where the RF field is generated by a transmit array with e.g. 8 or 16 elements that are each driven with independent phase and/or amplitude. The challenge is to design transmit arrays that have good transmit efficiency at the depth of the imaging target with minimum local tissue heating to avoid hotspots with potentially dangerous temperature rise. One particular design that has been used extensively for various applications is the fractionated dipole antenna [2]. The use of intersegment inductances in a segmented dipole antenna design has demonstrated lower effective SAR levels. However, in spite of this, peak local SAR levels are still a severely limiting factor for most applications when compared to 3T imaging. This study presents alternative designs on the fractionated dipole antenna that will further reduce peak local SAR levels while maintaining the same transmit efficiency.

**Increase of antenna-subject spacing (antenna thickness)** An obvious approach to reducing local SAR levels is to increase the spacing from the antenna to the imaging subject. However, this will also increase inter-element coupling because the load to the elements is reduced. The impact of an increased spacing on coupling and SAR levels has been studied by numerical simulations (Sim4Life, ZMT, Zurich). The simulation setup consists of two fractionated dipole antennas on an elliptical ASTM phantom with tissue-equivalent properties. The $S_{12}$ parameter between the antennas was simulated for various inter-element distances and antenna-phantom spacing h (figure 1). These results indicate that lower SAR levels can be reached without too much losses from inter-element coupling if the spacing between antenna and subject is increased. A 8-element array of fractionated dipole antennas has been realized with 45 mm spacing. Simulated SAR distributions and imaging results are presented in figure 2. Clearly, the maximum SAR level is decreased by 45% while the image quality in the prostate remains the same.

**Alternative antenna shape** An alternative approach to reduce SAR levels is to adapt the shape of the antenna. A new dipole antenna design is proposed, in which the dipole legs are formed as continuous sinusoids

that are growing in amplitude towards the end of the antenna. This design has been called the 'snake antenna'. The resulting antenna shape is indicated in figure 3, along with simulated SAR distributions. An antenna array of 8 elements has been realized for prostate imaging, resulting in a substantial SAR improvement over the fractionated dipole antenna (figure 5).

**Conclusions** These results show that both methods are capable of reducing local SAR levels while maintaining image quality. Future designs will combine both approaches for even further SAR reduction.

**Acknowledgements**, This work is supported by the Dutch Technology Foundation STW project #13783

## REFERENCES

1. Vaughan J. T. et al. "Whole-body imaging at 7T: preliminary results" *Magn Reson Med* Vol. 61, No. 1, 244-8, 2009.
2. Raaijmakers A. J. E. et al. "The fractionated dipole antenna: A new antenna for body imaging at 7 Tesla" *Magn Reson Med* Vol. 75, No. 3, 1366-74, 2016.

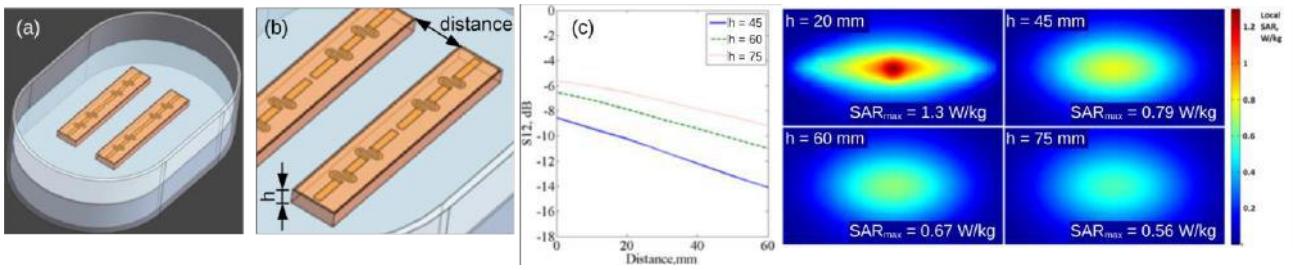



*Figure 1: Simulation study on antenna-phantom spacing h. (a) Setup (b) Definition of antenna-phantom spacing h and inter-element distance (c) Simulated $S_{12}$ as a function of inter-element distance for various values of h in mm. (d) SAR levels for various values of h.*

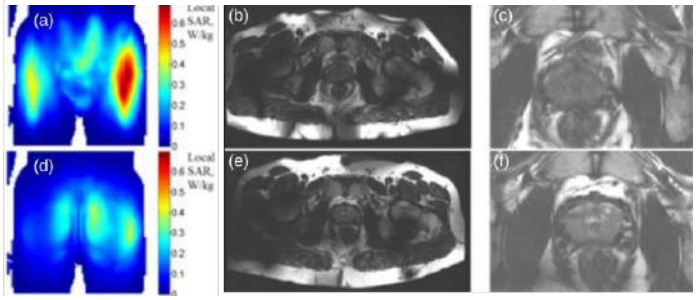



*Figure 3: Local SAR distribution and MR imaging results for 20 mm (top) and 45 mm spacing (bottom).*

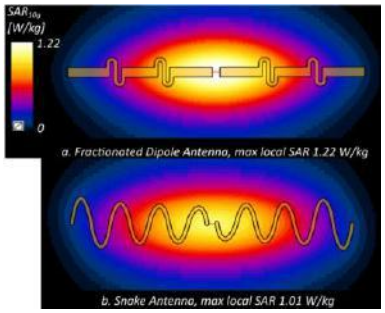



Figure 4: Currently used antenna design, fractionated dipole antenna (top) and proposed antenna design, snake antenna (bottom). SAR distributions are shown underneath both elements.

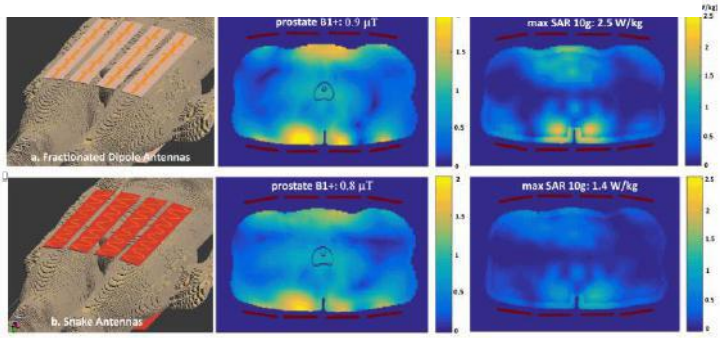



*Figure 5: Simulation results for the fractionated dipole antenna array (top) and the snake antenna array (bottom) in human model Duke*. The voxelized models (left),the B1-field distributions (middle) and the $SAR_{10g}$ distributions (right) are depicted. (*ITIS foundation, Zurich, CH)*

# ***REALIZATION OF A MAGNETIC COIL BASED ON MODE HYBRIDIZATION AND APPLICATION TO MAGNETIC RESONANCE IMAGING***

C. Jouvaud[1,2], R. Abdeddaim[1,3], B. Larrat[1], and J. de Rosny[1]

*[1]ESPCI ParisTech, CNRS, PSL Research University, Institut Langevin, 1 rue Jussieu, F-75005 Paris, France [2]CEA, DAM, GRAMAT, F-46500 Gramat, France*

*[3]Aix-Marseille Universite, CNRS, Centrale Marseille, Institut Fresnel, UMR 7249, Avenue Escadrille Normandie-Niemen, 13397 Marseille Cedex, France*

**Abstract:**

An original concept of Ultra High Field MRI coil is presented. We take the benefit of the hybridization between four half-a-wavelength resonators to transform a simple surface coil antenna into a volume coil. The device acting as a magnetic field enhancer (MFE) considerably increases the performance of a loop coil for magnetic resonance imaging. MFE is analyzed in terms of coupling of 4 "electrical" modes. This model is confirmed with a full-wave simulation. The device is shown to be efficient to image a "phantom" cylindrical gel and the head of a rat.

Usual surface coils offer high signal-to-noise ratio but they fall short in their ability to produce a uniform RF field and the depth of the image of surface coils is generally limited to about one coil radius. The magnetic field enhancer (MFE) described here is based on the hybridization of 4 half-wavelength electric resonators. The wires are placed in a square configuration in close vicinity of a loop coil. The hybridization resulting from the near-field interaction between the wires induces 4 modes. Two of them mainly interact with the magnetic field because of their current distribution symmetry.

FDTD simulations and experimentations were performed to quantify the improvement in terms of field homogeneity and signal to noise ratio brought by the enhancer. All experiments were performed in a 7T small animal MRI scanner (Pharmascan, Bruker Biospin, Germany) equipped with 300mT/m gradient coils. The length of the half-wavelength rods can be adjusted manually to finely tune the hybridized modes. MRI protocols were performed on homogeneous gel phantoms and on rodents.

Experimental results obtained on a rat head with and without the MFE are presented on Figure 1.

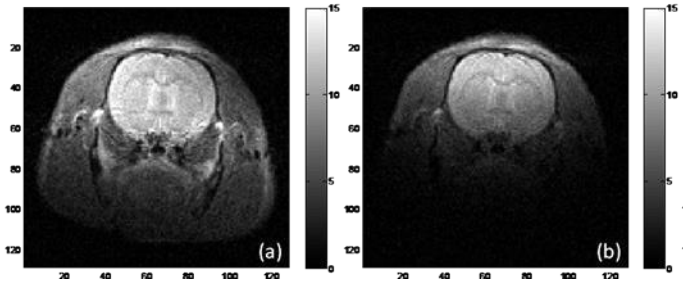



Figure1: Gradient echo image of a rat brain at 7T, acquired with (a) and without the MFE (b).

In silico, in vitro and in vivo results show a major improvement of global SNR (up to a 2 fold increase) as well as of magnetic field homogeneity in front of the loop coil. This technology is efficient and inexpensive. It does not require any electronic connections between the loop coil and the MFE. Therefore, it could bring new solutions to the MR imaging at high magnetic fields.

# Multiwave Technologies AG
## Dielectric shimming optimization

**T. Antonakakis**[1]

[1]Multiwave Technologies AG, Switzerland
tryfon@multiwave.ch

**Abstract**— A major challenge of Ultra High Field Magnetic Resonance Imaging is the homogeneity of the $B_1^+$. Homogenization of the field can be achieved in two ways, namely, parallel transmission and dielectric shimming and only latter will be studied herein. Dielectric shimming consists of adding dielectric pads. They act as a secondary source that interferes with the primary to yield a homogeneous resultant field. The geometry of the pad as well as its relative permittivity are the governing factors for the secondary field and by consequence the resultant $B_1^+$. The pad's optimal relative permittivity for a homogeneous $B_1^+$ field can be obtained by [3]. Another important factor on the field's homogeneity is the shape of the pad in the macroscale or the microscale. One can combine the method in [3] with a variation of the macroscopic shape of the pads and obtain new results for $B_1^+$ homogeneity.

Design of structured materials is hindered by lengthy computational time and a plethora of possible microstructures. Modeling a structured material is expensive in terms of computing memory, time and cost. One needs to have the right structure or topology combined with the adequate materials responding to engineering requirements of permittivity, permeability. We demonstrate the use of a proprietary software used to find the material and shape that yield the required relative permittivity. We have developed algorithms in the fields of homogenization reducing structured material analysis to analyzing solely the microscale.

To demonstrate the capabilities of our software we elucidate the homogenization procedure that forms a crucial component of one of our post-processing algorithms. We illustrate the latter by examining case studies applicable to single polarization electromagnetism [1, 2, 4] where the medium is composed of a periodic array of shaped rods. Our algorithms can be applied in two or three dimensional models and allow for an engineer or physicist to query for the optimal shape and/or material given a specified permittivity, that would render $B_1^+$ homogeneous.

The new design process would then be free of the iterative process required to obtain the best geometry structuration, material combinations and positioning of the pads for a wanted permittivity. The required permittivity is directly sought using our software. One can set constraints on materials and geometric shapes present and restrict the optimization problem. Further developments are planned to account for lossy materials.

Multiwave's proprietary algorithms and software allow for an acceleration of shimming pads design by several orders of magnitude, taking MRI one step further in medical imaging.

**REFERENCES**

1. T. Antonakakis, R. V. Craster, S. Guenneau,
"Asymptotics for metamaterials and photonic crystals"
*Proceedings of the Royal Society A*, Vol. 469, No. 2152, 2013.

2. T. Antonakakis, R. V. Craster, S. Guenneau,
"High-frequency homogenization of zero-frequency stop band photonic and phononic crystals"
*New Journal of Physics*, Vol. 15, No. 10, 2013.

3. W. M. Brink, R. F. Remis, A. G. Webb,
"A Theoretical Approach Based on Electromagnetic Scattering for Analyzing Dielectric Shimming in High-Field MRI"
*Magnetic Resonance in Medicine*, 2015.

4. L. Ceresoli et al.,
"Dynamic effective anisotropy: Asymptotics, simulations and microwave experiments with dielectric fibers"
*Physical Review B*, Vol. 92, No. 17, 2015.

# Flexible and compact metamaterials for high field in vivo magnetic resonance imaging

**R.Schmidt, and A.G.Webb**
C.J.Gorter Center for High Field MRI, Leiden University Medical Center, The Netherlands.
*corresponding author: a.webb@lumc.nl

**Abstract**- In this work we design a metamaterial tuned with a high permittivity material to produce a flexible and compact method for concentrating the transmit field in an MRI experiment. The particular example used in this study was a single pad placed behind the head to increase the efficiency and sensitivity in the visual cortex region of the brain.

Metamaterial structures can be used to focus or refract the magnetic field in MRI (1,2). Recent work demonstrated a simple structure built from copper strips, which was used to increase the efficiency of traveling wave MRI in the brain at very high field, 9.4 Tesla (3). Significant increases in signal-to-noise have also been demonstrated at clinical field strengths (4). In this work we propose the combination of high permittivity materials and metamaterials to provide a flexible, compact structure which can be used for in vivo imaging at 7 Tesla. The particular example used in this study was a single pad placed behind the head to increase the efficiency and sensitivity in the visual cortex region of the brain.

3D electromagnetic simulations were performed using finite integration technique (FIT) software (CST Microwave Studio, Darmstadt, Germany). All $B_1^+$ maps were normalized to an accepted power of 1 watt. The metamaterial/high permittivity pad structure is shown in Figure 1. The pad was constructed from a flexible aqueous suspension of calcium titanate in water, with a relative permittivity of ~110 (5). In vivo $B_1$+ maps were acquired using a DREAM sequence (6) with the following scan parameters: FOV 24x24 cm2, spatial resolution 2.5 x 2.5 x 5.0 mm3, TR/TE 3/1.7 ms, $B_1^+$ encoding tip angle 50° and imaging tip angle 10°.

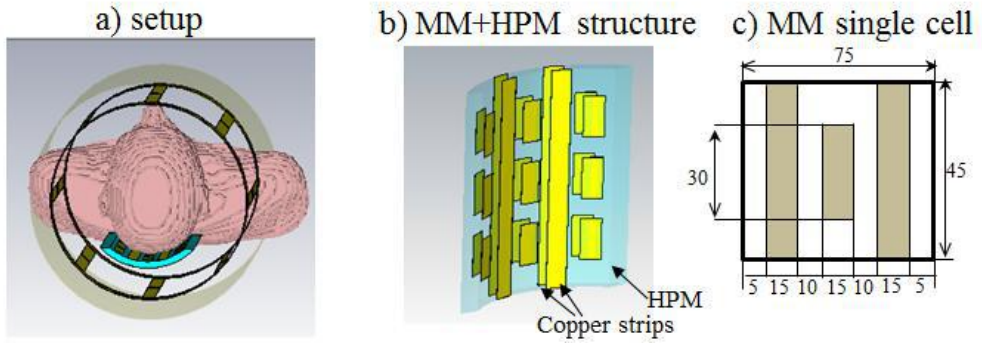



Figure 1. a) Physical setup for the simulations and experiments with the subject placed in a 7 Tesla MRI scanner and a 16-leg birdcage coil used for RF excitation. The tuned metamaterial/high permittivity pad was placed behind the head. b) close-up of metamaterial/high permittivity material, c) metamaterial single cell dimensions in mm,

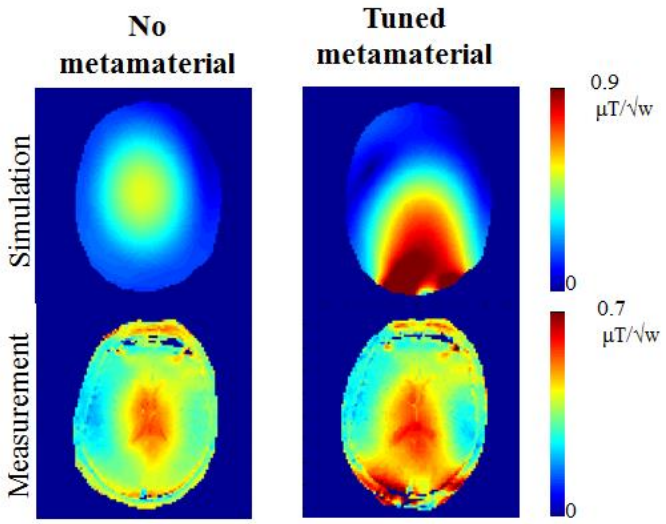



Figure 2. $B_1^+$ maps comparing simulation and experimental results without metamaterial (left) and with the metamaterial in place (right).

A MM structure combined with HPM layer has been shown to be a new type of structure which enables control of the local RF. Such a combination enables a small, simple MM structure to be designed for 7 T MRI. In this study it was shown to be beneficial for visual cortex imaging, relevant for example for functional MRI experiments.

**Acknowledgements**, This work was supported in part by the Netherlands Organization for Scientific Research (NWO) under NWO TOPGO 700.10.351.

**REFERENCES**

1. Algarin, J.M. et al.. "Metamaterial magnetoinductive lens performance as a function of field strength.," *J.Magn.Reson*, Vol. 247, 9-14, 2014.
2. Radu X. et al. "Toward a wire medium endoscope for MRI imaging", *Metamaterials*, Vol. 3, 90-99, 2009.
3. Zivkovic I and Scheffler K., "Metamaterial Cell for $B_1^+$ Field Manipulation at 9.4T MRI," in *Proceedings of International Society of Magnetic Resonance in Medicine*, Salt Lake City, USA, May 2014, 22
4. Slobozhanyuk A. et al., "Enhancement of Magnetic Resonance Imaging with Metasurfaces," *Advanced Materials*, Vol. 29, No. 9, 1832-1838, 2016.
5. Haines K., Smith N.B. and Webb, A.G., "New high dielectric constant materials for tailoring the $B_1^+$ distribution at high magnetic fields.," *J.Magn.Reson.*, Vol. 203, 323-327, 2010.
6. Nehrke K. and Boernert P. "DREAM--a novel approach for robust, ultrafast, multislice $B_1$ mapping", Magn.*Reson.Med*, Vol 68, 1517-1526, 2012.

**A bottom-up approach towards metamaterials and plasmonics**

# Hierarchical Oriented Assembly of Gold Nanorods

**L. M. Liz-Marzán**[1,2,3*]

[1] CIC biomaGUNE, Paseo de Miramón 182, 20009 Donostia – San Sebastian, Spain

[2] Ikerbasque, Basque Foundation for Science, 48013 Bilbao, Spain

[3] Ciber-BBN, Spain

[*]corresponding author: llizmarzan@cicbiomagune.es

**Abstract**-A method is presented that allows the preparation of hierarchical supercrystal structures made of oriented gold nanorods, with a suitable control of patterning, lateral dimensions and number of nanorod monolayers. The plasmonic properties are fully analyzed for supercrystals made of few layers, via simulations and experiments.

The integration of nanoparticle superstructures into daily life applications faces major challenges including the simplification of the self-assembly process, reduced cost and scalability. It is however often difficult to improve on one aspect without losing on another. Stamping and templated assembly have been used to create single- and multi-particle patterns, but these are typically limited to a small number of particles. We have recently developed a bench-top method that allows patterning a macroscopic substrate with gold nanoparticle supercrystals in a one-step process. The method allows parallelization and patterned substrates can be made with high throughput. The self-assembly of a variety of building blocks into crystalline superstructures takes place upon solvent evaporation and their precise placement over millimeter scale areas is induced by confinement of the colloidal suspension in micron sized cavities. We mainly focus on gold nanorods and demonstrate their hierarchical organization up to the device scale. The height of the formed nanorod supercrystals can be tuned by simply varying nanorod concentration, so that the topography of the substrate and the resulting optical properties can be readily modulated. The crystalline order of the nanorods results in homogeneous and high electric field enhancements over the assemblies, which is demonstrated by surface enhanced Raman scattering spectroscopy.

**Acknowledgements**, if any, including all funding information, should be gathered into a brief statement at the end.

**REFERENCES**

1. C. Hamon, S. Novikov, L. Scarabelli, L. Basabe-Desmonts, and L.M. Liz-Marzán, "Hierarchical Self-Assembly of Gold Nanoparticles into Patterned Plasmonic Nanostructures", *ACS Nano*, Vol. 8, 10694-10703, 2014.
2. C. Hamon, S.M. Novikov, L. Scarabelli, D.M. Solís, T. Altantzis, S. Bals, J.M. Taboada, F. Obelleiro, and L.M. Liz-Marzán, "Collective Plasmonic Properties in Few-Layer Gold Nanorod Supercrystals," *ACS Photonics*, Vol. 2, 1482–1488, 2015.

# Optical magnetism in a self-assembled 3D isotropic metamaterial.

**S. Gomez-Graña[1], M. Tréguer-Delapierre[1], E. Duguet[1], V. Kravets[2], A. Grigorenko[2], J. Leng[3], J.-B. Salmon[3], A. Baron[4], D. Torrent[4], P. Richetti[4], P. Barois[4], and V. Ponsinet[4*]**

[1]Univ. Bordeaux - CNRS, ICMCB, UPR 9048, Pessac, France

[2]School of Physics and Astronomy, University of Manchester, Manchester, UK

[1]Univ. Bordeaux - CNRS - SOLVAY, Laboratoire du Futur, UMR 5258, Pessac, France

[4]Univ. Bordeaux - CNRS, Centre de Recherche Paul Pascal, UPR 8641, Pessac, France

[*]corresponding author: ponsinet@crpp-bordeaux.cnrs.fr

**Abstract** (limited to 80 words max) - Magnetism at optical frequencies is one of the biggest challenges of the metamaterials research field. Artificial magnetic response was obtained at visible frequencies in resonating nanostructures like fishnets or nanopillar arrays, which are essentially two-dimensional and highly anisotropic, therefore inducing the entanglement of artificial magnetism and spatial dispersion. Combining nanochemistry, colloidal physics, numerical simulations and experimental optics, we demonstrate the fabrication of a large three-dimensional isotropic magnetic metamaterial, exhibiting non-natural values of the magnetic permeability between 0.8 and 1.4.

Plasmonic nano-clusters made of metallic satellites surrounding a dielectric core (so-called “plasmonic raspberries”) constitute a specific class of 'meta-materials', which are predicted[1] to exhibit artificial optical magnetism and open a path towards bulk materials presenting magnetic permeability different from 1. The magnetic response of such plasmonic raspberries depends on governing parameters like the sizes (core, satellites), the choice of materials and the number of satellites. We synthesized complex colloids made of spherical silver satellites distributed around a silica core, with a global size of 150 nm, and first studied experimentally their suspensions using a polarization resolved spectroscopic light scattering experiment[2]. We measured separately the scattering of the electric dipole and of the magnetic dipole and electric multipoles, as they occur with orthogonal polarizations.

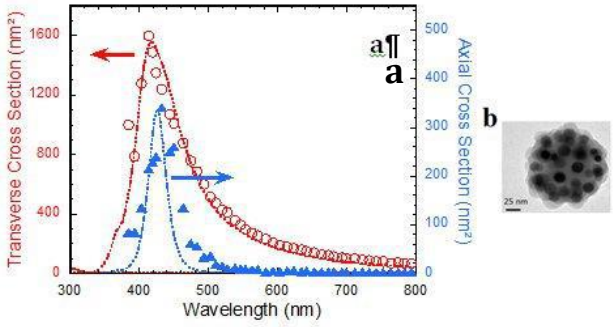



**Figure 1.** **(a)** Electric dipole (red) and magnetic dipole (blue) differential scattering cross sections measured at a scattering angle of $\pi/2$. Experimental data (symbols) obtained after normalization by a reference suspension of silica nanoparticles. Corresponding numerical simulations (lines) for a MNC with 22 Ag satellites of diameter 25 nm capped with 5 nm of silica. **(b)** Transmission electron microscopy image of a silver raspberry.

Numerical simulations of the MNC scattering cross sections computed by a T-Matrix code helps identifying the contributions of the magnetic dipole and electric multipole modes separately, and extracting a full determination[3] of the experimental dipole scattering cross-sections as plotted in Figure 1. These results demonstrate that the individual MNCs present a significant magnetic response related to coupled plasmon resonances of the satellites. These objects were then assembled with a microfluidic device[4] into dense 3D isotropic samples, with overall dimensions (μm) much larger than visible wavelengths. In particular, the assembled material is thick enough to behave like a semi-infinite sample, therefore enabling the analytic extraction of the permeability $\mu(\lambda)$ and the permittivity $\varepsilon(\lambda)$ from variable angle spectroscopic ellipsometry (VASE). Simultaneous analysis of spectroscopic ellipsometry data taken at five different angles of incidence shows that spatial dispersion is weak, and provides physical solutions $\mu(\lambda)$ and $\varepsilon(\lambda)$, both presenting a resonant behavior at $\lambda$ = 400 nm. The magnetic permeability deviates notably from 1 and reaches a value as high as $\mu$ = 1.46 - 0.55i (see Figure 2). This work paves the way to the large scale production of magnetic metamaterials of arbitrary shape and size, as required for the manipulation of the flow of light by transformation optics.

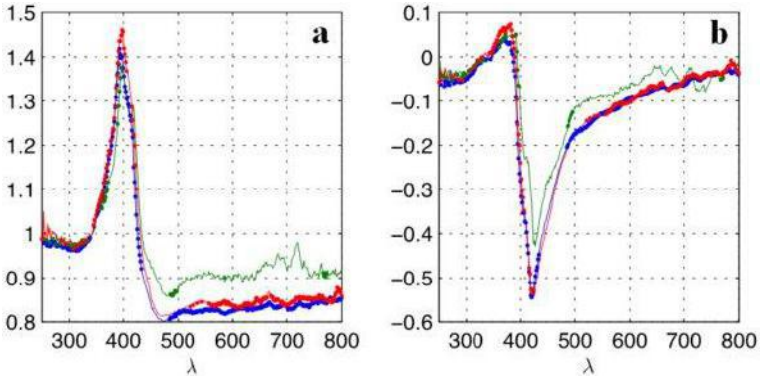



**Figure 2.** **(a)** Real part and **(b)** imaginary part of the magnetic permeability $\mu(\lambda)$, extracted from the VASE data. Three different curves (red, blue, green) correspond to data collected at three different positions on the sample.

**Acknowledgements**. This work was supported by the LabEx AMADEus (ANR-10-LABX-42) in the framework of IdEx Bordeaux (ANR-10-IDEX-03-02), France..

**REFERENCES**

[1] Simovski, C. R. and S. A. Tretyakov, "Model of isotropic resonant magnetism in the visible range based on core-shell clusters," *Phys. Rev. B*, Vol. 79, No. 4, 045111, 2009.

[2] Sharma, N. L. "Nondipole Optical Scattering from Liquids and Nanoparticles," *Phys. Rev. Lett.*, Vol. 98, No. 21, 217402, 2007.

[3] Ponsinet, V., P. Barois, S. M. Gali, P. Richetti, J.-B. Salmon, A. Vallecchi, M. Albani, A. Le Beulze, S. Gomez-Grana, E. Duguet, S. Mornet, and M. Treguer-Delapierre, "Resonant isotropic optical magnetism of plasmonic nanoclusters in visible light," *Phys. Rev. B*, Vol. 92, No. 22, 220414(R), 2015

[4] Angly, J., A. Iazzolino, J.-B. Salmon, J. Leng, S. P. Chandran, V. Ponsinet, A. Desert, A. Le Beulze, S. Mornet, M. Treguer-Delapierre and M. A. Correa-Duarte, "Microfluidic-induced growth and shape-up of 3D extended arrays of densely packed nanoparticles," *ACS Nano*, Vol. 7, No. 8, 6465–6477, 2013.

# Semiconductor Nanowire antennas

J. Gómez Rivas[1,2], D. van Dam[2], J.E.M. Haverkort[2], E.P.A.M Bakkers[2], D. Romero Abujetas [3] and J.A. Sánchez Gil[3]

[1]Dutch Institute for Fundamental Energy Research, DIFFER, P.O. Box 6336, 5600 HH Eindhoven, The Netherlands
[2]Eindhoven University of Technology, P.O. Box 513, 5600 MB Eindhoven, The Netherlands
[3]Instituto de Estructura de la Materia, CSIC, Madrid, Spain
E-mail: j.gomezrivas@amolf.nl

The absorption and emission of light can be modified and enhanced by its resonant interaction with nanostructures. We demonstrate experimentally and describe theoretically the strong directional emission and absorption of light by III-V semiconductor nanowires mediated by the resonant coupling to guided and leaky modes in the cylindrical structure. The coupling to these eigenmodes of the nanowires depends strongly on their diameter and length, which opens a rich spectrum of possibilities for the control of the direction, efficiency and polarization of the emission and absorption of light [1]. The emission experiments have been performed with Fourier microscopy [2], i.e., by imaging the back focal plane of a microscope objective to map the emission of single nanowires and of arrays. We also introduce a technique termed time-reversed Fourier microscopy that enables the detection of the directional absorption of polarized light by individual nanowires [3].

**Acknowledgements**. This research was financed by the Dutch Technology Foundation STW.

**References**

[1] R. Paniagua-Domínguez, G. Grzela, J. Gómez Rivas, and J.A. Sánchez-Gil, Nanoscale **5**, 10582–90 (2013).

[2] G. Grzela, R. Paniagua-Domínguez, T. Barten, Y. Fontana, J.A Sánchez-Gil and J. Gómez Rivas, Nano Letters **12**, 5481–5486 (2012).

[3] G. Grzela R. Paniagua-Domínguez, T. Barten, D. van Dam, J.A Sánchez-Gil and J. Gómez Rivas, Nano letters **14,** 3227−3234 (2014).

# Bulk rigid terahertz metamaterials based on dielectric microspheres

**C. Kadlec[1], M. Šindler[1,3], F. Dominec[1], P. Kužel[1], C. Elissalde[2], U.-C. Chung[2], P. Mounaix[3], and H. Němec[1]**

[1]Institute of Physics, ASCR, Prague, Czech Republic
[2]ICMCB, Univ. Bordeaux, CNRS, France
[3]IMS, Univ. Bordeaux, CNRS, France
kadlecch@fzu.cz

**Abstract**— Rigid metamaterials were prepared by embedding $TiO_2$ microspheres into polyethylene. These structures exhibit a series of Mie resonances where the lowest one is associated with a strong dispersion in the effective magnetic permeability. Using time-domain terahertz spectroscopy, we experimentally demonstrated the magnetic nature of the observed resonance. The presented approach shows a way for low-cost mass fabrication of mechanically stable terahertz metamaterials based on dielectric microresonators.

We focus on the investigation of THz metamaterials based on $TiO_2$ microsphere resonators. Titanium dioxide $TiO_2$ is a suitable dielectric material due to its high permittivity and low dielectric losses. In our previous work, the microspheres were dispersed in air, forming nearly a single-layer sample enclosed between two sapphire wafers [1]. Here we embedded the $TiO_2$ microspheres into a polyethylene (PE) matrix which enabled us to prepare a rigid bulk metamaterial with a controllable concentration of microresonators. We performed measurements using time-domain THz spectroscopy to characterize fully the response of such structures and to confirm its magnetic character. The retrieved spectra of effective dielectric permittivity and magnetic permeability are discussed within Mie theory and Maxwell-Garnett effective medium model.

$TiO_2$ microspheres with a diameter of a few tens of micrometers were prepared by the bottom up approach described in [1]. They were mixed with PE powder and a pressure of 14 MPa was used to prepare rigid pellets with random spatial distribution of the $TiO_2$ microspheres. Pellets with thicknesses of 1 and 3 mm were prepared.

First of all, we employed a finite-difference time-domain (FDTD) simulation software package MEEP [2] to calculate the transmission and reflection spectra of $TiO_2$ microspheres with diameter $d = 35$ µm arranged in a square lattice with period $a = 50$ µm and embedded in a medium with dielectric permittivity $\varepsilon_H$. In order to account for the losses and for the porosity of the microspheres, the permittivity of $TiO_2$ was considered as $92 + 2if$, where $f$ is the frequency in THz [1]. The Nicolson-Ross-Weir method [3] was used to retrieve the effective dielectric permittivity $\varepsilon$ and effective magnetic permeability $\mu$ from the simulated spectra of the metamaterial.

We investigated how the contrast between the permittivity of the microspheres and the host matrix affects the position and the strength of the magnetic response associated with the lowest Mie mode. This resonance is located around 0.9 THz and its position changes

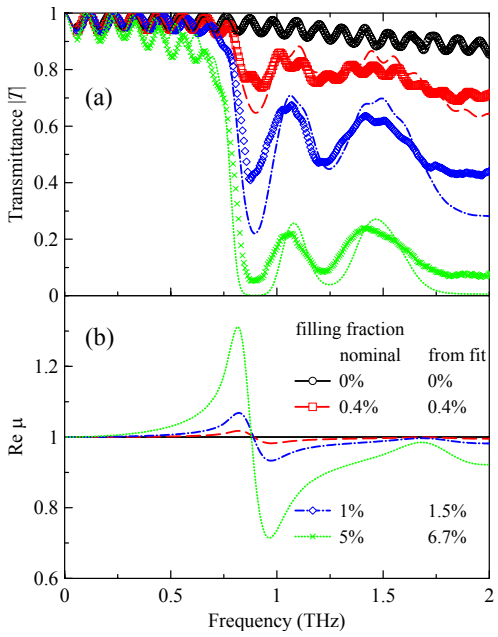



Figure 1: (a) Transmittance spectra of one-mm-thick PE pellets with various concentrations of $TiO_2$ spheres. Symbols: experimental data, lines: fits using Maxwell-Garnett theory. (b) Effective permeability corresponding to the fitted transmission spectra. Filling fractions were obtained from the component weights (nominal values) and from the fits.

only weakly for $\varepsilon_H < 3$. However, the strength of the resonance and the minimum negative value of the effective permeability decrease with increasing $\varepsilon_H$. For the filling factor of 18%, the range of the negative effective permeability completely disappears for the host material permittivity exceeding $\sim 5$.

Time-domain THz experiments were performed using a custom-made setup described in [4] and a commercial Teraview THz spectrometer. We verified that such pure PE pellets exhibit a constant permittivity ($\varepsilon_H = 1.98$) and negligible losses ($\tan\delta \sim 0.002$ around 1 THz). For a 3-mm thick pellet with a very low filling fraction of $TiO_2$ microspheres (0.15%) we extracted the complex dielectric permittivity $\varepsilon$ and magnetic permeability $\mu$ from the transmittances $T_0$ and $T_1$ corresponding to the direct pass and to the first echo in the sample, respectively [5]. A magnetic resonance around 0.9 THz is clearly resolved. This confirms the effective magnetic behavior of the metamaterial associated with this lowest Mie mode. Since $T_1$ dramatically decreases for higher filling fractions, we carried out further investigations based exclusively on the transmittance amplitude obtained from long time-domain scans which involved the sum of all measurable Fabry-Pérot reflections. In order to gain further insight into the properties of the metamaterial, we employed a dynamic Maxwell-Garnett theory [6], in which we account for the distribution of sizes of the microspheres. We found that a good match between the calculated and measured spectra is found when two mean particle radii are considered $r_1 = 17\,\mu m$, $r_2 = 13.5\,\mu m$ with a distribution width $\sigma = 1\,\mu m$ (see Fig. 1). These parameters are supported by the optical microscope analysis, which revealed a comparable ellipticity of the microparticles. Furthermore, the filling fractions obtained from the fit by the Maxwell-Garnett theory are in good agreement with those determined from the weights of the components.

Using a bottom up approach, we fabricated rigid metamaterials made of $TiO_2$ microresonators embedded in polyethylene. We experimentally confirmed the magnetic effective response in the vicinity of the lowest Mie resonance near 0.9 THz. Using FDTD calculations of the effective response we found out that a range of negative effective magnetic permeability can be achieved for sufficiently high filling fractions and contrasts between the permittivities of the resonators and the embedding medium. The developed structures are prototypes of cheap mechanically stable terahertz metamaterials.

**ACKNOWLEDGMENT**

This work was supported by the LabEx AMADEus (ANR-10-LABX-42) and by the Czech Science Foundation under Grant No. 14-25639S.

**REFERENCES**

1. Němec H., C. Kadlec, F. Kadlec, P. Kužel, R. Yahiaoui, U-C. Chung, C. Elissalde, M. Maglione, and P. Mounaix, "Resonant magnetic response of $TiO_2$ microspheres at terahertz frequencies," *Appl. Phys. Lett.*, Vol. 100, No. 6, 06 1117, 2012.
2. Oskooi A. F., D. Roundy, M. Ibanescu, P. Bermel, J. D. Joannopoulos, and S. G. Johnson, "MEEP: A flexible free-software package for electromagnetic simulations by the FDTD method," *Comput. Phys. Commun.*, Vol. 181, No. 3, 687–702, 2010.
3. Smith D. R., S. Schultz, P. Markoš, and C. M. Soukoulis, "Determination of effective permittivity and permeability of metamaterials from reflection and transmission coefficients," *Phys. Rev. B*, Vol. 65, No. 19, 195104, 2002.
4. Kužel P., H. Němec, F. Kadlec, and C. Kadlec, "Gouy shift correction for highly accurate refractive index retrieval in time-domain terahertz spectroscopy," *Opt. Exp.*, Vol. 18, No. 15, 15338–15348, 2010.
5. Němec H., F. Kadlec, P. Kužel, L. Duvillaret, and J.-L. Coutaz, "Independent determination of the complex refractive index and wave impedance by time-domain terahertz spectroscopy," *Opt. Comm.*, Vol. 260, No. 1, 175–183, 2006.
6. Yannopapas V., and A. Moroz, "Negative refractive index metamaterials from inherently non-magnetic materials for deep infrared to terahertz frequency ranges," *J. Phys.: Condens. Matter.*, Vol. 17, No. 25, 3717–3734, 2005.

# Assembling plasmonic nanoparticles through supramolecules

**A. Guerrero-Martínez**
Departamento de Química Física I, Universidad Complutense de Madrid, Avda. Complutense s/n, 28040, Madrid, Spain
* aguerrero@quim.ucm.es

**Abstract**- The gold nanoparticle supramolecular self-assembly strategy under controlled temperature and concentration conditions proposed in this work, shows a battery of chemical approaches to prepare new defined plasmonic superstructures in both aqueous and organic media, and their interfaces, with potential applications in plasmonic nanoparticle sensing.

The development of nanoplasmonics has been tremendous during the past two decades, driven in part by improvements in colloidal synthesis of nanocrystals and manipulation of nanoparticle surface functionalities. This has granted access not only to exquisite control over the morphology of nanoparticles but also to novel multiparticle nanostructures with a variety of organizational motifs.[1] Driven by such new possibilities, completely unforeseen plasmonic effects have been found, which let us think about applications in a variety of fields. In this work, we discuss the evolution of plasmonic nanomaterials and their corresponding properties and correlations with supramolecular concepts that have been around for a long time. Additional thinking along these lines may lead to further expansion of nanoplasmonics and to multiple surprising discoveries in this field.

The self-assembly of small molecules into large, functional nanostructures has led to the construction of supramolecular systems, both in solution and on solid substrates, with defined dimensions that display unique properties through collective interactions, much like natural systems. In this work, we show how one assembles gold plasmonic nanoparticles through supramolecular chemistry for the purpose of producing novel materials that can be used for optical devices and sensors.[2] In a stepwise process, we discuss the design and synthesis of the molecular and nanoparticle components, their optical behaviour, and finally the properties arising form the assembly in superlattices. We then move from simple supramolecular interactions, based on polyrotaxanes and supramolecular polymers,[3] with gold nanoparticles to more complex nanostructures such as gold colloidal membranes that can be used as nanocontainers and functionalized in different ways. We show how it is possible to organize such membranes of micron length in a space-controlled manner on surfaces.

Additionally, we propose here a light controlled synthetic procedure that allows obtaining selected plasmonic oligomers through coordinative bonds in high yield and with reaction times in the scale of minutes by irradiation with low fluence near-infrared (NIR) femtosecond laser pulses.[4] Selective inhibition of the formation of gold nanorod n-mers (trimers) with a longitudinal localized surface plasmon in resonance with a 800 nm Ti:sapphire laser, allowed efficient trapping of the (n−1)-mers (dimers) by hot spot mediated photothermal decomposition of the interparticle molecular linkers. Finally, laser irradiation at higher energies produced near-field enhancement at the interparticle gaps, which is large enough to melt gold nanorod tips, offering a new pathway toward tip-to-tip welding of gold nanorod oligomers with a plasmonic response at the NIR.

**Acknowledgements**. This work has been funded by the Spanish MINECO (MAT2014-59678-R). A.G.-M. acknowledges receipt of a Ramón y Cajal Fellowship from the Spanish MINECO.

**REFERENCES**


1. Guerrero-Martínez A., M. Grzelczak and L. M. Liz-Marzán, "Molecular thinking for nanoplasmonic design," *ACS Nano*, Vol. 6, No. 5, 3655–3662, 2012.
2. Coelho J. P., G. González-Rubio, A. Delices, J. Osío Barcina, C. Salgado, D. Ávila, O. Peña-Rodríguez, G. Tardajos and A. Guerrero-Martínez, "Polyrotaxane-mediated self-assembly of gold nanospheres into fully reversible supercrystals," *Angew. Chem. Int. Ed.*, Vol. 53, 12751–12755, 2014.
3. Coelho J. P., G. Tardajos, V. Stepanenko, A. Rödle, G. Fernández and A. Guerrero-Martínez, "Cooperative self-assembly transfer from hierarchical supramolecular polymers to gold nanoparticles," ACS Nano, Vol. 9, No. 11, 11241–11248, 2015.
4. González-Rubio G., J. González-Izquierdo, L. Bañares, G. Tardajos, A. Rivera, T. Altantzis, S. Bals, O. Peña-Rodríguez, A. Guerrero-Martínez and L. M. Liz-Marzán, "Femtosecond laser-controlled tip-to-tip assembly and welding of gold nanorods" Nano Lett., Vol. 15, 8282–8288, 2015.

# Self-collapsed meta-structures of alumina and $TiO_2$ nanowires for energy harvesting applications

**Kyuyoung Bae[1], Gumin Kang[1], Yunha Ryu[1] and Kyoungsik Kim[1*]**
[1]School of Mechanical Engineering, Yonsei University,
50 Yonsei-ro, Seodaemun-gu, Seoul 03722, Republic of Korea
[*]corresponding author: kks@yonsei.ac.kr

**Abstract**

We present novel meta-structures via self-collapsed nanowires which can be readily fabricated by aggregation due to the capillary force between the nanowires. We apply aluminum oxide and titanium dioxide nanowires to characterize both dielectric and semi-conductor materials. The self-collapsed alumina nanowire arrays exhibit high optical transmission haze to enhance the efficiency of optoelectronic devices. Ultra-broadband absorption and high photocatalyst efficiency can be also achieved by plasmonic nanostructure with metal coated nanowires for solar energy harvesting.

**REFERENCES**

1. Kang, G., Yoo, J., Ahn, J., and Kim, K., "Transparent dielectric nanostructures for efficient light management in optoelectronic applications," *Nano Today*, Vol. 10, No. 1, 22-47, 2015.
2. Kang, G. et al. "Broadband and ultrahigh optical haze thin films with self-aggregated alumina nanowire bundles for photovoltaic applications", *Energy & Environ. Sci.*, Vol. 8, 2650–2656, 2015.
3. Bae, K. et al. "Flexable thin-film black gold membranes with ultrabroadband plasmonic nanofocusing for efficient solar vapour generation", *Nat. Commun.*, Vol. 6, 10103, 2015.
4. Baek, S. et al. "Improvement of Light Extraction Efficiency in Flip-Chip Light Emitting Diodes on SiC Substrate via Transparent Haze Films with Morphology-Controlled Collapsed Alumina Nanorods", ACS Appl. Mater. Interfaces, Vol. 8, No. 1, 135-141, 2016.

# Photocatalysis through anisotropic plasmonic nanoparticles with hot spots in Au-$TiO_2$ nanoarchitectures

**M. Comesaña-Hermo,[1*] A. Sousa-Castillo,[1] M. Comesaña-Hermo,[1] B. Rodríguez-González,[1] M. Pérez-Lorenzo,[1] X.-T. Kong,[2,3] Z. Wang,[3] A. O. Govorov,[2] M. A. Correa-Duarte[1]**

[1] Department of Physical Chemistry, Biomedical Research Center (CINBIO), and Institute of Biomedical Research of Ourense-Pontevedra-Vigo (IBI), Universidade de Vigo, 36310 Vigo, Spain

[2] Department of Physics and Astronomy, Ohio University, Athens, Ohio 45701, United States

[3]Institute of Fundamental and Frontier Sciences, University of Electronic Science and Technology of China, Chengdu 610054, PR China; State Key Laboratory of Electronic Thin Films and Integrated Devices, University of Electronic Science and Technology of China, Chengdu 610054, PR China

[*]corresponding author: miguel.comesana@uvigo.es

The use of plasmonic metal nanoparticles as photosensitizers has undergone a strong development in the last few years given their ability to increase the activity of semiconductors into the visible and near infrared regions. The present work reports an experimental and theoretical study on the critical influence that shape anisotropy of gold nanoparticles exerts on the photocatalytic performance of Au-$TiO_2$ nanoarchitectures. The obtained results show that for a given amount of metallic material, Au nanostars endow titania with a strongly-enhanced catalytic efficiency compared to that found in the presence of Au nanospheres or nanorods. This is ascribed to the ability of nanostars to locally create extremely large electromagnetic field enhancements around their spikes (plasmonic hot-spots), which ensures an increased population of hot electrons close to the interface between the metal and the semiconductor. Numerical simulations confirm that the hot electron injection is a feasible mechanism behind the photosensitization process and that the nanostars should have the strongest photochemical response. These results pave the way for a more rational design of the plasmonic component in the search for high-performance photocatalytic nanoreactors operating under visible and NIR light.[1]

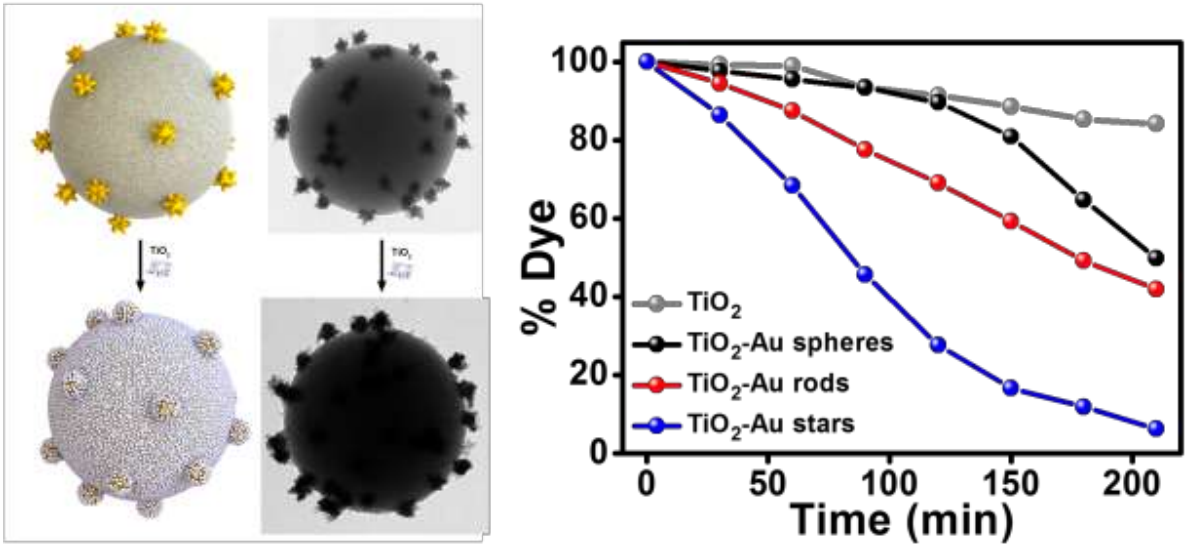


**Figure 1.** Schematic diagram of the composites synthesized (left) together with their photocatalytic behavior for the degradation of Rhodamine B (right).

**REFERENCES**

1. Sousa-Castillo A., Comesaña-Hermo M., Rodríguez-González B., Pérez-Lorenzo M., Wang Z., Kong X.-T., Govorov A. O., Correa-Duarte M. A., *submitted*.

# Comparing the Potential of Gallium and Bismuth Nanostructures for Switchable Optical Filtering

**A. Cuadrado[1], J. Toudert[1, 2], , R. Serna[1]**
[1] Instituto de Óptica, CSIC, Madrid, Spain
[2] Present address: ICFO - The Institute of Photonic Sciences, Castelldefels (Barcelona), Spain

**Abstract** Using numerical simulations, we compare the performance of plasmonic gallium and bismuth nanostructures for switchable optical filtering. They present a spectrally localized optical extinction that shifts upon solid-liquid transition, thus allowing a relevant extinction contrast at selected photon energies that depend on their nature and geometry.

Plasmonic metamaterials have attracted the attention of a broad community of scientists thanks to their capability to support resonant optical meta-effects that are especially interesting for filtering applications (resonant perfect absorbers or reflectors). The next step in the evolution of plasmonic metamaterial-based filters requires making them switchable. Gallium and bismuth are interesting candidates for building such metamaterials, due to their plasmonic properties in the ultraviolet and visible [1,2] that can be switched upon solid-liquid transition [3-5]. Using numerical simulations (finite element method), we show that gallium and bismuth nanostructures present a spectrally localized optical extinction that shifts upon solid-liquid transition, thus allowing a relevant extinction contrast at selected photon energies. We report the dependence of the extinction contrast spectrum on the nature (gallium or bismuth) and geometry of the nanostructures in order to assess their suitability for integrated switchable filters in the ultraviolet and visible.

**REFERENCES**

1. Knight M.W., Coenen T., Yang Y., Brenny B.J.M., Losurdo M., Brown A.S., Everitt H.O., and Polman A., "Gallium plasmonics: deep subwavelength spectroscopic imaging of single and interacting gallium nanoparticles", *ACS Nano* 9, 2049, 2015.
2. Toudert J., Serna R., and Jiménez de Castro M., "Exploring the optical potential of nano-bismuth: tunable surface plasmon in the near ultraviolet-to-near infrared range, *Journal of Physical Chemistry C* 116, 20530, 2012.
3. Waters R. F., Hobson P. A., MacDonald K. F., and Zheludev N. I., "Optically switchable photonic metasurfaces", *Appl. Phys. Lett.* 107, 081102, 2015.
4. Jimenez de Castro M., Cabello F., Toudert J., Serna R., and Haro-Poniatowski E. "Potential of bismuth nanoparticles embedded in a glass matrix for spectral-selective thermo-optical devices", *Applied Physics Letters* 105, 113102, 2014.
5. Cuadrado A., Toudert J., and Serna R., Polaritonic-to-plasmonic transition in optically resonant bismuth nanospheres for high-contrast switchable ultraviolet meta-filters, *arXiv.1511.04606*, 2015.

# Invited Paper: Optical Metamaterials based on p-block Elements for Switchable Nanophotonics

**J.Toudert[1, 2], A. Cuadrado[1], R. Serna[1]**
[1] Instituto de Óptica, CSIC, Madrid, Spain
[2] Present address: ICFO - The Institute of Photonic Sciences, Castelldefels (Barcelona), Spain

**Abstract** We explore the potential of p-block elements (especially Bi, Ga, Sb) for the fabrication of switchable plasmonic nanostructures and metamaterials, and demonstrate switchable plasmonic properties in nanostructured metamaterials based on such elements.

Plasmonic metamaterials have attracted the attention of a broad community of scientists thanks to their capability to support resonant optical meta-effects, such as perfect absorption [1], plasmonic phase flips [2,3], non-specular reflection or refraction [4] that provide solutions for light trapping, lensing, filtering or optically-monitored sensing. The next step in the evolution of such metamaterials requires making their plasmonic properties *switchable*. This will allow designing switchable optical components and sensors with enhanced performance. In this context, technology can profit from the use of alternative plasmonic elements or compounds that are unconventional in the plasmonic field, beyond the traditional noble metals. In this talk we will explore the potential of p-block elements for the fabrication of switchable plasmonic metamaterials. Especially, Bi, Ga and Sb display a plasmonic response in the ultraviolet – visible [5, 6] together with a switching capability upon solid-liquid transition. We will assess the plasmonic switching performance in nanostructures with different geometries. Finally we will report the fabrication and switchable response of metamaterials based on such nanostructures.

**REFERENCES**

1. Liu N., Mesch M., Weiss T., Hentschel M., and Giessen H., "Infrared perfect absorber and its application as plasmonic sensor", *Nano Lett.* 10, 2342, 2010.
2. Kravets V., Schedin F., Jalil R., Britnell L., Gorbachev R., Ansell D., Thackray B., Novoselov K., Geim A., Kabashin A., and Grigorenko A., "Singular phase nano-optics in plasmonic metamaterials for label-free single- molecule detection", *Nature Mater.* 12, 304, 2013.
3. Toudert J., Wang X., Tallet C., Barois P., Aradian A., and Ponsinet V., "Plasmonic Optical Interferences for Phase-Monitored Nanoscale Sensing in Low-Loss Three-Dimensional Metamaterials", *ACS Photonics* 2, 1443-1450, 2015.
4. Yu N., Genevet P., Kats M.A., Aieta F., Tetienne J.P., Capasso F., Gaburro Z., Light propagation with phase discontinuities: generalized laws of reflection and refraction, *Science* 334, 333, 2011.
5. Toudert J., and Serna R., Interband plasmonics with p-block elements, *arXiv.1601.01606*, 2015.
6. Cuadrado A., Toudert J., and Serna R., Polaritonic-to-plasmonic transition in optically resonant bismuth nanospheres for high-contrast switchable ultraviolet meta-filters, *arXiv.1511.04606*, 2015.

# Plasmon Enhanced Luminescence Upconversion in Self-Assembled Nanostructures

**Dawei Lu,[1] Chenchen Mao,[1] Suehyun Cho[1] and Wounjhang Park[1,2*]**

[1]Department of Electrical, Computer & Energy Engineering, University of Colorado, Boulder, United States

[2]Materials Science & Engineering Program, University of Colorado, Boulder, United States

[*]Corresponding author: won.park@colorado.edu

**Abstract**- We present a comprehensive theoretical and experimental study on plasmon enhancement of energy transfer upconversion in rare earth activated upconversion nanoparticles (UCNPs). The UCNPs and plasmonic nanostructures were coupled by electrostatic self-assembly or nucleic acid directed self-assembly. A detailed spectroscopic study together with a theoretical study based on quantum electrodynamics revealed the mechanisms involved in the plasmon enhancement and quantitatively determine the contribution by each mechanism. This study provides a clear pathway for advanced engineering of plasmon enhanced upconversion materials.

Frequency conversion is one of the most important phenomena in optics with a wide variety of applications. Frequency conversion by optically active ions is of special interest because it exhibits efficiencies far higher than the better known counterpart using nonlinear susceptibility.[1] Thanks to the high efficiency, these processes do not require phase matching and can be excited by incoherent light source at low intensities. This unique feature naturally opens doors to many new applications including solar energy conversion and bioimaging. However, despite the recent progress in the synthesis of high quality UCNPs, their efficiencies remain too low to impact the targeted applications in significant ways. Coupling with surface plasmon offers a promising way to dramatically enhance the conversion efficiency. While there has been a rapid increase in number of publications on this topic, the precise enhancement mechanism has remained elusive. This paper reports the recent progress that sheds light on the mechanism of plasmon enhancement of ETU process.

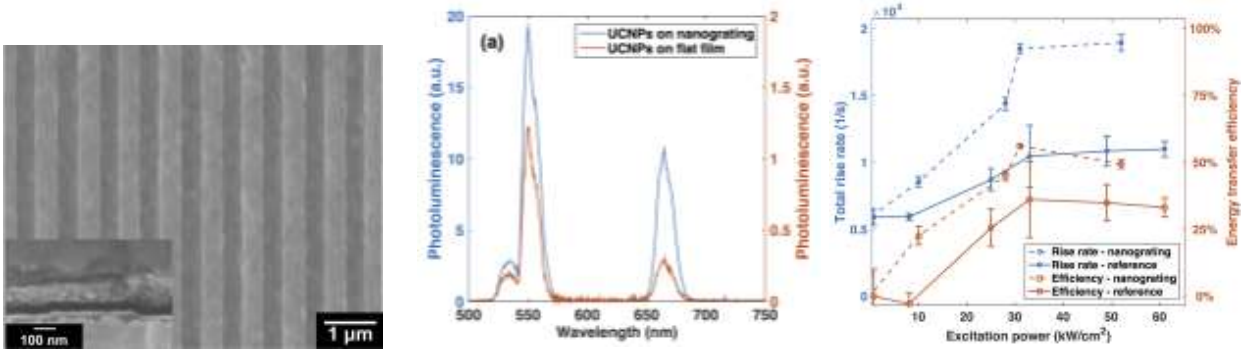
We used the thermal decomposition technique to synthesis UCNP nanoparticles with highly monodispersed size distributions ranging from 10 to 70 nm.[2] For further processing, the as-synthesized UCNPs are coated with poly(maleic anhydride-*alt*-1-octadecene) (PMAO). The amphiphilic polymer serves two functions. First it makes the hydrophobic surface of as-synthesized UCNPs hydrophilic, turning the UCNPs water soluble. Additionally, PMAO provides negative charge, enabling electrostatically driven layer-by-layer deposition of UCNPs with precise control of thickness. Using the latter characteristic, we deposited 3 monolyaers of UCNPs on a sliver nanograting fabricated by the laser interference lithography (LIL).[3] To alleviate quenching, a thin $Si_3N_4$ spacer layer was deposited between the nanograting and UCNP layers. The nanograting and UCNP deposited on nanograting are shown in Fig. 1(a). The grating is designed in such a way that, after $Si_3N_4$ and UCNP deposition, it exhibits a strong plasmon resonance at 980 nm, the absorption wavelength of UCNP. Photoluminescence (PL) spectroscopy revealed that the green and red emission bands are enhanced by 14x and 39x, respectively, by the plasmon resonance supported by the nanograting structure, as shown in Fig. 1(b).

In order to elucidate the enhancement mechanism, we set up a system of rate equations describing the ETU process in $NaYF_4:Yb^{3+},Er^{3+}$.[3,4] The theoretical analysis showed that the enhancement is entirely due to

absorption enhancement in the strong excitation limit while it depends on both absorption enhancement and energy transfer enhancement.

$$F_{weak} = F_{ET} F_{abs}^2, \quad F_{strong} = F_{abs}$$

The quadratic dependence on the absorption enhancement in the weak excitation regime shows the possibility of dramatic enhancement due to the nonlinear nature of the ETU process. This is why we were able to observe sizable PL enhancement despite that the absorption enhancement in our structure is rather modest, ~3x. Also, one of the long standing dispute in the field is whether plasmon resonance can actually enhance energy transfer rate. To address this issue, we conducted a comprehensive time-resolved PL spectroscopy and experimentally showed that the plasmon resonance does enhance the energy transfer process.[5] From direct measurement of rise and decay of infrared emission, we were able to quantitatively determine the energy transfer rate and found that the plasmon resonance enhanced the energy transfer rate and efficiency by 2.7x and 1.6x, respectively, in the strong excitation regime. In the weak excitation regime where the density of ions in the intermediate level is low, the energy transfer rate was too low to be measured but for the same reason the enhancement could be much higher. In summary, this study presents two crucial conclusions: (1) plasmon enhancement of luminescence upconversion is dominated by the absorption enhancement and (2) plasmon resonance does enhance energy transfer processes but to a lesser degree than absorption.




(a) (b) (c)

**Figure 1. (a) SEM micrograph of silver nanograting fabricated by laser interference lithography (inset: cross sectional SEM of UCNPs deposited on nanograting), (b) photoluminescence spectra of UCNPs on nanograting and flat film, and (c) experimentally measured energy transfer rate and efficiency as a function of excitation power density.**

**Acknowledgements** This work was supported in part by the Army Research Office through the grant W911NF-14-1-0211 and also by the National Science Foundation through the grant CHE-1125935 and the Soft Materials Research Center MRSEC Grant DMR-1420736.

## REFERENCES

1. F. Auzel, Chem. Rev. **104**, 139 (2004).
2. Z. Li, W. Park, G. Zorzetto, J. S. Lemaire, and C. J. Summers, Chem. Mater. **26**, 1770 (2014).
3. D. Lu, S. K. Cho, S. Ahn, L. Brun, C. J. Summers, and W. Park, ACS Nano **8**, 7780 (2014).
4. W. Park, D. Lu, and S. Ahn, Chem. Soc. Rev. **44**, 2940 (2015).
5. D. Lu, C. Mao, S. K. Cho, S. Ahn, and W. Park, Sci. Rep. **6**, 18894 (2016).

# Optical and Opto-electronic Properties of Self-Assembled Meta Systems.

**A.M. Urbas**
[1]Air Force Research Lab, USA
[*]corresponding author: augustine.urbas@gmail.com

**Abstract-** Metamaterials provide the ability to design materials properties to meet the unique needs of applications beyond what is possible with conventional materials. From spatially tailored dielectrics to tunable, dynamic material properties and unique nonlinear behavior, these systems offer tremendous flexibility to application engineers. Fabrication of these material systems has remained a key challenge, though significant progress has been made. The incorporation of multiple functional material types into patterned and structured materials is the principle route to leveraging the potential of metamaterials to provide active and widely tunable response. Self-assembly offers a suite of capabilities for forming and arranging multi-material systems in complex, three dimensional and precise structures. Decades of work in self-assembly has yielded a toolbox of materials and techniques to enable fabrication, even at nanometric dimensions. In this presentation, we will explore systems that leverage self-assembly primarily and as a component of hybrid assembly techniques to produce meta-systems with new properties in linear and nonlinear optics as well as opto-electronic applications. The materials and effects span wavelength ranges and demonstrate the potential for precise and localized fabrication and large area complex materials synthesis.

# Band-edge photonics: a promising approach for next-generation light emitters

**Kyungtaek Min**[1,2] **and Heonsu Jeon**[1,2*]

[1]Department of Physics and Astronomy, Seoul National University, Seoul 08826, Korea

[2]Inter-university Semiconductor Research Center, Seoul National University, Seoul 08826, Korea

[*]corresponding author: hsjeon@snu.ac.kr

Photonic crystal band-edge mode has an intriguing property: its optical mode profile is periodically bunched over an extended area. The most common application have been band-edge lasers, which can be obtained by tuning a band-edge mode to the emission wavelength of gain material. In this talk, we present a new approach in utilizing band-edge modes, where a band-edge mode is tuned to excitation wavelength. By properly designing the photonic crystal structure, we could obtain a large enhancement in optical absorption and therefore subsequent fluorescence, which is particularly suitable for phosphor applications.

# Ultra-confined acoustic THz graphene plasmons revealed by photocurrent nanoscopy

Pablo Alonso-González[1,2], Alexey Y. Nikitin[1,3], Yuanda Gao[4], Achim Woessner[5], Mark B. Lundeberg[5], Alessandro Principi[6], Nicolò Forcellini[7], Wenjing Yan[1], Saül Vélez[1], Andreas. J. Huber[8], Kenji Watanabe[9], Takashi Taniguchi[9], Luis E. Hueso[1,3], Marco Polini[10], James Hone[4], Frank H. L. Koppens[5,11], and Rainer Hillenbrand[3,12]

[1]*CIC nanoGUNE, E-20018, Donostia-San Sebastián, Spain,* [2]*Departamento de Física, Universidad de Oviedo, Oviedo 33007, Spain,* [3]*IKERBASQUE, Basque Foundation for Science, 48011 Bilbao, Spain,* [4]*Department of Mechanical Engineering, Columbia University, New York, NY 10027, USA,* [5]*ICFO-Institut de Ciencies Fotoniques, The Barcelona Institute of Science and Technology, 08860 Castelldefels (Barcelona), Spain,* [6]*Radboud University, Institute for Molecules and Materials, NL-6525 AJ Nijmegen, The Netherlands,* [7]*Department of Physics, Imperial College London, London SW7 2AZ, United Kingdom,* [8]*Neaspec GmbH, Martinsried, Germany,* [9]*National Institute for Materials Science, 1-1 Namiki, Tsukuba 305-0044, Japan,* [10]*Istituto Italiano di Tecnologia, Graphene labs, Via Morego 30 I-16163 Genova, Italy,* [11]*ICREA – Institució Catalana de Recerça i Estudis Avancats, Barcelona, Spain,* [12]*CIC NanoGUNE and EHU/UPV, E-20018, Donostia-San Sebastian, Spain*

The interaction of terahertz (THz) radiation with graphene has a vast application potential in many technologies, including imaging, communications, sensing, or photo-detection, among others. Recently, it has been shown that the excitation of localized THz plasmons in graphene can strongly enhance light-matter interactions, opening the door to more efficient optoelectronic devices. Here, we will present on the first visualization of propagating graphene plasmons (GPs) at THz frequencies, which can also be controlled by metallic (split) gates. Intriguingly, due to the coupling of GPs with the metal gate underneath we observe a linearization of the plasmon dispersion (thus revealing acoustic plasmons), which comes along with an extreme confinement of the plasmon fields [1]. These extraordinary GPs properties are very promising for sensing and communication technologies. To map the THz GPs, we introduce nanoscale-resolved THz photocurrent nanoscopy as a novel tool for studying fundamental and applied aspects of local THz photocurrent generation with a resolution of 25 nm, nearly 4 orders of magnitude below the diffraction limit.

References

[1] P. Alonso-González, A. Y. Nikitin, Y. Gao, A. Woessner, M. B. Lundeberg, A. Principi, N. Forcellini, W. Yan, S. Vélez, A. J. Huber, K. Watanabe, T. Taniguchi, L. E. Hueso, M. Polini, J. Hone, F. H. L. Koppens, and R. Hillenbrand, arXiv:1601.05753 [cond-mat.mes-hall], (2016).

**Nanophotonics, optical forces and the momentum of light**

# Manipulation of optical gradient forces for reconfigurable and selective assembly of gold nanoplates.

**Delphine Coursault[1*], Ying Bao[1], Patrick Figliozzi[1], Zijie Yan[1,2] and Norbert F. Scherer[1]**

[1] The James Franck Institute and Department of Chemistry, The University of Chicago, 929 East 57th Street, Chicago, Illinois 60637, USA.

[2] Department of Chemical and Biomolecular Engineering, Clarkson University, Potsdam, NY 13699, USA.

[*]corresponding author: dcoursault@uchicago.edu

**Abstract** We investigate directed-assembly of plasmonic nanoplates in a tightly focused beam. We demonstrate the reconfigurability of the assembly by altering the phase gradient achieved via holographic beam shaping. The slower motion of the nanoplates as compared with plasmonic nanospheres allows for a precise study of their assembly/disassembly dynamics. We observe a strong correlation of their motion far from the center of the trap that we are using to create extended arrays of plasmonic nanoparticles without collapsing the so-called "optical matter" structures.

Organization of matter into well-controlled and ordered structures is one of the main pursuits of nanoscience, especially for applications in nanophotonics. Top-down techniques such as e-beam or focused ion beam lithography and bottom-up ones such as self-assembly are widely used to create static ordered nanostructures. However, the research agenda is now shifting towards achieving tunable, switchable or nonlinear functionalities, which requires dynamic or reconfigurable nanostructures. To achieve this goal, the next generation of optical tweezers coupled with spatial light modulators (SLMs) for phase control, offers tremendous opportunities.[1-3]

Here we investigate optical trapping of plasmonic nanoplates. We are able to trap and orient the nanoplates in minimally shaped optical beams and can assemble/disassemble and orient them along unique directions. The optical phase gradients driven assembly and disassembly of the nanoplates over tens of micron are achieved via holographic beam shaping using a spatial light modulator[3-5] by inverting the phase gradient.

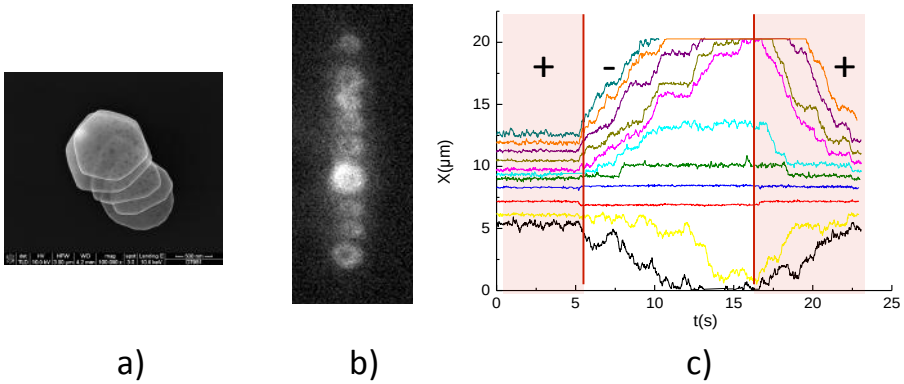



**Figure 1: a) TEM image of the gold nanoplates; b) Dark field image of the gold nanoplates linearly trapped in solution; c) Trajectories of the trapped nanoplates by inverting the phase gradient.**

This result corroborates recent findings on the importance of the phase gradient contribution to the optical gradient forces[6]. While the nanoplates exhibit a slower motion as compare to the plasmonic nanospheres[6], we conclude that sensitivity to the phase gradient versus the intensity gradient can be tuned. As opposed to the transition from 1D to 2D or amorphous organization of nanospheres[6], the compressive force imposed by the phase gradient[6] is decreased in the case of the nanoplates.

The smaller velocity of the nanoplates allows us to observe a strong correlation of their linear motion during the assembly and disassembly process. Remarkably, this correlated motion occurs as far as tens of micron away from the center of the line trap. The light scattered by each plasmonic nanoplate is thus strong enough to generate significant forces on neighboring ones. This phenomenon is known as optical binding[7,8]. We recently utilized it to direct the assembly of spherical metal nanoparticles (with sizes satisfying the Rayleigh criterion) into optically-bonded supra-crystals[8]. We show here that it can be extended to highly anisometric nano-objects (aspect ratio≥10).

Our findings demonstrate that control over the phase gradient force opens the route on the one hand for stabilizing large scale assembly, and on the other hand for sorting nanoparticles of various sizes (and shapes) in polydispersed colloidal solution.

**Acknowledgements**: This work was supported by a grant from the Department of Defense (National Security Science and Engineering Faculty Fellowship).

**REFERENCES**

1. Grier, D. G., "A revolution in optical manipulation ", *Nature*, Vol.424, 810-816, 2003.
2. Čžimár, T. Romero, L. C. D., Dholakia, K. & Andrews, D. L., "Multiple optical trapping and binding: new routes to self-assembly", *J. Phys. B: At. Mol. Opt. Phys.* Vol.43, 102001, 2010.
3. Yan, Z. J. et al, "Hierarchical photonic synthesis of hybrid nanoparticle assemblies", *J. Phys. Chem. Let.*, Vol.4, 2630-2636, 2013.
4. Yan, Z. et al., Shah, R. A., Chado, G., Gray, S.K., Pelton, M. and Scherer, N.F., "Guiding Spatial Arrangements of Silver Nanoparticles by Optical Binding Interactions in Shaped Light Fields", *ACS Nano*, Vol. 7, 1790-1802, 2013.
5. Bao, Y et al, 2014 *J. Phys. Chem. C*, Vol. 118, No.33, 19315–21, 2013.
6. Yan, Z., Sajjan, M. and Scherer, N.F., "Fabrication of a Material Assembly of Silver Nanoparticles Using the Phase Gradients of Optical Tweezers", *Phys. Rev. Lett.*, Vol. 114, 143901, 2015.
7. Roichman, Y., Sun, B., Roichman, Y., Amato-Grill, J., and Grier, D.G., "Optical Forces Arising from Phase Gradients", *Phys. Rev. Lett.*, Vol. 100, 013602, 2008.
8. Burns, M. Fournier, J. M. and Golovchenko, J. A., "Optical binding", *Phys. Rev. Lett.*, Vol.63, 1233-1236, 1989.
9. Yan, Z., Gray, S.K. and Scherer, N.F., "Potential energy surfaces and reaction pathways for light-mediated self-organization of metal nanoparticle clusters", *Nat.Com*. Vol.5, 3751, 2014.

# Significance of the electromagnetic spin and orbital-angular-momentum conservation: The optical torque.

*Manuel Nieto-Vesperinas*
**www.icmm.csic.es/mnv**
**Instituto de Ciencia de Materiales de Madrid, CSIC**
**Cantoblanco, Madrid 28049**
**mnieto@icmm.csic.es**

## ABSTRACT

We address the scattering of an electromagnetic field by a small particle, dipolar in the wide sense. We put forward a scattering component ST of the optical torque exerted on the body [1,2] which has been overlooked in all research so far. This ST cancels the usually called extinction torque ET, which was often considered to be responsible for the particle spinning. Also we show the contribution of the spatial structure and polarization of the wave to this torque, unknown to this date, demonstrating that it often leads to a negative torque on a single particle, so producing an orbital motion contrary to its spinning. Furthermore, we establish a decomposition of the electromagnetic torque into conservative and nonconservative components in which the helicity and the spin angular momentum play a role analogous to the energy and its flux for electromagnetic forces.

1. M. Nieto-Vesperinas, Opt. Lett. **40**, 3021 (2015).

2. M. Nieto-Vesperinas, Phys. Rev. A **92**, 043843 (2015).

# Optical negative forces on particles near plasmonic interfaces

**S.V. Sukhov[1,2,3] , M.I. Petrov[2] , A.A. Bogdanov[2,4], A.S. Shalin[2,3,5*] , and A. Dogariu[1]**

[1] CREOL, University of Central Florida, Orlando, Florida, USA

[2] ITMO University, St. Petersburg, Russia

[3] Kotelnikov Institute of Radio Engineering and Electronics of Russian Academy of Sciences (Ulyanovsk branch), Ulyanovsk, Russia

[4] Ioffe Institute, St Petersburg, Russia

[5] Ulyanovsk State University, Ulyanovsk, Russia

[*]corresponding author: alexandesh@gmail.com

**Abstract**- We demonstrate that gradientless light fields can exert pulling force on a dipolar particle located on a plasmonic interface. The forces acting against the propagation of light arise due to the amplification of the photon linear momentum when surface plasmon polaritons are excited at the plasmonic interface. This effect can be utilized for effective optomechanical control of nano-objects over metallic surfaces.

Optical "tractor beams" have attracted much interest recently because of their intriguing capabilities for micromanipulation [1]. A tractor beam can exert a "negative" force (NF) that pulls the scatterer in a direction opposite to the propagation of light, in contrast to the usually "positive" push exerted by radiation pressure. The fundamental requirement for NF to occur is the increase of the momentum of light during the process of light scattering. Previously we demonstrated that stable NFs are possible for objects placed at the interface of liquid dielectric media [2]. In this case, momentum of light increases when light goes from medium with lower to higher refractive index. This approach does not work for solid interfaces when manipulated particle should be completely outside the substrate. In present work we show theoretically that optical pulling force is still possible if nanoparticle is placed in the vicinity of plasmonic interface.

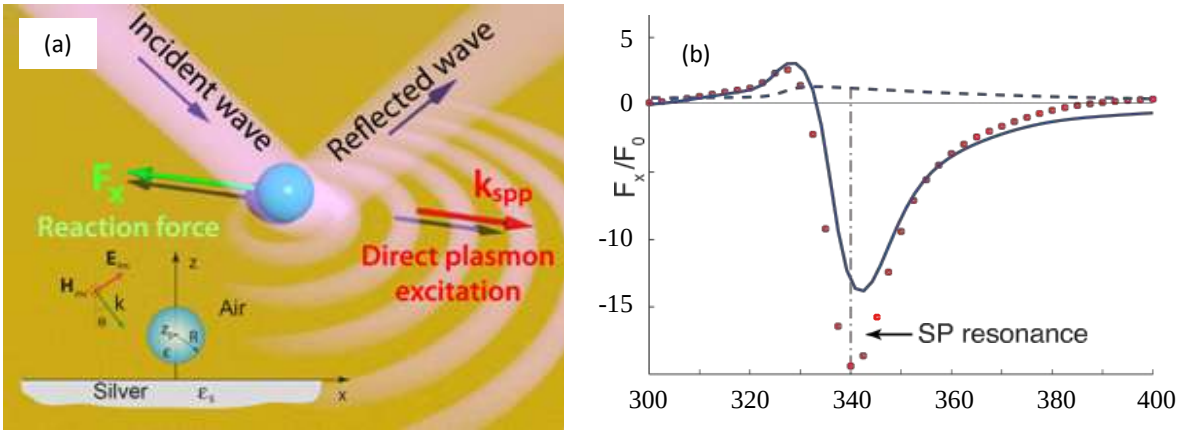



**Figure 1**. (a) The geometry of the problem; (b) The spectral dependence of the longitudinal force $F_x$ acting on a dielectric nano-particle placed in air above a silver surface. The solid line corresponds to the dipole model of Eq.(1), the dotted line corresponds to the numerical calculations. The dashed line corresponds to the dipole model without contribution of SPP. The dash-dotted line shows to the SP resonance wavelength.

We consider a spherical dielectric nanoparticle located in air at certain height $z_0$ above a substrate with permittivity $\varepsilon_s$ (Figure 1a). The particle is illuminated with unstructured wave having wavenumber $k$. Theoretical analysis of the optical force acting on a particle in a vicinity of a plasmonic interface can be provided in a framework of point dipole approximation using the Green function technique [3]. After some algebra, the expression for the force acting along the interface becomes

$$F_x = F_x^0 + F_x^D, \tag{1}$$

$$F_x^0 = \tfrac{1}{2} k_x \left( \mathrm{Im}\,\alpha_x \,|\, E_x^0 \,|^2 + \mathrm{Im}\,\alpha_z \,|\, E_z^0 \,|^2 \right), \quad F_x^D = -\frac{k^2}{\varepsilon_0} \mathrm{Im}(p_x^* p_z)\, \mathrm{Im}(\partial_x G_{xz}^R),$$

where $\hat{\alpha}$ is the polarizability of dipole particle, $\mathbf{E}^0$ is the amplitude of incident field, $\hat{G}$ is the Green's function for a particle located near the substrate. The first term in the right hand side of Eq.(1) corresponds to the ordinary radiation pressure and is always positive. The second term corresponds to the interaction of the particle with the substrate; we show that this term can become negative in certain cases. As one can see from the expression for $F_x^D$, two main factors contribute to the appearance of negative force. The interference between the incident and reflected waves produces a phase difference between the components of dipole moment $\mathbf{p}$. This rotating dipole with asymmetric scattering pattern produces directional excitation of surface plasmon polaritons (SPPs) [4] and enhances the linear momentum of scattered light. The strongly asymmetric SPP excitation is determined by spin-orbit coupling of the rotating dipole and SPP. As a result of the total momentum conservation, the force acting on the particle points in a direction opposite to the incident wave propagation. Figure 1b shows longitudinal force $F_x$ calculated for different wavelengths of incident wave. Both analytical and numerical calculations confirm the appearance of negative force in the conditions of SPP excitation.

In summary, we have demonstrated that paraxial optical fields can act as a "tractor beam" along a plasmonic interface. The asymmetric excitation of surface plasmon polaritons induces the amplification of the forward scattering momentum leading to negative scattering forces pulling objects in the direction opposite to the beam propagation. This simple scheme may find applications for developing novel nano-manipulation approaches.

**ACKNOWLEDGEMENT**

This work has been supported by the Russian Fund for Basic Research within the projects #15-02-01344, #14-02-01223, #16-52-00112, and #16-37-60064. The numerical simulation of optical pulling force has been supported by the Russian Science Foundation Grant No. 14-12-01227. The analytical calculations of field and forces distributions have been supported by the Russian Science Foundation Grant No. 16-12-10287.

**REFERENCES**

1. Dogariu, A., S. Sukhov and J. J. Saenz, "Optically induced 'negative forces'," *Nature Photon*. Vol. 7, No.1, 24-27, 2013.
2. Kajorndejnukul, V., W. Ding, S. Sukhov, C.-W. Qiu and A. Dogariu, "Linear momentum increase and negative optical forces at dielectric interface," *Nature Photon*. Vol.7, No.10, 787-790, 2013.
3. Petrov, M.I., S.V. Sukhov, A.A. Bogdanov, A.S. Shalin and A. Dogariu, "Surface plasmon polariton assisted optical pulling force," *Laser Photon. Rev*. V.122, No.1, 116-122, 2016.
4. Mueller, J. P. B., F. Capasso, "Asymmetric surface plasmon polariton emission by a dipole emitter near a metal surface," *Phys. Rev. B*, Vol.88, No.12, 121410(R), 2013.

# Boundary optical stress: pressure or tension?

**Shubo Wang**[1], **and C. T. Chan**[1*]
[1] Department of Physics and Institute for Advanced Study,
The Hong Kong University of Science and Technology, Hong Kong.
[*]corresponding author: phchan@ust.hk

**Abstract**-Using a generic microscopic model, we show that the boundary stress induced by an electromagnetic plane wave in a negative-refractive-index metamaterial depends not only on the macroscopic effective permittivity and permeability but also on the microscopic lattice symmetry of the polarizable units that constitute the metamaterial. The lattice effect is attributed to electrostriction and magnetostriction which can be accounted for by the Helmholtz stress tensor within the context of effective medium theory.

It is well known that light carrying momentum $\hbar\mathbf{k}$ exerts a positive photon pressure on an object in vacuum. With the advent of metamaterials which can have negative refractive indices, does photon pressure become photon tension in such a kind of material?

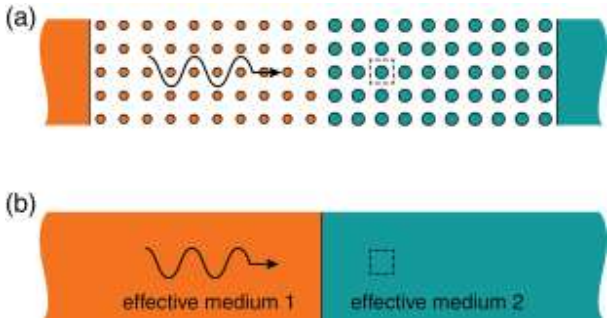



Figure 1. (a) The microscopic model system and (b) the effective medium system.

To answer the question we use a generic microscopic model as shown in Fig.1 (a), where two kinds of materials carrying different microstructures form a boundary in the middle. Near the boundary the materials are discretized into a lattice consisting of polarizable units (electric/magnetic dipoles), say for example, a square lattice here. The incident electromagnetic plane wave propagates from the left hand side to the right hand side and we are interested in the optical stress exerted on the boundary region. In the long wavelength limit the lattice system can be approximated as an effective medium system [Fig. 1(b)] characterized by the macroscopic effective permittivity and permeability. In the microscopic model system, the boundary stress is determined as follows. We first solve for the total field by using an analytical Green's function method. Then the optical force acting on each polarizable unit is calculated by using the Maxwell stress tensor approach. The boundary stress is obtained by summing the force acting all the units within the boundary region. We considered three kinds of lattice system: square lattice, triangle lattice and amorphous lattice and found that they have different boundary stress, although they are designed to have the same effective permittivity and permeability and hence correspond to the same effective medium system. This means that the boundary stress is, in fact, indeterminate if only the

macroscopic effective parameters are specified. Light can either push or pull a metamaterial boundary, depending also on the microscopic lattice structure of the polarizable units that constitute the medium.

Within the effective medium theory, the corresponding boundary stress can be determined using the Helmholtz stress tensor [1-3]:

$$\left\langle T_{ij}^{\mathrm{H}} \right\rangle = \frac{1}{2}\mathrm{Re}\left[ \varepsilon_0 \varepsilon_{\mathrm{eff}} E_i E_j^* + \mu_0 \mu_{\mathrm{eff}} H_i H_j^* - \frac{1}{2}\left( \varepsilon_0 \varepsilon_{\mathrm{eff}} E^2 + \mu_0 \mu_{\mathrm{eff}} H^2 \right)\delta_{ij} - \frac{1}{2}\left( \varepsilon_0 \frac{\partial \varepsilon_{\mathrm{eff}}}{\partial u_{ij}} E^2 + \mu_0 \frac{\partial \mu_{\mathrm{eff}}}{\partial u_{ij}} H^2 \right) \right] , \quad (1)$$

where $\partial \varepsilon_{\mathrm{eff}} / \partial u_{ij}, \partial \mu_{\mathrm{eff}} / \partial u_{ij}$ are electrostriction and magnetostriction terms that take into account the microscopic lattice information and they can be analytically derived using multiple scattering theory or numerically retrieved based on the band structure of the lattice. Using this stress tensor one can predict the boundary stress that match the results of the microscopic model system very well. Other forms of stress tensors such as Abraham, Minkowski or Einstein-Laub cannot predict the correct results for boundary optical stresses due to the absence of lattice-structure dependent terms.

Our results may shed light on the study of optical force density inside dielectric medium and may find applications in the field of biophysics (e.g., how the electromagnetic stress will deform a biological cell).

**Acknowledgements**

We thank Prof. Z. Q. Zhang and Dr. W. J. Sun for their valuable comments and suggestions. This work was supported by the Hong Kong Research Grants Council (AoE/P-02/12).

**REFERENCES**

1. Landau, L. D., E. M. Lifshitz and L. P. Pitaevskii, *Electrodynamics of Continuous Media*, Elsevier, Singapore, 1960.
2. Sun, W. J., S. B. Wang, J. Ng, L. Zhou and C. T. Chan, "Analytic derivation of electrostrictive tensors and their application to optical force density calculations," *Phys. Rev. B*, Vol. 91, 235439, 2015.
3. Wang, S. B., J. Ng, M. Xiao and C. T. Chan, "Electromagnetic stress at the boundary: Photon pressure or tension?", *Sci. Adv*., accepted.

# THz polarization control with chiral metamaterials

**M. Kafesaki[1,2], G. Kenanakis[1], A. Xomalis[1,2], M. Farsari[1], G. Konstantinidis[1], E. N. Economou[1], C. M. Soukoulis[1]**

[1]Foundation for Research and Technology Hellas (FORTH), Institute of Electronic Structure and Laser (IESL), N. Plastira 100, 70013 Heraklion, Crete, Greece

[2]University of Crete, Department of Materials Science and Technology, Crete, Greece

[3]Ames Laboratory and Dept. of Physics and Astronomy, Iowa State University, Ames Iowa, 50011

[*]corresponding author: kafesaki@iesl.forth.gr

**Abstract**- We discuss our studies on THz planar chiral metamaterials and the potential they show for THz polarization control. Besides planar structures we discuss also 3D bulk chiral metamaterial structures enabling additional functionalities, such as asymmetric transmission, asymmetric perfect absorption, and broadband polarization conversion for both linear and circularly polarized waves.

Chiral metamaterials, showing chirality orders of magnitude larger than that of natural chiral materials, offer great potential for the manipulation of wave polarization. Such potential is extremely useful in THz and far-infrared (IR) ranges, where natural materials do not show strong response and therefore they are not offered for the realization of optical components, while there is great potential in applications. Combining chirality (magnetoelectric coupling) with structural anisotropy one can get an even richer response compared to that of bi-isotropic chiral structures, allowing phenomena such as asymmetric transmission, asymmetric perfect absorption, giant polarization conversion etc.

In this work we studied, both theoretically and experimentally, a variety of THz and far-IR chiral metamaterials, both planar isotropic [1,2] and anisotropic three-dimensional ones [3]. The isotropic planar structures, which were fabricated by UV lithography on flexible substrates and operate in few THz, showed giant optical activity, large circular dichroism and negative index of refraction, offering promising candidates for the realization of various THz polarization control components and systems, like wave-plates and polarizers. The three-dimensional anisotropic structures, which were fabricated by direct laser writing, demonstrated a variety of polarization dependent phenomena, including asymmetric transmission, asymmetric polarization conversion, asymmetric narrow-band perfect absorption and others, showing unique potential in functionalities such as polarization isolation, and polarization conversion and filtering.

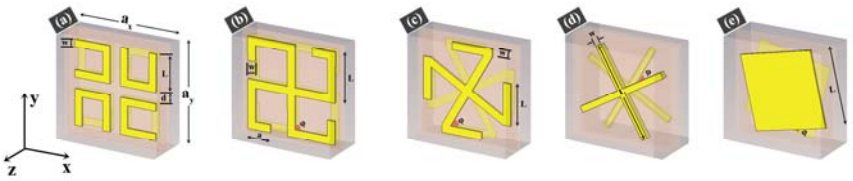



Fig. 1: The unit cell of the planar isotropic chiral metamaterials under study (yellow color indicates metal, grey indicates polyimide). The characteristic geometrical features marked on the figure are of the order of few microns. The wave propagation is along the z axis.

**Acknowledgements**. We acknowledge financial support by the EU projects ERC-PHOTOMETA, FET project Graphene Flagship, and EU-RUS project EXODIAGNOS.

**REFERENCES**

1. G. Kenanakis, R. Zhao, A. Stavrinidis, G. Konstantinidis, N. Katsarakis, M. Kafesaki, C. M. Soukoulis, E. N. Economou, "Flexible chiral metamaterials in the terahertz regime: a comparative study of various designs", *Opt. Mat. Express*, Vol. 2(12), 1702-1712, 2012.
2. G. Kenanakis, R. Zhao, N. Katsarakis, M. Kafesaki, C. M. Soukoulis, E. N. Economou, Optically controllable THz chiral metamaterials, *Opt. Express*, Vol. 22(10), 12149-12159, 2014.
3. G. Kenanakis, A. Xomalis, A. Selimis, M. Vamvakaki, M. Farsari, M. Kafesaki, C. M. Soukoulis, and E. N. Economou, "Three-dimensional infrared metamaterial with asymmetric transmission", *ACS Photon*., Vol. 2, 287-294, 2015.

# Strong coupling between waveguide-modes of opposite directionality: nearly-frozen light modes

**S. Foteinopoulou**[1*]
[1]Univ. of New Mexico, USA
[*]corresponding author: sfoteino@unm.edu

**Abstract**-Conventional dielectric waveguides support forwards light modes, where the phase velocity is parallel to the energy velocity. On the other hand, metamaterial waveguides having a negative refractive index support backwards light modes, with anti-parallel phase and energy velocities. We will discuss, how these two individual native modes can strongly couple into a new exotic "nearly-frozen" light mode. This unconventional light mode gives rise to an extra-ordinary mesoscale EM enhancement that is important to harnessing a strong light-matter interaction.

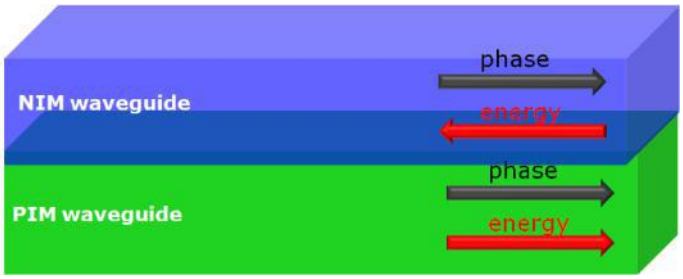



**Figure 1:** The exotic heterostructure waveguide comprising two waveguides made of a positive refractive index material (PIM) and a negative refractive index material (NIM) respectively.

We know that dielectric slab waveguides behave essentially like an optical fiber, where light is confined and guided through the slab area, with EM energy exponentially decaying outside. Conversely, negative-refractive-index slab waveguides, act very much similarly to dielectric waveguides, albeit the phase-fronts and EM energy of the light mode propagate in opposite directions (backward-wave propagation). Now, if we join together two waveguides of opposite refractive index into a hetero-structure waveguide we observe a remarkable phenomenon. A new exotic light mode emerges from strong coupling of the individual native modes in the NIM, PIM waveguides. This mode does not share the characteristics of either of the native modes in the constituent waveguides and appears "nearly-frozen," with an ultra-low energy velocity, 300 times smaller the vacuum speed of light, as calculated with ab-initio EM simulations [1].

Ultra-slow light is not a new concept; other paradigms have been reported before, based on either engineering the back-scattering and diffraction in periodically patterned materials [2] or relying on polar resonant atomic systems [3]. However, neither of the latter systems is capable of an electric-field enhancement covering a mesoscale area, demonstrated by the system of Fig. 1. This is because of either high insertion and radiation losses (for the systems of Ref. [2]) or because of energy storage into the atomic polarization rather than the electric field itself (for the systems of Ref. [3]). Thus, the paradigm of Fig. 1 exhibits a unique capability for intensity enhancement which can extend over large mesoscopic areas.

It is therefore important to understand how this photonic slow "super-mode" is formed. We will discuss the formation of such slow super-mode in the context of the interaction between the native modes in the two waveguides of opposite wave-handiness, as this transitions from the weak- to the strong- coupling regime. Our

analysis aims to bring about systematic ways of harnessing pulse delay, that is relevant to optical computing applications.

**REFERENCES**


1. Foteinopoulou, S. and Vigneron, JP, "Extended slow-light field enhancement in positive-index/negative-index heterostructures," *Phys. Rev. B* Vol. 85, 195144-1-8, 2013.
2. Gersen, H., Karle T. J., Engelen , R. J. P., Bogaerts, W., Korterik, J. P., Van Hulst, N.F., Krauss, T. F., and Kuipers, L., "Real-space observation of ultraslow light in photonic crystal waveguides," *Phys. Rev. Lett.* Vol. 94**,** 073903 (2005).
3. Khurgin, J., "Slow light in various media: a tutorial," *Adv. Opt. Mat.* Vol. 2, 287 (2010).

# Measurement of Sub-femtonewton forces at the thermal limit in fluid

**L. Liu**[1], **S. Kheifets**[1], **V. Ginis**[1,2], and **F. Capasso**[1]

[1]Harvard University, USA
[2]Vrije Universiteit Brussel, Belgium

**Abstract**— We present the first measurements of sub-femtonewton forces in fluid. The measurements, which we show to be limited only by room temperature thermal noise, are about two orders of magnitude more sensitive than has been previously reported. We apply our technique to measure the optical force on a microsphere in the presence of an evanescent wave. The results are in quantitative agreement with Mie theory predictions and the first such confirmation of its kind.

Pico-newton force spectroscopy is well-covered by existing methods such as atomic force microscopy (AFM). They have enabled position-dependent force measurements which have enhanced our understanding of various physical, chemical, and biological systems. However, especially in liquid media, the sensitivity of AFM's is limited by the large damping coefficient of a typical cantilever. This fundamental thermal limit cannot be circumvented by simply introducing more compliant cantilevers. We must reduce the footprint of our probe.

An existing technique called photonic force microscopy (PFM) aims to do just this with an optically trapped microsphere as probe. In this scheme, the probe is trapped in two dimensions and allowed to move freely (under the influence of gravity) in the third. In its free motion, the probe samples the trapping volume. By inverting the Boltzmann formula, independent samples of its position may be converted into a potential energy landscape. A derivative of this potential energy profile then gives a position-dependent force. This technique, though slightly more sensitive than the AFM, is unable to measure at the thermal limit, which remains about two orders of magnitude beyond reach.

By combining an optical tweezer to precisely position the microsphere probe in 3D, a capacitive sensor-piezo loop to control drift, and a lock-in detection scheme to minimize the effect of 1/f noise in our system, we demonstrate, for the first time, thermal-limited force measurements in a microsphere probe system. We demonstrate this with a measurement of Mie scattering optical forces on the microsphere in the presence of an evanescent field. We are able to achieve sub-fN force resolution in measurements of about 100 seconds in length.

## ACKNOWLEDGMENT

We acknowledge the support of NSF GFRP grant number DGE1144152 and the Research Foundation Flanders grant number 12O9115N. All fabrication was done in the Harvard Center for Nanoscale Sciences (CNS) clean room facility. We kindly thank the groups of Evelyn Hu and David Weitz at Harvard University for shared equipment and lab access, and Alexander Woolf for his contributions.

## REFERENCES

1. Liu, L., et. al,"Sub-femtonewton Force Spectroscopy at the Thermal Limit in Liquids," *under review*, 2016.
2. Liu, L., et. al,"Absolute position total internal reflection microscopy with an optical tweezer." *PNAS*, 2015.

# General Design Approaches in Geometrical Optics, Graded-Index Lenses, and Tracing of Optical Force

**A. J. Danner**[1*], **A. Akbarzadeh**[2], **and T. Tyc**[3]

[1]Department of Electrical and Computer Engineering, National University of Singapore, Singapore 117583

[2]Institute of Electronic Structure & Laser, Foundation for Research & Technology – Hellas, Heraklion, Greece

[3]Faculty of Science and Faculty of Informatics, Masaryk University, Kotlářská 2, 61137 Brno, Czech Republic

[*]corresponding author: adanner@nus.edu.sg

**Abstract**-Graded-index lenses that exhibit strict global behavior, such as absolute optical instruments (where all ray trajectories must be closed) can be difficult to mathematically construct because of the inherent one-way nature of lens design: it's easy to carry out raytracing when given an index profile, but much more difficult to design a lens with a specified desired behavior. A few approaches to this problem will be discussed, along with an extension of some techniques to optical force.

We are interested in the global behavior of lenses and designing lenses that have specific functions that are often difficult to express mathematically. In the case of absolute optical instruments, for example, in which a region of space is required to be imaged stigmatically, the known number of extant example lenses has until recently been very limited. The main reason for this is the inherent difficulty in converting the stated lens goal (all ray trajectories must be closed) into a useful mathematical form from which an expression for the refractive index can be derived. In 2006, J. C. Minano [1] discovered that many lenses that were already known, such as Eaton or Luneburg lenses, were also absolute optical instruments, and in 2011 T. Tyc et al. [2] presented a general method of designing other absolute optical instruments. In 2013 [3] and 2015 [4], new methods further extended design techniques to three dimensional lenses. However, the question remains – how can one start with a goal expressed in terms of ray behavior and end up with a refractive index profile?

In the specific case of absolute optical instruments, we will start with an analogy between classical mechanics and geometrical optics [5],

$$n(\vec{r}) = \sqrt{2[E - U(\vec{r})]}, \tag{1}$$

where $U(\vec{r})$ represents the potential (analogous to the refractive index) in which a particle of energy $E$ moves with the Lagrangian $L = v^2/2 - U(\vec{r})$. For systems with isotropic refractive index, we can first design the potential in a mechanical problem. If the potential is separable in a given coordinate system, then the Lagrangian is also separable, yielding conservation laws useful for lens design. Specifically, if the ratio of periodic oscillation periods along different coordinates is a rational number, then all ray trajectories will be closed [6]. The lens shown in Figure 1 was designed with such a method.

A more useful method is to assume that the Hamilton-Jacobi Equation is separable and following a similar line of reasoning – by calculating the frequency of oscillation along each (separated, orthogonal) coordinate direction and ensuring that they are rational-number ratios – we ensure closed trajectories for all orbits at a given energy, or at all energies. (For the optical problem, having closed trajectories for just a single energy is

sufficient to create an absolute optical instrument, representing a major difference with the requirement for a mechanical system to yield closed orbits for particles at all energies.) Lenses constructed with such design techniques will be described in the conference presentation associated with this abstract.

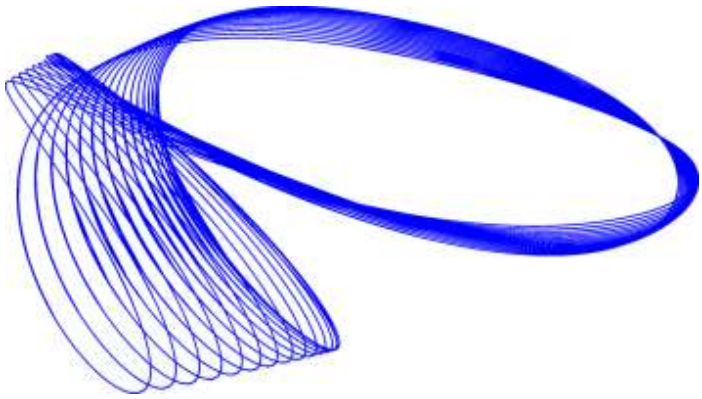


**Figure 1.** Ray trajectories of an asymmetric 3-dimensional lens with potential $U(\vec{r}) = \frac{1}{2}x^2 + \frac{1}{8\beta^2}y^2 + \frac{1}{2}z^2$ where $\beta = 1.7$ if $y \geq 0$, and $\beta = -0.3$ otherwise. The potential is clearly separable in Cartesian coordinates, and with care in the design, all ray trajectories in this example are closed.

We will also consider the case of tracing optical forces within a graded-index medium [7]. While it is not difficult to trace optical force distributions within a lens, it is much more difficult to reverse the problem – to require that a lens contain a certain distribution of optical force or radiation pressure throughout its bulk and find the corresponding refractive index distribution. However, conservation laws can still be found that permit this, and some simple cases will be shown.

**Acknowledgements:** A. Danner acknowledges partial support by the Singapore National Research Foundation under the 10 Tb/in$^2$ density storage project under award no. NRF-CRP 4-2008-06.

**REFERENCES**

1. Minano, J. C., "Perfect imaging in a homogeneous three-dimensional region," *Opt. Express*, vol. 14, 9627-9635, 2006.
2. Tyc, T., L. Herzanova, M. Sarbort, and K. Bering, "Absolute instruments and perfect imaging in geometrical optics," *New J. Phys*, Vol. 13, 115004, 2011.
3. Sarbort, M. and T. Tyc, "Multi-focal spherical media and geodesic lenses in geometrical optics," *J. Opt*., vol. 15, 125716, 2013.
4. Danner, A. J., H. L. Dao, and T. Tyc, "The Lissajous lens: a three-dimensional absolute optical instrument without spherical symmetry," *Opt. Express*, vol. 23, 5716-5722, 2015
5. Leonhardt, U. and T. Philbin, *Geometry and light: The science of invisibility*, (Dover, Mineola, 2010).
6. Tyc, T., H. L. Dao, and A. J. Danner, "Absolute optical instruments without spherical symmetry," *Phys. Rev. A*, vol. 92, 053827, 2015.
7. Akbarzadeh, A., C.-W. Qiu, and A. J. Danner, "*Force tracing versus ray tracing*" in META 2014 Conference, 20-23 May 2014, Singapore.

# Polarization Engineering in Photonic Crystal Waveguides for Spin-Photon Entanglers

A. B. Young[1], A. C. T. Thijssen[2], D. M. Beggs[2], P. Androvitsaneas[2], L. Kuipers[3], J. G. Rarity[1], S. Hughes[4], and R. Oulton[1,2]

[1] *Department of Electrical and Electronic Engineering, University of Bristol, Merchant Venturers Building, Woodland Road, Bristol BS8 1UB, United Kingdom*

[2] *Centre for Quantum Photonics, H.H. Wills Physics Laboratory, University of Bristol, Tyndall Avenue, Bristol BS8 1TL, United Kingdom*

[3] *Center for Nanophotonics, FOM Institute AMOLF, Science Park 104, 1098 XG Amsterdam, Netherlands*

[4] *Department of Physics, Queen's University, Ontario, Canada K7L 3N6*

**Abstract**-We present our work on QD spin emitters in photonic crystal waveguides, demonstrating that by placing a QD spin emitter at a C-point polarization singularity, one may achieve perfect unidirectional emission of a photon from the emitter, whose direction is determined by the spin direction.

Quantum dots are semiconductor artificial atoms. They are nanoscale structures that trap single electrons and holes, and their quantized energy level structure results in atomic-like transitions and single photon emission. These quantum dots act as a solid-state interface that is useful for quantum information applications, and for the past decade, semiconductor physicists have been attempting to replicate atomic cavity quantum electrodynamics in a practical semiconductor form. One can embed quantum dot into micron-sized photonic structures to capture and control the light emission, in order to use the single photon emission in quantum communication and quantum circuits.

One of the most exciting applications of quantum dots is to use their electron spins as a quantum memory. This involves transferring spin information from an electron spin to the polarization of a photon. However, as I shall explain, the definition of "polarization" for nanophotonic structures is far more complex than for a beam of light. In fact, we find that point-like "spin" emitters couple to a photonic structure in surprising ways: unlike any phenomenon observed in bulk material, simply changing the position of an emitter or the spin direction controls completely in which direction photons propagate. Suddenly, a rich variety of behaviour has arisen in the semiconductor/photonic domain which has no equivalent in atomic cavity QED, including a fundamental difference between how a classical dipole and a quantum dipole emitter interfere with incoming light [1].

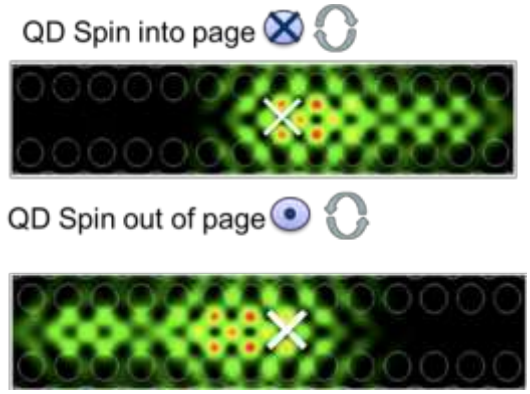



*Figure 1. Finite-difference time-domain simultion of circular dipole emission at a polarization singularity. showing unidirectional emission whose direction depends on dipole helicity.*

**Acknowledgements**

The authors acknowledge helpful discussions with P. Lodahl, B. Lang, and R. Ge. EM simulations were carried out using the computational facilities of the Advanced Computing Research Centre, University of Bristol. This work has been funded by Future Emerging Technologies(FET)-Open FP7-284743 [project Spin Photon Angular Momentum Transfer for Quantum Enabled Technologies (SPANGL4Q)]. R. O. was sponsored by Engineering and Physical Sciences Research Council (EPSRC) Grant No. EP/G004366/1, and J. G. R. is sponsored under European Research Council (ERC) Grant No. 247462 Quantum Optics in Wavelength Scale Structures (QUOWSS). This work is part of the research program of the Stichting voor Fundamenteel Onderzoek der Materie, which is financially supported by the Nederlandse Organisatie voor Wetenschappelijk Onderzoek. D. M. B. acknowledges support from a Marie Curie individual fellowship, and S. H. acknowledges funding from the Natural Sciences and Engineering Research Council of Canada.

**REFERENCES**

1. A. Young et al., Phys Rev Lett 115, 153901 (2015)

# Tunable and nonlinear metamaterials made of superconducting thin films.

**C. Kurter**[1*], **S. M. Anlage**[2]
[1]Department of Physics, Missouri University of Science and Technology, Rolla MO, USA
[2]Department of Physics, University of Maryland, College Park MD, USA
[*]corresponding author: kurterc@mst.edu

**Abstract**-Metamaterials made of thin-film superconducting resonators are rich playground for not only studying fundamental electrodynamics of superconductors but also novel applications. Here, we present an overview of the research on tunable and non-linear superconducting metamaterials with various functionalities such as artificial magnetism and electromagnetically induced transparency.

Metamaterials are engineered structures composed of sub-wavelength elements that form a homogeneous effective medium for the electromagnetic waves propagating through them. This effective response can be described by a coarse-grained electric permittivity and the magnetic permeability [1]. By manipulating these two electromagnetic parameters, unusual phenomena such as negative refractive index and artificial magnetism have been demonstrated [2].

Superconducting metamaterials combine the advantages of low-loss, extreme tunability and non-linearity compared to their normal metal counterparts. Therefore, they allow realization of compact and exotic device designs operating at low frequencies [3].

We have studied a hybrid metamaterial (Nb/Au) displaying a microwave response analogous to a quantum mechanical-electromagnetically induced transparency. In this design, the interference of two distinct resonators having extreme degrees of loss leads to narrow transparency windows with significantly enhanced group delays [4]. Due to the superconducting nature of the niobium thin film used in the hybrid metamaterial, the transparency windows in transmission was precisely tuned with temperature (see Fig. 1a). We also observed a non-linear response from the metamaterial with microwave power as demonstrated in Fig. 1b. The transparency windows are dramatically switched off at a critical power at which the local current density in Nb exceeds the critical current density and drives the superconducting Nb into ohmic regime.

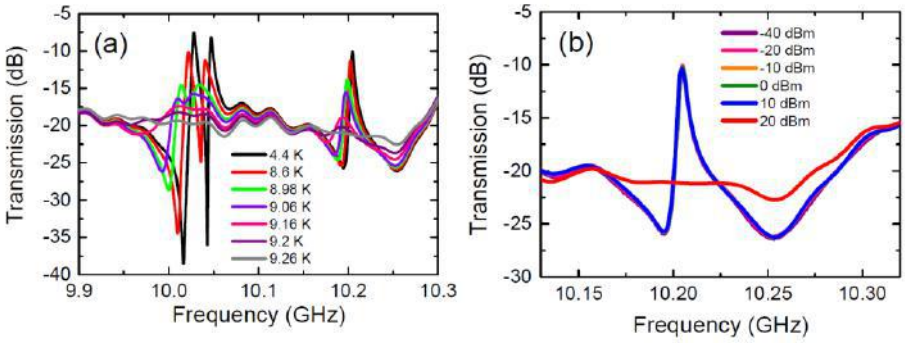



**Figure 1:** (a) Temperature and (b) microwave power evolution of transmission obtained from a hybrid superconducting metamaterial.

Moreover, we reported tunable artificial magnetism in a metamaterial made of three dimensional array of Nb thin film spirals [5]. The created medium showed a narrow frequency band where the real part of the complex effective permeability is negative up to 8.3 K, beyond which it starts to show near-zero and then positive values.

We demonstrated a precise and in-situ tuning of this frequency band with temperature until the metamaterial is driven into the resistive regime. Due to electrically small spacing ($\lambda_0/1875$) between the individual spirals - $\lambda_0$ is the free space wavelength- we treated the metamaterial with an effective medium approach [6]. Figure 2 shows the temperature dependence of the fitting parameters obtained by fitting the complex permeability with the Lorentzian function characterizing magnetic response of sub-wavelength split ring resonators [7]. The dramatic drop in resonant frequency $f_r$ is a result of a decrease in the density of superconducting electrons (superfluid density) with temperature, which is inversely proportional to the square of magnetic penetration depth.

As the fields of the electromagnetic waves penetrate deeper into the metamaterial with increasing temperature, the total inductance of the individual spirals increases due to the enhanced kinetic inductance, which leads to a reduction in the resonant frequency. Moreover, transmission decreases in magnitude and is smeared as transition temperature is approached due to the increasing ohmic losses arising from normal carriers, characterized by Γ.

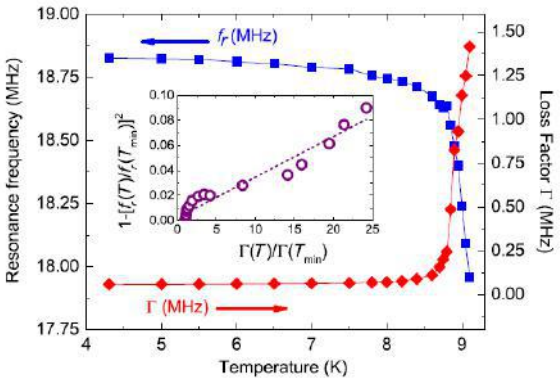



**Figure 2:** Temperature evolution of the extracted resonance frequency (blue squares) and damping factor Γ (red diamonds) by fitting the retrieved permeability of the 3D metamaterial.

Our work contributes to ongoing research on tunable and nonlinear metamaterials and demonstrates a novel electromagnetic properties where the sensitive tunability can be accomplished without use of lumped elements.

**REFERENCES**


1. Smith, D. R., Pendry, J. B. and Wiltshire, M. C. K. "Metamaterials and Negative Refractive Index," Science, Vol. 305, pp. 788-792, 2004.
2. Shelby, R. A., Smith, D. R. and Schultz, S. "Experimental Verification of a Negative Index of Refraction," Science, Vol. 292, pp. 77-79, 2001.
3. Anlage, Steven M., "The Physics and Applications of Superconducting Metamaterials," J. Opt., Vol. 13, 024001, 2011.
4. Kurter, C. K., Tassin, P., Zhang, L., Koschny, T., Zhuravel, A. P., Ustinov, A. V., Anlage, S. M. and Soukoulis, C. M. "Classical Analogue of Electromagnetically Induced Transparency with a Metal-Superconductor Hybrid Metamaterial," Phys. Rev. Lett., Vol. 107, p. 043901, 2011.
5. Kurter, C. K., T. Lan, L. Sarychev and S. M. Anlage, "Tunable negative permeability in a three-dimensional superconducting metamaterial," Phys. Rev. Appl., Vol. 3, p. 054010, 2015.
6. Kurter, C. K., J. Abrahams, S. M. Anlage, "Miniaturized superconducting metamaterials for radio frequencies,"Appl. Phys. Lett, Vol. 96, 253504, 2010.
7. Pendry, J. B., Holden, A. J., Robbins, D. J. and Stewart, W. J. "Magnetism from conductors and enhanced nonlinear phenomena," IEEE Trans. Microwave Theory Tech., Vol. 47, p. 2075, 1999.

# Enhancing optical forces between coupled waveguides using complex effective gauge fields

**L. Descheemaeker[1], V. Ginis[1*], S. Viaene[1,2], J. Danckaert[1], and P. Tassin[2,1]**
[1]Applied Physics, Vrije Universiteit Brussel, Belgium
[2]Department of Physics, Chalmers University, Sweden
[*]corresponding author: vincent.ginis@vub.ac.be

**Abstract**-We propose a novel mechanism to enhance the optical gradient forces between closely spaced waveguides based on the effective gauge potential for photons. We show that the modal field distribution of two coupled waveguides can be manipulated using a specifically engineered effective gauge potential. As one of the most interesting results of this phenomenon, we demonstrate that the electric field can be concentrated at the inner boundaries of the coupled waveguide system. Indeed, the optical gradient forces between the waveguides, which are proportional to the field intensity inside the enclosed region, can be enhanced considerable using this technique.

# Van der Waals forces at surfaces

**J. Pendry[1*] and K Sasihithlu[1]**

[1] Condensed Matter Theory Group, The Blackett Laboratory, Imperial College, United Kingdom

[*]corresponding author: j.pendry@imperial.ac.uk

**Abstract** A hot surface can lose heat by radiation but if in close proximity to another surface, phonons can also tunnel across the gap mediated by van der Waals forces. We have developed a new formulism for calculating this contribution to heat flow and will compare to other mechanisms such as near field heat transfer and conventional thermal radiative cooling.

# Chiral Optics and Chiral Materials: Interplaying Structures

# Electromagnetic Duality Symmetry in Optical Activity

**I. Fernandez-Corbaton**[1], **M. Fruhnert**[2], **C. Rockstuhl**[1,2]

[1]Institute of Nanotechnology, Karlsruhe Institute of Technology, 76021 Karlsruhe, Germany
[2]Institut für Theoretische Festkörperphysik, Karlsruhe Institute of Technology, 76131 Karlsruhe, Germany
ivan.fernandez-corbaton@kit.edu

**Abstract**— Recent research shows that the lack of spatial inversion symmetries is not the only necessary condition for a system to be optically active. For general illumination / scattering directions, electromagnetic duality symmetry is an additional necessary condition. We use these two conditions to design structures exhibiting optical activity in general scattering directions.

In 1848, Pasteur identified a necessary condition for optical activity (polarization rotation): Absence of any mirror plane of symmetry in the molecule or the unit cell of the crystal. Until very recently, the lack of spatial inversion symmetries was the only known necessary condition. New work in this field [1, 2] has proven that there is another one: For a system to be optically active *it shall not couple the two states of definite polarization handedness*. This additional condition ensures that the rotation angle is independent of the input polarization angle.

In the particular case of normal incidence and if only the forward propagation direction is relevant, the zero coupling of the two polarization handedness can be enforced by geometrical means: It is enough for the system to have a higher than 2-fold discrete rotational symmetry around the optical axis [3]. For example, a solution of a chiral molecule is, in effect, cylindrically symmetric ($\infty$-fold) [2]. However, in the general case, e.g focused beams and/or relevant scattering into general directions [5], zero coupling of the polarization handedness cannot be achieved by rotational symmetries. Crucially though, the new necessary condition is tightly connected to a fundamental symmetry in electromagnetism: Electromagnetic duality symmetry. A system is dual symmetric if and only if the two states of polarization handedness (helicity) remain uncoupled for all input/scattered directions.

In [1], we demonstrate how to design nanostructures exhibiting optical activity in general scattering directions by taking into account both necessary conditions. The lack of spatial inversion symmetries is achieved by designing a chiral nanostructure. The requirement of electromagnetic duality symmetry is met to an excellent approximation by fashioning the structure out of electromagnetically small individual nanoparticles which are dual symmetric in the dipolar limit. Even though exact duality requires materials with balanced electric and magnetic responses ($\epsilon = \mu$) [4], electromagnetically small scatterers like dielectric spheres can be tailored so that their electric and magnetic *dipolar* responses are balanced [6]. We have shown in [1] that a tetrahedral arrangement of four different dipolarly dual dielectric spheres exhibits optical rotation in general scattering directions (see Fig. 1). As far as we know, this is the first time that an optically active structure in this general sense has been proposed.

Our results show that the consideration of the electromagnetic duality symmetry is a valuable addition to the research in optical activity, for both its fundamental and practical sides. For example, by providing design principles for dielectric optically active metamaterials.

**REFERENCES**

1. I. Fernandez-Corbaton, M. Fruhnert, and C. Rockstuhl, "Dual and Chiral Objects for Optical Activity in General Scattering Directions", *ACS Photonics* **2**, 376384 (2015).
2. I. Fernandez-Corbaton, X. Vidal, N. Tischler, and G. Molina-Terriza, "Necessary symmetry conditions for the rotation of light", *J. Chem. Phys.* **138**, 214311 (2013).
3. I. Fernandez-Corbaton, "Forward and backward helicity scattering coefficients for systems with discrete rotational symmetry", *Opt. Express* **21**, 29885 (2013).
4. I. Fernandez-Corbaton *et al.*, "Electromagnetic Duality Symmetry and Helicity Conservation for the Macroscopic Maxwells Equations", *Phys. Rev. Lett.* **111**, 060401 (2013).
5. X. Vidal, *et al.*, "Polarization properties of light scattered off solutions of chiral molecules in non-forward direction", *App. Phys. Lett.*, **107**, 21 2015.
6. X. Zambrana-Puyalto, X.Vidal M. Juan, and G. Molina-Terriza, "Dual and anti-dual modes in dielectric spheres", *Opt. Express* **21**, 17520 (2013).

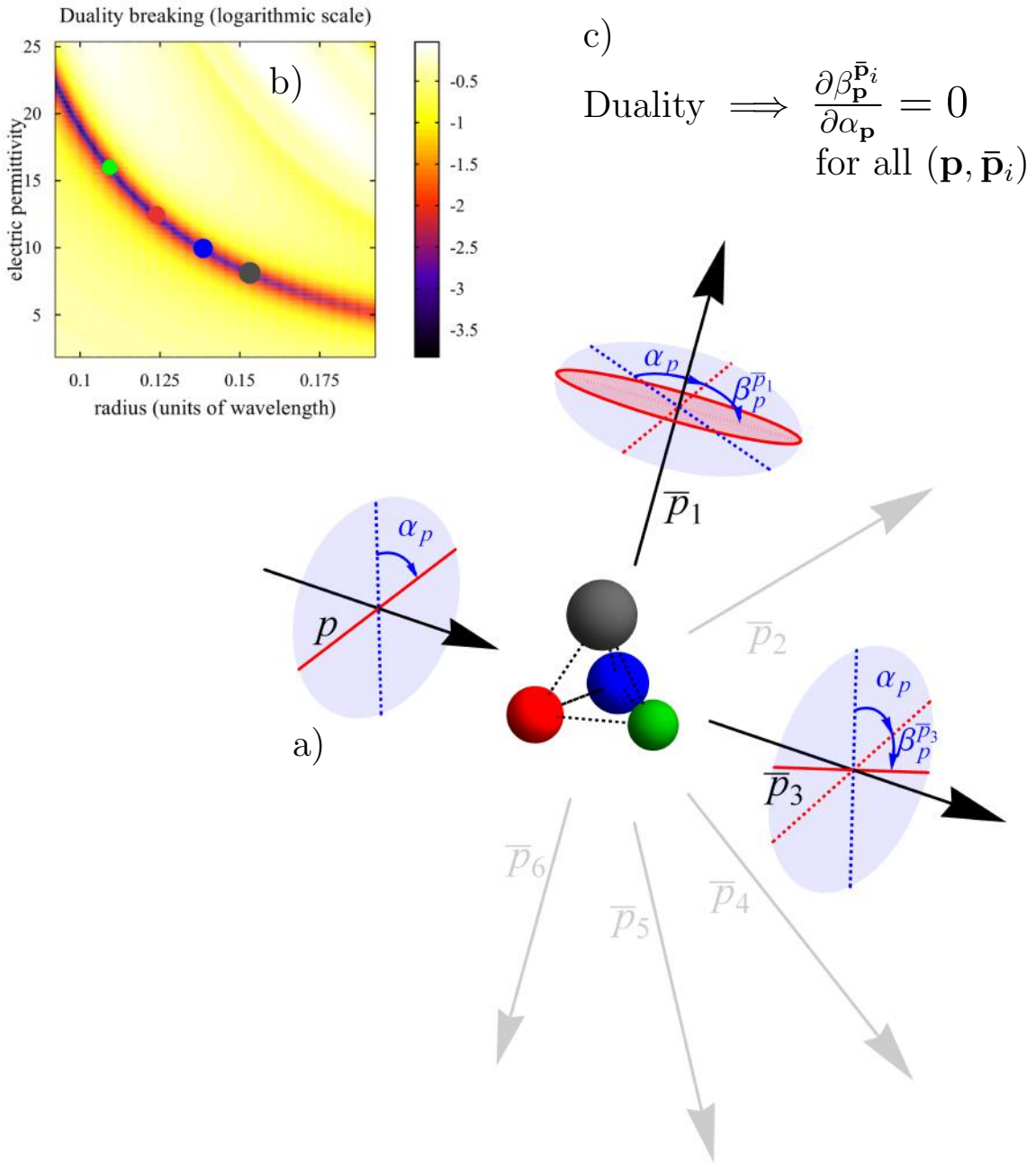



Figure 1: (a) Four different spheres in a tetrahedral arrangement form a chiral scattering system. (b) When the spheres are chosen to have a balanced electric and magnetic dipolar response, the system is also dual symmetric to good approximation. (c) Duality symmetry, equivalent to the zero coupling of polarization handedness, ensures that the polarization rotation angles of the scattered plane waves do not depend on the input polarization.

# Chiral Rotational Spectroscopy

**R. P. Cameron[1,2*], J. B. Götte[1,2], and S. M. Barnett[2]**
[1]Max Planck Institute for the Physics of Complex Systems, Dresden D-01187, Germany
[2]School of Physics and Astronomy, University of Glasgow, Glasgow G12 8QQ, United Kingdom
[*]corresponding author: robert.cameron@glasgow.ac.uk

**Abstract**-Chiral molecules illuminated by circularly polarised light reveal their orientated chiroptical responses and much more besides via their rotational spectrum.

Chirality pervades the natural world and is of particular importance to life, as the molecules that comprise living things are chiral and their chirality is crucial to their biological function. Our ability to probe and harness molecular chirality remains incomplete in many respects, however, and new techniques for chiral molecules are, therefore, highly sought after.

The basic property of a chiral molecule that is probed in typical optical rotation experiments using fluid samples is the isotropic sum

$$(G'_{XX}+ G'_{YY+} G'_{ZZ})/3 \tag{1}$$

with $G'_{XX}$, $G'_{YY}$ and $G'_{ZZ}$ components of the electric-dipole / magnetic-dipole polarisability [1]. These experiments do not yield the components $G'_{XX}$, $G'_{YY}$ and $G'_{ZZ}$ individually. Moreover, they yield no information about components such as $A_{X,YZ}$, $A_{Y,ZX}$ and $A_{Z,XY}$ of the electric-dipole / electric-quadrupole polarisability, which can make contributions to optical rotation that are individually comparable in magnitude to those from $G'_{XX}$, $G'_{YY}$ and $G'_{ZZ}$ but which together vanish upon isotropic averaging. Other well-established chiroptical techniques such as circular dichroism and Raman optical activity yield other chirally sensitive molecular properties but the fact remains that it is the isotropically averaged forms of these that are probed in typical experiments.

The ability to determine orientated rather than isotropically averaged chiroptical information, in particular the *individual* optical activity polarisability components $G'_{XX}$, $G'_{YY}$, $G'_{ZZ}$, $A_{X,YZ}$, $A_{Y,ZX}$ and $A_{Z,XY}$, is highly attractive, as these offer a wealth of information about molecular chirality which is only partially embodied by the isotropic sum (1). At present such information can only be obtained, however, using an orientated sample as in a crystalline phase. The preparation of such samples is often unfeasible and even when it can be achieved, signatures of chirality are usually swamped by other effects. Indeed, it was noted in 2012 that "*we have a shockingly small amount of data on the chiroptical responses of orientated molecules, a vast chasm in the science of molecular chirality*" [2].

Chiral rotational spectroscopy [3] is a new technique that enables the individual determination of $G'_{XX}$, $G'_{YY}$, $G'_{ZZ}$, $A_{X,YZ}$, $A_{Y,ZX}$ and $A_{Z,XY}$, in a manner that reveals the enantiomeric constitution of a sample whilst yielding an incisive signal even for a racemate. Chiral rotational spectroscopy could find particular use in the analysis of molecules that are chiral by virtue of their isotopic constitution and molecules with multiple chiral centres. The

principles that underpin chiral rotational spectroscopy might be exploited moreover in the search for molecular chirality in space, which, if found, may add weight to hypotheses that biological homochirality and indeed life itself are of cosmic origin.

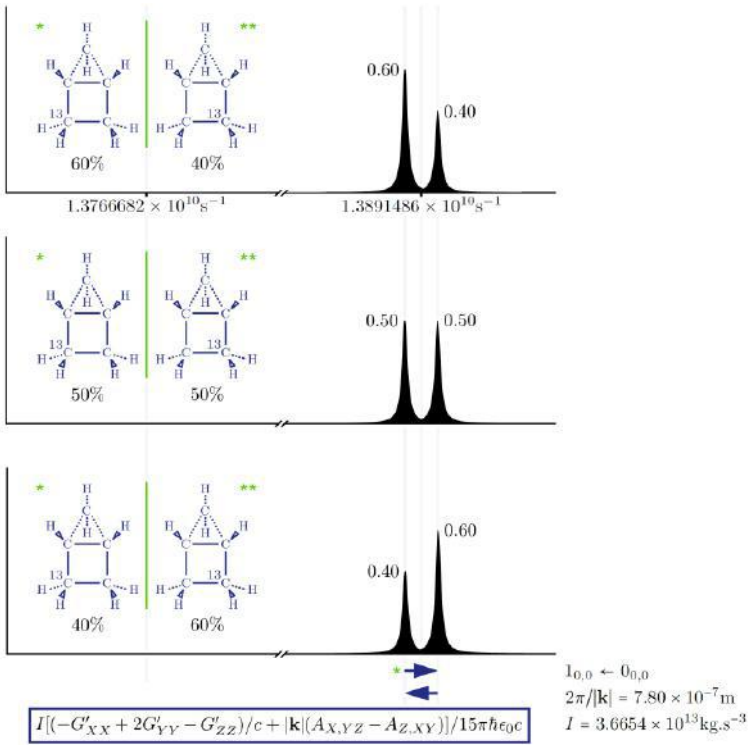



**Figure-**A rotational line for samples of isotopically chiral housane of different enantiomeric constitution in the presence of left-handed circularly polarised light. The separation between the two components of the line yields orientated chiroptical information whilst the relative heights of the components reflect the relative populations of the opposite molecular enantiomers. Note the middle plot in particular: we have here a clear and revealing signature of chirality from a racemate of a molecule that is chiral solely by virtue of the placement of a single neutron, which constitutes but 1% of the total mass of the molecule. Techniques such as electronic optical rotation and electronic circular dichroism in contrast are nearly double blind under such circumstances and even vibrational circular dichroism and Raman optical activity would yield a vanishing signal.

**Acknowledgements-**This work was supported by the Engineering and Physical Sciences Research Council grants EP/M004694/1 and EP/101245/1, the alumnus programme of the Newton International Fellowship and the Max Planck Institute for the Physics of Complex Systems.

**REFERENCES**

1. Barron, L. D., *Molecular Light Scattering and Optical Activity*, Cambridge University Press, 2004.
2. Kahr, B. and O. Arteaga, "Arago's best paper," *Phys. Chem.* **13**, 79-88, 2012.
3. Cameron, R. P., Götte, J. B. and S. M. Barnett, "Chiral rotational spectroscopy," *Phys. Rev. X* (submitted).

# “Chirality in evanescent near fields”

Euan Hendry, University of Exeter

We demonstrate the generation of short-range, chiral electromagnetic fields by the excitation of chiral arrays of nanoslits and nanorods [1]. These electromagnetic near fields, which can exhibit a chirality density greater than that of circularly polarized light, have some unusual properties; for example, they are spatially inhomogeneous, and do not exhibit time harmonic rotation of the electric field vector, as in circularly polarized light. We discuss the features of nanostructure symmetry required to obtain such chiral fields, and explicitly show how one can decompose the field to gain some understanding of its chiral properties.

However, recent demonstrations of chiroptical interactions of molecules in the chiral near fields of metallic nanoparticles are poorly understood [2], and there is much theoretical development required to understand the mechanisms essential to even the interaction of even the simplest chiral molecules. Here, we present proof of principal experiments using chiral microwave antennas and small “probe” helices to represent chiral molecules. By building up a physical understanding of both the generation of chiral near fields and their interaction with chiral matter, one can begin to harness the potential for sensing, measurement and characterization.

[1] E. Hendry et al Nano Letters 12, 3640 (2012)

[2] E. Hendry et al, Nature Nano 5, 783 (2010)

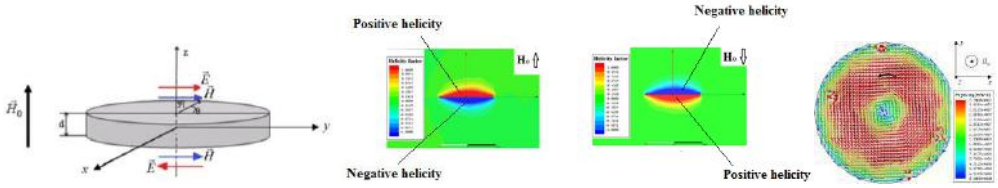
# Chirality of microwave fields

**E. O. Kamenetskii*, M. Berezin, E. Hollander, and R. Shavit**
Microwave Magnetic Laboratory
Department of Electrical and Computer Engineering
Ben Gurion University of the Negev, Beer Sheva, Israel
*kmntsk@bgu.ac.il

**Abstract**- In optics, the field chirality on the subwavelength scales can be obtained based on special-form plasmonic structures [1]. Recently, it was shown that with use of quasi-2D ferrite disks with magnetic-dipolar-mode (MDM) oscillations one can observe near-field chirality in microwaves. The MDMs are energy-eigenstate quantized oscillations [2]. The fields originated from a MDM ferrite disk, – called magnetoelectric (ME) fields – carry both spin and orbital angular momentums. They are characterized by power-flow vortices and non-zero helicity [3]. Because of chiral topology of ME fields in a near-field region, far-field orbital angular momenta can be observed. In this paper, we consider ME-field chirality in the near- and far-field regions of microwave radiation. We focus both on physics and application of this effect.

Maxwell added an electric displacement current to put into a symmetrical shape the equations coupling together the electric and magnetic fields. In a small ferrimagnetic sample [with sizes much less than the free-space electromagnetic (EM) wavelength], one has negligibly small variation of electric energy and microwave dynamical processes are described by Maxwell equations with neglect of an electrical displacement current [4]. Maxwell's symmetry becomes broken in this case. Nevertheless, specific unified-field (with coupled electric- and magnetic-field components) retardation effects exist in such a sample. There are MDM oscillations. The fields originated from MDM oscillations we term ME fields, to distinguish them from regular EM fields. Both the electric and magnetic fields in vacuum near a ferrite disk have spin and orbital angular momentums. These fields are not mutually perpendicular. The quadratic forms characterizing the ME fields are power-flow and helicity densities. The ME-field helicity density is defined as [3] $F = \frac{\varepsilon_0}{2}\vec{E}\cdot\nabla\times\vec{E}$. Formally, this parameter can be considered as a particular case of the EM-field chirality [5] $\chi = \frac{\varepsilon_0}{2}\vec{E}\cdot\nabla\times\vec{E} + \frac{1}{2\mu_0}\vec{B}\cdot\nabla\times\vec{B}$, when an electrical displacement current is negligibly small. At the MDM resonances ($\omega = \omega_{MDM}$), one observes active and reactive power flows [6]. The active power flow has vortex topology. The helicity parameter is calculated as $F = \frac{\omega_{MDM}\varepsilon_0}{4}\mathrm{Im}\left\{i\vec{E}\cdot\vec{B}^*\right\} = \frac{\omega_{MDM}\varepsilon_0}{4}\mathrm{Re}\left\{\vec{E}\cdot\vec{B}^*\right\} = \frac{\omega_{MDM}}{4c^2}\mathrm{Re}\left\{\vec{E}\cdot\vec{H}^*\right\}$. A sign of the helicity parameter depends on a direction of a bias magnetic field: $F^{\vec{H}_0\uparrow} = -F^{\vec{H}_0\downarrow}$. An integral of the ME-field helicity over the entire near-field vacuum region of volume *V* should be equal to zero: $H = \int_V F dV = \frac{\omega_{MDM}\varepsilon_0}{4}\int_V \mathrm{Re}\left\{\vec{E}\cdot\vec{B}^*\right\} dV = 0$.

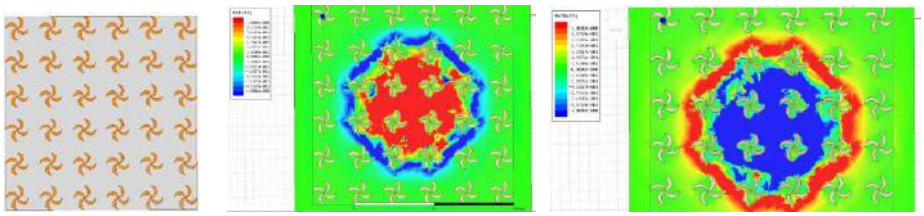
The helicity parameter $F$ is a pseudoscalar and ME fields can be considered as axion-electrodynamics fields [7]. Fig. 1. illustrates the topological structures of the ME field for the main MDM.




(*a*) (*b*) (*c*)

Fig. 1. Topological structures of the ME field near a MDM ferrite disk. (*a*) Rotating electric and magnetic fields; (*b*) helicity factor *F* for opposite directions of a bias magnetic field; (*c*) power flow vortex.

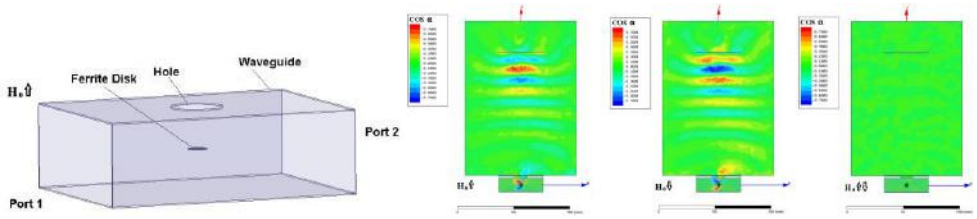
The helicity properties of ME fields allow chirality discrimination of material structures. This is illustrated in Fig. 2.



(*a*) (*b*) (*c*)

Fig. 2. Helicity-parameter distributions for microwave ME-fields near a chiral metasurface. (*a*) Chiral metasurface; (*b*), (*c*) helicity factor *F* for opposite directions of a bias magnetic field.

Topological ME effects are observed in microwave far-field radiation regions. This is shown in Fig. 3.




(*a*) (*b*) (*c*) (*d*)

Fig. 3. (*a*) A microwave radiating structure with a ferrite disk embedded in a rectangular waveguide. (*b*), (*c*) Normalized ME-field helicities in a far-field region for the MDM resonance frequency and opposite directions of a bias magnetic field. (*d*) Absence of the ME-field helicity in a far-field region at non-resonance frequency.

**REFERENCES**


1. E. Hendry *et al*, Nat. Nanotechnol. **5**, 783 (2010).
2. E. O. Kamenetskii, M. Sigalov, and R. Shavit, J. Phys.: Condens. Matter **17**, 2211 (2005).
3. E. O. Kamenetskii, R. Joffe, R. Shavit, Phys. Rev. E **87**, 023201 (2013).
4. L. D. Landau and E. M. Lifshitz, *Electrodynamics of Continuous Media*, 2nd ed. (Pergamon, Oxford, 1984).
5. Y. Tang and A. E. Cohen, Phys. Rev. Lett. **104**, 163901 (2010).
6. E. O. Kamenetskii, M. Berezin, R. Shavit, Appl. Phys. B: Lasers Opt. **121**, 31 (2015).
7. F. Wilczek, Phys. Rev. Lett. **58**, 1799 (1987).

# Helicity transfer between particles

*Manuel Nieto-Vesperinas*
**www.icmm.csic.es/mnv**
**Instituto de Ciencia de Materiales de Madrid, CSIC**
**Cantoblanco, Madrid 28049**
**mnieto@icmm.csic.es**

## ABSTRACT

Due to the conservation of the electromagnetic helicity [1,2], I will show the consequence for energy transfer of a recent optical theorem [3] that I established for the helicity of wave-fields, (equivalent to the so-called optical chirality [4] for time-harmonic waves), on scattering with chiral structures. In analogy with a FRET process, the helicity is transferred between a donor and acceptor thus conveying information of their respective chirality properties.

1. D. M. Lipkin, J. Math. Phys. **5**, 696 (1964).

2. R. P. Cameron, S. M. Barnett, and A. M. Yao, New J. Phys. **14**, 053050 (2012).

3. M. Nieto-Vesperinas, Phys. Rev. A **92**, 023813 (2015).

4. Y. Tang and A. E. Cohen, Phys. Rev. Lett. **104**, 163901 (2010).

# Chiral Tips and Nanoparticles for Visible and Ultraviolet Plasmonics.

**David J. Norris**[1]
[1]ETH Zurich, Switzerland
[*]corresponding author: dnorris@ethz.ch

**Abstract**-In an effort to produce chiral plasmonic structures beyond helices and nanoparticle aggregates, we recently developed a simple route to produce pyramidal tips and nanoparticles with a chiral shape. These structures, which are made from either gold or aluminum, can exhibit plasmonic resonances with intense chiral near fields. In this talk, we will discuss the fabrication, characterization, and use of these structures.

Because plasmonic structures have optical properties strongly influenced by their shape, various routes to complex geometries have been developed. Despite these advances, chiral shapes, those not superimposable on their mirror image, remain challenging. Metallic nanoparticle aggregates and solid helices are possible, but other chiral shapes that may be interesting for sensing, catalysis, and nonlinear optics, have not yet been fully explored. In this talk, we will discuss our recent efforts to investigate "non-standard" chiral structures. In particular, by exploiting the general fabrication technique known as template stripping [1], we can create high-quality solid chiral plasmonic nanopyramids of a specific handedness [2]. The resulting structures can either be tips on a surface (see e.g., Figure 1) or nanoparticles dispersed in a liquid. Such structures allow the exploration of superchiral electromagnetic fields. Made from gold, they exhibit record circular dichroism at red wavelengths. From aluminum, ultraviolet chirality resonant with biomolecules is obtained [3]. Thus, in addition to other

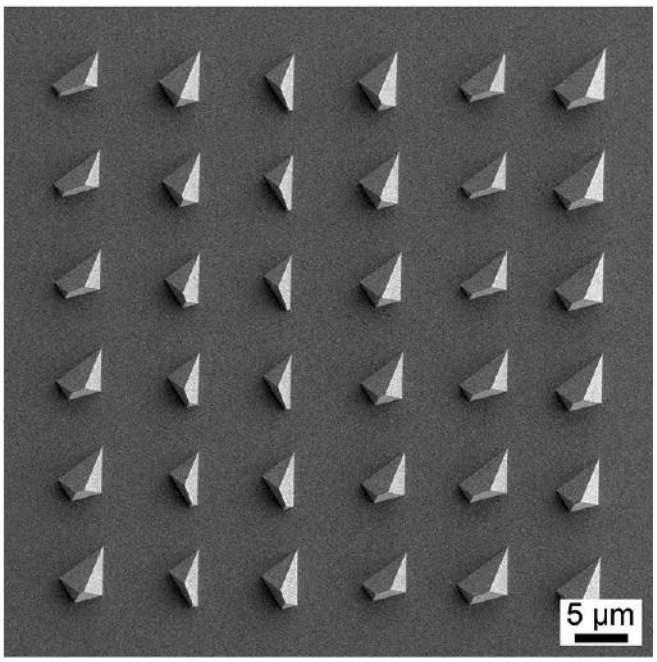



Figure 1. An electron micrograph showing a design palette of possible chiral Au pyramids that are fabricated via our template stripping technique. Each pyramid is sitting on a Au surface. A related technique can be used to obtain chiral Au and Al nanoparticles of ~150 nm that can be dispersed in liquids. The structures can have sharp (~10 nm) tips or edges that produce intense chiral near fields.

applications, they may provide new routes to detecting structural chirality in chemistry and biology. During the talk, we will also briefly touch upon two related issues: (i) what are the best deposition strategies to obtain the best plasmonic metals [4], and (ii) what are the best far-field probes for characterizing superchiral near fields.

**Acknowledgements**. This work was supported by the Swiss National Science Foundation under Award Number 200021-146747 and from the European Research Council under the European Union's Seventh Framework Programme (FP/2007-2013)/ERC Grant Agreement No. 339905 (QuaDoPS Advanced Grant).

**REFERENCES**

1. Nagpal, P., N. C. Lindquist, S.-H. Oh and D. J. Norris, "Ultrasmooth patterned metals for plasmonics and Metamaterials," *Science*, Vol. 325, 594–597, 2009.
2. McPeak, K. M., C. D. van Engers, M. Blome, J. H. Park, S. Burger, M. A. Gosálvez, A. Faridi, Y. R. Ries, A. Sahu and D. J. Norris, "Complex chiral colloids and surfaces via high-index off-cut silicon," *Nano Lett.*, Vol. 14, 2934–2940, 2014.
3. McPeak, K. M., C. D. van Engers, S. Bianchi, A. Rossinelli, L. V. Poulikakos, L. Bernard, S. Herrmann, D. K. Kim, S. Burger, M. Blome, S. V. Jayanti and D. J. Norris, "Ultraviolet plasmonic chirality from colloidal aluminum particles exhibiting charge-selective protein detection," *Adv. Mater.*, Vol. 14, 6244–6250, 2015.
4. McPeak, K. M., S. V. Jayanti, S. J. P. Kress, S. Meyer, S. Iotti, A. Rossinelli and D. J. Norris, "Plasmonic films can easily be better: Rules and recipes," *ACS Photonics*, Vol. 2, 326–333, 2015.
5. Poulikakos, L. V., P. Gutsche, K. M. McPeak, S. Burger, J. Niegemann, C. Hafner and D. J. Norris, "The optical chirality flux as a useful far-field probe of chiral near fields," in preparation.

# Formation of chiral nanostructures by optical angular momentum transfer effects

**T. Omatsu**[1,2*]
[1]Gradaute School of Advanced Integration Science, Chiba University, Japan
[2] Molecular Chirality Research Center, Chiba University, Japan Author Affiliation, Country
[*]corresponding author: omatsu@faculty.chiba-u.jp

**Abstract**- Optical vortices, e.g. helical lights, enable us to twist various materials, e.g., metal, silicon, and azo-polymer, by orbital angular momentum transfer effects. This allows us to form the chiral nanostructures in the atmosphere and at room temperature. The physical parameters (chirality, spiral structure, height, and diameter etc.) of such chiral nanostructures can also be controlled by the optical parameters (handedness, orbital angular momentum, optical vortex intensity etc..) of the optical vortices. The illumination of optical vortices will allow us to develop chiral metasurfaces, such as nanoscale chemical reactors and sensors with chiral selectivity, at high cost and time efficiencies.

Chiral nanostructures, which are difficult to fabricate, even by utilizing advanced chemical techniques, provide a variety of novel applications, such as nanoscale chemical reactors and sensors with chiral selectivity, chiral metasurfaces with optical rotation, and ultrahigh-efficiency photovoltaic cells.
Optical vortices carry an annular spatial form and an orbital angular momentum, $\ell\hbar$, ($\ell$ is an integer known as the topological charge) arising from a helical wavefront. In recent years, we and our co-workers discovered that the optical vortices can twist various materials, e.g., metal, silicon, and azo-polymer, by orbital angular momentum transfer effects, so as to form the chiral nanostructures in the atmosphere and at room temperature (see Figure). Also, the physical parameters (chirality, spiral structure, height, and diameter etc.) of the chiral nanostructures can be then determined by the optical parameters (handedness, orbital angular momentum, optical vortex intensity etc..) of the optical vortices.
Such chiral nanostructures fabricated merely by the illumination of optical vortices (without any chemical and/or advanced manufacturing processes) will play an important role in the above-related applications.
In this presentation, we report on the state of the art of forming chiral nanostructures by utilizing optical vortex illumination. We here also address the demonstration of an achiral monocrystalline silicon needle with a height of ~40 μm and a tip curvature radius of ~200 nm formed by picosecond optical vortex pulse illumination. The monocrystalline silicon needle will also be applied to devices, such as core–shell structures for silicon photonics and photovoltaic devices and nanoelectromechanical systems.
Further, the dynamics of such silicon needle formation was investigated by utilizing an ultrahigh-speed camera. We revealed that the melted silicon was confined in the dark core of the optical vortex to create the needle on a sub-microsecond time scale.

**Acknowledgements**, The author acknowledges a financial support from the Japan Science and Technology Agency (JST-CREST) and a Grant-in-Aid for Scientific Research (No. 24360022) from the Japan Society for the

Promotion of Science.

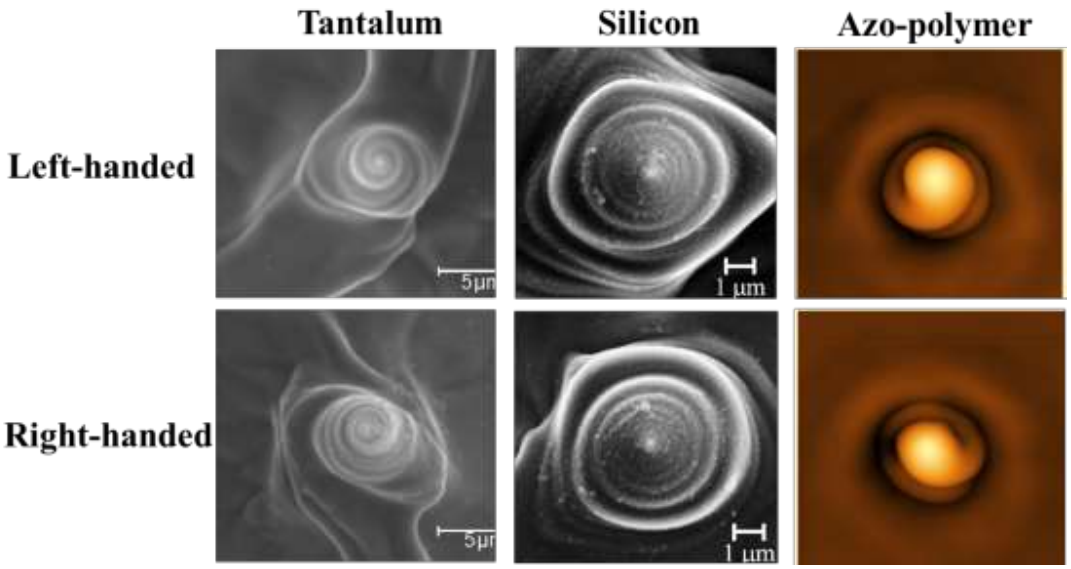



Figure Chiral nanostructures of metal, silicon and azo-polymer.

**REFERENCES**


1. Allen, L., et.al. "Orbital angular momentum of light and the transformation of Laguerre-Gaussian laser modes," *Physical Review A*, **45**, 8185–8189 (1992).
2. Toyoda, K. et al, "Using optical vortex to control the chirality of twisted metal nanostructures." *Nano Letters*, **12**, 3645 (2012).
3. Toyoda, K. et al, "Transfer of Light Helicity to Nanostructures," *Physical Review Letters* **110**, 146303, 1-5 (2013).
4. Watabe, et.al., "Light induced conch-shaped relief in an azo-polymer film," *Scientific Reports*, **4**, 4281 (2014).
5. Takahashi, F. "Optical vortex pulse illumination to create chiral monocrystalline silicon nanostructures," *Physica Status Solidi (A)* (in press).
6. Omatsu, T. et al, "Metal microneedle fabrication using twisted light with spin," *Optics Express*, **18**, 17967-17973 (2010).

# Helicity of Structured Light

**A. M. Yao**[1], **R. P. Cameron**[2], **C. J. Gibson**[1], **S. M. Barnett**[2] **and G.-L. Oppo**[1]

[1]SUPA and Department of Physics, University of Strathclyde, Glasgow G4 0NG, U. K.
[2]School of Physics and Astronomy, University of Glasgow, Glasgow G12 8QQ, U. K.
alison.yao@strath.ac.uk

**Abstract**— Light with spatially inhomogeneous states of polarization, such as vector and Poincaré beams, can also have non-uniform helicity density. The resultant gradients in helicity density will generate a force that will interact differently with opposite enantiomers of chiral molecules. By propagating these structured beams through nonlinear self-focusing media we can enhance this "chiral force" with the potential for manipulating chiral molecules.

The polarization state of light is of fundamental relevance in many applications in optics. In 1909, Poynting inferred that a beam of circularly polarised light carries spin angular momentum [1] and in 1996 it was demonstrated that this spin angular momentum could be transferred from a circularly polarised laser beam to macroscopic particles [2]. In addition to the spin angular momentum of light, we can also identify the *helicity* of light, which is often referred to as being equivalent to the value of the particle's spin in the direction of propagation [3]. In optics, however, it is more natural to work with a helicity written in terms of the potentials $\mathbf{A}$ and $\mathbf{C}$ [4, 5, 6]:

$$\mathcal{H} = \frac{1}{2}\int (\mathbf{A}^{\perp}\cdot\mathbf{B} - \mathbf{C}^{\perp}\cdot\mathbf{E})\, dV. \tag{1}$$

Identifying the helicity of light is not purely an academic point as it plays an important part in the coupling between electromagnetic fields and *chiral* molecules, i.e. molecules that have forms that distinguish them from their mirror images. Many molecules that comprise living things, including amino acids and sugars, are chiral and this is crucial to their biological function.

It has recently been suggested that the force $\mathbf{F}$ exerted upon a chiral molecule by light is proportional to the gradient of the helicity density of the beam [7]. Thus, manipulating the helicity density may allow chiral particles to be trapped and manipulated in much the same way as the gradient force can be used to trap and manipulate micron-sized particles [8]. Moreover, as this force has opposite signs for the mirror-image forms, or enantiomers, of a molecule, the "chiral force" may also be the key to separating objects with opposite chirality [9, 7].

For paraxial beams, the helicity density as defined in (1) is closely related to the $S_3$ Stokes's parameter [10] which in the circular basis takes the form $S_3 = |E_R|^2 - |E_L|^2$, where the subscripts $R, L$ denote the right and left circular components of the electric field. Thus, by spatially-varying the circular polarization, one may be able to produce beams with helicity density gradients. Beams with spatially inhomogeneous states of polarization can be generated by superposing two Laguerre-Gaussian (LG) modes with orthogonal polarisations [11, 12, 13]:

$$\mathbf{E}_p(\rho,\phi,z) = E_1|R\rangle + E_2|L\rangle, \tag{2}$$

where $E_{1,2} = LG_{0,\ell_{1,2}}(\rho,\phi,z)$ are normalised Laguerre-Gaussian modes [14, 15]. If $\ell_1 = -\ell_2 = 1$ this is a cylindrical vector beam and if $\ell_1 = \pm 1, \ell_2 = 0$ it is a full Poincaré beam.

It is known that in comparison with linearly polarized beams these display beneficial behaviour such as tighter focusing [16] and improved micromachining [17]. Here we investigate if the resultant spatially-varying helicity density may also be beneficial in controlling and manipulating opposite enantiomers of chiral molecules. In particular, we study the affect of propagation through a *nonlinear* medium with a self-focusing, $\chi^{(3)}$, nonlinearity, which we simulate using a two-dimensional Nonlinear Schrödinger equation with saturating nonlinearity. As we are dealing with vector beams our model consists of two coupled equations that interact through the cross phase modulation term characterized by the parameter $\nu$, which takes the value of $2/3$ for orthogonally polarized beams

and 2 for like polarized beams [18]:

$$\frac{\partial E_1}{\partial \zeta} = \frac{i}{2}\nabla_\perp^2 E_1 + i\gamma \frac{|E_1|^2 + \nu|E_2|^2}{1+\sigma(|E_1|^2+|E_2|^2)}E_1,$$
$$\frac{\partial E_2}{\partial \zeta} = \frac{i}{2}\nabla_\perp^2 E_2 + i\gamma \frac{|E_2|^2 + \nu|E_1|^2}{1+\sigma(|E_1|^2+|E_2|^2)}E_2. \tag{3}$$

The fields $E_{1,2}$ are dimensionless and have been normalised such that their power is equal to unity and the nonlinear parameter, $\gamma$, and the saturation parameter, $\sigma$ are given by

$$\gamma = \frac{k_0^2 n_2 P_0}{n_0}\,; \qquad \sigma = \frac{2P_0}{I_{sat} w_0^2}\,, \tag{4}$$

where $n_0$ and $n_2$ are the linear and nonlinear refractive indices ($n_2 > 0$ for self-focusing), and $I_{sat}$ is the saturation intensity.

**REFERENCES**


1. Poynting J. H., "The wave motion of a revolving shaft and a suggestion as to the angular momentum in a beam of circularly polarised light", *Proc. R. Soc. A*, Vol. 82, 560-7, 1909.
2. Friese M. E. J., J. Enger, H. Rubinstein-Dunlop and N. R. Heckenberg, "Optical angular-momentum transfer to trapped absorbing particles", *Phys. Rev. A*, Vol. 54, 1593-6, 1996.
3. S. S. Schweber, "An Introduction to Relativistic Quantum Field Theory", Dover, New York, 2005.
4. Cohen-Tannoudji,C., J. Dupont-Roc and G. Grynberg, "Photons and Atoms: Introduction to Quantum Electrodynamics", Wiley, New York, 1989.
5. Bateman, H., "The Mathematical Analysis of Electrical and Optical Wave-motion on the Basis of Maxwell's Equations", Cambridge University Press, Cambridge, UK, 1915.
6. Cameron R. P., S. M. Barnett and A. M. Yao, "Optical helicity, optical spin and related quantities in electromagnetic theory", *New J. Phys.*, Vol. 14, 053050, 2012.
7. Cameron R. P., S. M. Barnett and A. M. Yao, "Discriminatory optical force for chiral molecules", *New J. Phys.*, Vol. 16, 013020, 2014.
8. Ashkin A., J. M. Dziedzic, J. E. Bjorkholm and S. Chu, "Observation of a single-beam gradient force optical trap for dielectric particles", *Opt. Lett.*, Vol. 11, 288-90, 1986.
9. Canaguier-Durand A., J. A. Hutchison, C. Genet and T. W. Ebbesen, "Mechanical separation of chiral dipoles by chiral light", *New J. Phys.*, Vol. 15, 123037, 2013.
10. Dennis M. R., K. O'Holleran and M. J. Padgett, "Singular Optics: Optical Vortices and Polarization Singularities", *Prog. Opt.*, Vol. 53, 295, 2009.
11. Zhan Q., "Cylindrical vector beams: from mathematical concepts to applications" *Adv. Opt. Photon*, Vol. 1, 1, 2009.
12. Beckley A. M., T. G. Brown and M. A. Alonso, "Full Poincaré beams", *Opt. Exp.*, Vol. 18, 10777, 2010.
13. Galvez E. J., and S. Khadka, "Poincaré modes of light", *Proc. SPIE*, Vol. 8274, 82740Y, 2012.
14. Lugiato L. A., G.-L. Oppo, J.R. Tredicce, L. M. Narducci and M. A. Pernigo, "Instabilities and spatial complexity in a laser", *J. Opt. Soc. Am. A*, Vol. 7, 1019, 1990.
15. Barnett S. M. and R. Zambrini, "Quantum Imaging", Springer, Singapore, p 284, 2007.
16. Dorn R., S. Quabis and G. Leuchs, "Sharper Focus for a Radially Polarized Light Beam", *Phys. Rev. Lett.*, Vol. 91, 233901, 2003.
17. Allegre, O. J., W. Perrie, S.P. Edwardson, G. Dearden, and K.G. Watkins, "Laser microprocessing of steel with radially and azimuthally polarized femtosecond vortex pulses", *J. Opt.*, Vol. 14, 085601, 2012.
18. Agrawal G. P., "Nonlinear fiber optics", Fourth edition, Academic Press, 2007.

# One-way waveguide by self-collimation in photonic crystals.

**Rui-Xin Wu**[1*], **Qing-Bo Li**[1], **Yin Poo**[1]
[1]School of Electronic Sciences and Engineering, Nanjing University, China
[*]corresponding author: rxwu@nju.edu.cn

**Abstract**-We demonstrate that by breaking the parity and time-reversal symmetries electromagnetic waves can self-collimate and propagate unidirectionally in magnetic photonic crystals, which can be consider as a one-way wavguide. Experimentally, the one-way propagation in such magnetic photonic crystals is observed.

Guiding wave beam propagation unidirectionally as diodes guide current in electronics is of great interest for all optical signal processing systems. Several schemes, such as the optical nonlinearity [1] have been proposed. Recently, studies have determined that gyromagnetic photonic crystals (GPCs) have EM one-way bulk states in which the EM body waves in the GPCs propagate unidirectional [2]. Here, we present a new scheme for one-way wave beam guiding by using self-collimation effects of GPCs.

We consider a gyromagnetic array composed of semicylindrical ferrite rods in an air background, as displayed in Fig. 1(a). In applied bias magnetic field, such unit cell configuration breaks the mirror symmetry in x-direction and time reversal symmetry. The band structure calculations show in a certain frequency range the energy bands are asymmetric due to the symmetries breaking [3]. Figure 1(b) plots the equi-frequency contours (EFCs) of the energy band cover the frequencies 17.7 to 19.2 GHz. We can observe a shift of EFCs along ky direction, which indicates for certain incident angles wave beams in GPC will propagate in one direction. Because of the flat contour curve except at the corners, the wave beam will be self-collimated. Then the wave beam has not a noticeable change in its beam profile when it propagates, as displayed in Fig. 1(c). As a result, GPC can be used as a one-way waveguide.

Experimentally, we fabricated a GPC sample with 16x5 unit cells. Each unit cell consists of alumina and the ferrite YIG square pillars. We measured the electric field distribution along the exit surface of the sample in a parallel plate waveguide. Figure 3 displays the results. It shows in the frequency range 13.5 to 14.5 GHz the incident wave beam obliquely impinges on the sample from left can transmit through the sample. However, when wave beam comes from the opposite direction, as showed in Fig. 3(b), the incident wave is almost prohibited going through the sample, showing a one-way wave beam transmission.

**Acknowledgements**, This work is supported by NSFC (61271080 and 6130106), Jiangsu Key Laboratory of Advanced Techniques for Manipulating Electromagnetic Waves.

**REFERENCES**

1. A. Rostami, "Piecewise linear integrated optical device as an optical isolator using two-port nonlinear ring resonators," *Opt. Laser Technol*, Vol. 39, No. 5, 1059–1065, 2007.
2. C. He, M. H. Lu, X. Heng, L. Feng, and Y. F. Chen, "Parity-time electromagnetic diodes in a two-dimensional nonreciprocal photonic crystal," *Phys. Rev. B*, Vol. 83,075117, 2011.
3. Qing-Bo Li, Zhen Li, and Rui-xin Wu, "*Bending self-collimated one-way light by using gyromagnetic photonic crystals*," *Appl. Phys. Lett.*, Vol 107, 241907, 2015.

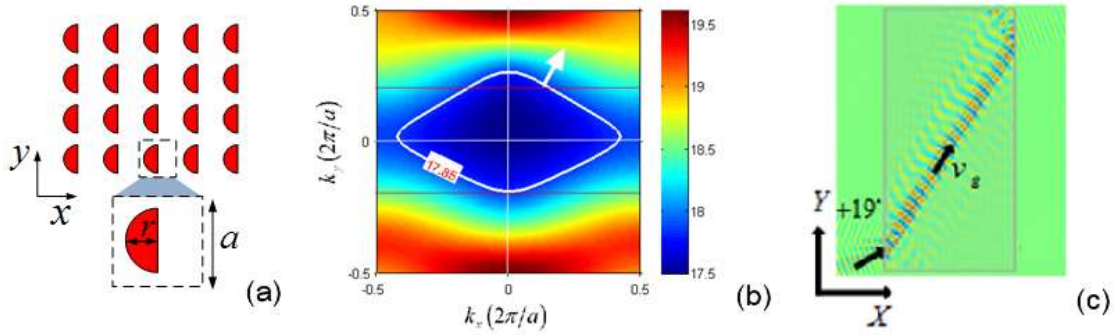



Figure 1. (a) Schematic of gyromagnetic photonic crystals (GPCs) consisting of semicylindrical ferrite rods. The lattice constant is a=10 mm, and the radius is r=3 mm. (b) Equi-frequency contours of the band covering frequency range 17.7 to 19.2 GHz. (c) Self-collimated wave beam in GPC.

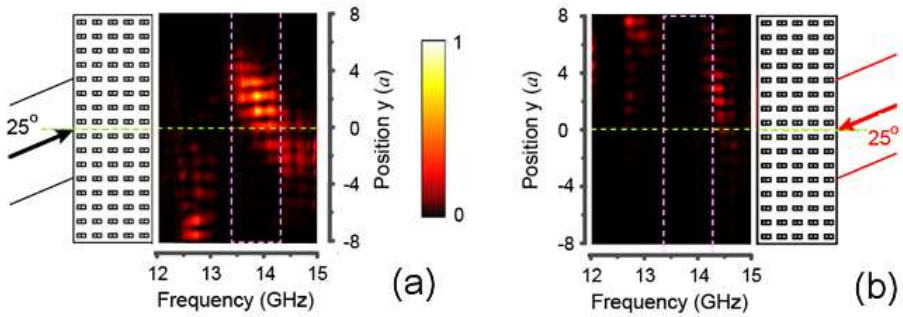



Figure 2. Electric field distribution measured along the exit surface of the sample as a function of frequency when wave beam obliquely incident from (a) left, and (b) opposite direction.

# Chirality control at the nanoscale

**X. Zambrana-Puyalto**[1], **and N. Bonod**[1]

[1]Aix-Marseille Université, CNRS, Centrale Marseille, Institut Fresnel UMR 7249, 13013 Marseille, France
xavislow@protonmail.com

**Abstract**— We present a simple analytic formalism to model the interaction between a chiral emitter and a nanoantenna. We compare the performances of metallic and dielectric spherical antennas to tailor the chirality of light emission. It is observed that, due to their strong electric dipolar response, metallic spherical nanoparticles spoil the chirality of light emission by yielding achiral fields. In contrast, thanks to the combined excitation of magnetic and electric modes, dielectric Si-based particles feature the ability to inhibit or boost the chirality of light emission. In particular, we show that dual modes in dielectric antennas preserve the chirality of light emission.

## 1. INTRODUCTION

Tailoring light-matter interactions at the nanometer scale is at the core of nanophotonics. Lately, much effort has been devoted to chiral light-matter interactions [1, 2, 3]. Here we investigate the interaction between a chiral emitter and a spherical resonator. We aim at studying how the antenna modifies the chirality of the emitted field. For this purpose, we present a simple formalism to analyze the chirality of the scattered light. The formalism, which is analytic and valid for antennas of any size, is developed using the Mie theory in the helicity basis [4]. Then, we apply it to gold and silicon-based spherical nanoantennas [5, 6]. It will be shown that the interplay between electric and magnetic modes of the resonators is required to tailor the chirality of light.

## 2. RESULTS

A chiral emitter illuminates a spherical nanoresonator. Let $C(\alpha)$ be a measure of the chirality of the emitter, where $|\alpha|^2$ is the power emitted into modes of helicity $+1$ ($\mathtt{W}_+$) [2, 4]. Then, $C(\alpha)$ can be computed as $(\mathtt{W}_+ - \mathtt{W}_-)/\mathtt{W}_+ - \mathtt{W}_-) = 2|\alpha|^2 - 1$. In a similar way, a measure of the scattered field by the antenna can be computed as:

$$\frac{\mathtt{W}^{\mathrm{s}}_+ - \mathtt{W}^{\mathrm{s}}_-}{\mathtt{W}^{\mathrm{s}}_+ + \mathtt{W}^{\mathrm{s}}_-} = C^s(\underbrace{\alpha, r_0, m_z, \lambda_0}_{\text{emitter}}, \underbrace{R, \epsilon, \mu}_{\text{antenna}}) \in [-1, 1] \tag{1}$$

where $\mathtt{W}^{\mathrm{s}}_\pm$ is the scattered power into modes with helicity $\pm 1$. Here, we assume that the two antennas (gold and silicon) whose performance we want to compare have a radius $R = 100$. We assume that the emitter has $|\alpha|^2 = 0.9$, it is located at $r_0 = 10$nm of the surface of the antenna, and it is oriented along the z axis, $m_z = 0$. Changes in $r_0$ and $m_z$ and $\alpha$ do not qualitatively change the results of this study [7]. The results are plotted in Fig.1. It is observed that the gold antenna yields an achiral response ($C^s \approx 0$) for the whole visible range, whereas the Si-based antenna has a very rich and $\lambda$-dependent response. In fact, for the Si-based antenna $C^s$ oscillates from $[-1, 1]$. Indeed, at $\lambda = 808$nm, the Si antenna yields a field with almost a pure helicity $+1$ state; and at $\lambda = 532$nm, the chirality of the emitter is almost reversed. Now, looking at the scattered power given by $Q^s$, it is not entirely clear why the antennas behave in such a way. In [7], we show that the duality properties of the antenna play a key role.

## 3. CONCLUSIONS

We have presented a general formulation to quantify the chirality of the field emitted by a chiral dipolar emitter coupled with an optical nanoresonator. It is seen that gold spherical antennas do not feature the ability to tailor the chirality of emitted fields since they yield the same achiral response in the whole visible/near infrared range (see Fig.1). This is due to the fact that plasmonic spherical nanoparticles behave mainly as electric dipoles. A very different behavior is observed for Si-made spherical nanoantennas. We have seen that Si-based nanoantennas are highly efficient to manipulate chiral fields emitted by quantum emitters. They can yield scattered fields which almost

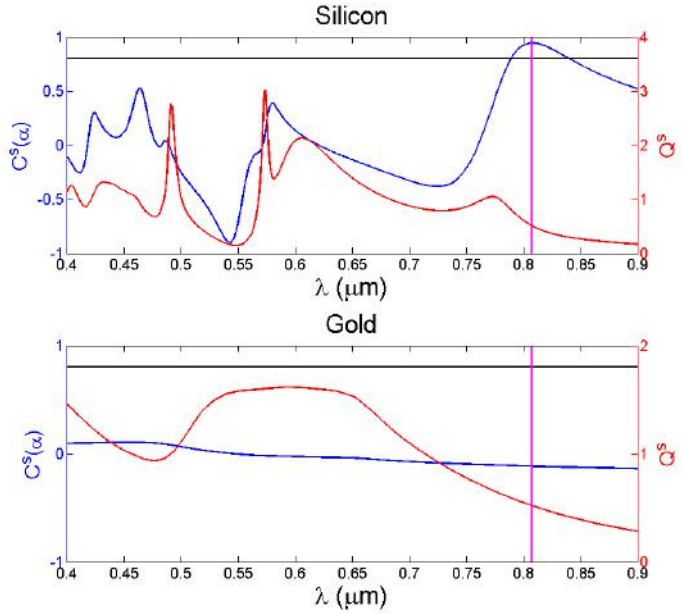



Figure 1: Scattered chirality ($C^s$) in blue and power ($Q^s$) in red, as a function of $\lambda$. The two antennas made of Au and Si have $R = 100$nm. The horizontal black line represents the initial chirality of the emitter $C = 0.8$, and the magenta vertical line highlights the $\lambda$ at which $C^s$ reaches the absolute maximum.

encompass all the possible values of chirality, from $C^s = -1$ to $C^s = +1$ (see Fig.1). Given a chiral emitter with an intrinsic chirality, the antenna can boost, reduce or even inverse the chirality in the far field region. In particular, the antenna can yield a field with the exact same chirality of the emitter at the dual condition, and it can also yield completely achiral field at the electric/magnetic resonant conditions. This result shows that transparent mono-disperse colloidal solutions could potentially be used to produce strong chiral effects with chiral emitters.

## ACKNOWLEDGMENT

This work has been carried out thanks to the support of the A*MIDEX project (n° ANR-11-IDEX-0001-02) funded by the Investissements d'Avenir French Government program managed by the French National Research Agency (ANR).

## REFERENCES

1. García-Etxarri, A. and J. A. Dionne "Surface enhanced circular dichroism spectroscopy mediated by non-chiral nanoantennas," *Phys. Rev. B*, Vol. 87, 235409, 2013.
2. Fernandez-Corbaton, I., M. Fruhnert, and C. Rockstuhl, "Dual and chiral objects for optical activity in general scattering directions," *ACS Phot.*, Vol. 2, No. 3, 376–384, 2015.
3. Poulikakos, L. V., P. Gutsche, K. M. McPeak, S. Burger, J. Niegemann, C. Hafner, and D. J. Norris, "The Optical Chirality Flux as a Useful Far-Field Probe of Chiral Near Fields," *arXiv:1601.06716*, 2016.
4. Zambrana-Puyalto, X., I. Fernandez-Corbaton, M. L. Juan, X. Vidal, and G. Molina-Terriza, "Duality symmetry and Kerker conditions," *Opt. Lett.*, Vol. 38, No. 11, 1857-1859, 2013.
5. Yoo, S. and Q. Park, "Enhancement of chiroptical signals by circular differential Mie scattering of nanoparticles," *Sci. Rep.*, Vol. 5, 14463, 2015.
6. Zambrana-Puyalto, X. and N. Bonod, "Purcell factor of spherical Mie resonators," in *Phys. Rev. B*, Vol. 91, No. 19, 195422, 2015.
7. Zambrana-Puyalto, X. and N. Bonod, *submitted* (2016).

# Classical electromagnetic scattering response of topological insulators

**Tom G. Mackay**[1,2] and **Akhlesh Lakhtakia**[2]

[1]School of Mathematics and Maxwell Institute for Mathematical Sciences, University of Edinburgh, Edinburgh EH9 3FD, UK

[2]NanoMM — Nanoengineered Metamaterials Group, Department of Engineering Science and Mechanics, The Pennsylvania State University, University Park, PA 16802–6812, USA

email: T.Mackay@ed.ac.uk

**Abstract**— Classically, a topological insulator may be modelled either as (i) an achiral nonreciprocal biisotropic dielectric-magnetic material, or (ii) an isotropic dielectric-magnetic material whose surface is endowed with charge and current densities characterized by a surface admittance. In terms of electromagnetic scattering responses from a topological-insulator half-space and from a topological-insulator sphere, the two models yield the same results. However, only model (ii) is consistent with topological insulators having protected conducting states at their surfaces.

The characteristic electromagnetic responses of a topological insulator are due to protected conducting states existing on its surface [1]. Two alternative classical models have been proposed to characterize this behaviour, labelled as (i) and (ii) in the following. Suppose that all space is partitioned into the disjoint regions $\mathcal{V}_{\rm out}$ and $\mathcal{V}_{\rm in}$ which are separated by the surface $\mathcal{S}$, and that a homogeneous topological insulator occupies the region $\mathcal{V}_{\rm in}$.

(i) The topological insulator is an achiral nonreciprocal biisotropic material specified by frequency-domain constitutive relations of the form [2]

$$\left.\begin{array}{l} \mathbf{D}(\mathbf{r}) = \varepsilon \mathbf{E}(\mathbf{r}) + \Psi \mathbf{B}(\mathbf{r}) \\ \mathbf{H}(\mathbf{r}) = \mu^{-1} \mathbf{B}(\mathbf{r}) - \Psi \mathbf{E}(\mathbf{r}) \end{array}\right\} , \qquad \mathbf{r} \in \mathcal{V}_{\rm in} \, , \tag{1}$$

with the surface of the topological insulator, namely $\mathcal{S}$, being charge-neutral and current-neutral.

(ii) The topological insulator is an isotropic dielectric-magnetic material specified by frequency-domain constitutive relations of the form of Eqs. (1) but with the Tellegen nonreciprocity parameter $\Psi = 0$. On the surface of the topological insulator there exists a surface charge density $\rho_s$ and a surface current density $\mathbf{J}_s$. Accordingly, the boundary conditions

$$\left.\begin{array}{l} \hat{\mathbf{n}}(\mathbf{r}_{\rm S}) \bullet [\mathbf{B}_{\rm out}(\mathbf{r}_{\rm S}) - \mathbf{B}_{\rm in}(\mathbf{r}_{\rm S})] = 0 \\ \hat{\mathbf{n}}(\mathbf{r}_{\rm S}) \times [\mathbf{E}_{\rm out}(\mathbf{r}_{\rm S}) - \mathbf{E}_{\rm in}(\mathbf{r}_{\rm S})] = \mathbf{0} \\ \hat{\mathbf{n}}(\mathbf{r}_{\rm S}) \bullet [\mathbf{D}_{\rm out}(\mathbf{r}_{\rm S}) - \mathbf{D}_{\rm in}(\mathbf{r}_{\rm S})] = \rho_s(\mathbf{r}_{\rm S}) \\ \hat{\mathbf{n}}(\mathbf{r}_{\rm S}) \times [\mathbf{H}_{\rm out}(\mathbf{r}_{\rm S}) - \mathbf{H}_{\rm in}(\mathbf{r}_{\rm S})] = \mathbf{J}_s(\mathbf{r}_{\rm S}) \end{array}\right\} , \qquad \mathbf{r}_{\rm S} \in \mathcal{S} \, , \tag{2}$$

apply at the surface of the topological insulator. Herein, the unit normal vector $\hat{\mathbf{n}}(\mathbf{r}_{\rm S})$ at $\mathbf{r}_{\rm S} \in \mathcal{S}$ points into $\mathcal{V}_{\rm out}$ and the subscripts $_{\rm in}$ and $_{\rm out}$ label the fields in $\mathcal{V}_{\rm in}$ and $\mathcal{V}_{\rm out}$, respectively. The non-null surface admittance $\gamma$, introduced per

$$\left.\begin{array}{l} \rho_s(\mathbf{r}_{\rm S}) = \gamma \, \hat{\mathbf{n}}(\mathbf{r}_{\rm S}) \bullet \mathbf{B}_{\rm in}(\mathbf{r}_{\rm S}) \\ \mathbf{J}_s(\mathbf{r}_{\rm S}) = -\gamma \, \hat{\mathbf{n}}(\mathbf{r}_{\rm S}) \times \mathbf{E}_{\rm in}(\mathbf{r}_{\rm S}) \end{array}\right\} , \qquad \mathbf{r}_{\rm S} \in \mathcal{S} \, , \tag{3}$$

may depend upon the geometry of $\mathcal{S}$, the constitution of the topological insulator, as well as the free-space wavenumber. However for simple configurations (e.g., $\mathcal{S}$ being spherical or planar with the topological insulator being homogeneous), it is reasonable to assume that $\gamma$ does not vary on $\mathcal{S}$. Most likely, a minimum radius of curvature of $\mathcal{S}$ is required for the existence of $\gamma \neq 0$. In addition, since tiny volumes are unlikely to support significant surface states, it is likely that $\gamma = 0$ in the long-wavelength approximation [3], as is supported by recent experimental results [4] on very thin films of the topologically insulating chalcogenide $Bi_2Se_3$.

Classical electromagnetic scattering was considered for the following two scenarios with $\mathcal{V}_{\text{out}}$ taken to be vacuous.

(A) Scattering by a planar half-space; i.e., $\mathcal{V}_{\text{out}} = \{(x, y, z) : z < 0\}$, $\mathcal{V}_{\text{in}} = \{(x, y, z) : z > 0\}$, and $\mathcal{S} = \{(x, y, z) : z = 0\}$. With the incident planewave fields in $\mathcal{V}_{\text{out}}$ decomposed in terms of their $s$- and $p$-polarized components, the reflected and refracted fields were calculated by solving the corresponding boundary-value problem for models (i) and (ii) [5]. It was found that the parameters $\Psi$ and $\gamma$ arise identically in the reflection and transmission coefficients. Also, there is cross-polarized reflection and cross-polarized refraction, entirely due to $\Psi + \gamma$. Thus, either $\Psi = 0$ or $\gamma = 0$ is admissible in order to predict reflection characteristics.

(B) Scattering by a sphere of radius $a$; i.e., $\mathcal{V}_{\text{out}} = \{(x, y, z) : r > a\}$, $\mathcal{V}_{\text{in}} = \{(x, y, z) : r < a\}$, and $\mathcal{S} = \{(x, y, z) : r = a\}$. With the incident fields in $\mathcal{V}_{\text{out}}$ decomposed in terms of vector spherical wavefunctions of the toroidal and poloidal types, the scattered fields were determined by solving the corresponding boundary–value problem for model (ii) [6]. The results were then compared with those for model (i) [7]. Again, the parameters $\Psi$ and $\gamma$ arise identically in the expressions of the scattered fields. Also, there is toroidal–poloidal mixing on scattering entirely ascribable to either $\Psi$ or $\gamma$. We note that while the surface-admittance boundary condition represented in Eqs. (2) and (3) gives rise to toroidal–poloidal mixing on scattering from a topological-insulator sphere, such mixing would not arise if the boundary conditions for a charged sphere or for an impedance sphere were used in lieu of Eqs. (2) and (3).

Thus, models (i) and (ii) cannot be distinguished on the basis of any scattering scenario. The mixing of fields that occurs on scattering, which is a characteristic of nonreciprocal biisotropic mediums, also arises for isotropic dielectric-magnetic materials endowed with a surface admittance. Furthermore, model (i) does not encapsulate the essential physics of topological insulation which is manifest not inside a volume but on its surface. In fact, the Tellegen parameter $\Psi$ disappears from the Maxwell equations applicable to $\mathcal{V}_{\text{in}}$ [8] (indeed, it would even do so if the topological insulator were bianisotropic [9]), and its existence by itself leads to a contradiction [10]. In contrast, the surface admittance of model (ii) is consistent with the existence of protected conducting states at the surfaces of topological insulators. Therefore, we conclude that model (ii), and not model (i), is the appropriate classical model for a topological insulator.

**REFERENCES**


1. M. Z. Hasan and C. L. Kane, "Topological insulators," Rev. Mod. Phys. **82**, 3045–3067 (2010).
2. X.-L. Qi, T. L. Hughes, and S.-C. Zhang, "Topological field theory of time-reversal invariant insulators," Phys. Rev. B **78**, 195424 (2008).
3. H. C. van de Hulst, *Light Scattering by Small Particles* (Dover Press, New York, NY, USA, 1981), Sec. 6.4.
4. M. Autore, F. D'Apuzzo, A. Di Gaspare, V. Giliberti, O. Limaj, P. Roy, M. Brahlek, N. Koirala, S. Oh, F. J. García de Abajo, and S. Lupi, "Plasmon-phonon interactions in topological insulator microrings," Adv. Optical Mater. **3**, 1257–1263 (2015).
5. A. Lakhtakia and T. G. Mackay, "Classical electromagnetic model of surface states in topological insulators," J. Nanophoton. **10**, 033004 (2016).
6. A. Lakhtakia and T. G. Mackay, "Electromagnetic scattering by homogeneous, isotropic, dielectric-magnetic sphere with topologically insulating surface states," J. Opt. Soc. Amer. B (accepted for publication).
7. C. F. Bohren, "Light scattering by an optically active sphere," Chem. Phys. Lett. 29, 458–462 (1974).
8. J. F. Nieves and P. B. Pal, "Third electromagnetic constant of an isotropic medium," Am. J. Phys. **62**, 207–216 (1994).
9. A. Lakhtakia and T. G. Mackay, "Axions, surface states, and the Post constraint in electromagnetics," Proc. SPIE **9558**, 95580C (2015).
10. A. Lakhtakia and W. S. Weiglhofer, "On a constraint on the electromagnetic constitutive relations of nonhomogeneous linear media," IMA J. Appl. Math. **54**, 301–306 (1995).

# Manipulating the hybridisation of chiral plasmonic metamaterials using molecular and macromolecular stereostructure

Calum Jack, Affar S. Karimullah , Ryan Tullius, Vincent M. Rotello[A], Graeme Cooke, Nikolaj Gadegaard[B], Laurence D. Barron, Malcolm Kadodwala,*.

School of Chemistry, Joseph Black Building, University of Glasgow, Glasgow, G12 8QQ, UK.

[B]School of Engineering, Rankine Building, University of Glasgow, Glasgow, G12 8QQ, UK.

[A]Department of Chemistry, 710 Nt. Pleasant Street, University of Massachusetts Amherst, MA 01003, USA.

.

The plasmonic response of a complex nanostructure can be understood using an electromagnetic analogue of molecular orbital theory. Within this framework a complex nanostructure is broken down into simpler elementary units, each of which support plasmonic modes. The plasmonic properties of the overall complex structure is then determined through hybridisation of the modes of elementary units. As with molecules, the hybridisation of the plasmonic modes is dependent upon the spatial and symmetry properties of the elementary units.

Here we show that the hybridisation of plasmonic modes (electric and magnetic) in a chiral metamaterial (inverse –solid hybrid) can be manipulated using chiral (bio)materials, and the effects are dependent both on the molecular and macromolecular stereochemical structure. As a demonstration of the potential application of the phenomena we have utilised it to characterise the secondary structure of femtomole quantities of proteins. Biomaterials with different secondary structure motifs (i.e. $\alpha$-helical, $\beta$-sheet and random coil structures) have differing effects on the level of coupling and thus provide unique fingerprints of biomacromolecular structure.

# Selectively Driving Optical Magnetism

**U. Manna[1], Jung-Hoon Lee[2], J. Parker[1,3], N. Shepherd[1,2], Tiansong Deng[2], Y. Weizmann[2], N. F. Scherer[1,2,*]**

[1]The James Franck Institute, [2]Department of Chemistry, [3]Department of Physics,
University of Chicago, 929 East 57th Street, Chicago, Illinois 60637, USA.

[*]corresponding author: nfschere@uchicago.edu

**Abstract** We induce magnetic responses in nano- and meso-scale materials by exploiting the Maxwell-Faraday law of induction through the design of the structure, by employing an electric field with instantaneous curl or do both to produce an instantaneous displacement current. We employ cylindrical vector beams with azimuthal polarization to create a cylindrical electric field, and selectively induce optical frequency magnetic responses in metal nanoparticle-based nanomaterials. We demonstrate this in 2- and 3-dimensional systems that do not have to possess cylindrical symmetry.

It is well known that one can create a magnetic field by passing a DC or AC electric current through a coil of conductor (i.e., a wire); a phenomenon described by the Maxwell-Faraday's law of electromagnetic induction[1]. NMR or ESR (nuclear magnetic resonance or electron spin resonance) spectroscopies involve the interaction of a spin (nuclear or electron, respectively) with a magnetic field[2-4]. Mathematically, these phenomena can be understood as the *curl* of the electric field (i.e., the current or spin) producing a (time varying) magnetic field or vise versa. Thus, one should also be able to induce a magnetic response in nano- and meso-scale materials by exploiting Maxwell-Faraday's law of induction through the design of the structure,[5-8] by employing an electric field with instantaneous curl or do both to produce an instantaneous circulating current. Here we employ cylindrical vector beams[9] with azimuthal polarization to create an angular (cylindrical) electric field,[10] and selectively drive magnetic resonance in metal nanoparticle-based nanomaterials at optical frequencies. This time-varying magnetic field at optical frequencies is induced in systems that do not possess spin or orbital angular momentum. Moreover, with the vector beam spectroscopy we also selectively drive electric dipole modes by excitation with a radially polarized light, and show that the strength of the electric and magnetic modes can be equal in magnitude in individual metal nano-structures. This work opens new opportunities for the selective spectroscopic investigation of "dark modes" and Fano resonances in nanomaterials, metamaterials, and control of nanomaterial molecular excitations and dynamics.

Figure 1a shows a schematic of the optical setup for vector beam spectroscopy. The light source is white light continuum from a fiber laser/nonlinear fiber. This has high spatial coherence but low temporal coherence. Figure 1b show images of the intensity distributions of azimuthally and radially polarized (spectrally broadband) beams obtained using a linear polarizer for analysis. The arrows indicate the analyzer orientation. Figure 3c shows the spectral responses obtained from the mesoscale core-shell cluster (300nm dia. $SiO_2$ core/ 43nm dia. Ag nanoparticles) shown in the inset. The focused azimuthally polarized beam selective excites magnetic modes (dipolar, quadrupolar) in such structures while the radially polarized beam selectively excites electric modes. Linearly polarized light creates complicated mixtures of both. This selectively is not limited to structures with cylindrical symmetry, as will be discussed in this presentation.

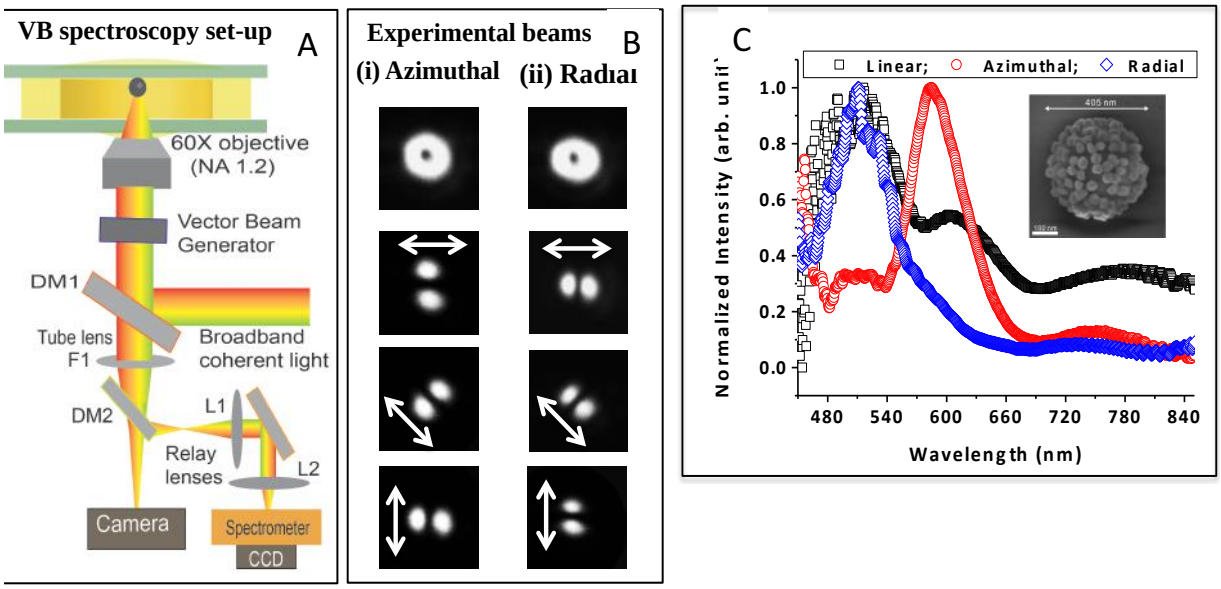



**Figure 1: a) schematic of the setup for vector beam spectroscopy; b) experimental characterization of spectrally broadband vector beams using a polarizer/analyzer - the double headed arrows indicate the analyzer direction. c) Backscattering spectra obtained for the particular mesoscale $SiO_2$ core - Ag nanoparticle shell cluster shown in the inset. The focused azimuthal beam selective drives magnetic modes (red open circles).**

**Acknowledgements**: This work was supported by a grant from the Department of Defense National Security Science and Engineering Faculty Fellowship (NSSEFF).

## REFERENCES

1. Maxwell, J. C. A Dynamical theory of the electromagnetic field. *Philosophical Transactions of the Royal Society of London* **155**, 459-512 (1865).
2. Bloch, F., Hansen, W. W. & Packard, M. Nuclear Induction. *Physical Review* **69**, 127-127 (1946).
3. Purcell, E. M., Torrey, H. C. & Pound, R. V. Resonance Absorption by Nuclear Magnetic Moments in a Solid. *Physical Review* **69**, 37-38 (1946).
4. Zavoisky, E. Ralaxation of liquid solutions for perpendicular fields. *J. Phys. USSR* **9**, 211-216 (1945).
5. Alù, A., Salandrino, A. & Engheta, N. Negative effective permeability and left-handed materials at optical frequencies. *Opt. Express* **14**, 1557-1567, (2006).
6. Simovski, C. R. & Tretyakov, S. A. Model of isotropic resonant magnetism in the visible range based on core-shell clusters. *Physical Review B* **79**, 045111 (2009).
7. Sheikholeslami, S. N., Alaeian, H., Koh, A. L. & Dionne, J. A. A Metafluid Exhibiting Strong Optical Magnetism. *Nano Letters* **13**, 4137-4141, (2013).
8. Fruhnert, M., Mühlig, S., Lederer, F. & Rockstuhl, C. Towards negative index self-assembled metamaterials. *Physical Review B* **89**, 075408 (2014).
9. Toussaint, K. C., Park, S., Jureller, J. E. & Scherer, N. F. Generation of optical vector beams with a diffractive optical element interferometer. *Opt. Lett.* **30**, 2846-2848, (2005).
10. Youngworth, K. S. & Brown, T. G. Focusing of high numerical aperture cylindrical-vector beams. *Opt. Express* **7**, 77-87, (2000).

# Probing chirality of molecule in the presence of nanoparticles

**T. Wu**[1*]**, X. D. Zhang**[1]

[1]School of Physics and Beijing Key Laboratory of Nanophotonics & Ultrafine Optoelectronic Systems, Beijing Institute of Technology, 100081, Beijing, China

[*]corresponding author: wutong1121@sina.com

**Abstract**- *We present a T-matrix method to study the interaction between optical waves and the chiral molecule in a cluster of nanoparticles. We find the plasmon mediated interaction between two molecules is strong when two molecules are inserted into plasmonic hot spots of nanostructures. Furthermore, large circular dichroism may be aroused from structure chirality of nanocomposites. We also investigate the interaction exists between the optical orbital angular momentum and the chiral cluster.*

Chirality plays a pivotal role in biochemistry and the evolution of life itself. Many biomolecules are chiral in nature. Recently, probing the chirality of molecules with the aid of nanoparticles (NPs) has been a topic of intense interest for researchers. Here we present a T-matrix method to study the interaction between optical waves and the chiral molecule in a cluster of nanoparticles.

We first consider a hybrid system consisting of two molecules and an Ag trimmer [1]. When the two-level molecule is located in the hot spot, radiation from its electric dipole is strongly enhanced, and the interaction between the molecule and NPs become strong. Our results show that the total circular dichroism (CD) of the system with two chiral molecules is not the sum for two cases when two chiral molecules inserted separately into the hot spots of NP clusters. From Fig.1 (a), it is seen clearly that not only are they different in amplitude for CD spectra but also the positions of resonance peaks also shift. This phenomenon is caused by the strong interaction between molecules mediated by surface plasmonic excitations of the NPs.

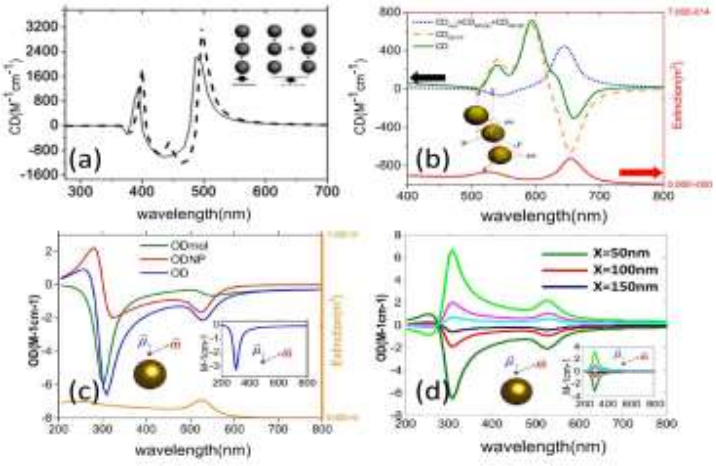
CD not only can be induced by chiral molecules but also depends on the spatial arrangements of NPs. If the chiral molecules are put in the hot spots of the chiral structures shown in inset of Fig.1 (b), the CD spectra of the system include two contributions, the structure chirality (CD FF) and the molecule-induced plasmon chirality (CD mol + CD NP − DD+CD NP−DF). A comparison between them is given in Fig.1(b). The dashed line in Fig.1(b) represents the structure chirality; the dotted line corresponds to the molecule-induced plasmon chirality, and the total CD is described by the green solid line. It can be seen that the molecule-induced plasmon chirality is completely suppressed by the structure chirality. If we want to detect chirality of chiral molecules by using surface plasmon resonances, we have to overcome the structure chirality, for example, by controlling all nanoparticles in the same plane.

The T-matrix theory is further extended [2] to study the interaction between optical orbital angular momentum (OAM) and the chiral molecule in a cluster of nanoparticles. Such an interaction could be observed if we define the OAM dichroism (OD) to be the difference of absorption rates between two focused linear polarized OAM beams with opposite topological indices.

Fig. 1(c) shows the calculated orientation averaged OD as a function of wavelength for a chiral molecule being placed in the vicinity of a single gold sphere (see the inset) for the OAM incident beams with topological indices $l = \pm 1$. Comparing the present OD spectra with that of pure chiral molecular (see the inset), we find that the molecular OD signal (ODmol) around $\lambda = 300$nm is improved about 2 times. Moreover, a new OD band (ODNP) appears in the plasmon resonance spectral region (520nm). These results reveal not only a plasmon-enhanced chiral molecule-OAM interaction at the molecule resonance frequency, but also an OD effect at the plasmonic resonant frequency of metallic

NP. Considering that the EM field of the OAM beam is nonuniform in space, we investigate the OD signal at different position of the OAM beams for the system discussed above. The olive/red/black blue line in Fig. 1(d) represents the orientation averaged OD when the molecule is put at x= 50 nm/100 nm/150 nm in the focal plane (origin of the coordinate is set to be the focal center of the OAM beams, and the beam is propagating). The corresponding OD for the mirror reflected samples are also plotted as green, pink and sky blue lines, as expected these signals are of same values but opposite signs. With the position of the nanocomposite shifting away from the beam center, the OD signal decreases. This phenomenon can be explained as decreasing of helicity density with the increase of the relative distance between nanocomposites and the center of the beam.

It's worth noting that the previous theoretical investigations [3] have shown that only the spin angular momentum leads to a differential absorption, there is no interaction of the OAM of the beam with the chirality of the molecule. This is because the signals calculated in these works are the average of contributions from all the molecules in spaces. In fact, the OD signals do not exist in the case of the whole spatial average either.




**Figures 1:** (a) Calculated CD signals as a function of wavelength for molecule − NP complexes with three spheres. The solid lines describe the case when two chiral molecules are inserted at the same time into two hotspots of the linearly arranged silver trimer; the dashed lines correspond to the CD signals two times for the case when only one chiral molecule is put in the hotspot of the trimer. (b) Calculated CD and extinction as a function of wavelength for the Au spheroid trimer chiral structure caused by dislocation of nanoparticles. The solid line, dashed line, and dotted line represent the total CD, the structure chirality (CD NP − FF ), and the molecule-induced plasmon chirality (CD mol + CD NP − DD +CD NP − DF ), respectively; the red line is extinction. (c) Orientation averaged OD as a function of wavelength for a metal nanoparticle and chiral molecule under the OAM incident beam with l = ±1. The insets represent the calculated results for the single chiral molecule without NPs. (d) Orientation averaged OD as a function of wavelength under the OAM incident beam when the nanocomposites locate at different positions.

## REFERENCES


1. Wu, T., J. Ren, R. Y. Wang and X. D. Zhang, "Competition of Chiroptical Effect Caused by Nanostructure and Chiral Molecules," *J. Phys. Chem. C*., Vol. 118, No. 35, 20529–20537, 2014.
2. Wu, T., J. Ren, R. Y. Wang and X. D. Zhang, "Plasmon-induced strong interaction between chiral molecules and orbital angular momentum of light," *Sci. Rep.*, Vol. 5, 18003, 2015.
3. Bliokh, K. Y. and F. Nori, "Characterizing optical chirality," Phys Rev. A, Vol. 83, 021803, 2011

# Optical and acoustical radiation torque and forces: overview, applications, and selected recent developments

**P. L. Marston[1*] and L.-K. Zhang[2]**

[1] Physics & Astronomy Dept., Washington State Univ., Pullman, WA, United States

[2] Physics Dept., University of Texas, Austin, TX, United States

[*]corresponding author: marston@wsu.edu

**Abstract**-Beginning with Marston and Crichton's analysis of optical radiation torque from the 1980s, the generation and analysis of acoustical beams carrying axial angular momentum (from the 1990s) is surveyed along with developments from the past decade involving negative radiation forces. Acoustical radiation forces are also well suited for controlling the shape of liquid objects (as used for exploring light scattering caustics) and for the suppression of capillary instabilities.

Marston and Crichton[1] analyzed the radiation torque of circularly polarized light on an isotropic sphere through the evaluation of the flux of angular momentum directly from the time-averaged Maxwell stresses associated with the combined incident and scattered fields (of radian frequency $\omega$) giving the torque as,

$$T = P_{abs}/\omega. \qquad (1)$$

They also evaluated the angular momentum flux of the scattering using the Humblet decomposition of fluxes into orbital and spin projections and showed that the result is consistent with the aforementioned analysis.[2,3] Hefner and Marston[4] introduced ways of generating acoustical beams that carry axial angular momentum in fluids. An effective source consisted of an appropriately phased array of transducers. While the angular momentum flux was only analyzed in the paraxial approximation, the analysis suggested that for an isotropic axisymmetric object placed on the beam's axis, the torque is also proportional to the absorbed power,

$$T = m P_{abs}/\omega, \qquad (2)$$

where the complex velocity potential of the incident wave and the one scattered by the object both depend on the azimuthal angle $\varphi$ in proportion to $\exp(im\varphi - i\omega t)$ and the integer m is known as the topological charge. Zhang and Marston[5] derived the result in (2) without using the paraxial approximation and generalized it to a much broader class of wave fields including acoustical vortex standing waves. Subsequently the dependence on m in (2) was experimentally confirmed.[6] Zhang and Marston[7] also recovered and generalized an early analysis of the low frequency radiation torque of an acoustic standing wave having m = 1 for a sphere in a viscous fluid by explicit evaluation of $P_{abs}$. Such wave fields were used in the 1980s and 1990s to spin liquid drops in reduced gravity. In the formal derivation[5] of (2) the scattered wave is a form of spiral wave having a phase factor $\exp(im\varphi)$. Spiral waves themselves carry angular momentum[5] and have other useful properties.[8]

In related research Marston[9] and Zhang and Marston[10] analyzed the scattering and associated acoustical radiation forces on spheres placed on the axis of acoustic Bessel beams and vortex Bessel beams. Situations

were found where the axial radiation force was opposite the beam's propagation direction (a form of tractor beam) and these results were explained by analyzing the axial projections of momentum.[10,11] The acoustical effect was demonstrated using a simplified beam and optimized target[12] and the optical effect based on similar properties is now well known. When analyzing the scattering and radiation forces and torques on isotropic spheres, we find[10] it advantageous to retain the traditional notation (from quantum mechanics) of expressing the nth partial wave scattering amplitude as proportional to $(s_n-1)$ where for a non-absorbing object $|s_n| = 1$. Recent experiments have demonstrated the utility of acoustic vortex beams for trapping and manipulation.[13]

The low speed of sound in fluids facilitates using acoustical radiation forces for controlling the shape of levitated drops for light scattering experiments[14] and for suppressing capillary instabilities of liquid columns.[15]

**REFERENCES**


1. Marston, P. L. and J. H. Crichton, "Radiation torque on a sphere caused by a circularly-polarized electromagnetic wave," *Phys. Rev. A*, Vol. 30, 2508–2516, 1984.
2. Marston, P. L. and J. H. Crichton, "Radiation torque on a sphere illuminated with circularly polarized light and the angular momentum of scattered radiation," in *Proceedings of the CRDC's 1984 Scientific Conference on Obscuration and Aerosol Research*, Aberdeen Proving Ground, MD, USA, 1985, 233–238.
3. Crichton, J. H. and P. L. Marston, "The measurable distinction between the spin and orbital angular momenta of electromagnetic radiation," *Electronic J. of Differential Equations*, Vol. Conf. 04, 37–50, 2000.
4. Hefner, B. T. and P. L. Marston, "An acoustical helicoidal wave transducer with applications for the alignment of ultrasonic and underwater systems," *J. Acoust. Soc. Am*, Vol. 106, 3313–3316, 1999.
5. Zhang, L. and P. L. Marston, "Angular momentum flux of nonparaxial acoustic vortex beams and torques on axisymmetric objects," *Phys. Rev. E*, Vol. 84, 065601, 2011.
6. Demore, C. E., M., Z. Yang, A. Volovick, S. Cochran, M. P. MacDonald, *et al.*, "Mechanical evidence of the orbital angular momentum to energy ratio of vortex beams," *Phys. Rev. Lett.* Vol. 108, 194301, 2012.
7. Zhang, L. and P. L. Marston, "Acoustic radiation torque on small objects in viscous fluids and connection with viscous dissipation," *J. Acoust. Soc. Am*, Vol. 136, 2917–2921, 2014.
8. Hefner, B. T. and B. R. Dzikowicz, "Acoustic propagation from a spiral wave front source in an ocean environment," *J. Acoust. Soc. Am*, Vol. 131, 1978–1986, 2012.
9. Marston, P. L. "Axial radiation force of a Bessel beam on a sphere and direction reversal of the force," *J. Acoust. Soc. Am*, Vol. 120, 3518–3524, 2006.
10. Zhang, L. and P. L. Marston, "Geometrical interpretation of negative radiation forces of acoustical Bessel beams on spheres," *Phys. Rev. E*, Vol. 84, 035601, 2011.
11. Zhang, L. and P. L. Marston, "Axial radiation force exerted by general non-diffracting beams," *J. Acoust. Soc. Am*, Vol. 131, EL329–EL335, 2012.
12. Démoré, C. E., P. M. Dahl, Z. Yang, P. Glynne-Jones, A. Melzer, S. Cochran, M. P. MacDonald and G. C. Spalding, "Acoustic tractor beam," *Phys. Rev. Lett.* Vol. 112, 174302, 2014.
13. Baresch, D., J.-L. Thomas and R. Marchiano, "Observation of a single-beam gradient force acoustical trap for elastic particles: acoustical tweezers," *Phys. Rev. Lett.* Vol. 116, 024301, 2016.
14. Marston, P. L. and E. H. Trinh, "Hyperbolic umbilic diffraction catastrophe and rainbow scattering from spheroidal drops," *Nature* Vol. 312, 529–531, 1984.
15. Marr-Lyon, M. J., D. B. Thiessen and P. L. Marston, "Passive stabilization of capillary bridges in air with acoustic radiation pressure," *Phys. Rev. Lett.* Vol. 86, 2293–2296, 2001; (E) Vol. 87, 209901, 2001.

# Directionality in coherent dipole-dipole interactions

**J. B. Götte[1,2,3], G. Sun[1], K. C. van Kruining[1] and T. Pohl[1]**

[1]Max Planck Institute for the Physics of Complex Systems, Dresden 01187, Germany

[2]School of Physics and Astronomy, University of Glasgow, Glasgow G12 8QQ, United Kingdom

[3]College of Engineering and Applied Sciences, Nanjing University, Nanjing 210093, China

[*]corresponding author: joerg.goette@physics.org

**Abstract**-We investigate the photon mediated interaction of atoms trapped in the evanescent field of a waveguide or nanofibre. The evanescent field features a locking between the spin and the direction of propagation which we employ to drive selectively coherent dipole-dipole interactions between the trapped atoms.

For plane waves we are very familiar with the notion that the momentum is determined by the wavevector and that is independent of the polararization, while the spin is directly associated with circular polarization and aligned with the direction of propagation. However, for an inhomogeneous field, these familiar connections between the wavevector, linear and angular momentum no longer hold true [1]. On of the simplest and ubiquitous examples of an inhomogeneous field is an evanescent wave, which gives rise to a spin component, which is independent of the polarization and is orthogonal to the wave vector [2]. In addition, there exists a locking between the sense of rotation of the spin and the direction of propagation.

This directionality is interesting to exploit in light-matter interaction between the extraordinary spin of the evanescent fields an atoms trapped close to a nanofibre [3]. In this context we examine the photon mediated coherent dipole-dipole interactions between two or more atoms trapped in an evanescent field of a nanofibre and laser written waveguides [4]. We show how the atoms can interact directly or via emission into the guided modes. Using different wavelengths for trapping and addressing the atoms we can greatly enhance the interaction and reach a strong coupling regime while retaining a flexible geometry offered by laser written waveguides

**Acknowledgements**-This work was supported by the alumnus programme of the Newton International Fellowship and the Max Planck Institute for the Physics of Complex Systems.

**REFERENCES**

1. Aiello, A., Lindlein, N., Marquardt, C. and G. Leuchs, “Transverse Angular Momentum and Geometric Spin Hall Effect of Light”. *Phys. Rev. Lett.* **103,** 100401, 2009.
2. Bliokh, K. Y., Bekshaev, A. Y. and F. Nori, F. Extraordinary momentum and spin in evanescent waves. *Nature Communications* **5,** 3300, 2014.
3. Junge, C., O'Shea, D., Volz, J. and A. Rauschenbeutel, “Strong Coupling between Single Atoms and Nontransversal Photons”. *Phys. Rev. Lett.* **110,** 213604,2013.
4. Jukić, D., Pohl, T. and J. B. Götte, “Evanescent fields of laser written waveguides”. in Proceedings of the SPIE (eds. Galvez, E. J., Glückstad, J. & Andrews, D. L.) **9379,** 93790R, 2015.

# Mechanical effects of highly twisted light interacting with two-level atoms.

**V. E. Lembessis**[1], **M. Babiker**[2], **D. Ellinas**[3]

[1]Department of Physics Astronomy, College of Science, King Saud University, Riyadh 11451, Kingdom of Saudi Arabia

[2]Department of Physics, University of York, Heslington, York YO10 5DD, United Kingdom

[3]Technical University of Crete, Department of Electronic Computer Engineering, QLab , GR 73 100, Chania Crete Greece

vlempesis@ksu.edu.sa

**Abstract**— We consider the interaction of a two-level atom with a Laguerre-Gaussian (LG) light beam with high values of radial index, $p$, and/or winding number $l$. We focus on the effects of the Gouy phase together with other phase contributions due to the curvature in a LG beam when it interacts with atoms at near resonance.

It has been shown that when LG laser light interacts with a two-level atom it carries not only a linear momentum but also a quantised orbital angular momentum vector along the beam propagation axis [1]. In all these works researchers were limited to cases of small values of the winding number $l$ and they also ignore modes with non-zero values of the radial mode index $p$. Recent advances in experimental techniques allowed the generation of twisted light with very large radial index, $p$, and/or winding number $l$ [2] [3]. The importance of the 'ignored quantum number' $p$ in quantum communications and quantum Hall physics has been emphasized in [4] and [5] respectively.

The large size of indices $p$, and $l$ implies that the Gouy and the curvature phase terms, which have so far been ignored in the analysis, become of significant magnitudes and cannot be ignored from the analysis of the mechanical effects of LG beams on atoms. In the paraxial approximation the electric field associated with a Laguerre-Gaussian mode propagating in the positive $z-$direction with its wave polarisation in the $x-$ direction and wavelength $\lambda = 2\pi/k$, is given by $\mathbf{E} = u_p^{|l|} e^{i\Theta_{klp}(z)}\hat{\mathbf{x}}$ where $u_p^{|l|}$ is the amplitude or mode distribution function

$$u_p^{|l|} = \mathcal{E}_{k00}\sqrt{\frac{2p!}{2\pi(|l|!+p!)}}\frac{1}{(1+z^2/z_{R^2})^{1/2}}\left(\frac{\sqrt{2}r}{\mathrm{w}(z)}\right)^{|l|} L_p^{|l|}\left(\frac{2r^2}{w^2(z)}\right)e^{-r^2/w^2(z)} \tag{1}$$

and $\Theta_{klp}$ is the phase function

$$\Theta_{klp}(z) = kz + l\phi - (2p+|l|+1)\tan^{-1}(z/z_R) + \frac{kr^2 z}{2(z^2+z_R^2)}. \tag{2}$$

The quantity $z_R$ is the Rayleigh range of the beam and $w(z) = w_0\sqrt{1+z^2/z_R^2}$ with $w_0$ the beam waist. The third and fourth terms in Eq.(2) are the Gouy and curvature phases respectively. Physical quantities like the scattering force, the atomic momentum diffusion coefficients and the effects of atomic diffraction through light masks depend on the gradient of the field phase in Eq.(2). In our case this gradient is given by:

$$\nabla\Theta_{klp} = k\left[1-(2p+|l|+1)\frac{1}{kz_R}+\frac{r^2}{z_R^2}\right]\hat{\mathbf{z}} + \frac{l}{r}\hat{\phi}. \tag{3}$$

The beam now has a "modified" wavevector $\mathbf{k} = \nabla\Theta_{klp}$ and hence a modified axial wave-number $k_{eff}$ given by:

$$k_{eff} = k\left[1-\frac{(2p+|l|+1)}{kz_R}+\frac{r^2}{2z_R^2}\right]. \tag{4}$$

From the above equation we see that $k_{eff}$ is different than the wavenumber $k$ which has been used so far in the relevant literature. This difference is shown from the following numerical estimation. We consider an LG mode of wavelength $\lambda = 2\pi/k = 852.35nm$ and beam waist $w_0$ with indices $l = 300$, $p = 5$. This beam has its maximum intensity at a radial distance $r \approx 11w_0$ . We consider four different values of beam waists, $w_0 = 3\lambda$ $(2.56\mu m)$ , $5\lambda$ $(4.26\mu m)$, $10\lambda$ $(8.52\mu m)$ and $20\lambda$ $(17.04\mu m)$ and seek to find out the values of the effective wave vector at the point of maximum intensity. The values are presented in TABLE 1. It is interesting to check that when the beam is tightly focused to a $w_0 = 3\lambda$ then $k_{eff}$ takes a negative value and this is to be interpreted by saying that locally the atom "sees" a beam travelling in the opposite direction. Also there is a radial position where $k_{eff} = 0$. We must, however, be careful with such conclusions since, as has recently been pointed out, when the focussing is very tight then the electric field of the LG beam should be supplemented by a component along the $z-$direction which destroys the paraxial expression for the field given in Eqs. (1) and (2) [5]. In our numerical examples the paraxial approximation is ensured at an amount above 95 % for the cases of beam waist equal to $10\lambda$ and $20\lambda$ and around 85% for beam waists of $3\lambda$ and $5\lambda$ [6].

Table 1: Values of effective wave vector at maximum intensity points for a LG beam with indices $p = 5$ and $l = 300$.

| $w_0$ | $k_{eff}/k$ |
|---|---|
| $3\lambda$ | $-0.07$ |
| $5\lambda$ | 0.61 |
| $10\lambda$ | 0.90 |
| $20\lambda$ | 0.98 |

Based on the above analysis in our work we show modified expressions for scattering force and atomic momentum coefficients. We also show modifications to the momentum and orbital angular momentum of atom vortex beams generated by atomic diffraction through properly tailored light masks generated by LG beams with large indices $l$ and $p$ [7]. The reduction of the value of the axial wavenumber $k_{eff}$ when $l$ increases shows an interesting "competition" between momentum and angular momentum of the atom. When the atom absorbs a high helicity photon it is "heated azimuthally" while is "cooled" axially.

**ACKNOWLEDGMENT**

This project was funded by the National Plan for Science, Technology and Innovation (MAARIFAH), King Abdulaziz City for Science and Technology, Kingdom of Saudi Arabia, Award No.15-MAT5110-02.

**REFERENCES**

1. Babiker. M, D. L. Andrews, and V. E. Lembessis in *The Angular Momentum of Light*, edited by D. L. Andrews and M. Babiker Cambridge University Press, Cambridge, 2013.
2. Campbell, G, B. Hage, B. Buchler, and P. K. Lam, "Generation of high-order optical vortices using directly machined spiral phase mirrors ," *Applied Optics*, Vol. 51, No. 7, 873-876, 2012.
3. Shen, Y., G. T. Campbell, B. Hage, H. Zou, B. C. Buchler, and P. K. Lam, "Generation and interferometric analysis of high charge optical vortices," *J. Opt.* , Vol. 15, 044005-07, 2013.
4. Fickler, R., R. Lapkiewicz, W. N. Plick, M. Krenn, C. Schaeff, S. Ramelow and A. Zeilinger, "Quantum Entanglement of High Angular Momenta," *Science*, Vol. 338, 640, 2012.
5. Lacki, M., H. Pichler, A. Sterdyniak, A. Lyras, V. E. Lembessis, O. Al-Dossary, J. C. Budich, and P. Zoller, "Quantum Hall physics with cold atoms in cylindrical optical lattices," *PRA*, Vol. 93, 013604, 2016.
6. Krenn, M., N. Tischler, and A. Zeilinger, "On small beams with large topological charge," *New J. Phys.* , Vol. 18, 033012, 2016.
7. Lembessis, V. E., D. Ellinas, M. Babiker, and O. M. Al-Dossary, "Atom vortex beams," *Phys. Rev. A* , Vol. 89, 053616, 2014.

# Cold atoms and optical vortex beams

**Sonja Franke-Arnold**
Physics and Astronomy University of Glasgow, UK

**Abstract.** Atoms that are exposed to a magnetic field display behaviours similar to chiral media. I will discuss the interaction of cold rubidium atoms with optical vortex beams, and report on our measurements of magnetic field mediated EIT (electro-magnetically induced transparency). We observed that the local opacity of the cold atoms is dictated by the structure of the optical vortex and the applied magnetic field.

# Plasmonics and propagation of electromagnetic radiations in low-dimensional materials

Title: Plasmonic excitations in thin topological insulators

Author: T. Stauber

Affiliation: Departamento de Teoría y Simulación de Materiales, Instituto de Ciencia de Materiales de Madrid, CSIC, 28049 Cantoblanco, Spain

Abstract:
We discuss plasmonic excitations in thin slabs of topological insulators. These structures can be ideally modeled as a double layer of Dirac electrons and we show that there is spin-charge separation of the collective excitation in the case of equal electronic density of the upper and lower layer. We will also point out that the plasmonic modes usually depend on the sample thickness and on the dielectric constant of the bulk - only for very small wave numbers, the universal Dirac dispersion is recovered. In order to explain recent experiments, we propose to also consider the influence of the Schrödinger-like depletion layer underneath the two Dirac systems.

# Effect of Remote Impurity Layer on THz gain in Graphene Bilayers with Population Inversion

**M. Ryzhii[1*], T. Otsuji[2], V. Ryzhii[2], V. Mitin[3], and M. S. Shur[4]**
[1]University of Aizu, Japan
[2]Research Institute of Electrical Communication, Tohoku University, Japan
[3]University at Buffalo, SUNY, USA
[4]Rensselaer Polytechnic Institute, USA
[*]corresponding author: m-ryzhii@ieee.org

**Abstract**-We demonstrate that the indirect interband generation of photons in hybrid graphene bilayer structures with population inversion can surpass their intraband (Drude) absorption, resulting in rather large absolute values of the negative dynamic conductivity in a wide range of terahertz frequencies at room temperatures. Thus, the hybrid graphene heterostructures under consideration can be perspective for THz lasers.

Heterostructures based on graphene layers (GL) and graphene bilayers (GBL) with population inversion enabled by optical pumping or injection can serve as the active media in the terahertz (THz) lasers [1, 2]. One of the options to increase the THz gain is to use GL- or GBL-heterostructures with an extra remote impurity layer [3, 4]. Figures 1a and 1b show the schematic view of the GBL-heterostructure with the remote impurity layer on the top and its band diagram with arrows indicating radiative electron transitions. The scattering of electrons and holes on long-range potential created by the remote impurity layer reinforces the indirect interband radiative transitions. Such transitions can dominate over the indirect intraband transitions [3]. We show that the net dynamic conductivity Re σ can become negative in a rather wide frequency range where it overcompensates the Drude absorption. The absolute value of Re σ can be larger than the contribution of direct interband transitions (Fig. 1c).

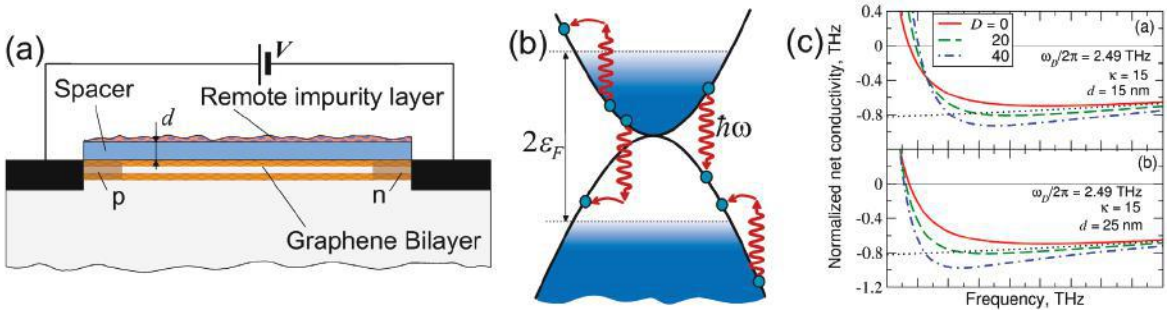



Figure 1. (a) Schematic view of the GBL-heterostructure with remote impurity layer, (b) its energy band diagram under optical pumping (b), and (c) calculated frequency dependences of normalized net THz conductivity for different structural parameters (effective dielectric constant $k$ of the substrate and spacer, thickness of the spacer $d$, remote impurity layer doping parameter $D$). Dotted line corresponds to normalized THz conductivity due to direct interband transitions only.

**Acknowledgement.** This work was supported by the Japan Society for Promotion of Science (Grant-in-Aid for Specially Promoting Research, #23000008), Japan, and by the Air Force Laboratory, USA.

**REFERENCES**

1. Ryzhii, V., M. Ryzhii, and T. Otsuji, "Negative dynamic conductivity of graphene with optical pumping," *J. Appl. Phys*., Vol. 101, 083114, 2007.
2. Ryzhii, M., and V. Ryzhii, "Injection and population inversion in electrically induced p–n junction in graphene with split gates," *Jpn. J. Appl. Phys*., Vol. 46, L151, 2007.
3. Svintsov, D., T. Otsuji, V. Mitin, M. S. Shur, and V. Ryzhii, "Negative terahertz conductivity in disordered graphene bilayers with population inversion," *Appl. Phys. Lett.*, Vol. 106, 113501, 2015.
4. Ryzhii, V., M. Ryzhii, V. Mitin, M. S. Shur, and T. Otsuji, "Negative terahertz conductivity in remotely doped graphene bilayer heterostructures," *J. Appl. Phys*., Vol. 118, 183105, 2015.

# Enhanced Sensing and PT-Symmetry in Photoexcited Graphene Nanostructures

**Pai-Yen Chen**
[1]Department of Electrical and Computer Engineering, Wayne State University,
Detroit, Michigan 48202, USA
[*]corresponding author: pychen@wayne.edu

**Abstract**- We present here the parity-time (PT) symmetric Terahertz (THz) system based on an optically-pumped, active graphene metasurface. We theoretically demonstrate that the combination of the spectral singularity in a PT-symmetric system and the chemical sensitivity of graphene may give rise to exotic scattering responses, strongly influenced by the presence of charged impurities in graphene at the spontaneous PT symmetry-breaking point.

Significant attention has been recently devoted to PT-symmetry [1], which is originally conceived in quantum physics and extended to optics and electronics by means of the spatial modulation of gain and loss. In this work, we will theoretically explore the THz amplification using graphene nanostructures for realizing PT symmetric systems in the THz regime. Graphene is of great interest as a novel material for integrated photonics and optoelectronics, as it can exhibit strong optical absorption, up to 2.3% for a single monolayer [2] and ultrafast modulation of its conductivity by electrostatic gating [3]-[4]. Its optical properties are especially interesting in the THz regime, where the population inversion and thus negative dynamic conductivity (THz lasing) can take place in an optically pumped graphene monolayer, due to the cascaded optical phonon emission and interband transitions around the Dirac point, as shown in Fig. 1a. The dynamic conductivity of a graphene monolayer under infrared pumping can be calculated using the non-equilibrium Kubo formula [2]-[4], of which the Fermi level $E_F$ is split into quasi-Fermi levels $E_{Fn}$ and $\underline{E_{Fp}}$. Figure 1b shows the real-part conductivity Re[σ] as a function of THz frequency and temperature. Even at room temperature, a negative Re[σ] can be obtained, which effectively implies that THz gain may be realized over a single layer of atoms, necessary for achieving the PT symmetry condition.

By using a pair of negative-resistance (optically pumped graphene) and positive-resistance (lossy silver thinfilm) surfaces separated by a proper distance, as schematically shown in Fig. 1c, the PT-symmetric THz system can be realized, with the scattering matrix S that possesses the special parity-time symmetry: $(\mathrm{PT})\mathbf{S}(\omega^*)(\mathrm{PT}) = \mathbf{S}^{-1}(\omega)$. A condition of special interest resides in the exceptional points (EP), for which we obtain unidirectional transparency, with zero reflection at port 1 ($|S_{11}| = 0$), unitary reflection at port 2 ($|S_{22}|=1$), and unitary transmittance at both ports ($|S_{12}|=|S_{21}| = 0$). Explicit criteria for the spontaneous PT symmetry-breaking transition can be derived using the transmission-line model, where the uni-modular and nondegenerate eigenvalues (λ±) transit to non-unimodular ones, by tuning the surface resistance $R$ (levels of gain and loss). Here we employ the metasurface structure in Fig. 1c to provide enhanced light-matter interactions in graphene and to tune out the kinetic inductance of graphene with metasurface's surface capacitance such that the overall surface impedance is purely real and negative (with a zero surface reactance). Here we assume a pristine graphene with $E_F$ = 0 eV, an optically transparent spacer (air here), and an ultrathin amorphous NiCr film at the bottom.

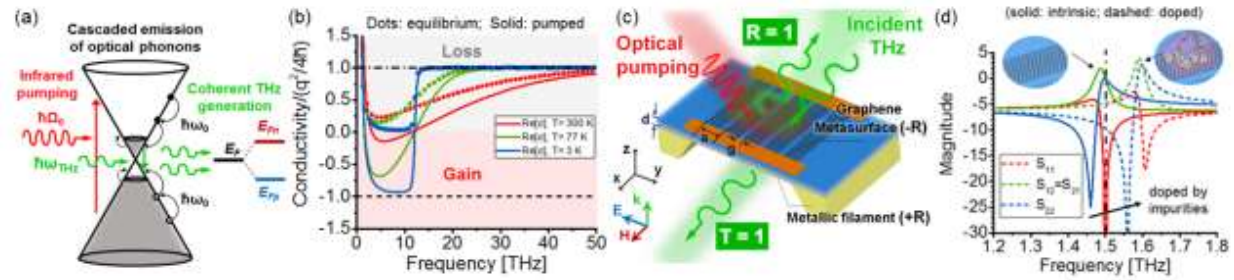



Figure 1 (a) Schematics of THz lasing in intrinsic graphene under optical pumping. (b) Theoretical THz conductivity of graphene with and without pumping. (c) Schematic integration of a chemical-sensitive PT-symmetric THz system using graphene metasurface. (d) Scattering parameters versus frequency for intrinsic and doped graphene.

Figure 1d illustrates the concept of the proposed PT-sensor for molecules/gas/chemical/ionic liquid sensing, using this graphene-based PT-symmetric THz system. In this framework, the unidirectional transparency condition, typically existing only at a singular frequency point, could be very sensitive to variations in the impedance of the active metasurface, yielded by the impurity doping in non-equilibrium graphene. When graphene is exposed to chemical agents, the negative dynamic conductivity can be varied, which dramatically modulates the THz scattering at the exceptional point. The analytical results in Fig. 1d are based on practical metasurface geometry and realistic loss/gain properties in materials. The theoretical results confirm not only the unidirectional transparency in this THz PT-symmetric system, but also the potential of an ultrasensitive THz sensor. When n-/p-type dopants attached on the graphene surface (0.05 eV in $\Delta E_{Fn}$ or $\Delta E_{Fp}$), the change in scattering coefficient $S_{11}$ can be dramatic, more than 40 dB at the EP frequency. For a fair comparison, an optimized passive graphene-metasurface sensor (without optical pumping) is also studied, which, however, shows a reduced sensitivity.

We have presented the THz PT-symmetric system using an optically-pumped graphene metasurface that has an interesting negative surface resistance and thus gain effect in the low-THz region. By engineering the geometry of graphene metasurface, the unidirectional reflectionless propagation can be observed at a singular frequency. Thanks to the sharp spectral singularities of the PT-symmetric system and the tunable THz gain in graphene, we have shown that even a low-level chemical doping may dramatically modulate scattering properties of a graphene-based PT-sensor at the exceptional point. Our findings may drive new directions and fundamentally novel effects by breaking the sensitivity limitations of conventional micro-/nano-sensors.

**REFERENCES**

1. C. M. Bender and S. Boettcher, "Real spectra in non-Hermitian Hamiltonians having PT symmetry," Phys. Rev. Lett. 80, 5243 (1998).
2. V. Ryzhii, M. Ryzhii, and T. Otsuji, "Negative dynamic conductivity of graphene with optical pumping," J. Appl. Phys. 108, 083114 (2007).
3. P. Y. Chen, and A. Alù, "Atomically thin surface cloak using graphene monolayers," ACS Nano 5, 5855-5863 (2011).
4. P. Y. Chen, H. Huang, D. Akinwande, and A. Alù, "Graphene-based plasmonic platform for reconfigurable terahertz nanodevices," ACS Photonics 1, 647-654 (2014).

# Terahertz Photogalvanics and Opto-Electronic Characterization of Topological Insulators

**S. D. Ganichev**

Terahertz Center, University of Regensburg, Regensburg, 93051 Germany
sergey.ganichev@physik.uni-regensburg.de

**Abstract**— The paper overviews experimental and theoretical studies of photocurrents excited by polarized terahertz radiation in $(Bi_{1-x}Sb_x)_2Te_3$ and HgTe based 3D and 2D topological insulators.

Much attention in condensed-matter physics is currently directed towards understanding electronic properties of Dirac fermions in three dimensional (3D) topological insulators (TIs), which challenge fundamental concepts and hold a great potential for electronic, optic and optoelectronic applications, see e.g. Ref. [1, 2, 3, 4, 5]. Recently nonlinear high frequency electron transport phenomena in TI systems, in particular photocurrents induced by infrared/terahertz radiation, have attracted growing interest. Here we show that the photocurrents in TIs are caused by photogalvanic, photon drag or, in the presence of magnetic field, magneto-photogalvanic effects: nonlinear transport effects yielding a *dc* electric current proportional to the square of the *ac* electric field [6, 7]. We discuss the phenomenological and microscopic theory of these phenomena, present the state-of-the-art of the experiments and show that nonlinear transport excited by terahertz laser radiation opens up new opportunities for probing of Dirac electrons in 3D TI even in the materials with substantial conductance in the bulk.

The photogalvanic effects is caused by asymmetric scattering of Dirac fermions driven back and forth by terahertz electric field which results in a dc electric current [8]. A selective excitation of dc current in TI surface states becomes possible due to the specific feature of photogalvanics, whose prerequisite is a lack of inversion center. As $(Bi_{1-x}Sb_x)_2Te_3$ crystals, like most of the 3D TI, are centrosymmetric, this requirement is fulfilled for the surface states only. Because of the symmetry filtration the dc current is generated by the surface electrons only. The photocurrent, being sensitive to the surface symmetry and scattering details, provides a simple method to determine the orientation of the surface domains, to probe high frequency conductivity in TI, and to study details of electron scattering the surface states even at room temperature. Further interesting access to spin transport in TI yields circular photogalvanic effect solely driven by the light's helicity and yielding photocurrent whose sign reverses upon switching the radiation handedness from left- to right-handed circularly polarized light [9]. A particular attention will also be paid to the helicity sensitive edge photogalvanic currents in HgTe-based 2D TIs [10].

Magneto-photogalvanic, in particular cyclotron resonance induced photocurrents [11, 12], can also be efficiently generated in the topologically protected surface states of 3D TI. We show that the effect belongs to the class of magnetic quantum ratchet effects. It emerges due to the joint orbital action of the ac electric and static magnetic fields on the 2D Dirac fermions in the system with structure inversion asymmetry. The latter leads to an asymmetric scattering of carriers in the momentum space resulting in a fully spin polarized dc electric current. Studying CR induced photocurrent in the gated samples enables us to probe the effective masses and the momentum relaxation times of 2D Dirac surface states, when the Fermi energy lies in the bulk energy gap or even in the conduction band [12].

## ACKNOWLEDGMENT

The support from the DFG priority program SPP1666 and Virtual Institute for Topological Insulators, the Elite Network of Bavaria (K-NW-2013-247).

## REFERENCES

1. Hasan M. Z., and Kane C. L., "Colloquium: Topological insulators," Rev. Mod. Phys. Vol. 82, No. 4, 3045–3067, 2010.
2. Moore J. E., "The birth of topological insulators," Nature Vol. 464, 194–198, 2010.

3. Qi X. L. and Zhang S. C., "Topological insulators and superconductors," Rev. Mod. Phys. Vol. 83, No. 4, 1057– 1110, 2011.
4. J. H. Bardarson and J. E. Moore, "Quantum interference and Aharonov-Bohm oscillations in topological insulators," Rep. Prog. Phys. Vol. 76, 056501/1-21, 2013.
5. *Topological Insulators Contemporary Concepts of Condensed Matter Science* eds. Franz M., and Molenkamp L., Elsevier Ltd, Oxford, 2013.
6. Glazov M.M., and Ganichev S.D., "High frequency electric field induced nonlinear effects in graphene," Physic Reports Vol. 535, No. 3, 101–138, 2013.
7. S. D. Ganichev and W. Prettl, *Intense Terahertz Excitation of Semiconductors*, Oxford University Press, Oxford, 2006.
8. P. Olbrich, L.E. Golub, T. Herrmann, S.N. Danilov, H. Plank, V.V. Bel'kov, G. Mussler, Ch. Weyrich, C.M. Schneider, J. Kampmeier, D. Gruetzmacher, L. Plucinski, M. Eschbach, and S.D. Ganichev, "Room temperature high frequency transport of Dirac fermions in epitaxially grown $Sb_2Te_3$ and $Bi_2Te_3$-based topological insulators," Phys. Rev. Lett. Vol. 113, 096601/1–5, 2014.
9. J. W. McIver, D. Hsieh, H. Steinberg, P. Jarillo-Herrero, and N. Gedik, "Control over topological insulator photocurrents with light polarization," Nature Nanotech., Vol. 7, 96–100, 2012.
10. Z.D. Kvon, K.-M. Dantscher, C. Zoth, D.A. Kozlov, N.N. Mikhailov, S.A. Dvoretsky, and S.D. Ganichev, "Terahertz electron transport of two-dimensional topological insulator in HgTe quantum wells," JETP Lett. Vol. 99, No. 5, 290–294, 2014.
11. C. Zoth, P. Olbrich, P. Vierling, K.M. Dantscher, V.V. Bel'kov, M.A. Semina, M.M. Glazov, L.E. Golub, D.A. Kozlov, Z.D. Kvon, N. Mikhailov, S.A. Dvoretsky, S.D. Ganichev, "Quantum oscillations of photocurrents in HgTe quantum wells with Dirac and parabolic dispersions,"Phys. Rev. B Vol. 90, 205415/1–15, 2014.
12. K.-M. Dantscher, D.A. Kozlov, P. Olbrich, C. Zoth, P. Faltermeier, M. Lindner, G.V. Budkin, S.A. Tarasenko, V.V. Belkov, Z.D. Kvon, N.N. Mikhailov, S.A. Dvoretsky, D. Weiss, B. Jenichen, and S.D. Ganichev, "Cyclotron Resonance Assisted Photocurrents in Surface States of a 3D Topological Insulator Based on a Strained High Mobility HgTe Film," Phys. Rev. B Vol. 92, 165314/1–10, 2015.

# Atomic scale meta-surfaces based on graphene and hexagonal boron nitride

**D.N. Basov**
Department of Physics, Columbia University, New York, NY, USA
*corresponding author: db3056@coumbia.edu

**Abstract**- We have investigated meta-surfaces comprised of graphene and hexagonal boron nitride. These structures show tunable hyperbolic response and are well suited to control flow of surface plasmons with electrostatic gating and/or photo-excitation.

We have implemented and investigated the tunable hyperbolic response in heterostructures comprised of a monolayer graphene deposited on hexagonal boron nitride (G-hBN) slabs. Electrostatic gating of the graphene layer enables electronic tunability of phonon polaritonic properties of hBN: a layered material with well-documented hyperbolic response in the mid-infrared (mid-IR) frequencies. The tunability originates from the hybridization of surface plasmon polaritons in graphene to hyperbolic phonon polaritons in hBN: an effect that we examined via nano-IR imaging and spectroscopy. The hybrid polaritons possess combined virtues from plasmons in graphene and phonon polaritons in hBN. Therefore, G-hBN structures fulfill the definition of the electromagnetic metamaterial since the attained property of these devices is not revealed by its constituent elements. Our results uncover a practical approach for realization of broadly tunable nano-photonic metamaterials by exploiting the interaction of distinct types of polaritonic modes hosted by different constituent layers of van der Waals heterostructures. [1]

Moire superlattices formed by graphene on hBN also present interesting opportunities for IR meta-surfaces. In these structures moire superlattice domain coexist with regions of plain graphene. The boundaries of the two types of domains act as efficient plasmonic reflectors. Most notably, the plasmonic reflectivity can be tuned by a single gate electrode applied to the entire structure [2]. I will discuss two additional approaches for controlling plasmonic flow in graphene-based devices including gating with carbon nanotubes [3] and gate electrodes and ultra-fast photo-excitation [4].

**REFERENCES**

1. S.Dai et al. “Graphene on hexagonal boron nitride as a tunable hyperbolic metamaterial,” *Nature Nanotechnology* Vol. 10, 682-685, 2015.
2. G. Ni et al., “Plasmons in graphene moiré superlattices,” *Nature Materials* Vol. 14, 1217-1220, 2015.
3. B.Y.Jiang, et al. “Optical signatures of a hypercritical 1D potential in a 2D Dirac metal,” arXive1602:03232.
4. Ni et al. “Ultrafast optical switching of infrared plasmon polaritons in high-mobility graphene” *Nature Photonics* 10, 244 (2016).

# Surface Electromagnetic Waves on Metamaterial Absorbers

**W. J. Padilla**[*1], **and A. E. Cardin**[1]

[1]Department of Electrical and Computer Engineering, Duke University, USA
[*]willie.padilla@duke.edu

**Abstract**— In metamaterial absorbers, absorption for transverse electric polarization falls off much more rapidly than transverse magnetic for increasing angle of incidence. In the present work we demonstrate through computational study that the broad-angle TM behavior cannot be associated with periodicity, instead it is the result of coupling with a surface electromagnetic. Previous experimental results are consistent our computational study and we highlight the potential augment absorber response by tailoring the surface wave.

Metamaterial absorbers (MMAs) are a well developed technology, having been demonstrated overmuch of the electromagnetic spectrum from radio frequencies to visible wavelengths [1, 2]. The scalable nature and symmetries available in MMAs offer for simple and polarization sensitive designs, which has led to great progress recently.

The operating principle of the MMA is fairly simple: achieve an impedance match to free space while providing a high loss. Fundamentally this response is achieved as a combination of a Drude like term from the ground plane and a Lorentz resonant term from the geometry of the metamaterial for the electric response, and time-varying anti-parallel currents on the ground plane and metamaterial driven by the incident magnetic field. The MMA can often be profitably discussed in terms of a frequency dependent effective permittivity ($\epsilon_{eff}(\omega)$) and effective permeability ($\mu_{eff}(\omega)$), and we consider here a regime where this description is valid.

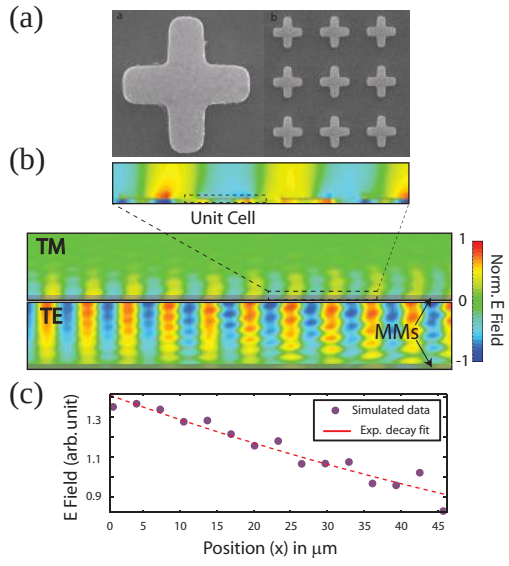



Figure 1: (a) SEM image of a cross type MMA of the same dimensions as the simulated case (b) plot shows the E-field in the $xz-$plane for the TE and TM cases; zoomed portion shows the coupled wave in the TM case (c) Electric field intensity of the surface wave falls off exponentially in the propagation direction.

It is known that MMAs maintain high absorption for transverse magnetic (TM) polarized waves, even for angles of incidence above 80° from the surface normal; a stark contrast to transverse electric (TE) waves whose absorption diminishes around 45°. This was explained as a reduction of the magnetic response due to the magnetic field rotating out of plane in the TE case [3]. However, recent work has introduced surface electromagnetic waves (SEWs) in to the description of these absorption [4]. The addition of this phenomena provides an important piece of the picture, and here we present a study that elucidates some aspects of the SEW and its role in absorption.

We perform 3D full wave electromagnetic field simulations in order to explore the nature of the polarization dependant absorption response. We use a Drude model for all metallic components [5], and a layer of benzocyclobutene (BCB) as the dielectric. Unit cell boundary conditions are employed allowing for angular variation in the incident wave. Our simulations provide the complex scattering parameters and we calculate the absorption as $A = 1 - R = 1 - |S_{11}|^2$.

We simulate a one dimensional array consisting of unit cells with a total length of 102.4$\mu$m, see Fig. 1. The orientation of the simulation domain is as follows: the surface normal of the MMA lies in the $\hat{z}$-direction, the one dimensional array is oriented in the $\hat{x}$-direction, and the $\hat{y}$-direction serves as the boundary by which the incident mode is enforced. Along the $\hat{z}$-direction, an open boundary is assigned to the top of the bounding box and a perfect electric boundary to the bottom

in place of the metallic ground plane. We simulate the TE and TM polarizations by setting perfect electric or magnetic boundaries along the sides of the simulation domain. In Figs. 1 we plot the electric field over the simulation volume for TE and TM polarized waves at the absorption peak. It can be seen that the TE polarized wave does not couple to the surface and retains its plane wave like appearance. TM polarized waves however have a dramatically different appearance, and are strongly confined to the surface of the MMA. In Fig. 1 (c) we note how the electric field strength falls off as a function of distance along the metamaterial, and note that it does so exponentially.

The results presented in Fig. 2 demonstrate that TE and TM polarized waves exhibit drastically different behavior. Our results allow us to approximate quantities such as loss, wavelength, and propagation distance of the SEWs [6, 7]. From a decaying exponential fit to max$|E_z|$ (Fig. 1 (c) we calculate the propagation length $L_{SEW}$ by determining where max$|E_z|$ has fallen to 1/e of its initial value. In this case the SEW realizes a propagation length of 64.5 $\mu$m.

A seen in Fig. 1 (a), an infrared MMA was fabricated using thin-film processing combined with UV photolithographic patterning. We use a 190 nm thick layer of BCB as the dielectric spacer and 80nm of gold for the ELC elements and ground plane. The cross shaped pattern has a linewidth of w = 500 nm, side length of L = 1.95 $\mu$m, and a unit cell size of a = 3.2 $\mu$m. A large area MMA was fabricated with a total lateral size of 2.54×2.54 cm$^2$. The experimental and computational results are found to be in good agreement.

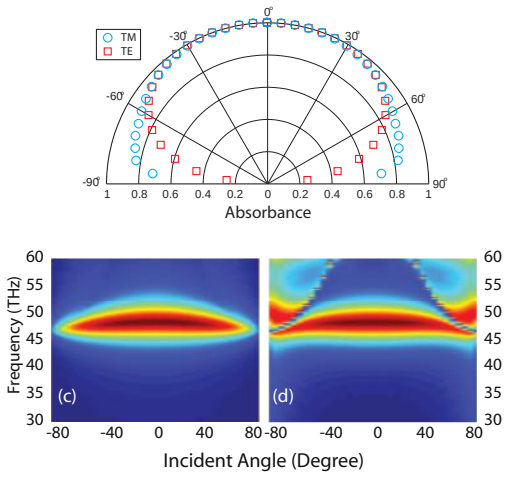



Figure 2: (a) the angle dependence of the TE and TM modes at peak absorption (b) frequency dependant absorption for the TE mode and (c) the TM

We have demonstrated the existence and contribution of a SEW to the stability of the absorbing response in the TM polarization. We note that it may be possible to tailor the angular response of an absorber by modifying the effective response of the MMA, which could lead to novel absorber design. Furthermore the symmetry of Maxwells equations suggests that absorbers dual to the presented configuration could leverage a SEW in the TE polarization using a structure that supports magneto-plasmons [8].

## ACKNOWLEDGMENT

Research was funded by the Office of Naval Research (N00014-10-C-0437), the NSF (ECCS-1002340), and the Department of Energy (DE-SC0005240).

## REFERENCES

1. Shrekenhamer, D., et al., "Metamaterial perfect absorber microwave focal plane array," Phys. Rev. Lett. **109**, 177401 (2012).
2. Hao, J., et al., "High performance optical absorber based on a plasmonic metamaterial," Appl. Phys. Lett. **96**, 251104 (2010).
3. Watts,C. M., el al., " Metamaterial electromagnetic wave absorbers," Adv. Mat. **24**, OP181 (2012).
4. Chen, W.C., et al., "The role of surface electromagnetic waves in metamaterial absorbers," Opt. Exp. **34**, 6783-6792 (2016).
5. Ordal, M. A., et al., "Optical properties of fourteen metals in the infrared and far infrared: Al, Co, Cu, Au, Fe, Pb, Mo, Ni, Pd, Pt, Ag, Ti, V, and W.," Appl. Opt. **24**, 4493 (1985)
6. Reinhard, B. , et al., "Experimental and numerical studies of terahertz surface waves on a thin metamaterial film," Opt. Lett. **35**, 1320 (2010).
7. Chen, C.-F., et al., "Controlling inelastic light scattering quantum pathways in graphene," Nature **471**, 617 (2011).
8. Gollub, J., et al., " Experimental characterization of magnetic surface plasmons on metamaterials with negative permeability," Phys. Rev. B **71**, 195402 (2005).

# Controlled signal propagation in a metamaterial analogue of tripod EIT medium.

**S. Zielińska - Raczyńska**[1], **D. Ziemkiewicz**[1]

[1]Institute of Mathematics and Physics, UTP University of Science and Technology, Al. Kaliskiego 7, 85-789 Bydgoszcz, Poland
david.ziemkiewicz@utp.edu.pl

**Abstract**— The metamaterials mimicking the electromagnetically induced transparency (EIT) are a new class of artificially structured materials which provide unprecedented opportunity to study EIT-related phenomena at room temperature. The Finite Difference Time Domain (FDTD) method widely used in studies of wave propagation in metamaterials can be extended to simulate complex EIT media such as a four level tripod, giving new insight into the dynamics of such systems.

## 1. INTRODUCTION

The Electromagnetically Induced Transparency (EIT) is a quantum optical phenomenon which significantly alters the conditions for pulse propagation in the medium. In particular, a four level tripod configuration allows for the creation of double transparency windows characterized by low absorption and very significant reduction of the group velocity within the windows. Nowadays, much interest has been put on a classical analogue of EIT phenomenon in metamaterials. Such structures are scalable to various frequency ranges, allowing for high flexibility, and also have the advantage of room temperature operation. Therefore, it is of interest to investigate the signal propagation in such media, the examples of which are coupled split-ring resonators or metal strips. Recently, it has been shown that the Doppler shift exhibits many unusual properties in classical analog of EIT $\Lambda$ type medium [1]. One can expect that a tripod medium might allow for even richer phenomena, including controlled generation of multiple frequency modes from monochromatic source.

## 2. SIMULATION OF TRIPOD METAMATERIAL

We employ the Finite Difference Time Domain (FDTD) method to study the light propagation in EIT metamaterial. The medium description is based on the coupled resonator model [2], accurately describing both the absorption spectrum of tripod medium (Fig. 1a) as well as the group velocity connected with the medium dispersion (Fig. 1b).

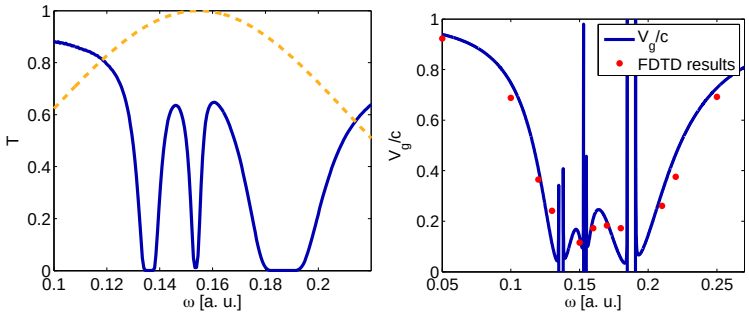



Figure 1: a) Calculated transmission spectrum, with two easily visible transparency windows, incident pulse is marked by a dashed line. b) The dependence of the group velocity on frequency inside the window.

## REFERENCES

1. S. Zielińska and D. Ziemkiewicz, "Frequency shifts of radiating particles moving in EIT metamaterial", JOSA B **33**, 412-419, (2016)
2. P. Tassin, Lei Zhang, Th. Koschny, E. N. Economou, and C. M. Soukoulis, "Low-Loss Metamaterials Based on Classical Electromagnetically Induced Transparency," Phys Rev. Lett. **102**, 053901 (2009)

**Microcavity Polaritons: fundamental physics and devices**

# Spin selective filtering and spin textures in quasi-one-dimensional polariton condensates.

**C. Antón[1,2], T. Gao[3,4], S. Morina[5], T. C. H. Liew[5], M. D. Martín[1,2], Z. Hatzopoulos[6], P. S. Eldridge[3], P. G. Savvidis[3,4], and L.Vina[1,2,7*]**

[1]Departamento de Física de Materiales, Universidad Autónoma de Madrid, Madrid 28049, Spain
[2]Instituto de Ciencia de Materiales "Nicolás Cabrera," Universidad Autónoma de Madrid, Madrid 28049, Spain
[3]FORTH-IESL, P.O. Box 1385, 71110 Heraklion, Crete, Greece
[4]Department of Materials Science and Technology, University of Crete, 71003 Heraklion, Crete, Greece
[5]School of Physical and Mathematical Sciences, Nanyang Technological University, 637371, Singapore
[6]Department of Physics, University of Crete, 71003 Heraklion, Crete, Greece
[7]Instituto de Física de la Materia Condensada, Universidad Autónoma de Madrid, Madrid 28049, Spain
[*]corresponding author: luis.vina@uam.es

**Abstract**- We report on the realization of a novel spin-selective spatial filter mediated by propagating exciton-polariton condensate bullets in a quasi-one-dimensional (1D) semiconductor microcavity. We also show that, under circularly polarized, continuous-wave, non-resonant excitation, spin textures whose phase depends on the emission energy are formed.

The use of polariton condensates in all optical logic devices has been the subject of intense research in recent years, promising ultrafast switching times, low losses, spin information transport and low power consumption. The control of polariton condensate propagation and their polarization [1] provide the necessary ingredients for future optical circuits. New schemes for the realization of spinoptronics devices and "polariton neurons" in circuits, the building blocks of all-optical integrated logic circuits, have been recently proposed. Quasi-1D patterned high- finesse microcavities provide an ideal platform for all-optical manipulation, ballistic propagation and amplification, and gating of polariton condensates [2,3]. The waveguide nature of these structures induces the channeling of polariton propagation, while the discretization of energy levels results in a rich relaxation dynamics [4].

Here we report on the realization of a spin-selective spatial filter mediated by propagating Bose-Einstein exciton-polariton condensates in a quasi-1D semiconductor microcavity [5]. The switch is achieved using a controllable spin-dependent gating barrier: a non-resonant laser beam provides the source of propagating polaritons, while a second circularly polarized weak beam imprints a spin dependent potential barrier, which gates the polariton flow and generates polariton spin currents. A complete spin-based control over the blocked and transmitted polaritons is obtained by varying the gate polarization.

Furthermore, the discretization in energy of the lower polariton branch in our structure has notable consequences in the coherent transport of the spin vector. The confinement renders a TE-TM mode splitting, which remains for zero in-plane wave vector, and it acquires larger values than the TE-TM splitting in two-dimensional (2D) MCs. A spectral analysis of the spin transport reveals different polariton spin textures from those observed in 2D systems [1]. The richness of these textures is related to the energy-dependent speed of propagation of polaritons in our system with lowered dimensionality. The ballistic propagation of spin-polarized polaritons along the ridge is observed over distances of $\sim$100 $\mu$m [6].

The experiments are compared with simulations of the spinor-polariton condensate dynamics based on a generalized Gross-Pitaevskii equation, modified to account for incoherent pumping, decay, and energy relaxation within the condensate.

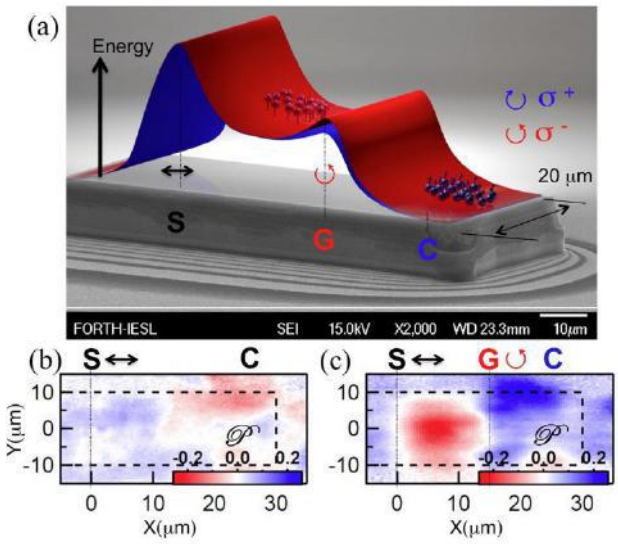



**Figure 1:** (a) A schematic of the spin filter with the red and blue slopes depicting the energy landscape for σ+ and σ- polaritons for a σ- (↺) gate (G). The source beam (S) has linear polarization. The degree of circular polarization, $\wp$, in real space (b) without and (c) with G present where the black dashed line shows the region of interest of the ridge.

**Acknowledgements:** P.S. acknowledges the Greek GSRT program "ARISTEIA" (1978) and EU ERC "Polaflow" for financial support. The work was partially supported by the Spanish MINECO MAT2014-53119-C2-1-R and EU-FP7 ITN INDEX (289968) projects.

## REFERENCES

1. E. Kammann, T. C. H. Liew, H. Ohadi, P. Cilibrizzi, P. Tsotsis, Z. Hatzopoulos, P. G. Savvidis, A. V. Kavokin, and P. G. Lagoudakis, "Nonlinear Optical Spin Hall Effect and Long-Range Spin Transport in Polariton Lasers" *Phys. Rev. Lett.* **109**, 036404, 2012.
2. T. Gao, P. S. Eldridge, T. C. H. Liew, S. I. Tsintzos, G. Stavrinidis, G. Deligeorgis, Z. Hatzopoulos, and P. G. Savvidis, "Polariton condensate transistor switch", *Phys. Rev. B* **85**, 235102, 2012.
3. C. Antón, T. C. H. Liew, G. Tosi, M. D. Martin, T. Gao, Z. Hatzopoulos, P. S. Eldridge, P. G. Savvidis, and L. Vina, "Dynamics of a polariton condensate transistor switch", *Appl. Phys. Lett.* **101**, 261116, 2012.
4. C. Antón, T. C. H. Liew, G. Tosi, M. D. Martín, T. Gao, Z. Hatzopoulos, P. S. Eldridge, P. G. Savvidis, and L. Vina, "Energy relaxation of exciton-polariton condensates in quasi-one-dimensional microcavities", *Phys. Rev. B* **88**, 035313, 2013.
5. T. Gao, C. Antón, T. C. H. Liew, M. D. Martín, Z. Hatzopoulos, L. Vina, P. S. Eldridge, and P. G. Savvidis, "Spin selective filtering of polariton condensate flow", *Appl. Phys. Lett.* **107**, 011106, 2015.
6. C. Antón, S. Morina, T. Gao, P. S. Eldridge, T. C. H. Liew, M. D. Martín, Z. Hatzopoulos, P. G. Savvidis, I. A. Shelykh, and L. Vina, "Optical control of spin textures in quasi-one-dimensional polariton condensates", *Phys. Rev. B* **91**, 075305, 2015.

# Instabilities of polariton condensates in patterned microcavities

**M. Wouters[1], V. N. Gladilin[1], and D. De Bernardis[2]**

[1]Universiteit Antwerpen, Belgium
[2]University of Trento, Italy
michiel.wouters@uantwerpen.be

**Abstract**— We present a theoretical analysis of the instability of polariton condensates. When the repulsive interactions between polaritons and reservoir excitons are sufficiently strong, the effective polariton-polariton interaction becomes attractive. For lossless bose gases this instability leads to the formation of bright solitons. With gain and losses present, a chaotic steady state arises. We discuss the different regimes, which include phase chaos, described by the Kuramoto-Sivashinsky equation, and defect chaos.

Microcavity polaritons are quasi-particles that arise from the strong coupling of a quantum well exciton with a microcavity photon. These hybrid light-matter quasi-particles inherit a light effective mass from their photonic component and significant interactions from their excitonic component. Thanks to their bosonic nature, Bose-Einstein condensation is possible at sufficiently large density and low temperature. Due to the finite quality factor of the microcavity, the polaritons have however a finite life time. This requires a continuous replenishing of polaritons in order to reach a steady state. A regime closest to equilibrium Bose-Einstein condensation is reached when injecting photons at an energy much higher than the band gap [1]. A fast relaxation then leads to the formation of an exciton reservoir, from where a slower relaxation creates new polaritons.

Apart from providing gain to the polariton condensate, the exciton reservoir also shifts the polariton energy due to exciton-polariton interactions. This shift of the polariton energy gives rise to effective polariton-polariton attractions [2, 3]. As it is well known in equilibrium condensation, attractive interactions cause a dynamical instability of the condensate due to collapse, which leads to the formation of bright solitons. Out of equilibrium, the instability is saturated and gives rise to a chaotic steady state. In the regime of weak instability, the condensate phase dynamics is well described by the Kuramoto-Sivashinsky equation.

The study of the spatio-temporal instability of polariton condensates becomes even richer when a periodic potential is applied. The resulting band structure can have states with negative effective mass. When a positive mass state is unstable, the negative mass state will be stable. This results in a rich interplay between the instability and external potentials.

In the presence of disorder, which is to some extent unavoidable in practice, the instability is shown to lead to larger modulations in the density. We elucidate the interplay between disorder and modulational instability of polariton condensates and point out the experimental implications.

**ACKNOWLEDGMENT**

M. Wouters acknowledges financial support from FWO.

**REFERENCES**

1. Kasprzak J., Richard M., Kundermann S., Baas A., Jeambrun P., Keeling J. M. J., Marchetti F. M., Szymańska M. H., André R., Staehli J. L., Savona V. , Littlewood P. B. , Deveaud B. and Le Si Dang, "BoseEinstein condensation of exciton polaritons," *Nature* 443, 409–414, 2006.
2. Wouters M. and Carusotto I., "Excitations in a Nonequilibrium Bose-Einstein Condensate of Exciton Polaritons," *Phys. Rev. Lett.* 99, 140402, 2007.
3. Bobrovska N. and Matuszewski M., "Adiabatic approximation and fluctuations in exciton-polariton condensates", *Phys. Rev. B* 92, 035311, 2015.

# Exciton-polariton lasers based on biologically produced fluorescent proteins

**S. Höfling[1,2], C. P. Dietrich[1,2], A. Steude[1], L. Tropf[1], M. Schubert[1], N. M. Kronenberg[1], K. Ostermann[3], and M. C. Gather[2]**

[1]SUPA, School of Physics and Astronomy, University of St Andrews, St Andrews, United Kingdom

[2]Technische Physik, Wilhelm-Conrad-Röntgen-Research Center for Complex Material Systems, Universität Würzburg, Würzburg, Germany

[2]Insitut für Genetik, Technische Universität Dresden, Dresden, Germany

[*]corresponding author: sven.hoefling@physik.uni-wuerzburg.de

**Abstract** Under adequate conditions, cavity-polaritons can form a Bose-Einstein condensate (BEC). Here, we demonstrate room-temperature BEC of cavity-polaritons in simple laminated microcavities filled with biologically produced enhanced green fluorescent protein (eGFP). The unique molecular structure of eGFP prevents exciton annihilation even at high excitation densities, thus facilitating BEC. BEC is clearly evidenced by a distinct threshold, an interaction-induced blue shift of the condensate and the presence of a second threshold at higher excitation density, which is associated with the onset of photon lasing.

Under adequate conditions, cavity-polaritons can form a Bose-Einstein condensate (BEC).[1,2] Compared to Wannier-Mott polaritons in inorganic semi-conductors, the localised Frenkel polaritons in organic emitter materials show weaker interaction[3] but stronger coupling[4] which recently enabled the first realisation of BEC at room temperature.[5,6] However, this required ultrafast optical pumping which limits the applications of organic BECs.

In recent work, we have investigated a distinctly different and novel class of organic solid-state emitter with unique optical properties – the biologically produced fluorescent proteins. In contrast to many other organic materials, the special molecular structure of these proteins ensures that in solid-state the protein fluorophores have a fixed interspacing of 3-4 nm. This suppresses concentration quenching and enables strong optical amplification (g = 22 cm-1) in thin protein films.[7] We have used protein films to fabricate efficient solid-state vertical cavity surface emitting micro-lasers.[8]

We now demonstrate room-temperature BEC of cavity-polaritons in simple laminated microcavities filled with biologically produced enhanced green fluorescent protein (eGFP).[9] The unique molecular structure of eGFP prevents exciton annihilation even at high excitation densities, thus facilitating BEC under conventional nanosecond pumping. BEC is clearly evidenced by a distinct threshold, an interaction-induced blue shift of the condensate, long-range coherence and the presence of a second threshold at higher excitation density which is associated with the onset of photon lasing and results from thermalization of the exciton reservoir.

The authors acknowledge  nancial support from the European Research Council (ERC StG 640012), the Scottish Funding Council (through SUPA), the studentship funding through the EPSRC CM-DTC (EP/L015110/1) and the EPSRC Hybrid Polaritonics program grant (EP/M025330/1).

**REFERENCES**


1. Kasprzak, J. et al., „Bose-Einstein condensation of exciton polaritons," *Nature*, Vol. 443, 409-414, 2006.
2. Balili, R. et al., "Bose-Einstein Condensation of Microcavity Polaritons in a Trap," *Science*, Vol. 316, 1007-1010, 2007.
3. Kéna-Cohen, S, Forrest, S.R., "Room-temperature polariton lasing in an organic single-crystal microcavity," *Nature Photon.*, 4, 371-375, 2010.
4. Kéna-Cohen, S., Maier, S.A., Bradley, D.D.C., "Ultrastrongly coupled exciton-polaritons in metal-clad organic semiconductor microcavities," *Adv. Opt. Mater.*, Vol. 1, 827-833, 2013.
5. Plumhof, J.D. et al., „Room-temperature Bose-Einstein condensation of cavity exciton polaritons in a polymer," *Nature Mater.*, Vol. 13, 247-252, 2014.
6. Daskalakis, K.S. et al., *"Nonlinear interactions in an organic polariton condensate," Nature Mater*, Vol. 13, 271-278, 2014.
7. Gather, M. C., Yun S. H., "Bio-optimized energy transfer in densely packed fluorescent protein enables near-maximal luminescence and solid-state lasers," *Nature Commun*, Vol. 5, 5722, 2014.
8. Dietrich, C. P., Höfling, S., Gather, M.C., "Multi-state lasing in self-assembled ring-shaped eGFP microcavities," *Appl. Phys. Lett.*, Vol. 105, 233702, 2014.
9. [9] arXiv:1601.06983

# Towards strongly confined exciton-polariton Bose-Einstein condensates with a polymer at ambient conditions

**D. Urbonas**[1], **F. Scafirimuto**[1], **L. Mai**[1], **R. F. Mahrt**[1], **and T. Stöferle**[1*]
[1]IBM Research – Zurich, Säumerstrasse 4, 8803 Rüschlikon, Switzerland
[*]corresponding author: tof@zurich.ibm.com

**Abstract**-We create exciton-polaritons in a microcavity filled with a ladder-type conjugated polymer. At room temperature, we observe thermalization and, above a critical excitation density, Bose-Einstein condensation of the polaritons, as evidenced through nonlinear emission, interaction-induced blue-shift and long-range macroscopic coherence. Our approach demonstrates a radically simplified route to investigate Bose-Einstein condensation physics at ambient conditions with easy-to-process non-crystalline materials. Finally, we discuss recent experiments on tunable nanoscale defect cavities to produce strongly confined condensates and possible ways towards quantum simulation.

In a microcavity with a spin-coated thin layer of ladder-type conjugated polymer (MeLPPP) embedded between dielectric distributed Bragg reflectors (DBR), we observe the avoided crossing of the cavity mode with the exciton energy characteristic of the strong coupling regime. We create exciton-polaritons by off-resonant excitation with incoherent picosecond laser pulses. At room temperature thermalization of these quasi-particles occurs while it is suppressed at low temperature because of a relaxation bottleneck. Above a certain excitation threshold, we observe the emergence of non-equilibrium Bose-Einstein condensation (BEC) in the lower polariton branch [1]. This is evidenced by several distinct features such as a blue-shifted emission peak at zero in-plane momentum, accompanied by a nonlinear increase in the emission intensity and a sudden drop of the linewidth. Furthermore, the emission becomes polarized and the emission dynamics is drastically shortened. In contrast to conventional lasing, we find a strong increase in threshold when decreasing the temperature, which can be explained by the peculiar thermalization properties.

Spatially-resolved measurements with a Michelson interferometer show a macroscopic phase relation over almost the whole excitation area. The interference fringe pattern exhibits non-flat phase fronts and fork-like dislocations, indicating a large number of vortices and excitations. As we are able to obtain single-shot measurements of the spectrum and the interference patterns, we can study single realizations of the condensate. This gives access to non-averaged properties from each individual condensation process.

In a first step towards realizing potential landscapes for the polaritons, we employ a novel cavity concept based on nanoscale Gaussian-shaped defects [2]. They are fabricated with focused ion beam milling [3], and allow strong lateral confinement of the photonic mode on the order of the wavelength. We mount the two cavity DBRs on separate XYZ positioners, one mirror including the Gaussian nanostructure on a mesa and the other one with the spin-coated polymer on top (Figure 1a). This results in a microcavity that is tunable down to half-wavelength mirror separation. We observe the avoided crossing of the cavity mode and the exciton energy,

demonstrating that this laterally confined cavity is in the strong light matter interaction regime at room temperature (Figure 1b). In further experiments, we study in more depth the emission properties in real space and momentum space for the weak and the strong excitation regime.

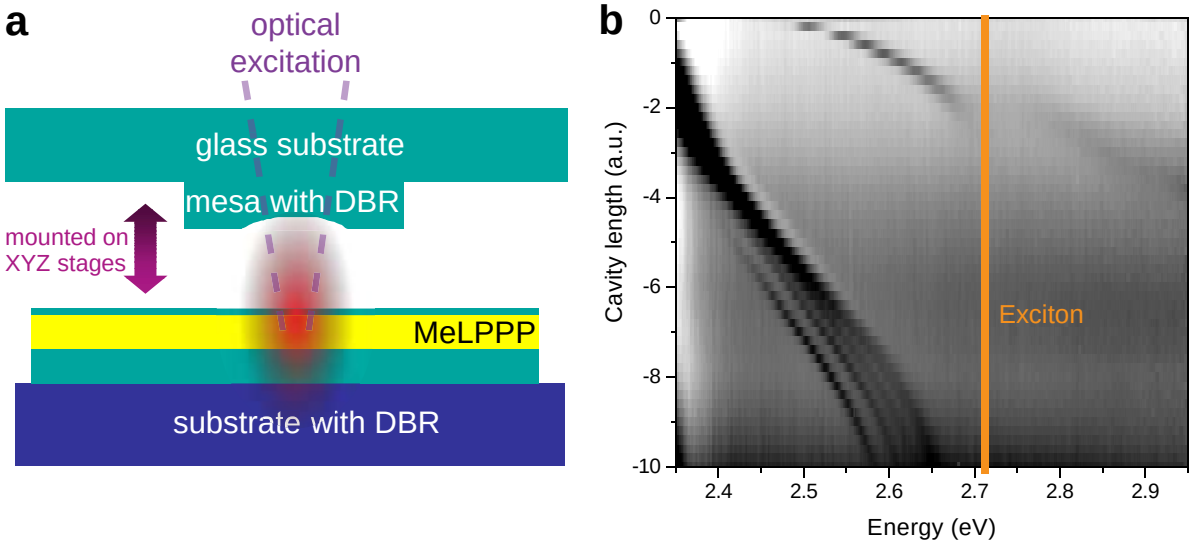



**Figure 1.** a) Sketch of the tunable microcavity with Gaussian-shaped deformation and MeLPPP polymer. b) An avoided crossing is observed in reflection when tuning the cavity resonance across the exciton energy, which is a hallmark feature of the strong light-matter coupling regime**.**

In conclusion, we show a polariton condensate at ambient conditions with an amorphous polymer. As no crystal growth is involved, our approach radically reduces the complexity of experiments to investigate BEC physics. In combination with tunable Gaussian-defect cavities, this opens the door to study quantum fluids at room temperature in strongly confined geometries and arbitrary potential landscapes that can mimic crystal lattices.

**ACKNOWLEDGMENT**

We acknowledge funding from EU projects ICARUS (FP7-ITN-237900), PHONSI (H2020-MSCA-ITN-642656) and SYNCHRONICS (H2020-MSCA-ITN-643238).

**REFERENCES**

1. Plumhof, J. D., T. Stöferle, L. Mai, U. Scherf and R. F. Mahrt, "Room-temperature Bose–Einstein condensation of cavity exciton–polaritons in a polymer," *Nature Materials*, Vol. 13, 247–252, 2014.
2. Ding, F., T. Stöferle, L. Mai, A. Knoll and R. F. Mahrt, "Vertical microcavities with high Q and strong lateral mode confinement," *Phys. Rev. B*, Vol. 87, 161116(R), 2013.
3. Mai, L., F. Ding, T. Stöferle, A. Knoll and R. F. Mahrt, "Integrated vertical microcavity using a nano-scale deformation for strong lateral confinement," *Appl. Phys. Lett.*, Vol. 103, 243305, 2013.

# Unitary dynamics of a propagating quantum fluid of light in a cavityless nonlinear optical medium

**P.-É. Larré**[1] **and I. Carusotto**[1]

[1] INO-CNR BEC Center and Dipartimento di Fisica, Università di Trento, I-38123 Povo, Italy
carusott@science.unitn.it pierre.larre@unitn.it

**Abstract**— We discuss the potential of bulk nonlinear optical media in cavityless configurations for quantum statistical mechanics studies of the unitary many-body dynamics in a gas of interacting photons. A critical comparison with more usual driven-dissipative dynamics in microcavity devices is made.

After several decades during which the study of systems of many interacting particles has focused on matter fluids such as liquid helium, electron gases in solid-state materials, ultracold atom vapors, nuclear-matter fluids, or quark-gluon plasmas in colliders, quantum fluids of light are presently attracting a growing interest as a novel platform to investigate many-body physics. So far, most experimental observations have been performed in microcavity devices, including the demonstration of Bose-Einstein condensation of polaritons and photons and of superfluid light [1].

An alternative platform for studying this physics is offered ny light propagation in a transparent bulk Kerr-nonlinear optical medium [2]. From elementary classical optics, it is well known that the paraxial propagation of a spectrally narrow beam of light around $\omega_0$ can be described at mean-field level within the so-called paraxial and slowly-varying-envelope approximations by a nonlinear wave equation formally analogous to the Gross-Pitaevskii equation for the order parameter of a dilute Bose-Einstein condensate. Building atop the pioneering theoretical works [3], we report here a fully general quantum field theory of the propagating photon fluid.

In this approach, the roles played by the optical-axis coordinate $z$ and the time $t$ are exchanged. Assuming that the medium is perfectly transparent with no absorption losses, light propagation in the $z$ direction at a carrier group velocity $v_0$ is naturally described in terms of an evolution equations as a function of the new time coordinate $\tau = z/v_0$ while the $t$ direction corresponds to a third spatial dimension $\zeta = v_0 t$ in addition to the transverse $x$ and $y$ directions. In a paraxial-propagation configuration, light diffraction provides an effective mass to the photons in the $(x, y)$ plane and chromatic dispersion $D_0$ leads to a, typically different, effective mass in the $\zeta$ direction. As usual, the Kerr nonlinearity of the medium gives rise to photon-photon interactions of intensity $g$.

In contrast to microcavity configurations where driving and dissipation play a major role in the photon-fluid dynamics and can hardly be avoided in a realistic experiment [1], in propagation geometries the quantum fluid of light obeys a fully conservative Hamilton dynamics starting from an initial condition determined by the spatial profile and the coherence properties of the incident beam. In a second-quantization formalism the Hamilton operator describing the evolution in the new time coordinate $\tau = z/v_0$ has the usual many-body form with binary interactions,

$$\hat{H}(\tau) = \mathcal{N} \int d\mathbf{r} \left[ \frac{1}{2\,\beta_0} \nabla_\perp \hat{\mathcal{E}}^\dagger \cdot \nabla_\perp \hat{\mathcal{E}} - \frac{v_0^2\, D_0}{2} \frac{\partial \hat{\mathcal{E}}^\dagger}{\partial \zeta} \frac{\partial \hat{\mathcal{E}}}{\partial \zeta} + \frac{i}{2} \left( \frac{\partial \hat{\mathcal{E}}^\dagger}{\partial \zeta}\, \hat{\mathcal{E}} - \hat{\mathcal{E}}^\dagger \frac{\partial \hat{\mathcal{E}}}{\partial \zeta} \right) + \frac{g}{2}\, \hat{\mathcal{E}}^\dagger\, \hat{\mathcal{E}}^\dagger\, \hat{\mathcal{E}}\, \hat{\mathcal{E}} \right].$$

where the fields obey same-$\tau$ bosonic commutation rules,

$$[\hat{\mathcal{E}}(\mathbf{r}, \tau), \hat{\mathcal{E}}^\dagger(\mathbf{r}', \tau)] = \frac{\hbar\, v_0}{\mathcal{N}}\, \delta(\mathbf{r} - \mathbf{r}') \qquad \text{and} \qquad [\hat{\mathcal{E}}(\mathbf{r}, \tau), \hat{\mathcal{E}}(\mathbf{r}', \tau)] = 0, \tag{1}$$

with a normalization

$$\mathcal{N} = \frac{\sqrt{1 + \chi_0}}{c\, \mu_0\, \omega_0}. \tag{2}$$

in terms of the medium linear dielectric susceptibility $\chi_0$ and magnetic constant $\mu_0$. As a result, the Heisenberg equation of motion for the field has the form of a quantum nonlinear Schödinger

equation,

$$\frac{i}{v_0}\frac{\partial\hat{\mathcal{E}}}{\partial\tau} = -\frac{1}{2\,\beta_0}\nabla_\perp^2\hat{\mathcal{E}} + \frac{v_0^2\,D_0}{2}\frac{\partial^2\hat{\mathcal{E}}}{\partial\zeta^2} - i\,\frac{\partial\hat{\mathcal{E}}}{\partial\zeta} + g\,\hat{\mathcal{E}}^\dagger\,\hat{\mathcal{E}}\,\hat{\mathcal{E}}. \tag{3}$$

The quantum state of the optical field at the end of the evolution can then be read out from the statistical properties of the light transmitted past the nonlinear medium.

As a most remarkable example of application of this formalism, we then study the transmission of a coherent light across a finite slab of weakly nonlinear medium [2]. In this very simple configuration, the photons experience a pair of sudden jumps of the interaction parameter upon crossing the front and the back faces of the nonlinear medium. As a result of these two quantum quenches, the fluid of light gets excited and its quantum state after the conservative evolution across the nonlinear material can be reconstructed from the statistical properties of the transmitted light. Signatures of this exciting physics are found in both angular intensity distribution and in the near- and the far-field two-body correlation functions and can be understood in analogy with the Dynamical Casimir effect of quantum field theory. In reduced dimension systems such as one-dimensional waveguides, this physics sets an intrinsic limitation to the propagation of optical coherence along nonlinear waveguides [4].

Future work will further develop these ideas in the direction of generating, detecting, and manipulating strongly correlated quantum phases of matter in photon gases, of studying quantum dynamical features of many-body systems, and of exploiting the many-body dynamics to realize new sources of coherent light.

## ACKNOWLEDGMENT

This work was supported by the ERC through the QGBE grant, by the EU-FET Proactive grant AQuS, Project No. 640800, and by the Autonomous Province of Trento, partly through the SiQuro project (On Silicon Chip Quantum Optics for Quantum Computing and Secure Communications).

## REFERENCES

1. I. Carusotto and C. Ciuti, "Quantum fluids of light", *Rev. Mod. Phys.* **85**, 299, 2013.
2. P.-É Larré and I. Carusotto, "Propagation of a quantum fluid of light in a cavityless nonlinear optical medium: General theory and response to quantum quenches", *Phys. Rev. A* **92**, 043802, 2015.
3. Y. Lai and H. A. Haus, "Quantum theory of solitons in optical fibers. I. Time-dependent Hartree approximation", *Phys. Rev. A* **40**, 844, 1989.
4. P.-É Larré and I. Carusotto, "Prethermalization in a quenched one-dimensional quantum fluid of light", *Eur. Phys. Journ. D*, in the press, 2016.

# Quantum Statistics of Bosonic Cascades

**T. C. H. Liew[1*], Y. G. Rubo[2], A. S. Sheremet[3,4],**
**S. De Liberato[5], I. A. Shelykh[1,3,6], F. P. Laussy[4,7] and A. V. Kavokin[4,5,8,9]**

[1]Division of Physics and Applied Physics, Nanyang Technological University, Singapore.
[2]Instituto de Energías Renovables, Universidad Nacional Autónoma de México, Morelos, Mexico.
[3]National University for Information Technology, Mechanics and Optics (ITMO), St.-Petersburg, Russia.
[4]Russian Quantum Center, Novaya 100, Skolkovo, Moscow Region, Russia.
[5]School of Physics and Astronomy, University of Southampton, Highfield, Southampton, UK.
[6]Science Institute, University of Iceland, Dunhagi-3, IS-107, Reykjavik, Iceland.
[7]Departamento de Física Teórica de la Materia Condensada and Condensed Matter Physics Center (IFIMAC), Universidad Autónoma de Madrid, E-28049, Spain.
[8]Spin Optics Laboratory, St.-Petersburg State University, 198504 Peterhof, St.-Petersburg, Russia
[9]CNR-SPIN, Viale del Politecnico 1, Rome I-00133, Italy.

[*]corresponding author: tchliew@gmail.com

**Abstract** - Bosonic cascades formed by lattices of equidistant energy levels sustaining radiative transitions between nearest layers represent a unique system to study correlated optical phenomena. We show how the light emitted by condensates in the visible range introduces a new regime of emission for cascade systems. Namely, the quantum statistics of bosonic cascades exhibits superbunching plateaus.

By merging the concepts of electronic quantum cascade lasers [1] and bosonic stimulation, a bosonic cascade laser was proposed a few years ago [2]. The device is based on a set of equidistant exciton states in a parabolic trapping potential, in which THz transitions between neighbouring levels are possible. Such transitions allow a cascade of multiple THz emission steps, theoretically allowing quantum efficiencies exceeding unity.

Here we extend previous theoretical work and study the quantum dynamics of bosonic cascades. By using stochastic Langevin equations, we demonstrate that bosonic cascades are able to produce extremely high values of photon bunching. The peculiar nature of the system, where coherence is transferred between single states, accounts for superbunching, which develops in the phase where one condensate empties suddenly into the state below.

**REFERENCES**

1. Faist, J., F. Capasso, D. L. Sivco, C. Sirtori, A. L. Hutchinson, and A. Y. Cho, "Quantum cascade laser", *Science*, Vol. 264, 553, 1994.
2. Liew, T. C. H., M. M. Glazov, K. V. Kavokin, I. A. Shelykh, M. A. Kaliteevski, and A. V. Kavokin, "Proposal for a Bosonic Cascade Laser", *Phys. Rev. Lett.*, Vol. 110, 047402, 2012.
3. Liew, T. C. H., Y. G. Rubo, A. S. Sheremet, S. De Liberato, I. A. Shelykh, F. P. Laussy, and A. V. Kavokin, "Quantum statistics of bosonic cascades", *New J. Phys.*, Vol. 18, 023041, 2016.

# Nonlocal Fluids of Light.

**Daniele Faccio**[1], **David Vocke**[1], **Kali Wilson**[1], **Thomas Roger**[1], **Francesco Marino**[2], **Calum Maitland**[1], **Iacopo Carusotto**[3], **Brian P. Anderson**[4], **Ewan M. Wright**[4,1].

[1] Institute of Photonics and Quantum Sciences, Heriot-Watt University, Edinburgh EH14 4AS, UK
[2]CNR-Istituto Nazionale di Ottica, L.go E. Fermi 6, I-50125 Firenze, Italy
[3]INFN, Sez. di Firenze, Via Sansone 1, I-50019 Sesto Fiorentino (FI), Italy
[3] INO-CNR BEC Center and Dipartimento di Fisica, Universitá di Trento, I-38123 Povo, Italy
[4] College of Optical Sciences, University of Arizona, Tucson, USA
d.faccio@hw.ac.uk

**Abstract**— The transverse spatial profile of an intense light beam propagating in a thermal nonlinear medium evolves following the hydrodynamical equations of a superfluid. The interplay between the geometry of the light beam and the nonlocal thermal response strongly affects superfluid behaviour, as shown by experiments studying quantised vortex nucleation from an obstacle. A properly tailored nonlocal response and beam geometry is also used to simulate the Newton-Schrödinger equation and provide an experimental testbed for astrophysical studies e.g. of boson stars.

*Introduction*:
Fluids of light or photon fluids have come to the forefront due to their versatility in simulating a wide variety of physical phenomena observed or predicted in other systems and also, due to some features that are specific to photon fluids themselves. A broadly studied class of such fluids relies on the exciton-polaritons in semiconductor cavities. A slightly less studied system of photon fluids is based on a propagating (i.e. cavity-less) geometry, where fluid-like behaviour is observed in the transverse profile of an optical beam propagating in a nonlinear medium.

In our experimental system, heating induced by a laser beam leads to a change in the refractive index of the medium and a consequent defocusing effect (for media with a negative thermo-optic coefficient), i.e., a nonlocal, repulsive photon-photon interaction. For a monochromatic beam, the transverse beam profile acts as a two-dimensional (2D) fluid and is fully described by hydrodynamical equations, where the propagation direction maps into an effective time coordinate. The Bogoliubov dispersion relation for small oscillations of frequency $\Omega$ and wavevector $K$ within the photon fluid has the form,

$$(\Omega - vK)^2 = \frac{c^2|n_2|\rho}{n_0^3}\hat{R}(K, n_0\Omega/c)K^2 + \frac{c^2}{4k^2n_0^2}K^4, \quad (1)$$

with the first term corresponding to a superfluid component with linear dispersion, and the second term corresponding to a single-particle component. Here $c$ is the speed of light in vacuum, $n_0$ is the linear index of refraction, $k = 2\pi n_0/\lambda$ is the optical wavenumber, with wavelength $\lambda$, $n_2$ is the nonlinear index of refraction, and $\rho = |E|^2$ is the density of the photon fluid, with $E$ the amplitude of the propagating electric field. $\hat{R}(K)$ is the 2D $k$-space response function: all of the physics discussed here lie within the details response function.

*The role of geometry in nonlocal superfluids*:
We performed a series of experiments in various materials, following those of Ref. [1] that allowed us to a very good approximation $\hat{R}(k_x, k_y) = [1 + \sigma^2k_x^2 + \sigma^2k_y^2]^{-1}$, i.e. $\hat{R}$ is a Lorentzian response function in $k$-space as a result of heat-diffusion in a bound 2D system. Here $\sigma$ is the nonlocal length associated with the fluid and is determined by the transverse boundary of the medium, with $\sigma = R = 1$ cm for our experiment, where $R$ is the radius of the cylinder confining the nonlinear medium, i.e. methanol containing a weak solution of graphene nano-flakes (introduced to slightly increase light absorption). Our measurements show that $\sigma = 1$ cm and thus the single-particle (non-superfluid) dispersion will dominate for all but the lowest wavevectors $K < 1/\sigma$. Such low wavevectors are not experimentally observable in our system, and hence, superfluid behaviour will not be observable under these conditions.

However, we then show that with a highly elliptical beam with $1/e^2$ beam radii $w_y << w_x$,

the smaller beam dimension ($y$-axis) effectively limits wavevectors along the $y$-axis to $k_y \sim 1/w_y$, while allowing for the full spectrum of oscillations along the $x$-axis. We find the elliptical beam geometry thus significantly reduces the effective nonlocal length to $\bar{\sigma} \sim w_y$. We have observed this reduced nonlocality in pump-probe measurements of the dispersion relation [2], which clearly show a linear, sonic region of the dispersion relation, consistent with superfluidity. Such tailoring of beam geometry gives unexpected and intriguing control over the effective nonlocal length, a defining parameter for the photon fluid. Choosing a beam with high ellipticity allows us to circumvent the high degree of nonlocality imposed by the system boundary, and to access a more local regime where superfluidity is experimentally observable. For example, we investigate the breakdown of superfluid flow around an extended obstacle, manifested as a clearly visible nucleation of quantised vortices in the wake of the obstacle.

*Light as a medium for simulations of the Newton-Schrödinger equation*:
A remarkable example of the connection between gravity and optics is the recent demonstration, using an optical system based on a thermally excited medium, of a laboratory-based system that allows to reproduce the physics of the Newton-Schrödinger equation (SNE) [3]. The SNE can be written as

$$i\hbar\psi_t + \frac{\hbar^2}{2m}\nabla_\perp^2\psi + m\phi\psi = 0, \qquad \nabla_\perp^2\phi = -4\pi G m|\psi|^2, \tag{2}$$

which describes the evolution of a particle with mass $m$ defined by a wavefunction $\psi$, coupled to the gravitational potential $\phi$, determined by the Poisson equation. This equation bears an obvious analogy with the evolution equation for an optical beam in a nonlinear *focusing* medium:

$$i\frac{\partial\mathcal{E}}{\partial z} + \frac{1}{2k}\nabla_\perp^2\mathcal{E} + k_0\Delta n\mathcal{E} = 0, \qquad \nabla_\perp^2(\Delta n) = -\frac{\alpha\beta}{\kappa}|\mathcal{E}|^2 \tag{3}$$

where the second equation is the Poisson equation that governs heat diffusion and $\beta = \partial n/\partial T$ is the medium thermo-optic coefficient, $\kappa$ is the thermal conductivity and $\alpha$ the material absorption.

In our experiments we now use a lead-glass that exhibits a focusing nonlinearity (as opposed to the defocusing methanol medium described above), and show that in the limit of a beam that contains only large transverse wave-vectors, i.e. $\sigma K_\perp \gg 1$, the medium response effectively reproduces the same $1/K^2$ behaviour expected in a gravitational field. As an example, we study the evolution of a beam with orbital angular momentum that effectively reproduces the dynamics of a rotating boson star. We observe oscillations of the star density that evolve over time and that for high powers, rather than collapsing towards the centre, are strongly repulsed by the central topological phase singularity. These studies hint at the fact that boson or Bose-Einstein condensate stars that are also forced to have quantised angular momentum, would not form black holes as a result of the gravitational collapse being counterbalanced by this new mechanism.

*Conclusions*: In conclusion, the propagation of light nonlocal thermal media allows a series of studies related to superfluidity in the presence of nonlocality and also astrophysical studies of a peculiar class of objects that are predicted to exist yet to date lack experimental confirmation. In all cases, the beam geometry plays a central role in determining the physics of the system.

**REFERENCES**


1. A. Minovich, D. N. Neshev, A. Dreischuh, W. Krolikowski, and Y. S. Kivshar, "Experimental reconstruction of nonlocal response of thermal optical media," *Opt. Lett.* **32**, 1599 (2007).
2. D. Vocke, T. Roger, F. Marino, Ewan M. Wright, I. Carusotto, M. Clerici, and D. Faccio,"Experimental characterization of nonlocal photon fluids," *Optica* **2**, 484 (2015).
3. R. Bekenstein, R. Schley, M. Mutzafi, C. Rotschild, M. Segev, "Optical simulations of gravitational effects in the Newton-Schrödinger system," Nature Physics, **11**, 872-878 (2015)

# Dynamic Control of Polariton States in Spin-Orbit Poincaré Spheres using Ultrafast Stark Pulses

**E. Cancellieri [1,*], F. Li [1], G. Buonaiuto [1], D. N. Krizhanovskii [1], M. S. Skolnick [1] and D. M. Whittaker [1]**

[1]Department of Physics and Astronomy, University of Sheffield, Sheffield S3 7RH, UK

[*]corresponding author: e.cancellieri@sheffield.ac.uk

**Abstract**-In this work we demonstrate the complete dynamical control of polariton spin-vortex states, with orbital angular momentum equal to plus or minus one, on a Poincaré sphere and among different ones. More specifically, we use red-detuned ultrafast Stark pulses to modulate, in time, the energy of the excitonic resonances. This, due to the double light-matter nature of cavity polaritons, allows controlling the phase and the state of polarization of the polariton field.

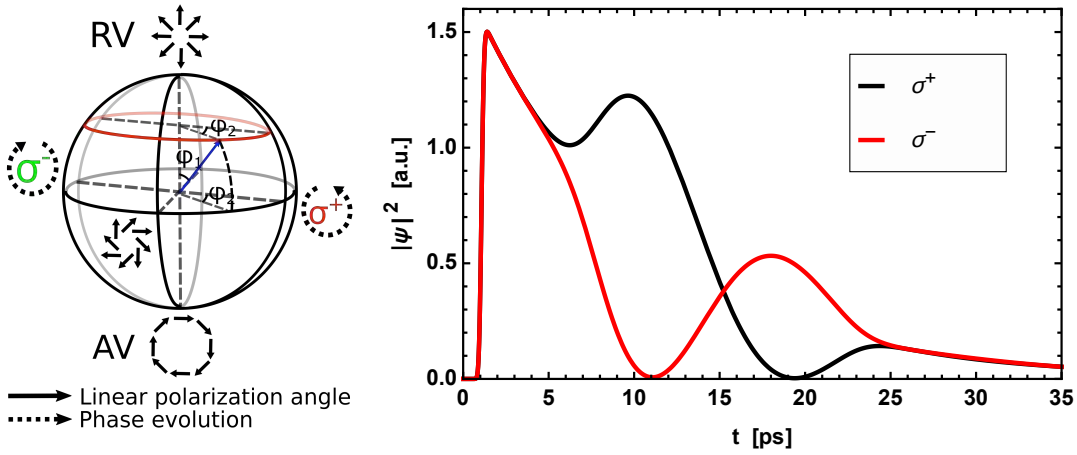
Light and light-beams are at the centre of our modern technological society since they allow fast and precise control of both classical and quantum systems. The first step change in the use of light for physical and technological applications has been the exploitation of its polarisation degree of freedom. More recently, particular attention has been devoted to the exploitation of the orbital angular momentum (OAM) of light beams with inhomogeneous spatial profiles, since are believed to have the potential to achieve higher dimensions of quantum information processing [1]. In particular, significant quantum effects such as high-dimensional, high quanta, multi-photon OAM entanglement [2] and OAM Hong-Ou-Mandel interference [3] have been experimentally demonstrated. The next natural step is the study, and exploitation, of states of light where the polarization and the OAM are coupled.

A particular kind of polarisation-OAM coupled states, also called spin-orbit coupled states, has been recently reported in Bragg-cavity systems, where the strong coupling between cavity photons and quantum-well excitons leads to the formation of polaritons. In these systems the coherent coupling between OAM and spin, induced by the transverse-electric transverse-magnetic splitting, has lead to the observations of vector vortex beams, referred to as spin vortices [4-6].

In this work we demonstrate that, due to the polaritons half-light and half-matter nature, it is possible to control a vector spin-vortex state using ultrafast dynamic Stark pulses red-detuned with respect to the exciton frequency. First we study the particular case of the Poincaré sphere relative to the two orthogonal states constituted by a radial (RV) and by an azimuthal (AV) spin vortices, and shown that its complete span can be achieved simply using Stark pulses polarised either $\sigma^+$ or $\sigma^-$ (see Figure).

Secondly, we demonstrate that the polariton state can be moved to another two different Poincaré spheres defined using different pairs of the systems eigenstates (the Hilbert space is four dimensional and therefore a maximum of 6 different Poincaré spheres can be defined), and that also for these two new spheres the complete span can be achieved by means of Stark pulses either linearly or circularly polarised.

Finally, we address the problem of the observation of topological Pancharatnam-Berry phases in these polarisation-OAM coupled states [7].




**Figures:** (Left) Poincaré sphere with the two orthogonal radial (RV) and azimuthal (AV) spin vortices lying at the poles. In this scheme, the two l=-1 $\sigma^+$ and l=1 $\sigma^-$ vortices lies at the equator. (Right) Plot of the $\sigma^+$ and $\sigma^-$ polariton population as a function of time. The system is initialised in the RV state and two 1ps-long Stark pulses, with opposite polarisation, at t1=7.5ps and t2=23ps, are used to flip it to the equator and then back to the RV state. Pulses with different lengths and intensities allow reaching any point of the Poincaré sphere.

We acknowledge support by EPSRC Grant No. EP/ J007544, ERC Advanced Grant EXCIPOL, and the Leverhulme Trust.

**REFERENCES**

1. A. Mair, A. Vaziri, G. Weihs and A. Zeilinger "*Entanglement of the orbital angular momentum states of photons*", Nature, Vol. 412, 313 (2001).
2. R. Fickler, T. Coudreau, P. Milman, D. B. Ostrowsky and S Tanzilli "*Entanglement-Enabled Delayed-Choice Experiment*", Science, Vol. 338, 640 (2012).
3. X. Wang, X. Cai, Z. Su, M. Chen, D. Wu, L. Li, N. Liu, C. Lu and J. Panet "*Quantum teleportation of multiple degrees of freedom of a single photon*", Nature, Vol. 518, 516 (2015).
4. V. Sala, D. D. Solnyshkov, I. Carusotto, T. Jacqmin, A. Lemaître, H. Terças, A. Nalitov, M. Abbarchi, E. Galopin, I. Sagnes, J. Bloch, G. Malpuech and A. Amo "*Spin-Orbit Coupling for Photons and Polaritons in Microstructures*", Phys. Rev. X, Vol. 5, 011034 (2015).
5. F. Manni, Y. Léger, Y.G. Rubo, R. André and B. Deveaud "*Hyperbolic spin vortices and textures in exciton–polariton condensates*", Nat. Comm., Vol. 4, 10.1038/ncomms3590 (2013).
6. S. Dufferwiel, Feng Li, E. Cancellieri, L. Giriunas, A. A. P. Trichet, D. M. Whittaker, P. M. Walker, F. Fras, E. Clarke, J. M. Smith, M. S. Skolnick and D. N. Krizhanovskii "*Spin Textures of Exciton-Polaritons in a Tunable Microcavity with Large TE-TM Splitting*", Phys. Rev. Letter, Vol. 115, 246401 (2015).
7. G. Milione, S. Evans, D. A. Nolan and R. R. Alfano "*Higher Order Pancharatnam-Berry Phase and the Angular Momentum of Light*", Phys. Rev. Letter, Vol. 108, 190401 (2012).

# Microcavity polaritons: fundamental physics and devices

**Benoit Deveaud**[1*]
[1]Physics Institute, Ecole Polytechnique Fédérale de Lausanne, CH1015 Switzerland
[*]corresponding author: benoit.deveaud@epfl.ch

Polaritons are half-light half matter quasiparticles resulting from the strong coupling of photons confined in a microcavity with excitons confined in a quantum well. Polariton condensates may be created both spontaneously through a "*standard*" phase transition towards a Bose Einstein condensate [1], or be resonantly driven with a well-defined initial phase, speed and spatial distribution [2].

Thanks to the photonic component of polaritons, the properties of the quantum fluid may be accessed very directly, with in particular the possibility of detailed interferometric studies. This allows for example to probe the long-range coherence properties of a quantum fluid with unprecedented ease. This also allows testing superfluid properties with great precision in space and time [3].

I will describe the static and dynamics of superfluid flow in polariton condensates, obtained with a picosecond time resolution, in different configurations, with in particular their phase configuration. I will show in particular the dynamics of the creation of dark solitons [4] and quantized vortex pairs. Implications for possible device structures will also be discussed.

**Acknowledgements**, This work has been performed at EPFL by a dream team of Postdocs, PhD students and collaborators: H. Abbaspour, A. Adiyatullin, R. Cerna, V. Kohnle, K. Lagoudakis, G. Grosso, F. Manni, G. Nardin, T. Paraiso, C. Plamondon, N. Takemura, M. David, Y Léger, S. Trebaol, G. Sallen, M. Portella Oberli, D. Oberli, F. Morier-Genoud and the help of our theorists friends V, Savona, M. Wouters and T. Liew.

**REFERENCES**

1. J. Kasprzak, M. Richard, S. Kundermann, A. Baas, P. Jeambrun, J. Keeling, F. M. Marchetti, M. H. Szymańska, R. André, J. L. Staehli, V. Savona, P. B. Littlewood, B. Deveaud, Le Si Dang, *Bose-Einstein Condensation of Exciton Polaritons*, *Nature* **443**, 409 (2006)
2. A. Amo, J. Lefrère, S. Pigeon, C. Adrados, C. Ciuti,, I. Carusotto, R. Houdré, E. Giacobino, and A. Bramati, *Superfluidity of polaritons in semiconductor microcavities*, *Nat. Phys.*, **5**, 805 (2009)
3. G. Nardin, G. Grosso, Y. Leger, B. Pietka, F. Morier-Genoud,, B. Deveaud-Plédran, *Quantum turbulence in a polariton Fluid, Nature Physics,* **7**, 635 (2011)
4. G. Grosso, G. Nardin, Y. Léger, F. Morier-Genoud, and B. Deveaud-Plédran, *Soliton Instabilities and Vortex Streets Formation in a Polariton Quantum Fluid, Phys. Rev. Lett.*, **107**, 245301 (2011)

# Transport properties of electromagnetically dressed graphene

**I.A. Shelykh[1,2,3,*], S. Morina[1], K. Kristinsson[1], K. Dini[2], and O.V. Kibis[2,4]**

[1]Nanyang Technological University, Singapore
[2]Science Institute, University of Iceland, Reykjavik, Iceland
[3]ITMO University, Saint Petersburg, Russia
[4]Department of Applied and Theoretical Physics, Novosibirsk State Technical University
[*]e-mail: shelykh@hi.is

**Abstract**— We demonstrated theoretically that high-frequency electromagnetic field leads to renormalization of the spectrum of graphene near Dirac point. The effect depends strongly on the polarization of the dressing field. As a consequence, the stationary dc electronic transport becomes polarization dependent, and conductance of a sample exhibits periodic oscillations as function of the intensity for the case of linear polarized pump and monotonously decreases for the case of circular polarized pump. We also show that such a non-resonant dressing field substantially modifies the magnetoelectronic properties such as profile of Shubnikov-de Haas oscillations. The effect is due to the renormalization of the structure of Landau levels in the presence of the dressing field.

## INTRODUCTION

Usually, the electron-field interaction is considered within the regime of weak light-matter coupling, where the electron energy spectrum is assumed to be unperturbed by photons. However, the opposite regime of strong light-matter coupling, where the energy spectrum of electromagnetically dressed electrons is strongly modified by high-frequency field is also of great interest, as variety of novel physical phenomena can emerge. In this work we consider transport properties of monolayer graphene in the regime of electromagnetic dressing. Solving the non-stationary Schrdinger equation with full inclusion of the EM field vector potential, we found the eigenfunctions and the eigenenergies of the system electron+field. The frequency, $\omega$, of the field is assumed to be much higher than the disorder induced broadening and lie far away from any resonance so that no energy is absorbed via optical transitions, neither inter-band nor intra-band.

## 1. DC TRANSPORT

We found that illuminating of monolayer graphene with circularly polarized light opens a band-gap in the spectrum of dressed quasiparticles and corresponding dispersion is given by the expression $\varepsilon_{\mathbf{g}} = \sqrt{(\hbar\omega)^2 + (\hbar v k)^2}$. For linearly polarized field we find that the Dirac cone is transformed into an elliptic cone with the major axis being perpendicular to the polarization direction which lies, say, along the x-direction, $\varepsilon_{\mathbf{g}} = \hbar\sqrt{k_x^2 + J^2(2vE_0/\hbar\omega^2)k_y^2}$. The modifications of the dispersion strongly affect the transport characteristics such as conductivity tensor. Additional impact to the effect comes from the renormalization of the disorder scattering matrix element by the dressing field. Solving the Boltzmann transport equation, we found that for circular polarized illumination the conductivity $\sigma_c$ remains isotropic. The band-gap opening leads to the slow suppression of $\sigma_c$ with intensity of the dressing field. For the case of the linear polarization, we demonstrated the onset of strong anisotropy in the conductivity tensor related to the corresponding anisotropy of the Dirac cones of dressed quasiparticles [1]. The profiles of the conductance for both cases are shown at Fig. 1.

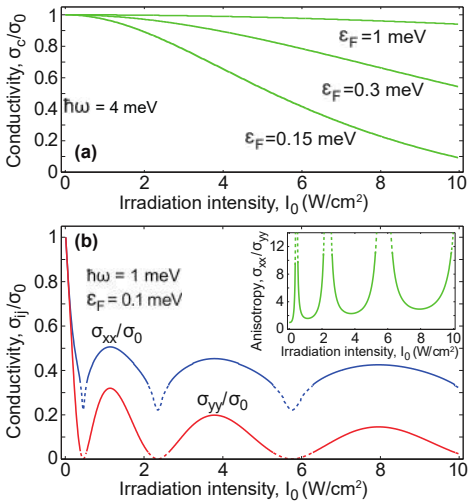



Figure 1: The DC conductivity in graphene is highly affected by dressing with a nonabsorptive EM field. In the case of circular polarization, a field induced gap causes the conductivity $\sigma_c$ to decrease with increasing field intensity while for a linear polarization, a huge anisotropy is introduced and oscillations of the conductivity are revealed.

## 2. MAGNETOELECTRONIC PROPERTIES

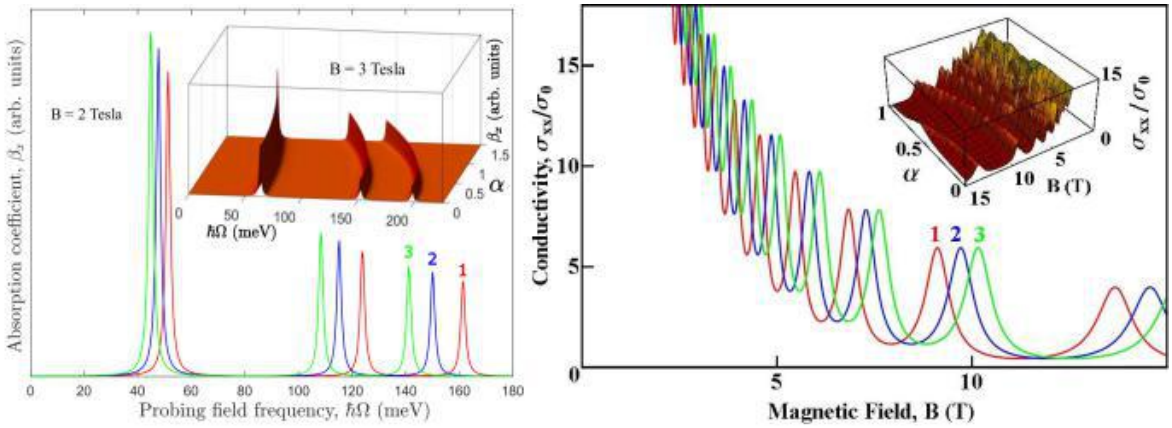



Figure 2: (**Left**). The absorption coefficient for dressed graphene in magnetic field plotted for three different dressing field intensities I = 0, 3.51 and 6.24 W/cm$^2$ represented by the curves 1, 2 and three, respectively. In the insert $\alpha = 2vE_0/\hbar\omega^2$. (**Right**). The conductivity plotted for the intensities I = 0, 1.56 and 2.63 W/cm$^2$ represented by the curves 1, 2 and three, respectively. For both figures, the dressing field photon energy is $\hbar\omega = 3$ meV.

We considered the geometry where constant magnetic field normal to the graphene sheet is applied to a monolayer graphene dressed by linear polarized field. The latter modifies the inter-Landau level separation as the levels are renormalized to

$$\varepsilon_n = sgn(n)\hbar\omega_B\sqrt{|n|}\sqrt{|J_0(2vE_0/\hbar\omega^2)|}, \tag{1}$$

where $\omega_B$ is the cyclotron frequency. In Fig. 2 we have plotted the absorption coefficient where we see that the absorption peaks are shifted. Formally, this effect results from $|J_0(2vE_0/\hbar\omega^2)|$ being always less than one. As to the Shubnikov-de Haas oscillations of the conductivity plotted in Fig. 2, their maxima correspond to the crossing of the Landau levels and the Fermi level. Since the distance between Landau levels depends on a dressing field, the field-induced shifting of the maxima of the conductivity curves takes place [2].

## 3. CONCLUSIONS

We have shown that the transport properties of electrons in graphene are strongly affected by dressing field. Circularly polarized dressing field leads to the monotonous decreas of the iconductivity, whereas linearly polarized field results in the oscillatory behavior of the conductivity and onset of giant anisotropy. Magneto-electronic properties of graphene are also strongly modified by dressing. In particular, optical absorption and Shubnikov-de Haas oscillations are very sensitive to the field intensity and polarization.


## ACKNOWLEDGMENT

The work was supported by FP7 ITN NOTEDEV and Singapore Ministry of Education under AcRF Tier 2 grant MOE2015-T2-1-055.


## REFERENCES


1. Kristinsson, K., Morina, S., Kibis, O. V. and Shelykh, I. A., "Control of electronic transport in graphene by electromagnetic dressing," *Sci. Rep.*, Vol. 6, No. 20082, 2016.
2. Kibis, O. V., Morina, S., Dini, K. and Shelykh, I. A., " Magnetoelectronic properties of graphene dressed by a high-frequency field", arXiv:1511.03522, 2016.

# Polariton lasing in hybrid organic-inorganic microcavity

**G. Paschos[5], N. Somaschi [1,2], G. Christmann[1] , D. Coles [3], D. G. Lidzey [3], Z. Hatzopoulos [1,4], S. I. Tsintzos [1], P. G. Lagoudakis[2], P. G. Savvidis [1,5]**

[1]Institute of Electronic Structure & Laser-FORTH, PO Box 1527, 71110 Heraklion, Greece

[2]Department of Physics and Astronomy, University of Southampton, Southampton SO17 1BJ, UK

[3]Department of Physics and Astronomy, University of Sheffield, Sheffield S37RH, UK

[4]Department of Physics, University of Crete, 71300 Heraklion, Greece

[5]Department of Materials Science and Technology, University of Crete, 71300 Heraklion, Greece

Cavity polaritons are formed when a confined optical mode within a high Q cavity strongly couples with exciton within the same cavity. Strong coupling regime has been observed in microcavity structures incorporating both inorganic quantum wells (QWs) as well as organic materials such as J-aggregates, molecular crystals and polymers[1].

In this work we study hybrid exciton-polaritons that arise from mixing of two different organic-inorganic excitonic species with the resonant photon mode[2]. A planar microcavity structure consists of GaAs QWs and Jaggregate molecular dye assembled together in a multi-layered stack to form the active region. Angle-resolved photoluminescence at 80K, when the system is excited almost-resonantly by a low repetition laser pulse at 780nm reveals clear anticrossing Figure 1(a). Furthermore, through power dependent measurements we demonstrate for the first time strong nonlinear emission and onset of hybrid polariton lasing regime with simultaneous line narrowing and interaction induced energy blueshift shown in Figure 1(b).

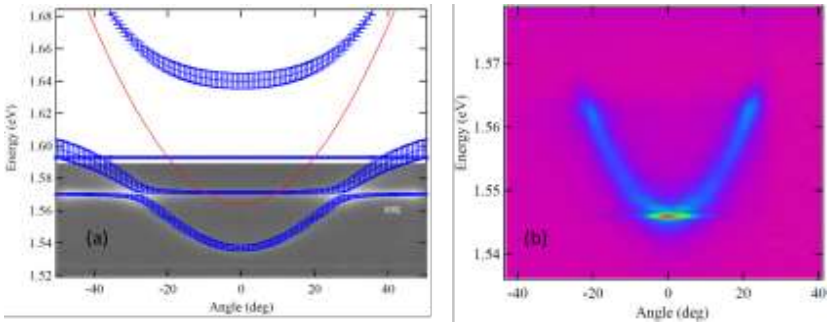



**Figure 1:** PL images recorded with Fourier plane projection technic. In left figure, 1(a), clear polariton dispersion is revealed at 80K while in the right hand figure, 1(b), clear polariton lasing obtained in similar detuning at 20K.

Such hybrid excitonic system presents an ideal playground for engineering nonlinear interactions and at the same time offers concrete possibilities for optoelectronics application. For example, laser diode designs combining high electrical conductivity of inorganic semiconductors with exciton robustness of organic compounds to maintain strong coupling regime at room temperature could provide efficient means to achieve electrically pumped organic polariton lasers.

**REFERENCES**

[1] D. Coles et al., Polariton mediated energy transfer between organic dyes in a strong-coupled optical microcavity, Nature Materials 13, 712 (2014)

[2] V.M. Agranovich et al., Organic and inorganic quantum wells in a microcavity: Frenkel-Wannier-Mott excitons hybridization and energy transformation, *Solid State Communications* **102,** 631-636 (1997).

# Polariton condensation phase diagram in a ZnO microcavity: What else besides room-temperature?

**J. Zuniga-Perez[1,*], O. Jamadi[2], F. Reveret[2], R. Hahe[3], F. Li[1], M. Leroux[1], F. Semond[1], J. Leymarie[2], P. Disseix[2], F. Medard[2], M. Mihailovic[2], T. Guillet[3], C. Brimont[3], S. Bouchoule[4], X. Lafosse[4], D. Solnyshkov[2] and G. Malpuech[2]**

[1] CRHEA-CNRS, Rue Bernard Gregory, 06560 Valbonne, France
[2] Clermont Université/CNRS UMR6602, Institut Pascal (IP), BP 10448, F-63000 Clermont-Ferrand, France
[3] Laboratoire Charles Coulomb (L2C), UMR 5221, CNRS-Université de Montpellier, Montpellier, France
[4] LPN-CNRS, Route de Nozay, 91460 Marcoussis, France

[*]corresponding author: jzp@crhea.cnrs.fr

**Abstract***:* The experimental determination of the condensation phase diagram in a ZnO microcavity shows that in wide bandgap microcavities, contrary to a common assumption, the strong exciton-LO phonon interaction does not necessarily lead to a reduction of the polariton condensation threshold. In fact the importance of this relaxation mechanism is largely dependent on the polariton relaxation time to polariton lifetime ratio. Most important, the condensation threshold is found to be a strongly varying function of the excitation spot size and to display an absolute minimum, for this microcavity and at room-temperature, for an excitation spot diameter of about 12μm.

In order to obtain polariton condensation at room-temperature materials with large oscillator strengths and large exciton binding energies must be employed as active regions. This is the reason why so much attention has been paid lately to organic semiconductors, van der Waals materials (e.g. $WSe_2$ or $MoSe_2$), GaN and ZnO. Furthermore, since in the fabrication of strongly-coupled microcavities distributed Bragg reflectors are most often employed, GaN and ZnO offer the additional advantage of being compatible with growth techniques such as molecular beam epitaxy (MBE) or metal organic vapor phase epitaxy. Indeed, MBE has contributed to establish GaAs-based microcavities as the benchmark system.

In this communication epitaxial ZnO cavities, grown by MBE on patterned silicon substrates [1], will be used to illustrate some of the particularities of polariton condensation in large Rabi splitting microcavities (typically larger than 100meV), which enable to access in one and the same microcavity polariton condensates very different in nature (i.e. from almost photon-like to almost exciton-like) [2]. In determining the condensation phase diagram of this microcavity it has been found that, contrary to a common assumption in wide-bandgap microcavities, the strong exciton-LO phonon interaction [2,3] does not necessarily lead to a reduction of the polariton condensation threshold. For this to hold two conditions, and not only one, are necessary: first, the bottom of the LPB and the exciton reservoir must be resonant (i.e. energetically separated by a number of LO phonons) and, second, the detuning must be such that the polariton lifetime and the polariton relaxation time are similar (“trade-off zone”) [4]. These different regimes and parameters are illustrated in Figure 1.

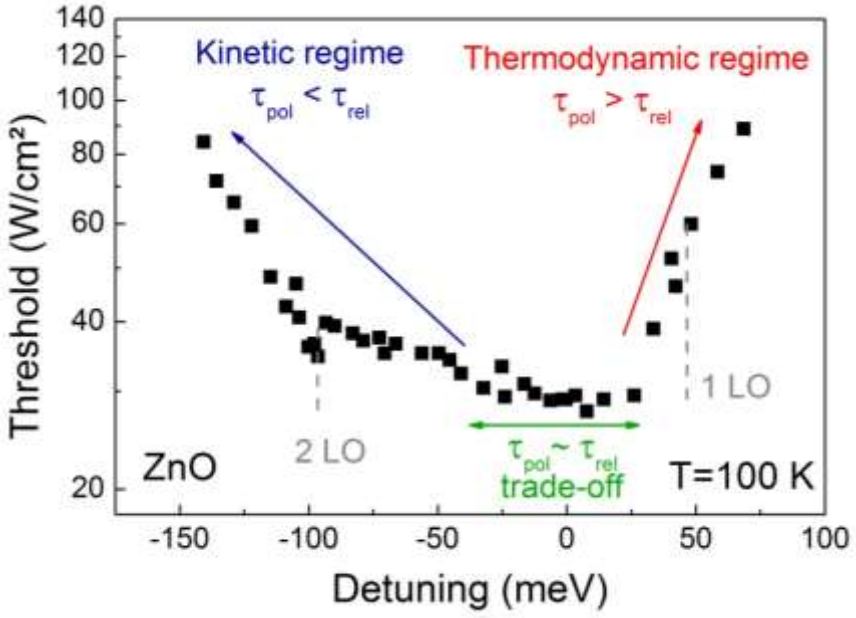



***Figure 1****: Condensation threshold of a ZnO microcavity as a function of detuning at a temperature of 100 K. The different regimes of the condensation phase diagram are recalled: positive (negative) detunings correspond to the thermodynamic (kinetic) regime. Between these two regimes a trade-off zone can be defined where the polariton lifetime is close to the relaxation time. The vertical dashed lines indicate the resonant condition, assisted by 1 or 2 LO phonons, between the reservoir and the bottom of the LPB at k=0.*

Furthermore, thanks to a homogenous photonic potential, with variations of the bare cavity mode smaller than 4% of the Rabi at a micrometer scale, we have been able to study experimentally how does the condensation threshold varies with the excitation spot size. This has allowed us to go from the "tightly-focused" excitation regime, in which the threshold is determined by the ejection of polaritons from below the excitation spot [5], to a large spot diameter regime. The optimum spot size, which for a given detuning results in an absolute condensation threshold minimum, is found in between the two regimes [4]. At 300K, and for a photonic fraction of about 75%, the optimum excitation spot diameter is about 12μm. The parameters determining the exact optimum size have not been yet clearly identified. In this sense, to study if photonic disorder and the associated inhomogeneous broadening play a role, a new class of monolithic epitaxial ZnO/ZnMgO microcavities has been developed. In the last part of the talk we will discuss the main characteristics of this new generation of cavities and their effect on the condensation threshold.

[1] J. Zuniga-Perez *et al*., *Appl. Phys. Lett.* **104** (2014) 241113.
[2] Feng Li *et al*., *Phys. Rev. Lett.* **110** (2013) 196406
[3] L. Orosz *et al., Phys. Rev. B* **85** (2012) 121201
[4] O. Jamadi *et al*., *Phys. Rev. B* ***accepted*** (2016)
[5] R. Hahe *et al., Phys. Rev. B* **92** (2015) 235308

# Spatio-temporal polariton phenomena in GaAs-based slab waveguides with giant optical nonlinearity

P.M. Walker[1] , C.Whittaker[1], L. Tinkler[1] , M.Sich[1], E.Cancelliery[1], D.V. Skryabin[2,3], A. Yulin[3], B. Royall[1] , I. Farrer[4,5], D.A. Ritchie[4], M.S. Skolnick[1] and D.N. Krizhanovskii[1]

[1]Department of Physics and Astronomy, University of Sheffield, Hounsfield Road, S3 7RH Sheffield, UK.
[2]Department of Physics, University of Bath, BA2 7AY Bath, UK.
[3]ITMO University 197101, Kronverksky pr. 49, St. Petersburg, Russian Federation.
[4]Cavendish Laboratory, University of Cambridge, J J Thomson Avenue, CB3 0HE Cambridge, UK.
[5]Present address: Department of Electronic & Electrical Engineering, University of Sheffield, Sheffield, S1 3JD, UK
corresponding author: d.krizhanovskii@sheffield.ac.uk

**Abstract-**

In this paper we review the physics of nonlinear polariton phenomena in GaAs-based semiconductor waveguides in the strong exction-photon coupling regime. We report the experimental observation of temporal bright polariton solitons formed at ultra-low excitation powers confirming giant optical nonlinearity of polariton system. Spatio-temporal modulational instability and dark-bright solitons are also investigated.

When light propagates through an optically active semiconductor material hybridisation of the optical and electronic excitations (photons and excitons) may occur. Such strong exciton-photon coupling leads to the formation of novel quasi-particles, so-called polaritons. Two photons colliding in free space do not interact: light beams just pass through each other with no effect on their propagation paths. By contrast the exciton component in the polariton wavefunction leads to giant repulsive interactions between the two colliding quasi-particles[1], which enable control of light by light at ultrafast speeds. This is potentially useful for applications in all-optical signal processing. The strong polariton $\chi^{(3)}$ nonlinearity also enables many-body phenomena ranging from superfluid-like behaviour, Bose-Einstein condensation to soliton physics[2] and to the study of inter-particle interactions in photonic analogs of important physical systems such as photonic topological insulators[3] or optical analogs of quantum Hall systems.

In this work we address giant polariton optical nonlinearity by studying ultra-low-power optical solitons in a novel slab waveguide geometry (Fig.1 a), where photons of waveguide mode are strongly coupled to quantum-well excitons[1]. On-chip applications require that solitons form and interact over small distances, which requires that both the group velocity dispersion (GVD) and nonlinear effects develop on very short length scales. In polariton waveguides the wavelength-dependent transition of polaritons from photon-like to matter-like leads to GVD on the order of 1,000 $ps^2$ $m^{-1}$ (Fig.1 b), which is comparable to that achieved in photonic crystal waveguides and fibre Bragg gratings. Using excitation pulse with a duration of 350 fs we demonstrate formation of bright picosecond temporal polariton solitons with pulse energies of 0.5 pJ. From the soliton formation threshold, we deduce a nonlinear refractive index three to four orders of magnitude larger than in any other ultrafast optical systems, for example, based on Si or InGaAsP, which verifies the highly nonlinear nature of our platform. Furthermore, using an excitation pulse of a

longer duration of ~2 ps polariton self-phase modulation is observed followed by the development of modulational instability with the resultant generation of a nonlinear polariton emission in a broad range of wavelengths ~10-15 nm (Fig.1 c, d). Such modulational instability probably indicates the formation of a soliton train in real space accompanied by coupling to dispersive spatio-temporal polariton modes.

As we achieve giant polariton nonlinearity with the transverse photonic confinement we are able to study spatio-temporal effects as well as purely temporal ones. Using an excitation pulse with a notch across the excitation spot dark–bright spatio-temporal polariton solitons are experimentally demonstrated: due to polariton-polariton interactions the notch develops into a pair of dark solitons accompanied by a nonlinear phase jump across the soliton profiles, whereas the temporal profile of polariton background also exhibits compression in time. To our knowledge this has not previously been seen in any experimental setting with either photons or polaritons. We note that bright[4] and spatial dark exciton-polariton solitons have previously been reported in Bragg semiconductor microcavities. Compared with these, our system has the advantages of simplicity of design and fabrication, compatibility with existing designs of high-performance waveguide photonic circuit elements, an order of magnitude faster soliton velocity. Crucially, in contrast to Bragg microcavities the polariton waveguide system also does not require external continuous wave pumping to balance loss for soliton formation to be possible. The intrinsic nature of the large dispersion and giant nonlinearity is also advantageous for the study of two-dimensional effects in hybrid-light matter system, such as X-waves[5].

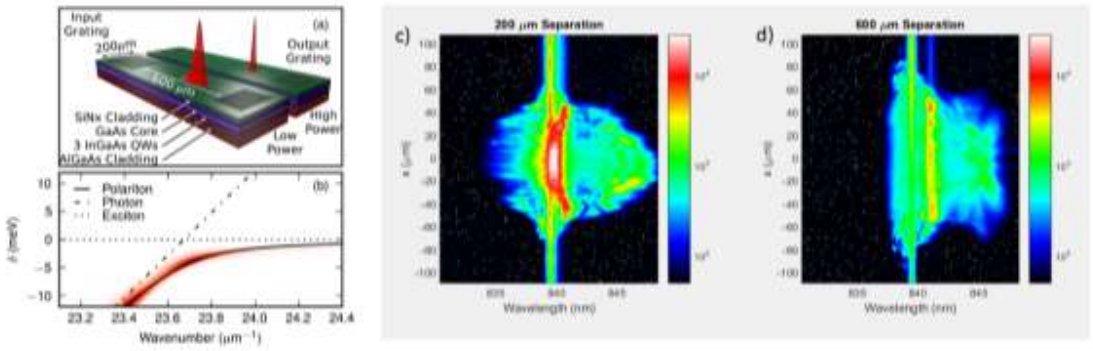



Fig.1 a) Scheme of GaAs slab waveguide showing soliton formation at high power using 350 fs pulse. Polariton mode is excited and detected through the grating coupler. b) Experimental dispersion of the lower polariton mode. c)-d) Intensity of quasi-continuum generation as a function of wavelength and transverse direction for polaritons propagated the distance of 200 μm (c) and 600 μm (d)

**Acknowledgements**: This work has been funded by UK EPSRC, the Leverhulme Trust and ERC.

## REFERENCES

[1] P. M. Walker, L. Tinkler, D. V. Skryabin, A. Yulin, B. Royall, I. Farrer, D. A. Ritchie, M. S. Skolnick, D. N. Krizhanovskii Nature Communications 6, 8317 ( 2015)

[2] I Carusotto, C Ciuti Reviews of Modern Physics 85 (1), 299

[3] Torsten Karzig, Charles-Edouard Bardyn, Netanel H. Lindner, and Gil Refael Phys. Rev. X 5, 031001

[4] M. Sich, D. N. Krizhanovskii, M. S. Skolnick et al., Nature Photonics 6, 50-55 (2012)

[5] C. Conti et al., Phys. Rev. Lett. 90, 170406 (2003)

**Spin-orbit coupling in photonic systems: from Optical Spin Hall Effect to Z topological insulator**

**G. Malpuech**, A. Nalitov, D. Solnyshkov
*Institut Pascal, PHOTON-N2, Clermont Université, University Blaise Pascal, CNRS, France*

Exciton-polaritons are bosonic hybrid exciton-photon quasi particles with 2 spin projections. In microcavities the polariton spin dynamics is governed by an effective spin-orbit coupling associated with the polarisation splittings between TE and TM polarised eigen mode, Zeeman splitting, and, in the non-linear regime by spin-anisotropic interactions. These two combines specificities makes of this system a unique platform to demonstrate and study original spin dependent phenomena, such as the Optical Spin Hall effect [1,2,3], Half integer topological defects [4,5,6,7,8], Magnetricity [9], Artificial Gauge fields [10]. These potentialities have been recently reinforced by the realisation of polariton mollecule and polariton lattices [11], which combined with the above mentioned degrees of freedom allowed to observe spontaneous and persistent spin currents [12], and to predict the feasability of emergent gauge field acting on Dirac quasi-particles [13] and of photonic/polaritonic topological insulators [14]. In this presentation, I will review, in a comprehensive way the above mentioned phenomena with a special focus on the scheme of polariton Z topological insulator based on polariton graphene. I will show how the TE-TM splitting breaks the symmetry between the two Dirac points in reciprocal space. The Zeeman splitting reveals this symmetry breaking opening a gap between topologically non trivial bands with integer Chern number -/+2. The band structure of a polariton ribbon calculated with a tight binding approach is shown on the **figure 1-a**. Each surface supports two unidirectional modes (blue: left surface, red: right surface). The **figure 1-b** shows a snapshot image taken after pulsed resonant excitation at the gap energy and at the position shown by the white circles. One can clearly see the one way propagation with opposite propagation directions on each edge of the ribbon. This topological insulator scheme is not based on the appearance of Landau Levels and has many similarities with the Haldane proposals of 1988 [15] and 2008 [16].

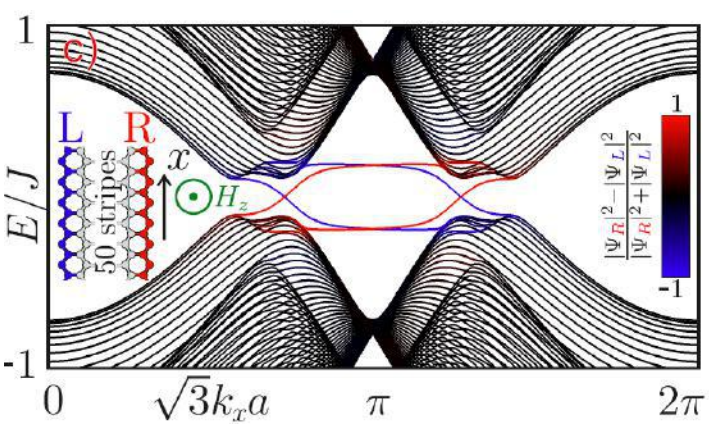



Figure 1-a

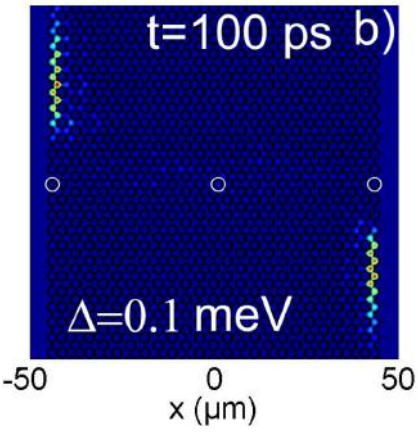



Figure 1-b

[1] Alexey Kavokin, Guillaume Malpuech, and Mikhail Glazov, **Phys. Rev. Lett. 95**, 136601 (2005).
[2] C. Leyder et al., **Nature Physics 3**, 628 (2007).
[3] H. Flayac, D. Solnyshkov, I.A. Shelykh, G. Malpuech., **Phys. Rev. Lett**., 110, 016404, (2013).
[4] Y. Rubo, **Phys. Rev. Lett., 99**, 106401, (2007).
[5] K. Lagoudakis et al. **Science 326**, 974, (2009).
[6] H. Flayac, D. Solnyshkov and G. Malpuech, **Phys. Rev. B 83**, 193305, (2011).
[7] D. D. Solnyshkov, H. Flayac, and G. Malpuech, **Phys. Rev. B 85**, 073105 (2012).
[8] R. Hivet, et al., **Nature Physics 8**, 724 (2012).
[9] H. Terças, D.D. Solnyshkov, G. Malpuech, **Phys. Rev. Lett**., 113, 036403, (2014).
[10] H. Terças, H. Flayac, D. D. Solnyshkov, and G. Malpuech, **Phys. Rev. Lett. 112**, 066402 (2014).
[11] T. Jacqmin et al., **Phys. Rev. Lett. 112**, 116402, (2014).
[12] V. Sala et al., **Phys. Rev. X 5**, 011034 (2015).
[13] A. Nalitov, G. Malpuech, H. Terças and D. Solnyshkov, **Phys. Rev. Lett. 114**, 026803, (2015).
[14] A. Nalitov, D. Solnyshkov, G. Malpuech, **Phys. Rev. Lett. 114**, 116401, (2015).
[15] F.D.M Haldane, **Phys. Rev. Lett. 61**, 2015, (1988),
[16] F.D.M. Haldane and S. Raghu, **Phys. Rev. Lett. 100**, 013904, 2(2008).

# Manipulating and controlling polariton superfluid vortices

**Simon Pigeon**[1]

[1]Centre for Theoretical Atomic, Molecular and Optical Physics, School of Mathematics and Physics, Queen's University Belfast, Belfast BT7 1NN, United Kingdom
s.pigeon@qub.ac.uk

**Abstract**— We report recent advances concerning the control of topological excitations in out-of-equilibrium microcavity polariton superfluids. These excitations, which include vortices and solitons that may be created on the vicinity of a localised potential barrier, propagate along the direction of the polariton flow but can also be optically trapped, as has been shown in Refs. [1, 2, 3, 4]. Here we present the next step in controlling these fundamental excitations, reporting an optical method to (i) enhance their propagation, and (ii) control their interaction strengths.

Polariton superfluids created via coherent pumping have been shown to exhibit topological excitations, similar to those found in equilibrium superfluids [1, 2, 3, 4]. However, the non-equilibrium nature of polaritons requires the system to be continuously pumped in order to compensate for losses. This driving plays a key role in the formation and dynamics of such topological excitations. Excited through a resonant pumping, the coherent field driving the system imposes a phase on the polariton fluid which inhibits the formation of vortices or solitons [1]. This unique feature of coherently driven polariton superfluids has been used to trap vortices. To that purpose an engineered pumping profile, alternating between spatial driven and non driven regions was proposed and successfully implemented [1, 2, 5].

Based on this same idea of spatially engineered pumping profils, many works done lately focused spontaneous formation of vortices in polariton superfluids. For practical experimental reasons, such as high speeds, small propagation length and a short lifetimes, the hydrodynamics of these vortices propagating were largely ignored.

I will present a recent investigation of an optical method allowing us to overcome these difficulties, together with giving the unique opportunity to directly control and manipulate the properties of the vortices. The general idea is to sustain the superfluid polariton flow, something which generally does not last long outside the excitation region, with a secondary excitation of low intensity. This way the flow may propagate over a much longer distance. The vortices formed in the superfluid are still permitted due to the weakness of the secondary pump. This allows their propagation along large distances and the observation of their hydrodynamic behaviour. However, the second coherent pump acting as a support, allows for some other rich and unique features. At the same time as increasing the propagation length, the same secondary pump gives direct control over the vortex-antivortex interaction, offering a unique opportunity to manipulate vortex properties locally. This optical control of some essential properties of vortices allows us to envisage a new class of devices based on these excitations, and gives a unique system where such fundamental excitations, i.e. vortices, can be manipulated locally.

The new approach proposed allows for the observation of hydrodynamic behaviour of superfluid vortices, and initiates a new step regarding the control of such fundamental entities, thus paving the way toward their practical use.

## ACKNOWLEDGMENT

This research was supported by the ANR France project ACHN C-Flight.

## REFERENCES

1. Pigeon, S., I. Carusotto and C. Ciuti, "Hydrodynamic nucleation of vortices and solitons in a resonantly excited polariton superfluid," *Phys. Rev. B*, Vol. 83, No. 14, 1–6, 2010.
2. Amo, A., S. Pigeon, D. Sanvitto, V. G. Sala, R. Hivet, I. Carusotto, F. Pisanello, G. Leménager, R. Houdré, E. Giacobino, C. Ciuti and A. Bramati, "Polariton superfluids reveal quantum hydrodynamic solitons," *Science* Vol. 332, No. 6034, 1167–1170, 2011.

3. Nardin, G., G. Grosso, Y. Léger, B. Piętka, F. Morier-Genoud and B. Deveaud-Pldran, Benot "Hydrodynamic nucleation of quantized vortex pairs in a polariton quantum fluid," *Nat. Phys.* Vol. 7, No. 8, 635–641, 2011.
4. Sanvitto, D., S. Pigeon, A. Amo, D. Ballarini, M. De Giorgi, I. Carusotto, R. Hivet, F. Pisanello, V. G. Sala, P. S. S. Guimaraes, R. Houdr, E. Giacobino, C. Ciuti, A. Bramati and G. Gigli, "All-optical control of the quantum flow of a polariton condensate," *Nature Photon.* Vol. 5, No 10, 610–614, 2011.
5. Hivet, R., E. Cancellieri, T. Boulier, D. Ballarini, D. Sanvitto, F. M. Marchetti, M. H. Szymanska, C. Ciuti, E. Giacobino and A. Bramati *Phys. Rev. B* Vol. 89, No. 13, 134501, 2014.

# Discrete vortex solitons in polariton lattices

**N.G.Berloff**

Skolkovo Institute of Science and Technology Novaya St., 100, Skolkovo 143025, Russian Federation and Department of Applied Mathematics and Theoretical Physics, University of Cambridge, Cambridge CB3 0WA, United Kingdom

E-mail: *n.g.berloff@damtp.cam.ac.uk*

***Keywords*:** *quantized vortex, exciton-polariton, Bose-Einstein condensation, superfluid turbulence, discrete vortex solitons*

Quantized vortices are fundamental topological objects playing an important role in most of the branches of physics from superfluids and superconductors to high energy physics and optics. They exist in classical matter fields described by a classical smooth complex-valued field signifying the points (in 2D) or lines (in 3D) where the amplitude of the field becomes zero and the phase winds around in multiples of h/m. The formation, structure, dynamics, turbulence of the quantised vortices has been a subject of intense research in the last 40 years (see Pismen 1999 or Fetter and Svidzinsky, 2001) but many aspects of the vortex motion even in the simplest settings as an advection of a single vortex of unit charge by a constant superflow are a subject of recent discussions and revisions.

I will discuss quantized vortices as they occur in non-equilibrium solid–state condensates such as exciton-polariton condensates. Apart from quantized vortices that exist on the otherwise nonzero and usually uniform background a new class of vortices has been studied theoretically and obtained experimentally in optics and atomic physics and very recently detected in exciton-polariton condensates. Optical lattices in ultra cold Bose-Einstein condensates, periodic photonic structures for light waves and pumped lattice polariton condensates support a quite different vortex class, termed discrete vortex solitons (DVS) (Neshev et al. 2004; Fleischer et al. 2004). The core of such vortices lies on a negligible density background between the sites and the phase winds to provide spatially localized circular energy flows between the sites. In the experimental realization the phase that corresponds to singly- and multiply charged vortices can be directly imprinted by polarized laser beams resulting in the stationary DVSs or appear during condensation depending on the parameters and distances between the excitation spots in exciton–polariton condensates (Tosi et al. 2012, Ohadi et al. 2016); .

In my talk I will show that exciton-polariton condensates arranged in lattices are capable of supporting spontaneous discrete vortex solitons. The transition between a vortex free and vortex states of different winding number can be controlled by changing the pumping strength or the distance between the lattice sites. I illustrate this by considering several condensates arranged in a circle where the interactions between distant condensates can not be neglected.

***References***

L. M. Pismen, Vortices in Nonlinear Fields, Clarendon, Oxford (1999).

A. L. Fetter and A. A. Svidzinsky, J. Phys.: Condens. Matter 13, R135 (2001)

D. Neshev et al., Phys. Rev. Lett. 92, 123903 (2004); J. W. Fleischer et al., Phys. Rev. Lett. 92, 123904 (2004).

G. Tosi, et al. Nat. Physics, 8, 190 (2012); H. Ohadi, et al."Simulated coupling of polariton multiplets," in review by Phys. Rev. B (2016).

# Control of the generation and propagation of polariton condensates at 300K in ZnO microcavities

**R. Hahe[1], H. Gargoubi[1], C. Brimont[1], B. Guizal[1], S. Jaziri[2], S. Bouchoule[3], X. Lafosse[3], F. Li[4], M. Leroux[4], F. Semond[4], J. Zuniga-Perez[4], T. Guillet[1*]**

[1] Laboratoire Charles Coulomb (L2C), UMR 5221, CNRS-Université de Montpellier, Montpellier, F-France

[2] LPM, Faculté des Sciences de Bizerte, 7021 Jarzouna, Bizerte, Tunisia

[3] LPN-CNRS, Route de Nozay, 91460 Marcoussis, France

[4] CRHEA-CNRS, Rue Bernard Gregory, 06560 Valbonne, FRANCE

[*]corresponding author: Thierry.Guillet@umontpellier.fr

**Abstract**-The spatial dynamics of the formation of a polariton condensate under a tightly focused excitation is imaged through 2D near-field and far-field 2D tomography in a ZnO microcavity, up to room temperature. The modelling exhibits the role of the outwards polariton flux caused by the reservoir repulsion, that leads to a 3 to 10 fold increase of the condensation threshold and is imprinted in the shape of the polariton condensate.

ZnO is a wide bandgap semiconductor with strong excitonic properties, in particular a large oscillator strength and a large exciton binding energy. Together with GaN, CuBr and some organic semiconductors, it raises a strong interest for the generation and control of polariton condensates up to room temperature. Such condensates were achieved over a wide range of exciton-photon composition and from cryogenic to room temperature in a hybrid microcavity consisting of a bulk ZnO active layer and two dielectric Bragg mirrors [1].

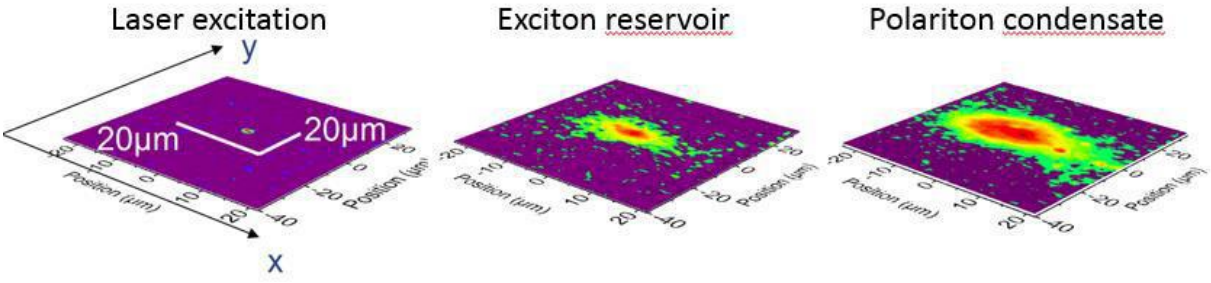



**Figure 1**: Formation and propagation of a polariton condensate in a ZnO microcavity at T=80K and a positive detuning comparable to the Rabi splitting. False color real space images under pulsed excitation (4.66 eV/266 nm, 400 ps, 1nJ/pulse).

The present work is devoted to the spatial dynamics of the condensate formation under the so-called "tightly focused excitation regime" [2] that is commonly used when optically pumping a polariton laser. The non-resonant laser excitation is focused over a few microns, and generates an exciton reservoir which feeds the polariton condensate, as shown by the experiment presented in figure 1. Using the terms of the laser physics, the threshold of the polariton laser is reached when the stimulated scattering from the reservoir to the condensate balances not only the polariton losses (related to the photon lifetime), but also the outwards polariton flux since

polaritons are repelled by the reservoir through the Coulomb interaction. The interplay between the condensate ballistic propagation and the tighly focused excitation is investigated as a function of the detuning, and its dependence on the polariton lifetime and the polariton effective mass is modelled through a resolution of the Gross-Pitaevskii in the cylindrical geometry [3]. This analysis shows that the threshold exciton density for condensation is 3 to 10 times larger for a 4 µm spot than for a large spot in the 2D limit, as also reported recently [4]. We show that the polariton current has a major influence on the spatial profile of the polariton condensate. The prospects concerning the optical control of the shape of the polariton condensate will be discussed.

**Acknowledgements**. H. Gargoubi acknowledges financial support from the Campus France PHC-Utique Program (Grant 29111XF).

**REFERENCES**

1. Li, F. *et al.*, Phys. Rev. Lett. **110**, 196406 (2013)
2. Wouters, M. *et al.*, Phys Rev B **77**, 115340 (2008)
3. Hahe, R. *et al.*, Phys Rev B **92**, 235308 (2015)
4. Jamadi, O. *et al.*, arXiv:1512.05985 (2015)

# Quantum Spin Hall phase and topologically protected edge states in the polariton rings lattices

**M. Hasan**[1], **I. Iorsh**[1], **and I.A. Shelykh**[1,2,3]

[1]National Research University of Information Technologies, Mechanics and Optics (ITMO), St. Petersburg 197101, Russia,

[2]Science Institute, University of Iceland, Dunhagi-3, IS-107 Reykjavik, Iceland,

[3] Division of Physics and Applied Physics, Nanyang Technological University 637371, Singapore.

i.iorsh@phoi.ifmo.ru

**Abstract**— We study the dispersion and topological properties of the two-dimensional arrays of the coupled polaritonic rings in the presence of the external magnetic field. We show that these structures can be characterized by the nontrivial Chern numbers $\mathcal{C}_n = \pm 1, \pm 2$ and demonstrate the emergence of the topologically protected chiral edge states at the interfaces of these structures.

The novel and rapidly emerging field of *spinoptronics* aims to find the way of the efficient optical control over the spin transport in nanostructures through the strong light-matter coupling. Excitons-polaritons [1], the quasiparticles originating from the strong light-matter coupling in microcavities, seem to be the most suitable platform for the realization of the spinoptronic devices. Exciton polaritons posses the spin degree of freedom, which can be flexibly controlled with the external light, exhibit strong nonlinearity and are characterized by much larger coherent propagation lengths than the carriers in semiconductors.

Recently, a concept of polariton rings as a basic element for the polariton spinoptronic devices has been put forward [2]. It has been shown that inherent polariton spin-orbit coupling originating due to TE-TM splitting in the microcavity, allows to realize a novely type of the polaritonic Berry phase interferometer. Later, the experimental realization of the polariton ring interferometer has been presented [3].

In this work, we studied how the polariton spin-orbit coupling and Berry phase would affect the topological properties of the lattices of polaritonic rings. We consider the structure shown in Fig. 1(a): a two-dimensional square lattice of microcavity rings subject to the perpendicular magnetic field. The geometry of the unit cell is shown in Fig. 1(b). We have calculated the band structure and the Chern numbers of the structure using the approach developed in [4]. For that, we have first derived the basis eigenfunctions both in the rings and in the leads. The polaritons both in the ring and in the lead experience a total magnetic field which is the combination of the real magnetic field aligned along the growth axis and the momentum dependent effective magnetic field originating due to the polariton TE-TM splitting. After that the scattering matrix of the single quantum point contact has been derived parametrized by a single parameter corresponding to the contact transparancy. Finally, the scattering matrix of the single period of the structure has been obtained, from which we derived the dispersion equation. The dispersion equation of the infinite two-dimensional structure yields:

$$-2\cos\left(2dq_{\pm}\right)+\cos\left(2dq_{\pm}-2\Theta_{\mathrm{B},\pm}\right)-2\cos\left(2\Theta_{\mathrm{B},\pm}\right)+\cos\left(2\left(dq_{\pm}+\Theta_{\mathrm{B},\pm}\right)\right)$$
$$+2\Bigg[1-8\cos\left(2q_{\pm}\left(d+\pi R\right)\right)+8\cos\left(q_{\pm}\left(2d+\pi R\right)\right)-8\cos\left(\Theta_{\mathrm{B},\pm}\right)\left[\cos\left(dq_{\pm}\right)-\cos\left(q_{\pm}\left(d+\pi R\right)\right)\right]$$
$$\left[\cos\left(K_xT_x\right)+\cos\left(K_yT_y\right)\right]-16\cos\left(K_xT_x\right)\cos\left(K_yT_y\right)\sin^2\left(\frac{q_{\pm}\pi R}{2}\right)\Bigg]=0,$$

where $q_{\pm}=\sqrt{(E\mp E_0)}$, $E_0=\sqrt{\Delta_{\mathrm{LT}}^2+\Delta_z^2}$, $\Delta_z$ and $\Delta_{LT}$ are the Zeeman and TE-TM splitting values respectively, the two signs refer to different spin-projections with respect to z-axis, and $\Theta_B$ is the Berry phase in the ring given by

$$\Theta_{\mathrm{B},\pm}=\pm\pi\left[1-\frac{\Delta_z}{\sqrt{\Delta_{\mathrm{LT}}^2+\Delta_z^2}}\right]. \tag{1}$$

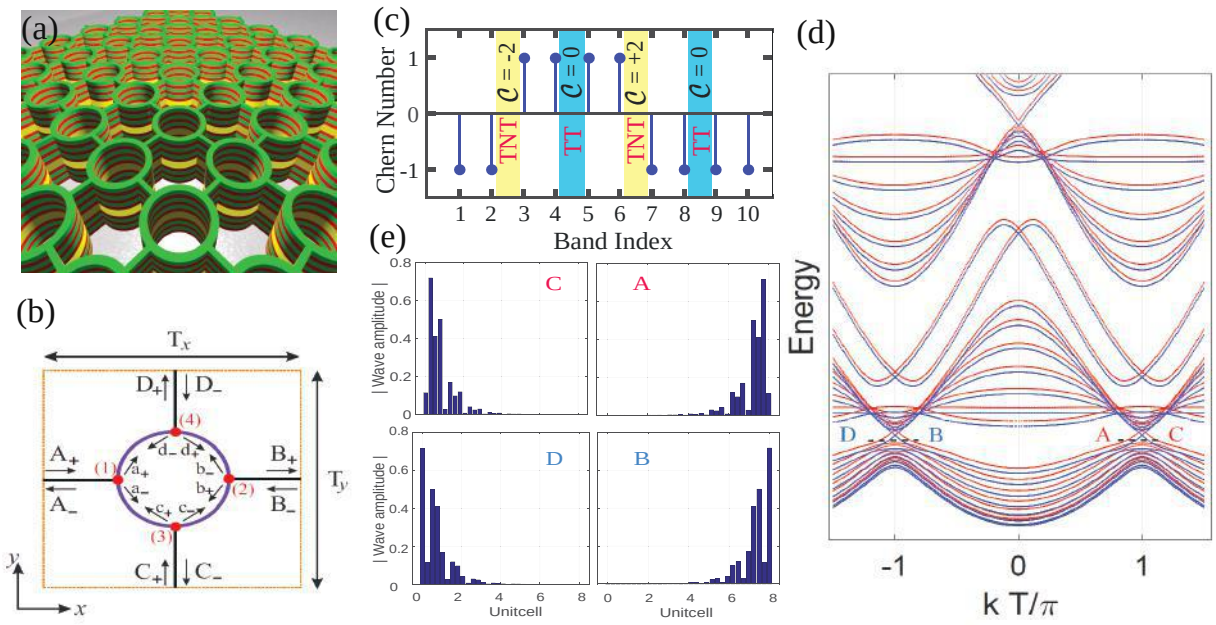



Figure 1: (a) Geometry of the structure: two-dimensional square lattice of the exciton-polariton ring resonators; (b) Unit cell of the structure: polariton rings are connected via leads at quantum point contacts (QPCs) which are shown as red filled-dots. (c) the Chern numbers of each band. The Chern invariants at bulk gaps are $\mathcal{C} = \pm 2$ for topologically non-trivial (TNT) gaps and $\mathcal{C} = 0$ for topologically trivial (TT) gaps. (d) Band structure of the stripe consisting of the 8 periods in $y$ directions. (e) Field profiles of the edge states marked at the band diagram

Note that all the energies are normalized by $\tilde{E} = \frac{\hbar^2}{2mT_x^2}$, where $T_x$ is the period of the structure. As can be seen in Fig. 1(c) the system is characterized by the non-trivial Chern numbers with the Chern invariants possible values $\mathcal{C}_n = -2, 0, +2$. In Fig. 1(d). It can be seen that the each edge of the stripe is characterized by the two counter-propagating topologically protected edge modes each characterized by different spin projections. The system thus exhibits a polariton realization of the Quantum Spin Hall insulator phase. The profiles of the polariton amplitude for the four edge modes marked in Fig. 1(d) are shown in Fig. 1(e).

To conclude, we have shown that a two-dimensional array of the polariton rings is characterized by the non-trivial Chern invariants and supports topologically protected chiral edge states analogously to the case of Quantum Spin Hall insulator. The topologically protected states carrying the specific spin projection would doubtlessly find its applications in the perspective spinoptronic devices.

**REFERENCES**


1. Kavokin, A. V., J. J. Baumber, G. Malpuech, and F. P. Laussy, *Microcavities*, Oxford University Press, 2007.
2. Shelykh, I. A., G. Pavlovic, D. D. Solnyshkov, and G. Malpuech, "Proposal for a Mesoscopic Optical Berry-Phase Interferometer," *Phys. Rev. Lett.*, Vol. 102, 046407, 2009.
3. Sturm, C. D. Tanese, H.S. Nguyen, H. Flayac, E. Galopin, A. Lematre, I. Sagnes, D. Solnyshkov, A. Amo, G. Malpuech, and J. Bloch, "All-optical phase modulation in a cavity-polariton MachZehnder interferometer", *Nat. Comm.*, Vol. 5, 3278, 2014.
4. Pasek, M. and Y. D. Chong "Network models of photonic Floquet topological insulators," *Phys. Rev. B* Vol. 89, no. 7, 075113, 2014.

# Nonequilibrium thermodynamics of quantum fluids of polaritons.

**S. Klembt**[1,2]**, T. Klein**[3]**, A. Minguzzi**[4]**, and M. Richard**[1*]
[1]Institut Néel – CNRS,UGA,CEA, 38042 Grenoble, France
[2] Würzburg University, Am Hubland, D-97074 Würzburg, Germany
[3]University of Bremen, 28334 Bremen, Germany
[4]LPMMC – CNRS,UGA, 38042 Grenoble, France

[*]corresponding author: maxime.richard@neel.cnrs.fr

**Abstract**- Owing to their mixed light-matter nature and their lifetime usually shorter than their thermalization time, exciton-polaritons in semiconductor microcavity constitute a very specific type of quantum fluids. In this work we present some experimental investigation focused on the nonequilibrium properties of such a fluid, and more specifically, on the way it is transports and stores heat.

Under suitable experimental conditions, the many-body properties of exciton-polaritons in semiconductor microcavities is accurately captured by the term "quantum fluid of light" [1]. Indeed, as a result of their ultra-light mass and sizeable interaction strength, polaritons exhibit a strikingly rich physics as a degenerate Bose gas. Their quantum hydrodynamics properties in particular have been thoroughly investigated over the last decade. Thus for instance, a superfluid phase in Landau's sense has been demonstrated [2], as well as the spontaneous/controlled generation of a large variety of spin-dependent topological excitations (cf. e.g. ref. [3]).

In a recent set of experiments, we have examined polariton fluids from another point-of-view, that of nonequilibrium thermodynamics. Indeed polaritons provides a unique opportunity to investigate a Bose gas exhibiting quantum phase transitions, and a variable amount of thermal equilibration within itself or with its environment. We have thus focused our attention on how it interacts with a genuine heat source.

In this experimental investigation, we have shown for instance that a polariton fluid can be used to pump efficiently heat out of its solid-state host microcavity [4]. At higher lattice temperature, we have shown that we could increase the coupling between a polariton quantum fluid and the thermal lattice vibrations, up to a point where thermal equilibration between the two is half way achieved. This equilibration mechanism results in a large increase of the evaporation rate of the polariton condensate which is directly visible in its spatial coherence properties [5].

**REFERENCES**

1. I. Carusotto and C. Ciuti, "Quantum fluids of light" *Rev. Mod. Phys.* Vol. 85, 299, 2013.
2. A. Amo *et al*., "Superfluidity of polaritons in semiconductor microcavities" *Nat.Phys.* Vol. 5, 805-810, 2009.
3. V. G. Sala *et al.* "Spin-Orbit Coupling for Photons and Polaritons in Microstructures" *Phys. Rev. X* Vol. 5, 011034, 2015.

4. S. Klembt *et al.* “Exciton-Polariton Gas as a Nonequilibrium Coolant” *Phys. Rev. Lett.* Vol. 114, 186403, 2015.
5. S. Klembt *et al. in preparation.*

# Fractal and topological properties of Fibonacci quasi-crystals for polaritons

**F. Baboux**[1], **D. Tanese**[1], **T. Jacqmin**[1], **A. Lemaître**[1], **E. Galopin**[1], **I. Sagnes**[1], **A. Amo**[1], **J. Bloch**[1]
[1]LPN-CNRS, Université Paris-Saclay, route de Nozay, F-91460 Marcoussis, France
**E. Levy**[2], **E. Gurevich**[2], **E. Akkermans**[2]
[2]Technion Israel Institute of Technology, Haifa 32000, Israel

**Abstract**- Waves propagating in a spatially varying potential present modifications of their spectral properties, which depend on the symmetry of this potential. Of particular interest is the case of a quasi-periodic potential. For instance, a potential modulated according to a Fibonacci sequence is predicted to produce a fractal energy spectrum, having a profound impact on many physical properties [1]. Fibonacci quasi-crystals are also expected to manifest topological properties characterized by Chern numbers [2]. I will show that cavity polaritons provide an excellent platform to probe these fractal and topological features [3,4], illustrating the great interest of semiconductor microcavities for quantum simulation.

Our samples are obtained by modulating the lateral profile of 1D cavities [Fig. 1(a)]. Low temperature (10 K) micro-photoluminescence experiments allows direct imaging of the Fibonacci eigenmodes both in real and momentum space.

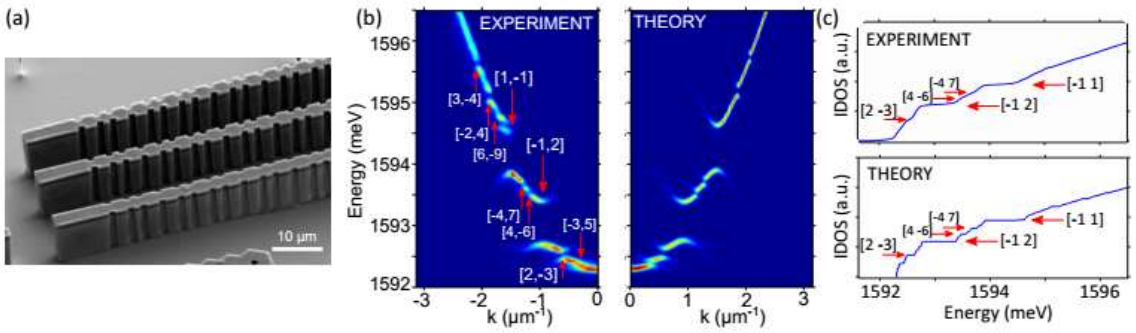



**Figure 1:** (a) SEM image of 1D cavities laterally modulated following a Fibonacci sequence. (b) Spectrally resolved far field emission and (c) integrated density of states (IDOS) of a single modulated wire

Fig. 1(b) shows the spectrally resolved far field emission of a Fibonacci wire (left panel). A complex band structure appears, with the opening of gaps not regularly spaced unlike the case of a periodic modulation. The momentum (k) position of theses gaps (red arrows) are topologically stable quantities characterized by two integers [p, q] such that $k=(p+q/\sigma)*\pi/a$,

with a the quasi-period and σ the golden mean, in accordance with the gap labeling theorem [5]. Calculations based on a 1D effective model (right panel) reproduce very well the experiment. Further insight into the fractal character of the spectrum is gained by extracting the integrated density of states [IDOS, Fig. 1(c)]. Here gaps appear as plateaus whose values are, again, topological invariants, as we have verified by studying various sample realizations. We also evidenced for the first time log-periodic oscillations in the IDOS, which constitutes a direct signature of the fractal character of the Fibonacci spectrum. Finally I will discuss the recent observation of topological edge stages in these structures and their connection with Chern numbers and gap-labelling. These results establish cavity polaritons as a promising platform for further exploring topological effects in higher synthetic dimensions [6] and in interplay with non-linear interactions [7].

**REFERENCES**


1. E. Akkermans, "Statistical mechanics and quantum fields on fractals", *Contemporary Mathematics* 601, 1-22 (2013).
2. E. Levy, A. Barak, A.Fisher and E. Akkermans, "Topological properties of Fibonacci quasicrystals: A scattering analysis of Chern numbers", *arXiv:1509.04028.*
3. D. Tanese, E. Gurevich, F. Baboux, T. Jacqmin, A. Lemaître, E. Galopin, I. Sagnes, A. Amo, J. Bloch, and E. Akkermans, "Fractal Energy Spectrum of a Polariton Gas in a Fibonacci Quasiperiodic Potential", *Phys. Rev. Lett.* 112, 146404 (2014).
4. F. Baboux, E. Levy, A. Lemaître, E. Galopin, I. Sagnes, L. Le Gratiet, A. Amo, J. Bloch, and E. Akkermans, *Under preparation.*
5. J. Bellissard, A. Bovier and J.M. Ghez, "Gap labelling theorems for one dimensional discrete Schrödinger operators", *Reviews in Math. Physics* 4, 1-37 (1992).
6. Y.E. Kraus, Z. Ringel, and O. Zilberberg, "Four-Dimensional Quantum Hall Effect in a Two-Dimensional Quasicrystal", *Phys. Rev. Lett.* 111, 226401 (2013).
7. A.J. Martínez and M.I. Molina, "Surface solitons in quasiperiodic nonlinear photonic lattices", *Phys. Rev. A* 85, 013807 (2012).

# Exciton-polariton condensates in non-Hermitian potentials

**Elena A. Ostrovskaya**[1*]

[1] Nonlinear Physics Centre, Research School of Physics and Engineering, The Australian National University, Canberra, ACT 2602, Australia

[*]corresponding author: elena.ostrovskaya@anu.edu.au

**Abstract** – Spatial shaping of an optical pump has been long recognized as a versatile tool for controlling and directing the flow of condensed microcavity polaritons. An off-resonant, incoherent optical pump creates both exciton-polaritons and an effective non-Hermitian trapping potential. We show that optically induced potentials enable exploration of non-Hermitian quantum physics with microcavity polaritons. In particular, we demonstrate, both experimentally and theoretically, non-trivial mode selection in tailored potentials, observation of exceptional points, and visualization of the topological Berry phase.

Bose-Einstein condensate of exciton-polaritons in semiconductor microcavities is a highly controllable macroscopic quantum system, which enables spectacular demonstrations of fundamental many-body quantum effects, and offers a novel platform for ultrafast optoelectronics [1]. Although confining potentials are not necessary for condensation, various methods for trapping of polaritons via their light (photon) or matter (exciton) constituents have been developed [2]. Of these, optically-induced trapping [3] is of particular interest.

Remarkably, a far off-resonant optical pump both continuously injects exciton-polaritons into the system, and traps them due to a strong, repulsive interaction with a spatially inhomogeneous excitonic reservoir created in the gain region. This pump-induced potential is non-Hermitian: exciton-polaritons exhibit a complex potential landscape due to the radiative loss and spatially inhomogeneous gain. The critical role of the non-Hermitian nature of polariton potentials in the formation and dynamics of the trapped polariton condensates is starting to emerge in various contexts [4].

In this talk, we summarize our experimental and theoretical studies of non-Hermitian effects on the spatial and spectral structure of polariton condensate in two-dimensional optically-induced potentials. We demonstrate that reconfigurable polaritonic potentials allow for manipulation of both real (energy) and imaginary (linewidth) parts of the modal eigenvalues. We show that such manipulation allows for targeted mode selection, and, for example, enables controlled creation of a vortex state with non-zero orbital angular momentum [5]. Furthermore, optically induced quantum billiards for exciton-polaritons [6] enable observation of *diabolical* and *exceptional points* in the spectra of quantum light-matter systems. Exceptional points are a direct consequence of non-Hermiticity, and are associated with nontrivial topology of the eigenstates, characterized by the *topological Berry phase* (as observed in [6]). Peculiar transport and mode-switching properties, akin to those observed in optical *PT*-symmetric systems, are therefore anticipated for optically trapped exciton-polaritons.

Our work shows that exciton-polariton condensates in semiconductor microcavities represent a robust solid-state platform for experimental and theoretical studies of open (non-Hermitian) quantum systems.

**REFERENCES**


1. Carusotto, I. and Ciuti, C. “Quantum fluids of light”, *Rev. Mod. Phys.* Vol. 85, 299, 2013; Byrnes, T., Kim, N. Y. , and Yamamoto, Y. “Exciton-polariton condensates,” *Nat. Phys.*, Vol. 10, 803, 2014; Liew, T. C. H., Shelykh, I. A., Malpuech, G. “Polaritonic Devices”, *Physica E,* Vol. 49, 1543, 2011.
2. Schneider, C., Winkler, K., Fraser, M.D., Kamp, M., Yamamoto, Y., Ostrovskaya, E.A., Höfling, S. ‘Exciton-Polariton Trapping and Potential Landscape Engineering’, *arXiv:1510.07540*
3. Tosi, G. *et al.*, “Sculpting oscillators with light within a nonlinear quantum fluid”, *Nat. Phys.* Vol. 8, 190, 2012; Cristofolini, P. *et al.* “Optical superfluid phase transitions and trapping of polariton condensates”, *Phys. Rev. Lett.* Vol. 110, 186403, 2013; A. Askitopoulos, *et al.* “Polariton condensation in an optically induced two-dimensional potential”, *Phys. Rev. B* Vol. 88, 041308, 2013.
4. Zhang, L. *et al.* “Weak lasing in one-dimensional polariton superlattices”, *PNAS*, Vol. 112, 1516, 2015; Baboux, F. *et al.* “Bosonic condensation and disorder-induced localization in a flat band” *arXiv:1505.05652*; Sun, Y. et al., “Stable Switching among High-Order Modes in Polariton Condensates”, *arXiv: 1602.03024*.
5. Dall, R., Fraser, M. D., Desyatnikov, A. S., Li, G., Brodbeck, S., Kamp, M., Schneider, C., Höfling, S., and Ostrovskaya, E. A., “Creation of orbital angular momentum states with chiral polaritonic lenses”, *Phys. Rev. Lett.*, Vol 113, 200404, 2014.
6. Gao, T., Estrecho, E., Bliokh, K.Y., Liew, T.C.H., Fraser, M.D., Brodbeck, S., Kamp, M., Schneider, C., Höfling, S., Yamamoto, Y., Nori, F., Kivshar, Y.S., Truscott, A., Dall, R., Ostrovskaya, E.A., ‘Observation of non-Hermitian degeneracies in a chaotic exciton-polariton billiard‘, *Nature* Vol. 526, 554–558, 2015.

# Exploring the potential of microcavity polariton physics for photonic devices

**O. Lafont[1], P. Lewandowski[2], M. H. Luk[3], N. H. Kwong[4], K.P. Chan[5], P.T. Leung[5], E. Galopin[6],A. Lemaitre[6], P. Roussignol[1], S. Schumacher[2], R. Binder[3,4], J. Tignon[1] and E. Baudin[1*]**

[1]Laboratoire Pierre Aigrain, École Normale Supérieure - PSL Research University, CNRS, Université Pierre et Marie Curie - Sorbonne Universités, Université Paris Diderot - Sorbonne Paris Cité,
24, rue Lhomond, 7523 Paris Cedex 05, France
[2]Physics Department and Center for Optolelectronics and Photonics Paderborn (CeOPP) Paderborn, Germany
[3]Department of Physics, University of Arizona, Tucson, USA
[4]College of Optical Sciences, University of Arizona, Tucson, USA
[5]Department of Physics, The Chinese University of Hong Kong SAR, China
[6]Laboratoire de Photonique et de Nanostructures, CNRS, Marcoussis, France

[*]corresponding author: baudin@lpa.ens.fr

*Key advantages and figures of merits of microcavity polaritons for photonic applications will be reviewed and as an illustration, two recent experiments will be detailed: a polaritonic lighthouse and a THz-detector.*

Microcavity exciton-polaritons are composite light-matter excitations, which result from the strong coupling of the optical modes of a cavity to the excitons of a quantum well. As composite bosons, they exhibit a BEC phase transition (up to room temperatures with recently developed materials), which has been subject to intense research in fundamental physics. They can also experience giant optical nonlinearities which, beyond fundamental physics, can lead to major breakthroughs for photonic devices. In this talk I shall explain why microcavity polaritons (in particular in coupled microcavities[1]) are good candidates for photonic devices and illustrate this in two different contexts:

(i) The possibility to orient light with a non-mechanical device has attracted much attention in the last decade[2]. In a previous work[3], we have shown that light can self-organize in a microcavity due to the polariton-polariton interaction in a similar fashion to Turing patterns.
I will present the basic principles and proof of concept of an optical device capable of reemitting light in a direction orthogonal to the input beam polarization, i.e., the equivalent of a lighthouse without mechanical parts. I will explain how the specific physics of polaritons is able to provide this intriguing function and how such concept can be extended to develop fast light manipulators (down to the picosecond switching time).

(ii) Detectors and emitters in the THz range have revealed to be very challenging, partly because of the competition between radiative and non-radiative transitions (i.e., induced by thermal phonons). To reduce the non-radiative transition rates, it is necessary to work at low temperature, e.g., with detectors based on Si impurities in Ge. I will explain how finely designed polaritons, thanks to their particularly short lifetime and

reduced thermalization rate due to a specific energy-momentum dispersion, can help to overcome this low temperature requirement for THz detection.

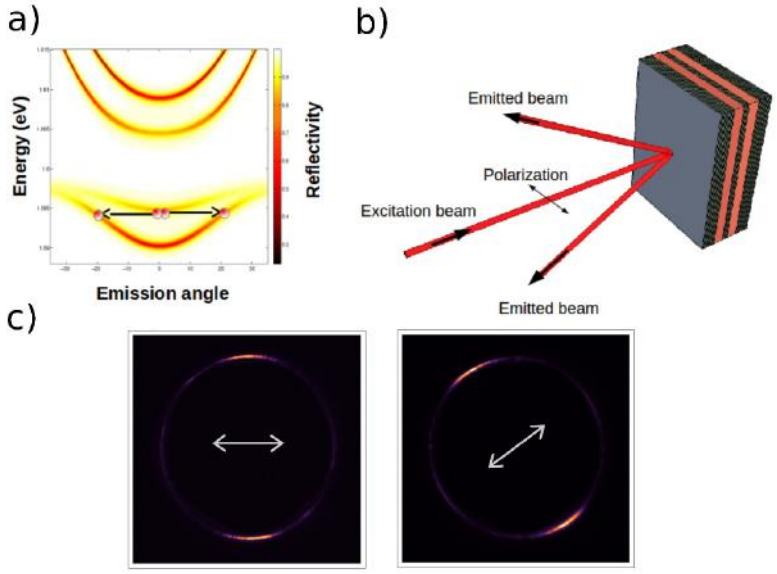



**Figure1:** a) Exciton-polariton dispersion curves for double-microcavity system. The parametric scattering process at stake is indicated by horizontal arrows, b) Schematic representation of the experimental configuration. c) Far field emission for two incident linear polarizations indicated by white arrows. A highly directive signal-idler beam pair is observed in the orthogonal direction to the incident pump polarization.

**Acknowledgements :** Work supported in part by NSF (ECCS-1406673), TRIF Photonics, DFG (research center TRR142 and SCHU 1980/5-1 and 5-2) and DFG Heisenberg programme.

**REFERENCES**

1. Diederichs, C. et al., "Parametric oscillation in vertical triple microcavities", *Nature, Vol. 410*, pp 904 (2006).
2. Wheeler, J.A. et al., "Attosecond lighthouses from plasma mirrors", *Nat. Phot., Vol.* 6, pp 828-832 (2012), note that in this case, the lighthouse effect is radial and the control degree of freedom is the wavefront profile.
3. Ardizzone, V. et al., "Formation and control of Turing patterns in a coherent quantum fluid", *Sci. Rep., Vol. 3* , 3016 (2013).

# Exciting polaritons with quantum light.

**J. C. López Carreño[1], C. Sánchez Muñoz[1], E. del Valle[1], and F. P. Laussy[1,2]**

[1]Departamento de Física Teórica de la Materia Condensada, Universidad Autónoma de Madrid, Spain
[2]Russian Quantum Center, Novaya 100, 143025 Skolkovo, Moscow Region, Russia
fabrice.laussy@gmail.com

**Abstract**— The excitation of polaritons is usually done by classical light (e.g., a laser). Here, we study their excitation by quantum light instead. We focus on a particular application of great interest in this field: the direct and accurate measurement of polariton-polariton interactions. The relevance of such an approach beyond polaritons is also addressed.

One of the great assets of polaritons [1] is their self-interaction. This brings these particles in the nonlinear regime, opening them wide open the physics of interacting quantum fluids [2]. Many of the important results of this field—including parametric scattering [3], superfuidity [4, 5], superconductivity [6], solitons [7], devices [8, 9], etc.—rely on this property. Still, the polariton-polariton interaction is a largely unknown quantity that has met with various degrees of conflicting statements [10, 11] if not controversies [12, 13]. Pioneering calculations that set the reference value of the interaction [14] have been challenged based on the composite nature of the underlying exciton [15]. Experimentally, despite ingenious and powerful methods to measure this quantity [16, 17, 18], the situation still remains unsettled due to the complexity that a strongly-driven highly dissipative solid-state system far from equilibrium can present [10]. The magnitude, sometimes even the nature (attractive/repulsive) [19, 20] and even up to the existence of the polariton interaction is thus an embarrassing unknown in a field that largely relies on it.

We propose a radically new approach to this question. Thanks to our theory of frequency-resolved photon correlations [21], we are able to characterize fully the dynamics of quantum sources (combining time *and* energy). Recent results on the generic problem of exciting optical targets with quantum light [22] shows that this can result in new regimes for the target, not available with classical excitation or even in the strong-coupling regime where light can become quantized as it interacts with the target. Here, we focus on its application to the particular case of interest in this Special Session, namely, the case where the target is the interacting and dissipative polariton field. We introduce a spectroscopic technique with quantum light [23] where the tunable photon statistics that is provided by, e.g., the Mollow triplet (other quantum sources are possible [24]), leads to an optimum probing of polariton-polariton interactions, namely: non-fluctuating two-photon packets excite the system and thus bring neither more nor less energy than is needed to query the two-polariton response. We show how, in this condition, a precise measurement of the polariton-polariton interaction strenght can be made, even if it is weak and dominated by large damping of the particles. The technique is also free of several complications due to strong pumping, such as heating, populating the exciton reservoirs, tearing apart the light-matter constitution of the polaritons, etc. Other applications of the general thematic of quantum excitations of polaritons will be overviewed.

In conclusion, we present a new concept of spectroscopy by exciting with quantum light, that could settle the crucial open problem of measuring accurately the polariton interaction strength.

**ACKNOWLEDGMENT**

We acknowledge funding by the POLAFLOW project.

**REFERENCES**

1. Kavokin, A., Baumberg, J. J., Malpuech, G. & Laussy, F. P. *Microcavities* (Oxford University Press, 2011), 2 edn.
2. Carusotto, I. & Ciuti, C. Quantum fluids of light. *Rev. Mod. Phys.* **85**, 299 (2013).
3. Savvidis, P. G. *et al.* Angle-resonant stimulated polariton amplifier. *Phys. Rev. Lett.* **84**, 1547 (2000).
4. Amo, A. *et al.* Collective fluid dynamics of a polariton condensate in a semiconductor microcavity. *Nature* **457**, 291 (2009).

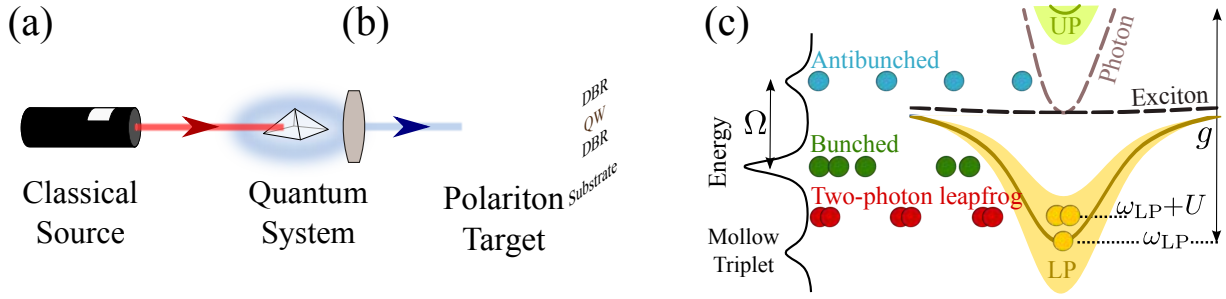



Figure 1: Scheme of our proposal: (a) a typical optical excitation scenario of quantum optics, a laser excites a quantum system, e.g., a quantum dot. (b) Instead of the conventional scenario of also exciting polaritons with a laser, we excite polaritons with quantum light, specifically, from the output of the quantum system excited by the laser. (c) Mollow spectroscopy: a strongly-driven two-level sytem provides the Mollow triplet, shown on the left with energy on the vertical axis. Various spectral windows provide different types of photon correlations, sketched here as "photon balls" with different temporal spacing. Exciting the Lower Polariton (LP) with leapfrog photon pairs allows to measure accurately very small values of the interaction.


5. Amo, A. *et al.* Superfluidity of polaritons in semiconductor microcavities. *Nat. Phys.* **5**, 805 (2009).
6. Laussy, F. P., Kavokin, A. V. & Shelykh, I. A. Exciton-polariton mediated superconductivity. *Phys. Rev. Lett.* **104**, 106402 (2010).
7. Sich, M. *et al.* Observation of bright polariton solitons in a semiconductor microcavity. *Nat. Photon.* **6**, 50 (2012).
8. Ballarini, D. *et al.* All-optical polariton transistor. *Nat. Comm.* **4**, 1778 (2013).
9. Antón, C. *et al.* Quantum reflections and shunting of polariton condensate wave trains: Implementation of a logic AND gate. *Phys. Rev. B* **88**, 245307 (2013).
10. Rossbach, G. *et al.* Impact of saturation on the polariton renormalization in iii-nitride based planar microcavities. *Phys. Rev. B* **88**, 165312 (2013).
11. Sun, Y. *et al.* Polaritons are not weakly interacting: Direct measurement of the polariton-polariton interaction strength. *arXiv:1508.06698* (2015).
12. Amo, A. *et al.* Comment on "linear wave dynamics explains observations attributed to dark solitons in a polariton quantum fluid". *Phys. Rev. Lett.* **115**, 089401 (2015).
13. Cilibrizzi, P. *et al.* Cilibrizzi *et al.* reply. *Phys. Rev. Lett.* **115**, 089402 (2015).
14. Ciuti, C., Savona, V., Piermarocchi, C., Quattropani, A. & Schwendimann, P. Role of the exchange of carriers in elastic exciton-exciton scattering in quantum wells. *Phys. Rev. B* **58**, 7926 (1998).
15. Combescot, M. & Betbeder-Matibet, O. Scattering rates and lifetime of exact and boson excitons. *Phys. Rev. Lett.* **93**, 016403 (2004).
16. Kavokin, K. *et al.* Linear polarisation inversion: A signature of Coulomb scattering of cavity polaritons with opposite spins. *Phys. Stat. Sol. C* **2**, 763 (2005).
17. Takemura, N., Trebaol, S., Wouters, M., Portella-Oberli, M. T. & Deveaud, B. Heterodyne spectroscopy of polariton spinor interactions. *Phys. Rev. B* **90**, 195307 (2014).
18. Takemura, N. *et al.* Two-dimensional Fourier transform spectroscopy of exciton-polaritons and their interactions. *Phys. Rev. B* **92**, 125415 (2015).
19. Dominici, L. *et al.* Real-space collapse of a polariton condensate. *Nat. Comm.* **6**, 8993 (2015).
20. Vishnevsky, D. V. & Laussy, F. Effective attractive polariton-polariton interaction mediated by an exciton reservoir. *Phys. Rev. B* **90**, 035413 (2014).
21. del Valle, E., González-Tudela, A., Laussy, F. P., Tejedor, C. & Hartmann, M. J. Theory of frequency-filtered and time-resolved $n$-photon correlations. *Phys. Rev. Lett.* **109**, 183601 (2012).
22. López Carreño, J. C. & Laussy, F. P. Exciting with quantum light. i. exciting an harmonic oscillator. *arXiv:1601.06187* (2016).
23. López Carreño, J. C., Sánchez Muñoz, C., Sanvitto, D., del Valle, E. & Laussy, F. P. Exciting polaritons with quantum light. *Phys. Rev. Lett.* **115**, 196402 (2015).
24. Sánchez Muñoz, C. *et al.* Emitters of $N$-photon bundles. *Nat. Photon.* **8**, 550 (2014).

# Advances on strongly correlated photonic systems

**C. Ciuti**[1]
[1]Université Paris Diderot, Sorbonne Paris Cité,
Laboratoire Matériaux et Phénomènes Quantiques,
CNRS-UMR 7162, 75013 Paris, France
[*]email: cristiano.ciuti@univ-paris-diderot.fr

**Abstract**-In this invited talk, I will present recent advances on the theory of strongly correlated photonic (polaritonic) systems. Applications and perspectives will be discussed.

The manybody physics of photons (polaritons) is attracting a considerable deal of interest for the fundamental study of non-equilibrium collective phenomena and for the realization of exotic quantum fluids of light[1]. I will show that already with a single cavity rich collective driven-dissipative effects can be achieved such as dynamical hysteresis[2] and generation of Schrödinger cats[3]. For the description of lattices with coupled nonlinear cavities, I will describe the corner-space renormalization method[4], as well as recent developments and applications, including the description of enhanced correlations in systems with geometric frustration[5].

**Acknowledgements**, Support from ERC (via the Consolidator Grant "CORPHO" No. 616233) is gratefully acknowledged.

**REFERENCES**

***1.*** I. Carusotto, C. Ciuti, "Quantum fluids of light", *Rev. Mod. Phys*. 85, 299 (2013) and references therein.
2. W. Casteels, F. Storme, A. Le Boité, C. Ciuti, "Power-laws in the dynamic hysteresis of quantum nonlinear photonic resonators", arXiv:1509.02118
3. F. Minganti, N. Bartolo, J. Lolli, W. Casteels, C. Ciuti, "Uncanny Schrödinger's cats in driven-dissipative photonic systems", arXiv:1601.02861.
4. S. Finazzi, A. Le Boité, F. Storme, A. Baksic, and C. Ciuti, "Corner-Space Renormalization Method for Driven-Dissipative Two-Dimensional Correlated Systems", Phys. Rev. Lett. 115, 080604 (2015)
5. W. Casteels, R. Rota, F. Storme, C. Ciuti, "Probing photon correlations in the dark sites of geometrically frustrated cavity lattices," *arXiv:1512.04868.*

# Collective Scattering of an Incoherently Driven Exciton-Polariton Condensate in Disordered Environment

**M. Pieczarka[1*], M. Syperek[1], Ł. Dusanowski[1], J. Misiewicz[1], F. Langer[2], M. Kamp[2], C. Schneider[2] S. Höfling[2,3], A. V. Kavokin[4,5] and G. Sęk[1]**

[1]Laboratory for Optical Spectroscopy of Nanostructures, Division of Experimental Physics, Faculty of Fundamental Problems of Technology, Wrocław University of Science and Technology, Wrocław, Poland

[2]Technische Physik, University of Würzburg and Wilhelm-Conrad-Röntgen-Research Center for Complex Material Systems, Würzburg, Germany

[3]SUPA, School of Physics and Astronomy, University of St. Andrews, St. Andrews, UK

[4]Spin Optics Laboratory, Saint Petersburg State University, St Petersburg, Russia.

[5]Physics and Astronomy School, University of Southampton, Southampton, UK.

[*]corresponding author: maciej.pieczarka@pwr.edu.pl

**Abstract** We observe renormalization of excitation branches of an expanding polariton condensate, generated by a tightly focused nonresonant laser pump. Polaritons scattered on the intrinsic sample disorder occupy normal and ghost branches, revealing peculiar polarization properties in collective microscopic scattering processes of polaritons. We track the time evolution of highly excited polariton condensate and resolve the evolution of the excitation branches.

In an exciton-polariton condensate the interactions between particles result in parametric scattering processes, which occur to scattering bands, normal branches (NB) and ghost branches (GBs), the latter ones being populated by the virtual off-branch exciton-polaritons with negative energy with respect to the condensate. This phenomenon is closely linked to interactions within the condensate of these quasi-particles [1] and Bogoliubov transformation of the excitation branches. The GB has been evidenced in a resonant excitation scheme in a complex geometry of four wave mixing experiment [2]. However, in case of the nonresonant excitation when the incoherent reservoir feeds and strongly interacts with the polariton condensate, the Bogoliubov-like dispersions were observed [3], surprisingly, with no signal from the GB being detected. This raised the question, if the GB can be observed under the influence of excitonic reservoir at all, and what are the reasons of absence of virtual GB states in such experimental conditions.

In this work we explain these issues and present the observation of a PL signal of a spontaneously formed NB and GB in a polariton condensate [3]. We investigate photoluminescence form a polariton gas excited nonresonantly with a pulsed laser focused to a diffraction limited spot of approx. 2 μm. The studied sample is a GaAs-based microcavity containing high indium content $In_{0.27}GaAs$ quantum wells, emitting in the near infra-red spectral range. The investigated system is characterized by a significant disorder (comparable to II-VI material based microcavities), induced by the Bragg mirrors imperfections (moderate quality factor of the microcavity, below 1000) and localization centers of the InGaAs quantum well. Our excitation scheme provided a repulsive potential, forming a ballistic flow of polaritonic wave packets propagating outside the pump spot. Under sufficient pump power we observe a distinct renormalization of a polariton momentum dispersion and record strong signal of virtual off-branch states, comparable to the signal intensity originating from the thermally

populated NB (Figure 1). This observation is verified in polarization-resolved measurements, were we explore the peculiar polarization nature of the two coupled branches, according to polarization selection rules in polariton-polariton scattering processes [5]. Further insight is provided by time-resolved measurements of full dispersion evolution after a pump pulse, where in particular time range we resolve signal from the NB and GB. Additionally we discuss the influence of modulational instabilities on the observed scattering features, which can enhance the GB signal and strongly modify the excitation spectrum.

Our results pave the way for studies of highly disordered bosonic condensates and show potential of moderate quality cavities to give new insights into the physics of exciton-polaritons.

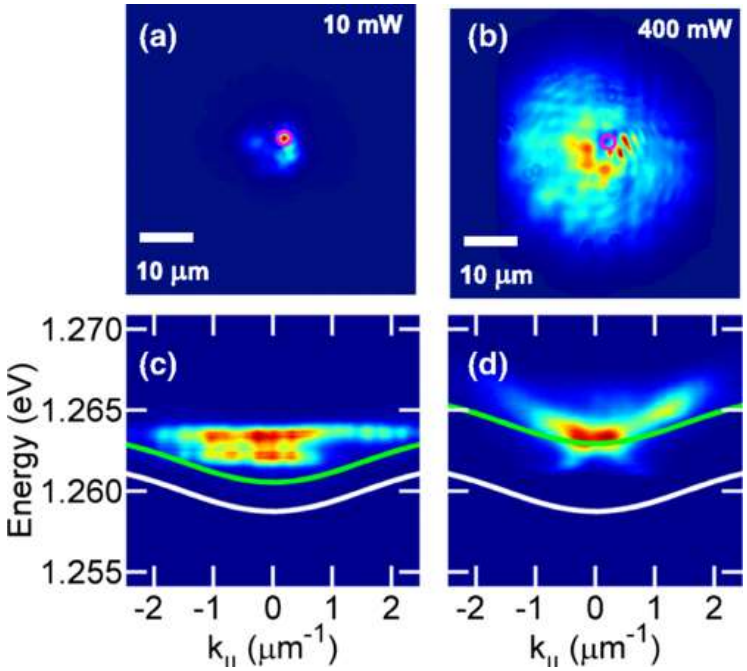



**Figure 1 Real (a and b) and wave vector space (c and d) luminescence maps of highly excited exciton-polariton condensate scattered against disorder. At moderate pump intensities (a and c) one can observe localization of polaritons within the disorder centers. At high density (b and d) polariton cloud spreads on macroscopic distances and scatter on disorder. Scattered polaritonic waves occupy normal and ghost branches in the wave vector space.**

## REFERENCES


1. J. Kasprzak et al., "Bose-Einstein Condensation of Exciton-Polaritons", *Nature*, Vol. 443, 409-414, 2006
2. V. Kohnle et al., "From Single Particle to Superfluid Excitations in a Dissipative Polariton Gas", *Phys. Rev. Lett.*, Vol. 106, 255302, 2011
3. S. Utsunomiya et al., "Observation of Bogoliubov excitations in exciton-polariton condensates", *Nat. Phys.*, Vol. 4, 700-705, 2008
4. M. Pieczarka et al., "Ghost Branch Photoluminescence From a Polariton Fluid Under Nonresonant Excitation", *Phys. Rev. Lett.* 115, 186401, 2015
5. T. Ostatnicky et al., "Theory of Polarization-controlled polariton logic gates", *Phys. Rev. B.*, Vol. 81, 125319, 2010

# Ultra-strong coupling with the free space: the superradiance

**C. Sirtori[1,*], A. Vasanelli[1], and Y. Todorov[1]**

[1] Université Paris Diderot, Sorbonne Paris Cité, Laboratoire Matériaux et Phénomènes Quantiques, UMR7162, 75013 Paris, France

[*]corresponding author: carlo.sirtori@univ-paris-diderot.fr

**Abstract**- We report on a phenomenon of non-perturbative spontaneous emission taking place in the absence of optical confinement, when a collective electronic excitation superradiantly decays into free space radiation.

Light-matter interaction, usually considered only as a weak probe, becomes the dominant energy relaxation mechanism for collective excitations in a two-dimensional electron gas. Indeed, when the concentration is sufficiently high, electrons respond to the solicitation of photons as a whole, with an absorption spectrum presenting a unique resonance at a completely different energy with respect to that of the electronic transitions.[1] This optical resonance corresponds to a many-body excitation of the system that ties together all dipoles, thus presenting a phenomenal interaction with light.[2] The spontaneous emission rate becomes proportional to the number of particles of the collective excitation, a phenomenon known as superradiance.[3] In systems with very high electronic density the spontaneous emission becomes therefore the dominant relaxation mechanism and is a sizable part of the linewidth of the emission spectrum. This physical situation is correctly described only by taking into account the anti-resonant terms of the light-matter interaction Hamiltonian in analogy to the ultra-strong coupling regime in micro-cavities.

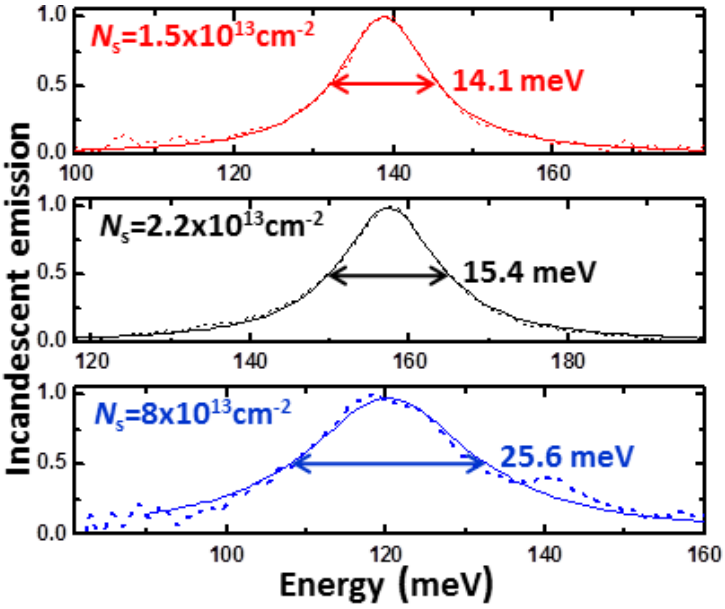



**Figure 1:** Normalized incandescent emission spectra, for three GaInAs/AlInAs quantum wells with three different electronic densities Ns, measured at an angle of 55° with respect to the growth axis. Note the increased width due to enhanced radiative decay.

By conducting thermal emission experiments, we have indeed observed a strong dependence of the linewidth as a function of the emission direction and electronic density (see figure 1). Due to superradiance phenomena, spontaneous emission lifetimes shorter than 100 fs have been deduced for collective excitations in a 2-dimensional electron gas.[4] These excitations have radiative decays more than six orders of magnitude faster than the spontaneous emission lifetime of a single particle at the same wavelength. This extremely fast radiative decay has important consequences on the characteristics of the incandescent emission that we have modelled by solving quantum Langevin equations, including coupling of the collective excitations with electronic and photonic baths.[5].

**Acknowledgements**. We acknowledge financial support from ERC (grant ADEQUATE) and Agence Nationale de la Recherche (grant ANR-14-CE26-0023-01).

**REFERENCES**

1. A. Delteil, A. Vasanelli, Y. Todorov, C. Feuillet-Palma, M. Renaudat St-Jean, G. Beaudoin, I. Sagnes and C. Sirtori, "Charge-Induced Coherence between Intersubband Plasmons in a Quantum Structure", *Phys. Rev. Lett.* Vol. 109, 246808, 2012.
2. G. Pegolotti, A. Vasanelli, Y. Todorov, and C. Sirtori, "Quantum model of coupled intersubband plasmons", *Phys. Rev. B* Vol. 90, 035305, 2014.
3. R. H. Dicke, "Coherence in Spontaneous Radiation Processes", *Phys. Rev.* Vol. 93, 99, 1954.
4. T. Laurent, Y. Todorov, A. Vasanelli, A. Delteil, I. Sagnes, G. Beaudoin, and C. Sirtori, "Superradiant electroluminescence from a collective excitation in a semiconductor", *Phys. Rev Lett.* Vol. 115, 187402, 2015.
5. S. Huppert, A. Vasanelli, T. Laurent, Y. Todorov, G. Pegolotti, G. Beaudoin, I. Sagnes, and C. Sirtori, "Radiatively broadened incandescent sources", *ACS Photonics* Vol. 2, 1663, 2015

# Polariton Stirring and Storage of Quantized Vortices

**N. D. Sangouard**[1], **T. Boulier**[1], **E. Cancellieri**[2], **Q. Glorieux**[1], **D. M. Whittaker**[2], **A. V. Kavokin**[3,4], **E. Giacobino**[1] & **A. Bramati**[1]

[1]Laboratoire Kastler Brossel, UPMC-Sorbonne Universités, CNRS, ENS-PSL Research University, Collège de France, Paris, France
[2]Department of Physics and Astronomy, University of Sheffield, Sheffield, United Kingdom
[3]School of Physics and Astronomy, University of Southampton, Southampton, United Kingdom
[4]CNR-SPIN, Viale del Politecnico, Rome, Italy
sangouard@lkb.upmc.fr

**Abstract**— We report the experimental investigation and theoretical modeling of a rotating polariton superfluid relying on an innovative method for the injection of angular momentum. Four coherent lasers arranged in a square resonantly create four polariton populations propagating inwards. Controlling the direction of the superflows allows injecting optical angular momentum. In the linear regime (low density), optical singularities coming from the interference between the four fluids are visible in the phase. In the superfluid regime (nonlinear), the interference pattern disappears and only same sign vortices remain. Remarkably, the number of vortices inside the superfluid region can be controlled by controlling the angular momentum injected by the pumps.

Exciton-polaritons are quasiparticles arising from the strong coupling between an exciton and a photon in a planar semiconductor microcavity. These bosons have specific properties inherit from both their matter and light components such as nonlinear interactions and low effective mass. They are easily controllable by optical techniques and offer a handy system to study light-matter interaction and nonlinear behaviors such as condensation, superfluidity and vortices. They are also of a big interest to study out-of-equilibrium phenomena.

We have been studying these polariton fluids in particular propagation geometries. As shown in Fig. 1 we investigate the propagation of four polariton flows towards the center of a square geometry [1]. In this configuration, the polariton wave vector can be easily changed both in direction and in modulus using the laser beams incident angle $\theta$ and the azimuthal angle $\varphi$. This way we can merge four polariton fluids with a continuous and controllable orbital angular momentum. By tuning the density of polaritons (changing the laser pump intensity), we can achieve a complete control of the nonlinearities. This allows to study the transition between the linear regime, where polaritons behave as optical waves, and the nonlinear regime where polaritons can form a superfluid (see Fig. 2). In the latest, the polariton-polariton interaction is dominant and we observe the vanishing of the interference pattern. This disappearance is accompanied by the annihilation of all vortex-antivortex pairs [2].

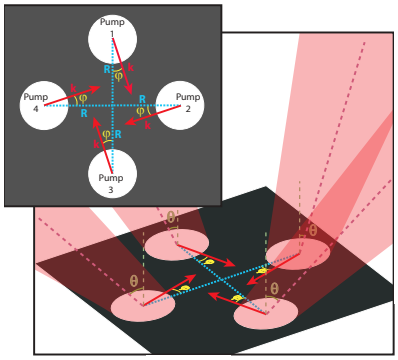



Figure 1: Schematic representation of the four pumps arriving on the sample and the propagation of the corresponding superfluids.

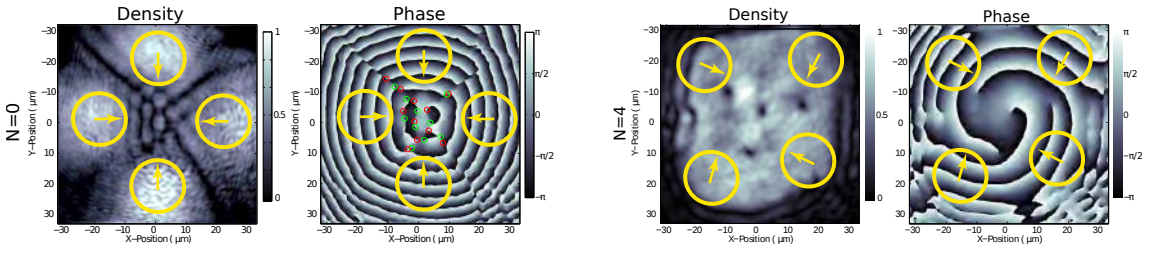



Figure 2: Density and phase of merging of four polaritons fluid. In the linear regime with the azimuthal angle $\varphi = 0$ (left hand side). In the nonlinear superfluid regime with $\varphi = 21^{o}$ (right hand side).

As shown in Ref. [1], the integer part of the continuous orbital angular momentum injected by the pump corresponds to the quantized number of vortices $N$ in the superfluid phase. This allows to store quantized vortices (topological charges) by injecting a classical orbital angular momentum in a controllable way. Moreover, our study indicates that, in the steady-state regime, the angular momentum continuously injected by the pumps compensates the loss of angular momentum by the system.

We have also measured the distribution of polaritons wave vectors in the superfluid regime (see Fig. 3). One can notice the presence of four bright spots corresponding to the four pumps, as well as a spreading of polaritons to lower wave vector values. We are currently investigating the physics of the merging of several polariton superfluids under the Bogoliubov perturbation approach. This could help us to fully understand this slow down phenomenon.

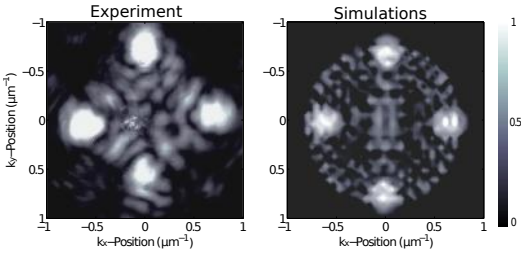



Figure 3: Reciprocal space in the four pumps configuration in the superfluid regime.


## ACKNOWLEDGMENT

We acknowledge the financial support of the ANR Quandyde (ANR-11-BS10-001) and EPSRC Grant No. EP/J007544.


## REFERENCES


1. Boulier, T., E. Cancellieri, N. D. Sangouard, Q. Glorieux, A. V. Kavokin, D. M. Whittaker, E. Giacobino and A. Bramati, "Injection of Orbital Angular Momentum and Storage of Quantized Vortices in Polariton Superfluids," *Phys. Rev. Lett.*, Vol. 116, 116402, 2016.
2. Cancellieri, E., T. Boulier, R. Hivet, D. Ballarini, D. Sanvitto, M. H. Szymanska, C. Ciuti, E. Giacobino and A. Bramati, "Merging of vortices and antivortices in polariton superfluids," *Phys. Rev. B*, Vol 90, 214518, 2014.

# Quantum Simulations with Polariton Graphs

Pavlos Lagoudakis
Department of Physics & Astronomy, University of Southampton, UK

Finding the ground state of physical systems is the natural quantum analogue of classical constraint satisfaction problems that are mapped into various optimization problems in technology and life sciences. Most of these problems belong to the non-deterministic polynomial time (NP)-complete or NP-hard complexity classes and cannot be solved efficiently using classical digital computers. By calculating the ground state energies of a physical system of a given complexity class one can solve any problem in the same complexity class according to the Cook-Levin theorem [1-3]. It has been established that quantum generalisation of constraint satisfaction problems is provided by the k-local Hamiltonian problem [4], which is quantum Merlin-Arthur (QMA)-complete for $k \geq 2$ [5], where QMA is the quantum analogue of NP. For QMA-complete (NP-complete) problems there are no classical or quantum polynomial-time algorithms to solve them. One way to tackle such computationally intractable problems is to construct a controllable quantum system - a quantum simulator -- for which the calculation of the ground state provides the solution for one and thus all of the NP-complete or NP-hard problems. Apart from potentially solving classical NP-complete or NP-hard problems a major motivation for constructing a quantum simulator for the k-local Hamiltonian problem is in simulating quantum mechanics in large condensed-matter, cosmological, high-energy, atomic, and other systems described in terms of k-local Hamiltonians with restricted types of interactions. Here, I will present recent advances on quantum simulations of 1-D Ising chains and 2-D frustrated classical magnetism utilising polariton graphs.

References:
[1] S. Cook, Proc. of the Third Ann. ACM Symp. on Theory of Computing, 151, (1971).
[2] L. Levin, Problems of Information Transmission (in Russian), **9**, 115, (1973).
[3] M. R. Garey and D. S. Johnson, Computers and Intractability: A Guide to the Theory of NP-Completeness (Freeman, San Francisco, 1979).
[4] A. Yu. Kitaev, A. H. Shen, and M. N. Vyalyi, Graduate Studies in Mathematics, AMS, vol. 47, 2002.

[5] J. Kempe, A. Kitaev, and O. Regev, SIAM J. Comput., **35**,1070 (2006).

# Subwavelength grating structures and metamaterials for integrated photonics

# Spatial Heterodyne Fourier-transform Spectroscopy: from fundamentals to array waveguide interferometers

**M. L. Calvo[1], A. V. Velasco[2], P. Cheben[3] and M. Florjańczyk[3]**
[1]Facultad Ciencias Físicas, Universidad Complutense de Madrid, Madrid, Spain
[2]Consejo Superior de Investigaciones Científicas, CSIC, Madrid, Spain.
[3]National Research Council of Canada (NRC), Ottawa, Canada.
[*]corresponding author: mlcalvo@ucm.es

**Abstract**- Since the 60's of the 20th C. the Fourier-transform (FT) spectroscopy has rapidly become a powerful and widespread research tool. This spectral analysis technique is based on the well-known Michelson interferometer set-up. By scanning the interferometer optical delay, a wavelength-dependent pattern is obtained. From it, the input spectrum is calculated by applying a Fourier transformation. FT spectroscopy provides highly resolved spectral measurements in the IR, visible and UV ranges. Current key challenges include implementing larger optical delays in a reduced footprint for higher resolutions.

Based upon this fundamental interferometric technique, the so called Spatial Heterodyne FT Spectroscopy (SHFTS), or stationary FT spectroscopy, avoids the use of moving scanning mirrors, by generating a stationary spatial output pattern containing the information equivalent to an optical delay line sweep [1]. Furthermore, the so-called *étendue* is improved, providing a large radiant throughput. According to the fundamentals of FT spectroscopy, the power of the output interferometric pattern is:

$$Y(y) = I_0 + I_0 \frac{2J_1(z)}{z} cos\left(\frac{2\pi}{\lambda} 4y\alpha\right) \quad (1)$$

Where, $I_0$: proportional to transmittance and radiance of the source, $y$: coordinate along the detection plane, $J_1$: Bessel function of first order, $\lambda$: input signal wavelength, $z$: parameter related to the angular aperture of the interferometer, $\alpha$: tilt angle. The input spectral density is computed as a cosine Fourier transform of the interferogram:

$$B(\sigma) = \int_{-\infty}^{+\infty} Y(y) cos(2\pi\sigma y) dy \quad (2)$$

Where the symmetry of the spectra holds and $\sigma$ is the wavenumber. These fundamentals open a wide variety of designs for SHFTS. Configurations can provide a large amount of applications from spatial instrumentation to design of micro-spectrometers in photonic devices. For example, since the SHFT configuration only requires stationary and passive components, it can be implemented in integrated optics by using planar waveguide interferometers. Waveguide SHFTS can be designed with an array of $N$ independent interferometers [2], as shown in Figure 1.. The output stationary interferogram can be measured in a single detection process. The device can be implemented with two different input configurations, namely, a single input waveguide feeding all the MZI and a multiple aperture scheme with an independent input for each MZI By using a separate input for each interferometer, a $N$-fold increase in *étendue* is achieved.

According to Eq.(2), and by applying the superposition principle, the total spectral power can be obtained from the integration of $B(\sigma)$:

$$P_i^{out} = \int_0^{+\infty} B_i^{out}(\sigma) d\sigma \quad (3)$$

Figure 2 shows the ideal response of the output interferogram for an input signal at Littrow wavelength [1]. Applications of this technique for space-borne instrumentation have been reported [3].

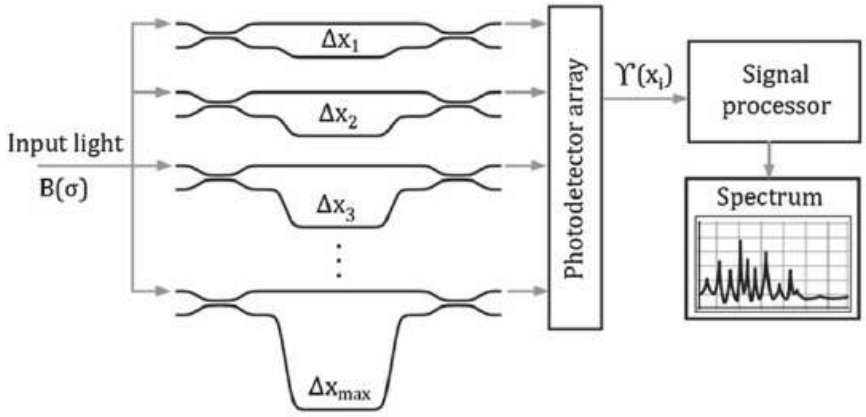



Figure 1.- Schematic of a SHFTS based on an array of *N* Mach-Zehnder interferometers. The arms of the interferometers are designed as to have a linear increase in the optical path across the array.

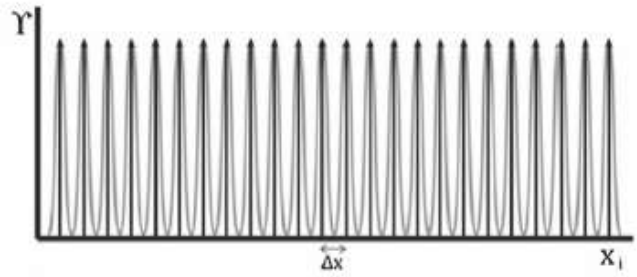



Figure 2.- Output interferogram associated to an array of *N* Mach-Zehnder interferometers (MZI) without phase or amplitude distortion.

**Acknowledgements**, M.L.C. acknowledges financial support from Spanish Ministry of Economy Grant TEC2014-57394-P. A.V.V. acknowledges financial support from Spanish Ministry of Economy (TEC2012-37958-C02-02, TEC2012-37958-C02-01), Community of Madrid (S2013/MIT-2790) and EURAMET (JRP IND14 FREQUENCY, JRP-i22 14IND13-PhotInd). P.C. acknowledges financial support from NRC, Canada.

**REFERENCES**

1. A. V. Velasco et al., "*Progress in Optics*, Vol. 59, 159-208, 2014.
2. M. Florjanczyk et al., *Opt. Express*, Vol. 15, 18176-18189, 2007.
3. M. Florjanczyk et al., *Opt. And Quant. Elect.*, Vol. 44, 549-556, 2012.

# On-chip Bragg gratings for Bloch surface waves

**L. L. Doskolovich**[1,2*], **E. A. Bezus**[1,2], **and D. A. Bykov**[1,2]
[1]Image Processing Systems Institute of the Russian Academy of Sciences, Samara, Russia
[2]Samara State Aerospace University, Samara, Russia
[*]corresponding author: leonid@smr.ru

**Abstract—** On-chip Bragg gratings (BG) and phase-shifted Bragg gratings (PSBG) for Bloch surface waves (BSW) propagating along the interface between a one-dimensional photonic crystal and a homogeneous medium are theoretically and numerically studied. Rigorous simulation results demonstrate the possibility of using the proposed on-chip PSBG for temporal and spatial differentiation of BSW pulses and beams. The obtained results can find application in the design of the prospective on-chip systems for all-optical analog computing.

Bloch surface waves are surface electromagnetic waves propagating along the interfaces between a photonic crystal and a homogeneous medium or between two different photonic crystals [1]. Along with surface plasmon polaritons (SPP), they are considered as potential candidates for the utilization in novel optical information processing devices as information carriers, as well as in other applications such as chemical and biological sensors [2, 3]. As opposed to SPP, BSW are supported by all-dielectric structures, so the absorption losses upon the surface wave propagation can be negligibly small.

In the present work, we propose and study numerically and theoretically Bragg gratings and phase-shifted Bragg gratings for BSW. The studied structures consist of a set of dielectric ridges located on the photonic crystal surface, the height of which is chosen so that they encode the required distribution of the effective refractive index. Rigorous simulation results of the surface wave diffraction on the proposed structures are compared with the plane wave (PW) diffraction on a conventional BG and PSBG.

Geometry of the considered PSBG for BSW (bottom) and the conventional PSBG for PW (top) is shown in Fig. 1(a). The middle panel in Fig. 1(a) shows the effective refractive index profile of the BSW in the PSBG. The refractive index profile of the conventional PSBG is the same. We consider a PSBG for normal incidence with the following parameters: central wavelength $\lambda_{\text{B}} = 800$ nm, TE-polarization, $\varepsilon_d = 1$, $\varepsilon_1 = 7$, $\varepsilon_2 = 2.25$, $h_1 = 120$ nm, $h_2 = 200$ nm, $h_{\text{gr},1} = 54$ nm and $h_{\text{gr},2} = 37$ nm (correspond to $n_1 = n_{\text{def}} = 1.6$, $n_{\text{sup}} = n_2 = 1.44$), $l_1 = 125$ nm, $l_2 = 139$ nm, and $l_{\text{def}} = 250$ nm. Fig. 1(b) shows the calculated amplitude and phase of the complex reflection coefficient of the PSBG for BSW and PW consisting of Bragg gratings with the number of periods 4 and 5 on the each side of the defect layer. According to Fig. 1(b), the reflection spectra of a conventional PSBG and a PSBG for BSW are in good agreement: the Pearson correlation coefficient between the spectra exceeds 0.99 both for the structures with 4 and 5 periods. Thus, similarly to conventional PSBG [4], the BSW PSBG can be used for temporal differentiation of optical pulses. Fig. 1(c) shows the incident 0.2 ps Gaussian BSW pulse envelope and the absolute values of the envelope of the pulse reflected by the 4-period PSBG and the analytically calculated derivative of the Gaussian function. It is evident from that the studied

PSBG enables high-quality differentiation of a BSW pulse. For the considered example, the Pearson correlation coefficient between the reflected pulse envelope and the exact derivative exceeds 0.999.

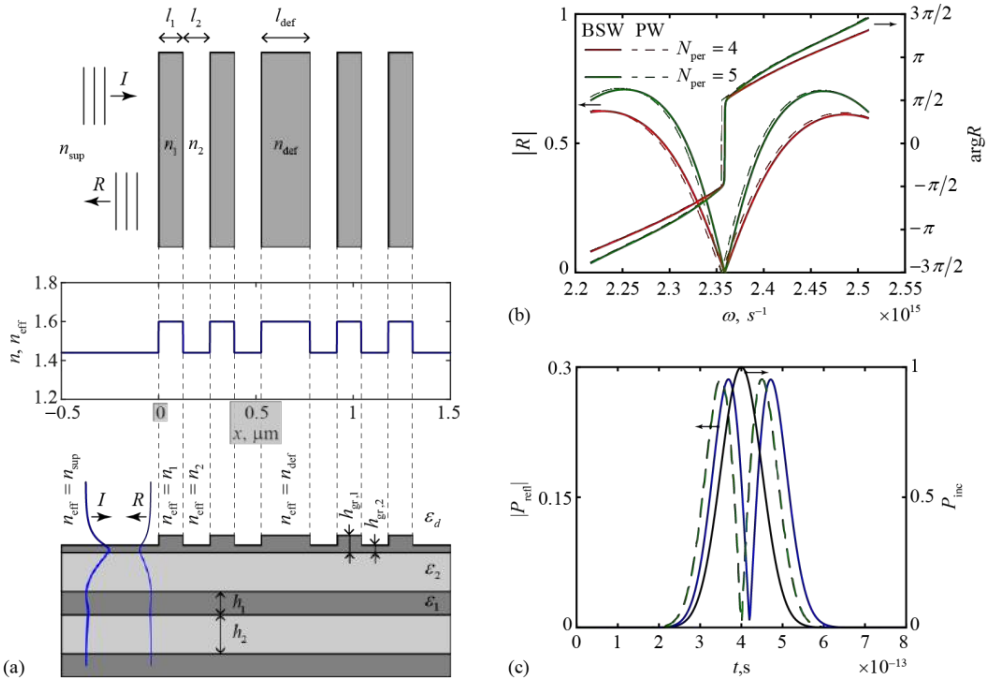



Figure 1. (a) Geometry of a PSBG for plane waves (top) and BSW (bottom), refractive/effective refractive index profile (middle), (b) spectra of the complex reflection coefficient of PSBG for BSW and PW, (c) envelopes of the incident and reflected BSW pulses and the analytically computed derivative.

Application of the studied PSBG for the optical computation of the spatial derivative of the envelope of BSW beams is also discussed. The obtained results are partially described in our recent paper [5]. The presented results can be applied for the design of new on-chip systems for all-optical analog information processing.

**Acknowledgements.** This work was funded by the Russian Science Foundation grants 14-31-00014 (design of the BSW BG and PSBG) and 14-19-00796 (application of the BSW PSBG for on-chip differentiation of optical pulses and beams).

## REFERENCES

1. Vinogradov, A. P., A. V. Dorofeenko, A. M. Merzlikin and A. A. Lisyansky, “Surface states in photonic crystals,” *Phys. Usp.*, Vol. 53, No. 3, 243–256, 2010.
2. Yu, L., E. Barakat, T. Sfez, L. Hvozdara, J. Di Francesco and H. P. Herzig, “Manipulating Bloch surface waves in 2D: a platform concept-based flat lens,” *Light Sci. Appl.*, Vol. 3, e124, 2014.
3. Sinibaldi, A., A. Fieramosca, R. Rizzo, A. Anopchenko, N. Danz, P. Munzert, C. Magistris, C. Barolo and F. Michelotti, “Combining label-free and fluorescence operation of Bloch surface wave optical sensors,” *Opt. Lett.*, Vol. 39, No. 10, 2947–2950, 2014.
4. Berger, N. K., B. Levit, B. Fischer, M. Kulishov, D. V. Plant and J. Azaña, “Temporal differentiation of optical signals using a phase-shifted fiber Bragg grating,” *Opt. Express*, Vol. 15, No. 2, 371–381, 2007.
5. Doskolovich, L. L., E. A. Bezus and D. A. Bykov, “Phase-shifted Bragg gratings for Bloch surface waves,” *Opt. Express*, Vol. 23, No. 21, 27034–27045, 2015.

# Dielectric on-chip diffraction gratings for surface plasmon polaritons

**E. A. Bezus**[1,2*], **L. L. Doskolovich**[1,2], **and V. A. Soifer**[1,2]
[1]Image Processing Systems Institute of the Russian Academy of Sciences, Samara, Russia
[2]Samara State Aerospace University, Samara, Russia
[*]corresponding author: evgeni.bezus@gmail.com

**Abstract—** On-chip diffraction gratings for surface plasmon polaritons (SPP) consisting of a periodic set of dielectric ridges located on the metal surface are studied. Simulation results demonstrate that the SPP diffraction on an on-chip grating with parasitic scattering suppression is very close to the diffraction of a TE-polarized plane wave on a conventional grating. Presented results can be used for the design of efficient 2D optical elements for steering SPP propagation.

Since the fabrication of first diffraction gratings more than 200 years ago and the discovery of resonant effects in gratings a century ago, diffraction gratings have found numerous applications as spectral filters, beam splitters, radiation absorbers etc. [1]. While the optical properties of the gratings have been exhaustively studied in the diffraction (large-period) and in the effective-medium regimes, it is the so-called near-wavelength regime that has attracted considerable attention over the past couple of decades and demonstrates the most interesting optical properties such as high quality-factor resonances or broadband high reflection or transmission [2].

Another rapidly developing area of nanophotonics is plasmonics. While various 2D optical elements including dielectric prisms lenses and Bragg mirrors were proposed for this purpose, diffraction gratings for SPP, to the best of our knowledge, were studied only in the effective-medium regime for the creation of gradient-index lenses [3]. In the present work, we investigate the optical properties of the near-wavelength on-chip dielectric plasmonic gratings within the framework of rigorous electromagnetic diffraction theory and compare their performance with the conventional diffraction gratings for free-space radiation. To decrease the SPP parasitic scattering, we adopt the two-layer configuration proposed in our previous works [4, 5].

Geometry of the studied low-scattering plasmonic grating is shown in Fig. 1(a). The grating consists of a periodic set of two-layer dielectric ridges on the metal surface. Let us consider an example with the following parameters: $\varepsilon_m = -24.06 + 1.51i$ (Au), $\varepsilon_d = 1$, $\varepsilon_1 = 1.45^2$, $\varepsilon_2 = 1.7^2$, and $h_2 = 1\ \mu\text{m}$. The thickness $h_1 = 70$ nm was chosen to minimize average scattering losses for the considered gratings. SPP with $\lambda = 800$ nm is normally incident on the structure. The calculated reflectance spectra of the plasmonic grating and an equivalent conventional grating (in the case of TE-polarization) at $w/d = 0.5$ are shown in Fig. 1(b). Normalized propagation constants of the SPP were used as refractive indices of the conventional grating. It is evident that the SPP diffraction with parasitic scattering suppression is both qualitatively and quantitatively close to the plane wave (PW) diffraction. As a particular example, we consider a reflecting grating (asterisk in Fig. 1(b)) with the following parameters: $d = 711$ nm, $l = w = 355$ nm. The calculated normalized electric field

distributions for the SPP grating and the corresponding PW grating are shown in Fig. 1(c). The reflectance of the SPP grating is as high as 0.84 and the transmittance is less than 0.003. This example demonstrates high reflectance with subwavelength footprint in the propagation direction ( $l < 0.45\lambda$ ) which is by an order-of-magnitude smaller than the lateral size of plasmonic Bragg gratings with comparable efficiency.

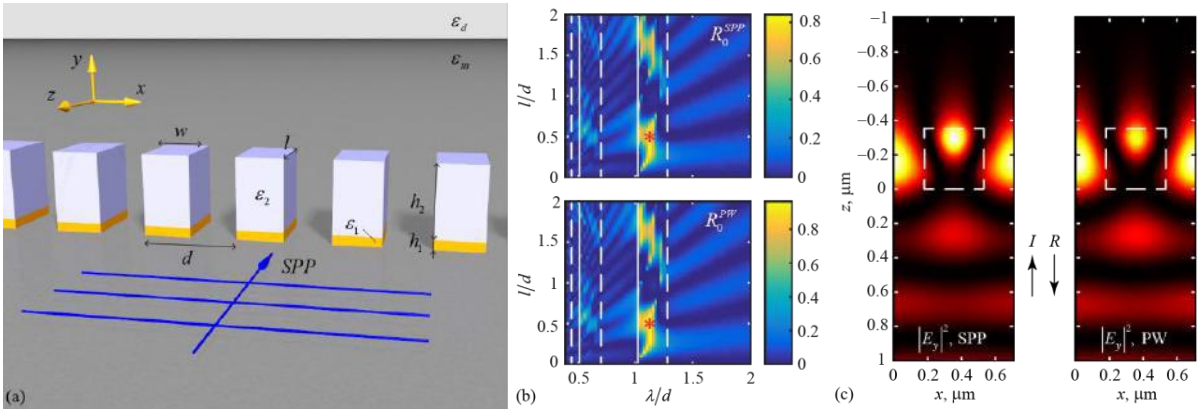



Figure 1. (a) Geometry of the studied plasmonic grating, (b) reflectance spectra of plasmonic and equivalent conventional gratings vs. normalized ridge length and wavelength (asterisk corresponds to the example in (c)), (c) electric field distributions in a plasmonic reflecting grating and the corresponding conventional grating (arrows show the propagation directions of the incident wave *I* and the reflected wave *R*).

Application of the studied SPP gratings for on-chip analog transformations of optical signals and preliminary experimental results are also discussed. The presented results are partially described in our recent paper [6]. The obtained results suggest that various results of the conventional diffraction grating theory can be extended to plasmonic gratings and lead to the creation of compact and efficient optical elements for controlling SPP propagation such as reflectors, spectral filters, beam splitters and deflectors.

**Acknowledgements.** This work was partially supported by Russian Foundation for Basic Research (projects 15-07-00548, 16-29-11683) and Russian Academy of Sciences (Presidium Programs 1 and 1.19P). The work concerning the application of SPP gratings for on-chip analog transformations of optical signals was funded by Russian Science Foundation grant 14-19-00796.

## REFERENCES

1. Collin, S. “Nanostructure arrays in free-space: optical properties and applications,” *Rep. Prog. Phys.*, Vol. 77, No. 12, 126402, 2014.
2. Karagodsky, V. and C. J. Chang-Hasnain, “Physics of near-wavelength high contrast gratings,” *Opt. Express*, Vol. 20, No. 10, 10888–10895, 2012.
3. Grajower, M., G. M. Lerman, I. Goykhman, B. Desiatov, A. Yanai, D. R. Smith and U. Levy, “Subwavelength plasmonics for graded-index optics on a chip,” *Opt. Lett.*, Vol. 38, No. 18, 3492–3495, 2013.
4. Bezus, E. A., L. L. Doskolovich and N. L. Kazanskiy, “Scattering suppression in plasmonic optics using a simple two-layer dielectric structure,” *Appl. Phys. Lett.*, Vol. 98, No. 22, 221108, 2011.
5. Bezus, E. A., L. L. Doskolovich and N. L. Kazanskiy, “Low-scattering surface plasmon refraction with isotropic materials,” *Opt. Express*, Vol. 22, No. 11, 13547–13554, 2014.
6. Bezus, E. A., L. L. Doskolovich and V. A. Soifer, “Near-wavelength diffraction gratings for surface plasmon polaritons,” *Opt. Lett.*, Vol. 40, No. 21, 4935–4938, 2015.

# Effect of “jitter” in subwavelength grating waveguides and devices

**J. Čtyroký***
Czech Academy of Sciences, Institute of Photonics and Electronics, Prague, Czech Republic
*corresponding author: ctyroky@ufe.cz

**Abstract**-Subwavelength grating waveguides are important building blocks of modern Si-based integrated-optical circuitry. However, accurate fabrication of structures composed of submicrometer-size Si blocks is challenging. Good understanding of the influence of fabrication imperfections on the device performance is thus required. To this end, a systematic numerical study of the effect of pseudo-random errors in size and position of Si nanoblocks on subwavelength grating waveguides and devices was performed. Results will be presented, analyzed, and physically justified, and some conclusions for the device design will be drawn.

Within last years, subwavelength grating (SWG) waveguides and structures [1] have been successfully implemented in a number of integrated-optic devices based on silicon on insulator (SOI) platform. Smart implementation of the SWG principle has led to significant improvement of technical performance of some kinds of waveguide devices and has simultaneously enabled their fabrication in a single photolithographic step [2-4]. As it follows from their very principle, SWG structures consist of a number of high-index (typically silicon) nanoblocks of subwavelength size that are (quasi)periodically arranged and embedded into a low-index medium (mostly silica). Low-loss propagation of waves in such structures in the form of Bloch modes requires that both position and size of the nanoblocks are met with deeply subwavelength accuracy.

To get some insight into the influence of random fabrication errors on SWG devices, transmittances and reflectances of fundamental Bloch modes of SWG waveguides with 200 periods and of different widths were numerically calculated using our proprietary 2D and 3D Fourier Modal Methods (FMM) [5, 6]. The length, width, and position of the nanoblocks were varied using the same sequence of pseudorandom numbers with normal distribution but with different values of standard deviation. The nominal Si nanoblock and gap lengths are 100 nm, the widths are 450 nm and 3000 nm. Standard thickness of the Si layer of 220 nm is considered.

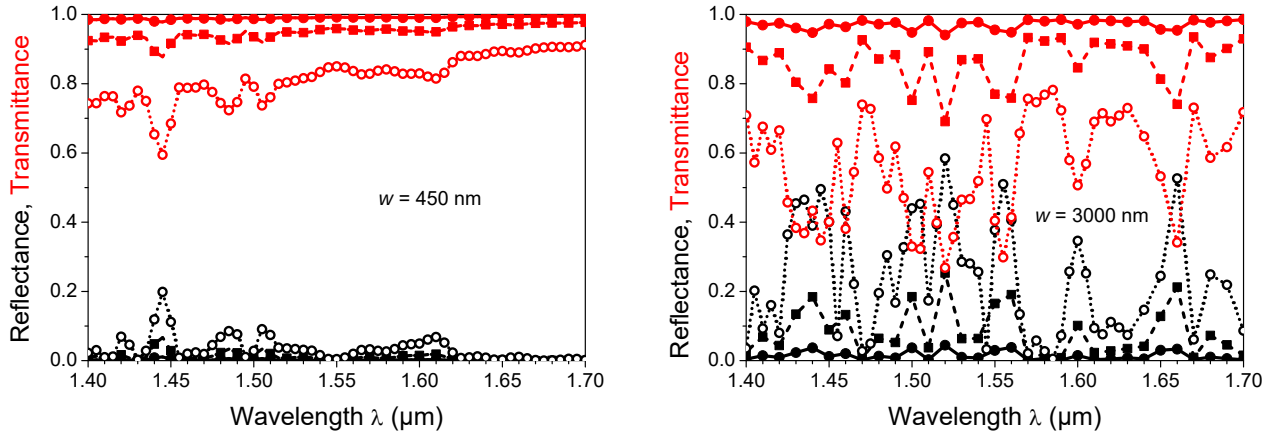



Figure 1. Transmittance (red) and reflectance (black) of a fundamental Bloch mode in a SWG waveguide with 200 periods. Lengths of the Si nanoblocks are randomized. Left: waveguide width 450 nm, right: waveguide width 3000 nm. Full circles and solid line – σ = 2 nm, squares and dashed lines – σ = 5 nm, empty circles and dotted lines – σ = 10 nm.

As an example, Figure 1 shows calculated spectral transmittances and reflectances of the fundamental Bloch modes for two SWG waveguides of different widths, in which the length of Si nanoblocks are pseudo-randomly changed according to the normal distribution. Results for standard deviations $\sigma$ = 2 nm, 5 nm and 10 nm are shown. It is apparent that the effect of random variations is rather detrimental, especially for wider waveguides used e.g., in the MMI couplers based on SWG waveguides [2].

More results will be shown, their characteristic features will be analyzed and physically justified, and some conclusions for the device design will be drawn at the presentation.

**Acknowledgements-**The author is grateful to Pavel Cheben from NRC Canada for his suggestion to study this topic and also to Robert Halir and Alejandro Ortega Moñux from the University of Málaga in Spain for many stimulating discussions, comparative calculations and experimental investigation of these effects. This work was financially supported by Czech Science Foundation under Project No. 16-00329S.

**REFERENCES**

1. Cheben, P., P. J. Bock, J. H. Schmid, J. Lapointe, S. Janz, D.-X. Xu, et al., "Refractive index engineering with subwavelength gratings for efficient microphotonic couplers and planar waveguide multiplexers," *Optics Letters*, vol. 35, 2526-2528, 2010.
2. Maese-Novo, A., R. Halir, S. Romero-Garcia, D. Perez-Galacho, L. Zavargo-Peche, A. Ortega-Moñux, et al., "Wavelength independent multimode interference coupler," *Optics Express*, vol. 21, 7033-7040, 2013.
3. Glesk, I., P. J. Bock, P. Cheben, J. H. Schmid, J. Lapointe, and S. Janz, "Picosecond all-optical switching using nonlinear Mach-Zehnder with silicon subwavelength grating and photonic wire arms," *Optical and Quantum Electronics*, vol. 44, 613-621, 2012.
4. Cheben, P., J. H. Schmid, S. Wang, D.-X. Xu, M. Vachon, S. Janz, et al., "Broadband polarization independent nanophotonic coupler for silicon waveguides with ultra-high efficiency," *Optics Express*, vol. 23, 22553-22563, 2015.
5. Čtyroký, J., "Improved bidirectional-mode expansion propagation algorithm based on Fourier series," *Journal of Lightwave Technology*, vol. 25, 2321-2330, 2007.
6. Čtyroký, J., "3-D Bidirectional Propagation Algorithm Based on Fourier Series," *Journal of Lightwave Technology*, vol. 30, 3699-3708, 2012.

# Directing OLED emission via subwavelength aluminium grating

**V. Tretnak**[1], **M. Auer-Berger**[2], **and J.R. Krenn**[1]

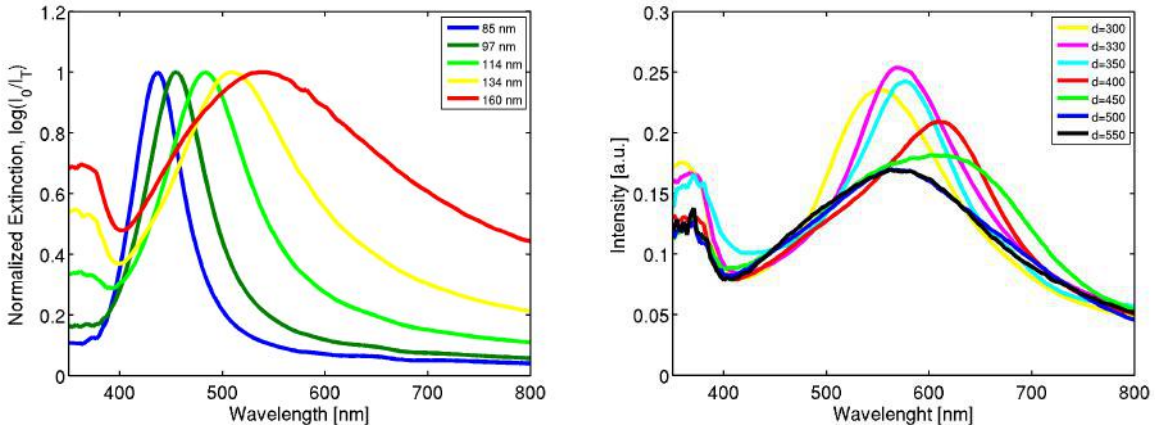
[1]Institute of Physics, University of Graz, Austria
[2]NanoTecCenter Weiz, Austria
veronika.tretnak@uni-graz.at

**Abstract**— LEDs and organic LEDs (OLEDs) are on the way to take over the lightning and display market. As with other light emitting or collecting devices, micro- and nanostructures for enhanced light control and thus increased efficiencies have already found their way into OLEDs. We chose plasmonic nanostructures due to their particularly high mode densities and enhanced optical fields. In addition, their spectral properties can be tuned by tailoring the nanostructure geometry while regular lattice arrangements can lead to higher efficiency.

In plasmonics, the traditional materials as gold and silver offer field enhancement only for wavelenghts larger than about 500 $nm$. In the blue spectral region, however, they show damping due to interband transitions which strongly supress near field enhancement. Here, we discuss aluminium as a plasmonic material for enhancing the light emission from a blue OLED.

Aluminium nanoparticles are designed by numerical simulation, fabricated by electron beam lithography and characterized by extinction spectroscopy. Disk-like nanoparticles show a spectrally narrow plasmonic peak that can be tuned throughout the visible range by changing the particle size (1a). We furthermore demonstrate that the emission dynamics of the organic light emitter can be controlled by the plasmonic modes, potentially enhancing the emission efficiency.

In addition, aluminum nanodisks were arranged in a lattice with different lattice constants to find the best parameters, due to appearing grating effects in the range of the emission wavelength of the particles (1b). The effect of the nanoparticle grating on the blue OLED is determined by fluorescence spectroscopy and lifetime measurements.




(a) Different diameters as indicated, grating constant 200 $nm$.

(b) Different grating constants as indicated, diameter 140 $nm$.

Figure 1: Extinction spectroscopy on aluminium disks.

By adding particularly designed nanostructures arranged in a lattice, we will be able to enhance the fluorescence efficiency of the molecules and direct the radiated light, thus increase the emitted light of a blue OLED.

**ACKNOWLEDGMENT**

This project is funded by the FFG (project number A28165301040).

# Optimization of Subwavelength Structures for Efficient Couplers and Hyperuniform Disordered Integrated Polarizers

**Hon Ki Tsang*, Wen Zhou, Bing Qing Zhu and Linghai Liu**
Department of Electronic Engineering, The Chinese University of Hong Kong, Hong Kong, P.R.China
*corresponding author: hktsang@ee.cuhk.edu.hk

**Abstract**-We compare integrated photonic devices which have been designed using conventional physics-based models with devices designed by direct numerical optimization. Examples include apodized gratings for improved mode matching in grating couplers, plasmonic slot waveguide couplers and integrated polarizers using the polarization-dependent photonic bandgap of hyperuniform disordered structures. These will be compared with devices designed by direct numerical optimization. Results from devices fabricated using electron beam lithography will be presented.

Integrated photonic devices have conventionally been successfully designed with the application of physical concepts such as the apodization of gratings for mode-matching to improve coupling efficiency of grating couplers [1-3], bottom reflectors and constructive interference to improve the directionality of grating couplers [4], the use of birefringence of subwavelength structures to compensate the waveguide birefringence for polarization independent grating couplers [5], use of subwavelength structure to reduce the effective index of the grating region to increase its optical bandwidth [6], improving the matching of effective refractive index to improve coupling efficiency to plasmonic slot waveguides [7] or the use of the polarization dependence of photonic bandgaps in hyperuniform disordered structures to make high extinction ratio integrated polarizers [8]. However an interesting alternative approach for the design of these devices is the direct use of numerical optimization techniques such as the direct binary search algorithm that has been applied to the design of integrated waveguide polarizers [9]. In this paper we compare the performance of grating couplers, plasmonic slot waveguide coupler and integrated polarizers designed by the conventional approaches and some recent devices which have been designed from direct numerical optimization.

The design of a subwavelength grating coupler, Fig.1 illustrates the difference in the two approaches considered in this paper. The length of the grating region is determined by the size of the mode field from the optical fiber in general each grating period has four independent parameters: the fill factors $f_x$, $f_y$ and the "periods" $\Lambda_x$ and $\Lambda_y$, could vary for each period. By using different fill factors for each period to ensure efficient matching of the diffracted mode with the optical fiber mode, we achieved an "optimized" design that experimentally 76% (-1.2dB) coupling efficiency [3]. Careful selection of etch depths in that design also ensured that the upwards diffracted light constructive interfered with the reflected downwards diffracted light to achieve good directionality [3]. However some parameters were not varied in that earlier work, for example the effective optical period was determined simply by the desired wavelength of peak coupling efficiency and thus the achieved coupling efficiency may not be the best possible. An alternative to this design approach is to consider the grating coupler design as a numerical optimization problem to optimize the four fill independent parameters for each of the 25 grating (periods 11 variable grating strength periods and 14 constant grating strength periods) [3]. There are thus

100 free parameters in the optimization problem. If we were to search only 10 possible values for each of the parameters there will be $10^{100}$ possible combinations of free parameters, which makes the numerical optimization problem too large for a brute force search. However inspired by the success of the direct binary search algorithm [9], we implemented a direct numerical optimization of the apodized grating coupler and obtained a further 0.26dB improvement in coupling efficiency.

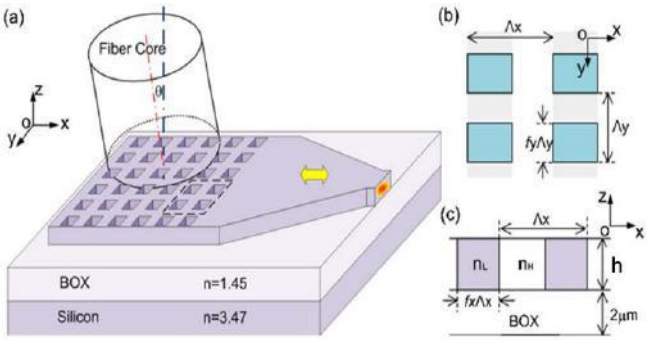



Fig. 1 (a) Subwavelength grating coupler [3] (b) plan view of grating (c) side view of grating

We shall also consider examples from other devices including the optimization of the coupler to a plasmonic slot waveguide [7] and the design of an integrated polarizer based on the polarization dependent bandgap of a hyperuniform disordered wall network [8], and compare them with devices designed by direct numerical optimization. In summary our talk will present results that show when a direct numerical approach can sometimes attain better performance than conventional design methods.

**Acknowledgements:** This work was supported by Hong Kong Research Grants Council project 14205515.

**REFERENCES**

1. D. Taillaert, P. Bienstman, and R. Baets, "Compact efficient broadband grating coupler for silicon-on-insulator waveguides," *Opt. Lett.*, Vol.29, No.23, pp.2749-2751, 2004.
2. R. Halir, P. Cheben, S. Janz, D.-X. Xu, I. Molina-Fernández and J. G. Wangüemert-Pérez, "Waveguide grating coupler with subwavelength microstructures," Opt. Lett. Vol. 34 No.9, 1408-1410, 2009.
3. X. Chen, C. Li, C. K. Fung, S. M. Lo, and H. K. Tsang, "Apodized waveguide grating couplers for efficient coupling to optical fibers," *IEEE Phot.Technol. Lett*., Vol. 22, pp. 1156-1158, 2010.
4. F. Van Laere, G. Roelkens,M. Ayre, J. Schrauwen, D. Taillaert, Dries Van Thourhout, T. F. Krauss,and R. Baets, "Compact and Highly Efficient Grating Couplers Between Optical Fiber and Nanophotonic Waveguides," *J. of Lightwave Technology*, Vol. 25, pp.151-156, 2007.
5. X. Chen and H.K. Tsang, "Polarization-independent grating couplers for silicon-on-insulator nanophotonic waveguides," *Optics Lett.*, Vol. 36, pp.796-798, 2011.
6. X. Chen, K. Xu, Z. Cheng, C. K.Y. Fung and H.K. Tsang, "Wideband subwavelength gratings for coupling between silicon-on-insulator waveguides and optical fibers," *Optics Lett.*, Vol.37, pp.3483-3485, 2012.
7. B.Q. Zhu and H.K. Tsang, "High coupling efficiency silicon waveguide to metal-insulator-metal waveguide mode converter," accepted for publication in *J. Lightwave Technology*, 2016.
8. W. Zhou, Z. Cheng, B. Zhu, X. Sun, and H.K. Tsang, "Hyperuniform Disordered Network Polarizers," accepted by *IEEE J. of Sel. Topics in Quant. Electronics*, 2016.
9. B. Shen, P. Wang, R. Polson, and R. Menon, "An integrated-nanophotonics polarization beamsplitter with 2.4× 2.4 μm$^2$ footprint," *Nature Photonics* Vol. 9, pp. 378-382, 2015.

# Transmitting and reflective subwavelength azimuthal micropolarizers

**S. S. Stafeev[1,2*], A. G. Nalimov[1,2], L. O'Faolain[3], M. I. Kotlyar[2] , and V. V. Kotlyar[1,2]**

[1]Image Processing Systems Institute, Russia

[2]Samara State Aerospace University, Russia

[3]School of Physics and Astronomy of the University of St. Andrews, Scotland

[*]corresponding author: sergey.stafeev@gmail.com

**Abstract**- we have investigated two binary subwavelength grating-micropolarizers that operate in reflection and transmission modes and transform linearly polarized light to the azimuthally polarized beam.

Using subwavelength grating is one way to obtain cylindrical vector beams. Correctly matched height of relief allows using the grating as a half-wave plate (or quarter-wave plate), and the direction of relief specify the orientation of this plate in space. Papers [1,2] are the first investigations, in which subwavelength gratings were used to convert circularly polarized light with a wavelength of 10.6 um to azimuthally polarized beam. Radially polarized light beam with wavelength of 1064 nm was obtained in [3] using subwavelength grating. Previously we investigated four-zone grating-polarizer that was used to obtain radially polarized light focused to subwavelength focal spot with size of $(0{,}35\times0{,}38)\lambda$ [4] by Fresnel zone plate.

In this paper we have investigated two subwalength four-zone grating-polarizers. The first polarizer (Fig. 1a) operates in reflection mode and was manufactured in a gold film; the second polarizer (Fig. 1b) operates in transition mode and was manufactured in silica on a glass substrate. It was shown experimentally that the first polarizer illuminated by laser light with wavelength of 532 nm forms azimuthally polarized beam. Figure 2 shows the intensity distribution of the beam reflected from polarizer. To check a polarization state of the reflected beam a linear polarizer was located before a camera in Figure 2. An angle between the axis of polarizer and incident light polarization equals to 0° (fig. 2a), 90° (fig. 2b), -45° (fig. 2c) and 45° (fig. 2d). The second polarizer illuminated by linearly polarized light with wavelength of 633 nm forms azimuthally polarized beam in transmission mode (Figure 3).

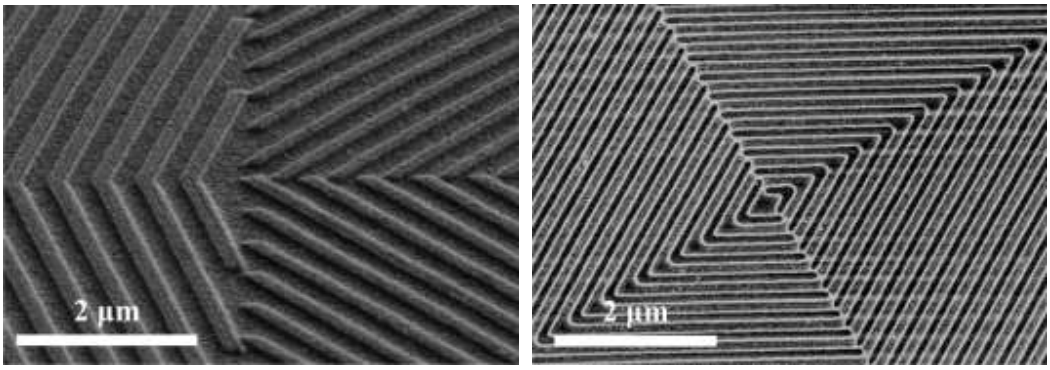



Figure 1. SEM Image of the central part of reflected (a) and transmitted (b) polarizers

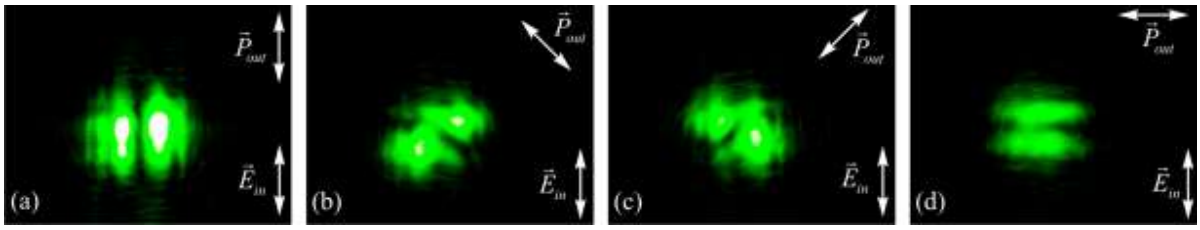



Figure 2. Image of the laser beam reflected from polarizer (Fig. 1a) in far field. A linear polarizer is located before the camera; an angle between the axis of polarizer and incident light polarization equals to 0° (a), 90° (b), -45° (c) and 45° (d). Image size is 6.2 mm × 4.2 mm.

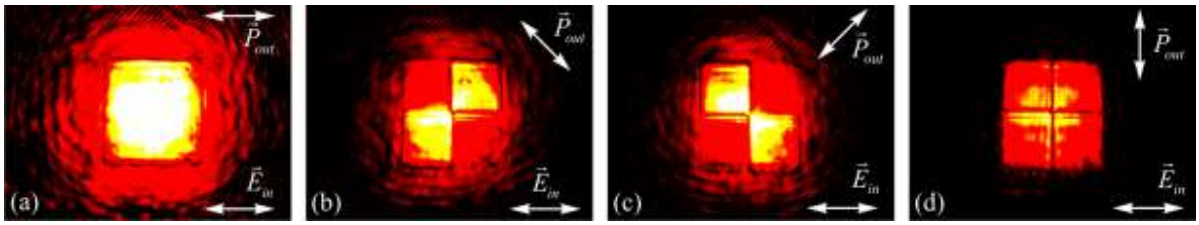



Figure 3. Image of the transmitted micropolarizer (Fig. 1b) in laser light. A linear polarizer is located before the camera; an angle between the axis of polarizer and incident light polarization equals to 0° (a), 90° (b), -45° (c) and 45° (d).

The work was partially funded by the Russian Federation Ministry of Education and Science, Presidential grants for support of leading scientific schools (NSh 4128.2016.9) and Russian Foundation of Basic Research Grants (14-29-07133, 14-07-97039, 15-07-01174, 16-07-00990).

**REFERENCES**

1. Bomzon, Z., V. Kleiner, E. Hasman, "Pancharatnam-Berry phase in space-variant polarization-state manipulations with subwavelength gratings," Opt. Lett., Vol. 26, No. 18, 1424-1426, 2001.
2. Bomzon, Z., G. Biener, V. Kleiner, E. Hasman, "Radially and azimuthally polarized beams generated by space-variant dielectric subwavelength gratings," Opt. Lett., Vol. 27, No. 5, 285-287, 2002.
3. Lerman, G.M., U. Levy, "Generation of a radially polarized light beam using space-variant subwavelength gratings at 1064 nm," Opt. Lett., Vol. 33, No. 23, 2782-2784, 2008.
4. Stafeev, S. S., L. O'Faolain, V. V. Kotlyar, A. G. Nalimov, 'Tight focus of light using micropolarizer and microlens." Appl. Opt., Vol. 54, No. 14, 4388-4394, 2015.

# Subwavelength-engineered interferometer arrays for Fourier-transform spectrometry

**A. V. Velasco[1], P. J. Bock[2], P. Cheben[2], J. H. Schmid[2], A. Delâge[2], J. Lapointe[2], D.-X. Xu[2], M. Vachon[2], S. Janz[2], M. L. Calvo[3], A. Herrero-Bermello[1] and P. Corredera[1]**

[1]Consejo Superior de Investigaciones Científicas, 28006 Madrid, Spain

[2]National Research Council Canada, Ottawa K1A 0R6, Canada

[3]Faculty of Physics, Universidad Complutense de Madrid, 28040 Madrid, Spain

[*]corresponding author: a.villafranca@csic.es

**Abstract**- We report the application of refractive index engineering through subwavelength gratings to a spatial heterodyne Fourier-transform spectrometer in planar silicon waveguides. Subwavelength gratings are used to produce linearly increasing optical path differences in a Mach-Zehnder interferometer array without waveguide bends. Subwavelength grating couplers are used at the chip facets for optimized fiber coupling and reduced Fabry–Perot effect. A fabricated device comprising an array of 32 interferometers is demonstrated, yielding a spectral resolution of 50 pm with minimized loss imbalance along the array.

Spatial heterodyne Fourier-transform (SHFT) spectrometry is an interferometric technique which circumvents the need of moving elements and provides an increased étendue [1]. The SHFT scheme can be implemented with a waveguide array of Mach-Zehnder interferometers (MZI) with linearly increasing optical path differences [2]. Instead of modifying the MZI physical length, optical path differences can be controlled by refractive index engineering through subwavelength gratings (SWG) [3]. As shown in Figure 1, each Mach-Zehnder interferometer comprises one arm with a strip waveguide of a constant length, and a second arm in which a section of the strip waveguide is replaced by the subwavelength grating (metamaterial) waveguide. The length of the SWG waveguide is linearly increasing across the array to provide spectrometer dispersion property. 50-μm-long SWG waveguide mode converters are used to connect strip waveguides with subwavelength grating waveguides (MZI second arm), allowing an adiabatic transition of the guided mode in these two types of waveguides. Efficient subwavelength grating couplers [4] were included at the input and output facets of the chip for optimized fiber coupling while at the same time reducing Fabry-Perot effect due to the reflectivity at the facets

Strip waveguide propagation loss was measured as -3.1 dB/cm while the SWG waveguide propagation loss was -3.0 dB/cm. This negligible propagation loss difference ensures high interference contrast in the MZI's spectral transmittance. Spectral retrieval was performed from a single measurement of the stationary spatial interferogram formed at the output waveguides of the array, with a wavelength resolution of 50 pm within a free spectral range of 0.75 nm near 1550 nm wavelength. The phase and amplitude errors arising from fabrication imperfections were compensated using a transformation matrix spectral retrieval algorithm [2]. Chip dimensions were approximately 6 mm x 2.5 mm, showcasing the potential of this approach for compact high-resolution integrated spectrometry.

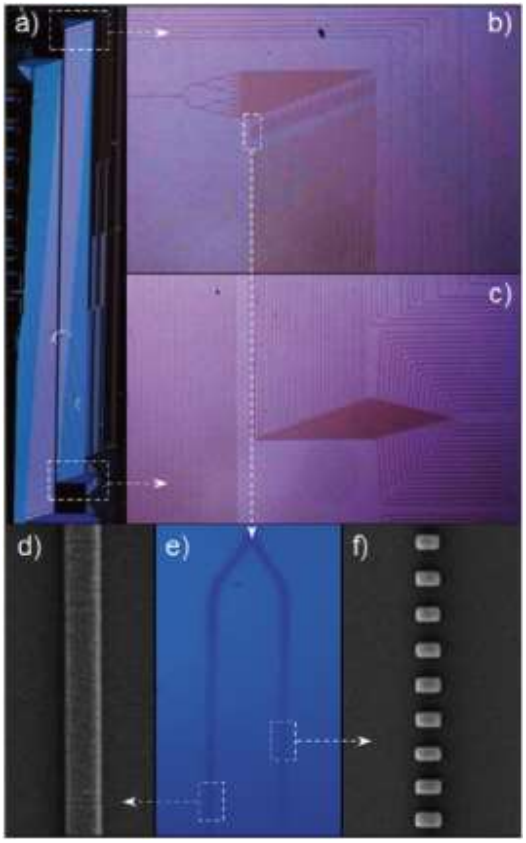



**Figure 1.** Optical and SEM images of the fabricated FT spectrometer including: a) chip, b) input cascaded Y-splitters, c) output fanout, d) strip waveguide detail, e) individual MZI, and f) SWG detail.

**Acknowledgements**: We acknowledge the support from the National Research Council of Canada and Spanish Ministry of Economy through projects TEC2015-71127-C2-1-R and TEC2014-57394-P, Community of Madrid through project S2013/MIT-2790, and EURAMET through project EMRP: JRP IND14 FREQUENCY and JRP-i22 14IND13-PhotInd.

**REFERENCES**

1. P. Cheben, I. Powell, S. Janz, and D.-X. Xu, "Wavelength-dispersive device based on a Fourier-transform Michelson-type arrayed waveguide grating," *Opt. Lett.* 30, 1824-1826 (2005).
2. A. V. Velasco, P. Cheben, P. J. Bock, A. Delâge, J. H. Schmid, J. Lapointe, S. Janz, M. L. Calvo, D.-X. Xu, M. Florjańczyk, and M. Vachon, "High-resolution Fourier-transform spectrometer chip with microphotonic silicon spiral waveguides" *Opt. Lett.* 38, 706-708 (2013).
3. P.J. Bock, P. Cheben, A. V. Velasco, J. H. Schmid, A. Delâge, M. Florjańczyk J. Lapointe, D.-X. Xu, M. Vachon, S. Janz and M. L. Calvo, "Subwavelength grating Fourier-transform interferometer array in silicon-on-insulator. *Laser Photon. Rev.* 7, L67–L70 (2013).
4. P. Cheben, P. J. Bock, J. H. Schmid, J. Lapointe, S. Janz, D.-X. Xu, A. Densmore, A. Delâge, B. Lamontagne, and T. J. Hall, "Refractive index engineering with subwavelength gratings for efficient microphotonic couplers and planar waveguide multiplexers" *Opt. Lett.* 35, 2526-2528 (2010).

# Inverse dispersion engineering in integrated waveguides

**D. Castelló-Lurbe**[1,*], **V. Torres-Company**[2], **and E. Silvestre**[3]

[1]Photonics Team (B-PHOT), Department of Applied Physics and Photonics (IR-TONA), Vrije Universiteit Brussel, Belgium

[2]Department of Microtechnology and Nanoscience (MC2), Chalmers University of Technology, Sweden

[3]Departament d'Òptica, Universitat de València, Spain

[*]david.castello-lurbe@vub.ac.be

**Abstract**— We present a differential tool to find the cross-section geometry of integrated waveguides that matches a target dispersion profile. Our approach is more efficient than usual trial-and-error procedures, particularly for geometries with several degrees of freedom. By applying our strategy, we find several ultraflattened dispersion curves over 350 nm bandwidth in a silicon-on-insulator waveguide in less than 10 iterations.

On-chip integration of optical functionalities traditionally developed in fiber is a very active research field nowadays. Integrated waveguides are key components to carry out such functions. Typically, their material constituents possess very different refractive indices. This high index contrast makes their geometries significantly affect the physical properties of these waveguides. It allows engineering waveguide's features like effective refractive index, dispersion or nonlinear coefficient by means of suitable designs of the cross section. Nevertheless, it is not straighforward to evaluate the impact of geometrical changes on these properties. Indeed, these tasks are often based on the systematic numerical calculation of the property of interest, *e.g.*, the dispersion, for a huge number of configurations [1]. Consequently, this strategy becomes time-consuming when the cross section have two or more degrees of freedom. Therefore, alternative approaches that improve the efficiency of the design are highly desirable.

Gradient-based algorithms is one of the preferred optimization methods if the derivatives of the property to be optimized are available [2]. Firstly, a suitable merit function that quantify the similarity between the target feature and that shown by a particular configuration is defined. Secondly, a local approximation of the merit function in the parameter space must be calculated somehow. Finally, the point in the parameter space (close to the initial point to keep the local approximation valid) where the merit function becomes minimum is selected as a new starting point. This procedure can be iterated until achieving the target (provided it can be reached). Our approach belongs to this class of optimization methods. Particularly, the points in the parameter space, $p$, represent different configurations in our case. Furthermore, we present a proposal to evaluate the above derivatives in high-index-contrast waveguides that removes numerical inaccuracies related to their tight light confinement.

Here we are interested in the waveguide's dispersion, $\beta_2 = \partial^2_\omega \beta$, where $\beta$ is the propagation constant of a waveguide mode. We define the local approximation of our merit function as

$$\chi^2(p;p_{(\mathrm{m})}) = \frac{1}{N_\omega}\sum_{k=1}^{N_\omega}\Big(\big[\beta_2(p_{(m)};\omega) + \partial_p\beta_2(p_{(m)};\omega)\cdot(p-p_{(m)})\big] - \beta_2^{\mathrm{target}}(\omega_k)\Big)^2. \tag{1}$$

Note that a linear approximation of $\beta_2$ in the parameter space is explicitly included inside the squared brackets. If $\chi^2$ becomes minimum at $p_{(\mathrm{m}+1)}$, then $p_{(\mathrm{m}+1)}$ represents a new configuration closer to the target and the procedure can be repeated. Of course, Eq. (1) assumes $\partial_p\beta_2$ is known. We propose to evaluate $\partial_p\beta_2 = \partial^2_\omega(\partial_p\beta)$ based on

$$\partial_p\beta = \frac{\varepsilon_0\omega}{2}\frac{\displaystyle\int_S\left((\partial_p\varepsilon^{-1}_{nn})d_n^2 - (\partial_p\varepsilon_{TT})e_T^2 + (\partial_p\varepsilon_{zz})e_z^2\right)\mathrm{d}S}{\displaystyle -\int_S(\mathbf{e}_\mathrm{t}\times\mathbf{h}_\mathrm{t})\cdot\hat{\mathbf{z}}\,\mathrm{d}S}, \tag{2}$$

where $d_n$ is the component of the electric displacement field normal to the interface, $e_T$ is the component of the electric field tangent to the interface in the transverse plane, $\mathbf{e}_\mathrm{t}$ and $\mathbf{h}_\mathrm{t}$ indicate

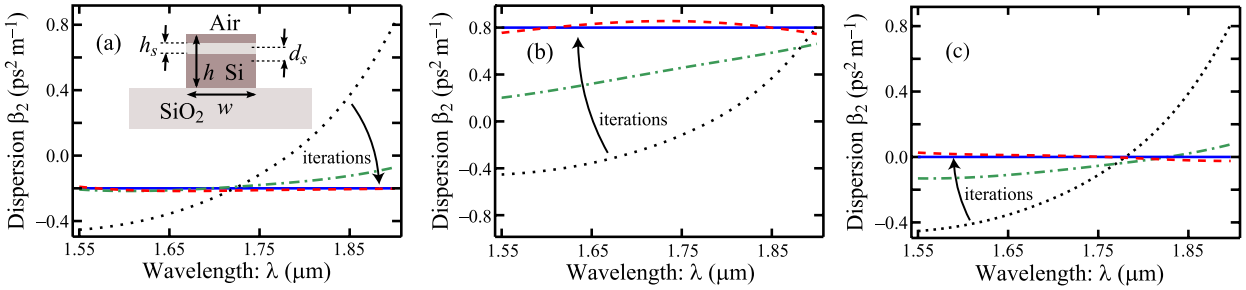



Figure 1: Three examples of optimization starting from the same geometry (dotted black curve) and with three different flattened dispersion profiles as a goal (solid blue line): (a) $\beta_2 = -0.2\,\mathrm{ps^2m^{-1}}$, (b) $\beta_2 = 0.8\,\mathrm{ps^2m^{-1}}$, and (c) $\beta_2 = 0$. The inset in (a) represents the cross-section of the waveguide.

the transverse components of the electric and magnetic fied, respectively, and $\varepsilon$ represents the permittivity tensor. It must be evaluated at several frequencies $\omega$ to compute numerically its second derivative with respect to $\omega$. It is worth noting that $\partial_p\beta$ does not depend on $\partial_p e$, where $e$ is the electric field. This result corresponds to a generalization of the Hellmann-Feynman theorem for nonself-adjoint operators [3]. From a practical point of view, it allows us to calculate $\partial_p\beta$ by means of the mode fields at $p$ (no additional calculations at $p + \delta p$ are required). Furthermore, Eq. (2) takes explicitly into account the vectorial nature of the mode fields through the axial term $(\partial_p\epsilon_{zz})e_z^2$, that is imperative in high-index-contrast waveguides. Moreover, it deals with $d_n$ instead of $e_n$ to avoid numerical inaccuracies related to the abrupt transition of $e_n$ around interfaces in high-index-contrast waveguides [4].

To illustrate our inverse dispersion engineering approach, we consider in Fig. 1 several target dispersion profiles in a cross section with four degrees of freedom [see inset in Fig. 1(a)]. It corresponds to a strip silicon waveguide with a silica slot [1]. Starting from a dispersion profile far from the targets, our algorithm finds in less than 10 iterations dispersions in close agreement to the targets. Note that these targets range from low negative dispersion, see Fig. 1(a), to high normal dispersion, see Fig. 1(b), also including zero dispersion, see Fig. 1(c). We also emphasize that despite we have targeted notably different dispersion curves, the number of iterations does not vary significantly with the target. Of course, the targets can be recovered to different extent [compare Fig. 1 (a) with Fig. 1 (b)] and it also depends on the geometry that is considered. From this point of view, our algorithm becomes a tool to check, in an efficient way, the capabilities of the available geometry for offering the dispersion curve that is required by an application.

In conclusion, we have proposed an inverse dispersion engineering approach that improves the efficiency of design tasks, particularly when trial-and-error procedures become time-consuming. It relies on the calculation of the gradient of the propagation constant with respect to all geometrical parameters by means of the analysis of only one geometry. It allows us to modify simultaneously all degrees of freedom of the structure to shape progressively the dispersion profile towards the target.

## ACKNOWLEDGMENT

This work has been financially supported by the Spanish Government (research project TEC2013-46643-C2-1-R) and by the Generalitat Valenciana (grant PROMETEO II/2014/072). V. T.-C. acknowledges funding from the Swedish Research Council (VR). D. C.-L. gratefully acknowledges funding from the ERC-FP7/2007-2013 grant 336940.

## REFERENCES

1. L. Zhang, *et al.*, Flattened dispersion in silicon slot waveguides, *Opt. Express* Vol. 18, No. 19 20529–20534, 2010.
2. W. H. Press, *et al.*, Numerical Recipes, 3rd ed. (Cambridge, 2007).
3. E. Silvestre, *et al.*, Differential toolbox to shape dispersion behavior in photonic crystal fibers, *Opt. Lett.* Vol. 31, No. 9, 1190–1192, 2006.
4. D. Castelló-Lurbe, *et al.*, Inverse dispersion engineering in silicon waveguides, *J. Opt. Soc. Am. B*, Vol. 1, No. 8, 1829–1835, 2014.

# Photonic crystal slot cavities; high-sensitivity nanotweezers

**S. Hamed Mirsadeghi, Jonathan Massey-Allard, and Jeff F. Young**

Department of Physics and Astronomy, University of British Columbia, Canada
young@phas.ubc.ca

**Abstract**— A silicon photonic circuit, composed of grating couplers and waveguides coupled to a photonic crystal slot cavity, is designed and fabricated for optical trapping and sensing applications. Experiments with Au nanospheres and nanorods demonstrate that these devices can optically trap nanoparticles as small as thirty nanometers with sub-mW laser power. By modelling the time-series transmission data while single nanoparticles are trapped in the cavity, it is possible to quantify the size and anisotropy of the particles with nanometer precision.

Optical tweezers are invaluable sensing tools in biology and material sciences due to their ability to manipulate and study individual nanoscale objects in-situ in a non-contact manner [1]. To trap and sensitively study such objects below the diffraction limit without damaging them, one can harness the strong light confinement available in photonic crystal slot-cavities [2]. The small mode volume and high in-solvent Q of the modes supported by these slot-cavities make them excellent devices for trapping nanoparticles that are well below $100nm$ in size [3].

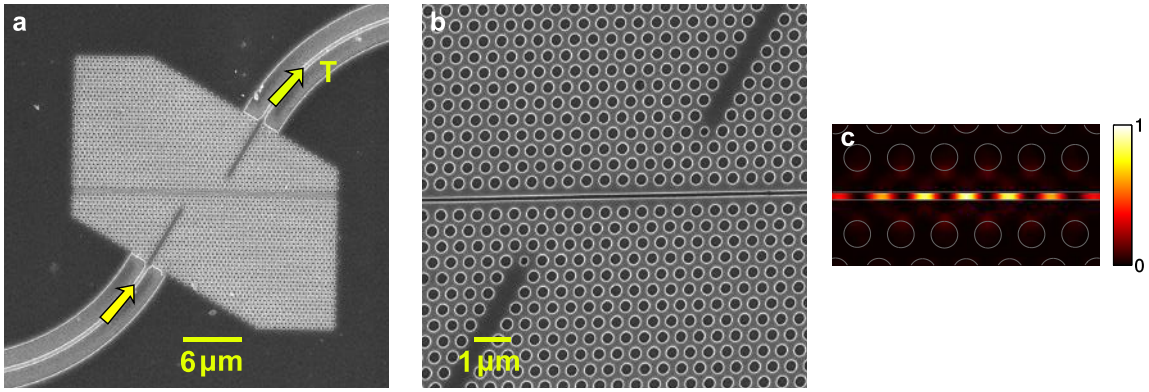



Figure 1: **a-b** Scanning electron microscope (SEM) images of a photonic crystal slot cavity used for optical trapping. Slot widths of different devices are in the range of 90-100nm. **c** Normalized electric field intensity profile of the cavity mode, showing the strong light confinement at the center of the slot.

Fig. 1a-b shows the SEM image of a fabricated photonic crystal slot-cavity along with its simulated electric field intensity profile. Once we immerse a device in a solution of Au nanoparticles, the transmission through the photonic circuit changes every time a particle is transiently trapped in the cavity (Fig. 2a). The Brownian motion of the trapped particle causes a shift in the resonance of the cavity and therefore changes the amount of light that gets transmitted through the cavity at the laser wavelength. This process called "backaction"[4] results in high amplitude fluctuations in the transmission signal. The histogram representing the transmission signal (Fig. 2b) during a trapping event can be modelled to extract the particle size and shape. Fig. 3a-c demonstrate 3 different experimental histograms associated with 3 distinct trapping events of Au nanorods at the same laser power and wavelength. These histograms are fit with a statistical model that self-consistently calculates the trapping potential energy (including backaction) when a particle of a certain shape and size moves (via both translation and rotation) in the trap. The nanorod sizes extracted using this method agree with measurements based on scanning electron microscope (SEM) images of the particles.

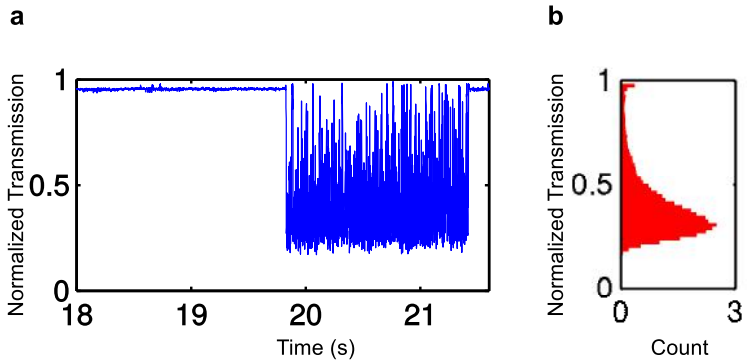



Figure 2: **a** A normalized experimental transmission signal of a 90 nm slot width device exhibiting large fluctuations when a nanosphere is transiently trapped in the cavity. For all trapping experiments, the injected laser power in the input ridge waveguide is less than a $0.5mW$. **b** Histogram corresponding to the distribution of transmission signal amplitudes during the transient trapping event.

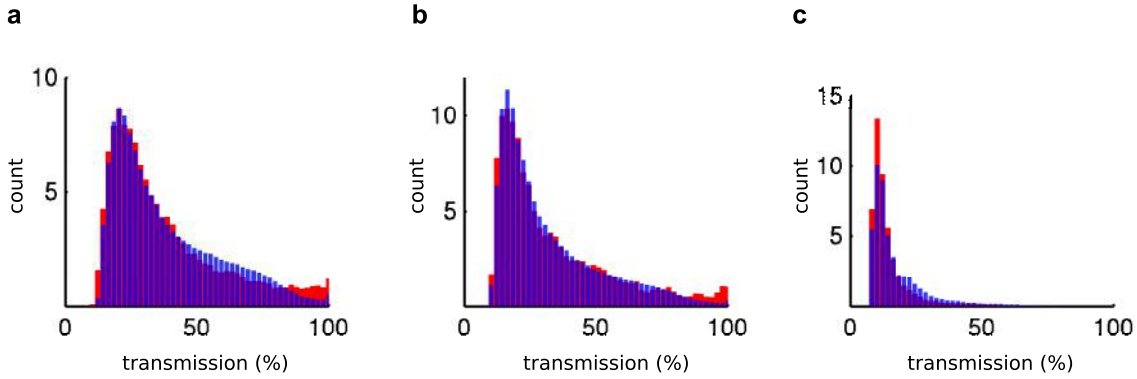



Figure 3: **a-c** 3 different experimental (red) histograms of Au nanorod trapping events are illustrated along with their fits (blue). The estimated nanoparticle sizes ($\pm 1nm$ uncertainty) based on the fits are $12nm \times 47nm$, $13nm \times 48nm$ and $35.1nm \times 35.3nm$ respectively.

In conclusion, a slot cavity-based nanotweezer is introduced that can trap Au nanoparticles, as small as $30nm$ at sub-mW power. We demonstrate not only excellent nanoscale trapping capabilities, but also a rigorous model of the devices' transmission signal that allows for highly sensitive measurements of both the size and anisotropy of trapped particles.

## ACKNOWLEDGMENT

The authors acknowledge financial support from the Natural Science and Engineering Research Council (Canada) and thank Dr. Lukas Chrostowski and Richard Bojko, as part of this work was conducted at the University of Washington Microfabrication/Nanotechnology User Facility, a member of the NSF National Nanotechnology Infrastructure Network. Computational support was provided by Lumerical Solutions Inc. and grid-enabled computational resources were provided by WestGrid.

## REFERENCES

1. Ashkin, A., J. M. Dziedzic, J. E. Bjorkholm, and S. Chu, "Self-induced back-action optical trapping of dielectric nanoparticles," *Opt. Lett.***11**, 288–290, 1986.
2. Mirsadeghi, S. H., E. Schelew and J. F. Young, "Photonic crystal slot-microcavity circuit implemented in silicon-on-insulator: High Q operation in solvent without undercutting," *App. Phy. Lett.* **102**, 131115–131115-4, 2013.
3. Mirsadeghi, S. H. and J. F. Young, "Ultrasensitive Diagnostic analysis of Au nanoparticles optically trapped in silicon photonic circuits at sub-milliwatt powers," *Nano Lett.* **14 (9)**, 5004–5009, 2014.
4. Juan, M. L., R. Gordon, Y. Pang, F. Eftekhari and R. Quidant, "Self-induced back-action optical trapping of dielectric nanoparticles," *Nat. Phys.* **5**, 915–919, 2009.

# High-efficiency single etch step surface grating couplers engineered by subwavelength structured metamaterials

**D. Benedikovic[1,*], C. Alonso-Ramos[1], L. Vivien[1]**
**P. Cheben[2], J. H. Schmid[2], S. Wang[2], D.-X. Xu[2], B. Lamontagne[2], J. Lapointe[2], S. Janz[2]**
**R. Halir[3], A. Ortega-Moñux[3], J.-G. Wangüemert-Pérez[3], I. Molina-Fernández[3]**
**J.-M. Fédéli[4]**
**M. Dado[5]**

[1]Institut d'Electronique Fondamentale, Université Paris Sud, CNRS, UMR 8622, Université Paris-Saclay, Bat. 220, Orsay Cedex, France
[2]National Research Council Canada, Information and Communication Technologies, Canada
[3]Dpto. de Ingeniería Comunicaciones, ETSI Telecomunicación, Universidad de Málaga, Spain
[4]CEA-LETI, Minatec, CEA-Grenoble, France
[5]University of Žilina, Department of Telecommunications and Multimedia, Slovakia
[*]daniel.benedikovic@u-psud.fr

**Abstract**-We report our recent developments of high-efficiency fiber-chip surface grating couplers engineered by subwavelength grating structuration. The intriguing technological concept of subwavelength grating index engineering provides extraordinary degree of freedom in designing and fabricating high-performance optical coupling interfaces for sub-micrometric silicon-on-insulator technology. We present an overview of various demonstrations of high-efficiency surface grating couplers, particularly develop for silicon photonics applications in the near-infrared spectral range (near 1.3 μm and 1.55 μm wavelengths) such as datacom and telecom optical interconnects.

Efficient optical coupling interfaces are one of the key building blocks in photonics integrated circuitry. Coupling of light to and from microphotonic waveguides has been recognized as a major practical challenge since the early years of integrated optics. The coupling is particularly difficult for silicon-on-insulator technology, since the cross-sectional area of silicon waveguides is more than two orders of magnitude smaller than that of a standard single-mode fiber. The surface grating couplers are an effective approach to circumvent this issue [1-5].

We have demonstrated by theory and experiments a series of subwavelength refractive index engineered surface grating couplers that require only a one fabrication step of lithography patterning and reactive ion etching, while providing the state-of-the-art coupling performance [2-5]. Specifically, we have reported various apodized grating couplers with an optimized directionality, with a coupling efficiency of up to -2.2 dB and -2.5 dB for wavelengths near 1.55 and 1.3 μm, respectively [2-4]. The grating couplers were implemented in a standard 220-nm-thick silicon-on-insulator substrates, as typically offered by silicon photonics foundries. In addition, a sub-decibel fiber-chip coupling efficiency of -0.7 dB has been experimentally realized for the first time in 220-nm silicon-on-insulator waveguides by utilizing the complementary metal-oxide-semiconductor-compatible manufacturing via backside processing [5].

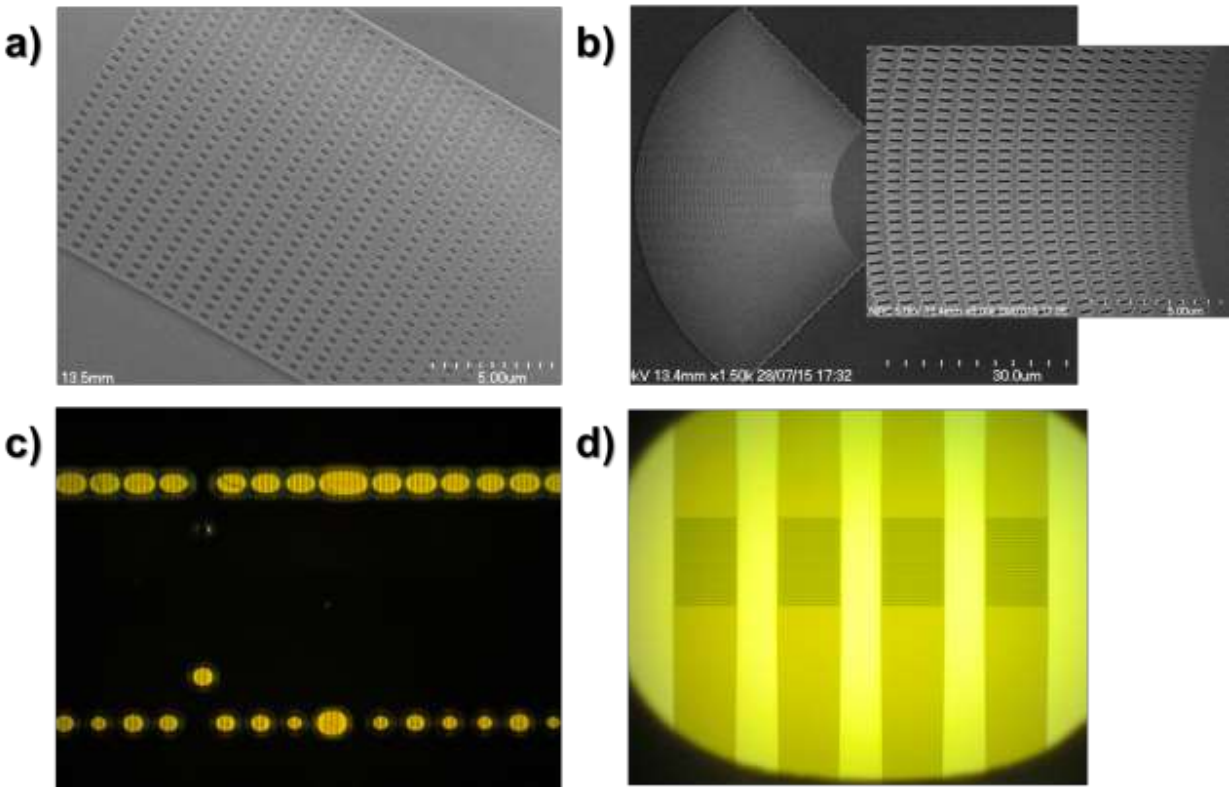



**Figure:** Single-etch apodized surface grating couplers in (a) linearly-tapered and (b) curved layout configurations, and subwavelength grating nanostructure inside the trenches. (c) Optical micrograph image of the surface grating couplers layout with metal reflector underneath. (d) Detail view of the surface grating coupler with metal reflector.

**REFERENCES**


1. Halir, R., et al., "Waveguide sub-wavelength structures: a review of principles and applications," *Laser Photon Rev*, Vol. 9, No. 1, 25–49, 2015.
2. Benedikovic, D., et al., "High-efficiency single etch step apodized surface grating coupler using subwavelength structure," *Laser Photon Rev*, Vol. 8, No. 6, 93–97, 2014.
3. Benedikovic, D., et al., "High-efficiency fully etched fiber-chip grating couplers with subwavelength structures for datacom and telecom applications," *Proc. of SPIE: OPTICS AND OPTOELECTRONICS*, Integrated Optics: Physics and Simulations II, Vol. 9516, 95160I–1 – 95160I-9, Prague, Czech Republic, 2015.
4. Benedikovic, D., et al., "Single-etch subwavelength engineered fiber-chip grating couplers for 1.3 μm datacom wavelength band," *Opt. Express*, (to be submitted), 2016.
5. Benedikovic, D., et al., "Subwavelength index engineered surface grating coupler with sub-decibel efficiency for 220-nm silicon-on-insulator waveguides," *Opt. Express*, Vol. 23, No. 17, 22628–22635, 2015.

# On leakage losses in subwavelength grating devices

**J. D. Sarmiento-Merenguel**[1], **A. Ortega-Moñux**[1], **J-M. Fédéli**[2], **J. G. Wangüemert-Pérez**[1], **C. Alonso-Ramos**[3], **E. Durán-Valdeiglesias**[3], **P. Cheben**[4], **Í. Molina-Fernández**[1], **R. Halir** [1]

[1] Universidad de Málaga, Dept. de Ingeniería de Comunicaciones, ETSI Telecomunicación, Campus de Teatinos s/n, 29071 Málaga, España, Spain

[2] Institut d'Electronique Fondamentale, Université Paris Sud, CNRS, UMR 8622, Université Paris-Saclay, Bât. 220, 91405 Orsay Cedex, France

[3] CEA, LETI, Minatec Campus, 38054 Grenoble, France

[4] National Research Council of Canada, Ottawa, K1A 0R6, Canada

jdsm@ic.uma.com

**Abstract**— Subwavelength gratings (SWGs) are periodic structures with a pitch small enough to suppress diffraction effects. SWG waveguides are lossless in theory, but implementations in the SOI platform have shown that they can exhibit additional losses, coming from the leakage to the substrate. This work provides the first thorough analysis of leakage losses in SWG waveguides, establishing a direct relation between the synthesized effective index of the guided mode and its leakage losses. This relation is furthermore shown to be independent of the geometrical parameters that define the SWG waveguide. We numerically and experimentally demonstrate this relation and provide simple design guidelines to avoid excessive leakage losses. Thus, for a BOX thickness of 2 (3) $\mu$m we found negligible leakage losses when the synthesized effective index is higher than 1.65 (1.55).

SWG waveguides are z-periodic structures, consisting of interleaved segments of two different materials with different refractive indexes as shown in Fig. 1.a. In SWG waveguides light propagates through the excitation of the Bloch-Floquets modes, which are theoretically lossless [1], as are the modes excited in a conventional waveguide. SWG approaches have enabled tolerant fiber-chip edge couplers, high efficiency gratings couplers, high-performance MMI design, among others [2, 3]. However, SWG designs hold a drawback: as the modal confinement diminishes in comparison to the silicon wire, the leakage losses become an important factor to take into account. The rigorous calculation of this leakage losses can be rather challenging in periodic structures as it is required to include the substrate into the simulation. An alternative to ease the design process is based on considering that the BOX layer is infinite, thus ignoring the substrate. For this purpose, an estimation of the leakage losses as a function of the effective index, which can be easily obtained, is however required. In this contribution we provide a solution to estimate the leakage losses in SWG waveguides, for the SOI platform, providing a relation between leakage losses and effective index. This relation is numerically and experimentally demonstrated, and fits an exponential curve, which is completely independent of the geometrical parameters defining the SWG waveguide.

To investigate the relation between effective index and leakage losses, we have performed a complete set of simulations, considering the geometrical parameters that define the SWG waveguide: pitch ($\Lambda$), duty cycle (DC), width (W), height (H) and the thickness of the BOX layer ($t_{BOX}$), as shown in Fig.1.a. In this study we only consider TE polarization operating in the wavelength range $1.5 - 1.6\ \mu m$, for two different BOX thicknesses, 2 and 3 $\mu m$. These simulations have been performed using FEXEN, our in-house Fourier-type 2D vectorial simulation tool [4]. Note that, as we continuously check that the SWG waveguide is working far from the Bragg regime, there are no back-reflections and the only source of propagation losses is the leakage to the substrate. Plotting the effective index versus leakage losses for all combination of geometrical parameters (except $t_{BOX}$) yields a virtually perfect fit to an exponential curve, and each $t_{BOX}$ value fixes a different exponential curve. Thus, given the value of $t_{BOX}$, leakage losses will only depend on the synthesized effective index, regardless the SWG geometrical parameters. For the most common BOX thickness of 2 and 3 $\mu$m, negligible leakage losses are found when the effective index is higher than 1.65 and 1.55, respectively. Since we obtain group index instead of the effective index from the measurements, we have also studied the relation between leakage losses and group index, which is also found to fit an exponential curve.

To experimentally demonstrate this relation, different SWG waveguides, whose nominal height and width are 220 nm $\times$ 450 nm, were fabricated in the Silicon-On-Insulator platform, with a $SiO_2$

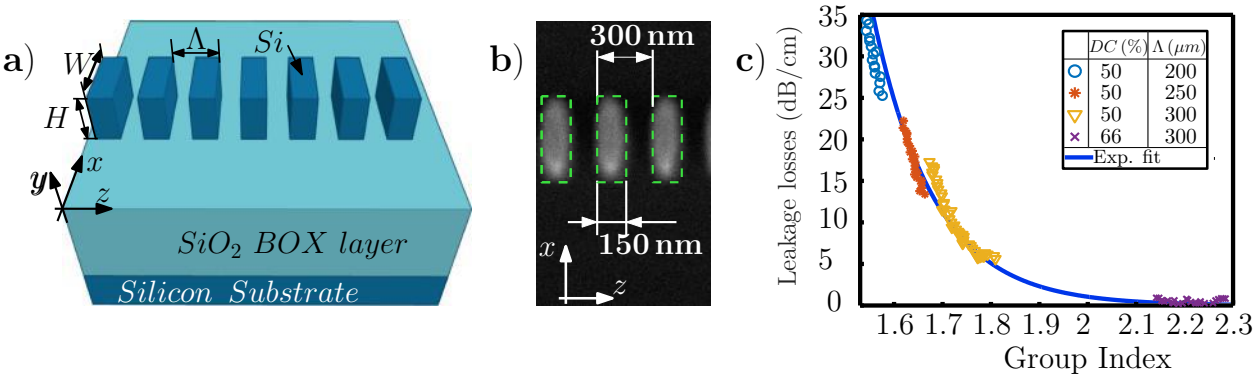



Figure 1: a) Schematic geometry of the SWG waveguide, the upper cladding is not shown. b) Top view scanning electron microscope (SEM) image of a fabricated SWG waveguide. c) Measured leakage losses vs group index for different waveguides, sweeping the wavelength in the range [1.5-1.6] $\mu$m.

BOX of 2 $\mu$m. Figure 1.b shows the top view of a fabricated waveguide. These waveguides have been overexposed during the etching process, so that as the duty cycle becomes smaller, leakage losses become significant. However, we have realized that this over-exposition also erodes the silicon segment, increasing the propagation losses. For both group index and leakage losses to be measured, SWG waveguides have been placed in one of the arms of a Mach-Zehnder Interferometer (MZI), while in the other arm a silicon photonic wire is placed. Thus, through the interferogram of this structure, information about the difference of losses and group index between the two waveguidess have been obtained. Raw measurement gives differential values of leakage losses and group index. Therefore we have estimated the group index of the silicon wire through simulation, which has been found to be around 4.2 for the measured wavelength range. Referring to the leakage losses, it has been assumed that they are negligible for $n_g^{SWG} > 2.2$. For this waveguide the measured differential losses were found to be around 5 dB/cm, which is attributed to the roughness due to the aggressive etching and the radiation losses coming from the silicon wire to SWG waveguide tapers. Figure 1.c shows the result of the measurements, after their processing. This figure shows the relation between group index and losses for every SWG waveguide, as a function of the wavelength, which fits an exponential curve, as predicted numerically.

The results provided in this contribution constitute a simple and easy approach to estimate SWG waveguide leakage losses for the SOI platform, allowing designers to estimate leakage losses from the synthesized effective index, which enables the simulation of SWG structures considering and infinite BOX.

## ACKNOWLEDGMENT

Ministerio de Economía y Competitividad, "Programa Estatal de Investigación, Desarrollo e Innovación Orientada a los Retos de la Sociedad (cofinan. FEDER)", Proyecto TEC2013-46917-C2-1-R.

## REFERENCES

1. P. J. Bock, P. Cheben, J. H. Schmid, J. Lapointe, A. Delâge, S. Janz, G. C. Aers, D.-X. Xu, A. Densmore, and T. J. Hall, "Subwavelength grating periodic structures in silicon-on-insulator: a new type of microphotonic waveguide," *Opt. Express*, Vol. 18, No. 19, 20251-20262, 2010.
2. R. Halir, P. J. Bock, P. Cheben, A. Ortega-Moñux, C. Alonso-Ramos, J. H. Schmid, J. Lapointe, D.-X. Xu, J. G. Wangüemert-Pérez, Í. Molina-Fernández *et al.*, "Waveguide subwavelength structures: a review of principles and applications," *Laser & Photonics Reviews*, Vol. 9, No. 5, 25–49, 2015.
3. V. Donzella, A. Sherwali, J. Flueckiger, S. T. Fard, S. M. Grist, and L. Chrostowski, "Subwavelength grating components for integrated optics applications on soi chips," *Opt. Express*, Vol. 22, No. 17, 21037–21050, 2014.
4. L. Zavargo-Peche, A. Ortega-Moñux, J. G. Wangüemert-Pérez, and Í. Molina-Fernández, "Fourier based combined techniques to design novel sub-wavelength optical integrated devices," *Progress In Electromagnetics Research*, Vol. 123, 447–465, 2012.

# Sub-wavelength engineered high directionality fiber-to-chip blazed grating couplers

**C. Alonso-Ramos[1,*], D. Benedikovic[1], P. Cheben[2], D. Pérez-Galacho[1], J. H. Schmid[2], S. Wang[2], D.-X. Xu[2], B. Lamontagne[2], J. Lapointe[2], S. Janz[2], R. Halir[3], A. Ortega-Moñux[3], J.-G. Wangüemert-Pérez[3], I. Molina-Fernández[3], J.-M. Fédéli[4], M. Dado[5], E. Cassan[1], D. Marris-Morini[1] and L. Vivien[1].**

[1]Institut d'Electronique Fondamentale, Université Paris Sud, CNRS, UMR 8622, Université Paris-Saclay, Bat. 220, Orsay Cedex, France

[2]National Research Council Canada, Information and Communication Technologies, Canada

[3]Dpto. de Ingeniería Comunicaciones, ETSI Telecomunicación, Universidad de Málaga, Spain

[4]CEA-LETI, Minatec, CEA-Grenoble, France

[5]University of Žilina, Department of Telecommunications and Multimedia, Slovakia

[*]carlos.ramos@u-psud.fr

**Abstract**- We report on development of fiber-chip grating couplers that exploit the blazing effect by interleaving standard full and shallow etch trenches in the silicon layer. Utilizing this concept, grating directionality in excess of 90% can be achieved independent of bottom oxide thickness, obviating the need of high-index overlays or bottom mirrors. The coupler also includes a subwavelength-engineered index matching region, designed to reduce the reflectivity at the interface between the injection waveguide and the grating. Blazed grating coupler fabricated in 220-nm thick Si platform demonstrated a remarkably large fiber-chip coupling efficiency of -1.3 dB at 1550 nm wavelength.

Silicon-on-insulator (SOI) offers an unprecedented miniaturization capability and unique potential compatibility with complementary metal-oxide-semiconductor (CMOS) technology. Unfortunately, the typically small waveguide cross-sectional area enabled by the high refractive index contrast poses a serious challenge for coupling light to and from external ports. Grating couplers are a promising solution that provide robust alignment tolerances and allow wafer-scale device testing [1]. The efficiency of such couplers is mainly limited by back reflections, mode mismatch between the radiated field and the optical fiber mode, and power loss due to radiation to the substrate. The back reflections and mode-mismatch limitations can be alleviated by apodization based on subwavelength grating (metamaterial) engineered structures [2]. However reducing power loss to the substrate requires the implementation of comparatively complex techniques like high-index overlays or bottom reflectors.

We have recently shown that by interleaving the standard full (220 nm) and shallow etch (70 nm) trenches in a 220 nm thick silicon layer, power loss to the substrate can be reduced below 5%, independent of the bottom oxide thickness [3,4]. The high-directionality is obtained by controlling the separation between the deep and shallow trenches to achieve constructive interference in the upward direction and destructive interference towards the silicon substrate. The coupler also includes a short index matching region with a grating strength controlled by subwavelength grating index engineering (Fig. 1), designed to reduce the reflectivity at the interface between the injection waveguide and the grating region. Interestingly, the interleaved grating approach

can be applied in other SOI platforms that employ different Si and BOX layers thicknesses or etch depths, with dimensions tolerances within the typical range of control in silicon photonic foundries.

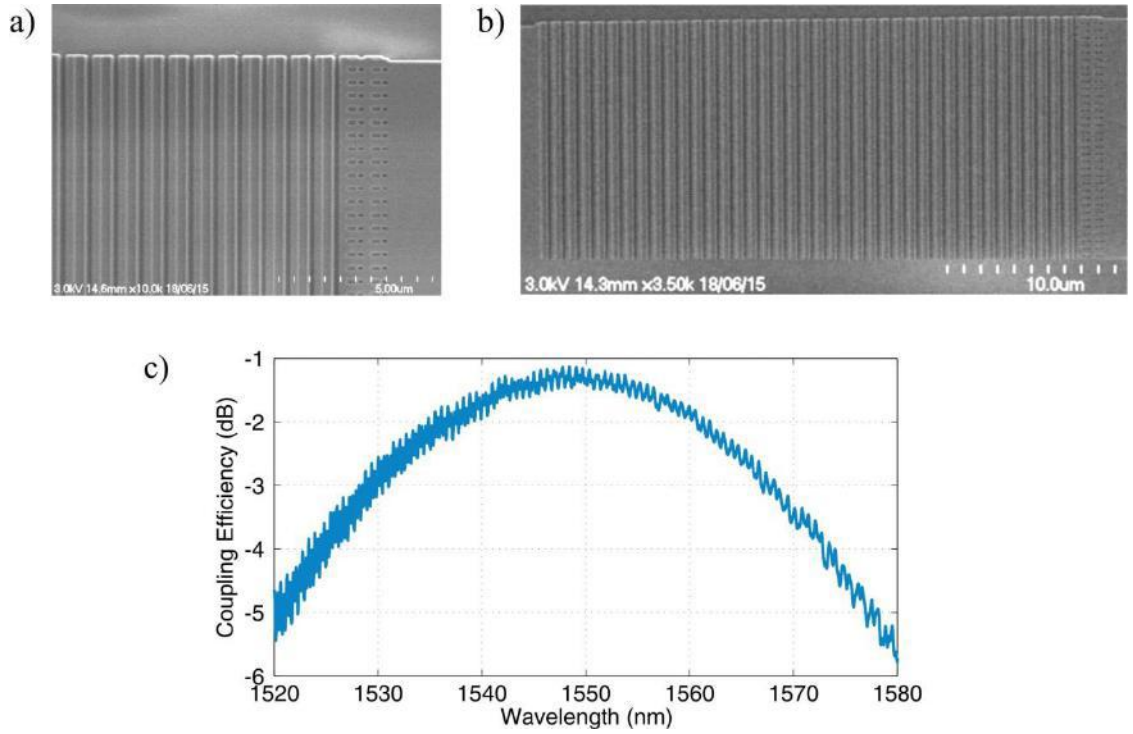



**Figure 1:** Scanning electron microscopy images of a) complete grating coupler and b) detail of the subwavelength grating index matching region. c) Measured coupling efficiency as a function of wavelength of dual-etch coupler with interleaved deep and shallow etched trenches.

**REFERENCES**


1. C. Gunn, "CMOS photonics for high-speed interconnects," IEEE Micro 26(2), 58-66, 2006.
2. R. Halir, et al., "Waveguide sub-wavelength structures: a review of principles and applications," Laser Photonic Reviews, Vol. 9, No. 1, 25–49, 2015.
3. C. Alonso-Ramos, et al., "Fiber-chip grating coupler based on interleaved trenches with directionality exceeding 95%," Optics Letters 39(18), 5351-5354, 2014.
4. D. Benedikovic, et al., "High-directionality fiber-chip grating coupler with interleaved trenches and subwavelength index-matching structure," Optics Letters 40(18), 4190-4193, 2015.

# Sub-wavelength cladded suspended silicon photonic components for the mid-infrared: fabrication and experiments

**M. Nedeljkovic[1], A. Ortega-Moñux[2], J. Soler Penadés[1], G. Wangüemert-Pérez[2], A. Z. Khokhar[1], R. Halir[2], Z. Qu[1], W. Cao[1], C. Mitchell[1], S. Stanković[1], F. Gardes[1], C. Alonso-Ramos[3], P. Cheben[4], and I. Molina-Fernández[2]**

[1]University of Southampton, United Kingdom
[2]ETSI Telecomunicación, Universidad de Málaga, Spain
[3]University of Paris Sud and CNRS, Paris, France
[4]National Research Council, Ottawa, Canada
E-mail: m.nedeljkovic@soton.ac.uk

**Abstract**- We report on development of a library of silicon membrane based photonic integrated circuits operating at the mid-infrared wavelength of 3.8 μm. Waveguides are formed with a lateral cladding consisting of etched sub-wavelength grating holes, which allow wet etching of the underlying buried oxide layer and formation of a suspended waveguide core. Experimental realizations of low-loss waveguides, bends, s-bends, and multimode interferometers in the platform will be presented. Our recent work on mid-infrared devices in silicon-on-insulator and germanium-on-silicon will also be discussed.

The mid-infrared (MIR) wavelength range (here defined as 2-14 μm) is of great interest for many applications such as environmental monitoring, toxic chemical detection, and industrial process control, because many gases and chemicals have clearly distinct MIR absorption spectra. New material platforms that have wide transparency windows in this range are required for the creation of photonic integrated circuits for sensing. For example, silicon-on-insulator (SOI) uses a $SiO_2$ lower cladding layer that absorbs light in much of the MIR. We have developed a library of components in a suspended silicon material platform where the $SiO_2$ layer is removed, which is expected to allow full use of silicon's transparency range (approximately 1.1-8 μm) [1, 2].

These components are based on waveguides in which the lateral cladding is formed by a sub-wavelength grating made by etching through the top Si layer and exposing the underlying buried oxide (BOX) layer. This lateral cladding serves three simultaneous functions: 1) it creates an area with lower refractive index than the Si waveguide core for optical confinement; 2) the grating holes enable buffered hydrofluoric acid (HF) to reach the BOX and thus remove it from underneath the waveguide; 3) the un-etched Si in the grating provides mechanical support for the Si waveguide core, creating a suspended membrane. Low loss suspended waveguides, bends, s-bends, and 2x2 multimode interferometers will be presented.

Progress on SOI and germanium-on-silicon photonic components that offer access to an even wider MIR range will also be discussed.

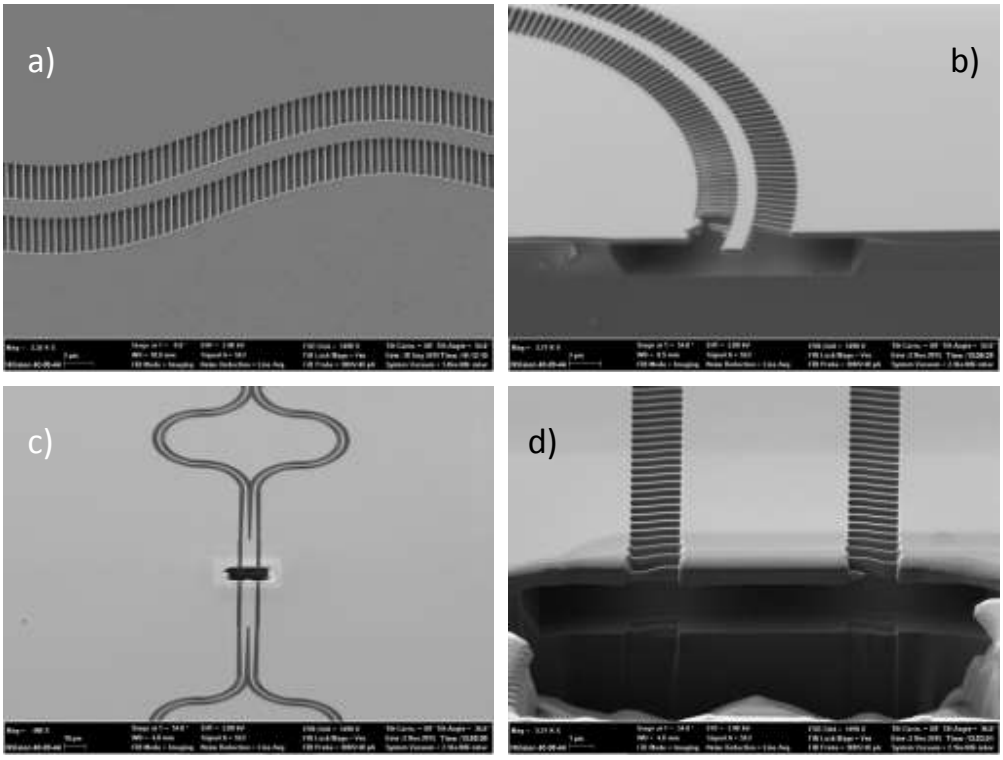



**Figure 1:** Scanning electron microscope images of passive silicon membrane devices with subwavelength grating lateral cladding: a) S-bend, b) cleaved facet showing suspended bend, c) multimode interference (MMI) coupler where a hole has been made using a focused ion beam (FIB), and d) close-up view of the FIB-made cross-section in the same device, showing that the structure is suspended.

**REFERENCES**

1. J. Soler Penades et al., "Suspended SOI waveguide with sub-wavelength grating cladding for mid-infrared," Optics Letters, pp. 5661-5664 (2014).
2. J. S. Penades et al., IEEE Group IV Photonics Conference (2015).

# Sub-wavelength Grating Components for the Silicon-on-insulator Platform

**Yun Wang**[1], **Jonas Flueckiger**[2], **Zeqin Lu**[1], **Han Yun**[1], **Minglei Ma**[1], **Fan Zhang**[1], **Valentina Donzella**[1,3], **Nicolas A. F. Jaeger**[1], **and Lukas Chrostowski**[1]

[1]University of British Columbia, Canada
[2]Lumerical Solutions Inc., Canada
[3]WMG, University of Warwick, UK
yunw@ece.ubc.ca

**Abstract**— Sub-wavelength structures introduce new flexibility to engineer the index and dispersion properties of silicon-on-insulator (SOI) photonic devices [1]. In this paper, we present four types of sub-wavelength grating enabled devices for the SOI platform, including a broadband sub-wavelength grating coupler, a broadband sub-wavelength directional coupler, a sub-wavelength polarization splitter-rotator, and a sub-wavelength microring resonator.

Grating couplers find wide applications in silicon-on-insulator (SOI) photonic integrated circuits (PICs). The insertion loss (IL) and bandwidth are the two most important figures of merit for a grating coupler. Sub-wavelength gratings (SWGs) have been used in grating couplers to engineer the index profile of the grating couplers to achieve high coupling efficiencies. Sub-wavelength grating couplers (SWGCs) with sub-dB ILs have been demonstrated [2, 3]. Bandwidth is the other important figure of merit for a grating coupler. We found the expression for the 1-dB bandwidth, $\Delta\lambda_{1dB}$, of a grating coupler, as a function of its wavelength dependent diffraction angle, $\theta$, and its group index, $n_g$, to be [4]:

$$\Delta\lambda_{1dB} = \Delta\theta_{1dB} \cdot 2\left|\frac{-\, n_c \cdot cos(\theta) \cdot \lambda}{n_g - n_c \cdot sin(\theta)}\right| \tag{1}$$

where $\Delta\theta_{1dB}$ is a constant that depends on the fiber parameters and $n_c$ is the refractive index of the cladding. From Eq. 1, we can see that the bandwidth of a grating coupler can be improved by reducing $n_g$. We used SWGs to obtain both the high and low index regions in our SWGC, so that both the effective index and dispersion of the grating were reduced. Therefore, a smaller $n_g$ was obtained. Following the methodology shown in [4], we demonstrated broadband SWGCs with $\Delta\lambda_{1dB}$ ranging from 50nm to 90nm.

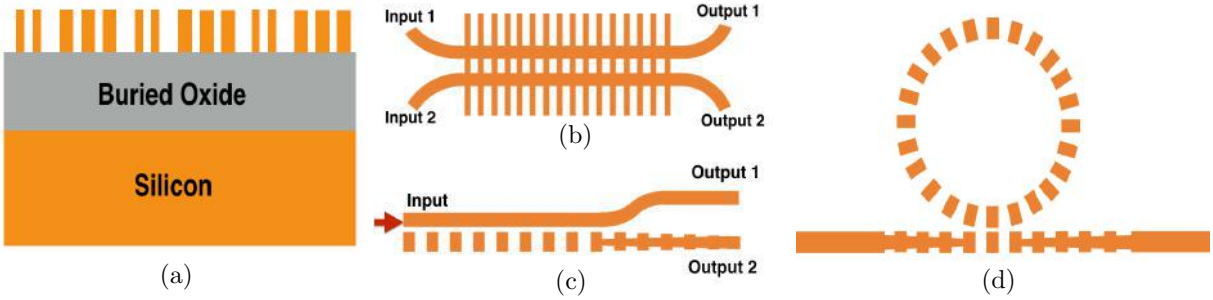



Figure 1: Schematic of (a) cross-section of an SWGC, (b) a SWG directional coupler, (c) a SWG polarization splitter-rotator, and (d) a SWG microring resonator.

Directional couplers are essential components in PICs and are used to couple light between waveguides. Directional couplers are typically compact, but when compact they are found to be very sensitive to wavelength and polarization, with a low tolerance to fabrication errors. SWGs have been used to engineer the dispersion properties of traditional directional couplers [5, 6], so that a broad operating bandwidth can be achieved. We have designed and fabricated broadband SWG directional couplers with various power splitting ratios for an SOI wafer with a 220nm silicon layer. A finite-difference time-domain (FDTD) method was used to calculate the band structure

of the SWG directional coupler, where the material dispersion of the structure has been included. Following our design methodology, we fabricated and measured SWG directional couplers with power splitting ratios of 50/50, 40/60, 30/70, and 20/80, that have operation bandwidths of 100nm and device lengths less than 15µm.

Polarization splitter-rotators (PSRs) are key components in polarization diversity systems. PSRs using asymmetrical directional couplers are, again, typically compact in size, but the compactness again, makes them sensitive to waveguide dimension variations. It has been proposed to use an SWG waveguide in a directional coupler-based PSR to obtain better tolerance to waveguide dimension variations [7]. However, the taper and S bend waveguide used in the proposed design were much larger than the PSR itself, which significantly increases the overall size of the proposed device. We designed and fabricated an SWG PSR with a TM-to-TE polarization conversion loss of 0.45dB and an overall device length of 34µm. To achieve the compact design, we first designed a compact, high efficiency taper to connect the SWG waveguide and the strip waveguide, which has length of 9µm with an IL less than 0.01dB. Then we used an FDTD based band structure calculation to obtain the dimensions of the SWG waveguide and the length of the PSR, which includes the material dispersion in the design process for a more accurate calculation.

Silicon microring resonators have been extensively investigated as biosensors, with the advantages of design simplicity and ease of fabrication [8]. Due to the high index contrast in such mirroring sensors, optical modes can be highly confined to the sub-micron waveguides, with portions of the electric field extending outside the silicon. The electric field outside the waveguide is sensitive to external refractive index changes. This sensitivity to external refractive index changes allows microrings to be used in applications such as biosensing. The sensitivity of a biosensor is determined by the overlap of the external electric field with the analyte. By replacing a conventional strip waveguide based microring resonator with an SWG based ring resonator, the effective refractive index of the waveguide can be reduced so that the optical modes are less confined within the silicon. Therefore, the overlap of the electrical field and the analyte can be increased and the sensitivity can be improved. We have designed and fabricated a 30µm diameter SWG waveguide-based microring resonator, which has a Q factor of $7 \cdot 10^3$, a bulk sensitivity of 490nm/RIU, and a system limit of detection of $2{\cdot}10^{-6}$ RIU. These SWG based sensors demonstrated the highest sensitivity performance of any waveguide-based sensor on the same SOI platform.

In conclusion, many conventional components in silicon photonic circuits can be replaced with SWG-based components, resulting in tailored response improved performance.

## ACKNOWLEDGMENT

This work was supported by the Natural Sciences and Engineering Research Council of Canada (NSERC), including the NSERC CREATE SiEPIC program. The devices were fabricated by Washington Nanofabrication Facility at the University of Washington, part of the National Science Foundations National Nanotechnology Infrastructure Network. We acknowledge Lumerical Solutions, Inc., and Mentor Graphics for the design software.

## REFERENCES

1. R. Halir, et al., "Waveguide sub-wavelength structures: a review of principles and applications", *Laser Photonics Rev.* , Vol. 9, No. 1, 25–49, 2015.
2. Y. Ding, et al., "Fully etched apodized grating coupler on the SOI platform with -0.58 dB coupling efficiency," *Opt. Lett.* , Vol. 39, No. 18, 5348–5350, 2014.
3. D. Benedikovic, et al., "Subwavelength index engineered surface grating coupler with sub-decibel efficiency for 220-nm silicon-on-insulator waveguides," *Opt. Express* , Vol. 23, No. 17, 22628–22635, 2015.
4. Y. Wang, et al., "Design of broadband subwavelength grating couplers with low back reflection," *Opt. Lett.* , Vol. 40, No. 20, 4647–4650, 2015.
5. R. Halir, et al., "Colorless directional coupler with dispersion engineered sub-wavelength structure," *Opt. Express* , Vol. 20, No. 12, 13470–13477, 2012.
6. V. Donzella, et al.,"Sub-wavelength grating components for integrated optics applications on SOI chips," *Opt. Express* , Vol. 22, No. 17, 21037–21050, 2014.
7. Y. Xiong, et al., "Polarization splitter and rotator with subwavelength grating for enhanced fabrication tolerance," *Opt. Lett.* , Vol. 39, No. 24, 6931–6934, 2014.
8. V. Donzella, et al., "Design and fabrication of SOI micro-ring resonators based on sub-wavelength grating waveguides" *Opt. Express* , Vol. 23, No. 4, 4791–4803, 2015.

# High efficiency, ultra-broadband fiber-to-chip coupler based on subwavelength gratings

**A. Sánchez-Postigo**[1], **A. Ortega-Moñux**[1], **J. M. Luque-González**[1], **C. Alonso-Ramos**[2], **R. Halir**[1], **J. H. Schmid**[3], **P. Cheben**[3], **J. G. Wangüemert-Pérez**[1] **and Í. Molina-Fernández**[1]

[1]Universidad de Málaga, ETSI Telecomunicación, Spain
[2]Université Paris-Sud, Institut d'Electronique Fondamentale, France
[3]National Research Council, Ottawa, Canada
asp@ic.uma.es

**Abstract**— A new grating coupler is presented to overcome the natural limitation in bandwidth that conventional grating couplers exhibit. By using subwavelength structures, the effective index of the grating waveguide can be engineered to enlarge the bandwidth. Our proposed grating coupler achieves a 3-dB bandwidth of about 200 nm. A sub-decibel coupling efficiency (below -0.3 dB) is accomplished.

The silicon-on-insulator (SOI) platform has become one of the most promising platforms for developing integrated optical devices. Its high index contrast, together with its compatibility with the CMOS fabrication processes, make it very attractive for achieving large scale photonic integration [1]. Nonetheless, the coupling of light between the photonic chip, with submicron dimensions, and the optical fiber, whose dimensions are of tens of microns, is still an important challenge. Two different solutions are usually employed: facet (edge) coupling and surface grating coupling. When testing at a wafer-scale, grating couplers are the preferred solution [2]. They are based on a periodic perturbation applied to a conventional waveguide, so that there is a phase matching between the effective index of its Bloch-Floquet mode and the plane wave of the upper cladding [3]. There are novel designs in the bibliography with which is possible to attain subdecibel coupling efficiencies [4]. However, all of them exhibit a limited operating bandwidth of about 60 nm for a 3 dB penalty.

In this paper we present an ultra-broadband sub-decibel grating coupler based on subwavelength structures. We have achieved a 3-dB broadband operation of around 200 nm, while the peak coupling efficiency is lower than $-0.3$ dB.

## ACKNOWLEDGMENT

This work has been funded by the Spanish Ministerio de Economía y Competitividad (MINECO) under project TEC2013-46917-C2-1-R. The first author is a Formación de Profesorado Universitario (FPU) scholarship holder by the Spanish Ministerio de Educación, Cultura y Deportes (MECD).

## REFERENCES

1. Soref, R., "The past, present, and future of silicon photonics", *IEEE J. Sel. Top. Quant.*, Vol. 12, No. 6, 1678–1687, 2006.
2. Van Laere, F., et al., "Compact and Highly Efficient Grating Couplers Between Optical Fiber and Nanophotonic Waveguides", *J. Lightwave Technol.*, Vol. 25, 151–156, 2007.
3. Tamir, T. and Peng, S. T., "Analysis and design of grating couplers", *App. Phys.*, Vol. 14, No. 3, 235–254, 1986.
4. Benedikovic, D. et al., "Subwavelength index engineered surface grating coupler with sub-decibel efficiency for 220-nm silicon-on-insulator waveguides", *Opt. Express*, Vol. 23, 22628–22635, 2015.

# Recent advancements towards all-optical signal processing.

**I. Glesk[1*], J. Wang[2], and L. Chen[2]**

[1]Electronic and Electrical Engineering Dept, University of Strathclyde, 204 George St, Glasgow, G1 1XW, UK

[2] Electrical and Computer Engineering Dept, McGill University, 480 University St, Montreal, H3A 0E9, Canada

[*]corresponding author: ivan.glesk@strath.ac.uk

**Abstract**-Recent years have seen a rapid growth in demand for ultra high speed data transmission with end users expecting fast, high bandwidth network access. However as data rates increase, present technology based on well-established CMOS electronics is becoming increasingly difficult to scale and consequently optical data networks are struggling to satisfy current user demands. Recently a number of advanced approaches have been reported developed to overcome this bottleneck based on all optical signal processing using silicon photonics devices.

It is becoming evident that the fundamental limits on electronic switching speeds are becoming severely affecting data communications both quantitatively and qualitatively. At present time we do not have any technological solution for immediate implementation to overcome this problem. However, to mitigate this problem a number of approaches have been proposed. One such approach has been the introduction of all-optical processing schemes. It has been also shown that optical signal processing can improve latency, connectivity and scalability of optical networks and interconnects, but undoubtedly its technological implementations are still required to further improve existing processing speed and to take full advantage of the potential serial data rates increases optical networks can offer and support. The requirement for a new disruptive technology is therefore inevitable. Namely, a development of a photonic transistor enabling superfast switching speeds and being compatible with CMOS fabrication techniques would allow much cheaper solutions than developing an all new fabrication technology. Silicon photonics devices can be fabricated using present CMOS fabrication techniques and therefore this technology has been under the microscope for possibilities to develop the future optical signal processing systems.

However, a key missing elements for developing the all-optical CPU are a silicon photonic transistor and its supporting optical interconnect technology which is necessary to carry out logic operations and provide the necessary buffering and timing. Some progress in these tasks has been reported and several research groups have been successful in demonstrating what one day may become possible future solutions to this great challenge. For example, Chen et al have demonstrated an optical transistor where a single stored gate photon can control the transmission of applied source photons [1]. However, the transistor is clearly not compatible with CMOS fabrication and since it requires three lasers for the gate and source, and lasers to allow super-cooling of the cesium gas, it is unlikely to provide a practical solution in the foreseeable future. Note, he terms ‘gate’ and ‘source’ are used as an analogue to the CMOS FET transistor terminology. Another approach reported by Varghese et al is the development of a silicon optical transistor which uses an asymmetric coupled add/drop filter consisting of a micro-ring resonator next to an optical waveguide representing the source [2]. The device is reported to operate at 10GHz. A notable advantage of this technology is compatibility with current state of the art CMOS fabrication techniques allowing scalability and avoiding the need to develop new fabrication techniques from the ground up. However it is clear that the development of the optical CPU and the all-optical

data signal processing is still in the very distant future.

Given a future where networks will need to perform ultra-high speed serial data processing all optically there will be basic requirements for all optical Mux/DeMux devices capable of performing at speeds well beyond that are available today.

To overcome the current electronic bottleneck Glesk et al developed a CMOS compatible ultrafast all optical photonic switch [3-4] which does not suffer from the currier recovery time limitations affecting all optical switches based on Semiconductor Optical Amplifiers, SOAs [5] demonstrated previously. This all optical photonic switch has a Mach-Zehnder interferometric structure with one arm composed of a Si nanowire. The second arm is a subwavelength waveguide grating (SWG) structure. Tapered sections are added to properly balance device properties and the loss to help achieve complete interferometric switching.

But there is also a need to develop a library of integrated devices for performing a variety of supporting all optical signal processing functions supporting its application in data centers and elsewhere. One key function required is an efficient wavelength filtering. By taking advantage of the ability to tailor the effective index of SWG waveguides, Wang et al [6] proposed a CMOS compatible type of integrated filtering device (which can also provide an Add/Drop functionality) based on combination of SWG waveguides and ring resonators. The biggest advantage for these SWG Bragg grating filtering devices is that the peak reflection wavelength can be tuned very easily by adjusting the duty cycle of the SWG. Optical fibre networks have a vast potential data handling capacity. However this capability is becoming severely limited by serial data processing speed abilities of currently available CMOS electronics. Speed-up using parallel signal processing is confounded by the fundamental limits of Amdahl's Law. This scenario will soon hinder the ability of data networks to scale up to meet exponentially increasing demand for capacity. While all-optical wavelength routing can help improve data network throughput, ultimately at network endpoints any such improvement will be choked by fundamentally limited CMOS electronic signal processing capabilities. Therefore there is a need for the development of a disruptive technology to overcome this bottleneck. A promising candidate is all-optical signal processing. Progress has been made in the development of CMOC compatible photonic devices necessary to achieve this goal. However any further progress depends on speedy development of ultrafast "all-optical transistor" based photonic logic gates.

**REFERENCES**


1. Chen, W., "All-Optical Switch and Transistor Gated by One Stored Photon," *Science,* Vol. 341, No. 6147, 68-770, 2013.
2. Varghese, L., "A Silicon Optical Transistor," in *Frontiers in Optics 2012/Laser Science XXVIII,* OSA Technical Digest (online) (Optical Society of America, 2012), paper FW6C.6.
3. Glesk, I., Bock, P. J., Cheben, P., Schmid, J. H., Lapointe, J. and Janz, S., "All-optical switching using nonlinear subwavelength Mach-Zehnder on Silicon," *Optics Exp.*, Vol. 19, No. 15, 14031-14039, 2011.
4. I. Glesk, I., Bock, P. J., Cheben, P., Schmid, J. H., Lapointe, J. and Janz, S., "Picosecond all-optical switching using nonlinear Mach-Zehnder with silicon subwavelength grating and photonic wire arms," *Optical and Quantum Electron.*, Vol. 44, No. 12, 613-621, 2012. Invited paper.
5. Sokoloff, J. P., Prucnal, P. R., Glesk, I. and Kane, M., "A terahertz optical asymmetric demultiplexer (TOAD)," *IEEE Photon. Tech. Lett.*, Vol. 5, No. 7, 787-790, 1993.
6. Wang, J., Glesk, I. and Chen, L., "Subwavelength grating filtering devices," *Optics Exp.,* Vol. 22, No. 13, 15335-15345, 2014.

# Subwavelength structures in silicon-on-insulator waveguides for efficient and broadband fiber-chip coupling

**J.H. Schmid, P. Cheben, D.-X. Xu, S. Janz, J. Lapointe, M. Rahim, S. Wang, M. Vachon, R. Halir, A. Ortega-Moñux, G. Wangüemert-Pérez, I. Molina-Fernández, J. Pond, D. Benedikovic, Y. Painchaud, M.-J. Picard, M. Poulin, M. Dado, J. Müllerová, W.N. Ye, M. Pápeš and V. Vašinek**

National Research Council, Ottawa, Canada
ETSI Telecomunicación, Universidad de Málaga, Spain
Lumerical, Inc., Vancouver, Canada
University of Paris Sud and CNRS, Paris, France
University of Žilina, Slovak Republic
Ciena, Québec, Canada
Carleton University, Canada
VSB – Technical University of Ostrava, Czech Republic
E-mail: jens.schmid@nrc-cnrc.gc.ca

**Abstract**- We report our results in developing highly efficient and broadband fiber-chip couplers for silicon photonic wire waveguides using subwavelength engineered metamaterial structures. We experimentally demonstrate a subwavelength structure with a coupling efficiency of -0.4 dB and polarization independent operation for a broad spectral range exceeding 100 nm for optical fiber with a core diameter of 3.2 μm. For coupling to standard SMF-28 fiber with 10.4 μm mode field diameter we numerically demonstrate a subwavelength engineered overlayer structure composed of $SiO_2$ and $Si_3N_4$ which exhibits an overall coupling efficiency exceeding 90%.

Efficient input and output coupling interfaces between silicon photonic chip and optical fiber or lasers are a fundamental prerequisite for successful implementations of such photonic chips for processing, modulating and detecting light. We present an optimized design of a metamaterial subwavelength grating (SWG) nanocoupler and demonstrate that SWG couplers can outperform inverse taper couplers in efficiency and polarization dependent loss. Specifically, we report on the design and experimental demonstration of an SWG coupler with a loss of 0.4 dB and negligible polarization dependence fabricated on a silicon-on-insulator chip with a standard 220 nm silicon thickness and silicon dioxide cladding [1]. We first designed the cross section of the metamaterial taper tip such that a mode size with maximum overlap with an optical fiber mode of diameter 3.2 μm is achieved. The subwavelength coupler tip is connected to the silicon wire waveguide with an adiabatic mode size transformation section to assure a smooth low-loss transition from the mode of a photonic wire to the Bloch mode of a periodic SWG waveguide. In this section, the effective index of the waveguide mode is modified by gradually changing the grating duty ratio from about 0.5 at the coupler tip to 1 at the junction with the silicon wire. The structure is shown in the SEM micrographs in Fig. 1. We also report coupling to a buried heterostructure laser operating at 1.3 μm with a coupling loss of 1.5 dB.

To avoid optical loss due to substrate leakage, for coupling to the larger mode size of standard SMF-28 fiber, we have

developed a silicon taper coupler with a $SiO_2$-$Si_3N_4$ overlayer structure incorporating a SWG in the $Si_3N_4$ to achieve low loss mode conversion. The cross section of the overlayer structure, which serves to pull the optical mode up away from the substrate as is expands is shown near the facet in Fig. 2. We present numerical calculations of the mode evolution with 3D-FDTD simulations, which demonstrate an overall coupling efficiency >90%.

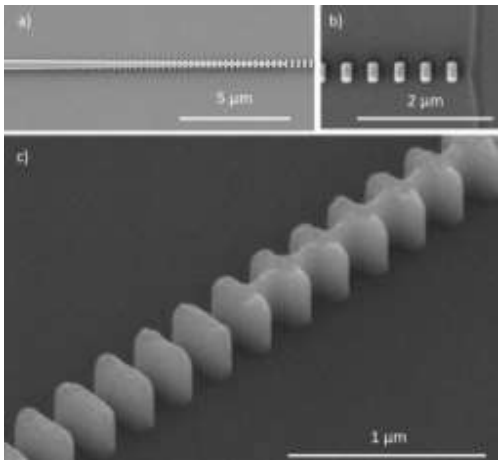



**Figure 1:** (a) SEM image of the nanocoupler, (b) detail view of the coupler tip and (c) intermediate section positioned at 15 µm from the junction with silicon wire waveguide.

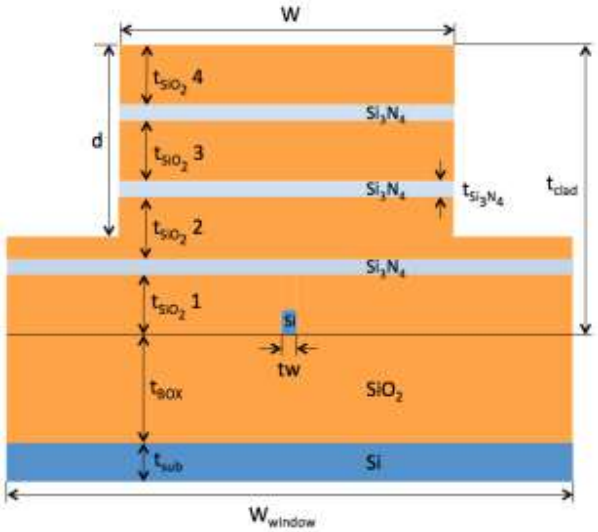



**Figure 2:** Cross-section schematics of the $SiO_2$-$Si_3N_4$ overlayer coupler design near the chip facet.

**REFERENCES**


1. P. Cheben et al., *Optics Express*, Vol. 23, 22553-22563 (2015).
2. M. Papes et al., *Optics Express*, submitted.

# Design of integrated photonic devices based on subwavelength structures for Near and Mid-Infrared applications

**A. Ortega-Moñux[1], J. G. Wangüemert-Pérez[1], R. Halir[1] and I. Molina-Fernández[1]**
**J. Soler Penadés[2], M. Nedeljkovic[2], A. Z. Khokhar[2], Z. Qu[2], W. Cao[2], C. Mitchell[2], S. Stanković[2], F. Gardes[2], G.Z. Mashanovich[2], C. Alonso-Ramos[3] and P. Cheben[4]**

[1] ETSI Telecomunicación, Universidad de Málaga, Spain
[2] University of Southampton, United Kingdom
[3] University of Paris Sud and CNRS, Paris, France
[4] National Research Council, Ottawa, Canada
E-mail: aom@ic.uma.es

**Abstract**- We report our progress in the design of high performance devices using subwavelength grating (SWG) structures for the NIR and the MIR wavelength ranges. We mainly focus on the development of a library of basic components based on a novel type of suspended silicon waveguide with SWG lateral cladding for MIR applications.

Silicon photonics is nowadays one of the leading technological platforms for the development of high performance Photonic Integrated Circuits (PICs) at telecommunication and datacom wavelengths (1.55μm and 1.3μm respectively) [1]. A conventional waveguide fabricated on the silicon-on-insulator (SOI) platform is basically composed of a high refractive index silicon core ($n_{Si}$ ~3.5) placed over a thick, low refractive index silicon dioxide layer ($n_{SiO2}$ ~1.45). The top cladding is usually air or any other compatible low index material, such as $SiO_2$ or SU8 polymer ($n_{SU8}$ = 1.58). Since SOI is a very high contrast platform (Δn ~2), single mode operation requires submicron waveguide cores. These waveguides are usually called photonic-wires (PW) and they allow for the integration of very compact devices and systems (e.g. losses for a 5μm 90º bend are typically below 0.01dB/bend). The extraordinary success of silicon photonics can be justified taking into account: 1) the potential of an extremely high integration density, 2) the compatibility with some of the very well-known CMOS fabrication processes and 3) the recent advances in the development of high speed photodetectors and optical modulators.

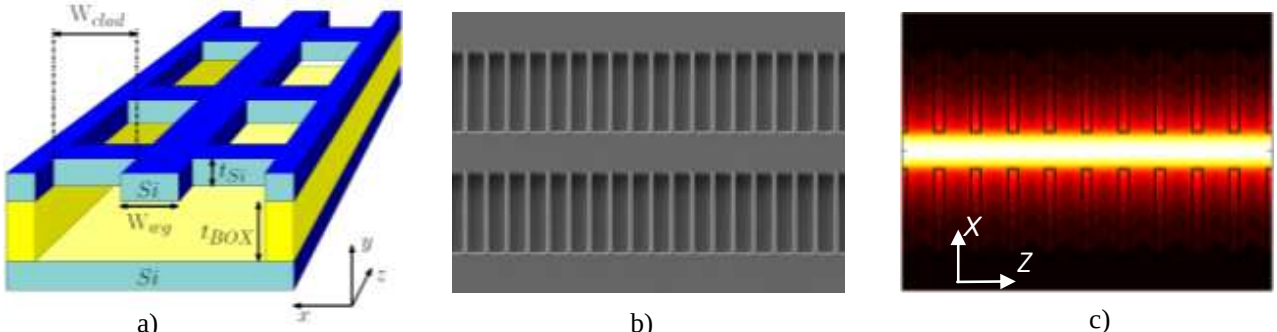
On the other hand, the use of a properly designed pattern of holes in the Si layer at a subwavelength scale allows for the implementation of artificial materials with arbitrary refractive index and/or specific dispersion properties [2-6]. These subwavelength grating (SWG) structures can be used in combination with conventional waveguides, thus providing to the designer an additional degree of freedom. The applications of SWG structures in the near-infrared (NIR) band are huge: low loss waveguides and crossings, highly efficient fiber-to-chip couplers, evanescent field sensors, ultra-broadband couplers, optimized transceiver hybrids, planar lenses, etc. [4].

Although much of the research in silicon photonics has been focused on the NIR wavelengths, the potential of this platform for the mid-infrared (MIR) band has lately attracted the attention of the scientific community. It must be highlighted that many gases have specific absorption peaks in the MIR band (2μm -20μm), thus

allowing a myriad of sensing applications: environmental pollution monitoring, homeland security, chemical detection or medical diagnostics [7-9]. Since the wavelength in the MIR band is longer than in the NIR, the potential of SWG design techniques at MIR is much higher (because the subwavelength condition is more easily fulfilled) and additionally, fabrication tolerances are much more relaxed.

The main limitation for using the SOI platform beyond 4μm comes from the $SiO_2$ layer, since this material is very lossy for longer wavelengths. To overcome this limitation, a new type of suspended waveguide, where the $SiO_2$ layer is removed, has been recently proposed, thus extending the operation range of the SOI platform up to the transparency limit of the Si (8μm) [10]. The suspended waveguide (see Fig. 1) is composed on a homogeneous Si core with a lateral SWG cladding which implements three different functions: 1) It enables the flow of the hydrofluoric acid (HF) through the Si layer to remove the $SiO_2$, 2) it mechanically supports the Si core, 3) it provides the lateral refractive index contrast necessary for guiding.

In this work we will describe our advances in the design of optimized SWG based devices at the NIR and the MIR wavelength ranges. We will focus on our most recent results: the development of a library of basic components for the aforementioned suspended waveguide platform for MIR applications.




a) b) c)

**Figure 1:** Suspended waveguide with SWG lateral cladding. a) Schematic geometry, b) Scanning electron microscope image of one of the fabricated devices (top view), c) Simulated field propagation through a suspended waveguide (top view).


**ACKNOWLEDGMENTS**

Ministerio de Economía y Competitividad, "Programa Estatal de Investigación, Desarrollo e Innovación Orientada a los Retos de la Sociedad (cofinanciado FEDER)", Proyecto TEC2013-46917-C2-1-R.


**REFERENCES**


1. Reed, G. T., & Knights, A. P. *Silicon photonics: an introduction*. John Wiley & Sons (2004).
2. P. Cheben et al., *Optics Express*, Vol. 14, 4695-4702 (2006).
3. P. Cheben et al., *Optics Letters*, Vol. 35, 2526-2528 (2010).
4. R. Halir et al., *Laser and Photonics Reviews*, Vol. 9, 25-49 (2015).
5. A. Ortega-Moñux et al., *Laser and Photonics Reviews*, Vol. 7, L12-L15 (2013).
6. G. Wangüemert-Pérez et al., *Optics Letters*, Vol. 39, 4442-4445 (2014).
7. M. Nedeljkovic et al. *Opt. Mater. Express*, Vol. 3, 1205-1214 (2013).
8. R. A. Soref, et al., *J. Opt. A*, Vol. 8, 840-848 (2006).
9. R. Soref, *Nature Photonics*, Vol. 4, 495-497 (2010).
10. J. Soler Penades et al., *Optics Letters*, Vol. 39, 5661-5664 (2014).

# Homogenisation of sub-wavelength grating waveguides

**T. J. Hall**[1*]**, and H. Nikkhah**[1]

[1]Photonics Technology Laboratory, Centre for Research in Photonics, School of Electrical Engineering & Computer Science, University of Ottawa, Advanced Research Complex, 25 Templeton Street, Ottawa, Ontario K1N 6N5, Canada

[*]corresponding author: trevor.hall@uottawa.ca

**Abstract**- The design of sub-wavelength planar light structures is challenging because nanoscale simulation over the full device may be unreliable. Rather reliance must be placed on a simple homogenisation procedure that captures properties pertinent to the larger scale while smoothing over the smaller scale detail. A homogenisation approach is described that combines available tools with simple design rules to accurately model subwavelength grating waveguides even closed to Bragg resonance provided proper account is taken of temporal and spatial dispersion.

Growing technical capabilities of photonic integration with novel algorithms, architectures and components is making coherent photonic integrated circuit implementation practical; introducing a new and very interesting category of highly functional optical systems having wide application including data centre interconnect; wired and wireless communications, and quantum optics. Great care is required to control the phase of light propagation as performance of coherent circuits can be severely degraded by small imperfections of optical components. Subwavelength waveguide gratings (SWG) offer the opportunity to perfect components by engineering the dispersion and anisotropy of integrated components. SWG have been applied with great success to a wide variety of applications of Si photonics to radically reduce coupling loss, excess insertion loss and crosstalk; and to dramatically increase the operational bandwidth of components [1].

The photonic integrated circuit designer is fortunate to have access to a wide variety of software tools. The tools assist the design process by verifying through simulation the behaviour of a preliminary design. Some tools support automatic refinement of a design using an optimisation algorithm. However, the design problem is typically so complex that any automated optimisation can at best be accomplished starting from a good preliminary design. There is therefore no substitution for the intuition of the designer in an iterative design-verification cycle and the application of design rules to the formulation of the initial design. Simplifications of the theory backed up by experimental results are critical to the acquisition of intuition and the formulation of design rules.

Components exploiting SWGs have two disparate scales to their structure; one scale small and one scale large compared to the wavelength. This provides a challenge to the designer because no single software tool spans the two scales. The simulation of sub-wavelength nanostructure over scales of many wavelengths requires an abstraction of the properties of the nanostructure, which summarises its properties pertinent to the larger scale and smooths over the detail at the smaller scale. This abstraction is known as homogenisation.

There is a vast literature on homogenisation. Its classical roots are the Clausius-Mossotti equation that links the electrodynamics of continuous media to their atomic structure and the mixture formulae of Maxwell-Garnet for the constitutive parameters of composite materials. A resurgence of interest in homogenisation can be traced to an influential paper by Smith & Pendry [2], which pointed out that the electromagnetic fields in a PhC unit

cell may be calculated advantageously using commercial software tools.

An approach to homogenization that combines available software tools with simple design rules is presented. The problem controlling phase in coherent circuits is used to illustrate the application of the method and the intuition it can provide. The method can accurately model subwavelength grating waveguide even closed to Bragg resonance provided proper account is taken of temporal and spatial dispersion. A justification for the design rule is found from the exact theory by a judicious choice of approximations. The method may be extended to SWG that are periodic on the scale of a sub-wavelength lattice with parameters that vary on a scale larger than a wavelength. This enables a multi-scale approximation to be applied to the modelling of graded metamaterial components, such as a Lüneburg lens for waveguide cross-overs [3] and Fourier Optics on-a-chip [4], and the refractive index and geometrical tapers that permit SWG to interface with each other and with standard waveguides [5].

**REFERENCES**


1. Halir, R., P. J. Bock, P. Cheben, A. Ortega- Moñux, C. Alonso-Ramos, J. H. Schmid, J. Lapointe, D. X. Xu, J. G. Wangüemert-Pérez , Í. Molina-Fernández, S. Janz, "Waveguide sub-wavelength structures: a review of principles and applications," *Laser & Photonics Reviews*, Vol. 9, No. 1, 25-49, 2015.
2. Smith D. R. and J. B. Pendry, "Homogenization of metamaterials by field averaging (invited paper)," *J. Opt. Soc. Am. B*, Vol. 23, No. 3, 391-403, 2006.
3. Nikkhah, H. and T. J. Hall, "A transpose optical interconnect utilising metamaterial Luneburg waveguide lenses for switch fabric on-a-chip applications," *Proc. of SP*IE, Vol. 8627, art. 86270V, 2013.
4. Nikkhah, H. and T. Hall, "Metamaterial Lüneburg lens for Fourier optics on-a-chip," *Proc. SPIE* , Vol. 8988, art. 89880J, 2014
5. Nikkhah, H., and T. J. Hall, "Subwavelength Grating Waveguides for Integrated Photonics," *Appl. Phys. A*, Vol.122 No. 4, 368, 2016.

# Efficient optimization of subwavelength gratings for photonic integrated circuits

**J. Pond[1*], A. Liu[1], J. Niegemann[1], X. Wang[1] and P. Cheben[2]**
[1]Lumerical Solutions, Inc., Canada
[2]National Research Council, Canada
[*]corresponding author: jpond@lumerical.com

**Abstract**-Subwavelength gratings provide additional design flexibility compared to conventional waveguide-based devices and are particularly useful for applications such as mode conversion, wavelength selective mirrors and dispersion engineering. However, subwavelength grating structures have some design and manufacturing challenges, in part due to the small features which are near the diffraction limit of most optical lithography systems used for integrated photonics. We discuss methods to design and optimize these devices and provide specific examples of edge couplers and frequency selective mirrors.

Subwavelength gratings (SWGs) can provide important design flexibility for integrated photonic components and can be used for applications such as mode conversion, frequency selective mirrors and dispersion engineering [1-2], to name a few. However, SWGs have some design, simulation and manufacturing challenges due to the required small feature sizes when compared with conventional waveguide-based devices. With respect to simulation, the small features must be resolved by the simulation mesh which can make it challenging to simulate larger devices, let alone optimize them. With respect to manufacturing, the small features are close to the critical dimension of most optical lithography systems used for photonics, leading to geometric discrepancies between the manufactured and original design. Here we show how subwavelength devices can be efficiently optimized through two specific examples.

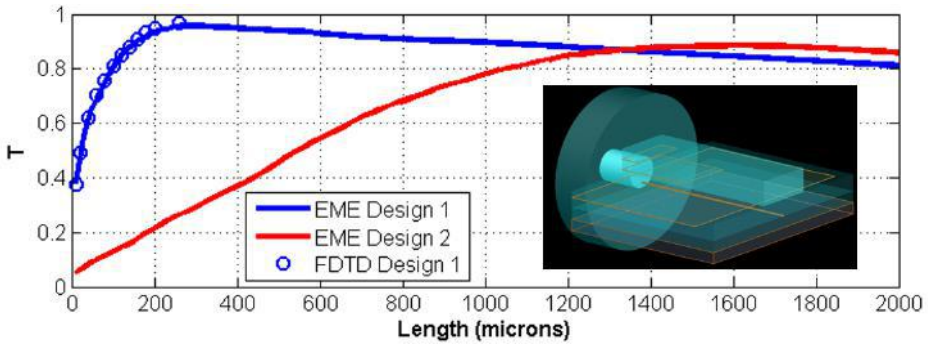



**Figure 1:** Comparison of the FDTD and EME transmittance for a fiber-chip edge coupler for a high numerical aperture fiber (Design 1), and EME results for an edge coupler for SMF-28 fiber (Design 2). A schematic view of the edge coupler is shown in the inset. The devices comprise two and three thin silicon nitride layers, respectively, which are patterned with a SWG to continuously vary the effective material index from silicon nitride to silicon dioxide. In these designs, the silicon waveguide is inversely tapered. Both designs are described in more detail in another publication [3].

Edge couplers using SWGs can achieve highly efficient, broadband mode conversion between optical fibers and silicon photonic waveguides [3-5]. An example device is shown in the inset of Figure 1, and uses SWG-

patterned thin silicon nitride layers to efficiently couple an SMF-28 fiber and a silicon waveguide [3]. We verify agreement between 3D FDTD and the eigenmode expansion method (EME), then show how the device can be optimized with EME in a very short simulation time (typically a few seconds), even for devices with lengths up to several millimeters as shown in Figure 1.

Waveguide Bragg gratings can be used for creating frequency selective mirrors with high reflectivity over a narrow bandwidth [6-8], which is useful for many applications including lasers [9]. The bandwidth of these devices is extremely sensitive to photolithography [10], and we show how to simulate these effects. We then show how finite sized mirrors and cavities can be simulated with EME and how the number of periods can be efficiently optimized for a target quality factor and peak transmission, as shown in Figure 2.

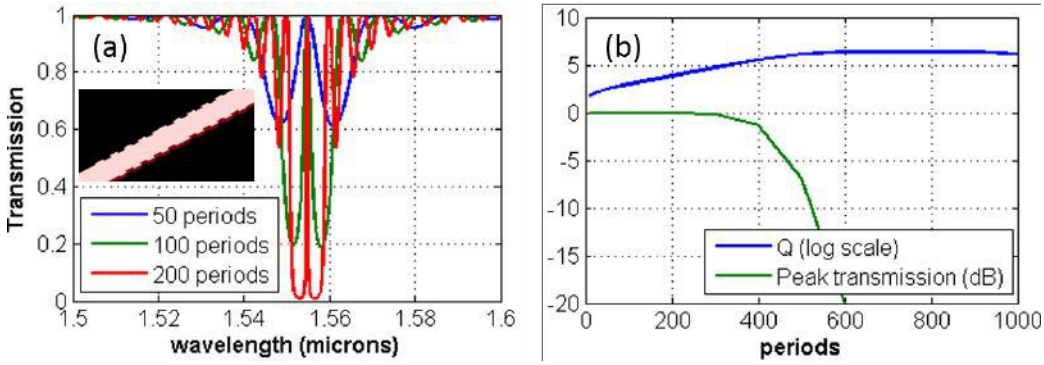



**Figure 2:** (a) The transmission spectrum for the waveguide Bragg grating cavity device (shown schematically in the inset) for different numbers of periods. (b) The quality factor and peak transmission at resonance as a function of the mirror periods.

## REFERENCES


1. Halir, R. *et al.*, "Waveguide sub-wavelength structures: a review of principles and applications," *Laser & Photonics Rev.*, Vol. 9, No. 1, 25-49, 2015.
2. Bock. P.J. *et al.*, "Subwavelength grating periodic structures in silicon-on-insulator: a new type of microphotonic waveguide," *Opt. Express*, Vol. 18, No. 19, 20251-2026, 2010.
3. Papes, M. *et al.*, "Fiber-chip edge coupler with large mode size for silicon photonic wire waveguides," *Opt. Express*, Vol. 24, No. 5, 5026–5038, 2016.
4. Barwicz, T. *et al.*, "An O-band metamaterial converter interfacing standard optical fibers to silicon nanophotonic waveguides," in *OFC, OSA technical Digest*, Los Angeles, USA, March 2015, Th3F.3.
5. Cheben, P. *et al.*, "Broadband polarization independent nanophotonic coupler for silicon waveguides with ultra-high efficiency," *Opt. Express*, Vol. 23, No. 17, 22553-22563, 2015.
6. Wang, X. et *al.*, "Lithography Simulation for the Fabrication of Silicon Photonic Devices with Deep-Ultraviolet Lithography", *IEEE Group IV Photonics (GFP)*, San Diego, USA, August 2012, 288-290.
7. Wang, X. *et al.*, "Narrow-band waveguide Bragg gratings on SOI wafers with CMOS-compatible fabrication process," *Opt. Express*, Vol. 20, No. 14, 15547-15558, 2012.
8. Wang, X. *et al.*, "Precise control of the coupling coefficient through destructive interference in silicon waveguide Bragg gratings," *Opt. Lett.*, Vol. 39, No. 19, 5519-5522, 2014.
9. Fang, A.W., *et al.*, "A Distributed Bragg Reflector Silicon Evanescent Laser," *IEEE Photon. Technol. Lett.*, Vol 20, No. 20, 1667-1669, 2008.
10. Pond, J. et al., "Design and optimization of photolithography friendly photonic components", Proc. SPIE 9751, Photonics West, San Francisco, USA, March 2016.

# Dielectric metasurfaces for beam shaping, mode matching and polarization selection

**Meir Grajower, Boris Desiatov, David Ohana, Jonathan Bar David, Noa Mazurski and Uriel Levy**

[1]Department of Applied Physics, The Benin School of Engineering and Computer Science, The Center for Nanoscience and Nanotechnology, The Hebrew University of Jerusalem, Jerusalem, 91904, Israel

*Corresponding author: ulevy@cc.huji.ac.il

**Abstract**-We present our recent results related to high index metasurfaces with applications in mode matching, beam shaping and polarization selectivity

While metallic metasurfaces are attracting growing attention, dielectric metasurfaces are a in fact a promising alternative primarily due to their lower losses, allowing to operate not only in reflection but also in transmission mode and even in an in plane propagation. Hereby, we present our recent results related to metasurfaces. Specifically, we describe an in plane propagation configuration allowing for light focusing and mode matching to take place. Furthermore, we present our results related to dielectric metasurfaces in transmission mode, with focus on the capability of achieving polarization selective beam shaping, whereby exchanging polarization states allows for displaying different images in the Fresnel domain.

# Silicon Nitride for Integrated Photonic Applications

**T. Domínguez Bucio[1*], A. Z. Al-Attili[1], K. Debnath[1], S. Saito[1], G. Mashanovich[1], A. Sánchez-Postigo[2], G. Wangüemert-Pérez[2], A. Ortega-Moñux[2], R. Halir[2], P. Cheben[3] and F. Y. Gardes[1]**

[1]University of Southampton, Optoelectronics Research Centre, UK

[2]University of Malaga, Spain

[3]National Research Council Canada

[*]Tdb2g12@soton.ac.uk

**Abstract**-Due to its flexible optical properties silicon nitride is an attractive material for integrated photonic circuits. In this paper, we review the results we have obtained on near-infrared photonic devices including low loss waveguides based on SiN layers deposited with low temperature PECVD using an ammonia-free chemistry. In particular, we discuss the fabrication of subwavelength suspended structures to extend the use of SiN to mid-infrared photonic devices.

Silicon nitride (SiN) is a CMOS compatible material that provides a wide range of possibilities for integrated photonics due to its flexible material composition that can be tuned to achieve the physical, chemical and optical properties required for different applications. In particular, the refractive index of SiN can be easily tailored to achieve tight optical confinement for densely integrated structures with low sensitivity to surface and sidewall roughness [1, 2]. Also, SiN has a high non-linear Kerr coefficient, which makes it a viable material for non-linear applications especially because it does not suffer from two-photon absorption in the near-infrared wavelengths [3]. Furthermore, SiN has an improved transparency window at visible and mid-infrared wavelengths [4], which are important for biosensing applications.

Under this context, we have studied the deposition of SiN using plasma enhanced chemical vapour deposition with an ammonia-free chemistry to fabricate films with low hydrogen content for multilayer platforms at maximum substrate temperatures of 350ºC. We have also designed and demonstrated a variety of photonic devices including low loss waveguides, splitters and MMIs working in the near-infrared spectral region. Specially, we have studied the fabrication of subwalength suspended structures that can potentially be used to extend the results obtained with the near-infrared devices to the mid-infrared spectral region. The demonstrated suspended structures can be used to fabricate photonic devices for communications and sensing applications, using a similar approach to non-suspended structures that have already been demonstrated using SiN in the visible wavelength region.

## REFERENCES

1. Daldosso, N. et al. “Comparison Among Various Si3N4 Waveguide Geometries Grown within a CMOS Fabrication Pilot Line,” *Mat. Sci. Semicon. Proc.*, Vol. 22, No. 7, 1734–1740, 2004.
2. Sacher, W. D. et al. “Multilayer Silicon Nitride-on-Silicon Integrated Photonic Platforms and Devices”, *J. Lightwave Technol*. Vol. 33, No. 4, 901-910, 2015.
3. Moss, D. J. et al. “New CMOS-compatible platforms based on silicon nitride and Hydex for nonlinear optics”, *Nature Photon*, Vol. 7, No. 8, 597-607, 2013.
4. Soref, R. “Mid-infrared photonics in silicon and germanium”, *Nature Photon*, Vol. 4, 495-497, 2010.

# Photonic crystal member lasers with integrated beam routing gratings and metasurfaces

**Weidong Zhou[1]*, Shichia Liu[1], Deyin Zhao[1], Hongjun Yang[1], Zhenqiang Ma[2]**
[1]Department of Electrical Engineering, University of Texas at Arlington, TX 76019, USA
[2]Department of Electrical and Computer Engineering, University of Wisconsin-Madison, WI 53706, USA
*corresponding author: wzhou@uta.edu

**Abstract**-We report here vertically integrated surface-emitting lasers with integrated beam routing structures based on photonic crystal cavities and dielectric gratings. Heterogeneous integration of III-V quantum well structures with silicon based photonic crystal cavities on silicon were demonstrated based on transfer printing techniques. Such multi-layer stacked nano-structures offer a powerful platform for integrated photonics for both in-plane and 3D photonic integrated on silicon.

CMOS compatible lasers on silicon (Si) remain to be an active and challenging area of research for integrated Si photonics. Recently, we demonstrated two types of ultra-compact planar surface-emitting membrane lasers on silicon substrates [1, 2], based on photonic crystal Fano resonance membrane reflectors and band-edge effects. We report here vertically integrated surface-emitting lasers with integrated beam routing structures based on photonic crystal cavities and dielectric gratings. Heterogeneous integration of III-V quantum well structures with silicon based photonic crystal cavities on silicon were demonstrated based on transfer printing techniques. Such multi-layer stacked nano-structures offer a powerful platform for integrated photonics for both in-plane and 3D photonic integrated on silicon.

Work is supported by US ARO (W911NF-15-1-0431), NSF (ECCS-1308520), and AFOSR (FA9550-16-1-0010).

**REFERENCES**

1. Yang, H., Zhao, D., Chuwongin, S., Seo, J.H., Yang, W., Shuai, Y., Berggren, J., Hammar, M., Ma, Z., and Zhou, W., 'Transfer-Printed Stacked Nanomembrane Lasers on Silicon', *Nat.Photon.*, 2012, 6, (9), p. 615-620.
2. Zhao, D., Liu, S., Yang, H., Ma, Z., Reuterskiold-Hedlund, C., Hammar, M., and Zhou, W., 'Printed Large-Area Single-Mode Photonic Crystal Bandedge Surface-Emitting Lasers on Silicon', *Sci Rep*, 2016, 6, p. 18860.

# Monolithic Subwavelength High-index Contrast Surface Gratings for ultra-thin VCSELs

**M. Gebski[1,2], E. Haglund[3], P. Moser[2],M. Riaziat[4],, M. Dems[1], A. Larsson[3], T. Czyszanowski[1], J. A. Lott[2]**

1. Lodz University of Technology, Institute of Physics, Photonics Group, Łódź, Poland
2. Technische Universität Berlin, Institut für Festkörperphysik and Zentrum für Nanophotonik, Berlin, Federal Republic of Germany
3. Photonics Laboratory, Department of Microtechnology and Nanoscience, Chalmers University of Technology, Göteborg, Sweden
4. OEpic Semiconductors Inc., Sunnyvale, California, 94089, United States of America

*corresponding author: marcin.gebski@p.lodz.pl

**Abstract:** We present reduced-vertical-dimension VCSEL designs that employ subwavelength monolithic high index contrast surface gratings (MHCGs) and distributed Bragg reflectors (DBRs). We show results of computer simulations of the optical field intensity distribution in these structures and the measured power reflectance of GaAs MHCGs designed for 980 nm.

## INTRODUCTION

Gallium-arsenide-based ~600-1100 nm vertical-cavity surface-emitting lasers (VCSELs) typically have physical vertical thicknesses of ~7-11 μm, nanometer-length optical cavities, and micrometer-length lateral dimensions. These devices are used in many applications of which short-reach and very-short-reach (about 2 m and less) system-in-a-package (SiP) optical interconnects is one of our primary interests. We believe VCSELs will also play a critical role in the emerging technology of integrated optical-electronic-photonic integrated circuits and systems, where massive numbers of very small volume, energy efficient, temperature stable, ultra-short-reach on-chip optical interconnects are desired. Surface normal emission, the potential for lateral emission via gratings, low threshold current, low cost per device, on-wafer testing, , and the potential for single-mode emission are key VCSEL attributes for the envisioned SiP. State-of-the-art data and computer communication VCSELs require the growth of hundreds of precisely defined epitaxial layers where multilayer distributed Bragg reflector (DBR) mirrors are typically >95% of the vertical thickness. By replacing the DBR mirrors with monolithic high-index contrast surface gratings (MHCGs) we may reduce the vertical dimensions of a VCSEL down to about 2λ. Our approach could enable InP-based (~1300-1600 nm) and GaN-based (~390-580 nm) MHCG VCSELs wherein semiconductor DBRs are highly problematic, and where dielectric DBRs or wafer-fusion techniques increase the VCSEL processing complexity and production cost, while jeopardizing reliability and temperature stability.

## RESULTS

Ultrathin-VCSEL structures can be realized with the use of thin MHCG mirrors as has been shown theoretically in [1, 2]. In our META 2016 presentation we analyze our novel designs of GaAs MHCG and DBR VCSELs. In Fig.1a), b), and c) we show a schematic cross-section diagram, an SEM image after oxidation, and 1D and 2D (scalar) simulated optical field intensity distributions for a 980 nm MHCG DBR VCSEL with 2.5 DBR periods between the optical cavity and the surface grating. We note the increase in optical field intensity in the MHCG, which increases relative to the optical field intensity in the QWs as the number of top DBR periods decreases. We propose a new grating optical confinement factor, which takes into account the field distribution inside the grating which is highly non-uniform over each grating period. Our approach leads to the conclusion that a classical 1D confinement factor definition is not suitable for fair comparisons of DBR MHCG VCSELs. We use a TE-polarized MHCG surface grating created using electron-beam lithography and standard dry etching, with a targeted design that includes a fill factor $F \sim 0.35$ (i.e. a stripe width of ~286 nm a trench width of~531 nm), a grating period $L \sim 817$ nm, and a stripe height of

This work is supported by the German Research Foundation (Deutsche Forschungsgemeinschaft - DFG) via the Collaborative Research Center (CRC) 787 (Sonderforschungsbereich 787). M. Gębski acknowledges support from the Polish National Science Centre within the projects PRELUDIUM 2013/11/N/ST7/02826 and ETIUDA 2015/16/T/ST7/00514.

*h* ~ 164 nm. In Fig. 2. We show the measured and simulated power reflectance (R) of an (u)GaAs TE-polarized MHCG, where R > 0.93 (93%) at ~1030 nm. We show via simulation how R > 0.99 (99%) at ~980 nm may be achieved by accounting for the actual physical shape of the surface-etched MHCG. Additionally, we present simulation results of various novel VCSEL designs (such as the structure shown in Fig. 1 a) and several variations of this structure as compared to an all-semiconductor VCSEL design. We show the impact of the lateral size of the MHCG mirror on the simulated Q-factor of the VCSEL cavity modes in Fig. 2 b. In Fig. 1 c we plot the impact of the number of top DBR pairs in a combined DBR MHCG mirror on the power reflectance as seen from the optical cavity looking up toward the combined DBR and MHCG. In the presentation we report our progress toward producing oxide-confined, all-semiconductor electrically-injected ~980 nm MHCG DBR VCSELs.

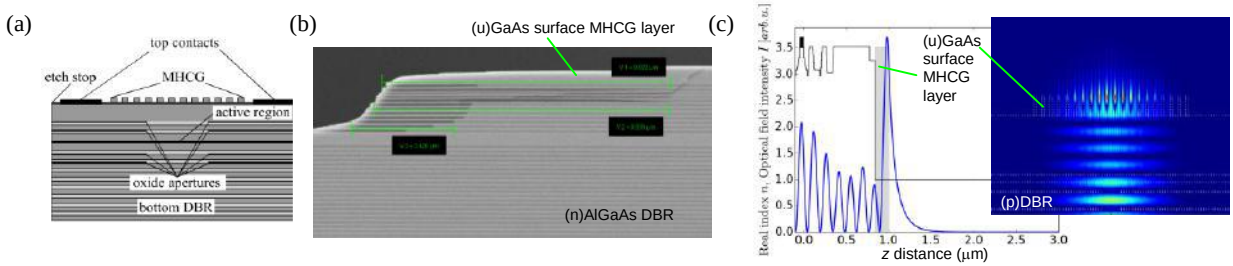



**Fig. 1** a) Schematic cross-section diagram of an MHCG DBR VCSEL; b) scanning electron micrograph of a 980 nm MHCG DBR VCSEL epitaxial structure with 2.5 top DBR periods under the topmost (not yet processed) (u)GaAs surface grating layer; and c) simulated 1D and 2D (scalar) optical-field intensity and real refractive index of the VCSEL in b). The 2D optical-field intensity plot is for a TE-polarized MHCG DBR VCSEL structure with a 20-period surface grating.

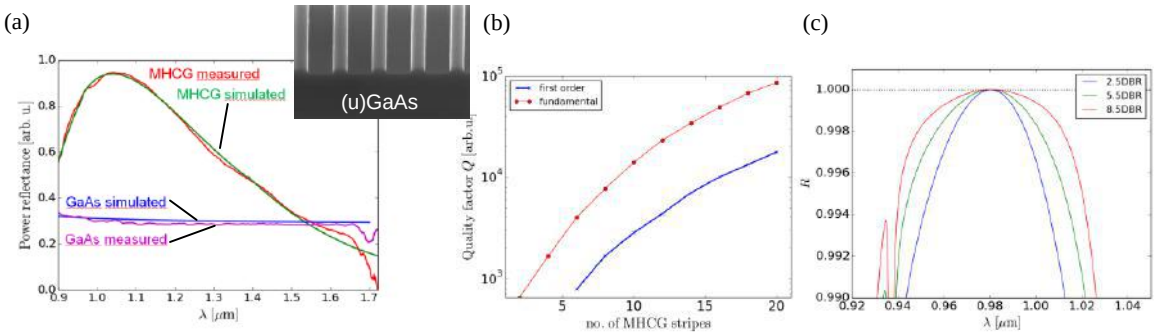



**Fig. 2** a) Power reflectance (R) spectrum of a bulk (u)GaAs MHCG mirror thinned to ~200 μm with a SiN AR coating opposite to the surface grating. We account for the actual shape of the experimental MHCG structure as may be seen in the SEM inset; b) calculated Q-factor as a function of the number of grating stripes of the top mirror for a 980 nm MHCG VCSEL; and c) calculated R as a function of wavelength for the different number of top DBR mirror pairs.

## REFERENCES


[1] Gębski, M., Dems, M., Szerling, A., Motyka, M., Marona, L., Kruszka, R., Urbańczyk, D., Walczakowski, M., Pałka, N., Wójcik-Jedlińska, A., Wang, Q. J., Zhang, D. H., Bugajski, M., Wasiak, M., and Czyszanowski, T., "Monolithic high-index contrast grating: a material independent high-reflectance VCSEL mirror," *Optics Express*, Vol. 23, No. 9, 11674-11686, 2015.

[2] Gębski, M., Dems, M., Wasiak, M., Lott, J. A., and Czyszanowski, T., "Monolithic subwavelength high-index-contrast grating VCSEL," *IEEE Photonics Technology Letters*, Vol 27, No. 17, 1953-1956, 2015.

**Nanophotonics and plasmonics for information applications**

# Photonic spin Hall effect in waveguides composed of two kinds of single-negative metamaterials

**Z. W. Guo, K. Yu, H. T. Jiang*, and H. Chen**

*MOE Key Laboratory of Advanced Micro-Structured Materials, School of Physics Science and Engineering, Tongji University, Shanghai, 200092, China*

*corresponding author: jiang-haitao@tongji.edu.cn

**Abstract**- In this work, we experimentally demonstrate the photonic spin Hall effect in waveguides composed of two kinds of single-negative metamaterials. We find that a source with a linear polarization couples equally with the two guided modes oppositely propagating along the interface. However, a circularly rotating source only couples with one guided mode with a specific propagating direction, which is determined by the rotation direction of the source.

The photonic spin Hall effect (i.e. photons of different circular polarizations (optical spin) may take different trajectories, in analogy to the spin Hall effect for electrons) via the excitation of localized optical modes have been realized based on the surface plasmon polaritons at air-metal interfaces [1], the guided modes in the nanofiber [2] and the subwavelength modes in hyperbolic metamatarials [3]. In 2015, Bliokh et al. theoretically reveal that the photonic spin Hall effect realized in the waveguides is essentially due to the transverse spin property of evanescent waves [4]. In this work, we experimentally demonstrate that the photonic spin Hall effect can occur in waveguides composed of $\varepsilon$-negative (ENG) metamaterial ( $\varepsilon < 0, \mu > 0$ ) and $\mu$-negative (MNG) metamaterial ( $\varepsilon > 0, \mu < 0$ ) (i.e. two kinds of single-negative metamaterials). Based on two-dimensional transmission lines loaded with lumped circuit elements, we fabricate the ENG/MNG waveguides. Then we verify the unidirectional excitation of guided modes in the ENG/MNG interface by using a circularly polarized source with a specific rotation direction. In Fig. 1(a), we see that a source with a linear polarization couples equally with the two guided modes oppositely propagating along the interface. However, by controlling the spin of the source, it is possible to break this symmetry and select one guided mode with a specific propagating direction. In Fig. 1(b) ((c)), a circularly rotating source with anti-clockwise (clockwise) rotation direction only couples with one guided mode propagating from the left (right) side to the right (left) side, which demonstrate the photonic spin Hall effect. Our work allows for the control of electromagnetic wave propagation by tuning the polarization degree of freedom.

**Acknowledgements**, This work is supported by the National Basic Research Program of China (No. 2011CB922001), the NSFC (No. 11234010 and No. 11474220), Innovation Program of Shanghai Municipal Education Commission (No. 14ZZ040).

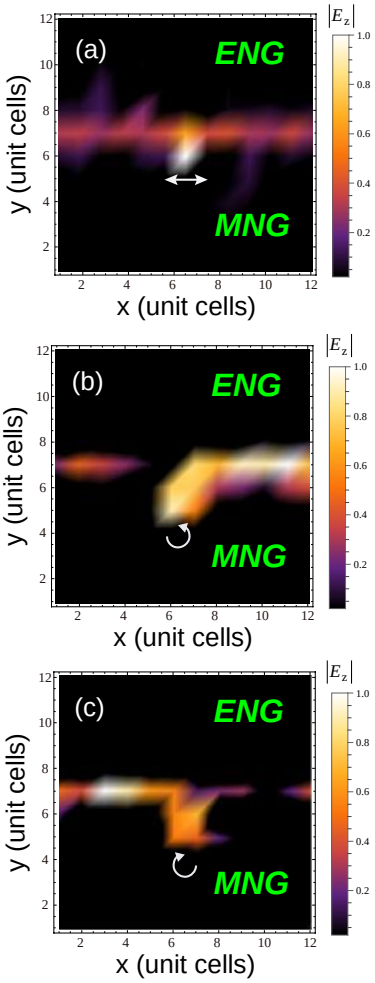



Fig. 1. The measured normalized $|E_z|$ patterns in the ENG/MNG waveguides at 2.88 GHz. White arrows denote the polarization of source.

**REFERENCES**


1. Rodríguez-Fortuño, F. J., Marino, G., Ginzburg, P., ÓConnor, D., Martínez, A., Wurtz, G. A and Zayats, A.V, "Near-field interference for the unidirectional excitation of electromagnetic guided modes," Science , Vol. 340, 328–330 (2013).
2. Petersen, J., Volz, J and Rauschenbeutel, A, "Chiral nanophotonic waveguide interface based on spin-orbit interaction of light," Science, Vol. 346, 67–71 (2014).
3. Kapitanova, P. V., Ginzburg, P., Rodríguez-Fortuño, F. J., Filonov, D. S., Voroshillov, P.V., Belov, P.A., Poddubny, A. N., Kivshar, Y. S., Wurtz, G. A and Zayats, A. V, "Photonic spin Hall effect in hyperbolic metamaterials for polarization-controlled routing of subwavelength modes," Nat. Commun, Vol. 5, No.3226 (2014).
4. Bliokh, K. Y., Smirnova, D and Nori, F, "Quantum spin Hall effect of light," Science, Vol. 348, 1448–1451 (2015).

# Efficient spectral and spatial manipulation of optical field hot spots via plasmonic mode hybridization in hierarchical nanostructures

**Benfeng Bai**[1*] **and Zhendong Zhu**[2]

[1] State Key Laboratory of Precision Measurement Technology and Instruments, Department of Precision Instrument, Tsinghua University, Beijing 100084, China

[2] National Institute of Metrology, Beijing 100029, China

[*]corresponding author: baibenfeng@tsinghua.edu.cn

**Abstract**- Utilizing plasmonic mode hybridization and cascaded field enhancement, we present the construction of novel plasmonic hierarchical nanostructures that can generate extremely enhanced and tightly confined optical field hot spots at target resonance wavelengths and accurate spatial positions. Two plasmonic hierarchical nanostructures, including an M-shaped nanograting and a nanoparticle-in-cavity nanoantenna array, are designed and fabricated. The greatly enhanced light-matter interaction and potential application of these devices are demonstrated by surface enhanced Raman spectroscopic experiments.

Plasmonic nanostructures with tightly confined and greatly enhanced optical field (i.e., the optical field "hot spots") are quite demanded in various applications based on enhanced light-matter interactions, such as surface enhanced Raman spectroscopy (SERS). In such applications, it is crucial to steer the spectral resonance of the field enhancement as well as the spatial distribution and/or localization volume of the field hot spots. As the tunability of the localized surface plasmon resonance (LSPR) of simple plasmonic nanoparticles (NPs) are quite limited, it is an effective way to tune or generate plasmonic resonance at an expected wavelength via plasmonic mode hybridization by properly designing some complex shaped nanostructures.[1] On the other hand, some specially designed hierarchical nanostructures, such as the self-similar gold NP chain of decreasing size,[2] can generate the cascaded field enhancement (CFE) effect so that strong field hot spots can be confined in very small spatial nano-volumes.

In this talk, we present our recent advance on the construction of some plasmonic hierarchical nanostructures that can realize the tunability of spectral resonance and the spatial distribution of field hot spots simultaneously, by utilizing both the mode hybridization and the CFE effect. Two plasmonic hierarchical nanostructures are introduced, including an M-shaped grating and a nanoparticle-in-cavity (PIC) nanoantenna array, as shown in Fig. 1. In the M-grating, CFE is realized via the hybridization of LSPR modes of two adjacent V-shaped grooves; while in the PIC array, by utilizing the hybridization between a plasmonic dark mode of the gold NP and a high-order cavity bright mode of the nanovoid, strong Fano resonance can be generated at a target wavelength under normal incidence, which then significantly boost the CFE. In these structures, the enhancement factor of the localized field amplitude is as high as $10^3$, which can significantly enhance the light-matter interaction.

We have developed a reliable, efficient, and cost-effective fabrication method based on room-temperature nanoimprinting lithography and anisotropic reactive ion etching to fabricate these hierarchical nanostructures. It is shown that high-quality M-grating and PIC array can be readily fabricated with this method. By controlling the etching process, the key geometrical features of these nanostructures can be well controlled. Furthermore, the

method has shown potential to fabricate such kind of hierarchical nanostructures in large area.

The greatly enhanced light-matter interaction in the M-grating and the PIC array are verified by conducting SERS experiments using the fabricated M-grating and PIC array as active SERS substrates. The experimentally attained SERS enhancement factor can reach as high as $10^8$, showing the great potential of these devices for SERS applications.

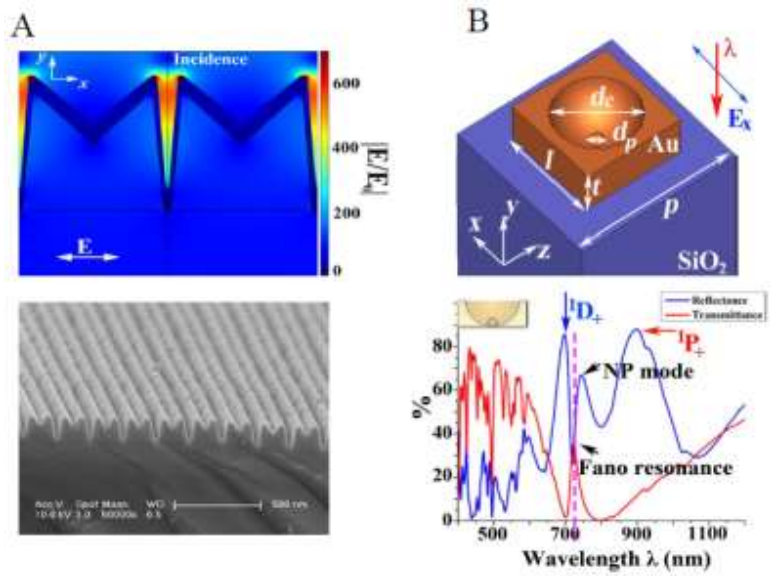



Figure 1. Two plasmonic hierarchical nanostructures with mode hybridization and CFE effect. (A) The enhanced optical field hot spots in the M-grating and the fabricated device; (B) Schematic of a PIC nanoantenna unit cell and the Fano resonance in the transmittance and reflectance spectra of a PIC array.

**Acknowledgements** We acknowledge the support by the National Natural Science Foundation of China (Projects No. 11474180 and No. 61227014) and the Ministry of Science and Technology of China (Project No. 2011BAK15B03).

**REFERENCES**

1. E. Prodan, C. Radloff, N. J. Halas, and P. Nordlander, "A hybridization model for the plasmon response of complex nanostructures," *Science*, Vol. 302, 419–422, 2003.
2. C. Höppener, Z. J. Lapin, P. Bharadwaj, and L. Novotny, "Self-similar gold-nanoparticle antennas for a cascaded enhancement of the optical field," *Phys. Rev. Lett.*, Vol. 109, 017402, 2012.
3. Z. Zhu *et al*., "M-shaped grating by nanoimprinting: A replicable, large-area, highly active plasmonic surface-enhanced Raman scattering substrate with nanogaps," *Small*, Vol. 10, 1603-1611, 2014.
4. Z. Zhu *et al*., "Fano-resonance boosted cascaded field enhancement in a plasmonic nanoparticle-in-cavity nanoantenna array and its SERS application," *Light: Science & Applications*, Vol. 4, e296, 2015.

# Efficient generation of prominent and robust plasmonic Fano resonances in a 3D metamaterial

**Jiafang Li,* Zhiguang Liu, and Zhi-Yuan Li**
Laboratory of Optical Physics, Institute of Physics, Chinese Academy of Sciences, Beijing, China, 100190
*Email: jiafangli@aphy.iphy.ac.cn

**Abstract**- We report our recent experimental and theoretical works on the efficient generation of prominent and robust Fano resonances in a 3D metamaterial. The observed Fano resonances are highly scalable, universal, robust and immune against both fabrication and illumination imperfections.

In this talk, we report our recent experimental and theoretical works on the efficient generation of prominent and robust Fano resonances in 3D metamaterials (MMs). The 3D MMs are formed by integrating vertical structures along a planar metallic hole array with extraordinary optical transmission (EOT). In such a configuration, intensified vertical E-field is induced along the metallic holes and naturally excites the electric resonances of the vertical structures, which form non-radiative "dark" modes due to the symmetry constraints. These 3D conductive "dark" modes strongly interfere with the "bright" resonance mode of the EOT structure, which generate significant Fano resonances with both prominent destructive and constructive interferences. Moreover, compared with the capacitive and inductive coupled Fano resonances that degrade drastically upon small structural deviations, the demonstrated 3D conductive coupling induced Fano resonances are highly scalable, universal, robust and immune against both fabrication and illumination imperfections.

**REFERENCES**

1. Ajuan Cui,[#] Zhe Liu,[#] Jiafang Li,[#] Tiehan H. Shen, Xiaoxiang Xia, Zhiyuan Li, Zhijie Gong, Hongqiang Li, Benli Wang, Junjie Li, Haifang Yang, Wuxia Li,* and Changzhi Gu,* "Directly patterned substrate-free plasmonic 'nanograter' structures with unusual Fano resonances," *Light: Science &Applications 4*, e308 (2015).
2. Zhiguang Liu,[#] Zhe Liu,[#] Jiafang Li,* Wuxia Li, Junjie Li, Changzhi Gu, and Zhi-Yuan Li, "3D conductive coupling for robust generation of prominent Fano resonances in metamaterials", *Scientific Report*, 2016 (accepted).

# Surface plasmon model for the radiation enhancement by resonant optical dipole antennas

**Haitao Liu**[1*]**, Hongwei Jia**[1]**, and Ying Zhong**[2]

[1]Key Laboratory of Optical Information Science and Technology, Ministry of Education, Institute of Modern Optics, Nankai University, Tianjin 300071, China

[2]State Key Laboratory of Precision Measuring Technology and Instruments, Tianjin University, Tianjin 300072, China

[*]corresponding author: liuht@nankai.edu.cn

**Abstract**-We report an intuitive model based on a multiple scattering of surface plasmon polaritons (SPPs) that can comprehensively predict the emission properties of a dipole antenna. The enhancement of the antenna radiation is shown to be due to surface waves that are resonantly excited on the two antenna arms and that are further coupled into the nano-gap. Both SPPs and other surface waves contribute to the antenna radiation for the lowest-order resonance while only SPP dominates at higher-order resonances.

Resonant dipole antennas, which are made of two metallic nano-wires separated by a nano-gap [1], show superior properties in enhancing the radiation of emitters such as molecules or quantum dots in the vicinity of the antenna. Concepts of impedance and resistance are proposed for dipole antennas [2] for reproducing quantities such as the resonance frequency and the quantum efficiency. The dipole antennas are also modeled as one-dimensional micro-cavities [3], and the enhancement effect is attributed to the resonance of SPPs. It is commonly believed that the enhancement effect of the antenna radiation is due to a resonant excitation of SPPs on the antenna arms. This intuitive belief, which plays a central role in present antenna theories, will be checked at a quantitative level in the present work, and the relevant physical picture will be clarified.

In this work [4], we theoretically investigate the emission of an electric dipole source in the nano-gap of a gold dipole antenna [as sketched in Fig. 1(a)]. A pure-SPP model is built up by considering a dynamical launching and multiple-scattering process of SPPs on the antenna arms. The SPP model can comprehensively reproduce the electromagnetic features of the antenna radiation, such as the total and radiative emission rates [Figs. 1(b) and 1(c)] and the far-field radiation pattern. The model is self-sufficient and does not rely on any fitting process with the use of rigorous numerical or experimental data. The model is highly accurate at high orders of resonance ($m$=1, 2, … in Fig. 1) which yields the dominant contribution from the SPP to the antenna radiation. While the model shows error at the lowest order of resonance ($m$=0), unveiling the contribution from surface waves other than SPPs. The present model is helpful for clarifying the underlying physics of the radiation enhancement with resonant optical antennas and may provide recipes for an intuitive design of relevant devices. With the model, the electromagnetic field in the nano-gap can be expressed as,

$$\mathbf{E}_{\text{gap}} = \mathbf{E}_{\text{source}} + b_1 u \mathbf{E}_{\text{SPP},+}^{\text{coupling}} + b_2 u \mathbf{E}_{\text{SPP},-}^{\text{coupling}}, \tag{1}$$

where $\mathbf{E}_{\text{source}}$ denotes the field excited by the dipole source for infinite-length antenna, $\mathbf{E}_{\text{SPP},+}^{\text{coupling}}$ or $\mathbf{E}_{\text{SPP},-}^{\text{coupling}}$

represents the field coupled from a right-going or a left-going SPP into the nano-gap, $u=\exp(ik_0 n_{\text{eff}} L)$ is the phase shift of the SPP accumulated over one antenna arm ($k_0=2\pi/\lambda$, $n_{\text{eff}}$ being the complex effective index of the SPP), and $b_1$ and $b_2$ are the coefficients of right-going and left-going SPPs [as sketched in Fig. 1(a)] expressed as

$$b_1 = b_2 = \frac{\beta u r}{1-u^2 r(\rho+\tau)}. \tag{2}$$

Here $\beta$ denotes the SPP excitation coefficient by the dipole source, $\rho$ and $\tau$ are the SPP reflection and transmission coefficients at the nano-gap, and $r$ is the SPP reflection coefficient at the antenna termination. Equation (2) shows that the antenna emission rate peaks under a phase-matching condition,

$$2k_0 \,\text{Re}(n_{\text{eff}})L + \arg(r) + \arg(\rho+\tau) = 2m\pi\,, \tag{3}$$

where $m$ is an integer corresponding to different orders of resonance. Equation (2) is related to a constructive interference of the excited SPPs on antenna arms.

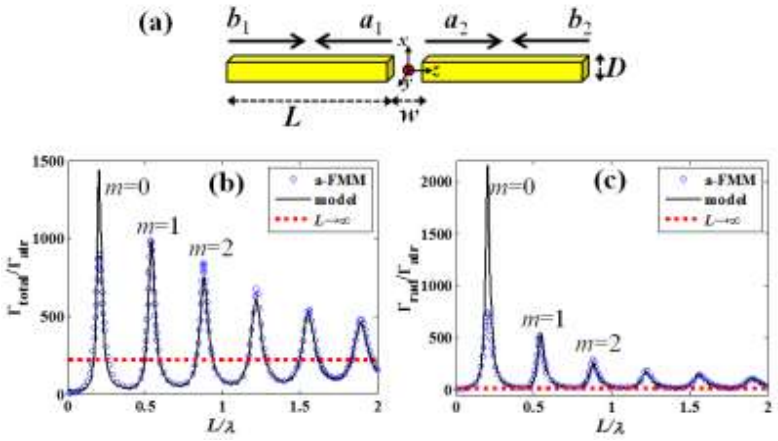



**Figure 1** (a) Sketch of the dipole antenna, where a *z*-polarized point source is placed in the nano-gap. (b)-(c) Total ($\Gamma_{\text{total}}$) and radiative ($\Gamma_{\text{rad}}$) emission rates for different antenna lengths $L$, normalized by the emission rate $\Gamma_{\text{air}}$ of the dipole source in air. The horizontal dotted lines show the results for antennas with infinite-length arms, for which impact of surface waves on antenna arms are excluded. The results are obtained with the full-wave aperiodic Fourier modal method (a-FMM) and the model for wavelength $\lambda$=1μm, $D$=0.04$\lambda$ and $w$=0.03$\lambda$.

**Acknowledgements** This work is financially supported by the National Key Basic Research Program of China (973 Program) under Grant No. 2013CB328701, and by the Natural Science Foundation of China under Grant No. 61322508.

**REFERENCES**

1. Mühlschlegel, P. et al, "Resonant optical antennas," *Science*, Vol. 308, 1607-1609, 2005.
2. Alù, A. and N. Engheta, "Input impedance nanocircuit loading and radiation tuning of optical nanoantennas," *Phys. Rev. Lett.*, Vol. 101, 043901, 2008.
3. Mousavi, S. S., P. Berini and D. McNamara, "Periodic plasmonic nanoantennas in a piecewise homogeneous background," *Opt. Express*, Vol. 20, 18044-18065, 2012.
4. Jia, H. W., H. T. Liu and Y. Zhong, "Role of surface plasmon polaritons and other waves in the radiation of resonant optical dipole antennas," *Sci. Rep.*, Vol. 5, 8456, 2015.

# 3D optical nanofabrication in glass

**Y. Liao[1], J. Ni[1], and Y. Cheng[1*]**

[1]State Key Laboratory of High Field Laser Physics, Shanghai Institute of Optics and Fine Mechanics, Chinese Academy of Sciences, China

[*]corresponding author: ya.cheng@siom.ac.cn

**Abstract**-Femtosecond laser has been widely used for fabricating various types of 3D functional structures on the micrometer scale. Here, we demonstrate fabrication of 3D nanostructures in a controllable manner by exciting self-induced plasmonic waves with far-field interaction of an ultrafast laser beam with glass. We reveal the mechanism by observing the gradual formation of the nanostructure under the irradiation of multiple femtosecond laser pulses.

As a direct and maskless fabrication technique, femtosecond laser micromachining provides a straightforward approach for space-selective modification inside transparent materials with micrometer resolutions through nonlinear optical absorption. Recently, we have developed a technique which further enables rapid fabrication of 3D nanostructures in glass for nanofluidic and nanophotonic applications [1].

To reveal the physical mechanism, we take the high-fidelity snapshots during the nanostructures formation [2]. It is observed that far-field excitation of plasmonic waves with nanoscale defects induced by femtosecond laser irradiation in glass is responsible for the formation of nanostructures with feature sizes down to ~30 nm, as shown in Fig. 1. The unique characteristic allows breaking the diffraction limit in the far-field optical nanofabrication and opens up opportunities for innovative applications such as 3D metamaterials.

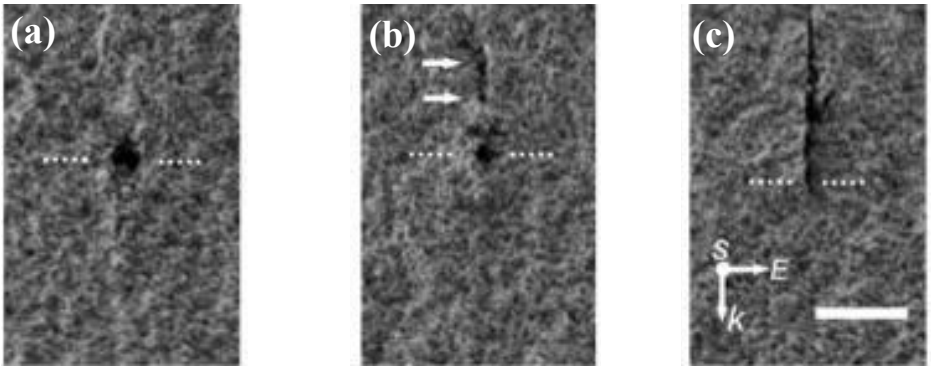



**Fig. 1:** Formation of an individual nanocrack during the continuous irradiation of multiple laser shots in glass. The transverse width of the fabricated nanocrack is ~30 nm. To gradually raise the number of laser shots at the laser irradiation spot, the scan velocities in (a)–(c) are 25, 5, and 1 mm/s, respectively, Scale bar: 1 μm. The laser incident direction ($k$), polarization direction ($E$), and the writing direction ($S$) are indicated.

**REFERENCES**

1. Y. Liao and Y. Cheng, "Femtosecond Laser 3D Fabrication in Porous Glass for Micro- and Nanofluidic Applications", *Micromachines* Vol. 5, 1106-1134, 2014.
2. Y. Liao, J. Ni, L. Qiao, M, Huang, Y. Bellouard, K. Sugioka, and Y. Cheng, "High-fidelity visualization of formation of nanogratings in porous glass by femtosecond laser irradiation," *Optica*, Vol. 2, 329-334, 2015.

# Dynamic plasmonic tweezers for nanoparticles and nanowires

**Xiujie Dou[1], Changjun Min[1*], Lichao Zhang[1], Yuquan Zhang[1], and Xiaocong Yuan[1]**

[1]Nanophotonics Research Centre, Shenzhen University & Key Laboratory of Optoelectronic Devices and Systems of Ministry of Education and Guangdong Province, College of Optoelectronic Engineering, Shenzhen University, Shenzhen 518060, China

[*]corresponding author: cjmin@szu.edu.cn

**Abstract**-The hybrid plasmonic mode between a nanoparticle and a metal film strongly enhances the electromagnetic field and the induced optical forces. Here, we employ the plasmonic mode to achieve a dynamic plasmonic tweezers for trapping and manipulation of nanoparticles and nanowires on a flat metal surface. The plasmonic tweezers can trap metallic, dielectric and semiconductor nano-objects, and control its position and orientation. Finally we show its potential applications in surface-enhanced Raman scattering and lab-on-a-chip nanowire devices.

Instead of being repulsed by a conventional optical tweezers due to high scattering force, we found that metallic particles can be attracted and steadily trapped in a plasmonic tweezers excited by a highly focused radially polarized beam [1]. This approach can attract and trap both Rayleigh and Mie type metallic and dielectric particles in the diameter range of 0.06~2.2 μm. In particular, trapping of mesoscopic/Mie metallic particles is particularly successful. Compared with other plasmonic tweezers based on fixed metallic nanostructures, this setup benefits from the structureless excitation of surface plasmon in a dynamic configuration. We can also use a radially polarized optical vortex as incident beam to excite the whirlpool-like plasmonic vortex to build a plasmonic spanner for metal particle manipulation in the microscopic system [2, 3].

Besides nanopartiles, we also used the plasmonic tweezers to trap and manipulate nanowires. We found that plasmonic hybridization achieved by exciting plasmonic tweezers with a linearly polarized laser beam could induce strong trapping forces and large rotational torques on a single metallic nanowire [4]. The position and orientation of the nanowire could dynamically be controlled by the enhanced nonisotropic electric field in the gap. Based on this technique, a plasmonic swallow tail structure is built to demonstrate its potential in the fabrication of lab-on-a-chip plasmonic devices. We also achieved the in-plane trapping and manipulation of a single ZnO nanowire by focused plasmonic tweezers on a flat metal surface. In contrast, when a ZnO nanowire is trapped by conventional laser beam tweezers, it tends to be aligned with the trapping beam axis rather than confined in the horizontal plane, and this limits the application of these nanowires in many in-plane nanoscale optoelectronic devices.

Finally, we introduce the application of the plasmonic tweezers in SERS. By trapping and dragging a single gold nanoparticle with the plamonic tweezers, we demonstrate a dynamic single-particle-film SERS system [5], which produces a high SERS enhancement factor of ~$10^9$, and therefore provides a promising approach to controllable SERS detection and imaging. These works could provide a profound influence on manipulating various metallic, dielectric and semiconductor nano-objects and have an important contribution to lab-on-a-chip devices for quantum optics, optical characterization, spectroscopy, and sensing applications.

**REFERENCES**

1. Min, C. J., Shen, Z., Shen, J. F., Zhang, Y. Q., Fang, H., Yuan, G. H., Du, L. P., Zhu, S. W., T. Lei and X.-C. Yuan, "Focused plasmonic trapping of metallic particles," *Nature Communications*, Vol. 4, 2891, 2013.
2. Shen, Z., Hu, Z. J., Yuan, G. H., Min, C. J., H. Fang and X.-C. Yuan, "Visualizing orbital angular momentum of plasmonic vortices," *Optics Letters*, Vol. 37, No. 22, 4627-4629, 2012.
3. Zhang, Y. Q., Shi, W., Shen, Z., Man, Z. S., Min, C. J., Shen, J. F., Zhu, S. W., H. P. Urbach and X.-C. Yuan, "A Plasmonic Spanner for Metal Particle Manipulation," *Scientific Reports*, Vol. 5, 15446, 2015.
4. Zhang, Y. Q., Wang, J., Shen, J. F., Man, Z. S., Shi, W., Min, C. J., Yuan, G. H., Zhu, S. W., H. P. Urbach and X.-C. Yuan, "Plasmonic hybridization induced trapping and manipulation of a single Au nanowire on a metallic surface," *Nano Letters*, Vol. 14, No. 11, 6430-6436, 2014.
5. Shen, J. F., Wang, J., Zhang, C. J., Min, C. J., Fang, H., Du, L. P., S. W. Zhu and X.-C. Yuan, "Dynamic plasmonic tweezers enabled single-particle-film-system gap-mode Surface-enhanced Raman scattering," *Applied Physics Letters*, Vol. 103, No. 19, 191119, 2013.

# Lithium-niobate-based micro-resonators

**Guoquan Zhang[1,2,*], Fang Bo[1], Jie Wang[1], Jiao Cui[1], Yongfa Kong[1,2], Jingjun Xu[1,2]**

[1]The MOE Key Laboratory of Weak Light Nonlinear Photonics, TEDA Applied Physics Institute and School of Physics, Nankai University, Tianjin 300457, China

[2]Collaborative Innovation Center of Extreme Optics, Shanxi University, Taiyuan, Shanxi 030006, China

[*]corresponding author: zhanggq@nankai.edu.cn

**Abstract**-We reported on our recent progresses on lithium-niobate-based micro-resonators, including the fabrication of high quality monocrystalline or hybrid lithium niobate micro-resonators, the electro-optical or all-optical light modulation, and the thermo-optically induced oscillations. The results show that high quality lithium-niobate-based micro-resonators are of excellent active light modulation capability and therefore have numerous potential applications in optical information process.

Optical micro-cavity or micro-resonator has attracted great attention recently because of its high quality and strong spatial confinement of light within a microscale-mode volume, which enable enhanced light-matter interaction and long circulating time duration of photons within the micro-cavity [1]. It is important from the view point of not only fundamental physics [2] but also practical applications such as high sensitive sensors [3], novel light sources [4], and nonlinear optical effects at low light power or energy [5,6]. Various materials such as dielectrics and semiconductors were employed to fabricate high quality micro-cavities, in which silica-based micro-resonators are of the characteristics of ultrahigh Q values but inherently lack of electro-optical modulation capability and $\chi^{(2)}$ nonlinearity [1]. As compared to silica, lithium niobate is of large electro-optical coefficients and high $\chi^{(2)}$ nonlinearity, therefore, it is a good candidate for active photonic devices. Here, we reported on our recent progresses on the fabrication of high-Q lithium-niobate-based micro-resonators and their various tunable resonant characteristics.

Two different types of lithium-niobate-based micro-resonators were fabricated [7,8] and their electro-optical, all-optical and thermo-optical tunability were presented. Monocrystalline lithium-niobate micro-resonators with a record Q-value over $10^6$ were fabricated using a microfabrication method in compatible with the traditional semiconductor manufacturing technique, and therefore allowing for mass production. The resonator was fabricated on a lithium niobate/silica/lithium niobate wafer (LNOI) prepared by ion slicing and wafer bonding techniques. The SEM image of a typical monocrystalline lithium niobate micro-resonator is shown in Fig. 1(a), which shows a very smooth surface, leading to a high Q value. The resonators exhibited very good electro-optical tunability on the resonant properties such as the resonant wavelength (see Fig. 1(b)). In addition, thermo-optically induced oscillations were observed in the monocrystalline lithium niobate micro-resonators when the resonators were pumped with a relatively high pump power, as shown in Fig. 1(c). This oscillation was attributed to the interplay between a fast thermo-optical nonlinearity within the mode volume and a slow thermal relaxation of the micro-resonator as a whole.

Another type of lithium-niobate-based micro-resonator was a hybrid one with a heterojunction structure, in which a layer of lithium niobate thin film was deposited on the top surface of a high-Q, inverted-wedge silica micro-resonator using an excimer laser ablation method. There were always modes with parts of its energy

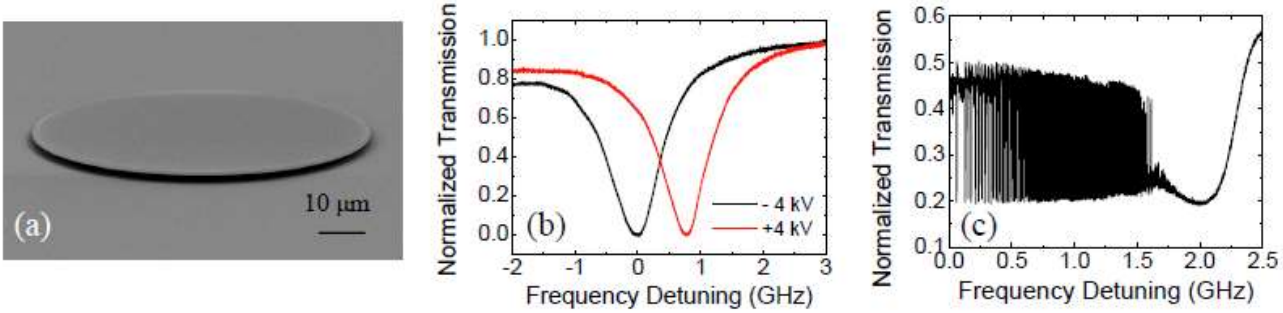



Figure. 1 (a) The SEM image of a typical monocrystalline lithium niobate micro-resonator. (b) Typical electro-optical tuning on the resonant wavelength of a monocrystalline lithium niobate micro-resonator sandwiched between two parallel transparency electrodes forming a parallel-plate capacitor. (c) Thermo-optically induced oscillations in the transmission spectrum of a monocrystalline lithium niobate micro-resonators with a 1.8-mW pump power at 1550 nm.

distributed in the top lithium niobate thin film, therefore, any change of lithium niobate film will also have effects on the resonant behavior of the whole hybrid resonator. Note that the thin lithium niobate film was in the polycrystalline state, but it still retained partially the electro-optical effect although with a coefficient much smaller than that in the monocrystalline state, which enables the device capable of active electro-optical modulation. Such a heterojunction structure combines the advantages of high Q value of silica micro-resonator and the active control capability of lithium niobate together, therefore, may have great potential applications in active photonic devices.

**Acknowledgements** The authors thank Prof. Lan Yang and Prof. Sahin Kaya Özdemir from Washington University for fruitful discussions. This project is supported by the 973 Program of China (Grant No. 2013CB328702), the National Natural Science Foundation of China (Grant Nos. 11174153, 11374165 and 61475077) and the 111 project (Grant No. B07013).

**REFERENCES**

1. Vahala, K. J., "Optical microcavities," *Nature*, Vol. 424, 839–846, 2003.
2. Haroche, S. and Kleppner, D., "Cavity Quantum Electrodynamics," *Phys. Today*, Vol. 42, 24–30, 1989.
3. Zhu, J. et al., "On-chip single nanoparticle detection and sizing by mode splitting in an ultrahigh-Q microresonator," *Nat. Photonics*, Vol. 4, 46–49, 2010.
4. Jiang, X.-F., Zou, C.-L., Wang, L., Gong, Q. and Xiao, Y.-F., "Whispering-gallery microcavities with unidirectional laser emission," *Laser & Photonics Reviews*, Vol. 10, 40–61, 2016.
5. Fürst J. U. et al., "Naturally Phase-Matched Second-Harmonic Generation in a Whispering-Gallery-Mode Resonator," *Phys. Rev. Lett.*, Vol. 104, 153901, 2010.
6. Marquardt C. et al., "Nonlinear Optics in Crystalline Whispering Gallery Resonators," *Opt. & Photon. News*, Vol. 24, 38–45, 2013.
7. Bo, F. et al. "Lithium-niobate-silica hybrid whispering-gallery-mode resonators," *Adv. Mater.*, Vol. 27, 8075–8081, 2015.
8. Wang, J. et al., "High-Q lithium niobate microdisk resonators on a chip for efficient electro-optic modulation," *Opt. Express*, Vol. 23, 23072–23078, 2015.

# Quasi-normal mode formalism for the radiation properties of nanoparticles in optical stacks

**K. Vynck**[1], **R. Faggiani**[1], **J. Yang**[1], **and P. Lalanne**[1]

[1]LP2N, CNRS - Institut d'Optique Graduate School - Univ. Bordeaux, F-33400 Talence, France
kevin.vynck@institutoptique.fr

**Abstract**— We propose to exploit the concept of quasi-normal modes (QNMs) to predict *rapidly* and *accurately* the radiation properties of small resonant nanostructures (e.g. individual nanoparticles, nanoparticle aggregates) deposited on or embedded in optical stacks. Once the QNMs of a resonant system are (numerically) calculated, the radiation pattern in free space and in the stack guided modes is known analytically for any excitation. This method opens the route towards a smart design of hybrid "nanoparticle/stack" systems with new optical functionalities.

Light interaction with nanoparticles deposited on or embedded in planar geometries, such as thin-film stacks, is paramount in photonics research and devices. Let us mention, for instance, the control of the efficiency and directivity of light emission using plasmonic nano-antennas [1], the engineering of nanoparticles to improve the light coupling to guided modes in solar cells [2], or inversely, to optimize the light extraction from layered organic light-emitting diodes [3].

Since Maxwell's equation solvers can in general compute only the near-field around a nanostructure, radiation properties are typically obtained using near-field to far-field transformation methods, which, in the case of nanostructures in layered media, can be quite tedious. While many groups have contributed to the elaboration of well-suited numerical tools (see, e.g., Ref. [4], where the near-to-far-field transformation are computed using a method based on reciprocity arguments using a freely available software package), the radiation properties of a specific nanostructure are always predicted by computing its optical response to a specific excitation (planewave, focused beam or dipole source; specific wavelength and polarization). Hence, a full knowledge of radiation properties can only be obtained by performing a series of numerical simulations, which can be very time-consuming.

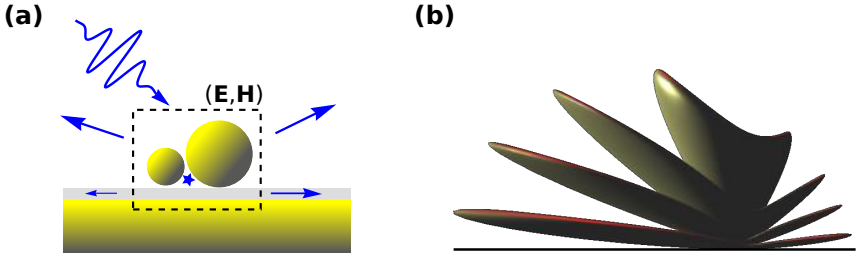



Figure 1: Radiation properties of nanoparticles in optical stacks. **(a)** Two nanoparticles, deposited on a thin-film stack, are excited by a far-field or a near-field source (incident blue arrow or blue star, resp.). The scattered light can radiate to free space and be coupled to the stack guided modes. **(b)** The far-field radiation pattern is obtained from the electric and magnetic fields, **E** and **H**, evaluated on a box surrounding the nanostructure in its near-field, see the black dashed box in panel (a).

Our group has recently introduced a formalism that allows predicting *analytically* the optical properties of arbitrary nanoparticles for *all* excitations from the sole knowledge of their optical resonances [5, 6]. These resonances, known as quasi-normal modes (QNMs), are solutions of Maxwell's equations without source and can be calculated numerically using any solver. Upon proper normalization of the QNMs fields, the optical response of a nanoparticle to an excitation is typically expressed as overlap integrals between the excitation field and the QNMs. The QNM formalism has been applied to predict the Purcell factor in the vicinity of nanoparticles [5], the scattering and absorption cross-sections of nanoparticles [6], and their interaction with quantum emitters [7].

In this communication, we will discuss the generalization of the QNM formalism to predict the radiation properties of resonant nanoparticles in optical stacks. Owing to its rapidity, we believe that this method constitutes a formidable tool for the design of hybrid "nanoparticle/stack" systems and could deeply impact photonics research.

**ACKNOWLEDGMENT**

This study has been carried out with financial support from the French State, managed by the French National Research Agency (ANR) in the frame of "the Investments for the future" Programme IdEx Bordeaux – LAPHIA (ANR-10-IDEX-03-02), from the "Mission for Interdisciplinarity" of CNRS through the project NanoCG and from the French "Direction Générale de l'Armement" (DGA).

**REFERENCES**

1. Biagioni, P., J. S. Huang and B. Hecht, "Nanoantennas for visible and infrared radiation," *Rep. Prog. Phys.*, Vol. 75, No. 2, 024402, 2012.
2. Mokkapati, S., F. J. Beck, R. de Waele, A. Polman and K. R. Catchpole, "Resonant nanoantennas for light trapping in plasmonic solar cells," *J. Phys. D: Appl. Phys.*, Vol. 44, No. 18, 185101, 2011.
3. Zhmakin, A. I., "Enhancement of light extraction from light emitting diodes," *Phys. Rep.*, Vol. 498, No. 4-5, 189-241, 2011.
4. Yang, J., J. P. Hugonin and P. Lalanne, "Near-to-far field transformations for radiative and guided waves," *ACS Photon.*, Just Accepted Manuscript, doi:10.1021/acsphotonics.5b00559, 2016.
5. Sauvan, C., J. P. Hugonin, I. S. Maksymov and P. Lalanne, "Theory of the Spontaneous Optical Emission of Nanosize Photonic and Plasmon Resonators," *Phys. Rev. Lett.*, Vol. 110, No. 23, 237401, 2013.
6. Bai, Q., M. Perrin, C. Sauvan, J. P. Hugonin and P. Lalanne, "Efficient and intuitive method for the analysis of light scattering by a resonant nanostructure," *Opt. Express*, Vol. 21, No. 22, 27371, 2013.
7. Yang, J., M. Perrin and P. Lalanne, "Analytical Formalism for the Interaction of Two-Level Quantum Systems with Metal Nanoresonators," *Phys. Rev. X*, Vol. 5, No. 2, 021008, 2015.

# Spatiotemporal 3D pulse shaping using phase-shifted Bragg gratings.

**N. V. Golovastikov**[1,2*], **D. A. Bykov**[1,2], **and L. L. Doskolovich**[1,2]
[1]Samara State Aerospace University, Samara, Russia
[2]Image Processing Systems Institute of the Russian Academy of Sciences, Samara, Russia
[*]corresponding author: nikita.golovastikov@gmail.com

**Abstract** We propose a simple theoretical model that analytically describes spatiotemporal transformations of a three-dimensional optical pulse diffracted on a phase-shifted Bragg grating (PSBG). The diffraction of the pulse is described in terms of a linear system with pulse's transformations determined by the system's transfer function and impulse response. It is theoretically demonstrated and numerically verified that a PSBG can perform complex pulse transformations, such as simultaneous spatial and temporal differentiation of the optical pulse envelope.

Optical elements performing laser pulse shaping are of great interest for a wide range of applications, including ultrafast optical information processing, analog optical computing, laser material processing, and coherent control. Previously, various cases of pulse transformations with Bragg gratings were investigated including such fundamental operations as temporal [1-2] and spatial [3] differentiation of an incident pulse envelope. The recently obtained spatiotemporal approximation of transmission and reflection spectra of a resonant diffraction grating [4] makes it possible to analytically describe spatiotemporal 2D and 3D pulse transformations.

Following the description of the grating spectrum as a function of frequency and in-plain wave vector component of the incident wave [4], we consider the diffraction of an incident pulse in terms of passing a signal through a linear system. Simple analytical approximations for the transfer function and the impulse response of said system are derived. These approximations contain three independent parameters, which can be estimated for a certain PSBG using the rigorous coupled-wave analysis. In this model we assume that the central frequency of the incident pulse lies in the vicinity of the grating's resonance frequency.

The present work generalizes previous research [1-3] in a way that it provides analytical description of simultaneous spatial and temporal transformation of an incident pulse envelope. In particular, we show that a low-Q resonance Bragg grating performs simultaneous temporal and spatial differentiation of the incident pulse in reflection.

The theoretical conclusions are supported with numerical simulation of a normally incident Gaussian pulse diffracting on a Bragg grating. The parameters of the grating under investigation are as follows (see figure 1): $n_1 = n_{def} = 2.45$, $n_2 = 1.45$, $h_1 = 150\,\text{nm}$, $h_2 = 260\,\text{nm}$, $h_{\text{def}} = 300\,\text{nm}$, the complex frequency of the structure mode $\omega_p = 1255.77 - 17.57\text{i}\,\text{ps}^{-1}$, $Q = 35.7$.

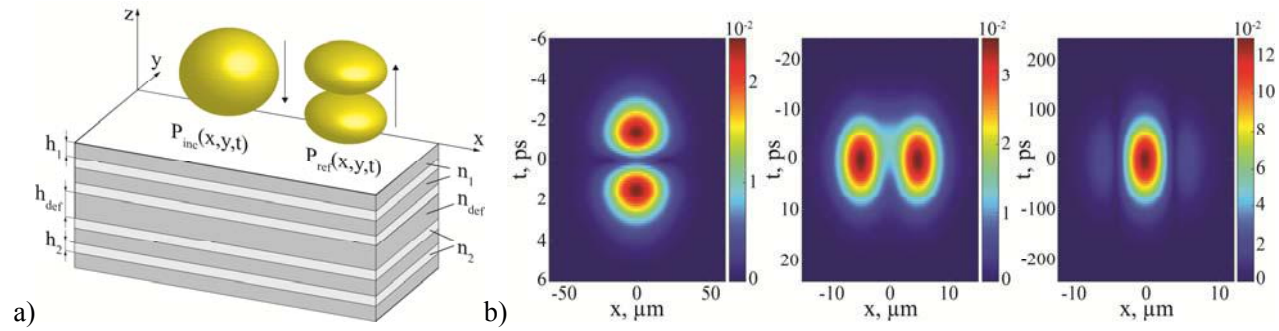



Figure 1. (a) Diffraction of a 3D pulse by a PSBG: incident pulse $P_{\text{inc}}(x,y,t)$ and reflected pulse $P_{\text{ref}}(x,y,t)$. (b) Numerically calculated reflected pulse envelope corresponding to different pulse transformations: temporal derivative (left), spatial derivative (right) and a superposition of both (centre).

Numerical simulation results in figure 1 prove that a single Bragg grating can perform first order temporal or second order spatial differentiation of an incident pulse envelope as well as superposition of both these transformations. The difference in outcome is determined by the incident pulse's width, duration and central frequency value. The root mean square deviation between the rigorously calculated pulse and analytical estimate in all three cases does not exceed 6%.

In conclusion, a new theoretical model to describe the spatiotemporal transformation of a 3D pulse by a Bragg grating is proposed. The diffraction of the pulse is described in terms of passing a signal through a linear system with simple analytical approximations of the system's transfer function and impulse response. The presented results of the rigorous numerical simulation completely confirm the proposed theoretical model and demonstrate that resonant gratings can perform complex pulse transformations, including simultaneous temporal and spatial differentiations of the pulse envelope. We believe that the proposed approach will be useful for pulse shaping and all-optical signal processing.

**Acknowledgements**

This work was funded by the Russian Science Foundation grant 14-19-00796.

**REFERENCES**

1. Berger, N. K., B. Levit, B. Fischer, M. Kulishov, D. V. Plant and J. Azaña, "Temporal differentiation of optical signals using a phase-shifted fiber Bragg grating," *Opt. Exp.*, Vol. 15, No. 2, 371-381, 2007.
2. Preciado, M. A. , X. Shu, P. Harper and K. Sugden "Experimental demonstration of an optical differentiator based on a fiber Bragg grating in transmission," *Opt. Lett.*, Vol. 38, No. 6, 917-919, 2013.
3. Bykov, D. A., L. L. Doskolovich, E. A. Bezus and V. A. Soifer, "Optical computation of the Laplace operator using phase-shifted Bragg grating," *Opt. Exp.*, Vol. 22, No. 21, 25084-25092, 2014.
4. Bykov, D. A. and L. L. Doskolovich, "$\omega - k_x$ Fano line shape in photonic crystal slabs," *Physical Review A*, Vol. 92, 013845, 2015.

# The Exceptional Point in Plasmonic Waveguide Arrays

**Shaolin Ke**[1], **Bing Wang**[1*], **and Peixiang Lu**[1]

[1] School of Physics, Huazhong University of Science and Technology, Wuhan 430074, China

[*] wangbing@hust.edu.cn

**Abstract**-We investigate the exceptional points (EPs) in non-parity-time-symmetric plasmonic waveguide arrays composed of monolayer graphene sheets. The intrinsic loss of graphene deforms the diffraction relation in the vicinity of the Dirac point. The optical EPs emerge as the wave vectors of the propagating and radiation modes coalesce.

Recently, the parity-time (PT) symmetry has attracted much attention in optical systems. Such non-Hermitian systems with balanced loss and gain may have real eigenvalues. The arranged potential is not enough to guarantee the realness of spectrum, leading to PT symmetry broking points, which are also known as EPs. Many intriguing phenomena are found associated with EPs, such as loss-induced transparency and unidirectional light reflectionless propagation. However, the EPs are much more general and could be found in the systems with loss, gain or open systems. They are singularities of the spectrum when both eigenvalue and eigenstate coalesce. Great attempt has been made to study EPs in optical cavity and photonic crystal, but not yet in waveguide arrays. Graphene sheet arrays (GSAs) attract intensive interest due to its two dimensional feature and flexible optical properties. In this work, we show that intrinsic loss of graphene can greatly affect the diffraction relation of Bloch modes and can transform the Dirac point into EPs.

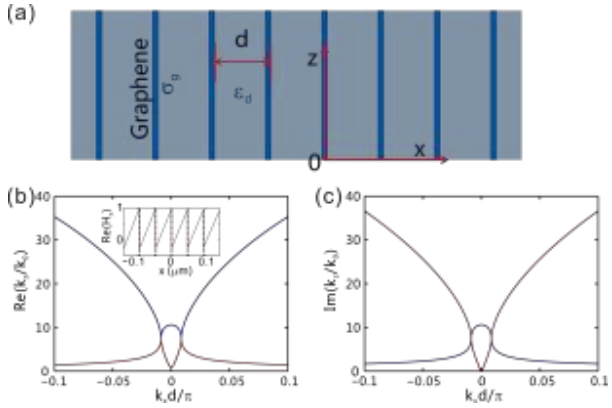



**FIG. 1** Schematic of graphene sheet arrays and diffraction relations of propagation and radiation modes.

Figure 1(a) shows the diagram of GSAs with period $d$. The incident wavelength $\lambda$ = 10 μm is assumed. The chemical potential is $\mu_c$ = 0.15 eV and relaxation time is $\tau$ = 0.5 ps at room temperature. The dispersion relation of TM modes can be derived as

$$\cos(\varphi) = \cosh(\kappa d) - \frac{\kappa\xi}{2}\sinh(\kappa d) \qquad (1)$$

where $\varphi = k_x d$ represents the Bloch momentum, $\xi = \eta_0\sigma_g/(i\varepsilon_d k_0)$ = 46.05- 0.72$i$ nm characterizes the effective mode width of SPPs in a single graphene sheet with $k_0$ denoting the wave vector of air, and $\kappa = (k_z^2 - \varepsilon_d k_0^2)^{1/2}$ with $k_z$ being the propagating constant. When not considering graphene loss, Eq. (1) has one real set and many imaginary solutions, corresponding to propagation and radiation modes. At $\varphi = 0$ and $d = \xi$, the propagation and lowest radiation modes coalesce as $\kappa = 0$. This point can be regarded as Dirac point. As the loss considered, the diffraction relation line

reshaped. Figure 1(b) illustrates $k_z$ as a function of $k_x$ at $d$ = 46.06 nm. The blue line represents the propagation mode and the red one the radiation mode. The enginvalue $k_z$ of two modes are the same at $d \approx \xi$ and $\varphi = \pm 0.0086\pi$, which are EPs. On the hand, the field distributions at EPs are shown in the insert, indicating the same eigenstate.

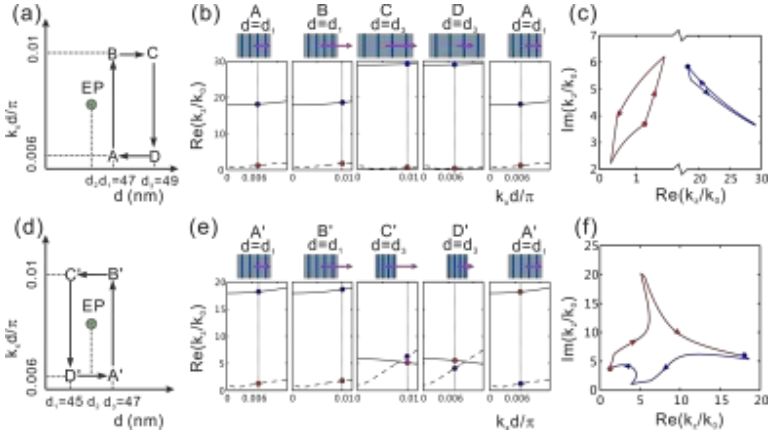



**FIG. 2** The loop properties of EPs.

We then investigate the topological property of EPs. A loop is created by adiabatically changing the system parameters. As show in Fig. 2(a), A, B, C, and D represent the points ($d$, $\varphi$) in the parametric space and the loop A→B→C→D→A don't encircle an EP. The blue and red dots in Fig. 2(b) indicate the eigenvalues at different parameters. It is found that without enclosing the EP, the blue dot and red dot come back to themselves at the end of loop, which also can be seen clearly in Fig. 2(c). On the other hand, when the other one encloses the EP (A'→B'→C'→D'→A'), the two eigenvalues switch their positions at the end of the loop as shown in Fig. 2(d)-2(f).

The position of EP is denoted as ($d_0$, $\varphi_0$). Because the Dirac point always locates at ($\xi$, 0) and the EPs are the perturbation results, we can get $d_0 \approx \mathrm{Re}(\xi)$, relating to $\sigma_g$ and $\lambda$. By using perturbation method, we get $\varphi_0 \approx a\mathrm{Re}(\sigma_g)/\mathrm{Im}(\sigma_g)$ and $a$ should be further determined by numerical fitting. As a result, the location of EP relates to surface conductivity of grphene and can be tuned via chemical potential and incident wavelength.

In conclusion, we have investigated the EPs in GSAs. The position of EPs can be tuned by chemical potential and incident wavelength. The loop property of EPs makes the arrays quite proper for sensor and may find applications in mode conversion.

**ACKNOWLEDGMENT**

This work is supported by the 973 Program (No. 2014CB921301), the National Natural Science Foundation of China (Nos. 11304108 and 11104095), and the Specialized Research Fund for the Doctoral Program of Higher Education of China (No. 20130142120091).

**REFERENCES**

1. Klaiman, S., U. Günther, and N. Moiseyev, "Visualization of branch points in p t-symmetric waveguides," Phys. Rev. Lett., Vol.101, No.8, 080402, 2008.
2. Zhen, B., C. W. Hsu, Y. Igarashi, L. Lu, I. Kaminer, A.Pick, and M. Soljačić, "Spawning rings of exceptional points out of Dirac cones," Nature, Vol. 525, No. 7569, 354-358, 2015.
3. Wang, B., X. Zhang, F. J. García-Vidal, X. Yuan, and J. Teng, "Strong coupling of surface plasmon polaritons in monolayer graphene sheet arrays," Phys. Rev. Lett., Vol. 109, N0.7, 073901, 2012.

# Surface Plasmon Polariton Manipulation in Graphene Sheet Arrays

**Bing Wang***
School of Physics, Huazhong University of Science and Technology, Wuhan 430074, China
*corresponding author: wangbing@hust.edu.cn

**Abstract**-Surface plasmon polaritons (SPPs) propagation in graphene sheet array (GSA) consisting of periodic arrays of spatially separated graphene sheets is investigated. The Talbot effect of SPPs is realized in the GSA when the incident field has a few selected periods. The Talbot distance increases exponentially with the array period. Bloch oscillations can also be observed in GSAs as the chemical potential of graphene undergoes a lateral gradient. By varying the lateral distribution of chemical potentials, we demonstrate the SPP beam routing effects in the GSAs. The same effects can also be realized by varying the interlayer spaces of graphene. The GSA should be a promising platform to manipulate SPPs on deep subwavelength scale.

Surface plasmon polaritons (SPP) can be supported in graphene as the photon energy of incident light is less than twice the Fermi level. When the graphene sheets are periodically stacked to form a waveguide array, the SPP Bloch mode can be existed in the graphene sheet array (GSA). Different from traditional dielectric and metallic waveguide arrays, SPPs in GSAs manifest unique diffraction behaviors. For example, as the interlayer space between graphene in the GSA is less than a critical value, there might be a Dirac point in the Brillouin zone center, where the SPPs experience diffraction free propagation and beaming splitting effect [1].

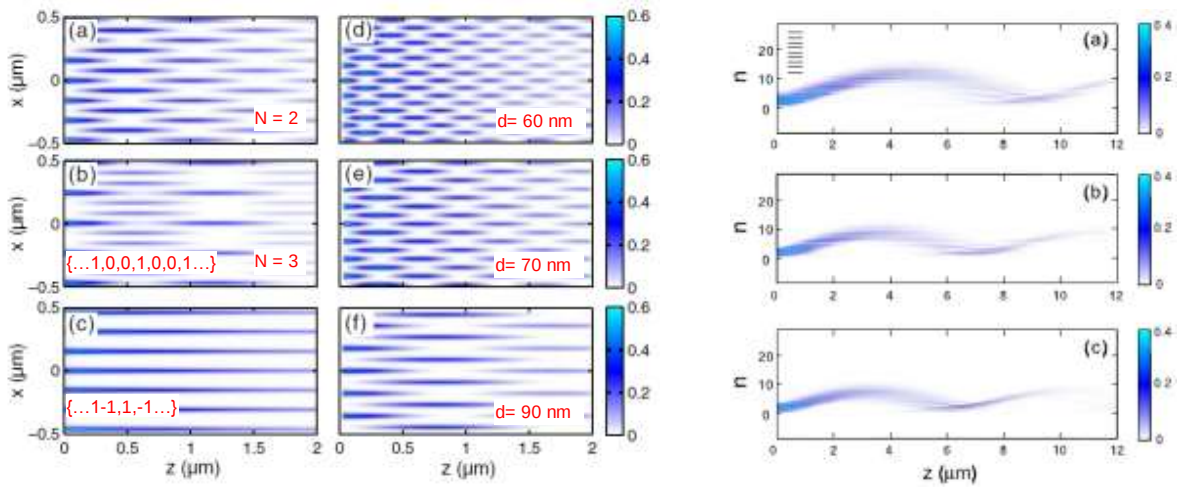



Figure 1. Left: Talbot effect of SPPs in GSAs. *N* denotes the incident field period in the unit of the array period *d*. Right: Bloch oscillations of SPPs in GSAs for different gradient of the inverse of chemical potential.

We firstly investigate the Talbot effect in the GSAs when SPPs between graphene experience weak coupling. The Talbot effect occurs only when the incident field has a pattern with a few selected periods, as shown in the left side of Fig 1. The Talbot distance is found to decrease exponentially with the decreasing period of the GSA and can be as small as 1/20 of the incident wavelength. By increasing the chemical potential of graphene, the Talbot distance can be further reduced [2]. On the other hand, the spatial plasmonic Bloch oscillations (BOs) can

also demonstrated in the GSAs by changing the chemical potentials of the graphene sheets [3]. The BOs occur when the SPPs reach the edge of the GSA and Brillouin zone edge at the same time. The period of BOs increases as the variation gradient of the chemical potential of the GSA decreases, as shown in the right side of Fig.1. The plasmonic BOs may find potential applications in graphene-based routing and switching devices on deep-subwavelength scale.

We also generally study the routing effect of SPPs in aperiodic GSAs, which are constructed by varying either the interlayer spaces between graphene or the individual graphene chemical potentials [4]. The SPP beams experience deep-subwavelength, low-loss, and diffraction-free propagation and can be accelerated or decelerated in the a-GSAs, resulting in beam routing in different paths, as shown in Fig. 2. The wave fronts of the beams are always parallel to the propagation direction, allowing the generation of transverse radiation pressure.

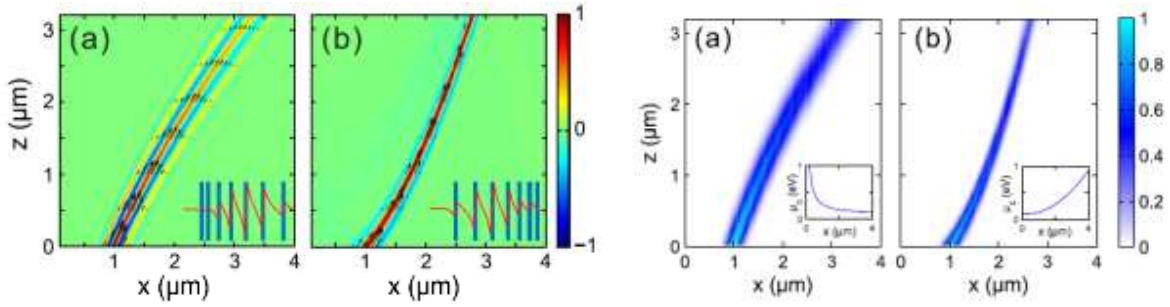



Figure 2. Left: The field distribution of SPPs propagating the aperiodic GSAs as the beam is accelerated (a) and decelerated (b). The insets show the structure of the aperiodic GSAs. Right: Intensity of SPPs in the aperiodic GSAs.

In conclusion, we investigate the Talbot self-imaging, Bloch oscillation, and beam routing effects of SPPs in GSAs. The Talbot effect can be observed in the weakly coupled GSAs. The Bloch oscillations and beam routing effects are realized in aperiodic GSAs constructed by varying either the interlayer spaces between graphene or the individual graphene chemical potentials. The GSA could be a promising platform to manipulate SPPs and find great applications in optical imaging, signal processing, and switches.

**Acknowledgements**-We acknowledge financial support by the National Natural Science Foundation of China (No.11304108), the 973 Program (No. 2014CB921301), and the Specialized Research Fund for the Doctoral Program of Higher Education of China (No.20130142120091).

**REFERENCES**

1. B. Wang, X. Zhang, F. J. García-Vidal, X. Yuan, and J. Teng, "*Strong coupling of surface plasmon polaritons in monolayer graphene sheet arrays*," Phys. Rev. Lett. 109, 073901 (2012).
2. Y. Fan, B. Wang, K. Wang, H. Long, and P. Lu, "*Talbot effect in weakly coupled monolayer graphene sheet arrays*," Opt. Lett. 39, 3371 (2014).
3. Y. Fan, B. Wang, H. Huang, K. Wang, H. Long, and P. Lu, "*Plasmonic Bloch oscillations in monolayer graphene sheet arrays*," Opt. Lett. 39, 6827 (2014).
4. B. Wang, H. Huang, K. Wang, H. Long, and P. Lu, "*Plasmonic routing in aperiodic graphene sheet arrays*," Opt. Lett. 39, 4867 (2014).

# Overcoming Quenching in Plasmonic Nanoantennas

**C. Sauvan**

[1]Laboratoire Charles Fabry, Institut d'Optique Graduate School, CNRS, Université Paris-Saclay, France

christophe.sauvan@institutoptique.fr

**Abstract**-We have developed a self-consistent electromagnetic theory of the link between light-matter interactions and optical resonances. The theory that relies on the concept of quasinormal modes is capable of accurately handling any photonic or plasmonic nanoresonator. We have used the modal formalism to analyze the mechanisms of spontaneous emission in plasmonic nanoantennas and to unravel the interplay between the decay into the antenna mode and the quenching. We provide guidelines to design plasmonic nanoantennas able to overcome quenching.

The development of micro- and nanotechnologies has recently opened a wide range of possibilities for controlling light at the wavelength scale or below. A fine control of the light (emission, transport and detection) in small volumes is at the heart of various applications, such as high performance sensors, light focusing below the diffraction limit, nanolasers, solid-state single-photons sources, or photovoltaic devices. Most of these applications rely on the use of localized optical resonances supported by photonic or plasmonic micro and nanoresonators.

In recent years, numerous works have been devoted to plasmonic nanoantennas because of their ability to provide extremely large field exaltations associated to nanoscale confinement volumes. In the context of spontaneous emission, these properties lead to huge enhancement factors. Unfortunately, very large enhancement factors usually correspond to emitters located only a few nanometers away from a metal surface. As a consequence, quenching through non-radiative energy transfer to the nearby metal constitutes the dominant relaxation process [1,2]. The resulting radiative efficiency is low and it is thus often thought that extremely large spontaneous decay rates in plasmonic nanoantennas are not of practical interest.

However, recent experimental demonstrations have shown that it is possible to obtain large enhancement factors (typically above 1000) with non-negligible radiative efficiencies (a few tenths of percent) [3,4]. These works have used a particular type of antenna geometry based on a nanogap between two metals. Very recently, a theoretical work has provided an explanation of these unexpectedly large radiative efficiencies in nanogap emitting devices [5].

We have developed a self-consistent electromagnetic theory that is able to unravel the interplay between the decay into the antenna mode and the quenching. The theory that is valid for any plasmonic nanoantenna relies on a modal formalism recently developed for photonic and plasmonic nanoresonators [6]. In particular, we show that overcoming the quenching is possible in different types of metallo-dielectric nanoantennas, not only in nanogap devices. We provide guidelines to design plasmonic nanoantennas that are able to overcome quenching and provide large spontaneous decay rate and large radiative efficiencies.

**REFERENCES**


1. Anger, P., P. Bharadwaj and L. Novotny, “Enhancement and quenching of single-molecule fluorescence,” *Phys. Rev. Lett.*, Vol. 96, 113002 (2006).
2. Kühn, S., U. Hakanson, L. Rogobete and V. Sandoghdar, “Enhancement of single-molecule fluorescence using a gold nanoparticle as an optical nanoantenna,” *Phys. Rev. Lett.*, Vol. 97, 017402 (2006).
3. Russel, K.J., T.L. Liu, S. Cui and E.L. Hu. “Large spontaneous emission enhancement in plasmonic nanocavities,” *Nat. Photonics*, Vol. 6, 459 (2012).
4. Akselrod, G.M., C. Argyropoulos, T.B. Hoang, C. Ciraci, C. Fang, J. Huang, D.R. Smith and M.H. Mikkelsen, “Probing the mechanisms of large Purcell enhancement in plasmonic nanoantennas,” *Nat Photonics*, Vol. 8, 835 (2014).
5. Faggiani, R., J. Yang and P. Lalanne, “Quenching, plasmonic and radiative decays in nanogap emitting devices,” *ACS Photonics*, Vol. 2, 1739 (2015).
6. Sauvan, C., J.P. Hugonin, I.S. Maksymov and P. Lalanne, “Theory of the spontaneous optical emission of nanosize photonic and plasmon resonators,” *Phys. Rev. Lett.*, Vol. 110, 237401 (2013).

# Plasmonic and Dielectric Nanoantennas for Integrated Photonic Circuitry

**Yuanqing Yang[1], Jingyi Tian[1], Hang Zhao[1], Qiang Li[1] and Min Qiu[1]***

[1]State Key Laboratory of Modern Optical Instrumental, College of Optical Science and Engineering, Zhejiang University, Hangzhou 310027, China

*corresponding author: minqiu@zju.edu.cn

**Abstract**- Nanoantennas, analogues of microwave and radiowave antennas at optical frequencies, have become a subject of great interest in recent years. Here we review our recent work on both plasmonic and dielectric nanoantennas. Different designs such as nanohorns, patch dimers and stair-like configurations are presented. In particular, we discuss how to control and functionalize the far-field radiation characteristics of these nanoantennas and nanoantenna-quantum-emitter coupled systems. These studies are expected to open new avenues for integrated photonic circuitry and optical wireless communications.

The widespread use of microwave and radiowave antennas could be found in almost all areas of modern technology, playing indispensable roles in our daily life. In particular, they function as the most efficient and essential components in various types of wireless communications, ranging from satellite communications to cellphones. Their optical counterparts, however, are still in its infancy in spite of intensive studies over the last decade [1]. Here we summarize our recent work on nanoantennas [2-6] and explore their potential in broadband optical wireless communications and integrated photonic nanocircuits.

## 1. On-chip nanoantennas for broadband nanophotonics wireless communication

Here we propose an on-chip plasmonic horn nanoantennas, as illustrated in Fig. 1(a). Different from most of nanoantennas that based on plasmonic resonances with narrow bandwidths, the presented horn nanoantennas are non-resonant type and could provide a natural impedance matching between localized plasmon modes and the free-space radiation. With a high coupling efficiency of 95%, the horn nanoantenna could also exhibit a high directivity of more than 20 [2, 3], which makes it a very promising building block for efficient wireless nanolinks. As depicted in Fig.1 (b) and (c), the horn-based nanolink shows a remarkably more pronounced power transmission than that of an optimized dipole-based nanolink with a 100-fold enhancement. More importantly, the horn-based nanolink even possesses an ultra-broad bandwidth that can cover the entire telecommunication range of more than 600 nm with nearly constant transmission characteristics.

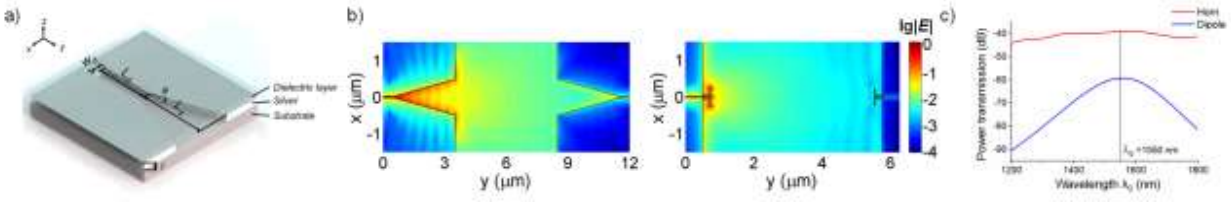



**Figure 1. (a)** The schematic diagram of the plasmonic horn nanoantenna **(b)** The electric-field distributions of wireless nanolinks using optimized horn and dipole nanoantennas at λ = 1550 nm **(c)** Spectral power transmission of horn-based (red) and dipole-based (blue) nanolinks at distance $d$ = 50 μm.

## 2. Directional Control of far-field radiation using plasmonic and Mie resonances of nanoantennas

In addition to the obtained high directivity and broad bandwidth, directional control of far-field radiation is also of central importance for many applications such as integrated optical circuitry and quantum communications. By exploiting plasmonic resonances of anisotropic nanodimers, we can achieve a linear-to-circular polarization conversion with an oblique directional radiation, making the nanoantenna-based devices an efficient background-free quarter-wave plate [4].

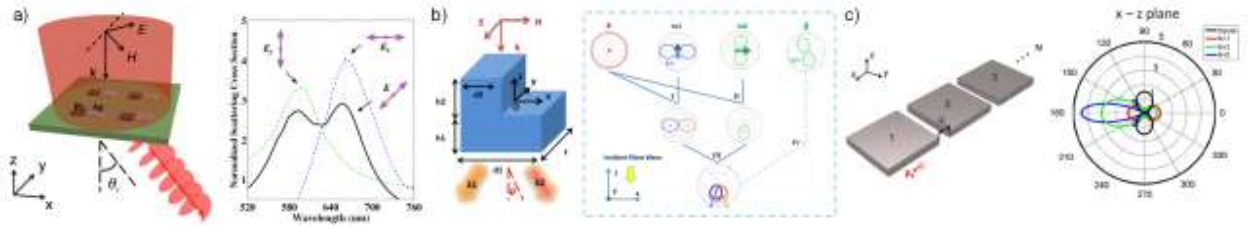



**Figure 2. (a)** Background-free quarter-wave plate based on anisotropic plasmonic nanodimers **(b)** Frequency-dependent directional scattering of silicon stair-like nanoantennas **(c)** All-dielectric patch nanoantennas and rotated unidirectional scattering from a quantum emitter.

Given the high intrinsic loss of metals involved in plasmonic regime, dielectric nanoantennas which are nearly lossless and could support both strong electric and magnetic responses are becoming a noteworthy and encouraging alternative. Here we realize frequency-dependent beam steering by introducing symmetry-breaking in silicon cubic nanoantennas and apply multipolar decomposition method to interpret the phenomenon, as illustrated in Fig. 2(b) [5]. Besides, we also investigate how to directionally control the radiation from a quantum emitter using electric and magnetic resonances of dielectric patch nanoantennas. The results clearly show that we can not only enhance but also rotate the far-field radiation of such an antenna-emitter coupled system. The underlying physics is also fully revealed by a semi-analytical equivalent model [6].

**Acknowledgements** This work is supported by the National Natural Science Foundation of China (Grant Nos. 61235007, 61205030, 61425023, 6157517 and 61275030).

## REFERENCES

1. L. Novotny and N. van Hulst, “Antennas for light,” *Nat. Photon.* Vol. 5, 83–90, 2011
2. Y. Yang, D. Zhao, H. Gong, Q. Li and M. Qiu, “Plasmonic sectoral horn nanoantennas” *Opt. Lett.*, 39(11), 3204–3207, 2014.
3. Y. Yang, Q. Li and M. Qiu, “Broadband nanophotonic wireless links and networks using on-chip integrated plasmonic antennas,” *Sci. Rep.*, Vol. 6, 19490, 2016.
4. H. Zhao, Y. Yang, Q. Li and M. Qiu, “Sub-wavelength quarter-wave plate based on plasmonic patch antennas”, *Appl. Phys. Lett.*, Vol. 103, No. 26, 261108, 2013
5. J. Tian, Q. Li, Y. Yang and M. Qiu, “Tailoring Unidirectional Angular Radiation through Multipolar Interference in a Single-element Subwavelength All-Dielectric Stair-like Nanoantenna,” *Nanoscale*, Vol. 8, 4047–4053, 2016
6. Y. Yang, Q. Li and M. Qiu, “Controlling the angular radiation of single emitters using dielectric patch nanoantennas,” *Appl. Phys. Lett.*, Vol. 107. No. 3, 031109, 2015

# Topological photonics

# Weyl Points and Topological Notions in Electromagnetic Waves

**Wen-Jie Chen[1*], Meng Xiao[1], Wen-Yu He[1], Z. Q. Zhang[1], and C. T. Chan[1]**

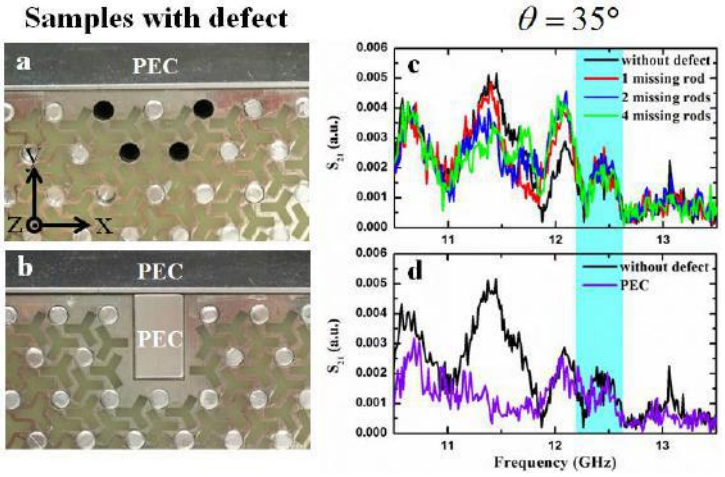
[1] Department of Physics and the Institute for Advanced Study, The Hong Kong University of Science and Technology, Hong Kong, China

[*]corresponding author: wjchen@ust.hk

**Abstract**- We designed, fabricated and experimentally characterized a Weyl photonic crystal with both single and double Weyl points. Nontrivial 2D bulk band gaps for fixed kz and Weyl points were confirmed by angle-resolved transmission spectra. The robustness of the associated surface states against kz-preserved scattering was experimentally observed. In addition, we propose a pseudospin-polarized waveguide without using bulk materials. Wave propagation in the waveguide is robust against deformations that do not induce spin flip, which were experimentally observed.

The analogues of 2D quantum Hall effect and quantum spin Hall effect have been proposed and realized in various kinds of classical wave systems. In our previous work[1], we create an effective gauge flux for acoustic waves in a reduced two-dimensional system by engineering interlayer couplings, achieving an acoustic analogue of the Haldane model. We showed that the synthetic gauge flux is closely related to the existence of Weyl points in the three-dimensional band structure and the system supports chiral edge states for fixed values of kz.

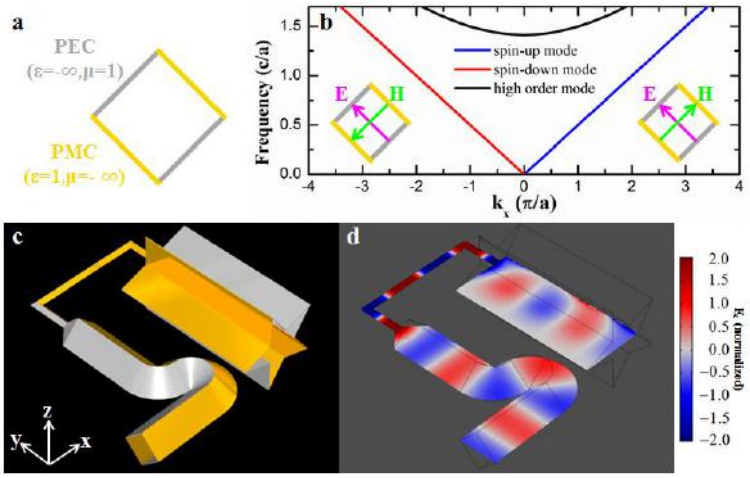
In the first part of this talk, we extend this idea to electromagnetic wave systems[2]. We designed and fabricated a Weyl photonic crystal by introducing chiral interlayer coupling in microwave regime. Nontrivial 2D bulk band gap for fixed kz and Weyl point were confirmed by angle-resolved transmission spectra. Owing to the topological charge of Weyl points, the surface between Weyl photonic crystal and perfect metal (trivial gap material) supports $k_z$-preserved robust surface state which is guaranteed by bulk-surface correspondence. To demonstrate the robustness against kz-preserving scattering, we fabricated two kinds of defects, as shown in Fig. 1a and 1b. The measured transmissions are illustrated in Fig. 1c and 1d, where black or colored curves correspond to the sample without or with defect. In the frequency region of nontrivial band gap (highlighted by light cyan box), no obvious reflection were introduced by both kinds of defects.




**Figures 1. Robust surface states between Weyl photonic crystal and PEC.** For a fixed nonzero kz, the surface only supports surface states in one direction. Hence the surface states are robust against scattering that

preserves kz. **a**. Photograph of the sample when 4 PEC rods (highlighted by black circles) near the surface are removed. **b**. Photograph of the sample with a PEC bar inserted into the crystal. **c**, **d**. The measured transmission spectra for two kinds of defect when the incident angle $\theta$=35° ($k_z$=0.2581$\pi/d$ for 12.5GHz).

In the second part, we propose a pseudospin-polarized waveguide without using bulk materials[3]. Wave propagation in the waveguide is robust against deformations that do not induce spin flip. On the basis of our spin-polarized waveguide, a broadband field concentrator was designed and realized experimentally. The realization of pseudospin transport simply by imposing boundary conditions has the obvious advantages of using less bulk material and being less lossy as the wave is guided in air.




**Figures 2. Concept of pseudospin-filtered waveguide. a**. Cross-sectional view of a square waveguide with PEC and PMC boundaries. **b**. Waveguide dispersion. Only two TEM modes are allowed below the cutoff frequency of a spin-degenerate high order waveguide mode. The forward mode propagating along the $+x$ direction is pseudospin-up polarized while the backward mode is pseudospin-down polarized (see the eigenfield in left inset). The square waveguide is hence a spin-filtered channel. Its transport is robust against backscattering unless the scatterer or deformation flips the pseudospin. **c**. Geometry of a deformed waveguide. EM wave with 45°-tilted polarization enters the bottom of the deformed waveguide, which consists of a square waveguide successively connected to an S-shaped bend, another square waveguide with very small (1/25) cross section and a star-shaped waveguide. As the $\varepsilon(x,y,z)=\mu(x,y,-z)$ symmetry is preserved despite these deformations, the spin-up mode and the spin-down mode are decoupled, and no backscattering can occur. **d**. $E_z$ field pattern in the deformed waveguide normalized by the incident field amplitude.

**Acknowledgements**, This work was supported by Research Grants Council Hong Kong (AoE/P-02/12).

**REFERENCES**

1. Xiao, M., Chen, W.-J., He, W.-Y. and Chan, C. T. "Synthetic gauge flux and Weyl points in acoustic systems." *Nat. Phys.* Vol. 11, No. 10, 920-924, 2015.
2. Chen, W.-J., Xiao, M. and Chan, C. T. "Experimental observation of robust surface states on photonic crystals possessing single and double Weyl points." Preprint at // http://arxiv.org/abs/1512.04681, 2015.
3. Chen, W.-J., Zhang, Z. Q., Dong, J.-W. and Chan, C. T. "Symmetry-protected transport in a pseudospin-polarized waveguide." *Nat. Commun.* Vol. 6, 9183, 2015.

# Synthetic dimensions in multi-mode ring-resonator arrays

**Tomoki Ozawa**[1], **Hannah M. Price**[1], **Nathan Goldman**[2], **Oded Zilberberg**[3], **and Iacopo Carusotto**[1]

[1]INO-CNR BEC Center and Dipartimento di Fisica, Università di Trento, I-38123 Povo, Italy
[2]CENOLI, Faculté des Sciences, Université Libre de Bruxelles (U.L.B.), B-1050 Brussels, Belgium
[3]Institute for Theoretical Physics, ETH Zurich, 8093 Zürich, Switzerland
tomoki.ozawa@unitn.it

**Abstract**—

We propose a method to produce synthetic dimensions in arrays of multi-mode ring-resonators. This method allows one to use d-dimensional arrays of resonators to simulate (d+1)-dimensional lattice models with synthetic magnetic fields. Applying the method to one-dimensional array of resonators, we show that such a structure can be used as an optical isolator. Applying the method to three-dimensional lattices of resonators, we show that the system exhibits the four-dimensional quantum Hall effect.

Recent advances in the study of multi-mode ring-resonator arrays have spurred the development of topological lattice models with photons with potential applications in integrated photonics. In this talk, we discuss how one can push the boundary even further by realizing synthetic dimensions in coupled arrays of ring-resonators [1]. We treat different modes of a ring-resonator as an extra "synthetic" dimension for photons. Tunneling along the synthetic dimension is implemented via an external time-dependent modulation of the dielectric constant. By appropriately choosing the phase of the modulation, one can obtain the complex tunneling phase in the synthetic dimension, which allows one to simulate the effect of a "magnetic" field for photons. We present how this approach can be used to generate a variety of topologically nontrivial lattices.

In particular, we show how a 1D chain of resonators can be used to simulate physics of a 2D lattice with a perpendicular magnetic field. Such a 2D lattice model, known as the Harper-Hofstdter model, is topologically nontrivial and exhibits topologically protected chiral edge states in appropriate frequency ranges. We show that, making a particular mode of resonators very lossy, one can effectively engineer an edge in the synthetic 2D lattice through the Zeno effect. We discuss that, making use of the chiral edge states at the effective edge, such a 1D chain can be used as an optical isolator.

Furthermore, we show that a 3D lattice of resonators can be used to simulate a 4D lattice with magnetic fields, which exhibits the 4D quantum Hall effect. In the 4D quantum Hall system, the Hall current in response to the external perturbative electric and magnetic fields is proportional to the 4D topological invariant known as the second Chern number. We show that it is possible to estimate the second Chern number in photonic systems with drive and dissipation, where the information of the Hall current is embedded in the steady-state distribution of photons.

**REFERENCES**

1. Ozawa, T., Price, H. M., Goldman, N., Zilberberg, O. and Carusotto, I., "Synthetic dimensions in integrated photonics: From optical isolation to 4D quantum Hall physics," *arXiv:1510.03910*.

# Topological effects based on spin-orbit coupling of cavity polaritons

**D.D. Solnyshkov[1*], A.V. Nalitov[1], and G. Malpuech[1]**
[1]Institut Pascal, Université Clermont Auvergne, Université Blaise Pascal/CNRS, Clermont-Ferrand, France
[*]corresponding author: dmitry.solnyshkov@univ-bpclermont.fr

**Abstract**- We show that the TE-TM splitting of planar cavities leads to a special type of spin-orbit coupling for patterned cavities. Under an applied magnetic field, polariton graphene behaves as a Z topological insulator with chiral surface states, which can be evidenced by direct resonant excitation. In zigzag chains of pillar cavities, this coupling brings about the topological edge states and stable dark-bright solitons, allowing to study the Kibble-Zurek mechanism in condensation.

Exciton polaritons – the quasiparticles formed from the strong coupling of a quantum well exciton and a cavity photon in planar microcavities – are a subject of active research since the demonstration of their Bose-Einstein condensation in 2006 [1]. Their most important properties include light effective mass, two spin projections, and strong spin-anisotropic interactions. They can be created by non-resonant excitation, allowing to study condensation, or by quasi-resonant excitation, allowing to precisely control the wavefunction, which can then be fully analyzed by studying the photons decaying from the cavity.

The main origin of the spin-orbit coupling for polaritons is the TE-TM splitting, arising from the difference in the reflection coefficients of the cavity for TE and TM polarizations, which is enhanced by a difference in the exciton-photon coupling. The TE-TM splitting is at the origin of the Optical Spin Hall effect [2,3,4], consisting in the spatial separation of opposite spin projections.

Polaritons can be confined in an in-plane potential, engineered by patterning the microcavity or by other means [5-7]. The TE-TM splitting is usually enhanced by the in-plane confinement and the strain. Recent structures include a polariton benzene molecule (6 coupled pillars) [8] and, finally, polariton graphene [9]: a large hexagonal array of overlapping pillar cavities etched from a larger planar cavity. The presence of the spin-orbit coupling was experimentally and theoretically demonstrated by its dramatic effects in the benzene molecule, while the polariton graphene was proven to have a band structure similar to that of the electronic graphene, including the Dirac points. The major difference with the electronic graphene arises from the original type of the spin-orbit coupling in polariton graphene. Unlike the well-known Rashba or Dresselhaus fields, or the Kane-Mele term acting as an out-of-plane magnetic field in monolayer graphene [10], the TE-TM splitting presents a double rotation, with the direction of the field rotating twice faster than the polar angle.

In our recent works, we have shown that the TE-TM effective field leads to a strong modification of the band structure of polariton graphene [11], including the trigonal warping. In presence of a magnetic field, the polariton graphene becomes a Z topological insulator [12], with integer band Chern numbers equal ±2. The bulk-to-boundary correspondence predicts the existence of chiral states on the surface of such insulator, which we have demonstrated, confirming their one-way nature and their topological protection from backscattering. Such states can be used for an optical non-return valve, isolating the inputs and the outputs of logical devices.

In a 1D zigzag chain of overlapping pillar cavities, the spin-orbit coupling means basically a difference between the tunneling coefficients through neighboring junctions for a given polarization, equivalent to the dimerization of the chain, with corresponding consequences, such as the splitting of a single band into two

topologically distinct ones [13], the existence of a topological invariant (the Zak phase [14]) characterizing these bands, and the associated topologically protected edge states, whose polarization depends on the parity of the chain. They can be evidenced via polariton condensation under focused pumping, because of their localized nature.

Dimer chains can support dimerization domains separated by domain walls – the Su-Schrieffer-Heeger solitons [15]. For polaritons, such domains are characterized by orthogonal polarization, and the domains walls are the dark-bright solitons, whose stability is provided by topological protection. This should allow to observe them in CW experiments, contrary to the usual dark solitons or half-solitons, which require single-shot experiments. Such feature is very useful for the study of universal scaling of the density of the solitons formed via the Kibble-Zurek mechanism during the condensation under homogeneous pumping [16]. Numerical simulations confirm our analytical predictions for the scaling exponent of 1/4.

We acknowledge the support of ITN INDEX (289968) and ANR Labex GANEX (ANR-11-LABX-0014).

**REFERENCES**

1. J. Kasprzak *et al*, "Bose-Einstein condensation of exciton-polaritons", *Nature*, Vol. 443, 409, 2006.
2. A. Kavokin, G. Malpuech, M. Glazov, "Optical Spin Hall Effect", *Phys. Rev. Lett.*, Vol. 95, 136601, 2005.
3. C. Leyder *et al*, "Observation of the optical spin Hall effect", *Nature Physics*, Vol. 3, 628, 2007.
4. H. Flayac, D.D. Solnyshkov, I.A. Shelykh, and G. Malpuech, "Transmutation of Skyrmions to Half-Solitons Driven by the Nonlinear Optical Spin Hall Effect", *Phys. Rev. Lett.*, Vol. 110, 016404, 2013.
5. E. Wertz *et al*, "Spontaneous formation and optical manipulation of extended polariton condensates", *Nature Physics*, Vol. 6, 860, 2010.
6. E.A. Cerda-Méndez et al, "Polariton Condensation in Dynamic Acoustic Lattices", *Phys. Rev. Lett.*, Vol. 105, 116402, 2010.
7. G. Tosi *et al*, "Sculpting oscillators with light within a nonlinear quantum fluid",*Nat. Phys.*,Vol.8,190, 2012.
8. V.G. Sala et al, "Engineering spin-orbit coupling for photons and polaritons in microstructures", *Phys. Rev. X*, Vol. 5, 011034, 2015.
9. T. Jacqmin *et al*, "Direct Observation of Dirac Cones and a Flatband in a Honeycomb Lattice for Polaritons", *Phys. Rev. Lett.*, Vol. 112, 116402, 2014.
10. C.L. Kane and E.J. Mele, "Quantum Spin Hall Effect in Graphene", *Phys. Rev. Lett.*, Vol. 95, 226801, 2005.
11. A.V. Nalitov, G. Malpuech, H. Terças, D. Solnyshkov, "Spin-Orbit Coupling and the Optical Spin Hall Effect in Photonic Graphene", *Phys. Rev. Lett.*, Vol. 114, 026803, 2015.
12. A.V. Nalitov, D.D. Solnyshkov, G. Malpuech, "Polariton Z Topological Insulator", *Phys. Rev. Lett*., Vol. 114, 116401, 2015.
13. P. Delplace, D. Ullmo, and G. Montambaux, "Zak phase and the existence of edge states in graphene", *Phys. Rev. B*, Vol. 84, 195452, 2011.
14. J. Zak, "Berry's Phase for Energy Bands in Solids", *Phys. Rev. Lett.*, Vol. 62, 2747, 1989.
15. W.P. Su, J.R. Schrieffer, A.J. Heeger, "Soliton excitations in polyacetylene", *Phys. Rev. B*, Vol. 22, 2099, 1980.
16. D.D. Solnyshkov, A.V. Nalitov, G. Malpuech, "Kibble-Zurek Mechanism in Topologically Nontrivial Zigzag Chains of Polariton Micropillars", *Phys. Rev. Lett*., Vol. 116, 046402, 2016.

# Topological Properties of Quasicrystals: A Scattering Analysis

**E. Levy**[1,2,*]**, A. Barak**[2]**, A. Fisher**[1] **and E. Akkermans**[1]
[1]Department of Physics, Technion Israel Institute of Technology, Haifa 32000, Israel
[2]Rafael Ltd., P.O. Box 2250, Haifa 32100, Israel
[*]corresponding author: mrelilevy@gmail.com

**Abstract** - We present a study of topological properties of dielectric Fibonacci quasicrystals. Chern numbers which label the dense set of spectral gaps correspond to an underlying palindromic symmetry. These spectral topological features are related to the two independent phases of the scattering matrix. Conveniently designed gap modes allow to directly measure these Chern numbers via spectroscopy. Existing experimental realizations will be addressed, and results will be shown which extend beyond the dielectric Fibonacci sequence.

Topology plays an important role in many topics in physics by providing a general classification of some physical phenomena in terms of a small number of topological invariants. These numbers appear to be ubiquitous in modern physics and particularly in condensed matter. Chern topological numbers, for instance, are instrumental to understand the Hall conductance in quantum Hall effects, anomalies in Dirac systems and topological insulators. This correspondence has also motivated the study of topological aspects of quasicrystals [1, 2]. For example, in substitution rules based quasicrystals, Chern integers label the dense set of gaps in the energy (frequency) spectrum through the gap labeling theorem [1], leading to a large number of topological invariants, uncommon phenomenon in most natural physical systems. For the Fibonacci test-case, these numbers show up as [1]

$$\mathcal{N}(\varepsilon_{gap}) = p + q\tau^{-1}, \qquad (1)$$

where $\mathcal{N}$ is the normalized integrated density of states, τ is the golden mean, and {p,q} are integers (see Figure 1a). However, for quasicrystals such as the Fibonacci chain, the physical origin underlying the existence of Chern numbers has not yet been identified in the most basic terms as the winding of a phase with respect to some field variable.

The current work [3] has addressed this point and has proposed new expressions and possible measurements of Chern numbers using the scattering approach. The unitary scattering matrix has been shown to consist of two independent phases. The first phase is the well-known total phase shift describing bulk spectral properties. The second phase is a newly defined chiral phase sensitive to the asymmetry of a finite quasicrystal. The chiral phase has been shown to have an integer winding number with respect to a structural degree of freedom called the modulation phase shift. This modulation phase shift, also known as a phason, has been shown to drive a cycle of structural palindromic symmetry (see Figure 1b). The winding of the chiral phase with respect to the modulation phase shift has been shown to be identical to Chern integers of the gap labeling theorem calculable through the total phase shift. A structural scheme to induce edge states, sensitive to the chiral phase, has been proposed as a spectroscopic measurement of Chern numbers (see Figure 1b). We shall present results for the specific case of Fibonacci chains, but we will stress their generality. Experimental progress on the measurement of the topological invariants and prospects will be also addressed [4,5].

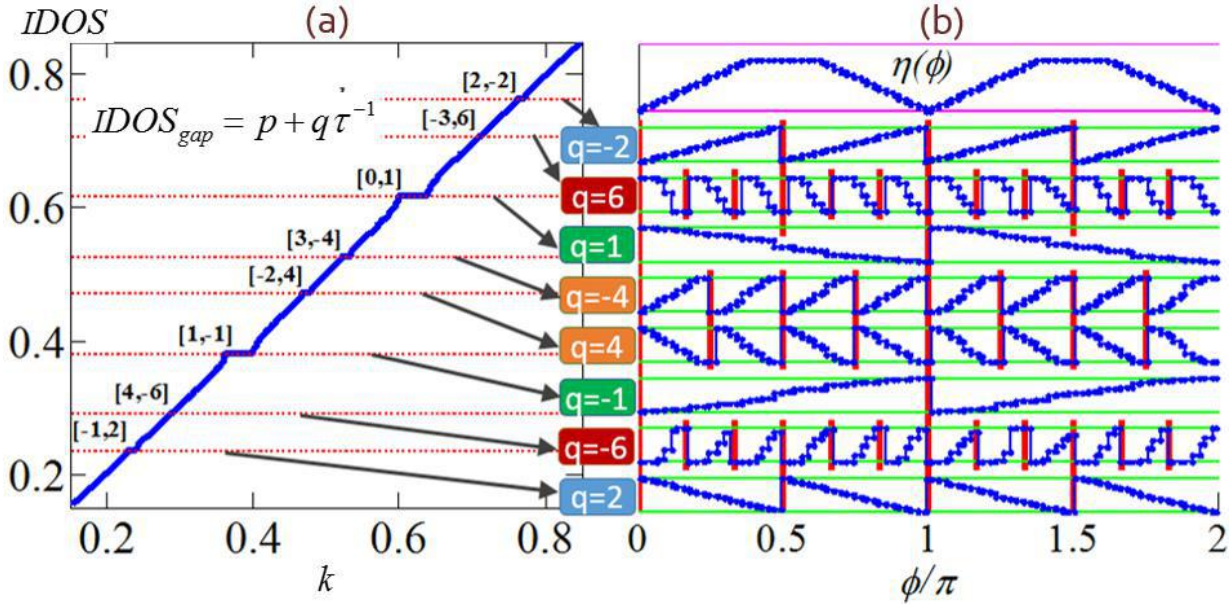



Figure 1: (a) Normalized integrated density of modes (IDOS) as a function of wavenumber for a dielectric Fibonacci chain. The location of 8 selected gaps using their topological numbers [p,q] are indicated in accordance to (1). (b) The corresponding gap modes relative spectral position within the gap as a function of the modulation phase shift $\phi$, and compared to the palindromic symmetry parameter $\eta(\phi)$ (top).

**REFERENCES**


1. J. Bellissard, A. Bovier and J.M. Ghez, Reviews in Math. Physics, Vol. 4, No. 1, 1-37 (1992) and J. Bellissard, Les Houches, Springer, J.M. Luck, P. Moussa and M. Waldschmidt Eds., (1993), S. Ostlund, R. Pandit, D. Rand, H.J. Schellnhuber and E.D. Siggia,Phys. Rev. Lett. 50, 1873 (1983) and S. Ostlund, D. Rand, J. Sethna and E.D. Siggia, Physica 8D, 303 (1983).
2. B. Simon, Adv. Appli. Math. 3, 463 (1982), M. Shubin, Russian Math. Surveys 34, 109 (1979), R. Johnson and J. Moser, Commun. Math. Phys. 84, 403 (1982), R. Johnson, Acta Applicandae Mathematicae, 1, 241 (1983) and K. Bjerklov and T. Jager, J. of American. Math. Soc. 22, 353 (2009)
3. E. Levy, A. Barak, A. Fisher, E. Akkermans, arXiv 1509.04028 (2015)
4. F. Baboux, E. Levy, A. Lemaître, E. Galopin, I. Sagnes, L. Le Gratiet, A. Amo, J. Bloch, and E. Akkermans, (in preparation 2016).
5. A. Dareau, E. Levy, M. Bosch Aguilera, R. Bouganne, E. Akkermans, F. Gerbier, and J. Beugnon (in preparation 2016).

# Metamaterial structures to realize real-space gauge-field

**Fu Liu and Jensen Li** *

School of Physics and Astronomy, University of Birmingham, Birmingham B15 2TT, UK

*corresponding author: j.li@bham.ac.uk

**Abstract**- By using metamaterials to mimic a pseudo gauge field and pseudo magnetic field to bend light, we can achieve optical spin Hall effect, one-way topological edge states, which will be useful in spin-dependent and spoof-magneto optics. In this talk, we will discuss the underlying metamaterial structures to realize such a gauge field. Reduced parameter approximation is established as a useful tool to simplify experiments without employing magnetic responses.

Conventional optical media bend light by changing the sizes and the shapes of the dispersion surfaces. We have recently introduced a gauge-field approach [1-4] by shifting the centers of the dispersion surfaces instead [5, 6]. The associated pseudo magnetic force, with opposite signs for the two pseudo-spins, can then be used to bend light into cyclotron-like motion. Optical spin Hall effect and one-way topological edge states can be achieved as a result of the pseudo magnetic field in the real space.

In this talk, we will discuss the underlying metamaterial structures in order to materialize such a shifting of dispersion surface, termed as the gauge field. In its ideal case, it requires generally an anisotropic metamaterial with dedicated balance of electric and magnetic responses. For a metamaterial in realizing a gauge field $\vec{A} = A_y\hat{y}$, with associated pseudo magnetic field $\vec{B} = \nabla \times \vec{A}$, we need an effective medium, in $x-y-z$ components, of the following form:

$$\epsilon = \begin{pmatrix} \epsilon_1 & 0 & A_y \\ 0 & \epsilon_2 & 0 \\ A_y & 0 & \epsilon_3 \end{pmatrix}, \qquad \mu = \eta^2 \begin{pmatrix} \epsilon_1 & 0 & -A_y \\ 0 & \epsilon_2 & 0 \\ -A_y & 0 & \epsilon_3 \end{pmatrix}. \tag{1}$$

To realize such a gauge field medium for two dimensional in-plane wave propagation, one of the principal axes of the medium and the associated metamaterial structures has to be tilted away from the vertical z-axis by 45 degrees. Figure 1(a) shows a design to fulfil the above form of effective medium with $\epsilon_1 = \epsilon_3 = 1.33$, $\epsilon_2 = 1/\eta^2 = 1.19$ at a frequency around 6.7GHz. It consists of a split-ring to get the magnetic response with an electric bar-resonator as a tuning for the detail balance. The associated split dispersion surfaces are plotted in Fig. 1(b) with a splitting of magnitude given by the gauge field $A_y = 0.13$.

To facilitate experimental realizations, we will further develop the so-called reduced parameter approximation on the material parameters so that only the shapes and locations of the shifted dispersion surfaces rather than the impedances are realized, in a similar spirit to transformation optics where an invisibility cloak can be experimentally realized with electric-only or magnetic-only responses. In our case, metamaterials with only electric responses can be designed to realize the gauge field. The associated effective medium can now be written as

$$\epsilon = \begin{pmatrix} \epsilon_1 & 0 & \epsilon_{13} \\ 0 & \epsilon_2 & 0 \\ \epsilon_{13} & 0 & \epsilon_3 \end{pmatrix}, \qquad \mu = 1. \tag{2}$$

As an example, Fig. 2(a) shows the metamaterial design composed of a two-level fractal structure in each unit cell. It only has electric response on the $x-z$ plane while the magnetic response is neglible. In this case, the associated dispersion surface is plotted in Fig. 2(b). It is approximated very well by two elliptical dispersion surfaces with a splitting of $A_y \cong 0.4$. With such a gauge field, we also discuss different spin-dependent optical devices based on the concept of gauge field. We will also extend the framework of transformation optics. Invisibility cloaks and transformation optical devices with unidirectional propagation characteristics can be designed as examples.

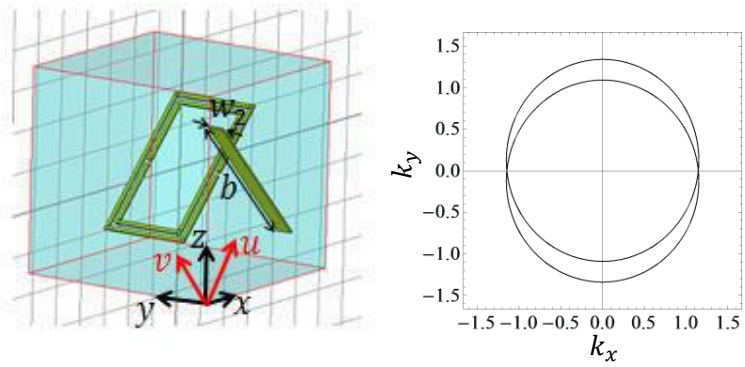



Figure 1 (a) A unit cell of tiled anisotropic metamaterial structure with detailed balance of electric and magnetic responses to achieve an ideal gauge field. The unit cell is repeated in all three directions. (b) The associated dispersion surface with gauge field $A_y = 0.14$.

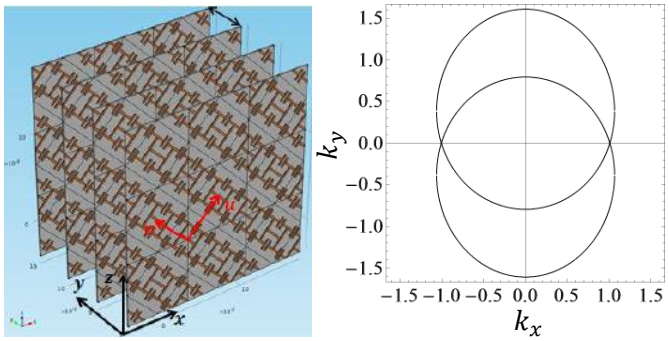



Figure 2 (a) Tilted metamaterial with electric-only responses to achieve an approximated gauge field. (b) The associated elliptic dispersion surfaces with splitting $A_y \cong 0.4$ in the y-direction in the reciprocal space.

**REFERENCES**


1. M. Hafezi, S. Mittal, J. Fan, A. Migdall and J. M. Taylor, Nature Photon. 7, 1001 (2013).
2. K. Fang, Z. Yu, and S. Fan, Nat. Photonics 6, 782 (2012).
3. Q. Lin, S. Fan, Phys. Rev. X 4, 031031 (2014).
4. M. C. Rechtsman, J. M. Zeuner, A. Tünnermann, S. Nolte, M. Segev, and A. Szameit, Nature Photon. 7, 153 (2013).
5. F. Liu, and J. Li, Phys. Rev. Lett. 114, 103902 (2015).
6. F. Liu, S. Wang, S. Xiao, Z. H. Hang, and J. Li, Appl. Phys. Lett. 107, 241106 (2015).

# Metasurface Laser

**B. Kanté**
*Department of Electrical and Computer Engineering, University of California San Diego, La Jolla, CA 92093-0407, USA*
*bkante@ucsd.edu*

**Abstract:** We have designed a high quality factor cavity that is based on a bound state in the continuum at a metasurface and harnessed its properties to demonstrate a novel type of surface emitting laser. We have experimentally demonstrated lasing action in this compact nanophotonic laser at room temperature and for a very low threshold power.

## 1. Introduction

In 1929, von Neumann and Wigner showed that Schrödinger's equation can have, somewhat surprisingly, bound states above the continuum threshold [1]. These bound states represent the limiting case of quasi-bound states with an infinite lifetime, *i.e.*, resonances that do not decay. It was recently realized that bound states in the continuum (BICs) are intrinsically a wave phenomenon and are thus not restricted to quantum mechanics. Since then, they have been shown to occur in many different fields of wave physics such as acoustics and photonics [2,3].

In photonics' terminology, BICs are eigenmodes of an open system with an infinite radiation quality factor, $Q_{rad}$. To take advantage of this unique property to design high quality resonant cavities, most investigations have focused on dielectric structures that, unlike their plasmonic counterparts, are not limited by their material quality factor, $Q_{mat}$ [3-5]. To investigate the properties of BICs, various platforms have been used such as 1D gratings [3], waveguide arrays [4], and 2D photonic crystal slabs [5].

In this contribution, we have designed a high quality cavity based on a BIC and harnessed its novel properties to achieve a compact low-threshold nanophotonic laser.

## 2. Laser Design

Our design consists of a 2D suspended array of nanoresonators (membrane). The membrane itself is composed of a square lattice of cylinders interconnected by a network of bridges as shown in the inset of Figure 1. This membrane contains epitaxially grown layers of InGaAsP which include quantum wells specially designed to operate around telecommunication wavelengths (λ=1550 nm). Figure 1 shows the evolution of the total quality factor for the BIC eigenmode in an infinite array with varying cylinder radius and for different $Q_{mat}$.

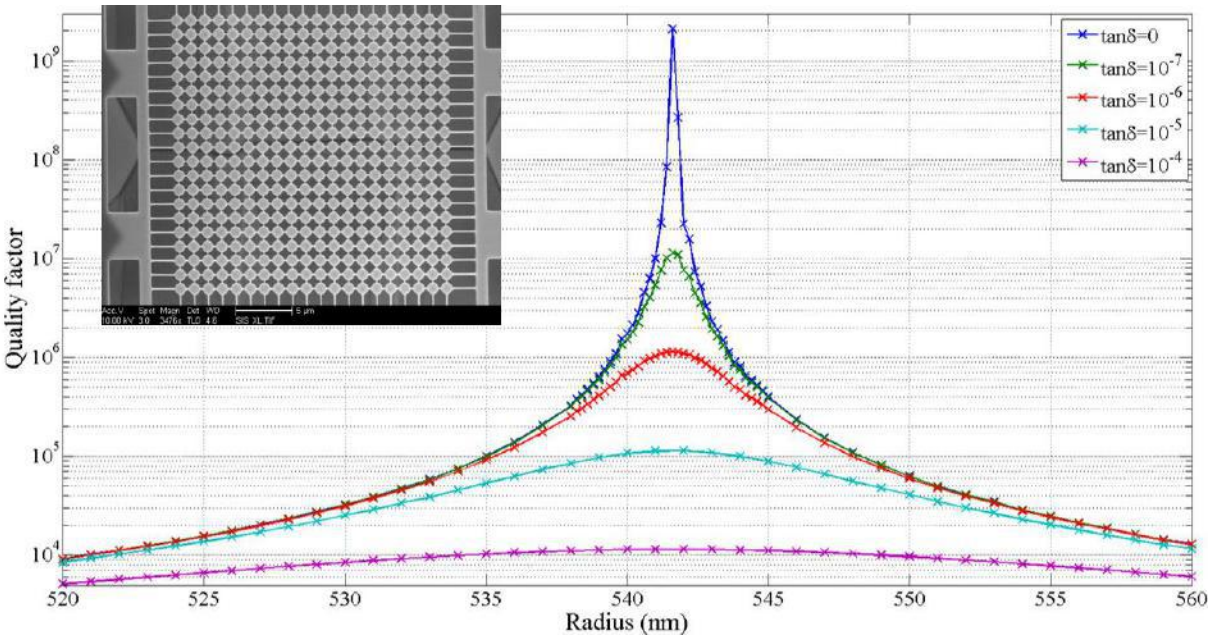



**Figure 1: (inset) scanning electron microscope (SEM) image of a finite 20x20 photonic crystal membrane; evolution of the total quality factor of the BIC eigenmode in an infinite array with varying radius for different material quality factors (Qmat=1/tanδ)**

Propagating and evanescent plane waves in the air surrounding the medium (top and bottom) can be interpreted as open and closed decay channels, respectively. Since we consider a subwavelength periodic structure, there is only one open decay channel. In a nutshell, the periodic nature of the slab couples all decay channels and as a result BICs arise due to destructive interferences, which can only occur for specific coupling values [6].

Our nanoresonators array surface emitting laser relies on a BIC, which is a very different mechanism than those previously demonstrated in band edge PCSELs [7]. Previously, eigenmodes that are symmetry-mismatched to free space were used for their high $Q_{rad}$ with the drawback that this only happens at a single point in k-space. In our design, we achieve a high $Q_{rad}$ in a much larger region of k-space thus enabling low-threshold, compact lasers [8].

## 3. Experimental Demonstration

To demonstrate lasing action, we optically pump our membrane at room temperature with a pulsed laser ($\lambda_{pump}$=1064 nm, 12 ns pulse at 300 kHz repetition rate) and record the photoluminescence emission. At low powers, we observe a spectrally broad emission continuum. At higher powers, we observe a drastic narrowing of the emission spectrum, *i.e.*, only a narrow peak with a linewidth below 1 nm remains at 1600 nm. Figure 2(a) shows the evolution of output power as a function of both input power and wavelength. We observe lasing action at room temperature with a threshold of only 100 μW. Figure 2(b) shows the evolution of output power as a function of input power at the lasing wavelength with a clear threshold behavior.

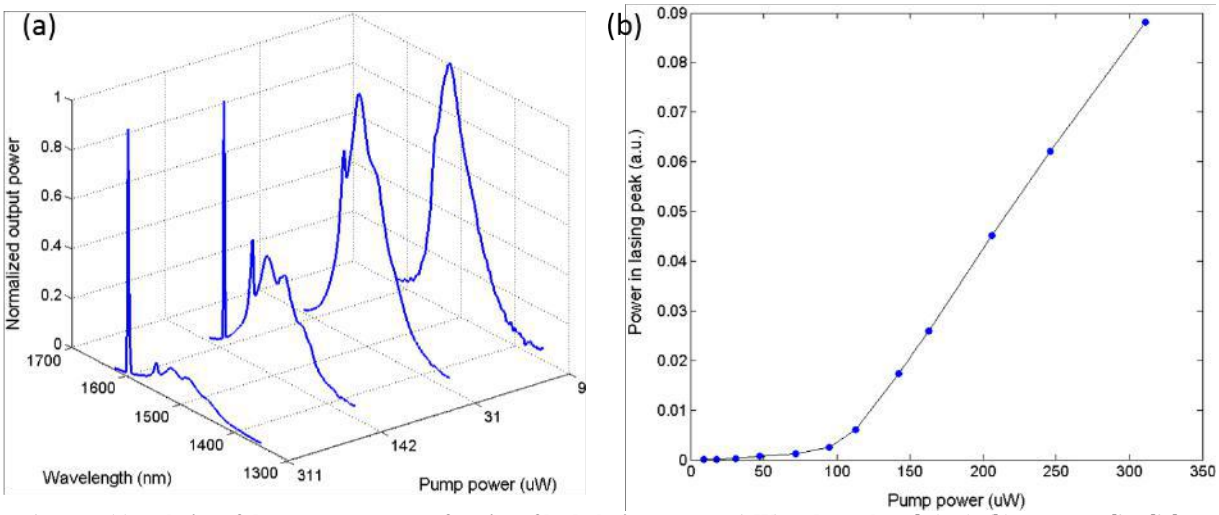



**Figure 2: (a) evolution of the output power as a function of both the input power (μW) and wavelength (nm); (b) corresponding light-light curve at 1550 nm indicating clear threshold behavior.**

Moreover, we have fabricated a series of samples with varying radius to demonstrate the BIC nature of our laser. We have observed a conclusive trend of decreasing laser threshold as the radius approaches the BIC point (r=540 nm).

## 4. Conclusion

We have demonstrated for the first time lasing action in a BIC-based cavity. We have achieved this result with an ensemble of dielectric resonators platform that is compatible with electrical pumping. Lasing action was observed at room temperature in a compact array with a footprint of only 24x24 $\mu m^2$. Furthermore, this work pave the way for future investigation into the intriguing topological properties of BICs.

## 5. References


[1] J. von Neumann and E. Wigner, "On some peculiar discrete eigenvalues" Phys. Z**,** 465 (1929).

[2] C. Linton *et al.*, "Embedded trapped modes in water waves and acoustics" Wave Motion **45**, 16 (2007).

[3] D. C. Marinica *et al.*, "Bound states in the continuum in photonics" Phys. Rev. Lett. **100**, 183902 (2008).

[4] Y. Plotnik *et al.*, "Experimental observation of optical bound states in the continuum" Phys. Rev. Lett. **107**, 183901 (2011).

[5] C. W. Hsu *et al.*, "Observation of trapped light within the radiation continuum" Nature **499**, 188 (2013).

[6] T. Lepetit and B. Kanté, "Controlling multipolar radiation with symmetries for electromagnetic bound states in the continuum" Phys. Rev. B **90,** 241103(R) (2014).

[7] K. Hirose *et al.*, “Watt-class high-power, high-beam-quality photonic-crystal lasers” Nat. Phot. **8,** 406 (2014).

[8] T. Lepetit, Q. Gu, A. Kodigala, B. Bahari, Y. Fainman and B. Kanté, “Resonantly trapped bound state in the continuum laser” Arxiv (2015).

# Nonlinear topological states of interacting photons

**Alexander N. Poddubny**[1,2]
[1]ITMO University, St. Petersburg, Russia
[2]Ioffe Institute, 194021 St. Petersburg, Russia
a.poddubny@metalab.ifmo.ru

**Abstract**-We discuss nonlinear topological states of light in the quantum and classical regimes. As two main examples, we consider (i) zero-dimensional quantum edge states of photon pairs in the chains of quantum microcavities and (ii) topological phases in the arrays of bianisotropic scatterers, induced by the optomechanical configurational nonlinearity.

The concept of topological states has recently propagated from the domain of solid states physics into optics, mechanics and acoustics. Electromagnetic disorder-robust topological states have been experimentally demonstrated from optical to microwave spectral domains using both plasmonic and dielectric structures. Yet, so far all the studies have been focused on the regime of linear classical optics. The concept of nonlinear topological states remains mainly unexplored, neither theoretically nor experimentally. Its understanding has fundamental importance and would open the pathway for nonlinear control and tuning of scattering-immune electromagnetic waves.

Here, we examine two models of the effect of interaction on the topological edge states in the quantum and classical regimes. First, we consider the chains of tunneling-coupled resonant quantum microcavities described by the generalized Bose-Hubbard model with the photon-photon repulsion. The simple Bose-Hubbard chain A-A-A… possesses bound states of quanta pairs, that have been experimentally realized in optical lattices. We focus on the states of photon pairs localized at the edges of the binary A-A=A-A=A-A=A… chain, where the tunneling constants assume of the two values. The single-photon excitations in this system are described by the Su-Schrieffer-Heeger model, being the simplest example showing the topological states. We develop a general Green function approach to calculate the eigenstates and the scattering coefficients of the photons pairs [1]. Our results indicate that the spectrum of the two-photon excitations is much richer than in the one-photon model. Depending on the tunneling constants and the nonlinearity strength the spectrum includes a complex mixture of various kinds of states where none, one, or both photons are localized at the edge. We show that the bound two-photon edge states can emerge for arbitrary weak nonlinear interaction strength.

Second, we examine the effect of interaction on the spectrum of the two-dimensional topological metamaterial with bianisotropic scatterers, introduced in Ref. [2]. We consider the model, where the bianisotropy is induced by the spontaneous symmetry breaking through the configurational optomechanical nonlinearity. Edge propagation and scattering of classical waves in this regime is studied numerically and analytically.

**Acknowledgements**. This work has been supported by the Russian President Grant No. MK-8500.2016.2.

**REFERENCES**

1. Poshakinskiy, A.V. and Poddubny, A.N. "Biexciton-mediated superradiant photon blockade", arXiv:1511.03627.
2. Khanikaev, A.B., *et. al.*, "Photonic topological insulators", *Nature Materials*, Vol. 12, 233 (2013).

# Topological Transport in Photonic Quasicrystals

**Miguel A. Bandres**[1], **Mikael C. Rechtsman**[2], **and Mordechai Segev**[1]
[1]Physics Department and Solid State Institute, Technion, Haifa 32000, Israel
[2]Department of Physics, The Pennsylvania State University, University Park, PA, USA

**Abstract**- We show that it is possible to have topological transport in a two-dimensional photonic quasicrystal. Hence, these lattices have unidirectional edgestates that are topologically protected against backscattering as they pass through defects or around corners. We find that the fractal-like spectrum of the quasicrystal is endowed with topological band gaps at all energy scales manifesting an entirely new physics phenomenon. These new fractal topological aspects lay the groundwork for new conceptual ideas involving topological phases in quasicrystals.

Topological insulators are materials that insulate in their bulk, but allow extremely robust flow of current on their surfaces [1]. In two dimensions, they possess one-way edge currents that that are immune to scattering and imperfections. Recently, the ongoing theoretical effort to realize topological insulation and protection in optics [2-6] culminated in the first experimental observation of photonic topological insulators in optics [7], as demonstrated in a honeycomb array of evanescently coupled helical waveguides. This effect was also demonstrated in a silicon-chip platform using a lattice of coupled ring resonators [8]. Introducing topological protection into photonics not only brings technology closer to employing the unique properties of topological phases in real applications but also provides an entirely new platform for probing and understanding topological protection.

Quasicrystals are unique structures with long-range order but no periodicity. They constitute an intermediate phase between crystals and disordered media, because the modes of a quasicrystal are neither extended throughout the whole lattice nor localized. Moreover, the energy spectrum of these modes is fractal-like. In principle, a topological phase with zero magnetic field is not expected in a two-dimensional or a three-dimensional QC. This because topological insulators must have at least one extended unidirectional edge state, whereas the eigenstates of QCs exhibit a power-law self-similar (fractal-like) decay and are generally stationary ("immobile" Anderson states in a random potential).

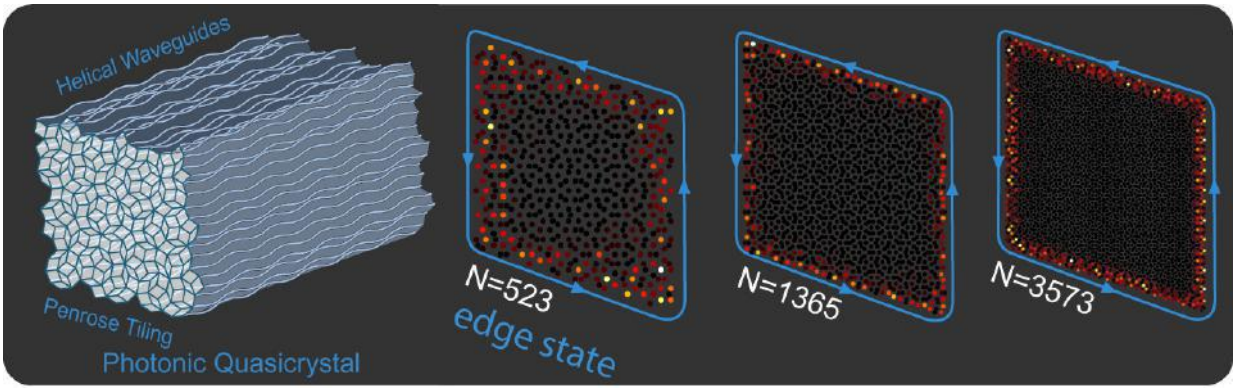



Figure 1. (Left) Sketch of the photonic Floquet quasicrystal formed by introducing a helical waveguide in each vertex of a Penrose tiling. (Right) Topological edge states for increasing size of the quasicrystal. The energy flow is always unidirectional as indicated by the blue lines.

Here, we show that a two-dimensional photonic quasicrystal have a topological insulating phase that exhibit one-way extended edge states that are topologically protected against backscattering as they pass through defects or around corners. These topologically protected (scatter-free) edge states are extended along the system's perimeter and have unidirectional energy flow (see Fig. 1); contrary to the states of a general QC system, which have power-law decay and are stationary.

Our specific model is a photonic quasicrystal created by a Penrose lattice of helical optical waveguides (depicted in Fig. 1). We demonstrate the existence of this topological phase both by using a discrete topological index, i.e., the Bott index [10], and also by studying the topologically protected dynamics (robust unidirectional transport) of the gapless edge states. Importantly, we find an entirely new phenomenon: the fractal-like spectrum of the quasicrystal is endowed with topological band gaps at all energy scales, hence new topological gaps appear as the system size increases. Hence, the quasicrystal topological structure emerges as a function of the system size, in contrary to periodic systems where the topological phase can be completely characterized using its unit cell.

We expect this new topological quasicrystal phase to be universally applicable to a variety of quasicrystalline structural variants, including those with higher-order noncrystallographic rotational symmetries. The fractal topological aspects discovered in this study lay the groundwork for new conceptual ideas involving topological phases in quasicrystals.

The research leading to these results has received funding from the European Union's – Seventh Framework Programme (FP7/2007-2013) under grant agreement n◦ 629114 MC–Structured Light.

## REFERENCES

1. C. Kane and E. Mele, "Quantum spin hall effect in graphene," Phys. Rev. Letters 95, (2005).
2. Z. Wang, Y. Chong, and M. S. JD Joannopoulos, "Observation of unidirectional backscattering-immune topological electromagnetic states," Nature 461, 772 (2009).
3. A. B. Khanikaev, et al., "Photonic topological insulators," Nature materials (2012).
4. K. Fang, Z. Yu, and S. Fan, "Realizing effective magnetic field for photons by controlling the phase of dynamic modulation," Nature Photonics 6, 782–787 (2012).
5. R. O. Umucalılar and I. Carusotto, "Artificial gauge field for photons in coupled cavity arrays," Phys. Rev. A 84, 043804 (2011).
6. F. D. M. Haldane and S. Raghu, "Possible realization of directional optical waveguides in photonic crystal with broken time-reversal symmetry," Phys. Rev. Lett. 100, 013,904 (2008).
7. M. C. Rechtsman, et al., "Photonic Floquet topological insulators," Nature 496, (2013).
8. M. Hafezi, et al., "Imaging topological edge states in silicon photonics," Nature Photonics 7, (2013).
9. D. Shechtman, et al., "Metallic Phase with Long-Range Orientational Order and No Translational Symmetry," Phys. Rev. Lett 53, (1951)
10. T.A. Loring and M.B. Hastings, "Disordered topological insulators via C-algebras," EPL, 92 (2010).

# Two-dimensional topological photonic crystals

**S. Barik[1,2], H. Miyake[1], W. DeGottardi[1,3], E. Waks[1,3], M. Hafezi[1,3]**

(1) Joint Quantum Institute, NIST and University of Maryland, USA
(2) Department of Physics, University of Maryland, USA
(3) Department of Electrical and Computer Engineering and Institute for Research in Electronics and Applied Physics, University of Maryland, USA

## Abstract

We propose a design for photonic crystals with topological properties. Both Finite-difference-time-domain simulations and tight-binding model show topological protection as controllable directional light propagation with circularly-polarized dipole excitations and backscattering-free propagation around sharp corners.

Topological phenomena such as chiral edge states have been extensively studied in condensed matter systems [1], and recently analogous phenomena have been studied in photonic systems [2, 3]: with microwaves [4], near-infrared light in silicon [5] and visible light in fused silica [6]. One reason topologically-protected edge states are interesting is that they allow backscattering-free propagation of light which can reduce loss due to disorder in photonic integrated circuits. We propose a new design for dielectric slab nanophotonic crystals which possess topological edge states that can be integrated with nonlinear quantum emitters such as color centers and quantum dots and could be used for robust on-chip quantum information processing [7] and quantum simulation of fractional quantum Hall states [8, 9].

Prior theoretical works have shown that two-dimensional electromagnetic systems with a honeycomb-lattice-like structure could give rise to non-trivial helical topological properties [10]. Here, we propose and analyze a two-dimensional photonic crystal with nanoscale triangular holes which possess non-trivial topological properties. Such an architecture is suitable for photonic integrated systems where dielectric materials such as gallium arsenide, silicon and diamond, can be integrated with quantum emitters, such as diamond color centers [11] and quantum dots [12].

Our structure is based on a honeycomb lattice of equilateral triangular holes, shown in Fig. 1(a). This photonic crystal can be considered a triangular lattice of hexagonal cells each consisting of six triangular holes. This lattice could be also considered as honeycomb lattice with $R = a_0/3$, where $a_0$ is the spacing between the cells and $R$ is the distance from the center of the hexagonal cell to the centroid of the triangular holes. Finite-difference-time-domain simulations show a Dirac cone at the $\Gamma$ point in the band structure for TE modes, shown in Fig. 1(c). By shrinking ($R < a_0/3$; Fig. 1(b)) and expanding ($R > a_0/3$; Fig. 1(d)) the cells, a gap can be opened at the $\Gamma$ point, indicating

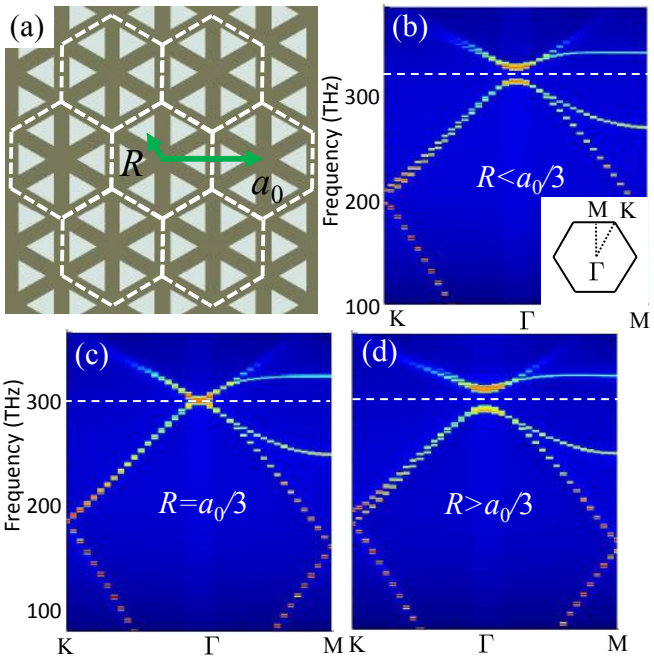



Figure 1: Design of triangular photonic crystal with equilateral triangular holes and the corresponding TE mode band structures. (a) The lattice of triangular holes can be considered as a triangular lattice of hexagonal cells each composed of six triangles, outlined by white dotted lines. The parameters $a_0$ is the lattice constant of the triangular lattice and $R$ is the distance from the center of a cell to the centroid of a triangular hole of the cell. When $R = a_0/3$, the system is exactly a honeycomb lattice with a Dirac cone. (b) Band structure when $R = 0.95 \times a_0/3$. Inset shows the Brillouin zone. (c) Band structure when $R = a_0/3$. (d) Band structure when $R = 1.05 \times a_0/3$. There is a Dirac cone in (c), but a band gap is opened for (b) and (d). The calculations were performed with $a_0 = 400$ nm and triangular hole edge lengths of 140 nm in a GaAs structure.

that these modifications can tune the system between different band topologies. To verify this, the band structure close to the Dirac point was analyzed with the Bernevig-Hughes-Zhang model for the Spin Quantum Hall effect [13], where it can be seen that the mass term changes sign when the lattice is shrunken/expanded around $R = a_0/3$ and the band orbitals are inverted. Consequently, the bands acquire nonzero Chern numbers that are the direct indication of nontrivial topological properties.

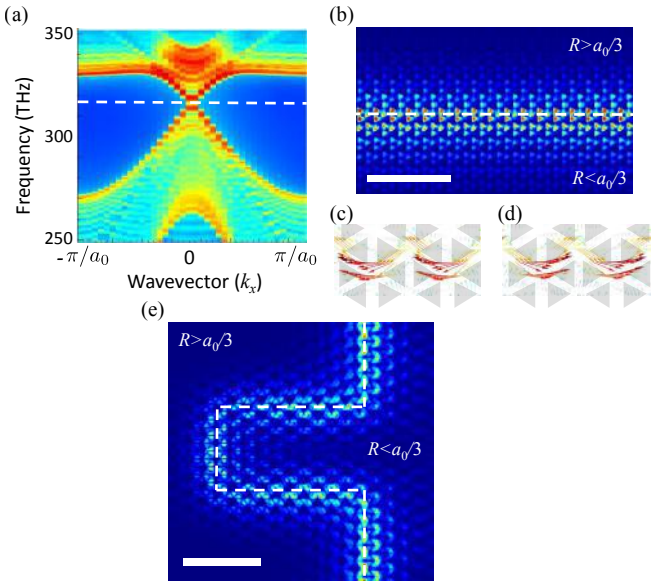



Figure 2: Topological edge states. (a) TE mode band structure of a system with one region $R < a_0/3$ and another $R > a_0/3$. There is a band crossing where formerly there was a band gap (centered at white dotted line), due to the different topologies of the two regions. (b) Intensity of an edge state between the boundary (white dotted line) of two regions. (c) and (d) correspond to the close up of the time-averaged Poynting vector of (b), which point left or right depending on excitation with positive or negative circularly polarized dipoles, respectively. (e) Intensity of an edge state around four 90° bends shows there is essentially no scattering. In (b) and (e) the white scale bar represents 2 $\mu$m.

A manifestation of non-trivial topological properties can be observed by combining two topologically distinct materials with a common band gap. At the interface region, a topological helical edge state emerges. Our numerical simulations indicate that this structure gives rise to TE mode helical edge states. In particular, the band structure of a system with one region having $R < a_0/3$ and another region having $R > a_0/3$ shows a band crossing where formerly there was a gap, shown in Fig. 2(a). The intensity of the mode existing in the band crossing region is shown in Fig. 2(b) and indicates the edge state. Furthermore, there are two guided modes propagating in opposite directions (Figs. 2(c) and (d)) which can be controllably excited by dipoles with positive and negative circular polarization respectively. Sharp bends can be introduced into the system and still the light propagates without backscattering as in Fig. 2(e). This would not be possible with photonic crystals whose modes are not topologically protected [14]. In Fig. 2, simulations with $a_0 = 400$ nm and triangular hole edge length 140 nm in GaAs, which can be fabricated with established techniques, give rise to edge states at 949 nm, which is ideal to interface with Indium Arsenide quantum dots [12].

## Acknowledgement

We thank Sunil Mittal, Mikael Rechtsman, Alberto Amo, Jay Sau for fruitful discussions. This research was supported by Air Force Office of Scientific Research grant no. FA9550-14-1-0267, Sloan Foundation, Office of Naval Research and the Physics Frontier Center at the Joint Quantum Institute.

## References

[1] M. Z. Hasan and C. L. Kane, "Colloquium: Topological insulators," Rev. Mod. Phys. **82**, 3045 (2010).

[2] L. Lu, J. D. Joannopoulos, and M. Soljačić, "Topological photonics," Nature Photon. **8**, 821 (2014).

[3] M. Hafezi and J. Taylor, "Topological physics with light," Physics Today, **67**, 68 (2014).

[4] Z. Wang, Y. Chong, J. D. Joannopoulos, and M. Soljačić, "Observation of unidirectional backscattering-immune topological electromagnetic states," Nature **461**, 772 (2009).

[5] M. Hafezi, S. Mittal, J. Fan, A. Migdall, and J. M. Taylor, "Imaging topological edge states in silicon photonics," Nature Photon. **7**, 1001 (2013).

[6] M. C. Rechtsman *et al.*, "Photonic Floquet topological insulators," Nature **496**, 196 (2013).

[7] P. Lodahl, S. Mahmoodian, and S. Stobbe, "Interfacing single photons and single quantum dots with photonic nanostructures," Rev. Mod. Phys. **87**, 347 (2015).

[8] M. Hafezi, M. D. Lukin, and J. M. Taylor, "Non-equilibrium fractional quantum Hall state of light," New J. Phys. **15**, 063001 (2013).

[9] R. O. Umucallar and I. Carusotto, "Fractional Quantum Hall States of Photons in an Array of Dissipative Coupled Cavities," Phys. Rev. Lett. **108**, 206809 (2012).

[10] L.-H. Wu and X. Hu, "Scheme for Achieving a Topological Photonic Crystal by Using Dielectric Material," Phys. Rev. Lett. **114**, 223901 (2015); T. Ma, A. B. Khanikaev, S. H. Mousavi, and G. Shvets, "Guiding Electromagnetic Waves around Sharp Corners: Topologically Protected Photonic Transport

in Metawaveguides," Phys. Rev. Lett. **114**, 127401 (2015); T. Ochiai, "Topological properties of bulk and edge states in honeycomb lattice photonic crystals: the case of TE polarization," J. Phys.: Condens. Matter **22**, 225502 (2010); M. Polini, F. Guinea, M. Lewenstein, H. C. Manoharan, and V. Pellegrini, "Artificial honeycomb lattices for electrons, atoms and photons," Nature Nanotech. **8**, 625 (2013).

[11] A. Sipahigil,1, K. D. Jahnke, L. J. Rogers, T. Teraji, J. Isoya, A. S. Zibrov, F. Jelezko, and M. D. Lukin, " Indistinguishable Photons from Separated Silicon-Vacancy Centers in Diamond", Phys. Rev. Lett. 113, 113602 (2014).

[12] H. Kim, R. Bose, T. C. Shen, G. S. Solomon, and E. Waks, "A quantum logic gate between a solid-state quantum bit and a photon," Nature Photon. **7**, 373 (2013).

[13] B. A. Bernevig, T. L. Hughes, and S.-C. Zhang, "Quantum Spin Hall Effect and Topological Phase Transition in HgTe Quantum Wells," Science **314**, 1757 (2006).

[14] I. Söllner *et al.*, "Deterministic photon-emitter coupling in chiral photonic circuits," Nature Nanotech. **10**, 775 (2015).

# Pseudospin-mediated phenomena in photonic graphene

**Zhigang Chen**
*The MOE Key Laboratory of Weak-Light Nonlinear Photonics, TEDA Applied Physics Institute and School of Physics, Nankai University, Tianjin 300457, China*
*Department of Physics and Astronomy, San Francisco State University, San Francisco, California 94132, USA*

**Abstract:** We report on pseudospin-mediated phenomena in photonic graphene, including topological charge flipping due to selective excitation associated with sublattice and valley degrees of freedom, as well as Aharonov-Bohm-like interferences due to deformation of honeycomb lattices.

Graphene and associated 2D materials with Dirac cones have attracted tremendous attention in condensed matter physics and quantum physics due to their importance in fundamental sciences and applications [1-2]. The band gap structure of graphene exhibits six Dirac points in the first Brillouin zone (BZ). At these Dirac points (valleys), the energy extrema are degenerated, leading to a new discrete degree of freedom in momentum space better named "valley pseudospin". In addition to the linear dispersion relation, the wavefunction around the Dirac cones has a geometrical Berry phase, which gives rise to many unique phenomena in graphene [3-4]. For instance, the Berry phase in the two inequivalent valleys is opposite, which has led to valley-dependent phenomena and development of new valleytronics-based applications. For such applications, a controllable way to selectively fill or deplete valleys to generate valley polarization is desirable, albeit nontrivial.

Photonic graphene - the photonic analog of graphene constructed with waveguide arrays arranged in honeycomb geometry [5] - has provided a powerful platform to emulate graphene physics while discovering new phenomena that would otherwise be inaccessible in real graphene. In our recent work, we have experimentally demonstrated pseudospin-mediated vortex generation due to the sublattice degree of freedom in photonic graphene, and observed topological charge flipping when different sublattices are selectively excited in the same valley [6]. In this talk, we will discuss pseudospin-mediated phenomena in photonic graphene, including the Aharonov-Bohm-like interferences arising from the deformation of a photonic graphene lattice. Moreover, we will present our recent demonstrations of vortex generation due to the valley degree of freedom when the same sublattice is excited, unveiling the topological charge flipping when the two inequivalent valleys are selectively excited. Our results may bring about a new way to manipulate the valley degree of freedom in graphene and related artificial graphene systems.

In short, we have observed in photonic graphene the vortex generation and topological charge flipping due to the pseudospins associated with different degrees of freedom in photonic graphene. Our results may open up a new way to manipulate the pseudospin and valley-dependent effects in photonic graphene [7-10].

[1] K.S. Novoselov, et al., Nature 438, 197 (2005).
[2] A.H.C. Neto., et al, Rev. Mod. Phys. 81, 109 (2009).
[3]X. Xu et al. Nat. Phys. 10, 343 (2014).
[4] R. V. Gorbachev et al., Science 346, 448(2014)
[5] O. Peleg , et al., Phys. Rev. Lett. 98, 103901 (2007).
[6] D. Song et al., Nat. Commun. 6,6272 (2015)
[7] C.-H. Park,et al. Phy. Rev. B 84,2054401(2011)
[8] H. Zeng et al., Nat. Manotech. 7, 490 (2012).
[9] D. Pesin et al., Nat. Materials, 11, 409 (2012)
[10] F. Deng et al., Opt. Lett. 40, 3380 (2015).

# $Z_2$ Topological Photonics derived from Crystal Symmetry

**Xiao Hu**
International Center for Materials Nanoarchitectonics (WPI-MANA)
National Institute for Materials Science (NIMS), Tsukuba 305-0044, Japan
*corresponding author: Hu.Xiao(at)nims.go.jp

**Abstract**-We demonstrate that a $Z_2$ topological photonic state can be achieved in a system made of conventional dielectric material, such as silicon. We explore the $C_6$ crystal symmetry to compose pseudospin and pseudo time-reversal (TR) symmetry similar to that for electrons. With band inversion between photonic bands characterized by opposite parities with respect to spatial inversion, nontrivial topology emerges similarly to the quantum spin Hall effect in electronic systems. The present topological photonic system has the advantage of easy integration with other electronic devices.

We consider a two-dimensional (2D) honeycomb lattice of dielectric cylinders as shown in Fig. 1. The electromagnetic wave propagating through the photonic crystal takes the transverse magnetic (TM) mode with finite $E_z$ and $H_{x,y}$ fields.

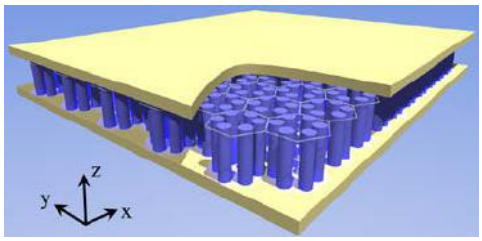



Fig. 1: Schematics for the 2D photonic crystal made of dielectric cylinders.

Grouping the cylinders into hexagons formed by six neighboring ones, and squeezing and stretching the separation between hexagons with the $C_6$ symmetry preserved, we obtain three photonic crystals as shown in Fig. 2. The corresponding photonic bands can be evaluated by solving the Maxwell equations, where the unit cell is taken as the one of hexagonal shape including six sites. Two degenerate Dirac cones appear at the Γ point in Fig. 2b for honeycomb lattice, due to folding from the well-known Dirac dispersions at K and K' points in the first Brillouin zone associated with the primitive rhombic unit cell of two sites. Photonic band gap opens when the honeycomb lattice is deformed as seen in Figs. 2a and 2c.

It is interesting to observe that the photonic bands close to the band gap exhibit two-fold degeneracy at the Γ point, which originates from the two 2D representations E' and E'' of the $C_6$ point group. As a matter of fact, one can assign the two states below and above the band gap in Fig. 2a respectively as

$$p_{\pm} = \frac{1}{\sqrt{2}}\left(p_x \pm i p_y\right), \quad d_{\pm} = \frac{1}{\sqrt{2}}\left(d_{x^2-y^2} \pm i d_{xy}\right) \qquad (1)$$

in terms of the in-plane distribution of the $E_z$ field, which are nothing but the Mie modes accommodated at an isolated hexagon.

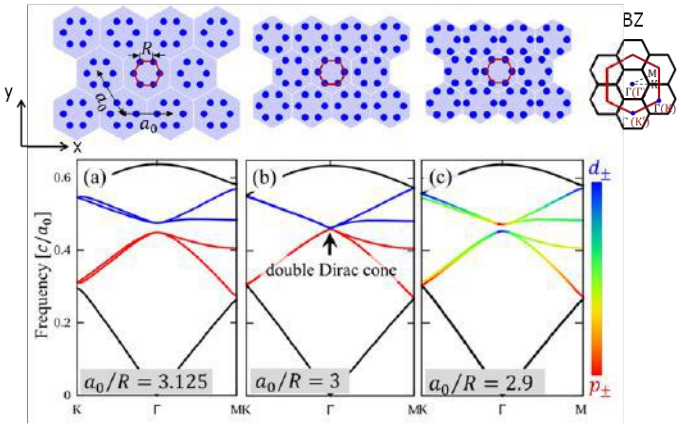



Fig. 2: Photonic crystals with different lattice constants and the corresponding photonic bands.

We notice that the orbital angular momentum of the *p* and *d* orbits plays the role of pseudospin in the present photonic system. A pseudo TR operator defined by $\mathcal{T} = \mathrm{i}\sigma_z\mathcal{K}$ with $\sigma_z$ the Pauli matrix and $\mathcal{K}$ the complex conjugating operator flips the pseudospin in the following way

$$\mathcal{T}p_\pm = \mp ip_\mp, \quad \mathcal{T}d_\pm = \mp id_\mp \qquad (2)$$

One can then confirm $\mathcal{T}^2 = -1$, which is the property of TR symmetry of fermionic systems. It is interesting that in the present photonic crystal, a fermionic degree of freedom emerges due to the crystal symmetry.

This pseudo TR symmetry leaves an important consequence to the system in Fig. 2c, where a band inversion between *p* and *d* bands takes place at the Γ point and the two bands mix with each other at finite momenta. It is easy to check that two skyrmion textures referring to the weights of *p* and *d* orbits appear in pseudospin up and down channels. With opposite Berry phases they yield the $Z_2$ topological index.

Calculating a ribbon-shaped photonic crystal given in Fig. 2c surrounded by two pieces of that given in Fig. 2a, one can obtain topological edge states with counter propagations of electromagnetic (EM) waves carrying up and down pseudospin, which characterizes the helical edge states associated with $Z_2$ topology. We also confirmed that the topological edge EM propagation is strong against defects. Since the present topological photonic crystal is made of conventional dielectric material such as silicon, does not require application of external magnetic field, and can be fabricated easily, it has a great advantage in integration with well-established electronic devices.

This work was supported by the WPI Initiative on Materials Nanoarchitectonics, MEXT of Japan.

**REFERENCE**

1. Wu, L.-H. and Hu, X., "Scheme to Achieve Topological Photonic Crystal by Dielectric Material," *Physical Review Letters*, Vol. 114, 223901, 2015.

# Topologically Non-Trivial States in Photonic Crystals

**M. Soljačić**[1*]
[1] Department of Physics, MIT; USA
[*]corresponding author: soljacic@mit.edu

**Abstract** - Topologically non-trivial photonic states will be surveyed. Our recent progress on Chiral Edge States, Weyl points, and Bound States in Continuum will be presented. Their properties and potential applications will be discussed.

In last few years, electronic community has witnessed a large interest in topologically non-trivial states because of their novel and unique properties. Similarly, topological states in photonics display an equally diverse range of novel and surprising phenomena. For example, many of interesting properties of graphene emerge from its Dirac electronic dispersion relation. While Dirac dispersion in graphene is a 2D phenomenon, we present one of its 3D analogues in photonics: Weyl points [1]. Weyl points were predicted in 1929 (one year after Dirac points), but have not been experimentally observed until 2015 [2]. In addition, we also discuss embedded eigenvalues in photonic crystal systems [3], whose robustness can also be understood as emerging from certain topological properties [4]. Finally, we will present our work on QAHE system which has Chern number >1 [5].

**REFERENCES**

1. "Weyl points and line nodes in gyroid photonic crystals" Ling Lu, Liang Fu, John D. Joannopoulos, and Marin Soljacic. *Nature Photonics*, **7**, 294, (2013).
2. "Experimental observation of Weyl points" L. Lu, Z. Wang, D. Ye, L. Ran, L. Fu, J.D. Joannopoulos, and M. Soljacic. *Science*, **349**, 622 (2015).
3. "Observation of trapped light within the radiation continuum" Chia Wei Hsu, Bo Zhen, Jeongwon Lee, Song-Liang Chua, Steven G. Johnson, J.D.Joannopoulos, and Marin Soljacic. *Nature* **499**, 188, (2013).
4. "Topological Nature of Optical Bound States in the Continuum" Bo Zhen, Chia Wei Hsu, Ling Lu, A. Douglas Stone, and Marin Soljacic. *Phys. Rev. Lett.*, **113**, 257401, (2014).
5. "Experimental Observation of Large Chern Numbers in Photonic Crystals" Scott A. Skirlo, Ling Lu, Yuichi Igarashi, Qinghui Yan, John D. Joannopoulos, and Marin Soljacic. *Phys. Rev. Lett.*, **115**, 235901, (2015).

# Anomalous Topological Phases and Unpaired Dirac Cones in Photonic Lattices

**Y. D. Chong**[1], **D. Leykam**[1], **and M. C. Rechtsman**[2]

[1]Nanyang Technological University, Singapore
[2]The Pennsylvania State University, USA
yidong@ntu.edu.sg

**Abstract**— This talk describes a class of photonic Floquet topological insulators based on staggered helical lattices, which exhibits anomalous Floquet topological insulator phases and an easily controllable topological transition between trivial and nontrivial phases. At the critical point of the topological transition, the bandstructure features a single unpaired Dirac cone, which yields a variety of unusual transport effects never previously observed, including weak antilocalization not limited by short-range disorder. Possible applications for controlling and switching topological photonic states are discussed.

Photonic topological insulators are an emerging class of photonic devices possessing topologically-nontrivial bandstructures, analogous to the electronic bandstructures of topological insulators [1]. Recently, a photonic topological insulator was demonstrated based on a photonic lattice containing helical optical waveguides [2], operating in the technologically important optical frequency regime. Here, we describe a class of photonic lattices with novel and potentially useful topological properties not found in the design of Ref. [2]. Our design is based on "staggered" lattices of helical waveguides, with each of the two sublattices having a different helix phase, as shown in Fig. 1(a).

By tuning continuous lattice parameters, such as the lattice period, it is possible to continuously tune the system between a topologically trivial and non-trivial phase [Fig. 1(b)]. To our knowledge, a continuously tuned transition between trivial and nontrivial topological phases has never before been observed in a 2D photonic lattice (in particular, the lattice in Ref. [2] was always strictly topologically non-trivial). This feature can be used to realize topological optical waveguides and switches that are actively controllable.

Furthermore, this photonic lattice can access the so-called "anomalous Floquet insulator" phase, in which all bands have non-zero Chern number but are topologically non-trivial [4]. Such a phase has previously been studied in microwave structures [5, 6], but such behavior has never before been found in optical waveguide lattices.

At the critical point of a topological phase transition, the photonic lattice can exhibit an interesting phenomenon that has hitherto been unobserved in topological photonics: an unpaired Dirac

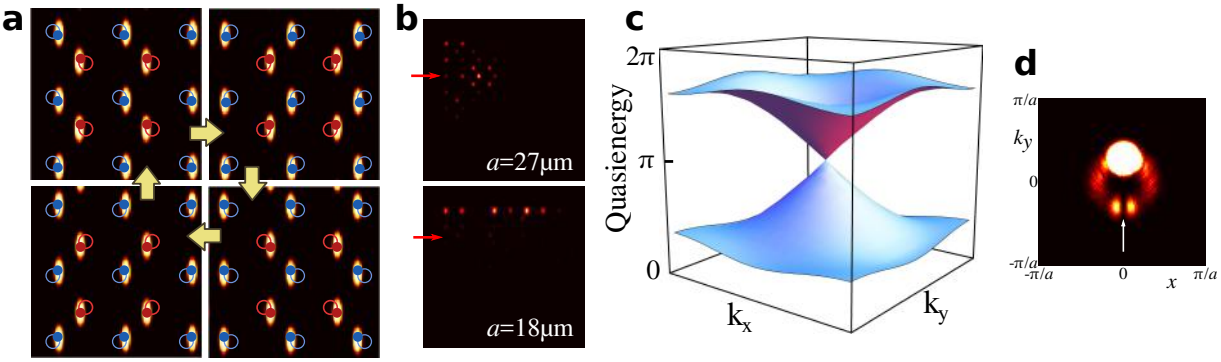



Figure 1: (a) Design of a staggered square lattice of helical waveguides, showing the lattice potential at each helix quarter-cycle. The helix trajectories are shown as red and blue overlays. (b) Output intensity profile (after 5 cycles), after exciting an edge waveguide, with the lattice in the topologically trivial phase (top) and a non-trivial phase (bottom). (c) Tight-binding Floquet quasienergy spectrum at the phase transition, showing a single (unpaired) Dirac cone. (d) Fourier spectrum intensity of a probe beam following propagation through a weakly disordered lattice, displaying a weak antilocalization dip in the backscattering direction

cone [Fig. 1(c)]. All previously-observed photonic band-crossing points have involved either paired Dirac points or quadratic dispersion. With an unpaired Dirac cone, wave propagation becomes immune to the inter-valley scattering processes that occur in bandstructures with pairs of Dirac cones. We can use this to demonstrate a novel "discrete" conical diffraction effect, generated by exciting a single unit cell, as well as weak antilocalization in the presence of short-range disorder.


## ACKNOWLEDGMENT

This research was supported by the Singapore National Research Foundation under grant No. NRFF2012-02, and by the Singapore MOE Academic Research Fund Tier 3 grant MOE2011-T3-1-005. M.C.R. acknowledges the support of the National Science Foundation under grant number ECCS-1509546.


## REFERENCES


1. L. Lu, J. D. Joannopoulos, and M. Soljačić, Nature Photon. **8**, 821 (2014).
2. M. C. Rechtsman *et al.*, Nature **496**, 196 (2013).
3. D. Leykam, M. C. Rechtsman, and Y. D. Chong, arxiv:arXiv:1601.01764.
4. T. Kitagawa, E. Berg, M. Rudner, and E. Demler, Phys. Rev. B **82**, 235114 (2010).
5. W. Hu *et al.*, Phys. Rev. X **5**, 011012 (2015).
6. F. Gao *et al.*, arXiv:1504.07809.

`

# Reconfigurable and all-dielectric photonic topological insulators in two and three dimensions

**Alexander B. Khanikaev**[1,2,3]

[1]*Department of Physics, Queens College of The City University of New York, Queens, NY 11367, USA*
[2]*Graduate Center of The City University of New York, New York, NY 10016, USA*
[3]*Department of Nanophotonics and Metamaterials, ITMO University, St. Petersburg 197101, Russia*
**corresponding author: khanikaev@gmail.com*

**Abstract**-It is shown that a symmetry protected topological phases can be engineered in the presence of the electromagnetic duality, which can be achieved by careful meta-atoms design. Synthetic gauge field induced by magneto-electric coupling gives rise to spin-polarized edge states in 2D and surface states in 3D systems with linear and conical Dirac dispersion. The ability to control and reconfigure gauge fields in these platform enables reflectionless routing of electromagnetic states along arbitrarily shaped pathways.

**Introduction.** Following the footsteps of condensed matter topological systems, a significant progress has been recently made in understanding and realizing topological states of light [1]. Here I present the results demonstrating that that topological states protected by the electromagnetic duality can be engineered in 2D and 3D metacrystals. The duality, which is reflected in the symmetry of the Maxwell equations with respect to electric and magnetic field components, responsible for the SPT phase of the electromagnetic eigenmodes, otherwise broken by materials response [2,3], is restored by careful design of building blocks of the 3D photonic lattice – meta-atoms. We demonstrate 2D and 3D photonic topological insulators based on the meta-waveguide and all-dielectric metamaterial platform, which is thus free of very restrictive requirement earlier concepts of time-reversal violating systems, where magnets or temporal modulation are required [1].

**Reconfigurable 2D photonic meta-crystals.** Endowed with topological robustness, photonic edge modes can avoid back-reflection from structural imperfections and disordered regions. Although several successful experimental implementations of topological states of light with TR symmetry have been reported recently, one important property of true external fields available in condensed matter systems has evaded emulation in photonics – the control of topological states. The possibility of such control through reconfigurable synthetic gauge fields would usher in a broad range of practical applications from spin/helicity filtering to tunable photonic devices. Based on this idea, here we demonstrate experimentally that the electromagnetic radiation can be steered and delivered to any point within a reconfigurable topological metacrystal without back-reflection. This is achieved by exploiting adjustable gauge fields defining arbitrarily-shaped pathways for topological edge states.

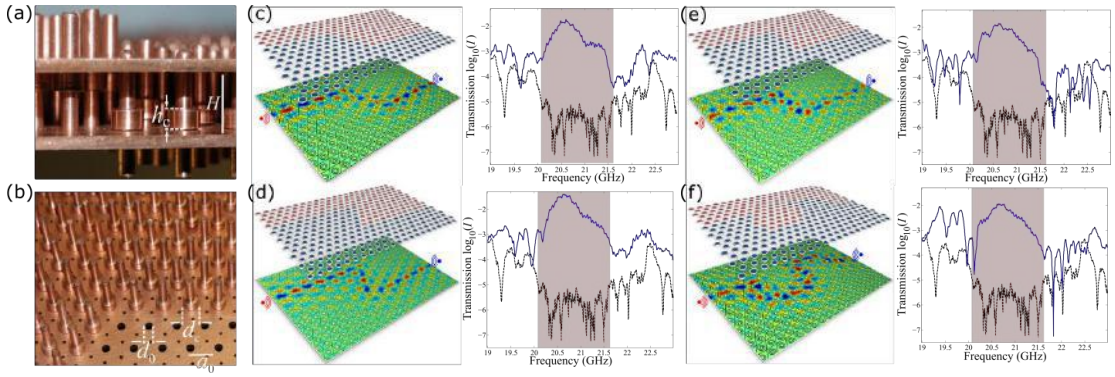



Fig. 1. (a) Geometric arrangement of metallic rods and collars inside the PPE. (b) The metacrystal without the top copper plate. (c-f) Domain walls with $60^o$, $90^o$, and $120^o$ bends, and random shape, respectively.

`

Here, we realize a reconfigurable topological photonic lattice implemented in the parallel plate waveguide shown in Figs. 1a-b [3]. The reconfigurable topological structure studied here is formed between two parallel copper plates through which holes are drilled to support a periodic triangular array of copper rods with ring collars. The rods can be moved up or down so that the collar of each rod can be positioned anywhere between the top and bottom plates. Lattices can be formed with the collar touching either the upper or lower plate and structures with arbitrarily-shaped domain walls can be created.

The main property of topological edge states that differentiates them from their topologically trivial counterparts is their robustness against defects and disorder. In order to test the robustness of photonic transport along reconfigurable pathways enabled by the design of the metacrystal, propagation was measured in samples with a variety of bends and shapes of the topological domain wall, as shown in Fig. 1c-f. The experimental spectra for different domain wall configurations exhibit high transmission mediated by the edge modes over the frequency range of the band gap. The high transmission observed for all domain wall contours, including an irregularly shaped wall with multiple bends, shows that transport is topologically robust.

**Three-dimensional all-dielectric photonic topological insulators.** In order to bring these ideas to three-dimensions, we introduce an all-dielectric topological photonic metacrystal shown in Fig. 2a, which represents a 3D hexagonal lattice of dielectric disks [4]. The domain wall within such 3D photonic topological insulator represents an interface between two crystals inverted with respect to each other along the z-direction, which results in the reversal of bianisotropy. The schematic view of the corresponding structure is shown in Fig. 2a with the photonic band structure presented in Fig. 2b-c. The surface states appear within the band gap region and cross it such that they interconnect lower and upper bulk bands. The 3D band diagram shown in Fig. 2c exposes one of the Dirac cones corresponding to the surface states near K-point. The confinement of the surface states to the domain wall was confirmed by their field profiles for all directions within the domain wall plane. As in the case of 3D electronic topological insulators, the surface states in our system also have a property analogous to spin-locking which endows them with topological robustness.

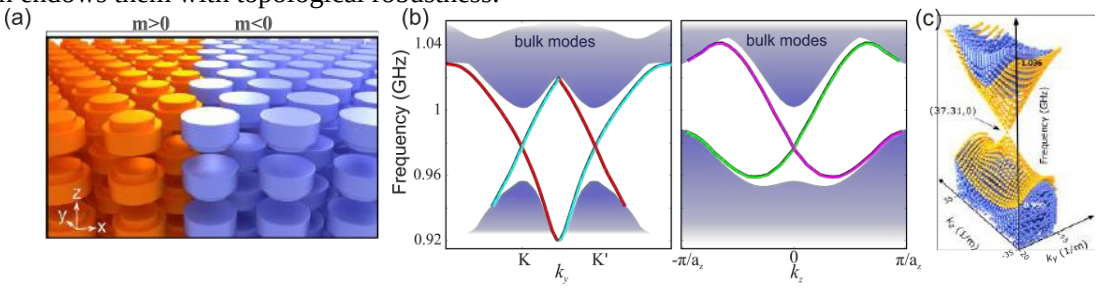



Fig 2. (a) The schematics of the domain wall formed by the reversal of the mass term induced by the bianisotropy in the middle of the metacrystal. (b) Band diagrams of topological surface states supported by the domain wall. (c) The conical Dirac-like dispersion of the surface states.

**Conclusion.** In summary, we propose a photonic platform which can be used to implement reconfigurable and topologically robust 2D and 3D photonic circuitry in the entire electromagnetic spectrum, from microwave frequencies to optical domain. The proposed all-dielectric platform may allow avoiding undesirable effects of Ohmic loss unavoidable in metallic and plasmonic structures. In addition, the SPT order facilitates topological protection in photonics-compatible materials, thus allowing one to escape technical difficulties associated with the use of magnetic materials, external magnets, and temporal modulation, which are required to induce topological order in systems with broken TR symmetry.

**REFERENCES**

1. L. Lu, J. D. Joannopoulos, and M. Soljaćić, Nat. Photon. **8**, 821-829 (2014).
2. A. B. Khanikaev, S. H. Mousavi, W.-K. Tse, M. Kargarian, A. H. MacDonald, G. Shvets, Nat. Mater. **12**, 233–239 (2013).
3. X. Cheng, C. Jouvaud, X. Ni, S. H. Mousavi, A. Z. Genack, and A. B. Khanikaev, Nat. Mater. (2016). doi:10.1038/nmat4573.
4. A. Slobozhanyuk, S. H. Mousavi, X. Ni, D. Smirnova, Y. S. Kivshar, A. B. Khanikaev, arXiv:1602.00049 (2016).

# Topological excitons, plexcitons, and polaritons in organic materials

**Joel Yuen-Zhou**[1]

[1]Department of Chemistry and Biochemistry, University of California San Diego, La Jolla, CA 92093, USA

[*]corresponding author: joelyuen@ucsd.edu

**Abstract**- The control of energy transfer at the nano- and mesoscales is one of the main goals for the development of efficient light-harvesting architectures and photonic circuitry. Here, we describe our proposals for the design of topological edge states in excitonic and polaritonic systems composed of organic materials. We shall discuss models of porphyrin thin films, molecular crystals coupled to plasmonic metals, and organic dyes in an optical microcavity, which we believe, can be readily implemented experimentally.

When molecular excitations in an aggregate strongly couple with electromagnetic fields, new hybrid quantum states arise, known as polaritons. These quasiparticles enjoy long coherence lengths from their electromagnetic component, but also exhibit interesting few and many-body phenomena stemming from the material counterpart. An interesting class of polaritons are *plexcitons*, which result from the coupling between surface plasmons and molecular aggregates. In this talk, I will describe how to simulate topological phases of matter (featuring one-way edge currents robust against disorder), such as the Quantum Hall Effect or topological insulators, using accessible hybrid molecular nanostructures in plexcitonic systems (see Figs. 1 and 2) or excitonic films alone [1,2], hence paving the way to the design and study of exotic solid state phenomena in easily realizable molecular environments at room temperature. Our study is the first to introduce solid state concepts of topological phases to Chemistry, and anticipates exciting developments along this frontier, in terms of quantum simulation, photonics, plasmonics, and control of energy flow at the nanoscale. I will finish my talk discussing some new ideas on how to carry out coherent control of nanoscale energy transport using polaritonic systems, where the phase coherence of the electromagnetic modes gets imprinted onto the molecular states that couple with them [3].

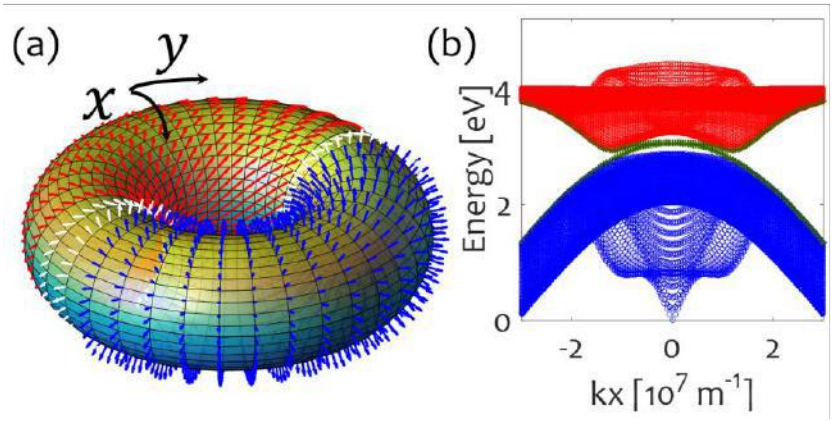



**Fig. 1.** *Topologically protected edge modes in plexcitons.* (a) Simulation of edge modes where magneto-SPs are computed in the torus geometry. Two domains of organic layers are placed on top of it (just like "two icings" on a donut). In-plane (red) and out-of-plane (blue) transition dipoles yield topologically nontrivial and trivial plexcitons, respectively. Topologically protected one-way plexcitons

appear at the interfaces (white domains). Each interface features a different plexciton direction of motion. (b) 1D dispersion relation for the setup in (a). Bulk lower polaritons (blue) and upper polaritons (red) separated by edge modes (green) featuring positive and negative dispersions, respectively, and localized along each interface.

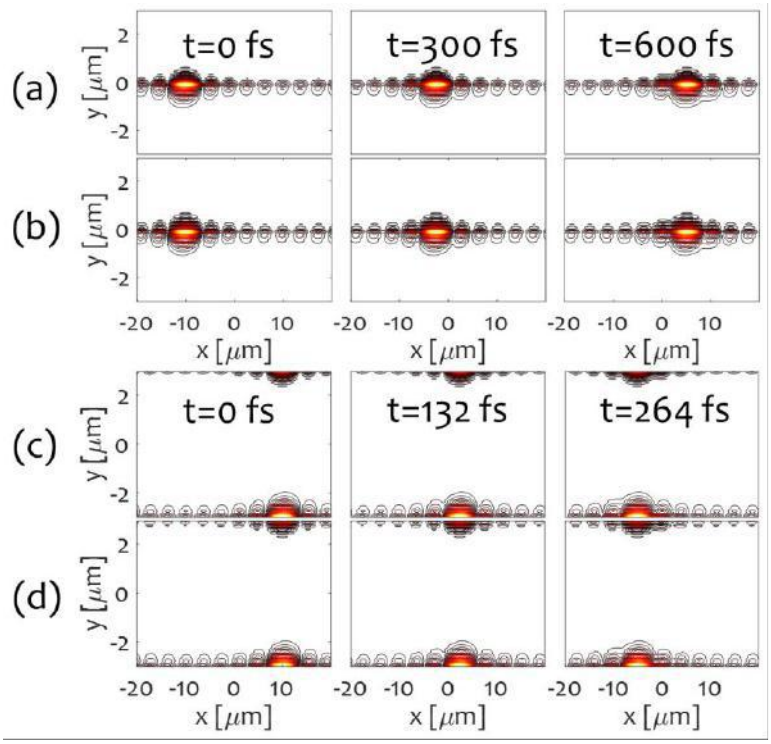



**Fig. 2.** *Snapshots of dynamics of topologically-protected plexciton modes.* (a,b) and (c,d) depict the dynamics of an initially localized plexciton along the y=0 and y= ± Ly/2 = ± 3 μ m interfaces of our simulation for the plexciton setup in Fig. 1. (a,c) and (b,d) show the exciton and magneto-surface-plasmon components, respectively. These modes, which are robust to disorder, have substantial excitonic and magneto-surface-plasmon components, travel in opposite directions along different interfaces (see Fig. 1b), and are robust against disorder.

**Acknowledgements**. J.Y.-Z acknowledges support from startup funds at UC San Diego as well as the Energy Frontier Research Center funded by the US Department of Energy, Office of Science, Office of Basic Energy Sciences under Award Number DESC0001088.

**REFERENCES**

1. Yuen-Zhou, J., S. K. Saikin, T. Zhu, M. C. Onbasli, C.A. Ross, V. Bulovic, M. A. Baldo, Plexciton Dirac points and topological modes, Nat. Comm., in press (2016).
2. Yuen-Zhou, J., S. K. Saikin, N. Yao, A. Aspuru-Guzik, Topologically protected excitons in porphyrin thin films, Nature Mater. 13, 1026 (2014).
3. Hu, Z., R. de León Montiel, V. Menon, J. Yuen-Zhou, Plexciton energy transfer, in preparation (2016).

# Advances in plasmonic and metamaterial devices

**JONG G. OK**, Ph.D.
Invited Talk – SP26. Advances in plasmonic and metamaterial devices
META 2016, Jun 25-28, 2016

# Scalable Nanoarchitecturing for Commercially-feasible Applications in Electronics, Photonics, and Metastructures

## SEMINAR ABSTRACT

The exceptional properties and features particularly emerging from micro- and nano-scale materials and structures are called for in many applications in mechanics, electronics, photonics, and energy and biological engineering. However, the typically-low fabrication throughput along with limited applicability out of each nanomaterial has been a roadblock to step toward practical nanomanufacturing from lab-scale nanofabrication. This seminar will address these issues while focusing on two main topics: (1) how multiple micro/nano-scale structures and materials can be complementarily assembled into more functional hybrid nanoarchitectures having broader applicability; and (2) how these systems can be engineered in a continuous and scalable manner to increase the manufacturing throughput towards commercially-feasible level.

In part one of this talk, carbon nanotubes, graphene, and metal oxide nanowires (NWs) will be considered as small-scale building blocks. Assembling these complementary functional components, three-dimensional (3D) hybrid nanoarchitectures comprising ZnO and VOx NWs hierarchically integrated with CNT constructs will be demonstrated for advanced energy and sensing applications based on photonic and electrochemical conversion. In the second part, a series of continuous and high-throughput micro/nano-manufacturing techniques will be presented based around roll-to-roll (R2R) lithography as well as seamless and template-free nanopatterning, along with direct photonic applications. R2R nanoimprint lithography (R2R NIL) and Photo Roll Lithography (PRL) will exhibit the scalable nanofabrication of various sub-wavelength-scale features by combining NIL and photolithography with continuous rolling principle. Further, the seamless nanopatterning enabled by continuous inscribing of a cleaved grating mold edge on a polymer substrate will be demonstrated, which will be followed by the template-free nanopattering via vibrational indentation of a simple flat edge over a softer substrate.

Moving forward, we will discuss how nanomaterials/nanostructures and nanopatterning methodologies can be mingled with each other towards more scalable and multidimensional nanoarchitectures. For instance, the mechanically-rolled 2D CNT sheets will be introduced for direct fabrication of NW/CNT hybrid thin-film devices. Then we will demonstrate PRL-fabricated metal mesh patterns can be incorporated to the transparent graphene films for flexible nanoelectronics. It will also be presented various 2D micro/nanopatterns can be continuously fabricated by sequential 1D patterning strokes enabled by nanoinscribing and vibrational indentation. In particular, how the aforementioned nanoarchitecturing methodologies can be utilized in novel metastructures and metamaterials will be envisioned through several specific concepts.

* This work is supported by the National Research Foundation of Korea (NRF) Grant funded by the Korean Government (MSIP) (No. 2015R1A5A1037668).

# Versatile and controllable excitation of SPPs by a metasurface composed of triangular nanoantennas

**Benfeng Bai*** **and Oubo You**

State Key Laboratory of Precision Measurement Technology and Instruments, Department of Precision Instrument, Tsinghua University, Beijing 100084, China

*corresponding author: baibenfeng@tsinghua.edu.cn

**Abstract**- We present a metasurface approach that can realize versatile and controllable excitation of surface plasmon polaritons (SPPs). The metasurface consists of triangular shaped nanoantennas that can directionally excite SPPs under normal incidence. By properly arranging the nanoantennas according to the required phase and amplitude distribution of a SPP wavefront, any SPP beam with even complex profile can be generated. The metasurface can also be designed to realize broadband, polarization-controlled tunable directional excitation of SPPs.

The efficient and directional excitation of surface plasmon polaritons (SPPs) is a key issue in various plasmonic applications such as plasmonic circuitry. It is favorable if the SPP wave or beam can be excited to any desired direction under normal incidence of an excitation light beam. On the other hand, the generation of SPP wave with required wavefront or the shaping of SPP wavefront are also quite demanded for plasmonic circuitry, which however is less explored so far.

In this talk, we present a metasurface approach that can realize versatile and controllable excitation of SPPs. The metasurface is composed of Δ-shaped nanoantennas that have the special property of efficient unidirectional excitation of SPPs under normal incidence.[1] By studying the radiation property of the Δ-antenna thoroughly, we can use it as a unit source to generate SPP wave with designed amplitude and initial phase. Then, by arranging the Δ-antenna unit cells into a lattice, the metasurface can generate SPP beam with any required wavefront profile, as shown in Fig. 1(A). Since the amplitude and phase of the SPP wavefront can be modulated separately, it is a general device that can produce any SPP beam with complex wavefront. We take the second-order Hermite-Gauss SPP beam as an example to demonstrate the effectiveness of the method.[2] The high quality of the generated SPP beam is verified by near-field characterization using a scanning near-field optical microscope.

Furthermore, based on the similar principle, the metasurface SPP launcher can be designed to achieve two symmetry SPP excitation states with two orthogonal linear polarization incidences, as shown in Fig. 1(B). By combining these two polarization states with different complex coefficients properly, one can achieve complete unidirectional SPP excitation. For different incident wavelengths, the unidirectional SPP excitation can still be maintained just by tuning the coefficients of the two orthogonal incident polarizations, whose combination is usually an elliptical polarization and can be easily achieved by using a linear polarizer and a quarter-wave plate. Therefore, in this way, one can realize broadband unidirectional SPP excitation easily with this metasurface. In addition, if the incident wavelength is fixed, one can achieve different excitation ratio of the SPPs propagating to two opposition directions by changing the incident polarization coefficient pair.

In conclusion, we have proposed a straightforward and efficient metasurface approach to the design of versatile and efficient SPP launchers that can generate SPP beams with arbitrary wavefront profiles or

polarization-controllable SPP waves. Since the principle is intuitive and straightforward and the fabrication of the metasurface is well adaptive to the mature nanofabrication technique nowadays, the approach may find wide applications in functional plasmonic devices and systems.

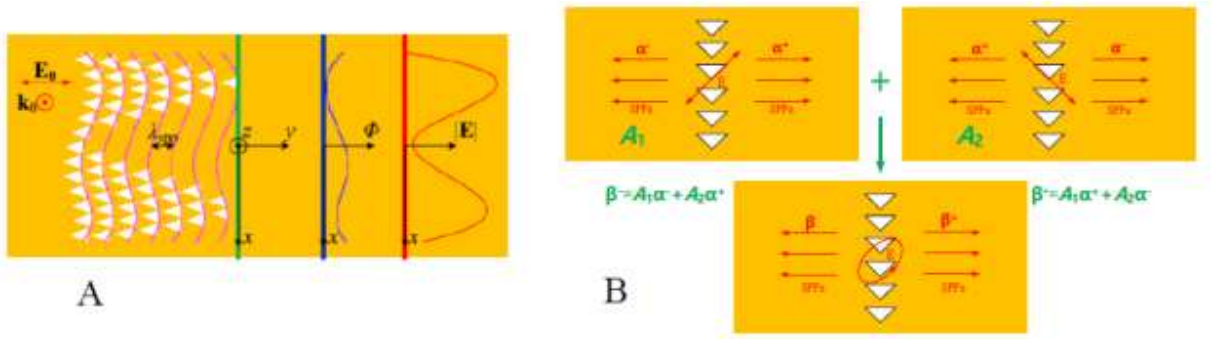



Figure 1. Δ-antenna metasurfaces for (A) the unidirectional excitation of SPP beam with arbitrary wavefront profile, and (B) the polarization-controlled tunable directional excitation of SPP wave.

**Acknowledgements** We acknowledge the support by the National Natural Science Foundation of China (Projects No. 11474180 and No. 61227014) and the Ministry of Science and Technology of China (Project No. 2011BAK15B03).

**REFERENCES**

1. O. You, B. Bai, and X. Li, "Experimental study of unidirectional excitation of SPPs by binary area-coded nanohole arrays," *Chin. Opt. Lett.*, Vol. 12, No. 8, 082401, 2014.
2. O. You, B. Bai, X. Wu, Z. Zhu, and Q. Wang, "A simple method for generating unidirectional surface plasmon polariton beams with arbitrary profiles," *Opt. Lett.*, Vol. 40, No. 23, 5486-5489, 2015.

# Wavefront shaping through emulated curved space

**Chong Sheng1, Rivka Bekenstein2, Hui Liu1,*, Shining Zhu1 and Mordechai Segev2,***

[1]National Laboratory of solid State Microstructures & Department and Physics, National Center of Microstructures and Quantum Manipulation, Nanjing University 210093, China

[2]Physics Department and Solid State Institute, Technion, 32000 Haifa, Israel

[*]corresponding author: liuhui@nju.edu.cn

**Abstract**- We propose wavefront shaping by exploiting General Relativity effects and concepts of curved space in waveguide settings. We use this technique to construct a very narrow non-diffracting beam and also design shape-invariant accelerating beams propagating along arbitrary trajectories. Finally, we demonstrate the phenomenon of Einstein's Rings, and find that the diameter of the rings in our setting follows exactly Einstein's 1936 formula.

Wavefront shaping for generating non-diffracting optical beams can be achieved by various methods, ranging from annular slits, axicon lenses, holograms, spatial light modulators, gratings, metasurfaces and diffraction from nanoparticles. Importantly, non-diffracting beams can also be generated in inhomogeneous media, such as photonic crystals and photonic lattices. All these require wavefront shaping, that is typically done externally, outside the medium within which the beam is propagating. However, wavefront shaping can also be done by shaping the EM environment in which the wave is propagating. The fact that the propagation of EM waves in static curved space is analogous to that in inhomogeneous media is the underlying principle of emulating General Relativity (GR) phenomena [1-2]. In artificial structures, the refractive indexs are structured to vary according to the curvature of space, giving rise to unique trajectories and controlling the diffraction of light [3-5].

Here, we show that using ideas inspired by GR yields efficient beam shaping in waveguide settings (figure (a)) [6]. First, we fabricate the micro-structured optical waveguide with the specific refractive index emulating the curved space environment generated by a massive gravitational object. This dielectric structure yields a very narrow beam that remains non-diffracting for many Rayleigh lengths (figure (b)). Second, with the same experiment system, we demonstrate the Einstein's rings phenomenon, matching Einstein's 80 years old formula (figure (d)). Finally, we present a general formalism to transform broad Gaussian beams to shape-invariant beams accelerating (bending) along arbitrary trajectories (figure (b)). The concept is general, applicable to many cases where wavefront beam shaping in a waveguide platform is required.

**REFERENCES**

1. A. Einstein, "Lens-like action of a star by the deviation of light in the gravitational field," Science 84, 506 (1936).
2. U. Leonhardt and T. G. Philbin, "General relativity in electrical engineering," New J. Phys. 8, 247 (2006).
3. C. Sheng et al., "Trapping light by mimicking gravitational lensing," Nature Photonics 7, 902 (2013).
4. R. Bekenstein et al., "Shape-Preserving Accelerating Electromagnetic Wave Packets in Curved Space," Phys. Rev. X 4, 011038 (2014)

5. R. Bekenstein et al., “Optical simulations of gravitational effects in the Newton–Schrödinger system”, Nature Physics 11, 872 (2015)
6. C. Sheng, et al., “Wavefront Shaping through Emulated Curved Space”, Nature Communications, DOI: 10.1038/ncomms10747 (2016)

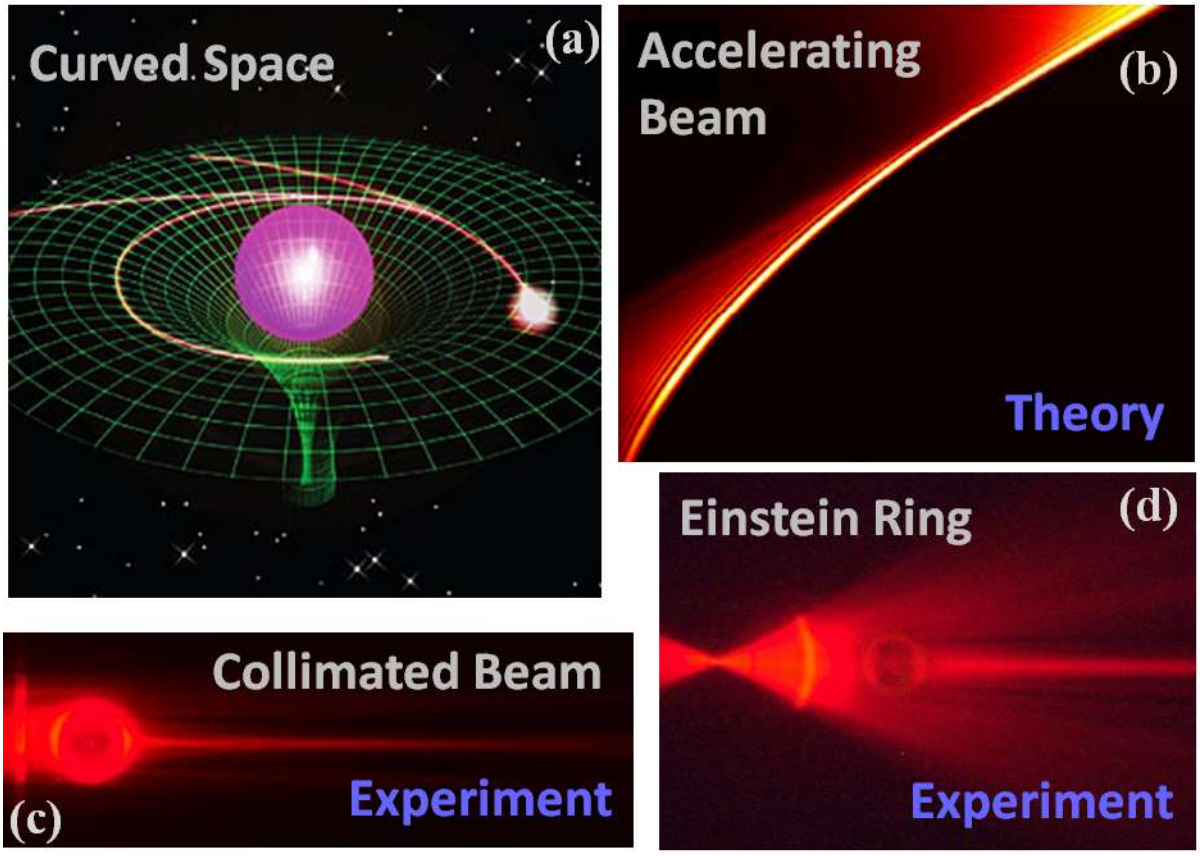



Figure (a) Curved space in general relativity; (b) Accelerating Beam in curved space; Wavefront shaping in our experiment: (c) Collimated beam and (d) Einstein ring.

# Metasurfaces for refractomatric sensing and advanced functionalities

**R.Verre[1*], M. Svedendahl[1], T. Antosiewicz[1, 2] and M. Käll[1]**

[1] Department of Applied Physics, Chalmers University of Technology, 412 96 Göteborg, Sweden

[2]Center of New Technologies, University of Wasaw, Warsaw, Poland

[*]corresponding author: ruggero.verre@chalmers.se

**Abstract-** Layers of closely spaced nanoparticles can behave as homogeneous surfaces characterized by well-defined specular reflection and transmission coefficients. By exploiting the properties of the individual constituents, in this case metallic nanoparticles supporting localized surface plasmon resonances (LSPRs), a variety of advanced functionalities can be obtained. Here, we provide several such examples based on advanced nanofabrication and optical characterization methodologies. Various types of plasmonic metasurfaces were produced and utilized for refractometric LSPR sensing based on novel phase and polarization-contrast methods with sensitivities comparable to state-of-the-art classical systems. We also demonstrate directionality and artificial magnetism, which can be induced and controlled by properly engineering the nanoscopic plasmonic elements composing the metasurface.

The prefix “meta” derives from greek μετά, which means“after”or “beyond”. A metasurface is a layer of closely spaced sub-wavelength objects on a substrate. The metasurface looks homogeneous to an incident light-wave but may possess advanced functionalities due specifically designed sub-wavelength structuring. The possibility to manipulate light at the nanoscale using metasurfaces constructed from plasmonic nanostructures is of high current interest. We will discuss several examples of plasmonic metasurfaces with different functionalities and possible applications.

Figure 1a) shows the simplest type of metasurfaces constructed from supported nanoparticle layers. In this case, we demonstrate the possibility of achieving complete light absorption using a metasurface composed of short-range ordered gold nanodisks on a cover glass [1]. Complete absorption is achieved due to Fano interference between the plasmonic resonances and the glass reflectance, which act as a continuum. We use this effect for facile refractometric sensing based on monitoring phase changes of the reflected light [2]. Advantages in comparison to normal colorimetric sensing will be discussed. We also demonstrate similar sensitivities using anisotropic metasurfaces composed of dimers. In this case, the polarization rotation induced using normal incidence illumination is analyzed by a polarization sensitive detection scheme that renders the method self-referenced.

Figure 2) shows a layer of tilted nanopillars. This kind of metasurface present a strong directionality caused by the complex charge oscillation induced in each individual nanopillar, which essentially acts as a tilted dipole above a dielectric interface. We demonstrate that fluorescence excitation and emission from dye molecules deposited on the metasurface is enhanced in specific directions determined by the tilt angle of the nanopillars. Cathodoluminescence spectroscopy was used to reveal the optical properties of the systems with a sub-wavelength resolution of ~10nm.

The metasurfaces discussed above were fabricated using a cheap production method called hole-mask colloidal lithography. This technique only allows one to produce structures that are semi-randomly dispersed on a substrate, while many advanced functionalities may require metasurfaces with much more well-defined structural parameters. We give an example in Figure 1 c), which shows a plasmonic oligomer in which each unit is a metal-insulator-metal (MIM) composite particle. The system possesses multiple Fano resonances that are the signature of quasi-broadband optical magnetism at visible wavelengths [4].

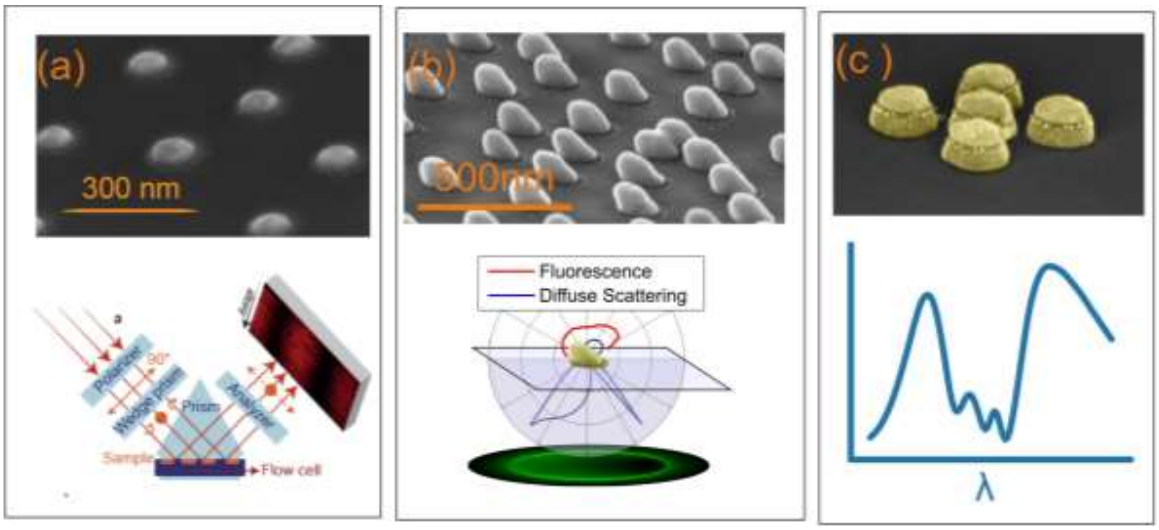



**Figure 1:** (a) A metasurface composed of simple nanodisks can cause complete light absorption and strong modulation of the polarization state of reflected light. This effect was used to constructe a simple interferometric plasmon sensor for biomolecular analysis. (b) Using the same production method, a metasurface composed of tilted nanopillars can be fabricated. When fluorophores are coupled to the nanoparticle layer, a directional emission similar to the diffuse scattering pattern is observed. (c) SEM image of a MIM plasmonic pentamer: the structure exhibits multiple Fano resonances and quasi-broadband optical magnetism.

**REFERENCES**


1. Svedendahl, M. Johansson, P and Käll, M., "Complete Light Annihilation in an Ultrathin Layer of Gold Nanoparticles", *Nano Lett.* 13, 3053–3058, 2013
2. Svedendahl, M., Verre, R., and Käll, "Refractometric biosensing based on optical phase flips in sparse and short-range-ordered nanoplasmonic layers", *LSA*, 3, e220, 2014
3. R. Verre, M. Svedendahl, N. Odebo Länk, Z. J. Yang, G. Zengin, T. J. Antosiewicz, and M. Käll, "Directional Light Extinction and Emission in a Metasurface of Tilted Plasmonic Nanopillars", *Nano Lett.*, 2015
4. Verre, R, Yang, Z.J., Shegai, T. and Käll, M., " Optical Magnetism and Plasmonic Fano Resonances in Metal–Insulator–Metal Oligomers", *Nano Lett.*, 2015

# Hybrid graphene-plasmonic antenna arrays for the fast detection of terahertz quantum cascade lasers

**R. Degl'Innocenti[1*], D. S. Jessop[1], L. Xiao[1,2], S. J. Kindness[1], Y. Ren[1], H. Lin[3,4], J. A. Zeitler[3], P. Braeuninger-Weimer[2], S. Hofmann[2], H. E. Beere[1] and D. A. Ritchie[1]**

[1]Department of Physics, University of Cambridge, J. J. Thomson Avenue, Cambridge CB3 0HE, UK

[2]Department of Engineering, University of Cambridge, J. J. Thomson Avenue Cambridge, CB3 0FA, UK

[3]Department of Chemical Engineering and Biotechnology, University of Cambridge, Pembroke St, Cambridge, CB2 3RA, UK

[4]Department of Engineering, Lancaster University, Lancaster LA1 4YW, UK

[*]corresponding author: rd448@cam.ac.uk

**Abstract**-We present an integrated room temperature terahertz detector based on asymmetrically doping interdigitated bow-tie antennas that are in contact with graphene which shunt the two arms. The device was tested with a quantum cascade laser emitting around 2 THz yielding a responsivity of 0.5 μA/W, and implemented in an imaging system.

THz research holds great promise for many applications in diverse fields such as spectroscopy, security screening, communications and biomedical imaging. The lack of suitable active and fast optoelectronic devices has so far hindered THz technology from reaching its full scientific and commercial potential. Detection of terahertz radiation, remains particularly elusive and has relied on intrinsically slow (< 100 Hz) detectors such as pyroelectric detectors or Golay cells. Graphene and other bidimensional nanomaterials have been recently investigated as viable terahertz detection materials in a range of detection schemes. In the photovoltaic effect, for instance, the unbalance between photogenerated carriers at differently doped graphene regions leads to a detectable photocurrent. We followed this approach and in order to overcome the intrinsically low efficiency of the graphene detection process, we designed a device architecture based on plasmonic bow-tie antennas, capable of enhancing the terahertz light to the graphene area shunting the two arms, as shown in Fig. 1 a) and Fig. 1 b). The detector was integrated in an imaging system, and tested with a bound to continuum quantum cascade laser (QCL) emitting in single frequency at 2 THz, matching the plasmonic resonance of the bow-tie antennas

The fabrication starts with monolayer graphene grown by chemical vapor deposition and transferred onto a $SiO_2$/Si substrate. The Si substrate was Boron-dope to allow electrostatic gating of the device. Two distinct steps of electronic beam lithography, metal evaporation and lift-off allowed the definition of interdigitated source and drain pads and bow-tie antennas, contacting the graphene region, as shown in Fig. 1 a) and b). The two elements of the bow-ties are fabricated with different metal evaporations, Pd/Au (60/15 nm) to obtain p-doping, and Ti/Au (60/15 nm) to achieve n-doping of the contacted graphene. The source and drain current has been monitored at different gate bias, showing a Dirac point around 100 V. The QCL was operated in pulsed mode with a repetition rate of 10 kHz and 30% duty cycle at 5 K. The detector's source and drain were biased with a constant voltage of 7 mV and at the Dirac point where the detector yielded the highest responsivity of 0.5 μA/W and allowed the fast acquisition of large objects. The terahertz image of a leaf acquired in these biasing conditions is shown in

Fig. 1 c) together with a picture of the same object acquired in the visible spectrum, reported for completeness in Fig. 1 d).

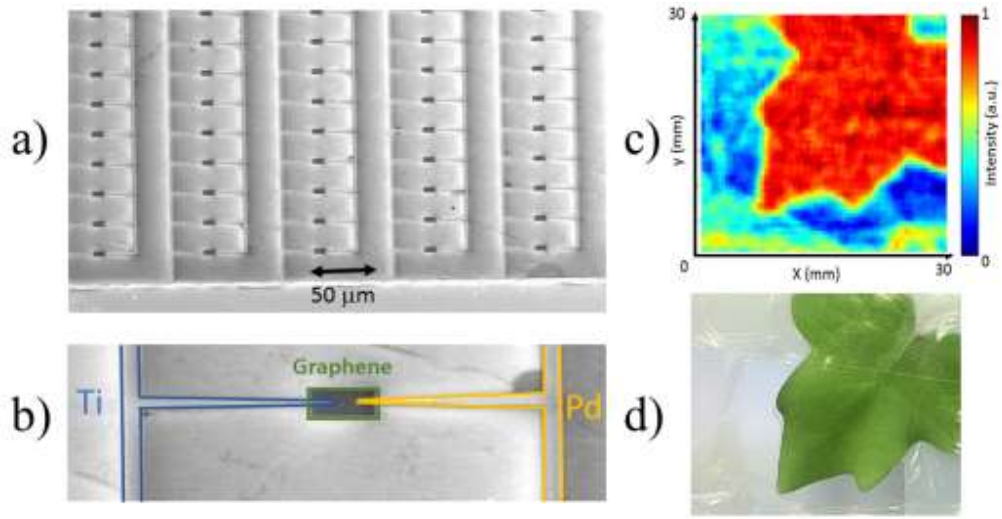



Figure 1: a), b) Scanning electron microscope pictures of the interdigitated bow-tie arrays based on Pd and Ti metallic arms, shunted by graphene area. c) A terahertz image of a leaf acquired with a QCL is reported, d) together with a picture in the visible of the same object d).

In summary we presented the realization of a terahertz imaging system utilizing a quantum cascade laser as source and hybrid graphene/bow tie antenna integrated arrays detectors.

**Acknowledgements**: We would like to acknowledge financial support from the Engineering and Physical Sciences Research Council (EPSRC); RD, HEB and DAR acknowledge the grant EP/J017671/1 - Coherent Terahertz Systems (COTS), PBW and SH acknowledge EP/K016636/1 – GRAPHTED and HL and JAZ acknowledge EP/L019922/1.

**REFERENCES**

1. Koppens, F. H. L., T. Mueller, P. Avouris, A. C. Ferrari, M. S. Vitiello and M. Polini "Photodetectors based on graphene, other two-dimensional materials and hybrid systems" *Nature Nanotech*. Vol. 9, 780-793, 2014.

# KERR EFFECT IN HYBRID PLASMONIC WAVEGUIDES

**S. Palomba[1*], F. J. Diaz[1], G. Li[1], C. Martijn de Sterke[1,2], B. T. Kuhlmey[1,2]**

Institute of Photonics and Optical Science (IPOS), School of Physics, The University of Sydney, NSW 2006, Australia.

[2]Center for Ultrahigh Bandwidth Devices for Optical Systems (Cudos), Australia

[*]corresponding author: stefano.palomba@sydney.edu.au

**Abstract** We report a detailed theoretical study of a Kerr effect in a hybrid plasmonic waveguide (HPWG), constituted by a nonlinear dielectric material, sandwiched between a metallic layer and a Si nanowire.

Optical nonlinearities have already enabled a range of capabilities, such as signal switching, de-multiplexing, wavelength conversion, light amplification and supercontinuum generation. Integrating these abilities in an on-chip photonic platform will lead to benefits in terms of cost, footprint, energy consumption and performance. These will in turn help meeting current demands of larger bandwidth, enabling all-optical signal processing vastly overcoming the electronic bottlenecks.

The current leading platform for integrated nonlinear optics is silicon-on-insulator (SOI). However, silicon suffers from a fundamental material limit imposed by strong two-photon absorption (TPA). As a consequence, alternative platforms which do not suffer from a large TPA are investigated. One alternative platform, the hybrid plasmonic platform, has gained attention as it generates strongly compressed fields [1]. The simplest structure of this kind is represented by a nonlinear dielectric material, sandwiched between a metallic layer and a Si nanowire, for which the first experimental evidence of third order nonlinearities we recently reported [2]. Here the plasmonic and photonic modes are combined to generate a hybridized fundamental mode which has been shown to possess a high field confinement, associated with the plasmonic mode, and reduced propagation losses, associated with the photonic mode [3]. The high confinement and modest loss is required for producing strong nonlinearities, which may be further increased through the incorporation of highly nonlinear polymers. Although the geometry with the largest theoretically reported nonlinear parameter is of this type [1], the origin for such a high nonlinearity remains somewhat unclear. In order to gain more insight we have analyzed the Kerr nonlinear parameter of HPWGs, which quantifies the strength of the nonlinear effect, and its dependence on the energy velocity, effective area and the average nonlinear refractive index, with and without the presence of the nonlinear polymer. In addition, in order to efficiently evaluate their Kerr nonlinear performance we propose a simple figure of merit (FOM) for Kerr nonlinear effects in plasmonic waveguides, including degenerate four wave mixing (DFWM). The effectiveness of the FOM is verified with an all-plasmonic waveguide and a hybrid-plasmonic waveguide configuration. Rigorous results show that the length for optimal DFMW efficiency is equal to the attenuation length, and that the FOM provides the obtainable upper limits of the DFWM efficiency and the nonlinear phase shift. These results provide fundamental theory and useful guidance in exploring plasmonic waveguides for nonlinear optical applications.

**Acknowledgements**. This work has been funded through the Australian Research Council (ARC) Discovery Project number DP150100779.

## REFERENCES

1. Pitilakis and E.E. Kriezis, "Highly nonlinear hybrid silicon-plasmonic waveguides: analysis and optimization," J. Op. Soc. Am. B 30(7), 1954-1965 (2013).
2. F. J. Diaz, T. Hatakeyama, J. Rho, Y. Wang, K. O'Brien, X. Zhang, C. Martijn de Sterke, B. T. Kuhlmey and S. Palomba. " Sensitive method for measuring third order nonlinearities in compact Dielectric and Hybrid Plasmonic Waveguides," Opt. Ex. 24(1), 545-554 (2016).
3. R.F. Oulton, V.J. Sorger, D.A. Genov, D.F.P. Pile and X. Zhang, "A hybrid plasmonic waveguide for subwavelength confinement and long-range propagation," Nat. Photon. 2(8), 496-500 (2008).Yikai, S., *Communications and Photonics Conference and Exhibition (ACP)*, 732, (2010).

# Coplanar isolator based on gap plasmon resonators

**E. Djekounyom[1,2], E. Verney[1*], D. Piétroy[1] and J.P. Chatelon[1]**
[1] Univ Lyon, UJM-Saint-Etienne, CNRS, LHC UMR 5516, F-42023, SAINT-ETIENNE, France
[2] Institut National Supérieur des Sciences et Techniques of Abéché, Tchad
[*]eric.verney@univ-st-etienne.fr

**Abstract**- The isolation function in coplanar technology can be carried out by a CPW line with an asymmetric geometry, in which one of the ground planes is engraved by an array of gaps with micrometric width. Such a structure shows a good isolation in the X and Ku band, about 50 dB, and relatively weak insertion losses. The influence of the parameters of the array - like the distance between the gaps, width and length of the gaps - over device performances is explored.

## 1. Introduction

Since C.P. Wen proposed the first structure of coplanar isolator for microwave applications in 1969 [1], which had the advantage of beeing simply interconnected to other circuits, propositions have been developed with interesting results regarding their ability to isolate [2]. Anyway, on the path to marketable devices, some challenges still need to be taken up in terms of performances on insertion losses or passband.
Our paper presents the study of a new structure of coplanar isolator, based on gap plasmon resonators as absorbers. The study was first realized with HFSS, and demonstrators have then been realized and measured on a spectral band between 5 and 15 GHz.

## 2. Properties of the structure

For some years, studies have shown the possibility of controlling electromagnetic waves transmission by absorption on a material surface thanks to sub-wavelength gaps. Gap plasmon resonators have been designed and realized to efficiently absorb electromagnetic waves in visible and infrared domains, under specific conditions for light polarisation's [3-5]. Despite a totally different configuration of modes in coplanar waveguides compared to these studies, and thus different conditions regarding gap plasmon resonator excitation, we dimensioned and simulated resonators which could work around 10 GHz.
As indicated in figure 1, the base structure is a classical copper coplanar waveguide engraved on a magnetical substrate of YIG (Yttrium Ion Garnet). Conductors are 3µm thick and the substrate is 1mm. The dimensions of the gap and signal of the CPW are respectively 200 µm and 400 µm. The isolator is 8 mm long and ground planes have a width of 5.1 mm. In one of the ground plane, an array of micrometric gaps is engraved with a LASER, in which evanescent modes could propagate at the interface metal-dielectric. The length of these gap plasmon resonators is proportional to half-wavelength of the chosen work frequency and their width is about 15 µm. The step of the array is about 400 µm.

This structure shows isolation properties only when the magnetic layer is polarized with a static magnetic field $H_0$ normal to the plane of the CPW. The magnetization of the layer generates a field displacement of the propagating wave, which acts in opposite directions for both directions of the propagation. Regarding the way of the energy propagation, gap plasmon resonators will be excited by funneling or not [5], and a non-reciprocal behavior of the structure will be achieved on the (Ox) axis at the resonance frequency of the gaps, the resonators acting like a metamaterial absorber [3-5].

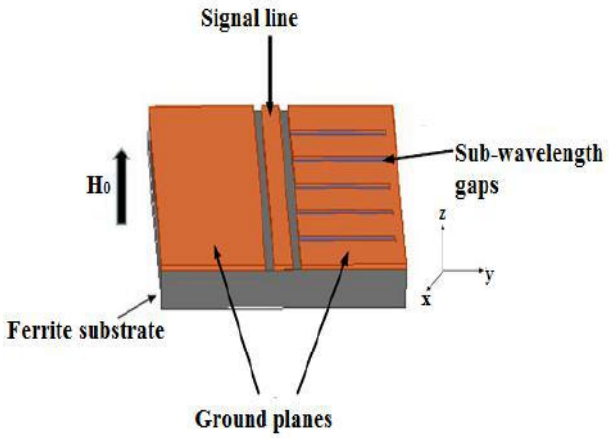



**Figure 1:** Structure of the gap plasmon resonators based isolator

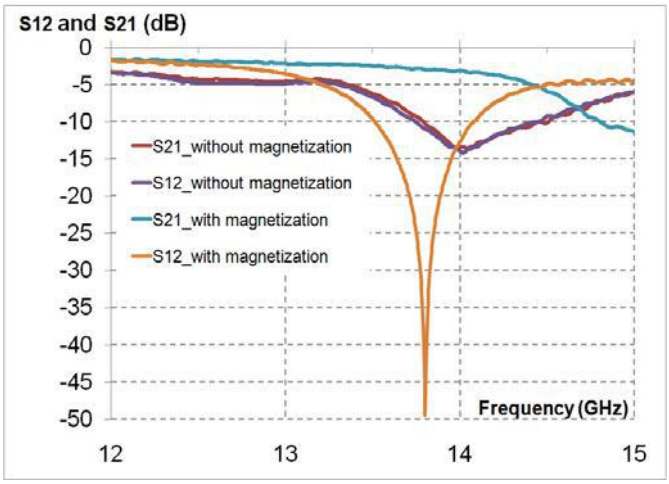



**Figure 2:** Measurements of the transmission S-parameters of the isolator under a 200 mT magnetization

## 3. Results and conclusion

After the validation of our structure by simulating it with HFSS, we fabricated a demonstrator with the dimensions indicated in the second paragraph. As shown in figure 2, under a 200 mT static field chose to obtain a saturated magnetic layer, we obtain an isolation of -50 dB around 13.7 GHz corresponding to the resonance of the gap length of 4.7 mm of our demonstrator. Insertion losses are about 3dB and could be lowered in a further study. Without magnetization, the structure is reciprocal and shows losses in both directions at 14 GHz. A second demonstrator shows the same results around 10 GHz with gap lengths about 6 mm.

So we have demonstrated that the principle of gap plasmon resonators, firstly proposed at optical wavelength to make absorbing surfaces, could be adapted at microwave frequencies in propagated mode to make non-reciprocal devices like isolators. The ratios of absorbed power in that structure are similar as those mentioned in literacy for optical frequencies.

**REFERENCES**

1. C.P. Wen, "Coplanar waveguide: a surface strip transmission line suitable for non reciprocal gyromagnetic device application", IEEE Trans. Microwave. Theor. Technol., 17(2), 1087- 1090 (1969).
2. S. Kirouane, D. Vincent, E. Verney, O. Zahwe, B. Payet and A. Chaabi, "Design of a new coplanar isolator made from YIG film operating in the X-frequency band", The European Physical Journal Applied Physics, 57, 01, 10602 (2011).
3. P.N. Stavrinou and L. Solymar, "The propagation of electromagnetic power through subwavelength slits in a metallic grating", Opt. Commun., Vol. 206, pp. 217-223, 2002.
4. J. Le Perchec and al, "Why metallic surfaces with grooves a few nanometers deep and wide may strongly absorb visible", Phys. Rev. Lett. 100, 066408 (2008).
5. F. Pardo and al, "Light Funneling Mechanism Explained by Magnetoelectric Interference", Phys. Rev. Lett. 107, 2011.

# Backward spoof surface plasmonic wave propagation and waveguide devices utilizing structured ultra-thin metallic films

**Y. J. Feng*, X. Y. Liu, J. M. Zhao, B. Zhu, and T. Jiang**
School of Electronic Science and Engineering, Nanjing University, Nanjing, 210093, China
*corresponding author: yjfeng@nju.edu.cn

**Abstract**-Backward spoof surface plasmonic wave with anti-parallel phase and group velocities is demonstrated experimentally in a single-conductor waveguide composed of plasmonic metamaterial of structured ultra-thin metallic film. As an application, a contra-directional coupler in the microwave band is designed and verified that can route the input signal to opposite directions with forward or backward coupling at different frequencies. These results could contribute to the development of more complicated surface circuitry for microwave and terahertz wave.

Backward wave with anti-parallel phase and group velocities is one of the basic properties associated with negative refraction and sub-diffraction image that have attracted considerable interest in the context of photonic metamaterials [1, 2]. It has been predicted theoretically that some plasmonic structures can also support backward wave propagation of surface plasmon polaritons (SPPs) [3-5], however direct experimental demonstration has not been reported, to the best of our knowledge. Here we report the successful realization and experimental demonstration of backward wave in a specially designed plasmonic metamaterial.

In this presentation, first we will propose a new design of a plasmonic metamaterial composed of single ultra-thin corrugated metallic film, which can support backward wave propagation of spoof SPP wave. Thanks to the low loss of the proposed structure, we have successfully demonstrated the backward wave propagation by both simulation and the transmission measurement of the fabricated prototype. The dispersion analysis, the full electromagnetic field simulation and the transmission measurement of the plasmonic metamaterial waveguide have clearly validated the backward wave propagation with dispersion relation possessing negative slope and opposite directions of group and phase velocities.

As a further validation and a direct application of the backward wave propagation, a microwave contra-directional coupler has been designed and tested that could route the signal to opposite terminals through forward or backward coupling at different operating frequencies. The proposed coupler is composed of a straight symmetric corrugated metallic film strip with the interdigital slots and a bending traditional symmetric strip with ordinary straight slots. The two strip waveguides are placed together with a small coupling gap at the middle forming a four port microwave device, as shown in Fig. 1. As the odd mode in the straight waveguide supports the backward wave, therefore the EM energy coupled from the traditional bending waveguide will propagate backwardly and result in an output to the port at the same end of the input port, as shown in Fig. 1. Detailed description of the design, analysis and measurement of the fabricated prototype will be given in the presentation.

Backward wave is the fundamental of many peculiar electromagnetic phenomena such as the negative refraction or the sub-diffraction imaging, therefore our findings can lead to many exciting applications based on the backward surface wave propagation. We also believe that the proposed planar plasmonic structure can be easily extended to higher frequency range and may be very promising for further development of practical

ultrathin surface circuitry for terahertz radiation.

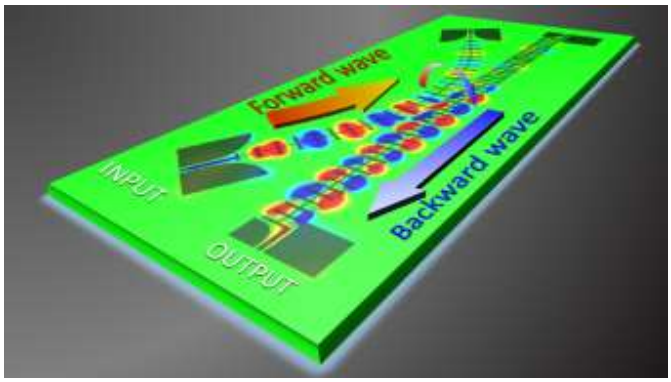



Fig. 1. The simulated transverse electric field distribution at 6.03 GHz along the microwave contra-directional coupler composed of corrugated metallic thin film strip waveguides for the backward coupling of the input power to the output port, indicating the backward wave propagation in the straight thin film waveguide.

In the rest of the presentation, we will report in detail our recent works on waveguide devices based on the conformal spoof surface plasmon (CSP) thin film structures. We have designed both a CSP frequency splitter and a coupler based on the symmetric CSP structure in the microwave frequency range. The designed devices exhibit good performance that is validated through both electromagnetic simulation and the experimental test on fabricated prototypes. We believe that such single-conductor CSP structure and related waveguide devices may be scaled down to other frequencies such as the millimeter wave, or even the terahertz range.

**Acknowledgements**

This work is partially supported by the National Nature Science Foundation of China (61371034, 61301017, 61571218), and partially supported by the Priority Academic Program Development of Jiangsu Higher Education Institutions (PAPD), Jiangsu Key Laboratory of Advanced Techniques for Manipulating Electromagnetic Waves.

**REFERENCES**

1. Shelby, R. A., Smith, D. R., and Schultz, S., "Experimental verification of a negative index of refraction," *Science*, Vol. 292, 77-79, 2001.
2. Pendry, J. B., "Negative refraction makes a perfect lens," *Phys. Rev. Lett.*, Vol. 85, 3966-3969, 2000.
3. Tournois, P., and Laude, V., "Negative group velocities in metal-film optical waveguides," *Opt. Commun.*, Vol. 137, 41-45, 1997.
4. Dionne, J. A., Verhagen, E., Polman, A., and Atwater, H. A., "Are negative index materials achievable with surface plasmon waveguides? A case study of three plasmonic geometries," *Opt. Express*, Vol. 16, 19001-19017, 2008.
5. Quesada, R., Martín-Cano, D., García-Vidal, F. J., and Bravo-Abad, J., "Deep-subwavelength negative-index waveguiding enabled by coupled conformal surface plasmons," *Opt. Lett.*, Vol. 39, 2990–2993, 2014.

# Quantum plasmons in nanoscale waveguides

**Xi-Feng Ren*, Yong-Jing Cai, Ming Li, Chang-Ling Zou, Xiao Xiong, Hua-Lin Lei, Bi-Heng Liu, Guo-Ping Guo, and Guang-Can Guo**

Key Lab of Quantum Information, University of Science and Technology of China, CAS, Hefei, Anhui, 230026, China

Synergetic Innovation Center of Quantum Information and Quantum Physics, University of Science and Technology of China, Hefei, Anhui 230026, China

Email:

*corresponding author: renxf@ustc.edu.cn

**Abstract**- Here we introduce two works on quantum plasmonics: high-visibility on-chip quantum interference of single surface plasmons and transmission of quantum polarization entanglement in a nanoscale hybrid plasmonic waveguide. Our works can bridge nanophotonics and quantum optics.

Quantum photonic integrated circuits (QPICs) based on dielectric waveguides have been widely used in linear optical quantum computation [1]. Recently, surface plasmons have been introduced to this application because they can confine and manipulate light beyond the diffraction limit [2-4].

Here, the on-chip quantum interference of two single surface plasmons was achieved using dielectric-loaded surface-plasmon-polariton waveguides [5]. The high visibility (greater than 90%) proves the bosonic nature of single plasmons and emphasizes the feasibility of achieving basic quantum logic gates for linear optical quantum computation. The effect of intrinsic losses in plasmonic waveguides with regard to quantum information processing is also discussed. Although the influence of this effect was negligible in the current experiment, our studies reveal that such losses can dramatically reduce quantum interference visibility in certain cases; thus, quantum coherence must be carefully considered when designing QPIC devices.

Photonic quantum technologies have been extensively studied in quantum information science, owing to the high-speed transmission and outstanding low-noise properties of photons. However, applications based on photonic entanglement are restricted due to the diffraction limit.

We demonstrate for the first time the maintaining of quantum polarization entanglement in a nanoscale hybrid plasmonic waveguide composed of a fiber taper and a silver nanowire [6]. The transmitted state throughout the waveguide has a fidelity of 0.932 with the maximally polarization entangled state $\phi+$. Furthermore, the Clauser, Horne, Shimony, and Holt (CHSH) inequality test performed, resulting in value of $2.495\pm0.147>2$, demonstrates the violation of the hidden variable model. Since the plasmonic waveguide confines the effective mode area to subwavelength scale, it can bridge nanophotonics and quantum optics, and may be used as near-field quantum probe in a quantum near-field micro/nano-scope, which can realize high spatial resolution, ultra-sensitive, fiber-integrated, and plasmon-enhanced detection.

## REFERENCES

1. Politi, A., Cryan, M. J., Rarity, J. G., Yu, S. & O'Brien, J. L. Silicaon-silicon waveguide quantum circuits, *Science* 320, 646-649 (2008).

2. Reinier W. H., Leo P. K. & Valery Z. *Nat. Nanotechnol*. 8, 719-722 (2013).
3. Fakonas, J. S.; Lee, H.; Kelaita, Y. A.; Atwater, H. A. *Nat. Photon.* 8, 317-320 (2014).
4. Martino, G. D.; Sonnefraud, Y.; Tame, M. S.; Ka-Cohen, S.; Dieleman, F.; Ozdemir, S. K.; Kim, M. S.; Maier, S. A. *Phy. Rev. Applied* 1, 034004 (2014).
5. Cai, Y. J.; Li, M.; Ren, X. F.; Zou, C. L.; Xiong, X.; Lei, H. L.; Liu, B. H.; Guo, G. P.; Guo, G. C. *Phys. Rev. Applied* 2, 014004 (2014).
6. Li, M.; Zou, C. L.; Ren, X. F.; Xiong, X.; Cai, Y. J.; Guo, G. P.; Tong, L. M. and Guo, G. C. Nano Lett. 15, 2380 (2015).

# Optimal and reproducible surface-enhanced Raman scattering with precisely-controlled nanometer-scale gaps

**J. M. Katzen*, A. Murphy, R. Pollard, and F. Huang**
[1]School of Mathematics and Physics, Queen's University Belfast, United Kingdom
*corresponding author: jkatzen01@qub.ac.uk

**Abstract**- We report achieving optimal and reproducible surface-enhanced Raman scattering (SERS) with plasmonic systems of nanoparticle-on-mirror geometry. Such systems produce robust nanometer-scale interparticle gaps that can be precisely controlled with dielectric spacing layers. A systematic investigation is carried out with a variety of nanoparticles, excitation wavelengths and molecules, which demonstrates that optimal and reproducible SERS is achievable at separations around 1 nm. The results are significantly important for developing ultrasensitive molecular sensors and many other plasmonic applications, including nonlinear effects.

Surface-enhanced Raman scattering (SERS) is an immensely useful technique for the detection of small amounts of molecules, such as illegal drugs, pesticides and explosives. However, a long-standing problem is that it is vey challenging to reproduce and optimize SERS signals, as the local field enhancements that are responsible for the enormously enhanced Raman signals are crucially dependent on interparticle distance, which is hard to tune and reproduce at the nanometer-scale.

Here we use the nanoparticle-on-mirror geometry (Figure 1a) to precisely control the interparticle distance and to find the distance at which the SERS intensity will be at its maximum. The plasmons in the gold nanoparticle couple to its image particle in Au film, in analogy to the particle-particle coupling dimer system, which has been demonstrated to be able to generate extremely strong field enhancement and resonant plasmonic coupling effects enabling a wide range of research and applications.[1,2] The electrodynamics of optics within nanometer-scale cavities is critically dependent on the interparticle separation. Classical theory indicates that enhancement should increase dramatically with decreasing separations, however, recently new theories suggest that at very close distances, the field enhancement will be smaller than that predicted by classical electrodynamics due to the nonlocality and quantum tunneling effects. So finding the distance at which optimal SERS can be achieved will not only be significant for important applications like molecular sensing, but also critical for understanding the fundamentals of optics in the non-classical regime.

Thin layers of gold films are sputtered on silicon substrates, followed by a $Ta_2O_5$ spacing layer of thickness varying from 0 to 10 nm. Gold nanoparticles are then drop cast on the surface to create the nanoparticle-on-mirror plasmonic structures (Figure 1 a). Optical dark-field scattering spectroscopy is used to mark the plasmonic resonance properties of the nanosystems and surface-enhanced Raman scattering spectroscopy of molecules adsorbed on Au nanoparticles is measured to characterize the local field enhancement. The results show that optimum SERS signals are achieved at separations around 1 nm (Figure 1b). It further shows that SERS is a phenomenon mainly confined to very small gaps. When interparticle

distance is larger than 2.5 nm, the SERS signals become negligible. A systematic investigation is carried out on a variety of nanoparticles, excitation wavelengths of lasers and different species of molecules, which consistently demonstrate that the plasmonic systems are robust and reproducible.[3] The results could pave the way for developing ultrasensitive plasmonic sensors for reproducible single molecule detection.

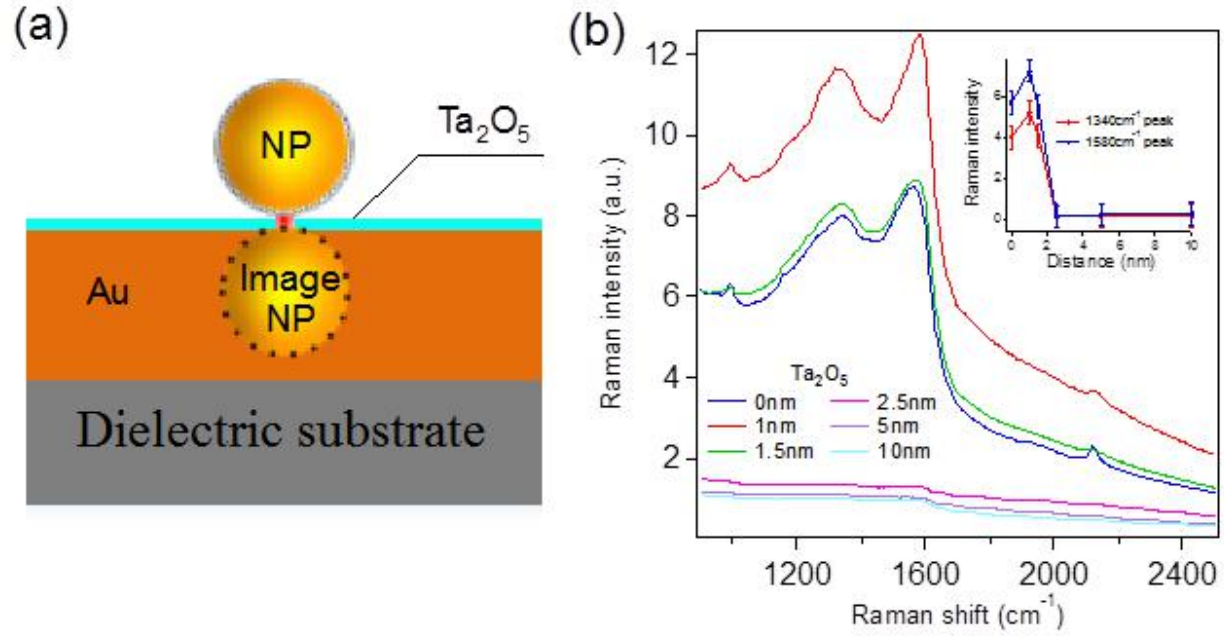



Figure 1 (a) Diagram illustrating the nanoparticle-on-mirror geometry, with a nanoparticle coupling to its image. (b) Raman spectra of citrate molecules adsorbed on Au nanoparticles measured with various $Ta_2O_5$ spacing layers ranging in thickness from 0-10 nm. Inset shows graphical how the Raman intensity changes with increasing separations.

**Acknowledgements** J. M. Katzen would like to thank the Department for Education and Learning of Northern Ireland for financial support.

**REFERENCES**

1. Mertens, J., Eiden, A.L., Sigle, D.O., Huang, F.M., Lombardo, A., Sun, Z., Sundaram, R.S., Colli, A., Tserkezis, C., Aizpurua, J., and Milana, S. “Controlling subnanometer gaps in plasmonic dimers using graphene”, Nano Letters, Vol. 13, 5033-5038, 2013.
2. Li, L., Hutter, T., Finnemore, A.S., Huang, F.M., Baumberg, J.J., Elliott, S.R., Steiner, U., and Mahajan, S. “Metal oxide nanoparticle mediated enhanced Raman scattering and its use in direct monitoring of interfacial chemical reactions”, Nano Letters, Vol. 12, 4242-4246, 2012.
3. Katzen, J. M., Bennington, J., Murphy, A., Pollard, R., and Huang, F. “Optimizing surface-enhanced Raman scattering with precisely-controlled nanometer-scale gaps”, submitted to ACS Photonics, 2016.

Disposable Plasmonics: Plastic Templated Plasmonic Metamaterials with Tunable Chirality

Affar S. Karimullah, , Calum Jack, Ryan Tullius, Vincent M. Rotello[A], Graeme Cooke, Nikolaj Gadegaard[B], Laurence D. Barron, Malcolm Kadodwala,*.

School of Chemistry, Joseph Black Building, University of Glasgow, Glasgow, G12 8QQ, UK.

[B]School of Engineering, Rankine Building, University of Glasgow, Glasgow, G12 8QQ, UK.

[A]Department of Chemistry, 710 Nt. Pleasant Street, University of Massachusetts Amherst, MA 01003, USA.

.

Artificially engineered plasmonic metamaterials can manipulate light in unique ways affording new opportunities in optics and for spectroscopic detection and characterisation of matter.[1–5] These plasmonic phenomena can be exploited to create new sensing, data storage and photovoltaic technologies.[6–10] With improved understanding of plasmonic phenomena, nanostructures with complex form factors can be designed for specific applications.[5,11–13] To date the tuning of optical properties of metamaterials has been achieved through the design of the shape and symmetry of the constituent nanostructures. This form-factor driven manipulation of optical functionality is inherently limited in versatility since there is no scope for post-fabrication tuning of properties unless complex ferroelectric / magnetic / molecular materials are incorporated.[14,15] Thus tailoring optical properties using geometric design parameters and with low-throughput lithographic fabrication methods is both time consuming and expensive.

Here we present a novel material, a continuous plasmonic metafilm consisting of periodic arrays of chiral nanostructures with optical properties that are significantly dependent on film thickness. These metafilms are grown on nano-indented polycarbonate substrates which are fabricated using high-throughput injection molding, a technique used for Blu-Ray manufacturing. The cost effectiveness and reproducibility of injection molding provide advantages over nano-imprinting and e-beam fabrication.[16–22] Thus these ‘Templated Plasmonic Substrates’ (TPS) offer low cost high-throughput fabrication, effectively a disposable consumable, with properties which can be easily tuned in the production process.

# Ultra narrow resonances, giant field enhancement and sensitivity by low-loss waveguide modes for sensing applications

**D. V. Nesterenko[1*], S. Hayashi[1,2], and Z. Sekkat[1,3,4]**

[1]Moroccan Foundation for Science, Innovation and Research (MAScIR), Rabat, Morocco

[2]Kobe University, Kobe, Japan

[3]University Mohamed V, Rabat, Morocco

[4]Osaka University, Osaka, Japan

[*]corresponding author: dtnesteren@gmail.com

**Abstract**- The resonance response of waveguide modes supported by a dielectric waveguide separated from a thin metal film by a low-index dielectric spacer layer in Kretschmann configuration is studied numerically. The impact of the loss degree in the waveguide to the resonance lineshape is demonstrated for *s* and *p* polarizations. Ultra narrow resonances, giant sensitivity and intensity enhancement are discovered in the attenuated total reflection angular spectra as a result of low-loss waveguide modes excitation allowing potential applications in surface-enhanced sensing.

Various propagating leaky modes are widely employed in sensing structures for detecting changes in the optical properties of an environment. The sensitivity of the sensors based on surface plasmon polariton (SPP) modes, which propagates along metal/insulator interfaces, symmetric SPP and antisymmetric SPP modes supported by insulator-metal-insulator and metal-insulator-metal structures, waveguide modes (WMs) of dielectric waveguide (WG) layers surrounded by metallic and lower-index dielectric claddings has been studied extensively for over a few decades.

Low-loss waveguide modes (LLWG) are supported by a 1D structure in Kretchmann configuration shown in Fig. 1 [1]. In the structure, the WG layer separated from the metal film by the dielectric spacer layer supports zeroth-order transverse electric ($TE_0$) and transverse magnetic ($TM_0$) WMs. We assumed a multilayer stack consisting of a BK7 substrate, a thin gold film, a Cytop spacer layer, a PMMA WG layer of $d$ = 0.5 μm and water superstrate as sensing media. The thickness of the gold film was set to 42 nm for $TE_0$ case and to 50 nm for $TM_0$ case to achieve the maximum height of resonance lineshape. The attenuated total reflection angular spectra were calculated by 2×2 transfer-matrix method for both *s*- and *p*-polarized incident plane waves at 632.8 nm wavelength. The resonances, which appear from excitation of these WMs, exhibit U-type and Fano lineshapes, respectively. The appearance of Fano resonances in *p* polarization case is an apparent effect of the coupling between a SPP mode, which is appeared at the metal layer/spacer layer interface, and a TM WM [1,2]. We experimentally demonstrated the generation of sharp Fano resonances by the structure in [3]. The coupling strength between WM field and field in the metal layer, and therefore the loss degree of the WM, is determined by the spacer layer thickness *t*. Another possible sources of losses are the

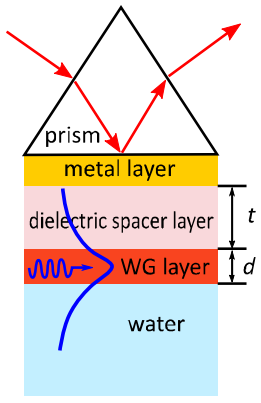



**Figure. 1.** Structure supporting low-loss WMs

intrinsic absorption and unevenness of the interfaces of layers. In the simulations, these weak losses can be represented by the non-zero imaginary part $\kappa$ of effective refractive index of the layers.

In sensing applications, sensitivity by intensity of a sensor can be estimated by figure of merit FOM = $|S|H/W$, where $S$ is the angular sensitivity, $W$ is the width and $H$ is the height of resonance lineshapes. The characterization of the resonance lineshape features was performed for a wide range of $t$ and several values of $\kappa$ from 0 up to $1\times10^{-4}$. The results are compared to the structure without spacer layer ($t$ = 0), which can be regarded as metal-clad waveguide. As $t$ increases, effective refractive indeces of the WMs increase in the strong coupling region (small $t$). In contrast, the angular sensitivity of the resonance angle to the bulk refractive index changes of water decreases in the strong coupling region. In the weak coupling region (large $t$), the effective refractive indices and angular sensitivities approach these of WMs of the WG with dielectric claddings. The angular sensitivities and effective refractive indices of the WMs demonstrate insensitivity to $\kappa$.

The height of the WM resonances remains constant for small $t$. For large $t$, the incoupling and the outcoupling strengths of the light energy to and from the modes by evanescent waves decrease exponentially with $t$, resulting in the exponential decay of $H$. $W$ decreases exponentially as $t$ increases for $s$ polarization. For $p$ polarization, $W$ increases with $t$ to a maximum at $t$ = 160 nm. Further increase in $t$ results in exponentially decaying $W$ with successive approaching the horizontal asymptotes for large $t$. As $\kappa$ increases, the transitions of $W$ from the decay stage to the stabilization stage and $H$ from the constant stage to the decay stage occur at lower values of $t$. The decrease in $\kappa$ leads to the proportional decrease in the minimum value of $W$.

The giant enhancement in the sensitivity by intensity in the absence of the losses ($\kappa$ = 0) of ~$10^5$-fold higher than that of conventional SPR and metal-clad waveguide sensors has been estimated by FOM for both polarizations exhibiting $H$ of ~0.6 and $W$ of ~ $2\times10^{-7}$ deg at $t$ of 1340 nm and 1840 nm for $TE_0$ and $TM_0$ cases, respectively. The giant intensity enhancement of $10^7$-fold on the WG surface has been revealed at resonance conditions and optimal parameters of the structure. The intensity of electromagnetic field localized in the WG region demonstrates almost perfect correlation with the sensitivity by intensity.

We theoretically demonstrated the giant intensity enhancement and possibility of achievement and control the extremely narrow deep resonances resulting in the giant sensitivity by intensity enhancement in simple planar structures. In general, the materials, which can be implemented for the structure, are not limited to the ones considered in the study. The structure composed of a variety of dielectrics and metals with properly chosen thicknesses can exhibit extremely sharp resonances. Our results may provide a significant improvement of detection limits in biosensing, Raman and fluorescence spectroscopy.

**Acknowledgements.** This work was partially supported by Osaka University International Joint Research Promotion Program.

**REFERENCES**

1. Hayashi, S., Nesterenko, D. V. and Z. Sekkat, "Waveguide-coupled surface plasmon resonance sensor structures: Fano lineshape engineering for ultrahigh-resolution sensing," *J. Phys. D: Appl. Phys.*, Vol. 48, 325303, 2015.
2. Hayashi, S., Nesterenko, D. V. and Z. Sekkat, "Fano resonance and plasmon-induced transparency in waveguide-coupled surface plasmon resonance sensors," *Appl. Phys. Express,* Vol. 8, 022201, 2015.
3. Hayashi, S., Nesterenko, D.V., Rahmouni, A. and Z. Sekkat, "Observation of Fano line shape arising from coupling between surface plasmon polariton and waveguide modes," *Appl. Phys. Lett.*, Vol. 104, 051101, 2016.

# Hot spot engineering in 3D Multibranched Nanostructures: realization of ultrasensitive platforms for Raman spectroscopy

**Manohar Chirumamilla[1],* Anisha Gopalakrishnan[2], Alexander S. Roberts[3], Remo Proietti Zaccaria[2], Francesco De Angelis[2], Peter Kjær Kristensen[1], Roman Krahne[2], Sergey I. Bozhevolnyi[3], Kjeld Pedersen[1] and Andrea Toma[2]**

[1]Department of Physics & Nanotechnology, Aalborg University, Skjernvej 4A, 9220 Aalborg Øst, Denmark

[2]Nanostructures Department, Istituto Italiano di Tecnologia, Via Morego 30, Genova, 16163, Italy

[3]Centre for Nano Optics, University of Southern Denmark, Campusvej 55, 5230 Odense M, Denmark

*Corresponding author: mch@nano.aau.dk

**Abstract**-Nanofabrication of bimetallic 3D multi-branched nanostructures enables the detection of analyte molecules down to single molecule level with the aid of hot-spots generated on the structure. Here we present fabrication and characterization of multi-branched nanostructures (up to 10 branches) for ultra-sensitive detection of Rhodamine-6G and p-Aminothiophenol molecules.

The fabrication of innovative plasmonic architectures supporting extremely large electric field enhancement has gained increasing attention over the last few years, especially for the detection of molecules in highly diluted liquids[1-3], and/or the spectral signature collection of single/few molecules concentrated in nanogaps. The application of the "hot spot" concept, induced by localized surface plasmon resonances, has been successfully exploited for surface-enhanced infrared absorption (SEIRA) and surface-enhanced Raman spectroscopy (SERS)[1-5]. Within this context, we introduced novel complex bimetallic 3D nanostructures, endowed with multiple tips and raised from the substrate by means of standing silicon pillars[4]. The elevated geometry, here adopted, allows for very efficient decoupling of the plasmonic field from the underlying substrate. Moreover, 3D configurations allow maskless recycling of SERS substrates by chemical etching and re-metallization.[2] Multi-branched nanostructures with sharp protrusions (up to 10) have been fabricated by electron beam lithography and reactive ion etching techniques. A schematic diagram, representative SEM images of multi-branched nanostructures and SERS spectrum of p-Aminothiophenol taken on 3D nanostructure with 6 branches are shown in the Figure 1. So far, a low molecular detection limit with high specificity and consistency has been reported only in the present case (i.e. multi-branched nanostructures). In addition, it is worth to be noticed that nanostructures endowed with multiple hot-spots show enormous importance in hyperspectral Raman imaging, where the intrinsically dense amount of active sites can promote the identification of probe molecules with high contrast and spatial resolution at trace level. A typical SERS spectrum of p-Aminothiophenol in the range of 900-1750 $cm^{-1}$ shows several prominent Raman bands of p-Aminothiophenol including C-S stretching band at 1077 $cm^{-1}$. Precise control on generation of multiple hot-spots is achieved by tailoring the number of branches of the nanostructure. In particular, an average electric field enhancement of $10^8$ has been demonstrated. Multi-branched nanostructures exhibit excellent uniformity and morphological homogeneity, thus allowing for unprecedented reproducibility in the SERS signals. The versatility of the proposed plasmonic architecture has been confirmed by testing with two different molecules with concentrations down to 1 fM.

In summary, we have demonstrated a systematic fabrication and characterization of 3D multi-branched nanostructures for hot-spot engineering. The far-field and near-field properties of these configurations have been

investigated by reflection spectroscopy and numerical calculations, thus confirming the formation of multiple hot-spots with highly enhanced local EM fields. The detection of probe molecules at extremely low concentrations (p-Aminothiophenol and Rhodamine-6G, concentrations down to 1 fM) has been attained by means of surface-enhanced Raman spectroscopy.

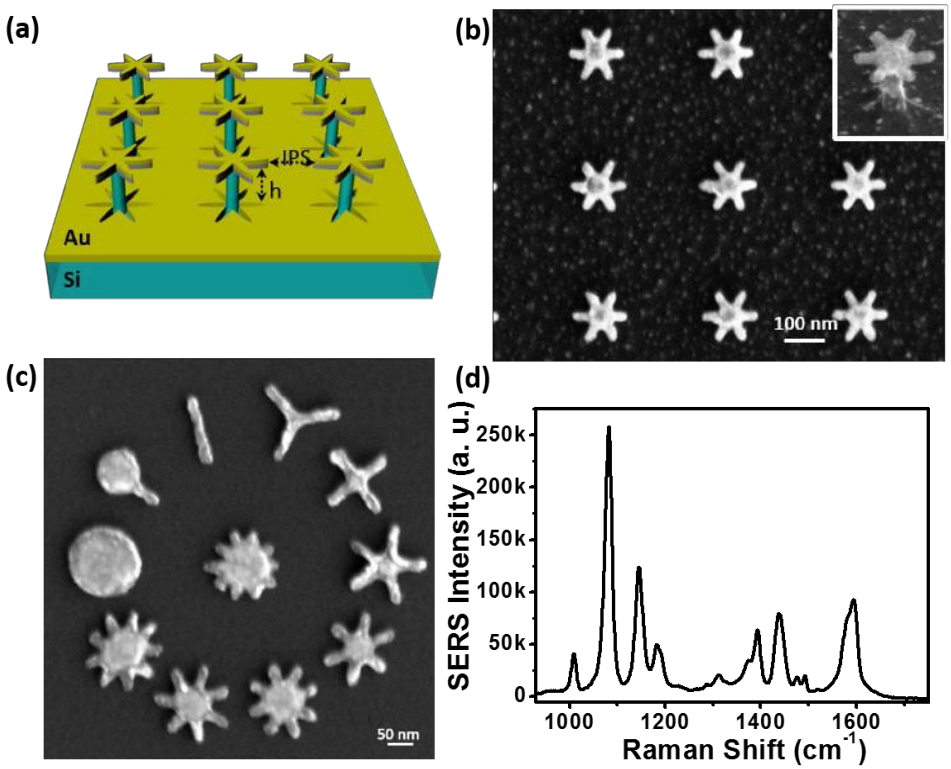



**Figure 1.** a). Schematic representation of 6 branch nanostar with inter-particle separation (IPS) and height h. b). Normal-incidence SEM image of 6 branched nanostar with 200 nm IPS. The inset represents the 54º tilted view of 3D nanostar with 150 nm structure height. c) Overview of the fabricated multibranch nanostructures. d). SERS spectrum of p-Aminothiophenol chemisorbed at 1 μM concentration taken on 3D nanostructure with 6 branches.

## REFERENCES


1. Chirumamilla, M.; Toma, A.; Gopalakrishnan, A.; Das, G.; Zaccaria, R. P.; Krahne, R.; Rondanina, E.; Leoncini, M.; Liberale, C.; De Angelis, F.; Di Fabrizio, E. "3D Nanostar Dimers with a Sub-10-nm Gap for Single-/Few-Molecule Surface-Enhanced Raman Scattering". *Advanced Materials* 2014, 26, 2353-2358.
2. Gopalakrishnan, A.; Chirumamilla, M.; De Angelis, F.; Toma, A.; Zaccaria, R. P.; Krahne, R. "Bimetallic 3D Nanostar Dimers in Ring Cavities: Recyclable and Robust Surface-Enhanced Raman Scattering Substrates for Signal Detection from Few Molecules". *ACS Nano* 2014, 8, 7986-7994.
3. Chirumamilla, M.; Gopalakrishnan, A.; Toma, A.; Zaccaria, R. P.; Krahne, R. "Plasmon resonance tuning in metal nanostars for surface enhanced Raman scattering". *Nanotechnology* 2014, 25, 235303.
4. Huck, C.; Toma, A.; Neubrech, F.; Chirumamilla, M.; Vogt, J.; De Angelis, F.; Pucci, A. "Gold Nanoantennas on a Pedestal for Plasmonic Enhancement in the Infrared". *ACS Photonics* 2015, 2, 497-505.
5. Chirumamilla, M.; Gopalakrishnan, A.; S. Roberts, A.; Proietti Zaccaria, R.; De Angelis, F.; Kjær Kristensen, P.; Krahne, R.; I. Bozhevolnyi, S.; Pedersen, K.; Toma. A. "Hotspot Engineering in 3D Multibranched Nanostructures: Ultrasensitive Substrates for Surface Enhanced Raman Spectroscopy", Submitted.

# The applications of propagating surface plasmon waves in the SERS

L. R. Yuan, L. Zhang, Y. Y. Zhu, Y. Q. Lu and X. J. Zhang

National Laboratory of Solid State Microstructures, Nanjing University, Nanjing 210093, P. R. China

## ABSTRACT

Surface plasmon polaritons (SPPs) have low loss with great potential for surface-enhanced Raman scattering (SERS) applications. We take subwavelength metallic grating as an example, which is a simple and effective structure to increase the enhancement factor (EF) of the SERS. Enormous electric field enhancement can be realized by the optimization of material, structure and technology, which is investigated by both finite-difference time-domain simulation and SERS EF measurements.

# Integrated Photonics Engineered Around Exceptional Points

**Liang Feng**[1*]
[1]Department of Electrical Engineering, The State University of New York at Buffalo, Buffalo, NY 14260, USA
[*]corresponding author: fengl@buffalo.edu

**Abstract**- Exceptional point is a fundamental notion in quantum field theories and enables new functionalities in photonics. In this talk, I will discuss harnessing parity-time (PT) symmetry to realize optical exceptional points using the state-of-the-art integrated nanophotonics technology for novel optoelectronic functionalities. I will present unidirectional light transport and coherent light control at PT exceptional points on a passive silicon platform and effective control of cavity resonant modes for stable lasing performances on a III-V semiconductor platform.

An intriguing characteristic of non-Hermitian quantum systems is their intrinsic asymmetry near a quantum exceptional point. In the realm of optics and photonics, recent investigations on parity-time (PT) symmetry [1] provides effective strategies of emulating quantum exceptional points on an integrated photonic platform. For PT symmetric systems, these exceptional points can either represent asymmetric transmission resonances [2-4] or a violation of energy conservation in the scattering eigenstates [5], depending on the formulation of the scattering matrix[15]. Here, we delicately design the interplay between index and absorption to explore the former type of exceptional points.

The non-Hermitian optical modulation by PT symmetry is effectively introduced along the length of waveguide with the index-absorption engineering, and reads

$$\Delta\varepsilon = \Delta\varepsilon_0 \left(\cos(qz) + i\delta \sin(qz)\right) \quad (1)$$

where $\Delta\varepsilon_0$ denotes the modulation amplitude and $\delta$ is designed exactly at or close to 1 ($\delta = 1$ corresponds to the exceptional point in Eq. 1 [2-4]) to have the device operating at or around the exceptional point. On both passive silicon and active III-V semiconductor platforms, the optical modulation in Eq. (1) at or around exceptional points have been successfully realized, leading to unique optical effects including unidirectional light transport and strongly asymmetric light-light interactions. The experimental validations further demonstrated effective control of drastic optical modulation and stable lasing oscillation, suggesting unique non-Hermitian photonics building blocks for next generation of all-optical information processing for optical communications and computing.

The work is supported by US Army Research Office (W911NF-15-1-0152) and National Science Foundation (DMR-1506884 and ECCS-1507312).

**REFERENCES**

1. El-Ganainy, R., Makris, K. G., Christodoulides, D. N., Musslimani, Z. H., "Theory of coupled optical PT-symmetric structures," *Opt. Lett.*, Vol. 32, No. 17, 2632-2634 (2007).
2. Lin, Z., Ramezani, H., Eichelkraut, T., Kottos, T., Cao, H., and Christodoulides, D. N., "Unidirectional invisibility induced by PT-symmetric periodic structures," *Phys. Rev. Lett.*, Vol. 106, No. 21, 213901, 2011.

3. Regensburger, A., Bersch, C., Miri, M. A., Onishchukov, G., Christodoulides, D. N., and Peschel, U., "Parity-time synthetic photonic lattices," *Nature*, Vol. 488, No. 7410, 167-171, 2012.
4. Feng, L., Xu, Y. L., Fegadollic, W., Lu, M. H., Oliveira, J. B. E., Almeida, V. R., Chen, Y. F., and Scherer, A., "Experimental demonstration of a unidirectional reflectionless parity-time metamaterial at optical frequencies," *Nature Mater.*, Vol 12, No. 2, 108-113 (2013).
5. Ge, L., Chong, Y. D., and Stone, A. D., "Conservation relations and anisotropic transmission resonances in one-dimensional PT-symmetric photonic heterostructures," *Phys. Rev. A*, Vol. 85, No. 2, 023802, 2012.

# A flexible THz random reflector by 1 bit coding metamaterial

**B. B. Jin[1*], W. W. Liu[2] and T. J. Cui[3]**

[1]Research Institute of Superconductor Electronics (RISE), School of Electronics Science and Engineering, Nanjing University, 210093 Nanjing, China

[2]Institute of Modern Optics, Nankai University, Tianjin 300071, China

State Key Laboratory of Millimeter Wave, Southeast University, Nanjing 210096, China

[*]corresponding author: bbjin@nju.edu.cn

**Abstract**- We present here a flexible 1-bit coding metamaterial to shape the reflection and scattering of THz wave. By adjusting the sequences, this metamaterial can easily form different reflection and scattering pattern. A wideband and low-reflection-and-scattering THz metamaterial is exampled to demonstrate the use and ability of the coding metamaterial. Both the simulation and experiments show the reflectivity less than -10 dB is achieved in a wide frequency range of 0.8-1.4 THz and is insensitive to the polarization of incident wave.

Terahertz (THz) radar has great advantages over microwave radar system in remote sensing and homeland security because of its high spatial resolution and extremely wide band [1]. At microwave the coating on the object with some structure design can effectively reduce the reflective wave to make the object invisible. However, such coating materials have no strong response in THz, the design of low-reflection surface is the main consideration. Some new designs are proposed to realize broadband electromagnetic wave absorption in the THz. These methods include perfect metamaterial absorber, saw-tooth multilayer anisotropic metamaterial and two-dimensional grating structure based on a heavily doped Si substrate and so on. These designs are all EM wave-thermal transformation, and the induced thermal effect can be detected easily. In addition, most of the metamaterial absorbers were fabricated on a rigid substrate, they were difficult conformal to the covered object. Very few reports on flexible THz absorbers only show the narrow band behavior, which obviously may limit its practical application. Therefore, a flexible and wideband low-reflection surface with new design idea remains a challenge in the terahertz frequencies.

Using the digital metamaterial concept recently developed [2-3], we design in this paper a flexible wideband low-reflection metamaterial by coding the “0”and “1”elements at terahertz frequencies. The coding metamaterial is shown in Fig. 1, which consists of three layers. The top layer is metallic structure with a number of rings, which is patterned on a flexible polyimide film, the bottom layer is metallic film. The “0”and “1”elements are realized by a unit cell without any metallic covering and with a metallic ring covering on the substrate, respectively. The reflection phase difference between “0” and “1”elements is about 180° in our interested frequency range. Unlike the metamaterial absorbers mentioned above, the reduction of the reflection is attributed to scattering of the incident wave in various directions, resulting in the small intensity and uniform distribution in space.

The metamaterial is fabricated by a lift-off process. Firstly, the liquid polyimide (PI) is spin-coated on silicon substrate to form 40 μm-thick PI film layer. Then, a lift-off technique is employed to get a metallic pattern. Finally, the PI layer is peeled off from the silicon substrate, and a 200-nm thick gold layer is deposited on the other side of PI layer. The reflection feature of the metamaterial is measured by a home-made fiber-coupled THz time domain spectroscopy (THz-TDS) system. The reflection was normalized to that of a gold mirror with the

same size of the sample. The reflection of the sample is measured at various incidence angles between 13 and 80 degrees with an increment of 5 degree.

The simulated and reflection spectrum at a reflection angle 13° are shown in Fig.1b. The good agreement can be obtained. The reflectivity less than -10dB is achieved in a wide frequency range from 0.8 to 1.4 THz for TE polarization. The similar spectrum is also observed for TM polarization. This indicates our structure is insensitive to the polarization of the incident wave. Also, this wideband property can keep up to the incident angle less than 40 degree. We also measured the reflection from a metallic cylinder which is wrapped by the above coding metamaterial and found the similar reflection spectrum compared with the flat case. These results imply that our metamaterial can be conformal to the object which can satisfy requirement in practical applications.

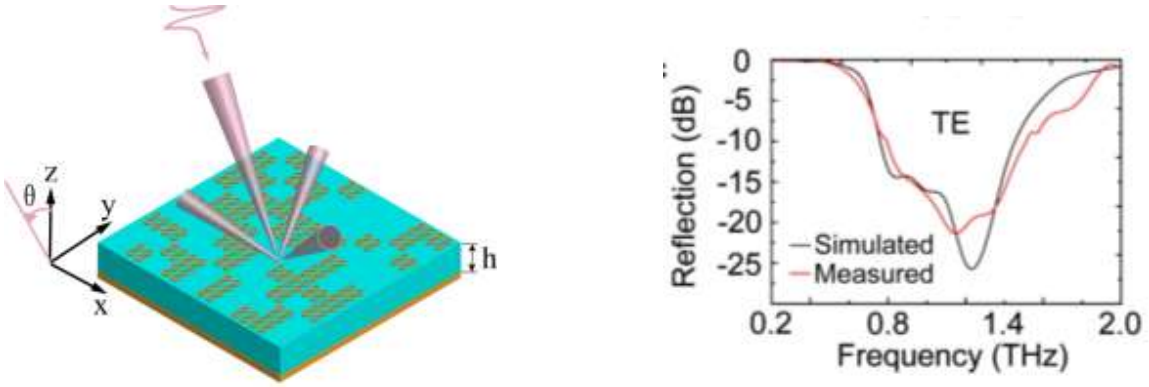



Fig.1(a) Schematic of a 1-bit coding metamaterial; (b) The simulated (black lines) and measured (red lines) reflection spectra under the incidence angle of 13° for TE polarization

**Acknowledgements** This work is supported by MOST973 (2014CB339800), National Natural Science Foundation (Nos. 61371035,61521001, 11227904), National Instrumentation Program under grant No. 2012YQ14005, the Priority Academic Program Development of Jiangsu Higher Education Institutions (PAPD), and Jiangsu Provincial Key Laboratory of Advanced Manipulating Technique of Electromagnetic Wave.

**REFERENCES**

1. J. S. Ding, M. Kahl, O. Loffeld and P. H. Bolivar, " THz 3D image formation using SAR techniques :simulation, processing and experimental results," *IEEE Trans. THz science and Technology*, vol.3, p.606, 2013
2. C. Della Giovampaola and N. Engheta, "Digital Metamaterials", *Nat. Mater*. vol.13, p.1115, 2014
3. T. J. Cui, M.Q. Qi, X. Wan, J. Zhao, Q. Cheng, " Coding metamaterials, digital metamaterial and programmable metamaterials," *light: Sci. Appl*. vol.3, p.218, 2014

# An MOS platform for sub-wavelength focusing and shaping of visible light

**Guy Bartal, Technion**

The ability to shape and focus optical waves to dimensions smaller than their wavelength has intrigued the scientific community both for its physical challenges and its potential applications. Resonant elements, , have provided deep-subwavelength control at long wavelength in the form of Metamaterials, while at optical frequencies light could be focused to specific points by nano-antenna and Nanofocusing elements, breaking the so-called diffraction limit. Alternatively, achieving similar focusing dimensions by scaling the diffraction limit rather than breaking it allows flexible and dynamic control over the type and shape of the focusing without specifically patterning the medium, hence can provide super-resolution capabilities for bio-imaging, nanolithography and spectroscopy. We have devised an MOS platform, utilizing the high refractive index of Silicon to scale the diffraction limit by 4-fold compression of the wavelength thereby achieving resolution at the order of 10-s of nanometers at visible light - comparable to that of single-molecule microscopy techniques. Utilizing this scaled diffraction limit, we present phase-resolved near-field observations of propagating-waves bright and dark focusing below 70 nm at 671nm illumination (λ/10), and direct observation of short-wavelength Super-Oscillations in planar 2D Hybrid Silicon-plasmon waveguides.

# Plasmon Lasers for Sensing

Ren-Min Ma*

* State Key Lab for Mesoscopic Physics and School of Physics, Peking University, Beijing 100871, China
renminma@pku.edu.cn

Lasers are the coherent sources of high frequency electromagnetic radiation with applications spanning all physical sciences and technology. In contrast to classical lasers, plasmon lasers amplify light coupled to oscillating electrons enabling their physical size and mode volume to shrink below the diffraction limit [1-10]. With unprecedented small physical size and mode volume, new features of plasmon laser are evident. The recent emergence of plasmon lasers also stimulates the exploration of nanometer-scale science and application towards the rich physics of deep sub-wavelength optics and the development of high performance devices. In this talk we will review our recent work on plasmon lasers for sensing [9, 10]

[1] Bergman, D. J. & Stockman, M. I. “Surface plasmon amplification by stimulated emission of radiation: quantum generation of coherent surface plasmons in Nanosystems” Phys. Rev. Lett. 90, 027402 (2003).

[2] Hill, M. T. et al. “Lasing in metal–insulator–metal sub-wavelength plasmonic waveguides.” Opt. Express 17, 11107–11112 (2009).

[3] Noginov, M. A. et al. “Demonstration of a spaser-based nanolaser” Nature 460, 1110–1113 (2009).

[4] Oulton, R. F. et al. “Plasmon lasers at deep subwavelength scale” Nature 461, 629–632 (2009).

[5] Ma, R-M., Oulton, R. F., Sorger, V. J., Bartal, G. & Zhang, X. “Room temperature sub-diffraction-limited plasmon laser by total internal reflection” Nature Mater. 10, 110–113 (2011).

[6] Khajavikhan, M. et al. “Thresholdless nanoscale coaxial lasers” Nature 482, 204–207 (2012).

[7] Lu, Y-J. et al. “Plasmonic nanolaser using epitaxially grown silver film” Science 337, 450–453 (2012).

[8] Ma, R-M., Yin, X. B., Oulton, R. F., Sorger, V. J. & Zhang, X. “Multiplexed and electrically modulated plasmon laser circuit” Nano Lett. 12, 5396–5402 (2012).

[9] Ma, R. M., Ota, S., Li, Y. M., Yang, S. and Zhang, X., “Explosive Detection in a Lasing Plasmon Nanocavity” Nature Nanotechnology, 9, 600, 2014.

[10] X.-Y. Wang, Y.-L. Wang, S. Wang, B. Li, X.-W. Zhang, L. Dai*, R.-M. Ma*, Lasing Enhanced Surface Plasmon Resonance Sensing, Nanophotonics DOI: 10.1515/nanoph-2016-0006, 2016.

# Physical Scaling Laws of Nanophotonics.

Ke Liu[1,4], Arka Majumdar[2,3], Volker J. Sorger[1*]

[1]Department of Electrical and Computer Engineering, The George Washington University, Washington, D.C. 20052, USA

[2]Department of Electrical Engineering, University of Washington, Seattle, WA 98195, USA

[3]Physics Department, University of Washington, Seattle, WA 98195, USA

[4]The Key Laboratory of Optoelectronics Technology, Ministry of Education, College of Electronic Information and Control Engineering, Beijing University of Technology, Beijing 100124, P.R. China

[*]corresponding author: sorger@gwu.edu

**Abstract**-Here we report fundamental scaling laws for optoelectronic devices including nanophotonics and plasmonics. We show how the underlying optical cavities directly influences the performance of four classes of photonic devices, namely laser sources, electro-optic-modulators, photodetectors, and all-optical switches. We observe non-monotonic performance behavior upon down-scaling, which is a result of balancing the optical losses and providing cavity feedback highlighting the physical tradeoff between optical loss management and field confinement.

Scaling laws based on fundamental physics predict a high potential to improve optoelectronic devices relative to the state-of-the-art when applying the FOM = {Datarate/bit} / {Power/bit x Area x Cost}. Ignoring engineering-limited device design constrains, basic physics dictates a lower-bound power consumption for optoelectronic devices of about 0.1aJ/bit. The general switching speed depends on the chosen switching effect, and both the optical and electrical dynamics penalty. Here we discuss scaling laws and benchmarks [1] of three prominent opto-electronic devices, namely, laser [2-4], electro-optic modulator [5], and photodetector. The work is based on underlying light-matter-interaction enhancement via optical resonators to include the microring, Fabry-Perot, and plasmonic nanocavity. We raise questions towards establishing a roadmap for optical information processing (i.e. logic and communication) including noise considerations at the detector, quantum entanglement, and realistic integration aspects such as technology hybridization [6] at the link level for high bit-flow-density metrics.

With previous investigations being ad-hoc in their approach to exploit nanoscale device functionality, an understanding leading to fundamental scaling behavior for this new class of devices is outstanding. Here we investigate the performance behaviors for nanophotonic devices as a function of nominal device length given by the underlying cavity geometry. Performance criteria of three critical interconnect devices are analyzed with respect to their scaling behavior. Underling to all devices are three types of optical cavities that support enhancing the fundamentally weak interaction between light and matter, namely, microring resonators, Fabry Perot cavities, and plasmonic metal particle-based cavities. An interesting, but actually expected find is, that all cavity types do not perform well for vanishing cavity lengths due to dominance of loss channels. However this critical length is strongly dependent on the cavity properties and varies by more than two orders of magnitude. With the high Purcell factors that can be realized despite high losses in nanoscale cavities, we investigate fundamental achievable optoelectronic device performance.

In our results we find that the thought ‘smaller-is-better’ is not true for nanophotonics and non-monotonic

scaling is found. With a goal for down-scalability in mind, key results show the possibility the ability to design; 1) laser sources with threshold currents at 1 uA and 100 GHz fast modulation, 2) electro-optic modulators with 10's aJ/bit energy efficiencies and THz fast modulation speeds, and 3) photodetectors with responsivities approaching 1 A/W and ~ps-fast response times. Understanding the potential and limits for Nanophotonics is a guiding insight not only for device designers, but increasingly also at the circuit level, since a true comparison between both the electronic and photonic technology options is enabled.

**Acknowledgements**, A.M. is supported by Air Force Office of Scientific Research-Young Investigator Program under grant FA9550-15-1-0150 and Startup fund provided by University of Washington. V.S. is supported by Air Force Office of Scientific Research-Young Investigator Program under grant FA9550-14-1-0215.

**REFERENCES**

1. K. Liu, A. Majumdar, V. J. Sorger, "Fundamental Scaling Laws in Nanophotonics" (in review).
2. R.-M. Ma, R. F. Oulton, V. J. Sorger and X. Zhang "Plasmon lasers: coherent light source at molecular scales", *Laser & Photonics Reviews* doi: 10.1002/lpor.201100040 (2012).
3. K. Liu, N. Li, D. K. Sadana, V. J. Sorger, "Integrated nano-cavity plasmon light-sources for on-chip optical interconnects" *ACS Nano***,** DOI: 10.1021/acsphotonics.5b00476 (2016).
4. N. Li, K. Liu, D. K. Sadana, V. J. Sorger, "Nano III-V Plasmonic Light-Sources for Monolithic Integration on Silicon", *Nature: Scientific Reports*, 5, 14067 (2015).
5. K. Liu, Z.R. Li, S. Khan, C. Ye, V. J. Sorger, "Ultra-fast electro-optic modulators for high-density photonic integration" *Laser & Photonics Review***,** 10, 11-15 (2015).
6. S. Sun, A. Badaway, T. El-Ghazawi, V. J. Sorger, "Photonic-Plasmonic Hybrid Interconnects: Efficient Links with Low latency, Energy and Footprint", *IEEE Photonics*, 7, 6, 15 (2015).

# PT symmetric Bragg gratings operating with long-range surface plasmons

**Elham Karami Keshmarzi[1], R. Niall Tait[1], and Pierre Berini[2,3,4]**
[1]Department of Electronics, Carleton University, 1125 Colonel By Dr., Ottawa, Ontario K1S 5B6, Canada
[2]School of Electrical Engineering and Computer Science, University of Ottawa, Ottawa, Ontario K1N 6N5, Canada
[3]Department of Physics, University of Ottawa, Ottawa, Ontario K1N 6N5, Canada
[4]Center for Research in Photonics, University of Ottawa, Ottawa, Ontario K1N 5N6, Canada

**Abstract-** Parity Time (PT) symmetric Bragg gratings operating with long-range surface plasmons are investigated in the near-infrared. It is shown that at the threshold for PT symmetry breaking there is unidirectional reflectance and dispersion-less group delay in transmittance. Optical gain provided by optically-pumped IR-140 is balanced with plasmonic loss in this structure to access PT symmetric structures. The fabrication of PT symmetric gratings is discussed and preliminary measurements are presented.

Parity-time (PT) symmetric optical materials have attracted great attention in recent years due to the extraordinary performance they exhibit at PT symmetry breaking threshold. Unlike other synthetic optical materials such as photonic crystals, which are engineered by tweaking the real part of refractive index, PT symmetric materials include modulation of both the real and imaginary refractive indices to the same order of magnitude. It is shown that the complex refractive index in a PT symmetric material must produce an even-symmetrical distribution of real refractive index and odd-symmetrical distribution of imaginary refractive index, so that the refractive index as a function of position obeys the condition $n(z) = n^*(-z)$[1]. The unusual optical properties, such as unidirectional energy transport[1], asymmetric reflectance[2] and Bloch power oscillations[3] are found around the breaking threshold for PT symmetry, at the so-called as exceptional point, where gain is perfectly balanced with loss in the system.

In this paper, we discuss the realization and performance of a PT symmetric Bragg grating operating at the exceptional point (near 880 nm) in a long-range surface plasmon polariton (LRSPP) structure. The balanced perturbation of real and imaginary refractive indices having even and odd symmetry is provided in a LRSPP structure comprising a 20 nm thick Au stripe stepped-in-width, on a silica layer, and covered with a 600 nm thick film having alternate passive and active regions. The fabrication process includes electron-beam lithography for defining the Au pattern on silica, followed by development, thermal Au deposition, and lift-off. Then a 600 nm thick passive PMMA layer is deposited on top of the Au stripes, and patterned using a second e-beam lithography step, followed by development, and finally, the active regions are created using a fluidic layer consisting of IR-140 dye molecules in a mixture of ethylene glycol and dimethyl sulfoxide. The gain fluid is index-matched to PMMA at 880 nm and dispensed on the sample using accurate pipetting such that the gain regions and passive regions have the same final thickness.

The reflectance/transmittance spectra of the PT symmetry Bragg are computed using the Transmission Matrix Method showing symmetric transmittance and unidirectional reflectance at 880 nm. Computations of group and energy velocity for the PT symmetry Bragg shows a dispersionless response when Bragg is at the breaking threshold. As soon as the gain/loss balance is disturbed, the PT phase switches from unbroken to broken with an inversion in group delay response. The proposed PT symmetry broken Bragg can provide new functionality in optical data processing by providing distortionless pulse transmission in these systems.

## REFERENCES

1. C. E. Rüter, K. G. Makris, R. El-Ganainy, D. N. Christodoulides, M. Segev, and D. Kip, "Observation of parity–time symmetry in optics," Nat. Phys., vol. 6, no. 3, pp. 192–195, Jan. 2010.
2. L. Feng, M. Ayache, J. Huang, Y.-L. Y. Xu, M. M.-H. Lu, Y.-F. Chen, Y. Fainman, and A. Scherer, "Nonreciprocal light propagation in a silicon photonic circuit," Science, vol. 333, no. 6043, pp. 729–733, Aug. 2011.
3. A. Regensburger, C. Bersch, M.-A. Miri, G. Onishchukov, D. N. Christodoulides, and U. Peschel, "Parity–time synthetic photonic lattices," Nature, vol. 488, no. 7410, pp. 167–171, Aug. 2012.

# CMOS THz On-chip Surface-wave Resonator and Oscillator

**Yuan Liang, Hao Yu* and Xiaojian Fu**

School of Electrical and Electronic Engineering, Nanyang Technological University, Singapore, 639798

*corresponding author: haoyu@ntu.edu.sg

**Abstract**-A compact high-Q surface-wave resonator is demonstrated at sub-THz in 65nm CMOS. By introducing sub-wavelength periodic corrugation structure, surface plasmon polaritons (SPP) is established to propagate signals with strongly localized surface-wave. Such a magnetic metamaterial achieves a significant reduction of radiation loss at sub-THz by further stacking additional resonator unit-cell which has opposite placement with respect to the existing resonator. A 140GHz fundamental oscillator is then designed by incorporating the surface-wave resonator as low loss loading. Simulation results show that the surface-wave oscillator has the ability of strongly confining EM energy with high-Q factor which easily start-up the 140GHz oscillator in low power. The simulated phase noise is -116dBc/Hz at 10MHz offset under 0.7V power supply by consuming only 3.5mW power. This low power and low phase noise oscillator design facilitates future fully integrated surface-wave I/O realization in CMOS at THz without mode converter.

Recently, surface-wave transmission has been demonstrated on-chip for THz communication [1, 2], which shows less crosstalk, low power consumption and high data rate that potentially replaces existing transmission line (T-line) based approaches. One example of on-chip surface-wave I/O design is illustrated in Fig. 1, in which all THz components are realized by surface-wave devices. The THz resonator can be hereby realized by surface-wave technique as the field confinement is essential as well for a low loss design. By employing surface-wave resonator, the *Q*-factor of load can be effectively improved while saving considerable silicon area. A sub-THz surface-wave oscillator was designed achieving lower than -116dBc/Hz phase noise by consuming only 3.5mW power that has not been realized so far.

Here, the on-chip SPP T-line structure [1] is designed as shown in Fig. 1(b) with comparison to conventional on-chip T-line. The *E*-field of surface-wave T-line is now tightly confined by the periodical grooves while conventional T-line presents highly delocalized nature. Illustrated in Fig. 1(c), the loss of SPP T-line is considerably lower than conventional T-line at mm-wave to THz frequency, demonstrating the potential of surface-wave T-line as THz interconnects.

By integrating both surface-wave transmission line and surface-wave resonator [2], we can develop a SPP oscillator by SPP T-line loaded SRR as shown in Fig. 2(a). The resonator structure is based on the stacked SRR resonator, while its lanes have been shaped by arrays of periodical grooves around the structure. Fig. 2(b) shows the current distribution, which has been considerably suppressed, an evidence of stacked SRR physics. Fig. 2(c) further provides the magnetic field distribution that is now dominating inside the grooves (due to surface-wave propagation) and the geometry center (due to the *M*-field enhancement by the SRR structure), proving that the structure has already combined both physical advantage of surface-wave T-line and stacked SRR resonator. Fig. 2(d) depicts the *E*-field distribution around the structure. The *E*-field is now mainly localized by the periodical grooves. Fig. 2(e) illustrates a very sharp stopband realized by this design, showing a good reflection at

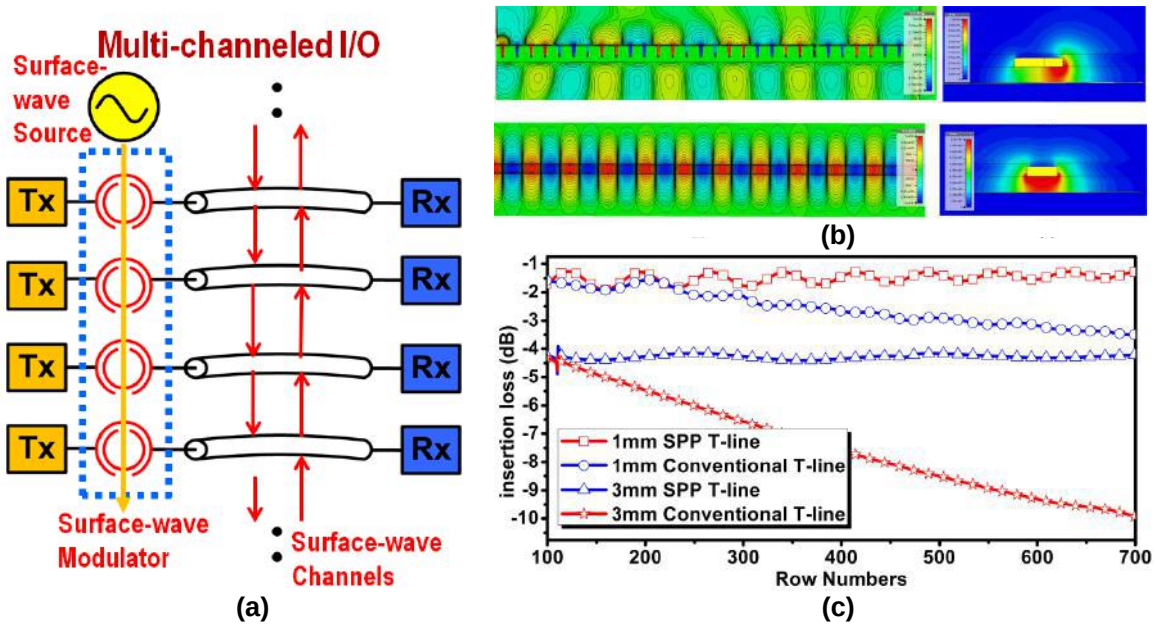



Fig. 1. An on-chip surface-wave THz I/O architecture, (b) *E*-field distribution for both surface-wave and conventional T-line, (c) The simulated insertion loss of surface-wave/conventional T-line with different length at mm-wave to THz.

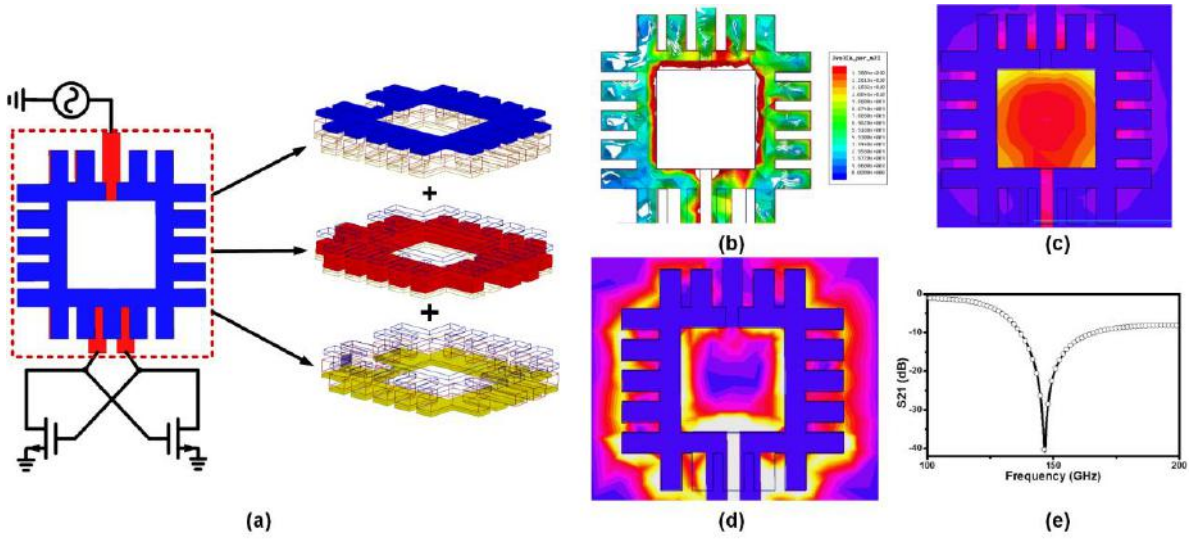



Fig. 2. The proposed sub-THz surface-wave oscillator, (b) current density, (c) *M*-field (d) *E*-field distribution of the proposed surface-wave resonator, (e) insertion loss the surface-wave resonator demonstrating huge reflection at resonance.

resonance. The sub-THz oscillator can be hereby designed by incorporating surface-wave resonator achieving -116dBc/Hz at 10MHz offset under 0.7V power supply by consuming only 3.5mW power.

## REFERENCES


1. Y. Liang. *et al*. "On-chip sub-terahertz surface plasmon polariton transmission lines in CMOS." *Sci. Rep.* 5, 14853; doi: 10.1038/srep14853 (2015).
2. Y. Liang, H. Yu, J. Zhao, W. Yang and Y. Wang, An Energy Efficient and Low Cross-talk CMOS Sub-THz I/O with Surface-wave Modulator and Interconnect. *ACM/IEEE ISLPED*, 110-115 (2015).

# Magnetic Surface Polaritons: interactions between the magnetic, plasmonic, acoustic surface waves

# Switching of the Magnetic Moment by Mechanical Motion

**Eugene M. Chudnovsky**
Department of Physics and Astronomy
Lehman College and Graduate School, The City University of New York
250 Bedford Park Boulevard West, Bronx, NY 10468-1589, USA
Eugene.Chudnovsky@CUNY.Lehman.edu

Research on spin-based quantum information processing and the emergence of nanoelectromechanical systems rejuvenated interest to microscopic mechanisms of the Einstein – de Haas effect [1-9]. It has been shown that spin-rotation coupling dictated by the conservation of the total angular momentum limits the quality factor of a nanocantilever and is responsible for recently observed non-trivial quantum mechanics of a magnetic molecule grafted on a carbon nanotube. The concept of a phonon spin, similar to a photon spin, has been recently introduced and applied to achieve better understanding of the conservation of angular momentum in magnetic relaxation. Related problems of practical interest include switching of the magnetic moment in a nanoresonator by the combined effect of the spin-polarized current and mechanical kick, possibility of the electromechanical magnetization switching in multiferroics, and switching of the magnetization by surface acoustic waves. This research has been supported by grants from the U.S. National Science Foundation.

**REFERENCES**

1. E. M. Chudnovsky, J. Tejada, and R. Zarzuela, *Quantum Forces in Solids with Two-State Systems: An Example of a Molecular Magnet*, Physical Review B **88**, 220409(R) (2013).
2. M. F. O'Keeffe, E. M. Chudnovsky, and D. A. Garanin, *Landau-Zener Dynamics of a Nanoresonator Containing a Tunneling Spin*, Physical Review B **87**, 174418 (2013).
3. S-H. Lim, A. Imtiaz, T. M. Wallis, S. Russek, P. Kabos, L. Cai, and E. M. Chudnovsky, *Magneto-Mechanical Investigation of Spin Dynamics in Magnetic Multilayers*, Europhysics Letters **105**, 37009 (2014).
4. E. M. Chudnovsky and D. A. Garanin, *Damping of a Nanocantilever by Paramagnetic Spins*, Physical Review B **89**, 174420 (2014).
5. E. M. Chudnovsky, *Spin Tunneling in Magnetic Molecules That Have Full or Partial Mechanical Freedom* (Ch. 3 in "Molecular Magnets: Physics and Applications", Springer 2014).
6. L. Cai, R. Jaafar, and E. M. Chudnovsky, *Mechanically-Assisted Current-Induced Switching of the Magnetic Moment in a Torsional Oscillator*, Physical Review Applied **1**, 054001 (2014).
7. D. A. Garanin and E. M. Chudnovsky, *Angular Momentum in Spin-Phonon Processes*, Physical Review B **92**, 024421 (2015).
8. E. M. Chudnovsky and R. Jaafar, *Electromechanical Magnetization Switching*, Journal of Applied Physics **117**, 103910 (2015).
9. E. M. Chudnovsky and R. Jaafar, *Manipulating Magnetization of a Nanomagnet by Surface Acoustic Waves: Spin-Rotation Mechanism*, Condensed Matter arXiv:1601.01016 (2016).

# Tunable magneto-acoustic crystals

**F. Allein, V. Tournat, V. E. Gusev, and G. Theocharis**

LAUM, UMR CNRS 6613, Université du Maine, Avenue O. Messiaen, Le Mans, 72085, France.
georgiostheocharis@gmail.com

**Abstract**— We study the dynamics of 1D magneto-acoustic crystals composed of a chain of steel spherical beads inside a properly designed magnetic field. The latter is induced by an array of permanent magnets, located in a holder and at a distance from the chain. We display the theoretical dispersion relations considering all six degrees of freedom of the individual beads, three translational and three rotational, and compare with the obtained experimental results. We present experimental evidence of transversal-rotational modes of propagation and tunability of the response by changing the strength of the magnetic field. The combination of the non-contact tunability with the potentially strong nonlinear behavior of the granular systems, makes magneto-granular crystals suitable nonlinear tunable mechanical metamaterials for the control of elastic wave propagation.

Envisioning the next generation of elastic devices, it is necessary to introduce a certain degree of frequency tunability of the phononic properties. In recent years, numerous solutions have been proposed by several authors including geometric changes of the structure by applying external stress [1] or external stimuli, like magnetic field [2]. Among the different proposed phononic crystals, a great amount of work has been devoted the last years to the study of granular crystals [3], which are closely packed, ordered arrangements of elastic particles (spheres in most of the cases) in contact. Due to the Hertzian contact interaction between the particles, the dynamic vibrational response of these structures can be nonlinear and tunable. In adition, due to the finite size of the particles and the friction between them, coupled rotational-translational elastic waves exist and were observed in three dimensional, hexagonal close-packed granular crystals [4].

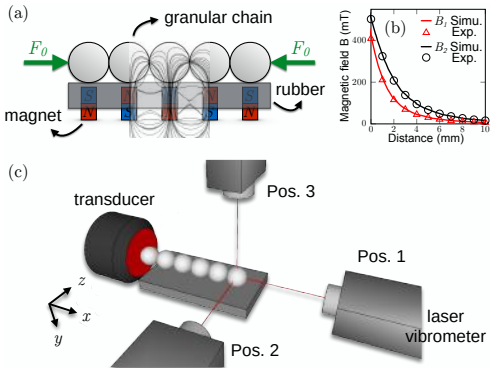



Figure 1: (a) Schematic of the granular chain on top of permanent magnets within a substrate. (b) Magnetic flux density (mTesla) as a function of the distance from the upper surface of the magnet for $B_1 = 1.32$ T (red) and $B_2 = 1.37$ T (black). (c) Schematic of the experimental setup.

In this work, we design and study tunable magneto-acoustic crystals. Tunability is demonstrated by employing granular chains made of ferromagnetic material and applying an external magnetic field. By changing the strength of the applied magnetic field, one can tune the interparticle forces at will. The latter will result in programmable elastic deformations at the contact points which determine the dynamic response of the granular crystal. Thus, by changing the magnetic field, one can tune the dynamic response of the granular crystal. The proposed magneto-acoustic crystal is shown in Fig. 1(a). It is composed of a chain of stainless steel spherical beads on top of a rubber substrate in which permanent neodymium magnets (NdFeB) are located in a linear array.

In Fig. 1(b), we plot the simulated (FEM analysis) and experimentally measured magnetic field as a function of the distance from the upper surface of the cylindrical magnet for $B_1 = 1.32$ T and $B_2 = 1.37$ T. Strong variations of the magnetic field strength, and thus of the normal forces

between the spheres, are possible by either placing the permanents magnets at different distances or by changing their remanent magnetization.

We use two kinds of transducers which allow us to drive the chain in three different directions $(x, y, z)$. The measurement of the last particle velocity is made by a laser vibrometer placed in three different positions to be able to detect all directions of translational motion of a particle. The experimental setup is presented in Fig. 1(c). The granular chain is composed of 5 and 15 beads of diameter $d = 15.875$ mm, made of stainless steel (Young's modulus $E = 200$ GPa, poisson ratio $\nu = 0.3$. The permanent magnets are NdFeB cylinders of remanent magnetization $B_2 = 1.37\ T$, located 10 mm from the center of the spheres. For this case, the precompression force measured to be $F_0 = 1$ , resulting to a normal stiffness of $K_N = 6.60 \cdot 10^6$ N/m, to a shear stiffness $K_S = 5.44 \cdot 10^6$ N/m, and to a torsional stiffness of $K_T = 1.12 \cdot 10^{-2}$ mN ($K_S R^2 = 3.42 \cdot 10^2$ mN $\approx 3 \times 10^4\ K_T$). In Fig. 2, we plot the theoretical dispersion curves for each plane (sagittal and horizontal) together with the relevant experimental linear spectra.

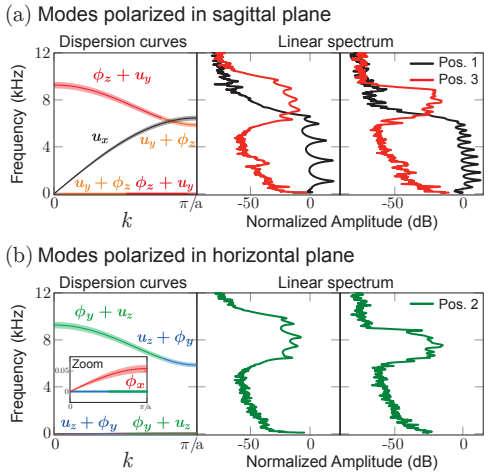



Figure 2: Dispersion curves (left) for the infinite free granular chain considering the experimentally measured $F_0 = 1$ N (solid line) with an error of $\pm 0.15$ N (shadow zone). Experimental linear spectrum for a chain composed of 5 beads (center) and 15 beads (right) (a) in the sagittal plane ($x$,$y$) and (b) in the horizontal plane ($x$,$z$).

To conclude, we have presented the realization and dynamics analysis of a magneto-acoustic crystal composed of spherical ferromagnetic spheres in contact in the presence of a properly designed magnetic field. The latter is imposed by strong permanent magnets arranged in line within a rubber holder at a distance from the granular chain. By considering all the degrees of freedom, we derive the full dispersion relations. Experiments reveal for the first time very clearly the existence of TR branches in a granular chain which can in addition be tuned by the external magnetic field. The combination of the non-contact tunability and the potential strong nonlinear behavior opens the way for the construction of novel nonlinear tunable mechanical metamaterials for the control of elastic wave propagation.

## ACKNOWLEDGMENT

G. T. acknowledges financial support from FP7-CIG (Project 618322 ComGranSol).

## REFERENCES

1. K.Bertoldi and M. C. Boyce, "Mechanically triggered transformations of phononic band gaps in periodic elastomeric structures," *Phys. Rev. B*, Vol. 77, 052105, 2008.
2. J.-F. Robillard, O. Bou Matar, J. O. Vasseur, P. A. Deymier, M. Stippinger, A.-C. Hladky-Hennion, Y. Pennec, and B. Djafari-Rouhani, "Tunable magnetoelastic phononic crystals," *Appl. Phys. Lett*, Vol. 95, 124104, 2009.
3. G. Theocharis, N. Boechler, and C. Daraio, in Acoustic Metamaterials and Phononic Crystals (Springer, New York, 2013), pp. 217-251.
4. A. Merkel, V. Tournat, V. Gusev, " Experimental evidence of rotational elastic waves in granular phononic crystals," *Phys. Rev. Lett*, Vol. 105, 225502, 2011.

# Inverse Magneto-Optical Effects in Cylindrical Graphene-Coated Nanowires.

**D. A. Kuzmin**[1], **I. V. Bychkov**[1*], **V. G. Shavrov**[2], **V. V. Temnov**[3], **H. I. Lee**[4], **and J. Mok**[5]

[1]Chelyabinsk State University, Chelyabinsk, Russian Federation

[2]Kotel'nikov Institute of Radio Engineering and Electronics of RAS, Moscow, Russian Federation

[3]Institut des Molécules et Matériaux du Mans, UMR CNRS 6283, Université du Maine, Le Mans cedex, France

[4]Research Institute of Mathematics, Seoul National University, Seoul, Korea

[5]Department of Industrial and Management Engineering, Sunmoon University, Asan, Choongnam, Korea

[*]corresponding author: bychkov@csu.ru

**Abstract**-We have investigated an inverse Faraday effect caused magnetic field distributions in cylindrical graphene-covered nanowire. The possibility of using of mode composition for controllable change in such distribution has been shown. Results may be used for magnetic memory applications as well as for design of plasmonically reconfigurable magnonic nanostructures.

In this work we present details of our recent results of investigation on plasmonically induced magnetic field $\mathbf{H}_{eff}$ in graphene-covered nanowire due to inverse Faraday effect[1].

An effective magnetic field induced by electric field of light may be calculated[2, 3]:

$$\mathbf{H}_{eff} = \alpha \, \mathrm{Im}\left[\mathbf{E} \times \mathbf{E}^{*}\right], \tag{1}$$

where $\alpha$ is the magneto-optical susceptibility, operation * means the complex conjugation.

Dispersion characteristics have been investigated in details recently[4]. Investigation showed that graphene-coated nanowire has a much higher mode index and a better mode confinement than metal-coated one.

We consider dielectric nanowire with radius $R$ and dielectric permittivity $\varepsilon_{in}$ covered by graphene layer and embedded in medium with dielectric permittivity $\varepsilon_{out}$. Graphene layer is represented as infinitely thin layer with surface conductivity $\sigma_g$. We consider monochromatic plasmons propagating along nanowire axis ($z$-axis) by putting electric and magnetic fields $\mathbf{E}$, $\mathbf{H} \propto \exp[i(\beta z - \omega t)]$ into Maxwell's equations ($\beta = \beta' + i\beta''$ is a complex propagation constant, $\omega$ is a circular frequency).

For mode with $m = 0$ electromagnetic waves may be divided onto TE- and TM- modes. TE- mode cannot produce any magnetic field, while TM- mode induces azimuthal magnetic field. Such magnetic vortex-like field is localized near graphene layer and exponently decays in $z$-axis direction. Magnetic field components induced by any single mode do not depend on azimuthal angle $\varphi$. For modes with $m \neq 0$ all components of magnetic field are non-zero. Change in propagation direction leads to change of $\mathbf{H}_{eff}$ rotation direction.

Fig. 1 shows magnetic field distributions for $m = 0, \pm 1, \pm 2$ at frequency $f = 100$ THz. One can see that distribution has a vortex-like type. Rotational direction is opposite for the field induced inside and outside of nanowire. Increasing in azimuthal mode number leads to increase of longitudinal component of induced field. Direction of this component is opposite for the field induced inside and outside of nanowire as well.

The work was supported by RFBR grants ## 16-37-00023, 16-07-00751. Numerical calculations were supported by RScF grant # 14-22-00279.

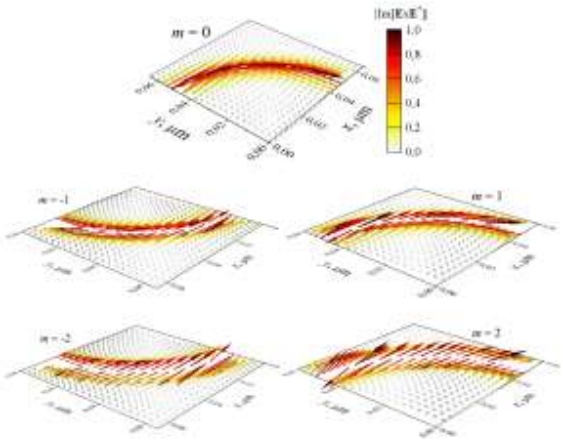


Figure 1. Magnetic field distribution for different azimuthal modes *m*.

**REFERENCES**


1. Kuzmin, D. A., I. V. Bychkov, V. G. Shavrov, V. V. Temnov, H. I. Lee, J. Mok "Plasmonically induced magnetic field in graphene-coated nanowires," *Optics Letters*, Vol. 41, No. 2, 396-399, 2016.
2. Pitaevskii, L. P., "Electrical forces in a transparent dispersive medium," *Sov. Phys. JETP*, Vol. 12, 1008, 1961.
3. Van der Ziel, J. P., P. S. Pershan, and L. D. Malmstrom, "Optically-Induced Magnetization Resulting from the Inverse Faraday Effect," *Phys. Rev. Lett.*, Vol. 15, No. 5, 190–193, 1965.
4. Gao, Y., G. Ren, B. Zhu, H. Liu, Y. Lian, and Sh. Jian, "Analytical model for plasmon modes in graphene-coated nanowire," *Opt. Expr.*, Vol. 22, No. 20, 24322–24331, 2014.

# Nonlinear surface photonics in hybrid magnetic structures.

**I. Razdolski**[1], **D. Makarov**[2], **A. Paarmann**[1], **M. Wolf**[1],**and V. V. Temnov**[3]

[1]Fritz-Haber-Institut der Max-Planck-Gesellschaft, Phys. Chemie, Faradayweg 4-6, 14195 Berlin, Germany
[2]Helmholtz-Zentrum Dresden-Rossendorf e.V., Institute of Ion Beam Physics and Materials Research, 01328 Dresden, Germany
[3]Institut des Molécules et Matériaux du Mans, UMR CNRS 6283, Université du Maine, 72085 Le Mans cedex, France
razdolski@fhi-berlin.mpg.de

**Abstract**— Nonlinear magneto-plasmonics [1] offers a considerable expansion of control over the magneto-optical response of a system supporting surface polaritons. Here we demonstrate enhanced magneto-optical modulation of the second harmonic generation output from hybrid plasmonic structures and comparatively analyze the advantages of nonlinear surface polaritons excitation. Further, we discuss possible application of this concept to metal-free polar dielectrics where low-losses surface phonon polaritons can be excited in the Reststrahlen band in the THz spectral range.

The recent achievements of magneto-plasmonics have opened the door for nonlinear magneto-plasmonics which utilizes magnetic field as a convenient control knob for tailoring the nonlinear-optical response of plasmonic systems. It can be shown that transversal magnetization $\vec{M}$ modulates the surface plasmon-polariton (SPP) wavevector $\vec{k}_{\rm spp}$ which acquires a magnetization-dependent contribution $\Delta\vec{k}(\vec{M})$:

$$\vec{k}_{\rm spp}(\pm M) = \vec{k}^{(0)}_{\rm spp} \pm \Delta\vec{k}(\vec{M}) \tag{1}$$

where $\vec{k}^{(0)}_{\rm spp}$ is the SPP wavevector in the absence of the magneto-optical effects. This effectively shifts the SPP resonant conditions thus giving rise to the SPP-induced magneto-optical effects [2]. However, these effects are rather small rarely exceeding 1% and thus representing a fundamental challenge of magneto-plasmonics. In turn, nonlinear magneto-optics is known for its large magnitude of the magnetic field-induced effects which *e.g.* in the case of magnetic second harmonic generation (SHG) can readily surpass dozens of percents. Complimented by the high SHG sensitivity to the inversion symmetry breaks at surfaces and interfaces where the SPPs are primarily localized, this technique holds high potential for the future development of magneto-photonics and plasmonics.

A number of experiments on nonlinear magneto-plasmonics [3, 4, 5, 6] demonstrated large magnetization-induced modulations of the SHG intensity. Magnetic SHG (mSHG) modulation is achieved with the help of the SPP-driven phase shifts between the crystallographic and magnetization-induced contributions arising when the SPP at the fundamental frequency $\omega$ is excited. However, an alternative approach utilizing SPP excitations at the double frequency $2\omega$ appears to be much more promising [7]. Here we consider Kretschmann configuration and fundamental light of 800 nm wavelength. A multilayer system shown in Fig. 1,a supports SPP excitation at both $\omega$ and $2\omega$ albeit at different angles, while the Co layer ensures the magneto-optical activity of the structure. Linear magneto-plasmonic effect barely reaches 0.5%, whereas in nonlinear response the mSHG output modulation exhibits two orders of magnitude enhancement.

Interestingly, the largest magnetization-induced variations of the mSHG intensity occur at the angles of about 44°–45°, when the SPP is excited at the double frequency $2\omega$ (Fig. 1,b). This observation hold true in a broad range of excitation wavelengths as long as the SPP at the double frequency is still supported. As soon as the interband transitions in Ag start to play a role and the SPP losses increase, the mSHG modulation experiences a sizeable decrease (see the red curve in, 760 nm excitation wavelength). This fact, along with the dispersive shift of mSHG maximum, reinforces our conclusion that the 33% large mSHG contrast (which is equivalent to the increase of the SHG intensity by a factor of 2 upon the magnetization reversal) is dominated by the SPP resonance at the SHG frequency. The complex shapes of the angular dependence of mSHG contrast as well as the SHG intensities for the two opposite directions of the Co magnetization (see inset

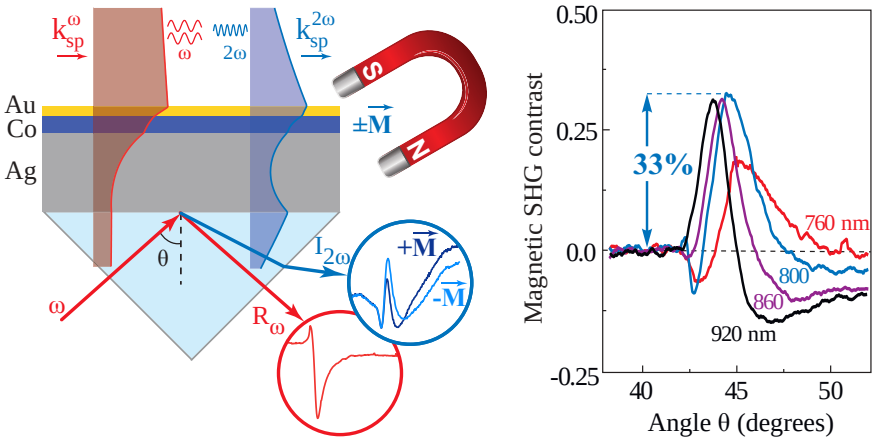



Figure 1: Figure 1. (a) Excitation of SPPs in a trilayer Au/Co/Ag structure in the Kretschmann geometry. Shaded areas represent the calculated distributions of the electric field when the SPPs are excited at the fundamental (red) and SHG (blue) frequencies. Insets demonstrate the angular spectra of linear reflectivity $R_\omega$ and SHG intensities for the two opposite directions of the magnetization $I_{2\omega}(\pm M)$. (b) Angular spectra of the mSHG magnetic contrast $\rho_{2\omega}$ for the four fundamental wavelengths.

in Fig. 1,a) can be explained as a result of the interference of the SPP-driven SHG and the SHG contribution from the bottom Ag/substrate interface largely unaffected by the SPP excitation [8].

Despite the large mSHG modulation, considerable losses induced by the presence of the Fe layer hamper the SPP excitation and decrease the total SHG output. Higher quality excitations can be driven in the Reststrahlen band in polar dielectrics [9], where longitudinal and transversal optical phonons ensure the spectral region of negative permittivity. There, surface phonon polaritons (SPhP) can be effectively excited offering higher quality factors Q as compared to surface plasmon polaritons in metals. The maximum attainable Q is limited by the intrinsic damping due to phonon-phonon scattering. One of the prominent example is SiC demonstrating large SPhP lifetimes and sharp resonances in the Reststrahlen band. Applying the concepts of nonlinear magneto-plasmonics to polar dielectrics with magnetic order could potentially open a new chapter in nonlinear surface photonics.

## ACKNOWLEDGMENT

The authors are indebted to Prof. Dr. A. Kirilyuk, Prof. Dr. Th. Rasing, Prof. Dr. O. G. Schmidt, Dr. W. Schöllkopf, and Dr. S. Gewinner.

## REFERENCES

1. Zheng, W. *et. al.*, "Nonlinear Magneto-Plasmonics," *Opt. Mater. Expr.*, Vol. 5, No. 11, 2597-2607, 2015.
2. Armelles, G. M. *et. al.*, "Magnetoplasmonics: Combining Magnetic and Plasmonic Functionalities," *Adv. Opt. Mater.*, Vol. 1, No. 1, 10–35, 2013.
3. Pavlov, V. V. *et. al.*, "Observation of magneto-optical second-harmonic generation with surface plasmon excitation in ultrathin Au/Co/Au films," *Appl. Phys. Lett.*, Vol. 75, No. 2, 190–192, 1999.
4. Razdolski, I. *et. al.*, "Nonlocal nonlinear magneto-optical response of a magnetoplasmonic crystal," *Phys. Rev. B*, Vol. 88, No. 7–15, 075436, 2013.
5. Zheng, W. *et. al.*, "Control of magnetic contrast with nonlinear magneto-plasmonics," *Sci. Rep.*, Vol. 4, 6191, 2014.
6. Krutyanskiy, V. L. *et. al.*, "Giant nonlinear magneto-optical response of magnetoplasmonic crystals," *Phys. Rev. B*, Vol. 91, No. 12–15, 121411(R), 2015.
7. Razdolski, I. *et. al.*, "Nonlinear Surface Magnetoplasmonics in Kretschmann Multilayers," *ACS Phot.*, Vol. 3, No. 2, 179–183, 2016.
8. Palomba, S. and L. Novotny, "Nonlinear Excitation of Surface Plasmon Polaritons by Four-Wave Mixing," *Phys. Rev. Lett.*, Vol. 101, No. 5, 056802, 2008.
9. Caldwell, J. D. *et. al.*, "Low-loss, infrared and terahertz nanophotonics using surface phonon polaritons," *Nanophotonics*, Vol. 4, No. 1, 44–68, 2015.

# Propagating magnons with sub-100 nm wavelength excited by microwaves in nanostructured metal/insulator thin-film magnets.

**H. Yu[1, 2], O. d'Allivy Kelly[3], V. Cros[3], R. Bernard[3], P. Bortolotti[3], A. Anane[3], F. Brandl[1], F. Heimbach[1], and D. Grundler[4*]**

[1]Physik Department E10, Technische Universität München, James-Franck-Strasse 1, D-85748 Garching b. München, Germany

[2]Fert Beijing Research Institute, Department of Electrical Engineering, Beihang University, Xueyuan Road 37, 100191 Beijing, China

[3]Unité Mixte de Physique CNRS/Thales and Université Paris Sud, 1 avenue Augustin Fresnel, Palaiseau, France

[4]Laboratory of Nanoscale Magnetic Materials and Magnonics, Institute of Materials, Ecole Polytechnique Fédérale de Lausanne, CH-1015 Lausanne, Switzerland

[*]corresponding author: dirk.grundler@epfl.ch

**Abstract**-Magnetic nanodevices will allow for the creation of smart GHz-to-THz devices operated at low power consumption if spin waves (magnons) are generated and manipulated on the sub-100 nm scale. We report how magnons with a wavelength of a few 10 nm are created by conventional microwave antenna in that we combine insulating yttrium iron garnet and specifically tailored metallic nanomagnets. We demonstrate magnonic devices at a wavelength of 88 ± 2 nm. At the same time we show that our microwave-to-magnon transducers are reconfigurable and thereby provide additional functionalities.

Collective spin excitations have the potential to provide beyond-CMOS applications via e.g. parallel processing in cellular networks [1]. However, magnonic devices realized so far from metallic ferromagnets such as permalloy suffer from the relatively short damping length δ. Insulating magnetic oxides improve the situation. Here we report on spin excitations in the insulating thin-film ferrimagnet yttrium iron garnet (YIG) that offers δ of several 100 μm at room temperature [2]. Based on such YIG, we excite propagating GHz spin waves with wavelengths λ down to 88 nm, when applying the recently reported nanomagnonic grating coupler [3]. In our case the grating coupler consists of an array of metallic nanomagnets with large saturation magnetization (permalloy or CoFeB) that are prepared between YIG and an integrated microwave antenna. A large spin-wave signal strength is obtained when we drive the grating coupler at its own ferromagnetic resonance frequency. The wavelength of the propagating magnons is smaller by five orders of magnitude compared to the electromagnetic wave that is used for excitation (in free space). The findings are straightforwardly extended to even smaller wavelengths by further optimizing nanomagnets and array parameters. The results are important for the implementation of nanomagnonic devices combined with conventional microwave circuits.

**Acknowledgements**. Financial support by the German Excellence Cluster Nanosystems Initiative Munich (NIM), the DFG via project GR1640/5-2 in the priority programme SPP1538, ANR-12-ASTR-0023 Trinidad and NSF China under Grant No. 11444005 are gratefully acknowledged.

**REFERENCES**


1. Khitun, A., Bao, M. and Wang, K. L., "Magnonic logic circuits", *J. Phys. D: Appl. Phys*., Vol. 43, 264005, 2010.
2. Yu, H. et al., "Magnetic thin-film insulator with ultra-low spin-wave damping for coherent nanomagnonics", *Scientific Reports*, Vol. 4, 6848, 2014.
3. Yu, H. et al., "Omnidirectional spin-wave nanograting coupler", *Nat. Commun*., Vol 4, 2704, 2013.

# Ultrafast Surface Magnetoelastic Waves

**J. Janusonis[1], C.L. Chang[1], A.M. Lomonosov[2], V. Shalagatskyi[2], V. S. Vlasov[2], V. V. Temnov[2], and R.I. Tobey[1*]**

[1]Zernike Institute for Advanced Materials, University of Groningen, The Netherlands

[2]IMMM CNRS, Universite du Maine, France

[*]corresponding author: r.i.tobey@rug.nl

**Abstract-** Surface magnetoelastic waves are generated using a hybrid magnetooptic / transient grating technique. This approach allows us to measure the structural and magnetic degrees of freedom independently and demonstrate resonant coupling between these disparate degress of freedom. We show the excitation of two distinct elastic waves in the transient grating geometry, and the selective resonant coupling to the magnetization of each individually. At resonance, large amplitude magnetization precession is shown.

We detail a unique approach to studying magnetoelasticity[1,2], the coupling of high frequency elastic waves to materials magnetization. We generate and detect surface elastic waves using the all-optical transient grating geometry, and then monitor in real time the coupling between the elastic waves and material magnetization. We measure simultaneously the elastic distortion using conventional transient grating spectroscopy and the average magnetization of the material by Faraday rotation of a transmitted beam, as shown in figure 1a. Our experiment provides for the application of a magnetic field in the plane of the sample and we thus show the field-tuned resonant excitation of a ferromagnetic resonance (FMR) by the passing elastic wave. The all-optical approach provides for a flexible excitation geometry of a variety of elastic waves which can be easily tuned from 1GHz to roughly 10GHz.

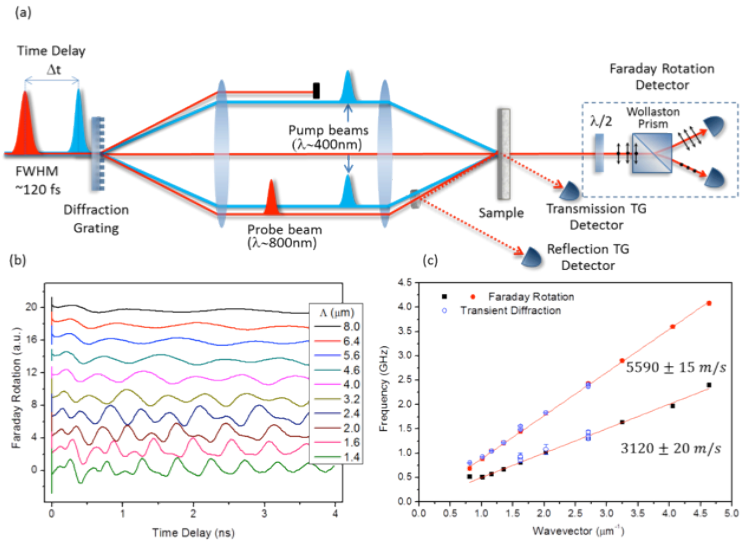



**Fig. 1**: (a) Transient grating geometry including diffraction and Faraday rotation measurement. (b) Grating dependence of the Faraday rotation shows that the precession frequency and amplitude reduces as the excitation grating wavelength is increased. (c) The dispersion relation shows good correspondence between the Faraday and transient grating measurements allowing us to identify the two elastic waves, the Rayleigh Surface Acoustic Wave (SAW) and the Surface Skimming Longitudinal Wave (SSLW). Both elastic distortions drive magnetization precession.

When excited in the TG configuration, the Faraday response (figure 1b) exhibits a series of oscillations that decrease in amplitude and frequency as the grating wavelength is increased. When the frequency of oscillation is plotted relative to the imposed wavevector, a dispersion relation, we can extract the velocity of propagation of the excitation. In comparing the dispersion measured in diffraction and Faraday channels, a near perfect correspondence is observed, allowing us to identify the observed modes as the Rayleigh Surface Acoustic Wave (SAW) with a velocity of 3120m/s and a Surface Skimming Longitudinal Wave (SSLW) with a velocity of 5590m/s. In both instances, since the response is observed in the Faraday detection channel, we conclude that the elastic waves drive a magnetization precession.

To emphasize the magneto-optical nature of our measurements, we apply an in-plane magnetic field to tune the magnitude of Faraday rotation signal, as shown in figure 2. Here the grating periodicity is fixed at 1.1mm and the applied field $H$ is swept from +700G to -700G while the amplitude of the precession oscillation is displayed (the FFT amplitude). Based on the dispersion relationship and extracted frequencies from figure 1c, we identify the two elastic waves, SAW and SSLW, by the two horizontal lines, while the increase in amplitude is observed when the elastic frequency matches that of the field-tuned ferromagnetic resonance (FMR) of the film with frequency given by Kittel's formula: $f_{FMR} \sim \sqrt{H(H+M)}$ (red).

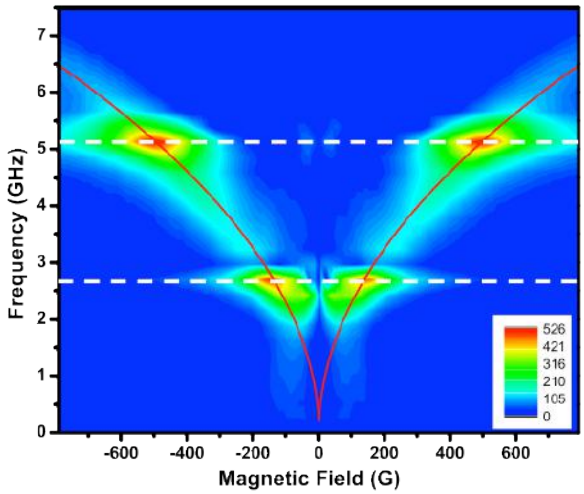



**Fig. 2**: (a) Field-tuned resonance. Applying a magnetic field in the plane of the sample tunes the ferromagnetic resonance condition to match the applied effective field generated by the passing elastic wave. Here, two resonance conditions are shown, at ~2.7GHz and 150G, the SAW wave resonantly drives the magnetic precession, while at ~5.1GHz and 500G, the SSLW resonantly drives precession.

In summary, we have demonstrated a novel experimental scheme for studying magnetoelastic dynamics using an all - optical method. We demonstrated the elastically driven FMR precession induced by two surface acoustic transients, the Rayleigh SAW and the SSLW. The TG geometry allows for the facile excitation and characterization of surface magneto-elastic waves, while the time resolved nature uniquely probes the resonant coupling between the magnetic and elastic counterparts in these polaritonic eigenwaves. More broadly, these experiments open the door to a number of research directions that study the interaction of dynamic structural transients at surfaces and interfaces with range of material properties, including magnetization or electronic properties.

**REFERENCES**

[1] J. Janusonis *et.al.* "Frequency Tunable Surface Magneto Elastic Waves" APL **106**, 181601 (2015).

[2] J. Janusonis *et.al.* "Ultrafast Magnetoelastic Probing of Surface Acoustic Transients" arXiv:1601.04350 (2016).

# Tunable plasmonic heterostructures: magnetic and optical-pump ultrafast control

**V.I. Belotelov**[1,2*]
[1]Russian Quantum Center, Moscow, Russia
[2] Lomonosov Moscow State University, Moscow, Russia
[*]corresponding author: v.belotelov@rqc.ru

**Abstract** - One should find different ways to control wavenumber, phase and polarization of surface plasmons. At this point, 'active plasmonics' comes to play. There are different methods and approaches of active plasmonics. In this talk, we shall discuss how to influence on the surface plasmons by means of direct and inverse magneto-optical effects, photoexcitation of electrons in a metal, gain media, optical phonons, and acoustic waves.

Currently, there is great research interest in the area of plasmonics, since surface plasmon-polaritons, coupled oscillations of electrons and light localized at a metal surface, are very promising as information carriers for next-generation nanophotonic devices. If such applications are anticipated, one should find different ways to control wavenumber, phase and polarization of surface plasmons. At this point, 'active plasmonics' comes to play.

There are different methods and approaches of active plasmonics. In this talk, we shall discuss how to influence on the surface plasmons by means of direct and inverse magneto-optical effects, photoexcitation of electrons in a metal, gain media, optical phonons, and acoustic waves. In all cases we consider Fano resonances in light transmitted or reflected from periodic plasmonic structures – plasmonic crystals – consisting of a metal nanograting of slits or holes and a smooth dielectric. Such type of resonances originates from excitation of surface plasmons.

Magnetic field control of light is among the most intriguing methods for modulation of light intensity and polarization on sub-nanosecond timescales. The implementation in nanostructured hybrid materials provides a remarkable increase of magneto-optical effects [1,2]. Highest figure of merit of resonances and enhancement of the magnetooptical effects are achieved for magnetic dielectrics like iron garnets.

However, not only the enhancement of already known effects has been demonstrated in plasmonic crystals. Recently, we postulate a novel magneto-optical phenomenon that originates solely from suitably designed magneto-plasmonic crystal [3]. In this material, an incident light excites coupled plasmonic oscillations and a waveguide mode. An in-plane magnetic field allows excitation of an orthogonally polarized waveguide mode that modifies optical spectrum of the magnetoplasmonic crystal and increases its transparency. The experimentally achieved light intensity modulation reaches 24%. As the effect can potentially exceed 100%, it may have great importance for applied nanophotonics. Further, the effect allows manipulating and exciting waveguide modes by a magnetic field and light of proper polarization.

Magnetization of the magnetoplasmonic crystal can be modified by either an external magnetic field or by laser pulse of circular polarization [4]. In the later case, inverse Faraday effect is involved thus allowing to switch magnetization on picosecond time scales.

Alternatively, optical properties of the plasmonic crystals can be tuned by femtosecond laser pulses. As a result, surface plasmons propagation through the plasmonic crystal are modified and

corresponding differential transmittance and reflectance changes of the order of 5% are observed [5]. The response time of plasmonic crystals can be varied widely from 200 to 800 fs by tuning the relative spectral positions of the probe and the SPP resonance.

Another approach of the active plasmonics uses coherent sub-THz phonons incident on a gold grating that is deposited on a dielectric substrate. They undergo diffraction and thereby induce an alteration of the surface plasmon-polariton resonance. This results in efficient high-frequency modulation (up to 110 GHz) of the structure's reflectivity for visible light in the vicinity of the plasmon-polariton resonance [6]. High modulation efficiency is achieved by designing a periodic nanostructure which provides both plasmon-polariton and phonon resonances. Our theoretical analysis shows that the dynamical alteration of the plasmon-polariton resonance is governed by modulation of the slit widths within the grating at the frequencies of higher-order phonon resonances.

Moreover, it is possible to achieve an efficient 3.6 THz modulation of light reflected from hybrid metal/semiconductor plasmonic crystals caused by lattice vibrations in a few-nm-thick layer of elemental tellurium [7]. We observe that surface plasmon polaritons contribute significantly to the photoinduced formation of this thin layer at the interface between a telluride-based II-VI semiconductor, such as (Cd,Mg)Te or (Cd,Mn)Te, and a one-dimensional gold grating. The change in interface composition is monitored via the excitation and detection of coherent optical tellurium phonons of $A1$ symmetry by femtosecond laser pulses in a pump-probe experiment. The patterning of a plasmonic grating onto the semiconductor enhances the transient signal which originates from the interface region. This allows one to monitor the layer formation and observe the shift of the phonon frequency caused by confinement of the lattice vibrations in the nm-thick segregated layer. Efficient excitation and detection of coherent optical phonons by means of surface plasmon polaritons are evidenced by the dependence of the signal strength on polarization of the pump and probe pulses and its spectral distribution.

**Acknowledgements** - This work was supported by the Russian Science Foundation (grant N 14-32-00010).

[1] V.I. Belotelov, I.A. Akimov, A.K. Zvezdin et. al, *Nature Nanotech.* **6**, 370 (2011).
[2] V.I. Belotelov, L.L. Doskolovich, A.K. Zvezdin: *Phys. Rev. Lett.*, **98**, 77401 (2007).
[3] V.I. Belotelov, L.E. Kreilkamp, I.A. Akimov, et al. *Nature Comm.* **4**, 2128 (2013).
[4] V.I. Belotelov and A.K. Zvezdin, *Phys. Rev. B* **86**, 155133 (2012).
[5] M. Pohl, V.I. Belotelov, I.A. Akimov, S. Kasture, A.S. Vengurlekar, A.V. Gopal, A.K. Zvezdin, M. Bayer, *Phys. Rev. B* **85**, 081401(R) (2012).
[6] C. Brüggemann, A.V. Akimov, V.I. Belotelov, et. al, *Phys. Rev. B* **86**, 121401(R) (5) (2012).
[7] L.E. Kreilkamp, I.A. Akimov, V.I. Belotelov, et. al, *Phys. Rev. B* (2016) (to be published).

**Localized Surface Plasmons and Magnetooptical Activity Enhancement**

G. Armelles

IMM-Instituto de Microelectrónica de Madrid (CNM-CSIC)
Isaac Newton 8, PTM, Tres Cantos, Madrid, 28760 (Spain)
E-mail: gaspar@imm.cnm.csic.es

Active plasmonic systems have exceptional potential in a wide range of applicabilities. Recently, endorsing this active character by incorporating magnetic functionality has received a great deal of attention. Combining plasmon resonances and magnetooptical activity allows enhancing the Magneto Optical (MO) response by electromagnetic field localization of the plasmon resonance in the MO active element,. In this talk we will review the different approaches that have been followed to increase the MO activity by electromagnetic field enhancement.

" Magnetoplasmonics: Combining Magnetic and Plasmonic Functionalities". G. Armelles et al. Adv. Op. Mat 1, 10 (2013).

"Magnetic Field Modification of Optical Magnetic Dipoles". G. Armelles et al. Nano Letters 15, 2045 (2015).

"From disk to ring: Aspect ratio control of the magnetoplasmonic response in Au/Co/Au nanostructures fabricated by hole-mask colloidal lithography". Feng H.Y. et al. Appl. Phys Lett 106, 083105 (2015).

"Magnetoplasmonic Nanorings as Novel Architectures with Tunable Magneto-optical Activity in Wide Wavelength Ranges". Feng H.Y. Adv Op Mat 2, 612 (2014).

"Interaction effects on the magneto-optical response of magnetoplasmonic dimers". De Sousa N. et al. Phys. Rev B 89, 205419 (2014).

# Curvilinear magnetism

**D. Makarov**[1*]

[1]Helmholtz-Zentrum Dresden-Rossendorf e.V., Institute of Ion Beam Physics and Materials Research, Bautzner Landstraße 400, 01328 Dresden, Germany

[*]corresponding author: d.makarov@hzdr.de

**Abstract**-Extending planar two-dimensional structures into the three-dimensional space has become a general trend in electronics, photonics, plasmonics and magnetics. In magnetism, a consequence of the curvilinear geometry is the appearance of novel curvature-driven effects including magnetochiral effects and topologically induced magnetization patterning, resulting in theoretically predicted unlimited domain wall velocities, chirality symmetry breaking and Cherenkov-like effects for magnons. These theoretical predictions and the application potential of 3D-shaped magnetic objects will be presented in this talk.

While conventionally magnetic films and structures are fabricated on flat surfaces, the topology of curved surfaces has only recently started to be explored and leads to new fundamental physics as well as applied device ideas. In particular, novel effects occur when the magnetization is modulated by curvature providing a new degree of freedom that leads to new magnetization configurations (see for instance [1,2]) and is predicted to have major implications on the spin dynamics due to topological constraints for instance in circular tubes and rolls [3].

Advances in this novel field solely rely on the understanding of the fundamental aspects behind the modifications of magnetic responses of 3D-curved magnetic thin films. The lack of an inversion symmetry and the emergence of a curvature induced anisotropy and Dzyaloshinskii-Moriya-like (DM-like) interaction are characteristic of bent and curved surfaces [4-6], leading to curvature-driven magnetochiral effects [7-9] and topologically induced magnetization patterning [6,10], including unlimited domain wall velocities in hollow tubes [3], chirality symmetry breaking [6-9] and Cherenkov-like effects for magnons [11]. In addition to these rich physics, the application potential of 3D-shaped objects is currently being explored as magnetic field sensorics for magnetofluidic applications [12], spin-wave filters [13], advanced magneto-encephalography devices [14] and for energy-efficient high-speed racetrack memory devices [3].

Recent advances in nanofabrication allowed to realize magnetic cap structures [1,2], Swiss rolls [12-17] and artificial complex helimagnetic-like configurations, namely hollow-bar-, corkscrew-, and radial-magnetized 3D micro-helix coils [15,18]. The microscopic characterization of those 3D-shaped objects is challenging and the magnetization configuration is commonly derived by integral means. To access the true 3D magnetization patterns, we put forth the concept of magnetic soft x-ray tomography as a unique approach providing sufficient spatial resolution, magnetic sensitivity and the capability to penetrate the 3D architectures [16,17].

These recent developments starting from the theoretical predictions to the fabrication of 3D-curved magnetic thin films, hollow cylinders or wires as well as their characterization using integral means but also advanced tomography approaches are in the focus of this talk.

**Acknowledgements**: This work is financed in part via the European Research Council under European Union's Seventh Framework program (FP7/2007-2013)/ERC grant agreement n.306277 and the Future and Emerging Technologies (FET) programme under FET-Open grant number 618083.

**REFERENCES**


1. Albrecht, M., Hu, G., Guhr, I. L., Ulbrich, T. C., Boneberg, J., Leiderer, P. and G. Schatz, "Magnetic multilayers on nanospheres," *Nat. Mater.*, Vol. 4, 203, 2005.
2. Ulbrich, T. C., Makarov, D., Hu, G., Guhr, I. L., Suess, D., Schrefl, T. and M. Albrecht, "Magnetization reversal in a novel gradient nanomaterial," *Phys. Rev. Lett.*, Vol. 96, 077202, 2006.
3. Yan, M., Kákay, A., Gliga, S. and R. Hertel, "Beating the Walker Limit with massless domain walls in cylindrical nanowires," *Phys. Rev. Lett.*, Vol. 104, 057201, 2010.
4. Gaididei, Y., Kravchuk, V. P. and D. D. Sheka, "Curvature Effects in Thin Magnetic Shells," *Phys. Rev. Lett.*, Vol. 112, 257203, 2014.
5. Sheka, D. D., Kravchuk, V. P. and Y. Gaididei, "Curvature effects in statics and dynamics of low dimensional magnets," *J. Phys. A: Math. Theor.*, Vol. 48, 125202, 2015.
6. Pylypovskyi, O. V., Kravchuk, V. P., Sheka, D. D., Makarov, D., Schmidt, O. G. and Y. Gaididei, "Coupling of chiralities in spin and physical spaces: The Möbius ring as a case study," *Phys. Rev. Lett.*, Vol. 114, 197204, 2015.
7. Hertel, R. "Curvature-induced magnetochirality," *SPIN*, Vol. 03, 1340009, 2013.
8. Yan, M., Andreas, C., Kákay, A., García-Sánchez, F. and R. Hertel, "Chiral symmetry breaking and pair-creation mediated Walker breakdown in magnetic nanotubes," *Appl. Phys. Lett.*, Vol. 100, 252401, 2012.
9. Otalora, J. A., Lopez-Lopez, J. A., Vargas, P. and P. Landeros, "Chirality switching and propagation control of a vortex domain wall in ferromagnetic nanotubes," *Appl. Phys. Lett.*, Vol. 100, 072407, 2012.
10. Kravchuk, V. P., Sheka, D. D., Streubel, R., Makarov, D., Schmidt, O. G. and Y. Gaididei, "Out-of-surface vortices in spherical shells," *Phys. Rev. B*, Vol. 85, 144433, 2012.
11. Yan, M., Kákay, A., Andreas, C. and R. Hertel, "Spin-Cherenkov effect and magnonic Mach cones," *Phys. Rev. B*, Vol. 88, 220412, 2013.
12. Mönch, I., Makarov, D., Koseva, R., Baraban, L., Karnaushenko, D., Kaiser, C., Arndt, K.-F. and O. G. Schmidt, "Rolled-up magnetic sensor: Nanomembrane architecture for in-flow detection of magnetic objects," *ACS Nano*, Vol. 5, 7436, 2011.
13. Balhorn, F., Mansfeld, S., Krohn, A., Topp, J., Hansen, W., Heitmann, D. and S. Mendach, "Spin-wave interference in three-dimensional rolled-up ferromagnetic microtubes," *Phys. Rev. Lett.*, Vol. 104, 037205, 2010.
14. Karnaushenko, D., Karnaushenko, D. D., Makarov, D., Baunack, S., Schäfer, R. and O. G. Schmidt, "Self-assembled on-chip integrated giant magneto-impedance sensorics," *Adv. Mater.*, Vol. 27, 6582, 2015.
15. Smith, E. J., Makarov, D. and O. G. Schmidt, "Polymer delamination: Towards unique three-dimensional microstructures," *Soft Matter*, Vol. 7, 11309, 2011.
16. Streubel, R., Lee, J., Makarov, D., Im, M.-Y., Karnaushenko, D., Han, L., Schäfer, R., Fischer, P., Kim, S.-K. and O. G. Schmidt, "Spin structures of rolled-up single-layer ferromagnetic nanomembranes," *Adv. Mater.*, Vol. 26, 316, 2014.
17. Streubel, R., Kronast, F., Fischer, P., Parkinson, D., Schmidt, O. G. and D. Makarov, "Retrieving spin textures on curved magnetic thin films with full-field soft x-ray microscopies," *Nat. Commun.*, Vol. 6, 7612, 2015.
18. Smith, E. J., Makarov, D., Sanchez, S., Fomin, V. M. and O. G. Schmidt, "Magnetic micro-helix coil structures," *Phys. Rev. Lett.*, Vol. 107, 097204, 2011.

# Spin transport and manipulation in GaAs quantum wells by surface acoustic waves

**A. Hernández-Mínguez**[1], **K. Biermann**[1], **R. Hey**[1], **and P. V. Santos**[1*]
[1]Paul-Drude-Institut für Festkörperelektronik, Berlin, Germany
[*]corresponding author: santos@pdi-berlin.de

**Abstract** - The fields of a surface acoustic wave (SAW) produce a moving potential modulation on semiconductor structures. This modulation can capture photo-excited, spin-polarized electrons and holes in an intrinsic semiconductor structure and transport them with the acoustic velocity. Here, we review recent results on the acoustic transport and manipulation of optically excited spins in (Al,Ga)As quantum wells at high (i.e. above liquid nitrogen, LN) temperature.

Moving vibrations in form of surface acoustic waves can be generated on a GaAs QW structure by applying a radio-frequency voltage to interdigital transducers (IDTs) deposited on the sample surface [cf. Fig. 1(b)]. Their piezoelectric potential $\Phi_{SAW}$ creates the type-II modulation of the conduction (CB) and valence band (VB) edges sketched in Fig. 1(a), which propagates with the acoustic velocity $v_{SAW}$. When applied to quantum well (QW) structures, this modulation can store photo-excited electrons and holes in spatially separated positions and transport them along the SAW propagation direction [cf. Fig. 1(a)].[1] After transport, photons can be retrieved by forcing the electrons and holes to recombine. The acoustic transport has been exploited for the realization of single electron pumps[2] and single-photon sources.[3] If the incoming photons are circularly polarized, spin-polarized carriers can be excited and subsequently transported while maintaining their spin polarization.[4-7] Finally, since the moving spins can be manipulated during transport via the spin-orbit interaction or external fields, the scheme illustrated in Fig. 1(b) becomes a spin processors for optical information.

The acoustic spin transport presupposes spin lifetimes considerably larger than the inverse SAW frequency $f_{SAW}$ (on the order of 1 GHz) in order to ensure transport over several acoustic wavelengths $\lambda_{SAW}$ (~1 μm). The spatial separation of electrons and holes essentially eliminates spin scattering due to the exchange interaction.[4] The major mechanisms limiting the spin lifetime then becomes the spin-orbit interaction: as a consequence of the coupling between electron spins and orbital motion, a moving spin experiences an effective magnetic field, which depends on its momentum. Spins thermally drifting along random trajectories will then undergo different precession angles under the effective spin-orbit field, thus leading to a reduction of the average spin of the ensemble (the Dyakonov-Perel (DP) spin dephasing). We discuss here two approaches to reduce DP spin dephasing during acoustic transport at high temperatures (i.e., LN). The first uses QWs grown along non-conventional crystallographic orientations such as along the [110] or [111] crystallographic axes. In particular, the symmetry of [110] QWs reduces the impact of the spin-orbit interaction for spins oriented along the [110] axis, leading to a significant enhancement of the spin lifetime (to values approaching 100 ns).[6] The second approach explores the fact that DP relaxation can be significantly reduced by controlling the electron orbital motion on a micrometer scale. By reducing the width $L_W$ to a few μm (i.e., to values smaller than the spin orbit precession length in the QW), it becomes possible to transport spins at high temperatures over several tens of μm along the plane of a QW.

The acoustic transport of spins at 105 K combining these two approaches is illustrated in Figs. 1(c)-(d).

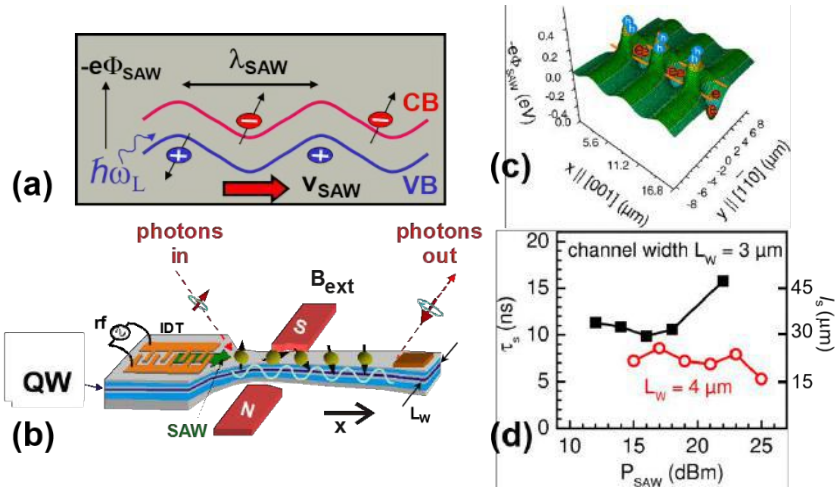



*Figure 1(a) Band structure modulation by a (b) SAW propagating on a (Al,Ga)As QW. (c) Calculated potential in a piezoelectrically defined narrow transport channel and (d) dependence of the spin lifetime ($\tau_s$) and of the acoustic transport length ($l_s$) on SAW power ($P_{SAW}$) and on the width ($L_W$) of a transport channel defined on a (110) GaAs QW.[8]*

Transport was carried out along a narrow piezoelectrically defined channel in a (110) GaAs QW with the potential profile illustrated in Fig. 1(c).[8] The spin transport length $l_s$ and the spin lifetime $\tau_s = l_s/v_{SAW}$ were then measured at difference temperatures by spatially resolved photo-luminescence. The dependence of these quantities on the acoustic power $P_{SAW}$ applied to the acoustic transducer displayed in Fig. 1(d) demonstrate that spin transport lengths increases with decreasing channel widths. In particular, $l_s$ values exceeding 30 µm can be achieved at 105 K. The application of similar concepts for the manipulation of single spins will be discussed.

**Acknowledgements**: we thank the German Physical Society for support.

**REFERENCES**

[1] C. Rocke, S. Zimmermann, A. Wixforth, J. P. Kotthaus, G. Böhm, and G. Weimann, "Acoustically driven storage of light in a quantum well," *Phys. Rev. Lett.*, vol. 78, p. 4099, 1997.

[2] J. M. Shilton, V. I. Talyanskii, M. Pepper, D. A. Ritchie, J. E. F. Frost, C. J. B. Ford, C. G. Smith, and G. A. C. Jones, "High-frequency single-electron transport in a quasi-one-dimensional GaAs channel induced by surface acoustic waves," *J. Phys.: Condens. Matter*, vol. 8, p. L531, 1996.

[3] O. D. D. Couto, Jr., S. Lazic, F. Iikawa, J. Stotz, R. Hey, and P. V. Santos, "Photon anti-bunching in acoustically pumped quantum dots," *Nat. Phot.*, vol. 3, p. 645, 2009.

[4] T. Sogawa, P. V. Santos, S. K. Zhang, S. Eshlaghi, A. D. Wieck, and K. H. Ploog, "Transport and lifetime enhancement of photoexcited spins in GaAs by surface acoustic waves," *Phys. Rev. Lett.*, vol. 87, pp. 276601–1, 2001.

[5] J. A. H. Stotz, R. Hey, P. V. Santos, and K. H. Ploog, "Coherent spin transport via dynamic quantum dots," *Nat. Mater.*, vol. 4, p. 585, 2005.

[6] O. D. D. Couto, Jr., F. Iikawa, J. Rudolph, R. Hey, and P. V. Santos, "Anisotropic spin transport in (110) GaAs quantum wells," *Phys. Rev. Lett.*, vol. 98, p. 036603, 2007.

[7] H. Sanada, T. Sogawa, H. Gotoh, K. Onomitsu, M. Kohda, J. Nitta, and P. V. Santos, "Acoustically induced spin-orbit interactions revealed by two-dimensional imaging of spin transport in GaAs," *Phys. Rev. Lett.*, vol. 106, p. 216602, May 2011.

[8] A. Hernández-Mínguez, K. Biermann, R. Hey, and P. V. Santos, "Spin transport and spin manipulation in (110) and (111) GaAs quantum wells," *Phys. Status Solidi B*, vol. 251, p. 1736, 2014.

# Enhanced Magneto-optical Effect in Magnetoplasmonic Ring-Split ring structures

**H. Y. Feng[1], F. Luo[1], R. Arenal[2], Fernando García[3], G. Armelles[3*], A. Cebollada[3]**

[1]IMDEA Nanoscience, Faraday 9, Ciudad Universitaria de Cantoblanco, 28049, Madrid, Spain

[2] Laboratorio de Microscopias Avanzadas (LMA), Instituto de Nanociencia de Aragon (INA), Universidad de Zaragoza, and Fundacion ARAID, C/ Mariano Esquillor, 50018, Zaragoza, Spain

[3] IMM-Instituto de Microelectrónica de Madrid (CNM-CSIC),Isaac Newton 8, PTM, Tres Cantos, 28760, Madrid, Spain

[*]gaspar@imm.cnm.csic.es

**Abstract-**Large enhancements of the magneto-optical (MO) activity by the localized surface plasmon resonance (LSPR) have been reported in structures like nanodisks, core-shell nanoparticles, dimers, etc. In this contribution, we extend this application to the magnetoplasmonic split ring-ring structure. With the hole-mask colloidal lithography method, a split Au ring is generated on top of a Au ring in which a Co-dot has been embedded. By properly optimizing the gap angle of the split ring, the electromagnetic field is redistributed and focused in the MO active Co area, therefore the MO activity obtains a boost and is maximized for the structure with a gap of 60deg angle, exhibiting an enhancement factor of 3 compared to the one without gap. The EM field redistribution and focus around the gap area is confirmed via EELS-TEM mapping

Metallic nanostructures supporting the localized surface plasmonic resonance (LSPR) allow confining light in subwavelength regions and producing a subsequent enhancement of the electromagnetic (EM) field at resonance. Using LSPR, large enhancements of the magneto-optical (MO) activity have been reported in structures like nanodisks, core-shell nanoparticles, dimers, etc., which is currently an active branch in the so-called magnetoplasmonics field and has been reviewed in Ref. (1). In this contribution, we extend this concept to a novel ring-split ring structure. The bottom Au ring structure holds the MO active component (a Co nanodot), while the Au split ring on top serves as a fine tuned enhancer of the electromagnetic field in the Co nanodot region. A series of nanostructures, based on this concept, have been fabricated, for which both of the optical and MO responses are characterized and analyzed. By properly modifying and optimizing the nanostructure, a boost in the MO activity is obtained, with a further enhancement by a factor of 3 with respect to the structure without a split ring gap.

The nanostructures are fabricated with the hole-mask colloidal lithography method (2). In our previous work the evolution of the plasmonic resonance and MO activity from single mode of disk to bimodal ring were studied and well explained with the plasmon hybridization model in Ref. (3,4). Based on the nanoring structure, the distribution of the Co and Au layers can be tuned independently and simultaneously. The resulting redistribution of the electromagnetic field will modify both of the optical and MO responses of the nanoparticles, even give a rise to the MO effect (5). The ring-split ring structure with the inserted Co dot below the gap is schematically shown in Fig. 1(a). The optical extinction spectra (Fig. 1(b)) depict optical anisotropy for s- and p-polarized incident light (5). The gap opening creates a focus of the EM field in the area around the Co dot at plasmonic resonances, which can be optimized by the gap opening angle, with a maximum of the EM field focus at 60deg as well as the optimized MO activity at this angle (Fig. 1(b) and (c)). A further and maximum enhancement in

MO activity of 3 times larger than the structure without gap (0deg) is obtained (Fig. 1(c)). The EM field redistribution and focus caused by the gap is confirmed with EELS-TEM mapping (inset Fig. 1(c)).

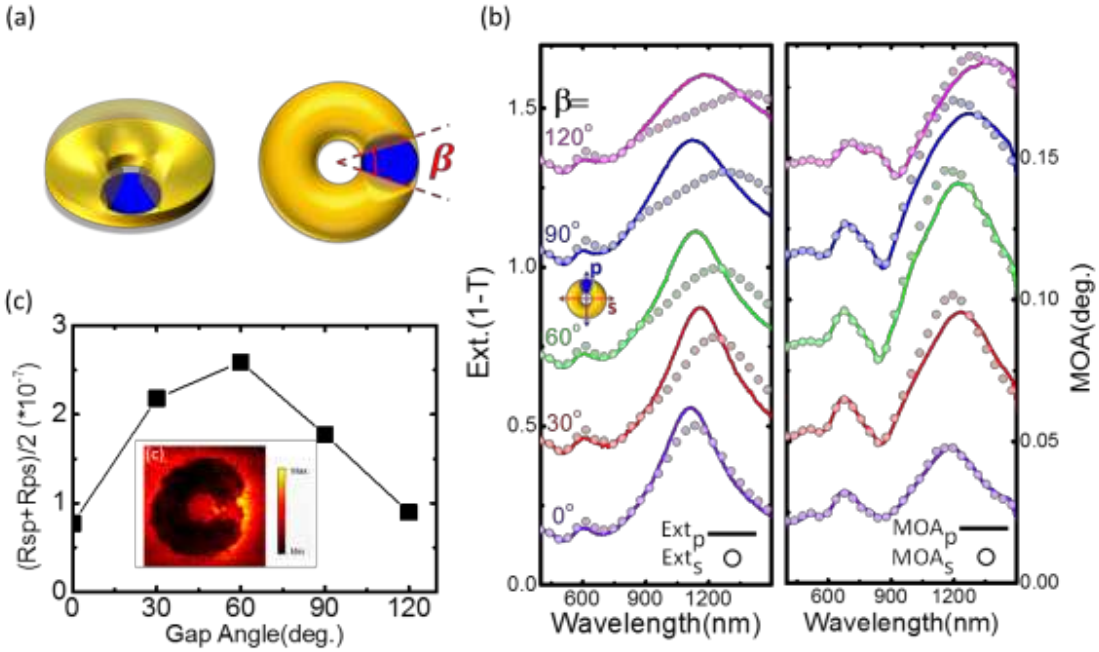



Fig. 1 (a) Sketches of the fabricated ring-split ring nanostructures. (b) Optical extinction and MO activity for the ring-split ring structures with Co embedded and below the gap. (c) Evolution of the MO activity as the gap angle increases and EELS-TEM mapping for the structure with a gap of 60deg angle (inset).

**REFERENCES**


1. Armelles, G., Cebollada, A., García-Martín, A., and González, M. U., "Magnetoplasmonics: Combinging Magnetic and Plasmonic Functionalities," *Adv. Opt. Mater*. Vol. 1, No. 1, 10-35, 2013.
2. Fredriksson, H., Alaverdyan, Y., Dmitriev, A., Langhammer, C., Sutherland, D., Zäch, M., Kasemo, B., "Hole-Mask Colloidal Lithography," *Adv. Mater.*, Vol. 19, No. 23, 4297, 2007.
3. Feng, H.Y., Luo, F., Kekesi, R., Granados, D., Meneses-Rodríguez, D., García J. M., García-Martín A., Armelles, G., and Cebollada, A., "Magnetoplasmonic Nanorings as Novel Architectures with Tunable Magneto'optical Activity in Wide Wavelength Ranges," *Adv. Opt. Mater.*, Vol. 2, No. 7, 612-617, 2014.
4. Feng, H. Y., Luo, F., Meneses-Rodríguez, D., Armelles, G., Cebollada, A., "From disk to ring: Aspect ratio control of the magnetoplasmonic response in Au/Co/Au nanostructures fabricated by hole-mask coloidal lithography," *Appl. Phys. Lett.*, Vol. 106, No. 8, 083105, 2015.
5. Feng, H. Y., Luo, F., Arenal, D., García, F., Armelles, G., Cebollada, A., "Active magnetoplasmonic split ring/ring nanoantennas," *Submitted*.

# Ultrafast spin-lattice coupling investigation in magnetostrictive Terfenol films by picosecond shear acoustic pulses

**T. Parpiiev[1,*], A. Hillion[2], V. S. Vlasov[1], V. Polewczyk[1], V. V. Temnov[1], K. Dumensil[2], S. Andrieu[2], A. Anane[3], V. Gusev[1], T. Pezeril[1]**

[1]Institut Molécules et Matériaux du Mans, UMR CNRS 6283, Université du Maine, 72085 Le Mans, France
[2]Institut Jean Lamour, UMR CNRS 7198, Université de Lorraine, 54506 Vandoeuvre, France
[3]Unité Mixte de Physique CNRS/Thales, UMR CNRS 137, 91767 Palaiseau, France
[*]corresponding author: tymur.parpiiev.etu@univ-lemans.fr

**Abstract**-We experimentally and theoretically demonstrate that, upon femtosecond demagnetization of magnetostrictives materials, the ultrafast release of the built-in strains generates ultrashort longitudinal and shear acoustic pulses. These ultrashort acoustic pulses gather new crucial information on the spin-lattice coupling at ultrafast timescale.

Since the pioneering demonstration of subpicosecond demagnetization by a 60 fs laser pulse by Beaurepaire and coworkers [1], manipulating and controlling magnetization with ultrafast laser pulses has become a big challenge. These findings triggered the new and booming field of ultrafast laser manipulation of magnetization [2,3]. Although there is a clear evidence that using fs laser pulses, a ferromagnetic thin film can be demagnetized within timescale of the order of ~100 fs, the physical mechanisms operating are still controversial [4]. Recent results demonstrating all-optical switching in a broad variety of rare earth-transition metal compounds with pronounced magnetostriction [5,6] challenge present theories of ultrafast optical switching and arise fundamental questions about the role of the spin-lattice coupling in such type of magnetostrictive compounds. In particular the role of phonons during the demagnetization/remagnetization process is getting more and more attention [7,8,9,10].

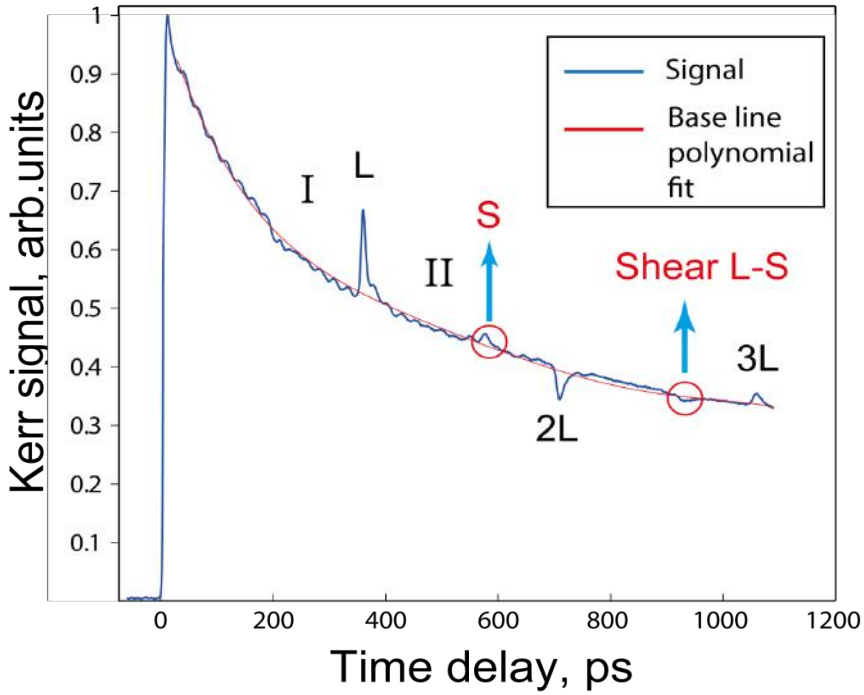



Fig. 1. Time resolved pump-probe experiment with a Terfenol hybrid sample structure of 480 nm TbFe2/ 1 micron SiO2. The ultrafast pump-probe Kerr signal shows a shear acoustic pulse at 536 ps which is consequent to the laser mediated ultrafast release of the magnetostrictive strains at the TbFe2/SiO2 interface.

In the present work, by probing the excited ultrafast longitudinal and shear acoustic pulses - rather than the magnetization dynamics, as it is already the case - during ultrafast demagnetization of Terfenol, we demonstrate the possibility to assess crucial information on the spin-lattice relaxation channel.We have conducted experiments with Terfenol (TbFe2 ) which is known as one of the most magnetostrictive materials [10]. The (110) single crystals TbFe2 thin films have been grown on sapphire substrates from molecular beam epitaxy and coated with a transparent dielectric layer of SiO2. The samples were laser excited with a 800 nm 150 fs pump pulse focused on the TbFe2 layer where, upon both thermoelastic transient heating and ultrafast release of magnetostriction mechanisms, the acoustic waves were launched in the surrounding SiO2 layer. These acoustic waves were detected by a time delayed probe pulse while propagating back and forth in the top SiO2 layer.

An example of a time resolved Kerr signal obtained with such sample is shown in Fig. 1. On top of the demagnetization background, we can distinguish several acoustic echoes (L, S, 2L …) which acoustic polarization (L longitudinal or S shear) and arrival time can be discriminated knowing the longitudinal and shear acoustic speeds in SiO2 as well as the film thickness. The most interesting echoes correspond to the shear acoustic pulses which are detected at 536 ps and at 870 ps. The first one of few ps duration evidences the ultrafast release of magnetostriction which is the only possible mechanism of shear generation in the present sample [11], while the second corresponds to an interesting mechanism of magneto-acoustic conversion of the longitudinal pulse at 335 ps into a shear pulse from the acoustic reflection at the interface.

Our results give the proof of concept of ultrafast laser demagnetostriction for the excitation of ultrashort shear acoustic pulses. For the moment, efficient and simple ultrafast shear transducers are lacking [11,12] and a new generation of THz shear transducers based on laser-mediated release of magnetostrictive stresses would be of great interest for the viscoelastic investigation of many materials (liquids [13-14], glasses, mixed multiferroics, correlated electron systems and magnetic materials).

**Acknowledgements**. The authors thank Agence Nationale de la Recherche for financial support under grant ANR-14-CE26-0008.

**References**

[1] E. Beaurepaire et al., *Phys. Rev. Lett.* **76**, 4250 (1996).
[2] Aeschlimann et al., *Phys. Rev. Lett.* 79, 5158 (1997).
[3] A. Scholl et al, Phys. *Rev. Lett*. **79**, 5146 (1997).
[4] B. Koopmans et al., *Nature Physics* **9**, 259 (2009).
[5] A. Hassdenteufel et al., *Adv. Mat.* **25**, 3122 (2013).
[6] S. Mangin et al, *Nature Materials* **13**, 286 (2014).
[7] A.V. Scherbakov et al., *Phys. Rev. Lett.* **105**, 117204 (2010).
[8] L. Thevenard et al., *Phys. Rev. B* **82**, 104422 (2010).
[9] J.-W. Kim, M. Vomir, J.-Y. Bigot, *Phys. Rev. Lett.* **109**, 166601 (2012).
[10] O. Kovalenko, T. Pezeril, V.V. Temnov, *Phys. Rev. Lett.* **110**, 266602 (2013).
[11] T. Pezeril et al., *Phys. Rev. B* **75**, 174307 (2007).
[12] T. Pezeril, C. Klieber, S. Andrieu, K. A. Nelson, *Phys. Rev. Lett.* **102**, 107402 (2009).
[13] C. Klieber, T. Pezeril, S. Andrieu, K. A. Nelson, *J. Appl. Phys.* **112**, 013502 (2012).
[14] C. Klieber, T. Hecksher, T. Pezeril et al., *J. Chem. Phys.* **138**, 12A544 (2013).

# Magneto-elastic Symmetry Breaking with Surface Acoustic Waves

**A.M. Lomonosov[1], V.S. Vlasov[2], J. Janusonis[3], C.L. Chang[3], R.I. Tobey[3], T. Pezeril[2] and V.V. Temnov[2,4*]**

[1]LAUM CNRS 6613, Université du Maine, 72085 Le Mans cedex, France

[2]Institut des Molécules et Matériaux du Mans, UMR CNRS 6283, Université du Maine, Le Mans cedex, France

[3] Zernike Institute for Advanced Materials, University of Groningen, Groningen, The Netherlands

[4]Abteilung Physikalische Chemie, Faradayweg 4-6, 14195 Berlin, Germany

[*]corresponding author: vasily.temnov@univ-lemans.fr

**Abstract**- Surface magneto-elastic waves (SMEW) are polaritons consisting of the coupled surface acoustic waves (SAW) and ferromagnetic resonance (FMR) precession. Here we theoretically analyze the dispersion of SMEW propagating on nickel films. The magneto-elastic symmetry nonreciprocity manifests itself in the dependence of SMEW phase velocity on the direction of the in-plane magnetic external magnetic field. A simplified analytical approach, where FMR-resonance is driven by a standing SAW modes (geometry of the typical transient grating experiments) provide a complimentary view on the observed symmetry breaking. The developed theory is applied to describe the signatures of symmetry breaking observed in ultrafast transient grating experiments.

Elastic properties of ferromagnetic materials depend on their magnetic state, a phenomenon known as magneto-striction. Very recently the dynamic interactions between ultrashort acoustic transients and FMR precession both in the bulk[1,2] and at ferromagnetic surfaces[3,4] attracted a renewed attention. The complex spatio-temporal behavior of acoustic transients makes the physical interpretation of elastically-induced FMR precession rather difficult. A first step towards understanding the non-stationary behavior is to understand the property of SMEW eigenmodes, where the acoustic and magnetic excitations form the polaritonic eigenmode propagating along the surface. To do so we solve the coupled system of the acoustic wave equations (for three components of acoustic displacement) and magnetic Landau-Lifschitz-Gilbert equation (for three components of magnetization vector) for small-amplitude FMR excitations around the equilibrium magnetization direction. Solving the secular equation leads to the dispersion relation of SMEW eigenmodes. It can be best visualized in the diagram in Fig. 1 displaying the anisotropy of SMEW phase velocity $v$ as a function of the tilt angle φ with respect to the external in-plane magnetic field $\vec{H}$. Two counterpropagating acoustic waves at frequency ω with wavevectors

$$\left|\vec{k}_{1,2}\right| = \frac{\omega}{v_{1,2}}$$

correspond to two different velocities $v_{1,2}$. The angular anisotropy in Figure 1 aims to demonstrate the intrinsic non-reciprocity of SMEW induced by magneto-striction and the maximum anisotropy is observed for φ~45 degrees. The angular variation of phases velocity is very small and it does not make sense to try in case of non-stationary processes. In the view of transient grating experiments[3,4] it appears to be reasonable to consider the excitation of FMR precession by elastic strains $\varepsilon_{xx}(t), \varepsilon_{zz}(t), \varepsilon_{xz}(t)$ formed by two counterpropagating

SMEW modes of equal amplitude (standing wave), assuming that SMEW strains are identical to those of non-magnetic SAWs. Within this approach the symmetry becomes broken by the non-zero shear strain $\varepsilon_{xz}(t)$ in a standing SAW resulting in non-zero excitation of FMR precession in φ=0. The preliminary TG measurements focused n the angular range of a few degrees around φ=0 indicate the signatures of such asymmetry. We expect that the results of magneto-elastic symmetry breaking can boost similar investigations in magneto-plasmonics.

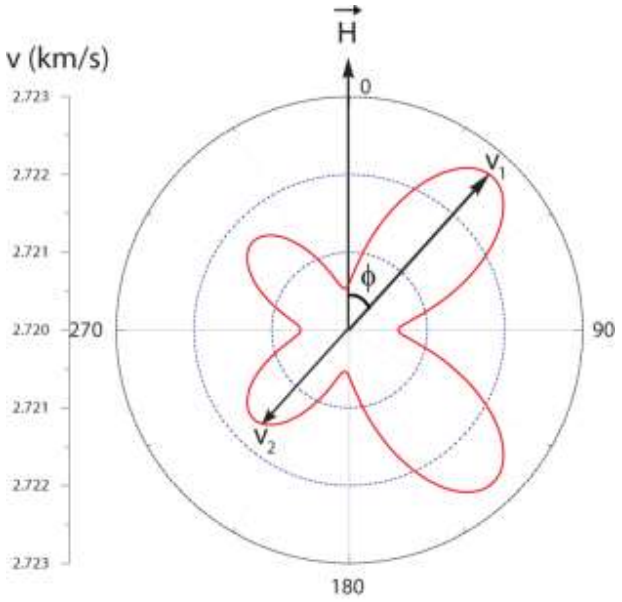



Figure 1. The phase velocity of surface magneto-elastic waves depend on their propagation direction. Counterpropagating SMEWs may have different speeds, indication the magneto-elastic non-reciprocity.

The work was partially supported by Stratégie Internationale NNN-Telecom and Alexander von Humboldt Foundation.

**REFERENCES**

1. A. Scherbakov et al., *Phys. Rev. Lett.*, Vol. 105, 111204 (2010); L. Thevenard et al., *Phys. Rev. B*, Vol. 82, 104422 (2010) ; J. Kim et al., *Phys. Rev. Lett.*, Vol. 109, 166601 (2012).
2. O. Kovalenko, T. Pezeril, V.V. Temnov, *Phys. Rev. Lett.*, Vol. 110, 266602 (2013).
3. J. Janusonis et al., *Appl. Phys. Lett.*, Vol. 106, 181601 (2015).
4. J. Janusonis et al., arxiv :1601.04350 (2016).

# Harnessing magnetoplasmons to induce topological excitations

**Joel Yuen-Zhou**[1]

[1]Department of Chemistry and Biochemistry, University of California San Diego, La Jolla, CA 92093, USA

[*]corresponding author: joelyuen@ucsd.edu

**Abstract**- I will discuss how to couple magnetoplasmons with excitons in an organic molecular crystals to obtain topologically protected edge states.

Plexcitons are hybrid polaritonic states composed of plasmons and excitons. We consider plexcitons arising from the coupling of plasmons in a metal film with organic excitons in a molecular crystal. The anisotropy of the exciton-plasmon interaction gives rise to Dirac points which can be lifted by interfacing the metal with a magneto-optical material such as a bismuth-garnet oxide (BIG), yielding magnetoplasmons in the metal layer. This gives rise to topologically protected edge modes akin to those found in Quantum Hall systems. We discuss our recent efforts to enhance the magneto-optical effects induce larger gaps to host the topological excitations. These topological excitations give novel capabilities for the control of energy transfer in the nanoscale [1,2].

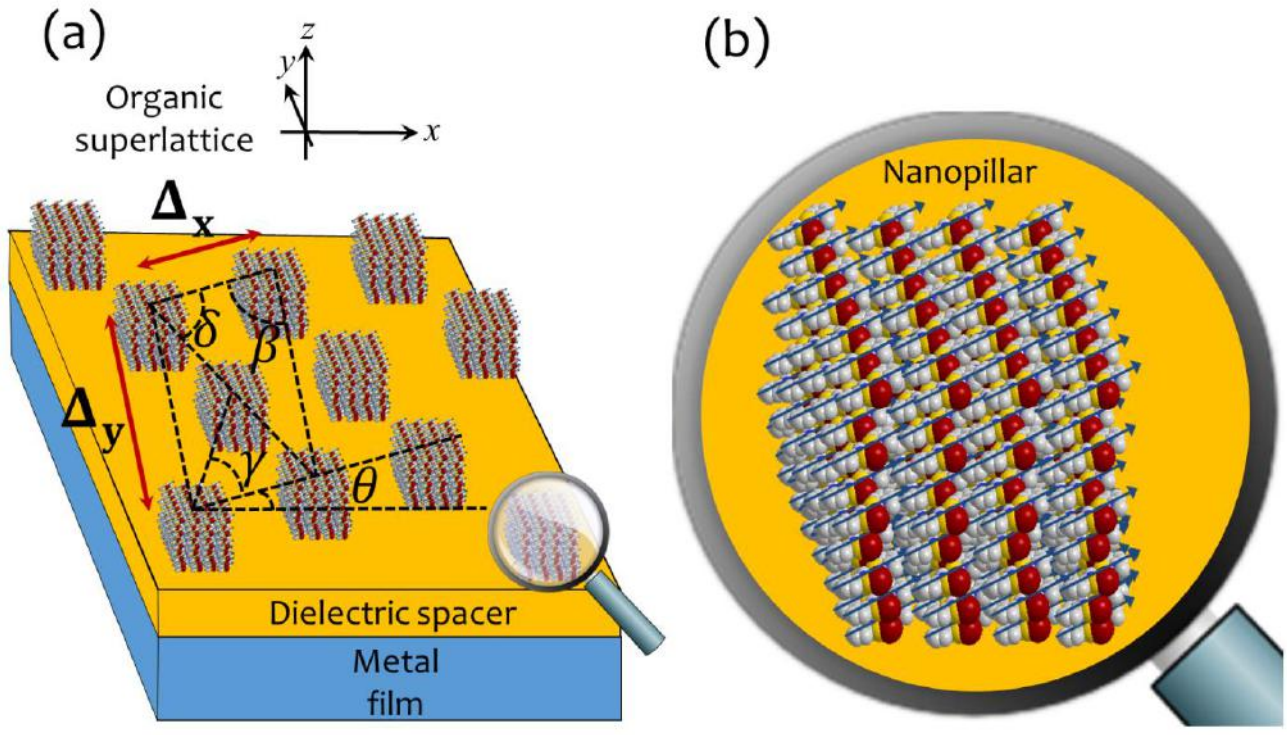



**Fig. 1.** *Plexciton setup.* It consists of a plasmonic metal film, a dielectric spacer, and an organic layer. The latter is taken to be a monoclinic superlattice which makes an angle θ with respect to the x axis, and is further characterized by angles β , γ , δ as well as distances between nanopillars Δ h and Δ v . Each element in the superlattice is a nanopillar of organic emitters of dimensions W i along each axis. When the density of emitters is big enough, the coupling between the excitons in the organic layer and the

surface plasmons in the metal becomes larger than their linewidths, giving rise to polaritonic eigenmodes that are superpositions of excitons and plasmons, or more succintly, plexcitons. We shall also consider the case where the dielectric spacer is a magneto-optical (MO) material. The superlattice design is not essential for our purposes, except for guaranteeing a global gap for topological modes spanning all wavevectors. Hence, one may substitute it with a standard molecular crystal with some trade-offs.

**Acknowledgements**. J.Y.-Z acknowledges support from startup funds at UC San Diego as well as the Energy Frontier Research Center funded by the US Department of Energy, Office of Science, Office of Basic Energy Sciences under Award Number DESC0001088.

**REFERENCES**

1. Yuen-Zhou, J., S. K. Saikin, T. Zhu, M. C. Onbasli, C.A. Ross, V. Bulovic, M. A. Baldo, Plexciton Dirac points and topological modes, Nat. Comm., in press (2016).
2. Yuen-Zhou, J., S. K. Saikin, N. Yao, A. Aspuru-Guzik, Topologically protected excitons in porphyrin thin films, Nature Mater. 13, 1026 (2014).

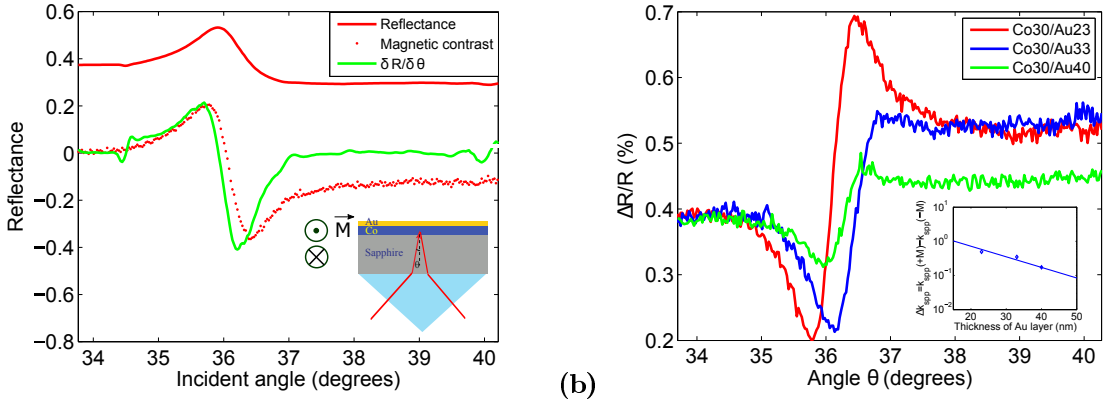
# Static and dynamic properties of hybrid magnetoplasmonic structures

**N. M. Tran[1], T. Seifert[2], T. Parpiiev[1], G. Vaudel[1], T. Pezeril[1], D. Makarov[3], T. Kampfrath[2] and V. Temnov[1,2]**

[1]Institut des Molécules et Matériaux du Mans CNRS 6283, Université du Maine, 72085 Le Mans, France
[2]Department of Physical Chemistry, Fritz-Haber Institut der MPG, 14195 Berlin, Germany
[3]HZDR Institute of Ion Beam Physics and Materials Research, 01328 Dresden, Germany
ngoc_minh.tran@univ-lemans.fr

**Abstract**— In this work, we study magnetoplasmonic as well as dynamic properties of bilayered ferromagnetic/nonmagnetic heterostructure. While the ultrafast dynamics of this system have been actively investigated for spintronics [1] and acoustics [2], their magnetoplasmonic properties are rarely explored. We demonstrate that this bilayered structure exhibits magnetoplasmonics, and would be a promising target for further research, such as nonlinear magnetoplasmonics or coupling with other ultrafast properties.

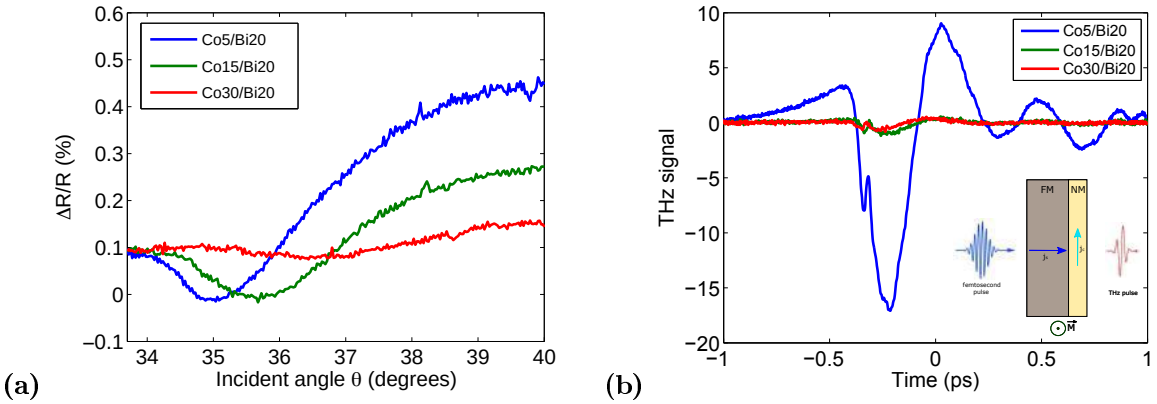
Magnetoplasmonic structures refer to the hybrid nanostructures, which are tailored for the purpose of combining magnetic and plasmonic functionalities. They allow mutual interactions between magnetism and plasmonics, specifically the active control of surface plasmons by external magnetic field and the influence of plasmon resonance on magneto-optical (MO) properties [3]. These effects have been demonstrated on the multilayered nanostructures comprised of a ferromagnetic layer, which gives large MO response, and noble metallic layers, which aid the coupling of incident light and surface plasmon. The trilayer of noble metal/ferromagnetic/noble metal is highly preferred compared to the simple bilayer of ferromagnetic/noble metal according to an argument that ferromagnetic metals have high losses, hence would not support plasmon resonance efficiently [3, 4]. Nevertheless, our experimental results show that the coupling of SPP and MO in this bilayer is possible and can be enhanced by appropriate design of nanostructure.




**Figures 1: a.** The reflectance and corresponding transversal MOKE for Co(30 nm)/Au(23 nm) are plotted with respect to incident angle. The MOKE contrast fits well with the angle derivative of reflectance, proving the effect of SPP on MOKE **b.** MOKE signal ($\Delta R/R$) for Co/Au with different thickness of capping Au layer. The maximal contrast is plotted versus the thickness of Au in the inset and coincident with the decay of SPP into metallic layer.

In order to investigate the magnetoplasmonic properties of the bilayered structure, a set of Co/Au is used with a fixed thickness of 30 nm for Co and varying thickness of capping Au. The thickness of Au layer is verified by ultrafast acoustics, which measures the time it takes for an

acoustic pulse generated from Co layer to travel across Au layer [2]. The surface plasmon polariton (SPP) is excited by conventional Kretschmann–Raether configuration and the external magnetic field is applied perpendicularly to the incident plane and parallelly to the bilayer, as illustrated in the inset of Fig. 1a. The incident light is p–polarized light at wavelength 632 nm from HeNe laser, and the transversal magneto–optical Kerr effect (MOKE) signal is recorded as shown in Fig. 1a, and it represents a clear dependence of MOKE signal on the incident angle, i. e. on the coupling to SPP. The maximal contrast for this set of samples is 0.5%, compared to 1–2% in trilayered structures. Under the effective medium approximation [5], the maximal contrast of MOKE signal versus the thickness of the top-most Au layer, or the depth of Co layer underneath the gold/air interface, fits the exponential decay of SPP into the metallic heterostructure, as plotted in the inset of Fig. 1b.




**Figures 2**: **a.** Transversal MOKE signal under SPP excitation of Co capped with Bi with varying thickness of Co. **b.** Terahertz emission from these samples. The inset shows the inverse spin Hall effect (ISHE) in ferromagnetic (FM)/nonmagnetic (NM) bilayer , which converts spin current $j_s$ into charge current $j_c$ and generates THz pulse.

Under the excitation of SPP, transversal MOKE contrast is also observed for Co capped with 20-nm-thick bismuth (Bi), a semi-metal, as shown in Fig. 2a. The optical loss in this case is higher than the bilayer Co/Au, and is indicated by broader peak. The dynamic property of this bilayer is demonstrated below.

Excitation with an ultrafast injects a transient current of majority-spin electrons across the ferromagnetic layer [6]. This spin current can be inspected via its emitted THz spectrum, based on inverse spin Hall effect (ISHE) [1]. Because of the spin-orbit interaction in the nonmagnetic layer, spin-up and spin-down electrons are deflected into different directions, which results in an in-plane charge current and a respective transient THz pulse, as shown in the inset of Fig. 2b. This mechanism is applicable for the heterostructure of Co/Bi. The waveform of THz electromagnetic field is recorded by electro-optic sampling, and shown in Fig. 2b for three samples of Co/Bi bilayer structure with varying thickness of Co and 20 nm of Bi. The reduction in amplitude of THz spectra as the thickness of metallic layer increases is consistent with the model for thickness dependence of THz emission [7]. When these spectra are normalized, no difference in dynamics of spin-polarized electrons are observed regardless of the thickness of Co layer.


## ACKNOWLEDGMENT

The authors would like to acknowledge the financial support from the project *Stratégie internationale* "NNT-Telecom" of Région Pays de la Loire, France.


## REFERENCES


1. Kampfrath, T. et. al., "Terahertz spin current pulses controlled by magnetic heterostructures," *Nature Nanotechnology 8*, 256–260, 2013.
2. Shalagatskyi, V. et. al., "Ultrafast electron-phonon-magnon interactions at noble metal-ferromagnet interfaces," *arXiv:1511.09060*, 2015.
3. Armelles, G. et. al., "Magnetoplasmonics: Combining Magnetic and Plasmonic Functionalities," *Advanced Optical Materials*, Vol. 1, No. 1, 10–35, 2013.

4. Zheng, W. et. al., "Surface plasmon-enhanced transverse magnetic second-harmonic generation," *Opt. Express*, Vol. 21, No. 23, 28842–28848, 2013.
5. Temnov, V., "Ultrafast acousto-magneto-plasmonics," *Nature Photonics*, Vol. 6, 728–736, 2012.
6. Battiato, M., K. Carva and P. M. Oppeneer, "Superdiffusive Spin Transport as a Mechanism of Ultrafast Demagnetization," *Phys. Rev. Lett.*, Vol. 105, 027203, 2010.
7. Seifert, T. et. al., "Efficient metallic spintronic emitters of ultrabroadband terahertz radiation," *arXiv:1510.03729*, 2015.

# On-chip Integrated Quantum Photonics

# A heterogeneous III-V / $Si_3N_4$ quantum photonic integration platform

**M. Davanco[1], J. Liu[1,2], C.-Z. Zhang[3], L. Liu[3], K. Srinivasan [1]**

[1]Center for Nanoscale Science and Technology, National Institute of Standards and Technology, USA
[2]Maryland NanoCenter, University of Maryland, College Park, USA
[3]China Academy of Advanced Optoelectronics, South China Normal University, Guangzhou, China
marcelo.davanco@nist.gov

**Abstract**— We develop a heterogeneous III-V/$Si_3N_4$ integration platform for photonic integrated circuits incorporating on-chip, InAs quantum dot-based single-photon sources.

There is currently a great interest in the development of chip-scale photonic devices for quantum information. Chip-based integration can provide unprecedented scalability, stability, and functionality for photonic quantum information science, and in addition can enable exploration of quantum-level optical nonlinearities with highly improved efficiency through nanoscale photonic structures. Here, we develop a heterogeneous III-V / Silicon photonic integration platform to produce photonic circuits, based on $Si_3N_4$ waveguides, which incorporate on-chip triggered single-photon sources based on single InAs/GaAs quantum dots (QDs). InAs QDs are to date the most promising solid-state light sources for quantum information, offering pure, bright and indistinguishable triggered single-photon emission, and allowing electronic and photonic radiation control [1]. In counterpoint, $Si_3N_4$ waveguides offer low-loss propagation with tailorable dispersion and relatively high Kerr nonlinearities, which can be explored for linear and nonlinear optical signal processing, down to the quantum level [2].

The core of our integration platform is the vertical directional coupler shown in Fig. 1 (a), consisting of a GaAs waveguide, which hosts an InAs QD, stacked over a Si3N4 waveguide. The GaAs waveguide is designed so that QD emission is efficiently coupled to its fundamental mode, shown in Fig. 1(b). As illustrated in Fig. 1(c), careful tapering of both waveguide widths can lead to almost complete optical power transfer from the GaAs guided mode into the underlying Si3N4 waveguide. The GaAs waveguide thus acts as an on-chip source of single photons, which can be efficiently ($> 90\%$) launched into low-loss $Si_3N_4$ waveguide-based photonic circuits. Figure 2(a) shows a false-color scanning electron micrograph (SEM) of a preliminary test device fabricated based on our integration platform, which uses thin adhesive bonding to combine the GaAs and $Si_3N_4$ layers. Figure 2(b) shows an optical micrograph of the same device.

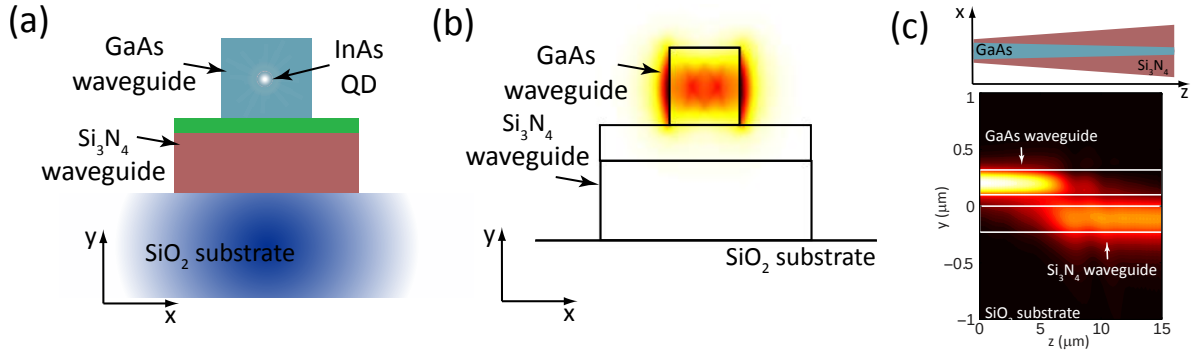



Figure 1: (a) Cross-section schematic of vertical GaAs/$Si_3N_4$ waveguide directional coupler. (b) Fundamental guided mode of the GaAs waveguide. (c) Top: top view of waveguide width taper for power transfer from GaAs to $Si_3N_4$. Bottom: electric field amplitude across the x=0 plane, for a GaAs waveguide mode launched at z=0.

We believe that, together with our recently developed photoluminescence imaging-based technique, which allows the creation of GaAs devices with deterministically positioned InAs QDs [3],

our integration platform will enable a new class of highly efficient and versatile integrated quantum photonic chip-scale devices.

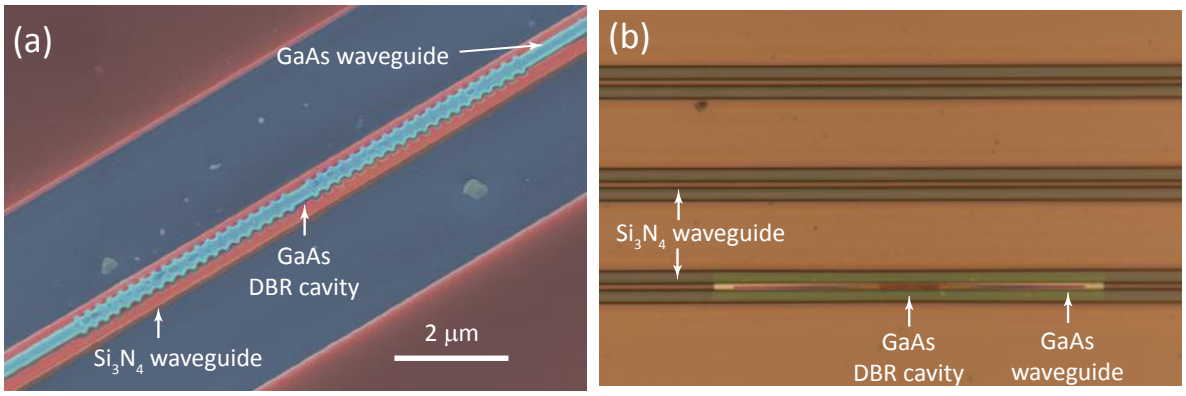



Figure 2: (a) False-color SEM of fabricated GaAs distributed-feedback cavity on top of a $Si_3N_4$ waveguide. (b) Optical microscope image of the same device.


## ACKNOWLEDGMENT

J.L. acknowledges support under the University of Maryland and NIST-CNST Cooperative Agreement


## REFERENCES


1. N. Somaschi, V. Giesz, L. De Santis, J. Loredo, M. Almeida, G. Hornecker, S. Portalupi, T. Grange, C. Anton, J. Demory, et al., "Near optimal single photon sources in the solid state," arXiv preprint arXiv:1510.06499 (2015).
2. Q. Li, M. Davanco, and K. Srinivasan, "Efficient and low-noise single-photon-level frequency conversion interfaces using silicon nanophotonics," arXiv preprint arXiv:1510.02527 (2015).
3. L. Sapienza, M. Davanço, A. Badolato, and K. Srinivasan, "Nanoscale optical positioning of single quantum dots for bright and pure single-photon emission," Nature communications **6** (2015).

# Resonant laser spectroscopy of localized bright and dark excitons in monolayer $WSe_2$

**S. Kumar[1], M. Brotons-Gisbert[2], R. Al-Khuzheyri[1], A. Kaczmarczyk[1], G. Ballesteros-Garcia[1], J. F. Sánchez-Royo[2], and B. D. Gerardot[1*]**

[1]Institute of Photonics and Quantum Science, SUPA, Heriot-Watt University, UK
[2] Departamento Física Aplicada y Electromagnetismo, Universidad de Valencia, Spain
[*]corresponding author: b.d.gerardot@hw.ac.uk

**Abstract**-Resonance and near-resonance fluorescence of isolated quantum emitters in a two-dimensional semiconductor is investigated. Resonance fluorescence and bright (> 3 MHz detected count rates at saturation), stable high-purity single photon emission is achieved. High resolution photoluminescence excitation spectroscopy is used to characterize the bright exciton fine-structure. Moreover, localized dark exciton states blue-shifted by approximately 5 meV from the bright exciton states is directly observed. These results open a path towards future investigations of spin-valley and exciton coherence in 2D semiconductors.

Near-resonance optical excitation of quantized matter underpins the field of quantum photonics. It enables the initialization, coherent manipulation, and read-out of the quantum states and, via resonance fluorescence, the generation of indistinguishable single photons that are an important resource for future quantum technologies. In the solid-state, such quantum optical demonstrations have been made using self-assembled quantum dots, single molecules, and defects in diamond and other semiconductors. An alternative, emerging quantum photonic platform is two-dimensional transition metal dichalcogenide (2D-TMD) semiconductors which have a direct band-gap near visible wavelengths and optically addressable exciton valley pseudo-spins. Recently, spatially localized excitons which emit quantum light have been discovered in monolayer $WSe_2$ [1]. Here we perform resonance and near-resonance excitation of isolated, localized 2D excitons to reveal near ideal single photon fluorescence and uncover dark exciton states ~ 5meV blue-shifted from the bright exciton states. The high-purity single photon emission is stable and bright, yielding detected count rates up to 3 MHz. We take advantage of spectral fluctuations to perform high-resolution photoluminescence excitation spectroscopy of the localized exciton fine-structure. The high-resolution characterization of the bright exciton fine-structure and the experimental observation of the dark exciton provide important information to unravel the precise nature of these localized excitons while the demonstration of resonance fluorescence paves the way to probe the coherence of the localized excitons via the first and second order correlation functions. Moreover, these results yield a route for intriguing investigations of the spin and valley coherence of 2D-TMD localized excitons.

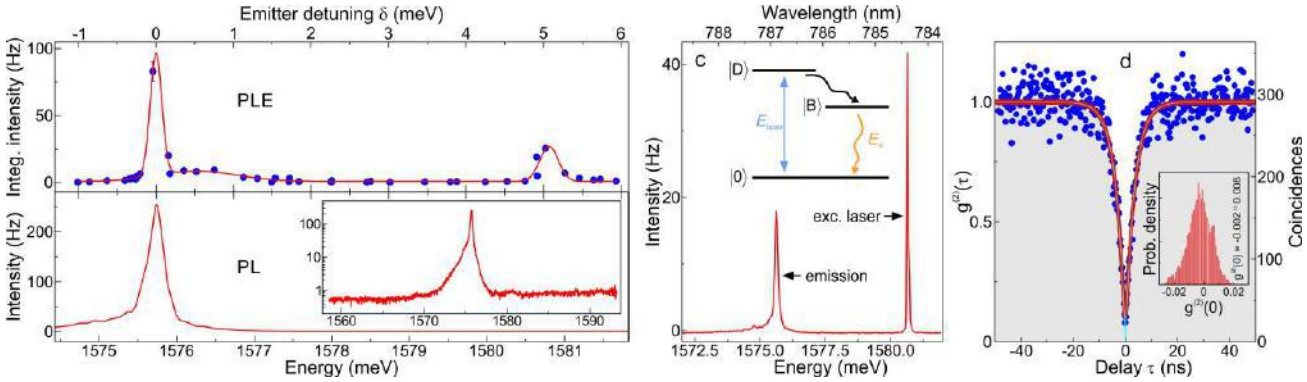



**Figure 1:** (a) PLE spectrum of an emitter identifying the "dark" exciton at an energy of ~5 meV higher than the bright-exciton. (b) The fluorescence spectrum of the same emitter under non-resonant excitation. The spectrum matches the energy range for which PLE is performed in (a). Inset: a high-resolution, high dynamic range PL spectrum. (c) The fluorescence spectrum of the emitter under resonant excitation of the dark-exciton (emitter detuning □ = ~5 meV). Inset: Schematic of resonant excitation to the dark-exciton and emission via the bright-exciton. (d) g(2)(□) of the bright-exciton fluorescence under resonant CW excitation of the dark-exciton showing the high purity single photon emission.

## REFERENCES


1. Srivastava et al., Nat. Nanotechnol. **10**, 491 (2015); He et al., Nat. Nanotechnol. **10**, 497 (2015); Koperski et al., Nat. Nanotechnol. **10**, 503 (2015); Chakraborty et al. Nat. Nanotechnol. **10**, 507 (2015); Tonndorf et al., Optica **2**, 347 (2015); Kumar et al., Nano Lett. **15**, 7567 (2015).

# Quantum nanophotonics: controlling spins with single photons on-a-chip.

**Edo Waks[1*], Shuo Sun[1], Tao Cai[1], Ranojoy Bose[1], Hyochul Kim[1], and Glenn S. Solomon[2]**
[1]University of Maryland, Joint Quantum Institute, College Park, MD 20742-3511
[2]Joint Quantum Institute, NIST and University of Maryland, Gaithersburg, MD 20742
[*]corresponding author: edowaks@umd.edu

**Abstract**-I will describe our recent work on coupling spin in single quantum dots to photonics using integrated nanophotonic devices. We implement a quantum phase switch, the fundamental building block for quantum information processing. I will also discuss our efforts to extend devices to telecom wavelengths.

The implementation of quantum networks and distributive quantum information processing relies on interaction between stationary matter qubits and flying photons [1]. The spin of a single electron or hole confined in a charged quantum dot is considered as a promising matter qubit as it possesses microsecond coherence time [2, 3] and allows picosecond timescale control using optical pulses [4, 5]. The quantum dot spin can also interact with a photon by controlling the optical response of a strongly coupled cavity. So far most experimental demonstrations of the cavity spectrum control have used neutral quantum dots. Spin-dependent cavity spectrum has not been reported yet. Here, we report an experimental realization of a spin-photon transistor using a strongly coupled quantum dot and cavity system. We show large modulation of the cavity reflectivity by manipulating the spin states of the quantum dot. The spin-photon transistor is crucial for realizing a quantum logic gate or generating hybrid entanglement between a quantum dot spin and a photon. Our results represent an important step towards semiconductor based quantum logic devices and on-chip quantum networks.

We perform measurements on a singly charged InAs quantum dot coupled to a GaAs photonic crystal cavity. In the presence of a magnetic field applied in the quantum dot growth direction (Faraday configuration), the quantum dot exhibit four energy levels with two optically allowed transitions, as shown in Fig. 1(a).

Figure 1(b) shows the scanning electron microscope image of a typical fabricated photonic crystal cavity device. The initial wafer is composed of a 160 nm GaAs membrane with a single layer of InAs quantum dots at its center. A small portion of the quantum dots are naturally charged during the growth of the wafer. The membrane layer is grown on top of a 900 nm $Al_{0.78}Ga_{0.22}As$ sacrificial layer. The GaAs is patterned by electron beam lithography, followed by chlorine based dry etching. After dry etching, a selective wet etching removes the sacrificial layer, creating a suspended membrane. The cavity design is based on a three-hole defect in a triangular photonic crystal where the inner three holes adjacent to the defect are shifted to optimize the quality factor.

Figure 1(c) shows the device photoluminescence at different magnetic fields. At 0 T we observe both the cavity mode (labeled as CM) and several quantum dot emission lines (labeled as QD1, QD2, QD3 and QD4). As we increase the magnetic field, all of the quantum dot emission lines split into two peaks. At this stage the charge properties of these dots are not clear yet. The experiment results shown in the next section (Fig. 1d) demonstrate that the second quantum dot (QD2) is a charged quantum dot. The two peaks that are split from QD2 correspond to the $\sigma_+$ and $\sigma_-$ transitions of a charged quantum dot, as labeled in the figure. We also observe anti-crossing between the $\sigma_+$ transition and the cavity mode as we further increase the magnetic field, demonstrating strong coupling between the $\sigma_+$ transition and the cavity.

## 3. Spin-dependent cavity reflectivity

We measure the cavity reflectivity at 6 T with a temperature of 16 K. At this condition the $\sigma_+$ transition of the quantum dot is resonant with the cavity. We use a broad-band light-emitting diode as an excitation source, which has dominant emission in the range of 900 nm to 950 nm. We excite the sample with vertical polarization and collect only the horizontal polarization component of the reflected signal. We orient the cavity axis to be about 45 degree with respect the vertical direction to ensure maximum signal to noise ratio.

In addition to the broad-band excitation, we also use a continuous-wave narrow-band tunable diode laser to manipulate the spin state of the quantum dot. We tune the wavelength of the diode laser close to the quantum dot $\sigma_-$ transition. The black solid lines in Fig. 1(d) show the cavity reflectivity when the pump laser is red detuned by 0.1 nm, resonant, and blue detuned by 0.1 nm with respect to the quantum dot $\sigma_-$ transition respectively. When the pump laser is resonant with the $\sigma_-$ transition, it initializes the quantum dot into the spin-up state via optical pumping. The cavity reflectivity shows two polariton peaks and a central dip due to its strong coupling with the $\sigma_+$ transition. The strong coupling behavior is no longer apparent as the pump laser is blue or red detuned from the $\sigma_-$ transition, as the quantum dot is not well initialized into the spin-up state at these conditions. These results demonstrate our ability to control the cavity reflectivity via manipulation of a quantum dot spin. They also serve to verify that the quantum dot we measured is charged, since the neutral quantum dot would behave differently when we pump the decoupled transition [6]. The red solid lines in Fig. 1(d) show the cavity feeding effect induced by the pump laser. We observe that the feeding effect is enhanced when the pump laser is resonant with the $\sigma_-$ transition.

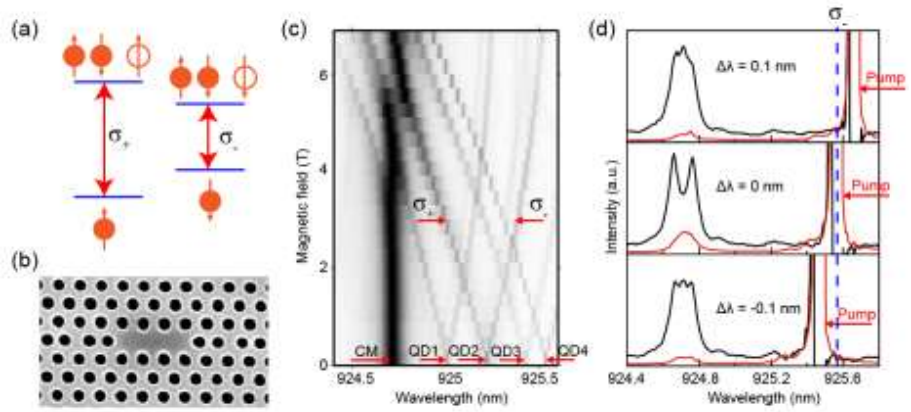



FIG. 1. (a) Energy level structure of a charged quantum dot in the presence of a magnetic field applied in the Faraday geometry. (b) Scanning electron microscope of a typical fabricated photonic crystal cavity device. (c) Photoluminescence spectrum of the device as a function of applied magnetic field. The sample temperature is fixed at 14 K for this measurement. (d) Cavity reflectivity with different pump laser detunings. The sample temperature is fixed at 16 K for this measurement.


[1] Kimble, H. J. "The quantum network," Nature **453**, 1023-1030 (2008).

[2] Xu, X. et al. "Optically controlled locking of the nuclear field via coherent dark-state spectroscopy," Nature **459**, 1105-1109 (2009).

[3] Press, D. et al. "Ultrafast optical spin echo in a single quantum dot," Nature Photon. **4**, 367-370 (2010).

[4] Berezovsky, J. et al. "Picosecond Coherent Optical Manipulation of a Single Electron Spin in a Quantum Dot," Science **320**, 349-352 (2008).

[5] Press, D. et al. "Complete quantum control of a single quantum dot spin using ultrafast optical pulses," Nature **456**, 218-221 (2008).

[6] Kim, H. et al. "A quantum logic gate between a solid-state quantum bit and a photon," Nature Photon. **7**, 373-377 (2013).

# Integrated Quantum Frequency Comb Source of Entangled Qubits

**Michael Kues,[1,*] Christian Reimer,[1] Piotr Roztocki,[1] Benjamin Wetzel,[1,2] Yaron Bromberg,[3] Brent E. Little,[4] Sai T. Chu,[5] David J. Moss,[6] Lucia Caspani,[1,7] and Roberto Morandotti[1]**

[1]*INRS-EMT, Varennes, Québec J3X 1S2, Canada*

[2]*Department of Physics and Astronomy, University of Sussex, Falmer, Brighton BN1 9RH, United Kingdom*

[3]*Department of Applied Physics, Yale University, New Haven, Connecticut 06520, USA.*

[4]*Xi'an Institute of Optics and Precision Mechanics of CAS, Xi'an, China*

[5]*Department of Physics and Material Science, City University of Hong Kong, Hong Kong, China*

[6]*Centre for Micro Photonics, Swinburne University of Technology, Hawthorne, VIC, 3122 Australia*

[7]*School of Engineering and Physical Sciences, Heriot-Watt University, Edinburgh EH14 4AS, United Kingdom*

[*]corresponding author: michael.kues@emt.inrs.ca

**Abstract**- We demonstrate the simultaneous generation of multiple time-bin entangled photon pairs on a CMOS-compatible photonic chip. We measure quantum interference and perform state tomography, confirming entangled qubits with fidelities above 86% and 99.9% purity.

Entangled photon pair sources form one of the key building blocks for applications in quantum information processing and computing [1], quantum communication [2], as well as imaging and sensing with resolutions exceeding the classical limit [3]. The generation of entangled photon pairs in various forms (i.e. polarization entanglement, time-energy entanglement and time-bin entanglement) has been demonstrated through spontaneous parametric down-conversion (SPDC) in a diverse range of second-order nonlinear media and through spontaneous four wave-mixing (SFWM) within third-order nonlinear media. To deliver the compactness, scalability and efficiency required by future optical quantum circuit devices, solutions focusing on an integrated (on-chip) approach have been recently studied and developed, including integrated quantum circuits, sources, and detectors [4]. The use of micro-ring resonators [5,6] with narrow resonances and high Q-factors are of special interest since, in contrast to waveguides, they offer an enhancement in photon pair generation efficiency as well as a narrow photon pair bandwidth, rendering them compatible with quantum optical devices. More importantly, resonant nonlinear cavities such as ring resonators offer the possibility of generating correlated photon pairs on multiple signal/idler frequency channels [7] due to the periodic and equidistant resonance structure. Here we demonstrate the first simultaneous generation of multiple entangled photon pairs distributed over a quantum frequency comb.

**Experiment setup-** We realized the quantum frequency comb using a 4-port integrated micro-ring resonator with a free spectral range of 200 GHz, and resonances exhibiting Q-factors of 235,000 (820 MHz resonance bandwidth). The integrated micro-ring resonator was fabricated in a CMOS-compatible high refractive index silica glass [8]. The experimental setup used a pulsed mode-locked fiber laser (10 MHz repetition rate) to optically pump the resonator. An imbalanced phase-stabilized Michelson interferometer was used to generate the double pulses required for the time-bin entanglement scheme, which relies on the coherent superposition of photon pairs generated in the first or second pulse (i.e. first or second time-bin) [9]. The double pulses were then coupled into the ring resonator, where their center frequency was matched with a bandpass filter to a single ring resonance. Due to the high field enhancement and high nonlinearity, photon pairs were generated through SFWM on several frequency channels (corresponding to the ring resonances) symmetrically with respect

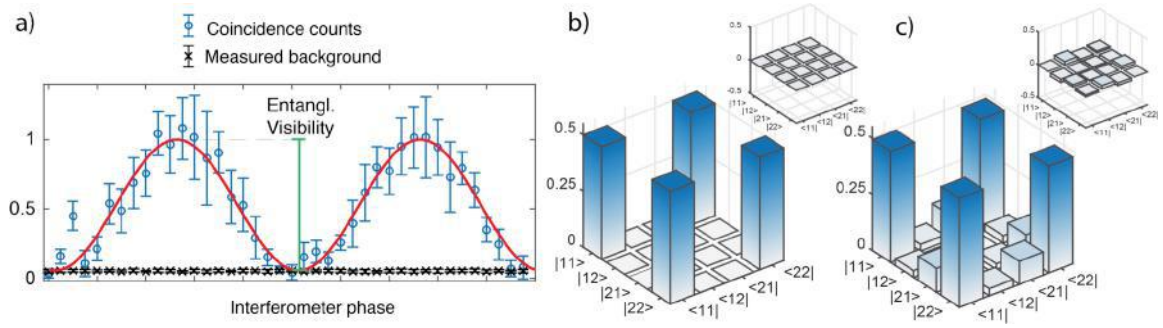



Fig. 1: a) Quantum interference measurement. Real (large) and imaginary part (small) of an ideal (b) and the measured (c) density matrix of time-bin entangled qubits.

to the pump frequency [7]. We measured the single photon output spectrum, confirming the ultra broadband nature of the quantum comb, with photon pairs emitted over the full S, C, and L telecommunication band. To verify entanglement through quantum interference, we additionally added interferometers with the path length difference matched to the first interferometer. Using coincidence detection, this setup allowed to measure quantum interference, as well as to perform full quantum state tomography, fully characterizing the entangled photon pairs.

**Results-** The interference pattern shown in Fig. 1b was measured for the first signal-idler frequency pair closest to the pump frequency. The extracted quantum visibility of 86.9% (98% with background correction) violates the Clauser-Horne-Shimony-Holt (Bell-like) inequality (86.9% > 71%≈1/√2) [10], and therefore confirms the observation of time-bin entanglement from our integrated photon pair source (see Fig. 1a). We repeated the measurement for 5 different spectral mode couples symmetric to the pump frequency and always measured a visibility above 86% (94% background corrected). To fully characterize the generated quantum state, we performed quantum state tomography [11] (see Fig. 1b and c), revealing that the generated entangled photon pairs form time-bin entangled qubits with a measured fidelity of above 86% and a purity of 99.9%.

**Conclusions-** We report the first generation of a quantum frequency comb of time-bin entangled photon pairs. The fully integrated device emits high-quality entangled qubits over an extremely broadband quantum comb, covering the full S, C, and L telecommunication bands. The unique features make the comb particularly appealing for multiplexed and multi-channel quantum communications, as well as for quantum computation, where additional channels increase the information capacity [12].

## REFERENCES

[1] P. Walther et al., "Experimental one-way quantum computing," Nature 434, 169 (2005).

[2] H. J. Kimble, "The quantum internet," *Nature* 453, 1023 (2008).

[3] M. Kolobov, "The spatial behavior of nonclassical light," *Rev. Mod. Phys*. 71, 1539 (1999).

[4] D. Bonneau et al., "Silicon quantum photonics," in Silicon Photonics III, L. Pavesi, D.J. Lockwood, Springer, pp. 41-82.

[5] D. Grassani et al., "Micrometer-scale integrated silicon source of time-energy entangled photons," *Optica* 2, 88 (2015).

[6] C. Reimer et al., "Cross-polarized photon-pair generation and bi-chromatically pumped optical parametric oscillation on a chip," *Nature Commun.* 6, 8236 (2015).

[7] C. Reimer et al., "Integrated frequency comb source of heralded single photons," *Opt. Express* 22, 1023 (2014).

[8] D. J. Moss et al., "New CMOS-compatible platforms based on silicon nitride and Hydex for nonlinear optics," *Nature Photon.* 7, 597 (2013).

[9] J. Brendel et al., "Pulsed energy-time entangled twin-photon source for quantum communication," *Phys. Rev. Lett.* 86, 1392 (2001).

[10] J. F. Clauser et al., "Proposed experiment to test local hidden-variable theories," *Phys. Rev. Lett.* 23, 880 (1969).

[11] D. F. V. James et al., "Measurement of qubits," *Phys. Rev. A.* 64, 052312 (2001).

[12] P. C. Humphreys et al., "Linear optical quantum computing in a single spatial mode," *Phys. Rev. Lett.* 111, 150501 (2013).

# Fully-tuneable, cavity-enhanced waveguide single-photon sources.

**A. Fiore[1*], M. Petruzzella[1], S. Birindelli[1], F.M. Pagliano[1], Ž. Zobenica[1], L.H. Li[2] and E.H. Linfield[2]**

[1] COBRA Research Institute, Eindhoven University of Technology, The Netherlands

[2] School of Electronic and Electrical Engineering, University of Leeds, United Kingdom

[*]corresponding author: a.fiore@tue.nl

**Abstract**- Efficient sources of indistinguishable single photons are required for integrated quantum photonics. We present an integration scheme which enables the funneling of photons emitted by single semiconductor quantum dots from nanophotonic cavities into waveguide circuits and the combined tuning of the emitter energy and cavity frequency. This allows bringing distinct sources in resonance with each other and therefore the on-chip production of indistinguishable single-photons.

Quantum dots (QDs) in photonic crystal cavities (PCCs) enable the efficient generation of single photons, which can be efficiently coupled to waveguides in quantum photonic integrated circuits [1]. However, their implementation in multiphoton experiments requires the photons generated by distinct sources to be indistinguishable, which is made very challenging by the natural dispersion of the QD size, resulting in varying exciton energies, and by the disorder in the PCC pattern, producing random variations in the cavity frequency. A method for the real-time control of both the exciton energy and the cavity frequency is therefore needed. We have recently shown that the combination of Stark tuning and electromechanical actuation enables the full control of the QD-PCC system and thereby tuneable, Purcell enhanced QD sources [2]. Here we show that these structures can be efficiently integrated in a quantum photonic integrated circuit, leading to tuneable waveguide-coupled sources. The cavity tuning is realized through the electromechanical actuation of a double-membrane PCC, while the exciton tuning is obtained through the quantum-confined Stark effect by applying an electric field on the QDs, within the same cavity structure (see Fig. 1(a)). The double-membrane PCC is then coupled to a ridge waveguide via suspended nanobeams. Fig. 1(b) shows two independently controllable waveguide-coupled QD sources integrated side-by-side. Multi-mode interference couplers have also been fabricated on this platform and their operation as beamsplitters demonstrated. The large-scale integration of tuneable single-photon sources, passive optics and waveguide detectors [3] may enable the implementation of boson sampling circuits [4] at the scales of tens of photons.

**REFERENCES**

1. Fattah poor, S. et al. “Efficient coupling of single photons to ridge-waveguide photonic integrated circuits,” *Appl. Phys. Lett.*, Vol. 102, 131105, 2013.
2. Petruzzella, M. et al., “Fully tuneable, Purcell-enhanced solid-state quantum emitters,” *Appl. Phys. Lett.*, Vol. 107, 141109, 2015.
3. Sprengers, J.P. et al., “Waveguide superconducting single-photon detectors for integrated quantum photonic circuits,” *Appl. Phys. Lett.*, Vol. 99, 181110, 2011.
4. Aaronson, S. and Arkhipov, A., “The Computational Complexity of Linear Optics,” *Theory of Computing*, Vol.4, 143, 2013.

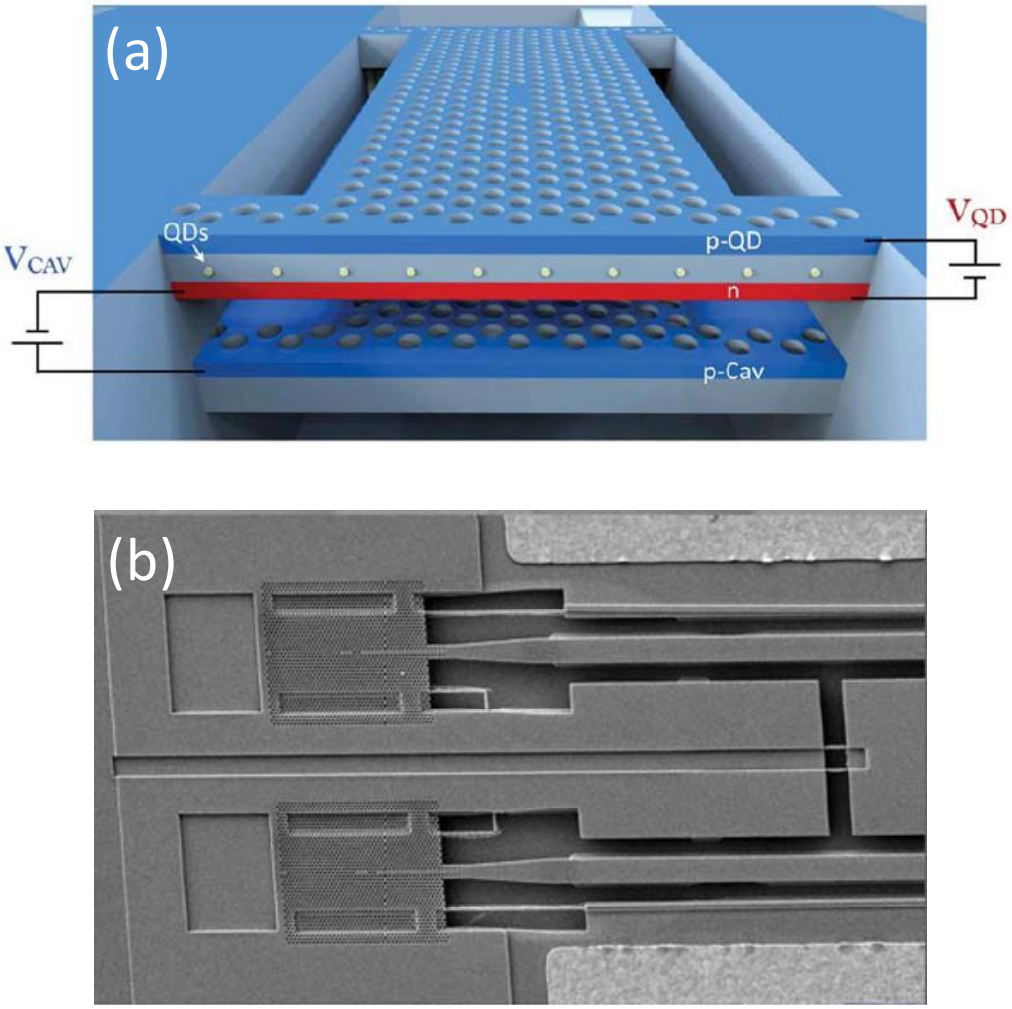



Fig. 1: (a) Schematics of tuneable double-membrane photonic crystal cavity. (b) Electron microscope image of two fabricated waveguide-coupled tuneable cavities.

# Comparison of four computational methods for computing Q factors and resonance wavelengths in photonic crystal membrane cavities

**Jakob Rosenkrantz de Lasson[1], Lars Hagedorn Frandsen[1], Sven Burger[2], Philipp Gutsche[2], Oleksiy S. Kim[3], Olav Breinbjerg[3], Ole Sigmund[4], Jesper Mørk[1] and Niels Gregersen[1*]**

[1]DTU Fotonik, Department of Photonics Engineering, Technical University of Denmark

[2]Zuse Institute Berlin, Germany

[3]DTU Elektro, Department of Electrical Engineering, Technical University of Denmark

[4]DTU Mekanik, Department of Mechanical Engineering, Technical University of Denmark

[*]corresponding author: ngre@fotonik.dtu.dk

**Abstract –** We benchmark four state-of-the-art computational methods by computing quality factors and resonance wavelengths in photonic crystal membrane L5 and L9 line defect cavities. The convergence of the methods with respect to resolution, degrees of freedom and number of modes is investigated. Special attention is paid to the influence of the size of the computational domain. Convergence is not obtained for some of the methods, indicating that some are more suitable than others for analyzing line defect cavities.

The photonic crystal (PhC) membrane represents a platform for planar integration of components, where cavities and waveguides may play a key role in realizing compact optical components with classical functionality[1] such as switches, lasers[2], and amplifiers or quantum optical functionality such as integrated sources of quantum light[3]. By leaving out a row of holes in an otherwise perfect PhC membrane lattice, a line defect is created in which light may be guided. If the waveguide is terminated at both ends, the finite-length waveguide forms an L*n* cavity, where *n* denotes the length of the cavity. Such L*n* cavities support spectrally discrete optical modes, and the fundamental cavity mode profile of an L9 cavity is shown in Fig. 1. Light may be confined to such an L*n* cavity for extended periods, as quantified by the quality (Q) factor. For laser applications, the Q factor governs the onset of lasing, and for cavity quantum electrodynamics applications, it governs the onset of strong coupling. The Q factor thus represents a key parameter in the design of a PhC membrane cavity.

The combination of the large size of the PhC L*n* cavity and the full 3D nature of the geometry makes the

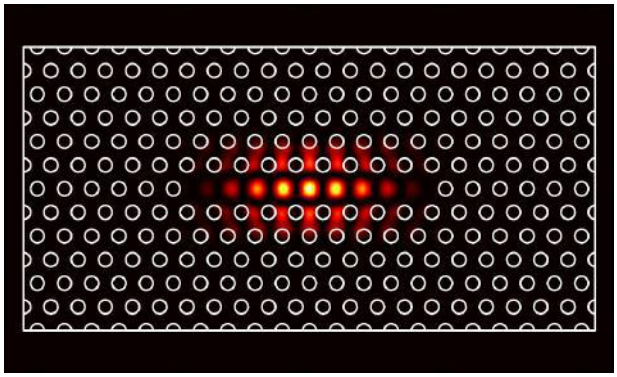


**Fig. 1:** Optical field $|E_y|^2$ profile in the $z = 0$ plane for the fundamental L9 cavity mode.

calculation of the cavity Q factor an extremely demanding numerical challenge. No matter which numerical method is used, careful convergence checks with respect to the degrees of freedom must be made. Additionally, most numerical simulations methods rely on a closed simulation domain, and here the influence of the boundary conditions requires carefully study. A study of PhC nanobeam cavities using four numerical techniques has previously been reported[4], where cavity frequencies and Q factors were investigated as function of structural parameters. While qualitative agreement between the methods was found, quantitative discrepancies were in some cases as large as an order of magnitude, and estimates for the computational error and the influence of the size of the computational domain were not given.

In this work, we focus on two structures, a low-Q L5 cavity and a high-Q L9 cavity. We employ four different computational methods[5], the finite-difference time-domain (FDTD) technique, the finite-element method (FEM), the surface integral equation (SIE) approach and the Fourier modal method (FMM), to compute the cavity Q factor and the resonance wavelength for both structures. For each method, the relevant computational parameters are systematically varied to quantify the computational errors. In particular, we investigate the influence of the size of the computational domain.

**Table 1:** Calculated Q factors and resonance wavelengths λ.

| | FDTD | FEM | SIE | FMM |
|---|---|---|---|---|
| $\lambda^{L5}$ (nm) | 1567.7 | 1571 | 1572 | 1567 |
| $\lambda^{L9}$ (nm) | 1583 | 1578 | 1579 | 1572 |
| $Q^{L5}$ | 1670 | 1700 | 1696 | 1700 |
| $Q^{L9}$ | 90,000 | 105,000 | 103,000 | 50,000 |

The final results summarized in Table 1 show that both the resonance wavelength and the Q factor agree fairly well for the L5 cavity among the four methods. On the other hand, significant deviations are observed for the Q factor in the L9 cavity. Our study highlights the importance of careful convergence checks and systematic estimation of the computational error, both of which are generally missing in the literature.

**Acknowledgements**. Support from the Villum Foundation via the VKR Centre of Excellence NATEC II is gratefully acknowledged.

**REFERENCES**

1. Notomi, M., A. Shinya, K. Nozaki, T. Tanabe, S. Matsuo, E. Kuramochi, T. Sato, H. Taniyama, and H. Sumikura, "Low-power nanophotonic devices based on photonic crystals towards dense photonic network on chip," *IET Circuits Devices Syst*., Vol. 5, No. 2, 84-93, 2011.
2. Xue, W., Y. Yu, L. Ottaviano, Y. Chen, E. Semenova, K. Yvind, and J. Mørk, "Threshold Characteristics of Slow-Light Photonic Crystal Lasers," *Phys. Rev. Lett.*, Vol. 116, No. 6, 063901, 2016.
3. Lodahl, P., S. Mahmoodian and S. Stobbe, "Interfacing single photons and single quantum dots with photonic nanostructures," *Rev. Mod. Phys.*, Vol. 87, No. 2, 347-400, 2015.
4. Maes, B., J. Petráček, S. Burger, P. Kwiecien, J. Luksch, and I. Richter, "Simulations of high-Q optical nanocavities with a gradual 1D bandgap," *Opt. Express*, Vol. 21, No. 6, 6794-6806, 2013.
5. Lavrinenko, A. V., J. Lægsgaard, N. Gregersen, F. Schmidt and T. Søndergaard, *Numerical Methods in Photonics*, CRC Press, Boca Raton, 2015.

# Fundamental limitations to the coherence of single-photon sources due to phonon scattering

**Jesper Mork, Dara P. S. McCutcheon, Jake Iles-Smith and Niels Gregersen**
DTU Fotonik, Department of Photonics Engineering, Technical University of Denmark

**Abstract –** We discuss the effect of phonons on the coherence of single-photon sources. In particular, the role of non-Markovian effects, arising from the colored nature of the phonon reservoir, is elucidated. The photon-indistinguishability of cavity- and waveguide-based sources is compared.

A semiconductor quantum dot embedded in an optical cavity or a waveguide is a promising system for realizing solid-state sources that emit on-demand indistinguishable single-photons. The development of such sources is important, e.g., for the realization of quantum simulators and quantum computers. However, since the emitter, the quantum dot, is realized in a solid-state matrix, phonons perturb the quantum dot energy levels, leading to decoherence and jeopardizing the indistinguishability of subsequently emitted photons. In the talk we will discuss how the characteristic features of different types of structures affect the degree of indistinguishability that can be obtained.

Fig. 1 shows example calculations of the variation of the indistinguishability of a quantum dot (QD) embedded in a microcavity [Kaer et al., Phys. Rev. B, **87**, 081308(R), 2013], which may be a photonic-crystal defect or a micropillar structure. Considering the indistinguishability of the cavity-emitted field, Fig. 1(d), a conventional

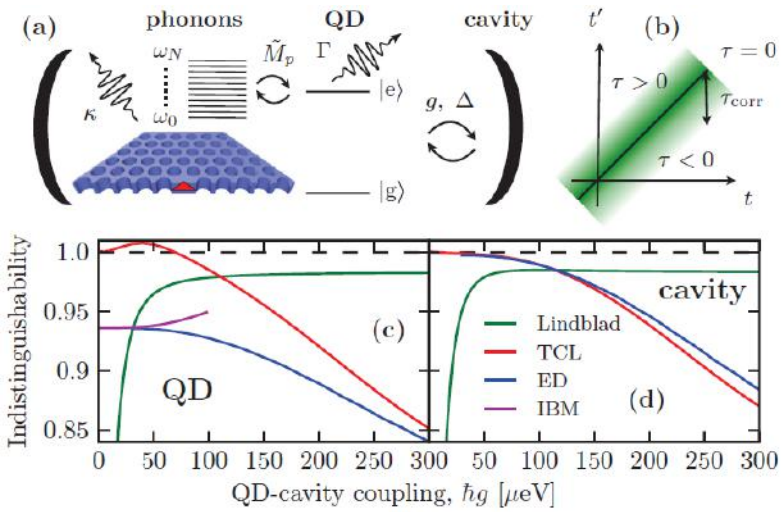



**Fig. 1:** (a) Schematic of the coupled system of cavity and quantum dot, subject to interaction with a reservoir of phonons. Calculated indistinguishability of (c) quantum dot and (d) cavity emission versus coupling constant using different approaches and approximations. TCL: Time convolution less approach, ED: Exact diagonalization, IBM: Independent boson model. From [Kaer et al., Phys. Rev. B, **87**, 081308(R), 2013].

Lindblad-type model of phonon scattering predicts that it is advantageous to increase the QD-cavity coupling strength, $g$. Physically, this appears reasonable, since a larger value of $g$ implies a faster QD decay rate, and "less time" for phonon scattering to perturb the coherence of the field emitted by the QD. However, more accurate calculations, taking into account the structure of the phonon environment, using either an exact-diagonalization (ED) approach or a time-convolutionless (TCL ) approximation, give quite the opposite result! The explanation can be found considering the polaritons of the coupled system. A larger value of $g$ increases the polariton splitting, which leads to an increase of phonon scattering between the branches. We will discuss the importance of such real scattering events as well as virtual phonon scattering, probing a larger energy range.

Another important effect to consider is the different degrees of spectral filtering exercised by narrow-band cavity-based single photon sources as opposed to broad-band waveguide-based sources. At the conference we will discuss the implications of these differences on the indistinguishability and efficiency, in particular emphasizing the importance of the structure of the phonon reservoir.

# A modal approach to light emission and propagation in coupled cavity waveguide systems

**P. T. Kristensen**[1], **J. R. de Lasson**[2], **N. Gregersen**[2], **and J. Mørk**[2]

[1]Institut für Physik, Humboldt Universität zu Berlin, Berlin D-12489, Germany
[2]DTU Fotonik, Technical University of Denmark, Lyngby DK-2800, Denmark

**Abstract**— We theoretically investigate systems of optical cavities coupled to waveguides, which necessitates the introduction of non-trivial radiation conditions and normalization procedures. In return, the approach provides simple and accurate modeling of Green functions, Purcell factors and perturbation corrections, as well as an alternative approach to the so-called coupled mode theory. In combination, these results may form part of the foundations for highly efficient, yet physically transparent models of light emission and propagation in both classical and quantum integrated photonic circuits.

Integrated systems of coupled optical waveguides and cavities hold a great potential for future classical and quantum signal processing. Theoretically, the properties of resonant but leaky cavities can be described in terms of quasinormal modes (QNMs), defined as solutions to the electromagnetic wave equation subject to a suitable radiation condition, which depends on the physical system. For cavities embedded in a homogeneous background, the radiation condition is the Silver-Müller condition, which causes the solutions to behave as outgoing waves at large distances. For cavities coupled to waveguides, one can formulate a radiation condition by demanding that the solutions behave as waveguide modes traveling in the directions *away* from the cavity [1, 2]. The left panel in Fig. 1 shows an example of a QNM in a photonic crystal cavity side coupled to a waveguide [2]. The radiation condition results in a discrete spectrum of complex resonance frequencies, $\tilde{\omega}_\mu = \omega_\mu - \mathrm{i}\gamma_\mu$, from which the quality factors can be obtained as $Q_\mu = \omega_\mu/2\gamma_\mu$. The radiative behavior in combination with the complex resonance frequency results in an exponential divergence of the fields in the waveguides, which complicates the formulation of a suitable QNM normalization. Nevertheless, one can regularize the normalization integral via the theory of divergent series [2] and use the QNMs for perturbation calculations [2] as well as simple yet accurate models for the Purcell factor [2, 3]. The right panel in Fig. 1 shows the enhancement in the local density-of-states (LDOS) in the cavity center as a function of frequency [3]. At resonance, the LDOS enhancement equals the Purcell factor as calculated from the $Q$-value and the effective mode volume [2].

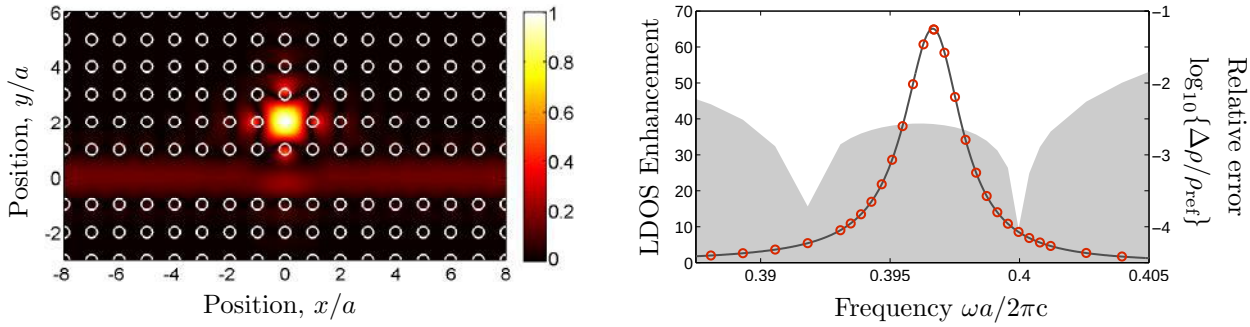



Figure 1: Left: Absolute value of the QNM in a cavity side-coupled to an infinite waveguide in a photonic crystal with lattice constant $a$. Right: Spectrum of LDOS enhancement for a z-oriented dipole positioned in the center of the cavity. Black solid curve and red circles (left axis) show the QNM approximation $\rho_{\mathrm{QNM}}$ and independent reference calculation $\rho_{\mathrm{ref}}$, respectively. Gray shading (right axis) shows the relative error in the single QNM approximation as calculated from the difference $\Delta\rho = \rho_{\mathrm{QNM}} - \rho_{\mathrm{ref}}$.

For applications in classical and quantum optical calculations, the Green function conveniently describes the propagation of light between two different positions. For coupled cavity-waveguide systems, this calls for a hybrid formulation, in which light in the cavities is described in terms of QNMs, and light in the waveguides is treated in terms of waveguide modes. The two families of

modes can be coupled using the field equivalence principle, by which an incident field through the waveguide is known to be identical to the field from certain electric and magnetic current sources in a plane intersecting the waveguide. In this way, the complex coupling of light from the waveguide to the cavity can be approximated to high accuracy from properties of the QNMs only [4]. In a simple and illustrative one dimensional example, Fig. 2 shows a comparison between the field in the cavity center as calculated based on QNMs and by traditional scattering methods. In the time domain, this naturally provides an alternative approach to the so-called temporal coupled mode theory, which is typically derived from energy conservation arguments [5], and to which the formulation reduces in the limit of high $Q$-values [4].

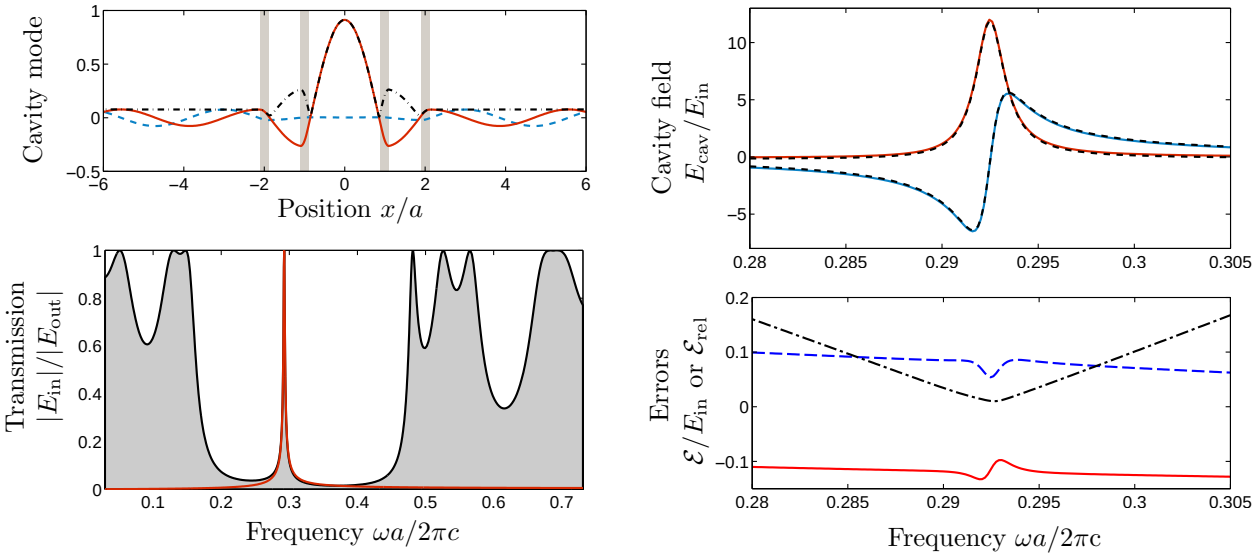



Figure 2: Left top: Real (solid red), imaginary (dashed blue) and absolute (dashed-dotted black) value of the normalized cavity mode of interest in a finite sized one-dimensional photonic crystal (indicated in gray). Left bottom: Transmission spectrum of the cavity. Red line indicates the single mode approximation to the transmission, which is the underlying assumption of the QNM formulation. Right top: Real (solid red) and imaginary (blue) parts of the field in the cavity center when illuminated by a plane wave from the left. Dashed black curves show the result of the QNM formulation. Right bottom: Real (solid red) and imaginary (blue) parts of the error $\mathcal{E} = E_{\rm cav}^{\rm QNM} - E_{\rm cav}^{\rm ref}$ between the two calculations in the top panel. Black dashed-dotted curve shows the relative error $\mathcal{E}_{\rm rel} = |E_{\rm cav}^{\rm QNM} - E_{\rm cav}^{\rm ref}|/|E_{\rm cav}^{\rm ref}|$.

In conclusion, we have investigated light emission and propagation in integrated photonic circuits consisting of optical cavities coupled to waveguides. Light in the cavities may be conveniently described by use of QNMs, providing relatively simple but very accurate modeling of Green functions, Purcell factors and perturbation corrections, and an alternative approach to the so-called temporal coupled mode theory. In combination, these results may form part of the foundation for highly efficient, yet physically transparent models of light emission and propagation in both classical and quantum integrated photonic circuits.

**REFERENCES**


1. de Lasson, J. R., P. T. Kristensen, J. Mørk and N. Gregersen, "Roundtrip matrix method for calculating the leaky resonant modes of open nanophotonic structures," *JOSA A*, Vol. 31, No. 10, 2142–2151, 2014.
2. Kristensen, P. T., J. R. de Lasson and N. Gregersen, "Calculation, normalization, and perturbation of quasinormal modes in coupled cavity-waveguide systems," *Optics Letters*, Vol. 39, No. 22, 6359–6362, 2014.
3. de Lasson, J. R., P. T. Kristesnen, J. Mørk and N. Gregersen, "Semianalytical quasi-normal mode theory for the local density of states in coupled photonic crystal cavity-waveguide structures," *Optics Letters*, Vol. 40, No. 24, 5790–5793, 2015.
4. Kristensen, P. T., J. R. de Lasson, M. Heuck, N. Gregersen and J. Mørk, "Theory of coupled modes in optical cavity-waveguide structures," *In preparation*, 2016.
5. Joannopoulos, J. D., S. G. Johnson, J. N. Winn and R. D. Meade, *Photonic Crystals, 2nd Ed.*, Princeton, New Jersey, 2008.

# Photonic Crystal-Based Single Photon Infrared Detectors and Sources in Silicon-on-Inuslator Photonic Circuits.

**Mohsen K. Akhlaghi**[1], **Ellen Schelew**[1], **and Jeff F. Young**[1]
[1]Department of Physics and Astronomy, University of British Columbia, Canada
young@phas.ubc.ca

**Abstract**— High efficiency, low noise single infrared photon detectors and high-rate single infrared photon sources that can be integrated in silicon-on-insulator photonic circuits are highly desirable to enable scalable photonic-based quantum information processing. Here we report recent progress on using photonic crystal microcavities to a) realize near unity quantum efficiency superconducting nanowire single photon detectors, and b) develop an ultra-compact source of spontaneously generated photon pairs, all at wavelengths $\sim 1.55\mu m$.

## 1. INTRODUCTION

The goal of realizing scalable photonic-based quantum information processing in a silicon-on-insulator (SOI), CMOS compatible platform desperately requires the development of high-efficiency low noise single infrared photon detectors and high-rate, high-quality single infrared photon sources. Photonic crystal microcavities offer one of the best approaches for enhancing the light-matter interaction strength necessary to achieve both of these goals in a compact format. A single photon detector has been realized by locating an 8 nm by 35 nm cross section NbTiN superconducting nanowire on the surface of a 190 nm by 500 nm cross section silicon waveguide in SOI [1]. The absorbing region of the nanowire is located within a microcavity defined by etching 1D arrays of holes entirely through the silicon waveguide (see Fig. 1a); an $\sim 100\%$ reflectivity Bragg mirror is placed on back side, and the reflectivity of the input-side mirror is set to match the absorption rate of the superconducting nanowire when light is trapped in the cavity. Waveguided light incident on this "coherent perfect absorber" [2] is then almost perfectly absorbed if it is at the resonant cavity frequency, and almost perfectly reflected otherwise. The structure itself limits the bandwidth over which the absorption and quantum efficiencies peak (see Fig. 1b), thus minimizing the need for separate filters to reject stray photons. The microcavity reduces the nanowire length required for efficient light absorption as compared to an unpatterned waveguide, thus enabling efficient and fast conversion of absorbed photons to electrical pulses. Biased at 0.9 of the experimental critical current at $T = 2.05$ K, the detector quantum efficiency for $\sim 1545$ nm photons peaks close to unity, while its intrinsic dark count rate, recovery time and timing jitter stay at $\sim 0.1$ Hz (see Fig. 1c), $\sim 7$ ns (see Fig. 1d), and $\sim 55$ ps full-width-at-half-maximum, respectively.

A spontaneous four-wave-mixing source of single photon pairs is realized by embedding three "local defects" in a 2D photonic crystal host with bandgap energies modulated in one direction to form a heterostructure cavity [3, 4] (see Fig. 1a). The defects support three coupled microcavity modes with the lowest and highest energy modes equally spaced from the central mode, thus maximizing the efficient generation of photon pairs produced by light coupled into the central mode via an input-waveguide that selectively excites that mode (see Fig. 1b and c). The device is designed to maximize the coupling of the photon pairs into a single output waveguide.

## ACKNOWLEDGMENT

Financial support from the Natural Sciences and Engineering Research Council is acknowledged. The support of Lukas Chrostowski and Richard Bojko is also acknowledged, as part of this work was conducted at the University of Washington Microfabrication/Nanotechnology User Facility, a member of the NSF National Nanotechnology Infrastructure Network. Computational support was provided by Lumerical Solutions Inc. and grid-enabled computational resources were provided by WestGrid.

## REFERENCES

1. Akhlaghi, M. K., E. Schelew and J. F. Young, "Waveguide integrated superconducting single-photon detectors implemented as near-perfect absorbers of coherent radiation," *Nat. Commun.*, Vol. 6, 8233, 2015.

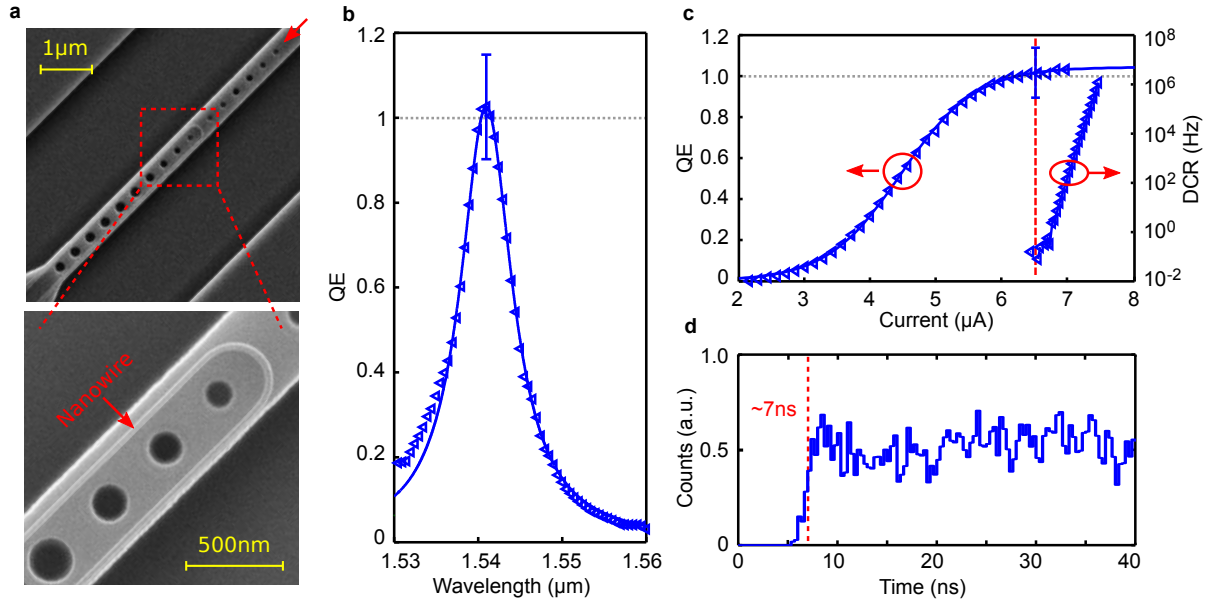



Figure 1: (a) A superconducting nanowire single photon detector in a photonic crystal microcavity. (b) Quantum efficiency vs. wavelength measured at 0.9 of the experimental critical current. (c) Quantum efficiency at $\sim 1545$ nm and intrinsic dark count rate vs. bias current. (d) Histogram of detection restoration after an initial detection at $t = 0$. All measurements were done at 2.05 K.

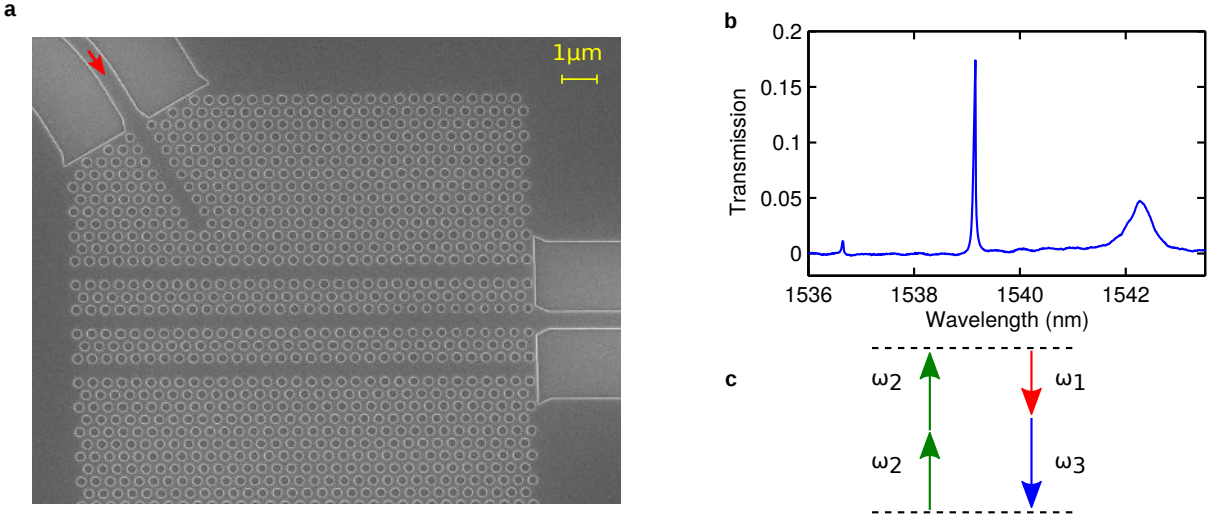



Figure 2: (a) Heterostructure triple cavity designed for spontaneous four-wave mixing (SFWM). (b) Linear transmission from the input to the output channel waveguide measured by scanning the wavelength of the input light. (c) Schematic of SFWM.


2. Chong, Y. D., L. Ge, H. Cao and A. D. Stone, "Coherent perfect absorbers: Time-reversed lasers," *Phys. Rev. Lett.*, Vol. 105, 053901, 2010.
3. Song, B.-S., S. Noda, T. Asano and Y. Akahane, "Ultra-high-Q photonic double-heterostructure nanocavity," *Nat. Mater.*, Vol. 4, No. 3, 207–210, 2005.
4. Azzini, S., D. Grassani, M. Galli, D. Gerace, M. Patrini , M. Liscidini, P. Velha and D. Bajoni, "Stimulated and spontaneous four-wave mixing in silicon-on-insulator coupled photonic wire nano-cavities," *App. Phys. Lett.*, Vol. 103, 031117, 2013.

# Quantum-dot-based on-chip functionality in III-V circuits

M S Skolnick,
*Department of Physics and Astronomy,*
*University of Sheffield, Sheffield S3 7RH, UK*
Corresponding author: m.skolnick@sheffield.ac.uk

This talk will describe recent work on III-V quantum dots incorporated in nano-photonic circuits. The first topic will describe chiral behaviour found in structures with wavelength scale lateral confinement, where spin up recombination leads to photon propagation in one direction only, and spin down in the opposite direction (see Fig 1). This forms the basis for spin-photon interfaces and long term for photon-mediated spin networks. Further on-chip functions to be described will include resonance fluorescence, 50:50 on-chip beam splitting (Fig 2), single photon routing and single photon interference, further steps towards larger scale circuits. An important step towards long scalability, namely deterministic registration of quantum dots to achieve desired properties including spin readout, will also be demonstrated.

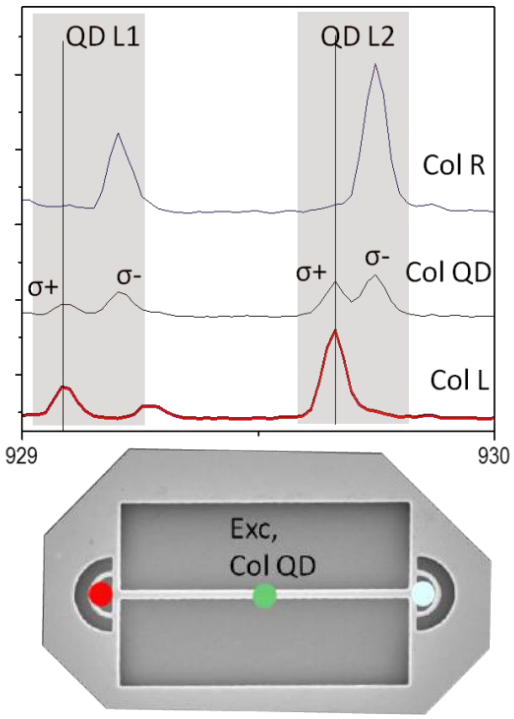



Fig 1 Spin to path conversion in nano-photonic waveguide

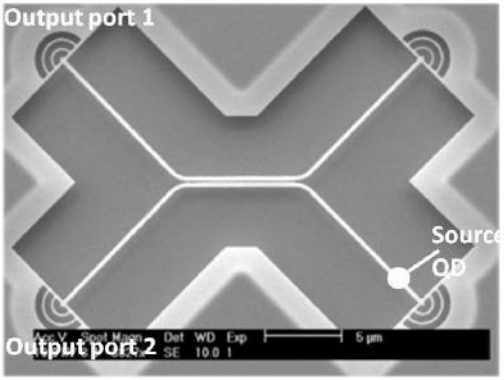



Fig 2 On-chip beam splitter

**Quantum correlations of light and matter through environmental transitions**

One aspect of solid-state photonic devices that distinguishes them from their atomic counterparts is the unavoidable interaction between system excitations and lattice vibrations of the host material. I shall explain how this coupling may lead to surprising departures in emission properties between solid-state and atomic systems. Specifically, I shall show that in solid-state cavity quantum electrodynamics, interactions with the host vibrational environment can generate quantum cavity–emitter correlations in regimes that are semiclassical for atomic systems. This behavior, which can be probed experimentally through the cavity emission properties, heralds a failure of the semiclassical approach in the solid state, and challenges the notion that coupling to a thermal bath supports a more classical description of the system. Furthermore, it does not rely on the spectral details of the host environment under consideration and is robust to changes in temperature. It should thus be of relevance to a wide variety of photonic devices.

# New approaches in the design of quantum sources.

**C. Sánchez Muñoz**[1], **J. C. López Carreño**[1], **F. P. Laussy**[1,2] **and E. del Valle**[1]

[1]Departamento de Física Teórica de la Materia Condensada, Universidad Autónoma de Madrid, Spain
[2]Russian Quantum Center, Novaya 100, 143025 Skolkovo, Moscow Region, Russia
elena.delvalle.reboul@gmail.com

**Abstract**— We present a guiding principle to enhance quantum emitters or even bring them to new regimes of operation, that consists in exploiting their correlations in energy instead of indiscriminately averaging over the full lineshape of emission. We propose an $N$-photon emitter based on the mere Purcell enhancement of such processes and show how—using quantum light not only as the output but also as part of a device—one can greatly increase its figures of merit.

Recent theoretical and experimental works [1, 2, 3] have evidenced how families of physical processes giving rise to strong photon correlations are revealed in the usual second-order correlation function $g^{(2)}$ by retaining the energy degree of freedom. In the case of quantum emitters under coherent driving, these strong correlations have been demonstrated to violate both Cauchy-Schwarz and Bell inequalities [4] to a much greater extent than when averaging over all the light emitted by the source. These strongly correlated photons can be Purcell-enhanced in a cavity QED device, in effect providing a new type of light that delivers all of its energy exclusively in groups, or "*bundles*", of $N$-photons [5]. Such a strongly quantum light presents obvious advantages for a wealth of applications (it is a natural input for a boson sampling circuit, for instance). This approach of exploiting frequency-resolved photon correlations can be applied to all quantum emitters, and therefore constitutes, in our view, an important framework for future quantum devices. For instance, considering the popular bi-exciton configuration [6], we show how the same mechanism can be extended to exploit other degrees of freedom such as polarization, allowing for different excitation schemes and for greatly enhanced emission of entangled photon pairs [7].

Furthermore, we propose to use the quantum light emitted by a source to drive another source. For instance, we consider a scheme that consists in cascading a chain of two-level emitters (e.g.,

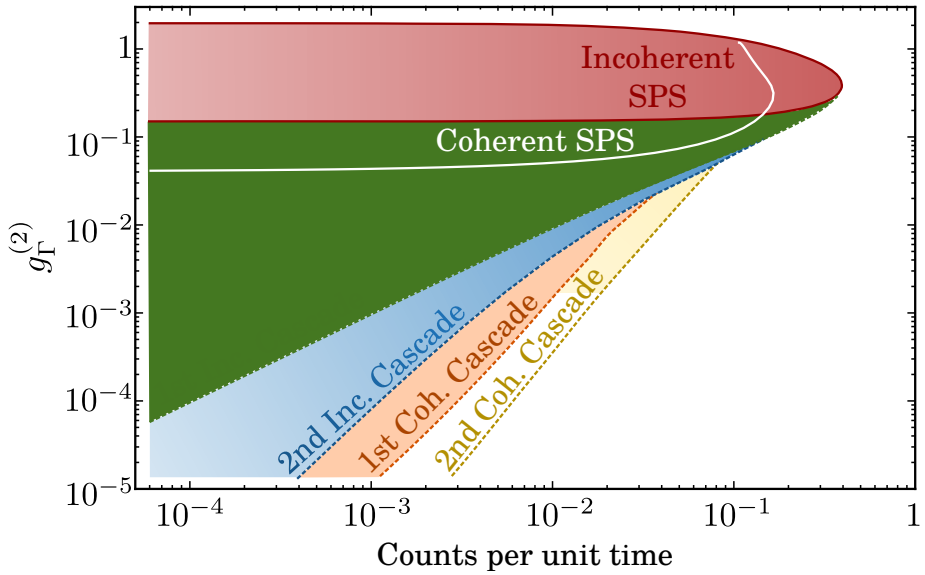



Figure 1: An example of the improvement brought by our architecture to implement better single-photon sources (SPS). In solid (red and white) lines, the conventional scheme where a two-level system is excited incoherently and coherently, respectively. In dashed lines, the result of a chain of two-level systems each exciting the next in a cascaded scheme. As a result, much stronger *suppression of multiple-photon emission* (antibunching) are achieved, at a slight cost of the emission rate.

quantum dots) with each emitter exciting the next one in the sequence. The output of the last emitter in the chain can beat the Fourier transform limit thanks to the driving by quantum light, and thus achieve much stronger suppression of multiple-photon emission (antibunching, cf. Fig. 1). We explain the underlying mechanism in terms of suppression of tail events and, in particular, identify why coherent excitation of a two-level system provides better antibunching than its incoherent counterpart, bringing another viewpoint to the physics of driven two-level systems even without this cascading concept.

In conclusion, we provide new approaches for the engineering of quantum sources. Their successful implementation in the laboratory could have important applications for technology by opening additional routes based on new ideas (dressing with quantum light) rather than incremental progress of making better samples.

**ACKNOWLEDGMENT**

We acknowledge support of the CLAQUE project.

**REFERENCES**

1. del Valle, E., González-Tudela, A., Laussy, F. P., Tejedor, C. & Hartmann, M. J. Theory of frequency-filtered and time-resolved $n$-photon correlations. *Phys. Rev. Lett.* **109**, 183601 (2012).
2. González-Tudela, A., Laussy, F. P., Tejedor, C., Hartmann, M. J. & del Valle, E. Two-photon spectra of quantum emitters. *New J. Phys.* **15**, 033036 (2013).
3. Peiris, M. *et al.* Two-color photon correlations of the light scattered by a quantum dot. *Phys. Rev. B* **91**, 195125 (2015).
4. Sánchez Muñoz, C., del Valle, E., Tejedor, C. & Laussy, F. Violation of classical inequalities by photon frequency filtering. *Phys. Rev. A* **90**, 052111 (2014).
5. Sánchez Muñoz, C. *et al.* Emitters of $N$-photon bundles. *Nat. Photon.* **8**, 550 (2014).
6. del Valle, E. Distilling one, two and entangled pairs of photons from a quantum dot with cavity QED effects and spectral filtering. *New J. Phys.* **15**, 025019 (2013).
7. Sánchez Muñoz, C., Laussy, F. P., Tejedor, C. & del Valle, E. Enhanced two-photon emission from a dressed biexciton. *New J. Phys.* **17**, 123021 (2015).

# Site-controlled quantum dots coupled to photonic crystal waveguides

**B. Rigal[1*], J. R. de Lasson[2], C. Jarlov[1], B. Dwir[1], A. Rudra[1], A. Lyasota[1], I. Kulkova[1], N. Gregersen[2], J. Mørk[2] and E. Kapon[1]**

[1]Laboratory of physics of nanostructures (LPN), Ecole Polytechnique Fédérale de Lausanne, Switzerland

[2]DTU Fotonik, Department of Photonics Engineering, Technical University of Denmark, Denmark

[*]corresponding author: bruno.rigal@epfl.ch

**Abstract**- We demonstrate selective optical coupling of multiple, site controlled semiconductor quantum dots (QDs) to photonic crystal waveguide structures. The impact of the exact position and emission spectrum of the QDs on the coupling efficiency is elucidated. The influence of optical disorder and end-reflections on photon transport in these systems are discussed.

The challenging goal of realizing on-chip quantum circuits in which spins are interfaced with photons that are then routed, processed and detected has triggered significant research efforts over the past decades [1]. InGaAs/GaAs quantum dots (QDs) integrated in photonic crystal (PhC) circuits are one of the most advanced technologies in this direction [2]. Most of the work has focused on Stranski-Krastanow QDs that nucleate at random positions [3], while achieving truly scalable quantum circuits requires a precise deterministic integration of an entire QD system in a photonic circuit. However, the inhomogeneous broadening inherent to QD systems makes the simultaneous efficient coupling of several QDs to a given photonic mode difficult to accomplish. On the contrary, the finite spectral bandwidth of photonic waveguides should facilitate the simultaneous optical coupling of QD systems. Such structures could be used, e.g., to increase the emission rate of single photon sources by efficiently coupling multiple QD single photon sources to the same optical channel.

In this work, we demonstrate the deterministic coupling of five site-controlled QDs placed at different positions within a $W_1$ semi-waveguide with a reflective termination and an out-coupler on its ends (see Fig. 1a). We study the spectra emitted by the s-states of each single QD and how they evolve during the propagation through the waveguide. In Fig. 1b) spectrally resolved near-field pattern in which light is emitted by a selectively excited QD positioned 20.5µm away from the out-coupler, propagates in the waveguide and is collected at the out-coupler. This constitutes the first direct observation of light emission by a site-controlled QD in a PhC waveguide.

Next, we analyze the fraction of light collected at the out-coupler relative to the intensity collected directly from the QD emission (by exciting each QD separately). We perform the same study on each QD of eleven structures with systematic variations in the PhC hole radii r such that the QDs s-states (with an energy around 1.31eV) were tuned into (r<72nm) and out of (r>72nm) resonance with the fundamental waveguide mode. As shown in Fig. 1c), the emission of QDs in the bandgap (r>72nm) is not efficiently channeled to the out-coupler. For QDs resonant with the waveguide photonic band (r<72nm), the fraction of light collected at the out-coupler $I_{outc}/I_{QD}$ reaches values up to 10, evidencing an efficient coupling of the QDs with the waveguide modes. The intensity of the emission collected from the out-coupler for QDs in resonance with the waveguide band varies with the PhC hole radius. This is explained by the formation of Fabry Pérot-like modes in the waveguide due to

the significant reflection at the out-coupler [4]. This effect is already observed in the QD spectra collected at the out-coupler in Fig. 1b: only QD lines near resonance with a Fabry Pérot line are efficiently channeled to the out-coupler. A minimal reflection at the out-coupler is thus required in this case to ensure a truly broadband coupling of the QD to the waveguide. This brings to light the need for alternative designs of out-couplers with very low reflection into the waveguide. Photon correlation measurements confirm the emission of single photons by the integrated QDs. The impact of PhC waveguide disorder on the propagation along the PhC channel will also be demonstrated and discussed. We show that mode localization can be avoided when propagation via modes of high enough frequency is used.

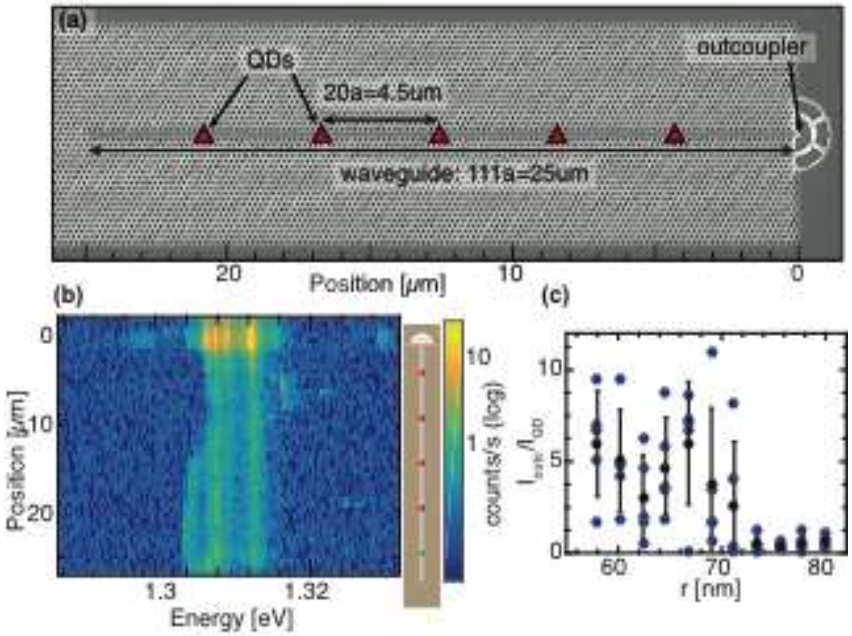



**Figure 1: (a) SEM picture of a 25µm long semi-waveguide with indications of QD positions, (b) Spectrally-resolved near field pattern of the structure in (a) (Excitation power: P=5µW, T=10K, r=61nm), only one QD (shown in green) is excited. (c) Effect of tuning the QD emission through the bandgap: fraction of the intensity extracted from the outcoupler divided by the intensity collected directly from the QD s-states as a function of the PhC hole radius (Excitation power: P=5µW, T=10K, for each PhC hole radius, each data point corresponds to the emission of only one of the five QDs).**

**REFERENCES**


1. R.-B. Liu, W. Yao, and L. J. Sham, "Quantum computing by optical control of electron spins," Adv. Phys. **59**, 703–802 (2010).
2. C. P. Dietrich, A. Fiore, M. Thompson, M. Kamp, and S. Höfling, "GaAs integrated quantum photonics: Towards dense and fully-functional quantum photonic integrated circuits," ArXiv160106956 Cond-Mat Physicsquant-Ph (2016).
3. P. Lodahl, S. Mahmoodian, and S. Stobbe, "Interfacing single photons and single quantum dots with photonic nanostructures," Rev. Mod. Phys. **87**, 347 (2015).
4. M. Arcari, I. Söllner, A. Javadi, S. L. Hansen, S. Mahmoodian, J. Liu, H. Thyrrestrup, E. H. Lee, J. D. Song, S. Stobbe, and P. Lodahl, "Near-unity coupling efficiency of a quantum emitter to a photonic-crystal waveguide," Phys. Rev. Lett. **113**, (2014).

# Polarization Engineering in Photonic Crystal Waveguides for Spin-Photon Entanglers

**A. B. Young[1], A. C. T. Thijssen[2], D. M. Beggs[2], P. Androvitsaneas[2], L. Kuipers[3], J. G. Rarity[1], S. Hughes[4], and R. Oulton[1,2]**

[1]Department of Electrical and Electronic Engineering, University of Bristol, Merchant Venturers Building, Woodland Road, Bristol BS8 1UB, United Kingdom

[2]Centre for Quantum Photonics, H.H. Wills Physics Laboratory, University of Bristol, Tyndall Avenue, Bristol BS8 1TL, United Kingdom

[3]Center for Nanophotonics, FOM Institute AMOLF, Science Park 104, 1098 XG Amsterdam, Netherlands

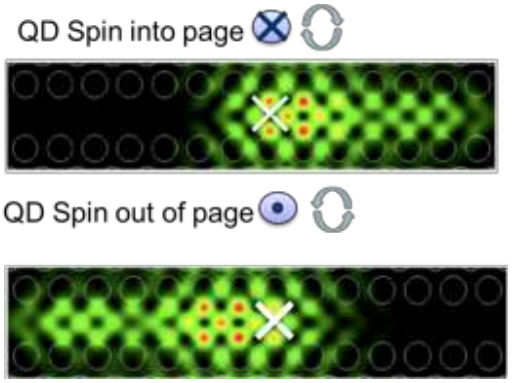
[3]Department of Physics, Queen's University, Ontario, Canada K7L 3N6

[*]corresponding author: ruth.oulton@bristol.ac.uk

**Abstract**-We present our work on QD spin emitters in photonic crystal waveguides, demonstrating that by placing a QD spin emitter at a C-point polarization singularity, one may achieve perfect unidirectional emission of a photon from the emitter, whose direction is determined by the spin direction.

Quantum dots are semiconductor artificial atoms. They are nanoscale structures that trap single electrons and holes, and their quantized energy level structure results in atomic-like transitions and single photon emission. These quantum dots act as a solid-state interface that is useful for quantum information applications, and for the past decade, semiconductor physicists have been attempting to replicate atomic cavity quantum electrodynamics in a practical semiconductor form. One can embed quantum dot into micron-sized photonic structures to capture and control the light emission, in order to use the single photon emission in quantum communication and quantum circuits.

One of the most exciting applications of quantum dots is to use their electron spins as a quantum memory. This involves transferring spin information from an electron spin to the polarization of a photon. However, as I shall explain, the definition of "polarization" for nanophotonic structures is far more complex than for a beam of light. In fact, we find that point-like "spin" emitters couple to a photonic structure in surprising ways: unlike any phenomenon observed in bulk material, simply changing the position of an emitter or the spin direction controls completely in which direction photons propagate. Suddenly, a rich variety of behaviour has arisen in the semiconductor/photonic domain which has no equivalent in atomic cavity QED, including a fundamental difference between how a classical dipole and a quantum dipole emitter interfere with incoming light.




**Acknowledgements:** The authors acknowledge helpful discussions with P. Lodahl, B. Lang, and R. Ge. EM simulations were carried out using the computational facilities of the Advanced Computing Research Centre, University of Bristol. This work has been funded by Future Emerging Technologies (FET)-Open FP7-284743 [project Spin Photon Angular Momentum Transfer for Quantum Enabled Technologies (SPANGL4Q)]. R. O. was sponsored by Engineering and Physical Sciences Research Council (EPSRC) Grant No. EP/G004366/1, and J. G. R. is sponsored under European Research Council (ERC) Grant No. 247462 Quantum Optics in Wavelength Scale Structures (QUOWSS). This work is part of the research program of the Stichting voor Fundamenteel Onderzoek der Materie, which is financially supported by the Nederlandse Organisatie voor Wetenschappelijk Onderzoek. D. M. B. acknowledges support from a Marie Curie individual fellowship, and S. H. acknowledges funding from the Natural Sciences and Engineering Research Council of Canada.

# Quantum dots in monolayered $WSe_2$ : A new class of high purity solid state single photon sources

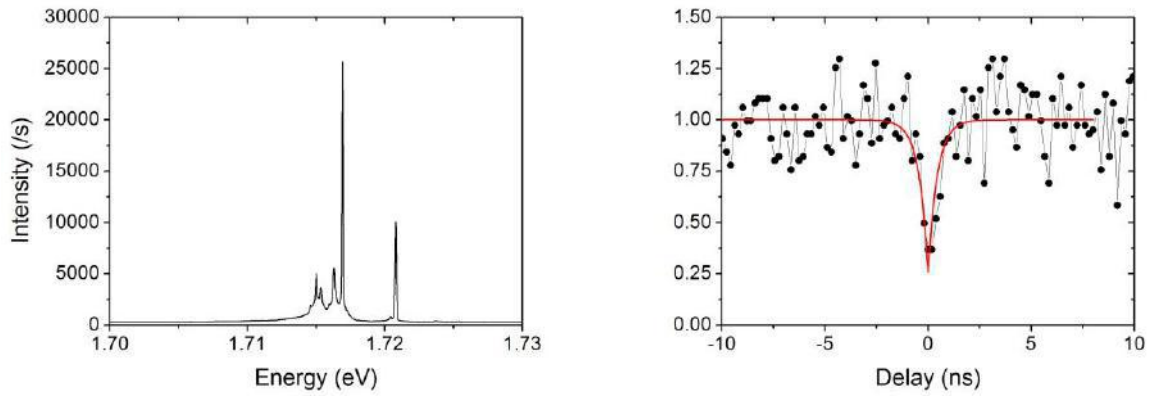
**Yu-Ming He, Oliver Iff, Nils Lundt, Sven Höfling, and Christian Schneider**

*Technische Physik and Wilhelm Conrad Röntgen Research Center for Complex Materials, University of Wuerzburg, Germany*

* Corresponding author: cnschnei@physik.uni-wuerzburg.de

**Abstract:** Solid state quantum emitters are excellent candidates for on-chip quantum light emission, as they promise ultra-compact integration into complex devices and a vast flexibility of engineering their properties via advanced crystal growth and lithography techniques. While In(Ga)As quantum dots probably can still be considered as the prime example of a quantum emitter in solid, the emergent class of two dimensional transition metal dichalcogenides has recently emerged as an interesting alternative. Surprisingly, monolayers of WSe2 exposed to an open surface have been identified to host optically active defects which promote single photon emission, and as such represent a class of solid state which do not suffer from a dramatic reduction of brightness via total internal reflection on the air interface.

Here, we study the properties of optically active defects in $WSe_2$, exfoliated on $SiO_2$ as well as GaInP substrates. We unambiguously demonstrate single photon emission from such defects by measuring second order autocorrelation function yielding a value of $g^2(0) < 0.3$. By investigation the decay dynamics of such emitters, we map out a significant contribution of the dark state contribution, which the ground state in $WSe_2$, to the emission process. We furthermore verify, that the integration of monolayers of transition metal dichalcogenides with epitaxially grown semiconductor material leads a strong reduction of detrimental environmental effects, such as spectral jittering and uncontrolled charging, which paves the way towards a generation of high quality, bright quantum emitters and pair emitters in emerging two dimensional materials.




(left) High resolution microphotoluminescence spectrum of quantum dot like emitter in $WSe_2$. (right) second order autocorrelation function of the emitter.

Acknowledgement: We thank the state of Bavaria, and the ERC grant UnLiMIt-2D for financial support.

# Quantum entanglement between distant quantum dot spins

**E. Togan[1*], J. Klaers[1], A. Delteil[1], Z. Sun[1], and A. Imamoglu[1]**
[1]ETH Zurich, Switzerland
[*]corresponding author: togane@phys.ethz.ch

**Abstract**- Controllably generating entanglement between distant qubits is an important milestone for distributed quantum computation. We will discuss recent results demonstrating heralded entanglement between hole spins of quantum dots, as well as new approaches for generating entanglement between qubits.

Single optically active solid state spins are promising candidates for qubits due to their individual addressability and the prospect for integrating many qubits on a single chip. A number of such solid state systems possess optical transitions that allow for initialization, manipulation and readout of their spin states. The same optical transitions can be used to entangle the state of a single photon with the spin state of the emitter. Such entangled states are useful for implementation of quantum information protocols such as generation of heralded entanglement between two separate qubits. We will review recent progress in this field focusing on demonstration of entanglement between two distant hole spins heralded by detection of a single-photon that projects the distant spins onto an entangled state[1].

A complementary approach for entangling nearby spins is to use the interaction of each emitter with a common localized mechanical mode. We will discuss coupling between mechanical modes of nanostructures fabricated in GaAs and states of quantum dots embedded in the nanostructures. Recent results and prospects of using such a hybrid system for quantum information will be discussed.

**REFERENCES**

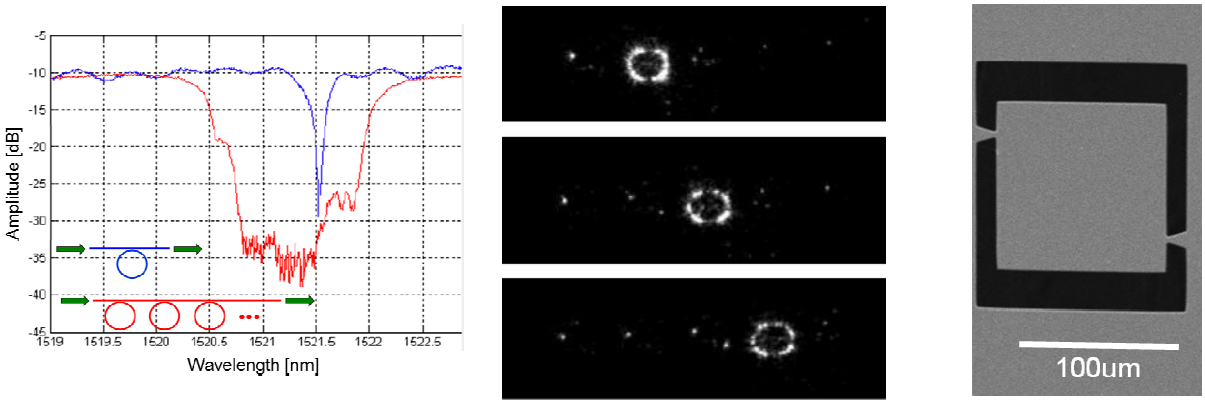
1. Delteil, A., Sun, Z., Gao, W., Togan, E., Faelt, S., Imamoglu, A. "Generation of heralded entanglement between distant hole spins," *Nature Physics*, DOI: 10.1038/NPHYS3605 (2015).

# Heterogeneous integration and trimming of complex silicon photonic circuits

**G.J. Sharp[1], L. Meriggi[1], C. Klitis[1], B.M. Holmes[1], Y. Ding[1], S. May[1], G. Cantarella[2], M. Strain[2], M.Sorel[1]**
[1]School of Engineering, University of Glasgow, G12 8LT Glasgow, United Kingdom
[2]Institute of Photonics, University of Strathclyde, G1 1RD Glasgow, United Kingdom
[*]corresponding author: marc.sorel@glasgow.ac.uk

**Abstract** – The rapid increase in the complexity of integrated photonic circuits demands the development of new tools and technologies for performance monitoring and device integration. We present recent advances in post-fabrication trimming of photonic circuits through local laser annealing and transfer printing for bonding III-V material platelets to silicon chips.

Integrated photonics on silicon-on-insulator (SOI) is currently regarded as one of the most promising solutions for the development of quantum circuits, thanks to its unique potential for integration, volume production, energy efficiency and scalability [1]. In the last few years, the establishment of generic and accessible foundry models has propelled a phenomenal growth in silicon photonic research activities, with the demonstration of several circuits with unprecedented level of functionality. However, such increase in chip complexity can only be sustained with a shift from today's "device" level to a full "system-on-a-chip" that will require the development of adequate tools to reliably control the manufacture and operation of the circuits, as well as approaches for efficient chip integration. In this talk, we will discuss recent progress in post-fabrication trimming and parallel transfer printing of III-V devices on SOI chips, which can offer very appealing solutions for future development of complex and multi-functional chips.




a) b) c)

**Figure 1:** a) Transfer functions of a single (blue curve) and of 64 cascaded micro-ring resonators (red curve); b) Infrared image of a chip showing the scattered light from three cascaded rings when tuned to resonance; c) SEM picture of a suspended III-V membrane attached to the substrate via two lateral mechanical anchors.

The strongly confining nature of SOI waveguides provides extreme compactness, albeit at the expense of a

very large dependence on fabrication tolerance, which translates into large variability and non-uniformity between devices [2]. A typical example of this is shown in Fig. 1a, which compares the transfer functions of a single all-pass filter (APF) micro-ring resonator, with that of 64 identical cascaded APFs. The increase in the FWHM of the transfer function from ~0.1 nm to ~0.6 nm is a direct measure of this fabrication non-uniformity. A popular approach to manage such variations is to include a thermo-optical element on each device so as to re-tune the whole circuit to the desired working point. However, the scalability of this technique is limited because of the power consumption of the heaters and the complexity in controlling cross-talk in large numbers of closely packed devices. To this end, a number of post-fabrication trimming techniques have been explored, including the use of photo-sensitive or liquid crystal claddings, material compaction by electron beam irradiation, back etching of SiN over claddings or local oxidation of Si using a heated AFM tip [3]. Here, we will present an effective solution to these difficulties that monitors the status of the elements by collecting the light scattered from the chip (see Fig. 1b) and trims the circuit through re-crystallization of a thin layer of amorphous silicon by local laser heating.

The creation of on-chip light sources and detectors on silicon photonic circuits is a crucial technology for the future scalable systems. Although progress has been made towards the generation of light in Si and Ge, the real advances towards this goal have been in the field of heterogeneous III-V on SOI integration. We will discuss the development of a transfer printing method for bonding III-V material platelets to SOI chips, which allows the parallel transfer of large numbers of III-V platelets to non-native substrates using pre-patterned elastomer stamps (see Fig.1c). Transfer stamps can be manufactured to match complex PIC layouts giving flexibility for circuit design whilst maintaining a parallel process with sub-μm positional accuracy [4].

The authors acknowledge support from the technical staff of the James Watt Nanofabrication Center at Glasgow University. The research is supported by the European Union “BBOI” project (grant no. 323734) and by the EPSRC “Cornerstone” project (EP/L021129/1).

**REFERENCES**

1. J.W. Silverstone, et al., “On-chip quantum interference between silicon photon-pair sources”, Nature Photonics 8 (2), 104-108
2. L. Chrostowski, et al., “Impact of fabrication non-uniformity on chip-scale silicon photonic integrated circuits," in Optical Fiber Communication Conference. OSA, 2014
3. A. Canciamilla, et al., “Photo-induced trimming of chalcogenide-assisted silicon waveguides,” Opt. Express 20(14), 15807– 15817 (2012) S. Srinivasan, et al. *IEEE J. Sel. Top. Quantum Electron.*, vol. 20, no. 4, 2014.
4. A. J. Trindade, et al. *Appl. Phys. Lett.*, vol. 103, no. 25, p. 253302, 2013.

# Efficient parametric interactions in Photonic Crystals Waveguides and Resonators.

**A. Martin**[1,2], **G. Moille**[1], **T. Debuisschert**[1], **A. P. Mosk**[3], **G. Eisenstein**[4], **S. Combrié**[1], **and A. De Rossi**[1]

[1]Thales Research and Technology, France
[2]Laboratoire de Photonique et de Nanostructures, CNRS, Université Paris-Saclay, France
[3]Complex Photonic Systems (COPS), MESA+ Institute for Nanotechnology, University of Twente, Enschede, The Netherlands
[4]Technion Institute of Technology, Haifa, Israel
alfredo.derossi@thalesgroup.com

**Abstract**— Enhanced Kerr nonliner response in semiconductor photonic crystals is exploited for wavelength conversion, ultra-fast gating, phase-sensitive amplification and correlated photon pairs. In waveguides, Four Wave Mixing and related effects can be controlled through dispersion-engineering to a very broad extent. In coupled resonators, we show efficient parametric interactions and intense spontaneous emission of photons with an optical pump below 100 $\mu W$.

## 1. INTRODUCTION

Nonlinear frequency conversion processes are attractive for the generation of light at arbitrary colours. Integrated photonic devices based on four-wave mixing (FWM) are of particular interest due to the promise of compact all-optical signal processing metrology and quantum information sources. This talk will focus on a class of photonic nanostructures where *structural slow light* enhances the effective nonlinearity, which has been reported to be close to $10^4 m^{-1}W^{-1}$, i.e. more than six orders of magnitude larger than in optical fibres.
We have introduced a Photonic Crystal (PhC) technology based on a large band-gap semiconductor, Gallium Indium Phosphide, which virtually removes nonlinear absorption when operating in the practical Telecom spectral range, and this has opened the access to a strongly nonlinear regime, as it can bear fairly large peak power densities. This is favourable to the observation of a strong nonlinear dynamic, similarly to optical fibers, but just scaled down. A striking example is on-chip pulse compression resulting from the the evolution of higher order solitons[1].
The specific property of PhC waveguides is the ability to control and tailor the dispersion to a very broad extent: e.g. setting one or more zero dispersion wavelength (ZDW) to prescribed values, and this just by design. Besides applications in linear signal processing, this property is fundamental for controlling the dynamics of nonlinear waves[2] and parametric processes, namely FWM.

## 2. DISPERSION-CONTROLLED PHASE-SENSITIVE AMPLIFICATION

Phase-sensitive Amplification (PSA) occurs when (all) the inputs of the parametric interaction are frequency and phase locked (fig. 1a). It is crucial for all-optical processing of phase-encoded signals, since they can selectively process the two complex quadratures of the optical field. PSA has been demonstrated in ultra-compact Silicon PhC waveguides[3], Here we show that phase-sensitive amplification in GaInP waveguides strictly obeys the pure Kerr nonlinear dynamics, in contrast with Silicon, where it is necessary to remove the generated carriers to prevent PSA to be perturbed. Large (15 dB) extinction ratio is achieved with a peak pump power of 600 mW (Fig 1b). We discuss the role of the waveguide dispersion on the PSA process, which is apparent in (Fig 1c).
PSA is related to the manipulation of the quantum states of light, specifically to squeezing. Output coupling losses are about 3 dB, however, this will not be a concern for exploing quantum effects in future fully integrated photonic circuits.

## 3. TRIPLY-RESONANT FWM AND SPONTANEOUS EMISSION OF PHOTONS.

Parametric fluorescence arising from parametric down-conversion in non-centrosymmetric crystals and from FWM in optical fibres, semiconductor or other nonlinear waveguides and resonators leads to the generation of correlated photons pairs. Spectrally bright sources of photon pairs has been

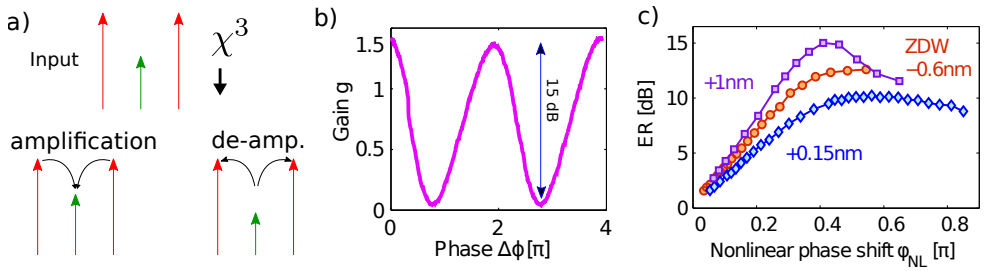



Figure 1: Phase-Sensitive Amplification in GaInP PhCs. a) power flow in phase-sensitive interactions; b) measured parametric gain as a function of the mutual phase of the inputs; c) dependence of the phase-sensitive extinction ratio as a function of the phase.

demonstrated with silicon ring resonators[4]. Indeed, when FWM is triply resonant, the efficiency of frequency conversion due to four wave mixing (FWM) scales as $Q^4$, provided the pump, the probe and the idler are all spectrally matched with a resonance.
It is however notoriously difficult to obtain equally spaced resonances in PhC resonators, however it has been demonstrated in coupled resonators[5, 6].
Here, we consider a chain of 10 resonators and select three resonances spaced approximatively equally (168 GHz and 169 GHz). Owing to an average Q factor of $7 \times 10^4$, a conversion efficiency $P_{idler}/P_{signal}$ close to -17 dB has been achieved (fig. 2a) by injecting about 100 $\mu$W in the photonic chip (coupling losses are about 5 dB). Then, the rate of photons emitted in the spontaneous process (without signal input) is estimated from the count rate of a superconducting bolometer, leading to a maximum of about 14 MHz (fig. 2b).

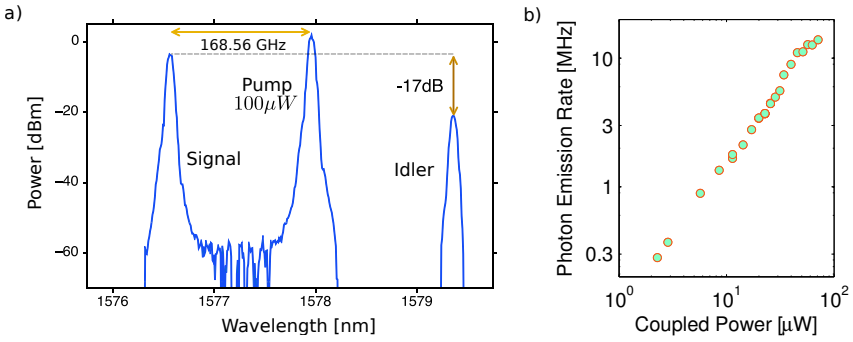



Figure 2: Resonant FWM in coupled PhC resonators: a) output spectra; b) estimated rate of spontaneously emitted photons

**REFERENCES**


1. P. Colman, C. Husko, S. Combrié, I. Sagnes, C. Wong, and A. De Rossi, "Temporal solitons and pulse compression in photonic crystal waveguides," *Nature Photonics*, vol. 4, p. 862, 2010.
2. P. Colman, S. Combrié, G. Lehoucq, A. De Rossi, and S. Trillo, "Blue self-frequency shift of slow solitons and radiation locking in a line-defect waveguide," *Phys. Rev. Lett.*, vol. 109, p. 093901, 2012.
3. Y. Zhang, C. Husko, J. Schröder, S. Lefrancois, I. H. Rey, T. F. Krauss, and B. J. Eggleton, "Phase-sensitive amplification in silicon photonic crystal waveguides," *Optics letters*, vol. 39, p. 363, 2014.
4. D. Grassani, S. Azzini, M. Liscidini, M. Galli, M. J. Strain, M. Sorel, J. E. Sipe, and D. Bajoni, "Micrometer-scale integrated silicon source of time-energy entangled photons," *Optica*, vol. 2, p. 88, Feb 2015.
5. N. Matsuda, H. Takesue, K. Shimizu, Y. Tokura, E. Kuramochi, M. Notomi, "Slow light enhanced correlated photon pair generation in photonic-crystal coupled-resonator optical waveguides", *Opt. Expr.*, vol. 21, p. 8596, 2013
6. S. Azzini, D. Grassani, M. Galli, D. Gerace, M. Patrini, M. Liscidini, P. Velha, and D. Bajoni, "Stimulated and spontaneous four-wave mixing in silicon-on-insulator coupled photonic wire nano-cavities," *Appl. Phys. Lett.*, vol. 103, no. 3, p. 031117, 2013.

# Quantum photonics with quantum dots in photonic wires

**Mathieu Munsch[1], Andreas Kuhlmann[1], Davide Cadeddu[1], Jean Teissier[1], Martino Poggio[1], Niels Gregersen[2], Jean-Michel Gérard[3,4], Julien Claudon[3,4], Richard J. Warburton[1]**

[1] Department of Physics, University of Basel, Basel, Switzerland

[2] DTU Fotonik, Department of Photonics Engineering, Technical University of Denmark

[3] Université Grenoble Alpes, France

[4] CEA, INAC-SP2M, 17 rue des Martyrs, France

mathieu.munsch@unibas.ch

**Abstract-** We present results from the spectroscopy of a single quantum dot in a photonic wire. The device presents a high photon extraction efficiency, and strong hybrid coupling to mechanical modes. We use resonance fluorescence to probe the emitter's properties with the highest sensitivity. We perform a detailed analysis of the noise in the device and reveal in particular the thermal excitation of mechanical modes at 4 K.

Our approach to engineering both photonic and phononic properties involves the top-down fabrication of 1D photonic waveguides. The proper engineering of the wire's dimension and shape forces the QD to emit into a specific mode of the electromagnetic field, a mode propagating along the wire axis [1,2]. In addition, a tapered section results in adiabatic deconfinement of the mode and limits diffraction losses at the top facet [3]. Optimum coupling between the emitter and the fundamental mode of the waveguide requires lateral dimensions of the photonic structure on the order of $\lambda/n$, the light wavelength in the semiconductor. Whether the relative proximity of surfaces affects the coherence properties of the embedded emitter or not has remained an open question so far. Furthermore, photonic wires display reasonably high-Q mechanical resonances which affect the QD state. More specifically, material strain intrinsically couples the mechanical resonator with an embedded QD, resulting in a hybrid QD-opto-mechanical system [4].

Efficient adiabatic deconfinement demands a taper with a very small angle which is cumbersome to fabricate and work with. We present here an alternative, the photonic trumpet, where the deconfinement takes place in the semiconductor itself. The taper angle can be much larger in this case. We demonstrate single photon emission from a single QD with high extraction efficiency [5]. To characterize the QD-in-trumpet properties with the highest sensitivity we drive the QD optical transition with a highly coherent resonant laser. Rejection of scattered laser light is realized with a dark-field microscope based on cross-polarized excitation and detection. The key enabling feature for this experiment is the large top facet of the photonic trumpet, which allows for excellent suppression of the back-scattered laser light. At resonance, count rates on a silicon avalanche photodiode approach 1 MHz. We measure small QD linewidths similar to the ones in the bulk material showing that there is little if any additional dephasing due to the nanowire surfaces. Using noise spectroscopy of the resonance fluorescence signal, we reveal signatures of the Brownian motion of the nanowire even at a temperature of 4K. This new approach allows us to determine the characteristics of the hybrid QD-opto-mechanical system with ultra-high sensitivity and opens new perspectives in terms of precision sensing: mechanical sensing proceeds by detecting the QD photons and not by an interferometric approach. We show theoretically that this new approach achieves the Heisenberg limit once the device operates perfectly (transform-limited emission and 100% detection efficiency).

Finally, we show that it is possible to eliminate all the optics between the photonic trumpet and a single-mode optical fibre (typically two expensive objective lenses and a three-axis nano-positioning stage). We achieve excellent trumpet-to-fibre coupling by realizing a "quantum fiber-pigtail" [6]. The device consists of a QD in a photonic trumpet with the end facet bonded directly to the cleaved facet of a single-mode fibre. Proof-of-principle experiments yield an efficiency of 6% and this can be increased with simple modifications. Such a structure is particularly appealing not just for quantum optics experiments but also for surface scanning, the quantum dot acting as a highly sensitive electrometer. Furthermore, the approach can be translated to other materials, for instance diamond, opening the way to creating a simple but highly sensitive magnetometer.

**REFERENCES**

1. Bleuse J. et al, "Inhibition, Enhancement, and Control of Spontaneous Emission in Photonic Nanowires" in Phys. Rev. Lett. 106, 103601 (2011).
2. Munsch M. et al, "Linearly Polarized, Single-Mode Spontaneous Emission in a Photonic Nanowire" in Phys. Rev. Lett. 108, 077405 (2012).
3. Stepanov P. et al, "Highly directive and Gaussian far-field emission from a giant photonic trumpet" in Appl. Phys. Lett. 107, 141106 (2015).
4. Yeo I. et al, "Strain-mediated coupling in a quantum dot-mechanical oscillator hybrid system" in Nat. Nanotech 9, 106 (2014)
5. Munsch M. et al, "Dielectric GaAs Antenna Ensuring an Efficient Broadband Coupling between an InAs Quantum Dot and a Gaussian Optical Beam" in Phys. Rev. Lett. 110, 177402 (2013)
6. Cadeddu, D. et al , "A fiber-coupled quantum dot on a photonic tip" in Appl. Phys. Lett. 107, 141106 (2015).

# Quantum photonic circuits using single photons from a quantum dot.

**A. J. Bennett[1], J. P. Lee[1,2], D.J. P. Ellis[1], E. Murray[1,3], F. Floether[1,3], J. Griffiths[3], T. Meany[1], I. Farrer[3], D. A. Ritchie[3] and A. J. Shields[1]**

[1] Toshiba Research Europe Limited, Cambridge Research Laboratory, 208 Science Park, Milton Road, Cambridge, CB4 OGZ, United Kingdom.

[2] Engineering Department, University of Cambridge, 9 J. J. Thomson Avenue, Cambridge, CB3 0FA,United Kingdom.

[2] Cavendish Laboratory, Cambridge University, J. J. Thomson Avenue, Cambridge, CB3 0HE, United Kingdom.

[*]corresponding author: anthony.bennett@crl.toshiba.co.uk

**Abstract**-Leveraging the advantages of integrated optics for quantum photonics (1) has led to a new functionality and complexity. The inclusion of a source that delivers high efficiency single photons, such as a quantum dot, is particularly attractive. We show here how a resonantly driven quantum dot can create indistinguishable photons for use in on-chip quantum optics experiments. Further, we present a device where the source and circuit, bonded together, create and manipulate quantum light at cryogenic temperatures.

We report the resonant excitation of a pillar microcavity containing a single weakly-coupled quantum dot. Using co-linear excitation and collection along the efficient axis of the cavity, crossed polarisers can suppress the collected laser intensity to a negligible level, relative to the fluorescence intensity of the dot. We show that Resonant Rayleigh Scattering from the $X^+$ transition creates anti-bunched light a factor of 16 beyond the time-bandwidth limit (2).

Alternatively, a pulsed laser can be used to create on-demand indistinguishable single photons with wave-packet overlap as high as 0.9. Guiding these photons to a Silicon-Oxynitride (SiON) photonic circuit held under ambient conditions we create a two-photon N00N state, and confirm its phase super-resolving ability (Figure 1).

In future, it will be advantageous to integrate the source directly onto the photonic circuit. We discuss a device (3), where the emitter is bonded to a SiON optical circuit creating a highly stable source of path encoded single photons. The inclusion of couplers and reconfigurable elements on our circuit allows us to perform a Hanbury-Brown and Twiss measurement, confirming the quantum nature of the emitted light, or to create qubits in a superposition of two paths on the chip. We will discuss the possibilities for scaling to a greater number of optical elements.

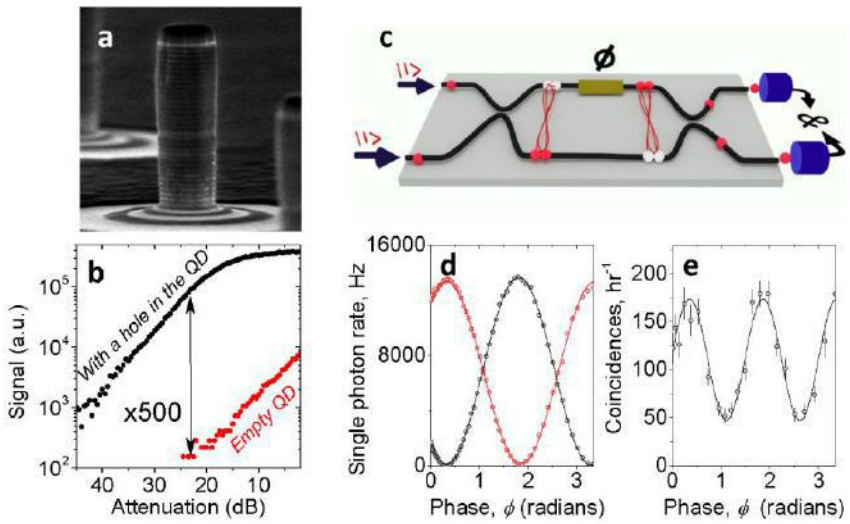



Figure 1: Resonant excitation of a charged quantum dot in a micro-pillar. (a) SEM image of a micro-pillar of 1.75 micron diameter, (b) signal intensity as a function of laser attenuation dependent on whether the dot is charged or not. (c) A reconfigurable $SiO_xN_y$ photonic waveguide circuit is injected with indistinguishable photons from the dot. (d) Single photon rates at each detector as a function of phase in the circuit and (e) demonstration of super-resolution at the circuit output using the 2-photon *N00N* state.

**Acknowledgements**, The EPSRC partly funded the MBE machine used to grow the sample. JL acknowledges support from the EPSRC CDT in Photonic Systems Development.

**REFERENCES**

1. Politi, A. Cryan, M. Rarity, J. Yu, S. O'Brien, J. "Silica on Silicon quantum circuits," *Science*, Vol. 320, No. 5876, 646-649, 2008.
2. Bennett, A. J. *et al*, "Cavity enhanced light scattering from a quantum dot", accepted for publication in *Science Advances*, 2016.
3. Murray, E. *et al*, "Quantum Photonics Hybrid Integration Platform" *Appl. Phys. Lett.* **107**, 171108, 2015.

# Silica on silicon planar photonic circuits for Quantum Information Processing.

**Peter G.R. Smith[1], James C. Gates, Corin B.E. Gawith, Christopher Holmes, Lewis G. Carpenter, Samuel A. Berry, Teresa I. Ferreiro, Paolo L. Mennea, Matthew T. Posner, Peter A. Cooper, Stephen G. Lynch, Rex Bannerman, Miranda Turvey, Alexander Jantzen**

[1]Optoelectronics Research Centre, University of Southampton,
Highfield, Southampton, SO17 1BJ, United Kingdom
[*]corresponding author: peter.smith@soton.ac.uk

**Abstract**- Quantum Information Processing makes use of quantum mechanics to achieve useful information processing functions. This invited talk will review work carried out at the University of Southampton on the fabrication of optical waveguide elements to realize essential functions for all optical quantum information handling. Utilizing silica-on-silicon as a platform and direct UV writing of waveguides, results will be presented on the key elements including single photon sources, waveguide circuits and waveguide sensors.

Quantum information processing offers potential for harnessing quantum mechanics to achieve unprecedented scale-up in information technology. While some applications, such as quantum-secure communication are already starting to see deployment, others are much longer term, with the potential of a universal quantum computer being an ultimate goal. To realize these breakthroughs it is necessary to develop bespoke optical components featuring low-loss, and suited to operate with the unique requirements of Quantum Information Processing. Low-loss is particularly important for quantum applications, as loss of photons cannot be compensated by the use of amplifiers. This means that the accepted paradigms within optical telecommunications no longer apply, so for example, while in a telecomm system an insertion loss of 3dB for a lithium niobate modulator is acceptable in a transmitter because erbium fibre amplifiers are routinely used as pre-amplifiers before transmission and the loss from the modulator has negligible effect. However in quantum applications, operating at single photon level such approaches are unacceptable. Further complications come from the fact that for many quantum systems, based on trapped ions or trapped atoms, the photons carrying quantum information are at shorter wavelengths – in the 780nm region and even the blue or near UV for ions. Hence standard integrated optics cannot easy be used, and some approaches such as silicon photonics cannot be used at all due to band-gap absorption.

Results will be presented on a range of topics, including optical circuits for demonstration of quantum teleportation, on boson sampling, and on non-classical interferometry. As well as circuits, results will be presented on sources and on single photon detectors. All of the results presented were conducted in collaborative work with the University of Oxford and with NIST, Boulder, Co. The emphasis of this work will be on the fabrication and design of devices, and in showing how optical telecommunication approaches such as Bragg gratings can be used to enhance and improve Quantum Information Processing.

**Acknowledgements**, This work has been supported by EPSRC, UK.

# Superconducting Nanowire Single Photon Detectors Integrated with GaAs Waveguide Circuits

Robert Kirkwood[1], Chandra M. Natarajan[1], Alessandro Casaburi[1], Mike Tanner[2], Robert Hadfield[1]

[1]University of Glasgow, Glasgow, G12 8LT, UK.
[2]Heriot-Watt University, Edinburgh, EH14 4AS, UK.

The field of photonic quantum information processing has recently been progressing towards single chip integration of components necessary to demonstrate a quantum information processor. Central to this architecture are single photon sources, waveguides, and single photon detectors. A practical scalable device requires detectors that have high detection efficiency, low dark counts, low timing jitter and sensitivity into the infrared. Superconducting nanowire single photon detectors (SNSPDs) combine these favoured properties with the ability to be monolithically integrated with waveguide circuits. We present an SNSPD fabricated from NbTiN on top of a GaAs single mode waveguide and demonstrate the operation of these integrated components. The use of III-V semiconductors as a platform for photonic circuits is advantageous as it allows the inclusion of quantum dot single photon sources to be embedded within waveguides. Taking advantage of recent progress in development of GaAs waveguide technology we demonstrate a single photon detector operating at 3.7K on a suspended nanobeam single mode waveguide and present progress towards additional integration of filters and beam splitters on a single chip. Low temperature electrical and nano-optical characterisation reveals a high yield of detectors with uniform photo-response and viable waveguide components (**Figure 1**).

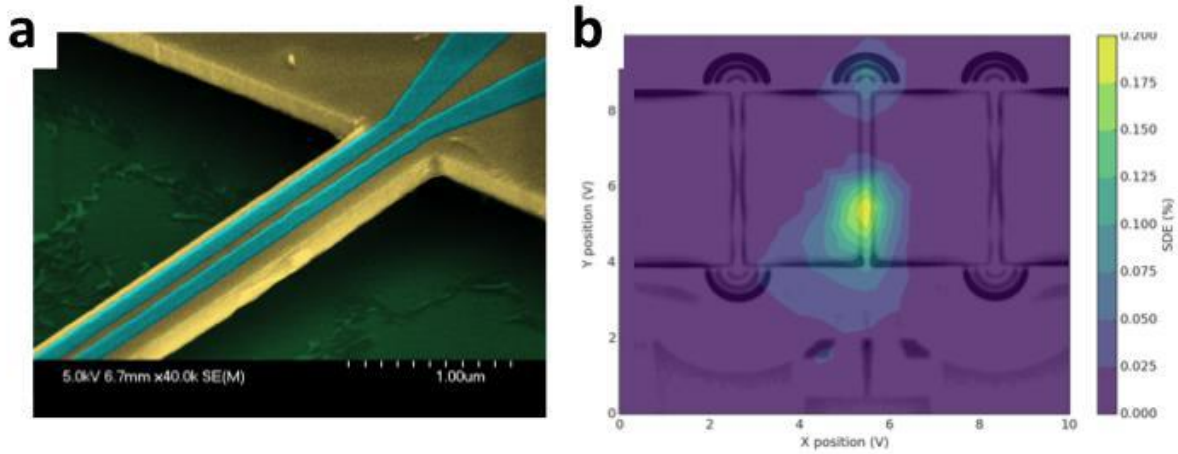



**Figure 1 a.** Scanning electron microscope image (false coloured) showing a NbTiN nanowire (blue) fabricated on top of GaAs (yellow). The active area of the detector is covering a single mode nanobeam waveguide that has been under-etched to separate it entirely from the substrate below (green). **b.** A photo-response map records detector counts (yellow) as an attenuated focussed laser beam is scanned over the area of a waveguide-integrated detector at perpendicular incidence. An optical micrograph transparency is overlaid to indicate the location of the detector and of the waveguide with grating input coupler.

# Nonlinear photonic crystals and metamaterials

# High-efficiency Ultra-Broadband Supercontinuum High-Harmonic Generation from a Single Nonlinear Crystal

**Chen-Yang Hu[1], Bao-Qin Chen[2], Jiafang Li[1,*], Zhi-Yuan Li[1,*]**

[1]Laboratory of Optical Physics, Institute of Physics, Chinese Academy of Sciences, Beijing 100190, China

[2]School of Physics and Optoelectronics, South China University of Technology, Guanzhou 510640, China

[*]Emails: lizy@aphy.iphy.ac.cn, jiafangli@ aphy.iphy.ac.cn

**Abstract**-We report the generation of an ultrabroadband visible white light beam corresponding to $5^{th}$–$8^{th}$ HG with a record high conversion efficiency of 18%, by using a single chirped periodic poled lithium niobate (CPPLN) nonlinear crystal.

Since the invention of the laser, nonlinear optics has become a popular and efficient routine for expanding the frequency window of lasers from ultraviolet to visible, infrared, and terahertz bands, and for generating broadband coherent light sources and ultrafast pulse lasers. However, it's still difficult to realize high-harmonic generation (HHG) in a single crystal, because more and more nonlinear up-conversion processes must be simultaneously adopted with phase matching. Instead, a chain of two or more individual nonlinear crystals with cascaded SHG and SFG is used, but with a complicated experimental setup and low conversion efficiency.

In recent years, our group makes effort to accomplish high-efficiency frequency conversion by quasi-phase-matching (QPM) technology. We have realized multi-direction high-efficiency second harmonic generation [1] and simultaneous broadband generation of second and third harmonics [2] by nonlinear photonic crystals. More recently, our group has accomplished simultaneous $5^{th}$–$8^{th}$ harmonic generation (HG) from a single chirped periodic poled lithium niobate (CPPLN) nonlinear crystal [3]. The CPPLN crystal offers a series of broad QPM bands with a considerably large effective nonlinear susceptibility $\chi_{eff}$ and freely designated spectral position to support SHG and SFG in the different wavelength bands that are necessary for various-order HHG. Upon illumination of a mid-IR femtosecond pulse laser, we have observed the generation of an ultrabroadband visible white light beam corresponding to $5^{th}$–$8^{th}$ HG with a record high conversion efficiency of 18%.

The CPPLN nonlinear crystal with HHG hints a new avenue for greatly expanding the power to engineer high-order nonlinear interactions in solid state materials and can find application in supercontinuum generation, ultrafast lasers, frequency combs, large-scale laser displays, and short-wavelength laser sources.

**REFERENCES**

1. Bao-Qin Chen, Chao Zhang, Rong-Juan Liu, and Zhi-Yuan Li,* "Multi-direction high-efficiency second harmonic generation in ellipse structure nonlinear photonic crystals", *Appl. Phys. Lett.* **105**, 151106 (2014).
2. Bao-Qin Chen, Ming-Liang Ren, Rong-Juan Liu, Yan Sheng, Bo-Qin Ma, Chao Zhang, and Zhi-Yuan Li*, "Simultaneous Broadband Second and Third Harmonic Generation in Chirped Nonlinear Photonic Crystal", *Light: Science & Application* **3**, e189 (1-6) (2014)
3. Bao-Qin Chen, Chao Zhang, Chen-Yang Hu, Rong-Juan Liu, and Zhi-Yuan Li*, "High-Efficiency Broadband High-Harmonic Generation from a Single Quasi-Phase-Matching Nonlinear Crystal", *Phys. Rev. Lett.* **115**, 083502 (2015)

# Topological Description and Nonlinearity Enhancement for Optical Mirrors

**Hong Chen**
School of Physics, Tongji University, Shanghai 200092, China
hongchen@tongji.edu.cn

Optical materials can be classified, analog to electronic materials, into two catalogues depending on the sign of the product of permittivity $\varepsilon$ and permeability $\mu$, i.e. optical conductors for both double-positive materials ($\varepsilon > 0, \mu > 0$) and double-negative materials ($\varepsilon < 0, \mu < 0$); optical insulators or mirrors for both $\varepsilon$-negative (ENG) materials ($\varepsilon < 0, \mu > 0$) and $\mu$-negative (MNG) materials ($\varepsilon > 0, \mu < 0$). Metals, as typical ENG optical mirrors, have much larger third-order nonlinear susceptibility than those of typical dielectrics. However, such novel nonlinear properties are inaccessible due to high reflectance of the mirrors. In this talk we will discuss our recent studies on nonlinearity enhancement of an optical thick metal slab based on the mechanism of the topological edge states. Inspired by recent studies on novel properties of electronic topological insulators, we have developed a topological description for optical mirrors by mapping Maxwell's equation to the Dirac equation in 1D systems [1,2]. It is shown that there exists topological difference between ENG and MNG mirrors as the result of mass inversion in the Dirac equation. Photonic analogs of topological excitations of the Dirac equation have been observed, such as edge states coming from the Berry phase in a 1D stack of ENG-MNG mirrors. Applications based on the edge states in pairing structures made of a metal slab and a MNG-like 1D photonic crystal, e.g., enhancing nonlinearity, realizing all-optical diode action, and nonlinear excitation of SPP's are also discussed.

**Reference**

[1] S.Q. Shen, *Topological insulators: Dirac Equation in Condensed matters*, Springer-Verlag, Berlin, 2012.

[2] Tan, W., Sun, Y., Chen, H. & Shen, S.-Q. Photonic simulation of topological excitations in metamaterials. Sci. Rep. 4, 3842; DOI:10.1038/srep03842 (2014).

# Self-accelerating Pulses and Their Nonlinear Dynamics

**Yi Hu[1,2*], Zhigang Chen[1,2,3], and Jingjun Xu[1,2]**

[1]The MOE Key Laboratory of Weak-Light Nonlinear Photonics, TEDA Applied Physics Institute and School of Physics, Nankai University, Tianjin 300457, China

[2]Collaborative Innovation Center of Extreme Optics, Shanxi University, Taiyuan, Shanxi 030006, China

[3]Department of Physics and Astronomy, San Francisco State University, San Francisco, California 94132, USA

[*]corresponding author: yihu@nankai.edu.cn

**Abstract**-Self-accelerating pulses are reviewed together with the development of areas associated with self-accelerating wave packets, and our study on the control of these pulses as well as on their nonlinear dynamics are presented in this talk.

Self-accelerating wave packets have been receiving lots of attention in recent years. Fueled by themselves, they are able to propagate in a curved trajectory in free space, or evolve in an accelerating configuration in time in a dispersive system, without using any special structure or nonlinearity. Such a concept of self-acceleration offers a new perception on waves and hence shows not only fundamental interest but also fascinating prospect in applications. Since the first experimental realization of self-accelerating wave packets in optics, namely Airy beams [1,2], such a new wave packet has successively become real in plasmonics, matter waves, acoustics and hydrodynamics. Self-accelerating pulses, as one of the family members, exhibit the common features of these packets including accelerating, non-spreading and self-healing properties, which have been ingeniously applied in producing linear optical bullets [3,4], manipulating soliton interactions [5], and controlling supercontinuum generation [6] as well as intra-pulse Raman scattering [7]. In this talk, we will present our recent study on self-accelerating pulses, ranging from the control of these pulses to their intriguing nonlinear dynamics under the effect of high-order nonlinearities/dispersions.

**REFERENCES**

1. Siviloglou, G. A., Broky J., Dogariu A., et al, "Observation of Accelerating Airy Beams," *Phys. Rev. Lett.*, Vol. 99, No. 213901, 1–4, 2007.
2. Hu Y., Siviloglou G. A., Zhang P., et al, Self-accelerating Airy Beams: Generation, Control, and Applications, Springer, New York, 2012.
3. Chong A., Renninger W. H., Christodoulides. D. N., et al, "Airy–Bessel wave packets as versatile linear light bullets," *Nat. Phonics*, Vol. 4, 103–106, 2010.
4. Abdollahpour D., Suntsov S., Papazoglou D. G., et al, "Spatiotemporal Airy Light Bullets in the Linear and Nonlinear Regimes," *Phys. Rev. Lett.*, Vol. 105, No. 253901, 1–4, 2010.
5. Cai W., Mills M. S., Christodoulides D. N., et al, "Soliton manipulation using Airy pulses," Opt. Commun., Vol 316, No. 1, 127–131, 2014.
6. Ament C., Polynkin P., and Moloney J. V., "Supercontinuum Generation with Femtosecond Self-Healing Airy Pulses," *Phys. Rev. Lett.*, Vol. 107, No. 243901, 1–5, 2011.
7. Hu Y., Tehranchi A., Wabnitz S., et al, "Improved Intrapulse Raman Scattering Control via Asymmetric Airy Pulses," *Phys. Rev. Lett.*, Vol. 114, No. 073901, 1–5, 2015.

# Optical control of patterns and polariton flow in semiconductor microcavities

**S. Schumacher**[1*]

[1] Department of Physics and CeOPP, University of Paderborn, 33098 Paderborn, Germany

[*]corresponding author: stefan.schumacher@uni-paderborn.de

**Abstract**-Polaritons in semiconductor microcavities are composite particles formed from photons and excitons. Through their photonic component they can be efficiently optically controlled. Their excitonic part gives rise to intriguing nonlinear behavior. Here we will discuss schemes to efficiently control self-organization and flow of polaritons with light.

With long-lived coherences and strong nonlinearities, polaritons in semiconductor quantum-well microcavities have recently proven an ideal playground for nonlinear optical physics. Recent studies have focussed both on direct resonant excitation of polaritons and on off-resonant excitation of coherent polariton condensates through an exciton reservoir. The interest in polaritons is fueled both by an interest in fundamental physics as well as by their promise for future applications.

In the presentation I will discuss our recent work in the area of self-organization and pattern formation of coherently driven polariton systems [1,2]. In particular the spinor character of the polariton quantum fluid distinguishes the patterns formed from patterns previously studied in other systems. Apart from being of fundamental interest, this also opens up new possibilities to optically control the patterns. In the second part I will discuss off-resonant excitation of polariton condensates with spatially structured excitation profiles [3]. In this scenario the spatial shape of the exciton reservoir density can be re-configured by changing the optical excitation profile which can be used to control the flow of the polaritons in the two-dimensional plane.

**REFERENCES**

1. V. Ardizzone, P. Lewandowski, M. H. Luk, Y. C. Tse, N. H. Kwong, A. Lücke, M. Abbarchi, E. Baudin, E. Galopin, J. Bloch, A. Lemaître, P. T. Leung, Ph. Roussignol, R. Binder, J. Tignon, and S. Schumacher, "Formation and control of Turing patterns in a coherent quantum fluid," *Scientific Reports*, Vol. 3, 3016, 2013.
2. A. M. C. Dawes, D. J. Gauthier, S. Schumacher, N. H. Kwong, R. Binder, and A. L. Smirl, "Transverse optical patterns for ultra-low-light-level all-optical switching," *Laser & Photonics Reviews*, Vol. 4, 221, 2010.
3. J. Schmutzler, P. Lewandowski, M. Assmann, S. Schumacher, M. Kamp, C. Schneider, S. Höfling, and M. Bayer, "All-optical flow control of a polariton condensate using only non-resonant excitation," *Physical Review B*, Vol. 91, 195308, 2015.

# Shaping optical absorption in disorder gold nanorod assemblies

**Yi Xu[1*⊥], Jin-Xiang Li[2⊥], Qiao-feng Dai[2], Shao-long Tie[3] and Sheng Lan[2*]**

[1] Department of Electronic Engineering, College of Information Science and Technology, Jinan university, China

[2] School of Information and Optoelectronic Science and Engineering, South China Normal University, China

[3] School of Chemistry and Environment, South China Normal University, Guangzhou, China

[*]corresponding author: e_chui@qq.com slan@scnu.edu.cn, [⊥]equal contribution

**Abstract**-We demonstrate that the relevance between the linear and the nonlinear optical absorption of a gold nanorod assembly can be modulated by plasmonic coupling. The strongly localized modes induced by random coupling play a crucial role in determining the optical absorption of the plasmonic systems.

Gold nanorods (GNRs) are the most intensively and extensively studied nanoparticles [1,2]. The plasmonic coupling between GNRs will modify the optical properties of GNRs and the coupling of two GNRs has been extensively investigated [3-8]. However, less attention has been paid to the effects of plasmonic coupling on the nonlinear optical properties of GNRs assembly [9,10]. To data, several groups have shown independently that the nonlinear absorption peak coincides with the linear one for GNR assemblies with low optical densities [2,11]. However, an intuitive conclusion will be not true when strong plasmonic coupling is introduced.

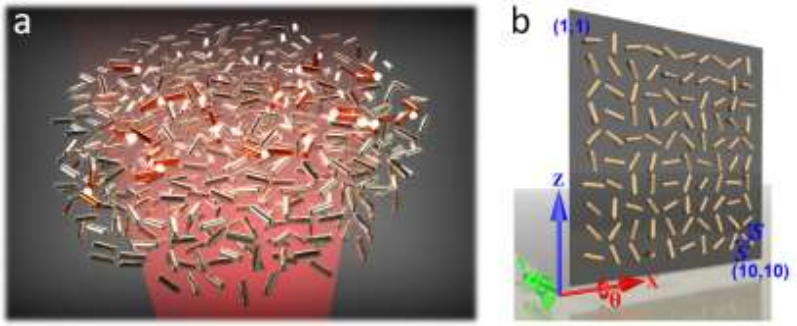



**Figure 1** (a) Sketch of the plasmonic hot spots created in a coupled gold nanorod assembly. (b) Schematic of the physical model which is used to qualitatively model the coupling effect on the TPA of a gold assembly. The square GNR array composed of 10 x 1 x 10 randomly oriented GNRs. The diameter and length of GNRs are 6 and 25 nm. θ and ψ indicate the random rotational angles of the GNRs referring to x and y axes, respectively.

The structure under consideration is schematically shown in Fig. 1 (a). We use a simplified version shown in Fig. 1 (b) to study the effect of plasmonic coupling on the optical absorption. The normalized single photon absorption (SPA) spectra of the GNR arrays with different lattice constants are shown in Fig. 2 (a). With decreasing S, a slight redshift of the SPA peak as well as a significant broadening of the longitudinal SPRs is observed. We also present the normalized two photon absorption (TPA) spectra for the corresponding GNR arrays in Fig. 2 (a). For the GNR array with weak coupling (S = 2L), the SPA and TPA peaks coincide (λ = 910 nm). For the GNR array with larger coupling (S = L), they are separated. In Fig. 2 (b), we present the corresponding experimental result measured in the GNR-PVA films. The TPA peaks for the GNR-PVA film with optical density (OD) = 3 appear at λ = 800 nm [locations $C_0$ and $C_1$], consistent with the SPA peak. In sharp contrast, the TPA peaks for the GNR-PVA film with OD = 24 exhibit a strong dependence on the local volume density of GNRs and appear at a longer wavelengths ranging from 880 to 920 nm [locations $C_2$, $C_3$ and $C_4$]. A large redshift (~120 nm) of the TPA peak with respect to the SPA peak is experimentally observed for the

location $C_4$. Such experimental observation indicates that the coupling induced modulation of TPA is substantial. The maximum TPA is no longer achieved at the SPA peak for the GNR assembly with strong enough coupling.

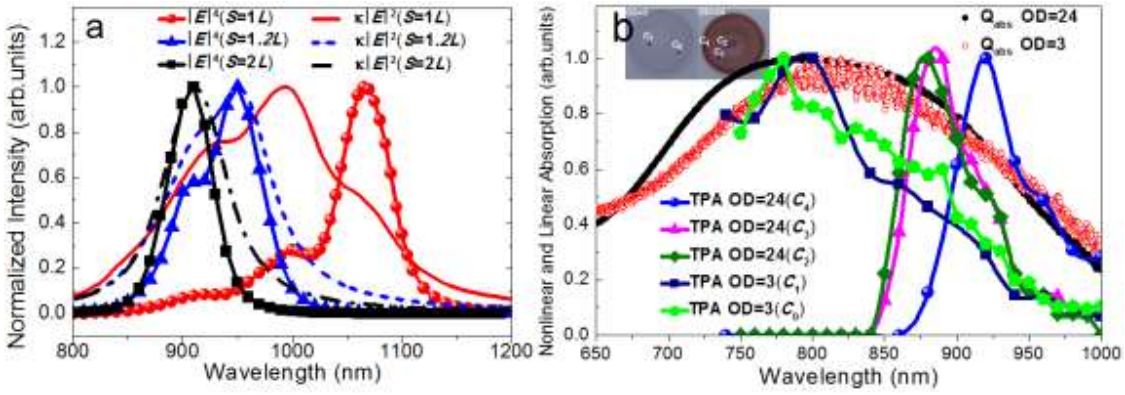



**Figure 2** (a) Normalized SPA and TPA spectra calculated for GNR arrays with different lattice constants. (b) Excitation spectra of the TPL measured for GNR-PVA films with OD = 3 and 24 at different locations ($C_0$ to $C_4$). $Q_{abs}$ stands for the Normolized SPA. The photos of GNR-PVA films and the measured positions are shown by the insets of (b).

Our results provide a guideline for engineering the optical absorption in disorder plasmonic systems. The authors acknowledge the financial support from the National Natural Science Foundation of China (Grant Nos. 51171066, 11374109 and 11304047).

**REFERENCES**

1. Prasad P. N., *Nanophotonics*, John Wiley, Sons, Inc.: New York, 2004.
2. Chon J. W. M., Bullen C., Zijlstra P., and Gu M., "Spectral encoding on gold nanorods doped in a silica sol-gel matrix and its application to high-density optical data storage," *Adv. Funct. Mater.*, Vol.17, No. 6, 875-880, 2007.
3. Halas N. J., Lal S., Chang W.-S., Link S., and Nordlander P., "Plasmons in strongly coupled metallic nanostructures," *Chem. Rev.*, Vol. 111, No. 6, 3913-3961, 2011.
4. Nordlander P., Oubre C., Prodan E., Li K., and Stockman M. I., "Plasmon hybridization in nanoparticle dimers," *Nano Lett.*, Vol. 4, No.5, 899-903, 2004.
5. Funston A. M., Novo C., Davis T. J., and Mulvaney P., "Plasmon coupling of gold nanorods at short distances and in different geometries," *Nano Lett.*, Vol. 9, No. 4, 1651-1658, 2009.
6. Tabor C., Haute D. V., and El-Sayed M. A., "Effects of orientation on plasmonic coupling between gold nanorods," *ACS Nano* Vol. 3, No. 11, 3670-3678, 2009.
7. Shao L., Woo K. C., Chen H., et al, "Angle- and energy-resolved plasmon coupling in gold nanorod dimers," *ACS Nano*, Vol. 4, No. 6, 3053-3062, 2010.
8. Krasnok A. E., Maksymov I. S., Denisyuk A. I., Belov P. A., Miroshnichenko A. E., Simovski C. R., and Kivshar Y. S., "Optical nanoantennas," *Phys. -Usp*. Vol. 56, No. 6, 539-564, 2013.
9. Klaer P., Razinskas G., Lehr M., et al, "Robustness of plasmonic angular momentum confinement in cross resonant optical antennas," *Appl. Phys. Lett.*, Vol. 106, No. 26, 261101, 2015.
10. Deng H., Chen X., Xu Y. and Miroshnichenko A. E., "Single protein sensing with asymmetric plasmonic hexamer via Fano resonance enhanced two-photon luminescence," *Nanoscale*, Vol. 7, No. 48, 20405-20413, 2015.
11. Wang H., Huff T. B., Zweifel D. A., et al, "In vitro and in vivo two-photon luminescence imaging of single gold nanorods," *Proc. Natl. Acad. Sci.*, Vol. 102, No. 44, 15752- 15756, 2005.

# Third harmonic emission from self-organized dielectric meta-surfaces.

**S. V. Makarov[1], T. Voitova[1], A. Tsypkin[1], V. A. Milichko[1], I. S. Mukhin[1,2], A.V. Yulin[1*], E. Putilin[1], M. Baranov[1], A. E. Krasnok[1], and P. A. Belov[1]**

[1]ITMO University, St. Petersburg 197101, Russia

[2]St. Petersburg Academic University, St. Petersburg 194021, Russia

[*]corresponding author: alex.v.yulin@gmail.com

**Abstract-** The process of laser induced self-organization of silicon clusters is used to fabricate large scale meta-surfaces showing pronounced optical resonances in the infrared range of wavelengths. It is experimentally demonstrated that the efficiency of third harmonic generation in these systems can be 30 times higher than in spatially uniform non-resonant films. We managed to generate 40 fs pulses of ultraviolet coherent light with total energy of 1.3nJ at the wavelength of 266nm. A simple theory describing the phenomenon is developed.

In recent time nonlinear optics of high refractive index nanoparticles attracts much of attention because of both the fundamental and practical importance. Strong spatial localization of the field in the particles at the resonant frequencies opens a way to enhance nonlinear optical effects greatly. In this work a process of third harmonic generation in nanostructured films is studied. We show that 5nJ femtosecond ultraviolet pulses can be formed by third harmonic generation in Si-based resonant structures with the conversion efficiency$10^{-6}$. The wavelength of the generated light is 266nm and thus the process of third harmonic generation in the considered nanostructures can be used for the development of compact sources of ultraviolet light.

To fabricate the periodically arranged arrays of nano-particles we use self-organizing laser-induced nano structuring of thin Si:H films. The method is schematically illustrated in Fig. 1.

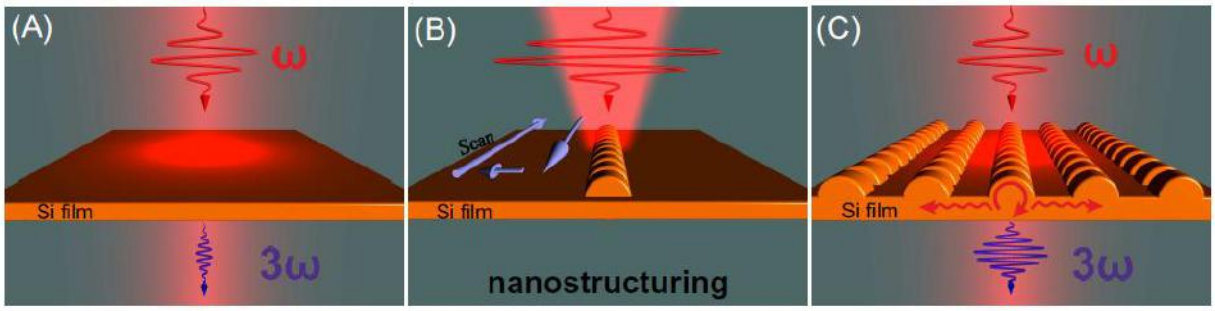



**Figure 1** Schematic views of third harmonic generation from smooth (A) and nanostructured (C) Si film. (B) Illustration of the principle of Si film laser-induced nanostructuring.

To produce the metasurfaces we use silicon films with the thickness varying from 30nm to 200nm. After the processing the film transforms into an array of periodically arranged quasi-elliptical particles with the sizes 130nm x 330nm, the period of the array is 260nm along one dimension and 700 along another dimension.

To generate the third harmonic we use 40 fs laser pulses with the wavelength 780 nm and having energy up to 1.3mJ. The third harmonic signal was filtered from the fundamental frequency and then measured by a power meter.

We measure the power of third harmonics generated from the metasufaces of different thicknesses, see panel (A) of Fig. 2. The non-monotonic behavior can be explained by Fabry-Perot resonances in the silicon film. The panel (B) shows the dependence of the power of the third harmonic on the power of the pump at the fundamental frequency. The dependencies are plotted in double-log scale and it is clearly seen that the experimental points fit well to the cubic dependency expected for the third harmonic generation.

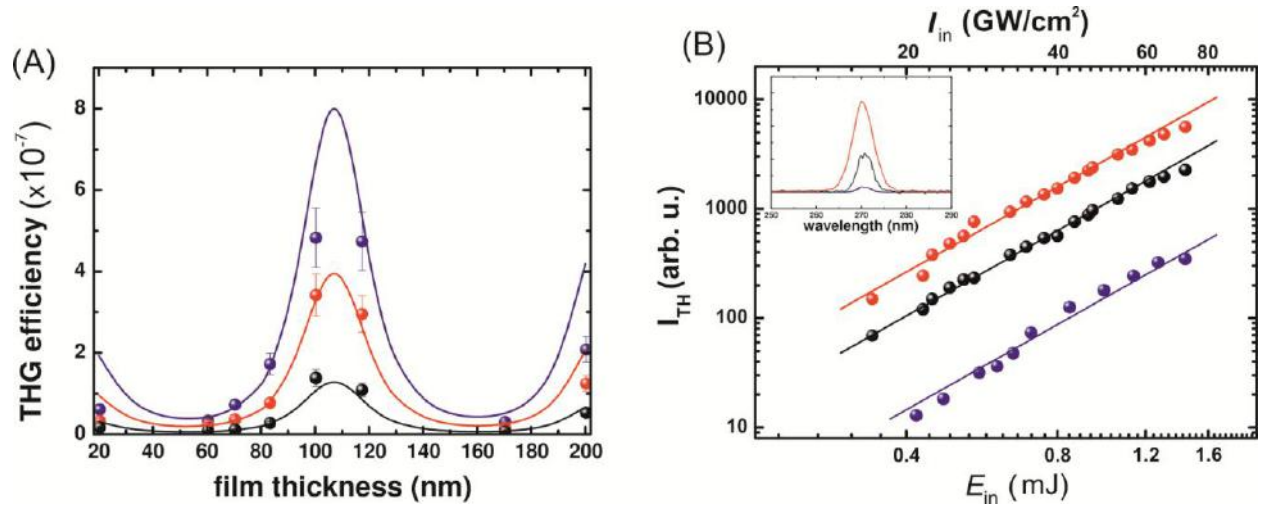



**Figure 1** (A) Dependencies of third harmonic power on a film thickness for different pump intensities. (B) Experimental dependencies of third harmonic intensity on the pump power for the non-structured (black curve), resonant structured (red curve) and non-resonant structured (blue curve) films of 100-nm thickness deposed on thick fused silica substrate. Inset: the spectrum of the third harmonics.

The measurements show that in our structures the efficiency of the third harmonic generation is as high as $10^{-6}$. This value is about 2 times higher than that value for the films supporting only Fabry-Perot resonances and about 30 times higher than the generation efficiency in spatially uniform non-resonant films. The increase of the efficiency can be explained by local enhancement of the filed caused by the nanoparticles.

To conclude we briefly summarize the main results of the work. Self-organizing laser-induced nanostructuring of thin Si:H films is used to fabricate arrays of subwavelength structures with pronounced resonances at optical frequencies. The efficiency of the third harmonic generation in the nanostructured metasurfaces is much higher comparing to their spatially uniform counterparts due to the enhancement of the field at the resonant frequencies.

**Acknowledgements:** The work was supported by Russian Science Foundation №15-19-30023. SVM and AVY acknowledge the support from the Government of the Russian Federation (Grant 074-U01) through ITMO Early Career Fellowship scheme.

# Improved nonlinear plasmonic slot waveguides

**Mahmoud M. R. Elsawy**, **Gilles Renversez**

Aix–Marseille Université, CNRS, Ecole Centrale, Institut Fresnel, 13013 Marseille, France
mahmoud.elsawy@fresnel.fr, gilles.renversez@fresnel.fr

**Abstract**— We study the main properties of TM modes in an improved symmetric metal slot waveguide with a Kerr-type nonlinear dielectric core, adding linear dielectric buffer layers between the metal cladding and the core. The stability of the main modes has also been demonstrated numerically. Our model is extended to consider complex waveguides with nonlinear hyperbolic metamaterials embedded between two metal cladding.

Nonlinear plasmonic slot waveguides (NPSWs) have drawn attention in the last decade due to the strong light confinement in the nonlinear dielectric core ensured by the surrounding metal regions, and to their peculiar nonlinear effects [1, 2]. Nevertheless, the experimental observation of plasmon-soliton waves in these NPSWs is still lacking, and the loss is still a fundamental issue. In our work, we propose and study the improvement of the symmetric metal-nonlinear dielectric-metal waveguides by the inclusion of two lateral linear dielectric buffer layers between the nonlinear dielectric core of focusing Kerr-type and the two semi-infinite metal cladding see Fig. 1. These supplementary buffer layers have two principle consequences. First, they reduce the overall losses, and allow the losses to decrease with the power. Secondly, they modify the types of solutions that propagate in the simple structures [3, 5]. We use the fixed power algorithm in the finite element method (FEM) to compute the nonlinear stationary solutions and their nonlinear dispersion curves [4]. In the linear case, our improved structure provides two different families of modes.

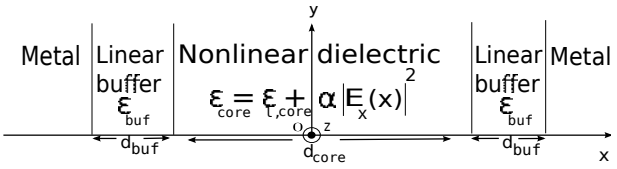



Figure 1: Improved NPSW with supplementary buffer layers between the core and the metal region.

The plasmonic type modes, where the effective index of the guided wave is above the core linear refractive index. These modes are similar to what already obtained in the simple structure [3]. For well-chosen refractive indices or thicknesses of the buffer layers, new type of linear modes can be found in our improved structure in which the effective index of the guided wave is below the core linear refractive index. They follow the cosine profile in the linear high-index core with plasmonic tails in the metal regions. For the nonlinear study, we start with the case such that the effective index of the linear modes is below the core linear refractive index. The real parts of effective indices of the first three main modes: symmetric, asymmetric and antisymmetric denoted respectively by S0-solI, AS1-solI, and AN0-solI, are shown in Fig. 2(a) while their imaginary parts and losses are shown in Fig. 2(b). In the two previous figures, the three main nonlinear plasmonic modes for a simple NPSW made from the improved NPSW by removing the buffer dielectric layers are also shown in grey for comparison (symmetric S0-plas, asymmetric AS1-plas, antisymmetric AN0-plas). As it can be seen, in the improved NPSW, the global shape of the dispersion curves is similar to what already obtained in the simple structures [3, 5]. Nevertheless, the field profiles now are of solitonic type with plasmonic tails in the metal regions see Fig. 3(a), (b), and (c). We also note that losses are at least three times smaller than the ones of the simple NPSW and they decrease with the increase of the power (see Fig. 2(b)). We now study the nonlinear dispersion curves of the improved NPSW such that the effective index of the linear modes is above the core linear refractive index. The corresponding curves are given in Fig. 2(c) and (d). The global shape of these dispersion curves is similar to the ones already studied for the three main modes of the simple NPSW but the mode field profiles now exhibit a spatial transition from a plasmonic type profile to a solitonic type one see Fig. 3(d), (e), and (f). Furthermore, at low powers, the losses are reduced, at least, by a factor two compared to the associated simple NPSW, and they are now decreasing with the power for the main symmetric and antisymmetric modes leading to low loss solutions at high powers (see

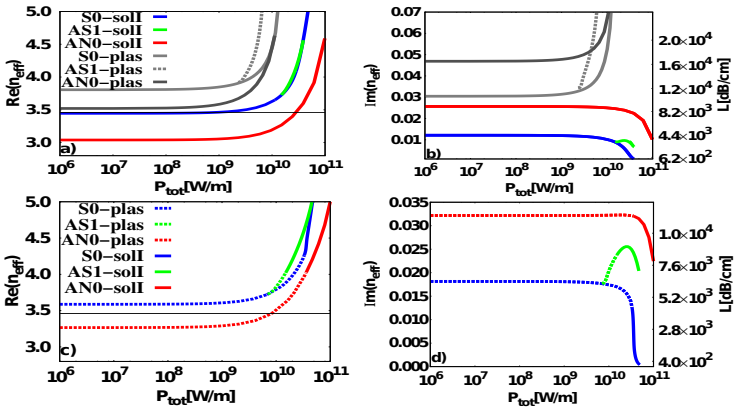



Figure 2: Nonlinear dispersion curves for the simple NPSW (grey curves) and for the improved one (color curves). The blue, green, and red colors indicate the symmetric, asymmetric and antisymmetric nonlinear modes respectively. $d_{core} = 400$ nm, $d_{buf} = 15$ nm. For $\varepsilon_{buf} = 2^2$: (a) for $\Re e(n_{eff})$ and (b) for $\Im m(n_{eff})$ and the associated losses. For $\varepsilon_{buf} = 2.5^2$: (c) for $\Re e(n_{eff})$ and (d) for $\Im m(n_{eff})$ and the associated losses.

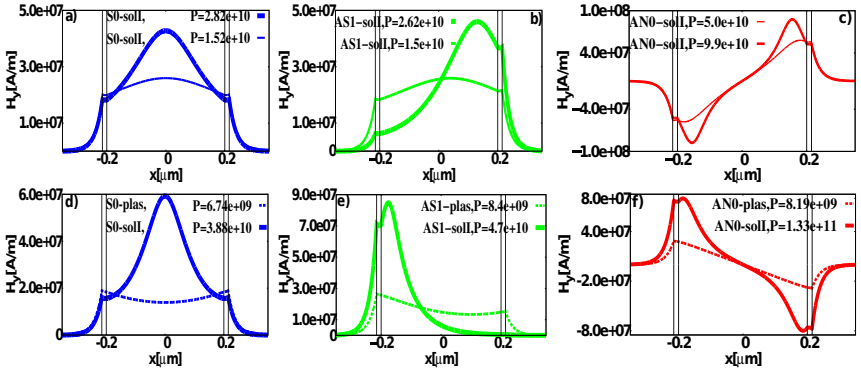



Figure 3: Typical nonlinear magnetic field profiles at different powers for the improved structure. First row for $\varepsilon_{buf} = 2^2$ (see Fig 2(a) and (b)). Second row for $\varepsilon_{buf} = 2.5^2$ (see Fig 2(c) and (d)).

Fig. 2(d)). For the asymmetric mode, loss first increases with power and then decreases. This loss increase is linked to the fact that, in this case, the field first tends to increase near one of the metal interface, increasing the fraction of field in a highly lossy region. Then, the mode moves gradually from a plasmonic type to a solitonic type asymmetric profile, and when the peak of the soliton is far enough from the metal interface the losses start to decrease see Fig 3(e). Using our numerical method, we obtained the phase diagrams for the improved NPSW for the main modes as a function of the total power, buffer, and core thicknesses. The stability of the main modes has been also demonstrated numerically using the FDTD method. Our model is extended to treat complex waveguides with nonlinear anisotropic core embedded between two semi-infinite metal cladding. Depending on the sign of the diagonal elements of the linear permittivity tensor, we can achieve novel nonlinear effects. Interestingly, starting from a focusing Kerr-nonlinearity, one can obtain a defocusing effect which can be tuned by the power. This peculiar nonlinear effect can be obtained, when one of the elements of the linear diagonal tensor is negative (Hyperbolic metamaterials). For positive diagonal elements, this structure is shown to enhance the focusing nonlinearity in most of the cases. Our new structures could be fabricated and characterized experimentally.

**REFERENCES**


1. E. Feigenbaum and M. Orenstein, "Plasmon-soliton," Opt. Lett. **32**, 674–676 (2007).
2. A. R. Davoyan, I. V. Shadrivov, and Y. S. Kivshar, "Self-focusing and spatial plasmon-polariton solitons," Opt. Express **17**, 21732–21737 (2009).
3. W. Walasik and G. Renversez, "Plasmon-soliton waves in planar slot waveguides. i. modeling," Phys. Rev. A **93**, 013825 (2016).
4. F. Drouart, G. Renversez, A. Nicolet, and C. Geuzaine, "Spatial Kerr solitons in optical fibres of finite size cross section: beyond the Townes soliton," J. Opt. A: Pure Appl. Opt. **10**, 125101 (2008).
5. W. Walasik, G. Renversez, and F. Ye, "Plasmon-soliton waves in planar slot waveguides. ii. results for stationary waves and stability analysis," Phys. Rev. A **93**, 013826 (2016).

# Still azimuthal doughnuts in near-zero-index media

**A. Marini**[1,*] **and F. J. García de Abajo**[2]

[1]ICFO-Institut de Ciencies Fotoniques, The Barcelona Institute of Science and Technology,
08860 Castelldefels (Barcelona), Spain

[2]ICREA-Institució Catalana de Recerca i Estudis Avançats,
Passeig Lluís Companys 23, 08010 Barcelona, Spain

[*]corresponding author: andrea.marini@icfo.es

**Abstract** - Optical beams are generally unbound in bulk media. Here we reveal the existence of still doughnut-shaped and azimuthally polarized solitons with vanishing Poynting vector and angular momentum in near-zero-index media with Kerr nonlinearity. Our results suggest applications in optical data processing and storage, quantum optical memories, and soliton-based lasers without cavities. Additionally, near-zero-index conditions can also be found in the interplanetary medium and in the atmosphere, where we provide a complementary explanation to the rare phenomenon of ball-lightning.

Spatial and temporal self-trapping of light beams occur in several optical systems, including photorefractive media, liquid crystals, and metamaterials. Remarkably, nonlinearity can act simultaneously on temporal and spatial domains to compensate for both diffraction and dispersion, thus enabling the formation of light bullets, spatio-temporal doughnuts, and X-shaped waves. Physical systems enabling either slow or fast light naturally enhance radiation-matter interaction, thus boosting nonlinear processes that can be efficiently used for active light control, all-optical switching, and modulation. In particular, near-zero-index (NZI) media can slow down light propagation [1,2] and enable extreme nonlinear dynamics, enhanced second and third harmonic generation, active control of tunneling, optical switching, and bistable response. These materials naturally exist in nature, for example plasmas, transparent conductors, and metals near their bulk plasma frequency $\omega_p$. Besides, they can be artificially realized as waveguides close to modal cutoff, using surface phonon polaritons in GaAs quantum wells, or by engineering subwavelength metallic nanowires, nano-spheres, or nano-circuits embedded in dielectric matrices. The latter strategy has enabled the development of epsilon-near-zero (ENZ) metamaterials, which have been investigated for applications such as enhanced transmission, cloaking, energy squeezing in narrow channels, and subwavelength imaging. The ENZ regime is inevitably associated with high dispersion and is therefore accompanied by absorption, which can be suppressed by embedding externally pumped active inclusions in the NZI medium.

Here we theoretically investigate self-organization of light in NZI media with Kerr-like instantaneous nonlinearity. In particular, we reveal the existence of fully confined doughnut-shaped solitons with vanishing Poynting vector and angular momentum. In practice nonlinearity enables digging a three-dimensional cavity for light, which in turn remains frozen and self-trapped. We study the effect of loss on stationary light doughnuts by developing a soliton perturbative theory, finding that they evaporate over time due to absorption: their amplitude decreases, their frequency blueshifts slightly, and their radius increases. These findings demonstrate the possibility to freeze light beams in NZI media, with potential applications in optical data processing and storage, quantum optical memories, and NZI lasers operating without cavities [2].

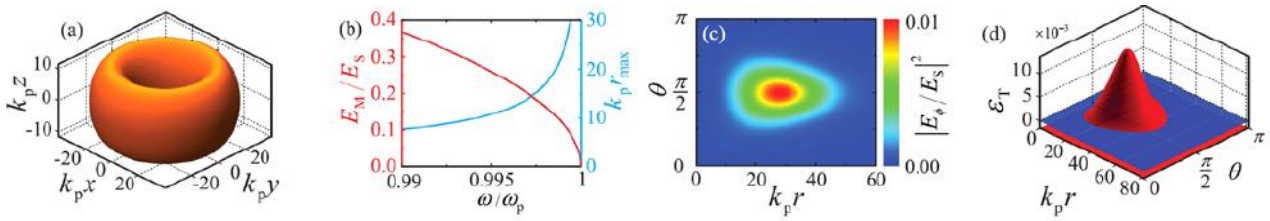



**Figure 1:** (**a**) Iso-surface $|E_\varphi(\mathbf{r})/E_S|^2$ = 0.005 of a still doughnut with maximum squared amplitude $|E_M/E_S|^2$ = 0.01, where $E_S = \chi_3^{-1/2}$ is the scaling field amplitude, excited at an angular frequency $\omega/\omega_p$ = 0.9992. (**b**) Soliton maximum amplitude $E_M/E_S$ (red left *y*-axis) and its corresponding radius $r_{max}$ (cyan right *y*-axis) as a function of angular frequency $\omega/\omega_p$. (**c**) Contour-plot in the *r*-$\theta$ plane of the dimensionless intensity profile $|E_\varphi(r,\theta)/E_S|^2$ and (**d**) total dielectric permittivity profile including Kerr nonlinearity $\varepsilon_T(r,\theta)$ (red surface) associated with the still doughnut of (**a**). The blue plane in (**d**) represents the metal-dielectric transition plane $\varepsilon_T(r,\theta)$ = 0. All quantities are plotted in dimensionless units: the angular frequency $\omega$ is normalized to the plasma frequency $\omega_p$, while spatial coordinates are normalized to the inverse of the plasma wave-vector $k_p^{-1}$.

This phenomenology appears rather similar to ball-lighnings (BLs), rare lightning events with hitherto unknown theoretical explanation. Among the several theories trying to explain their nature, the so-called maser-caviton theory suggests that BLs are localized high-field solitons forming a cavity surrounded by plasma. Indeed, during thunderstorms, atmosphere can get ionized and become a NZI medium with a plasma frequency falling in the terahertz-microwave spectral region, where rotational levels of water can be excited. The ensuing emitted radiation is thought to remain self-trapped and heat up the air, thus emitting broadband blackbody radiation. Following our rigorous calculations, as suggested by the maser-caviton theory, we speculate that BLs may actually ensue from a self-organization process in the ENZ regime, where we theoretically demonstrate the existence of still doughnut solitons [2]. The ENZ condition would explain the infrequency of the phenomenon and provides an insightful signature for experimental investigations.

**Acknowledgements**

This work has been partially supported by the Spanish MINECO (MAT2014-59096-P and SEV-2015-0522) and the European Commission (Graphene Flagship CNECT-ICT-604391 and FP7-ICT-2013-613024-GRASP). A.M. is supported by an ICFOnest+ Postdoctoral Fellowship (Marie Curie COFUND program).

## REFERENCES

1. A. Ciattoni, A. Marini, C. Rizza, M. Scalora and F. Biancalana, “Polariton excitation in epsilon-near-zero slabs: Transient trapping of slow light,” *Phys. Rev. A*, Vol. 87, 053853, 2013.
2. A. Marini and F. J. Garcia de Abajo, “Self-organization of frozen light in near-zero-index media with cubic nonlinearity,” *Sci. Rep.*, Vol. 6, 20088, 2016.

# Structured Light in Nonlinear Colloidal Media

**S. Z. Silahli,[1] W. Walasik,[2] and N. M. Litchinitser,*[1]**

[1]University at Buffalo, The State University of New York, Buffalo, New York 14260, United States

*corresponding author: natashal@buffalo.edu

**Abstract**- We theoretically and experimentally investigate the possibility of necklace beam generation originating from spatial modulational instability of vortex beams in engineered colloidal nonlinear media with different types of exponential nonlinearity.

Self-focusing of optical vortices in various nonlinear optical media was investigated and the azimuthal modulation instability (MI) for ring-shaped vortices was shown to result in the beam breakup into a ring of filaments [1-4]. A majority of the previous studies focused on light-matter interactions in self-focusing Kerr media. Recently, the optical nonlinearity of colloidal suspensions, despite the initial belief that it was of the Kerr type, was found to be exponential [5]. Moreover, this exponential nonlinearity can be saturable or super-critical with intensity, depending on the sign of the particle polarizability in the suspension.

Here we theoretically and experimentally study spatial MI in soft-matter nonlinear media with these two distinct types of nonlinearity using beams with an orbital angular momentum (OAM). An optical beam propagating in the nano-colloidal system can be described by the nonlinear Schrödinger for the slowly varying electric field envelope φ [6]

$$i\frac{\partial\varphi}{\partial Z}+\frac{1}{2k_0n_b}\nabla_\perp^2\varphi+k_0\left(n_p-n_b\right)V_p\rho_0e^{\frac{\alpha}{4k_BT}|\varphi|^2}\varphi+\frac{i}{2}\sigma\rho_0e^{\frac{\alpha}{4k_BT}|\varphi|^2}\varphi=0. \qquad (1)$$

The particle polarizability is denoted by α, and $k_BT$ is the thermal energy. $V_p$ is the volume of a particle, $\rho_0$ is the unperturbed particle concentration, σ is the scattering cross-section, and $k_0=2\pi/\lambda_0$ is the wave number.

Equation (1) for the case of positive polarizability particles ($n_p > n_b$) can be written as follows

$$i\frac{\partial U}{\partial\xi}+U_{XX}+U_{YY}+e^{|U|^2}U+i\,\delta e^{|U|^2}U=0, \qquad (2)$$

while for the negative polarizability particles ($n_p < n_b$) is takes the following form

$$i\frac{\partial U}{\partial\xi}+U_{XX}+U_{YY}+\left(1-e^{-|U|^2}U\right)U+i\,\delta e^{-|U|^2}U=0. \qquad (3)$$

In order to understand the reason behind these different types of nonlinearity, we note that colloidal suspensions can be created by two kinds of particles: with positive polarizabilities corresponding to a particle refractive index greater than the background index ($n_p > n_b$) or with negative polarizability, with the corresponding refractive index of a particle lower than that of the background material ($n_p < n_b$) [6]. Positive polarizability dielectric particles are attracted towards the high-intensity regions of the beam, whereas negative polarizability particles are repelled (Fig. 1). At the same time, in the positive polarizability case, the nonlinear

scattering losses increase in the high-intensity region of the beam. In contrast, in the negative polarizability case, the nonlinear losses decrease with the increase of intensity since the particle concentration decreases.

In our initial studies [7], we predicted that different types of the exponential optical nonlinearity in the positive polarizability and negative polarizability cases lead to very different dynamics of beam propagation and to the formation of different spatial distributions of so-called necklace beams. Our results may be of interest for imaging and spectroscopic applications using light propagating in highly scattering biological and chemical colloidal media.

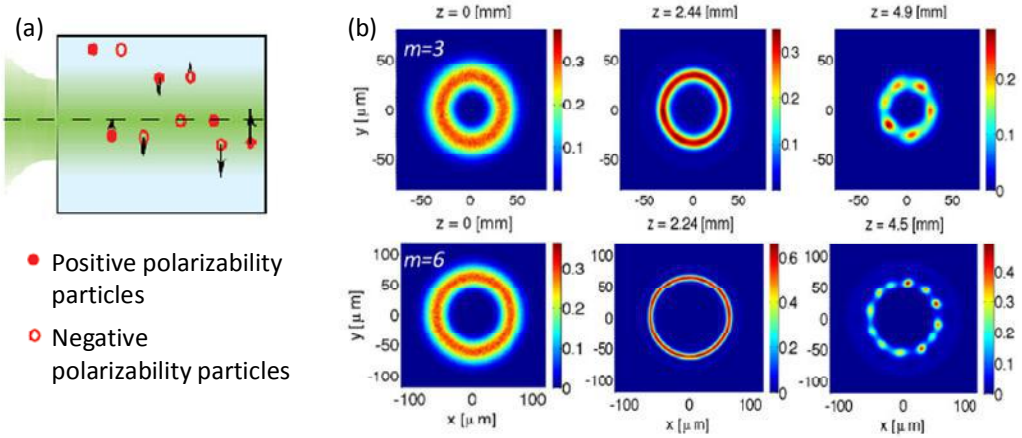



Figure 1 (a) Schematic illustration of light-particle interaction in colloidal suspensions. Arrows represent optical force acting on each of the particles. (b) Distribution of the electric field intensity presenting the dynamics of the necklace beams for different topological charges $m$=3,6 in the NP particle-based system.

**Acknowledgements**

This work was supported by the U.S. Army Research Office Awards No. W911NF-15-1-0146 and W911NF-11-1-0297.

**REFERENCES**

1. Soljacic, M., Sears, S., and Segev, M., “Self-Trapping of “Necklace” Beams in Self-Focusing Kerr Media,” Phys. Rev. Lett. 81, 4851-4854, 1998.
2. He, Y. J., Malomed, B. A. and Wang, H. Z., "Fusion of necklace-ring patterns into vortex and fundamental solitons in dissipative media," Opt. Express 15, 17502-17508, 2007.
3. Kartashov, Y. V., Malomed, B. A., Vysloukh, V. A., and Torner, L., Stabilization of multibeam necklace solitons in circular arrays with spatially modulated nonlinearity,” Phys. Rev. A 80, 053816(4), 2009.
4. Gaeta, A. L., “Collapsing Light Really Shines,” Science 301, 54-55, 2003.
5. Man, W., Fardad, S., Zhang, Z., Prakash, J., Lau, M., Zhang, P., Heinrich, M., Christodoulides, D. N., and Chen, Z., “Optical Nonlinearities and Enhanced Light Transmission in Soft-Matter Systems with Tunable Polarizabilities,” Phys. Rev. Lett. 111, 218302(5), 2013.
6. El-Ganainy, R., Christodoulides, D. N., Musslimani, Z. H., Rotschild, C., and Segev, M., "Optical beam instabilities in nonlinear nanosuspensions," Opt. Lett. 32, 3185-3187, 2007.
7. Silahli, S. Z., Walasik, W., and Litchinitser, N. M., "Necklace beam generation in nonlinear colloidal engineered media," Opt. Lett. 40, 5714-5717, 2015.

# All-optical light storage in nonlinear Fabry-Perot resonator and release by demand

**Konstantin Pichugin**[1] **and Almas Sadreev**[1*]

[1]Kirensky Institute of Physics, 660036 Krasnoyarsk, Russia
*corresponding author, E-mail: almas@tnp.krasn.ru

## Abstract

In the framework of the temporal coupled mode theory we consider bound states mbedded in the continuum (BSC) of photonic crystal waveguide as a capacity for light storage. A symmetry protected BSC occurs in two off-channel microresonators positioned symmetrically relative to the waveguide. We demonstrate that this BSC captures a fraction of a light pulse due to the Kerr effect as the pulse passes by the microresonators. However the amount of captured light is found to be extremely sensitive to the shape of the light pulse. In contrast to the above the BSCs in the Fabry-Perot resonator formed by nonlinear Fano mirrors accumulates a fixed amount of light but independent of the light pulse. Addition of auxiliary nonlinear off-channel resonator between the mirrors makes the process of light storage robust relative to the distance between mirrors. We also show that the accumulated light can be released by a secondary pulse. These phenomena pave a way for all-optical storage and release of light.

## 1. Introduction

One of the most technologically attractive approaches for light storage is the use of slow wave designs of optical periodic structures to slow down the light pulse [1, 1, 2]. Various methods and designs such as direct-coupled resonators [1, 3, 4] and photonic crystal (PhC) waveguides [5] have been proposed to slow down the group velocity of light. Slow light waveguides composed of left-handed materials have been also proposed [6, 7]. In these waveguides, the time average power in the left-handed material layer flows in an opposite direction of that in the normal dielectric layer. For the case when light flows are almost equal, slow light and even trapping can be achieved [8]. The frequency of the slow light regime varies with the thickness of the layer resulting in so-called trapped rainbow [9, 10, 11].

In this paper we propose to employ bound states in the continuum (BSC) as a novel capacity for light storage. Recently the BSCs have attracted much interest in photonics owing to a possibility to trap light in various photonic systems [12, 13, 14, 15, 16, 17, 18, 19, 20, 21, 22, 23, 24, 25, 26, 27, 28, 29]. The BSC is a localized solution of the Maxwell equations with a discrete eigenfrequency coexisting with the extended modes of continuous spectrum of the PhC waveguide or radiation continuum. Our main goal is to demonstrate that the BSCs are able to capture light due the Kerr effect in the microresonators. Moreover we demonstrate that the application of a secondary light pulset releases trapped light making the BSC potentially interesting for all-optical light storage and release.

The physics of the light storage by the BSCs is the following. Assume for a moment that the amplitude of the injected wave is so small that we can neglect the nonlinearity. Because the BSC is completely decoupled from the continuum it can not be probed by the incoming wave. However with the increase of the injected power the Kerr effect of the microresonators becomes important killing two birds with one stone. First, there is no necessity for tuning material parameters because the Kerr effect in the microresonators results in occurrence of self-induced BSCs [30, 31, 32]. Second, the nonlinearity couples the BSC with the continuum so that the injected wave excites the BSC transforming it into a quasi-BSC. Once the pulse has passed by the microeresonator the quasi-BSC is again decoupled from the waveguide and becomes a true BSC. As a result some amount of light is trapped in the true BSC opening an opportunity for light storage. Finally, the application of a secondary pulse again transforms the true BSC into a quasi-BSC with finite life-time and releases the light with substantial or even $100\%$ efficiency. Below we inspect these ideas on the basis of three simplest 2D PhC designs which realize the self-induced BSCs. The present paper develops the ideas and methods in Ref. [33] in application to Fabry-Perot resonator with nonlinear resonant mirrors and auxiliary nonlinear off-channel microresonator in linear PhC waveguide. The last adjusts optical length between mirrors in self-induced way and makes the process of light storage fully robust.

## 2. Symmetry protected BSC

We begin with the most obvious system in which light can be trapped by the symmetry protected BSC [15, 19, 22, 34]. For clear visualization of such a BSC we present in Fig. 1 (a) 2D photonic crystal (PhC) layout. However interested reader can easily design different layouts based for instance on nano resonators with extremely high Q-factors in air-hole 2D PhC system [35, 36, 37]. In order to present the mechanism of light storage in the BSC in the most comprehensive form we assume that among all eigenmodes of the micro resonator only the lowest monopole TM mode has the eigenfrequency $\omega_0$ embedded into the first TM propa-

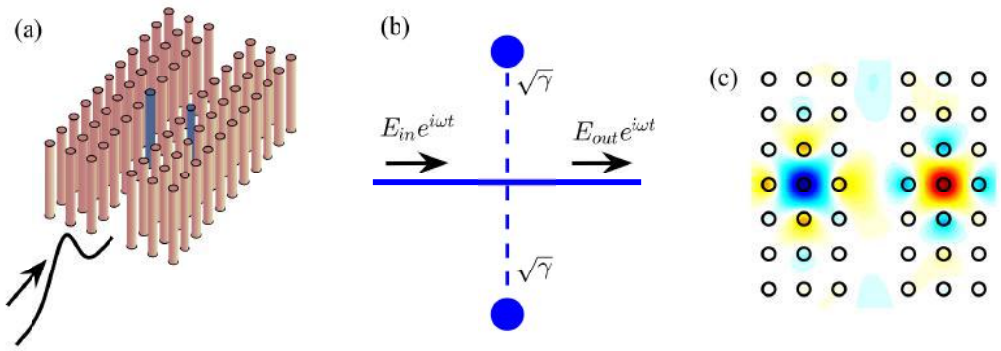



Figure 1: (a) Square lattice of dielectric rods of GaAs with $n_0 = 4.3, n_2 = 2 \cdot 10^{-12} W/cm^2, a = 0.5\mu m$, radius $0.18\mu m$ shown in pink where $a$ is the lattice unit. The single row of the rods is removed from the PhC to form a directional photonic waveguide which supports a band of guided even TM mode. Two defect rods shown in gray with the Kerr effect are inserted symmetrically relative to the waveguide to form identical off-channel optical microresonators coupled with the waveguide. (b) Equivalent CMT presentation for PhC layout. (c) Electric field profile in the symmetric protected BSC.

gation band of the directional PhC waveguide. Then the eigenmodes of the total system of two resonators can be classified as symmetric and antisymmetric modes

$$A_{s,a} = (A_1 \pm A_2)/2, \;\; \omega_{s,a} = \omega_0 \pm u \tag{1}$$

where variable $A_j, j = 1, 2$ present the amplitudes of the single modes in the j-th microresonator. For simplicity we disregard the dispersion properties of the waveguide and consider that light with the amplitude $E_{in}$ is injected into the waveguide as shown in Fig. 1. We assume the injected light is symmetrical relative to the direction cross to the waveguide. Then the temporal coupled mode theory (CMT) equations has the following form [38, 39]

$$\begin{aligned} -i\dot{A}_s &= (\omega_s + 2i\gamma)A_s - i\sqrt{\gamma}E_{in}, \\ -i\dot{A}_a &= \omega_a A_a, \end{aligned} \tag{2}$$

where the term $\sqrt{\gamma}$ is responsible for the coupling of the off-channel resonators with the waveguide. Thus, these CMT equations constitute by the most obvious and simple way that the antisymmetric mode of two microresonators symmetrically coupled with the waveguide is the symmetry protected BSC. This antisymmetric BSC mode calculated for PhC structure shown in Fig. 1 (a) and experimentally observed by Plotnik *et al* [19] is shown in Fig. 1 (c).

If the waveguide can support only the symmetrical propagating mode then injected light can not probe the BSC. However that is truth for the linear case. If the microresonators are nonlinear owing to the Kerr effect of the rod's material there is a nonlinear shift of the eigenfrequency $\omega_0 \to \lambda|A_j|^2$ where $I_j = |A_j|^2$ are the intensities of light in the j-th microresonators. We considering that the scales of the defect rods much less the light wavelength and disregard an inhomogeneity of electromagnetic field inside the microresonators. Substituting Eq. (1) into the CMT equations (2) we obtained the CMT equations modified with account of the Kerr effect as follows

$$\begin{aligned} -i\dot{A}_1 &= (\omega_0 + \lambda|A_1|^2)A_1 + i\gamma(A_1 + A_2) + uA_2 \\ &\quad -i\sqrt{\gamma}E_{in}(t)e^{i\omega t}, \\ -i\dot{A}_2 &= (\omega_0 + \lambda|A_2|^2)A_2 + i\gamma(A_1 + A_2) + uA_1 \\ &\quad -i\sqrt{\gamma}E_{in}(t)e^{i\omega t}, \end{aligned} \tag{3}$$

where $\lambda$ is the nonlinear coefficient equal [35, 40]

$$\lambda = \frac{\omega_0 n_0 c^2 n_2^2}{8\pi a^2 N_m^2} \int E_m^4(x,y)dxdy, \tag{4}$$

$$N_m = \int \epsilon(x,y)E_m^2(x,y)dxdy = \frac{a^2}{cn_2}$$

with integration over the cross-section of the defect rod. $E_m(x,y)$ is the monopole eigenmode with the normalization constant $N_m$. The profiles of the monopole mode are clearly seen in the BSC mode shown in Fig. 1 (c). Estimations based on numerics for the PhC structure in Fig. 1 (a) give the following order in magnitude for the equivalent CMT layout: $\gamma \approx 0.01, u \approx 0.001, \lambda \approx 10^{-4}$.

We rewrite Eqs. (3) in terms of symmetric and antisymmetric modes as follows

$$\begin{aligned} -i\dot{a}_s &= (\nu + \lambda[|a_s|^2 + 2|a_a|^2])a_s + \lambda a_a^2 a_s^* + 2i\gamma a_s \\ &\quad -i\sqrt{\gamma}E_{in}, \\ -i\dot{a}_a &= (\nu + \lambda[|a_a|^2 + 2|a_s|^2])a_a + \lambda a_s^2 a_a^*, \end{aligned} \tag{5}$$

where $\nu = \omega_0 - \omega$ is the detuning parameter. One can see from the above equations that although the antisymmetric mode $a_a$ is decoupled from the injected light it can be excited via the nonlinear terms.

In order to trap light we apply a gaussian pulse of light

$$E_{in}(t) = E_0 \exp(-t^2/2\sigma^2). \tag{6}$$

Fig. 2 (a) shows that the injected gaussian pulse excites the symmetric mode $a_s$ which follows the amplitude of the

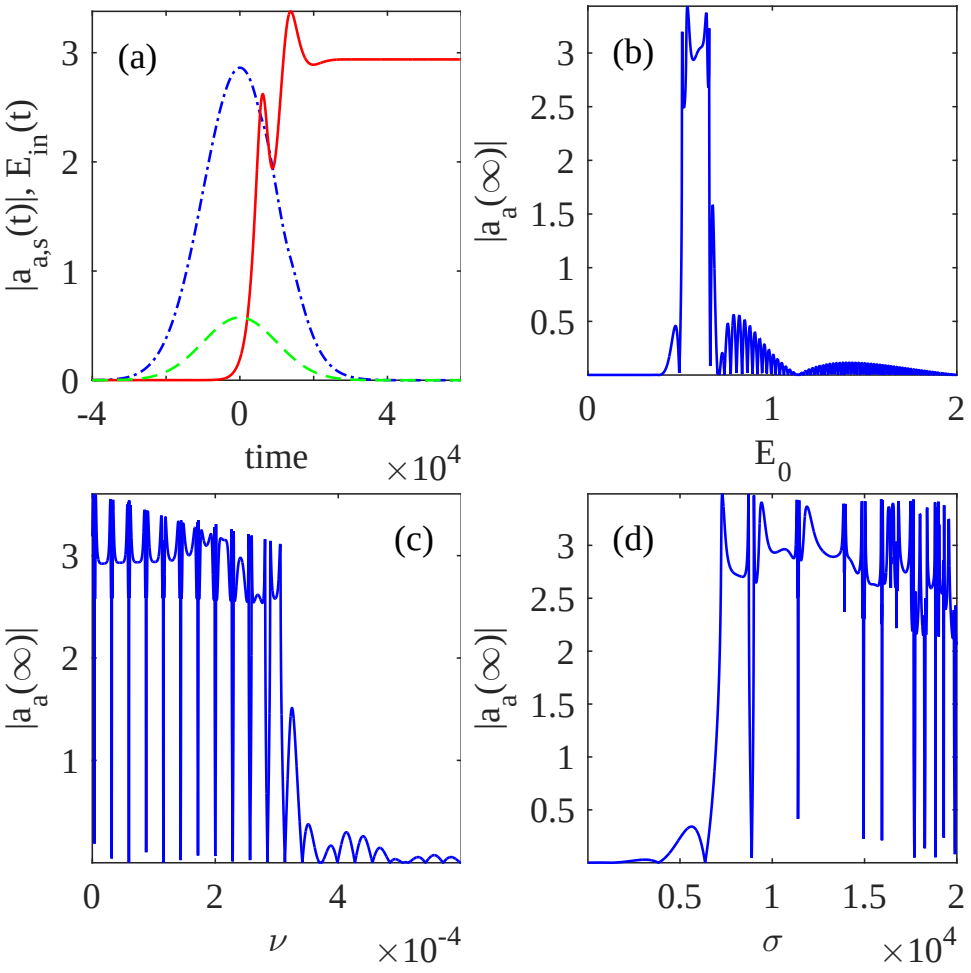



Figure 2: (a) Amplitudes of eigenmodes of resonators under application of a gaussian pulse in the PhC waveguide shown in Fig. 1. The amplitude of trapped light $|a_a(\infty)|$ in the symmetry protected BSC as dependent on (b) the amplitude $E_0$ and (c) the tuning parameter $\nu = \omega - \omega_0$ of the gaussian pulse Eq. (6) with $\sigma = 50$. (d) The release of light from BSC after application of a secondary gaussian pulse with $\sigma = 100, \omega = 1.25, E_0 = 0.8$. Green dash line shows the profile of the injected pulse with amplitude $E_0 = 1.25$ and basic frequency $\omega = 1.25$, dash-dot line shows the symmetric mode amplitude $|a_s|$ and red solid line shows the amplitude of the antisymmetric $|a_a|$ BSC mode. Parameters of the resonators are $\gamma = 0.2, \omega_0 = 1, \lambda = 0.1$.

injected light pulse. Fig. 2 (b) shows that when the injected amplitude $E_0$ reaches a certain threshold it triggers the excitation of the antisymmetric mode through the nonlinear terms in Eq. (5). From the first equation (5) we have the following estimation for $|a_s| \sim \sqrt{\gamma} E_0/\nu$ and respectively from the second equation (5) we obtain that the threshold for the amplitude of injected wave

$$E_{0c} \sim \sqrt{\frac{\nu^3}{\lambda\gamma}}. \qquad (7)$$

Substitution of parameters listed in Figure caption of Fig. 2 into this estimation demonstrates reasonable agreement with Fig. 2 (b). More accurate estimations for the threshold are given in Ref. [41]. After the pulse has passed by the resonator the symmetric mode leaks into the waveguide and the antisymmetric mode becomes isolated from the waveguide, i.e., becomes a true BSC with trapped amplitude $|a_a(\infty)|$ as shown in Fig. 2 (a). Fig. 2 (b) shows that light is trapped above a certain threshold in the amplitude of the pulse $E_0$. As Eq. (7) shows the threshold is growing with the increase of the frequency. Respectively, Fig. 2 (c) demonstrates that there is a frequency window in which light storage takes place with the window width strongly dependent on the injected amplitude. Therefore the robust symmetric BSC is capable for light trapping, however the amount of storage energy proportional to $A_a(\infty)|^2$ [35] is highly irregular over the detuning parameter $\nu$ and the injected amplitude $E_0$ as it is plotted in Figs. 2 (b) and (c). Therefore we can conclude that the symmetry protected BSCs make the process of the light storage in the nonlinear microresonators non-robust. The application of the secondary pulse again opens the BSC according to Eq. (5) and the symmetry protected BSC leaks into the waveguide as shown in Fig. 2 (d).

## 3. Light storage in BSCs in Fabry-Perot resonator

The next design is close to that considered in section 2, however two defect nonlinear rods are positioned at some distance $L$ between each other as shown in Fig. 3 (a). Each

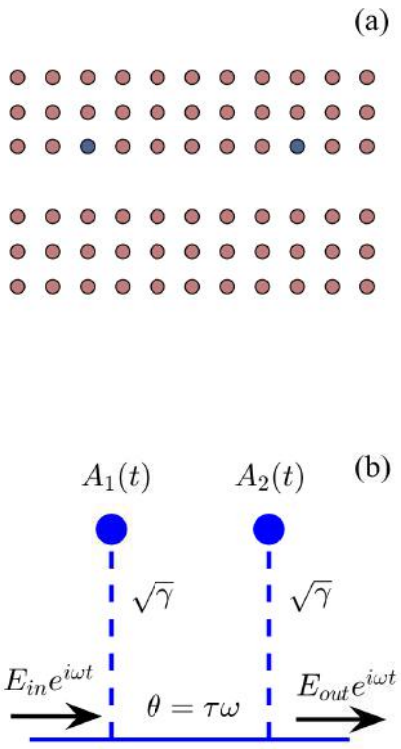



Figure 3: (a) Layout of 2D PhC which forms the Fabry-Perot resonator. Two defect rods shown by gray with the Kerr effect are inserted near by PhC waveguide. (b) Equivalent CMT presentation for PhC layout.

defect rods presents off-channel nonlinear microresonator which gives rise to a full reflection at the frequency dependent on the intensity of light [42]. Therefore these two off-channel resonators form a Fabry-Perot resonator. Then if the distance between the microresonators is tuned to fulfill the integer half-wavelength condition [31] the system supports a BSC. For simplicity we consider that only defect rods shown by gray in Fig. 3 (a) are subjected to the Kerr effect and neglect by the nonlinear phase shift in the waveguide. The CMT equations have the following form [12, 43]

$$\begin{aligned} -i\dot{A}_1 &= (\omega_0 + \lambda|A_1|^2 + i\gamma)A_1 + i\gamma A_2 e^{i\theta} \\ &\quad -i\sqrt{\gamma}E_{in}(t)e^{i\omega t}, \\ -i\dot{A}_2 &= (\omega_0 + \lambda|A_2|^2 + i\gamma)A_2 + i\gamma A_1 e^{i\theta} \\ &\quad -i\sqrt{\gamma}E_{in}(t)e^{i\omega t+i\theta}, \end{aligned} \tag{8}$$

where $\theta$ is the phase shift incurred as the wave travels from the first defect to the second one. For a monochromatic wave $\theta = k(\omega)L$. However for a light pulse which is an expansion over monochromatic waves these equations (8) are not valid. Therefore we have to modify Eqs. (8) taking into consideration the delay time $\tau$ for travelling from one microcavity to another:

$$\begin{aligned} -i\dot{A}_1 &= (\omega_0 + \lambda|A_1|^2 + i\gamma)A_1 + i\gamma A_2(t-\tau) \\ &\quad -i\sqrt{\gamma}E_{in}(t)e^{i\omega t}, \\ -i\dot{A}_2 &= (\omega_0 + \lambda|A_2|^2 + i\gamma)A_2 + i\gamma A_1(t-\tau) \\ &\quad -i\sqrt{\gamma}E_{in}(t-\tau)e^{i\omega(t-\tau)}. \end{aligned} \tag{9}$$

For stationary process with $A_j(t) = A_j e^{i\omega t}$, $\theta = \tau\omega$. Eqs. (9) can be obtained from Eqs. (8) after the substitution $\omega$ with the differential operator $i\frac{\partial}{\partial t}$. Then we have $A_j(t-\tau) = \exp[i\tau\frac{\partial}{\partial t}]A_j(t) = \exp(i\theta)A_j(t)$. The BSC occurs if the determinant of the matrix in the stationary CMT equations

$$\begin{pmatrix} \omega_0 + \lambda|A_1|^2 - \omega + i\gamma & i\gamma e^{i\tau\omega} \\ i\gamma e^{i\tau\omega} & \omega_0 + \lambda|A_2|^2 - \omega + i\gamma \end{pmatrix}$$

equals zero [31]. That condition gives us

$$\tau\omega = \pi n,\ |A_{1c}|^2 = |A_{2c}|^2 = \frac{1}{\lambda}\left(\frac{\pi n}{\tau} - \omega_0\right), \tag{10}$$

where $n$ is an integer. For some arbitrary model case $\omega_0 = 1, \gamma = 0.01, \lambda = 10^{-4}, \nu = \omega - \omega_0 = 10^{-5}, \tau = \pi/\omega$ we obtain the amplitudes $|A_{jc}|$ of the BSC take discrete value defined by the ratio $\frac{\nu}{\lambda}$ for $n = 1$. They are are shown in Fig. 4 by straight dash lines. The numerical solution of Eqs. (9) shows as injected gaussian pulse is captured at this BSC (the first inset in Fig. 4). Application of the secondary pulse releases captured light. However the secondary pulse is to be at least two times shorter in order the process of release was efficient as second inset shows in Fig. 4. Moreover in contrast to the previous case of single microresonator the intensity of the secondary pulse should also be high enough that shows high stability of the light storage in the Fabry-Perot design. The second important difference is a possibility to trap multiple discrete amounts of light defined by equation (10) for $n = 1, 2, 3, \ldots$.

## 4. Fabry-Perot resonator with two nonlinear resonant mirrors and self-tuning optical length between mirrors

For the previous case of the FPR with two off-channel resonators there were no necessity to tune the resonant mirrors $\omega_0 + \lambda I$ due to the Kerr effect. Then the condition for the Fano mirror is satisfied $\omega = \omega_0 + \lambda I$ without necessity to tune the material parameters or the frequency $\omega$. However, we still have to adjust the distance between the mirrors. In this section we show a possibility of stable light trapping in the nonlinear FPR without necessity to tune the resonant frequency of the Fano mirrors and the optical length

$$
\begin{aligned}
-i\dot{A}_1 &= (\omega_0+\lambda|A_1|^2+i\gamma)A_1+i\sqrt{\gamma\Gamma}A_2(t-\tau)+i\gamma A_3(t-2\tau)-i\sqrt{\gamma}E_{in}(t)e^{i\omega t},\\
-i\dot{A}_2 &= i\sqrt{\gamma\Gamma}A_1(t-\tau)+(\omega_0+\lambda|A_2|^2+i\Gamma)A_2+i\sqrt{\gamma\Gamma}A_3(t-\tau)-i\sqrt{\Gamma}E_{in}(t-\tau)e^{i\omega(t-\tau)},\\
-i\dot{A}_3 &= i\gamma A_1(t-2\tau)+i\sqrt{\gamma\Gamma}A_2(t-\tau)+(\omega_0+\lambda|A_3|^2+i\gamma)A_3-i\sqrt{\gamma}E_{in}(t-2\tau)e^{i\omega(t-2\tau)}.
\end{aligned}
\tag{11}
$$

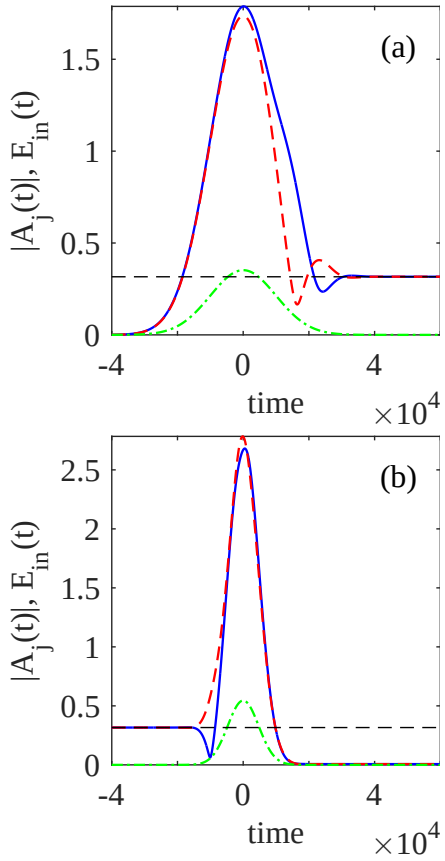



Figure 4: Time evolution of mode amplitudes $|A_1|$ (blue solid line) and $|A_2|$ (red dash line) after the injection of a first gaussian pulse shown by green dash-dot line with $\sigma = 10000, E_0 = 0.3522, \nu = 10^{-5}$ (a) and a secondary pulse with $\sigma = 4705, E_0 = 0.545, \nu = -10^{-5}$. Black dash lines show the BSC amplitude given by Eqs. (10).

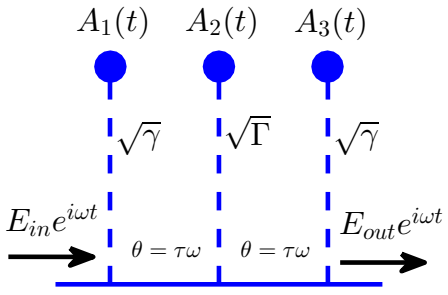



Figure 5: The nonlinear Fabry-Perot resonator with an auxiliary central nonlinear off-channel resonator.

Fig. 6 demonstrates that process of light storage for injection of gaussian pulse (6) is robust relative to choice of the parameters of the Fabry-Perot resonator with nonlinear resonant mirrors and auxiliary central nonlinear off-channel resonator.

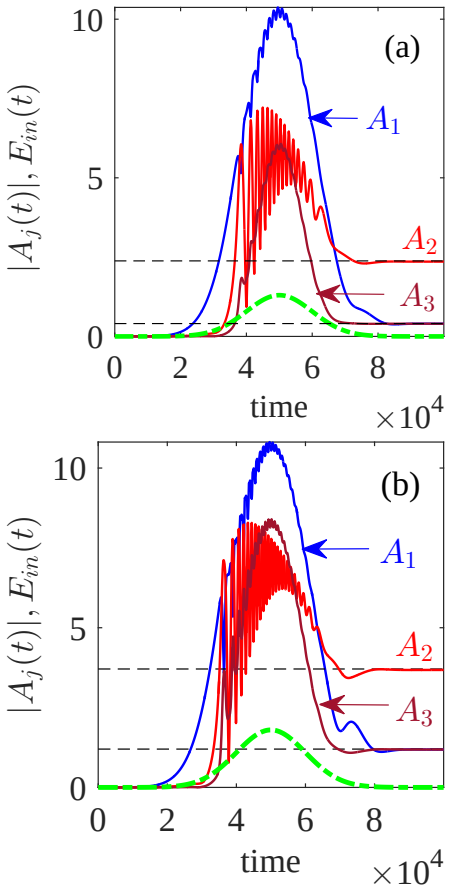



Figure 6: Time evolution of mode amplitudes after the injection of a gaussian pulse for (a) $\tau\omega = 0.3\pi$ and (b) $\tau\omega = 0.4\pi$. Other parameters substituted into CMT equations (11) are the following: $\gamma = 0.1, \Gamma = 0.02, \omega_0 = 1, \lambda = 10^{-4}$.

## 5. Discussion and conclusions

In regard to stability the approaches based on stopping light in linear PhC designs briefly discussed in the introduction are preferable compared to the light storage in the symme-

try protected BSC. Moreover the linear system can operate at any light intensity while the light storage in the self-induced BSCs (sections 3 and 4) is possible only if the amplitude of injected pulse exceeds a certain threshold. Although the symmetry protected BSC (section 2) does not have this restriction. However the process of light slowing demands tuning of operational frequency of light to the specific points of the frequency spectrum of waveguide where the group velocity of light tends to zero.

Another strategy to trap light is exploring of two nonlinear off-channel microresonators in linear PhC waveguide which serve as the resonant Fano mirrors. It is important to lay stress that frequency of full reflection of such nonlinear mirror can vary in wide range as dependent on the intensity of trapped light between the mirrors forming self-induced BSCs. However still the process of light storage in this nonlinear Fabry-Perot resonator is not fully robust because of necessity to adjust a distance between the mirrors in order to fulfill the condition $k\omega = \pi n, n = 1, 2, 3, \ldots$. Implementation of an auxiliary nonlinear resonator between the mirrors makes the process of light storage free from a necessity to adjust the distance between the mirrors. Important advantage of exploiting of the self-induced BSC in nonlinear systems is that the light can be easily released by a secondary pulse rendering the process of storage and release by demand all-optical.

Let us estimate the values of the power of injected light which is necessary to achieve the all-optical storage and release by demand. The constant of nonlinearity for the rods fabricated from GaAs we have $\lambda$ in order of magnitude $10^{-4}$. Then the unit of injected amplitude in terms of CMT equations $E_0 = 1$ corresponds to $25W/a$ where $a = 0.5\mu m$ is the lattice unit. Therefore in order to storage light in the symmetry protected BSC (section 2) by gaussian impulse its power should exceed $E_0^2 \cdot 25W/a$. The same approach is applicable for other PhC designs in Sections 3 and 4.

In the present paper we considered the phenomenon of light storage and release by the bound states in the continuum in the framework of temporal coupled mode equations although with the parameters of models borrowed from numerical calculations of real 2d PhC structures. Direct study of these processes in PhC designs needs extremely time consumed computing even for the case when nonlinearity is accounted only in the defect rods. There are processes of irreversible light emission due to finite $h$ and sizes of 2D PhC as well as due to imperfectness of the design which take place for any approach. However nonlinearity of the system has a risk of switching of TE channel for the light emission by spontaneous switching of TE modes of the nonlinear micro resonator. Also light can decay from the micro resonator through modulation instability of enough long nonlinear defect rod. These processes can be readily involved into the CMT approach by expansion of number of modes of the microresonator and number of channels coupled with the modes. But it is clear that a criteria to exclude these unwanted modes is the frequency distance between useful modes and unwanted modes should substantially exceed the perturbation due to the Kerr effect.

It is very important to notice the Kerr effect is small $\lambda \sim 10^{-4}$. Therefore to compensate this smallness we have to imply very accurate tuning $\nu$ of order of $\lambda$ beforehand. This requirement strongly restricts functional possibilities of the presented way for light storage in the BSCs. We can imply effectiveness as a ratio of energy accumulated in the BSC proportional its intensity and passed energy proportional $\sigma E_0^2$. This gives us the effectiveness around one percent for $\sigma \sim 100$.

## Acknowledgement

This work was supported by Russian Scientific Foundation through Grant 14-12-00266. We acknowledge discussions with E.N. Bulgakov and D.N. Maksimov.

## References

[1] T.F. Krauss, Slow light in photonic crystal waveguides, *J. Phys. D* **40**: 2666–2670, 2007.

[1] T. Baba, Slow light in photonics crystals, *Nature Photonics* **2**: 465–473, 2008.

[2] M. Notomi, Manipulating light with strongly modulated photonic crystals, *Rep. Progr. Phys.* **73**: 096501, 2010.

[3] A. Melloni, F. Morichetti, and M. Martinelli, Optical slow wave structures, *Opt. Photonics News* **14**: 44-48, 2003.

[4] F. Morichetti, C. Ferrari, A. Canciamilla, and A. Melloni, The first decade of coupled resonator optical waveguides: bringing slow light to applications, *Laser and Photonics Rev.* **6**: 74–96, 2012.

[5] H. Gersen, T.J. Karle, R.J.P. Engelen, W. Bogaerts, J.P. Korterik, N.F. van Hulst, T.F. Krauss and L. Kuipers, Real-space observation of ultraslow light in Photonic Crystal Waveguides, Phys. Rev. Lett. **94**: 073903, 2005.

[6] I.V. Shadrivov, A.A. Sukhorukov, and Y.S. Kivshar, Guided modes in negative-refractive-index waveguides, *Phys. Rev. E* **67**: 057602, 2003.

[7] Jinlong He, Yi Jin, Zhi Hong, and Sailing He, Slow light in a dielectric waveguide with negative-refractive-index photonic crystal cladding, *Opt. Express* **16**: 11077–11082, 2008.

[8] Sailing He, Yingran He, and Yi Jin, Revealing the truth about trapped rainbow storage of light in metamaterials, *Science Rep.* **583**: 1–9, 2012.

[9] K.L. Tsakmakidis , A.D. Boardman, and O. Hess, Trapped rainbow storage of light in metamaterials, *Nature* **450**: 397–401, 2007.

[10] V.N. Smolyaninova, I.I. Smolyaninov, A.V. Kildishev, and V.M. Shalaev, Experimental observation of the trapped rainbow, *Appl. Phys. Lett.* **96**: 211121, 2010.

[11] Rui Yang, Wenkan Zhu, and Jingjing Li, Realization of trapped rainbow in 1D slab waveguide with surface dispersion engineering, *Opt. Express* **23**: 6326–6335, 2015.

[12] S. Fan, P.R. Villeneuve, J. D. Joannopoulos, M. J. Khan, C. Manolatou, and H. A. Haus, Theoretical analysis of channel drop tunneling processes, *Phys. Rev. B* **59**: 15882–15892, 1999.

[13] S.P. Shipman and S. Venakides, Resonant transmission near nonrobust periodic slab modes, *Phys. Rev. E* **71**: 026611, 2005.

[14] D. C. Marinica, A. G. Borisov, and S.V. Shabanov, Bound States in the Continuum in Photonics, *Phys. Rev. Lett.* **100**: 183902, 2008.

[15] E.N. Bulgakov and A.F. Sadreev, Bound states in the continuum in photonic waveguides inspired by defects, *Phys. Rev. B* **78**: 075105, 2008.

[16] S. Longhi, Transfer of light waves in optical waveguides via a continuum, *Phys. Rev. A* **78**: 013815, 2008.

[17] S. Longhi, Optical analogue of coherent population trapping via a continuum in optical waveguide arrays, *J. Mod. Optics* **56**: 729–737, 2009.

[18] F. Dreisow, A. Szameit, M. Heinrich, R. Keil, S. Nolte, A. Tünnermann, and S. Longhi, Adiabatic transfer of light via a continuum in optical waveguides, *Opt. Lett.* **34**: 2405–2407, 2009.

[19] Y. Plotnik, O. Peleg, F. Dreisow, M. Heinrich, S. Nolte, A. Szameit, and M. Segev, Experimental Observation of Optical Bound States in the Continuum, *Phys. Rev. Lett.* **107**: 183901, 2011.

[20] G. Corrielli, G. Della Valle, A. Crespi, R. Osellame, and S. Longhi, Observation of Surface States with Algebraic Localization, *Phys. Rev. Lett.* **111**: 220403, 2013.

[21] S. Weimann, Yi Xu, R. Keil, A.E. Miroshnichenko, A. Tunnermann, S. Nolte, A.A. Sukhorukov, A. Szameit, and Yu.S. Kivshar, Compact Surface Fano States Embedded in the Continuum of Waveguide Arrays, *Phys. Rev. Lett.* **111**: 240403, 2013.

[22] Chia Wei Hsu, Bo Zhen, Song-Liang Chua, S.G Johnson, J.D. Joannopoulos, and M. Soljačić, Bloch surface eigenstates within the radiation continuum, *Light: Science and Applications* **2**: 1–5, 2013.

[23] Chia Wei Hsu, Bo Zhen, Jeongwon Lee, Song-Liang Chua, ,S.G. Johnson, J.D. Joannopoulos, and M. Soljačić, Observation of trapped light within the radiation continuum, *Nature* **499**: 188–191, 2013.

[24] E.N. Bulgakov and A.F. Sadreev, Robust bound state in the continuum in a nonlinear microcavity embedded in a photonic crystal waveguide, *Opt. Lett.* **39**: 5212–5215, 2014.

[25] Yi Yang, Chao Peng, Yong Liang, Zhengbin Li, and S. Noda, Analytical Perspective for Bound States in the Continuum in Photonic Crystal Slabs, *Phys. Rev. Lett.* **113**: 037401, 2014.

[26] Bo Zhen, Chia Wei Hsu, Ling Lu, A.D. Stone, and M. Soljačić, Topological nature of bound states in the radiation continuum, *Phys. Rev. Lett.* **113**: 257401, 2014.

[27] E.N. Bulgakov and A.F. Sadreev, Bloch bound states in the radiation continuum in a periodic array of dielectric rods, *Phys. Rev. A* **90**: 053801, 2014.

[28] Maowen Song, Honglin Yu, Changtao Wang, Na Yao, Mingbo Pu, Jun Luo, Zuojun Zhang, and Xiangang Luo, Sharp Fano resonance induced by a single layer of nanorods with perturbed periodicity, *Opt. Express* **23**: 2895–2903, 2015.

[29] Mingda Zhang and Xiangdong Zhang, Ultrasensitive optical absorption in graphene based on bound states in the continuum, Scientific Rep. **5:8266**: 1–6, 2015.

[30] E.N. Bulgakov and A.F. Sadreev, Resonance induced by a bound state in the continuum in a two-level nonlinear Fano-Anderson model, *Phys. Rev. B* **80**: 115308, 2009.

[31] E.N. Bulgakov and A.F. Sadreev, Bound states in photonic Fabry-Perot resonator with nonlinear off-channel defects, *Phys. Rev. B* **81**: 115128, 2010.

[32] M.I. Molina, A.E. Miroshnichenko, and Yu.S. Kivshar, Surface Bound States in the Continuum, *Phys. Rev. Lett.* **108**: 070401, 2012.

[33] E.N. Bulgakov, K.N. Pichugin, and A.F. Sadreev, All-optical light storage in bound states in the continuum and release by demand, *Opt. express* **23**: 22520–22531, 2015.

[34] E.N. Bulgakov, K.N. Pichugin, and A.F. Sadreev, Symmetry breaking for transmission in a photonic waveguide coupled with two off-channel nonlinear defects, *Phys. Rev. B* **83**: 045109, 2011.

[35] J. Joannopoulos, R. D. Meade, and J. Winn, *Photonic Crystals* Princeton University, Princeton, N.J., 1995.

[36] D. Englund, I. Fushman, and J. Vuckovic, General recipe for designing photonic crystal cavities, *Opt. Express* **13**: 5961–5975, 2005.

[37] M. Notomi, E. Kuramochi, and H. Taniyama, Ultrahigh-Q Nanocavity with 1D Photonic Gap, *Opt. Express* **16**: 11096–11102, 2009.

[38] Sh. Fan, W. Suh, and J.D. Joannopoulos, Temporal coupled-mode theory for the Fano resonance in optical resonators, *J. Opt. Soc. Am. A* **20**: 569–572, 2003.

[39] W. Suh, Z. Wang, and S. Fan, Temporal Coupled-Mode Theory and the Presence of Non-Orthogonal Modes in Lossless Multimode Cavities, *IEEE J. of Quantum Electronics* **40**: 1511–1518, 2004.

[40] E. N. Bulgakov and A. F. Sadreev, All-optical diode based on dipole modes of Kerr microcavity in asymmetric L-shaped photonic crystal waveguide, *Opt. Lett.* **39**: 1787–1790, 2014.

[41] K.N. Pichugin and A.F. Sadreev, Frequency comb generation by symmetry- protected bound state in the continuum, *J. Opt. Soc. Am. B* **32**: 1630–1636, 2015.

[42] A.E. Miroshnichenko, S.F. Mingaleev, S. Flach, and Yu.S. Kivshar, Nonlinear Fano resonance and bistable wave transmission, *Phys. Rev. E* **71**: 036626, 2005.

[43] Zh. Wang and Sh. Fan, Compact all-pass filters in photonic crystals as the building block for high-capacity optical delay lines, *Phys. Rev. E* **68**: 066616, 2003.

[44] H. Friedrich and D. Wintgen, Interfering resonances and bound states in the continuum, *Phys. Rev. A* **32**: 3231-3242, 1985.

# Plasmonics and metamaterials beyond pure noble metals

# Advances in Nano-aperture Optics and Ultrathin Overcoats for Heat-assisted Magnetic Recording

**Reuben J. Yeo[1], Sajid Hussain[1], Neeraj Dwivedi[1], Shreya Kundu[1], Hyunsoo Yang[1], Aaron J. Danner[1] and C. S. Bhatia[1*]**

[1]Department of Electrical and Computer Engineering, National University of Singapore, Singapore

[*]corresponding author: elebcs@nus.edu.sg

**Abstract**-In heat-assisted magnetic recording (HAMR), a near-field transducer (NFT) is required to deliver sufficient power to heat a highly localized spot on high anisotropy magnetic media. We show that a C-shaped nano-aperture can provide much higher transmission efficiency compared to conventional designs to successfully demonstrate HAMR. Separately, the media overcoat has to withstand aggressive heating conditions at ultrathin levels. We demonstrate the thermal stability of an ultrathin carbon overcoat for HAMR and also explore graphene as a possible overcoat.

To accommodate the areal density growth for future generation hard disk drives (HDDs), heat assisted magnetic recording (HAMR) is widely regarded as the next step forward to push the HDD areal density above 1 Tb/in$^2$. HAMR employs a laser to locally heat the media up to the Curie temperature, such that the media coercivity becomes low enough for data to be written by the magnetic field produced by the write head. This requires high laser powers to be delivered from the head onto extremely small localized spots on the media. A nano-aperture type near-field transducer (NFT) is seen as a possible solution for laser light delivery to the media by functioning as a plasmonic nano-antenna. However, conventional nano-aperture shapes such as square or circular designs have not been able to achieve transmission efficiencies high enough for HAMR. Several non-conventional shaped apertures have been developed to enhance transmission efficiency while simultaneously maintaining a small spot size [1, 2].

Based on finite-difference time-domain simulations, the best transmission and focusing characteristics were found for C-shaped nano-apertures as compared to the other shapes. Hence in this work, C-shaped nano-apertures were fabricated and characterized, and their performance for HAMR was compared with the conventional square-shaped nano-aperture design. Alternating square-shaped and C-shaped nano-aperture arrays were patterned on a 100-nm thick gold film via an electron beam lithography process. The laser source was a vertical cavity surface-emitting laser (VCSEL). The required power density of the laser for HAMR was first calibrated to be 1.4 mW/μm$^2$ on iron platinum (FePt) media using a pump-probe magneto-optic Kerr effect (MOKE) setup. This power density of the laser was then applied through the C-shaped and square-shaped nano-aperture arrays onto FePt media, as shown in the schematic in Figure 1(a). The Kerr microscope image of the FePt media after the experiment is shown in Figure 1(b), where the black areas represent the domains which were magnetically switched during laser irradiation. It was observed that there was no switching in the areas exposed to the square nano-apertures due to the insufficient power density transmitted. In contrast, the C-shaped nano-apertures exploited plasmonic effects to transmit higher power densities to the media, which successfully caused switching. This demonstrated the effectiveness of the C-shaped nano-aperture design for HAMR.

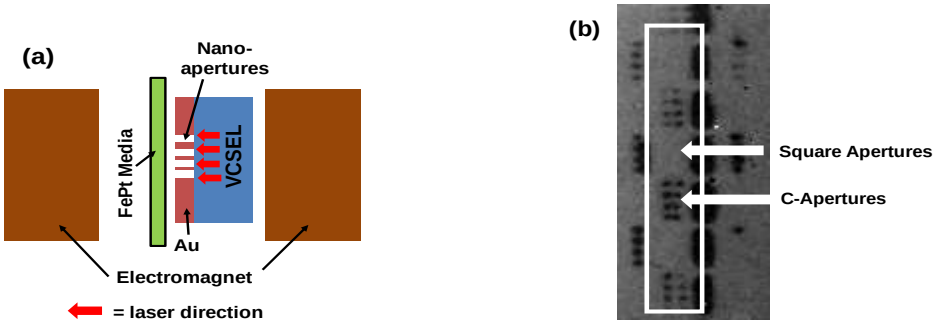



**Figure 1.** (a) Schematic showing the arrangement of laser irradiation of FePt media through the nano-apertures using a VCSEL. (b) Kerr microscope image showing the magnetically switched regions of the media as indicated in black, corresponding to the areas exposed through the C-shaped nano-apertures.

At the same time, due to the exposure of the media to such high power densities and repeated thermal cycling, it is critical for the thermal stability of the media overcoat to be maintained without degradation, especially with decreasing overcoat thicknesses. Conventional carbon overcoats (COCs) for media fabricated by plasma-based chemical vapor deposition have shown to degrade under such aggressive thermal conditions due to their relatively low $sp^3$ carbon ($sp^3C$) content [3, 4]. However, by utilizing the filtered cathodic vacuum arc (FCVA) technique, an ultrathin (~ 1.5 nm) COC was fabricated on FePt media containing higher $sp^3C$ content than a sputtered COC with similar thickness. FCVA-processed COC demonstrated high thermal stability under HAMR-like conditions as observed by Raman spectroscopy, making it a promising media overcoat for HAMR [4, 5]. To accommodate the further reduction in magnetic spacing, we are also currently exploring graphene, without and with a perfluoropolyether lubricant [6, 7], as a possible media overcoat. Despite being only an atomic layer of carbon, graphene has shown advantageous properties for corrosion and tribological protection, and has also demonstrated thermal stability in air to at least 500 °C [8, 9]. Work is ongoing in this area in applying graphene onto media and evaluating its performance for HAMR.

**Acknowledgements**- This work is supported by the National Research Foundation, Prime Minister's Office, Singapore under its Competitive Research Programme (CRP Award No. NRF-CRP-4-2008-06).

**REFERENCES**

1. Jin, E. X. and X. Xu, "Finite-difference time-domain studies on optical transmission through planar nano apertures in a metal film," *Jpn. J. Appl. Phys.*, Vol. 43, No. 1, 407–417, 2004.
2. Xu, J., T. Xu, J. Wang and Q. Tian, "Design tips of nanoapertures with strong field enhancement and proposal of novel L-shaped aperture," *Opt. Eng.*, Vol. 44, No. 1, 018001, 2005.
3. Pathem, B. K., X. C. Guo, F. Rose, N. Wang, K. Komvopoulos, E. Schreck and B. Marchon, "Carbon overcoat oxidation in heat-assisted magnetic recording," *IEEE Trans. Magn.*, Vol. 49, No. 7, 3721–3724, 2013.
4. Samad, M. A., S. Xiong, L. Pan, H. Yang, S. K. Sinha, D. B. Bogy and C. S. Bhatia, "A novel approach of carbon embedding in magnetic media for future head/disk interface," *IEEE Trans. Magn.*, Vol. 48, No. 5, 1807–1812, 2012.
5. Kundu, S., N. Dwivedi, N. Satyanarayana, R. J. Yeo, J. Ahner, P. M. Jones and C. S. Bhatia, "Probing the role of carbon microstructure on the thermal stability and performance of ultrathin (< 2 nm) overcoats on L10 FePt media for heat-assisted magnetic recording," *ACS Appl. Mater. Interfaces*, Vol. 7, 158–165, 2015.

6. Chen, C.-Y., D. Bogy and C. S. Bhatia, “Effect of lubricant bonding fraction at the head-disk interface,” *Tribol. Lett.*, Vol. 10, No. 4, 195-201, 2001.
7. Ambekar, R. P., D. B. Bogy and C. S. Bhatia, “Lubricant depletion and disk-to-head lubricant transfer at the head-disk interface in hard disk drives,” *J. Tribol.*, Vol. 131, No. 3, 031901, 2009.
8. Shin, Y. J., R. Stromberg, R. Nay, H. Huang, A. T. S. Wee, H. Yang and C. S. Bhatia, “ Frictional characteristics of exfoliated and epitaxial graphene,” *Carbon*, Vol. 49, 4059–4073, 2011.
9. Nan, H. Y., Z. H. Ni, J. Wang, Z. Zafar, Z. X. Shi and Y. Y. Wang, “The thermal stability of graphene in air investigated by Raman spectroscopy,” *J. Raman Spectrosc.*, Vol. 44, 1018–1021, 2013.

# Alternative Materials for Plasmonic Applications.

**PK Petrov*[1], AP Mihai[1], B Zou[1], L Braic[1], N Vasilantonakis[2], SA Maier[3], N Alford[1] and AV Zayats[2]**

[1]Department of Materials, Imperial College London, Prince Consort Road, London SW7 2AZ, UK,
[2]Department of Physics, King's College London, Strand, London WC2R 2LS, UK,
[3]Department of Physics, Imperial College London, Prince Consort Road, London SW7 2BB, UK

*corresponding author: p.petrov@imperial.ac.uk

**Abstract**- Several new plasmonic materials have recently been introduced in order to achieve better temperature stability than conventional plasmonic metals and control field localization with a choice of plasma frequencies in a wide spectral range. Here, epitaxial $SrRuO_3$ TiN and TiON thin films with low surface roughness are studied. It is demonstrated that SrRuO3 thin films exhibit plasmonic behavior in the near-infrared spectral range with the plasma frequency in 3.16 – 3.86 eV range and epsilon-near-zero wavelength in 1.11 – 1.47 μm range that could be controlled by the deposition conditions.

$SrRuO_3$ (SRO), a material with perovskite-type crystal structure, has been the subject to intense research due to its high thermal and electrical conductivity, and high thermal and chemical stability (up to 1200 K in oxidizing or inert-gas atmospheres).[1] For these reasons $SrRuO_3$ is widely used as electrode material for ferroelectric devices and semiconductors.[2] Also, it can be grown on Si substrates[3], or used as a standard substrate for the epitaxial growth of $SrTiO_3$ and other functional materials.

The most recent experimental results promoted $SrRuO_3$ as an attractive candidate for application plasmonic devices.[4] It exhibits carrier dynamic similar to that of the cuprate superconductors. The experimental results for itinerant electron systems on the kinetic energy of the electrons, as derived from optical conductivity data are in good agreement with band-structure calculations with the deviations due to strong spin-orbit coupling, which are specific for many intermetallic compounds with d and f electrons.

In the search for alternative plasmonic materials, titanium nitride (TiN) was proposed as a possible candidate to be used in the visible and near infrared domains.[5] The colour of stoichiometric TiN films[6] hints at their similarity to gold. In turn, its counterpart Titanium dioxide ($TiO_2$) is a well-known semiconductor with many applications in important research areas such as solar energy harvesting or photocatalysis. Also, a number of intermediate phases of general composition $TiO_xN_y$ called Titanium oxynitrides are found midway between TiN and $TiO_2$. Their properties are similar to those of the respective parent materials when the composition is near that of pure systems. They change in properties when they evolve from one pure phase to the other. However, there are several questions about these intermediate oxynitride phases that still need to be answered. In particular, whether they are stable and their optical properties depend on the $TiO_xN_y$ composition.

This paper examines the potential of the above materials (in thin film form) for plasmonic applications in the near-infrared spectral range, including optical telecommunication frequencies. We show that the optical properties of the films can be controlled via growth conditions changing working gas partial pressure during film deposition, and the epsilon-near-zero condition can be controllably achieved in the wavelength range 1.11- 1.47 μm, so that a negative permittivity and plasmonic behavior are observed at longer wavelengths.

The balance of plasmonic properties and loss in the telecom wavelength range makes this material competitive for design of ENZ and perfect-absorber-type metamaterial applications.

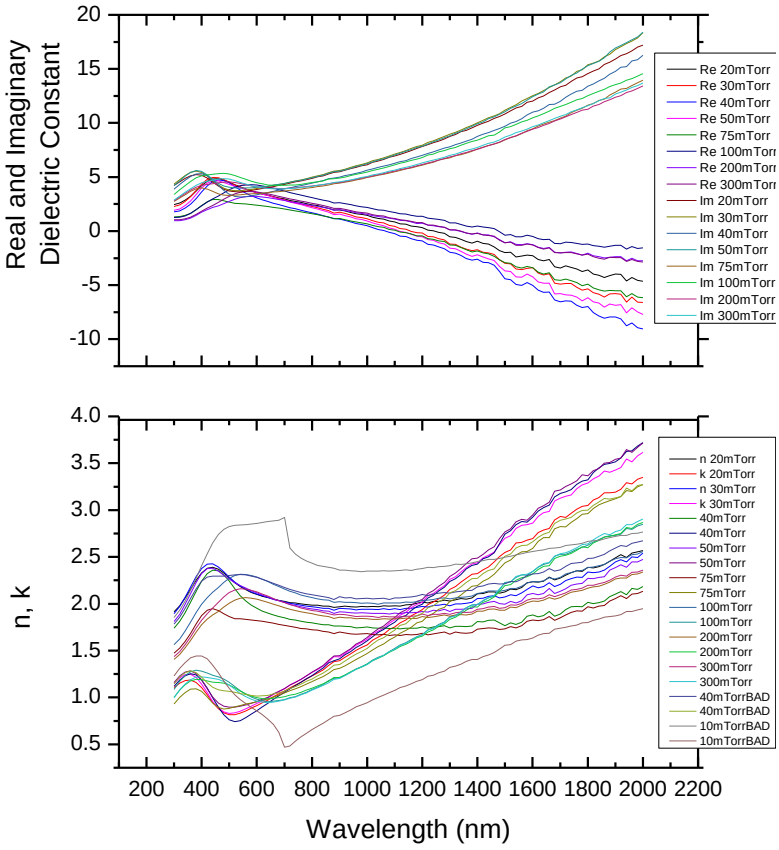



Figure 1 Optical response of $SrRuO_3$ thin films deposited at various oxygen partial pressures measured at wavelengths from 600 nm (VIS) to 1800 nm (IR).

**REFERENCES**


1. Bensch, W., Schmalle, H. & Reller, A.: Structure and thermochemical reactivity of $CaRuO_3$ and $SrRuO_3$. Solid State Ionics, 43, 171 – 177 (1990)
2. Morimoto, T., et al..Ferroelectric Properties of Pb(Zi, Ti)$O_3$ Capacitor with Thin $SrRuO_3$ Films within Both Electrodes. Jpn. J. Appl. Phys. 39 2110-2115 (2000)
3. Higuchi, T. Y. et al.Fabrication of Pseudocubic $SrRuO_3$ (100) Epitaxial Thin Films on Si by Pulsed Laser Deposition. Jpn. J. Appl. Phys. 41, L481-3 (2002)
4. Braic, L., et al. Optimizing Strontium Ruthenate Thin Films for Near-Infrared Plasmonic Applications. Scientific reports, 5, (2015).
5. Naik, G. V., Shalaev, V. M. and Boltasseva, A. Alternative plasmonic materials: beyond gold and silver, Advanced Materials, vol. 25, no. 24, 3264-3294 (2013)..
6. Niyomsoan, S., Grant, W., Olson, D.L., Mishra, B. Variation of color in titanium and zirconium nitride decorative thin films, Thin Solid Films, 415, Issues 1–2, 187-194 (2002).

# Hot carrier excitation in transition metal nitrides

**S. Ishii**[1,2*], **S. L. Shinde**[1,2], **M. Kumar**[1,2], **R. P. Sugavaneshwar**[1,2], **T. D. Dao**[1,2], **T. Yokoyama**[1,2], **N. Umezawa**[1,2] **and T. Nagao**[1,2]

[1] International Center for Materials Nanoarchitectonics (MANA), National Institute for Materials Science (NIMS), Tsukuba, Ibaraki 305-0044, Japan

[2] CREST, Japan Science and Technology Agency, Kawaguchi, Saitama 332-0012, Japan

[*]corresponding author: sishii@nims.go.jp

**Abstract** High carrier concentrations and optical losses of transition metal nitrides make them suitable for light absorption and photo-excited hot carrier applications. We show experimentally that titanium nitride nanoparticles absorb sunlight efficiently and photocurrent is generated from titanium nitride thin films by optical illumination. Our calculations based on first-principles density functional theory are successful in calculating optical properties of transition metal nitrides.

The use of noble metals in nanophotonics is not limited to plasomonic localization or propagation. Photons which go through non-radiative decay processes excite hot carriers and a number of novel applications with photo- or plasmon- induced hot carriers have been studied in the past decade [1].

Recently it has been shown that highly conductive ceramics can be alternative materials of noble metals. Among them titanium nitride (TiN) is one such material which becomes plasmonic in visible and longer wavelength range [2]. Previous studies have shown that TiN seems to be best suited for non-radiative decay related applications such as perfect absorbers [3] and photothermal effects [4].

To further explore the possibility of TiN for photo-absorption related applications, here we present our preliminary results on nano-structured TiN for photothermal [5] and photoelectric applications. We also show the dielectric functions of transition metal nitrides including TiN calculated from first-principles density functional theory (DFT) which are used to compare their expected performances for particular applications [6].

When using nanoparticles (NPs) for photothermal applications, absorption efficiency (absorption cross section divided by the particle cross section) is a measure for comparison. In Fig. 1(a) the absorption efficiencies of TiN, carbon and gold NPs are plotted together with the normalized solar irradiance. Among the three NPs, the absorption efficiency of the TiN NP has a large broad peak due to lossy plasmonic resonances and it overlaps well to solar irradiance plot. This feature makes TiN NP as an appropriate material for solar phtothermal applications. Figure 1(b) shows steam generation from water containing TiN NPs at room temperature. TiN NPs dispersed into water allow us to efficiently use solar heat for water heating as well as water distillation.

In photoelectric demonstration, a metal-insulator-metal structure was fabricated using TiN thin films instead of metals. Upon visible light illumination to the sample, photocurrent was observed as shown in Fig. 1(c). The photon energies were smaller than the bandgap of the insulator, hence the photo-excited electrons were generated not at the insulator film but at the top TiN film. This result opens a door for using TiN to harvest light and generate photo-excited carriers.

First-principles DFT studies have been performed for various transition metal nitrides [6]. Figures 2(a) and 2(b) show the DOS and complex permittivity of TiN calculated based on the first-principles DFT study. The permittivity obtained from DFT is in reasonable agreement with the experiment [2]. Theoretical calculations of

complex permittivity is powerful in predicting the intrinsic properties of materials and studying element substitution [7].

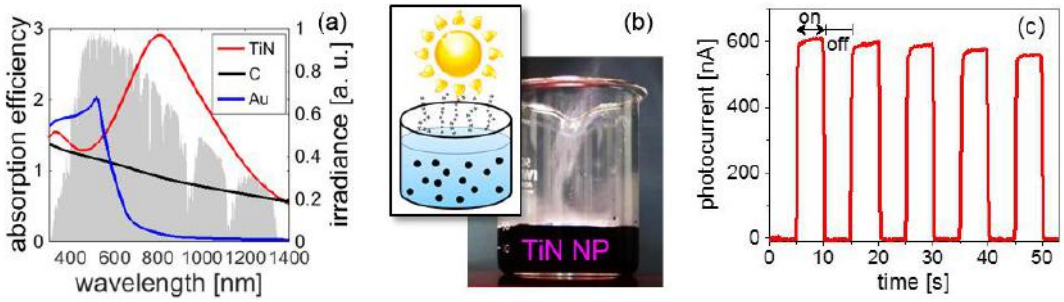



**Figure 1:** (a) Absorption efficiencies of TiN, carbon and gold nanoparticles of 65 nm in radius. (b) Steam generation from water containing TiN NPs by the illumination of focused artificial sunlight. Inset shows the schematic of the experiment. (c) Photocurrent from TiN-oxide-TiN trilayers upon visible light irradiation.

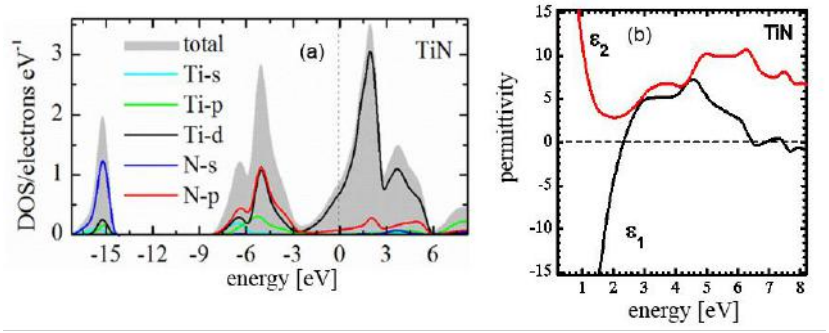



**Figure 2:** (a) DOS of TiN. (b) Complex permittivity of TiN calculated from first-principles DFT study.

**Acknowledgements** This work is partially supported by the JSPS KAKENHI Grant Number 15K17447.

## REFERENCES

1. M. L. Brongersma, N. J. Halas, and P. Nordlander, "Plasmon-induced hot carrier science and technology," Nat. Nanotechnol. **10**, 25-34 (2015).
2. G. V. Naik, V. M. Shalaev, and A. Boltasseva, "Alternative Plasmonic Materials: Beyond Gold and Silver," Adv. Mater. **25**, 3264-3294 (2013).
3. W. Li, U. Guler, N. Kinsey, G. V. Naik, A. Boltasseva, J. Guan, V. M. Shalaev, and A. V. Kildishev, "Refractory Plasmonics with Titanium Nitride: Broadband Metamaterial Absorber," Adv. Mater. **26**, 7959-7965 (2014).
4. U. Guler, G. V. Naik, A. Boltasseva, V. M. Shalaev, and A. V. Kildishev, "Performance Analysis of Nitride Alternative Plasmonic Materials for Localized Surface Plasmon Applications," Appl. Phys. B **107**, 285-291 (2012).
5. S. Ishii, R. P. Sugavaneshwar, and T. Nagao, "Titanium Nitride Nanoparticles as Plasmonic Solar-Heat Transducers," J. Phys. Chem. C **120**, 2343-2348 (2016).
6. M. Kumar, N. Umezawa, S. Ishii, and T. Nagao, "Examining the Performance of Refractory Conductive Ceramics as Plasmonic Materials: A Theoretical Approach," ACS Photonics **3**, 43-50 (2016).
7. M. Kumar, S. Ishii, N. Umezawa, and T. Nagao, "Band engineering of ternary metal nitride system $Ti_{1-x}Zr_xN$ for plasmonic applications," Opt. Mat. Express **6**, 29-38 (2016).

# Plasmonic and thermal properties of transition metal nitride/noble metal core-shell nanoparticles

**Fumin Huang*, S. Drakeley, M. Ali, W. Hendren, and R. Bowman**
[1]School of Mathematics and Physics, Queen's University Belfast, Belfast, BT7 1NN, United Kingdom,

[*]corresponding author: f.huang@qub.ac.uk

**Abstract** We report a systematic investigation on the optical and thermal properties of core-shell nanoparticles composed of noble metal nanoparticles coated with transition metal nitrides. Plasmonic properties of such core-shell nanoparticles are strongly dependent on the thickness and the materials of the coating layer. We also investigate the thermal properties of such hybrid nanoparticles and compare them to bare noble nanoparticles. The results show significantly improved stability, which could be important for key applications such as heat-assisted magnetic recording.

Traditionally noble metals, such as gold and silver, are the most popular materials that are widely used in plasmonics and metamaterials, due to their strong optical response. However, noble metals have some limitations, for instance, silver is easy to be oxidized in air and gold is too soft. Gold atoms are easy to diffuse and migrate at elevated temperatures and become unstable, which makes it not a reliable material in high-temperature applications, such as heat-assisted magnetic recording (HAMR) [1]. Recently there is increasing interest in the search of alternative plasmonic materials that can work at extreme conditions, such as high pressure, high temperature, and have long lifespans [2].

Transition metal nitrides, such as TiN and ZrN, have appeared to be promising alternative plasmonic materials [2]. The plasmonic properties of those metallic nitrides are close to those of gold at visible and near-infrared (NIR) frequencies, but they have much higher melting temperatures and significantly stronger hardness, which are appealing for HAMR and other plasmonic and metamaterials applications at elevated temperatures. Here we report a systematic investigation of hybrid plasmonic nanoparticles composed of noble metal nanoparticles coated with transition metal nitrides.

Core-shell nanoparticles were prepared by depositing transition nitrides onto noble metal nanoparticles by reactive magnetron sputtering from a Ti target in an atmosphere of nitrogen gas. The nitride coating layer significantly shifts the plasmonic resonance of noble metal nanoparticles. Figure 1 shows the measured scattering spectra of 80 nm Au nanoparticles coated with various thickness of TiN films. The plasmonic resonant peaks shift to longer wavelengths with increasing thickness of TiN layer. The inset in Figure 1 shows the TEM image of one of such core-shell nanoparticles. The outer TiN shell is clearly distinguished, which is quite uniform. We provide a systematic investigation of the plasmonic properties of the hybrid core-shell nanoparticles, studying a range of film thickness of a number of transition metal nitrides on gold and silver nanoparticles. We also investigate the thermal properties of such hybrid core-shell nanoparticles. The evolution

of nanoparticle morphologies is investigated at a range of temperatures. The thermal stability of such core-shell nanoparticles is compared to that of bare noble metal nanoparticles, which show much improved reliability. These results provide important implication for the development of alternative plasmonic materials for applications under harsh conditions, such as high temperature, high pressure and long-durance.

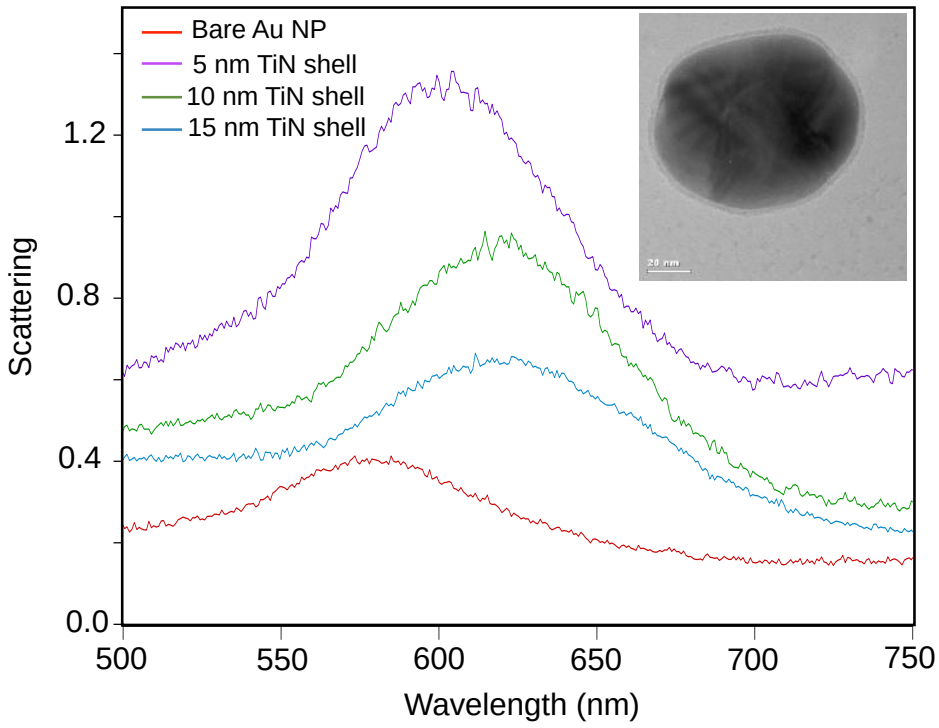



Figure 1 Measured optical scattering spectra of TiN-coated Au nanoparticles. Inset: TEM image of a TiN-coated Au nanoparticle.

**REFERENCES**


1. Challener, W. A., C. Peng, A. V. Itagi, D. Karns, W. Peng, Y. Peng, X. Yang, X. Zhu, N. J. Gokemeijer, Y. -T. Hsia, G. Ju, R. E. Rottmayer, M. A. Seigler and E. C. Gage, "Heat-assisted magnetic recording by near-field transducer with efficient optical energy transfer," *Nature Photonics*, Vol. 3, 220-224, 2009.
2. G. V. Naik, V. M. Shalaev, and A. Boltasseva, Adv. Mater. 25, 3264 (2013).

# Comparing the efficiency of plasmonic materials. The case of metal nitrides.

**Adrien Lalisse[1,2], Gilles Tessier[2], Jérôme Plain[1], Guillaume Baffou[3,*]**

[1]ICD/LNIO, UMR 6281, CNRS, Technological University of Troyes, 10004 Troyes, France

[2]Laboratoire de Neurophotonique UMR8250, CNRS, Faculté des sciences biomédicales et fondamentales, Université Paris Descartes, 75270 Paris, France

[3]Institut Fresnel, UMR 7249, CNRS, Aix-Marseille Université, Ecole Centrale Marseille, Marseille, France

[*]corresponding author: guillaume.baffou@fresnel.fr

**Abstract**-In this presentation, I will first introduce two new figures of merit intended to quantify the efficiency of a plasmonic material to respectively enhance the near-field and generate heat under illumination. In a second part, I will focus on the case of metal nitrides and explain in which conditions they can replace and eventually outperform gold in plasmonics.

Following recent advances in nanoplasmonics related to heat-assisted magnetic recording, hot-electron processes, nanochemistry, sensing, and active plasmonics, new materials have been introduced, reducing the supremacy of gold and silver in plasmonics. The variety of possible materials in nanoplasmonics is now so wide that selecting the best material for a specific application at a specific wavelength may become a difficult task.

In this context, we recently introduced two dimensionless parameters acting as figures of merit to simply compare the plasmonic capabilities of different materials [1]. These numbers, which we named Faraday and Joule numbers, aim at quantifying the ability of a nanoparticle to respectively enhance the optical near field and produce heat (see Table below). The benefit of these numbers compared to previously defined figures of merit, such as / , is that (i) they possess simple close-form expressions and can be simply calculated without numerical simulations, (ii) they give quantitative estimations in the non-retarded regime, and (iii) they take into account the nature of the surrounding medium. These numbers read

$$\mathrm{Fa} = 9\left|\frac{\epsilon}{\epsilon + 2\epsilon_s}\right| \qquad \mathrm{Jo} = 9\frac{e\epsilon''}{n_s}\left|\frac{\epsilon_s}{\epsilon + 2\epsilon_s}\right|$$

where $\epsilon$ is the metal permittivity, $\epsilon''$ its imaginary part, $\epsilon_s$ and $n_s$ the surrounding permittivity and refractice index and $e = 1$ eV.

In the first part of this presentation, I will introduce and discuss the Faraday and Joule numbers and demonstrate how they can be conveniently used in plasmonics and what kind of information they can provide. In a second part, I will focus on metal nitrides (TiN and ZrN) and discuss their possible use as refractory materials in applications such as heat-assisted magnetic recording.

| | | $\lambda_{res}^{out}$ (nm) | $Fa^0$ | $\lambda_{res}^{in}$ (nm) | $Jo^0$ | $T_s$ (°C) |
|---|---|---|---|---|---|---|
| gold | Au | 528 | 19.6 | 507 | 6.32 | 1064 |
| silver (Palik) | Ag | 357 | 118 | 354 | 52.0 | 961 |
| silver (J&C) | Ag | 355 | 476 | 354 | 111 | |
| aluminum (Rakic) | Al | 140 | 1290 | 140 | 477 | 660 |
| copper | Cu | 585 | 15.2 | 538 | 2.65 | 1085 |
| cobalt | Co | 366 | 10.9 | <200 | >12 | 1495 |
| chromium | Cr | 289 | 10.6 | <200 | >11 | 1907 |
| iron | Fe | 337 | 9.38 | <200 | >11 | 1538 |
| molybdenum | Mo | 154 | 18.3 | 140 | 41.3 | 2623 |
| manganese | Mn | 380 | 9.82 | <200 | >9.2 | 1246 |
| nickel | Ni | 218 | 11.6 | 141 | 21.4 | 1455 |
| palladium | Pd | 223 | 13.3 | <200 | >21 | 1555 |
| platinum | Pt | 323 | 10.5 | 210 | 12.0 | 1768 |
| rhodium | Rh | 199 | 18.4 | 173 | 31.5 | 1964 |
| tantalum | Ta | 735 | 11.8 | 640 | 2.45 | 3017 |
| tantalum | Ta | 177 | 11.6 | 77 | 52.3 | |
| titanium | Ti | 274 | 11.2 | <200 | >13 | 1668 |
| titanium nitride | TiN | 566 | 12.0 | 488 | 5.55 | 2930 |
| tungsten | W | 159 | 14.2 | 131 | 25.6 | 3422 |
| zirconium nitride | ZrN | 467 | 28.6 | 437 | 16.6 | 2952 |

**Table:** Values of the Faraday and Joule numbers at the plasmonic resonance wavelength for a large set of plasmonic materials. The melting temperature is also indicated. Reproduced from Ref. [1].

## REFERENCES


1. Lalisse, Tessier, Plain, Baffou "Quantifying the Efficiency of Plasmonic Materials for Near-Field Enhancement and Photothermal Conversion," *J. Phys. Chem. C*, Vol. 119, 25518–25528, 2015.

# Fully-integrated Light Delivery System for Heat Assisted Magnetic Recording

(invited paper)

**Qian Wang, Kim Peng Lim, Vivek Krishnamurthy, Jing Pu**

Data Storage Institute, Agency for Science, Technology and Research, Singapore

*corresponding author: wang_qian@dsi.a-star.edu.sg

**Abstract:** A fully-integrated light delivery system for heat assisted magnetic recording is presented. The proposed system consists of two key features: 1) a high-index nanowaveguide is integrated with a tapered plasmonic near field transducer (NFT), which has a much higher waveguide-NFT-media efficiency due to the improved waveguide-NFT coupling; 2) the III-V semiconductor laser is heterogonous integrated on slider through bonding the epitaxial layers and light is efficiently coupled to the nanowaveguide through an ultra-compact adiabatic coupling structure. Optical coupling, integration architecture and overall power budgeting is discussed and analyzed.

Heat assisted magnetic recording (HAMR) technology increases the storage density by incorporating a so-called light delivery system to momentarily heat the media over Curie temperature [1]. The light delivery system includes a laser source, nanowaveguide and plasmonic near field transducer (NFT). The laser beam is coupled to waveguide and focused to a spot of tens of nanometer through the NFT to heat the media. An efficient light delivery system ($\eta=P_{abs}/_{Plsr}$) and cost-effective/compact integration solution is very critical for success of HAMR technology.

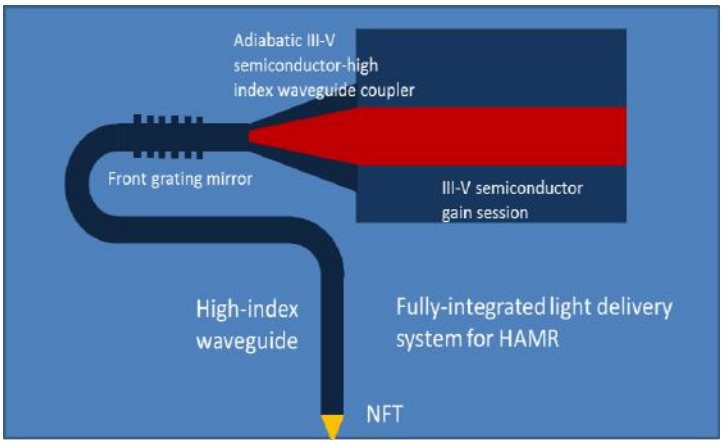



Fig.1 fully-integrated light delivery system

In this paper, we present a fully-integrated light delivery system solution for HAMR as shown in Fig.1. The system consists of a high-index nanowaveguide integrated with a tapered plasmonic NFT. The high-index waveguide enables a high-efficiency waveguide mode to NFT plasmonic mode coupling as compared to the case using low/medium index waveguide. Therefore, it enables a much higher waveguide-NFT-media efficiency as compared to the prior art [2].

Laser source is currently attached to slider through assembling, in which the laser diode is bulky as compared to the slide and also costly/low-efficiency due to the strict light coupling requirement. In this paper, the III-V semiconductor laser is designed to be heterogonous integrated on slider through bonding the epitaxial layers and fabricated after the bonding [3]. The on-chip laser can be only a few micrometers thick. Based on the high index waveguide used, high-efficiency/compact adiabatic coupler between laser and the waveguide is designed.

**REFERENCES**

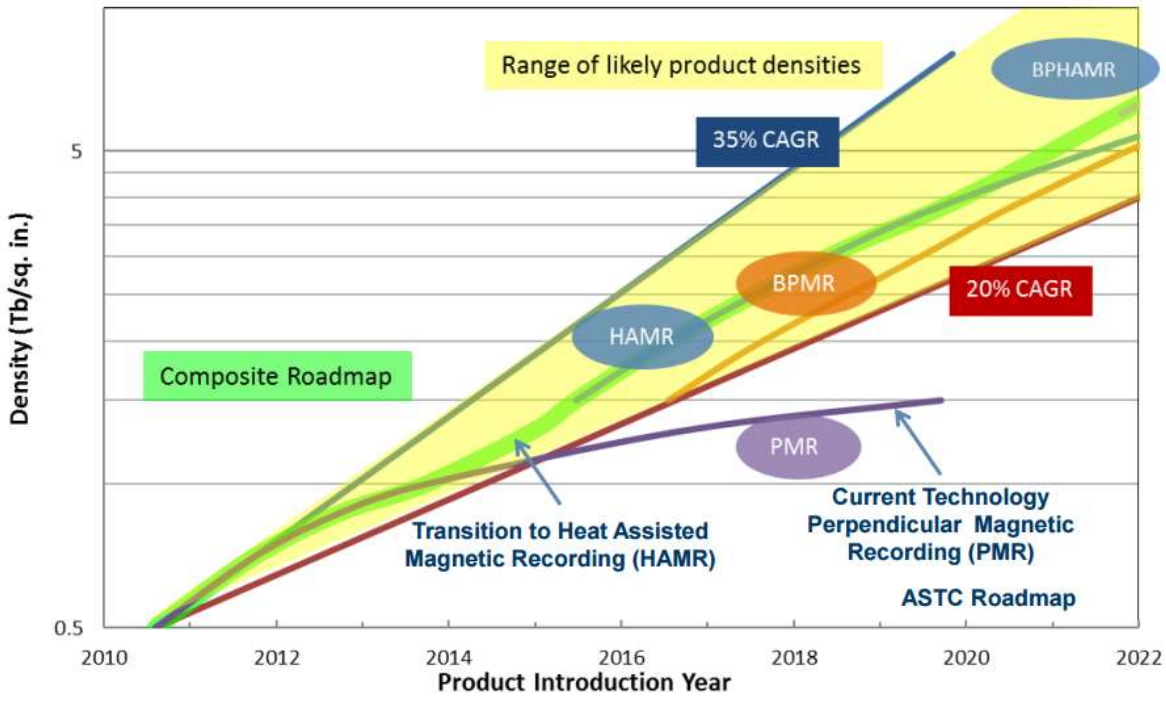

1. M. H. Kryder, E. C. Gage, T. W. McDaniel, et.al, “Heat Assisted Magnetic Recording”, Proceedings of the IEEE, Vol.96, No.11, pp. 1810-1834, 2008.
2. V. Krishnamurthy, D. Ng, Z. H. Cen, et.al., “Maximizing the Plasmonic Near-Field Transducer Efficiency to Its Limit for HAMR”, Journal of Lightwave Technology, Vol.34, No.4, pp.1184-1190, 2015.
3. J. Pu, K. Lim, D. Ng, et.al., “Heterogeneously Integrated III-V Laser on Thin SOI with Compact Optical Vertical Interconnect Access”, Optics Letters, Vol.40, No.7, pp.1378-1381, 2015

# HAMR and the Future of Hard Drives

Dr Roberto Fernandez Garcia, Seagate technology

**Data storage is one of the key enabling technologies for future economic growth. Key to providing future data storage requirements are improvements in the information capacity and areal density of hard disk drives. Heat-assisted magnetic recording (HAMR) is the next-generation hard drive recording technology. We report significant areal density improvement over previous demos. It is an important milestone for the development of such a new technology. HAMR recording heads consist of advanced integrated photonic elements such as the plasmonic transducer allowing light to be focused to sub-50nm spot sizes and heating the disk in the HAMR hard drive to temperatures over 400C.**

**Hard drives with HAMR technology will store significantly higher areal densities around 1.5Tbit per square inch initially and will be able to store noticeably more data than today's HDDs featuring perpendicular recording technology. Eventually we expect that HAMR will help to increase bit densities of hard disk drives to 5Tbit per square inch. In this presentation, we will give an introduction to the HAMR technology and its impact on the actual hard disk technology industry.**




**Advanced storage consortium technology road map for the future storage densities in hard disk drives.**

# All-dielectric light concentrator for heat assisted magnetic recording

**A.K. Sarychev**[1], **S.S. Vergeles**[2], **and G. Tartakovsky**[3]

[1]Institute for Applied and Theoretical Electrodynamics of RAS, Moscow, 125412, Russia
[2]Institute for Theoretical Physics of RAS, Chernogolovka, 142432, Russia
[3]Advanced Systems and Technologies, Inc., Irvine, CA 92618, USA
sarychev_andrey@yahoo.com

**Abstract**— We propose a novel all-dielectric near field transducer, which focuses the light, pumped through the waveguide, into a hot spot, which is much smaller than the wavelength, without dissipative loss inevitable in the plasmonic nanoantennae. Therefore, the detrimental thermal effects almost vanish, which gives an opportunity to use the concentrator for the heat-assisted magnetic recording (HARM).

In the proposed new device [1], the electric field is much enhanced at the vertex of the dielectric tip attached to the specially tuned dielectric resonator as it is shown in Fig. 1. The electric field enhancement and concentration is achieved by longitudinal polarization of the vertex, which is exposed to the resonator field. Concentration of light into nanospots much smaller than the wavelength is beneficial for HAMR [2] and for many other very important applications: biomedical imaging and sensing, optical microscopy with single-molecule resolution, QED studies, nanolasing, etc. Until now, plasmonic metal nanoantennae or metallic near field concentrators have been used for this purpose. Optical field enhancement and concentration is achieved by the excitation of the surface plasmons. The main advantage of the metal nano-antennae is their capabilities to localize plasmonic modes, which can be excited by the incident transverse em wave. Yet, the metal nanoparticles have large optic loss. The proposed novel all-dielectric transducer allows to focus light into a hot spot much smaller than the wavelength without the dissipative loss.

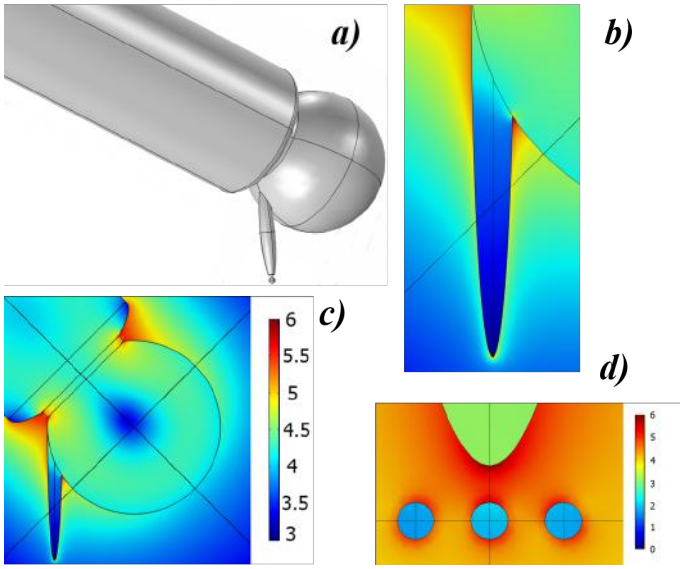



Figure 1: ***a)*** Near field transducer consisting of cylindrical silicon waveguide (radius $\rho$), spherical resonator (radius $a$), and prolate ellipsoidal nanotip (length $b$); ***b), c)*** numerical simulation of electric field which is pumped in the resonator through the waveguide ($\rho = 107\,nm, a = 111\,nm, \lambda = 900\,nm$); magnetic dipole resonance is excited in the spherical resonator; electric field of the resonance excites vertical tip of $b = 130\,nm$ length; ***d)*** tip heats $2\,nm$ magnetic nanoparticles made of alloy FePt; heat production inside the core magnetic particle is 1.4 times greater than in its neighbors.

The longitudinal electric field enhancement at the tip's vertex can be achieved for any optically dense material, including a transparent dielectric. The problem is how to convert the incident light into a longitudinal electric field. A simple waveguide does not produce a considerably localized longitudinal electric field, which is necessary to excite the tip. In the recently proposed metal Fresnel lens, the specially designed plasmonic lens produce the longitudinal electric field [3]. In contrast to the previous works we propose to excite the dielectric tip through the waveguide ended by the optic resonator. The waveguide is matched with the resonator, which accumulates em energy. The em field, pumped in the resonator, effectively excites the tip.

**REFERENCES**


1. Vergeles S. S. and Sarychev A. K., "Silicon plasmonics and optical field concentration at nanometer scale", *Metadevices and Metasystems*, Eds. N. Engheta, M. A. Noginov, I. N. Zheludev, SPIE **9544**, 954415 (2015).
2. Vedantam S., Lee H., Tang J., Conway, M. Staffaroni, E. Yablonovitch, "A Plasmonic Dimple Lens for Nanoscale Focusing of Light", *Nano Lett.* **9**, 3447 (2009).
3. Y. Wang, Z. Du, Y. Park, C. Chen, X. Zhang, L. Pan, "Quasi-3D plasmonic coupling scheme for near-field optical lithography and imaging", *Optics letters* **40**, 3918 (2015).

# Antenna-assisted picosecond control of the vanadium dioxide phase transition through resonant near-field excitation.

**Otto L. Muskens[1], Yudong Wang[1], Kees C. H. de Groot[1], Luca Bergamini[2], Nerea Zabala[2], Javier Aizpurua[2], Geoffrey Gaskell[3], David W. Sheel[3]**

[1] Zepler Institute, Physical Sciences & Engineering, University of Southampton, UK

[2] DIPC and CSIC-UPV/EHU, San Sebastian, Spain

[3] University of Salford, UK

[*]corresponding author: userid@institution.edu

**Abstract**-We demonstrate that plasmonic nanoantennas enable control of a local phase transition in vanadium dioxide through resonant local field enhancement and enhanced absorption at the nanoantenna tips. Optical pumping using picosecond laser shows a large modulation of up to 20% of the plasmon resonance, where the antenna is used both to enhance the excitation and readout of the nanoscale phase transition.

Efficient and reversible control of plasmonic modes at visible and near-infrared wavelengths is one of the key desirable properties for tunable devices. We investigate how plasmonic local field enhancement can be used to efficiently drive an optical nonlinear material and to enhance the readout of the nonlinear response. To achieve order-unity effects in the optical modulation, materials with large changes in dielectric response are needed. Several materials under investigation include highly doped metal oxides with a tunable, metallic Drude response in the near-infrared. Indium-tin-oxide (ITO) was shown to provide a large nonlinear response caused by the optical pumping of free carriers [1,2].

Phase-change materials offer technologically relevant opportunities as they can provide very large changes in the dielectric response. Vanadium oxide ($VO_2$) provides an ultrafast, reversible phase transition at only modestly elevated temperatures around 68°C. Most studies so far have reported the effects of a global phase transition of a $VO_2$ layer on the plasmonic response of nanoparticles and metamaterials.

Here, we exploit nanometer-scale plasmonic hot-spots to induce highly localized phase-changes in a plasmonic nanoantenna [3]. These studies are enabled by the fabrication of high quality thin films of $VO_2$ with low surface roughness of around 5nm [4]. Figure 1 shows a helium-ion microscopy image of the gold nanoantenna array fabricated onto a $VO_2$ film of 50 nm thickness. The arrays show an excellent thermochromic switching response (Figure 1). The crossed array of horizontal and vertical antennas of varying lengths allows independently studying the resonant excitation and readout, while the polarization of the incident light controls coupling to the two individual antenna sub-arrays.

Optical experiments were performed using a picosecond pump-probe scheme, using 11ps laser pulses with pulse energies from 100 pJ to 13 nJ, focused to a diffraction limited spot of around 2 $\mu m^2$ area onto the array. Readout was done using the synchronized output of a white light supercontinuum, allowing detection over a wide spectral range from 1100nm-2100nm. The repetition rate of the experiment was controlled between 0.1 MHz and 10 MHz using a pulse picker. Our experiments show

that fully reversible switching of antenna resonances with >1 million cycles per second are possible using resonant pumping schemes. The recovery time of the antenna-$VO_2$ system was 5 times faster than the pure $VO_2$ film. Furthermore, resonant pumping of the half-wave dipole resonance of a plasmonic nanoantenna results in a threshold energy for the phase transition which is 20 times lower than for the pure $VO_2$.

Our results are in quantitative agreement with microscopic numerical simulations taking into account the resonant nature of light absorption in the hybrid antenna-$VO_2$ system, combined with picosecond local heating using an equilibrium description.The nanoantenna-$VO_2$ hybrids enable new directions in all-optical switching at picojoule energy levels, and open up the possibility for plasmonic memristor-type devices exploiting nanoscale thermal memory.

**Acknowledgements**, This work was supported by EPSRC through research grant EP/J011797/1. L. B., N. Z. and J. A. acknowledge financial support from Project No. FIS2013-41184-P of the Spanish Ministry of Economy and Competitiveness, project ETORTEK IE14-393 NANOGUNE'14 of the Department of Industry of the Government of the Basque Country, and support from the Basque Department of Education and the UPV-EHU (Grant No. IT-756-13).

**REFERENCES**

1. M. Abb, P. Albella, J. Aizpurua, O. L. Muskens, "All-optical control of a single plasmonic nanoantenna-ITO hybrid," *Nano Lett.* Vol. 11, 2457-2463, 2011.
2. M. Abb, Y. Wang, C. H. de Groot, O. L. Muskens, "Hotspot-mediated ultrafast nonlinear control of multifrequency plasmonic nanoantennas," *Nature Communications* Vol. 5, 4869, 2014.
3. O. L. Muskens, L. Bergamini, Y. Wang, J. M. Gaskell, N. Zabala, C. H. de Groot, D. W. Sheel, J. Aizpurua, "Antenna-assisted picosecond control of nanoscale phase transition in $VO_2$," submitted (2016).
4. J. M. Gaskell, M. Afzaal, D. W. Sheel, H. M. Yates, K. Delfanazari, O. L. Muskens, "Optimised atmospheric pressure CVD of monoclinic VO2 thin films with picosecond phase transition," Surf. Coat. Techn. Vol. 287, 160 – 165, 2016.

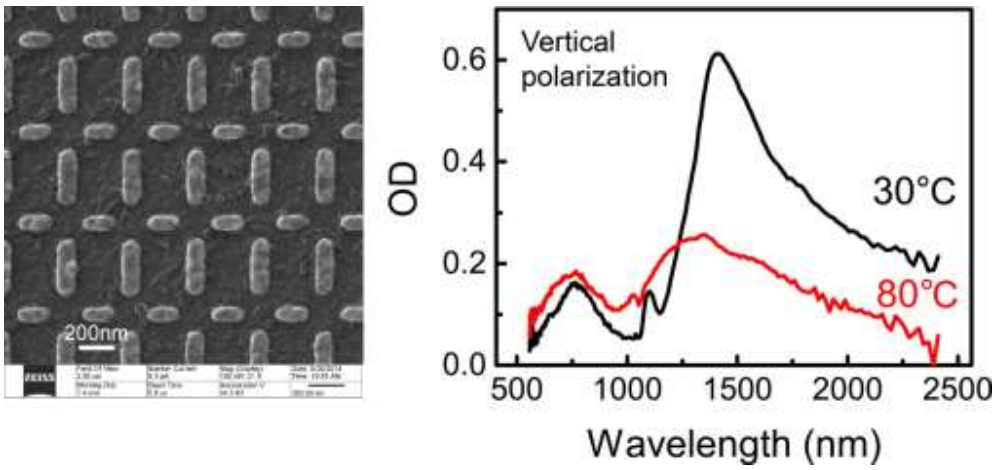



Figure 1 shows gold antennas fabricated on a $VO_2$ film of high quality (left), with (right) excellent switching performance between 30°C and 80°C at telecommunication wavelengths using an external heater.

# Refractory Plasmonic Materials for Heat Assisted Magnetic Recording

**Alexandra Boltasseva**[1], **Urcan Guler**[1,2], **Alexander V. Kildishev**[1], **Ernesto E. Marinero**[1,2,3*] **and Vladimir M. Shalaev**[1,2]

[1]School of Electrical and Computer Engineering and Birck Nanotechnology Center, Purdue University, USA; [2] Nano-Meta Technologies, Inc., West Lafayette, Indiana, USA; [3]School of Materials Engineering, Purdue University, USA; [*]corresponding author: eemarinero@purdue.edu

**Abstract**-Refractory plasmonic materials offer superior mechanical, thermal and structural stability advantages over noble metal plasmonic antennas for heat assisted magnetic recording (HAMR). Whereas these inherent advantages position these materials as leading candidates for potential replacement of Au in HAMR nano-antenna fabrication, their bulk optical properties result in significant self-heating. In this presentation we will describe our progress in manipulating the optical properties of refractory plasmonic nanostructures to circumvent this limitation.

The thermal stability of nanoscale magnetic materials for Tb/in$^2$ recording and beyond requires the use of high magnetic anisotropy materials to meet data retention requirements. As the available fields from the recording head are insufficient to switch the magnetization of said high anisotropy materials, recording is accomplished with the assistance of heat. To this end, Au nano-antennas have been shown to be effective transducers in generating the desired nanoscale thermal footprints in the recording medium. High light coupling efficiencies into the magnetic thin films are obtained with modest or little self-heating. This is an important requirement in order to avoid deleterious heating of the magnetic properties of the thin films comprising the write and read elements of the recording head. However, Au is a soft material, easily damaged upon unintended contact with the metallic layers of the recording medium. In addition, Au ultrathin films have a propensity to form coarse, discontinuous grains whose optical properties can be expected to largely differ from bulk Au. In contrast, refractory materials such as TiN and ZrN are mechanically robust (they are routinely employed to protect drill bits), thermally stable up to 2700 °C and are readily fabricated with conventional growth techniques such as sputter deposition. In this work we report on single crystal growth of refractory plasmonic materials by sputter deposition exhibiting plasmonic resonances in the visible and near infrared regions. We find that the optical properties of TiN and ZrN can be manipulated through judicious growth conditions and can potentially be optimized to closely match those of noble metals. This is corroborated experimentally and our simulations indicate that in terms of plasmonic properties, TiN and ZrN can perform very similarly. We demonstrate also the high temperature operation stability of nanoscale devices in air employing optically matched thin ceramic overcoats.

**Acknowledgements**, The authors acknowledge generous support from NSF SBIR grant IIP-1416232, ONR MURI grant N00014-10-1-0942, and NSF MRSEC grant DMR-1120923.

**REFERENCES**

1. Guler, U., Kildishev, A.V., Boltasseva, A. and Shalaev, V.M. "Plasmonics on the slope of enlightment: the role of transition metal nitrides," *Faraday Discussions*, Vol. 178, 71 - 86, 2015.
2. Guler, U., Boltasseva, A. and Shalaev, V.M. "Refractory Plasmonics" *Science*, Vol. 344, 263 - 264, 2014.
3. Guler, U., Kildishev, A.V., Shalaev, V.M., Boltasseva, A., Stocks D., Gururaj, N., "Near Field Transducer for HAMR," *US Patent*, 2015-0287425

# Metal alloys for plasmonics applications

**Marina S. Leite**[1,2*]

[1]Department of Materials Science and Engineering, University of Maryland, MD, USA

[2]Institute for Research in Electronics & Applied Physics, University of Maryland, MD, USA

[*]corresponding author: mleite@umd.edu

**Abstract**- We determine the optical properties of noble metal thin-film alloys composed by Ag, Au, Cu and Al, by combining ellipsometry and SPP measurements and calculations, and find an excellent agreement between the two experimental methods. Surprisingly, in some cases, the quality factor of the alloy is substantially higher than their pure counterparts. We also quantify the dispersion relation for the alloys, providing a library of the alloys' optical response.

To date, the understanding and control of light-matter interactions is essential for the implementation of game-changing plasmonics devices. For instance, hot carrier devices and perfect absorbers require a high $\varepsilon_2$ (light absorption) while for low-loss metamaterials based devices a low $\varepsilon_2$ is needed to enable surface plasmons effective propagation. Despite the successful use of metals in plasmonics, their pre-defined dielectric function ($\varepsilon = \varepsilon_1 + \varepsilon_2$) currently restricts its application in devices for operation in the visible range of the spectrum. To overcome this limitation, distinct materials have been explored, including ceramics, intermetallics, and semiconductors.

Here, we demonstrate how the alloying of metal thin films formed by Ag, Au, Cu and Al, can modify their optical response [1]. For that, we fabricated a sequence of thin films with a controlled gradient in chemical composition by co-sputtering (see Figure 1). Although the deposition conditions were not optimized, the alloyed samples represent a valid model system to investigate how one can modulate $\varepsilon$ by varying the content of each metal. We performed transmission and reflection measurements of the alloyed thin films and used a B-spline model (Kromers−Kronig relation enforced) to determine their dielectric function. For the experimental conditions used here, we found that some alloys can deliver a higher SPP quality factor (QSPP) than their corresponding pure counterparts. By measuring the SPP coupling angle through the Kretschmann configuration we independently determined $\varepsilon_1$, as shown in Figure 1.

We investigate the near-field response of alloyed nanostructures by NSOM to determine the spectral dependence of their optical response. Further, by using the measured dielectric function of the alloyed thin films, we simulate light-matter interactions of alloyed nanostructures for potential applications in perfect absorbers. Our results demonstrate that the chemical composition of metallic thin films and nanostructures is an effective extra knob to control their optical properties.

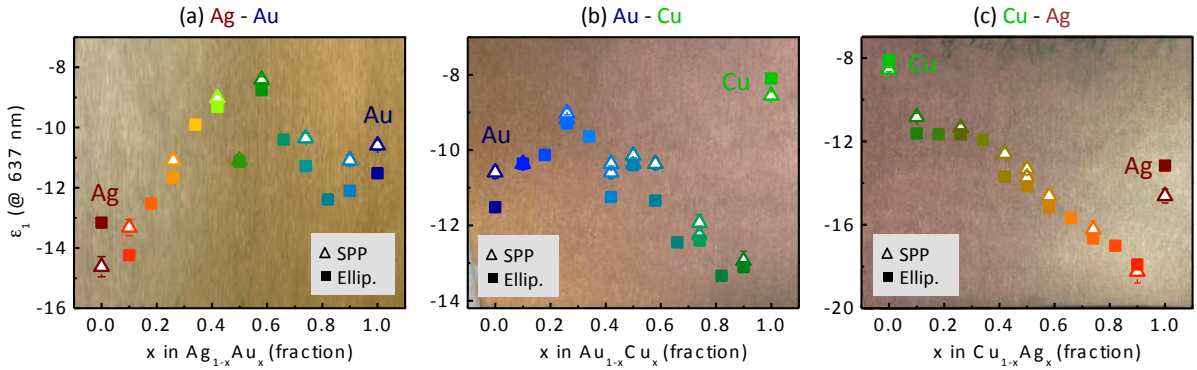



**Figure 1:** Real part of the dielectric function ($\varepsilon_1$) of (a) $Ag_xAu_{1-x}$, (b) $Au_xCu_{1-x}$, and (c) $Cu_xAg_{1-x}$ alloyed thin-films determined by ellipsometry (Ellip., solid squares) and by surface plasmon polariton excitation (SPP, open triangles) measurements overlaid with photographs of the thin film samples.

**Acknowledgements**, Funding support from the National Science Foundation under Grant No. HRD1008117 and by the UMD ADVANCE program, the 2014 Minta Martin Award at the Clark School of Engineering and the University of Maryland 2015 Graduate School's Summer Research Fellowship program.

## REFERENCES

1. Gong, C. and M. S. Leite. "Metal Alloys for Plamonics," *ACS Photonics*, Vol. 3, 507-513, 2016. COVER.

# Physics, Signal, and Noise in Heat-Assisted Magnetic Recording

**Jian-Gang (Jimmy) Zhu**[1*] **and Hai Li**[1]
[1]Data Storage Systems Center, Carnegie Mellon University, USA
[*]corresponding author: jzhu@.cmu.edu

In this paper, we primarily review the fundamental recording physics of heat-assisted magnetic recording (HAMR), the leading candidate for next generation of hard disk drives. Multiple noise origins and its underlying mechanism are discussed and compared, along with recently focused noise, transition curvature. From grain behavior to system optimization, various aspects are visited to validate and apply the recording physics theorem via systematic micromagnetic modeling.

To reach beyond the physical limit of conventional magnetic recording technology, heat assisted magnetic recording (HAMR) was proposed for future hard disk drives [1]. HAMR has been under intensive development effort for the past decade and systematic micromagnetic modeling has provided some of the critical fundamental understanding of the recording process [2][3].

One of the intended advantage of HAMR is the magnetic grains in the media can have extremely high anisotropy field, usually > 70kOe, such that the grain size can be scaled down to significantly increase area storage density capability while maintaining thermal stability. However, the actual dynamic magnetization process as medium cools down to below Curie temperature is critically important. Micromagnetic modeling analysis show that time duration, referred to as recording time window (RTW), between Curie temperature and the temperature magnetization freezes needs to be adequate [2]. If too short, magnetization actually will have a finite probability to be not in the direction of recording field. If too long, the sharpness of the magnetization transition will degrades due to thermally activated magnetization reversal [2]. RTW is a combined function of recording head field, thermal recording profile, disk speed, and medium anisotropy field temperature dependence. This phenomenon becomes more pronounced for smaller size grains. Ideally, higher field amplitude combining with higher thermal gradient is the direction of system optimization. As shown in Fig. 1, lower recording fields lead to insufficient RTW, resulting incomplete magnetization reversal and higher fields lead to erasure after write. Figure 2 illustrates the effect of grain magnetic property distribution on the energy barriers of the grains away from recording zone at the trailing side.

Thermal profile produced by near field transducers (NFT) in HAMR often yields transitions with significant curvature. Associated with curved thermal profile, the maximum temperature becomes non-uniform across the track width, the thermal gradient degrades away from track center, and erasure after write becomes more severe at high linear densities. Figure 3 shows calculated signal amplitude cross-track profile at various linear densities for a circular (left) and straight (right) thermal recording profile.

In HAMR, although the effective recording field gradient is substantially higher than that of the conventional magnetic recording, transition jitter noise remains to be the dominant medium noise due to Curie temperature variations from grain to grain [3][4]. Reducing medium Curie temperature distribution and raising recording thermal gradient are critical for increasing linear density performance.

Figure 4 shows an analysis instance with a generic industrial design, which provides application and validation of the developed dynamic micromagnetic models [5].

This series of work has been generously supported by the industrial sponsors of Data Storage Systems Center at Carnegie Mellon University.

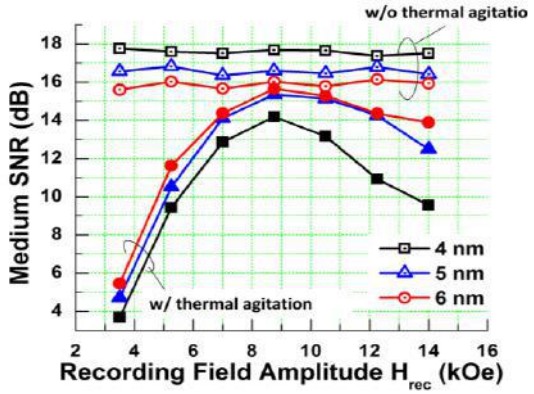



**Figure 1 Size effect of field dependence.**

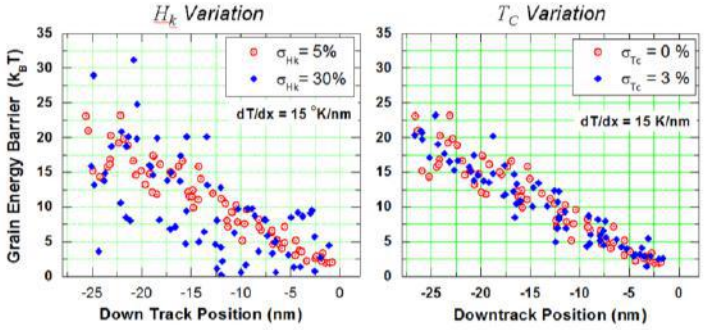



**Figure 2 Energy barrier dispersion of $H_k$ / $T_c$ variation noise.**

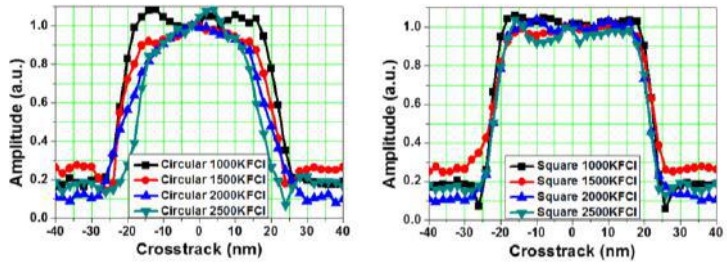



**Figure 3 Crosstrack profile with circular or square thermal profiles.**

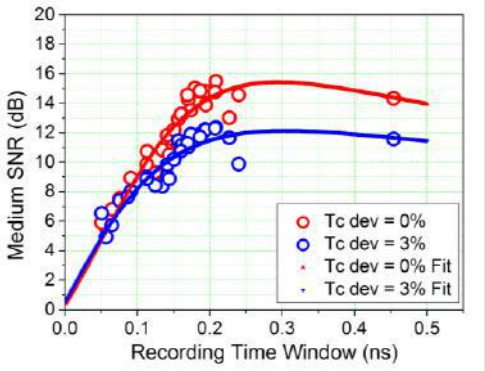



**Figure 4 The recording time window optimization with generic industrial writer design**

## REFERENCES

[1] M.H. Kryder, et al, "Heat assisted magnetic recording," Proc. IEEE, 96, 1810-1834 (2008), W.A. Challener, et al, "Heat assisted magnetic recording by a near-field transducer with efficient optical energy transfer," Nature Photonics, 3, 220-224 (2009). B.C. Stipe, et al, "Magnetic recording at 1.5 Pbm-2 using an integrated plasmonic antenna, " Nature Photonics, 4, 484-488 (2010).

[2] J.-G. Zhu and H. Li, "Understanding Signal and Noise in Heat Assisted Magnetic Recording," *IEEE Trans. Magn.*, vol. 49, no. 2, pp. 765–772, Feb. 2013.

[3] H. Li and J.-G. Zhu, "Understanding the impact of Tc and Hk variation on signal-to-noise ratio in heat-assisted magnetic recording," *J. Appl. Phys.*, vol. 115, no. 17, p. 17B744, May 2014.

[4] H. Li and J.-G. Zhu, "The Role of Media Property Distribution in HAMR SNR," *IEEE Trans. Magn.*, vol. 49, no. 7, pp. 3568–3571, 2013.

[5] H. Li, B. Johnson, M. Morelli, M. Gibbons, and J.-G. (Jimmy) Zhu, "Analysis of signal-to-noise ratio impact in heat assisted magnetic recording under insufficient head field," *J. Appl. Phys.*, vol. 117, no. 17, p. 17D133, 2015.

# Plasmonic Nanocircuits: Fundamentals and Devices

# Plasmonic vector near-field for composite interference, SPP switches and optical simulators

**Tao Li*, Yulin Wang, Qingqing Cheng and Shining Zhu**
National Laboratory of Solid State Microstructures, College of Engineering and Applied Sciences, School of Physics, Nanjing University, Nanjing 210093, China
*corresponding author: taoli@nju.edu.cn

**Abstract**-Plasmonic offers people not only the strong field confinement and field enhancement within nanostructures, but also a versatile configuration of the vector near-field. Here, we would like to show several interesting optical phenomena arising from the vector field coupling effect. One is the composite interference of surface plasmon polaritons (SPPs) within two crossed strip waveguides, and the other is optical simulations for massless Dirac Fermion and topological interface states.

Plasmonic has provided versatile solutions to confine the light at sub-wavelength scale together with strong field enhancement, which enables great possibilities for compact photonic integration and other applications. Besides these useful properties, its vector near-field configurations supported by the nanostructure's geometries also gives rise to novel optical phenomena and functionalities. In this talk, I would firstly show an interesting composite plasmonic interference resulted from two crossed strip-metallic waveguides with a narrower gap, where the vectorial field configuration gives rise to two quite different interferences - synchronous and antisynchronous. Based on this interference effects, compact SPP switches are proposed and demonstrated with respect to external phase modulations [1]. Secondly, such kind of the vectorial SPP field is found to play a crucial role in determine the coupling coefficient in coupled strip waveguide system. Here, a positive/negative alternating coupling scheme is theoretically proposed in plasmonic waveguide array to simulate the massless Dirac Fermion behaviors with nondispersive propagations. Moreover, in experiments, a strong/weak coupling system in plasmonic waveguide array was experimentally realized to simulate the SSH mode with a robust topological interface mode [2]. All of results are closely related with the vectorial configuration of the plasmonic near field that would offer people new avenues in steering the optical field and photons in more degrees of freedom.

**Acknowledgements** This work was supported by the National Key Projects for Basic Researches of China (No. 2012CB933501) and the National Natural Science Foundation of China (Nos. 11174136, 11322439, 11321063, and 91321312). This work was also supported by the Dengfeng Project B of Nanjing University.

**REFERENCES**

1. Y. Wang, T. Li, L. Wang, H. He, L. Li, Q. Wang, and S. N. Zhu, "Plasmonic switch based on composite interference in metallic strip waveguides," *Laser Photon. Rev.* Vol. 8, No. 4, L47–L51, 2014.
2. Q. Q. Cheng, Y. Pan, Q. Wang, T. Li, and S. N. Zhu, "Topologically protected interface mode in plasmonic waveguide arrays," *Laser Photon. Rev.* Vol. 9, No. 4, 392–398, 2015.

# Mechanisms of plasmon-mediated light emission in biased nanoscale constrictions

**A. V. Uskov[1,2*], I. V. Smetanin[1], I. E. Protsenko[1], J. B. Khurgin[3], M. Buret[4], and A. Bouhelier[4]**

[1]P. N. Lebedev Physical Institute, Leninsky pr. 53, 119991 Moscow, Russia

[2]ITMO University, Kronverkskiy pr. 49, 197101 Sankt-Petersburg, Russia

[3]Department of Electrical & Computer Engineering, John Hopkins University, Baltimore, Maryland, USA

[4]Laboratoire Interdisciplinaire Carnot de Bourgogne, CNRS-UMR 6303,
Université Bourgogne Franche-Comte, 21078 Dijon, France

[*]corresponding author: alexusk@lebedev.ru

**Abstract**-We investigate spontaneous light emission by electrons passing through a nanoscale metal constriction. We find that the emission is caused by two distinct mechanisms. The first mechanism is driven by electron colliding with the effective potential of the mesoscopic contact. The second emission process involves collisions of electrons with the walls of the constriction. We find that multiple collisions with the walls can lead to the orders-of-magnitude higher light emission probability in comparison to a single collision with the effective potential.

Electrically-driven optical nanoantennas [1-3] attract growing interests due to their potential use as nanosources of plasmons integrated in optical nano-circuitries. Physics of plasmon excitation in metal-barrier-metal (MBM) structures was understood many years ago on the basis of inelastic electron tunneling [4]. On the other hand, recent experimental results are suggesting that a nanoscale mesoscopic contact between two electrodes also emits photons. The constriction is obtained from the electromigration of a nanowire [3]. In the present paper, we discuss the possible mechanisms leading to the emission of photons by electrons passing through mesoscopic constrictions.

Emission of photons by free electrons requires momentum conservation; hence an electron must collide with a "third body". In MBM structures, the tunneling barrier is the third body, and the emission can be thought as a "bremsstrahlung" process during electron tunneling. The strong localization of excited plasmonic modes may also promote emission of plasmons, which may decay radiatively into photons. Figure 1 shows an electron passing through a nanoscale constriction with a width $W(x)$. The constriction is assumed to have the potential walls of infinite height, which is typical in the theory of quantization of conductivity in mesoscopic contacts [5]. This is a valid approximation as long as work function of the metal exceeds a few electron-volts. The constriction is positioned inside a localized surface plasmon polariton (SPP) mode of the metallic structure. The effective volume of the mode $V_{mode} \sim L^3$ is outlined by the dashed line in Fig. 1. The passage of the electron through the constriction is assumed *ballistic*: the electron does not experience any collisions inside the constriction; the electron's motion is governed only by the potential walls and the field of the mode.

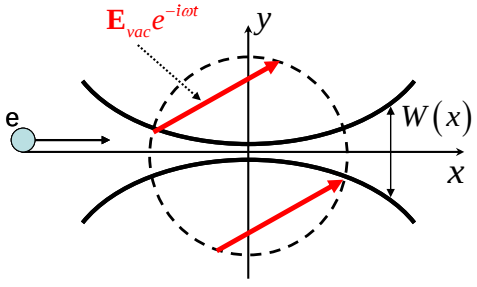



**Figure 1: Simplified picture of an electron passing through a nanoscale contact and interacting with a plasmonic field with a modal volume outlined by the dashed line.**

Our analysis shows that the mechanisms of plasmon emission strongly depends on the polarization of the field in the mode shown by red arrows in Fig. 1. If the field is polarized along the constriction (*parallel* to the x-axis), an electron may emit a photon (or absorb) due to its collision with the *effective* confinement potential $U_n(x) = n^2\hbar^2\pi^2 / \left[2mW^2(x)\right]$, where $n$ is the number of a channel in which the electron moves [5]. The probability of emission (for electron energy $u_{ox}$ higher then $U_{n\max}$) can be estimated as $p^{\parallel}_{e-spon} = e^2 \left|E_{vac}\right|^2 u_{ox} / \left(m\omega^4\hbar^2\right)$ where $E_{vac}$ is the "vacuum" field of the mode: $\left|E_{vac}\right|^2 \sim \hbar\omega / \left(2\varepsilon_o V_{\text{mode}}\right)$. Estimation with $u_{ox} \sim \varepsilon_F$(Fermi energy)~5eV, $\hbar\omega \sim 1$eV, $L$~100nm gives $p^{\parallel}_{e-spon} \sim 10^{-5}$. Such a low probability is caused by the fact that an electron only experiences a *single* collision in the mechanism.

On other hand, if the field in the mode is *perpendicular* to the constriction, then plasmon excitation occurs each time the electron experiences one of the *multiple* collisions with the walls of constriction. Then the probability of spontaneous emission can be estimated as $p^{\perp}_{e-spon} = \tau_o^2 e^2 \left|E_{vac}\right|^2 / \left(m\hbar\omega\right)$, where $\tau_o = L/\mathrm{v}_{ox}$ is the characteristic time of electron interaction electron with the mode, and $\mathrm{v}_{ox}$ is the electron velocity. We estimate $p^{\perp}_{e-spon} \sim 0.1$ for $L$~100nm. One can show that $p^{\perp}_{e-spon}$ exceeds $p^{\parallel}_{e-spon}$ by the factor ~$N^2$, where $N = \omega \cdot L/\mathrm{v}_{ox}$ is the number of collisions of electron with the walls of constriction.

In conclusion, we have shown that electrons passing through a nanoscale metal constriction may excite plasmon mode by colliding with the effective potential or with the walls depending on the polarization of the plasmonic mode. Because the electrons may collide multiple times with the walls in contrast to a single collision with the effective potential, the probability to emit plasmon by interaction with the walls can reach ~0.1. Thus nanoscale metallic constrictions are promising alternatives for developing efficient nanosource of plasmons

**Acknowledgements**-This work was financially supported in part by the Government of the Russian Federation (Grant 074-U01) through ITMO Visiting Professorship program. The research leading to these results has received funding from the European Research Council under the European Community's Seventh Framework Program FP7/ 2007-2013 Grant Agreement No. 306772.

**REFERENCES**

1. Bharadwaj, P., A. Bouhelier and L. Novotny, "Electrical Excitation of Surface Plasmons", Phys. Rev. Lett., Vol. 106, No. 22, 226802, 2011.
2. Kern, J., R. Kullock, J. Prangsma, M. Emmerling, M. Kamp and B. Hecht, "Electrically driven optical antennas", Nature Photonics, Vol. 9, No. 9, 582-586, 2015.
3. M. Buret, A. V. Uskov, J. Dellinger, N. Cazier, M.-M. Mennemanteuil, J. Berthelot, I. V. Smetanin, I. E. Protsenko, G. Colas-des-Francs and Alexandre Bouhelier, "Spontaneous Hot-Electron Light Emission from Electron-Fed Optical Antennas", Nano Lett., Vol. 15, No. 9, 5811-5818, 2015.
4. Davis, L. C., "Theory of surface-plasmon excitation in metal–insulator–metal tunnel junctions", Phys. Rev. B, Vol. 16, No. 6, 2482–2490 (1977).
5. Datta, S., Electronic Transport in Mesoscopic Systems, Cambridge University Press 1995.

# Composite interference based plasmonic switches and logical gates

**Yulin Wang, Tao Li* and Shining Zhu**

National Laboratory of Solid State Microstructures, School of Physics, College of Engineering and Applied Sciences, Nanjing University, Nanjing 210093, China

*corresponding author: taoli@nju.edu.cn

Abstract– Full optical switch is an important element in developing photonic on-chip integration. In this talk, compact switches were proposed and demonstrated based on the interference of surface plasmons polaritons (SPP) on free metal surface and in waveguides. Additionally, an interesting composite interference was observed and discussed in the waveguide device. By cascading two kinds of different interference components, a novel interference phenomenon of phase-insensitivity was finally achieved.

Full optical switch is an important element in developing photonic on-chip integration [1, 2]. Traditional approaches are always suffering from the large spatial occupation that severely limits the massive integration. Thanks to the strong confinement of the optical field, surface plasmons provide a possible solution to achieve compact photonic elements. In this talk, I will demonstrate compact switches based on the interference of surface plasmons polaritons (SPP) on free metal surfaces and in waveguides. A 2×2 ports switch devices composed of strip waveguides, in which the BS is shortened within a small cross region (the green box in an area of $6\times6\mu m^2$) were achieved with a maximum modulation depth of about 80%[3]. Additionally, an interesting composite interference was observed and analyzed in the waveguide device, which is proved from an anti-synchronous transmission/reflection interference and a synchronous field superposition interference (see Fig. 1). Samples of Bragg gratings and slits with different parameters were investigated in further experiments, which provided convincible evidences supporting the composite interference model. Furthermore, its logical functions implemented by the switch on synchronous and anti-synchronous interference have already been discussed and proved. However, optical switches based on interference are phase-sensitive, may becoming a key restriction factor for optical integrated circuits for computing and information process. By cascading two kinds of interference components, a novel interference phenomenon of phase-insensitivity was finally achieved (see Fig. 2), exhibiting a good function of phase-insensitive NOR logical gate. It would probably inspire new modulating methods on the guided SPPs and hold the possibility for designing new types of photonic devices at the micro/nanoscale.

**Figures and Tables:**

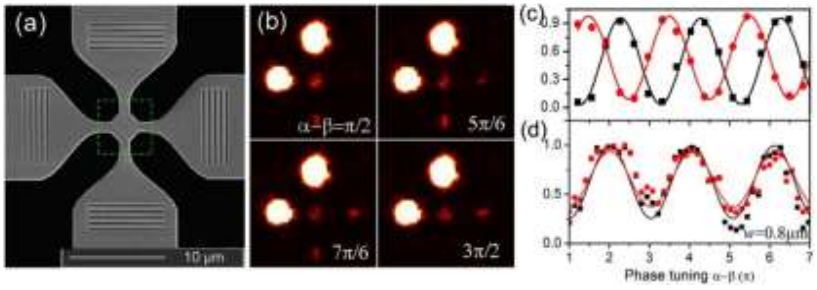


Fig.1. (a) SEM image of plasmonic switch device, (b) Interference results with different input phases, (c) and (d) anti-sychronous and sychronous intereference between two output ports, respectively.

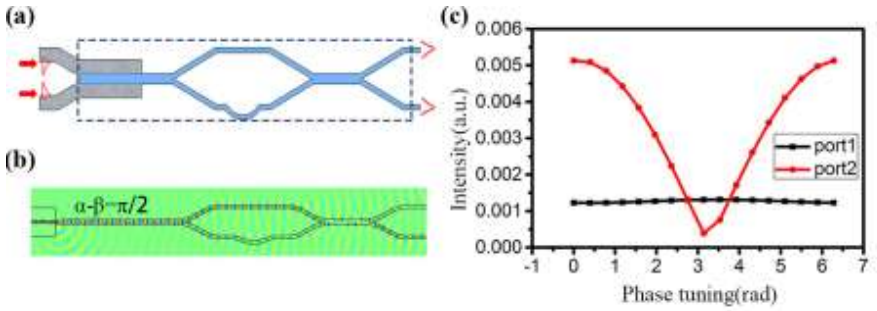



Fig.2. (a) The schematic structure of the phase-insensitive device. (b) The field distribution of the phase-insensitive interference with the phase lag of π/2. (c) The interference curves with phase tuning.

**Acknowledgements** This work was supported by the National Key Projects for Basic Researches of China (No. 2012CB933501) and the National Natural Science Foundation of China (Nos. 11174136, 11322439, 11321063, and 91321312). This work was also supported by the Dengfeng Project B of Nanjing University.

## REFERENCES

[1] H. Wei, Z. Wang, X. Tian, M. Käll, and H. Xu, "Cascaded logic gates in nanophotonic plasmon networks," *Nature Communications*, vol. 2, pp. 503-507, 2011.

[2] Y. Fu, X. Hu, C. Lu, S. Yue, H. Yang, and Q. Gong, "All-optical logic gates based on nanoscale plasmonic slot waveguides," *Nano Letters*, vol. 12, pp. 5784-5790, 2012.

[3] Y. Wang, T. Li, L. Wang, H. He, L. Li, Q. Wang, *et al.*, "Plasmonic switch based on composite interference in metallic strip waveguides," *Laser & Photonics Review*, vol. 8, pp. L47–L51, 2014.

# Subwavelength scale lasers at room temperature by top-down fabrication

**N. Liu[1*], and B. Corbett[2]**

[1]Department of Physics and Energy, Materials and Surface Science Institute, University of Limerick, Ireland

[2]Tyndall National Institute, Ireland

[*]corresponding author: ning.liu@ul.ie

**Abstract**- Hybrid plasmonic mode, a special optical mode at the semiconductor-insulator-metal interface, has demonstrated its unprecedented mode confinement (tens of nanometer) and relatively low propagation loss and is regarded as one of the most promising candidates for integrated plasmonics. Lasing at deep subwavelength scale have been realized through hybrid plasmonic modes. However, most of the lasing cavities reported so far are fabricated using bottom-up approaches, which limits the scalability and reproducibility of the plasmonic devices. In this talk, I will present the recent progresses made in our groups on utilizing bottom-up approach to fabricate various subwavelength laser cavities that are suitable for large scale production. These subwavelength cavities demonstrate low lasing threshold and can operate at room temperature, showing great promise for future high density integrated plasmonic applications.

# Localized surface plasmon enhanced and modulated nonlinear optical processes: second harmonic generation and upconversion emissions

**D. Y. Lei**
Department of Applied Physics, The Hong Kong Polytechnic University, Hong Kong, China
*corresponding author: dylei@polyu.edu.hk

**Abstract**-This talk will present our recent theoretical and experimental investigations on using localized surface plasmons to significantly enhance several nonlinear optical processes, including second harmonic generation, two-photon luminescence and upconversion emissions, and their applications in bioimaging and biosensing.

In the first part of this talk, I will show our experimental investigation on the linear and nonlinear optical properties of metal film-coupled nanosphere monomers and dimers both with nanometric gaps. We have developed a new methodology - polarization resolved spectral decomposition and color decoding to "visualizing" unambiguously the spectral and radiation properties of the complex plasmonic gap modes in these hybrid nanostructures. Single-particle spectroscopic measurements indicate that these hybrid nanostructures can simultaneously enhance several nonlinear optical processes, such as second harmonic generation, two-photon absorption induced luminescence, and hyper-Raman scattering. In the second part, I will show how the polarization state of the emissions from sub-10 nm upconversion nanocrystals (UCNCs) can be modulated when they form a hybrid complex with a gold nanorod (GNR). Our single-particle scattering experiments expose how an interplay between excitation polarization and GNR orientation gives rise to an extraordinary polarized nature of the upconversion emissions from an individual hybrid nanostructure. We support our results by numerical simulations and, using Förster resonance energy transfer theory, we uncover how an overlap between the UCNC emission and GNR extinction bands as well as the mutual orientation between emission and plasmonic dipoles jointly determine the polarization state of the UC emissions.

# Taming single solid-state quantum systems and mesoscopic objectives at the nanoscale.

**Xuewen Chen**
School of Physics, Huazhong University of Science and Technology, Wuhan, P.R. China
E-mail: xuewen_chen@hust.edu.cn

**Abstract**- *We report on controllable and highly efficient coherent and incoherent interactions of propagating photons and single quantum systems in solid state. Depending on the configuration and the regime of interactions, a single emitter show great impact on a mesoscopic objective (or vice versa ) by cloaking, or by enhancing extinction cross section of a few orders of magnitude, or by starting coherent oscillation. We present new experimental efforts on building highly bright single-photon sources.*

In the past decade, we have witnessed tremendous development of the concept and technologies of photonics, which allow unprecedented manipulation of the light fields at the mesoscopic scale. In the meanwhile, precision spectroscopy, quantum physics and material science have advanced at a spectacular pace, offering great flexibilities in the detection, microscopy and control of single quantum systems in the solid state. In this context, efficient and precise interfacing of novel photonic structures and complex quantum systems in the mesoscopic scale becomes important and highly prospective for novel functional quantum devices. In this talk, we will present our recent efforts in achieving controllable and efficient coherent and incoherent interactions between propagating photons and single emitters in open systems. We show that depending on the configuration and interaction regime single emitters could cloak a large nanostructure, or enhance by a few orders of magnitude of the extinction of a small particle, or start coherent oscillations. In the incoherent interaction regime, we present some experimental results towards making ultrabright single-photon sources based on colloidal quantum dots enhanced by simple nanoantennas. We may also talk about how two photons can strongly interact in an open structure via a single emitter.

**Acknowledgements**
This work is partially supported by National Science Foundation of China (NSFC, No. 11474114).

# Nanometric imaging of the few-cycle plasmonic near-field within single nanoobjects

**A. Losquin[1*], E. Mårsell[1], E. Lorek[1], R. Svärd[1], C. Guo[1], A. Harth[1], M. Miranda[1], C. L. Arnold[1], H. Xu[2], A. L'Huillier[1], J. Mauritsson[1], and A. Mikkelsen[1]**

[1]Department of Physics, Lund University, Lund, Sweden
[2]School of Physics and Technology, and Institute for Advanced Studies, Wuhan University, Wuhan, China

[*]corresponding author: arthur.losquin@fysik.lth.se

**Abstract**-We combined PhotoEmission Electron Microscopy with a few-femtosecond laser system to image the few-cycle plasmonic near-fields within single nanoobjects.

Ultrafast applications of nanoplasmonics such as near-field coherent control are attracting a growing attention, stimulated by the progressive availability and mastering of ultrashort laser pulses [1]. In particular, the combination of nanoplasmonics and broadband few-femtosecond laser pulses open up the regime of few-cycle plasmonics [2]. Possible applications require characterization tools to access the plasmonic near-fields induced by few-cycle pulses, ultimately at a nanometer spatial scale. We recently combined PhotoEmission Electron Microscopy (PEEM) with a few-femtosecond laser system to image the few-cycle plasmonic near-fields within single nanoparticles.

Fig. 1 illustrates the results obtained on single silver nanocubes (Fig. 1(a)) and nanorice particles (Fig. 1(b)). The nanocube experiments were performed by rotating the polarization of the laser pulses. The near-field intensity is localized at different corners of the cube depending on the polarization (Fig. 1(a)). The nanorice experiments were performed by splitting and delaying the laser pulses with respect to each other through an interferometer. Two intensity spots are visible at both ends of the particle. The intensity oscillations as a function of the delay between the pulses are different, reflecting a different time evolution of the near field at both ends (Fig. 1(b)).

We thus demonstrated control of the localization of the near-field intensity within single nanoobjects through the polarization of the laser pulses (Fig. 1 (a)) [3]. Using an interferometric time-resolved setup [4], we showed that the near-field dynamics of single nanoobjects strongly depend on their shape [5, 6]. Furthermore, we demonstrated that the near-field dynamics can show significant differences *within* single nanoobjects [6].

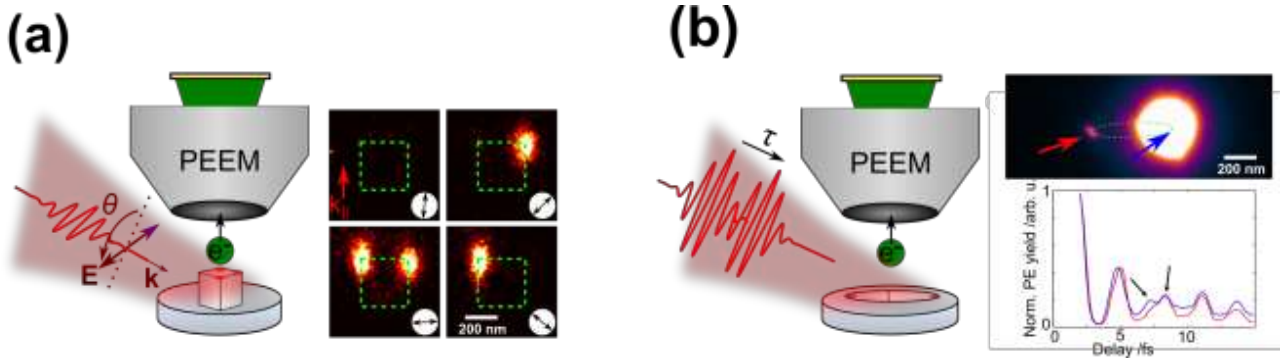



Fig. 1. (a) Imaging of the near-field localization control within single silver nanocubes. Left: sketch of the experiment. θ is the deviation of the laser polarization from p-polarization. Right: PEEM images of a silver nanocube for different polarizations. The polarizations are indicated with arrows depicting the electric field component parallel to the sample plane. (b) Imaging of the near-field dynamics within single silver nanorice particles. Left: sketch of the experiment. τ is the delay applied between the two excitation pulses. Right: PEEM image of a silver nanorice particle, and PEEM intensity integrated over the left end (red) and right end (blue) of the particle as a function of the delay between the two excitation pulses.

**REFERENCES**

1. M. I. Stockman et al., Phys. Rev. Lett. **88**, 067402 (2002)
2. P. Dombi et al., Opt. Express **18**, 24206 (2010)
3. E. Mårsell et al., Appl. Phys. Lett. **107**, 201111 (2015)
4. A. Kubo et al., Nano Lett. **5**, 1123 (2005)
5. E. Lorek et al., Opt. Express **23**, 31460 (2015)
6. E. Mårsell et al., Nano Lett. **15**, 6601 (2015)

We acknowledge Hong Wei for nanoparticle synthesis. This work was supported by NanoLund, the Swedish Research Council (VR), the Swedish Foundation for Strategic Research (SSF), the Crafoord Foundation, the Knut and Alice Wallenberg Foundation, and the European Research Council (ERC) (startup grant ElectronOpera and advanced Grant PALP).

# Plasmonic metasurfaces for polarization and phase sensing

**E. Panchenko[1], J. J. Cadusch[1], P. Achmari[1], K. Singh[1], T. D. James[1], D.E. Gomez[1, 2], T. J. Davis[1] and A. Roberts[1]**

[1]School of Physics, The University of Melbourne, 3010, Australia

[2]CSIRO Materials Science and Engineering, Private Bag 33 Clayton, Victoria 3168, Australia

[*]corresponding author: ann.roberts@unimelb.edu.au

**Abstract**- Metasurfaces are artificially fabricated, ultrathin films that exhibit a tailored response to incident electromagnetic radiation. Here theoretical, computational and experimental progress toward the design and demonstration of phase and polarization-sensitive metasurfaces for applications in optical image processing will be presented.

The properties of optical wavefields, such as polarization and phase, can be utilised in applications ranging from information processing, communications and imaging. Two aspects of metasurface physics will be presented here. Firstly, the utilization of subradiant modes of nanostructures to create metasurfaces to directly manipulate the angular spectrum of a transmitted or reflected optical field will be discussed. These devices provide an avenue for the development of ultracompact devices that will perform on-chip, real-time, single-shot conversion of wavefield information to readily measured intensity distributions. Secondly, the integration of plasmonic antennas with the capacity to discriminate between different states of polarization onto an MSM photodetector will be demonstrated. This device, compatible with standard CMOS fabrication processes, demonstrates the capacity for metasurfaces to play a significant role in future optoelectronic systems.

Metasurfaces consist of arrays of subwavelength nanostructures that exhibit characteristic resonances. While attention has been focused on taking advantage of the lowest order electric dipole mode, resonators exhibit a range of higher order modes. While the dipole mode can be easily excited with a normally incident plane wave, many modes are ‘dark’ or ‘subradiant’ precluding their excitation with a uniform field. Such modes can, however, be excited with fields possessing non-uniform polarization [1] or phase [2] distributions, suggesting an avenue for converting optical information carried in the form of phase or polarisation into variations in the intensity of a wavefield that can be detected using conventional camera technology. In particular, the sensitivity of a metasurface to phase gradients in a wavefield can be characterized by its optical transfer function. As an example, Fig. 1 shows the computed transmission of horizontally polarised plane waves through an array of coaxial apertures in a perfectly electrically conducting (PEC) film when either the dipole $TE_{11}$ mode (a) or the radial TEM coaxial waveguide mode (b) is excited. The high fidelity of the transmission of spatial frequency information by the dipole mode is apparent, as is the suppression of low-spatial frequency information when the TEM mode is on resonance. The sensitivity of dark mode excitation to phase gradients in the incident field suggests their potential as elements in ultra-compact optical systems for image processing operations such as edge detection or the visualization of transparent objects.

There is also considerable interest in integrating metasurfaces with photodetectors to realize their potential in semiconductor applications. Here, recent progress in the development of a planar Metal-Semiconductor-Metal (MSM) device integrated with plasmonic elements that can sense different states of polarisation will be discussed [6]. Through the incorporation of arrays of metallic nanostructures onto the surface between two

back-to-back MSM photodetectors on n-type silicon, the difference between the photocurrents produced by each detector provides information about the state of polarization of the incident light. Three leads forming the two photodetectors (one lead being common) are wrapped into a spiral to match the circular profile of an incident beam and the surface of the Si between each pair of leads is decorated with aluminium nanoantennas that selectively reflect different polarization states leading to a polarization-dependent photocurrent. We have developed two photodetectors with one using nanorods, to sense different states of linear polarization, and a second, using chiral antennas [6], to preferentially reflect left or right circularly polarized light.

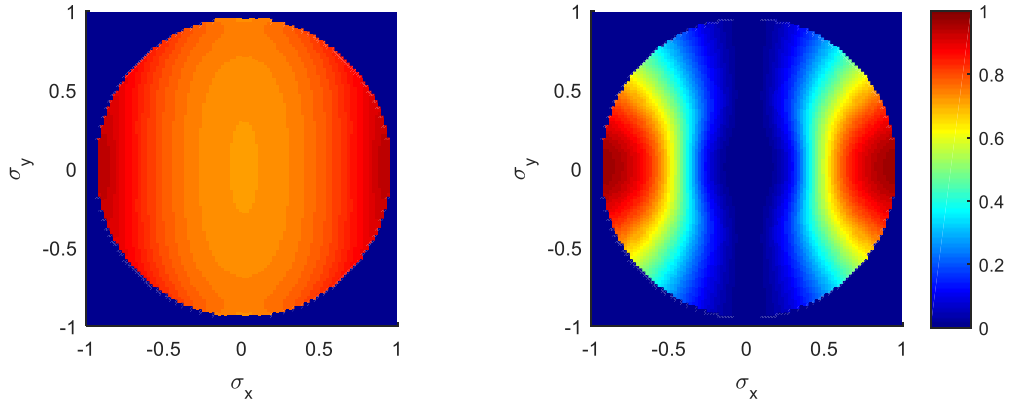



Figure 1. Plane wave transmission through a square array (period $d$) of annular apertures in a PEC of thickness 2.7$d$ as a function of normalised wavevector. The outer and inner radii of the apertures are 0.375$d$ and 0.333$d$ respectively. The figure on the left is at a wavelength of 2.22$d$ ($TE_{11}$ coaxial waveguide mode resonance), while on right the wavelength is 2.78$d$, a TEM mode resonance.

**Acknowledgements:** This work was performed in part at the Melbourne Centre for Nanofabrication (MCN) in the Victorian Node of the Australian National Fabrication Facility (ANFF). This research was also supported under the Australian Research Council's Discovery Projects funding scheme project numbers DP110100221 and DP160100983.

**REFERENCES**

1. D.E. Gómez, Z.Q. Teo, M. Altissimo, T. J. Davis, S. Earl, and A. Roberts, "The Dark Side of Plasmonics," *Nano Lett*. Vol. 13, 3722-3728 (2013)
2. A. Roberts, "Beam Transmission Through Hole Arrays," *Opt. Exp*., Vol. 18, 2528-2533 (2010)
3. F. Eftekhari, D.E. Gómez and T.J. Davis, "Measuring subwavelength phase differences with a plasmonic circuit--an example of nanoscale optical signal processing," *Opt. Lett.* Vol. 39, 2994-2997 (2014)
4. W. Li, Z. J. Coppens, L. V. Besteiro, W. Wang, A. O. Govorov and J. Valentine, "Circularly polarized light detection with hot electrons in chiral plasmonic metamaterials," *Nature Comm.* Vol. 6, 8379 (2015)
5. L. Du, S. S. Kou, , E. Balaur, J. J. Cadusch, A. Roberts, B. Abbey, X.-C. Yuan, D. Tang & J. Lin, "Broadband chirality-coded meta-aperture for photon-spin resolving," *Nature Comm.* Vol. 6, 10051 (2015)
6. E. Panchenko, J. J. Cadusch, T. D. James and A. Roberts, "Plasmonic antenna-enabled differential photodetectors for broadband polarisation-sensitive optical signaling," *submitted* 2016.
7. F. Eftekhari and T.J. Davis, "Strong chiral optical response from planar arrays of subwavelength metallic structures supporting surface plasmon resonances," *Phys. Rev. B*, Vol. 86, 075428 (2012)

# Optical Stark-effect in J-aggregate-metal hybrid nanostructures

**Parinda Vasa***
Department of Physics, Indian Institute of Technology Bombay, Mumbai, India
*corresponding author: parinda@iitb.ac.in

**Abstract** We report on the observation of optical Stark effects in J-aggregate–metal hybrid nanostructures exhibiting strong exciton-surface-plasmon-polariton coupling. For red-shifted nonresonant excitation, pump-probe spectra show characteristic features of pump-induced Stark shift of the polariton resonances. For larger coupling strengths, we observe largely enhanced Stark shift with opposite sign caused by a transient reduction in normal mode splitting. Such a strong coherent interaction may be useful for applications in ultrafast all-optical switching.

The optical Stark effect (OSE) is a fundamental, coherent nonlinear interaction involving transient shifts of energy levels in the presence of a non-resonant light field [1]. Being a coherent interaction, it is promising for implementing quantum information processing and for gaining insights into the quantum dynamics of optical excitations. Molecular aggregates have recently received considerable interest [2-4]. Because of their large optical dipole moment they serve as prototypes [2,3] for exploring dipolar coupling between excitons (Xs) and surface plasmon polaritons (SPPs).

We investigate hybrid nanostructures consisting of a ~50 nm thick J-aggregated cyanine dye layer spin coated onto a periodic nanogroove array with a 400 nm period in a gold film [3,4]. The linear optical response of such hybrid nanostructures is governed by the coupling of excitonic transition dipole moments to vacuum fluctuations of the groove array SPP modes. Because of this coupling, the isolated J-aggregate and SPP resonances are transformed into strongly coupled higher (UP) and lower energy (LP) with normal mode splitting, $\Omega_{NMS}$ ~110 meV [3,4]. For excitation with off-resonant ultrashort pump pulses [Figure 1(a)], we observe fully coherent X-SPP optical nonlinearities. For systems with $\Omega_{NMS}$ ~60 meV, they reflect the expected transient dressing of the X resonances [Figure 1(b)]. For large mode splitting, however, our results indicate a different type of response, greatly enhancing the OSE [4].

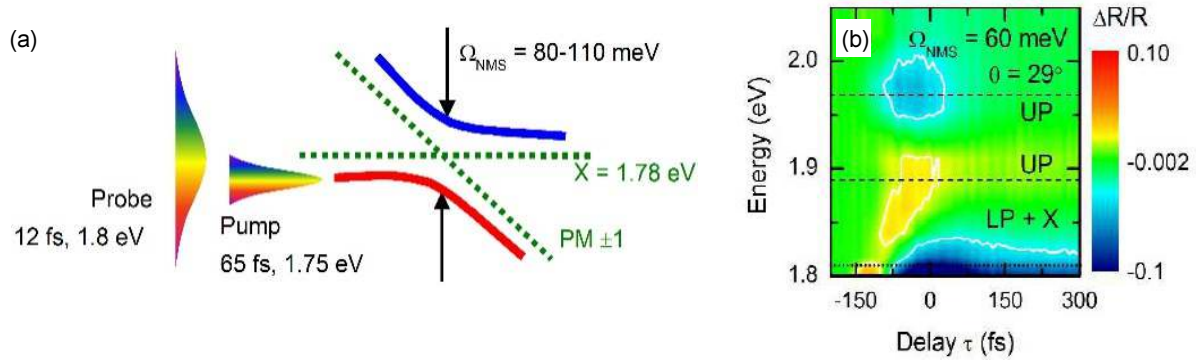



**Figure 1** (a) Schematic of the pump-probe experiment. (b) Transient reflectivity map showing OSE induced shift of UP.

Our results offer a very interesting approach for coherently controlling and enhancing OSEs in strongly coupled hybrid materials by transiently reducing the $\Omega_{NMS}$ rather than dressing X resonances. It can greatly enhance OSEs making hybrid nanostructures interesting, not only for applications but also for exploring the underlying physics [4]. Our experiments on large ensembles of Xs have been performed with nanojoule pulse energies. We anticipate ultrafast coherent switching with femtojoule pulse energies for reduced sample area $\leq 1$ $\mu m^2$, even without considering plasmonics field enhancement.

This work was carried out in collaboration with Wei Wang, Robert Pomraeneke, Christoph Lienau (Carl von Ossietzky Universitet Oldenburg, Germany) and Margherita Maiuri, Cristian Manzoni, Giulio Cerullo (Politecnico di Milano, Italy).

**REFERENCES**

1. B. R. Mollow, "Optical stimulated emission and absorption near resonance for driven systems", *Phys. Rev. A*, Vol. 5, 2217, 1972.
2. J. Bellessa, C. Bonnand, J. C. Plenet, and J. Mugnier, "Strong coupling between surface plasmons and excitons in an organic semiconductor interaction", *Phys. Rev. Lett.*, Vol. 93, 036404, 2004.
3. P. Vasa, W. Wang, R. Pomraenke, M. Lammers, M. Maiuri, C. Manzoni, G. Cerullo, and C. Lienau, "Real-time observation of ultrafast Rabi oscillations between excitons and plasmons in metal nanostructures with J-aggregates", *Nature Photon.*, Vol. 7, 128, 2013.
4. P. Vasa, W. Wang, R. Pomraenke, M. Maiuri, C. Manzoni, G. Cerullo, and C. Lienau, "Optical Stark effects in J-aggregate–metal hybrid nanostructures exhibiting a strong exciton–surface-plasmon-polariton interaction", *Phys. Rev. Lett.*, Vol. 114, 036802, 2015.

# Interaction of quantum dots and plasmonic nanoparticle dimers

**M. Gašparić, A. Hohenau, U. Hohenester, J. R. Krenn**

Institute of Physics, University of Graz, Austria
marija.gasparic@uni-graz.at

**Abstract**— The coupling of single photon emitters like quantum dots (QDs) and metal nanoparticles (MNPs) give us the possibility to investigate light matter interaction. Our study is focused on developing a plasmon enhanced photo detector using a (single) QD and MNPs. Resonant MNPs generate an enhanced near field that strongly influences the absorption rate of the QDs placed in the MNPs' vicinity.

Coupling single photon emitters to plasmonic nanostructures allows the detailed study of strong light-matter interaction. In our work, we aim at the lithographically controlled combination of (single) QDs and silver or gold MNPs. Therefore, we first tailor triangle dimers in a bow-tie geometry by electron beam lithography. In the Figure we show measured and simulated extinction spectra for bow-tie structures with a different gap size. Simulations are performed using the Matlab MNPBEM toolbox [1]. When light is polarized along the gap, there is a particularly strong influence on the resonance peak position due to the high field enhancement in the bow-tie gap.

In a second lithography step we fabricate a polymer mask for placing the QDs into the gap. On the one hand, this places the QDs in the plasmonic hot spot influencing the QDs' properties. On the other hand, we aim at contacting the QDs electrically using a bow-tie structure with electrodes turning the system into a photoconductive device.

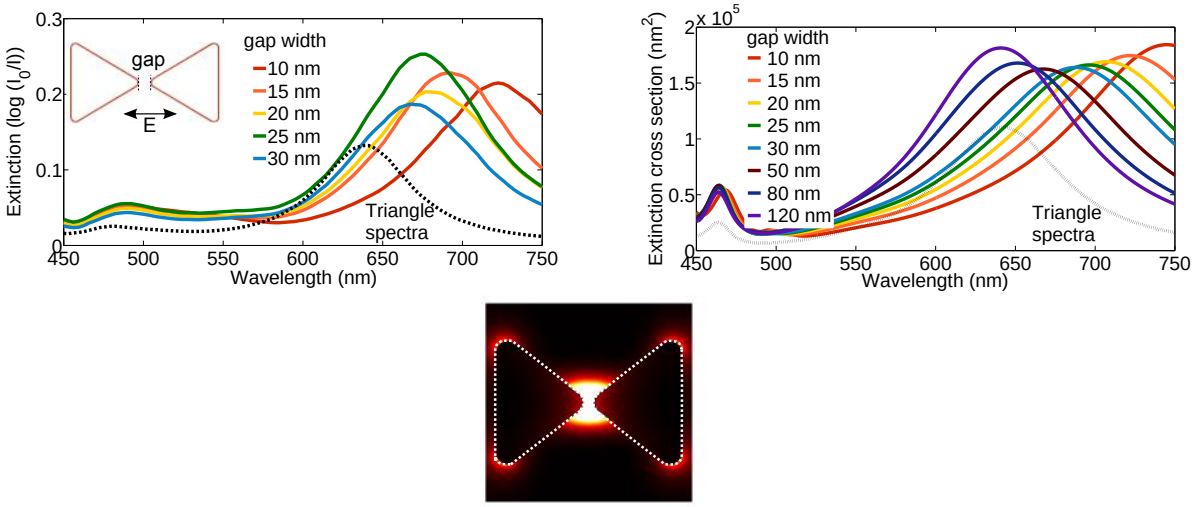



Figure 1: Measured (top left) and simulated (top right) extinction spectra of silver triangle dimers excited with light polarized along the gap (indicated with a double arrow in the inset). The side length of equilateral triangles was 120 nm and the height 40 nm. The bottom figure shows the electric field enhancement associated with the resonant bow-tie structures.

By placing a semiconductor QD in the gap between electrically connected bow-tie structures, we aim to enhance the absorption of QDs and extract the charge carriers by applying a bias voltage. Ultimately, we envisage investigating the feasibility and performance of a single-quantum-dot photodetector.

## ACKNOWLEDGMENT

Support from the Austrian Science Found (FWF - SFB) NextLite is acknowledged.

## REFERENCES

1. Hohenester, U., "Computer Physics Communications," *Comput. Phys. Commun.* , Vol. 183, No. 2, 370–381, 2012.

# Strong plasmon-exciton coupling on individual nanoantenna level

**G. Zengin[1], M. Wersäll[1], T. J. Antosiewicz[1,2], M. Käll[1] and T. Shegai[1,*]**
[1]Department of Physics, Chalmers University of Technology, 421 96 Göteborg, Sweden
[2]Centre of New Technologies, University of Warsaw, Banacha 2c, 02-097 Warsaw, Poland
[*]corresponding author: timurs@chalmers.se

**Abstract**-We demonstrate strong coupling between plasmonic nanocavities and molecular excitons at room temperature on a single plasmonic nanoparticle level. These results open up possibilities for room temperature quantum optics as opposed to previous experiments that have been performed at cryogenic temperatures and in vacuum using various cavity-emitter configurations in atomic and solid state systems.

We have studied nanoparticle plasmons coupled to molecular excitons in J-aggregates on a single nanoantenna level. Several types of plasmonic nanoantennas have been studied. For the case of silver nanorods (Fig. 1a) strong suppression of scattering at the J-aggregate absorption line has been observed, implying strong plasmon-exciton interactions. Upon photodegradation of chromophores under laser illumination, a recovery to a single peak plasmon resonance of a nanorod occurred. We studied these hybrid systems as a function of geometrical parameters of the nanorods and found that for smaller rods the interaction was approaching the strong coupling limit due to efficient suppression of radiative damping.

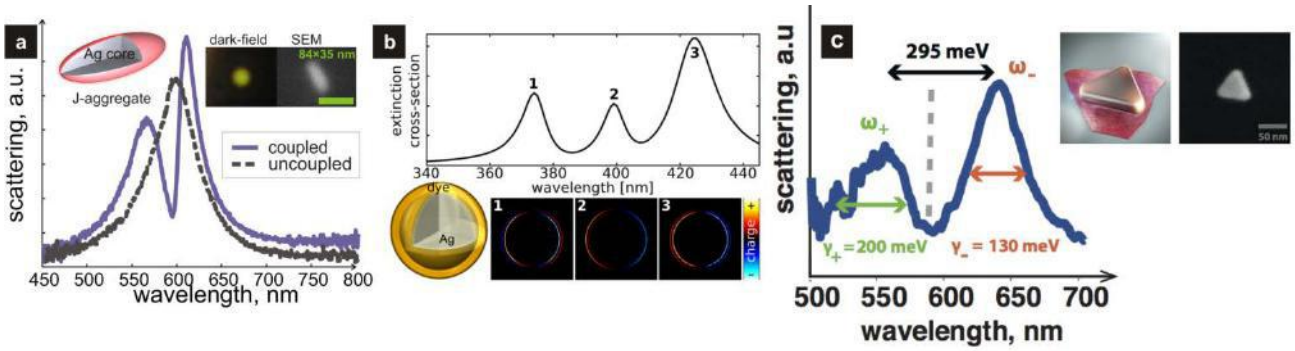



**Figure 1.** (a) Single silver nanorod strongly interacting with a J-aggregate before and after photodegradation of the molecules [1]. (b) Theoretically studied plasmon-exciton interaction in core-shell geometry. In the limit of high oscillator strength a 3-peaked spectrum emerges [2]. (c) Single silver nanoprism gives rise to Rabi splitting of 300 meV at room temperature [3].

These findings have been further confirmed by numerical simulations, which showed emergence of transparency dips not only in scattering but also in absorption and extinction of a single nanoparticle [1, 2]. Extensive simulations using Mie theory, FDTD and analytical covered spheroid model have revealed that (*i*) spectral dips in scattering spectra and mode anti-crossing cannot be used as undisputable argument of strong coupling, but rather it should be dips and anti-crossing in absorption and (*ii*) in the limit of high oscillator strength 3-peaked spectra emerge as a result of the core-shell structure resonating as a whole (Fig. 1b).

We have further reduced the nanoparticle volume and thus suppressed radiative losses by using silver nanoprisms (Fig. 1c). In this study we have unambiguously shown that individual nanoparticle plasmons can reach the strong coupling limit with about 70-80 excitons in molecular J-aggregates at room temperature [3]. Moreover, we have discussed the possibility to lower the number of excitons down to truly quantum regime. These findings open up prospects for room temperature quantum optics research and applications.

**REFERENCES**


1. Zengin, G. *et al.*, "Approaching the strong coupling limit in single plasmonic nanorods interacting with J-aggregates," *Sci. Rep.*, Vol. 3, 3074, 2013.
2. Antosiewicz, T. J., Apell, S. P., and Shegai, T. "Plasmon-exciton interactions in a Core-Shell Geometry: From Enhanced Absorption to Strong Coupling," *ACS Photonics*, Vol. 1, 454–463, 2014.
3. Zengin, G. *et al.* "Realizing Strong Light-Matter Interactions between Single-Nanoparticle Plasmons and Molecular Excitons at Ambient Conditions," *Phys. Rev. Lett.*, Vol. 114, 157401, 2015.

# Multimodal plasmonics devices in crystalline colloidal systems.

**Sviatlana Viarbitskaya[1,2], Alexandre Teulle[1], Upkar Kumar[1], Jadab Sharma[1], Kargal Gurunatha[1], Aurélien Cuche[1], Michel Bosman[3], Alexandre Bouhelier[2], Gérard Colas des Francs[2], Arnaud Arbouet[1], Christian Girard[1], Erik DUJARDIN[1]***

[1] *CEMES CNRS UPR 8011 and Université Fédérale de Toulouse, 29 rue J. Marvig, 31055 Toulouse, France.*

[2] *LICB, CNRS UMR 6303, Université de Bourgogne, 9 Av. A. Savary, Dijon, France.*

[3] *Institute of Materials Research and Engineering, A*STAR, 3 Research Link, 117602 Singapore, Singapore.*

*corresponding author: dujardin@cemes.fr

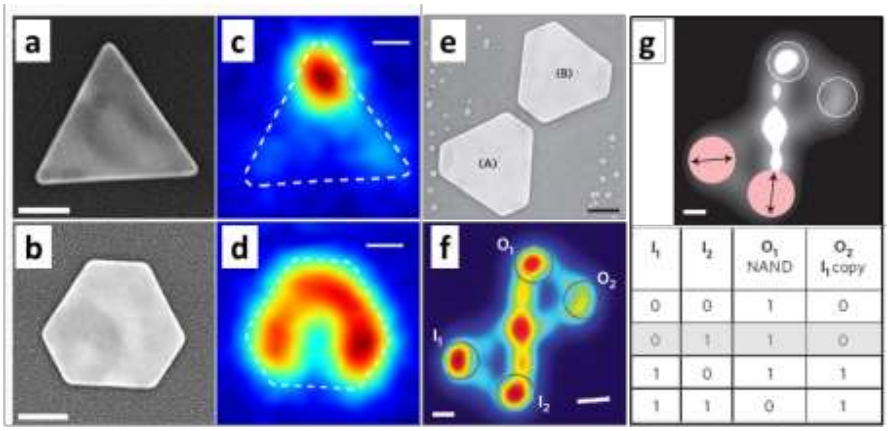
**Abstract**-Two-dimensional crystalline Au colloidal structures with mesoscale lateral dimensions act as cavities that sustain higher order plasmon modes with well-defined spatial and spectral characteristics. This multimodal optical behavior can be directly evidenced and explained but also tailored both spatially and spectrally. This intermediate regime that combines propagative and local modes is exploited for a new implementation of information processing devices, including complex Boolean logic gates.

Plasmonics has opened ways to tailor optical properties both at the macroscopic scale, by allowing propagation, waveguiding and routing of plasmon polaritons, but also at the nanometer-scale by exploiting evanescent fields, strong confinement volumes and localized plasmonic resonances. While both regimes have been extensively studied and led to numerous applications, much less scrutiny has so far focused on the intermediate regime of micrometer-sized systems supporting a large number of confined higher order surface plasmon (SP) modes. Multimodal plasmonic systems open a new realm in which the modal behavior is better described by the SP local density of states (SP-LDOS), which is solely governed by the material properties and the boundary conditions set by the structure shape but is independent of the illumination parameters. The SP-LDOS can therefore be rationally designed to tailor the local spatial and spectral characteristics of the SP modes, while allowing information transfer over micrometer-sized distances. To reveal and exploit such spatio-modal engineering of plasmons, dissipation must be reduced by exploiting the enhanced performances of crystalline metal colloids.[1] Our approach is applied to localized hot electron generation,[2] modal logic gates [3] and information transfer and routing.[4, 5]

We will first present strategies to chemically tailor the plasmonic properties of anisotropic 1D and 2D plasmonic microstructures composed of either single crystalline Au colloids [2, 3] or self-assembled superstructures [4] sustaining higher order plasmonic modes. We will then demonstrate that the SP-LDOS distribution of mesoscale 2D structure can be conveniently imaged by all-optical technique such as two-photon luminescence (TPL) microscopy and closely matched with descriptive models implemented in numerical tools based on the Green Dyadic Method. [2, 3, 6] We will illustrate that further insight can be obtained by more invasive techniques such as plasmonic hot-printing [2] and electron energy loss spectroscopy,[4] with the extra benefit of much improved spatial resolution.

Next, we propose to exploit the spectral and spatial behavior of individual or assembled 2D

colloids to implement a new holistic approach of optical information processing. Two routes will be presented. Physical reshaping of the colloidal prisms by focused ion beam [7] and near-field coupling between colloidal building blocks [8] lead to modal plasmonic devices able to guide and route information in guides as narrow as 10 nm, [4, 5] or even implement complex Boolean logic gates [2, 5] for which principles and first experimental evidence will be exposed.




| $I_1$ | $I_2$ | $O_1$ NAND | $O_2$ $I_1$ copy |
|---|---|---|---|
| 0 | 0 | 1 | 0 |
| 0 | 1 | 1 | 0 |
| 1 | 0 | 1 | 1 |
| 1 | 1 | 0 | 1 |

**Figures:** (a,b) SEM images of triangular and truncated triangular Au nanoprisms. (c, d) Confocal TPL images recorded with horizontally polarized, 700 nm exciatation. (e, f) SEM of an Au nanoprism dimer and simulated TPL image for 5° polarized, 700 nm excitation. (g) Scheme and truth table of a proposed implementation of modal plasmonic Boolean logic gates. Scale bars are 200 nm. [3,6]

**Acknowledgements.** The authors acknowledge R. Menzegga (ETH Zurich, Switzerland), S. Mann (Univ. Bristol, UK), R. Quidant (ICFO, Barcelona, SP) for fruitful collaborations. The financial support of the European Research Council (ERC) (contract number ERC-2 2007-StG Nr 203872 COMOSYEL), Agence Nationale de la Recherche (ANR) (Grants ANR-09-BLAN-0049-Plastips and ANR-13-BS10- 0007-PlaCoRe), the CPER “Gaston Dupouy” 2007−2013, and the computing center CALMIP in Toulouse.

**REFERENCES**

1. C. Girard, E. Dujardin, G. Baffou and R. Quidant. "Shaping and manipulation of light fields with bottom-up plasmonic structures." *New J. Phys.* 10, 105016, 2008.
2. S. Viarbitskaya, A. Cuche, A. Teulle, J. Sharma, C. Girard, A. Arbouet, E. Dujardin." Plasmonic hot printing in gold nanoprisms." *ACS Photonics*, 2, 744, 2015
3. S. Viarbitskaya, A. Teulle, R. Marty, J. Sharma, C. Girard, A. Arbouet and E. Dujardin. "Tailoring and imaging the plasmonic local density of states in crystalline nanoprisms." *Nature Materials* 12, 426, 2013.
4. A. Teulle, M. Bosman, C. Girard, K. L. Gurunatha, M. Li, S. Mann, E. Dujardin, "Multimodal plasmonics in fused colloidal networks." *Nature Materials*, 14, 87, 2015.
5. U. Kumar, S. Viarbitskaya, A. Cuche, A. Bouhelier, G. Colas des Francs, C. Girard, E. Dujardin. in prep.
6. S. Viarbitskaya, A. Teulle, A. Cuche, J. Sharma, C. Girard, E. Dujardin, A. Arbouet. "Morphology-induced redistribution of surface plasmon modes in 2D crystalline gold platelets." *Appl. Phys. Lett.* 103, 131112, 2013.
7. A. Cuche, S. Viarbitskaya, J. Sharma, A. Arbouet, C. Girard, E. Dujardin. "Modal engineering of surface plasmons in apertured Au Nanoprisms." *Sci. Rep.*, 5, 16635, 2015.
8. A. Cuche, S. Viarbitskaya, U. Kumar, J. Sharma, A. Arbouet, C. Girard, E. Dujardin, in prep.

# Strong Plasmon-Emitter Coupling: Beyond the Jaynes-Cummings Model

**Ben Lawrie[1*], Roderick B Davidson II[1,2], Pavel Lougovski[1]**

[1] Quantum Information Science Group, Oak Ridge National Laboratory, Oak Ridge, TN, USA

[2] Department of Physics and Astronomy, Vanderbilt University, Nashville, TN, USA

[*]corresponding author: lawriebj@ornl.gov

**Abstract**-Strong plasmon-emitter coupling has received growing attention over the past decade because of the potential of engineering a plasmonic analogue to cavity quantum electrodynamics (cQED) that exploits mode volumes well below the diffraction limit. However, the demonstration of a true plasmonic cQED platform remains elusive. Here, we will compare current descriptions of strongly coupled systems with experimentally recorded femtosecond plasmon dynamics in order to move towards an accessible platform for high efficiency nonlinear optics at the single photon scale.

CQED utilizes coherent interactions between a single mode of an optical cavity and a single, trapped quantum emitter in the strong coupling regime in order to transduce high efficiency nonlinearities at the single photon scale. Quantum limited nonlinear efficiencies are possible with cQED platforms ranging from quantum dots and trapped ions in photonic crystal cavities and microcavities to superconducting transmons coupled to microwave waveguides, but all current implementations require low operating temperatures in order to achieve dephasing times longer than the light-matter interaction time described by the Rabi period. Replacing photonic cavities with plasmonic nanoresonators exhibiting sub-diffraction limited mode volumes could enable cQED-like effects with low quality factor systems under ambient conditions, but a true plasmonic analog to cQED exhibiting vacuum Rabi oscillations between a single plasmonic mode and a single quantum emitter has not yet been demonstrated. The Jaynes Cummings model is routinely used to describe light matter interactions in photonic cQED systems with a master equation given by:

$$\frac{d}{dt}\rho_{EP} = -\frac{i}{\hbar}\left[H_{0E} + H_{0P} + H_{EPint}, \rho_{EP}\right] + \frac{\Gamma_0+\Gamma_{pl}}{2}\mathcal{L}_1\rho_{EP} + \frac{\kappa}{2}\mathcal{L}_2\rho_{EP}, \quad (1)$$

where $\mathrm{H_{0E}} = \hbar\omega_{ab}\sigma^{\dagger}\sigma$ is the Hamiltonian describing a two level quantum emitter with the transition frequency $\omega_{ab}$ and $\mathrm{H_{0P}} = \hbar\sum_k \omega_k a_k^{\dagger}a_k$ is the Hamiltonian for the free modes supported by the photonic cavity enumerated by the index k. The interaction Hamiltonian $\mathrm{H_{EPint}} = \hbar\sum_k g_k (a_k^{\dagger}\sigma + a_k\sigma^{\dagger})$ describes the dipole interaction between the emitter and photon in the rotating wave approximation and $g_k$ are correspondent coupling constants. The Lindblad operators $\mathcal{L}_1$ and $\mathcal{L}_2$ describe the decoherence channels due to spontaneous emission ($\Gamma_0$), and non-radiative decay ($\Gamma_{pl}$) of the quantum emitter ($\mathcal{L}_1$) and cavity ($\kappa$) due to thermal effects ($\mathcal{L}_2$).

The Jaynes Cummings model has been increasingly used to model strong plasmon-emitter coupling, with appropriate substitutions for the nonlinear plasmonic dispersion, nanoscale mode volume, and poor quality factor relative to photonic systems, yielding reasonable agreement with the femtosecond dynamics of aggregates of

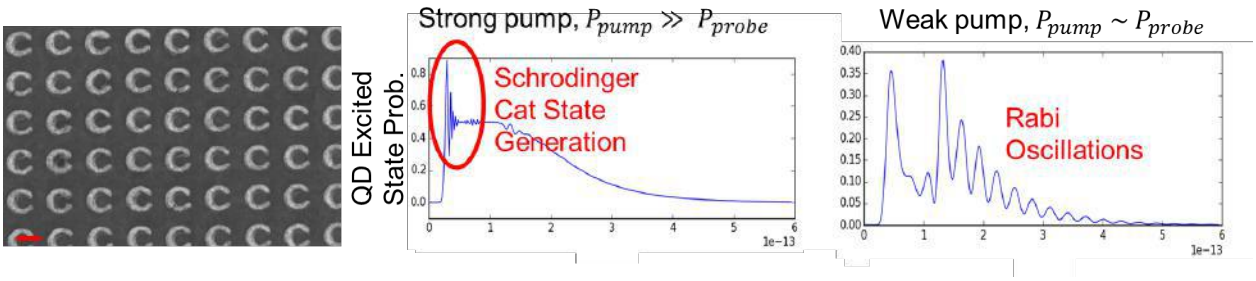



**Figure 1.** (left) SEM of Aluminum split ring resonators with a 200 nm scale bar. (middle) Calculated quantum dot excited state dynamics in the presence of a strong optical pump for a single quantum dot deposited within the plasmonic hot spot. (right) Calculated dynamics in the weak optical pump limit.

emitters coupled to delocalized plasmon modes [1]. Applying this model to individual CdSe quantum dots deterministically placed within the plasmonic hot spot of lithographically fabricated aluminum split ring resonators shown in the middle of Fig. 1 resulted in the prediction of a plasmon-emitter Schrodinger cat state in the strong optical pumping regime and of vacuum Rabi oscillations at the single plasmon/single emitter scale in the weak pumping regime. This model ultimately predicted that a cooperativity in excess of 1000 is possible for the experimental parameters described by this system, and femtosecond pump probe spectroscopies are ongoing in an attempt to verify this model. However, the Jaynes Cummings model relies on a plane wave expansion of modes within the optical cavity that is invalid below the diffraction limit. In lieu of such an expansion, the local density of states can be determined from the imaginary part of the Green's function for a given plasmonic nanoresonator, calculated by finite difference time domain (FDTD) simulations, and current efforts to incorporate this plasmonic density of states in the Jaynes Cummings model are ongoing. Despite the apparent experimental agreement with the Jaynes Cummings model in the limit of many coupled emitters, it makes sense to pursue a model with none of the assumptions of the Jaynes Cummings model. We will compare semi-classical, pseudo-Jaynes Cummings, and novel plasmonic master equation models with the experimental dynamics and energetics of plasmonic modes supported in the split ring resonator that are strongly coupled to CdSe quantum dots. Achieving a true plasmonic analog to cQED would enable high efficiency optical nonlinearities at the single photon scale without recourse to the cryogenic temperatures required to achieve high quality factors in photonic cQED.

**Acknowledgements**: This work was performed at Oak Ridge National Laboratory, operated by UT-Battelle for the U.S. Department of Energy under contract no. DE-AC05-00OR22725. The nanofabrication was conducted at the Center for Nanophase Materials Sciences, which is a DOE Office of Science User Facility. The authors recognize support from the Laboratory Directed Research and Development program.

## REFERENCES

1. Vasa, P., et al. "Real-time observation of ultrafast Rabi oscillations between excitons and plasmons in metal nanostructures with J-aggregates." *Nature Photonics* **7,** 128-132, 2013.

# Plasmon-mediated generation of continuum emission in metal nanoparticle hot spots

**S. Bange[1*], T. Haug[1], P. Klemm[1], and J. M. Lupton[1]**
[1]Institut für Experimentelle und Angewandte Physik, Universität Regensburg, 93051 Regensburg, Germany
[*]corresponding author: sebastian.bange@ur.de

**Abstract –** Ultrafast near-infrared laser pulses can excite localized broadband luminescence on disordered noble-metal nanoparticle surfaces. The nonlinear emission from individual hot spots spans a continuum covering both the near-infrared (Stokes) and visible (anti-Stokes) spectral range, and its spectroscopic signatures can be explained by radiative relaxation of hot electrons within the conduction band of individual nanoparticles. Despite the presence of electron-lattice scattering, the electron gas in the emitting particles is heated to several thousand Kelvin, since the plasmonic environment enhances the excitation cross section and funnels additional energy into the hot spot.

Disordered noble metal nanoparticle surfaces provide a plasmonic landscape that can induce strong localization and enhancement of the electromagnetic field. This effect is well known to enable Raman spectroscopy down to the single-molecule level [1] – more surprisingly, under femtosecond infrared excitation localized emission arises even in absence of analyte molecules [2]. Such hot spots exhibit ultrafast non-linear white-light emission from diffraction-limited volumes [3] and provide an alternative to SNOM in superresolution optical transmission microscopy [4]. The excitation of these continuum-emitting hot spots can be studied both in the frequency and in the time domain, by either observing the emission as a function of excitation wavelength or by Fourier autocorrelation of the exciting laser pulses [5]. Both techniques reveal the hybridization of bright, localized plasmon modes with propagating polariton modes. In contrast to experiments on isolated nanoparticles, the excitation cross-section for individual emissive sites is strongly enhanced by long-range transport of electromagnetic field energy over dozens of µm across the rough metal surface.

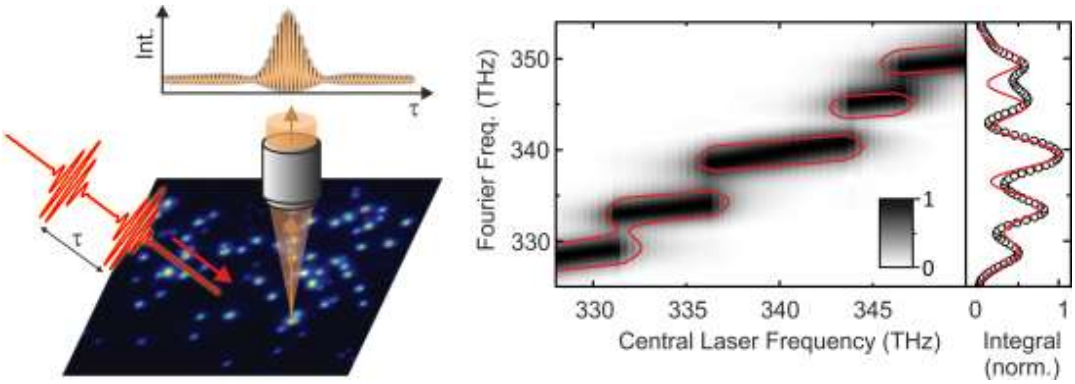



**Figure 1:** The emission of single white-light emitting hot spots under double-pulse excitation can be studied as a function of interpulse delay to provide an autocorrelation probe of the excitation field modes (left). Fourier analysis of autocorrelation excitation spectroscopy of single hot spots reveals the interplay of surface plasmon

propagation and interference in near-field subdiffraction continuum generation (right).

While the absorption of ultrashort laser pulses on a metal surface is known to heat its electron gas through intraband transitions, the role of these conduction-band transitions in radiative relaxation has previously been largely ignored [6]. The enhanced excitation cross-section associated with single nanoscale emitter sites strongly enhances the excitation energy funneled into the electron gas of individual metal nanoparticles and thus the achievable electron temperatures. The spectroscopic signatures of intraband luminescence are very similar to blackbody radiation and are clearly identified by observing the excitation-power dependence as a function of emitted photon energy [7].

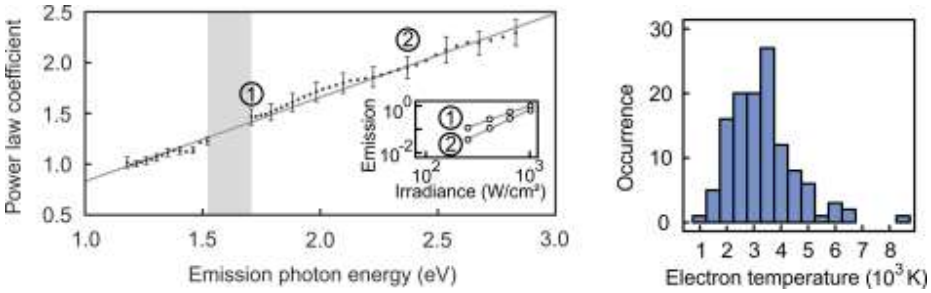



**Figure 2:** Continuum emission is an approximate power-law with respect to the excitation intensity. Analysis of the power-law as a function of emitted photon energy reveals a tell-tale linear relationship that is directly related to the temperature of the hot electron gas (left). Even under the same excitation conditions, the effective temperature of the electron gas in different hot spot sites scatters over a wide range due to the impact of the plasmonic environment on the excitation cross-section (right).

Electron-lattice scattering limits the time available for radiative relaxation to a few ps. Continuum-emission hot spots on disordered noble-metal nanoparticle surfaces thus effectively constitute ultrafast, sub-diffraction, optically-addressable incandescent light sources. With obvious applicability to nanoscopic pump-probe techniques, the spectroscopy of hot electrons in metal nanoparticles is also relevant to energy harvesting and photocatalysis.

**Acknowledgements** This work was inspired by a Scialog Fellowship of the Research Corporation for Science Advancement. Financial Support by the European Research Council (ERC) through the Starting Grant MolMesON (305020) is gratefully acknowledged.

**REFERENCES**

1. Walter et al., Phys. Rev. Lett. 98, 137401 (2007)
2. Borys et al., Phys. Rev. B 80, 161407(R) (2009)
3. Borys et al., J. Phys. Chem. C 115, 13645 (2011)
4. Chaudhuri et al., Nano Lett. 9, 952 (2009)
5. Klemm et al., Phys. Rev. Lett. 113, 266805 (2014)
6. Beversluis et al., Phys. Rev. B 68, 115433 (2003)
7. Haug et al., Phys. Rev. Lett. 115, 067403 (2015)

# CMOS copper plasmonic nanocircuitry

**D. Yu. Fedyanin,[1,*] D. I. Yakubovsky,[1] R. V. Kirtaev,[1] and V. S. Volkov[1,2]**

[1]Laboratory of Nanooptics and Plasmonics, Moscow Institute of Physics and Technology, Russian Federation

[2]Department of Technology and Innovation, University of Southern Denmark, Denmark

[*]corresponding author: dmitry.fedyanin@phystech.edu

**Abstract -** Plasmonics is widely considered to be the most promising candidate for the next generation of chip-scale technology. However, at telecommunication wavelengths, characteristics acceptable for practical implementation have been demonstrated only with noble metals, which are not compatible with industry-standard fabrication processes. In this work, we present ultralow-loss deep-subwavelength copper plasmonic waveguides fabricated in a CMOS compatible process, which can outperform gold waveguides. These results create the backbone for practical implementation of plasmonic nanocircuits in both silicon photonics and silicon microelectronics.

Implementation of plasmonic components, such as waveguides and cavities, in nanophotonic circuits fundamentally requires a low-loss material with a large negative dielectric function in the telecommunication spectral range. To date, characteristics acceptable for practical applications have been demonstrated only with noble metals – gold and silver, – which combine a high real part $\varepsilon'$ of permittivity and a low imaginary part $\varepsilon'' \ll -\varepsilon'$ responsible for SPP losses [1]. However, these materials are not compatible with industry-standard fabrication processes, such as CMOS technology.

Here, we experimentally demonstrate for the first time deep-subwavelength copper plasmonic waveguides, which can outperform gold plasmonic waveguides providing the same level of mode confinement and lower propagation losses [2] (Figure 1). The waveguide fabrication process is remarkably simple and CMOS compatible, which makes the presented copper plasmonic platform highly attractive for optical nanocircuitry.

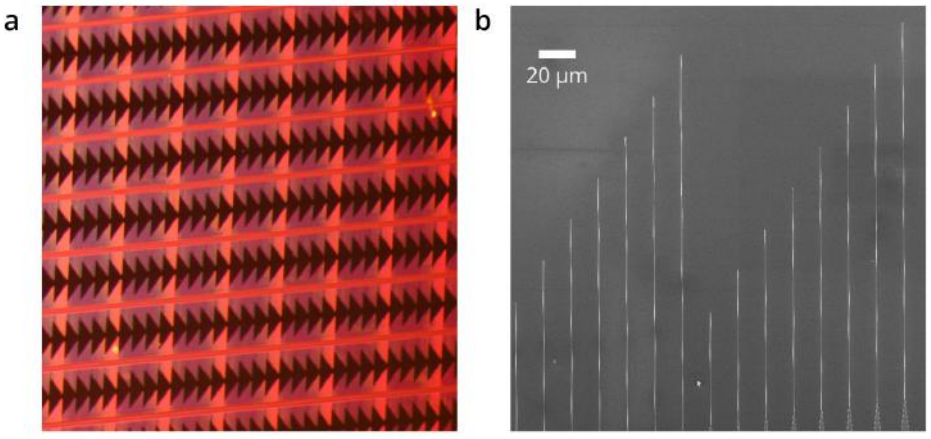



**Figure 1.** (a) Silicon chip with nanoscale copper plasmonic waveguides. (b) Scanning electron microscopy (SEM) image of the waveguides.

## ACKNOWLEDGEMENTS

This work was supported by the Russian Science Foundation (14-19-01788).

## REFERENCES

1. Blaber, M. G., Arnold, M. D. and Ford, M. J., "A review of the optical properties of alloys and intermetallics for plasmonics," *J. Phys.: Condens. Matter*, Vol. 22, 143201, 2010.
2. Fedyanin, D. Yu., Yakubovsky, D. I., Kirtaev, R. V. and Volkov, V. S., "Ultralow-loss CMOS copper plasmonic waveguides," *Nano Letters*, Vol. 16, 362-366, 2016.

# Optical nanoantenna excitation through the dissipative instability of DC current in a quantum well near a metal surface

**I. V. Smetanin[1*], A. Bouhelier[2] , I. E. Protsenko[1], A. V. Uskov[1,3]**

[1]P. N. Lebedev Physical Institute, Leninskiy pr. 53, 119991 Moscow, Russia

[2]Laboratoire Interdisciplinaire Carnot de Bourgogne, CNRS-UMR 6303,
Universite Bourgogne Franche-Comte, 21078 Dijon, France

[3]ITMO University, Kronverkskiy pr. 49, 197101 Sankt-Petersburg, Russia

[*]corresponding author: smetanin@sci.lebedev.ru

**Abstract**- We propose a novel physical mechanism for the excitation of optical nanoantenna which utilizes the dissipative instability of DC electric current in the quantum well. Realization of this approach in nanoplasmonics can lead to a new device – *nanoresotron.*

The effective electrical excitation of surface plasmon waves becomes an extremely important challenge for developing integrated elements for on-chip nanophotonics technology [1]. However, the prospects for solution of this problem are related to a number of fundamental issues in the physics of optical nanoantennas.

In the following we propose a novel approach to excite optical nanoantennas based on the dissipative instability of DC electric current in quantum well. Primarily, the idea to use this instability for light generation had been realized in the concept of *resotron*, free-electron laser in which electromagnetic wave is amplified by magnetically guided high-current relativistic electron beam, moving above the surface of a resonance absorbing material [2, 3]. Light amplification in this scheme emerges as a result of electron beam plasma self-consistent oscillations when the signal frequency lies within the material' resonant absorption line. Instability is absent at frequencies at which the material is transparent (Imε→0). This effect takes place not only in relativistic electronics: the dissipative instability of the DC current in superconductor film was analyzed in [4].

Realization of above principle of light generation in nanoplasmonics can lead to developments of a new device – *nanoresotron.* Below, in order to demonstrate how the idea can work in nanoplasmonics, we consider the simplest planar configuration, which includes carrying DC current quantum well (QW) and the metal film, separated with the spacer d between them as shown in Fig.1. Electromagnetic mode with the field components $E_z, E_x, H_y \propto \exp[i(hz-\omega t)]$ propagates along the z axis. Moreover, for sake of simplicity, we assume that metal film has infinite thickness, and neglect the thickness of the spacer, i.e., $d$=0, Δ→∞ in Fig.1. We solve self-consistently Maxwell's equations for the electromagnetic mode and Euler hydrodynamics equations for the current-carrying 2D electron liquid [5]. To the first order in perturbation theory over the field amplitude, we are coming to the following dispersion equation

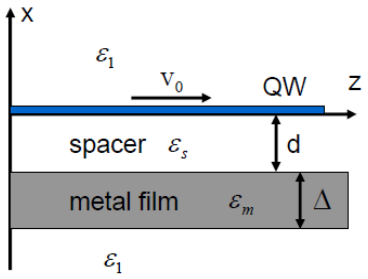



**Figure 1: Simplified scheme of the resotron in which plasma oscillations in carrying DC current QW result in surface wave amplification near metal film.**

$$\left(\frac{\varepsilon_1}{q_1}+\frac{\varepsilon_m}{q_m}\right)=\frac{4\pi n_0 e^2/m}{[(h\mathrm{v}_0-\omega)(h\mathrm{v}_0-\omega-i\gamma)-s^2h^2]} \qquad (1)$$

where $n_0$ is the 2D electron density, $\mathrm{v}_0$ is the electron drift velocity, $\gamma$ is the momentum relaxation rate, $s\approx \mathrm{v}_F/\sqrt{2}$ is the speed of sound, and $\mathrm{v}_F$ is the Fermi velocity of 2D electron gas. The electromagnetic field of the mode is exponentially vanishing with the distance x from surface with the transverse wavenumbers $q_1=(h^2-\varepsilon_1\omega^2/\mathrm{c}^2)^{1/2}$ in the upper half-space $x>0$ and $q_m=(h^2-\varepsilon_m\omega^2/\mathrm{c}^2)^{1/2}$ in the metal, where $\varepsilon_1$ and $\varepsilon_m$ are the dielectric permittivities of the upper dielectric and metal, respectively.

The dispersion equation (1) has two kinds of roots. The conventional rapidly decaying surface wave solution is determined by the left hand side of Eq. (1) when $n_0\to 0$. The presence of DC current leads to appearance of another pair of much more slower solutions with $h\to\omega/\mathrm{v}_0$. Then, the transverse wavenumbers are close to each other, $q_1\approx q_m\approx h$ and we find that the largest increment is

$$\mathrm{Im}\,h\approx -\frac{s^2}{(\mathrm{v}_0^2-s^2)}\frac{\mathrm{Im}\,\varepsilon_m}{|\varepsilon_1+\varepsilon_m|^2}\frac{4\pi n_0 e^2}{ms^2}\,. \qquad (2)$$

The amplification effect Im $h<0$ arises if the 2D electrons drift velocity $\mathrm{v}_0$ exceeds the sound velocity $s$, i.e., $\mathrm{v}_0>s$. Assuming for estimation GaAs QW with the 2D electron density $n_0=10^{12}\mathrm{cm}^{-2}$, and electron mass $m=0.067m_0$, the Fermi velocity is $\mathrm{v}_F\approx 4.2\cdot 10^7$cm/s and, as far as $\mathrm{Im}\,\varepsilon_m/|\varepsilon_1+\varepsilon_m|^2\sim 10^{-2}\div 10^{-3}$ in the optical domain, we find the increment is rather large, of the order $\mathrm{Im}h\sim 10^5$- $10^6$ cm$^{-1}$, which makes the proposed scheme extremely attractive. Note, however, the nonzero gap $d$ and finite thickness $\Delta$ will result in corrections to Eq.(1) leading to lower amplification increments.

In conclusion, the proposed nanoresotron scheme can be extended from planar metal films to nano-sized structures. The approach may be a very promising alternative to electrically excited optical nanoantennas by a DC electric current flowing in nanocircuits.

**Acknowledgements**-This work was financially supported in part by the Government of the Russian Federation (Grant 074-U01) through ITMO Visiting Professorship program. The research leading to these results has received funding from the European Research Council under the European Community's Seventh Framework Program FP7/ 2007-2013 Grant Agreement No. 306772.

**REFERENCES**

1. Cohen, M., Z. Zalevsky and R. Shavit, "Towards integrated nanoplasmonic logic circuitry", *Nanoscale*, Vol. 5, No. 3, 5442-5449, 2013.
2. Oraevsky, A. N. and I. V. Smetanin, "Intensification of light by an electron beam near an absorbing surface," *JETP Lett.*, Vol. 62, No. 3, 258-261, 1995.
3. Oraevsky, A. N. and I. V. Smetanin, "Resotron − a new concept of IR free-electron laser driven by low-voltage electron beam," *Laser Physics*, Vol. 7, No. 1, 155-158, 1997.
4. Smetanin, I. V., "Free-electron lasers driven by supercurrent", *Nuclear Instrum. Meth. Phys. Res. A*, Vol.429, 445-450, 1999.
5. Fetter, A. L., "Electrodynamics of a Layered Electron Gas. I. Single Layer," *Annals of Physics*, Vol. 81, 367-393, 1973.

# Surface plasmon enabled fast LED, compact waveguide device and OAM demultiplexor

**Jinghua Teng**
Institute of Materials Research and Engineering, A*STAR, Singapore
*corresponding author: jh-teng@imre.a-star.edu.sg

**Abstract**-This talk will introduce several photonic devices enabled by plasmonic structures including surface plasmon coupled high speed light emitting diodes, compact waveguide devices using graphene and semiconductor, and the multiplexing of optical angular momentum in optical vortices.

The unique properties of surface plasmon (SP) such as the strong field localization and enhancement bring many opportunities to optoelectronics in terms of functionality, performance and compactness. In this talk, I will introduce several plasmonic enabled devices developed in the group, including a fast electrically modulated InGaN light emitting diode (LED) by plasmonic coupling [1], the waveguide, splitters and modulators made from graphene [2, 3], the loss compensation in an electrically pumped plasmonic waveguide [4], the generation, focusing and multiplexing of optical angular momentum (OAM) in optical vortex beams by plasmonic nano-structures [5, 6].

There is growing interest in using LEDs for LiFi by taking the advantages of their ubiquitous existence as solid state lighting source, besides the inherent merits on speed and security of light communication. The key limiting factor is the slow spontaneous emission rate of LEDs. The coupling of surface plasmon polaritons (SPPs) with the excitons in a semiconductor quantum wells has show the capability in affecting the carrier dynamics. However, the requirement of near field interaction places a fundamental restriction on its implementation in LEDs. We show that the carrier recombination rate can be significantly enhanced by 23 times in Ag coated InGaN LED. Due to the high density of sharp hexagonal V-pits, a large proportion of photons emitted can directly couple into SP modes with extremely high density of states. The photon-SPs coupling range can be as long as 400nm. The electrically modulated LEDs is 65% faster than those without the Ag coating.

Graphene can support transverse magnetic polarized SPPs in mid-IR range. With its very large model index, relatively low loss and flexibility in dynamic tuning, graphene is another promising candidate in making compact plasmonic waveguide and devices. Here we show the analytical study on SPP coupling among spatially separated graphene sheets and the ultracompact optical splitter, 1x2 digital optical switch and M-Z interferometer based modulator with the coupling region far below the diffraction limit. We have also analyzed the unique properties of SPPs in multi-layer graphene sheet arrays. For Au based plasmonic waveguide at near infrared wavelength, electrically pumped InGaAsP multiple quantum wells are used as the gin media to compensate the SPP propagation loss. The SPP propagation greatly benefits from the modal gain for the long-range hybrid SPP mode that is optimized by adopting an amorphous Si cladding layer accompanied with minimal degradation of mode confinement.

The OAM of light has potentially important applications in optical communication, quantum information processing and particle manipulation. The generation, focusing and multiplexing/demultiplexing of OAM modes in a compact way is a big challenge for traditional strategies. By employing the concept of controllable interfacial phase discontinuity and the Babinet-inverted nanovoids, we demonstrated an ultrathin OAM generator with multiple focal planes. The number of focal planes, corresponding topological charges, and focal lengths can be easily tailored for different requirements. By using semi-ring shaped plasmonic nanoslits and the constructive interference of a helical phase modulated surface wave, we also demonstrated the on-chip nano-scale separation and sorting of OAM modes with ~120 nm intervals on the metallic surface.

**Acknowledgements**, The works reported here are partially supported financially by IMRE and A*STAR. People contributed to the works include Ee Jin Teo, Chengyuan Yang, Hui Hui Kim, Michael Bosman, Hui Ru Tan, Bing Wang, Hong Liu, Kun Huang and Siew Lang Teo from IMRE, Andrew Bettiol, M. Q. Mehmood, Mei Shengtao, Kun Huang, Fei Qin, Minghui Hong, S. Y. Siew, Aaron Danner and Cheng-Wei Qiu from the National University of Singapore, Xiang Zhang from Wuhan University, Xiaocong Yuan from Nankai University, F. J. Garcia-Vidal from Autonomous University of Madrid, Yicen Li, Zhengji Xu and Dao Hua Zhang from Nanyang Technological University, and Ting Mei from Northwestern Polytechnic University,

**REFERENCES**

1. Chengyuan Yang, Hui Hui Kim, Andrew Bettiol, Jing Hua Teng and Ee Jin Teo, "An ultrafast and highly efficient surface plasmon coupled light emitting diode," *Advanced Optical Materials*, 2015, DOI: 10.1002/adom.201500210
2. Bing Wang, Xiang Zhang, Xiaocong Yuan, F. J. Garcia-Vidal and Jinghua Teng, "Negative Coupling and Directional Splitting of Surface Plasmons in Monolayer Graphene Sheet Arrays," *Physical Review Letters*, Vol. 109, 073901, 2012.
3. Bing Wang, Xiang Zhang, Xiaocong Yuan, and Jinghua Teng, "Optical Coupling of Surface Plasmons between Graphene," *Applied Physics Letters*, Vol.100, 131111, 2012
4. Yicen Li, Hui Zhang, Ning Zhu, Ting Mei, Dao Hua Zhang, and Jinghua Teng "Mode engineering for loss compensation in electrically-pumped plasmonic waveguide," *Optics Express*, Vol. 22, 25599-25607, 2014.
5. M. Q. Mehmood, Mei Shengtao, Sajid Hussain, Kun Huang, S. Y. Siew, Hong Liu, Jinghua Teng, Aaron Danner, and Cheng-Wei Qiu, "Visible-frequency Metasurface for Structuring and Spatially Multiplexing Optical Vortices," *Advanced Materials*, 2016. DOI: 10.1002/adma.201504532
6. Shengtao Mei; Kun Huang; Hong Liu; Fei Qin; Muhammad Qasim Mehmood; Aaron Danner; Zhengji Xu; D. H. Zhang; Minghui Hong; Jinghua Teng; Cheng-Wei Qiu, "On-Chip Discrimination of Orbital Angular Momentum of Light with Plasmonic Nanoslits," *Nanoscale*, Vol. 8, 2227-2233, 2016.

# Control of Gap Plasmon Resonance in a Suspended Nanowire By Electrostatic Force

**J. Takahara[1,2*], A. Kaijima[2], Y. Nagasaki[2] and M. Miyata[2]**
[1]Photonics Advanced Research Center, Osaka University, Japan
[2] Graduate School of Engineering, Osaka University, Japan
[*]corresponding author: takahara@ap.eng.osaka-u.ac.jp

**Abstract**- We demonstrate a reconfigurable plasmonic resonator based on a metal nanowire (NW) suspended on a metal substrate. The suspended gold NW can be pull down by electrostatic force induced by applying voltage to the NW. Such electromechanical response dramatically changes the plasmonic resonance between the NW and the substrate. We observe the change of scattering spectra, which is attributed to Fabry-Perot interference of surface plasmon inside the gap.

For realizing active plasmonic devices, it is desirable to have the capability to electrically tune optical resonant properties of plasmonic structures over a wide spectral range to achieve dynamic functionalities. More recently, electromechanically reconfigurable plasmonic metamaterials have been proposed as an alternative pathway for achieving tunable plasmonic characteristics [1,2]. Achieving electrical tuning of plasmon resonances in visible wavelengths remains a challenge, in contrast to the great success of tunable plasmonic nanostructures in the other spectral regimes. Recently, we have reported static gap plasmon resonance in various gap sizes of a plasmonic NW suspended on a metal substrate [3]. Such structure has a great potential for the dynamic control of gap plasmon resonance.

In this study, we propose and demonstrate a novel reconfigurable plasmonic resonator based on a metal NW suspended on a metal substrate. Figure 1 shows the schematic of the device, where applying voltage induces the vertical deformation of NW, resulting in significant change of the scattering spectra. Figure 2 shows SEM image of a Au NW on $Al_2O_3$/Au/$SiO_2$ substrate.

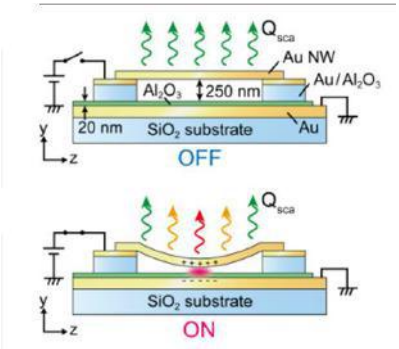



Fig. 1 Schematic of a suspended NW on a metal substrate. (a) off, (b) on.

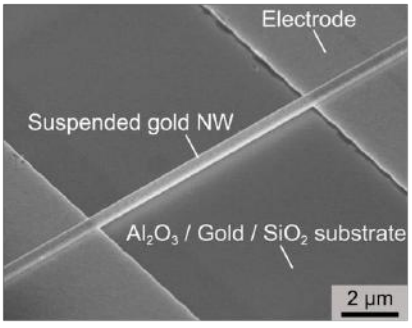



Fig. 2 SEM image of a gold suspended NW.

**REFERENCES**

1. J.-Y. Ou, E. Plum, J. Zhang, and N.I. Zheludev, *Nat. Nanotechnol.* 8, 252 (2013).
2. P. Pitchappa, C.P. Ho, Y. Qian, L. Dhakar, N. Singh, and C. Lee, *Sci. Rep.* 5, 11678 (2015).
3. M. Miyata, A. Holsteen, Y. Nagasaki, M.L. Brongersma and J. Takahara, *Nano Lett.*, Vol. 15, 5609 (2015).

# New Building Blocks for Quantum Technologies: Doped Carbon Nanotubes and Plasmonically Coupled Quantum Dots Molecules

**H. Htoon**
Center for Integrated Nanotechnologies, Materials Physics and Applications Division,
Los Alamos National Laboratory, USA
*corresponding author: htoon@lanl.gov

**Abstract**- I will present two novel systems capable of serving as new building blocks for Quantum Information Technologies. First, I will present that solitary oxygen dopant covalently attached to the carbon nanotubes can serve as the room temperature single photon emitters in telecommunication wavelength. I will then show that the plasmonic field of a gap-bar nano-antenna can induced coupling between two thick-shell quantum dots separated by more than 30 nm, forcing them to emit as a single quantum emitter.

A solid state system capable of mimicking a two-level atom can enable multiple quantum technologies ranging from eavesdropping proof quantum communication to sub-diffraction imaging, ultra-sensitive absorption measurements and linear quantum computing. Coupling of two or more such solid-state artificial atoms through charge tunneling or dipole-dipole interaction (i.e. artificial molecule) can further expand their functionalities as coupled qubits of a solid-state quantum computer and active elements of photon switches that are needed for realization of quantum communication networks. Solid-state artificial atoms and molecules can therefore be considered as the building blocks for quantum technologies. In this talk I will present our recent discoveries of two new nanomaterial systems that can serve as such building blocks: namely, doped carbon nanotubes[1,2] and plasmonically coupled quantum dot molecules.[3]

In doped carbon nanotubes, solitary oxygen functional group (ether or epoxide) are attached covalently to their side wall. These dopants create a localized state capable of trapping and re-emitting 1 dimensional excitons at the energies 150-300 meV below the bandedge. We preformed the first quantum optic experiment on these individual oxygen dopant states and demonstrate that they can emit stable stream of single photons exhibiting near perfect photon antibunching at room temperature in 1100 to 1300 nm wavelength range.[2] We can extend the single photon emission to cover 1500 nm telecommunication wavelengths by doping large diameter nanotubes with smaller bandgaps. This work is enabled by our key discovery that electron-beam (e-beam) deposition of SiO2 on surfactant wrapped, undoped (6,5) SWCNTs leads to creation of isolated

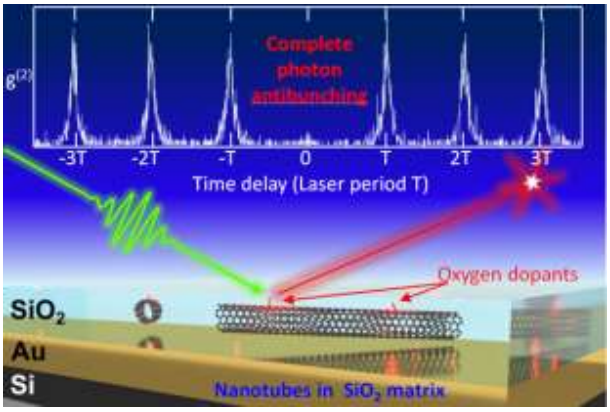



Fig. 1. Doped CNT encapsulated in $SiO_2$ matrix (lower) and $g^{(2)}$ trace showing complete photon antibunching (single photon emission) (upper).

oxygen dopant states with PL emission that is free of fluctuation and bleaching.[1] Because this $SiO_2$ matrix is fully compatible with well-developed $Si/SiO_2$ based micro-/nano-device fabrication techniques, one can now envision straight-forward integration of our doped nanotubes into field effect transistor structures and photonic/dielectric meta-materials for the development of electrically driven single photon sources and integrated quantum photonic circuits.

Plasmonically coupled quantum dot molecules (Fig. 2) compose of a pair of gap bar antenna and a small cluster of 2-3 core/ thick-shell (CdSe/CdS) giant nanocrystal quantum dots (gQDs) over coated by a 10 nm thick Silica shell.[3] The nanocrystal clusters were placed deterministically at the center of the gap-bar using a 2 step e-beam lithography. Because our silica coated gQDs of the clusters are separated from one another by 30 nm of CdS and silica shell materials, dot-to-dot coupling via either charge tunneling or dipole-dipole interaction is completely impossible for a free standing cluster. However, our quantum optics experiment conducted in direct correlation with SEM imaging surprisingly revealed that the single exciton emission of a cluster of 2-3 gQDs trapped at the center of a gap-bar antenna can exhibit complete photon antibunching, a characteristic of a single quantum emitter. Through a detailed analysis of their photoluminescence (PL) emissions characteristics, we confirmed that all the gQDs of the clusters are optically active and the observed antibunching is the evidence of the formation of quantum dot molecules (QDM).[3] Since QDM formation cannot occur for the clusters of gQDs placed away from the antenna, we conclude that the observed formation of QDM is resulted from the plasmonic enhancement of the dipole-dipole interaction. These QDMs present a very exciting opportunity to further investigate other quantum optical as well as coherent properties of QDMs such as entanglement generation. These QDMs also open the path to realize QDM-based quantum plasmonic devices such as single photon switches. We are currently improving the design and fabrication processes to push plasmon-QDM interaction to a strong interaction regime where these phenomena are expected to manifest.

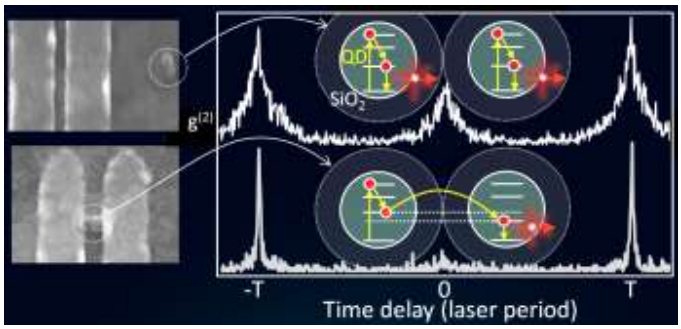



Fig. 2 While two gQD not coupled to the antenna behave as two independent emitters, two gQDs trapped in the gap bar exhibiting single photon emission indicating the formation of quantum dot molecules.

**Acknowledgements**, We acknowledge the support of by Los Alamos National Laboratory Directed Research and Development Fund for the work on doped carbon nanotube and a Single Investigator Small Group Research Grant (2009LANL1096), Division of Materials Science and Engineering (MSE), Office of Basic Energy Sciences (OBES), Office of Science (OS), U.S. Department of Energy (DOE) for the work on plasmonically coupled quantum dot molecules. Both works were performed at the at the Center for Integrated Nanotechnologies (CINT), a U.S. DOE, OBES Nanoscale Science Research Center and User Facility

## REFERENCES

1 Ma, X. *et al.* Solid‐State Approach for Fabrication of Photostable, Oxygen‐Doped Carbon Nanotubes. *Advanced Functional Materials*, Vol. 25, No. 39, 6157-6164, 2015.

2 Ma, X. *et al.* Room Temperature Single-Photon Generation from Solitary Dopants of Carbon Nanotubes. *Nature Nanotechnology*, Vol. 10, 671, 2015.

3 Wang, F. *et al.* Quantum Optical Signature of Plasmonically Coupled Nanocrystal Quantum Dots. *Small*, Vol. 11, No. 38, 5028-5034, 2015.

# Revealing Optical Properties of Two-Dimensional Semiconductors at Relevant Length Scales.

**P. J. Schuck**[1*]
[1]Molecular Foundry, Lawrence Berkeley National Lab, Berkeley, California, USA
[*]corresponding author: pjschuck@lbl.gov

**Abstract**- Reduced-dimensionality materials for photonic and optoelectronic applications including energy conversion, solid-state lighting, sensing, and information technology are undergoing rapid development. The search for novel materials based on reduced-dimensionality is driven by new physics. Understanding and optimizing material properties requires characterization at the relevant length scale, which is often below the diffraction limit. I will describe recent near-field advances that lay groundwork for generally-applicable nano-optical studies of these low-D materials, and will show recent results on 2D semiconductors.

I will describe the first nano-optical investigations of 2D transition metal dichalcogenides (TMDCs). By using plasmonics to establish a solution to the "nanospectroscopy imaging" problem for these materials, we cross the boundary from insufficient to sufficient resolution, mapping critical optoelectronic properties in these exciting materials at their native length scales [1]. In doing so, we and others have uncovered new optoelectronic regions and spatially-varying features in TMDCs that were hidden in prior optical studies [2]. These findings have broad implications for the development of atomically thin transistors, quantum optical components, photodetectors and light-emitting devices based on high-quality ML-TMDCs.

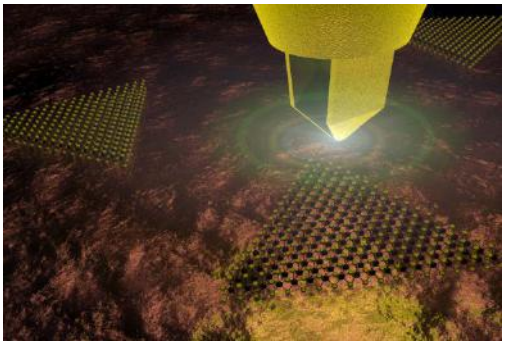


**Figure 1:** Nano-optical imaging of PL in ML-$MoS_2$. Illustration of near-field excitation and collection of the PL from ML-MoS2 using the Campanile near-field probe where the optical laser excitation and collection of sample emission are confined to the apex of the tip to produce high-resolution optical maps. At each pixel a full PL spectrum is acquired.

**REFERENCES**

1. Bao, W., Melli, M. *et al*. "Mapping Local Charge Recombination Heterogeneity by Multidimensional Nanospectroscopic Imaging," *Science*, Vol. 338, 1317–1321, 2012.
2. Bao, W., Borys, N. J. *et al*. "Visualizing nanoscale excitonic relaxation properties of disordered edges and grain boundaries in monolayer molybdenum disulfide," *Nature Commun.*, Vol. 6, 7993, 2015.

# Quantum Yield of Single Surface Plasmons Generated by a Quantum Dot Coupled with a Silver Nanowire

**Hong Wei[1*], Qiang Li[1], and Hongxing Xu[2]**
[1]Institute of Physics, Chinese Academy of Sciences, Beijing 100190, China
[2]School of Physics and Technology, Wuhan University, Wuhan 430072, China
[*]corresponding author: weihong@iphy.ac.cn

**Abstract** - The interactions between surface plasmons in metal nanostructures and excitons in quantum emitters lead to many interesting phenomena that are strongly dependent on the quantum yield of surface plasmons. The experimental measurement of this quantum yield is hindered due to the difficulty in distinguishing all the possible exciton recombination channels. By utilizing the propagation of surface plasmons, we experimentally determined the quantum yield of single surface plasmons generated by a quantum dot coupled with a silver nanowire.

The interactions between surface plasmons (SPs) and excitons in the coupled systems of metal nanostructures and quantum emitters (QEs) lead to many interesting phenomena and potential applications, which are strongly dependent on the efficiency of excitons converting to SPs, i.e., the quantum yield of SPs. As is known, there are three channels for the recombination of the excitons in coupled plasmonic systems, which are the direct free space radiation channel, SP generation channel and nonradiative damping channel. The difficulty in distinguishing all the possible exciton recombination channels hinders the experimental determination of SP quantum yield.

The propagating SPs supported by the metal nanowire (NW) make it possible to separate the directly radiative photons and the generated SPs in the QE-NW coupling structure, which provides a suitable system to disentangle the exciton recombination channels and obtain the SP quantum yield [1]. Here, we carefully analyzed the exciton-plasmon coupling process in the coupled system of a single quantum dot (QD) and a silver NW. The quantum yield of single SP generation is experimentally determined for the first time by disentangling all the exciton recombination channels. Moreover, we used $Al_2O_3$ film of different thickness to control the QD-NW separation and studied the distance-dependent exciton recombination dynamics. Our results show that the optimum QD-NW coupling distance for the largest SP quantum yield is about 10 nm, resulting from the different distance-dependent decay rates of the three channels, as shown in Figure 1 [2].

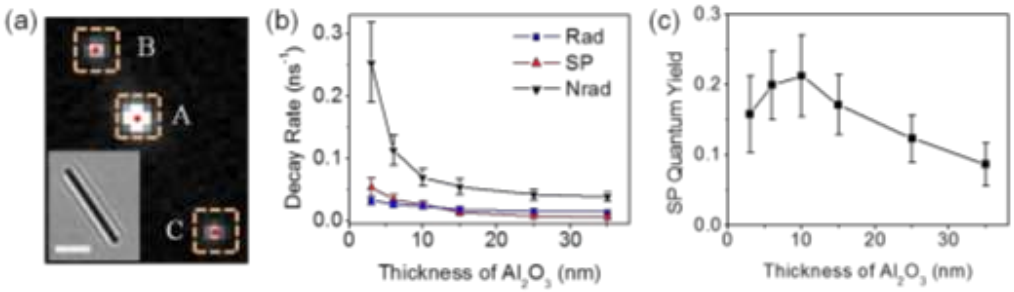



**Figure 1.** (a) Fluorescence image of a single QD coupled with a silver NW coated with $Al_2O_3$ film of 15 nm

thickness. The inset is the optical transmission image of the silver NW. The scale bar is 2 μm. The red dots are the accurate positions of QD A and the NW ends obtained using single molecule localization method. (b) Exciton decay rates as a function of $Al_2O_3$ thickness. The legends "Rad", "SP", and "Nrad" correspond to the free space radiation channel, SP generation channel, and nonradiative damping channel, respectively. (c) Experimentally extracted SP quantum yield as a function of $Al_2O_3$ thickness.

**Acknowledgements** - This work was supported by the Ministry of Science and Technology of China (Grant No. 2015CB932400), and the National Natural Science Foundation of China (Grant Nos. 11422436, 11374012, 11227407, and 11134013)

**REFERENCES**

1. Li, Q., Wei, H., and Xu, H. X., "Resolving single plasmons generated by multiquantum-emitters on a silver nanowire", *Nano Lett.*, 14, 3358-3363, 2014.
2. Li, Q., Wei, H., and Xu, H. X., "Quantum yield of single surface plasmons generated by a quantum dot coupled with a silver nanowire", *Nano Lett.*, 15, 8181–8187, 2015.

# VO2-driven switchable-beam directional antenna for micro/nano scale optical communications

**E. Rahimi[1] and K. Sendur[1*]**

[1] Sabanci University, Faculty of Engineering and Natural Sciences, Istanbul, Turkey

[*]corresponding author: sendur@sabanciuniv.edu

**Abstract -** In this study, we propose a switchable-beam directional antenna for micro/nano scale intrachip optical communications. Vanadium dioxide phase transition controls antenna's beam by affecting director's resonance frequency in a Yagi-Uda array and transforming them to reflector elements. A considerable gain manipulation is achievable by this method depending on array size.

Intrachip micro/nano scale communication fascinated researchers to develop optical antennas for wireless purposes due to a huge metallic absorption losses of plasmonic waveguides [1]. Yagi-Uda array antenna which consists of a feed radiator and some parasitic elements can provide directive emission in this regime [2,3]. Controlling antennas directivity facilitate the communication system with a useful nano-scale switch that may be employed for different purposes[4,5] including signal modulation [6].

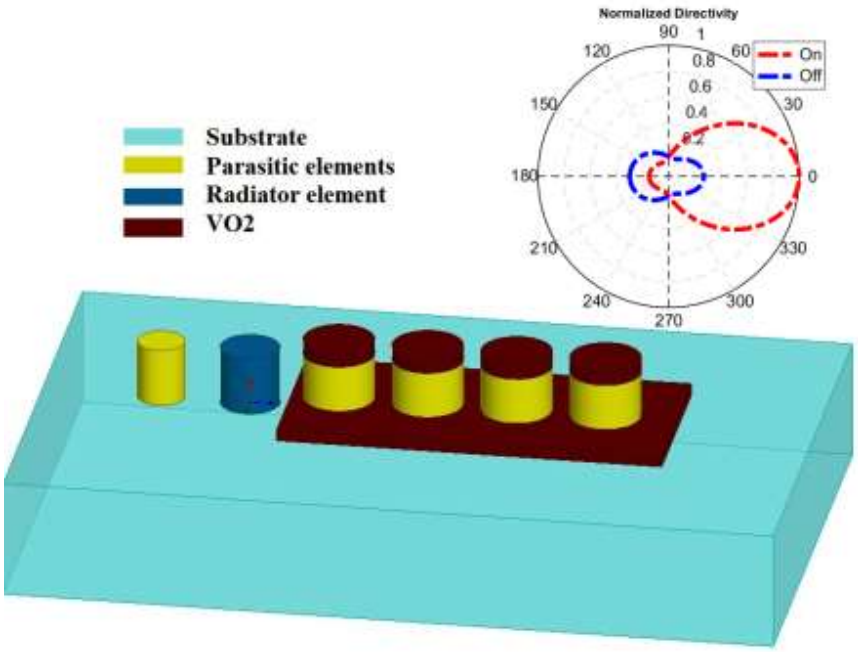



Figure **(1)** VO2-driven switchable-beam Yagi-Uda antenna array

This work proposes a switchable-beam directional antenna for micro/nano scale wireless communication. Phase transition of vanadium dioxide covering due to temperature variations shifts the resonance frequency [7] of parasitic elements in a Yagi-Uda array. Depending on the resonance frequency of the parasitic elements they may act as directors or reflectors; consequently, they can add to or reduce radiation in specific direction. As a

result, a control over radiation gain is achieved by manipulating phase transition of the phase change material.

**REFERENCES**


1. Alù A. and N. Engheta, "Wireless at the nanoscale: optical interconnects using matched nanoantennas," *Phy. Rev. Let*. Vol. 104, No. 21, 2010.
2. Kosako, T., Y. Kadoya, and H.F. Hofmann, "Directional control of light by a nano-optical Yagi–Uda antenna," *Nature Photonics*, Vol. 4, No. 5, 312-315, 2010.
3. Coenen, T., E.J.R. Vesseur, A. Polman, and A.F. Koenderink, "Directional emission from plasmonic Yagi–Uda antennas probed by angle-resolved cathodoluminescence spectroscopy," *Nano letters*, Vol. 11, No. 9, 3779-3784, 2011.
4. Chen, Y., P. Lodahl, and A.F. Koenderink, "Dynamically reconfigurable directionality of plasmon-based single photon sources," *Phys. Rev. B*,Vol. 82, No. 8, p.081402, 2010.
5. Kim, S.J., K. Lee, S.Y. Lee, and B. Lee, "Directional switching of surface plasmon polaritons by vanadium dioxide-gold hybrid antennas," *InSPIE OPTO*, 975621-975621, 2016.
6. Zhu, Q., S. Yang, R. Yao and Z. Nie, "Directional modulation based on 4-D antenna arrays," *Ant. & Prop. IEEE Trans*., Vol. 62, No. 2, pp.621-628, 2014.
7. Kats, M.A., R. Blanchard, P. Genevet, Z. Yang, M.M. Qazilbash, D.N. Basov, S. Ramanathan and F. Capasso, "Thermal tuning of mid-infrared plasmonic antenna arrays using a phase change material," *Optics letters*, Vol. 38, No. 3, pp.368-370, 2013.

# Novel photonic and plasmonic structures: theory and applications

# Optoelectronic applications of graphene-integrated silica nanowires

**Fei Xu**

National Laboratory of Solid State Microstructures and College of Engineering and Applied Sciences, Nanjing University, Nanjing 210093, P. R. China

*Email: feixu@nju.edu.cn

Abstract- Sub-wavelength silica nanowires(SNs) are attractive for integration with graphene, which can be realized by covering a graphene sheet on the side and even the endface of a straight SN, or wrapping a SN on a graphene-coated micro-rod. Here we will show several kinds of graphene-SN-hybrid devices and their optoelectronics applications.

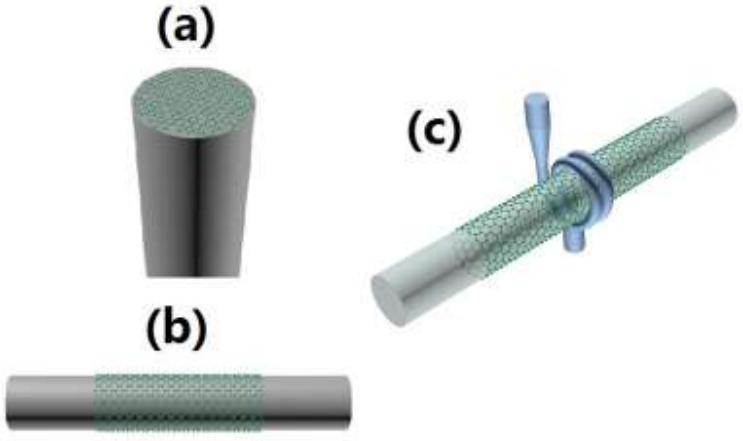



Fig. 1 Graphene-integrated SNs based on (a) edface coupling,(b) side coupling,(c) wrap on a rod.

Low-dimensional material, in particular, Graphene, which has received considerable attention recently due to many extraordinary electrical, mechanical, and optical properties, is being applied in numerous fields. Regarding the exceptional optical properties, for example, 2.3% linear absorption, saturable absorption, and a tunable Fermi level have been demonstrated for a number of optical devices such as mode-lock lasers, ultrafast photo-detectors, and modulators. Most practical applications require graphene to be integrated with optical waveguides for sufficient length and strength of interaction. Subwavelength-diameter silica nanowires (SNs) with a strong evanescent field are attractive for integration, which can be realized by transferring graphene flake onto a SN end face, covering or wrapping a graphene sheet on a straight SN and even wrapping a SN on a graphene-coated rod. The first method is the simplest but the light-graphene interaction length is very small because of normal-incidence. Utilizing the second method, moderate light-graphene interaction length because of the evanescent field coupling. This third method is much simpler because we only need to coat a small piece of graphene on a thick rod and can obtain unique stereo geometry with sufficient length and strength of interaction between the graphene and optical fields. Here we will show several kinds of 1D and 3D graphene-SN-integrated devices and the optoelectronic applications such as lasering, sensing, modulating, and detecting will also be discussed [1,2].

**REFERENCES**

1. J.-l. Kou, J.-h. Chen, Y. Chen, F. Xu, and Y.-q. Lu, "Platform for enhanced light-graphene interaction length and miniaturizing fiber stereo-devices," Optica, 1,307,2014

2. J.-h. Chen, B.-c. Zheng, G.-H. Shao, S.-j. Ge, F. Xu, and Y.-q. Lu," All-optical modulator based on a stereo graphene-microfiber structure," Light: Science & Applications 4，e360，2015.

# Light-trapping in perovskite solar cells

**Qingguo Du* and Ching Eng Png**

Institute of High Performance Computing, A* STAR, Singapore, 138632, Singapore
*duq@ihpc.a-star.edu.sg

**Abstract**-A new type of inverted vertical cone photonic crystal nanostructure based perovskite solar cell has been proposed. For optimized structure with $a$ = 600 nm and $R$ = 380 nm, the maximum MAPD of 24.0 mA/cm$^2$ has been realized, the efficacy of our light-trapping architecture was shown by its ability to absorb sunlight slightly beyond the Lambertian limit in the wavelength range of 300 nm – 800 nm.

Organometallic halide perovskites have been intensively studied in solar cell applications since the first perovskite solar cell was reported [1]. The excellent optical and electrical properties of perovskites make them among the most promising next generation solar cells. Both mesostructured and planar perovskite architectures have been proposed and their power conversion efficiency (PCE) has improved very rapidly in recent years. There are currently two distinct perovskite family materials, $CH_3NH_3PbI_3$ and $CH(NH_2)_2PbI_3$, used in solar cell research. The absorption spectrum of $CH_3NH_3PbI_3$ is from 300 nm to 800 nm while $CH(NH_2)_2PbI_3$ has a broader spectrum from 300 nm to 850 nm. Consequently, $CH(NH_2)_2PbI_3$ enables higher power conversion efficiency than $CH_3NH_3PbI_3$ based solar cells. Most recently, a 20.1% PCE solar cell has been certified in a $CH(NH_2)_2PbI_3$ planar device architecture [2]. While previous attention has been focused on improving electronic quality of the perovskite layer, there remain opportunities to optimize optical absorption through light-trapping.

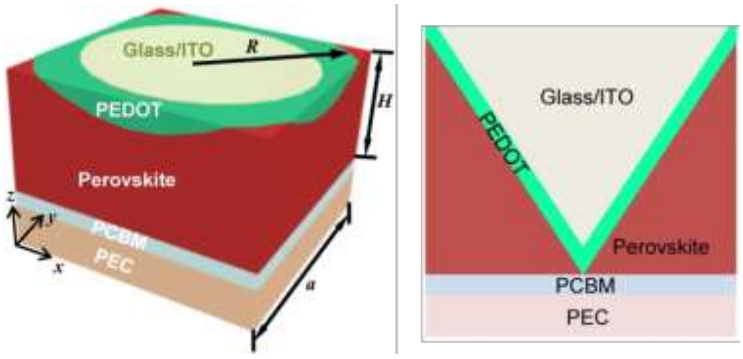



Fig. 1 (a) Three-dimensional perspective of the inverted vertical cone perovskite unit cell, (b) Two-dimensional side view of the device unit cell.

We numerically simulate solar absorption in nanostructured perovskite solar cells. By direct solution of Maxwell's equations, we identify optimized light-trapping architectures consisting of inverted-vertical-cone arrays. The active layer thickness is limited to about 300 nm of perovskite material to ensure charge carrier collection. This corresponds to an "equivalent bulk thickness" of 180 nm. Absorption and reflection are calculated using the finite-difference time-domain (FDTD) method for the absorption wavelength ranges of both perovskites using a 5 nm step size. The

simulated structure is shown in Fig.1. The refractive index of CH3NH3PbI3 is taken from Ref. [3].

In our numerical simulation of sunlight absorption, the thicknesses of PCBM and PEDOT are both fixed at 10 nm. The total height of the active perovskite region is fixed at $H$ = 300 nm (see Fig. 1a) to ensure reasonable carrier collection efficiency. The optimization process is performed by varying the lattice constant $a$ from 200 nm to 1000 nm and the base radius $R$ of the inverted cone from $a/4$ to $3a/4$. The MAPD map is shown in Fig. 2. When $a$ = 600 nm and $R$ = 380 nm, the maximum MAPD of 24.0 mA/cm$^2$ is realized. The total equivalent bulk thickness of perovskite material in this case is 180 nm of a corresponding planar device.

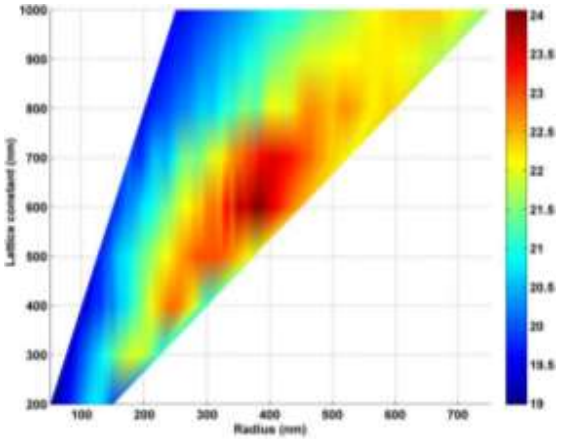



Fig.2 MAPD optimization map for $CH_3NH_3PbI_3$ based perovskite photonic crystal with lattice constant $a$ from 200 nm to 1000 nm and cone base radius $R$ from $a/4$ to $3a/4$.

In summary, we have designed vertical, inverted cone, photonic-crystal light-trapping architectures for $CH_3NH_3PbI_3$ based perovskite solar cells. In our calculations, we have limited ourselves to perovskite film thicknesses in which the carrier collection probability (internal quantum efficiency) is close to unity. When $a$ = 600 nm and $R$ = 380 nm, the maximum MAPD of 24.0 mA/cm$^2$ is realized, the efficacy of our light-trapping architecture was shown by its ability to absorb sunlight slightly beyond the Lambertian limit in the wavelength range of 300 nm – 800 nm.

References:


1. A. Kojima, K. Teshima, Y. Shirai and T. Miyasaka, "Organometal Halide Perovskites as Visible-Light Sensitizers for Photovoltaic Cells," J. Am. Chem. Soc. **131**, 6050-6051, (2009).
2. W. S. Yang, J. H. Noh, N. J. Jeon, Y. C. Kim, S. Ryu, J. Seo and S. I. Seok, "High-performance photovoltaic perovskite layers fabricated through intramolecular exchange," Sci. **348**, 1234-1237, (2015).
3. P. Löper, M. Stuckelberger, B. Niesen, J. Werner, M. Filipič, S.-J. Moon, J.-H. Yum, M. Topič, S. De Wolf and C. Ballif, "Complex Refractive Index Spectra of CH3NH3PbI3 Perovskite Thin Films Determined by Spectroscopic Ellipsometry and Spectrophotometry," The Journal of Physical Chemistry Letters **6**, 66-71, (2015).

# Optical Periodic Structures with Double Spatial Resonance

**G. Alagappan*, and C. E. Png**
Department of Electronics and Photonics, Institute of High Performance Computing, Agency for Science, Technology, and Research (A-STAR), Fusionopolis, 1 Fusionopolis Way, #16-16 Connexis, Singapore 138632
*corresponding author: gandhi@ihpc.a-star.edu.sg

**Abstract**-This article summarizes the intriguing optical properties of a periodic structure that has double spatial resonance. Such periodic structures exhibit a unique dispersion curve that is fundamentally different from the conventional periodic structures.

Dielectric periodic structures [1] are usually characterized by a single period $a$, and they are well known for their ability to provide a stopband – spectral region for which light propagation is forbidden. The fundamental spatial resonance of the single period structure (SPS) occurs at the frequency $2\pi/a$. For a doubly resonant periodic structure (DPS) [2], we have two closely spaced spatial resonances at frequencies $2\pi/a$ and $2\pi/ra$, where $r$ is a rational number close to 1. The conservation of the translational symmetry in the DPS requires $r = R/(R\text{-}1)$, where $R$ is a huge integer. Assuming a weak dielectric modulation, the dielectric function of the DPS can be casted as

$$\varepsilon(x) = \varepsilon_0 + \varepsilon_1 \cos\left(\frac{2\pi}{a}x\right) + \varepsilon_1 \cos\left(\frac{2\pi}{ra}x\right) \tag{1}$$

Figure 1 shows the dispersion curve of a DPS with $\varepsilon_0 = 2.56$, and $\varepsilon_1 = 0.16$ for a huge value of $R$ (i.e., in the limit $r \to 1$). The figure also compares the dispersions of the homogenous medium (dielectric constant = 2.56) and SPS ($r$ = 1). As we can clearly see from this figure, the dispersion of the DPS is remarkably different from the dispersion of the SPS despite the limit $r \to 1$. This intriguing dispersion is the result of the destructive interference between the two cosine waves in Eqn. 1, which occurs regardless of the proximity of $r = R/(R\text{-}1)$ to one.

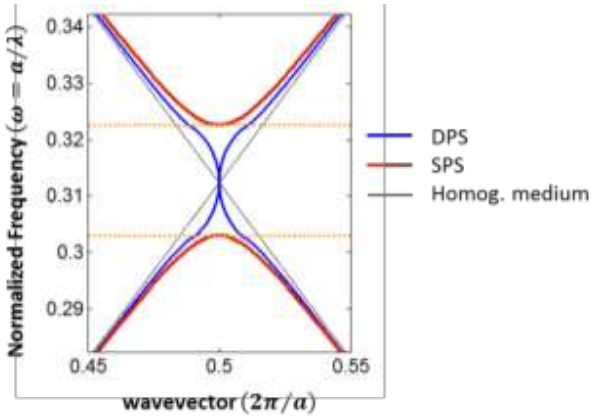



Fig. 1 Dispersions of the conventional single period structure (SPS), doubly resonant periodic structure (DPS), and the homogenous medium

**REFERENCES**


1. J. D. Joannopoulos, S. G. Johnson, J. N. Winn, R. D. Meade, "Photonic Crystals: Molding the Flow of Light" (Second Edition, Princeton University Press, New Jersey, 2008).
2. G. Alagappan, and C. E. Png, "Doubly Resonant Optical Periodic Structure," *Sci. Rep.*, Vol. 6, 20590, 2016.

# Manipulating polarization of radially polarized beams by anisotropic Kerr media

**Bing Gu[1,*], Bo Wen[1], Guanghao Rui[1], Yuxiong Xue[2], Qiwen Zhan[3], and Yiping Cui[1]**

[1]Advanced Photonics Center, Southeast University, Nanjing 210096, China

[2]Science and Technology on Vacuum Technology and Physics Laboratory, Lanzhou Institute of Physcis, Lanzhou 730000, China

[3]Electro-Optics Program, University of Dayton, 300 College Park, Dayton, OH, 45469-2951 USA

[*]corresponding author: gubing@seu.edu.cn

**Abstract**: We propose the manipulation of the states of polarization and the spin angular momentum (SAM) flux of radially polarized beams (RPBs) by anisotropic nonlinear Kerr media. We investigate the vectorial self-diffraction behavior of the RPBs induced by an anisotropic Kerr nonlinearity. Numerical studies demonstrate that the self-diffraction patterns with a four-fold rotational symmetry have hybrid polarization and the interaction of RPBs with the anisotropic Kerr media results in a redistribution of the SAM flux in the far-field plane.

Light fields with structured polarization distribution interacting with structured media will result in many novel optical effects in both the linear and nonlinear regimes. In this work, we consider a focused RPB incidents normally on the surface of an optically thin crystal and propagates parallel to the [001] crystallographic axis, as shown in Fig. 1. For this specific geometry, the effective third-order nonlinear refraction index is expressed as [1]

$$n_2(\theta) = n_2^0[1 + 2\sigma(\sin^4\theta - \sin^2\theta)], \tag{1}$$

where $n_2^0$ is the third-order nonlinear refraction index, $\sigma$ is the anisotropy coefficient, and $\theta$ is the incident polarization angle with respect to the [100] crystallographic axis.

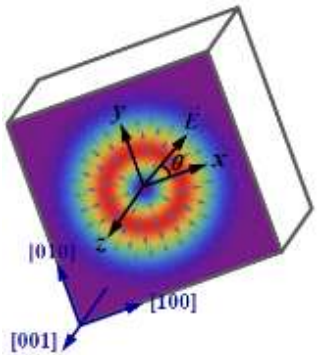



Fig. 1 The coordinate system associated to the crystal orientation with respect to the focused RPB in the analysis.

Based on the vectorial Rayleigh-Sommerfeld formulas under the paraxial approximation [2], we can obtain the electric field distribution in the far-field observational plane. Figure 2 presents the intensity patterns of RPBs at the far-field observational plane when an anisotropic Kerr medium is located at the focal plane of the lens with

different values of σ and ΔΦ. It was shown that hybridly polarized self-diffraction patterns with a four-fold rotational symmetry can be induced by the anisotropic optical nonlinearity. Moreover, the interaction of RPBs with the anisotropic nonlinear Kerr media leads to the redistribution of the SAM flux at the far-field plane. The presented work opens up new avenues for manipulating polarization and SAM by the anisotropic optical nonlinearity.

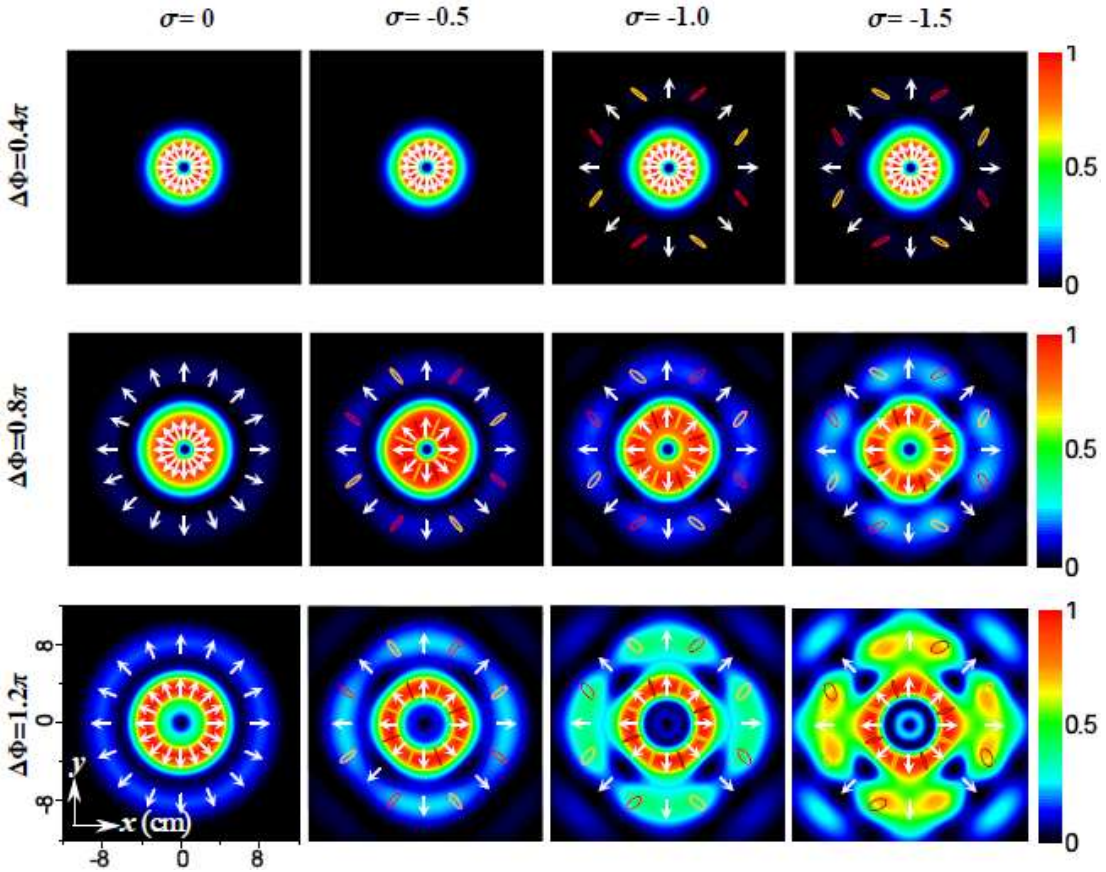



Fig. 2. Normalized far-field intensity patterns and schematics of SoPs (Deep red: LH polarization; Deep blue: RH polarization; White arrows: linear polarization) of radially polarized beams for an anisotropic Kerr medium with different values of σ and ΔΦ.

**Acknowledgements** This work was supported by the National Science Foundation of China (Grant Nos: 11474052, 11504049) and the National Key Basic Research Program of China (Grant No: 2015CB352002).

**REFERENCES**

1. R. DeSalvo, M. Sheik-Bahae, A. A. Said, D. J. Hagan, and E. W. Van Stryland, "Z-scan measurements of the anisotropy of nonlinear refraction and absorption in crystals," *Opt. Lett.* Vol. 18, 194--196 (1993).
2. R. K. Luneburg, *Mathematical Theory of Optics*, University of California, 1966.

# Plasmonic design for enhanced light emission and detection

**F.-F. Ren[1,2*], G.-G. Zhang[2], M. Yang[2], W.-Z. Xu[1,2], J.-D. Ye[1,2], H. Lu[2], R. Zhang[2], Y. Shi[2], H. H. Tan[1], and C. Jagadish[1]**

[1]Department of Electronic Materials Engineering, Research School of Physics and Engineering, The Australian National University, Canberra, ACT 2601, Australia

[2]School of Electronic Science and Engineering, Nanjing University, Nanjing 210093, China

[*]corresponding author: fangfang.ren@anu.edu.au

**Abstract**-We report on the plasmonic nanostructures design for enhanced blue light emission from InGaN/GaN light-emitting diode structures, and also the plasmonic antenna design for enhanced responsivity of high-speed photodetectors in the spectral range from visible to mid-infrared. The mechanisms of different enhancement features have been theoretically analyzed based on three-dimensional finite-difference time-domain simulations, and the results are well supported by the experimental observation.

Plasmonic structures have a wide range of application in optoelectronic devices by concentrating wave electromagnetic energy into a deep-subwavelength volume. Examples include light-emitting diode (LED), photodetectors, solar cells, sensors and many others. The principles that govern such structures, including antennas and arrays of metallic particles, can be extended from radio-frequency to the ultraviolet range. As will be shown in this work, the InGaN/GaN LED structures are proposed with integration of Al-coated GaN nanorods[1]. The intensity of light emission was found to be greatly enhanced due to the strong near-field confinement at the interface of Al/GaN and its extension to the multiple quantum wells (MQWs) active region. To address the unique properties of plasmonic antennas, we developed split bull's eye (SBE) structures to enhance the responsivity of high-speed photodetectors [2-4]. The investigation was conducted over a wide spectral range from visible to mid-infrared range.

**Enhanced light emission.** InGaN/GaN MQW LED structures with Al-coated GaN nanorods were fabricated by using soft ultraviolet nanoimprint lithography. The low-cost Al metal exhibits superior performance in the blue spectral region. The photoluminescence (PL) intensity was found to be enhanced by 2.6 times at 467 nm, which is exactly the wavelength of the surface plasmon mode excited on the interface of the Al layer and p-GaN. We believed that the higher PL intensity is due to the increase of the spontaneous emission rate and internal quantum efficiency via surface plasmon-coupling. The phenomena of faster radiative recombination rate and enhanced Raman scattering are also observed and discussed. Our findings provide the foundation for rapid development of high-efficiency and low-cost LED devices.

**Enhanced light detection.** We studied the transmission enhancement mechanisms of SBE antennas based on three-dimensional finite-difference time-domain simulations from visible to mid-infrared. By taking a subwavelength slit as the central aperture, the cutoff function of SBE antennas is improved mainly due to the change in transmission mode from evanescent to propagating. By further combining the concentration

capability of circular grooves and F-P resonances in the slit, the transmission though SBE antennas can be enhanced by 6 orders of magnitude at the wavelength of 4 μm, exhibiting excellent advantages in the mid-infrared region. In the visible region, a high transmission can be maintained by properly narrowing the slit. Therefore, SBE antennas have the ability to efficiently funnel incident light into an ultra-small area from visible to mid-infrared, which is especially applicable for high-speed photodetectors.

**Acknowledgements**, The authors would like to thank the funding support from Australian Research Council and the Fundamental Research Funds for the Central Universities (China) under Grant No. 021014380033.

**REFERENCES**

1. Zhang G. G., Zhuang Z., Guo X., Ren F. F., Liu B., Ge H. X., Xie Z. L., Sun L., Zhi T., Tao T., Li Y., Zheng Y. D., and Zhang R., Bloch surface plasmon enhanced blue emission from InGaN/GaN light-emitting diode structures with Al-coated GaN nanorods, *Nanotechnology*, Vol. 26, No. 12, 125201, 2015.
2. Yang M., Ren F. F., Pu L., Xiao L., Sheng Y., Wang J., Zheng Y., and Shi, Y. Split Bull's Eye Antenna for High-Speed Photodetector in the Range of Visible to Mid-Infrared, *IEEE Photonics Technology Letters,* accepted, 2016.
3. Ren F. F., Xu W. Z., Ye J. D., Ang K. W., Lu H., Zhang R., Yu M. B., Lo G. Q., Tan H. H., and Jagadish C., Second-order surface-plasmon assisted responsivity enhancement in germanium nano-photodetectors with bull's eye antennas, *Opt. Express*, Vol. 22, No. 13, 15949-15956, 2014.
4. Ren F. F., Ang K. W., Ye J. D., Yu M. B., Lo G. Q., and Kwong D. L., Split bull's eye shaped aluminum antenna for plasmon-enhanced nanometer scale germanium photodetector, *Nano Letters*, Vol. 11, No. 3, 1289-1293, 2011.

# The applications of macro-optical elements in micro/nano scale

**H. T. Dai**[1*], and **M. X. Run**[1]

[1] Tianjin Key Laboratory of Low Dimensional Materials Physics and Preparing Technology, School of Science, Tianjin University, Tianjin 300072, China

[*]corresponding author: htdai@tju.edu.cn

**Abstract**- Until now, many mature optical designs in geometric optics, such as Luneburg lens, Yagi-Uda antenna, have been found promising applications in photonics, in which the scale of devices are reduced to micro/nano range. In this report, we investigated kinds of applications in photonic field by employing subsistent macro optical devices, for example modified Luneburg lens and Maxwell fish-eyes lens, to achieve nanojet or tightly focusing. Numerical analysis results show that the multi-focus Luneburg lens enable tunable nanojet by engineering the focal lengths. Additional, Maxwell fish-eyes lens was also found some novel applications in photonics. The related research opens a way to design functional photonic devices by means of subsistent gradient index optical devices.

The Luneburg lens (LLs), which is rotationally symmetric graded refractive index lens, is able to manipulate the ray paths so that, for example, an omnidirectional source can be transformed into a directive beam [1]. By engineering the refractive index distribution, the generalized Luneburg lens (GLLs), of which focal point can be tuned either inside or at a distance from the surface of the lens, can be formed. Multiple focal points of GLLs also can be generated by tailoring the refractive index distribution [2]. The index distribution of GLLs for single focal point can be expressed as follow:

$$n(r) = n_0 \left[ 1 + f^2 - \left( \frac{r}{\mathrm{R}} \right)^2 \right]^{1/2} \Big/ f \tag{1}$$

The double-focus GLLs has a more complex form, which can be described as below:

$$n(\rho) = \begin{cases} \exp\left[ \omega_1(\rho, f_2) + \omega_2(\rho, f_1, P_a) + \omega_3(\rho, f_2, P_a) \right], 0 \le \rho \le P_a \\ \exp\left[ \omega_1(\rho, f_2) \right], P_a \le \rho \le 1 \end{cases} \tag{2}$$

$$\omega_1(\rho, f_2) = \frac{1}{\pi} \int_{\rho}^{1} \frac{\arcsin\left(k / f_2\right) dk}{\left(k^2 - \rho^2\right)^{1/2}} \tag{3}$$

$$\omega_2\left(\rho, i, P_a\right) = \frac{1}{\pi} \int_{\rho}^{P_a} \frac{\arcsin\left(k / i\right) dk}{\left(k^2 - \rho^2\right)^{1/2}} \tag{4}$$

As we knew, the GLLs can generate focal points in geometric optics. In micro scale, however, the behavior of electromagnetic wave has to be checked according to fullwave theory. To verify this situation, numerical simulation is performed by means of finite-difference time-domain (FDTD) method. The size of the computational cell in our numerical experiment is selected as 0.01 μm and perfectly matched layers (PMLs) are

chosen as the boundary conditions to minimize non-physical reflections. Figure 1 shows the electric field intensity envelopes of double-focus GLLs with different focal lengths. To explore the effect of double-focus GLLs on PNJ, one focal length has to be set as fixed and then the other focal length is varied to observe the properties of PNJ. First, we scan $f_2$ with a fixed $f_1$. Figures 1(a)-1(d) show the intensity distribution of GLLs with $f_2$ = 1.7, 2.2, 2.7, and 3.2, respectively. The first focal length is set as fixed value ($f_1$ = 1.2). Similar to the single-focus GLLs, the increasing $f_2$ leads to elongated PNJ, accompany with decreased peak intensity and broadened FWHM. Figures 1(e) and 1(f) show the corresponding L and FWHM for Figs. 1(a)-1(d). According to Figs. 1(e) and 1(f), the L of PNJ extend from 6.10$\lambda$ to 12.10$\lambda$ while the FWHM increase from 0.6625$\lambda$ to 0.97$\lambda$. Certainly, the longitudinal waist L of PNJ and the corresponding FWHM are mutual contradiction, a trade-off has to be decided according to specific application.

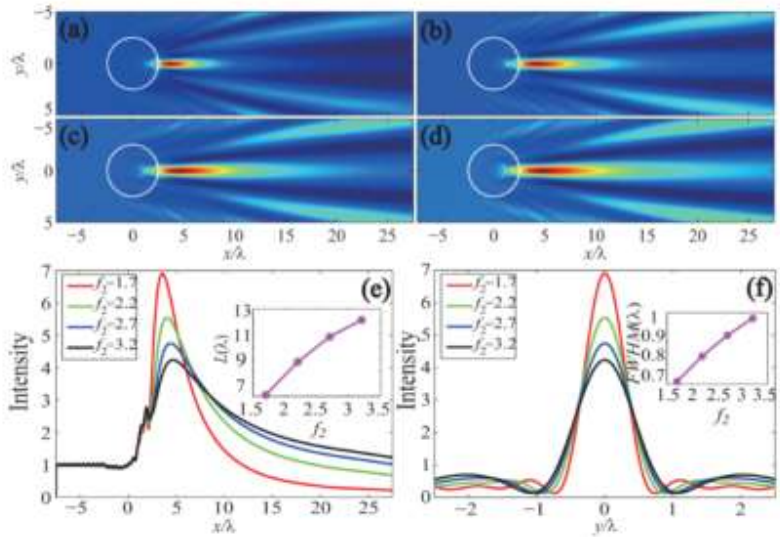



Fig. 1 Intensity distributions of double-focus GLLs with various normalized focal length for (a) $f_2$ = 1.7, (b) $f_2$ = 2.2, (c) $f_2$ = 2.7, and (d) $f_2$ = 3.2 when the first focal length $f_1$ is set as 1.2 for a 400 nm incident wavelength. Intensity distributions of double-focus GLLs (e) along the x axis passing through center of GLLs, and (f) along the y axis at maximum intensity spots. The insets of the right upper corner each figure correspond to the concrete value of L and FWHM with different normalized focal length $f_2$.

We also discussed the properties of Maxwell fish-eyes lens in microscale numerically. Numerical results show that Maxwell fish-eyes lens can be used as superresolution focusing or imaging.

**Acknowledgements**, This work was supported in part by the National Natural Science Foundation of China (Grant No. 61177061, 11204208 and 61405088); the Open Research Fund of the State Key Laboratory of Transient Optics and Photonics (Chinese Academy of Sciences); Key project of Nature Science Foundation of Tianjin No. 14JCZDJC31400.

**REFERENCES**

1. J. A. Lock, "Scattering of an electromagnetic plane wave by a Luneburg lens. I. Ray theory," *J. Opt. Soc. Am. A* Vol. 25, No. 12, 2971–2979, 2008.
2. J. Sochacki, "Multiple-foci Luneberg lenses," *Appl. Opt.* Vol. 23, No. 23, 4444–4449 ,1984.

# Refractory metal based broadband, omnidirectional and polarization-insensitive light absorber for high-temperature applications

**Manohar Chirumamilla[1],* Alexander S. Roberts[2], Fei Ding[1], Deyong Wang[1], Sergey I. Bozhevolnyi[2], Kjeld Pedersen[1]**

[1]Department of Physics & Nanotechnology, Aalborg University, Skjernvej 4A, 9220 Aalborg Øst, Denmark

[2]Centre for Nano Optics, University of Southern Denmark, Campusvej 55, 5230 Odense M, Denmark

[*]Corresponding author: mch@nano.aau.dk

**Abstract** Perfect broadband absorbers based on metal-insulator-metal resonators using refractory materials (tungsten and alumina) are reported for energy harvesting/conversion applications. The absorption efficiency is higher than 90% over a broad spectral region with a maximum of 98% around 500 nm. Omnidirectional and polarization-insensitive absorption of incident light is observed for broad angles of incidence. Thermal stability of the substrate is tested at high working temperature (800 ºC).

Broadband absorbers composed of tungsten/alumina/tungsten/alumina layers stack are fabricated by a simple deposition method. A schematic representation of the continuous MIM cavity structure with a protective coating layer of alumina is shown in Figure 1a. The protective coating layer minimizes the melting point depression of the thin film relative a bulk material. Two lossy metallic (tungsten) layers separated by a dielectric spacer layer (alumina) placed over a polished silicon substrate, serves as the Fabry-Perot (FP) photonic resonator. The bottom layer should be thick enough (100 nm) to act as a reflector, whereas the thickness of the top layer should be ultrathin (10 nm) for transmitting the incident light and further generating the resonances. The dielectric layer serves as an optical cavity, and the thickness of the dielectric layer (optical cavity length) determines the resonance position. Since tungsten is a high lossy metal with a positive real part and large imaginary part of the dielectric constant, instead of the narrow band observed in noble metals based resonators, a broadband absorption around a center resonance defined by the optical cavity length is observed.[1-4]

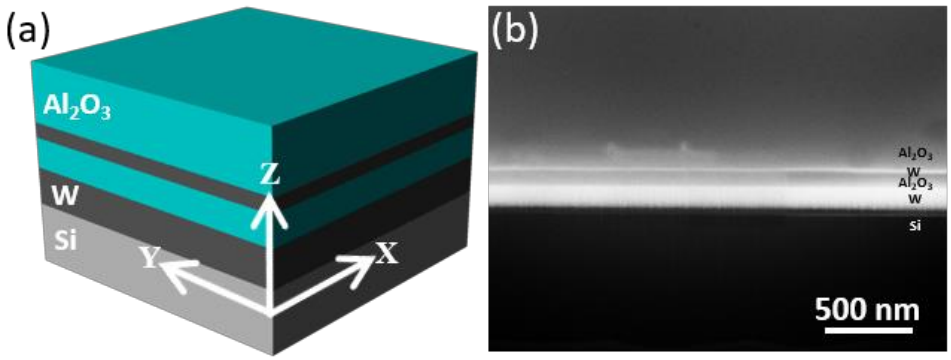



**Figure 1.** a). Schematic representation of MIM resonator with a protective coating layer of alumina. b) Cross-sectional SEM image of the resonator.

Tungsten is deposited onto a silicon substrate by DC sputtering and alumina is deposited by e-beam evaporation. A 30 nm alumina adhesion layer (not shown in Figure 1a) is deposited between bottom

tungsten film and the polished silicon substrate. All layers are deposited with a deposition rate of 0.3 Å/s. Reflection measurements are performed on a Perkin Elmer Lambda 950 spectrometer equipped with 150 mm integrating sphere. Figure 2 shows the absorption spectrum of the resonator for tungsten/alumina/tungsten/alumina stack of 100/50/8/100 nm thickness under normal incidence. The red trace shows the absorption spectrum without protective coating layer, where a narrow band absorption around 625 nm is seen. When the resonator with alumina protective coating layer (black trace) a broadband absorption spectrum spanning from visible to near-infrared spectral regions is observed due to the impedance matching. Figure 1b shows the cross-sectional scanning electron microscope (SEM) image of the resonator. COMSOL simulations are performed to identify the power dissipation, the phase of the light and the electric field distribution, and the calculated absorption spectra show good agreement with experimental results. Angular and polarization insensitive broadband absorption is observed over a broad spectral region.

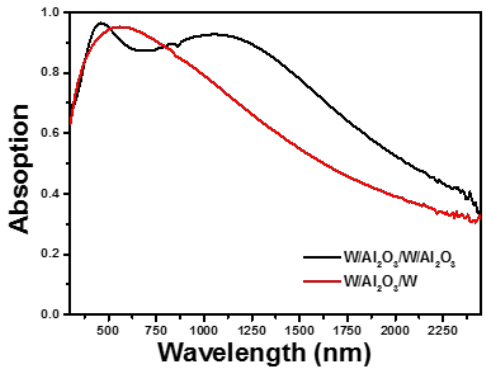



**Figure 2.** The broadband absorption spectrum for 50 nm alumina, 8 nm top tungsten and 100 nm protective coating film of the resonator.

In summary, this work demonstrates the feasibility of lithography-free, broadband, omnidirectional and polarization-insensitive broadband absorbers based on tungsten and alumina multilayered stacks with low-cost wafer-scale fabrication methods. Due to the planar configuration of the resonator and thermal stability, it can be easily implemented in high-temperature energy harvesting applications.

**Acknowledgments:** We acknowledge financial support from the Danish Council for Independent Research (the FTP project PlasTPV, contract no. 1335-00104).

**REFERENCES**

1. Roberts, A. S.; Chirumamilla, M.; Thilsing-Hansen, K.; Pedersen, K.; Bozhevolnyi, S. I. "Near-infrared tailored thermal emission from wafer-scale continuous-film resonators". *Optics Express* 2015, 23, A1111-A1119.

2. Roberts, A. S.; Søndergaard, T.; Chirumamilla, M.; Pors, A.; Beermann, J.; Pedersen, K.; Bozhevolnyi, S. I. "Light extinction and scattering from individual and arrayed high-aspect-ratio trenches in metals". *Physical Review B* 2016, 93, 075413.

3. Li, Z.; Palacios, E.; Butun, S.; Kocer, H.; Aydin, K. "Omnidirectional, broadband light absorption using large-area, ultrathin lossy metallic film coatings". *Scientific Reports* 2015, 5, 15137.

4. Ding, F.; Mo, L.; Zhu, J.; He, S. "Lithography-free, broadband, omnidirectional, and polarization-insensitive thin optical absorber". *Applied Physics Letters* 2015, 106, 061108.

5. Chirumamilla, M.; Roberts, A. S.; Wang, D.; Bozhevolnyi, S. I.; Pedersen, K. " Tungsten based tunable broadband and omnidirectional polarization-independent light absorber for high-temperature applications" submitted.

# Whispering Bloch Modes

**B. Maling**[1], **R. V. Craster**[1]

[1]Imperial College London, UK
ben.maling12@imperial.ac.uk

**Abstract**— Using illustrative examples, we discuss the properties of whispering Bloch modes, which are spatially-confined eigenstates of open wave systems with high orders of rotational symmetry. We explore the potential application of whispering Bloch resonators as integrated photonic components and in other cases where cylindrical whispering gallery mode resonators are currently employed. The effect of slightly perturbing the geometry of the system is investigated, leading to asymmetric field patterns and other potentially desirable consequences.

Whispering gallery modes (WGMs), ubiquitous in wave systems with circular or spherical cavities [1], have found application as sensors, spectral filters and integrated circuit components [2]. In most instances, these quasi-normal modes are partially confined due to a material boundary, and are characterised by complex frequencies, implying a decay of the field in time. In contrast to this, we consider systems in which no surrounding material boundary is necessary to achieve confinement, which is induced instead by a geometric structure arranged periodically around a circle. It is straightforward to prove that the quasi-normal modes of such systems exhibit discrete Bloch-like angular periodicity and hence we refer to them as whispering Bloch modes (WBMs) [3]. In Fig. 1 we illustrate a WGM in a two-phase photonic system, and a WBM in a system of radial conducting spokes embedded in a homogeneous background material. Note that in this case, the radiative quality factor, defined as $Q = \mathrm{Re}(\omega)/|2\,\mathrm{Im}(\omega)|$, is significantly higher for the WBM.

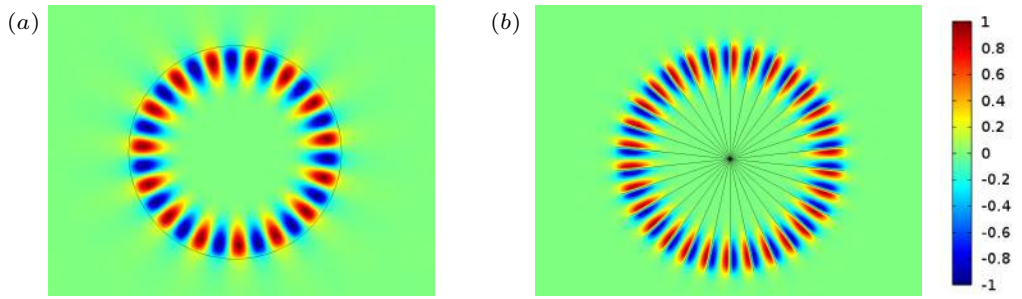



Figure 1: WGM vs. WBM. Frame (a) shows a WGM for a high refractive index ($n = 2$) cylinder in a low refractive index ($n = 1$) background, in TE polarisation. Frame (b) shows a WBM in the same polarisation, induced by an array of perfectly conducting spokes in a homogeneous background. In each case, the real part of the out-of-plane magnetic field $H_z$ is plotted, normalised to the colour bar shown.

Using illustrative examples, we discuss the properties of WBMs, as well as their potential applications in photonics and in other physical systems. We focus on two geometries: the array of spokes shown in Fig. 1(b), and also a periodic ring of cylindrical holes in a homogeneous background medium. In both cases, we note the existence of standing wave solutions with very high $Q$-factors. At frequencies close to these, solutions are found with wide-angle Bloch modulation, offering possibilities such as frequency-based switches for integrated photonics. We investigate these phenomena from a practical point of view in terms of potential applications, and also theoretically using asymptotic analysis. We go on to consider what happens if the geometry of a WBM system is perturbed such that the rotational symmetry of the system is broken, and discuss cases in which the resulting geometries could be used to build photonic components with desirable properties.

**ACKNOWLEDGMENT**

The authors thank the EPSRC (UK) for their support through the Programme Grant EP/L024926/1.

**REFERENCES**


1. A. B. Matsko, A. A. Savchenkov, D. Strekalov, V. S. Ilchenko, and L. Maleki. "Review of applications of whispering-gallery mode resonators in photonics and nonlinear optics," *IPN Progress Report*, 2005.
2. D. G. Rabus. *Integrated ring resonators*, Springer-Verlag, Berlin, 2007.
3. B. Maling and R. V. Craster "Whispering Bloch modes," *Proc. R. Soc. A*, 2016 (under review)

# Sub-THz Optical antenna in a Standard CMOS Technology

**X.Ji, Y.Liao, Q.Lou, R.Wu, and F.Yan**
School of Electronic Science and Engineering, Nanjing University, Nanjing, China.
corresponding author: fyan@nju.edu.cn

**Abstract**-A high-performance optical antenna for Terahertz detectors is demonstrated using standard CMOS technology. By introducing the bowtie optical antenna patterned by Si material, surface plasmon polaritons (SPP) are excited and propagate THz signals to MOSFETs via a strongly localized surface wave. The maximum response of the CMOS detector having the optical antenna is about 60 times larger than the design without the antenna. The antenna design open a wide range of possibilities for highly dense on-chip THz detectors in CMOS technologies.

For Si MOSFETs to detect sub-THz waves, FETs are usually integrated with the antennas for collecting THz signals [1-4]. In order to obtain high-performance detection, matching of the input impedance of the antenna and FETs should be carefully considered. However, there remain the challenges to realize antenna with ideal power matching for CMOS devices in THz region [1-2]. We propose the new antenna designs exploiting plasmonic effects to overcome this trade-off by converting the input waves into the localized surface plasmon polaritons (SPP) resonances.

Optical antenna by Si material in standard CMOS technology is designed as the modified bowtie structure which combines the advantages of both rod and bowtie to achieve the high localized field enhancement for THz radiation. By monitoring the SPP modes observed at maximum in electrical field with HFSS simulator, we get the structural parameters of antenna for frequency of 0.65 GHz. To verify the above design, such antenna-coupled nMOSFET detector is fabricated using 0.18 μm CMOS process. The maximum response of the detector is about 650 uV, which is about 60 times larger than that of the detector without the antenna. Such enhancement of response is a direct experimental evidence of plasmonic effect from Si optical antenna without the need of matching of the antenna and FET receivers. The demonstrated antenna design open a wide range of possibilities for the ease of realization of highly dense on-chip THz detectors in CMOS technologies.

## REFERENCES

[1] F. Schuster, H. Videlier, A. Dupret, D. Coquillat, M. Sakowicz, J. Rostaing, M. Tchagaspanian, B. Giffard, and W. Knap, "A broadband THz imager in a low-cost CMOS technology," Int. Solid-State Circuits Conf. (ISSCC) Dig. Tech. Papers, 2011.

[2] E. ¨ Ojefors, U. R. Pfeiffer, A. Lisauskas, and H. G. Roskos, "A 0.65 THzfocal-plane array in a quarter-micron CMOS process technology," *IEEE J. Solid-State Circuits*, vol. 44, no. 7, pp. 1968–1976, 2009.

[3] Franz Schuster *et al*, "Broadband terahertz imaging with highly sensitive silicon CMOS detectors" Optics Express, 19,7827 ,2011

[4] R. Hadi, H. Sherry, J. Grzyb, Y. Zhao, W. Forster, H. M. Keller, A. Cathelin, A. Kaiser, and U. Pfeiffer, "A 1 k-pixel video camera for 0.7–1.1 terahertz imaging applications in 65-nm CMOS," IEEE J.Solid-State Circuits, vol. 47, no. 12, pp. 2999–3012, 2012

# Broadband absorption enhancement in ZnTe nanowire intermediate solar cells with plasmonic bowtie antennas

**Kui-Ying Nie, Fang-Fang Ren, Jing Li, Jiandong Ye*, Kun Tang, Shulin Gu, Rong Zhang, Youdou Zheng**
School of Electronic Science and Engineering, Nanjing University, Nanjing 210093, China
*corresponding author: yejd@nju.edu.cn

**Abstract**- A plasmonic bowtie antenna design is investigated numerically to enhance a broad spectral absorption of zinc telluride (ZnTe)/zinc oxide (ZnO) core/shell single nanowire intermediate solar cells. Compared to a single-bowtie antenna, triple-bowtie antennas demonstrate much higher absorption enhancement in multiple spectra regimes, especially in 680nm, which is corresponding to the intermediate level of ZnTe:O materials. It provides a promising approach to improve the poor absorption of low-energy photons and improve the conversion efficiency of single nanowire solar cells.

In recent years, one-dimensional (1D) semiconductor nanowires (NWs) received much attention due to their potential applications in a number of nanoscale optoelectronic devices, such as photodetectors [1], solar cells [2], optical switches and modulators [3]. In particular, the NWs with engineered materials, size, and morphology can support distinctive structural resonances, which offers the possibility to control the optical properties of semiconductor materials [4]. It has been demonstrated that plasmonic nanoantennas and arrays can strongly concentrate and increase light absorption over engineered nanoscale spatial domains and spectral bandwidth. Here, bowtie plasmonic antennas are designed to enhance a broadband absorption in red-green-blue multiple spectral regimes in a zinc telluride (ZnTe)/zinc oxide (ZnO) core/shell nanowire structure. With a single-bowtie antenna, the absorption could be enhanced by 1.2 and 1.8 times at the wavelengths of 550 nm (2.25eV) and 680 nm (1.8eV) due to the excitation of plasmonic resonances, and it could be further improved to 1.5 and 2.7 times if using a triple-bowtie antenna. The plasmonic resonance at 1.8eV is exactly corresponding to the optical transition from valence band to intermediate band induced by O-doping in ZnTe mateials, and thus this provide an effective way to enable the absorption of the low-energy photons and thus improve the opto-electronic conversion efficiency of the final solar cells.

**Acknowledgements** This research was supported by National Natural Science Foundation of China (Nos. 61274058 and 61322403), the Natural Science Foundation of Jiangsu Province (Nos. BK2011437 and BK20130013), the Six Talent Peaks Project in Jiangsu Province (2014XXRJ001).

**REFERENCES**

1. Soci, C., Zhang, A., and Xiang, B. *Nano Lett.*, Vol.7, No.4, 1003-1009, 2007.
2. Tsakalakos, L., Balch, J., Fronheiser, J., and Korevaar, B.A., *Appl. Phys. Lett.* Vol 91, 233117, 2007.
3. Krogstrup, P. et al. *Nat. Photon.* Vol 7, 306-310, 2013.
4. Casadei, A., Pecora, E.F., et al. *Nano Lett.*, Vol.14, No.5, 2271-2278, 2014.

# Optical and mechanical properties of chitosan-based interpenetrating polymer networks

**C. C. Ryan[1], M. Bardosova[1*], and M. E. Pemble[1]**

[1]Tyndall National Institute, University College Cork, Lee Maltings, Prospect Row, Cork, Ireland

[*]corresponding author: catherine.ryan@tyndall.ie

**Abstract** – Chitosan is a versatile polymer derived from the naturally-occurring polysaccharide chitin[1]. It is pH-sensitive due to its cationic polyelectrolyte structure- a characteristic of chitosan which is commonly utilized in applications. Due to instability in solution chitosan is generally cross-linked with separate chemical entities to form a stronger interpenetrating polymer network[2]. In the case of the work presented here tetraethylorthosilicate (TEOS) has used for cross-linking. We present here the results of our studies of the structural, mechanical and optical properties of various chitosan/ TEOS networks combined with nanostructured colloidal particles.

Chitosan-tetraethylorthosilicate interpenetrating polymer networks (Chi-TEOS IPNs) were formed by a solution polymerization technique. The structural and pH-sensitive properties of these IPNs were studied, varying chitosan molecular weight and TEOS cross-linker density. It was observed that swelling ability of the IPN increased with increasing chitosan molecular weight, as expected due to increasing chain length. Increasing TEOS cross-linker density resulted in an increase in mechanical strength of the membranes, causing the membranes to become brittle and break. Figure 1 shows the decreasing quality of the IPN with increasing cross-linker density.




Figure 1. 1:1, 1:2 and 1:3 LMWChi-TEOS IPNs respectively.

A composite structure consisting of a $SiO_2$ photonic crystal surrounded by the IPN was prepared by a drop-casting technique. The original photonic crystal was produced by controlled evaporation of monodisperse colloidal $SiO_2$ particles[3]. The resulting fcc structure was then infilled by the IPN hydrogel. Figure 2 displays a free-standing Chi-TEOS-$SiO_2$ composite. The swelling ability of the composite was studied together with optical analysis. Figure 2 shows a shift in Bragg diffracted wavelength as a function of pH[4].

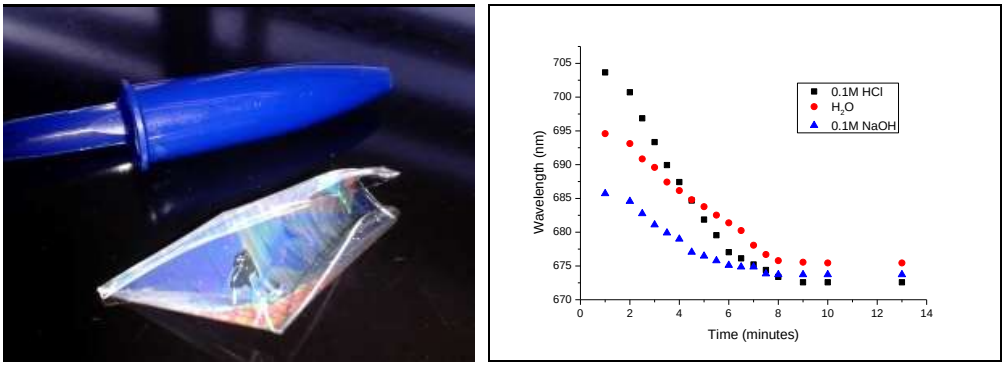



Figure 2. MMWChi-TEOS-$SiO_2$ composite constructed with particles of 312nm diameter and a graph of shift in Bragg diffracted wavelength as a function of pH.

Further tests were carried out on the mechanical properties of the IPNs to establish whether they could be enhanced by incorporating nanoparticles into the system. Colloids such as $SiO_2$ and polystyrene were tested using a surface grafting tecnique and also by completely incorporating particles into the network. Results from the different variables show that the tensile stength can be further enhanced by the presence of nanoparticles in the network and also that there is an increase in tensile strength as the particle size decreases, due to enhanced bonding interactions over a larger surface area. The tensile strength of the IPN is enhanced by a factor of 3 in the presence of 100nm colloidal particles, a factor of 2 in the presence of 250nm particles and a factor of 1.3 in the presence of particles > 500nm. These results are for networks with particles embedded throughout the system. The networks with surface grafting alone did not show enhanced mechanical effects.

Overall, the cross-linked Chi-TEOS IPN prepared provides a versatile polymer network which is both flexible and mechanically stable. A free-standing composite suitable for optical sensing of pH was developed by combining the IPN with a $SiO_2$ photonic crystal structure. The tests carried out on the mechanical properties of the IPNs show that the tensile strength can be enhanced up to three times by embedding colloidal $SiO_2$ or polystyrene nanoparticles in the IPN system.

**Acknowledgements** - The authors would like to extend gratitude to Science Foundation Ireland (PI Grant No. 11/PI/1117 and ISCA Grant No. 12/ISCA/2494) and the European Union's Seventh Framework Programme (FP7/2007-2013) under grant agreement n° FP7-IRSES-295182.

**REFERENCES**

1. Goosen, M. F., *Applications of Chitin and Chitosan*. CRC Press, 1996.
2. Leceta, I., P. Guerrero and K. de la Caba, "Functional properties of chitosan-based films",*Carbohydr. Polym.*, Vol. 93, No. 1, 339-346, 2013.
3. Jiang, P., J. Bertone, K. Hwang and V. Colvin, "Single-crystal colloidal multilayers of controlled thickness", *Chem. Mater.*, Vol. 11, No. 8, 2132-2140, 1999.
4. Ryan, C. C., J. Delezuk A. Pavinatto, O. Oliveira Jr., H. Fudouzi, M. Pemble and M. Bardosova, "Silica-based photonic crystals embedded in a chitosan-TEOS matrix: preparation, properties and proposed applications", *J. Mater. Sci.*, Vol. 51, No. 11, 5388–5396, 2016.

# Towards Single Antenna On-Chip Surface Enhanced Raman Spectroscopy: Arch Dipole Antenna

**A. Raza**[1,2*], **F. Peyskens**[1,2], **S. Clemmen**[1,2] **and R. Baets**[1,2]

[1]Photonics Research Group, INTEC Department, Ghent University-imec, Technologiepark-Zwijnaarde, 9052 Ghent, Belgium

[2]Center for Nano- and Biophotonics, Ghent University, Belgium.

[*]corresponding author: ali.raza@ugent.be

Plasmonic antennas have recently been combined to nanophotonic silicon nitride (SiN) waveguides for demonstrating all-on-chip Surface Enhanced Raman Spectroscopy (SERS). This achievement relied on bowtie antennas engineered to maximize the generated Raman signal. Here, we present numerical investigation of an arch dipole (AD) antenna identically patterned on a rib waveguide and compare it to the best engineered bowtie antenna. Our study shows a 23 fold improvement over the state of the art thus promising shorter integration time and high Signal-to-Noise Ratio which should ultimately enable the detection of on-chip SERS signals originating from a single antenna.

Plasmonic nanostructures have attracted a lot of attention in recent years because of their remarkable ability to enhance dipole excitation and emission near their hotspots. To avoid large and expensive free same optics for excitation and collection of the Raman signal, a great deal of research is going on to integrate plasmonic nanostructures with other nano/micro technologies [1,2]. Recently [3], our group demonstrated indeed that bowtie plasmonic antennas could couple efficiently to a silicon nitride waveguide so that the Raman spectrum of a thin layer of 4-Nitrothiophenol (NTP) was recorded by excitation and collection within the nanophotonic chip. For an antenna gap of 48 nm, pump to Stokes signal conversion efficiency (η) was reported as $2.19 \times 10^{-15}$. This means that for 1W pump power, 2.19 fW Stokes power from NTP molecules will couple back into the waveguide. Due to the relatively low efficiency, long integration time and several antennas were required to detect weak Raman signal. Arch dipole (AD) antennas on other hand were shown to exhibit higher SERS enhancements as compared to more simple antennas [4]. In this work, we numerically analyze the same arch dipole (AD) antennas integrated on a single mode SiN rib waveguide and shows that they provide 23 times higher conversion efficiency as compared to the recently published bowtie for the same gap dimension. An enhancement by this factor reduces the integration time and the required number of antennas to just one.

The schematic of the AD is shown in Fig.1. In this work numerical simulations are performed with Lumerical FDTD Solutions. We consider a SiN rib waveguide with refractive index of 1.89 at 785 nm wavelength and a geometry of 700 × 220 nm$^2$ supporting a single TE mode. The waveguide is surrounded by a bottom silica cladding, a top air cladding and the AD antenna. A 1 nm thin NTP layer with refractive index of 3 is also defined at the surface of AD [3] and constitutes the Raman medium under investigation. The figure of merit (FOM) for on-chip SERS which incorporates pump to Stokes conversion efficiency as well as the extinction induced by the antenna at pump and Stokes wavelength is defined [3] as $FOM = \eta \times e_s^{1-N} \times (1-t^N)/(1-t)$, where $t = e_s/e_p$, N is number of antennas, $e_s$ and $e_p$ are linear extinctions at $\lambda_s$ and $\lambda_p$ respectively. The FOM reaches a maximum at an optimum number of antennas $N_{opt} = log(log(e_s)/log(e_p))/log(e_s/e_p)$.

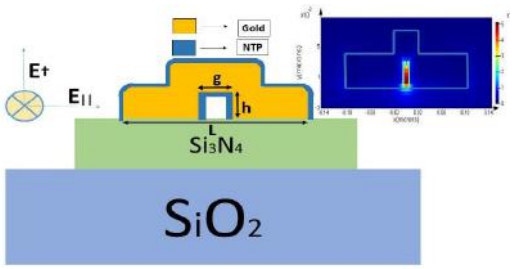



Fig. 1. Schematic of AD antenna on a SiN waveguide. The inset shows the field distribution in the arch.

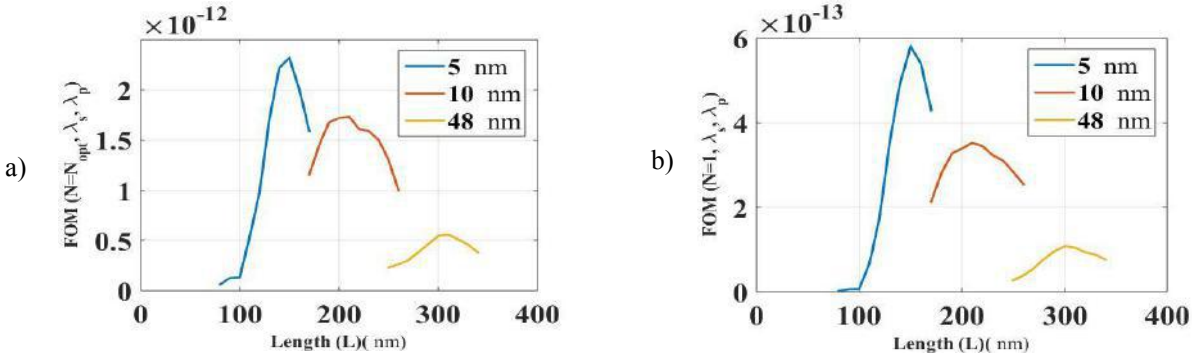



Fig. 2. FOM for on-chip AD antennas as a function of length for an arch height h=30 nm, longitudinal width=30nm (along the propagation direction) and gap of 48 nm. (a) FOM evaluated at $N_{opt}$ and (b) N=1

The *FOM* evaluated at $N_{opt}$, for an AD antenna for different gaps and lengths is shown in Fig. 2(a). The *FOM* for smaller gaps changes abruptly with length owing to the large plasmon resonance sensitivity to length variations. Increasing the gap from 5 nm to 48 nm reduces the *FOM* just by a factor of 4. This is attributed to the fact that the *FOM* incorporates an average Raman enhancement which is less sensitive to the antenna gap.

For an on-chip BT antenna with 48 nm gap coated with a 1nm NTP layer and with 2 nm Ti adhesive layer, a single antenna conversion efficiency ($\eta_{BT}$) of $2.19\times10^{-15}$ is reported in [3]. By using same simulation parameters, it has been noticed that $\eta_{BT}$ for a bowtie antenna (gap=48 nm) without Ti layer improves by a factor of 2.2 i.e. $\eta_{BT} = 4.82 \times10^{-15}$. A single antenna conversion efficiency for AD antennas is shown in Fig. 2(b). Hence, for a gap of 48 nm without Ti layer, $\eta_{AD} \approx 23\times\eta_{BT}$. The increased enhancement is attributed to the dense population of charges along the side walls which is expected to lead to a better localization of the electric field inside the nano-arch. An enhancement by this factor should capacitate low integration time, high Signal-to-Noise Ratio and eventually enable detection of SERS signals using single antenna.

The authors acknowledge FWO and ERC-InSpectra for financial support.

**REFERENCES**

1. Peyskens, F., et al. “Bright and dark plasmon resonances of nanoplasmonic antennas evanescently coupled with silicon nitride waveguides,” *Opt. Express*, Vol. 23, No. 3, 3088–3101, 2015.
2. Measor, P., et al. “On-chip surface-enhanced Raman scattering detection using integrated liquid-core waveguides,” Appl. Phys. Lett. 90, 211107-1U-211107-3, 2007.
3. Peyskens, F., et al. “Surface enhanced Raman spectroscopy using a single mode nanophotonic-plasmonic platform,” *ACS Photonics*, Vol. 3, No. 1, 102–108, 2016.
4. Seok, T. J., et al. “Mass producible and efficient optical antennas with CMOS-fabricated nanometer-scale gap,” *Opt. Express*, Vol. 21, No. 14, 16561–16569, 2013.

# Synthesis of ZnO Nanoparticles and their Application in Quantum Dot Light Emitting Diodes

**Jiangyong Pan[1], Jing Chen[1*], Yuning Zhang[1], Qianqian Huang[1], Yan Tu, Chao He[2], Kaifeng Zhou[2] Wei Lei[1*]**

[1] School of Electronic Science and Engineering, Southeast University, Nanjing, 210096, China
[2] Shenzhen China Star Optoelectronics Technology Co., Ltd, ShenZhen 518132

*corresponding author, E-mail: chenjing@seu.edu.cn; lw@seu.edu.cn

## Abstract

In this paper, the ZnO nanoparticles (NPs) has been synthesized by sol-gel method and used as electron transport layer (ETL) in quantum dot light emitting diode (QLED). The effect of solvent types and film thickness of ZnO NPs on QLED performance has been studied. It has been found that the optimal solvent and thickness of ZnO NPs is butanol and 35 nm, respectively.

## 1. Introduction

Quantum dot LEDs (QLEDs) have been attracting much attention in the past few years since they possess unique properties of the tunable emission wavelengths by controlling the size of QDs, highly saturated emission, narrow emission with small full width at half maxima (FWHM), solution process, and compatible with flexible substrates. After about two decades of research and development, QLEDs are reaching the performance of organic LEDs (OLEDs) and emerging as a candidate for single-material, full-color light sources. It is noted that in the past few years, much effort has been made to improve the efficiency of QLEDs by optimization of the active materials and the employment of novel structures.[1-4]

In this paper, the ZnO nanoparticles (NPs) has been synthesized by sol-gel method and used as electron transport layer (ETL) in QLED. The effect of solvent types and film thickness of ZnO NPs on QLED performance has been studied. It has been found that the best solvent and thickness of ZnO NPs is butanol and 35 nm respectively.

## 2. Method

The ZnO NPs were synthesized through a solution-precipitation process using Zn acetate and tetramethylammonium hydroxide (TMAH) precursors. The reaction process proceeds as follows: a solution of 0.5 M TMAH in ethanol and a solution of 0.1 M zinc acetate in dimethyl sulphoxide (DMSO) were mixed and stirred for 1 hour in an ambient atmosphere. The prepared product was collected by centrifugation and then washed. The obtained transparent precipitate was dispersed in butanol at a concentration of 30 mg/ml.

The QLEDs were fabricated on glass substrates covered with indium tin oxide (ITO). The substrates were first cleaned with de-ionized water, acetone and iso-propanol, consecutively, for 15 min each, and then treated with ultraviolet light generated ozone for half an hour to increase the work function and modify the surface energy of the ITO. Poly(ethylenedioxythiophene):poly styrenesulphonate (PEDOT:PSS) solutions were spin-coated onto the ITO substrates at 5000 rpm for 30 s and baked at 120°C for 20 min under ambient conditions. The PEDOT:PSS-coated substrates were transferred into a nitrogen-filled glove box (O2< 0.1 ppm, H2O < 0.1 ppm) for spin-coating of the sequential layers. The TFB used as the hole transport layer (1 wt% in chlorobenzene) was spin-coated at 2500 rpm for 30 s, followed by baking at 110°C for 30 min. After that, QDs (10 mg/ml in toluene) were layered at 800 rpm for 30 s followed by baking at 120°C for 15 min. Then the ZnO NPs (30 mg/ml in different solvent) were spin coated at 4000 rpm for 30 s and baked at 120°C. The thicknesses of the PEDOT:PSS, TFB, ZnCdSeS QD and ZnO NPs are 30 nm, 30 nm, 28 nm, and 35 nm, respectively. Finally, the top Al cathode was deposited in a custom high-vacuum deposition chamber (background pressure, 6*10-4 torr) with an active device area of 4 mm2.

## 3. Discussion

The structure and schematic energy band diagram of the QLED are shown in Fig. 1(a) and (b), respectively. Here, the multilayer device consists of layers of ITO/PEDOT:PSS / TFB/ZnCdSeS QD /ZnO NPs /Al, in which PEDOT:PSS was used as the hole injection layer (HIL), TFB as the hole transport layer (HTL), ZnCdSeS QD as the emission layer (EML), and ZnO NPs as the electron transport layer (ETL).

According to Fig. 1(b), the small conduction band offset and large valence band offset at the QD/ZnO nanoparticle interface stems from the ~4.3 eV electron affinity and ~7.6 eV ionization potential of ZnO NPs. Thus, the ZnO NPs layer not only facilitates efficient electron injection from the Al cathode into QDs, but also prevents leakage of holes to the adjacent ZnO NPs layer. This confines the excitation-recombination region, thereby improving charge recombination efficiency.

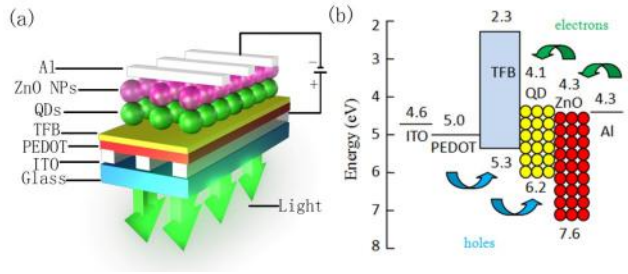



Fig. 1 (a) Structure and (b) energy level diagram for the various layers of the QLED

### 3.1. Influence of solvent types

To illustrate the effect of solvent type on the wetting ability of ZnO NPs on QD layer, we measured the contact angles of the ZnO NPs with different solvent (butanol, methanol, ethanol and isopropanol) on the QD surface. The results are displayed in Table 1, and the images of the drops of ZnO NPs on the QD surface are shown in Figure 2 for (a) butanol, (b) methanol, (c) ethanol and (d) isopropanol. These results indicate that the wetting of the ZnO NPs with the solvent of butanol on the surface of QD is the best.

Table 1. Contact angle data for ZnO NPs with various solvent on QDs layer

| The solvent of ZnO NPs | Left contact angle (deg) | right contact angle (deg) | average contact angle (deg) |
|---|---|---|---|
| butanol | 7.92 | 7.92 | 7.92 |
| methanol | 16.25 | 16.25 | 16.25 |
| ethanol | 22.34 | 22.34 | 22.34 |
| isopropanol | 15.01 | 15.01 | 15.01 |

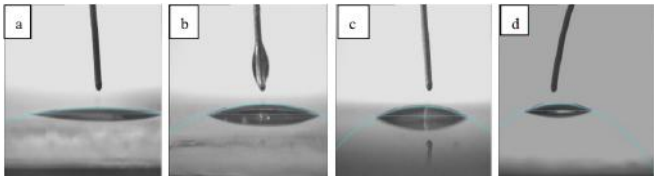



Fig. 2 Contact angle images of ZnO NPs on QDs layer with the solvent of (a) butanol, (b) methanol, (c) ethanol, and (d) isopropanol.

### 3.2. Influence of thickness

It is noted that the device performance show a strong dependence on the thickness of the ZnO nanoparticle layer. Because the thickness of ZnO NPs has a great impact on the electron injection of device, influencing the charge balance of device further.[5] To verify the effect of ZnO NPs thickness on the electronic properties of QLED device, the current density versus voltage, luminance versus driving voltage, current efficiency and power efficiency were displayed in Fig. 3. It can be found from Fig. 3(a) that the current density is the largest of ZnO layer with the thickness

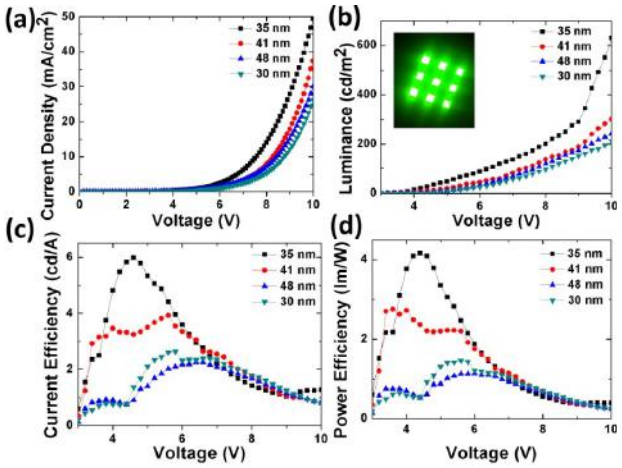



Fig. 3 Electroluminescence performance of QLEDs with different thickness of ZnO NPs. (a) Current density versus driving voltage; (b) luminance versus driving voltage. Inset shows the real photo of working QLED ; (c) current efficiency and (d) power efficiency versus driving voltage

of 35 nm, which indicates that the charge transport is optimal on this occasion. Fig. 3 (b) shows the luminance versus driving voltage characteristic of QLED with different thickness of ZnO NPs. It is displayed that the luminance of device with 35 nm-thick ZnO increases most fast with voltage and reaches the largest value at last. Fig. 3(c) and 3(d) show the characteristic of current efficiency-current density and power efficiency-current density, respectively. It is obvious that the current efficiency and power efficiency of device with 35 nm-thick ZnO NPs increases remarkably compared to the device based on the other thickness of ZnO, reaching 5.99 cd/A and 4.16 lm/W, respectively.

## 4. Conclusions

According to the experiment above, it is found that both of the solvent of ZnO NPs and the thickness of ZnO NPs layer have the great impact on the performance of QLED, by influencing the wetting ability between ZnO NPs and the under layer, as well as the thickness of ZnO NPs leading to the different internal electric field. By comparison among the experiments, it can be concluded that the performance of QLED can be largely improved by using of butanol solvent and the optimized ZnO NPs thickness of 35 nm.

## Acknowledgements

This work was supported partially by the National Key Basic Research Program 973 (2013CB328804, 2013CB328803), the National High-Tech R&D Program 863 of China (2012AA03A302, 2013AA011004), National Natural Science Foundation Project (51120125001, 61271053, 61306140, 61405033, 91333118, 61372030, and 61307077), Natural Science Foundation Project of Jiangsu Province (BK20141390, BK20130629, and BK20130618), Jiangsu College Graduate Research Innovation Program (3206006701, 3206006705) and Shenzhen China Star Optoelectronics Technology Co., Ltd.

## References


1. Anikeeva, P. O. *et al*. Electroluminescence from a mixed red-green-blue colloidal quantum dot monolayer. Nano Lett.7, 2196–2200 (2007).
2. Supran, G. J. *et al*. QLEDs for displays and solid-state lighting. MRS Bull. 38, 703–711 (2013)..
3. Mashford, B. S. *et al*. High-efficiency quantum-dot light-emitting devices with enhanced charge injection. Nature Photon. 7,407–412 (2013)
4. Cho, K. S. *et al*. High-performance crosslinked colloidal quantum-dot light emitting diodes. Nature Photon. 3,341–345 (2009)
5. Qian, L., Zheng, Y., Xue, J. & Holloway, P. H. Stable and efficient quantum-dot light-emitting diodes based on solution-processed multilayer structures.Nature Photon.5,543–548 (2011)

# Incorporation of graphene as the hole transfer layer for quantum dot light emitting diode

**Qianqian Huang[1], Jing Chen[1]*, Yuning Zhang[1] , Jiangyong Pan[1], Wei Lei[1]*, Chao He[2],Kaifeng Zhou[2]**

[1] School of Electronic Science and Engineering, Southeast University, Nanjing, China, 210096
[2] Shenzhen China Star Optoelectronics Technology Co., Ltd

*corresponding author, E-mail: chenjing@seu.edu.cn, lw@seu.edu.cn

## Abstract

We report a color-saturated, red quantum dot light-emitting diode (QLED) using graphene oxide doped PEDOT: PSS as the hole injection layer (HTL) to optimize the band offset between the HTL and emitting layers. The QLEDs show a maximum luminance of up to 4200 cd/m2, corresponding to 7.5 lm/W in power efficiency and turn on voltage of 1.9V. Overall, there is a six-fold enhancement in the performance of the QLED with graphene oxide due to the higher hole injection/transfer rate.

## 1. Introduction

Quantum dot LEDs (QD-LEDs) have been attracting much attention in the past few years since they possess unique properties of the tunable emission wavelengths by controlling the size of QDs, highly saturated emission, narrow emission with small full width at half maxima (FWHM), solution process, and compatible with flexible substrates[1-3]. Ever since the first demonstration of QD-LEDs, great efforts have been made to achieve better device performance, including seeking suitable charge transporting or injection materials and optimizing device structures. Peng et al. reported a solution-processed, multilayer quantum-dot-based LED with high external quantum efficiencies of up to 20.5 per cent, using bilayer-structured hole-transport interlayers to realize efficient hole injection into the quantum dot layers and the relatively high hole mobility of poly-TPD to achieve low turn-on voltage and high power efficiency[4]. Dai et al. tried deoxyribonucleic acid (DNA) complexed with cetyltrimetylammonium (CTMA) (DNACTMA) as a combined hole transporting and electron-blocking layer (HTL/EBL) to realize highly efficient QD-LEDs with a high color purity[5].

Due to its excellent thermal stability and can be cast on rigid or flexible substrate through solution process, Poly(3,4-ethylenedioxythiophene):poly(styrenesulfonate) (PEDOT:PSS) is a promising material for optoelectronic device applications[6]. On the other hand, graphene materials have attracted much attention due to their fascinating physical properties, such as quantum electronic transport, a tunable band gap and extremely high mobility[7-10]. The possibility of using hybrid nanocomposites to fabricate QD-LEDs suggests the feasibility of narrowing the energy barrier between the highest occupied molecular orbital (HOMO) of PEDOT:PSS and the conductive band (CB) of the QD.

In this work, we report on a low-voltage driven, red QD-LED by addition of graphene oxide (GO) into the hole injection layer. Due to the more favorable alignment of energy levels and higher carrier mobility, our device exhibits color-saturated, deep-red emission, along with a sub-gap turn-on of 1.9 volts, a maximum luminance of 4200 cd/m2 and power efficiency of 7.5 lm/W.

## 2. Experimental

### 2.1. Preparation of red ZnCdSeS QDs

ZnCdSeS QDs were synthesized according to a modified method reported previously [11]. Here, 1.0 mmol of CdO, 4 mmol of zinc acetate, 4 mmol of oleic acid (OA), and 20mL of 1-octadecne were mixed in a 100mL round flask. The mixture was heated to 150 °C in high-purity N2 flowing for 30 min, and further heated to 300 °C to form a clear solution of Cd(OA)2 and Zn(OA)2. At this temperature, a stock solution containing 3mL of trioctylphosphine, 1.0 mmol of Se, and 2.5 mmol of S was quickly injected into the reaction flask. After the injection, the reaction temperature was maintained for 10 min to promote the growth of QDs. The reaction was subsequently cooled down to room temperature to stop further growth. The QDs were washed with acetone three times, and finally dispersed in toluene at a concentration of 10 mg/ml.

### 2.2. Preparation of graphene oxide (GO)

GO was prepared from exfoliated graphite powder according to a modified Hummer's method [12]. Briefly, expandable graphite powder (2 g) and sodium nitrate (1 g) were added to sulfuric acid (46mL, 98 wt%) in sequence at a temperature of 0 °C. Following this, $KMnO_4$ (6 g) was gradually added to the mixture over a period of 1 h. Later, the mixture was transferred to an oil bath at a temperature of 35 °C for 8 h. Then, deionized water (DW, 92 mL) was gradually added to the mixture. At the same time, the temperature was increased to 98 °C for 15 min in order to increase the degree of oxidation of the GO products. Subsequently, it was further treated by adding DW (280 mL) and 30 wt% $H_2O_2$ (15mL). After this, the product was filtrated by 5wt% of HCl solution and washed for several times in water. Finally, the GO product was deposited by concentrating the as-synthesized product.

### 2.3. Device fabrication

ITO glass substrates with a sheet resistance of about 6–8*V*/square was cleaned by successive ultrasonic treatments in detergent, de-ionized water, acetone, and iso-propanol for 15 min, respectively, followed by UV-ozone treatment for half an hour. The graphene with concentration of 1wt% doped

into PEDOT:PSS (Baytron P VP AI4083) as hole injection layer (HIL), was spin coated onto the ITO-coated glass substrate (5000 rpm, 30 s), followed by baking at 150 °C for 15 min. Thereafter, TFB as the hole transport layer (HTL) was spin-coated at 2000 rpm, followed by annealing at 130 °C for 10 min. The emissive layer of colloidal ZnCdSeS QDs was spin-coated on the HTL (1000 rpm, 30 s) and annealed at 120 °C for 30min. Then $TiO_2$ solution was deposited on the layer of QDs (at 4000 rpm and 30 s) and annealed at 150 °C in air. Finally, a 100 nm aluminum (Al) electrode was thermally evaporated under high vacuum (4×10^-6 Torr) on top of the $TiO_2$ ETL, followed by post-annealing at 100 °C for 20 min.

Thin film transistor (TFT) structures were considered with fabrication process as follows:1-2 top-contact bottom-gate geometry was prepared on heavily doped Si substrates used as the common gate electrode with thermally grown 300 nm-thick $SiO_2$ gate dielectric layer (unit area capacitance: 11.5 nF cm-2). Then PEDOT-GO film were deposited on the $SiO_2$/Si substrates by spin-casting at a rate of 4000 rpm for 30 s. Patterned Al source-drain electrodes were thermally evaporated on top of the PEDOT-GO film through a shadow mask.

### 2.4. Material and device characterization

The current density–voltage (J–V) characteristics were measured with a Keithley-2400 source-meter. The absorption and photoluminescence (PL) spectra were measured by a U-4100 UV-visible and NIR-300 spectrophotometer, respectively.

## 3. Discussion

The schematics of our device structure and corresponding energy level diagram are shown in Fig. 1a and b. The device consists of a patterned ITO as the anode, graphene doped poly(ethylenedioxythiophene):polystyrene sulfonate (PEDOT-GO) as the HIL, poly[(9,9-dioctylfluorenyl-2,7-diyl)-co-(4,4- (N-(4-secbutylp-henyl))diphenylamine)] (TFB) layer as the HTL, ZnCdSeS QD as the emitting layer, $TiO_2$ layer as the ETL, and aluminum (Al) layer as the cathode. The $TiO_2$ layer not only provides efficient electron injection from the Al cathode into QDs, but also facilitates to confine holes within the QD layer due to the valence band offset. Overall, the QD-LED structure effectively blocks electrons and holes that pass through the QD layer, ensuring the charge recombination efficiency.

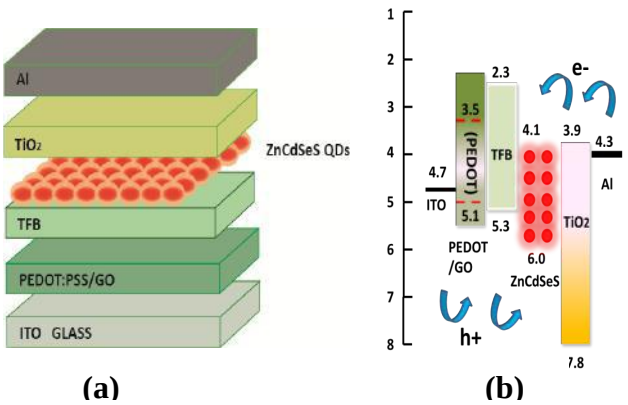



Figure 1. (a) Schematic of device structure and (b) corresponding energy band diagram of red QD-LED.

Figure 2 shows the absorption and photoluminescence (PL) spectra of ZnCdSeS QDs used in this study. The absorption spectrum clearly shows the first excitonic transition peak at 595 nm. The PL spectrum shows a

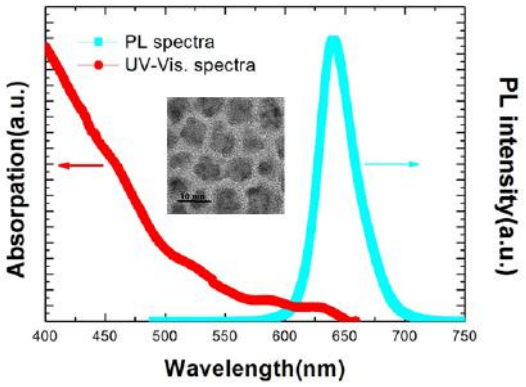



Figure 2. UV–Vis absorption and PL spectra of ZnCdSeS QDs dispersed in toluene.

Gaussian-shaped peak located at 640 nm with a narrow FWHM of 35 nm. The quantum yield (QY) of ZnCdSeS QDs can be calculated as 84%, using Rhodamine 6G as reference. The HRTEM image indicates that ZnCdSeS QDs were with an average diameter of 8 nm.

Figure 3 shows the current density–voltage (J–V) of the devices under forward bias. Compared to the QD-LED without graphene, the turn-on voltage is clearly reduced to

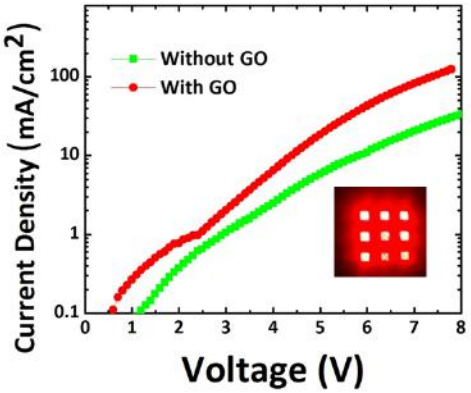



Figure 3. Current density as a function of driving voltage.

1.9V, which is primarily attributed to the reduced injection barrier for holes, leading to a balanced hole and electron transfer rate.

Figure 4 shows the brightness and power efficiency for driving voltages varying from 2 to 14V. A maximum brightness of 4200 cd/m$^2$ and power efficiency of 7.5 lm/W are achieved. This power efficiency constitutes a six fold

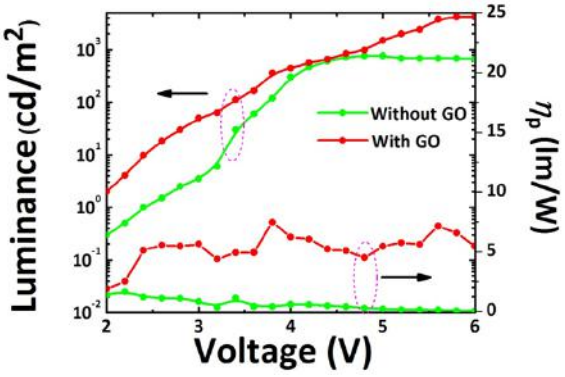



Figure 4. Luminance as a function of driving voltage and power efficiency as a function of driving voltage for samples with and without GO.

enhancement compared to that without GO, because of the balanced electron and hole injection coupled with the enhanced conductivity of PEDOT-GO.

To find out the mobility of the PEDOT-GO film , we fabricate a thin film transistor. As Figure 5 shows, the aspect ratio (ratio of channel width to length, W/L) of the TFT is 20.

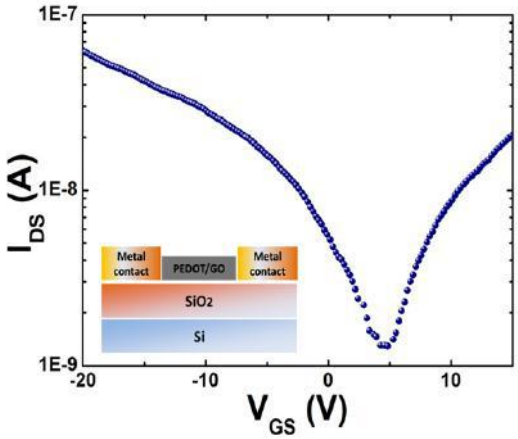



Figure 5. TFT characteristics of PEDOT-GO film. Inset shows TFT structure.

The equation for mobility calculation is as followed,

$$\mu = \frac{L}{V_d C_{ox} W} \frac{dI_d}{dV_g}$$

Where L and W are the device channel length and width, $V_d$=30 V, and $C_{ox}$ is the gate capacitance per unit area. The mobility of the PEDOT-GO film can be calculated as 0.04 cm2/Vs, which is much higher than that of pure PEDOT (0.0095 cm$^2$/Vs).

## 4. Conclusions

In this work, we demonstrated enhanced performance of QD-LED using PEDOT-GO as the hole injection/transfer layer. The turn-on voltage is as low as 1.9V,which is lower than the normal device. A maximum brightness of 4200 cd/ m2 and power efficiency of 7.5 lm/W are achieved. The technique can be extended to band gap engineer blue or white light QD-LED by doping graphene into the HTL.

## Acknowledgements

This work was supported partially by the National Key Basic Research Program 973 (2013CB328804, 2013CB328803), the National High-Tech R&D Program 863 of China (2012AA03A302, 2013AA011004), National Natural Science Foundation Project (51120125001, 61271053, 61306140, 61405033, 91333118, 61372030, and 61307077), Natural Science Foundation Project of Jiangsu Province (BK20141390, BK20130629, and BK20130618), Jiangsu College Graduate Research Innovation Program (3206006701, 3206006705) and Shenzhen China Star Optoelectronics Technology Co., Ltd.

## References

1. Coe S, Woo W K, Bawendi M, et al. Electroluminescence from single monolayers of nanocrystals in molecular organic devices[J]. Nature, 2002, 420(6917): 800-803.
2. Coe−Sullivan S, Steckel J S, Woo W K, et al. Large−Area Ordered Quantum−Dot Monolayers via Phase Separation During Spin−Casting[J]. Advanced Functional Materials, 2005, 15(7): 1117-1124.
3. Colvin V L, Schlamp M C, Alivisatos A P. Light-emitting diodes made from cadmium selenide nanocrystals and a semiconducting polymer[J]. Nature, 1994, 370(6488): 354-357.
4. Dai X, Zhang Z, Jin Y, et al. Solution-processed, high-performance light-emitting diodes based on quantum dots[J]. Nature, 2014, 515(7525): 96-99.
5. Sun Q, Subramanyam G, Dai L, et al. Highly Efficient Quantum-Dot Light-Emitting Diodes with DNA−CTMA as a Combined Hole-Transporting and Electron-Blocking Layer[J]. ACS nano, 2009, 3(3): 737-743.
6. Kim Y H, Sachse C, Machala M L, et al. Highly conductive PEDOT: PSS electrode with optimized solvent and thermal post−treatment for ITO−free organic solar cells[J]. Advanced Functional Materials, 2011, 21(6): 1076-1081.
7. Novoselov K S A, Geim A K, Morozov S V, et al. Two-dimensional gas of massless Dirac fermions in graphene[J]. nature, 2005, 438(7065): 197-200.
8. Zhang Y, Tan Y W, Stormer H L, et al. Experimental observation of the quantum Hall effect and Berry's phase in graphene[J]. Nature, 2005, 438(7065): 201-204.
9. Novoselov K S, Geim A K, Morozov S V, et al. Electric field effect in atomically thin carbon films[J]. science, 2004, 306(5696): 666-669.
10. Lee C, Wei X, Kysar J W, et al. Measurement of the elastic properties and intrinsic strength of monolayer

graphene[J]. science, 2008, 321(5887): 385-388.
11. Bae W K, Char K, Hur H, et al. Single-step synthesis of quantum dots with chemical composition gradients[J]. Chemistry of Materials, 2008, 20(2): 531-539.
12. Hummers Jr W S, Offeman R E. Preparation of graphitic oxide[J]. Journal of the American Chemical Society, 1958, 80(6): 1339-1339.

# Metamaterial structures for healthcare applications

# Microwave Devices for Theranostic Applications

**M. Puentes[1*], C. Reimann[1], M. Schüßler[1] and R. Jakoby[1]**

[1] Institute of Microwave Engineering and Photonics, Technische Universität Darmstadt
Merckstrasse 25, 64283 Darmstadt, Germany.

[*]corresponding author: puentes@imp.tu-darmstadt.de

**Abstract**- The evolution from a large demonstrator into a minimal invasive microwave device for theranostic applications in healthcare environments is presented. The sensor element is based on microstrip/coplanar excited SRR. The initial prototypes were bulky and could only detect the dielectric properties of organic tissue. Extensive work was done to reduce the size and its packaging to include them in a minimal invasive tool and create a second operation mode where the tissue could also be ablated with the same device.

In any process, it is desired to streamline its execution, reduce costs and increase performance. Healthcare processes are no different and the trend is to give patients a custom made treatment. To achieve this goal electromagnetic devices in life sciences have gained a lot of interest in the past years. Therefore, metamaterial sensor elements at micro-, millimeter- and THz waves are very promising because of the combination of high sensitivity, good penetration and spatial resolution as well as marker- and reactionless operation. For example, a cancer diagnosis can be made due to the difference between healthy and malignant tissue in terms of its water content and consequently its dielectric properties. In addition, electromagnetic sensor-based methods can also be used for treatment using a different operation mode. For example, in the eradication of cancer by a thermal ablation procedure, sensor and applicator are based on identical electromagnetic interaction principles and can therefore be combined in a single theranostic instrument. The theranostic instrument can deliver the right therapy for a specific patient at a specific point in time. As a result, state of the art devices that can perform diagnosis, treatment or both with great advantages over classical methods are explored with great interest and will be possibly available in the next years. Some of these advantages are minimal invasive procedures, reduction of risk for the patient and secondary surgeries, faster recovery time and lower costs. In this paper, it is shown the evolution of such a device. The principle of operation is depicted in Fig. 1 where the two modes can be selected with the frequency and input power. In Fig. 2 the diagnostic mode is depicted with the change of the resonance frequencies of the SRRs when loaded with tissue. The actual prototypes from its initial demonstrator created in 2011 to the minimal invasive tool in 2016 are seen in Fig. 3. Finally the thermal ablation treatment mode is shown in Fig.4.

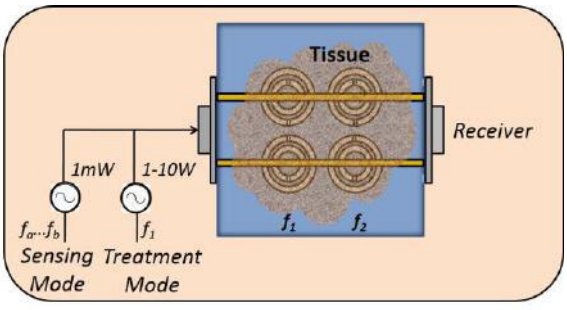



Fig. 1 Theranostic principle of operation for the minimal invasive microwave applicator.

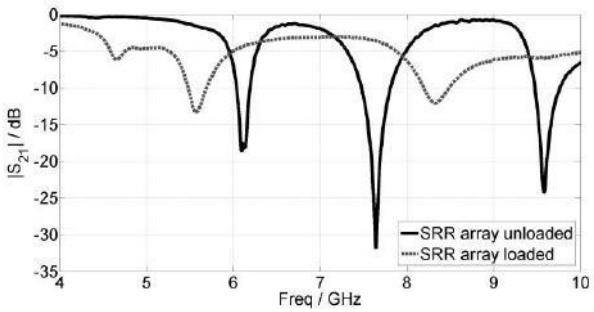



Fig.2 Diagnostic Mode: The dielectric loading of the tissue shifts the resonance frequencies of the SRRs [1].

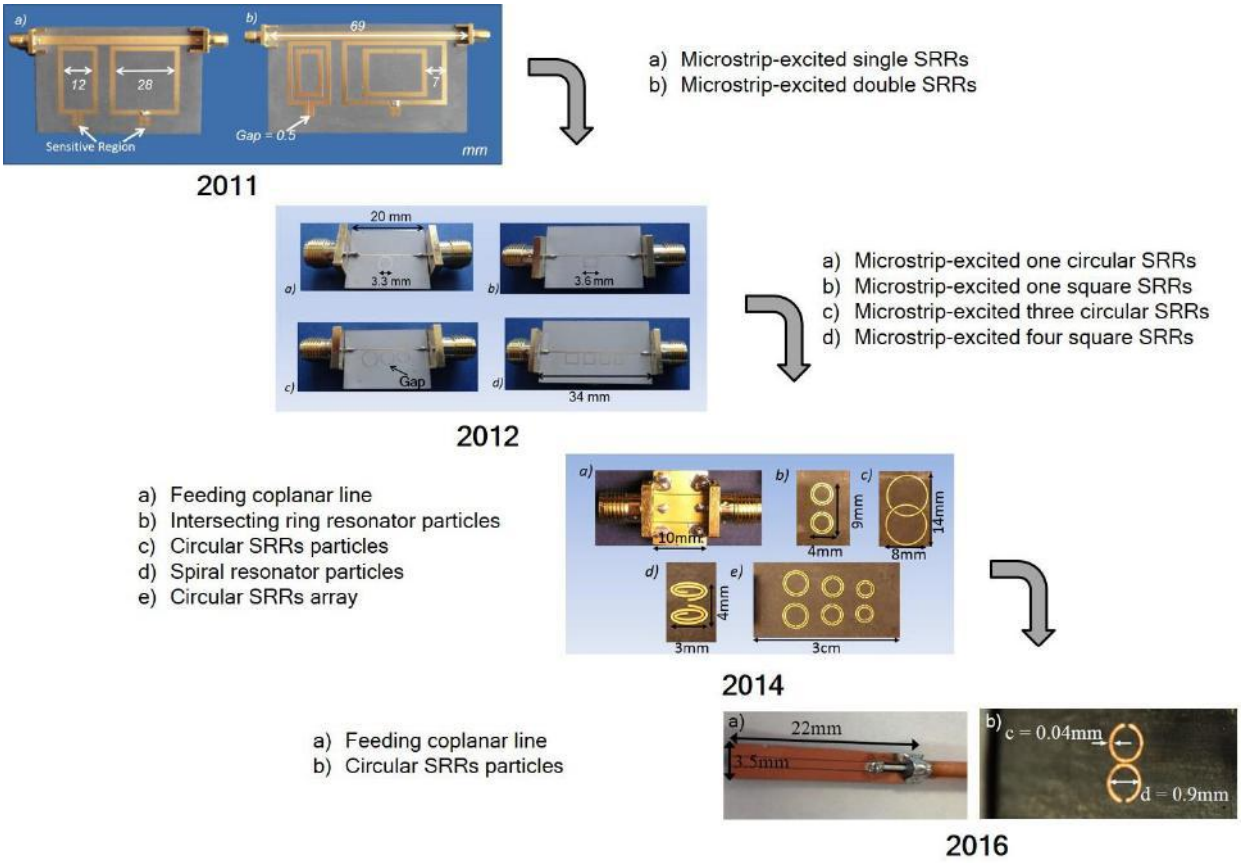



Fig. 3 Evolution from a large demonstrator into a minimal invasive microwave device for theranostic applications in healthcare environments [1,2,3].

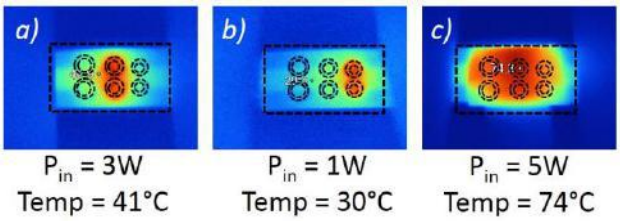



Fig. 4 Treatment Mode. With a low power is reached the appropriate temperature to perform thermal ablation treatment. The heat can also be focus on a single SRR pair [1].

**REFERENCES**


1. Puentes, M., Maasch, M., Schüßler, M., Damm, C. and Jakoby, R., "Analysis of Resonant Particles in a Coplanar Microwave Sensor Array for Thermal Ablation of Organic Tissue," *International Microwave Symposium*. Tampa Bay, Florida, USA. June 2014.
2. Puentes, M., Maasch, M., Schüßler, M., and Jakoby, R., "Frequency multiplexed2-dimensional sensor array based on split-ring resonators for organic tissue analysis*," IEEE Transactions on Microwave Theory and Techniques*, Vol 60, Issue 6, pp: 1720 – 1727, June 2012.
3. Reimann, C., Puentes, M., Huebner, F., Bazrafshan, B., Vogl, T. and Jakoby, R., "Design and Realization of a Microwave Applicator for Diagnosis and Thermal Ablation Treatment of Cancerous Tissue", *German Microwave Conference*. Bochum, Germany. March 2016.

# Large-Scale Metamaterial Anti-Reflection Coating for Biological Tissues at 60 GHz

**H. Cano-García[1, 2*], S. Saha[1], P. Kosmas[2], and E. Kallos[1, 3]**
[1]Medical Wireless Sensing Ltd., United Kingdom
[2]King's College London, United Kingdom
[3]Metamaterial Technologies Inc., Canada
[*]corresponding author: helena.cano_garcia@kcl.ac.uk

**Abstract**-While metamaterials are usually designed assuming plane wave excitation, in practice they are often placed closed to a finite source or an antenna. This paper presents simulation results of a large but finite metamaterial-based antireflection coating for biological tissues excited by a patch antenna working at 60 GHz. Additionally, the minimum number of metamaterial cells necessary to obtain similar performance as a unit cell (infinitely periodic) simulation is determined.

Most non-invasive biomedical applications face a major impedance mismatch problem in the interaction between the electromagnetic (EM) radiation and the human tissue, which is due to the high value of relative permittivity and conductivity of the skin compared to air. Previous work by the authors has proposed using metamaterials-based antireflection coatings to address this problem [1, 2]. The work in [1] presents a metamaterial unit cell designed to work at 60 GHz and in contact with lossy skin. The metamaterial design of [1] consisted of a Jerusalem cross and a regular cross made out of perfect electric conductor material, both of them separated by an Ultralam 3850 substrate and covered on either side with a thin layer made of the same material. This design was similar to the structure presented in [3], and under plane wave incidence achieved a reduction in the reflected power by 39% (from 39% to 0.16% relative to the input power), and an increase in the transmitted power by 1.8% (from 4.5% to 6.3%).

The main motivation for this antireflection coating design has been to enhance the resolution of a non-invasive glucose sensor working at millimeter waves, where the metamaterial will be excited using patch antennas (1.5 x 1.5 mm in size) operating at 60 GHz. It is therefore essential to determine the performance of our previously proposed design [1] for a more realistic scenario where EM radiation is due to a patch antenna instead of plane waves.

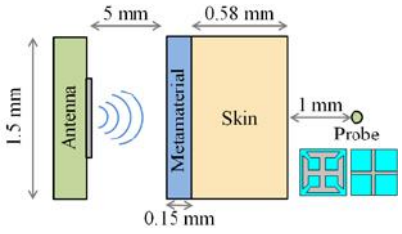



Figure 1. Schematic of the setup. A patch antenna is used as an excitation source. This figure also shows the location of the electric probe. On the corner of the figure, under the probe, there is the front and back view of the metal crosses that are part of the metamaterial design.

The antireflection coating metamaterial consists of a transversely repeating pattern of a multilayer metallodielectric unit cell, as designed in [1] for plane wave excitation. As a first step, we determine the minimum number of unit cells necessary for a finite metamaterial to resemble the performance of the infinitely periodic metamaterial under plane wave excitation. A set of full wave simulations consisting of metamaterial cells of varying extend and open boundary conditions were performed. The electric field results were collected using a

dielectric probe located after the skin slab (see Figure 1).

To quantify the performance of the metamaterials, two simulations were run for each case: I) metamaterial and skin, II) only skin. From these two simulations the relative power changes at the probe location were calculated to determine the effect produced by the metamaterial when it is added in front of the tissue. Three different metamaterial sizes were simulated: 10x10, 20x20 and 30x30 unit cells. These were compared with a 1x1 unit cell simulation (0.7 mm x 0.7 mm).

Figure 2a shows that there is a relative increase in the power transmitted at 60 GHz when the metamaterial is added, as designed. This relative increase in transmission appears because of the antireflection effect produced at this frequency. The results shown that the 30x30 structure presents only 1.4% relative error in the metamaterial performance at 60 GHz compared to the 1x1 unit cell structure. The other two large structures, 10x10 and 20x20 unit cells, present larger errors, 168.2% and 51.2% respectively. Therefore, a 30x30 unit cells metamaterial is going to be used for the simulations that use a patch antenna as excitation source.

Subsequently, the 30x30 unit cell metamaterial was simulated using a patch antenna as an excitation source, placed 5 mm away from the first metamaterial interface. Figure 2b presents the obtained results at the probe location. These results showed that a 39% relative power increase in transmission is also achieved around 60 GHz when using antennas.

These results suggest that a 30x30 unit cell metamaterial produces reflections and transmissions enhancements that are comparable to the performance of an infinite cell structure in front of plane waves.

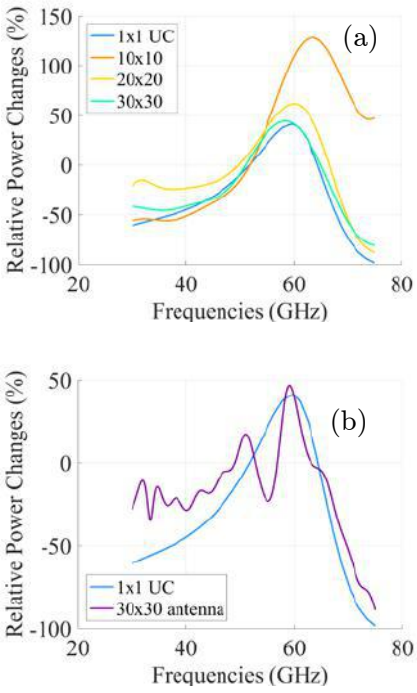



Figure 2. (a) Relative power changes at the probe location for four different metamaterial sizes: 1x1, 10x10, 20x20 and 30x30 unit cells excited by plane wave. The 1x1 unit cell simulation was performed using infinitely periodic boundary conditions. The 10x10, 20x20 and 30x30 simulations were performed using open boundary. (b)Relative power changes at the probe location for two different simulations, the infinite periodic unit cell structure of (a) and the 30x30unti cells structure excited by a patch antenna.

## REFERENCES


1. Cano-Garcia, H., Kosmas, P. and Kallos, E. "Metamaterial Antireflection Coating for Biological Tissues at Millimeter Waves", in META'15 6th International Conference on Metamaterials, Photonic Crystals and Plasmonics, New York, USA, August 2015.
2. Cano-Garcia, H., Kosmas, P. and Kallos, E. "Enhancing electromagnetic transmission through biological tissues at millimeter waves using subwavelength metamaterial antireflection coatings," in 9th International Congress on Advanced Electromagnetic Materials in Microwaves and Optics (METAMATERIALS), 2015, Oxford, UK, Sept. 2015, pp.43-45.
3. Chen, H.-T., J. Zhou, J. F. O'Hara, F. Chen, A. K. Azad, and A. J. Taylor, "Antireflection Coating Using Metamaterials and Identification of Its Mechanism," Physical Review Letters, Vol. 105, No. 7, 073901, 2010.

# A NOVEL MICROWAVE IMAGE SLICES TECHNIQUE FOR EARLY BREAST TUMORS DETECTION BASED ON METALENSES

**Mazhar B. Tayel** [1], **Mohamed I. Badwai** [2], **Heba Tallah A. Hasan**[3*]

[1]Electrical Department, Faculty of Engineering, Alexandria University, Egypt
[2] Medical equipment Department, Pharos University, Egypt
[3] Medical equipment Department, Pharos University , Egypt
[*]hebatallah.ali@pua.edu.eg

**Abstract**-Microwave imaging (MWI) is an attractive alternative technique for mamograph breast imaging. The procedures are comfortable, and the clinical system cost is a small fraction of the Magnetic resonance imaging (MRI), making it affordable for widespread screening. The procedures offer no hazards and the potential is significant for detecting very small tumors in early stages of cancer progress . The proposed configurations consist of 40 metamaterial array lenses, each array consist of 20 split ring resonator (SRR).Total of 800 SRR used to illuminate a proposed cylindrical breast model. To effectively test this configuration, a Finite-element Time-Domain (FETD) adaptive analysis is considered and is used to simulate the refocused backscattered microwave. The proposed system showed that tumors, as small as 2 mm in breast model, can be clearly detected. The modeling and simulation was performed in CST STUDIO SUITE electromagnetic simulation software.

## 1. INTRODUCTION

Breast cancer become one of the most common cancers in women and recently in men. Fortunately, early detection and treatment can significantly improve the survival rate. Ultrasound, mammography and magnetic resonance imaging (MRI) are currently used clinically for breast cancer diagnosis [1]. However, these techniques have many limitations, such as high rate of missed detections, ionizing radiation (mamography), too expensive to be widely available, and so on. Compared with conventional mammography, microwave imaging of breast tumors is a nonionizing, potentially low-cost, comfortable and safe alternative [2]. The motivation for developing microwave (MW) imaging technique for detecting breast cancer is the significant change in contrast between normal vs. malignant breast tissue and the reduction of patient exposure rate to X-ray doses [3, 4]. The microwave breast tumor detection also has the potential to be both sensitive and specific, to detect small tumors, and to be less expensive than methods such as MRI.

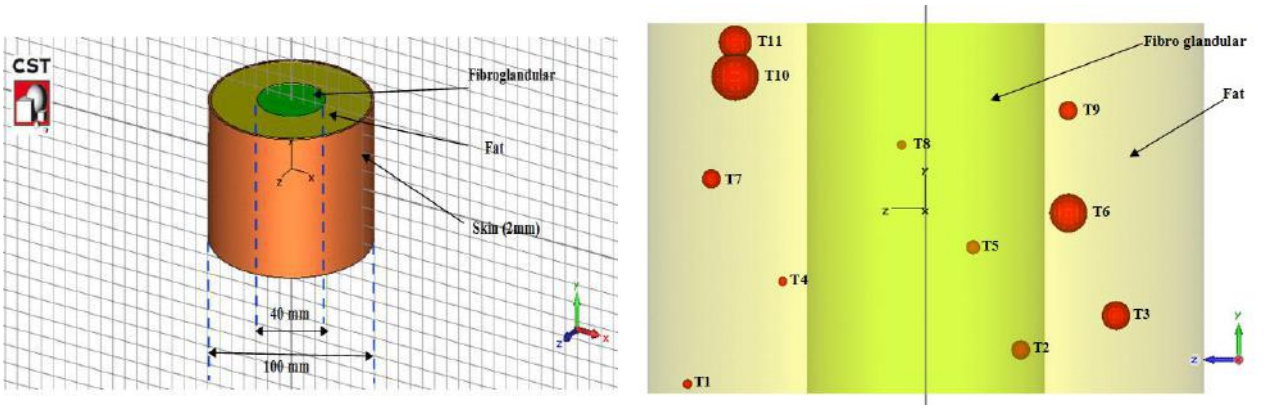
## 3. MICROWAVE IMAGING ADVANTAGES

MW is electromagnetic waves with frequencies ranging from 300 MHz up to 30 GHz. The breast can easily be radiated from outside and is translucent to MW in this regime, up to a certain degree.
MW radiation, as used in the screening process, contains insufficient energy to directly change biological tissue by ionization or similar effects, and consequently, is a very harmless radiation. Most of the studies conclude that it is perfectly safe for the human health [1,4].
In response to the increasing interest in microwaves for breast cancer detection, new studies have been prepared and published recently containing and analyzing the breast data of a large group of patients [5-7]. The result of this work is that the contrast between the healthy and tumors tissue is lower than it was reported in earlier studies. In particular, the contrast in dielectric properties is less significant for breasts with higher content of dense fibroglandular tissue. Nevertheless, a majority of breasts can be classified as mostly 'fatty' (fatty tissue is from 3 up to 10 times less dense than fibbroglandular tissue), with approximately 70% of fatty and 30% of fibbroglandular tissue [9]. This important circumstance supports that in a majority of the cases, the possibility of the successful detection of very small tumors via microwave imaging exists.

## 3. BREAST AND TUMOR CONFIGURATION AND DIELECTRIC PROPERTIES

Knowing the dielectric properties of breast tissues and malignant tumors in the MW frequency range is necessary. Most of the reported studies found that there is a large change in contrast between normal and malignant breast tissues [9,10]. Water content level plays the major role in the value of dielectric properties

of tissue. Low water content tissues (such as fat) have lower conductivity and permittivity values. A large scale study of breast tissue dielectric properties revealed that the dielectric contrast is as large as 10:1 between malignant and normal fat breast tissues. The normal breast has a complex tree-like architecture, composed of fibroglandular and fatty tissues, surrounded by skin layer. Figure (1) illustrates a proposed cylindrical breast model (PCBM). Table (1) presents the main parameters of the PCBM [12-14], while table (2) shows the locations of introduced 11 tumors.




**(a):** 3D view of the PCBM. **(b):** Location of 11 tumors in a breast model side view.

**Figure 1**: The proposed cylindrical breast model (PCBM).

**Table 1:** The parameters of the PCBM layers.

| Parameter / Layer | Conductivity $\sigma$ (S/m) | Permittivity $\varepsilon_r$(F/m) | Layer Dimension (mm) |
|---|---|---|---|
| Skin | 1.49 | 37.9 | 2 |
| Fat | 0.7 | 10 | 100 |
| Tumor | 1.20 | 43 | table.2 |
| Fibroglandular | 1.18 | 39 | 40 |

**Table 2:** Introduced tumor locations in the PCBM layers.

| Parameters / Tumors | diameter (mm) | location in the PCBM (mm) | | | Breast layer |
|---|---|---|---|---|---|
| | | X | Y | Z | |
| T1 | 2 | 0 | -36 | 50 | Fat |
| T2 | 4 | 0 | -29 | -20 | Fibroglandular |
| T3 | 6 | 0 | -22 | -40 | Fat |
| T4 | 2 | 0 | -15 | 30 | Fat |
| T5 | 3 | 0 | -8 | -10 | Fibroglandular |
| T6 | 8 | 30 | -1 | -30 | Fat |
| T7 | 4 | -30 | 6 | 45 | Fat |
| T8 | 2 | 15 | 13 | 5 | Fibroglandular |
| T9 | 4 | -30 | 20 | -30 | Fat |
| T10 | 10 | 0 | 27 | 40 | Fat |
| T11 | 7 | 0 | 34 | 40 | Fat |

The proposed microwave imaging system is composed of two main structures, mainly an array antenna set and a left handed meta lenses set. From table.2 and figure 1.b, it is shown the presence of three tumors in the Fibroglandular layer of dimensions 2 and 3 mm , and eight tumors in the fat layer of dimensions 2 to 10 mm . The tumors T10 and T11 are inserted in order to evaluate the potential of detection.

## 4. PROTOTYPE MODEL STRUCTURE AND DESIGN

It is necessary to construct a microwave imaging system able to transmit/receive (TR-RX) the scattered microwaves at one or more antennas. The purpose of this article is to develop a (TR-RX) medical microwave imaging system suitable for breast-cancer detection.

### 4.1 ARRAY ANTENNA CONFIGURATION

Figure (2) shows the front view layout of a rectangular microstrip patch antenna (RMSPA) with the patch and ground plane layers. The parameters of the rectangular patch antenna are shown in table (3).

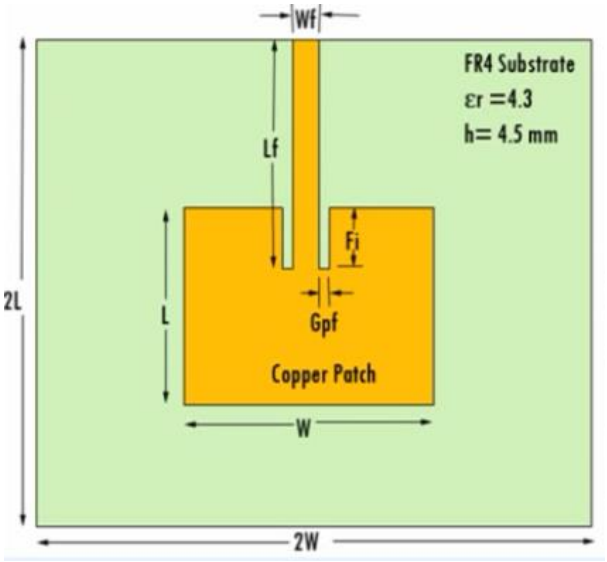



**Figure 2:** Front view of the proposed insert fed rectangular microstrip patch antenna (RMSPA).

The following relations are used to determine the patch antenna dimensions [17]:

and
$$L = \frac{c}{2 f_r \sqrt{\varepsilon_r}} \quad (1)$$

$$W = \frac{c}{2 f_r} \sqrt{\frac{2}{\varepsilon_r + 1}} \quad (2)$$

For $f_r$ = 1.18 GHz , $\varepsilon_r$=4.3 and $c = 3 \times 10^8$, then L≈ 38 mm and W≈51mm.

**Table 3:** The parameters of the proposed insert fed rectangular microstrip patch antenna (RMSPA).

| Parameter | Description | Dimension (mm) |
|---|---|---|
| L | length | 38 |
| W | width | 51 |
| $L_f$ | Feed length | 31.5 |
| $F_i$ | Insert feed length | 12.5 |
| $W_f$ | Feed width | 8.7 |
| $G_{pf}$ | Gap distance | 1 |
| 2L | Substrate length | 76 |
| 2w | Substrate width | 102 |
| h | Substrate thickness | 4.5 |

To obtain full illumination of the PCBM model, eight RMSPA are used with 45° angles separation, as shown in figure 3.

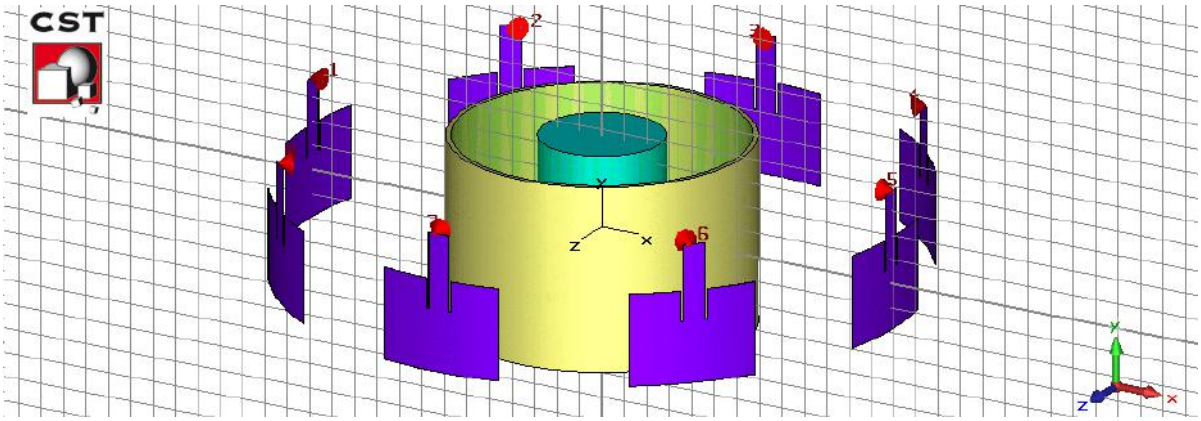



**Figure 3:** An eight RMSPA is used with 45° angles separation.

## 4.2 PROPOSED METALENSES (MTL)

### 4.2.1 LATTICE WIRE STRUCTURE

In metamaterial (left handed material ) (LHM) , negative permittivity and negative permeability can be realized separately, negative permittivity materials exist in nature. Plasma media, e.g., all the metals, have negative permittivity up to the plasma frequency. However, the usage of solid metal in metamaterial is limited by the fact that the absolute value of the negative ε is too large at the target frequency. So, one must determine a method to scale the value of ε to a reasonable value on the order of -1. Usually the permittivity of a metal can be described by the Drude model [15]:

$$\varepsilon(\omega) = 1 - \frac{\omega_p^2}{\omega(\omega + j\omega_c)} \tag{3}$$

where $\omega_c$ is the damping frequency and $\omega_p$ is the plasma frequency given by :

$$\omega_p^2 = \frac{ne^2}{\varepsilon_0 m_{eff}} \tag{4}$$

where $n$ is the electron concentration and $m_{eff}$ is the effective mass of free electrons.

The plasma frequency is extremely high in metals, therefore, not suitable for metamaterial. However Pendry had proposed a wire array structure of periodically arranged "infinite" long wires with separation, $a$, and radius, $r$ , as shown in figure (4) , which can significantly decrease the plasma frequency and realize negative permittivity ε ≈-1 at MW frequencies.

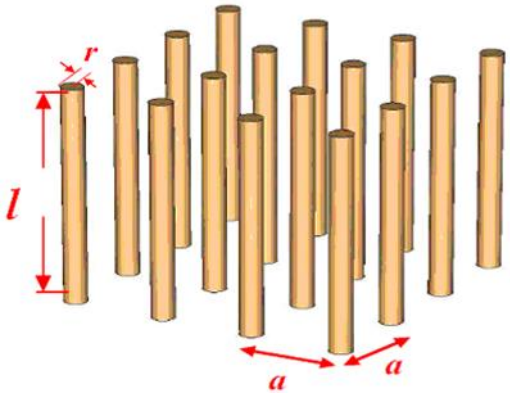



**Figure 4:** The metallic wire array structure.

Thus, the plasmon frequency, $\omega_{pn}$, of the wire array is completely controllable via the geometrical parameters and is given by :

$$\omega_{pn}^2 = \frac{2\pi c^2}{a^2 \ln(a/r)} \tag{5}$$

where c is the speed of light in vacuum, r is the radius of wire, and a is the lattice constant.

### 4.2.2 SPLIT RING RESONATOR UNIT CELL AND ARRAY CONFIGURATION

Although negative permittivity can be realized by a plasmon medium such as metallic structures, one cannot achieve the negative medium, due to the fact that no material exists in nature with both negative permittivity and permeability. Subsequently, Pendry had proposed a split ring resonator (SRR) design [16], which can provide a narrow frequency band with negative permeability under certain polarization of incident EM wave. If an incident EM wave is applied with a magnetic field, (H), perpendicular to the plane of SRR, circular currents will be induced on both the inner and outer rings, and also charges will accumulate across the gaps in both the inner and outer rings, respectively. Thus, each individual SRR acts as a series LRC circuit with the inductance, (L), of the rings and the capacitance, (C), between the two rings, table(4) and figure (5) show the parameters and construction of SRR.

**Table 4 :** The parameters of the proposed SRR.

| Parameter | Description | Dimension (mm) |
|---|---|---|
| $r_i$ | inner ring radius | 2.5 |
| $r_o$ | outer ring radius | 3.6 |
| d | space between inner and outer rings | 0.2 |
| g | gap of the rings | 0.2 |
| w | thickness of rings | 0.9 |
| ax | unit cell lattice constant in X axis | 8.8 |
| ay | unit cell lattice constant in Y axis | 8.8 |
| t | substrate thickness | 2.5 |

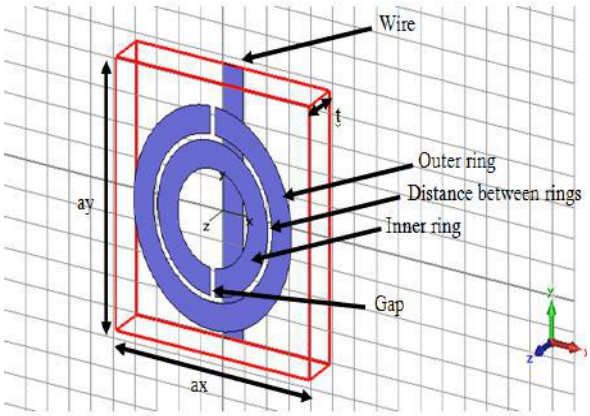



**Figure 5:** Single unit cell of the used SRR.

The effective permeability, μeff , can be approximated as [16] :

$$\mu_{eff} = \frac{R}{1-(\omega_m/\omega)^2 + i(\Gamma_m/\omega)} \tag{6}$$

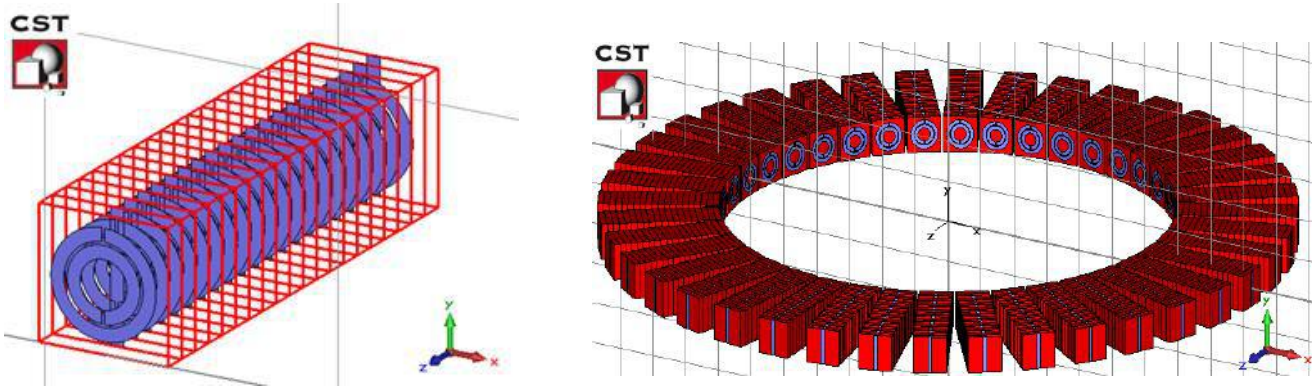
$$\omega_m = \frac{3ac_0^2}{\pi \ln \frac{2\omega}{d} r^3} \quad (7)$$

Where $\omega_m$ is the resonance frequency and Γm is the damping factor, $\Gamma_m = \frac{2a\sigma}{r\mu_0}$ (8) and $\boldsymbol{R} = \frac{\pi r^2}{a^2}$ (9).

Both $\omega_m$ and $\Gamma_m$ are functions of the geometric parameters, (*a*, *d*, and *r*) and the conductivity, (σ), of the metal.

### 4.2.3 THE STRUCTURE OF THE PROPOSED METALENSES (MTL)

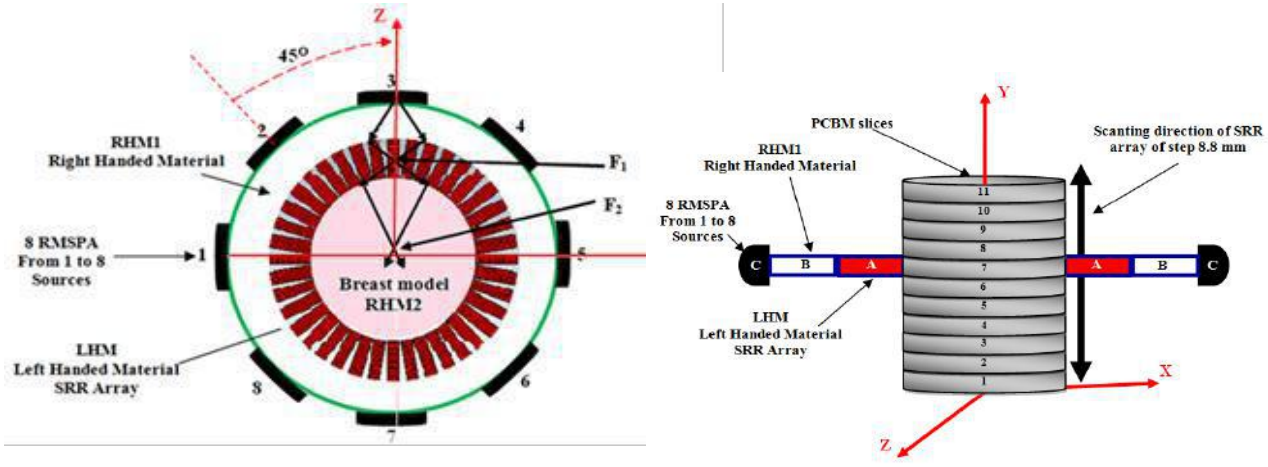
A metamaterial ring design consists of periodically arranged 20 copper SRR unit cells which are supposed to surround the PCBM, with a separation equals to the substrate thickness = 1.6 mm, so the total depth of the SRR array is 50 mm which equal to the depth of the PCBM to achieve full volume focusing of the PCBM. Figure (6) shows the structure of the proposed SRR array.




(a) (b)

**Figure 6**: (a) Single SRR array , (b) Metalens ring consisting of 40 SRR.

Figure 7.a shows the focusing pattern of a MW ray emitted from an eight RMSPA with 45° angel separation inside the PCBM and the corresponding two focal spots, F1 in the left handed material (LHM) and F2 in the PCBM. Figure 7.b illustrates side view of MW breast cancer detection system based on image slices technique and shows the slices distribution along a PCBM of 100 mm height. Accordingly, the PCBM is divided into 11 slices depending on the metalens length in the direction of scanning (ay=8.8 mm). The movable ring shaped metalens starts moving from y=0 towards the chest wall, precisely the scanning process ends when the metalens reaches the full height of the PCBM 8.8mm × 11 slices ≈ 100 mm.




(a): Plan view (b): Slices side view

**Figure 7** : PCBM,SRR Lens Array and RMSPA.

### 4.2 DETAILED DESCRIPTION OF THE PROPOSED PROTOTYPE

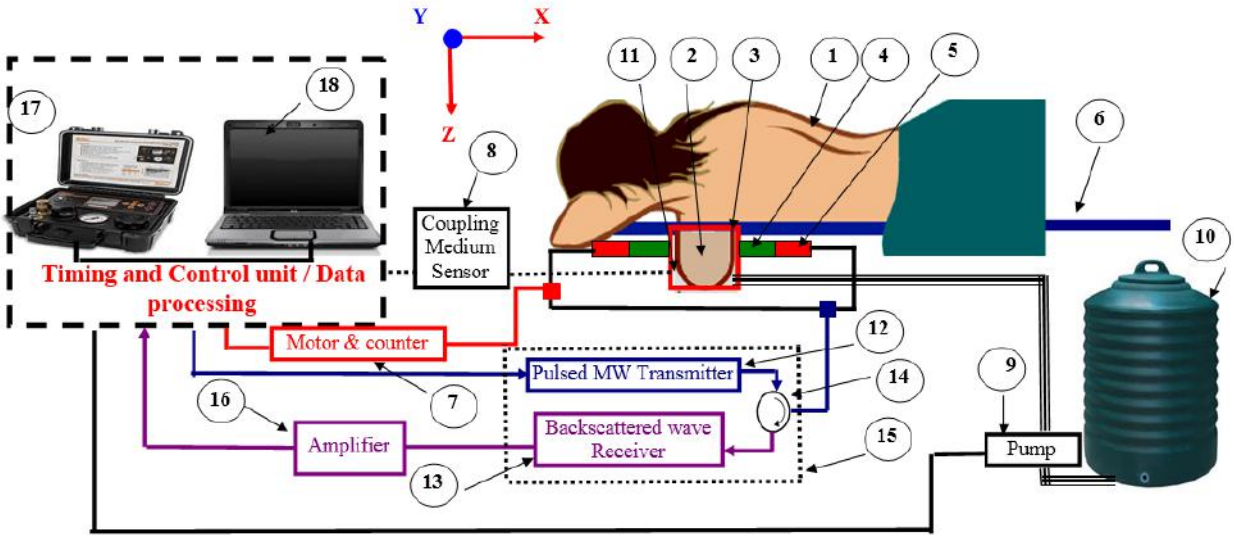



**Figure 8**: The proposed MIS prototype.

**Table 5 :** The proposed MIS prototype parts

| No | Name | No | Name |
|---|---|---|---|
| **1** | Patient | **10** | Coupling medium container |
| **2** | Breast | **11** | Coupling medium |
| **3** | Imaging chamber | **12** | MW transmitter |
| **4** | Ring shaped metalens | **13** | Backscattered wave collector |
| **5** | Microstrip patch antennas | **14** | Circulator |
| **6** | Screening table | **15** | Transceiver unit |
| **7** | Motor & movement counter | **16** | Amplifier |
| **8** | Coupling medium sensor | **17** | Timing and Control unit / Data processing |
| **9** | Pump | **18** | Display |

## 5. TUMORS DETECTION

### 5.1 SIMULATION RESULTS

Full illumination of breast under detection is achieved using the new MW imaging slices technique. The system offers easy in-depth scanning, high-resolution imaging and tumor early detection. Tumors as small as 2 mm in fat layer or fibroglandular layer can be clearly detected due to changes in their dielectric properties, which show a distinguished contrast from the surrounding normal tissue. The modeling and simulation is performed using CST STUDIO SUITE electromagnetic simulation software. Figure 9 shows the electric field distributions in PBM containing 11 spherical tumors of different diameters. slice 1 distinguishes tumor of diameter 2mm T1 located in fat layer at Z=50mm and depth Y=-36mm and tumor T2 of diameter 4mm appears in slice 2 in fibroglandular layer at Z=-20 and depth Y=-29. Tumor of diameter 6mm T3 appears in slice 3 and located in the fat layer at Z=-40mm and depth Y=-22mm, also in slice 4, tumor T4 of diameter 2mm appears in the fat layer at Z=-30 and Y=-15. slice 5 shows the existence of tumor T5 with diameter 3mm in the fibroglandular layer at Z=-10mm and depth Y=-8mm ,also in slice 6 tumor T6 appears with diameter 8mm in the fat layer at X= 30mm ,Z=-30mm and depth Y=6mm. slice 7 distinguishes tumor of diameter 4mm T7 located in fat layer at X=-30, Z=45mm and depth Y=6mm, and tumor T8 of diameter 2mm appears in slice 8 in fibroglandular layer at X=15, Z=5 and depth Y=13. Three more tumors T9,T10 and T11 on fat layer can be clearly detected in slices 9,10,11.

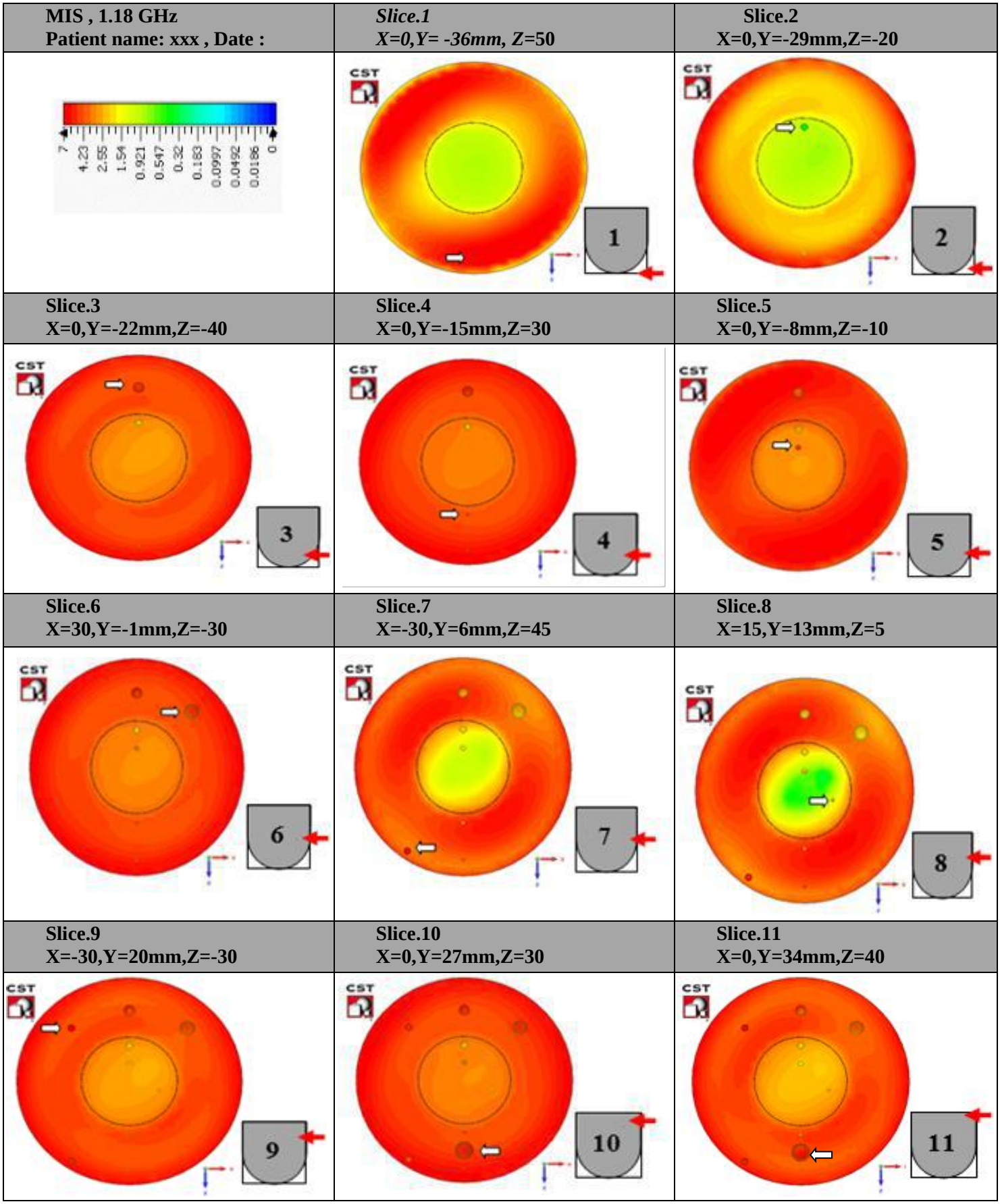
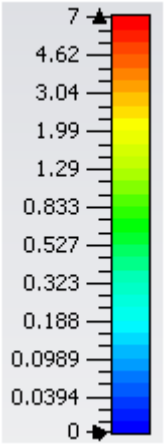



**Figure 8**: Filming of the 11 tumors.




## CONCLUSION

Breast cancer is a globally major health problem for women, causing 13.9% of the yearly female death. There is growing need for engineers and physicists to concentrate and develop devices specifically suitable for early diagnosis of breast cancer and continuous monitoring of the uncontrolled growth of the malignant cells. Microwave imaging is an efficient diagnostic tool for non-invasively visualizing dielectric properties of non-metallic bodies. The basic principle behind the cancer detection is, a small change in the water content of biological tissues produces changes in the permittivity ($\varepsilon$) and conductivity ($\sigma$) values of the tissues. The malignant cells have significantly higher water content than normal tissues. Hence the permittivity and the conductivity of the tumor are higher than those ones of a normal tissue at microwave frequencies.

Metamaterials are key components of the active field of research in the past decade which has potential application in healthcare, their electromagnetic properties altered to something beyond what can be found in nature. Hence metamaterials have been attracted great interest among MW engineers and physicists, due to showing exotic EM properties at microwave frequencies. By developing microwave devices and combining it with structures inspired by metamaterials, it can lead to a very cost-effective device that can localize with high precision an abnormality within the human body. Considering the fact that malignant tumors generally have larger scattering cross-sections than the comparably sized normal breast tissue. A new design for breast cancer detection system is proposed based on image slices technique, by combining multi-point source MWI system to achieve full illumination of breast under detection with movable ring shaped metamaterial structure consisting of 40 arrays of 20 metallic metamaterial split-ring resonators (SRRs) surrounding a layered beast (according to the large majority of female breast tissue structures, fat 70% , fibroglandular 30%) . The New MW imaging method for early detection of breast cancer using the proposed metamaterial offering easy in-depth scanning, high-resolution for detection and imaging, scanning a merged focal spot of area under detection and screening the backscattered MW refocused by the proposed method. The system shows that tumors as small as 2 mm on fat layer and fibroglandular layer can be clearly detected due changes in their dielectric properties, which shows a distinguished contrast from the surrounding normal tissue.

## REFERENCES

1. Fear, E. C., S. C. Hagness, and P. M. Meaney, “Enhancing breast tumor detection with near-field imaging," IEEE Microwave Mag., Vol. 3, No. 1, 48-56, 2002.
2. Fear, E. C., P. M. Meaney and M. A. Stuchly, “Microwave detection of breast cancer,” IEEE Trans. Microwave Theory Tech., Vol.22, 12-18, 2003.
3. Liu, Q. H., Z. Q. Zhang, T. Wang, G. Ybarra, L. W. Nolte, J. A. Bryan and W. T. Joines, “Active microwave imaging I: 2-D forward and inverse scattering methods,” IEEE Trans. Microwave Theory Tech., Vol. 50, No. 1, 123-133, 2002.
4. Fear, E. C., P. M. Meaney, and M. A. Stuchly, “Microwaves for breast cancer detection,” IEEE Potentials, Vol. 22, No. 1, 12-18, 2003.
5. Lazebnik , M., L.McCartney, D. Popovic, C. Watkins, M. Lindstrom, J. Harter, S. Sewall, A. Magliocco, J. Booske, M. Okonievki and S. Hagness, “A large-scale study of the ultrawideband microwave dielectric properties of normal breast tissue obtained from reduction surgeries ,” Phys. Med. Biol., Vol. 52, No. 10, 2637-2656, 2007.

6. Lazebnik, M., D. Popovic, L. McCartney, C. Watkins, M. Lindstrom, J. Harter, S. Sewall, T. Ogilvie, A. Magliocco, T. Breslin, W. Temple,D. Mew, J. Booske, M. Okonievki and S. Hagness, “A large-scale study of the ultrawideband microwave dielectric properties of normal, benign and malignant breast tissues obtained from reduction surgeries ,” Phys. Med. Biol., Vol. 52, 6093-6115, 2007.
7. Lazebnik, M., M. Okoniewki, J. Booske and S. Hagness, “Highly Accurate Debye Models for Normal and Malignant Breast Tissue Dielectric Properties at Microwave Frequencies,” IEEE Microwave and Wireless Components Letters, Vol. 17, No. 12, 822-824, 2007.
8. Nelson, T. R., L. Cervino, J. M. Boone and K. K. Lindfors,“Classification of breast computed tomography data,” Med. Phys., Vol. 35, No. 3, 1078-1086, 2008.
9. Schwan, H. P., Electrical properties measured with alternating currents body tissues, Handbook of Biological Data, Philadelphia , 1956.
10. Firoozabadi, R. and E. L. Miller, “A Shape-Based Inversion Algorithm Applied to Microwave Imaging of Breast Tumors,”IEEE Transactions on Antennas and Propagation, Vol.59, No. 10, 3719 - 3729 2011.
11. Lazebnik, M., et.al, “A large-scale study of the ultrawide band microwave dielectric properties of normal breast tissue obtained from reduction surgeries,” Phys. Med. Biol., Vol. 52, 2637-2656, 2007.
12. Tayel, M. B., A. T. Ibrahim, M. I. Badwai, "A Finite Element-Adaptive Meshing Sweep for Early Detection of Breast Tumors using A Proposed Metamaterial lens," Canadian Journal on Biomedical Engineering & Technology, Vol. 2, No. 4, 32-37, October 2011.
13. Tayel M. B., A. T. Ibrahim, M. I. Badwai, " Early Detection of Tumors In a Multi Layered Breast Model Using The Proposed Metamaterial lens Array," Canadian Journal on Biomedical Engineering & Technology. ,Vol. 2, No. 4, 32-37, December 2011.
14. AlShehri, S. A. and S. Khatun “UWB Imaging for Breast Cancer Detection Using Neural Network,” Progress In Electromagnetics Research,Vol. 7, 79-93, 2009.
15. Jacjson, J. D. ,Classical Electrodynamics, John Wiley & Sons, New York,1998.
16. Pendry, J.B. ,A. J. Holden, W. J. Stewart, and I. Youngs, “Extremely low frequency plasmons in metallic microstructures,” Physical Review Letters, Vol. 76, No. 25,4773– 4776, 1996.
17. Bhalla, D. and Bansal, K., “ Design of a Rectangular Microstrip Patch Antenna Using Inset Feed Technique,” IOSR-JECE, Vol.7, No. 4, 08-13, 2013.

# Fano resonances in optics and microwaves: Physics and application

# Demonstration of true electromagnetically induced transparency in a metamaterial

**T. Nakanishi And M. Kitano**

Department of Electronic Science and Engineering, Kyoto University, Japan
t-naka@kuee.kyoto-u.ac.jp

**Abstract**— We propose a way to realize electromagnetically induced transparency (EIT) in a metamaterial. The incidence of auxiliary electromagnetic waves renders the metamaterial transparent exactly in the same way as the case of original EIT effect in an atomic medium. We show the design of the metamaterial loaded with nonlinear capacitances and demonstrate the EIT effect in the metamaterial in microwave region.

Electromagnetically induced transparency (EIT) effect has been investigated in atomic physics to realize extremely slow-light propagation and to store light in a medium by dynamical modulation of the group velocity. The EIT effect is a nonlinear optical phenomenon, which renders opaque medium transparent for a probe light by the incidence of an auxiliary light, called control light. The transparent region is quite narrow and the group velocity of light is significantly reduced. It is also possible to realize the narrow transparency and resulting slow-light propagation in metamaterials, and various types of metamaterials with EIT-like property have been proposed and demonstrated [1, 2]. Recently, we proposed a metamaterial with EIT-like property controlled by DC electric field and demonstrated the storage of electromagnetic waves in the metamaterial [3]. However, the EIT-like effects, or the sharp transparency and slow-light effect, are implemented in a different way from the original EIT effect in atomic systems. In this paper, we propose a metamaterial, which realizes *true* EIT effect in that an auxiliary electromagnetic wave, or control light, induces transparency [4].

In order to realize the true EIT effect, nonlinear elements are required, because the EIT effect is induced by nonlinear interaction between a probe light and a control light. For the demonstration in microwave region, we utilize nonlinear capacitors called varactor diodes whose capacitance depends on the applied voltage. Figure 1(a) shows a unit cell of the metamaterial. This structure has three resonant modes as shown in Figs. 1(b)(c)(d), which are referred to as a radiative mode, a trapped mode, and a control mode, respectively. These three modes oscillating different resonant frequencies are coupled through three-wave mixing owing to the nonlinearity of the capacitors. As a result, the probe light and the control light interfere in the metamaterial, and the absorption of the probe light is suppressed. Figure 1(e) shows the transmission spectra for probe light without the control light (left) and with 11dBm control light (right). It is confirmed that the opaque metamaterial becomes transparent in a narrow spectral region by the incidence of the control light. The width of the transparent region can be controlled by the power of the control light. In addition, we can control the position of the transparent region by changing the frequency of the control light, and the transmission spectrum shows asymmetric shape unique to Fano resonance.

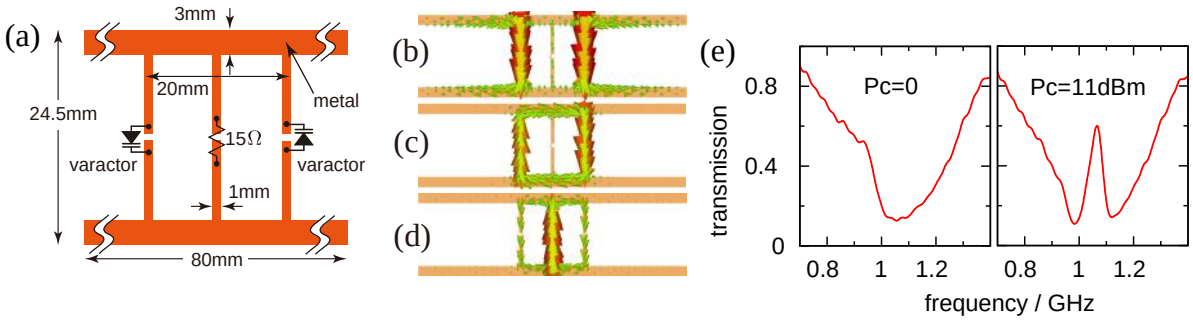



Figure 1: (a) Unit structure. (b) Radiative mode. (c) Trapped mode. (d) Control mode. (e) Transmission spectra with or without the control wave.

We have demonstrated the proof-of-principle experiment concerned with true EIT effect in the metamaterial for the first time, using the nonlinearity of the varactor diodes. The basic idea of three-mode coupling via three-wave mixing could be applied for higher frequency regions. The controllability of the EIT effect by propagating electromagnetic waves is quite important for practical applications including the storage of light, and various properties unique to atomic EIT systems can be also implemented in the metamaterial.

## ACKNOWLEDGMENT

This research was financially supported by JSPS KAKENHI Grants No. 22109004, No. 25790065, and No. 25287101.

## REFERENCES

1. V. A. Fedotov, M. Rose, S. L. Prosvirnin, N. Papasimakis, and N. I. Zheludev, "Sharp trapped-mode resonances in planar metamaterials with a broken structural symmetry," *Phys. Rev. Lett.* Vol. 99, No. 14, 147401, 2007.
2. S. Zhang, D. A. Genov, Y. Wang, M. Liu, and X. Zhang, "Plasmon-induced transparency in metamaterials," *Phys. Rev. Lett.* Vol. 101, No. 4, 047401, 2008.
3. T. Nakanishi, T. Otani, Y. Tamayama, and M. Kitano, "Storage of electromagnetic waves in a metamaterial that mimics electromagnetically induced transparency," *Phys. Rev. B*, Vol. 87, No. 16, 161110, 2013.
4. T. Nakanishi and M. Kitano, "Implementation of Electromagnetically Induced Transparency in a Metamaterial Controlled with Auxiliary Waves," *Phys. Rev. Applied*, Vol. 4, No. 2, 024013, 2015.

# The nanofabrication and unusual Fano resonances of 3D metamaterials

**C. Z Gu[1,2*], Z. Liu[1], A. J. Cui[1], W. X. Li[1] and J. J. Li[1]**

[1]Beijing National Laboratory for Condensed Matter Physics, Institute of Physics, Chinese Cademy of Sciences, Beijing 100190, China

[2]Collaborative Innovation Center of Quantum Matter, Beijing, China

[*]corresponding author: czgu@iphy.ac.cn

**Abstract**-We developed a novel nanofabrication technology of 3D metamaterials based on focused-ion-beam irradiation-induced folding of thin film, which can similarly constructed 3D free-standing nanostructures in the research and development of photonics. The optical characteristics of 3D plasmonic ‘‘nanograters’’ composed of free-standing Au films was studied, and the unusual and well-scalable Fano resonances at wavelengths ranging from 1.6 to 6.4 mm were observed.

The 3D metamaterials (MMs) can realize the effective constituent properties and be tuned in all propagation directions at various frequencies. Specially, nanoscaled 3D MMs responded at higher frequencies, such as in the infrared and visible regimes, remains an active focus of research. Many 3D nanofabrication technologies have been developed in decades, such as layer-by-layer stacking, multilayer electroplating, direct laser writing and ion-beam irradiation, etc. However, the fabrication technology of nanoscale 3D MMs with a hierarchical geometry remains challenging. Here, we developed a fabrication method of focused-ion-beam (FIB) folding of metallic cantilevers to construct self-supporting 3D MMs. The fabrication process employed FIB nanopatterning combined with in situ irradiation-induced folding of metallic thin-film structures. The result indicated that this method can be used to produce complex 3D metamaterials with ease and is also feasible for the production of 2D arrays of millimeter-sized 3D elements, which have practical uses in many optical applications.

Our works focused on metamaterials of U-type nanograters consisting of an array of vertical U-shape splitring resonator patterns standing along an edge of horizontal subwavelength rectangular holes. The 3D metamaterials exhibited scalable unusual Fano resonances, a very strong dependence on the refractive index of the surrounding medium, with a high refractive index sensitivity, was observed. These suggested that the local modifications to the phase and amplitude of the light wave front on a subwavelength scale induced by the nanograter structures profoundly influence the propagation of the incoming light, thereby suggesting that such nanostructures may be applied in a wide range of optical applications, including high-performance plasmonic sensing.

**REFERENCES**

1 Wu C, Khanikaev AB, Adato R, Arju N, Yanik AA et al. Fano-resonant asymmetric metamaterials for ultrasensitive spectroscopy and identification of molecular monolayers. Nat Mater 2012; 11: 69–75.

2 Liu N, Hentschel M, Weiss T, Alivisatos AP, Giessen H. Three-dimensional Plasmon rulers. Science 2011; 332: 1407–1410.

# Explicit demonstration of how path interference can enhance plasmonic nonlinearity

Mehmet Emre Tasgin[1]

[1]Institute of Nuclear Sciences, Hacettepe University, 06800 Ankara, Turkey
metasgin@hacettepe.edu.tr

**Abstract**— We demonstrate why nonlinear frequency generation, e.g. second harmonic generation and four-wave mixing, can be enhanced via interference of conversion paths. We derive a single equation for the amplitude of the generated nonlinear oscillations. On this equation we show that cancellation in the denominator gives rise to conversion enhancement. We utilize this phenomenon to obtain further enhancement using interference of the multiple conversion paths.

Fano resonances on the linear response are shown to enhance the lifetime of plasmon oscillations and can lead to enhanced florescence of the molecules [1, 2]. Enhancement in the plasmon lifetime leads to the observation of spaser [3] —surface plasmon amplification by stimulated emission of radiation. Fano resonances in plasmonic materials are also shown to enhance the degree of the quantum entanglement [4].

Besides the linear response, Fano resonances are shown to enhance and suppress the nonlinear frequency conversion processes [5, 6]. 2 to 3 orders of magnitude enhancement can be achieved on top of the enhancement due to field localization [6, 7]. We explicitly demonstrate —on an expression for the steady-state SHG amplitude— how the presence of a Fano resonance leads to cancellation of nonresonant terms in a SHG process. Cancellation in the denominator gives rise to enhancement in the nonlinearity. The explicit demonstration, we present here, guides one to a method for achieving even larger enhancement factors by introducing additional coupling terms. The method is also applicable to Fano resonances induced by all-plasmonic couplings [8], which are easier to control in experiments.

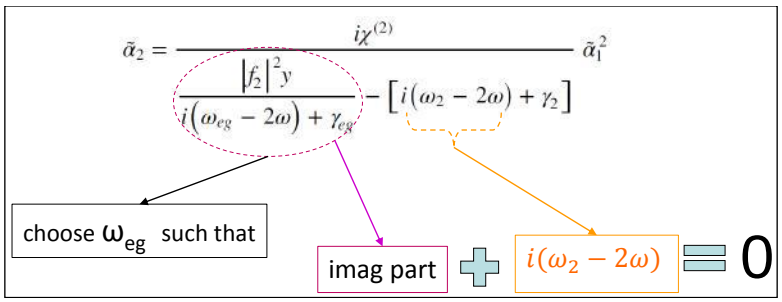



Figure 1: A quick demonstration of how cancellation in the denominator enhances the second harmonic generated plasmons, that is $|\tilde{\alpha}_2|^2$. $\omega_{eg}$ ($\gamma_{eg}$) is the level spacing (spectral width) of the quantum-emitter (QE), $f_2$ is the MNP-QE coupling strength, $\omega_2$ ($\gamma_2$) is the resonance plasmon frequency (damping rate) of the MNP converter into which SHG take place, $y$ is the population inversion in the QE, $\chi^{(2)}$ is proportional with the nonlinear susceptibility.

## ACKNOWLEDGMENT

We acknowledge support from TUBITAK-1001 Project No. 114F170 and Hacettepe University.

## REFERENCES

1. M. E. Taşgın, Nanoscale **5**,*Metal nanoparticle plasmons operating within a quantum lifetime*, 8616 (2013).
2. P.Anger, P. Bharadwaj, and L. Novotny,*Enhancement and quenching of single-molecule fluorescence*, Phys. Rev. Lett. **96**, 113002 (2006).

3. M. A. Noginov, G. Zhu, A. M. Belgrave, R. Bakker, V. M. Shalaev, E. E. Narimanov, S. Stout, E. Herz, T. Suteewong and U. Wiesner, *Demonstration of a spaser-based nanolaser*, Nature **490**, 1110 (2009).
4. Guang-Yin Chen and Yueh-Nan Chen, *Correspondence between entanglement and Fano resonance of surface plasmons*, Opt. Lett. **37**, 4023 (2012).
5. D. Turkpence, G. B. Akguc, A. Bek, and M. E. Tasgin, *Engineering nonlinear response of nanomaterials using Fano resonances*, J. Opt. **16**, 105009 (2014).
6. S. K. Singh, M. Kurtulus Abak, and Mehmet Emre Tasgin, *Enhancement of Four-Wave Mixing via interference of multiple plasmonic conversion paths*, Phys. Rev. B **93**, 035410 (2016).
7. M. E. Tasgin, I. Salakhutdinov, D. Kendziora, M. K. Abak, D. Turkpence, L. Piantanida, L. Fruk, M. Lazzarino, Alpan Bek, *Fluorescence Excitation by Enhanced Plasmon Upconversion under Continuous Wave Illumination*, arXiv:1402.5244.
8. B. C. Yildiz, M. E. Tasgin, M. K. Abak, S. Coskun, H. E. Unalan, and A. Bek, *Enhanced Second Harmonic Generation from Coupled Asymmetric Plasmonic Metal Nanostructures*, J. Opt. **17**, 125005 (2015).

# Highly contrasted structural colors for industrial applications using the Fano lineshape

**B. Gallinet**
CSEM SA, Muttenz , Switzerland
benjamin.gallinet@csem.ch

**Abstract**- The fabrication of plasmonic nanostructures using up-scalable and cost-efficient processes is reported. Their optical response features the characteristic Fano lineshape, which allows them to generate strong structural colors. Wafer-scale fabrication and process compatibility with roll-to-roll embossing are demonstrated, which paves the road towards their industrial implementation. These plasmonic nanostructures are expected to be used in particular for anticounterfeiting, optical security and solar light management.

The Fano lineshape takes it origin from the interference between a spectrally narrow resonance and a broad continuum. It became of high interest in the past few years in plasmonics thanks in particular to its high modulation depth [1]. Plasmonic resonators combining highly contrasted spectra with light confinement at the nanoscale are obtained using Fano resonances and numerous application opportunities are foreseen. However, the control of the Fano lineshape is technologically highly demanding and the up-scalability of the fabrication processes of such complex plasmonic nanostructures remains a challenge.

Here, the fabrication of plasmonic nanostructures using up-scalable and cost-efficient processes is reported. Their optical response features the characteristic Fano lineshape, which allows them to generate strong structural colors. No etching or lift-off processes are needed. Wafer-scale fabrication and process compatibility with roll-to-roll embossing are demonstrated, which paves the road towards their industrial implementation.

Ultra-violet nanoimprint lithography (UV-NIL) combined with two tilted evaporations of aluminum or gold are used to generate plasmonic nanostructures at visible wavelengths [2]. These structures have the shape of hollow nanowires and generate a strong response in most of the visible spectrum thanks to a highly modulated Fano lineshape. Similar plasmonic nanowires are fabricated using hot embossing of stretchable polyurethane substrates [3]. The observed Fano lineshape is very sensitive to the spacing between the wires and responds to strain with a spectral shift as well as an attenuation of the resonance amplitude. A clearly visible color change from purple to green is achieved through optimization of the structural parameters, which enables colorimetric or even visual sensing with possibility of a remote read-out using e.g. a camera.

In another family of devices, a single tilted evaporation of aluminum generates an array of plasmonic nanolamellas [4]. The strong coupling between localized and propagating plasmon resonances leads to characteristic Fano lineshape with tunable spectral positions and widths. Distinct colors covering the entire visible spectrum are generated by tuning the structural parameters. The asymmetry of nanolamellas gives rise to a strong color rendering effect with broken symmetry, for which colors are observed only at a particular tilt angle. In particular, this unique visual effect is foreseen to be implemented in anticounterfeiting, optical security and solar light management.

**REFERENCES**


1. Luk'yanchuk B., Zheludev N. I., Maier S. A., Halas N. J., Nordlander. P., Giessen H. and Chong C. T., "The Fano resonance in plasmonic nanostructures and metamaterials," *Nature Materials*, Vol. 9, 707-715, 2010.
2. Lütolf, F., O. J. F. Martin and B. Gallinet, "Fano-resonant aluminum and gold nanostructures created with a tunable, up-scalable process," *Nanoscale*, Vol. 7, No. 43, 18179–18187, 2015.
3. Lütolf, F.., D. Casari and B. Gallinet, "Low-cost and large-area strain sensors based on plasmonic Fano resonances," *Advanced Optical Materials*, 2016.
4. Duempelmann, L., D. Casari., A. Luu-Dinh, B. Gallinet and L. Novotny, "Color rendering plasmonic aluminum substrates with angular symmetry breaking," *ACS Nano*, Vol. 9, No. 12, 12383–12391, 2015.

# Fano resonances, their relation to exceptional points, and applications

**H. Cartarius**[1], **L. Schwarz**[1], **G. Wunner**[1], **W. D. Heiss**[2,3], **and J. Main**[1]

[1]Institut für Theoretische Physik, Universität Stuttgart, Pfaffenwaldring 57, 70569 Stuttgart, Germany
[2]Department of Physics, University of Stellenbosch, 7602 Matieland, South Africa
[3]National Institute for Theoretical Physics (NIThePP), Western Cape, South Africa
Holger.Cartarius@itp1.uni-stuttgart.de

**Abstract**— We show for a model Hamiltonian that the interference of the first and second order pole of the Greens function at an exceptional point, as well as the interference of the first order poles in the vicinity of the exceptional point, gives rise to asymmetric scattering cross section profiles which are well described by the Beutler-Fano formula, and thus are genuine Fano resonances. An outlook to possible applications in optics is given.

While Fano resonances were first discovered in atomic physics [1, 2], they also appear in cross sections in nuclear physics and are called Feshbach resonances [3]. Their characteristic features are asymmetric line shapes, caused by the interaction between a discrete state and a continuum of states, as described by the formula derived by Fano in his landmark work in 1961 [4]. In this work we take a fundamental perspective on Fano resonances and investigate how they can be understood to be the result of coalescing resonances at a so-called exceptional point [5, 6, 7, 8], i.e. points in a physical parameter space at which two resonances pass through a branch point singularity as functions of these parameters. As a consequence the energies *and* the wave functions become identical.

Similar to the well-established description of an isolated resonance by a pole in the complex plane of the scattering function, an exceptional point is characterized by an additional second-order pole. The interference of the first- and second-order poles gives locally, i.e. close to the resonance energy, raise to Fano profiles [8], which we demonstrate in this work numerically by means of an elementary matrix model [9]. However, the result is not restricted to an exact realization of an exceptional point. Indeed, we can show that in the vicinity of an exceptional point the interference of the two first-order poles generated by the two almost coalescing resonances leads to exactly the same effect. Thus, we can state that exceptional points constitute genuine Fano resonances. Moreover, the cross sections can globally be described by the Beutler-Fano formula, if energy-dependent Fano parameters are introduced.

Fano line shapes created in the vicinity or at exceptional points have shown to be important for the sensitivity of optical detectors. The signal produced by perturbations of an evanescent light field of optical resonators can be enhanced by several orders of magnitude if the cavities are operated close to an exceptional point [10, 11].

## REFERENCES

1. Beutler, H., "Über Absorptionsserien von Argon, Krypton und Xenon zu Termen zwischen den beiden Ionisierungsgrenzen $^2P^o_{3/2}$ und $^2P^o_{1/2}$," *Z. Phys.*, Vol. 93, 177, 1935.
2. Fano, U., "Sullo spettro di assorbimento dei gasi nobili presso il limite dello spettro d'arco," *Nuovo Cim.*, Vol. 12, 154, 1935.
3. Feshbach, H., "Unified theory of nuclear reactions," *Ann. Phys. (N.Y.)*, Vol. 5, 357, 1958.
4. Fano, U., "Effects of configuration interaction on intensities and phase shifts," *Phys. Rev.*, Vol. 124, 1866, 1961.
5. Kato, T., *Perturbation theory for linear operators*, Springer, Berlin, 1966.
6. Moiseyev, N., *Non-Hermitian Quantum Mechanics*, Cambridge University Press, Cambridge, 2011.
7. Heiss, W. D., "The physics of exceptional points," *J. Phys. A*, Vol. 45, 444016, 2012.
8. Heiss, W. D. and Wunner, G., "Fano-Feshbach resonances in two-channel scattering around exceptional points," *Eur. Phys. J. D*, Vol. 68, 284, 2014.

9. Schwarz, L., Cartarius, H., Wunner, G., Heiss, W. D. and Main, J., "Fano resonances in scattering: an alternative perspective," *Eur. Phys. J. D*, Vol. 69, 196, 2015.
10. Wiersig, J., "Enhancing the Sensitivity of Frequency and Energy Splitting Detection by Using Exceptional Points: Application to Microcavity Sensors for Single-Particle Detection," *Phys. Rev. Lett.*, Vol. 112, 203901, 2014.
11. Li, J., Yu, R., Ding, C., Wu, Y., "$\mathcal{PT}$-symmetry-induced evolution of sharp asymmetric line shapes and high-sensitivity refractive index sensors in a three-cavity array," *Phys. Rev. A*, Vol. 93, 023814, 2016.

# Interference of nano-vortex fields formed by plasmonic cavities

**Keiji Sasaki** [*]
[1]Research Institute for Electronic Science, Hokkaido University, Japan
[*]corresponding author: sasaki@es.hokudai.ac.jp

**Abstract**- We demonstrate the capability of forming the single-nanometer-sized optical vortex fields using designed plasmonic nanostructures. The orbital and spin angular momenta provided by a Laguerre-Gaussian beam are transferred to localized plasmons of a metal multimer structure and then confined into a nano-gap. Nano-scale position dependent Fano resonance spectra are observed, which are caused by interference of multiple vortex modes having different angular momenta.

The Laguerre-Gaussian (LG) beam, called as optical vortex, that possesses helical wave-front and doughnut beam profile has recently attracted significant attention because of the unique characteristics of carrying the orbital angular momentum in addition to the spin angular momentum corresponding to circular polarization. Recently, we demonstrated that multipolar plasmons of metal nano-disks can be selectively excited by circularly-polarized optical vortex beams [1]. The orbital and spin angular momenta are transferred from LG-mode photons to localized plasmons. This plasmonic field localized by the nano-disk just corresponds to the whispering gallery mode (WGM), where the angular mode number is determined by the total angular momentum of the LG beam. Unfortunately, the mode volume of this plasmonic resonator is sub-micrometer dimension that is restricted by the diffraction limit of the surface plasmon wave [2].

In order to realize the WGM nano-cavity, we design the tailored plasmonic structure consisting of metal multimer surrounding a single-nanometer-sized gap (Fig. 1). This metal structure makes it possible to localize the optical vortex field into the nanogap space with conserving the high-order orbital and spin angular momenta. We discussed on the relation between the degrees of freedom in the multimer structure and the transferable angular momenta, i.e., the angular mode number of the WGM nanocavity. By mixing multiple LG-modes of the excitation beam, the nano-vortex fields having different WGM modes interfere with each other, which result in Fano resonances [3,4]. The characteristic spectra of the Fano resonances are observed within the nano-gap, and the line shape drastically varies depending on the nano-scale position. We also demonstrate efficient and selective excitation of the optical forbidden states in an artificial molecule placed in the nano-vortex fields.

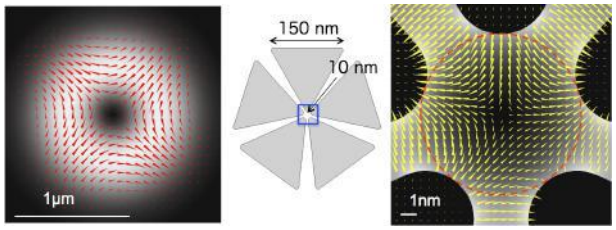



Fig. 1 The electric field of the incident LG beam (left), the plasmonic multimer structure (middle), and the nano-sized optical vortex field (right).

**REFERENCES**

1. K. Sakai, K. Nomura, T. Yamamoto, and K. Sasaki, *Sci. Rep.* 5, 8431 (2015).
2. Y. Tanaka, S. Kaneda, and K. Sasaki, *Nano Lett.* 13, 2146 (2013).
3. Y. Tanaka, A. Sanada, and K. Sasaki, *Sci. Rep.*, 2, 764 (2012).
4. Y. Tanaka, M. Komatsu, H. Fujiwara, and K. Sasaki, *Nano Lett.* 15, 7086 (2015).

# Exploring Fano-Resonance Phenomenology with Quantum Point Contacts

**J. Fransson[1] and J. P. Bird[2]**

[1]Uppsala University, Sweden
[2]University at Buffalo, USA
Jonas.Fransson@physics.uu.se

**Abstract**— A critical aspect of quantum mechanics is the nonlocal nature of the wavefunction, a characteristic that may yield unexpected coupling of nominally isolated systems. The capacity to detect this coupling can be vital in many situations, especially those in which its strength is weak. In this work we demonstrate an approach to such detection by making use of one of the most ubiquitous of wave-interference phenomena, namely the Fano resonance. The focus of this joint experimental and theoretical work is on demonstrating a novel form of *nonequilibrium* Fano resonance, that is very different in nature to the usual (quasi-equilibrium) implementations of this phenomenon. The essential idea of our approach is to exploit the strong sensitivity of the Fano resonance to the presence of additional transmission pathways, as a means to identify the coupling of some host system to an *intruder*. Crucially, our nonequilibrium scheme allows us to detect the presence of *hidden* components within some system, even while they remain *invisible* in near-equilibrium transport. For a proof-of-concept demonstration of this phenomenon, we implement an electron-wave interferometer from mesoscopic quantum point contacts. The wave-based origins of the Fano resonance imply, however, that our scheme should be widely realizable across a variety of physical platforms.

**ACKNOWLEDGMENT**

FRs are observed in wave systems in which the transmission from an initial to a final state is governed by the interference between a continuum and a narrow level. Broadly realized in a variety of systems [1, 2, 3], the essential features of the Fano geometry are indicated schematically in Fig. 1(a). This shows a problem in which waves propagate between points $A$ and $B$ (in some configuration space), with the transmission either occurring directly (matrix element $w$) or being mediated (with matrix element $v$) by a discrete level ($D$) that serves as an intermediate state. In this doubly-connected geometry, resultant wave interference causes the transmission ($T$) to exhibit a rapidly-varying resonant modulation (Fig. 1(a), right panel), as the energy (or frequency) of the incoming wave is swept through that of the discrete level. The lineshape of the resonance takes a universal form whose profile is determined by an asymmetry parameter ($q$), which in turn is governed by the matrix elements $w$ and $v$ [1, 2]. Dependent upon the value of $q$ a variety of different lineshapes may be obtained, ranging from Lorentzian ($q = \infty$) and near-symmetric ($q \gg 1$) forms, to fully antisymmetric ($q \sim 1$) and "window" resonances (or antiresonances, with $q = 0$). The capacity to manipulate the form of the FR via its asymmetry parameter, combined with the ability to very effectively modulate the transmission of an incident wave, are the features that make this phenomenon of such interest for use in the various applications alluded to above.

In this work we describe a form of nonequilibrium Fano resonance (NEFR), which we observe in a mesoscopic system in which the two-path Fano interferometer is *already* established under equilibrium conditions. By monitoring the distortions of its FR that arise when the system is subjected to strong nonequilibrium electrical driving (see Fig.1(b), right panel), we are able to infer the presence of coupling between the Fano interferometer and an *additional* continuum. The realization of this phenomenon in an all-electrically-controlled scenario and we provide combined experimental and theoretical assessment of our observations.

The generalized concept of the NEFR is indicated schematically in Fig. 1(b). In this relatively-straightforward extension of Fig. 1(a), the usual two-path Fano interferometer (see, also, the left schematic of Fig. 1(c)) is modified by coupling it (with matrix element $t$) to an additional continuum ($I$). As we indicate in the right schematic of Fig. 1(c), this *intruder* [4] continuum is taken to be separated energetically from the discrete level by an energy detuning $\Delta$. In a situation in which mono-energetic waves are injected into the system to realize an equilibrium FR (at $E = E_o$), the

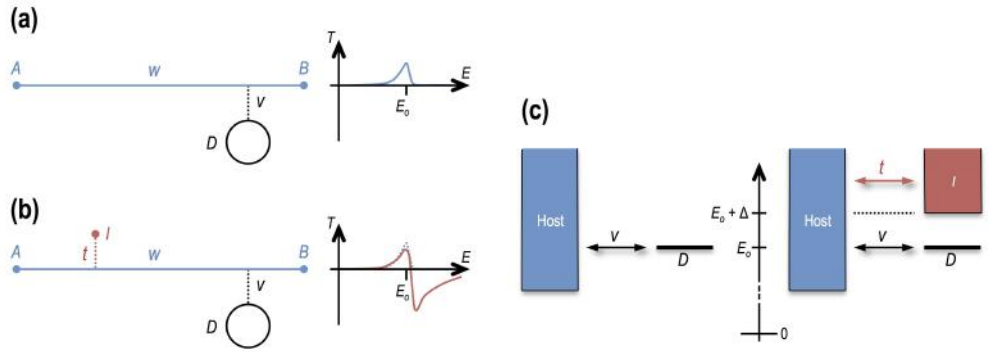



Figure 1: (a) Shown left is a schematic representation of the standard two-path FR, while on the right we represent the possible variation of transmission as a function of energy ($E$) for such a system. The lineshape of the resonance reflects the relative values of the matrix elements $w$ and $v$, which in this case are shown to yield a weakly asymmetric peak. (b) The schematic on the left indicates the situation in which the Fano system of (a) is coupled to an additional, intruder, continuum ($I$). On the right we sketch the expected variation of $T(E)$ for this system. The dotted line represents the FR in the absence of the intruder, while the solid line indicates the lineshape distortion that can be induced by the coupling to $I$. (c) The left panel is a schematic representation of the energy alignment in the standard FR. The host continuum connects points $A$ and $B$ and is coupled to the discrete level ($D$) by the matrix element $v$. A FR results when mono-energetic waves are injected into the system with an energy close to $E_o$. The right panel shows the corresponding alignment relevant to discussions of the NEFR. Here, the host is coupled to the discrete level and the intruder ($I$), with respective matrix elements $v$ and $t$. The NEFR occurs when waves with a spread of energies, ranging from $E_o$ to $E_o + \Delta$, are simultaneously injected into the system to access both $D$ and $I$. The dotted line in the figure indicates the energy alignment of the intruder.

intruder will therefore be energetically inaccessible and will consequently not participate in the resonant interference. However, if waves are injected into the same system with a spread of energy, chosen such that it matches the value of the detuning ($\Delta$), transmission via both the discrete level and the intruder can be activated simultaneously (see Fig. 1(c)). Under such conditions, a three-path interferometer is established and it is this modification to the Fano geometry that results in the distortion of the resonance that we indicate schematically in Fig. 1(b). The NEFR therefore provides a means to detect the coupling of the host to the intruder; put more simply, it allows us to detect the presence of *hidden* components within a Fano system, even when they are undetectable in near-equilibrium transmission.

**REFERENCES**


1. U. Fano, *Effects of Configuration Interaction on Intensities and Phase Shifts*, Phys. Rev. **124**, 1866 (1961).
2. U. Fano and A. R. P. Rau, *Atomic Collisions and Spectra* (Academic Press, Orlando, FL, 1986)
3. A. E. Miroshnichenko, S. Flach, and Y. S. Kivshar, *Fano Resonances in Nanoscale Structures*, Rev. Mod. Phys. **82**, 2257 (2010).
4. J. Fransson, M.-G. Kang, Y. Yoon, S. Xiao, Y. Ochiai, J. L. Reno, N. Aoki, and J. P. Bird, *Tuning the Fano Resonance with an Intruder Continuum*, Nano Lett. **14**, 788 (2014).

# Multivariable Fano line shape in guided-mode resonant gratings

**D. A. Bykov**[1,2*], **L. L. Doskolovich**[1,2], **and N. V. Golovastikov**[1,2]

[1]Image Processing Systems Institute of the Russian Academy of Sciences, Samara, Russia
[2]Samara State Aerospace University, Samara, Russia
*corresponding author: bykovd@gmail.com

**Abstract**—We study generalizations of the Fano line shape that describe the scattering amplitude as a function of several variables. In particular, we obtain simple approximations for the transmission coefficient of guided-mode resonant (GMR) gratings as a function of both frequency and in-plane wave vector components of the incident wave. The approximations take into account symmetries of the structure, causality and energy conservation conditions. The proposed theory describes angular tolerances of GMR filters and spatio-temporal pulse transformations implemented by GMR gratings.

Resonances in various optical structures are usually described in terms of the Fano line shape. Conventional Fano line shape provides a simple relation for the scattering amplitude as a function of a single argument (either angular or spatial frequency of the incident light) [1]:

$$T(\omega) = t + \frac{b}{\omega - \omega_{\mathrm{p}}}. \tag{1}$$

Here $T$ is the complex scattering amplitude, $\omega$ is the incident light's angular frequency, $\omega_{\mathrm{p}}$ is the complex frequency of the eigenmode. Of particular interest is studying Fano resonances, taking several arguments into account. In paper [1] resonances in subwavelength diffraction gratings were studied, considering the scattering amplitude as a function of both in-plane wave vector $k_x$ and grating thickness $h$. In papers [2, 3] the authors obtained simple expressions for the grating's transmission coefficient as a function of both $k_x$ and $\omega$.

In the present work, we study optical properties of guided-mode resonant gratings (or photonic crystal slabs; see Fig. 1(a)). We consider different generalizations of the Fano line shape that take into account light's angular frequency $\omega$ and in-plane wave-vector components, $k_x$ and $k_y$. We also study the consequences of symmetry, causality, reciprocity and energy conservation law.

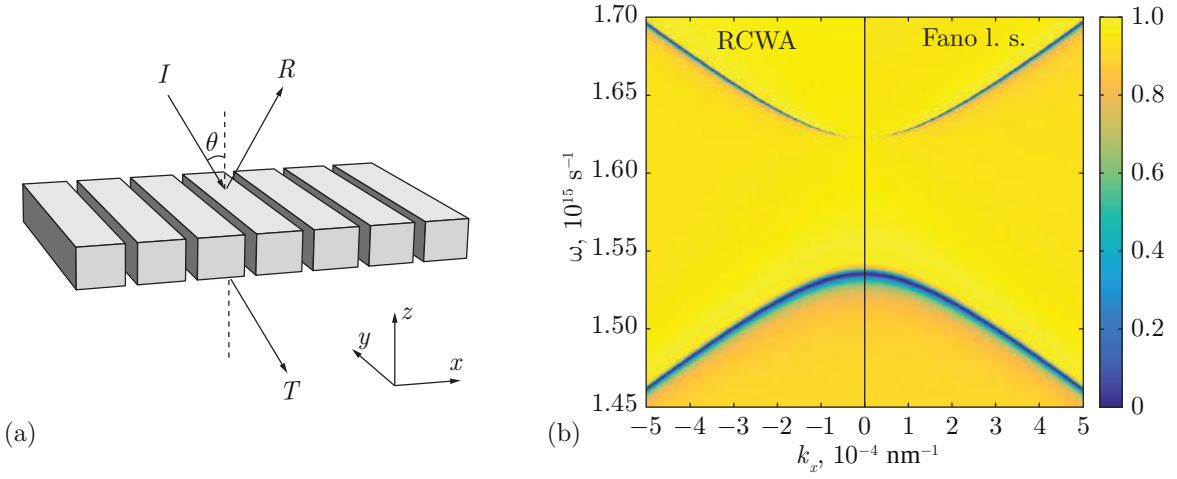



Figure 1. (a) Guided-mode resonant grating. (b) Transmission coefficient $|T(k_x, \omega)|^2$: calculated using rigorous coupled-wave analysis (at $k_x < 0$) and approximated using $\omega$–$k_x$ Fano line shape (2) (at $k_x > 0$)

The spatio-temporal formulation of the coupled mode theory provides the most intuitive way to obtain the following $\omega$–$k_x$ Fano line shape for guided-mode gratings [4]:

$$T(k_x,\omega) = t\frac{v_{\mathrm{g}}^2 k_x^2 + (\omega-\omega_{\mathrm{z}})(\omega-\omega_{\mathrm{p2}})}{v_{\mathrm{g}}^2 k_x^2 + (\omega-\omega_{\mathrm{p1}})(\omega-\omega_{\mathrm{p2}})}. \tag{2}$$

Here $T$ is the grating's complex transmission coefficient; $v_{\mathrm{g}}$ is the mode's group velocity; $\omega_{\mathrm{z}}$ is the zero of the scattering amplitude at $k_x = 0$; $\omega_{\mathrm{p1}}$ and $\omega_{\mathrm{p2}}$ are the complex frequencies of the modes of the structure (at $k_x = 0$). Note that at fixed $k_x$ Eq. (2) can be represented as $T(\omega) = t + b_1/(\omega-\omega_p) + b_2/(\omega-\omega_q)$, which is a form of Eq. (1) for two Fano resonances. Similarly, at fixed $\omega$ Eq. (2) can also be represented as conventional two-resonance Fano line shape (with the argument $k_x$). Hence Eq. (2) can be referred to as the generalization of the Fano line shape (1).

Let us note that Eq. (2) was obtained taking into account the symmetry of the structure [4] and it satisfies the causality condition [5]. Besides, one can write the special form of Eq. (2) that takes into account the energy conservation law [5].

We considered the guided-mode resonant grating (see Fig. 1(a)) with the following parameters: period $d = 1000\,\mathrm{nm}$, height $h = 700\,\mathrm{nm}$, fill-factor $f = 4/5$, surrounding medium refractive index $n_{\mathrm{s}} = 1$, grating permittivity $\varepsilon_{\mathrm{gr}} = 2$. The left part of Fig. 1(b) shows the rigorously calculated transmission coefficient of the grating. The approximated transmission coefficient (2) (right part of Fig. 1(b)) is in good agreement with the rigorously calculated one. In particular, the approximation error does not exceed 0.1 in the $|k_x| < 4\times10^{-4}\,\mathrm{nm}^{-1}$, $\omega \in [1.5, 1.65]\times10^{15}\,\mathrm{s}^{-1}$ area. According to Fig. 1(b), approximation (2) describes such optical phenomena as "bright" and "dark" resonances, and mode coupling.

The coupled mode theory used to obtain Eq. (2) considers two coupled unidirectional wave equations for dispersive medium [4]. The use of *paraxial* unidirectional wave equations allows one to obtain the transmission coefficient as a function of $\omega, k_x$ and $k_y$. This $\omega$–$k_x$–$k_y$ Fano line shape describes angular properties of guided-mode resonant gratings, taking into account the polarization of the incident light and the polarization of the excited mode. Another generalization of the Fano line shape can be formulated for magneto-optical structures: the analysis of the symmetries of the structure allows one to include structure's magnetization as an argument of Eq. (2). This approach can be used to explain resonant magneto-optical effects in magnetized guided-mode gratings.

In conclusion, we obtained generalizations of the Fano line shape that describe the transmission coefficient of guided-mode resonant gratings, taking into account both frequency and direction of the incident light. These line shapes are obtained taking symmetry, causality and energy conservation law into account. The proposed theory can be used to describe angular tolerances of guided-mode resonant filters. Other applications include spatio-temporal pulse shaping using guided-mode resonant gratings [6], and describing magneto-optical properties of guided-mode resonant gratings.

**ACKNOWLEDGMENT**

This work was funded by the Russian Science Foundation grant 14-19-00796.

**REFERENCES**

1. Nevière, M., E. Popov, and R. Reinisch, "Electromagnetic resonances in linear and nonlinear optics: phenomenological study of grating behavior through the poles and zeros of the scattering operator," *J. Opt. Soc. Am. A*, Vol. 12, No. 3, 513–523, 1995.
2. Shipman, S. P. and S. Venakides "Resonant transmission near nonrobust periodic slab modes," *Phys. Rev. E*, Vol. 71, No. 2, 026611, 2005.
3. Liu, H. and P. Lalanne "Microscopic theory of the extraordinary optical transmission," *Nature*, Vol. 452, 728–731, 2008.
4. Bykov, D. A. and L. L. Doskolovich "Spatiotemporal coupled-mode theory of guided-mode resonant gratings," *Opt. Express*, Vol. 23, No. 15, 19234–19241, 2015.
5. Bykov, D. A. and L. L. Doskolovich "$\omega - k_x$ Fano line shape in photonic crystal slabs," *Phys. Rev. A*, Vol. 92, 013845, 2015.
6. Golovastikov, N. V., D. A. Bykov, and L. L. Doskolovich "Spatiotemporal pulse shaping using resonant diffraction gratings," *Opt. Lett.*, Vol. 40, No. 15, 3492–3495, 2015.

# Fano effects in hybrid nanostructures

**Wei Zhang**[1*]
[1]Institue of Applied Physics and Computational Mathematics, Beijing 100088, China
[*]corresponding author: zhang_wei@iapcm.ac.cn

**Abstract**-We discuss various aspects of Fano effects in hyrid nanostructures made of metallic nanoparticles, semiconductor quantum dots and molecules. The interaction between excitons and plasmons leads to the formation of the hybrid exciton. Moreover, the interference between the exciton and plasmon channels leads to the nonlinear Fano effect, which appears in the strong field regime and can be tuned by the incident field. The Fano effect in nanoparticle arrays with near field interaction and collective behavior has also been addressed.

Modern nanotechnology opens the possibility of combining nanocrystals of various materials with very different characteristics in one superstructure. Here we present semiclassical and complete quantum theories on the optical properties of nanocomplex composed of semiconductor quantum dots, molecules, and metallic nanoparticles. Excitons and plasmons in such hybrid structures become strongly coupled, which leads to the formation of new excitation-the hybrid exciton with interaction renormalized frequency and lifetime. Moreover, the interference between the exciton channel and plasmon channel leads to the nonlinear Fano effect, which appears in the strong field regime and can be tuned by the incident field[1]. The usual linear Fano effect is recovered in the weak field limit. We establish the relation between quantum and semiclassical theory[2]. The combination of the nonlinearity of exciton and plasmon leads to a transition from saturated absorption to anti-saturated absorption[3].

The collective dynamics in nanoparticle arrays, such as metallic nanoparticle dimer chains, may lead to new features. The strong near field in the dimer gap and the far field interactions among the metallic nanoparticles lead to anomalous collective hotspots with dual enhancement of the electromagnetic field. In particular, the interference between the incident field and the induced internal field leads to Fano-type effect with Wood anomaly related destructive interference and the strong resonance with an extremely narrow width. Our systematic study shows that the correlation between the local structure and the global structure leads to an optimal orientation of the dimer for the largest gap field enhancement[4].

**REFERENCES**

1. Zhang, W., Govorov A. O., and Bryant G.W., "Semiconductor-metal nanoparticle molecules: hybrid exciton and nonlinear Fano effects," *Phys. Rev. Lett.* Vol. 97, No. 14, 146804, 2006.
2. Zhang, W. and Govorov A. O., "Fano effect in hybrid metal-semiconductor nanostructures: The case of strong nonlinearity," *Phys. Rev. B* Vol. 84, No. 8, 081405, 2011.
3. Nan F., Zhang Y. F., Li, X. F., Zhang X. T., Li H., Zhang, X. H., Jiang, R.B., Wang J. F., Zhang, W., Zhou, L., Wang, J. H., Wang, Q. Q. and Zhang, Z. Y., "Unusual and Tunable One-Photon Nonlinearity in Gold-Dye Plexcitonic Fano Systems," *Nano Lett.*, Vol. 15, No. 4, 2705–2710, 2015.
4. Song, G. and Zhang W., "Fano Resonance Induced Anomalous Collective Hotspots in Metallic Nanoparticle Dimer Chains," *arxiv*: 1602.04896.

# Sharp Fano resonances arising from coupling between surface plasmon polariton and waveguide modes

**S. Hayashi[1,2*], D. V. Nesterenko[2], A. Rahmouni[2] and Z. Sekkat[2,3,4]**

[1]Kobe University, Japan

[2]Morrocan Foundation for Advanced Science, Innovation and Research, Morroco

[3]University Mohammed V, Morroco

[4]Osaka University, Japan

[*]corresponding author: s.hayashi@dragon.kobe-u.ac.jp

**Abstract**-Fano resonances arising from coupling between the surface plasmon polariton and planar waveguide modes supported by multilayer planar structures are studied theoretically and experimentally. Sharp Fano resonances with high Q values in angle-scan attenuated total reflection (ATR) spectra are theoretically predicted and confirmed experimentally. The multilayer structures can easily be fabricated without nanofabrication techniques and allow potential applications in sensing and enhanced spectroscopy.

In spite of the intensive work done to generate Fano lineshapes in plasmonic nanostructures and metamaterials, the fabrication of the nanostructures is not always easy and time consuming, preventing their real applications. Here, we present theoretical and experimental results on Fano lineshapes generated in simple planar multilayer systems that do not require nanofabrication techniques.

The structure studied and it's analogy with coupled harmonic oscillators are shown in Fig.1. The structure is a combination of a metal-dielectric interface, which supports surface plasmon polariton (SPP) modes, and a waveguide structure, which supports planar waveguide (PWG) modes. Based on the electromagnetic (EM) theory, we have shown that the structure allows coupling between SPP and PWG modes when the optical constants and the thicknesses of the layers are appropriately chosen [1,2]. The layer of dielectric 1 acts as a spacer layer and the coupling strength can be controlled by its thickness. A remarkable consequence of the coupling is the appearance of the Fano resonance and plasmon-induced transparency (PIT) in the angle-scan attenuated total reflection (ATR) spectra [1,2]. Results of EM calculations can be well reproduced by the mechanical model of two coupled oscillators as schematically shown in Fig.1 (b). The Fano lineshape is much narrower than the conventional SPP resonance, implying that the proposed structure is very much promising for realizing optical sensors with high sensitivities.

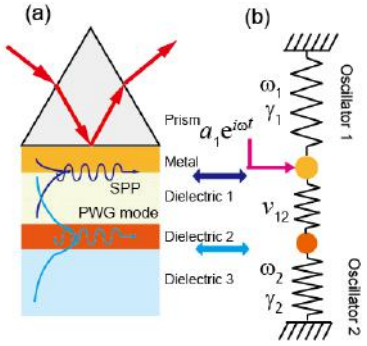



**Fig.1** (a) Structure studied and (b) analogy with coupled harmonic oscillators.

To demonstrate experimentally the generation of the Fano lineshape in the proposed structure, we fabricated the sample schematically shown in Fig. 2 and performed angle-scan ATR measurements using a 632.8 nm line of a He-Ne laser [3]. The sample consists of a 45 nm thick Ag film prepared by vacuum evaporation, a

fluoropolymer Cytop layer and a PMMA layer spin coated successively onto the Ag film. The sample attached to a SF11 prism was mounted on a rotating stage and the reflectance was measured as a function of the incident angle. The polarization of the incident light was set to the p-polarization. Figure 3 (a) shows an ATR spectrum obtained for a sample without the Cytop spacer layer. The thickness of the PMMA layer was estimated to be $d$ = 1790 nm. The sample can be regarded as a metal-clad waveguide and exhibits sharp dips corresponding to the $TM_0$ and $TM_1$ PWG modes as well as a broad dip corresponding to the SPP resonance. For this metal-clad waveguide structure, the coupling between the SPP and PWG modes is not achieved because their propagation constants do not coincide and the resonances are separated from each other.

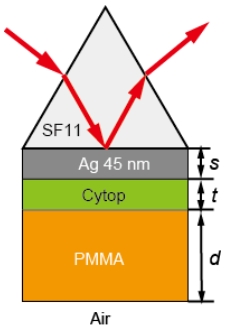



**Fig.2** Sample prepared for ATR measurements.

The introduction of a Cytop spacer layer (estimated thickness of $t$= 400 nm) allows the coupling and leads to a pronounced Fano resonance located around 55° in Fig. 3(b). The Fano resonance is due to the coupling between the SPP mode at the Ag/Cytop interface and the $TM_0$ PWG mode supported by the PMMA layer ($d$= 920 nm) surrounded by the Cytop layer and air. Figure 3(c) demonstrates that the experimental line shape (dots) can be fitted very well to the Fano lineshape function (black solid line). A Q factor calculated from the fitting parameters is as high as ~350. The experimental spectra in Figs. 3 (a) and (b) are fairly well reproduced by the EM calculations presented by blue solid lines.

We demonstrated both theoretically and experimentally the generation of sharp Fano resonances in simple planar multilayer structures. Our results may open a new avenue for realizing optical sensors with extremely high sensitivities and enhanced spectroscopies with extremely high enhancement factors.

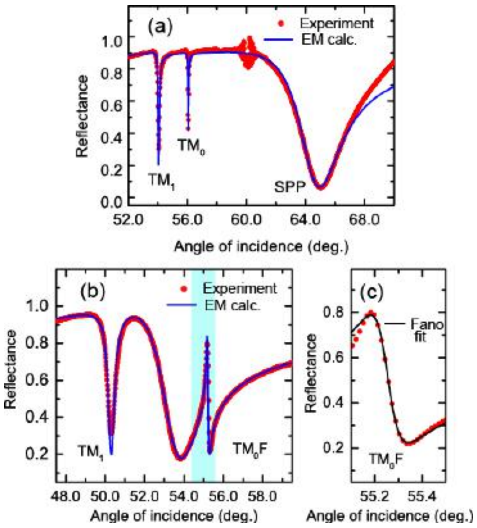



**Fig.3** (a) ATR spectrum obtained for a metal-clad waveguide structure. (b) ATR spectrum obtained for a coupled SPP-PWG structure with a spacer layer. (c) Fano fit to the experimental points.

**Acknowledgements**, This work was supported by an Osaka University International Joint Research Promotion Program: the Handai project.

## REFERENCES

1. Hayashi, S., D.V. Nesterenko and Z. Sekkat, "Fano resonance and plasmon-induced transparency in waveguide-coupled surface plasmon resonance sensors," *Appl. Phys. Express*, Vol. 8, 022201, 2015.
2. Hayashi, S., D.V. Nesterenko and Z. Sekkat, "Waveguide-coupled surface plasmon resonance sensor structures: Fano lineshape engineering for ultrahigh-resolution sensing," *J. Phys. D: Appl. Phys.*, Vol. 48, 325303, 2015.
3. Hayashi, S., D.V. Nesterenko, A. Rahmouni and Z. Sekkat, "Observation of Fano line shape arising from coupling between surface plasmon polariton and waveguide modes," *Appl. Phys. Lett*, Vol. 104, 051101, 2016.

# Utilizing Fano resonances in chiral and dielectric nanoparticle oligomers

**B. Hopkins**[1,*], **F. Monticone**[2],**A. E. Miroshnichenko**[1], **A. Alù**[2] **and Y. S. Kivshar**[1]

[1] Nonlinear Physics Centre, Australian National University, Australia
[2] Department of Electrical and Computer Engineering, University of Texas at Austin, USA
* ben.hopkins@anu.edu.au

**Abstract**— We present recent results on the use of Fano resonances to provide (i) circularly-dichroic behavior in planar chiral nanoparticle oligomers, and (ii) strong enhancement of magnetic response from silicon nanoparticles. This work thereby illustrates a more directed use of Fano resonances to produce novel optical behavior in nanoantenna and metasurface scattering geometries.

A growing proportion of metamaterials research is being devoted toward planar metasurfaces; ultrathin functional surfaces that avoid the complication of structural design related to three-dimensional fabrication. However, planar devices are also subject to limitations owing to the stronger symmetry constraints involved with being essentially two-dimensional. Perhaps one of the most recognized of these limitations is the absence of circular dichroism at normal incidence; the extinction of left- and right-handed circularly polarized light remains identical. Here we present a recent realization that planar chiral plasmonic nanostructures still offer substantial capacity to change their chiral optical response through Fano resonances [1]. As seen in Figure 1, a planar chiral oligomer that exhibits a Fano resonance will produce dominantly material absorption losses or scattering losses depending entirely the handedness of an incident circular polarization.

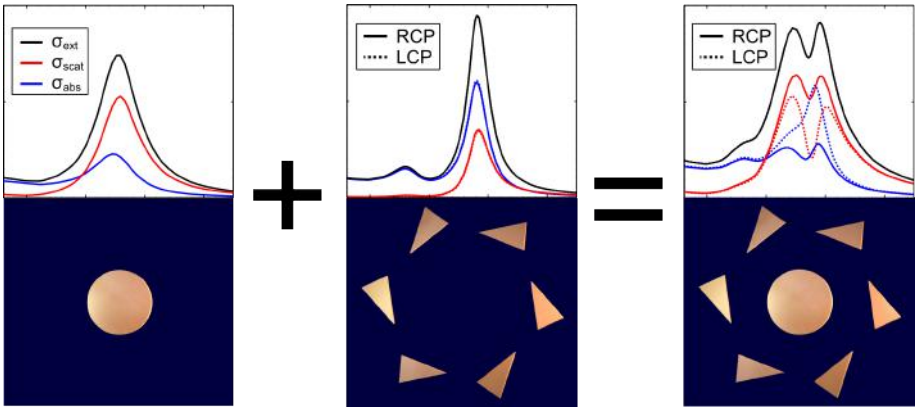



Figure 1: Simulation results showing the formation of Fano resonance induced circular dichroism in the scattering and absorption spectra of a gold planar chiral oligomer at normal incidence. Simulations were performed with *CST Microwave Studio*.

This demonstrates a promising avenue by which planar structures can offer circular-polarization dependent optical response to rival those of true chiral nanostructures. However, a large area of interest behind chiral nanostructures regards their optical interaction with chiral proteins or chemical agents, for which metals are generally hindered by their strong chemical activity. Simultaneously, the material losses in plasmonic nanostructures inherently limits their efficiency, particularly in the transmission regime. One option to circumnavigate these issues is to use nanostructures made from silicon or other dielectric materials. In doing so, we are inherently drawn to account for the propensity of individual nanoparticles made from high-index dielectric materials to exhibit both electric and magnetic responses [2]. A particular consequence of this in a symmetric quadrumer geometry is that the magnetic dipoles of individual silicon nanospheres can be made to interact with the magnetic dipole produced by the collective circulation of electric dipoles [3]. As is illustrated in Fig. 2(a,b), such a quadrumer geometry is able to provide two basis vectors that radiate

as per magnetic dipoles. In Fig. 2(c,d) we further show the formation of a Fano resonance from these these two dimensions of magnetic dipolar response in a ceramic ($\epsilon = 16$) microwave analog of silicon nanospheres. This effectively shows that we are able to produce a Fano resonance that will radiate as per a pure magnetic dipole.

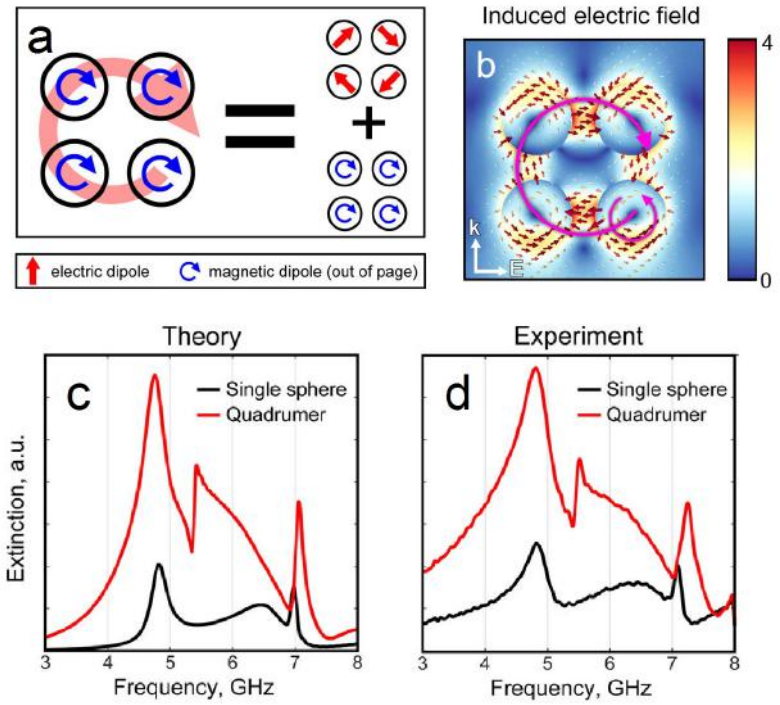



Figure 2: (a) Schematic showing the two basis vectors of electric and magnetic dipoles in a symmetric dielectric quadrumer that contribute towards the structure's collective magnetic dipole response. (b) CST numerics of the electric near-field showing evidence of such a, two-dimensional, magnetic response. (c) Simulation and (d) experimental results showing the formation of a Fano resonance in the magnetic dipole response of an equivalent quadrumer at GHz frequencies using $\epsilon = 16$ ceramics.

This interaction in dielectric oligomers demonstrates the truly intertwined nature of electric and magnetic driving fields in dielectric oligomers and thereby presents a host of opportunities for future work on bianisotropic behavior in chiral dielectric oligomer geometries. In this regard, it is worth recognizing that both systems we presented here have utilized discrete rotational symmetry, which, for normal-incidence operation, conserves the handedness of circularly polarized plane waves in transmision and flips the handedness of the reflected wave [4]. Such symmetry-enforced helicity opens possibilities for realizing *uniform enhancement* of near-field helicity, such as was originally proposed for dual nanoparticles [5]. Indeed, the work we present here illustrates how a more directed use of Fano resonances permits the development of both novel and useful optical behavior from nanoparticle oligomer scattering geometries.

**REFERENCES**


1. B. Hopkins, A. N. Poddubny, A. E. Miroshnichenko and Y. S. Kivshar, "Circular dichroism induced by Fano resonances in planar chiral oligomers," *Laser Photon. Rev.*, Vol. 10, No. 1, 137–146, 2016.
2. A. I. Kuznetsov, A. E. Miroshnichenko, Y. H. Fu, JB. Zhang and B. Lukyanchuk "Magnetic Light," *Sci. Rep.*, Vol. 2, 492, 2012.
3. B. Hopkins, D. S. Filonov, A. E. Miroshnichenko, F. Monticone, A. Alù and Y. S. Kivshar, "Interplay of Magnetic Responses in All-Dielectric Oligomers To Realize Magnetic Fano Resonances," *ACS Photon.*, Vol. 2, 724–729, 2015.
4. I. Fernandez-Corbaton, "Forward and backward helicity scattering coefficients for systems with discrete rotational symmetry," *Opt. Express*, Vol. 21, No. 24, 29885, 2013.
5. I. Fernandez-Corbaton and C. Rockstul, "Objects of maximum electromagnetic chirality," *arXiv:1508.04049*, 2015.

# Lineshape inheritance and coherent absorption at the boundary between weak and strong critical coupling in lossy coupled oscillators

**S. Zanotto**[1*] **and A. Tredicucci**[2,3]

[1]Istituto Nazionale di Ottica – CNR, and LENS, Via Nello Carrara 1, 50019 Sesto Fiorentino (FI), Italy

[2]NEST, Istituto Nanoscienze - CNR, P.za S. Silvestro 12, 56127 Pisa, Italy

[3]Dipartimento di Fisica "E. Fermi", Università di Pisa, Largo Pontecorvo 3, 56127 Pisa, Italy

[*]corresponding author: simone.zanotto@ino.it

**Abstract**- We discuss a model describing key features concerning the lineshapes and the coherent absorption conditions in Fano-resonant dissipative coupled oscillators. The model treats on the same footing the weak and strong coupling regimes, and includes the critical coupling concept, hence enabling to explore the borders between these regimes, usually considered as separate frameworks. Due to the wide generality of the model, which can be adapted to various fields like nanophotonics, plasmonics, and optomechanics, we envisage that the analytical formulas presented here will be crucial to effectively design devices and to interpret experimental results.

Among the resonance lineshapes, Fano lineshapes deserve a special interest since they first enabled to interpret atomic and molecular physical processes, and subsequently the response of nanostructured systems like photonic crystals and plasmonic resonators [1,2]. In general, resonances may be absorptive, in the sense that part of the energy vehicled by the excitation field is converted into other forms. While absorption, in the sense of losses, is usually an undesired effect, in other frameworks it can be harnessed to enable functional operations like detection, wavelength conversion or quantum state transfer. Absorbing systems also exhibit a rich physics, as for instance that of coherent perfect absorption (CPA) which shares some key mathematical aspects with non-Hermitian quantum systems and parity-time symmetry breaking [3].

In its original formulation, the theory of CPA is very general, as it relies on fundamental properties of the scattering matrices [4]; when dealing with specific systems, appropriate modeling tools are needed. However, due to the possibly complex nature of the systems under analysis, microscopical approaches are often time-consuming, and an analytical model would be an advantage both for the interpretation of experimental results and as a guide to target ab-initio simulations. We analyzed the CPA in a two-lossy-oscillator coupled-mode model with a non-resonant background, which, thanks to its generality, can be applied to a number of emergent frameworks like photon- or plasmon-exciton coupled systems, multiplasmon resonators, coupled photonic cavities, and optomechanic devices.

In the literature there is a plenty of works about the interpretation of resonances in those systems as Fano resonances. However, to our knowledge there is no systematic analysis of the simultaneous presence of a non-resonant background and two coupled resonances having similar lifetimes, arranged in a two-port configuration. The presence of two coupled resonances opens up the possibility to describe the well-known *strong coupling* regime, and the possibility to handle losses enables to deal with the *critical coupling* regime, of great relevance in several applications. The exploration of the border between weak, strong, critical and

non-critical coupling regimes proved to be fruitful, in that two effects, which to our knowledge have not been reported before, were observed. The first is what we named *lineshape inheritance*. This consists in the fact that the Fano transmittance and reflectance resonances typical of a single, uncoupled resonator are inherited by the two-coupled-resonator system. Furthermore, it turns out that absorption lineshapes are described by another, *universal* lineshape, depending on few, physically meaningful parameters.

These findings are summarized in Fig. 1 and commented in the figure caption.

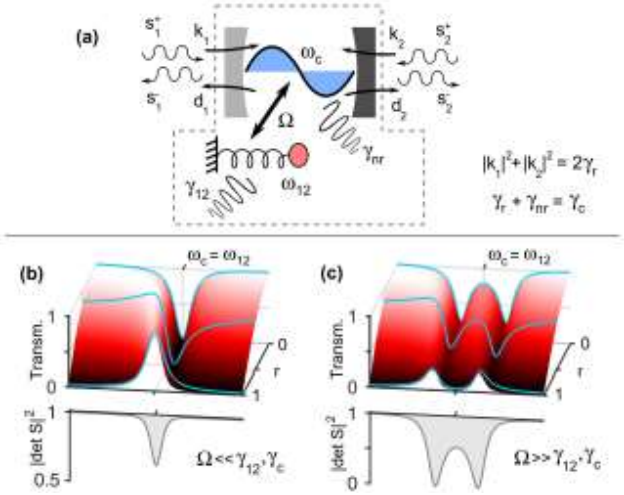



**Fig. 1.** Panel (a): sketch of the coupled oscillator model under analysis. Panels (b-c): spectral lineshapes of the weakly (b) and strongly coupled (c) system. The transmittance lineshape can be tuned through a parameter *r*, which quantifies the non-resonant scattering, and is inherited from the weakly to the strongly coupled case. The S-matrix determinant, instead, is given by a universal function, independent of the trasmittance (and reflectance) lineshapes. The S-matrix determinant is eventually connected to the absorption lineshape and to the CPA poles, which are, as well, independent of any Fano-like lineshape behavior.

In conclusion, we developed a model of wide generality, which we believe to be of great significance in the development of many active research topics like nanophotonics, plasmonics or optomechanics, where the modeling of a complex system would draw advantage from analytical expressions depending on few parameters of direct interpretation.

**Acknowledgements.** The authors gratefully acknowledge Raffaele Colombelli for precious suggestions and insights on the application of coupled-mode models to strongly-coupled systems.

## REFERENCES

1. Luk'yanchuk, B. et al. "The Fano resonance in plasmonic nanostructures and metamaterials". *Nature materials* **9**, 707–15
2. Miroshnichenko, A. E., Flach, S. and Kivshar, Y. S., "Fano resonances in nanoscale structures". *Rev. Mod. Phys.* **82**, 2257–2298 (2010).
3. Longhi, S., "PT-symmetric laser absorber". *Physical Review A* **82**, 1–4 (2010).
4. Chong, Y. D., Ge, L., Cao, H. & Stone, A. D., "Coherent perfect absorbers: Time-reversed lasers". *Phys. Rev. Lett.* **105**, 053901 (2010).

# Ultra-High *Q* Fano Resonances and its Figure of Merit in metasurfaces

**Manukumara Manjappa[1], Longqing Cong[1], Yogesh Kumar Srivastava[1], Ningning Xu[2], Ibraheem Al-Naib[3], Weili Zhang[2], and Ranjan Singh[1,*]**

[1] Center for Disruptive Photonic Technologies, Division of Physics and Applied Physics, School of Physical and Mathematical Sciences, Nanyang Technological University, 21 Nanyang Link, Singapore 637371.

[2] School of Electrical and Computer Engineering, Oklahoma State University, Stillwater, OK, USA.

[3] Biomedical Engineering Department, College of Engineering, University of Dammam, Dammam 31441, Saudi Arabia

[*]corresponding author: ranjans@ntu.edu.sg

**Abstract**

Metamaterial resonators offer a unique advantage of shape and size dependent resonance properties that has been hugely favored in controlling and manipulating the light matter interaction with a great precision. Symmetry within these resonator structures play a significant role in dictating the nature of observed resonances and breaking the symmetry of the structure gives rise to the excitation of very sharp Fano resonances that remain inaccessible in the case of symmetric resonators. Fano resonances have an asymmetric line shape that results from the destructive interference between the discrete background and the broad resonant scattering processes.

Fano resonances offer exciting features like high quality (*Q*) factors and strong field enhancement that are exploited in the resonant ultrasensitive sensors in bio-sensing applications and are used for enhancing the gain in the plasmonic laser and nonlinear systems. Here, we present an overview of our research on high *Q*-Fano resonances using the metamaterials at terahertz frequencies and our recent investigation on the strong influence of material conductivity on the ultra high *Q* Fano resonances. These results demonstrate that the choice of the material becomes extremely important in exciting the very sharp Fano resonances with higher figure of merit in the far infrared frequencies.

**REFERENCES**

1. L Cong, M Manjappa, N Xu, I Al-Naib, W Zhang and R Singh, "Fano Resonances in Terahertz Metasurfaces: A Figure of Merit Optimization," *Advanced Optical Materials*, 3 (11), 1537-1543, 2015.

2. Y K Srivastava, M Manjappa, L Cong, W Cao, I Al-Naib, W Zhang and R Singh, "Ultrahigh-Q Fano Resonances in Terahertz Metasurfaces: Strong Influence of Metallic Conductivity at Extremely Low Asymmetry," *Advanced Optical Materials*, DOI: 10.1002/adom.201500504, 2015.
3. R Singh, W Cao, I Al-Naib, L Cong, W Withayachumnankul, W Zhang, "Ultrasensitive terahertz sensing with high-Q Fano resonances in metasurfaces," *Applied Physics Letters*, 105 (17), 171101, 2014.
4. R Singh, I Al-Naib, W Cao, C Rockstuhl, M Koch and W Zhang., "The Fano resonance in symmetry broken terahertz metamaterials," *Terahertz Science and Technology, IEEE Transactions on*, 3 (6), 820-826, 2013.

# Broken Symmetry Dielectric Resonators for Scalable, High Quality-Factor Fano Metasurfaces

**M. B. Sinclair[1,*], S. Campione[1,2], S. Liu[1,2], L. I. Basilio[1], L. K. Warne[1], W. L. Langston[1], T. S. Luk[1,2], J. R. Wendt[1], J. L. Reno[1,2], G. A. Keeler[1], and I. Brener[1,2]**

[1]Sandia National Laboratories, Albuquerque NM 87185 USA

[2]Center for Integrated Nanotechnologies, Sandia National Laboratories, Albuquerque NM 87185 USA

[*]corresponding author: mbsincl@sandia.gov

**Abstract**-We present a new, all-dielectric metasurface design that yields very high quality-factor Fano resonances, and is scalable from radio frequencies to near infrared wavelengths. In contrast to other recently demonstrated designs, our approach features a single resonator in the unit cell. We will present the theoretical underpinnings of the new design and present several experimental demonstrations of near-infrared Fano metasurfaces, including a gallium-arsenide based design that achieves a quality-factor of 600 at a wavelength of 1 μm.

Using metasurfaces to achieve high quality-factor (Q-factor) reflection and transmission resonances is desirable for a host of applications including sensing, optical detection, and optical modulation. However, it is difficult to achieve narrow spectral resonances with traditional metasurfaces due to: Ohmic losses in metal-based metasurfaces; and strong radiative coupling in all-dielectric metasurfaces. Recently, metasurface designs have emerged that exploit Fano resonances between "bright" and "dark" resonances [1-5]. Such designs have led to only modest improvements in Q-factor for metal designs [1,2], but for all-dielectric designs have produced high Q-factor resonances [3-5]. However, most all-dielectric designs demonstrated to date rely on multiple resonators per unit cell, and near-field coupling between the resonator elements.

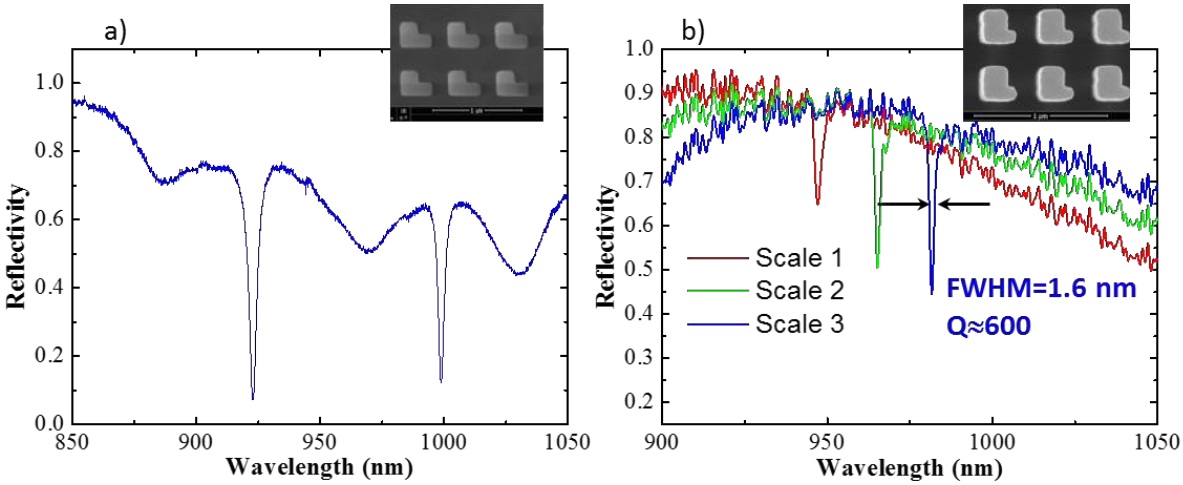



Figure 1. Experimental reflectivity spectra for: (a) Si-based Fano metasurface exhibiting a Q-factor of ~350 near 1 μm; and (b) GaAs-based Fano metasurfaces with three different size scales. Scale 3 exhibits a Q-factor of ~600 near 1 μm. The insets show SEMs of the respective structures.

Our design utilizes small geometric perturbations to reduce the symmetry of otherwise high-symmetry resonators such as cubic resonators. The symmetry breaking allows a coupling of a bright transverse electric dipole resonance (which couples strongly to the external field) to a dark longitudinal magnetic dipole resonance. The longitudinal magnetic resonance does not couple to the external field and its radiative decay is inhibited due to the local field arising from the other resonators in the two-dimensional array [6]. As a result, the losses of the longitudinal magnetic resonance are primarily limited by residual absorption, and very high Q-factors can be achieved. Importantly, since our approach relies on dielectric resonators, it is scalable to any spectral region in which transparent, high permittivity dielectric materials are available.

We will present a series of numerical simulations that unravel the origin of the Fano effect in our metasurfaces, including simulations of finite resonator arrays that demonstrate the increasing inhibition of radiative decay with increasing array size. We will also present the results of experimental studies of two Fano metasurfaces operating in the near infrared. The first is based on silicon-on-insulator arrays and achieves a Q-factor of ~350 near 1 μm (Fig. 1(a)). The second experimental demonstration is based upon arrays of GaAs resonators and achieves an even larger Q-factor of ~600 near 1 μm (Fig. 1(b)) due to the low absorptive losses of the direct bandgap GaAs. To our knowledge, this is the largest Q-factor ever reported for metasurfaces operating in this spectral range.

The achievement of such high-Q resonances along with their large field enhancements in GaAs is particularly exciting since it opens up new avenues to exploit the active and nonlinear properties of GaAs for devices such as lasers, photodetectors, modulators, nonlinear frequency converters, and sensors.

**Acknowledgements:** This work was supported by the U.S. Department of Energy, Office of Basic Energy Sciences, Division of Materials Sciences and Engineering and performed, in part, at the Center for Integrated Nanotechnologies, an Office of Science User Facility operated for the U.S. Department of Energy Office of Science. Sandia National Laboratories is a multi-program laboratory managed and operated by Sandia Corporation, a wholly owned subsidiary of Lockheed Martin Corporation, for the U.S. Department of Energy's National Nuclear Security Administration under contract DE-AC04-94AL85000.

**REFERENCES**

1. Wu, C.; Khanikaev, A. B.; Adato, R., Arju, N., Yanik, A. A., Altug, H. and Shvets, G., "Fano-resonant asymmetric metamaterials for ultrasensitive spectroscopy and identification of molecular monolayers," *Nat. Mater.*, Vol. 11, No. 1, 69-75, 2012.
2. Singh, R., Cao, W., Al-Naib, I., Cong, L., Withayachumnankul, W. and Zhang, W., "Ultrasensitive terahertz sensing with high-Q Fano resonances in metasurfaces," *Appl. Phys. Lett.*, Vol. 105, No. 17, 171101, 2014.
3. Wu, C., Arju, N., Kelp, G., Fan, J. A., Dominguez, J., Gonzales, E., Tutuc, E., Brener, I. and Shvets, G., "Spectrally selective chiral silicon metasurfaces based on infrared Fano resonances," *Nat. Commun.*, Vol. 5, 2014.
4. Yang, Y., Kravchenko, I. I.; Briggs, D. P. and Valentine, J., "All-dielectric metasurface analogue of electromagnetically induced transparency," *Nat. Commun.*, Vol. 5, 2014.
5. Zhao, W., Leng, X. and Jiang, Y., "Fano resonance in all-dielectric binary nanodisk array realizing optical filter with efficient linewidth tuning," *Opt. Express*, Vol. 23, No. 5, 6858-6866, 20156.
6. Tretyakov, S., *Analytical Modeling in Applied Electromagnetics*, Artech House: London, UK, 2003.

# Photonic crystal Fano structure for all-optical switching

**Y. Yu*, W. Q. Xue, H. Hu, L. K. Oxenløwe, K. Yvind, and J. Mork**
DTU Fotonik, Technical University of Denmark, Denmark
*corresponding author: yiyu@fotonik.dtu.dk

**Abstract**-We present experimental investigations on nonlinear photonic crystal Fano structures based on a waveguide coupled to a nanocavity. We show that the use of Fano resonance in combination with spatial symmetry breaking can enable significant improvement in high-speed low-energy all-optical switching.

Ultra-compact photonic structures performing optical switching at high-speed with low-energy consumption are essential for enabling integrated photonic chips that can meet the growing demand for information capacity [1]. In resonator based switches, the transmission of a data signal can be controlled by shifting the cavity resonance via an optical pump signal [2]. The extended tails of a Lorentzian spectrum imply large switching energies, since the resonance needs to be shifted significantly to properly switch the signal. In contrast, a Fano resonance [3] may show an asymmetric spectrum, featuring a large transmission change within a narrow wavelength range, determined by the transition from constructive to destructive interference between the discrete resonance and the continuum. Here we present our investigations on photonic crystal (PhC) Fano structures and show that the use of Fano resonances can significantly enhance the performance of all-optical switching.

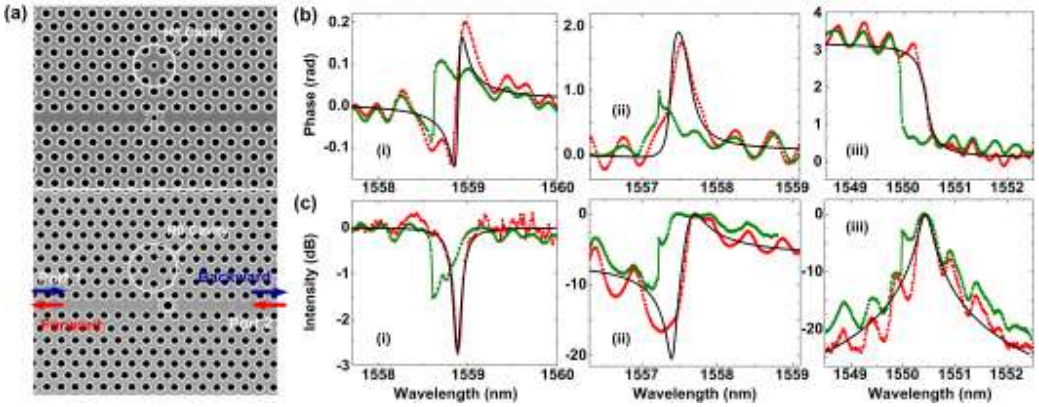



Fig. 1. (a) Upper: A symmetric Fano structure with an H1 nanocavity. Lower: an asymmetric Fano structure with an H0 nanocavity. Measured (b) phase and (c) intensity spectra of (i) open ($t_B^2$=1), (ii) partially-blocked ($t_B^2$=0.1) and (iii) blocked ($t_B^2$=0) structures with similar cavity Q-factor for two different input powers. Red/green dotted lines are experimental data at low/high input powers, respectively, and black solid lines are theoretical fits to the low-power, linear case.

Fig. 1(a) shows a fabricated PhC InP membrane where an H1 nanocavity is side-coupled to a waveguide. We add below the nanocavity a blockade hole (BH) as a partially transmitting element (PTE) that allows controlling the amplitude of the continuum-path [3], with a transmission coefficient $t_B$ that can be varied via the radius of the BH. By tuning $t_B$ between 0 to 1, cf. Figs. 1(b), (c), the transmission spectrum can be varied between a symmetric Lorentzian ((i) and (iii)) and an asymmetric Fano (ii) shape. For higher input power, a small nonlinear blueshift of the Fano resonance imposes a larger intensity change than for a Lorentzian, while the phase shifts are similar, which suggests that the Fano structures are promising for realizing intensity modulators with large modulation contrast and small chirp-parameter. In addition, by displacing the BH by one lattice constant towards port 2, we break the mirror symmetry of the Fano structure, cf. Fig. 1(b) where a smaller H0 nanocavity is

employed here. We find that the device transmission becomes nonreciprocal above a threshold input power (Fig. 2(a)), reflecting that the coupling rate between port 2 and cavity is larger than the coupling rate between port 1 and cavity so that different energies are excited in the cavity, leading to different nonlinear resonance shifts for the two directions [4,5]. This gives an advantage in optical switching since larger energy can be coupled into the nanocavity without scarifying the cavity Q-factor.

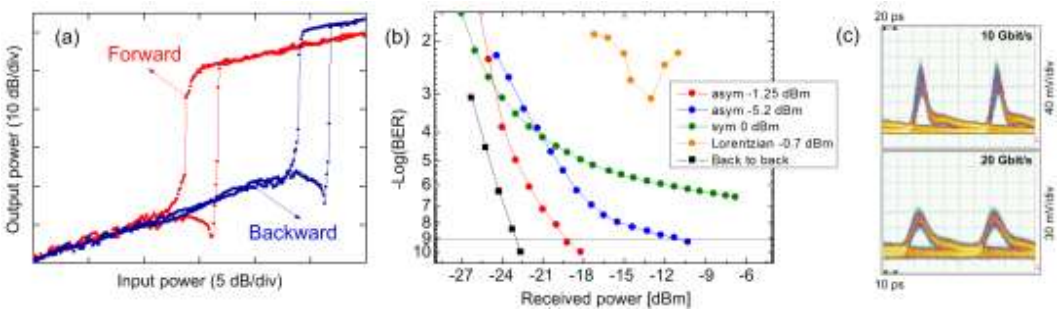



Fig. 2. (a) Output vs. input power in forward (red) and backward (blue) direction for a certain signal detuning in an asymmetric Fano structure. (b) BER measurements of modulated signal for different pump energies at 10 Gbit/s operation. The (red and blue)/green dotted lines correspond to the asymmetric/symmetric Fano structure and the yellow dotted line corresponds to the Lorentzian structure. (c) Corresponding eye diagrams of the asymmetric Fano structure.

To confirm this, we compare the switching performance between Lorentzian, symmetric and asymmetric Fano structures at 10 Gbit/s (Fig. 2(b)). Patterning effects are significantly suppressed and the energy consumption is reduced in the asymmetric Fano structure, enabling modulation rates higher than the carrier relaxation rate, which originates from the regeneration characteristics of the nonlinear transfer function of the Fano resonance [2]. Error-free operation can be achieved only in the asymmetric Fano structure whose BER increases somewhat at 20 Gbit/s, but still well below the threshold for employing forward error correction schemes [6].

In conclusion, we present experimental investigations on nonlinear photonic crystal Fano structures and show that the use of Fano resonances significantly enhances the switching performance and provides additional design freedom, which may also find other applications, e.g., within sensor and laser [7].

**REFERENCES**


1. Nozaki, K. *et al.* "Sub-femtojoule all-optical switching using a photonic-crystal nanocavity." *Nat. Photonics*, vol. 4, no. 7, 477–483, 2010.
2. Yu. Y. *et al.* "Fano resonance control in a photonic crystal structure and its application to ultrafast switching.," Appl. Phys. Lett., vol. 105, 061117, 2014..
3. Heuck, M. *et al.* "Improved switching using Fano resonances in photonic crystal structures.," *Opt. Lett.*, vol. 38, 2466–2468, 2013.
4. Fan, S. H. *et al.* "Temporal coupled-mode theory for the Fano resonance in optical resonators.," *J. Opt. Soc. Am. A.*, vol. 20, 569–572, 2003.
5. Yu, Y. *et al.* "Nonreciprocal transmission in a nonlinear photonic-crystal Fano structure with broken symmetry.," *Laser & Photonics Reviews*, vol. 9, 241–247, 2015.
6. Yu, Y. *et al.* "Ultrafast all-optical modulation using a photonic-crystal Fano structure with broken symmetry.," *Opt. Lett.*, vol. 40, 2357–2360, 2015.
7. Mork, J. *et al.* "Photonic crystal Fano laser: terahertz modulation and ultrashort pulse generation.," *Phys. Rev. Lett.* 113, 163901 (2014).

# High-*Q* perfect absorption based on coherent Fano resonances

**Xianji Piao*, Sunkyu Yu, and Namkyoo Park**
Photonic Systems Laboratory, School of ECE, Seoul National University, Seoul 08826, Korea
**E-mail*: xjpiao227@gmail.com

**Abstract** We realize narrowband perfect absorption of light by applying Fano resonances to guided-wave structures. By transplanting the stub structure of microwave theory into the optical platform we derive the Fano resonance for coherent incident waves, which allows the low-loss and high-*Q* perfect absorption. Its application as a simplest but fundamental building block in opto-thermal devices such as absorptive switch and opto-thermal emitter will be discussed.

Stub structures in microwave engineering[1] have received much attention in nanophotonics and plasmonics[2] due to their resonant-less design, alleviating the significant radiative loss of resonator structures from the abrupt potential change in their boundaries. However, most works have focused only on the optical reproduction of the signal filtering functionality of the microwave stub structure, ignoring the optics-specific property related to localized modes in visible and IR regimes. In this presentation, we introduce the Fano interference using the local mode of the optical stub structure, and demonstrate its application to opto-thermal devices: the high-*Q* perfect absorption at the scattering singularity.

Figure 1a,b shows the schematic of the proposed device. While the stub structure being resonant-less, its conversion to a highly-sensitive signal filtering[3,4] device can be achieved relatively easily; by applying the coherent incident condition realizing the interference-based mirror, to the Fano-resonant stub structure which derives the Fano 'time-reversed lasing'[5]. Results show a drastic improvement in the spectral *Q*-factor (Fig. 1c vs 1d vs 1e) in sharp contrast to general broadband applications of perfect absorption, and also an order of reduced material loss for the complete conversion from optical to thermal energy.

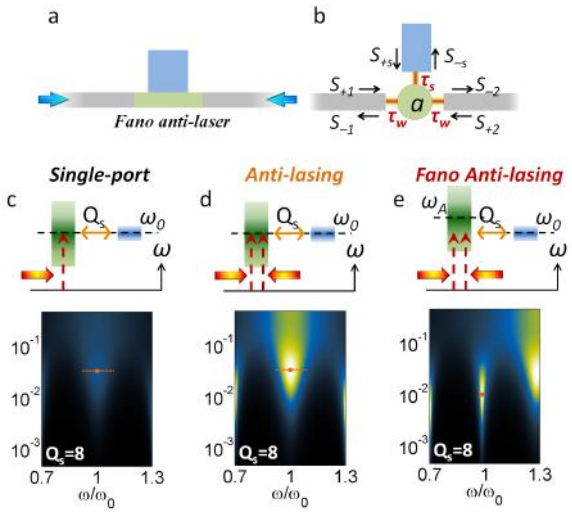



Figure 1. (a) Schematic and (b) its coupled mode modelling of low-loss Fano anti-laser. Absorption spectra of (c) a single-port incident absorber, (d) a non-Fano antilaser, and (e) a Fano antilaser.

The proposed dynamics of Fano anti-lasing can also be applied to the spatio-spectrally localized generation of thermal energy, for the realization of ultrahigh-*Q* absorptive switch, thermal emitter, and hyperspectral imaging; especially in the guided wave platform for example using photonic crystals. Figure 2 shows the example of dielectric photonic crystal anti-laser based on the platform of 2D square lattice of square rods. The spatio-spectral selectivity providing strong heat generation only inside the stub, selectively at the anti-lasing frequency with the scattering singularity.

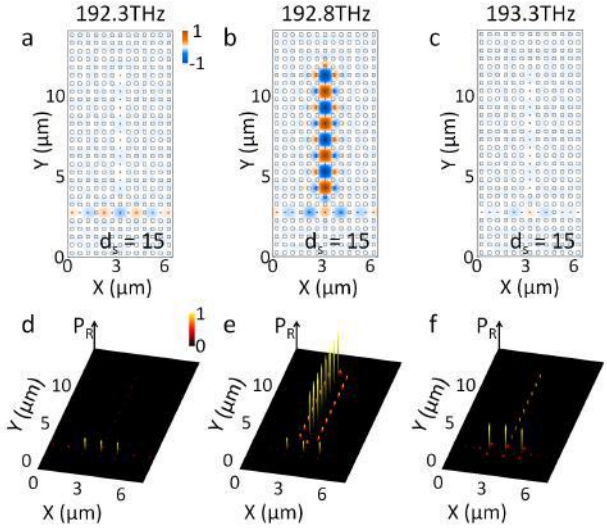



Figure 2. Photonic crystal anti-laser: (a-c) field distributions and (d-f) heat generation maps around the perfect absorption (b,e).

**REFERENCES**


1. Pozar, D. M., *Microwave Engineering*, John Wiley & Sons, 2005.
2. Matsuzaki, Y., Okamoto, T., Haraguchi, M., Fukui, M., and Nakagaki, M., "Characteristics of gap plasmon waveguide with stub structures," Opt. Express, Vol. 16, 16314-16325, 2008.
3. Piao, X., Yu, S., Koo, S., Lee, K., and Park, N., "Fano-type spectral asymmetry and its control for plasmonic metal-insulator-metal stub structures," *Opt. Express*, Vol. 19, No. 11, 10907–10912, 2011.
4. Piao, X., Yu, S., Park, N., "Control of Fano asymmetry in plasmon induced transparency and its application to plasmonic waveguide modulator," *Opt. Express*, Vol. 20, No. 17, 18994–18999, 2012.
5. Yu, S., Piao, X., Hong, J., and Park, N., "Progress toward high-Q perfect absorption: A Fano antilaser," *Phys. Rev. A*, Vol. 92, No. 1, 011802(R), 2015.

# Optical spin-dependent Fano resonances

**Xianji Piao, Sunkyu Yu, and Namkyoo Park***
Photonic Systems Laboratory, School of ECE, Seoul National University, Seoul 08826, Korea
*corresponding author: nkpark@snu.ac.kr

**Abstract** We introduce optical spin-dependent Fano resonance, using a chiral resonator enclosed within a pair of designed birefringent mirrors. It is shown that the interference between two nondegenerate resonances from the presence of birefringent mirrors develops differentiated Fano resonance for each spin. We also prove that these spin-dependent antisymmetric Fano line shapes originate from the counter-rotating spin eigenvectors. Utilizing the spectral separation between different spin, we propose a route to achieve optical spin angular momentum without the aid of circular dichroism or magneto-optical effect.

Fano resonance leads to asymmetric line shapes from the constructive and destructive interference between resonant states of different bandwidth[1,2]. Optical Fano resonance has been intensively studied with its advantage in high-$Q$ spectral sensitivity, for the applications including sensors, modulators, and switches[3-5].

In this presentation, extending past works on Fano resonances - mostly focusing on the spectral sensitivity at the fixed polarization state - we show that implementation of Fano resonance in the polarization space could open the pathway toward the manipulation of optical spin state. Using a chiral resonator enclosed within highly birefringent mirrors (Fig. 1a,b), we show that two suitably-designed resonant states with different resonant positions and bandwidth can provide Fano antisymmetric line shape for the reflectance of each spin[6] (Fig. 1c). Figure 1d shows the spin density $\sigma = (R_{e-}-R_{e+})/(R_{e-}+R_{e+})$, where $R_{e\pm}$ is the reflectance for each spin.

To clarify the origin of the observed spin-dependent Fano resonances, we develop an optical spin-form analytical equation based on the temporal coupled mode theory (CMT). For the material chirality with the natural rotation of $\theta$, we then have the spin-form CMT formula as

$$\frac{d}{dt}\begin{bmatrix} a_+ \\ a_- \end{bmatrix} = i\begin{bmatrix} \omega_s & \omega_d \\ \omega_d & \omega_s \end{bmatrix}\cdot\begin{bmatrix} a_+ \\ a_- \end{bmatrix} + \begin{bmatrix} \kappa_s e^{-i\theta} & \kappa_d e^{i\theta} \\ \kappa_d e^{-i\theta} & \kappa_s e^{i\theta} \end{bmatrix}\vec{S}_{in} \quad , \tag{1}$$

where $a_\pm$ is the amplitude of resonant mode for each handedness, $\boldsymbol{S}_{in}$ is the incidence, $\omega_s = (\omega_h+\omega_v)/2$, $\omega_d = (\omega_h-\omega_v)/2$, $\kappa_s=(\kappa_h+\kappa_v)/2$, $\kappa_d=(\kappa_h-\kappa_v)/2$, and $\omega_{h(v)}$ and $\kappa_{h(v)}$ are resonant frequency and coupling coefficient of horizontal (vertical) resonance, respectively. Equation (1) clearly reveals the underlying physics of the spin-dependent Fano resonances: the phase evolutions through $\kappa_d e^{\pm i\theta}$ for each spin, which is the origin of antisymmetric Fano response.

In Figure 1e and f, we also propose and demonstrate 'optical spin switching', utilizing the sharp transition of the optical spin density $\sigma$, reversing its sign from +1 to -1 (Fig. 1d). Figure 1e shows the spin density as a function of material chirality and applied refractive index tuning. Our results pave the way to nonmagnetic spin excitation both in IR and THz regimes.

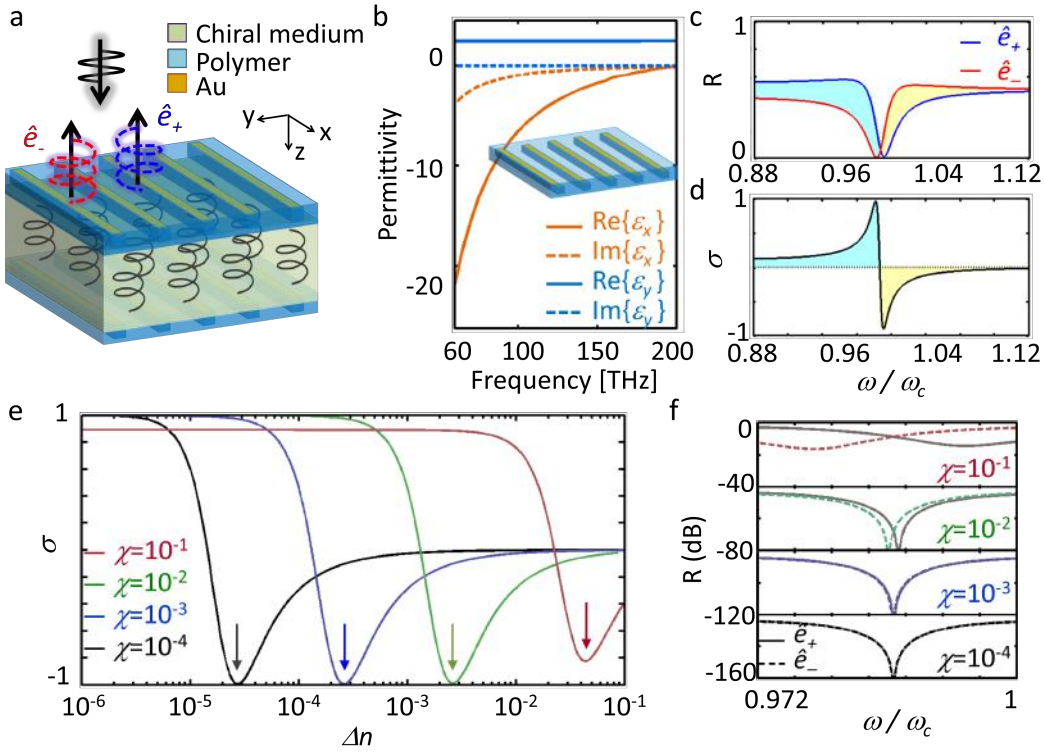



Figure 1. (a) Schematics of chiral resonator enclosed within birefringent mirrors. (b) Design of metamaterial birefringent mirror. (c) Reflectance and (d) spin density spectra. (e) Optical switching with the spin density as a function of optical chirality $\chi$ and modulated refractive index $\Delta n$, and (f) corresponding reflectance.

## REFERENCES


1. Fano, U., "Effects of Configuration interaction on intensities and phase shifts," *Phys. Rev.*, Vol. 124, 1866, 1961.
2. Miroshnichenko, A. E., Flach, S., and Kivshar, Y. S., "Fano resonances in nanoscale structures," *Rev. Mod. Phys.*, Vol. 82, No. 3, 2257–2298, 2010.
3. Piao, X., Yu, S., Koo, S., Lee, K., and Park, N., "Fano-type spectral asymmetry and its control for plasmonic metal-insulator-metal stub structures," *Opt. Express*, Vol. 19, No. 11, 10907–10912, 2011.
4. Piao, X., Yu, S., Park, N., "Control of Fano asymmetry in plasmon induced transparency and its application to plasmonic waveguide modulator," *Opt. Express*, Vol. 20, No. 17, 18994–18999, 2012.
5. Yu, S., Piao, X., Hong, J., and Park, N., "Progress toward high-Q perfect absorption: A Fano antilaser," *Phys. Rev. A*, Vol. 92, No. 1, 011802(R), 2015.
6. Piao, X., Yu, S., Hong, J., and Park, N., "Spectral separation of optical spin based on antisymmetric Fano resonances," *Sci. Rep.*, Vol. 19, No. 11, 10907–10912, 2011.

# Modal Fano resonances and off-diagonal photonic Lamb shift in reactively coupled waveguide-resonator systems

M. Ghulinyan[1], M. Bernard[1,2], F. Ramiro Manzano[2], G. Pucker[1], L. Pavesi[2] and I. Carusotto[3]

[1] Centre for Materials and Microsystems, Fondazione Bruno Kessler, I-38123 Povo, Italy

[2] Department of Physics, Nanoscience Laboratory, University of Trento, I-38123 Povo, Italy

[3] INO-CNR BEC Center and Department of Physics, University of Trento, I-38123 Povo, Italy

The coupling between a physical system and its environment is known to activate new channels through which the system may dissipate energy. Along this, the coupling may induce a shift of energy levels of the system. In atomic context, the manifestation of these phenomena are described through well known examples of the Coherent Population Trapping for decay channels and the electronic Lamb shift of electronic states of the Hydrogen atom.

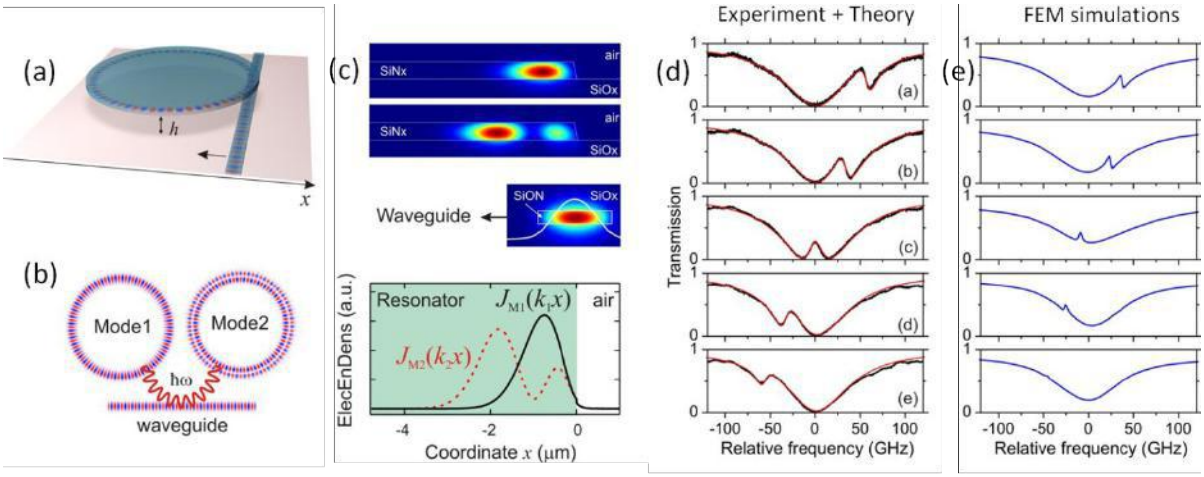



**Figure 1. (a) A sketch of the microphotonic device. (b) A sketch for the waveguide-assisted inter-mode reactive coupling. (c) The radial intensity profiles of first and second order mode families and the mode profile in the waveguide. (d) Experimentally measured Fano-shaped spectra of coupled modes and the theoretical model fits. (e) Finite Elelment Method simulations confirm the predicted and measured lineshapes.**

Here we report on a joint theoretical and experimental study of such coupling for an integrated microresonator device which is vertically coupled to the waveguide (Fig.1(a)). The developed theory predicts that the presence of a neighboring waveguide induces a reactive indirect coupling between the resonator modes, which are intrinsically orthogonal and, therefore, should not couple directly in the absence of the waveguide (Fig.1(b,c)). Such a coupling, analogous to an off-diagonal Lamb shift known from atomic physics, alters the bare optical frequencies of the modes and manifests as peculiar Fano lineshapes in the transmission spectra

of the waveguide. These theoretical predictions are both validated by 3D numerical simulations and confirmed in the experiments (Fig.1(d,e)).

Moreover, we demonstrate experimentally the possibility to induce thermo-optically clear features of Electromagnetically Induced Transparency by tuning the Fano lineshape of coupled resonator modes (Fig. 2).

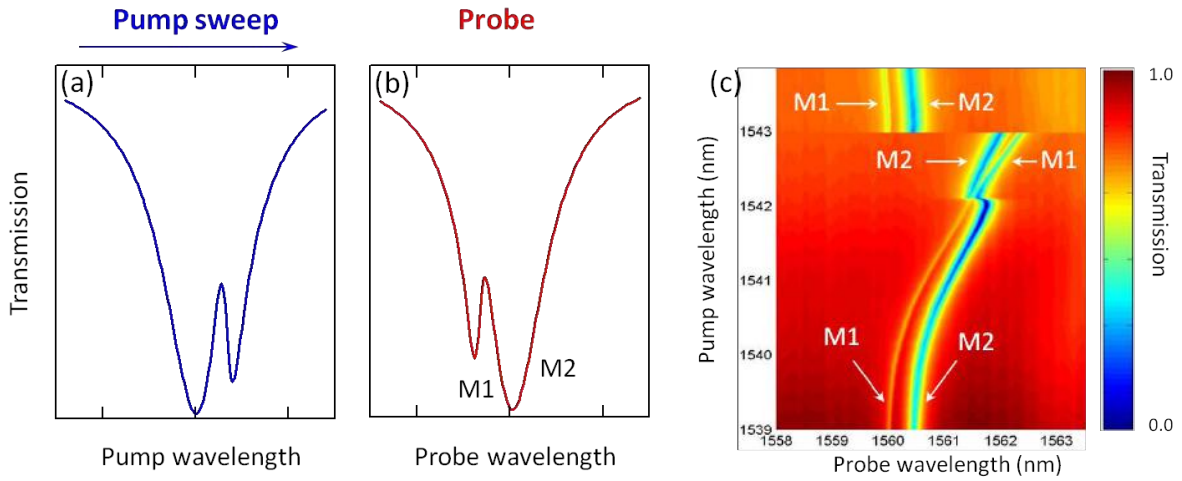



**Figure 2. Thermo-optical tuning pump-probe experiments. (a) The pump laser wavelength is swept across a pair of coupled modes and (b) the Fano spectrum of another pair of coupled modes is probed dynamically. The different mode families undergo a different amount of thermo-optical red shift (the narrow mode red-shifts faster and further) which permit to dynamically alter the relative detuning. (c) The map of the dynamical tuning shows a complete inversion of the relative detuning, i.e. a clear EIT-like crossing of the narrow and broad modes of the probe spectrum.**

Our study provides an important insight on the phenomenon of inter-mode dissipative and reactive couplings due to the neighboring waveguide. This phenomenon may find applications in designing resonator devices with nonlinear and quantum functionalities. From a broader perspective, our work provides a generic model which may be useful to study a fundamental feature of the theory of open systems, namely, the environment-mediated couplings – the off-diagonal photonic Lamb shift – between different modes of a system.

References


[1]. M. Ghulinyan *et al.*, "Oscillatory vertical coupling between a whispering-gallery resonator and a bus waveguide," **Phys. Rev. Lett. 110**, 163901 (2013).

[2]. M. Ghulinyan *et al.*, "Inter-mode reactive coupling induced by waveguide-resonator interaction", **Phys. Rev. A 90**, 053811 (2014).

[3]. M. Bernard *et al.*, "Off-diagonal photonic Lamb shift in reactively coupled waveguide-resonator system", **Proc. SPIE 9520** (2015).

[4]. M. Bernard *et al.*, (submitted, 2016)

# Degenerate Fano resonance between multipole surface plasmons in a metallic nanohole array

**M. Nishida**[1], **N. Hatakenaka**[2], **and Y. Kadoya**[1]

[1]Graduate School of Advanced Science of Matter, Hiroshima University, Higashi-Hiroshima, 739-8530, Japan

[2]Graduate School of Integrated Arts and Science, Hiroshima University, Higashi-Hiroshima, 739-8521, Japan

mnishida@hiroshima-u.ac.jp

**Abstract**— When the size of a nanohole occupies relatively large portion of the unit cell of an array of nanoholes perforated in thin metallic film, the surface plasmon polaritons (SPPs) are combined by the higher order waveguide modes of the holes to produce multipole surface plasmons (MSPs): coupled SPPs with multipole texture on the electric field distributions. It is shown that the degeneracy between MSPs with different symmetries produces sharp Fano resonance and causes nearly perfect absorption with strong field enhancement.

At the interface between a metal and a dielectric, a kind of surface bound state, called surface plasmon polariton (SPP), is created by the coupling between the plasma oscillation in the metal and the electromagnetic wave in the dielectric. The SPP excitation confines electromagnetic fields near the interface, and causes strong enhancement, which depends strongly on the environment near the metallic surface. Utilizing this peculiarity of SPP, many researches have been conducted aiming to realize high-sensitivity biosensors and nanoscale optical devices, controlling the SPP characteristics by metallic nanostructures. A metallic nanohole array is one of the simplest nanostructures; a metallic film perforated by a periodic array of subwavelength holes. As was found by Ebbessen et al. [1], the light transmission through this system can be resonantly enhanced by orders of magnitude larger than the expectation of the usual theory. There are some interpretations of this extraordinary optical transmission (EOT) [2], but the Fano resonance seems to give a unified view of the origin of EOT [3,4]. A metallic nanohole array fulfills the condition of the Fano resonance; direct transmissions through the holes and leaky bound states, i.e., SPPs coupled with the external radiation by the periodic array of holes as a diffraction grating.

Another peculiarity of this system is that external light can penetrate into the metal region using evanescent waveguide modes of the holes, and produce a kind of surface bound state that has similar property with SPP, even when the metal behaves as a perfect electric conductor (PEC) where SPP does not exist [5]. Therefore, the surface bound states in nanohole arrays of real metals are considered to be hybrid modes between SPPs of metal surface and the evanescent waveguide modes of holes, whose detailed characterization is necessary to understand fully the Fano resonance phenomena in this system.

In recent paper [6], we have shown that when the size of the nanohole occupies a large portion of the unit cell, the SPPs at both sides of the film are combined by the higher order waveguide modes of the holes to produce multipole surface plasmons (MSPs): coupled surface plasmon modes with multipole texture on the electric field distributions. Due to the multipole nature of these modes, multiple dark modes coexist to produce a variety of Fano resonance structures on the transmission and reflection spectra. When the Fano resonance occurs, the MSP is excited strongly, and confines electromagnetic field near the metallic surface. Thus, the Fano resonances also appear as absorption peaks due to the loss of metal. Figure 1(a) shows the absorption spectra together with the band structure of MSPs calculated using the coupled mode method [2, 6]. You can see the correspondence between the absorption peaks and the dispersion relations of MSPs.

The most striking feature in Figure 1(a) is that nearly perfect absorption occurs when a pair of MSPs are degenerate due to the difference of symmetry. This phenomenon can be considered as a result of degenerate Fano resonance. It is known that the Fano resonance by a pair of degenerate modes in lossless multimode cavities produce a quite sharp resonance peak [7]. Figure 1(b) shows the transmission and reflection spectra calculated by omitting the imaginary part of the dielectric function of the metal. We can see that a sharp reflection peak with the same property also appears in lossless nanohole array systems when MSPs are degenerate. The sharpness of the resonance

means that the energy remains in the localized modes in a long period of time. If the metal loss is included, almost all the incident energy is consumed around the metal region before it is radiated back, as shown by the transmission and reflection spectra in Figure 1(c). The electric field enhancement at the surface of metal film, $|E|^2/|E_0|^2$, is also shown in Figure 1(c). We can see that the field enhancement is increased strongly by the occurrence of degenerate Fano resonance. Thus, the high degrees of freedom of multipole surface plasmons in metallic nanohole arrays will open the possibility to improve the functionality of plasmonic sensors and devices via degenerate Fano resonances.

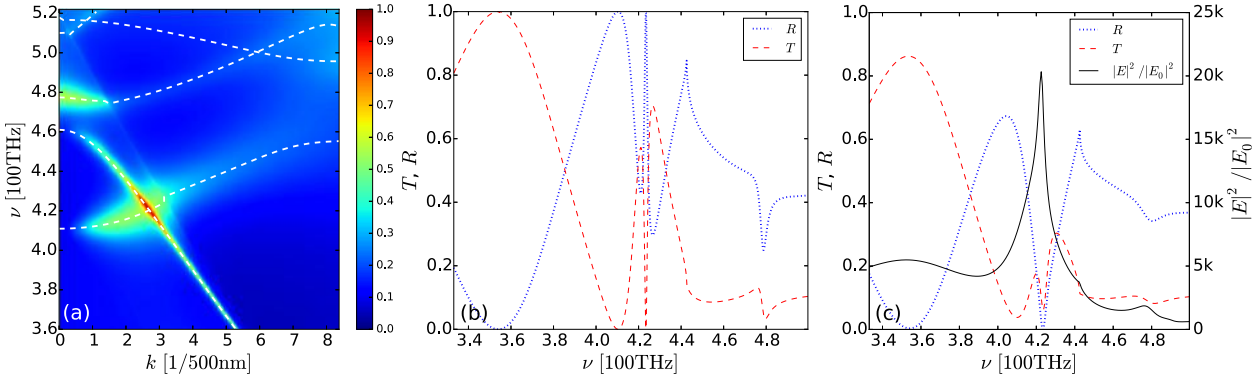



Figure 1: (a) Absorption spectra and dispersion relations of multipole surface plasmons. (b) Transmission ($T$) and reflection ($R$) spectra for a lossless metal film. (c) Transmission ($T$), reflection ($R$) and field enhancement ($|E|^2/|E_0|^2$) spectra for a real metal film.

**REFERENCES**


1. Ebbesen, T. W., H. J. Lezec, H. F. Ghaemi, T. Thio, and P. A. Wolff, "Extraordinary optical transmission through sub-wavelength hole arrays," *Nature (London)*, Vol. 391, No. 6668, 667–669, 1998.
2. García-Vidal, F. J., L. Martí-Moreno, T. W. Ebbesen, and L. Kuipers, "Light passing through subwavelength apertures," *Rev. Mod. Phys.*, Vol. 82, No. 1, 729–787, 2010.
3. Sarrazin, M., J.-P. Vigneron, and J.-M. Vigoureux, "Role of Wood anomalies in optical properties of thin metallic films with a bidimensional array of subwavelength holes," *Phys. Rev. B*, Vol. 67, No. 8, 085415, 2003.
4. Genet, C., M. van Exter, and J. Woerdman, "Fano-type interpretation of red shifts and red tails in hole array transmission spectra," *Opt. Commun.*, Vol. 225, No. 4-6, 331–336, 2003.
5. Pendry J. B., L. Martn-Moreno, and F. J. Garcia-Vidal, "Mimicking Surface Plasmons with Structured Surfaces," *Science*, Vol. 305, No. 5685, 847–848, 2004.
6. Nishida, M., N. Hatakenaka, and Y. Kadoya, "Multipole surface plasmons in metallic nanohole arrays," *Phys. Rev. B*, Vol. 91, No. 23, 235406, 2015.
7. Suh, W., Z. Wang, and S. Fan, "Temporal Coupled-Mode Theory and the Presence of Non-Orthogonal Modes in Lossless Multimode Cavities," *IEEE J. Quantum Electron.*, Vol. 40, No. 10, 1511–1518, 2004.

# Electromagnetically Induced Transparency and Absorption in Metamaterials

**P. Tassin**
Department of Physics, Chalmers University, Sweden

**Abstract**-I will review our work on electromagnetically induced transparency and absorption in metamaterials. By combining dark and radiative resonators in the unit cell, it is possible to create dispersion-engineered metamaterials with transmission spectra reminiscent of electromagnetically induced transparency. While these metamaterials are a completely classical analogue of electromagnetically induced transparency, they exhibit a transmission maximum and high group delay at the same frequency. We show how the response can be improved by designing both the radiative and the dissipative loss of the constituent resonators. When the radiative coupling of the bright resonator is small, it is possible to obtain a narrow peak in absorption, still combined with large group delay. We then speak of electromagnetically induced absorption. We will review a series of different metamaterial designs exhibiting these properties and present a model incorporating all necessary aspects to understand electromagnetically induced transparency and absorption in metamaterials.

**REFERENCES**

1. Jain, A., P. Tassin, T. Koschny, and C. M. Soukoulis, "Large Quality Factor in Sheet Metamaterials Made from Dark Dielectric Meta-atoms," *Phys. Rev. Lett.*, Vol. 112, 117403, 2014.
2. Tassin, P., L. Zhang, R. Zhao, A. Jain, T. Koschny, and C. M. Soukoulis, "Electromagnetically Induced Transparency and Absorption in Metamaterials: The Radiating Two-Oscillator Model and Its Experimental Confirmation," *Phys. Rev. Lett.*, Vol. 109, 187401, 2012.
3. Kurter, C., P. Tassin, A. P. Zhuravel, L. Zhang, T. Koschny, A. V. Ustinov, C. M. Soukoulis, and S. M. Anlage, "Switching Nonlinearity in a Superconductor-Enhanced Metamaterial," *Appl. Phys. Lett.*, Vol. 100, 121906, 2012.
4. Kurter, C., P. Tassin, L. Zhang, T. Koschny, S. M. Anlage, and C. M. Soukoulis, "Classical Analogue of Electromagnetically Induced Transparency with a Metal-Superconductor Hybrid Metamaterial," *Phys. Rev. Lett.*, Vol. 107, 043901, 2011.
5. Zhang, L., P. Tassin, T. Koschny, C. Kurter, S. M. Anlage, and C. M. Soukoulis, "Large group delay in a microwave metamaterial analogue of electromagnetically induced transparency," *Appl. Phys. Lett.*, Vol. 97, 241904, 2010.
6. Tassin, P., L. Zhang, T. Koschny, E. N. Economou, and C. M. Soukoulis, "Planar designs for electromagnetically induced transparency in metamaterials," *Opt. Express*, Vol. 17, 5595–5605, 2009.
7. Tassin, P., L. Zhang, T. Koschny, E. N. Economou, and C. M. Soukoulis, "Low loss metamaterials based on classical electromagnetically induced transparency," *Phys. Rev. Lett.*, Vol. 102, 053901, 2009.

# Excitation of non-radiating anapole mode with focused radially polarized beams

**Lei Wei*, Zheng Xi, Nandini Bhattacharya and H. Paul Urbach**
Optics Research Group, Delft University of Technology, the Netherlands
*corresponding author: l.wei-11@tudelft.nl

**Abstract** A method to excite the non-radiating anapole mode of a high index isotropic dielectric nanosphere is presented. With tightly focused radially polarized beam illumination, the main-contributing electric dipole mode and magnetic modes can be zero with only a weak electric quadruple contributing to the total scattering. Further, with a standing wave illumination formed by two counter-propagating focused radially polarized beam under 4π configuration, the ideal radiationless anapole can be excited.

The study of non-radiative sources has been a part of fundamental physics for a long time. In Mie scattering theory, under certain conditions a specific multipole mode from the vector spherical harmonics decomposition of the scattering field of an illuminated particle can be completely suppressed. For example, the scattering coefficient of the spherical electric dipole moment can be zero at certain wavelength for a high index dielectric nanosphere under plane wave illumination. This is a case radiationless anapole is excited since the Cartesian electrical dipole and toroidal dipole moment of the induced current inside the particle form a nontrivial destructive interference. However, a strong and broadband magnetic dipole resonance can be excited at the same time. The nonradiating anapole mode of a nanosphere is therefore difficult to observe under plane wave illumination. That's why the first experimental demonstration of anapole in the visible wavelength range[1] is done with a specially designed nanodisk, instead of a sphere. In spite of constructing the nanodisk for the specific anapole condition, the scattering from the particle cannot be completely reduced to zero due to the simultaneous excitation of a magnetic quadrupole mode.

Instead of specifically designed structures, in this work we propose an alternative way to excite the anapole mode of an isotropic nanosphere with tightly focused radially polarized beams. The focused radially polarized beam with a pure electric field component Ez and zero magnetic fields at the focal point can efficiently excite electric dipole and toroidal moment of the induced current at the anapole condition while keeping the magnetic modes suppressed. With a single focused beam excitation, the anapole dipole mode can be excited but there is still a weak contribution of electric quadruple radiation in the total scattering power. However, an ideal radiationless anapole can be excited by a 4π configuration, where the two conter-propagating radially polarized beams have the same amplitude but a π phase difference. This approach shows for the first time how a radiationless anapole mode can be realized inside the un-engineered isotropic spherical Mie particle.

**REFERENCES**

1. Miroshnichenko, Andrey E., et al. "***Nonradiating anapole modes in dielectric nanoparticles***." *Nature communications* 6 (2015).
2. Wei, L., et al. **"*Excitation of radiationless anapole mode of isotropic dielectric nanoparticles with tightly focused radially polarized beam*."** arXiv preprint arXiv:1602.08145 (2016).

# Fano resonances and band structure of two-dimensional photonic structures

**Peter Markoš**

Department of Experimental Physics, Faculty of Mathematics, Physics and Informatics,
Comenius University in Bratislava, Slovakia
peter.markos@fmph.uniba.sk

**Abstract**— We calculate the transmission of the electromagnetic wave propagating through a linear array of dielectric, metallic and metamaterial cylinders and show that frequencies of observed Fano resonances coincide with the position of very narrow frequency bands found in the spectra of corresponding two-dimensional photonic crystals. We discuss some other consequences of excited Fano resonances to the frequency spectrum of two-dimensional photonic crystals.

Electromagnetic wave propagating through periodic photonic structure excites Fano resonances when its frequency coincides with the frequency of eigenmodes of the structure [1, 2]. Excited Fano resonances significantly influences the transmission and reflection spectra already for the linear chain of cylinders [3, 4, 5, 6]. An example is shown in the top panel of Figure 1 for a linear chain of dielectric cylinders.

We investigate numerically the propagation of plane electromagnetic wave through periodic structures made from dielectric, metallic and metamaterial cylinders. For linear array of cylinders we calculate the transmission spectra and identify the position of Fano resonance and observe the one-to one correspondence between obtained resonant Fano frequencies and flat frequency bands in the frequency spectra of two dimensional periodic structure (Figure 1). Owing to the resonant character of these bands, the intensity of propagating electromagnetic field is strongly enhanced inside cylinders. Consequently, the propagating field is strongly absorbed even if cylinders are made from weakly absorbing dielectrics.

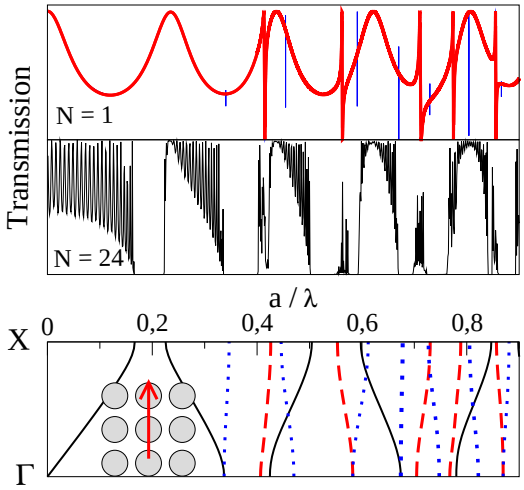



Figure 1: Top: Transmission coefficient (thick red line) of the plane wave (with $\vec{E}$ parallel to the cylinder axes) propagating across the linear array of dielectric cylinders with radius $R = 0.4\times a$ ($a$ is the spatial period) and permittivity $\varepsilon = 12$. Five even Fano resonances excited by the incident field can be identified. Odd resonances (thin blue line) can be excited only in the case of non-perpendicular wave incidence. Middle panel: Transmission through 24 rows of cylinders. Fano resonances, found in the linear array of cylinders develop to very narrow transmission bands. Bottom panel shows the frequency spectrum of the two dimensional photonic crystal along the ΓX direction. Dashed red and dotted blue lines represent even and odd frequency bands, respectively, which originate from Fano resonances described above.

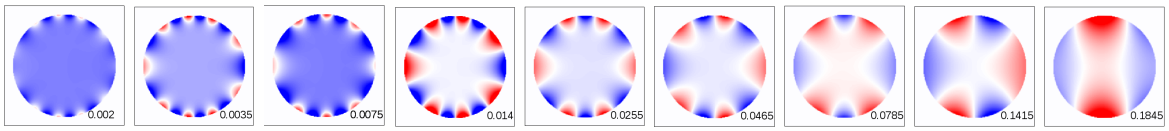



Figure 2: Electric intensity $E$ inside the left-handed cylinders for frequencies corresponding to nine even Fano resonances excited in the linear array. Cylinders have negative permittivity $\epsilon = -12$ and permeability $\mu = -1$. Legends give the ratio $a/\lambda$. Note that the order of resonance decreases when the frequency $a/\lambda$ increases.

Narrow Fano bands observed in Figure 1 can be easily identified with frequency bands since resonant Fano frequencies lye in gaps between two periodic (Bragg) frequency bands. In more general case, observed for instance in photonic structures composed from thinner dielectric cylinders, Fano resonances can overlap with periodic Bragg bands; resulting frequency and transmission spectra of two dimensional structures exhibit a series of non-standard features [4].

Of particular interest are photonic structures composed from metallic [5] and left-handed [6] cylinders. Here, the spectrum of Fano resonances is much reacher thanks to a possibility to excite a series of surface plasmon resonances along the cylinder circumference (Figure 2).

The analysis of Fano resonances enables us to understand a physical origin of flat frequency bands in the spectra of two dimensional photonic structures and provides us with physical interpretation of various irregularities observed in frequency spectra of two-dimensional photonic structures.

## ACKNOWLEDGMENT

This work was supported by the Slovak Research and Development Agency under Contract No. APVV-0108-11 and by Agency VEGA under Contract No. 1/0372/13.

## REFERENCES

1. Fan, S. and J. D. Joannopoulos, "Analysis of guided resonances in photonic crystal slabs," *Phys. Rev. B*, Vol. 65, 235112, 2002.
   Fan, S., W. Suh, and J. D. Joannopoulos, "Temporal couple-mode theory for the Fano resonance in optical resonators," *J. Opt. Soc. Am. A*, Vol. 20, 569, 2003
2. Astratov, V. N., I. S. Culshaw, R. M. Stevenson, D. M. Whittaker, M. S. Skolnick, T. F. Krauss, and R. M. De La Rue, "Resonant coupling of near-infrared radiation to photonic band structure waveguides" *J. Lightwave Technol.*, Vol 17, 2050 1999.
3. Ohtaka, K., and H. Numata, "Multiple scattering effects in photon diffraction for an array of cylindrical dielectrics", *Phys. Lett. A* Vol. 73, n. 5,6, 411, 1979.
4. Markoš, P.,"Fano resonances and band structure of two-dimensional photonic structures," *Phys. Rev. A*, Vol. 92, N. 04, 043814, 2015.
5. Markoš, P. and V. Kuzmiak, unpublished
6. Markoš, P., "Photonic crystals with left-handed components," *Optics Communications*, Vol. 361, 65, 2016.

# Microwave magnetoelectric fields and Fano resonances

**E. O. Kamenetskii**
Microwave Magnetic Laboratory
Department of Electrical and Computer Engineering
Ben Gurion University of the Negev, Israel
kmntsk@bgu.ac.il

**Abstract-**Similar to electromagnetism, described by the Maxwell equations, the physics of magnetoelectric phenomena deals with the fundamental problem of the relationship between electric and magnetic fields. Recently it was shown that microwave near fields in the proximity of a small ferrite particle with magnetic-dipolar-mode (MDM) oscillations have the space and time symmetry breakings and topological properties of these fields are different from topological properties of free-space electromagnetic fields. Such MDM-originated fields – called magnetoelectric (ME) fields – carry both spin and orbital angular momentums. The topology of ME fields is strongly correlated with properties of the Fano-resonance spectra observed at terminals of a microwave structure.

Hybrid systems consisting of resonantly coupled spin ensembles and microwaves received much attention recently [1, 2]. In a ferromagnetic sample with finite dimensions, dipolar interaction dominates the long-wavelength limit, and the boundary condition at the surface defines rigid discrete modes called magnetostatic (MS) waves or magnetic-dipolar modes (MDM) [3]. Collective excitations of electron spins in a ferromagnetic sample dominated by the magnetic dipole-dipole interaction strongly influence the field structure of microwave radiation.

A small quasi-two-dimensional ferrite disk with MDM oscillation spectra can behave as a source of specific fields in vacuum, termed magnetoelectric (ME) fields. The ME fields are quantized fields. These fields are characterized by strong energy confinement, topologically distinctive power-flow vortices, and helicity parameters [4]. Interaction of electromagnetic radiation with such a topological singularities of subwavelength scales results in appearance of the MDM polariton states of open quantum systems which are described by a non-Hermitian Hamilton operator. Topological properties of ME fields arise from the presence of geometric phases on a border circle of an MDM ferrite disk. Due to geometrical phases, the power-flow vortices appear. It is evident that, in accordance with the thermodynamics laws, power cannot flow along a closed circle. So we have helices of the power-flow distributions. The incident wave power flow goes from peripheral regions to the vortex center. The scattered-wave power flow goes from the vortex center to peripheral regions. There are or right-handed, or left-handed helices. When, for example, the incident wave power flow is a right-handed helix, the scattered-wave power flow is a left-handed helix.

Long radiative lifetimes of MDMs combine strong subwavelength confinement of electromagnetic energy with a narrow spectral linewidth. Due to these effects, MDMs may carry the signature of Fano resonances. The multiresonance Fano interference effects in microwave scattering by a MDM ferrite particle were shown in Refs. [5, 6]. The MDM Fano resonances exhibit very strong sensitivity to changes of the local environment and so could be very informative in study of properties of ME fields. As the local environment with varying parameters,

different dielectric samples abutting a ferrite disk can be used [7].

The topology of ME fields is strongly correlated with properties of the Fano-resonance spectra observed at terminals of a microwave structure. Due to a topological structure of ME fields one can observe unidirectional multi-resonant tunneling for electromagnetic waves propagating in microwave structures with embedded quasi-2D ferrite disks [8]. The resonances manifest themselves as peaks in the scattering matrix parameters at the stationary states of MDM oscillations in a ferrite disk. The effect of unidirectional tunneling is exhibited as multiresonance Fano-resonance interferences, which are different for oppositely directed bias magnetic fields. Fig. 1 illustrates these properties of the Fano-resonance interferences.

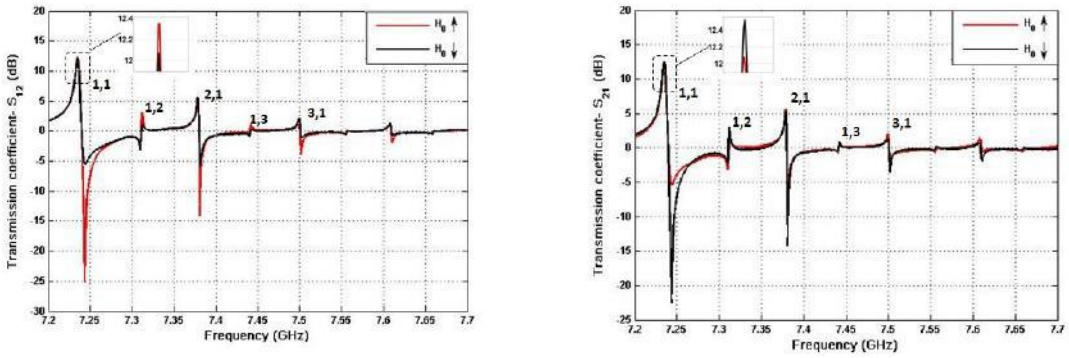



Fig. 1. Frequency characteristics of modules of the transmission coefficients for two opposite orientations of a normal bias magnetic field $\vec{H}_0$. The resonances are classified as follows. The first number characterizes a number of radial variations for the MDM spectral solution. The second number is a number of azimuth variations. Microwave radiation in a two-port structure can be described by the formula for the scattering-matrix parameters: $S_{ij}^{\vec{H}_0\uparrow} = S_{ji}^{\vec{H}_0\downarrow}$.

MDM oscillations with the spin and orbital rotational motions are the Lorentz-violation excitations. The Lorentz violation is associated with rotations of localized field configurations in a fixed observer inertial frame. There are $\mathcal{PT}$ violated oscillations. Microwave radiation can potentially couple to MDM oscillations if the ferrite sample in which the magnetostatic magnons reside shows a confined structure to satisfy conservation of energy and angular momentum. So, microwave radiation in a cavity should be $\mathcal{PT}$ violated as well. The ME-field excitations can be considered as Lorentz-violating extension of the Maxwell equations.

**REFERENCES**


1. H. Zhang, C.-L. Zou, L. Jiang, and H. X. Tang, Phys. Rev. Lett. **113**, 156401 (2014).
2. J. A. Haigh, N. J. Lambert, A. C. Doherty, and A. J. Ferguson, Phys. Rev. B **91**, 104410 (2015).
3. A. G. Gurevich and G. A. Melkov, *Magnetic Oscillations and Waves* (CRC Press, New York, 1996).
4. E. O. Kamenetskii, R. Joffe, and R. Shavit, Phys. Rev. E **87**, 023201 (2013).
5. E. O. Kamenetskii, A. K. Saha, and I. Awai, Phys. Lett. A **332**, 303 (2004).
6. E. O. Kamenetskii, G. Vaisman, and R. Shavit, J. Appl. Phys. **114**, 173902 (2013).
7. M. Berezin, E. O. Kamenetskii, and R. Shavit, Phys. Rev. E **89**, 023207 (2014).
8. E. O. Kamenetskii, E. Hollander, R. Joffe, and R. Shavit, J. Opt. **17**, 025601 (2015).

# Trapping of light with angular orbital momentum above the light cone in a periodic array of dielectric spheres

**Evgeny Bulgakov**[1,2], **Almas Sadreev**[1*]

[1]Kirensky Institute of Physics, 660036 Krasnoyarsk, Russia,
[2]Siberian State Aerospace University, Krasnoyarsk 660014, Russia
*corresponding author, E-mail: almas@tnp.krasn.ru

## Abstract

We consider bound states in the radiation continuum (BSC) above the light cone in a one-dimensional periodic array of dielectric spheres in air. The BSCs are classified by azimuthal number $m$, Bloch wave vector $\beta$ directed along the array, and polarization. The most simple symmetry protected BSCs have $m = 0, \beta = 0$ and occur in a wide range of the radius of spheres and dielectric constant. More sophisticated BSCs with $m \neq 0, \beta = 0$ exist only for a selected radius of spheres at a fixed dielectric constant. We also show an existence of robust Bloch BSCs with $\beta \neq 0, m = 0$. The BSCs with $m = 0$ can be easily detected by the collapse of Fano resonance for scattering of plane wave of linear polarization. The BSCs with orbital angular momentum $m \neq 0$ can be excited by plane wave with circular polarization and accumulate giant vortical EM power.

## 1. Introduction

Recently guiding of electromagnetic waves by a linear array of dielectric spheres below the diffraction limit attracted considerable attention. There were two types of considerations: finite arrays [1, 2, 3, 4] and infinite arrays which were studied by means of the coupled-dipole approximation [5, 6, 7, 8, 9, 10]. A consummate analysis of electromagnetic waves propagating along linear arrays of dielectric spheres below the light cone was provided by Linton *et al* [11]. It is widely believed that only those modes whose eigenfrequencies lie below the light cone, are confined and the rest of the eigenmodes have finite life times. Recently confined electromagnetic modes above the light cone were shown to exist in various periodical arrays (i) of long dielectric cylindrical rods [12, 13, 14, 15, 16], (ii) photonic crystal slabs [17, 18, 19, 20] and (iii) two-dimensional arrays of spheres [21, 22]. Similar one may expect light trapping in the one-dimensional array of spheres with the bound frequencies *above light cone*. Such localized solutions of the Maxwell equations are known as the bound states in the continuum (BSC) and were first reported by von Neumann and Wigner [23]. The BSCs are of immense interest in optics thanks to experimental opportunity to confine light despite that outgoing waves are allowed in the surrounding medium [20, 22, 24, 25, 26, 27].

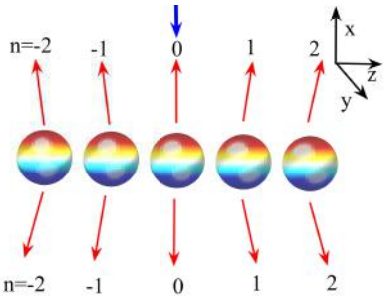



Figure 1: A periodic infinite array of dielectric spheres illuminated by a plane wave (blue arrow). The wave can be transmitted and reflected to discrete diffraction continua enumerated by integers $m$ and $n$ in accordance with Eqs. (8) and (12) shown by red arrows.

## 2. Basic equations for EM wave scattering by a linear array of spheres

We formulate the scattering theory by a periodic array of dielectric spheres in the form of the Lippmann-Schwinger equation similar to the approach developed for a periodic array of dielectric cylinders [15]

$$\widehat{L}\mathbf{\Psi} = \mathbf{\Psi}_{inc}. \tag{1}$$

where the matrix $\widehat{L}$ is defined by the scattering matrix of the isolated sphere and mutual scattering events between the spheres, $\mathbf{\Psi}_{inc}$ is given by the incident wave, and the column $\mathbf{\Psi}$ consists of amplitudes $a_l^m$ and $b_l^m$ of the multipole expansion of the scattering function.

The exact expression of the matrix $\widehat{L}$ was derived by Linton *et al* [11] for EM guided waves on a periodic array of dielectric spheres. For the reader's convenience we present a set of equations and notations from this reference. We seek the solutions of the Maxwell equations, which obey the Bloch theorem

$$\mathbf{E}(\mathbf{r} + \mathbf{R}_j) = e^{i\beta\mathbf{R}_j}\mathbf{E}(\mathbf{r}), \mathbf{H}(\mathbf{r} + \mathbf{R}_j) = e^{i\beta\mathbf{R}_j}\mathbf{H}(\mathbf{r})$$

with the Bloch wave vector $\beta$ directed along the array aligned with the z-axis (see Fig. 1). Here $\mathbf{R}_j = j\mathbf{e}_z$ is the position of the center of the j-th sphere and $\mathbf{e}_z$ is the unit vector along the array. Scattered electromagnetic fields are

expanded in a series over vector spherical harmonics $\mathbf{M}_n^m$ and $\mathbf{N}_n^m$ [11, 28]

$$\mathbf{E}(\mathbf{r}) = \sum_{j,lm} e^{i\beta\mathbf{R}_j}[a_l^m \mathbf{M}_l^m(\mathbf{r}-\mathbf{R}_j) + b_l^m \mathbf{N}_l^m(\mathbf{r}-\mathbf{R}_j)],$$
$$\mathbf{H}(\mathbf{r}) = -i\sum_j e^{i\beta\mathbf{R}_j}\sum_{lm}[a_l^m \mathbf{N}_l^m(\mathbf{r}-\mathbf{R}_j) + b_l^m \mathbf{M}_l^m(\mathbf{r}-\mathbf{R}_j)].$$

Here the first/second terms presents TE/TM spherical vector EM fields.

In absence of an incident wave Linton *et al* [11] derived the homogeneous matrix equation for the amplitudes $a_l^m, b_l^m$

$$\begin{aligned} Z_{TE,l}^{-1} a_l^m - \textstyle\sum_\nu (a_\nu^m \mathcal{A}_{\nu l}^{mm} + b_\nu^m \mathcal{B}_{\nu l}^{mm}) = 0, \\ Z_{TM,l}^{-1} b_l^m - \textstyle\sum_\nu (a_\nu^m \mathcal{B}_{\nu l}^{mm} + b_\nu^m \mathcal{A}_{\nu l}^{mm}) = 0, \end{aligned} \quad (2)$$

where summation over $\nu$ begins with $max(1, m)$, and $Z_{TE,l}$ and $Z_{TM,l}$ are the so-called Lorenz-Mie coefficients can be found in Stratton's book [28]. Mathematical expressions of matrix elements $\mathcal{A}_{l\nu}^{mm}$ and $\mathcal{B}_{l\nu}^{mm}$ are rather cumbersome. The reader can find explicit expressions for them in Refs. [11].

The next step is to account incident plane wave which can be expanded over vector spherical harmonics [28, 29]

$$\begin{aligned} \mathbf{E}^\sigma(\mathbf{r}) = \textstyle\sum_{l=1}^\infty \sum_{-l}^{l} [q_{lm}^\sigma \mathbf{M}_l^m(\mathbf{r}) + p_{lm}^\sigma \mathbf{N}_l^m(\mathbf{r})], \\ \mathbf{H}^\sigma(\mathbf{r}) = -i\textstyle\sum_{lm}[p_{lm}^\sigma \mathbf{M}_l^m(\mathbf{r}) + q_{lm}^\sigma \mathbf{N}_l^m(\mathbf{r})]. \end{aligned} \quad (3)$$

Here index $\sigma$ stands for plane TE/TM wave.

$$\begin{aligned} p_{lm}^{TE} = -F_{lm}\tau_{lm}(\alpha), \;\; q_{lm}^{TE} = F_{lm}\pi_{lm}(\alpha), \\ p_{lm}^{TM} = -iF_{lm}\pi_{lm}(\alpha), \;\; q_{lm}^{TM} = iF_{lm}\tau_{lm}(\alpha), \end{aligned} \quad (4)$$

$k_x = -k_0 \sin\alpha, k_y = k_0 \cos\alpha,$

$$\begin{aligned} F_{lm} = (-1)^m i^l \sqrt{\tfrac{4\pi(2l+1)(l-m)!}{(l+m)!}}, \\ \tau_{lm}(\alpha) = \tfrac{m}{\sin\alpha} P_l^m(\cos\alpha), \\ \pi_{lm}(\alpha) = -\tfrac{d}{d\alpha} P_l^m(\cos\alpha). \end{aligned} \quad (5)$$

For a particular case of normal incidence $k_z = 0, \alpha = -\pi/2$ we obtain from Eqs. (5)

$$\tau_{lm} = -mP_l^m(0), \pi_{lm} = -\frac{d}{d\alpha}P_l^m(0). \quad (6)$$

The general equation for the amplitudes $a_l^m, b_l^m$ which describe the scattering by a linear array of spheres takes the following form

$$\begin{aligned} Z_{TE,l}^{-1} a_l^m - \textstyle\sum_\nu (a_\nu^m \mathcal{A}_{\nu l}^{mm} + b_\nu^m \mathcal{B}_{\nu l}^{mm}) = q_{lm}^\sigma, \\ Z_{TM,l}^{-1} b_l^m - \textstyle\sum_\nu (a_\nu^m \mathcal{B}_{\nu l}^{mm} + b_\nu^m \mathcal{A}_{\nu l}^{mm}) = p_{lm}^\sigma. \end{aligned} \quad (7)$$

Here the left hand term formulates explicitly the matrix $\widehat{L}$ in Eq. (1) and the right hand term corresponds the vector of incident wave $\mathbf{\Psi_{inc}}$ in the space of vector spherical functions notified by two integers $l, m$ and polarization.

## 3. The diffraction continua of vector cylindrical modes

Thanks to the axial symmetry of the array we can exploit the vector cylindrical modes for description of the diffraction continua which are doubly degenerate in TM and TE polarizations $\sigma$. The modes can be expressed through a scalar function $\psi$ [28]

$$\psi_{m,n}(r, \phi, z) = H_m^{(1)}(\chi_n r) e^{im\phi + ik_{z,n}z}. \quad (8)$$

Then for the TE modes we have [28]

$$\begin{aligned} E_z = 0, \;\; H_z = \psi_{m,n}, \\ E_r = \tfrac{ik_0}{\chi_n^2}\tfrac{1}{r}\tfrac{\partial\psi_{m,n}}{\partial\phi}, \;\; H_r = \tfrac{ik_z}{\chi_n^2}\tfrac{\partial\psi_{m,n}}{\partial r}, \\ E_\phi = \tfrac{-ik_0}{\chi_n^2}\tfrac{\partial\psi_{m,n}}{\partial r}, \;\; H_\phi = \tfrac{ik_z}{\chi_n^2}\tfrac{1}{r}\tfrac{\partial\psi_{m,n}}{\partial\phi}, \end{aligned} \quad (9)$$

and for the TM modes

$$\begin{aligned} E_z = \psi_{m,n}, \;\; H_z = 0, \\ E_r = \tfrac{ik_z}{\chi_n^2}\tfrac{\partial\psi_{m,n}}{\partial r}, \;\; H_r = \tfrac{-ik_0}{\chi_n^2}\tfrac{1}{r}\tfrac{\partial\psi_{m,n}}{\partial\phi}, \\ E_\phi = \tfrac{ik_z}{\chi_n^2}\tfrac{1}{r}\tfrac{\partial\psi_{m,n}}{\partial\phi}, \;\; H_\phi = \tfrac{ik_0}{\chi_n^2}\tfrac{\partial\psi_{m,n}}{\partial r}, \end{aligned} \quad (10)$$

where

$$\chi_n^2 = k_0^2 - k_{z,n}^2 \quad (11)$$

and

$$k_{z,n} = \beta + 2\pi n, \;\; n = 0, \pm1, \pm2, \ldots. \quad (12)$$

In what follows we consider the BSCs in the diffraction continua specified by two quantum numbers $m$ and $n$ where the $m$ is the result of the axial symmetry and $n$ is the result of translational symmetry of the infinite linear array of the dielectric spheres. Note each diffraction continuum is doubly degenerate relative to the polarization $\sigma$. The interplay between the frequency $k_0$ and the wave number $k_{z,n}$ the continua can be open ($\chi$ is real) or closed ($\chi$ is imaginary). In the present paper we restrict ourselves by the case of one, two and three open continua.

## 4. Symmetry classification of BSCs

In previous section we presented theory of scattering of plane wave by periodic array of dielectric spheres based on formalism by Linton *et al* [11]. Situation when there is no incident plane wave: $\mathbf{\Psi}_{inc} = 0$ gives the homogeneous equation $\widehat{L}\mathbf{a} = 0$ whose solution are responsible for bound modes of the array. There might be two kinds of the bound modes. The first type of modes have wave number $\beta > k_0$ and describe guided waves along the array. These solutions found by Linton *et al* exist in some interval of material parameters of spheres, dielectric constant $\epsilon$ or radius $R$ and the Bloch wave number $\beta$ [11]. The second type of bound modes have wave numbers $\beta < k_0$ embedded into the diffraction continua above the light cone (BSCs). It is much more difficult to establish the existence of the second type of bound states because of tuning of material parameters. However there might be a class of symmetry protected

BSC which are free of tuning of the material parameters but exist only for selected values of Bloch vector $\beta$. These BSC have been already considered in the linear array of infinitely long dielectric rods [12, 14, 18, 20, 15, 22, 25].

First, axial symmetry of the array implies that the matrixes $\mathcal{A}$ and $\mathcal{B}$ split over the irreducible representations of magnetic quantum number $m$ which therefore classifies the BSCs. Second, discrete translational symmetry along the z-axis implies that respective wave vector component $\beta$ specifies the BSC with discrete $k_0$ too. At last, additional optional symmetries arise due to the inversion symmetry transformation $\widehat{K}f(x,y,z) = f(x,y,-z)$ for $\beta = 0, \pi$. The selection rules for the amplitudes $a_l^m,\ b_l^m$ were established in Ref. [30] and listed in 1. In turn, the symmetry properties of the cartesian components of vector spherical functions under the inversion of $z$ allow to establish the symmetric properties of EM fields collected in Table II.

Table 1: Classification of the BSCs.

| $m$ | $\beta$ | I type of BSC | II type of BSC |
|---|---|---|---|
| $\neq 0$ | 0 | $(a_{2k}^m,\ b_{2k+1}^m)$ | $(a_{2k+1}^m,\ b_{2k}^m)$ |
| 0 | $\neq 0$ | $(a_l^0,\ 0), E_z = 0$ | $(0,\ b_l^0), H_z = 0$ |
| 0 | 0 | $(a_{2k}^0,\ 0), E_z = 0$ | $(0,\ b_{2k}^0), H_z = 0$ |
| 0 | 0 | $(0,\ b_{2k+1}^0), H_z = 0$ | $(a_{2k+1}^0,\ 0), E_z = 0$ |

Table 2: Symmetry properties of the eigenmodes for $\beta = 0$.

| I type | II type |
|---|---|
| $E_{x,y}(-z) = (-1)^{m+1}E_{x,y}(z)$ | $E_{x,y}(-z) = (-1)^m E_{x,y}(z)$ |
| $E_z(-z) = (-1)^m E_z(z)$ | $E_z(-z) = (-1)^{m+1}E_z(z)$ |
| $H_{x,y}(-z) = (-1)^m H_{x,y}(z)$ | $H_{x,y}(-z) = (-1)^{m+1}H_{x,y}(z)$ |
| $H_z(-z) = (-1)^{m+1}H_z(z)$ | $H_z(-z) = (-1)^m H_z(z)$ |

Light can be trapped above the light cone due to the most simple symmetry mechanism in symmetry protected BSCs with $m = 0, \beta = 0$. They constitute the majority of the BSCs. The symmetry-protected BSCs are either pure TE spherical vector modes (Type I in Table I) which are pure TE spherical vector modes (the I type in Table I) with $a_{2k}^0 \neq 0, b_k^0 = 0$ and TM spherical vector modes (the II type) with $a_k^0 = 0, b_{2k}^0 \neq 0$. Numerical results for the coefficients $a_l, b_l$ are given in Ref. [30]. Here we show only two examples of the symmetry protected BSCs, one the TE BSC in Fig. 2 (a) and second the TM BSC in Fig. 2 (b). Note the profiles are periodic over the chain. Hereinafter we plot real parts of electromagnetic fields.

## 5. Robust Bloch BSCs with $\beta \neq 0, m = 0$

Could the Bloch BSC occur at $\beta \neq 0$ in the continuum of free-space modes? This question was first answered positively by Porter and Evans [31] who considered acoustic trapping in the array of rods of rectangular cross-section. Marinica *et al* [13] demonstrated the existence of the Bloch BSC with $\beta \neq 0$ in two parallel dielectric gratings and

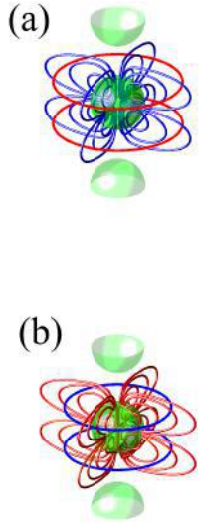



Figure 2: Patterns of the symmetry protected TE BSC (a) and TM BSC (b) with $m = 0$. Electric force lines are in red and magnetic force lines are in blue.

Ndangali and Shabanov [14] in two parallel arrays of dielectric rods. In a single array of rods positioned on the surface of bulk 2d photonic crystal multiple BSCs with $\beta \geq 0$ were considered by Wei *et al* [18]. Also the Bloch BSCs in a single array of cylindrical dielectric rods in air were presented in Ref. [15]. Such a running Bloch BSCs with the eigenfrequencies above the light cone are interesting by that the array serves as a waveguide for electromagnetic waves however for the only fixed $\beta$ (see summary of BSCs in Fig. 5) in contrast to the bound states below the light cone [11].

According to Table I the Bloch BSCs with $\beta \neq 0, m = 0$ have only components $a_l^0$ or $b_l^0$. Let us first consider the type I of BSC with $b_l^0 = 0$ which has $E_z = 0$ and, therefore, is decoupled with the TM continuum but is coupled with the TE $n = 0, m = 0$ continuum. However numerically we show that this coupling can be achieved to be zero for variation of $\beta$ with pattern of EM fields profiles shown in Fig. 3.

This BSC occurs for tuning $\beta$ but there is no necessity to tune material parameters of spheres and therefore the BSC can be defined still as the robust that is attractive from experimental point of view. We managed to find only the type I of the BSCs for $\epsilon = 15$ but not the type II. Such a difference between types of the BSC is related to different boundary conditions for electric and magnetic fields at the dielectric sphere.

## 6. Orbital angular momentum BSCs

The BSCs with orbital angular momentum (OAM) $m \neq 0$ are of primary interest in the present paper. The mechanism

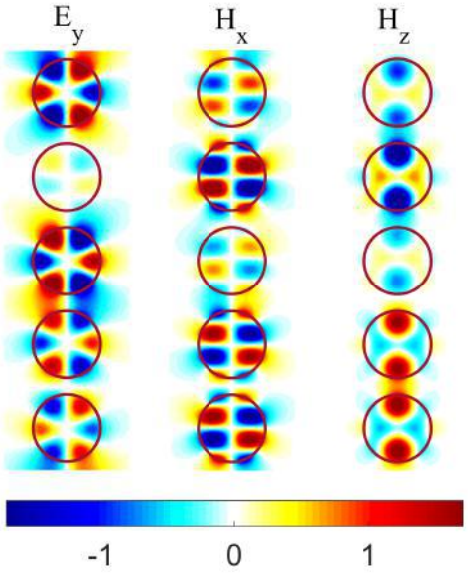



Figure 3: (Color online). EM field configurations of the Bloch BSC with $\beta = 1.2074$.

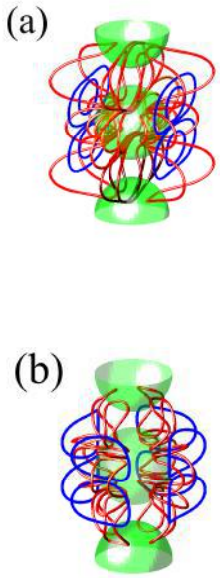



Figure 4: BSCs with OAM (a) $m = 1$ and (b) $m = 2$.

for partially symmetry protected BSCs allows us to understand how to realize the BSCs with $m \neq 0, \beta = 0$ which are embedded into the diffraction continuum with the same $m$ and $n = 0$. Obviously, the system has the time reversal symmetry that implies that such BSCs are degenerated over $\pm m$. Let us start with the BSC of the I type with $m = 1$ which has the odd $E_z$ and the even $H_z$ according to Tables I and II. The diffraction TE and TM continua $m = 1, n = 0$ is independent of $z$ and therefore as it follows from Eqs. (9) and (10) the solutions of type I are mismatched with the TM continuum but are coupled with the TE continuum. However the coupling can be cancelled by tuning the radius. The results of computation of this partially symmetry protected BSC of type I $(a_{2k}, b_{2k+1})$ are given in Ref. [30] and shown in Fig. 4 (a) for $m = 1$.

The next type of BSC $(a_{2k+1}, b_{2k})$ with $m = 2$ belongs to type II with even $E_z$ and odd $H_z$. It is symmetry protected against decay into the TE continuum with $m = 2, n = 0$. A decay into the TM continuum is can be eliminated by tuning the sphere radius and shown in Fig. 4 (b). All components of electric and magnetic fields of the BSCs are nonzero and localized around the array as shown in Fig. 4. We show EM fields around one sphere because patterns are periodic along the z-axis. One can see that the value of OAM $m$ reflects the structure of force lines in the xy-plane while number of sufficient amplitudes in orbital momentum $l$ reflects in the structure along the z-axis.

## 7. Emergence of the BSC in scattering

Scattering of plane waves by periodic two-dimensional arrays of dielectric spheres has been in focus of researches since pioneering papers by Ohtaka *et al* [32]. Scattering by aggregates of finite number of spheres was considered in the framework of multisphere Mie scattering [29, 33, 34], however to our knowledge the scattering by the one-dimensional infinite array of dielectric spheres has not been considered yet. This section aims to present results of numerical calculation of differential and total cross-sections of the infinite array with focus to follow resonant traces of the BSCs in the cross-sections similar to the scattering by array of dielectric rods [15, 18, 20].

General theory of scattering in terms of the amplitudes $\mathbf{\Psi} = (a_l^m, b_l^m)$ is formulated in the form of Eq. (7) which allows to find the amplitudes via inverse of the matrix $\widehat{L}$

$$\mathbf{\Psi} = \widehat{L}^{-1}\mathbf{\Psi}_{inc}. \tag{13}$$

This equation is the Green equation in which a source presented by incident wave $\mathbf{\Psi}_{inc}$ unambiguously gives the solution as the scattered wave $\mathbf{\Psi}$. However there can be an exception when the inverse of the matrix $\widehat{L}$ becomes singular. That occurs if one of complex eigenvalues of $\widehat{L}$ turns to zero giving rise to the BSC as the null eigenvector of $\widehat{L}$

$$\widehat{L}\mathbf{\Psi}_{BSC} = 0. \tag{14}$$

Then the general solution of Eq.(7) can be presented as linear superposition of the BSC and particular solution [35, 36]

$$\mathbf{\Psi} = \alpha\mathbf{\Psi}_{BSC} + \mathbf{\Phi} \tag{15}$$

where $\alpha$ is an arbitrary constant that makes the BSC invisible for probing incident plane wave at exact BSC point. However as soon as one deviates from the BSC point the BSC manifests in the form of collapsing Fano resonance

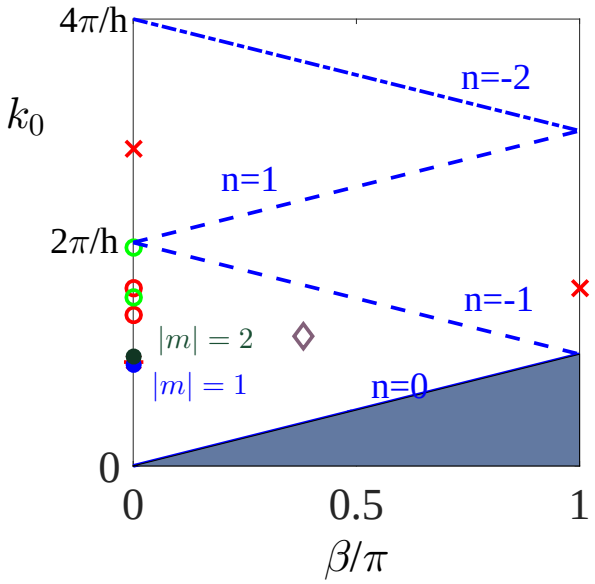



Figure 5: (Color online). BSC frequencies and Bloch vector $\beta$ relative to the light line $k_0 = \beta$. Dash and dash-dot lines show thresholds where the next continua $n = \pm 1$ and $n = -2$ are opened. Fully symmetry protected BSCs are marked by open circles (Type I by, Type II by green), two OAM BSCs are marked by closed circles, Bloch BSC with $\beta \neq 0$ is marked by rhombus, BSCs embedded into two and three continua are marked by cross.

for approaching to the BSC point in parametric space. That phenomenon was observed for scattering of EM waves by array of rods [14, 15, 18, 20, 21, 22]. The Fano resonance for the present system can be interpreted as interference of paths through the spheres and paths between the spheres. In what follows we present briefly a mathematical tool to highlight these features of the BSCs using the biorthogonal basis of eigenvectors of the non Hermitian matrix $\widehat{L}$ [15, 37]

$$\widehat{L}\mathbf{X}_f = L_f\mathbf{X}_f,\ \ \widehat{L}^+\mathbf{Y}_f = L_f^*\mathbf{Y}_f,\ \ \mathbf{Y}_f^+\mathbf{X}_{f'} = \delta_{ff'}. \quad (16)$$

It immediately follows that

$$\widehat{L}^{-1} = \sum_f \mathbf{X}_f \frac{1}{L_f}\mathbf{Y}_f^+. \quad (17)$$

Because of axial symmetry matrix $\widehat{L}$ has block structure in the preserving OAM $m$

$$L_{ll'}^{(m)} = \begin{pmatrix} Z_{TE,l}^{-1}\delta_{ll'} - \mathcal{A}_{ll'}^{mm} & -\mathcal{B}_{ll'}^{mm} \\ -\mathcal{B}_{ll'}^{mm} & Z_{TM,l}^{-1}\delta_{ll'} - \mathcal{A}_{ll'}^{mm} \end{pmatrix}. \quad (18)$$

In the nearest vicinity of the BSC point one of the complex eigenvalues $L_c$ is very close to zero. That allows us to substantially simplify Eq. (17) leaving in the sum only the leading contribution related to the $L_c$. Respectively the scattering state in Eq. (13) is simplified as follows

$$\mathbf{\Psi}^\sigma \approx \frac{1}{L_c}\mathbf{X}_c(\mathbf{Y}_c^+ \cdot \mathbf{\Psi}_{inc}^\sigma), \quad \sigma = TE/TM. \quad (19)$$

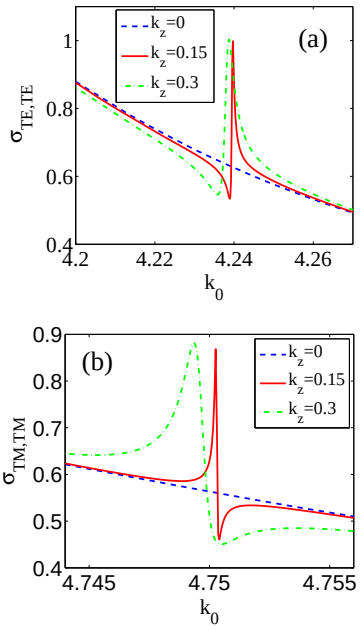



Figure 6: Total cross-section for scattering of TE (a)/TM (b) plane wave incident under angle to the array of dielectric spheres strongly effected by presence of the symmetry protected type I/II BSC shown in Fig. 2 (a).

This equation manifests a remarkable property of the BSCs to enormously enhance the incident wave $\mathbf{\Psi}_{inc}$ by the factor $1/L_c$. First we present this effect for the symmetry protected BSCs with $m = 0$ shown in Fig. 2 when plane wave with the wave vector in plane $x, z$ and TE polarizations with electric field along the y-axis illuminates the array. Small complex eigenvalue $L_c$ in the denominator of scattering wave function (19) results in sharp resonant contribution in the cross-section $\sigma_{TE,TE}$ as shown in Fig. 6 (a). When the plane incidents normally to the arrow of spheres $k_z = 0$ (dash line) the BSC of type I is fully invisible in respect to the cross-section. Alternatively, the symmetry protected type II of the symmetry protected BSCs with the only amplitudes $b_k$ can be observed via the cross-section $\sigma_{TM\to TM}$ which shows similar anomalies in the cross-section $\sigma_{TM,TM}$ as seen from Fig. 6 (b). Thus, although the BSCs have no effect for the normal incidence they are detected by collapse of Fano resonances in total cross-sections for $k_z \to 0$.

## 8. Transfer of spin momentum of circularly polarized wave into orbital momentum of the BSC with $m \neq 0$

Scattering of circularly polarized plane wave by the OAM BSCs is the main issue of the next section. It is well known that EM fields can carry not only energy but also angular momentum. The angular momentum is composed of spin angular momentum (SAM) and OAM describing its polarization state and the phase structure distribution, re-

spectively. The research on OAM of EM fields was not attractive until Allen *et al.* investigated the mechanism of OAM in laser modes [38, 39]. In contrast to SAM, which has only two possible states of left-handed and right-handed circular polarizations, the theoretical states of OAM are unlimited owing to its unique characteristics of spiral flow of propagating EM waves [40]. There were many proposals to generate OAM beams by use of ferrite particles [41], by chiral plasmonic nanostructures [42] and by designer metasurfaces [43]. Here we show that the BSCs with OAM are capable to generate spinning currents in response to illumination of the array by circularly polarized plane wave.

Because of time-reversal symmetry BSCs with OAM are degenerate in a sign of $m$. That modifies Eq. (19) as follows

$$\mathbf{\Psi}_{\sigma}^{m} \approx \frac{1}{L_c}\sum_{\pm}[\mathbf{X}_c(\pm m)(\mathbf{Y}_c(\pm m)^{+}\cdot\mathbf{\Psi}_{inc}^{\pm m,\sigma})] \quad (20)$$

where the incident wave according to Eq. (7) is given

$$\mathbf{\Psi}_{inc}^{m,\sigma} = \begin{pmatrix} \mathbf{p}_m^{\sigma} \\ sgn(m)\mathbf{q}_m^{\sigma} \end{pmatrix}, \quad (21)$$

and subvectors $\mathbf{p}^m$ and $\mathbf{q}^m$ are given by Eqs. (4). From Eq. (18) and property $\mathcal{B}_{ll'}^{(m)} = -\mathcal{B}_{ll'}^{(-m)}$ the eigenvectors can be decomposed over the polarizations as follows

$$\mathbf{X}_c(\pm m) = \begin{pmatrix} \mathbf{x}_{TE}^m \\ \pm\mathbf{x}_{TM}^m \end{pmatrix}, \mathbf{Y}_c(\pm m) = \begin{pmatrix} \mathbf{y}_{TE}^m \\ \pm\mathbf{y}_{TM}^m \end{pmatrix}. \quad (22)$$

As a result substitution of Eqs. (21) and (22) into Eq. (20) gives

$$\mathbf{\Psi}_{\sigma} \approx \frac{1}{L_c} D_{\sigma}(\mathbf{X}_c^{+m} \pm \mathbf{X}_c^{-m}) \quad (23)$$

where the sign $\pm$ refers to the TE/TM polarizations and

$$D_{\sigma} = \mathbf{y}_{TE}^{+}\mathbf{p}_{|m|}^{\sigma} + \mathbf{y}_{TM}^{+}\mathbf{q}_{|m|}^{\sigma}. \quad (24)$$

Asymptotically $D_{TM} \to 0$ for $k_z \to 0$. Assume that the elliptically polarized plane wave $\mathbf{\Psi}_{inc}^{TE} + \alpha\mathbf{\Psi}_{inc}^{TM}$ is incident almost normally to the array with small $k_z$. Instantly from Eq. (23) we obtain that

$$\mathbf{\Psi}_{\sigma} \approx F\mathbf{X}_c^{+m}, F = \frac{2D_{TE}}{L_c} \quad (25)$$

for

$$D_{TE} = \alpha D_{TM} \quad (26)$$

the scattering wave function has only a contribution with the positive OAM $m > 0$. Here we introduced the enhancement factor $F$ which defines to what extent the incident wave amplitude enhances near by the array. Respectively for $D_{TE} = -\alpha D_{TM}$ the scattering wave function has only a contribution with the negative OAM $m < 0$. Fig. 7 illustrates the behavior enhancement factor in the plane of the frequency $k_0$ and $k_z$ for elliptically polarized plane waves with the polarization parameter $\alpha$. In particular $\alpha = -0.3133 + i0.9496$ corresponds to the circularly polarized wave.

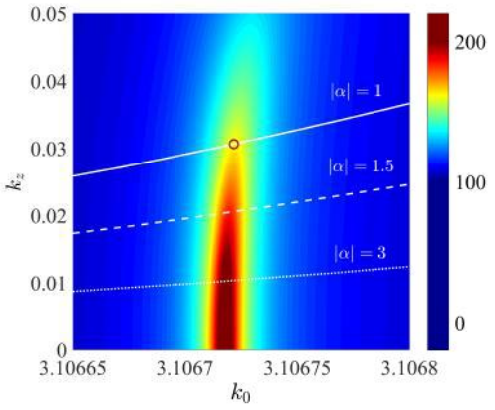



Figure 7: The enhancement factor $|F|$ vs frequency and $k_z$. The parameter $\alpha$ controls polarization of incident wave $\mathbf{\Psi}_{inc}^{TE} + \alpha\mathbf{\Psi}_{inc}^{TM}$. Open circle marks point $k_z = 0.0306, k_0 = 3.1067$.

Let us examine the scattering wave function as we pass by the BSC point $\omega_{BSC} = 3.086, R = 0.471, \epsilon = 15$ [30] where the radius of spheres is measured in terms of the period of array. The solution for the BSC with $m = 2$ is the following [30]

$$(a_l^2,\, b_l^2) = \begin{pmatrix} 0 & 0.6545 + 0.2013i \\ -0.2142 + 0.6964i & 0 \\ 0 & -0.0057 - 0.0018i \\ 0 & 0 \\ 0 & 0 \end{pmatrix} \quad (27)$$

where $, l \geq 2$ and shown in Fig. 4 (b). In what follows we take $R = 0.468$ and sweep the frequency of incident wave $k_0$ in the nearest vicinity of the BSC frequency 3.086. Then because of smallness of the eigenvalue $L_c$ in Eq. (23) EM fields given by the scattering wave function can reach extremal high values near by spheres. It is clearly a property of the extremely high quality of the BSCs, that presents a possibility to enhance the incident light [21, 22] that is illustrated in Fig. 8 (a). Besides carrying OAM the BSC with $m \neq 0$ provide an opportunity to create giant spinning Pointing currents [44] as demonstrated in Fig. 8 (b). Fig. 9 shows as the giant Pointing current circulates around the array when the light with polarization $\alpha = -0.3133 + i0.9496$ and angle of incidence $\beta = 0.0306$ illuminates the array illustrating transformation of SAM into OAM.

## 9. Discussions and summary

Recently the BSCs above the light cone were shown to exist in various systems of one-dimensional arrays of dielec-

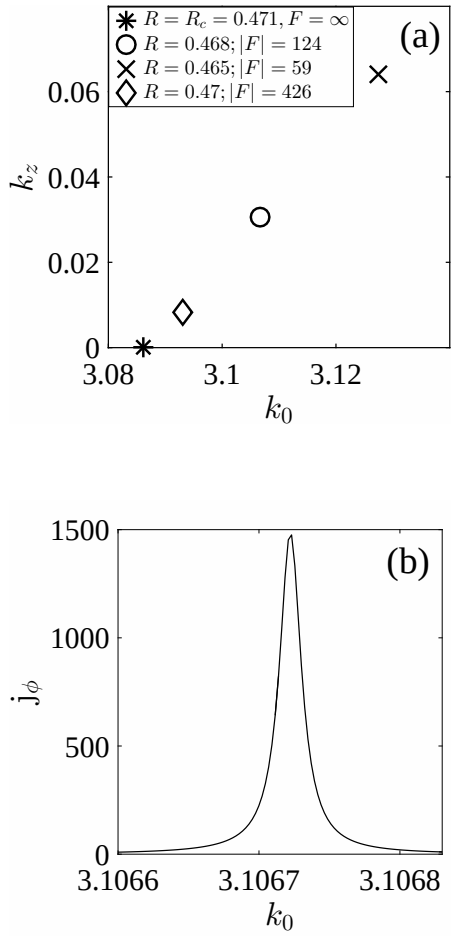



Figure 8: (a) Values of the enhancement factor $|F|$ vs $k_z$ and $k_0$ as dependent on radius of spheres. (b) Value of the angular component of Pointing current for the $r = 0.571$ close to parameters of the BSC with OAM $m = 2$ (27). $k_z = 0.0303$.

tric rods and holes in the dielectric slab [12, 14, 13, 18, 20, 19, 15, 16] and of dielectric spheres [30]. One can ask themselves why BSCs can occur in periodic (grating) dielectric structures but not in homogeneous structures like slab or rod which can support only guiding EM modes below the light cone. Let us begin with the simplest textbook system of dielectric slab infinitely long in the $x, y$ plane with the dielectric constant $\epsilon > 1$. The Maxwell equations can be solved by separation of variables for scalar function $\psi(x, y, z) = e^{ik_x x + ik_y y}\psi(z)$ to result in bound states below the light cone $k_0^2 = k_x^2 + k_y^2$ [46]. Situation can be cardinally changed if to substitute the continual translational symmetry by discrete one $\epsilon(x, y, z) = \epsilon(x + ph, y, z)$ where $p = 0, \pm1, \pm2, \ldots$, $h$ is the period of the structure. Then the radiation continua are quantized $k_{x,n} = \beta + 2\pi n/h, \quad n = 0, \pm1, \pm2, \ldots$ which are outgoing plane waves $e^{ik_{x,n}x + ik_y y + ik_z z}$ with the frequency $k_0^2 = k_{x,n}^2 + k_y^2 + k_z^2$. $\beta$ is the Bloch wave vector along the x-axis and the integer $n$ refers to diffraction continua [14]. Physical interpretation of this statement is related to

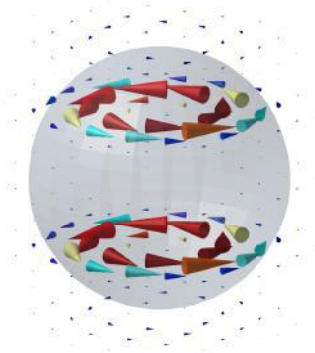


Figure 9: Pointing current circulates around the sphere when circularly polarized light illuminates the array. Currents around other spheres are repeating periodically.

that the slab with discrete translational symmetry can be considered as one-dimensional diffraction lattice. Let us take for simplicity $\beta = 0, k_y = 0$. Assume there is the bound solution with the eigenfrequency $k_{0BSC} > 0$ which is coupled with all diffraction continua enumerated by $n$. Let $k_{0BSC} < 2\pi/h$, i.e., the BSC resides in the first diffraction continua but below the others (see Fig. 5). Because of the symmetry or by variation of the material parameters of the modulated slab we can achieve that the coupling of the solution with first diffraction continuum equals zero [18, 20, 19, 15, 16]. However the solution is coupled with continua $n = 1, 2, \ldots$ which are evanescent that give rise to exponential decay of the solution over $z$-axis. The length of localization $L \sim \frac{1}{\sqrt{2\pi^2/h^2 - k_{0BSC}^2}}$. Therefore the evanescent diffraction continua play principal role in space configuration of the BSCs.

In the present paper we chose another strategy to quantize the radiation continuum. We break a continual translational symmetry of infinitely long single rod along its axis z. In particular we have substituted the infinite long circular rod by periodic array of dielectric spheres that allowed us to use the the Mie scattering theory for single sphere contributed by multiple events of mutual scattering processes between spheres. Such a theory is well developed recently by Linton *et al* [11] for consideration of guiding electromagnetic modes below the light cone which shown by gray color in Fig. 5. As soon as the continual translational symmetry along the z-axis is substituted by discrete one the continua is quantized specified by two quantum numbers, magnetic quantum number $m$ and $n$. The last quantum number leads to discrete directions of outgoing cylindrical waves from the array given by the wave vector $k_{z,n} = \beta + 2\pi n/h$ in each sector $m$ where $\beta$ is the Bloch

vector along the array.

We have performed symmetry analysis of the BSCs which are listed in tables I and II. The BSCs are labelled by two quantum numbers $m$ , azimuthal number of continuum and $\beta$ which defines Bloch wave vector of the BSC solution along the array. (1) The symmetry protected BSCs constitute the vast majority of BSCs which are symmetry mismatched with the first diffraction continuum $m = 0, n = 0$ of both polarizations. The EM field configurations of BSCs presented in Fig. 6 show hybridizations of a few orbital quantum numbers $l = 2, 4, 6, \ldots$ that specifies the BSCs as multipoles of high order. The most remarkable property in view of experimental visualization of the BSCs is their robustness relative to choice of material parameters of the dielectric spheres, the radius and dielectric constant.

(2) We demonstrated that the BSC can be established not only by variation of the material parameters but also by variation of Bloch wave vector $\beta$ along the array axis. Patterns of the Bloch BSCs are presented in Fig. 4.

(3) An advantage of dielectric structures is high quality factor and wide range of BSC wavelengths from microns (photonics) to centimeter (microwave range) as dependent on choice of the radius of spheres. Although the BSCs exist in a selected points in the parametric space, radius and dielectric constant there is a domain in the vicinity of the BSC point where the BSC mostly contributes into the cross-section and the EM field in near field zone as Figs. 7. That leads to extremely efficient light harvesting capabilities [45]. The BSCs with OAM $m \neq 0$ demonstrate the most striking effect of transformation of incident SAM beam with elliptic polarization into the OAM solution with giant spinning Pointing current in the near field zone of the array. It is worthy to note that the direction of current circulation can be easily inverted by changing the angle of incidence.

## Acknowledgement

The work was supported by Russian Science Foundation through grant 14-12-00266. We acknowledge discussions with D.N. Maksimov.

## References

[1] A. Quirantes, F. Arroyo, and J. Quirantes-Ros, Multiple Light Scattering by Spherical Particle Systems and Its Dependence on Concentration: A T-Matrix Study, *J. Colloid and Interface Sc.* **240**: 78-82, 2001.

[2] Pi-Gang Luan, Kao-Der Chang, Transmission characteristics of finite periodic dielectric waveguides, *Opt. Express* **14**: 3263–3272, 2006.

[3] R. Zhao, T. Zhai, Z. Wang, and D. Liu, Guided Resonances in Periodic Dielectric Waveguides, *J. Lightwave Tech.* **27**: 4544–4547, 2009.

[4] J. Du, S. Liu, Z. Lin, J. Zi, and S.T. Chui, Guiding electromagnetic energy below the diffraction limit with dielectric particle arrays, *Phys. Rev. A***79**: 051801R, 2009.

[5] A.L. Burin, H. Cao, G.C. Schatz and M.A. Ratner, High-quality optical modes in low-dimensional arrays of nanoparticles: application to random lasers, *J. Opt. Soc. A.*: 21, 121–131, 2004.

[6] M. Gozman, I. Polishchuk, and A. Burin, Light propagation in linear arrays of spherical particles, *Phys. Lett. A***372**: 5250–5253, 2008.

[7] G.S. Blaustein, M.I. Gozman, O. Samoylova, I.Ya. Polishchuk, A.L. Burin, Guiding optical modes in chains of dielectric particles, *Opt. Express* **15**: 17380–17391, 2007.

[8] B.T. Draine and P.J. Flatau, Discrete-dipole approximation for periodic targets: theory and tests, *J. Opt. Soc. Am. A* **25**: 2693–2703, 2008.

[9] R.S. Savelev, A.P. Slobozhanyuk, A.E. Miroshnichenko, Yu.S. Kivshar, and P.A. Belov, Subwavelength waveguides composed of dielectric nanoparticles, *Phys. Rev. B* **89**: 035435, 2014.

[10] A. Krasnok, S. Makarov, M. Petrov, R. Savelev, P. Belov, and Yu. Kivshar, Towards all-dielectric metamaterials and nanophotonics, *SPIE*: **9502**: 950203, 2015.

[11] C.M. Linton, V. Zalipaev, and I. Thompson, Electromagnetic guided waves on linear arrays of spheres, *Wave Motion* **50**: 29–40, 2013.

[12] S.P. Shipman and S. Venakides, Resonant transmission near nonrobust periodic slab modes, *Phys. Rev. E* **71**: 026611, 2005.

[13] D. C. Marinica, A. G. Borisov, and S.V. Shabanov, Bound States in the Continuum in Photonics, *Phys. Rev. Lett.* **100**: 183902, 2008.

[14] R.F. Ndangali and S.V. Shabanov, Electromagnetic bound states in the radiation continuum for periodic double arrays of subwavelength dielectric cylinders, *J. Math. Phys.* **51**: 102901, 2010.

[15] E.N. Bulgakov and A.F. Sadreev, Bloch bound states in the radiation continuum in a periodic array of dielectric rods, *Phys. Rev. A* **90**: 053801, 2014.

[16] Zhen Hu and Ya Yan Lu, Standing waves on two-dimensional periodic dielectric waveguides, *J. Optics* **17**: 065601, 2015.

[17] J. Lee, B. Zhen, S.-L. Chua, W. Qiu, J.D. Joannopoulos, M. Soljačić, and O. Shapira, Observation and Differentiation of Unique High-Q Optical Resonances Near Zero Wave Vector in Macroscopic Photonic Crystal Slabs, *Phys. Rev. Lett.* **109**: 067401, 2012.

[18] C.W. Hsu, B. Zhen , Song-Liang Chua , S.G. Johnson, J.D.Joannopoulos, and M. Soljačić, Bloch surface eigen states with in the radiation continuum, *Light: Science and Applications* **2**: 1–5, 2013.

[19] Y. Yang, C. Peng, Y. Liang, Z. Li, and S. Noda, Analytical Perspective for Bound States in the Continuum in Photonic Crystal Slabs, *Phys. Rev. Lett.* **113**: 037401, 2014.

[20] Bo Zhen, Chia Wei Hsu, Ling Lu, A.D. Stone, and M. Soljačić, Topological Nature of Optical Bound States in the Continuum, *Phys. Rev. Lett.* **113**, 257401, 2014.

[21] M. Zhang and X. Zhang, Ultrasensitive optical absorption in graphene based on bound states in the continuum, *Scientific Rep.* **5:8266**: 1–6, 2015.

[22] M. Song, H. Yu, C. Wang, N. Yao, M. Pu, J. Luo, Z. Zhang, and X. Luo, Sharp Fano resonance induced by a single layer of nanorods with perturbed periodicity, *Opt. Express* **23**: 2895–2903, 2015.

[23] J. von Neumann and E. Wigner, Über merkwüdige diskrete eigenwerte, *Z. Physik* **50**: 291–293, 1929.

[24] Y. Plotnik, O. Peleg, F. Dreisow, M. Heinrich, S. Nolte, A. Szameit, and M. Segev, Experimental observation of optical bound states in the continuum, em Phys. Rev. Lett. **107**: 183901, 2011.

[25] M. López-García, J.F. Galisteo-López, C. López, and A. García-Martín, Light confinement by two-dimensional arrays of dielectric spheres, *Phys. Rev. B* **85**: 235145, 2012.

[26] G. Corrielli, G. Della Valle, A. Crespi, R. Osellame, and S. Longhi, Observation of surface states with algebraic localization, *Phys. Rev. Lett.* **111**: 220403, 2013.

[27] S. Weimann, Yi Xu, R. Keil, A.E. Miroshnichenko, A. Tünnermann, S. Nolte, A.A. Sukhorukov, A. Szameit, and Yu.S. Kivshar, Compact surface fano states embedded in the continuum of waveguide arrays, *Phys. Rev. Lett.* **111**: 240403, 2013.

[28] J. A. Stratton, *Electromagnetic Theory*, McGraw-Hill, New York, 1941.

[29] J.H. Bruning and Y.T. Lo, Multiple scattering of EM waves by spheres Part I - multipole expansion and ray-optical solutions, *IEEE Trans. Antennas and Propagation* **AP-19**: 378–390, 1971.

[30] E.N. Bulgakov and A.F. Sadreev, Light trapping above the light cone in one-dimensional array of dielectric spheres, *Phys. Rev. A* **92**: 023816, 2015.

[31] R. Porter and D.V.Evans, Embedded RayleighBloch surface waves along periodic rectangular arrays, *Wave Motion* **43**: 29–50, 2005.

[32] K. Ohtaka, Scattering theory of low-energy photon diffraction, *J. Phys. C: Solis State Phys.* **13**: 667–680, 1980.

[33] K.A. Fuller and G.W. Kattawar, Consummate solution to the problem of classical electromagnetic scattering by an ensemble of spheres. I: Linear chains, *Opt. Lett.* **13**: 90–92, 1988.

[34] Yu-lin Xu, Electromagnetic scattering by an aggregate of spheres, *Appl. Optics* **34**: 4573–4588, 1995.

[35] A.F. Sadreev, E.N. Bulgakov, and I. Rotter, Bound states in the continuum in open quantum billiards with a variable shape, *Phys. Rev. B* **73**: 235342, 2006.

[36] E. N. Bulgakov , K. N. Pichugin , A. F. Sadreev , and I. Rotter, Bound States in the Continuum in Open AharonovBohm Rings, *JETP Lett.* **84**, 430–435, 2006.

[37] A. F. Sadreev and I. Rotter, S-matrix theory for transmission through billiards in tight-binding approach, *J. Phys. A: Math. Gen.* **36**: 11413–11433, 2003.

[38] L. Allen, M.W. Beijersbergen, R.J.C. Spreeuw, and J.P. Woerdman, Orbital angular momentum of light and the transformation of Laguerre-Gaussian laser modes, *Phys. Rev. A* **45**: 8185–8189, 1992.

[39] L. Allen, M.J. Padgett, The Poynting vector in Laguerre-Gaussian beams and the interpretation of their angular momentum density, em Opt. Comm. **184**: 67–71, 2010.

[40] A.M. Yao and M.J. Padgett, Orbital angular momentum: origins, behavior and applications, *Adv. Opt. Photon.* **3**: 161–204, 2011.

[41] M. Berezin, E. O. Kamenetskii, and R. Shavit, Magnetoelectric-field microwave antennas: Far-field orbital angular momenta from chiral-topology near fields, *arXiv preprint*: 1512.01393, 2015.

[42] Yu. Gorodetski, A. Drezet, C. Genet, and T.W. Ebbesen, Generating Far-Field Orbital Angular Momenta from Near-Field Optical Chirality, *Phys. Rev. Lett.* **110**, 203906, 2013.

[43] N. Yu, F. Capasso, Optics with designer metasurfaces, *Nature Materials* **13**: 139–150, 2014.

[44] E. N. Bulgakov and A. F. Sadreev, Giant optical vortex in photonic crystal waveguide with nonlinear optical cavity, *Phys. Rev. B*: **85**: 165305, 2012.

[45] A. I. Fernandez-Dominguez, S.A. Maier, and J. B. Pendry, Collection and Concentration of Light by Touching Spheres: A Transformation Optics Approach, *Phys. Rev. Lett.* **105**: 266807, 2010.

[46] J.D. Jackson, *Classical Electrodynamics*, N.Y., 1962.

# A wideband resonant cavity antenna based on Fano resonance effect in a two-layer patch array superstrate

**Komsan Kanjanasit[1], Changhai Wang[2*], and Paul Record[2]**

[1]Department of Computer Engineering, Faculty of Engineering, Prince of Songkla University, Phuket Campus, 83120, Thailand

[2]Institute of Sensors, Signals and Systems, School of Engineering & Physical Sciences, Heriot-Watt University, Edinburgh EH14 4AS, UK

*corresponding author, E-mail: c.wang@hw.ac.uk

## Abstract

This paper presents the first demonstration of a wideband resonant cavity antenna (RCA) antenna enabled by the Fano resonance effect in a two-layer patch array based metamaterial as the superstrate. In this device gain enhancement over a wideband was achieved by utilizing two effects associated with the superstrate, the effect of the cavity formed between the ground plane of the feed antenna and the superstrate due to the finite reflectivity associated with the Fano resonance effect of the superstrate and the effect of the finite superstrate size around the resonance frequency at which the reflectivity of the superstrate is zero. By combining the two gain enhancement mechanisms, a compact RCA device for wideband operation with enhanced gain has been designed and constructed. A wideband patch antenna was designed and used as the feed source for the RCA device. For an RCA device using a superstrate consisting of two patch arrays each on a thin film liquid crystal polymer (LCP) substrate and separated by an air gap, a gain of ~13 dBi was obtained with the 3dB bandwidth of 46%. The device shows a good flat band response with 1-dB-ripple bandwidth as wide as 40%.

## 1. Introduction

The resonant cavity antenna (RCA) has been studied for many years due to its ability to provide a narrow beam response with enhanced directivity over the conventional single element antenna devices [1-16]. In a typical RCA device the feed (source) antenna is placed inside a resonator which is usually a Fabry-Perot (FP) based cavity structure. The bottom reflector is commonly made of a blank metal surface or a patterned (defected) surface or an impedance surface which also acts as the ground plane of the feeding antenna device. The top reflector (superstrate) can be a single dielectric substrate or more dielectric layers called an electromagnetic band gap (EBG) structure. The required high reflectivity is obtained using a high permittivity dielectric material with a quarter wavelength thickness [1-4]. In the EBG based superstrates, Weily et al. used a three layer EBG structure as the superstrate in a RCA device fed by a slot array [7]. The gain and bandwidth of the RCA device were 22.7 dBi and 13.2% respectively. Al-Tarifi et al. proposed a double cavity RCA device consisting of two dielectric superstrates [8] which has a bandwidth of 17.9% based on the results of simulation work as compared to 9% of a single cavity device. The recent work by Hashmi et al. [9] demonstrated a wideband RCA device using an all dielectric superstrate consisting of 3 layers of dielectric substrates. A large 3-dB bandwidth of 22% was achieved with a peak gain of 18.2 dBi. Although the dielectric material based superstrate is easy to design, the resultant antenna device is bulky. The lack of choice in dielectric slab materials with the required thicknesses also restricts design flexibility.

In recent years it has been shown that a partially reflecting surface (PRS) consisting of one or more layers of periodic metallic or aperture elements on a dielectric substrate known as a frequency selective surface (FSS), can be used effectively as the superstrate leading to low-profile RCA devices [10-13]. Wideband capability of RCA devices based on one FSS layer as the PRS was studied by Feresidis et al. [11] but the available bandwidth was limited by the intrinsic characteristics of the magnitude and phase of the reflection characteristics of the single layer FSS based PRS designs. Therefore bandwidth enhancement has been a subject of significant interest using double FSS layer based PRS structures for RCA devices. Feresidis and Vardaxoglou [14] proposed a double layer superstrate design consisting of two FSS layers with different dimensions of patch elements on each dielectric board. An enhanced bandwidth of 9% was obtained using a waveguide based feed source. Ge et al. [15] investigated a double layer superstrate for bandwidth enhancement of a RCA device utilizing two dissimilar dipole arrays printed on each side of a dielectric board. A monopole antenna was used as the feed source and a bandwidth of 13.6% was achieved. In [16], Wang et al. has reported a wideband RCA device using a two layer metamaterial superstrate consisting of a patch array and a perforated metal layer with periodic square holes, the two FSS layers were printed on each side of a dielectric board. In their work a wideband microstrip fed patch antenna with a suspended patch element [17] was used as the feed source.

The measured impedance bandwidth was about 25% and the gain bandwidth was 28%. In addition a dual-band RCA device using a two layer metallo-dielectric superstrate has also been investigated [18], the metamaterial superstrate design was based on two dissimilar rectangular patch arrays one on each side of a dielectric board.

In this paper, we present the results of design and implementation of a wideband RCA device using a double layer metamaterial based superstrate (PRS) consisting of identical periodic metallic patch elements on thin film liquid crystal polymer (LCP) substrates [19]. Impedance and gain bandwidth as large as 44% and 46% have been obtained from a practical device. The results were achieved using an optimized wideband patch antenna as the feed source with the two layer metamaterial superstrate.

## 2. Design and modelling

In this section, the configuration and design principle of the resonant cavity antenna for gain enhancement and wideband operation are discussed. The design and modelling work was carried out using the Ansys-HFSS software tool. An aperture coupled CPW fed patch antenna with a suspended patch was designed for wideband operation. The design and characteristics of a two layer metamaterial are studied for application as a superstrate for a wideband RCA device. The metamaterial substrate structure is then incorporated into the RCA configuration for modelling and optimization of the resultant antenna device.

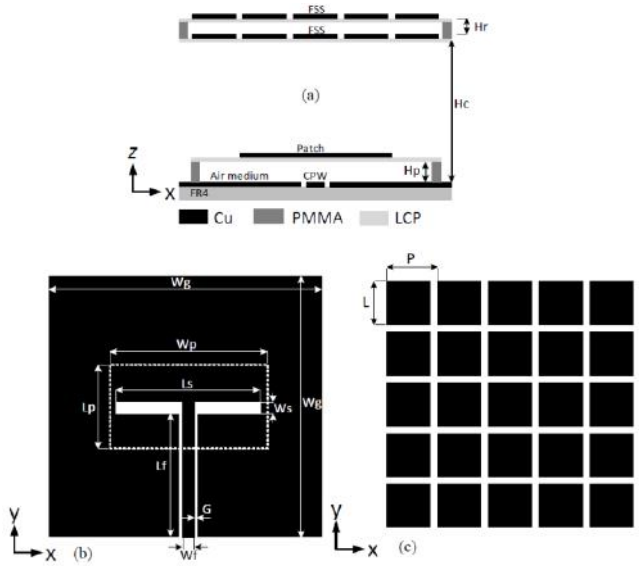



Figure 1: Geometry of the broadband resonance cavity antenna, (a) cross sectional view, (b) plane view of the CPW feed structure, the coupling aperture and the patch element, and (c) the square patch array in each layer of the PRS.

### 2.1. Configuration of the RCA antenna design

Fig. 1(a) shows a schematic cross-sectional view of the resonant cavity antenna for high directivity and wideband operation. The primary source is a wideband CPW fed patch antenna using a suspended patch design on an FR4 substrate. The patch element is on a thin film liquid crystal polymer (LCP) substrate. The latter is supported using a laser micromachined PMMA (polymethyl methacrylate) based polymer rim. The thickness of the PMMA rim and hence the air gap between the LCP and the FR4 substrates, is denoted by Hg. The layout of the aperture for coupling and the coplanar waveguide for feeding is shown in Fig. 1(b). The PRS is a two-layer metamaterial and is separated from the ground plane of source antenna by the cavity height, Hc. Unlike the PRS designs in the previous work, our PRS consists of two identical layers of square patch based arrays each printed on the same thin film LCP material as that used in the source antenna. Fig. 1(c) shows a schematic layout of the patch array on the LCP film. Two such LCP film substrates are combined together using a PMMA based rim structure by aligning and bonding the LCP films to each side of the PMMA rim.

### 2.2. Design of a CPW-fed aperture-coupled patch antenna as a wideband primary source

For wideband operation of a RCA device, it is necessary to use a wideband antenna as the source element. In our previous work [17], [20] we showed that wideband patch antenna devices can be obtained by using an aperture coupled design and a suspended patch [17] or patches in the case of stacked patch antennas [20]. Using a microstrip feed design, a bandwidth of ~20% was obtained for a single patch based design [17]. In this work we developed a CPW based feed design to obtain increased bandwidth using a short end CPW line. In the CPW fed configuration shown in Fig. 1, a wide impedance bandwidth can be obtained based on the coupling of the resonances associated with a double tuned aperture [21] and the suspended patch. The design and simulation work was carried out in a similar approach as described in our previous work [17]. Briefly the aperture was designed in the first step, the total length of the aperture was one guided wavelength at 10 GHz and the width was one tenth of the length [17]. Then a short-end CPW was added to the aperture on the ground plane as the feeding structure. The CPW line acts as an impedance transformer and was designed to obtain a double-tuned aperture with wide impedance bandwidth. By studying the reflection characteristic of the CPW fed aperture, it was found that the desired length for the CPW line was one wavelength for wideband impedance operation of the double tuned aperture. In the last design step, a rectangular patch was added to the CPW fed aperture with an air gap between the thin film LCP substrate of the patch and the aperture. The length of the patch was half wavelength at 10 GHz, the patch resonance was coupled to those of the double tuned aperture resulting in triple resonances thus broadening the impedance bandwidth of the antenna design. The air gap determines the coupling between the patch and the aperture. A range of air gap values was investigated and it was found that the air gap of 3 mm provides the best impedance bandwidth. The material properties and design parameters are given in Table 1 and 2 respectively.

The simulation results of the reflection coefficient and directivity of the wideband patch antenna are shown in Fig.

2. An impedance bandwidth of about 46% has been achieved. It is believed that this is the widest bandwidth obtained for a single patch based antenna device. The directivity is higher than that of the conventional printed patch antenna on a PCB board by using the air gap based design and a low loss LCP thin film substrate [17].

Table 1: Properties of dielectric substrates.

| | LCP [22] | FR4 [23] | PMMA [24] |
|---|---|---|---|
| $\varepsilon_r$ | 2.9 | 4.1 | 2.6 |
| tanδ | 0.0025 | 0.02 | 0.008 |

Table 2: Design dimensions of patch antenna.

| Lp | Wp | Ls | Ws | Wf | Lf | G | Hg | Wg |
|---|---|---|---|---|---|---|---|---|
| 10 | 20 | 17 | 1.0 | 1.4 | 20 | 0.2 | 3 | 45 |

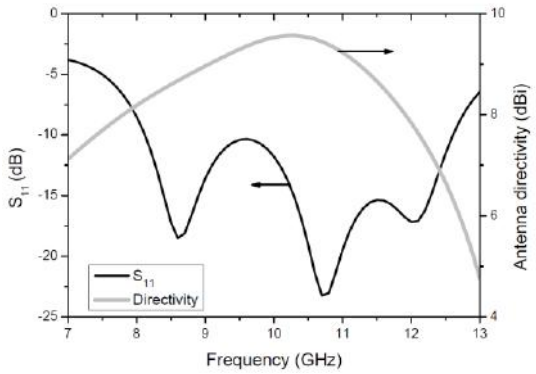



Figure 2: Simulation results of reflection coefficient ($S_{11}$) and the directivity of the patch antenna source.

### 2.3. Design of the metamaterial based PRS

In this work we have studied design of an effective PRS using a two-layer metallo-dielectric based metamaterial as shown in Fig. 1. The metamaterial based PRS consists of two identical patch arrays each printed on an LCP film substrate and separated by an air gap. In our previous work [25], we investigated Fano resonance in such metamaterials with a narrow bandwidth for high-Q applications. In this paper we demonstrate that the same metamaterial design but with broad resonance characteristics can be used to design an effective PRS for a wideband RCA device. Unlike in [25], in this work patch arrays with approximately quarter wavelength pitch have been found to provide suitable reflection characteristics for incorporating into a RCA device for broadband operation. The resonant frequency of the metamaterial PRS was chosen to be 10 GHz matching that of the source antenna as discussed previously. The resonant frequency of the two-layer material PRS depends on the pitch of the patch array, the dimensions of the square patch element and the gap between the two LCP film substrates. The design work was carried out using a unit cell based approach thus assuming an infinite array size [12]. The implementation of the unit cell for design and simulation work is shown in Fig. 3. Full wave EM simulation was performed based on the Floquet's theorem using the Ansys HFSS software tool. It has been shown that this method is accurate and efficient in study of infinite size two dimensional periodic arrays [26].

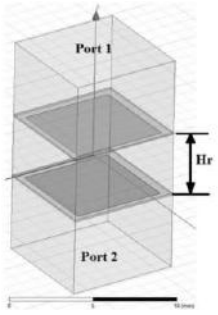
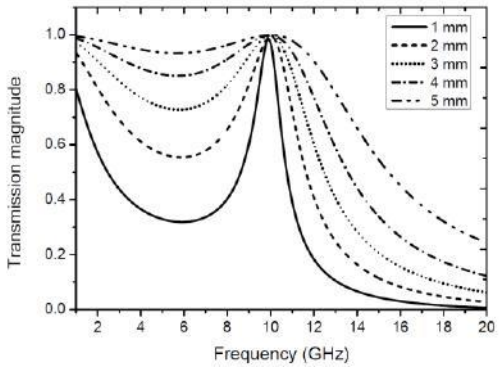
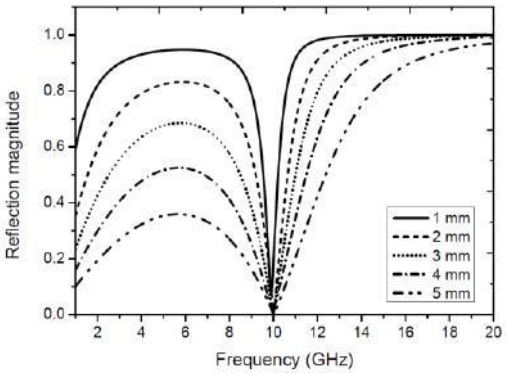



Figure 3: Unit cell structure for simulation of PRS design consisting of two identical patch arrays each on a thin film LCP substrate.




**(a)**




**(b)**

Figure 4: Simulation results for the PRS design based on the unit cell shown in Fig. 3, (a) transmission magnitude and (b) reflection magnitude.

Five such metamaterial designs have been considered for PRS applications. The pitch of the patch array was 7 mm in all cases. The values of the air gap between the two arrays are 1, 2, 3, 4 and 5 mm respectively. To maintain the resonant frequency of the material structures, the dimensions of the square patch elements were adjusted in the design

process. The corresponding values were found to be 6.95 mm, 6.77 mm, 6.45 mm, 6 mm and 5.3 mm respectively. Fig. 4 shows the transmission and reflection characteristics of the two-layer metamaterial designs. The resonant behavior has a strong dependence on the air gap thickness between the two array layers. As the air gap increases, the effect of Fano resonance decreases since the electromagnetic coupling between the scattered waves becomes weaker [25].

#### 2.4. Design of RCA

The design of a wideband RCA device was carried out by implementing the corresponding 3D structure of the cross-sectional view as shown in Fig. 1(a) in Ansys HFSS environment. The source antenna as described in section 2 was incorporated in the RCA design without modification. Since the actual PRS structure in a RCA device has a finite array of patch elements. Therefore the RCA synthesis work was carried out using a finite element based full wave simulation approach to take into account of the effect of the finite size of the PRS. For compactness both of the PRS and the substrate of the primary source should be small while maintaining a wideband performance.

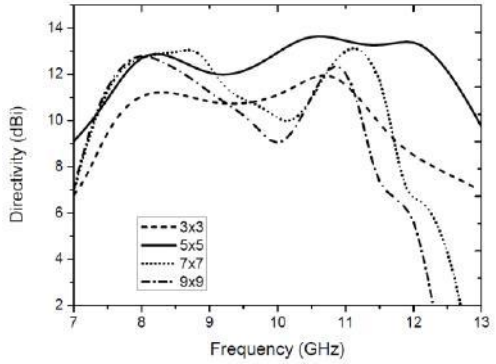



Figure 5: Comparison of broadside directivity of the RCA design for different arrays in the finite-size PRS. The cavity height (Hc) is 20 mm.

Fig. 5 shows the results of broadside directivity as a function of frequency for array sizes of 5x5, 7x7 and 9x9 in the superstrate respectively. It can be seen that the bandwidth of directivity is strongly affected by the size of the superstrate. This effect has already been observed in other RCA devices [6], [13] and has been discussed in detail in [9]. A larger superstrate results in lateral propagation within the cavity and phase non-uniformity across the radiation aperture thus causing degradation in antenna performance. Hence a smaller superstrate is better for a RCA device, the leaked wave from the edges of the superstrate also increases the radiation bandwidth [9]. In our work this effect is used to obtain gain enhancement at 10 GHz at which the superstrate is at resonance exhibiting zero reflectivity and thus gain enhancement cannot be achieved using the cavity effect. It was found that the optimum array size for a wideband RCA device is 5x5. Further reduction of superstrate size weakens the effect of the Fabry-Perot resonator and thus reducing the performance of the RCA device at frequencies below and above the resonant frequency (10 GHz) of the superstrate. As shown in Fig. 5 as the superstrate becomes very large (e.g. 9x9 array) no enhancement in directivity can be obtained at 10 GHz since the effect of gain/directivity enhancement of the superstrate is small.

Fig. 6 shows the results of both radiation and reflection characteristics of the RCA device with the 5x5 array based PRS design for different cavity heights. It can be seen that the cavity height has a significant effect on the radiation response of the cavity. The best RCA performance is obtained at the cavity height of 20 mm with the lowest ripple response in antenna directivity. The corresponding impedance bandwidth is 45% as shown in Fig. 6(b).

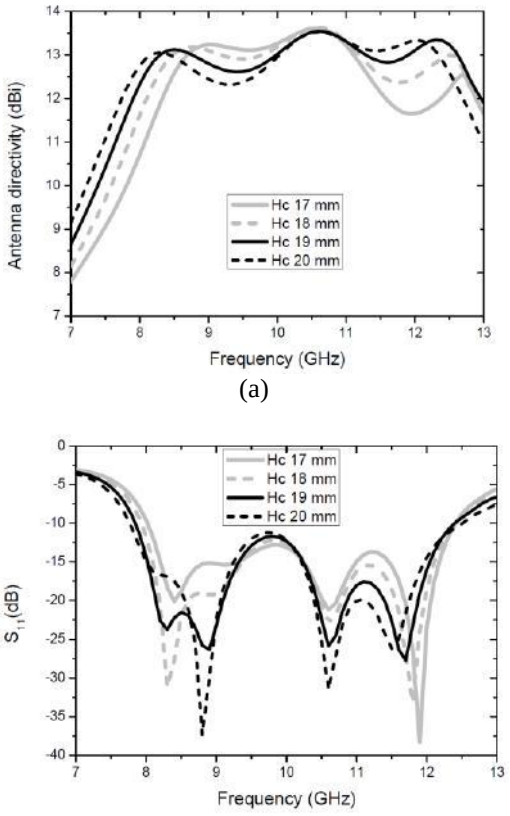



Figure 6: Radiation (a) and reflection (b) characteristics of the RCA device with 5x5 patch arrays in the superstrate.

## 3. Fabrication and measurements

#### 3.1. Fabrication of patch antenna

The wideband patch antenna was produced on an FR4 substrate. The thickness of the substrate was 1.6 mm. A similar fabrication approach as in our previous work was used [20]. However a laser micromachined PMMA rim was used in this work to obtain a suspended patch instead of the SU8 based polymer rim that was produced by a surface micromachining based method. The new approach is efficient and better for producing millimeter thick polymer structures than the previous method. The CPW feed line and the coupling aperture was produced on a copper clad FR4 board using a microfabrication approach. The patch was

fabricated on a thin film (100 μm) copper clad LCP substrate. The PMMA rim for supporting the patch on the LCP substrate was produced using a $CO_2$ laser based micromachining system. The inner dimensions of the rim were 36 x 36 $mm^2$ and the width of the PMMA track was 2 mm. A PMMA plate of 3 mm of thickness was used in this work to match the design requirement for wideband operation of the resultant patch based source antenna. In the assembly process, the PMMA rim was aligned to the aperture on the FR4 substrate and attached to it using the SU8 based bonding method [20]. The patch on the LCP film substrate was then aligned to the coupling aperture and the LCP substrate was bonded to the PMMA rim using the same method as for bonding of the PMMA rim to the FR4 substrate. Finally a SMA connector was mounted to the FR4 board by soldering to complete the construction of a wideband patch antenna as the primary source for a wideband RCA device.

### 3.2. Fabrication of PRS

Based on the results of design and simulation work as described in section 2, the PRS design with a 5x5 array of square patch elements in each FSS layer was chosen for construction of a RCA device. As shown in Figs. 5 and 6, the best performance for a RCA device is expected from incorporation of this PRS design. The 5x5 array of square patch elements was fabricated on a copper clad LCP film substrate. The patch array was the fabricated on the LCP substrate using the same microfabrication method as for fabrication of the primary source antenna. Two arrays were fabricated each on an LCP film as necessary for construction of the double layer metamaterial based PRS. Two 2 mm thick laser machined PMMA rims were prepared and stacked together to a total rim thickness of 4 mm as the spacer between the two patch arrays. The two LCP layers were then aligned and attached to each side of the stacked PMMA rim to complete the construction of the PRS structure.

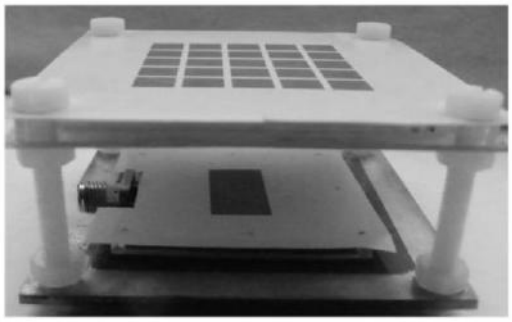


Figure 7: A photograph of the assembled RCA device showing a CPW-fed aperture coupled patch antenna and the PRS superstrate. The cavity height is 20 mm.

### 3.3. Assembly of RCA device

The primary source antenna and the PRS as described in the above sections were assembled to complete the construction of the wideband RCA device. A screw based method was used to mount the PRS on the FR4 substrate of the source antenna. Alignment was made using 4 pre-drilled matching holes on the FR4 substrate and the PRS structure. The holes were located on each corner of the square FR4 board and the PRS assembly. Fig. 7 shows an optical image of the assembled wideband RCA device. The cavity height can be controlled by adjusting the position of the screws securing the PRS structure.

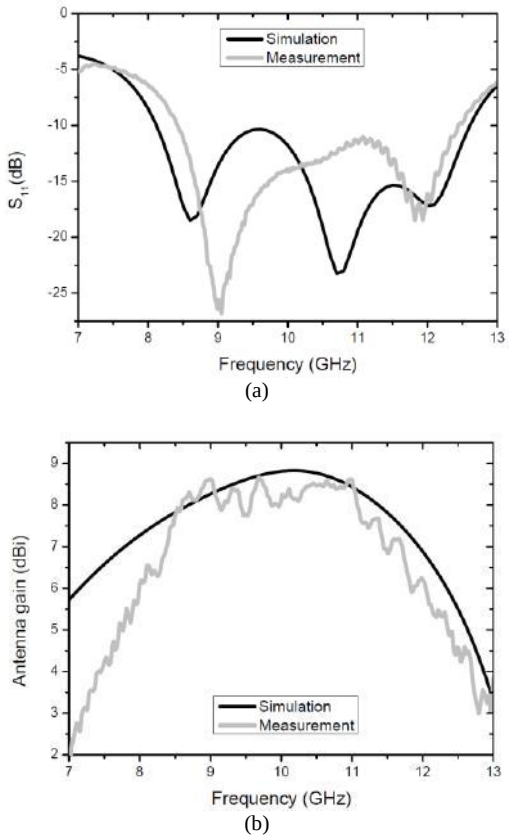
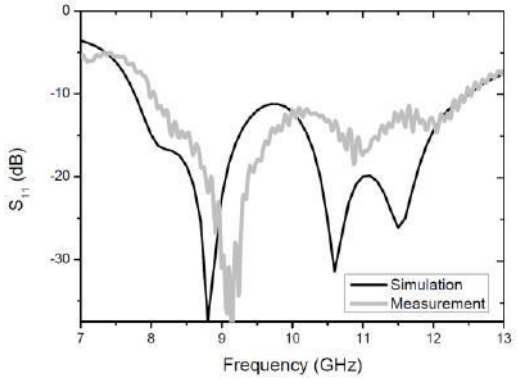



Figure 8: The measured and simulation results of reflection (a) and radiation (b) characteristics of the broad band feed antenna

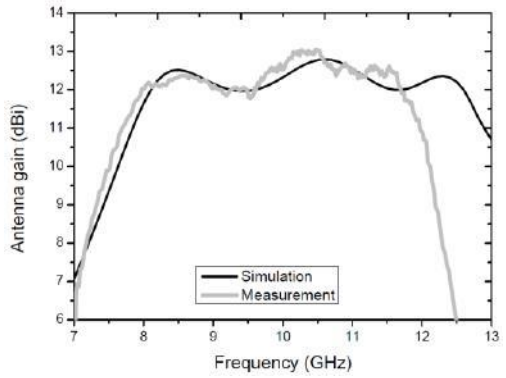
### 3.4. Antenna characterization

Microwave measurements for antenna characterization were made in an anechoic chamber using a vector network analyzer (HP 8510). Fig. 8 shows the results of reflection and gain measurements for the source (feed) antenna. Good impedance matching through coupling of multiple resonances was obtained with an impedance bandwidth of 43%. The 3dB gain bandwidth is 40% covering the X-band with a peak gain of 8 dBi. To our knowledge the results are the largest bandwidth values obtained for a patch antenna device. It provides the necessary feed source for a wideband RCA device. Fig. 9 presents the results of measurement and simulation of the far-field radiation pattern for the RCA antenna device shown in Fig. 7. A good agreement between the measurement and simulation results has been obtained. The cavity height was 20 mm. The measured impedance bandwidth is 44% between 8 GHz and 12.4 GHz. The measured 3dB gain bandwidth is 46%. The device has

excellent flat-ripple response with a 1-dB-ripple gain bandwidth as wide as 40% over the frequency band between 7.6 and 11.6 GHz




(a)




(b)

Figure 9: (a) Results of reflection from measurement and simulation, and (b) results of gain from measurement and simulation.

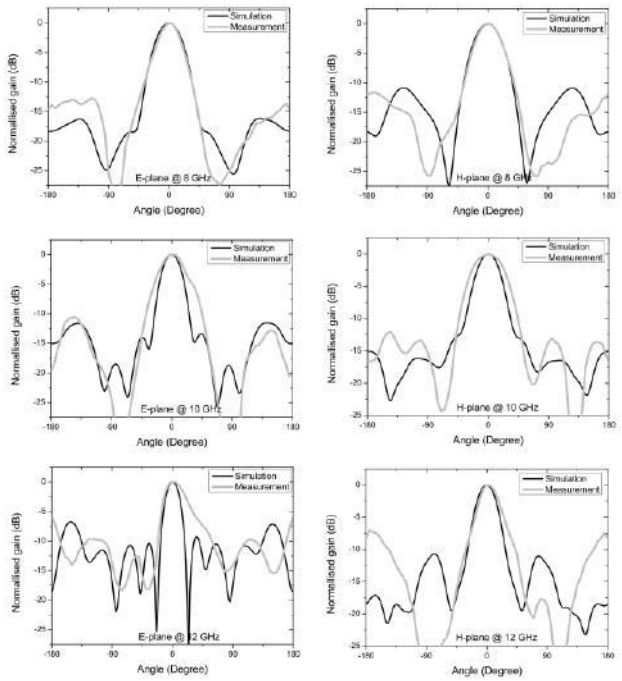



Figure 10: E- and H-plane far-field radiation patterns of the RCA device at three different frequencies of 8 GHz, 10 GHz and 12 GHz respectively.

To investigate the spatial characteristics of the radiation, angle dependent measurements were carried out at selected frequencies and the results are shown in Fig. 10. In general the measured results are in good agreement with the predicted performance, except the E-plane results at 10 and 12 GHz which may be due to the fact that the SMA connector of the source antenna was on the E-plane and was not included in the model of the simulation work. The results of E-plane and H-plane measurements show the same value of 40° for the 3dB bandwidth at the frequencies of both 8 GHz and 10 GHz. It is slightly barrower at 12 GHz with a value of 30°. Therefore the results illustrate the desirable radiation behavior of the RCA design for broadband applications maintaining similar radiation patterns over the band of operation.

## 4. Conclusion

A resonance cavity antenna with the characteristics of the broad radiation bandwidth has been proposed and demonstrated successfully. The effects of Fano resonance in the PRS consisting of two identical arrays of square patch elements and the finite PRS size was combined to achieve gain enhancement over a wideband. A wideband patch antenna was designed and used as the feed source for the RCA device. Thin film LCP substrates were used in construction of the RCA device enabling high performance and light weight devices. The impedance and 3 dB radiation bandwidth of the device were measured to be 44% and 46% respectively representing considerable improvement over the bandwidth of similar devices reported in the previous work. The peak gain of the device was about 13 dBi. The RCA device is also very compact with dimensions of only 45x45x26 $mm^3$.


## Acknowledgements

The authors would like to thank Rogers Corp. for providing the LCP film substrate material used in this work.


## References


[1] D.R. Jackson, N.G. Alexopoulos, Gain enhancement method for printed circuit antennas, *IEEE Trans. Antennas Propag*. 33: 976-987, 1985.

[2] D.R. Jackson, A.A. Oliner, A. Ip, Leaky-wave propagation and radiation for a narrow-beam multiple-layer dielectric structure, *IEEE Trans. Antennas Propag*. 41: 344 -348, 1993.

[3] C. Cheype, C. Serier, M. Thevenot, T. Monediere, An electromagnetic bandgap resonator antenna, *IEEE Trans. Antennas Propag*. 50: 1285-1290, 2002.

[4] A.R. Gardelli, M. Albani, F. Capolino, Array thinning by using antennas in a Fabry-Perot cavity for gain enhancement, *IEEE Trans. Antennas Propag.* 54: 1979-1990, 2006.

[5] A.R. Weily, L. Horvath, K.P. Esselle, B.C. Sanders, T. S. Bird, A planar resonator antenna based on a woodpile EBG material, *IEEE Trans. Antennas Propag.* 53: 216-223, 2005.

[6] Y.J. Lee, J. Yeo, R. Mittra, W.S. Park, Application of electromagnetic bandgap (EBG) superstrates with controllable defects for a class of patch antennas as spatial angular filters, *IEEE Trans. on Antennas Propag*. 53: 224-235, 2005.

[7] A.R. Weily, K.P. Esselle, T.S. Bird, B.C. Sanders, Dual resonator 1-D EBG antenna with slot array feed for improved radiation bandwidth, IET Micow. Antennas Propag., 1: 198-203, 2007.

[8] M.A. Al-Tarifi, D.E. Anagnostou, A.K. Amert, K.W. Whites, Bandwidth enhancement of the resonant cavity antenna by using two dielectric superstrates, *IEEE Trans. Antennas Propag*. 61: 1898–1908, 2013.

[9] R.M. Hashmi, B.A. Zeb, and K.P. Esselle, Wideband high-gain EBG resonator antennas with small footprints and all-dielectric superstructures, *IEEE Trans. on Antennas Propag*. 62: 2970-2977, 2014.

[10] G.V. Trentini, Partially reflecting sheet arrays, *IRE Trans. Antennas Propag.* 4: 666-671, 1956.

[11] A.P. Feresidis and J.C. Vardaxoglou, High gain planar antenna using optimised partially reflective surfaces, *Proc. Inst. Elect. Eng. Microw. Antennas Propag.* 148: 345-350, 2001.

[12] N. Guerin, S. Enoch, G. Tayeb, P. Sabouroux, P. Vincent, H. Legay, A metallic Fabry-Perot directive antenna, *IEEE Trans. on Antennas Propag.* 54: 220-224, 2006.

[13] A. Foroozesh, L. Shafai, Investigation into the effects of the patch-type fss superstrate on the high-gain cavity resonance antenna design, *IEEE Trans. Antennas Propag.* 58: 258-270, 2010.

[14] A.P. Feresidis, J.C. Vardaxoglou, A broadband high gain resonant cavity antenna with single feed, *Proc. 1st Eur.Conf. Antennas Propag. (EuCAP)*, Nice, France, 2006.

[15] Y. Ge, K. P. Esselle, T. S. Bird, The Use of Simple Thin Partially Reflective Surfaces With Positive Reflection Phase Gradients to Design Wideband, Low-Profile EBG Resonator Antennas, *IEEE Trans. On Antennas Propag*. 60: 743–750, 2012.

[16] N. Wang, Q. Liu, C. Wu, L. Talbi, Q. Zeng, J. Xu, Wideband Fabry-Perot resonator Antenna with two complementary FSS layers, *IEEE Trans. on Antennas Propag*. 62: 2463–2471, May 2014.

[17] S.K. Pavuluri, C.H. Wang, A.J. Sangster, High-performance aperture-coupled patch antenna supported by a micromachined polymer ring, *IEEE Antennas Wireless Propag. Lett.* 7: 283–286, 2008.

[18] D.H. Lee, Y.J. Lee, J. Yeo, R. Mittra, W.S. Park, "Design of novel thin frequency selective surface superstrates for dual-band directivity enhancement, *IET Microw., Antennas & Propag*. 1: 248-254, 2007.

[19] K. Kanjanasit and C.H. Wang, A high directivity broadband aperture coupled patch antenna using a metamaterial based superstrate, *Proc. Antennas and Propagation Conference (LAPC2012)*, Loughborough, UK, 2012.

[20] S.K. Pavuluri, C.H. Wang, and A.J. Sangster, High efficiency wideband aperture-coupled stacked patch antennas assembled using millimeter thick micromachined polymer structures, *IEEE Trans. on Antennas Propag*. 58: 3616-3621, 2010.

[21] A.R. Lopez, Double-tuned impedance matching, *IEEE Antennas and Propag. Mag.* 54: 109–116, 2012.

[22] D.C. Thompson, O. Tantot, H. Jallageas, G.E. Ponchak, M.M. Tentzeris, J. Papapolymerou, Characterization of liquid crystal polymer (LCP) material and transmission lines on LCP substrates from 30 to 110 GHz, *IEEE Trans. Microw. Theory Tech*. 52: 1343–1352, 2004.

[23] E.L. Holzman, Wideband measurement of the dielectric constant of an FR4 substrate using a parallel-coupled microstrip resonator, *IEEE Trans. on Microw. Theory Tech*. 54: 3127-3130, 2006.

[24] B. Riddle, J. Baker-Jarvis, J. Krupka, Complex permittivity measurements of common plastics over variable temperatures, *IEEE Trans. on Microw. Theory Tech*. 51: 727-733, 2006.

[25] K. Kanjanasit and C.H. Wang, Fano resonance in a metamaterial consisting of two identical arrays of square metallic patch elements separated by a dielectric spacer, *Appl. Phys. Lett*. 102: 251108, 2013.

[26] L.E.R. Petersson, J.M. Jin, A three-dimensional time-domain finite element formulation for periodic structures, *IEEE Trans. Antennas Propagat*. 54: 12–19, 2006.

# Multiple electric and magnetic Fano resonances in core-shell particles

**Tiago J. Arruda[1*], Alexandre S. Martinez[1], and Felipe A. Pinheiro[2]**

[1]Faculdade de Filosofia, Ciências e Letras de Ribeirão Preto, Universidade de São Paulo, Brazil
[2]Instituto de Física, Universidade Federal do Rio de Janeiro, Brazil
*corresponding author, E-mail: tiagoarruda@pg.ffclrp.usp.br

## Abstract

Using the Lorenz-Mie theory, we derive an analytical condition for the occurrence of mutiple Fano resonances in single scattering by coated spheres composed of magnetic materials [*Phys. Rev. A* 92: 023835, 2015]. This condition establishes that Fano-comb scattering response depends uniquely on material parameters and thickness of the shell, provided that it is magnetic and thin compared to the scatterer radius. We argue that both position and profile of these Fano resonances could be externally tuned by engineering magnetic materials.

## 1. Multiple Fano resonances

Recently, a great deal of attention has been devoted to the Fano resonance in plasmonic nanostrutures due to its sensitivity to both geometry and local environment changes [1, 2]. The interference between broad and narrow resonance modes, supported by plasmonic nanostrutures, gives rise to the Fano resonance, which has a characteristic, asymmetric lineshape with a narrow bandwidth [2]. By properly choosing the materials and/or the system design, it is possible to generate *e.g.* multiple Fano, comblike scattering resonances in plasmonic nanoparticles [3, 4]. The design of these Fano-comb nanoparticles may enable several applications at different spectral ranges, such as improving the resolution in comb-spectroscopy techniques and optical tagging [3].

Here, we propose an alternative approach [1], based on magnetic materials, for generating comblike scattering response in concentric, single-layered core-shell nanoparticles, which can exhibit Fano resonances [5]. Instead of inducing Fano-comb resonances by the geometrical symmetry breaking in single-layered core-shell nanostructures [4], we suggest the use of high permeability covers [6, 7] in center-symmetric scatterers. Indeed, in the long-wavelength limit, the presence of a ferromagnetic layer breaks the isotropy of the Rayleigh scattering [8], and allow us to obtain multiple Fano, comblike scattering resonances composed of both electric and magnetic dipole resonances in the extinction cross-sections. These Fano-like resonances, known as "unconventional" Fano resonances [5], are different from the conventional Fano ones [2], since they are polarization-independent and arise from the interference between EM modes with the same multipole moment.

With this aim, let us consider a center-symmetric, core-shell sphere, with inner radius $R_1$ and outer radius $R_2$, interacting with a plane EM wave in free space. The refractive and impedance indices are $n_q \equiv \sqrt{\varepsilon_q \mu_q}$ and $\widetilde{n}_q \equiv \sqrt{\varepsilon_q/\mu_q}$, with $q = 1$ for core and $q = 2$ for shell, so that $\widetilde{n}_q = n_q$ for nonmagnetic materials ($\mu_q = 1$) [6, 7, 8]. The scattering efficiency is $Q_{\rm sca} = 2\sum_{\ell=1}^{\infty}(2\ell+1)(|a_\ell|^2 + |b_\ell|^2)/(kR_2)^2$, where $a_\ell$ and $b_\ell$ are the electric and magnetic Lorenz-Mie coefficients, respectively, and $k = 2\pi/\lambda$ is the wave number of the incident wave [9].

With a little bit of algebra (for details, see Ref. [1]), it is possible to demonstrate that the combination of small-particle and ferromagnetic limits for the shell ($kR_2 \ll 1$ and $|n_2|kR_2 \gg 1$) with the Rayleigh limit for the core ($kR_1 \ll 1$ and $|n_1|kR_1 \ll 1$) leads to multiple Fano, comblike resonances in the scattering cross-section. With a proper choice of parameters and assuming $\zeta \equiv R_1/R_2 \approx 1$, one can obtain electric and magnetic Fano-like resonances with a scattering minimum (cloaking [10]) at the same frequency. The cloaking condition ($Q_{\rm sca} \approx 0$) leads to a mutual dependence between $\varepsilon_2$ and $\mu_2$, for $kR_2 \ll 1$, $|n_1|kR_1 \ll 1$, $|n_2|kR_2 \gg 1$, and $\zeta \approx 1$:

$$\varepsilon_2\mu_2 \approx \left[\frac{\pi N}{kR_2(1-\zeta)}\right]^2, \quad N = 1,\ 2, \ldots \qquad (1)$$

These integer numbers $N$ can roughly be interpreted as indicating the "cavity modes" of the magnetic shell. In fact, being $\lambda_2$ the wavelength inside a nanoshell with thickness $d \equiv b - a$, the EM cloaking occurs for $\lambda_2 \approx 2d/N$. Note that this is the same condition for resonant modes in a Fabry-Pérot cavity with $d$ being the separation distance between its mirrors. Since this analytical result is typical of resonant optical cavities, it suggests that the cloaking condition does not depend on the geometry of the particle (optical cavity), but rather the magnetic material parameters, shell thickness, and irradiation schemes.

Also, due to the electric and magnetic Fano-like resonances, the cloaking frequencies given by Eq. (1) are spectrally near to a pair of scattering resonance peaks. Each of these scattering, Fano-comb resonances are associated with a mode number $N$ and are referred to as morphology-dependent resonances of first order ($\ell = 1$). These Fano-comb resonances are plotted in Fig. 1 as a function of the input frequency $\omega$ and $\mu_2$.

It is important to mention that the profile and the position of the comblike resonances can be externally tuned in engineered magnetic materials, such as metamaterials made

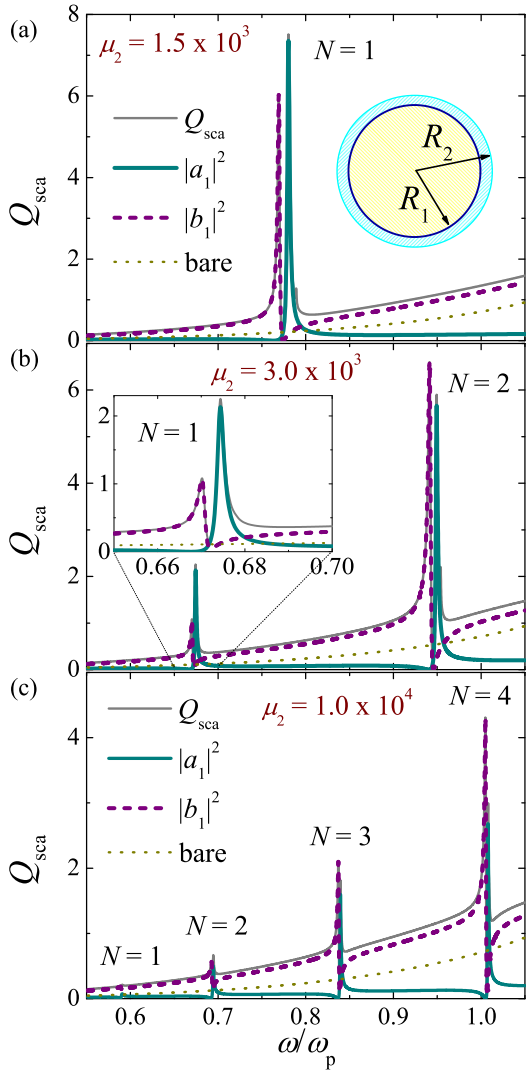



Figure 1: Scattering efficiency $Q_{\rm sca}$ for a dielectric sphere with refractive index $n_1 = 3.1$ coated with a plasmonic, lossy magnetic shell with $\mu_2 \gg 1$ and $\varepsilon_2(\omega) = \varepsilon_\infty - \omega_{\rm p}^2/[\omega(\omega + i\Gamma)]$, where $\varepsilon_\infty = 3.3$, $\omega_{\rm p} = 2213.2$ THz, and $\Gamma = 0.002\omega_{\rm p}$ [3], embedded in vacuum. The inner sphere has radius $R_1 = 100$ nm and aspect ratio $\zeta = R_1/R_2 = 0.9$ [1]. The dotted line represents the sphere without coating ($\zeta = 1$). The cloaking occurs at $\varepsilon_2$ values given by Eq. (1). The $|a_1|^2$ and $|b_1|^2$ curves refer to the electric and magnetic dipole contributions in the exact Lorenz-Mie theory. (a) $\mu_2 = 1.5 \times 10^3$. (b) $\mu_2 = 3 \times 10^3$. (c) $\mu_2 = 10^4$.

of ferroelectric compounds [6, 7]. Indeed, by applying an external magnetic field and/or varying the temperature, one can change the value of $\mu_2$. This possibility of tuning the value of $\mu_2$ has influence not only on the resonance position but also on the number of resonances that compose the comblike scattering response at a given spectral range, as illustrated in Fig. 1.

We emphasize that, to the best of our knowledge, this tunability is not found in previous proposals involving comblike resonances in core-shell nanoparticles, which are based mainly on nonmagnetic materials [3, 4]. In these previous systems, the position and profile of comblike resonances are determined *a priori* by the nanostructure design, either by varying the plasma frequencies with a gradient of doping level in multilayered spheres [3] or by constructing nonconcentric core-shell nanowires [4]. This fact, which distinguishes our proposal from the previous ones, allows for tunable, versatile comblike scattering response in concentric, single-layered core-shell nanoparticles.

## Acknowledgement

The authors acknowledge the Brazilian agencies for support. T.J.A. holds grants from FAPESP (2010/10052-0) and CAPES/PNPD (1564300). A.S.M. holds grants from CNPq (307948/2014-5, 485155/2013). F.A.P. holds grants from CNPq (303286/2013-0) and CAPES (BEX 1497/14-6).

## References

[1] T.J. Arruda, A.S. Martinez, F.A. Pinheiro, Tunable multiple Fano resonances in magnetic single-layered core-shell particles, *Phys. Rev. A* 92: 023835, 2015.

[2] A.E. Miroshnichenko, S. Flach, Y.S. Kivshar, Fano resonances in nanoscale structures, *Rev. Mod. Phys.* 82: 2257–2298, 2010.

[3] F. Monticone, C. Argyropoulos, A. Alù, Multilayered plasmonic covers for comblike scattering response and optical tagging, *Phys. Rev. Lett.* 110: 113901, 2013.

[4] J. Zhang, A. Zayats, Multiple Fano resonances in single-layer nonconcentric core-shell nanostructures, *Opt. Express* 21: 8426–8436, 2013.

[5] T.J. Arruda, A.S. Martinez, F.A. Pinheiro, Unconventional Fano effect and off-resonance field enhancement in plasmonic coated spheres, *Phys. Rev. A* 87: 043841, 2013.

[6] F.A. Pinheiro, A.S. Martinez, L.C. Sampaio, New effects in light scattering in disordered media and coherent backscattering cone: system of magnetic particles, *Phys. Rev. Lett.* 84: 1435–1438, 2000.

[7] F.A. Pinheiro, A.S. Martinez, L.C. Sampaio, Vanishing of energy transport velocity and diffusion constant of electromagnetic waves in disordered magnetic media, *Phys. Rev. Lett.* 85: 5563–5566, 2000.

[8] T.J. Arruda, A.S. Martinez, Electromagnetic energy within a magnetic sphere, *J. Opt. Soc. Am. A* 27: 992–1001, 2010.

[9] T.J. Arruda, F.A. Pinheiro, A.S. Martinez, Electromagnetic energy within coated spheres containing dispersive metamaterials, *J. Opt.* 14: 065101, 2012.

[10] A. Alù and N. Engheta, Multifrequency optical invisibility cloak with layered plasmonic shells, *Phys. Rev. Lett.* 100: 113901, 2008.

# (Nano)Plasmonic Biosensors

# Selective detection of elevated IgG in human blood serum using surface modified chiral plasmonic metamaterials.

**R. Tullius[1*], A. S. Karimullah[1], C. Jack[1], M. Rodier[1], G. Cooke[1], V. M. Rotello[2] and M. Kadodwala[1]**
[1]School of Chemistry, Joseph Black Building, University of Glasgow, Glasgow, G12 8QQ, UK
[2]Department of Chemistry, University of Massachusetts, 710 North Pleasant Street, Amherst, MA, 01003, USA
[*]corresponding author: r.tullius.1@research.gla.ac.uk

**Abstract**-Protein levels in human serum are an attractive target for early diagnostics and sensors due to the direct correlation of these protein concentrations to diseases/infections. Due to human serum containing more than 20,000 different proteins, detecting a change in these levels can be challenging. Here, we present a method to selectively detect a physiologically relevant increase in the Immunoglobulin G concentration in human blood serum.

Human blood serum contains >20,000 different proteins, with an overall protein concentration of ~1 mM. These proteins vary largely in their relative concentrations, with some being in the 50 g/l range all the way down to under 1 ng/l, with the most abundant protein being serum albumin. This can make it increasingly difficult to selectively detect an elevated level of a specific protein within biological sera [1]. In serum, roughly 20 proteins make up 99% of the mass of serum, the chosen protein to study here, Immunoglobulin G (IgG), makes up ~15% of that.

| HUMAN SERUM | | |
|---|---|---|
| Proteins in the reconstituted material [1)] | Mass concentration | |
| | Certified value [2)] [g/L] | Uncertainty [3)] [g/L] |
| $\alpha_2$ macroglobulin (A2M) | 1.43 [4)] | 0.06 |
| $\alpha_1$ acid glycoprotein (AAG) | 0.617 [5)] | 0.013 |
| $\alpha_1$ antitrypsin (AAT) | 1.12 [5)] | 0.03 |
| albumin (ALB) | 37.2 [4)] | 1.2 |
| β-2-microglobulin (B2M) | 0.00217[6)] | 0.00007 |
| complement 3c (C3c) | 1.00 [4)] | 0.04 |
| complement 4 (C4) | 0.162 [4)] | 0.007 |
| haptoglobin (HPT) | 0.889 [4)] | 0.021 |
| immunoglobulin A (IgA) | 1.80 [4)] | 0.05 |
| immunoglobulin G (IgG) | 9.17 [4)] | 0.18 |
| immunoglobulin M (IgM) | 0.723 [4)] | 0.027 |
| transferrin (TRF) | 2.36 [5)] | 0.08 |
| transthyretin (TTR) | 0.220 [5)] | 0.018 |

**Table 1:** Table of most common proteins present in human serum, along with their concentrations in g/L.

To study the effects of spiking human serum with an increased level of IgG, reflectivity spectra from both left and right handed chiral gold nanostructures were recorded. Similar looking spectra are seen for both the left and the right handed chiral nanostructures, where there is a dip with a peak of enhanced reflectivity within that dip. These peaks of enhanced reflectivity within reflectance dips have previously been attributed to an electromagnetically induced transmission (EIT)-like phenomena in hybrid solid-inverse systems [2]. The origin of this effect is due to the coupling between bright and dark modes of the hybrid structures.

The separation between the reflectance dips in the spectra are sensitive to chiral molecules absorbed on the surface of the chiral gold nanostructures. Various dilutions of a serum standard (15.3% IgG) were run over injection moulded chiral shuriken structures covered in a 100nm gold film, and reflectance spectra measured for each solution. After that, 3 different spiked solutions were used (16.7% IgG, 18.1% IgG and 21.8% IgG total) and reflectance spectra measure for each concentration. The separation between the reflectance dips were measured for both left and right handed nanostructures and then a separation asymmetry was calculated (right separation – left separation) for each solution.

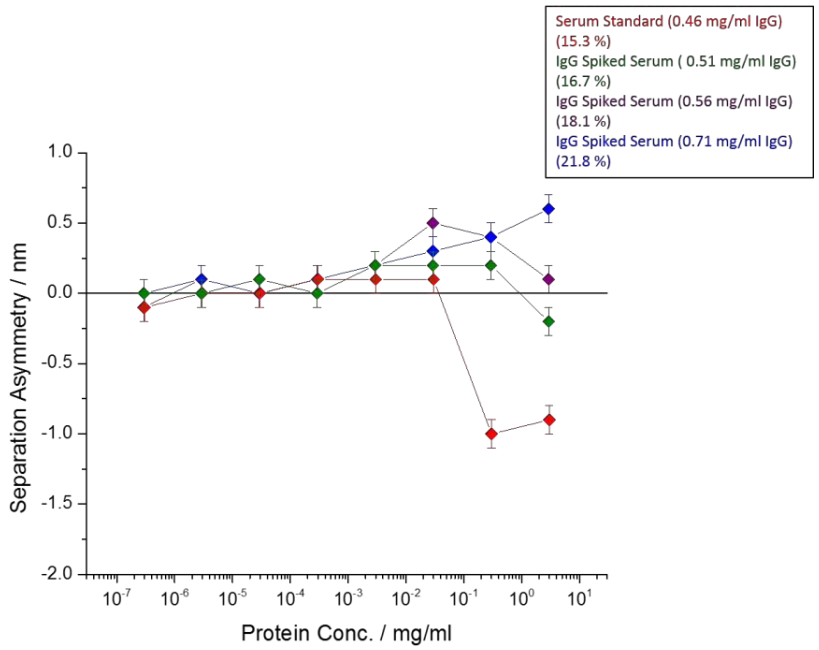



**Figure 1:** Graph showing separation asymmetry for each concentration of standard (red) and spiked serum (green, purple and blue) solutions.

Figure 1 shows that even a small increase in IgG from a standard serum solution can be detected, and as the percentage of spiked IgG increases, so does the separation asymmetry relative to the standard. This sensitive detection of physiologically relevant concentrations of altered IgG from serum samples using injection moulded chiral metamaterials is a step forward in making low cost disease diagnostics a reality.

**Acknowledgements**, The authors acknowledge financial support from the Engineering and Physical Sciences Research Council (EPSRC), National Science Foundation (NSF) and the University of Glasgow. The authors also thank the technical support staff of the James Watt Nanofabrication Centre (University of Glasgow).

## REFERENCES

1. De, M., "Sensing of proteins in human serum using conjugates of nanoparticles and green fluorescent protein," *Nature Chem.*, Vol. 1, 461 – 465, 2009.
2. Hentschel, M., "Babinet to the half: coupling of solid and inverse Plasmonic structures," *Nano Lett.*, Vol. 13, No. 9, 4428 – 4433, 2013.

# 3D Flexible and Tunable Plasmonic Platforms for Optical Biosensing.

**M. Focsan[1*], M. Potara[1], C. Leordean[1], A. M. Craciun[1], D. Maniu and S. Astilean[1,2]**

Nanobiophotonics and Laser Microspectroscopy Center, Interdisciplinary Research Institute on Bio-Nano-Sciences, Babes-Bolyai University, Treboniu Laurean Str. 42, Cluj-Napoca 400271, Romania

[2]Biomolecular Physics Department, Faculty of Physics, Babes-Bolyai University, M Kogalniceanu Str. 1, Cluj-Napoca 400084, Romania

[*]corresponding author: monica.iosin@phys.ubbcluj.ro

**Abstract**- There is an urgent need for the development of new optical, ultrasensitive, robust biosensor for the detection of specific disease biomarkers in order to enable early diagnostics and improve diseases treatment [1].

Here we describe a novel method to fabricate 3D flexible and tunable plasmonic biosensors and their implementation as Localized Surface Plasmon Resonance/Surface Enhanced Raman Scattering (LPSR/SERS) platforms for the real time detection of anti-human Immunoglobulin G (anti-IgG) in buffer solution. In particular, the substrates were prepared by combining the nanosphere lithography that uses polystyrene spheres to obtain a template for lithography and soft lithography that uses polydimethylsilane (PDMS). The as-fabricated flexible substrates were subsequently coated with a 50 nm Au thin film to obtain large area plasmonic platforms (see Fig. 1). Moreover, the plasmonic properties of the flexible plasmonic platforms can easily be tuned by changing the size of polystyrene spheres used here as mold. The plasmonic tunability is further evaluated both experimentally and theoretically.

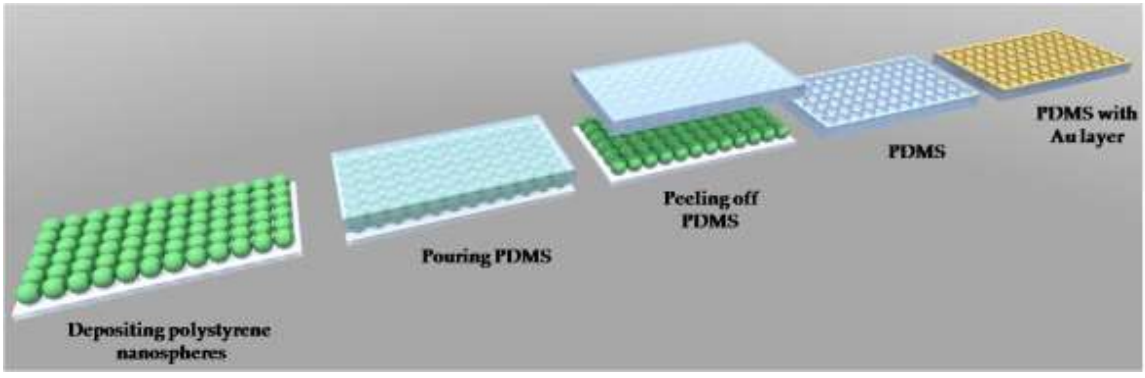



Fig. 1 Schematic illustration of fabrication steps of the 3D plasmonic platform.

Finally, in order to demonstrate the biosensing performance of our flexible plasmonic substrates in view of future detection assays on real biological samples, the as-designed biosensor was successfully implemented as LSPR platform for the detection of anti-IgG molecules. Specifically, the capture IgG molecules were immobilized on flexible plasmonic substrate and then incubated with anti-IgG molecules. In addition, we

demonstrate the feasibility of this biosensor to detect and identify anti-IgG molecules through SERS, a molecular identification technique that offers qualitative information about the IgG-anti-IgG interaction.

We are confident that these efficient LSPR/SERS platforms will pave the way to optical biosensors that are simple, transparent and flexible.

**Acknowledgments.** This work was supported by CNCS - UEFISCDI Romania, under the project number PN-II-PT-PCCA-2013-4-1961.

**REFERENCES**

1. Mayer, K. M. and J. H. Hafner "Localized Surface Plasmon Resonance Sensors," *Chem. Rev.*, Vol. 111, 3828–3857, 2011.

# Plasmonic (Nano)biosensors for Clinical Chemistry

**Jean-Francois Masson**[1]
[1]Departement de chimie, Université de Montréal, Canada

[*]corresponding author: jf.masson@umontreal.ca

**Abstract**-In this presentation, our efforts towards the development of novel nanomaterials applied for sensing molecules in crude biofluids will be discussed. Specifically, plasmonic nanoparticles and nanostructured surface were applied to the detection of molecules for therapeutic drug monitoring, for therapeutic response monitoring and for sensing other important biomarkers.

In this presentation, the properties of different plasmonic nanomaterials will be discussed in the context of clinical and biological sensing. In our research, we have studied and integrated novel plasmonic materials based on nanoparticle and hole arrays, surface chemistry relying on peptide monolayers and unique instrumental designs for sensing biomolecules of importance in disease detection, monitoring the course of treatment of patients during ongoing therapies or of general interest in biological systems. The plasmonic properties of nanohole and microhole arrays were studied in different excitation modes (transmission and attenuated total reflection) for plasmonic sensing and in surface-enhanced excitation. The nanohole and microhole were arrayed using photolithography on a 4" wafer and the nanohole arrays were integrated in a 96-well plate reader. This platform was used to screen antibodies for PSA sensing and to monitor methotrexate, an anticancer agent used in chemotherapy. We have also developed a SPR and LSPR sensing platform based on a small and portable instrument. Competition assays were validated for therapeutic drug quantitation, such as methotrexate and antibiotics and for monitoring therapeutic responses of patients undergoing leukemia treatments.

**Acknowledgements**

The author would like to thank the Natural Science and Engineering Research Council of Canada for financial support.

# Detecting Variations in Serum Composition through Chiral Plasmonic Metafilms

**A. S. Karimullah[1], R. Tullius[1], C. Jack[1], M. Rodier[1], G. Cooke[1], V.M. Rotello[2] and M. Kadodwala[1*]**
[1]School of Chemistry, Joseph Black Building, University of Glasgow, G12 8QQ, Glasgow, UK
[2]Department of Chemistry, University of Massachusetts, 710 North Pleasant Street, Amherst, MA, 01003, USA
[*]corresponding author: Malcolm.Kadodwala@glasgow.ac.uk

**Abstract-** The composition of blood serum is sensitive to the medical physiology of patients. Monitoring this composition leads to diagnosis of diseases such as cancer, organ failure, and malnutrition. We present a new methodology to detect changes in the globular proteins composition of blood serum utilizing chiral plasmonic metafilms. This new technique provides a unique platform for rapid detection of disease and medical diagnosis through optical detection of serum variations.

The composition of globular proteins in the blood is an important marker of a patient's condition. Detecting the changes is often used to diagnose conditions that include cancer, kidney or liver problems, irregularities in the immune system and poor nutrition.[1] The composition of blood serum is hence measured as variations indicate deviation from regular physiological conditions. The prominent components of blood serum are globular proteins dominated by a large quantity of Albumin. The commonly used clinical methods to distinguish variations in the composition include gel electrophoresis, mass spectrometry, precipitation and paper chromatography. However, these techniques can be slow and cumbersome. We have used plastic templates to create chiral plasmonic metafilms that are sensitive to protein structure, to detect changes in the composition of serum through optical reflectivity measurements.[2,3] We measure the reflectivity of these metafilms that show reflectivity profiles of electromagnetic induced transmission in coupled systems. The variation in the coupling causes changes in the optical behavior that can then be detected through the reflection measurement.

A common results of any infection is the increment in the levels of immunoglobulins (antibodies) in the blood. We show the detection of IgG spiked serum samples that relate to possible markers for diseases. This unique new methodology enables detection of changes in the blood serum using microliter quantities of sample with an all optical measurement.

**Acknowledgements:** We would like to acknowledge financial support from the Engineering and Physical Sciences Research Council (EPSRC EP/K034936/1), National Science Foundation (NSF grant CHE-1307021), JSPS Core to Core, and the Leverhulme Trust.

**REFERENCES**

1. K. P. Rosenblatt, P. B. Greenwood, J. K. Killian, A. Mehta, D. Geho, V. Espina, E. F. Petricoin, L. Liotta, "Serum proteomics in cancer diagnosis and management." *Annual Review of Medicine*. Vol. 55, 97–112, 2004.
2. R. Tullius, A. S. Karimullah, M. Rodier, B. Fitzpatrick, N. Gadegaard, L. D. Barron, V. M. Rotello, G. Cooke, A. Lapthorn, and M. Kadodwala, ""Superchiral" Spectroscopy: Detection of Protein Higher Order

Hierarchical Structure with Chiral Plasmonic Nanostructures", *Journal of the Americal Chemical Society*. Vol. 137, 8380-8383, 2015.

3. A. S. Karimullah, C. Jack, R. Tullius, V. M. Rotello, G. Cooke, N. Gadegaard, L. D. Barron, and M. Kadodwala, "Disposable Plasmonics: Plastic Templated Plasmonic Metamaterials with Tunable Chirality", *Advanced Materials*, Vol. 27, 5610-5616, 2015.

# Graphene plasmonics for tunable mid-infrared biosensors

**Daniel Rodrigo[1*], Odeta Limaj[1], Davide Janner[2], Dordaneh Etezadi[1], F. Javier García-de-Abajo[2,3], Valerio Pruneri[2,3], Hatice Altug[1*]**

[1] Institute of BioEngineering, École Polytechnique Fédérale de Lausanne (EPFL), Lausanne, Switzerland

[2] ICFO - Institut de Ciències Fotòniques, The Barcelona Inst. of Science and Technology, Castelldefels, Spain

[3] ICREA - Institució Catalana de Recerca i Estudis Avançats, 08010 Barcelona, Spain

[*]corresponding author: daniel.rodrigo@epfl.ch, hatice.altug@epfl.ch

**Abstract**- Infrared spectroscopy provides chemical information of biomolecules by detecting their vibrational fingerprints. Here, we use graphene plasmons to enhance infrared absorption and to demonstrate a tunable biosensor with high sensitivity for label-free and chemically-specific detection of protein monolayers. We show that the tunability and extreme light confinement of graphene offer great possibilities for biosensing.

The vibrational fingerprints of common biomolecules lie in the mid-infrared region of the spectrum, making infrared spectroscopy a key tool in chemical-specific biosensing. One of the most effective approaches to

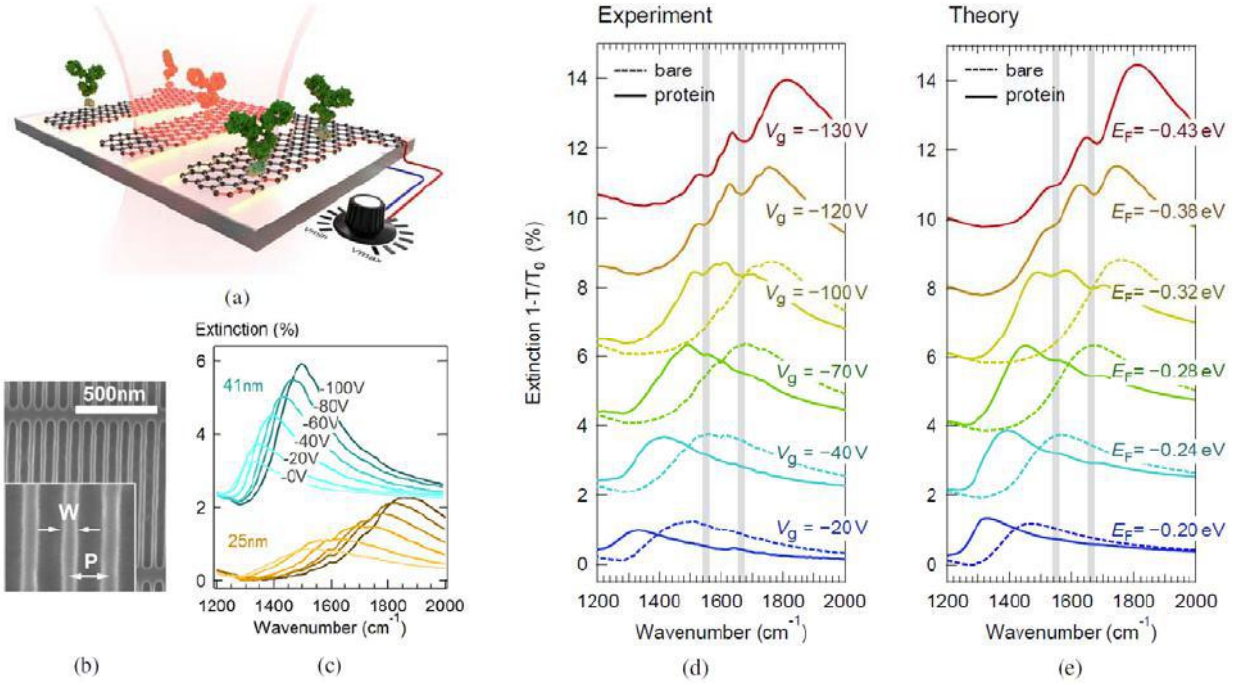



Fig. 1: (a) Conceptual view of the tunable graphene biosensor. (b) SEM micrograph of a GNRA. (c) Infrared extinction spectra of GNRAs for different ribbon widths and biasing voltages. (d, e) Extinction spectra of the graphene biosensor (W=30nm) before and after protein immobilization obtained from experiments and an analytic model.

enhance vibrational absorption signals is to exploit the strong electric near-fields in metallic nano-antennas [1]. However, this technique is able to enhance only those vibrations matching the antenna resonance frequency and the levels of enhancement are limited by the relatively poor field confinement of metals in the infrared. In contrast to metals, graphene is able to sustain tunable and highly-confined long-lived plasmons in the infrared [2]. We present the first infrared biosensor using graphene and show the potential of its unique opto-electronic properties for plasmon-enhanced biosensing [3]. In particular, we demonstrate a graphene biosensor with dynamic spectral tunability and with an unprecedent sensitivity in detecting simultaneously the refractive-index and vibrational fingerprints of nanometric biological layers.

The conceptual view of the graphene infrared biosensor is shown in Fig.1a. A graphene nanoribbon array (GNRA) is illuminated with infrared light to excite a localized surface plasmon resonance, which is dynamically tuned by applying a biasing variable voltage Vg (Fig.1c). The biological target of our biosensor are protein molecules. The performance of the sensor is tested by forming a well-defined protein bilayer (protein A/G and IgG antibody). The extinction spectra of the biosensor before and after protein immobilization is shown in Fig.1d. evidencing dramatic changes upon protein physisorption. The first effect is a strong redshift of the plasmonic resonance corresponding to the detection of the protein refractive index. The second effect corresponds to the two spectral dips appearing at the characteristic vibrational bands of proteins (amide I-II, 1660-1550$cm^{-1}$). These fingerprints are only detectable when the graphene plasmonic resonance is spectrally tuned to overlap with the amide bands. The results are in good agreement with an analytical model for dielectric-coated graphene nanoribbons [3].

Our results, based upon a simple sensor design, show the big potential of graphene for biosensing and clearly leave plenty of room for improvement. Careful design of the nanoresonator geometry combined with higher graphene mobility will lead to even sharper plasmonic resonances, improved field enhancement, larger sensitivity, and higher spectral resolution. The graphene tunability expands the spectral range of plasmon-based IR biosensing and offers hyper-dimensional spectral information that demands the development of new fingerprint identification algorithms. In conclusion, we have shown that graphene brings new spectrally-dynamic and highly-confined plasmonics to mid-IR, opening exciting and unforeseen possibilities for biosensing.

Acknowledgements:
This work was funded in part by European Commission under project FP7-IEF-2013-625673-GRYPHON

**REFERENCES**

1. F. Neubrech, A. Pucci, T.W. Cornelius, S. Karim, A. Garcia-Etxarri, and J. Aizpurua, “Resonant plasmonic and vibrational coupling in a tailored nanoantenna for infrared detection,” Phys Rev Lett 101, 157,403 (2008).
2. H. Yan, T. Low, W. Zhu, Y. Wu, M. Freitag, X. Li, F. Guinea, P. Avouris, and F. Xia, “Damping pathways of mid-infrared plasmons in graphene nanostructures,” Nat Photon 7, 394–399 (2013).
3. D. Rodrigo, O. Limaj, D. Janner, D. Etezadi, F. J. García de Abajo, V. Pruneri, and H. Altug, “Mid-infrared plasmonic biosensing with graphene,” Science 349, 165–168 (2015).

**Biological and chemical sensing within plasmonic nano-gaps**

Dr Anna Lombardi*, Dr Bart de Nijs, Dr Setu Kasera, Dr Daniel Sigle,
Felix Benz, Rohit Chikkaraddy, Cloudy Carnegie, Prof Jeremy J. Baumberg

NanoPhotonics Centre, Cavendish Laboratory, University of Cambridge, UK
al716@cam.ac.uk, jjb12@cam.ac.uk,

Detection of low concentrations of chemical and biological agents plays a fundamental role in biomedical, environmental and material sciences. The development of real-time, ultra-sensitive, and label-free sensors requires advanced technologies coupled with fundamental knowledge in chemistry, physics and biology. Plasmonic nanosensors for molecular optical detection have been widely investigated in the past - their sensitivity has been greatly improved over the years, opening unique possibilities for single molecule spectroscopy under ambient conditions.

We present here the development of a practical implementation capable of low-cost robust real-time single-molecule sensitivity. Experimental SERS-based studies are shown where the strong localized field enhancement associated with plasmonic nanoparticles is exploited for biomolecule detection and real-time chemical reaction tracking.

We use nano-assembling aggregates of gold nanoparticle with cucurbit[n]urils (CB[n]s) molecules [1,2] to measure small quantities of organic molecules (e.g. neurotransmitters) in aqueous environments such as human urine.[1] Gold nanorod-CB[n] aggregates and DNA-origami-based assemblies are also synthesized and exploited to detect low concentration of dye molecules.[3,4]
In a different set of studies we investigate individual gold nanoparticles deposited on a gold film (nanoparticle-on-mirror geometry, NPoM).[5,6] By placing a lipid bilayer spacer between the nanoparticle and the film, we are able to show in-situ high-speed single molecule dynamics, crucial to better understand the changes in conformation and orientation of lipids composing bio-membranes.[7] We use host-guest chemistry to align dye molecules in the particle-substrate nano-cavity: this allows us to reach the strong coupling regime with only single molecules at room temperature and under ambient conditions.[8] Finally, we exploit NPoM plasmonic nanogaps for in-situ SERS monitoring of chemical reactions, such as selective photodimerization, photoisomerism,[9] and single molecule oxidation processes.






[1] *Scientific Reports* **4**, 6785 (2014); Quantitative multiplexing with nano-self-assemblies in SERS
[2] *J.Phys.Chem.Lett.* **7**, 704 (2016); Observing Single Molecules Complexing with CB[7] through Nanogap-SERS
[3] *Small* **10**, 4298 (2014); Au nanorods with sub-nm separation using CB[n] for SERS applications
[4] *Nature Comm*. **5**, 3448 (2014); DNA origami based assembly of gold nanoparticle dimers for SERS detection
[5] *Nano Lett* **13**, 5033 (2013); Controlling sub-nm plasmonic gaps using graphene
[6] *Nano Letters* **15**, 669 (2015); Nano-optics of molecular-shunted plasmonic nanojunctions
[7] *Science Reports* **4**, 5490 (2014); Watching individual molecules flex within lipid membranes using SERS
[8] R. Chikkaraddy et al. under review
[9] *Nano Lett* **13**, 5985 (2013); In-situ SERS monitoring of photochemistry within a nano-junction reactor

# Quantitative Reflection Imaging for Morphology and Dynamics of Live *Aplysia Californica* Pedal Ganglion Neurons on Nanostructured Plasmonic Crystals

**S. Kang[1], A. Badea[2], S. S. Rubakhin[2,3], J. V. Sweedler[2,3], J. A. Rogers[1,2], and R. G. Nuzzo[*1,2]**

[1]Department of Materials Science and Engineering, University of Illinois at Urbana-Champaign, USA

[2]Department of Chemistry, University of Illinois at Urbana-Champaign, USA

[3] Beckman Institute for Advanced Science and Technology, University of Illinois at Urbana-Champaign, USA

[*]corresponding author: r-nuzzo@illinois.edu

**Abstract** - Live cell imaging, essential in monitoring dynamic cell functions, is difficult due to the optical transparency of cells. Stain-based imaging, however, often impacts the cell functions being observed, creating a need for live cell imaging techniques with minimal physical and chemical effects on the cell. We herein describe a simple reflection imaging system consisting of a plasmonic crystal, a common laboratory microscope, and band-pass filters, and demonstrate its capabilities for quantitative imaging and *in-situ* monitoring of live cells.

Real-time imaging of biological processes and morphological changes within living cells provides essential information about cellular events that may escape the static observation typically performed on fixed cells.[1,2] Most current live cell imaging strategies heavily rely on staining or tagging different components of the cell, because cells are optically transparent.[3] The high intensity light illumination associated with these techniques may induce temperature fluctuations and/or damage DNA via UV light absorption, ultimately affecting the cell functions being observed.[4] There is, therefore, a need for live cell imaging techniques designed to minimize damage to the cell by sustaining physical and chemical conditions suitable for the local biological environment.

To meet this need, a number of optics-based analytical tools have been developed for the study of dynamic phenomena of living cells that bypass the need for fluorescent labels. Phase contrast microscopy[5, 6] and differential interference contrast microscopy,[7, 8] while effective in visualizing unstained biological specimens with enhanced contrast and resolution, are limited by their two-dimensional projections of data, which cannot fully quantitatively capture live cell morphology. Digital holographic microscopy[9] and spatial light interference microscopy,[10] both extremely powerful analytical methods able to provide label-free quantitative dynamical live cell imaging, can obtain three-dimensional images. The main drawback of these optical techniques is that they require complex instrumental setups and non-trivial data processing capacities.

The work presented describes the operation of a simple reflection imaging system which consists of a plasmonic crystal, a common laboratory microscope, and band-pass filters for quantitative imaging and *in-situ* real-time analysis of live cells and their interactions with the substrate. Surface plasmon resonance (SPR) is highly sensitive to local optical profile changes at the interface between the metal and dielectric coating. Thus, variations in the thin film thickness or dielectric properties near the surface of the plasmonic crystal can be detected by analyzing the plasmonic optical responses. We construct a reference system to calibrate the film thickness-dependent variations in reflection contrast by depositing polyelectrolyte thin films using the

layer-by-layer (LBL) self-assembly method. Finite-difference time-domain (FDTD) simulations were performed to confirm the viability of the optical responses measured experimentally from the polyelectrolyte reference system as a calibration for quantitative studies investigating live cell structure and function in culture. The utility of this plasmonic imaging technique was exemplified on a model biological system using live *Aplysia californica* pedal ganglion neurons immersed in artificial sea water (ASW). Our findings show that the morphology of peripheral structures (smaller than ~80 nm in thickness) of live *Aplysia* pedal neurons can be analyzed quantitatively and their structural changes during processes such as cell detachment induced by trypsinization can be optically monitored. These results show the quantitative capabilities of plasmonic reflection imaging as a valuable real-time analytical tool for monitoring the morphology and dynamics of ultrathin cellular systems in their environment.

**Acknowledgements**

This work was supported by the U.S. Department of Energy under prime Award No. DE-SC0001293 via subcontract 67N-1087758 from California Institute of Technology as part of the DOE Energy Frontier Research Center on Light-Material Interactions in Energy Conversion and was performed using resources at the Frederick Seitz Materials Research Laboratory Central Facilities at the University of Illinois, including the Center for Microanalysis of Materials; the Micro/Nanofabrication Facility; and the Laser and Spectroscopy Facility.

**REFERENCES**

1. Conn, P. M., "Imaging and spectroscopic Analysis of Living Cells: Optical and Spectroscopic Techniques," *Method. Enzymol.*, Vol. 504, 1-506, 2012.
2. Jaiswal, J. K.; Goldman, E. R.; Mattoussi, H.; Simon, S. M., "Use of quantum dots for live cell imaging," *Nat. Methods*, Vol. 1, No. 1, 73-78, 2004.
3. Frigault, M. M.; Lacoste, J.; Swift, J. L.; Brown, C. M., "Live-cell microscopy - tips and tools," *J. Cell Sci.*, Vol. 122, No 6, 753-767, 2009.
4. Squirrell, J. M.; Wokosin, D. L.; White, J. G.; Bavister, B. D., "Long-term two-photon fluorescence imaging of mammalian embryos without compromising viability," *Nat. Biotechnol.*, Vol. 17, No. 8, 763-767, 1999.
5. Barty, A.; Nugent, K. A.; Paganin, D.; Roberts, A., "Quantitative optical phase microscopy," *Opt. Lett.*, Vol. 23, No. 11, 817-819, 1998.
6. Liang, C. C.; Park, A. Y.; Guan, J. L., "In vitro scratch assay: a convenient and inexpensive method for analysis of cell migration in vitro," *Nat. Protoc.*, Vol. 2, No. 2, 329-333, 2007.
7. Allen, R. D.; Allen, N. S.; Travis, J. L., "Video-Enhanced Contrast, Differential Interference Contrast (Avec-Dic) Microscopy - a New Method Capable of Analyzing Microtubule-Related Motility in the Reticulopodial Network of Allogromia Laticollaris," *Cell Motil. Cytoskel.*, Vol. 1, No. 3, 291-302, 1981.
8. Dodt, H. U.; Zieglgansberger, W., "Visualizing Unstained Neurons in Living Brain-Slices by Infrared Dic-Videomicroscopy," *Brain Res.*, Vol. 537, No. 1-2, 333-336, 1990.
9. Marquet, P.; Rappaz, B.; Magistretti, P. J.; Cuche, E.; Emery, Y.; Colomb, T.; Depeursinge, C., "Digital holographic microscopy: a noninvasive contrast imaging technique allowing quantitative visualization of living cells with subwavelength axial accuracy," *Opt. Lett.*, Vol. 30, No. 5, 468-470, 2005.
10. Wang, Z.; Millet, L.; Mir, M.; Ding, H. F.; Unarunotai, S.; Rogers, J.; Gillette, M. U.; Popescu, G., "Spatial light interference microscopy (SLIM)," *Opt. Express*, Vol. 19, No. 2, 1016-1026, 2011.

# Responsive hydrogel-metallic nanostructures for plasmonic biosensing

**N. G. Quilis[1], P. Kögler[2], C. Petri[2], U. Jonas[2], W. Knoll[1], and J. Dostalek[1*]**

[1]AIT - Austrian institute of Technology GmbH, Muthgasse 11, Wien 1190, Austria

[2]Macromolecular Chemistry, Department of Chemistry, University of Siegen, Adolf-Reichwein-Strasse 2, Siegen 57076, Germany

[*]corresponding author: jakub.dostalek@ait.ac.at

**Abstract**- Hybrid materials composed of photo-crosslinkable thermo-responsive hydrogel and metallic nanostructures are presented. These materials are prepared by using UV laser interference lithography. The responsive hydrogel serves as a binding matrix that is functionalized with ligand molecules for selective capture of target analyte at a plasmonic hotspot. Such structures are promising for biosensors relying on surface plasmon-enhanced fluorescence detection.

Plasmonics concerns manipulating of light at nanoscale and it offers attractive means for sensitive detection and interaction analysis of chemical and biological species. In particular, metallic nanostructures supporting localized surface plasmons (LSPs) allow enhancing intensity of electromagnetic field by its confining at so called "plasmonic hotspot". This intense field can efficiently probe specific analyte binding and it enables detection of the binding events by using of plasmonically-enhanced optical spectroscopy techniques such as surface plasmon-enhanced fluorescence or surface-enhanced Raman spectroscopy. This paper reports on the implementation of photo-crosslinkable responsive hydrogel materials for selective functionalization of metallic nanostructures. *N*-isopropylacrylamide-co-methacrylic acid-co-4-methacryloyloxy benzophenone polymer [pNIPAAm, see Fig 1 a) below] is employed to serve as a responsive binding matrix. UV laser interference lithography [1] is used to align pNIPAAm-coated areas with arrays of metallic nanoparticles and nanoholes [see Fig b)]. In its swollen state, the polymer structure is modified with biomolecules by using the amine coupling and can accommodate large amounts of biomolecules [2]. By raising the temperature above the pNIPAAm lower critical solution temperature, the matrix is collapsed and biomolecules are compacted in vicinity to metallic nanostructure where the maximum field intensity enhancement occurs. Combined localized surface plasmon resonance (LSPR) and plasmonically-enhanced fluorescence spectroscopy is employed for the studies of biomolecular binding into the pNIPAAm-based hydrogel binding matrix capping the plasmonic hotspot.

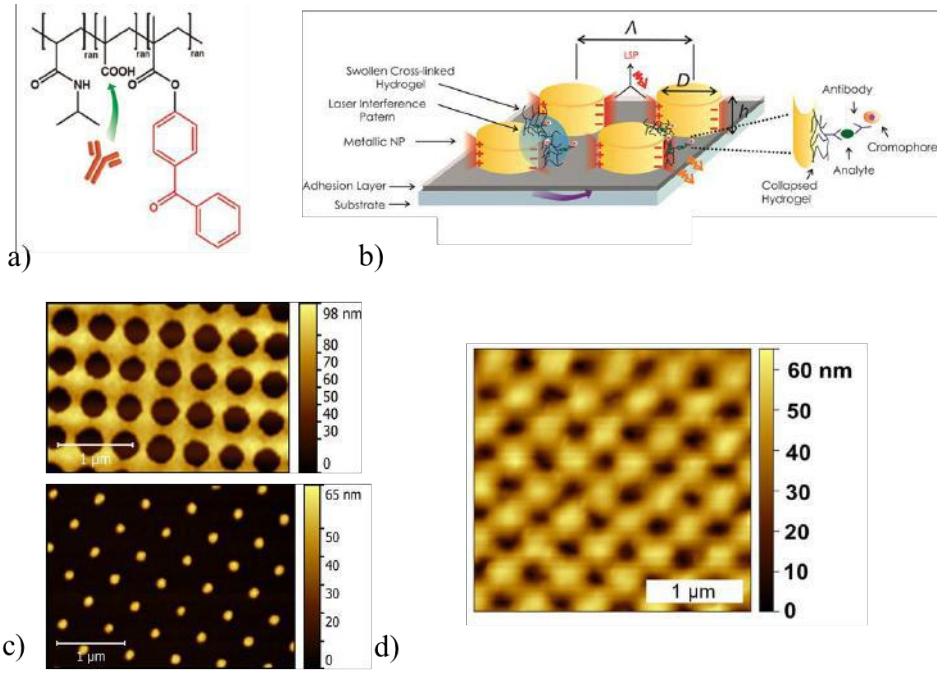



**Figure 1: a)** Chemical structure of poly (N-isopropylacrylamide-co-methacrylic acid-co-4-methacryloyloxy benzophenone - pNIPAAm, b) schematic of a metallic nanoparticle selectively capped by a responsive hydrogel matrix, c) examples of Au arrays of nanoholes and nanoparticles with period around 450 nm prepared by LIL and d) pNIPAAm grating structure prepared by LIL.

**Acknowledgements**, this project has received funding from the European Union's Horizon 2020 Research and Innovation Programme under grant agreement No. 642787, Marie Sklodowska-Curie Innovative Training Network BIOGEL. In addition, the presented work was supported by European Union's Horizon 2020 Research and Innovation Programme through project ULTRAPLACAD, grant agreement No. 633937.

**REFERENCES**

1. N. Sharma, C. Petri, U. Jonas, J. Dostalek, Reversibly tunable plasmonic bandgap by responsive hydrogel grating, Opt. Express, Vol. 24, No. 3, 2457-2465, 2016.
2. M. Toma, U. Jonas, A. Mateescu, W. Knoll, J. Dostalek, Active control of SPR by responsive hydrogels: towards active plasmonics for biosensor applications, J. Phys. Chem. C, Vol. 117, No.22, 11705- 11712, 2013.

# Lattice localized plasmons for fluorescence immunosensing

**S. Fossati**[1], **S. Hageneder, M. Bauch**[2], **W. Knoll and J. Dostalek**[1*]
[1]Biosensors Technologies, AIT - Austrian Institute of Technology, Austria
[2]Energy Department, AIT - Austrian Institute of Technology, Austria

[*]corresponding author: jakub.dostalek@ait.ac.at

**Abstract** – The detection of chemical and biological analytes is important in numerous fields including medical diagnostics, environmental science and food safety. Fluorescence spectroscopy provides an established means for such sensitive analysis by the utilization of fluorescent labels. Here, a method for the enhancement of detected fluorescence signal by collective localized plasmons supported by regular arrays of gold capped nanopillars is studied and a reader with epifluorescent readout geometry is suggested.

Immunoassays make use of the highly specific interaction of antibodies and their respective antigens. By decorating a recognition element in the assay with a fluorophore, the molecular binding event becomes detectable as localized fluorescent light emission. By combining the assay with plasmonic nanostructures, the amount of detected fluorescence can be amplified significantly [1]. This phenomenon is based on the strong enhancement of electromagnetic field intensity and local density of optical states which originates from the excitation of surface plasmons. Here, a periodic plasmonic structure of gold capped nanopillars supporting multiple resonant modes enhancing both, the fluorescence excitation at the fluorophore absorption wavelength, as well as providing directional emission at the emission wavelength, is studied. By this diffraction coupled emission, the fluorescence photons are emitted in a narrow solid angle, thus simplifying the optical system required for rapid readout of fluorescence kinetics in an array sensor format [2]. Structures are studied and optimized for dyes in the red and near infra-red part of the spectrum using numerical simulations and are subsequently prepared using nanoimprint lithography. Experimental results supporting the simulation results are shown and a reader geometry supporting the analysis of array format assays is presented.

**Acknowledgements**
This project has received funding from the European Union's Horizon 2020 research and innovation programme under grant agreement No 633937, project ULTRAPLACAD.

**REFERENCES**

1. Bauch, M., K. Toma, M. Toma, Q. Zhang and J. Dostalek, "Plasmon-enhanced fluorescence biosensors: a review", *Plasmonics*, Vol. 9, No. 4, 781-799, 2014.
2. Bauch, M., S. Hageneder and J. Dostalek "Plasmonic amplification for bioassays with epi-fluorescence readout", *Optics Express*, Vol. 22, No. 26, 32026-32038, 2014.

# Plasmonically amplified fluorescence for biomarker analysis

**J. Dostalek**[1*]

[1]Biosensors Technologies, AIT - Austrian Institute of Technology GmbH, Muthgasse 11, Vienna Austria

[*]corresponding author: jakub.dostalek@ait.ac.at

**Abstract** – The detection of biomarkers present in bodily fluids by using surface plasmon-enhanced fluorescence will be discussed. Novel hybrid materials composed of metallic nanoparticles and responsive hydrogels enabling efficient capturing and probing of target analytes will be presented. Ultrasensitive detection of markers for colon and ovarian cancer will be reported and routes for pushing the assay sensitivity to below femtomolar concentrations will be addressed.

Confined electromagnetic field of surface plasmons offers attractive means for improving performance characteristics of various fluorescence–based analytical technologies. The near-field coupling of fluorophores that are used as labels with surface plasmons can increase the signal-to-noise ratio of detected fluorescence signal by the combination of increased excitation rate, improved quantum yield of emitter, and directional fluorescence emission. This amplification strategy translates to the ability to detect lower amounts of specifically captured analyte from investigated samples at the sensor surface, which leads to an improved limit of detection [1].

The paper will discuss implementation of surface plasmon-enhanced fluorescence for the analysis of minute amounts of biomarkers in bodily fluids. The interfacing of metallic nanostructures with hydrogel materials in order to serve as a responsible 3D binding matrix as well as a filter that enables only target analyte reaching the surface and preventing unspecific interaction is presented. Tuning of probing depth of surface plasmon field in order to maximize sensitivity of assays for the analysis of species that vary in size from several nanometers (e.g. biomolecules) to around hundred nanometers (exosome vesicles) and even several micrometers (bacterial pathogens) will be addressed. Novel applications of surface plasmon-enhanced fluorescence for the analysis of trace amounts of biomarkers will be discussed. These include analysis exosomes and autoantibodies against tumor associated antigens present in blood serum for the ovarian and colon cancer diagnostics. In addition, plasmonically amplified fluorescence sensor with aptamer for continuous monitoring of small molecules will be presented in the context of a tool for drug administration.

**Acknowledgements**

This project has received funding from the European Union's Horizon 2020 research and innovation programme under grant agreement No 633937 (project ULTRAPLACAD) and No 642787 (Marie Sklodowska-Curie Innovative Training Network BIOGEL). This work was partially supported by the Austrian Science Fund (FWF), project ACTIPLAS (P 244920-N20)

**REFERENCES**

1. Bauch, M., K. Toma, M. Toma, Q. Zhang and J. Dostalek, "Plasmon-enhanced fluorescence biosensors: a review", *Plasmonics*, 1-19, 2014.

# Bioanalytics using single plasmonic nanostructures

**T. Schneider, J. Jatschka, N. Jahr, D. Zopf, A. Dathe, J. Wirth, F. Garwe, A. Csaki, O. Stranik, W. Fritzsche***

Leibniz Institute of Photonic Technology (IPHT) Jena, Germany
*corresponding author: wolfgang.fritzsche@ipht-jena.de

**Abstract**- Plasmonic nanostructures promise to provide sensing capabilities with the potential for ultrasensitive and robust assays in a high parallelization, and without the need for marker. Upon binding of molecules, the localized surface plasmon resonance (LSPR) of these structure is changed, and can be used as sensoric readout. By using single plasmonic nanostructures as sensor, an ultimate miniaturisation as well as paralellization (multiplexing) is possible.

Novel requirements for bioanalytical methods emerge due to trends such as personalized medicine or pathogen detection in environment and food. Here, innovative tools for diagnostics are needed, to be used outside of dedicated laboratories and with less qualified personnel, and with minimal costs. Here the use of individual nanostructures (such as gold nanoparticles) for the detection and manipulation of biomolecules (e.g. DNA) based on optical approaches is presented [1].

Holes in a Cr layer present an interesting approach for bioanalytics. They are used to detect even single plasmonic nanoparticles as labels or to sense the binding of DNA on these particles. This hybrid system of hole and particle allows for simple (just using RGB-signals of a CCD [2]) but a highly sensitive (one nanoparticle sensitivity) detection [3].

The change in LSPR of individual metal nanoparticles is utilized to monitor the binding of DNA directly or via DNA-DNA interaction. The influence of different size (length) as well as position (distance to the particle surface) is thereby studied [4] using a dark-field approach developed a century ago [5]. The established serial approach is now further developed into a parallel readout using imaging spectrometric sensing based on interferometry and Fourier transformation [6]. So a parallelization of the assay is realized, which enables a much higher throughput for bioanalytical applications.

Besides sensing, individual plasmonic nanostructures can be also used to optically manipulate biomolecular structures such as DNA. Attached particles can be used for local destruction [7] or cutting as well as coupling of energy into (and guiding along) the molecular structure upon laser irradiation [8]. The resonance wavelength of these particles can not only manipulated by their inherent properties (material, geometry) or their surrounding, but also by coupling with adjacent metal films due to interferometric effects [9] or gap modes.

## REFERENCES

1. A. Csaki, T. Schneider, J. Wirth, N. Jahr, A. Steinbrück, O. Stranik, F. Garwe, R. Müller and W. Fritzsche, *Philosophical Transactions A* 369, 3483-3496 (2011).

2. N. Jahr, N. Hädrich, M. Anwar, A. Csaki, O. Stranik and W. Fritzsche, Int J Env Anal Chem 93, 140-151 (2013).
3. N. Jahr, M. Anwar, O. Stranik, N. Hädrich, N. Vogler, A. Csaki, J. Popp, W. Fritzsche. J Phys Chem C 117, 7751-7756 (2013)
4. T. Schneider, N. Jahr, A. Csaki, O. Stranik and W. Fritzsche, J Nanopart Res 15, 1531 (2013)
5. T. Mappes, N. Jahr, A. Csaki, N. Vogler, J. Popp, W. Fritzsche. Angew Chem Int Ed 51, 11208-11212 (2012)
6. D. Zopf, J. Jatschka, A. Dathe, W. Fritzsche, O. Stranik. Biosensors and Bioelectronics 2016 (in press)
7. A. Csaki, F. Garwe, A. Steinbrück, G. Maubach, G. Festag, A. Weise, I. Riemann, K. König and W. Fritzsche, *Nano Letters* 7 (2), 247-253 (2007).
8. J. Wirth, F. Garwe, G. Haehnel, A. Csaki, N. Jahr, O. Stranik, W. Paa and W. Fritzsche, Nano Letters 11 (4), 1505-1511 (2011).; J. Toppari, J. Wirth, F. Garwe, O. Stranik, A. Csaki, J. Bergmann, W. Paa, W. Fritzsche, ACS Nano 7, 1291-1298 (2013); J. Wirth, F. Garwe, J. Bergmann, W. Paa, A. Csaki, O. Stranik, W. Fritzsche. Nano Letters 14, 570-577 (2014)
9. J. Wirth, F. Garwe, R. Mayer, A. Csaki, O. Stranik, W. Fritzsche: Nano Letters 14, 3809-3816 (2014)

**Towards Sensitive, Selective Point-Of -Care Plasmonic Diagnostic Devices**

Debrina Jana, Jie He, Ian Bruzas, Sarah Unser, and **Laura Sagle***

Department of Chemistry, College of Arts and Sciences, University of Cincinnati, 301 West Clifton Court, Cincinnati OH 45221-0172
Corresponding author Tel: +1 513 556 1034; Fax: +1 513 556 9239. E-mail: saglela@uc.edu

Localized Surface Plasmon Resonance shows excellent promise as next generation biosensing materials, since they provide sensitive, label-free, rapid, colorimetric detection that is amenable to on-chip devices.[1-3] However, challenges such as biofouling in complex media, detection of membrane-associated species, and incorporation of plasmonic materials into multiplexed and microfluidic devices have proven difficult in recent years. This presentation will highlight three projects in the Sagle group in which approaches were taken to overcome these issues. The first project involves the incorporation of shape complementarity at the nanoparticle surface for improved selectivity in complex media based on size. The second project develops an inexpensive and ultrasensitive platform for the detection of membrane-associated species, using colloidal lithography and sol-gel chemistry. Lastly, the incorporation of lithography-fabricated, uniform nanoparticle arrays into microfluidic and multiplexed devices will be discussed.[4] These uniform nanoparticle arrays can be fabricated on a number of substrates including flexible polymers, and show excellent promise towards applications such as drug screening and pathogen detection.

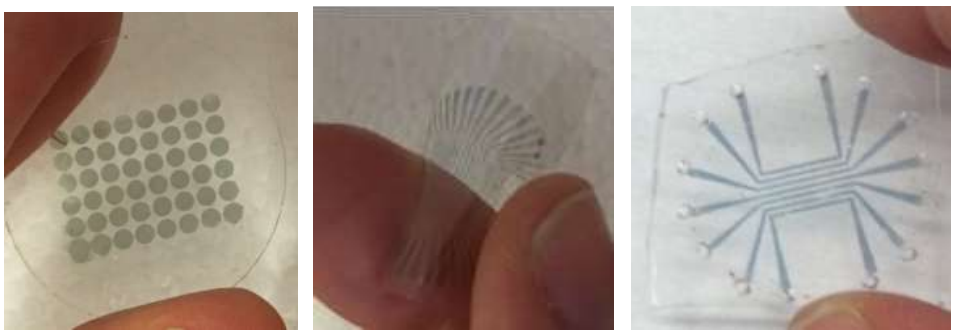


**Figure 1.** Images of multiplexed, miniaturized spot plates and microfluidic devices made on both glass and flexible plastic substrates.

**Acknowledgements**

The authors gratefully acknowledge University Start-Up Funds for supporting this work.

**REFERENCES**

1. Sagle, Laura B., Ruvuna, Laura K., Ruemmele, Julia A., and Van Duyne, R. P., "Advances in Localized Surface Plasmon Resonance Biosensing" *Nanomedicine*, Vol. 6, No. 8, 1447-1462, 2011.
2. Unser, S., Bruzas, I., He, J., and Sagle, L., "Localized Surface Plasmon Resonance Biosensing: Current Challenges and Approaches" *Sensors*, Vol. 15, No. 7, 15684-15716, 2015.
3. Tokel, O., Inci, F., and Demirci, U. "Advances In Plasmonic Technologies For Point Of Care Applications" *Chem. Rev.*, Vol. 114, No. 11, 5728-5752, 2014.
4. He, J., Boegli, M., Bruzas, I., Lum, W., and Sagle, L., "Patterned Plasmonic Nanoparticle Arrays For Microfluidic And Multiplexed Biological Assays" *Analytical Chemistry*, Vol. 87, No. 22, 11407-11414, 2015.

# Plasmonic Biosensors and Their Bioanalytical Applications

**J. Homola**
Institute of Photonics and Electronics of the CAS, Prague, Czech Republic
homola@ufe.cz

**Abstract** Plasmonic biosensors represent the most advanced and mature optical label-free biosensor technology. This paper reviews selected recent advances in plasmonic biosensors, including advances in the method, optical instrumentation, microfluidics, functionalization and detection methodology. Examples of bioanalytical applications illustrating performance and potential of plasmonic biosensors in medical diagnostics and food safety are also presented.

Since their conception in the 1980's, optical biosensors based on surface plasmons propagating along the surface of a metal (sometimes referred to as surface plasmon resonance (SPR) biosensors) have made significant advances both in terms of technology and applications. SPR biosensors have become a central tool for characterizing and quantifying biomolecular interactions and have shown vast potential for (bio)analytics [1]. In recent years, the sensing potential of surface plasmons supported by various kinds of nanostructures have been also studied and numerous sensor platforms based on plasmonic modes supported by metallic nanoparticles or their arrays have been developed. In this paper we discuss selected recent advances in the development of plasmonic biosensors and their bioanalytical applications.

Advances in optical platforms for plasmonic biosensors discussed in this contribution will include developments towards compact optical plasmonic platforms for portable biosensors and plasmonic imaging sensors; fabrication of plasmonic nanostructures by means of multiple-beam interference lithography will be also discussed [2, 3]. In addition, we shall investigate effects of mass transport and molecular interaction on performance of plasmonic biosensors. We analyzed molecular interactions occurring between analyte molecules in a flow-through microfluidic cell and biorecognition elements immobilized on a continuous as well as nanostructured metallic films. We demonstrated that the flow-cell geometry and parameters of nanostructured surfaces have potentially significant effect on analytical performance of plasmonic biosensors [4, 5]. Furthermore, advances in the development of functional coatings for plasmonic biosensors will be discussed; in particular, functionalized polymer brushes with ultra-high resistance to fouling from complex biological samples (e.g. bodily fluids, foods) will be covered [6, 7]. Finally, bioanalytical applications of plasmonic biosensors will be discussed with focus on detection of chemical and biological species in real-world complex samples. Recent advances in detection methodologies (referencing [8], amplification strategies [9]) will be presented and examples of bioanalytical applications will be given. These examples will include the detection of analytes implicated in food safety (antibiotics residues, toxins and bacterial pathogens) [7] and the detection of disease biomarkers (microRNA and proteins) in bodily fluids [8-10].

This research was supported by Praemium Academiae of the Academy of Sciences of the Czech Republic and the Czech Science Foundation (contract # P205/12/G118).

**REFERENCES**

1. Homola, J (editor), *Surface Plasmon Resonance Based Sensors*, Springer, 2006.

2. Piliarik, M., H. Šípová, P. Kvasnička, N. Galler, J. R. Krenn and J. Homola, "High-resolution biosensor based on localized surface plasmons", *Opt. Express*, 20, 672–680, 2012.
3. Vala, M. and J. Homola, "Flexible method based on four-beam interference lithography for fabrication of large areas of perfectly periodic plasmonic arrays", *Opt. Express*, 22, 18778–18789, 2014.
4. Lynn, N. S. and J. Homola, "Biosensor enhancement using grooved micromixers: part I, numerical studies", *Anal. Chem.*, 87, 5516–5523, 2015.
5. Lynn, N. S., M. Bocková, P. Adam and J. Homola, "Biosensor enhancement using grooved micromixers: part II, experimental studies", *Anal. Chem.*, 87, 5524-5530, 2015.
6. Vaisocherová, H., V. Ševců, P. Adam, B. Špačková, A. S. Pereira, C. Rodriguez-Emmenegger, T. Riedel, E. Brynda and J. Homola, "Functionalized ultra-low fouling carboxy- and hydroxy-functional surface platforms and their fouling resistance from undiluted biological media and biorecognition capability", *Biosen. Bioel.*, 51, 150–157, 2014.
7. Vaisocherová-Lísalová, H., I. Víšová, M. L. Ermini, T. Špringer, X. Song, J. Mrázek, J. Lamačová, N. S. Lynn Jr., P. Šedivák and J. Homola, "Low-fouling surface plasmon resonance biosensor for multi-step detection of foodborne bacterial pathogens in complex food samples", *Biosen. Bioel.*, 80, 84–90, 2016.
8. Špringer, T., M. Bocková and J. Homola, "Label-free biosensing in complex media: a referencing approach", *Anal. Chem.*, 85, 5637–5640, 2013.
9. Špringer, T., M. L. Ermini, B. Špačková, J. Jabloňků and J. Homola, "Enhancing sensitivity of SPR biosensors by functionalized gold nanoparticles – size matters", *Anal. Chem.*, 86, 10350−10356, 2014.
10. Vaisocherová, H., I. Víšová, M. Bocková, T. Špringer, M. L. Ermini, X. Song, Z. Krejčík, L. Chrastinová, O. Pastva, K. Pimková, M. Dostálová Merkerová, J. E. Dyr and J. Homola, "Rapid and sensitive detection of multiple MicroRNAs in cell lysate by low-fouling surface plasmon resonance biosensor", *Biosen. Bioel.*, 70, 226–231, 2015.

# Ultrasensitive plasmonic biosensors platforms-from conception to controllable biofunctionalization and detection of target (bio)molecules

**Rodica Elena Ionescu, Pierre-Michel Adam, Jean-Louis Bijeon**
Université de Technologie de Troyes, France

**Abstract**- The talk will discuss different cost-effective approaches enabling the design of controllable metallic micro- and nano-structured glass substrates using either natural micrometric labels such as Escherichia coli bacteria, metallic staples, scotch tape “barcode-like” or microscopic TEM grids for further high throughtput and multiplexing plasmonic sensitive detection of (bio)molecules.

# Nanoplasmonic Sensor Arrays for Rapid Detection of Biomolecules and Nanoparticles

**Avijit Barik[1,2], Shailabh Kumar[1], Daehan Yoo[1], Yong-Sang Ryu[1], Xiaoshu Chen[1], Daniel A. Mohr[1], Daniel J. Klemme[1], Christopher T. Ertsgaard[1], Nathan J. Wittenberg[1], and Sang-Hyun Oh[1,2*]**

[1]Department of Electrical and Computer Engineering and [2]Biomedical Engineering, University of Minnesota, Minneapolis, United States

[*]corresponding author: sang@umn.edu

**Abstract** This presentation will focus the application of nanoplasmonic devices for rapid capture and detection of biomolecules and nanoparticles. We employ unconventional nanofabrication techniques - template stripping and atomic layer lithography - to mass produce high-density plasmonic sensor arrays and combine them with rapid sample concentration schemes.

Nanoplasmonic devices have shown great promise for sensitive on-chip detection of biomolecules.[1] For surface-based biosensors, diffusion of analytes into the sensing zone is typically a slow process, and the problem is compounded for miniaturized plasmonic sensors with nanoscale sensing 'hot spots'. In parallel, many groups have tackled the challenges of speeding up the capture and detection of biomolecules. Various schemes have been attempted to accelerate mass transport, such as electrokinetic pre-concentration of charged molecules, dielectrophoresis, evaporation-driven concentration of sample droplets, or 'flow-through' nanohole sensors to shrink the diffusion distance. Here we employ dielectrophoresis to accelerate the mass transport of biomolecules and nanoparticles toward nanoplasmonic sensors, in particular nanoholes[2] and ultra-sharp pyramids,[3] which reduces detection time and lowers detection limits. We also present magnetic nanofocusing[4] via ultra-sharp ferromagnetic tips to trap iron oxide nanoparticles for biosensing applications.

Our devices are fabricated via two unconventional fabrication techniques: template stripping[5] for making ultra-smooth patterned metals and atomic layer lithography[6] for mass-producing ultra-small (< 10 nm) gaps with angstrom-scale control.

In template stripping, instead of directly patterning noble metal films, which are difficult to plasma-etch, we create inverse patterns such as holes and V-grooves in a silicon template. After metal deposition and peeling, precisely patterned geometries in the silicon template, such as nanoholes, pyramids, and wedges are faithfully replicated onto a deposited metal film. These nanoscale features serve a twofold purpose: to function as electrodes for generating the non-uniform electrical fields required for dielectrophoretic mass transport, and to concentrate optical energy for plasmonic sensing. Template stripping is also used to create bilayer metallic films with the ability to concentrate external magnetic fields.

Another emerging fabrication technique, called atomic layer lithography, has demonstrated wafer-scale production of ultra-long (> mm) and ultra-small (< 1 nm) slits in metal films. The resulting slits and resonant loops show extremely high field enhancements via gap plasmons and tunable resonances at visible, infrared, and terahertz frequencies. We will describe broader sensing applications of this powerful lithography technique.

**Acknowledgements**. The authors acknowledge support from the U.S. National Science Foundation (NSF CAREER Award #1054191 and CMMI #1363334).

## REFERENCES

1. Brolo, A. G.; Gordon, R.; Leathem, B.; Kavanagh, K. L. "Surface Plasmon Sensor Based on the Enhanced Light Transmission through Arrays of Nanoholes in Gold Films," *Langmuir*, 20 (12), 4813-4815 (2004).
2. Barik, A.; Otto, L. M.; Yoo, D.; Jose, J.; Johnson, T. W.; Oh, S.-H. "Dielectrophoresis-enhanced plasmonic sensing with gold nanohole arrays," *Nano Letters*, 14, 2006-2012 (2014).
3. Barik, A.; Cherukulappurath, S.; Wittenberg, N. J.; Johnson, T. W.; Oh, S.-H. "Dielectrophoresis-assisted Raman Spectroscopy of Intravesicular Analytes on Metallic Pyramids," *Analytical Chemistry*, 88, 1704-1710 (2016).
4. Kumar, S.; Johnson, T. W.; Wood, C. K.; Qu, T.; Wittenberg, N. J.; Otto, L. M.; Shaver, J.; Long, N. J.; Victora, R. H.; Edel, J. B.; Oh, S.-H. "Template-stripped Multifunctional Wedge and Pyramid Arrays for Magnetic Nanofocusing and Optical Sensing," *ACS Applied Materials & Interfaces*, 8, 9319-9326 (2016).
5. Nagpal, P.; Lindquist, N. C.; Oh, S.-H.; Norris, D. J. "Ultrasmooth Patterned Metals for Plasmonics and Metamaterials," *Science*, 325, 594-597 (2009).
6. Chen, X.; Park, H.; Pelton, M.; Piao, X.; Lindquist, N. C.; Im, H.; Kim, Y. J.; Ahn, J. S.; Ahn, K. J.; Park, N.; Kim, D.-S.; Oh, S.-H. "Atomic layer lithography of wafer-scale nanogap arrays for extreme confinement of electro-magnetic waves," *Nature Communications* 4:2361 (2013).

# Plasmonic sensing, imaging, and other active functions in biology and medicine

# Surface Plasmon Resonance Behaviors of Gold Nanoring and Their Application to Photothermal and Photodynamic Therapies

**Chih-Ken Chu, Che-Kuan Chu, Yi-Chou Tu, Jen-Hung Hsiao, Jian-He Yu, Y. W. Kiang, and C. C. Yang***
Institute of Photonics and Optoelectronics, National Taiwan University, Taipei, 10617 Taiwan
*corresponding author: ccycc@ntu.edu.tw

**Abstract**-Bio-conjugated gold nanorings are fabricated on substrate and then transferred into solution for showing the localized surface plasmon resonance in the spectral range of 1000-1300 nm, in which light can penetrate into tissue deepest. The combined effects of photothermal and photodynamic therapies are demonstrated through cancer cell necrosis and apoptosis based on the enhanced absorption and strong local field of the gold nanorings.

Au nanorings (NRIs), which have the localized surface plasmon resonance (LSPR) wavelength around 1058 nm, either with or without linked antibodies, are applied to SAS oral cancer cells for cell inactivation through the LSPR-induced photothermal effect when they are illuminated by a laser of 1065 nm in wavelength. Different incubation times of cells with Au NRIs are considered for observing the variations of cell uptake efficiency of Au NRI and the threshold laser intensity for cell inactivation. In each case of incubation time, cell sample is washed for evaluating the total Au NRI number per cell adsorbed and internalized by the cells based on inductively coupled plasma mass spectrometry measurement. Also, the Au NRIs remaining on cell membrane are etched with $KI/I_2$ solution to evaluate the internalized Au NRI number per cell. The threshold laser intensities for cell inactivation before washout, after washout, and after $KI/I_2$ etching are calibrated from the circular area sizes of inactivated cells around the illuminated laser spot center with various laser power levels. By using Au NRIs with antibodies, the internalized Au NRI number per cell increases monotonically with incubation time up to 24 hrs. However, the number of Au NRI remaining on cell membrane reaches a maximum at 12 hrs in incubation time. The cell uptake behavior of an Au NRI without antibodies is similar to that with antibodies except that the uptake NRI number is significantly smaller and the incubation time for the maximum NRI number remaining on cell membrane is delayed to 20 hrs. By comparing the threshold laser intensities before and after $KI/I_2$ etching, it is found that the Au NRIs remaining on cell membrane cause more effective cancer cell inactivation, when compared with the internalized Au NRIs. Also, the more effective inactivation of oral cancer cell SAS through the combination the photothermal therapy (PTT) and photodynamic therapy (PDT) effects based on the LSPR around 1064 nm in wavelength of Au NRI under femtosecond (fs) laser illumination is demonstrated. The PTT effect is caused by the LSPR-enhanced absorption of Au NRI. The PDT effect is generated by linking Au NRI with the photosensitizer of AlPcS for producing singlet oxygen through the LSPR-enhanced two-photon absorption (TPA) excitation of AlPcS. The laser threshold intensity for cancer cell inactivation with the applied Au NRI linked with AlPcS is significantly lower, when compared to that with the Au NRI not linked with AlPcS. The comparison of inactivation threshold intensity between the cases of fs and continuous laser illuminations at the same wavelength and with the same average power confirms the crucial factor of TPA under fs laser illumination for producing the PDT effect.

# Recent progress in chirality-based biomolecular sensing and hyperlens-based biological imaging

**Minkyung Kim[1], Jungho Mun[2], Inki Kim[1], Dasol Lee[1] and Junsuk Rho[1,2*]**
[1]Department of Mechanical Engineering, POSTECH, Korea
[2]Department of Chemical Engineering, POSTECH, Korea
[*]corresponding author: jsrho@postech.ac.kr

**Abstract**

In this abstract, we will discuss recent progress of biomolecular sensing such as peptides and proteins using chiral nanostructures. Also, recent advancement of super-resolution live imaging based on hyperlens for biological applications will be discussed.

Biomolecular sensors have been active research area with high importance. There are many important factors such as sensitivity, effectiveness, functionality and compactness. Especially, the sensitivity which is defined as the minimum mass of biomolecules is one of the most important as the sensor applications. In this abstract, we will discuss the current effort for the chirality based nanosensors which detects biomolecules such as peptides and proteins with very high sensitivity and reliability. Chiral nanostructures in 2D and 3D are both used for the different purposes. Also, we will discuss the recent progress of real-time super-resolution imaging with hyperlens which has shown promising application because it directly converts evanescent waves to propagating waves and thus allow far-field imaging beyond diffraction limit. Using such an imaging device, real-time imaging of live biological machineries such as neurons, cells and DNA could be possible. We will discuss recent development of large-scale hyperlens array fabrication and its direct neuron live imaging without any existing bioimaging techniques.

**Acknowledgements**

This work is supported by the National Research Foundation of Korea (NRF) Grant funded by the Korean Government (MSIP) (No. 2015R1A5A1037668 and No. 2015R1C1A1A02036464)

**REFERENCES**

1. E. Hendry et al., “Ultrasensitive detection and characterization of biomolecules using superchiral fields,” *Nature Nanotechnology*, 5, 783-787. 2010.
2. M. Kim et al., “Chirality assisted ultra-high sensitive biomolecules direct sensing,” *in preparation.*
3. Rho, J. et al., “Spherical hyperlens for two-dimensional sub-diffractional imaging at visible frequencies,” *Nature Communications*, 1, 143, 2010.
4. Rho, J. et al., “Sub-diffractional hyperlens imaging for real-time biological imaging” *in preparation.*

# Metamaterial Integrated Microfluidic Terahertz Sensors

**Xin Hu[1], Gaiqi Xu[1,2], Yaxin Zhang[2], David R. S. Cumming[3], Qin Chen[1]***

[1]Key Lab of Nanodevices and Applications, Suzhou Institute of Nano-Tech and Nano-Bionics, Chinese Academy of Sciences, P. R. China

[2]Terahertz Science Cooperative Innovation Center, University of Electronic Science and Technology of China, P. R. China

[3]School of Engineering, University of Glasgow, United Kindom

*corresponding author: qchen2012@sinano.ac.cn

**Abstract**-By constructing a metallic microstructure array-dielectric-metal structure, a metamaterial integrated microfluidic sensor is demonstrated in terahertz range, where the dielectric layer is hollow with the strongest electric field distribution and acts as the microfluidic channel. A record high sensitivity of 3.5THz/RIU is predicted by numerical simulation due to the confined field sensing rather than the regular exponential field sensing. Normalized the sensitivity to the working frequency, the calculated and measured normalized sensitivity is 0.55/RIU and 0.31/RIU, respectively.

Recently, terahertz (THz) sensing has arisen as a promising technique for biomedical research because some inter-strand vibrational modes of DNA molecules provide a specific fingerprint of double strands in the THz frequency range. However, the widespread use of THz sensing is hampered by the lack of high-performance THz sources and limited sensitivity due to the mismatch between the large wavelengths of THz waves (>30μm) and the analyte sizes. Plasmonic and metamaterial sensors with strong interaction between light and analytes have been widely investigated [1,2]. Nearly all these sensors use exponential electromagnetic fields to detect the analytes, irrespective of surface plasmon resonances or cavity resonances. Because the exponential field intensity quickly decreases with the distance away from the surface, the sensitivity is greatly reduced in the case that molecules are not attached on the surface.

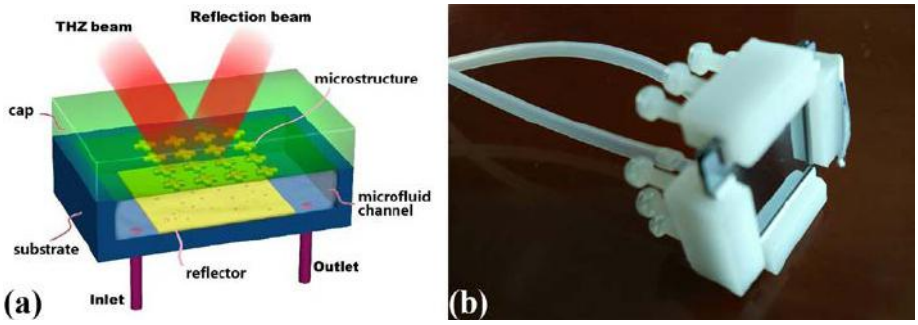



Figure 1. a) Schematic diagram and b) optical image of the MIM sensor.

A novel metamaterial integrated microfluidic THz sensor as shown in Figure 1 was proposed and demonstrated. The microfluidic channel is sandwiched between metal microstructure array and metal reflector. The metal microstructure array is attached on the cap and the metal reflector is on the substrate. The analyte in the channel flows in from the inlet and out from the outlet. THz beam is incident from the cap side and the reflected THz beam is measured for sensing. By tuning the electromagnetic impedance of the Metal-Dielectric-Metal metamaterial, a resonant perfect absorption can be obtained with the incident wave fully trapped between the two metallic layers, which is called metamaterial perfect absorber (MPA). Compared to the

previous work on MPA sensors [3-5], in the proposed device the microfluidic channel is spatially overlapped with the confined field in MPA and therefore leads to improved sensitivity as shown in Figure 2. The excellent overlap induces a record high sensitivity of 3.5THz/RIU. The sample was fabricated with a working frequency around 1THz and measured by THz-TDS system. A normalized (to frequency) sensitivity of 0.31/RIU was obtained.

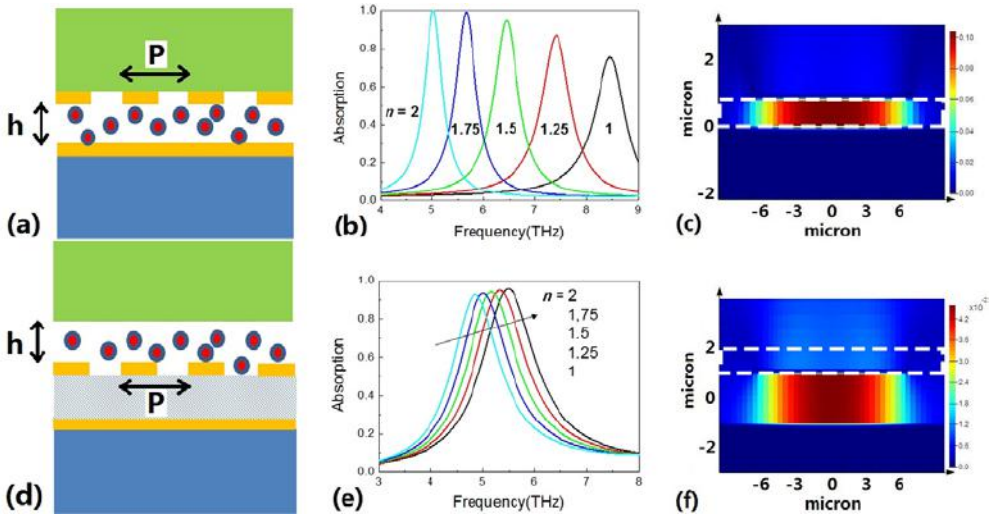



Figure 2. Simulation results of metamaterial based microfluidic sensors. a) and d) are the calculation models for the proposed device and the reference device as Ref. [3,5], respectively. The former has the microfluidic channel inside the MDM stack and the latter has the channel on top of the stack. The channel is modeled as a uniform material with a height of $h$ = 1μm. b) and e) are the calculated absorption spectra for both devices with refractive index of channel $n$ = 1, 1.25, 1.5, 1.75, 2. c) and f) are the magnetic field cross-section distributions in a unit cell with $n$ = 1.5. White dashed lines indicate the positions of the channels. For both devices, reflector is alumimium film with a thickness of 200 nm, and the microstructure is cross array with a period P=22μm, where the long and short sidelengths of both arms are 15 and 6μm, respectively. For the reference device, the dielectric layer is chosen to be polyimide (1.8+i0.06). The thickness of this layer is set to be 2μm.

**Acknowledgements** This work is supported by the grants from the National Natural Science Foundation of China (No. 11274344 and 61574158), Suzhou Science and Technology Development Program Foundation (No. ZXG201425) and the Royal Society Newton Advanced Fellowship.

**REFERENCES**

1. A. G. Brolo, “Plasmonics for future biosensors,” *Nature Photonics*, VOL. 6, NO. 11, 709-713, 2012.
2. Chen T., Li S., Sun H., “Metamaterials application in sensing,” *Sensors*, VOL. 12, NO. 3, 2742-2765, 2012.
3. Liu N., Mesch M., Weiss T., Hentschel M., Giessen H., “Infrared perfect absorber and its application as plasmonic sensor,” *Nano Letter*, VOL. 10, No. 7, 2342-2348, 2010.
4. Xie L., Gao W., Shu J., Ying Y., Kono J., “Extraordinary sensitivity enhancement by metasurfaces in terahertz detection of antibiotics,” *Scientific Reports*, VOL. 5, 8671, 2015.
5. Wang B.-X., Zhai X., Wang G.-Z., Huang W.-Q., Wang L.-L., “A novel dual-band terahertz metamaterial absorber for a sensor application,” *Journal of Applied Physics*, VOL.117, NO. 1, 014504, 2015.

# Plasmon-Enhanced Raman Spectroelectrochemistry

**K. Okubo**[1], **L. Le Thi Ngoc**[2], **and E. T. Carlen**[1,2,*]

[1]Graduate School of Pure and Applied Sciences, University of Tsukuba, Japan
[2]University of Twente and MESA+ Institute for Nanotechnology, The Netherlands
*ecarlen@ims.tsukuba.ac.jp

**Abstract**— An analysis system based on plasmon-enhanced Raman spectroelectrochemistry is presented that consists of a microfluidic sample chamber integrated into a three-electrode cell for in situ Raman spectroelectrochemistry. The key elements of the spectroelectrochemical analysis system are a nanostructured gold surface that serves as the electrochemical working electrode and surface-enhanced Raman scattering (SERS) substrate, microfabricated counter electrode, and reference electrode. The system has the merits of wide range of target molecules, small sample volume, and low detection limit.

There is great demand for analytical tools that can quantify the concentration of an analyte, in combination with specific molecular identification, and both with high spatial and temporal resolution. In situ surface-enhanced Raman spectroelectrochemistry (SEC), a hybrid of electrochemistry and surface-enhanced Raman spectroscopy, is well-suited for this type of analysis and applications such as biochemical analytics, surface science, and neuroscience. In situ surface-enhanced Raman SEC enables molecular identification in combination with electrochemical quantitation, thus enabling quantitative time-resolved monitoring of molecular dynamics.

A surface-enhanced Raman spectroelectrochemical analysis system is presented that consists of a microfluidic sample chamber integrated with a compact three-electrode configuration. We recently reported a SERS surface well-suited for surface-enhanced Raman SEC [1]. Figure 1(a) shows an example of a SERS spectrum of a mercapto-benzene (MB) SAM chemisorbed on a nanostructured gold surface irradiated with a HeNe laser with an energy density of $1.3\times10^4$ J cm$^{-2}$, which produces a similar integrated band intensity as a conventional Raman measurement from a neat MB solution irradiated with a 2000× greater energy density (Figure 1(b)). The nanostructured gold surfaces are realized with a simple nanofabrication technology that is based on template-guided film growth to form large aspect ratio metal nanowire arrays with dimensions down to 50 nm and nanogaps down to 5 nm. Figures 1(c) and 1(d) show representative scanning electron microscopy (SEM) images of the nanostructured gold surfaces. The SERS surface can be precisely tuned to achieve extremely large ($10^8$) and uniform (less than 10% spatial variation) SERS enhancements.

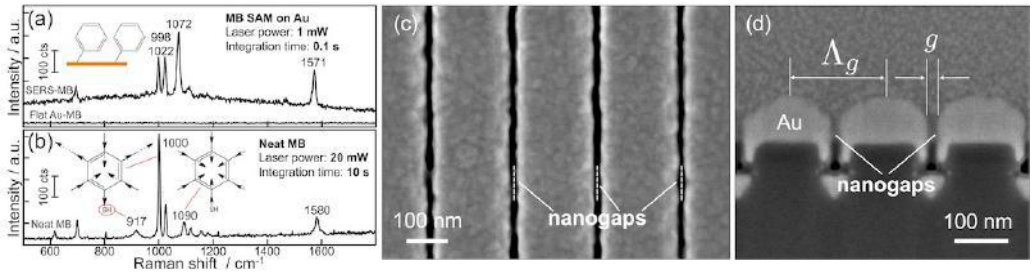



Figure 1: (a) Top: SERS spectrum of MB SAM from nanostructured gold surface, Bottom: Raman spectrum from planar gold surface (b) Conventional Raman spectrum of neat MB, (c),(d) SEM images of nanostructured gold surface. (c) Top view, (d) Cross section view showing pitch $\Lambda_g$ and nanogap $g$.

The nanostructured gold surfaces enable highly sensitive in situ SERS vibrational spectroscopy through large and uniform SERS enhancements, thus eliminating the need for surface-enhanced resonance Raman scattering (SERRS), which has been used extensively for in situ Raman spectroelectrochemistry in order to resolve small quantities of adsorbed species. SERRS requires that the laser wavelength be resonant with the surface plasmon resonance wavelength of the nanostructured metal surface as well as the electronic absorption band of the molecule of interest, thus limiting its application to molecules with absorption wavelengths in the visible spectrum. Such large Raman

scattering enhancements by the nanostructured Au surfaces enable the measurement of SERS spectra from sub-monolayers within milliseconds on chemically stable gold surfaces. The in situ SERS SEC system consists of a SEC-cell interfaced to the Raman microscope and electrically interfaced to a potentiostat (Figure 2(a)). The SEC-cell consists of the nanostructured Au working electrode (WE) and microfabricated Pt counter electrode (CE), directly bonded to the microfluidic sample chamber that is optically interfaced to the Raman spectrometer (Figure 2(b)), and an external reference electrode (RE) (Figure 2(c)). A SEM image of a nanostructured Au WE surface is shown in Figure 2(d). Figure 3 shows in situ SERS SEC measurements of the metalloporphyrin hemin

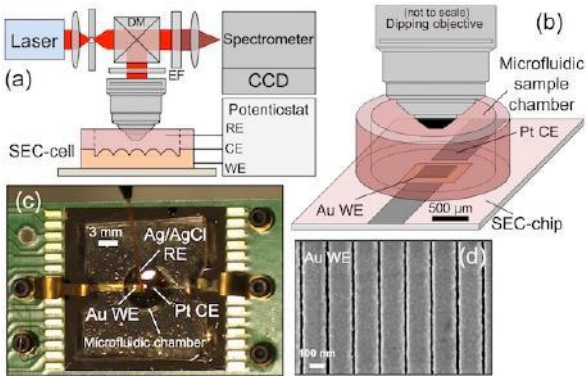



Figure 2: SERS SEC analysis system. (a) Schematic of SEC system, (b) SEC-cell comprised of a SEC-chip directly bonded to a small-volume microfluidic sample chamber with an optical interface to a microscope objective, (c) SEC-cell consisting of a Pt CE and a nanostructured Au WE patterned on the silicon SEC-chip, and external Ag/AgCl RE, (d) SEM image of the nanostructured Au WE.

that indicates shifts of the iron oxidation marker band with the nanostructured gold WE under potential control [2].

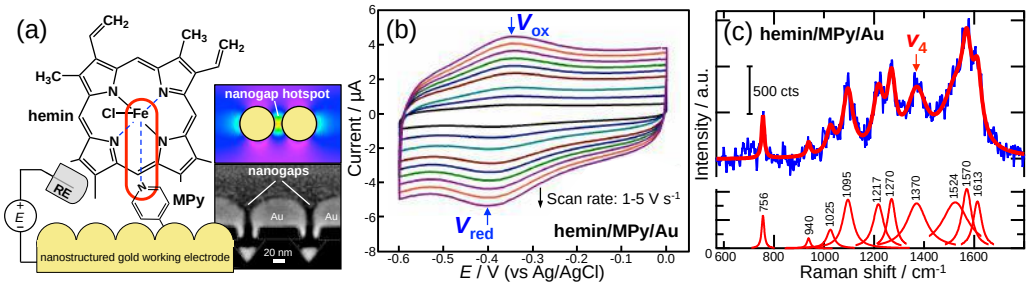



Figure 3: In situ SERS SEC of hemin coordinated to a mercapto-pyridine (MPy) self-assembled monolayer on a nanostructured gold WE, (a) Measurement configuration, (b) Cyclic voltammogram, (c) SERS spectrum with $E$=-0.5 V

In conclusion, an in situ SERS spectroelectrochemical analysis platform is presented that is composed of a small volume sample chamber and a nanostructured Au WE for simultaneous SERS and electrochemical investigation of any modified electrode surface with low laser power.

## ACKNOWLEDGMENT

The authors thank Johan Bomer for assistance with device fabrication.

## REFERENCES

1. Le Thi Ngoc, L., M. Jin, J. Wiedemair, A. van den Berg, and E. T. Carlen, "Large area metal nanowire arrays with tunable sub-20 nm nanogaps," *ACS Nano*, Vol. 7, No. 6, 5223-5234, 2013.
2. Yuan, Y., L. Le Thi Ngoc, J. van Nieuwkasteele, M. Odijk, A. van den Berg, H. Permentier, R. Bischoff, and E. T. Carlen, "In situ surface-enhanced Raman spectroelectrochemical analysis system with a hemin modified nanostructured gold surface," *Anal. Chem.* Vol. 87, No. 5, 2588-2592, 2015.

# Three-dimensional plasmonic metastructures for sensing and imaging

**J. Shin*, N. Lee, R. H. Kim, T. Y. Chang, J. Y. Kim, and H. W. Kim**
Department of Materials Science and Engineering, KAIST, Republic of Korea
*corresponding author: qubit@kaist.ac.kr

**Abstract**-While plasmonic metasurfaces with a monolayer metallic pattern are promising many novel applications, extending the geometry to three dimensions allow even more diverse optical properties and applications. At the same time, the fabrication becomes more challenging due to sub-ten nanometer scale alignment accuracy typically required for such three-dimensional structures. Here we introduce examples of extreme optical properties enabled by three-dimensional structures designed in our lab and demonstrate that some of these structures can be facilely fabricated by current nanofabrication technology.

Optical devices utilizing surface plasmon-polariton (SPP) waves have seen much research interest in the last decades because SPP allows manipulation of light in a deep-subwavelength scale, impossible with conventional optics based on dielectric materials only. The main difference between SPP waveguides and conventional dielectric waveguides is that the former is composed of materials with both positive and negative signs in their real parts of the electric permittivities. This allows the existence of electrostatic resonances that is only dependent on the permittivities and the geometrical shape and is invariant under spatial scaling (size change). Hence, optical resonance phenomena can occur in very small metallic elements such as five nanometer gold particles. This is in stark contrast to purely dielectric resonators that rely on phase retardation effect for the occurrence of resonances, which require physical sizes at least on the order of a half wavelength.

The ability to control the electromagnetic fields and resonances in a truly nanometer scale has important consequences in many macroscopic optical functions such as imaging resolution, solar energy conversion, optical nonlinearity, and sensing. First, the imaging resolution is directly determined by the maximum wavenumber that can be recorded locally or transmitted to farfield optics. An artificial material composed of three-dimensionally patterned metallic inclusions may possess a very high index of refraction and it may allow super-resolution imaging because the maximum wavenumber is directly proportional to the refractive index. In this talk, it is shown that three-dimensionality is important in achieving a high refractive index over broad wavelength range. Also, it is numerically confirmed that a resolution of one-tenth of a wavelength or better is possible in the optical range.

Second, the large wavenumber achievable in SPP waveguides allows a design of very small optical Fabry-Perot resonators. In this talk, an extremely small three-dimensional SPP resonator that can be facilely fabricated over a large area is introduced. The three-dimensional design makes it possible to expose the high field intensity sites of the resonators on a flat surface which is beneficial in sensing applications. Large area arrays of these resonators are fabricated with good uniformity across the sample. The sensing performance of the design is demonstrated by SERS measurements.

**Acknowledgements**-This work is supported by the Samsung Science & Technology Foundation (Grant: SSTF-BA1401-06) and by the Ministry of Science, ICT & Future Planning through the National Research Foundation of Korea (2014M3A6B3063708, 2013M3C1A3063598, 2012M3A7B4035327).

**REFERENCES**

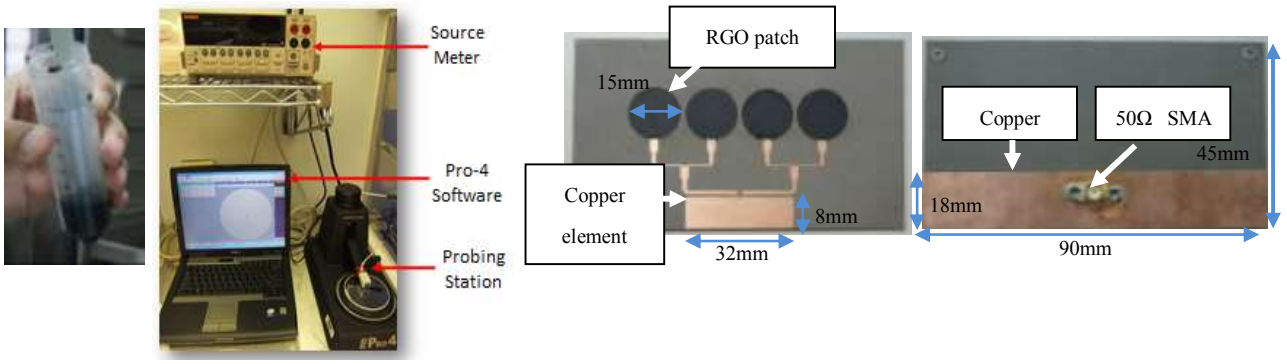
1. Mayergoyz, I. D., D. R. Fredkin and Z. Zhang, "Electrostatic (plasmon) resonances in nanoparticles," *Phys. Rev. B*, Vol. 72, No. 15, 155412/1–15, 2005.
2. Baek, K. M, J. M. Kim, J. W. Jeong and Y. S. Jung, "Sequentially Self-Assembled Rings-in-Mesh Nanoplasmonic Arrays for Surface-Enhanced Raman Spectroscopy," *Chem. Mater.*, Vol. 27, No. 14, 5007–5013, 2015.
3. Shin, J., J. T. Shen and S. Fan, "Three-dimensional metamaterials with an ultrahigh effective refractive index over broad bandwidth," *Phys. Rev. Lett.*, Vol. 102, No. 9, 093903/1–4, 2009.

# Reduced Graphene Oxide (RGO) Sensor for Confocal Microwave Imaging Technique in Detecting Human Brain Tumor

**M. A. Jamlos**[1*], **A. H. Ismail**[2], and **M. V. Schleusingen**[3]
[1,2,3]Faculty of Technology Engineering (F-Tech), UniCITI Alam Campus, Universiti Malaysia Perlis (UNIMAP), Malaysia
[*]mohdaminudin86@gmail.com

**Abstract**-RGO sensor is successfully identifying tumor in human brain using confocal microwave imaging technique. The sensor consists of RGO as patch and conventional copper for the rest radiating element parts as well as Taconic as the substrate. The sensor operated within ultra-wide band radiation frequency (2.5 GHz-12.2 GHz) with high energy produced (5.5dB-14.5dB) in order for the signal to reach tumor located inside human head phantom. The image produces indicated tumor present with the highest intensity spot (reddish in colour).

Graphene is the promising radiating material for the sensor for cancer detection purpose [1]. Since graphene is very expensive to buy, having reduced graphene oxide originated from cheap graphite which has almost the same performance with pure graphene is the ultimate solution for that particular matter. Graphene oxide, a derivative of pure graphene loses most of its electrical conductivity properties during oxidation process. In order to restore back its electrical conductivity, special reduction procedures need to be done [2]. Two unique methods using a two stepped chemical and microwave method to reduce graphene oxide done for that purpose. Figure 1 shows RGO in liquid form. RGO has conductivity of 3.38 $\times 10^{7}$ s/m, resistivity of 2.01 $\times 10^{-3}$ Ω.m, voltage of 0.2 V and current of 9.48 $\times 10^{-1}$ I. Test have been done using Four Point Probe device. Meanwhile figure 1 (c) and (d) show sensor views from front and back respectively.




(a) (b) (c) (d)

Figure 1: (a) RGO in liquid form, (b) Four Point Probe, (c) sensor front view, (d) sensor back view

The most intensive peak at $26.6^{0}$ is recorded by pure graphite [3] as shown in figure 2(a) for XRD pattern. Due to oxidation reaction, the characteristic peak for graphite becomes broader and shifts toward $12.7^{0}$. However, XRD pattern for RGO display an increasing broader peak which reveals the

disappearance of multilayer structures and the formation of graphene single sheets [4] where the broad hump at $2\theta = 20\text{-}30^0$ indicated the smaller sheet size and an amorphous structure as shown in figure 2(b). The two-stepped processed product for RGO exhibit adequate reduction as seen in other reduction methods [5]. RGO sensor successfully detected the tumor indicated by the highest intensity spot, reddish in colour as shown in figure 3 (b).

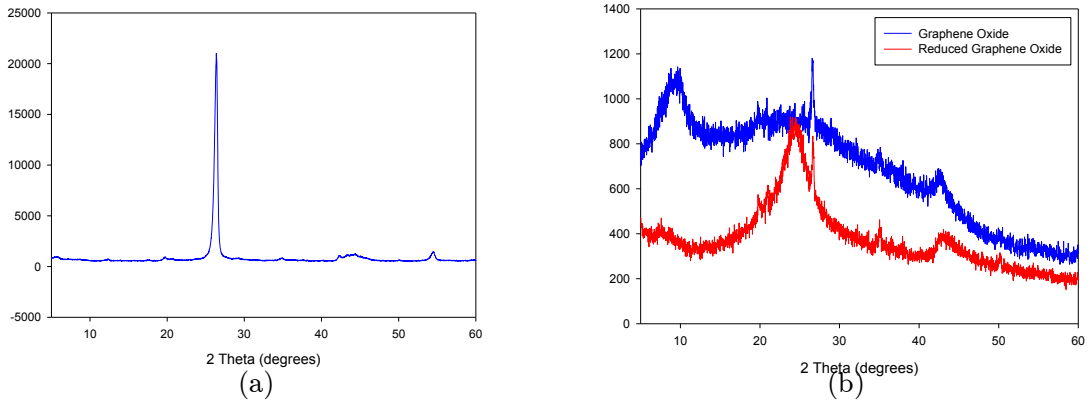



Figure 2: XRD pattern for (a) graphite, (b) graphene oxide and reduced graphene oxide

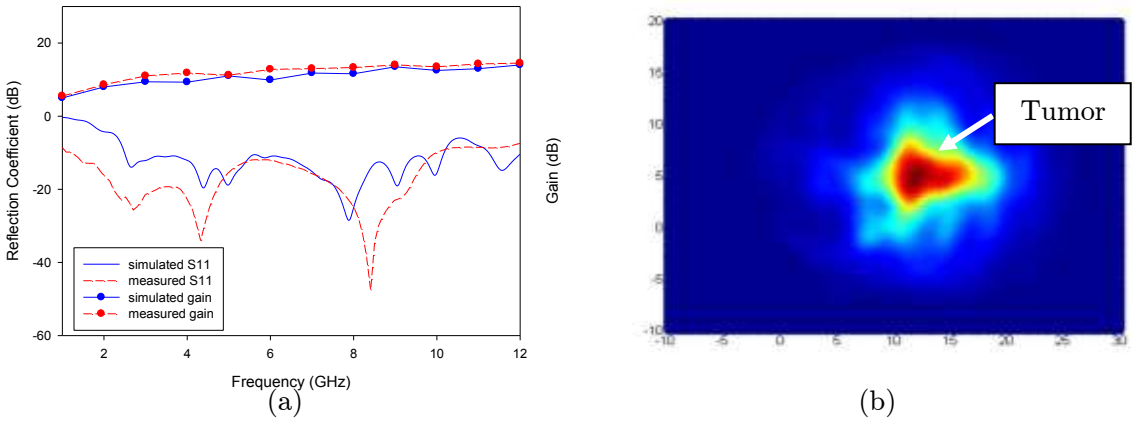



Figure 3: (a) Sensor's measured and simulated S11 and gain, (b) image result with tumor in brain

## REFERENCES


1. Moon, J. S. and Gaskill, D. K. "Graphene: Its Fundamentals To Future Applications", IEEE Transactions On Microwave Theory And Techniques, Vol. 59, No. 10, 2011.
2. Vashist, S. K. and Luong, J. H. T, "*Recent Advances in Electrochemical Biosensing Schemes Using Graphene and Graphene-based Nanocomposites*", Carbon 2015, 84, 519-550, 2015.
3. M. M. Viana, M. C. F. S. Lima, J. C. Forsythe, V. S. Gangoli, M. Cho, Y. Cheng, G. G. Silva, M. S. Wong, and V. Caliman, "*Facile Graphene Oxide Preparation by Microwave-Assisted Acid Method*", J. Braz. Chem. Soc, 26, 978-984, 2015.
4. W.Chen, L. Yan, P. R. Bangal, "*Preparation of graphene by the rapid and mild thermal reduction of graphene oxide induced by microwaves*", Carbon. 48, 1146-1152, 2010.
5. N. Zhao, X. Cheng, J. Yang, M. Yang, and S. Zheng, "*Experimental study on the preparation, characterization and conductivity improvement of reduced graphene-oxide papers*", Journal of Physics and Chemistry of Solids. 75, 1141-1146, 2014.

# Sensing the surface plasmon resonance at the quantum noise limit

**K. Pufahl, J. Heckmann, U. Woggon, and N. B. Grosse**

Technical University of Berlin, Germany
nicolai.grosse@tu-berlin.de

**Abstract**— The mono-layer deposition of molecules onto a substrate leads to perturbations in the local refractive index. These can be tracked via surface plasmon resonance (SPR) sensing. We show that the commonly-employed incoherent detection scheme (locating the intensity centroid after Gaussian illumination) is only 86% efficient when compared to an optimal coherent scheme operating at the quantum-noise-limit. We derive expressions for the detectability, and advise how the spatial modes for illumination and detection are best tailored to the SPR resonance.

The most common realization of surface plasmon resonance (SPR) sensing employs a gold-coated glass prism in the Kretschmann-Raether geometry; see Fig. 1(a). Novel schemes that aim to improve the sensitivity of detecting the shift in the SPR have been proposed in the literature and demonstrated in practice [1, 2, 3]. Some theoretical bounds for the limit in sensitivity have been investigated using a semi-classical treatment of detector shot-noise [4]. However, a quantum optical analysis of the signal strength and measurement noise-floor that incorporates the non-commuting quadratures of the illumination field, and the identification of the optimal detection scheme in the context of quantum information, has hitherto been lacking.

In this contribution, we develop a quantum noise model of SPR sensing that involves the field fluctuations that originate from a monochromatic illumination field of arbitrary mode shape, and the vacuum fluctuations that arise from the SP mode and its propagation losses. We derive the quantum-noise-limited detectability of a shift in the resonance, given the available quantum resources; and identify the illumination function and mode-specific detection scheme that yields the optimal sensitivity. We compare the performance of the two competing SPR technologies: *incoherent* split detection in Fig. 1(b), and *coherent* homodyne detection in Fig. 1(c); and discuss the possible role of nonclassical light in further improving the sensitivity.

The mean-field response of the Kretschmann-Raether geometry, described by a Fresnel coefficient model, is approximated near the SPR by a Lorentzian function [5]; see Fig. 2(a). Quantum harmonic oscillator operators $\hat{a}$ and $\hat{b}$ are assigned to the illumination and local-oscillator modes, respectively, which are in specific spatial mode functions (defined over $\kappa$); see Fig. 2(b-d). The SP vacuum state and losses in the metal are incorporated into one fluctuation operator $\hat{c}$. The system's response

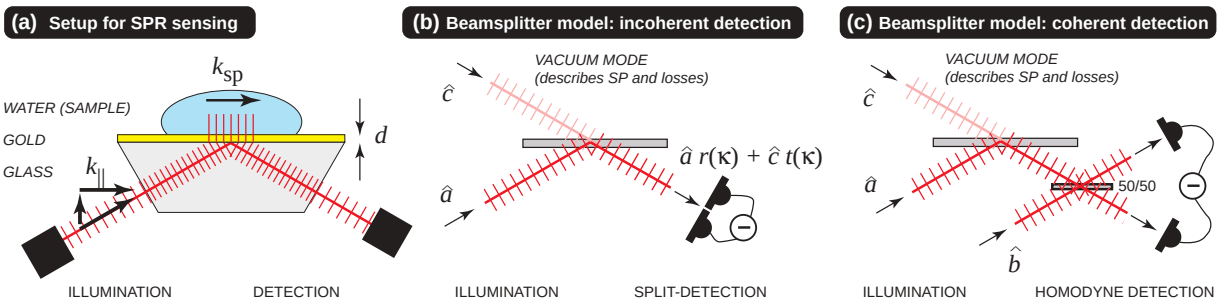



Figure 1: **(a)** Typical setup for SPR sensing using the Kretschmann-Raether geometry, where the k-vector $k_{||}$ is matched to that of the SP given by the material dielectrics: $k_{\rm sp} = (\omega/c)[\epsilon_{\rm gold}\epsilon_{\rm water}/(\epsilon_{\rm gold} + \epsilon_{\rm water})]^{1/2}$. **(b)** An equivalent far-field beamsplitter model for the mean field and quantum fluctuations. A vacuum mode accounts for the SP vacuum state and absorption/losses from the metal. These sources are merged into one operator $\hat{c}$ which is set to the vacuum state $|0\rangle$. The incident light is in a coherent state: $\hat{a}|\alpha\rangle = \alpha|\alpha\rangle$. The reflection and transmission of the beamsplitter must satisfy $|r|^2 + |t|^2 = 1$ and $r^*t - rt^* = 1$. Incoherent detection of the SPR shift relies on the centroid being located using split-detection. **(c)** Homodyne detection, being phase-sensitive and mode-specific, is achieved via interference with a local oscillator in a bright coherent state: $\hat{b}|\beta\rangle = \beta|\beta\rangle$ and $|\beta| \gg |\alpha|$.

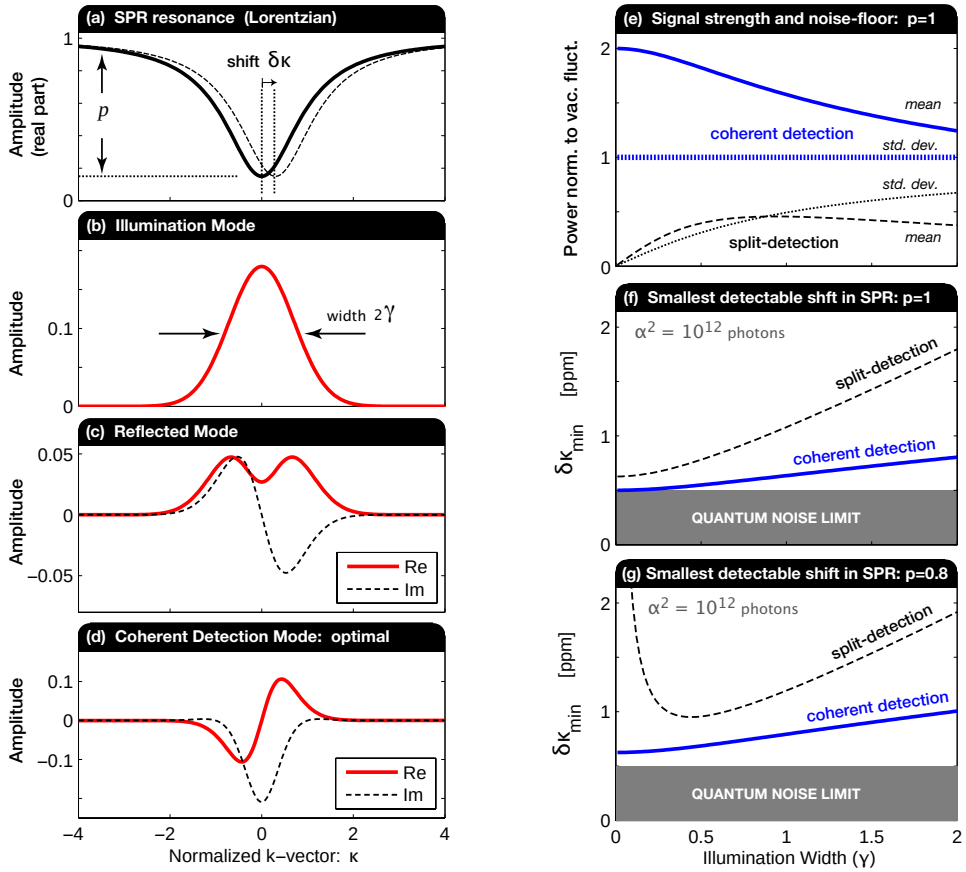



Figure 2: **(a)** The SPR resonance is treated as a Lorentzian function $r(\kappa) = 1 - (p/(\mathrm{i}\kappa + 1))$ defined over the normalized k-vector $\kappa = (k_{||} - \Re\{k_{\mathrm{sp}}\})/\Im\{k_{\mathrm{sp}}\}$; with coupling-strength $p$. A shift in resonance $\delta\kappa$ is indicated. **(b)** Illumination using a Gaussian beam of width $\gamma$. **(c)** The resulting reflected field's complex amplitude. **(d)** The optimal choice of mode for the local oscillator field. **(e)** Comparison of the signal strength (mean) and noise-floor (standard deviation) for the two detection schemes. **(f)** The resulting smallest detectable shift in SPR in parts-per-million (ppm), relative to the SPR width, for an illumination of $10^{12}$ photons ($\approx$1 mW visible laser power, integrated for 1 ms). In the limit of narrow-beam illumination, the coherent scheme reaches the quantum noise limit ($\delta\kappa_{\mathrm{min}} = 0.5$ ppm). Incoherent detection of the centroid location attains only 86% of this sensitivity ($\delta\kappa_{\mathrm{min}} = 0.58$ ppm). **(g)** A more realistic case having a weaker SPR, for which the best sensitivity for split-detection uses a Gaussian beam-width approximate to the SPR width.

function yields a complex field in reflection; see Fig. 2(c). Standard techniques in continuous-variable quantum optics are used to arrive at the main results in Fig. 1(e). We compare the performance of the two detection schemes for an ideal SPR in Fig. 2(f), and a weaker SPR in Fig. 2(g); where the signal-to-noise ratio (SNR) has been translated into a sensitivity bound, i.e. a minimum detectable shift $\delta\kappa_{\mathrm{min}}$ for which the SNR=1. The quantum-noise-limit has been defined using classical states (coherent states and vacuum states), leading to $\delta\kappa_{\mathrm{min}} = 1/(2\alpha)$, where the sensitivity can only improve by increasing the photon number $|\alpha|^2$ of the illumination.

**REFERENCES**


1. Wu, S. Y., Ho, H. P., Law, W. C., Lin, C., Kong, S. K., "Highly sensitive differential phase-sensitive surface plasmon resonance biosensor based on the Mach-Zehnder configuration", *Optics Letters*, Vol. 29, No. 20, 2378–2380, 2004.
2. Slavík, R., Homola, J., "Ultrahigh resolution long range surface plasmon-based sensor", *Sensors and Actuators B*, Vol. 123, 10–12, 2007.
3. Hastings, J. T. , Guo, J., Keathley, P. D., Kumaresh, P. B., Wei, Y., Law, S., Bachas, L. G., "Optimal self-referenced sensing using long- and short- range surface plasmons", *Optics Express*, Vol. 15, No. 26, 17661–17672, 2007.
4. Piliarik, M., Homola, J., "Surface plasmon resonance (SPR) sensors: approaching their limits?", *Optics Express*, Vol. 17, No. 19, 16505–16517, 2009.
5. Raether, H., "Surface plasmons on smooth surfaces", Springer Berlin Heidelberg, 1988.

# Ordered Arrays of Au NP on Nanopipettes for SERS Sensing

**H. Zhu[1], J. P. Spatz[2], J.-F. Masson[1*] and C. G. Bazuin[1*]**

[1]Département de chimie, Centre de recherche sur les matériaux auto-assemblés (CRMAACSACS), Université de Montréal, Montréal (QC), Canada

[2]Department of New Materials and Biosystems, Max-Planck Institute for Intelligent Systems, Stuttgart, Germany

[*]corresponding author: jf.masson@umontreal.ca, geraldine.bazuin@umontreal.ca

**Abstract.** Incorporating plasmonic nanoparticles to patch clamp nanopipettes is a promising technology for miniature SERS biosensors for cell biology, due to its potential sensitivity and spatio-temporal resolution. Here, we demonstrate a bottom-up approach to create ordered arrays of nanoparticles deposited on the curved surface of nanopipettes of pulled optical fibers or capillaries that is essential for stable plasmonic responses in SERS studies.

The recent advances in plasmonic materials have transformed Raman, a conventionally weak light scattering event, into a highly sensitive spectroscopic technique using the surface enhanced Raman spectroscopy (SERS) effect. Raman is particularly interesting for cell biology experiments, as it provides a unique vibrational fingerprint of molecules that can be distinguished from the complex biology background. To investigate cells in their native environment, novel nanosensors must be designed for capturing cellular communication events. A platform for miniature SERS sensing probes uses pulled glass nanopipettes (NPPs), because their unique geometry extends from mm at the stem (facilitating manipulation) down to nm at the tip (giving a small probe volume that minimizes disturbance to cells). Therefore, we predict that SERS-enabled NPPs will become an important tool to spectroscopically detect biochemical molecules in cell biology with high sensitivity and spatio-temporal resolution.[1]

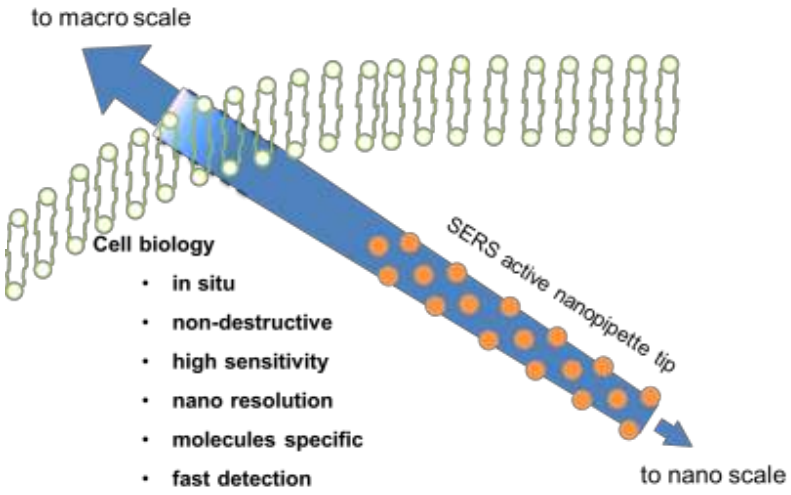



**Figure 1.** SERS-enabled nanopipette for cell biology.

The most critical aspect of SERS measurements is to engineer surface nanostructure arrays to maximize signal strength and ensure reproducibility. Block copolymer self-assembly (BCSA) in thin films forms suitable

templates for this purpose.[2] It is an inexpensive bottom-up approach that can produce nanostructured arrays with long-range order and tunable nanoparticle size and inter-particle spacing. A representative BCSA template, shown in Figure 2a-c where it is deposited on a flat silicon substrate, is composed of a polystyrene (PS) matrix in which are embedded AuNP-host block surface micelles [poly(4-vinyl pyridine)] in a quasi-hexagonal array. On the small and highly curved surface of NPP tips, weak surface energetics prevent direct deposition of BCSA-AuNP arrays. Therefore, we implemented unique surface functionalization through carbon vapour deposition and laser illumination to enhance the adhesion between PS and the NPP tip. As shown in Figure 2d, high surface coverage and uniform distribution of AuNPs were thus achieved at the tip. This approach can be extended to PS-grafted AuNPs, which is easily synthesized via colloidal chemistry in various AuNP shapes and which is also capable of producing ordered AuNP arrays. We are currently investigating the detailed mechanism of the surface functionalization, in order to optimize the immobilization of AuNPs on the surface, to thereby enhance the stability and reproducibility of SERS signals from the SERS-enabled nanopipette biosensor.

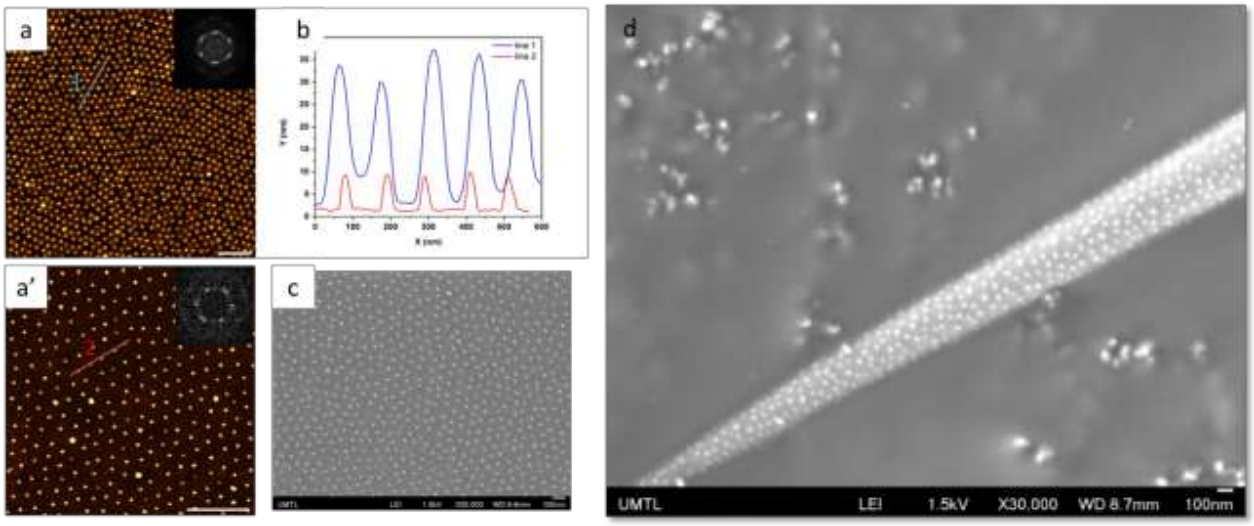



**Figure 2.** AFM height images (a, a'), their corresponding line profiles (b), and SEM image (c) of a BCSA-templated AuNP array on a flat silicon wafer; SEM image (d) of a BCSA-templated AuNP array on a nanopipette.

**Acknowledgement.** The authors acknowledge funding from le Fonds de recherche du Québec - Nature et technologies (FRQNT). HZ thanks Guangzhou Elite Project for a PhD scholarship.

**REFERENCES**

1. Masson, J. F., J. Breault-Turcot, R. Faid, H. P. Poirier-Richard, H. Yockell-Lelievre, F. Lussier and J. P. Spatz, "Plasmonic nanopipette biosensor," *Anal. Chem*, 86, 8998-9005, 2014.

2. Lohmueller, T., E. Bock and J. P. Spatz, "Synthesis of Quasi-Hexagonal Ordered Arrays of Metallic Nanoparticles with Tuneable Particle Size," *Adv. Mater.*, 20, 2297-2302, 2008.

# Multiplexed molecular imaging with targeted SERS nanoparticles for intraoperative guidance of tumor resection

**Y. Wang[1], S. Kang[1], and J.T.C. Liu[1,*]**
[1]University of Washington, Seattle, WA 98195, USA
[*]corresponding author: jonliu@uw.edu

**Abstract**- We are developing a wide-area imaging strategy to enable the imaging of multiple cell-surface protein biomarkers in freshly excised tissues during surgery. This technique utilizes surface-enhanced Raman scattering (SERS) nanoparticles (NPs) that are targeted to various disease biomarkers and which are topically applied on surgical specimens to provide molecular-imaging contrast. We demonstrate that the technology is able to visualize the expression of a panel of protein biomarkers at the surfaces of fresh tissues following a rapid topical staining (10-min) and rinse removal (15-s) protocol that is appropriate for intraoperative use.

In order to guide the complete resection of tumors, intraoperative imaging techniques are needed to identify residual tumor at the surgical margins. A highly specific means of identifying tumor is to image disease-related biomarkers. However, due to the heterogeneity of biomarker expression in tumors, assessing a panel of relevant biomarkers is advantageous for accurate tumor detection. Surface-enhanced Raman-scattering (SERS) nanoparticles (NPs), a contrast agent with great multiplexing capabilities, have attracted interest in recent years [1]. Although basic experiments to assess the sensitivity [2, 3], targeting ability [4, 5] and multiplexing potential [6] of SERS NPs have been performed, there is a need to demonstrate that multiplexed biomarker imaging is possible with SERS NPs topically applied on fresh tissues under time-limited clinical settings.

Here, we demonstrate that the topical application and quantification of a multiplexed cocktail of biomarker-targeted SERS NPs offers the potential for rapid (15 min) molecular phenotyping of the freshly excised tissues to determine the presence of tumor. A topical-staining procedure as well as a raster-scanned fiber-optic imaging system were developed to comprehensively image fresh tissue specimens. In addition, a ratiometric strategy was employed to distinguish biomarker-specific binding from nonspecific binding caused by off-target accumulation and uneven delivery of the NPs [3, 5].

*Ex vivo* studies with tumor xenografts and human breast tissues (Fig. 1) were performed to demonstrate the SERS-NP-based molecular imaging technique. For breast tissue imaging, each tissue specimen was stained with an equimolar mixture of HER2-NPs and isotype-NPs (10 min), followed by a quick rinse in PBS (20 s). After that, the stained tissue surface was raster-scanned within 2 min. The entire procedure was performed in less than 15 min, a time frame that is consistent with current intraoperative guidance techniques such as X-ray CT examination of surgical excisions and frozen-section pathology. Figure 1b shows that the HER2 vs. isotype ratio measured from 4 tumor specimens is significantly elevated compared to the ratio from 4 normal specimens, clearly revealing the expression level of the HER2 cell-surface receptor. Figs. 1d–1g show images of one tissue specimen that contained both tumor and normal regions. Measurements of absolute NP concentrations are misleading due to nonspecific accumulation of the topically applied NPs (Fig. 1e), where the HER2-NPs accumulate more on normal tissue regions than on tumor regions. However, the ratiometric image (Fig. 1f)

accurately quantifies HER2 expression levels in agreement with IHC validation data (Fig. 1g).

In summary, we have demonstrated that the topical application and quantification of receptor-targeted SERS NPs allows for rapid (< 15 min) molecular phenotyping at the surface of freshly resected tissues, and that the unambiguous detection of biomarkers is achievable through the ratiometric quantification of targeted NPs vs. untargeted NPs, as recently published [7,8]. These tools have the potential to enable the accurate intraoperative detection of residual tumors at the resection margins.

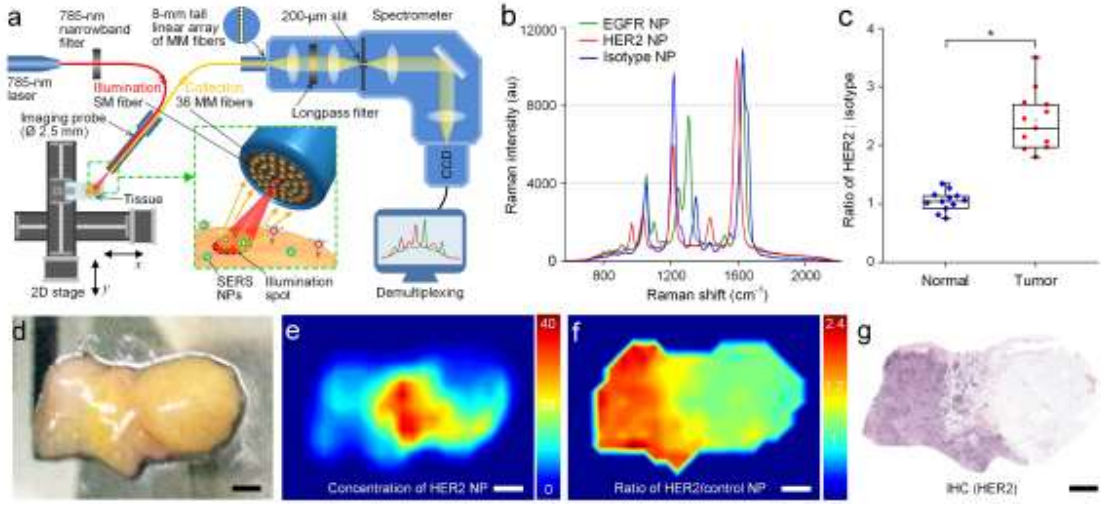



**Figure 1.** Multiplexed molecular imaging of fresh breast tissues *ex vivo* with targeted SERS nanoparticles. **(a)** Schematic illustration of a customized raster-scanned imaging system to detect bioconjugated NPs topically applied on a tissue surface (zoom-in panel: distal end of fiber bundle for Raman spectral measurements). **(b)** Raman spectra of the three NP contrast agents used in this study. **(c)** Concentration ratio of targeted vs. untargeted NPs topically applied on normal breast tissues and HER2+ tumors (4 tissue samples from two patients). **p*<0.001. **(d)** Photograph of a breast tissue sample containing both tumor and normal tissue regions (tissue size: 1×1.8 $cm^2$). Images showing **(e)** concentration of HER2-NPs (ambiguous due to nonspecific accumulation), **(f)** concentration ratio of HER2-NPs vs. isotype-NPs and **(g)** IHC staining with an anti-HER2 mAb. The scale bars are 2 mm.

**Acknowledgements**. We acknowledge funding support from the NIH/NIBIB (R21 EB015016).

## REFERENCES

1. Wang, Y. et al., *Chem. Rev.* 113, 1391 (2013)
2. Bohndiek, S. et al., *Proc. Natl. Acad. Sci. U.S.A.* 110, 12408 (2013)
3. Wang, Y. et al., *Biomed. Opt. Exp.* 5, 2883 (2014)
4. Jokerst, J. et al., *Small* 7, 625-633 (2011)
5. Wang, Y. et al., *Technology* 02, 118 (2014)
6. Zavaleta, C. et al. *Proc. Natl. Acad. Sci. U.S.A.* 106, 13511 (2009)
7. Wang, Y. et al., *Scientific Reports* (2016)
8. Wang, Y. et al., *IEEE J.S.T.Q.E.* (2016)

# Vertical dimer antennas for microfluidic biosensing

**A. Horrer[1], K. Krieg[2], K. Freudenberger[2], S. Rau[2], L. Leidner[2], G. Gauglitz[2], D. P. Kern[1], and M. Fleischer[1*]**

[1]Institute for Applied Physics and Center LISA[+], University of Tübingen, Auf der Morgenstelle 10, 72076 Tübingen, Germany

[2]Institute of Physical and Theoretical Chemistry, University of Tübingen, Auf der Morgenstelle 18, 72076 Tübingen, Germany

[*]corresponding author: monika.fleischer@uni-tuebingen.de

**Abstract-** In plasmonic nano-sensors, the sensitive dependence of the plasmon resonance wavelength on the refractive index near the surface of an optical nano-antenna can be used as a detection principle. In the presented work, lithographically fabricated arrays of vertical dimer antennas are integrated in microfluidic channels. The dimer surfaces are functionalized by antibodies for the specific binding of target molecules from the liquid. Shifts of the symmetric, antisymmetric and lattice modes of the nano-antennas are observed upon binding.

One main potential area of application of optical antennas is their implementation for optical sensors.[1-4] Nanostructured surfaces support localized surface plasmon polaritons (LSPP) upon illumination. The energy of an incoming electromagnetic field is concentrated at the positions of the nanostructures, leading to high electrical near-fields, which can be harnessed for high sensitivity detection.

As one approach LSPP sensors are integrated in microfluidic channels. The nanostructure surfaces are functionalized with recognition structures. When analyte from the solution binds to the surface, the resonance frequency of the LSPP is slightly shifted with a concentration-dependent wavelength shift. The shift is used as a signal for detecting the specific binding.

In this work, arrays of vertical gold-$SiO_2$-gold dimers are fabricated in microfluidic channels. These coupled nanostructures show three distinct resonances in the visible wavelength range, a symmetric and an asymmetric plasmon mode as well as a lattice resonance from their symmetric arrangement.[5] Shifts of the three resonances are observed and evaluated upon functionalization and binding. As an example, a microfluidic testosterone sensor was demonstrated.[6] The preparation, numerical analysis and experimental results will be shown.

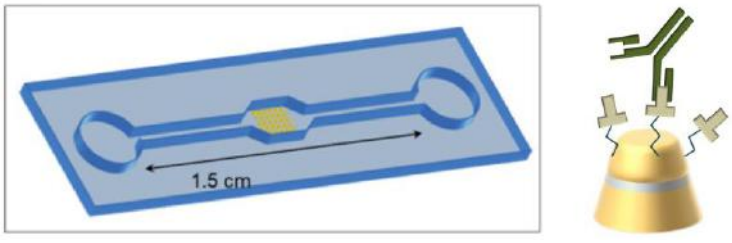



**Figure 1:** Arrays of vertical dimer antennas in a microfluidic channel (left) are functionalized for specific analyte binding (right), which is detected via shifts in the plasmon resonance wavelengths of the different antenna modes.

**Acknowledgements**: This work was financially supported by the Baden-Württemberg Foundation as part of the project GRIN-SEN in the research program Optical Technologies, and by the Deutscher Akademischer Austauschdienst (DAAD) within the scope of the program PROCOPE. The project was performed in the framework of the European Cooperation in Science and Technology COST Action MP1302 Nanospectroscopy.

**REFERENCES**

1. Haes, A. J., Hall, W. P., Chang, L., Klein, W. L., Van Duyne, R. P., "A localized surface plasmon resonance biosensor: first steps toward an assay for Alzheimer's disease", *Nano Lett.*, Vol. 4, 1029–1034, 2004.
2. Englebienne, P., "Use of colloidal gold surface plasmon resonance peak shift to infer affinity constants from the interactions between protein antigens and antibodies specific for single or multiple epitopes", *Analyst*, Vol. 123, 1599–1603, 1998.
3. Fleischer, M., "Plasmonics and detection", in the Topical Review "Roadmap on biosensing and photonics with advanced nano-optical methods" edited by di Fabrizio, E., *Journal of Optics*, accepted, 2016.
4. Yanik, A. A., Cetin, A. E., Huang, M., Artar, A., Mousavi, S.H., Khanikaev A., Connor, J., Shvets, G., Altug, H., "Seeing protein monolayers with naked eye through plasmonic Fano resonances", *Proc. Natl. Acad. Sci. USA*, Vol. 108, 11784–11789, 2011.
5. Dmitriev, A., Pakizeh, T., Käll, M., Sutherland, D.S., "Gold-silica-gold nanosandwiches: tunable bimodal plasmonic resonators", *Small*, Vol. 3, 294–299, 2007.
6. Horrer, A., Krieg, K., Freudenberger, K., Rau, S., Leidner, L., Gauglitz, G., Kern, D. P., Fleischer, M., "Plasmonic vertical dimer arrays as elements for biosensing", *Anal. Bioanal. Chem.*, Vol. 407, No. 27, 8225-8331, 2015.

# The longitudinal magnetophotonic effect in a magnetoplasmonic crystal for magnetic field sensing

**A.E. Rogachev[1,2], M.A. Kozhaev[1,3], P.M. Vetoshko[1], S. Dagesian[2], A.N. Kalish[1,2], A.K. Zvezdin[1,3], V.I Belotelov[1,2*]**

[1]Russian Quantum Center, Moscow, Russia

[2]Lomonosov Moscow State University, Moscow, Russia

[3]Prokhorov General Physics Institute of the Russian Academy of Sciences, Moscow, Russia

[*]corresponding author: v.belotelov@rqc.ru

**Abstract** – Here we investigate the longitudinal magneto-photonic intensity effect (LMPIE) in a magnetoplasmonic structure of one dimensional gold grating and smooth iron-garnet film in regards to its application for a novel type of magneto-optical sensor. The concept was developed theoretically and the samples were designed and fabricated. The performed measurements of the LMPIE proved the ability of magnetic sensing.

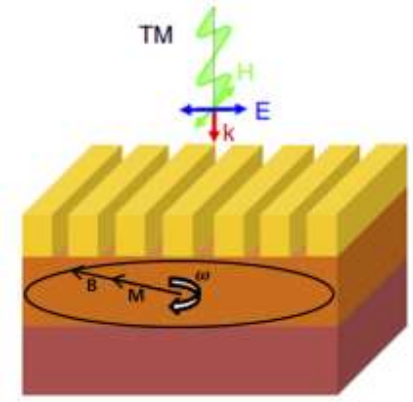



Fig. 1. The magnetoplasmonic crystal used for magnetic sensing. Yellow, brown and purple colors correspond to gold, ferromagnetic dielectric film and dielectric substrate, respectively.

Nowadays creation of high-sensitive magnetic sensors is of great interest for many applications. The magneto-optical methods of sensing provide such advantages as contactless, wide dynamic range and the absence of electrical connections. In addition, magneto-optical sensors have benefit of immediately obtaining measurement data directly above the surface of the magnetic material. It can be used for the effective visualizing of the magnetic field distribution in materials.

Here we propose a novel type of magnetic field sensor based on a magnetoplasmonic crystal that consists of ferromagnetic dielectric film which is covered by gold periodic grating (Fig. 1). It is based on the recently discovered longitudinal magnetophotonic intensity effect (LMPIE) that is a resonant change in transmittance or reflectance induced by magnetic field directed in-plane perpendicularly to the slits [1]. The achieved change of transmittance was 24 percent and can be potentially increased. Moreover, at normal incidence the Faraday effect is absent, the polarization remains unchanged. The distinctive feature of the LMPIE is that it is sensitive to the

in-plane magnetization component even if the structure is illuminated by light at normal incidence. It is of prime importance for magneto-optical magnetic field sensors and visualizers.

In the present work the LMPIE is used for design of the magnetic field sensor. The in-plane rotating magnetic field is applied as strong as to keep the sample saturated and the intensity of the transmitted light is measured. Due to the LMPIE the second harmonic in signal occurs. The presence of a small additional in-plane constant external magnetic field leads to distortion of the signal. The other harmonics appear, in particular the 1-st and the 3-rd, with their amplitudes being proportional to the constant field. Thus by observing the quantitative changing of the harmonics amplitudes and phases we determine the values of two planar components of the constant magnetic field.

In order to prove this concept we designed and fabricated the samples with rather low saturation magnetization of the dielectric. The samples had different parameters of the gold grating: the period differs from 320 nm to 340 nm and the air slit width differs from 70 nm to 140 nm. The rotating magnetic field of 10 Oe was formed by Helmholtz coils. The light is normally incident on the sample. The spectrum of the LMPIE for one of the samples is shown in Fig. 2. The obtained light modulation is 5%.

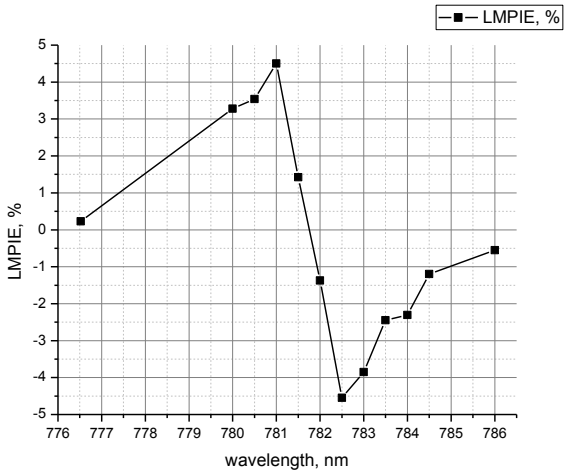



Fig. 2. The measured LMPIE spectrum.

Our next step was adding the constant in-plane magnetic field. The performed experiments proved the concept that observing the odd harmonics of the transmittance one can detect the value and the direction of the magnetic field.

**Acknowledgements** - This work was supported by the Russian Science Foundation (grant N 14-32-00010).

**REFERENCES**

1. V. I. Belotelov, et al., Plasmon-Mediated Magneto-Optical Transparency, Nat. Commun. **4**, 2128 (2013).

# Miniaturized Motor-Sensor Unibody Devices for Tunable Biochemical Release, DNA Removal, and Microfluidic Manipulation

**Donglei (Emma) Fan*[1,2], K. Kim[2], J. H. Guo[1], X. B. Xu[1]**

[1] *Materials Science and Engineering Program, University of Texas at Austin, Austin, TX, USA*
[2] *Department of Mechanical Engineering, University of Texas at Austin, Austin, TX, USA*
*dfan@austin.utexas.edu

In this talk, I will discuss our recent progress on innovative design, assembling and operation of new types of miniaturized rotary motor-sensor unibody devices made from micro/nanoscale building blocks, such as nanowires, nanodisks, nanodots, and microrods. Arrays of micor/nanomotors can be efficiently assembled and rotated with controlled angle, chirality and speed to 18,000 rpm, the same level of that of jet engine. The nanomotors have all dimensions less than 1 μm. They are one of the smallest rotary Nanoelectromechanical System (NEMS) Devices. They can operate for 80 hours over 1.1 million cycles, the longest device lifetime reported to the best of our knowledge. The micro/nanomotors are further equipped with sensing components, such as plasmonic Ag nanoparticles and applied in tunable biochemical release, DNA purification, as well as microfluidic manipulation. These results are relevant to single cell stimulation, cell-cell communication, and system biology.

# Nanoparticle mediated photo-protection and -therapy

**V. V. Tuchin**
Research-Education Institute of Optics and Biophotonics, Saratov National Research State University, Russia
Institute of Precision Mechanics and Control of Russian Academy of Sciences, Russia
Interdisciplinary Laboratory on Biophotonics, Tomsk National Research State University, Russia
tuchinvv@mail.ru

**Abstract**-Nanoparticle mediated laser treatment of diseases is a novel modality in the field of nanomedicine. We will discuss protection of humans from UV light and microorganisms, cancer and inflammatory diseases treatment, and cell optoporation/transfection using plasmonic gold nanoparticles, photocatalytic $TiO_2$ nanoparticles, and plasmonic nanocomposites.

Nanoparticle mediated laser diagnostics and therapy of diseases is a novel modality realizing principles of theranostics formulated and overviewed recently [1-3]. The $TiO_2$-nanoparticles are on use to protect skin from UV light for years due to their unique scattering and absorption properties. Plasmonic gold nanoparticles are efficient for cancer treatment. Both plasmonic gold and photocatalytic $TiO_2$ nanoparticles are prospective for protection of humans from pathogens. Tissue engineering and disease treatment technologies could be improved significantly by the development of optoporation/transfection techniques of tissue and cell membranes with the help of the appropriate nanoparticles and laser irradiation protocols. The goal of this study is to summarize recent results in the field of interaction of laser radiation with nanoparticles embedded into a tissue or cell in order to design technologies for protection of humans from UV light and microorganisms, treatment of cancer and inflammatory diseases, and tissue and cell optoporation for drug and biomaterial delivery.

The distributions of differential and integral absorbing power of gold spherical nanoparticles, temperature increment, and Arrhenius damage integral were used to quantify biological action of laser-heated nanoparticles [4]. The effectiveness of biological response was presented in the two-dimensional space "laser wavelength ($\lambda$) × radius of nanoparticles (R)." Such consideration allows one to select an optimal irradiating protocol at laser treatment.

The efficiency of NIR laser radiation (808 nm) and gold nanorods on methicillin-sensitive *Staphylococcus aureus* (MSSA) and methicillin-resistant (MRSA) microorganisms was studied. Nanorods having the dimensions 10×44 nm with the absorption maximum in the NIR, functionalized with human immunoglobulins IgA and IgG were used [5]. The killing efficiency up to 97 % of the population of microorganisms was demonstrated for both strains at the laser fluence of 180 J/cm$^2$.

Nanocomposites (NCs) (gold nanorod core with mesoporous silica shell doped with hematoporphyrin) were used to improve the efficiency of inactivation of *Staphylococcus aureus* and cancer treatment by combining photothermal and photodynamic therapies (PTT/PDT) [6,7]. A suspension of NCs was directly injected into xenografted solid tumor of rat model *in vivo* [7]. Under 633-nm laser exposure, singlet oxygen was generated, as under 808-nm NIR laser irradiation, heat was produced. The efficiency of the combined therapy was evaluated by optical coherence tomography (OCT), histological analysis, and by measurements of the tumor volume. This treatment resulted in the large-area tumor necrosis and dramatic decrease in the tumor volume. Application of multifunctional Au nanoclusters for targeted imaging and enhanced photodynamic inactivation of

*Staphylococcus aureus* was also demonstrated [8].

The development of antibacterial coatings based on photocatalytic nanomaterials is a promising route towards potential environmentally friendly applications in public buildings and health care facilities. Various types of $TiO_2$ nanofiber-based photocatalytic materials (nitrogen-doped and/or palladium nanoparticle decorated) and their composites with gypsum were demonstrated their excellent antimicrobial properties by killing both MSSA and MRSA strains under the blue LED light (405 nm) [9,10]. In the case of MSSA cells, the palladium nanoparticle-decorated and nitrogen-doped $TiO_2$ composites demonstrated the highest antimicrobial activity.

**Acknowledgements**

The study supported by grant No. 14-15-00186 of the Russian Science Foundation.

**REFERENCES**

1. Tuchin V.V., Drezek R., Nie S., and Zharov V.P. (Guest Eds.), "Nanophotonics for Diagnostics, Protection and Treatment of Cancer and Inflammatory Diseases," *J. Biomed. Opt.*, Vol. 14, No.2, 2009.
2. Huang X., Jain P. K., El-Sayed I. H., El-Sayed M. A., "Plasmonic photothermal therapy (PPTT) using gold nanoparticles," *Lasers Med Sci.* Vol. 23(3), 217–228, 2007.
3. Dykman L. A. and Khlebtsov N. G., "Gold nanoparticles in biomedical applications: recent advances and perspectives," *Chem. Soc. Rev*., Vol. 41, No. 6, 2256–2282, 2012.
4. Yakunin A.N., Avetisyan Y.A., and Tuchin V.V., "Quantification of laser local hyperthermia induced by gold plasmonic nanoparticles," *J. Biomed. Opt*., Vol. 20, No. 5, 051030, 2015.
5. Tuchina E.S., Petrov P.O., Kozina K.V., Ratto F., Centi S., Pini R., and Tuchin V.V., "Using gold nanorods labelled with antibodies under the photothermal action of NIR laser radiation on *Staphylococcus aureus*," *Quantum Electronics* Vol. 44, No. 7, 683 – 688, 2014.
6. Khlebtsov B. N., Tuchina E. S., Khanadeev V. A., E. V. Panfilova, P. O. Petrov, V. V. Tuchin, N. G. Khlebtsov, "Enhanced photoinactivation of Staphylococcus aureus with nanocomposites containing plasmonic particles and hematoporphyrin," *J. Biophotonics*, Vol. 6, No. 4, 338–351, 2013.
7. Terentyuk G., Panfilova E., Khanadeev V., Chumakov D., Genina E., Bashkatov A., Tuchin V., Bucharskaya A., Maslyakova G., Khlebtsov N., and Khlebtsov B., "Gold nanorods with hematoporphyrin-loaded silica shell for dual-modality photodynamic and photothermal treatment of tumors in vivo," *Nano Research., Vol.*7, No.3, 325–337, 2014.
8. Khlebtsov B., Tuchina E., Tuchin V., and Khlebtsov N., "Multifunctional Au nanoclusters for targeted bioimaging and enhanced photodynamic inactivation of *Staphylococcus aureus*," *RSC Advances* Vol. 5, 61639–61649, 2015.
9. Sarkar A., Shchukarev A., Leino A.-R., Kordas K., Mikkola J.-P., Petrov P. O., Tuchina E. S., Popov A. P., Darvin M. E., Meinke M. C., Lademann J., and Tuchin V. V., Photocatalytic activity of $TiO_2$ nanoparticles: effect of thermal annealing under various gaseous atmospheres, *Nanotechnology*, Vol. 23, 475711-1-8, 2012.
10. Mohl M., Dombovari A., Rautio A.-R., Tuchina E. S., Petrov P. O., Bibikova O. A., Skovorodkin I., Popov A. P., Sarkar A., Mikkola J.-P., Valtanen A., Huuhtanen M., Vainio S., Keiski R. L., Prilepskyi A., Kukovecz A., Konya Z., Tuchin V. V., and Kordas K., "Gypsum-titaniafiber nanocomposites for indoor antimicrobial coatings," *J. Mater. Chem. B.*, Vol. 2, 1307-1316, 2014.

# Plasmon-enhanced molecular sensing and imaging on nanoporous gold disks

**Fusheng Zhao[1], Greggy Santos[1], Arnob Masud[1], and Wei-Chuan Shih[1*]**

[1]Department of Electrical and Computer Engineering, University of Houston, Houston, TX 77204

[*]corresponding author: wshih@uh.edu

**Abstract**- We have demonstrated that disk-shaped nanoporous gold (NPG) nanoparticles are a unique class of plasmonic nanomaterials with tunable LSPR, 3-dimensional near-field hot-spot distribution, large surface area, excellent SERS and SEF enhancement factors, and high sensitivity to local index changes. By taking advantage of the abundance of hot-spots in NPG disks, we have developed several applications in molecular sensing and imaging.

To fabricate NPG disks, we take advantage of both top-down lithographic patterning and bottom-up atomic dealloying, which together demonstrate great synergy in precisely tuning the plasmonic properties of nanoporous materials. As shown in Fig. 1, a film of gold and silver alloy approximately 120 nm thick was first sputter deposited onto a substrate (e.g., silicon wafer or glass slide) using an $Ag_{82.5}Au_{17.5}$ (atomic percentage) alloy target. A monolayer of 460-1100 nm size polystyrene beads (PS) was then formed on top of the alloy film. In our experience, over 90% of the alloy surface covered with close-packed PS beads can be achieved reproducibly (Fig. 1a). Next, a timed oxygen plasma treatment was employed to shrink the PS beads, thus separating them from neighboring beads. The sample was then sputter-etched in Argon plasma to transfer the bead pattern into the alloy film (Fig. 1b). Once the pattern transfer was completed, the PS beads were removed (Fig. 1c). The alloy disks were dealloyed in concentrated nitric acid, followed by rinsing in deionized (DI) water (Fig. 1d) to produce the *random array* format NPG disks. There was substantial size shrinkage during the PS bead etching step as well as the dealloying process. Scanning electron microscopy (SEM) images (Fig. 1e to h) show the corresponding nanostructures through the fabrication steps. To produce suspended colloidal NPG disks, high-density NPG disk arrays on a 3-inch Si wafer were further sonicated in DI water [1].

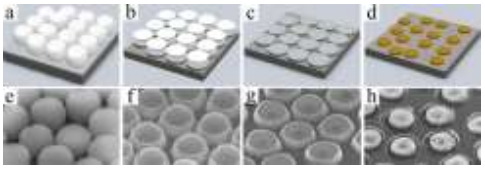



**Figure 1.** Fabrication process used to prepare NPG disks on a silicon (or glass) substrate.

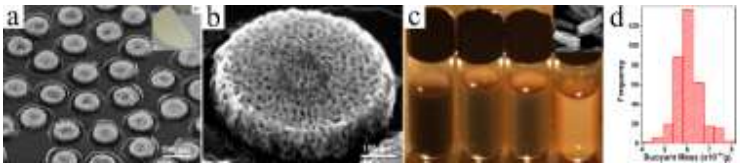



**Figure 2.** SEM images of NPG disks, stored in DI water, and single disk buoyant mass measurements.

Figure 2 displays three different views of NPG disks to further show the capability of preparing the both arrayed and colloidal NPG disks. Figure 2a and b show of high-density NPG disk random arrays on a 3-inch Si wafer and SEM image of a single NPG disk, respectively. With the aid of sonication, NPG disks were released from the substrates into DI water to form colloidal NPG disk suspensions (Figure 2c). The inset shows colloidal NPG disks dried on a Si wafer. To our surprise, *surfactant-free* NPG disks were easily transferred to DI water without aggregation. Therefore, by flowing individual colloidal NPG disks in microfluidic channels, single disk (400 nm diameter) buoyant mass was determined to be $6.04\times10^{-14} \pm 7.6\times10^{-15}$ g as shown in Figure 2d.

The plasmonic properties of NPG disks can be characterized by extinction spectra in Figure 3a, where three peaks have been assigned as NPG LSPR ("▲"), out-of-plane resonance ("■"), and in-plane resonance ("●"). The NPG LSPR mode originated from the nanoporous structures, whereas the in-plane and out-of-plane modes were

associated with the external disk shape. Size-dependent plasmonic shifts in these peaks have been observed when the disk diameter was increased from 300 to 700 nm. Among these peaks, the in-plane resonance clearly dominates and *only* exists in NPG disks but *not* in semi-infinite NPG thin films.

To further elucidate the observed extraordinary size- and environment-dependent plasmonic behavior of NPG disks, we performed finite difference time domain (FDTD) simulations and compared with Au disks having identical external shape parameters: 500 nm in diameter and 75 nm in thicknesses. The NPG disk model shown in Figure 3b was constructed directly from the SEM image shown earlier. Figure 3c displays the calculated electric-field (E-field) distribution for 1300 nm incident wavelength, matching the in-plane resonance previously discussed. "Hot-spots" in the pores around the edges are observed with a maximum E-field enhancement factor ~100. In contrast, uniformly distributed hot-spots within the entire disk are observed with a maximum E-field enhancement factor about 32 for 785 nm incident wavelength, matching the NPG LSPR peak previously discussed. These features are distinct from non-porous nanoparticles.

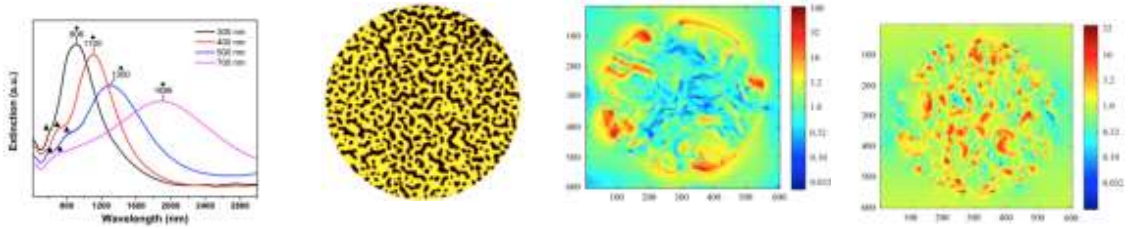


**Figure 3.** Extinction spectra and electrical field distribution.

In the presentation, we will further show our recent results on using NPG disks for molecular imaging and sensing based on three different reporting mechanisms: surface-enhanced Raman scattering (SERS) [2-4], surface-enhanced fluorescence (SEF) [5], and localized surface-plasmon resonance (LSPR) [6].

**References:**


1. Zhao, F., et al., *Monolithic NPG nanoparticles with large surface area, tunable plasmonics, and high-density internal hot-spots.* Nanoscale, 2014. **6**: p. 8199-8207.
2. Li, M., et al., *Reagent- and separation-free measurements of urine creatinine concentration using stamping surface enhanced Raman scattering (S-SERS).* Biomedical Optics Express, 2015. **6**(3): p. 849-858.
3. Li, M., et al., *Stamping surface-enhanced Raman spectroscopy for label-free, multiplexed, molecular sensing and imaging.* Journal of Biomedical Optics, 2014. **19**(5): p. 050501.
4. Qi, J., et al., *Surface-enhanced Raman spectroscopy with monolithic nanoporous gold disk substrates.* Nanoscale, 2013. **5**: p. 4105-4109.
5. Santos, G.M., et al., *Label-free, zeptomole cancer biomarker detection by surface-enhanced fluorescence on nanoporous gold disk plasmonic nanoparticles.* Journal of Biophotonics, 2015. **9999**(9999): In press.
6. Zeng, J., et al., *Morphological control and plasmonic tuning of nanoporous gold disks by surface modifications.* Journal of Materials Chemistry C, 2015. **3**(2): p. 247-252.

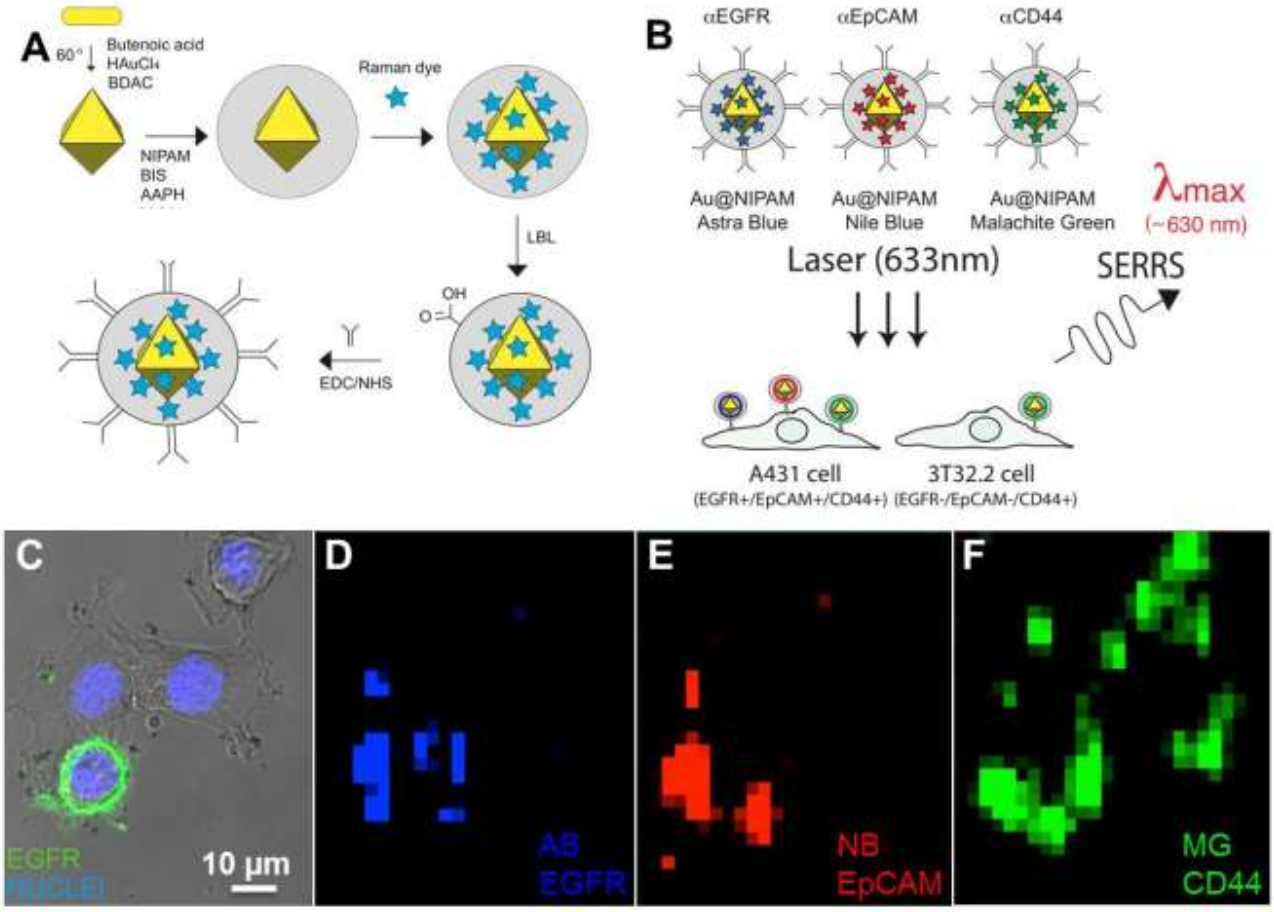
# Multiplex Detection and Imaging of Tumor Cells using Gold-based SERS platforms.

**Gustavo Bodelón,[1] Verónica Montes-García,[1] Cristina Fernández-López,[1] Jorge Pérez-Juste,[1] Luis M. Liz-Marzán,[1,2,3] Isabel Pastoriza-Santos[1]**

[1] Departamento de Química Física, Universidade de Vigo, 36310 Vigo, Spain.
[2]BioNanoPlasmonics Laboratory, CIC biomaGUNE, Paseo de Miramón 182, 20009 San Sebastián, Spain
[3]Ikerbasque, Basque Foundation for Science, 48013 Bilbao, Spain
[*]corresponding author: pastoriza@uvigo.es

**Abstract**- Surface-enhanced resonance Raman scattering (SERRS)-encoded tags have gained much interest toward clinical diagnostics and drug discovery, but the portfolio of available systems is still limited. We report the fabrication of novel SERRS-encoded particles based on gold octahedra coated with poly(N-isopropylacrylamide) microgels for the identification and imaging of proteins expressed in cells. Thus, three tumor-associated surface biomarkers were simultaneous detected and imaged. The plasmonic microgels are able to discriminate tumor A431 and nontumor 3T3 2.2 cells while cocultured in vitro.

The development of high sensitive platforms with plasmonic responses will allow the simultaneous detection of multiple protein receptors which has a great potential for imaging and diagnostics.[1] In this context, we have designed a new type of SERRS tags fabricated followed the strategy displayed in Figure 1A. It is based on poly(N-isopropylacrylamide) (pNIPAM) encapsulated gold nanoparticles. The SERRS tags were fabricated by direct pNIPAM polymerization, via a grafting-through route, on butenoic acid-functionalized Au octahedra and the subsequent encoding with Raman reporters (by addition of Raman active dyes (astra blue (AB), Nile blue (NB), or malachite green isothiocyanate (MGI)).[2] Finally, the microgel surface was coated with a polyelectrolyte by layer-by-layer to seal the porous-encoded particles while facilitating covalent conjugation with three different antibodies. The selected antibodies were specific against three different tumor biomarkers: epithelial cell adhesion molecule (EpCAM), epidermal growth factor receptor (EGFR), and homing cell adhesion molecule (CD44) (Figure 1B). Then we demonstrated the multiplexing capability of our SERRS-encoded microgels for the simultaneous detection of these three tumor-associated biomarkers (EGFR, EpCAM, and CD44) in cocultures of tumor A431 and nonturmor 3T3 2.2 cells with a single excitation laser line (633 nm) Figure 1B and 1C-F. The SERRS labels presented in this work may be applied to high throughput, multiplex assays involving encoded particles for in vitro screening and diagnostics such as flow cytometry, enzyme-linked immunosorbent assay (ELISA), or automated microscopy.




**Figures 1**: A) Schematic representation of the preparation of Au@pNIPAM SERRS-encoded tags B) Schematic representation of the SERRS tags indicating their Raman codification and targeting entities and of the immunophenotype detection of A431 and 3T3 2.2 cells by SERRS C) Bright field and confocal fluorescence microscopy image showing A431 (EGFR positive) and 3t3 2.2 (EGFR negative) cells. D–F) SERRS mappings recorded in the same area using the B) 748 cm−1 peak of AB, C) 592 cm−1 peak of NB**.**

**Acknowledgements**, This work was supported by the European Research Council (PLASMAQUO, 267867), Spanish MINECO (MAT2013-45168-R and MAT2013-46101-R), and Xunta de Galicia/FEDER (Grant No. GPC2013-006; INBIOMED-FEDER "Unha maneira de facer Europa"). V.M.-G. acknowledges FPU scholarship from the Spanish MINECO.

## REFERENCES

1. Wang, Y. Q., Yan, B. and Chen, L. X. *Chem. Rev.*, Vol. 113, No. 3, 1391–1428, 2013.
2. Bodelón G., Montes-García V., Fernández-López C., Pastoriza-Santos I., Pérez-Juste J., Liz-Marzán L.M. *Small*, Vol. 11, No. 33, 4149–4157, 2015.

# 3 Dimensionally Stacked Surface Enhanced Raman Scattering (SERS) Substrates with pico-Molar Sensitivity: Experimental and Simulation Studies

Daejong Yang, Hyunjun Cho, Sukmo Koo, Sagar Vaidyanathan, Kelly Woo, and Hyuck Choo

Electrical Engineering & Medical Engineering, Division of Engineering and Applied Science, California Institute of Technology, Pasadena, CA 91125, USA

We have demonstrated a surface-enhanced Raman scattering (SERS) substrate capable of detecting 1 pM of benzenethiol (BT) and developed better understanding of its enhancing mechanism by varying the fabrication process and also performing detailed simulation studies. The extreme enhancement originates from the three dimensionally fabricated and optimized substrate, which is made of Au-nanoparticle (NP) clusters stacked using vertically standing ZnO nanowires (ZnO-NW) as skeletal frames that completely dissolve away during the synthesis procedure and leave vertical light passages among clusters, allowing light to reach deeper into the stacks for higher sensitivity.

Our straightforward two-step-fabrication process involves (1) the hydrothermal synthesis to create ZnO-NWs perpendicularly standing on the substrate and (2) the liquid phase deposition (LPD) to create Au NPs on ZnO-NWs: (1) to grow ZnO-NWs, we coat a Si substrate in a ZnO-seed solution consisting of zinc acetate dihydrate in ethanol and anneal at 350 °C, followed by immersion in a ZnO-NW precursor solution made of zinc nitrate hydrate, hexamethylenetetramine, and polyethylenimine in DI water at 95 °C; and (2) to grow Au-NP clusters using the LPD process, we submerged the ZnO-NW substrate in a Au-NP precursor solution consisting of sodium tetrachloroaurate(III) dihydrate, sodium citrate dihydrate and sodium hydroxide in DI water at 90 °C. The LPD process was repeated 1 -8 times to systematically vary the thickness of the Au-NP layers.

After the ZnO-NW synthesis, we used the scanning electron microscopy (SEM) to examine the substrate and observed 1 μm-tall perpendicularly synthesized ZnO NWs. We also observed after the Au-NP deposition process that 20nm-diameter Au NPs were uniformly coated on the surface of ZnO NWs, and increasing the iterations of the LPD process resulted in thicker Au-NP-cluster stacks.

To characterize SERS performance, we incubated the substrates with 1-8 iterations of the Au-NP synthesis in 1mM BT solution. The SERS intensity of BT consistently increased with the increasing number of LPD iterations up to 5 and then saturated due to the increase in the effective sensing area and plasmonic interactions among NPs. After 5 iterations, the most laser power was absorbed in the upper layers of the Au-NPs, and the additional layers had almost no effect. If Au-NPs were cumulated on Si substrates without ZnO-NWs, the SERS intensity never saturated even after 8 iterations and was about ½ the intensity from the 3D stacked substrates. Numerical simulation also showed good agreement with our experimental results and provided helpful insight into the SERS mechanism, including the roll of the ZnO-NWs. The substrate also generated clear BT Raman peaks down at 1 pM, and its enhancement factor was ~$10^8$. Because of the excellent SERS performance and simple two-step wafer-scale fabrication using wet chemistry, our approach will prove to be very useful in various sensing applications.

**Biocompatible, Liposome-Based Surface Enhanced Raman Spectroscopy (SERS) Substrates**

Ian Bruzas, William Lum, Sarah Unser, and **Laura Sagle***

Department of Chemistry, College of Arts and Sciences, University of Cincinnati, 301 West Clifton Court, Cincinnati OH 45221-0172
Corresponding author Tel: +1 513 556 1034; Fax: +1 513 556 9239. E-mail: saglela@uc.edu

Surface enhanced Raman spectroscopy (SERS) is a powerful technique capable of probing single molecules with unprecedented detail for processes ranging from biological sensing and chemical transformation to optical waveguides and electronics.[1-2] Unfortunately, most currently used SERS substrates contain <10 nm gaps between gold or silver particles, in which probe molecules are inserted.[3-4] Although this strategy often leads to single molecule detection of the probe molecule, it also results in denaturation and inactivation of these molecules, which severely limits the use of SERS for biophysical measurements.[5-6] In the Sagle group, we are working with novel liposome-based SERS substrates, in which probe molecules are encapsulated in the liposome component, rather than tethered to or sandwiched between metallic surfaces. Initial characterization of these substrates shows extremely high field enhancement of $10^8$-$10^9$, and good measurement reproducibility. Measurements of substrate fidelity and temperature changes associated with laser illumination are also carried out and show the substrates are robust. Lastly, the biocompatibility of these substrates is evaluated through incorporation of horse heart cytochrome *c*, and comparison of the structure to that of the same protein in solution and absorbed onto aggregated silver colloids. These novel SERS substrates should find tremendous use in *in vitro* interrogations of various biological phenomena including protein-nanoparticle interactions, protein structure and catalysis, and protein-small molecule interactions.

**Acknowledgements**

The authors gratefully acknowledge University Start-Up Funds for supporting this work.

**REFERENCES**

1. Haynes, C. L.; McFarland, A. D.; Van Duyne, R. P., "Surface-enhanced Raman spectroscopy" *Anal. Chem.,* Vol. 77, 338a-346a, 2005.
2. Kneipp, J.; Kneipp, H.; Kneipp, K., "SERS - a single-molecule and nanoscale tool for bioanalytics" *Chem. Soc. Rev.,* Vol. 37, 1052-1060, 2008.
3. Futamata, M.; Maruyama, Y.; Ishikawa, M., "Critical importance of the junction in touching Ag particles for single molecule sensitivity in SERS" *J. Mol. Struct.,* Vol. 735, 75-84, 2005.

4. Michaels, A. M.; Jiang, J.; Brus, L., “Ag nanocrystal junctions as the site for surface-enhanced Raman scattering of single Rhodamine 6G molecules” *J. Phys. Chem. B,* Vol. 104, 11965-11971, 2000.
5. Otto, A. “What is observed in single molecule SERS, and why?” *J. Raman. Spectrosc.,* Vol. 33, 593-598, 2002.
6. Banerjee, V.; Das, K. P. “Structure and Functional Properties of a Multimeric Protein alpha A-Crystallin Adsorbed on Silver Nanoparticle Surface” *Langmuir,* Vol. 30, 4775-4783, 2014.

# Manipulating Light using Integrated Nanophotonic Devices

# Signal storage in tripod structure metamaterial.

**S. Zielińska - Raczyńska**[1], **D. Ziemkiewicz**[1]

[1]Institute of Mathematics and Physics, UTP University of Science and Technology, Al. Kaliskiego 7, 85-789 Bydgoszcz, Poland
sziel@utp.edu.pl

**Abstract**— The quantum optical phenomenon of electromagnetically induced transparency can be modeled in suitably structured metamaterials, allowing for signal storage and manipulation. Classical description of the light stopping phenomenon facilitates the application of numerical methods typically used in simulation of wave propagation in metamaterials, giving new insight into the process.

## 1. INTRODUCTION

The Electromagnetically Induced Transparency (EIT) is an effective tool in quantum optics, providing means of realization of various experiments such as light stopping. The possibility of signal storage, manipulation and release in one or many parts might lead to many applications in quantum information processing. Recently, the classical analogue of EIT in metamaterials received much attention, and the storage of a signal in metamaterial has been demonstrated [1]. Such media provide benefits of room temperature operation and scalability to various frequency regimes. Therefore, it is of interest to study the light stopping process and the means of signal control and manipulation in classical EIT metamaterial.

## 2. SIMULATION OF LIGHT STOPPING

We use the Finite Difference Time Domain (FDTD) algorithm which is a common tool in studies of electromagnetic field propagation. The medium description, based on the coupled resonator model [2], allows for the time domain simulation of signal stopping and manipulation, giving insight into the dynamics of these phenomena. We model a tripod medium (Fig. 1a) with an electrical, RLC circuit model (Fig. 1b). The manipulation of the coupling capacitances allows for signal storage and release, as shown on the Fig. 1c.

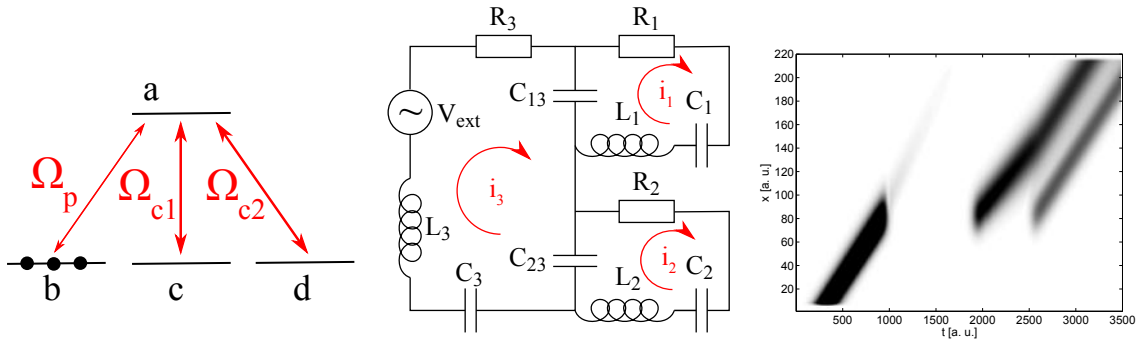



Figure 1: a) Schematics of a three-level tripod configuration; b) Electric circuit model of EIT metamaterial; c) Simulation results of signal stopping, showing time and space dependence of field strength.

## REFERENCES

1. T. Nakanishi, T. Otani, Y. Tamayama, M. Kitano, "Storage of electromagnetic waves in a metamaterial that mimics electromagnetically induced transparency," Phys Rev. B **87**, 161110(R) (2013)
2. S. Zielińska-Raczyńska, D. Ziemkiewicz, "Controlled processing of signal stored in metamaterial with tripod structure," arXiv: 1604.00757 [physics.optics] (2016)

# Silicon-graphene hybrid devices for signal modulations

**Ciyuan Qiu[1], Yong Zhang[1], Ruili Liu[1], Yikai Su[1]**

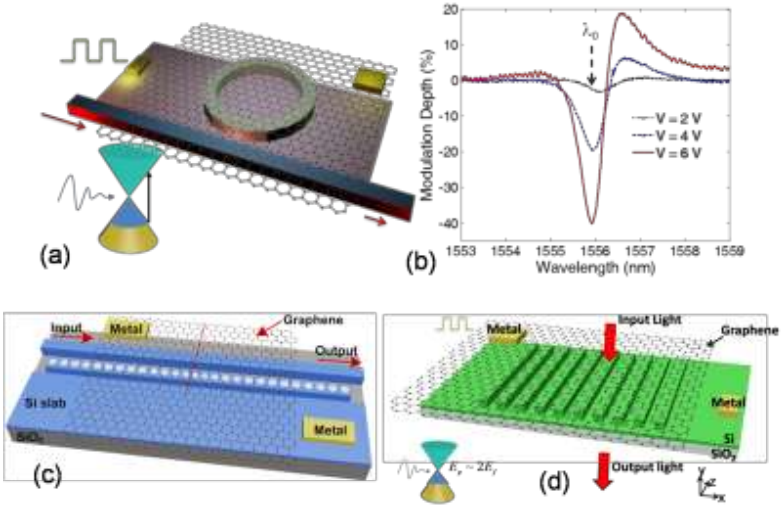
[1] state Key Lab of Advanced Optical Communication Systems and Networks, Department of Electronic Engineering, Shanghai Jiao Tong University, China

[*]corresponding author: qiuciyuan@sjtu.edu.cn

**Abstract**- Here we present our works on silicon-graphene hybrid devices for signal modulations. By tuning the fermi level of the graphene, we have demonstrated a silicon-graphene micro-ring electro-optic (EO) modulator with modulation depth about 40%. We also have proposed a nanobeam EO modulator and a spatial light modulator (SLM) based on silicon-graphene hybrid structure. Their modulation speeds are calculated to be higher than 45 GHz with the modulation depths larger than 10 dB.

Graphene is considered to be a promising material to build active optoelectronic device. Recently, various graphene based optoelectronic devices have been proposed and demonstrated such as electro-optic (EO) modulator[1] and photodetector[2]. They have the merits including broadband, high speed and low power consumption.

We have proposed and built a micro-ring modulator based on silicon-graphene hybrid structure. The schematic of the device is shown in Figure 1(a). By changing the the Fermi level of the graphene, the permittivity of the graphene can be largely changed. This introduces strong effect on the effective index ($n_{eff}$) of the silicon-graphene hybrid waveguide. Thus both the real part and imaginary part of $n_{eff}$ can be tuned. Since the real part determines the resonant wavelength and the imaginary part determines the loss of the resonant cavity, lightwave can be effectively modulated. The transmission spectra under different gate voltage are shown in Figure 2(b). A large modulation depth about 40% is observed at $\lambda_0$ = 1555.97 nm. Thanks to the high electron mobility of the graphene, the device is expected to work at tens of GHz based on RC circuit model.




**Figures 1:** (a) Schematic diagram of microring modulator based on silicon-graphene hybrid structure. (b) Gate-voltage-induced differential transmission spectra at different voltages. (c) Schematic diagram of nanobeam modulator based on silicon-graphene hybrid structure. (d) Schematic diagram of spatial light modulator based on silicon-graphene hybrid structure.

We also have proposed a nanobeam EO modulator and a spatial light modulator (SLM) based on silicon-graphene hybrid structure. Their device schematic diagrams are shown in Figure 1(c) and 1(d) respectively. The nanobeam modulator has ultra-wide FSR about 125.6 nm and has only one resonant wavelength in the communication band which could eliminate the channel crosstalk in the Dense Wavelength Division Multiplexing (DWDM) system. The spatial light modulator could couple the normal incident light and change its amplitude by tuning the Fermi level of the graphene. Their modulation speeds are calculated to be higher than 45 GHz with the modulation depths larger than 10 dB.

In conclusion, we have demonstrated micro-ring EO modulator and have proposed a nanobeam EO modulator as well as a SLM based on silicon-graphene hybrid structure. Their speeds are expected to be tens of GHZ and would have application in future telecommunications.

**REFERENCES**


1. M. Liu, X. B. Yin, E. Ulin-Avila, B. S. Geng, T. Zentgraf, L. Ju, F. Wang, and X. Zhang, "A graphene-based broadband optical modulator," *Nature*, Vol. 474,64-67, 2011.
2. X Gan, RJ Shiue, Y Gao, I Meric, TF Heinz, K. Shepard, J. Hone, S. Assefa and D. Englund. "Chip-integrated ultrafast graphene photodetector with high responsivity ," *Nature Photonics*, Vol. 7, 883–887 (2013).
3. C. Qiu, W. Gao, R. Vajtai, P. M. Ajayan, J. Kono, and Q. Xu, "Efficient Modulation of 1.55 μm Radiation with Gated Graphene on a Silicon Microring Resonator," Nano Letters, Vol. 14, No. 12, 6811–6815, 2014.
4. T. Pan, C. Qiu, J. Wu, X. Jiang, B. Liu, Y. Yang, H. Zhou, R. Soref, and Y. Su, "Analysis of an electro-optic modulator based on a graphene-silicon hybrid 1D photonic crystal nanobeam cavity," Optics Express, Vol. 23, No. 18, 23357-23364, 2015.
5. C. Qiu, T. Pan, W. Gao, R. Liu, Y. Su, and R. Soref, "Proposed High Speed Micron-Scale Spatial Light Valve Based on a Silicon-Graphene Hybrid Structure," *Optics Letters*, Vol. 40, No. 19, 4480–4483, 2015.

# Nonlinear applications in the mid-infrared regime based on germanium on silicon platform

**L. Shen[12*], N. Healy[1], C. J. Mitchell[1], J. S. Penades[1], M. Nedeljkovic[1], G. Z. Mashanovich[1] and A. C. Peacock[1]**

[1]Optoelectronics Research Centre, University of Southampton, Southampton SO17 1BJ, United Kingdom

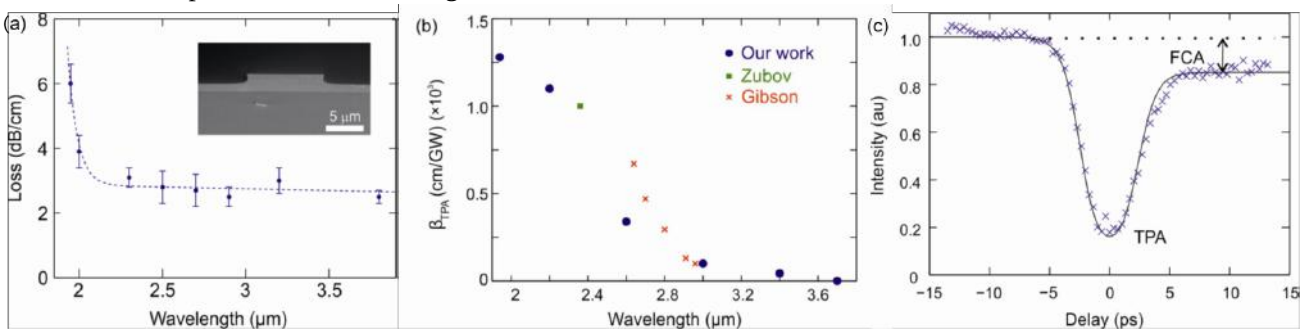
[2]Wuhan National Laboratory for Optoelectronics, School of Optical and Electronic Information, Huazhong University of Science and Technology, Wuhan 430074, Hubei, China

[*]corresponding author: lishen@hust.edu.cn

**Abstract**-This abstract reviews our progress in characterizing nonlinear properties of low loss germanium-on-silicon waveguides in the mid-infrared wavelength. All-optical modulation is demonstrated in these waveguides and indicates the suitability of this platform for nonlinear applications in this long wavelength regime.

Group IV mid-infrared photonics is currently attracting considerable attention for applications in gas sensing and spectroscopy. Recently, low loss germanium-on-silicon (Ge-on-Si) waveguides have emerged and have been demonstrated to have advantages in the mid-infrared wavelength regime, e.g. broad transmission window and CMOS compatible [1]. Here we review our progress in characterizing the nonlinear transmission properties of the Ge-on-Si rib waveguides and demonstrate the first ultrafast all-optical modulation in these waveguides.

Our Ge-on-Si waveguides were fabricated using lithographic patterning and reactive-ion etching methods and have an etch depth of 1.2 μm and a core width of 2.25 μm [2]. The rib structure is shown in the inset of Fig. 1(a). A summary of the loss measurements taken by an effective cut-back method over the wavelength range 1.9-3.8 μm is provided in Fig. 1(a). Fig. 1(b) plots the results of the measured two-photon absorption (TPA) parameter for selected pump wavelengths and the results of bulk germanium by Zubov et al. [4] and Gibson et al. [5]. Fig. 1(c) plots the modulation of the weak probe as a function of delay using a simple pump-probe experiment based on cross-absorption modulation (XAM) process [3]. In conclusion, we have characterized the nonlinear transmission properties of low loss Ge-on-Si waveguides in the 2−3.8mm regime and demonstrated their use for all-optical modulation using XAM schemes.




**REFERENCES**

1. Y. Chang et al., Opt. Lett., Vol. 37, No. 14, 2883-2885, 2012.
2. L. Shen et al., Opt. Lett., Vol. 40, No. 2, 268-271, 2015.
3. L. Shen et al., Opt. Lett., Vol. 40, No. 10, 2213-2216, 2015.
4. B. V. Zubov et al., JETP Letters, Vol. 9, No. 4, 130-132, 1969.
5. A. F. Gibson et al., J. Phys. C, Vol. 9, No. 17, 3259-3275, 1976.

# Approach total absorption in critically coupled photonic crystal structures with monolayer 2D materials

**Weidong Zhou[1]*, Yonghao Liu[1], Xiaochen Ge[1], Xiuling Li[2], Shanhui Fan[3]**
[1]University of Texas at Arlington, TX 76019, USA
[2] University of Illinois at Urbana-Champaign, Urbana, Illinois, 61801, USA
[3]Stanford University, Stanford, California, 94305, USA
*corresponding author: wzhou@uta.edu

**Abstract**-We review recent progresses in spectrally selective absorption enhancement in ultra-thin semiconductor nanomembranes and monolayer 2D materials integrated with defect-free dielectric photonic crystal cavities. Based on local field enhancement and critical coupling concept, total absorption from ultra- and monolayer dispersion materials can be obtained. Experimental results will also be discussed based on transfer printed single crystalline silicon and silicon nitride photonic crystal Fano resonance filters on glass and quartz substrates.

Over the past decade, the unique electronic and optical properties of graphene have generated strong interests in developing optoelectronic and electronic devices based on graphene and other layered two–dimensional material. [1] However the nature of ultra-thin monolayer structure limits their optical properties on light absorption and emission. Increasing the light-matter interactions in graphene is highly desirable for high-performance graphene-based optical devices. *Total* absorption is indeed feasible by coupling unpatterned monolayer graphene or other 2D materials with patterned defect-free photonic crystal slab (PCS) via critical coupling with guided resonance.[2] . Measured peak absorptions of 35% and 85% were obtained from cavity coupled monolayer graphene for the structures without and with back reflectors, respectively. [3] These measured values agree very well with the theoretical values predicted with the coupled mode theory based critical coupling design. We will also discuss recent progresses in graphene and other 2D materials integrated with different types of photonic crystal cavities. Such strong light-matter interactions can lead to extremely compact and high performance photonic devices based on large area monolayer graphene and other 2D materials.

Work is supported by US AFOSR (FA9550-16-1-0010).

**REFERENCES**

1. Xia, F., Wang, H., Xiao, D., Dubey, M., and Ramasubramaniam, A., 'Two-Dimensional Material Nanophotonics', *Nat Photon*, 2014, 8, (12), pp. 899-907.
2. Piper, J.R. and Fan, S., 'Total Absorption in a Graphene Monolayer in the Optical Regime by Critical Coupling with a Photonic Crystal Guided Resonance', *ACS Photonics*, 2014, 1, (4), pp. 347-353.
3. Liu, Y., Chadha, A., Zhao, D., Piper, J.R., Jia, Y., Shuai, Y., Menon, L., Yang, H., Ma, Z., Fan, S., Xia, F., and Zhou, W., 'Approaching Total Absorption at near Infrared in a Large Area Monolayer Graphene by Critical Coupling', *Applied Physics Letters*, 2014, 105, (18), p. 181105.

# Recent advances in light manipulation using plasmonic and dielectric metasurfaces

**(Invited Paper)**

**Jian Wang***

Wuhan National Laboratory for Optoelectronics, School of Optical and Electronic Information, Huazhong University of Science and Technology, Wuhan 430074, Hubei, China

*Corresponding author: jwang@hust.edu.cn

**Abstract**-Metasurfaces, a new type of optical interfaces with patterned nanostructures, can provide great flexibility in light manipulation. Plasmonic and dielectric metasurfaces can facilitate flexible manipulation of structured light. We review our recent research progress in light manipulation using plasmonic and dielectric metasurfaces: 1) metasurfaces-based broadband generation of orbital angular momentum (OAM) carrying vector beams; 2) on-chip N-fold OAM multicasting using V-shaped antenna array metasurfaces; 3) chip-scale OAM beams generation and detection using nanophotonic dielectric metasurface array; 4) design and fabrication of metasurfaces on conventional optical fiber facet for linearly polarized mode ($LP_{11}$) generation at visible light wavelength.

Metasurfaces, i.e. a single layer of resonant elements, can introduce abrupt phase changes along the propagation of light to facilitate flexible light manipulation (phase, amplitude, polarization) over sub-wavelength propagation distances. The metasurfaces approach provides new opportunities to control the wavefront of light and could open up new types of interesting applications in photonics. Very recently, we have witnessed the rapid development of plasmonic and dielectric metasurfaces, which can enable flexible manipulation of structured light when meeting the structured metasurfaces [1-4]. In this paper, we review our recent research progress in light manipulation using plasmonic and dielectric metasurfaces [5-10].

**Broadband Generation of Orbital Angular Momentum Carrying Vector Beams [5-7]:** We propose a simple approach to broadband generation of orbital angular momentum (OAM) carrying vector beams based on compact metasurfaces. It consists of two concentric rings in a gold film, where each ring is composed of sub-wavelength rectangular apertures with gradually varied orientation. The sub-wavelength rectangular aperture serves as a localized spatial polarizer. We show the generation of different OAM-carrying vector beams with OAM charge number and polarization order varying from −3 to +3 using a 11.2 × 11.2 μm device. The extinction ratio can exceed 20 dB, and the operation bandwidth (1500 nm) can cover from 1000 to 2500 nm (from near-infrared to mid-infrared).

**On-Chip N-Fold Orbital Angular Momentum Multicasting Using V-Shaped Antenna Array [8]:** We design a V-shaped antenna array to realize on-chip multicasting from a single Gaussian beam to four OAM beams. A pattern search assisted iterative (PSI) algorithm is used to design an optimized continuous phase pattern which is further discretized to generate collinearly superimposed multiple OAM beams. Replacing the designed discrete phase pattern with corresponding V-shaped antennas, on-chip N-fold OAM multicasting is achieved. The designed on-chip 4-fold OAM multicasting exploiting V-shaped antenna array shows favorable

operation performance with low crosstalk less than -15 dB.

**Chip-Scale Orbital Angular Momentum Beams Generation and Detection Using Nanophotonic Dielectric Metasurface Array [9]:** We design and experimentally investigate the generation of OAM beams with topological number from $l$ = -4 to 4 at the wavelength of 632.8 nm utilizing the nanophotonic dielectric metasurface array. We also detect the generated OAM beams using the dielectric metasurface array corresponding to their inverted topological number.

**Metasurface on Conventional Optical Fiber Facet for Linearly Polarized Mode ($LP_{11}$) Generation [10]:** We design and fabricate metasurface on the facet of conventional G.652 single mode fiber (SMF). We also experimentally investigate the linearly polarized mode ($LP_{11}$) generation in SMF using the fabricated metasurface at the wavelength of 632.8 nm.

**Acknowledgements**: This work was supported by the National Natural Science Foundation of China (NSFC) under grants 11574001, 11274131 and 61222502, the National Basic Research Program of China (973 Program) under grant 2014CB340004, the Program for New Century Excellent Talents in University (NCET-11-0182), the Wuhan Science and Technology Plan Project under grant 2014070404010201, and the seed project of Wuhan National Laboratory for Optoelectronics (WNLO).

## REFERENCES

1. Jahani, S. and Jacob, Z. "All-dielectric metamaterials," *Nature Nanotech.*, Vol. 11, No. 1, 23–36, 2016.
2. Genevet, P. and Capasso, F. "Holographic optical metasurfaces: a review of current progress," *Rep. Prog. Phys.*, Vol. 78, No. 10, 024401, 2015.
3. Yu, N. F. and Capasso, F. "Flat optics with designer metasurfaces," *Nature Mater.*, Vol. 13, No. 2, 139–150, 2014.
4. Yu, N. F., Genevet, P., Kats, M. A., Aieta, F., Tetienne, J.-P., Capasso, F. and Gaburro, Z. "Light propagation with phase discontinuities: generalized laws of reflection and refraction," *Science*, Vol. 334, No. 6054, 333–337, 2011.
5. Wang, J. "A review of recent progress in plasmon-assisted nanophotonic devices," *Front. Optoelectron.*, Vol. 7, No. 3, 320–337, 2014.
6. Zhao, Z., Wang, J., Li, S. H. and Willner, A. E. "Metamaterials-based broadband generation of orbital angular momentum carrying vector beams," *Opt. Lett.*, Vol. 38, No. 6, 932–934, 2013.
7. Zhao, Z., Wang, J., Li, S. H. Willner, A. E. "Selective broadband generation of orbital angular momentum carrying vector beams using metamaterials," *Proc. CLEO2013*, Optical Society of America (OSA), paper QM4A. 7, 2013.
8. Du, J. and Wang, J. "Design of on-chip N-fold orbital angular momentum multicasting using V-shaped antenna array," *Sci. Rep.*, Vol. 5, 9662, 2015.
9. Du, J., Li, X. H., Li, S. H., Zhu, L., Zhou, N., Liu, J., Chen, S., Zhao, Y. F. and Wang, J. "Experimental demonstration of chip-scale orbital angular momentum (OAM) beams generation and detection using nanophotonic dielectric metasurface array," *Proc. OFC2016*, Optical Society of America (OSA), paper W2A.13, 2016.
10. Du, J., Chen, S., Liu, J., Li, S. H., Zhu, L., Zhao, Y. F. and Wang, J. "Design and fabrication of metasurface on conventional optical fiber facet for linearly polarized mode ($LP_{11}$) generation at visible light wavelength," *Proc. CLEO2016*, Optical Society of America (OSA), paper JTu5A.120, 2016.

# Reconfigurable Integrated Optical Signal Processing

Ming Li
Institute of Semiconductors, Chinese Academy of Sciences, No. 35, Tsinghua East Road, Beijing, China
*E-Mail: ml@semi.ac.cn;*

All-optical implementations of signal processing have attracted a great deal of attention due to the unique potential of this approach to overcome the bandwidth and speed bottleneck of electronic devices. Many all-optical signal processing techniques, offering processing bandwidths up to several THz, have been proposed and successfully employed in a wide range of areas, such as ultrafast telecommunications, optical computing, microwave photonics and bio-photonics etc.

To build up an all-optical signal-processing and computing platform with complex functionality, a promising solution is to emulate the developments in the electronic domain using photonic technologies. For this purpose, photonics counterparts of fundamental components that form basic building blocks in electronic circuits need to be designed and realized. This is a key step toward the practical realization of all-optical information processing and computing circuits. Recently, some fundamental signal operators, such as all-optical temporal differentiators and integrators, and real-time Fourier and Hilbert transformers, have been experimentally demonstrated by employing fiber- and integrated-optic platforms. Based on the state of art electronics technology, the achievable bandwidth of electronics operators is limited to about 1 GHz. On the other hand, the photonics-based signal operators can easily realize an operation bandwidth larger than 1 THz [1]. In particular, an optical differentiator with a record bandwidth up to 25 THz has been recently reported based on a wavelength-selective directional coupler [2]. Therefore, the key advantage of a photonics-assisted signal operator is that the achievable operation bandwidth can be largely increased.

In this talk, very recent progresses on reconfigurable integrated optical signal processing will be introduced and reviewed [3-4]. These works represent an important step towards the realization of efficient optical signal-processing circuits.

References

1. L. Venema, “Photonics technologies,” Nat. Insight **424**, 809 (2003).
2. J. Azaña, C. K. Madsen, K. Takiguchi, and G. Cincontti, eds., Special issue on "Optical signal processing," J. Lightwave Technol. 24, 2484-2767 (2006).
3. W. Liu, M. Li, R. S. Guzzon, E. J. Norberg, J. S. Parker, M. Lu, L. A. Coldren, and J. P. Yao, "A fully reconfigurable photonic integrated signal processor," Nature Photon., vol. 10, no. 3, pp. 190-195, Mar. 2016.
4. M. Li, Y. Deng, J. Tang, S. Sun, J. P. Yao, J. Azaña and N. Zhu, "Reconfigurable optical signal processing based on a distributed feedback semiconductor optical amplifier," Sci. Rep., vol. 6, paper number 19985, Jan. 2016.

# Photonic integrated devices for the emission and detection of optical vortex beams

**L. Meriggi[1], C. Klitis[1], X. Cai[2], S. Li[2], J. Zhu[3], S. Yu[2,3], M. Strain[4], M.Sorel[1]**

[1]School of Engineering, University of Glasgow, G12 8LT Glasgow, United Kingdom

[2]State Key Laboratory of Optoelectronic Materials and Technologies and School of Physics and Engineering, Sun Yat-Sen University, Guangzhou 510275, China

[3]Faculty of Engineering, University of Bristol, Woodland Road, Bristol B68 1UB 8LT, UK

[4]Institute of Photonics, University of Strathclyde, G1 1RD Glasgow, United Kingdom

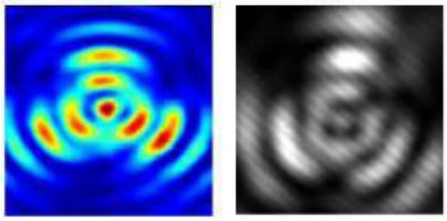
[*]corresponding author: marc.sorel@glasgow.ac.uk

**Abstract** –Emerging applications exploiting the orbital angular momentum of light will require compact and functional devices for the emission, detection and manipulation of these beams. We will discuss recent progress on the development of silicon-on-insulator micro-ring resonators for the emission of multiple OAM states with fast reconfigurability.

.

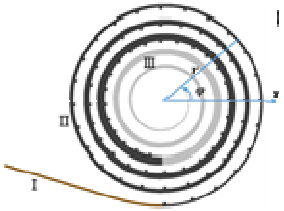
The orbital angular momentum (OAM) is an additional degree of freedom of a light beam with interesting applications in micromanipulation, microscopy[1] and free-space communications[2]. So far, OAM states have been generated, detected and manipulated by complex and bulky components that prevented the full exploitation of the OAM dimension. Recently, a number of research groups have used photonic integrated technologies to demonstrate very compact and low-cost components that meet the requirements for large volume manufacturing[3,4].

We will discuss recent research progress on the development of ultra-compact and tunable integrated OAM devices fabricated on a silicon photonic technology. The emitters consist of microring resonators that incorporate periodic scattering elements to couple the waveguide propagating beams to vertically emitted beams carrying OAM[4]. The devices to be presented will include tunable emitters that offer fast switching between the OAM modes, resonators integrated with superposed gratings for the simultaneous emission of multi-OAM states (fig. 1a), spiral-shaped waveguides to improve the detection efficiency (fig. 1b) and resonators integrated with Mach-Zehnder interferometer for the emission of +/- *l* OAM states (fig. 1c).

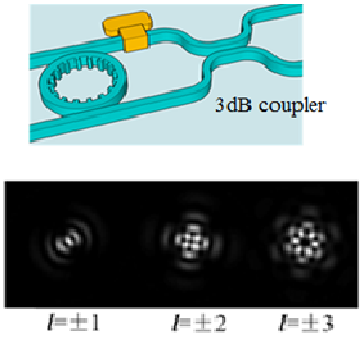


**|-4>+|-1>**

a)




b)




c)

**Figure 1:** a) Emission pattern of an OAM beam composed by a superposed $l$=-4 and $l$=-1 order. The beam is generated by a microring that incorporates two different gratings; b) A spiral-shaped waveguide to increase the active surface of an OAM detector; c) A resonator for the emission of OAM beams integrated with a Mach-Zehnder interferometer to tune the relative phase between $+l$ and $-l$ beams.

## REFERENCES


[1] D. G. Grier et al., "A revolution in optical manipulation", *Nature* **424**, 810 (2003).

[2] G. Gibson et al., "Free-space information transfer using light beams carrying orbital angular momentum", *Opt. Express* **12**, 5448 (2004).

[3] C. R. Doerr et al., "Circular grating coupler for creating focused azimuthally and radially polarized beams", *Opt. Lett.* **36**, 1209 (2011).

[4] X. Cai et al., "Integrated compact optical vortex beam emitters", *Science* **33**, 363 (2012).

# Hybrid Plasmonics and Functional Nanomaterials

# Hyperlensing at NIR Frequencies Using a Hemi-spherical Metallic Nanowire Lens in Sea-urchin Geometry

**Ankit Bisht,[1,2] Wei He,[2] Xiaotian Wang,[1] Linda Y. L. Wu,[2] Xiaodong Chen[1] and Shuzhou Li[1*]**
School of Materials Science and Engineering, Nanyang Technological University, Singapore 639798
[2]Singapore Institute of Manufacturing Technology, 71 Nanyang Drive, Singapore 638075
[*]corresponding author: lisz@ntu.edu.sg

**Abstract**- Label-free and real time far-field super-resolution imaging (hyperlensing) at the nanoscale is of significant interest where sub-λ imaging remains a constraint because of Abbe's diffraction limit. Though by utilizing anisotropic permittivities, metal-dielectric multilayers have been successful in reconstructing the high-frequency components from sub-λ objects, yet they remain cumbersome and expensive to make. Most of the multilayer structures require multiple vacuum deposition cycles and are plagued by stringent requirements on surface roughness of metallic layers. In contrast to the multilayer structure here we propose a 3D hyperbolic metamaterial model composed of metallic nanorods arranged in sea-urchin geometry as a hyper-lensing device, which is capable of projecting and magnifying diffraction limited information into the far-field at Near-infrared (NIR) frequencies. The hyperlens generates a band of flat hyperbolic dispersions in spherical coordinates, which in turn supports the propagation of high wave-vector spatial harmonics leading to far-field super-resolution imaging. Using full-wave Finite-difference time-domain (FDTD) simulations with diffraction limited trimer, quadrumer and ringed objects etched on thin perfect electric conductor (PEC) films, we show that the hyperlens model can achieve magnification factors of up to 10X in the far-field (~4.5λ from object's surface) under a light source with a wavelength of 1 μm, with successful resolution down to 220 nm (~λ/5). The magnified image field distribution projected into the far-field is shown to follow the object under reduction in symmetry. These results are important for making progress in the realization of real-time bio-molecular imaging systems, eliminating the need for near-field scanning, destructive electron microscopy and various image post-processing techniques.

For next generation MMs, indefinite mediums composed of metallic nanowires embedded in dielectric matrices are considered as one of the promising candidates since they are easily tuneable and have lesser energy losses. More importantly, they are not constrained by the ubiquitous metamaterial requirement of magnetic resonance.[1,2] They have been previously shown to produce all angle negative refraction[1,2] and sub-wavelength imaging.[3-5] Endoscopes made from tapering nanowire arrays have been shown in the past but they can only reproduce the fields near the surfaces.[6,7] Kawata et al[8] numerically showed colour imaging using stacked nanorod arrays and the idea of magnification using tapered nanorod arrays. Nevertheless, the imaging capabilities of these nanorod array based hyperlenses still remain largely unexplored. Tapered arrays of metallic wires were shown theoretically[6] to magnify electromagnetic information on one of its edge to the other, but the resultant magnified image was shown to be limited to the near-field of the nanowires. Here we propose a sea-urchin hyperlens (SHL) composed of hexagonally arranged metallic nanorods embedded in a dielectric

medium and arranged in sea-urchin geometry as a hyperlens design working in the NIR. We show numerically that when conformed to a hemispherical surface the hyperlens is capable of projecting images from sub-λ objects into the far-field, which in turn can be easily brought to focus by conventional microscope objectives. Magnification factors up to 10X were achieved at a distance of 2.5λ from the hyperlens.

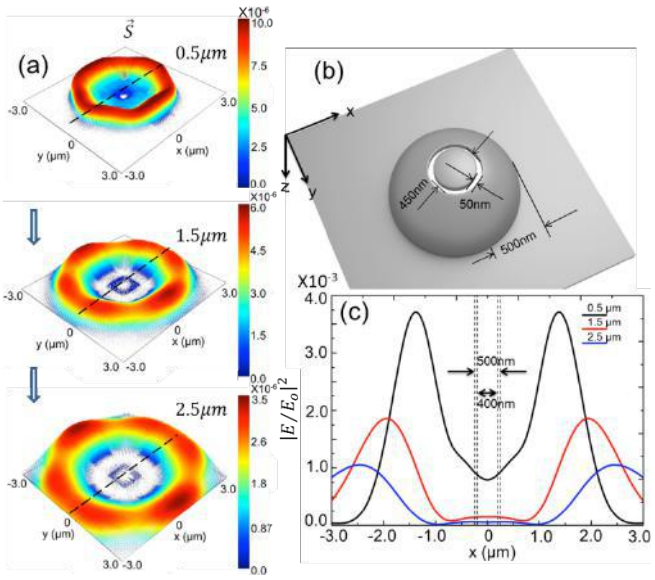



**Figure 1:** Nanoring object imaged through SHL. (a) 3D Poynting vector plots at different image planes, magnified using SHL at various distances from the hyperlens. (b) 3D schematic of the nanoring sub-wavelength object used to obtain images in (a), the centre-to-centre separation is 450 nm (<λ/2) while the thickness of the ring is 50 nm (~λ/20). (c) E-field intensity at different distances from the hyperlens, corresponding to power flow vector plots in (a), shown with dashed lines. The vertical dashed lines in (c) represent the nanoring object with centre-to-centre separation of ~450 nm.

**Acknowledgements**, Y.L.W. acknowledges financial support by the Metamaterials Programme: Superlens (0921540099) funded by Agency for Science, Technology and Research of Singapore (A*Star). S.L. acknowledges support from MOE Tier 2 (ACR12/12) and MOE Tier 1.

## REFERENCES

(1) Yao, J.; Liu, Z.; Liu, Y.; Wang, Y.; Sun, C.; Bartal, G.; Stacy, A. M.; Zhang, X. *Science* **2008**, *321*, 930.

(2) Liu, Y.; Bartal, G.; Zhang, X. *Opt. Express* **2008**, *16*, 15439.

(3) Lu, W. T.; Sridhar, S. *Phys. Rev. B: Condens. Matter Mater. Phys.* **2008**, *77*, 233101.

(4) Casse, B. D. F.; Huang, Y. J.; Lu, W. T.; Gultepe, E.; Menon, L.; Sridhar, S. In *Proc. SPIE 8034, Photonic Microdevices/Microstructures for Sensing III* Orlando, Florida, USA 2011; Vol. 8034, p 803407.

(5) Wu, L. Y. L.; Leng, B.; Bisht, A. *Appl. Phys. A: Mater. Sci. Process.* **2014**, *116*, 893.

(6) Shvets, G.; Trendafilov, S.; Pendry, J. B.; Sarychev, A. *Phys. Rev. Lett.* **2007**, *99*, 053903.

(7) Tuniz, A.; Kaltenecker, K. J.; Fischer, B. M.; Walther, M.; Fleming, S. C.; Argyros, A.; Kuhlmey, B. T. *Nat. Commun.* **2013**, *4*, 2706.

(8) Kawata, S.; Ono, A.; Verma, P. *Nat. Photonics* **2008**, *2*, 438.

# Nanoscale surface chemistry directs the tunable assembly of silver octahedra into three two-dimensional plasmonic superlattices

**Yih Hong Lee,[1] Wenxiong Shi,[2] Ruibin Jiang,[3] Jianfang Wang,[3] Shuzhou Li[2] & Xing Yi Ling[1]**

[1] Division of Chemistry and Biological Chemistry, School of Physical and Mathematical Sciences, Nanyang Technological University, Singapore 637371, Singapore.

[2]Division of Materials Science, School of Materials Science and Engineering, Nanyang Technological University, Singapore 639798, Singapore.

[3] Department of Physics, The Chinese University of Hong Kong, Shatin, Hong Kong, China.

[*]corresponding author: xyling@ntu.edu.sg

**Abstract**-A major challenge in nanoparticle self-assembly is programming the large-area organization of a single type of anisotropic nanoparticle into distinct superlattices with tunable packing efficiencies. Here we utilize nanoscale surface chemistry to direct the self-assembly of silver octahedra into three distinct two-dimensional plasmonic superlattices at a liquid/liquid interface. Systematically tuning the surface wettability of silver octahedra leads to a continuous superlattice structural evolution, from close-packed to progressively open structures. Notably, silver octahedra standing on vertices arranged in a square lattice is observed using hydrophobic particles. Simulations reveal that this structural evolution arises from competing interfacial forces between the particles and both liquid phases. Structure-to-function characterizations reveal that the standing octahedra array generates plasmonic 'hotstrips', leading to nearly 10-fold more efficient surface-enhanced Raman scattering compared with the other more densely packed configurations. The ability to assemble these superlattices on the wafer scale over various platforms further widens their potential applications.

# 3D DNA Plasmonics

**Maximilian J. Urban**[1*] **and Na Liu**[1,2*]

[1]Max Planck Institute for Intelligent Systems, Stuttgart, Germany

[2]Kirchhoff Institute for Physics, University of Heidelberg, Im Neuenheimer Feld 227, D-69120, Heidelberg, Germany

[*]corresponding authors: laura.liu@is.mpg.de, urban@is.mpg.de

**Abstract**- Deterministic placement and dynamic manipulation of individual plasmonic nanoparticles with nanoscale precision feature an important step towards active nanoplasmonic devices with prescribed levels of performance and functionalities at optical frequencies. We demonstrate the precise organization and the controlled motion of nanoparticles by using the toolbox of DNA nanotechnology.

Realization of three-dimensional (3D) plasmonic nanoarchitectures exemplifies one of the key challenges in nanotechnology. Bottom-up self-assembly approaches, which often involve molecular recognition characters, offer large-scale fabrication, biochemical compatibility, and many other benefits. Among a variety of materials for self-assembly, DNA represents one of the most attractive building blocks largely due to its unprecedented programmability. In particular, the DNA origami technique allows for rational 3D organization of metal nanoparticles with nanometer precision, allowing for engineering complex plasmonic architectures with tailored optical response.

First, we demonstrate hierarchical assembly of plasmonic toroidal metamolecules, which exhibit tailored optical activity in the visible spectral range.[1] Each metamolecule consists of four identical origami-templated helical building blocks. Such toroidal metamolecules show stronger chiroptical response than monomers and dimers of the helical building blocks. We also demonstrate that given the circular symmetry of the toroidal metamolecules, distinct chiroptical response along their axial orientation can be uncovered via simple spin-coating of the metamolecules on substrates.

Next we show the creation of active plasmonic systems, in which plasmonic nanorods can execute directional, progressive and reverse nanoscale walking on two or three-dimensional DNA origami.[2,3] Such a walker comprises an anisotropic gold nanorod as its 'body' and discrete DNA strands as its 'feet'. Specifically, our walker carries optical information and can *in situ* optically report its own walking directions and consecutive steps at nanometer accuracy, through dynamic coupling to a plasmonic stator immobilized along its walking track. We demonstrate that two gold nanorod walkers can independently or simultaneously perform stepwise walking along a shared DNA origami track.[3]

Our studies exemplify the power of plasmonics, when integrated with DNA nanotechnology for realization of advanced artificial nanomachinery with tailored optical functionalities.

**REFERENCES**

1. Urban, M. J., P. K. Dutta, P. Wang, X. Duan, X. Shen, B. Ding, Y. Ke and N. Liu, submitted 2016.
2. Zhou, C. M., X. Duan and N. Liu, "A plasmonic nanorod that walks on DNA origami," *Nat. Commun.*, Vol. 6, 8102, 2015.
3. Urban, M. J., C. Zhou, X. Duan and N. Liu, "Optically Resolving the Dynamic Walking of a Plasmonic Walker Couple," *Nano Lett.*, Vol. 15, No. 12, 8392-9396, 2015.

# Optically active nanomaterials

**Yurii K. Gun'ko[1,2*] Finn-Purcell Milton,[1] Joseph E. Govan,[1] Alexander Loudon,[1] Olan Cleary,[1] Maria Mukhina, [2] Alexander Baranov, [2] Anatoly Fedorov [2]**

[1] School of Chemistry and CRANN, Trinity College Dublin, Dublin 2, Ireland.

[2] ITMO University, 197101 Saint Petersburg, Russia.

*corresponding author, E-mail: igounko@tcd.ie

**Abstract:** The main goal of our research is to develop new types of technologically important optically active nanomaterials, study their properties and explore their applications. The utilisation of chiral stabilisers allowed the preparation of new water soluble white emitting quantum dots, rods, nano-tetrapods and nano-sheets, which demonstrated circular dichroism in the band-edge region of the spectrum. Biological testing of chiral nanotetrapods displayed a chiral bias for an uptake of the D- enantiomer stabilised nano-tetrapods by cancer cells. We have also developed a range of ZnS, ZnSe, CdSe and 2D $MoS_2$ based optically active nanostructures. These nanostructures can find a range of potential application in nanobiotechnology, photonics, medicine and optical chemo- and bio-sensing.

The area of optically active metal nanoparticles has received a great deal of attention due to the range of potential applications offered by these materials in chiral sensing, catalysis and as metamaterials in advanced optical devices [1, 2]. The use of stereospecific chiral stabilising molecules has also opened another avenue of interest in the area of optically active quantum dot (QD) research. Initially, optically active CdS QDs have been prepared by us using microwave induced heating with the racemic (Rac), D- and L-enantiomeric forms of penicillamine as stabilisers [3]. Circular dichroism (CD) studies of these QDs have shown that D- and L-penicillamine stabilised particles produced mirror image CD spectra, while the particles prepared with a Rac mixture showed only a very weak signal It was also found that all three types of CdS particles (D-, L-, and Rac penicillamine) show very broad emission bands between 400 and 700 nm due to defects or trap states on the surfaces of the nanocrystals. The density functional calculations of the electronic states have demonstrated that the longer-wavelength circular dichroism is associated with near-surface metal atoms that are enantiomerically distorted by the chiral ligands, which translate an enantiomeric structure to the surface layers and associated electronic states [4], while the quantum dot core is found to remain undistorted and achiral. We have also reported chiral CdSe QDs [5] and chiral CdS nanotetrapods [6, 7]. All of these chiral nanostructures also showed a very broad distribution of photoluminescence which originates from emissive defect states and characteristic CD responses within the band-edge region of the spectrum. More recently we have reported intrinsic chirality of CdSe/ZnS QDs, which is caused by the presence of naturally occurring chiral defects (e.g. dislocations) and not by the presence of chiral ligands [8]. Using theoretical modeling we have also demonstrated that optical activity can be inherent to many semiconductor nanostructures (e.g. nanowires and nanorods), as it is induced by chiral screw dislocations naturally developing during their growth [9]. Finally, using a combination of exfoliation and phase transfer techniques, we have developed a range of optically active two dimensional (2D) nanostructures

such as $MoS_2$ and $WS_2$. These nanostructures have demonstrated strong unique CD responses and very interesting structural morphology. It is expected that optically active nanomaterials will find a range of potential uses in the chemistry, nanobiotechnology, photonics and optical chiral chemo- and bio-sensing. In addition, optically active quantum nanostructures can find applications as circular polarized light emitters and new metamaterials.

**Acknowledgements**, The authors gratefully acknowledge financial support from EU FP7 programme (Future Nanoneeds grant), the Science Foundation of Ireland (Grant SFI 12/IA/1300),and the Ministry of Education and Science of the Russian Federation (Grant No. 14.B25.31.0002).

## REFERENCES

1. Ben-Moshe, A., Maoz, B. M., Govorov, A. O. & Markovich, G. "Chirality and chiroptical effects in inorganic nanocrystal systems with plasmon and exciton resonances", *Chem. Soc. Rev.*, Vol.42, 7028-7041, 2013.
2. Govorov, A. O., Gun'ko, Y. K. , Slocik, J.M., Gerard, V. A., Fan, Z.N. & Rajesh, R. "Chiral nanoparticle assemblies: circular dichroism, plasmonic interactions, and exciton effects", *J. Mater. Chem*., Vol. 21, 16806-16818, 2011.
3. Moloney, M. P., Gun'ko, Y. K. & Kelly, J. M. "Chiral highly luminescent CdS quantum dots", *Chem. Comm*., 3900-3902, 2007.
4. Elliott, S. D., Moloney, M. P. & Gun'ko, Y. K. "Chiral shells and achiral cores in CdS quantum dots", *Nano Lett*. , Vol.8, 2452-2457, 2008.
5. Gallagher, S. A. Moloney, M. P., Wojdyla, M., Quinn, S. J., Kelly, J. M. & Gun'ko, Y. K. "Synthesis and spectroscopic studies of chiral CdSe quantum dots", *J. Mater. Chem.* , Vol. 20, 8350-8355, 2010.
6. Govan, J. E., Jan, E., Querejeta, A., Kotov, N. A. & Gun'ko, Y. K. "Chiral luminescent CdS nano-tetrapods", *Chem. Comm.*, 6072-6074, 2010.
7. Moloney, M. P. Govan, J. Loudon, A. Mukhina, M. & Gun'ko, Y. K., "Preparation of chiral quantum dots", *Nature Protocols*, Vol. 10, 558-573, 2015.
8. Mukhina, M. V., Maslov, V. G., Baranov, A. V., Fedorov, A. V., Orlova, A. O., Purcell-Milton, F., Govan, J. & Gun'ko, Y. K., "Intrinsic Chirality of CdSe/ZnS Quantum Dots and Quantum Rods", *Nano Lett.*, Vol. 15, 2844–2851, 2015.
9. Baimuratov, A. S., Rukhlenko, I. D., Gun'ko, Y. K., Baranov, A. V. & Fedorov, A. V., Dislocation-Induced Chirality of Semiconductor Nanocrystals, *Nano Lett.*, Vol. 15, 1710-1715, 2015.

# Single-Particle Absorption Spectroscopy of Plasmonic Nanostructures

**S. Link**
Department of Chemistry, Rice University, USA
slink@rice.edu

**Abstract**- Single-particle absorption spectroscopy on strongly scattering plasmonic nanoparticles is investigated by photothermal microscopy with a supercontinuum laser. The absorption spectra are compared to scattering spectra of the same individual gold nanoparticles and correlated with electron microscopy images that characterize the size and shape of the nanostructures. For many applications of plasmonic nanostructures, absorption and scattering cross sections and lineshapes are important to distinguish, possible with single-particle spectroscopy that also removes nanoparticle heterogeneity.

Applications of plasmonic nanostructures take advantage of their large absorption and scattering cross sections that depend sensitively on the nanoparticle size, shape, and local environment. Effects due to distributions in these parameters can be understood using single particle spectroscopy techniques, especially when combined with structural imaging and electromagnetic simulations. Single particle spectroscopy methods have, however, been mostly developed to investigate the scattering or extinction of plasmonic nanostructures. The latter equals the absorption, but only if the nanoparticles of interest are small and do not scatter significantly. Photothermal imaging is capable of measuring the absorption only of nanostructures, and is based on the heating of the local environment following absorption and nonradiative decay [1]. Photothermal imaging is typically limited to a single wavelength though as it requires a coherent light source for excitation. Here we show how with the use of a white light supercontinuum source we are able to record absorption spectra of plasmonic nanoparticles of different sizes/shapes and compare the results to the scattering response [2]. Furthermore, time-resolved transient absorption spectroscopy is employed to follow in real time the nonradiative decay of the initially absorbed photon energy in single plasmonic nanostructures [3].

**Acknowledgements.** Financial support from the Robert A. Welch Foundation (C-1664), the Office of Naval Research (N00014-10-1-0989), the Army Research Office (MURI W911NF-12-1-0407), and a DURIP equipment grant (N00014-12-1·0727) is acknowledged.

**REFERENCES**

1. D. Boyer, P. Tamarat, A. Maali, B. Lounis, M. Orrit, *Science* 297, 1160-1163 (2002).
2. M. Yorulmaz, S. Nizzero, A. Hoggard, L.-Y. Wang, Y.-Y. Cai, M. N. Su, W.-S. Chang, S. Link, *Nano Lett.* 15, 3041-3047 (2015).
3. W.-S. Chang, F. Wen, D. Chakraborty, M.-N. Su, Y. Zhang, B. Shuang, P. J. Nordlander, J. E. Sader, N. J. Halas, S. Link, *Nat. Comm.* DOI 10.1038/ncomms8022 (2015).

# Colloidal Plasmonic Metasurfaces for Nonlinear Optics

Shangjr Gwo,[1,5] Chun-Yuan Wang,[1] Hung-Ying Chen,[1] Liuyang Sun,[2] Xiaoqin Li,[2] Wei-Liang Chen,[3] Yu-Ming Chang,[3] and Hyeyoung Ahn[4]

[1]Department of Physics, National Tsing-Hua University, Hsinchu 30013, Taiwan
[2]Department of Physics, The University of Texas at Austin, Austin, TX 78712, USA
[3]Center for Condensed Matter Sciences, National Taiwan University, Taipei 10617, Taiwan
[4]Department of Photonics, National Chiao-Tung University, Hsinchu 30010, Taiwan
[5]National Synchrotron Radiation Research Center, Hsinchu 30076, Taiwan

Plasmonic metasurfaces consist of two-dimensional arrays of plasmonic "meta-atoms", which exhibit collective and tunable resonance properties controlled by in-plane coupling. Here, we focus on the applications of metasurfaces with precisely engineered plasmonic properties for nonlinear optics. In practice, these applications are susceptible to material losses and structural imperfections, such as variations in size, shape, periodicity of meta-atoms, and their material states. We show that silver crystals synthesized by a "green" chemical process are excellent materials for fabrication of plasmonic metasurfaces. Utilizing focused ion-beam milling, we are able to generate uniform and precisely engineered metasurfaces for broadband tunable second-harmonic generation.

# Significant enhancement of the chiral correlation length in nematic liquid crystals by gold nanoparticles capped with axially chiral binaphthyl ligands

**T. Mori[1], A. Sharma[1*], and T. Hegmann[1,2]***

[1]Chemical Physics Interdisciplinary Program, Liquid Crystal Institute, Kent State University, Kent, OH 44242-0001, U.S.A.

[2]Department of Chemistry and Biochemistry, Kent State University, Kent, OH 44242-0001, U.S.A.

[*]Corresponding author: thegmann@kent.edu

**Abstract.** To investigate how chirality propagates from a chiral nanoscale surface, we studied gold nanoparticles functionalized with axially chiral binaphthyl molecules. In particular, we synthesized three enantiomeric pairs of chiral ligand-capped gold nanoparticles differing in size, curvature, and ligand density that allowed us to tune the chirality transfer from nanoscale solid surfaces to a bulk anisotropic liquid crystal (nematic) medium.[1] Ultimately we are examining how far the chirality from a nanoparticle surface reaches into a soft, self-assembled bulk material.[2]

Circular dichroism spectra of the gold nanoparticles decorated with binaphthyl thiols confirmed that the binaphthyl moieties form a *cisoid* conformation in isotropic organic solvents. In the chiral nematic liquid crystal phase, induced by dispersing these gold nanoparticles into an achiral nematic liquid crystal host as an anisotropic solvent, the binaphthyl moieties on the nanoparticle surface form a *transoid* conformation as determined by imaging the helical twist direction of the induced cholesteric phase. This suggests that the ligand density on the nanoscale metal surfaces provides a dynamic space to alter and adjust the helicity of binaphthyl derivatives in response to the ordering of the surrounding medium. The helical pitch values of the induced chiral nematic phase were determined, and the helical twisting power (*HTP*) of the chiral gold nanoparticles calculated to elucidate the chirality transfer efficiency of the axially chiral binaphthyl ligand-capped gold nanoparticles. Remarkably, the *HTP* increases with increasing diameter of the particles, *i.e.* the efficiency of the chirality transfer of the binaphthyl units bound to the nanoparticle surface is diminished as the size of the particle is reduced. However, in comparison to the free ligands, per chiral molecule, all tested gold nanoparticles induce helical distortions in a 10- to 50-times larger number of liquid crystal host molecules surrounding each particle, indicating a significantly enhanced chiral correlation length.

We propose that both the helicity and the chirality transfer efficiency of axially chiral binaphthyl derivatives can be controlled at metal nanoparticle surfaces by adjusting the nanoparticle size and curvature as well as the number and density of the chiral ligands to ultimately measure and tune the chiral correlation length (Figure 1).

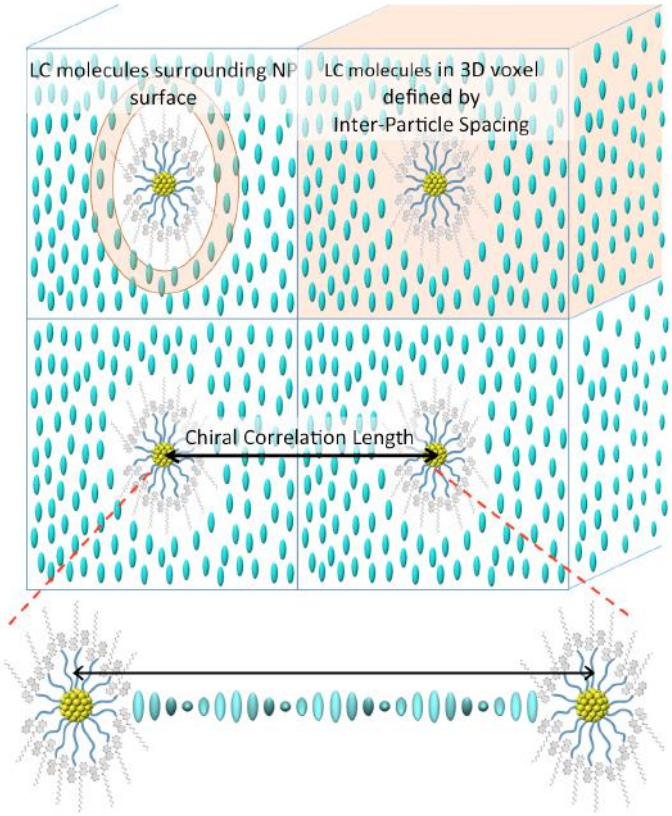



**Figure 1.** Schematic representations highlighting the number of nematic liquid crystal (**5CB**, Cr 25 N 35 Iso) molecules surrounding the gold nanoparticle surface (top left) and in the 3D space (voxel, top right) defined by the inter-particle distance (bottom), defining the chiral correlation length, assuming well-dispersed gold nanoparticles in the 5CB matrix. For simplicity, the helical arrangement of the 5CB molecules in the induced chiral nematic liquid crystal (N*-LC) phase is shown underneath.

**Acknowledgements.** This work was supported by the National Science Foundation (NSF, DMR-1506018), the Ohio Third Frontier (OTF) program for Ohio Research Scholars "Research Cluster on Surfaces in Advanced Materials" (T.H.), which also supports the cryo-TEM facility at the Liquid Crystal Institute (Kent State University), where current TEM data were acquired. Finally, T.M. acknowledges financial support (postdoctoral scholarship) from the Japan Society for the Promotion of Science (JSPS). We also thank L.C. Chien at the Liquid Crystal Institute for access to cell gap measurements.

## REFERENCES

1. Mori, T., Sharma, A., Hegmann, T., "Significant enhancement of the chiral correlation lengths in nematic liquid crystals by gold nanoparticle surfaces featuring axially chiral binaphthyl ligands," *ACS Nano* 10, 1552-1564, 2016.
2. Sharma, A., Mori, T., Lee, H.-C., Worden, M., Bidwell, E., Hegmann, T., "Detecting, visualizing, and measuring gold nanoparticle chirality using helical pitch measurements in nematic liquid crystal phases," *ACS Nano* 8, 11966-11976, 2014.

# Recent advances and perspectives of magnetoplasmonic metamaterials.

**P. Vavassori**[1,2*]
[1]CIC nanoGUNE, 20018 San Sebastian, Spain
[2]IKERBASQUE Basque Foundation for Science, 48013 Bilbao, Spain
[*]corresponding author: p.vavassori@nanogune.eu

**Abstract**- The rapidly developing field of magnetoplasmonics merges concepts from plasmonics and magnetism to realize novel and unexpected phenomena and functionalities for the manipulation of light at the nanoscale. This talk will cover recent advances in the field arising from the interplay between which contributed to broaden the understanding and control of optics at the nanoscale in ferromagnetic nanostrucutres owing to the intertwined optical and magneto-optical properties. Applications of such multifunctional optical metamaterials to variety of emerging technologies are presented as an example of their broad scientific and technological perspectives.

Magnetoplasmonics combines strong local enhancements of electromagnetic fields in surface plasmon excitations with magneto-optically active ferromagnetic materials enabling plasmonic nanostructures, called magnetoplasmonic nanoantennas, that can be controlled by external magnetic fields. Such magnetoplasmonic nanoantennas offer a smart toolbox for the realization of actively tuneable optical metasurfaces. Here we review recent advances in the field showing that magnetoplasmonic metamaterials open a clear path towards applications to variety of emerging technologies as, e.g., ultrasensitive molecular sensing and ultrathin optical metadevices.

The fundamentals aspects of the physics underlying the optical behavior of magnetoplasmonic metamaterials are first introduced [1-3]. Then, some relevant realizations of magnetoplasmonic metamaterials are presented as examples of the broad scientific and technological perspectives enabled by such multifunctional optical metamaterials.

- Systems allowing label-free molecular detection are expected to have enormous impact on biochemistry and biomedicine, and are therefore subject to intense investigation. We propose an innovative and alternative route based on magneto-plasmonic nanoantennas, which enables radically improved sensitivity, clearly outperforming recently reported plasmon based sensors [4-6]. Most remarkably, we achieved a local raw surface sensitivity of two orders of magnitude higher than the best values reported for nanoplasmonic sensors.

- Light polarization rotators and non-reciprocal optical isolators are essential building blocks in photonics technology. The control of the non-reciprocal light propagation displayed by magnetoplasmonic nanoantennas offer a promising route to bring these devices to the nanoscale, thanks to their ability to tailor the amplitude and sign of magneto-optical light polarization manipulation over a broad spectral range[7]. We present a novel concept of magnetically tunable plasmonic crystal based on the excitation of Fano-like lattice surface modes in periodic arrays of hybrid ferromagnetic and noble metal[8] as well as ferromagnetic and optically anisotropic nanoantennas [9]. In these metamaterials, the excitation of the magnetic field-induced lattice surface modes leads to highly tunable and amplified magneto-optical effects as compared to disordered systems. The concepts

presented here can be exploited to design novel magnetoplasmonic sensors based on coupled localized plasmonic resonances and non-reciprocal optical devices that allow for an enhanced tuneability and control of light polarization states.

- Two-dimensional magnetoplasmonic crystals, namely plasmonic crystals with a periodic array of cylindrical holes in a ferromagnetic layer, support surface plasmon polariton modes and display a two-dimensional photonic band structure. We demonstrate that under proper conditions incident light can couple to selected surface plasmon polariton modes through the synergistic action between diffracted coupling and magneto-optical induced polarization conversion. Our results suggest a novel path to the design of metamaterials with tailored and enhanced magneto-optical response by engineering the plasmonic band structure via lattice design [10].

**Acknowledgements**, support from Basque Government under the Project n. PI_2015_1_19 is acknowledged.

**REFERENCES**

1. Chen, J., et al., "Plasmonic nickel nanoantennas", *Small* Vol. 7, No. 16, 2341-2347, 2011.
2. Maccaferri, N,. et al., "Tuning the magneto-optical response of nanosize ferromagnetic Ni disks using the phase of localized plasmons", *Phys. Rev. Lett.*, Vol. 111, No. 16, 167401, 2013.
3. Maccaferri, N., et al.," Polarizability and magnetoplasmonic properties of magnetic general nanoellipsoids", *Opt. Express*, Vol 21, No. 8, 9875-9889, 2013.
4. Bonanni, V., et al., "Designer magnetoplasmonics with nickel nanoferromagnets", *Nano Lett.*, Vol. 11, No. 12 , 5333-5338 , 2011.
5. Maccaferri, N., et al., "Ultrasensitive and label-free molecular-level detection enabled by light phase control in magnetoplasmonic nanoantennas", *Nature Commun.*, Vol. 6, 6150, 2015.
6. Zubritskaya, I., et al., "Active magnetoplasmonic ruler", *Nano Lett.*, Vol. 15, No. 5, 3204-3211, 2015.
7. Lodewijks, K., et al., "Magnetoplasmonic Design Rules for Active Magneto-Optics", *Nano Lett.*, Vol. 14, No. 12, 7207-7214, 2014.
8. Maccaferri, N., et al., "Anisotropic nanoantenna-based magnetoplasmonic crystals for highly enhanced and tunable magneto-optical activity", submitted to *Nano Lett.*
9. Kataia, M., et al., "Hybrid plasmonic lattices with tunable magnetooptical activity", *Opt. Express*, Vol. 24, No. 4, 3652-3261, 2016.
10. Maccaferri, N., et al., "Resonant Enhancement of Magneto-Optical Activity Induced by Surface Plasmon Polariton Modes Coupling in 2D Magnetoplasmonic Crystals", *ACS Photonics*, Vol. 2, No. 12, 1769-1779, 2015.

# Assembling Plasmonic Nanoantennas on DNA

**Sébastien Bidault***
ESPCI Paris, PSL Research University, CNRS, Institut Langevin, Paris, France
*corresponding author: sebastien.bidault@espci.fr

**Abstract**- Plasmon-based optical antennas have become ubiquitous in photonics with numerous biomedical applications in sensing, imaging and spectroscopy. Their sub-wavelength size means that their structural properties must be controlled at the nanometer scale to successfully engineer their optical responses. DNA has recently emerged as the building material of choice to mass-produce plasmonic resonators with controlled geometries and chemical environments, allowing their reproducible coupling to single quantum emitters and the dynamic modulation of their photonic properties.

To enhance the fluorescence properties of single molecules, we assemble them in the center of gold nanoparticle (AuNP) dimers, using a short DNA double-strand, which are obtained in large scale as a purified colloidal suspension (figure 1-a) [1-3]. Confocal luminescence lifetime measurements in microfluidic conditions demonstrate that these nanostructures are single photon-emitters with picosecond lifetimes (figure 1-b) [1]. Furthermore, molecules with a dipolar transition moment parallel to the dimer axis can be selected with radially-polarized Laguerre-Gauss beams for antennas oriented perpendicularly to our sample plane [2]. A conjunction of time-resolved luminescence and fluorescence correlation spectroscopy allows us to fully characterize the photophysical properties of these hybrid emitters that feature excitation cross-sections and decay rates enhanced by more than one order of magnitude with respect to isolated organic dyes [3].

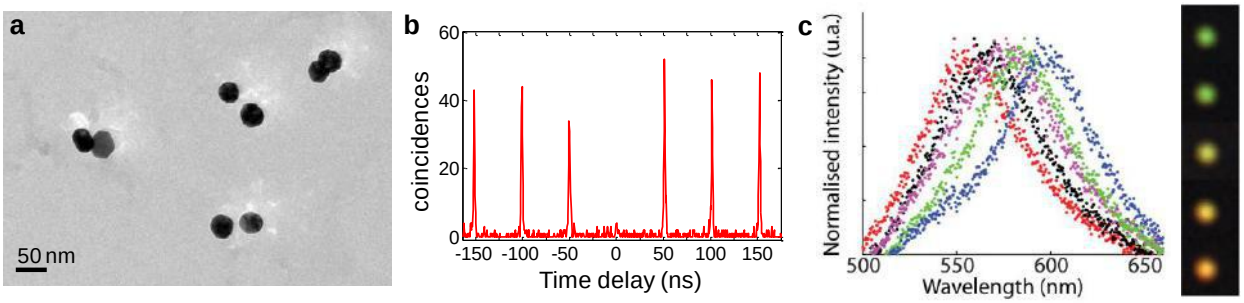



**Figure 1**: (a) Cryo-EM image of 40 nm AuNP dimers linked by a 30 base-pair DNA strand. (b) Photon antibunching from a single molecule in the center of a 40 nm AuNP dimer, that features a fluorescence lifetime of a few tens of ps. (c) Evolution of the scattering signal from a single 40 nm AuNP dimer, when increasing the salt concentration, measured with a confocal spectrometer (left) or a color camera (right).

Furthermore, the nanometer-scale sensitivity of plasmon coupling allows the translation of minute morphological changes in nanostructures into macroscopic optical signals. In particular, single nanostructure scattering spectroscopy provides a direct estimation of interparticle distances in gold nanoparticle dimers linked by a short DNA double-strand [4]. This spectroscopic information can be inferred from simple widefield

measurements on a calibrated color camera (figure 1-c) [5]. This allows us to analyze the influence of electrostatic and steric interparticle interactions, as well as amphiphilic surface chemistries, on the morphology of DNA-templated AuNP groupings [6]. We apply this spectroscopic characterization to identify dimers featuring two different conformations of the same DNA template. In practice, the biomolecular scaffold contains a hairpin-loop that opens after hybridization to a specific DNA sequence and increases the interparticle distance [7]. These results open numerous perspectives for the parallel colorimetric sensing of single biomolecules using dynamic plasmon rulers.

**Acknowledgements**, This work was supported by Agence Nationale de la Recherche via projects ANR 11 BS10 002 02 and ANR 11 JS10 002 01, by LABEX WIFI (Laboratory of Excellence within the French Program "Investments for the Future") under references ANR-10-LABX-24 and ANR-10-IDEX-0001-02 PSL* and by Region Ile de France in the framework of DIM Nano-K.

**REFERENCES**

1. M. P. Busson, B. Rolly, B. Stout, N. Bonod, and S. Bidault, *Nat. Commun.* 3, 962, 2012.
2. M. P. Busson and S. Bidault, *Nano Lett.* 14, 284, 2014.
3. M. P. Busson, B. Rolly, B. Stout, N. Bonod, J. Wenger, and S. Bidault, *Angew. Chem. Int. Ed.* 51, 11083, 2012.
4. M. P. Busson, B. Rolly, B. Stout, N. Bonod, E. Larquet, A. Polman, and S. Bidault, *Nano Lett*. 11, 5060, 2011.
5. L. Lermusiaux, V. Maillard, and S. Bidault, *ACS Nano* 9, 978, 2015.
6. L. Lermusiaux and S. Bidault, *Small* 11, 5696, 2015.
7. L. Lermusiaux, A. Sereda, B. Portier, E. Larquet, and S. Bidault, *ACS Nano* 6, 10992, 2012.

# The Active Plasmonics Paradigm

**R. Caputo[1,2], L. De Sio[3], Ugo Cataldi[4], T. Maurer[2], R. Bachelot[2],**

[1] Department of Physics and CNR-NANOTEC
Università della Calabria,
87036 Arcavacata di Rende (CS), Italy

[2] Laboratoire de Nanotechnologie et d'Instrumentation Optique, ICD CNRS UMR n°6281,
Université de Technologie de Troyes,
CS 42060, 10004 Troyes, France

[3] Beam Engineering for Advanced Measurements Company,
Winter Park, Florida 32789, USA

[4] Dèpartement de Chimie Physique,
Universitè de Genève,
Quai Ernest-Ansermet 30, 1211 Gèneve, Switzerland

[*]corresponding author: roberto.caputo@fis.unical.it

**Abstract**- Remarkable properties are devised in systems exploiting plasmonic functionalities. After years of research in this direction, great results have been achieved in Photonics, Sensoristics, Bio-systems, Theragnostics and Metamaterials. Very often, despite the awesome functionality reported, these systems comprise an intrinsic limit in their "single use" applicability. The active plasmonics paradigm predicts, in a given plasmonic system, the presence of a tunable medium thus enabling the tunability of aforementioned functionalities. Following this design rule, a much wider scenario of possibilities is unveiled that breaks the gap between research, fundamental and/or applied, and realization of tangible "everyday use" devices.

The unique properties of plasmonic materials derive from the collective oscillation of free conduction electrons induced by the interaction of metal nanoparticles (NPs) with an external electromagnetic field, the so-called Localized Surface Plasmon Resonance (LSPR). The plasmonic response of a system containing NPs is usually evidenced by a very intense color, absent in the bulk material, as well as in individual atoms. Control of the spectral position of the plasmonic resonance is a hot-topic and can be enabled by modifying size and shape of NPs or their distribution. The intrinsic limit of such an approach is the realization of materials with possibly awesome but not adjustable functionalities: one sample, one function.

A very intriguing possibility is the use of an "active" host, through which it is possible to tune, in a dynamic and reproducible way, the spectral position of the NPs plasmonic resonance. Much effort has been recently spent to design host materials that can exercise such an influence on NPs. Here we report the scenario of possibilities considered up to now and suggest new ones. Attempts to realize tunable plasmonic systems often exploit the

combination of “hard” and “soft” matter. In this sense, the outstanding properties of Liquid Crystals (LCs) make them an ideal candidate for this role. Indeed, a convenient way to dynamically modify the plasmonic resonance frequency of a homogeneous (surface or bulk) distribution of mono-dispersed metal NPs is to vary the dielectric permittivity of the medium surrounding the NPs. LCs represent an excellent example of reconfigurable medium where the refractive index can be finely controlled by means of external stimuli (Electric or Magnetic field, Temperature). A demonstration of the use of LCs as a tunable host for gold NPs can be found in [1,2].
Another way to exploit the plasmonic tunability of a metal nanoparticles array is to act on NPs inter-distance. This idea has been implemented by coating a Polydimethylsiloxane (PDMS) substrate with mono- or multi-layers of gold NPs. The fabricated system is sensitive to mechanical stresses and, depending on NPs size and density, and on the number of gold layers, it is possible to induce a plasmonic shift as well as modifications of the shape of the resonance curves [3,4]. Finally, by precisely positioning emitters of different colors in the close vicinity of metal nanoparticles, it is possible to achieve another active control of plasmonic functionalities. In this case, the dominant emission wavelength of the metal/polymer anisotropic hybrid nanoemitter can be selected by altering the polarization state of the exciting light [5].

**REFERENCES**


1. L. De Sio, R. Caputo, U. Cataldi and C. Umeton, *J. Mat. Chem.* 21, 47, 18967 (2011).
2. L. De Sio, A. Cunningham, V. Verrina, C.M. Tone, R. Caputo, T. Bürgi and C. Umeton, *Nanoscale*, 4, 7619 (2012).
3. U. Cataldi, R. Caputo, Y. Kurylyak, G. Klein, M. Chekini, C. Umeton and T. Bürgi, *J. Mater. Chem. C*, 2, 7927 (2014).
4. T. Maurer, J. Marae-Djouda, U. Cataldi, A. Gontier, G. Montay, Y. Madi, B. Panicaud, D. Macias, P.-M. Adam, G. Lévêque, T. Bürgi and R. Caputo, *Front. Mat. Sci.* 9, 170 (2015).
5. X. Zhou, J. Wenger, F.N. Viscomi, L. Le Cunff, J. Béal, S. Kochtcheev, X. Yang, G.P. Wiederrecht, G. Colas des Francs, A. Singh Bisht, S. Jradi, R. Caputo, H. Volkan Demir, R.D. Schaller, J. Plain, A. Vial, X. Wei Sun and R. Bachelot, *Nano Lett.*, 15, 7458 (2015).



**Acknowledgements**

The author(s) would like to acknowledge networking support by the COST Action IC1208. www.ic1208.com

# Biocompatible Liquid Crystal Elastomers with Unique Properties for Cell Scaffolds.

**T. Mori, A. Sharma,[1] Y. Gao,[1] R. J. Clements,[3] E. J. Freeman,[3] C. Malcuit,[3] J. A. McDonough,[3] L. T. J. Korley,[4] T. Hegmann,[1] and E. Hegmann[1-3,*]**

*[1]Liquid Crystal Institute, Chemical Physics Interdisciplinary Program, [2]Department of Chemistry and Biochemistry, [3]Department of Biological Sciences, Kent State University, Kent, Ohio 44242, and [4]Macromolecular Science and Engineering Department, Case Western Reserve University, Cleveland (OH) 44106, USA*

[*]corresponding author: ehegmann@kent.edu

**Abstract**- Liquid crystal elastomers (LCEs), and liquid crystals (LCs) in general, combine order and mobility on a molecular (nanoscale level), and can respond rapidly to external stimuli such as temperature, elastic deformation, applied electric and magnetic fields, light, and thermal expansion[1]. LCEs responsiveness to external stimuli makes them excellent candidates for the replacement of human tissue[2,3] cellular delivery or as drug delivery systems.[4] We have already prepared series of smectic and nematic SC-LCEs, which have proven to be non-cytotoxic to soft tissue cell lines such as myoblasts, fibroblasts, and neuroblastomas.[5,6,7] These particularly designed LCEs show tunable internal morphology with either a porous 3D network spanning through the entire elastomer scaffold (inter-channels) or elastomers with a globular morphology. The tunable morphologies address a common issue in the area of tissue regeneration, necrosis (cell death) that is generally found in the center of most scaffolds due to a lack of tunable porosity. Tunable porosity allows for better mass transport of nutrients for healthier, viable cells throughout the scaffold.

LCEs comes to fulfill a need for creating new, more-adaptable scaffolds that would be able to report anisotropic growth of expanding cell lines back to the observer with an easily discernable optical response. The use of LCEs as porous scaffold for cell scaffolds would open up an entirely new area of application for LCEs where the LC properties can be exploited for the monitoring of cell attachment, expansion and tissue regeneration.

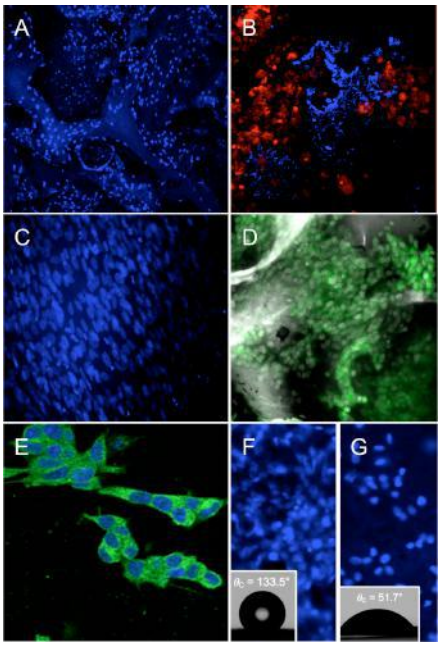



**Fig. 1** *C2C12 on: (A)* ***SC-LCE**$_{LBC}$* *foam and (B) globular* ***SC-LCE**$_{PhBz}$* *morphology. (C) HDFs on Swiss cheese* ***SC-LCE**$_{4\alpha\text{-}SBC}$* *morphology. SH-SY5Y on: (D)* ***SC-LCE**$_{3\gamma\text{-}SBC}$* *and (E)* ***SC-LCE**$_{3\alpha\text{-}SBC}$* *Swiss cheese morphology. C2C12s on* ***SC-LCE**$_{3\alpha SBC}$**: (F) before and (G) after $O_2$ plasma.*

In addition, changes in the birefringence of such elastomers due to an internal stress created by proliferating cells provides a unique means to non-invasively monitor cell expansion within these scaffolds without the need for cell fixing and staining.

We will present new and interesting optical and mechanical properties obtained by slight modifications on the choice of monomers and crosslinking moieties.

## References


1 Kim, Y. -K., Senyuk, B. and Lavrentovich, O. D., “Molecular reorientation of a nematic liquid crystal by thermal expansion”, *Nat. Commun.* Vol. 3, 1133, 2012.

2 Younes, H. M., Bravo-Grimaldo, E. and Amsden B. G., “Synthesis, characterization and in vitro degradation of a biodegradable elastomer”, *Biomaterials,* Vol. 25, 5261-5269, 2004.

3 Amsden, B., Misra, G., Marshall, M. andTurner, N., “Synthesis and characterization of biodegradable networks providing saturated-solution prolonged delivery,” *J. Pharmaceut. Sci.*, Vol. 97, 860-874, 2008.

4 Liu, X. H., Jin, X. B. and Ma, P. X., “Nanofibrous hollow microspheres self-assembled from star-shaped polymers as injectable cell carriers for knee repair,” *Nat. Mater*., Vol. 10, 398-406, 2011.

5 Sharma, A., Neshat, A., Mahnen, C. J., Nielsen, A. d., Snyder, J., Stankovich, T.L., Daum, B.G., LaSpina, E.M., Beltrano, G., Li, S., Park, B.- W., Clements, R. J., Freeman, E.J., Malcuit, C., McDonough, J. A., Korley, L. T. J., Hegmann, T. and Hegmann, E., “Biocompatible, biodegradable and porous liquid crystal elastomer scaffolds for spatial cell cultures”, *Macromol. Biosci*., Vol. 15, 200-2014, 2015.

6 Bera, T., Freeman, E. J., McDonough, J. A., Clements, R. J., Aladlaan, A., Miller, D.W., Malcuit, C., Hegmann, T. and Hegmann, E., *ACS Appl. Mater. Interfaces*, Vol. 7, 14528-14535, 2015.

7 Gao, Y., Manning, S., Zhao, Y., Nielsen, A. d., Mori, T., Neshat, A., Sharma, A., Mahnen, C. J., Everson, H. R., Crotty, S., Clements, R. J., Malcuit, C. and Hegmann, E., *ACS Macro Lett.*, Vol. 5, 4-9, 2016.

# Optical Activity in Organic-Silver Hybrid Nanoparticles

**F. Hidalgo**[1] **and Cecilia Noguez**[1*]

[1]Instituto de Fisica, Universidad Nacional Autonoma de Mexico, Mexico

[*]corresponding author: cecilia@fisica.unam.mx

**Abstract**- The optical activity in organic-metal hybrid nanoparticles (NP) is studied using a time-perturbed density functional theory that determines the electronic circular dichroism (CD) of chiral systems. The effects of the number of organic molecules, their chiral nature, and different chiral arrangements of they are analyzed in detail. CD spectra, along with results of the atomic distortions and electronic states allow identify the origin and consequences of the induced chirality of the arrangements in comparison with the intrinsic chirality of ligands, and when both act simultaneously. These results would be significant in the identification and discussion of the experimental chiroptical response of these organic-metal hybrid NPs. Additionally, this latter might allow develop new strategies to increase the sensitivity of chiroptical spectroscopies.

Chiral systems are optically active and exhibit circular dichroism (CD) in the same spectral region where optical absorption occurs. CD spectroscopy is capable to measure small differences in extinction between right and left circularly polarized-light, which makes it a very sensitive tool to account for small chiral asymmetries. However, CD signals are very small in intensity as compared to optical extinction itself, limiting the analysis to samples containing large concentrations of chiral molecules, and/or large excess of one enantiomer (pure left-handed or right-handed), being this latter very difficult and expensive to achieve. Therefore, increasing the limits of detection in chiral spectroscopies would have significant impact in pure and applied sciences, with direct consequences on pharmaceutics, bio- and/or nanotechnology, asymmetric catalysis, and other emerging fields.

The optical activity of chiral L-Cysteine, and achiral $SCH_3$ ligands adsorbed on icosahedral $Ag_{55}$ is investigated within a time-perturbed density functional theory. After atomic optimizations, the chiroptical response of these organic-metal hybrid nanoparticles is studied by analyzing: (i) the electronic circular dichroism (CD), (ii) the asymmetry of the atomic geometries, and (iii) the electronic density of states. Besides the intrinsic chiral nature of the ligands, CD spectra are examined as a function of the number of ligands adsorbed. Also, different low-energy achiral and chiral ligand arrangements are investigated, including both left- and right-handed arrays, as well as the racemic mixtures.

While separately $SCH_3$ and icosahedral $Ag_{55}$, the achiral organic and metal building parts are not optically active and consequently have null CD. The hybrid obtained by adsorbing the ligands in a chiral arrangement shows a large CD response at the visible and less intense at the UV region. The mirror image of the chiral arrangement can be also built, confirming that such hybrids behave as enantiomers, i.e., both CD spectra have alike line-shapes but with opposite sign, thus racemates have null CD. This result permits identify the visible spectral region as where the induced chirality by the ligand array is more evident.

When using chiral L-Cysteine ligands, the optimized low-energy hybrid nanoparticles are always chiral.

Their CD spectra remarkably differ from the single peak observed at the UV region when the L-Cysteine is alone. Now, new spectral features appear at the visible region (between 1–3 eV), together with an intense peak at the same energy where the CD signal of L-Cysteine was found. Analyzing the achiral arrangements it is concluded that the intensity of this particular peak, and the spectral features around the UV region (between 3–6 eV) are quite proportional to the number of adsorbed ligands. While at lower energies this proportionality is not observed.

Additionally, supramolecular chiral nanoparticles can be formed when the arrangement of the chiral ligands is also chiral. Now, CD spectra have contributions from both, the intrinsic chirality of the ligand and the induced chirality of the ligand array. The racemates in array using chiral ligands confirm that at the energy where the CD signal of L-Cysteine is present, the intensity is still proportional to the number of adsorbed ligands

**Acknowledgements**. Authors acknowledge the partial support from DGAPA-UNAM project PAPIIT IN107615 and CONACyT project 179454.

**REFERENCES**

1. Hidalgo, F.; Noguez, C. “Optical Activity of Achiral Ligand $SCH_3$ Adsorbed on Achiral $Ag_{55}$ Clusters: Relationship between Adsorption Site and Circular Dichroism,” *ACS Nano,* Vol. 7, No. 1, 513–521, 2013.
2. Hidalgo, F.; Noguez, C.; Olvera de la Cruz, M. “Metallic influence on the atomic structure and optical activity of ligand-protected nanoparticles: a comparison between Ag and Au,” *Nanoscale,* Vol. 6, No. 6, 3325–3334, 2014.
3. Noguez, C.; Sánchez-Castillo, A.; Hidalgo, F. J. “Role of Morphology in the Enhanced Optical Activity of Ligand-Protected Metal Nanoparticles”, *Phys. Chem. Lett.,* Vol. 2, No. 9, 1038–1044, 2011.

# Plasmonics of Dielectric−Metallic Hybrid Nanostructures

**H. J. Chen**[1*], **H. Wang,**[1] **Z.-K. Zhou**[2]

[1]State Key Laboratory of Optoelectronic Materials and Technologies, Guangdong Province Key Laboratory of Display Material and Technology, and School of Electronic and Information Technology, Sun Yat-sen University, Guangzhou 510275, China

[2]School of Physics and Engineering, Sun Yat-sen University, Guangzhou 510275, China

[*]corresponding author: chenhj8@mail.sysu.edu.cn

**Abstract**-Hybrid nanostructures composed of dielectric and metallic components can exhibit intriguing plasmonic properties, which can be utilized for tailoring and enhancing various light−matter interactions. Two recent progresses of our study will be presented. We will first show that Au−silicon nanosphere dimers can exhibit strong unidirectional light scattering behaviors in the visible range. Secondly, we will demonstrate the nonlinear optical properties of hybrid dielectric and plasmonic nanostructure arrays, which can further be utilized for enhancing the photocurrent generation of semiconductors.

Plasmonic structures can shape their surrounding electromagnetic environment and therefore tailor and enhance various optical processes, such as light absorption, emission, scattering, and nonlinear optical properties, at the nanoscale. In recent years, one type of plasmonic structure, i.e. hybrid nanostructures composed of dielectrics and plasmonic metals, has gain much attention due to its extraordinary plasmonic properties derived from the synergistic interactions between the different optical resonance modes in these two components.[1] In this presentation I will mainly talk about two of our recent progresses, which include the unidirectional scattering of dimers composed of Au and Si nanospheres, and plasmonic properties of metallic−dielectric nanostructure arrays.

Si nanosphere with high refractive index can exhibit magnetic resonance in the visible. By bringing the silicon nanosphere close to the Au nanosphere, strong hybridization will happen between the magnetic mode and dipolar plasmon mode. Such a hybridization gives rise to unidirectional light scattering with enhanced forward scattering and suppressed backward scattering in a specific narrow wavelength range.[2] The unidirectional scattering is strongly dependent on the sizes of the nanospheres as well as the separations between them. These results can be beneficial for nanoscale light routing and manipulating.

Hybrid nanostructure array is another topic that have gained much interest due to its potentials in large-area photonic device applications. We propose a centimeter-scale hybrid plasmonic arrays composed of dielectric@Au core−shell nanorods. Such hybrid nanorod arrays exhibit exotic collective plasmon modes dependent on the angles of the incidence light. Due to their ability of focusing free-space light, the hybrid nanorod arrays can exhibit strong nonlinear multiphoton avalanche emission. The luminescence band can cover ~300 nm from the visible into the near infrared region. Furthermore, the strong electric field enhancement of the nanorod array can be utilized for enhancing the photocurrent generation efficiency of a wide band-gap semiconductor. The enhancement factor can reach up to 220 times.

**Acknowledgements**. This work was supported in part by the National Natural Science Foundation of China

(Grant Nos. 11474364, 51290271), the Guangdong Natural Science Funds for Distinguished Young Scholars (Grant No. 2014A030306017).

**REFERENCES**

1. Schuller, J. A., Barnard, E. S., Cai, W. S., Jun, Y. C., White, J. S. and Brongersma, M. L., "Plasmonics for extreme light concentration and manipulation." *Nat. Mater.*, Vol. 9, 193–204, 2010.
2. Wang, H., Liu, P., Ke, Y. L., Su, Y. K., Zhang, L., Xu, N. S., Deng, S. Z. and Chen, H. J. "Janus magneto–electric nanosphere dimers exhibiting unidirectional visible light scattering and strong electromagnetic field enhancement." *ACS Nano*, Vol. 9, 436–448, 2015.
3. Zhou, Z.-K., Xue, J. X., Zheng, Z. B., Li, J. H., Ke, Y. L., Yu, Y., Han, J.-B., Xie, W. G., Deng, S. Z., Chen, H. J. and Wang, X. H. Centimeter-scale sub-10 nm gap plasmonic nanorod array film as a versatile platform for enhancing light–matter interactions." *Nanoscale*, Vol. 7, 15392–15403, 2015.

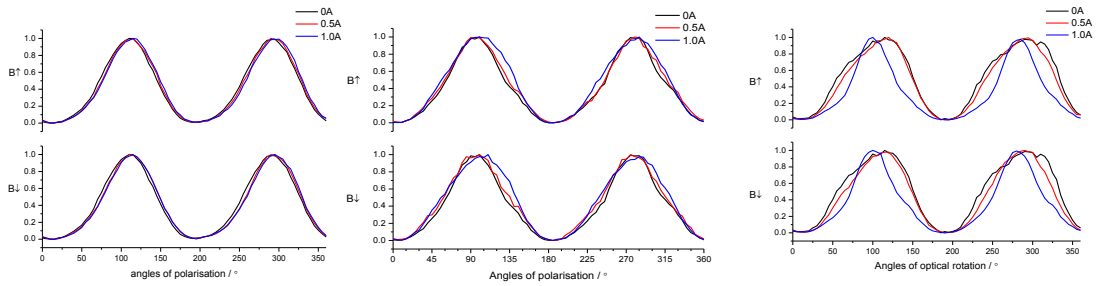
# Magneto-chiral Effect in Hybrid Plasmonic Nanostructures

**Marion Rodier[1], Christopher Kelly[1], Affar Karimullah[1], Calum Jack[1], Ryan Tullius[1] and Malcolm Kadodwala[1]**

[1]School of Chemistry, Joseph Black building, University of Glasgow, Glasgow G12 8QQ, UK.

**Abstract** The magneto-chiral effect occurs in magnetic chiral media, and can be detected by use of polarised light. Although this effect is of interest in the study of the light matter interaction, it has not been studied in depth because of the important magnetic field needed to observe it, and the weakness of the effect. Hybrid plasmonic nanostructures were used to detect a magneto chiral effect. The aim here was also to detect this effect at a low magnetic field with a high intensity.

The magneto-chiral effect has been observed, in molecules and crystals, using strong magnetisation (about 3T), and drastic conditions such as extremely low temperature[3]. We propose to study this phenomenon at low magnetic field (0.003T) and at ambient temperature. We therefore used a home design hybrid chiral plasmonic material, consisting of left and right handed nanostructures[4], coated by a layer of 100nm gold and 100nm nickel. The non-linear optical technique, second harmonic generation (SHG) was used to generate S-polarised and P-polarised light. Our material was set up with a magnetic field directed parallel or anti-parallel to the plane of the sample.The absorption of the polarised light, in the magnetised chiral material, relative to the direction of the magnetisation was recorded. We compared the results from the left and right handed structures with those of non-chiral media. The response changes between P-polarised and S-polarised light, because the light is respectively parallel and perpendicular to the magnetic field.




Gold Left-handed Right-handed

**Figure1: Optical rotation of the S-polarised light with an increasing magnetic field in two opposite directions.**

We can see in figure 1 that there is no change in the polarised light for the gold. The left handed structure shows that as we increased the magnetic field, the peak became broader, meaning that the contribution of the magnetic quadrupole increased. In the right handed structure the opposite effect was observed: as we increased the field the magnetic quadrupole contribution decreased. These results are summarised in figure 2 showing the chirality of the effect.

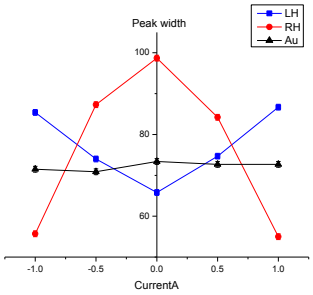
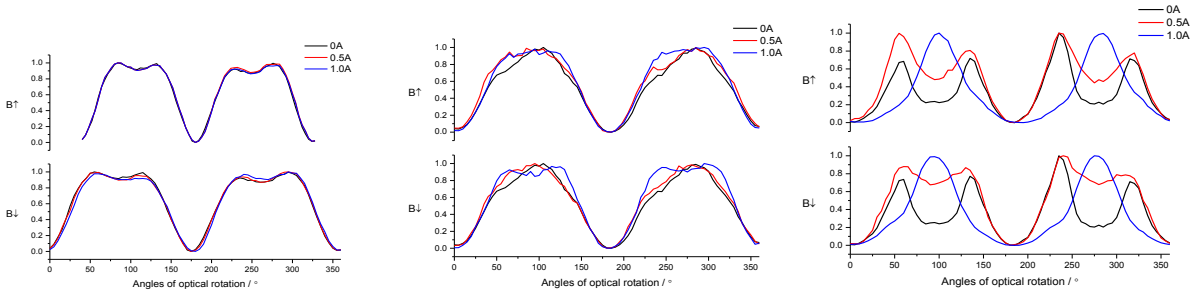



**Figure 2: Peak width relative to the magnetic field in the left-handed and right-handed structures, compared to the gold for the S-polarised light.**




Gold Left-handed Right-handed

**Figure 3: Optical rotation of the P-polarised light with an increasing magnetic field in two opposite direction.**

In figure 3 we can see that we observed a similar effect to the one for S-polarised. Here however the magnetic quadrupole contribution is changing due to the change in the direction of the light. Figure 4 shows a chiral response as well, except that the effect is less pronounced than for S-polarised light.

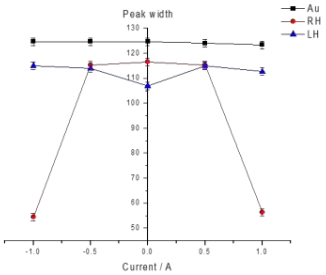



**Figure 4: Peak width relative to the magnetic field for the left-handed and right-handed structures compared to the gold for the P-polarised light.**

## REFERENCES


1. G. H. Wagnière. "*The magnetochiral effect and related optical phenomena*" Chem. Phys. 245 _1999. 165–173.
2. G. L. J. A. Rikken & E. Raupach "*Observation ofmagneto-chiral dichroism*" lett. Nat VOL 390 1997.
3. R. Sessoli, M. Boulon, A. Caneschi, M. Mannini, L. Poggini, F. Wilhelm and A. Rogalev. "*Strong magneto-chiral dichroism in a paramagnetic molecular helix observed by hard X-rays*" nat. Phys 10.1038 (2014).
4. A. S. Karimullah, C. Jack, R. Tullius, V. M. Rotello , G. Cooke, N. Gadegaard , L. D. Barron, and M. Kadodwala: Plasmonics: "*Disposable Plastic Templated Plasmonic Metamaterials with Tunable Chirality*" adv. Mater 201501816.

**Electrochemical control of plasmonic nanomaterial surface chemistry**

Christy F. Landes
Department of Chemistry, Department of Electrical and Computer Engineering
Rice University, Houston, TX 77005 USA

**Abstract**

Novel chemical and physical processes occur at nanoparticle surfaces, both aided and reported by the broad tunability of their plasmonic properties. Electrochemical tuning is one way to control both plasmon resonance shifts and underlying morphology, composition, and surface chemistry. We approach this challenge with electrochemical redox tuning of metallic nanoparticles and assembled structures. Our method allows us, for example, to electrodeposit silver and/or its salts on the surface of gold nanostructures and selectively grow silver metal on the surface of these structures. We demonstrate repeatable spectro-electrochemical tuning of single nanoparticles and dimers. Potential applications include novel heterogeneous catalysis routes, experimental tests of charge transfer plasmonics, and nanoscopic plasmonic switches.

# Enhancing Solar Cells and Photocatalysis via Plasmonic Nanostructures

**Dongling Ma**[1]

[1] Institut National de la Recherche Scientifique, Center of Energy, Materials and Telecommunications Quebec, Canada

[*]corresponding author: ma@emt.inrs.ca

**Abstract**- With unique surface plasmon resonance properties and high potential for many important applications, plasmonic nanostructures are attracting more and more attention in the past decade. In this presentation, the development of several types of plasmonic nanostructures by wet chemical method or pulsed laser ablation will be introduced first. Their interesting optical properties and their applications in solar cells and photocatalysis will then be presented and discussed.

Harvesting a wide range of solar photons from UV to visible and further to near infrared represents an attractive approach to improve the power conversion efficiency of photovoltaics, since most of the solar cells are only able to efficiently capture photons in the UV and visible ranges. The same dilemma exists in photocatalysis. With unique, size- and shape-tunable surface plasmon resonance, plasmonic nanostructures have recently been explored for enhancing the efficiency of solar cells and photocatalysis via improved light scattering, strong near field effect and/or hot electron injection. Herein, I will present some of our recent development in Au and Ag plasmonic nanostructures and their applications in solar cells (mainly quantum dot based solar cells and dye sensitized solar cells) and photocatalysis [1-5]. One example is about our recent synthesis of a new class of materials: plasmonic Au nanoparticle decorated upconverting- $NaYF_4$:$Yb^{3+}$, $Er^{3+}$, $Tm^{3+}$ -core@porous-$TiO_2$-shell microspheres with uniform size distribution, high surface area and excellent stability and reusability. The structure was rationally designed in such a way to simultaneously maximize the beneficial effects of plasmonics and upconversion towards largely enhanced broadband photocatalysis. As a consequence, the nanohybrid catalysts developed herein exhibit broadband absorption from UV up to near infrared and excellent photocatalytic activity, significantly better than the benchmark $TiO_2$ (Degussa P25). Different mechanisms were found to dominate under separate UV, visible and near infrared excitations and critical factors were identified. Optical and energy-transfer properties were further modeled theoretically to support our interpretations of the catalytic mechanisms. In addition to yielding novel and interesting materials and properties, the current work also provides physical insights that can contribute to the future development of plasmon-enhanced broadband catalysts.

**Acknowledgements.** The author would like to acknowledge financial support from the Natural Sciences and Engineering Research Council of Canada and Fonds de la recherche sur la nature et les technologies. The author sincerely thanks all co-authors shown below for their contributions.

**REFERENCES**

1. Liang, H., Rossouw, D., Zhao, H., Cushing, S. K., Shi, H., Korinek, A., Xu, H., Rosei, F., Wang, W., Wu, N., Botton, G. A. and Ma, D. *J. Am. Chem. Soc.*, 135, 9616-9619, 2013.
2. Xu, Z., Quintanilla, M., Vetrone, F., Govorov, A. O., Chaker, M., and Ma, D., *Adv. Funct. Mater.*, *25*, 2950-2960, 2015 **(*Front Cover*)**.
3. Liang, H., Zhao, H., Rossouw, D., Wang, W., Xu, H., Botton G. A. and Ma, D., *Chem. Mater*. 24, 2339-2346, 2012.
4. Liang, H., Li, Z., Wang, Z., Wang, W., Rosei, F., Ma, D. and H. Xu, *Small* 8, 3400-3405, 2012.
5. Li, S. Zhang, J., Kibria, M. G., Mi, Z., Chaker, M., Ma,* D., Nechache*, R and Rosei*, F. *Chem. Commun*. 49, 5856-5858, 2013.

# Plasmon-enhanced heteronanostructures for photocatalysis

**S. M. Bahauddin, H. Robatjazi, C. Doiron, X. Liu, T. Tumkur, P. Wray, W.-R. Wang, B. Jiang, I. Thomann***

Electrical and Computer Engineering, Department of Materials Science and Nanoengineering, Department of Chemistry, Rice University, Houston, Texas, USA

*corresponding author: isabell.thomann@rice.edu

**Abstract**-We will present optical cavity structures for efficient light absorption within plasmonic and low-dimensional thin films, resulting in efficient hot electron generation for solar water splitting. Furthermore, we will discuss fabrication of ultrathin AAO membranes to serve as generic templates for centimeter scale nanostructure fabrication with sub-100 nm feature sizes. Time permitting, I will discuss charge carrier dynamics and imaging of plasmon-enhanced heteronanostructures for photocatalysis.

We will present optical cavity structures for broadband or select light absorption within plasmonic [1], metallic/dielectric [2] and low-dimensional thin films [3]. Furthermore, we will discuss fabrication of ultrathin (200 nm) anodic aluminum oxide (AAO) membranes to serve as generic templates for centimeter scale nanostructure fabrication with sub-100 nm feature sizes [2]. Light absorption within plasmonic nanoparticles can be significantly enhanced by optical cavity structures, resulting in efficient hot electron generation. In the case of hot electron generation, we present a Schottky barrier-free photoelectrode architecture that allows for direct hot electron injection into the adjacent electrolyte [1] for solar water splitting. On the substrate side, the plasmonic particles are in contact with a wide band gap oxide film that serves as an electron blocking layer but accepts holes and transfers them to the counter electrode. The observed photocurrent spectra follow the plasmon spectrum, and demonstrate that the extracted electrons are energetic enough to drive the hydrogen evolution reaction. A similar structure can be designed to achieve broadband absorption enhancement in monolayer $MoS_2$ [3]. Time permitting, I will discuss charge carrier dynamics in hybrid nanoparticles composed of plasmonic / two-dimensional materials, and photo-induced force microscopy to image these nanostructures.

**Acknowledgements** We gratefully acknowledge support from the Robert A. Welch Foundation (Grant No. C-1825) and the National Science Foundation (NSF CAREER Award, CHE- 1352579, and the NSF MRI CHE-1428184).

**REFERENCES**

1. Robatjazi, H., Bahauddin, S.M., Doiron, C., and I. Thomann, "Direct Plasmon-Driven Photoelectrocatalysis," *Nano Lett.*, 2015, 15 (9), pp 6155–6161.
2. Robatjazi, H., Bahauddin, S.M., MacFarlan, L., Fu, S. and I. Thomann, "Ultra-thin AAO membrane as a generic template for sub-100 nm nanostructure fabrication," *submitted*.
3. Bahauddin, S.M., Robatjazi, H., and I. Thomann, "Broadband absorption engineering to enhance light absorption in monolayer $MoS_2$," *submitted*.

# Spatial Control of Chemical Processes on Nanostructures through Nano-Localised Water Heating

Calum Jack1, Affar S. Karimullah1,2*, Ryan Tullius1, Larousse Khosravi Khorashad4, Marion Rodier1, Brian Fitzpatrick1, Laurence D. Barron1, Nikolaj Gadegaard2, Adrian J. Lapthorn1, Vincent M. Rotello3, Graeme Cooke1, Alexander O. Govorov4, Malcolm Kadodwala1*

1School of Chemistry, Joseph Black Building, University of Glasgow, Glasgow, G12 8QQ, UK.

2School of Engineering, Rankine Building, University of Glasgow, Glasgow, G12 8LT, UK.

3Department of Chemistry, 710 Nt. Pleasant Street, University of Massachusetts Amherst, MA 01003, USA.

4Department of Physics and Astronomy, Ohio University, USA

*

Optimal performance of nanophotonic devices, including sensors and solar cells, requires maximising the interaction between light and matter. This efficiency is optimised when active moieties are localised in areas where electromagnetic (EM) fields are confined. Confinement of matter in these “hot spots” has previously been accomplished through inefficient “top-down” methods. Here we report a rapid “bottom-up” approach to functionalise selective regions of plasmonic nanostructures that utilises nano-localised heating of the surrounding water induced by pulsed laser irradiation. This localised heating is exploited in a chemical protection / de-protection strategy to allow selective regions of a nanostructure to be chemically modified. As an exemplar, we use the strategy to enhance the biosensing capabilities of a chiral plasmonic substrate. This novel spatially selective functionalisation strategy provides new opportunities for efficient high-throughput control of chemistry on the nanoscale over macroscopic areas for device fabrication.

# Engineering the Electromagnetic Properties of Plasmonic Nanohybrids for Solar Water Splitting

**L. Razzari[1]*, J. Zhang[2], X. Jin[1], P. I. Morales-Guzman[1], J. Claverie[2*]**

[1] INRS-EMT, 1650, Boul. Lionel-Boulet, Varennes, Quebec, J3X 1S2, Canada
[2] NanoQAM, Department of Chemistry, UQAM Succ Centre Ville, CP8888, Montreal, Quebec, H3C 3P8, Canada
*corresponding authors: razzari@emt.inrs.ca, claverie.jerome@uqam.ca

**Abstract:** We will present engineered plasmonic nanohybrids featuring an enhanced photocatalytic activity in the solar spectral range. Details about their electromagnetic design and experimental evidences of their efficacy in water splitting experiments will be provided. Our findings show a possible route towards the design of full solar spectrum photocatalysts.

Surface plasmon resonance (SPR) effects have been recently exploited to build photocatalysts that are active in the visible spectral range [1,2]. In a typical arrangement, these plasmonic photocatalysts combine a semiconductor material, transparent in the visible region (such as nanospheres of titanium dioxide - $TiO_2$) and a nanoplasmonic counterpart (e.g. gold nanoparticles - Au NPs). However, specific SPRs cover the visible spectrum only partially and are generally endowed with weak light absorption. In our investigation, we aimed at optimizing the electromagnetic properties of plasmonic photocatalysts to increase their activity under solar illumination.

Using numerical simulations, and by properly tuning the relative position and size of the photocatalysts' constituents, we have designed nanohybrids with a reinforced plasmonic absorption, extending over the entire visible range, and with an enhanced local electric field at the Au-$TiO_2$ interface. Indeed, these properties can promote the generation of "hot electrons" (within the Au NP) and their transfer into the $TiO_2$ sphere, resulting in an increased photocatalytic activity [3,4]. The key ingredient of our design is the exploitation of resonant cavity modes (namely, "whispering gallery modes" [5]), which develop in the $TiO_2$ sphere when its size is properly adjusted.

Such structures have then been chemically synthesized and experimentally characterized by means of absorption spectroscopy and Raman measurements, which have confirmed the distinctive electromagnetic properties of the fabricated nanohybrids. In accordance with these evidences, such optimized plasmonic photocatalysts, when employed in water splitting experiments, have shown an enhanced activity under solar illumination.

Figure 1 shows the TEM image of one particular geometry that has been fabricated and tested: nanohybrids composed of Au multimers (Au NP diameter: 60 nm) half-embedded in $TiO_2$ spheres (440 nm in diameter). These WGM-assisted plasmonic photocatalysts have shown the ability to efficiently harvest photons with energies below the $TiO_2$ bandgap for hydrogen production.

Detailed results highlighting the role of the nanohybrids' geometry and size in the enhancement of the photocatalytic activity will be presented on site.

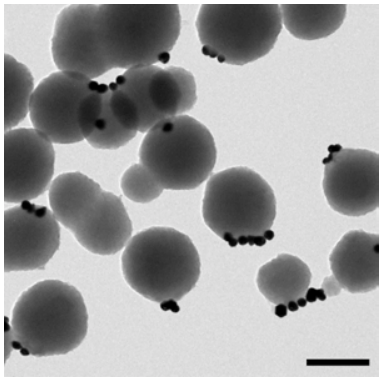


**Figure 1:** TEM micrograph of nanohybrids composed of Au multimers half-embedded in $TiO_2$ spheres. The scale bar is 500 nm.

**Acknowledgements** The authors are grateful for financial support from the Natural Sciences and Engineering Research Council of Canada (NSERC), the Fonds de Recherche du Québec − Nature et Technologies (FRQNT), and PRIMA Québec.

**REFERENCES**

1. Linic, S., Christopher, P., Ingram, D. B., "Plasmonic-Metal Nanostructures for Efficient Conversion of Solar to Chemical Energy," *Nat. Mater.* **2011**, *10*, 911–921.
2. Hou, W. and Cronin, S. B., "A Review of Surface Plasmon Resonance-Enhanced Photocatalysis," *Adv. Funct. Mater.* **2013**, *23*, 1612–1619.
3. Qian, K., Sweeny, B. C., Johnston-peck, A. C., Niu, W., Graham, J. O., Joseph, S., Qiu, J., Wang, Y., Engelhard, M. H., Su, D., Stach, E. and Wei, W. D., "Surface Plasmon-Driven Water Reduction : Gold Nanoparticle Size Matters," *J. Am. Chem. Soc.* **2014**, *136*, 9842–9845.
4. Seh, Z. W., Liu, S., Low, M., Zhang, S.-Y., Liu, Z., Mlayah, A., Han, M.-Y., "Janus Au-$TiO_2$ Photocatalysts with Strong Localization of Plasmonic near-Fields for Efficient Visible-Light Hydrogen Generation," *Adv. Mater.* **2012**, *24*, 2310–2314.
5. Yang, S., Wang, Y., Sun, H., "Advances and Prospects for Whispering Gallery Mode Microcavities," *Adv. Opt. Mater.* **2015**, *3*, 1136–1162.

# Plasmon-induced photoenergy conversion systems

**Hiroaki Misawa**[1,2*]

[1]Research Institute for Electronic Science, Hokkaido University, Sapporo 001-0021, Japan

[2]Department of Applied Chemistry & Institute of Molecular Science, National Chiao Tung University, 1001 Ta Hsueh R., Hsinchu 30010, Taiwan

[*]corresponding author: misawa@es.hokudai.ac.jp

We have demonstrated plasmonic photocurrent generation from visible to near-infrared wavelengths without deteriorating photoelectric conversion using electrodes in which gold nanorods are elaborately arrayed on the surface of a $TiO_2$ single crystal.[1-3] We have also reported the stoichiometric evolution of oxygen via water oxidation by irradiating the plasmon-enhanced photocurrent generation system with near-infrared light.[4-6] In the present study, we developed a plasmon-assisted water splitting system that operates under irradiation by visible light; the system is based on the use of two sides of the same strontium titanate ($SrTiO_3$) single crystal substrate.[7] The water splitting system contains two solution chambers to separate hydrogen ($H_2$) and oxygen ($O_2$), respectively. To promote water splitting, a chemical bias was applied by pH values regulations of those chambers. The quantity of $H_2$ evolved from the surface of platinum, which was used as a reduction co-catalyst, was twice of $O_2$ evolved from an Au nanostructured surface. Thus, the stoichiometric evolution of $H_2$ and $O_2$ was clearly demonstrated. The hydrogen evolution action spectrum closely corresponds to the localized surface plasmon resonance spectrum, indicating that the plasmon-assisted charge separation at the Au/$SrTiO_3$ interface promotes water oxidation and the subsequent reduction of a proton on the backside of the $SrTiO_3$ substrate.

According to the analogous method of the water splitting system, we have successfully constructed the artificial-photosynthesis system which produces the ammonia by a photofixation of a nitrogen molecule based on visible light irradiation.[8] Unlike the water splitting system, ruthenium is used as a co-catalyst instead of a platinum for the ammonia synthesis, and not a solution system but a gas system is used to reduce nitrogen gas. The action spectrum of the apparent quantum efficiency of ammonia evolution showed good agreement with the plasmon resonance spectrum. In addition, we revealed that ammonia can be obtained with ~100% selectivity by using zirconium/zirconium oxide cocatalyst.[9] These findings blaze new methods for energy-efficient photocatalytic production of ammonia using solar light, water, and nitrogen gas, which are entirely different from conventional methods of ammonia synthesis.

**REFERENCES**

1. Nishijima, Y., Ueno, K., Yokota, Y., Murakoshi, K., Misawa, H. *J. Phys. Chem. Lett.* **2010**, 1, 2031-2036.
2. Gao, S.; Ueno, K.; Misawa, H. *Accounts. Chem. Res.*, **2011**, 44, 251-260.
3. Shi, X., Ueno, K., Oshikiri, T., Misawa, H. *J. Phys. Chem. C*, **2013**, 117, 24733-24739.
4. Nishijima, Y., Ueno, K., Kotake, Y., Murakoshi, K., Inoue, H., Misawa, H. *J. Phys. Chem. Lett.*, **2012**, 3, 1248-1252.
5. Shi, X., Ueno, K., Takabayashi, N., Misawa, H. *J. Phys. Chem. C*, **2013**, 117, 2494-2499.
6. Ueno, K., Misawa, H. *NPG Asia Mater.*, **2013**, 5, e61.
7. Zhong, Y., Ueno, K., Mori, Y., Shi, X., Oshikiri, T., Murakoshi, K., Inoue, H., Misawa, H. *Angew. Chem. Int. Ed.*, **2014**, 53, 10350-10354.
8. Oshikiri, T., Ueno, K., Misawa, H., *Angew. Chem. Int. Ed.*, **2014**, 53, 9802-9805.
9. Oshikiri, T., Ueno, K., Misawa, H., *Angew. Chem. Int. Ed.*, **2016**, accepted for publication.

# Optical liquid biopsy in microfluidic devices

Ramón A. Álvarez-Puebla[a,b,c,d]

[a]Departamento de Química Física e Inorgánica, Universitat Rovira i Virgili, Avda. Països Catalans, Tarragona, Spain.
[b]Centro de Tecnología de la Química de Cataluña, Carrer de Marcel•lí Domingo, Tarragona, Spain
[c]Medcom Advance S.A., Viladecans, Barcelona, Spain
[d]ICREA, Avenida LLuis Companys, Barcelona, Spain

Detection of circulating tumor cells (CTCs) and their proteinic or nucleic acid markers in bloodstream has recently gained a clinical relevance since they suppose potential criteria for prognosis and diagnosis of cancer progression. Despite the efforts focused on developing methods for the direct identification of them, their extremely low concentration in blood have led to a generation of new technologies dedicated to their enrichment and capturing, taking advance of the presence of specific cell surface markers or other physical properties. These additional steps increase the operation time and require of advanced instrumentation.

Herein, we report a fast and direct optical methods for the identification of oncogenic proteins, DNA mutations and cell discrimination and quantifications using light in microfluidic devices.

# Modal engineering in plasmonic crystalline colloidal systems.

**Upkar Kumar[1*], Sviatlana Viarbitskaya[1,2], Aurélien Cuche[1], Alexandre Bouhelier[2], Gérard Colas des Francs[2], Jadab Sharma[1], Christian Girard[1], Erik Dujardin[1]***

[1] CEMES CNRS UPR 8011 and Université Fédérale de Toulouse, 29 rue J. Marvig, 31055 Toulouse, France.
[2] LICB, CNRS UMR 6303, Université de Bourgogne, 9 Av. A. Savary, Dijon, France.
[*]corresponding authors: kumar@cemes.fr, dujardin@cemes.fr

**Abstract**- We report on the engineering of the spatial and spectral distributions of plasmon modes in mesoscale 2D crystalline colloids by physical reshaping and dimer assembly. This approach allows us to match the plasmonic characteristics of the complex metallic structure to the specifications of emitters, for example, in order to optimize the resulting in hybrid plasmonics device.

Plasmonics research has traditionally focused on the macroscopic metallic structures that facilitate propagation, waveguiding and routing of surface plasmon polaritons (SPP) or on nanometer-scale particles producing evanescent field, strong confinement volumes by means of localized surface plasmon (LSP) resonances. Both regimes have been exploited in a broad range of technological areas and led to numerous applications, yet much less scrutiny has so far been focused on the intermediate regime of mesoscopic scale systems. These systems sustain higher order plasmonic modes in the visible/near-IR spectral window and combine together the advantages of both LSP and SPP. Multimodal plasmonic systems open a new realm in which the modal behavior is better described by the Surface Plasmon local density of states (SP-LDOS). SP-LDOS is solely governed by the material properties and the boundary conditions set by the structure shape, but is independent of the illumination parameters. The SP-LDOS can therefore be rationally designed to tailor the local spatial and spectral characteristics of the SP modes, while allowing information transfer over micrometer-sized distances. To reveal and exploit such spatio-modal engineering of plasmons, dissipation can be reduced by exploiting the enhanced performances of crystalline metal colloids [1].

We will start with the demonstration that the SP-LDOS distribution of mesoscale 2D nanoprisms (Fig. 1a,b) can be conveniently mapped by two-photon luminescence (TPL) microscopy (Fig. 1c,d) [2, 3, 4]. We will present results revealing the dependence of the spatial and spectral characteristics of the SP-LDOS on excitation wavelength, polarization, particle shape and interparticle coupling. Interestingly, when the excitation power is increased, non-linear thermal effects lead to extremely localized particle melting, which is shown to provide a well-resolved mapping of the SP-LDOS (Fig. 1i-j). [5] All results will be supported by theoretical analysis with our simulation tools based on the Green Dyadic Method (GDM) as shown in Figs. 1e-h. From the multimodal behavior of individual 2D colloids, we will derive two new ways to tailor the spatial/spectral behavior of the higher order SP modes. First, physical reshaping of the colloidal nanoprisms is performed by creating a hole defect by focused ion beam. [6] Depending on the diameter and location of the aperture, the SP-LDOS spectrum and in-plane distribution is moderately perturbated or significantly modified. This allows to selectively modify plasmonic features to be enhanced or suppressed for tailoring hybrid plasmonic systems. Alternatively, when individual colloidal nanoprisms are brought in the near-field coupling regime superstructures are formed that

exhibit new plasmonic modes. In particular, we show that the enhanced field in the gap region can be tuned independently from the higher order modes borne by the metallic prisms, therefore opening a new way to design multimodal antennas [7]. Time allowing, we will consider applying this approach to the tailoring of multimodal information transfer devices [8] as a first step to implement our proposed concept of modal plasmonic circuits. [2]

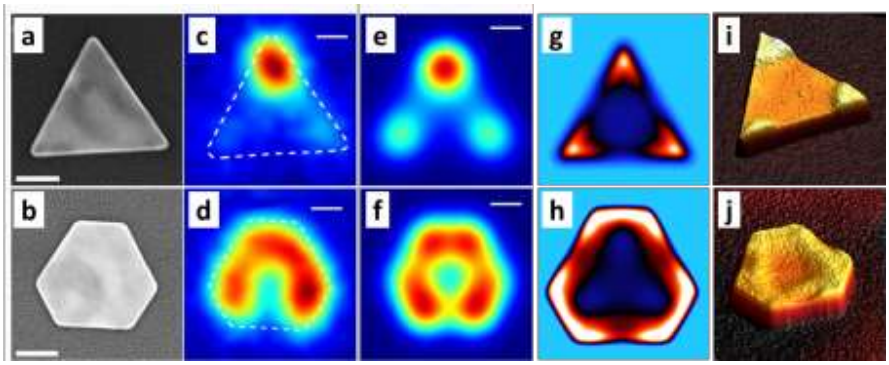



Figure 1: (a,b) SEM images of triangular and truncated triangular Au nanoprisms. Scale bars are 200 nm. (c, d) Confocal TPL images recorded with horizontally polarized, 700 nm excitation. (e, f) Corresponding simulated TPL images using the GDM [2,3] (g, h) Total SP-LDOS maps and (i, j) corresponding AFM images of prisms with modified surface induced by plasmonic hot printing. [5]

**Acknowledgements**

The authors acknowledge the financial support of the European Research Council (ERC) (contract number ERC-2 2007-StG Nr 203872 COMOSYEL), Agence Nationale de la Recherche (ANR) (Grant ANR-13-BS10-0007-PlaCoRe), and the computing center CALMIP in Toulouse.

**REFERENCES**

1. C. Girard, E. Dujardin, G. Baffou and R. Quidant. Shaping and manipulation of light fields with bottom-up plasmonic structures. *New J. Phys.* 10, 105016 (2008)
2. S. Viarbitskaya, A. Teulle, R. Marty, J. Sharma, C. Girard, A. Arbouet and E. Dujardin. Tailoring and imaging the plasmonic local density of states in crystalline nanoprisms. *Nature Materials* 12, 426 (2013)
3. S. Viarbitskaya, A. Teulle, A. Cuche, J. Sharma, C. Girard, E. Dujardin, A. Arbouet. Morphology-induced redistribution of surface plasmon modes in 2D crystalline gold platelets. *Appl. Phys. Lett.* 103, 131112 (2013)
4. T. Hoheisen, J. Cordeiro, O. Lecarme, V. Paillard, C. Girard, E. Dujardin, D. Peyrade, A Arbouet. Plasmonic Shaping in Gold Nanoparticle 3D Assemblies. *J. Phys. Chem. C*, **117**, 23126 (2013)
5. S. Viarbitskaya, A. Cuche, A. Teulle, J. Sharma, C. Girard, A. Arbouet, E. Dujardin. Plasmonic hot printing in gold nanoprisms. *ACS Photonics*, 2, 744 (2015)
6. A. Cuche, S.Viarbitskaya1, J. Sharma, A. Arbouet, C. Girard, E. Dujardin. Modal engineering of Surface Plasmons in apertured Au Nanoprisms, *Scientific Report*, 5:16635 (2015).
7. A Cuche et al, in prep (multimodal antenna)
8. U. Kumar, S. Viarbitskaya, A. Cuche, A. Bouhelier, G. Colas des Francs, C. Girard, R. Mezzenga, E. Dujardin. in prep

# Preparation of Au-Ag Alloy Nanoparticles via Ionic Liquid/Metal Sputter Deposition and Their Application to Plasmon-induced Photosensitization

**T. Kameyama**[1], **E. Kumazawa**[1], **S. Kuwabata**[2], **and T. Torimoto**[*1]

[1]NagoyaUniversity, Japan

[2]Osaka University, Japan

[*]corresponding author: torimoto@apchem.nagoya-u.ac.jp

**Abstract**- Au-Ag nanoparticles having tunable wavelength of LSPR peak, prepared by ionic liquid/metal sputter deposition, were loaded on porous $TiO_2$ electrodes. An anodic photocurrent was observed by the photoexcitation of LSPR peak of the resulting electrodes.

Noble metal alloy nanoparticles (NPs) have attracted much attention recently due to their unique optical, electronic and catalytic properties different from those of monometallic nanoparticles. Among them, Au-Ag alloy NPs have tunable optical properties depending on the composition of NPs in the visible light wavelength region due to localized surface plasmon resonance (LSPR) and then have been intensively investigated for the fabrication of the solar light energy conversion systems, such as the photosensitization of wide-gap semiconductors by photoexcitation of LSPR peak.[1] Although in most cases Au-Ag NPs were prepared in a solution phase by simultaneous chemical reduction of the corresponding metal ions or metal complexes, the chemical composition and nanostructure of the resulting alloy particles were difficult to be precisely controlled because of large difference in the reactivity of metal precursors used. On the other hand, we have recently reported a novel clean method for syntheses of ultrafine metal NPs, such as Ag, Au, Pd, and Pt, via sputter deposition of metals onto ILs under a reduced gas pressure (IL/metal sputtering).[2-5] This could be also applied for preparation of alloy NPs including Au-Pd, Au-Pt, Au-Cu, and Au-Ag, because the IL/metal sputtering technique did not require the chemical reduction of precursors[3, 5-7] In this study, we report the immobilization of Au-Ag alloy NPs sputter-deposited in ILs on porous $TiO_2$ photoelectrodes and investigate their photosensitization abilities.

Nanoparticles of Au, Ag, and Au-Ag were prepared by the sputter deposition of Au and Ag in an IL of 1-buthyl-3-methylimidazolium hexafluorophosphate (BMI-$PF_6$) with use of metal target plates having different fractions of Au surface area, $f_{Au}$, as shown in Fig. 1. The sputtering was carried out with a discharge current of 40 mA under Ar pressure of 10 Pa. A portion of IL containing metal NPs was spread on porous $TiO_2$ electrodes, followed by the heat treatment at 100 ˚C under vacuum. The resulting photoelectrodes were washed with acetonitrile and then calcined at 450 ˚C in $N_2$ for 30 min to remove strongly adsorbed IL. Thus-obtained photoelectrodes, denoted as Au-Ag($x$)/$TiO_2$ where $x$ is the value of $f_{Au}$ used for NP preparation, were irradiated in an aqueous solution containing triethanolamine as a hole scavenger with a 300 W Xe lamp ($\lambda$ > 350 nm). The potential was determined against an Ag/AgCl (sat. KCl) reference electrode and a Pt wire was used as a counter electrode.

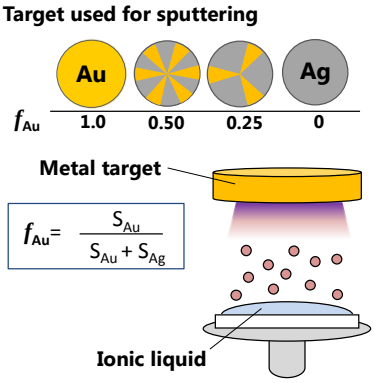



**Fig. 1** Schematic illustration of the preparation of Au-Ag NPs via sputter deposition.

Figure 2 shows a typical TEM image of Au NPs, Ag NPs and Au-Ag NPs. The simultaneous sputter deposition of Au and Ag produced spherical particles highly-dispersed in BMI-$PF_6$, regardless of $f_{Au}$ values. The average diameter of thus-obtained NPs increased from 1.8 to 6.2 nm with a decrease in the $f_{Au}$ value from 1 to 0. XRD measurements revealed that the thus-obtained NPs were AuAg alloy with *fcc* crystal structure.

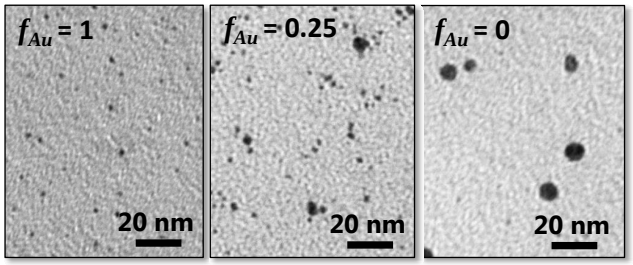



**Fig. 2** TEM image of Au ($f_{Au}$ = 1), Au-Ag NPs ($f_{Au}$ = 0.25) and Ag NPs ($f_{Au}$ = 0) sputter-deposited in BMI-$PF_6$.

The Au-Ag NPs were successfully immobilized on porous $TiO_2$ electrodes by spreading the IL containing metal NPs on the surface of $TiO_2$ followed by heat treatment. Figure 3a shows extinction spectra of thus-obtained Au-Ag($x$)/$TiO_2$ electrodes. An intense LSPR peak was observed in each photoelectrode except for $x$ = 0 in which only small amount of Au-Ag(0) NPs were immobilized on $TiO_2$. The wavelength of LSPR peak was slightly red-shifted from 498 nm to 550 nm with an increase in the value of $f_{Au}$. It was well-known that spherical Au-Ag alloy NPs exhibited a single LSPR peak, the wavelength of which was red-shifted with an increase in the fraction of Au in Au-Ag alloy NPs.[1] Therefore the present results indicated that the optical properties of the electrodes was successfully controlled by changing the composition of Au-Ag alloy NPs immobilized.

Anodic photocurrents were observed by the irradiation of Au-Ag($x$)/$TiO_2$ photoelectrodes with Xe lamp in an aqueous solution containing 0.1 mol $dm^{-3}$ triethanolamine and sodium sulfate under the potential application at +0.5 V vs. Ag/AgCl. Action spectra of photocurrents are shown in Fig. 3b. The peak wavelengths in the action spectra roughly agreed with those of LSPR peak in the extinction spectra of corresponding electrodes. The IPCE value at LSPR peak was enhanced by decreasing value of $f_{Au}$. These results indicated that Au-Ag NPs prepared by the IL/metal sputter deposition technique efficiently worked as a visible light photosensitizer.

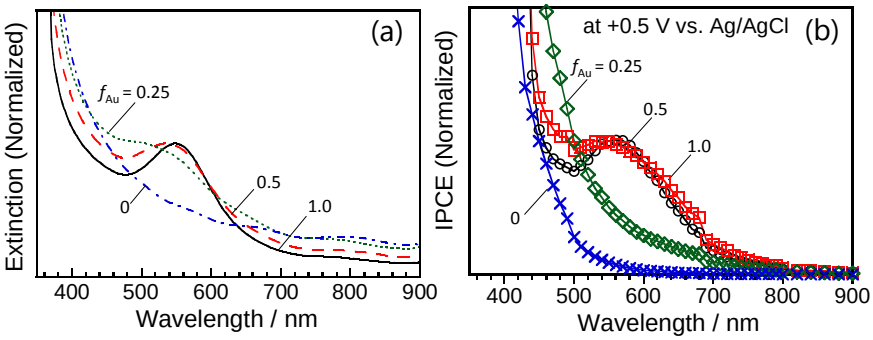



**Fig. 3** (a) Extinction spectra and (b) action spectra of Au-Ag($x$)/$TiO_2$ electrodes. .

**REFERENCES**


1. Nishi, H., Torimoto, T. and Tatsuma, T., *Phys. Chem. Chem. Phys.*, Vol. 17, No. 6, 4042-4046, 2015.
2. Torimoto, T., Okazaki, K., Kiyama, T., Hirahara, K., Tanaka, N. and Kuwabata, S, *Appl. Phys. Lett.*, Vol. 89, No. 24, 243117, 2006.
3. Okazaki, K., Kiyama, T., Hirahara, K., Tanaka, N., Kuwabata, S. and Torimoto, T., *Chem. Commun*., No. 6, 691-693, 2008.
4. Yoshii, K., Tsuda, T., Arimura, T., Imanishi, A., Torimoto, T. and Kuwabata, S., *RSC Adv.*, Vol. 2, No. 22, 8262-824, 2012.
5. Hirano, M., Enokida, K., Okazaki, K., Kuwabata, S., Yoshida, H. and Torimoto, T., *Phys. Chem. Chem. Phys.*, Vol. 15, No. 19, 7286-7294, 2013.
6. Suzuki, S., Suzuki, T., Tomita, Y., Hirano, M., Okazaki, K., Kuwabata, S. and T. Torimoto, *CrystEngComm*, Vol. 14, No. 15, 4922-4926, 2012.
7. Suzuki, S., Tomita, Y., Kuwabata, S. and Torimoto, T., *Dulton Trans.*, 44, 4186-4194, 2015.

# Plexitonic QED: Strong coupling effect in absorption and photoluminescence spectra of hybrid systems of gold nanorods and J-aggregates.

**D. Melnikau[1], R. Esteban[2], D. Savateeva[1], A. Sánchez-Iglesias[3], M. Grzelczak[3], M.K. Schmidt[1], L. M. Liz-Marzán[3,4], J. Aizpurua[1,2], Y.P. Rakovich[1,2,4*]**

[1] Centro de Física de Materiales (Materials Physics Center, CSIC-UPV/EHU), Donostia-San Sebastián, Spain
[2] Donostia International Physics Center (DIPC), Donostia-San Sebastián, Spain
[3] CIC biomaGUNE, Donostia-San Sebastián, Spain
[4] IKERBASQUE, Basque Foundation for Science, Bilbao, Spain
[*]corresponding author: yury.rakovich@ehu.eus

**Abstract**-We investigated the interactions between localized plasmons in gold nanorods and excitons in J-aggregates and were able to track an anticrossing behavior of the hybridized modes both in the extinction and in the photoluminescence (PL) spectra of this hybrid system. We followed the evolution of the two PL peaks as the plasmon energy was detuned from the excitonic resonance. Both extinction and PL results are in good agreement with the theoretical predictions obtained for a model of two interacting modes.

One of the main objectives of nanophotonics research is to control the light-matter interaction on the nanoscale. Phenomenon of plasmon-exciton resonance coupling is of the great importance for this research field in both the fundamental aspects and many practical applications. Especially attractive for these applications is so called strong coupling regime when the rate of periodic and coherent energy exchange between the excitonic and plasmonic systems exceeds the rate of the losses in the system. This periodic energy exchange has an analogy with two coupled oscillators where new eigenmodes of the system arise, manifesting itself in the appearance of a double-peaked feature in the extinction spectra. The spectral distance between these two peaks defines the value of the energy of Rabi splitting ($\Omega_R$) which is one of fundamental quantum-optics phenomena.

While observation of Rabi splitting in extinction or transmission spectra of plexitonic hybrid systems has been reported in a number of publications[1], photoluminescence properties of these systems in the strong coupling regime are more elusive to experimental investigation[2].

In this study, using extinction and PL spectroscopies, we investigated an exciton-plasmon interaction in the system consisting of J-aggregates of cyanine dye and gold nanorods in resonant and non-resonant regimes. In the last case overlap between exciton and plasmon bands was gradually reduced to a minimum in a step-by-step manner.

The main results of our study are presented in Figure 1. In resonant regime in the extinction spectrum of the hybrid structure the pronounced dip at 590 nm appears as a result of strong coupling of the excited states of J-aggregates and plasmon modes of the nanorods. Also left panel in Figure 1 demonstrates that the separation between upper resonance (UR) and lower resonance (LR) grows with the detuning of extinction bands of pure

gold nanorods with different aspect ratios from the excitonic resonance of J-aggregates. This separation reaches 710 meV for the biggest detuning achieved in our experiments (681 meV).

We estimated value of the Rabi splitting ($\Omega_R$>200 meV) at zero detuning from the anticrossing behavior of the bands in extinction spectra. This value is similar to the largest splittings observed in planar organic microcavities[3] or in plexitonic systems based on gold particles[1,2]. Next, we focused on the signature of the strong coupling in the evolution of the PL modes, which we can identify due to the pronounced emission from both the UR and LR branches. The evolution of the modes is consistent with the results from the extinction, which corroborates the interpretation of the modes in terms of an anti-crossing. Both the extinction and PL results are in good agreement with the results of theoretical calculations performed using a model of two interacting modes with a ratio between the coupling strength and the plasmonic losses close to 0.4, indicative of the strong coupling regime. We also used a theoretical model of emission to analyze lineshapes of the PL spectra and discuss their dependence on the excitation wavelength.

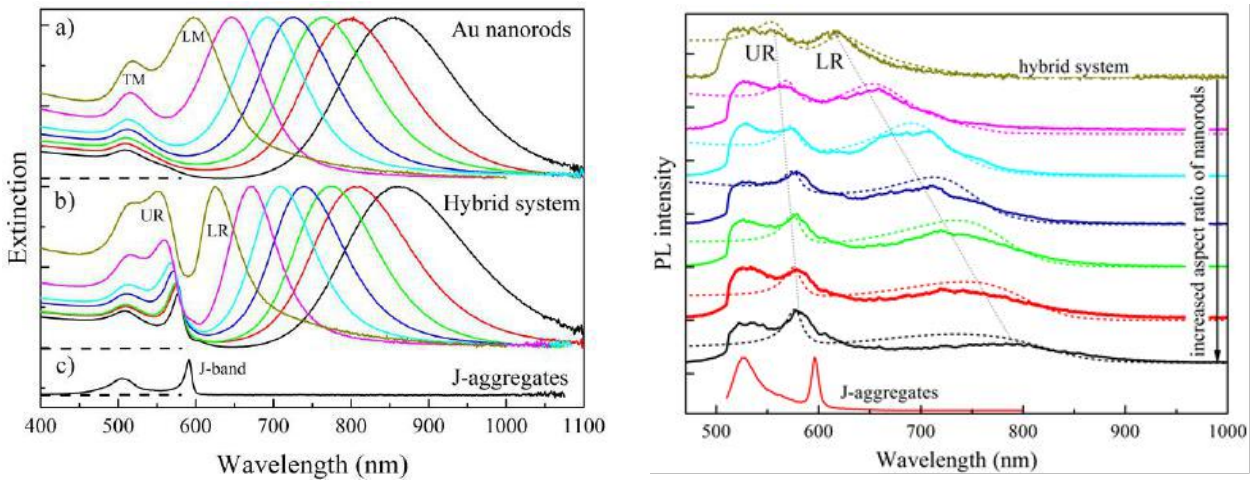



Figure 1 Left panel: Extinction spectra of gold nanorods of different aspect ratio (a), hybrid J-aggregates/gold nanorods complexes (b) and pure J-aggregates (c). Right panel: Normalized PL spectra of the hybrid system formed by nanorods of different aspect ratio and J-aggregates in comparison with the PL spectrum of pure J-aggregates. Dashed curves are results of the theoretical calculations.

**Acknowledgements**, We acknowledge financial support from Projects FIS2013-41184-P and MAT2013-46101-R of the Spanish Ministry of Economy and Competitiveness (MINECO) and ETORTEK project NANOGUNE'14. R.E. acknowledges funding as Fellow Gipuzkoa of the Gipuzkoako Foru Aldundia through Feder Funds of the European Union "Una manera de hacer Europa".

**REFERENCES**

1. Fofang, N. T., Park, T.-H., Neumann, O., Mirin, N. A., Nordlander, P., Halas, N. J. "Plexcitonic Nanoparticles: Plasmon-Exciton Coupling in Nanoshell-J-Aggregate Complexes," *Nano Lett.*, Vol.8, 3481−3487, 2008.
2. Melnikau, D., Esteban, R., Savateeva, D., Sánchez-Iglesias, A., Grzelczak, M., Schmidt, M.K., Liz-Marzán, L.M., J. Aizpurua, J. and Rakovich, Y.P. "Rabi Splitting in Photoluminescence Spectra of Hybrid Systems of Gold Nanorods and J‑Aggregates," *J. Phys. Chem. Lett.*, Vol.7, 354−362, 2016
3. Tischler, J. R., Bradley, M. S., Zhang, Q., Atay, T., Nurmikko, A., Bulovic, V. "Solid state cavity QED: Strong coupling in organic thin films," *Org. Electron.* Vol. 8, 94−113, 2007.

# Nanophotonic Designs for Photovoltaics and Luminescent Solar Concentrators

**Vivian E. Ferry**[1*]
[1]University of Minnesota, USA
[*]corresponding author: veferry@umn.edu

**Abstract**-Luminescent solar concentrators hold many advantages for future photovoltaic designs, but are limited by optical losses deriving from both the luminescent material and the optical geometry. In this paper we discuss ways that Bragg mirrors and metamaterials can be used in cooperation with tailored luminescent nanocrystals to achieve high concentration factors. In particular, we quantify the forms of the losses, and show how nanophotonics can be used to change the necessary tolerances on the luminescent materials to achieve high performance.

Light management strategies for photovoltaics can lead to both increased conversion efficiencies and reduced manufacturing costs. One such optical challenge in photovoltaic design stems from the solar spectrum itself, which is a spectrally broad and diffuse light source. Luminescent solar concentrators (LSCs) offer advantages over traditional light concentrators in this regard, as incident sunlight from a broad spectral distribution is downshifted through the absorption and luminescence process, and sunlight from a broad angular distribution is redirected and concentrated onto a single solar cell. These systems are also attractive as building integrated and architectural materials. However, their performance is limited by factors such as escape cone losses, non-unity quantum yields, and reabsorption.

In this paper we discuss several ways that nanophotonics can be used to improve the efficiency of LSCs, in combination with tailored luminescent nanocrystals. The luminophores used in this study are core-shell nanocrystals with tunable optical properties based on the size and geometry of the crystal. The concentrator consists of a large polymer sheet with embedded nanocrystals, and a solar cell mounted to the edge. A Bragg mirror designed to accept light within the absorption band of the shell and reflect light within the luminescence band is also included in the design.

With the aid of both experimental measurements and simulations, we show how nanophotonic elements can be combined with these nanocrystal materials to enhance the overall performance. We find that while achieving good dispersion of nanocrystals inside the polymer matrix is important, the use of additional light trapping and guiding elements can reduce the detrimental effects of light scattering due to aggregation. We also find that by considering the absorption and scattering of individual nanocrystals, specific target sizes and geometries can be determined that account for the tradeoff between Stokes shift and scattering. Nanophotonic designs that address different tradeoffs in the materials are also developed, showing how control over light propagation can be used to reduce losses due to reabsorption. Finally, by considering the propagation of light within the concentrator we show how metamaterials can be used to guide light effectively over large distances. By combining these principles with careful design of the luminescent materials into hybrid systems, concentration factors in excess of 30 are possible.

.

**REFERENCES**


1. Bronstein, N. D., Yao, Y., Xu, L., O'Brien, E., Powers, A. S., Ferry, V. E., Alivisatos, A. P., and Nuzzo, R. G. "Quantum dot luminescent concentrator cavity exhibiting 30-fold concentration," *ACS Photonics*, Vol. 2, No. 11, 1576 – 1583, 2015.
2. Bronstein, N. D., Li, L., Xu, L., Yao, Y., Ferry, V. E., Alivisatos, A. P., and Nuzzo, R. G. "Luminescent solar concentration with semiconductor nanorods and transfer-printed micro-silicon solar cells," *ACS Nano*, Vol. 8, No. 1, 44 – 53, 2013.
3. Smestand, G., Ries, H., Winston, R., and Yablonovitch, E., "The thermodynamic limit of light concentrators," *Solar Energy Materials*, Vol. 21, 99–111, 1990.
4. Debije, M. G., and Verbunt, P. P. C., "Thirty years of luminescent concentrator research: solar energy for the built environment," *Adv. Mater.*, Vol. 2, No. 1, 12 - 35, 2012.
5. Meinardi, F., Colombo, A., Velizhanin, K. A., Simonutti, R., Lorenzon, M., Beverina, L., Viswanatha, R., Klimov, V. I., and Brovelli, S., "Large-area luminescent solar concentrators based on 'Stokes-shift-engineered' nanocrystals in a mass-polymerized PMMA matrix," *Nature Photon.*, Vol. 8, No. 5, 392 – 399, 2014.
6. Rau, U., Einsele, F., and Glaeser, G. C. "Efficiency limits of photovoltaic fluorescent collectors," *Appl. Phys. Lett.*, Vol. 87, 171101, 2005.
7. Giebink, N. C., Wiederrecht, G. P., and Wasielewski, M. R. "Resonance-shifting to circumvent reabsorption loss in luminescent solar concentrators," *Nature Photon.*, Vol. 5, No. 11, 694 – 701, 2011.
8. Goldschmidt, J. C., Peters, M., Gutmann, J., Steidl, L., Zentel, R., Bläsi, B., and Hermle, M., "Increasing fluorescent concentrator light collection efficiency by restricting the angular emission characteristic of the incorporated luminescent material – the 'Nano-Fluko' concept," *Proc. SPIE*, Vol. 7725, 77250S, 2010.

# On the use of hybrid modal properties to design enhanced nonlinear and ultrafast optical properties.

**Cillian McPollin[1], Silvia Peruch[1], David J. Gosztola[2], Gary P. Wiederrecht[2], Gregory Wurtz[1,3], and Anatoly V. Zayats [1]**

[1] Department of Physics, King's College London, Strand, London WC2R 2LS, United Kingdom

[2]Center for Nanoscale Materials, Argonne National Laboratory, 9700 South Cass Avenue, Argonne, IL 60439, United States of America

[3]Department of Physics, University of North Florida, 1 UNF Drive, Jacksonville, FL 32224, United States of America

[*]corresponding author: g.wurtz@unf.edu

**Abstract**- In this presentation we present some of the unique opportunities hybrid plasmonic systems offer in the design of active plasmonic metamaterials and devices. In particular, we show that an active control over the modal coherence within hybrid system leads to enhanced nonlinear optical properties being triggered at ultrafast timescales.

Hybrid systems are commonly defined by the electromagnetic coupling between two or more entities to create a unique system with an optical signature determined by the dispersive attributes of the respective constituents. Carefully controlling the resonant properties of those constituents and their mutual interactions within a complex nanostructured system, enables one to design chosen optical properties not otherwise achievable by any of the constituents alone.[1]

Here we will review some of the unique optical properties of hybridized resonances in plasmonic nanostructured systems, including metamaterials and device architectures. The hybridization considered include *plasmon-plasmon* coupling,[2] *plasmon-polariton* coupling,[3] *plasmon-photon* coupling,[4] as well as *plasmon-exciton* coupling (e.g. in fig. 1).[5] The hybridization process for each of those geometries is unique and will be discussed on the basis of both analytical and numerical simulations. A particular focus of the presentation will be on assessing the potential gain hybridized modes provide when considering the nonlinear and ultrafast optical properties of nanostructured systems.

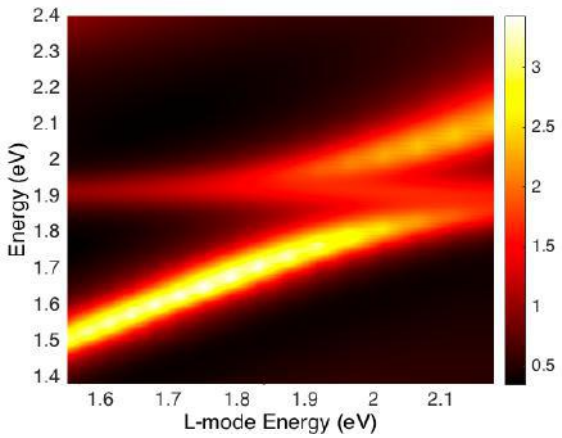



**Figure 1:** Dispersion plot for a metamaterial showing strong coupling between a delocalized plasmonic mode and a dispersion-less excitonic resonance.

**Acknowledgements**, This work was supported, in part, by EPSRC (UK). A.Z. acknowledges support from the Royal Society and the Wolfson Foundation. G.W. acknowledges the support from the EC FP7 Project No. 304179 (Marie Curie Actions). Use of the Center for Nanoscale Materials, an Office of Science user facility, was supported by the U. S. Department of Energy, Office of Science, Office of Basic Energy Sciences, under Contract No. DE-AC02-06CH11357.

## REFERENCES

1. Wiederrecht, G. P.; Wurtz, G. A.; Bouhelier, A., Ultrafast hybrid plasmonics. *Chemical Physics Letters* **2008,** *461* (4-6), 171-179.

2. G. A. Wurtz; R. Pollard; W. Hendren; G. Wiederrecht; D. Gosztola; V. A. Podolskiy; Zayats, A. V., Designed ultrafast optical nonlinearity in a plasmonic nanorod metamaterial enhanced by nonlocality. *Nature nanotechnology* **2011,** *6*, 107.

3. Neira, A. D.; Wurtz, G. A.; Ginzburg, P.; Zayats, A. V., Ultrafast all-optical modulation with hyperbolic metamaterial integrated in Si photonic circuitry. *Optics express* **2014,** *22* (9), 10987-94.

4. McPolin, C. P. T.; Olivier, N.; Bouillard, J.-S.; O'Connor, D.; Krasavin, A. V.; Dickson, W.; Wurtz, G. A.; Zayats, A. V., Universal Switching of Plasmonic Signals using Optical Resonator Modes, *under review* **2016**.

5. Wurtz, G. A.; Wiederrecht, G.; Zayats, A., Non-Linear Optical Properties of Hybrid Exciton-Plasmon Nanorod Arrays. *under review* **2016**.

# Manipulation of Molecules adsorbed on Metal Nanostructures under Plasmon Excitation

**K. Murakoshi**
Department of Chemistry, Hokkaido University, Sapporo, Hokkaido, 060-0810, Japan
*corresponding author: kei@sci.hokudai.ac.jp

**Abstract**- *In-situ* surface-enhanced Raman scattering spectroscopy was used for the quantitative characterization of the number of molecules in highly localized electromagnetic fields on the surface of metal nanostructure under electrochemical potential control at room temperature. Increment in the Raman scattering intensity was correlated with the change in the surface diffusion behaviour of the molecules adsorbed on the metal nanostructure.

Manipulation of molecules at room temperature in an atmosphere or a solution is generally difficult, because the thermal fluctuation acts as a noise to destroy controlled motion of molecule. Optical force is one of the choices to control the motion of molecules selectivity. Specific polarizability of molecule may result in the control of the molecule motion by optical force under light illumination. We may expect that relatively intense electromagnetic field can generate enough force which can overcome random fluctuation induced by Brownian motion of molecules and/or nanomaterials. Recently developed manipulation techniques using the plasmonic field now have been regarded as a promising approach to control objects less than micrometer in size [1]. However, optical trapping of molecule at room temperature unfortunately has not been achieved yet. We have shown that highly localized electromagnetic field generated by plasmon resonance of metal nanostructure emerges very characteristic resonant excitation of molecules. Ultra small sizes of the localized field also contribute to induce anomalous resonance of the optical excitation [2]. Such unusual interactions between the electromagnetic fields and the electronic states of molecules can be monitored by the intensity of surface-enhanced Raman scattering (SERS). Vibrational spectrum observed by Raman scattering provides the quantitative information on the electronic excitation of molecules, not only on molecule structure and its orientation. In this presentation, possibility of the molecule trapping in the plasmonic field will be discussed based on the evolution of SERS bands from molecules adsorbed on metal surface under electrochemical potential control at room temperature.

In-situ SERS spectra were measured using the substrate immersed in an aqueous solution containing 1 mM 4,4'-bipyridine under electrochemical potential control to define the orientation of molecules. Observed SERS bands are attributable to the vibrational modes of the ring breathing around 1016 $cm^{-1}$, the in-plane ring deformation coupled with the C-H bending at 1060 $cm^{-1}$, the inter-ring stretching at 1300 $cm^{-1}$, and the ring bending at 1600 $cm^{-1}$. The Raman intensities of respective bands increased gradually during the observation for 10 s. This band evolution became slow and saturated at the maximum value during 20 – 30 s illumination. The change in the band intensity was reversible. After turn off the illumination for a few tens seconds, repeated illumination resulted in the same behavior of the SERS band evolution from the same initial intensity to the maximum intensity as those at the first illumination At the gap of metal nanodimer, the enhancement ratio of the electromagnetic filed reaches to the order of $10^4$ -$10^5$. Expected gradient force applied to the molecule in the

field was estimated to be in the order of tens pN under the illumination of the light intensity with ca. 1 mW $mm^{-2}$. In our previous experiments to segregate molecules using the steep gradient of the chemical potential at metal nanogate less than 100 nm in width [3, 4], the force of <fN applied to a single molecule is enough to control the translational motion of molecules at room temperature [5]. Although we need further precise estimation about the net polarizability of molecules on the surface, the force of <pN could contribute to retard Brownian motion of molecules at room temperature. Applied force to molecules is quite sensitive to the polarizability of molecules. Thus, the additional resonance induces the SERS depolarization could be also considered as the origin to apply the forces to molecules with distinct adsorbed orientations in the anisotropic electromagnetic field.

**REFERENCES**


1. Nabika, H.; Takase, M.; Nagasawa, F.; Murakoshi, K., "Toward Plasmon-Induced Photoexcitation of Molecules", *J. Phys. Chem. Lett.***,** 1, 2470-2487 (2010).
2. Takase, M.; Ajiki, H.; Mizumoto, Y.; Komeda, K.; Nara, M.; Nabika, H.; Yasuda, S.; Ishihara, H.; Murakoshi, K., "Selection-Rule Breakdown at Plasmon-Induced Electronic Excitation of an Isolated Single-Walled Carbon Nanotube", *Nat. Photo.*, 7, 550-554 (2013).
3. Nabika, H.; Iijima, N.; Takimoto, B.; Ueno, K.; Misawa, H.; Murakoshi, K., "Segregation of Molecules in Lipid Bilayer Spreading Through Metal Nano-Gates", *Anal. Chem.*, 81, 699-704 (2008).
4. Nabika, H.; Sasaki, A.; Takimoto, B.; Sawai, Y.; He, S.; Murakoshi, K., "Controlling Molecular Diffusion in Self-Spreading Lipid Bilayer Using Periodic Array of Ultra-Small Metallic Architecture on Solid Surface", *J. Amer. Chem. Soc.*, 127, 16786-16787 (2005).
5. Takimoto, B.; Nabika, H.; Murakoshi, K., "Force Applied to a Single Molecule at a Single Nanogate Molecule Filter", *Nanoscale*, 2, 2591-2595 (2010).

# Self-aligned fabrication and spectroscopy of coupled hybrid antenna-nanoemitter-structures

**A. Bräuer[1], R. Jäger[2], J. Fulmes[1], K. Scherzinger[2], S. Jäger[2], S. zur Oven-Krockhaus[2], D. A. Gollmer[1], A. J. Meixner[2], D. P. Kern[1], M. Fleischer[1*]**

[1]Institute for Applied Physics, University of Tübingen
Auf der Morgenstelle 10, 72076 Tübingen, Germany
[2]Institute of Physical and Theoretical Chemistry, University of Tübingen
Auf der Morgenstelle 18, 72076 Tübingen, Germany
[*]corresponding author: monika.fleischer@uni-tuebingen.de

**Abstract**- Plasmonic nanostructures act as optical nanoantennas with shape- and size-dependent plasmon resonances. By positioning individual nano-emitters in the high near-field regions of such antennas, the emitter properties can be strongly modified. Techniques for the self-aligned fabrication of individual hybrid antenna-emitter-structures are demonstrated, and the optical characteristics of single or few semiconductor quantum dots coupled to specifically designed metallic nanoantennas are evaluated.

Plasmonic nanostructures that act as optical nanoantennas for visible light offer interesting opportunities for locally concentrating and enhancing the electric near-field of an incident light wave, or of spectrally tuning the antenna characteristics via their size, shape and material. By combining the antennas with a second component in hybrid configurations, such as quantum dots, fluorescent molecules, or organic thin-films, the antennas can be employed to modify the absorption and emission characteristics of these objects in the coupled system.[1-3] Key challenges in this context are the optimization of the antenna properties in view of the envisaged application, as well as achieving selective coupling of the nano-emitters to the high near-field regions of individual antennas.

In this presentation procedures for selectively coupling few or single nano-emitters to the tips of lithographically fabricated conical nanoantennas will be shown (see Figure 1).[4,5] The plasmon resonance of the antennas is adapted to the emission of the quantum dots. The resulting individual hybrid antenna-emitter structures are investigated in terms of their optical characteristics.[6] The modified intensity trajectories, emission enhancement and lifetime reduction of single quantum dots coupled to nano-antennas will be illustrated.

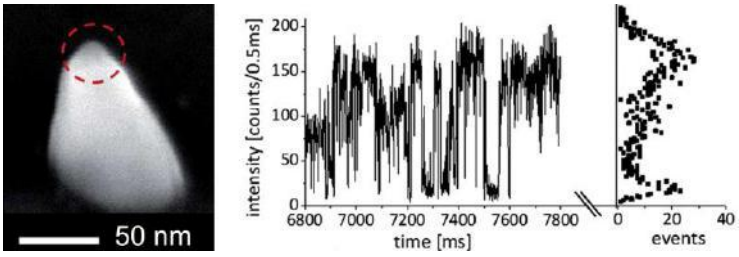



**Figure 1:** CdSe/ZnS quantum dot at the tip of a conical gold nanoantenna (left) and intensity trajectory of a quantum dot coupled to the tip of an antenna (right), modified from Ref. 6.

**Acknowledgements**: This work was performed in the context of the European COST Action MP1302 Nanospectroscopy. Financial support from the German Research Foundation DFG and by Carl Zeiss Foundation are gratefully acknowledged.

**REFERENCES**

1. Curto, A. G., Taminiau, T. H., Volpe, G., Kreuzer, M. P., Quidant, R. and van Hulst, N. F., *Nat. Commun.*, "Multipolar radiation of quantum emitters with nanowire optical antennas", Vol. 4, 1750, 2013.
2. Viste, P., Plain, J., Jaffiol, R., Vial, A., Adam, P. M. and Royer, P., "Enhancement and quenching regimes in metal-semiconductor hybrid optical nanosources", *ACS Nano*, Vol. 4, No. 2, 759-764, 2010.
3. Kern, A. M., Zhang, D., Brecht, M., Chizhik, A. I., Failla, A. V., Wackenhut, F. and Meixner, A. J., "Enhanced single-molecule spectroscopy in highly confined optical fields: from λ/2-Fabry-Perot resonators to plasmonic nano-antennas", *Chem. Soc. Rev.*, Vol. 43, 1263-1286, 2014.
4. Fleischer, M., Stanciu, C., Stade, F., Stadler, J., Braun, K., Heeren, A., Häffner, M., Kern, D. P., Meixner, A. J., "Three-dimensional optical antennas: Nanocones in an apertureless scanning near-field microscope", *Appl. Phys. Lett.*, Vol. 93, No. 11, 111114, 2008.
5. Fulmes, J., Jäger, R., Bräuer, A., Schäfer, C., Jäger, S., Gollmer, D. A., Horrer, A., Nadler, E., Chassé, T., Zhang, D., Meixner, A. J., Kern, D. P., Fleischer, M., "Self-aligned placement and detection of quantum dots on the tips of individual conical plasmonic nanostructures", *Nanoscale*, Vol. 7, 14691-14696, 2015.
6. Meixner, A. J., Jäger, R., Jäger, S., Bräuer, A., Scherzinger, K., Fulmes, J., zur Oven Krockhaus, S., Gollmer, D. A., Kern, D. P., Fleischer, M., "Coupling single quantum dots to plasmonic nanocones: optical properties", *Faraday Discussions*, Vol. 184, 321-337, 2015.

# High Resolution Technique for Simultaneous Proteins and Nanoparticles Patterning

**Lourdes Basabe-Desmonts[1,2]***

[1] BIOMICs Research Group, Lascaray Ikergunea research center, University of the Basque Country, Spain
[2] Ikerbasque, Basque Foundation of Science, Spain
[*] corresponding author: lourdes.basabe@ehu.eus

**Abstract**- We present a novel methodology to create micro-scaled patterns of gold nanoparticles (GNP) adjacent to micro-scaled patterns of proteins on a planar substrate. This methodology is the combination of microfluidic vacuum soft lithography and micro-contact printing. Such multicomponent patterns enabled controlled cell adhesion on discrete locations surrounded by GNP. Given the inherent properties of GNP, which may act as optical sensors and topographic cues, these high-resolution multicomponent patterns could enable new cellular studies with high spatio-temporal resolution.

Lithographic techniques have enabled the fabrication of chemical and physical nano and microstructures. Through lithography, protein patterns on a planar substrate can be formed. Those can be used to control the physical position of cells on a surface, enabling the creation of cell arrays, what may find applications in single cell or cell populations studies. Integration of cell arrays on microfluidic structures allows further control on the cellular microenviroment through controlled delivery of nutrients and drugs. Cellular studies on microsystems are a highly promising field appearing as a new toolbox for biology providing spatiotemporal control on cellular microenvironments (1). Despite the promise of microsystems to become a platform technology for high throughput cellular studies, a challenge remains, *continuous monitoring* of cell activity with good spatiotemporal resolution. Gold nanoparticles are excellent candidates as optical nanosensors thanks to the unique tunable optical properties (2). With the aim of enabling controlled adhesion of cells, and control of cell – cell contact, while providing each cell or group of cells, with an adjacent sensing area, we have developed a methodology for positioning cells and nanoparticles in close proximity. It is the combination of microfluidic vacuum soft lithography and micro-contact printing. It was used to create adjacent patterns of biomolecules and metal nanoparticles, this constituting a high-resolution methodology to create combined physical and chemical patterns on solid substrates.

## REFERENCES

1. Weaver, W. M., Tseng, P., Kunze, A., Masaeli, M., Chung, A. J., Dudani, J. S. ;Kittur, H., Kulkarni, R. P., Di Carlo, D., “Advances in high-throughput single-cell microtechnologies,” *Current Opinion in Biotechnology*, Vol. 25, 114 –123, 2014

2. Wang, S., Ota, S., Guo, B., Ryu, J., Rhodes, Christopher, Xiong, Y., Kalim, S., Zeng, L., Chen, Y. ; Teitell, M. A., Zhang, X. “ Subcellular Resolution Mapping of Endogenous Cytokine Secretion by Nano-Plasmonic-Resonator Sensor Array,” *Nano Letters*, Vol. 11, No. 8, 3431–3434, 2011

# Fano resonance in self-organized embedded metallic nanoparticle gratings and application as optical security features

**S. Bakhti[1], G. Baraldi[1], Z. Liu[1] and N. Destouches[1*]**

[1]Univ Lyon, UJM-Saint-Etienne, CNRS, Laboratoire Hubert Curien UMR 5515, F-42023, SAINT-ETIENNE, France

*nathalie.destouches@univ-st-etienne.fr

**Abstract**-We demonstrate that the singular colored effects of laser induced self-organized metallic nanoparticle gratings embedded in a high index film result from the excitation of Fano-like resonances. The latter originate from the coupling of the localized surface plasmon mode of metallic nanoparticles and a waveguide mode. They create strongly asymmetric spectral absorber whose color in reflection can be tuned differently on both sides of samples. This self-structuring technique is a fast a low-cost process that can provide color marking on large areas and offers promising transparent platforms for a new range of optical variable devices.

The plasmon resonances of metallic nanoparticles widely demonstrated over last decades their ability to find many domains of applications, driven by the development of sophisticated fabrication techniques and supported by a theoretical deepening of their nanoscale optical properties. While complex coupling effects are observed and studied on the nanometer or micrometer scale, one of the current challenges is to extend to macroscopic scale these unique properties using low-cost and reliable fabrication techniques. In this context, we recently demonstrated the possibility to induce the self-organized growth of silver nanoparticles by scanning a laser beam on silver loaded titania thin films[1] and to draw centimeter wide colored patterns.[2] In this work, we demonstrate that the original color rendering of such self-organized structures results from Fano resonances whose position can be tuned in the visible range. We show the strong sensitivity of such resonances in our asymmetric system to the illumination and observation conditions. This leads us to design transparent optical variable devices which can exhibit different drawing depending on the side from which they are illuminated and observed.

The self-organized structures consist of silver nanoparticle gratings embedded in a $TiO_2$ thin film whose parameters can be tuned by varying the laser exposure conditions. The nanoparticles size and their depth in the $TiO_2$ film mainly depend on the scanning speed and writing laser intensity, the grating period on the laser wavelength and the grating orientation on polarization. Two kinds of modes can be excited in such structures, the localized surface plasmon mode of silver nanoparticles and a waveguide mode. The latter can be seen as a lattice plasmon mode that extends partly in the waveguiding adjacent $TiO_2$ film. A lattice plasmon mode corresponds to a collective resonance mode mediated by diffractive coupling of localized plasmons, which propagates parallel to the grating plane. In our case, it has the specificity to be preferentially excited with a TE polarized incident light and propagates perpendicular to the grating lines. The localized plasmon mode is an optical bright mode that directly couples to the external electric field. In contrast, the waveguide mode is an nearly optical dark mode, which is excited via the localized plasmon mode. Their coupling results in a Fano-like resonance with a characteristic asymmetric spectral lineshape.

Simulations are carried out for both perfectly regular lattices of homogeneous nanoparticles and true

self-organized nanoparticle gratings. We first investigate the coupling strength of the Fano-like resonance by varying its position by means of a variable grating period. Extinction spectra obtained for both TE and TM polarizations are compared. Only TE polarization allows the excitation of the waveguide mode and gives rise to a Fano-like resonance. The asymmetric lineshape of the latter is characterized by a spectral range with a strongly decreased absorption and an adjacent spectral range with an enhanced absorption. We interpret such spectral features thanks to near field intensity maps.

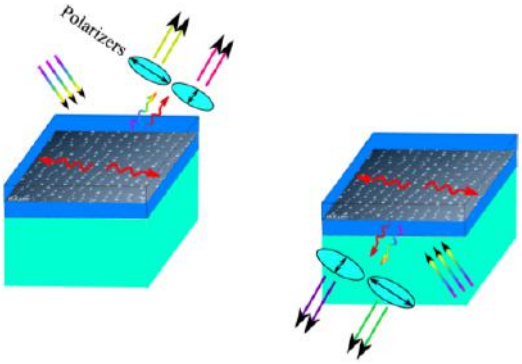



**Figure 1**. Schematic of color rendering effects of self-organized silver nanoparticle gratings in a $TiO_2$ thin film. Sensitivity of the reflected color to the observed side of the sample.

Another interesting feature of such self-organized systems is their ability to exhibit an asymmetric spectral absorption. If the transmission spectrum ($T(\lambda)$) of structures is always independent on the side from which they are illuminated, their color in reflection ($R(\lambda)$) strongly varies if they are observed and illuminated from the front side (film side) or from the back side (substrate side) (Figure 1). This means that their absorption $A=1-R-T$ varies in the same way. Simulation results provide an explanation for such an effect resulting from a more pronounced damping of Fano-like resonances on one side of the asymmetric multilayer sample.

Controlling the laser writing parameters not only gives access to a wide range of dichroic colors but also allows to design couples of colors that have close hue and luminance when observed from one side and different ones from the other side. This can therefore provide optical variable devices for security applications on transparent substrate where the same drawing could appear with different shapes on both sides of the sample.

**Acknowledgements**. This work was supported by the LABEX MANUTECH-SISE (ANR-10-LABX-0075) of Université de Lyon, within the program "Investissements d'Avenir" (ANR-11-IDEX-0007) operated by the French National Research Agency (ANR). The authors thank ANR for its financial support in the framework of project PHOTOFLEX n°12-NANO-0006.

**REFERENCE**

1. Destouches, N. et al. "Self-organized growth of metallic nanoparticles in a thin film under homogeneous and continuous-wave light excitation", *J. Mater. Chem. C*, Vol. 2, 6256-6263, 2014.
2. Destouches, N. et al. "Dichroic colored luster of laser-induced silver nanoparticle gratings buried in dense inorganic films", *J. Opt. Soc. Am. B*, 31, 11, C1-C7, 2014.

# Scalable Fabrication of 2 nm-Wide Plasmonic Nanotrench Arrays For Strong Field Enhancements

**Joel K.W. Yang**[1,2]

[1]Pillar of Engineering Product Development, Singapore University of Technology and Design, 8 Somapah Road, Singapore 487372, Singapore

[2]Institute of Materials Research and Engineering (IMRE)

2 Fusionopolis Way, Innovis, #08-03

Singapore 138634

[*]corresponding author: joel_yang@sutd.edu.sg

**Abstract**-Plasmonic field enhancements intensifies with decreasing gaps between metallic nanostructures. However, the scalable fabrication of nanogaps in the 10-nm scale remains challenging. We present a process to scale-up the fabrication of nanotrench arrays in Au. Combining top-down and bottom-up techniques, double-gap structures were patterned, with gaps measuring ~2 nm. These structures exhibit ultrasmooth surfaces, as achieved with template stripping with reusable templates. The double-gap structure increases the surface area where light is localized thus enabling enhanced second-harmonic generation (SHG).

As a research tool, the electron-beam lithography (EBL) system allows computer-designed patterns to be rapidly prototyped with dimensions approaching the atomic scale[1–3]. Several processes have been developed using EBL to reliably pattern sub-10-nm gaps in Au, e.g. liftoff[4,5], nano-stenciling[6], and template-assisted dewetting[7]. Direct patterning techniques using helium ion beam lithography [8], and indirect approaches using atomic-layer deposition[9] are complementary to EBL with comparable resolution. On the other hand, bottom-up techniques, such as self-assembled nanoparticle dimers[10], provides a means to control the gap size via selection of the molecular ligands used. The combination of top-down, bottom-up, and pattern replication methods such as template stripping[11] can thus result in a scalable process that produces computer-designed structures with molecularly controlled gap sizes.

A schematic and SEM image of a double-gap structure is as shown in Fig. 1. It consists of a 50-nm deep trench in Au patterned by template stripping, and gold nanoparticles self-assembled within the trenches. The self-assembly process was recently developed[12]. These structures produce an intensity enhancement in the gaps in the order of ~1,000x for 878 nm laser polarized across the double gaps in the trench. Compared to gold nanoparticles self-assembled on a flat gold surface, the double-gap structures produced a 4,200x enhancement in SHG. The effective second-order susceptibility of the structures was determined to be ~6.1 pm/V, comparable to typical nonlinear crystals, but acting on the nanoscale and potentially removing the need for phase matching.

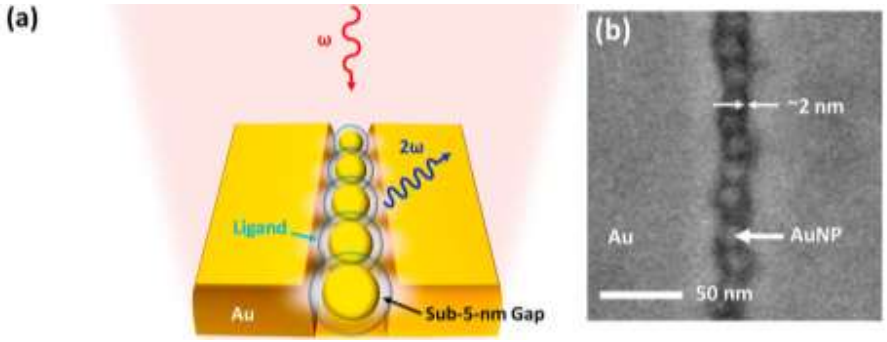



**Figure 1.** [Reproduced and adapted from Ref.[13]] (a) Schematic of the double-gap structure in Au achieved by self-assembly of gold nanoparticles (AuNP) within trenches made by template stripping. Structures provide strong field enhancement and second-harmonic generation. (b) Top-down SEM image of a segment of a trench with particles trapped inside with gaps measuring ~2-nm.

**Acknowledgements** We acknowledge funding support from Agency for Science, Technology and Research (A*STAR) Young Investigatorship (grant 0926030138), SERC (grant 092154099), Singapore University of Technology and Design (grant RGDM1530302), and National Research Foundation (grant NRF-CRP 8-2011-07).

**REFERENCES**

1. Yang, J. K. W. & Berggren, K. K. Using high-contrast salty development of hydrogen silsesquioxane for sub-10-nm half-pitch lithography. *J. Vac. Sci. Technol. B.* **25,** 2025 (2007).
2. Yang, J. K. W. *et al*. Understanding of hydrogen silsesquioxane electron resist for sub-5-nm-half-pitch lithography. *J. Vac. Sci. Technol. B.* **27,** 2622 (2009).
3. Manfrinato, V. R. *et al.* Resolution limits of electron-beam lithography toward the atomic scale. *Nano Lett.* **13,** 1555–1558 (2013).
4. Duan, H., Hu, H., Kumar, K., Shen, Z. & Yang, J. K. W. Direct and reliable patterning of plasmonic nanostructures with sub-10-nm gaps. *ACS Nano* **5,** 7593–7600 (2011).
5. Duan, H., Fernandez-Dominguez, A. I., Bosman, M., Maier, S. A. & Yang, J. K. W. Nanoplasmonics: Classical down to the nanometer scale. *Nano Lett.* **12,** 1683–1689 (2012).
6. Duan, H., Hu, H., Hui, H. K., Shen, Z. & Yang, J. K. W. Free-standing sub-10 nm nanostencils for the definition of gaps in plasmonic antennas. *Nanotechnology* **24,** 185301 (2013).
7. Wang, Y. M. *et al.* High aspect ratio 10-nm-scale nanoaperture arrays with template-guided metal dewetting. *Sci. Rep.* **5,** 9654 (2015).
8. Kuznetsov, A. I. *et al.* Split-ball resonator as a three-dimensional analogue of planar split-rings. *Nat. Commun.* **5,** 3104 (2014).
9. Im, H., Bantz, K. C., Lindquist, N. C., Haynes, C. L. & Oh, S. H. Vertically oriented sub-10-nm plasmonic nanogap arrays. *Nano Lett.* **10,** 2231–2236 (2010).
10. Tan, S. F. *et al.* Quantum Plasmon Resonances Controlled by Molecular Tunnel Junctions. *Science* **343,** 1496–1499 (2014).
11. Nagpal, P., Lindquist, N. C., Oh, S.-H. & Norris, D. J. Ultrasmooth patterned metals for plasmonics and metamaterials. *Science* **325,** 594–7 (2009).
12. Asbahi, M. *et al.* Large Area Directed Self-Assembly of Sub-10 nm Particles with Single Particle Positioning Resolution. *Nano Lett.* **15,** 6066–6070 (2015).
13. Dong, Z. *et al.* Second-Harmonic Generation from Sub-5 nm Gaps by Directed Self-Assembly of Nanoparticles onto Template-Stripped Gold Substrates. *Nano Lett.* **15,** 5976–5981 (2015).

# Ultrafast hot electrons spice up localized plasmons

**B. Palpant[1*], T. Labouret[1], J. F. Audibert[2], R. Pansu[2]**

[1]Laboratoire de Photonique Quantique et Moléculaire, CentraleSupélec, ENS Cachan, CNRS, Université Paris-Saclay, Grande Voie des Vignes, 92290 Châtenay-Malabry, France

[2]Laboratoire de Photophysique et Photochimie Supramoléculaires et Macromoléculaires, ENS Cachan, CNRS, Université Paris-Saclay, 61, avenue du Président Wilson, 94230 Cachan, France

[*]corresponding author: bruno.palpant@centralesupelec.fr

**Abstract**- Ultrashort light pulses absorbed by plasmonic nanostructures are not only able to transiently modulate their optical properties, but can also lead to the production of a nanoscale plasma, which in the enhanced local electromagnetic field may generate reactive oxygen species in water over a large area, opening interesting outlooks for photodynamic therapy. We demonstrate this process on single gold nanorods by fluorescence imaging and explain the mechanisms involved by an appropriate theoretical model.

Nanostructures exhibiting localized plasmon resonance under light excitation are widely developed for their ability to strongly enhance the local electromagnetic field or to convert light into heat at the nanoscale. Beyond, new properties can be generated when such plasmonic nanostructures absorb ultrashort light pulses. Indeed, the electron distribution is modified by such a strong energy input, leading to a hot electron gas which then relaxes back to equilibrium by radiation, electron emission and electron-phonon scattering. The electromagnetic properties of the nanostructures evolve along these transient processes, resulting in the modulation of both their optical response and the local field enhancement.[1] Besides, their very close environment can also be affected by electron transfer, electron ejection, and overheating.

In this communication, we demonstrate the production of a nanoscale plasma around single gold nanorods (AuNRs) in water irradiated by subpicosecond laser pulses tuned to their longitudinal plasmon mode. Electrons ejected from the metal as their energy exceeds the work function gain further kinetic energy by inverse Bremsstrahlung in the strong electric field localized around the nanorods.[2] They are then able to ionize oxygen and water molecules over an area several micrometer wide, succeeding in the effective production of reactive oxygen species (ROS) which are known to induce cell death in a living environment. If the AuNR aspect ratio is chosen so that the longitudinal plasmon resonance matches the transparency window of biological tissues, ultrashort laser pulse irradiation of AuNRs can constitute a relevant tool for photodynamic therapy.

By using a fluorescent probe sensitive to the presence of •OH and $^1O_2$, we show by fluorescence imaging that the production of ROS by a single AuNR varies with the polarization of light relative to the nanorod orientation (Fig. 1).[3] This result is correlated to the far-field emission of a white light continuum which follows a 3-photon absorption process and extends over the whole visible spectrum. In order to interpret the pulse-induced production of ROS, a theoretical approach is carried out which accounts for the electron ejection, acceleration and ionization of water. The emission of electrons mainly stems from thermionic emission, and to a lesser extent to multiphoton ionization. We show that the transient modification of the electron distribution results in the

real-time evolution of the NR absorption cross section, preventing the NR from melting. In addition, we show that the athermal nature of the electron distribution has a strong influence on the plasma generation.

Further, we will briefly demonstrate the effect of the hot electron distribution on the ultrafast optical response of AuNRs[4] and show how this transient optical response can be efficiently enhanced by coupling plasmon modes with localized photonic modes in a microcavity.[5]

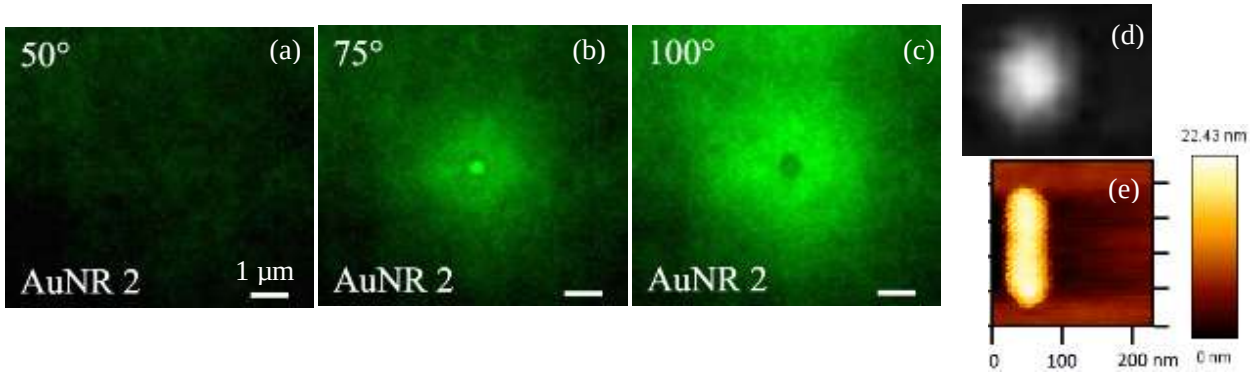



**Figure 1.** (a)-(c) Fluorescence microscopy images demonstrating the production of reactive oxygen species by a single gold nanorod in water irradiated by 400-fs laser pulses at 3 different polarization angles. The ROS amount clearly depends on light polarization relative to the NR orientation. The bright central spot in (b) corresponds to the NR photoluminescence. The black central spot in (c) corresponds to the fluorescence darkening due to ROS excess. (d) Dark-field microscopy image of a single nanorod under pulse irradiation, without fluorescent molecule, showing the diffraction-limited luminescence emission. (e) AFM image of the same AuNR as in (d).

**Acknowledgements**. This work was financially supported by Région Ile-de-France, French Agence Nationale de la Recherche (project ANR-13-BS10-0008-01), and Institut d'Alembert (FR CNRS 3242).

**REFERENCES**

1. Guillet, Y., M. Rashidi-Huyeh and B. Palpant, "Influence of laser pulse characteristics on the hot electron contribution to the third-order nonlinear optical response of gold nanoparticles", *Phys. Rev. B*, Vol. 79, 045410, 2009.
2. Boulais, E., R. Lachaine and M. Meunier, "Plasma-mediated nanocavitation and photothermal effects in ultrafast laser irradiation of gold nanorods in water", *J. Phys. Chem. C*, Vol. 117, 9386–9396, 2013.
3. Labouret, T., J.-F. Audibert, R. Pansu and B. Palpant, "Plasmon-assisted production of reactive oxygen species by single gold nanorods", *Small*, Vol. 11, 4475-4479, 2015.
4. Wang, X., Y. Guillet, P. R. Selvakannan, H. Remita and B. Palpant, "Spectral signature of the ultrafast optical response of gold nanorods", *J. Phys. Chem. C*, Vol. 119, 7416-7427, 2015.
5. Wang, X., R. Moreira, J. Gonzalez and B. Palpant, "Coupling localised plasmonic and photonic modes tailors and boosts ultrafast light modulation by gold nanoparticles", *Nano Letters*, Vol. 15, 2633–2639, 2015.

# Infrared and THz plasmonics using nano-engineered gold structures

**K. Ueno***

Research Institute for Electronic Science, Hokkaido University, Japan

*corresponding author: k-ueno@es.hokudai.ac.jp

**Abstract**- Terahertz (THz) wave has received considerable attention for use in many applications such as transmission imaging and fingerprint spectra with an important contribution in the bioengineering and security field. We are interested in THz spectroscopy for a molecular science study because the energy of THz wave is almost corresponding to that of intermolecular interaction such as hydrogen bonding or van der Waals force. THz spectroscopy is promising because the lower frequency mode and even light molecules can be measured. However, the sensitivity of THz spectroscopy is low since absorption cross-section of molecule/substances in THz frequency region is very small. In this study, we proposed plasmon-induced near field enhances the signal of THz spectroscopy and demonstrated surface-enhanced THz spectroscopy using gold nanostructured THz antennae.

Gold rod (80 μm × 200 nm × 40 nm) structures whose plasmon resonance band is peaking at 24.7cm$^{-1}$ (0.74 THz) were fabricated on a silicon substrate by electron beam lithography and lift-off processes. L-glutamic acid was deposited on the substrate with a thickness of 150 nm by vacuum evaporation technique. The L-glutamic acid was converted to a crystal of L-Pyroglutamic acid as a result of vacuum vapor deposition. A conventional THz time-domain spectroscopy was employed for extinction spectrum measurement.

Figure 1 indicates extinction spectrum of L- Pyroglutamic acid crystal deposited on gold rod structured silicon substrate.

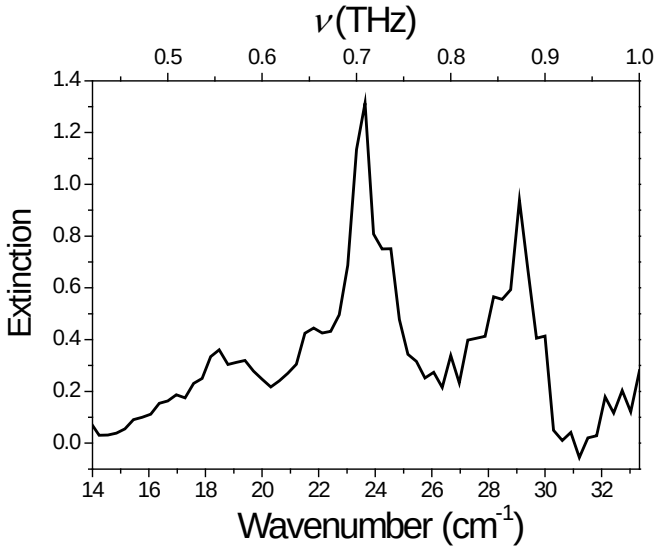



Figure 1. Extinction spectrum of L- Pyroglutamic acid crystal deposited on gold rod structured silicon substrate.

Two distinct peaks were clearly observed overlapping with a broad plasmon resonance spectrum as background. The spectrum measured under the incident polarization perpendicular to the rod was used for reference of the extinction spectrum measurement, so that we have successfully demonstrated surface-enhanced THz spectroscopy. It is considered that apparent absorption cross-section was enhanced due to the longer dephasing time of surface plasmon in THz frequency region and plasmon resonant spectrum was modulated by the change of dielectric function by coupling between plasmon dipole and dipole moment of molecular and intermolecular vibrational modes.

**Acknowledgements**, the author acknowledges Prof. Hiroaki Misawa and Mr. Sho Nozawa for fruitful discussions and experimental results. The author also acknowledgements financial supports from MEXT-KAKENHI Photosynergetics (No.15H01073), JSPS-KAKENHI (Nos. 23225006 and 15K04589), Nanotechnology Platform of MEXT (Hokkaido University).

**REFERENCES**

1. Ueno, K., Juodkazis, S., Mizeikis, V., Ohnishi, D., Sasaki, K. and Misawa H. “Inhibition of multipolar plasmon excitation in periodic chains of gold nanoblocks,” *Opt. Express*, Vol. 15, No. 25, 16527–16539, 2007.
2. Toma, A., Tuccio, S., Prato, M., Donato, F. D., Perucchi, A., Pietro, P. D., Marras, S., Liberale, C., Zaccaria, R. P., Angelis, F. D., Manna, L., Lupi, S., Fabrizio, E. D. and Razzari, L. “squeezing terahertz light into nanovolumes: nanoantenna enhanced terahertz spectroscopy (NETS) of semiconductor quantum dots,” *Nano Lett.*, Vol. 15, No. 1, 386–391, 2015.
3. Shalabney, A., George, J., Hutchison, J., Pupillo, G., Genet, C. and Ebbesen, T. W. “Coherent coupling of molecular resonators with a microcavity mode,” *Nat. Commun.*, Vol. 6, 5981, 2015.
4. Ueno, K., Nozawa, S. and Misawa, H. “Surface-enhanced terahertz spectroscopy using gold rod structures resonant with terahertz waves”, *Opt. Express.*, Vol. 23, No. 22, 28584–22592, 2015.

# Colloidal Nano-Assemblies for DNA Detection and Label-Free SERS Tagging.

**Jessica Rodríguez-Fernández**[1,2*]

[1] Department of Physics and Center for Nanoscience (CeNS), Ludwig-Maximilians-Universität (LMU), Munich, Germany

[2] Nanosystems Initiative Munich (NIM), Munich, Germany

[*]corresponding author: jessica.rodriguez@lmu.de

**Abstract**- This talk will report on the design and application of nano-assemblies recently devised in our group. Anisotropic metal NPs and DNA oligonucleotides are the corresponding NP and biomolecule building-blocks. It will be shown how optothermal effects can be used to selectively trigger the disassembly of metal NP-DNA assemblies, and thereby, enable the ultrafast detection of DNA. In another example, discrete nano-assemblies with strong directional interactions will be presented and proved as sensitive label-free SERS tags.

Several reasons make biomolecules beneficial in nanoscience. For instance, they can serve as morphological templates to induce the formation and growth of inorganic nanoparticles (NPs) with unconventional shapes and tailored properties.[1] Combining inorganic NPs and biomolecules is also advantageous from the perspective of nano-assembly design. Examples of nano-assemblies resulting from the combination of DNA and plasmonic NPs are particularly interesting, especially given the unprecedented properties and wide scope of applications recently demonstrated.[2, 3]

This talk will report on the design and application of nano-assemblies recently devised in our group.[4, 5] Anisotropic metal NPs and DNA oligonucleotides are the corresponding NP and biomolecule building-blocks. For instance, it will be shown how optothermal effects can be used to selectively trigger the disassembly of metal NP-DNA assemblies, and thereby, enable the ultrafast detection of DNA. In another example, discrete nano-assemblies with strong directional interactions will be presented and proved as sensitive label-free SERS tags.

**Acknowledgements.** We acknowledge the Federal Ministry of Economics and Technology (Germany) for financial support through the ZIM project KF2260002AJ1 and the Ludwig-Maximilians-Universität München for funding through the LMUexcellent Junior Researcher Fund (DFG's Excellence Initiative, project HE-Go-3D).

**REFERENCES**

1. Baumann, V., M. A. H. Muhammed, A. J. Blanch, P. Dey and J. Rodríguez-Fernández, "Biomolecules in metal and semiconductor nanoparticle growth", *Isr. J. Chem.*, doi: 10.1002/ijch.201500031, In press.
2. Roller, E.-M., L. K. Khorashad, M. Fedoruk, R. Schreiber, A. O. Govorov and T. Liedl, "DNA-assembled

nanoparticle rings exhibit electric and magnetic resonances at visible frequencies", *Nano Lett.*, Vol. 15, No. 2, 1368−1373, 2015.

3. Kuzyk, A., R. Schreiber, H. Zhang, A. O. Govorov, T. Liedl and N. Liu, "3D reconfigurable plasmonic metamolecules", *Nat. Mater.*, Vol. 13, 862−866, 2014.
4. Baumann, V., K. Lyons, F. Haase, K. Szendrei, P. J. F. Rötgermann, M. Gräßel, J. Stehr, L. Ullerich, F. Bürsgens and J. Rodríguez-Fernández, Submitted.
5. Dey, P., V. Baumann and J. Rodríguez-Fernández, In preparation.

# Hierarchical Plasmonic Nanostructured Materials: Synthesis and Applications

**Miguel A. Correa-Duarte**[1]

[1] Department of Physical Chemistry, Biomedical Research Center (CINBIO), and Institute of Biomedical Research of Ourense-Pontevedra-Vigo (IBI), Universidade de Vigo, 36310 Vigo, Spain

[*]corresponding author: macorrea@uvigo.es

**Abstract**- In the near future, hierarchically organized plasmonic nanostructured materials holding multiple functionalities, are expected to play a key role in many different fields, such as drug delivery, optics, catalysis, or sensing, among others. However, there is still an important lack of knowledge with regard to their fabrication which in the end, limits their applicability in the areas of interest. We report herein the implementation of novel strategies for the fabrication of such materials based on the confinement of plasmon-resonant nanoparticles. In a first example, the ability of plasmonic nanoparticles to concentrate light at the nanometer scale has been exploited for the simultaneous thermal activation and optical monitoring of high energy-demanding chemical reactions. As a proof of concept, a Diels-Alder cycloaddition reaction has been carried out into the inner cavities of plasmonic nanocapsules in order to evidence their efficacy as nanoreactors. Thus, it is demonstrated that this process can be performed in a confined volume with no alteration of the temperature of the bulk solvent, allowing at the same time a real time monitoring of the reaction progress. These plasmonic nanostructures have been also shown to be efficient nanoprobes for relevant signaling molecules. In this regard, an advanced hybrid SERS sensor has been implemented so as to perform the intracellular detection of NO. With this aim, a NO-chemoreceptor functionalization of plasmonic nanoparticles has been performed in order to engineer a quantitative fully biocompatible sensor capable of executing an in situ real time monitoring of the dynamics of NO in living cells. This sophisticated design prevents the interaction of cytosolic macromolecules with the active optical material and the enzymatic degradation of the sensing elements. Finally, anisotropic plasmonic nanoparticles with hot spots in Au-metal oxide hierarchical nanoarchitectures is discussed for enhancing hot electron-driven photocatalysis, as well as infrared shielding.

**REFERENCES**

1. Vázquez-Vázquez, C., Vaz, B., Giannini, V., Pérez-Lorenzo, M., Álvarez-Puebla, R. A. and Correa-Duarte, M. A.“ Nanoreactors for Simultaneous Remote Thermal Activation and Optical Monitoring of Chemical Reactions,” *J. Am. Chem. Soc.*, 135, 13616–13619, 2013.
2. Rivera-Gil, P, Vázquez-Vázquez, C., Giannini, V., Callao, M. P., Parak, W. J., Correa-Duarte, M. A. and Álvarez-Puebla, R. A., “Plasmonic Nanoprobes for Real-Time Optical Monitoring of Nitric Oxide inside Living Cells,” *Angew. Chem. Int. Ed.*, 52, 13694–13698, 2013.
3. Pérez-Lorenzo, M., Vaz, B., Salgueiriño,V. and Correa-Duarte,M. A, “Hollow-Shelled Nanoreactors Endowed with High Catalytic Activity,” *Chem. Eur. J.*, 19, 12196–12211, 2013.

# Spatial localization of plasmonic hot spots as probed by molecular nanomotors and atomic force microscopy

**Y. Zhang[1], J. Plain[1], G. Davy[1], G. Demesy[2], N. Bonod[2], and R. Bachelot[1*]**
[1]ICD-LNIO, CNRS, University of Technology of Troyes, France
[2] Institut Fresnel, CNRS, France
[*]corresponding author: renaud.bachelot@utt.fr

**Abstract**-Plasmonic hot spots can trigger molecular displacements. In this approach azobenzene-like molecules, covalently grafted onto a polymeric backbone, are used as optical nanomotors that act as local molecular probes of electromagnetic phenomena. The resulting local optically-induced motion is characterized by Atomic Force Microscopy. We used this unique method for visualizing tunable plasmonic hot spots at the gaps of plasmonic trimers in the near infrared.

A photochemical imaging method have been developed to realize near-field control of electromagnetic fields and hot spots in plasmonic nanostructures[1-3]. In this method azobenzene-like molecules, covalently grafted onto a polymeric backbone, are used as optical nanomotors driven by local electromagnetic fields: azo molecules moves at hot spots in a way that depends on the local polarization state. The resulting optically induced motion is characterized by Atomic Force Microscopy.

On the occasion of the META2016 conference, we summarize important achievements and report the recent use of this unique method for visualizing tunable plasmonic hot spots at the gaps of plasmonic trimers in the near infrared.

We have designed a nanotrimer that consists of three Au nanoparticles (Fig. 1, left). Different hot spots with different local positions have been observed and studied as a function of incident polarization and angles (cf. example on Figure 1, right). Interestingly, when the polarization of incident light is parallel to nanotrimer axis, a certain incident angle relative to nanotrimer axis induces a strong near-field enhancement in one nanogap while nullifying the near-field intensity in the other nanogap. In general, the localization of this hotspot turns out to depend on the direction of the incident beam.

The observations are interpreted in terms of plasmonic symmetric and antisymmetric mode balancing [4].

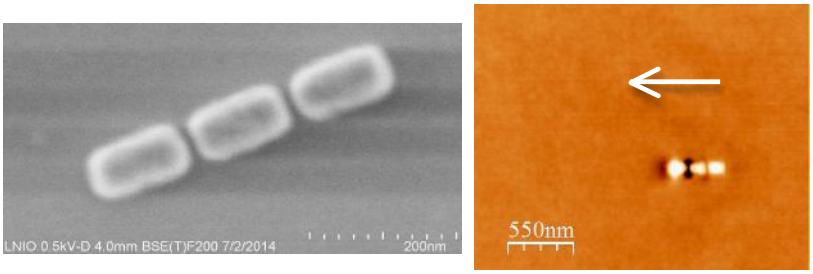



Figure 1. Left: SEM image of the plasmonic trimer. Right: AFM image of the optically-induced (at (λ=900 nm, p

polarization) topography in the vicinity of the plasmonic trimer. The white arrow is the in-plane projection of the incident wavevector. The left gap is a near-field enhanced area

**REFERENCES**


1. Hubert, C. et al. "Near-Field Photochemical Imaging of Noble Metal Nanostructures", *Nano Letters*, Vol. *5*, No. 4, 615-619, 2005.
2. Juan M. L. et al. "Multiscale Model for Photoinduced Molecular Motion in Azo Polymers", *ACS Nano*, Vol. 3, No. 6, 1573–1579, 2009.
3. Haggui, L. et al., "Spatial Confinement of Electromagnetic Hot and Cold Spots in Gold Nanocubes ", *ACS Nano*, Vol. 6, No. 2, 1299–1307, 2012.
4. Devilez et al., "Mode-balancing far-field control of light localization in nanoantennas", *Phys. Rev. B.*, Vol. 81, 245128, 2010.

# SERS inside Au@Ag nanocuboids and Au@Gap@Au nanomatryoshkas

**N. G. Khlebtsov**[1,2,*] **and B. N. Khlebtsov**[1,2]
[1]Institute of Biochemistry and Physiology of Plants and Microorganisms, Russian Academy of Sciences, Russia
[2]Saratov State University, Russia
[*]corresponding author: userid@institution.edu

**Abstract**- Raman-active 1,4-aminothiophenol (ATP) and benzenedithiol (BDT) molecules were embedded inside Au@ATP@Ag nanocuboids and Au@BDT@Au nanomatryoshkas with ~1-nm hollow or bridged gaps. The SERS enhancement factor for embedded molecules was about an order of magnitude higher than that for molecules on the particle surface. Multilayered Mie and FDTD simulations were used to explain the electromagnetic enhancement inside plasmonic nanogaps.

Recently, several research groups reported on highly efficient multilayer SERS tags, in which Raman molecules were trapped at the Au-Ag interface[1]or in a nanometer-sized interior gap between the metallic core and shell.[2-4] Such multilayered structures, also called nanomatryoshkas[5] (NMs) have great potential for biomedical applications due to several advantages: (1) Raman molecules are protected from desorption and environment conditions; (2) they are subjected to uniform and strongly enhanced electromagnetic field in the gap; (3) NMs produce stable SERS response irrespective of their aggregation; (4) highly uniform spectral pattern ensures a linear correlation between probe concentration and SERS intensity; (5) nanogap SERS probes can be multiplexed by incorporated different Raman molecules into multilayered NMs. The core-shell separation can be obtained by using dielectric or molecular spacers, consequently controlling the gap-field enhancement. However, the synthesis of such nanostructures with controllable parameters remains still challenging.

Here, we report on the preparation of uniform Au@Ag core/shell nanocuboids with a controllable Ag shell thickness from 1 to 25 nm. Successful embedding of ATP reporter molecules inside the core/shell nanoparticles was confirmed by the absence of selective oxidation of the amino groups, as measured by Raman spectroscopy. The dependence of Raman intensity on the inside/surface location of the reporter molecules was studied. The interior molecules showed a strong and uniform Raman intensity, at least an order of magnitude higher than that of the molecules on the nanoparticle surface. In contrast to usual surface-functionalized Raman tags, aggregation and clustering of nanoparticles with embedded molecules decreased the SERS signal. The findings from this study provide the basis for a novel technique of low analyte concentration detection based on high SERS response inside the core/shell metal nanostructures. As an example, we show robust SERS detection of the thiram fungicide in solution at a concentration as low as $10^{-9}$ M.

In the second part of this talk, we report on fabrication, characterization and electromagnetic simulations of Au NMs with a nanometer-sized interior gap between Au core and shell. We have found that the structure of nanogaps inside Au NMs strongly depends on the core surface morphology. Specifically, when the initially citrate-stabilized smooth Au 15- and 35-nm cores were functionalized further with 1,4 benzenedithiol (BDT) in the presence of cetyltrimethylammonium chloride (CTAC), the Au shell growth leads to formation of a sub-nanometer hollow interior gap containing BDT molecules. In contrast, the use of faceted polygonal

CTAC-stabilized 23-nm and 35-nm Au cores for Au shell growth resulted in NMs with small bridged gaps. The experimental SERS response from BDT molecules in bridged-gap NMs was one order higher than that for hollow-gap NMs, in agreement with finite-difference time-domain (FDTD) simulations predicting stronger electromagnetic fields inside nano-bridged gaps compared to hollow-gap NMs. The major SERS peaks from BDT inside NMs of both types (two sizes, four samples) was one order higher than the near-field SERS peaks recorded for corresponding 15CIT, 23CTAC, 35CIT, and 35CTAC cores alone after surface functionalization with BDT molecules. This observation is explained by a simple dipole approximation (DA) theory, which was developed to estimate the structural- and spectral-dependent electromagnetic SERS enhancement in the hollow gap NMs with a good accuracy as confirmed by comparison with exact multilayered Mie (ML Mie) calculations (Fig. 1). The physical insights acquired from this study open the way for rational design and efficient optimization of new SERS platforms based on electromagnetic field enhancement in sub-nanometer gaps within plasmonic nanostructures.

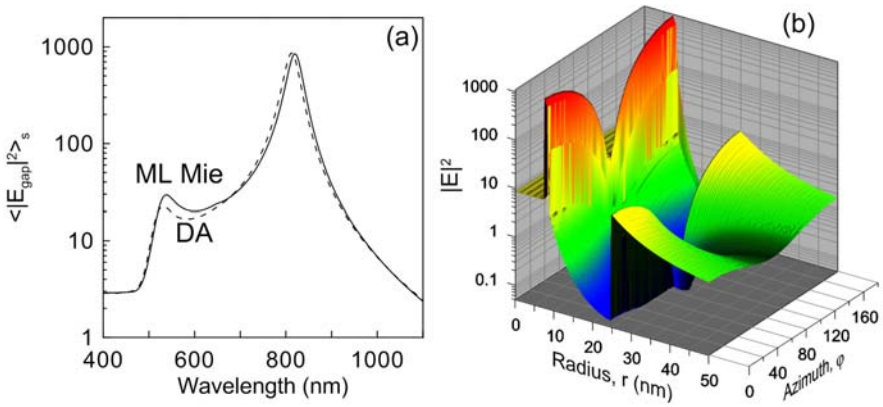



Figure 1. Spectra of the surface averaged field intensity in the gap (a) and the distribution of the internal field intensity (b) in equatorial plane (x, y). The incident field is propagated along the z-axis and polarized along the x-axis. Calculations by DA and ML Mie for an Au-dielectric ($n$ =1.40)-Au NM with radii 7.5, 8.5, 25 nm and the wavelength 785 nm by DA(a) and ML Mie solutions (a, b).

This work was supported by RNF grant no. 14-13-01167.

**REFERENCES**

1. Pinkhasova, P., B. Puccio,; T. Chou, S. Sukhishvili and H. Du, "Noble metal nanostructure both as a SERS nanotag and an analyte probe," *Chem. Commun.*, Vol. 48, 9750–9752, 2012.
2. Lim, D. K., K. S. Jeon, J. H. Hwang, H. Kim, S. Kwon, Y. D. Suh and J. M. Nam, "Highly uniform and reproducible surface-enhanced Raman scattering from DNA-tailorable nanoparticles with 1-nm interior gap. *Nat. Nanotechnol.*, Vol. 6, 452–460, 2011.
3. Gandra, N. and S. Singamaneni, "Bilayered Raman-intense gold nanostructures with hidden tags (BRIGHTs) for high-resolution bioimaging," *Adv. Mater.*, Vol. 25, 1022–1027, 2013.
4. Lin, L., M. Zapata, M. Xiong, Z. Liu, S. Wang, H. Xu, A. G. Borisov, H. Gu, P. Nordlander, J. Aizpurua and J. Ye, "Nanooptics of plasmonic nanomatryoshkas: shrinking the size of a core−shell junction to subnanometer," *Nano Lett.*, Vol. 15, 6419−6428, 2015.
5. Lin, L., H. Gu and J. Ye, "Plasmonic multi-shell nanomatryoshka particles as highly tunable SERS tags with built-in reporters," *Chem. Commun.*, Vol. 51, 17740–17743, 2015.

# Nano-optical Chemical and Structural Classification of Nucleic Acids via Label-free Surface-enhanced Raman Scattering Analysis

**Judit Morla-Folch**[1,2], **P. Gisbert-Quilis**[1,2], **A. Torres**[1,2], **R.A. Alvarez-Puebla**[1,2,3] **and L. Guerrini**[*1]

[1]Medcom Advance, Viladecans Business Park, Ed. Brasil, Bertran i Musitu 83-85, 08840 Viladecans (Spain).

[2] Centro Tecnológico de la Química de Catalunya, Carrer de Marcel•lí Domingo s/n, 43007 Tarragona (Spain).

[3] ICREA, Passeig Lluís Companys 23, 08010 Barcelona, Spain.

[*]corresponding author: luca.guerrini@ctqc.org

**Abstract**-We report a fast and affordable high-throughput screening direct SERS method for gaining detailed genomic information on nucleic acids (DNA and RNA) and for the characterization and quantitative recognition of DNA interactions with exogenous agents.

The exploring of the genetic information carried by nucleic acids has become a major scientific challenge, finding a vast set of applications in different fields, such as medical diagnostics, genomic screening, drug analysis, forensic and bioterrorism. Emerging technologies such as the optical sensing through plasmons have the potential of reshaping the detection and characterization scenario of the nucleic acids by offering simple, fast and highly sensitive platforms that overcome the limitations of PCR and Northern blot based microarrays. Among them, surface-enhanced Raman scattering (SERS) spectroscopy has developed into a mature, reliable technique combining the rich molecular information contained in the vibrational spectra with outstanding ultrasensitive, multiplexing and quantification capabilities. However, until today, most of the SERS application to nucleic acid analysis largely relied on indirect strategies. Although this approach has been demonstrated very effective for pure identification purposes, it completely dismisses the exquisite chemical and structural information provided by the direct acquisition of the vibrational fingerprint of the biomolecule. Contrarily, direct label-free SERS of nucleic acid shows an outstanding potential in terms of chemical-specific information. However, the final SERS of a complex biomolecule such as DNA is highly sensitive to a large set of interdependent multiple factors and experimental variables that are difficult to control and often case specific. As a result, the acquisition of reproducible SERS spectra at low DNA concentrations has usually represented a major challenge, especially in the case of double-stranded structures (dsDNA) where the negatively charged phosphate backbone (at the physiological pH) shields the direct interaction of the nucleobase with the metal surface.

To address these limitations, we developed a fast and affordable high-throughput screening direct SERS method for gaining detailed genomic information on nucleic acids (DNA and RNA) and for the characterization and quantitative recognition of DNA interactions with exogenous agents.[1-4] The simple strategy relies on the electrostatic adhesion of nucleic acids onto positively-charged silver colloids that promotes the nanoparticle aggregation into stable clusters yielding intense and reproducible SERS spectra (DNA sequences are selectively sandwiched between interparticle junctions, thus maximizing the intensification of the Raman signal, see Fig. 1A). The SERS spectra are acquired with high batch-to-batch reproducibility, providing truly spectral fingerprints of the nucleoside composition and organization within the helix as well as DNA complexes with

exogenous agents (chemotherapeutic drugs, intercalating agents, metal ions etc.), as depicted in Fig. 1B. The spectral changes associated with structural perturbations of nucleic acids are quantitatively correlated with the extent of the molecular modifications. Implementation of the sensing strategy into a microfluidic device further reduced the required amount of DNA per measurement to the picogram level while enabling fundamentally new applications, such as an increase in automation and parallelization. Thus, the analysis can be performed without the necessity of amplification steps providing realistic direct information of the nucleic acid in its native state. We anticipate this method to gain a vast impact and set of applications in different fields, including medical diagnostics, genomic screening, drug discovery, forensic science and even molecular electronics.

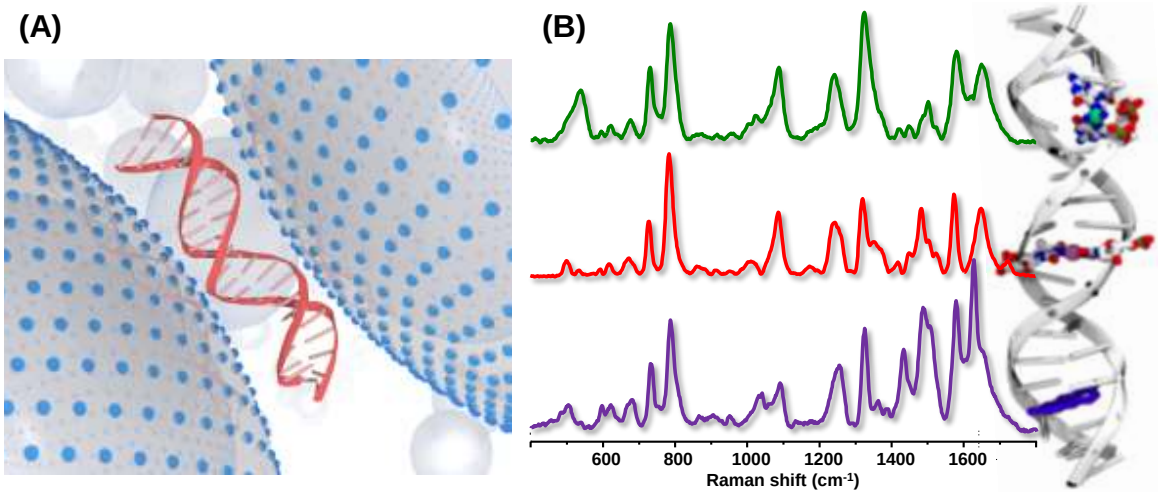



**Figure 1**. (A) dsDNA sandwiched between two positively charged silver nanoparticles. (B) SERS spectra of dsDNA complexes with cisplatin, $Hg^{2+}$ and methylene blue.

**Acknowledgements**. The work was funded by the European Research Council (CrossSERS, FP7/2013 329131, PrioSERS FP7/2014 623527), the Spanish Ministerio de Economia y Competitividad (CTQ2011-23167), and Medcom Advance SA.

**REFERENCES**

1. Morla-Folch, J.; Xie, H.; Alvarez-Puebla, R. A.; Guerrini, L. "Fast Optical Chemical and Structural Classification of RNA" *ACS Nano*, Vol. 10, 2834-2842, 2016.

2. Guerrini, L.; Krpetić, Ž.; van Lierop, D.; Alvarez-Puebla, R. A.; Graham, D. "Direct Surface-Enhanced Raman Scattering Analysis of DNA Duplexes" *Angew. Chem.-Int. Edit.*, Vol. 54, 1144-1148, 2015.

3. Masetti, M.; Xie, H.; Krpetić, Ž.; Recanatini, M.; Alvarez-Puebla, R. A.; Guerrini, L. "Revealing DNA Interactions with Exogenous Agents by Surface-Enhanced Raman Scattering" *J. Am. Chem. Soc.*, 137, 469-476, 2015.

4. Morla-Folch, J.; Xie, H.; Gisbert-Quilis, P.; Gómez-de Pedro, S.; Pazos-Perez, N.; Alvarez-Puebla, R. A.; Guerrini, L. "Ultrasensitive Direct Quantification of Nucleobase Modifications in DNA by Surface-Enhanced Raman Scattering: The Case of Cytosine" *Angew. Chem.-Int. Edit.* Vol. 54, 13650-13654, 2015.

**Plasmonics and nanophotonics**

# Fano and Induced Transparency in Plasmon Based Optical Sensors

**Zouheir Sekkat[1-3] and Shinji Hayashi[1]**
[1]*Optics and Photonics Center, Moroccan Foundation for Advanced Science, Innovation and Research (MAScIR)*
[2]*Faculties of Sciences, Mohammed V University, Rabat, Morocco*
[3] *Graduate School of Engineering, Osaka University, Suita, Japan*
*E-mail address: z.sekkat@mascir.com*

During the past few years, we have been involved in the study of optical sensors, in particular the plasmonic sensors, to achieve ultra-high sensitivities. As is well known, the sensitivity of the conventional surface plasmon resonance (SPR) sensor based on a single layer of Au is not very high because of the broad lineshape of the resonance. Several attempts have been made so far to improve the sensitivity by using long-range surface plasmons and waveguide (WG) modes. We propose here alternative ways to improve the sensitivity and to achieve extremely high sensitivities.

Based on our appropriate formulation of the figure of merit of sensor sensitivity, we performed extensive numerical calculations for Kretschmann's configurations constructed by Au, Ag, Cu and Al films [1]. The figures of merit obtained for a wide range of the wavelength from the ultraviolet to the infrared regions allow us to optimize the structure to achieve the best performance for bulk and thin film sensing..

We also studied both theoretically and experimentally multilayer structures that give sharper resonances and higher sensitivities. One of the promising structure is metal-insulator-metal structures that support symmetric and antisymmetric surface plasmon polaritons (SPPs) arising from the coupling between two SPPs at the metal-insulator interfaces. Experiments performed on Ag-PMMA-Ag structures demonstrated a reflectance dip much sharper than that exhibited by a single layer of Ag, in good agreement with results of theoretical calculations [2]. The appearance of the sharp dip can be explained by the anticrossing behavior of the SPP dispersion curves.

Recently, we have found that an alternative multilayer structure shown in Fig. 1 gives extremely narrow resonances and high sensitivities [3,4]. The structure can be regarded as a combination of a SPP structure presented in Fig. 1(a) and a WG structure shown in Fig. 1(b). In the structure shown in Fig. 1 (c), SPP and WG modes can interact with each other through the overlap of their evanescent fields inside the spacer layer (Dielectric 1). The coupling of the modes generates very sharp resonances as shown in Figs. 2(a) and 2(b). The lineshape seen in Fig. 2(a) is so-called plasmon-induced transparency and that seen in Fig. 2(b) is Fano lineshape. It should be stressed that these lineshape, in particular the Fano lineshape, are very much sharper than the conventional SPR and exhibit shifts when the refractive index of the surrounding medium (water) is changed. According to our estimations, the figure of merit of sensitivity by intensity of this type of sensor can be $10^7$ times as large as that of the conventional SPR and WG sensors, provided that the loss in the dielectric layers is sufficiently small. The proposed structure is very much suited for applications, because it does not require any nanofabrication procedure. Experimental confirmation of the ultra-high sensitivities is now underway in our laboratory.

[1] D. V. Nesterenko and Z. Sekkat, Plasmonics, **8**, 1585 (2013).
[2] S. Refki, S. Hayashi, A. Rahmouni, D. V. Nesterenko and Z. Sekkat, DOI 10.1007/s11468-015-0047-7.
[3] S. Hayashi, D. V. Nesterenko and Z. Sekkat, APEX, **8**, 022201 (2015)
[4] S. Hayashi, D. V. Nesterenko and Z. Sekkat, J. Phys. D: Appl. Phys., **48**, 325303 (2015).

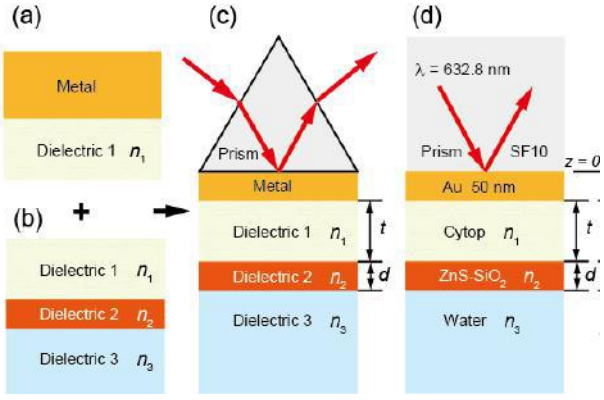



Fig.1 WG-coupled surface plasmon sensor

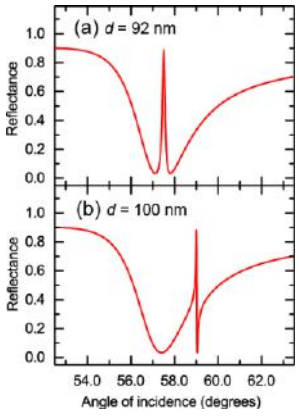



Fig. 2 PIT and Fano lineshapes

# Additive nano- and micro-structures towards perfect anti-reflector surfaces

**Y. Nishijima[1], R. Komatsu[1], S. Ohta[1], G. Seniutinas[1], A. Balčytis[1], and S. Juodkazis[2]**

[1]Department of Electrical and Computer Engineering, Graduate School of Engineering, Yokohama National University, 79-5 Tokiwadai, Hodogaya-ku, Yokohama 240-8501, Japan
[2]Centre for Micro-Photonics, Faculty of Engineering and Industrial Sciences, Swinburne University of Technology, Hawthorn, VIC 3122, Australia, and Melbourne Centre for Nanofabrication (MCN), Australian National Fabrication Facility, Clayton, VIC 3168, Australia
nishijima@ynu.ac.jp

**Abstract**— Engineering of surface texture and pattern is important for efficient light trapping and constructing anti-reflection surfaces. Here we demonstrate the nano-micro composite structures formed using combination of dry and wet etching processes on the surface of Si. Anti-reflection property has been dramatically improved towards perfect anti-reflectors as demonstrated by spectral measurements.

## 1. INTRODUCTION

Control of anti-reflection properties of semiconductor surfaces is sought after for solar cell applications. Recently, we have developed the nano needle structures made by an inductively coupled plasma etching - the black Si - and demonstrated its application for photo-thermal energy conversion system with plasmonic nanoparticles [1], for the surface enhanced Raman scattering spectroscopy [2], and bacteriacial effect [3]. Further functionalization of surfaces requires combination of two or three different nano-micro structuring techniques. Here we show that by combining micro texturing by wet etching with nano-needle structure is promising for formation of unrivaled low refectivity over broad spectral range.

## 2. EXPERIMENTS

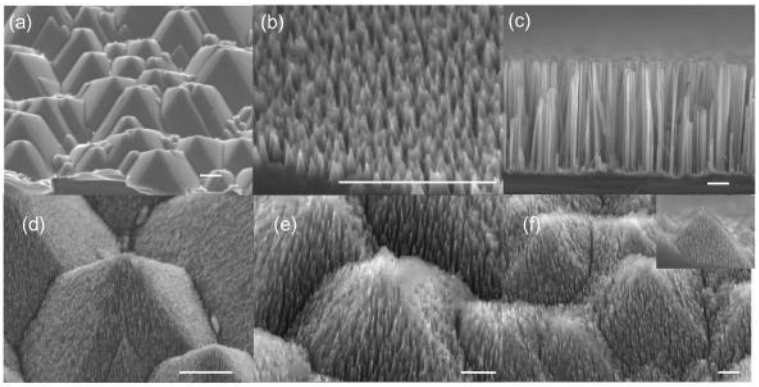



Figure 1: (a) Si textured surface which was formed using alkaline wet etching, (b) Si nano needle fabricated using ICP-RIE etching, (c) nanowire formed with Ag-metal assist etching, (d) nano-micro composite materials with texture formation and nano needle formation for 15min ICP etching, (e) 30min ICP etching and (f) 45 min etching. Scale bars, 1 $\mu$m.

Micro-pyramidal structures were fabricated using NaOH alkaline wet etching. The etching solution that is commercially available (Pure Etch T501S, Hayashi pure chemical, Ind. Ltd.). It was diluted 6 times by ion exchanged water. Si substrate, which has (100) top surface was dipped into the etching solution at 60°C for 10 min. Nano-pillar structures were fabricated using inductively coupled plasma reactive ion etching (ICP-RIE) with the mixture of $SF_6$ and $O_2$ plasma. Nano-wire structures were made by a metal assisted etching: Si was dipped into the $AgNO_3$ and HF mixed solution at room temperature for 20 min.

## 3. RESULTS AND DISCUSSION

Figure 1 shows scanning electron microscopic (SEM) image of each fabricated nano-micro structured surfaces. The size (height and separation) of micro pyramidal structures is in the range from 10 to 20 $\mu$m. Nano-needles have ∼100 nm width and ∼(200 - 300) nm height; the nano-wires have ∼(30- 40) nm width and more than 5 $\mu$m height. By combination of fabrication techniques nano-micro composite surfaces are formed by controlling the etching time. Pattern of pyramids made by ICP-RIE became similar to nano-needles that formed on flat surfaces by chemical metal-mediated etching. Micro-pyramids can be covered by nano-needles when 15 to 45 min dry etching was used over macro-textured Si.

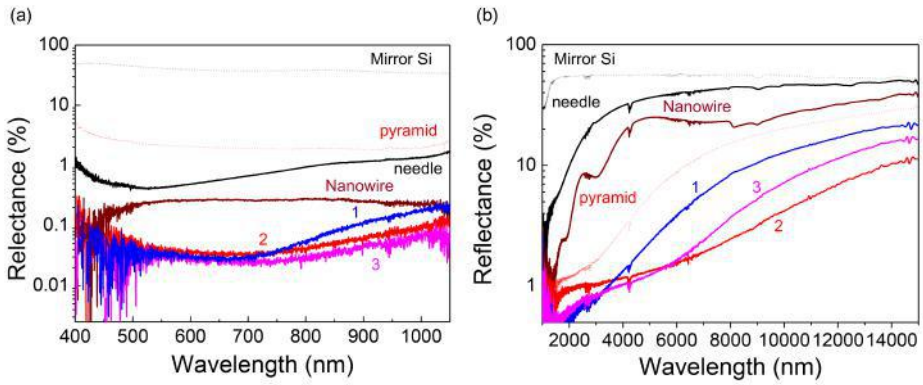



Figure 2: Reflection spectra of mirror Si (dashed black), micro-pyramidal (dashed red), nano-needle (solid black), nano-wire (solid brown), pyramid combined with: 15 min etched nano needle 1 (solid blue), 30 min 2 (solid red), and 45 min 3 (solid purple).

Figure 2 shows optical reflection spectra of each different surface. In the visible wavelength region, nano-micro composite material reflects less than 0.1% light, which is less than the other nano-needle and nano-wire pattern. Nano-micro composite structures can scatter and re-absorb light with higher efficiency in this wavelength region. Using FT-IR spectral measurements, less than 2% reflectivity was observed up to 8000 nm wavelengths into IR spectral range. There is no absorption by Si since it is transparent at those wavelengths. Low reflectivity is due to the scattering losses of the particular micro-nano textured surface. For the further qualitative and quantitative analysis, we will perform the fractal dimension analysis for the light absorption and scattering effects.

## 4. CONCLUSION

Combination of different Si structuring techniques has been successfully adopted for fabrication of nano-micro textured Si. The combination of micro pyramidal and nano-needle structure achieved lowest $< 1\%$ reflectivity from visible to infrared wavelengths.


## ACKNOWLEDGMENT

This work was financially JSPS KAKENHI. SJ is grateful for support via Australian Research Council DP130101205 project and startup funding for Nanolab by Swinburne University.


## REFERENCES


1. R. Komatsua, B. Armandas, G. Seniutinas, T. Yamamura, Y. Nishijima, and S. Juodkazis, "Plasmonic Photo-Thermoelectric Energy Converter with Black-Si Absorber," *Solar Energy Materials and Solar Cells* , vol. 143, 72-77, 2015.
2. G. Gervinskas, G. Seniutinas, J. S. Hartley, S. Kandasam, P. R. Stoddart, N. F. Fahim and S. Juodkazis, "Surface-enhanced Raman scattering sensing on black silicon," *Annalen der Physik* , vol. 525, 907-914, 2013
3. E. P. Ivanova, J. Hasan, H. K. Webb, G. Gervinskas, S. Juodkazis, V. K. Truong, A. H.F. Wu, R. N. Lamb, V. A. Baulin, G. S. Watson, J. A. Watson, D. E. Mainwaring and R. J. Crawford, "Bactericidal activity of black silicon," *Nature Communications* vol. 4, 2838, 2013.

# Full-spectrum solar light absorbtion and photothermal conversion with Ge-Sn on black silicon

**Y. Nishijima[1], R. Komatsu[1], T. Yamamura[1], G. Seniutinas[2], A. Balčytis[2], and S. Juodkazis[2]**

[1]Department of Electrical and Computer Engineering, Graduate School of Engineering, Yokohama National University, 79-5 Tokiwadai, Hodogaya-ku, Yokohama 240-8501, Japan
[2]Centre for Micro-Photonics, Faculty of Engineering and Industrial Sciences, Swinburne University of Technology, Hawthorn, VIC 3122, Australia
nishijima@ynu.ac.jp

**Abstract**— Harvesting entire solar light energy is desired for developing a sustainable energy supply for society. Solar cells still have unavoidable energy loss due to the heat generation. Also, transparency window for longer wavelength (i. e. 1100 nm for Si) is not utilised for the photo-current conversion. Here we demonstrate the photo-thermo-electric conversion system for the harvesting broad-band solar energy that can not be used in Si solar cell by direct absorption. Black silicon (b-Si) reducing the reflectivity of surface, and Ge-Sn layer is absorbing the full spectral wavelength of solar light.

## 1. INTRODUCTION

Efficient use of light absorption for solar energy harvesting is important for development of sustainable energy supply for society. Recently black silicon, which has the surface covered by nano needles is used for efficient light absorbers for photons over the band gap energy, Surface enhanced Raman scattering sensors[1], and bacteriacidal surfaces[2]. Solar cell technology has limitation of energy conversion efficiency; in case of Si, around 25% with other wavelengths falling into the transparency window and thermal generation loss. Those losses amounts up to 80% of total solar light energy. Therefore utilising the thermal energy, provides further advantages for solar energy harvesting.

In the previous our work, we have demonstrated the solar absorbers for thermal energy conversion system[3]. To improve the absorbing light efficiency we have added a Ge-Sn layer for infrared light absorbtion. Ge and Sn are IV group elements, same as Si and has smaller band gaps: Ge has 0.67 eV and Sn is $\tilde{0}$ eV at room temperature. Si has a 1.11 eV band gap could absorb the light at the shorter wavelength wing up to the 1100 nm. However, solar light reaching the surface of the earth is extended up to the 2500 nm (i. e. Air mass 1.5 condition). Those wavelengths are not harvested. Considering such limitation, narrower band gap materials are required for absorption of long wavelength light.

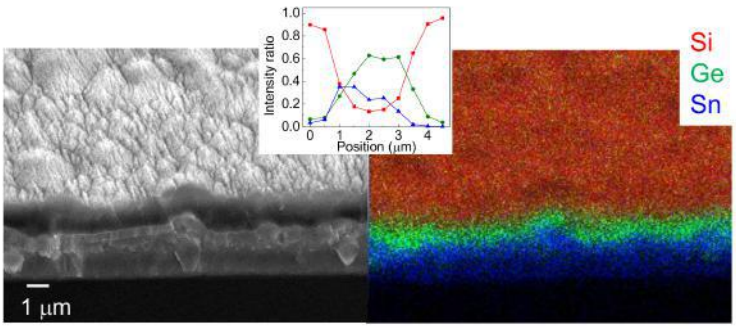



Figure 1: Black Si formation on the Ge-Sn, SEM and EDS

## 2. EXPERIMENTS

Ge and Sn are deposited by thermal evaporator from the same melting pot. The ratio of Sn is 20 atom% to the Ge. After evaporation of Ge and Sn, Si was sputtered on the surface of Ge-Sn.

Surface Si layer was dry etched by inductive coupling plasma reactive ion (ICP-RIE) etching. Photo thermal measurements were performed with Seebeck elements, that was reported in our previous study.

## 3. RESULTS AND DISCUSSIONS

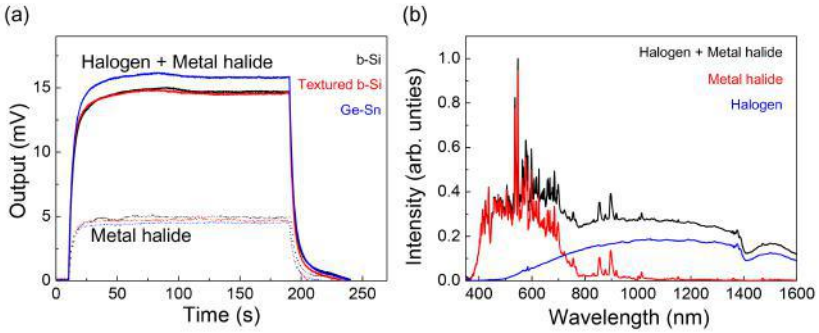



Figure 2: (a)Photo-thermal response of b-Si, Ge-Sn and textured b-Si and

Figure 1 shows the scanning electron microscopic (SEM) image and energy dispersive X-ray spectroscopic (EDS) imaging monitoring Si, Ge and Sn, respectively. From the EDS image, it is revealed that the composition is not homogeneously evaporated. The Ge/Sn composition changed form $Ge_{65}Sn_{35}$ to $Ge_{93}Sn_7$ gradually. This is due to the faster evaporation of Sn which has lower melting point than Ge. The top surface of b-Si has micron scale roughness. A leaf-like fractal surface with different scale roughness is effective in reduction reflectivity over spectrally broad spectral range. The fabricated surface shows less than 5% reflectivity till 3000 nm.

Figure 2 shows photo-thermal response from the b-Si and Ge-Sn/b-Si materials. As the reference of Ge-Sn/b-Si, textured b-SI, which is the composition of micro pyramidal texture structures of Si alkaline etching and b-Si formation (details will be discussed at the other our presentation[4]). This also have similar fractal like surface and have a lower reflectivity till near infrared wavelengths. Illumination by metal halide lamp, which has $\sim$ 1000 nm wide spectrum shows similar response using the all sample. This is mainly due to the b-Si absorption. Additional halogen lamp was co-illuminated with metal halide light source. The Ge-Sn shows larger output voltage response as compared to the other samples. Textured b-Si has the lowest reflection, but photo-thermal generation does not work at the sub-band gap wavelengths. From this result, it is clear that Ge-Sn layer works as the light absorber at longer than 1100 nm wavelengths.

## 4. CONCLUSION

In this study, we have demonstrated the photo-thermal response of b-Si with Ge-Sn light absorber. The Ge-Sn layer clearly works as absorbing layer for the near infrared longer than 1100 nm wavelengths and and contributes to thermal generation when placed over b-Si. Through this study, we demonstrate material composite that can harvest full spectrum of sunlight by absorption and conversion to the thermal energy.


## ACKNOWLEDGMENT

This work was financially JSPS KAKENHI. SJ is grateful for support via Australian Research Council DP130101205 project and startup funding for Nanolab by Swinburne University.


## REFERENCES


1. G. Gervinskas, G. Seniutinas, J. S. Hartley, S. Kandasam, P. R. Stoddart, N. F. Fahim and S. Juodkazis, "Surface-enhanced Raman scattering sensing on black silicon," *Annalen der Physik* , vol. 525, 907-914, 2013
2. E. P. Ivanova, J. Hasan, H. K. Webb, G. Gervinskas, S. Juodkazis, V. K. Truong, A. H.F. Wu, R. N. Lamb, V. A. Baulin, G. S. Watson, J. A. Watson, D. E. Mainwaring and R. J. Crawford, "Bactericidal activity of black silicon," *Nature Communications* vol. 4, 2838, 2013.
3. R. Komatsua, B. Armandas, G. Seniutinas, T. Yamamura, Y. Nishijima, and S. Juodkazis, Plasmonic Photo-Thermoelectric Energy Converter with Black-Si Absorber, *Solar Energy Materials and Solar Cells* , vol. 143, 72-77, 2015.
4. Y. Nishijima, R. Komatsu, S. Ohta, G. Seniutinas, A. Balčytis, and S. Juodkazis, "Composition of nano-micro structures toward perfect anti-reflector", will be presented at META'16

# Leakage imaging and tracking of ultrafast surface plasmon pulses.

**Y. Gorodetski[1*], T. Chervy[2], S. Wang[2], J. A. Hutchison[2], A. Drezet[3], C. Genet[2], T. W. Ebbesen[2]**

[1] Electrical Engineering and Electronics Department, Ariel University, 40700, Ariel, Israel

[2] ISIS & icFRC, Université de Strasbourg and CNRS (UMR 7006), 8 allée Gaspard Monge, 67000 Strasbourg, France

Institut Néel, CNRS and Université Joseph-Fourier (UPR 2940), 25 rue des Martyrs, 38042 Grenoble, France

[*]corresponding author: yurig@ariel.ac.il

**Abstract**-We introduce a new method for performing ultrafast imaging and tracking of surface plasmon wave packets that propagate on metal films. We demonstrate the efficiency of leakage radiation microscopy implemented in the time domain for measuring both group and phase velocities of near-field pulses with a high level of precision. The versatility of our far-field imaging method is particularly appealing in the context of ultrafast near-field optics.

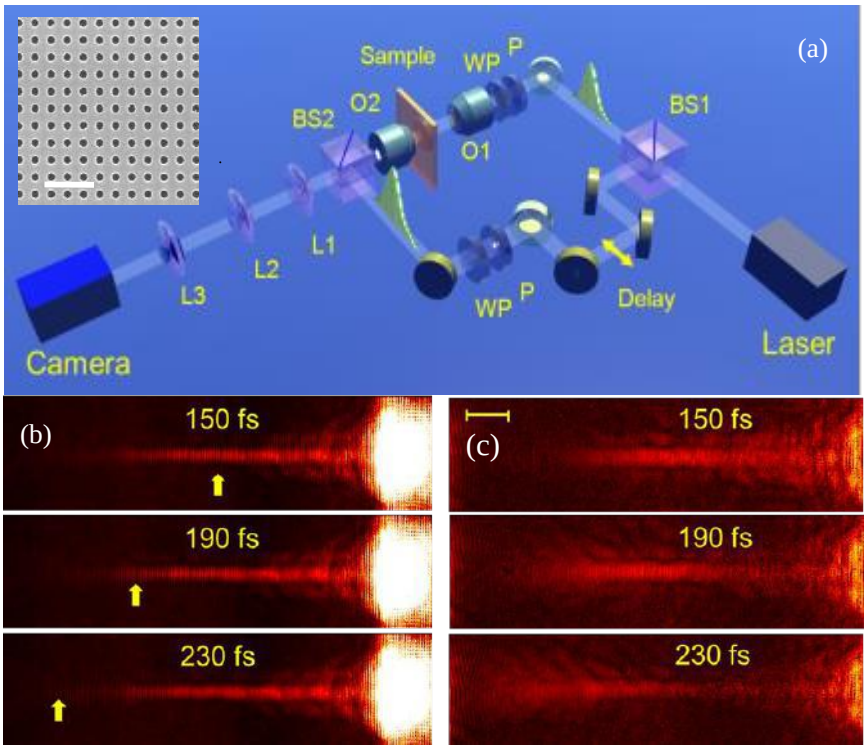



**Figure 1.** Time resolved images of SP propagation. (a) Setup scheme (O1 and O2 are objectives, L – lenses, BS – beam-splitter, WP – waveplate, P – polarizer). Inset – enlarged electron micrograph of the launching hole array. (b) Raw data from the system with different time-delays (the arrows denote the center of the pulse) (c) Extracted pulse envelope. Scale bar length is 10 microns.

Among the different surface plasmon imaging techniques, leakage radiation (LR) microscopy is a powerful method for imaging surface plasmon (SP) modes propagating on metal-dielectric interfaces [1-3]. This imaging method has been implemented in a great variety of plasmonic systems, ranging from surface plasmon circuitry [4,5] to near-field weak measurements [6], both at the classical and quantum levels [7]. Recently, this technique has been combined with interference microscopy, providing not only the amplitude but also the phase of the leakage signal [8].

Here we develop a system for time-resolved imaging of surface plasmon ultra-fast signals with 10

femto seconds (fs) resolution by using a heterodyne interference system combined with leakage radiation microscopy. The simplicity of our all-optical method, that does not involve any raster-scanned local probe nor non-linear detection processes, presents a clear advantage with respect to the sophistication of recently proposed near-field pulse tracking techniques (such as phase-sensitive time-resolved photon scanning tunneling microscopy [9], time-resolved two-photon photoemission electron microscopy [10,11] or pulse-tracking via far-field SP scattering interference imaging [12].

Our experimental scheme, described in details in Fig. 1a, consists of an LR microscope within a Mach-Zehnder interferometer. At the input a transform-limited laser pulse is evenly split into two beams. In one arm, the beam resonantly launches an SP wave packet on a thin metal film using an *(x,y)* square hole array (inset Fig. 1a) properly designed and milled through the film. This beam is linearly polarized in the *x* direction of the array, corresponding to the propagation direction of the SP wave packet. A high numerical aperture (NA) oil-immersion objective collects the plasmonic LR signal. This pulse is then combined with the reference pulse coming from the other arm of the interferometer that can be time-delayed using a motorized optical delay line. The both pulses interfere at the output of the interferometer. The visibility of the interference fringes then corresponds to the overlap of the pulses in time and space. Our system tracks the propagation of the pulse by monitoring the imaged interferograms visibility as a function of the delay time between the two pulses.

An imaged interferogram is displayed in Fig. 1b for a given time-delay between the leakage and the reference signals. The interference fringes are clearly visible on top of the leakage signal exactly where the two pulses overlap. We filter out the DC (non-oscillating) component by image processing and reveal the clean plasmonic pulse image as shown in Fig. 1c. Using these images, the propagation and spatial distribution of the pulse could be easily derived. Moreover we were able to precisely measure the group and phase velocity of the pulse which was shown to nicely match the theory.

In conclusion we have demonstrated a unique combination of LR microscopy with spatial heterodyne interference technique providing an access to the time-resolved plasmonic imaging.

**REFERENCES**


1. B. Hecht, H. Bielefeldt, L. Novotny, Y. Inouye, and D. W. Pohl, Phys. Rev. Lett **77**, 1889 (1996).
2. A. Drezet, et al. Mat. Sci. and Eng. B, **149**, 220 (2008).
3. A. Hohenau, et al, Opt. Exp. **19**, 25749 (2011).
4. A.-L. Baudrion, et al, Opt. Express **16**, 3420 (2008).
5. B. Stein, J.-Y. Laluet, E. Devaux, C. Genet, and T. W. Ebbesen, Phys. Rev. Lett. **105**, 266804 (2010).
6. Y. Gorodetski, K. Y. Bliokh, B. Stein, C. Genet, N. Shitrit, V. Kleiner, E. Hasman, and T. W. Ebbesen, Phys. Rev. Lett. **109**, 013901 (2012).
7. A. Cuche, O. Mollet, A. Drezet, and S. Huant, Nano Lett. **10**, 4566 (2010).
8. E. Descrovi, et al, Opt. Lett. **38**, 3374 (2013).
9. M.L.M. Balistreri, H. Gersen, J.P. Korterik, L. Kuipers, and N.F. van Hulst, Science, **294**, 1080 (2001).
10. A. Kubo, K. Onda, H. Petek, Z. Sun, Y.S. Jung, and H.K. Kim, Nano Lett. **5**, 1123 (2005).
11. C. Lemke, et al, Nano Lett. **13**, 1053 (2013).
12. R. Rokitski, K. A. Tetz, and Y. Fainman, Phys. Rev. Lett. **95**, 177401 (2005).

# Unravelling the optomechanical nature of plasmonic trapping

Pau Mestres[1,*], Johann-Berthelot[1], Srdjan S. Aćimović[1], and Romain Quidant [1,2]

[1] *ICFO- Institut de Ciencies Fotoniques, The Barcelona Institute of Science and Technology, 08860 Castelldefels (Barcelona), Spain*

[2] *ICREA - Institució Catalana de Recerca i Estudis Avançats, 08010 Barcelona, Spain*

[*]corresponding author: *pau.mestres@icfo.es*

**Abstract**-Non-invasive and ultra-accurate optical manipulation of nanometer objects has recently gained a growing interest as a powerful enabling tool in nanotechnology and biophysics. In this context, Self-Induced Back-Action (SIBA) trapping in nano-optical cavities has shown a unique potential for trapping and manipulating nanometer-sized objects under low optical intensities. Yet, the existence of the SIBA effect has so far only been evidenced indirectly by its enhanced trapping performances. In this article we present for the first time a direct experimental evidence of the self-reconfiguration of the optical potential experienced by a nanoparticle trapped in a plasmonic nanocavity. Our observations enable us to gain further understanding of the SIBA mechanism and to determine the optimum conditions to boost the performances of SIBA-based nano-optical tweezers.

Optical trapping and manipulation have emerged as powerful tools to investigate single microscopic objects in a controlled environment. Using the momentum carried by light, forces can be exerted to confine and manipulate objects in a wide range of conditions ranging from ultra-high pressures to high vacuum [(1)]. As the object decreases in size it becomes more challenging to obtain a stable potential that overcomes environmental fluctuations. Consequently, trapping nanoscale sized and light sensitive objects size requires new and more efficient trapping schemes.

A suggested strategy, inspired from the field of optomechanics, consists on building the optical trap inside an optical cavity. With this strategy, the specimen plays an active role in the trapping mechanism by modulating the optical potential with its position changes, the so called Self-Induced Back-Action (SIBA) effect [(2)]. Although this approach has shown longer-term stabilities as compared to a static potential, the modulation of the optical potential has never been observed.

By boosting the optomechanical interaction between an optical nano-cavity and an optically trapped gold nanoparticle we show for the first time a direct measurement of the optical potential reconfiguration in a nano-scale optical trap[(3)] (Figure 1 **a**, **b**).

Finally, studying the potential reconfiguration at different cavity resonance detuning regimes(Figure 2 **a**, **b**) we identify the optimum conditions that maximise the SIBA mechanism in optical traps.

Using finite-element simulations of our experimental system we retrieve an exceedingly high average optomechanical coupling constant of $2\pi \cdot 150$ GHz/nm, corresponding to half linewidth of the optical resonator.

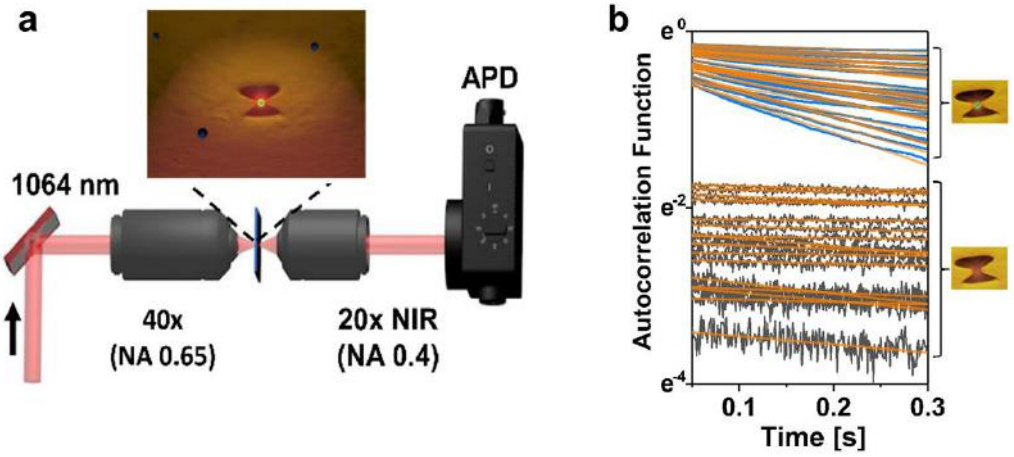



Figure 1. Schematic view of the experimental configuration (**a**) and continuous measurements of the stiffness of the optical trap (**b**).

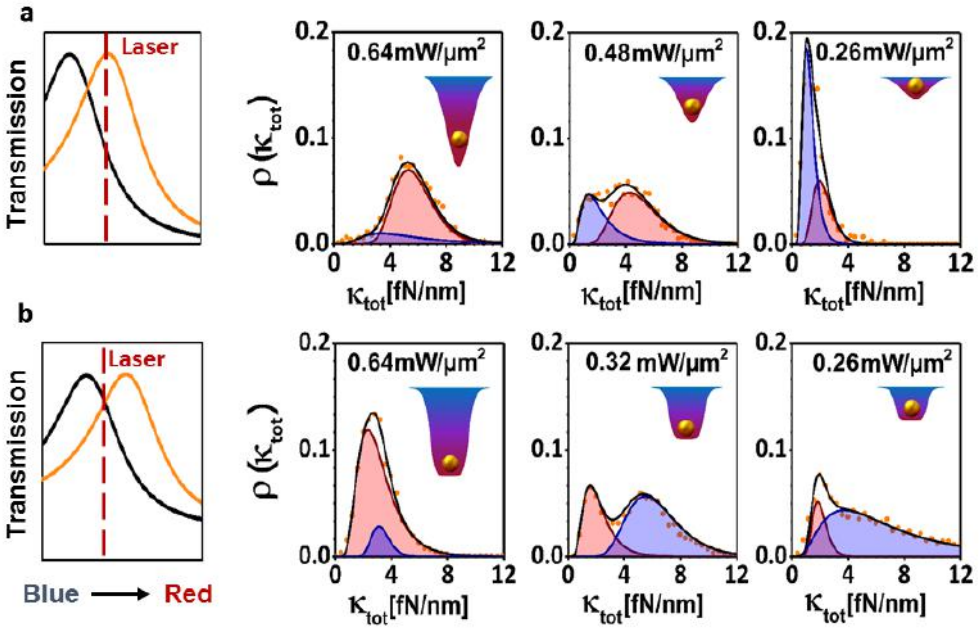



Figure 2. Stiffness probability distribution in the optical trap in a blue-shifted **(a**) and resonant (**b**) regimes**.**

**REFERENCES**


1. Mestres P, Berthelot J, Spasenović M, Gieseler J, Novotny L, Quidant R. Cooling and manipulation of a levitated nanoparticle with an optical fiber trap. Applied Physics Letters. 2015;107(15):151102.
2. Juan ML, Gordon R, Pang Y, Eftekhari F, Quidant R. Self-induced back-action optical trapping of dielectric nanoparticles. Nature Physics. 2009;5(12):915-9.
3. Mestres P, Berthelot J, Acimovic S, Quidant R, Unravelling the optomechanical nature of SIBA effect (To Appear in Light: Science & Applications).

# Fabrication of Hyperuniform Disordered Photonic Bandgap Materials

**N. Muller,[1] J. Haberko,[2] C. Marichy,[3] and F. Scheffold[1,*]**

[1]Departement of Physics and Fribourg Center for Nanomaterials, University of Fribourg, Chemin du Musée 3, CH-1700 Fribourg, Switzerland

[2]Faculty of Physics and Applied Computer Science, AGH of Science and Technology, al. Mickiewicza 30, 30-00059 Krakow, Poland

[3]Laboratoire des Multimatériaux et Interfaces CNRS, Université Claude Bernard Lyon 1, Université de Lyon, 69622 Villeurbanne Cedex, France

[*]corresponding author: nicolas.muller@unifr.ch

**Abstract-** Disordered photonic materials are structures characterized by a non-deterministic variation of the refractive index. Numerical calculations in two and three dimensions predict that under certain conditions such materials can exhibit a full photonic bandgap with zero density of states in the gap [1, 2]. Here we present experimental results for a candidate for such a disordered bandgap material, derived from hyperuniform point patterns. Complex three-dimensional freestanding network structures were fabricated in silicon by combining direct laser writing with the silicon double inversion method. The high quality of the structures is confirmed by focused ion beam milling as well as an isotropic transmittance dip in the spectral response, measured by Fourier Transform Infrared spectroscopy.

Structured dielectric materials in three dimensions can exhibit photonic properties that allow control of the propagation of light. For crystalline structures, a complete or incomplete photonic band gap emerges and the propagation of light is hindered or even completely suppressed over a certain range of wavelengths. Full photonic band gaps open up for dielectric materials with a sufficiently high refractive index contrast. The change in transport properties is accompanied by a reduction in the local density of states, which results in increased lifetimes for embedded light emitters such as fluorescent molecules. Interestingly, it appears that many of these unique properties are not tied exclusively to crystalline structures. In a recent numerical study Florescu et al. demonstrated that particular designer disordered materials could display large, complete photonic band gaps in two dimensions [3]. Mapping hyperuniform point patterns with short-range geometric order into tessellations allows the design of interconnected networks that give rise to enhanced photonic properties [3-5].

Here we present experimental results for the fabrication of disordered network structures with a pronounced gap in the shortwave infrared are presented. These structures can be derived from hyperuniform point patterns, patterns whose structure factor vanishes for $|q| \rightarrow 0$. Numerical simulations have shown that a significant depletion in the density of states can be obtained in such systems, a hallmark for the formation of an isotropic photonic bandgap. First, the structures were fabricated via direct laser writing in polymer by adapting the standard writing protocol presented in [4]. A substantial increase in the material refractive index is necessary to observe a photonic gap. To this end we employed the well-established silicon double inversion method [6]. This multi-step replication technique consists of successive infiltration and etching processes. Both atomic layer deposition (ALD) of ZnO and chemical vapor deposition (CVD) of amorphous silicon were used subsequently. The high quality of the resulting structures is illustrated by focused ion beam etching coupled to a scanning

electron microscopy images as well as a pronounced and angular independent transmittance dip in the spectral response, measured by Fourier Transform Infrared spectroscopy [7].

**Acknowledgements** - The present project has been financially supported by the National Research Fund, Luxembourg (project No. 3093332), the Swiss National Science Foundation through the National Centre of Competence in Research Bio-Inspired Materials and the Adolphe Merkle Foundation. We thank Bodo Wilts for help with the scanning electron microscopy.

**REFERENCES**

1. Liew, S. F., Yang, J.-K., Noh, H., Schreck, C. F., Dufresne, E. R., O'Hern, C.S., and Cao, H. (2011), "Photonic band gaps in three-dimensional network structures with short-range order", *Phys. Rev. A*, 84, 063818
2. Froufe-Pérez, L. S., Engel, M., Damasceno, P. F., Muller, N., Haberko, J., Glotzer, S.C., and Scheffold, F., "The role of Short-Range Order and Hyperuniformity in the Formation of Band Gaps in Disordered Photonic Materials", *submitted*
3. Florescu, M., Torquato, S., Steinhardt, P. J. (2009), "Designer disordered materials with large, complete photonic band gaps", *PNAS*, Vol. 106, 49 20658–20663
4. Haberko, J., Muller, N., and Scheffold, F. (2013), "Direct laser writing of three-dimensional network structures as templates for disordered photonic materials", *Phys. Rev. A*, 88, 043822
5. Muller, N., Haberko, J., Marichy, C., and Scheffold, F. (2014 ), "Silicon Hyperuniform Disordered Photonic Materials with a Pronounced Gap in the Shortwave Infrared", *Adv. Opt. Mat*, Vol. 2, 2, 115–119
6. Tétreault, N., von Freymann, G., Deubel, M., Hermatschweiler, M., Pérez-Willard, F., John, S., Wegener, M. and Ozin, G. A. (2006), "New Route to Three-Dimensional Photonic Bandgap Materials: Silicon Double Inversion of Polymer Templates," *Adv. Mater.*, Vol. 18, 457–460
7. Muller, N., Haberko, J., Marichy, C. and Scheffold, F., "Fabrication of strongly photonic hyperuniform disordered network materials using the silicon double inversion method," *manuscript in preparation*

# Multipolar behavior of hollow plasmonic nanospheres: obvious or mysterious?

**Ari Sihvola, Dimitrios C. Tzarouchis, and Pasi Ylä-Oijala**

Department of Radio Science and Engineering,
Aalto University School of Electrical Engineering, Espoo, Finland
E-mail: ari.sihvola@aalto.fi

**Abstract**— Localized surface plasmon resonances appear on spherical subwavelength nanospheres around a frequency for which the real part of the dielectric function is $-2$. For silver, this takes place at around 356 nm. As the size of the sphere increases, this resonance will be red-shifted. However, regarding this shift, the size matters much less than changes in shape and structure of the nanoscatterer. This presentation focuses on the resonance structure of negative-permittivity scatterers, including multipoles and plasmon hybridization.

For small solid plasmonic nanospheres, the localized multipolar resonances take place for wavelengths at which the real part of the relative permittivity has values $-1-1/n$, $n=1,2,3,\cdots$. The electric dipole dominates for $\varepsilon=-2$, quadrupole for $\varepsilon=-1.5$, etc. Full-wave electromagnetic analysis (Lorenz–Mie approach [1]) allows the view into the behavior of these resonances as function of the size of the sphere, showing that once the diameter $d$ increases into values no longer negligible compared with the wavelength $\lambda$, the resonances become softer and their positions migrate towards more negative values of permittivity. The shift is proportional to the square of the size parameter $x$ of the sphere ($x=\pi d/\lambda$).

Many plasmonic materials follow a Drude-type permittivity dispersion. This means that the (negative permittivity) increases with frequency, reaching zero at plasma frequency. Hence the effect of increasing size means a red-shift of the plasmonic peaks. Geometrical shape of the scatterer is another—and much more powerful—factor of shifting the resonances. From a static (Laplacian) analysis of a homogeneous solid dielectric ellipsoid [2], it can be seen that for example the dipolar resonance appears when the relative permittivity takes the value $\varepsilon=1-1/D$ where $D$ is the depolarization factor of the ellipsoid in the direction of the exciting electric field vector. For sphere, $D=1/3$ recovers the dipolar value $-2$. When the shape deviates from sphere or ellipsoid, no exact solution for the static solution can be found (excluding some exceptional cases), and the characteristics have to be studied numerically. For example, changing the spherical shape into a more cornered one, towards a cube, makes the peaks shift strongly and the resonance landscape becomes very diverse [3].

Apart from morphological effects on plasmonic resonances, also topology plays an important role. A hollow spherical plasmonic shell is a very interesting object, not least because its presence in an electromagnetic field can be exactly analyzed both in statics and full-wave dynamic setting. Consider the core-shell structure in Figure 1.

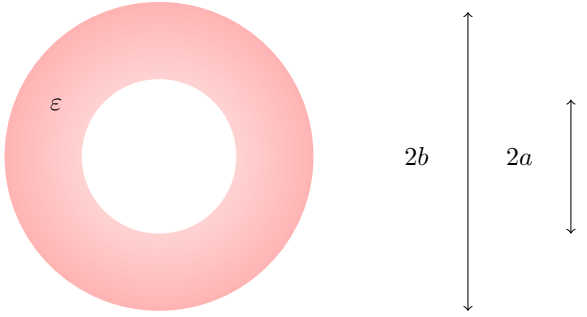



Figure 1: A hollow spherical shell with radius ratio of the core $r=a/b$.

In this structure, the static (di)-polarizability response has the form (normalized to be unity for infinity-permittivity solid sphere)

$$\alpha_1 = \frac{(\varepsilon - 1)(2\varepsilon + 1)(1 - r^3)}{(\varepsilon + 2)(2\varepsilon + 1) - 2r^3(\varepsilon - 1)^2} \tag{1}$$

where $r = a/b$ is the radius ratio between the core and the sphere. The denominator can now vanish for two (negative) permittivity values, giving rise to two resonances. This is due to the fact that there are now two separate surfaces of the metallic phase (sometimes this phenomenon of excitation of two resonances in the core-shell structure is called mode hybridization [4]). Likewise the quadrupole term can be seen to hybridize:

$$\alpha_2 = 2\frac{(\varepsilon - 1)(3\varepsilon + 2)(1 - r^5)}{(2\varepsilon + 3)(3\varepsilon + 2) - 6r^5(\varepsilon - 1)^2} \tag{2}$$

In the presentation, the behavior of the various size-, morphology-, and topology-dependent resonances will be discussed. As an example, Equation (1) shows that the dipolar effect vanishes for $\varepsilon = -1/2$, independently of the size of the core $r$. This fact leads us to find the spectral position where the nanoshell displays the strong and domimant quadrupolar response, as shown in Figure 2.

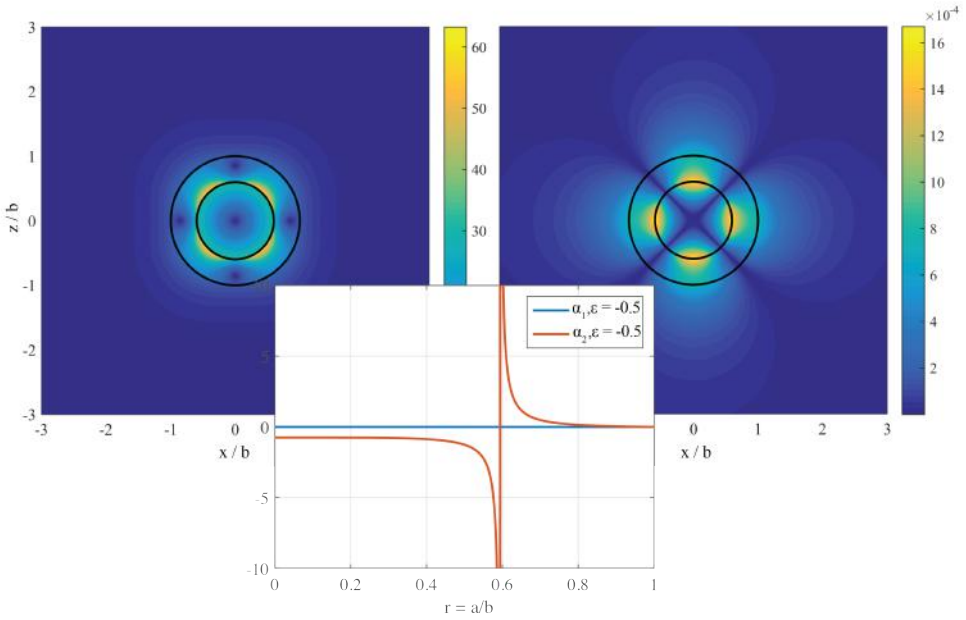



Figure 2: Vanishing of the dipolarizability of the nanoshell ($\varepsilon = -1/2$). Left: imaginary part of the scattered electric field; Right: real part of the scattered magnetic field; Center: amplitudes of the $a_1$ and $a_2$ terms.

**REFERENCES**


1. Bohren, C.F., and D.R. Huffman, *Absorption and Scattering of Light by Small Particles*, Wiley, New York, 1983.
2. Sihvola, A., *Electromagnetic Mixing Formulas and Applications*, IET, London, UK, 1999.
3. Tzarouchis, D.C., P. Ylä-Oijala, T. Ala-Nissila, and A. Sihvola, "Shape effects on surface plasmons in spherical, cubic, and rod shaped silver nano-particles," *Applied Physics A*, to appear, 2016.
4. Prodan, E., C. Radloff, N.J. Halas, and P. Nordlander, "A hybridization model for the plasmon response of complex nanostructures," *Science*, Vol. 302, No. 5644, 419-422, 2003.

# Spatial non-locality and Landau damping in the dynamics of a quantum dot coupled to surface plasmons.

**A. Vagov[1], I. A. Larkin[2], M. D. Croitoru[3], K. Keil[1], and V.M. Axt[1]**

[1]Bayreuth University, Bayreuth, Germany
[2]Minho University, Braga, Portugal
[3]Universiteit Antwerpen, Antwerp, Belgium
alexei.vagov@uni-bayreuth.de

**Abstract**— We investigate the dynamics of a quantum dot induced by the coupling to surface plasmons on a metal surface. Surface plasmons are described using a continuous media model with a non-local Lindhard-type dielectric response. Plasmon modes for this model are determined analytically. The time evolution of the quantum dot is found by solving quantum dynamical equations in the rotating wave approximation. The solution demonstrates that the non-locality in the dielectric response and the Landau damping notably change the system dynamics. The time evolution reveals Rabi oscillations and follows a two-time relaxation pattern.

Unique properties of surface plasmon excitations [1] can be used in many applications, many of which rely on the possibility to manipulate the electromagnetic field of the plasmon modes with high precision. Unlike conventional light waves, plasmons resolve scales below the diffraction limit [2] and this fact can be used to achieve a considerable enhancement of the field intensity and a better control of its spatial distribution. The Achilles heel in some of the applications is the weak coupling between plasmons and external light which can be remedied by introducing mediating quantum emitters such as strongly confined quantum dots [3], that are coupled to both incoming light-waves and surface plasmons. The strong coupling leads to a non-trivial dynamics of the quantum dot states which reveal quantum coherences.

In this work we study the dynamics of a quantum dot placed near a metal surface induced by the electromagnetic interactions with plasmons localized on the metal surface. The calculations are done using a continuous media model for a metal with linear electromagnetic response. Unlike many previous works we take into account the non-locality of the electromagnetic response. The non-locality is important for ultra-fast time-scales especially when the dimensions of the system are in the nano-scale. The electromagnetic response of the metal is modeled by a Lindhard-type permittivity function which is calculated for the chosen geometry of the system. It is demonstrated that the approach is valid in a wide range of system parameters. In particular the interval of acceptable dot-surface distances is estimated as $5 \lesssim a \lesssim 500$nm for the parameters of typical metals.

The analytical solution for the plasmon modes is obtained using the method of auxiliary boundary conditions [4, 5, 6]. In this work this method is extended beyond the quasi-static limit ($\omega \ll cq$, $c$ is the light velocity, $q$ denotes the plasmon wave-number). A detailed analysis reveals significant modifications of the frequency dispersion due to the non-locality of the response. Its $q$-dependence is linear in the intervals of small and large $q$ (see left panel of Figure 1). Surface plasmons reveal thus two group velocities, the larger velocity $v_p \sim c/\sqrt{\varepsilon}$ ($\varepsilon$ is the insulator dielectric constant) at small $q$ and a much smaller velocity $v_p \sim v_F$ ($v_F$ is the Fermi velocity in the metal) at larger $q$. It is also demonstrated that the largest contribution to the damping of plasmon modes in the interval of larger $q$-s is provided by the Landau damping mechanism in agreement with the earlier works [6, 7].

The coherent quantum time evolution is calculated for the case when the dot is initially excited by an ultra-fast external laser pulse. The analysis assumes that the plasmon modes are quantum bosonic excitations [8]. The linear dispersion together with the Landau damping at larger $q$ give rise to notable features in the time evolution. The time dependence of the dot occupation comprises two distinctive contributions: rapidly decaying oscillations at short times are followed by a much slower monotonic decay (see right panels of Figure 1). The existence of two very different relaxation rates is a consequence of the non-locality of the electromagnetic response. It is found that the time evolution pattern is controlled by two main parameters: i) the detuning between the surface plasmon frequency $\Omega_{sp}$ (derived within the Drude model) and the dot transition frequency and ii)

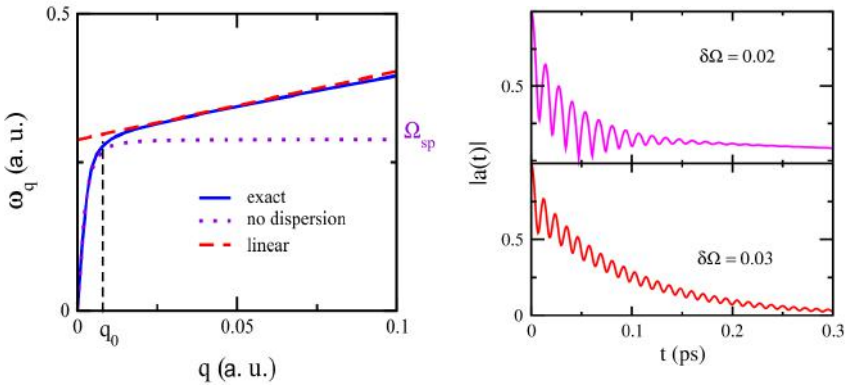



Figure 1: **Left panel:** The continuous blue line, labeled "exact", is the real part of the plasmon frequency dispersion, calculated with the Lindhard model for the metal dielectric response. The dispersion in intervals $q \lesssim q_0$ and $q \gtrsim q_0$ is approximately linear and is described by two significantly different group velocities. The dashed red line ("linear") is obtained obtained from the solution of a simplified dispersion equation. Plasmons with $q \gtrsim q_0$ provide the largest contribution to the quantum dot dynamics. The dotted magenta line ("no-dispersion") is a standard textbook result obtained for the Drude model without non-locality. **Right panels:** Typical time evolution patterns of the system (absolute value of the dot exciton occupation $|a(t)|$) calculated for two values of the frequency detuning $\delta\Omega$, here shown in units of the bulk plasma frequency $\Omega_p$. Initial ultra-fast Rabi oscillations decay rapidly, a much longer monotonic decay is observed at longer times. The lower-right panel illustrates the reduced decay of the Rabi oscillations which indicates the presence of a dynamical contribution with a power law decay.

the dot-metal coupling strength (the latter can be adjusted by the distance between the dot and the surface). It is shown that in a certain parameter range one of the dynamical contributions has a power-law long-time asymptote, which leads to a considerably reduced damping of the Rabi oscillations (see the lower-right panel in Figure 1). We also demonstrate that the two-velocity dispersion law leads to a peculiar spatial propagation of plasmons which forms two types of wave-packages, which have different shape and move with different speeds.

Finally, we have analyzed plasmon modes occurring at the surfaces of metal slabs with nanometer width. Our studies revealed qualitative modifications of the plasmon frequency dispersion, which in this case has several branches. One of the branches has an extended interval where the group velocity is negative leading to qualitative changes in both plasmon propagation and the dynamics of the dot.

**REFERENCES**


1. S. A. Maier, *Plasmonics: Fundamentals and Applications* (Springer, 2007).
2. M. S. Tame, K. R. McEnery, S. K. Özdemir, J. Lee, S. A. Maier, and M. S. Kim, Nature Physics **9**, 329 (2013).
3. D. E. Gomes, K. C. Vernon, P. Mulvaney, and T.J. Devis, Nano Lett. **10**, 274 (2010).
4. K.L. Kliewer and R. Fuchs, Phys. Rev. **172**, 607 (1968).
5. R. H. Ritchie and A. L. Marusak, Surface Science **4**, 234 (1966).
6. I. A. Larkin, M. I. Stockman, M. Achermann, and V. I. Klimov, Phys. Rev. B **69**, 121403(R) (2004).
7. I. A. Larkin and M. I. Stockman, Nano letters, **5**, 339 (2005).
8. D. Pines, Phys. Rev. **92**, 626 (1953).

# Hybrid surface plasmon modes in metallic nanostructures: Complete numerical analysis and application to bio-sensing.

**Mitradeep Sarkar[1*], Jean-Fr. Bryche[1,2], Raymond Gillibert[4,3,1], Julien Moreau[1], Mondher Besbes[1], Aurore Olivéro[1,3,4], Grégory Barbillon[2], Bernard Bartenlian[2], Marc Lamy de la Chapelle[4] and Michael Canva[1,5]**

[1]Laboratoire Charles Fabry, Institut d'Optique Graduate School, Université Paris Sud, CNRS, 2 Avenue Augustin Fresnel, 91127 Palaiseau, France

[2]Institut d'Électronique Fondamentale, Université Paris Sud, CNRS, Rue Ampère, 91405 Orsay, France

[3]Horiba Scientific, Avenue de la Vauve, Passage Jobin Yvon, CS 45002, 91120 Palaiseau, France

[4]Laboratoire Chimie, Structures, Propriétés de Biomatériaux et d'Agents Thérapeutiques, Université Paris-Nord, CNRS,74 Rue Marcel Cachin, 93017 Bobigny Cedex, France

[5] Current address: Laboratoire Nanotechnologies Nanosystèmes, CNRS, Université de Sherbrooke, Canada

[*]Corresponding author: mitradeep.sarkar@institutoptique.fr

Surface plasmons on metallic surfaces are excited by collective oscillations of free electrons. Such collective oscillations in nanometric scale have the ability to enhance local electromagnetic field in their vicinity. They satisfy certain resonance conditions with respect to the excitation frequency and the incident wave-vector of light and their dispersion can be considered as modes of the system in which such resonances are excited.

The plasmons at uniform metal-dielectric interfaces manifest as evanescent electromagnetic fields confined to a few hundreds of nanometers from the metallic surface and propagate along the interface. This mode is called the propagating surface plasmon (PSP) and is a fundamental plasmonic mode. Owing to the large dispersion of the PSP, they are conventionally used for SPR detections to probe local refractive index changes.

The other fundamental group of plasmonic modes, which are non-propagative, results from collective oscillations of free electrons on surfaces of metallic nano-particles. They are called localized surface plasmon (LSP) modes. They have been effectively used for numerous applications such as SERS, drug delivery, chemical sensing, cancer therapy, and new photonic devices. However unique nanoparticles have proved to be less efficient for SPR detection due to their low spectral dispersion and weak scattering cross-sections.

Our aim is to combine these two types of surface plasmons, namely the PSP and the LSP to exploit the advantages of both the modes: the high dispersion of the PSP and the strong field confinement of the LSP. To achieve this, a hybrid structure comprising of an array of metallic nano-structures (cylinders for example) along with an underlying thin metallic film was studied. A complete understanding of the different plasmonic modes that can be excited in such hybrid geometry is needed to optimize them for different applications.

**The plasmonic modes of a hybrid structure**: For the LSP supported by metallic nano-particles, we have shown that the polarizability of complex geometries with an underlying substrate can be calculated analytically and the results obtained closely approximate the resonance conditions for such geometries. Furthermore, in such structures, we demonstrated that the LSP can harmonically couple to the PSP mode to give rise to a new mode called the Hybrid Lattice Plasmon (HLP). In our recent publication, we have shown that the HLP has a high field confinement, characteristic of the LSP but at the same time a high dispersion similar to the PSP [1]. Apart from the HLP, another set of modes called the Bragg modes (BM), caused by the diffraction of the PSP by the periodic array is also excited at certain resonance conditions. We introduce a simple analytical model to predict the existence of all the different plasmonic modes and their dispersion in a hybrid nano-structured geometry.

**Properties of the HLP and BM**: The HLP has a large dispersion similar to the PSP as shown in Figure 1. Thus, the mode can be tuned over a wide range of excitation frequencies by changing the structural parameters. Also due to its high dispersion, the HLP mode can be used effectively for SPR detection in the Kretschmann configuration. Both the HLP and the BMs, like the LSP shows strong field confinement close to the nanocylinders. It is well-known that the SERS enhancement is roughly proportional to the fourth power of the local electric field and thus these modes can have an enhancement of SERS intensity by another order of magnitude compared to the sole NPs. This was experimetally verified and the experimental results closely support such theoretical hypothesis [2].

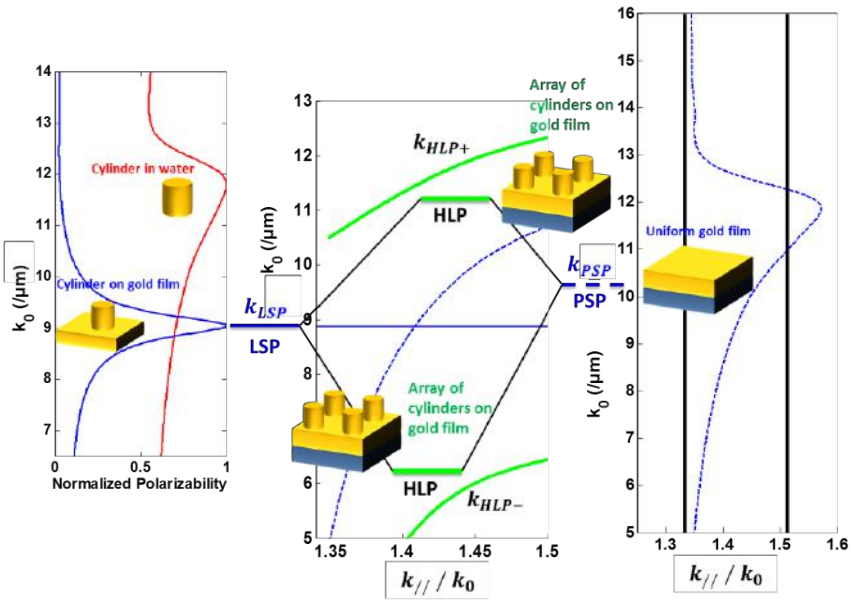



*Figure 1 : Schematic showing the coupling of the LSP (left) and the PSP (right) to give rise to the HLP mode (green) in an array of metallic nanocylinders on a thin metallic film.*

We have also demonstrated the experimental excitation of the different modes for the hyrid structure in the Kretschmann configuration. Such results yeild very close correspondence of the experimental and theoretical results as shown in our recent publication [3]. Such detailed description of plasmonic modes can offer a complete understanding of the surface plasmon resonance phenomena in such metallic structures and allows their optimization as per required for various applications such as SPR detection and SERS. The theories and models presented in this work can be used to effectively describe the EM properties of different geometries and experimental configurations.

**REFERENCES**


1. M. Sarkar, M. Besbes, J. Moreau, J.-F. Bryche, A. Olivéro, G. Barbillon, A.-L. Coutrot, B. Bartenlian, and M. Canva, "Hybrid plasmonic mode by resonant coupling of localized plasmons to propagating plasmons in a Kretschmann configuration," Acs Photonics **2**, 237-245 (2015).
2. R. Gillibert, M. Sarkar, J.-F. Bryche, R. Yasukuni, J. Moreau, M. Besbes, G. Barbillon, B. Bartenlian, M. Canva, and M..L de la Chapelle, "Directional surface enhanced Raman scattering on gold nano-gratings," Nanotechnology (2016).
3. M. Sarkar, J.-F. Bryche, J. Moreau, M. Besbes, G. Barbillon, B. Bartenlian, and M. Canva, "Generalized analytical model based on harmonic coupling for hybrid plasmonic modes: comparison with numerical and experimental results," Opt Express **23**, 27376-27390 (2015).

# Enhanced light emission in organic materials caused by constructive surface plasmon generation and scattering

**T. Inui[1], Y. Mizoguchi[1], T. Yoneda[1], T. Ishiguro[1], K. Kasahara[1], N. Ikeda[2], and Y. Sugimoto[2]**

[1]Ritsumeikan University, Kusatsu, Shiga 525-8577, Japan

[2]Nanotechnology Innovation Center, National Institute for Materials Science, Tsukuba, 305-0047, Japan

[*]corresponding author: kasahara@se.ritsumei.ac.jp

**Abstract**- Photoluminescence enhancement observed in $Alq_3$ with Ag was 3~3.8 at a peak wavelength, which could not be explained by the calculated scattering rate of surface plasmons. Experimental results suggested that surface plasmons were generated in phase at the same time, and scattered simultaneously. Aggregate behavior of the energy transfer of excitons to surface plasmons can happen, because excitons in the organic film exist mere nanometers apart.

The light emission efficiency of organic light emitters formed on metal has been reported to be enhanced by the surface plasmon (SP) absorption of excitons and the subsequent scattering which occurs due to submicrometer-scale roughness on the surface of a metal film. SP-mediated overall light enhancement was measured using an integration sphere[1)], and the SP scattering rate was calculated using a one dimensional model[2)]. However, it is not necessarily evident that the calculated scattering rate could account for the experimentally obtained light output increase, and a comprehensive understanding of how the SP generation and scattering rate is associated with enhanced light output is still lacking[3)]. In this research, we calculated the SP scattering rate using AFM-measured height and pitch of roughness on Ag, and investigated whether this could explain light enhancement measured for $Alq_3$ with Ag. The results suggest the possibility of constructive SP creation and scattering occurring on the surface of Ag. Simultaneous energy transfer of excitons to SPs can occur, because excitons in the organic film are only nanometers apart from each other.

In measuring overall light output of organic material on a metal film/glass substrate system with an integration sphere, one must note the following: a guided mode confined inside the organic layer and propagating in the lateral direction completely attenuates in the course of multiple reflections on the surface of the metal film. This is different from the case for organic material on a glass substrate without the metal film, and comparing total light emission between two devices with an integration sphere is not necessarily as easy as it seems. Thus, we measured luminous intensity dependence on output angle instead of using an integration sphere. We prepared $Alq_3$/glass/100-nm-Ag and $Alq_3$/100-nm-Ag/glass devices. The thickness of $Alq_3$ and glass was 60 nm and 1 mm, respectively. When comparing light output of organic material on a glass substrate and a metal film/glass substrate system in the forward direction, the latter emits four times as much light as the former structure due to a geometrical effect, leading to difficulty in direct comparison between them. Figure 1 shows that this was avoided by evaporating Ag on the rear surface of a glass substrate. Photoluminescence (PL) enhancement obtained by the light output of $Alq_3$/Ag/glass divided by that of $Alq_3$/glass/Ag is shown in Fig. 2 as a parameter of output angle in the air from 0 to 80 degrees. PL enhancement at 520 nm was 3 at 0 degree (i.e. in the normal direction) and 80 degree, although it increased to 3.8 at 40 degree.

The dependence of the SP scattering rate on scattering angle on a bump on the surface of Ag is shown in Fig.

3, where a p-polarized SP was assumed to propagate along a flat metal interface with a bump. The average height and pitch measured by AFM, which were 7 nm and 100 nm, respectively, were used in the calculation. The dashed line indicates the scattering rate for unidirectional SP propagation, and it reached its maximum at 35 degree. Actual scattering rate consists of the average of SPs propagating in all directions, and eventually the average of those from two SPs propagating in opposite directions, which is shown as a solid curve in Fig. 3 with a peak at $\theta$ = 0 degree. Because an output angle of 80 degree was equivalent to $\theta$ = 33 degree, the calculated result reasonably explained the dependence of PL enhancement on output angle shown in Fig. 2. Actually, one must furthermore take into an account the fact that SP experiences multiple bumps within the propagation length of the SP attenuating to 1/*e* due to ohmic loss, and the average scattering rate became 4%.

However, calculated scattering rate could not account for the PL enhancement which was expressed as $(p-(1-\eta)p_s+ (1-p)\zeta\eta)/p$ in a simple model. Here, $p$ is the radiative probability without metal, $p_s$ is SP generation rate, $\eta$ is SP scattering rate, and $\zeta$ is energy transfer probability of the nonradiative component to SP. $p$ for 60~100 nm thick GaAs layer was found to be 10% by measurements of an integration sphere. Since $\zeta$<1, one cannot explain PL enhancement as large as 3~3.8. This can be interpreted if constructive SP generation and scattering is assumed. The total energy that the original $N$ excitons possess is, of course, proportional to $N$, regardless of individual phase of generated SPs, whose electric field is expressed as $\sum_j E_j e^{i\theta_j}$. When the respective phase is the same, $p_s$ is proportional to the square of this term, and thereby becomes $N^2E^2$, and $E_j$ is equal to $E$. Therefore, the actual $\eta$ of one SPP should increase in proportion to $N$, and become $N\eta$.

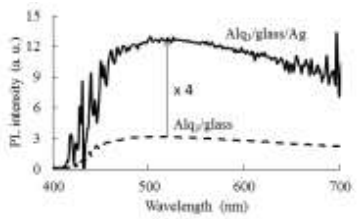



Fig. 1 PL intensity of $Alq_3$/glass and $Alq_3$/glass/Ag.

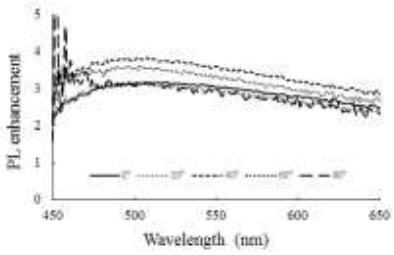



Fig. 2 PL enhancement obtained by light output of $Alq_3$/Ag/glass divided by that of $Alq_3$/glass/Ag. Output angles in the air were from 0 to 80 degrees.

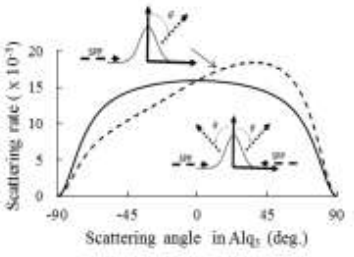



Fig. 3 Angular dependence of scattering rate. Dashed and solid curves show scattering rate for unidirectional SP and average rate, respectively.

**REFERENCES**


1. Tam, M.C., Su, H., Wong, K.S., Zhu, X. and Kwok, H.S. "Surface-plasmon-enhanced photoluminescence from metal-capped $Alq_3$ thin film," *Appl. Phys. Lett.*, Vol. 95, 051503, 2009.
2. Sanchez-Gil, J.A. and Maradudin, A.A. "Near field and far field scattering of surface plasmon polaritons by one-dimensional surface defects," *Phys. Rev. B*, Vol. 60, No. 11, 8359-8367, 1999.
3. Inui, T., Mizoguchi, Y., Yoneda, T., Kawase, H., Kasahara, K., Ikeda, N. and Sugimoto, Y. " Factors Determining the Light Amplification Spectra in Surface Plasmon-Enhanced Organic Light Emitters", in *Proceedings of META'15*, NY, USA, August 2015, 40.

# Plasmonic color printing combining conjugate twin phase modulation with plasmonic broadband absorption

**J. Xue[1,2], Z. K. Zhou[1,2*], and X. H. Wang[1,2*]**

[1] School of Physics and Engineering, Sun Yat-sen University, China

[2] State Key Laboratory of Optoelectronic Materials and Technologies, Sun Yat-sen University, China

[*]corresponding author: zhouzhk@mail.sysu.edu.cn (Z.K.Z.); wangxueh@mail.sysu.edu.cn (X.H.W.)

**Abstract**- Plasmonic color printing has a promising future as a new generation of color printing technology. As for practical application, the problems of color gamut and production area need to be addressed. Here, we realize scalable and full-color plasmonic color printing by combining conjugate twin phase modulation with plasmonic broadband absorption. Furthermore, we develop plasmonic color printing with reversibly color-changing capability, giving rise to enormous potentials in special label, anti-counterfeiting, and even high-density data encryption storage.

Our wonderful life is built on the basis of a colorful world, which is ascribed to the ubiquitous existence of natural and artificial colors. Among the artificial color technologies, plasmonic color printing has drawn wide attentions as a promising candidate for the next generation color printing technology, because of its admirable virtues such as high compactness, robust stability, high tunability, and compatibility of functionalization.[1-5] Despite the achieved excellent performances, several crucial problems still impede the practical application of this technology, including absence of efficient method to produce large-scalar sample, lack of easy-implemented strategy for full color generation, as well as scarcity in functionalizing device. To address these problems, we for the first time present a facile, scalable, full-color and controllable chromotropic plasmonic color printing strategy by combining conjugate twin phase modulation with a plasmonic broadband absorber (CTPM-PBA).[6]

We firstly theoretically investigated the mechanism of color generation on the CTPM-PBA panel, which is constructed by a conjugate twin phase modulation theory and a plasmonic broad-band absorber (Figure 1). Secondly, we experimentally realized the CTPM-PBA using a facile method by sputtering a plasmonic layer on an electrochemically grown anodized aluminum oxide (AAO) template. In addition, we succeeded in achieving full color output via the CTPM-PBA plasmonic color strategy, with the plasmonic layer consisting of aluminum, the third most abundant element on earth. Finally, we functionalized the CTPM-PBA panel with controllable chromotropic capability, i.e., the ability of reversible color transformations with on-demand color generation. Due to these functionalities, we further demonstrated our CTPM-PBA color strategy can serve as a practical strategy for wide application field, such as commercial coloration, anti-counterfeiting trademark fabrication, and high density data encryption storage. Our findings not only built new theory and concept of the plasmonic color printing, but also presented a practical method for turning the great potential of plasmonic color printing into realistic color applications, which will enrich our colorful world in an innovative way.

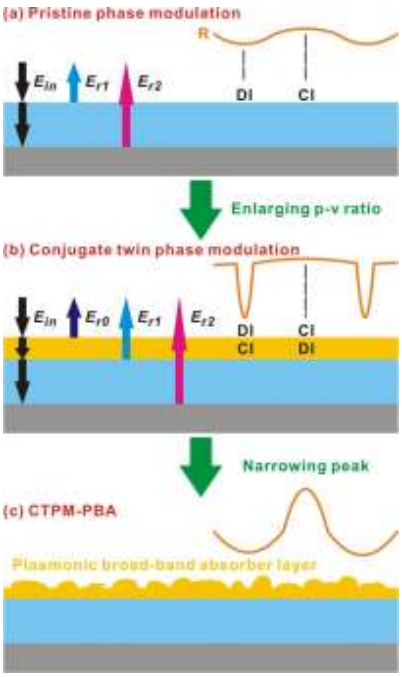



**Figure 1** The CTPM-PBA mechanism. (a) The pristine phase modulation in a thin dielectric film on an opaque substrate. Destructive interference (DI) and constructive interference (CI) between $E_{r1}$ and $E_{r2}$ render vague reflective valleys and peaks, respectively. (b) Enlarging peak-to-valley (p-v) ratio by the asymmetric phase modulation with a thin metal coating. Wavelengths of CI and DI in the metal layer conversely correspond to that of DI and CI of the reflected waves at the outer surface, respectively, resulting in distinct reflective valleys as well as wide and flat peaks. (c) Narrowing reflective peaks by CTPM-PBA with a metallic island film. The metallic island film works as a plasmonic broad-band absorber, making the reflective peaks much narrower.

**Acknowledgements:** This work was supported financially by National Natural Science Foundation of China (Grants 11334015, 11204385 and 11511130056) and National Basic Research Program of China (Grant 2010CB923200), the Guangdong Natural Science Foundation (Grant 2014A030313140).

**REFERENCES**

1. Kumar, K. *et al.* "Printing colour at the optical diffraction limit," *Nat. Nanotechnol.*, Vol. 7, No. 9, 557–561, 2012.
2. Roberts, A. S., Pors, A., Albrektsen, O. & Bozhevolnyi, S. I. "Subwavelength plasmonic color printing protected for ambient use," *Nano Lett.*, Vol. 14, No. 2, 783–787, 2014.
3. Tan, S.J. *et al.* "plasmonic color palettes for photorealistic printing with aluminum nanostructures," *Nano Lett*. Vol. 14, No. 7, 4023-4029, 2014.
4. Clausen, J.S. *et al.* "Plasmonic metasurfaces for coloration of plastic consumer products," *Nano Lett*. Vol. 14, No. 8, 4499-4504, 2014.
5. Goh, X.M. *et al.* "Three-dimensional plasmonic stereoscopic prints in full colour," *Nat. Commun.* Vol. 5, 5361, 2014.
6. Xue, J. *et al.* "Scalable, full-color, and controllable chromotropic plasmonic printing," *Nat. Commun.* Vol. 6, 8906, 2015.

# Optical properties of nanoparticle chains (Ag, Au, Ag-Au) embedded in a dielectric matrix

**A. Fafin**[1], **S. Yazidi**[1], **S. Camelio**[1], **and D. Babonneau**[1]

[1]Institut Pprime, Département Physique et Mécanique des Matériaux, UPR 3346 CNRS, Université de Poitiers, SP2MI, 11 Bvd M. et P. Curie, BP 30179, F-86962 Futuroscope Chasseneuil Cedex, France
alexandre.fafin@univ-poitiers.fr

**Abstract**— We investigate the optical properties of Ag-Au nanoparticle chains embedded in a dielectric matrix by the FDTD method. We show that it would be preferable to use pure metal (Ag or Au), instead of Ag-Au, to obtain a maximum field enhancement. We also study the optimal gap between nanoparticles to have a maximum field enhancement at the capping layer/air interface. It appears that a compromise has to be found to reach the best field-enhancement effect.

The excitation of a metal nanoparticle by an electromagnetic wave allows to generate a localized surface plasmon resonance (LSPR). The wavelength of LSPR depends on the morphology (shape and size) and composition of the nanoparticle as well as the permittivity of the host medium. An interesting property of the LSPR is the confinement and significant increase of the electromagnetic field in the vicinity of the nanoparticle. By minimizing the distance between particles (also called gap), coupling effects give rise to an increase of the amplitude of the electromagnetic field between two particles by several orders of magnitude compared to the incident field [1, 2]. This property can be used to detect molecules by surface-enhanced Raman spectroscopy (SERS). In this case nanoparticles can be coated with a dielectric capping layer, which provides stability against ageing effects and temperature, but also enables surface cleaning without modification of the optical properties. However, the capping layer must be as thin as possible because the electric field is evanescent. Silver nanoparticles are known to product an important field enhancement but also to have a hight mobility and a poor chemical stability, which may force to use a capping layer too thick to obtain an acceptable field enhancement at the capping layer/air interface. In contrast, gold nanoparticles present a lower field enhancement but also a lower atomic mobility and a better chemical stability against corrosive environments. Gold would therefore allow using a thinner capping layer, which could preserve sufficient electric field intensity at the surface of the capping layer. In order to combine the advantages of these two metals, it was recently proposed to produce gold-silver alloy nanoparticles that could present both chemical inertness and high field enhancement [3]. In this presentation, we will compare the near-field and far-field optical properties of isolated and coupled $Ag_xAu_{1-x}$ nanoparticles ($0 \leq x \leq 1$) sandwiched between dielectric layers. Particular attention will be paid to the influence of the nanoparticle composition, interparticle gap and capping-layer thickness on the amplitude and spatial extent of the hot spots.

We will first present the production process of $Ag_xAu_{1-x}$ alloy thin films (with a thickness of around 100 nm) and the determination of their complex permittivity by spectroscopic ellipsometry. Then, we will focus on simulations based on the finite-difference time-domain (FDTD) method, to study the near-field and far-field optical properties of individual $Ag_xAu_{1-x}$ nanoparticles embedded in various amorphous dielectric matrices. As shown in figure 1, our results highlight that pure metal nanoparticles have a larger field enhancement than alloy nanoparticles.

We will then discuss the optical response of Au or Ag nanoparticle chains embedded in $Al_2O_3$ matrix. For example, figures 2 and 3 show the field enhancement above a capping layer for two gaps (2 nm and 14 nm) and two capping layer thicknesses (3 nm and 5 nm). We can notice that the amplification is greater for Au nanoparticles with a 3 nm-thick layer than for Ag nanoparticles with a 5 nm-thick layer.

In conclusion, this study allows a better understanding of the near-field optical properties of plasmonic nanoalloys in order to increase the field enhancement for SERS-type applications with protected nanoparticles.

**ACKNOWLEDGMENT**

This work has been partially funded by the French National Agency (QMAX project no. ANR-09-NANO-031) in the frame of its 2009 programme in Nanosciences, Nanotechnologies and Nanosystems (P3N2009).

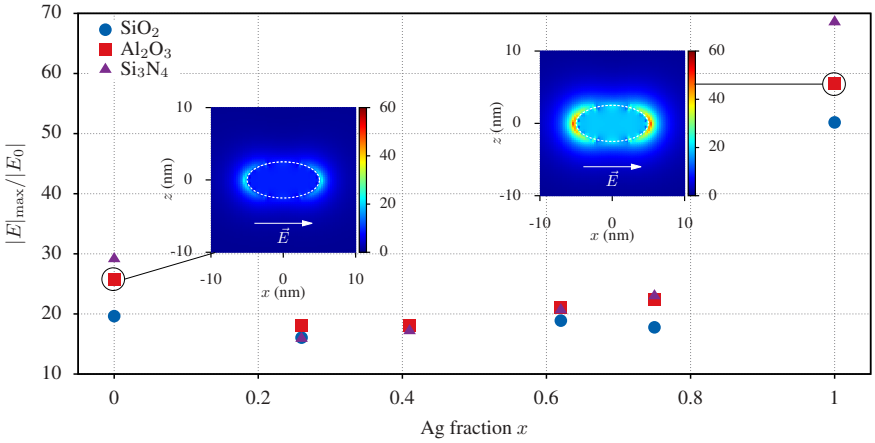



Figure 1: Maximum of the field enhancement $|E|_{\max}/|E_0|$ obtained at the LSPR energy as a function of the Ag fraction $x$ for isolated nanoparticles embedded in $SiO_2$, $Al_2O_3$ and $Si_3N_4$ matrices. Insets: field enhancement $|E(x,z)|/|E_0|$ maps calculated at the LSPR energy for Ag and Au nanoparticles in $Al_2O_3$ matrix. Dotted lines indicate dimensions and position of the nanoparticle.

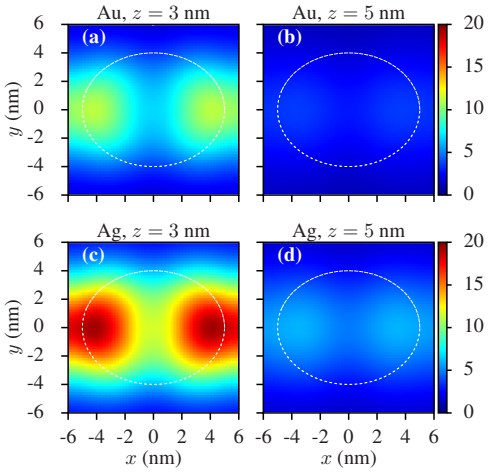



Figure 2: Field enhancement $|E|/|E_0|$ maps for a gap $g_x = 2$ nm above the capping layer/air interface at (a),(c) $z = 3$ nm and (b),(d) $z = 5$ nm for (a),(b) Au nanoparticles and (c),(d) Ag nanoparticles. Dotted lines indicate dimensions and position of the nanoparticle at $z = 0$ nm.

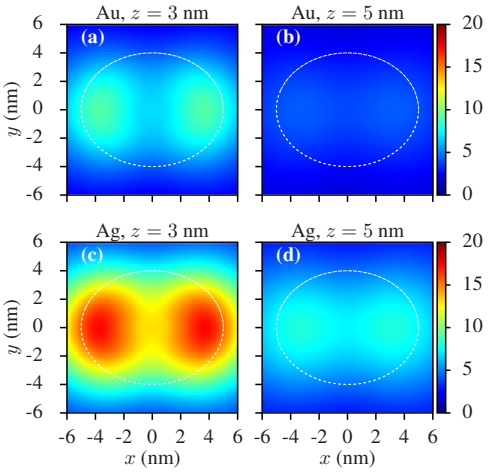



Figure 3: Field enhancement $|E|/|E_0|$ maps for a gap $g_x = 14$ nm above the capping layer/air interface at (a),(c) $z = 3$ nm and (b),(d) $z = 5$ nm for (a),(b) Au nanoparticles and (c),(d) Ag nanoparticles. Dotted lines indicate dimensions and position of the nanoparticle at $z = 0$ nm.

**REFERENCES**


1. L. A. Sweatlock, S. A. Maier, H. A. Atwater, J. J. Penninkhof, and A. Polman, "Highly confined electromagnetic fields in arrays of strongly coupled Ag nanoparticles," *Phys. Rev. B*, Vol. 25, 235408, 2005
2. S. Camelio, E. Vandenhecke, S. Rousselet, D. Babonneau, "Optimization of growth and ordering of Ag nanoparticle arrays on ripple patterned alumina surfaces for strong plasmonic coupling," *Nanotechnology*, Vol. 25, 035706, 2014.
3. C. Gao, Y. Hu, M. Wang, M. Chi, and Y. Yin, "Fully Alloyed Ag/Au Nanospheres: Combining the Plasmonic Property of Ag with the Stability of Au," *J. Am. Chem. Soc.*, Vol. 136, 7474-7479, 2014.

# UV Circular Polarization Selection using Aluminum Nano-Spirals

**M.S. Davis[1, 2, 3], J. Strait[2], J.K. Lee[1], S. Blair[4], A. Agrawal[2,3], and H. J. Lezec[2]**

[1]Department of Electrical Engineering and Computer Science, Syracuse University, Syracuse, NY 13244, USA

[2]Center for Nanoscale Science and Technology, National Institute of Standards and Technology, Gaithersburg, MD 20899, USA

[3]Maryland Nanocenter, University of Maryland, College Park, MD, 20742, USA

[4]Department of Electrical and Computer Engineering, University of Utah, Salt Lake City, UT 84112, USA

msdavi01@syr.edu

**Abstract**: Manipulating ultraviolet light presents unique challenges in technology. Here we demonstrate circular polarization selection at ultraviolet wavelengths over subwavelength distances using a flat-optical device consisting of Al chiral nanospirals periodically patterned on a glass substrate.

As plasmonics continues to play an integral role in the development of technologies from the infrared to the visible frequency range, there is an increasing interest in plasmonic applications at ultraviolet (UV) wavelengths. The high energy and short wavelengths associated with UV light are of interest in many technologies such as optical communications, chemical/biological sensing, and advanced nanofabrication techniques enabled by UV lasers [1]. Key to the development of UV technology is the ability to manipulate the polarization and phase properties of light at such short wavelengths. Recently plasmonic metasurfaces have demonstrated the ability to introduce abrupt phase changes to incident light over subwavelength distances [2]. Experimental work has focused on infrared and visible wavelength due to the fabrication challenges in scaling Au and Ag to shorter wavelengths [2]. Al is preferred for UV applications due to its high plasma frequency enabling a Drude like electron response at UV wavelengths. Some computational work has been done to understand the potential applications of nanoscale Al devices at UV wavelengths, though to the best of our knowledge these devices have yet to see experimental realization [3, 4]. Here we experimentally demonstrate circular diattenuation (CD) of circularly polarized (CP) UV light in the wavelength range 200 nm – 400 nm. CD-UV is accomplished with a periodic array of nanospirals fabricated using e-beam lithography and lift-off on a $SiO_2$ substrate coated with a 20 nm thick ITO layer. The nanospiral surface transmission and reflection responses to incident UV light are determined by incident light handedness (Figures 1a). Individual spiral dimensions (≈250 nm) are on the order of the UV wavelength, though elements of the spiral geometry near the origin are deep-subwavelength and play a crucial role in the device response. The spiral thickness of ≈80 nm is characteristic of flat-optical devices wherein the phase manipulation of light occurs on a subwavelength scale. Figures 1b-c whos scanning electron microscopy (SEM) images of the fabricated Al nanospirals on ITO coated $SiO_2$ surface with 25% spiral fill-factor. Current fabrication efforts are focused on increasing the fill-factor fto 100% for increasing CD response. Figures 2a-b show the FDTD calculated LSP modes for the right-circularly-polarized (RCP) and left-circularly-polarized (LCP) incident light at 300 nm. The normalized difference in reflected powers are

measured using a spectroscopic ellipsometer operating in reflection mode. Figure 2c shows the reflected power difference measurement made with light incident on the device at an angles 45°, 50°, and 55°. The peak value of ≈0.043 shows that ≈4.3% more RCP power is reflected in comparison to LCP at a wavelength of 300 nm, hence demonstrating CP selectivity. FDTD simulations using 100% nanospiral fill-factor suggest that CD as high as 20% is possible, and so current fabrication efforts are focused on increasing this fill-factor.

In this talk, we will discuss the computational design, nanofabrication process, and optical properties of the Al nanospirals. We will also discuss experimental characterization of the device at UV wavelengths; demonstrating the first experimental realization of a polarization selective flat-optical metasurface capable of manipulating UV light in both reflection and transmission.

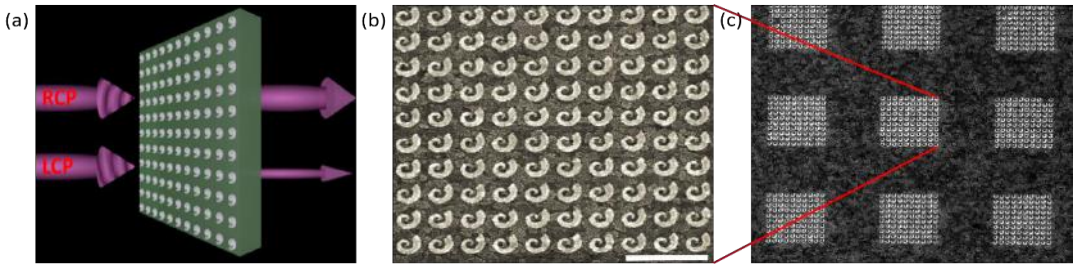



**Figure 1.** (a) Al nanospirals patterned on a fused silica substrate selectively pass circularly polarized light at UV wavelengths. Selectivity is determined by handedness of UV light. (b) SEM image of Al nanospirals patterned on a fused silica substrate coated with 20 nm thick ITO layer. Scale bar in (b) is 1 μm. Spirals were fabricated using e-beam lithography and a lift-off procedure. Spirals dimensions: 80 nm height, 250 nm lateral size, and 380 nm pitch. (c) Spirals are fabricated in 10 x 10 periodic squares with 25% fill factor.

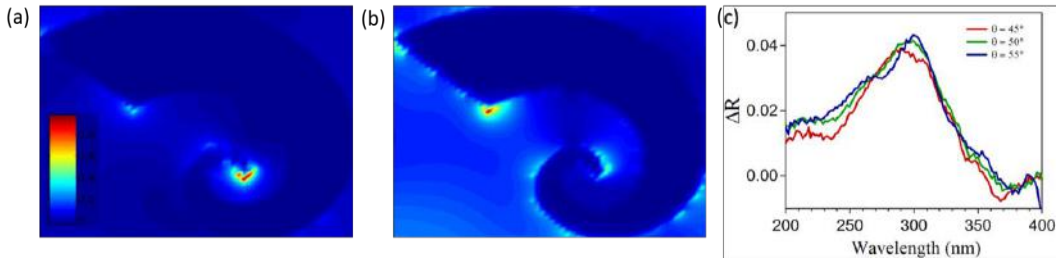



**Figure 2.** FDTD calculated normalized field intensity of the LSP modes at 300 nm for the Al nanospiral for (a) RCP and (b) LCP excitation. (c) The difference in reflected power, measured with a spectroscopic ellipsometer for LCP and RCP.

## REFERENCES


1. K. Liu, D. Ji, X. Zeng, N. Zhang, H. Song, Y. Xu and Q. Gam, "Super absorbing ultraviolet metasurface," *IEEE Photon. Tech. Lett.*, Vol. 27, No. 1, 1539–1542, 2015.
2. E. Hojlund-Nielson, X. Zhu, M.S. Carstensen, M.K. Sorenson, C. Vannahme, N.A. Mortensen and A. Kristensen, "Polarization-dependent aluminum metasurface operating at 450 nm," *Opt. Express*, Vol. 23, No. 22, 28829–28835, 2015.
3. J. Li, S. Chen, H. Yang, J. Li, P. Yu, H. Cheng, C. Gu, H.T. Chen and J. Tian, "Simultaneous control of light polarization and phase distributions using plasmonic metasurfaces," *Adv. Funct. Mater.*, Vol. 25, 704–710, 2015.
4. M. Rodriguez, C. Furse, J.S. Shumaker-Parry and S. Blair, "Scaling the response of nanocrescent antennas into the ultraviolet," *ACS Photonics.*, Vol. 1, 496–506, 2014.

# 3D toroidal metamaterial on suspended SiN film

**Z. Liu[1], S. Du[1], Z. C. Li[2], S. Q. Chen[2], J. J. Li[1*], and C. Z. Gu[1,3]**

[1] Beijing National Laboratory for Condensed Matter Physics, Institute of Physics, Chinese Academy of Sciences, Beijing 100190, China

[2]Laboratory of Weak Light Nonlinear Photonics Ministry of Education, School of Physics and Teda Applied Physics Institute, Nankai University

[3] Collaborative Innovation Center of Quantum Matter, Beijing 100871, China

[*]corresponding author: jjli@iphy.ac.cn

**Abstract**-Toroidal metamaterial on suspended SiN film was fabricated by focused ion beam induced bending technique. The SiN film plays the role of framework, while the metal patterns on the vertical SiN flakes comprise the toroidal molecule. Toroidal and magnetic dipole moments can be excited by vertical incident light, which can be distinguished by the current and magnetic field distribution. Compared to horizontally incidence, the resonance here has the same frequency but much larger transmission modulation depth.

Toroidal moments play an important role in nuclear and particle physics, but the relevant studies in the classical electromagnetic field has just started in recent years, due to the lack of toroidal responses in nature materials. Split ring resonator (SRR) is a basic element for magnetic response by optical excitation, which has been considered as a structural unit of toroidal metamaterial[1-5]. In order to construct toroidal molecule, the SRRs should be arranged appropriately in free space with specific orientation, and this has been achieved in microwave region[1]. However, it is hard to be achieved by traditional planar microfabrication techniques, especially in higher frequency region. The 3D configurational SRR-based toroidal metamaterial has been predicted to be a promising candidate for lasing spaser, dichroism and non-reciprocal refraction of light, which is worth studying in high frequency region.

In this paper, SRR pattern made of Au was first fabricated on suspended SiN film. Then focused ion beam (FIB) technique was used to cut square-shaped cantilevers and bend then up by scanning the bottom of the cantilevers[6], as shown in Figure 1. Each toroidal molecule contains four SRR-on-flake structures, two of which were open-side-up and the others open-side-down. The transmission and reflection spectra were simulated by FDTD method, and a toroidal response was found to be at 51 THz (Figure 2). The magnetic field distribution is shown in the inset, which proves to be a torus passing through the middle of the SRRs. It can be noted that the incident wave vector *k* in Fig. 1 is perpendicular to the plane where the structures lie, different from the former work of parallel incidence. Compare to parallel incidence, the toroidal response in this work shows the same resonance frequency, but much larger modulation depth, which mainly comes from the farfield radiation property of toroidal dipoles. The toroidal dipole also shows very large potentials on environment index sensing.

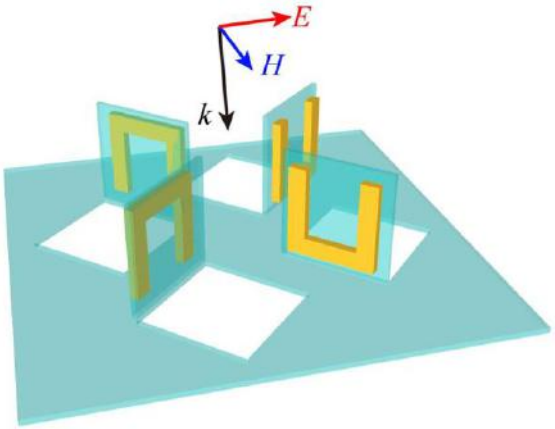



Figure 1 Schematic of toroidal metamaterial on suspended SiN film

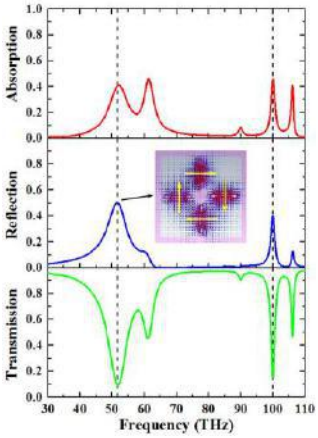



Figure 2 Spectra of the 3D toroidal metamaterial, with the magnetic field distribution in the inset

**Acknowledgements**: This work was supported by the National Natural Science Foundation of China (Grants Nos 91323304, 11174362, 61390503, 11574369, 11434017 and 11504414) and the Knowledge Innovation Project of CAS (Grant No. KJCX2-EW-W02).

**REFERENCES**

1. Kaelberer, T., Fedotov, V. A., Papasimakis, N., Tsai, D. P. and Zheludev, N. I. "Toroidal Dipolar Response in a Metamaterial," *Science*, Vol. 330, 1510-1512, 2010.
2. Huang, Y.-W. et al. "Design of plasmonic toroidal metamaterials at optical frequencies," *Optics Express*, Vol. 20, 1760-1768, 2012.
3. Fan, Y., Wei, Z., Li, H., Chen, H. and Soukoulis, C. M., "Low-loss and high-Q planar metamaterial with toroidal moment," *Phys. Rev. Lett.B*, Vol. 87, 115417, 2013.
4. Huang, Y.-W. et al, "Toroidal Lasing Spaser," *Sci. Rep.*, Vol. 3, 2013.
5. Guo, L., Li, M., Yang, H., Huang, X. and Wu, S., "Toroidal dipolar responses in a planar metamaterial," *Journal of Physics D: Applied Physics*, Vol. 47, 415501, 2014.
6. Cui A. J., et al, "Directly Patterned Substrate-free Plasmonic 'Nanograter' Structures with Unusual Fano Resonances," *Light: Science & Applications*, Vol. 4, e308, 2015.

# Ag and Au nanoparticles synthesis with pulsed laser ablation in monomer solution.

**I. Yu. Denisyuk, N.A. Zulina*, I. M. Pavlovets**

St. Petersburg National Research University of Information technologies, Mechanics and Optics, Russian Federation

*corresponding author: zulinatsu@mail.ru

**Abstract**- In this study Ag and Au nanoparticles were obtained with pulsed laser ablation method in liquid substance. As liquid monomer solutions of two different photocurable polymers were picked – carboxyethyl acrylate and isodecyl acrylate. UV-visible spectroscopy and SEM investigation showed that obtained nanoparticles have size distribution from 50 to 200 nm. Also, polymerization process was carried out for nanocomposite synthesis and its biomedical application study.

Ag and Au nanoparticles (AgNPs and AuNPs) are well known nanomaterials with plasmon resonance and attracted interest due to their potential applications. One of a most perspective direction is to synthesize nanocomposites based on photocurable polymers and metal nanoparticles. But nanoparticles incorporation in polymer matrixes is a quite difficult procedure. Most of metal nanoparticles have a colloid solution form and utilized solvents are very destructive for monomers. So, it is necessary to evaporate solvents for following nanoparticles utility, but such treatment leads to agglomeration of nanoparticles.

In this work AgNPs and AuNPs were obtained in monomer solutions with pulsed laser ablation method [6].

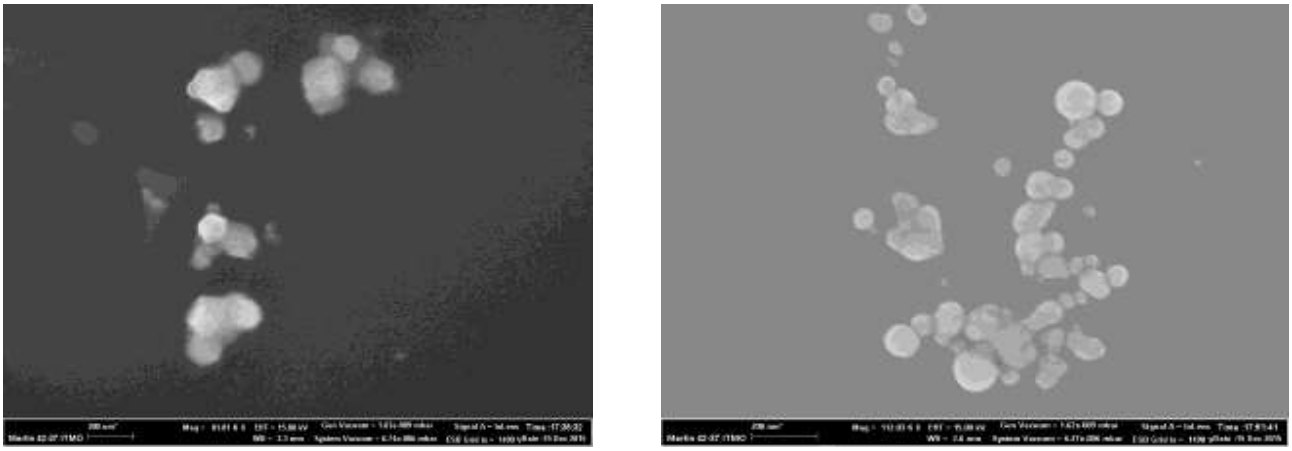
Pulsed laser ablation (PLA) in liquid is widely-used method of metal nanoparticles synthesis. This method includes quick substance evaporation or removing and its condensation to form nanoparticles. In this case, there is no need for chemical synthesis reactions, the method is more universal and consists no contamination of reaction products [1-5].

PLA of gold and silver patterns was carried out with Nd:YAG laser with 1064 nm wavelength and 10 ns pulse duration. Repetition rate was 10 Hz and power density was 11 MW/cm$^2$. Duration of irradiation (exposition time) was about 5 minutes for silver and 10 for gold.

Two different monomers – carboxyethyl acrylate and isodecyl acrylate - were used as liquids for PLA. Optical absorbance spectrums of obtained colloids were measured with UV and visible spectroscopy. Then colloids were poured on silicon substrate and heated up 180°C temperature during 2 hours, till monomer solution complete evaporation. PLA products were investigated with optical and scanning electron microscopy.

Obtained optical absorbance spectrums have a plasmon resonance picks at 400 nm for AgNPs and 530-560 nm - for AuNPs.

Fig. 1 demonstrates SEM images of obtained nanoparicles. All nanoparticles have size distribution from 50 to 200 nm.



a) b)

Fig. 1. SEM images of nanoparticles synthesized in monomer solution with pulsed laser ablation: a) AgNPs, b) AuNPs

Also, in this study photocurable polymerization of monomer-nanoparticles solutions was carried out and polymer nanocomposites based on Ag and Au nanoparticles were synthesize and prepared for following photonics and biomedical research.

**Acknowledgements**, The reported study was funded by RFBR according to the research project No. 16-32-00448.

**REFERENCES**

1. 1. Kassavetis**,** S.', Kaziannis**,** S., Pliatsikas**,** N., Avgeropoulos**,** A., Karantzalis**,** A.E., Kosmidis, C., Lidorikis, E., Patsalas, P., "Formation of plasmonic colloidal silver for flexible and printed electronics using laser ablation**",** Applied Surface Science, Vol. 336**,** 262–266, 2005.
2. 2. Bagga**,** K., McCann**,** R., Wang**,** M., Stalcup**,** A., Vázquez**,** M., Brabazon**,** D., "Laser assisted synthesis of carbon nanoparticles with controlled viscosities for printing applications", Journal of Colloid and Interface Science**,** Vol. 447, 263–268, 2005.
3. 3. Tamaki, Yo., Asahi, Ts., Masuhara, H., "Nanoparticle Formation of Vanadyl Phthalocyanine by Laser Ablation of Its Crystalline Powder in a Poor Solvent", J. Phys. Chem. A, Vol. 106, 2135-2139, 2002.
4. 4. Li, B., Kawakami, T., Hiramatsu, M., "Enhancement of organic nanoparticle preparation by laser ablation in aqueous solution using surfactants", Applied Surface Science, Vol. 210, № 3–4, 171–176, 2003.
5. 5. Elaboudi**,** I., Lazare**,** S.', Belin, C., Bruneel, J.L., Servant**,** L., "Organic nanoparticles suspensions preparation by underwater excimer laser ablation of polycarbonate", Applied Surface Science**,** Vol. 253, № 19**,** 7835–7839, 2007.
6. 6. Barcikowski, S., Hustedt, M., Chichkov, B., "Nanocomposite manufacturing using ultrashort-pulsed laser ablation in solvents and monomers", Polimery, Vol. 53, № 9, 2008.

# Dark chameleon nanomaterials for lasing and energy harvesting

**A. Fratalocchi**

PRIMALIGHT, Faculty of Electrical Engineering; Applied Mathematics and Computational Science, King Abdullah University of Science and Technology (KAUST), Thuwal, Saudi Arabia
andrea.fratalocchi@kaust.edu.sa

**Abstract**— By using a biomimetic approach, we engineered an ultra-dark metamaterial that behaves as a black-body at visible and near infrared wavelengths. This material is based on random aggregates of nanoparticles with unconventional shape. Through experiments and theory, we show that such black material allows to develop a new type of "laser", which spontaneously generates single color pulses through a process of light condensation. Energy harvesting applications of this nanomaterial are also discussed.

The concept of a traditional laser exploits a cavity with single or multiple resonant modes, and their coherent amplification in a feedback structure. With this contribution we endeavor to leave this path and investigate a new concept, where lasing does not result from a cavity or a resonance. In particular, we considered the possibility to achieve lasing from a black-body material. We fabricate the latter by taking inspiration from an Asian species of beetle, the Cyphochilus. This little insect possesses a sophisticated camouflage technique, which is based on ultrabrilliant scales that control a complex process of light scattering. By reversing this effect, we designed a new series of ultra-dark random nanoplasmonic structures. Measurements between 200 nm to 1400 nm under isotropic illumination angles, show that this material has a flat absorption between 99%-99.8%, behaving like an almost ideal back-body.
Such extremely dark metamaterial does not encompass any particular resonance, and opens the possibility to investigate a new type of laser. In performing our experiments, we diluted a standard dye inside the black-body metamaterial, and then illuminate the system by a pulsed laser operating at 532 nm, characterized by a repetition rate 10 Hz and pulse duration 10 ns. We selected Rhodamine B (RhB) as a gain material, with fluorescence peak at 625 nm. Stimulated emission spectra were then measured by employing a fiber spectrograph. We observed a strong emission peak that shifted from the amplified spontaneous emission (ASE) peak of the dye as the power increased. Further theory showed that such regime is the characteristic lasing of the system, which occurs by a new mechanism of light condensation that coherently gathers all energy from the amplifier, confining it to a single frequency. In our experiments, we observed this transition from an initial broadband emission characterized by 50 nm, to final lasing whose bandwidth is only 5 nm, despite the absence of any resonance and the complete randomness of the material.
Due to the high absorption of these nanoparticles, we recently applied this metamaterial platform to solar energy harvesting applications. A blackbody is in fact an ideal material to efficiently transfer radiation power into heat. As a first application of this concept, we ideate and characterized a water desalination device, which achieves record efficiency (75%) under the solar power of 1 kW/m$^2$.

**REFERENCES**

1. C. Liu, A. Di Falco, D. Molinari, Y. Khan, B. S. Ooi, T. F. Krauss, and A. Fratalocchi, "Enhanced energy storage in chaotic optical resonators," Nature Photonics, **7**(6), 473–478 (2013).
2. C. Liu, A. Di Falco, and A. Fratalocchi, "Dicke phase transition with multiple superradiant states in quantum chaotic resonators," Physical review X, **4**(2),021048 (2014).
3. C. Liu, R.E.C. van der Wel, N. Rotenberg, L. Kuipers, T. F. Krauss, A. Di Falco, A. Fratalocchi, "Triggering extreme events at the nanoscale in photonic seas," Nature Physics, **11**, 358–363 (2015).
4. J.Huang, C. Liu, Y. Zhu, S. Masala, E. Alarousu, Y. Han, and A. Fratalocchi, "Harnessing structural darkness in the visible and infrared wavelengths for a new source of light," Nature Nanotechnology **7**, 60–66 (2016).

# Shape and phase of surface plasmon lasers on an active metasurface

**V. T. Tenner, M. J. A. de Dood, and M. P. van Exter**

Huygens-Kamerlingh Onnes Laboratorium, Universiteit Leiden, The Netherlands
tenner@physics.leidenuniv.nl

**Abstract**— We study surface plasmon lasing in a simple metamaterial with gain, comprising a square metal hole array on a semiconductor gain layer. These lasers emit radially polarized vector-vortex beams. We study the origin of these beams by measuring the radiated intensity in both near and far field and reconstructing the phase of the emission. The reconstructed phase gives valuable information on the distributed feedback of these lasers and reveals the origin of the donut shaped laser beams.

In optical metamaterials the flow of light is altered by nano-structuring the materials. Many metamaterials consist of periodic lattices of sub-wavelength elements. Most often, metals are deployed in such systems in order to confine the light on a nano-scale by using their surface plasmon respons. However, ohmic loss in the metals limit the efficiency of such devices. These losses can be compensated by active gain materials. When the losses are fully compensated, surface plasmon lasing occurs [1].

We study such a meta-surface where the losses are compensated. We observe surface plasmon lasing at telecom wavelengths in a metal hole array with a square lattice [2]. The gain is provided by an optically pumped InGaAs layer closely spaced from the metal surface. We measure the profile of the emitted light in real- and k-space. Both in real and k-space the emitted beam is donut shaped and radially polarized. We performed a simple beam block experiment in order to obtain also information about phase of the emission. In this experiment we block half of the real space and observe the resulting k-space, shown in Fig. 1d. From these measurements we reconstruct the phase using an iterative algorithm [4].

The laser cavity is formed by distributed feedback (DFB) due to scattering of the surface plasmons on the air holes. We determined this feedback strength by observing the SP-dispersion relation and its avoided crossings. This dispersion relation reveals the 4 modes relevant for the laser action. Dark and bright modes are observed and radiation losses are identified as main discriminator in laser threshold [3].

We compare our observations with the standard DFB theory, and demonstrate that this theory is insufficient to explain the observed beam profiles. We identify two missing ingredients, being the position dependence of the gain and refractive index, and extend the standard theory to agree with the observations, shown in Fig. 1b-d.

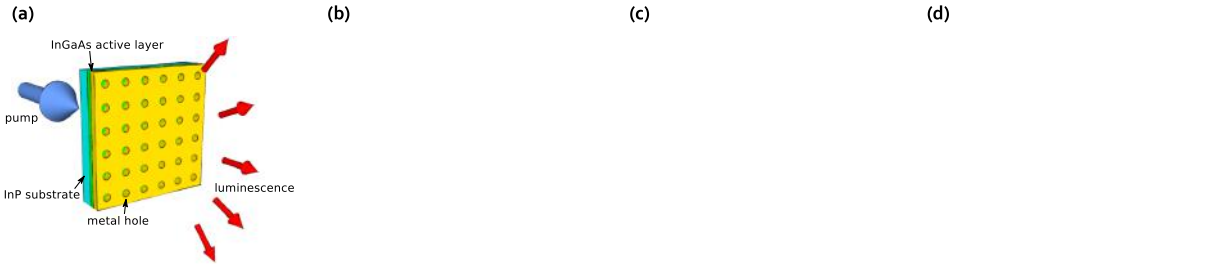



Figure 1: (a) Sketch of setup. The active layer is pumped optically through the substrate, while the emission is collected on the gold side, using a fiber coupled spectrometer or a CCD camera. (b-d) Cuts through k-space. (b) Standard DFB theory. (c) Extended theory. (d) Experimental data. The black curve the depicts the Fourier transform of full real space. The yellow (brown) show the resulting k-space, while blocking the right (left) half of the real-space.

**REFERENCES**


1. Mark Stockman. Spaser Action, Loss Compensation, and Stability in Plasmonic Systems with Gain. *Phys. Rev. Lett.*, 106(15):156802, April 2011.
2. Frerik van Beijnum, Peter J. van Veldhoven, Erik Jan Geluk, Michiel J. A. de Dood, Gert W. 't Hooft, and Martin P. van Exter. Surface Plasmon Lasing Observed in Metal Hole Arrays. *Physical Review Letters*, 110(20), May 2013.
3. V T Tenner, A N van Delft, M J A de Dood, and M P van Exter. Loss and scattering of surface plasmon polaritons on optically-pumped hole arrays. *Journal of Optics*, 16(11):114019, November 2014.
4. V T Tenner *Manuscript in preparation*

# Stokes Polarimetry using Silicon Nanoantennas.

**A. Espinosa-Soria[1*], F. J. Rodríguez-Fortuño[2], A. Griol[1], and A. Martínez[1]**

[1] Universitat Politècnica de València, Nanophotonics Technology Center, Camino de Vera s/n, 46022, Valencia, Spain

[2] King's College London, Department of Physics, Strand, London WC2R 2LS, UK

[*]corresponding author: alesso@ntc.upv.es

**Abstract -** In this work, we present an on-chip polarimeter working at telecom wavelengths that obtains the full state of polarization (SoP) of an incoming plane wave. The polarimeter has six outputs that allow for a direct synthesis of the Stokes parameters. This outputs come from three silicon nanoantennas coupled to three waveguides, so that each nanoantenna responds to a certain polarization state by changing the amount of optical power coupled to each direction of propagation along the coupled waveguide.

Polarization is a fundamental property of electromagnetic waves. The state of polarization (SoP) is an essential characteristic used in several disciplines (chemistry, astronomy, optical communications). It has been recently shown that the polarization of the source exciting a guided wave via near-field coupling plays a key role in determining the propagation direction of the guided wave [1]. We seize this concept to characterize the state of polarization of an incoming light beam using two types of dielectric scatterers, first type for linear polarization [2], and the second type for resolving the handedness (or spin) of a circular polarization [3]. This scatterers act as a nanoantennas, coupling the input light to silicon waveguides.

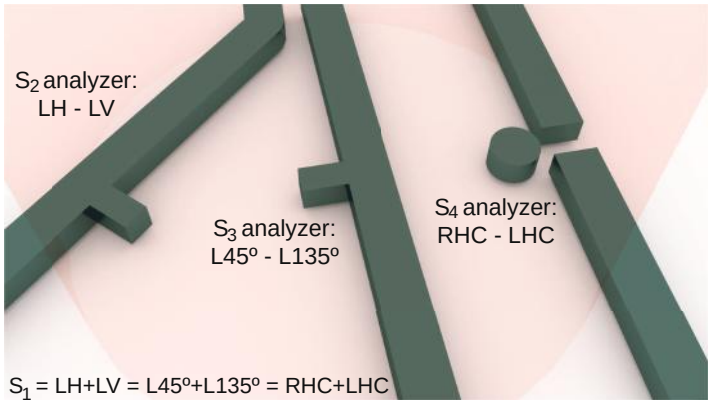



Figure 1. Scheme of the photonic circuit. The first Stokes parameter ($S_1$) can be obtained from any of the nanoantennas, while the others ($S_2$ to $S_4$) are obtained specifically from each one. Notice that the nanoantennas are put in close proximity in order to be all simultaneously illuminated.

Properly combining this three nanoantennas, it is possible to full measure the SoP of a light beam, on the basis of the Stokes parameters, in a single measurement. Exploiting the polarization-dependent characteristics of the nanoantennas described above, only three nanoantennas (two for lineal polarization and one for circular polarization) are required for full description of the four Stokes parameters defining the SoP of the incident light

beam. This three nanoantennas couple the impinging light in three waveguides, with two outputs each, so we have a six outputs device where direct combination of the power at each output result in the four Stokes parameters.

In conclusion, the methodology outlined allows a quick analysis of the incoming SoP in real time and over an ultrabroad bandwidth. Moreover, it could be used in an in-line configuration due to the small scattering losses, and the proposed technology allows high level of integration. Because of all this, our device could find application in polarimetry, spectrometry or high speed optical communications.

**ACKNOWLEDGMENT**

Financial support by Ministerio de Economía y Competitividad under the MEMENTO project (TEC2014-51902-C2-C-R) is acknowledged.

**REFERENCES**

1. Rodríguez-Fortuño, F. J., G. Marino, P. Ginzburg, D. O'Connor, A. Martínez, G. A. Wurtz, A. V. Zayats, "Near-field interference for the unidirectional excitation of electromagnetic guided modes," *Science*, Vol. 340, 328-330, 2013.
2. Rodriguez-Fortuño, F. J., I. Barber-Sanz, D. Puerto, A. Griol, and A. Martinez, "Resolving light handedness with an on- chip silicon microdisk," *ACS Photonics*, Vol. 1, No. 9, 762–767, 2014.
3. Rodriguez-Fortuño, F. J., D. Puerto, A. Griol, L. Bellieres, J. Marti, and A. Martinez, "Sorting linearly polarized photons with a single scatterer," *Opt. Lett.*, Vol. 39, No. 6, 1394–1397, 2014.

# Tailoring Resonances in Hybridized Plasmonic Systems

**Ashok Kodigala, Thomas Lepetit, Boubacar Kante**

[1]Department of Electrical and Computer Engineering, University of California San Diego, La Jolla, CA 92093, USA

akodigala@eng.ucsd.edu

**Abstract**- We present a plasmon hybridization picture for a system with coupled plasmonic bars and investigate its resonance dynamics by computing the complex poles of the scattering matrix for the purpose of designing better plasmonic devices.

Plasmonics and its applications have garnered ample attention over the years. These applications range from chemical and biological sensors to enhanced photovoltaics [1-2]. In order to advance these plasmonic devices, it is essential that we have the ability to control their respective resonances. These resonances are central to the devices' unique function. The conventional approach to analyzing plasmonic resonances has been to locate peaks and troughs of transmission and reflection spectra. This approach is qualitative in nature and fails for non-symmetric or Fano resonances. We use a quantitative approach based on effective Hamiltonian formalism to study and tailor resonances of plasmonic systems at optical frequencies described in greater detail in Ref. [3]. Using this approach, we compute the complex poles of the scattering matrix which directly correspond to both the resonance frequencies and linewidths. Therefore, we are able to quantitatively track the evolution of resonances and study the coupling behavior between multiple plasmonic bars.

A plasmonic system based on multiple coupled plasmonic bars, depicted in Figure 1(a), is considered. The dimensions of an individual gold bar are chosen such that the dipolar resonance falls in the optical domain at a wavelength of 1.55 μm. Placing these gold bars in close proximity hybridizes their individual plasmon modes into multiple system modes with different symmetries as shown in Figure 1(b) [4]. Here, the instantaneous current profiles of each mode are depicted for a plane wave excitation with the electric field along the length of the bars. The spectral locations of these hybridized plasmon modes can be tuned by spatially shifting one bar in relation to the other two. Essentially, we break the symmetry of the overall system by shifting one of the bars. Here, we chose to shift the middle bar by an amount 'dx'.

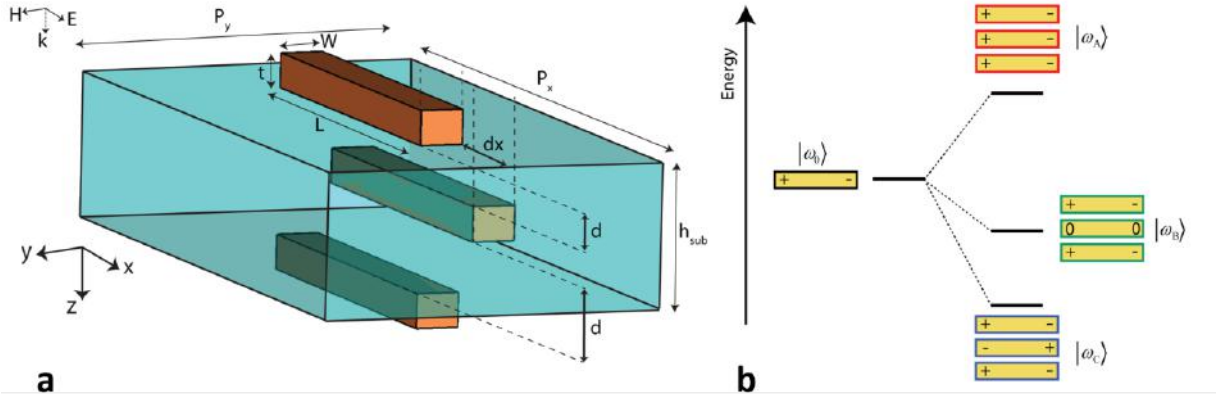



**Figure 1.** (a) Unit cell setup of plasmonic gold bars with a dielectric (SiO2) spacer given in blue with dimensions: L=450 nm, W=50 nm, t=40 nm, Py=400 nm, Px=800 nm, hsub, dx (variable). The gold bars are described using the Drude model with a plasma frequency ($\omega_p$=1.367x10$^{16}$ rad/sec) and collision frequency ($\omega_c$=6.478x10$^{13}$ rad/sec) based on values from Ref. [5]. (b) Energy-level diagram describing the plasmon hybridization in the shift-bar system with three modes: $\omega_A$, $\omega_B$, $\omega_C$ where $\omega_A > \omega_B > \omega_C$ for dx=0. $\omega_0$ is the decoupled resonance of an individual bar.

Initially at no shift, mode A, $\omega_A$, has current in all the bars oscillating in-phase and mode C, $\omega_C$, has current in all bars oscillating out-of-phase while mode B, $\omega_B$, has no field in the middle bar as seen in Figure 1(b). As such, mode A resides at

a higher energy (higher frequency) due to all repelling forces and mode C resides at a lower energy (lower frequency) as a result of repelling forces. Lastly, mode B resides in between mode A and mode C on the energy scale.

We now examine the effect of shifting the middle bar in the x-direction on all three modes of the plasmonic system. As the middle bar is progressively displaced, the repelling forces associated with mode A weaken to become attractive. Similarly, the attractive forces of mode C weaken to become repulsive. Lastly, the coulomb forces associated with mode B remain constant with shift. This behavior is noticeable in the figure below.

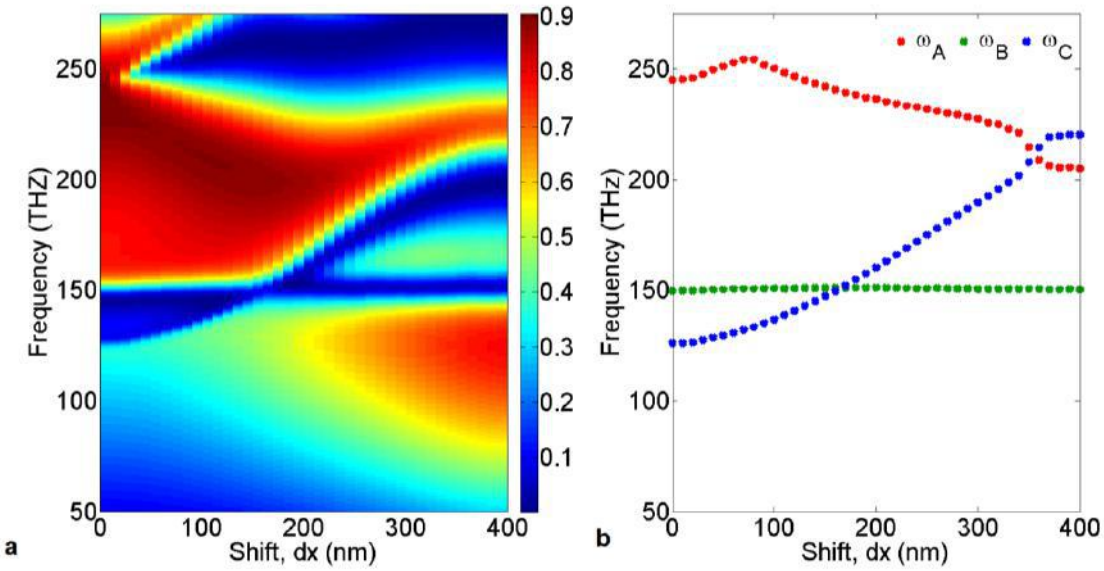



**Figure 2.** (a) Reflection spectra, $|S11|^2$, acquired from full-wave simulations plotted as a function of shift 'dx' for $p_x$=800nm and (b) corresponding resonance frequencies, complex poles, extracted from scattering parameters: $\omega_A$, $\omega_B$, $\omega_C$.

The location of the resonance frequencies are not easily apparent from the reflection spectra. Using the method mentioned in Ref. 3, we plot the extracted resonances in Figure 2(b). As explained earlier, $\omega_A$ decreases with increasing shift whereas $\omega_C$ increases and $\omega_B$ remains constant. Due to the immutable nature of mode B, this mode can serve as a frequency-reference for plasmonic devices. Unlike mode B, modes A and C share a symmetry with respect to the middle bar and as a result interact with each other when they are neighboring in frequency. As seen above, these two modes are degenerate in frequency for a shift dx=355nm and crisscross past that. The region where they crisscross, or where the modes are inverted, is of special interest for plasmonic devices such as biosensors, modulators, etc. Operating the system in this inversion region can allow for higher sensitivity and more robust modulators.

We have demonstrated that we can quantitatively observe resonances of hybridized plasmonic systems by computing the complex poles of the scattering matrix. Furthermore, we have shown that we can tailor the resonances of the system under study which allows for a large degree of tunability and exhibits interacting resonances at optical wavelengths (near-IR).


[1] H. A. Atwater and A. Polman, "Plasmonics for improved photovoltaic devices," Nature Mater. **9**, 205 (2010).

[2] N. Liu, M. Hentschel, T. Weiss, A. P. Alivisatos, and Harald Giessen, "Three-Dimensional Plasmon Rulers," Science **332**, 1407 (2011).

[3] A. Kodigala, T. Lepetit, and B. Kante, "Engineering Resonance Dynamics of Plasmon Hybridized Systems", J. Appl. Phys. (2014) (Accepted).

[4] E. Prodan, C. Radloff, N. J. Halas, P. Nordlander, "A Hybridization Model for the Plasmon Response of Complex Nanostructures," Science 302, 419 (2003).

[5] P. B. Johnson and R. W. Christy, "Optical Constant of the Noble Metals," Phys. Rev. B **6**, 4370 (1972).

# Optical Properties of Strained Metal Thin-Films

**J. K. D. Clark, N. P. Kherani***

Department of Electrical and Computer Engineering, University of Toronto, Toronto, Canada

*corresponding author: kherani@ecf.utoronto.ca

**Abstract***:* Development of tunable materials for use in photonic, plasmonic, and metamaterial devices is extremely important *vis-à-vis* their application to adaptive devices. Metal thin-films on flexible substrates represent a potential material wherein the optical properties can be actively tuned using mechanical strain. The present study reports on strain-induced variation of optical properties of metallic films on flexible substrates.

**Introduction:** Metallo-dielectric structures comprise an extremely versatile class of photonic devices that are used for a variety of applications including high-efficiency window coatings[1], passive cooling films[2], meta-material devices such as superlenses[3] and hyperbolic metamaterials[4]. These structures are composed of thin metallic and transparent dielectric layers[5]. The inability of tuning the properties of metallic layers has limited the potential of these devices. Considering recent work on flexible electronics which has shown that thin metal films can be deposited on elastomeric substrates and strained elastically up to 30%, thereby creating reversible structural changes at the micro and nano length scales[6], we have proposed that it is possible to develop tunable metallo-dielectric devices[7]. In order to develop understanding and insight that would enable effective design of tunable metallo-polymer optical devices, a theoretical study of optical resonances induced in these strained metal films is required.

Studies on mechanical and electrical properties of strained metal films have observed many different film structures the formation of which is principally attributed to deposition conditions of the metal films.[6,8]. This variability in film morphology is expected to exhibit a corresponding variation in optical properties. Herein, we report on the optical properties of strained metal films with nanoscale cracking patterns. We also compare these results to our recent work on the properties of metal films with microscale cracking patterns[7].

**Methods:** An initial undeformed metallic film structure was defined based on a two dimensional hexagonal close packed unit cell comprising of nanoscale tri-branched cracks in COMSOL. Lacour, *et al.*[6] have shown that this tri-branched structure is the resulting morphology of strained metal films deposited using *e*-beam lithography on polydimethylsiloxane (PDMS) with a chromium seeding layer. The metal film was then strained using the structural mechanics module in COMSOL. Finally, this new deformed geometry was imported into an electromagnetics wave frequency domain simulation, where treating it as a periodic unit cell a periodic port analysis was performed to determine the reflected and transmitted power.

**Results:** Using the structural mechanics module, we were able to create strained film structures similar to those observed in previous experimental studies[6]. The reflection and transmittance spectra of the unstrained and strained metal films, shown in Fig. 1 and Fig. 2, exhibit three unique phenomena. As strain is applied, at visible frequencies broad local surface plasmonic resonances are observed; around 1000nm an enhancement in the transmittance is observed; and in the long wavelength limit reflectance of the film decreases. These distinct changes in the optical properties of the film with small strains can be used to create tunable metallo-dielectric devices. The results shown in this abstract will be compared with experimental measurements on strained metal films on PDMS substrates exhibiting similar nanoscale cracking, as well as contrasted against our recent work on films with microscale cracking patterns.

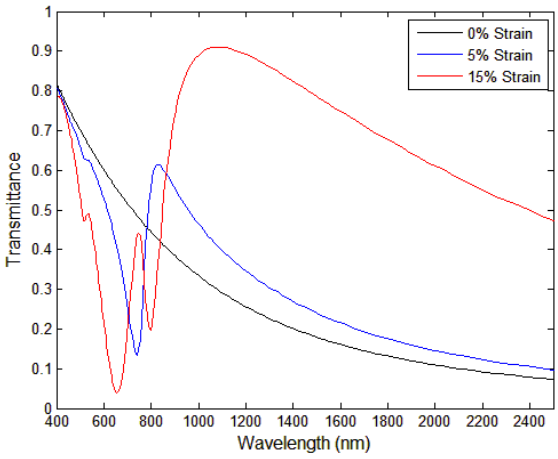



**Fig. 1:** Transmittance of a 10nm silver film under 0% strain (black), 5% strain (blue), and 15% strain (red).

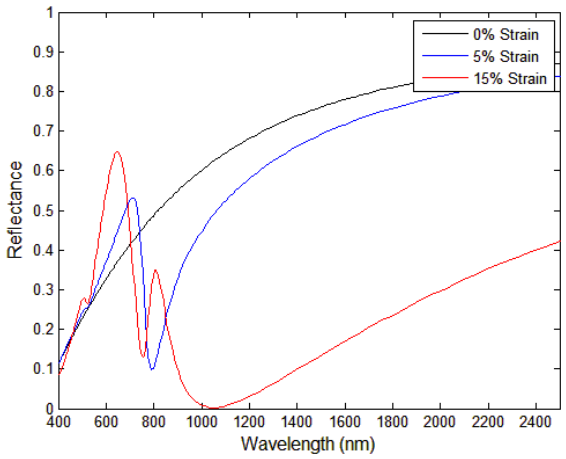



**Fig. 2:** Reflectance of a 10nm silver film under 0% strain (black), 5% strain (blue), and 15% strain (red).

**Conclusion:** This study clearly illustrates that cracking patterns created when metal thin-films are strained do yield unique optical resonances and changes in their infrared reflectivity. These variations in optical properties open the prospect of using strained metal films for tunable metallo-dielectric devices. Such tunable structures can potentially enable a variety of directly tunable photonic, plasmonic and metamaterial devices. The above results represent a first theoretical study into the optical properties of a new material, strained metal thin-films.

The authors gratefully acknowledge research support from the Natural Sciences and Engineering Research Council of Canada.

## REFERENCES

1. Mahtani, P., Leong, K. R., Xiao, I., Chutinan, A., Kherani, N. P. and Zukotynski, S. “Diamond-like carbon based low-emissive coatings,” *Sol. Energy Mater. Sol. Cells*, vol. 95, no. 7, pp. 1630–1637, Jul. 2011.
2. Raman, A. P., Anoma, M. A., Zhu, L., Rephaeli, E. and Fan, S. “Passive radiative cooling below ambient air temperature under direct sunlight,” *Nature*, vol. 515, pp. 540-544, 2014.
3. Xu, T., Agrawal, A., Abashin, M., Chau, K. J. and Lezec, H. J. “All-angle negative refraction and active flat lensing of ultraviolet light.,” *Nature*, vol. 497, no. 7450, pp. 470–4, May 2013.
4. Alaeian, H. and Dionne, J. A. “Parity-time-symmetric plasmonic metamaterials,” *Phys. Rev. A*, vol. 89, no. 3, p. 033829, Mar. 2014.
5. Allen, T. W. and Decorby, R. G. “Assessing the maximum transmittance of periodic metal-dielectric multilayers,” *J. Opt. Soc. Am.*, vol. 28, no. 10, pp. 12–15, 2011.
6. Lacour, S. P., Chan, D., Wagner, S., Li, T., and Suo, Z. “Mechanisms of reversible stretchability of thin metal films on elastomeric substrates,” *Appl. Phys. Lett.*, vol. 88, no. 20, pp. 1–3, 2006.
7. Clark, J.K.D., Kherani, N.P. to be published (2016).
8. Lambricht, N., Pardoen, T. and Yunus, S. “Giant stretchability of thin gold films on rough elastomeric substrates,” *Acta Mater.*, vol. 61, no. 2, pp. 540–547, Jan. 2013.

# Metal-Dielectric Flexible Films for Ultrahigh Transmission

**J. Y. Na, Y. J. Moon, D. S. Kim, and S. K. Kim***

Department of Applied Physics, Kyung Hee University, Gyeonggi-do 17104, Republic of Korea
*corresponding author: sunkim@khu.ac.kr

**Abstract**-We investigated high-transmittance dielectric-metal-ITO multilayer films for developing high-efficiency GaN-based light-emitting diodes using the scattering matrix method. An optically-thick (10-12 nm) metal layer sandwiched by a dielectric layer and an ITO layer yielded a transmittance of 0.94, which surpasses the maximum transmittance (0.91) of a single ITO film. Further, we investigated the transmission of metal-dielectric films depending on the refractive index and thickness of the dielectric layer.

The dielectric-metal-dielectric multilayer films are incorporated into a variety of photonic applications, including solar cells devices [1,2] and light-emitting diodes [3,4] due to their high transmittance and electrical conductivity. Even though the dielectric-metal-dielectric multilayer films have exhibited outstanding optical and electrical performances, design strategies on them are not completely understood as ever. In this paper, we investigated the optical properties of dielectric-Ag-ITO multilayer films as a function of the optical constant and thickness of each layer. A complex phasor diagram can account for the high transmittance in dielectric-metal films [5]

In the simulation model, dielectric, metal, ITO, and GaN ($n$= 2.5) were stacked sequentially and a normal plane wave ($\lambda$= 450 nm) was generated in the GaN medium [Fig. 1 (A)]. Fig. 1 (B) shows the transmittance of a dielectric-Ag-ITO multilayer films depending on the thickness of the used Ag ($t$) and dielectric ($d$) layers. The transmittance oscillates with $d$, which is due to the interference between reflected waves. Also, the overall transmittance is degraded with increasing $t$. Interestingly, the maximum peaks in transmittance of the multilayer film appear at the same thicknesses ($d$ ~ 30 and 140 nm), which are marginally influenced by the thickness ($t$) of metal. An optimized multilayer film with a substantially thick ($t$ = 10 nm) Ag layer exhibits a transmittance of 0.94, which surpasses the maximum transmittance (0.91) of a single ITO film. The design rules related to the dielectric-metal-dielectric multilayer films will provide a feasible strategy for improving transparent electrodes form solar cell and GaN-based LED devices.

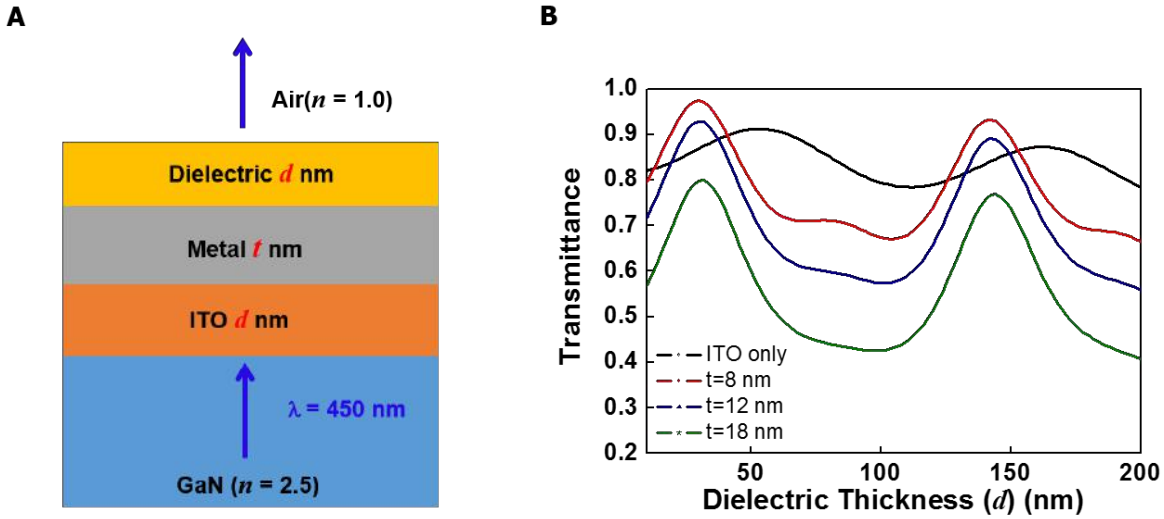



**Fig. 1** (A) Schematic illustration of a GaN structure with the dielectric-Ag-ITO multilayer films. (B) Transmittance (λ=450 nm) properties of the dielectric-Ag-ITO multilayer films placed on a GaN medium as function of dielectric thickness (*d*) for different Ag thickness (*t*).

**Acknowledgements**, We were supported by the Basic Science Research Program through the National Research Foundation of Korea (NRF-2013R1A1A1059423) funded by the Ministry of Science, ICT, and Future Planning.

**REFERENCES**

1. Kim A., Y. Won, C.-H. Kim and J. Moon "Highly transparent low resistance ZnO/Ag nanowire/ZnO composite electrode for thin film solar cells," ACS Nano 7 (2013) 1081-1091.
2. Morgenstern F. S. F., D. Kabra, S. Massip, T.J.K. Brenner and P.E. Lyons, "Ag-nanowire films coated with ZnO nanoparticles as a transparent electrode for solar cells," Appl. Phys. Lett. 99 (2011) 183307.
3. Lee J.-H., K.-Y. Woo, K.-H. Kim, H.-D. Kim and T.-G. Kim, "ITO/Ag/ITO multilayer based transparent conductive electrodes for ultraviolet light-emitting diodes," Opt. Lett. 38 (2013) 5055-5058.
4. Hong K., K. Kim, S. Kim, I. Lee, H. Cho, S. Yoo, H.-W. Choi, N.-Y. Lee, Y.-H. Tak and J.- L. Lee, "Optical properties of WO3/Ag/WO3 multilayer as transparent cathode in top-emitting organic light emitting diodes," J. Phys. Chem. C 115 (2011) 3453-3459.
5. Kats M. A., D. Sharma, J. Lin, P. Genevet, R. Blanchard, Z. Yang, M. Qazilbash, D. N. Basov, S. Ramanathan and F. Capasso, "Ultra-thin perfect absorber employing a tunable phase change material," Appl. Phys. Lett. 101 (2012) 221101.

# High-Index-Contrast Bubble Patterns for High-Efficiency Light Emitting Devices

**Y. J. Moon[1], J. Y. Na[1], D. S. Kim[1], D. W. Hwang[1], D. K. Bae[2], E. J. Yoon[3] and S. K. Kim[1*]**

[1]Department of Applied Physics, Kyung Hee University, Gyeonggi-do 17104, Republic of Korea

[2]Hexa Solution Co., Ltd., Gyeonggi-do 16229, Republic of Korea

[1]Department of Materials Science and Engineering, Seoul National University, Seoul 08826, Republic of Korea

[*]corresponding author: sunkim@khu.ac.kr

**Abstract**-Two-dimensional high-index-contrast dielectric gratings exhibit unconventional diffraction features. Here, we demonstrate monolithic growth templates capable of supporting enhanced outcoupling ability for light-emitting devices. Rationally-designed high-index-contrast air bubble patterns lead to intensified strength for the low order diffraction modes. Furthermore, we demonstrate a new type of economically viable InGaN/GaN LED devices outperforming state-of-the-art patterned sapphire substrate LED devices.

Two-dimensional (2D) dielectric gratings that are mainly characterized by their refractive index contrast and pitch have been utilized in photonic applications including semiconductor lasers and solar cells[1-2]. For light-emitting diodes (LEDs), rationally-designed 2D dielectric gratings diffract optical modes confined in high refractive index active layer, thereby enhancing the outcoupling efficiency[4]. Most lateral- and flip-chip-geometry GaN-based LED devices, which comprise the great majority of the current LED market[5], have adopted patterned sapphire substrates (PSSs). However, light extraction efficiency has remained a limited value for a few decades because the refractive index contrast between GaN and sapphire materials is fixed. Here, we report a new class of high-index-contrast bubble patterned substrates (BPSs) that act as monolithic growth templates to overcome the refractive index barrier encountered with PSSs. Our BPSs includes a 2D hexagonal array of hemispherical air cavities with conformal alumina shells, as shown in Fig. 1. A cross-section scanning electron microscopy (SEM) image of a single BPS object clearly shows a well-defined air cavity that is sustained by an 80-nm-thick alumina shell (inset, Fig. 1B).

To elucidate the optical features of GaN-grown BPS and PSS structures, we measured transmittance profiles by using a home-built spectrally resolved far-field scanner. The results highlight the different diffraction features between the BPS and PSS patterns (Fig. 2). Both GaN/BPS and GaN/PSS exhibit six-fold symmetry diffraction spots that are further spread at longer wavelengths. Interestingly, the centered spot (i.e., zeroth-order diffraction) and the nearest six spots (i.e., the first-order diffraction) are more visible for the BPS over the considered wavelengths. Finally, to investigate the practical importance of BPS patterns, we fabricated large-area (1075 x 750 $\mu m^2$) blue-emitting lateral-geometry InGaN/GaN LED devices. By exploiting InGaN/GaN epitaxial growth on these BPS templates, we establish the foundation of a new breakthrough for creating high-efficiency LEDs that surpass state-of-the-art PSS LEDs.

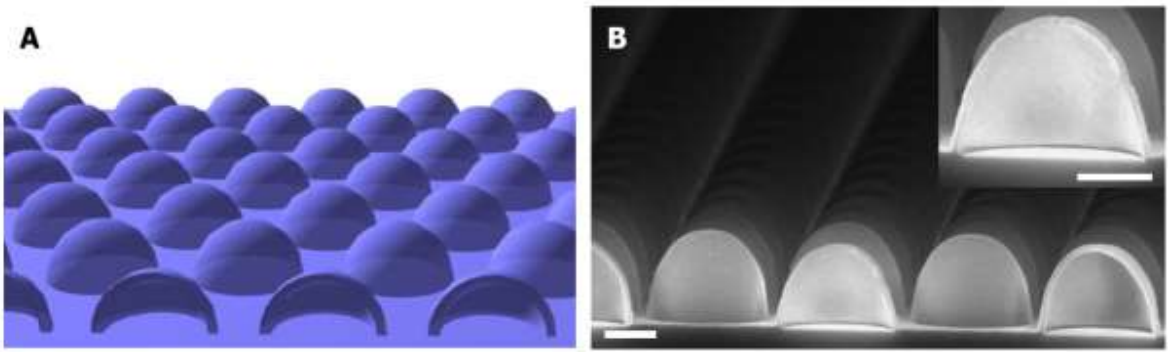



**Figure 1. (A)** Schematic of hemispherical BPS patterns. **(B)** Cross-section SEM image showing hemispherical BPS patterns: scale bar, 1 μm. Inset: SEM image magnifying an inner air cavity covered with a thin alumina shell: scale bar, 1 μm.

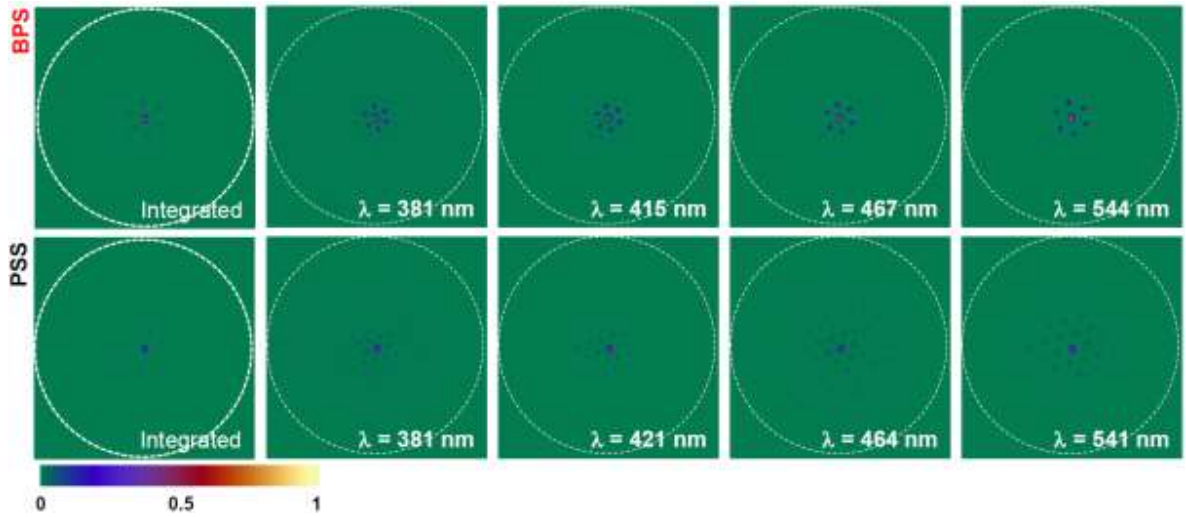



**Figure 2.** Integrated (λ = 380 – 800 nm) and wavelength-resolved diffraction profiles for GaN/BPS and GaN/PSS structures.

**Acknowledgement** We were supported by the Basic Science Research Program through the National Research Foundation of Korea (NRF-2013R1A1A1059423) funded by the Ministry of Science, ICT, and Future Planning.

**REFERENCES**

1. Huang, M. C. Y., Y. Zhou and C. J. Chang-Hasnain, "A surface-emitting laser incorporating a high-index-contrast subwavelength grating," *Nature Photon*, Vol. 1, 119-122, 2007.
2. Brongersmal, M. L., Y. Cui and S. Fan, "Light management for photovoltaics using high-index nanostructures," *Nature Mater*, Vol. 13, 451-460, 2014.
3. Yamada, M. et al., "InGaN-Based Near-Ultraviolet and Blue-light-Emitting Diodes with High External quantum Efficiency Using a Patterned Sapphire Substrate and a Mesh Electrode," *Jpn. J. Appl. Phys*, Vol. 41, L1431-L1433, 2002.
4. "LED Packaging Technology and Market Trends 2014" Yole Development Press, 2014.

# Optically-controlled local plasmonic nanosoldering of silver nanowires

**Qiang Li*, Guoping Liu, Hangbo Yang, Wei Wang, Si Luo, Shuowei Dai, Min Qiu***
Country State Key Laboratory of Modern Optical Instrumentation, College of Optical Science and Engineering, Zhejiang University, 310027, Hangzhou, China
*corresponding author: qiangli@zju.edu.cn

**Abstract**- An optically-controlled local plasmonic nanosoldering technique is proposed and demonstrated. By exploiting the strong photothermal effect in metal nanostructures, this soldering technique ensures the nanostructures to be bonded while their original structural integrity is retained. Typical elemental devices (V-shaped and T-shaped nanostructures) are formed with this nanosoldering technique. The conductivity of one V-shaped junction is enhanced by 500 times after plasmonic nanosoldering. This facile nanosoldering technique is expected to benefit the development of nanophotonics and nanoelectronics.

Nanojoining (including nanowelding, nanosoldering, etc.) of metal nanomaterials offers the opportunity of constructing complex structures and advanced functional devices at the nanoscale. In comparison with nanowelding, nanosoldering does not involve the melting of base metal and shows considerable mechanical strength, good thermal and electrical conductivity. So far, nanosoldering of metal nanowires (NWs) has been accomplished with several distinct strategies, including chemical soldering [1], electric joule heating soldering [2], thermal annealing soldering [3]. All these nanosoldering methods are constrained for locally nanosoldering individually arranged NW-based electronic and photonic devices, which are essential building blocks in nanophotonics and nanoelectronics. Therefore, it is of vital importance to develop new soldering processing with nanoscopic controllability for individually arranged NW-based electronic and photonic devices.

Here two fundamental NW devices (T-shaped or V-shaped NW junctions) are soldered out of two individual NWs. With the help of a nanofiber probe, two silver NWs could be manipulated to form T-shaped or V-shaped nanostructures. Here one segment of one NW is extended beyond the nanojunction and serves as solder in plasmonic nanosoldering; this nanosoldering is accordingly termed as "self-nanosoldering" in this study. When the laser is illuminated on the extended NW segment, it becomes liquid droplet and moves to the unilluminated nanojunction gradually. By displacing the exposing location, the liquid droplet meets the neighboring nanojunction finally and solders the two NWs together. Fig. 1(a) provides the SEM image of a soldered T-shaped nanostructure exploiting plasmonic self-nanosoldering. The visible roughness of the NW results from the sputtered thin gold film for enhancing the electrical conductivity of the substrate in order to clearly observe the sample in SEM imaging. Fig. 1(b) presents a zoom-in of the soldered junction. It can be explicitly seen that the extended segment of the horizontal NW effectively serves as the solder to bond the two NWs together. Importantly, apart from the solder bonding the NWs, no further morphological changes can be observed on the original NW junction, indicating that the junction is not directly affected by the illumination. Similarly, a V-shaped junction is also constructed using plasmonic self-nanosoldering, as displayed in Fig. 1(c and d).

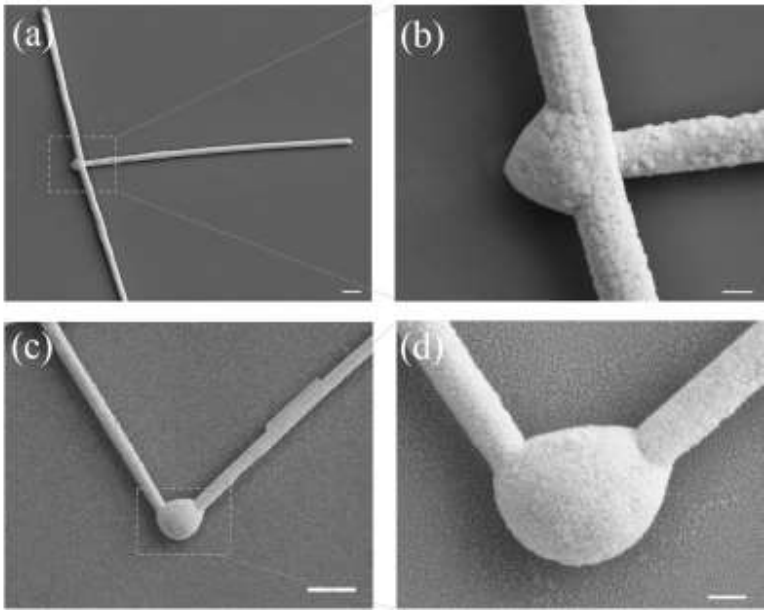



Fig. 1 Self-solder mediated plasmonic soldering of T-shaped and V-shaped nanostructures. (a, c) Plane-view SEM images of T-shaped and V-shaped nanojunctions after plasmonic nanosoldering. Scale bar is 1 μm. (b, d) Zoom-in images of T-shaped and V-shaped nanojunctions after plasmonic nanosoldering. Scale bar is 200 nm.

In summary, a new technique of optically-controlled local plasmonic nanosoldering of metal nanostructures is proposed and demonstrated. The local extreme plasmonic heating induces fusing of the NW solder, stimulates the process of phase change and solders the nanostructures together. Since these nanostructures are building blocks for composing complicated NW interconnected network and plasmonic integrated circuits, the optically-controlled plasmonic nanosoldering technique proposed here provides a new avenue to locally manipulate light, charge, heat and mass transport at the nanoscale and would benefit the development of nanophotonics and nanoelectronics.

**Acknowledgements**: This work is supported by the National Natural Science Foundation of China (Grant Nos. 61425023, 61575177, 61275030 and 61205030).

## REFERENCES

1. Lee, J., Lee, P., Lee, H. B., Hong, S., Lee, I., Yeo, J., Lee, S. S., Kim, T. S., Lee, D. and Ko, S. H. "Room-temperature nanosoldering of a very long metal nanowire network by conducting-polymer-assisted joining for a flexible touch-panel application," *Adv. Funct. Mater.*, Vol. 23, 4171-4176, 2013.
2. Peng, Y., Cullis, T. and Inkson, B. "Bottom-up nanoconstruction by the welding of individual metallic nanoobjects using nanoscale solder," *Nano Lett.*, Vol. 9, 91-96, 2008.
3. Gao, F. and Gu, Z. "Nano-soldering of magnetically aligned three-dimensional nanowire networks," *Nanotechnology*, Vol. 21, 115604, 2010.

# Dynamic Plasmonics with Aluminum-Doped Zinc Oxide

**M. Ferrera[1*], M. Clerici[2], N. Kinsey[3], A. M. Shaltout[3], C. DeVault[3,4], L. Caspani[1], J. Kim[3], R. Kaipurath[1], T. Roger[1], E. G. Carnemolla[1], D. Faccio[1], V. M. Shalaev[3], and A. Boltasseva[3,4]**

[1] Institute of Photonics and Quantum Sciences, Heriot-Watt University, SUPA, Edinburgh, EH14 4AS, UK

[2] School of Engineering, University of Glasgow, Glasgow, Scotland, G12 8LT, UK

[3] Dept. of Electrical and Computer Engineering, Purdue University, West Lafayette, IN, 47907, USA

[4] Dept. of Physics & Astronomy, Purdue University, West Lafayette, IN, 47907, USA

[*]corresponding author: M.Ferrera@hw.ac.uk

**Abstract**- Novel aluminum-doped zinc oxide thin films have been synthesized to maximize the intrinsic carrier density, setting the epsilon-near-zero point at telecom wavelengths (λ=1300nm) and shortening the recombination time of optically generated electron-hole pairs due to defects. When pumped, our material shows deep sub-picosecond recovery time (<300fs), large absolute changes of its refractive index (>10%), remarkable wavelength detuning of the probe signal, and large dynamic tunability of the crossover point (>130nm). All these results, combined with tunability in the static optical properties, are expected to impact many applications in active nano-photonics and tunable metamaterials.

Plasmonics relies on the possibility of coupling the electromagnetic radiation to the oscillations of the electron plasma at the metal-dielectric interface. The resultant modes are tightly localized and extremely susceptible to changes in the environmental conditions. Both these features are intrinsically useful for nano-photonic applications, but they normally come at the cost of fundamental limitations such as large optical losses, low damage threshold, lack of CMOS compatibility, and very limited tunability of the optical properties.

Because the previously listed weaknesses are generally linked to the use of noble metals in plasmonic technology, a large scientific community is working to develop alternative materials besides gold and silver. In this direction, transparent conducting oxides (TCOs), which during the last decade have been extensively used for industrial applications (e.g. touch screens, photovoltaics, etc.), have recently gained great interest, since they have the potential to overcome all the previously listed drawbacks. Among TCOs, aluminum doped zinc oxide (AZO) is very attractive because it is cheap (all its constituents are largely available in nature), it allows for a wide tunable range of its optical properties (i.e. its complex dielectric permittivity can be drastically changed by altering the doping concentration), and it exhibits low optical losses at telecom wavelengths [1].

In this work, we report a deep optical characterization of newly engineered AZO thin films, designed to possess epsilon-near-zero behavior at telecom wavelengths and ultra-fast electron-hole recombination dynamics [2]. By using pump and probe measurements (see Fig.1-a), tuned in both pump and probe wavelengths, we demonstrate numerous interesting effects, which are intrinsically useful for the development of dynamically tunable nanophotonic components. When excited by an optical pump, our material is capable of changing its refractive index by over 10% of its linear value, causing remarkable relative variations in both reflectance and transmittance. This change can be induced by either interband or intraband pumping due to the “hybrid” nature of AZO. The unprecedented magnitude in the variation of the optical properties is directly related to the epsilon-near-zero characteristics of our material, which is shown to be dynamically tunable over a wavelength

range larger than 130nm (see Fig. 1-b). In addition to this, by performing transient spectral detection, a remarkable overall induced frequency shift in the probe carrier frequency as large as the entire pulse bandwidth (≈20nm) was detected (see Fig.1-c). Such alterations of the signal's frequency content is in good quantitative agreement with a generalized law of reflection and refraction that accounts for the temporal phase-gradient induced by the pump [3-4].

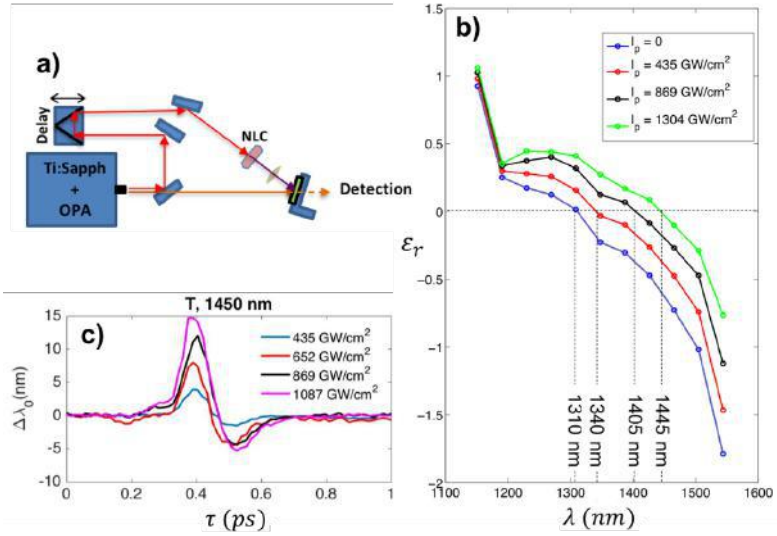



**Figure 1.** Experimental overview. a) Simplified scheme of the pump and probe setup for the characterization of the AZO thin films. b) Real part of the dielectric permittivity as a function of the probe wavelength for different values of the pump intensity. c) Wavelength shift of the probe carrier as a function of the pump-to-probe time delay for different values of the pump intensity.

Our experiments show that AZO is an efficient time-varying medium which brilliantly overcomes the typical nonlinear trade-off between amplitude and speed. By optical excitation we can induce large and ultra-fast changes in both the real and imaginary parts of AZO's dielectric permittivity. Such a change is very effective in tuning the ENZ operational wavelength, and shifting the carrier frequency of the propagating pulse on a sub-picosecond time scale. All these results are extremely promising for future integrated and tunable plasmonics devices.

**Acknowledgements**, The authors acknowledge support from AFOSR FA9550-12-1-0389, ARO W911 NF-13-1-0226, NSF DMR- 1120923 and the Marie Curie Actions IOF program - project n° [329346].

**REFERENCES**

1. Naik, G. V., Shalaev, V. M., and Boltasseva, A. "Alternative Plasmonic Materials: Beyond Gold and Silver," *Adv. Mater*, Vol. 25, No. 24, 3264–3294, 2013.
2. Kinsey, N., DeVault, C., Kim, J., Ferrera, M., Shalaev, V. M., Boltasseva, A., "Epsilon-near-zero Al-doped ZnO for ultrafast switching at telecom wavelengths," *Optica*, Vol. 2, No. 7, 616–622, 2015.
3. Shaltout, A., Kildishev, A., and Shalaev, V. M., "Time-varying metasurfaces and Lorentz non- reciprocity," *Opt. Mater. Express*, Vol. 5, No. 11, 2459–2467, 2015.
4. Mendonça, J. T., and Shukla, P. K., "Time Refraction and Time Reflection: Two Basic Concepts," *Phys. Scripta*, Vol. 65, 160–163, 2002.

# Applying the Otto geometry to access the intrinsic nonlinearity of propagating surface plasmon modes

**J. Heckmann**[1], **K. Pufahl**[1], **N. B. Grosse**[1], **J. E. Sipe**[2], **and U. Woggon**[1]

[1]Technical University of Berlin, Germany
[2]University of Toronto, Canada
jan.heckmann@tu-berlin.de

**Abstract**— A high resolution k-space-spectroscopy setup is applied to analyze linear and nonlinear surface plasmon resonances that are excited by evanescent fields in the Otto geometry. This non-invasive approach allows a detailed analysis of supported resonances in thin films as well as in bulk materials. The results are confirmed by theoretical calculations based on the hydrodynamic model.

The excitation of surface plasmons (SP) by attenuated total internal reflection (ATR) geometries has been of great interest since its first implementation by Otto[1] and Kretschmann et al.[2]. It has provided a basis for applications such as plasmonic sensor devices, waveguide couplers and modulators [3, 4, 5, 6]. Of all the methods of efficiently coupling a propagating SP mode directly to the optical far-field, the Otto geometry is the most non-invasive. It is well-known that the intrinsic SP mode properties are particularly sensitive to surface roughness and contamination of the metal surface — both of which significantly affect the SP's propagation speed, lifetime and resonant field enhancement. The latter property is valuable in boosting the yields of nonlinear frequency conversion, such as in harmonic generation and the sensing of molecular vibrations via surface enhanced Raman scattering (SERS) [7]. Although these ideas have been widely tested using

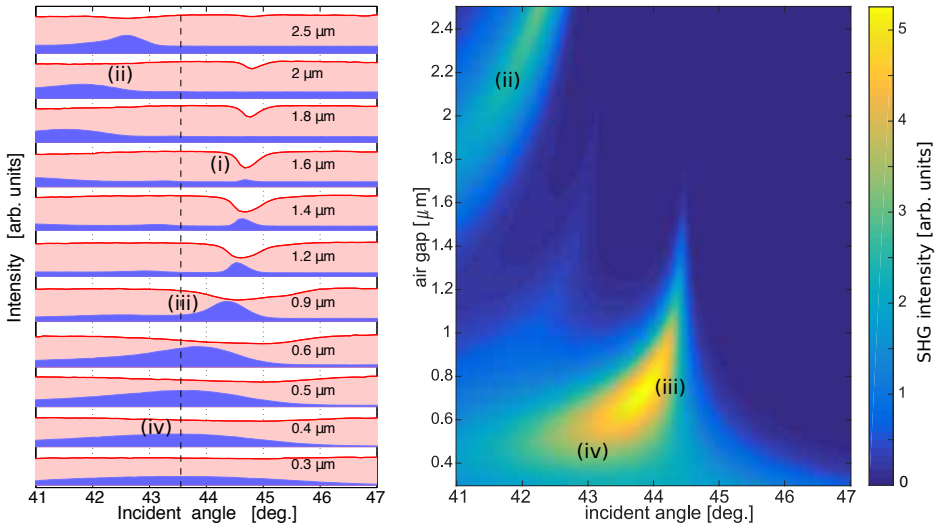



Figure 1: (a) Experimental data from the Otto geometry for varying air gaps. A Quartz prism was used for coupling and 200 nm of vapor deposited Au on BK7 glass as sample. Red is the reflected fundamental signal and blue the emitted second harmonic radiation, the dashed line represents the fundamental TIR angle. The excitation wavelength was 850 nm. (b) The correspondent calculation for the emitted second harmonic.

the competing technologies of grating coupling [8] and the Kretschmann-Raether geometry [9], it is the original Otto geometry that can give us access to the intrinsic material properties that lead

to long SP lifetimes and strong field enhancement. The Otto geometry is at an advantage because the surface of the material need not be structured as the coupling is achieved via evanescent fields, nor must it be prepared onto a transparent substrate in the form of a thin film; and furthermore, the coupling strength of the SP to the far-field is easily tuned.

In this contribution, we exploit the non-invasive nature of the Otto geometry to experimentally investigate the intrinsic nonlinear properties of the SP modes that propagate at the interface of bulk gold and the surrounding air. Applying a $k$-space analysis of second-harmonic generation (SHG), we observe a merger of the SP mode with a neighbouring dielectric-waveguide mode that can be tuned via the strength of coupling to the far-field. This hybridization behaviour — not readily visible in the data for ATR alone — thus highlights the value in examining the nonlinear frequency conversion of SP in the Otto geometry. These results are supported by a theoretical model based on the hydrodynamic description of the microscopic nonlinearity in the metal [10, 11].

The experimental results in Figure 1(a) show the reflected fundamental intensity and emitted SHG. A k-space spectrum over the relevant angular range was measured for different air gap spacings, while keeping all other parameters constant. Starting at an air gap of 2.5 $\mu$m and moving in, the linear coupling strength to the fundamental SP found a maximum (i) at 1.6 $\mu$m, while the lowest order Fabry-Pérot mode could be identified by its characteristic SHG peak (ii). Moving closer, the SP-related SHG (iii) improves at 0.9 $\mu$m, due to the better out-coupling efficiency for this wavelength. As the air gap is minimized still further, the absorption and SHG features in k-space broaden. Below 0.5 $\mu$m we observe the SP mode (as evidenced by its SHG peak) merge with the waveguide mode that lies exactly on the angle for total internal reflection. This evidence of strong coupling suggests that the photonic and plasmonic mode have hybridized (iv).

The results for SHG are supported by the theoretical model in Figure 1(b), which includes the peak characteristics and the mode hybridization. The combination of applying high-resolution nonlinear k-space spectroscopy to the non-invasive Otto geometry allows a highly sensitive analysis of supported modes and related resonances, especially for thin films and plasmonic structures. On this basis, other materials and waveguide structures can be investigated and characterized in terms of waveguide performance, coupling properties and mode lifetime.

**REFERENCES**


1. Otto, A., "Excitation of nonradiative surface plasma waves in silver by the method of frustrated total reflection." *Z. Physik* **216** (4), 398-410 (1968).
2. Kretschmann, E. and Raether, H., "Radiative decay of nonradiative surface plasmons excited by light", *Z. Physik* **23**a, 2135-2136 (1968).
3. Homola, J., Yee, S. S., and Gauglitz, G., "Surface plasmon resonance sensors: review." *Sensors and Actuators B: Chemical*, **54**(1), 3-15 (1999).
4. Ozbay, E. "Plasmonics: merging photonics and electronics at nanoscale dimensions." *Science* **311** (5758), 189-193 (2006).
5. Nikolajsen, T., Leosson, K., and Bozhevolnyi, S. I. "Surface plasmon polariton based modulators and switches operating at telecom wavelengths." *Applied Physics Letters*,**85**(24), 5833-5835 (2004).
6. Simon, H. J., Mitchell, D. E., and Watson, J. G., "Optical Second-Harmonic Generation with Surface Plasmons in Silver Films", *Phys. Rev. Lett.* **33**, 1531- 1534 (1974).
7. Kneipp, K., Wang, Y., Kneipp, H., Perelman, L. T., Itzkan, I., Dasari, R. R., and Feld, M. S., "Single molecule detection using surface-enhanced Raman scattering (SERS)." *Phys. Rev. Lett.* **78**(9), 1667- 1670 (1997).
8. López-Tejeira, F., Rodrigo, S. G., Martn-Moreno, L., García-Vidal, F. J., Devaux, E., Ebbesen, T. W., Krenn, J. R., Radko, I. P. ,Bozhevolnyi, S. I. , González, M. U., Dereux, A., and Weeber, J. C., "Efficient unidirectional nanoslit couplers for surface plasmons." *Nature Physics*, **3**(5), 324-328 (2007).
9. Grosse, N. B., Heckmann, J., and Woggon, U., "Nonlinear Plasmon-Photon Interaction Resolved by k-Space Spectroscopy", *Phys. Rev. Lett.* **108**, 136802 (2012).
10. Sipe, J. E., So, V. C. Y., Fukui, M., and Stegeman, G. I., "Analysis of second-harmonic generation at metal surfaces", *Phys. Rev. B* **21**, 4389- 4402 (1980).
11. Wang, F. X., Rodrguez, F. J., Albers, W. M., Ahorinta, R., Sipe, J. E., and Kauranen, M., "Surface and bulk contributions to the second-order nonlinear optical response of a gold film." *Phys. Rev. B* **80**(23), 233402 (2009).

# Hole arrays in metal film as distributed feedback plasmonic laser and its dynamics

**A. A. Pavlov[1,2*], I. V. Zabkov[1,3], and V. V. Klimov[1,2,4]**

[1]Dukhov Research Institute of Automatics (VNIIA), Moscow, Russia

[2]P.N. Lebedev Physical Institute, Russian Academy of Sciences, Moscow, Russia

[3]Moscow Institute of Physics and Technology (State University), Dolgoprudny, Russia

[4]National Research Nuclear University MEPhI, Moscow, Russia

[*]corresponding author: dron.pavlov@gmail.com

**Abstract**-In this work we have studied lasing characteristics of the array of nanoholes in silver film covered with gain medium. We have analyzed mode structure of the system with and without pump and determined lasing frequencies and non-interacting lasing thresholds for all modes. Varying angle and wavelength of pump field, we have found optimal pump conditions for lasing. Subsequent numerical time domain modeling of laser generation have showed that predicted values for the first lasing mode threshold are accurate.

The prospects that are opened by the emerging field of plasmonics allow one to create nanolocalized sources of coherent emission – so-called spasers (for surface plasmon amplification of stimulated emission of radiation) [1]. One approach to this is in utilizing strong coupling between gain molecules and localized surface plasmon resonances of single structures due to the high field enhancement in them. Another way is to use gratings formed of either plasmonic particles arranged in periodic arrays [2,3] or arrays of holes (or slits) perforated in the metallic film [4,5]. While there are several papers that demonstrated lasing in the systems such as the latter, optimal parameters for low-threshold lasing are yet to be determined. In this work we develop a method for fast determination of lasing threshold and lasing frequency values and apply it for the analysis of the system described in Figure 1.

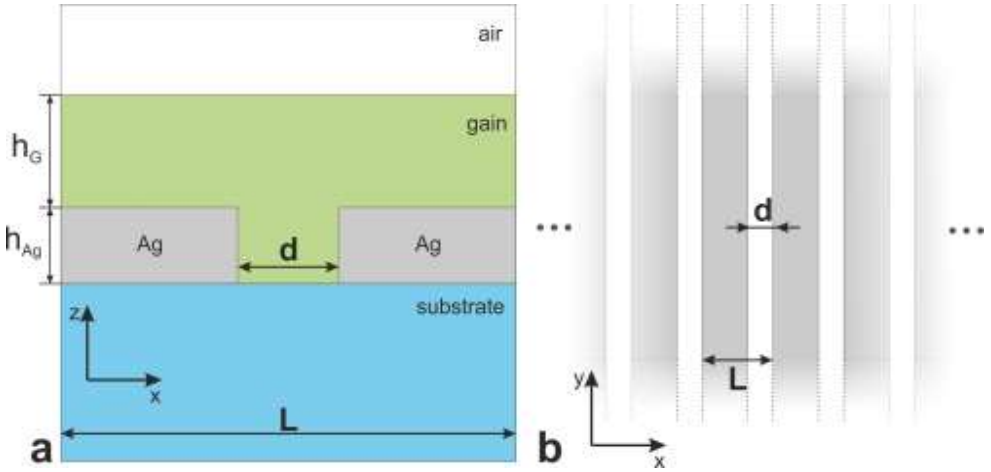



**Figure 1** Desing of the system under consideration: a) side view of the unit cell of the structure (*xz*-plane), b) top view (*xy*-plane). *d* is slit width, *L* is array period, $h_{Ag}$, $h_G$ is silver film and gain medium thicknesses, respectively.

First step of the algorithm is to obtain mode structure of the system and determine the modes that allow lasing. In our system, this mode is surface plasmon localized near the metal surface adjacent to the gain medium, while surface plasmon localized near the opposite metal interface has too weak coupling to the molecules that constitute gain medium. On the next step, we consider pump field impinging on the system from the air half-space, while gain medium is modelled as a saturating absorber. Then from the steady state solution for the pump field and the steady state form of Maxwell-Bloch equations, we calculate complex dielectric permittivity of gain medium and then we find eigenmodes and complex eigenfrequencies of such system. Iterating through the last steps one can find threshold value of the pump field intensity for which eigenfrequency will have zero imaginary part. As confirmed by the numerical modelling of the Maxwell-Bloch equations in time domain, this algorithm gives very accurate values of lasing frequencies and thresholds for the first mode that reaches threshold.

This algorithm is then used to find the optimal parameters for the laser geometry, pumping angle and wavelength. Particularly, we found that pumping at the angle corresponding to the excitation of the surface plasmon mode of the system is one order of magnitude more effective than at arbitrary angle that does not correspond to any mode.

**ACKNOWLEDGEMENTS**

The authors would like to thank the Advanced Research Foundation (7/004/2013-2018), the Russian Foundation for Basic Research (grants 14-02-00290, 15-52-52006) and the Presidium of the Russian Academy of Sciences for financial supports of the present work.

**REFERENCES**

1. J. Y. Suh, et al., “Plasmonic Bowtie Nanolaser Arrays,” *Nano Lett.*, Vol. 12, 5769–5774, 2012.
2. A. H. Schokker and A. F. Koenderink, “Lasing at the band edges of plasmonic lattices,” *PRB*, Vol. 90, 155452, 2014.
3. A. Yang, et al., “Real-time tunable lasing from plasmonic nanocavity arrays”, *Nat. Comm.*, Vol. 6, 2015.
4. F. van Beijnum, et al., “Surface Plasmon Lasing Observed in Metal Hole Arrays,” *PRL*, Vol. 110, 206802, 2013.
5. X. Meng, J. Liu, A. V. Kildishev, V. M. Shalaev, “Highly directional spaser array for the red wavelength region,” *Laser Photon. Rev.*, Vol. 8, No. 6, 2014.

# Probing the radiative and full electromagnetic local densities of states through electron energy loss spectroscopy and cathodoluminescence spectroscopy

**A. Losquin**[1*]**, and M. Kociak**[2]

[1] Department of Physics, Lund University, Lund, Sweden

[2]Laboratoire de Physiques des Solides, CNRS / Université Paris Sud, Orsay, France

[*]corresponding author: arthur.losquin@fysik.lth.se

**Abstract**-Electron Energy Loss Spectroscopy (EELS) and CathodoLuminescence spectroscopy (CL) have become popular to study the surface plasmon modes of metallic nanoparticles. By combining EELS and CL on single nanoobjects, we showed that EELS and CL signals differ. Whereas EELS measures a quantity close to the full ElectroMagnetic Local Density Of States (EMLDOS) projected along the electron trajectory, CL measures a quantity close to the radiative EMLDOS projected along the electron trajectory.

Electron Energy Loss Spectroscopy (EELS) and CathodoLuminescence spectroscopy (CL) map the surface plasmon modes of metallic nanoparticles at the nanometer scale [1]. Although they yield similar results, EELS and CL differ by nature. EELS measures the energy lost by fast electrons interacting with a sample whereas CL measures the energy of the light emitted from this interaction [2]. However, the consequence of this different nature has remained unexplored because combining EELS and CL on single nanoobjects could not be achieved.

We combined EELS and CL on single nanoobjects using a Scanning Transmission Electron Microscope [3]. We studied small gold triangular nanoprisms as a model system (Fig. 1a). We showed that CL only probes the dipolar mode, contrary to EELS that probes both the dipolar and quadrupolar modes. Furthermore, the dipolar mode resonates at slightly shifted resonances in EELS and CL (Fig. 1b). The magnitude of the shift relates to the mode damping.

Having demonstrated that EELS and CL signals differ, we showed that the full and radiative ElectroMagnetic Local Densities Of States (EMLDOS) differ similarly (Fig. 1c) [4]. Whereas EELS measures a quantity close to the full EMLDOS projected along the electron direction [5], CL measures a quantity close to the radiative EMLDOS projected along the electron direction [4]. Contrary to EELS, CL probes only the radiative modes, which are not necessarily dipolar for object sizes beyond the quasistatic limit. The ratio of the CL resonance to the EELS resonance quantifies the radiative weight of the mode damping. If the modes are damped and induce interfering radiation, CL resonant line shapes are shifted and asymmetric compared to EELS.

This work demonstrates the great interest of combining EELS and CL for plasmonics [3, 4].

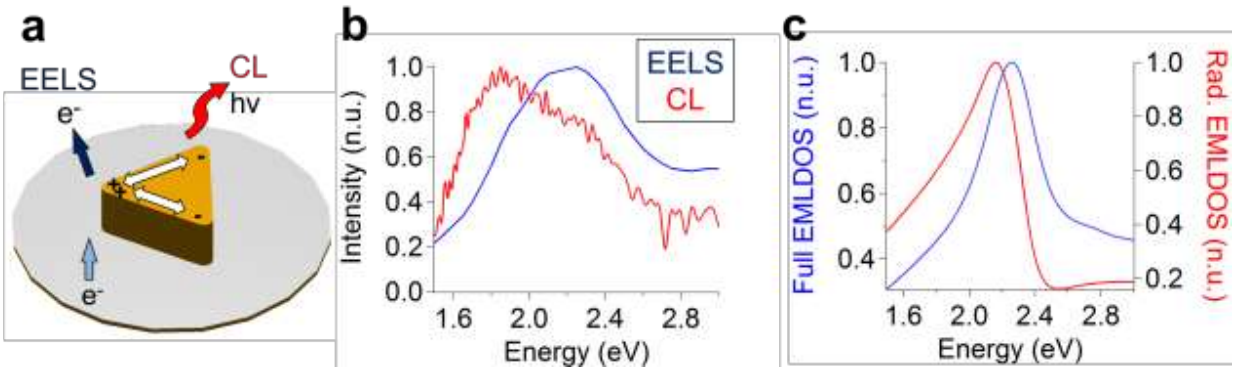



Fig. 1. a. Sketch of a combined EELS and CL experiment using a Scanning Transmission Electron Microscope. An electron probe is focused onto a gold nanoprism on a carbon substrate. The transmitted electrons are collected for EELS, while the emitted light is collected for CL. b. EELS (blue) and CL (red) spectra measured at the tip of a gold nanoprism. c. Full (blue) and radiative (red) EMLDOS spectra calculated at the tip of a similar gold nanoprism. As measured by EELS and CL, the radiative EMLDOS is redshifted compared to the full EMLDOS.

The research leading to these results has received funding from the European Union Seventh Framework Programme [No. FP7/2007-2013] under Grant Agreement No. n312483 (ESTEEM2).

**REFERENCES**

1. M. Kociak and O. Stéphan, Chem. Soc. Rev. **43**, 3865 (2014)
2. F. J. García de Abajo, Rev. Mod. Phys. **82**, 209 (2010)
3. A. Losquin et al., Nano Lett. **15,** 1229 (2015)
4. A. Losquin and M. Kociak, ACS Photonics **2,** 1619 (2015)
5. F. J. García de Abajo and M. Kociak, Phys. Rev. Lett. **100**, 106804 (2008)

# Surface plasmon generation by light scattering in terminated metallic slabs: interference effects between diffracted light and surface waves.

**L. A. Mayoral-Astorga, J. A. Gaspar-Armenta, and F. Ramos-Mendieta***
Departamento de Investigacion en Fisica, Universidad de Sonora,
Apartado Postal 5-088, Hermosillo, Sonora, 83190 Mexico
**corresponding author:* framos@cifus.uson.mx

**Abstract**- We use the Finite Difference Time Domain (FDTD) method to study the scattering of light at the edge of a metallic terminated slab. The first result is the generation of a surface plasmon polariton. Additionally, interference effects between the surface wave and the diffracted fields are observed. We report the formation of a series of low field intensity spots in the air region above the surface that result from this interference mechanism. In our numerical study the incident light is generated by a point source placed far away from the edge; the metal is simulated with the Drude model.

The surface plasmon polariton (SPP) is an excitation that propagates along a metallic-dielectric interface with exponentially decay electromagnetic fields on either interface side. For *plasmonics* and nanotechnology applications the SPPs have great potentialities for the miniaturization of optoelectronic devices for carrying information.[1] For fundamental physics, for instance, the SPPs have an important role in the light enhancement transmission.[2]

In plasmonics circuitry the way of excitation of a SPP results of crucial interest. Traditional optical methods involving prisms or grids could be inconvenient due to the spatial dimensions of the new nano-devices. For these reason it is important to revisit the alternative mechanisms to excite SPPs. In this paper we show that a SPP can be excited directly by light which is incident on the corner of a terminated metallic slab. We shall report some relevant characteristics of the excited SPP. The main new result is the interference phenomenon between the diffracted waves (oscillatory waves) and the surface wave (of evanescent fields). Notice that along the metallic surface, beyond the corner, both waves oscillate in the direction parallel to the surface, thus wave interference is possible.

In our numerical simulation we send an electromagnetic wave in direction of the slab direction using the next point source of TM waves

$$H_z(x_0, y_0, t) = e^{-\frac{1}{2}\left(\frac{t-t_0}{\sigma_t}\right)} \sin(\omega_0 t), \qquad (1)$$

where $y_0$ and $x_0$ are conveniently chosen to ensure that the incident waveform at the metallic edge approaches to a plane wave. The additional parameters $\sigma_t$, $t_0$ and $\omega_0$ are selected to guarantee sufficient temporal evolution of

the excitation. Then by Fourier transform we obtain the wave vector spectrum along the surface; this spectrum shows that a surface plasmon polariton is excited. In Fig.1 we present some of our main results. Fig. 1(a) shows dark spots (regions of low field amplitude) produced by interference between the surface plasmon polariton and the grazing diffracted waves.

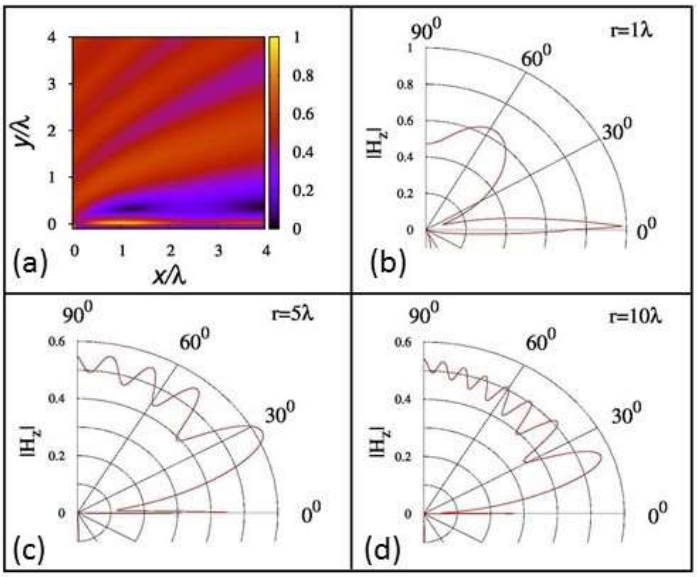



Figure 1

Note that the field intensity is high at the surface; it corresponds to the excited SPP. Then in Figures 1 (b)-(d) we show lobules of field amplitude in the first quadrant (above the metallic slab); the amplitude of the surface plasmon (the peak at 0°) decays with the distance, but it remains still excited at distances of the order of 10 $\lambda$.

In this presentation we give additional qualitative and quantitative characteristics of the excited SPP. In advance we can say that it is not an ordinary SPP because it appears modulated by the grazing diffracted fields.

**Acknowledgements**, This work was supported by PRODEP Mexico. LAMA thanks CONACYT Mexico for financial support.

**REFERENCES**

1. S. I. Bozhevolnyi, V. S. Volkov, E. Devaux, J. Y. Laluet and T. W. Ebbesen, "Channel plasmon subwavelength waveguide components including interferometers and ring resonators," *Nature* **440**, 508 (2006)

2. Ebbesen, T. W., Lezec, H. J., Ghaemi, H. F. , Thio, T. and Wolff, P. A., "Extraordinary optical transmission through sub-wavelength hole arrays," *Nature* **391**, 667 (1998)

# Theory and Experiment on Coherent Nanoscopic Light-sources: Spasers vs. Nano-Lasers

**G. Kewes[1], K. Herrmann[1], A. Ott[2], R. Rodriguez-Oliveros[1], A. Kuhlicke[1], Y. Lu[2], M. Ballauff[2], K. Busch[1,3], and O. Benson[1]**

[1]Institut für Physik, Humboldt-Universität zu Berlin, Germany
[2]Helmholtz-Zentrum Berlin für Materialien und Energie GmbH (HZB), Berlin, Germany
[3]Max-Born Institut, Berlin, Germany
gkewes@physik.hu-berlin.de

**Abstract**— We present experimental as well as theoretical results, which clearly demonstrate that particle-based spasers feature a much poorer performance than expected so far. On the other hand, we suggest that only a "renaissance" of low loss dielectrics as resonator material (with high index of refraction) will enable efficient nano-lasers.

Surface plasmons lasers (spasers) [1] have been considered as viable ultra-small sources of coherent near-fields with a vast number of potential new applications. Especially the fully nanoscopic version of a spaser, utilizing metal nano-particles as resonators is of interest due to its potential for ultra-compact packing on chip or in 3D arrangements. In 2009 laser-like features from 14 nm gold spheres with a dye-doped coating were observed [2]. In 2013 similar results were shown for gold nano-rods embedded in dye-doped polymers [3]. Here, we critically evaluate so far reported results on both an experimental and on a theoretical basis.

**Experiments**: Core-shell spasers were chemically synthesized or metal nano-particles were coated with dye-doped polymer films. Various excitation schemes were tested, yielding laser or laser-like signatures. All of them, however, were later identified to stem from sources other than spasing. From these findings we can conclude, that no unambiguous proof of particle-based spasing is possible in ensemble measurements unless "parasitic" laser effects can be ruled out with certainty.

**Theory**: A semi-classical model for spherical core-shell spasers was developed [4]: Within this model, we drop the widely used quasi-static approximation of the electromagnetic field in favor of fully electromagnetic Mie theory. This allows for precise incorporation of realistic gain relaxation rates (quenching and cavity-to-gain coupling) that so far have only been estimated (and massively underestimated) in spaser theory.
The model unravels multiple severe limitations that exist all over the VIS concerning the large pump threshold, the requirement of a medium with unrealistically large gain and unavoidable heat production. These limits basically result from the poor quality-factors and the surprisingly poor $\beta$-factors (ratio of gain-to-cavity coupling to the overall decay rate) in spasers.

The insights gained for spasers yield clear advice on how to construct a feasible alternative: ultra-small fully dielectric lasers. Especially nano-cavities made from high index dielectrics with low losses hosting electric and magnetic resonances promise energy-efficient solutions. We propose that Si or GaP nano-resonators will be the basis for nano- or micro-laser devices in the future.

**ACKNOWLEDGMENT**

Support by the German Research Foundation (DFG via SFB 951) is gratefully acknowledged.

**REFERENCES**

1. Stockman, M. I., "The spaser as a nanoscale quantum generator and ultrafast amplifier," *Journal of Optics*, Vol. 12, 024004, 2004. , Nature 460, 1110 (2009).
2. Noginov, M. A., Zhu, G., Belgrave, A. M., Bakker, R., Shalaev, V. M., Narimanov, E. E., Stout, S., Herz, E., Suteewong, T., and Wiesner, U., "Demonstration of a spaser-based nanolaser," *Nature*, Vol. 460, 2009.
3. Meng, X., Kilidishev, A. V., Fujita, K., Tanaka, K., and Shalaev, V. M., "Wavelength-Tunable Spasing in the Visible," *Nano Letters*, Vol. 13, 4106, 2013.

4. Kewes, G., Rodriguez-Oliveiros, R., Hermann, K., Kuhlicke, A., Benson, O. and Busch, K., "Threshold Limitations of the spaser," *arXiv*.1408.7054, 2014.

# Exploring scattering phenomena at the nano-scale by angle- and polarization-resolved cathodoluminescence spectroscopy and imaging.

**V. Myroshnychenko**[1], **N. Nishio**[2], **J. Förstner**[1], **and N. Yamamoto**[2]

[1]Institute of Electrical Engineering, University of Paderborn, Germany
[2]Physics Department, Tokyo Institute of Technology, Japan
viktor.myroshnychenko@gmail.com

**Abstract**— We fabricate single and coupled gold triangular nanoprisms using electron beam lithography. Plasmon modes of these nanostructures are investigated using an angle- and polarization - resolved cathodoluminescence (CL) measurements performed in a scanning transmission electron microscope. We demonstrate that powerful combination of angle- and polarization - resolved CL provides insight into the nature of the plasmon modes in the nanostructures. Our results show that dark modes in bow-tie antennas can be efficiently excited by electron beam and detected by photon detection system. Our experiments are supported by numerical simulations.

Localized surface plasmon resonances of single and coupled plasmonic nanoparticles have been deeply investigated due to their major role in a wide range of application such as enhanced fluorescence and surface-enhanced Raman scattering [1]. Experimental access to the electromagnetic field distribution associated with plasmon excitations in metal nanoparticles, with a high energy and spatial resolution, is of critical importance. In this work, we use cathodoluminescence, based on electron-induced radiation emission produced by interaction with an electron beam, to study plasmon excitations in sub-wavelength single and coupled gold triangular nanoparticles [2, 3, 4, 5, 6].

The nanoparticles are patterned onto $SiO_2$ using high-resolution electron-beam lithography. The CL spectra, beam-scan images, and plasmon maps are obtained on various configuration using an angle- and polarization-resolved cathodoluminescence (CL) measurements performed in a scanning transmission electron microscope (STEM) equipped with a parabolic mirror placed above the specimen (see Fig. 1 (b)). A polarizer selects emitted *s*- or *p*-polarized light. For an angle-resolved measurement, the light emitted from the sample is collected by a charge-coupled device (CCD) detector, with the direction specified by angles $\theta$ and $\phi$ selected through a movable mask.

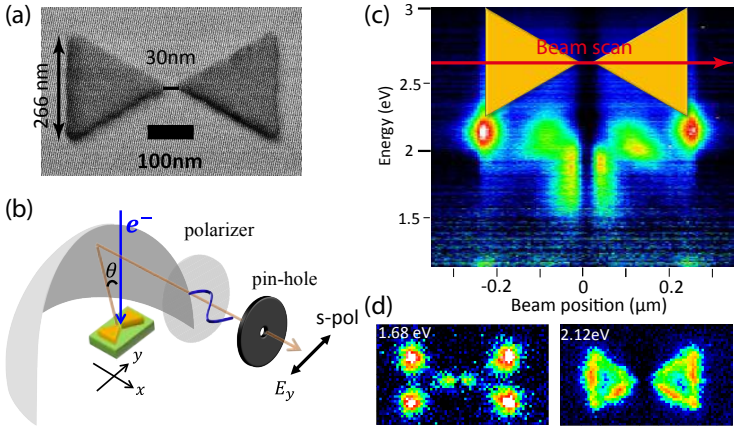



Figure 1: (a) TEM image of the lithographically fabricated bow-tie nanoantenna. (b) Geometry of the angle- and polarization-resolved measurement of radiation using a parabolic mirror. (c) Position and energy dependence of the CL intensity originating from a gold bowtie nanoantenna. (d) Plasmon maps obtained at resonance energies.

For example, Figure 1 (c) shows the position and energy dependence of the CL intensity originating from a gold bow-tie nanoantenna and corresponding plasmon maps at different energies

(Fig. 1(d)). We provide a theoretical description of this technique and numerical modeling of the spectral features and spatially resolved maps of nanoparticle plasmon modes by using boundary element method simulations.

In conclusion, surface plasmon modes of individual and coupled nanoprisms were investigated using electron-beam excitations in a STEM with CL. We demonstrate that combination of angle- and polarization-resolved CL provides the powerful technique allowing us to detect and identify a rich variety of plasmonic modes. In particular, we observed that the dark plasmon mode of gold bow-tie antennas can be efficiently excited by electron beam and detected by photon detection system. Our experimental results are in a good agreement with boundary element method simulations.

**ACKNOWLEDGMENT**

This work has been supported by the Deutsche Forschungsgemeinschaft (DFG) via TRR142.

**REFERENCES**

1. Halas, N. J., S. Lal, W-S. Chang, S. Link and P. Nordlander, "Plasmons in Strongly Coupled Metallic Nanostructures," *Chem. Rev.*, Vol. 111, 3913-3961, 2011.
2. García de Abajo, F. J., "Optical excitations in electron microscopy," *Rev. Mod. Phys.*, Vol. 82, 209–275, 2010.
3. Gómez-Medina, R., N. Yamamoto, M. Nakano and F. J. García de Abajo, "Mapping plasmons in nanoantennas via cathodoluminescence," *New J. Phys.*, Vol. 10, 105009, 2008.
4. Denisyuk A. I., G. Adamo, K. F. MacDonald, J. Edgar, M. D. Arnold, V. Myroshnychenko, M. J. Ford, F. J. García de Abajo and N. I. Zheludev, "Transmitting Hertzian optical nanoantenna with free-electron feed," *Nano Lett.*, Vol. 10, 3250–3252, 2010.
5. Losquin, A., L. F. Zagonel, V. Myroshnychenko, B. Rodríguez-Gonzalez, M. Tencé, L. Scarabelli, J. Förstner, L. M. Liz-Marzán, F. J. García de Abajo, O. Stéphan, and M. Kociak, "Unveiling Nanometer Scale Extinction and Scattering Phenomena through Combined Electron Energy Loss Spectroscopy and Cathodoluminescence Measurements," *Nano Lett.*, Vol. 15, 12291237, 2015.
6. Fung, K. H., A. Kumar and N. X. Fang, "Electron-photon scattering mediated by localized plasmons: A quantitative analysis by eigen-response theory," *Phys. Rev. B*, Vol. 89, 045408, 2014.

# Metal-insulator-metal plasmonic sensor for high sensing sensitivity

**Siham Refki [1, 2*], Shinji Hayashi[1, 3], Zouheir Sekkat[1, 2, 4], Hidekazu Ishitobi[4, 5] and Yasushi Inouye[4, 5].**

[1] Optics and Photonics Center, (MAScIR), Rabat 10100, Morocco
[2] Faculty of Sciences, University Mohammed V, Rabat 10010, Morocco
[3]Graduate School of Engineering, Kobe University, Kobe 657-8501, Japan
[4]Graduate School of Engineering, Osaka University, Osaka 585-0871, Japan
[5]Graduate School of Frontier Biosciences, Osaka University, Osaka 585-0871, Japan

[*] s.refki@mascir.com

**Abstract**

We propose a metal-insulator-metal (MIM) structure consisting of a thick insulator layer sandwiched with metal layers. This structure allows to couple surface-plasmon polaritons (SPP). Results of reflectivity calculations clearly show very sharp resonances attributed to the SPP mode compared to a conventional SPR, which may find potential applications in sensing problems.

Optical biosensors based on surface plasmon resonance (SPR) have attracted increasing attention over the past three decades. In SPR sensors, a single metal layer is commonly used, but the resolution is limited because of broad resonances.[1)] in metal-insulator-metal (MIM) structures, coupling between surface plasmon polaritons (SPPs) can be achieved and a sharp resonance can be expected.

In the present work, we propose a MIM structure consisting of a thick insulator layer sandwiched with metal layers[2)]. Theoretical results of the angle-scan ATR spectrum show two resonances: the first one is a sharp resonance corresponding to a SPP propagating along the Au/sensing medium interface modified by the MIM structures. The second one is a broad resonance which corresponds to a symmetric SPP arising from coupling between two SPP modes in the MIM structure.

Estimation of the sensitivity with intensity modulation indicates that the Figure of Merit of the MIM structure is six times larger than that of conventional SPR.

**REFERENCES**

1. Hayashi.S, Nesterenko. D. V, and Sekkat.Z, “Fano resonance and plasmon-induced transparency in waveguide-coupled surface plasmon resonance sensors" Physics Express, 8, 022201 ,2015.
2. Kyeong.S. L, Ju Myeong .S, DaeY. J, Taek .S. L and Won.M. K, “Resolution Enhancement in Surface Plasmon Resonance Sensor Based on Waveguide Coupled Mode by Combining a Bimetallic Approach” Sensors, 10, 11390-11399,2010.

# Metallic nanocylinder metasurfaces for filtering and reflecting properties in the visible spectrum

**H. Bertin[1*], Y. Brûlé[2], G. Demésy[2], A.-L. Fehrembach[2], B. Gralak[2], E. Popov[2], G. Tayeb[2], D. Barat[3], P. Gogol[1], V. Yam[1] and B. Dagens[1]**

[1]IEF, CNRS, Univ Paris-Sud, Université Paris-Saclay, 91405 Orsay, France

[2]Institut Fresnel, UMR 7249, CNRS, Aix-Marseille Université, Centrale Marseille, 13013 Marseille, France

[3]PSA Peugeot Citroën, Direction Scientifique, Centre technique de Vélizy, route de Gisy, F-78140 Vélizy-Villacoublay, France

[*]corresponding author: herve.bertin@u-psud.fr

**Abstract**-Plasmonic resonance in an array of silver nanoparticles is used to create a transparent reflective filter in the visible range. Transmittance and reflectance are measured from 400 to 900 nm.

Many applications in building or automotive domains require window glasses with specific optical properties which are usually obtained by surface treatments like thin layer stack deposition. But additional "on demand" properties can be obtained thanks to plasmonic resonances in nanostructures. Plasmonic metasurfaces allow for control and spatial modulation of the optical properties by playing on nanostructure surface density, size and shape [1,2].

In this article, the challenge was to obtain with few manufacturing steps increased reflectivity at two distinct wavelength and transparency in the whole visible spectrum for two 45° incident polarization. The presented samples are 1.2x0.6 mm arrays of silver cylindrical and elliptic nanoparticles on a glass (SiO2) substrate and encapsulated in PMMA, with different cross section ellipticity.

The dimensions were obtained by Finite Element Method (FEM) simulations [3] resulting in a square cell positioning of silver ellipses with typical dimension for major axis of 80 nm, minor axis of 60 nm, thickness of 30 nm and a spacing of 200 nm between cylinders. The 200 nm spacing is a compromise between the reflectivity and transmission over the whole visible range. This low spacing also avoids diffraction in the visible spectral range.

Silver nanoparticles are made by using e-beam lithography and lift-off technique using 30 nm of silver deposited by e-beam evaporation. On glass, compared to gold, silver has the advantage of not needing additional adherence layer (in Ti or Cr) that would otherwise increase absorption [4]. The last step of the process is to encapsulate the cylinders with 200 nm of PMMA.

The pictures in Fig.1(a,b,c,d) show the main resulting optical effects: the reflectivity wavelength is clearly tunable, with the nanocylinder sizes and incident light polarization. The transparency of the sample is correctly preserved. Transmission and reflection have been measured with a reflectometer at a 45 degrees incidence in p and s polarization for each case. Fig. 1e) shows a measured spectra for 93x70nm ellipse array, in this case a full

width at half maximum (FWHM) of 66-94 nm is obtained.

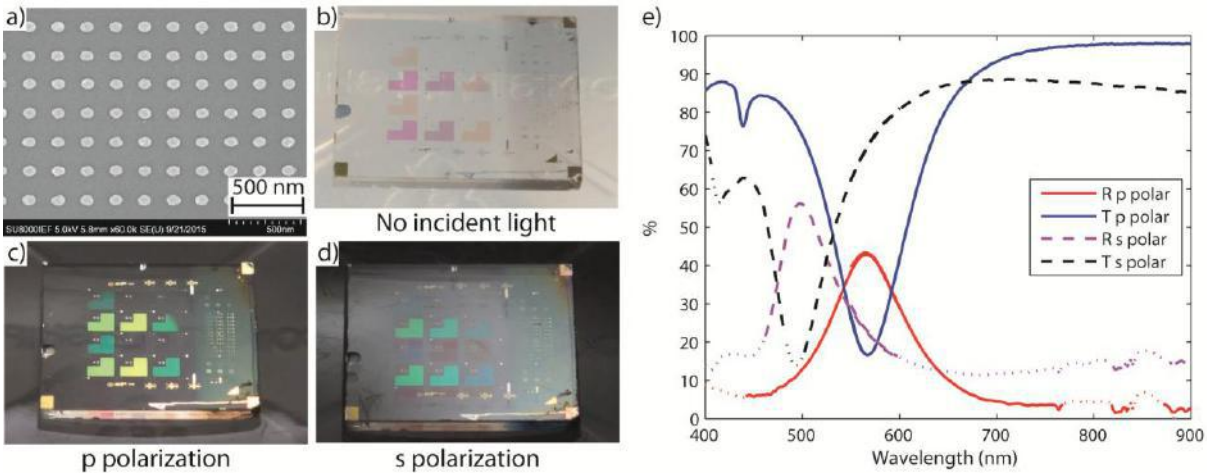



**Figure 1. a)** SEM image of 93x70 nm silver nanoparticles on glass. **b), c), d)** Multiple silver nanoparticles arrays with different ellipse dimensions for each axis (57 to 93 nm): **b)** with ambient illumination, **c)** with p polarized light, **d)** with s polarized light. **e)** Measured spectra normalized in air at two polarization (p and s) for ellipses of 93±3 nm and 70±3 nm (incident light parallel to the main axis), a thickness of 30 nm and a spacing of 201 ±1 nm.

To conclude we have shown the use plasmonic resonance in an array of silver nanocylinders as a mean to obtain transparent reflective mirrors in the visible range. Impact of dimension fluctuations on resonance wavelength is high, and the fabrication control must be accurate to reach precise values. In counterpart, the wavelength can be tuned on the whole visible spectrum. Further simulations will be made to evaluate the most tolerant design.

**Acknowledgements**, This work has been supported by the ANR funded project PLANISSIMO (ANR-12-NANO-0003) and by the french RENATECH network.

**REFERENCES**

1. Kumar K., Duan H., Hedge R. S., Koh S. C.W., Wei J. N., Yang J. K.W., "Printing colour at the optical diffraction limit", *Nature Nanotechnology*, vol. 7, , no. 9, pp557–561, Aug 2012.

2. Si G., Zhao Y., Lv J., Lu M., Wang F., Liu H., Xiang N., Huang T. J., Danner A.J., Teng J., Liu Y. J., "Reflective plasmonic color filters based on lithographically patterned silver nanorod arrays", *Nanoscale*, vol. 5, pp6243-6248, Apr 2013.

3. Brûlé Y., Demésy G., Fehrembach A.-L., Gralak B., Popov E., Tayeb G., Grangier M., Barat D., Bertin H., Gogol P., and Dagens B., "Design of metallic nanoparticle gratings for filtering properties in the visible spectrum", Applied Optics, vol. 54, issue 35, pp10359-10368, 2015

4. Barchiesi D., Macías D., Belmar-Letellier L., van Labeke D., Lamy de la Chapelle M., Toury T., Kremer E., Moreau L., Grosges T., "Plasmonics: influence of the intermediate (or stick) layer on the efficiency of sensors", *Appl. Phys. B*, vol.93, pp177-181, Aug. 2008

# Spin-controlled switching of near field excitation of optical nanoantennas

**Y. Lefier[1*], U. Fischer[2], R. Salut[1], M. Suarez[1], and T. Grosjean[1]**
[1]Femto-ST Institute, Besançon, France
[2]Interface physics group, WWU, Muenster, Germany
[*]corresponding author: yannick.lefier@femto-st.fr

**Abstract**- We demonstrate a new concept based on optical spin-orbit coupling for selectively addressing resonant nano-antennas by nanoscale plasmonic waveguiding. Two nanoantennas are placed at both ends of a bent subwavelength gap-plasmon waveguide avoiding spoiling background effects in nano-antenna addressing. Our aim is to reach new nano-optical functionalities in ultracompact optical devices such as remote (background free) excitation of nano-antennas and directional addressing in nano-antenna networks, etc.

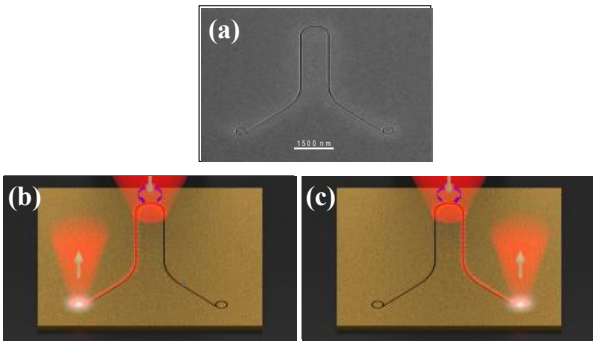



Figure 1 : MEB image (a) and illustrations (b) and (c) of the elaborated structure to show the concept of spin-controlled switching of remotely excitation of optical nanoantennas

Nanoantennas are nanoscopic structures that enhanced the local light-matter interaction [1,2]. A nanoantenna can act as a secondary source if it is directly excited by a (resonant) radiative light but can also be excited by near field interaction and emits radiative light (FIG.1). In a (radio-wave) classical view, this system can be seen as a generator + transmission line + antenna architecture (FIG.2).

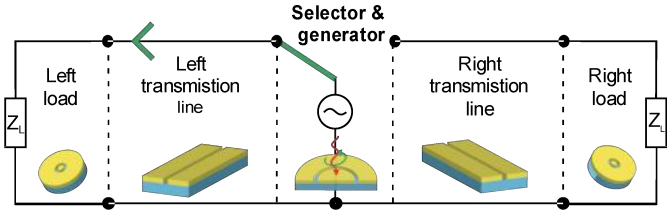



Figure 2 : Scheme of the whole chain of communication from the generator to the antenna. Here, the generator also plays the role of a selector to send the signal only in one transmission line

Subwavelength plasmonic waveguides show the unique ability of strongly localizing (down to the nanoscale) and guiding light [3]. We use here this waveguides to adress the energy from the generator to the nanoantennas. But this waveguides are intrinsically symmetric and here, we show that symmetry can be broken over a broad spectral bandwidth by using incident circularly polarized light, on the basis of a spin–orbital angular momentum transfer directly within waveguide bends (FIG.3). Such a phenomenon is a nanoscale manifestation of the optical the induced Pancharatnam-Berry phase [4,5] in polarized sensitive structures. We predict that up to 94% of the incoupled light is directed into a single propagation channel of a gap plasmon waveguide [5]. Unidirectional propagation of strongly localized optical energy, far the diffraction limit, becomes switchable by polarization, with no need of intermediate nanoantennas/scatterers as light directors (FIG.1). The experimental evidence of such a polarization-controlled adressing of resonant nanoantennas has been demonstrated by a far field experiment. As you can see on FIG.4, only one nanoantenna can be remotely excited thanks to the unidirectionnality process occurring in the waveguide.

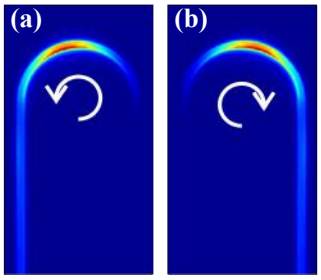



Figure 3 : Simulation of the electric intensity in the bend of a plasmon waveguide excited by left (a) and right (b) circularly polarized beam at the waveguide bend

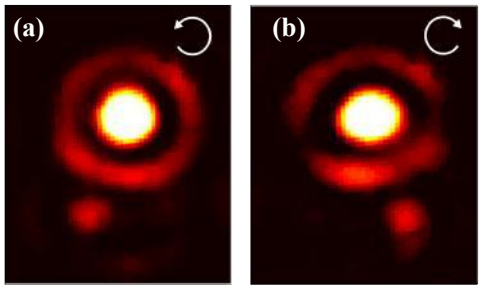



Figure 4 : Experimental far-field images of the light emitted by the structure illuminated in the bend by a left (a) and right (b) circularly polarized beam.

This study may open new perspectives in a large panel of scientific domains, such as nanophotonic circuitry, routing and sorting, optical nanosensing, and nano-optical trapping and manipulation.

This work is supported by the Labex ACTION.

**REFERENCES**

1. Mühlschlegel, P., Eisler, H.-J., Martin, O. J. F., Hecht, B.& Pohl, D. W. Resonant optical antennas. *Science* 308, 1607–1609 (2005).
2. Novotny, L. & Van Hulst, N. Antennas for light. *NaturePhotonics* 5, 83–90 (2011).
3. T. Ebbesen, et al, Physics Today **61**, 44 (2008)
4. Bliokh, K. Y.; Gorodetski, Y.; Kleiner, V. & Hasman, E.
5. Pancharatnam, S., Proceedings of the Indian Academy of Sciences, 1956
6. Lefier, Y. & Grosjean, Opt. Lett., 2015, 40, 2890-2893

# Tunable optomagnets in diamagnetic thin metal layers and plasmonic nano-antennas.

**Y. Lefier[1*], U. Fischer[2], and T. Grosjean[1]**
[1]Femto-ST Institute, Besançon, France
[2]Interface physics group, WWU, Muenster, Germany
[*]corresponding author: yannick.lefier@femto-st.fr

**Abstract**- We study the optical generation and tuning of highly confined DC magnetic fields directly in metals. We first predict the transfer of orbital angular moment of light to the free electrons of thin metal layers excited with tightly focused beams (leading to tiny loops of DC current). We also show that plasmonic nano-antennas can be magnetized by light and we study how the plasmonic resonances in play can enhance and control the optically induced magnetization.

The angular momentum of light [1] is a "quantity" that can be transferred to matter, leading to magnetization of the matter interacting with optical fields. The problem of optically-induced magnetization is often reduced to the inverse Faraday effect which involves the transfer of spin angular momentum of light to matter [2].

We focus here on the transfer of orbital angular momentum of light to free electrons in metals, leading to magnetization through the generation of tiny loops of DC currents. To this end, we use a hydrodynamic model of the free electron gas in metal [3] to predict and describe the non linear effects in light-matter interaction at the origin of DC electromotive forces.

We first show an optically-induced magnetization in diamagnetic thin metal layers under illumination with highly focused beams. By considering focused optical vortices carrying orbital angular momentum [4] or by exploiting the spin-orbit coupling in strongly focused circularly-polarized beams [5], we show the possibility to generate tunable nanoscale loops of DC current and quantify the resulting DC magnetic fields.

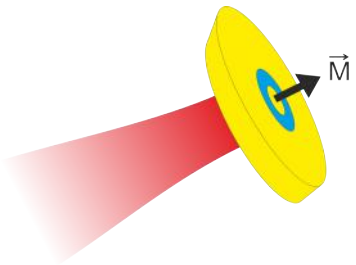



Figure 1 : Principle of optomagnets : when light is on, magnetization is induced. If light is off, magnetization disappear.

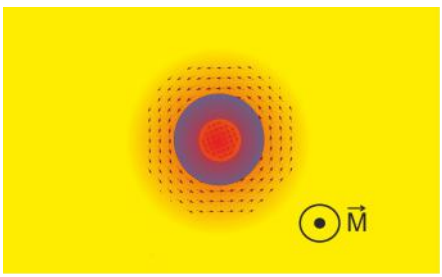



Figure 2 : The optical forces drives azimuthal steady currents leading to a magnetization orthogonal to the structure.

Optically induced magnetization has been also evidenced in arrays of subwavelength metallic holes [6]. The unprecedented control of light-matter interaction offered by plasmonic nano-antennas [7] offers promising perspectives in the generation of enhanced, highly localized and tunable optically-induced magnetization. We study here how spin-orbit coupling (on the basis of Pancharatnam Berry phase) [8] within plasmonic nano-antennas can induce nano-antenna magnetization.

This work open the way to the generation and control of nanoscale magnetization up to frequencies higher frequency than with magnetization controlled by the classical electrical way.

This work is supported by the Labex ACTION.

**REFERENCES**

1. Allen, L., Padgett, M. J., & Babiker, M. (1999). The orbital angular momentum of light. *Progress In Optics: Vol XXXIX*, *39*, 291-372.
2. Stanciu, C. D., Hansteen, F., Kimel, A. V., Kirilyuk, A., Tsukamoto, A., Itoh, A., & Rasing, T. (2007). All-optical magnetic recording with circularly polarized light. *Physical review letters*, *99*(4), 047601.
3. Shen, Y. R. (1984). Principles of nonlinear optics.
4. Allen, L., Beijersbergen, M. W., Spreeuw, R. J. C., & Woerdman, J. P. (1992). Orbital angular momentum of light and the transformation of Laguerre-Gaussian laser modes. *Physical Review A*, *45*(11), 8185.
5. Bliokh, K. Y.; Gorodetski, Y.; Kleiner, V. & Hasman, E.
6. Smolyaninov, I. I., Davis, C. C., Smolyaninova, V. N., Schaefer, D., Elliott, J., & Zayats, A. V. (2005). Plasmon-induced magnetization of metallic nanostructures. *Physical Review B*, *71*(3), 035425.
7. Novotny, L. & Van Hulst, N. Antennas for light. *NaturePhotonics* 5, 83–90 (2011).
8. Bekshaev, A., Bliokh, K. Y., & Soskin, M. (2011). *Journal of Optics*, *13*(5), 053001.

**Smith-Purcell radiation emission by non-periodic array nanostructures**

**J.R.M. Saavedra**[1], D. Castells[1], and F. Javier García de Abajo[1,2]

[1] ICFO Institut de Ciencies Fotoniques, The Barcelona Institute of Science and Technology, 08860 Castelldefels (Barcelona), Spain
[2]ICREA-Institució Catalana de Recerca i Estudis Avançats, Passeig Lluís Companys 23, 08010 Barcelona, Spain
jose.martinez@icfo.es

## Abstract

Smith-Purcell radiation (SPR) [1] arises when an electron moves parallel to a diffraction grating; the interaction between the electron's evanescent electric field and the grating's periodic corrugation makes the latter emit radiation along directions of constructive coherent superposition [2]. Its sensitivity to the electron beam's properties confers SPR a wide tenability range, from the X-rays to the THz regime. Additionally to this high tunability, SPR has also been used as a free-electron laser source [3], thanks to its superradiance capabilities [4]. However, all these appealing properties rely subtly on the grating's periodicity, which guarantees the constructive coherent superposition in the far-field regime.

In this work we study the possibility of SPR emission from non-periodic array structures: we analyze the necessary conditions for Smith-Purcell emission by arbitrary arrays which present long-range order, with focus on quasiperiodic and hyperuniform configurations, and compare them with the periodic array case. We conclude that SPR can appear not only in periodic structures but also in non-periodic structures as well, in the case the non-periodic structure presents long-range order properties.

## References

[1] S. J. Smith and E. M. Purcell, *Phys. Rev.* **92**, 1069 (1953).
[2] F. J. García de Abajo, *Rev. Mod. Phys.* **82**, 209 (2010).
[3] S. E. Korbly, A. S. Kesar, J. R. Sirigiri, and R. J. Temkin, *Phys. Rev. Lett.* **94**, 1 (2005).
[4] D. Li, K. Imasaki, Z. Yang, and G. S. Park, *Appl. Phys. Lett.* **88**, 201501 (2006).

## Figures

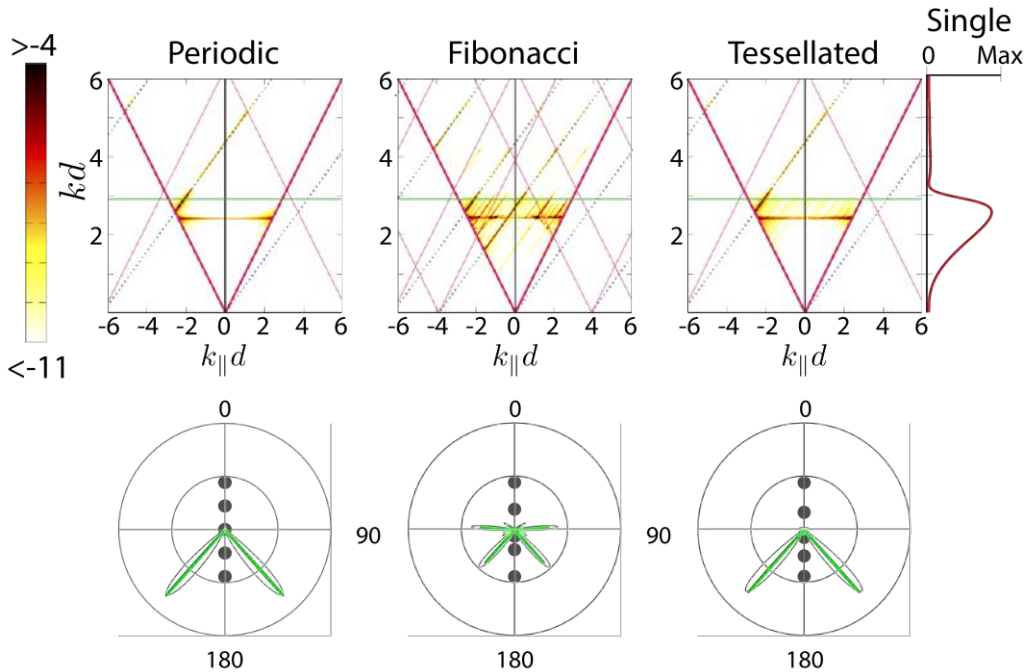



**Fig. 1.** Cathodoluminescence probability and angular emission profiles. Plots for the logarithm of the cathodoluminescence probability for 50-particles periodic, Fibonacci and tessellated arrays. The cathodoluminescence is normalized to the maximum cathodoluminescence probability for the periodic array. The polar plots correspond to the vertical sections of the contour plots (*i.e.*, fixed frequency), for 20- and 50-particles arrays. The electron beam has an impact parameter $b=75$ nm, and an energy $E=200$ keV ($v=0.7\,c$).

# Foerster resonance energy transfer in inhomogeneous non-dispersive nanophotonic environments

**M. Wubs[1*] and W. L. Vos[2]**

[1]Department of Photonics Engineering, Technical University of Denmark, Kgs. Lyngby, Denmark

[2]Complex Photonic Systems (COPS), MESA+, University of Twente, Enschede, The Netherlands

[*]corresponding author: mwubs@fotonik.dtu.dk

**Abstract**- A nondispersive inhomogeneous dielectric environment of a donor-acceptor pair of quantum emitters affects their Foerster resonance energy transfer (FRET) rate. We find that this rate does not depend on the emission frequency and hence not on the local optical density of states (LDOS) at that frequency, but that it can be expressed as a broad frequency integral over the optical LDOS. Our numerical results illustrate that even with the broadband LDOS it is hard to control the FRET rate.

There is currently an ongoing debate in Nanophotonics whether the famous Förster resonant energy transfer (FRET) rate between a donor and an acceptor depends on the local radiative density of states (LDOS): no [1] or yes [2]. Motivated by the debate we have initiated a study of an exactly solvable analytic model with essential features of nanophotonic energy transfer. Our model has a pair of ideal dipole emitters –donor and acceptor – that exhibit energy transfer (and spontaneous emission) near an ideal mirror, similar to the archetypal nanophotonic "Drexhage" geometry. The mirror is described by a dielectric planar scatterer, whose T matrix and dyadic Green functions are exactly known from scattering theory, even for vectorial Maxwell waves [3, 4].

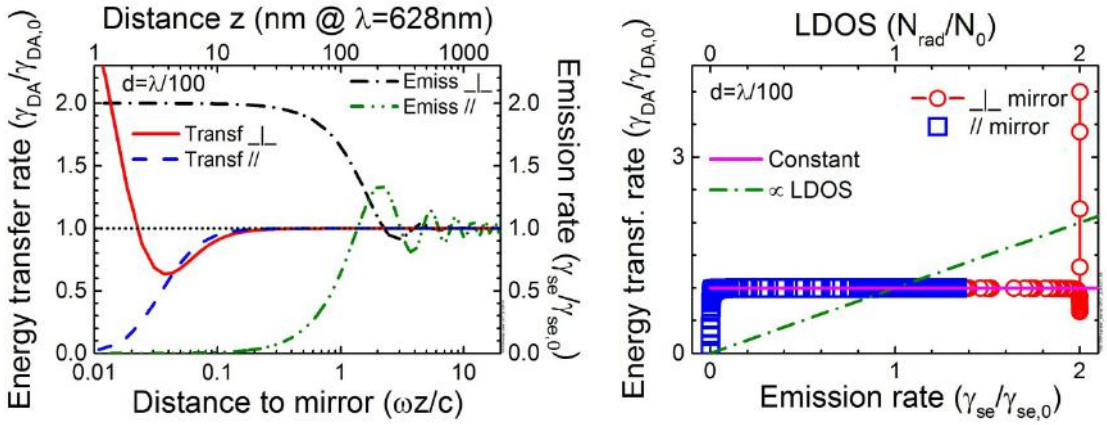



**Fig. 1** (Color) Left: Energy transfer and spontaneous emission rates (both scaled to free space) vs reduced distance to the mirror. Top abscissa shows distance in real units for a dipole resonance at wavelength $\lambda$=628 nm. Right: Scaled energy transfer rate vs. emission rate (bottom) and LDOS (top) for dipoles oriented perpendicular (red) or parallel (blue) to the mirror. The magenta line is constant at 1, the green dashed-dotted line shows a proportionality to the LDOS. Both panels are for donor-acceptor distance $d=\lambda/100$ (6.28 nm).

Fig. 1 (left) shows that the spontaneous emission rate reveals “Drexhage” oscillations versus distance to the mirror, with characteristic length scales of the order of the wavelength. The energy transfer rate also depends on distance to the mirror, yet at length scales up to about the donor-acceptor distance (d=λ/100), in other words 10-100 times smaller than the wavelength. Fig. 1 (right) is a parametric plot of energy transfer rate versus spontaneous emission rate and LDOS. Clearly, there is no correlation between FRET rate and LDOS: the FRET rate is constant and independent of LDOS over nearly the whole range. Deviations from 1 occur only when the dipoles are very close to the mirror (*cf.* left panel.) where the LDOS is nearly constant.

Our analytic model allows us to dissect arguments for these observations. To this end, we have derived a relation between the FRET rate and the LDOS. It appears that the LDOS is integrated over a huge frequency bandwidth, that extends from zero frequency ("DC") to about 10 times the emitter's resonance frequency, typically corresponding to the vacuum-ultraviolet (“VUV”). Remarkably, the contribution of the LDOS-integral to the FRET rate is small (< 7%). Thus FRET rates are in general hardly controlled by the LDOS in a realistic nanophotonic medium that is transparent up to the UV. The main controlling factor of FRET is the (quasi)static dipole-dipole interaction between donor and acceptor. Our analytical expressions yield transfer rates for an illustrative emission wavelength λ = 628 nm, that reveals typical nm-distances relevant to experiments (Fig. 1 (left), top abscissa).

## REFERENCES


1. E.g.: M.J.A. de Dood, J. Knoester, A. Tip, and A. Polman, *Phys. Rev. B*, Vol. 71, 115102, 2005; C. Blum, N. Zijlstra, A Lagendijk, M. Wubs, A.P. Mosk, V. Subramaniam, and W.L. Vos, *Phys. Rev. Lett.*, Vol. 109, 203601, 2012; F.T. Rabouw, S. den Hartog, T. Senden, and A. Meijerink, *Nat. Commun.*, Vol. 5, 3610, 2014.
2. E.g.: P. Andrew and W.L. Barnes, *Science*, *Vol.* 290, 785, 2000; T. Nakamura, M. Fujii, K. Imakita, and S. Hayashi, *Phys. Rev. B*, Vol. 72, 235412, 2005; P. Ghenuche, J. de Torres, S. Babu Moparthi, V. Grigoriev, and J. Wenger, *Nano Lett.*, Vol. 14, 4707 (2014).
3. M. Wubs, L.G. Suttorp, and A. Lagendijk, *Phys. Rev. E,* Vol. 69, 016616, 2004.
4. H.T. Dung, L. Knöll, and D.-G. Welsch, *Phys. Rev. A*, Vol. 65, 043813, 2002.

# Optical Multiple Bistability in Metal-Insulator-Metal Plasmonic Waveguides Side-coupled with Twin Resonators

**Ruei-Cheng Shiu[1], Yung-Chiang Lan[2], and Guang-Yu Guo[1*]**

[1]Department of Physics, National Taiwan University, Taipei 10617, Taiwan

[2] Department of Photonics, National Cheng Kung University, Tainan 701, Taiwan

[*]corresponding author: gyguo@phys.ntu.edu.tw

**Abstract**- We investigate the resonant transmissions surface plasmons that propagate in a metal-insulator-metal (MIM) waveguide side-coupled to two MIM racetrack resonators in which optical third-order nonlinear material is filled, by the coupling mode analyses and finite-difference time-domain simulations. We find the multiple bistabilities and the hysteresis phenomena in the transmission coefficient as the input intensity varies. Furthermore, the mode conversion between the bistable states can be controlled by varying the input-gate intensity with a short switching time of about 333 fs.

Nonlinear and switchable metamaterials, two kinds of the emergent materials of great interest [1], have widely been applied in nano-devices such as optical switches, rewritable memories, and logic operators. Metal-insulator-metal (MIM) plasmonic waveguides are a fundamental structure for surface plasmon polariton propagation, and provide low-loss propagation in a wide range of frequency. Therefore, several investigations based on MIM plasmonic waveguides to realize bistable effect in switchable systems with a nonlinear optical material have been reported recently [1-4]. In this paper, we build up a structure composed of a MIM plasmonic waveguide and two racetracks filled with optical Kerr nonlinear material to realize the multi-bistable effect. Such property may have valuable applications in multi-switches, optical logic operations.

We consider two racetrack resonators side-coupled to a silver MIM plasmonic waveguide as shown as Fig. 1. The resonators are filled with a Kerr nonlinear material, whose relative permittivity ($\varepsilon_d$) depends on the local intensity of electric field $|E|^2$: $\varepsilon_d = \varepsilon_0 + \chi^{(3)}|E|^2$, where $\varepsilon_0$ and $\chi^{(3)}$ are linear relative permittivity and third-order nonlinear susceptibility. In our simulations, the Drude model with the plasma frequency ($\omega_p$) and electron collision frequency ($\gamma_d$) set to $1.255\times10^{16}$ and $0.68\times10^{14}$, is used to describe the dielectric response of Ag, i.e., the relative permittivity of Ag is given by $\varepsilon_{ag}(\omega) = 1 - \omega_p^2 / (\omega^2 - 2i\omega\gamma_d)$. A TM-polarized plane wave (input-signal), of which the magnetic field is perpendicular to the *x*-*y* plane, is incident onto the waveguide from one end (Fig. 1), and the wavelength is 1540 nm.

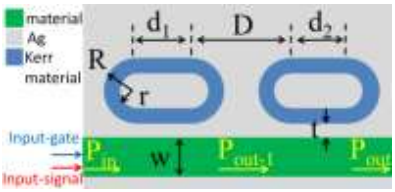



**Fig. 1:** Illustration of our proposed plasmonic waveguide.

First of all, we find that the eigen-wavelength of the first and second resonators are 1506 nm and 1495 nm respectively, as shown in Fig. 2(a). In addition, such structure has a strong resonance, $Q_1 = Q_2 = 72$, in the nonlinear

resonators at the signal wavelength, which can enhance the nonlinear Kerr effect. As a result, we choose 1540 nm as the signal wavelength. Based on our FDTD simulations, the multi-bistable effect is presented in Fig. 2(b), and the blue (green and red) line and points indicate that the power of the input-signal increases from 0 (decreases from 24 $MV^2/cm^2$ and decreases from 10 $MV^2/cm^2$). In Fig. 3(b), (i), (ii), (iii), and (iv) are the contours of $|H_z|^2$ normalized by the input power when the signal power increases to 7.8, 8.6, 12, and 16.4 $MV^2/cm^2$, respectively.

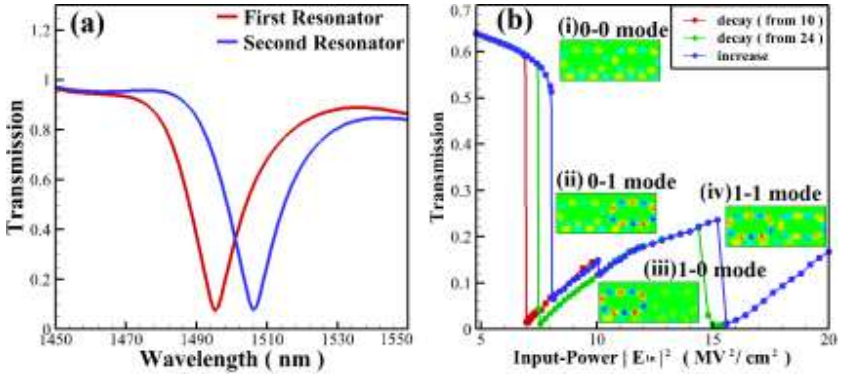



**Fig. 2:** (a) Transmission spectra of the first (red line) and second (blue line) racetrack resonators. (b) Transmission efficiency as a function of the power of input. The blue (green and red) line and points indicate that the power of input-signal increases from 0 (decreases from 24 $MV^2/cm^2$ and decreases from 10 $MV^2/cm^2$). (i), (ii), (iii), and (iv) are the contours of $|H_z|^2$ as $|E_{in}|^2$=7.8, 8.6, 12, and 16.4 $MV^2/cm^2$ on the blue line, respectively.

In this study, we have investigated the optical multi-bistable effect in two racetracks filled with an optical Kerr material on one side of a MIM plasmonic waveguides by two-dimensional FDTD simulations. Because of its multi-bistable effect, such system may find technological applications in multi-switches, optical logic operations, or even optical devices.

## REFERENCES


1. N. I. Zheludev, “The road ahead for metamarials,” Science, Vol. 328, 582–583, 2010.
2. Wang, X., Jiang, H., Chen, J., Wang, P., Lu, Y., and Ming, H., "Optical bistability effect in plasmonic racetrack resonator with high extinction ratio," Opt. Express, Vol. 19, 19415-19421, 2011.
3. Shen, Y. and Wang, G. P., "Optical bistability in metal gap waveguide nanocavities," Opt. Express, Vol. 16, 8421-8426, 2008.
4. Lin, X.-S., Yan, J.-H., Zheng, Y.-B., Wu, L.-J., and Lan, S., "Bistable switching in the lossy side-coupled plasmonic waveguide-cavity structures," Opt. Express, Vol. 19, 9594-9599, 2011.

# Plasmonic magneto-optical light modulator with the domain wall manipulation via giant magneto-electric effect

**N. E. Khokhlov[1,2*], A. E. Khramova[1], E. P. Nikolaeva[1], T. B. Kosykh[1], A. V. Nikolaev[1], A. P. Pyatakov[1], V. I. Belotelov[1,2]**

[1]Lomonosov Moscow State University, Moscow, Russia
[2]Russian Quantum Center, Skolkovo, Moscow reg., Russia
[*]corresponding author: n.e.khokhlov@yandex.ru

**Abstract**- We consider a new method of light modulation via the magneto-optical effects in magneto-plasmonic crystals. The modulation of the structure's magnetization in this case is induced by the electric field of the charged tip. So, the variations of the voltage on the needle produce the shift of a domain wall in the magnetic film due to the magnetoelectric effect and local magnetization switching. We demonstrated experimentally different regimes of modulation – linear and binary – with modulation depth up to 300% and more.

We consider a scheme of Faraday magneto-optical light modulator with magnetization control via magneto-electric effect. Our earlier researches of bismuth-substituted iron garnets films showed the giant domain wall (DW) movement in electric field of charged tip due to magneto-electric effect [1, 2]. The displacement of DW may be increased with in-plain magnetic field applied normally to the DWs. Observed displacements in this case are up to half of the domain's width (figure 1). The effect gives the opportunity to switch the film's magnetization on spatial scales 5-10 microns without inductive electromagnets.

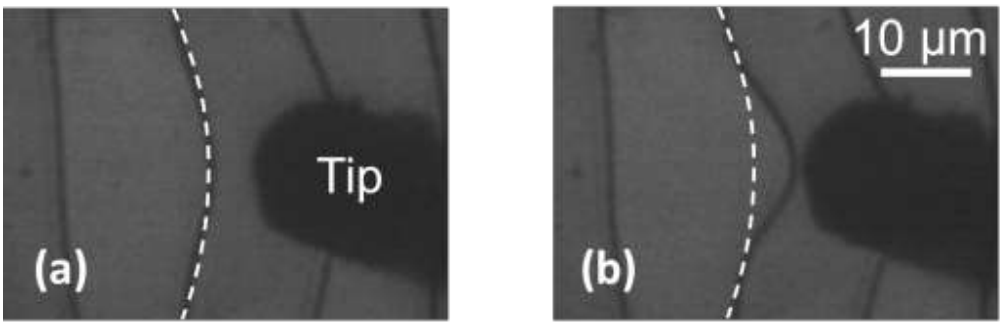
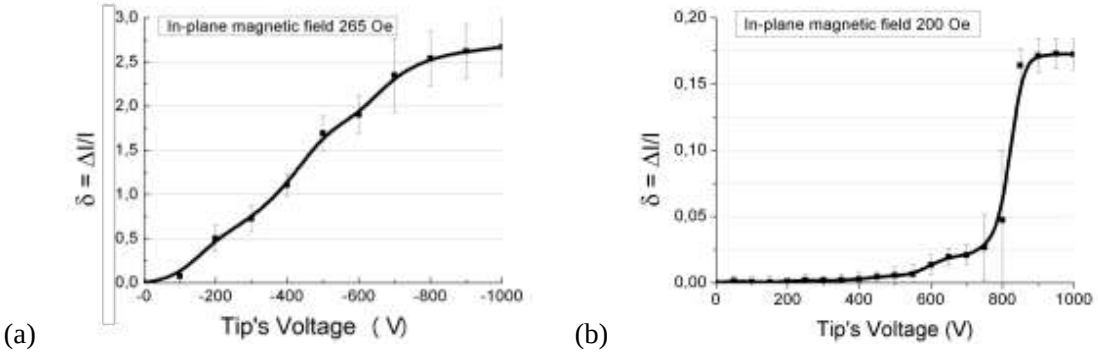



Figure 1. Domain wall displacement due to magneto-electric effect. Tip's voltage is (a) 0 V, (b) 1000 V.

Considering such giant DW displacement we proposed and realized the Faraday magneto-optical light modulator with local magnetization control. The ferromagnetic dielectric film with composition $(BiLu)_3(FeGa)_5O_{12}$ was deposed inside two electromagnets with fields orientation in-plane and normally to the film. The normal field is needed to tune the domains widths and to make they equal in non-zero in-plane field [1]. Laser beam passes through the polarizer – film – analyzer and its intensity is detected. Laser spot on the sample has the size about the domain width, 10-15 microns. So, two parts of the light spot pass through two domains with opposite magnetization orientations and obtain opposite polarization rotation due to Faraday effect. DW's displacement changes the ration between the parts of the

spot and the total light intensity passing through the analyzer, as a result.

Amplitude and sign of intensity modulation depends on spot size, angle between polarizer and analyzer, relative positions of the light spot, DW and tip. Varying the parameters we experimentally obtained the linear regime with the modulation depth $\delta$ = [I(V)-I(0)]/I(0) up to 300%, where V = 1000 V is tip's voltage (figure 2) [3].




(a) (b)

Figure 2. Intensity modulation $\delta$ = [I(V)-I(0)]/I(0) for transmitted light vs tip's voltage in different regimes of modulation: (a) linear regime with saturation, (b) binary regime.

We used the local magnetization changes for modulation the surface plasmon-polaritons (SPP) exited on the bottom side of the gold grating deposited on the magnetic film. As a result the sharp magneto-optical resonance near spectral feature of SPP is observed.

**Acknowledgements**. The work is supported by RFBR (grant 14-29-08216_ofi_m).

**REFERENCES**

1. Pyatakov A.P., Zvezdin A.K., "Magnetoelectric and multiferroic media", *Physics-Uspekhi*, Vol. 55, No 6, 557-581, 2012.
2. Pyatakov A.P., Sergeev A.S., Mikailzade F.A., Zvezdin A.K.," Spin flexoelectricity and chiral spinstructures in magnetic films", *Journal of Magnetism and Magnetic Materials*, Vol 383, 255-258, 2015.
3. Khokhlov N.E., Khramova A.E., Nikolaeva E.P., Kosykh T.B., Nikolaev A.V., Pyatakov A.P., Belotelov V.I., "Magneto-optical light modulator with the domain wall manipulation via giant magneto-electric effect" *Applied Physics Letters* (2016) *submitted*.

# Resonant nanophotonics with dielectric particles

**A. Devilez, X. Zambrana-Puyalto, B. Stout, N. Bonod***

Aix-Marseille Université, CNRS, Centrale Marseille, Institut Fresnel, UMR 7249, Domaine universitaire de Saint Jérôme, 13013 Marseille, France
*nicolas.bonod@fresnel.fr

**Abstract**— Dielectric and metallic nanoparticles feature the ability to resonantly interact with light thanks to the excitation of electromagnetic resonances. Metallic particles host localized surface plasmons while dielectric particles host morphologic resonances, also called Mie resonances. Dielectric subwavelength sized particles feature very reach scattering spectra since they host both electric and magnetic modes when the dielectric permittivity is typically larger than 7. The interplay between electric and magnetic resonances opens a novel route to tailor light scattering, and to engineer light matter interaction at the nanoscale with the design of all dielectric optical antennas. Here, we present our recent advances in the calculation of the Purcell factor of silicon spherical cavities doped with emitters, and in the understanding of the link and differences between surface plasmons and morphologic resonances. In particular, we show analytically how positive dielectric particles can reproduce the electromagnetic response of plasmonic particles characterized by a negative dielectric permittivity.

## 1. PURCELL FACTOR OF SI-BASED MIE RESONATORS

Subwavelength sized dielectric nanostructures made of semi-conductors have attracted a keen interest over the last 6 years due to their ability to feature electric and magnetic resonances in the visible and near infrared frequencies [1-2]. Silicon particles are very promising to design novel light cavities. We derived in [3] the analytic expression of the decay rates of emitters located in the vicinity (but outside) silicon particles. The expressions were derived for electric or magnetic dipoles coupled with a silicon resonator featuring electric and magnetic dipolar and quadrupolar modes [3].

Lastly, we considered the case of silicon particles homogeneously doped with quantum emitters. By taking advantage of the latest progress in modal analysis of optical nano-cavities [4,5], we derived the analytical expression of the effective volume of silicon Mie particles featuring electric and magnetic resonances. These effective volumes permit to calculate the decay rates of quantum emitters coupled to the cavity through the Purcell factor that is proportional to the ratio between the quality factor and the effective volume. Importantly, this method allows for the calculation of the final Purcell factor of a silicon particle homogeneously doped with quantum emitters modeled as electric or magnetic dipoles featuring random orientations [6].

## 2. "PLASMONICS" WITH POSITIVE DIELECTRICS

Now that dielectric particles are widely used to enhance light matter interaction at the nanometer scale, it still remains to know whether they can replace nanoparticles made of noble metals. The dielectric permittivity of noble metals is dominated by the free electrons in the conduction band leading to a negative real part and positive imaginary part, while insulators (without free electrons) are characterized by a dielectric permittivity with positive real and imaginary parts.

In order to show that the fields scattered by a silver particle can be reproduced with a positive dielectric particle, we need to equalize the electric dipolar scattering coefficients of the two different particles: $a_1(z_0, \varepsilon_{metal}) = a_1(z_0, \varepsilon_{insulator})$. The other scattering coefficients are negligeable. After some algebraic manipulations, this expression can be simplified to the following complex transcendental equation : $\frac{\varphi_1^{(1)}(z_{metal})}{\varepsilon_{z_{metal}}} = \frac{\varphi_1^{(1)}(z_{insulator})}{\varepsilon_{z_{insulator}}}$ (Eq.1). The $\varphi_1$ functions are defined as $\varphi_1^{(\pm)}(z) \equiv \frac{\left[zh_1^{(\pm)}(z)\right]'}{h_1^{(\pm)}(z)}, \varphi_1^{(1)}(z) \equiv \frac{[zj_1(z)]'}{j_1(z)}$. We used a factorized expression of the Bessel function to obtain a new formulation of the special function[7-8]: $\varphi_n^{(1)}(z) = n + 1 + \sum_{\alpha=1}^{\infty} \frac{2z^2}{z^2 - a_{n,\alpha}^2}$, where $a_{n,\alpha}$

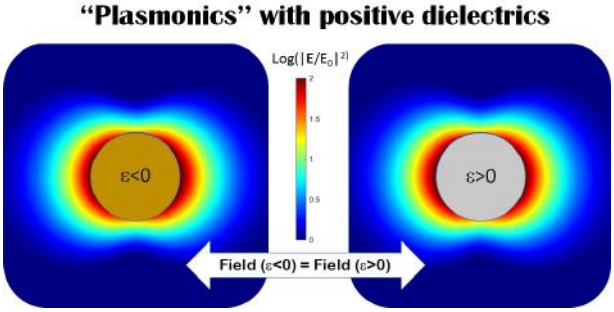



Figure 1: Enhancement of the near electric fields in the vicinity of a silver particle (left, $\epsilon = -2.5 + 0.5i$, $\phi$ = 50 nm, $\lambda = 373.6$ nm), and a positive dielectrics (left), $\epsilon = 111.815 + i0.464$, taken from Eq.1, with same ratio $\phi/\lambda$.

are the (tabulated) zeros of the Bessel function $j_n(x)$. By taking only the lowest zero, $a_{1,1}$, Eq. 1 can be cast:

$$\varepsilon_{\text{eq}} = \left(\frac{a}{z_0}\right)^2 \frac{1-(z_0/a)^2\varepsilon_{\text{in}}}{1-(z_0/b)^2\varepsilon_{\text{in}}}. \quad (1)$$

This analytic expression shows that two particles made of different materials can scatter the same electromagnetic field. Also, a study of the sign of the dielectric permittivity of the insulator, $\varepsilon_{z_{insulator}}$, shows that when $\varepsilon_{z_{metal}}$ depicts the dielectric permittivity of silver, $Re[\varepsilon_{z_{insulator}}]$ is positive (see Fig.1). In other words, the electromagnetic response of silver nanoparticles when excited at the surface plasmon resonance frequency can be reproduced with particles made of insulators [9].

**REFERENCES**


1. A. B. Evlyukhin, C. Reinhardt, and B. N. Chichkov, "Multipole light scattering by non-spherical nanoparticles in the discrete dipole approximation," *Phys. Rev. B* **84**, 235429 (2011).

2. A. Garcia-Etxarri, R. Gomez-Medina, L. S. Froufe-Perez, C. Lopez, L. Chantada, F. Scheffold, J. Aizpurua, M. Nieto-Vesperinas, and J. J. Saenz , "Strong magnetic response of submicron Silicon particles in the infrared," *Opt. Express* **19**, 4815 (2011).

3. B. Rolly, B. Bebey, S. Bidault, B. Stout, N. Bonod, "Promoting Magnetic Dipolar Transition in Trivalent Lanthanide Ions with Lossless Mie Resonances," *Phys. Rev. B* **85**, 245432 (2012).

4. C. Sauvan, J. P. Hugonin, I. S. Maksymov, and P. Lalanne, "Theory of the Spontaneous Optical Emission of Nanosize Photonic and Plasmon Resonators," *Phys. Rev. Lett.* **110**, 237401 (2013).

5. E. A. Muljarov, M. B. Doost, W. Langbein, "Exact mode volume and Purcell factor of open optical systems," arXiv:1409.6877.

6. X. Zambrana-Puyalto, N. Bonod, "Purcell factor of dielectric Mie resonators featuring electric and magnetic resonances," *Phys. Rev. B* **91**, 195422 (2015).

7. V. Grigoriev, A. Tahri, S. Varault, B. Rolly, B. Stout, J. Wenger, N. Bonod, "Optimization of resonant effects in nanostructures via Weierstrass factorization," *Phys. Rev. A* **88**, 011803(R) (2013).

8. V. Grigoriev, N. Bonod, J. Wenger, B. Stout, "Optimizing Nanoparticle Designs to Reach Ideal Light Absorption," *ACS Photonics* **2**, 263-270 (2015).

9. A. Devilez, X. Zambrana-Puyalto, B. Stout, N. Bonod, "Mimicking localized surface plasmons with dielectric particles," *Phys. Rev. B* **92**, 241412(R) (2015)

# Induced modulation instability of surface plasmon polaritons in an ultra-thin metal film

**S. Moiseev[1,2]*, D. Korobko[1], I. Zolotovskii[1], S. Sukhov[2]**

[1]Ulyanovsk State University, Ulyanovsk, Russia

[2] Kotelnikov Institute of Radio Engineering and Electronics, Russian Academy of Sciences, Ulyanovsk, Russia

*corresponding author: serg-moiseev@yandex.ru

**Abstract** - The effect of the modulation instability of surface plasmon polariton waves in an ultra-thin metal film is demonstrated. It is shown that the modulation instability effect could be used for the generation of signals with a repetition rate in the terahertz range and ultrafast trains of picosecond optical pulses.

In this work we propose a physical model of compact generator based on plasmon waveguides to produce short optical pulses with a controllable terahertz repetition rate. The pulse generation is produced by modulation instability of surface plasmon polaritons (SPPs) in a structure with a silver film of subwavelength thickness.

It is shown that during a time interval of a few picoseconds the slightly modulated SPP wave is transformed into a train of pulses due to nonlinear effects. In the case of the film thickness of 5 nm, the pulsation frequency equals 4.6 THz, the duration of each pulse is less than 0.1 ps (Fig. 1). For the film thickness of 10 nm the temporal dynamics at any given point looks like separated pulses of longer duration 0.5 ps attributed to a smaller group velocity of SPP. In this case the repetition rate of the pulse train is about 1.4 THz. In both cases the peak intensity is about 6 times higher than the intensity of the original SPP wave. Note, that the evolution of the modulated SPP wave is cyclical: the initial wave is transformed into a train of pulses that then transforms into a modulated wave to be decomposed into a sequence of pulses again, and so on. The period of the cycle depends on the relation between the dispersion and nonlinearity coefficient of system under consideration. For the used system parameters, the period of SPP wave evolution is few picoseconds. The SPPs of the required intensity and spatial period of modulation could be generated by using commercially available laser sources of moderate power.

This work was supported by the Ministry of Education and Science of the Russian Federation (Project No. 3.2202.2014/K).

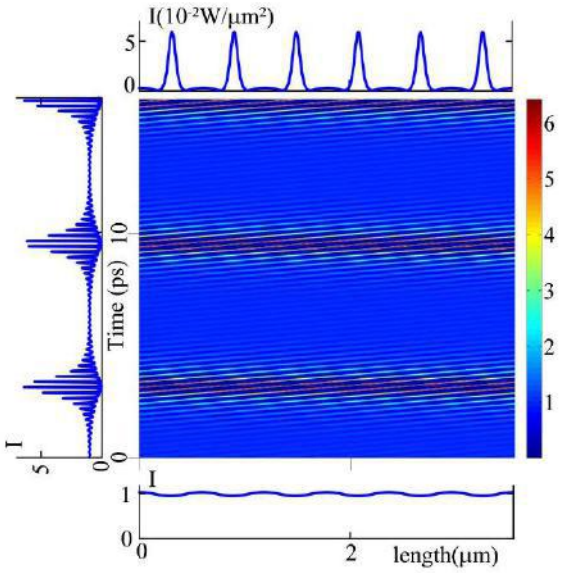



Fig. 1. Evolution of the SPP intensity in the film of thickness 5 nm; the initial wave (at $t$ = 0), modulated along $x$-coordinate (in bottom), time dynamics of the wave intensity at $x$=0 (left), spatial distribution of the SPP intensity (top) at $t$ = 16 ps.

# Excitation of quantum dot by femtosecond plasmon-polariton pulse focused by conducting cone

**P.A. Golovinski[1,2)] , V.A. Astapenko[1)] , E.S. Manuylovich[1)]**

[1)]Moscow Institute of Physics and Technology, Russia,
[2)] Physics Research Laboratory,
Voronezh State University of Architecture and Civil Engineering, Russia

**Abstract.** Surface plasmon-polariton is an electromagnetic wave that propagates along an interface between two materials with dielectric permittivity of opposite signs. Such waves can be focused by metal waveguides of special geometry. The spatial distribution for a near field strongly depends on a linear chirp of the laser pulse which can partially compensate the wave dispersion. Field distribution is calculated for different chirp values, opening angles and distances. The spatial selectivity of excitation of quantum dots (QDs) using focused field is shown using Bloch equations.

# Plasmonic hybridization investigated in non-local response regime

**S. Panaro*, S. D'Agostino, and C. Ciracì**
Center for Biomolecular Nanotechnologies, Istituto Italiano di Tecnologia, Italy
*corresponding author: simone.panaro@iit.it

**Abstract** - Plasmonic hybridization is an elegant way of describing the electromagnetic interaction of strongly coupled plasmonic systems. The smaller is the distance between two particles the greater is the degree of hybridization of the system. Ultra-strong coupling then, can be achieved in sub-nanometer gap systems. In this context, the nonlocal character of the free-electron response becomes critical. We investigate an elemental system, highlighting the effects that non-locality introduces in a complex hybridization scheme.

In recent years, significant efforts have been put in studying the electromagnetic (EM) response of complex plasmonic nano-assemblies and describing their behavior in strong coupling regime [1,2]. Intriguing applications have been envisaged from the possibility to hybridize *localized surface plasmons* (LSPs), especially for bio-sensing perspectives [3]. However, the necessity to increase the sensitivity of plasmonic systems unavoidably pushes the inter-particle gaps towards ultra-narrow regimes [4], requiring a more complex description of the electron optical response. The hydrodynamic approach is an ideal tool that allows investigating strongly coupled systems and in particular it allows to describe the EM response of deeply sub-wavelength plasmonic cavities [5].

The system we are presenting is a 2D rod-like antenna dimer that supports plasmonic resonances in the visible/near-infrared spectral range [6]. For conventional gap values ($g$ larger than 3 nm), this system shows a bi-modal EM response, due to the hybridization of the unperturbed long axis LSPs individually supported by each antenna (see left part of Figure 1(a)). Nevertheless, when the gap is pushed below 3 nm, a more complex hybridization diagram has to be considered (Fig. 1(a)). On the surface of the antennas, high order modes can be observed, with particular evidence in the gap region [7]. These modes are very sensitive to the gap and for this reason we indicate them as *gap modes*. Under particular geometrical conditions, these modes can spectrally overlap to the long axis hybrid modes, generating new hybridization schemes (Fig. 1(a)). We studied this system using a Finite Element Method software (Comsol Multiphysics) in a configuration that strongly promotes the long axis antibonding mode (see inset in Figure 1(a)). In Figure 1(b) we reported the evolution of the power scattered by the dimer as a function of the inter-particle distance. As we can appreciate, for gaps around $g$ = 3 nm, the far-field spectrum shows a quite broad peak around 800 nm wavelength. If we reduce the gap we can observe how the peak at 800 nm remains practically fixed, while a relatively sharp feature arises in the high energy side of the spectrum and red-shifts significantly. Finally, around $g$ = 0.5 nm, the two modes appear strongly overlapped.

We focused on the near-field distributions in correspondence of the two separate peaks. In particular, the narrow feature is characterized by a field distribution strongly localized in the gap region (Fig. 1(c)). Considering the high spectral evolution of this resonance as a function of the gap and the high field confinement observed, we ascribe it to a gap mode.

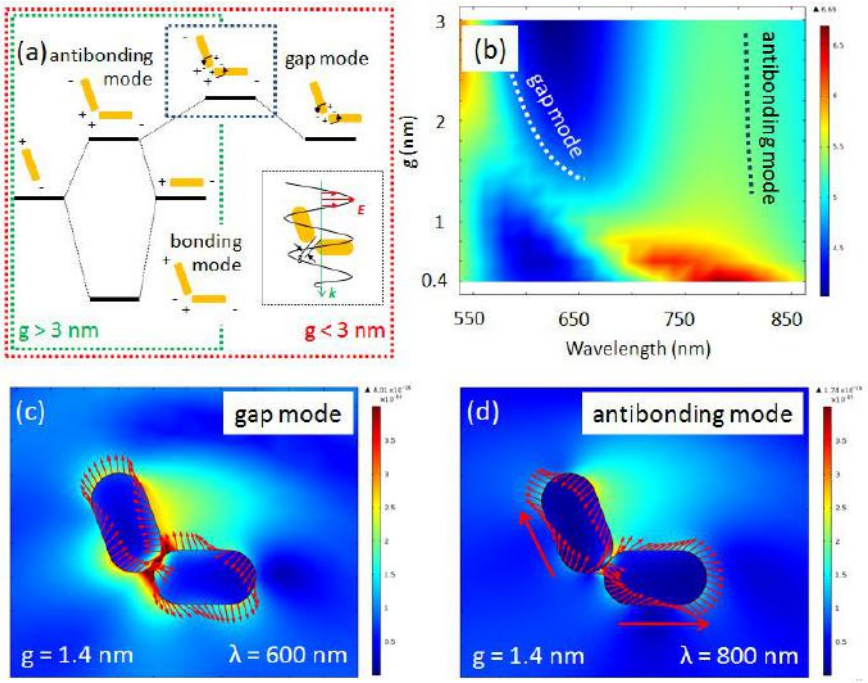



Figure 1. (a). Hybridization diagram of the 2D dimer respectively for $g$ > 3nm (left part) and $g$ < 3 nm. Inset in the lower right part: sketch of the system optical configuration. (b). 2D plot of the scattered power spectrum as a function of $g$. (c,d). Local response of respectively the gap mode and the long axis antibonding mode (the vectorial field corresponds to the surface current density distribution).

Instead, in correspondence of the 800 nm resonance (Fig. 1(d)) the surface current densities of the two antennas are present in mutual out-of-phase oscillation condition (we put arrows in the plot in order to help the view).

The fine control of two different plasmonic modes in ultra-small gap regimes opens the possibility to investigate complex hybridization phenomena taking into account non-local optical response. This provides a deep insight of the hybridization processes in an ideal framework, probing the sensitivity limits of plasmonic systems endowed with sub-nm gaps.

**REFERENCES**


1. Prodan, E., *et al.*, "A Hybridization Model for the Plasmon Response of Complex Nanostructures", *Science*, Vol. 302, No. 5644, 419–422, 2003.
2. Gómez, D. E., *et al.*, "The Dark Side of Plasmonics", *Nano Lett.*, Vol. 13, No. 8, 3722–3728, 2013.
3. Jian, Y. , *et al.*, "Plasmonic Nanoclusters: Near Field Properties of the Fano Resonance Interrogated with SERS", *Nano Lett.*, Vol. 12, No. 3, 1660–1667, 2012.
4. Jones, S. T., *et al.*, "Gold Nanorods with Sub-Nanometer Separation using Cucurbit[n]uril for SERS Applications", *Small*, Vol. 10, No. 21, 4298-4303, 2014.
5. Ciracì, C., *et al.*, "Probing the Ultimate Limits of Plasmonic Enhancement", *Science*, Vol. 337, No. 6098, 1072–1074, 2012.
6. Panaro, S., *et al.*, "Dark to Bright Mode Conversion on Dipolar Nanoantennas: A Symmetry-Breaking Approach", *ACS Photonics*, Vol. 1, No. 4, 310-314, 2014.
7. Lei, D. Y., *et al.*, "Revealing Plasmonic Gap Modes in Particle-on-Film Systems Using Dark-Field Spectroscopy", *ACS Nano*, Vol. 6, No. 2, 1380–1386, 2012.

# Direct coupling of InAs quantum dot excitons with surface plasmon polaritons

**F. W. A. Sobreira[1], Yu. I. Mazur[2], A. Xian Hu[2], G. J. Salamo[2] and E. Marega Jr[1*]**

[1] Instituto de Física de São Carlos, Universidade de São Paulo, 13560-970, São Carlos, SP, Brazil

[2] University of Arkansas, Institute for Nanoscience and Engineering, Fayetteville, Arkansas, 72701

[*]corresponding author: euclydes@ifsc.usp.br

**Abstract -** When placed near a thin metallic film, excitons in a quantum dot (QD) decay into surface plasmon polaritons (SPPs), guided modes of light confined at the interface of the metal/dielectric. It was reported that the interaction of SPPs with excitons in a QD may give rise to a modification in the photoluminescence (PL) spectra of the exciton energy levels, however the mechanism that explains this modification remains unclear. We propose a new methodology to excite many energy levels in an exciton by placing the QDs near a metallic array of slits fabricated onto a thin metallic gold (Au) film. By changing the position under the array where the QDs are excited we can resolve between the many energy levels. The unique features of the PL spectra obtained are the result of the strong electromagnetic field (EMF), the increase in the local density of states (LDOS) and the mesoscopic effects attributed to the gradient of the SPP field near the QDs.

The area of plasmonics has grown in the last decade as a promising successor for electronics and photonics, because we can in principle design devices as fast as in photonics and also as small as in electronics. To do so, the interaction of SPPs with matter has become of fundamental importance, even more because of the ability to control quantum emitters at low dimensional systems is a natural feature of plasmonics. For example, it has been reported that when SPPs interact with semiconductor quantum emitters such as excitons in QDs or quantum wells, they may give rise to an enhancement or quench in the PL spectrum of these emitters [1-4], although details about the conditions for each case are still lacking.

To probe the interaction of InAs quantum dots with surface plasmon polaritons InAs quantum dots were grown by Molecular Beam Epitaxy on (100)-oriented GaAs substrate. After the 300nm GaAs buffer layer we deposited 2.0 monolayers (ML) of InAs at 530ºC followed by a 30s annealing. Then a 12nm GaAs layer was grown. This process was repeated 5 times in order to produce a sample of stacked QDs to increase the density of QD emitters. The 12nm spacer layer is enough to prohibit electronic coupling between the QDs at different layers. After the QD growth a thin Au film of 120nm was deposited over the final GaAs surface by thermal evaporation. Then, we used a Focused Ion Beam (FIB) FEI Quanta 3D 200i system to mill a pattern over the Au film using a $Ga^+$ ion beam. The pattern consists of a slit array with 100nm width and period (distance between the center of two adjacent slits) of 400nm, as shown in figure 1.

In order to investigate the response of the system to the intensity of the SPPs we have focused the laser beam at the four different points shown in figure 1. We used a 785nm laser beam at full power and TM polarizations. The backscattered light from the grating is shown in figure 2. The differences observed in the PL spectra revels the mechanisms of exciton-SPP interaction.

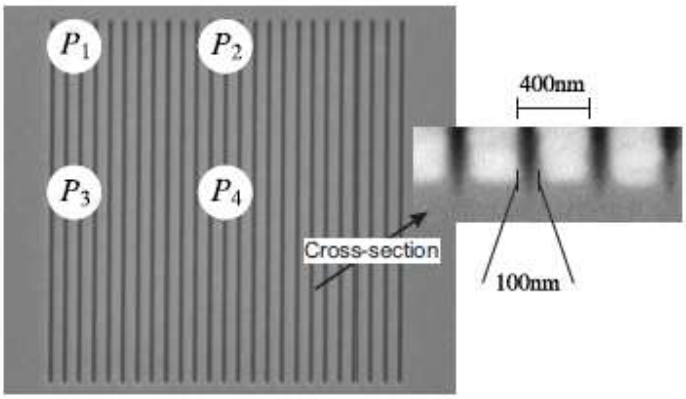



Figure 1: Secondary electron microscope image of the slit array patterned using FIB on a Au film of 120nm thickness deposited over a GaAs cap layer. The positions numbered $P_{1-4}$ represent the positions where the PL spectrum of the sample was taken with laser focused on the surface of the sample. The inset shows a cross-section image of the pattern. The slits are 100nm width, 10µm length and the period of the array is 400nm.

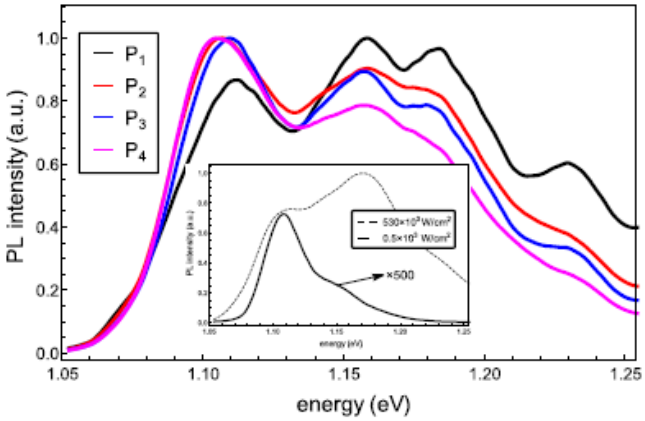



Figure 2: Normalized PL signal for each of the 4 points $P_{1-4}$ given by figure 1. The 785nm laser beam is focused at each point at maximum intensity of $530x10^3$ W/cm$^2$ and TM polarization mode. The inset shows the normalized PL spectra for the sample of UQDs at minimum ($0.5x10^3$ W/cm$^2$) and maximum ($530x10^3$ W/cm$^2$) laser power.

We thank the support from CEPOF (CEPID-FAPESP) under grant number 2013/07276-1. We are also grateful to the Brazilian agencies CNPq under grant number 140152/2011-3 for financial support.

**REFERENCES**

1. D. Chang, J. Thompson, H. Park, V. Vuleti_c, a. Zibrov, P. Zoller, and M. Lukin, Phys. Rev. Lett. 103, 123004 (2009).
2. D. K. Gramotnev and S. I. Bozhevolnyi, Nat. Photonics 4, 83 (2010).
3. J. B. Khurgin and G. Sun, Appl. Phys. Lett. 94, 191106 (2009).
4. O. Kulakovich, N. Strekal, A. Yaroshevich, S. Maskevich, S. Gaponenko, I. Nabiev, U. Woggon, and M. Artemyev, Nano Lett. 2, 1449 (2002).

# Plasmonic properties of metal-doped ZnO transparent conductive oxides for energy conversion

**A. Catellani[1], A. Ruini[1,2], and A. Calzolari[1*]**
[1]CNR-NANO, Instituto nanoscienze, Centro S3 Modena, Italy
[2]Dipartimento Fisica informatica Matematica, Univ. Modena e Reggio E., Modena Italy
[*]corresponding author: arrigo.calzolari@nano.cnr.it

**Abstract**- Using first principles calculations, we investigate the origin of near-infrared plasmonic activity in M-doped ZnO (MZO), one of the most promising TCO materials for optoelectronics and photovoltaics applications. Our results predict realistic values for the plasma frequency and the free electron density as a function of the M-doping, in agreement with recent experimental results. Then we characterize the plasmon properties of In-doped nanowires that have been envisaged as plasmonic nanoparticles for energy conversion applications.

Noble metals such as gold and silver are conventionally used as the primary plasmonic building blocks in the fields of the telecommunications and energy conversion. [1]. However, metals are plagued by large losses, especially in the UV–vis and IR spectral ranges, arising in part from interband electronic transitions and in part from dissipative scattering events. These losses are detrimental to the performance of plasmonic devices, seriously limiting the feasibility of many plasmonic applications. As an alternative, heavily doped semiconductors, such as transparent conductive oxides (TCOs), can exhibit a small negative real permittivity and very small losses at the infrared and longer wavelengths [2].

Transparent conducting oxides (TCOs) are electrical conductive materials with a low absorption of light in the visible range. The unique combination of metallicity and transparency makes TCOs appealing for a variety of applications, including photovoltaic cells, flat displays, invisible electronics and plasmonics. TCOs are obtained by doping wide band-gap semiconductors with metal ions. Yet, the remarkable combination of conductivity in an albeit wide-gap (i.e., transparent) material is not fully understood, along with the effect of dopants on charge transport.

Here, we present a first principles investigation of the optical and plasmonic properties of metal-doped ZnO systems (MZO), based on density functional theory, within the Random-Phase-Approximation. First, we investigate how doping [3-5] and defects [6] affects the optical and electronic properties of MZOs, up to the experimental solubility limit (3%–4%). Then, we study the origin of plasmonic activity in MZO transparent conducting oxides [7] and we provide a microscopic insight on the formation of surface-plasmon polaritons at the Al:ZnO/ZnO interfaces in terms of characteristic lengths that can be measured by experiments. These systems present tunable plasmonic activity in the near-IR range and in particular at wavelength relevant for telecommunications (1,5 μm), in agreement with the experimental results [8]. Finally, we investigated the optoelectronic properties of In-doped ZnO nanowires [9]. We show that the wires behave as 1D TCOs and low-loss plasmonic elements in the near IR and visible range. We discuss the possibility to develop

nanostructured energy converters in the form plasmon-heater/thermoelectric generator fully based on MZO nanowires.

**REFERENCES**


1. W. A. Murray and W. L. Barnes, "Plasmonic Materials", *Adv. Mater.,* Vol. 19, 3771-3782, 2007.
2. G.V. Naik, V. M. Shalaev, and A, Boltasseva, "Alternative Plasmonic Materials: Beyond Gold and Silver", *Adv. Mater.,* Vol. 25, 3264–3294, 2013.
3. M. Bazzani, A. Neroni, A. Calzolari, A. Catellani, "Optoelectronic properties of Al:ZnO: Critical dosage for an optimal transparent conductive oxide", *Appl. Phys. Lett.,* Vol. 98, 121907, 2011.
4. A. Catellani, A. Ruini, G. Cicero, and A. Calzolari, F. M. "First principles description of the electronic properties of doped ZnO", *Phys. St. Sol. B,* Vol. 10, 2106-2109, 2013.
5. A. Catellani, A. Calzolari and A. Ruini, "Effect of ultrathin gold on the Ohmic-to-Schottky transition in Al/ZnO contacts: A first-principles investigation", *J. Appl. Phys.,* Vol. 115, 043711, 2014.
6. A. Catellani, A. Ruini, and A. Calzolari, "Optoelectronic properties and color chemistry of native point defects in Al:ZnO transparent conductive oxide", *J. Mater Chem. C,* Vol. 3, 8419-8424, 2015.
7. A. Calzolari, A. Ruini, and A. Catellani, "Transparent conductive oxides as near-IR plasmonic materials: the case of Al-doped ZnO derivatives" *ACS Photonics,* Vol. 1, 703-709, 2014.
8. G. V. Naik, J. Liu, A. V. Kildishev, V. M. Shalaev, A. Boltasseva, "Demonstration of Al:ZnO as a plasmonic component for near-infrared metamaterial, *Proc. Natl. Acad. Sci. USA* Vol. 109, 8834-8838, 2012.
9. A. Catellani, A. Ruini, M. Buongiorno Nardelli and A. Calzolari, "Unconventional co-existence of plasmon and thermoelectric activity in In:ZnO nanowires", *RSC Advances,* Vol. 5, 44865-44872, 2015.

# Luminescence upconversion of $Er^{3+}$ doped tellurite glass through subwavelengh metallic nanostructures

**O. B. Silva, V. A. G. Rivera, S. Pratavieira and E. Marega Jr***
Instituto de Física de São Carlos, Universidade de São Paulo, 13560-970, São Carlos, SP, Brazil
*corresponding author: euclydes@ifsc.usp.br

**Abstract** - This manuscript addresses the upconversion excitation and emission obtained from an $Er^{3+}$-doped tellurite glass through nanostructured metallic surfaces consisting of a square lattice of subwavelengh slits fabricated on a gold thin film. The periodic nanostructures were fabricated with a Focused Gallium Ion Beam on a gold thin film deposited onto an $Er^{3+}$-doped tellurite glass. The $Er^{3+}$ ion was excited using 980nm and the luminescence spectra measured at the far-field (in the 400−700 nm wavelength range). The emission observed through the metallic nanostructure is caused by: (i) Upconversion excitation of the $Er^{3+}$ ions via extraordinary optical transmission through the grating. (ii) The coupling between the excited $Er^{3+}$ ions and the surface plasmon polariton on the gold/glass interface.

Surface plasmons enable the localization of light at nanoscale and provide an effective way of controlling the excitation and emission properties of quantum systems. Such characteristic is important for diverse applications, e.g., nanophotonics, biosensing, biotechnology, medical imaging and others. The most fascinating aspects of metallic nanostructures for plasmonics are their linear and nonlinear optical properties [1, 2]. In addition, the optical properties of metallic nanostructures are strongly dependent on the shape, depth and thickness of the films [3]. Electromagnetic surface waves propagating in the parallel direction of metal/dielectric interfaces have been extensively investigated for a wide range of applications [4]. Including engineering and light transport on a subwavelength scale, owing to their ability to significantly enhance optical and electromagnetic field intensities around metallic nanostructures, which can change the excitation and emission properties of locally excited quantum systems, such as $Er^{3+}$ ions. In this frame, we can build experimental setups for a variety of fascinating physical processes in a plasmonic and quantum system, known today as quantum plasmonics [5,6]. Nevertheless, the properties of metallic nanostructures (LSPR, SPP, plasmon intensity, tuning of the plasmon wavelength and others) depend on both geometry of the nanostructure and the substrate. In this work we investigated the luminescence of Erbium ions in a glass matrix. The $Er^{3+}$ ion was excited using 980nm and the luminescence spectra measured at the far-field (in the 400−700 nm wavelength range). The emission observed through the metallic nanostructure is caused by: (i) Upconversion excitation of the $Er^{3+}$ ions via extraordinary optical transmission through the grating. (ii) The coupling between the excited $Er^{3+}$ ions and the surface plasmon polariton on the gold/glass interface. The glass substrate content 1 mol% $Er_2O_3$ concentration, i.e., 10000 ppm in weight of erbium. A gold thin film with thickness of 120 nm was thermally evaporated onto the substrate. The metallic nanostructure array is composed by a 10μm length slit with 100nm width fabricated by means of a focused gallium ion beam milling. The array area is $10\mu m^2$ and the slit periods are 500, 700 and 900nm.

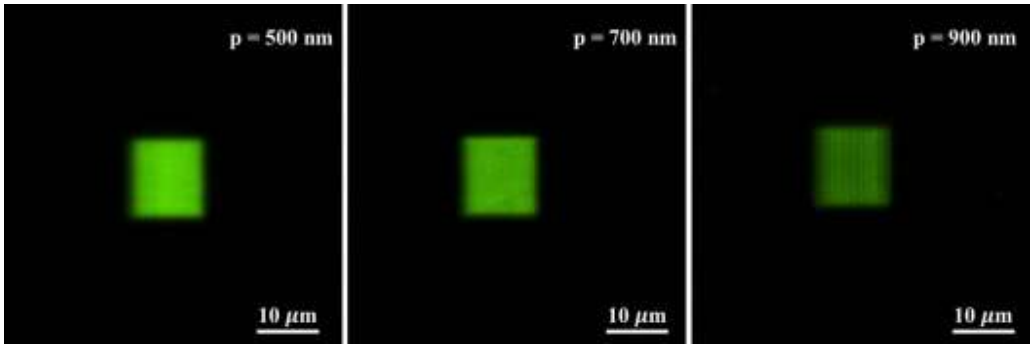



Figure 1: Confocal scanning microscopy images of the 10x10 μm metallic gratings showing the luminescence (total intensity in the range of 400-700nm) using a 980nm excitation wavelength. The slit width is 100nm and the period is denoted by p. The laser was polarized in the TM mode (transverse to the slit length).

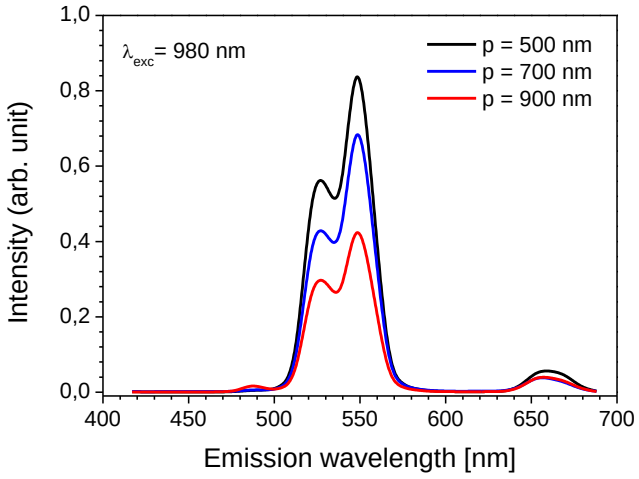



Figure 2: Visible luminescence spectra collected from the entire grating for three grating periods.

We thank the support from CEPOF (CEPID-FAPESP) under grant number 2013/07276-1.

**REFERENCES**

1. A. Henglein, Chem. Rev. Small-particle research: physicochemical properties of extremely small colloidal metal and semiconductor particles, 89, 1861-1873 (1989).
2. A. A. Lazarides, K. Lance Kelly, T.R. Jensen, G.C. Schatz, Optical properties of metal nanoparticles and nanoparticle aggregates important in biosensors, J. of Mol. Struc. (Theochem) 529, 59–63 (2000).
3. F.A. Ferri, V.A.G. Rivera, S.P.A. Osorio, O.B. Silva, A.R. Zanatta, B.H.V. Borges, J. Weiner, E. Marega Jr, Influence of film thickness on the optical transmission through subwavelength single slits in metallic thin films, Appl. Opt. 50(31):G11-G16 (2011).
4. P.N. Prasad, Nanophotonics (Wiley, 2004).
5. V.A.G. Rivera, O.B. Silva, Y. Ledemi, Y. Messaddeq, E. Marega Jr, *Collective Plasmon-Modes in Gain Media - Quantum Emitters and Plasmonic Nanostructures* (*Springer*, 2014).
6. V.A.G. Rivera, F.A. Ferri, L.A.O. Nunes, A.R. Zanatta, E. Marega Jr, Focusing surface plasmons on $Er^{3+}$ ions through gold planar plasmonic lenses, Appl Phys A **109**, 1037-1041 (2012).

# Coherent and non-coherent interactions between quantum emitters induced by plasmonic hot spots

**J. Ren[*] and X. D. Zhang**

School of Physics and Beijing Key Laboratory of Nanophotonics & Ultrafine Optoelectronic Systems, Beijing Institute of Technology, 100081, Beijing, China

[*]corresponding author: swhgywhz2008@126.com

**Abstract**-The theoretical method to study strong interactions between an ensemble of quantum emitters mediated by plasmonic nanoparticle cluster has been presented by using a rigorous first-principles electromagnetic Green's tensor technique. We find that strong coherent and non-coherent interactions could be observed in the same plasmonic hot spots system under different frequencies. These two interactions could lead to multifrequency multi-qubit entanglement and coherent energy transfer between emitters respectively in the hot spot systems.

Figure 1 presents multifrequency multi-qubit genuine entanglement[1] with long duration quantum beats derived from non-coherent interaction under coupling resonance frequencies (Figure 2). Strong coherent interaction (large $\delta\omega_{12}/\Gamma_{11}$ in Figure 3(a)) could shift the energy levels of emitters and lead to coherent resonance energy transfer[2] (Figure 3(b)).

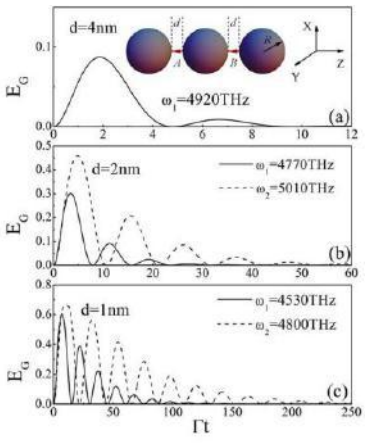



**Figure 1**

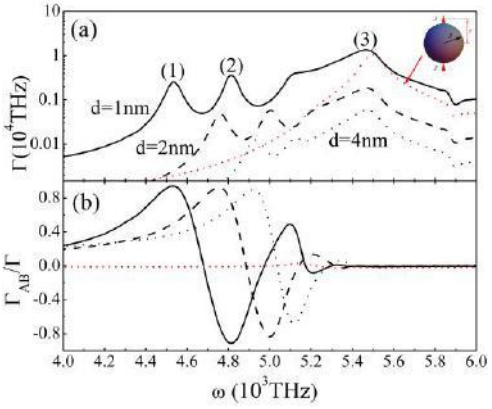



**Figure 2**

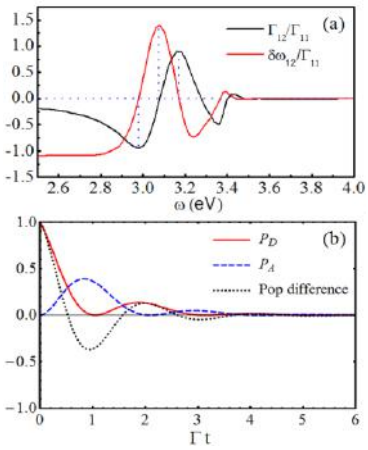



**Figure 3**

**Figure 1:** Genuine entanglement of two quantum emitters inserted in the gaps of a silver trimer (see inset) with different separation distances. (a) d=4nm, (b) d=2nm, (c) d=1nm. **Figure 2:** (a) Spontaneous decay rate $\Gamma$ and (b) interference term $\Gamma_{AB}/\Gamma$ of quantum emitters described in Fig. 1. **Figure 3:** (a) Non-coherence interaction term $\Gamma_{12}/\Gamma$ and coherent term $\delta\omega_{12}/\Gamma_{11}$. (b) Populations of donor and acceptor and their difference.

## REFERENCES

1. Ren, J., T. Wu and X. D. Zhang, "Multifrequency multi-qubit entanglement based on plasmonic hot spots," *Sci. Rep.*, Vol. 5, 13941, 2015.
2. Ren, J. and X. D. Zhang, "Coherent energy transfer mediated by plasmonic excitation," *preparing*.

# Study of Surface Plasmons in 1D and 2D Structured Metallic Surfaces

**R. García-Llamas[1,*], S. L. Gastélum-Acuña[1], D. Morales-Cruz[2], and A. S. Ramírez-Duverger[3]**

[1]Research Physics Department, University of Sonora, México

[2]Mechanical and Electrical Engineering Higher School, National Polytechnic Institute of México, México

[3]Physics Department, University of Sonora, México

[*]corresponding author: ragal@cifus.uson.mx

**Abstract**-The one-dimensional (1D) structures were fabricated by means of the two-beam interference technique. The surfaces were covered with an aluminum thick film. Transverse magnetic reflection spectra were measured for metallic gratings. The experimental spectra exhibited a minimum due to the excitation of surface plasmons, which was coupled by light via the gratings. The experimental results are compared with Rayleigh theory.

The surface plasmons (SPs) are electromagnetic waves localized at the interface between a metal and dielectric medium and they have a transverse magnetic (TM) character. The field intensity is maximum at the interface and decays exponentially for distances perpendicular to the interface. This field confinement together with adequate manipulation the light permit the possibility to go at subwavelength scale achievable with SPs. For achieved this, the structure requires an efficiently coupling SPs from space light and to control the propagation in predetermined direction [1-6]. Plasmonic promises potential applications[7].

In this paper, the problem of diffraction of light, based on Rayleigh criterion for SPs to excite by metallic gratings, is presented. The Rayleigh hypothesis restrict the values of the peak-to-peak $h$ respect to the period $a$ of any function profile $z = f(y)$ and $h/a < 0.143$ [8-11] . Gratings reflect the incident wave and the orders $r_n$ satisfy the following equation,

$$\Sigma\, C_{m,n}\, \mathrm{I}\,\{-[\beta_1(\alpha_n)-\beta_2(\alpha_m)]\} r_n = D_{m,0}\, \mathrm{I}\,\{+[\beta_1(\alpha_0)+\beta_2(\alpha_m)]\} u_0 \qquad (1)$$

**Numerical Results**: The eq. (1) is solved by assuming that the 1D structured metallic surface has a sinusoidal profile with period $a$ = 555 nm, which is determined for the experimental technique. Besides, electromagnetic incident waves as Gaussian beams and plane waves were considered. The values of the complex refractive index for the aluminum were interpolated from the data presented in [12].

**Experimental results**: The spectra of the experimental specular reflection $R_{exp}$ was measured from 250 to 800 nm for $\Delta\lambda$=1 nm resolution and for different angles of incidence from 16 to 35°, in steps of $\Delta\theta = 1^o$. The Figure 1 shows the specular reflection as a function of wavelength for a fixed angle of incidence $\theta_i = 20^o$. The purple, red and blue curves correspond to the experimental, the theoretical, calculated for a Gaussian beam, and the theoretical, calculated for a plane wave, respectively. To obtain both theoretical curves the peak-to-peak height was $h$ = 120 nm for plane wave and was $h$ = 80 nm for Gaussian beam, respectively. It is possible to see minima in the experimental and theoretical curve; these minima are associated with the excitation of SPs by

gratings. The experimental reflection spectrum shows two minima, and it is compared with the theoretical reflection spectrum calculated for a Gaussian beam and a plane wave.

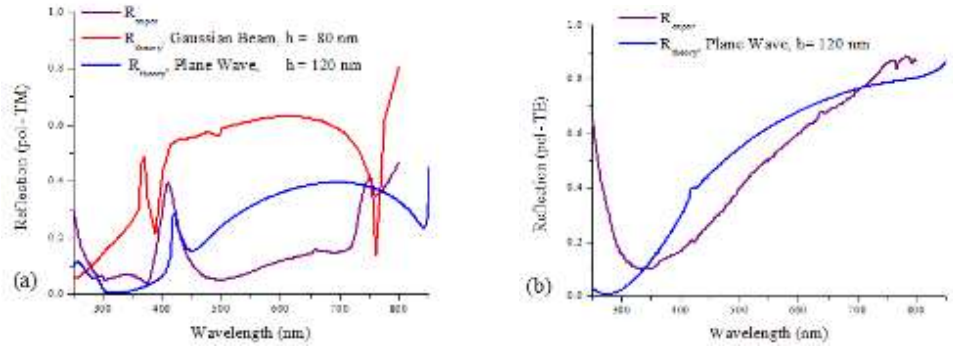



Figure 1. (a) The TM Specular reflection versus wavelength for an angle of incidence of 20$^{o}$, a period $a$ = 555 nm. The theoretical curve was calculated with $h$ = 80 nm for Gaussian beam and $h$ = 120 for a plane wave, respectively. The purple, red and blue correspond to the experimental, theoretical for a Gaussian beam and theoretical for a plane wave. (b) A transverse electric (TE) Specular reflection versus wavelength for an angle of incidence of a 20$^{o}$, a period $a$ = 555 nm. The purple and blue correspond to the experimental, and theoretical for a plane wave.

Results of the reflection spectrum and light diffraction for a 2D structured metallic surface or bigrating will be presented during the meeting.

**Acknowledgements**, to the National Council of Science and Technology of México (CONACYT), Catedras Funds. References 244041 y 245524.

**REFERENCES**

1. Petit, D., *Electromagnetic Theory of Gratings*, Springer Verlag, New York, 1980.
2. Raether, H., *Surface Plasmons on Smooth and Rough Surfaces and on Gratings*, Springer, Berlin 1988.
3. Maiers, S. A., *Plasmonics: Fundamentals and applications*, Springer, 2007.
4. Bar-Lev, D., A. Arie, J. Scheuer and I. Epstein, "Efficient excitation and control of arbitrary surface plasmon polariton beams using one-dimensional metallic gratings", *J. Opt.Soc.Am.B*, Vol. 32, No. 5, 923-932, 2015.
5. Brongersma, M.L. and V.M. Shalaev, "The Case for Plasmonics", *Appl. Phys.*, Vol. 428, 440-441, 2010.
6. Gramotnev, D. K and S. I. Bozhevolny, "Plasmonic beyond the diffraction limit", *Nat. Phot.* Vol. 4, 83-91, 2010.
7. Roszkiewicz, A., W. Szabelak and W. Nasalski, "Surface plasmon polariton applications in selected branches of modern science and technology", *J. Tech. Phys*., Vol. 50, No. 1, 3-16, 2009.
8. Popov, E., N. Bonod and S. Enoch, "Comparison of plasmon surface waves on shallow and deep metallic 1D and 2D gratings", *Opt. Exp.* Vol. 15, No. 7, 4224-4237, 2007.
9. Worthing, P. T. and W. L. Barnes, "Efficient coupling of surface plasmon polaritons to radiation using a bi-gratings", *Appl. Phys. Lett.* Vol. 79, No. 19, 3035-3037, 2001.
10. García-Llamas, R. and J. Félix Aguilar, "Analysis of experimental reflection spectra from diffraction gratings using the Rayleigh theory and a rigorous method," in *Proc. SPIE 4780, Surface Scattering and Diffraction for Advanced Metrology II,153* Seattle, USA, October 2002, 153-160.
11. Toigo, F., A. Marvin, V. and N. R. Hill, "Optical properties of rough surfaces: General theory and the small roughness limit", *Phy. Rev. B*, Vol. 15, No. 12, 5618-5626, 1977.
12. Palik, E. D. ed., *Handbook of Optical Constants of Solids I*, Academic Press. Inc., 1991.

# Towards a quantitative description of the plasmonic character of optical excitations in nanostructures.

**L. Bursi**[1,2], **A. Calzolari**[2], **S. Corni**[2], **and E. Molinari**[1,2]

[1]Dipartimento di Fisica, Informatica e Matematica, Università di Modena e Reggio Emilia, Italy
[2]Istituto Nanoscienze CNR-NANO-S3, I-41125 Modena, Italy
luca.bursi@unimore.it

**Abstract**— The excited states of molecular-sized systems have an intrinsic quantum nature. How to recognize plasmonic excitations microscopically in these systems is still an open issue. Here we introduce approaches that allow the quantification of the plasmonic character for each excitation based on first-principles simulations. Our results on isolated and hybrid prototypical nanostructures shed some light on the nature of plasmons at the nanoscale.

Localized surface plasmon resonances are collective electronic excitations of nanostructures that couple strongly with electromagnetic radiation allowing its confinement down to deep subwavelength regions, below the diffraction limit[1]. Thus they represent a powerful tool to manipulate light at the nanoscale and are the basis of a wide variety of applications ranging from light harvesting[2] to medicine[3].

On the theoretical side, plasmons can be classically defined as the collective charge density oscillations of the electrons in metals driven by their strong induced electromagnetic field. Metal nanoparticles are the most traditional plasmonic materials and their optical properties are generally described by semiclassical models of the frequency-dependent dielectric function[4]. This description has been very useful for designing applications, but fails to convey a microscopic understanding of what plasmons are. In particular, when the system size reaches a few nanometers, quantum finite-size effects become important and classical descriptions break down, unraveling the intrinsic quantum nature of plasmons. Indeed, nanoparticles are composed of electrons and nuclei like ordinary molecules. Therefore, their excited states, which include plasmons, must be understood in terms of the same elementary electron-hole excitations routinely used to interpret molecular excited states. In solid-state physics the electronic excitations are classified as single-particle and plasmonic ones. However, at the nanoscale, they are indissolubly mixed[5], and the identification of plasmonic excitations in small nanosystems is currently an unsolved problem and a highly debated research topic[6, 7, 8, 9, 10, 11, 12].

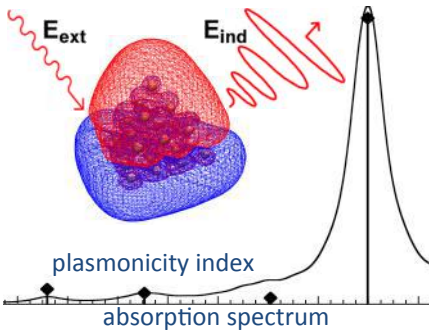



Figure 1: TDDFT absorption spectrum averaged over the three spatial polarizations (in arbitrary units) of $Ag_{20}$ cluster (black line) and plasmonicity index (black diamonds and vertical lines) computed for selected peaks in the spectrum. The inset shows a selected isosurface plot of the imaginary part of the TDDFT response charge density.

Recently, we have introduced a number, the plasmonicity index[13], which quantifies the plasmonic character of the excitations of a nanosystem. The rigorous theoretical definition of this index leads to the physically sound result that the measure of the plasmonicity of an excitation is proportional to its capability of enhancing locally an external electromagnetic radiation[10].

The mathematical expression of the plasmonicity index is based on the interaction of matter with electromagnetic field at the microscopic level and therefore it is general and applicable to any finite system. Moreover, it can be computed directly from the results of standard first-principles simulations, thus making it easily accessible, versatile and promising for the extension to other frameworks. We validated our approach on the few paradigmatic systems where the classification of plasmonic and single-particle excitations was established before[6]. Then, we applied it to metal nanostructures, such as the $Ag_{20}$ cluster shown in Figure 1, polycyclic aromatic hydrocarbons as molecular models of graphene nanoflakes which host "molecular plasmons"[7], and prototypical hybrid systems composed of plasmonic and molecular portions. The electronic, optical absorption and plasmonic properties of all these systems are investigated through (TD)DFT-based state-of-the-art first-principles approaches[14]. In all cases the results are, *a posteriori*, conforming with intuition and provide insights into the microscopic origin of the plasmonic resonances in small plasmonic and hybrid nanosystems, thus paving the way for the analysis of complex nanostructured materials whose plasmonic properties are unknown a priori.

In conclusion, the definition of the plasmonicity index points out the role of the induced Coulomb potential and represents a step forward in the fundamental understanding of the concept of plasmon in a molecular-sized system.

**ACKNOWLEDGMENT**

Computer resources were provided by the CINECA supercomputing center through the *ISCRA C PlasmInd* project.

**REFERENCES**

1. Tame, M. S., K. R. McEnery, Ş. K. Özdemir, J. Lee, S. A. Maier and M. S. Kim, "Quantum plasmonics", *Nat. Phys.*, Vol. 9, 329–340, 2013.
2. Atwater, H. A. and A. Polman, "Plasmonics for improved photovoltaic devices", *Nat. Mater.*, Vol. 9, No. 3, 205–213, 2010.
3. Halas, N. J., S. Lal, W.-S. Chang, S. Link and P. Nordlander, "Plasmons in strongly coupled metallic nanostructures", *Chem. Rev.*, Vol. 111, No. 6, 3913–3961, 2011.
4. della Sala, F. and S. D'Agostino, *Handbook of Molecular Plasmonics*, Pan Stanford Publishing, Pte. Ltd., 2013.
5. Zheng, B. Y., H. Zhao, A. Manjavacas, M. McClain, P. Nordlander and N. J. Halas, "Distinguishing between plasmon-induced and photoexcited carriers in a device geometry", *Nature Comm.*, Vol. 6, No. 7797, 1–7, 2015.
6. Bernadotte, S., F. Evers and C. R. Jacob, "Plasmons in Molecules", *J. Phys. Chem. C*, Vol. 117, No. 4, 1863–1878, 2013.
7. Guidez, E. B. and C. M. Aikens, "Origin and TDDFT Benchmarking of the Plasmon Resonance in Acenes", *J. Phys. Chem. C*, Vol. 117, No. 41, 21466–21475, 2013.
8. Townsend, E. and G. W. Bryant, "Which resonances in small metallic nanoparticles are plasmonic?", *J. Opt.*, Vol. 16, No. 11, 114022, 2014.
9. Guidez, E. B. and C. M. Aikens, "Quantum mechanical origin of the plasmon: From molecular systems to nanoparticles", *Nanoscale*, Vol. 6, No. 20, 11512–11527, 2014.
10. Bursi, L., A. Calzolari, S. Corni and E. Molinari, "Light-Induced Field Enhancement in Nanoscale Systems from First-Principles: The Case of Polyacenes", *ACS Photonics*, Vol. 1, No. 10, 1049–1058, 2014.
11. Krauter, C. M., J. Schirmer, C. R. Jacob, M. Pernpointner and A. Dreuw, "Plasmons in molecules: Microscopic characterization based on orbital transitions and momentum conservation", *J. Chem. Phys.*, Vol. 141, No. 10, 104101 (1–10), 2014.
12. García de Abajo, F. J., R. Sapienza, M. Noginov, F. Benz, J. Baumberg, S. Maier, D. Graham, J. Aizpurua, T. Ebbesen, A. Pinchuk, J. Khurgin, K. Matczyszyn, J. T. Hugall, N. van Hulst, P. Dawson, C. Roberts, M. Nielsen, L. Bursi, M. Flatté, J. Yi, O. Hess, N. Engheta, M. Brongersma, V. Podolskiy, V. Shalaev, E. Narimanov and A. Zayats, "Plasmonic and new plasmonic materials: general discussion", *Faraday Discuss.*, Vol. 178, 123–149, 2015.
13. Bursi, L., A. Calzolari, S. Corni and E. Molinari, submitted.
14. Ge, X., S. J. Binnie, D. Rocca, R. Gebauer and S. Baroni, "turboTDDFT 2.0 - Hybrid functionals and new algorithms within time-dependent density-functional perturbation theory", *Comput. Phys. Commun.*, Vol. 185, No. 7, 2080–2089, 2014.

# Optical spin-orbit interaction in plasmonic structures

**Feng Lin***

School of Physics, State Key Laboratory for Mesoscopic Physics, Peking University, Beijing 100871, China

*corresponding author: linf@pku.edu.cn

**Abstract**-Au nanostructures can be fabricated to intentionally guide the propagation of surface plasmon polaritons (SPPs), which leads to the varying of propagating directions for the SPP beams, and thus generates the orbital angular momentum (AM) of SPPs. Here, we investigated the coupling of such plasmonic orbital AM with optical spin AM, and found that the chiral characteristics of Au nanostructures impose great effects on the electromagnetic modes of SPPs under this spin-orbit interactions.

The optical spin-orbit interaction is that a coupling of the intrinsic angular momentum (photon spin) and the extrinsic momentum (orbital angular momentum) [1-2]. The effect is usually observed when the light passes through an anisotropic and inhomogeneous medium. For instances, the optical spin Hall effect, beam displacement and momentum shift due to the optical spin, was observed at the medium interface. In plasmonic structures, the surface plasmon polaritons travel along the path that can be defined to within a subwavelength scale by the geometric patterns of the structures, which generate a significant optical orbital angular momentum. In our work, on the Au thin film deposited on glass substrates, we fabricate the subwavelength holes by focused ion beam, which form the ring shape. Using the scanning near-field optical microscope, the different propagation modes of surface plasmon polaritons has been observed for the excitation light with the left and right handed circular polarization, respectively. Based on the conservation of total optical angular momentum in this circular system, the coupling effect of the spin and orbital angular momentum can be deduced from the measured and simulated distribution of electric fields.

**REFERENCES**

1. Shitrit, N., Bretner, I., Gorodetski, Y., Kleiner, V. and Hasman, E., "Optical spin Hall effects in plasmonic chains," Nano Lett., Vol. 11, 2038-2042, 2011.
2. Shitrit, N.; Yulevich, I.; Maguid, E.; Ozeri, D.; Veksler D.; Kleiner, V.; Hasman, E., "Spin-optical metamaterial route to spin-controlled photonics," Science, Vol. 340, 724-726, 2013.

# The “on” and “off” of optical waves in planar multilayer stacks

**Yikuan Wang**[1]

[1]School of Clean Energy and Electrical Engineering, Yancheng Teachers University, Jiangsu, 224002, China

[*]corresponding author: wangyk@yctu.edu.cn

**Abstract**- The transmittance of two planar multilayer stacks is computed. When 537nm red light impinges on the stacks with an incident angle of 46°, the transmittance of $Si_3N_4$/Ag(46nm)/water stack vanishes, while the transmittance of $Si_3N_4$/Ag(46nm)/water(2nm)/$Si_3N_4$ is about 0.13%. If we combine these two stacks in parallel with each other, the composite structure can turn photons “on” and “off” in far field distances. This suggests that the beam size and intensity of SPCE rely on the choice of dielectric material.

Recent progress in plasmonics has brought about a number of applications at the molecule level, such as dipole optical antennae, sensitive SERS technique etc. Bringing a fluorophore to a continuous metallic film within 200nm distance results in a directional beam called Surface Plasmon coupled emission (SPCE) [1-3]. As a high sensitive technique, SPCE has been used to study bio-molecule interactions in laboratories with fluorophores and metallic films dependent on appropriate spectral range [4]. However, the role played by the dielectric materials near the metal-dielectric interface remains to be explored.

To understand how dielectric interacts with metal film in SPCE, we choose to study optical properties of planar $Si_3N_4$/Ag/water/$Si_3N_4$ multilayer stacks using plane-wave propagation model described elsewhere [5-6]. First we calculated the reflectance of $Si_3N_4$/Ag (46nm)/water for visible light. The reflectance of light at wavelength of 537nm for the multilayer stack is at minimum at an incidence angle of 46°, and the transmittance vanishes, as shown in Fig. 1. Light cannot travel through this structure because it is trapped at the Ag/water interface as SPPs [7].

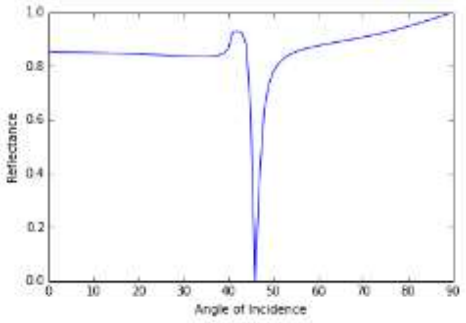



**Figure 1 Reflectance vs the angle of incidence in $Si_3N_4$/Ag/water stack.**

Then we calculate the transmittance of $Si_3N_4$/Ag(46nm)/water(2nm)/$Si_3N_4$ stack from monochromatic light with $\lambda$=537nm, keeping the Ag thickness and the incidence angle unchanged. We set the water layer as thin as 2nm, and got a transmittance of about 0.13%. Even though this value is so small, it is significant as compared to the transmittance of the tri-layer stack we mentioned above. Detection of this transmitted light is possible at far-field.

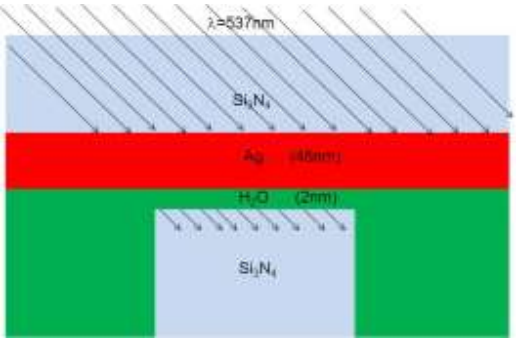



**Figure 2 $Si_3N_4$/Ag/water/(water,$Si_3N_4$,water) structure**

If these two structures are hybridized to form $Si_3N_4$/46nm Ag/2nm water/(water,$Si_3N_4$,water) stack, as shown as Fig.2, SPPs are generated at the silver-water interface. A certain amount of SPP energy is transformed into SPCE in the outside $Si_3N_4$. Because of wavevector compensation in high refractive index dielectric($Si_3N_4$), one would also expect some SPP photons from left side of water-$Si_3N_4$ are converted into the same SPCE while entering $Si_3N_4$ region, thus makes SPCE stronger. Since photon-scattering effect takes place at $Si_3N_4$-water boundary, this does not affect the SPCE direction at all. Therefore SPCE beam size depends on the dielectric material which turns SPCE "on".

In a summary, by calculating the transmittance of optical waves in planar metal-dielectric stacks, we show that different dielectric materials coupled with metal can turn "on" and "off" SPCE, thus the wave-fronts of light is modified through these metal-dielectric structures. It is the dielectric material which turns SPCE "on" that determines the SPCE beam size.

The author acknowledges the start-up funding from Yancheng Teachers University for this study.

**REFERENCES**

1. Lakowicz JR,Malicka J,Gryczynski I, Gryczynski Z. "Directional surface plasmon–coupled emission:a new method for high sensitivity detection". *Biochem. Biophys. Res. Commun*. Vol 307, 435–39, 2003.
2. Geddes CD, Gryczynski I, Malicka J, Gryczynski Z, Lakowicz JR. 2004. Directional surface Plasmon coupled emission. *J. Fluoresc*. Vol 14, 119–23, 2004.
3. Kostov Y.,D.S. Smith, L. Tolosa, G. Rao,I. Gryczynski,Z. Gryczynski,J.Malicka, and Joseph R. Lakowicz, "Directional Surface Plasmon-Coupled Emission from a 3 nm Green Fluorescent Protein Monolayer", *Biotechnol. Prog.*, Vol 21, 1731-1735, 2005.
4. Cao, S, Wei-Peng Cai, Qian Liu, and Yao-Qun Li, "Surface Plasmon-coupled emission: what can directional fluorescence bring to the analytical sciences?", *Annu. Rev. Anal. Chem.* Vol 5, 317–36, 2012.
5. Windt, D.L., "IMD—Software for modeling the optical properties of multilayer films", *Computers in phys.*, Vol. 12, NO. 4, 360-70, 1998.
6. Morales, E. H.,Y. Wang, D. Lederman, A. J. Kellock and M. J. Carey, "Inter-diffusion and exchange bias in the MnxPt1-x/Co system", *J. Appl. Phys.* 93, 4729-33, 2003.
7. Born, M. and E. Wolf, Principles of Optics, 6th ed. Pergamon, Oxford, 1980.
8. Yalcin, S. E., Y. Wang, M. Achermann, "Spectral bandwidth and phase effects of resonantly excited ultrafast surface plasmon pulses", *Appl. Phys. Lett.* 93, 101103, 2008.

# Resonance Coupling between Excitons and Magnetic Dipole Resonances in Hybrid Nanostructure Composed of J-Aggregate and Dielectric Nanoparticle

**Hao Wang[1,2,4], Huanjun Chen[1,2,3*]**

[1]State Key Laboratory of Optoelectronic Materials and Technologies, [2]Guangdong Province Key Laboratory of Display Material and Technology, [3]School of Electronics and Information Technology, [4]and School of Physics, Sun Yat-sen University, Guangzhou 510275, China

[*]corresponding author: chenhj8@mail.sysu.edu.cn

**Abstract** We investigated theoretically and experimentally the resonance coupling between the magnetic dipole resonances of silicon nanospheres and molecular excitons. By coating the silicon nanosphere with a dye molecule layer, we demonstrated that hybrid states were induced around the magnetic dipole resonance mode due to magnetic field mediated Fano-type energy transfer. We further observed a Rabi splitting of 100 meV by spin coating the silicon nanospheres with J-aggregates (TDBC).

The plasmon−exciton coupling, known as plexciton,[1] in hybrid nanostructures composed of noble metal nanostructures and aggregate molecules has been a subject of intense study for tailoring the light−matter interactions. In these hybrid systems, the localized surface plasmon resonances (LSPRs) of the metallic nanostructures can concentrate light into deep-subwavelength volumes and induce large electromagnetic field enhancement around the nanostructures. Strong interaction phenomena from Fano-type energy transfer to strong coupling can be induced due to the coupling between the molecular excitons and plasmon resonances. Such interaction forms the basis of many practical applications, such as high-performance sensing, subwavelength signal processing and transmitting, and single-photon sources. However, the noble metal nanostructures usually suffer from the intrinsic losses at the visible wavelength region. Recently, high-refractive-index dielectric nanoparticles have been demonstrated to support both electric and magnetic resonant modes in the entire visible and near-IR spectral regions.[2, 3] The interference of the electric and magnetic resonances in these dielectric nanoparticles opens up a novel approach to manipulation of light at the nanoscale,[4] which is important for many applications like solar cells, ultrasensitive sensing, and light emitting devices. Besides, various resonance interactions at the nanoscale mediated by the magnetic resonances have been achieved. In comparison with the plasmonic metals, the dielectric nanoparticles exhibit lower loss and are more CMOS compatible, making them promising for the future applications of on-chip nanophotonics.

In our study, we demonstrated that localized magnetic dipole resonance (LMDR)−exciton coupling can be realized in hybrid nanostructures composed of dielectric nanoparticle and molecular J-aggregates. We applied Mie theory to calculate the resonance coupling effect, where the hybrid structure was modeled by coating the silicon nanosphere with a molecule layer. The exciton resonance of the molecule shell was modeled with Lorentzian line shape. The theoretical results indicated that new hybrid energy states can be induced around the magnetic dipole resonance of the silicon nanosphere. Furthermore, for relatively large oscillator strength, a

blue-shifted cavity resonance mode emerges in the dye shell, which can strongly couple with the electric dipole resonance in the silicon nanosphere. These interactions were manifested by Fano-resonance-like dip structure in the scattering and extinction spectra. The optical near-field properties of the hybrid nanostructure was then calculated via finite element method, which indicated that for coupling between the electric dipole mode of the silicon nanosphere and cavity mode of the dye shell, the Fano dip was resulted from electric field-induced energy transfer from the silicon core to the dye shell, while magnetic field-induced energy transfer dominated at the Fano dip in the exciton−LMDR coupling region. This is significant different from that of the plexcitonic. To verify the theoretical calculations, we have experimentally measured the coupling between individual silicon nanospheres and J-aggregates using dark-field scattering spectroscopy.

In conclusion, we have demonstrated that exciton−LMDR resonance coupling in dielectric hybrid nanostructures can generate Fano-type energy transfer associated with the novel magnetic response, which is distinctly different from plasmon-induced energy transfer in plexcitonic nanostructures. Such coupling effect in low-loss dielectric nanoparticles opens up a novel approach to the strong light−matter interaction at the nanoscale and make it promising for the various applications in future nanophotonic devices and circuits.

**REFERENCES**


1. Fofang, N. T.; Park, T.-H.; Neumann, O.; Mirin, N. A.; Nordlander, P.; Halas, N. J. "*Plexcitonic Nanoparticles: Plasmon-Exciton Coupling in Nanoshell-J-Aggregate Complexes*," *Nano Lett.*, Vol. 8, No. 10, 3481−3487, 2008.
2. Kuznetsov, A. I.; Miroshnichenko, A. E.; Fu, Y. H.; Zhang, J.; Luk'yanchuk, B. "*Magnetic Light*," *Sci. Rep.*, Vol. 2, 492, 2012.
3. Evlyukhin, A. B.; Novikov, S. M.; Zywietz, U.; Eriksen, R. L.; Reinhardt, C.; Bozhevolnyi, S. I.; Chichkov, B. N. "*Demonstration of Magnetic Dipole Resonances of Dielectric Nanospheres in the Visible Region*," *Nano Lett.*, Vol. 12, No. 7, 3749−3755, 2012.
4. Wang, H.; Liu, P.; Ke, Y.; Su, Y.; Zhang, L.; Xu, N.; Deng, S.; Chen, H. "*Janus Magneto–Electric Nanosphere Dimers Exhibiting Unidirectional Visible Light Scattering and Strong Electromagnetic Field Enhancement*," *ACS Nano*, Vol. 9, No. 1, 436−448, 2015.

# Extension of standard transfer-matrix method for three-wave mixing for plasmonic structures

**A. Loot**[1*] **and V. Hizhnyakov**[1]
[1]Institute of Physics, University of Tartu, Estonia
[*]corresponding author: ardi.loot@ut.ee

**Abstract**-Fast and accurate modelling of three-wave mixing processes in arbitrary stratified medium has significant practical and scientific importance. Several attempts to generalize transfer-matrix method (TMM) for nonlinear interactions have been made, however none suits for easy-to-use modelling of plasmonic structures which requires oblique angle of incidence, p-polarization and minimal approximations. In this work, an easy-to-use extension to standard TMM is proposed. The proposed method is used to study the strength of unconventional plasmonic enhancement of second harmonic generation (SHG).

Without any derivation here, we state the differences in comparison to the standard TMM [1]. For compact notation, only results regarding the p-polarized SHG will be presented, however generalization to any three-wave mixing process is straightforward. The appropriate field component $U_{(i)}$, $E_{y(i)}$ in case of s-polarization and $H_{y(i)}$ for p-polarization, inside a layer number $i$ is defined as a sum of forward and backward propagating fields $U_{(i)} = U_{(i)}^{+} + U_{(i)}^{-}$ in usual way, which are given by a sum of a homogeneous wave and inhomogeneous wave $U_{(i)}^{\pm} = A_{(i)}^{\pm} e^{\pm i k_{z(i)} z} + B_{(i)}^{\pm} e^{\pm i k_{sz(i)} z}$. The amplitudes of inhomogeneous waves are found to be expressed as

$$\begin{bmatrix} B_{(i)}^{+} \\ B_{(i)}^{-} \end{bmatrix} = -\frac{\omega}{k_{(i)}^2 - k_{s(i)}^2} \begin{bmatrix} k_{sz(i)} p_{sx(i)}^{+} - k_{sx(i)} p_{sz(i)}^{+} \\ \left( k_{sz(i)} p_{sx(i)}^{-} - k_{sx(i)} p_{sz(i)}^{-} \right) e^{i k_{sz(i)} d_{(i)}} \end{bmatrix}, \tag{1}$$

where $\omega$ denotes the frequency of the SHG wave, $c$ is the speed of light, $\varepsilon_0$ is the permittivity of a vacuum and $d_{(i)}$ is the thickness of layer $i$. The magnitudes of the wavevectors of homogeneous and inhomogeneous waves are defined by $k_{z(i)} = \omega n_{(i)}(\omega)/c$ and $k_{s(i)} = \omega n_{(i)}(\omega/2)/c$, where $n_{(i)}(\omega)$ denotes the refractive index of layer $i$. $\mathbf{p}_{s(i)}^{\pm}$ is defined through equation for nonlinear polarization $\mathbf{P}_{NL(i)}^{\pm} = \mathbf{p}_{s(i)}^{\pm} e^{\pm i k_{sz(i)} z} = \varepsilon_0 \chi_{(i)}^{(2)} \mathbf{E}_{p(i)}^{\pm} \mathbf{E}_{p(i)}^{\pm}$, where $\chi_{(i)}^{(2)}$ is the second order nonlinear susceptibility tensor and $\mathbf{E}_{p(i)}^{\pm}$ denotes the electrical field of fundamental wave. All the waves are taken to depend only on z-coordinate. As usual, all the wavevectors are taken to be in xz-plane and the x-dependence is harmonic.

The propagation matrix, which relates the field amplitudes in the beginning of a layer $i$ to the amplitudes at the end of the layer, has just additional nonlinear term $\mathbf{P}_{NL(i)}$

$$\begin{bmatrix} U_{(i)}^{+}(d_{(i)}) \\ U_{(i)}^{-}(d_{(i)}) \end{bmatrix} = \mathbf{P}_{L(i)} \cdot \begin{bmatrix} U_{(i)}^{+}(0) \\ U_{(i)}^{-}(0) \end{bmatrix} + \begin{bmatrix} P_{NL(i)}^{+} \\ P_{NL(i)}^{-} \end{bmatrix} \tag{2}$$

$$P_{NL(i)}^{\pm} = B_{(i)}^{\pm} \left( e^{\pm i k_{sz(i)} d_{(i)}} - e^{\pm i k_{z(i)} d_{(i)}} \right), \tag{3}$$

where $\mathbf{P}_{L(i)}$ denotes the ordinary propagation matrix. Another important component is transfer matrix, which relates the field components at the interface between the layers. Again, it was possible to express the nonlinear term as an extension of standard TMM:

$$\begin{bmatrix} U^{+}_{(i+1)}(0) \\ U^{-}_{(i+1)}(0) \end{bmatrix} = \mathbf{T}_{L(i,i+1)} \cdot \begin{bmatrix} U^{+}_{(i)}\left(d_{(i)}\right) \\ U^{-}_{(i)}\left(d_{(i)}\right) \end{bmatrix} + \begin{bmatrix} T^{+}_{NL(i,i+1)} \\ T^{-}_{NL(i,i+1)} \end{bmatrix} \tag{4}$$

$$T^{\pm}_{NL(i,j)} = \pm \frac{1}{2\varepsilon_{(i)} k_{z(j)}} \Big[ \varepsilon_{(j)} \left(k_{sz(i)} - k_{z(i)}\right)\left(B^{+}_{(i)} e^{ik_{sz(i)}d_{(i)}} - B^{-}_{(i)}\right) + \varepsilon_{(i)} \left(k_{sz(j)} - k_{z(j)}\right)\left(B^{-}_{(j)} e^{ik_{sz(j)}d_{(j)}} - B^{+}_{(j)}\right) - \\ -\omega\varepsilon_{(j)} \left(p^{-}_{x(i)} e^{-ik_{sz(i)}d_{(i)}} + p^{+}_{x(i)} e^{ik_{sz(i)}d_{(i)}}\right) + \omega\varepsilon_{(i)} \left(p^{-}_{x(j)} + p^{+}_{x(j)}\right) \Big]. \tag{5}$$

The system matrix, which describes the whole system, could be easily found by multiplying the propagation and transfer matrices of all the layers and interfaces. Finding the power of reflected and transmitted SHG signal is straightforward, if assuming that there is no incident SHG signal. This newly developed nonlinear TMM (NL-TMM) was formed as an easy-to-use python library.

NL-TMM was used to study alternative, generally not studied, process for plasmonic enhancement of SHG. The common process for the plasmonic enhancement of SHG is described by $2f_{\omega} \rightarrow 2p_{\omega} \rightarrow f_{2\omega}$, where two pump-photons excites two plasmons at the fundamental frequency (with enhanced electrical field) which will decay to the SHG signal due to a nonlinear interaction. This kind of process is well studied and understood. However, an alternative process for plasmonic enhancement also exists, where two pump photons will excite plasmons at the double frequency directly ($2f_{\omega} \rightarrow p_{2\omega} \rightarrow f_{2\omega}$). The results in Fig. 1 show, that such effect (corresponding angle denoted by $p_{2\omega}$) exists, however, as expected it is a few orders of magnitude smaller than alternative process (denoted by $p_{\omega}$), that is why it is generally experimentally not observed. Additional analysis will be presented.

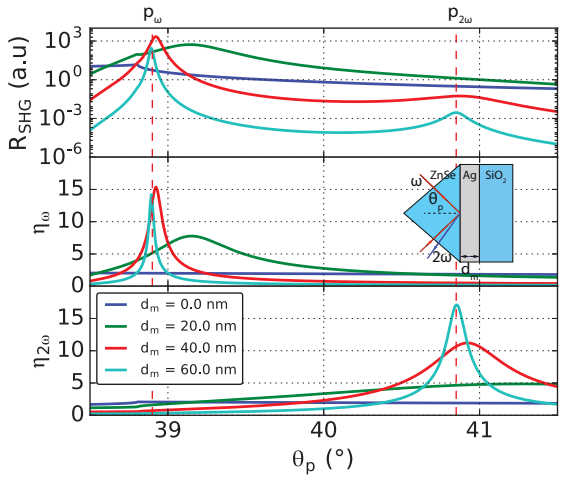



Figure 1. Reflected SHG intensity ($R_{SHG}$), fundamental (λ=1550 nm) and second harmonic field enhancement ($\eta_{\omega}$ and $\eta_{2\omega}$) in $SiO_2$ crystal for the ZnSe-Ag-$SiO_2$ structure shown in inset. Crystallograpic x-axis is aligned to be perpenticular to metal-crystal interface.

NL-TMM derived in this study has vast potential in many studies. It could be used to model the plasmon-enhanced spontaneous parametric down-conversion described in Ref. [2] more precisely, if assuming that SPDC is a difference frequency generation process initiated by a vacuum fluctuations. If NL-TMM will be generalized to take into account anisotropy as well, then it would be beneficial to precisely estimate the SGH generated in the setup described in Ref. [3] which employs leaky Dyakonov SPPs for surface-wave excitation without a prism.

**Acknowledgements** The research was supported by the Estonian research project IUT2-27.

## REFERENCES

[1] O. S. Heavens, "Optical properties of thin films," *Reports Prog. Phys.*, vol. 23, no. 1, p. 301, 1960.

[2] A. Loot and V. Hizhnyakov, "Enhanced spontaneous parametric down-conversion in a metal-dielectric interface," *IEEE*, vol. 7342484, pp. 451–453, 2015.

[3] A. Loot and V. Hizhnyakov, "Leaky Dyakonov surface plasmon polaritons for birefringent crystals," *Appl. Phys. A*, vol. 122:327, no. 4, pp. 1–8, 2016.

# Tuning the optical response of dewetted silver films through nanopatterning.

**P. Jacquet**[1,2,3], **I. Gozhyk**[3], **J. Teisseire**[3], **J. Jupille**[1,2] **and R. Lazzari**[1,2]

[1]CNRS, UMR 7588, Institut des NanoSciences de Paris, 4 place Jussieu, F-75252 Paris, France
[2]Sorbonne Universités, UPMC Univ Paris 06, UMR 7588, Institut des NanoSciences de Paris, 4 place Jussieu, F-75252 Paris, France
[2]Surface du Verre et Interfaces, UMR 125 CNRS/Saint-Gobain Recherche, 39 quai Lucien Lefranc, F-93303 Aubervilliers, France
paul.jacquet@saint-gobain.com

**Abstract**— Thin metallic films can be unstable upon deposition. A phenomenon called dewetting leads to hole appearance and propagation until only isolated particles remain. We studied the optical response of the system during the dewetting process and the possibilities to tune the optical response of the particles through substrate nanopatterning.

A major issue in glass industry concerning the use of thin metallic layers is their instability at reasonable temperatures (i.e. below metal melting point). A phenomenon, called dewetting, takes place, transforming thin layers into isolated particles [1]. However, dewetting is also an affordable and scalable way to produce nano-particles (NP) suitable for applications in various domains such as photovoltaics [2], optoelectronics [3] and plasmonics [4].

Dewetting can be controlled, for example via the substrate patterning prior to the deposition of metallic film [5]. As a result, regular arrays of NP are obtained. The first demonstration of this method [5] was made with a silicon, and thus opaque substrate, preventing complete optical characterization. It was later shown [6], that using the Nano-Imprint technique for surface patterning allows to combine the advantages of controlled dewetting and substrate transparency, here silica (see Fig.1).

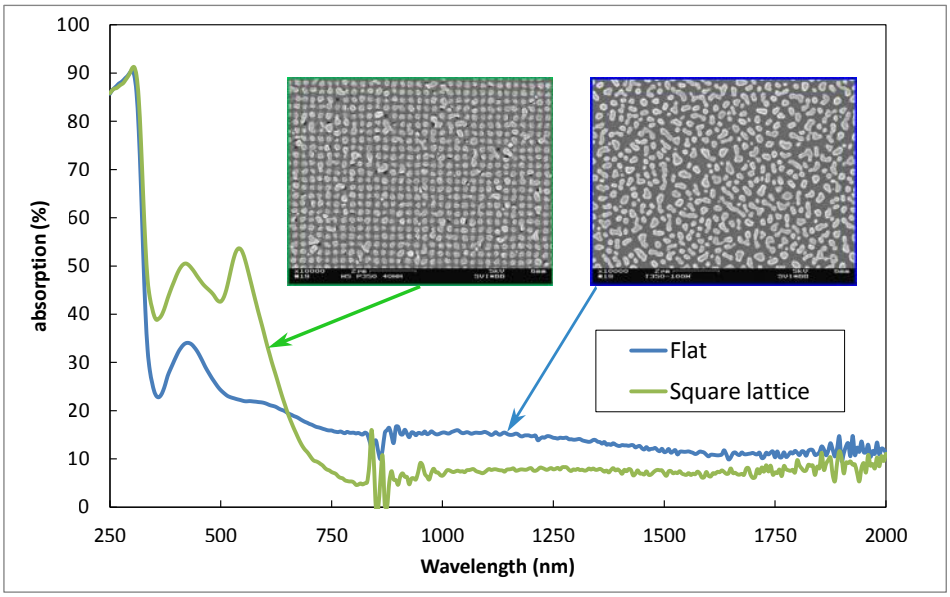



Figure 1: Comparison of the absoprtion in silver NP arrays obtained from solid state dewetting on flat (blue) at surface vs. patterned (green) surface. Image width is 10 µm.

A recent study on silver dewetting [7] has been applied to produce ordered arrays of silver nano-particles. The optical response of such systems was measured in transmission, reflection and

absorption. We observed the modification of the absorption signal with changes in the array of metallic NP, determined by tunable operating conditions: substrate pattern or silver deposition parameters. The results are also compared to dewetting on flat surfaces.

On flat surfaces, an absorption peak is observed at 420 nm. It remains unchanged on patterned surfaces, and a second peak appears. Its position is influenced by the pattern of the substrate.

**REFERENCES**


1. Thompson, C. V., "Solid State Dewetting of Thin Films," *Annu. Rev. Matter.*, Vol. 42, 399, 2012.
2. Morawiec, S., M. J. Mendes, S. Mirabella, F. Simone,F. Priolo,I. Crupi,"Self-assembled silver nanoparticles for plasmon-enhanced solar cell back reflectors: correlation between structural and optical properties," *Nanotech.*, Vol. 24, No. 26, 265601, 2013.
3. Abbarachi, M., M. Naffouti, B. Vial, A. Benkouider, L. Lermusiaux, I. Berbezier, N. Bonod, L. Favre, A. Ronda, "Wafer Scale Formation of Monocrystalline Silicon-Based Mie Resonators via Silicon-on-Insulator Dewetting," *ACS Nano*, Vol. 8, No. 11, 11181–11190, 2014.
4. Atwater, H., A. Polman,"Plasmonics for improved photovoltaic devices," *Nature materials*, Vol. 9, No. 3, 205–213, 2010.
5. Giermann, A., C. V. Thompson,"Requirements for graphoepitaxial alignment through solid-state dewetting of Au films," *J. App. Phys.*, Vol. 109, No. 8, 083520, 2011.
6. Le Bris, A., F. Maloum, J. Teisseire, F. Sorin, "Self-organized ordered silver nanoparticle arrays obtained by solid state dewetting," *App. Phys. Lett.*, Vol. 105, No. 20, 203102, 2014.
7. Jacquet, P., R. Podor, J. Ravaux, J. Teisseire, I.Gozhyk, J. Jupille, R.Lazzari, "Grain growth: The key to understand solid-state dewetting of silver thin films," *Scripta Mater.*, Vol. 115, 128–132, 2016.

# Chiral Au-crescents fabricated by angled hole-mask colloidal lithography for plasmon-enhanced CD measurements

**G. Klös[1*], and D. S. Sutherland[1]**
[1]iNano Aarhus University, Denmark
[*]corresponding author: gunnarkloes@inano.au.dk

**Abstract**-I report a new fabrication technique for chiral metal nanoparticles based on hole-mask colloidal lithography and angled evaporation. These plasmonic particles show a significant circular dichroism (CD) response and are promising candidates for plasmon-enhanced molecular CD measurements.

The electronic resonances of a plasmonic metal nanoparticle (NP) do not only depend on its structure and composition but, due to near field interactions, also on the attributes of the surrounding materials, especially the refractive index. Therefore, metal NPs are widely used for high sensitivity refractive index sensing [1]. The near field interactions are also exploited in more specific ways, one of which is through the creation of super chiral electromagnetic fields for enhancing the sensitivity of chiroptical measurements, allowing not only the detection but also the characterization of very dilute amounts of chiral material such as many biomolecules. It was shown that such fields are generated by optically exciting planar plasmonic chiral NPs [2].

The state-of-the-art fabrication technique of NPs with chiral responses involves time consuming methods such as layer-by-layer electron-beam lithography [3]. More simplicity and higher throughput is achieved when using instead a method based on self-assembled colloidal particles allowing to efficiently and reliably produce NPs of various geometries and sizes over large area surfaces [4].

In this contribution I am presenting a novel fabrication method of planar plasmonic chiral Au nanocrescents based on hole-mask colloidal lithography [4]. This method standardly involves the self-assembly of charged polystyrene nanospheres onto a spin coated PMMA layer covered with a triple layer of polyelectrolytes. The orthogonal physical vapor deposition (PVD) of a metal layer and subsequent tape stripping and oxygen-plasma etching leaves behind a hole-mask of randomly distributed holes with diameters given by the polystyrene nanospheres. The final structures are then created by angled PVD through these holes, whereby the novelty of the system presented here lies in utilizing the fact that the cross section of the hole is shrinking when evaporating material through it. For a deposition under a constant tilt angle with constant rotation speed around the axis of evaporation and a constant deposition rate this leads to semi rings with steady decrease in width and height from one end to the other.

Measuring the absorbance of Au crescents fabricated as described above (see fig. 1) shows a broad plasmonic response at a wavelength of about 780 nm which fits to previous results for Au structures [1]. Furthermore, when measuring the absorbance with circular polarized light, the resonance wavelength shifts and this shift also shows significant differences when comparing the two cases of clockwise and anti-clockwise circular polarization.

These newly designed nanostructures are therefore promising tools for the detection and structural analysis of chiral materials, yielding high sensitivity combined with a time- and cost-efficient fabrication method.

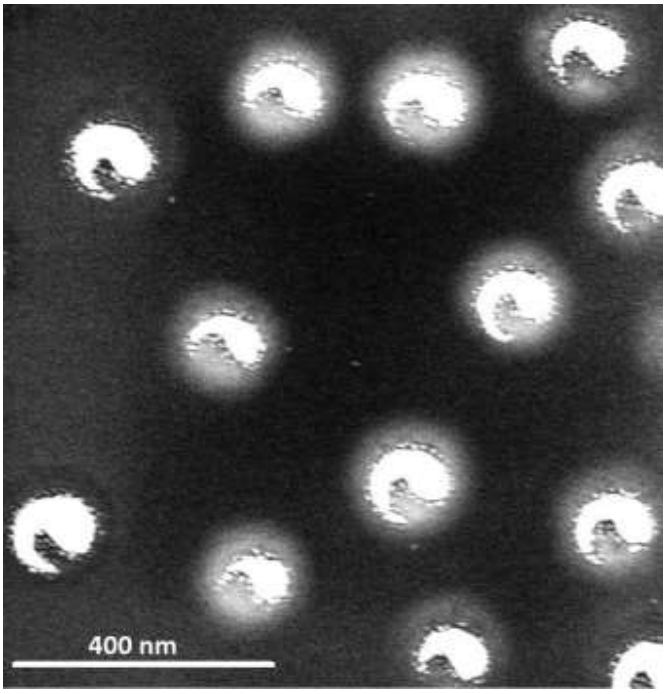



**Figure 1** Scanning electron microscope (SEM) image of the Au nanocrescents.

**REFERENCES**

1. Guerreiro, J. R. L. et al. "Multifunctional Biosensor Based on Localized Surface Plasmon Resonance for Monitoring Small Molecule-Protein Interaction," *ACS nano*, Vol. 8, No. 8, 7958–7967, 2014.
2. Hendry, E. et al., "Ultrasensitive detection and characterization of biomolecules using superchiral fields," *NNANO*, Vol. 5, 783-786, 2010.
3. Hentschel, M. et al., "Three-Dimensional Chiral Plasmonic Oligomers," *NanoLett*, Vol. 12, 2542-2547, 2012.
4. Bochenkov, V. E. and Sutherland, D. S. "From Rings to Crescents: A Novel Fabrication Technique Uncovers the Transition Details," *NanoLett*, Vol. 13, 1216-1220, 2013.

# Optical Nanofilters Based on Plasmonics Waveguide with Archimedes' Spiral Nanostructure

**Youwen Liu[1*], Yuncai Feng[1], Daxing Dong[1], and Xiaohua Wang[1]**

[1] Department of Applied Physics, Nanjing University of Aeronautics and Astronautics, Nanjing 210016, China

[*]corresponding author: ywliu@nuaa.edu.cn

**Abstract**- A plasmonics nanofilter based on the Metal-insulator-metal waveguide with an Archimedes' Spiral nanostructure is proposed and demonstrated by FDTD method. The simulation results indicate that the transmission valley and peak can be tuned by the rotation angle of the right-handed Archimedes (RAS) spiral structure and the number of channel can be adjusted by the number of the RAS ring. The unique feature may have potential applications in filter, sensor and photonic integrated circuits.

Surface plasmon polaritons (SPPs) propagating at the metal/dielectric interface has deep mode confinement, which has been considered as the promising solution to reduce the transverse dimension of the optical devices. Metal-insulator-metal (MIM) waveguide is demonstrated to be the best way to guide light with nanoscale mode confinement and low loss. The nanoscale filters were achieved in MIM waveguide structure consisting of different structures such as the plasmonic stubs, rectangle ring resonators, nano-capillary resonators, slot cavities, nanodisk and so on [1-3].

In this contribution, the nanofilter based on plasmonics waveguide with Archimedes spiral nanostructure is proposed, and the filter characteristics is investigated by using the finite-difference time-domain (FDTD) method. Fig.1 shows the 2D schematic drawing of the proposed structure, where the spiral air groove is surrounded by the silver substrate. To ensure the SPPs mode with strong confinement is excited, the width of MIM waveguide is set to w = 50 nm. In the cylindrical coordinates, right-handed Archimedes spiral (RAS) slot structure can be described as $\rho = a + b\theta/2\pi$, where a is the start radius of the spiral structure and b is the screw pitch. The wavelength $\lambda_m$ of the notch of the transmission is given as

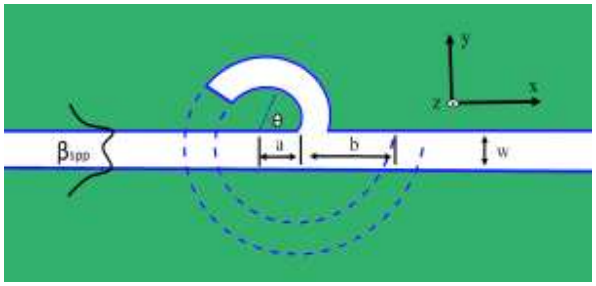



Fig. 1. Schematic diagram of the proposed nanofilter

$$\frac{2\pi}{\lambda_m}(2n_{\text{eff}}L(\theta)_{eff} + w) + \Delta\phi = (2m+1)\pi \tag{1}$$

where L $(\theta)_{\text{eff}}$ is the equivalent arc length of the slot, $\triangle\varphi$ is the phase shift caused by the reflection on the interface of the silver and air, $n_{\text{eff}}$ is the real part of the effective index, it can be obtained by the dispersion of the SPPs.

To further study the transmission characteristics, the FDTD method is used. Figure 2 show the transmission spectra of the with the RAS structure with different angle when the start radius of the spiral structure is set a = 100nm and the screw pitch is set b = 100 nm. The FDTD simulation results also reveal that the central wavelength of the bandgap as a function of the rotation angle of the RAS. Figure 3 shows the central wavelength of the bandgap shifts toward long wavelength with the increasing of the rotation angle, which is in accordance with the Eq. 1.

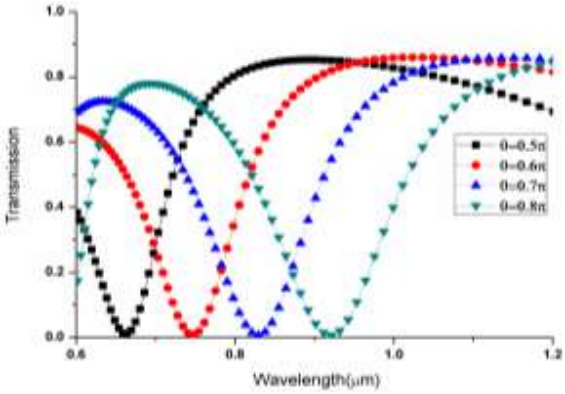



Fig. 2. Transmission spectra of the plasmonic waveguide with different angular.

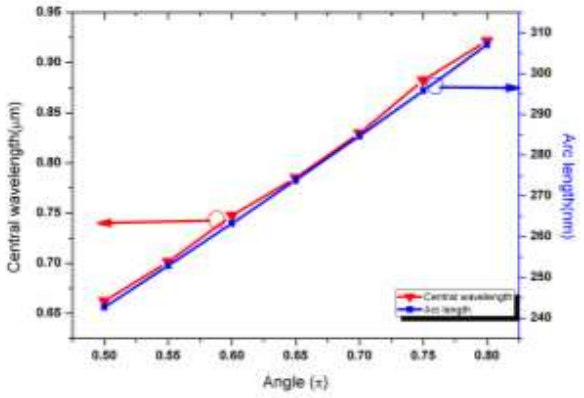



Fig. 3. The central wavelength of the bandgap and the arc length of the RAS as a function of the angle

Moreover, we design another waveguide structure to avoid overlapping between the RAS and the bus waveguide as shown in Fig. 4(a). Figure 4(b) shows the transmission spectra for a regular spiral ring and number of the filter channels of this structure becomes more than the previous one. The position of minimum transmittance shifts to longer wavelength with the increase of screw pitch b. Of course, we employ two regular spiral rings coupled to the MIM waveguide to obtain more channels, as shown in Figure 4(c).

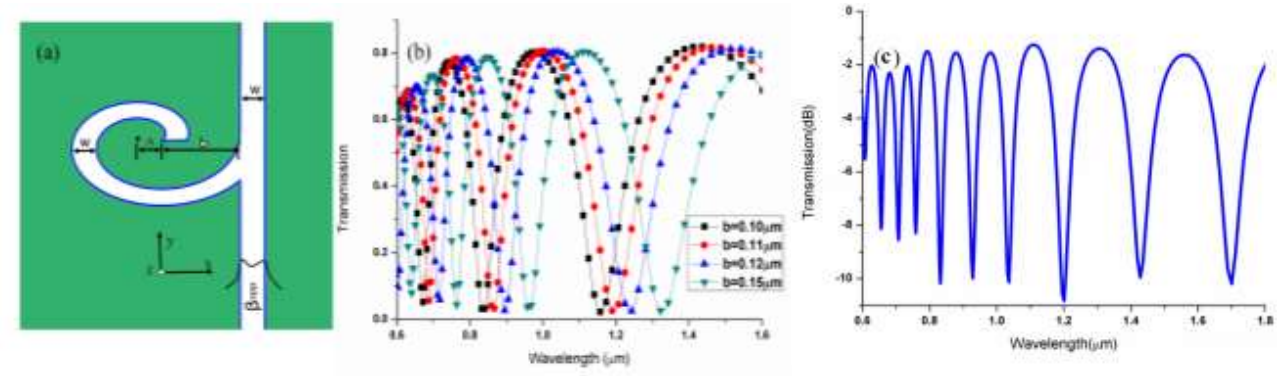



Fig. 4. (a) The schematic diagram of the bus waveguide with a regular spiral ring, (b) the transmission spectrum of nanofilter with a regular spiral ring for different screw pitch, (c) the transmission spectrum of nanofilter with two regular spiral rings.

In conclusion, an optical nanofilter based on MIM waveguide with RAS structure is proposed and studied numerically. The results reveal that the transmission valley and peak can be tuned by the rotation angle $\theta$ of the RAS structure.

**Acknowledgements**: the authors gratefully acknowledge the support of K. C. Wong education foundation, Hong Kong.

## REFERENCES

1. Lin, X.-S. and X.-G. Huang, "Tooth-shaped plasmonic waveguide filters with nanometeric sizes". Opt. Lett.,. **33**(23): 2874-2876, 2008.
2. Guo, Y., et al., "A plasmonic splitter based on slot cavity". Opt Exp., **19**(15):13831-13838, 2011..
3. Pang, S., et al., "The filter characteristic research of metal-insulator-metal waveguide with double overlapping annular rings". Plasmonics, **10**(6):1723-1728, 2015

# Minimum Forward Light Scattering by Silicon nanopillars

**J. F. Algorri[1*], R. Vergaz[1], A. Cuadrado[2], J. M. Sánchez-Pena[1], and B. García-Cámara[1]**
[1] Group of Displays and Photonic Applications (GDAF-UC3M), Carlos III University of Madrid, Spain.
[2] Laser Processing Group, Instituto de Óptica, CSIC, C/Serrano 121, 28006 Madrid, Spain
[*]corresponding author: jalgorri@ing.uc3m.es

**Abstract**- In this paper, we demonstrate that for silicon nanopillars an optimum aspect ratio can be found, at which the overlapped electric and magnetic dipole resonances provide an optimized minimum forward scattering. This optimum shape depends on the aspect ratio, wavelength and refractive index of the surrounding medium. We work in the frame of numerical simulations based on Maxwell equations solved by finite element method. These results are promising for design and create novel flat optical devices.

Kerker's conditions were theoretically proposed for spherical particles in 1983 [1]. Two possible conditions were predicted, in this work the second condition (minimum forward) is sought. This condition appears when a constructive interference in the backscattering direction is produced while almost cancel each other in the forward direction. This theoretical work was experimentally demonstrated at micrometric wavelengths in 2012 [2] and at nanometric wavelengths in 2013 [3]. In addition, a significant greater overlap of the electric and magnetic-dipole resonances, and in consequence a higher forward scattering, can be realized if spheroidal [4] and disks [5] are considered. In this paper, we demonstrate that for silicon nanopillars also an optimum aspect ratio can be found for an enhanced forward scattering condition.

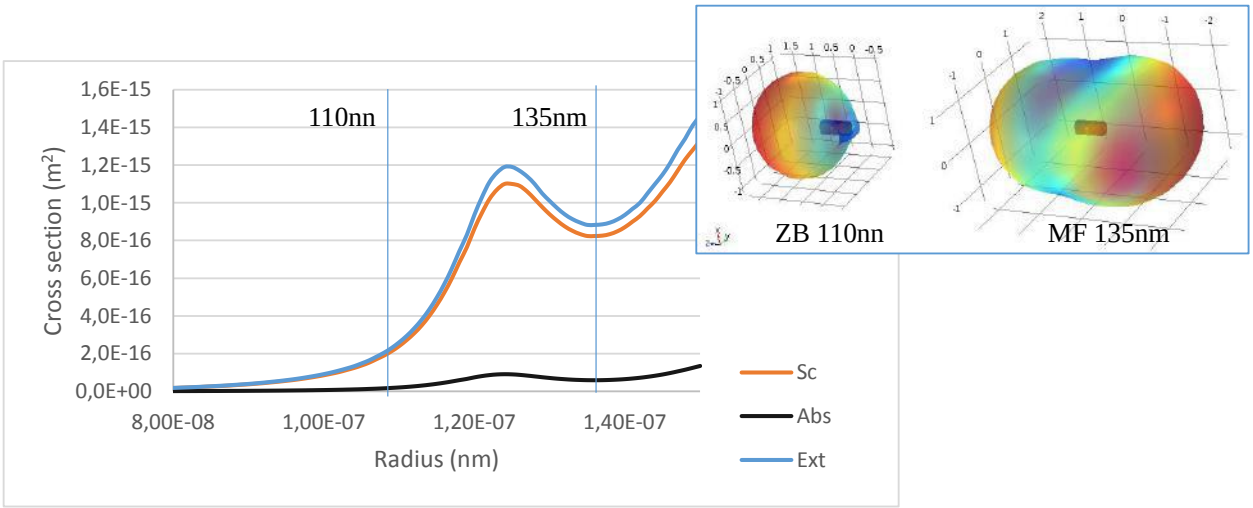



Figure 1. Extinction, scattering and absorption cross sections for a nanopillar with height of 480nm. The inset shows the far field scattering for two radius satisfying Kerker's conditions.

From this study, the forward condition can be easily extracted because it is produced when both dipolar contributions, electric and magnetic, intersect. Although there are several intersections, the minimum forward condition can be found at the minimum value between peaks (Fig. 1, R=135nm). For example, for a determined

wavelength of 1250 nm the results are shown in Fig.1 (a). As can be observed, by studying the far field [Fig. 1 (b)] the intersection of both contributions produce a minimum forward scattering. By studying all of the scattering profiles for each height, radius and wavelengths, the minimum forward condition is extracted. The result is a graph at which all the relations can be observed (Fig. 2). A linear behavior is observed when the aspect ratio is of a nanopillar (height higher than diameter). Also, for this aspect ratio the minimum forward has a higher value.

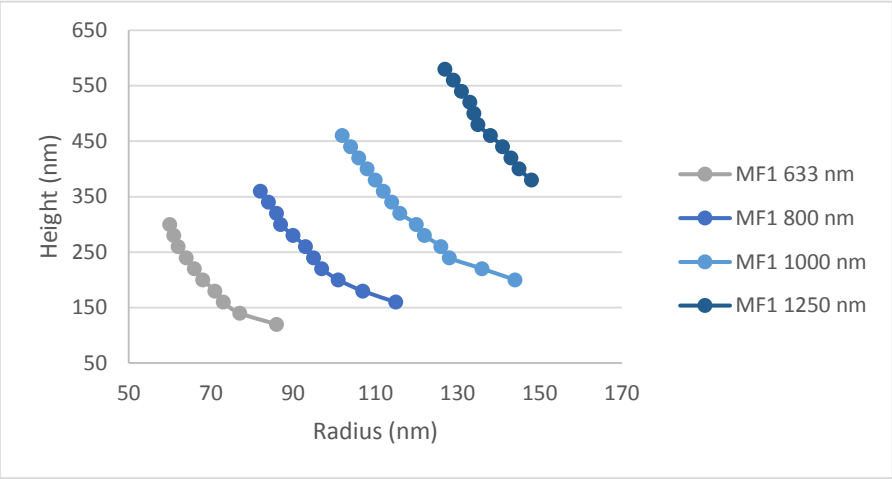



Figure 2. Parameters at which minimum zero forward condition is satisfied.

We have demonstrated that the use of Si nanopillars are easy to design due to a linear relation between the aspect ratio and the minimum forward condition. Moreover, a higher forward scattering than usual spherical nanoparticles can be obtained. These results are of great value in order to design very efficient, low-loss flat-optical devices.

**Acknowledgements.** This work has been supported by Ministerio de Economía y Competitividad of Spain (grant no. TEC2013-50138-EXP & TEC2013-47342-C2-2-R) and the R&D Program SINFOTON S2013/MIT-2790 of the Comunidad de Madrid

**REFERENCES**

1. Kerker, M., D. S. Wang and C. L. Giles, *J. Opt. Soc. Am.*, vol. 73, pp. 765-767, 1983.
2. Geffrin, J.M., et al., *Nature Commun.*, vol. 3, 1171, 2012.
3. Fu, Y. H., A. I. Kuznetsov, A. E. Miroshnichenko, Y. F. Yuand B. Luk'yanchuk, *Nature Commun.*, vol . 4, pp. 1527, 2013.
4. Boris S. Luk'yanchuk, Nikolai V. Voshchinnikov, Ramón Paniagua-Domínguez, and Arseniy I. Kuznetsov, *ACS Photonics*, vol. 2, no. 7, pp. 993-999, 2015.
5. I. Staude, A. E. Miroshnichenko, M. Decker, N. T. Fofang, S. Liu, E. Gonzales, J. Dominguez, T. S. Luk, D. N. Neshev, I. Brener, and Y. S. Kivshar, *ACS Nano*, vol 7, no. 9, pp. 7824-7832, 2013.

# Large Radiative Decay Rate Enhancement of Single Quantum Dots by a Gold Nanocone Antenna

**K. Matsuzaki[1*], H.-W. Liu[1], B. Hoffmann[1], A. Dutschke[1,2], S. Christiansen[1,3], S. Götzinger[4,1], and V. Sandoghdar[1,4]**

[1]Max Planck Institute for the Science of Light, Erlangen, Germany

[2]Carl Zeiss Microscopy GmbH, Oberkochen, Germany

[3]Helmholtz-Zentrum Berlin für Materialien und Energie GmbH, Berlin, Germany

[4]Friedrich Alexander University of Erlangen-Nürnberg, Germany

[*]corresponding author: korenobu.matsuzaki@mpl.mpg.de

**Abstract**-The fluorescence enhancement of a single quantum dot by a plasmonic gold nanocone antenna was studied experimentally. We first show that the photophysics of the quantum dot is modified by the large enhancement of the radiative decay rate. By taking the modified photophysics into account, we extract the radiative and nonradiative decay rates from the experimental data. We demonstrate that a large radiative decay rate enhancement of the order of one hundred and a high quantum efficiency are achieved simultaneously.

Control of the spontaneous emission of a quantum emitter is important in many domains of science. Plasmonic antennas are often utilized to modify the spontaneous emission rate. In a previous work, we used a gold nanosphere as a plasmonic antenna, and we experimentally demonstrated that the fluorescence lifetime of a molecule could be reduced by a factor of 22 [1]. In order to obtain a large enhancement of the radiative decay rate, the emitter needs to be positioned very close to the antenna. However, that makes the ohmic loss in the metal significant, resulting in a lower quantum efficiency. In order to overcome this problem, we theoretically explored various alternatives, including a nanocone structure [2,3]. It turns out that a gold nanocone antenna allows one to enhance the radiative decay rate by a factor of 1000 while keeping a high quantum efficiency. Here we present the experimental realization of this concept.

The gold nanocones were fabricated by focused ion beam milling of a thin gold film deposited on a glass substrate (Fig. 1a) [4]. As shown in Fig. 1b and c, the wavelength for the plasmon resonance can be tuned by varying the dimension of the nanocone, in good agreement with the theoretical calculations. Therefore, we can choose a nanocone with an appropriate plasmon resonance wavelength to match the emission wavelength of the emitter.

As emitter, we used single colloidal quantum dots attached to the end of a glass fiber tip. Using shear-force control, the quantum dot can be approached and kept close to the glass surface, on which the nanocones are fabricated (Fig. 2). This configuration allows us to move the quantum dot and the nanocone with nanometer precision with respect to each other.

We first studied the fluorescence emission of a quantum dot as a function of its position relative to a nanocone. By analyzing the change in the fluorescence lifetime and the degree of second-order coherence ($g^{(2)}$), we elucidated how the acceleration of the radiative decay caused by the nanocone antenna affects the photophysics of the quantum dot. Furthermore, by measuring the fluorescence emission as a function of the

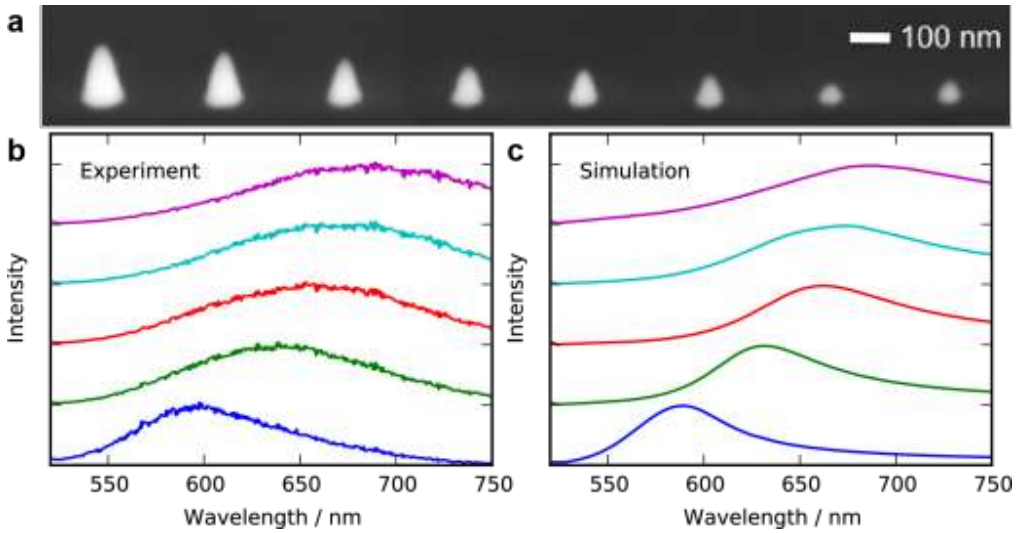



**Figure 1.** (a) Scanning electron microscope (SEM) images of gold nanocones with different sizes and aspect ratios. (b) Experimental and (c) theoretical plasmon spectra of five gold nanocones with different dimensions.

excitation power, we could extract the radiative and nonradiative decay rates of the quantum dot in the presence and absence of the nanocone antenna. The extracted decay rates demonstrate that our nanocone antenna is indeed capable of achieving a large radiative decay rate enhancement while keeping the quantum efficiency high. The details of our analysis will be discussed in the presentation.

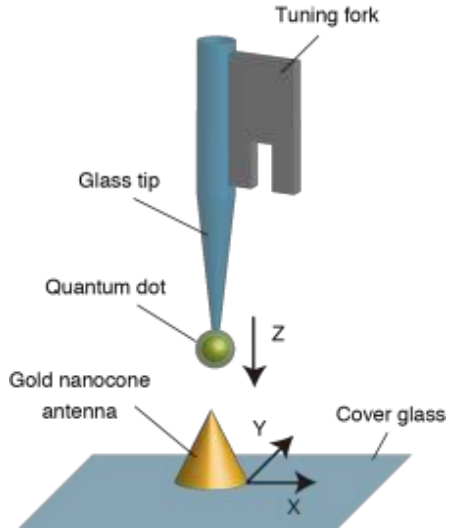



**Figure 2.** Schematics of the experiment.

**REFERENCES**


1. Kühn, S., U. Håkanson, L. Rogobete and V. Sandoghdar, "Enhancement of Single-Molecule Fluorescence Using a Gold Nanoparticle as an Optical Nanoantenna," *Phys. Rev. Lett.*, Vol. 97, 017402, 2006.
2. Mohammadi, A., F. Kaminski, V. Sandoghdar and M. Agio, "Fluorescence Enhancement with the Optical (Bi-) Conical Antenna," *J. Phys. Chem. C*, Vol. 114, 7372, 2010.
3. Chen, X.-W., V. Sandoghdar and M. Agio, "Metallodielectric Hybrid Antennas for Ultrastrong Enhancement of Spontaneous Emission," *Phys Rev. Lett.*,, Vol. 108, 233001, 2012.
4. Hoffmann, B., S. Vassant, X.-W. Chen, S. Götzinger, V. Sandoghdar and S. Christiansen, "Fabrication and characterization of plasmonic nanocone antennas for strong spontaneous emission enhancement," *Nanotechnology*, Vol. 26, 404001, 2015.

# Out-of-Plane Optical Interactions of Nanohole Trimers Milled in Stacked Gold Films

**M. Janipour** [1,2*], **and K. Sendur**[1*]

[1] Faculty of Engineering and Natural Science, Sabancı University, Orhanlı – Tuzla, Istanbul, Turkey

[2] Department of Electrical Engineering, Iran University of Science and Technology, Tehran, Iran

[*]corresponding authors: mjanipour@sabanciuniv.edu, sendur@sabanciuniv.edu

**Abstract**- Optical interactions of symmetric nanohole trimers milled in stacked gold films are investigated. A dispersive finite-difference time-domain (D-FDTD) model is used to study the presented system through numerical simulations. The normalized scattering spectrum of the presented structure demonstrates two distinct resonant peaks. The scattering spectrum of the stacked structure is compared with the scattering spectrum of a symmetric nanohole trimer. It can be seen that for the stacked trimers the resonant peaks are blue shifted in comparison to a nanohole trimer milled in a single metallic film.

It has been shown theoretically and numerically [1], through the normalized electric and magnetic power amplitudes, and also experimentally [2], using SNOM measurements, that the output radiated power from a nanohole milled in a metallic film is dominated by magnetic power. Thus, each nanohole can be considered as a radiating magnetic dipole [3]. In other words, the nanoholes may radiate through surface plasmon polaritons (SPPs) at the dielectric-metal interface [4]. However, nanoholes may have in-plane or out-of-plane near-field interactions [5], which affect the scattering spectrum of the structure. Figure 1(a), and 1(b) demonstrate the schematic representation of the structure and scattering spectrum for symmetric nanoholes milled in a single (solid-line) and two stacked (dashed-line) gold films, achieved from D-FDTD numerical simulations, respectively. It is clear that two distinct resonant peaks are obvious according to Fig. 1(b). In addition, Figures 1(c), and 1(d) show the phase variations of the magnetic field component (i.e. $\angle H_y$) for the layered nanoholes at the first (short-wavelength), and second (long-wavelength) resonant peaks which correspond to $\lambda = 600$ nm, and $\lambda = 817$ nm, respectively. According to Figs. 1(c), and 1(d), it can be seen that at $\lambda = 600$ nm the out-of-plane nanoholes may interact out-of-phase (antibonding mode) and at $\lambda = 817$ nm the nanoholes can interact in-phase (bonding mode).

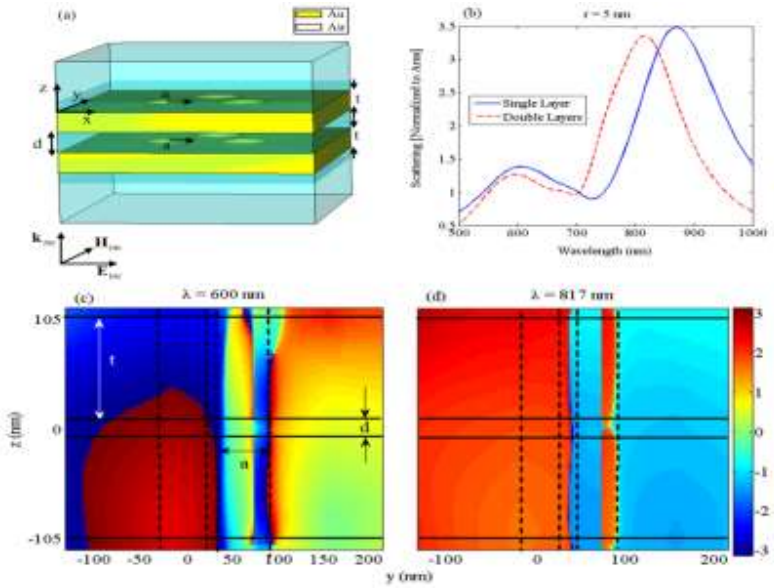



**Figure 1 (a).** The schematic representation of the stacked symmetric nanohole trimers. **(b)** The normalized scattering spectrum for the nanohole trimers milled in a single (solid-line), and double stacked (dashed-line) layers of gold film obtained by simulations. (c), and (d) phase variations of $\angle H_y$ component at $\lambda = 600\,\text{nm}$, and $\lambda = 817\,\text{nm}$, respectively.

**Acknowledgements**, Dr. Mohsen Janipour acknowledges the support of TUBITAK under the 2216- Research Fellowship Program.

**REFERENCES**

1. Janipour, M., T. Pakizeh and F. Hodjat-Kashani, "Strong optical interaction of two adjacent rectangular nanoholes in a gold film," *Opt. Express*, Vol. 21, No. 26, 31769-31781, 2013.
2. Permyakov, D. V., I. S. Mukhin, I. I. Shishkin, A. K. Samusev, P. A. Belov and Yu. S. Kivshar, "Mapping Electromagnetic Fields Near a Subwavelength Hole," *JETP Lett.*, Vol. 99, No. 11, 622-626, 2014.
3. Janipour, M., T. Pakizeh and F. Hodjat-Kashani, "Optical Interaction of a Pair of Nanoholes in Au Film via Surface Plasmon Polaritons," *IEEE Phot. J.*, Vol. 6, No. 3, 4800913-1--4800913-3, 2014.
4. S. H. Chang, S. Gray, and G. Schatz, "Surface plasmon generation and light transmission by isolated nanoholes and arrays of nanoholes in thin metal films," *Opt. Express*, Vol. 13, No. 8, 3150–3165, 2005.
5. Janipour, M., K. Sendur, "Optical Transmission Enhancement of Stacked Plasmonic Apertures," *J. Light. Tech.*, Vol. 34, No. 3, 961-968, 2016.

# Far-field control of hot-spots on random metal-dielectric networks

**P. Bondareff[1], G. Volpe[2], S. Gigan[3] and S. Gresillon[1*]**

[1]Institut Langevin, Université Pierre et Marie Curie, ESPCI Paris and CNRS, 1 rue Jussieu, 75005 Paris, France

[2]Department of Chemistry, University College London, 20 Gordon Street, London WC1H 0AJ, United Kingdom

[3]Laboratoire Kastler Brossel, UMR8552 of CNRS and University Pierre et Marie Curie, Ecole Normale Supérieure and Collège de France, 24 rue Lhomond, 75005 Paris, France

[*]corresponding author: Samuel.gresillon@espci.fr

**Abstract**- Efficient control of carefully designed nanostructure has been achieved recently, but fabrication and accessibility of the modes addressed from the far-field still represent open challenges. It has been shown on disordered media that disorder can be turned into an advantage to control light propagation. We propose a new experimental scheme where plasmonics modes on random metal-dielectric networks are tuned by wavefront shaping which allows to extract information about the extension of the modes and also far field control of hot-spots.

Addressing the nanoscale through far field control is tailored by dynamic control onto smaller and smaller objects[1]. Efficient control of carefully designed nanoscale devices has been achieved in the past years[2], but fabrication and accessibility of the modes addressed from the far-field still represent open challenges. It has been shown recently on random dielectric media that disorder can be turned into an advantage to control light propagationcite[3]. Combining metal and dielectric in a random system would allow to couple plasmon modes and to control their propagation from the far-field. Random metal-dielectric films which are particularly easy to fabricate and show interesting intrinsic behavior, such as intense subwavelength near-field features[4] and broadband optical response[5] could therefore be used to achieve such far-field dynamical control of the optical near-field of a nanosystem.

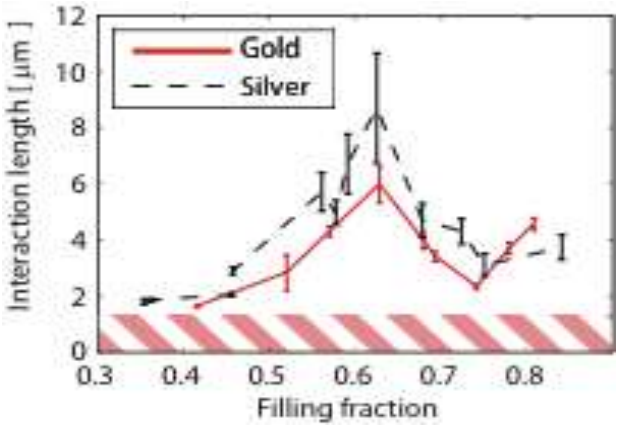



**Figure 1:** Comparison of the interaction length measured on gold and silver films for different filling fractions *ff*. Percolation is around *ff*=0.65. The shaded stripe shows the detection limit of our detection system.

We propose a new experimental scheme where plasmonics modes are controlled by wavefront shaping of the incident beam with a spatial light modulator directly imaged on a random metal-dielectric film. This allows us to extract information about the extension of the modes, a key parameter for the far-field control of such films. Experimental results on the control of the propagation of surface plasmons polaritons on the surface will be presented. In particular, we will show that the filling fraction influences the efficiency of the coupling between far-field excitation and the plasmonic modes. Therefore, by choosing the right filling fraction for the metal film far-field control of hot-spots has been successively implemented[6].

**REFERENCES**


1. M.L. Brongersma and V. M. Shalaev, The case for Plasmonics, *Science* Vol. 328, 440-441, 2010; L. Novotny and N. van Hulst, Antennas for light, *Nat. Photonics* Vol. 5, 83-90, 2011.
2. M.I. Stockman et al, Coherent Control of Femtosecond Energy Localization in Nanosystems, *Phys Rev Lett* Vol. 88, No. 067402, 2002; M. Aeschlimann et al., Adaptative subwavelength control of nano-optical fields, *Nature* Vol. 446, 301-304, 2007; G. Volpe et al. Contrling the optical near-field of nanoantennas with spatial phase-shaped beams *Nano letters* Vol. 9, 3608-3611, 2009; B. Gjonaj et al, Active spatial control of plasmonic fields *Nat Photon* Vol. 5, 360-363, 2011; T. S. Kao et al "Digitally" addressable focusing of light into a Subwavelength Hot Spot *Nano letters* Vol. 12, 2728-2731, 2012.
3. W. Wenseleers et al, Five Orders-of-Magnitude Enhancement of Two-Photon Absorption for Dyes on Silver Nanoparticles Fractal Clusters, *J Phys Chem B* Vol. 106, 6853-6863, 2002; A. Sanchot et al, Plasmonic Nanoparticle Networks for Light and Heat Concentration *ACS Nano* Vol. 6, 3434-3440, 2012.
4. C. Grandqvist and O. Hunderi, Optical properties of ultrafine gold particles, *Phys Rev B* Vol. 16, 3513-3534, 1977; A. K. Sarychev and V. M. Shalaev, Electromagnetic field fluctuations and optical nonlinearities in metal-dielectric composites. *Phys Rep* Vol. 335, 275-371, 2000.
5. M. Stockman et al, Giant fluctuations of local optical fields in fractal clusters, *Phys Rev Lett* Vol. 72, 1-4, 1994; F. Brouers et al, Giant field fluctuation of local opticl fields in fractal clusters, *Phys Rev B* Vol. 58, 15897-15903, 1998.
6. P. Bondareff, G. Volpe, S Gigan, S Gresillon, Probing Extended Modes on Disordered Plasmonic Networks by Wavefront Shaping, *ACS Photonics* Vol. 2, 1658-1662, 2015.

# Double Hot-Spot Dual-Polarization Elliptical Crescent Nanoantenna for Near-Infrared Detection Applications

**A. Y. Elsharabasy*, M. H. Bakr, and M. Jamal Deen**
Department of Electrical and Computer Engineering, McMaster University, Canada
*corresponding author: elsharay@mcmaster.ca

**Abstract**- In this work, we introduce a novel design for a gold nanoantenna array. The nanoantenna consists of an elliptical aperture etched out from a rectangle. A less-than-half elliptical patch is placed inside the aperture. The geometrical dimensions are properly selected such that two symmetrical small gaps are created. The electric field intensity has significant enhancement in these two gaps (hot-spots) at the same resonance frequency within the near-infrared (NIR) regime for both orthogonal polarizations. The new design offers an improved performance for IR detection and applications.

Nanoantennas have the ability to confine the light into sub-wavelength volumes [1]. Their unique performance due to light-matter interaction has recently lead to numerous applications in energy harvesting [2], photothermal heat generation [3], heat assisted magnetic recording [4], and infra-red (IR) detection [5]. The light, in general, is propagating in a random polarized manner. Therefore, the efficiency of light detection applications relies on ability to receive different polarizations through the same antenna. Here, we propose a new design for an elliptical crescent nanoantenna which supports dual polarization. Moreover, the electric field intensity undergoes a large enhancement at two hot spots simultaneously.

Our design geometrical parameters are presented in Fig. 1. The nanoantenna array has been simulated using COMSOL Multiphysics. The simulations are carried out on one cell of the array by defining two floquet ports with an incident power of 1 W, in addition to periodic boundary conditions at the sides. Perfect matched layer (PML) has been utilized on top and bottom of the simulation volume. The 30-nm thick gold nanoantenna has been designed using Drude model with physical constants from [6]. The electric field enhancement at the hot spot center is shown in Fig. 2 corresponding to both X-polarized and Y-polarized incident electric fields. The spatial electric field intensity distribution at the resonance frequency is presented in Fig. 3(a) for the Y-polarized incident field. Fig. 3(b) shows the field intensity distribution for the X-polarized incident field. A third weaker hot spot is also observed in the horizontal gap between both ellipses. Also, HFSS is utilized to validate all the simulation results.

**REFERENCES**

1. Novotny, L. and N. van Hulst, "Antennas for light", *Nature Photonics*. , Vol. 5, No. 2, 83–90, 2011.
2. Atwater, H. A. and Polman , A., "Plasmonics for improved photovoltaic devices", *Nature Materials*, Vol. 9, No. 3, 205–213, 2010.
3. Coppens, Z. J., Li, W., Walker, D. G. and Valentine, J. G., "Probing and controlling photothermal heat generation in plasmonic nanostructures", *Nano Letters* , Vol. 13, No. 3, 1023–1028, 2013.

4. Challener, W. A., et al., "Heat-assisted magnetic recording by a near-field transducer with efficient optical energy transfer", *Nature Photonics* , Vol. 3, No. 4, 220–224, 2009.
5. Neubrech, Frank, et al., "Resonant plasmonic and vibrational coupling in a tailored nanoantenna for infrared detection", *Physical Review Letters*, Vol. 101, No.15, 2008.
6. Soliman, E. A., "Wideband nanocrescent plasmonic antenna with engineered spectral response", *Microwave and Optical Technology Letters*, Vol. 55, 624–629, 2013.

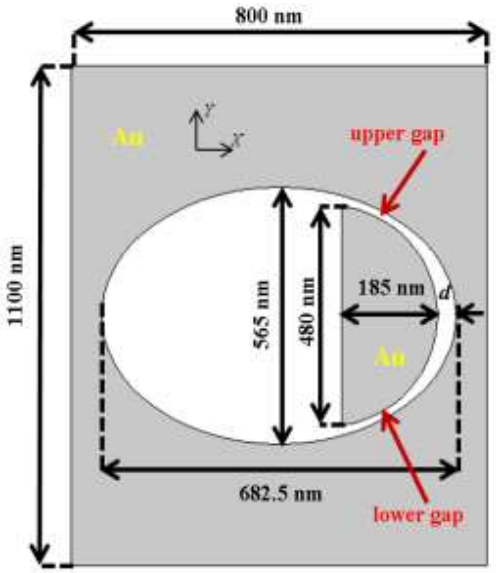



Fig. 1. A schematic top view for the proposed nanoantenna.

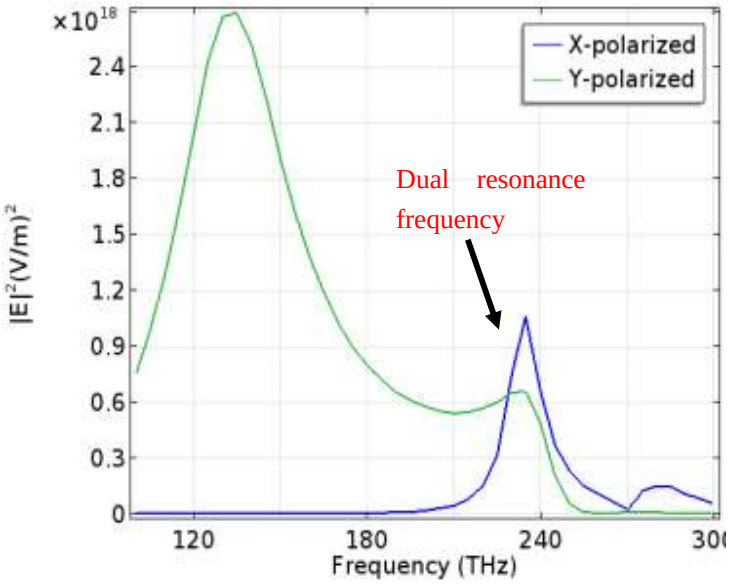
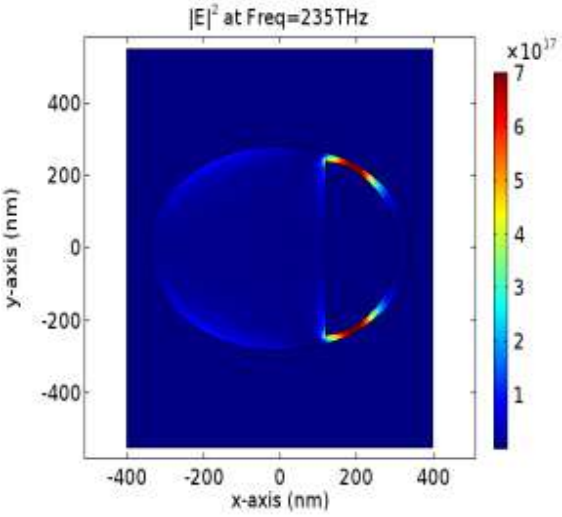
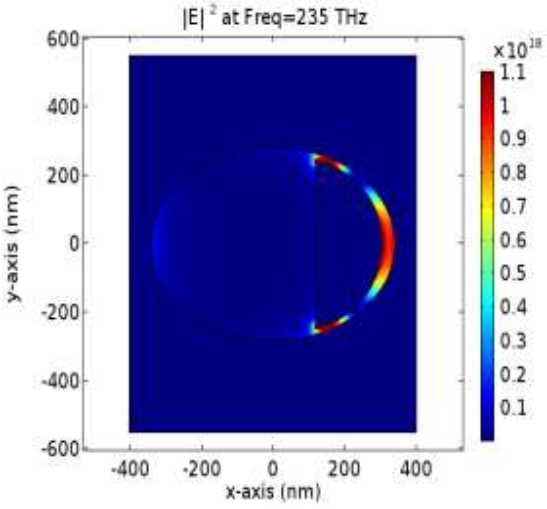



Fig. 2. Electric field intensity versus frequency.




(a)




(b)

Fig. 3. Electric field intensity distribution in the xy-plane normal to incident wave (a) with y-polarized electric field, and (b) with x-polarized electric field.

# Hybrid plasmonic directional coupler switches and modulators

**D. C. Zografopoulos[1*], M. A. Swillam[2], L. A. Shahada[3], and R. Beccherelli[1]**

[1]Consiglio Nazionale delle Ricerche, Istituto per la Microelettronica e Microsistemi (CNR-IMM), Roma 00133, Italy

[2] Department of Physics, School of Science and Engineering, The American University in Cairo, New Cairo, 11835, Egypt

3 Department of Chemistry and Earth Sciences, College of Arts and Science, Qatar University, P.O. Box 2713, Doha, Qatar

[*]corresponding author: dimitrios.zografopoulos@artov.imm.cnr.it

**Abstract**- The design of a hybrid plasmonic modulator based on directional couplers enhanced with a layer of electro-optic polymer is presented. The modulator shows very broad operating window with low crosstalk values and very small footprint with respect to similar couplers and switches of the silicon photonics platform.

Owing to their capacity for sub-wavelength light confinement, plasmonics enable the miniaturization of integrated optical signal processing units in a platform compatible with traditional CMOS technology. In such architectures, modulators and switches are essential elements for fast and low-power optical signal processing. Here, we present the design of a hybrid plasmonic modulator in a directional coupler configuration [1], based on the extended version of conductor-gap-silicon plasmonic waveguides [2]. The device features high modulation depths, very low modulation crosstalk, and moderate insertion losses and power consumption.

**Acknowledgements**. This work was made possible by a NPRP award [NPRP 7456-1-085] from the Qatar National Research Fund (member of the Qatar Foundation). The statements made herein are solely the responsibility of the authors.

**REFERENCES**

1. M. Wu, Z. Han, and V. Van, "Conductor-gap-silicon plasmonic waveguides and passive components at subwavelength scale," *Opt. Express*, vol. 18, pp. 11728-11736 (2010).
2. D. C. Zografopoulos, M. A. Swillam, L. A. Shahada, and R. Beccherelli, "Hybrid electro-optic plasmonic modulators based on directional coupler switches", *Appl. Phys. A*, Vol. 12, art. no. 344 (2016).

# Ultrafast dynamics of plasmonic vortices

**D. Kilbane[1,2*], G. Spektor[3], A. K. Mahro[1], B. Frank[4], L. Gal[3],**
**H. Giessen[4], F.-J. Meyer zu Heringdorf[5], M. Orenstein[3], M. Aeschlimann[1]**
[1]Department of Physics, University of Kaiserslautern, 67663 Kaiserslautern, Germany
[2]School of Physics, University College Dublin, Belfield, Dublin 4, Ireland
[3]Department of Electrical Engineering, Technion – Israel Institute of Technology, 32000 Haifa, Israel
[4]4th Physics Institute and Research Centre SCoPE, University of Stuttgart, D-70569 Stuttgart, Germany
[5]Faculty of Physics and CENIDE, University of Duisburg-Essen, 47057 Duisburg, Germany
[*]corresponding author: dkilbane@physik.uni-kl.de

**Abstract**- We map the spatiotemporal evolution of plasmonic vortices with < 40 nm and 100 as resolution using time-resolved photoemission electron microscopy. The resulting sub-optical cycle snapshot images reveal the ultrafast dynamics of orbital angular momentum leading to the formation of these vortices.

Optical vortices are a topic of great interest in many fields of research and have led to several novel applications such as optical tweezers in biology[1] and orbital angular momentum (OAM) multiplexing in communication[2]. In plasmonics, OAM has also been controlled by illuminating Archimedean spirals[3] and plasmonic vortex lenses (PVLs)[4] with light of different circular helicity. Here we observe the ultrafast dynamics of the formation of plasmonic vortices in these structures.

PVLs are prepared by focused ion beam milling into thin atomically flat mono-crystalline gold platelets. Near-field imaging is performed using time-resolved photoemission electron microscopy (TR-PEEM) under normal incidence illumination with an ultrashort pulse Ti:Sa laser[5]. Snapshot images are recorded every 100 as of the different plasmonic vortices formed by illumination with left and right handed circularly polarized light. Sequences of such sub-optical cycle snapshots show the ultrafast dynamics of these plasmonic vortices.

**REFERENCES**

1. Padgett, M. & Bowman, R. "Tweezers with a twist," *Nature Photon.*, Vol. 5, 343–348, 2011.
2. Bozinovic, N. et al., "Terabit-scale orbital angular momentum mode division multiplexing in fibers," *Science*, Vol. 340, 1545–1548, 2103.
3. Gorodetski, Y., Niv, A., Kleiner, V. & Hasman, E. "Observation of the spin-based plasmonic effect in nanoscale structures," *Physical Review Letters*, Vol. 101, 043903, 2008.
4. Kim, H., et al. "Synthesis and dynamic switching of surface plasmon vortices with plasmonic vortex lens," *Nano Letters*, Vol. 10, 529–536, 2010.
5. Kahl, P., et al. "Normal-incidence photoemission electron microscopy (NI-PEEM) for imaging surface plasmon polaritons," *Plasmonics*, Vol. 9, 1401–1407, 2014.

# Propagation of nolinear surface waves through metamaterial waveguide structure

**B. Mokhtari[1*], N. Hissi[2], Mohammed. M. Shabat[3], N.Cherkaoui Eddeqaqi[4], S. Bahsine[5]**

1, 2, 4, 5 Physics department, Faculty of Sciences, Moulay Ismail University, Morocco

3 Physics department, Islamic University, Gaza, Palestine

**J.Atangana**

Physics department, University of Yaounde I, Yaounde, Cameroon

*nicet2012@hotmail.com

**Abstract** - Recent studies of novel composite materials with a negative refractive index of refraction opens up a unique possibility to design novel types of devices, where electromagnetic waves propagate in a nonconventional way. We present an investigation of nonlinear electromagnetic surface waves propagating in a new ferrite slab made of a metamaterial, where the permittivity is selected in the form of the commonly used function for plasmon investigations, the metamaterial film is surrounded by a nonlinear cover cladding and a ferrite substrate, we calculate the associated propagation index and the film-cover interface nonlinearity. Results show that the propagating characteristics in the above three layers can be tuned and controlled by selecting the film thickness and the film-cover interface nonlinearity. It is also shown that the use of the singular solutions to the electric-field equation allows to identify several new properties of surface waves which do not exist in conventional waveguide.

Keywords: Metamaterial; Nonlinear electromagnetic surface waves; Ferrite substrate; Waveguide.

# Nanoparticle multilayers and colloidal solutions of silver nanoparticles synthesized by femtosecond pulsed laser ablation

**Ovidio Peña-Rodríguez,[1,*] Pablo Díaz-Núñez,[1,2] Jesús González-Izquierdo,[2] Guillermo González-Rubio,[2,3] Gabriel Balabanian,[4] Andrés Guerrero-Martínez,[2] Antonio Rivera,[1] José Olivares,[5] José Manuel Perlado,[1] and Luis Bañares[2]**

[1]Instituto de Fusión Nuclear, Universidad Politécnica de Madrid, José Gutiérrez Abascal 2, E-28006 Madrid, Spain

[2]Departamento de Química Física I, Facultad de Ciencias Químicas, Universidad Complutense de Madrid, 28040 Madrid, Spain

[3]BioNanoPlasmonics Laboratory, CIC biomaGUNE, Paseo de Miramón 182, 20009 Donostia - San Sebastián, Spain

[4]Carl Zeiss Microscopy GmbH, Geschäftsführung: Dr. Frank Stietz., Sitz der Gesellschaft: 73447 Oberkochen, Germany

[5]Instituto de Óptica, Consejo Superior de Investigaciones Científicas, C/ Serrano 121, E-28006 Madrid, Spain

[*]Corresponding author: ovidio.pena@upm.es

**Abstract**-In this work we report the synthesis of silver nanoparticles by Femtosecond Pulsed Laser Ablation. Those nanoparticles can be either deposited on a substrate (and subsequently embedded) or obtained as a colloidal solution. In both cases the nanoparticles have spherical shapes with an average diameter around 6 nm and a narrow size distribution.

In this work Femtosecond Pulsed Laser Ablation (fs-PLA) has been applied in vacuum or liquid environment to fabricate embedded silver nanoparticle multilayers and highly concentrated colloidal solution of silver nanoparticles, respectively. In vacuum, deposits of exposed and embedded silver nanoparticles were grown on Si(100) and silica substrates by laser ablating high-purity silver and $SiO^2$ targets using a femtosecond Ti:Sapphire laser delivering 45 fs pulses at 804 nm and 1 kHz repetition rate. The effect of the laser fluence and irradiation time on the obtained nanostructures was investigated using several fluences between 650 mJ/cm$^2$ and 3.2 J/cm$^2$ and deposition times in the range of 1-20 minutes. Optical response of the deposits was characterized using optical absorption spectroscopy and the surface morphology was studied by scanning electron microscopy (SEM). Samples with the optimal optical response were obtained by depositing three successive Ag/$SiO_2$ bilayers (Figure 1, left) using the main laser wavelength (804 nm) under vacuum and with the substrate at room temperature. They were composed of silver nanoparticles with an average diameter of 6 nm and a narrow size distribution; each layer of these nanoparticles was then separated by silica layers of approximately 100 nm [1]. The laser fluence and deposition time for Ag ($SiO_2$) were 650 mJ/cm$^2$ (3.2 J/cm$^2$) and 1 min (10 min), respectively. When applied in a liquid environment, fs-PLA is able to synthesize colloidal solutions of nanoparticles from the ablated material in a complex process [2]. Low-concentration colloidal solutions of silver nanoparticles fabricated by femtosecond laser ablation were first reported by Tsuji et al. [3]. In this work we have used femtosecond laser ablation to generate highly concentrated silver colloidal nanoparticle solutions (Figure 1, right). When performed in pure water, such concentrations usually lead to a high level of

agglomeration making the solutions nearly useless. To avoid this problem, we have employed two different organic stabilizers, namely hexadecyl-trimethyl-ammonium bromide (CTAB) and polyvinylpyrrolidone (PVP), and studied its effect on the size distribution, structural characteristics and concentration of the solutions by means of transmission electron microscopy and optical absorption spectroscopy. Our results show that the agglomeration can be considerably reduced or even completely eliminated with those stabilizers.

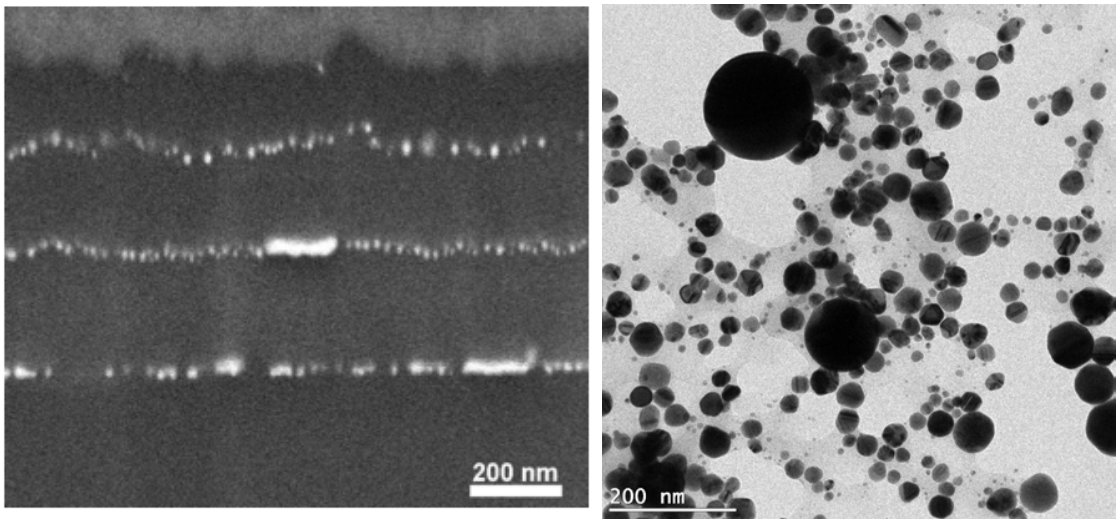



**Figure 1:** (Left) SEM micrograph of the transversal section of a multilayer structure deposited on a silica substrate. (Right) TEM micrograph of silver nanoparticles fabricated by pulsed laser ablation in $H_2O$+PVP.

**Acknowledgements**: This work was partially funded by the Spanish ministry MINECO, projects AIC-A-2011- 0718, MAT-2012-38541, CTQ2008-02578 and CTQ2012-37404-C02-01. O.P.R. is grateful with Moncloa Campus of International Excellence (UCM-UPM) for the PICATA postdoctoral fellowship. Facilities provided by the Centro de Láseres Ultrarrápidos at Universidad Complutense de Madrid are gratefully acknowledged.

**REFERENCES**

1. O. Peña-Rodríguez, J. González-Izquierdo, A. Rivera, G. Balabanian, J. Olivares, J. M. Perlado, and L. Bañares, “Embedded silver nanoparticle multilayers fabricated by femtosecond pulsed laser deposition,” *Opt. Mater. Express*, vol. 4, no. 9, pp. 1943–1952, Sep. 2014.
2. V. Amendola and M. Meneghetti, “What controls the composition and the structure of nanomaterials generated by laser ablation in liquid solution?,” *Phys. Chem. Chem. Phys.*, vol. 15, no. 9, pp. 3027–3046, Feb. 2013.
3. T. Tsuji, T. Kakita, and M. Tsuji, “Preparation of nano-size particles of silver with femtosecond laser ablation in water,” *Appl. Surf. Sci.*, vol. 206, no. 1–4, pp. 314–320, Feb. 2003.

**Quantum Plasmonics with Finite Carbon Nanotubes**

**S. de Vega Esteban**[1], J. D. Cox[1], F. Javier García de Abajo[1,2]

[1]ICFO - Institut de Ciencies Fotoniques, The Barcelona Institute of Science and Technology, 08860 Castelldefels (Barcelona), Spain
[2]ICREA - Institució Catalana de Recerca i Estudis Avançats, Passeig Lluís Companys 23, 08010 Barcelona, Spain
sandra.devega@icfo.es

**Abstract**
Inspired by recent advances in graphene plasmonics, and following previous developments in their use for nanophotonics [1], highly doped carbon nanotubes (CNTs) have been recently argued to show excellent tunable plasmonic properties in the visible and near-infrared [2], including propagation distances exceeding those of graphene [3]. Interestingly, the coupling of optical quantum emitters to infinitely long CNTs has been shown to be also more efficient than in graphene [3].

Finite CNTs appear as an intermediate situation between large-scale graphitic structures and small polycyclic aromatic hydrocarbons, so they are good candidates to push the robustness and tunability of graphene plasmons towards the visible and near-infrared parts of the spectrum [2], while sustaining modes that are localized in all three space dimensions, in contrast to infinite tubes.

In this work we study finite size effects of highly doped CNTs on their optical spectrum and compare classical and quantum approaches to describe these structures [Fig. 1]. We focus on the investigation of the strength of the interaction of a CNT plasmon with quantum emitters, as well as the interaction between two emitters mediated by that plasmon. For this purpose, we calculate the enhancement of the radiative decay rate and hence predict a Purcell factor of the order of $10^7$ for a plasmon lifetime of 65 fs. We also predict record-high coupling between two emitters placed at the opposite ends of the tube.

**References**
[1] P. Avouris, M. Freitag and V. Perebeinos, Nat. Phot. **2**, 341 (2008).
[2] F. J. García de Abajo, ACS Photon. **1**, 123020 (2014).
[3] L. Martín-Moreno, F. J. García de Abajo, F. J. García-Vidal, Phys. Rev. Lett., **115**, 173601 (2015).

**Figures**

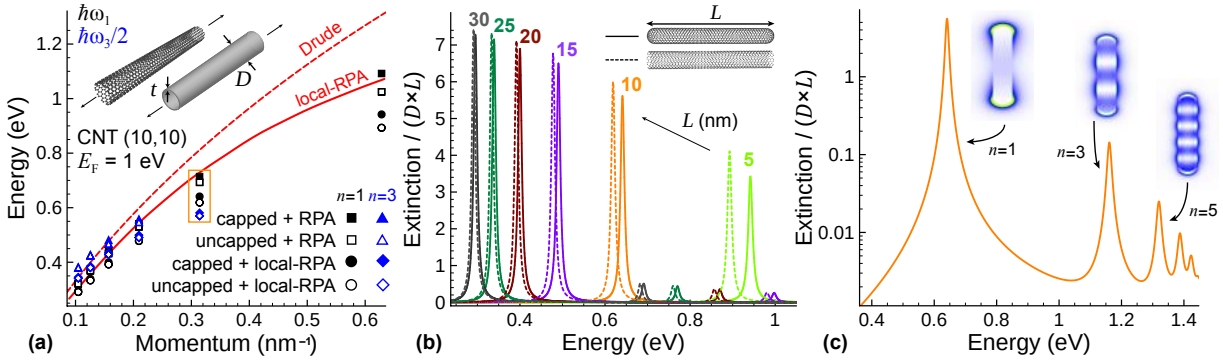



**Fig. 1. Plasmons in CNTs**. **(a)** Plasmon dispersion relation for an infinite CNT, compared with the values of the frequency and momentum obtained from a Fabry-Perot model for finite tubes of various lengths. The figure shows classical electromagnetic calculations for two different models of the surface conductivity, taken from the Drude and local-RPA approximations for extended graphene. We also compared tubes with open and closed ends. See legend and text insets for further details. **(b)** Extinction cross-section for capped (solid) and uncapped (dashes) (10,10) CNTs of various lengths within the local-RPA approximation. **(c)** Overview of the extinction spectrum for one of the tubes, along with near-field plots for the different plasmon modes. The damping is taken as 10 meV in all cases.

# Near infrared distributed feedback surface plasmon lasers

**Elham Karami Keshmarzi[1], R. Niall Tait[1], and Pierre Berini[2,3,4]**
[1]Department of Electronics, Carleton University, 1125 Colonel By Dr., Ottawa (ON) K1S 5B6, Canada
[2]School of Electrical Eng. and Computer Science, University of Ottawa, Ottawa (ON) K1N 6N5, Canada
[3]Department of Physics, University of Ottawa, Ottawa (ON) K1N 6N5, Canada
[4]Center for Research in Photonics, University of Ottawa, Ottawa (ON) K1N 5N6, Canada

**Abstract-** Distributed feedback lasers are realized at near-infrared wavelengths using Bragg gratings in a long range surface plasmon polariton structure. DFB lasers comprise a 20 nm thick, stepped-in-width Au stripe on a silica substrate, covered with 600 nm thick dye-doped (IR-140) PMMA layer. The lasers are pumped optically using 10 ns laser pulses at 810 nm and emit at about 880 nm with a full width half maximum (FWHM) linewidth of about 3 nm.

Distributed feedback (DFB) lasers are compact optical sources commonly used in optical integrated circuits. These lasers are normally realized in semiconductor quantum well structures using dielectric waveguides. Surface plasmon waveguides are interesting alternatives to dielectric waveguides, enabling different device architectures and functions. Amplification and lasing with surface plasmon waves have been demonstrated in guiding structures; indeed significant progress has recently been achieved in this area[1,2].

Long range surface plasmon polariton (LRSPP) laser concepts were previously proposed and the requirements for single mode lasing were investigated[2]. In this paper we describe DFB lasers realized according to this concept and present experimental results of lasing. The DFB lasers consist of a 20 nm thick Au stripe on a thick silica layer and covered with 600 nm IR-140-doped PMMA layer which acts as the laser's active medium. The Au stripe is stepped in width in a pitch of $\Lambda \sim 300$ nm forming a Bragg grating with a center wavelength of $\lambda_B \sim 880$ nm, corresponding to the peak emission wavelength of IR-140 dye molecules. A scanning electron microscopy image of a Bragg grating is given in Fig.1, showing the steps in width of the Au stripe (1 μm, 0.5 μm) and the grating pitch.

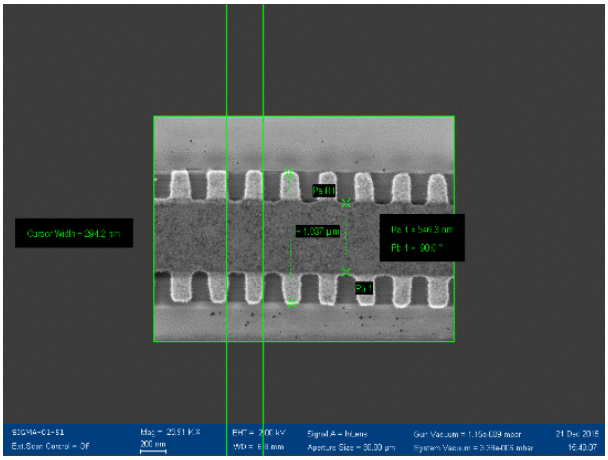


Fig.1 Scanning electron microscope image of a step-in-width grating in a 20 nm Au stripe on Silica.

The lasers are pumped optically from the top using 10 ns laser pulses at 810 nm with a peak energy density of ~40 mJ/cm$^2$. Multimode and singlemode lasing around 880 nm is observed for various grating pitches, laser length and pump intensities.

## REFERENCES

1. P. Berini, and I. De Leon, Surface plasmon-polariton amplifiers and lasers, Nat. Photonics 6, 16–24, (2012).
2. E. K. Keshmarzi, R. N. Tait, and P. Berini, Long-range surface plasmon single-mode laser concepts, J. Appl. Phys. 112, 063115 (1–5), (2012).

# Plasmonic nanoparticles fabricated on a wave shape flexible substrate

**Di Feng[1,2]*, Ningfang Song[1], Hui Fang[2], Hui Zhang[3], Dewei Yang[1], Yue Zheng[1], Haowei Li[1], and Shaobo Zhang[1]**

[1] School of Instrumentation Science and Optoelectronics Engineering, Beihang University, Beijing 100191, China
[2] Department of Materials Science and Engineering, Frederick Seitz Materials Research Laboratory, University of Illinois at Urbana-Champaign, Urbana, Illinois 61801, USA
[3] Department of Electrical and Computer Engineering, Rice University, Houston, Texas 77005, USA
*corresponding author, E-mail: fengdi@buaa.edu.cn

## Abstract

In this paper, we report on detailed fabrication process and analytical studies of plasmonic nanoparticles on flexible substrates of polydimethylsiloxane (PDMS) that are fabricated with non-flat, wavy features of surface relief. The fabrication process, like making patterns of nano circle particles by using PDMS stamp, etching patterns in a silicon wafer, and transferring metal nanoparticles from the silicon substrate to a sinusoidal wavy elastomer PDMS substrate, is described, and this flexible material can be used to mechanically control the inter-particle spacing by applying strain, then this device's optical properties at different strain values are characterized also. The tunability of optical resonance peaks is observed at near-infrared wavelengths with different stain values.

## 1. Introduction

Plasmonic nanoparticles have attracted great attention in the field of optical and plasmonic sensing devices applications, due to their ability to produce enhance surface electromagnetic fields through the excitation of localized surface plasmon resonances[1-2].The optical response of metamaterial can be controlled by manipulation of the size, pattern, and composition of its nano unit particles. But this response is usually fixed when fabricated on a hard substrate. Flexible plasmonic devices generally refer to plasmonic nano structures fabricated on flexible polymer substrates which can be mechanically deformed (bending, folding, tilting, and stretching). Mechanical flexibility is the key attribute of these devices enabling emerging applications such as flexible display arrays [3-5], wearable photonic textiles [6], broadband tunable photonic devices[7] and optical systems conformably integrated on curved surfaces [8] or biological tissues [9-10]. But recently the progress in exploiting such functionalities with photonics, particularly at dimensions relevant to nano plasmonics operating in visible and infrared frequencies is still limited. The mean reason is the difficulty of fabricating nanophotonic structures with dimensions below several hundred nanometers on flexible, nonplanar, and mechanically compliant surfaces with traditional nanofabrication techniques. Polydimethylsiloxane (PDMS) is one of the popular polymers for a variety of applications because it is optically transparent, flexible, stretchable, and inexpensive. In 2015, Li Gao et al. reported a large-scale arrays of plasmonic nanodisks on PDMS by using advanced transfer printing techniques, and this device has the ability to tune plasmonic resonances at near-infrared wavelengths[11], where the fabrication of devices employed a flat substrate, as in most studies in literature. In this paper, we use a sine curve surface as devices' substrate and transform the traditional flat nanoparticle arrays into three-dimensional, non-coplanar layout, resulting in the 3D mechanical tuning of optical response. Experimental measurements and theoretical simulations demonstrate the influence of these 3D curve substrates on the optical resonance peaks.

## 2. Experimental

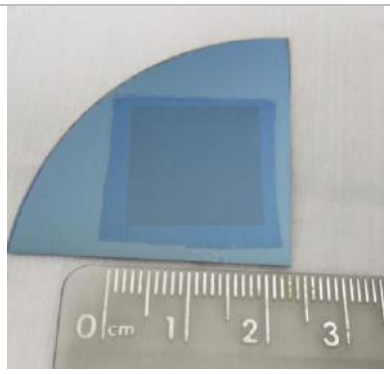
### 2.1. A masking layer for ICP etching

In order to make the metal nanoparticle, firstly, we need to prepare the mask layer for etching Si substrate. A 4% SU8 photo resist is spin coated on a silicon wafer at a speed of 500 rpm for 5 seconds followed by 2000 rpm for 30 seconds. The pattern of a square array dots (nano particle arrays, with period 300nm, and each circle particle's diameter 200nm) is imprinted on the layer of SU8 using a 2 cm by 2 cm hard PDMS stamp, as shown in Fig. 1. After that, the reactive ion etching (RIE) system is used to etch the pattern with oxygen gas and control the diameter size, and in order to do it, the SU8 layer should be etched as more as possible. After RIE, the top view SEM image is shown in Figure 2.

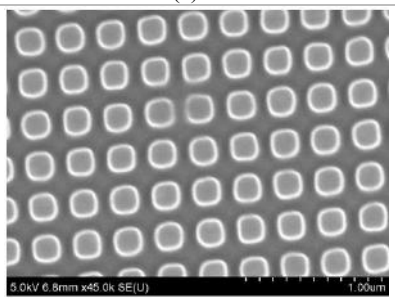
### 2.2. Preparation of nano patterns on the Silicon substrate

The ICP-RIE system deep etches the substrate with the SU8 acting as a masking layer to create 300nm posts with a diameter of a little less than 200nm in the silicon wafer. After this, the SU8 is etched off the substrate with oxygen

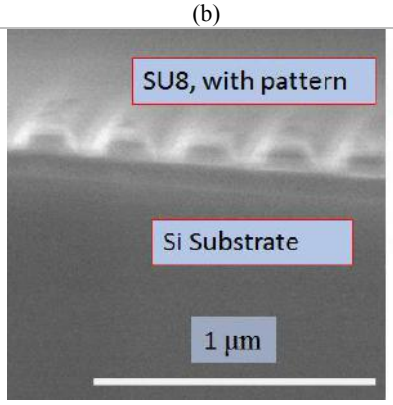
gas using the RIE system again, as shown in Fig. 3, (a) top view SEM image, (b) side view SEM image.




(a)




(b)




(c)

Figure 1: Patterns on the layer of SU8, (a) optical images of patterns on SU8 layer, (b) top view SEM image of nano patterns, (c) side view SEM image of nano patterns.

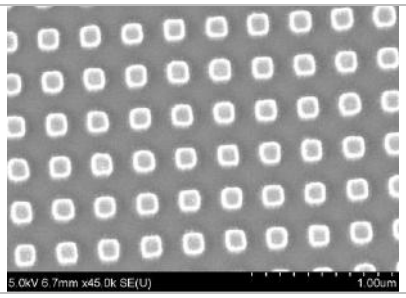
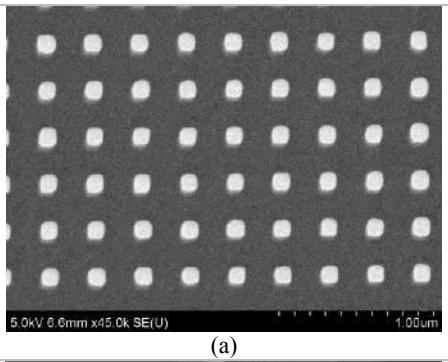
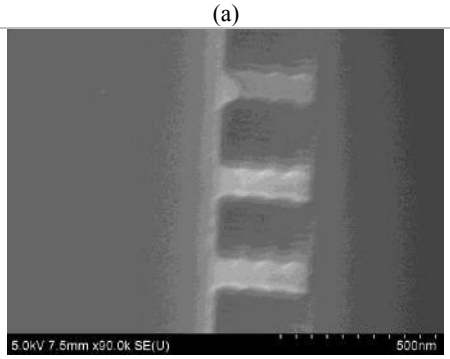



Figure 2: Top view SEM image of nano patterns after RIE.




(a)




(b)

Figure 3: SEM image of nano patterns on the silicon substrate, (a) top view, (b) side view.

For easy release of the metal (Au/Ti) patterns from the donor (silicon) substrate, it is essential to form an anti-adhesion layer on the substrate before metal deposition. Here UVO and perfluorodecyltrichlorosilane (FDTS) were used to form an ultrathin anti-adhesion layer, about 10 nm, on a silicon wafer.

After that, using e-beam thermal evaporation, 25nm of Au film is deposited on the silicon substrate as the functional plasmonic material; 5nm of Ti is deposited on top of the Au particles as an adhesion promoter. The Ti allows for an easy transfer of the gold nanoparticles from the silicon substrates to a PDMS substrate. And the whole deposition process is monitored by a quartz crystal microbalance.

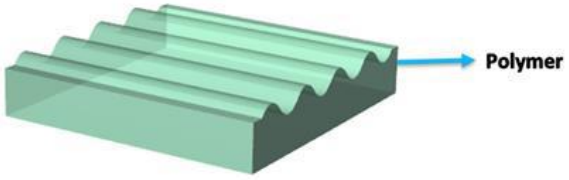
### 2.3. Wave PDMS formation and peel-off process

The very critical step is fabrication of stable Au/Ti particles embed in wave PDMS. In order to fabricate a three dimensional sinusoidal PDMS substrate, we use a plane holographic reflection gratings (sine surface with a period about 900nm, and the height about 300nm) as the mold, and then the silicone PDMS material is spin coated on this grating mold at a speed of 250rpm for 60 seconds. Then it is cured in an oven at $80^0$C for 4 hours, and maintained at room temperature for 8 hours. Finally, the grating sine surface will be transferred to the PDMS substrate (shown in Fig. 4(a)). In this study, the PDMS substrate is made from a DOW Corning Sylgard 184 kit with a base to curing agent ratio of 30:1. For the transfer printing method, the PDMS is treated with UV light for 3.5 minutes to make –OH group on the silicone and to create strong bonds. It is then placed on the silicon substrate with the nanoparticle array and

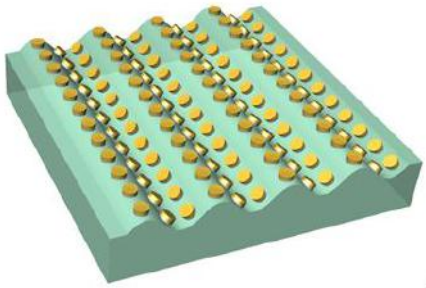
heated for 25 seconds at 110° C. Once cooled down, the PDMS substrate is peeled off and the nanoparticle array is transferred from the silicon wafer to the 3-D sinusoidal PDMS substrate (as shown in Fig.4 (b)).

In order to control the inter-particles, before transfer printing, we use the PDMS substrate without pre-stretching, that means nano particles can be transferred to the 3-D substrate directly, and to get the sample device (as shown in Fig. 4(b)).

The sample can be done by removing the silicon stamp leaves the entire array of Au/Ti nanoparticles well adhered to the 3-D surface of the polymer substrate, with exceptionally high yields (Figure 5, (a) is SEM image for top view, and (b) is SEM image for 45 degree tilted view, which is clear to see a 3-D sinusoidal surface adhered by nanoparticles).




(a)



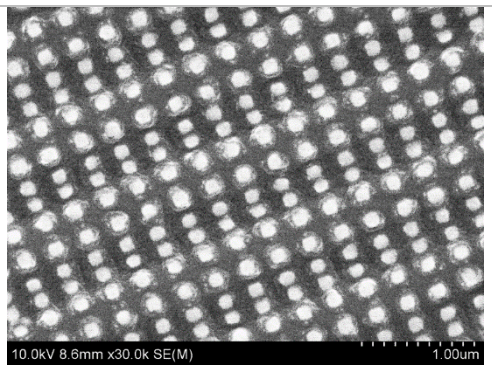
(b)

Figure 4: Schematics of 3-D wave PDMS polymer and nanoparticles, (a) the sinusoidal curve PDMS polymer; (b) transfer printing nanoparticles to curve polymer substrate.

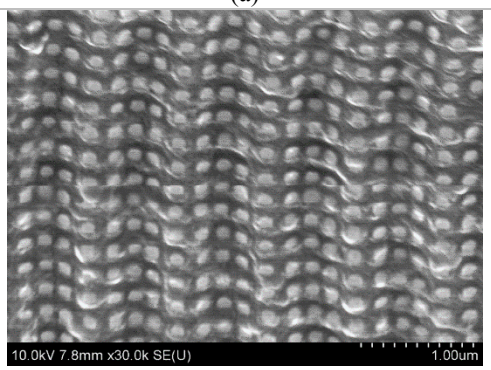
## 3. Results and discussion

The final samples consist of a 2 cm by 2 cm nanoparticle array with a particle diameter of about 200nm, as shown in Fig. 6(a), and in Fig. 6(b) we can see the diffractive stripes made by wave substrate and nanoparticles clearly. The mechanical system for straining is shown in Figure 7, and using it, the sample can be stretched along one direction.

The samples are optically characterized using spectrophotometry to observe the shift in the resonance peaks with stretching, normalized to a bare silicone substrate. Spectrophotometry is a method that allows measuring the fraction of light of different wavelengths transmitted through a medium in comparison with a control sample. Strain is applied on the samples by clamping both ends of the sample between two metal plates and varying the distance between the clamps (shown in figure 7) [11]. A varian Cary5G spectrophotometer is used for data collection.



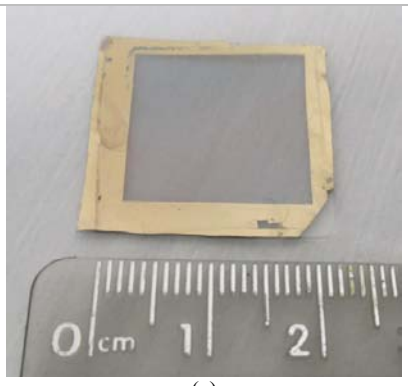

(a)



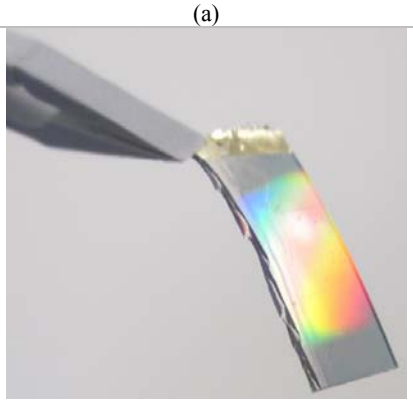

(b)

Figure 5: SEM images of nano particle array on 3-D PDMS substrate. (a) Top view SEM image of gold nano particle array. (b) Tilted view (45 degree) SEM image of gold nano particle array.

The light source is polarized perpendicular to the stretching direction and different strains from 0% to 30% are applied to the sample at intervals of 15%. As the strain increases, the inter-particle spacing perpendicular to stretching decreases and the result is an enhancement of local electric field and lowering of the resonant frequency, so red-shifting appears. The resulting transmission spectra are shown in Figure 8. There is a clear redshift in the plasmon resonance peaks from 0% to30% of $\Delta\lambda$ = 72 nm (Figure 8(a)). The direction of the resonance shift can be determined by considering the Coulomb forces associated with the polarization of the particles. The nanoparticle arrays can be modeled as an array of interacting point dipoles. So for comparison, simulation results by using Coupled Dipole Approximation (CDA) are shown in Figure 8 (b) for the light source is polarized perpendicular to the stretching direction, which is quite similar to experimental results (Figure 8(a))




(a)



(b)

Figure 6: Optical image of the final plasmonic nanoparticles sample that consists of Au/Ti nano particles, (a) top view, (b) tilted view.

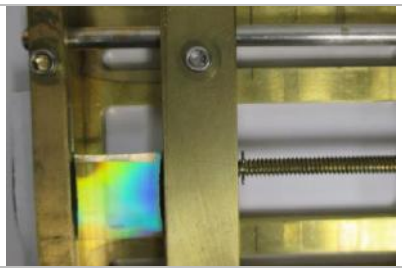
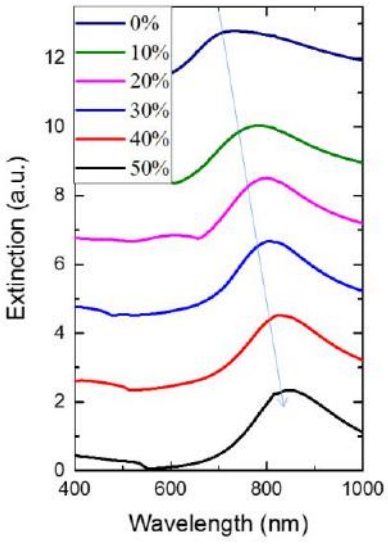


Figure 7: The mechanical system for straining.

(a)




(b)

Figure 5: Optical transmission measured with polarization aligned perpendicular to the stretching direction, for different strains from 0% (no strain) to 30% strain, (a) experimental results, (b) simulated results.

## 4. Conclusions

Thin Au/Ti plasmonic nano particle arrays have been fabricated on a three-dimensional, high-stretchable and large-area polymer substrate by using advanced transfer printing method. The sample's plasmonic resonance tunability has been tested and analyzed also. With light polarized perpendicular to the stretching direction, the sample without pre-stretching shows a large tunability range. This tuning capability will make this kind of samples or devices have potential applications for strain sensors, and low-cost wearable plasmonic sensors, etc.

## Acknowledgements

This research is supported by China Scholarship Council （CSC）,the National Natural Science Foundation of China (No. 61573039), and the Special fund on Major Instruments of the Ministry of Science and Technology of China (No. 2013YQ040877)

## References

[1] S. A. Maier, M. L. Brongersma, P. G. Kik, S. Meltzer, A. A. G. Requicha and H. A. Atwater, Plasmonics - A route to nanoscale optical devices, *Adv. Mater.* 13: 1501−1505, 2001

[2] J. A. Schuller, E. S. Barnard, W. S. Cai, Y. C. Jun, J. S. White,and M. L. Brongersma, Plasmonics for extreme

light concentration and manipulation, *Nat. Mater.,* 9: 193-204, 2010.

[3] Kim. Dae-Hyeong, Rogers. John A, Stretchable Electronics: Materials Strategies and Devices. *Adv. Mater*, 20:4887-4892, 2008.

[4] Yu, Zhibin, Niu, Xiaofan, Liu, Zhitian, Intrinsically Stretchable Polymer Light-Emitting Devices Using Carbon Nanotube-Polymer Composite Electrodes. *Adv. Mater,* 23:3989-3993, 2011.

[5] Juejun Hu, Lan Li, Hongtao Lin, Ping Zhang, Weidong Zhou, and Zhenqiang Ma, Flexible integrated photonics: where materials, mechanics and optics meet [Invited]. *Opt. Mater. Express,* 3: 1313-1331, 2013

[6] Mack. S, Meitl. MA, Baca. AJ, Zhu. ZT, Rogers. JA, Mechanically flexible thin-film transistors that use ultrathin ribbons of silicon derived from bulk wafers. *Appl. Phys. Lett*, 88: 213101, 2006.

[7] Pryce. IM, Aydin. K, Kelaita.YA, Briggs. RM. Atwater. HA, Highly Strained Compliant Optical Metamaterials with Large Frequency Tunability. *Nano Letters*, 10: 4222-4227, 2010.

[8] Ko. HC, Stoykovich. MP, Song. JZ, Malyarchuk. V, Choi. WM, Yu. CJ, Geddes, JB. Xiao, JL. Wang, SD. Huang. YG, Rogers. JA, A hemispherical electronic eye camera based on compressible silicon optoelectronics. *Nature*, 454: 748-753,2008.

[9] D. H. Kim, N. Lu, R. Ma, Y. S. Kim, R. H. Kim, S. Wang, J. Wu, S. M. Won, H. Tao, A. Islam, K. J. Yu, T. I. Kim, R. Chowdhury, M. Ying, L. Xu, M. Li, H. J. Chung, H. Keum, M. McCormick, P. Liu, Y. W. Zhang, F. G. Omenetto, Y. Huang, T. Coleman, and J. A. Rogers, Epidermal electronics, *Science*, 333: 838–843, 2011

[10] Aksu. S, Huang. M, Artar. A, Yanik. AA, Selvarasah.S, Dokmeci. MR, Altug. H, Flexible Plasmonics on Unconventional and Nonplanar Substrates. *Adv. Mater*, 23:4422-4430, 2011.

[11] Li Gao, Yihui Zhang, Hui Zhang, Sage Doshay, Xu Xie, Hongying Luo, Deesha Shah, Yan Shi, Siyi Xu, Hui Fang, Jonathan A. Fan, Peter Nordlander, Yonggang Huang, and John A. Rogers, Optics and Nonlinear Buckling Mechanics in Large-Area, Highly Stretchable Arrays of Plasmonic Nanostructures. *ACS Nano*, 9:5968-5975, 2015.

# Focusing of EM Wave through Square-microhole Aperture

**Santosh Kumar Maurya[1], Suyog R. Hawal[1], Raghvendra Pratap Chaudhary[1], Shobha Shukla[1] and Sumit Saxena[1*]**

[1]Nanostructures Engineering and Modeling laboratory, Department of Metallurgical Engineering and Materials Science, Indian Institute of Technology Bombay, MH, India 400076
* Corresponding author: - sumit.saxena@iitb.ac.in

**Abstract-**Utilization of surface plasmons has drastically increased the performance of Photodevices due to increased light matter interactions. Recently, we have reported circular micro-hole patterned on gold thin layer. It exhibited extraordinary transmission in the visible range. Radiative surface plasmons couple incident waves at the transmitting edges of the microhole aperture, results in extraordinary transmission. In this report, using FDTD method, we comparatively studied the focusing abilities of square shaped micro hole and circular microhole.

# Complete Picture of Dispersion Relation for Surface Plasmon Polaritons in Layered Media

**H. S. Tetikol**[1], **M. I. Aksun**[1]

[1]Graduate School of Sciences and Engineering, Koc University, Istanbul, Turkey
htetikol@ku.edu.tr

**Abstract**— We show that both the wavevector and the frequency of surface plasmon polaritons (SPPs) can simultaneously assume complex values, providing better resolution and confinement than previously thought. As an example, we analyze SPPs in layered media and ascertain the true nature of their dispersion. We prove that a dispersion *curve* constitutes only a subset of the solutions to the dispersion equation, and the entire solution set can be represented as a *surface* in the complex frequency–wavevector domain.

All the salient features of surface plasmon polaritons (SPPs), such as energy confinement and enhancement, very high resolution and sensitivity, negative group velocity and refraction, can be deduced from a simple equation describing the relationship between an SPP's evolution in time and its spatial distribution: The dispersion relation. The dispersion relation, most commonly expressed in terms of the frequency $\omega$ and the wave vector $k$ of the wave, is of fundamental importance in understanding the nature of all types of electromagnetic modes, including SPPs, supported by a given geometry or structure. Therefore, it is vital to capture the whole picture, literally and figuratively, of the dispersion relation for the SPP in order to understand and exploit it to its fullest in a given structure, which is exactly what this paper aims to achieve.

We investigate the Kretschmann-Raether configuration (KRC) which consists of glass, metal and air layers as shown in Figure 1. Since metals must be dispersive and lossy, due fundamentally to the causality principle, SPPs propagating along the interface between such a metal and a dielectric material (lossy or lossless) always suffer from attenuation, resulting in a rather limited range of propagation. Considering the functional form of the modes, i.e. $e^{j\omega t - jkx}$, it is only natural to introduce an imaginary part either to the frequency $w$ or to the wavevector $k$ or to both in order to account for the loss mechanisms in metals. However, the usual practice has been to introduce the imaginary part to $w$ or to $k$, but not to both. For brevity of the later referrals, the former will be called the *real* $k$ choice and the latter the *real* $\omega$ choice. Although there have been some justifications for these choices based on how the modes are excited [1], they are far from being conclusive and irrefutable, as they give rise to different dispersion curves [2]. For example, while the *real* $\omega$ choice predicts infinite resolution and confinement of SPPs, the *real* $k$ choice predicts an upper limit on resolution/confinement and, as a result, negative group velocity over a frequency band. The current consensus on this issue is that these two cases correspond to different experiments with different modes of excitation. However, the confusion about which case should be applied to which problem remains unresolved in many studies such as SPPs in linear chains of metallic nanospheres [3], SPPs in cylindrical metallic nanowires [4], SPPs in layered media [5], and SPPs on grating structures [6].

In this study, upon constructing the whole *surface* of the dispersion relation for the SPPs, we have demonstrated that the *real* $\omega$ and *real* $k$ choices are only the two elements of the entire solution set in which both $k$ and $\omega$ assume complex values. In order to find the SPP modes, the generalized reflection coefficient (1) from the glass side is calculated and the locations where it diverges are seeked in the complex $\omega$–complex $k$ domain. In equation (1), $r_{12}$ and $r_{23}$ are the reflection coefficients at the first ($z = 0$) and the second ($z = d$) interfaces, respectively, $k_{z2}$ is the normal component of the wave vector in the metal film and $d$ is the thickness of the metal film.

$$\tilde{r} = \frac{r_{12} + r_{23}e^{-jk_{z2}2d}}{1 + r_{12}r_{23}e^{-jk_{z2}2d}} \tag{1}$$

For the dielectric function of the metal, the Drude model (2), fitted to the experimental data for aluminum, is used [7].

$$\epsilon_m = 1 - \frac{\omega_p^2}{\omega^2 - j\gamma\omega} \tag{2}$$

The SPP dispersion surface proves that the SPP modes occupy a much larger portion of $\omega$-$k$ domain than what is conventionally thought. By properly designing the exciting electromagnetic field to have a complex $\omega$ or $k$ or both, any mode on the dispersion surface might be excited, enabling the designer to finetune the resolution and confinement of SPP fields. Furthermore, by fixing the imaginary part of $\omega$ or $k$, a whole new dispersion curve may be extracted from the dispersion surface, giving a new resolution limit, group velocity, confinement and back-bending characteristics. This way, the effective dispersion curve may be tuned to the desired shape.

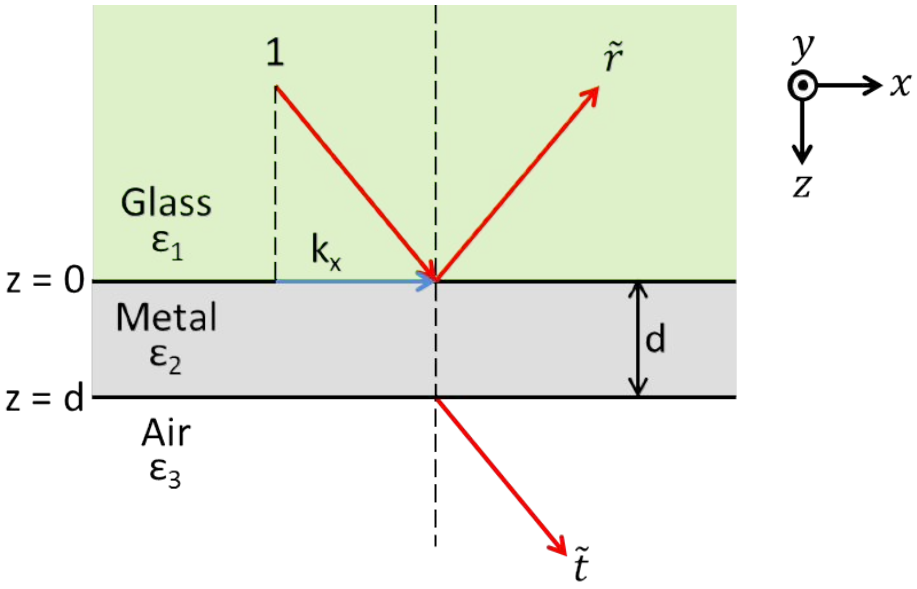



Figure 1: The Kretschmann-Raether configuration. 1, $\tilde{r}$ and $\tilde{t}$ represent the incident wave, the generalized reflection coefficient and the generalized transmission coefficient, respectively.

**REFERENCES**


1. E. Le Ru and P. Etchegoin, *Principles of Surface-Enhanced Raman Spectroscopy: and related plasmonic effects*. Elsevier, 2008.
2. G. Kovener, R. Alexander Jr, and R. Bell, "Surface electromagnetic waves with damping. i. isotropic media," *Physical Review B*, vol. 14, no. 4, p. 1458, 1976.
3. I. B. Udagedara, I. D. Rukhlenko, and M. Premaratne, "Complex-$\omega$ approach versus complex-k approach in description of gain-assisted surface plasmon-polariton propagation along linear chains of metallic nanospheres," *Physical Review B*, vol. 83, no. 11, p. 115451, 2011.
4. L. Wan, Y.-M. Huang, C.-K. Dong, and H.-J. Luo, "Analytical solutions to zeroth-order dispersion relations of a cylindrical metallic nanowire near the backbending point," *The European Physical Journal B*, vol. 85, no. 1, pp. 1–6, 2012.
5. A. Archambault, T. V. Teperik, F. Marquier, and J.-J. Greffet, "Surface plasmon fourier optics," *Physical Review B*, vol. 79, no. 19, p. 195414, 2009.
6. W. Barnes, T. Preist, S. Kitson, and J. Sambles, "Physical origin of photonic energy gaps in the propagation of surface plasmons on gratings," *Physical Review B*, vol. 54, no. 9, p. 6227, 1996.
7. K. M. McPeak, S. V. Jayanti, S. J. Kress, S. Meyer, S. Iotti, A. Rossinelli, and D. J. Norris, "Plasmonic films can easily be better: rules and recipes," *ACS photonics*, vol. 2, no. 3, pp. 326–333, 2015.

# Refractive index sensitivity characteristics of dual-resonant plasmonic perfect absorber

**M. Turkmen[1,2,*], S. Kaya[1,2], S. Korkmaz[1], and E. Aslan[1,2]**

[1]Department of Electrical and Electronics Engineering, Erciyes University, 38039, Kayseri, Turkey
[2]Department of Electrical and Computer Engineering, and Photonics Center of Boston University, Boston, MA 02215, USA
[*]corresponding author: turkmen@bu.edu

## Abstract

We proposed double bowtie shaped plasmonic nanoantenna arrays based on dual-band plasmonic perfect absorber (PPA) operating in mid-infrared regime. We investigated the spectral responses and surface-enhanced infrared absorption (SEIRA) enhancements of nanostructures by using finite difference time domain (FDTD) method. We studied refractive index sensing characteristics by embedding nanostructures into different cladding media. Owing to strong absorption peaks, high SEIRA enhancements, and refractive index sensitivity, designed PPA can be utilized in mid-infrared sensing applications.

## 1. Introduction

Perfect absorber based on plasmonic nanostructures simultaneously minimizing the reflectance with perfect impedance matching and eliminating the transmittance by maximizing material losses. PAs typically consist of three functional layers that comprise a dielectric layer sandwiched between two metal layers. The top layer is mainly a periodically patterned metallic nanostructure that serves as an electric resonator. The bottom layer is mostly the thick metal plane which is used as an optical mirror that significantly reduces transmittance. The coupling between two metallic layers results in magnetic resonance depending on the thickness and dielectric constant of the dielectric layer [1].

In this work, we present double bowtie shaped plasmonic nanoantenna arrays based on perfect absorber. Designed structure consists of magnesium fluoride ($MgF_2$) interlayer which separates four gold (Au) nanoantennas from thick gold film. Theoretical analyses are performed by using finite difference time domain (FDTD) method. The spectral response of the system has dual-resonant under x-polarization illumination source. Periodic boundary conditions are used for x- and y-axes and perfectly matched layers are used along z-axis. In order to understand the amount of the confined energy on the nanoantennas, we analyze theoretical surface-enhanced infrared absorption (SEIRA) enhancement at the corresponding resonance frequency values [2,10]. Intense SEIRA enhancements are observed at the metal-dielectric interface. We study refractive index sensing characteristics of the nanostructures by embedding into different cladding media with the thickness of 150 nm. In the last decade, plasmonic nanoantennas and PPAs have been studied in GHz and THz regimes [3-10].

## 2. Numerical Analysis

Fig. 1.a shows the schematic view of the proposed PPA structure. It consists of an interlayer ($MgF_2$) between nanoparticle based on top layer and gold (Au) film on a dielectric substrate (Si). The isosceles triangles at the *y*-axis have 2100 nm base length and 1050 nm height. The smaller isosceles triangles at the *x*-axis have 1720 nm base length and 860 nm height. Periodicities of the structures are 2600 nm. The distance between the corners of isosceles triangles at the center of structure is 200 nm. In the numerical calculations dielectric constants of the metals are taken from ref. [11]. Fig. 1.b shows the reflection, transmission and absorption spectra of the perfect absorber. Nearly 100% absorption observed in the 52 THz and 91 THz frequencies.

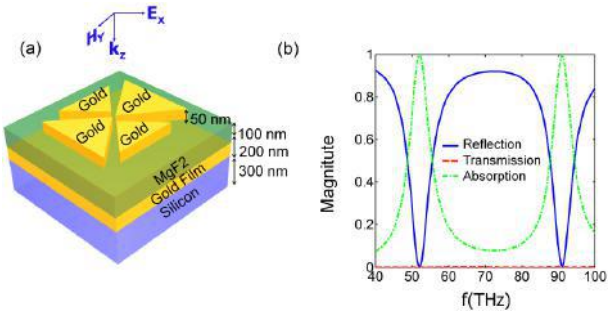



Figure 1. (a) Schematic view of double bowtie based perfect absorber. (b) Spectral response of the proposed PPA structure.

Fig. 2 illustrates the distributions of the SEIRA enhancement for obtained strong absorption resonance frequencies. The electric fields are concentrated at the corners of the metal particles. As seen from the Fig. 2, the near-field enhancements are larger than 5000 times for the two resonance frequencies. This is highly desirable for light-matter interaction applications [2, 10].

To analyze the sensing capability of proposed PPA, the sensitivity and spectral tunability characteristics are analyzed by loading different refractive indexed dielectric

cladding media with thickness of 150 nm as shown in Fig. 3.a.

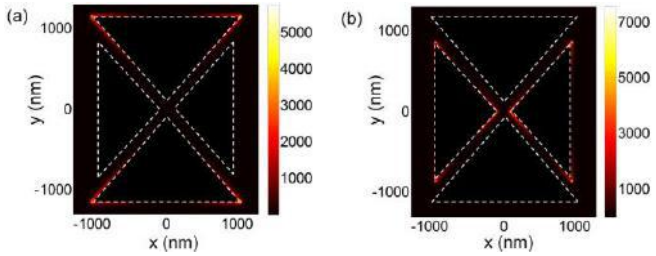



Figure 2. SEIRA enhancements of PPA under *x*-polarized illumination at resonances (a) 52 THz (b) 91 THz.

In Fig. 3.b, we tune the spectral response by loading easily depositable dielectric materials with different refractive indices, such as de-ionized water (DIW) (n=1.3325), acetone (n=1.3591) and glycerol (n=1.4722). Dielectric constants of the cladding medium are taken from ref. [7]. It is observed that the spectral responses of designed PPA are so sensitive to refractive index variations. Due to the high SEIRA enhancements and strong absorption peaks, proposed PPA can be utilized in refractive index sensing applications.

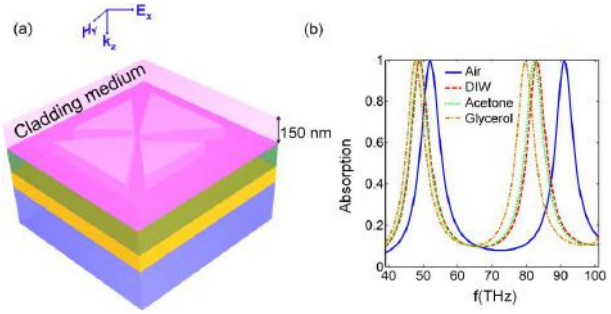



Figure 3. (a) Perspective view of the PPA in cladding medium. (b) Absorption spectra of the PPA in different cladding medium.

## 3. Discussion

We obtain strong absorption peaks, SEIRA enhancements in the mid-IR regime. We determine highly sensitive refractive index sensing characteristics of the nanostructures. These fundamental properties of light-matter interactions show us that designed plasmonic nanostructures can be used in molecular finger-print region applications.

## 4. Conclusions

In conclusion, we present a dual-resonant PA for mid-infrared light-matter interaction applications. We theoretically investigate the physical origin of the dual-resonant behavior by using finite difference time domain method. We determine intense near-field enhancements at the corresponding resonance frequency values. We also carry out refractive index sensitivity of PA by embedding the nanostructure into different dielectric refractive indexed cladding media. We observe dual-resonant reflectance in mid-IR spectra of the electromagnetic spectrum.


## Acknowledgements

The work described in this paper is supported by The Scientific and Technological Research Council of Turkey (Project No: 113E277) and Scientific Research Project Center of Erciyes University (Project No: FYL-2014-5075).


## References


[1] H. Lee, J. Wu, A wide-angle dual-band infrared perfect absorber based on metal–dielectric–metal split square-ring and square array, *J. Phys. D: Appl. Phys.* 45: 205101, 2012.

[2] L.V. Brown, X. Yang, K. Zhao, B.Y. Zheng, P. Nordlander, N.J. Halas, Fan-shaped gold nanoantennas above reflective substrates for surface-enhanced infrared absorption (SEIRA), *Nano Lett*. 15: 1272-1280, 2015.

[3] A.E. Cetin, M. Turkmen, S. Aksu, H. Altug, Nanoparticle-based metamaterials as multiband plasmonic resonator antennas, *IEEE Trans. Nanotechnol.* 11: 208-212, 2012.

[4] E. Aslan, M. Turkmen, Novel dual-band resonator nanoantenna array for infrared detection applications, *Sens. Mater.* 25: 689-696, 2013.

[5] M. Turkmen, Characterization of x-shaped nano-aperture antenna arrays operating in mid-infrared regime, *Chin. Opt. Lett*. 11: 070501, 2013.

[6] E. Aslan, M. Turkmen, Refractive index sensing characteristics of dual resonances in rectangular fractal nano-apertures, *Opt. Mater*., 46: 1-8, 2015.

[7] A.E. Cetin, S. Kaya, A. Mertiri, E. Aslan, S. Erramilli, H. Altug, and M. Turkmen, Dual-band plasmonic resonator based on Jerusalem cross-shaped nanoapertures, *Phot. Nano. Fund. Appl*. 15: 73-80, 2015.

[8] A.E. Cetin, M. Turkmen, S. Aksu, D. Etezadi, H. Altug, Multi-resonant compact nanoaperture with accessible large nearfields, *Appl. Phys. B: Lasers Opt.* 118: 29-38, 2015.

[9] N.I. Landy, S. Sajuyigbe, J.J. Mock, D.R. Smith, and W.J. Padilla, Perfect metamaterial absorber, *Phys. Rev. Lett.* 100: 207402, 2008.

[10] K. Chen, R. Adato, H. Altug, Dual-band perfect absorber for multispectral plasmon-enhanced infrared spectroscopy, *ACS Nano*, 6: 7998-8006, 2012.

[11] E. Palik, *Handbook of Optical Constants of Solids*, Academic Press, Orlando, 1985.

# Utilization of Hybrid Plasmonic Modes to Investigate Surface Interactions Between Nanocubes and Polymer Substrates

**Adam Bottomley, Michael Bushell, Daniel Prezgot, Jason Coyle, Anatoli Ianoul***

Department of Chemistry, Carleton University, Ottawa, Ontario, Canada
* anatoli.ianoul@carleton.ca

## Abstract

Silver nanocube monolayers deposited on polymer films were heated past the glass transition temperature of the polymer. Surface interactions between the cubes and substrate dictate the depth and rate of incorporation into the polymer. Silver nanocubes support hybrid plasmonic modes that are spatially separated when there is anisotropy in the local refractive index. Using this measure, it becomes possible to monitor the position of the cubes relative to the surface and tune spectral features in the visible spectrum.

## 1. Introduction

Nanoparticles on top of polymer supports are of great interest due to their unique: catalytic [1], electrical [2] and optical properties [3]. Metal nanoparticles can support localized surface plasmons which yield high optical extinction and extreme sensitivity to particle size, geometry, chemical composition and local environment [4]. This high sensitivity to changes in the local environment of the nanoparticle allows monitoring of polymer surface properties such as: the glass transition temperature ($T_g$) and polymer interface properties such as viscoelasticity [5]. This sensitivity also allows nanoparticle-polymer nanocomposites to be used as nanorulers for sub-diffraction measurements using far-field optics [6–8]. Nanoparticles can be used to enhance properties of polymers when embedded, such as thin film stability [9] and embedding can also enhance particle properties such as controlling the orientation of nanocubes forming controllable silver nanocube dimers [10].

Silver nanocubes have increased charge accumulation at their vertices and edges allowing high intensity electric fields [11] and subsequently high refractive index sensitivity [12], making silver nanocubes an excellent candidate for monitoring the embedding process. When silver nanocubes are placed on a dielectric substrate such as a polymer film, hybridization of the dipolar mode into hybrid dipolar (D) and quadrupolar (Q) modes occur [13], where the quadrupolar mode is confined to the top of the cube and the dipolar mode is confined to the bottom. Subsequently, this spatial separation makes the D mode more sensitive to the refractive index of the substrate, while the Q mode is more sensitive to changes above the substrate.

Noble Metal nanoparticles such as silver and gold have been found to embed into polymer thin films when heated above the polymers glass transition temperature [6,5,9,14]. The physical process can be modeled by the Helmholtz free energy [15] as seen in equation (1), where the driving force of embedding is described by the free energy decrease as determined by Kovacs *et al* [15]. For equation (1) $\Delta A_{surface}$ is the Helmholtz surface free energy, $a$ is the area of the particle, $\gamma_p$ is the surface free energy of the particle, $\gamma_s$ is the surface free energy of the polymer substrate and $\gamma_{p,s}$ is the interfacial surface energy between the particle and the substrate.

$$\Delta A_{surface} = a(\gamma_{ps} - \gamma_p) \quad (1)$$

For embedding to occur, two constraints must be fulfilled. One constraint is the spontaneity condition that the Helmholtz free energy is negative, $\Delta A_{surface} < 0$; satisfying the inequality in equation (2). The second constraint is a kinetic factor; the polymer chains local to the particle must be above their $T_g$, which represents the activation energy of polymer chain motion and reorganization.

$$\gamma_p > \gamma_{ps} \quad (2)$$

Equation (2) only describes the requirements for the process of embedding to begin, but fails to describe the conditions required for full incorporation of the particle into the polymer film. If the system reaches a local minimum before the particle fully embeds, the sinking will become unfavorable causing the particle to stop while only partially embedded. In order for full incorporation of the particle, the polymer must reform around the particle expressed as the polymers surface free energy ($\gamma_s$); thus, a new inequality arises for full embedding of the polymer (3).

$$\gamma_p > \gamma_s + \gamma_{ps} \quad (3)$$

The glass transition temperature of a polymer is affected by anything that restricts the free rotation of the polymer chains [16,17]. In general: a higher molecular weight polymer reduces free rotation and increases the $T_g$ of the polymer [18], A thinner film tends to increase free rotation and decrease the $T_g$ of a polymer [19]. The tacticity of the polymer can also effect free rotation and change the $T_g$ [20,21]

In the case of silver nanocubes the embedding process causes a red shift in the dipolar resonance due to an increase in the refractive index surrounding the cubes. When the cubes are approximately half way embedded the D mode no longer shifts as it no longer senses the increase in refractive index. However, the Q mode starts to sense an increase in refractive index causing it to red shift. Full embedding by UV-Vis measurements is represented by the Q mode overlapping onto the D mode as they are both experiencing the same local environment. Therefore, a series of peak position from a UV-Vis spectra vs temperature or time gives information on the local surface $T_g$ of the polymer as well as relative position of the silver nanocubes in respect to the polymer film.

## 2. Experimental

Polymer films were spin coated using a homemade spin coater at ≈ 4000 RPM. Silver Nanocubes were synthesized using the polyol process [22] and were deposited using Langmuir-Schaefer deposition. Heating experiments were conducted at 1 minute time intervals on a hot plate varying the temperature after each interval. The embedding process was monitored using: atomic force microscopy (AFM, Ntegra NTMDT, Russia) before and after heating, and using UV-Vis (Shimadzu, UV-2450) after each temperature interval.

## Results and Discussion

Silver nanocube embedding was monitored by use of atomic force microscopy (AFM) and UV-Vis spectroscopy. AFM analysis was done before heating and after heating to gain an understanding of how far the silver nanocubes embedded and to determine if the silver nanocubes undergo rounding or aggregation under the high temperatures. UV-Vis spectroscopy was performed to analyze the plasmonic shifts as the silver nanocubes embed into the polymer thin films.

### 1.1 Polystyrene-silver nanocube nanocomposite

AFM analysis of a silver nanocube-PS nanocomposite can be seen in Figure 1. The AFM images show the morphology of the nanocomposite over a 20x20 micron scale. Before heating (A) and after heating (B) there is a relatively uniform monolayer of silver nanocubes. The corresponding histograms (D, E) were used to analyze the embedding depth. In (D) two peaks are seen, since the silver nanocubes are currently on top of the polymer substrate the peak on the right is seen as the height distribution of cubes + polymer thickness, whereas the peak on the left is the height distribution of the polymer on a glass slide. The average cube height therefore, is the difference between these two peaks, which on average for all polymers was 85 nm. The peaks were fit using a bi-Gaussian curve as seen in (D) and (E), where the green and red curves represent the individual Gaussian distributions and the blue curve represents the net bi-Gaussian fit. The peaks maxima were subtracted to render the cube height before and after heating and the amount embedded is the difference of the cube height before and after heating. The average of 6 AFM images gave the distance embedded of 83 +/- 4 nm. This suggests the

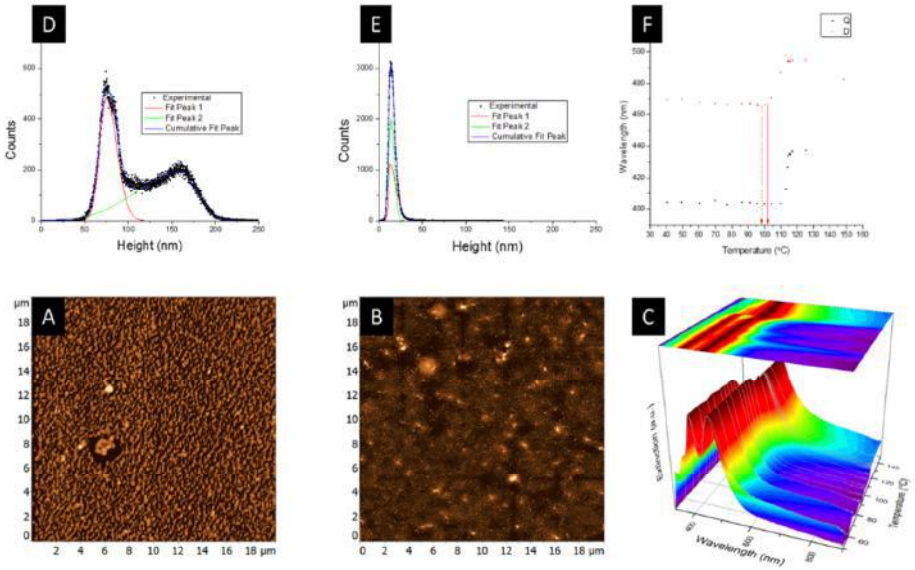



Figure 1 : The AFM and UV-Vis analysis and of a silver nanocube-PS nanocomposite heating experiment. (A) the AFM image of silver nanocubes on PS at room temperature. (B) The AFM image of silver nanocubes on PS after heating was completed. (D) and (E) are the histograms for the before heated and after heated AFM images respectively with corresponding Bi-Gaussian fitting. (C) the temperature dependent UV-Vis extinction spectra. (F) Illustrating the change in the dipolar mode in respect to temperature, with experimental $T_g$ is signified in the red line and the bulk $T_g$ as the dotted red line.

cubes became fully or near fully embedded.

The embedding process was also monitored using UV-Vis spectroscopy after each temperature interval. The UV-Vis extinction spectra can be seen in Figure 1 (C) with a contour map on top to help accentuate the peak shifts. Image (F) illustrates the dipolar and quadrupolar modes plotted with respect to temperature. The red line signifies where the dipolar mode starts red-shifting, which represents the silver nanocubes started to embed into the polymer. The point at which the D mode starts red shifting was found by fitting (F) with two linear equations, one before the redshift and one at the section with the highest slope, with the intersection representing a standard $T_g$ calculation. Since the cube has started to embed, it can also be said that at this point the temperature of the polymer is at least at its glass transition temperature. The surface glass transition temperature ($T_g$) was considered to be 103 +/- 2 $^oC$ for PS as represented by the solid red line, while the dotted red line represents the bulk $T_g$ of PS [23]. The red shift of the quadrupolar mode at ~111 $^oC$ indicates the cubes are approximately half way embedded. As can be seen, the D and the Q modes overlap onto each other forming an asymmetrical peak signifying near complete incorporation of the silver nanocube into the PS thin films. Therefore, the UV-Vis analysis shows near full incorporation of the silver nanocubes, while the AFM analysis shows on average near complete incorporation of the silver nanocubes into the PS thin film.

**1.2 PMMA-silver nanocube nanocomposite**

The AFM data for PMMA can be seen in Figure 2. Before heating (A) the silver nanocubes are on top of the PMMA thin film. As represented by the histogram (D), due to the presence of two well defined peaks. After heating the histogram (E) appears to be a single asymmetric peak which signifies a homogeneous height distribution characteristic of particle incorporation. The amount embedded was calculated as 76 +/- 4 nm, which suggests incomplete incorporation of the silver nanocubes into the PMMA substrate.

UV-Vis analysis was done on the PMMA-silver nanocube composite as seen in figure 2 (C). An initial blue shift for both the D and the Q mode can be seen and is represented clearer in (F). Typically, blue shifting of the D and Q modes infers cube rounding or a decrease in the refractive index. The AFM image supports a cubic shape after heating, and the UV-Vis shows a relatively consistent multipolar mode (350 nm) characteristic of the cubic shape thus, cube rounding didn't happen. It is possible that cube tilting upon embedding caused a relative decrease in refractive index causing a blue shift in the dipolar mode, however the Q mode would be expected to red shift [6]; since the Q mode didn't red shift cube tilting is not the cause for the blue shift. Further analysis on the origin of the blue shift for the D and Q modes is required to understand this discrepancy. The main issue with the blue shift is that it adds to the error of the measurements, making determining the temperature where the D mode started to red shift challenging, since the blue shift could be obscuring the true magnitude of the red shift. The experimentally determined surface $T_g$ of 122 +/- 12 $^oC$ is potentially higher than the expected surface $T_g$

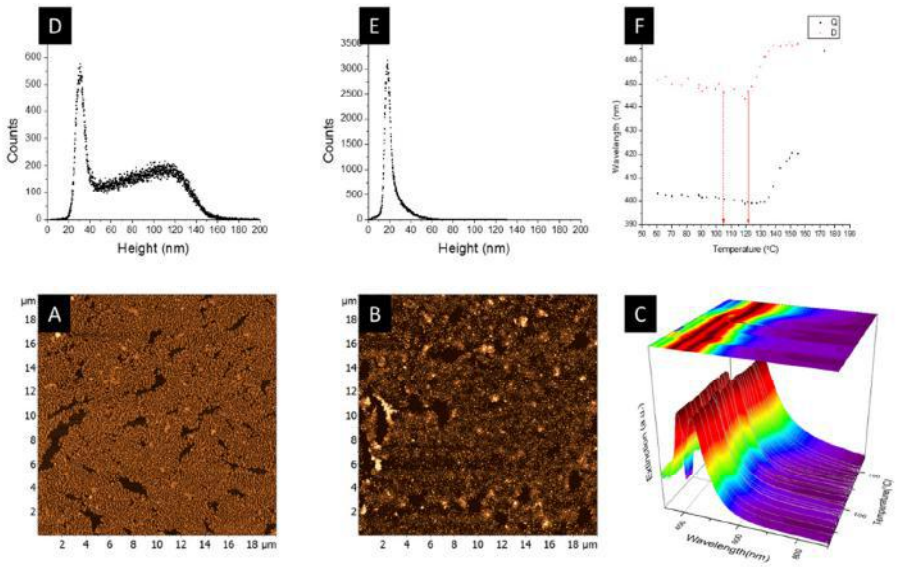



Figure 2 : The AFM and UV-Vis analysis and of a silver nanocube-PMMA nanocomposite heating experiment. (A) the AFM image of silver nanocubes on PMMA at room temperature. (B) The AFM image of silver nanocubes on PMMA after heating was completed. (D) and (E) are the histograms for the before heated and after heated AFM images respectively. (C) the temperature dependent UV-Vis extinction spectra. (F) Illustrating the change in the dipolar mode in respect to temperature, with experimental $T_g$ is signified in the red line and the bulk $T_g$ as the dotted red line.

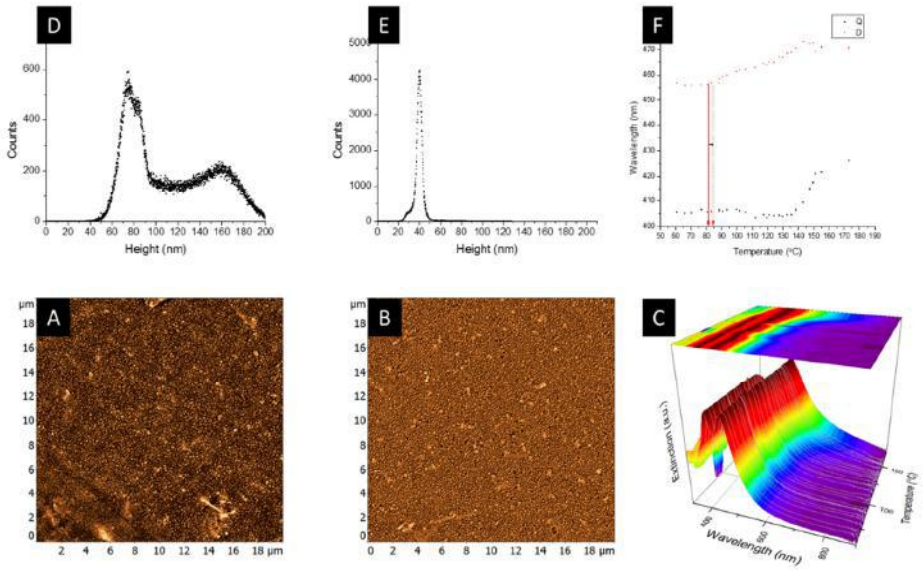



Figure 3: The AFM and UV-Vis analysis and of a silver nanocube-PVC nanocomposite heating experiment. (A) the AFM image of silver nanocubes on PVC at room temperature. (B) The AFM image of silver nanocubes on PVC after heating was completed. (D) and (E) are the histograms for the before heated and after heated AFM images respectively. (C) the temperature dependent UV-Vis extinction spectra. (F) Illustrating the change in the dipolar mode in respect to temperature, with experimental $T_g$ is signified in the red line and the bulk $T_g$ as the dotted red line

### 1.3 PVC-silver nanocube nanocomposite

The AFM data for PVC is shown in Figure 3. Before heating (A) two well defined peaks in the histogram (D) are observed. This is characteristic of a discreet layer of silver nanocubes deposited on top of a polymer thin film. After heating, the histogram appears to be a sharp symmetric peak with a small tail. The amount embedded was calculated to be 80 +/- 7 nm, which represents near full incorporation of the silver nanocubes into the polymer thin film.

UV-Vis analysis was done on the PVC-silver nanocube composite as seen in Figure 3 (C). A relatively slow dipolar red shift cab be seen in (F) where the transition occurs over a large 66 $^{o}$C temperature range. The quadrupolar mode however shifted over a smaller period of time and at such higher temperature. Since the red shift in the Q mode signifies approximately halfway embedding of the silver nanocubes. The greater separation in temperature between the onset for both trends, and the relatively extended features for the D mode suggest that while the process remains spontaneous, it is kinetically slower than the other composites. This observed trend is an artifact of ramping temperature program. This is consistent with the polymer chains gaining more energy and kinetic movement on an order of the ramp rate, allowing for quicker reorganization of the polymer chains. The Q mode was found to overlap onto the D mode forming an asymmetric peak representing near full incorporation of the cube into the PVC film. The $T_g$ was found to be 81 +/- 2 $^{o}$C, which matches the reference bulk $T_g$ of 81.0 $^{o}$C.

Table 1: Experimental $T_g$, and bulk $T_g$

| Polymer | Experimental $T_g$ ($^{o}$C) | *Reference $T_g$ ($^{o}$C) |
|---|---|---|
| PS | 103 +/- 2 | 99.8 |
| PMMA | 122 +/- 12 | 105 |
| PVC | 81 +/- 2 | 81.0 |

*Bulk references from [23]

### 1.4 Refractive index and Dipolar mode

As the refractive index increases the hybridized dipolar mode redshifts, this relationship can be considered linear over small ranges. Figure 4 shows the relationship between the dipolar mode and the bulk refractive index of each polymer. The left image represents the silver nanocubes deposited onto the corresponding polymer thin films, whereas the right image shows the dipolar mode in respect to the bulk refractive index of the polymer, a linear relationship can be seen with a $R^2$ value of 0.995 signifying a very linear relationship between the dipolar mode and the refractive index as expected [24,25]. The Q mode was found to stay approximately constant (left) which is supported by literature that the quadrupolar mode is insensitive to the refractive index when the silver nanocube in on top of the substrate [24,25].

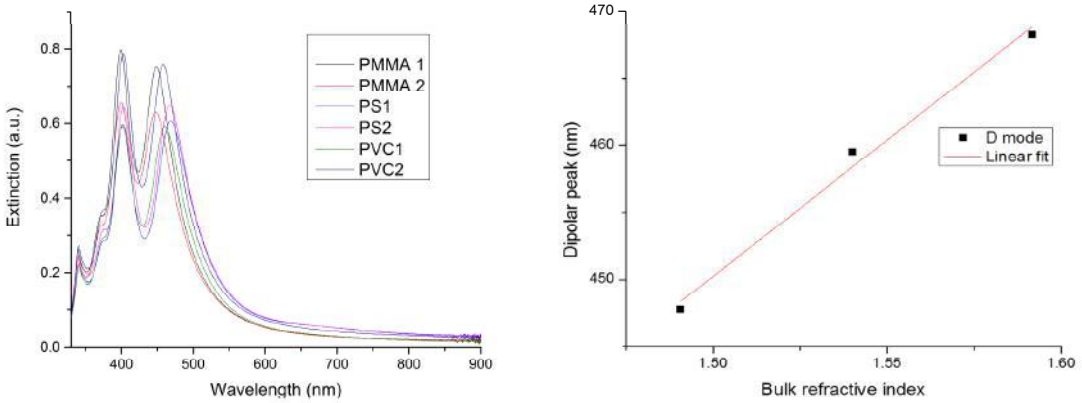



Figure 4: (left) UV-Vis of the various silver nanocube-polymer nanocomposites. (right) showing the relationship between bulk

## 3. Conclusions

Thermosensitive silver nanocube polymer nanocomposites were produced and used to locally probe the glass transition temperature of various polymers. The glass transitions of the polymers were found by monitoring the red shift in the Dipolar mode and were found to be: 103 +/- 2 $^{o}$C for PS, 122 +/- 12 $^{o}$C for PMMA, and 81 +/- 2 $^{o}$C for PVC. In comparison to the bulk $T_g$ values of: 99.8 $^{o}$C, 105 $^{o}$C and 81.0 $^{o}$C for PS, PMMA and PVC respectively. For silver nanocubes on top of polymer films, the dependence of the dipolar mode on the bulk refractive index of each polymer was found to be linear, while the quadrupolar mode was insensitive to the bulk refractive index. Further analysis by monitoring the embedding process by UV-Vis continuously at a constant temperature will give more insight on the polymer dependence on the kinetics. The use of polymer blends may give insight on polymer-polymer surface properties and glass transition temperatures. It is also interesting to use polymers of different properties such as very high refractive index like polycarbodimide. The use of particle embedding can be done to produce anisotropic particles and possibly control particle aggregation upon solvent annealing forming controllable particle dimers.

## Acknowledgements

Funding provided by NSERC. Special thanks to Jim Logan for help with constructing the spin coater.

## References

[1]. T. F. Jaramillo, S.-H. Baeck, B. R. Cuenya, and E. W. McFarland, J. Am. Chem. Soc. **125**, 7148 (2003).
[2]. W. A. Lopes and H. M. Jaeger, Nature **414**, 735 (2001).
[3]. I. Tokareva, S. Minko, J. H. Fendler, and E. Hutter, J. Am. Chem. Soc. **126**, 15950 (2004).
[4]. C. Noguez, J. Phys. Chem. C **111**, 3806 (2007).
[5]. J. Teichroeb and J. Forrest, Phys. Rev. Lett. **91**, 016104 (2003).
[6]. A. Bottomley, D. Prezgot, J. P. Coyle, and A. Ianoul, Nanoscale (2016).
[7]. X. Wang, S. Li, P. Zhang, F. Lv, L. Liu, L. Li, and S. Wang, Adv. Mater. **27**, 6040 (2015).
[8]. J. Butet and O. J. F. Martin, ACS Nano **8**, 4931 (2014).
[9]. G. Amarandei, I. Clancy, C. O'Dwyer, A. Arshak, and D. Corcoran, ACS Appl. Mater. Interfaces **6**, 20758 (2014).
[10]. B. Gao, G. Arya, and A. R. Tao, Nat. Nanotechnol. **7**, 433 (2012).
[11]. C. Boerigter, R. Campana, M. Morabito, and S. Linic, Nat. Commun. **7**, 10545 (2016).
[12]. K. M. Mayer and J. H. Hafner, Chem. Rev. **111**, 3828 (2011).
[13]. S. Zhang, K. Bao, N. J. Halas, H. Xu, and P. Nordlander, Nano Lett. **11**, 1657 (2011).
[14]. R. D. Deshmukh and R. J. Composto, Langmuir **23**, 13169 (2007).
[15]. G. J. Kovacs and P. S. Vincett, J. Colloid Interface Sci. **90**, 335 (1982).
[16]. C. B. Roth and J. R. Dutcher, J. Electroanal. Chem. **584**, 13 (2005).
[17]. R. M. Overney, C. Buenviaje, R. Luginbühl, and F. Dinelli, J. Therm. Anal. Calorim. **59**, 205 (n.d.).
[18]. C. A. Daniels and E. A. Collins, Polym. Eng. Sci. **19**, 585 (1979).
[19]. G. Vignaud, M. S. Chebil, J. K. Bal, N. Delorme, T. Beuvier, Y. Grohens, and a Gibaud, Langmuir **30**, 11599 (2014).
[20]. G. Greyling and H. Pasch, Anal. Chem. **87**, 3011 (2015).
[21]. L. Chang and E. M. Woo, Polym. Chem. **1**, 198 (2010).
[22]. S. E. Skrabalak, L. Au, X. Li, and Y. Xia, Nat. Protoc. **2**, 2182 (2007).
[23]. J. Brandrup, E. Immergut, and E. a Grulke, *Polymer Handbook*, 4th ed. (Wiley, 1999).
[24]. A. Bottomley, D. Prezgot, and A. Ianoul, Appl. Phys. A **109**, 869 (2012).
[25]. N. Ahamad, A. Bottomley, and A. Ianoul, J. Phys. Chem. C **116**, 185 (2012).

# Disordered plasmonic nanoholes in Ag thin films

**Piragash Kumar R M, Venkatesh A and V H S Moorthy***

Research Laboratory for Plasmonics, Department of Electronics and Communication, Manipal Institute of Technology, India
*corresponding author, E-mail: vhsmoorthy@gmail.com vhs.moorthy@manipal.edu

## Abstract

Extraordinary transmission of light through subwalength holes in a metallic thin film offers potential applications in optoelectronic and sensing devices. Here, we present the optical properties of disordered nanoholes in optically thick silver thin films – fabricated by a novel technique. The disordered nanoholes exhibit strongly enhanced broadband optical transmission and highly localized electric fields which find potential applications in photovoltaic and sensing devices respectively.

## 1. Introduction

Subwavelength holes in a metallic thin film exhibit enhanced transmission of light due to the phenomenon of coupling of light with surface plasmons of the patterned metal film. Periodic arrays of nanoholes in an optical thick metal film have been widely studied owing to the spectral tunability of light transmission – by changing the size, shape and period of the holes. The optically active subwavelength holes – in which incident light gets converted into surface waves – in metal films find applications in optical filters, light-emitting diodes, photovoltaic devices and sensors. The widely studied system of periodic arrays (or ordered) of nanoholes in a metal film are mainly fabricated using focused ion beam, electron beam lithography and photolithography [1]. Recently, disordered nanoholes have gained importance owing to their non-linear optical response, high bandwidth field concentration (hotspots) in nanoscopic volume and possible optical Anderson-localization effects [2].

Disordered nanoholes are fabricated through a low-cost colloidal lithography technique which possesses its own limitations to be realized at wafer-scale. We have developed a novel technique to fabricate disordered nanoholes in optically thick silver thin films [3]. The technique is facile, inexpensive and wafer-scale compatible. Here, in this paper, we present the optical properties of the disordered nanoholes and discuss the advantages of utilizing them in photovoltaic and sensing applications.

## 2. Experimental

Disordered nanoholes in Ag thin films are prepared by a novel technique. Ag thin films of 180nm thickness are prepared using DC Magnetron sputtering with rate of deposition (1.5 nm/s) calibrated using thickness profilometer (Dektek XT). The disordered nanoholes are characterized using Scanning Electron Microscopy (Zeiss EVO-18 SEM), Optical microscopy (Nikon Eclipse LV-100), UV-Vis-NIR spectroscopy (Shimadzu UV-3600 with ISR200) and Scanning Near-field Optical Microscopy (WITec Alpha RS 300).

## 3. Results

Figure 1 (a-b) show the SEM micrograph of the disordered nanoholes in Ag thin films.

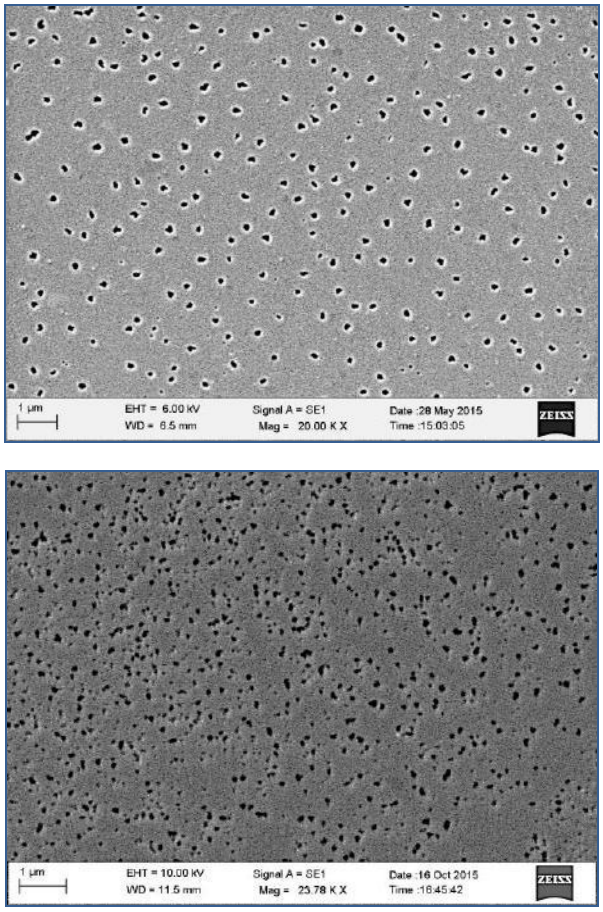



**Fig. 1.** Imaging of disordered nanoholes in optically thick silver thin films. **a-b)**SEM micrographs showing the

structural morphology and disordered arrangement of low and high densities of nanoholes respectively.

The SEM data reveal that the nanoholes in 180nm Ag thin films have different sizes and shapes and possess disordered arrangement. Also, fig. 1b show that the density of the nanoholes can be increased.

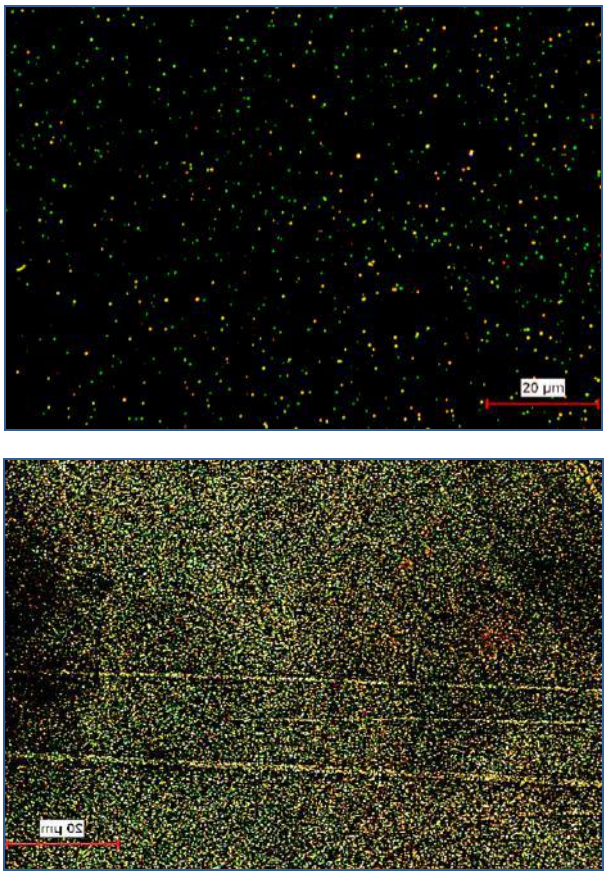



**Fig. 2**. Imaging of disordered nanoholes in optically thick silver thin films. **a-b)** Optical micrographs showing the spectrally filtered optical transmission through disordered nanoholes – observed as coloured dots.

The optical micrographs were obtained in the bright field transmission mode. The black background in the micrograph results from the opaqueness of the optically thick Ag thin film. In fig. 2a, individually colored dots in the green to red range are observed and are few in number – pertaining to the low density of the nanoholes. In fig. 2b, the colored dots are very high in number – due to high density of nanoholes- and various colors are observed.

Fig. 3. Shows the transmittance spectra of low density of nanoholes (blue) and high density of nanoholes (black) acquired using integrating sphere. The low density of nanoholes transmit only 0.035% of light in the green to red regime of the spectrum. The high density of nanoholes show a 25 fold increase in transmission of light to that of low density of nanoholes. The transmission of light through high density of nanoholes exhibit broadband nature in the 500 – 750 nm region.

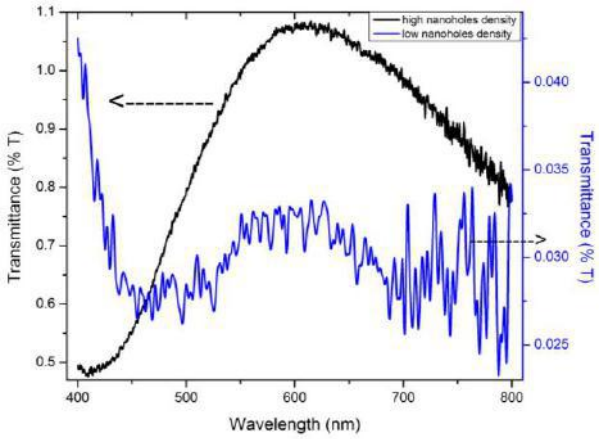



Fig. 3. Optical studies of disordered nanoholes. Transmittance spectra exhibiting broadband enhanced transmission for high density nanoholes. Transmittance of low density nanoholes is also given for comparison.

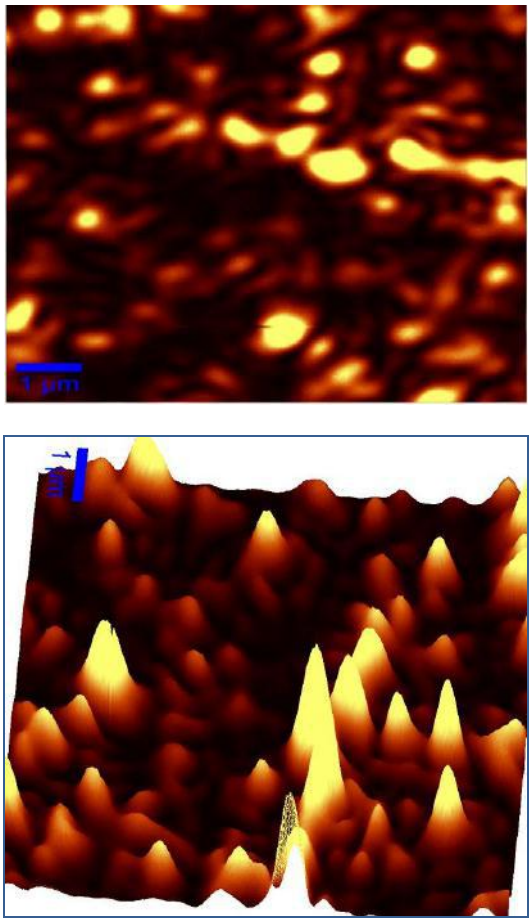



Fig. 4. Optical studies of disordered nanoholes. **a-b)** Two – and Three – dimensional Scanning Near-field Optical Microscope images showing the localized electric field profile on disordered nanholes respectively.

The fig. 4 show the SNOM micrographs of disordered nanoholes acquired in collection mode with 532nm laser illumination source. The SNOM data indicates the confinement of electric fields in and around the nanoholes.

## 4. Discussion

The structural morphology of the disordered nanoholes for two different densities – number of nanoholes per unit area - in optically thick silver thin films vary in shape, size (from 80 – 200 nm) and possess disordered arrangement. The high density of nanoholes exhibit broadband enhanced transmission of light over a wide wavelength range from 500 – 750nm. Partly, this enhanced transmission can be attributed to the variation in size and shape although disorder in the arrangement influences the optical response the most. The disordered nanoholes showcase spectrally filtered optical transmission – observed as coloured dots – in the entire visible region correlating to the broadband transmission.

The enhanced light transmission is more pronounced in the near-field regime, as shown in figure 2 b-c, where hotspots of high intensity electric fields are observed.

## 5. Conclusions

In conclusion, the disordered nanoholes in optically thick silver thin films fabricated using the novel technique show strongly enhanced broadband transmission of light and hotspots with localized electric fields which can be utilized for photovoltaic and sensing applications.

## Acknowledgements

The authors would like to thank the Department of Science & Technology (DST) and Department of BioTechnology (DBT), New Delhi, India for funding the research work.

## References

1. C. Genet & T. W. Ebbesen, *'Light in tiny holes'*, Nature, vol. 445 (2007), 39 – 46.
2. Luca Dal Negro and Svetlena V. Boriskina "Deterministic aperiodic nanostructures for photonics and plasmonic applications" *Laser Photonics Rev.,* 1-41, 2011.
3. Piragash Kumar R. M, Venkatesh A & Moorthy V. H. S, ***'Patent document submitted'*** to Department of Science and Technology(DST) New Delhi, India.

# Plasmonic Induced Transparency in a MIM Waveguide with Two Side Coupled Cavities

**Adnane Noual[1,2], Ossama El Abouti[1], El Houssaine El Boudouti[1,3], Abdellatif Akjouj[3], Yan Pennec[3], Bahram Djafari-Rouhani[3]**

[1]LPMR, Département de Physique, Faculté des Sciences, Université Mohamed Premier, 60000 Oujda, Morocco

[2]Ecole Normale Supérieure de Tétouan, Université Abdelmalek Essaadi, Tétouan, Morocco

[3]Institut d'Electronique, de Microélectronique et de Nanotechnologie, UMR CNRS 8520, UFR de Physique, Université de Lille 1, 59655 Villeneuve d'Ascq, France,

*corresponding author, E-mail: noualad@yahoo.fr

**Abstract** We investigate numerically the classical analogue of electromagnetically induced transparency in a nano-plasmonic structure constituted by two side-coupled cavities. Two configurations are considered: *i*) two cavities connected symmetrically on each side of the waveguide; *ii*) two cavities situated on the same side. In the first case the EIT resonance occurs as a consequence of the destructive interference between the two cavities (playing the role of two coupled radiative oscillators), whereas in the second situation the phenomenon arises due to a coupling between dark and radiative resonators. By detuning the sizes of the two cavities (i.e., the length difference ΔL, keeping their width *w* similar), we show that the position, width and quality factor of the EIT resonance depend strongly on ΔL. The effect of the metal gap separating the two cavities from the waveguide is also discussed. These results may have important applications for designing integrated devices such as narrow-frequency optical filters, novel sensors and high-speed switches.

## 1. Introduction

Electromagnetically induced transparency (EIT) is a quantum interference phenomenon that renders an opaque medium transparent in a narrow spectral region with low absorption and steep dispersion [1, 2]. These properties have been exploited to show different applications in these systems such as: slow light, sensing and data storage [2-5]. However, it was realized that EIT-like behaviors are not uniquely associated to quantum systems and can be extended to classical systems [2-4]. In this context, several classical systems have been designed to demonstrate the classical analogue of EIT. Among these systems one can cite: plasmonic nanostructures [6-11], planar metamaterials [12-14], photonic crystal waveguides coupled to cavities [15-19], coupled microresonators [20-25], micro and radiowave circuits [26-28] and acoustic slender tube waveguides [29-31]. The EIT resonance can be obtained using two coupled resonators (or oscillators) with closely spaced frequencies.

The resonators with high (dark resonator) and low (radiative resonator) Q factors give rise to the so-called Λ-type configuration [1] in three atomic levels, whereas the resonators with low Q factors (radiative resonators) give rise to the so-called V-type configuration [6, 8, 27-31]. In few recent works, the V-type resonances in double stub resonators connected at the same site along a waveguide have been shown in photonic [27-28] acoustic [29-30] and plasmonic [32-33] structures.

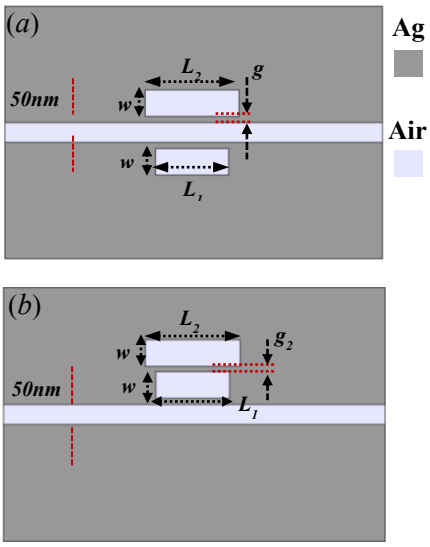



Figure 1: (*a*) Geometry of a Metal-Insulator-Metal waveguide side-coupled (through a metallic gap *g*) to two cavities situated symmetrically on each side of the bus waveguide. (*b*) Same as in (*a*) but such as both cavities are placed on the same side of the main waveguide, and coupled to each other through a metallic gap $g_2$.

In this work, we studied the plasmonic analogue of EIT in a two side-coupled cavities to a waveguide. The geometry of the system is considered in either Λ or V-like configuration. This is to provide a plasmonic system design giving rise to EIT-like resonance in both configurations. The cavities are embedded in a metal and filled with air, and are considered to have the same width (*w*=100 nm), whereas their lengths $L_1$ and $L_2$ can be detuned. We show the possibility of existence of EIT resonance by detuning the size of the two cavities in Λ and V-type configurations

(Figs. 1a and 1b). Their separation from the waveguide is referred to as g (metallic gap that enables evanescent coupling).

## 2. Method of numerical simulation

The cladding of the waveguide and the cavities is a silver metal whose dielectric function is described by the lossy Drude model

$$\varepsilon(\omega) = \varepsilon_\infty - \frac{\omega_p^2}{\omega^2 + i\Gamma\omega}, \quad (1)$$

where $\varepsilon_\infty$ is the relative permittivity at infinite frequency, $\omega_p$ is the plasma frequency and $\Gamma$ is the collision frequency. The corresponding values are given by [34]: $\varepsilon_\infty = 12.5$, $\omega_p = 2.05 \times 10^{16}$ rad/s and $\Gamma = 10^{14}$ rad/s. The waveguide width ($d$) is set out to be equal to 50 nm and the incident plane wave is a TM polarized one, i.e. the magnetic field is perpendicular to the plane of Fig. 1 ($\vec{H}//\vec{z}$). The frequency domain we are interested in here corresponds to the vacuum wavelength ranging from 600 nm to 820 nm. In this frequency interval the waveguide is strictly monomode and antisymmetric [35]. It corresponds to a surface plasmon-polariton (SPP)-like mode in which the electric field is strongly confined along the dielectric-metal interface and decays exponentially away from it [36].

The optical properties of the structure such as transmission (T), reflection (R) and absorption (A) are obtained using finite-element method (Comsol-Multiphysics package) [37]. R and T are calculated, respectively, by means of the scattering matrix elements of the system, namely:

$$R = |S_{11}|^2 \text{ and } T = |S_{21}|^2, \quad (2)$$

whereas the absorption is deduced by A = 1 – R – T.

## 3. Plasmonic design system in V-type state

In order to show the possibility of existence of EIT-resonance, i.e. a resonance squeezed between two transmission zeros, we have to take $L_1$ and $L_2$ slightly different. This is true whether the system design is set into a V or Λ-like configurations. We will focus first on the V-type system, and then treat the Λ-like case. Figures 2 (a), (b) and (c) give respectively the transmission, reflection and absorption spectra (pink curves) for $L_1$=240 nm and $L_2$=258 nm ($\Delta L = L_2 - L_1 = 18$ nm). One clearly notes, in Fig. 1(a), the emergence of a resonance peak at $\lambda_r = 672$ nm between the two dips situated at $\lambda_1 = 654$ nm and $\lambda_2 = 693$ nm. As a matter of comparison, we have also plotted the transmission, reflection and absorption for each resonator alone (black and red curves). While the zeros of transmission are originated from the resonances of the cavities [36], the peak of resonance is the consequence of an interaction between the cavities.

Figures 3(a) and 3(b) represent the magnetic field distribution at the incident wavelengths (of the dips) $\lambda_1 = 654\ nm$ and $\lambda_2 = 693\ nm$. At these wavelengths, the field is trapped in each cavity and do not propagate in the system. This result has already been explained and reported deeply in [36].

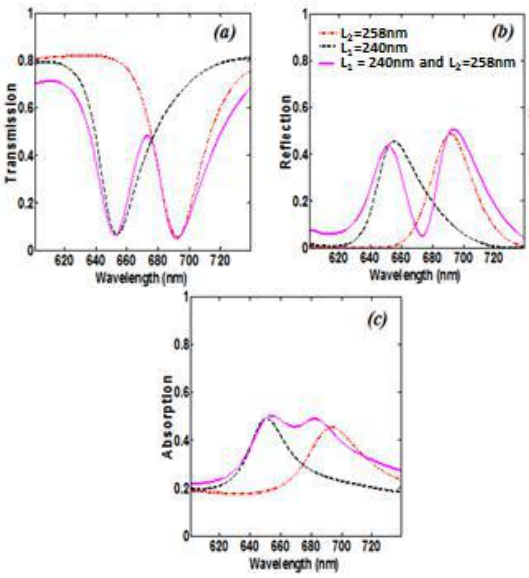



**Figure 2**: (a) Transmission spectra when a single cavity is coupled to the waveguide with $L_1$=240 nm (black curve) and $L_2$=258 nm (red curve). The pink curve corresponds to the case when both cavities are present in the system ($L_1$=240 nm and $L_2$=258 nm). (b) The same as in (a) but for the reflection. (c) The same as in (a) but for the absorption.

Besides, the magnetic field map at the wavelength of the resonant peak, i.e. $\lambda_r = 672$ nm is depicted in Fig. 3(c). It can be clearly seen that the wave is now transmitted through the waveguide. This phenomenon can be explained as an out of phase oscillation of one cavity with respect to the other. Indeed, the cavities, acting like radiative oscillators, interfere destructively (via the bus waveguide) at the wavelength of the EIT-resonance. As a result, the guided mode at the resonance is transmitted to the end of the waveguide giving rise to the EIT-phenomenon.

In addition to the study of the amplitudes of the transmission, it is interesting to analyze other information of the scattering parameters such as the dispersion behavior. The latter is related to the phase $\phi$ of the transmission. An example of the variation of the phase as a function of the wavelength is given in Fig. 4($a$) for $\Delta L = 18\ nm$. As predicted, the phase shows two phase drops around the transmission zeros (Fig. 2($a$)). The phase drops do not reach $\pi$ because of the large absorption in the metal. Similar behavior has been observed experimentally in coaxial cables [28]. A clear signature of the phase drops is observed in the delay time defined as $\tau = \frac{d\phi}{d\omega}$ giving rise to negative delay time in Fig 4($b$). The delay time gives the time spent by electromagnetic waves in the cavities (time of capture) before their transmission.

In order to study the effect of the detuning $\Delta L = L_2 - L_1$ on the EIT resonance, we have fixed the length of the lower cavity at $L_1$=240 nm and changed the length $L_2$ of the upper cavity. The results are depicted in Fig.5 for $\Delta L$ = 0 nm (Fig.5 (a)), 6 nm (Fig.5 (b)) and 18 nm (Fig.5(c)). As predicted, the dip associated with the fixed cavity falls at the same wavelength indicated by an arrow. However, the wavelengths induced by the second cavity and the EIT resonance increase when $\Delta L$ increases.

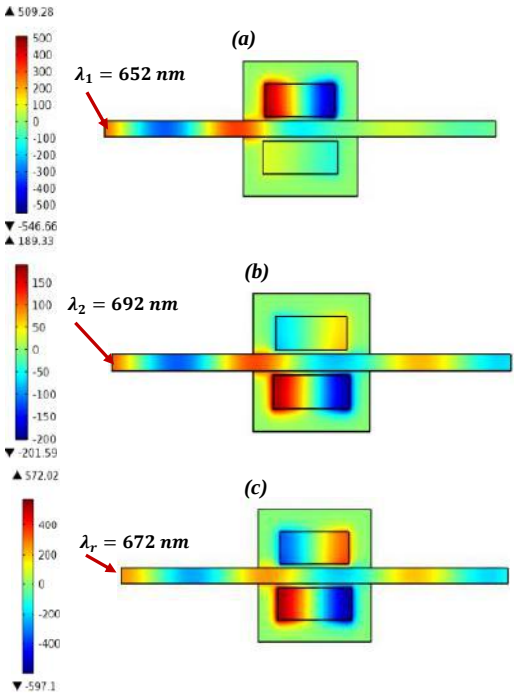



**Figure 3:** (a), (b) Magnetic field maps at the transmission dips wavelengths $\lambda_1 = 652$ nm and $\lambda_2 = 692$ nm respectively. (c) Same as (a) and (b) but for the resonance peak at $\lambda_r = 672$ nm. Notice the different color scales at the left hand side of the figures.

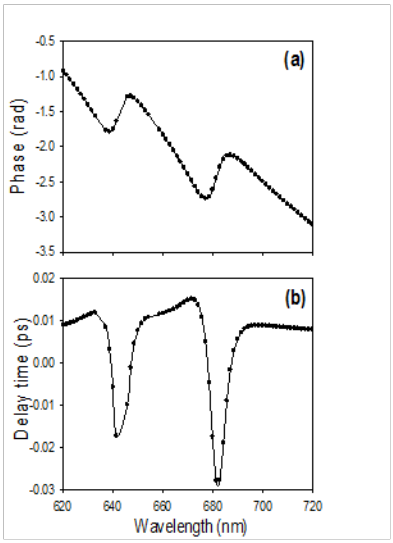



**Figure 4:** (a) Variation of the phase of the transmission as a function of the wavelength for the structure depicted in Fig.3 (a) with $L_1$ = 240 nm and $L_2$ = 258 nm. (b) Same as (a) for the delay time.

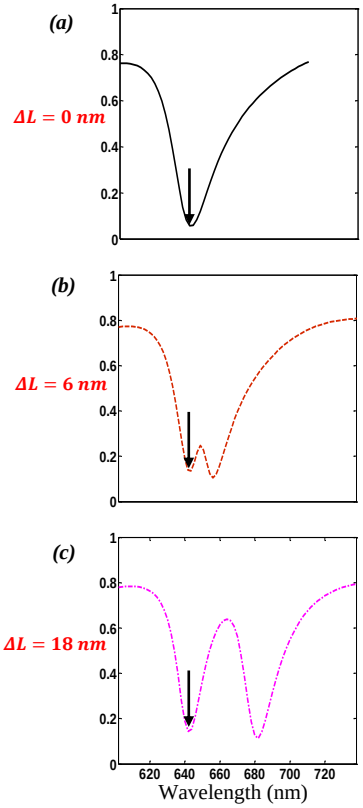



**Figure 5:** (a)-(c) Transmission spectra versus wavelength for different values of ΔL (4 nm (a), 6 nm (b) and 18 nm (c)) with g=16 nm and $L_1$=240 nm. The arrows indicate the position of the fixed size cavity mode.

We can also notice that around the EIT resonance, the transmission increases, whereas the reflection coefficient decreases and the absorption increases over a small amount of $\Delta L$ before decreasing (reflection and absorption data are not given here). These results are summarized in Fig.6 where we have plotted the magnitudes of transmission, reflection and absorption as a function of $\Delta L$ for the EIT resonance depicted in the insert. One can notice that the transmission and reflection coefficients cross each other when the absorption reaches its maximum value around $\Delta L \approx 5.5\ nm$. This is similar to the behaviour observed recently in photonic circuits [28]. In order to achieve a good transparency (i.e., a suppression of absorption), $\Delta L$ should be chosen larger. For instance, if one takes $\Delta L \approx 12\ nm - 18\ nm$ the resonance line width is rather reasonably small (which means good quality factor).

The characteristics of the EIT resonance depend strongly on the gap parameter g separating the cavities and the waveguide, as it is described in Fig. 7(a). When g decreases, i) the wavelengths associated with the transmission dips and the EIT resonance increase. ii) The width and the intensity of the resonance decrease which renders the system less

transparent because of the absorption. iii) The dips reach zero intensity which means that the system becomes more opaque at the cavities wavelengths.

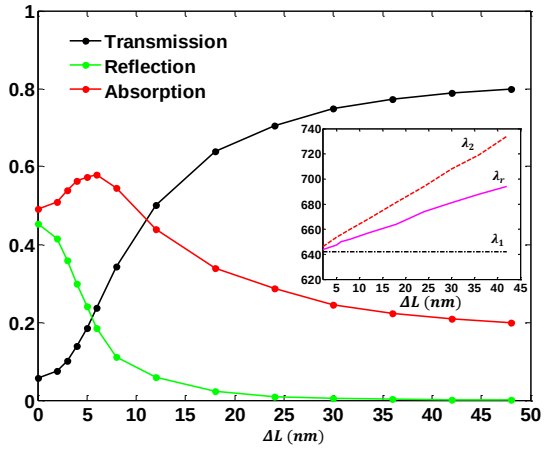



**Figure 6:** Transmission, reflection and absorption versus $\Delta L = L_2 - L_1$ for the EIT resonance depicted in the insert. The wavelengths of the transmission zeros $\lambda_1$ and $\lambda_2$ are also sketched in the insert. The length of the lower cavity is fixed to $L_1$ = 240 nm

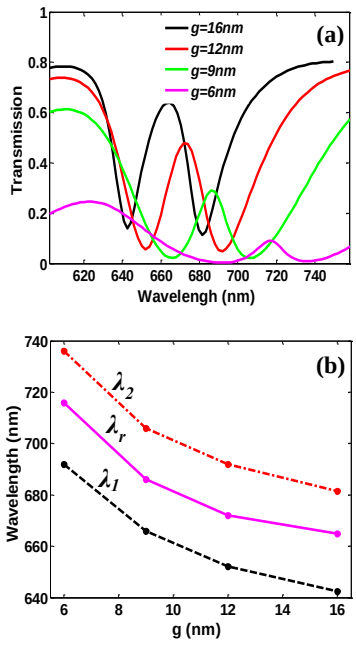



**Figure 7:** Transmission spectra versus wavelength for g=16 nm (black curve), 12 nm (red curve), 9 nm (green curve) and 6 nm (pink curve). The lengths of the two cavities are fixed to $L_1$=240 nm and $L_2$=258 nm. (b) Transmission zeros and EIT-resonance wavelengths versus *g*.

## 4. Plasmonic design system in a Λ-type state

After having grafted the cavities resonators aside of the bus waveguide in a V-like configuration, we now put both cavities on the same side of the waveguide as depicted in Fig. 1(b). In this shape, the system clearly resembles a Λ-like atomic state [1]. To make the comparison more evident we add upon the geometry of the system the corresponding three atomic-levels.

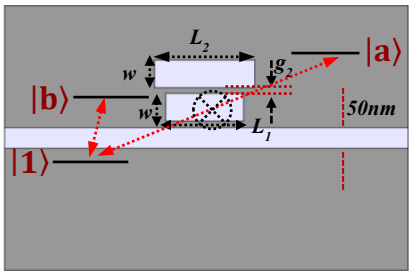



**Figure 8:** Geometry of the plasmonic design system following a Λ-type state. To make the analogy more apparent with atomic systems, the corresponding three atomic-levels are sketched within the structure.

It should be pointed out that the upper cavity ( labeled $|\mathbf{a}\rangle$) corresponds to the dark-mode (high quality factor Q) as it couples only evanescently with the guide through the lower cavity ( labeled $|\mathbf{b}\rangle$ ). The lower cavity exhibits a strong coupling with the waveguide giving rise to the bright mode (low Q) (*g* is usually taken small). In figure 9, we give the transmission spectra of such system for $L_1 = 240$ nm and $L_2 = 252$ nm (i.e. $\Delta L = L_2 - L_1 = 12$ nm), and $g=g_2=10$ nm. One notes the appearance of a relatively large transparency window (EIT-resonance) between the transmission zeros corresponding to each cavity mode.

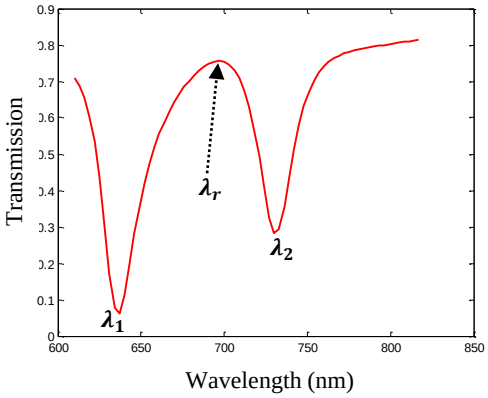



**Figure 9:** Transmission spectra versus wavelength of the system of fig. 7 for $L_1 = 240$ nm, $L_2 = 252$ nm and $g=g_2=10$ nm.

The high frequency mode (lower wavelength, $\lambda_1 = 630$ nm) is an eigenmode of the lower cavity, while the low frequency mode (higher wavelength, $\lambda_2 = 730$ nm) is an eigenmode of the upper cavity (of higher length). This is quite explicit in Figs. 10(a) and 10(b) where the magnetic field map is shown within the system at these specific wavelengths. As a matter of fact, at these frequencies the incident waves are trapped inside the cavities and reflected back to the entrance of the waveguide. The magnetic field map at the middle wavelength of the transmitted window ( $\approx \lambda_r = 700$ nm ), corresponding to the EIT-resonance

wavelength is also presented in Fig. 10(c). Clearly, the lower cavity mode gets extinct whereas the upper cavity mode remains trapped within. As a result, the incident wave is transmitted at the right end of the waveguide. To get a deeper insight of the physical mechanism behind the EIT-resonance in a Λ-like state, we turn back to the analogy with atomic systems. The EIT-resonance in such Λ-type configuration is inferred to quantum destructive interference (of transition amplitude). If we base our analysis on the three levels-system of Fig. 7, the transition $|\mathbf{1}\rangle \rightarrow |\mathbf{b}\rangle$ has two possible pathways to occur: (i) through a direct transition $|\mathbf{1}\rangle \rightarrow |\mathbf{b}\rangle$ or (ii) indirectly such as $|\mathbf{1}\rangle \rightarrow |\mathbf{b}\rangle \rightarrow |\mathbf{a}\rangle \rightarrow |\mathbf{b}\rangle$. The destructive interference between the two paths leads to EIT-resonance (suppression of absorption associated with $|\mathbf{1}\rangle \rightarrow |\mathbf{b}\rangle$).

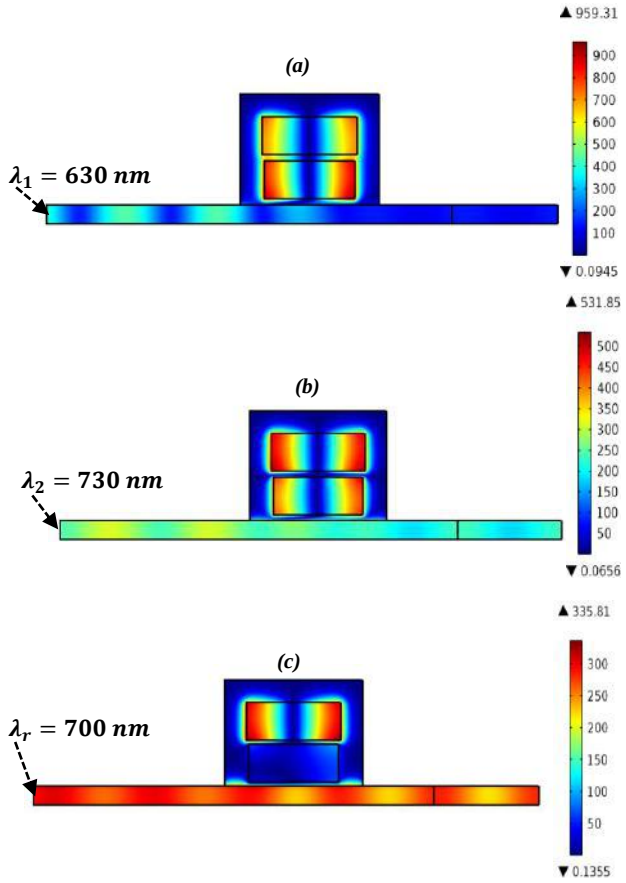



**Figure 10:** (a), (b) Modulus of the magnetic field maps at transmission dips at $\lambda_1 = 630$ nm and $\lambda_2 = 730$ nm respectively. (c) Same as (a) and (b) but for the EIT-resonance peak wavelength at $\lambda_r = 700$ nm. Notice the different color scales at the right hand side of the figures.

This means that, in our classical system, the EIT resonance can be understood as a destructive interference between the mode escaping from the upper cavity and the mode resonating within the lower cavity. Hence, the guided mode uncouples with both resonators and passes through the waveguide.

One could have noticed the relatively large width of the transparency window that opened up, which indicates a quite low quality factor of the EIT-resonance. In order to improve Q we studied the influence of the metallic gap $g_2$ on the full width at half maximum (FWHM) of the resonance. This parameter permits the control of the evanescent coupling intensity between upper and lower cavities. In Fig 11, we give the transmission spectra of the system versus wavelength for different values of $g_2$, and such that $L_1$=240 nm, $L_2$=252 nm and $g$=10 nm. We remark a significant decrease of the width of the EIT resonance with increasing $g_2$. Specifically, Q≈13 for $g_2$=10 nm and Q≈27 for $g_2$=20 nm. The drawback of increasing Q is the energy loss associated with EIT-peak. Indeed, one can see that at $g_2$=10 nm (Q≈13) approximately 75% of the incident power is transmitted while for $g_2$=20 nm only 60% of the power is transferred. Nonetheless, 60% of transmitted power is still quite reasonable value, and a trade-off should always be reached at that point.

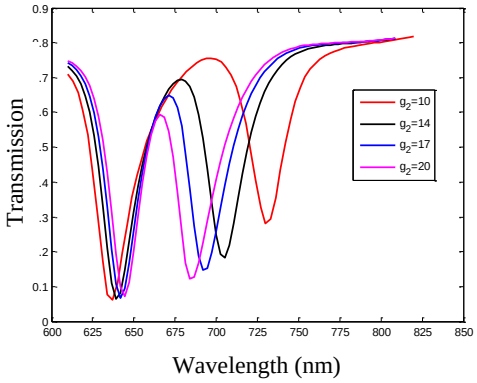



**Figure 11:** Transmission spectra versus wavelength of the system for different values of $g_2$ such that $L_1 = 240$ nm and $L_2 = 252$ nm and $g$=10 nm.

Another important feature of a classical analogue system of EIT is whether it is easy to tune the resonance peak or not. In order to show the possibility of EIT-resonance frequency tuning, we studied the effect of the upper cavity length on the transmission properties of the system. Specifically, we calculated the transmission spectra versus wavelength for $L_2$=246 nm, 252 nm, 258 nm and 264 nm, whereas $L_1 = 240$ nm, $g$=10 nm and $g_2$=20 nm are kept constant. As pointed out just above, the value of $g_2$=20 nm offers a good rate of transmitted power at EIT-resonance and a relatively small FWHM of the associated peak. The corresponding results are presented in Fig 12, where one can notice an almost linear increase of the EIT-resonance wavelength with increasing $L_2$.

Actually, it can be seen in Fig 11 that the intensity of the evanescent coupling between the two cavities resonators represented by $g_2$ enables the tuning of the EIT-resonance as well. Nevertheless, it also modifies the FWHM of the resonance peak, which might be undesirable. Consequently,

it is best to adjust $L_2$ such that only the wavelength resonance can be tuned.

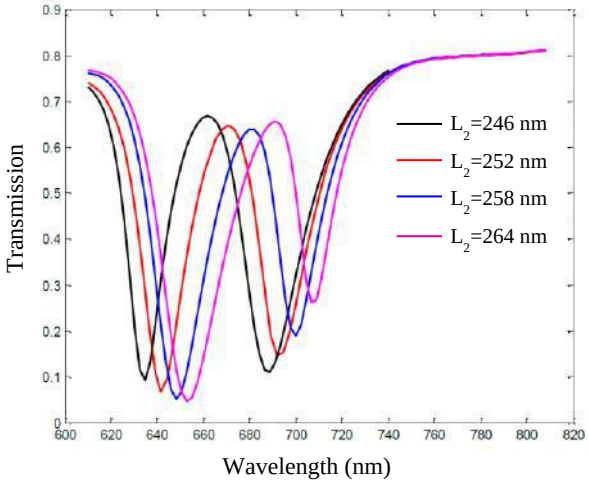



**Figure 12:** Transmission spectra versus wavelength of the system for different values of $L_2$ such that $L_1 = 240$ nm, $g_2 = 20$ nm and $g$=10 nm.

## 5. Conclusion

In this paper, we have demonstrated numerically the possibility of existence of plasmonic analogue of EIT in metal-air-metal waveguide coupled to two nano-cavities resonators placed in either V or Λ-type configurations. Both cavities are filled with air but with different sizes. The waveguide and the cavities are embedded in a metal and the interaction between the confined mode within the waveguide and the cavities depends on the type of configuration the system is set into. In a V-like state, the incident light-wave couples with both cavities (put aside) evanescently through a small metal gap. In this case, the EIT-resonance is shown and explained by destructive interference between the cavities acting like radiative oscillators. We have shown that the behavior of the EIT resonance in the transmission can be detuned via the difference in size of the two cavities depending on the value of the gap separating the cavities from the waveguide. On the other hand, when the same system is placed in a Λ-type state, the incident wave couples directly (evanescently) with the lower cavity, and only indirectly (via the former) with the upper one. In this situation, The EIT-resonance existence is proven as well and is explained analogously with atomic systems as destructive interference between the upper and lower cavities. The possibility of tuning the frequency and improving the quality factor of the EIT-resonance peak is demonstrated. As a matter of completeness of this work, we predict to use the properties of the EIT resonance in designing an optical demultiplexer made of one input waveguide and two output waveguides [38]. This work is in progress. Besides, the available results may have important applications for designing integrated devices such as narrow-frequency optical filters, novel sensors and high-speed switches.

## References


1. M. Fleischhauer, A. Imamoglu, and J.P. Marangos, Electromagnetically induced transparency: Optics in coherent media. Rev. Mod. Phys. **77**, 633 (2005)
2. S.E. Harris, Electromagnetically induced transparency. Phys. Today **50**, 36 (1997)
3. L.V. Hau, S. E.Harris, Z. Dutton, and C.H. Behroozi, Light speed reduction to 17 metres per second in an ultracold atomic gas. Nature **397**, 594 (1999)
4. C. Liu, Z. Dutton, C.H. Behroozi, and L.V. Hau, Observation of coherent optical information storage in an atomic medium using halted light pulses. Nature **409**, 490 (2001)
5. I. Novikova, R.L. Walsworth, and Y. Xiao, Electromagnetically induced transparency-based slow and stored light in warm atoms. Laser Photon. Rev. **6**, 333 (2012)
6. X. Piao, S. Yu, and N. Park, Control of Fano asymmetry in plasmon induced transparency and its application to plasmonic waveguide modulator. Opt. Express **20**, 18994 (2012)
7. N. Liu, L. Langguth, T. Weiss, J. Kastel, M. Fleischhauer, T. Pfau, and H. Giessen, Plasmonic analogue of electromagnetically induced transparency at the Drudedamping limit. Nat. Mater. **8**, 758 (2009)
8. Z. Han, S.I. Bozhevolnyi, Plasmon-induced transparency with detuned ultracompact Fabry-Perot resonators in integrated plasmonic devices. Opt. Express **19**, 3251 (2011)
9. A. Mahigir, P. Dastmalchi, W. Shin, S. Fan, and G. Veronis, Plasmonic coaxial waveguide-cavity devices. Opt. Express **23**, 20549 (2015)
10. R. Taubert, M. Hentshel, J. Kastel, and H. Giessen, "Classical analog of electromagnetically induced absorption in plasmonics", Nano Lett. **12**, 1367 (2012)
11. B. Yun, G. Hu, C. Jiawei, and Y. Cui, Plasmon induced transparency in metal–insulator–metal waveguide by a stub coupled with FP resonator. Materials Research Express **1**, 036201 (2014)
12. J. Wu, B. Jin, J. Wan, L. Liang, Y. Zhang, T. Jia, C. Cao, L. Kang, W. Xu, J. Chen, and P. Wu, Superconducting terahertz metamaterials mimicking electromagnetically induced transparency. Appl. Phys. Lett. **99**, 161113 (2011)
13. Y. Sun, H. Jiang, Y. Yang, Y. Zhang, H. Chen, and S. Zhu, Electromagnetically induced transparency in metamaterials: Influence of intrinsic loss and dynamic evolution. Phys. Rev. B **83**, 195140 (2011)
14. X. Zhang, N. Xu, K. Qu, Z. Tian, R. Singh, J. Han, G. S. Agarwal, and W. Zhang, Electromagnetically induced absorption in a three-resonator metasurface system. Sci. Rep. **5**, 10737(2015)
15. S. Fan, J.D. Joannopoulos, Analysis of guided resonances in photonic crystal slabs. Phys. Rev. B **65**, 235112 (2002)
16. M.F. Yanik, W. Suh, Z. Wang, and S. Fan, Stopping light in a waveguide with an all-optical analog of

electromagnetically induced transparency. Phys. Rev. Lett. **93**, 233903 (2004)
17. X. Yang, M. Yu, D-L. Kwong, C.W. Wong, All-optical analog to electromagnetically induced transparency in multiple coupled photonic crystal cavities. Phys. Rev. Lett. **102,** 173902 (2009)
18. J. Zhou, D. Mu, J. Yang, W. Han, and X. Di, Coupled-resonator-induced transparency in photonic crystal waveguide resonator systems. Opt. Express **19**, 4856 (2011)
19. Y. Sato, Y. Tanaka, J. Upham, Y. Takahashi, T. Asano, and S. Noda, Strong coupling between distant photonic nanocavities and its dynamic control. Nat. Photon. **6**, 56 (2012)
20. Q. Xu, S. Sandhu, M. L. Povinelli, J. Shakya, S. Fan, and M. Lipson, Experimental realization of an on-chip all-optical analogue to electromagnetically induced transparency. Phys. Rev. Lett. **96**, 123901 (2006)
21. K. Totsuka, N. Kobayashi, and M. Tomita, Slow light in coupled-resonator-induced transparency. Phys. Rev. Lett. **98**, 213904 (2007)
22. C.H. Raymond Ooi, C.H. Kam, Controlling quantum resonances in photonic crystals and thin films with electromagnetically induced transparency. Phys. Rev. B **81**, 195119 (2010)
23. B.B. Li, Y.F. Xiao, C.L. Zou, X.F. Jiang, Y.C. Liu, F.W. Sun, Y. Li, and Q. Gong, Experimental controlling of Fano resonance in indirectly coupled whispering-gallery microresonators. Appl. Phys. Lett. **100**, 021108 (2012)
24. W. Ding, B. Luk'yanchuk, and C.-W. Qiu, Ultrahigh-contrast-ratio silicon Fano diode Phys. Rev. A **85**, 025806 (2012)
25. P. Tassin, L. Zhang, T. Koschny, and C.M. Soukoulis, Low-loss metamaterials based on classical electromagnetically induced transparency. Phys. Rev. Lett. **102**, 053901 (2009)
26. Y. Yang, S. Saurabh, J. Ward, and S.N. Chormaic, Coupled-mode-induced transparency in aerostatically tuned microbubble whispering-gallery resonators. Opt. Lett. **40**, 1834 (2015)
27. A. Mouadili, E.H. El Boudouti, A. Soltani, A. Talbi, A. Akjouj, and B. Djafari-Rouhani, Theoretical and experimental evidence of Fano-like resonances in simple monomode photonic circuits. J. Appl. Phys. **113**, 164101 (2013)
28. A. Mouadili, E.H. El Boudouti, A. Soltani, A. Talbi, B. Djafari-Rouhani, Electromagnetically induced absorption in detuned stub waveguides: a simple analytical and experimental model. J. Phys.: Condens. Matter **26**, 505901 (2014)
29. E.H. El Boudouti, T. Mrabti, H. Al-Wahsh, B. Djafari-Rouhani, A. Akjouj, and L. Dobrzynski, Transmission gaps and Fano resonances in an acoustic waveguide: analytical model. J. Phys.: Condens. Matter **20**, 255212 (2008)
30. A. Santillan, S.I. Bozhevolnyi, Acoustic transparency and slow sound using detuned acoustic resonators. Phys. Rev. B **84**, 064304 (2011).
31. W. Tan, C.Z. Yang, H.S. Liu, Z.G. Wang, H.Q. Lin, and H. Chen, Manipulating classical waves with an analogue of quantum interference in a V-type atom. Europhys. Lett. **97**, 24003 (2012)
32. Z. Zhang, L. Zhang, P. Yin, and X. Han, Coupled resonator induced transparency in surface plasmon polariton gap waveguide with two side-coupled cavities. Physica B **446**, 55 (2014)
33. A. Noual, O. El Abouti, E.H. El Boudouti, A. Akjouj, B. Djafari-Rouhani, and Y. Pennec, Proceedings of the Mediterranean Conferenceon Information & Communication Technologies, 2015, Plasmonic Analogue of Electromagnetically Induced Transparency in Detuned Nano-cavities Coupled to a Waveguide. Lecture Notes in Electrical Engineering **380**, 539-544 (2016)
34. E. D. Palik, Handbook of Optical Constants of Solids, New York: Academic, 1985
35. M. L. Bah, A. Akjouj, and L. Dobrzynski, "Response functions in layered dielectric media", Surf. Sci. Rep **16**, 95–132 (1992)
36. A. Noual, Y. Pennec, A. Akjouj, B. Djafari-Rouhani, and L. Dobrzynski, Nanoscale plasmon waveguide including cavity resonator. J. Phys.: Condens. Matter **21**, 375301 (2009)
37. M. Dong, M. Tomes, M. Eichenfield, M. Jarrahi, and T. Carmon, Proceeding of Comsol Conference in Boston, 2013
38. Z. Chen, R. Hu, L. Cui, L. Yu, L. Wang, and J. Xiao, Plasmonic wavelength demultiplexers based on tunable Fano resonance in coupled-resonator systems. Opt. Commun., **320**, 6 (2014)

# Enhanced subwavelength focusing properties of Ag-Au hybrid plasmonic lens with outer slit design

**Kai-Hao Chang[1], Min-Hsiu Cheng[1], Po-Tsung Lee[1],**

[1]Department of Photonics and Institute of Electro-Optical Engineering, National Chiao Tung University, Hsinchu, Taiwan
*corresponding author, E-mail: openhowgood@gmail.com

## Abstract

We propose a Ag-Au hybrid plasmonic lens (*PL*) with outer slit design to obtain enhanced subwavelength focusing. The added outer slit can increase the power intensity and narrow down the focal spot. The measured focal spots of Ag-Au hybrid *PL* and Au *PL* with outer slit are 285 nm and 299 nm at working wavelength of 633 nm, which show the better subwavelength focusing property for the bimetallic nanostructure design.

## 1. Introduction

Recently, several approaches to achieve subwavelength focusing have been proposed to overcome the limit of resolution [1]. The plasmonic lens (*PL*) has become very appealing because of the super resolution image with extraordinary enhanced transmittance [2]. However, the subwavelength focusing of traditional plasmonic zone plate is usually underperformed in experiment owing to the weak evanescent wave approaching the focal point.

In this work, we propose a Ag-Au hybrid *PL* with outer slit design. The transmitted power and localized field enhancement of this bimetallic nanostructure can be tuned by varying the ratio of different metallic compositions which can increase the magnitude of evanescent wave, similar to other nanophotonic devices [3]. In addition, the outer slit can further increase the transmittance and enhance focusing effect. We fabricate Au *PL* and hybrid *PL* with outer slit and measured their plasmonic properties. For comparison, focusing properties of Au *PL* and hybrid *PL* without outer slit are simulated.

## 2. Design of the focusing effect

The focusing effect of plasmonic device are based on the principles of constructively interference and focusing wavefront [2,4]. Figure 1 shows the schematic illustration of Ag-Au hybrid *PL* with outer slit. Different circular slit width are arranged to generate the focusing beam with correspond phase delay distribution along the x direction which can be described by the equation in Fig. 1. The gold film deposited on the silver film is to prevent the oxidation and sulfuration of silver film.

The plasmonic focusing properties were investigated by using the Comsol Multiphysics Software. The gold and

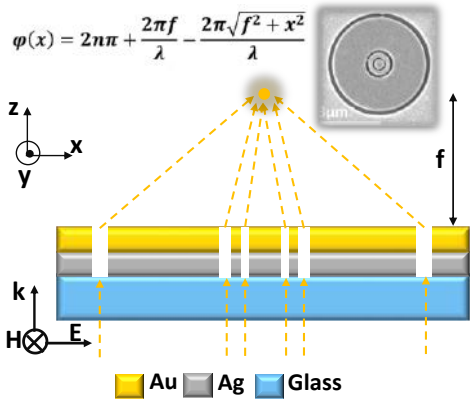



Figure 1: Schematic illustration of Ag-Au hybrid *PL* with outer slit. The insert plot shows a SEM image.

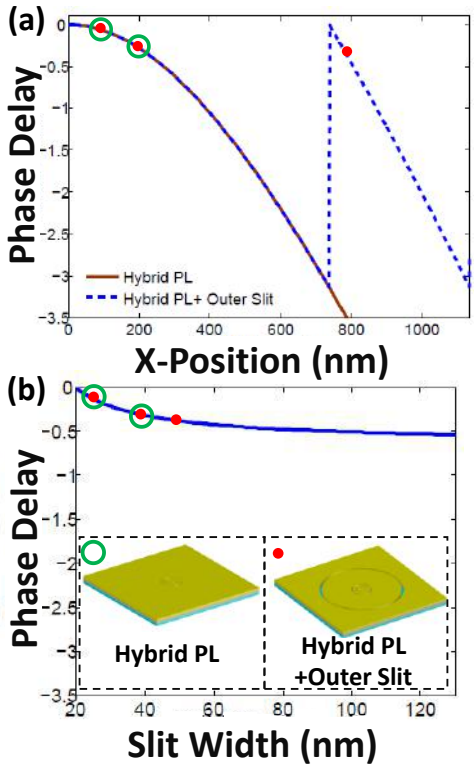



Figure 2: The phase delay for (a) x- directional distribution and (b) different slit widths of hybrid *PL*.

silver film thickness are both 50nm respectively. The TM polarized incident plane wave are focused at designed position after though the *PL*. The working wavelength is at 633nm. The insert Scanning Electron Microscope (SEM) image is shown with same structure parameters as simulating design.

Figure 2 shows the phase delay for the *PL* with focal length F = 500nm. However, few number of the circular slit are easy for fabrication but the targeted focal length will be changed [2]. New idea for choosing the proper slit width with phase delay shifted 2*π is used for our outer circular nanoslits design [5]. Two or three circular nanoslits are selected for hybrid *PL* to achieve the subwavelength focusing.

## 3. Plasmonic focusing properties analysis

The focusing performances are simulated for observing the enhanced focusing effect from the added outer slits. The power flows of focusing beam for each case are shown in Fig. 3. Stronger focusing beam is observed in hybrid *PL* with outer slit. The focusing wave fronts from outer slits not only enhance the power flow intensity but also narrow down the focal spot, which are shown near by the central focusing beam. Although the actual focal length is reduced almost hundreds of nanometer (compared with the idea design), the focal point is still around 100nm away with subwavelength focusing.

Four kinds of the *PLs* are simulated to analysis the influence of focus by different metal composition as shown in Fig. 4. The Au *PL* and that with outer slit are compared with the hybrid *PLs*. Figure 4(a) shows the power intensity distribution along the x-axis at the focusing spot. Figure 4(b) indicates the focusing properties of different nanostructures. The FWHM of focal spot of hybrid *PL* is slightly decreased compared with the Au *PL* (less evanescent wave attenuated in the silver). On the other side, the power intensity is increased for hybrid *PL* and the *PL* with outer slit design. By considering the two aspects of plasmonic focusing performance, the hybrid *PL* with outer slit design are seen to be the best choice for application. In addition, the four *PL* are demonstrated with subwavelength focusing and the hybrid *PL* with outer slit can achieve around 240nm FWHM with working wavelength at 633nm.

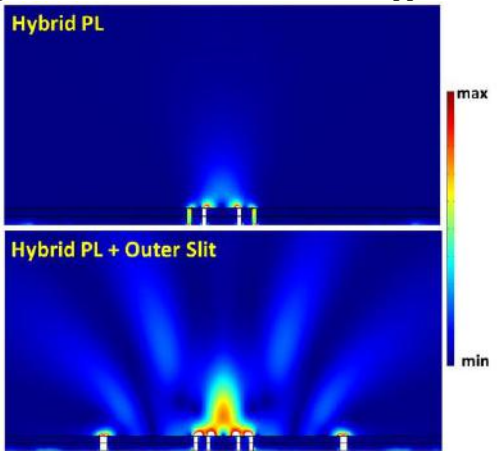



Figure 3: Power intensity distribution along x-z plane for hybrid *PL* and hybrid *PL* with outer slit.

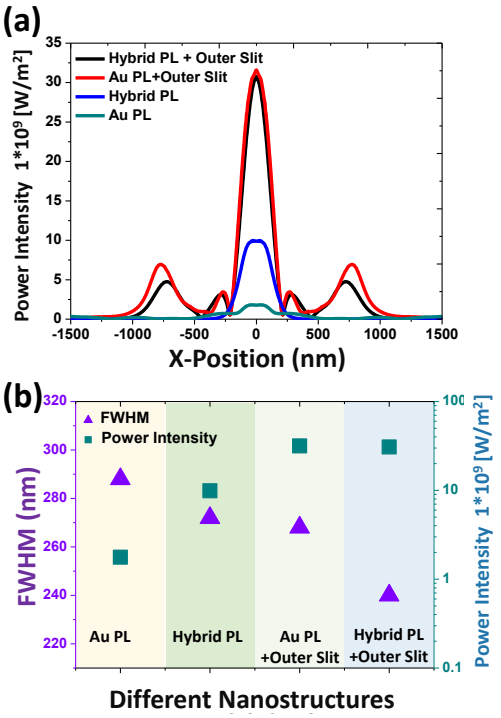



Figure 4: (a) Power intensity profiles of focal spot along x-axis and (b) focusing properties of FWHM and power intensity at focal point for four different *PL*s.

## 4. Fabrication and measurement

To fabricate these *PL*s, we deposit silver and gold film on glass substrate, and then the pattern is made using focus ion beam (FIB). For measurement, the near-field scanning optical microscopy (NSOM) measurements were performed by using self-made fiber mount on scanning head. The tunable white light laser with optical filter is used as light source. The optical near-fields are collected into photomultiplier (PMT) and recorded during the 2D plane scanning.

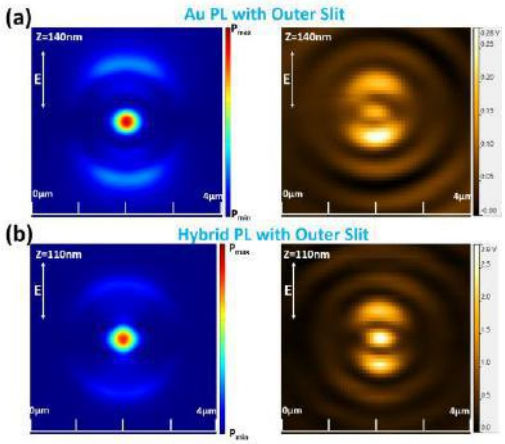



Figure 5: Simulated and experimental focusing spots for the (a) Au *PL* with outer slit and (b) hybrid *PL* with outer slit.

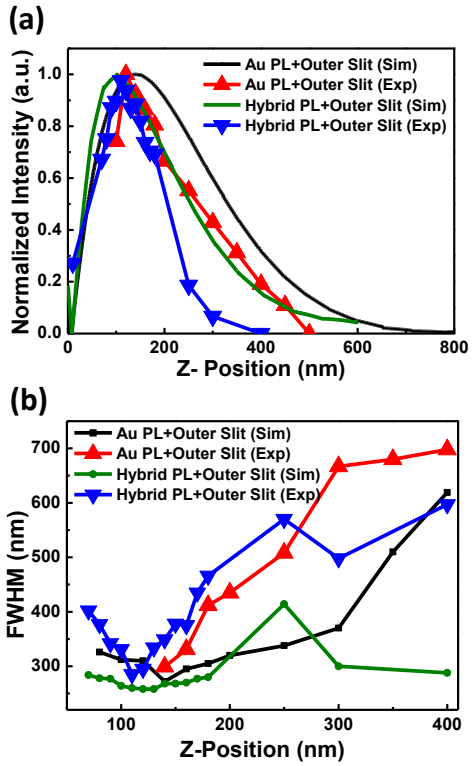



Figure 6: (a) normalized intensity profile and (b) FWHM of focusing beam for the two kinds of *PL* along z-axis.

In fig. 5, the focusing spots of the Au *PL* and Hybrid *PL* with outer slit are observed. Form the results of simulation and experiment, the central focal spot and the side lobes are shown and confirm the direction of polarization. In addition, the near-field cross sections of focusing beam are record along the z-axis at different heights.

Figure 6 shows the power intensity and FWHM of focal spot alone the z-axis. In fig. 6(a), the simulated and measured results indicate that the focal length is around 140nm for Au *PL* and 110nm for hybrid *PL* with outer slit design, which are shown with the strongest power flow. Fig. 6(b) plots the FWHM of focal spot along the z-position which also confirm the same results of focal length as fig. 6(a). In addition, the suddenly narrow FWHM around 300nm are observed both in simulation and experiment. This is understood as the outer slit providing the longer distance focus wavefront which is not observed in the case of the *PL* without the outer slit design. Finally, the small FWHM of focal spots for Au *PL* and hybrid *PL* are 295nm and 285nm respectively. This small subwavelength focusing spot is achieved and the focal length can be extended to around 100nm which are much longer than other subwavelength focusing devices as planar superlens. Furthermore, the plasmonic plasmonic zone plates with long focal length are seldom achieving the subwavelength focusing in experiment but the designed hybrid PL with outer slit can overcome this problem.

## 5. Conclusions

We have developed the Ag-Au hybrid *PL* with outer slit design. The stronger power intensity for both Au *PL* and hybrid *PL* with added outer slit are obtained in simulation. Furthermore, smaller subwavelength focusing spot of hybrid *PL* with outer slit are simulated and measured by comparison to that of Au *PL* with outer slit. The enhanced focusing properties can be applied into optical trapping, optical data storage and nanolithography.

## Acknowledgements

We would like to acknowledge the help of NSOM measurement from Prof. Wen-Hau Chang and Yen-Chun Chen at National Chiao Tung University, Taiwan. We also acknowledge the help of focus ion beam to pattern the plasmonic lens from Center For Nanotechnology, Materials Science, and Microsystems, NTHU.

## References

[1] J. B. Pendry, Negative refraction makes a perfect lens, *Phys. Rev. Lett.* 85: 3966−3969, 2000.

[2] L. Verslegers, P. Catrysse and S. H. Fan, Planar lenses based on nanoscale slit arrays in a metallic film, *Nano Lett.*9: 235-238, 2009.

[3] T. Cesca, N. Michieli, and G. Mattei, Nonlinear absorption tuning by composition control in bimetallic plasmonic nanoprism arrays, *Nanoscale* 7: 12411-12418, 2015.

[4] Y. Fu, T. Tsukahara, M. Motozawa, Near-field behavior of zone-plate-like plasmonic nanostructures, *J. Opt. Soc. Am. A* 25: 238−249, 2008.

[5] Q. Chen, A Novel Plasmonic Zone Plate Lens Based on Nano-Slits with Refractive Index Modulation, *Plasmonics* 6: 381-385, 2011.

# Metamaterials and negative index materials

# Soliton-induced transparency in one-dimensional non linear Kerr/metamaterial heterostructures

**E. Reyes-Gómez**[1], **S. B. Cavalcanti**[2], **and L. E. Oliveira**[3]

[1]Instituto de Física, Universidad de Antioquia UdeA, Calle 70 No. 52-21, Medellín, Colombia
[2]Instituto de Física, Universidade Federal de Alagoas, Maceió-AL, 57072-970, Brazil
[3]Instituto de Física, Universidade Estadual de Campinas - Unicamp, Campinas-SP, 13083-859, Brazil
oliveira@ifi.unicamp.br

**Abstract**— A theoretical study of non-Bragg gap solitons in one-dimensional non linear Kerr-metamaterial heterostructures is performed. A switching from states of no transparency in the linear regime to soliton-induced high-transparency states in the nonlinear regime is observed for various non-Bragg gaps. Soliton solutions are shown to be robust with respect to absorption effects.

The experimental realization of metamaterials, or left-handed materials (LHMs), has opened up interesting possibilities in the study of 1D plasmonic heterostructures. Recently, multi stability, transmission switching and soliton formation have been reported on Kerr-metamaterial superlattices at the band edge of the non-Bragg $< n > = 0$ gap [1], plasmon-polariton (PP) gap [2, 3] and Kerr polaritonic/metamaterial [4] heterostructures at the edge of the zero-$\phi_{eff}$ non-Bragg gap.

Here we are concerned with a heterostructured system composed by alternate building blocks A (of width $a$) and B (of width $b$) periodically arranged or in a quasi-periodic Fibonacci sequence [2, 3]. Layers A are characterized by a constant magnetic permeability $\mu_A$ and an electric permittivity given by $\epsilon_A = \epsilon_A^0 + \alpha|E(z)|^2$, where $E = E(z)$ is the electric-field amplitude of the electromagnetic field within the heterostructure. Slabs B represent the metamaterial whose frequency-dependent electric permittivity and magnetic permeability are given by $\epsilon_B = f_\epsilon + \frac{F_\epsilon}{\beta_\epsilon - \nu^2 - i\nu\gamma}$ and $\mu_B = f_\mu + \frac{F_\mu}{\beta_\mu - \nu^2 - i\nu\gamma}$, respectively, where $\nu$ is the linear frequency and $\gamma$ is a phenomenological damping parameter which accounts for absorption/loss effects in slabs B. We have chosen the electric and magnetic response parameters as in Hedge *at al* [1]. Without loss of generality we have focused on the study of transversal-electric (TE) electromagnetic modes in the heterostructure (cf. Figs. 1 and 2).

Moreover, a theoretical study of 1D heterostructures composed of alternate layers of a Kerr polaritonic material and a linear dispersive metamaterial is performed [4]. For frequency values at the edges of the non-Bragg zero-$\phi_{eff}$ gap of the heterostructure in the linear regime, a switching from very low to high transmission states is obtained and localized gap solitons of various orders are found (see Fig. 3), depending on the particular value of the incident power.

## ACKNOWLEDGMENT

We thank the Agencies Estrategia de Sostenibilidad (2014-2016) and CODI - Univ. of Antioquia and Brazilian Agencies CNPq, FAPESP and FAEPEX-UNICAMP for partial financial support.

## REFERENCES

1. R. S. Hedge and H. G. Winful, "Zero-n gap soliton," *Opt. Lett.*, Vol. 30, No. 14, 1852-1854, 2005.
2. E. Reyes-Gómez, S. B. Cavalcanti and L. E. Oliveira, "Absorption effects on plasmon polariton-gap solitons in Kerr/metamaterial superlattices," *Europhys. Lett.*, Vol. 106, 64001/1-6, 2014.
3. E. Reyes-Gómez, S. B. Cavalcanti and L. E. Oliveira, "Non-Bragg gap solitons in 1D Kerr-metamaterial Fibonacci heterostructures," *Phys. Rev. E*, Vol. 91, 063205/1-8, 2015.
4. E. Reyes-Gómez, S. B. Cavalcanti and L. E. Oliveira, "Zero-$\phi_{eff}$ non-Bragg gap solitons in 1D Kerr polaritonic/metamaterial heterostructures," *Physica E* (in press).

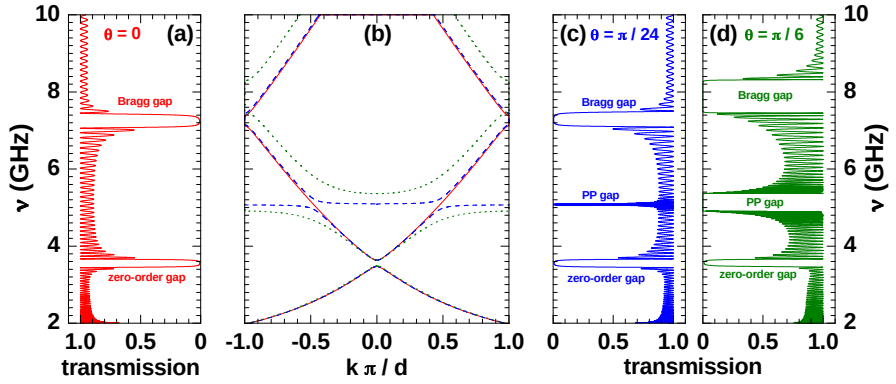



Figure 1: Transmission coefficient in a heterostructure of 32 AB bilayers ($a = b = 10$ mm) in the absence of absorption and nonlinearity, for (a) normal and TE-configuration oblique incidence with (c) $\theta = \pi/24$ and (d) $\theta = \pi/6$. Panel (b) shows the dispersion relation corresponding to the infinite heterostructure for normal and oblique incidence with $\theta = \pi/24$ and $\theta = \pi/6$ (solid, dashed, and dotted lines, respectively).

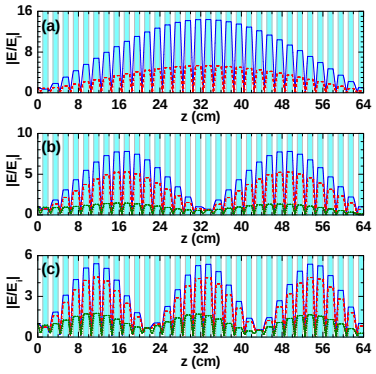



Figure 2: PP gap solitons for oblique incidence with $\theta = \pi/24$ obtained for the system considered in Fig. 1. Solid, dashed and dotted lines correspond to $\gamma = 0$, $\gamma = 10^{-5}$ GHz and $\gamma = 10^{-4}$ GHz, respectively. Results for each value of $\gamma$ were obtained for the values of $-\alpha|E_i|^2$ corresponding to the three first local maxima of the transmission coefficient as a function of the defocusing nonlinearity power at $\nu = 5.0662$ GHz.

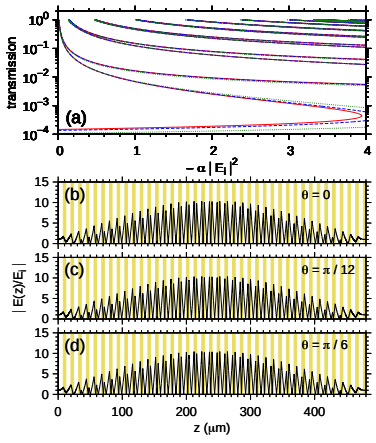



Figure 3: (a) Transmission coefficient as a function of the defocusing nonlinearity power. Results were obtained for a finite heterostructure [4] with N = 40 double AB layers, in the TE configuration (absorption effects were not considered) for $\nu$ at the bottom of the zero$-\phi_{eff}$ gap, with full, dashed, and dotted lines corresponding to $\theta = 0$, $\theta = \pi/12$, and $\theta = \pi/6$, respectively. The corresponding zero$-\phi_{eff}$-gap solitons, in the case of the defocusing nonlinearity power associated with the first maximum-transmission peak, for (b) $\theta = 0$ and oblique incidence with (c) $\theta = \pi/12$, and (d) $\theta = \pi/6$, are also displayed.

# Absorption effects and non-Bragg gap solitons in quasiperiodic Fibonacci and disordered Kerr-metamaterial heterostructures

**E. Reyes-Gómez**[1], **S. B. Cavalcanti**[2], **and L. E. Oliveira**[3]

[1]Instituto de Física, Universidad de Antioquia UdeA, Calle 70 No. 52-21, Medellín, Colombia
[2]Instituto de Física, Universidade Federal de Alagoas, Maceió-AL, 57072-970, Brazil
[3]Instituto de Física, Universidade Estadual de Campinas - Unicamp, Campinas-SP, 13083-859, Brazil
oliveira@ifi.unicamp.br

**Abstract**— The optical transmission properties of light in one-dimensional disordered nonlinear layered systems with metamaterial inclusions are theoretically studied. Layer widths of both nonlinear and metamaterial slabs are considered as random variables without any correlation between them. A thorough investigation is performed of soliton-induced transparency and influence of disorder in the vicinities of a Bragg gap and non-Bragg zero$-n$ and bulk-like longitudinal plasmon-polariton gaps. It is shown that the Bragg-gap soliton reveals itself as the most robust against disorder.

The experimental realization of metamaterials, or left-handed materials (LHMs), has opened up interesting possibilities in the study of one-dimensional (1D) plasmonic heterostructures. In this respect, periodic, quasiperiodic and disordered structures, made up of bilayers AB composed of materials with positive (RHM) and negative (LHM) indices of refraction, have been the subject of both experimental and theoretical investigations. Such a heterostructure with metamaterial inclusions exhibit a non-Bragg band gap associated to the $< n > = 0$ null average of the refractive index [1, 2]. Also, investigations on 1D RHM-LHM heterostructures have shown that, for oblique electromagnetic incidence, longitudinal bulk-like plasmon polaritons (PPs) may be excited along the growth direction of the heterostructure with the non-Bragg PP gap showing up in the corresponding transmission spectra [3].

Theoretical studies on nonlinear layered systems have also revealed novel results: non-Bragg $< n > = 0$ gap-soliton solutions have been reported [4] for frequencies at the edge of the linear gap, in 1D superlattices which alternates linear/nonlinear media: one finds a soliton-mediated transparency switching, from a state of no transparency at the linear regime to total transparency in the nonlinear regime. Similar results were obtained for PP gap solitons and multi stability, transmission switching and n-soliton formation have been reported both on Kerr-metamaterial superlattices at the band edge of the PP gap and on Kerr polaritonic/metamaterial heterostructures at the edge of the zero-$\phi_{eff}$ non-Bragg gap [5, 6, 7, 8, 9, 10]. In the present work, a theoretical study of non-Bragg gap solitons in 1D Kerr-metamaterial Fibonacci-quasiperiodic and disordered heterostructures is presented. The transmission coefficient is numerically obtained by combining the transfer-matrix formalism in the metamaterial layers with the numerical solution of the nonlinear differential equation in the Kerr slabs, and by considering the loss effects in the metamaterial slabs. A switching from states of no transparency in the linear regime to high-transparency states in the nonlinear regime is observed for the non-Bragg $< n > = 0$, PP, and zero-$\phi_{eff}$ gaps.

With respect to quasiperiodic Fibonacci structures, we have performed a detailed study of non-Bragg-gap solitons in one-dimensional Kerr-metamaterial heterostructures. More specifically, by considering both nonlinearity and absorption effects in the metamaterial slabs, we have studied the transmission properties of various $S_n$ generation sequences of Fibonacci heterostructures as a function of the defocusing nonlinearity power in the vicinity of the zero-order gap, for frequency values corresponding to a negligible transmissivity in the linear regime and for normal incidence. In all cases we demonstrated that the system transmissivity switches from a state of no transparency, in the linear regime, to high-transparency states in the nonlinear regime. The results reported here suggest that the effects of the quasiperiodicity do not considerably affect the spatial-localization properties of the zero-order gap solitons in the heterostructure. The spatial localization of the non-Bragg-gap solitons is also examined, and the symmetry properties of the soliton waves are briefly

discussed.

In the case of disordered Kerr-metamaterial heterostructures, disorder was introduced via a random variation of layer widths without any correlation between them. The transmission-switching phenomenon in heterostructures is observed for frequency values in the vicinity of zero$-n$, PP or Bragg gaps and for sufficiently low values of the disorder amplitude. As the disorder amplitude is increased we have observed the gradual extinction of soliton waves for frequency values in the vicinity of the zero$-n$, PP or Bragg gaps. The transmission properties in the vicinity of the Bragg gap are shown to be more robust against fluctuations than near non-Bragg gaps. This fact may be attributed to the interference origin of the Bragg gap in contrast with the non-Bragg ones. The most sensible PP gap depends on resonance effects and therefore one may expect it to be indeed quite sensible to fluctuations. Also, inclusion of absorption effects via a phenomenological damping constant leads to the decrease of the average of the transmission coefficient and to the extinction of soliton waves in the heterostructure. We have demonstrated that the average of the transmission coefficient of the heterostructure with $N$ double layers ($T_N$) as well as the occurrence of the transmission-switching phenomenon are very sensitive to the value of the disorder amplitude $\Delta$, a fact which is more remarkable for heterostructures with large number of layers. The extinction of soliton waves for relatively small values of $\Delta$ suggests possible difficulties for their experimental observation in a real system if a rigorous control of the system geometry is not taken into account.

## ACKNOWLEDGMENT

We thank the Agencies Estrategia de Sostenibilidad (2014-2016) and CODI - Univ. of Antioquia and Brazilian Agencies CNPq, FAPESP and FAEPEX-UNICAMP for partial financial support.

## REFERENCES

1. S. B. Cavalcanti, M. de Dios-Leyva, E. Reyes-Gómez, and L. E. Oliveira, "Photonic band structure and symmetry properties of electromagnetic modes in photonic crystals," *Phys. Rev. E*, Vol. 75, 026607/1-7, 2007.
2. L. Zhou, Z. Song, X. Huang, C. T. Chan, "Physics of the zero$-\bar{n}$ photonic gap: fundamentals and latest developments," *Nanophotonics*, Vol. 1, 181-198, 2012.
3. E. Reyes-Gómez, D. Mogilevtsev, S. B. Cavalcanti, C. A. A. Carvalho, and L. E. Oliveira, "Plasmon polaritons in photonic superlattices containing a left-handed material," *Europhys. Lett.*, Vol. 88, 24002/1-6, 2009.
4. R. S. Hedge and H. G. Winful, "Zero-n gap soliton," *Opt. Lett.*, Vol. 30, No. 14, 1852-1854, 2005.
5. S. B. Cavalcanti, P. A. Brandão, A. Bruno-Alfonso, and L. E. Oliveira, "Bulk plasmon polariton-gap soliton-induced transparency in one-dimensional Kerr-metamaterial superlattices," *Opt. Lett.*, Vol. 39, 178-181, 2014.
6. E. Reyes-Gómez, S. B. Cavalcanti and L. E. Oliveira, "Absorption effects on plasmon polariton-gap solitons in Kerr/metamaterial superlattices," *Europhys. Lett.*, Vol. 106, 64001/1-6, 2014.
7. E. Reyes-Gómez, S. B. Cavalcanti and L. E. Oliveira, "Non-Bragg gap solitons in 1D Kerr-metamaterial Fibonacci heterostructures," *Phys. Rev. E*, Vol. 91, 063205/1-8, 2015.
8. E. Reyes-Gómez, S. B. Cavalcanti and L. E. Oliveira, "Localization properties of photonic modes in disordered nonlinear-Kerr/metamaterial heterostructures," *Superl. Microstruct.*, Vol. 90, 1-7, 2016.
9. E. Reyes-Gómez, S. B. Cavalcanti and L. E. Oliveira, "Soliton-induced transparency in disordered Kerr-metamaterial heterostructures," *J. Opt. Soc. Am. B* (in press).
10. E. Reyes-Gómez, S. B. Cavalcanti and L. E. Oliveira, "Zero-$\phi_{eff}$ non-Bragg gap solitons in 1D Kerr polaritonic/metamaterial heterostructures," *Physica E* (in press).

# Recent experimental progress of reversed Cherenkov radiation in left-handed metamaterial

**Zhaoyun Duan[1*], Xianfeng Tang[1], Zhanliang Wang[1], Yabin Zhang[1], Xiaodong Chen[1, 2*], Min Chen[3*], and Yubin Gong[1]**

[1]National Key Laboratory of Science and Technology on Vacuum Electronics in Chengdu, Institute of High Energy Electronics, School of Physical Electronics, University of Electronic Science and Technology of China, No.4, Section 2, North Jianshe Road, Chengdu 610054, China

[2]School of Electronic Engineering and Computer Science, Queen Mary, University of London, London E1 4NS, UK

[3]Department of Physics, Massachusetts Institute of Technology, 77 Massachusetts Avenue, Cambridge, MA 02139, USA

[*]corresponding authors: zhyduan@uestc.edu.cn, xiaodong.chen@qmul.ac.uk, chenm@mit.edu

**Abstract**-Reversed Cherenkov radiation (RCR) in the left-handed metamaterial (LHM) has been detected at microwave frequencies for the first time by using a charged particle bunch as an excited source. This experiment has confirmed that the RCR will bring technology innovations in conventional particle physics, vacuum electronics, accelerator physics, material science, and optics.

The left-handed metamaterial (LHM) was first proposed in a seminal work in 1967 by Veselago. There are three novel electromagnetic phenomena: negative refraction index, reversed Cherenkov radiation (RCR), and reversed Doppler Effect in this hypothetical medium [1]. The negative refraction index was experimentally demonstrated in 2001 [2] and then the reversed Doppler effect was experimentally verified in 2003 [3]. However, there are many challenges in RCR experiment. For examples, due to the intrinsic anisotropy and strong dispersion of LHM, it is very difficult to realize and characterize it; there is no suitable couplers to connect the LHM for detection due to the special property of the LHM, hence the novel couplers have to be designed. Rigorous RCR experimental verification using real charged particles has not been reported, although some famous institutions in the world such as Argonne National Laboratory, Los Alamos National Laboratory and Massachusetts Institute of Technology were involved in this activity with most attempts [4]-[6].

Based on the theoretical works about the RCR in an either isotropic or anisotropic LHM in both lossy and dispersive cases [7]-[10], we have creatively constructed a suitable all-metal LHM [11]. It consists of a square waveguide loaded by complementary electric split ring resonators, which exhibits "*left-hand*" property in a narrow frequency band. We have also designed two identical output couplers being added to the two ends of the LHM presented here to output *backward* and *forward* microwave signals, respectively. And then, we have built the experimental needed components and used the Oscilloscope to detect the RCR and reflected signals at Ports 1 and 2, respectively. The experimental results clearly state that the power of signal at Port 2 is much lower than that at Port 1 and the frequency of the signal at Port 2 is almost the same as that at Port 1. According to these facts, we can conclude that the output signal at Port 1 is the RCR directly excited by the charged particles.

The present work paves the way for many applications such as particle detections in high-energy particle physics, high-power, high-efficiency radiation sources with smaller size in vacuum electronics and metamaterial

characterization in material science.

**Acknowledgements:** This work was supported by the Natural Science Foundation of China (Grant Nos. 61471091 and 6151101115).

**REFERENCES**

1. Veselago, V. G., "The electrodynamics of substances with simultaneously negative values of ε and μ," *Sov. Phys. Usp.*, Vol. 10, No. 4, 509-514, 1968.
2. Shelby, R. A., D. R. Smith and S. Schultz, "Experimental verification of a negative index of refraction," *Science*, Vol. 292, No. 5514, 77-79, 2001.
3. Seddon, N. and T. Bearpark, "Observation of the inverse Doppler effect," *Science*, Vol. 302, No. 5650, 1537-1540, 2003.
4. Antipov, S., L. Spentzouris, W. Gai, M. Conde, F. Franchini, R. Konecny, W. Liu, J. G. Power, Z. Yusof and C. Jing, "Observation of wakefield generation in left-handed band of metamaterial-loaded waveguide," *J. Appl. Phys.*, Vol. 104, No. 1, 014901, 2008.
5. Shchegolkov, D. Y., A. K. Azad, J. F. O'Hara and E. I. Smirnove, "A Proposed measurement of the reverse Cherenkov radiation effect in a metamaterial-loaded circular waveguide," in *International Conference on IRMMW-THz*, Pasadena, USA, September 2008.
6. Xi, S., H. S. Chen, T. Jiang, L. X. Ran, J. T. Huangfu, B.-I. Wu, J. A. Kong and M. Chen, "Experimental verification of reversed Cherenkov radiation in left-handed metamaterial," *Phys. Rev. Lett.*, Vol. 103, No. 19, 194801, 2009.
7. Lu, J., T. Grzegorczyk, Y. Zhang, J. Pacheco Jr., B.-I. Wu, J. Kong and M. Chen, "Cerenkov radiation in materials with negative permittivity and permeability," *Opt. Express*, Vol. 11 No. 7, 723-734, 2003.
8. Duan, Z. Y., B.-I. Wu, J. Lu, J. A. Kong and M. Chen, "Reversed Cherenkov radiation in a waveguide filled with anisotropic double-negative metamaterials," *J. Appl. Phys.*, Vol. 104, No. 6, 063303, 2008.
9. Duan, Z. Y., B.-I. Wu, J. Lu, J. A. Kong and M. Chen, "Reversed Cherenkov radiation in unbounded anisotropic double-negative metamaterials," *J. Phys. D: Appl. Phys.*, Vol. 42, No. 18, 185102, 2009.
10. Duan, Z. Y., C. Guo and M. Chen, "Enhanced reversed Cherenkov radiation in a waveguide with double-negative metamaterials," *Opt. Express*, Vol. 19, No. 15, 13825-13830, 2011.
11. Duan, Z. Y., J. S. Hummelt, M. A. Shapiro and R. J. Temkin, "Sub-wavelength waveguide loaded by a complementary electric metamaterial for vacuum electron devices," *Phys. Plasmas*, Vol. 21, No. 10, 103301, 2014.

# Magnetic Uniaxial Wire Medium

**Tiago A. Morgado**[1*], **João T. Costa**[2], **Mário G. Silveirinha**[1, 3]
[1]Instituto de Telecomunicações, University of Coimbra, Coimbra, Portugal
[2]CST AG, Bad Nauheimer Strasse 19, 64289 Darmstadt, Germany
[3]University of Lisbon, Instituto Superior Técnico, Lisboa, Portugal
[*]corresponding author: tiago.morgado@co.it.pt

**Abstract -** It is shown that a racemic array of helical-shaped metallic wires (magnetic wire medium) supports a nearly dispersionless transverse electric (TE) mode with phase velocity almost independent of the wave vector. The metamaterial may be characterized by an extreme magnetic anisotropy, and hence may be regarded as the magnetic analogue of the standard wire medium formed by straight wires. It is demonstrated with full-wave simulations that the magnetic wire medium enables channeling the near field of TE waves.

One of the most exciting possibilities provided by metamaterials is the manipulation of the near-field, which most notably enables to surpass the half-wavelength spatial resolution limit inherent to conventional imaging devices. Several metamaterial-based imaging systems with a subwavelength resolution have been proposed over the last decade [1-6]. In particular, it was demonstrated that uniaxial arrays of metallic wires may operate as nearly ideal endoscopes, performing a pixel-by-pixel channeling of the entire source spatial spectrum (i.e., both propagating and evanescent waves) with a subwavelength resolution [3-5]. However, despite all the remarkable imaging properties of these wire medium lenses, such structures have an important limitation: they are inherently polarization sensitive and only enable the transport of transverse magnetic (TM or *p*) polarized waves.

Achieving a similar channeling effect for TE (or *s*) polarized waves (with the electric field parallel to the interface) would require replacing the metallic wires by "perfectly magnetic conducting" (PMC) wires. However, materials with a PMC-type response are unavailable in nature, even as an imperfect approximation. Yet, it is possible to partially mimic the response of a PMC using metamaterials. This can be done using a "Swiss rolls" array – a periodic set of cylinders comprising a thin conducting sheet wrapped around a central mandrel [6]. It was demonstrated in [6] that at the resonant frequency, the Swiss rolls may behave as magnetic wires and enable the transport of a magnetic near-field distribution with a resolution identical to the roll diameter. However, the Swiss rolls lenses are only effective at MHz frequencies, since due to fabrication constraints this solution is unsuitable for higher oscillation frequencies.

Here, we suggest an alternative way to mimic the behavior of PMC wires that can be easily implemented in the microwave regime and possibly extended to the THz and IR domains. Specifically, we consider a metamaterial formed by a racemic array of PEC helical-shaped metallic wires (Fig. 1(a)) [7-8]. Notably, it is demonstrated that to some extent this metamaterial may be regarded as the magnetic analogue of the standard wire medium formed by straight wires. In particular, it supports an electromagnetic mode with a phase velocity nearly independent of the transverse wave vector (Fig. 1(b)), similar to what happens in the conventional wire medium for TM polarized waves [3-5]. One can see from Fig. 1(b) that the isofrequency contours are nearly flat so that $k_z$ is almost independent of $k_x$, which is the fingerprint of an extreme magnetic anisotropy. This suggests the existence of some kind of "canalization regime" [3-4] for TE-*z* polarized waves.

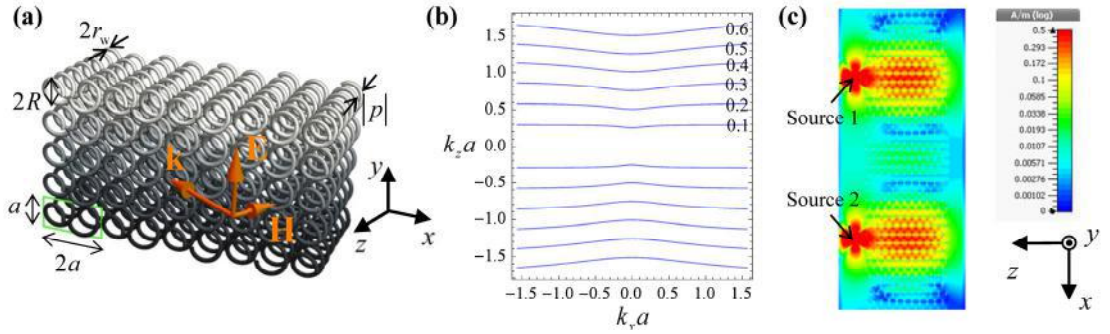



**Fig. 1** (a) Geometry of the magnetic wire medium: a periodic array of metallic helical-shaped wires arranged in an orthorhombic lattice (period $2a$ along the *x*-direction, period $a$ along the *y*-direction, and period $|p|$ along the *z*-direction). Each unit cell includes one right-handed helix and one left-handed helix. $R$ is the radius of the helices and $r_w$ is the radius of the wires. The helices stand in free-space. The plane of incidence is the *xoz* plane and the incident wave is TE-*z* polarized [ $\mathbf{k} = (k_x, 0, k_z^{\text{inc}})$, $\mathbf{E} = E^{\text{inc}}\hat{\mathbf{u}}_y$ ]. (b) Isofrequency contours of the nearly dispersionless TE mode supported by the magnetic wire medium with $R = 0.4a$, $r_w = 0.05a$, $|p| = 0.9a$. The number insets correspond to the value of $\omega a / c$. (c) Density plot of $|\mathbf{H}|$ for a magnetic wire medium with the same geometrical parameters as in (b), $a = 5$ mm and $f = 1.012$ GHz, obtained using CST Microwave Studio. The sources are placed at a distance $d_1 = a$ from the front interface of the lens, and are separated by a distance $\Delta_s = 0.3\lambda_0$.

To evaluate the potentials of the near-field transport by the magnetic wire medium lens, we simulated the electromagnetic response of the structure using CST Microwave Studio. We considered the scenario wherein the metamaterial lens is illuminated by two small magnetic loops parallel to the interface plane and separated by a distance $\Delta_s = 0.3\lambda_0$. Figure 1(c) clearly shows that the magnetic wire medium lens channels the electromagnetic field radiated by the sources along the axial direction, with a resolution approximately equal to $0.075\lambda_0 \simeq 4.45a$. At the conference, we will explain in detail the physics of the wave propagation in the magnetic wire medium based on an effective medium approach [9], and we will present further numerical results of the subwavelength imaging illustrated in Fig. 1(c) [9].

This work was funded by Fundação para a Ciência e a Tecnologia under project PTDC/EEI-TEL/4543/2014. T. A. Morgado acknowledges financial support by Fundação para a Ciência e a Tecnologia (FCT/POPH) and the cofinancing of Fundo Social Europeu under the Post-Doctoral fellowship SFRH/BPD/84467/2012.

## REFERENCES

1. J. B. Pendry, “Negative Refraction Makes a Perfect Lens,” *Phys. Rev. Lett.*, vol. 85, 3966-3969, 2000.
2. N. Fang, H. Lee, C. Sun, and X. Zhang, “Sub-diffraction-limited optical imaging with a silver superlens,” *Science*, vol. 308, 534-537, 2005.
3. P. A. Belov, Y. Hao, and S. Sudhakaran, “Subwavelength microwave imaging using an array of parallel conducting wires as a lens,” *Phys. Rev.* B, vol. 73, 033108, 2006.
4. P. A. Belov, Y. Zhao, S. Tse, P. Ikonen, M. G. Silveirinha, C. R. Simovski, S. Tretyakov, Y. Hao, and C. Parini, “Transmission of images with subwavelength resolution to distances of several wavelengths in the microwave range,” *Phys. Rev. B*, vol. 77, 193108, 2008.
5. T. A. Morgado, J. S. Marcos, M. G. Silveirinha, S. I. Maslovski, “Experimental verification of full reconstruction of the near-field with a metamaterial lens,” *Appl. Phys. Lett.*, vol. 97, 144102, 2010.
6. M. C. K. Wiltshire, J. V. Hajnal, J. B. Pendry, D. J. Edwards, and C. J. Stevens, “Metamaterial endoscope for magnetic field transfer: near field imaging with magnetic wires,” *Opt. Express*, vol. 11, 709-715, 2003.
7. M. G. Silveirinha, “Design of Linear-to-Circular Polarization Transformers Made of Long Densely Packed Metallic Helices,” *IEEE Trans. Antennas Propag.* vol. 56, 390 (2008).
8. T. A. Morgado, S. I. Maslovski, M. G. Silveirinha, “Uniaxial indefinite material formed by helical-shaped wires,” *New J. Phys.*, vol. 14, 063002, 2012.
9. T. A. Morgado, J. T. Costa, and M. G. Silveirinha, “Magnetic Uniaxial Wire Medium,” *Phys. Rev. B*, vol. 93, 075102, 2016.

# Reconfigurable holographic generation of non-Hermitian and parity-time symmetric photonic lattices

**Choloong Hahn, Youngsun Choi, Jae Woong Yoon, Cha Hwan Oh, Seok Ho Song***
Department of Physics, Hanyang University, Seoul 133-791, Korea
*corresponding author: shsong@hanyang.ac.kr

**Abstract**-Non-Hermitian optical systems require precisely controlled complex-valued optical potentials. Here, we generate such complex potentials on azo-dye-doped PMMA polymer thin film by using the reconfigurable holographic method. The purest exceptional point to our knowledge is generated and the skewness of eigenvectors of the complex potentials is characterized by observing the asymmetric diffraction. Also we present non-Hermitian trajectories in skewed vector space which implying this approach should enable the observation of non-Hermitian nature.

Several parity-time (PT) symmetric systems which are special cases of non-Hermitian systems have been proposed and investigated including experimental observation of unidirectional beam propagation in coupled fiber-optic network that satisfying PT-symmetry in time-domain [1]. They discussed about the extraordinary behaviors of light around PT-symmetric exceptional point (EP) which are the characteristic features of skewed eigenvector. Moreover, the eigenstates flipping features during encircling of EPs in exciton-polariton billiard system [2] also reported recently. To observe and applicate these features, the robust and reconfigurable generation methods of non-Hermitian systems are required.

Here we present a reconfigurable generation method of arbitrary complex potentials in optical domain by using the vector-field holography in azo-dye-doped polymer film. By illuminating the interfered pump light, the complex permittivity is generated as shown in Fig. 1(a). The physical migration due to the gradient force gives the real part modulation [3] and the reorientation due to the local polarization distribution gives the imaginary part modulation [4]. Therefore, the modulations can be written as

$$\Delta\varepsilon_{\mathrm{R}}(x) = C_{\mathrm{R}}\chi\frac{\partial}{\partial x}\left\langle \mathbf{E}_{\mathrm{P}}\cdot\nabla E_{\mathrm{P}x}\right\rangle_{t}, \tag{1}$$

$$\Delta\varepsilon_{\mathrm{I}}(x) = C_{\mathrm{I}}\frac{2}{1+\sqrt{1-\sin^{2}2\alpha\cdot\sin^{2}\varphi_{xy}}}\left(|E_{\mathrm{P}x}|^{2}-|E_{\mathrm{P}y}|^{2}\right). \tag{2}$$

Here, $C_{\mathrm{R}}$ and $C_{\mathrm{I}}$ are empirical constants, $\chi$ is the electric susceptibility of the host polymer, $\langle\cdots\rangle_{\mathrm{t}}$ denotes time-average, and $\alpha = \tan^{-1}(|E_{\mathrm{P}y}/E_{\mathrm{P}x}|^{2})$ and $\varphi_{xy} = \arg(E_{\mathrm{P}x})–\arg(E_{\mathrm{P}y})$ are local polarization parameters. $E_{\mathrm{P}x}$ and $E_{\mathrm{P}y}$ are $x$ and $y$ components of interfered pump light $\mathbf{E}_{\mathrm{P}} = \mathbf{E}_{1} + \mathbf{E}_{2}$. The modulation of complex permittivity of generated non-Hermitian photonic lattices can be conveniently expressed by the first-harmonic sinusoidal form which including Eqs. (1) and (2) as

$$\Delta\varepsilon(x) = \Delta\varepsilon_{\mathrm{R}}(x) + i\Delta\varepsilon_{\mathrm{I}}(x) = \Delta\varepsilon_{0}\left[(1-\xi)\cos(Kx) + i\xi\cos(Kx-\delta)\right], \tag{3}$$

Therefore, the non-Hermitian lattices can be characterized by the balance factor $\xi$ and phase difference

between real and imaginary modulation $\delta$. Note that the system is PT-symmetric (or exceptional point) when ($\xi$, $\delta$) = (0.5, $\pi$/2).

We experimentally confirm the generation of non-Hermitian lattices by observing the asymmetric diffraction due to skewing of eigenvectors. By scanning $\delta$ around $\pi$/2 with fixed $\xi$ = 0.5, we can clearly obseve the diverging of contrast ratio of ±1th-order diffractions implying extremely skewed eigenvectors as shown in Fig. 1(b). Moreover, by continuously evolving the parameters ($\xi$, $\delta$), the non-Hermitian lattices are reconfigured along certain path. Thus several interesting path such as presented in Fig. 1(c) are realizable by this method.

We will present theoretical and experimental details and interesting results, and it will clearly show that our suggested method could enable extending the experimental works on the non-Hermitian features, application to the switchable devices from its reconfigurable ability, and observation of non-Hermitian natures by optically reconfigurable generation and evolution of Hamiltonians which lies on the non-Hermitian quantum mechanics.

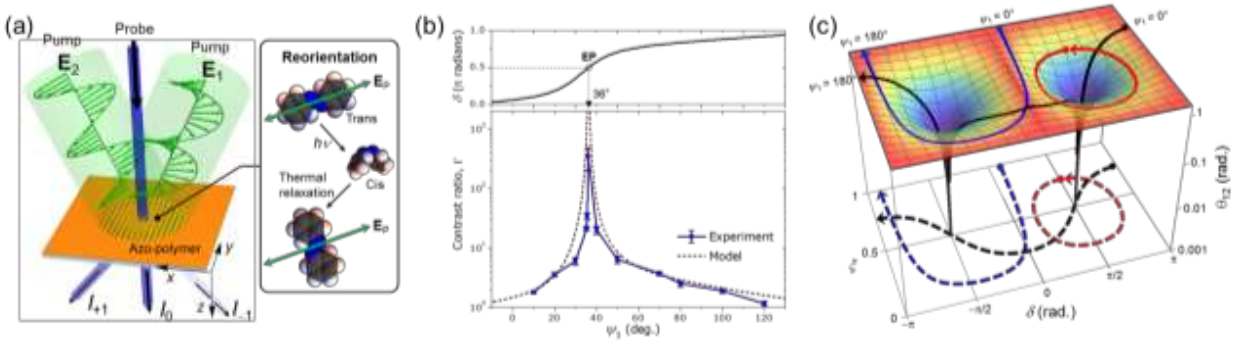



Figure 1. (a) Schematic illustration of complex photonic lattice formation. (b) Contrast ratio of asymmetric diffractions as function of polarization angle of pump beam. (c) Reconfigurable paths in skewed vector space.

**Acknowledgements**, This research was supported in part by the Basic Science Research Program (No. NRF-2015R1A2A2A01007553) and by the Global Frontier Program through the National Research Foundation (NRF) of Korea funded by the Ministry of Science, ICT & Future Planning (No. NRF-2014M3A6B3063708).

## REFERENCES

1. Regensburger, A., C. Bersch, M. A. Miri, G. Onishchukov, D. N. Christodoulides, and U. Peschel, "Parity-time synthetic photonic lattices," *Nature*, Vol. 488, No. 7410, 167-171, 2012.
2. Gao, T., E. Estrecho, K. Y. Bliokh, T. C. H. Liew, M. D. Fraser, S. Brodbeck, M. Kamp, C. Schneider, S. Höfling, Y. Yamamoto, F. Nori, Y. S. Kivshar, A. G. Truscott, R. G. Dall, and E. A. Ostrovskaya, "Observation of non-Hermitian degeneracies in a chaotic exciton-polariton billiard," *Nature*, Vol. 526, 554, 2015.
3. Kumar, J., L. Li, X. L. Jiang, D. Y. Kim, T. S. Lee, and S. Tripathy, "Gradient force: The mechanism for surface relief grating formation in azobenzene functionalized polymers," *Appl. Phys. Lett.*, Vol. 72, No. 17, 2096-2098, 1998.
4. Sutter, K. and P. Günter, "Photorefractive gratings in the organic crystal 2-cyclooctylamino-5-nitropyridine doped with 7, 7, 8, 8-tetracyanoquinodimethane," *JOSA B*, Vol. 7, No. 12, 2274-2278, 1990.

# Transparent conductive oxide-based hyperbolic metamaterials for telecommunication wavelengths

**E. Travkin**, **L. Orphal**, **O. Benson**, **S. Sadofev**, **and S. Kalusniak**

Institut für Physik, Humboldt-Universität zu Berlin, Newtonstr. 15, 12489 Berlin, Germany
kalus@physik.hu-berlin.de

**Abstract**— We report on realization of hyperbolic metamaterials operating at near- and mid-infrared frequencies using Ga-doped ZnO and Sn-doped $In_2O_3$ as metallic component. The hyperbolic dispersion is manifested by occurrence of negative refraction. Control of the doping level allows for systematic adjustment of the frequency range with hyperbolic dispersion from the mid-infrared up to almost one micrometer. As a prerequisite, we discuss the plasmonic properties of Ga-doped ZnO and Sn-doped $In_2O_3$.

Hyperbolic metamaterials (HMMs) have attracted much attention because they allow for broadband enhancement of spontaneous emission and imaging below the diffraction limit [1]. When fabricated out of traditional metals like Al or Ag, the frequency range of operation is typically restricted to the UV/VIS spectral range and for operation at longer wavelengths alternative materials are required [2]. Transparent conductive oxides with a metallic-like dielectric function in the infrared spectral range are promising candidates in this regard. Tunable free-electron concentration, small optical losses and the possibility of epitaxial growth are significant advantages compared to traditional metals.

Using molecular beam epitaxy, we have established growth regimes for fabrication of heavily doped ZnO:Ga [3] and $In_2O_3$:Sn [4]. The resultant infrared Drude-type dielectric function can be systematically tuned via the free-electron concentration allowing to extend the metallic range to wavelengths as short as 1.36 $\mu$m and 1.06 $\mu$m for ZnO:Ga and $In_2O_3$:Sn, respectively. The mean electronic damping rate ($2\gamma$) does not exceed 110 meV in the case of ZnO:Ga and is almost a factor of two smaller for $In_2O_3$:Sn. The fabricated ZnO/ZnO:Ga and $In_2O_3$/$In_2O_3$:Sn HMMs are of high quality and the frequency range with hyperbolic dispersion covered by both material classes extends from mid-infrared wavelengths to almost 1 $\mu$m. Figure 1 shows exemplarily characteristics of a ZnO/ZnO:Ga HMM designed for operation at telecommunication wavelengths [5]. The free-electron concentration of ZnO:Ga centers the spectral range with Type-I hyperbolic behavior to about 1.55 $\mu$m and its spectral width allows to cover the entire telecommunication band [Figure 1 (a)]. We identify the material's hyperbolic character by various optical measurements in combination with theoretical calculations. In particular, we demonstrate negative refraction of the extraordinary wave [Figure 1 (b)].

These HMMs can now be combined with a selected emitter material, e.g. rare-earth doped metal oxides, which is grown on top or even embedded between two HMMs. In this way, the effect of the hyperbolic high-$k$ states on the spontaneous emission can be studied and engineered. Moreover, by replacing the dielectric layer with this material, gain assisted reduction of the optical losses might be possible [6]. Another attractive application feasible is imaging below the diffraction limit with telecommunication light.

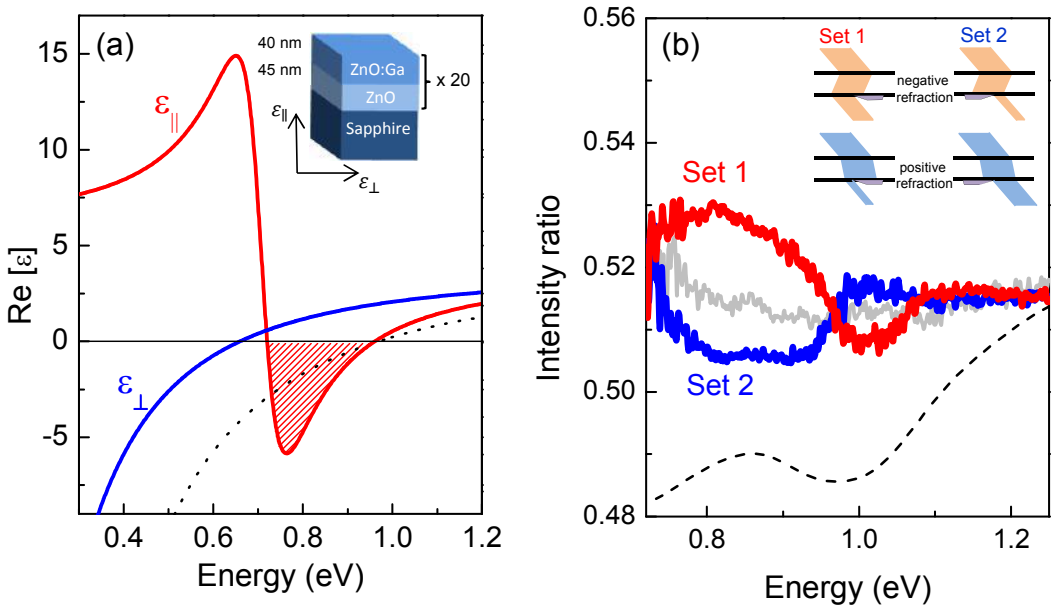



Figure 1: ZnO/ZnO:Ga HMM for telecommunication wavelengths. (a) Calculated real part of the dielectric function parallel (red) and perpendicular (blue) to the crystal axis using the effective medium approximation. The real part of the dielectric function of the sole ZnGaO is plotted for reference (black, dotted). The spectral range where $\mathrm{Re}[\epsilon_{\|}] < 0$ and $\mathrm{Re}[\epsilon_{\perp}] > 0$ is attained is 0.72 eV - 0.96 eV. Inset: Schematics of the sample and orientation of the dielectric functions. (b) Verification of negative refraction of the extraordinary wave transmitted through the sample. Inset: Schematics of the experimental configuration in which the transmitted beam is partly blocked by a razor blade. Depending on the exact configuration (Set 1 or 2), negatively or positively refracted frequency components shift away from the blade or behind the blade resulting in an increased or decreased signal in the spectrum. Main panel: Intensity ratio of the partly blocked transmitted beam and the unblocked transmitted beam for the two different configurations and for the ordinary wave in configuration 2 (light gray line). The unblocked transmission is shown for reference, too (black, dashed line). The angle of incidence is 25°


## ACKNOWLEDGMENT

The authors acknowledge financial support by the Deutsche Forschungsgemeinschaft in the frame of SFB 951 (HIOS).


## REFERENCES


1. A. Poddubny, I. Iorsh, P. Belov and Y. Kivshar, "Hyperbolic metamaterials," *Nat. Photonics*, Vol. 7, No. 12, 948–957, 2013.
2. P. Shekhar, J. Atkinson and Z. Jacob, "Hyperbolic metamaterials: fundamentals and applications," *Nano Convergence*, Vol. 1, No. 1, 14, 2014.
3. S. Sadofev, S. Kalusniak, P. Schäfer, H. Kirmse, and F. Henneberger, "Free-electron concentration and polarity inversion domains in plasmonic (Zn,Ga)O," *Phys. Status Solidi B*, Vol. 252, No. 3, 607–611, 2015.
4. S. Kalusniak, L. Orphal, P. Schäfer, and S. Sadofev, "Surface plasmon polaritons with plasma frequencies above 1 eV in Sn-doped $In_2O_3$," *Phys. Status Solidi B*, Vol. 253, No. 2, 361–365, 2016.
5. S. Kalusniak, L. Orphal, and S. Sadofev, "Demonstration of hyperbolic metamaterials at telecommunication wavelength using Ga-doped ZnO," *Opt. Express*, Vol. 23, No. 25, 30079–30087, 2015.
6. A. S. Kuznetsov, S. Sadofev, P. Schäfer, S. Kalusniak, and F. Henneberger, Single crystalline $Er_2O_3$:sapphire films as potentially high-gain amplifiers at telecommunication wavelength, *Appl. Phys. Lett.*, Vol. 105, No. 19, 191111, 2014.

# THE NATURAL WAY OF OBTAINING METAMATERIAL BY THERMORADIATION TREATMENT OF IRON OXIDE DOPED POTASSIUM-ALUMINUM-BORON GLASS

**A.N.Salakhitdinov[1], M.K. Salakhitdinova[2], N.S.Saydirasulov[1], A.A.Yusupov[2], E.M.Ibragimova[3]**

[1]-Tashkent University of Information Technologies, Samarkand branch, Uzbekistan;
[2]-Samarkand State University, Uzbekistan;
[3]-Institute of Nuclear Physics Academy of Science Republic of Uzbekistan,
**e-mail:** smaysara@yandex.ru

**Abstract** –The glass samples of $25K_2O{\cdot}25Al_2O_3{\cdot}50B_2O_3$ composition (mol. %) with addition of 3.0 mass.% $Fe_2O_3$ were gamma-irradiated to the dose of 1.7 MR at 423 K showed optical response characteristic for metamaterial. The effect was explained by the developed phenomenological theory of the radiation-induced processes at the thermoradiation treatment.

Obtaining metamaterials is actual now, although microwave treatment isn't the only way [1,2]. Here we considered another possible way, which is the dynamic nonlinear effect of self-organization at thermoradiation treatment.

The purpose of this work was to search for structural transformations in multicomponent oxide glasses at strong external impacts (for example, thermoradiation effects) which would result in obtaining "meta"-like material with non-linear optical properties.

We could find the negative differential absorption phenomenon [3] at gamma irradiation or thermoradiation treatment (TRT) which relates to metamaterials.

For determination of parameters of the negative induced absorption (self-transparency) we use the following phenomenological equation of TRT:

$$\frac{dN}{dt} + \left(\alpha + \alpha'\right)Nt + aN = \gamma_0 n - \frac{\alpha''}{t} \qquad (1)$$

where t - parameter of a radiation dose; N- concentration of the radiation-induced centers of coloring; n- concentration of initial defects on which the centers of coloring (CC) are created; $\gamma_0$- probability of CC formation at capture of charge carriers (electrons or holes). This equation gives a probability of destruction of CC; and also probabilities of CC disintegration under the influence of irradiation dose (radiation annealing) and heating (thermal annealing) at a fixed T. At some simplifying assumptions the general solution of (1) can be received in the form:

$$\Delta = (\Delta D) = D_{irrad} - D_{non-irrad} = N^{\max} e^{-\left(\frac{\alpha_0}{2}\right)t^2}\left\{\left(1+\frac{\alpha_0}{a^2}\right)\left(1-e^{at}\right)+\alpha_0+\left(\frac{2}{t}-\frac{1}{a}\right)\right\}$$
$$-\alpha'' e^{-\frac{\alpha_0}{2}t^2}\left\{\frac{2\ln t}{1+a}+\frac{\alpha_0(t-1)}{a}\right\} \qquad (2)$$

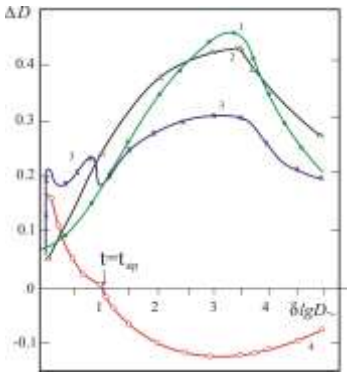



Fig.1.

In the solution (2) $\gamma_0$- probability of emergence of CC at capture of hole at oxygen vacancy, and also structural units like $[BO_4]$, $[AlO_4]$. In (2) probabilities of recombination and disintegration of CC hole $[BO_4]^{e+}$ ; $[AlO_4]^{e+}$ due to temperature mobility of the free electrons created by radiation are also considered. $\alpha''$ - valent transition $Fe^{3+} \Leftrightarrow Fe^{2+}$, which is caused by radiochemical process (reaction of zero order).

In figure 1 the dependence of the radiation induced optical density $(\Delta D)_\lambda$ ($\lambda$=340-770 nm) from logarithm of post-radiation dose ($\lg D_\sim$, $D_\sim$, Gy) calculated by generation-recombination model (1-2) is shown: 1 experiments, potash aluminoboron glass

($22,5P_2O_3$, $22,5Al_2O_3$, $55B_2O_3$) in mol. % with $Fe_2O_3$ additive - 0.1 mass. % $Fe_2O_3$; 2-theoretical calculation at $\alpha_2=0$; 3-theoretical calculation at $\alpha_2\neq0$, i.e. at TRT and dependence of the second part of the solution (2) on dose is also shown (curve 4).

It is seen from fig.1 that the thermoradiation contribution in the second term gives the curve corresponding to the critical dose of the subsequent irradiation then the induced absorption $(\Delta D)_\lambda$ becomes negative. In other words the glass sample after TRT and additional irradiation becomes non-linear (self-transparent). We believe that at usual radiation annealing or thermal annealing the positive absorption is compensated by the negative absorption, which was caused by self-organizing electron-hole processes at thermal radiation processing.

Experimental data on optical absorption spectra of the studied PAB glass - ($25P_2O_3$, $25Al_2O_3$, $50B_2O_3$) in mol.% with $Fe_2O_3$ oxide additives in mass. %, over 100% in section of changes of temperature of radiation in the range of 423-573 K are obtained. The dose rates of gamma irradiation were 286, 237 and 40 R/s. The obtained data confirmed the above considerations of negative differential absorption. The preliminary obtained data also showed that at thermoradiation processing with 423 K and power of gamma-radiation 237 R/s at 2-hour radiation in the gamma channel gives in $60^0$ angle of incidence the left rotating at the angle reflection on (5±0,5) of degrees.

Thus, it has been shown here that the thermoradiation phenomena in glasses, considering that the negative radiation-induced absorption at thermoradiation processing testifies to homogenization of structure of glass, which allow to obtain metamaterials in the natural way from multi oxide glasses with iron oxide. The thermoradiation effect can be useful for modifying magnetooptical glasses with new unique non-linear properties.

**Acknowledgements**

This research is supported by A-4-9 project of Ministry of High Education Republic of Uzbekistan.

**References**

1. Pendry J.B., Holden A.J., Robbins D.J., Stewart W.J. IEEE Trans. Microwave Theory Tech. 1999, vol.47, iss.11, pp.2075-2084.
2. Smith D.R., Padilla W.J., Vier D.C., Nemat-Nasser S.C., Schultz S. Phys.Rev.Lett. 2000, vol.84, iss.18, pp.4184-4187.
3. Salakhitdinov A.N., Salakhitdinova M.K., Yusupov A.A. Uzbek Journal of Physics, 2014, vol.16, iss.2, pp.144-148.

# Metal-Dielectric-Semiconductor Hyperbolic Metamaterial for selectable canalization wavelength

**V. Caligiuri**[1] **and A. De Luca**[1,*]

[1]Dept. of Physics and CNR-Nanotec - University of Calabria - 87036 - Rende (Italy)
*antonio.deluca@fis.unical.it

**Abstract**— Hyperbolic metamaterials (HMMs) are artificial structures whose extreme optical anisotropy opens the way for a broad range of applications in the visible range, from perfect lensing to attomolar biosensing. Recently, the possibility to engineer a structure showing a zero in the in-plane optical constant and, simultaneously, a pole in the out-of-plane one has been demonstrated for the so called "$\varepsilon_{NZP}$" HMMs. Unfortunately, once properly designed for only a few metal-dielectric pairs in the visible range, there is no way to shift the transition wavelength between these coexisting anisotropies and keep the same constituents. We present a simple way of overcoming this problem and set up a method to tune this transition point within almost the entire visible range without changing the constituent fundamental materials.

Hyperbolic Metamaterials (HMMs) constitute a new class of artificial, extremely anisotropic materials based on deeply subwavelength metal/dielectric building blocks, whose properties have been widely exploited in spontaneous emission enhancement,[1] subwavelength imaging [2] and biosensing [3]. Recently, a new configuration has been proposed allowing the coexistence of the type I and type II anisotropies and their complete inversion at a single wavelength called "canalization wavelength". This condition verifies if $Lm = Ld$ and $\varepsilon_m = -\varepsilon_d$. Unfortunately, once the materials are selected, there is no way to shift the canalization wavelength keeping the same components. In this paper we show how to overcome this limit and open a whole visible wide design tunability window by introducing a HMM based on a three materials building block [4]. In particular, five trilayers, each one consisting in a metal-semiconductor-oxide triplet, are considered. Si has been chosen as the high index material, $SiO_2$ as the low index dielectric and, as a metal, we have chosen silver. By fixing the thickness of the metal, it is possible to act on the other two to design the *type I/type II* transition wavelength at the desired position into the allowed range. In the case of a three materials HMM (TM-HMM), the expressions for $\tilde{\varepsilon}_{\parallel}$ and $\tilde{\varepsilon}_{\perp}$ are given in 1 and 2

$$\tilde{\varepsilon}_{\parallel} = \frac{\tilde{\varepsilon}_{d_1} t_{d_1} + \tilde{\varepsilon}_{d_2} t_{d_2} + \tilde{\varepsilon}_m t_m}{t_{d_1} + t_{d_2} + t_m} \tag{1}$$

$$\tilde{\varepsilon}_{\perp} = \frac{\tilde{\varepsilon}_{d_1}\tilde{\varepsilon}_{d_2}\tilde{\varepsilon}_m (t_{d_1} + t_{d_2} + t_m)}{t_{d_1}(\tilde{\varepsilon}_{d_2}\tilde{\varepsilon}_m) + t_{d_2}(\tilde{\varepsilon}_{d_1}\tilde{\varepsilon}_m) + t_m(\tilde{\varepsilon}_{d_1}\tilde{\varepsilon}_{d_2})} \tag{2}$$

Where $d_1, d_2$ and $m$ indicate respectively the first and the second dielectric and metal, $t_{d_1}, t_{d_2}$ and $t_m$ are their thicknesses. In order to obtain simultaneously $\tilde{\varepsilon}_{\parallel} = 0$ and $\tilde{\varepsilon}_{\perp} = \infty$ the system in equation 3 has to be solved.

$$\begin{cases} \tilde{\varepsilon}_{d_1} t_{d_1} + \tilde{\varepsilon}_{d_2} t_{d_2} + \tilde{\varepsilon}_m t_m = 0 \\ t_{d_1}(\tilde{\varepsilon}_{d_2}\tilde{\varepsilon}_m) + t_{d_2}(\tilde{\varepsilon}_{d_1}\tilde{\varepsilon}_m) + t_m(\tilde{\varepsilon}_{d_1}\tilde{\varepsilon}_{d_2}) = 0; \end{cases} \tag{3}$$

Once the three materials are selected, then $\tilde{\varepsilon}_{d_1}, \tilde{\varepsilon}_{d_2}$ and $\tilde{\varepsilon}_m$ are fixed. By fixing the thickness of the metal at 20nm, positive solutions for the thicknesses of the two dielectrics can be found by solving the system in equation 4.

$$\begin{cases} t_{d_1} = -\frac{\tilde{\varepsilon}_{d_2} t_{d_2} + \tilde{\varepsilon}_m t_m}{\tilde{\varepsilon}_{d_1}} \\ t_{d_2} = -t_m \frac{\tilde{\varepsilon}_{d_1}^2 - \tilde{\varepsilon}_m^2}{\tilde{\varepsilon}_{d_1}^2 - \tilde{\varepsilon}_{d_2}^2} \frac{\tilde{\varepsilon}_{d_2}}{\tilde{\varepsilon}_m} \end{cases} \tag{4}$$

By contemporary imposing the conditions $t_{d_1} > 0$ and $t_{d_2} > 0$ in system 4, we find $\tilde{\varepsilon}_{d_1} < |\tilde{\varepsilon}_m|$ and $\tilde{\varepsilon}_{d_2} > |\tilde{\varepsilon}_m|$. By merging these two conditions it is possible to reach the design relation for a three materials based $\varepsilon_{NZP}$ HMM:

$$\tilde{\varepsilon}_{d_2} > |\tilde{\varepsilon}_m| > \tilde{\varepsilon}_{d_1} \tag{5}$$

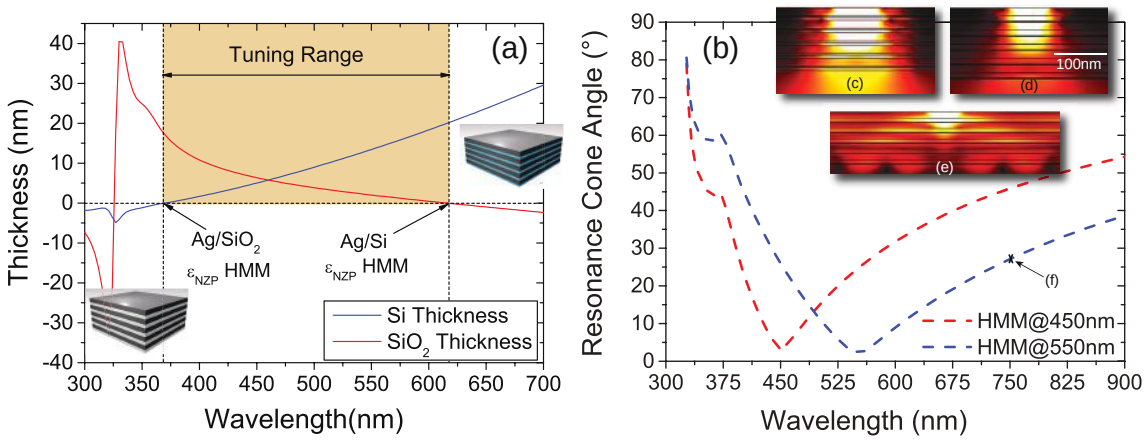



Figure 1: (a) *Si* and $SiO_2$ thicknesses as extracted by equation 4. At 365nm the system becomes an $Ag/SiO_2$ HMM, while at 620nm system falls down in the $Ag/Si$ bilayer HMM. Below 365nm and above 620nm solutions are not physical. (b) Resonance cones angle calculation for both the HMM systems showing a minimum very close to zero in correspondence of the two transition wavelengths. In the insets a FEM simulation of the electric field propagation inside the structures showing a canalization effect at the respective canalization wavelengths, manifested as a straight subwavelength confined light beam.

By using Ag as a metal, Si as high-index dielectric and $SiO_2$ as a low index dielectric, a tunability of 255nm is obtained (see figure 1.a).

Here we designed two systems, showing two different transition wavelengths. The first one, with $\lambda_{tr} = 450nm$, is made of 20nm Ag, 6.5nm $SiO_2$ and 5nm Si layers. The second, showing $\lambda_{tr}$ at 550nm, is made of 20nm Ag, 2nm $SiO_2$ and 13nm Si layers. The evaluation of the presence/absence of the Brewster angle, together with a complete Scattering Matrix Method (SMM) and Transfer Matrix Method (TMM) characterization of the response of the two systems, confirmed their good design. In the end, we evaluated the propagation of the light through the two structures by means of FEM based simulations. The presence of the well known resonance cones in the type II region for both the systems has been reported and the supercollimation effect appears for both the systems exactly at each transition wavelength. In conclusion, we demonstrated the possibility to overcome the lack of the design tunability of classic stack HMMs by introducing a third material in the one-dimensional (1D) periodicmultilayer lattice. By using a metal, a high-index and a low-index dielectric we engineered two different systems, showing two different transition wavelengths. For each of them we carried out a complete SMM and TMM characterization that confirmed the accuracy of our design. FEM models of our systems revealed the presence of the supercollimation effect inside our structures happening at the transition wavelengths, confirming the possibility to use our systems as perfect lenses within the visible range.

## ACKNOWLEDGMENT

The research leading to these results has received support and funding from the Italian Project "NanoLase" - PRIN 2012, protocol number 2012JHFYMC.

## REFERENCES

1. K. V. Sreekanth, A. De Luca, and G. Strangi, "Experimental demonstration of surface and bulk plasmon polaritons in hypergratings," *Scientific Reports*, vol. 3, p. 3291, 2013.
2. J. Rho, Z. Ye, Y. Xiong, X. Yin, Z. Liu, H. Choi, G. Bartal, and X. Zhang, "Spherical hyperlens for two-dimensional sub-diffractional imaging at visible frequencies," *Nat. Commun.*, vol. 1, pp. 143–, Dec. 2010.
3. A. V. Kabashin, P. Evans, S. Pastkovsky, W. Hendren, G. A. Wurtz, R. Atkinson, R. Pollard, V. A. Podolskiy, and A. V. Zayats, "Plasmonic nanorod metamaterials for biosensing," *Nat. Mater.*, vol. 8, no. 11, p. 871, 2009.
4. V. Caligiuri and A. De Luca, "Metal-semiconductor-oxide extreme hyperbolic metamaterials for selectable canalization wavelength," *Journal of Physics D: Applied Physics*, vol. 49, no. 8, p. 08LT01, 2016.

# Optical response of periodic/quasiperiodic structures containing a left-handed material.

**M. Toledo-Solano, M. A. Palomino-Ovando, and I. Paredes-Pérez**
Benemérita Universidad Autónoma de Puebla FCFM, México
*corresponding author: marthap@fcfm.buap.mx

**Abstract-** We investigated the optical properties of a one-dimensional photonic periodic/quasiperiodic (PC/QC) structure. This structure is composed of alternating layers of a right-handed material and a left-handed material. Using attenuated total reflectivity (ATR) geometry, we investigate the coupling of light with the plasmons on the surface of the metamaterial layers. Bands of surface modes with a significant selective spatial localization confined almost totally within the periodic or quasiperiodic section were observed.

Optical properties of materials have been investigated for many years provided that the knowledge of these properties defines the material applications in the optoelectronic industry. Plasmons, which are quanta of plasma oscillations, have been studied in metals since the pioneer work of Ritchie **Erreur ! Source du renvoi introuvable.**], and Stern and Ferrell **Erreur ! Source du renvoi introuvable.**]. Plasmons may propagate either in bulk or at the surface consequently they are termed as bulk or surface plasmons. Special attention has been paid to the interaction between S-polarized light and surface plasmons in left handed materials [3]. A one dimensional photonic crystal made up of alternating layers of a dielectric and a left handed material may support modes at the interfaces. Furthermore, these structure display novel properties such as zero energy gaps and the possibility to obtain omnidirectional non-Bragg gaps, and have exhibited bulk plasmon polariton modes, whether the stacking arrangement is periodic, quasiperiodic, or even disordered. It is because the disorder causes multiple light scattering that the extinction of coherent waves propagating through the photonic structure originate and this leads to a dramatic change in the localization properties of the electromagnetic modes. The surface modes can be amplified in photonic crystal with defect due to an increase in the density of states at the level of the defect [4]. Based on these results we use a hybrid structure, that is, we build a device composed of both periodic (PC) and quasiperiodic (QC) subunits each one exhibiting a different kind of topological ordering. The goal of this paper is to study the selective spatial localization of surface plasmons within a hybrid PC|QC|PC structure applying the attenuated total reflectivity technique. The presence of defects in the interior of the structure induces a coupling of the surface plasmons with modes associated to them on their interfaces.

Let us consider a metamaterial characterized by the dielectric permittivity $\varepsilon_2$ and magnetic permeability $\mu_2$ given by [5]

$$\varepsilon_2 = \varepsilon_0 - \frac{\omega_P^2}{\omega(\omega + i\gamma)} \quad \text{and} \quad \mu_2 = \mu_0 - \frac{\omega_P^2}{\omega(\omega + i\gamma)}$$

Here $\gamma$ is the damping factor, the boundary conditions yield the surface polariton dispersion relations.

In order to obtain the projected band structure and the reflectivity spectrum of the hybrid structure the transfer matrix method is used for both periodic and quasiperiodic structures.

We show the projected band structure as well as the dispersion curves of the surface modes for both polarizations, with composed cell of PC|QC|PC for PC build with four thin films and QC build for Fibonacci and Cantor sequence of order five. We calculated the distribution of the electric field in the hybrid structure and found the amplified of the electric field in the quasiperiodic superlattice. The introduction of a periodic photonic crystal permits the inclusion of an additional degree of order in the system, allowing more bands to exist compared to the case of the quasiperiodic structure alone. Reflection spectra obtained by the ATR technique show the existence of plasmons for these hybrid structures.

**Acknowledgements**, M. Toledo-Solano thanks to the Program Cátedras Conacyt, Mexico, and thanks the for financial support of VIEP-BUAP.

**REFERENCES**

1. Ritchie, R. H., "Plasma Losses by Fast Electrons in Thin Films," *Phys. Rev*., Vol. 106, Issue 5, 874-881, 1957.
2. Stern, E. A. and R. A. Ferrell, "Surface Plasma Oscillations of a Degenerate Electron Gas," *Phys. Rev*., Vol. 120, Issue 1, 130-136, 1960.
3. R. Ruppin, "Surface Polaritons of a left-handed medium", *Phys. Lett*., 85, 3966, (2000)
4. J.E. Pérez-Rodríguez, M. A. Palomino-Ovando, Gregorio H. Cocoletzi, "Surface modes coupling in one-dimensional metamaterial photonic crystals with defects", *Superlattices and Microstructures*, Vol 83, 383 – 389 (2015).
5. H. Jiang H. Chen, H. Li, Y.Zhang, S Zhu, "Omnidirectional gap and defect mode of one-dimensional photonic Crystal cibtaining negative-index materials", *Appl, Phys. Lett*. Vol. 83 5386 (2003)

# Optical metamaterial slabs based on hexagonal arrays of metallic nano-resonators with three-fold rotational symmetry

**Mircea Giloan*, Robert Gutt and Gavril Saplacan**
Company for Applied Informatics, Cluj-Napoca, Romania
*corresponding author: mircea_giloan@cianet.ro

**Abstract:** Metallic nano-resonators with three-fold rotational symmetry are used to design meta-atoms with different geometries distributed in hexagonal arrays separated by dielectric films. The nature of the hybridized plasmon modes allowed by the designed meta-atoms leads to extraordinary optical properties for the resulted metamaterial slabs like negative refractive index and high chirality.

In our study we analyzed the optical properties of different nanostructures made of gold nano- resonators with three-fold rotational symmetry arranged in two perfectly overlapping hexagonal lattices separated by a dielectric film. The optical behavior of the studied nanostructures derives from the nature (i.e. symmetry) and resonances of the hybridized plasmon modes excited by the incident light on the metallic surfaces of the constituent meta-atoms. Using meta-atoms with different geometries we designed optical metamaterials with negative index of refraction for linearly polarized light (see fig. 1(a)) [1], high chirality, and negative index of refraction for circularly polarized light (see fig. 1(d)) [2]. Optical properties of the considered nanostructures were studied by performing computer simulations using a three-dimensional finite-difference time domain (FDTD) algorithm [3].

The paired nano-resonators of the metamaterial slab depicted in fig. 1(a) are identical and perfectly overlapping. Due to the different size of the adjacent pairs of nano-resonators a symmetric respectively an anti-symmetric hybridized plasmon mode are induced into the large (see fig. 1(b)) respectively small (see fig. 1(c)) pair of nano-resonators at the same frequency of linearly polarized light. The presence of both symmetric and anti-symmetric plasmon modes at the same frequency leads to a negative refractive index for the studied metamaterial slab. The paired nano-resonators of the metamaterial slab depicted in fig. 1(d) are identical and placed in a conjugated arrangement. Due to this specific arrangement of the paired nano-resonators different hybridized plasmon modes are induced at the same frequency by the left (see fig. 1(e)) and right (see fig. 1(f)) circularly polarized light. The presence of different plasmon modes induced by the left and right circularly polarized light at the same frequency leads to a high chirality for the studied metamaterial slab.

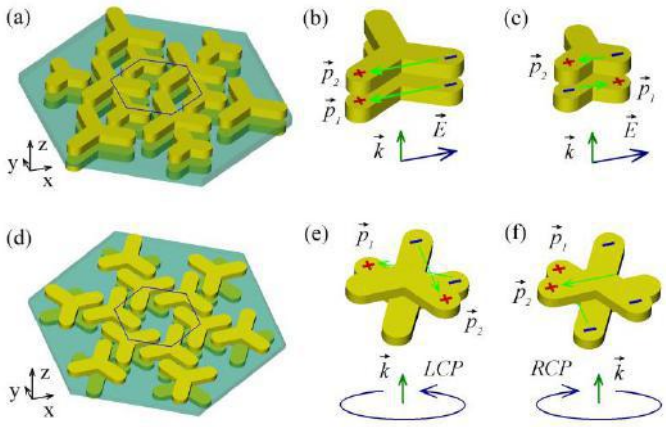



**Figure 1.** (a) 3D view of the studied negative index metamaterial. (b) Symmetric hybridized plasmon mode lodge by the large sized nano-resonators pair. (c) Anti-symmetric hybridized plasmon mode lodge by the small sized nano-resonators pair. (d) 3D view of the studied chiral metamaterial. (e) Hybridized plasmon mode induced by the LCP light. (f) Hybridized plasmon mode induced by the RCP light. Electric charge distributions (+, -) and electric dipole moments ($p_1$, $p_2$) are depicted for each nano-resonator.

**Acknowledgments:**
This work was supported by the Company for Applied Informatics through the project: "CERIA" - ID: 1542/SMIS: 44023, POSCCE-A2-O2.3.2-2012-1.

**References:**
[1] M. Giloan and R. Gutt, "Optical negative index metamaterial based on hexagonal arrays of metallic meta-atoms with threefold rotational symmetry," J. Opt. Soc. Am. B **33** (2016).
[2] M. Giloan, R. Gutt and G. Saplacan, "Optical chiral metamaterial based on metaatoms with three-fold rotational symmetry arranged in hexagonal lattice," J. Opt. **17** (2015).
[3] MEEP, http: //ab-initio.mit.edu/wiki/index.php/Meep.

# Simulation of graphene-negative index waveguide structure model for solar cell

**N. Hissi[1], S. Bahsine[2], B.Mokhtari[3*], N.Cherkaoui Eddeqaqi[4]**

1, 2, 3, 4 Physics department, Faculty of sciences, Moulay Ismail University, Meknes, Morocco

**Mohammed. M. Shabat**

Physics Department, Islamic University, Gaza, Palestine

**J.Atangana**

Physics department, University of Yaounde I, Yaounde, Cameroon.

*nicet2012@hotmail.com

**Abstract**-Graphene and negative index materials are newly artificial materials which could become the most key issues in design solar cells for energy applications. The aim of this work is to construct a novel waveguide structure which is acting as solar cell, containing graphene and negative index materials to minimize the reflection of the light incident on such structure and to increase the transmission and the absorption of light. Optical modeling and simulation based on the transfer matrix method are used to investigate the effects of the physical parameters of the proposed waveguide structure on the transmittance, reflectance and the absorptance. The numerical results are presented, analyzed and discussed.

We consider the graphene-sandwiched three-layer structure as shown in the inset of Figure 1.

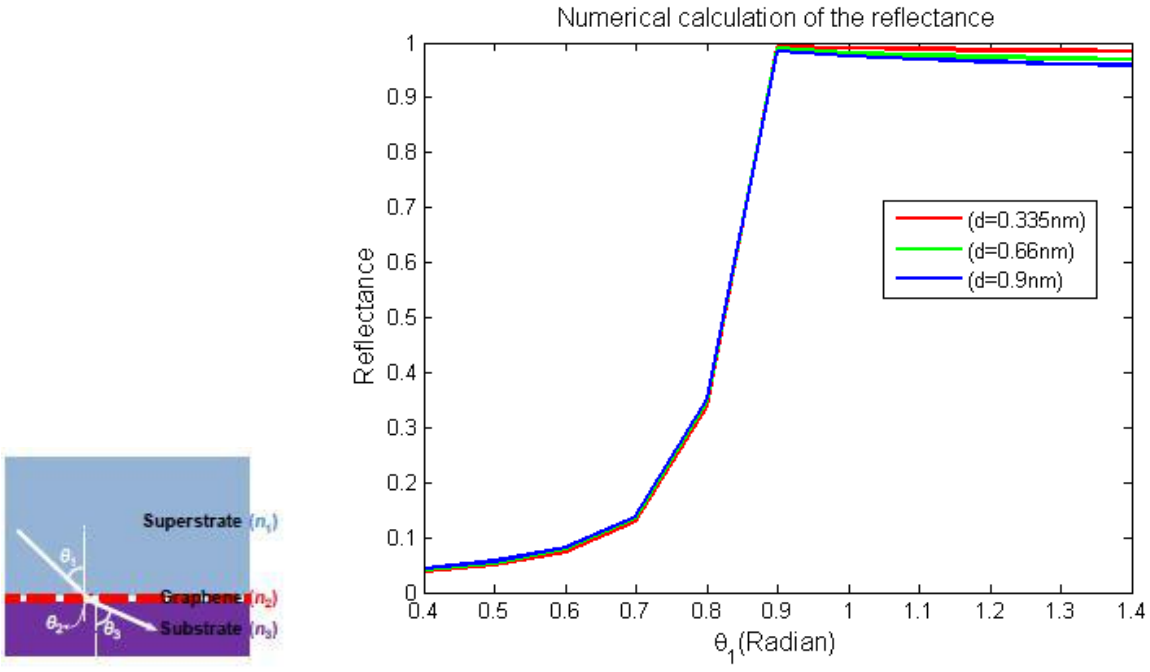



Figure 1. Numerical calculation of the reflectance as functions of incident $\theta_1$ angle, and the thickness d.

The top layer (MTM superstrate), graphene, and bottom layer (MTM substrate) have refractive indices $n_1$, $n_2$, and $n_3$, respectively. The refractive index of graphene is a complex number and can be calculated by $n_2 = \left(1 + j\frac{\sigma_g}{\varepsilon_0 \omega d}\right)^{\frac{1}{2}}$, where $\varepsilon_0$ is the permittivity of the free space, and $\omega$ is the angular frequency of the incident light wave. $n_1 = -1.12$ and $n_3 = -1.51$.

Assume that a plane wave is incident into the three-layer structure and the corresponding propagation angles to the normal are $\theta_1$, $\theta_2$, and $\theta_3$, respectively. Snell's law is held between layers, $n_q \sin\theta_q = n_1 \sin\theta_1$ ($q$=1, 2, 3). Based on the transfer matrix method, the amplitude reflectance can be calculated by

$$r = \frac{(\tilde{n}_3 - \tilde{n}_2)(\tilde{n}_2 + \tilde{n}_3)e^{j\tilde{\varphi}_2} + (\tilde{n}_3 + \tilde{n}_2)(\tilde{n}_2 - \tilde{n}_1)e^{-j\tilde{\varphi}_2}}{(\tilde{n}_3 + \tilde{n}_2)(\tilde{n}_2 + \tilde{n}_1)e^{j\tilde{\varphi}_2} + (\tilde{n}_3 - \tilde{n}_2)(\tilde{n}_2 - \tilde{n}_1)e^{-j\tilde{\varphi}_2}}$$

Where $\varphi_2 = n_2 k_0 d \cos\theta_2$ ($k$0 is the wavenumber of the light wave in free space; $d$≈0.335nm is the thickness of graphene). Also, $\tilde{n}_q = n_q \cos\theta_q$ ($q$=1, 2, 3) for $s$-polarized light.

Based on this three-layer model, the reflectance grows when the thickness of the graphene layer decreases as shown on figure (1). The reflectance increases when increasing the incidence angle $\theta_1$ and reaches it maximum value at $\theta_1 = 0.9$ rad. Moreover, we can also control the reflectance and the absorptance by changing the thickness of the graphene layer. Furthermore, the closer n3 and n1 are, the larger the critical angle, and the larger the absorptance are. The reason is because a larger critical angle decreases the incident power density on graphene.

**REFERENCES**


1. Manenkov, A.B. Scattering Froman Abruptly Terminated Planar Metamaterial Waveguide. Opt. Quantum Electron. 53, 210-220 (2010).

2. El-Khozondar, H.J., Al-Sahhar, Z.I., Shabat, M.M. Electromagnetic surface waves of a ferrite slab bounded by metamaterials, Int. J.Electron. Commun. (AEU) 64, 1063–1067 (2010).

3. H. M. Mousa and M.M. Shabat, Energy Procedia, Simulation of a Symmetry Metamaterial Waveguide Absorber(TE&TM), Vol. 74, 597-607, 2015.

# Coupled-Mode Equations for Third-Harmonic Generation in A One-Dimensional PIM/NIM Structure

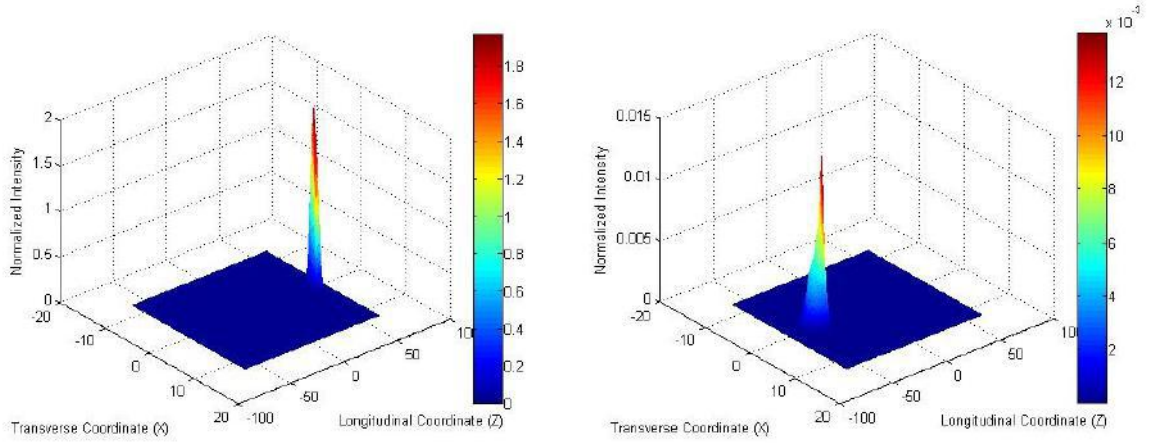
**S. Wicharn[1*], P. Buranasiri[2], and W. Yindeesook[2]**
[1]Department of Physics, Faculty of Science, Srinakharinwirot University, Bangkok 10110, Thailand
[2]Department of Physics, Faculty of Science, King Mongkut's Institute of Technology Ladkrabang, Bangkok 10520, Thailand
[*]corresponding author: surawutw@g.swu.ac.th

**Abstract**-We formulate a completed set of rigorous coupled-mode equations by using method of multiple-scale. These coupled-mode equations are used to describe a third-harmonic generation in a one-dimensional periodic structure containing stack of positive-index material (PIM) and third-order nonlinear negative-index material (NIM) layers. We found that the generated third-harmonic pulse amplitudes in forward- and backward-directions from PIM/NIM periodic structure can be enhanced due to backward phase matching technique and band-edge field enhancement.

Metamaterials are artificial electromagnetic structures providing unnatural properties, which can not be found in nature such as negative refraction or reversal of Snell's law, reversal of Doppler shift, and backward Cherenkov radiation [1-2]. The key feature of metamaterials is having negative refractive index, so this structure are often called negative-index materials (NIMs) due to their simultaneous negative electric permittivity and magnetic permeability. NIMs have become an interesting research topics because of the previous experimental demonstration of real-world photonics crystal structure with negative refractive index at optical and infrared frequencies [3-4]. After that, various type of NIM structure have been engineered and developed to create potential applications based on negative refraction and linear optical effects [5]. Not only linear optical effects can use the benefits of NIMs, but nonlinear optical effects can also take the benefits of negative-index of this material for improving the efficiency of nonlinear optical frequency mixing and conversions [6-8]. The nonlinear NIMs can possibly create the exact phase-matched conditions, which can be called "backward phase-matching", for counter-propagating energy flow waves when fundamental frequency and converted frequency waves lie in the negative-index and the positive-index frequency domain, respectively [8].

In this presentation, we formulate a completed set of coupled-mode equations corresponding to third-harmonic generation (THG) in rigorous form by using method of multiple-scale and then discuss a numerical modelling of the enhanced THG in one-dimensional (1D) PIM/NIM structure. Our PIM/NIM structure is a multilayered stack which composed of periodically alternating PIM and NIM embedded in third-order nonlinearity material layers. To enhance the THG process, the band-edge field enhancement, which is a benefit of periodic multilayered structure, is used for increasing the forward third-harmonic pulse amplitude [9] and the backward phase-matching technique, which is a benefit of containing nonlinear NIMs in the structure, is used for increasing the backward third-harmonic pulse amplitude. Therefore, this 1D PIM/NIM structure can give the strong THG in both forward- and backward-directions. The numerical result examples are shown in figure 1 where the 1D PIM/NIM structure is placed at origin point on z axis. Fig. 1(a) and 1(b) represent the output third-harmonic pulses in both forward- and backward-directions, which are induced with the fundamental frequency pumping pulse having the same intensity of previous work [9]. Especially, the intensity of backward third-harmonic pulse is more than backward pulse from normal 1D PIM/PIM structure in previous work [9].

The optimal design of choice of materials, material parameters, and structural geometry of the 1D PIM/NIM structure can apply as a component in intense third-harmonic frequency generator, high-sensitive nonlinear optical spectroscopy, efficient nonlinear mirrors.




(a) (b)

**Figure 1.** (a) Forward and (b) backward third-harmonic pulses from 1D PIM/NIM structure.

## REFERENCES


1. Veselago, V. G., "The electrodynamics of substance with simultaneously negative value of epsilon and mu," *Sov. Pays. Usp.*, Vol. 10, 509-514, 1968.
2. Caloz, C. and Itoh, T., *Electromagnetic Metamaterials: Transmission line theory and Microwave applications*, Wiley-Interscience, 2006.
3. Shalaev, V. M., Cai, W., Chattier, U. K., Yuan, H., Sarychev, A. K., Drachev, V. P., and Kildishev, V. M., "Negative index of refraction in optical metamaterials," *Opt. Lett.*, Vol. 34, No. 30, 3356–3358, 2005.
4. Berrier, A., Mulot, M., Swillo, M., Qiu, M., Thyl'en, L., Talneau, A., and Anand, S., "Negative refraction at infrared-wavelengths in a two-dimensional photonics crystal," *Phys. Rev. Lett.*, Vol. 93, 073902, 2004.
5. Ramakrishna, S. A. and Grzegorczyk, T. M., *Physics and Applications of Negative refractive index materials*, CRC Press, 2009.
6. Klein, M. W., Enkrich, C., Wegener, M., and Linden, S., "Second-harmonic generation from magnetic metamaterials," *Science*, Vol. 313, 502-504, 2003.
7. Klein, M. W., Wegener, M., Feth, N., and Linden, S., "Experiments on second- and third-harmonic generation in nonlinear metamaterials," *Opt. Express*, Vol. 15, 5238-5247, 2007.
8. Shadrivov, I. V., Zharov, A. A., and Kivshar, Yu. S., "Second-harmonic generation in nonlinear left-handed metamaterils," *J. Opt. Soc. Am. B*, Vol. 23, 529-534, 2006.
9. Wicharn, S. and Buranasiri, P., "Third-harmonic pulse generation in one-dimensional photonic crystal structure" *J. Nanophotonics*, Vol. 8, No. 1, 083893-1-083893-18, 2014.

# High-speed Detection of Microorganisms in Ambient and Aqueous Environments Using Metamaterials

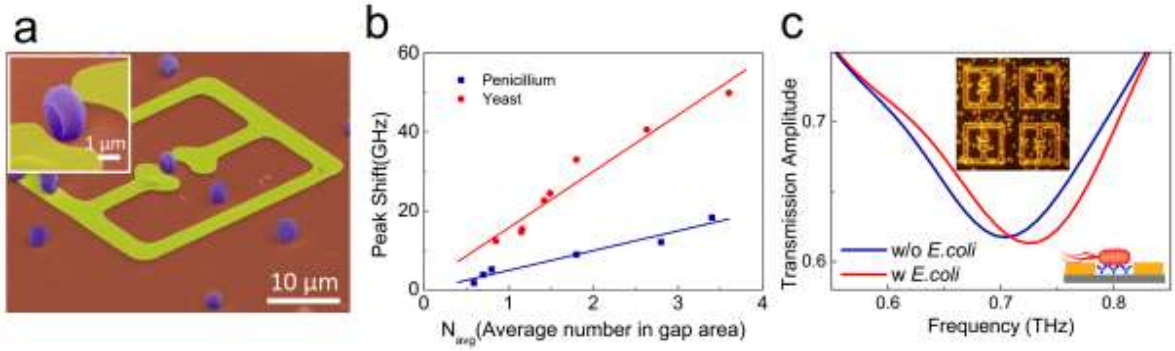
**S. J. Park and Y. H. Ahn***

Department of Physics and Department of Energy Systems Research, Ajou University, Suwon 151-749 Korea

*corresponding author: ahny@ajou.ac.kr

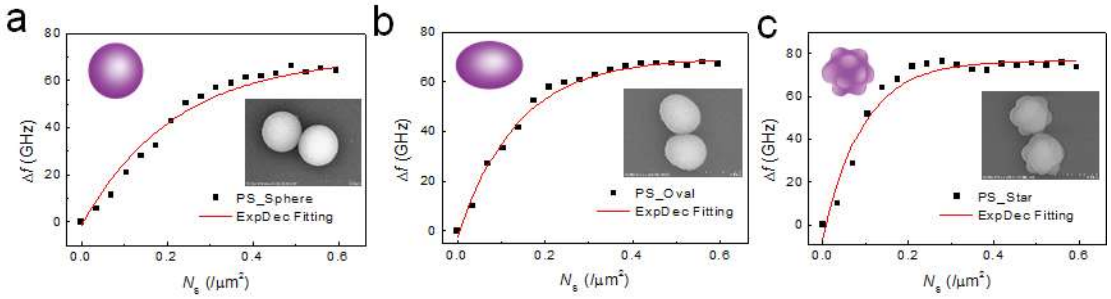
**Abstract**-We used terahertz metamaterials for the high-speed detection of microorganisms. Extremely small amounts of the microorganisms can be detected, because their sizes are on the same scale as the micro-gaps of the metamaterials. The resonant frequency shift of the metamaterials was investigated in terms of the number density and the dielectric constants of the microorganisms. To optimize the metamaterial sensors, we controlled the geometrical parameters such as gap width, substrate dielectric constant and target shapes.

Detections of biological substances such as fungi, bacteria, and virus have been of particular interests in the terahertz (THz) frequency range for the purpose of food and security inspection. There has been hardly any progress since they are mostly transparent against THz waves. On the other hand, metamaterials have been studied extensively to develop useful biosensors. In particular, THz metamaterials have gap structures typically with the size of 3 μm which is compatible with the sizes of the microorganisms. Here, we show that THz metamaterials can work as an efficient sensor for sensing microorganisms such as fungi, yeasts, bacteria, and viruses [1]. A clear shift in the resonant frequency is observed following the deposition of microorganisms on the THz metamaterials (Fig. 1a), and it rises up due to the change in the effective dielectric constant in a gap area of the metamaterials. Strong field localization and enhancement in the gap area enables us to detect the microorganisms with high sensitivity.




**Figures 1:** (a) SEM image of metamaterials coated by penicillia. (inset) Magnified image of the fungi located in the micro-gap. (b) A plot of resonant frequency shifts as a function of $N_{avg}$, for depositions of penicillia (blue boxes) and yeasts (red circles). Solid lines are linear fits to the data. (c) THz transmission before (blue line) and after (red line) the deposition of E. coli. on the functionalized metamaterials in aqueous environments. (Inset) A corresponding dark-field microscopic image obtained after the deposition of E. coli.

In particular, the resonant frequency shift is higher for the larger dielectric constants, which was supported by the dielectric constant measurements of individual fungi and bacteria. As shown in Fig. 1b, we found that yeast cells are more sensitive than the penicillium in terms of the frequency shift, which was successfully interpreted by the dielectric constant measurements of the individual fungi. In addition, as shown in Fig. 1c, our THz metamaterials sensors can be applied in aqueous conditions as easily as in ambient conditions, because THz metamaterial is extremely sensitive to the substances located near the surface. THz metamaterial sensing is a universal method because it is based on the dielectric sensing, while a selective detection is also possible by functionalizing the substrates with antibodies specific to the target substances.




**Figures 2:** Resonant frequency shift as a function of surface number density for various polystyrene types: (a) sphere, (b) oval, and (c) star.

To design optimized microbial sensor, the sensitivity of THz metamaterial sensor has been studied as a function of the substrate dielectric constant, gap size and the metal film thickness [2]. The frequency shift decreases with increasing gap width for a fixed coverage of yeast film, showing a field enhancement effect. Furthermore, the vertical range of the effective sensing volume has been studied by varying the thickness of the yeast film. Importantly, the frequency shift was higher for non-spherical microbeads, such as the star-shaped microbeads as shown in Fig. 2. Therefore, the shape of the individual target material was a crucial factor in determining metamaterial sensor sensitivity [3]. Finally, the experimental findings are in a good agreement with the results of finite-difference time-domain (FDTD) simulations. Our work shows promising potential for use in the fabrication of highly sensitive microbial detectors that are capable of high-speed on-site detection of hazardous microorganisms in various environments.

## REFERENCES


1. S. J. Park, J. T. Hong, S. J. Choi, H. S. Kim, W. K. Park, S. T. Han, J. Y. Park, S. Lee, D. S. Kim, and Y. H. Ahn, "Detection of microorganisms using terahertz metamaterials." *Scientific reports* 4, 4988 (2014).
2. S. J. Park, B. H. Son, S. J. Choi, H. S. Kim, and Y. H. Ahn, "Sensitive detection of yeast using terahertz slot antennas", *Opt. Express* 22 30467 (2014).
3. S. J. Park, S. W. Jun, A. R. Kim, Y. H. Ahn, "Terahertz metamaterial sensing on polystyrene microbeads: shape dependence", *Opt. Mater. Express* 5, 2150 (2015).

# Coupling effects between three dimensional split ring resonators

**Che-Chin Chen*, M. H. Shiao, Y. H. Lin and C. N. Hsiao**

[1] Instrument Technology Research Center, National Applied Research Laboratories, Hsinchu 30076, Taiwan

*corresponding author: ccchen@itrc.narl.org.tw

**Abstract**-In this study, the coupling effects between three dimensional split ring resonators (SRRs) were presented by changing the inter distance of SRRs. The transmission spectra revealed that the transmission amplitude and the resonance frequencies were increased with deceasing the inter distance of the SRRs. The simulations were evidentially retrieved as well. We conclude that the electric field strength inside the SRR dominated the couplings between the SRRs.

The exotic electromagnetic properties of artificial metamaterials are extensively demonstrated by tailoring the periodicity and geometry of the meta-atoms. Three-dimensional (3D) split ring resonator (SRR) is a commendatory meta-atom to obtain the magnetic resonance when the magnetic field oscillating in the SRR plane. However, the studies on the coupling effects between 3D SRRs are only present in GHz regime or simulation [1-2] since the difficulties to fabricate 3D structures. We recently demonstrated three dimensional SRRs by a simple fabrication method and showed its' unique optical properties [3-4].

Our simple strategy to construct 3D SRRs utilized metal stress driven method [4]. In current work, we design rectangle-arrayed SRRs by varying the distance in the normal direction of the SRR plane as shown in Fig.1. The transmission spectra were carried out by FTIR as shown in Fig. 2. The spectra clearly showed that the transmission amplitude and resonance frequencies were increased with decreasing distance. The transmission amplitudes could be easily explained by the filling factors of the arrays. The simulated results (not shown here) showed that the magnetic field strength in the SRR plane increased with decreasing distance while the current density decreased with decreasing distance. We conclude that the electric response was the key factor for the resonance frequency shift of varying distance SRRs. More details will be in the conference.

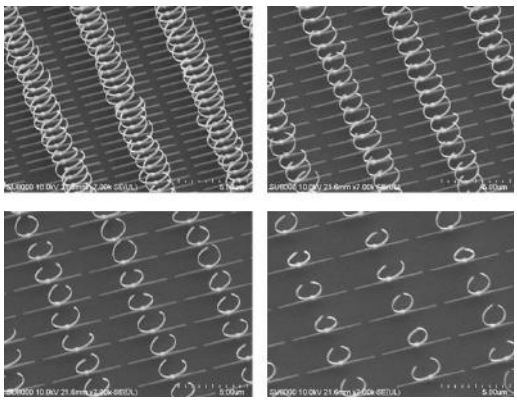


Fig. 1 The rectangle-arrayed SRRs with inter-distances of 0.5, 1, 2, and 3 $\mu$m, respectively.

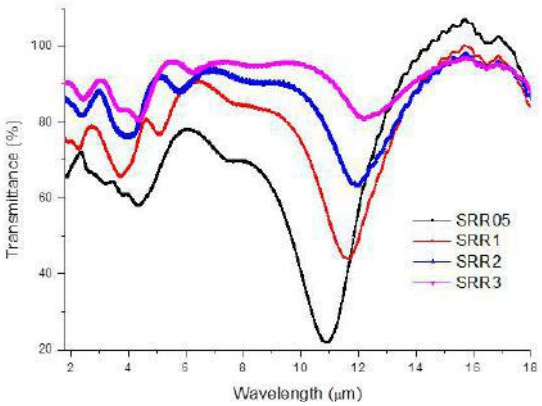



Fig. 2 The transmission spectra revealed the transmission amplitude and the resonance frequencies were increased with deceasing the inter distance of the SRRs.

**Acknowledgements**, This work was supported by Ministry of Science and Technology with grant number MOST 104-2112-M-492-004.

**REFERENCES**

1. Ilya V. Shadrivov et al,. "Scattering of electromagnetic waves in metamaterial superlattices," *Appl. Phys. Lett.*, Vol. 90, 201919, 2007.
2. Heinz Schweizer et al., "Title of the journal paper," *phys. stat. sol. (a)*, Vol. 204, 1760, 2012.
3. C. C. Chen et al., "Fabrication of three dimensional split ring resonators by stress-driven assembly method" *Opt. Express* , Vol. 20, 9415-9420. 2012
4. Che-Chin Chen et al., "Uniaxial-isotropic Metamaterials by Three-Dimensional Split-Ring Resonators" *Adv. Opt. Mater.* Vol. 3, 44-48, 2015

# Refraction at a flat interface of an optically anisotropic metamaterial

**A. Bregar**[1], **M. Ravnik**[1,2]

[1]Faculty of Mathematics and Physics, University of Ljubljana, Slovenia
[2]Jožef Stefan Institute, Ljubljana, Slovenia
anja.bregar@fmf.uni-lj.si

**Abstract**— Refraction at a boundary between isotropic dielectric and an anisotropic hyperbolic metamaterial is theoretically studied for different angles between the optical axis and the metamaterial surface. Different regimes of negative and positive refraction are explored and various cases of the dependence of refraction and absorption on the incident angle of light are shown. These examples are further illustrated with finite-difference time-domain simulations.

New possibilities for the fabrication of macroscopically large samples of an optical metamaterial are explored continuously [1]. One of the potential ways for the creation of novel metamaterials is taking advantage of the optically anisotropic nature of their building blocks [2]. For instance, in liquid crystal metamaterials, the orientational order inherently breaks the material symmetry and introduces optical anisotropy. The inclusion of metal nanoparticles into a liquid crystal matrix can result in negative permittivity of such a material, which can lead to innovative optical effects [3]. Another advantage of liquid-crystal-metamaterials is also that they are easily tunable with electric field [1].

In birefringent materials, the extraordinary angle of refraction $\beta$ depends among other on the angle of its optical axis $\gamma$ with respect to the surface of the crystal:

$$\beta = (\sin\alpha / n_e(\beta, \gamma)) \,, \tag{1}$$

where $\alpha$ is the impinging angle and extraordinary refractive index is connected to the permeability $\mu$, ordinary $\varepsilon_\perp$ and extraordinary value of permittivity $\varepsilon_\parallel$:

$$n_e = \pm\sqrt{1/\left(\sin^2(\beta-\gamma)/\mu\varepsilon_\parallel + \cos^2(\beta-\gamma)/\mu\varepsilon_\perp\right)} \tag{2}$$

All the used quantities are shown also in figure 1. The sign of refraction and whether the light will be absorbed depends on the sign of $\mu$, $\varepsilon_\perp$ and $\varepsilon_\parallel$. If the sign of one of them is different than that of the other two, the extraordinary ray will be totally absorbed for at least some angles of optical axis and the extraordinary angle of refraction will be smaller with respect to the case of equally signed $\mu$, $\varepsilon_\perp$ and $\varepsilon_\parallel$.

To model materials with different signs of permeability and ordinary and extraordinary value of permittivity we have utilised a numerical simulation of Maxwell's equations, following the finite-difference time-domain (FDTD) algorithm [4]. In order to simulate negative-index materials with frequency-dispersive permittivity function, we have used an auxiliary differential equation method (ADE) [5].

In our work we show that it is possible to simulate optically anisotropic double-negative materials with FDTD accurately using the ADE method – i.e. to simulate hyperbolic metamaterials not just as metal-dielectric bilayers or nanorod arrays, but as homogeneous anisotropic materials. In this manner, it is possible to devise a more realistic model for existent metamaterials, that are inherently optically anisotropic (i.e. have negative refractive index only around normal to metamaterial surface) and for metamaterials with liquid-crystal inclusions.

**REFERENCES**

1. Zheludev, N. I. and Kivshar, Y. S. , "From metamaterials to metadevices", *Nat. Mater.,* Vol. 11, No. 917, 2012.
2. Poddubny, A., Iorsh, I., Belov, P. and Y. Kivshar, "Hyperbolic metamaterials", *Nature Photon.,* Vol. 7, No. 948, 2013.

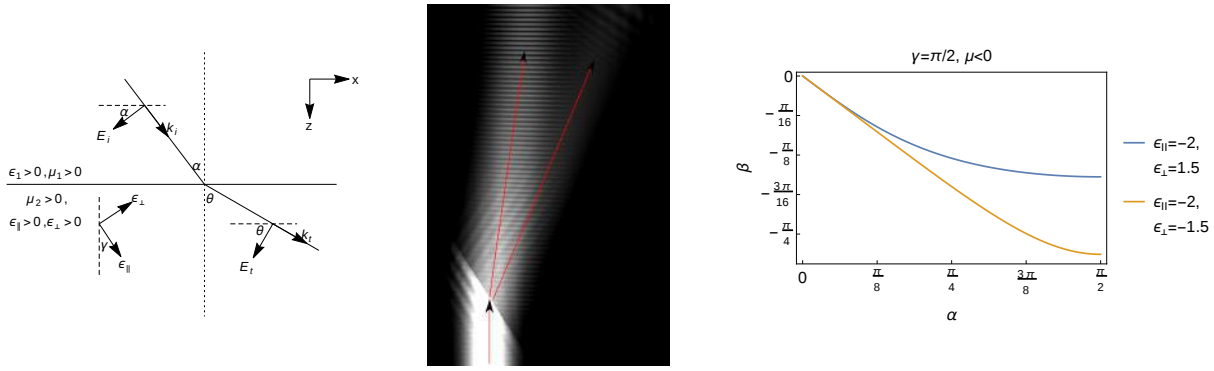



Figure 1: Leftmost figure: a sketch of the incoming and refracted wavevectors for positive signs of permeability and permittivity. Drawn are also the principal axes of permittivity tensor and the angle $\gamma$ between the normal on the surface and the optical axis. Middle: FDTD simulation of intensity of a Gaussian beam falling on a boundary between vacuum and a medium with material parameters $\varepsilon_\parallel = 1.1$, $\varepsilon_\perp = 1.8$, and $\mu = 1$. The beam is comes from belos, on the surface boundary it is partly reflected and part of it is doubly refracted. The refraction angles are in agreement with the theoretical prediction. Rightmost figure: comparison of negatively refracted angle $\beta$ of extraordinarily refracted beam on impinging angle $\alpha$ for $\gamma = \pi/2$ and different signs of $\varepsilon_\perp$ and $\varepsilon_\parallel$. If the material dispersion is hyperbolic, refracted angle will be smaller.


3. Jia, D., Yang, C., Li, X., Peng, Z., Liu, Y., Cao, Z., Mu, Q., Hu, L., Li, D., Yao, L., Lu, X., Xiang, X., Zhang, H. and Xuan, L., "Optical hyperbolic metamaterials based on nanoparticles doped liquid crystals", *Liq. Cryst.*, Vol. 41, No. 207, 2013.
4. Taflove, A. and Hagness, S. C., *Computational Electrodynamics: The Finite-Difference Time-Domain Method*, Third Edition, Artech House, Norwood, MA, 2005.
5. Taflove, A., Johnson, S. G., and Oskooi, A., *Advances in FDTD Computational Electrodynamics: Photonics and Nanotechnology*, Artech House, Norwood, MA, 2013.
6. Sayem, A. A., Mahdy, M. R. C. and Rahman, M. S., "Broad angle negative refraction in lossless all dielectric or semiconductor based asymmetric anisotropic metamaterial", *J. Opt.*, Vol. 18, No. 015101, 2016.

# All-optical phase-change tuning in hybrid dielectric EIT-like metamaterials.

**E. Petronijevic, R. L. Voti, A. Belardini, G. Leahu, G. Cesarini, and C. Sibilia**
La Sapienza University of Rome, Italy
*corresponding author: emilija.petronijevic@uniroma1.it

**Abstract** Here we investigate the all-optical tuning of the EIT-like resonances in dielectric metamaterials based on Si bright and dark resonators. The tuning is enabled by a thin layer of phase change material which changes its optical properties in optical telecommunications range.

Electromagnetically induced transparency (EIT) is an effect in atomic physics that leads to observation of a narrowband transparency window within an otherwise wide absorption line of the spectra. It is followed by dramatic dispersion and high Q resonances, which paves the way for the slow-light devices, the improvement of nonlinear effects' enhancement, optical sensors etc. A metamaterial classical analogue of this effect consists of a broadband, "bright" mode resonator, excited directly by the light, and a narrowband "dark" mode resonator, which is poorly accessible from the free space. When designed properly, the interference between these two and the low radiative loss of the dark mode could lead to very sharp, EIT-like resonances leading to the complete transmission or reflection. In the region of the optical telecommunications there have been many attempts to mimic this behavior by means of metal-based metamaterials. However, their main limitation are huge non-radiative losses from ohmic damping. The potential solution is to use high refractive index dielectric materials instead of metals – they can still provide magnetic and electric dipole response, while having low non-radiative losses. It has been experimentally shown that all-dielectric EIT-like metamaterials based on Si can lead to Q~130 in the near-infrared domain [1]. Additionally, the active all-optical non-volatile tuning of these resonances could lead to many practical applications in optical telecommunications, and the phase change materials are a possible solution [2].

In this work we investigate a possibility of active tuning of the EIT-like response of an all-dielectric metamaterial based on bright and dark resonators made of Si upon the SiO2 substrate. As an functional layer that changes the coupling or losses of our resonators, we exploit a vastly investigated and exploited $Ge_2Sb_2Te_5$ (GST). This material could be fastly and reversibly switched between the amorphous and the crystalline state by the control beam in the visible region. These states have different refractive indices and low losses in the near IR region, where we design the resonances of our dielectric metamaterial. Such a hybrid structure can be conventionally fabricated, very stable and with high cyclability, and the all-optical control of its resonances is very promising for the applications in photonics.

[1] Y. Yang, II. Kravchenko, DP. Briggs, J. Valentine, All-dielectric metasurface analogue of electromagnetically induced transparency, *Nat. Commun.* **5** (2014).
[2] B. Gholipour, J. Zhang, K. F. MacDonald, D. W. Hewak, N. I. Zheludev, An All-Optical, Non-volatile, Bidirectional, Phase-Change Meta-Switch, *Adv. Mater.* **25**, 3050–3054 (2013).

# Developing a FETD method for modeling of the optical black hole in metamaterials

**Wei Yang**[1], **Jichun Li**[2], **and Yunqing Huang**[1]

[1]Xiangtan University, China
[2]University of Nevada Las Vegas, USA
jichun.li@unlv.edu

**Abstract**— In this paper we propose a finite element time-domain (FETD) method for modeling the optical black holes (OBHs) in metamaterials. Stability analysis is carried out for the proposed scheme. Simulations of cylindrical, elliptical and square black holes demonstrate that our method is quite effective in modeling OBHs in time domain. To our best knowledge, this is the first OBHs simulation realized by the FETD method.

The modeling of the optical black hole is based on Faraday's Law and Ampere's Law: $\frac{\partial \boldsymbol{B}}{\partial t} = -\nabla \times \boldsymbol{E}$, $\frac{\partial \boldsymbol{D}}{\partial t} = \nabla \times \boldsymbol{H}$, and the constitutive relations $\boldsymbol{D} = \varepsilon_0 \varepsilon_r \boldsymbol{E}, \boldsymbol{B} = \mu_0 \mu_r \boldsymbol{H}$. Consider a 2D cylindrical optical black hole device, which is divided into two regions: the shell region is used to change the direction of wave propagation, and the core region is usually used to absorb the wave. The radially dependent permittivity distribution of the cylindrical black holes are:

$$\varepsilon_r(r) = \begin{cases} \varepsilon_1, & r > R_s \\ \varepsilon_1 \left(\frac{R_s}{r}\right)^2, & R_c \le r \le R_s \\ \varepsilon_2 + i\gamma & r < R_c \end{cases}, \tag{1}$$

where $\varepsilon_1$ is the relative permittivity of the surrounding medium, $\varepsilon_2 > \varepsilon_1$ is the relative permittivity of the core, $\gamma > 0$ is the loss, $r$ is the radial distance from the center of the black hole, and $R_s$ and $R_c$ are the radii of the shell and core of the black hole, respectively. To reduce the reflection of the electromagnetic waves, $R_c$ is chosen to satisfy $R_c = R_s \sqrt{\frac{\varepsilon_1}{\varepsilon_2}}$.

To simulate OBHs, we use an unsplit PML model developed in our previous work [1]:

$$\varepsilon_0 \varepsilon_r^* \frac{\partial \boldsymbol{E}}{\partial t} + \sigma^* \boldsymbol{E} = \nabla \times H_z, \tag{2}$$

$$\mu_0 \frac{\partial H_z}{\partial t} + \left(\sigma_{mx}^* + \sigma_{my}^*\right) H_z + \nabla \times \boldsymbol{E} + \sigma_{mx}^* \sigma_{my}^* Q_z + \sigma_{my}^* \frac{\partial P_y}{\partial x} - \sigma_{mx}^* \frac{\partial P_x}{\partial y} = 0, \tag{3}$$

$$\mu_0 \frac{\partial \boldsymbol{P}}{\partial t} = \boldsymbol{E}, \quad \mu_0 \frac{\partial Q_z}{\partial t} = H_z. \tag{4}$$

Here $\boldsymbol{P} = (P_x, P_y)'$ and $Q_z$ are auxiliary variables, and

$$\sigma^* = \begin{cases} \begin{bmatrix} \sigma & 0 \\ 0 & \sigma \end{bmatrix} & in\ \Omega_c, \\ \begin{bmatrix} \sigma_y & 0 \\ 0 & \sigma_x \end{bmatrix} & in\ \Omega_{pml}, \end{cases}, \ \varepsilon_r^* = \begin{cases} Re(\varepsilon_r), & in\ \Omega_c \\ \varepsilon_1, & in\ \Omega_{pml}, \end{cases}, \ \sigma_{m,i}^* = \begin{cases} 0, & in\ \Omega_c, \\ \sigma_{m,i}, & in\ \Omega_{pml}, \end{cases} (i = x, y),$$

where $\Omega_c$ denotes the black hole and surrounding medium region, and $\Omega_{pml}$ denotes the PML region.

Divide the time interval $I = [0, T]$ into N uniform subintervals $I_i = [t_{i-1}, t_i]$ by points $t_k = k\tau, k = 0, 1, ..., N$, where $\tau = \frac{T}{N}$. Introduce some difference operators:

$$\delta_\tau \boldsymbol{E}^{k+1} = \frac{\boldsymbol{E}^{k+1} - \boldsymbol{E}^k}{\tau}, \ \delta_\tau^2 \boldsymbol{E}^k = \frac{\boldsymbol{E}^{k+1} - 2\boldsymbol{E}^k + \boldsymbol{E}^{k-1}}{\tau^2}, \ \delta_{2\tau} \boldsymbol{E}^k = \frac{\boldsymbol{E}^{k+1} - \boldsymbol{E}^{k-1}}{2\tau}, \ \overline{\boldsymbol{E}}^{k+\frac{1}{2}} = \frac{\boldsymbol{E}^{k+1} + \boldsymbol{E}^k}{2}.$$

We construct a leap-frog scheme for (2)-(4): Find $\boldsymbol{E}_h^{k+1} \in \boldsymbol{V}_h^0$, $H_{z,h}^{k+\frac{3}{2}} \in U_h$ such that

$$\varepsilon_0 \left( \varepsilon_r^* \frac{\boldsymbol{E}_h^{k+1} - \boldsymbol{E}_h^k}{\tau}, \boldsymbol{\phi}_h \right) + \left( \sigma^* \overline{\boldsymbol{E}}_h^{k+\frac{1}{2}}, \boldsymbol{\phi}_h \right) = \left( H_{z,h}^{k+\frac{1}{2}}, \nabla \times \boldsymbol{\phi}_h \right), \tag{5}$$

$$\mu_0 \frac{\boldsymbol{P}_h^{k+\frac{3}{2}} - \boldsymbol{P}_h^{k+\frac{1}{2}}}{\tau} = \boldsymbol{E}_h^{k+1}, \quad \mu_0 \frac{Q_h^{k+1} - Q_h^k}{\tau} = H_{z,h}^{k+\frac{1}{2}}, \tag{6}$$

$$\begin{aligned} &\mu_0 \left( \frac{H_{z,h}^{k+\frac{3}{2}} - \boldsymbol{H}_{z,h}^{k+\frac{1}{2}}}{\tau}, \psi_h \right) + \left( (\sigma_{mx}^* + \sigma_{my}^*) \overline{H}_{z,h}^{k+1}, \psi_h \right) + \left( \nabla \times \boldsymbol{E}_h^{k+1}, \psi_h \right) \\ &+ (\sigma_{mx}^* \sigma_{my}^* Q_h^{k+1}, \psi_h) + \mu_0 \left( \nabla \times \overline{\boldsymbol{P}}_h^{*,k+1}, \psi_h \right) = 0, \end{aligned} \tag{7}$$

hold true for any $\phi_h \in \boldsymbol{V}_h^0$ and any $\psi_h \in U_h$, where $\boldsymbol{P}^* = (k_1 P_x, k_2 P_y)'$. Here $\boldsymbol{V}_h^0$ denotes the lowest-order edge element on either triangles and rectangles satisfying the PEC boundary conditions, and $U_h$ denotes the piecewise constant finite element space.

Our scheme can be proved to be conditionally stable under the constraint $\tau = O(h)$, and be convergent second order in both time and space. We simulated the cylindrical, elliptical and square optical black holes. Due to the page limit, we only present the cylindrical black hole example. We assume that the black hole is embedded in $S_iO_2$ with permittivity $\varepsilon_1 = 2.1$, and the core of the device is composed of n-doped silicon with permittivity $\varepsilon_2 + i\gamma = 12 + 0.7i$. The physical domain is chosen to be $[0, 45]\ \mu m \times [0, 45]\ \mu m$, and the physical parameters $R_{sh} = 8.4\mu m$, $R_c = R_{sh}\sqrt{\frac{\varepsilon_1}{\varepsilon_2}}$. The computational mesh is obtained by uniformly refining the coarse mesh given in Fig. 1 five times, and the time step is chosen as $\tau = 2.5 \cdot 10^{-17}$s, and the center frequency is $f = 100$THz.

To see how wave propagates in the black hole, we demonstrate one case with the incident source wave located at $x = 0, y \in [37.6, 41.5]\ \mu$m. In Figs. 1, we plot the calculated magnetic fields $H_z$ at different time steps. It is clear that the electromagnetic waves bend rapidly toward the core of the black hole, and the waves are totally absorbed inside the core of the device (cf. Figs. 1. Furthermore, we can easily see that there is almost no reflection, since the device is designed to match the surrounding material.

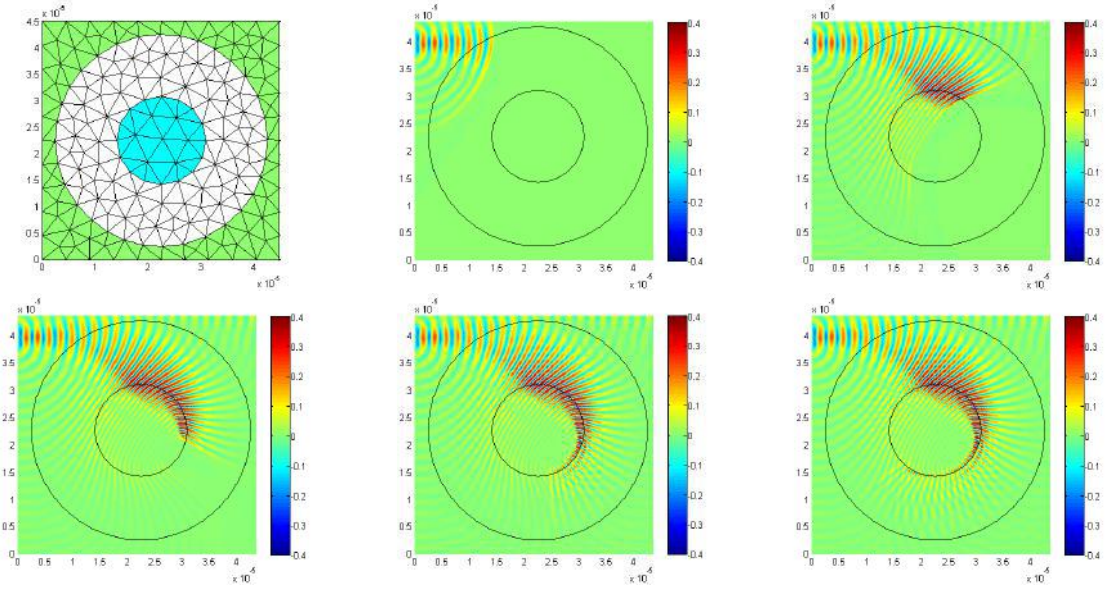


Figure 1: The sample coarse mesh, and snap shots of magnetic fields $H_z$ obtained at 2800, 8000, 12000, 16000, and 20000 steps.

**REFERENCES**


1. J. Li and Y. Huang, *Time-Domain Finite Element Methods for Maxwell's Equations in Metamaterials*, Springer, 2013.

# Optical diode based on unidirectional state exchange around an exceptional point

**Youngsun Choi, Choloong Hahn, Jae Woong Yoon, Seok Ho Song***

Department of Physics, Hanyang University, Seoul 133-791, Korea

*corresponding author: shsong@hanyang.ac.kr

**Abstract**-We theoretically propose optical diode design based on unidirectional state exchange. The proposed device consists of an index-modulated waveguide coupler in which the index profile is designed to encircle an exceptional point. Nonreciprocal transmission occurs as a result of inevitable non-adiabatic transition and unidirectional gain saturation. We explain the essential mechanism with non-Hermitian Hamiltonian formalism and numerically demonstrate 20 dB extinction ratio with experimentally presumable settings.

Exceptional point (EP) is a singular point of system's parameter space where system's eigenstates and eigenvalues are simultaneously degenerated. This singularity exists only in non-Hermitian systems. Recently, EP has attracted great attention because of its eigenvalue geometry which enable adiabatic state flip for evolution path encircling an EP [1, 2]. Dynamic states during encircling an EP do not necessarily follow adiabatic passages [3] as opposed to canonical Hermitian systems. Theoretical study on this subject has shown that the non-adiabatic evolution in the vicinity of an EP is due to inevitable instability of dissipating eigenstates in non-Hermitian systems and can be used for generating nonreciprocal quantum systems. This interesting property has been suggested for efficient unidirectional transfer of gas molecules between different vibrational states previously [4].

In this work, we utilize this non-Hermitian effect as a new principle for optical diodes. The proposed structure consists of two waveguide arms in which index profiles along the propagation axis mimic a quantum system adiabatically encircling an EP. Figure 1(a) summarizes the basic design generating such effect. In the proposed system, a symmetrically coupled mode incident from the left y-branch experiences anti-adiabatic evolution that maintains the mode's symmetry while the input from the right y-branch undergoes a normal-adiabatic state exchange that transfers the symmetry of the mode into the orthogonal, anti-symmetric output mode. Therefore, the left-to-right transmission yields efficient transmission of the optical signal and the right-to-left transmission is rejected due to symmetry mismatch at the output y-branch. The anti-symmetric output mode for the right-to-left transmission case is rejected due to symmetry mismatch occurring at the output y-branch. Through the y-branch, single waveguide mode and symmetrically coupled mode are converted to each other and anti-symmetrically coupled mode scattered out when encounter y-branch instead of coupled to single waveguide mode.

Two waveguide arms that mimic an encircling-an-EP evolution have core refractive indices $n_1 = n_c + \Delta n$ and $n_2 = n_c - \Delta n$, where $n_c$ is average index and index modulation $\Delta n$ is given by

$$\Delta n(z) = \Delta n_r \sin(2\pi z / L) + i\Delta n_i \left[1 - \cos(2\pi z / L)\right], \quad (1)$$

where $\Delta n_r$ and $\Delta n_i$ are real and imaginary modulation amplitudes, respectively, and $L$ is length of the arms. Real and imaginary core indices form two dimensional parameter space and EP is given by $(\mathrm{Re}\{\Delta n\}, \mathrm{Im}\{\Delta n\}) = (0, n_c\kappa/\beta)$ where $\kappa$ is average coupling constant and $\beta$ is average propagation constant of an isolated waveguide arm. Therefore, the circular parametric path encircles an EP for $2\Delta n_i > n_c\kappa/\beta$ and the unidirectional state exchange obtained during a state evolution through the waveguide arms.

Performance of an optimized device is numerically calculated using the finite element method included in Comsol Multiphysics package. In this calculation, we use parameters: $n_c = 1.55$, cladding index of 1.5, $\Delta n_r = \Delta n_i = 6\times10^{-4}$, waveguide core size of 1 μm, arm separation of 2 μm, arm length of 5 mm, and input power $I_0$ is 0.01 times of saturation intensity $I_s$. Note that we applied a saturated gain for the amplifying arm with a normal saturated gain of the form $\Delta n_i(I) = -\Delta n_i(0)(1-I/I_s)^{-1}$ to strictly break the time reversal symmetry between the left-to-right (forward) and right-to-left (backward) propagation through the

device. The result is shown in Figs. 1(b)~1(d). We obtain an extinction ratio of 20 dB as shown in Fig. 1(b). The extinction ratio and the device footprint are in-principle freely adjustable by optimizing desired coupling constant and index modulation amplitude. For example, the device footprint can be significantly reduced on Si-photonic or plasmonic waveguide platforms. It is worth mentioning that the proposed strategy for the nonreciprocal transmission is highly advantageous over the previous concepts based on parity-time symmetric Bragg gratings [5] and micro-resonator structure [6] since it is a wavelength-insensitive, broadband effect, not involving multiple interferences and phase-accumulative resonance excitations.

In this presentation, we will provide the basic principle of the proposed effect, device optimization, and fundamental performance limit in greater details. Specifically, the adiabatic condition for the state exchange and gain saturation for regulating over-amplified field will be intensively discussed as the main conceptual advance of our proposal. Experimental realization and associated practical device applications will be envisaged on this basis as well.

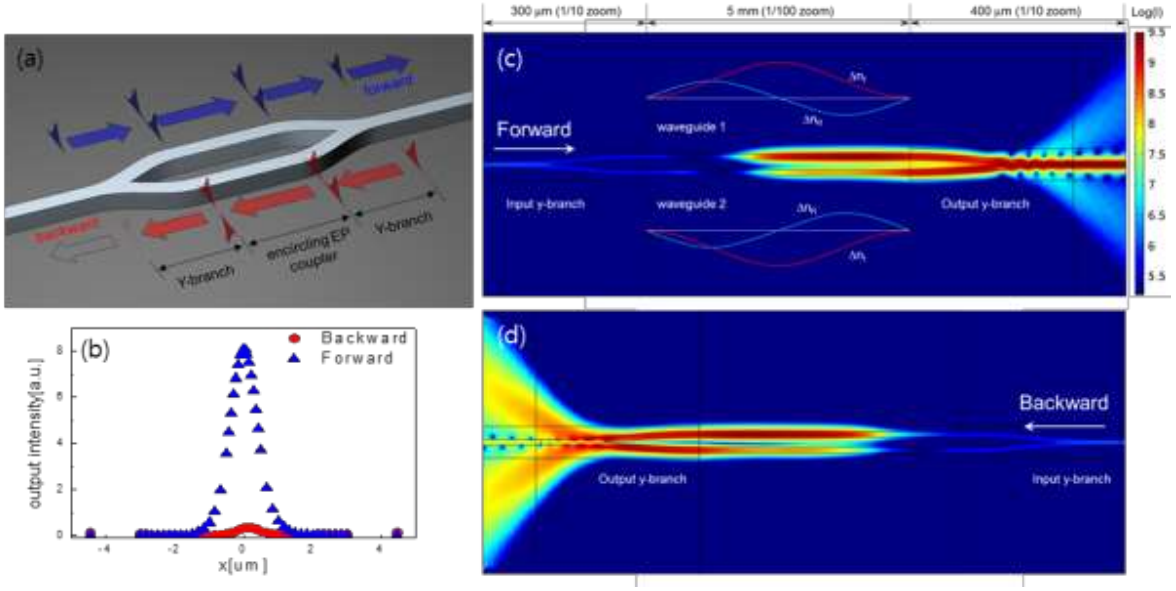



Figure 1. Schematic illustration of optical diode (a) and FEM simulation results: output intensities (b), field distribution for forward incidence (c) and backward incidence (d).

**Acknowledgements**, This research was supported in part by the Basic Science Research Program (No. NRF-2015R1A2A2A01007553) and by the Global Frontier Program through the National Research Foundation (NRF) of Korea funded by the Ministry of Science, ICT & Future Planning (No. NRF-2014M3A6B3063708).

## REFERENCES

1. C. Dembowski, H. D. Gräf, H. L. Harney, A. Heine, W. D. Heiss, H. Rehfeld, and A. Richter, "Experimental observation of the topological structure of exceptional points," Phys. Rev. Lett., Vol. 86, No. 5, 787–790, 2001.
2. T. Gao, E. Estrecho, K. Y. Bliokh, T. C. H. Liew, M. D. Fraser, S. Brodbeck, M. Kamp, C. Schneider, S. Höfling, Y. Yamamoto, F. Nori, Y. S. Kivshar, A. G. Truscott, R. G. Dall, and E. A. Ostrovskaya, "Observation of non-Hermitian degeneracies in a chaotic exciton-polariton billiard," Nature, Vol. 526, No. 7574, 554–558, 2015.
3. R. Uzdin, A. Mailybaev, and N. Moiseyev, "On the observability and asymmetry of adiabatic state flips generated by exceptional points," J. Phys. A Math. Theor., Vol. 44, No. 43, 435302, 2011.
4. I. Gilary and N. Moiseyev, "Asymmetric effect of slowly varying chirped laser pulses on the adiabatic state exchange of a molecule," J. Phys. B At. Mol. Opt. Phys., Vol. 45, No. 5, 051002, 2012.
5. Z. Lin, H. Ramezani, T. Eichelkraut, T. Kottos, H. Cao, and D. N. Christodoulides, "Unidirectional Invisibility Induced by P T -Symmetric Periodic Structures," Phys. Rev. Lett., Vol. 106, No. 21, 213901, 2011.
6. L. Chang, X. Jiang, S. Hua, C. Yang, J. Wen, L. Jiang, G. Li, G. Wang, and M. Xiao, "Parity–time symmetry and variable optical isolation in active–passive-coupled microresonators," Nat. Photonics, Vol. 8, No. 7, 524–529,

2014.

# Zero index metamaterial for enhanced transmission and beaming

**H. Hajian[1], E. Ozbay[1,2,3], and H. Caglayan[4*]**

[1]Nanotechnology Research Center, Bilkent University, 06800 Ankara, Turkey

[2]Department of Electrical and Electronics Engineering, Bilkent University, 06800 Ankara, Turkey

[3]Department of Physics, Bilkent University, 06800 Ankara, Turkey

[4]Department of Electrical and Electronics Engineering, Abdullah Gul University, 38080 Kayseri, Turkey

[*]corresponding author: humeyra.caglayan@agu.edu.tr

**Abstract**- Using a previously reported near-zero index (NZI) metamaterial, we theoretically investigate light transmission through a subwavelength metallic aperture. The NZI metamaterial is composed of two double-layer arrays of dissimilar metasurfaces of subwavelength dimensions which operates at 13-15 GHz. Our theoretical results show that the presence of the NZI system at the inner side of the aperture enhances the transmission of light through it. Moreover, when we use the metamaterial at the outer side, the light extraction from the aperture can be beamed.

Recently, metamaterials with near-zero refractive index have attracted much attention [1-2]. Light inside these materials experiences no spatial phase change and extremely large phase velocity, makes these peculiar systems applicable for realizing directional emission [3], tunneling waveguides [4], large-area single-mode devices [5] and electromagnetic cloaks [6]. In addition, epsilon-near-zero (ENZ) metamaterials can also enhance light transmission through a subwavelength aperture [7]. The previously demonstrated zero-index metamaterials have required the use of metallic inclusions which leads to large Ohmic losses, a serious impedance to device applications at high frequencies. Therefore, impedance-matched all-dielectric zero-index metamaterials which exhibit Dirac cone dispersions at center of the Brillouin zone, have been experimentally demonstrated at microwave regime [6] and optical frequencies [8] for transverse-magnetic (TM) polarization of light. More recently, it has been also proved that these systems can be realized in a miniaturized in-plane geometry useful for integrated photonic applications [9], i.e. these metamaterials can be integrated with other optical elements, including waveguides, resonators and interferometers.

In this abstract, using a previously a zero-index metamaterial at the inner and outer sides of a subwavelength aperture (2 mm width), we numerically study light transmission through and its extraction from the aperture. The metamaterial consists of a combination of two double-layer arrays of scatterers with dissimilar subwavelength dimensions (5.5 mm each unit cell) printed on either side of a dielectric sheet and separated by an air cavity. The unite cell of this system is schematically depicted in Fig. 1 of Ref. 1, and as it is shown in Fig. 2 of this paper, the metamaterial exhibits zero-index optical response in 13 to 15 GHz region. Our numerical investigation shows that the presence of the NZI metamaterial at the inner side of the aperture leads to a considerable increase in the transmission of light through the subwavelength aperture at $\lambda$=20 mm. This enhancement is related to the amplification of the amplitude of the electromagnetic field inside the metamaterial which drastically increases the coupling between free space and the slit. In case of having NZI structure at the both sides of the aperture, due to the inevitable Ohmic losses of the metallic inclusions of the metamaterial, there would be a decrease in the light transmission as compared with that of when we have metamaterial at only the inner side of the slit. However, a noticeable enhancement in the light transmission at 14.5 GHz can still be observed, in comparison

with that of a bare aperture. By obtaining the electric field profile of the light passing through the considered NZI/aperture/NZI system at this frequency we found out that in addition to the enhanced transmission there is an excellent beaming of the extracted light from the structure.

To conclude, we have theoretically shown that using a zero-index metamaterial at the inner and outer sides of a metallic subwavelength slit can considerably enhance the transmission of light through the aperture and beam its extraction, respectively.

**Acknowledgements**

This work has been supported by TUBITAK under Project No 114E505. The author H.C. also acknowledges partial support from the Turkish Academy of Sciences.

**REFERENCES**

1. Konstantinidis, K., and A. P. Feresidis, "*Broadband near-zero index metamaterials*", J. Opt. Vol. **17**, No. 10, 105104-1-7, 2015.
2. Soemphol, C., A. Sonsilphong, and N. Wongkasem, "*Metamaterials with near-zero refractive index produced using fishnet structures*" J. Opt. Vol. **16**, No. 1, 015104-1-6, 2014.
3. Enoch, S., G., Tayeb, P., Sabouroux, N., Gue´rin, and P., Vincent, "*A metamaterial for directive emission*". Phys. Rev. Lett. Vol. **89**, No. 21, 213902-1-4, 2002.
4. Silveirinha, M., and N. Engheta, "*Tunneling of electromagnetic energy through subwavelength channels and bends using1-near-zero materials*", Phys. Rev. Lett. Vol. **97**, No. 15, 157403-1-4, 2006.
5. Bravo-Abad, J., J. D., Joannopoulos, and M. Soljacic, "*Enabling single-mode behavior over large areas with photonic Dirac cones*", Proc. Natl Acad. Sci. USA, Vol. **109**, No. 25, 9761–9765, 2012.
6. Huang, X., Y. Lai, Z. H., Hang, H. Zheng, and C. T. Chan, "*Dirac cones induced by accidental degeneracy in photonic crystals and zero-refractive-index materials*", Nature Mater. Vol. **10**, 582–586, 2011.
7. Inampudi, S., D. C. Adams, T. Ribaudo, D. Slocum, S. Vangala, W. D. Goodhue, D. Wasserman, and V. A. Podolskiy, "*ε-near-zero enhanced light transmission through a subwavelength*", Phys. Rev. B Vol. **89**, No. 12, 125119-1-10, 2014.
8. Moitra, P., Y. Yang, Z. Anderson, I. I. Kravchenko, D. P. Briggs, and J. Valentine, "*Realization of an all-dielectric zero-index optical metamaterial*", Nature Photon. Vol. **7**, 791–795, 2013.
9. Li, Y., S. Kita, P. Muñoz, O. Reshef, D. I. Vulis, M. Yin, M. Lončar, and E. Mazur, "*On-chip zero-index metamaterials*" Nature Photon. Vol. **9**, 738–742, 2015.

# Dual Band Metamaterial Perfect Absorber with Nearly Polarization-Independent

**O. Ayop[1*], M. K. A. Rahim[1], N. A. Murad[1], N. A. Samsuri[1], F. Zubir[1], and H. A. Majid[2]**

[1]Faculty of Electrical Engineering, Universiti Teknologi Malaysia, Johor Bahru, Malaysia

[2]Faculty of Engineering Technology, Universiti Tun Hussein Onn Malaysia, Batu Pahat, Johor, Malaysia

[*]corresponding author: osman@fke.utm.my

**Abstract**-This paper presents the analysis of dual band metamaterial perfect absorber (MPA) with nearly polarization-independent in X-band frequency. The resonating elements are designed using a rectangular ring and slotted-cross structure. The resonating elements are printed on the top surface of FR4 substrate while a full copper layer is printed at the opposite surface. The performance of the dual band MPA is observed using CST software. From simulation, the proposed structure achieves almost perfect absorbance, which is 99.31% and 97.37% at 8 GHz and 12 GHz respectively for normal incident electromagnetic (EM) wave. For oblique incident angles, it is observed that the operating angle (50% absorption limit) is 77$^o$ for both TE and TM polarizations.

## INTRODUCTION

The use of metamaterials as EM absorber has attracted a lot of attention since recent years. This unusual behavior is first experimented by Landy [1] using a combination of electric resonator and cut wire. Thus, it performs the opposite of efficient EM reflectors [2] that are also designed based on metamaterial structure. Metamaterials can be represented using effective medium theory, involves effective permittivity and permeability [3]. One example of perfect dual band metamaterial absorber was proposed by H. Y. Zheng in [4] using Fabry-Perot cavity resonant. This metamaterial absorber achieved almost perfect absorbance for normal incident EM wave. However, the absorbing frequencies change into single resonant frequency when the incident angle is altered. The polarization-independent and wide operating angle metamaterial absorber has been presented in [5] based on circular ring structure. The resonant frequencies do not vary obviously with the different oblique incident EM wave but the operating angle is only up to 64$^o$. The proposed dual band PMA in this paper can improves the operating angle up to 77$^o$ with excellent absorbing performance.

## PROPOSED DESIGN, SIMULATION, AND DISCUSSION

The proposed dual band MPA is illustrated in Figure 1(a). The dimensions of the structure are $h=0.8mm$, $t=0.035mm$, $W=L=9mm$, $L_1=W_1=5.6mm$, $L_2=1.4mm$, $L_3=1.375mm$, $W_2=1.5mm$, and $w_e=0.25mm$. The performances of the dual band MPA are presented in Figure 1(b) (normal incident EM wave), Figure 2 (different polarization), Figure 3 (oblique: TE polarization), and Figure 4 (oblique: TM polarization). From Figure 1(b), since full copper plane is printed at the bottom surface of FR4 substrate, the transmittance, T(ω) is reduce to zero for all frequencies. Therefore the absorbance, A(ω) is determined only by reflectance, R(ω) where A(ω)=1-R(ω). Two peaks absorbance are observed at 8 GHz and 12 GHz with absorbencies of 99.31% and 97.37% respectively. The absorbing characteristic of dual band MPA for different polarization angle is shown in Figure 2. It shows that the absorbing characteristic of the dual band MPA is not much different for all observed polarization angles indicates that the structure is working nearly polarization-independent. The absorbing characteristic for different oblique angle of incident EM waves is shown in Figure 3 and Figure 4. It shows that the operating angle for TE polarization (Figure 3) and TM polarization (Figure 4) is 77$^o$. The operating angle for TE and TM polarization is the same due to the symmetrical structure.

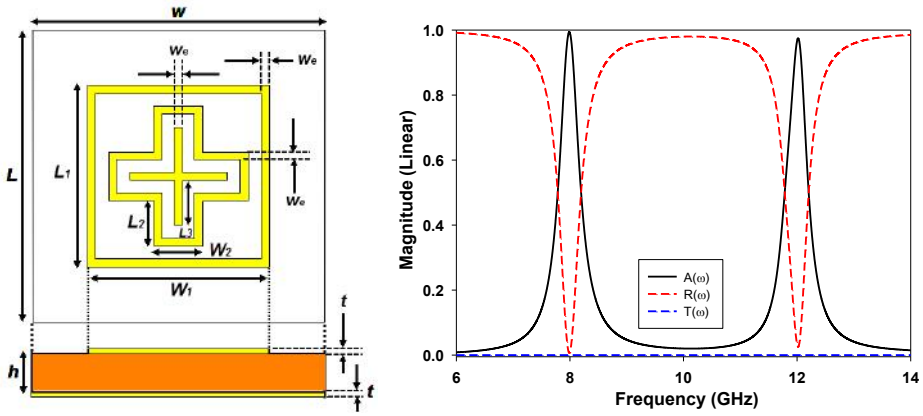



Figure 1: A unit cell of proposed dual band MPA (left) and the corresponding absorbing performance of dual band MPA for normal incident of EM wave (right).

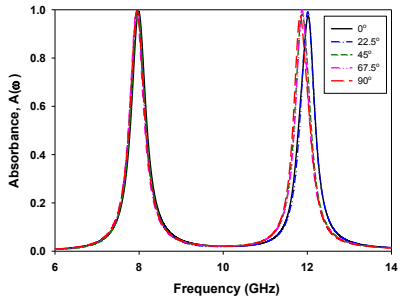



Figure 2: Simulated absorbance for different polarization angle.

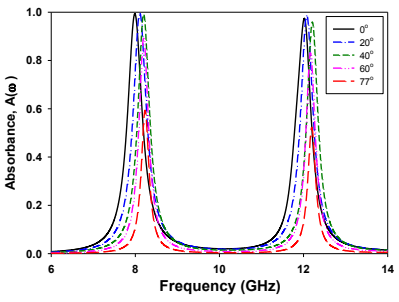



Figure 3: Simulated absorbance for TE polarization.

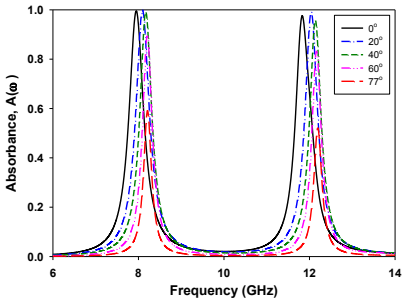



Figure 4: Simulated absorbance for TM polarization.

## CONCLUSION

A dual band metamaterial perfect absorber with nearly polarization-independent and wide operating angle in X-band has been presented. The symmetrical structure made this dual band MPA almost independent to any polarization state of incident EM wave.

## REFERENCES


1. Landy, N. I., S. Sajuyigbe, J. J. Mock, D. R. Smith, and W. J. Padilla, "Perfect metamaterial absorber," Physical Review Letters, Vol. 100, 207402, 2008.
2. Lee, S., N. Kim, and S. -Y. Rhee, "Design of novel artificial magnetic conductor as reflector and its SAR analysis," *Progress In Electromagnetics Research Sumposium Proceedings*, 325–328, 2012.
3. Zhang. X. and Y. Wu., "Effective medium theory for anisotropic metamaterials," *Scientific Reports*, Vol. 5, 7892, 2015.
4. Zheng. H. Y., X. R. Jin, J. W. Park, Y. H. Lu, J. Y. Rhee, W. H. Jang, H. Cheong, and Y. P. Lee, "Tunable dual-band perfect absorbers based on extraordinary optical transmission and Fabry-Perot cavity resonance," *Optics Express*, Vol. 20, No. 21, 24002−24009, 2012.
5. Ayop, O., M. K. A. Rahim, N. A. Murad, and N. A. Samsuri, "Dual-resonant polarization independent and wide-angle metamaterial absorber in X-band frequency," *Applied Physics A*, Vol. 122, No. 4, 2016.

# Metafilm consisting of spherical silica glass particles

**Zhanna Dombrovskaya[1], Anton Zhuravlev[2]**
[1]Lomonosov Moscow State University, Faculty of Physics, Russia
[*]corresponding author: dombzhanna@yandex.ru

**Abstract**-The polarizabilities of subwave spherical silica glass particles are investigated with taking material dispersion into account. It is shown that the ranges of negative values for electric and magnetic polarizabilities are practically coinciding. This permits to use such particles for constructing DNG medium. A method for simultaneously calculating the effective thickness and the effective refractive index of the metafilm is proposed.

# Wideband Metamaterial Absorber with Polarization-dependent Operation

**O. Ayop[1*], M. K. A. Rahim[1], N. A. Murad[1], N. A. Samsuri[1], F. Zubir[1], and H. A. Majid[2]**
[1]Faculty of Electrical Engineering, Universiti Teknologi Malaysia, Johor Bahru, Malaysia
[2]Faculty of Engineering Technology, Universiti Tun Hussein Onn Malaysia, Batu Pahat, Johor, Malaysia
[*]corresponding author: osman@fke.utm.my

**Abstract**-This paper presents the analysis of wideband metamaterial absorber (WBMMA). The behavior of the proposed WBMMA is polarization-dependent. The resonating elements are designed using a square patch with a circle shape removed at the center. A diamond slit is placed at the removed area and connected to the square patch with thin copper bridges. The resonating elements are printed on the top surface of FR4 substrate while a full copper layer is printed at the opposite surface. The performance of the WBMMA is observed using CST software. From simulation, the proposed structure achieves widest absorbing band which is 13.11% between 8.34 and 9.51 GHz for normal incident electromagnetic (EM) wave for polarization angle of $0^o$ and $90^o$. For oblique incident angles, it is observed that the operating angle (50% absorption limit) for wideband operation is limited to $20^o$ for both TE and TM polarizations.

## INTRODUCTION

For the recent years, a new branch of metamaterial (MM) research has been appeared which is metamaterial absorber (MMA). MMs have been proven to behave as perfect EM reflector [1]. However, by focusing to the imaginary part of refractive index of the structure, highly efficient EM absorber can be designed [2]. MMAs are normally working in very narrow bandwidth and need adjustment to increase its bandwidth [3]. A WBMMA with polarization-independent behavior has been presented in [4] based on modified circular ring structure. However, the wideband operation is only achieved for normal incident angle. Thus, this paper proposes a WBMMA that can improves the operating angle up to $20^o$ for wideband operation.

## PROPOSED DESIGN, SIMULATION, AND DISCUSSION

The proposed WBMMA is illustrated in Figure 1(a). The dimensions of the structure are $h=0.8mm$, $t=0.035mm$, $W=L=10mm$, $L_{sq}=W_{sq}=5.8mm$, $r=2.65$, $W_d=2.95mm$, $L_c=2.3mm$, $W_{rc}=0.24mm$, $L_s=1.2mm$, $W_s=0.2mm$, $L_b=0.68mm$, and $W_b=0.24mm$. The performances of the WBMMA are presented in Figure 1(b) (normal incident EM wave), Figure 2 (different polarization), Figure 3 (oblique: TE polarization), and Figure 4 (oblique: TM polarization). From Figure 1(b), $T(\omega)$ is zero for all frequencies due to the full copper plane. Therefore the absorbance, $A(\omega)=1-R(\omega)$ where $R(\omega)$ is refer to the reflectance value. Wideband absorption is observed between 8.34 and 9.51 GHz with full width half maximum bandwidth (FWHM) of 13.11%. The absorbing characteristic of WBMMA for different polarization angle is shown in Figure 2. It shows that the absorbing characteristic of the WBMMA is varied for different observed polarization angles indicate that the behavior of the structure is polarization-dependent. This is because the structure is not fully symmetrical for different rotating angle. The absorbing characteristic for different oblique angle of incident EM waves is shown in Figure 3 and Figure 4. It shows that the operating angle for TE polarization (Figure 3) and TM polarization (Figure 4) is $20^o$. The operating angle for TE and TM polarization is the same because the arrangement of the structure for $0^o$ (TM polarization) is the same with $90^o$ (TM polarization).

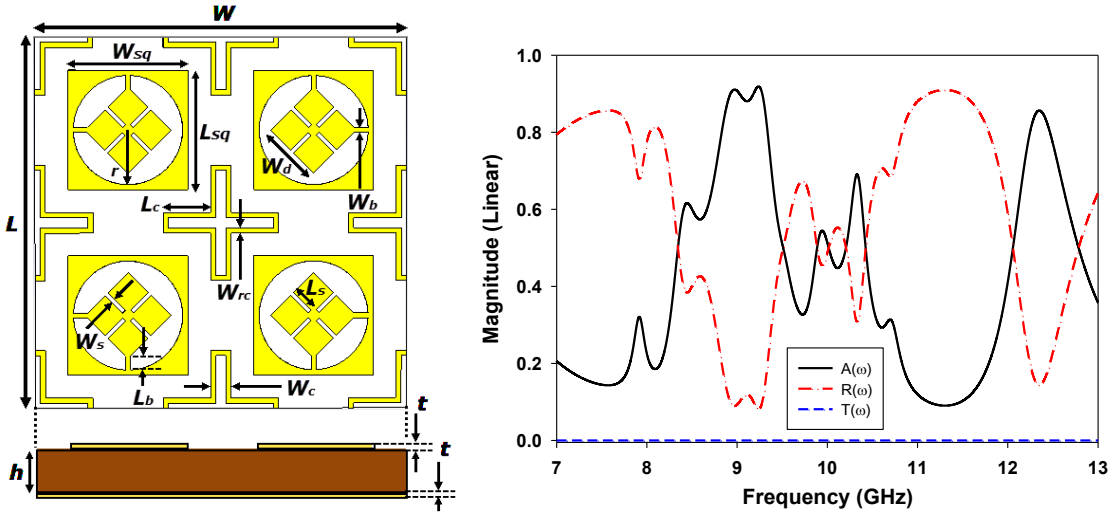



Figure 1: A unit cell of proposed dual band MPA (left) and the corresponding absorbing performance of dual band MPA for normal incident of EM wave (right).

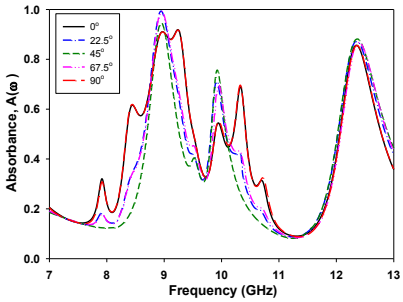



Figure 2: Simulated absorbance for different polarization angle.

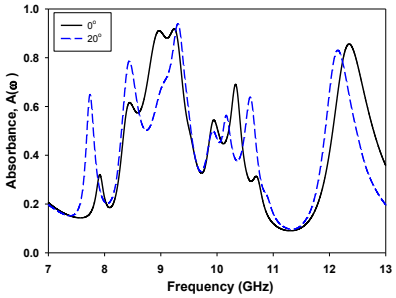



Figure 3: Simulated absorbance for TE polarization.

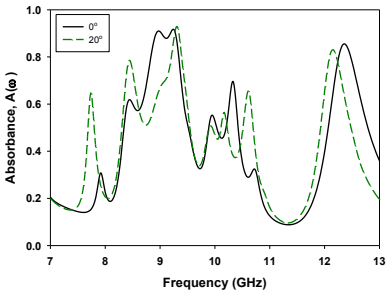



Figure 4: Simulated absorbance for TM polarization.

## CONCLUSION

The performance of new WBMMA is observed in term of polarization behavior and operating angle. From the investigation, the WBMMA is almost polarization-independent and maintain the wideband behavior up to $20^{o}$ incident angle.

## REFERENCES


1. Lee, S., N. Kim, and S. -Y. Rhee, "Design of novel artificial magnetic conductor as reflector and its SAR analysis," Progress In Electromagnetics Research Sumposium Proceedings, 325–328, 2012.
2. He. X.-J., Y. Wang, J.-M. Wang, and T.-L. Gui, "Dual-band terahertz metamaterial absorber with polarization insensitivity and wide incident angle," *Progress In Electromagnetics Research*, Vol. 115, 381−397, 2011.
3. Luo. H., Y.Z. Cheng, and R.Z. Gong, "Numerical study of metamaterial absorber and extending absorbance bandwidth based on multi-square patches," *Eur. Phys. Journal B*, Vol. 81, 387−392, 2011.
4. Ayop. O., M. K. A. Rahim, N. A. Murad, and N. A. Samsuri, "Wideband polarization-insensitive metamaterial absorber with perfect dual resonances," *Applied Physic A*, Vol. 122(4), 316, 1-7, March 2016.

# Transmission properties of electromagnetic waves incident to moiré superlattices exhibiting quasiperiodic interference patterns

**Jung-Wan Ryu[1*], Jae_hyung Han[2], Inbo Kim[2], and Muhan Choi[2]**

[1]Center for Theoretical Physics of Complex Systems, Institute for Basic Science, Daejeon 34051, South Korea

[2]School of Electronics Engineering, Kyungpook National University, Daegu, 702-701, South Korea

[*]corresponding author: jungwanryu@gmail.com

**Abstract**-We report the transmission properties of electromagnetic waves incident to moiré superlattices with arbitrary rotation angles, which exhibit quasiperiodic as well as periodic interference patterns. We also discuss the potential applications of the moiré superlattice, such as tunable metamaterials of which refractive index can be controlled macroscopically.

Metamaterials are artificial materials with the designed structures shorter than the wavelength of interests. These sub-wavelength structures produce the unique properties due to strong coupling through the electric and magnetic components of the incident electromagnetic waves. However, many applications of metamaterials are inhibited by the lack of tuning capabilities due to the predetermined nature of the sub-wavelength structures.

Recently, a new type of reconfigurable metamaterials in which the size and shape of the sub-wavelength cluster can be changed simultaneously using moiré interference was proposed [1]. The moiré pattern is formed by overlapping two transparent layers, each of which has a periodic metallic pattern. The periodicity, size, and shape of the resulting moiré pattern can be varied by changing the relative superposition angle of the two layers. The transmission of electromagnetic waves can be controlled via the structural change of the resulting moiré patterns because the geometrical periodicity, shape, and size of the meta-atom are the crucial factors that determine the resonance feature of the metamaterials.

In this work, we report the transmission properties of electromagnetic waves incident to moiré superlattices with arbitrary rotation angles, which exhibit quasiperiodic as well as periodic interference patterns. We also discuss the potential applications of the moiré superlattice, such as tunable materials of which refractive index can be controlled macroscopically.

**Acknowledgements**: This research was supported by Basic Science Research Program through the National Research Foundation of Korea (NRF) funded by the Ministry of Education (No.000). J.-W. Ryu was supported by Project Code (IBS-R024-D1).

**REFERENCES**

1. Han, J.-H., Kim, I., Ryu, J.-W., Kim, J., Cho, J.-H., Yim, G.-S., Park, H.-S., Min, B., and Choi, M., "Rotationally reconfigurable metamaterials based on moiré phenomenon," *Optics Express*, Vol. 23, No. 13, 17443–17449, 2015.

# Modeling of 1D Dc-SQUID Metamaterials

**O.V. Shramkova[*1], N. Lazarides[1], A.V. Ustinov[2,3], G.P. Tsironis[1,3]**
[1]Crete Center for Quantum Complexity and Nanotechnology, University of Crete, 71003 Heraklion, Greece
[2]Physikalisches Institut, Karlsruhe Institute of Technology, 76131 Karlsruhe, Germany
[3]National University of Science and Technology, MISiS, 119049 Moscow, Russia
[*]corresponding author: oksana@physics.uoc.gr

**Abstract**- We have created and examined the properties of superconducting metamaterial consisting of direct current (dc-) superconducting quantum interference device (SQUID) and superconducting rod meta-atoms.

A new generation of artificial superconducting materials has opened up new opportunities for engineering the media with the specified properties 1,2] . The recent studies indicate that metamaterial structures with superconducting elements provide both loss reduction and wideband tunability by varying the temperature or an external magnetic field. In the present work we consider one-dimensional superconducting metamaterials that is tunable over a broad frequency range. The building block of this metamaterial medium is a direct current (dc-) superconducting quantum interference device (SQUID) made of a superconducting loop interrupted by two Josephson junctions (JJ). A sketch of such a device is presented in Fig.1 (a). The time-dependent magnetic field **H**(t) is applied perpendicular to the area of the SQUID loop. As long as dc-SQUID can be considered like a single junction with an effective critical current, the equivalent lumped circuit for the dc-SQUID in a magnetic field comprises a flux source $\Phi_{ext}$ in series with the geometric inductance of the SQUID loop and JJ shunted by effective capacitor $C^*$ and effective resistor $R^*$ (Fig.1(b)). In order to find the medium with simultaneously negative permittivity and permeability, we combine the dc-SQUIDs with superconducting rods (Fig.1(c)). The propagation of waves in a one-dimensional array of meta-atoms is considered. We have

obtained the frequencies corresponding to the electrical and magnetic resonances. The dependence of the propagation characteristics on the parameters of meta-atoms was studied. Such metamaterials are tunable with dc magnetic field and frequency. Fig. 2 shows numerical results for transmission coefficient carried out by software package COMSOL Multiphysics.

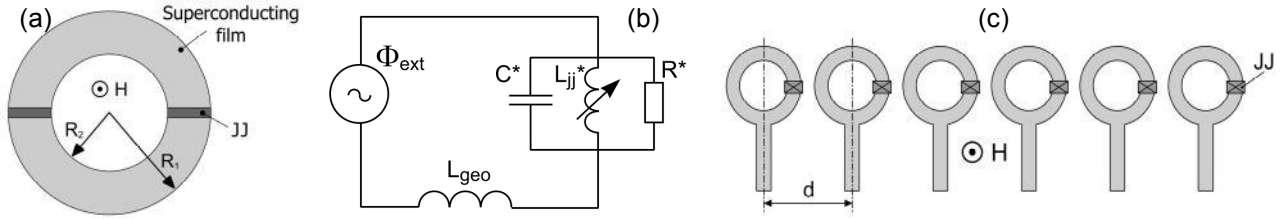



Fig.1. (a) – Schematic drawing of a dc-SQUID, (b) – Equivalent electrical circuit for a single SQUID, (c) – 1D SQUID metamaterials.

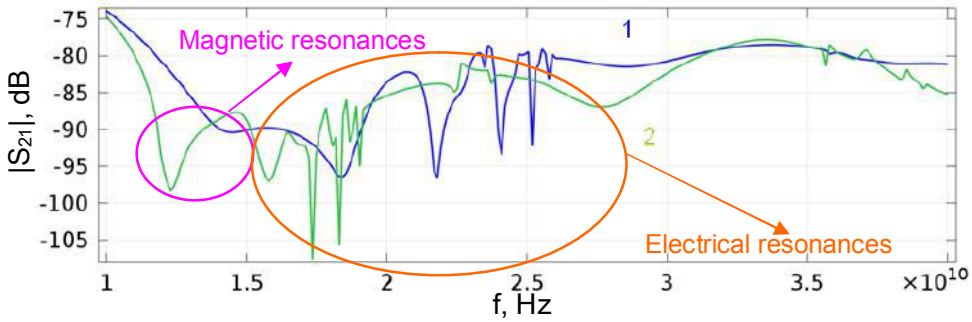



Fig.2. $|S_{21}|$ of the 12 dc-SQUID array as a function of frequency at $w_r$=250 μm ($w_r$ is the thickness of the rod), $R_1$=400 μm, $R_2$=150 μm, d=2400 μm; 1– $l_r$=4000 μm; 2 – $l_r$=6000 μm ($l_r$ is the length of the rod)

**Acknowledgements**: The research work was partially supported by the European Union Seventh Framework Program (FP7-REGPOT-2012-2013-1) under grant agreement No. 316165. Partial support by the Ministry of Education and Science of Russian Federation in the framework of Increase Competitiveness Program of the NUST MISIS (contracts no. K2-2014-025, K2-2015-002 and K2-2015-007 ) is gratefully acknowledged.

## REFERENCES

1. Lazarides, N. and Tsironis G. P. “rf superconducting quantum interference device metamaterials,” *Appl. Phys. Lett.*, Vol.90, No. 16, 163501, 2007.
2. Anlage S. M. “The physics and applications of superconducting metamaterials,” *J. Opt.* , Vol. 13 , 024001, 2011.

# Second-harmonic generation from toroidal moments of all-dielectric metasurfaces

**D. Timbrell**[1], **and N. C. Panoiu**[1]

[1]Department of Electronic and Electrical Engineering, University College London, Torrington Place, London, WC1E 7JE, United Kingdomm
uceedti@ucl.ac.uk

**Abstract**—
We present an all-dielectric metamaterial with a pronounced nonlinear electromagnetic field due to a strong toroidal dipole. A unit cell consisting of 4 GaAs cuboids is excited with a plane wave, causing the displacement currents of each component to couple, forming a toroidal moment. The power radiated by the dipoles is calculated at both the fundamental frequency and second harmonic. The engendered toroidal dipole is shown to be the primary origin of the second harmonic signal, which is magnetic in nature.

Since Zel'dovich's discovery in 1957[1], toroidal moments have been shown to be the third family class of electromagnetic excitations which must be separately considered alongside the electric and magnetic groups. The most primitive member of this group, the toroidal dipole, is formed from a closed loop of magnetic moments. While these electromagnetic moments have been shown to exist within natural media[2], they are usually justifiably neglected[3].

Toroidal metamaterials are often based on the plasmonic resonances of metallic meta-atoms[4], such as split ring resonators. Recently, toroidal moments have been shown to exist in all-dielectric structures[5][6]. In this paper, we theoretically and computationally demonstrate a metamaterial consisting of four GaAs cuboids, which exhibits a second harmonic (SH) resonance stemming primarily from the toroidal dipole. Dipoles are the most basic elements of the electromagnetic

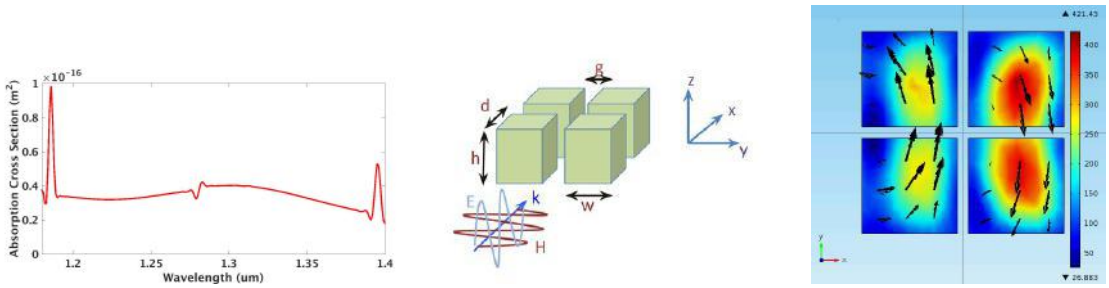



Figure 1: Left: The computed absorption cross section of the GaAs metamaterial. A distinct resonance at 1.28$\mu$m is present. Centre: The structure in question, with structural parameters in microns: d = 0.4 g = 0.05, h = 0.3, w = 0.4. Right: The computed normalised magnetic field, $|\mathbf{H}|$, at an incident wavelength of 1.25$\mu$m. Arrows show the instantaneous directions of the magnetic field.

multipole expansion. The electric, magnetic and toroidal dipoles are given, respectively, by the following expressions:

$$\mathbf{p} = \frac{1}{i\omega}\int \mathbf{J} d^3\mathbf{r} \tag{1}$$

$$\mathbf{m} = \frac{1}{2c}\int \mathbf{r}\times\mathbf{J} d^3\mathbf{r} \tag{2}$$

$$\mathbf{T} = \frac{1}{10c}\int ((\mathbf{r}\cdot\mathbf{J})\mathbf{r} - 2r^2\mathbf{J}) d^3\mathbf{r} \tag{3}$$

where $\mathbf{J}$ is the current density. In metamaterials made from noble metals such as gold and silver, the current density arises from the plasma electrons stemming from the Drude model. In

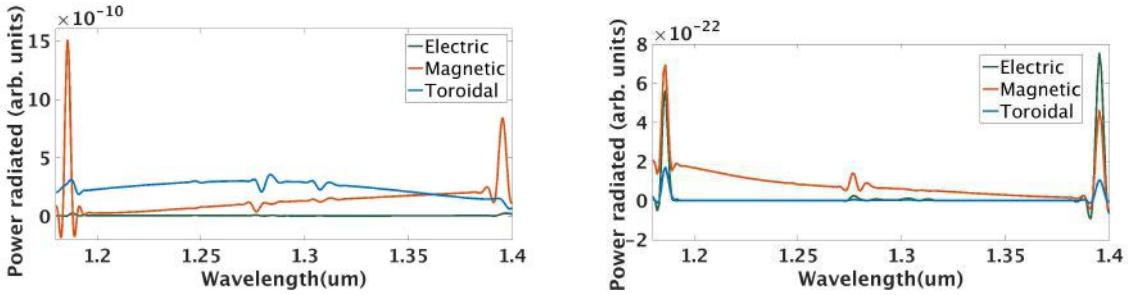



Figure 2: Left - The power radiated at the fundamental field by the structure. The toroidal dipole is clearly dominant for a range of frequencies. Right - The SH field produced by the toroidal field. The resonance at 1.28$\mu$m is still visible. In this regime, the emitted field is mostly magnetic in nature.

the context of dielectric structures, however, it is the displacement current resonances on which the metamaterial resonances rely.

An incident plane wave, with the electric field polarized along the $z$-direction causes displacement currents to arise within the structure, which form a loop. The four generated magnetic moments couple to produce this toroidal dipole.

Figure 1 contains the computed absorption cross section along with the structure and dimensions. The normalised magnetic field is also calculated for where the toroidal field is dominant, with the arrows depicting the instantaneous direction of the field. Figure 2 delineates the power radiated by the structure at both the fundamental frequency (FF) and SH. It is clear that the radiated power at the FF predominantly belongs to the toroidal dipole. While toroidal moments in nature are most often negligible, we present here an all-dielectric metamaterial which hosts a strong toroidal moment producing its own electromagnetic field at the SH, which, as can be seen in Figure 2, is primarily magnetic in nature.

This structure therefore allows the lesser-studied toroidal family to be more rigorously analysed.


## ACKNOWLEDGMENT

This work was supported by EPSRC.


## REFERENCES


1. Zel'dovich, Ya. B., "Title of the journal paper," *Zh. Eksp. Teor. Fiz.*, Vol. 33, No. 1531, 1957
2. Fedotov, V. A., K. Marinov, A. D. Boardman and N. I. Zheludev, 1, "On the aromagnetism and anapole moment of anthracene nanocrystals," *New Journal of Physics*, Vol. 9, No. 95, 2007.
3. Savinov, V., V. A. Fedotov and N. I. Zheludev, "Toroidal dipolar excitation and macroscopic electromagnetic properties of metamaterials" *Physical Review B* Vol. 89, No. 205112, 2014.
4. Kaelberer, T., V. A. Fedotov, N. Papasimakis, D. P. Tsai and N. I. Zheludev, "Toroidal Dipolar Response in a Metamaterial," *Science*, Vol. 330, No. 1510, 2010.
5. Basharin, A. A., M. Kafesaki,E. N. Economou, C. M. Soukoulis, V. A. Fedotov, V. Savinov and N. I. Zheludev. "Dielectric Metamaterials with Toroidal Dipolar Response," *Physical Review X* Vol. 5, No. 011036, 2015.
6. Miroshnichenko, A. E., A. B. Evlyukhin, Y. F. Yu, R. M. Bakker, A. Chipouline5, A. I. Kuznetsov, B. Lukyanchuk, B. N. Chichkov and Y. S. Kivshar, "Nonradiating anapole modes in dielectric nanoparticles," *nature communications*, Vol. 6, No. 8069, 2015.

# Simultaneous Phase-Matching in Dirac-Cone-Based Zero-Index Metamaterials

**O. Reshef, Y. Li, M. Yin, L. Christakis, D. I. Vulis, P. Camayd-Muñoz, S. Kita, M. Lončar, and E. Mazur**

John A. Paulson School of Engineering and Applied Sciences, Harvard University
mazur@seas.harvard.edu

**Abstract**— Zero-index metamaterials exhibit unique nonlinear properties. Using nonlinear scattering theory, we simulate nonlinear signal generation in 2-dimensional zero-index metamaterials based on a photonic Dirac cone at the Γ point. We observe phase-matching in multiple simultaneous directions, consistent with a refractive index of zero.

## 1. INTRODUCTION

Dirac cones at the center of the Brillouin zone have been used to achieve a metamaterial with a refractive index of zero[1, 2, 3]. Previously, simultaneous bi-directional phase-matching behaviour has been demonstrated using an anisotropic zero-index metamaterial (ZIM)[4]. Here, we use nonlinear scattering theory [5, 6] to simulate an isotropic on-chip ZIM based on photonic Dirac cones and demonstrate simultaneous phase-matching in all directions.

## 2. PHOTONIC DIRAC-CONE-BASED ZIM

We investigate two platforms: a 2D square array of silicon pillars in air (pitch = 845 nm, radius = 171 nm) and a 2D square array of air holes in a silicon bulk (pitch = 583 nm, radius = 182 nm). These metamaterials are designed to exhibit a Dirac cone at the center of their respective Brillouin zones (Fig. 1), indicating an effective refractive index of zero.

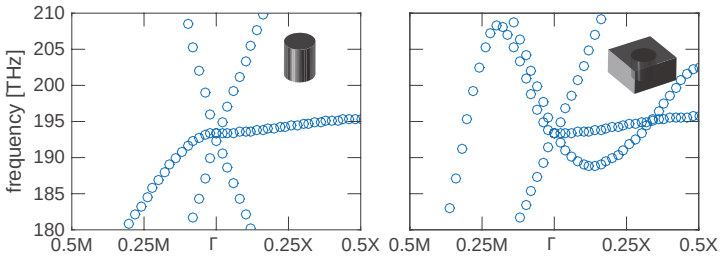



Figure 1: The band structures for 2D square arrays of rods (left) and air holes (right) are designed to exhibit Dirac cones at the center of the Brillouin zone, corresponding to an effective refractive index of zero.

## 3. NONLINEAR SCATTERING THEORY

Using nonlinear scattering theory, we calculate the relative intensity of the nonlinear signal generated within a medium using $I_{\mathrm{NL}} \propto \left| \chi^{(3)} \int \vec{E} \cdot \vec{P}_{\mathrm{NL}} \, dV \right|^2$ [5]. We verify this method by simulating degenerate four-wave mixing (FWM) within bulk materials with dispersionless refractive indices of $n = 2$, 1, 0.5, and 0.01 (Fig. 2). As expected, the coherence lengths for these interactions are infinite for light that is generated in the forward-propagating direction, regardless of the material index. On the other hand, the coherence length increases in the backward-propagating direction as the index decreases, in good agreement with the predicted value of $L_{\mathrm{coh}} = \pi c / 2\omega n \approx 400\,\mathrm{nm}/n$.

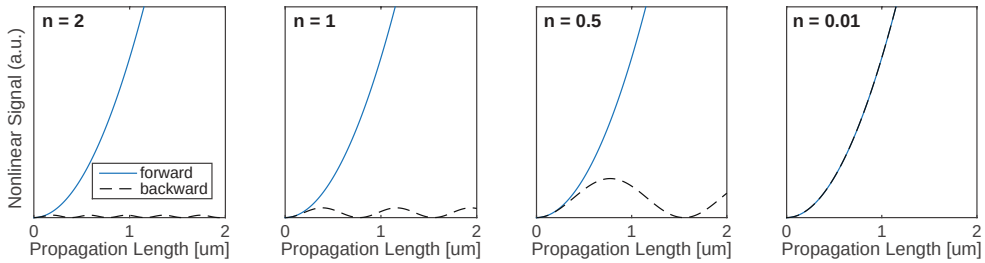



Figure 2: Generated nonlinear signal computed using the nonlinear scattering method for dispersionless bulk media, exhibiting different backward-phase-matching behavior as a function of index.

## 4. PHASE-MATCHING IN DIRAC-CONE-BASED ZIMS

Using the method outlined in Section 3, we calculate the nonlinear signal generated in both the rod-based and air hole-based ZIMs as a function of propagation length (Fig. 3a-b). We normalize the intensities to the peak intensity measured. The generated intensities all grow quadratically in all propagation directions, indicating perfect phase-matching. This result qualitatively resembles the $n = 0.01$ case in Fig. 2. We also observe phase-matching behavior when increasing the size of the ZIM laterally, orthogonally to the direction of the input pump (Fig. 3c).

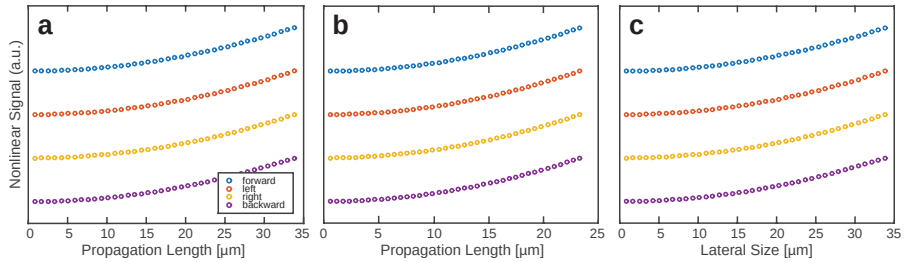



Figure 3: Nonlinear signals computed for (a) rod-based and (b) air hole-based ZIMs as a function of propagation length. The nonlinear signal also grows quadratically as the device increases in the lateral direction (c).

## 5. CONCLUSION

We have used nonlinear scattering theory in 2-dimensional Dirac-cone-based ZIMs to demonstrate the simultaneously phase-matched generation of nonlinear signal in multiple directions, consistent with a refractive index of zero. This phase-matched signal generation is independent of shape, ZIM size, and excitation direction.

## REFERENCES


1. Y. Li, S. Kita, P. Muñoz, O. Reshef, D. I. Vulis, M. Yin, M. Lončar, and E. Mazur, "On-chip zero-index metamaterials," Nature Photonics **9**, 738–742 (2015).
2. X. Huang, Y. Lai, Z. H. Hang, H. Zheng, and C. T. Chan, "Dirac cones induced by accidental degeneracy in photonic crystals and zero-refractive-index materials." Nature Materials **10**, 582–586 (2011).
3. P. Moitra, Y. Yang, Z. Anderson, I. I. Kravchenko, D. P. Briggs, and J. Valentine, "Realization of an all-dielectric zero-index optical metamaterial," Nature Photonics **7**, 791–795 (2013).
4. H. Suchowski, K. O'Brien, Z. J. Wong, A. Salandrino, X. Yin, and X. Zhang, "Phase Mismatch-Free Nonlinear Propagation in Optical Zero-Index Materials," Science **342**, 1223–1226 (2013).
5. K. O'Brien, H. Suchowski, J. Rho, A. Salandrino, B. Kante, X. Yin, and X. Zhang, "Predicting nonlinear properties of metamaterials from the linear response," Nature Materials **14**, 379–383 (2015).
6. J. Butet and O. J. F. Martin, "Evaluation of the nonlinear response of plasmonic metasurfaces: Miller's rule, nonlinear effective susceptibility method, and full-wave computation," Journal of the Optical Society of America B **33**, A8–A15 (2016).

# RF ENERGY HARVESTING STUDY USING VARIABLE METAMATERIAL STRUCTURE

**M. K. A Rahim, N. A. Samsuri, and M. S. Zainudin**
Faculty of Electrical, Universiti Teknologi Malaysia, Malaysia
mkamal@fke.utm.my

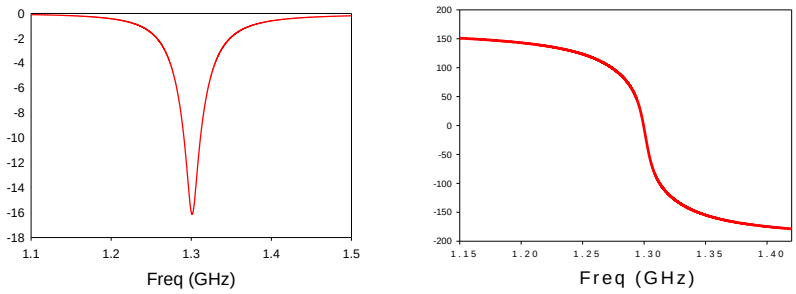
**Abstract**- A metamaterial Split Ring Resonators (SRR) structure for electromagnetic energy harvesting is presented. The resonance phenomenon inside the SRR structure indicates the capability to capture the electromagnetic energy from the electromagnetic wave. This paper shows the pattern of the energy radiation in the structure. Three structures are presented which is circle, square and hexagon with single ring structure. The SRR structures are operated at 1.3 GHz and the square structure shows highest density of electric field, which contribute in energy harvesting study.

The increasing of research in wireless communication systems nowadays continuously challenge antenna engineers to develop a novel antenna structure or improves the performance of existing antenna designs[1]. Energy harvesting put wireless communication world into another level in research field. Previous researches has proven that electricity can be harvested from the radio frequency wavelength in the atmosphere. For many years, the rectenna is the most popular method for energy harvesting from the microwave signal. A simple rectenna consists of a dipole antenna with an RF diode connected across the dipole element. A low power dual circularly polarized rectenna is presented by [2]. Operating at 2.45 GHz, the rectifier was optimized for -15dBm per access, with an output DC voltage of 215 mV.

In this research, the energy harvesting is approached with metamaterial structure, by using a single ring structure. Previous research [3] used the square design of single SRR structure. In this study, another two designs of single SRR structure are proposed, which is circle and hexagon. It is expected that different shape may affect the performance significantly. The proposed structures operate at 1.3 GHz with same material of patch, substrate and ground plane. The patch and ground plane uses a copper sheet with electrical conductivity of 5.8 × 107 and thickness of 0.035mm. The thickness, loss tangent, relative permittivity and permeability of the FR-4 substrate are 3.2 mm, 0.025, 4.3 and 1, respectively. The unit cell of the proposed SRR structure is shown in Table 1.0.

All structures considered in this study are simulated by using CST software. The waveguide port are using in this simulation, which the setting of electric field (E-field) propagate in the direction of xz-axis and magnetic field (H-field) propagate at yz-axis. Notice that magnetic permeability in only achievable via parallel polarization, where the vector is parallel to the SRR plane and the H-field is along the z-axis[4]. At the resonance, SRR plane perpendicular with the magnetic field and induces current loop. Since the wave vector is parallel to the SRR plane, the type of polarization is called parallel polarization for the convention.

Simulated result shows that the square shape give the highest value of E-field compared with the others two design. The result are influent by the bare surface per area that perpendicular with the H-field. Since the H-field

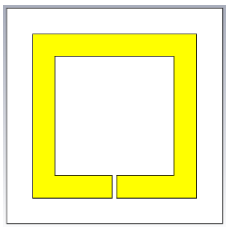
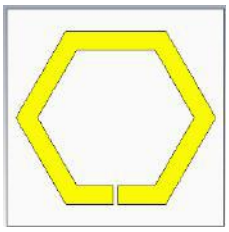
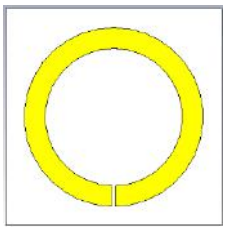
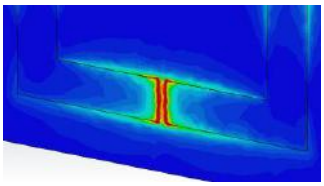
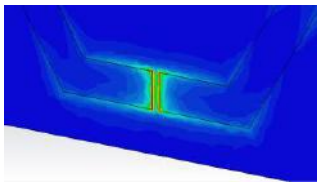
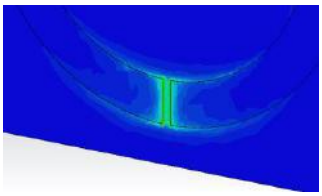



(a) (b)

Figure 1 : Simulated S-parameter for the unit cell (a) Magnitude and (b) Phase

oscillates at yz-plane, square shape has the highest surface per area that parallel with the H-field propagation. For hexagon, the bent shape at the left and right cause the H-field are not orthogonal with the structure. Hence, induces current are not fully generate for hexagon type. Same with circle, although it resonate at 1.3 GHz, the structure can't produce the highest induce current because bare surface area that parallel with the H-field are low compared others two design. Based on simulation, square SRR structure are chosen as the structure to harvest energy in electromagnetic wave.

Table 1 : The ilustration of single Split Ring Resonator for square, hexagon and circle design structure

| **Structure** | **Square** | **Hexagon** | **Circle** |
|---|---|---|---|
| **Ilustration** |  |  |  |
| Electric Field (V/m) | 128,500 | 99,990 | 93,909 |
| Electric Field Animation |  |  |  |

**Reference**


[1] M. K. Taher Al-Nuaimi and W. G. Whittow, "Novel planar AMC for low profile antenna applications," *Loughbrgh. Antennas Propag. Conf. LAPC 2009 - Conf. Proc.*, no. November, pp. 145–148, 2009.

[2] W. Haboubi, H. Takhedmit, J. L. S. Luk, S. Adami, and B. Allard, "An Efficient Dual-Circularly Polarized Rectenna for RF Energy Harvesting in the 2 . 45 GHz ISM Band," vol. 148, pp. 31–39, 2014.

[3] T. S. Almoneef and O. M. Ramahi, "Harvesting electromagnetic energy using metamaterial particles," *IEEE Antennas Propag. Soc. AP-S Int. Symp.*, pp. 1046–1047, 2013.

[4] K. Aydin and E. Ozbay, "Identifying magnetic response of split-ring resonators at microwave frequencies," *Opto-Electronics Rev.*, vol. 14, no. 3, pp. 193–199, 2006.

# Analysis of TM surface plasmons at Graphene-MTM interface

**R. J. El-Khozondar[1], H. J. El-Khozondar[2], M. M. Shabat[3]**

[1]Physics Department, Al-Aqsa University, Gaza, Palestine
[2]Electrical Engineering Department, Islamic University, Gaza, Palestine
[3]Physics Department, Islamic University, Gaza, Palestine
*corresponding author, E-mail: hkhozondar@iugaza.edu.ps

## Abstract

A new waveguide is proposed which consists of thin graphene layer on top of MTMs and covered by dielectric. The graphene conductivity ($\sigma$) is taken to be constant with positive imaginary part. Therefore, we studied the possible propagation of Transverse Magnetic (TM) surface plasmon (SP) in terahertz range of frequency. The effective refractive index as a function of frequency at different MTM's parameters is plotted using Maple 17. Results show that effective refractive index is hardly changing with frequency; however, it changes as MTM parameters change. The designed structure can be used as low dispersion and low attenuation waveguide which very useful for communication systems.

## 1. Introduction

THz radiation have several range of applications including astronomy to sense the interstellar, communications, and spectroscopic applications to classify the materials [1, 2]. THz science requires the development of novel materials to manufacture new device components. In our work, we proposed waveguide consists of graphene thin layer at the boundary between Metamaterials (MTMs) and dielectric. Graphene is a material composed of 2D hexagonal lattice of carbon atoms. It has special properties such as high mobility, optical transparency, and tunability by applied gate voltage. Numerous arrangements of antenna were designed built on graphene [3,4]. Further, surface plasmon modes in the terahertz and infrared ranges supported by graphene ribbon waveguides were investigated [5] which can be constructing material for MTMs. MTMs are synthetic material with negative permittivity and/ or permeability. A substantial amount of research were conducted to study these materials [6-8]. Several studies has studied their applications in sensors [9], isolators [10], and transmission lines [11].

The focus of this study is on understanding the effect of MTM parameters keeping the on the proposed structure keeping the product of the permittivity and permeability of MTM = 4 [12]. The proposed waveguide structure is introduced in section 2. Section 3 presents the results of the proposed structure. The conclusion is given in section 4.

## 2. Theoretical model

Fig. 1 shows the schematic of the proposed waveguide structure. The proposed structure is a graphene layer sandwiched between dielectric form above and MTM from below. The dielectric has positive permeability $\varepsilon_1$ and positive permeability $\mu_1$. MTM has both negative permeability $\varepsilon_2$ and positive permeability $\mu_2$. The graphene monolayer is characterized by a surface conductivity σ. In this model, σ is considered to have positive imaginary part. Thus, graphene can only support surface plasmons (SP) in Transvers Magnetic field (TM) [13].

When the imaginary part of graphene conductivity is positive, the graphene layer functions as a thin metal layer. The field components of TM modes are [14]

$$H_y = \begin{cases} A_1 e^{-\gamma_1 x} & 0 < x < \infty \\ A_2 e^{\gamma_2 x} & -\infty < x < 0 \end{cases} \quad (1)$$

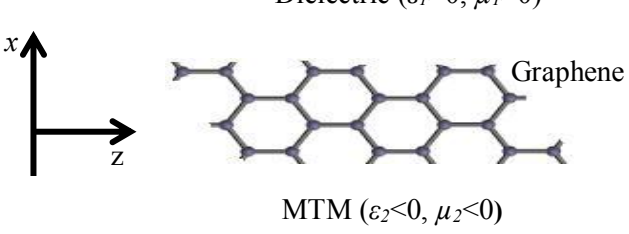



Figure 1. The schematic of the dielectric-graphene-MTM waveguide.

Using Maxwell's equation to obtain $E_x$ and $E_z$, the dispersion relation for TM modes can be written as [15]

$$\frac{\varepsilon_1}{\gamma_1} + \frac{\varepsilon_2}{\gamma_2} + j\,\frac{\sigma}{\omega\varepsilon_0} = 0, \quad (2)$$

where $\gamma_i = k_0\sqrt{N^2 - \varepsilon_i \mu_i}$ , $N$ is the effective refractive index and $k_0$ is the wave number in free space.

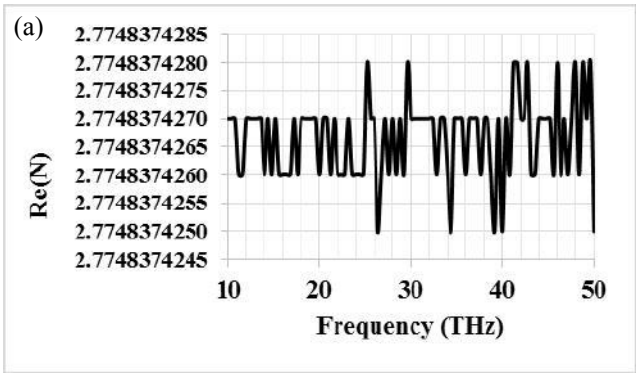
## 3. Results and Discussion

The dispersion equation presented in Equation (2) is solved numerically using Maple. The dispersion equation is solved at different values of $\varepsilon_2$ and $\mu_2$. The numerical values are chosen such that the multiplication $\varepsilon_2 \mu_2$=4. Table 1 presents the selected values of $\varepsilon_2$ and $\mu_2$. For the dielectric material, $\varepsilon_1$ is chosen to be equal 2.25. The graphene conductivity is taken from [13] as σ=0.772+j0.386 μS.m.

Table 1: Selected values of $\varepsilon_2$ and $\mu_2$.

| case | $\varepsilon_2$ | $\mu_2$ |
|---|---|---|
| 1 | -1 | -4 |
| 2 | -4 | -1 |
| 3 | -2 | -2 |
| 4 | -8 | -1/2 |
| 5 | -1/2 | -8 |

Case 1:



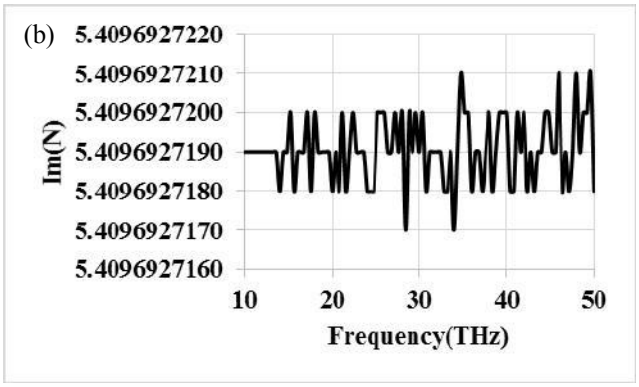
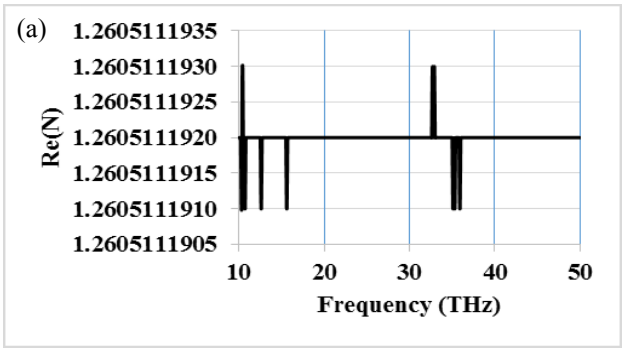




Figure 2: Effective refractive index (N) as function of frequency where case (1) is implanted. (a) real par and (b) Imaginary part.

In Fig.2 the values of $\varepsilon_2$ = -1 and $\mu_2$=-4. We realized that the variation of N is very small as frequency changes. We notice also that the values of the imaginary part is bigger than the real part indicating that the absorption is relatively big.

Case 2:



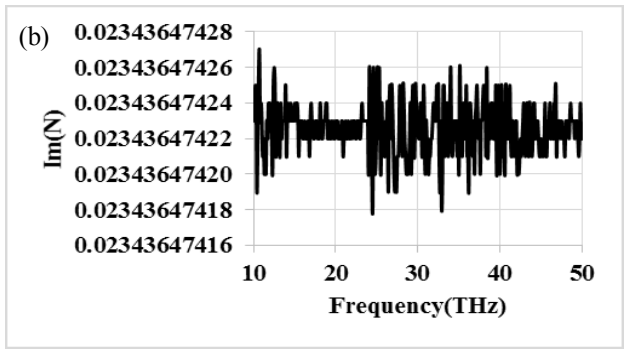



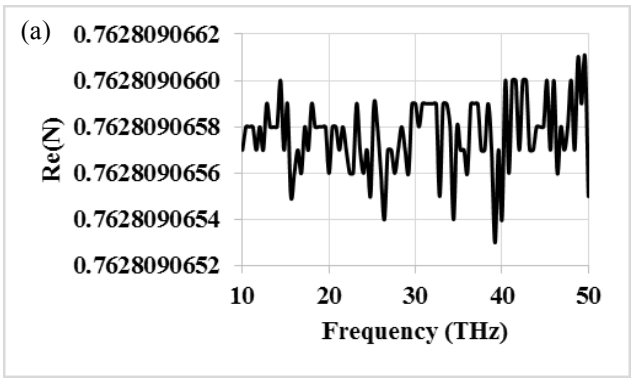

Figure 3: Effective refractive index (N) as function of frequency where case (2) is implanted. (a) real par and (b) Imaginary part.

In Fig.3 the values of $\varepsilon_2$ = -4 and $\mu_2$ = -1. We realized that the variation of N is very small as frequency changes. We also notice that the real part in this case is bigger than the imaginary part. Indicating that absorption is suppressed in this case. In Fig.4 the values of $\varepsilon_2$ = -2 and $\mu_2$ = -2. We realized that the variation of N is very small as frequency changes. We notice also that the values of the imaginary part is bigger than the real part indicating that the absorption is relatively big.

In Fig.5 the values of $\varepsilon_2$ = -8 and $\mu_2$ = -1/2. we can easily see that the changes in the refractive index is not noticeable. It is almost zero except at 47.9 THz where Re(N) is changes slightly. We can also see that the imaginary part is suppressed and the variation with frequency is also very small. This can be used for low dispersion and low attenuation waveguide. In Fig.6 the values of $\varepsilon_2$ = -1/2 and $\mu_2$ = -8. We realized that the variation of N is very small as frequency changes. We notice also that the values of the

imaginary part is bigger than the real part indicating that the absorption is relatively big.

Case 3:



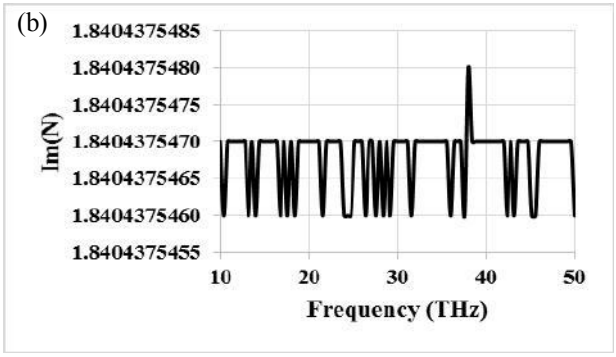




Figure 4: Effective refractive index (N) as function of frequency where case (3) is implanted. (a) Real par and (b) Imaginary part.

Case 4:

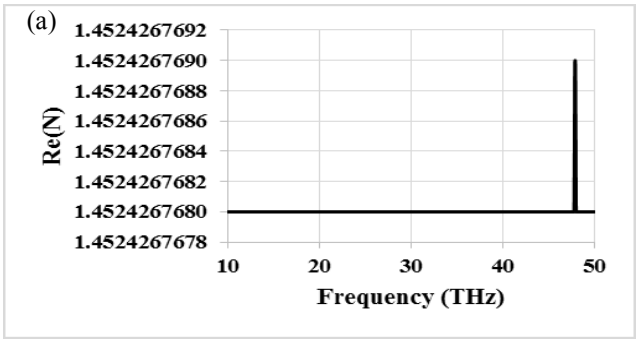



Figure 5: Effective refractive index (N) as function of frequency where case (4) is implanted. (a) real par and (b) Imaginary part.

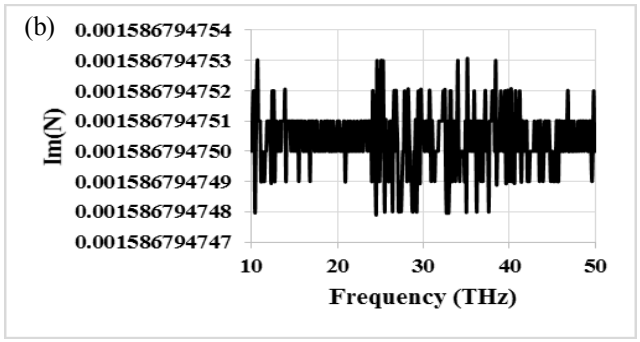
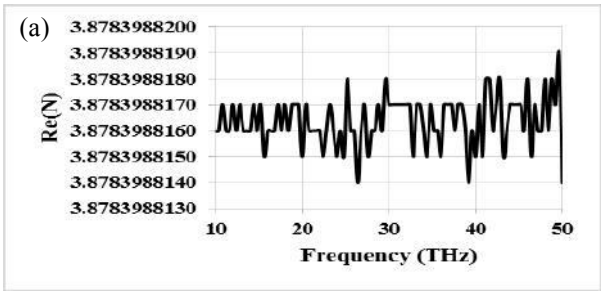



Figure 5: continue

Case 5:



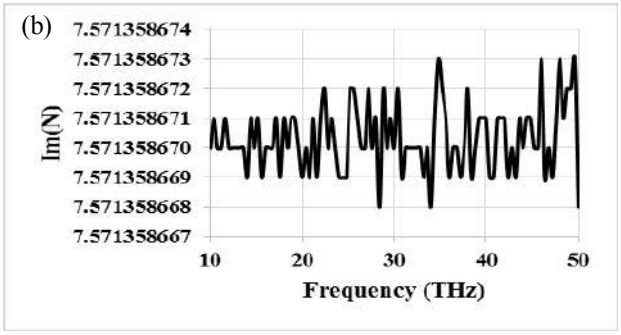




Figure 6: Effective refractive index (N) as function of frequency where case (5) is implanted. (a) Real par and (b) Imaginary part.

The relation between MTM parameter ($\varepsilon_2$) and the effective refractive index values is shown in Fig. 7. In the calculation, the multiplication $\varepsilon_2 \mu_2$=4, frequency is taken to be 20THz. The effective refractive index is dependent of the MTM parameter. As the absolute value of $\varepsilon_2$ increases the imaginary part of effective refractive index decrease creating low dissipation material as well as low dispersion materials.

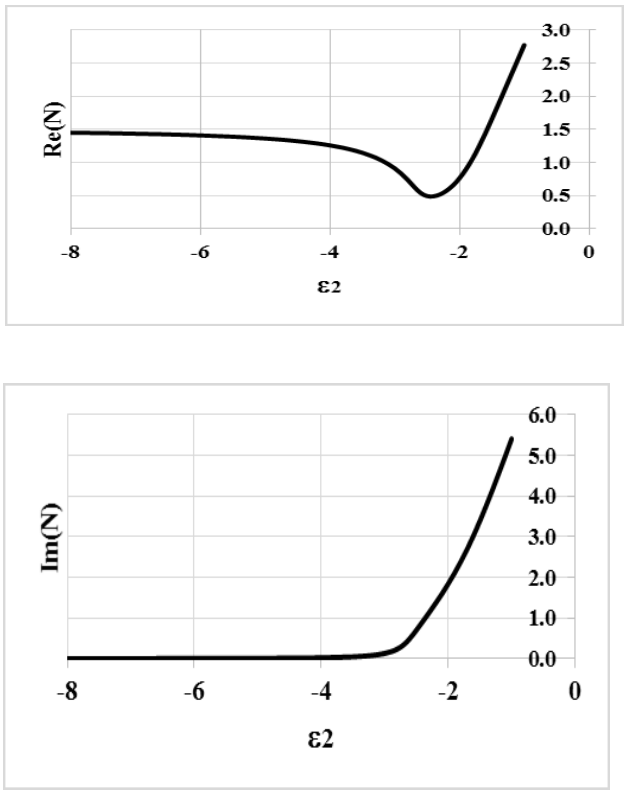



Figure 7: Effective refractive index (N) as function of MTM parameter ($\varepsilon_2$). (a) real par and (b) Imaginary part.

## 4. Conclusions

In this work, TE wave propagation is studied in the proposed waveguide which consists of a monolayer of graphene sandwiched between dielectric and MTM. The graphene conductivity is chosen such that its imaginary par is positive. The dispersion equation is solved numerically using Maple. The real and imaginary part of the effective refractive index are plotted as function of frequency at different MTM parameteres. Results show that the effective refractive index is hardly changing with frequency and vary as MTM parameters change. We also realized at specific values where $\varepsilon_2$ = -8 and $\mu_2$ = -1/2 the real part of effective refractive index in hardly changes and the imaginary part is very small. This structure can be used as low dispersion and low attenuation waveguide.

## References


[1] A. Andryieuski, and A. V. Lavrinenko, Graphene metamaterials based tunable terahertz absorber: effective surface conductivity approach, *Opt Express* 21: 9144-9155, 2013.

[2] H. Tao, N. I. Landy, C. M. Bingham, X. Zhang, R. D. Averitt, and W. J. Padilla, A metamaterial absorber for the terahertz regime: Design, fabrication and characterization, *Opt. Soc. Am.* 16: 7181-7188, 2008.

[3] M. Dragoman, A. A. Muller, D. Dragoman, F. Coccetti and R. Plana, Terahertz antenna based on graphene, *J. Appl. Phys*. 107: 104313, 2010.

[4] Y. Huang, L. Wu, M. Tang, and J. Mao, Design of a Beam Reconfigurable THz Antenna with Graphene-Based Switchable High-Impedance Surface, *IEEE Trans. Nanotechnol.* 11: 836–842, 2012.

[5] J. Chen, M. Badioli, P. Alonso-Gonzalez, S. Thongrattanasiri, F. Huth, J. Osmond, M. Spasenovi ´ c, A. Centeno, ´A. Pesquera, P. Godignon, A. Z. Elorza, N. Camara, F. J. Garc´ıa de Abajo, R. Hillenbrand, and F. H. L. Koppens, Optical nano-imaging of gate-tunable graphene plasmons, *Nature (London)* 487: 77–81, 2012.

[6] V. G. Veselago, The electrodynamics of substances with simultaneously negative values of ε and μ, *Soviet Physics* **10:** 509-514,1968.

[7] D. R. Smith, W. J. Padilla, D. C. Vier, S. C. Nemat-Nasser and S. Schultz, Composite medium with simultaneously negative permeability and permittivity, *Phys. Rev. Lett*. **84:** 4184-4187,2000.

[8] H. J. El-Khozondar, R. J. El-Khozondar and S. Zouhdi, Tunable MTMs consists of a single-walled nanotube thin film waveguide covered by nonlinear cladding, *Appl. Phys. A* 119: 451–453, 2015.

[9] H. J. El-Khozondar, R. J. El-Khozondar, M. M. Shabat, Double-Negative Metamaterial Optical waveguide Behavior Subjected to Stress, *Islamic university journal for natural science and Engineering* 16: 9-20, 2008.

[10] H. El-Khozondar, R. El-Khozondar, M. Shabat and A. Koch, Metallic nonlinear magnetooptical nonreciprocal isolator, *Optik* 122: 256–258, 2011.

[11] H. J. El-Khozondar, M. Abu-Marasa, R. J. El-Khozondar, M. Elbahri, S.Zouhdi, Design of Voltage control Oscillator using Nonlinear Composite Right/Left-Handed Transmission Line, *Advanced Electromagnetics* 5: 15-21, 2016.

[12] K. Y. Kim, Y. K. Cho and H. Tae, Guided Modes Propagations of Grounded Double-Positive and Double-Negative Metamaterial Slabs with Arbitrary Material Indexes, *Journal of the Korean Physical Society* **49**: 577-584,2006.

[13] X. He, J. Tao, B. Meng, Analysis of graphene TE surface plasmons in the terahertz regime, *Nanotechnol.* 24: 345203-345208, 2013.

[14] I. P. Kaminow, W. L. Mammel and H. P. Weber, Metal-Clad Optical Waveguides: Analytical and Experimental Study, *Apllied Optics* 13: 136-405, 1974.

[15] F. Wang, Y. Zhang, C. Tian, C. Girit, A. Zettl, M. Crommie and Y. R. Shen, Gate-variable optical transitions in graphene, *Science* 320: 206-209, 2008.

# A New Wideband Negative Refractive Index Metamaterial for Dual-band Operation

**S. S. Islam[1*], M. R.I. Faruque[1], M. T. Islam[2] and M. T. Ali[3]**

[1]Space Science Centre, Universiti Kebangsaan Malaysia, Malaysia
[2]Dept. of Electrical, Electronic and Systems Engineering, Universiti Kebangsaan Malaysia, Malaysia
[3]Centre for Communication Engineering Studies, Universiti Teknologi Mara, Shah Alam, Malaysia
[*]corresponding author: sikder_islam@yahoo.co.uk

## Abstract

A new wideband negative refractive index (NRI) metamaterial for dual-band operation is introduced in this study. Initially, a bare-H-shaped resonator was designed over the FR-4 substrate material. The refractive index curve for the unit cell, displays more than 3 GHz negative real peak from C-band to some portion of X-band. The proposed design also displays NRI property in the same frequency bands with wider bandwidth, when the Rogers RT 3010 substrate material was employed instead of FR-4 substrate material.

## 1. Introduction

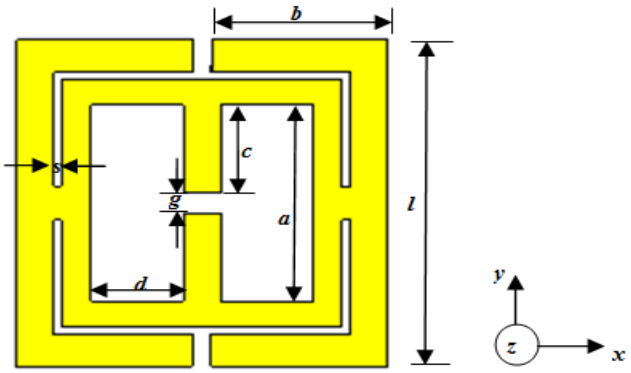
Materials having negative refractive index (NRI) has been a great concern in the scientific research community earlier in twenties. After the first idea was proposed by Victor Veselago [1] in 1967, exploration of such material of negative permittivity (ε) and negative permeability (μ) for negative refractive index was started. For the time being, the research on such topic was postponed due to lack of such natural materials until the material named 'metamaterial' was perfectly revealed by D. R. Smith and his colleagues in 2000 [2]. Metamaterial is an artificially produced extraordinary material where negative permittivity and negative permeability are tailored to have negative refractive index property in some certain frequencies. The negative refractive index property usually occurs where the permittivity and permeability is found negative. D. R. Smith and his colleagues constructed such composite material by utilizing repeated metallic wires and split ring resonators to have negative permittivity and permeability. They claimed that negative permittivity can be achieved by repeated metallic wire inclusion and negative permeability can be obtained by numerous magnetic structures like π-shape, S-shape, Z-shape and other interesting shapes [3-6]. It is well known that, metamaterials are formed by small unit cells those are arrange in a periodic form and the characteristics of each individual unit cell is very important for the overall material's performance. However, recently in some specific applications like, antenna design or filter design, utilization of single metamaterial unit cell is one of the promising approaches instead of bulk metamaterial or array of unit cells [7-9]. Beside this, it is being applied in specific absorption rate (SAR) reduction in human head, cloaking an object electromagnetically, designing polarizer or absorber and many other interesting applications [10-12]. According to the applications, different types of alphabetic metamaterial unit cells with NRI property were proposed in the literature but not all of these designs show negative refractive index property in the C-and X-band ranges with wide bandwidth. For example, Chang-Chun *et al.* in [3] demonstrated a π-shaped negative refractive index metamaterial but it works in the X-band only. Hayet Benosman *et al*. in [4], presented an 'S' shaped NRI metamaterial that operates in the $K_u$-band only. Abdullah Dhouibi *et al*. proposed a 'Z' shaped metamaterial for C-band only in [5] but it was not showing NRI property.

In this paper, a new bare-H-shaped metamaterial unit cell is proposed that has been designed on FR-4 substrate material. The material shows double negative property in the C- and X-band in conjunction with the negative refractive index property in those frequency bands. The material also exhibits negative refractive index property for the Rogers RT 3010 substrate material in the same frequency bands (C- and X-band).

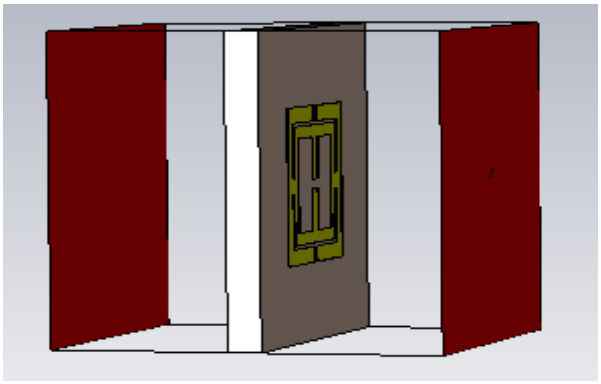
## 2. Methodology

In Fig. 1a, the proposed metamaterial unit cell is displayed. The proposed 'Bare-H-shaped' metamaterial unit cell was designed on a 20×20mm$^2$ FR-4 substrate material of thickness 1.60 mm that had dielectric constant of 4.3 and loss tangent of 0.025. The finite difference time domain method based 'CST Microwave studio' simulation software was utilized for the design and respective analysis of the unit cell.

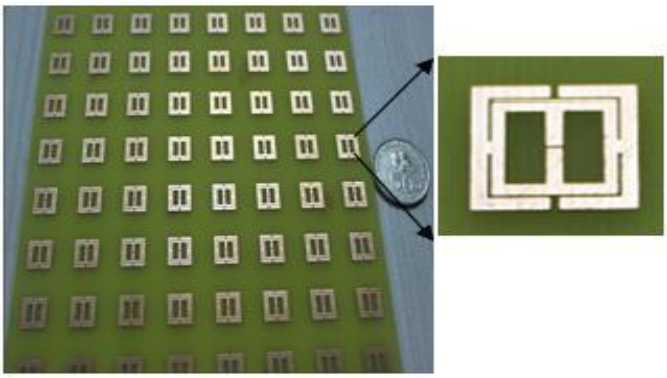
The structure was designed with two complementary split square resonators of copper layer with thickness of 0.035mm. From the Fig.1a, the parameters of the proposed metamaterials are as follows: $a$=6, $b$=4.77, $c$=2.77, $d$=2.50, $s$=0.2, $g$=0.66, $l$=10 all in mm scale. The gap between the inner and outer resonators is 0.2 mm and they were added two form a complementary bare-H-shape (i.e., empty H-shape) by a 1mm wide copper line in between them. The split between the two outer resonators were kept 1mm. The length of each arm is responsible for generating inductive effect whereas each split in resonator is the means




(a)



(b)



(c)

**Figure. 1 a** The schematic view of the proposed unit cell **b** simulation geometry of the unit cell **c** fabricated prototype for measurement

of generating capacitive effect. The mutual coupling capacitance originates between the gap of inner and outer resonator. By varying the coupling capacitance, the absorbing capacity of the material can be improved.

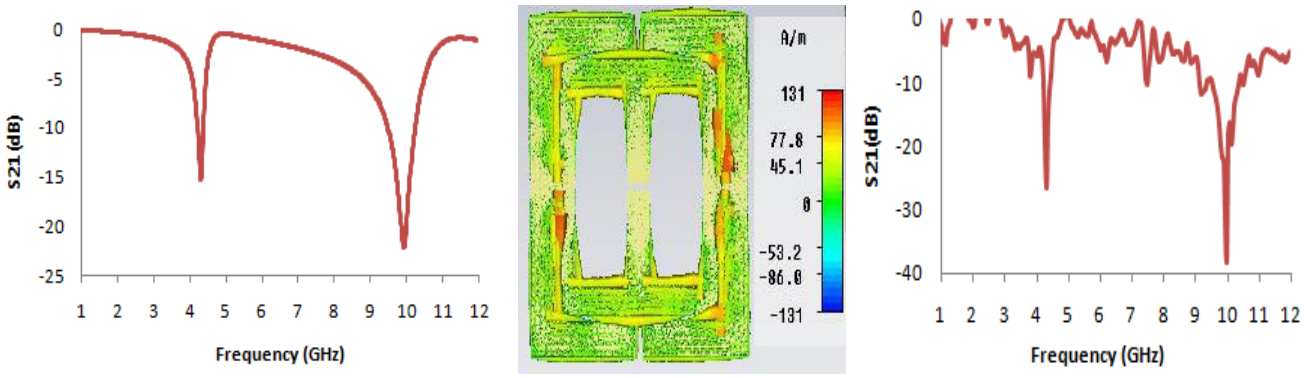
To calculate the S-parameter, the simulation was performed for the frequency range of 1-12 GHz. The transverse electromagnetic (TEM) wave was propagated through *z*-axis of the unit cell using two wave-guide ports. The simulation geometry is being displayed in the Fig. 1b. For the simulation purpose, the frequency domain solver was utilized after setting the normalized impedance at 50 ohm. The effective medium parameters permeability (μ) and permittivity (ε) were extracted from the simulated complex $S_{21}$ (transmission co-efficient) and $S_{11}$ (reflection co-efficient) parameters using Nicolson-Ross-Weir method [12].

The open space method was adopted for the measurement of the metamaterial. This method was chosen to see the practical effect of the material. A prototype of 180×200 $mm^2$ was built for the measurement purpose that contains 9×10 unit cells. The fabricated prototype is seen in the Fig. 1c. The fabricated prototype was placed between two horn antennas, which were working as transmitting and receiving antenna. These antennas were connected to an Agilent E8363D vector network analyzer to determine the S-parameters. To avoid the near field effect, 35cm distance was maintained from each antenna to the prototype. For the perfection of the test, with metamaterial and without metamaterial measurement were performed as well.

For further investigations, the FR-4 substrate was replaced by a Rogers RT 3010 substrate material of same size with thickness of 1.27 mm, dielectric constant of 11.2 and loss tangent of 0.0023 and the same numerical methodology was followed to see the impact of the change.

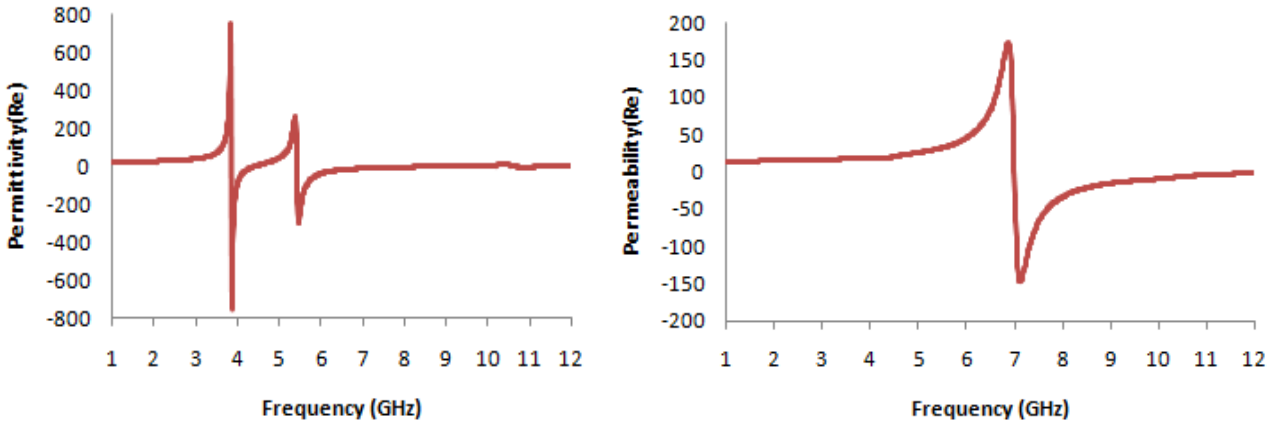
## 3. Results and Discussion

The Fig. 2a shows the magnitude of S-parameters for the proposed unit cell on FR-4 substrate material. The transmittance ($S_{21}$) resonances are seen at the frequency of 4.29 GHz and 9.93 GHz. The Fig. 2b displays the current distribution at the frequency of 7 GHz on FR-4 material. Unlike the split ring resonator, the current flows two opposite directions at the two sides of the unit cell. The major current is seen at the border of inner resonator near the gap between inner and outer resonators that has occurred due to the effect of strong coupling capacitance. The Fig. 2c shows the measured magnitude of transmission parameter ($S_{21}$) that clearly demonstrates good conformity with the




(a) (b) (c)

**Figure. 2 a** Transmission coefficient ($S_{21}$) for the proposed unit cell **b** current distribution at 7 GHz for the unit cell **c** measured transmittance ($S_{21}$) for the proposed unit cell




(a) (b)

**Figure. 3 a** Real magnitude of permittivity (ε) vs. frequency **b** Real magnitude of permeability (μ) vs. frequency

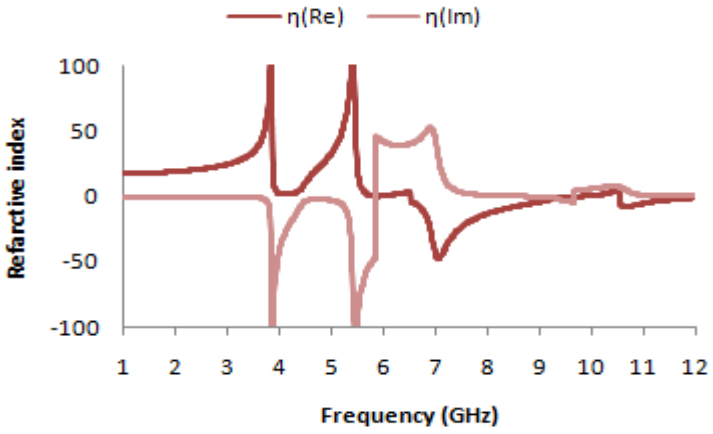
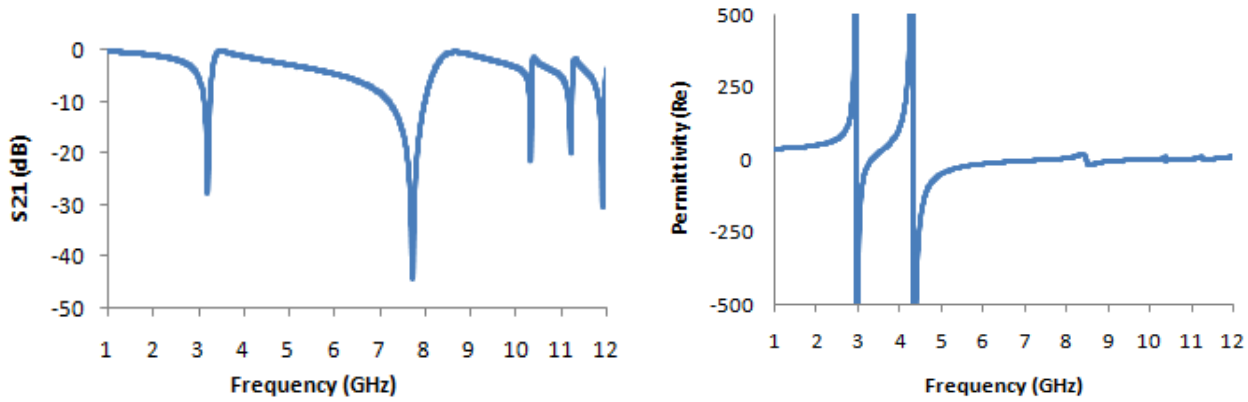



**Figure. 4** Magnitude of refractive index (η) vs. frequency for the unit cell on FR-4 material

simulated results. However, bit distorted and extended magnitude is seen in the measured resonance that most likely occurs due to open space measurement process or due to increased impendence for the array arrangement of measurement prototype.

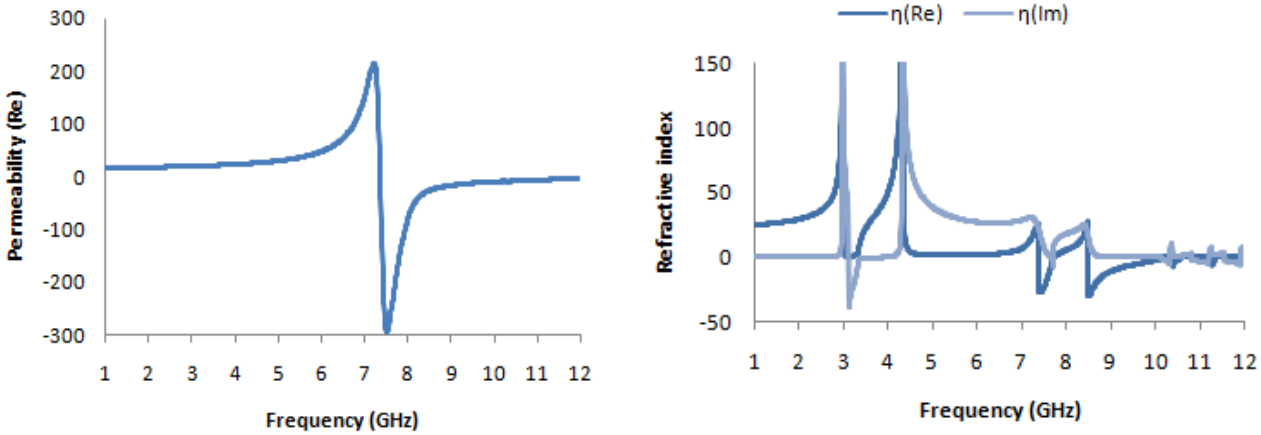
The real magnitudes of permittivity (ε) and permeability (μ) are expressed in the Fig. 3a and Fig. 3b respectively. In the Fig. 3a it is seen that the permittivity curve shows negative magnitude from the frequency of 3.85 GHz to 4.41GHz, 5.42 GHz to 9.26 GHz and 10.61 GHz to 12 GHz. It contains two resonances at the frequency of 3.85 GHz and




(a) (b)

(b)

**Figure. 5 a** Transmission coefficient ($S_{21}$) for the proposed unit cell on Rogers RT 3010 substrate material **b** Real magnitude of permittivity (ε) vs. frequency for Rogers RT 3010 substrate material




(a) (b)

**Figure. 6 a** Real magnitude of permeability (μ) vs. frequency for the proposed unit cell on Rogers RT 3010 substrate material **b** magnitude of refractive index(η) vs. frequency for Rogers RT 3010 substrate material

5.46 GHz. Similarly, the real curve of permeability in Fig. 3b displays negative peak from the frequency of 7 GHz to 12 GHz and only one sharp negative resonance at the frequency of 7.13 GHz. However, it is remarkable that, there is a wide negative bandwidth of 5 GHz in the permeability curve is rarely found and the curve trends to continue so on. Usually, in the varying magnetic field a charge is produced between the gap of inner and outer resonator and at the split in the middle line. At low frequency, the current remain in phase with the applied field but at the higher frequencies, the current cannot cope with the applied field and starts lagging which cause negative peak in the permeability curve.

The Fig. 4 reveals the magnitudes of refractive index curve against the frequency for the unit cell designed on FR-4 substrate material. It is evident that, the curve shows negative real peak from the frequency of 6.51 GHz to 9.72 GHz and from 10.61 GHz to exact 12 GHz. The imaginary peak for the curve is found reverse of the real in most of the positions. Nevertheless, it is noticeable that, the negative peak of the refractive index curve contains wide bandwidth of more than 3 GHz from C-band to some portion of X-band (6.51 GHz to 9.72 GHz). Another, wide bandwidth of more than 1 GHz (10.61GHz to 12 GHz) portion is found in the X-band. Therefore, the material can be characterized as a NRI material in these respective frequencies of negative peak region of refractive index. However, according to the Fig. 3a and Fig. 3b, the permittivity and the permeability curve also displays negative peak simultaneously with the negative peak portion of the refractive index curve. So, the material can be categorized as double negative (DNG) metamaterial in these respective frequencies as well.

The further study was done after replacing the Rogers RT 3010 substrate material instead of FR-4 substrate material. The same methodology was followed. For Rogers RT 3010 substrate material it is seen in Fig. 5a, the material exhibits

transmittance ($S_{21}$) at the frequency of 3.19GHz, 7.66 GHz, 10.33 GHz, 11.22 GHz and 11.92 GHz.

The Fig. 5b reveals the real magnitude of permittivity against frequency for the unit cell on Rogers RT 3010 substrate material. The permittivity curve shows two sharp negative resonances at the frequency of 3 GHz and 4.31 GHz and displays negative peaks from 2.97 GHz to 3.31GHz, 4.31 GHz to 7.66 GHz and 8.47 GHz to 10.12 GHz.

Equally, the Fig. 6a displays the real magnitude of permeability that has one sharp negative resonance at the frequency of 7.50 GHz. It has negative magnitude from the frequency of 7.37 GHz to over 12 GHz that covers more than 5 GHz wide bandwidth. The magnitude of refractive index against frequency is seen in the Fig. 6b. The refractive index curve exhibits two negative resonances at the frequency of 7.37 GHz in the C-band and 8.47 GHz in the X-band of microwave spectra. It also contains real negative magnitude from the frequency of 7.37GHz to 7.66 GHz, 8.47 GHz to 10.12 GHz, 10.39 GHz to 10.57 GHz and 11.26 GHz to 11.33 GHz. The imaginary peak shows nearly the opposite behavior. Moreover, the permittivity and permeability curve also displays negative magnitude in these negative real value regions of refractive index curve. Another mentionable point is, more than 1 GHz wide bandwidth (8.47 GHz to 10.12 GHz) of negative peak region is present in the X-band in conjunction with one or two smaller negative peak portions. Therefore, the material can be characterized as NRI or DNG material in these respective frequency ranges.

## 4. Conclusion

In this paper, a new bare-H-shape NRI metamaterial unit cell has been introduced that was designed initially on FR-4 substrate material. The material shows NRI property in the C-and X-band with more than 3 GHz wide bandwidth. The material exhibits NRI property in the same bands for Rogers RT 3010 substrate material as well. Moreover, one mentionable point is, for both of the substrate materials the permeability curve shows more than 5 GHz bandwidth of negative peak that is rarely found. C-band is widely used for long distance radio communications and X-band is popular for satellite applications. Therefore, the proposed unit cell can be utilized in the C-and X-band antenna for superior performance besides other applications in the proposed frequency regions.

## Acknowledgements

This work is supported by the Ministry of Education Malaysia (MOE) under grant no. FRGS TOPDOWN/2014/TK03/UKM/01/1 and DIP-2014-03.

## References

[1] V.G. Veselago, The electrodynamics of substances with simultaneously negative values of ε and μ. *Sov. Phys. Usp* 10(04), 509–514 ,1968.

[2] D. R. Smith, W. J. Padilla, D.C. Vier, S. C. Nemat-Nasser, and S. Schultz, Composite medium with simultaneously negative permeability and permittivity, *Phys. Rev. Lett.* 84(18), 4184 ,2000.

[3] Y. Chang-Chun, C. Yi-Ping, W. Qiong , Z. Shing-Chuang, 'Negative Refraction of a Symmetrical π-shaped Metamaterial', *Chin. Phys. Lett.* 25, 482-484, 2008.

[4] H. Benosman, N.B. Hacene, Design and Simulation of Double "S" Shaped Metamaterial; Int. J. Comput. Sci. Issues, 9, 534–537 ,2012.

[5] A. Dhouibi, S. N. Burokur, A. d. Lustrac, and A. Priou, Study and analysis of an electric Z-shaped meta-atom, Adv. Electromag.,1:64–70, 2012.

[6] S. S. Islam, M.R.I. Faruque and M. T. Islam; 'Design and analyses of a novel split-H-shaped metamaterial for multi-band microwave applications'; *Materials*,7,4994-5011,2014.

[7] M.A. Wan Nordin, M.T. Islam, N. Misran, A compact wideband coplanar waveguide fed metamaterial-inspired patch antenna for wireless application, *Appl. Phys. A*, 109,961–965(2012)

[8] L. Li, Y. Li, T.S. Yeo, J.R. Mosig, O.J.F. Martin, A broadband and high-gain metamaterial microstrip antenna. *Appl. Phys. Lett.*, 96, 164101:1–164101:3, 2010.

[9] J. Carver, V. Reignault, F. Gadot, Engineering of the metamaterial-based cut-band filter, *Appl. Phys. A*, 117,513–516, 2014.

[10] N. Landy, D.R. Smith, A full-parameter unidirectional metamaterial cloak for microwaves; *Nat. Mater.*, 12, 25–28 , 2013.

[11] M.T. Islam, M.R.I. Faruque, N. Misran, Study of specific absorption rate (SAR) in the human head by metamaterial attachment. *IEICE Electron. Express*, 7, 240–246 , 2010.

[12] O. Luukkonen, S.I. Maslovski, S.A. Tretyakov, A Stepwise Nicolson–Ross–Weir-Based Material Parameter Extraction Method. *IEEE Antennas Wirel. Propag. Lett.*, 10, 3588–3596 , 2011.

# Metamaterial Absorber Insensitive to Polarization and Incidence Angle Based on Multilayer Structure

**L. Belaïd[1], and R. Oussaid[1,2]**
[1] Houari Boumediene University of Science and Technologie,
Electronics and Computer Science Faculty, Instrumentation Laboratory, Algiers, Algeria
[2]ENPEI-Badji Mokhtar, Rouiba, Algeria
Corresponding author, E-mail: lbelaid.usthb@gmail.com

## Abstract

This paper presents a design of a metamaterial absorber insensitive to polarization and incidence angle. The full-wave electromagnetic simulation from CST Microwave Studio demonstrates a perfect microwave absorption around 10 GHz, with a maximum of 98% and a FWHM close to 4.97% for two types of polarization, for TE and TM modes. We have also studied the influence of the incidence angle on the absorption coefficient and FWHM. In addition, we have shown the improvement of the absorption coefficient and the FWHM by designing a three-layer model.

## 1. Introduction

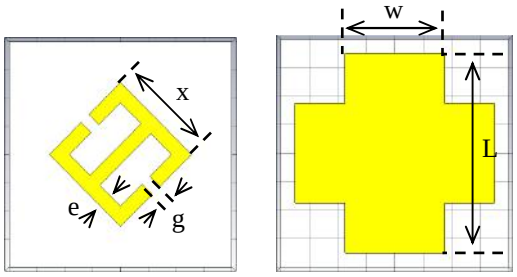
The metamaterial absorber (MA) is an artificial structure which has the capability of absorbing the electromagnetic (EM) waves at a specific frequency range [1]. In general, these structures can be fabricated in the desired EM spectrum from radio to optical frequencies. The concept is to adjust $\varepsilon$ and $\mu$ independently by varying the geometrical dimensions of the electric and magnetic resonant components in the unit cell. The purpose is to get the absorber impedance matching the free space impedance $Z_0$, and simultaneously to have a refraction index $n(\omega)$ with a large imaginary part. In this case, both reflection and transmission waves will be minimized within a certain frequency range. This property has been used to design EM absorbers with a nearly perfect absorption in microwave [2]-[6] and terahertz bands [7].

In this paper, the authors present a perfect metamaterial absorber (PMA) by integrating electric and magnetic resonators into the unit cell. We are presenting of design and simulation results at 10 GHz insensitive to two polarizations of the electric component for normal incident EM waves namely, along x-axis and at 45° in the x-y plane and simulations for a wide range of incident angles for both transverse electric (TE) and transverse magnetic (TM) modes. Furthermore, we are showing the improvement of the absorption magnitude and full width half maximum (FWHM) through the use of a 3-layers structure.

## 2. Design and Results

### 2.1. Design and simulations of single layer structure

The unit cell of 8mm x 8mm x 0.8mm was designed on the Rogers RO3010 ($\varepsilon_r$ = 10.2, tan = 0.0022). It consists of electric and magnetic resonators at the front side of the substrate Fig. 1(a), and a metallic cross at the back side of the substrate Fig. 1(b).




(a) (b)

Fig. 1: Metamaterial absorber: (a) electric and magnetic resonators ;(b) Metallic cross. Dimensions: x=3.5 mm, e=0.55 mm, g=0.32 mm, L=7 mm, w=3.5 mm.

Based on S-parameters, the microwave power absorption A could be expressed as:

$$A = 1 - |S_{11}|^2 - |S_{21}|^2 \quad (1)$$

Where, $S_{11}$ and $S_{21}$ are the reflection and transmission parameters, respectively.

By simultaneously minimizing both transmission and reflection parameters at a given frequency, a nearly perfect absorption can be achieved at a given frequency.

### 2.1.1. *Absorption for two polarizations*

The simulation is carried out with CST Microwave Studio using frequency solver, the S-parameters obtained by simulations are used to calculate the absorption magnitude A from the equation (1).
We have considered two different polarizations of a planar normal incident EM waves for the electric field component namely, along the x-axis and rotated by 45° in the x-y plane. The curves of the absorption magnitude at 10 GHz for RO3010 substrate are plotted in Fig. 2.

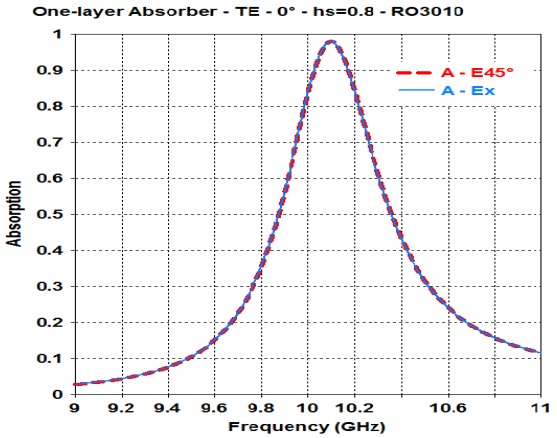
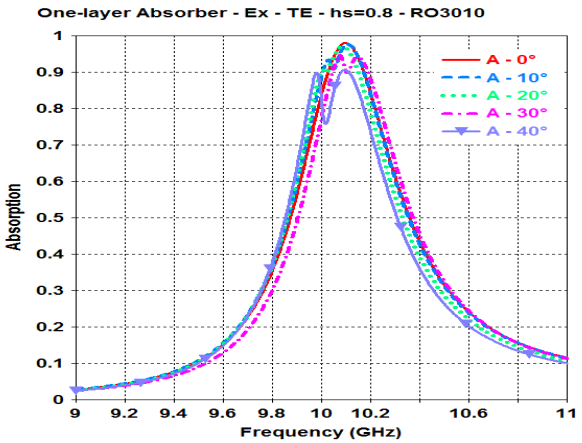



Figure 2: One-layer. Simulated absorption for electric field polarized along the x-axis and rotated by 45° in x-y plane, RO3010 substrate, for normal incidence and TE mode.

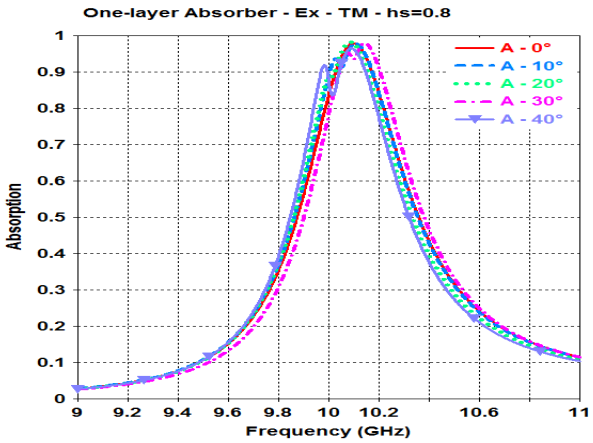
The curves are almost identical with an absorption peak of 98% and a corresponding FWHM is around 4.97%, this demonstrates a nearly perfect absorption and polarization insensitivity of the proposed design.

### 2.1.2. *Absorption related incident angle*

The operating angle is also concerned, the simulated results for electric field polarized along x-axis and different incidence angles ranging from 0° to 40°. The absorption curves for the TE and TM modes are shown in Fig. 3 (a) and (b), respectively. The simulated results are presented in Table 1, we see a small decrease in the absorption magnitude for TE mode when the incidence angle increases from 0° to 40° (i.e., a variation of 7.4%). While for TM mode, the values of the absorption are identical. The corresponding FWHM is practically the same around 4.9% for both modes.




(a)




(b)

Figure 3: One- layer. Simulated absorption for electric field polarized along x-axis and incidence angle varied from 0° to 40°, (a) TE and (b) TM modes

Table 1: Values of absorption peak for TE and TM modes.

| θ [°] | $A_{TE}$ [%] | $A_{TM}$ [%] | F [GHz] |
|---|---|---|---|
| 0 | 98 | 98 | 10.098 |
| 10 | 97.67 | 97.84 | 10.1 |
| 20 | 96.98 | 97.31 | 10.09 |
| 30 | 94.68 | 94.04 | 10.07 |
| 40 | 90.6 | 95.92 | 10.09 |

## 2.2. Design and simulations of the 3-layers structure

Considering a structure composed of three layers. The layers 1 and 3 designed on RO3006 ($\varepsilon_r$ = 6.15, tan δ= 0.002) with the same thickness $d_1$=0.64mm containing the structure described in paragraph 2.1 , and between these two layers there are a layer design on air with a thickness $d_2$=0.64mm. The unit cell of 13mm x 13mm x 1.92.mm is optimized at resonance frequency of 10 GHz (Fig. 4)

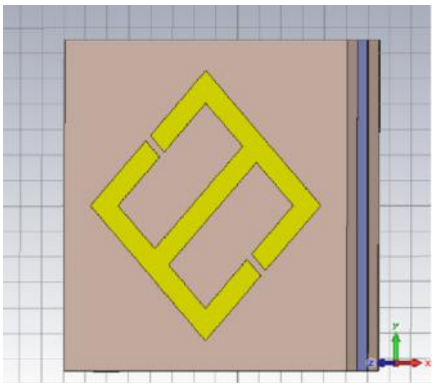


Figure 4: Unit cell of 3-layers metamaterial absorber

In order to prove the polarization insensitivity of our designed cell, two different polarizations of the planar normal incident EM waves were considered for the electric field component. The curves of the absorption in the case of TE mode (Fig. 5) are almost identical with an absorption peak of 99.8%. This, demonstrate the nearly perfect absorption and polarization insensitivity of the proposed design.

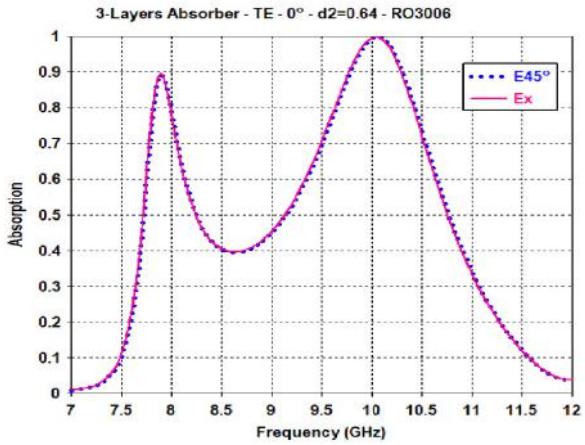



Figure 5: Unit cell of 3-layers. Simulated absorption for normal incidence and TE mode. Electric field polarized along the x-axis and rotated by 45° in the x-y plane.

In figure 6, we show the absorption magnitude for normal incidence and electric field polarized along x-axis. The absorption peak at 10 GHz was identical (of 99.83%) and 99.85% for TE and TM modes, respectively. The FWHM for two modes is 16.4%. From the results, we can see that absorption and FWHM have largely increased compared to the results for a single layer.

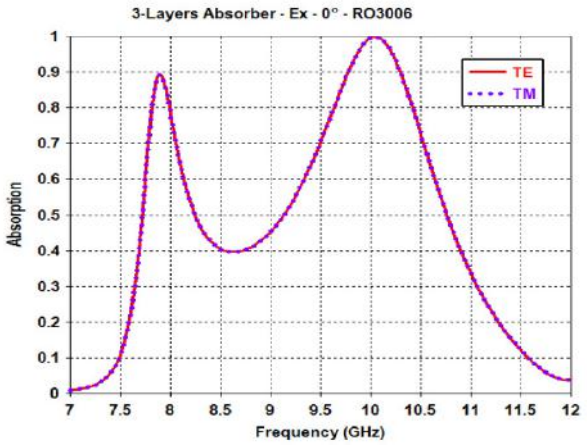
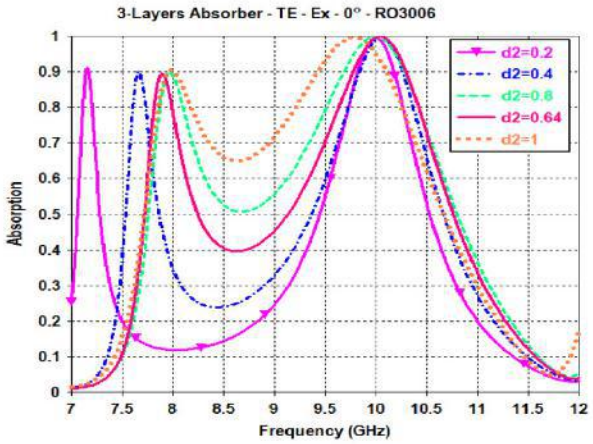
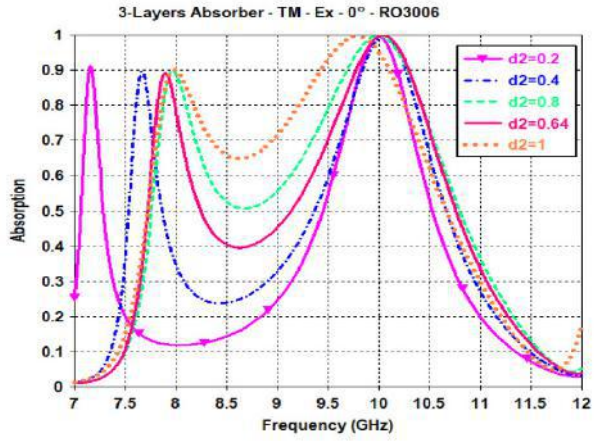



Figure 6: Unit cell of 3-layers. Simulated absorption for normal incidence and electric field polarized along the x-axis. For TE and TM modes

Furthermore, the structure is simulated for different thickness $d_2$ ranging from 0.2mm to 1mm. The simulated absorption magnitude for normal incidence and electric field polarized along the x-axis are presented in fig. 7, (a) TE and (b) TM modes, respectively.




(a)




(b)

Figure 7: 3-layers. Simulated absorption with electric field polarized along x-axis and angle incidence varied from 0° to 40°, (a) TE and (b) TM modes.

The simulated results are presented in Table 2 and Table 3. In the case of the two modes, for $d_2$=0.2mm we have 2-bands with the peaks of magnitude of 91% and 99.56%, and the FWHM of 0.238 GHz and 1.08 GHZ for $f_1$=7.15 GHz and $f_2$=10 GHz, respectively. The corresponding FWHM around of 10 GHz varies from 10.8% to 30% when $d_2$ varied from 0.2mm to 1mm, respectively.

Table 2: Simulated absorption of a 3-layers design at $F_1$

| $d_2$ [mm] | $A_{TE}$ [%] | $A_{TM}$ [%] | $FWHM_{TE}$ [GHz] | $FWHM_{TM}$ [GHz] |
|---|---|---|---|---|
| 0.2 | 91 | 91 | 0.238 | 0.247 |
| 0.4 | 89.91 | 89.6 | 0.372 | 0.374 |
| 0.64 | 89.45 | 89.1 | 0.625 | 0.637 |
| 0.8 | 89.76 | 89.76 | - | - |
| 1 | 90.38 | 89.96 | - | - |

Table 3: Simulated absorption of a 3-layers design at $F_2$

| $d_2$ [mm] | $A_{TE}$ [%] | $A_{TM}$ [%] | $FWHM_{TE}$ [%] | $FWHM_{TM}$ [%] |
|---|---|---|---|---|
| 0.2 | 99.56 | 99.52 | 10.8 | 10.8 |
| 0.4 | 99.77 | 99.77 | 12.9 | 12.9 |
| 0.64 | 99.83 | 99.85 | 16 | 16.24 |
| 0.8 | 99.82 | 99.81 | 30 | 30 |
| 1 | 99.60 | 99.56 | 30 | 30 |

But when the thickness $d_2$ increases, the frequency $f_1$ shifts to $f_2$ (Table 4), so we get a broader absorption curve.

Table 4: Simulated frequencies $F_1$ and $F_2$ for TE mode

| $d_2$ [mm] | $F_1$ [GHz] | $F_2$ [GHz] |
|---|---|---|
| 0.2 | 7.15 | 10 |
| 0.4 | 7.66 | 10.05 |
| 0.64 | 7.9 | 10.04 |
| 0.8 | 7.97 | 9.995 |
| 1 | 7.98 | 9.785 |

## 3. Conclusions

With its scalable geometry, this absorber can be designed to operate on various EM frequency ranges with almost perfect absorption. Compared to existing metamaterial absorbers [4-8], the designed structure exhibits a high absorption and a large FWHM at predefined frequencies. Its insensitivity to polarization and incident angle was demonstrated with almost identical responses for both TE and TM modes. We have also shown that the optimization of the unit cell allowed the design of a perfect absorber around a frequency of 10 GHz. The design of the 3-layers absorber has increased the absorbance magnitude of 1.6% and the FWHM of 25%, indicates that this structure can operate for several applications.

These characteristics suggest many applications, such as the electromagnetic cloaking, absorber, EM filters, electromagnetic shield, frequency selective heat transmitter, thermophotovoltaics…

## References


[1] S. Celozzi, R. Areno, G. Lovat, *Electromagnetic Shielding*, Wiley&Sons, New Jersey, 2008.

[2] B. Zhu, Z. Wang, C. Huang, Y. Feng, J. Zhao, and T. Jiang, Polarization insensitive metamaterial absorber with wide incident angle, *Progress In Electromagnetics Research*, vol 101, pp. 231-239, 2010.

[3] M. H. Li, H. L. Yang, and X. W. Hou, Perfect metamaterial absorber with dual bands, *Progress In Electromagnetics Research*, vol. 108, 37-49, 2010.

[4] Xu YQ, Zhang PH , Chen L, Deng LJ, A wide-angle planar metamaterial absorber based on split ring resonator coupling, *Journal of Applied Physics*; 110: 1-9, 2011.

[5] L. Huang, and H. Chen, Multi-Band and polarization insensitive metamaterial absorber, *Progress In Electromagnetics Research*, Vol. 113, 103-110, 2011.

[6] O. Ayop, M. K. Rahim, N. A. Murad, N. A. Samsuri, Polarization Insensitive and Wide Operating Angle Metamaterial Absorber at X-Banb, *IEEE Asia-Pacific Conference on Applied Electromagnetics*, 978-1- 4799-6603, 2014.

[7] Tao H, Landy NI, Bingham CM, Zhan X, Averitt RD, Padilla WJ. A metamaterial absorber for the terahertz regime: Design, fabrication and characterization, *Opt. Express*, **16**: 7181-7188, 2008.

[8] Wen D, Huang X, Guo L, Yang H, Han S, Zhang J. Quadruple- band polarization-insensitive wide-angle metamaterial absorber based on multi-layer structure, *Optik*, 126:1018-1020, 2015.

[9] He XJ, Yan ST, MA QX, Zhang QF, Jia P, Wu FM. Broadband and polarization-insensitive terahertz absorber based on multilayer metamaterials, *Optics Communications*, **340**: 44-49, 2015.

# Design and analysis of a new double C-shaped miniaturized metamaterial for multiband applications

**Mohammad Jakir Hossain[1], Mohammad Rashed Iqbal Faruque [1], Sikder Sunbeam Islam[1] Mohd Faizal Bin Jamlos[2], Mohammad Tariqul Islam[3]**

[1]Space Science Center (ANGKASA), Universiti Kebangsaan Malaysia, 43600 UKM, Bangi, Selangor, Malaysia
[2]School of Computer & Communication Engineeering, Universiti Malaysia Perlis, 02600 Arau, Perlis, Malaysia
[3]Department of Electrical, Electronic and Systems Engineering, Universiti Kebangsan Malaysia, 43600 UKM, Bangi, Selangor, Malaysia
*corresponding author, E-mail: rashed@ukm.edu.my

## Abstract

In this paper, a new double C-shaped compact structure of metamaterial was designed; fabricated and measured that can operate in a multi-band microwave frequency span. The proposed metamaterial structure offers miniaturization factor compared to traditional metamaterial unit-cells and obeys better effective medium ratio. Commercially available Computer Simulation Technology (CST) electromagnetic simulator is adopted to investigate the design of the metamaterial. The metamaterial displays multi-band response in conjunction with left handed property over the certain frequency band in the microwave regime. In addition, few parametric studies were done with the metamaterial and the effective medium parameters were analysed. The dimensions and scattering parameters of the proposed double C-shaped compact metamaterial are suitable for triple-band applications.

## 1. Introduction

Materials with relative negative permittivity ($\varepsilon$ less than 0) and permeability ($\mu$ less than 0) was some various properties compared to conventional materials has been depicted by Victor Veselago in 1968. Due to the non-appearance of the properties of the regular materials, this matter was less important until 1999. Negative permittivity properties of the materials could be found, but make engineered material with negative permeability was challenging work. Smith et al. achieved success to develop a new engineered material with unusual properties such as negative permeability and permittivity practically in 2000 [1]. Different type of unit-cell structure has been utilized to achieve metamaterial characteristics such as spiral resonators, double split-ring resonators and broad side–coupled SRRs [2-5]. On the other hand, most of the traditional unit-cell depicts single band response. It is important matter to utilize metamaterial in multiband antenna applications to achieve gain enhancement in all operating bandwidths of multiband antenna [6]. However, metamaterials were broadly utilized to develop many antennas. Using metamaterials, antenna performance was enhanced [7-9]. Due to specific applications, different types of alphabetic structures of metamaterials were proposed. "Z" shaped metamaterial was proposed by Abdallah Dhouibi *et al* in [10] that was found working at a single band only with single negative property. The compactness of the metamaterial is governed by improved effective medium ratio (EMR), which is the important factor of the metamaterial research. A diamond-shaped single-sided left handed metamaterial was proposed to show increased receive power and high transmission peak [11]. In addition, the dimension of the diamond-shaped unit-cell was large and EMR of the unit-cell was too small. In [12], a novel two-rectangular U-shaped double negative metamaterial analyzed was suggested for single band operation. Moreover, the design of unit-cell of metamaterial was very large in size and the effective medium ratio was less than standard value. Theodosius *et al*. in [13] depicted a double negative (DNG) metamaterial of compact size with 6.9 EMR but they utilized two different resonators at the two opposite sides of the substrate. Various analyses were performed for multi-band operation with a split-H-shaped metamaterial by Islam *et al*. [14], whereas the metamaterial design was very large the size and the EMR was too small. In microwave imaging applications, negative index metamaterial embedded miniaturized antenna with based on modified SRR and CLS unit cell was utilized for ultra-wideband operation [15], whereas the metamaterial size was big and the effective medium ratio was 6.38. A new dual band metamaterial unit-cell construction was proposed in [16] with EMR 7.14 but they argument single negative property for their dual band operation.

In this study, a new double-C-shaped metamaterial unit cell is being introduced for microwave triple-band applications with better EMR property. The proposed metamaterial demonstrates negative permittivity at S-band and double negative properties of C- and X-band applications. The structure of the metamaterial size is being miniaturized and follows the good EMR.

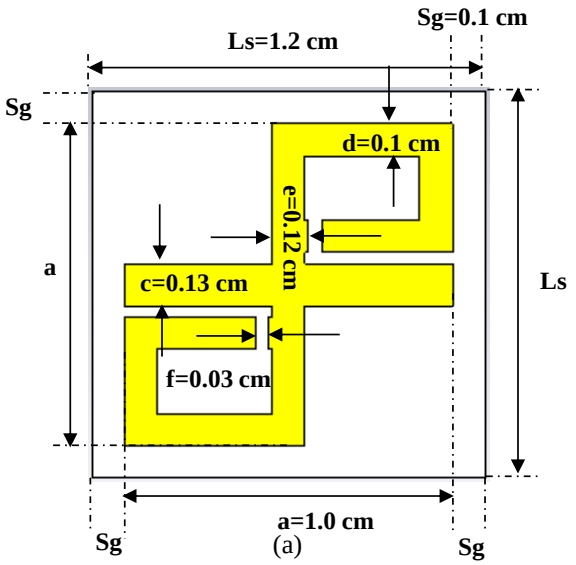
## 2. Methodology

### 2.1. Geometry of the metamaterial unit-cell

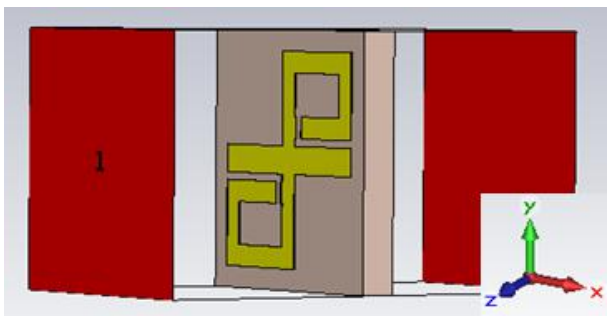
The proposed metamaterial unit-cell and structural parameters are illustrated in Fig. 1(a). The proposed design was developed using two C-shaped split-circular resonators connected to each other. The thickness of all elements of the metamaterials unit-cell is 0.035 mm and the substrate material is low cost FR4 lossy material. The unit-cell is fabricated on the substrate with a dielectric constant ε, 4.3 and dielectric loss tangent δ, 0.025. The width and height of the substrate of unit-cell is 1.2 cm and thickness is 0.16 cm. In Table 1, the design parameters of the unit-cell are reported.

Table 1: Dimensions of double C-shaped unit-cell [cm].

| Parameters | Value |
|---|---|
| Ls | 1.2 |
| a | 1.0 |
| c | 0.13 |
| d | 0.1 |
| e | 0.12 |
| f | 0.03 |
| Sg | 0.1 |



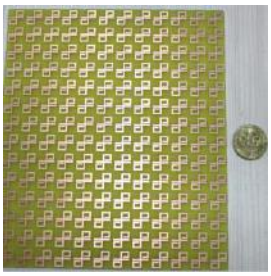

(a)



(b)

Figure 1. (a) The proposed double C-shape unit-cell structure; (b) Simulation set up of the proposed design.

In this paper, the CST Microwave studio (Thomas Weiland, Germany) based on finite-difference time-domain method is investigate this design where an incident electromagnetic wave travelling along the positive z-axis with an Electric field polarized along the y-axis. The boundary conditions of perfect magnetic conductor and the perfect electric conductor have been utilized along the x-axis and y-axis, respectively, and along the z-axis, two waveguide ports are placed. The simulation, schematic diagram of the proposed design is illustrated in Fig. 1(b). To determine the transmission coefficient and the reflection coefficient at simulation a frequency domain solver is utilized. The impedance matching was set to fifty ohms. The frequency range 1-15 GHz was used to simulate the design of metamaterials.



(a)



(b)

Figure 2. (a) The fabricated array of double C-shape structure; (b) Experimental set up.

A fabricated prototype was displayed in Fig. 2(**a**). The prototype contains 14 ×12 arrays of the unit-cell of copper materials and the size of the prototype are 16.8 × 14.4 $cm^2$. The measurement was performed [11] with two horn antennas in an anechoic chamber using free-space environment. To allow the incident electromagnetic wave travelling over the prototype that was positioned between the horn antennas in the identical plane, similar to the simulation geometry. In addition, the transmission co-efficient are determined from the Agilent E8363D vector network analyzer. The experimental setup of the proposed metamaterial characteristics measurement is shown in Fig. 2 (**b**).

### 2.2 Effective S-parameters Calculation

To determine the characteristics of the metamaterials such as relative permeability and relative permittivity that depends on the transmission coefficient ($S_{21}$) and reflection coefficient ($S_{11}$). The high superiority geometrical estimation can be achieved in this design using FDTD method based meshing scheme. The meshing scheme has to manage a simulation period to achieve convergent results. By using CST Microwave Studio, S-parameters of the reported unit-cell and array were calculated. To excerpt the effective permeability ($\mu$), permittivity ($\varepsilon$) from the simulated complex S-parameters the Nicolson Rose Weir (NRW) method [17] was used. The direct refractive index method [18] was utilized to extract effective refractive index ($\eta$) from the simulated complex S-parameters. The

simplified equation for the effective permeability, permittivity and refractive index are as follows:

Relative effective permeability, $\mu_r = \frac{2c(1-s_{21}+s_{11})}{j\omega d(1+s_{21}-s_{11})}$ (1)

Relative effective permeability, $\varepsilon_r = \mu_r + j\frac{2cs_{11}}{\omega d}$ (2)

Relative refractive index, $\eta \approx \frac{c}{j\pi fd}\{\frac{(s_{21}-1)^2 - s_{11}}{(s_{21}+1)^2 - s_{11}}\}^{1/2}$ (2)

Where, $S_{11}$ and $S_{21}$ are the reflection coefficient and transmission coefficient of the unit-cell metamaterial. c is the velocity of light, d is the thickness of the slab and $\omega$ is the angular frequency.

## 3. Results and Discussion

In this section, simulation and experimental result of double C-shaped compact metamaterial is presented. The scattering parameters and characteristics of various geometrical parameters of the design are also analyzed. The reflection coefficient ($S_{11}$), and transmission coefficient ($S_{21}$) of the unit-cell are illustrated in Fig. 3. Fig. 3 demonstrates the three frequency span of resonance frequencies namely 3.27-3.45 GHz, 7.76-9.03 GHz, and 11.263-11.816 GHz that indicates the S -band, C-band and X-band applications. The values of the transmission coefficient ($S_{21}$) at the three resonance frequencies such as 3.366 GHz, 8.574 GHz, and 11.57 GHz are -17.07 dB, -27.16 dB, -17.91 dB, respectively.

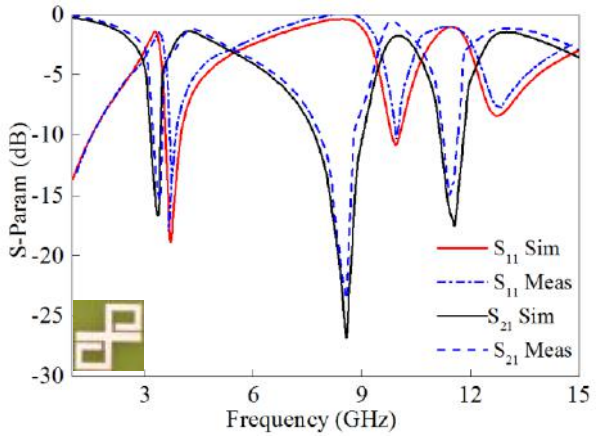



Figure 3. Simulated and measured S-parameters response of double C-shape structure.

From Fig. 3, it observed that the simulation and experimental results are good agreement with each other. Fig. 4 shows the surface current distributions and electric field of the unit-cell at 3.36 GHz, 8.58 GHz, and 11.57 GHz, where it reveals effective negative characteristics. Moreover, Fig. 4 (a), it is shown that the distribution of surface current at the lower frequencies is higher than the higher resonance frequencies of the unit-cell. According to the current distribution results, the current of the upper section are opposite to the lower section of the resonance frequency at 3.36 GHz. For that reason, the related magnetic fields nullify each other. It is also seen that weak local electric field at the same time at Fig. 4 (b). At resonance frequency 8.57 GHz, the current flow of the upper section is same as direction to the lower section. That is why; the related magnetic fields amplify each other and at the same time the strong electric field are observed at Fig. 4 (c) and (d). Hence, it is concluded that electric and magnetic resonances are exist at these frequencies, and negative refractive index is seen at that frequencies which is shown in Fig. 6. From Fig. 4 (e), it is seen that the behavior of the current distribution is asymmetrical. For that reason, the related magnetic fields nullify each other and make weak local electric field at the same time that is revealed in Fig. 4 (f).

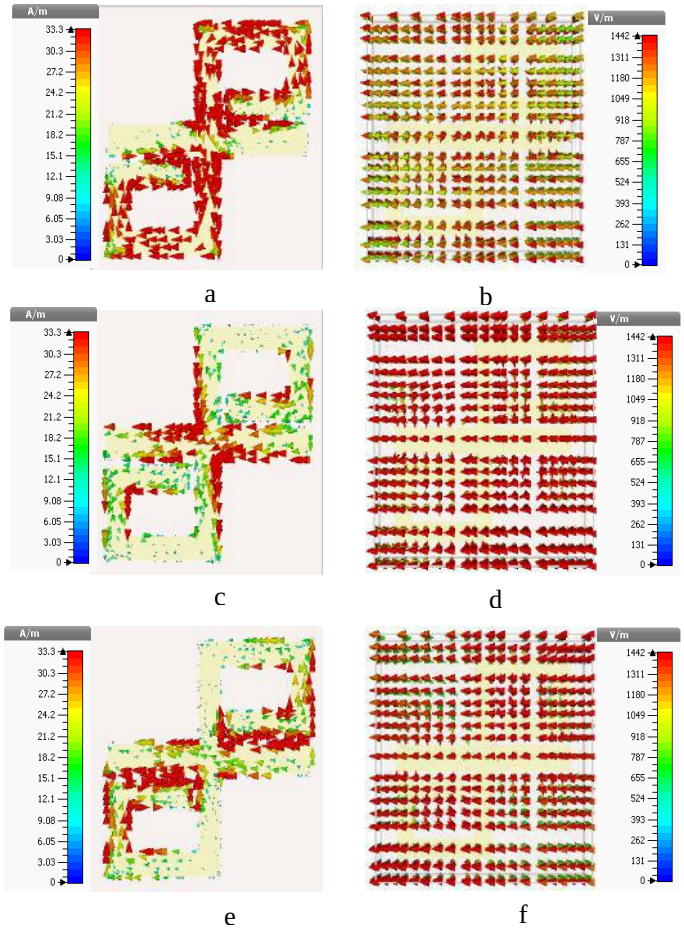
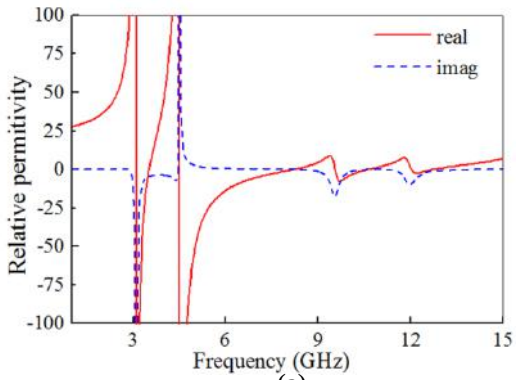


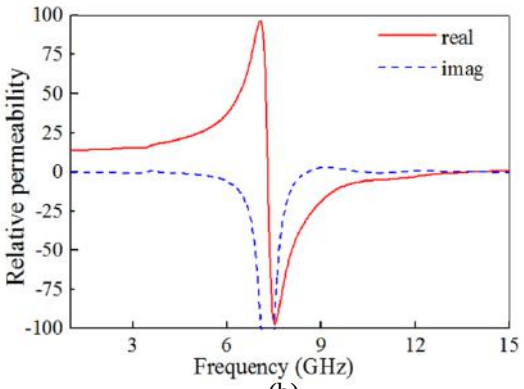

Figure 4. Current distribution and electric field at 3.36GHz, 8.58 GHz and 11.57 GHz of double C-shape structure.

Frequency span of relative permittivity ($\varepsilon$), relative permeability ($\mu$) and relative refractive index ($\eta$) of the unit-cell are 3.1-3.506, 4.5-8.224, 9.554-10.632, 12.046-12.732; 7.3-13.838 and 4.472-10.8, 11.304-13.796, respectively. Frequency span of double Negative region of the unit-cell is 7.3-8.224, 9.554-10.632, 12.046-12.732. It can be observed that the metamaterials unit-cell has a negative refractive index at different resonance frequencies

Fig. 5(a), (b) illustrates the real and imaginary curves of the relative permittivity, relative permeability of the metamaterials unit-cell.



(a)



(b)

Figure 5. Unit-cell (a) relative permittivity (b) relative permeability values of real and imaginary curves.

Fig. 6 illustrates the relative negative refractive index curve verses frequency. The relative negative refractive indices have been found to be negative for frequency span 4.472-10.8 GHz and 11.304-13.796 GHz. The double negative ($\varepsilon$ & $\mu$) region has been found at the frequency span 7.3 - 8.224 GHz, 9.554 - 10.632 GHz, and 12.046 - 12.732 GHz. The double negative region proves the unit-cell and array of the metamaterials act as a left handed metamaterials (LHM) that is applicable in many sophisticated areas such as electromagnetic cloaking operation, design of filters, sensors and detectors, antenna performance enhancers, electromagnetic absorber, imaging, noise reduction, and seismic protection etc.

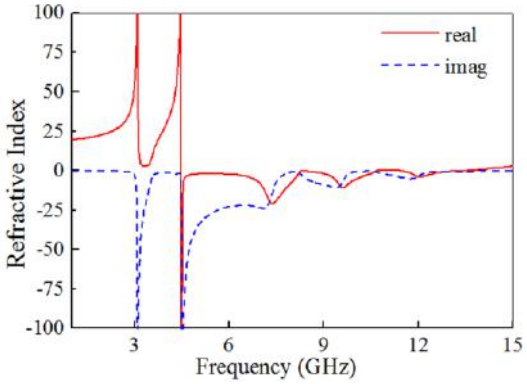



Figure 6. Relative refractive index values of real and imaginary curves of unit-cell.

The ratio between the wavelengths to unit-cell size is called effective medium ratio which is important to design compact metamaterial. The unit-cell can reveal negative permeability and/ or permittivity in the region of effective medium whether it is greater than 4. Due to the compactness of the metamaterial unit-cell, the effective medium ratio is an important matter in the field of metamaterial research. It can be seen that our proposed unit-cell size and effective medium ratio are 1.2 × 1.2 × 0.16 $cm^3$ and 7.44 respectively.

### 3.1. Role of the middle line width(c)

Fig. 7, Fig. 8 and Fig. 9 depicts the reduced width of the middle line(c) of the unit-cell from 0.13 mm to 0.07mm and corresponding scattering and effective medium parameters.

It is seen from Fig. 7 that the reduction of middle line of unit-cell leads to increase the electric resonance and reduce the magnetic resonance at 3.36 GHz and 8.57 GHz, respectively.

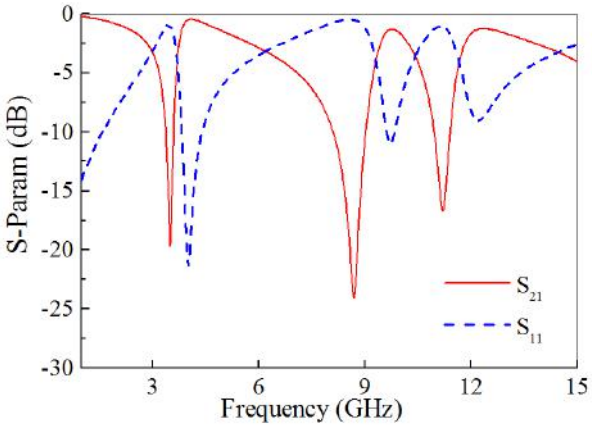
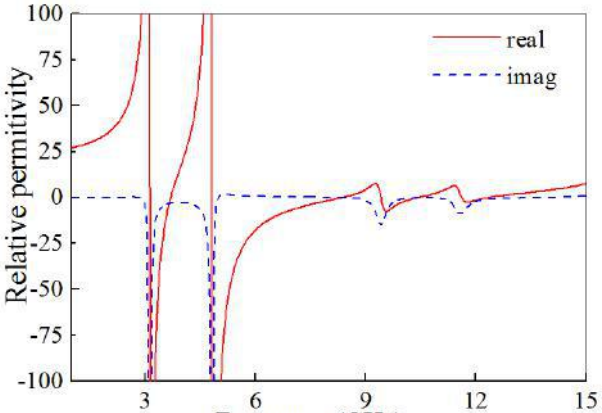
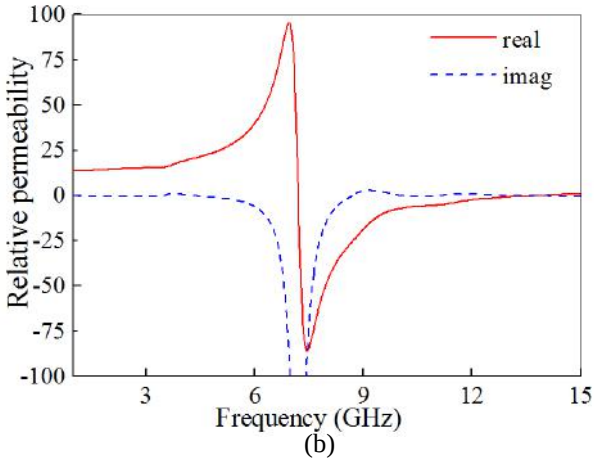



Figure 7. S-parameters response of double C-shape structure with middle slab width c = 0.7 mm.



(a)



(b)

Figure 8. Unit-cell with middle slab width c = 0.7 mm (a) Relative permittivity (b) relative permeability values of real and imaginary curves.

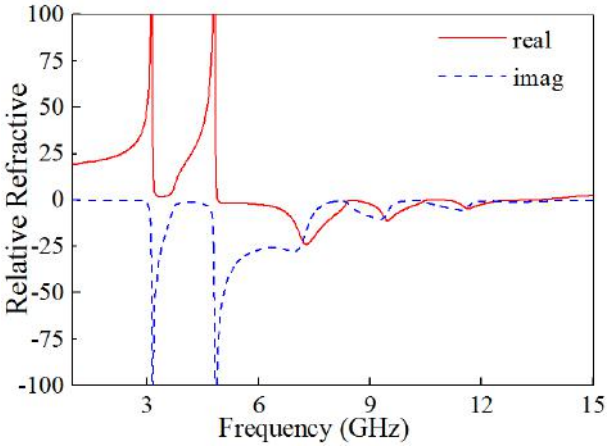



Figure 9. Relative refractive index values of real and imaginary curves of unit-cell with middle slab width c = 0.7 mm.

The decrease of width caused the reduction in capacitance between the mid-line and the resonator and it eventually shifted the permittivity curve bit left.

Table 2: Frequency span of negative index of the unit-cell (middle slab width c = 0.7 mm) of the relative effective parameters.

| Parameters | Value |
|---|---|
| Relative permittivity ($\varepsilon$) : | 3.142-3.688, 4.822-8.378, 9.428-10.45, 11.626-12.368; |
| Relative permeability ($\mu$) : | 7.202-13.866; |
| Relative refractive index ($\eta$) : | 4.906-10.632, 10.884-13.348; |
| Double Negative ($\varepsilon$ & $\mu$) region: | 7.202-8.378, 9.428-10.45, 11.626-12.368; |

Table 2 depicts the details of effective negative permeability, negative permittivity, negative refractive index, and double negative region of the unit-cell. It can be observed from Table 2 that the metamaterials unit-cell with middle slab width c = 0.7 mm has a negative refractive index at different resonance frequencies.

### 3.1 Role of the resonator width(d):

The width of the square resonator (d) of the unit-cell has been reduced from 1.0 mm to 0.5mm and investigating the scattering parameters and effective medium parameters that is shown in Fig. 10, Fig. 11 and Fig. 12.

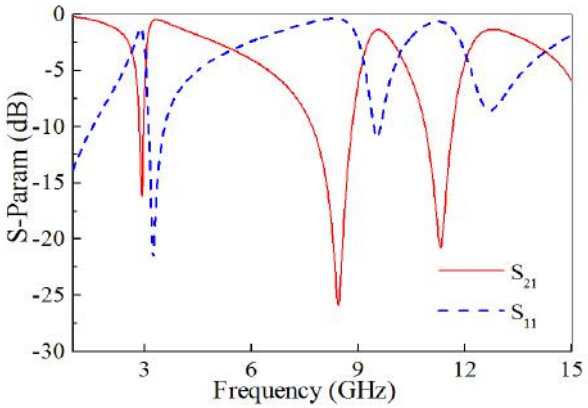
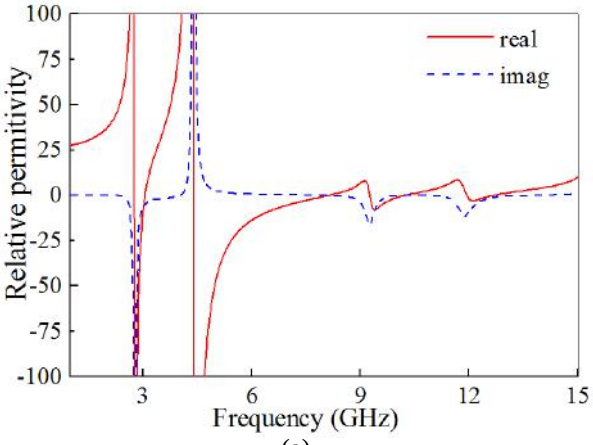


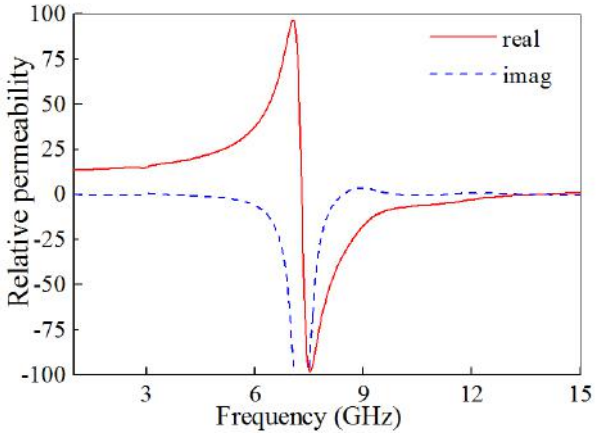

Figure 10. S-parameters response of double C-shape structure with resonator width d = 0.5 mm.

It can be observed from Fig. 10 that the reduction of square resonator at the inner side of unit-cell leads to decrease the electric resonance at 3.36 GHz and 11.57 GHz, respectively. It is also seen from Fig.10 that the resonance points were shifted a little bit at the left side compare to the basis unit-cell.

This has been happen due to increase the capacitance between the resonator and the mid-line. Similarly, the increment of width of the resonator at the outer side would shift the transmittance at the right side. Fig. 11 (a) and (b) demonstrates the Real and imaginary curves of the relative permittivity and relative permeability of unit-cell with resonator width d = 0.5 mm, simultaneously.



(a)




(b)

**Figure 11.** Unit-cell resonator width d = 0.5 mm. (**a**) permittivity (**b**) permeability values of real and imaginary curves

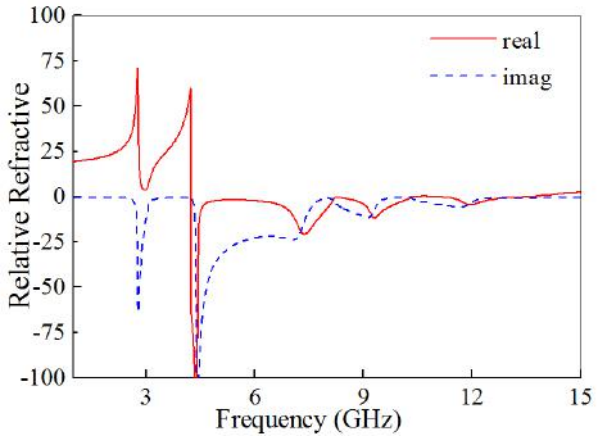



Figure 12. refractive index values of real and imaginary curves of unit-cell with resonator width d = 0.5 mm.

It is seen from the Fig. 11 (a) and (b) that the magnitude of the real and imaginary curves of the relative permittivity has shifted to left a little bit and amplitude of the real part has reached negative near 3 GHz frequency. The relative permeability of this unit-cell was found constant. On the other hand, the magnitude of the permittivity curves is stronger than basis unit-cell. Fig. 12 also illustrates the relative negative refractive index curve verses frequency of unit-cell. The relative negative refractive index originated to be negative for frequency span 4.234-10.352 GHz and 11.052-13.628 GHz. The double negative ($\varepsilon$ & $\mu$) region has been found at the frequency span 7.3-8.168 GHz, 9.26-10.268 GHz, 11.948-12.718 GHz. The magnitude of the relative refractive index curves is weaker than basis unit-cell because of reduction of inductive path. The effective negative values of the relative permittivity, relative permeability, and relative refractive index of unit-cell with resonator width d = 0.5 mm metamaterial can be observed from Table 3. The double negative properties are also seen from this Table 3 that makes the metamaterials to LHM.

Table 3: Frequency span of negative index of the unit-cell (resonator width d = 0.5 mm) of the relative effective parameters.

| Parameters | Value |
|---|---|
| Relative permittivity ($\varepsilon$) : | 2.778-3.044, 4.402-8.168, 9.26-10.268, 11.948-12.718; |
| Relative permeability ($\mu$) : | 7.3-13.88; |
| Relative refractive index ($\eta$) : | 4.234-10.352, 11.052-13.628; |
| Double Negative ($\varepsilon$ & $\mu$) region: | 7.3-8.168, 9.26-10.268, 11.948-12.718; |

Table 3 depicts the details of effective negative permeability, negative permittivity, negative refractive index, and double negative region of the unit-cell. It can be observed from Table 3 that the metamaterials unit-cell with middle slab width d = 0.5 mm has a negative refractive index at different resonance frequencies.

Table 4: Comparison of EMR with other unit-cell.

| Ref. No. | Unit-cell size ($mm^3$) | Effective medium ratio |
|---|---|---|
| Fabio Urbani *et al.* 2010 [11] | 20 × 25 × 0.25 | 1.2 |
| Theodosios *et al.* 2012 [13] | 5.3 ×4.3 × 1.5 | 6.9 |
| Anik Mallik *et al.* 2013 [12] | 25 × 25 × 1 | 1.99 |
| Sikder *et al.* 2015 [14] | 20 × 20 × 1.6 | 4.32 |
| Moinul *et al.* 2015 [15] | 5 × 3.2 × 1.6 | 6.38 |
| Abhishek *et al.* 2015 [16] | 7.5 × 7.5 × 0.8 | 7.14 |
| Proposed Metamaterial | 12.0×12.0×1.6 | 7.44 |

Due to the compactness of the metamaterial unit-cell, the effective medium ratio is an important matter in the field of metamaterial research. According to the Table 4, comparing the effective medium ratio of our proposed unit-cell with the other unit-cells, the proposed structure is found more suitable as a compact metamaterial.

## 4. Conclusions

A new compact metamaterial structure of the unit-cell for triple band is presented in this paper. The scattering parameters and effective parameters of the proposed metamaterial were analysed over the frequency range 1-15 GHz. The results exhibit negative refractive index properties for the unit-cell structure in multiband frequency range as well. The proposed unit-cell structure is compact in size and follows better effective medium ratio with value of 7.44 which are more applicable in microwave spectra. The

free-space measurement method was used to verify the results of the 14 ×12 arrays prototype of the unit-cell that was fabricated and measured. This unit-cell of metamaterial can be applied for many sophisticated areas such as electromagnetic cloaking operation, design of filters, sensors and detectors, antenna performance enhances, high data rate communications, and electromagnetic absorber.

## References


[1] D. R. Smith, W. J. Padilla, D. C. Vier, S. C. Nemat-Nasser, S. Schultz, Composite medium with simultaneously negative permeability and permittivity. *Phys. Rev. Lett.* 84: 4184–4187, 2000.

[2] L. Wang, X. Q. Lin, F. Cheng, Y. Fan, and Z. B. Zhou, Electric split-ring resonator based on double-sided parallel-strip line, *IEEE Antenna Wireless Propag. Lett.*, 12: 69–71, 2013.

[3] B. Zarghooni, and T. A. Denidni, New compact metamaterial unit-cell using SIR technique, *IEEE Lett. Microw. Theory Tech.*, 24: 315–317, 2014.

[4] R. Marques, F. Mesa, J. Martel, F. Medina, Comparative analysis of edge- and broadside-coupled split ring resonators for metamaterial design- theory and experiments, *IEEE Trans. Antennas Propag.*, 51: 2572–2581, 2003.

[5] J. D. Baena *et al.*, Equivalent-circuit models for split-ring resonators and complementary split-ring resonators coupled to planar transmission lines, IEEE Trans. Microw. Theory Tech., 53: 1451–1461, 2005.

[6] O. M. Khan, Z. U. Islam, Q. U. Islam, F. A. Bhatti, Multiband high-gain printed Yagi array using square spiral ring metamaterial structures for S-band applications, *IEEE Antenna Wireless Propag. Lett.*, 13: 1100–1103, 2014.

[7] C. Sabah, Multiband metamaterials based on multiple concentric open ring resonators topology, *IEEE J. Sel. Topics Quantum Electron.*, 19: 2013.

[8] O. Yurduseven, Y. AE, G. Turhan-Sayan, Hybrid-shaped singleloop resonator: A four-band metamaterial structure, *Electron. Lett.*, 47: 1381–1382, 2011.

[9] M. H. Ullah, M. T. Islam, M. R. I. Faruque, A near-zero refractive index meta-surface structure for antenna performance improvement, *Materials*, 6: 5058–5068, 2013.

[10] A. Dhouibi, S. N. Burokur, A. Lustrac, A. Priou, Study and analysis of an electric Z-shaped meta-atom. *Adv. Electromagn.*, 1: 64–70, 2012.

[11] F. Urbani, Experimental Analysis of Novel Single-Sided Left-Handed Metamaterial, *IEEE Antennas and Wireless Propagation Letters*, 9: 720-723, 2010.

[12] A. Mallik, A. S. Kundu, M. O. Goni, Design of a novel two-rectangular U-shaped double negative metamaterial. *Proc.ICIEV13*, Dhaka, Bangladesh, pp. 1-6, 2013.

[13] T. D. Karamanos, A. I. Dimitriadis, and N. V. Kantartzis, Compact Double-Negative Metamaterials Based on Electric and Magnetic Resonators, *IEEE Antennas And Wireless Propagation Letters*, 11: 480-483, 2012.

[14] S. S. Islam, M. R. I. Faruque, and M.T. Islam, A new double negative metamaterial for multi-band microwave applications. *Appl. Phys. A*, 116, 723-733, 2014.

[15] M. M. Islam, M. T. Islam, M. Samsuzzaman, M. R. I. Faruque, N. Misran, F. M Mansor, A miniaturized antenna with negative index metamaterial based on modified SAR and CLS unit cell for UWB microwave applications. *Materials*, 8: 92-407, 2015.

[16] A. Sarkhel, D. Mitra, S. Paul, S. R. B. Chaudhury, A Compact Meta Atom for Dual band negative Permittivity Metamaterial, *Microwave and Optical technology letter*, 57: 1152-1156, 2015.

[17] A. M. Nicolson, G. F. Ross, Measurement of the intrinsic properties of materials by time-domain techniques. *IEEE Trans. Instrum. Meas.*, 19: 377–382, 1970.

[18] S. S. Islam, M. R. I. Faruque, M. T. Islam, A new direct retrieval method of refractive index for the metamaterial. *Current Science*, 109: 337-342, 2015.

# A Complementary Chiral Metamaterial with Giant Electromagnetic Activity and Low Losses

**Ismael Barba[1*], Ana Grande[1], Ana C. López-Cabeceira[1], José Represa[1], Gregorio J. Molina-Cuberos[2], Óscar Fernández[3] & A. Gómez[3]**

[1]Universidad de Valladolid, Spain
[2]Universidad de Murcia, Spain
[3]Universidad de Cantabria, Spain
[*]corresponding author: ibarba@ee.uva.es

## Abstract

A planar complementary metamaterial, as well as its corresponding inverse structure, has been designed and characterized. Numerical results (using commercial software) are presented here. The structure shows a giant gyrotropy (chirality) as well as very low losses.

## 1. Introduction

The use of "complementary" structures in PCB to perform metamaterial response has been established during the last years [1, 2]. In [1] it is shown that their transmission characteristics should be complementary too, i.e., if the "original" shape shows a resonant decrease in transmission characteristics at the frequencies of interest, in the "complementary" shape the transmission is resonantly enhanced at the same frequencies instead.

In a previous conference [3], we designed and characterized numerically a partially complementary chiral metamaterial, which presented negative refraction index in a resonant band. In this paper we present an enhanced version of the structure, in order to reduce material losses, and we compare it with its "full complementary" shape.

Fig. 1 and 2 show the designed structures: the "original" (i.e., the one composed by a distribution of metallic segments on a dielectric substrate) and the "complementary" (the one composed by a distribution of slots on a metal plate): the dielectric substrate has been made transparent in order to highlight the two metal layers. Another structure, very similar to the first one, has been studied in [4]. We have studied different dielectric substrates, from the traditional FR4 as in [3] to low-losses materials, like TACONIC TLC-30 and Rogers RO4003C, in order to enhance the transmission.

Looking at the figures, it is straightforward that both structures are geometrically chiral: i.e., they lack any mirror symmetry. From an electromagnetic point of view, chirality can lead to a cross-coupling between the electric and magnetic fields [5], so the refractive index has different values for right circularly polarized (RCP) and left circularly polarized (LCP) waves, following the equation

$$n_{\pm} = n \pm \kappa , \qquad (1)$$

where $n_+$ is the refractive index for a RCP wave, while $n_-$ is the index for a LCP wave. $n$ is the usual refraction index ($\sqrt{\varepsilon_{eff}\mu_{eff}}$) and κ is the cross-coupling parameter, also known as Pasteur or chirality index [5,6].

Looking at that equation, we can see that one of both indexes, $n_+$ or $n_-$ would be negative if κ is high enough ($|\kappa| > n$, assuming n is positive) [6].

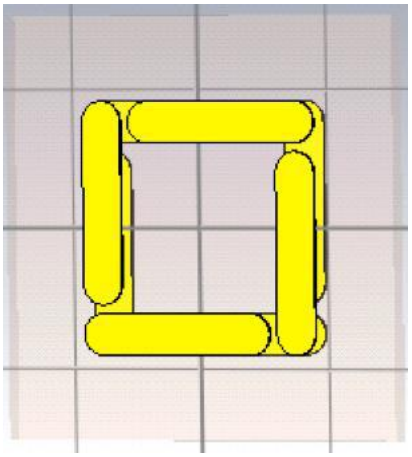


Figure 1: Geometry of the "original" planar metamaterial unit cell. It is composed by a dielectric substrate (removed) in the image, and metal (copper) traces on both its faces. The metal layer on the back face is the specular image of the front layer; so the geometry shows specular (chiral) asymmetry.

## 2. Design and characterization

In order to design a sample with a chiral electromagnetic response at microwave frequencies, we have used a basis cell of 16x16 mm, each segment/slot in Figs. 1 and 2 is 9.9x2 mm, and the minimum separation between them is 0.3 mm. That means the four segments/slots are enclosed inside a square of 12.2x12.2 mm. As mentioned, we have probed different dielectric plates between the two metal layers: TACONIC TLC-30 and Rogers RO4003C; both have similar properties (dielectric constant 3 and 3.38 respectively, and loss tangent 0.003 and 0.0027,

respectively, so the results are similar. We also have probed different widths of the dielectric slab (0.03 and 0.06 inches). The lateral boundaries are modeled by means of periodic conditions, in order to simulate a periodic arrangement of cells.

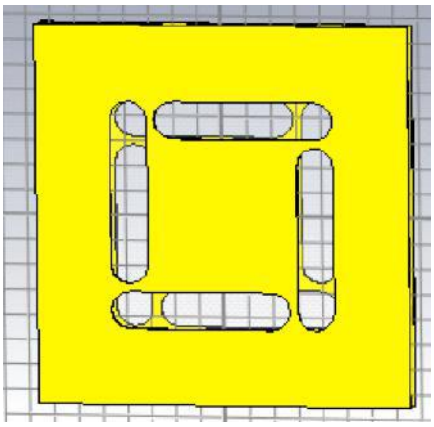


Figure 2: Geometry of the "complementary" planar metamaterial unit cell.

## 3. Results

We have modelled the response of our structure if a linear polarized plane wave incides normally on the slab. Due to the chirality of the structure, a rotation of the polarization plane is expected, and, therefore, we have measured the transmission coefficient in copolarization $T_{CO}$ (i.e. the transmitted signal in the same polarization plane of the incident wave) and crosspolarization $T_{CR}$ (polarization plane normal to the one of the incident wave), as well as the reflection coefficient R (the structure being reciprocal, no rotation was expected in the reflected wave and, indeed, it has not been found) [4]. Afterwards, we have used those results to calculate the effective Pasteur parameter of the structure.

### 3.1. Scattering Coefficients

In this paper, the results using two different dielectric slabs are presented. Figs 3 ("original" shape) and 4 ("complementary") show the scattering parameters when the dielectric slab is 0.03 inches width and it is made of Taconic TLC 30. The simulation has been performed using time-domain CST Studio software. In Fig. 3 there is a first resonance (minimum of R and $T_{CO}$ and maximum of $T_{CR}$), at 10.6 GHz, plus a second one (minimum of $T_{CO}$) at 12.4 GHz.. Fig. 4, instead, shows a first resonance (minimum of R and maximum of $T_{CR}$ and $T_{CO}$) at 10.7 GHz, and a second one (again, minimum of R and maximum of $T_{CR}$ and $T_{CO}$) around 12.1-12.2 GHz.

This results are in agreement with what is proposed in [1]: both shapes resonate in the same frequencies approximately but, while in the original shape, there is a minimum of the transmission for the (copolarization) transmission coefficient; in the complementary one there is a maximum of this coefficient.

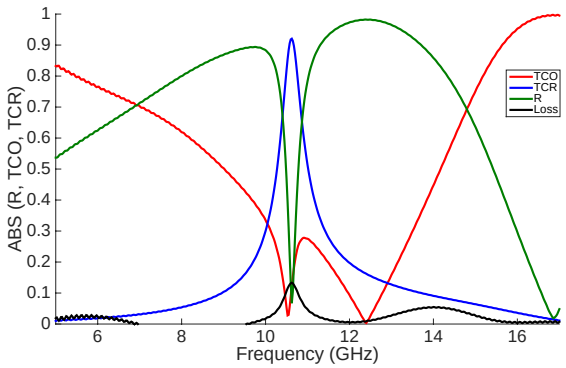



Figure 3: Reflection (R), Copolarization (TCO), and Crosspolarization (TCR) transmission coefficients, as well as relative losses for a plane wave normally incident over a periodic structure composed by cells as shown in Fig. 1. The dielectric slab is 0.03 inches width and it is made of Taconic TLC 30.

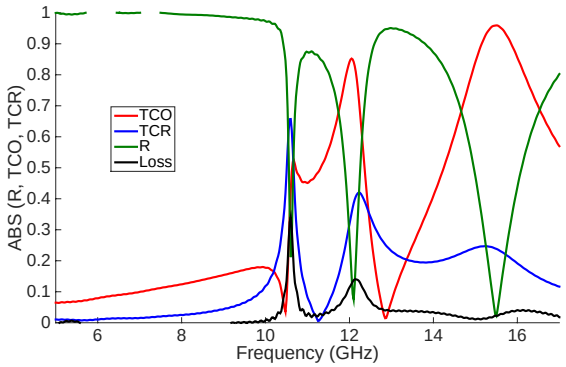



Figure 4: Reflection (R), Copolarization (TCO), and Crosspolarization (TCR) transmission coefficients, as well as relative losses for a plane wave normally incident over a periodic structure composed by cells as shown in Fig. 2. The dielectric slab is 0.03 inches width and it is made of Taconic TLC 30.

Figs. 5 and 6 show the scattering parameters when the dielectric slab is 0.06 inches width and it is made of Rogers RO4003C. In this case, the simulation has been performed using EMPRO software.

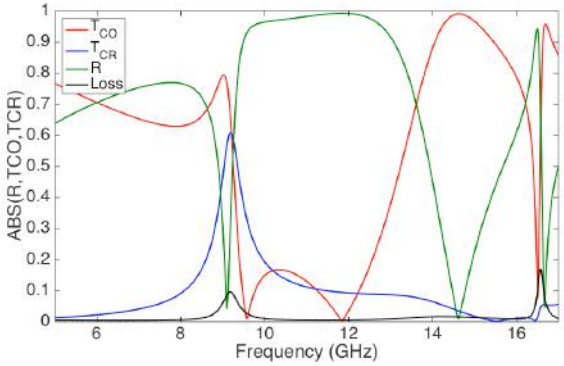



Figure 5: Reflection (R), Copolarization (TCO), and Crosspolarization (TCR) transmission coefficients, as well as relative losses for a plane wave normally incident over a periodic structure composed by cells as shown in Fig. 1. The dielectric slab is 0.06 inches width and it is made of Rogers RO4003C.

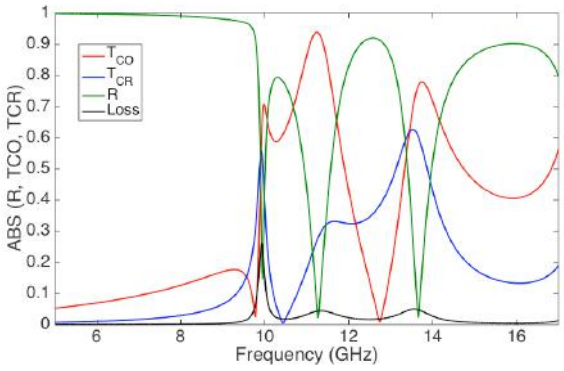



Figure 6: Reflection (R), Copolarization (TCO), and Crosspolarization (TCR) transmission coefficients, as well as relative losses for a plane wave normally incident over a periodic structure composed by cells as shown in Fig. 2. The dielectric slab is 0.06 inches width and it is made of Rogers RO4003C.

Looking at Figs. 5 and 6, the results are very similar to what was found in the first case: the resonances are placed now at slightly lower frequencies (9.1 GHz and 11.8 GHz in Fig. 5; 9.9 GHz and 10.4 GHz). The difference may be explained because of the higher dielectric constant of the slab.

In all the four figures, every resonance is associated with a strong rotation of the polarization plane (maximum value of $T_{CR}$). There are frequencies, coinciding with the resonances (Figs. 3 and 5) or close to them (Figs. 4 and 6) where the copolarization transmission coefficient is close to 0. That means the structures behave as a 90º polarization rotator, almost without dichroism (losses) at those frequencies.

At the same time, it is worth of noticing the high value of the total transmission coefficients in the resonant frequencies. To make them more evident, we have added in both figures the value of the energy losses ($1-R^2-T_{CO}^2-T_{CR}^2$). It is worth of being mentioned that those losses are almost negligible in most of frequencies, and stay in a low value even in the resonance frequencies.

### 3.2. Pasteur Parameter

The presence of a giant gyrotropy is, indeed, due to the chirality of both structures. We have calculated, too, the Pasteur parameter (κ) in every case; since the results are very similar, only the parameters for the first example (Taconic dielectric) are shown in Figs. 7 and 8.

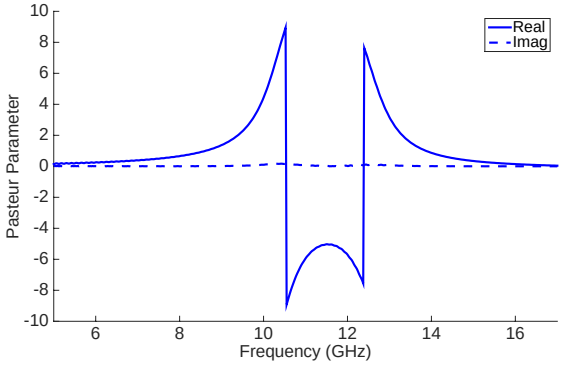



Figure 7: Effective Pasteur parameter (κ) of a periodic structure composed by cells like shown in Fig. 1. The dielectric slab is 0.03 inches width and it is made of Taconic TLC 30.

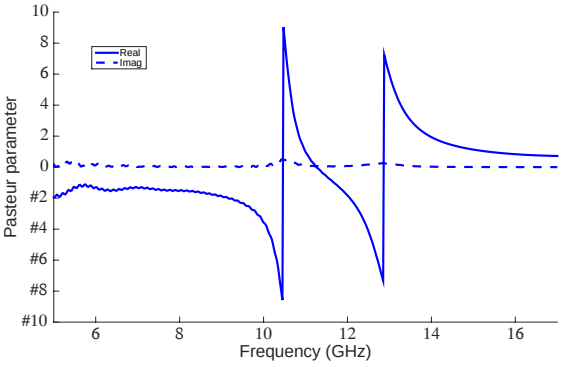



Figure 8: Effective Pasteur parameter (κ) of a periodic structure composed by cells like shown in Fig. 2. The dielectric slab is 0.03 inches width and it is made of Taconic TLC 30.

The chirality parameters show both resonant behaviors as predicted by the Condon model [5]. The resonances are placed too in similar frequencies: 10.5 GHz and 12.4 GHz for the “original” structure; 10.5 GHz and 12.8 GHz for the

"complementary" one. They are also placed, approximately, at the same frequencies of the resonances in the scattering parameters (minimums of $T_{CO}$ in Figs. 3 and 4). It is worth of noticing the change in the sign of the second resonance between the original and the complementary shapes.

In both cases the imaginary part (i.e., losses) is almost insignificant, even in resonance, while there is a huge real part (gyrotropy). Especially the "original" shape shows a significant real part (-5) during a wide band (11-12 GHz) virtually without losses.

## Conclusions

A planar complementary metamaterial has been designed and characterized. Its scattering parameters have been numerically calculated, and compared with the corresponding values for its complementary structure. The comparison between both cases is in good agreement with the theoretical predictions. Both structures show a giant gyrotropy as well as an almost negligible dichroism, so their Pasteur parameter has also been calculated. They indeed present a strong chirality, with a low imaginary part.

## Acknowledgements

This work has been supported by the Spanish Government (MINECO) through the Research Projects TEC2014-55463-C3-1-P, TEC2014-55463-C3-2-P, and TEC2014-55463-C3-3-P and also by the European Commission (ERDF).

## References

[1] H.-T. Chen, J.F. O'Hara, A.J. Taylor, R.D. Averitt, C. Highstrete, M. Lee, W.J. Padilla, Complementary Planar Terahertz Metamaterials, *Optics Express* 34, 10: 1084–1095, 2007.

[2] Z. Li, K.B. Alici, E. Colak, E. Ozbay, Complementary Chiral metamaterials with giant optical activity and negative refractive index, *Appl. Phys. Lett.* 98, 161907, 2011.

[3] I. Barba, A. Grande, A.C. López-Cabeceira, G.J. Molina-Cuberos, J. Represa, A partially complementary chiral metamaterial based on a four-cranks resonator, *9th European Conference on Antennas and Propagation, EuCAP'2015*, Lisbon, Portugal, 2015.

[4] Y. Yee, S. He, 90º polarization rotator using a bilayered chiral metamaterial with giant optic activity, *Applied Physics Letters*, 96: 20351, 2010.

[5] A.H. Sihvola, A.J. Viitanen, I.V. Lindell, S.A. Tretyakov, Electromagnetic *Waves in Chiral and Bi-Isotropic Materials*. Artech House, 1994.

[6] J.B. Pendry, A chiral route to negative refraction, *Science* 306, 5700: 1353-1355, 2004.

# A New Metasurface based on Meta-atom Cluster for Terahertz Applications

**M. M. Islam[1, *], M. F. Mansor[2], M. R. I. Faruque[3], and M. T. Islam[2]**

[1]Department of Software Engineering, Daffodil International University, Dhaka 1207, Bangladesh
[2]Deparment of Electrical, Electronic & Systems Engineering, Universiti Kebangsaan Malaysia, 43600 UKM, Bangi, Malaysia
[3]Space Science Centre (ANGKASA), Universiti Kebangsaan Malaysia, 43600 UKM, Bangi, Malaysia
*corresponding author, E-mail: mmoiislam@yahoo.com

## Abstract

In the manuscript, a new metasurface is presented for terahertz applications based on meta-atom cluster. The metasurface having magnetic and electric resonances shows left-handed metamaterial characteristics in the terahertz frequency. The meta-atom cluster consists of split-ring resonators based on conducting wire strip (a single loop) printed on RT5880LZ substrate material. The permeability and the permittivity are picked out from the complex scattering parameters. The calculation of the unloaded Q-factor is executed for the meta-atom cluster based metasurface in the terahertz frequency. The test of the metasurface has been performed using different dielectric samples loaded. Effective change has been realized in the transmission. This metasurface is novel in case of terahertz band due to left-handed characteristics. This metasurface is appropriate for high-performance filters and sensors due to high Q-factors.

## 1. Introduction

Metasurfaces are presented for terahertz applications as potential applicant in the field of high performance sensors and filters [1-3]. For these potentials, their low Q-factors are gradually improved. Metamaterials or meta-atoms can control the light waves in a wonderful way. The metamaterial is made of subwavelength resonating metal which is fabricated on dielectric materials. The metallic resonators provide the consequent electromagnetic behaviors than molecules or atoms [4].

Meta-atom is an electromagnetic metamaterial which is a subwavelength structure engineered artificially in a periodic array. Metamaterial characteristics are not found in ordinary materials which exhibit the positive permeability and permittivity, where, in the effective medium region, the meta-atoms can display negative permeability and/or permittivity. In the case, the ratio between unit cell size and wavelengths is > 4, which is called the effective medium ratio [5]. There are various types of meta-atoms such as metallic thin wires [6], cut-wire pairs [7], split-ring resonators[8], Ω type metallic inclusion [9], and electric-LC resonator[10] in the microwave frequency region. A negative permeability and permittivity is found at lower frequencies through metallic thin wires [6] shortening and changing the fundamental frequency to the spectrum's lower part. Meta-atoms create new route to observe left-handed properties where both permeability and permittivity are negative, simultaneous, which lead negative index features are not available in nature[11]. In order to point out the effective parameters (negative permeability and permittivity), transmission wires have been applied for testing the meta-atoms in the beginning stages [12]. In meta-atom field, negative index materials having extraordinary attitude play an important role for making metamaterial field attractive and for enhancing the operation in visible frequency spectrum[13].

Various types of opportunities have been stated with meta-atoms for raising the abilities of the running microwave and optical devices and components in terms of functional abilities. Invisibility cloaks [14], biosensors [15] and super lenses [16] have been explored with the running researches. Split-ring resonators (SRRs) having impressive features are extensively applied in various meta-atom as basic circuits. Negative resonances are pointed out at negative refractive index regions, with these artificial structures which are not possible for any natural material. Meta-atom resonators are also used in in imaging [17]. In sensor clusters, SRRs have been applied in different orientation as unit cell with a view to having extraordinary features (negative refractive index, permeability, and permittivity). At the high frequency, it is not possible to ignore the substrate material's effect owing to high loss which is reduced with the utilization of substrate material [18] of very low and thin permittivity. Different shapes of SRRs such as S-shape resonator[19], omega resonators[20], hexagon shape[21] have been mentioned in the literature for meta-atoms. In the terahertz frequency, researches on double negative meta-atoms are raised rapidly[22].

Condensed electromagnetic field is displayed with meta-atoms and plays an important role for achieving sensors of enhanced selectivity in terms of detecting analytes [23].In many applications, meta-atoms are used extensively instead of metallic conductors whereas surface plasmons are engaged [24]. At high frequency, meta-atoms of sized subwavelength have been applied as sensing devices[25].

In sensing applications, subwavelength resonators of two dimension are appropriate [26]. Narrow waveguide channels of electric permittivity near-zero have been applied to narrate meta-atoms for sensing [27]. For detecting materials with small fault, nondestructive evaluation sensor based on meta-atoms in comparison with a wavelength have been mentioned in [28].

In the research, a new metasurface has been mentioned for terahertz applications based on meta-atom cluster. The meta-atom cluster consists of split-ring resonators based on conducting wire strip printed on RT5880LZ substrate material. By using different dielectric samples loaded the measurement of the metasurface has been executed. Effective change has been realized in the transmission. This metasurface is novel in case of terahertz band due to left-handed characteristics.

## 2. Material and Methods

The proposed metasurface has been arranged periodically in the form of meta-atom cluster demonstrated in Fig 1. Spectral resolution is an important issue in the terahertz application. Most of the existing materials cannot be applied for sensing of minute samples in the terahertz frequency because of having poor magnetic and electric responses. The proposed metasurface operates in the terahertz frequency due to belonging high spectral resolution.

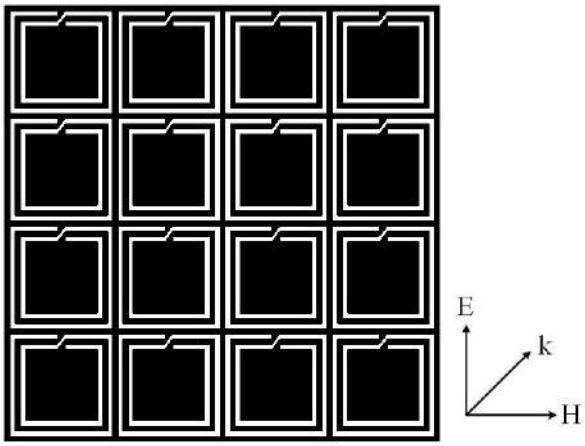


Figure 1: Metasurface based on 4 by 4 meta-atom cluster.

The meta-atom cluster is made of rectangular SRRs and is ordered periodically on a thin dielectric material. In order to attain strong magnetic and electric response from meta-atom cluster, perpendicular incidence external field has been used. The strong LC resonance has been realized. The surface current is dominantly distributed in the SRR rings and split gap provides increased capacitance.

Electromagnetic resonance is pointed out with SRR whereas capacitor contains the electric energy. In the way, the inductor contains the magnetic energy which is balanced with split gap. [29, 30]. Owing to loaded dielectric, the shift in inductance (L) and capacitance (C) conducts a reasonable change in the resonant frequency indicated in the equation (1).

$$f_c = \frac{1}{2\pi\sqrt{LC}} \quad (1)$$

A new shape of rectangular SRR has been used to design the unit cell of the proposed meta-surface based on meta-atom cluster. Two rectangular SRRs have been aligned face to face with modified gaps at the top and bottom spaced with 1.5 μm to each other on a thin dielectric substrate. The proposed modified SRR is indicated in Fig 2 with geometric dimensions. Computer Simulation Technology (CST) has been applied for the simulation of the mentioned met-atom cluster, which helps to compute the parameters with the complex scattering constitutive parameters. For retrieving the effective parameters, the simulated scattering parameters have been achieved.

The extraction of the effective parameters with SRRs have been executed applying Nicolson-Ross and Weir method[31, 32]. In addition, in order to achieve better results, the Kramers-Kronig relationship[33] have been utilized. 1.0 μm is the space between the width of the outer and inner gap. Gold strips have been used to design the SRRs including 11.9 permittivity. The gold strips have been printed on the substrate. The material strip is based on gold and annealed copper (5.8×10 Siemens per meter). 0.017 μm is the strip thickness. Deeper resonances have been created with the use of low permittivity materials at terahertz frequency [34]. For this reason, RT5880LZ of relative permeability 1 and permittivity 1.96 has been applied as a substrate for attaining smaller unit to wavelength ratio. The meta-atom unit cell configuration is listed in Table 1.

Table 1: configuration of meta-atom unit cell.

| parameters | dimensions[μm] |
|---|---|
| $W_1$ | 20 |
| $W_2$ | 14 |
| $W_3$ | 6.25 |
| $W_4$ | 9.25 |
| $L_1$ | 20 |
| $g_1$ | 1.5 |
| $g_2$ | 1.5 |
| $g_3$ | 1 |
| $g_4$ | 1 |
| $g_5$ | 1 |

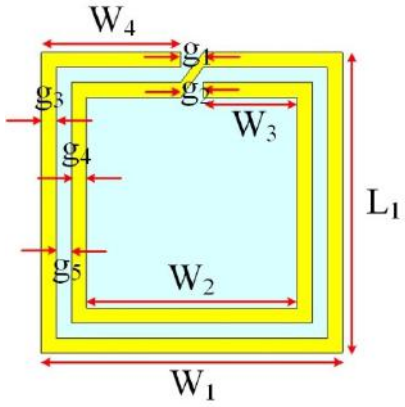



Figure 2: Design layout of Meta-atom unit cell.

By using the equation (2) & (3), the permittivity and permeability have been calculated as following

$$\mu_r = \frac{2}{jk_0 d} \times \frac{1-\nu_2}{1+\nu_1} \quad (2)$$

$$\varepsilon_r = \frac{2}{jk_0 d} \times \frac{1-\nu_1}{1+\nu_2} \quad (3)$$

In the equation (2) & (3), $k_0$ and d have been denoted as the wave number and the substrate thickness, respectively. The scattering parameters have been presented as following equations (4) and (5):

$$\nu_1 = S_{21} + S_{11} \quad (4)$$

$$\nu_2 = S_{21} - S_{11} \quad (5)$$

The sensitivity of the proposed meta-surface has been explained in terms of Q factor (Quality factor). The calculation of the Q factor with a dip or a resonance peak have been performed using the frequency bandwidth ($\Delta f$) and the resonant frequency ($f_0$) of the resonant peak at -3 dB power point [35] indicated in equation (6). Quality factors of the meta-atoms are realized approximately 10, which are operated in the terahertz frequency at the microwave portion [36]. Unloaded Q factor of the mentioned metasurface based on meta-atom cluster have been calculated using -3dB bandwidth formula, which is listed in the Table 2.

$$Q = \frac{f_0}{\Delta f} \quad (6)$$

Table 2: Q factor at the resonant frequency.

| Resonant frequency [THz] | Quality factor |
|---|---|
| 3.05 | 97 |

It can be observed that the Q factor is very high, this means that the reported meta-surface belongs to high sensibility. The value of Q factor depends on the sharpness of the transmission and the location of resonant frequency. The deeper the resonance the higher the value of Q can be achieved.

## 3. Results and Discussion

The proposed meta-surface has been made of rectangular SRRs, arranged periodically in the form of meta-atom cluster. For attaining stable magnetic and electric field response from the mentioned meta-surface based on meta-atom cluster, perpendicular incidence external field has been utilized. In order to realize the transmission spectra of the meta-atom unit cell, incidence direction is perpendicular to the meta-atom unit cell surface plane. The magnetic and electric fields have been polarized, which is parallel to the long edges of the meta-surface along z-axis and y-axis, respectively. When the long edges of the structure are parallel to the electric field polarization, electric response has been induced with the perpendicular incident waves. When a loop is existed in the SRR structure, for inducing the magnetic response, the parallel incident waves are comfortable. From the surface current distribution, it is realized that the LC resonance is very stable and the electric field is a dominant figure on the inner ring and the outer ring with capacitive gap area indicated in Fig. 3.

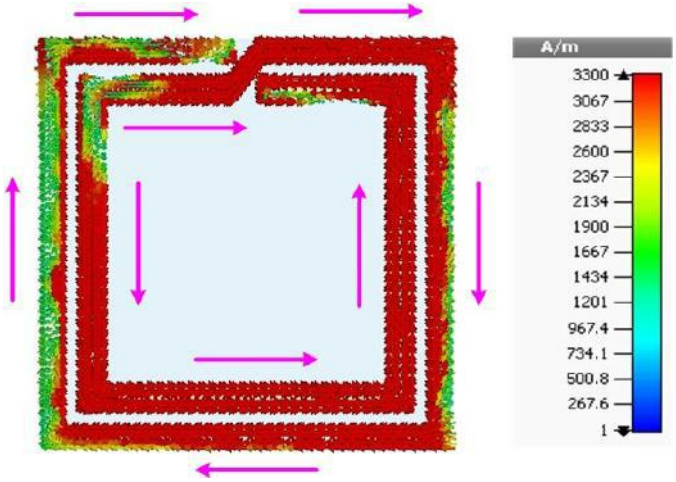



Figure 3: Surface current distribution at the resonant frequency 3.05 THz.

The concentration of the surface current is around the split gap due to having raised capacitance. The current flows entirely the meta-atom cluster including the split gap area.

Fig.4 demonstrates the effective permeability of the mentioned meta-surface. Fig. 5 indicates the effective permittivity of the mentioned meta-surface. Table 3 conducts the negative frequency area with details. It can be realized from the two figures that at the resonant frequency 3.05 THz, a sharp negative region exists in case of both permittivity and permeability. This proves the properties of double negative metamaterial or left-handed metamaterial.

Table 3: Parameters at the negative frequency area.

| parameter | Negative frequency region [THz] |
|---|---|
| permeability | 3.01-5 |
| permittivity | 2-2.25, 3-3.71 |

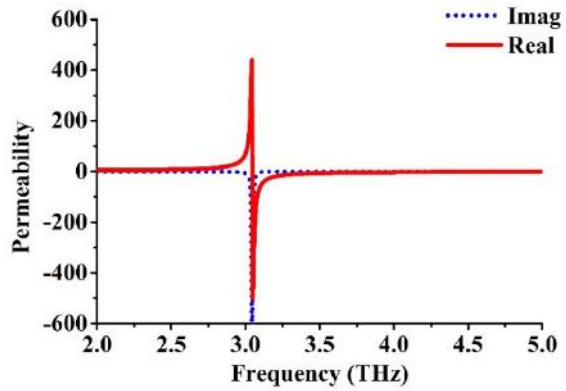



Figure 4: Effective permeability.

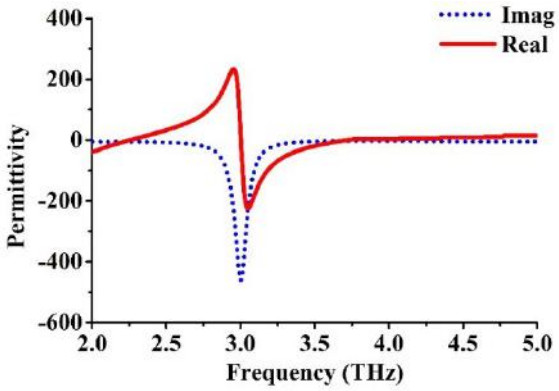



Figure 5: Effective permittivity.

SRRs are metamaterial structures which are extensively applied in terahertz applications due to having loop layout in the configuration. The current flows at the electric resonant frequency, which is parallel to the polarization direction. This means that the meta-atom split ring resonator acts like an electric dipole.

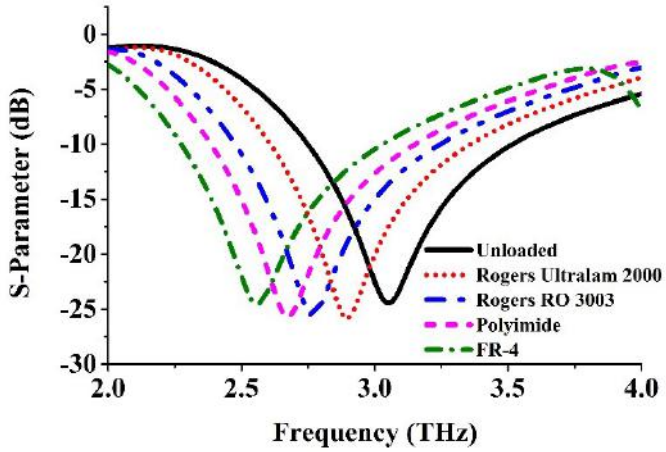



Fig. 6: Transmission spectra of the metasurface under loading and unloading conditions.

At the resonant frequency, a stop band has been noticed, when the sample layer has not been loaded on the mentioned meta-surface or under the unloading condition. During this period, both the real part of permeability and permittivity go to the frequency area with negative value, which indicates the properties of double negative metamaterial. The thickness and dielectric constant of the substrate have been remained constant in all the experimental simulations along with the sample thickness, which is maintained to 100 nanometer. The meta-surface has been scaled down to attain the optimum values, which conduct the presence of the thin sample layers for sensing applications. In case of unloaded transmission, resonance is observed at 3.05 THz frequency and but transmission is shifted when the meta-atom cluster have been loaded with FR4, Polyimide, Rogers RO 3003 and Rogers Ultralam 2000, indicated in Fig. 6. Simulations are executed under different loading conditions and listed in Table 4.

Table 4: Dielectric materials for sample loadings.

| material | permeability | permittivity | shift $\Delta f/f$ |
|---|---|---|---|
| FR4 | 1 | 4.6 | 0.49 THz |
| polymide | 1 | 3.5 | 0.38 THz |
| RO 3003 | 1 | 3 | 0.29 THz |
| Ultralam 2000 | 1 | 2.5 | 0.15 THz |

## 4. Conclusions

The proposed new meta-surface based on meta-atom cluster points out double negative or left-handed metamaterial characteristics for THz applications.The mentioned meta-surface is made of meta-atom cluster of split-ring resonators based on conducting wire strip (RT5880LZ material). It is found that the transmission has been shifted to the lower frequency due to the thin dry dielectric layers of the mentioned meta-surface. Significant changes were observed under loading samples with higher dielectric constants. This metasurface is novel in case of terahertz band due to left-handed characteristics to the 3.05 THz. This metasurface is appropriate for high-performance filters and sensors due to high Q-factors.

## Acknowledgements

This work was supported by the Research University (RU) grant, Malaysia under GUP-2016-028 and GUP-2016-029.

## References

[1] C. Jansen, I. A. Al-Naib, N. Born, and M. Koch, "Terahertz metasurfaces with high Q-factors," *Applied Physics Letters,* vol. 98, p. 051109, 2011.

[2] N. Naeem, A. Ismail, H. Alhawari, A. Reda, and M. A. Mahdi, "Terahertz Dielectric Sensor Based on Novel Hexagon Meta-Atom Cluster," *Applied Computational Electromagnetics Society Journal,* vol. 30, 2015.

[3] B. Luk'yanchuk, N. I. Zheludev, S. A. Maier, N. J. Halas, P. Nordlander, H. Giessen, *et al.*, "The Fano resonance in plasmonic nanostructures and metamaterials," *Nature materials,* vol. 9, pp. 707-715, 2010.

[4] J. Pendry, "Photonics: Metamaterials in the sunshine," *Nature Materials,* vol. 5, pp. 599-600, 2006.
[5] A. Sarkhel, D. Mitra, S. Paul, and S. R. B. Chaudhuri, "A compact meta-atom for dual band negative permittivity metamaterial," *Microwave and Optical Technology Letters,* vol. 57, pp. 1152-1156, 2015.
[6] J. Pendry, A. Holden, W. Stewart, and I. Youngs, "Extremely low frequency plasmons in metallic mesostructures," *Physical review letters,* vol. 76, p. 4773, 1996.
[7] D. A. Powell, I. V. Shadrivov, and Y. S. Kivshar, "Cut-wire-pair structures as two-dimensional magnetic metamaterials," *Optics express,* vol. 16, pp. 15185-15190, 2008.
[8] J. Pendry, A. Holden, D. Robbins, and W. Stewart, "Magnetism from conductors and enhanced nonlinear phenomena," *IEEE Transactions on Microwave Theory Techniques,* vol. 47, pp. 2075-2084, 1999.
[9] F. Zhang, G. Houzet, E. Lheurette, D. Lippens, M. Chaubet, and X. Zhao, "Negative-zero-positive metamaterial with omega-type metal inclusions," *Journal of Applied Physics,* vol. 103, p. 084312, 2008.
[10] D. Schurig, J. Mock, and D. Smith, "Electric-field-coupled resonators for negative permittivity metamaterials," *Applied Physics Letters,* vol. 88, p. 041109, 2006.
[11] J. B. Pendry and D. R. Smith, "Reversing light with negative refraction," *Physics today,* vol. 57, pp. 37-43, 2004.
[12] D. R. Smith, W. J. Padilla, D. Vier, S. C. Nemat-Nasser, and S. Schultz, "Composite medium with simultaneously negative permeability and permittivity," *Physical review letters,* vol. 84, p. 4184, 2000.
[13] G. Dolling, M. Wegener, C. M. Soukoulis, and S. Linden, "Negative-index metamaterial at 780 nm wavelength," *Optics letters,* vol. 32, pp. 53-55, 2007.
[14] R. Liu, C. Ji, J. Mock, J. Chin, T. Cui, and D. Smith, "Broadband ground-plane cloak," *Science,* vol. 323, pp. 366-369, 2009.
[15] C. Debus and P. H. Bolivar, "Frequency selective surfaces for high sensitivity terahertz sensing," *Applied Physics Letters,* vol. 91, p. 184102, 2007.
[16] X. Zhang and Z. Liu, "Superlenses to overcome the diffraction limit," *Nature materials,* vol. 7, pp. 435-441, 2008.
[17] B. Sensale-Rodriguez, S. Rafique, R. Yan, M. Zhu, V. Protasenko, D. Jena*, et al.*, "Terahertz imaging employing graphene modulator arrays," *Optics express,* vol. 21, pp. 2324-2330, 2013.
[18] J. F. O'Hara, R. Singh, I. Brener, E. Smirnova, J. Han, A. J. Taylor*, et al.*, "Thin-film sensing with planar terahertz metamaterials: sensitivity and limitations," *Optics Express,* vol. 16, pp. 1786-1795, 2008.
[19] H. Chen, L. Ran, J. Huangfu, X. Zhang, K. Chen, T. M. Grzegorczyk*, et al.*, "Left-handed materials composed of only S-shaped resonators," *Physical Review E,* vol. 70, p. 057605, 2004.
[20] B.-I. Wu, W. Wang, J. Pacheco, X. Chen, T. M. Grzegorczyk, and J. A. Kong, "A study of using metamaterials as antenna substrate to enhance gain," *Progress In Electromagnetics Research,* vol. 51, pp. 295-328, 2005.
[21] F. H. Wee, F. Malek, A. Al-Amani, and F. Ghani, "Effect of two different superstrate layers on Bismuth Titanate (BiT) array antennas," *Scientific reports,* vol. 4, 2014.
[22] Y. Yuan, C. Bingham, T. Tyler, S. Palit, T. H. Hand, W. J. Padilla*, et al.*, "Dual-band planar electric metamaterial in the terahertz regime," *Optics Express,* vol. 16, pp. 9746-9752, 2008.
[23] Z. Jakšić, S. Vuković, J. Matovic, and D. Tanasković, "Negative refractive index metasurfaces for enhanced biosensing," *Materials,* vol. 4, pp. 1-36, 2010.
[24] A. Ishimaru, S. Jaruwatanadilok, and Y. Kuga, "Generalized surface plasmon resonance sensors using metamaterials and negative index materials," *Progress In Electromagnetics Research,* vol. 51, pp. 139-152, 2005.
[25] M. Shamonin, O. Radkovskaya, C. Stevents, G. Faulkner, D. Edwards, O. Sydoruk*, et al.*, "Waveguide and sensor systems comprising metamaterial element," in *Proceedings of the DPG—Spring Meeting of the Division Condensed Matter*, 2006, pp. 114-118.
[26] T. Chen, S. Li, and H. Sun, "Metamaterials application in sensing," *Sensors,* vol. 12, pp. 2742-2765, 2012.
[27] A. Alu and N. Engheta, "Dielectric sensing in ϵ-near-zero narrow waveguide channels," *Physical Review B,* vol. 78, p. 045102, 2008.
[28] D. Shreiber, M. Gupta, and R. Cravey, "Comparative study of 1-D and 2-D metamaterial lens for microwave nondestructive evaluation of dielectric materials," *Sensors and Actuators A: Physical,* vol. 165, pp. 256-260, 2011.
[29] I. M. Rusni, A. Ismail, A. R. H. Alhawari, M. N. Hamidon, and N. A. Yusof, "An aligned-gap and centered-gap rectangular multiple split ring resonator for dielectric sensing applications," *Sensors,* vol. 14, pp. 13134-13148, 2014.
[30] M. T. Islam, M. M. Islam, M. Samsuzzaman, M. R. I. Faruque, and N. Misran, "A negative index metamaterial-inspired UWB antenna with an integration of complementary SRR and CLS unit cells for microwave imaging sensor applications," *Sensors,* vol. 15, pp. 11601-11627, 2015.
[31] A. Nicolson and G. Ross, "Measurement of the intrinsic properties of materials by time-domain techniques," *Instrumentation and Measurement, IEEE Transactions on,* vol. 19, pp. 377-382, 1970.
[32] W. B. Weir, "Automatic measurement of complex dielectric constant and permeability at microwave frequencies," *Proceedings of the IEEE,* vol. 62, pp. 33-36, 1974.
[33] Z. Szabo, G.-H. Park, R. Hedge, and E.-P. Li, "A unique extraction of metamaterial parameters based on Kramers–Kronig relationship," *Microwave Theory and Techniques, IEEE Transactions on,* vol. 58, pp. 2646-2653, 2010.

[34] C. Sabah and H. Roskos, "Terahertz sensing application by using planar split-ring-resonator structures," *Microsystem technologies,* vol. 18, pp. 2071-2076, 2012.
[35] X.-j. He, L. Qiu, Y. Wang, Z.-x. Geng, J.-m. Wang, and T.-l. Gui, "A compact thin-film sensor based on nested split-ring-resonator (SRR) metamaterials for microwave applications," *Journal of Infrared, Millimeter, and Terahertz Waves,* vol. 32, pp. 902-913, 2011.
[36] W. Cao, R. Singh, I. A. Al-Naib, M. He, A. J. Taylor, and W. Zhang, "Low-loss ultra-high-Q dark mode plasmonic Fano metamaterials," *Optics letters,* vol. 37, pp. 3366-3368, 2012.

# Left-Handed Compact MIMO Antenna Array Based on Wire Spiral Resonator for 5 GHz Wireless Applications

**A. S. M. Alqadami[1], M. F. Jamlos[2], P. J. Soh[3], S.K.A. Rahim[4]**

[1,2,3]Advanced Communication Engineering Centre (ACE), School of Computer and Communication Engineering, Universiti Malaysia Perlis (UniMAP), 01000, Kangar, Perlis, Malaysia.

[2]Faculty of Mechanical Engineering, Universiti Malaysia Pahang (UMP), Pekan, Malaysia.

[4]Wireless Communication Centre (WCC), Universiti Teknologi Malaysia, Johor Bharu, Malaysia.

[2]mohdfaizaljamlos@gmail.com

**Abstract-** A compact coplanar waveguide(CPW)-fed Multiple Input Multiple Output (MIMO) antenna array based on the left-handed wire loaded spiral resonators (SR) is presented. The proposed antenna consists of a 2×2 wire SR with two symmetrical microstrip feed lines, each line exciting a 1x2 wire SR. Left-handed (LH) metamaterial unit cells are placed on its reverse side and arranged in a 2×3 array. A reflection coefficient of less than -10 dB, mutual coupling of less than -20 dB, a 0.004 correlation coefficient, and high diversity gain of 9.99 dB are achieved at 5.0 GHz-5.20 GHz WLAN band.

Fig. 1 (a) and (b) shows the structure of the left-handed wire spiral resonator unit cells. The substrate is Taconic TLY-5 with $\varepsilon_r = 2.2$ and 1.57 mm thickness. The geometrical parameters of the proposed unit cell are tabulated in Table.1, while its characteristics are evaluated by the mathematical formulation in [1 - 2]. The negative index metamaterial parameters are produced by the excitation of electric and magnetic dipoles in the LH wire SR unit cells. Fig. 1 (c), (d), (e) and (f) illustrates the obtained real and imaginary values of refractive index, impedance, permittivity, and permeability, and is operable within the desired frequency range of 5.0 GHz to 5.20 GHz.

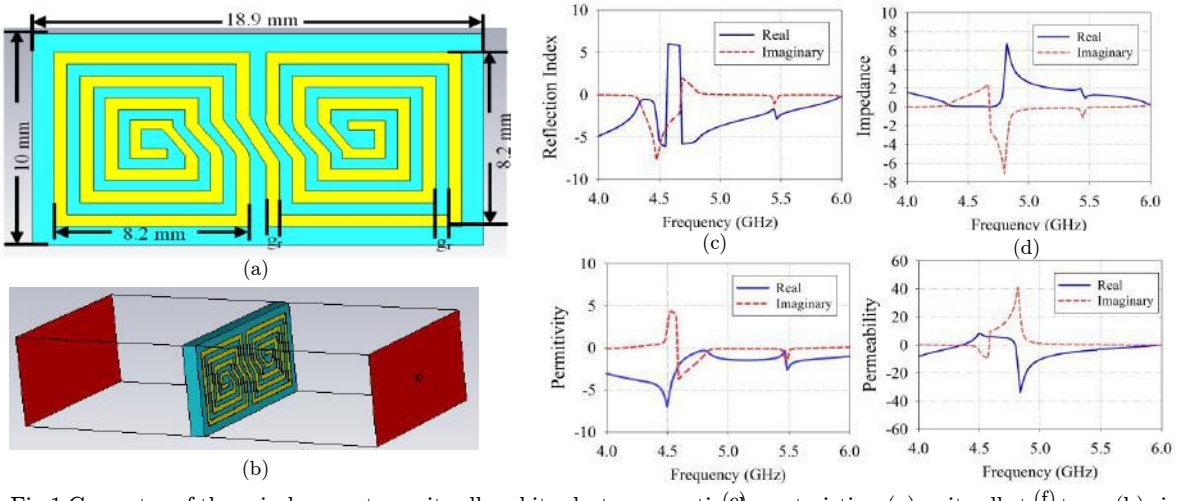



Fig.1 Geometry of the spiral resonator unit cell and its electromagnetic characteristics, (a) unit cell structure, (b) simulation setup, (c) reflective index, (d) impedance, (e) permittivity, (f) permeability.

Fig.2 illustrates the simulated setup of the proposed CPW-fed MIMO antenna array. It consists of a 2×2 wire SR fed by two symmetrical microstrip lines and connected using two 50Ω SMA connectors. The ground plane is located on the same face as its radiators, besides its feed line. The square slots on the ground planes are introduced

to improve the reflection coefficient and impedance bandwidth. Twelve left-handed SR unit cells are arranged in 2×3 array configuration for each port, and it is placed on the reverse side of the proposed, see Fig. 2 (c). Their dimensions are summarized in Table.1.

Fig.3 (a) shows a good reflection coefficient ($S_{11}$) and low mutual coupling ($S_{21}$) at the operating frequency. Fig.3 (b) and (c) demonstrates a low correlation coefficient (0.004), high diversity gain (9.99 dB) and satisfactory radiation patterns at 5.1 GHz. The proposed left-handed SR structure has enabled the concentration of the electromagnetic filed and currents nearby radiating elements instead of distributed them along the ground plane. This allows compact MIMO antenna arrays to be utilized with minim mutual coupling, and high diversity gain [3].

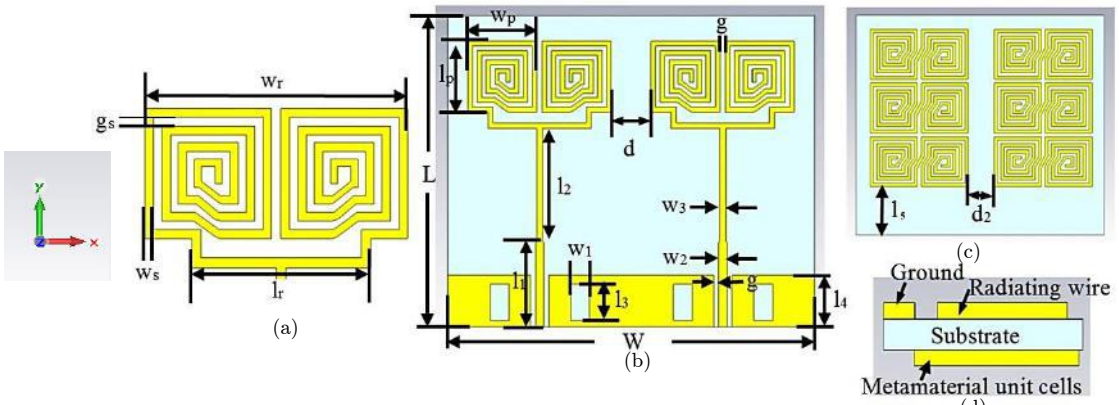



Fig.2 Geometry of the proposed antenna, (a) radiating elements, (b) front view, (c) back view, (d) layer structure.

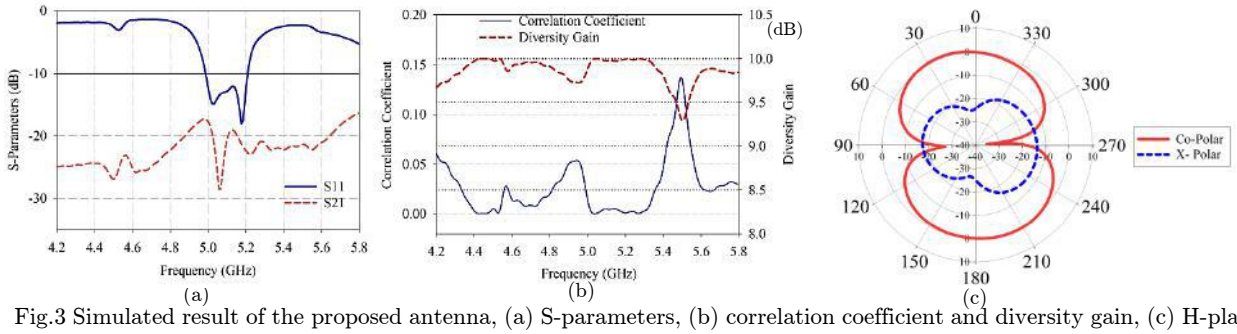



Fig.3 Simulated result of the proposed antenna, (a) S-parameters, (b) correlation coefficient and diversity gain, (c) H-plane radiation patterns.

Table.1 Dimensions of the proposed antenna and wire SR unit cells.

| Para. | Value (mm) | Para. | Value (mm) | Para. | Value (mm) | Para. | Value (mm) | Para. | Value (mm) | Para. | Value (mm) | Para. | Value (mm) |
|---|---|---|---|---|---|---|---|---|---|---|---|---|---|
| W | 36 | $l_p$ | 8.2 | $l_3$ | 4.2 | $w_1$ | 2.2 | d | 4.7 | $g_s$ | 0.55 | $l_r$ | 12.24 |
| L | 43.4 | $l_1$ | 9.6 | $l_4$ | 6 | $w_2$ | 1 | $d_2$ | 4.6 | $g_r$ | 0.55 | $w_s$ | 0.55 |
| $w_p$ | 8.2 | $l_2$ | 13 | $l_5$ | 7.9 | $w_3$ | 0.7 | g | 0.57 | $w_r$ | 17 | - | - |

## REFERENCES


1. Chen, X., T.M. Grzegorczyk, B.-I.Wu, Jr. Pacheco, and J.A Kong, Robust method to retrieve the constitutive effective parameters of metamaterials, *Physical Review E,* 70.1, 2004.
2. Smith, D., D. Vier, T. Koschny, and C. Soukoulis, Electromagnetic parameter retrieval from inhomogeneous metamaterials. *Physical Review E. 71*, 036617, 2005.
3. Lee, C. J., W. Huang, A. Gummalla, and M. Achour, Small antennas based on CRLH structures: Concept, design, and applications. *Antennas and Propagation Magazine, IEEE*, *53*(2), 10-25, 2011.

# Miniaturized Dual Band Antenna Array with Double Negative (DNG) Metamaterial for Wireless Applications

**A. S. M. Alqadami[1], M. F. Jamlos[2], P. J. Soh[3], S.K.A. Rahim[4]**

[1,2,3]Advanced Communication Engineering Centre (ACE), School of Computer and Communication Engineering, Universiti Malaysia Perlis (UniMAP), 01000, Kangar, Perlis, Malaysia.

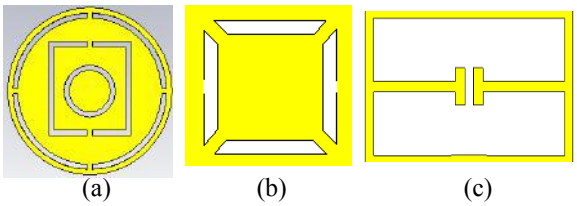
[2]Faculty of Mechanical Engineering, Universiti Malaysia Pahang (UMP), Pekan, Malaysia.

[4]Wireless Communication Centre (WCC), Universiti Teknologi Malaysia, Johor Bharu, Malaysia.

[2]mohdfaizaljamlos@gmail.com

**Abstract-** A miniaturized dual band antenna array using a negative index metamaterial is presented for WiMax and WLAN applications. A left-handed metamaterial unit cell is located on the rear side of the antenna array. The unit cell combined form spilt ring resonator (SRR), square electric ring resonator (SERR) and rectangular electrical coupled (ELC) resonator to obtain a metamaterial structure that exhibit both negative permittivity and permeability. The simulated reflection coefficient ($S_{11}$) shows a 40.25% bandwidth for the first band (2.119–3.058 GHz) and 3.36% for the second band and greater than 95% radiation efficiencies are obtained for both bands.

**In recent years,** negative index metamaterials have become a popular option in miniaturizing antennas due to their artificial electromagnetic properties that cannot be found in nature [1-2]. In this paper, left-handed metamaterial unit cells are utilized to obtain a negative refractive index by producing negative permittivity and permeability. The unit cells that have been used in this antenna are illustrated in Fig.1.



(a) (b) (c)

Fig. 1 Metamaterial unit cells, (a) SRR, (b) SERR, (c) ELC resonator

Fig. 2 (a) shows the front view of the combined unit cells structure. It consists of spilt ring resonator (SRR), square electric ring resonator (SERR) which both magnetic resonant structure. The perpendicular magnetic field produced by those cells generates negative permeability. Meanwhile, the rectangular electrical coupled (ELC) resonator is located between the abovementioned cells and is used to generate negative permittivity. The dimensions of the proposed unit cells are illustrated in Table.1. Fig. 2 (b), (c), (d) and (e) illustrate the real and imaginary values of impedance, refractive index, permeability, and permittivity. The result indicated that the proposed structure features a negative refractive index within 1.5 to 3.6 GHz.

Fig.3 (a) and (b) illustrates the simulated geometry of the proposed antenna. It is an array containing 10-elements; each rectangular element is is dimensioned at 4×4 $mm^2$. The antenna is fed using a combination of both series and corporate feed techniques. It designed on a 0.51 mm thick RT/duroid®5880 substrate. . The metamaterial unit cells and ground plane are located on the rear side of the antenna. The dimensions of the proposed antenna array are demonstrated in Table.1

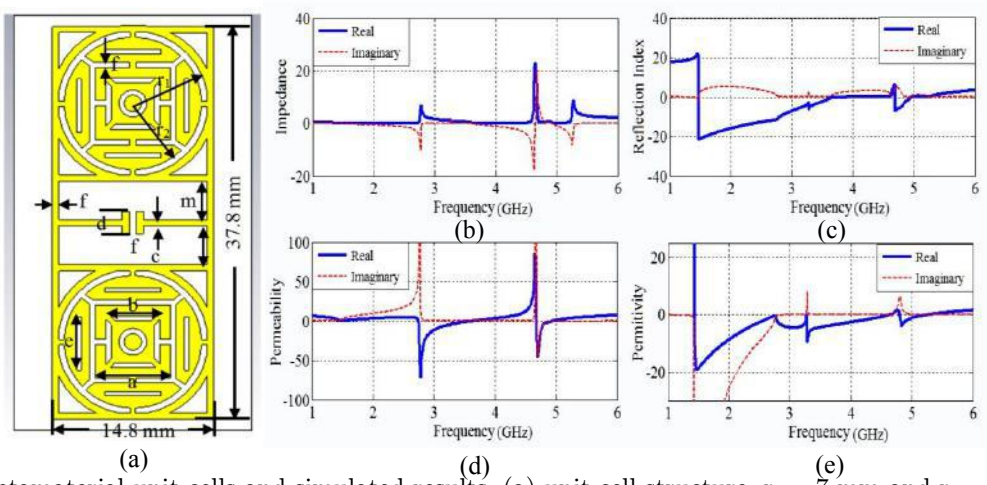



Fig. 2. Metamaterial unit cells and simulated results, (a) unit cell structure, $r_1 = 7$ mm and $r_2 = 6.4$ mm, (b) impedance, (c) reflective index, (d) permeability, (e) permittivity.

Table.1 Dimensions of the proposed metamaterial unit cells and antenna array elements and its feed.

| Para. | Value (mm) | Para. | Value (mm) | Para. | Value (mm) | Para. | Value (mm) | Para. | Value (mm) | Para. | Value (mm) | Para. | Value (mm) |
|---|---|---|---|---|---|---|---|---|---|---|---|---|---|
| a | 7 | d | 2.2 | $w_p$ | 4 | $w_2$ | 0.5 | $w_5$ | 0.6 | $l_2$ | 1.5 | $l_5$ | 2 |
| b | 4.2 | e | 5.2 | $l_p$ | 4.4 | $w_3$ | 0.7 | $w_6$ | 0.6 | $l_3$ | 2 | $l_6$ | 5 |
| c, f | 0.6 | m | 3.7 | $w_1$ | 1 | $w_4$ | 1 | $l_1$ | 10.4 | $l_4$ | 4.8 | $l_7$ | 1 |

Fig. 3(c) illustrates the simulated reflection coefficient ($S_{11}$). It shows a 40.25 % bandwidth for the first band (2.119–3.058 GHz). A gain greater than 2.5 dB and radiation efficiencies of more than 95% are obtained in both bands. The promising performance indicated that it is suitable for WiMax, WLAN as well as LTE applications.

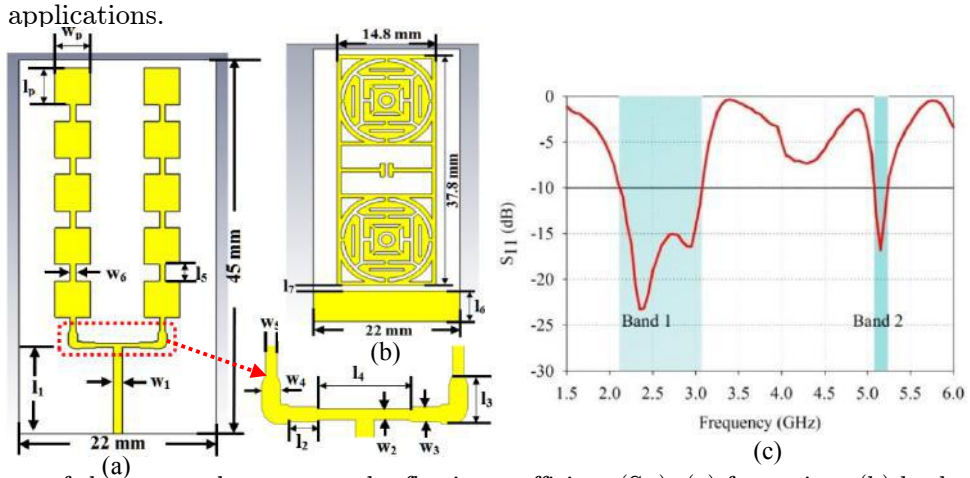



Fig. 3. Geometry of the proposed antenna and reflection coefficient ($S_{11}$), (a) front view, (b) back view, (c) $S_{11}$.

## REFERENCES


1. Schurig, D., J.J. Mock, and D.R. Smith, Electric-field-coupled resonators for negative permittivity metamaterials, *Appl. Phys. Lett.*, 88, (4), p. 041109, 2006.
2. Sajuyigbe, S., B.J. Justice, A.F. Starr, and D.R. Smith, Design and analysis of three-dimensionalized ELC metamaterial unit cell, *IEEE Antennas Wirel. Propag. Lett.*, 8, pp. 1268–1272009.

# Permeability tensor for a metamaterial adjacent to a metal

**Olga Porvatkina*, Alexey Tishchenko, and Mikhail Strikhanov**

National Research Nuclear University MEPhI, Moscow, Russia
*E-mail: OVPorvatkina@mephi.ru

**Abstract**

In our work we investigate magnetic properties of metamaterial-metal interface with help of the local field theory combined with the method of images. Proceeding from microscopic description of the substance and calculating its macroscopic properties, for the first time the modified Clausius-Mossotti relation has been obtained for permeability of the metamaterial bordering a metal.

## 1. Introduction

Metamaterials are artificially structured materials which do not exist in nature and are prospective to control and manipulate light [1,2]. For this reason, metamaterials based on different kind of particles has the advantage of being incorporated into composite structures. For example, metamaterial based on colloidal quantum dots can be successfully used in organic light emitting diodes (OLEDs) [3-5].

In only a few years, the studying of metamaterials has become one of the most exciting topics in the materials engineering with extremely interesting results thanks to combined advances in nanofabrication, numerical modeling and characterization tools [6]. Boundary problems play a vital part because they appear repeatedly in the analysis of metamaterial properties.

The boundary effects at the interfaces between metal and metamaterial, because these effects have a strong influence on the properties of metamaterials [7] and give the possibility of synthesizing such useful structures defined by boundary surfaces [8].

On the other hand, it is well-known that the polarization of a near-surface layer differs from its value in the bulk of the non-magnetic material. Optical anisotropy in near-surface layer is one of the reasons of this phenomenon, as demonstrated theoretically and experimentally in [9,10].

In case of metamaterial investigation of polarization of near-surface layer is also important, because of necessity to interpret correctly the calculations of the parameters of artificial materials.

In our previous work [11] we have considered semi-infinite metamaterial, and analogues of Clausius-Mossotti relations were obtained. These results allow us to analyze dielectric and magnetic properties of semi-infinite metamaterials and understanding influence of polarization of the near-surface layer of metamaterial on the optical phenomena in artificial medium.

To characterize magnetic properties of the boundary under the action of electromagnetic fields at an interface between metamaterial and metal, we introduce the modernized method of images, which is of great interest in the research of electric and magnetic fields in cases where there are reflecting boundaries [12,13]. This method allows us to analyze physical characteristics associated with a configuration of charges by replacing the conductors with image charges.

Thus, method of images is a powerful tool to solve a set of physical problems, constrained by specific symmetries: infinite plane, infinite cylinder, sphere *etc* [14].

Finally, we use the local field theory to link macroscopic properties of the medium and properties of its constituent particles. According to this theory, the local field acting on one of the particles of the medium is the sum of fields generated by all other particles of the medium except the field of considering particle [15]. The local field theory gives good results for 3d metamaterials [16], periodic metamaterials [17] and also for nonmagnetic medium [18].

To sum up, the aim of this research is to find out how the adjacent metal changes the magnetic properties of the metamaterial in the near-interface region.

## 2. Magnetic properties of the metamaterial adjacent to a metal

We consider metamaterial consisting of $N$ anisotropic particles with dielectric and magnetic properties:

$$\alpha_{ij}^{e}(\omega) = \alpha_{\perp}^{e}(\omega)\left(\delta_{ij} - e_i e_j\right) + \alpha_{l}^{e}(\omega) e_i e_j, \qquad (1)$$

$$\alpha_{ij}^{m}(\omega) = \alpha_{\perp}^{m}(\omega)\left(\delta_{ij} - e_i e_j\right) + \alpha_{l}^{m}(\omega) e_i e_j. \qquad (2)$$

The metamaterial is adjacent to a metal. The metamaterial occupies the half-space $z > 0$ and metal occupies the half-space $z < 0$ (Fig.1).

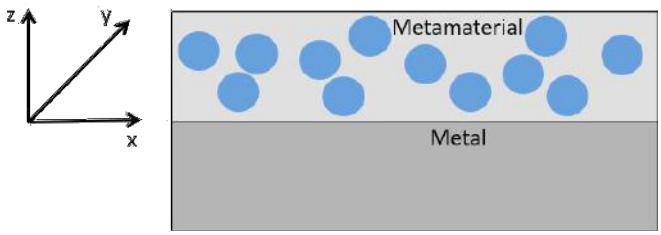



Figure 1: Schematic illustration of a boundary between metamaterial and metal. Particles of metamaterials with dielectric and magnetic polarizabilities $\alpha_{ij}^{e}(\omega), \alpha_{ij}^{m}(\omega)$ are blue circles.

The electromagnetic field $(\mathbf{E}_0, \mathbf{B}_0)$ acts on materials. The microscopic field of the $n$-th particle of the medium is the superposition of the primary field, generated by external source, and secondary fields, produced by all particles of the medium [19]. From Maxwell's equations one can obtain the equation for microscopic magnetic field, acting on the $n$-th particle:

$$
\begin{aligned}
H_i^{mic}(\mathbf{R}_n,\omega) = H_i^0(\mathbf{R}_n,\omega) + \frac{i}{2c\pi^2}\int d^3p \frac{1}{p^2-k^2} \\
\times\Bigg(-i\omega\alpha_{ij}^{e}(\omega)\Big[\mathbf{p}, \sum_b e^{-i\mathbf{p}(\mathbf{R}_b-\mathbf{R}_n)}\mathbf{E}^{mic}(\mathbf{R}_b,\omega)\Big]_j \\
-i\omega\alpha_{ij}^{\prime e}(\omega)\Big[\mathbf{p}, \sum_c e^{-i\mathbf{p}(\mathbf{R}_c-\mathbf{R}_n)}\mathbf{E}^{mic}(\mathbf{R}_c,\omega)\Big]_j \\
+c\alpha_{ij}^{m}(\omega)\Big[\mathbf{p}, rot\sum_b e^{-i\mathbf{p}(\mathbf{R}_b-\mathbf{R}_n)}\mathbf{H}^{mic}(\mathbf{R}_b,\omega)\Big]_j \\
+c\alpha_{ij}^{\prime m}(\omega)\Big[\mathbf{p}, rot\sum_c e^{-i\mathbf{p}(\mathbf{R}_b-\mathbf{R}_n)}\mathbf{H}^{mic}(\mathbf{R}_c,\omega)\Big]_j\Bigg),
\end{aligned}
\tag{3}
$$

where $k^2 = \frac{\omega^2}{c^2}$, $b$ is the number of the particle of metamaterial, $c$ is the number of the particle of metal.

We do our calculations with the method of images, which is founded on the uniqueness of the solution of the Laplace Equation in a region limited by equipotential surfaces. The basic requirement of this method is that the effect of the boundary should be correctly represented by the images [20]. Therefore, in our case one can replace the metal with fictitious charges-images (notice, that charges-images have the opposite sign). The field of the charges-images at $z<0$ will be identical with that defined both by the induced charges and the all particles the metamaterial consists of.

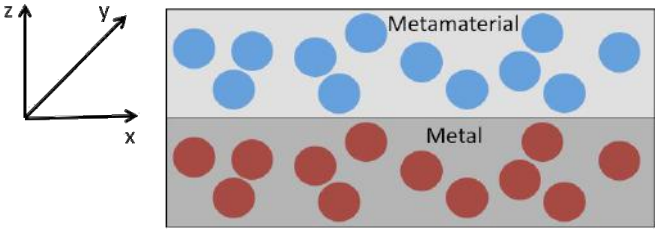



Figure 2: Schematic illustration of a boundary between metamaterial and metal with charges-images in a metal. Particles of metamaterials with dielectric and magnetic polarizabilities $\alpha_{ij}^{e}(\omega), \alpha_{ij}^{m}(\omega)$ are blue circles. The images in a metal with dielectric and magnetic polarizabilities $\alpha'^{e}_{ij}(\omega), \alpha'^{m}_{ij}(\omega)$ are dark red circles.

We next consider the so-called local field approach. The local field effects arise due to the fact that incident electromagnetic field polarizes particles of the medium surrounding the one of the interest. So, the local field acting on the $a$-th particle of the medium can be calculated by averaging over the positions of the remaining particles [21]. Then, the equation for the local magnetic field can be written as

$$
\begin{aligned}
H_i^{loc}(\mathbf{R}_a) = \int d^3R_{an_1}\ldots d^3R_{an_{N-1}} w(\mathbf{R}_{an_1})\ldots \\
\times w(\mathbf{R}_{an_{N-1}}) H_i^{mic}(\mathbf{R}_a;\mathbf{R}_{n_1},\ldots,\mathbf{R}_{n_{N-1}}),
\end{aligned}
\tag{4}
$$

where $w(\mathbf{R}_{an})$ is the function of distribution, which describes the probability density for the $n$th particle to be found at a position $\mathbf{R}_{an}$ relative to the $a$th one. This function contains dependence of the local field on the structure of the medium [15]. Notice, that equation for local electric field has the same form.

So, taking into account the local field effects and two-particle function of distribution

$$
w(\mathbf{R}_{an}) \equiv \frac{1}{V}\{1-f(\mathbf{R}_{an})\} \tag{5}
$$

one can obtain average Eq.(3)

$$
\begin{aligned}
B_i^{loc}(\mathbf{R},\omega) = B_i^0(\mathbf{R},\omega) \\
+\frac{n}{2c\pi^2}\int d^3p\int d^3R' \frac{e^{-i\mathbf{pR}'}(1-f(\mathbf{R}'))}{p^2-k^2} \\
\times\Big\{\theta_1(Z+Z')\Big(\omega\alpha_{ij}^{e}(\omega)\varepsilon_{jlm}p_l E_m^{loc}(\mathbf{R}+\mathbf{R}',\omega) \\
+c\alpha_{ij}^{m}(\omega)\Big(p^2\delta_{jk}-p_jp_k\Big)B_k^{loc}(\mathbf{R}+\mathbf{R}',\omega)\Big) \\
+\theta_2(Z+Z')\Big(\omega\alpha'^{e}_{ij}(\omega)\varepsilon_{jlm}p_l E_m^{loc}(\mathbf{R}+\mathbf{R}',\omega) \\
+c\alpha'^{m}_{ij}(\omega)\Big(p^2\delta_{jk}-p_jp_k\Big)B_k^{loc}(\mathbf{R}+\mathbf{R}',\omega)\Big)\Big\},
\end{aligned}
\tag{6}
$$

where

$$
\begin{aligned}
\theta_1(Z+Z') = \begin{cases} 1, & Z'>-Z \\ 0, & Z'<-Z \end{cases} \\
\theta_2(Z+Z') = \begin{cases} 1, & Z'<-Z \\ 0, & Z'>-Z \end{cases}
\end{aligned}
\tag{7}
$$

Function $\theta(Z)$ permits us to consider positional relationship of metal and metamaterial.

Notice, that in Eq.(5) $V$ is the volume of the medium, $f(\mathbf{R}_{an})$ is the radial distributional function, which can be found from independent experiment, e.g., using x-ray diffraction [19] or by simulating [22].

From Eq.(3) one can obtain equation for macroscopic magnetic field, by averaging over the positions of all the particles. Considering that particles of the metamaterial are in the half-space $Z_b > 0$ and particles of the metal are in the half-space $Z_c < 0$ we can write

$$\begin{aligned} B_i(\mathbf{R},\omega) &= B_i^0(\mathbf{R},\omega) \\ &+ \frac{n}{2c\pi^2}\int d^3p \int d^3R' \frac{1}{p^2-k^2} e^{-i\mathbf{p}\mathbf{R}'} \\ &\times\Big\{\theta_1(Z+Z')\Big(\omega\alpha_{ij}^{e}(\omega)\varepsilon_{jlm}p_l E_m^{loc}(\mathbf{R}+\mathbf{R}',\omega) \\ &+ c\alpha_{ij}^{m}(\omega)\theta_1\left(p^2\delta_{jk}-p_j p_k\right)B_k^{loc}(\mathbf{R}+\mathbf{R}',\omega)\Big) \\ &+ \theta_2(Z+Z')\Big(\omega\alpha'^{e}_{ij}(\omega)\varepsilon_{jlm}p_l E_m^{loc}(\mathbf{R}+\mathbf{R}',\omega) \\ &+ c\alpha'^{m}_{ij}(\omega)\left(p^2\delta_{jk}-p_j p_k\right)B_k^{loc}(\mathbf{R}+\mathbf{R}',\omega)\Big)\Big\}. \end{aligned} \tag{8}$$

Let us consider a long-wave limit. In accordance with this limit if the wavelength of the field is large in comparison with intermolecular distance $n^{-1/3}$ the effective field acting on a particle is formed by adding the fields of many molecules lying in some volume of the medium with linear dimensions $L$

$$n^{-1/3} << L << \frac{c}{w}. \tag{9}$$

This allows one to carry out the integration and neglect spatial dispersion in equations for local and macroscopic fields.

Substitution $B_i^0(\mathbf{R},\omega)$ from Eq.(8) in Eq.(6) gives the relation between local and macroscopic field:

$$\begin{aligned} B_i(\mathbf{R},\omega) &= B_i^{loc}(\mathbf{R},\omega) \\ &+ \frac{n}{2\pi^2}\int d^3p \frac{1}{p^2-k^2}\int d^3R' e^{-i\mathbf{p}\mathbf{R}'} f(\mathbf{R}') \\ &\times\Big\{\theta_1(Z+Z')\alpha_{ij}^{m}(\omega)\left(p^2\delta_{jk}-p_j p_k\right)B_k^{loc}(\mathbf{R}+\mathbf{R}',\omega)\Big) \\ &+ \theta_2(Z+Z')\alpha_{ij}'^{m}(\omega)\left(p^2\delta_{jk}-p_j p_k\right)B_k^{loc}(\mathbf{R}+\mathbf{R}',\omega)\Big)\Big\}. \end{aligned} \tag{10}$$

Taking into account that magnetization of material can be expressed through the local field

$$\begin{aligned} &M_j(\mathbf{R}+\mathbf{R}',\omega) = \\ &n\Big(\theta_1(Z+Z')\alpha_{jk}^{m}(\omega)+\theta_2(Z+Z')\alpha_{jk}'^{m}(\omega)\Big)B_k^{loc}(\mathbf{R}+\mathbf{R}',\omega) \end{aligned} \tag{11}$$

and using the following notation

$$F_{ij}(-\mathbf{R}',\omega) = \int d^3p \frac{p^2\delta_{ij}-p_i p_j}{p^2-k^2} e^{-i\mathbf{p}\mathbf{R}'} \tag{12}$$

we can write Eq. (10) in the form:

$$\begin{aligned} B_i(\mathbf{R},\omega) &= B_i^{loc}(\mathbf{R},\omega) \\ &+ \frac{1}{2\pi^2}\int d^3R' f(\mathbf{R}') F_{ij}(-\mathbf{R}',\omega)\mathrm{M}_j(\mathbf{R}+\mathbf{R}',\omega). \end{aligned} \tag{13}$$

Then, we can apply the inverse Fourier transform

$$\begin{aligned} B_i(\mathbf{q},z,\omega) &= B_i^{loc}(\mathbf{q},z,\omega) \\ &+ \frac{1}{2\pi^2}\int d^3R' e^{i\mathbf{q}\mathbf{R}'} f(\mathbf{R}') F_{ij}(-\mathbf{R}',\omega)\mathrm{M}_j(\mathbf{q},z+Z',\omega). \end{aligned} \tag{14}$$

The local field is varying more smoothly than the radial distributional function $f(\mathbf{R}')$, therefore one can obtain the relation between macroscopic and local magnetic field in form

$$G_{ij}(\mathbf{q},z,\omega)B_j^{loc}(\mathbf{q},z,\omega) = B_i(\mathbf{q},z,\omega), \tag{15}$$

where

$$\begin{aligned} G_{ij}(\mathbf{q},z,\omega) &= \delta_{ij} + \frac{n}{2\pi^2}\int d^3R' e^{i\mathbf{q}\mathbf{R}'} f(\mathbf{R}') F_{ij}(-\mathbf{R}',\omega) \\ &\times\Big(\theta_1(Z+Z')\alpha_{jk}^{m}(\omega)+\theta_2(Z+Z')\alpha_{jk}'^{m}(\omega)\Big). \end{aligned} \tag{16}$$

As is well known, the sum of the vector of magnetic field and the magnetization of the medium is called magnetic induction

$$H_i(\mathbf{q},z,\omega) = B_i(\mathbf{q},z,\omega) - 4\pi M_i(\mathbf{q},z,\omega) \tag{17}$$

while

$$H_i(\mathbf{q},z,\omega) = \mu_{ij}^{-1}(\mathbf{q},z,\omega)B_j(\mathbf{q},z,\omega). \tag{18}$$

From Eqs. (15)-(18) we can obtain equation for permeability taking into consideration that magnetization can be expressed in terms of both macroscopic and local fields

$$\begin{aligned} &\mu^{-1}{}_{ij}(\mathbf{q},z,\omega) = \delta_{ij} - 4\pi n \\ &\times\Big(\theta_1(Z+Z')\alpha_{ik}^{m}(\omega)+\theta_2(Z+Z')\alpha_{ik}'^{m}(\omega)\Big)G_{kj}^{-1}(\mathbf{q},z,\omega), \end{aligned} \tag{19}$$

where tensor $G_{kj}^{-1}(\mathbf{q},z,\omega)$ describes magnetic properties of the medium and in the long-wave limit. Recognizing that medium consists of anisotropic particles, finally, permeability tensor in our case can be written in the following form:

$$\mu_{ij}(\mathbf{q},z,\omega) = \mu_\perp(\mathbf{q},z,\omega)\left(\delta_{ij}-e_i e_j\right)+\mu_l e_i e_j, \tag{20}$$

where

$$\mu_\perp = \frac{1+4\pi n\left\{\alpha_\perp^{m}(\omega)\left(\frac{2}{3}-c_1(z)\right)+\alpha_\perp'^{m}(\omega)\left(\frac{2}{3}-c_2(z)\right)\right\}}{1-4\pi n\left\{\alpha_\perp^{m}(\omega)\left(c_1(z)+\frac{1}{3}\right)+\alpha_\perp'^{m}(\omega)\left(c_2(z)+\frac{1}{3}\right)\right\}} \tag{21}$$

$$\mu_l = \frac{1+4\pi n\left\{\alpha_l^{m}\left(2c_1(z)+\frac{2}{3}\right)+\alpha_l'^{m}(\omega)\left(2c_2(z)+\frac{2}{3}\right)\right\}}{1-4\pi n\left\{\alpha_l^{m}\left(\frac{1}{3}-2c_1(z)\right)+\alpha_l'^{m}(\omega)\left(\frac{1}{3}-2c_2(z)\right)\right\}} \tag{22}$$

$$c_1(z) = \frac{1}{4}\int d^2l_\perp l_\perp \mathrm{e}^{-zl_\perp}\int dp_z f(l_\perp,p_z)\frac{\mathrm{e}^{-izp_z}}{l_\perp+ip_z} \tag{23}$$

$$c_2(z) = \frac{1}{4}\int d^2l_\perp l_\perp \mathrm{e}^{zl_\perp}\int dp_z f(l_\perp,p_z)\frac{\mathrm{e}^{-izp_z}}{l_\perp-ip_z}. \tag{24}$$

The permeability tensor Eq.(20) is an analogue of the Clausius-Mossotti relation in case of metamaterial adjacent

to a metal. This relation connects permeability to the magnetic polarizability of the particles constituting the metamaterials and can be used to work out the magnetic polarizability if the permeability and number density are known (in our case we also have to know the radial distributional function).

It should be pointed out that Clausius-Mossotti relation one of the earliest formulas, which has been successfully used for relations macroscopic properties (permittivity) to microscopic properties (polarizability of particles of the medium) [23, 24].

In case of the boundary of metamaterial (without metal) from Eq.(19) we get

$$\mu_{ik}\left(\mathbf{q},\mathrm{z},\omega\right)=\mu_{\perp}\left(\mathrm{z},\omega\right)\left(\delta_{ik}-e_i e_k\right)+\mu_{l}\left(\mathrm{z},\omega\right)e_i e_k, \quad (25)$$

where

$$\mu_{\perp}\left(\mathrm{z},\omega\right)=\frac{1+4\pi n\left\{\frac{2}{3}-a\left(z\right)\right\}\alpha_{\perp}^{m}\left(\omega\right)}{1-4\pi n\left\{\frac{1}{3}+a\left(z\right)\right\}\alpha_{\perp}^{m}\left(\omega\right)}, \quad (26)$$

$$\mu_{l}\left(\mathrm{z},\omega\right)=\frac{1+4\pi n\left\{\frac{2}{3}-2a\left(z\right)\right\}\alpha_{l}^{m}\left(\omega\right)}{1-4\pi n\left\{\frac{1}{3}+2a\left(z\right)\right\}\alpha_{l}^{m}\left(\omega\right)}, \quad (27)$$

$$a\left(z\right)=\frac{1}{4}\int d^2 p_{\perp} p_{\perp}\,\mathrm{e}^{-zp_{\perp}}\int dl_z f\left(p_{\perp},l_z\right)\frac{\mathrm{e}^{-izl_z}}{p_{\perp}+il_z}. \quad (28)$$

Eqs. (25)-(28) describe properties of semi-infinite metamaterial and they are of interest for analyzing of many optical phenomena.

In case of non-magnetic medium our resulting equations for permeability take the value of 1.

## 3. Discussion

In this paper we have performed theoretical investigations of magnetic properties of metamaterial-metal boundary with local field theory and method of images.

We have obtained the permeability tensor (20) for metamaterial-metal boundary.

In Eqs. (26),(27) denominators are not vanishing, because magnetic polarizability is a complex value. Still, they can be very small, which leads to the maximum of permeability (the analysis similar to that was performed for dielectric properties in [25]) under conditions:

$$\begin{cases}\mathrm{Re}\left(\alpha_{l}^{m}\left(\omega_1\right)^{-1}\right)=4\pi n\left\{\frac{1}{3}+2a\left(z\right)\right\}\\ \mathrm{Re}\left(\alpha_{\perp}^{m}\left(\omega_2\right)^{-1}\right)=4\pi n\left\{\frac{1}{3}+a\left(z\right)\right\}\end{cases}. \quad (29)$$

At frequencies $\omega_1,\omega_2$ defined by conditions (29) one can observe sharp enhancement of the response of a metamaterial to the incident electromagnetic field.

Our results give the new expression for the Clausius-Mossotti relation for a metamaterial adjacent to a metal. This fact allows us to establish a direct relation between the macroscopic permeability $\mu$ and the microscopic magnetic polarizability $\alpha^{m}\left(\omega\right)$, which opens the new opportunities for constructing metamaterials with desired properties.

In case of infinite metamaterial our results passing on to our previous work [11] and coincide with those from the paper [26], obtained with help of another method.

## 4. Conclusions

Metamaterials are the key elements of interesting and potentially innovative applications in electromagnetism. A number of investigations on the determination of metamaterial characteristics (permittivity, permeability, refractive index) have appeared in recent years. [27].

Combination of local field theory and method of images provides new opportunities for manipulating the optical properties of magnetic medium and, consequently, serves as a source of interesting new phenomena in metamaterials, e.g. for subdiffraction limit imaging and focusing [28].

We comment finally, the results presented in this paper were motivated by the great interest in the boundary effects at the interface between metamaterial and convention material (particularly, metal) and they are a part of the general problem of study electromagnetic properties of metamaterials.


## Acknowledgements

This work was supported by the Ministry of Education and Science of the Russian Federation, the project 3.1110.2014/K, and by Competitiveness Growth Program of the Federal Autonomous Educational Institution of Higher Education National Research Nuclear University MEPhI (Moscow Engineering Physics Institute).


## References


[1] J.B. Pendry, Negative refraction makes a perfect lens, *Phys. Rev. Lett* 85: 3966–3969, 2000.

[2] V.M. Shalaev, Optical negative-index metamaterials, *Nature Photonics* 1: 41–48, 2007.

[3] O.V. Porvatkina, A.A. Tishchenko, M.I. Ryazanov, M.N. Strikhanov, Local field effects and metamaterials based on colloidal quantum dots**,** *IOP Conference Series* 643: 012074, 2015.

[4] M. LoCascio, S.M. Yang, Nanostructured layers, methods of making nanostructured layers, and application thereof, Patent US 8368048 B2, 2013.

[5] H. Lirong, S. Rong, Composite structure based on metamaterials and semiconductor low dimension quantum materials and application thereof , Patent CN103135151 A, 2013.

[6] W. Cai, V.M. Shalaev, *Optical Metamaterials: Fundamentals and Applications*, Springer, New York, 2010.

[7] S. Kim, E.F. Kuester, C.L. Holloway, A.D. Scher, J. Baker-Jarvis, Boundary Effects on the Determination of Metamaterial Parameters from Normal Incidence

Reflection and Transmission Measurements, *IEEE Transactions on Antennas and Propagation* 59(6): 2226-2240, 2011.

[8] I.V. Lindell, A.H. Sihvola, Electromagnetic boundary and its realization with anisotropic metamaterial, *Physical Review E* 79: 026604, 2009.

[9] M.I. Ryazanov, The effect of the natural variation in the polarization of a near-surface layer on electromagnetic surface waves, *JETP* 110: 959-965, 1996.

[10] W.L. Mochan, R.G. Barrera, Intrinsic Surface-Induced Optical Anisotropics of Cubic Crystals: Local-Field Effect, *Phys. Rev. Lett.* 55: 1192-1195, 1985.

[11] O.V. Porvatkina, A.A. Tishchenko, M.N. Strikhanov, Permittivity and permeability of semi-infinite metamaterial, *IOP Conference Series* 2016 (in print).

[12] R.A. Diaz, W.J. Herrera, J.V. Niño, Electrostatic internal energy using the method of images, *Eur. J. Phys.* 27: 1391-1398, 2006.

[13] D.J. Griffiths, *Introduction to Electrodynamics*, Prentice Hall, New Jersey,1999.

[14] M.T. de Oliveira, C.J.B. Pagan, The Method of Images applied to the grounded sphere: The problem of the ground wire, *Journal of Electrostatics* 70: 292-299, 2012.

[15] M.I. Ryazanov, A.A. Tishchenko, Clausius-Mossotti-type relation for planar monolayers, *JETP* 103: 539-545, 2006.

[16] O.V. Porvatkina, A.A. Tishchenko, M.I. Ryazanov, M.N. Strikhanov, Local field effects in anisotropic metamaterials, *IOP Conference Series* 541: 012024, 2014.

[17] O.V. Porvatkina, A.A. Tishchenko, M.N. Strikhanov, Local field effects in periodic metamaterials, *IOP Conference Series* (in print), 2016.

[18] M.N. Anokhin, A.A. Tishchenko, M.I. Ryazanov, M.N. Strikhanov, Dielectric permittivity of artificial periodic structure and local field effects *J. Phys.: Conf. Ser.* 643: 012066 2015.

[19] M.I. Ryazanov, *Electrodynamics of Condensed Matter*, Nauka, Moscow, 1984 (in Russian).

[20] P. Hammond, Electric and magnetic images, *Proc. Of the IEE - Part C: Monographs* 107: 306 – 313, 1960.

[21] M.I. Ryazanov, A.A. Tishchenko, Clausius-Mossotti-type relation for planar monolayers, *JETP* 103: 539-545, 2006.

[22] H. Touba, G.A. Mansoori, An Analytic Expression for the First Shell of the Radial Distribution Function, *International Journal of Thermophysics* 18: 1217-35, 1997.

[23] D.E. Aspnes, Local-field effects and effective-medium theory: A microscopic perspective, *Am. J. Phys.* 50: 704-709, 1982.

[24] M.N. Anokhin, A.A. Tishchenko, M.I. Ryazanov, M.N. Strikhanov, Permittivity of anisotropic dielectric near surface with local field effects, *J. Phys.: Conf. Ser.* 541: 012023 2014.

[25] M.I. Ryazanov, M.N. Strikhanov, A.A. Tishchenko, Local field effect in diffraction radiation from a periodical system of dielectric spheres, *Nucl. Instr. and Meth. B* 266: 3811-3815, 2008

[26] J. Kästel, M. Fleischhauer, Local-field effects in magnetodielectric media: Negative refraction and absorption reduction, *Phys. Rev.* A 76: 062509, 2007.

[27] D.R. Smith, S. Schultz, Determination of effective permittivity and permeability of metamaterials from reflection and transmission coefficients, *Phys. Rev. B* 65: 195104, 2002.

[28] J. Zhou, T. Koschny, M. Kafesaki, C.M. Soukoulis, Size dependence and convergence of the retrieval parameters of metamaterials, *Photon. Nanostruct. Fundam. Appl.* 6:, 96-101, 2008.

# Photonic crystals and cavities

# 2D photonic crystal-based double switch-divider

**Victor Dmitriev**[1], **and Leno Martins**[1]

[1]Department of Electrical Engineering, Federal University of Para, PO Box 8619, Agencia UFPA, 66075-900, Belem, Para, Brazil.
lenormartins@gmail.com

**Abstract**— We propose and investigate a new multifunctional component. It consists of a T-junction of three waveguides in 2D photonic crystal with square lattice. One of the waveguides is the input port and the other two serve as output ones. This component can fulfil three functions. Firstly, it can switch OFF the two output ports. Secondly, it can switch ON any one of the two output ports. Thirdly, our component can be used as a 3 dB divider of the input power. The changing of the regime is achieved by DC magnetic field which magnetizes a cylindrical ferrite resonator placed in the T-junction. We present analysis of the scattering matrices of the component and calculated frequency characteristics for the central frequency 98.46 GHz.

One of the ways to create highly integrated optical systems are PhC (photonic crystal) chips. Various active and passive components based on PhCs were suggested during last years. Among the passive components are switches [1], different types of circulators [2,3], two-way dividers [4,5]. In this work, we investigate a possibility of further integration of PhC chips. We suggest a new PhC component which fulfils simultaneously three functions, namely, switching OFF of the two output ports, division of the signals between two output channels, and also switching ON one or another of the two input ports. This component substituting three common elements, allows one to reduce losses, to increase density of components in the chips and, as a consequence, to reduce the dimensions of optical subsystems.

In the theoretical part of our paper, we consider ideal scattering matrices for different regimes of functioning. In the nonmagnetic state, the T-junction possesses the plane of symmetry $\sigma$ (Fig. 1a) but in the magnetized case it has the antiplane of symmetry $T\sigma$ [6] (Fig. 1b,c,d). Using these elements and also the unitary condition, one can calculate the structure of the scattering matrix [S]. In our theoretical part we have shown that considering separately these three regimes, there are no fundamental restrictions on the realizability of these regimes.

Regime 1 can be conceived with a nonmagnetized ferrite resonator. It is shown in Fig. 1a. If the dipole mode of the resonator has its nodes oriented along the axes of the output waveguides, the latters will not be excited. Thus, the incident wave will be reflected from port 1. This corresponds to switching OFF the two output waveguides.

It is well known that in a magnetized ferrite resonator placed in a photonic crystal, the rotating and standing dipole modes can be excited. Using rotating modes we can switch ON ports 2 and 3 with equal division between them (regime 2, see Fig. 1b). Notice that the mechanism of division in this case is different from that in reciprocal devices. Finally one can separately switch ON port 3 or port 2 (regime 3, see Fig. 1c,d). Regimes 2 and 3 are realized with different DC magnetic fields $\pm\mathbf{H}_1$ and $\pm\mathbf{H}_2$, respectively. With $\pm\mathbf{H}_1$, the rotating dipole mode provides the 3 dB division, and with $\pm\mathbf{H}_2$, the circulator regime. In regime 3, the transmission of the input wave to port 2 or port 3 can be achieved by changing the sign of the field $\mathbf{H}_2$, such as in any three-port circulator.

We demonstrate results of numerical modelling of the double switch-divider which is based on a ferrite resonator in a two dimensional PhC. In our example, the PhC is a square lattice of dielectric cylinders of radius $0.2a$ ($a$=1.065 mm is the lattice constant). The permittivity of the dielectric is 11.56. The guided electromagnetic wave in PhC waveguide is TM mode with the components $E_z, H_x$ and $H_y$. The ferrite material of the resonator is characterized by the electric permittivity $\epsilon_r$ =12.5 and in the regime with magnetization, by the magnetic permeability tensor $[\mu]$.

The frequency responses of the divider were calculated by the software COMSOL. The central frequency $f_0 = 98.46$ GHz of the component is defined by the dipole resonance of the nonmagnetized ferrite resonator in regime 1. Therefore, if the parameters of the nonmagnetized ferrite resonator and geometry of its environment are chosen, the external magnetic field is the only available parameter for adjustment of the device in regime 2 and regime 3. The given below results are obtained for $\mathbf{H}_1 = 990$ kA/m and $\mathbf{H}_2 = 2178$ kA/m.

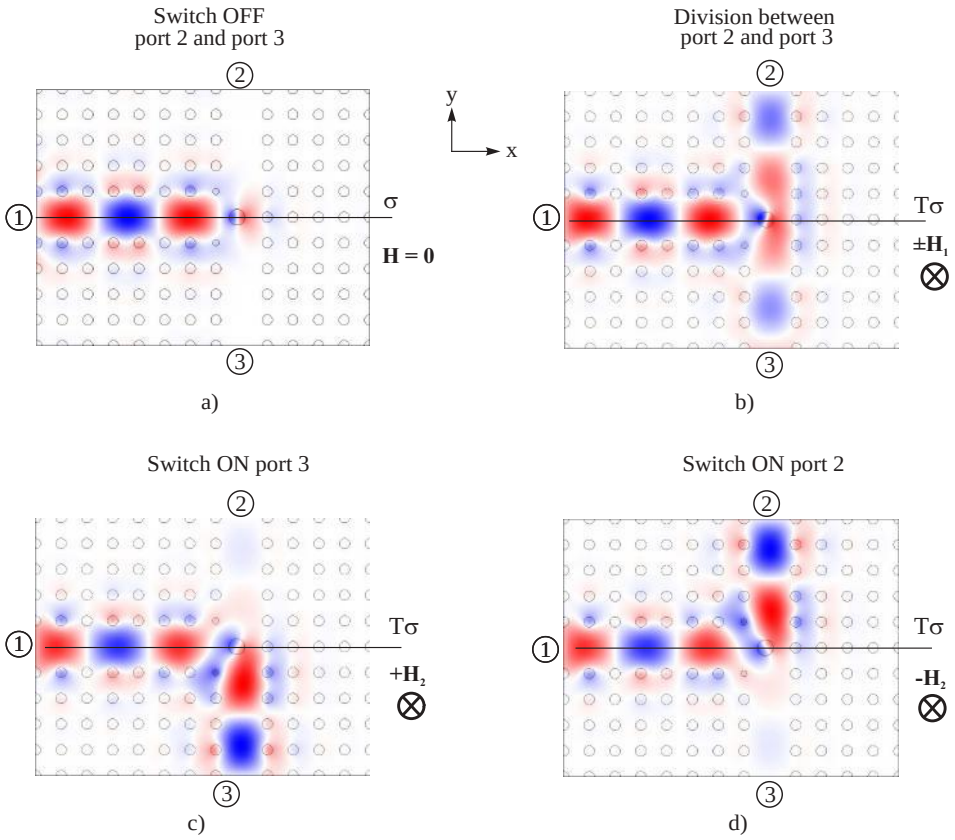



Figure 1: (Color online) Possible regimes of double switch-divider, a) switching OFF two output ports, b) 3 dB divider, c) switching ON port 3, d) switching ON port 2.

Summarizing, the scattering matrices of the component in the three possible regimes have been analysed from the point of view of realizability of them. The physical effects responsible for the functioning of the double switch-divider have been also discussed. The numerical simulations have confirmed our theoretical predictions. In the frequency band of about 1 GHz and the central frequency $f_0 = 98.46$ GHz, the double switch-divider has the following parameters: in regime 1 the isolation of ports 2 and 3 from port 1 is better than -30 dB. In regime 2 the division of the input signal is about -3.8 dB. The isolation in regime 3 is higher than -15 dB and the insertion loss is -0.7 dB. We believe that the suggested component can be scaled to higher frequencies.

## ACKNOWLEDGMENT

This work was supported by Brazilian agency CNPq.

## REFERENCES

1. Dmitriev, Victor, Marcelo N. Kawakatsu and Gianni Portela, "Compact optical switch based on 2D photonic crystal and magneto-optical cavity", *Optics Letters*, Vol. 38, 1016–1018, 2013.
2. 5 Wang, Z. and S. Fan, "Suppressing the effect of disorders using time-reversal symmetry breaking in magneto-optical photonic crystals: An illustration with a four-port circulator", *Photonics and Nanostructures Fundamentals and Applications*, Vol. 4, 1326–140, 2006.
3. Wang, Q. Z. Quyang, K. Tau, M. Lin and S. Ruan, "T-shaped optical circulator based on coupled magneto-optical rods and a side-coupled cavity in a square-lattice photonic crystal", *Phys. Lett. A*, Vol. 376, 646-649, 2012.
4. Boscolo, S., M. Midrio and T. F. Kraus, "Y junctions in photonic crystals channel waveguides: high transmission and impedance matching", *Optics Letters*, Vol. 27, 1001-1003, 2002.
5. Dmitriev, Victor and Marcelo N. Kawakatsu, "Nonreciprocal optical divider based on two-dimensional photonic crystal and magneto-optical cavity", *Applied Optics*, Vol. 51, 5917–5920, 2012.
6. Barybin A. A. and V. A. Dmitriev, *Modern Electrodynamics and Coupled-Mode Theory: Application to Guided-Wave Optics*, Rinton Press, Princeton (NJ), 2002.

# Spectral Scalability and Optical Spectra of Fractal Multilayer Structures: FDTD analysis

**S. Simsek[1], S. Palaz[2], A. M. Mamedov[3,4*], E. Ozbay[4]**

[1]Faculty of Engineering, Department of Material Science and Engineering, Hakkari University, Hakkari, Turkey

[2]Faculty of Science and Letters, Department of Physics, Harran University, Sanliurfa, Turkey

[3]International Scientific Center, Baku State University, Baku, Azerbaijan

[4]Nanotechnology Research Center, Bilkent University, Ankara Turkey

[*]corresponding author: mamedov@bilkent.edu.tr

**Abstract**-Quasi-periodic Fibonacci structures have given a rise to some interesting phenomena which are not observed in periodic structures and it is based on the Fibonacci generation scheme. The sequence is expressed as $S_{j+1}=\{S_jS_{j-1}\}$ for level $j\geq1$, with $S_0=\{B\}$ and $S_1=\{A\}$, the first few sequences are $S_2=\{AB\}$,$S_3=\{ABA\}$, $S_4=\{ABAAB\}$ and soon. In a Fibonacci quasi-periodic one- and two-dimensional photonic crystal, two types of layer, A and B are arranged in a Fibonacci sequence, where A and B are considered as the dielectric materials ($BaTiO_3$, $SrTiO_3$ and $LiTaO_3$) and conducting ($Sb_2Te_3$-as topological insulator) material respectively.

In this report we present an investigation of the optical properties and band structures for the photonic structures based on $BaTiO_3$, ($SrTiO_3$ and $LiTaO_3$) with a Fibonacci sequence that can act as a multi-wavelength birefringent (Solc) filter. The filtering wavelengths are analyzed by the indices concerning the quasi-periodicity of a Fibonacci sequence and the average lattice parameter. The transmittances of filtering wavelengths can be tuned by varying structure parameters such as the lengths of poled domains, filling factor, and dispersion relation. The optical spectra of Fibonacci multilayer dielectric structures have shown to possess spectral scalability, which has been found to be directly related to the structure's spatial self-similarity. In our simulation, we employed the finite-difference time domain technique which implies the solution of Maxwell equation with the centered finite-difference expressions for the space and time derivatives.

# Temporally resolved fourwave mixing in a photonic crystal switch

**P. Lunnemann**[1], **P. Colman**[2], **Y. Yu**[1], **and J. Mørk**[1]

[1]DTU Fotonik, Technical University of Denmark,
[2]Institut DElectronique Fondamentale, Universite Paris-Sud
plha@fotonik.dtu.dk

**Abstract**— We present a detailed experimental analysis of temporally resolved fourwave mixing in a photonic crystal cavity based optical switch. The origin of the parametric gain is analysed a model based on temporally coupled mode theory. The upper limit of the parametric gain is experimentally investigated and discussed.

Photonic crystal (PhC) cavities coupled to a PhC waveguide have recently been been demonstrated as an efficient structure for achieving all optical switching in a compact chip-compatible platform [1, 2, 3]. The principle is based on a strong pump pulse that induces a spectral shift of the cavity resonance, thus giving rise to drastic transmission changes of a subsequent signal pulse. A mechanism for changing the material refractive index is achieved by the carrier dispersion generated by two photon absorption (TPA). Here we report on such structures, with a detailed investigation of the generation of parametric gain, by fourwave mixing in a photonic crystal cavity. Since it potentially could lead to an alternative method for realization an ultra-fast PhC switch, we analyse the origin of the dynamics as well as the limitations of the parametric gain.

We use short $\sim 120$ fs laser pulses centred around 1.5 $\mu$m. Two acousto optical modulators are used for separating the laser pulses into a reference, pump, and probe pulse. A fibre-coupled pulse shaper is used for spectral filtering as well as dispersion compensation of both pump and probe. The structure is an InP-based photonic crystal (PhC) membrane similar to the one investigated in ref. [4] with a cavity linewidth of 1.5 nm. Spectral width (FWHM) of the signal and pump were set accordingly to 1.5 nm and 5.0 nm, respectively. The estimated in-coupled pulse energy were 2 fJ and 0.4 pJ for the probe and pump, respectively. The detection scheme is based on a heterodyne cross-correlation detection scheme [5], using a relatively short duration of the reference pulse ($\sim 120$ fs) thus giving a high temporal resolution of the transmitted response of the waveguide, see fig. 1a).

By sweeping the ref. stage for each pump-probe delay we may map out the full dynamics of the switch. An example of the probe envelope for a range of pump-probe delay values is presented in figure 1b) for the switch-off configuration. We notice the typically measured reduced transmission near 0 ps for positive values of the pump delay (pump arrives before probe). However, for slightly negative pump-probe delay (pump arrives after the probe) we notice an additional bump on the tail of the probe envelope. This is clearly illustrated in fig. 1c) showing the relative transmission, i.e. the ratio of the probe power with and without the pump pulse present, where red coloured areas indicate and increased transmission. We attribute the observed increase of transmission to a fourwave mixing effect. The overlap of the weak probe with a strong pump creates a beating that

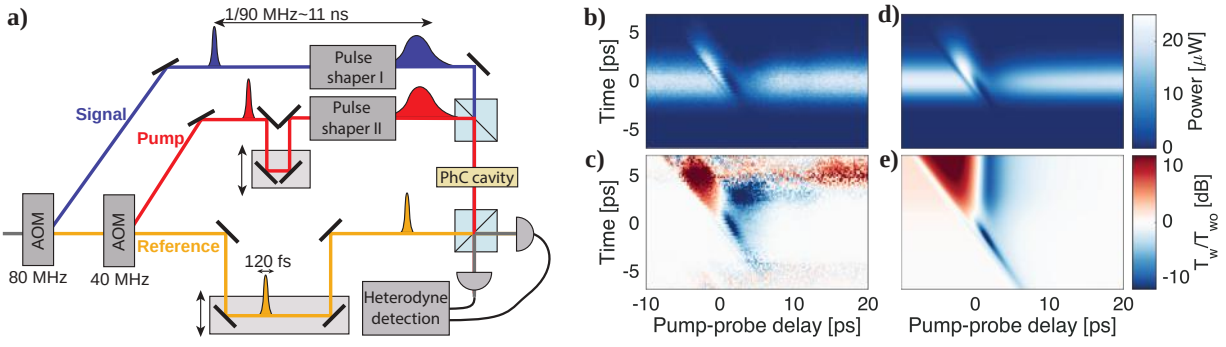



Figure 1: a) Sketch of the optical setup setup. b) Measured signal envelope as a function of pump-probe delay. c) Associated relative transmission. d) and e) Corresponding theoretical calculations based on TCMT.

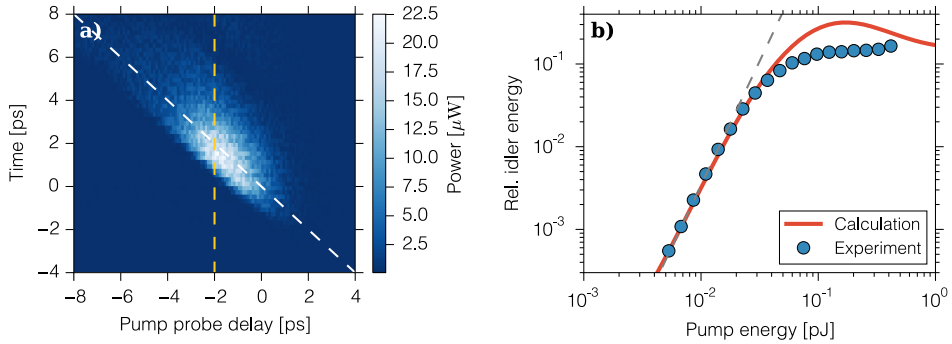



Figure 2: Measured idler envelope as a function of pump-probe delay. Dashed white line is a guide to the eye, with a slope of -1. c) Measured idler pulse energy relative to the estimated incoupled probe energy for a fixed pump-probe delay of -2 ps. Red solid line represent calculated values and dashed grey serve is as a guide to the eye for a scaling of the pump energy to the power of 3.

results in a modulation of the generation of free carriers and thus also the refractive index. The latter diffracts the pump into the signal and idler frequency. We validate this interpretation using a temporal coupled mode theory (TCMT) based on rate equations of the field and carrier density in the cavity. As opposed to previous models [4], we include terms associated with the beating between the pump and probe, giving rise to rate equations describing the response of the cavity field at the signal as well as the idler frequency. The calculated results are presented in fig. 1d)-e), showing good qualitative agreement with the measurements.

Direct evidence of the generation of an idler pulse is measured by applying the heterodyne detection at the corresponding idler frequency, $2\omega_p - \omega_{pr}$, where $\omega_p$ and $\omega_{pr}$ denotes the frequency of the pump and probe, respectively. The resulting idler envelope, as a function pump-probe delay, is presented in fig. 2a). Clearly, we notice that the signal peaks along a straight line with slope of -1, corresponding to overlapping pump and reference pulse. In order to examine the upper limit of the parametric gain, we measured the idler envelope as a function of pump pulse energy for a fixed pump delay of -2, see fig. 2b). The total idler energy, is found by integrating along the time axis, and is presented in fig. 2 scaled by the input probe pulse energy. The idler energy is seen to scale with the pump energy to the power of 3 for the lowest pump energies. For larger pump energies the idler generation is seen to saturate for increasing pump energies. This we ascribe a balance between a strong beating between the pump and probe and a shift of the resonance frequency. E.g. in the case of a very strong pulse, the cavity resonance shifts with only a fraction of the pulse envelope having entered the cavity. This prevents the remaining tail of the probe to enter the cavity, and thus hinders any further diffraction of the pump. Theoretical results show good agreement for the lowest energies. While the calculations do exhibit saturation they tend to overestimate the gain for the largest input energies. We attribute this discrepancy to the crude simplifications of the model, not taking into account the finite spectral width of the pulses or thermal effects.

In conclusion, we have presented experimental results on a photonic crystal switch showing parametric gain. The gain originates from an oscillating free carrier population giving rise to fourwave mixing between the pump and probe. The results were in good agreement with a model based on TCMC. We found an upper limit to the generated idler signal that we ascribe to a balance between efficient pump-probe beating and pump-induced shift of the resonance.

**REFERENCES**


1. Fushman, I. *et al.* "Ultrafast nonlinear optical tuning of photonic crystal cavities." *Appl. Phys. Lett.*, vol. 90, no. 9, 091118, 2007.
2. Heuck, M. *et al.* "Heterodyne pump probe measurements of nonlinear dynamics in an indium phosphide photonic crystal cavity." *Appl. Phys. Lett.*, vol. 103, no. 18, 181120, 2013.
3. Nozaki, K. *et al.* "Sub-femtojoule all-optical switching using a photonic-crystal nanocavity." *Nat. Photonics*, vol. 4, no. 7, 477–483, 2010.
4. Yu, Y. *et al.* "Switching characteristics of an InP photonic crystal nanocavity: Experiment and theory." *Opt. Express*, vol. 21, no. 25, 9221–9231, 2013.
5. Mecozzi, A. and Mørk, J. "Theory of heterodyne pump-probe experiments with femtosecond pulses." *J. Opt. Soc. Am. B*, vol. 13, no. 11, 2437–2452, 1996.

# Magnetic collinear holograms with magnetophotonic crystals

**Yuichi Nakamura[1,*], Ryosuke Isogai[1], Hiroyuki Takagi[1], Taichi Goto[1,2], Pang Boey Lim[1] and Mitsuteru Inoue[1]**

[1]Toyohashi University of Technology, 1-1 Tempaku-cho, Toyohashi, Aichi, 441-8580, Japan
[2]JST, PRESTO, 4-1-8 Honcho, Kawaguchi, Saitama, 332-0012, Japan
[*]corresponding author: nakamura@ee.tut.ac.jp

**Abstract**- Magnetic volumetric hologram is recorded as magnetization directions through thermomagnetic recording. To achieve bright reconstruction image, the use of magnetophotonic microcavity (MPM) for recording media is effective to achieve high diffraction efficiency through the enhancement of Faraday rotation angle and fringe depth. In this study, we demonstrated the effectiveness of MPM media to achieve bright reconstruction image. In addition we also propose the MPM with heat-sink layers for retaining well-defined magnetic fringes that results much high diffraction efficiency.

Holographic memory is a promising data-storage technology with fast transfer rates and high recording densities. Compared to conventional holographic memory using photopolymers as recording media, magnetic holograms provide rewritability and long-term stability. The magnetic holograms are recorded as a direction of magnetization in magnetic films using thermomagnetic writing process, while reconstruction involves using the magneto-optical effect. Previously, we demonstrated that a hologram can be magnetically written by using this thermomagnetic writing and reconstructed from transparent magnetic films of $Bi_{1.3}Dy_{0.85}Y_{0.85}Fe_{3.8}Al_{1.2}O_{12}$ (BiDyAlYIG); however, the diffraction efficiency was insufficient for applying this to actual data storage devices [1]. Recently we reported that the use of magnetophotonic microcavities (MPMs) or magnetophotonic crystals as recording media provides high diffraction efficiency through the increase in the Faraday rotation angle and the depth of the magnetic fringes [2–3]. The formation of deep hologram in the medium is needed for volumetric hologram and for further improvement of diffraction efficiency. However, thermomagnetic writing with high writing energy density for forming deep magnetic fringes produces excessively high temperature that results the merge of fringes through the lateral thermal diffusion. To suppress this heat diffusion effect and to control the fringes' shapes, a stacking structure composed of a magnetic garnet and transparent heat-sink layers (HSLs) is thought to be effective for controlling the thermal diffusion. In this work, we demonstrated the effectiveness of the MPM holographic medium to achieve a bright reconstructed image in magnetic collinear holography. In addition, the MPM with HSLs media for controlling the heat diffusion was also proposed to achieve much higher diffraction efficiency.

BiDyAlYIG single layer film (SLF) and MPM media with the BiDyAlYIG defect layer sandwiched between two pairs of $(Ta_2O_5/SiO_2)_2$ Bragg mirrors were prepared. The magnetic holograms were recorded and reconstructed in those media by collinear holography system. Figure 1 shows the reconstructed images from SLF and MPM medium. As clearly shown in this figure, the image from the MPM medium was brighter than that from SLF. This means that the use of MPM is effective to achieve bright reconstruction images through high diffraction efficiency [4]. As previously mentioned, the increase in depth of fringe is important for volumetric

hologram to achieve high diffraction efficiency for realizing bright image, but the depth was limited due to fringe merging near the surface as shown in Figure 2(a). For further improvement of diffraction efficiency, we investigated the insertion of HSLs in MPM media for retaining well-defined magnetic fringes by numerical simulation. The MPM+HSLs media had optical microcavities with BiDyAlYIG/alumina multilayers as defects, where alumina was used as a heat-sink material. When HSLs are inserted into the optical cavity, it is important to maintain the resonance condition and control the electric field distribution. That is, the thickness of each HSL should be designed thinking of both thermal and optical conditions to suppress the undesired localization of light between the HSLs in the cavity. In this work, the optical thickness of each HSL was set to be equal to an integral multiple of a half wavelength of light, which maintains the original intensity of electric field distribution in garnet layer after inserting HSLs. Figure 2 shows the calculated shapes of magnetic fringes written by the two-beam interferometer at 80 and 152 mJ/cm$^2$. The merge of fringes near the surface in MPM+HSLs media were prevented even written at larger energy density; thermal diffusion induced merging of magnetic fringes is effectively reduced in optical microcavities by HSLs. Figure 3 shows the diffraction efficiencies of the SLF, MPM, and MPM+HSLs media. The diffraction efficiency exhibited by the MPM+HSLs medium was approximately one order of magnitude higher than that of the conventional SLF. The insertion of HSLs enabled the formation of deep magnetic holograms and avoided the limitation on the hologram writing depth owing to the merging of magnetic fringes. This approach provides a method for accurately manipulating the magnetization by volumetric thermomagnetic recording even in MPM media.

**Acknowledgements**, This work was supported in part by the Grants-in-Aid for Scientific Research (S) 26220902, Grants-in-Aid for Scientific Research (A) 15H02240, and Grant-in-Aid for Japan Society for the Promotion of Science (JSPS) Fellows No. 25-8942.

**REFERENCES**

1. Y. Nakamura, H. Takagi, P. B. Lim, and M. Inoue, Opt. Express Vol. 22, 16439–16444, 2014.
2. R. Isogai, N. Sagara, T. Goto, Y. Nakamura, P. B. Lim, and M. Inoue, J. Magn. Soc. Jpn., Vol. 38, 119–122, 2014.
3. R. Isogai, T. Goto, H. Takagi, Y. Nakamura, P. B. Lim, and M. Inoue, J. Magn. Soc. Jpn. Vol. 39, 33–36, 2015.
4. R. Isogai, S. Suzuki, K. Nakamura, Y. Nakamura, H. Takagi, T. Goto, P. B. Lim, and M. Inoue, Opt. Express Vol. 23, 13153–13158, 2015.

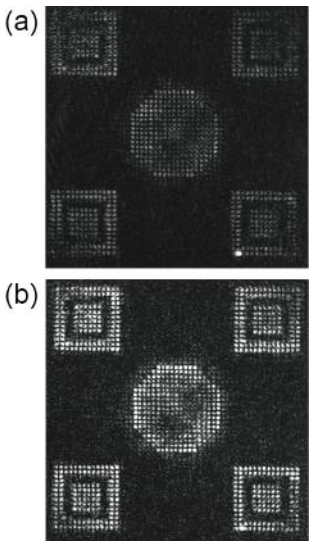



Figure 1 Reconstructed images from (a) SLF and (b) MPM medium.

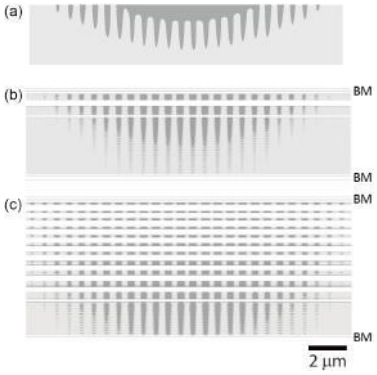



Figure 2 The shapes of magnetic fringes at (a) 80 mJ/cm$^2$ in SLF, (b) 80 mJ/cm$^2$ and (c) 152 mJ/cm$^2$ in MPM+HSLs media.

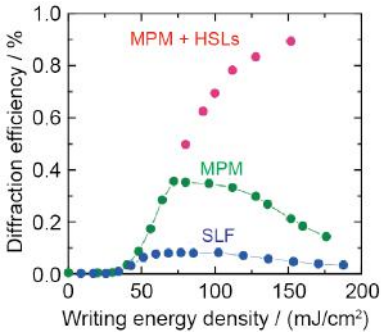



Figure 3 Dependence of the diffraction efficiency on the writing power density for SLF, MPM, and MPM + HSLs media.

# Full-k-space flat bands in photonic crystals beyond the tight-binding picture

**C.Q. Xu[1], and Y. Lai[1*]**

[1]Department of Physics, Soochow University, 1 Shizi Street, Suzhou 215006, China

[*]corresponding author: laiyun@suda.edu.cn

**Abstract**-Based on a band engineering method, we propose a theoretical prescription to create a full-k-space flat band in dielectric photonic crystals covering the whole Brillouin Zone. With wave functions distributed in air instead of in the dielectrics, such a flat band represents a unique mechanism for achieving flat dispersions beyond the tight-binding picture, which can enormously reduce the requirement of permittivity contrast in the system. Finally, we demonstrate a unique application based on the full-k-space coverage of the flat band.

In the past decades, a lot of attention has been focused on slow light and its applications such as optical information processing. One possible route to realize slow light is the creation of flat bands in photonic crystals [1-6], which exhibit dramatically small group velocities and high density of states (DOS), and thus provide an efficient method to slow down and control photons. In the typical band structures of photonic crystals, flat bands usually only appear in a small region in *k*-space, such as the Brillouin zone edge or center [7-10]. In order to expand the range of the flat bands so as to cover the whole Brillouin Zone, the conventional wisdom is to make the wave functions in the photonic crystal more localized in space. This can be easily understood within the framework of the tight-binding picture. When the wave functions on the sites are more localized, the coupling between neighboring sites becomes weaker, which in turn flattens the whole band.

Based on a band engineering method [11], we represents a general principle of full-k-space flat band engineering in classical wave systems beyond the tight binding picture. Comparing with normal flat bands with flatness only in one direction, such a full-k-space flat band can exhibit omnidirectional flatness, which leads to higher DOS and a unique application: ultra-sensitive detection of nearby small scatterers by enhancing the scattered waves in specific angles. Surprisingly, the wave function distributions of some eigenstates in such a flat band are concentrated in air (free space) instead of dielectrics. This corresponds to wave functions localized between the sites instead of on the sites in a quantum system. Further analysis reveals that the wave functions exhibit quite small inverse participation ratios (IPRs), which indicate an unusual feature of delocalization in space. By using full-wave simulations with a tiny gain, we have demonstrated ultra-sensitive detection of nearby small scatterers by such full-k-space flat bands, which can provide a convenient approach for detection and measuring of micro size particles. Finally, we discuss the topological properties of the photonic crystal with the full-k-space flat band.

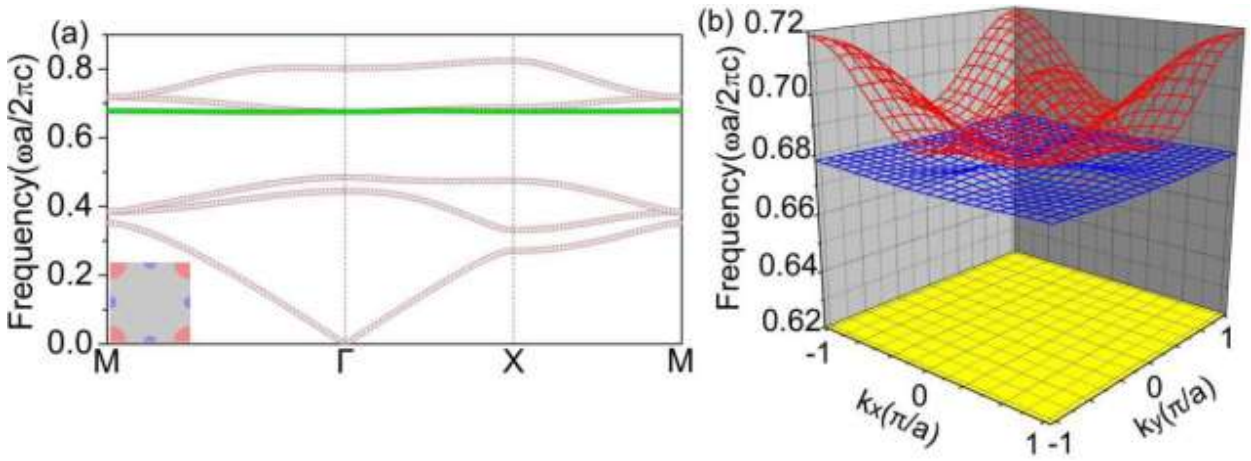



Fig. 1 (a) The designed band structure with a full-*k*-space flat band (green circles). (b) The fourth and fifth bands in the whole Brillouin zone.

**REFERENCES**


1. Krauss, T.F. "Why do we need slow light." *Nat. Photonics*, Vol. 2, 448-450, 2008.
2. Soljačić, M and S.G. Johnson, "Photonic-crystal slow-light enhancement of nonlinear phase sensitivity," *J. Opt. Soc. Am. B* Vol.19, 2052-2059, 2002.
3. Bayindir, M., B. Temelkuran, and E. Ozbay, "Tight-Binding Description of the Coupled Defect Modes in Three-Dimensional Photonic Crystals." *Phys. Rev. Lett.* Vol. 84, 2140-2143, 2000.
4. Gersen, H., et al. "Real-Space Observation of Ultraslow Light in Photonic Crystal Waveguides." *Phys. Rev. Lett.* Vol. 94, 073903, 2005.
5. Vlasov, Y.A., M. O'Boyle, H.F. Hamann, and S.J. McNab, "Active control of slow light on a chip with photonic crystal waveguides." *Nature* Vol. 438, 65-69, 2005.
6. Kondo, K., et al. "Ultrafast Slow-Light Tuning Beyond the Carrier Lifetime Using Photonic Crystal Waveguides." *Phys. Rev. Lett.* Vol. 110, 053902, 2013.
7. Baba, T. "Slow light in photonic crystals." *Nat. Photonics* Vol. 2, 465-473, 2008.
8. Huang, X., Y. Lai, Z.H. Hang, H. Zheng, and C.T. Chan, "Dirac cones induced by accidental Dirac cones induced by accidental zero-refractive-index materials." *Nat. Mater.* Vol. 10, 582-586, 2011.
9. Sakoda, K. "Universality of mode symmetries in creating photonic Dirac cones." *J. Opt. Soc. Am. B* Vol. 29, 2770-2778, 2012.
10. Mei, J., Y. Wu, C.T. Chan, and Z.Q. Zhang, "First-principles study of Dirac and Dirac-like cones in phononic and photonic crystals." *Phys. Rev. B* Vol. 86, 035141, 2012.
11. Zhang, X., Z.Q. Zhang, and L.M. Li, "Enlarging a photonic band gap by using insertion," *Phys. Rev. B* Vol. 61, 1892-1897, 2000.

# Nitride nanophotonics from the deep ultra-violet to the near infrared: non-linear optics and microlasers.

**J. Sellés[1], C. Brimont[1], B. Guizal[1], B. Gayral[2,3], M. Mexis[4], F. Semond[4], I. Roland[5], Y. Zeng[5], X. Checoury[5], P. Boucaud[5] and T. Guillet[1*]**

[1] Laboratoire Charles Coulomb (L2C), UMR 5221, CNRS-Université de Montpellier, Montpellier, F-France

[2] Univ. Grenoble Alpes, F-38000 Grenoble, France

[3] CEA, INAC-PHELIQS, "Nanophysique et Semiconducteurs" group, F-38000 Grenoble, France

[4] CRHEA-CNRS, Rue Bernard Gregory, 06560 Valbonne, FRANCE

5 Institut d'Electronique Fondamentale, CNRS, Univ Paris-Sud, Université Paris-Saclay, F-91405 Orsay, France

[*]corresponding author: Thierry.Guillet@umontpellier.fr

**Abstract**-The recent developments of nitride nanophotonics, based on photonic crystal membrane nanocavities and microdisk resonators, pave the way to a novel nanophotonic platform. Here we present two recent achievements: first we demonstrate the room-temperature operation of a nitride microlaser emitting in the deep UV spectral range (λ=275 nm) with GaN/AlN multiple quantum wells. Secondly we tailor the second-harmonic generation of a cw near infra-red radiation coupled to a high quality factor photonic crystal cavity.

Nitride semiconductors (GaN and nitride alloys) provide a spectrally-broad transparency -expanding from the near-infrared to the ultraviolet- as well as robust excitons that are efficiently interacting with light and stable up to room temperature. They offer a promising playground for non-linear optics and micro- or nano-lasers at 300K. Over the last decade, the progresses of the nitrides' processing has allowed fabricating nanophotonic resonators and devices such that the interaction between excitons and photons can be tailored on demand. We will review our recent achievements, ranging from near-UV high Q photonic crystal cavities [1], to UV-C GaN/AlN microdisk lasers [2] and second- and third-harmonic generation in photonic crystal cavities [3].

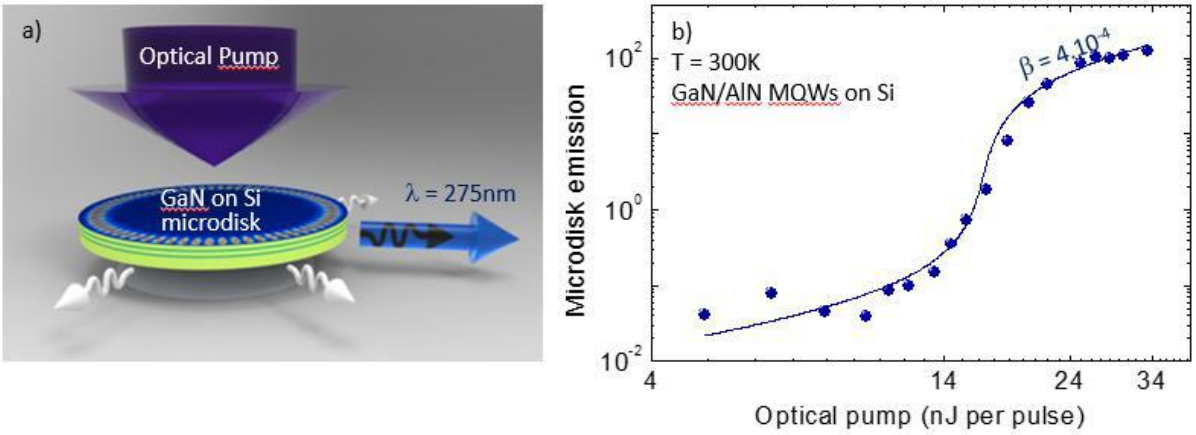



**Figure 1:** a) Scheme of the microlaser, with the optical pump from the top of the nitride microdisk and the emission collected from the edge ; b) Input-output characteristics of the microlaser, and its modelling through a microlaser rate equation model.

Figure 1 presents the demonstration of the first UV-C microlaser operating at room temperature [2]. It is based on an AlN microdisk photonic resonator with a quality factor of about 4000, embedding very thin GaN/AlN multiple quantum wells (MQWs). It operates at 4.5 eV/275 nm under pulsed quasi-resonant optical pumping (266nm, 400ps pulses), with a threshold excitation density of 17 nJ/pulse. The input-output characteristics of the microlaser and the line narrowing at threshold allow extracting the spontaneous emission coupling factor of the microlaser: $\beta=4\pm2\ 10^{-4}$. This demonstration underlines the interest of simple binary GaN/AlN MQWs, grown on a thin AlN buffer on a silicon substrate, compared to much more complex approaches based on thick engineered buffer layers, that are presently employed in UV-C ridge lasers. We exploit the possibility to selectively under-etch the silicon substrate in order to form membrane photonic resonators, that was previously only used in the visible and near-UV spectral range with bulk GaN and InGaN MQW active layers.

The same nanophotonic platform has been exploited without internal emitters, and operated within the GaN transparency window. Larger quality factors, up to 34000, have been obtained for photonic crystal membrane cavities in the near-infrared spectral range due to the larger dimension of the photonic pattern [4]. We have demonstrated the second and third harmonic generation of a 1.57 µm continuous-wave pump brought into resonance with such a suspended nanocavity [3]. The emission pattern is correlated to the simulated harmonic polarization and allows identifying the nonlinear process involved in the frequency conversion.

Those two results demonstrate the versatility of the nitride-on-silicon nanophotonic platform for future developments of integrated nanophotonics in the near-IR, visible and UV spectral range.

**Acknowledgements** The authors acknowledge support from the projects GANEX (ANR-11-LABX-0014) and QUANONIC (ANR-13-BS10-0010). GANEX belongs to the public funded 'Investissements d'Avenir' program managed by the French ANR agency. This work was also partly supported by the RENATECH network.

**REFERENCES**

1. Sam-Giao, D. *et al.*, Appl. Phys. Lett. **100**, 191104 (2012).
2. Sellés, J. *et al.*, Sci. Rep. **6**, 21650 (2016)
3. Zeng Y. *et al.*, Appl. Phys. Lett. **106**, 081105 (2015)
4. Roland I. *et al.*, Appl. Phys. Lett. **105**, 011104 (2014)

# Out-of-plane photonic band structures of two-dimensional photonic crystals: a study of the complete band gap

**J. D. Valenzuela-Sau[1*], and R. García-Llamas[2]**
[1]Physics Doctorate, Universidad de Sonora, México
[2]Physics Research Department, Universidad de Sonora, México
[*]corresponding author: daniel.valenzuela@live.com

**Abstract-**The out-of-plane photonic band structures (PBSs) of two-dimensional photonic crystals (PCs) are calculated. We focus the calculation of this study on the behavior of the complete forbidden band gaps. The PC is a rectangular (triangular) array of infinitely long vacuum rods of elliptical (circular) cross section surrounded by a high dielectric medium. The out-of-plane frequency modes are presented at the high symmetry points Γ, X, M and X' (Γ, M and K) for the rectangular (triangular) lattice.

Using the plane wave method [1], the eigenvalues matrix equation (1) is found and solved numerically to obtain the eigenfrequencies for both, in-plane (stationary) and out-of-plane (propagating) electromagnetic modes, for each propagation wave vector. (PBSs) are obtained for a rectangular (triangular) array of cylinders of elliptical (circular) cross section. In-plane (out-of-plane) band structure considers perpendicular (oblique) propagation according to the homogeneous axis of the system. Out-of-plane studies have been made [2,4,5], however, a rigorous study of the complete band gap has not been done. In-plane (PBSs) were compared with those presented in references [2] and [3]. Out-of-plane modes, for the triangular array, were compared with those presented in reference [2]. Equation (1) is presented next.

$$\sum_{m',n'} [\varepsilon_2^{-1}]_{m-m',n-n'} \left[ (\boldsymbol{k}_{m,n} \times \boldsymbol{v}_{m',n'}) h_{m',n'} - \boldsymbol{k}_{m,n} \times \boldsymbol{w}_{m',n'} |\boldsymbol{k}_{m',n'}|^2 e_{m',n'} \right] = \frac{\omega^2}{c^2} \left[ \boldsymbol{v}_{m,n} |\boldsymbol{k}_{m,n}| e_{m,n} + \boldsymbol{w}_{m,n} h_{m,n} \right] \quad (1)$$

Where $[\varepsilon_2^{-1}]_{m-m',n-n'}$ are the coefficients of the multiplicative inverse of the dielectric constant, and $\boldsymbol{v}_{m,n}$ and $\boldsymbol{w}_{m,n}$ are two orthogonal polarizations. $\boldsymbol{k}_{m,n}=k_x\boldsymbol{i}+k_y\boldsymbol{j}+\gamma\boldsymbol{k}$ is the wave vector which contains the Bloch vector, the reciprocal lattice vectors and the oblique propagation component; $\gamma$.

Figures 1 and 2, present the lowest frequency modes at the high symmetry points of the two PCs as a function of $\gamma$. Both figures show how some frequency modes, for a specific Bloch vector in the first Brillouin zone, became degenerated when γ is increased. The grey rectangles perimeters illustrate the complete band gaps for in-plane PBSs. The lower limit of the complete band gap, for the rectangular (triangular) lattice, is given by the upper limit of the second (first) frequency band in the Γ point (Γ point), meanwhile, the upper limit of the complete band gap, is given by the upper limit of the third (third) frequency band in the Γ point (M point). The extinction of the band, for the rectangular (triangular) lattice, occurs for $\gamma a_y/2\pi=0.37$ ($\gamma a_x/2\pi=0.86$), approximately, and is denoted by a dashed grey line.

We plan to calculate sufficient out-of-plane (PBSs) increasing γ, to clearly see the behavior of the complete

band gap that these PCs present. As γ is increased, it is expected that some limits of the complete band gap also became degenerated extinguishing the gap. This study could be useful to rise up, if necessary, the complete band gap of any photonic crystal for manufacturing and practical purposes.

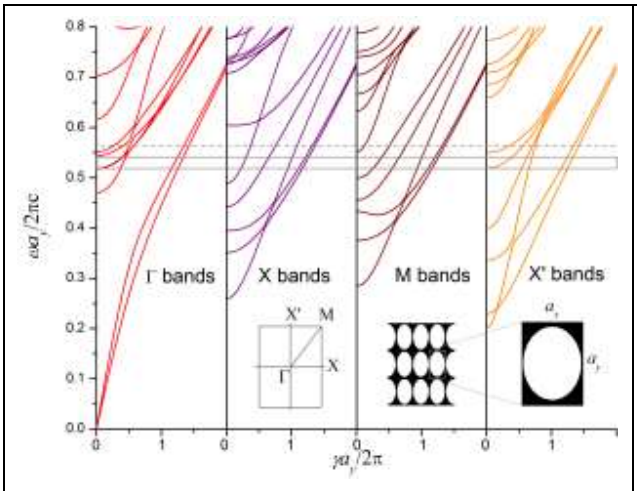



Figure 1. The frequency modes of the lowest bands as a function of $\gamma a_y/2\pi$ for the rectangular lattice: (a) Γ bands, (b) X bands, (c) M bands and (d) X' bands. The grey rectangle perimeter illustrates the complete band gap for in-plane PBSs. The left inset shows the first Brillouin zone with the high symmetry points. The centered inset shows a transversal cut of the PC. The right inset shows the unit cell of dimensions $a_x$ and $a_y = a_x/0.77$, minor radius $r_x=0.38a_y$, and mayor radius $r_y=0.45a_y$, where white represents vacuum ($\varepsilon_c = 1$) and black the high dielectric ($\varepsilon_e = 11.4$). Filling ratio is 0.696.

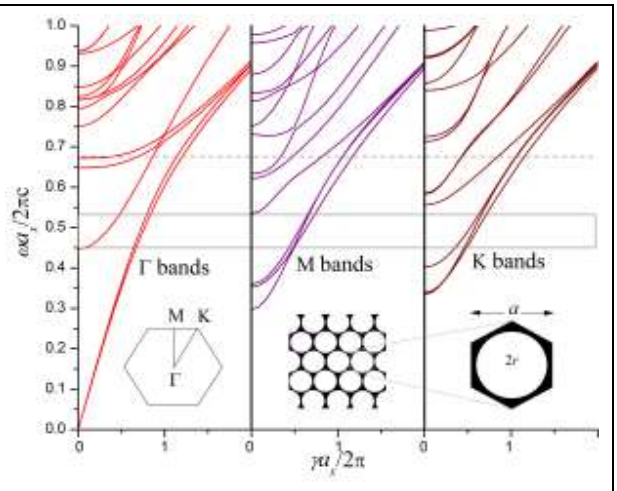



Figure 2. The frequency modes of the lowest bands as a function of $\gamma a_x/2\pi$ for the triangular lattice: (a) Γ bands, (b) M bands and (c) K bands. The grey rectangle perimeter illustrates the complete band gap for in-plane PBSs. The left inset shows the first Brillouin zone with the high symmetry points. The centered inset shows a transversal cut of the PC. The right inset shows the unit cell of hexagonal shape, with $2r=0.96a$, where white represents vacuum ($\varepsilon_c = 1$) and black the high dielectric ($\varepsilon_e = 13$). Filling ratio is 0.8358.

**Acknowledgements** J.D.V.S. is grateful for the scholarship granted for CONACYT.

**REFERENCES**

1. Ho, K. M., C. T. Chan and C. M. Soukoulis, "Existence of a Photonic Band Gap in Periodic Dielectric Structures," *Phys. Rev. Lett.*, Vol. 65, No. 25, 3152–3155, 1990.
2. Meade, R. D., K. M. Brommer, A. M. Rappe and J. D. Joannopoulos, "Existence of a Photonic Band Gap in Two Dimensions," *Appl. Phys. Lett.*, Vol. 61, No. 4, 495–497, 1992.
3. Qiu, M. and S. He, "Large complete band gap in two-dimensional photonic crystals with elliptic air holes," *Phys. Rev. B*, Vol. 60, No. 15, 10610–10612, 1999.
4. Zhou, L., M. Hu, F. Jia, C. Liao, Z. Feng and X. Feng, "Effect on Bandgap of Two-dimensional Square Photonic Crystal with Different Incidence Angle" *Acta Photonica Sinica*, Vol. 37, No. 11, 2213-2216, 2008.
5. Zhou, L., M. Hu, K. Zhang and X. Chen, "Band Structure of 2D Air-hole-type Triangular Photonic Crystal with Oblique Incidence," *Science & Technology Review*, Vol. 29, No. 7, 46-49, 2011.

# Optical correlations in 2D and 3D photonic crystals with weak and strong disorder

**O.S. Ojambati*, E. Yeganegi, A.P. Mosk, and W.L. Vos**

*Complex Photonic Systems (COPS)*

*MESA+ Institute for Nanotechnology*

*University of Twente,*

*P.O. Box 217, 7500 AE Enschede, the Netherlands.*

*corresponding author: o.s.ojambati@utwente.nl

**Abstract**- We investigate experimentally the effect of disorder in real photonic crystals. We studied three-dimensional (3D) silica opals, and two-dimensional (2D) silicon photonic crystals. The statistics of reflected light intensities strongly differs from the Rayleigh distribution typical of a completely disordered medium, indicative of intensity correlations. To investigate such correlations, we probe the spatial-dependent correlation function of the reflected intensity. We find that the reflected light from regions with low disorder correlates more than regions with higher disorder. Our method offers a new probe of the correlation length of the light in the crystal.

It is well-known that propagating light waves in a perfect and infinitely extended photonic crystal fulfill the Bloch condition [1]. In real photonic crystals, however, the spatial dependence of the waves is modified by the presence of unavoidable variations in size and position of the building blocks, as well as the finite crystal extent. Both effects result in scattering, which hampers the propagation of light through a crystal and eventually leads to Anderson localization [2,3]. Here, we propose a new experimental method to investigate the effects of disorder on the transport of light in periodic photonic crystals.

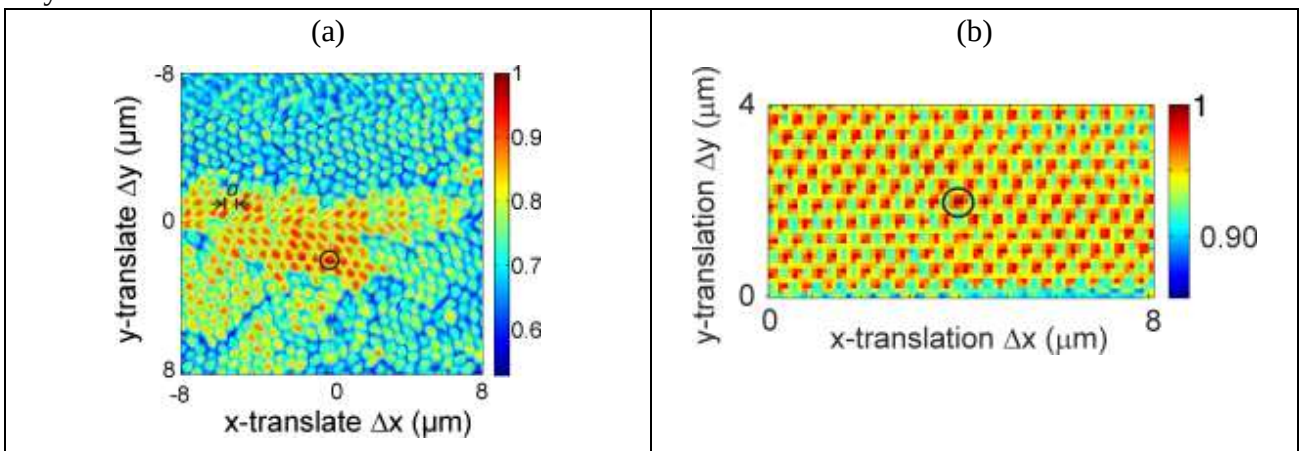



*Figure 1. Spatial correlation function of the reflected intensity (a) of a 3D opal made from silica nanoparticles, and (b) of a 2D photonic crystal consisting of deep pores etched in silicon. The correlation function is computed relative to the reflected intensity at the position of the black circle.*

*In the 2D Si crystal, the correlation function exceeds 0.95 over a long range.*

We investigate three-dimensional (3D) opals made by self-assembly, and two-dimensional (2D) silicon photonic crystals made by lithography and deep etching [4]. We collect intensity reflected by the crystals with an objective with a high numerical aperture. With increasing long-range order, the statistics of the reflected intensity increasingly deviates from the Rayleigh distribution of uncorrelated scattered intensities typical of statistically homogeneous media. Thus, the reflected intensities are correlated, as a result of the statistically periodic nature of the crystals.

To further investigate the optical correlations, we measure the correlation function as a function of translation across each crystal surface. We find that the correlation function depends on the disorder in different crystal grains within opal photonic crystals (see Fig. 1a). In contrast, the CMOS-fabricated 2D crystals show a very strong correlation in excess of 90% over a large range, shown in Figure 1b, typical for a system with long-range periodic order. Hence, our method provides a new way to characterize the correlation length of the waves - a central role in mesoscopic physics [5] - in photonic crystals with periodic structural order.

**References**


[1] N. W. Ashcroft and N. D. Mermin, *Solid State Physics* (Saunders College, 1976)

[2] A.F. Koenderink, A. Lagendijk, and W.L. Vos, Phys. Rev. B **72**, 153102 (2005)

[3] E. Kuramochi, M. Notomi, S. Hughes, A. Shinya, T. Watanabe, and L. Ramunno, Phys. Rev. B **72**, 161318 (2005)

[4] L.A. Woldering, R.W. Tjerkstra, H.V. Jansen, I.D. Setija, and W.L. Vos, Nanotechnology **19**, 145304 (2008)

[5] P. Sheng, *Introduction to wave scattering, localization and mesoscopic phenomena* (Springer, 2005)

# Active control of the vacuum field in nanomechanical photonic crystal structures

**M. Cotrufo[1], L. Midolo[1], M. Petruzzella[1], Z. Zobenica[1], F.W.M. van Otten[1], A. Fiore[1]**

[1]COBRA Research Institute, Eindhoven University of Technology, PO Box 513, 5600 MB Eindhoven, The Netherlands

[*]corresponding author: m.cotrufo@tue.nl

**Abstract**- We theoretically and experimentally investigate a nano-opto-electro-mechanical system which allows controlling the spatial distribution of the vacuum electromagnetic field. The system is based on a double-membrane photonic crystal waveguide. The bending of the top membrane, induced by an applied voltage, creates a spatial profile of the effective refractive index, which affects the localization of the electromagnetic modes. Large modulations of the optical quality factor are predicted by both theory and numerical calculations, and confirmed by experimental data.

The active control of light-matter interaction lies at the heart of cavity quantum electrodynamics. The strength of the interaction between a quantum emitter and the electromagnetic field depends both on the spatial alignment between emitter and field and on their spectral detuning. Nano-opto-electro-mechanical systems (NOEMS) have been used to implement spectral control on devices such as photonic crystal cavities (PCCs)[1,2]. So far, the work in PCC NOEMS has mostly been devoted to the wavelength tuning of optical modes, while the spatial distribution of the vacuum electromagnetic field is only weakly perturbed. In this work, we propose and investigate a NOEMS in which the spatial distribution of the optical field is greatly affected by the mechanical displacement of a membrane. In particular, we demonstrate that large variation of the quality factor Q can be obtained by increasing or decreasing the localization of the optical modes along a PCC structure. In perspective, the control of the vacuum field opens the way to the mechanical control of the emitter-photon interaction.

The device is schematically depicted in fig. 1a. It is composed by two GaAs membranes in which two identical photonic crystal waveguides have been etched. The membranes support two coupled guided modes, with a symmetric (S) and antisymmetric (AS) vertical field distribution, respectively. The corresponding effective refractive indices ($n_{eff}$) depend on the membrane distance and are different for the S and AS modes. When the membranes are parallel, $n_{eff}$ is uniform along the waveguide and the structure can be described as a Fabry-Perot cavity with weakly reflecting mirrors at the waveguide ends, which give rise to a discrete set of localized modes in the slow-light region of the dispersion curve. When the electrostatic force is applied, the top membrane bends and forms a region in the middle of the bridge where $n_{eff}$ is higher for the S modes and lower for the AS modes. This results in a large spatial modulation of $n_{eff}$ which induces a strong localization of the S modes at the center of the waveguide, while the AS modes are pushed towards the waveguide termination.

We developed an analytical theory based on an envelope function approach to investigate the behavior of the field profiles and the losses (that is, the Q factor) as a function of the mechanical bending. Our calculations (fig.1c and 1d) predict an increase (decrease) of the Q factor of the S (AS) modes of more than two orders of magnitudes as the membrane is bended from the equilibrium position to the maximum allowed deformation. 3D finite element method (FEM) calculations show, for the lowest-energy modes, good agreement with our theory.

Fig. 1b shows an electron microscope picture of the fabricated structure. The membranes are separated by a small air gap (200 nm). A layer of InAs quantum dots (QDs) is grown in the middle of the top membrane and

used as internal source to excite the modes. The membranes are doped to form an n-i-p diode, which is reverse biased in order to apply an electrostatic attractive force. The dimensions and the mechanical constraints are chosen so that, under the electrostatic force, the top membrane bends with a quasi-parabolic profile along the waveguide direction (inset of fig. 1b). In fig. 1(e-f) we show the evolution of the S and AS modes (in two different structures) as the applied voltage is increased. As expected, the spectral separation among the AS modes decreases, due to the modification of the index profile. Correspondingly, large modifications of the Q factors are observed (decrease by factor of ≈3 for the AS modes and increase by a factor of ≈ 2 for the S modes). The achieved Q modulation is much larger than the previous demonstrations based on, e.g., evanescently coupling a waveguide to a cavity.[3] The discrepancy between the experimental and theoretical values is mainly due to disorder effects, and to non-optimal bending of the real structures, as confirmed by FEM simulations.

These results demonstrate the mechanical control of the field distribution of nanophotonic cavities for the first time, and open the way to new regimes of opto-(electro)-mechanical coupling where the field, instead of the frequency, is coupled to the mechanical motion.

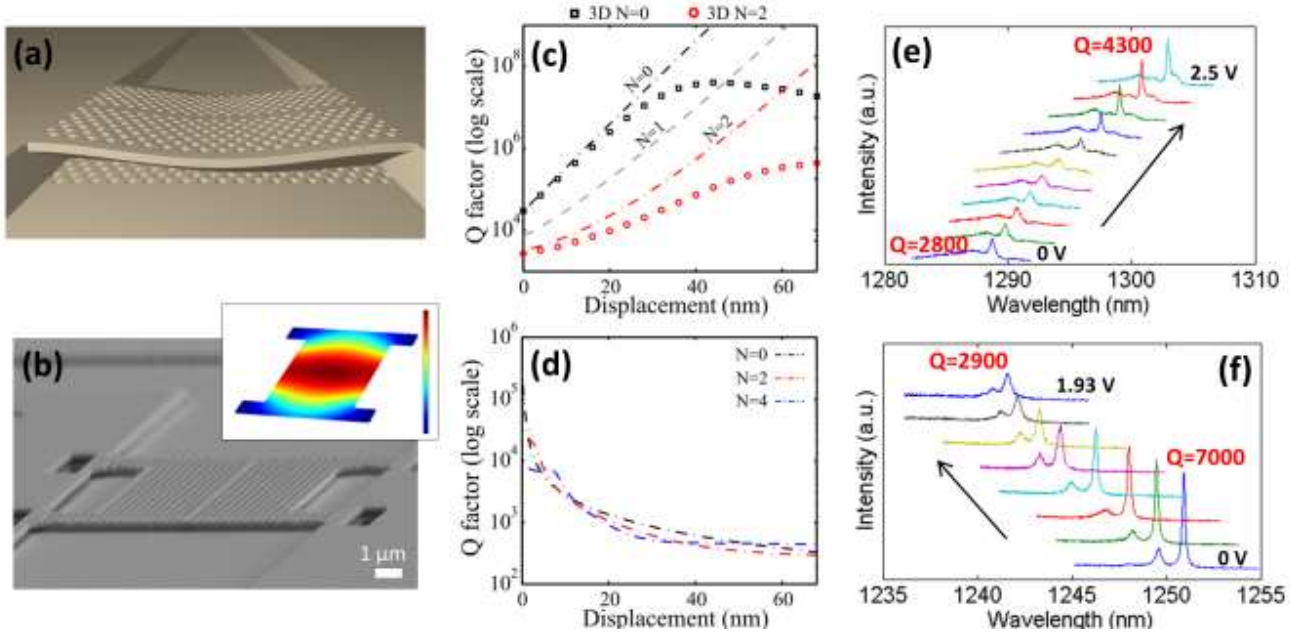



Fig1. (a) Sketch of the proposed structure. (b) SEM image of a fabricated device. The inset shows a numerical calculation of the top membrane's bending due to an applied uniform force. (c) Q-factor variation of the first 3 S modes with respect to the mechanical displacement of the center of the membrane. Lines indicate the results of our theory while symbols shows the results of FEM calculations.. (d) As in (c) but for the AS modes (without FEM calculations) and for the first 3 even modes. (e-f) Experimental data showing the increase of the symmetric mode's Q factor (panel e) and the decrease of the antisymmetric mode's Q factor (panel f). The initial and final Q factors, and corresponding applied voltages, are indicated in the figures.

**REFERENCES**


1. R. Perahia, J. D. Cohen, S. Meenehan, T. P. M. Alegre, and O. Painter, "Electrostatically tunable optomechanical zipper cavity laser", *Appl. Phys. Lett.*, 97, 191112 (2010).
2. Midolo, L., P. J. van Veldhoven, M. A. Dündar, R. Nötzel, and A. Fiore, "Electromechanical wavelength tuning of double-membrane photonic crystal cavities," *Appl. Phys. Lett.*, Vol. 98, 211120 1-3, 2011.
3. R. Ohta, Y. Ota, H. Takagi, N. Kumagai, K. Tanabe, S. Ishida, S. Iwamoto, and Y. Arakawa, "Electro-Mechanical Q Factor Control of Photonic Crystal Nanobeam Cavity", *Jpn. J. Appl. Phys.* 52, 04CG01 (2013).

# High-Emissivity Thermal Emitters on Patterned Dielectric Substrates for Thermophotovoltaics

**D. S. Kim[1], J. Y. Na[1], Y. J. Moon[1], Y. S. Kim[2], and S. K. Kim[1*]**

[1]Department of Applied Physics, Kyung Hee University, Gyeonggi-do 17104, Republic of Korea, [2]Display Components and Materials Research center, Korea Electronics Technology Institute, Gyeonggi-do 13509

[*]corresponding author: sunkim@khu.ac.kr

**Abstract**- We studied an optimal design of highly efficient thermal emitters fabricated on patterned dielectric substrates by conducting full-vectorial electromagnetic simulation. The simulation results revealed that two-dimensional (2D) photonic crystals that are composed of dielectric patterns covered with a metal (Ta and W) layer enhance the emissivity over a broad spectral range. This feature illustrates that each object in the 2D photonic crystals acts as an optical cavity, thus improving the light-matter interactions at every resonant frequency.

Recently, promising thermal-to-electrical solid-state energy conversion schemes have emerged, including thermophotovoltaics, supplied by heat sources such as combustion microreactors, radioisotope fuel, and solar energy [Fig. 1(A)] [1]. This concept permits efficient direct thermal to electrical energy conversion and enables low-mass, small-size devices with relatively high power densities, fundamentally limited only by Plank's blackbody law and the quantum efficiency (QE) of incorporated photovoltaic cells [Fig. 1(B)]. However, the mismatch between the radiation spectrum of a thermal emitter and the QE spectrum of photovoltaic cells causes low energy conversion efficiency of thermophtovoltaics. Thus, tailoring radiation spectrum of a thermal emitter is crucial for developing high-efficiency thermophotovoltaic devices.

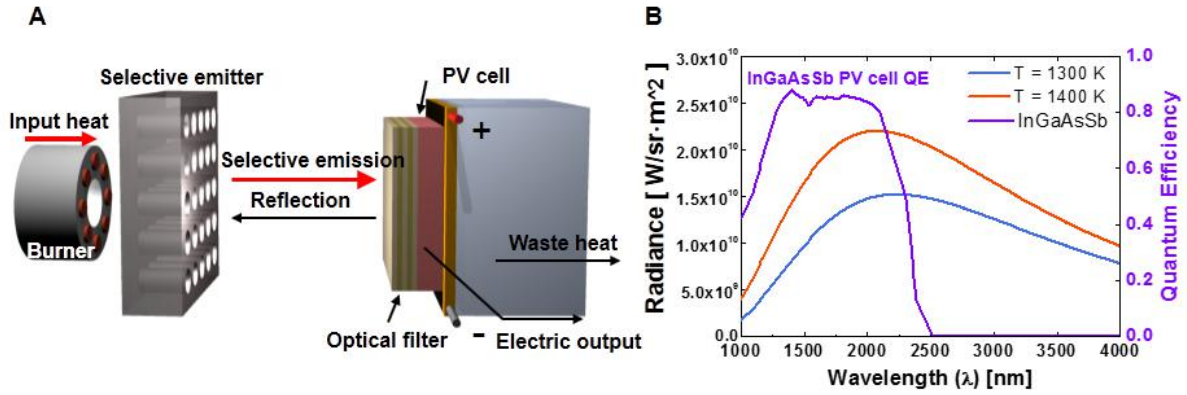



Fig. 1. (A) Schematic of a thermophotovoltaic system. (B) Blackbody radiation spectra at particular temperatures and the quantum efficiency of InGaAsSb photovoltaic cell[3].

To modify the radiation spectrum, various geometries of thermal emitters have been studied, including 2D metallic photonic crystals[1-3], 3D inverse opal structures[4], and metal-dielectric-metal metasurfaces[5]. In particular, 2D photonic crystals that possess periodic rod objects acting as an uncoupled optical cavity reliably enhance the

radiation efficiency and tune the cut-off wavelength. To attain high radiation efficiency, however, deep rod patterns must be prepared on a metal surface, which needs sophisticated fabrication and also causes the oxidation along a metal surface. To overcome existing problems, we propose dielectric patterned thermal emitters placed on a transparent substrate [Fig. 2(A)]. In our thermal emitters, a rationally designed dielectric pattern is defined on a substrate in prior to depositing a bulk metal. We highlight that this fabrication method can be used for realizing metasurfaces in which dielectric and metal materials are stacked alternatively along the predefined patterns [Fig. 2(B)].

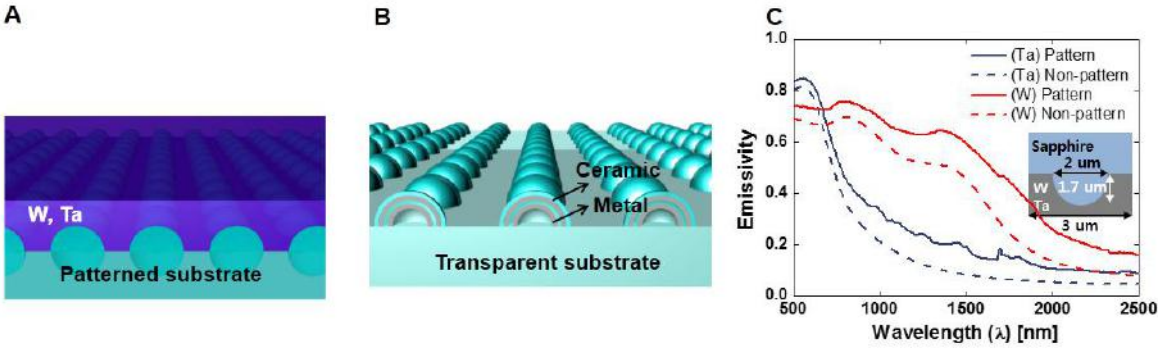



Fig. 2. (A) Schematic of dielectric patterned thermal emitters placed on a transparent substrate. (B) Schematic of meta-surfaces stacked on a 2D periodic patterned substrate. (C) Calculated radiation spectra of the proposed thermal emitters for W and Ta as shown in [Fig. 2. (A)].

For the first examination, we investigated W and Ta as a thermal emitter material to study their radiation spectra [Fig. 2(C)]. The radiation spectra show a dramatic enhancement of emissivity over the whole range of spectrum, compared to non-patterned structures. We expect that further improvement will be attainable if we seek for optimal structural parameters in a patterned substrate and also apply designed metasurfaces. These new findings on thermal emitters will pave the way toward highly efficient thermophotovoltaic systems.

**Acknowledgements**,

We were supported by the Basic Science Research Program through the National Research Foundation of Korea (NRF-2013R1A1A1059423) funded by the Ministry of Science, ICT, and Future Planning.

## REFERENCES

1. Rinnerbauer V. *et al*., "Recent developments in high-temperature photonic crystals for energy conversion," *Energy Environ. Sci*. Vol. 5, No. 8815-8823, 2012.

2. Celanovic I., N. Jovanovic, J. Kassakian, "Two-dimensional tungsten photonic crystals as selective thermal emitters," *Appl. Phys. Lett*. Vol. 91, 193101, 2008.

3. Stelmakh V. *et al*., "Tantalum-tungsten alloy photonic crystals for high-temperature energy conversion systems," *SPIE*. Vol. 9127, 91270Q-91270Q-9, 2014.

4. Kevin A. A. *et al*., "Three-dimensional self-assembled photonic crystals with high temperature stability for thermal emission modification, *Nat. Commun*. DOI: 10.1038 , 4:2630, 2013.

5. Liu X. *et al*., "Taming the blackbody with infrared metamaterials as selective thermal emitters," *Phys. Rev. Lett*. Vol. 107(4), 045901-041901-4, 2011.

# Fully optically built tunable photonic crystal

**O. Brzobohatý, L. Chvátal, and P. Zemánek**

Institute of Scientific Instruments of the CAS, v.v.i., Czech Republic
otobrzo@isibrno.cz

**Abstract**— We demonstrate experimentally that a tunable photonic colloidal crystal can be built fully optically. Polystyrene spheres, when illuminated by two counter-propagating laser beams, self-arranged due to the optical binding forces into chain-like structure. Our experiments, based on confocal microscopy, show tunability of optical response to unfocused supercontinuum laser. The spectrum of the scattered field varied along the photonic crystal showing localization of the field on the front part of the chain.

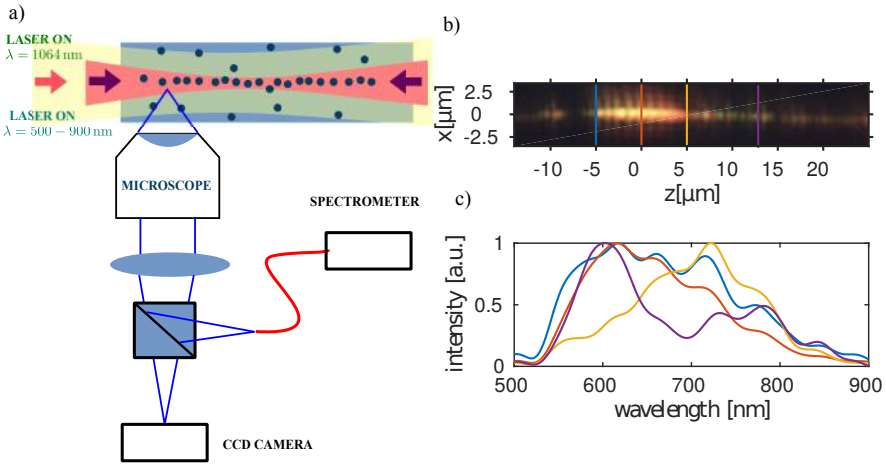



Figure 1: a) Two horizontally counter-propagating (C-P) laser beams (IPG, 1064 nm) were employed to optically confine polystyrene particles (520 nm; diluted in water). A supercontinuum white laser sources (NKT, 500-900 nm) were used to study optical response of self-arranged photonic chain-like structure. b) A colour CCD camera was employed to observe white light scattered on the structure. c) A spectrometer in confocal microscope arrangement was used characterize scattered light along the structure. The scattered spectrum varied along photonic structure. Most of the light was scattered from the front part of the structure. On the rear part of the chain some of the wavelengths are suppressed (650-750 nm).

Over the past few decades, the unusual optical properties of the periodic dielectric structures – *photonic crystals* – have been studied intensively [1]. Various remarkable optical responses can be designed and tailored, e.g., photonic bandgap, slow photons, negative refraction and others. Photonic structures can be nowadays prepared by several methods, e.g. colloidal self-assembly [1], conventional lithography process, and holographic photo-lithography.

A tightly focused laser beam can be used to create spatial optical field gradients which in turn can be used to trap colloids, hence this tool is called *optical tweezers* [2]. The rapid assembly of arbitrary materials into two-dimensional and three-dimensional quasicrystalline heterostructures with features suitable for obtaining interesting and potentially useful diffractive effects in infrared and visible light was demonstrated using the so-called holographic optical tweezers system [3]. Such devices tailor dynamically the laser beam wavefront using computer generated holograms and reached all degrees of freedom to vary the number of beam foci and their positions in 3D. However the performance of such holographic optical tweezers is limited when independent manipulation with higher number of objects is demanding.

Except tightly focused beams used in optical tweezers other geometries were developed. Here the mutual scattering of the trapping beam by the objects mediates new type of long-range interaction between these objects – *optical binding*. It leads to the spontaneous self-arrangement of micro-particles into stable formations with well defined inter particle distances – *optically bound matter*.

Here we present a formation and an optical response of a chain-like colloidal photonic structure. We employed recently developed flexible dual-beam optical trap [4] which enabled us to optically trap and self-arranged large number of colloids (polystyrene particles), see Fig. 1a). Two horizontally counter-propagating (C-P) laser beams (IPG, 1064 nm) were employed to optically confine polystyrene particles (520 nm; diluted in water). A supercontinuum white laser sources with relatively large beam waist and low power (NKT, 500-900 nm) were used as probe beam to study optical response of a self-arranged photonic chain-like structure. A colour CCD camera was employed to observe white light scattered on the structure, see Fig. 1 c). A spectrometer in confocal microscope arrangement was used to characterize scattered light along the chain. The scattered spectrum varied along photonic structure. Most of the light was scattered from the front part of the structure. On the rear part of the chain some of the wavelengths are suppressed (650-750 nm) The optical response on the supercontinuum white laser is highly sensitive to the separation of colloids. Since the separation between self-arranged colloids can be easily set [5] we can tune the optical response, see Fig. 2.

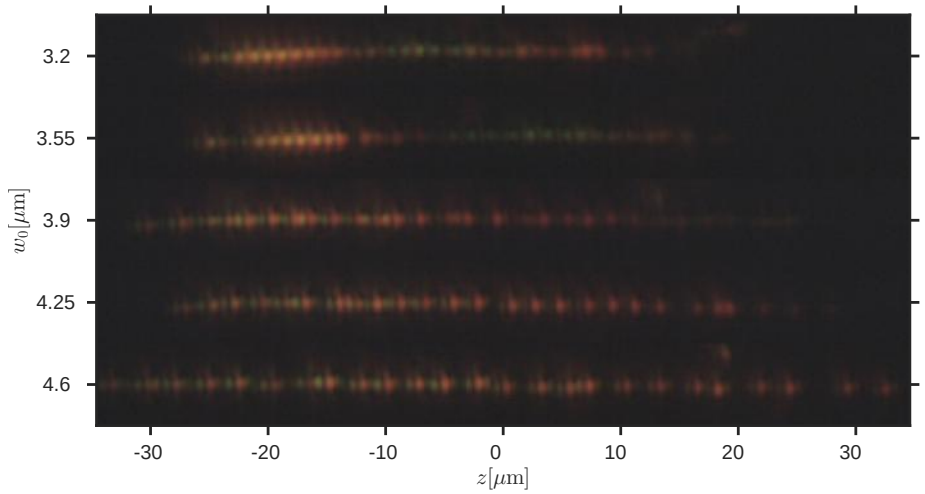



Figure 2: Tunability of the optical response of the photonic structure.

**ACKNOWLEDGMENT**

The research was supported by the Czech Science Foundation (project GA14-16195S), and its infrastructure by the Ministry of Education, Youth and Sports of the Czech Republic (LO1212), Academy of Sciences of the Czech Republic (RVO:68081731) and European Commission (CZ.1.05/2.1.00/01.0017).

**REFERENCES**

1. Kim, S. H., Lee, S. Y., Yang, S. M., and Yi, G. R., "Self-assembled colloidal structures for photonics," *NPG Asia Mater*, Vol. 3, No. 1, 25–33, 2011.
2. Ashkin, A., "Optical trapping and manipulation of neutral particles using lasers," *World Scientific*, London, 2006.
3. Roichman Y. and Grier, D. G."Holographic assembly of quasicrystalline photonic heterostructures," *Opt. Express*, Vol. 13, No. 14, 5434–5439, 2005.
4. Čižmár, T., Brzobohatý, O., Dholakia, K., and Zemánek, P. "The holographic optical micromanipulation system based on counter-propagating beams," *Laser Phys. Lett.*, Vol. 8, No. 1, 50–56, 2011.
5. Brzobohatý, O, Karásek, V., Čižmár, T., and Zemánek, P.. "Dynamic size tuning of multidimensional optically bound matter," *Appl. Phys. Lett.*, Vol. 99, No 10, 101105, 2011.

# Optimization of silicon slot waveguide micro-ring resonator cavities

**W. Zhang[1], S. Serna[1], X. Le Roux[1], C. Alonso-Ramos[1], L. Vivien[1] and E. Cassan[1,*]**

[1]Institut d'Electronique Fondamentale, Université Paris Sud, CNRS, UMR 8622, Université Paris-Saclay, Bat. 220, Orsay Cedex, France

[*]eric.cassan@u-psud.fr

**Abstract**- We report our recent results on the development of optimized silicon vertical slot micro-resonators, demonstrating remarkably low propagation loss of 1.32±0.87dB/cm at $\lambda$=1,550nm. We discuss on optical loss mechanisms in such resonators, with a special focus on the coupler loss contribution that turns out to be the key obstacle to achieve high *Q*-factors. We show ten-fold loaded Q-factor improvement, achieved by engineering the coupler region. These results open exciting new opportunities for the application of slot ring resonators for on-chip nonlinear optical processing or sensing in hybrid silicon photonics.

Silicon photonics, due to its very high index contrast, enables ultra-high mode confinement that poses a unique potential for the implementation of nonlinear optical processing with substantially reduced power consumptions, compared with optical fiber counterparts [1]. However, efficiency of nonlinear processes in silicon at telecommunication wavelengths is limited by the two-photon-absorption process. One possible solution to overcome this effect, while still benefiting from high index contrast in silicon, is to use slot waveguides that funnel the field within the void gap between two narrow silicon rails [2,3]. Interestingly, light recirculation in slot waveguide micro-resonators can be used to further enhance light matter interaction. Unfortunately, slot waveguides are known to suffer from larger roughness-induced scattering extrinsic losses than Si wires. This is due to a strong electric field interaction with the inner rails' walls defined by lithographic and etching technological processes. This results in ring resonators with a moderate *Q*-factor of typically a few thousands in standard situations.

To alleviate this intrinsic limitation in slot waveguide resonators we have worked in two directions: optimize the slot waveguide fabrication process, and engineer the coupler contribution to the overall ring losses. We have experimentally characterized different ratios of slot width to total slotted waveguide width and waveguide aspect ratio to analyze their linear loss. We have also designed various testing structures to properly extract the different waveguide-ring coupling coefficients directly from experiments. We used subwavelength grating couplers [4] at the input and output to minimize Fabry-Perot ripples in our measurements, easing the quality factor characterization. We have found that the micro-ring loaded quality factor greatly increases when the coupler gap approaches 500 nm. These results indicate that the coupler losses are significantly reduced for increasing gap values, probably due to the reduction of the waveguide side-wall scattering loss effects. Following the deduced guidelines, we then fabricated a 50μm radius add-drop slot waveguide ring resonator (see Fig. 1) with *Q*=30,600 in a silicon wafer with silicon thickness of 220nm and a 2μm thick box.

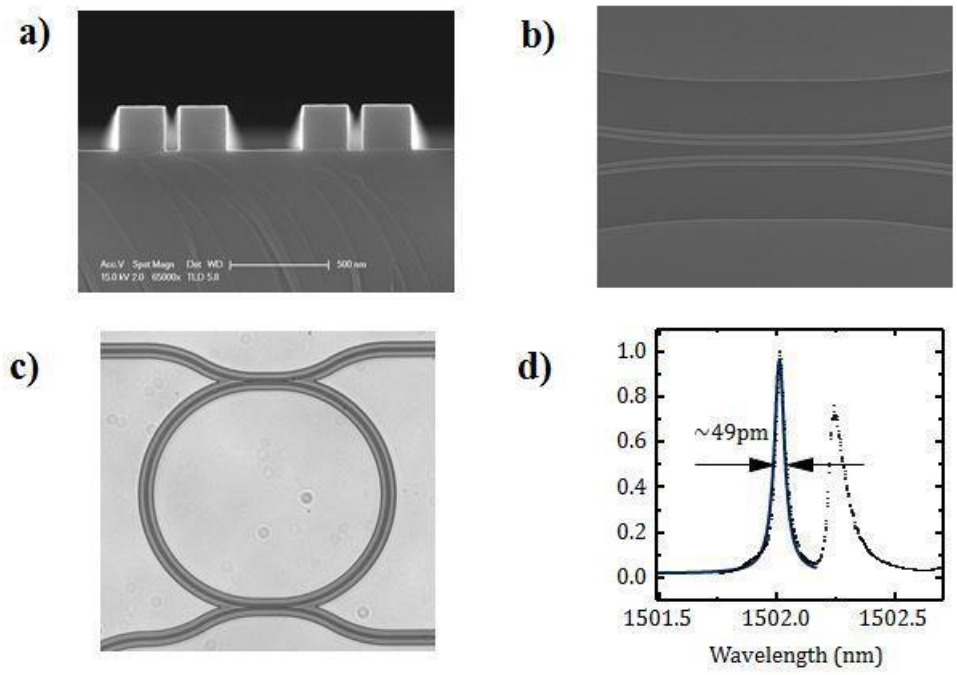



**Figure 1:** Scanning electron microscopy images of a) cross-section of ring coupler and b) symmetric bus-ring coupler region. c) Optical view of add-drop slot micro-ring resonator. c) Normalized transmission of slotted add-drop micro-ring resonator with 50 μm radius and symmetric coupler with 500 nm gap.

As a conclusion, in this work, we have experimentally observed a strong influence of the coupler losses on the overall slot ring performances. We have found that symmetric couplers with larger gaps minimize coupler losses yielding an up to ten-fold improvement in the *Q*-factor compared with normal non optimized straight bus-ring coupler.

**ACKNOWLEDGEMENT**

ANR Program Blanc International POSISLOT (2012, 9035RA13); CARTOON European project.

**REFERENCES**

1. L. Vivien and L. Pavesi, Handbook of Silicon Photonics, 2013.
2. V. R. Almeida, et al., "Guiding and confining light in void nanostructure," Opt. Lett. 29, 1209–1211, 2004.
3. W. Zhang, et al., "Nonlinear optimization of slot Si waveguides: TPA minimization with FOM TPA up to 425," Opt. Lett. 40, 1212, 2015.
4. D. Benedikovic, et al., "Subwavelength index engineered surface grating coupler with sub-decibel efficiency for 220-nm silicon-on-insulator waveguides," Opt. Express 23(17), 22628-22635, 2015.

# Magneto-optical nonreciprocity of the waveguide modes in one-dimensional magnetophotonic crystals

**D.A. Sylgacheva[1,2*], N.E. Khokhlov[1,2], A.N. Kalish[1,2], A.R. Prokopov[3], A.N. Shaposhnikov[3], V.N. Berzhansky[3], M. Nur-E-Alam[4], M. Vasiliev[4], K. Alameh[4], S.A. Dagesyan[1], and V.I. Belotelov[1,2]**

[1]M.V. Lomonosov Moscow State University, Moscow, Russia

[2]Russian Quantum Center, Skolkovo, Moscow Region, Russia

[3]V.I. Vernadsky Crimean Federal University, Simferopol, Russia

[4]Electron Science Research Institute, Edith Cowan University, Australia

[*]corresponding author: sylgacheva.darjja@physics.msu.ru

**Abstract**- We extend the theory of the waveguide modes' dispersion for the case of photonic crystals containing transverse magnetized layers. Obtained solutions of the dispersion equation are in good agreement with the experimentally measured spectral displacements of transverse magneto-optical Kerr effect's extrema.

Photonics is modern rapidly developing area of optics. Usage of multilayer planar waveguides opens new perspectives in this field. Systems of planar waveguides used, for example, in fiber-optic communication system. The optical properties of planar waveguides could be precisely varied with a Bragg structure or one-dimensional photonic crystals (PC). In particular, it allows obtaining the desired view of the transmission spectrum; Bragg structures as optical fiber shells allow to specify the necessary dispersion characteristics of eigenmodes.

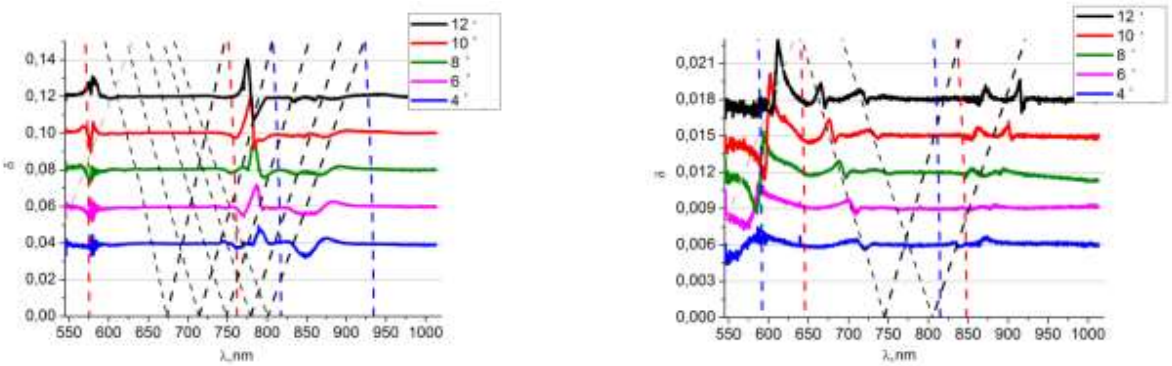
Waveguide structures based on one-dimensional PC are considered in [1, 2], for example, where the main attention was paid to the calculation of waveguide mode dispersion law, as well as assessing their optical losses. In other works, such as [3], a PC with microresonator layer was considered with the localization of electromagnetic waves within this layer as a microcavity. The optical properties of the defect layer can be changed by external influences: an external electric field, heating, etc. Magnetophotonic crystals (MPC) - PC with magnetic media - provide additional opportunities for the modulation of the optical signal by the magneto-optical effects [4].

In this work, we study the waveguide modes in the 1D PC with magnetic dielectric film on top (sample 1), and MPC, were a magnetic dielectric is used as one of the layers within the period of the PC (sample 2). The deposition of gold grating on top of the samples leads to the possibility to excite the waveguide modes within the structures with propagation along the layers. Since the samples contain the magnetically active materials at different positions, the spectral features of the transverse Kerr effect (TMOKE) have different spectral dependences (fig. 1).

The dispersion curves of waveguide modes are calculated by the method, which is similar to the one used in [5] through the recording of the scattering matrix and find non-trivial solutions of the homogeneous system of ordinary linear equations. We extended the method in accordance to take into account the transverse magnetization of the layers. The calculated curves are in good agreement with the experimental positions of TMOKE resonances. Therefore, it is convenient to determine the correlation between the fixed resonance and corresponding eigenmode. For example, for sample 1 TMOKE reaches the value $\delta=1.3\bullet10^{-3}$ at a wavelength

$\lambda_0$=916 nm and an angle of incidence $\theta = 10^0$, which corresponds to the excitation of the waveguide mode with diffraction order +1.

The new extended theory gives the opportunity to design and compare MPCs of different configuration and choose one more suitable for practical porpoises.




(a) (b)

Fig. 1. Spectra of transverse Kerr effect in the reflection of the sample 1 (a) and sample 2 (b) at different angles of incidence and TM-polarized light. $\delta$ = [R(+**M**) - R(-**M**)]/R(0). The angles of incidence $\theta$ are 4° (blue curves), 6° (purple curves ), 8° (green curves), 10° (red curves), 12° (black curves); spectra at different $\theta$ are plotted with different offsets for convenience. Dashed lines represent the dispersion curves of eigenmodes calculated numerically: waveguide modes (black lines), Rayleigh anomalies (gray lines), and photonic bang gap borders (red lines). Induction of the external magnetic field of 150 mT.

**Acknowledgements.** The research is supported by Russian Science Foundation (grant No 14-32-00010).

**REFERENCES**

1. Johnson S.G., Ibanescu M., Skorobogatiy M. “Low-loss asymptotically single-mode propagation in large-core OmniGuide fibers”, *Opt. Express*, Vol. 9 No 13, 748-779, 2001.
2. Mizrahi A., Schachter L. “Bragg reflection waveguides with a matching layer”, *Opt. Express*, Vol. 12, No 14, p. 3156-3170, 2004.
3. Fushman I., Waks E., Englund D., Stoltz N., Petroff P., and J. Vuckovic “Ultrafast nonlinear optical tuning of photonic crystal cavities”, *Appl. Phys. Lett*. Vol. 90, No 9, 091118, 2007.
4. Berzhansky V. N. et al “The Effect of Faraday Rotation Enhancement in Nanolayered Structures of Bi - Substituted Iron Garnets” *Solid State Phenom*. Vol. 200, No 233, 233-238, 2013.
5. P. Yeh, A. Yariv, “Electromagnetic propagation in periodic stratified media”, *J. Opt. Soc. Amer*., Vol. 67, No.4, 423-438, 1977.

# All-dielectric Zero-Index Metamaterial

**D. I. Vulis[1], Y. Li[1], O. Reshef[1], M. Yin[1],P. Camayd-Muñoz[1], S. Kita[1], M. Lončar[1], and E. Mazur[1]**

**[1]School of Engineering and Applied Sciences, Harvard University, 9 Oxford Street, Cambridge, Massachusetts 02138**
**dvulis@seas.harvard.edu**

**Abstract**— We present an on-chip Dirac-cone metamaterial with an impedance-matched zero refractive index at a wavelength of 1550nm. The design consists of a square array of air holes in 220-nm silicon-on-insulator (SOI) that can be fabricated using a single electron beam lithography procedure. This all-dielectric structure offers improved compatibility with current integrated silicon photonics platforms. In addition, this design enables mass production of zero-index-based photonic devices at low cost and high quality using standard complementary metal-oxide-semiconductor (CMOS) fabrication technology.

## 1. INTRODUCTION

Metamaterials with simultaneously zero effective permittivity and permeability offer uniform spatial phase and infinite wavelength [1, 2]. Such properties allow for a broad range of photonic applications including super-coupling and simultaneous phase matching in nonlinear optics [3, 4]. Zero-index metamaterials have been recently demonstrated in both out-of-plane and on-chip configurations [5, 6] by taking advantage of a photonic Dirac-cone dispersion at the center of the Brillouin zone. Such designs offer matched impedance and low losses. However, mass production of photonic devices necessitates integration with CMOS technology. Previously demonstrated configurations are inherently incompatible due to an out-of-plane configuration or metallic and high aspect-ratio structures, respectively.

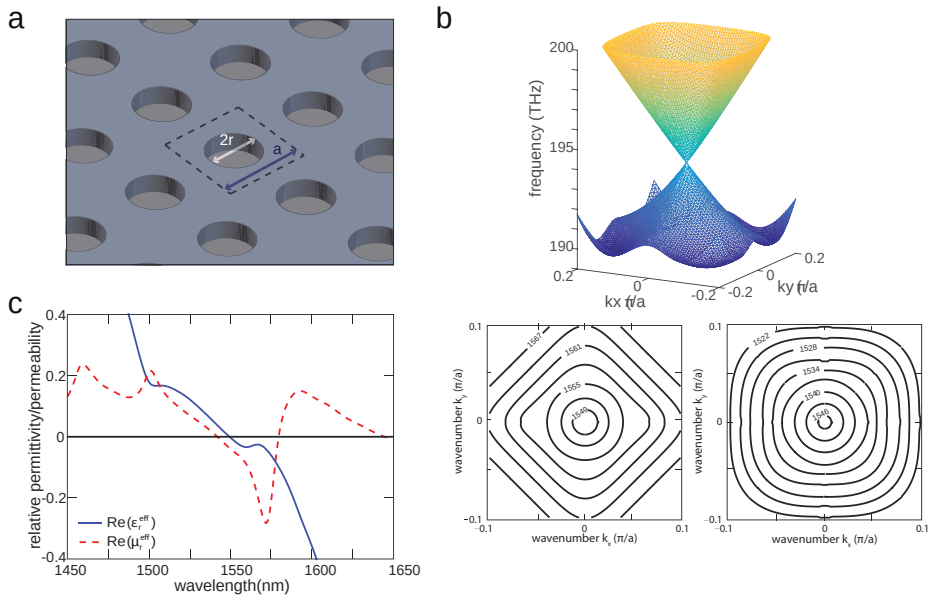



Figure 1: Material properties of the Dirac-cone metamaterial. a) Schematic of the air-holes-in-silicon-matrix metamaterial showing the unit cell and associated radius ($r$) and pitch ($a$) parameters. b) (top) Three-dimensional bandstructure of the metamaterial for transverse electric (TE) polarization; the flat band is filtered to show the Dirac-cone dispersion clearly. Isowavelength contours for wavelengths above (bottom left) and below (bottom right) the design wavelength of 1550nm. c) Effective permittivity and permeability of the metamaterial retrieved from reflection and transmission coefficients.

We present an on-chip zero-index metamaterial consisting of a square array of air-holes in a 220-nm-thick SOI wafer (Fig. 1a) designed through iteration of air-hole radius ($r$) and unit cell pitch ($a$) for transverse electric (TE) polarization.

## 2. DESIGN AND FABRICATION

The increased proportion of silicon in an air-hole configuration as compared to silicon pillars [6] allows for improved confinement in thinner silicon layers. The resulting structure produces a Dirac-cone dispersion with an improved quality factor. The three-dimensional TE bandstructure of the metamaterial is shown to have a Dirac-cone dispersion at the center of the Brillouin zone corresponding to the design frequency (Fig. 1b top). The degeneracy in the dispersion corresponds to a quadrupole mode and two dipole modes at the Gamma point. In this region, the zero-index metamaterial is also found to be isotropic (Fig. 1b bottom). We verify that the effective permittivity and permeability cross zero simultaneously and linearly at the design wavelength (Fig. 1c). These results indicate that this metamaterial possesses an impedance-matched, isotropic zero index at 1550 nm.

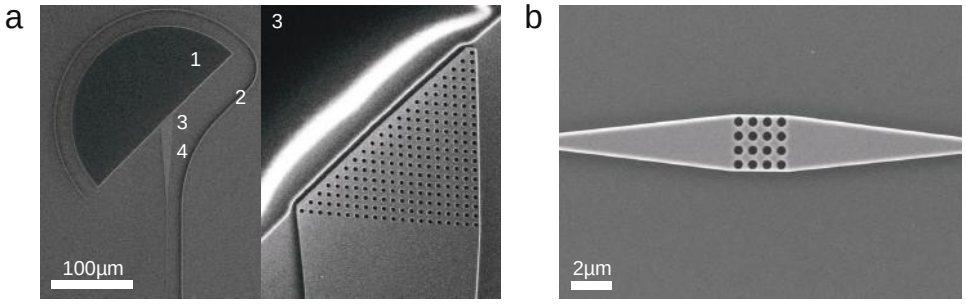



Figure 2: a) SEM of the fabricated prism device showing output SU-8 slab waveguide (1), calibration SU-8 waveguide (2), air hole prism (3) with closer view shown on right, and input silicon waveguide (4). b) SEM of the fabricated Mach Zehnder device.

To experimentally verify that the metamaterial has a refractive index of zero, we plan to measure refraction through a prism consisting of the metamaterial (Fig. 2a). In addition, we can extract the effective constitutive parameters of the metamaterial through measurement of the complex transmission and reflection coefficients using an on-chip Mach-Zehnder-interferometer-based setups (Fig. 2b).

The significant reduction in fabrication procedures will allow for mass implementation of zero-index-based photonic devices.

## REFERENCES


1. Huang, X., Y. Lai, Z.H. Hang, H. Zheng, and C.T. Chan, "Dirac cones induced by accidental degeneracy in photonic crystals and zero-refractive-index materials," *Nat. Materials*, Vol. 10, 582-586, 2011.
2. Engheta, N., "Pursuing near-zero response," *Science*, Vol. 340, 286-287, 2013.
3. Silveirinha, M. G. and N. Engheta, "Theory of supercoupling, squeezing wave energy, and field confinement in narrow channels and tight bends using epsilon-near-zero metamaterials," *Phys. Rev. B*, Vol. 76, 245109, 2007.
4. Suchowski, H., K. O'Brien, Z. J. Wong, A. Salandrino, X. Yin, and X. Zhang, "Phase mismatch-free nonlinear propagation in optical zero-index materials," *Science*, Vol. 342, 1223-1226, 2013.
5. Moitra, P., Y. M. Yang, Z. Anderson, I. I. Kravchenko, D. P. Briggs, and J. Valentine, "Realization of an all-dielectric zero-index optical metamaterial," *Nat. Photonics*, Vol. 7, 791-795, 2013.
6. Li, Y., S. Kita, P. Munoz, O. Reshef, D.I. Vulis, M. Yin, M. Loncar, and E. Mazur, "On-chip zero-index metamaterials," *Nat. Photonics*, Vol. 9, 738-742, 2015.

# Wave transmission and photonic frequency bands in graphene superlattices with sequentially modulated doping

**I. Fuentecilla-Carcamo,[1] M. A. Palomino-Ovando[1] and F. Ramos-Mendieta[2]**

[1]Benemerita Universidad Autonoma de Puebla, Mexico

[2]Universidad de Sonora, Mexico

[*]*corresponding author*: framos@cifus.uson.mx

**Abstract**- The propagation of light in periodic layered media constituted of equidistant and equally doped graphene sheets is described by band theory. We report that additional structure on the photonic bands is produced when the graphene doping is sequentially modulated along the superlattice axis. Transmission and reflection spectra of multilayer arrays with different doping modulation are presented.

It has been proved recently that a periodic array of graphene monolayers behaves as a 1D photonic crystal.[1-4] Therefore, a periodic stack of graphene sheets can forbid electromagnetic wave transmission in certain frequency ranges. It is an interesting result because graphene is a flat layer of practically zero thickness which means zero optical path length in the perpendicular direction. Consequently, the photonic bands will not include modes with oscillatory or evanescent fields inside the graphene layer. It is an important difference with respect to ordinary dielectric 1D photonic crystals where fields can penetrate into the constituent dielectric slabs. Thus, with homogeneous dielectric background it is graphene the solely responsible of band structure formation. In this paper we consider frequencies of oscillatory fields inside the background media; surface plasmons in graphene with exponentially decay field in the background media are not considered

Maxwell equations establish that tangential electric (magnetic) fields are continuous (discontinuous) when they traverse a graphene monolayer of conductivity $\sigma$ . Such discontinuity of the magnetic field is the principal mechanism leading to the bang gap formation in graphene superlattices. We have found quantitative changes in the band structure when the graphene doping changes uniformly through all the superlattice. However, as we shall prove in this presentation, a sequential modification of the graphene doping could lead to important qualitative differences. Notice that we are considering a periodic structured system (the graphene layers are equidistant); the doping modulation is over imposed to this system.

For instance, we present results for the wave transmission in graphene superlattices where three levels of graphene doping are used. Distinct graphene layers considered are labeled as A, B and C and their chemical potentials are $\mu_A = 0.2\,\mathrm{eV}$ , $\mu_B = 1.2\,\mathrm{eV}$ and $\mu_C = 1.0\,\mathrm{eV}$ , respectively. Figure 1 features transmission spectra for two cases: (a) for a stack of 55 homogeneously doped graphene layers of C type, and (b) for a stack of 55 graphene monolayers following the ninth order Fibonacci sequence with layers satisfying the basic order $S_0$ = A and $S_1$ = B. For numerical calculations we consider the typical

values for graphene losses[1] and the interlayer distance is $d$ = 10 μm.

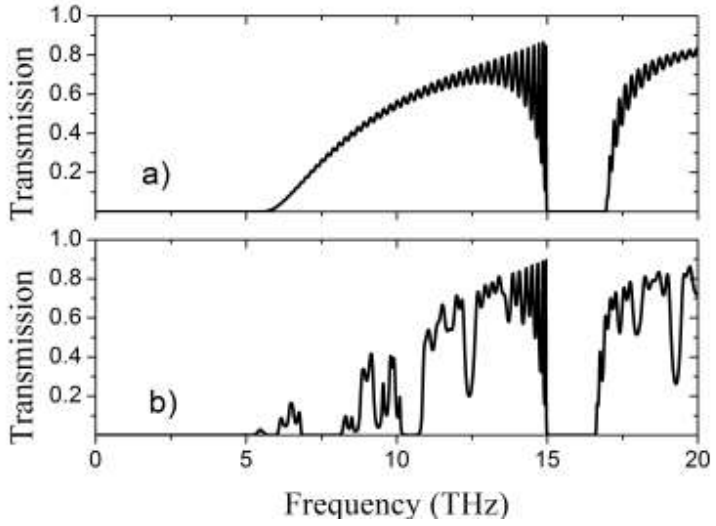



**Figure 1**

We notice in Figure 1 that both arrays generate the same *structural* band gaps (that depend mainly on the constant separation between the layers); they lay in the low frequency region and just above the frequency $f = 15$ THz. However additional band gaps appear for the structure with Fibonacci modulation.

More details on the formation of new photonic band gaps as function of the Fibonacci sequences and other type of sequences, will be given in this presentation.

**Acknowledgements**

One of the authors (I.F.C.) wishes to thank the Consejo Nacional de Ciencia y Tecnología (CONACyT) for financial support.

**REFERENCES**

1. Madani A. and Entezar S. R., *Physica B: Condensed Matter*, **431**, 1-5, 2013.
2. Zhan T., Shi X., Dai Y., Liu X.and Zi J., *Transfer matrix method for optics in graphene layers*, Journal of Physics: Condensed Matter, **25**, 215301, 2013.
3. Al-sheqefi F. U. Y., Belhadj W., *Photonic band gap characteristics of one-dimensional graphene-dielectric periodic structures*, Superlattices and Microstructures, **88**, 127-138,2015
4. Roshan Entezar S., Saleki Z., Madani A., *Optical properties of a defective one-dimensional photonic crystal containing graphene nanolayers*, **478**, 122-126, 2015

# Influence of microscale and nanoscale size effects on optoelectronic properties of metallic patterned structures

**M. Marus[1], A. Hubarevich[1], A. Smirnov[2*], X. W. Sun[1,3], H. Hui[4] and W. Fan[1]**

[1] School of Electrical and Electronic Engineering, Nanyang Technological University, Nanyang Avenue 50, 639798 Singapore

[2] Department of Micro- and Nano-Electronics, Belarusian State University of Informatics and Radioelectronics, P. Brovki 6, 220013 Minsk, Belarus

[3] Department of Electrical and Electronic Engineering, College of Engineering, South University of Science and Technology, 1088 Xue-Yuan Road, Nanshan, Shenzhen, Guangdong, 518055, China

[4] Singapore Institute of Manufacturing Technology, 71 Nanyang Drive, Singapore 638075

[*]corresponding author: smirnov@bsuir.by

**Abstract**-The impact of micro- and nanopores on the optoelectronic performance of aluminium and silver layers with hexagonal pore arrangement is demonstrated. Results show that the difference of optoelectronic properties between the aluminium and silver MP layers is negligible (less than 5%), while the NP silver layers demonstrate significantly higher transmittance (up to 20%) at the given sheet resistance. The results obtained allow to analyze which microscale or nanoscale pore size of patterned transparent conductive metallic layers is the most appropriate for each specific optoelectronic applications.

Transparent conductive layers (TCLs) with both good transmittance and electrical conductivity are the key components in optoelectronic applications such as liquid crystal cells, organic and quantum dot displays, solar panels, light emitting diodes, electrochromic windows, touch screens and other devices [1]. Commonly used TCLs based on indium-tin-oxide (ITO) do not meet the current criteria of flexibility, accessibility, ease of fabrication and low cost, which creates demand for alternative films [2]. Micro- and nanoporous (MP and NP) metallic layers have received particular interest due to the convenient methods of their preparation coupled with high optoelectronic performance and flexibility. Here, we analyze the change in optoelectronic properties of aluminium (Al) and silver (Ag) hexagonally arranged MP and NP layers in visible wavelength range, which takes place with gradual decrease of cells from the microscale to the nanoscale.

Figure 1 shows the geometrical model for TCLs based on MN and NP metallic layers. Both metallic layers were spread across the glass substrate within the same plane parallel to *X* and *Y* axes. MP and NP layers were arranged hexagonally with interpore distance *a* and diameter of pore *d*. The simulation area was narrowed to the unit cell and set to *a* and $a\sqrt{3}$ along X and Y axes, respectively. The optical properties were simulated using the finite-difference time-domain method (FDTD) which is commercially available within Lumerical software [3]. The sheet resistance was calculated by percolation model in accordance to [4]. Above mentioned methods were successfully applied by our group in [5-7].

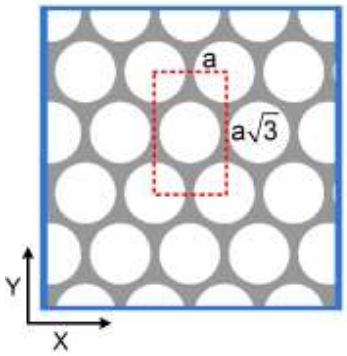



Figure 1: The geometrical model for TCLs based on MP and NP metallic layers on the glass substrate. Red rectangle is the unit simulation area for the hexagonal pore arrangement.

Figure 2 demonstrates the dependence of the transmittance of Al and Ag MP (a) and NP (b) layers on the sheet resistance. As can be seen, the difference of optoelectronic properties between Al and Ag MP layers is negligible (less than 5%). In case of NP, the transmittance of Ag layers is significantly higher (up to 20%) at the given sheet resistance. Such effect is explained by stronger influence of surface plasmons on the transmittance of Ag NP layer over the whole visible range.

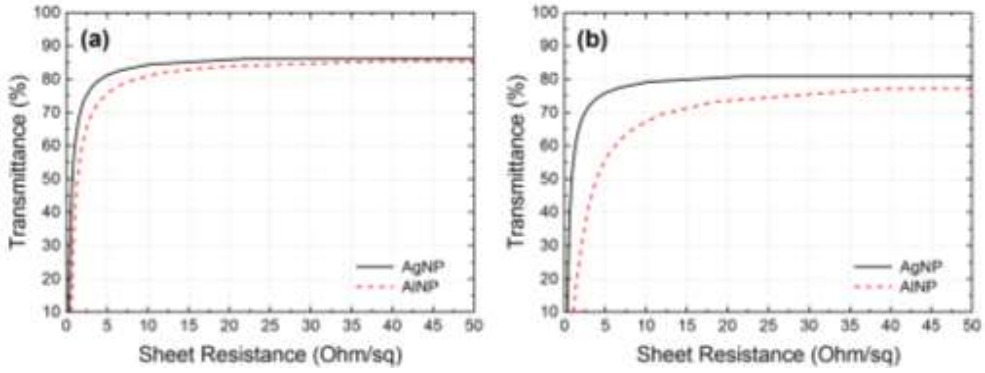



Figure 2: Dependence of the transmittance of Al and Ag MP (a) and NP (b) layers on the sheet resistance.

The given results grant the opportunities for more detailed analysis of the influence of size effects for micro- and nanoscale pores of patterned transparent conductive metallic layers chosen for different optoelectronic applications.

**REFERENCES**

1. Bae, S., J. Kim, D. Shin, J.-H. Ahn, and B. H. Hong, "Towards industrial applications of graphene electrodes," *Phys. Scr.*, Vol. 2012, No. T146, 14024–14031, 2012.
2. Van de Groep, J., P. Spinelli, and A. Polman, "Transparent conducting silver nanowire networks," *Nano Lett.*, Vol. 12, No. 6, 3138-3144, 2012.
3. Lumerical FDTD Solutions. Available from: https://www.lumerical.com/tcad-products/fdtd/.
4. Last, B. and D. Thouless, "Percolation theory and electrical conductivity," *Phys. Rev. Lett.*, Vol. 27, No. 25, 1719-1721, 1971.

5. Marus, M., A. Hubarevich, H. Wang, A. Smirnov, X. Sun, and W. Fan, “Optoelectronic performance optimization for transparent conductive layers based on randomly arranged silver nanorods,” *Opt. Express*, Vol. 23, No. 5, 6209-6214, 2015.
6. Hubarevich, A., M. Marus, W. Fan, A. Smirnov, X. W. Sun, and H. Wang, “Theoretical comparison of optical and electronic properties of uniformly and randomly arranged nano-porous ultra-thin layers,” *Opt. Express*, Vol. 23, No. 14, 17860-17865, 2015.
7. Marus, M., A. Hubarevich, H. Wang, A. Stsiapanau, A. Smirnov, X. W. Sun, and W. Fan, “Comparative analysis of opto-electronic performance of aluminium and silver nano-porous and nano-wired layers,” *Opt. Express*, Vol. 23, No. 20, 26794-26799, 2015.

# Highly efficient high-speed thermal emitters based on quantum wells and photonic crystals

**T. Inoue[1*], T. Asano[1], M. D. Zoysa[1], and S. Noda[1*]**
[1]Kyoto University, Japan
[*]corresponding author: t_inoue@qoe.kuee.kyoto-u.ac.jp, snoda@kuee.kyoto-u.ac.jp

**Abstract**- We demonstrate the drastic improvement of power utilization efficiency and modulation speed of thermal emitters, by utilizing intersubband transitions in multiple quantum wells and optical resonances in photonic crystal slabs. We realize a high-*Q* (>100) thermal emission peak whose intensity at a given input power is an order of magnitude higher than that of a reference blackbody emitter. We also demonstrate high-speed (~MHz) switching of thermal emission intensity, linewidth, and wavelength via electrical control of emissivity.

Thermal emission devices that operate over a wide range of frequencies are important for various sensing applications as well as thermo-photovoltaic power generation systems. However, conventional thermal emitters suffer from low power utilization efficiency due to their broadband emission spectra, and extremely slow modulation speed (1~100 Hz) due to their slow thermal response. In this talk, we describe the method of thermal emission control combining intersubband transitions in multiple quantum wells (MQWs) with optical resonant modes in photonic crystal (PC) slabs, and present our recent demonstrations of highly efficient high-speed thermal emitters.

In the first part of our talk, we focus on the realization of single-mode high-*Q* thermal emitters operating with high power-utilization efficiency. Although various thermal emitters based on optical nanostructures have been so far investigated, they exhibit low-*Q* emission peaks ($Q$<10) and broadband background emission due to the large optical losses inherent in the materials used (typically metals). In order to obtain much narrower thermal emission, we recently proposed the thermal emission control via simultaneous manipulation of the photonic states in the emitter and the absorption spectra of the materials. More specifically, we proposed using an intersubband transition in GaAs/AlGaAs MQWs to obtain a narrowband absorption spectrum around the target wavelength, and enhancing the light-matter coupling by using a band-edge resonant mode in a PC slab [1]. The emissivity and linewidth of the thermal emission peaks achieved with this method are determined by the decay rates of the modal energy due to the intersubband absorption and the far-field radiation from the PC slab. By carefully matching these two rates, we achieve a single-mode narrowband thermal emission peak with a *Q* factor of above 100 [2]. In addition, we demonstrate that the peak emission intensity of our device is an order of magnitude greater than that of a reference blackbody emitter under the same input power owing to the efficient increase in the emitter's temperature.

In the second part of our talk, we discuss the dynamic control of thermal emission spectra. Our concept is based on the electrical control of emissivity (absorptivity), which can be realized by extracting electrons from the quantum wells in the emitter described above. By changing the electron density in the MQWs using a pn junction with a reverse bias, we realize for the first time the ultrafast control of the thermal emission intensity at a modulation frequency of ~1MHz [3], which is four orders of magnitude faster than is possible using the

conventional temperature-modulation method. By using this electrical controllability, we also demonstrate the post-fabrication tuning of thermal emission linewidth [4] as well as high-speed switching of thermal emission wavelengths in the mid-infrared region on a single chip [5]. We believe that our demonstrations will pave the way towards arbitrary control of thermal emission both in the field of fundamental science and for practical applications.

**Acknowledgements**, This work was partially supported by a Grant-in-Aid for Scientific Research (S) from the Japan Society for the Promotion of Science (JSPS), and by Core Research for Evolutional Science and Technology (CREST) from the Japan Science and Technology Agency (JST). T.I. also acknowledges support by a Grant-in-Aid for JSPS Fellows.

**REFERENCES**

1. Zoysa, M. D., T. Asano, K. Mochizuki, A. Oskooi, T. Inoue and S. Noda, "Conversion of broadband to narrowband thermal emission through energy recycling," *Nature Photonics*, Vol. 6, No. 8, 535-539, 2012.
2. Inoue, T., M. D. Zoysa, T. Asano and S. Noda, "Single-peak narrow-bandwidth mid-infrared thermal emitters based on quantum wells and photonic crystals," *Appl. Phys. Lett.* Vol. 102, No. 19, 191110, 2013.
3. Inoue, T., M. D. Zoysa, T. Asano and S. Noda, "Realization of dynamic thermal emission control," *Nature Materials*, Vol. 13, No. 10, 928-931, 2014.
4. Inoue, T., M. D. Zoysa, T. Asano and S. Noda, "Electrical tuning of emissivity and linewidth of thermal emission spectra," *Phys. Rev. B*, Vol. 91, No. 23, 235316, 2015.
5. Inoue, T., M. D. Zoysa, T. Asano and S. Noda, "On-chip integration and high-speed switching of multi-wavelength narrowband thermal emitters," *Appl. Phys. Lett.*, Vol. 108, No. 9, 091101, 2016.

# Chiral photonic crystals to control the circular polarization of quantum dots' light emission.

**S. G. Tikhodeev[1,2,3*], S. V. Lobanov[1,4,5], N. A. Gippius[4,1], T. Weiss[6], C. Schneider[7], J. Geßler[7], M. Kamp[7], S. Höfling[7,8], A. A. Maksimov[2], E. V. Filatov[2], I. I. Tartakovskii[2], and V. D. Kulakovskii[2]**

[1]A. M. Prokhorov General Physics Institute, Russian Academy of Sciences, Vavilova Street 38, Moscow 119991, Russia
[2]Institute of Solid State Physics, Russian Academy of Science, Chernogolovka 142432, Russia
[3]M. V. Lomonosov Moscow State University, Leninskie Gory 1, Moscow 119991, Russia
[4]Skolkovo Institute of Science and Technology, Novaya Street 100, Skolkovo 143025, Russia
[5]School of Physics and Astronomy, Cardiff University, Cardiff CF24 3AA, UK
[6]4th Physics Institute and Research Center SCoPE, University of Stuttgart, Stuttgart D-70550, Germany
[7]Technische Physik, Physikalisches Institut and Wilhelm Conrad Röntgen Research Center for Complex Material Systems, Universität Würzburg, D-97074 Würzburg, Germany
[8]SUPA, School of Physics and Astronomy, University of St Andrews, St Andrews, KY16 9SS, UK
* corresponding author: tikh@gpi.ru

**Abstract**— We demonstrate a possibility to control the polarization state of radiation from quantum dots embedded in chiral photonic crystal structures made of achiral planar GaAs waveguides. A chiral partial etching of the waveguide layer modifies the electromagnetic mode structure and results in a high circular polarization degree of the quantum dot emission in the absence of external magnetic field.

The possibility to control the polarization state of radiation from quantum emitters has drawn attention of researchers in recent years as it opens various important applications in spin-optoelectronics, quantum information technology, chiral synthesis and sensing. A very effective method to produce the circularly polarized light emission is the fabrication of chiral nanostructures from achiral semiconductor materials [1-3].

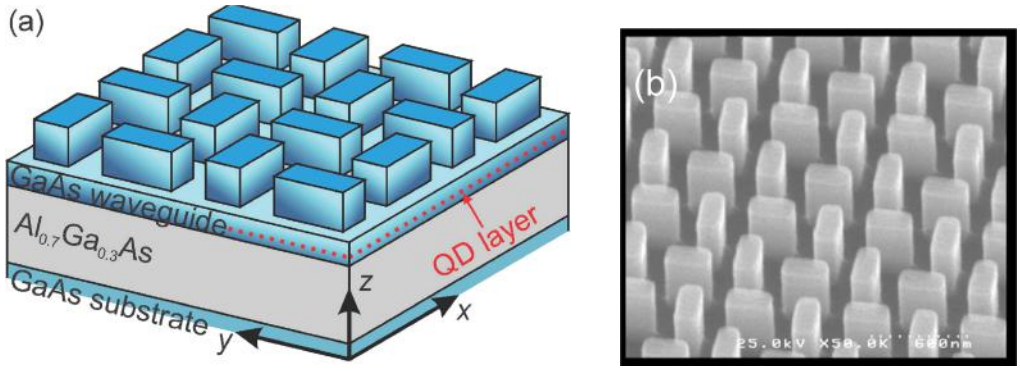



Figure 1: (a) Schematics of the structure with GaAs/air chiral photonic crystal slab, GaAs waveguide layer with a QD plane, and $Al_{0.7}Ga_{0.3}As$ cladding layer on GaAs substrate. (b) Scanning electron microscopy side view of the right-twisted chiral photonic crystal fabricated from the GaAs-based waveguide.

We have fabricated and studied [4] a structure with light emitting InAs quantum dots (QD) inside a GaAs waveguide with a chiral photonic crystal layer on top (see Fig. 1). The optimized structure demonstrates a strongly circularly polarized photoemission of QDs at zero magnetic field with the degree of circular polarization up to 81% and up to 96% if the unpolarized background due to the chiral photonic crystal imperfection is removed (see Fig. 2). This is in agreement with the theoretical expectations (98% for the optimized structure). The physical nature of the effect can be understood in terms of the reciprocity principle taking into account the structural symmetry.

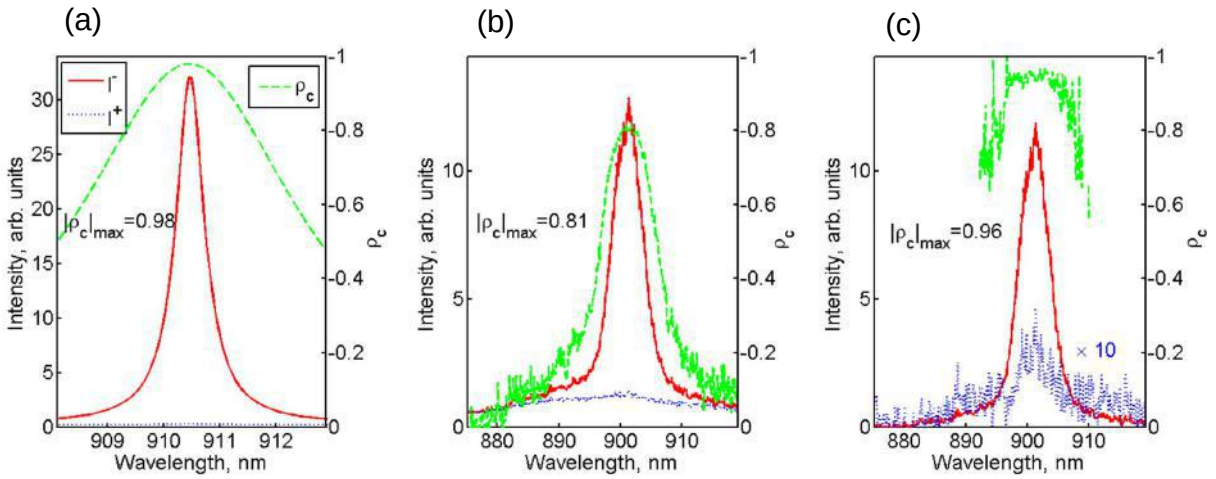



Figure 2: (a) Calculated circularly polarized spectra and circular polarization degree of QDs' emission from the chiral waveguide structure with right-twisted pillars. The sign of circular polarization is opposite for the left-twisted pillars. The emission intensity is normalized to the emission intensity of the same oscillating dipole in vacuum (without the structure). (b) Experimental circularly polarized spectrum of QDs' emission from the fabricated chiral waveguide structures with right-twisted pillars. (c) Same as in panel b, with subtracted unpolarized background.


## ACKNOWLEDGMENT

The authors acknowledge the support of the Russian Academy of Sciences and the Russian Basic Research Foundation.


## REFERENCES


1. Konishi, K., Nomura, M., Kumagai, N., Iwamoto, S., Arakawa, Y., and Kuwata-Gonokami, M., "Circularly Polarized Light Emission from Semiconductor Planar Chiral Nanostructures," *Phys. Rev. Lett.*, Vol. 106, 057402, 2011.
2. Lobanov, S. V., Weiss, T., Gippius, N. A., Tikhodeev, S. G., Kulakovskii, V. D., Konishi, K., and Kuwata-Gonokami, M., "Polarization control of quantum dot emission by chiral photonic crystal slabs," *Opt. Letters* , Vol. 40, No. 7, 1528–1531, 2015.
3. Maksimov, A. A., Tartakovskii, I. I., Filatov, E. V., Lobanov, S. V., Gippius, N. A., Tikhodeev, S. G., Schneider, C., Kamp, M., Maier, S., Höfling, S., and Kulakovskii, V. D., "Circularly polarized light emission from chiral spatially-structured planar semiconductor microcavities," *Phys, Rev. B*, Vol. 89, 045316, 2014.
4. Lobanov, S. V., Tikhodeev, S. G., Gippius, N. A., Maksimov, A. A., Filatov, E. V., Tartakovskii, I. I., Kulakovskii, V. D., Schneider, C., Geßler, J., Kamp, M., Höfling, S., and "Circularly polarized light emission from chiral spatially-structured planar semiconductor microcavities," *Phys, Rev. B*, Vol. 92, 205309, 2015.

# Coupling between Guided Spoof Surface Plasmon Polaritons

**S.-H. Kim**[1], **K.-J. Kim**[2], **and C.-S. Kee**[1]

[1]Integrated Optics Laboratory,Advanced Photonics Research Institute, GIST, Gwangju 61005, South Korea
[2]Electronics and Telecommunications Research Institute, Daejeon, 34129, South Korea
topofuni@gmail.com

**Abstract**— We investigate coupling behaviours between guided spoof surface plasmon polaritons in a form of line defect modes. We theoretically derive and numerically evaluate the coupling length, which indicates coupling strength, from dispersion relations of eigenmodes in coupled waveguides. The dispersion relations of the eigenmodes are calculated by the finite element method.

The spoof surface plasmon polaritons (SPPs)[1, 2], which can be exited on a structured metal surface, imitate the exotic features of optical SPPs as confining electromagnetic fields at a sub-wavelength scale. They have attracted great interest of controlling waves of far-IR, terahertz, and microwave radiations, such as waveguiding[3, 4, 5, 6], localization[4, 7, 8], and focusing[3]. Recently, we demonstrate guiding of spoof SPP modes with beam width in sub-wavelength scale, which is based on line defect modes inside spoof SPP bandgap of a two dimensional groove metal array (2D GMA)[6], shown in Fig.1 (a). This waveguide would be a great promise for highly dense integration in terahertz or microwave photonics because they support modes at sub-wavelength scale. For high density integration, crosstalk or coupling effect between waveguides should be minimised. Thus, it is important to understand coupling effects between guided spoof SPPs for integrated photonics applications. In this study, we investigate coupling effects between spoof SPP waveguides. Using interactions between two supermodes in coupled spoof SPP waveguides, we obtain transferred power and coupling length for coupled waveguides with various geometrical parameters. The dispersion relations of coupled spoof SPP waveguides are calculated by the finite element method (FEM).

To investigate coupling behaviours between coupled waveguides, we need to evaluate performance metrics such as crosstalk or coupling length. For this purpose, we consider two identical line defect waveguides which possess mirror symmetry to the center between them, shown in Fig. 1 (a). Note that, according to coupled mode theory[9], when phase velocities of two waveguides are matched, the coupling is the strongest. Therefore, this is the worst case for crosstalk. The coupled waveguides support two eigenmodes, which are orthogonal, with symmetric and antisymmetric magnetic field distributions ($|H_S(y,z)\rangle, |H_A(y,z)\rangle$) with respect to $y = 0$ plane, shown in Fig. 1 (b). The coupling effects depend on properties of these eigenmodes. In detail, the coupling length is determined by the beat length of the the two eigenmodes, which is defined as $l_c = \pi/|\beta_S - \beta_A|$, where $\beta_S$ and $\beta_A$ are wavevectors of symmetric and antisymmetric modes, respectively. After modes propagate over the coupling length $l_c$, power is transferred completely from one waveguide to the other waveguide. A larger coupling length means coupling effects of the two waveguides are weaker. For high density integration, the limitation of crosstalk should be $l << l_c$. The coupling length can be evaluated, as long as the wavevectors of two eigenmodes $\beta_S$ and $\beta_A$ are given. In this work, we calculate the dispersion relations of eigenmodes by using FEM method. Figure 1 (c) and (d) shows the frequency dependance of coupling lengths for various geometric parameters when the distance between waveguides is fixed at $2a$, which is the minimum distance in the 2D GMA. From Fig. 1 (c) and (d), one can see that waveguides with the deeper grooves (i.e. larger $h$) and smaller $h_d$ are more appropriate for dense integration. Even though the coupling length for the structure with $h_d = 0.9a$ is small, this coupled waveguide could be used for directional coupler.

In summary, we have studied coupling behaviours between identical spoof SPP waveguides with various geometric parameters. The coupling length for the coupled waveguides with various parameters was evaluated from numerical calculations. Since, overall, coupling between the coupled spoof SPP waveguides is not strong to provoke crosstalk, they have potential applications for dense integration in integrated photonics. Moreover, even the coupling is strong, the coupled spoof SPP waveguides could be utilised for a directional coupler.

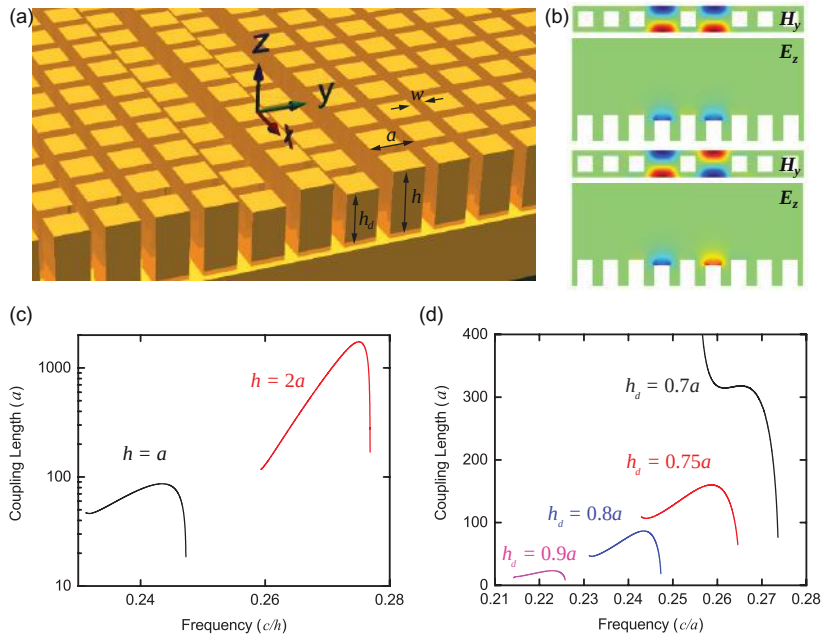



Figure 1: (a) Schematic diagram of the coupled spoof SPP waveguide.(b) Field distributions of symmetric (upper) and antisymmetric modes (lower). (c) The dependence of the coupling lengths on the frequency for the coupled waveguides with groove depths of $h = a$ and $2a$. (d) The dependence of the coupling lengths on the frequency and the defect height when $h = a$.


## ACKNOWLEDGMENT

This research was supported by the Basic Science Research Program through the National Research Foundation of Korea (NRF) funded by the Ministry of Education, Science and Technology (No. NRF- 2015R1D1A1A01060180 and NRF-2011-357-C00042) and by the GRI(GIST Research Institute) Project through a grant provided by GIST in 2016.


## REFERENCES


1. Pendry, J. B., Martin-Moreno L., and Garcia-Vidal, "Mimicking Surface Plasmons with Structured Surfaces," F. J., Science Vol. 305, No. 5685, 847-848 ,2004.
2. Hibbins, A. P. , Evans, B. R. and Sambles, J. R., "Experimental Verification of Designer Surface Plasmons," *Science*, Vol. 308 , No. 5722, 670-672, 2005.
3. Maier, S. A., Andrews, S. R., Martn-Moreno, L. and Garca-Vidal F. J., Terahertz Surface Plasmon-Polariton Propagation and Focusing on Periodically Corrugated Metal Wires, *Phys. Rev. Lett.* Vol. 97, No. 17, 176805, 2006.
4. Martin-Cano, D., Nesterov, M. L., Fernandez-Dominguez, A. I., Garcia-Vidal, F. J., Martin-Moreno L. and Moreno E., "Plasmons for subwavelength terahertz circuitry," *Opt. Express*, Vol. 18, No. 2, 754-764, 2010.
5. Kim, S.-H., Kim, T.-T., Oh, S., Kim, J.-E., Park, H. Y. and Kee C.-S.,"Experimental demonstration of self-collimation of spoof surface plasmons," *Phys. Rev. B*, Vol. 83, No. 16, 165109, 2011.
6. Kim, S.-H., Oh, S., Kim, K.-J. and Kee C.-S, "Waveguiding of spoof surface plasmon polaritons," in *Proceedings of 2015 Conference on Lasers and Electro-Optics Pacific Rim,*, Busan, South Korea, 24-28 August 2015, 26P_78.
7. Pors, A., Moreno, E., Martin-Moreno, Pendry, L., J. B. and Garcia-Vidal, F. J.,"Localized Spoof Plasmons Arise while Texturing Closed Surfaces," *Phys. Rev. Lett.*, Vol. 108, No. 22, 223905, 2012.
8. Kim, S.-H., Oh, S. S., Kim, K.-J., Kim, J.-E., Park, H. Y. Park, Hess, O. and Kee, C.-S., "Subwavelength localization and toroidal dipole moment of spoof surface plasmon polaritons," *Phys. Rev. B*, Vol. 91, No. 3, 035116, 2015.
9. Yariv, A., *Optical Electronics in Mordern Communications,* 5th edition, Oxford University Press, New York, 1997.

# Dielectric metamaterial fabricated from silicon pyramid grating as an effective optical sensor

**A. K. Sarychev**[1], **K. N. Afanasev**[1], **I. A. Boginskaya**[1], **I. A. Budashov**[2], **I. N. Kurochkin**[2,3], **I. A. Ryzhikov**[1], **A. V. Ivanov**[1], **M. V. Sedova**[1], **and A. N. Lagarkov**[1]

[1]Institute for Theoretical and Applied Electrodynamics of Russian Academy of Sciences, Russia
[2]Faculty of Chemistry of Lomonosov Moscow State University, Russia
[3]Emanuel Institute of Biochemical Physics of Russian Academy of Sciences, Russia
av.ivanov@physics.msu.ru

**Abstract**— Dielectric metamaterial composed of periodic silicon pyramid grating is investigated. We use the results of the numerical simulations as well as real experiment to demonstrate giant field fluctuations in the dielectric substrate due to the excitation of the dielectric resonances. We demonstrate the enhancement of the Raman signal from the complex of 5,5-dithiobis-[2-nitrobenzoic acid] molecules and gold nanoparticles (TNB-Au-NP), which are immobilized on the surface of the silicon pyramid grating.

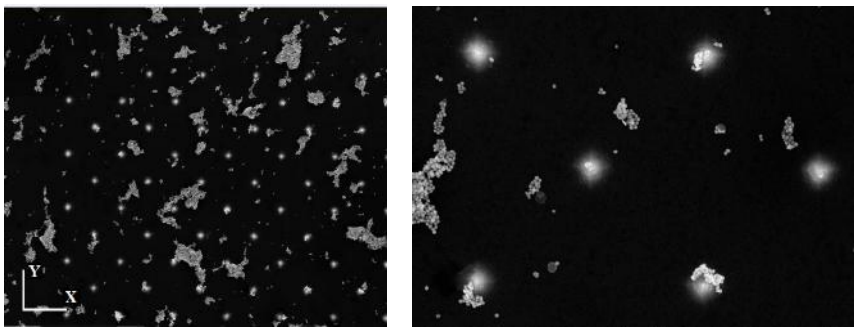
Electric field enhancement in the dielectric micro particles is well known phenomenon. The electric and magnetic resonances can be excited in the almost all particles made, for example, from silica, ceria and the other dielectrics [1].

The value of SERS signal, described enhancement factor (EF) $G$ is given by [2]

$$G = \frac{\langle |\mathbf{E}_\omega(\mathbf{r})|^2 \, |\mathbf{E}_{\omega-\Delta\omega}(\mathbf{r})|^2 \rangle}{|\mathbf{E}_0|^4} \simeq \frac{\langle |\mathbf{E}_\omega(\mathbf{r})|^4 \rangle}{|\mathbf{E}_0|^4}, \tag{1}$$

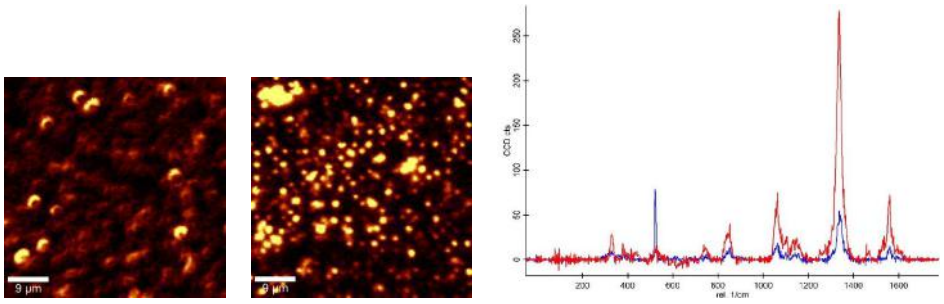
for $\Delta\omega << \omega$, where $\mathbf{E}_0$ - amplitude of the incident field, $\omega$ is the frequency of exciting radiation, $\Delta\omega$ is the frequency of the Stocks shift. EF factor is hardly depends on the shape and arrangement of the resonators and can be additionally increased by combination of plasmonic and dielectric resonators.

In this work we investigate dielectric metamaterial fabricated by NT-MDT made of silicon pyramid grating[3]. The geometric parameters are: period $(3.00 \pm 0.05)\mu m$, diagonal period 2.12 $\mu m$, height 0.3-0.7 $\mu m$, tip angle 30 degrees, tip curvature radius $\leq 10$ $nm$, effective area 2x2 $mm$. The surface of grating was modified by SERS-active tags - Au-nanoparticles (Au-NP) with average size $(56 \pm 1)nm$ covered by semicontinuous monolayer of 5.5-dithio-bis(2-nitrobenzoicacid) (Fig 1). Au-NP were prepared by well-known citrate method [4]. The conjugate Au-NP-TNB was adsorbed onto pyramid grating after deposition of polycation (polydiallyldimethylammonium chloride) according to the procedure described in [5] with some modifications. The conjugate of Au-NP with TNB (Au-NP-TNB) has series of well defined Raman peaks and can be used as an effective SERS indicator [6].




*a)* *b)*

Figure 1: SEM images of Au-NP-TNB deposited on silicon pyramid grating layer.




*a*) *b*) *c*)

Figure 2: (a) The optical mapping of the intensity distribution for TNB Raman band 1338 $cm^{-1}$ for - flat region.(b) - for structured region.(c) The intensity field distribution for band 1338 $cm^{-1}$. Blue line corresponds to flat region, red line - structured region. The excitation was performed in an epi configuration through a 100X objective (NA=0.9) on a microscope WITec.

A Raman spectrometer WITec (ABC Inc.)was used for the collection of spectra using an excitation wavelength of 785 nm with 100x objective (NA=0.9). Raman scattering $NO_2$ band of TNB was used to investigate the SERS signal. The optical mapping of the intensity distrubution for band 1338 $cm^{-1}$ is shown in Fig.2. We demonstrate huge enhancement of the intensity distribution in the grating (red line) with respect to flat region (blue line). It can be explain by excitation of surface plasmon and dielectric resonances while the pyramids behave as a resonators that convert the laser light into longitudinal electric field.

The fraction of surface occupied by the gold nanoparticles estimated as a 6.77% - the flat region, and 7.22% - in the structured region. The detailed research of spectra after normalization to the amount of Au-NP shows that EF depends on Au-NPs position at the surface. The intensity of Raman signal from Au-NP-TNB for the Stokes shift 1338 $cm^{-1}$ is larger up to 200 times in case of pyramid grating area with respect to flat layer of the same silicon material. It was reached by placing Au-NP at the top of pyramid.

We suggest using the proposed metamaterial as a core of the high sensitive optical sensing device.

## ACKNOWLEDGMENT

The work is partially supported by Russian Science Foundation (RSF) (grant 16-14-00209).

## REFERENCES

1. Lagarkov, A. N., Budashov, I. A., Chistyaev, V. A., Ezhov, A. A., Fedyanin, A. A., Ivanov, A. V., Kurochkin, I. N., Kosolobov, S. S., Latyshev, A. V., Nasimov, D. A., Ryzhikov, I. A., Shcherbakov, M. R., Vaskin, A. V. and A. K. Sarychev "SERS-active dielectric metamaterials based on periodic nanostructures," *Opt. Express*, Vol. 24, No. 7, 7133–7150, 2016.
2. Sarychev, A. K. and V. M. Shalaev *Electrodynamics of Metamaterials*, World Scientific, Singapore, 2007.
3. Bykov, V., Gologanov, A. and V. Shevyakov, "Test structure for SPM tip shape deconvolution," *Appl. Phys. A*, Vol. 66, 499–502, 1998.
4. Turkevich, J., Stevenson, P. S. and J. Hiller, "A study of the nucleation and growth processes in the synthesis of colloidal gold," *Discuss. Faraday Soc.*, Vol. 11, 55–75, 1955.
5. Gromova, M. G., Sigolaeva, L. V., Fastovets, M. A., Evtushenko, E. G., Babin, I. A., Pergushov, D. V., Amitonov, S. A., Eremenko, A. V. and I. N. Kurochkin, "Improved absorption of choline oxidase on a polyelectrolyte LBL film in the presence of iodine anions," *Soft Matter.*, Vol. 7, 7404–7409, 2011.
6. Tamer, U., Boyaci, I. H., Temur, E., Zengin, A., Dincer, I. and Y. Elerman, "Fabrication of magnetic gold nanorod particles for immunomagnetic separation and SERS application," *J. Nanopart. Res.*, Vol. 13, 3167–3176, 2011.

# Temperature dependence of band gap ratio and Q-factor defect mode in a semiconductor quaternary alloy hexagonal photonic-crystal hole slab

**R. Snchez-Cano[1], and N. Porras-Montenegro[2]**

[1]Departamento de Física, Universidad Autónoma de Occidente, AA 2790 Cali, Colombia
[2]Departamento de Física, Universidad del Valle, AA 25360 Cali, Colombia
rsanchez40@gmail.com

**Abstract**— We present numerical predictions for the photonic TE-like band gap ratio and the quality factors of symmetric localized donor defect as a function of the thickness-slab and temperature by the use of plane wave expansion and the finite-difference time-domain methods. The photonic-crystal hole slab is composed of a 2D-hexagonal array of identical air holes of circular cross-section, embedded in a non-dispersive III-V semiconductor quaternary alloy slab, which has a high value of dielectric function in the near-infrared region.

Optoelectronics devices operating in the infrared range arouse a growing interest due to their potential applications in optical telecommunications, atmospheric pollution monitoring, industrial process control, medical diagnoses, optomechanical systems, characterization of materials, analysis of biological samples, biomedical applications, and chip light manipulation [1, 2, 3]. A lot theoretical studies have been undertaken on binary semiconductor photonic crystal slabs. However, few theoretical results on quaternary semiconductor photonic crystal slabs have been reported [4, 5], and to our knowledge works in photonic crystals using $Ga_{1-x}In_xAs_ySb_{1-y}$ semiconductor quaternary alloy, has not been addressed. In this theoretical work using supercell plane wave expansion (SCPW) and the finite-difference time-domain (FDTD) methods [6] we have calculated the photonic band gap ratio and Q-factor as a function of temperature.
As suggested by Samara [7] it is not likely that the dielectric function $\varepsilon(\vec{r}, x, t)$ is really linearly dependent on temperature $t$, over a broad temperature range. Therefore, we fit the dependence of such quantity by Varshni-type equation given by

$$\varepsilon(\vec{r}, x_i, t) = \varepsilon(\vec{r}, x_i, 0) + \frac{\delta t^2}{\eta + t}, 0 \leq x_i \leq 1, \tag{1}$$

with $\delta = 4.8 \times 10^{-3} K^{-1}$, $\eta = 550K$, and we propose the dielectric constant as a function of the absolute temperature $t$, at $x = 0.16$ for the quaternary alloy, as

$$\varepsilon(\vec{r}, 0.16, t) = 13.6 + \frac{4.8 \times 10^{-3} t^2}{550 + t}. \tag{2}$$

Fig.1 shows a graph of the band gap ratio, $\triangle\omega/\omega_c$ for even modes as a function of slab thickness $T$ at room temperature for the $Ga_{0.84}In_{0.16}As_{0.14}Sb_{0.86}$, $\omega_c$ is the frequency at the center of the gap. As observed, there is an optimal thickness at $T = 0.6a$, which justifies the use of slab thickness $T = 0.6a$ in our calculations for $r = 0.45a$. The existence of an optimum thickness can be understood by considering two limiting cases of a very thin or very thick slab. If the slab is too thin, practically there are no guided modes and the lattice periodicity not affect the cladding. On the other hand, if the slab is very thick the photonic band gap approaches to the 2D-photonic crystal case. However, higher modes are pulled into the photonic band gap. Fig.2 shows a graph of the band gap ratio, $\triangle\omega/\omega_c$ for even modes as a function of the temperature for slab thickness, $T = 0.2a$, $T = 0.4a$, $T = 0.6a$, $T = 0.8a$, and $T = 1.0a$, radius $r = 0.45a$, Indium and Arsenic concentrations, x = 0.16 and y = 0.14 respectively. We see that in graphs the bad gap ratio depends linearly on the temperature. This result is due basically to the dielectric constant, which is strongly linked with the electronic energy band structure of the semiconductor quaternary alloy, and to the variation of the critical point energy levels, originated by the lattice thermal expansion and DebyeWaller effect. Furthermore, an analysis of Eq.(2) shows that the dielectric constant increase linearly with the temperature in $150 - 400K$ range.

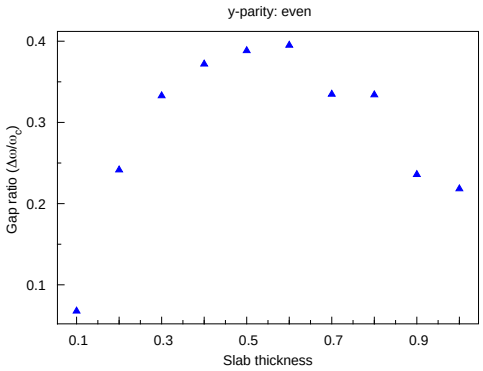



Figure 1: (Color online) Band gap ratio, $\triangle\omega/\omega_c$ for TE-like modes as a function of the slab thickness $T$, for $Ga_{0.84}In_{0.16}As_{0.14}Sb_{0.86}$ slab, $\omega_c$ is the frequency at the center of the gap. The slab dielectric constant is given by Eq.(2), $\varepsilon(\vec{r}, 0.16, 300) = 14.1$, the air rods radius is $r = 0.45a$, and the cladding background is air.

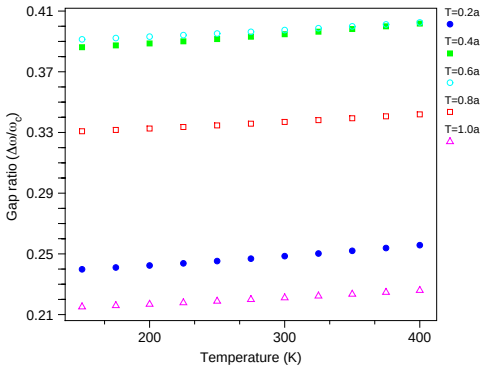



Figure 2: (Color online) Band gap ratio, $\triangle\omega/\omega_c$ for TE-like (even) modes as a function of the temperature for slab thickness $T = 0.2a$, $T = 0.4a$, $T = 0.6a$, $T = 0.8a$, and $T = 1.0a$, and the same parameters as in Fig. 1.

**REFERENCES**


1. Nazirizadeh, Y., J. Reverey, U. Geyer, U. Lemmer, C. Selhuber-Unkel, and M. Gerken, "Material-based three-dimensional imaging with nanostructured surfaces," *Appl. Phys. Lett.*, Vol. 102, 011116–011120, 2013.
2. De Tommasi, E., A. C. De Luca, S. Cabrini, I. Rendina, S. Romano, and V. Mocella, "Plasmon-like surface states in negative refractive index photonic crystals," Appl. Phys. Lett. Vol. 102, 081113–081115, 2013.
3. Erchak, A. A., D. J. Ripin, S. Fan, P. Rakich, J. D. Joannopoulos, E. P. Ippen, G. S. Petrich, and L. A. Kolodziejski, "Enhanced coupling to vertical radiation using a two-dimensional photonic crystal in a semiconductor light-emitting diode," *Appl. Phys. Lett.*, Vol. 78, No. 5, 563–565, 2001.
4. Fan, and J. D. Joannopoulos, "Analysis of guided resonances in photonic crystal slabs," *Phys. Rev. B*, Vol. 65, 235112–235118, 2002.
5. Vuŏković J., M. Lončar, H. Mabuchi, and A. Scherer, "Design of photonic crystal microcavities for cavity QED," *Phys. Rev. E*, Vol. 65, 016608–016611, 2001.
6. Oskooi, Ardavan F. et al. "Meep: A flexible free-software package for electromagnetic simulations by the FDTD method, *Computer Physics Communications*, 181.3, 687–702, 2010.
7. Samara, G. A., "Temperature and pressure dependences of the dielectric constants of semiconductors," *Phys.Rev.B*, Vol. 27, 3494–3505 1983.

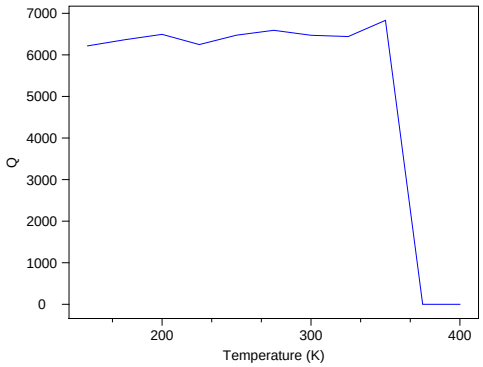



Figure 3: (Color online) Q-factor for TE-like mode as a function of the temperature for $\omega a/2\pi C = 0.24$, slab thickness $T = 0.6a$, defect-radius $r_d = 0.45a$ and lattice radius $r = 0.3a$.

# Nanophotonic devices with integrated color centers in diamond and silicon carbide

**David O. Bracher**[1*], **Evelyn L. Hu**[2]

[1] Department of Physics, Harvard University, United States

[2]John A. Paulson School of Engineering and Applied Sciences, Harvard University, United States

[*]corresponding author: dbracher@fas.harvard.edu

**Abstract**- Photonic crystal nanocavities have demonstrated extraordinary effectiveness in controlling and storing photons. Furthermore, coupling of cavities to embedded emitters has allowed augmented emission and extraction efficiencies. New opportunities and challenges for cavity-emitter coupling have arisen with "point-defect" emitters in materials such as diamond and silicon carbide (SiC). This talk will focus on the particular challenges in matching cavities to these emitters, as well as demonstrations of high quality cavities and cavity-emitter coupling.

Photonic crystal cavities (PCCs) enable a high degree of light confinement both spatially and temporally. As a result, they have found wide use in modern optical device research. For example, these cavities are instrumental in controlling the emission properties of emitters embedded within the cavity volume. Indeed, by modifying the local density of optical states, PCCs allow for increased or decreased spontaneous emission rates and improved light extraction from the emitters[1]. PCCs can therefore be used to improve single photon source properties and have been used to modify emission from quantum dots, atoms, and other systems. Recently, these cavities have also been of interest in controlling the emission of semiconductor point defects.

Spin-active point defects, particularly the diamond nitrogen-vacancy (NV) center, are of interest for quantum information and sensing applications, due to the optical read out and initialization of their spin state and their long spin coherence times[2]. The study of the NV has also led to the investigation of potential spin-active defects in other semiconductors. Silicon carbide (SiC) has been found to host a number of such defects. In particular, the 4H polytype contains both silicon vacancy[3] and divacancy centers[4], both of which emit photoluminescence (PL) in the near infrared and could be used for various forms of quantum sensing and for quantum computation.

These defect centers have great potential but suffer from low PL emission (<5%) into their zero phonon lines (ZPL). Due to the utility of the ZPL, it is crucial to embed the defects in high quality cavities to increase ZPL emission. Our group has previously demonstrated high quality photonic crystal cavities (PCCs) in diamond, with the cavity mode tuned into spectral resonance with the NV ZPL[5]. Given the well-developed fabrication protocols for SiC, we now seek to achieve similar results with cavities in 4H-SiC coupled to both species of point defects.

One major challenge in coupling point defects to optical cavities is that the defects are very sensitive to their environment, and care is needed to preserve the defect properties. Thus, to create PCCs in 4H-SiC, we make use of homoepitaxially grown material and a dopant-selective photoelectrochemical (PEC) etch to provide optical isolation. By ensuring high quality material (due to the homoepitaxy) and gentle removal of the underlying substrate, this PEC etch—as compared to wafer-bonded SiC-on-insulator techniques, for example—should preserve the properties of the embedded defect centers and yield high quality devices. Indeed, we have demonstrated nanobeam PCCs in 4H-SiC (fig. 1a) with high quality factors (up to Q ~7,000)[6]. Since the cavity emission must overlap the narrow-linewidth ZPLs, we have also developed two methods to spectrally tune the PCC modes, allowing for greater versatility in achieving cavity-defect coupling.

In addition to ensuring that the fabrication process is not disruptive to the point defects, another critical challenge in achieving cavity-defect coupling is in creation and placement of the defects near the cavity field maximum. The 4H-SiC defects can be created either through electron irradiation or ion implantation, but these methods are very difficult to achieve deterministic placement of defects with (unlike, for example, quantum dots which can be grown at specified locations). Moreover, it is important to introduce the defects with as little damage as possible to again preserve the quality of the defect and the optical cavities. Therefore, it is necessary to study which method is optimal for defect generation, given the above criteria (for example, ion implantation allows for better control of the depth of implanted defects but may be more damaging than electron irradiation).

Indeed, we have demonstrated PCCs in 4H-SiC coupled to defects generated using both methods, and we have also shown cavities coupled to both species of defects—silicon vacancy and divacancy (fig. 1b). Given the ability to generate high quality cavities and spectrally tune the resonant modes, we will seek to demonstrate full Purcell enhancement of the defect ZPLs, as we continue to study how best to incorporate the defects. Thus, with the coupling of spin-active defects to high quality cavities, our techniques will aid in the development of 4H-SiC as a platform for solid-state quantum information and sensing.

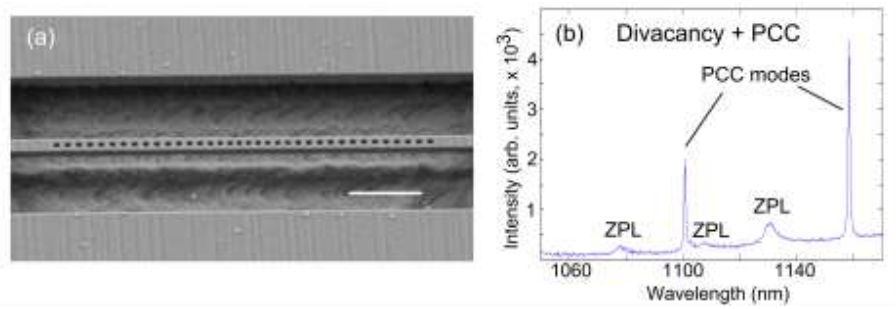



**Figure 1.** (a) SEM micrograph of nanobeam PCC in 4H-SiC. Scale bar indicates 2 μm. (b) Photoluminescence spectrum of divacancy defect coupled to PCC. Resonant modes and zero phonon lines (ZPL) are indicated.

**Acknowledgements**: The authors acknowledge funding from the Air Force Office of Scientific Research, under the QUMPASS program (Award No. FA9550-12-1-0004). This work was performed at the Center for Nanoscale Systems (CNS), a member of the National Nanotechnology Infrastructure Network (NNIN), which is supported by the National Science Foundation under NSF award no. ECS-0335765. CNS is part of Harvard University.

**REFERENCES**

1. Noda, S., M. Fujita and T. Asano, "Spontaneous-emission control by photonic crystals and nanocavities," *Nat. Phot.*, Vol. 1, No. 8, 449-458, 2007.

2. Childress, L. and R. Hanson, "Diamond NV centers for quantum computing and quantum networks," *MRS Bull.*, Vol. 38, 134-138, 2013.

3. Koehl, W. F., Buckley B. B., Heremans F. J., G. Calusine and D. D. Awschalom, "Room temperature coherent control of defect spin qubits in silicon carbide," *Nature*, Vol. 479, No. 7371, 84-87, 2011

4. Widmann, M., Lee, S. Y., Rendler, T., Son, N. T et al., "Coherent control of single spins in silicon carbide at room temperature," *Nat. Mat.*, Vol. 14, 164-168, 2015.

5. Lee, J. C., Bracher, D. O., Cui. S., Ohno, K., et al. "Deterministic coupling of delta-doped nitrogen vacancy centers to a nanobeam photonic crystal cavity," *Appl. Phys. Lett.*, Vol. 105, No. 26, 261101, 2014.

6. Bracher D. O. and E. L. Hu, "Fabrication of high-Q nanobeam photonic crystals in epitaxially grown 4H-SiC," *Nano Lett.*, Vol. 15, No. 9, 6202-6207, 2015.

# Coupling to Photonic Crystal Waveguide by Polarization Tailored Free Space Beam.

**A. Mahdavi[1*], P. Banzer[1,2], and F. Vollmer[1]**

[1] Max Planck Institute for the Science of Light, Günther-Scharowsky-Straße 1, 91058 Erlangen, Germany

[2] Institute of Optics, Information and Photonics,
Friedrich-Alexander-University Erlangen-Nuremberg, D-91058 Erlangen, Germany

[*]Corresponding author: ali.mahdavi@mpl.mpg.de

**Abstract**- Photonic crystals are an ideal choice for localizing light in micro-cavities, which exhibit sub-wavelength modal volumes and show quality factors of up to 2 million. Furthermore, waveguides with high dispersion and slow light characteristics can be realized. We demonstrate an alternative method for coupling to waveguide modes and for the excitation of microcavities by tailoring the state of polarization in the diffraction limited spot of a focused light beam impinging normally onto the waveguide.

Two dimensional silicon photonic crystal waveguides are well-established structures for exciting defect and random cavities. Defect cavities can be intentionally introduced by omitting lattice sites and by disordering the lattice of the photonic crystal. Hence, random microcavities along the waveguide with high quality factors can be created at arbitrary locations [1]. The photonic crystal structures under investigation comprise high refractive index silicon slabs with 2D arrays of air holes and exhibit a wide photonic crystal bandgap [2]. By removing a row of air holes, a typical W1 photonic crystal waveguide geometry is created (see Figure). In our studies, we investigate the coupling efficiency to such W1 photonic crystal waveguides as well as the excitation and properties of embedded defect and random microcavities by tailoring the state of polarization in the diffraction limited spot of a focused light beam impinging normally onto the waveguide [3]. In contrast to a tapered fiber where coupling is achieved by butt-coupling or evanescent field coupling, this free-space configuration offers a more flexible and robust arrangement with regards to sample scanning multiplexing and ease of coupling for different wavelengths [4]. More importantly this setup allows the excitation of random microcavities by polarization mixing, which can be used for stand-off detection and bio-sensing.

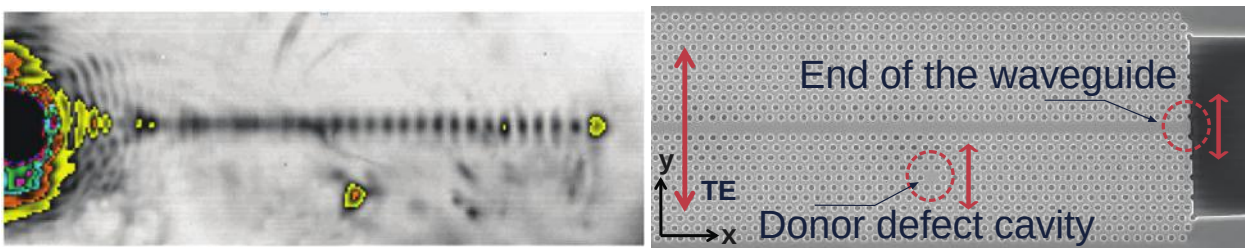



**Figure:** Experimental demonstration of a donor defect cavity coupled with TE polarization is shown on the left, and a schematic overview on the right. To confirm the polarization of the waveguide mode we analyze the

intensity and the polarization of light scattered from the end of the waveguide.

**REFERENCES**


1. Topolancik, Juraj, et al. "Out-of-plane scattering from vertically asymmetric photonic crystal slab waveguides with in-plane disorder." Optics Express 17.15 (2009): 12470-12480.
2. Mahdavi, Ali, et al. "Maximizing Photoluminescence Extraction in Silicon Photonic Crystal Slabs." Scientific Reports 6 (2016): 25135.
3. Banzer, Peter, et al. "On the experimental investigation of the electric and magnetic response of a single nano-structure." Optics Express 18.10 (2010): 10905-10923.
4. Topolancik, J., F. Vollmer, and B. Ilic. "Random high-Q cavities in disordered photonic crystal waveguides." Applied Physics Letters 91.20 (2007): 201102.

# Electromagnetic Mode Profile Shaping in Waveguides

**Jonathan Gratus[1,2*], Paul Kinsler[1,2*], Rosa Letizia[1,2*], Taylor Boyd[1,2*]**

[1]Physics Department, Lancaster University, Lancaster LA1 4YB, UK
[2]Engineering Department, Lancaster University, Lancaster LA1 4YW, UK
[3]Cockcroft Institute, Keckwick Ln, Daresbury, Warrington WA4 4AD
*corresponding author, E-mail: j.gratus@lancaster.ac.uk

## Abstract

Electromagnetic mode profile shaping would be a very useful technique, with applications including in accelerator science and data transmission. Two methods are proposed, one varying the permittivity, the other using a wire medium. By the use of Mathieu functions we demonstrate a flatter, a triangular and a peakier profile. The first two may be used to manipulate longer particle bunches, while the last could be used on shorter bunches and in data transmission. It is also demonstrated how further improvements can be achieved by going beyond Mathieu functions.

## 1. Introduction

Electromagnetic modes in a waveguide with uniform cross-section have a sinusoidal profile. There are many situation where a non sinusoidal waves may be particularly useful. In accelerator science, for example, one may wish to have a flatter profile. The waveform in Fig. 1 would accelerate a longer bunch, and therefore more electrons, for a given peak power. By contrast a peakier profile, Fig. 2 would accelerate shorter bunches for the same total power. In addition due to the steeper gradient, it would enable one to give a shorter bunch more chirp which is necessary for bunch compression. The peakier profiles would also be useful for data transmission where one can have the higher peak when the signal is being observed. Intermediate between the flatter and peakier profile is a triangular profile as given in Fig 3. This has the advantage of having a significant part of the profile having a constant slope. In terms of interactions with electron bunches this would give longer bunches a sustained chirp. Figs. 1-3 are all examples of waveforms based on Mathieu functions, which often have convenient properties. However we can go beyond Mathieu functions. In Figs. 4-5 we demonstrate how an even flatter profile can be achieved.

In this article we modify the mode profile by modifying the constitutive relations, in particular the permittivity. To simplify the analysis we consider the permittivity $\epsilon$ to be periodic in $z$ the direction of propagation.

We consider two scenarios. The first is for transverse waves, section 2. In this case we choose a permittivity which depends frequency and position. The use of varying the permittivity combined with the use of Mathieu functions was considered by Haddad [1], where the transmission

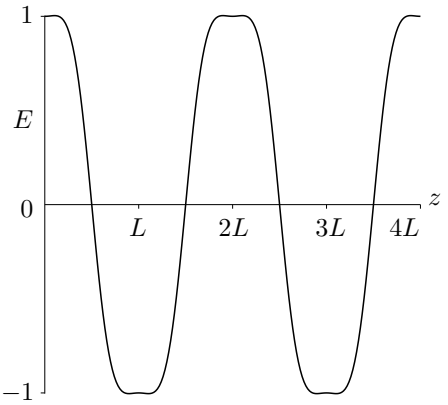



Figure 1: A flatter solution to Mathieu's equation: In (3) with $q = 0.8$ and $a = A_1(0.8) = 1.711$, where $A_n(q)$ is the Mathieu-A function.

functions were calculated. However the author did not consider the use of this to modify the profile. There are many methods for making such a medium. For example one can compose the medium from many thin slices of media, each with a different value of $\epsilon$, thereby approximating the continuous variation. Another method is to set up a standing wave in a non-linear material. The linearised permittivity about this solution would have the spatial dependence as desired. However for the examples in Fig. 1 and Fig. 4 given in this article to work would require regions to have negative permittivity, $\epsilon < 0$ which would require some kind of metamaterial [2, 3, 4, 5, 6, 7] . It also does not work for longitudinal waves.

A second scenario, section 3, is to make $\epsilon$ spatially dispersive as well as inhomogeneous. That is we set $\epsilon = \epsilon(\omega, k, z)$ where $k$ is the Fourier conjugate variable associated with $z$. It is natural to ask the meaning of a function depending on both $k$ and $z$. This is addressed in [8, 9, 10]. The method, as described below, is to replace the permittivity function with a differential equation. A wire medium [11, 12, 13, 14, 15] is naturally spatially dispersive and by varying the radius of the wires, periodically in $z$ will naturally give it the correct spatial inhomogeneity. See Fig. 12.

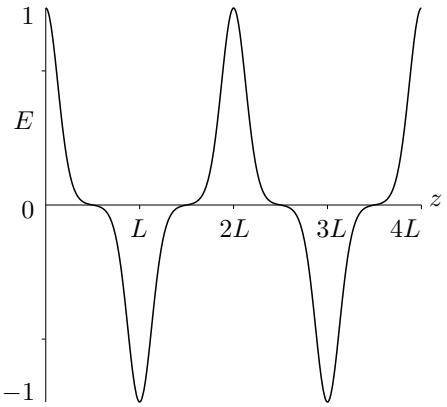



Figure 2: A peakier solution to Mathieu's equation: In (3) with $q = -10.0$ and $a = A_1(-10.0) = -13.937$.

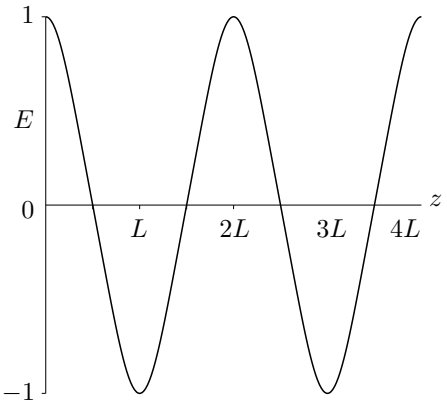



Figure 3: A triangular solution to Mathieu's equation which has the advantage of having a significant part of the profile having a constant slope: In (3) with $q = -0.329$ and $a = A_1(-0.329) = 0.658$

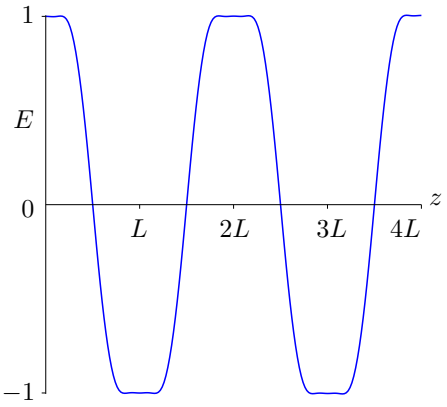



Figure 4: An even flatter profile: A solution to the equation $\pi^2 L^{-2} E'' + (1.9266 - 2.2\cos(2\pi Z/L) + 0.4\cos(8\pi Z/L))E = 0$.

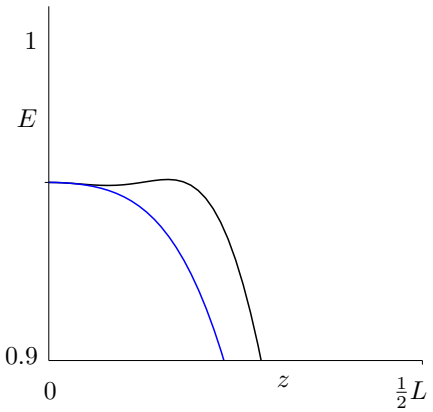



Figure 5: Close up showing difference between the profiles in Fig. 1 and Fig. 4.

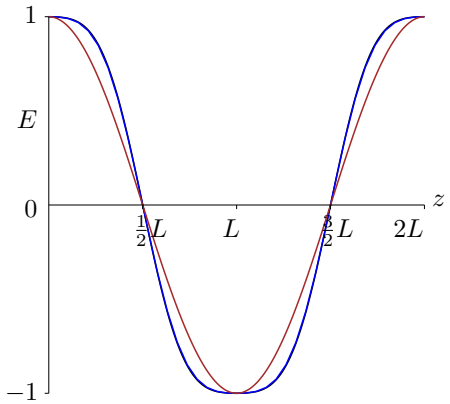



Figure 6: Comparison of the simulated $E_x$-field (blue) [Fig. 8] for a flatter profile, as in Fig 1, with the predicted curve (black). The two curves are almost identical. In comparison with the cosine (brown).

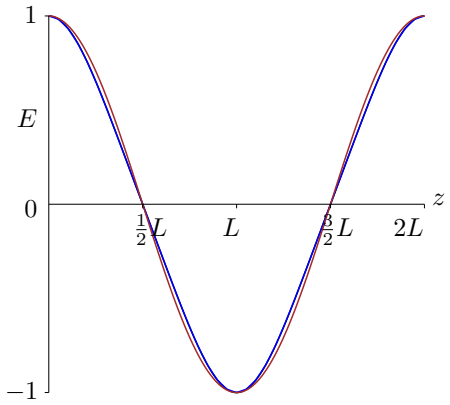



Figure 7: Comparison of the simulated $E_x$-field (blue) [Fig. 9] for a triangular profile, as in Fig 3, with the predicted curve (black). The two curves are almost identical. In comparison with the cosine (brown).

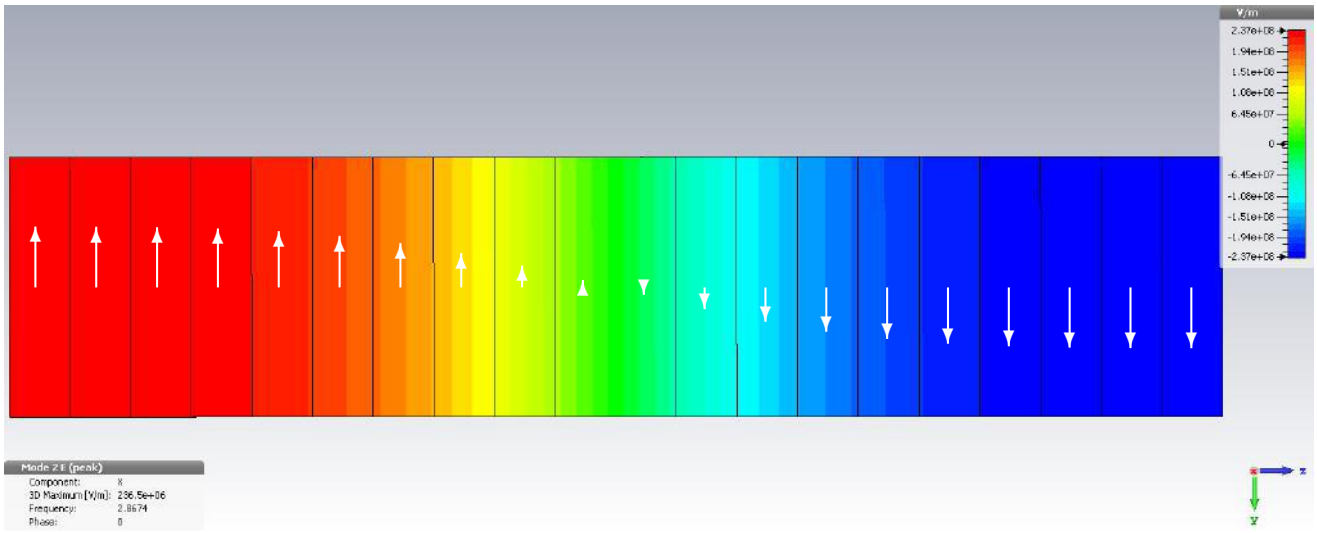



Figure 8: CST simulated contour plot of $E_x$ field for the flatter profile, as in Fig 1.

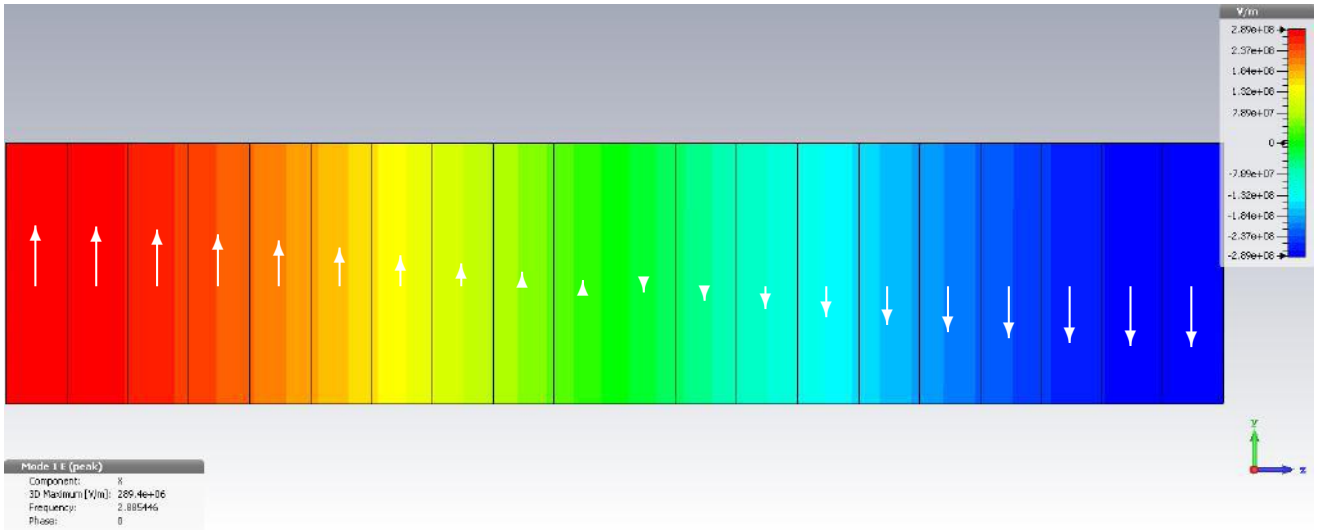



Figure 9: CST simulated contour plot of $E_x$ field for the triangular profile, as in Fig 3.

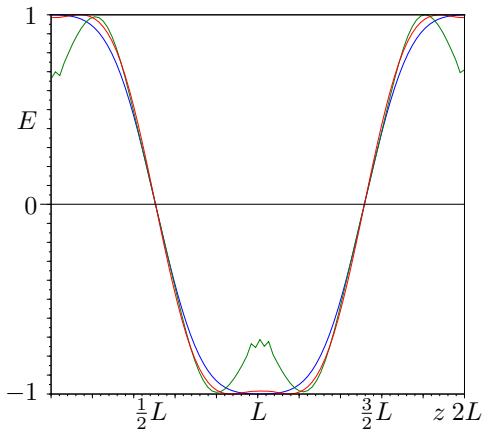



Figure 10: MPB calculation of the flatter modes with $q = 0.8$ (blue), $q = 0.9$ (green) and $q = 1.0$ (red). The Green curve shows numerical instability

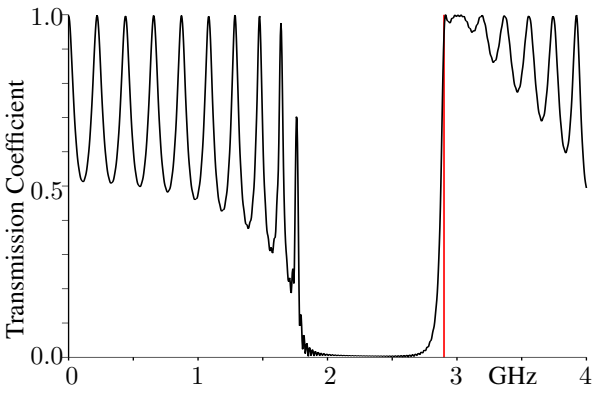



Figure 11: Transmission coefficients for a periodically varying permittivity as in Fig. 8. This is implemented in CST using 10 cells. The transmission is very high and corresponds to the right edge of the band gap at around 2.89 GHz (red).

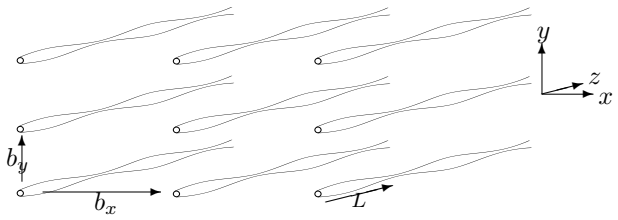



Figure 12: Wire medium with a periodic variation in the radius of the wires. The inter wire spacing are $(b_y, b_z)$ and the period of the longitudinal variation is $L$.

## 2. Transverse modes periodic inhomogeneous permittivity

Consider the single frequency transverse mode with $\boldsymbol{E} = e^{i\omega t}\tilde{E}(z)\boldsymbol{i}$, $\boldsymbol{P} = e^{i\omega t}\tilde{P}(z)\boldsymbol{i}$ and $\boldsymbol{H} = e^{i\omega t}\tilde{H}(z)\boldsymbol{j}$, together with the permittivity $\epsilon(\omega, z) = \epsilon_0\epsilon_{\rm r}(\omega, z)$ and vacuum permeability $\mu_0$. Then Maxwell's equations give

$$\tilde{E}'' + \omega^2 c^{-2}\epsilon_{\rm r}(\omega, z)\tilde{E} = 0 \tag{1}$$

where $' = \frac{d}{dz}$. Set

$$\epsilon_{\rm r}(\omega, z) = \pi^2 c^2 \omega^{-2} L^{-2}\big(a(\omega) - 2q(\omega)\cos(2\pi z/L)\big) \tag{2}$$

where $L$ is twice the period of the $\epsilon$ variation: $\epsilon(\omega, z) = \epsilon(\omega, z + L\pi)$. Then we get the (rescaled) Mathieu's equations

$$\pi^{-2}L^2\tilde{E}'' + \big(a - 2q\cos(2\pi z/L)\big)\tilde{E} = 0 \tag{3}$$

It is easy to model spatially varying permittivity numerically using the CST package [16], when $\epsilon > 0$. Since $a = A_1(q)$ where $A_n(q)$ is the Mathieu-A function, then from (2) we require that $A_1(q) > |q|$. This implies that

$$-0.329 < q < 0.889 \tag{4}$$

Conveniently the two limits of this range correspond to the triangular and flatter profiles. To validate these results, numerical simulations of these profiles have been performed using 20 slabs of constant $\epsilon_{\rm r}$ by the eigen mode solver of CST Microwave Studio [16]. Periodic, PEC and PMC boundary conditions are chosen along the $z$, $x$ and $y$ direction, respectively. Figs. 6-7 show the comparison between the $E$-field profile for the modelled and simulated modes, where a very good agreement can be observed. The simulated $E$-field profile on the $x - y$ plane is given in Figs. 8-9 for the flatter and triangular modes respectively.

These were implemented directly into CST, by using 20 slabs of constant $\epsilon_{\rm r}$. To confirm these modes we have run a CST simulation as shown in Figs. 6-9.

If we are allowed to have negative $\epsilon_{\rm r}$ then one can create more extreme shapes. For example in Figs. 4-5 we add a higher harmonic to produce an even flatter profile, whereas in figure 2 we obtain a much peakier solution. One must be careful however with simulating these. We have used MPB [17] to simulate the fields for $q = 0.8$ to $q = 1$, Fig. 10. We see that the region with negative $\epsilon_{\rm r}$ have numerical instabilities.

The oscillation of the permittivity at the order of the wavelength implies that the structure is similar to a one dimensional photonic crystal or Bragg mirror [18, 19, 20, 21, 22]. One can ask whether what the transmission coefficient is for waves coming from a vacuum into this media. In Fig. 11 we use CST to calculate the transmission coefficients for the flatter profile as in Fig. 8. We see that at the proposed frequency of 2.9GHz there is a high transmission and we are at the edge of a band gap.

## 3. Wire Media: Longitudinal modes with spatially dispersive inhomogeneous permittivity

Consider longitudinal modes so that the electric and polarization fields are longitudinal and the magnetic field vanishes, i.e. $\boldsymbol{E} = e^{i\omega t}\tilde{E}(z)\boldsymbol{k}$, $\boldsymbol{P} = e^{i\omega t}\tilde{P}(z)\boldsymbol{k}$ and $\boldsymbol{B} = \boldsymbol{0}$, then Maxwell's equations are automatically satisfied if

$$\epsilon_0\tilde{E} + \tilde{P} = 0 \tag{5}$$

I.e. $\boldsymbol{D} = \boldsymbol{0}$, thus we are looking for epsilon near zero (ENZ) media. When the medium is homogeneous we will use an empirical model of the permittivity via

$$\epsilon(\omega, k) = \epsilon_0 - \frac{\epsilon_0 k_{\mathrm{p}}^2}{L(\omega) - \beta^2 k^2} \tag{6}$$

Combining (5) and (6) we obtain the dispersion relation

$$L(\omega) - \beta^2 k^2 = k_{\mathrm{p}}^2 \tag{7}$$

Taking the Fourier transform of $\hat{P}(k) = \epsilon(\omega, k)\hat{E}(k)$ with respect to $k$ using $\tilde{P}(z) = \int_{-\infty}^{\infty} e^{ikz}\hat{P}(k)dk$ one obtains the differential equation

$$\beta^2\tilde{E}'' + L(\omega)\tilde{E} = k_{\mathrm{p}}(z)^2\tilde{E} \tag{8}$$

The simplest method to include an inhomogeneity in the permittivity is to let the plasma frequency $k_{\mathrm{p}}$ to depend on position $z$, that is $k_{\mathrm{p}} = k_{\mathrm{p}}(z)$. Thus (8) becomes

$$\beta^2\tilde{E}'' + \big(L(\omega) + k_{\mathrm{p}}(z)^2\big)\tilde{E} = 0 \tag{9}$$

Again by choosing the appropriate periodic function for $k_{\mathrm{p}}(z)$ one can replace (9) by the Mathieu equation.

As stated in the introduction this can be created with a wire medium, as described in more detail in [13].

## 4. Conclusion

Two methods of mode profile shaping are suggested. One using transverse waves and a varying permittivity. The second is by using a wire medium with periodic variation the radius of the wire. In the first method we observed that for the more extreme profiles such as the peakier profile, Fig. 2, and the flatter profile Fig. 4 require $\epsilon < 0$. This is challenging for the numerical solvers CST and MPB. In addition one would suspect it would also be challenging to implement experimentally. Since we have implemented a 1-dimensional photonic crystal we see from Fig.11 that there are band gaps and the the operating frequency is at the edge of this band gap. Fortunately the transmission is high.

We are currently implementing numerically the wire medium to optimise the shape of the wires to form the desired profile shape.

## Acknowledgement

The authors are grateful for the support provided by STFC (the Cockcroft Institute ST/G008248/1) and EPSRC (the Alpha-X project EP/J018171/1 and EP/N028694/1).

## References

[1] A EL Haddad. Exact analytical solution for the electromagnetic wave propagation in a photonic band gaps material with sinusoidal periodicity of dielectric permittivity. *Optik-International Journal for Light and Electron Optics*, 127(4):1627–1629, 2016.

[2] Filippo Capolino. *Theory and phenomena of metamaterials*. CRC Press, 2009.

[3] M Notomi. Theory of light propagation in strongly modulated photonic crystals: Refractionlike behavior in the vicinity of the photonic band gap. *Physical Review B*, 62(16):10696, 2000.

[4] L Mandelshtam. *Complete works. Vol. 5*. Academy of Scinces, USSR, 1950.

[5] Giacomo Oliveri, Douglas H Werner, and Andrea Massa. Reconfigurable electromagnetics through metamaterialsa review. *Proceedings of the IEEE*, 103(7):1034–1056, 2015.

[6] Tyler Rowe, John H Booske, and Nader Behdad. Metamaterial-enhanced resistive wall amplifiers: Theory and particle-in-cell simulations. *Plasma Science, IEEE Transactions on*, 43(7):2123–2131, 2015.

[7] Sebastian E Lauro, Alessandro Toscano, and Lucio Vegni. Symmetrical coupled microstrip lines with epsilon negative metamaterial loading. *Magnetics, IEEE Transactions on*, 45(3):1182–1185, 2009.

[8] Jonathan Gratus and Robin W Tucker. Covariant constitutive relations and relativistic inhomogeneous plasmas. *J. Math. Phys.*, 52:042901, 2011.

[9] Jonathan Gratus and Robin W. Tucker. Covariant constitutive relations, landau damping and non-stationary inhomogeneous plasmas. *Prog. Elec. Research M*, 13:145–156, 2010.

[10] Jonathan Gratus and Matthew McCormack. Spatially dispersive inhomogeneous electromagnetic media with periodic structure. *Journal of Optics*, 17(2):025105, 2015.

[11] PA Belov, R Marques, SI Maslovski, IS Nefedov, M Silveirinha, CR Simovski, and SA Tretyakov. Strong spatial dispersion in wire media in the very large wavelength limit. *Physical Review B*, 67(11):113103, 2003.

[12] Wei Song, Zhun Yang, Xin-Qing Sheng, and Yang Hao. Accurate modeling of high order spatial dispersion of wire medium. *Optics express*, 21(24):29836–29846, 2013.

[13] Jonathan Gratus, Matthew McCormack, and Rosa Letizia. Spatially dispersive inhomogeneous dielectric wire media with periodic structure. In *Proceedings of PIERS 2015 in Prague, July 6-9, 2015*, pages 675–680. The Electromagnetics Academy, 7 2015.

[14] Mário G Silveirinha. Additional boundary condition for the wire medium. *Antennas and Propagation, IEEE Transactions on*, 54(6):1766–1780, 2006.

[15] João T Costa and Mário G Silveirinha. Macroscopic electromagnetic response of arbitrarily shaped spatially dispersive bodies formed by metallic wires. *Physical Review B*, 86(7):075129, 2012.

[16] CST STUDIO SUITE. [Online]. CST AG, Germany. `http://www.cst.com`.

[17] Steven G. Johnson and the Joannopoulos Ab Initio Physics MIT. MIT photonic bands. `http://ab-initio.mit.edu/wiki/index.php/MIT_Photonic_Bands`.

[18] Judson D Ryckman and Sharon M Weiss. Localized field enhancements in guided and defect modes of a periodic slot waveguide. *Photonics Journal, IEEE*, 3(6):986–995, 2011.

[19] John D Joannopoulos, Steven G Johnson, Joshua N Winn, and Robert D Meade. *Photonic crystals: molding the flow of light*. Princeton university press, 2011.

[20] Ping Xie, ZQ Zhang, and KS Wong. Simultaneous high-efficiency second-and third-harmonic generation in a 1-d semiconductor photonic crystal. *Quantum Electronics, IEEE Journal of*, 43(9):804–809, 2007.

[21] Harry E Ruda, John C Polanyi, Jody SY Yang, Zhanghua Wu, Usha Philipose, Tao Xu, Susan Yang, KL Kavanagh, JQ Liu, L Yang, et al. Developing 1d nanostructure arrays for future nanophotonics. *Nanoscale Research Letters*, 1(2):99–119, 2006.

[22] L Pilozzi, A DAndrea, and K Cho. Spatial dispersion effects on the optical properties of a resonant bragg reflector. *Physical Review B*, 69(20):205311, 2004.

# Acoustic metamaterials

# Experimental demonstration of anomalous Floquet topological insulators for sound

**Yu-Gui Peng[1,2] and Xue-Feng Zhu[*1,2]**

[1]Department of Physics, Huazhong University of Science and Technology, Wuhan, 430074, China

[2]Innovation Institute, Huazhong University of Science and Technology, Wuhan, 430074, China

[*]corresponding author: xfzhu@hust.edu.cn

**Abstract**-Time reversal (*T*) invariant topological insulator is widely recognized as one of the fundamental discoveries in condensed matter physics, for which the most fascinating hallmark is perhaps a spin based topological protection, the total cancellation of scattering of conduction electrons with certain spins on matter surface[1-2]. Despite the growing interests in realizing topologically protected acoustic wave transport[3], *T*-invariant acoustic topological insulator has not yet been achieved. Here, we report the first experimental demonstration of anomalous Floquet topological insulator (AFI) for sound: a strongly coupled metamaterial ring lattice that supports one-way propagation of pseudo-spin-dependent edge states under *T*-symmetry, scattering immune to boundary defects, such as abrupt variations. The very unique thing is the formation of pseudo-spin-dependent interface states due to lattice dislocations. The mechanism underlying the formation of topologically protected boundary states in AFI is applicable in various other wave systems or higher dimensions.

**Acknowledgements**, X. F. Z. acknowledges the financial support from the Bird Nest Plan of HUST.

## REFERENCES

1. Kane, C. L. & Mele, E. J. Quantum spin Hall effect in graphene. *Phys. Rev. Lett.* **95**, 226801 (2005).
2. Bernevig, B. A. & Zhang, S. -C. Quantum spin Hall effect. *Phys. Rev. Lett.* **96**, 106802 (2006).
3. Yang, Z. *et al*. Topological acoustics. *Phys. Rev. Lett.* **114**, 114301 (2015).

# Coherent perfect absorption induced by the nonlinearity of coupled Helmholtz resonators

**V. A. Achilleos**[1], **O. Richoux**[1], **and G. Theocharis**[1]

[1]LUNAM Université, Université du Maine, CNRS, LAUM UMR 6613, avenue O. Messiaen, 72085
vassosnbi@gmail.com

**Abstract**— In this work we show that the nonlinear response of Helmholtz resonators, can be used to control coherent perfect absorption of sound waves in an acoustical waveguide. Three different configurations are studied, and in all cases we find analytical expressions for the conditions leading to perfect absorption for high amplitude incident waves. Experimental results are found in a good agreement with our predictions. The nonlinear control of perfect absorption opens new possibilities in the design of high amplitude sound attenuators.

## 1. INTRODUCTION

The improvement of low frequency sound absorption constitutes a real scientific challenge and resonant structures based on Helmholtz Resonators (HR), bubbles and membranes (sub-wavelength scatterers) provide excellent candidates for the design of efficient, thin and light absorbing structures. The inherent viscothermal losses of an acoustic system combined with wave interference can give rise to perfect absorption, a phenomenon which is of great applied interest. For the case of a two-port, resonator/waveguide system, it has been shown that Coherent Perfect Absorption (CPA) can be obtained under a so-called critical coupling condition, which is met when the leakage rate of energy out of the resonant system (resonant system-waveguide coupling) is balanced by the resonator losses [1, 2]. Typically, aforementioned resonators exhibit weak inherent losses, thus, for a *single* resonator/waveguide system, critical coupling condition can be fulfilled employing using either a highly lossy resonator, for example a poroelastic membrane [3] or viscous metascreens including bubbles [4], On the other hand, when the system is composed of several resonators, the interaction of two or more resonant modes of moderate Q-factor can be also used to achieve the critical coupling of the structure [5]. In this work we propose an alternative way to achieve and manipulate the occurrence of CPA, using nonlinear effects in a HR.

## 2. METHODS AND RESULTS

Nonlinear losses appear in HRs at high acoustic amplitudes, due to the conversion of acoustical energy into kinetic rotational energy at the resonators neck [6]. A simplified nonlinear model [6] can be found in the literature which describes the dynamics of the pressure inside the HR cavity, and it is employed in this work. In particular we study one dimensional plane wave scattering, in a waveguide with side-loaded resonators for the the three different settings shown in Fig. 1. Our scope is twofold, (i) to find analytical expressions describing the conditions for CPA for all the configurations and (ii) to study the influence of the nonlinear losses which serve as an amplitude dependent tuning parameter.

*Single scatterer.* The simplest case of a single HR is studied first and it is found that: although in the linear case the viscothermal losses of the resonator are inadequate to balance its leakage to the waveguide, nonlinear losses can lead to critical coupling [7]. More specifically, using the simplified nonlinear model for the HR, we analytically obtain the necessary conditions for CPA, quantifying the required amount of acoustic amplitude. These conditions correspond to incident waves from both ports of the system, and are equivalent to an absorption of $A = 0.5$ for a single incident wave. We experimentally confirm the critical coupling for the single incident case [panel (d) of Fig. 1], in good agreement with our analytical findings (vertical dashed line). Additionally a *nonlinear* acoustic impedance model is used to characterize the nonlinear scattering properties, and is in a good agreement with the experiments (solid line).

*A pair of scatterers.* We furthermore study the more complex case of two HRs where the presence of a second resonant mode allows for CPA even in the linear limit [5]. Here we derive a set of non-Hermitian $2 \times 2$ matrices whose (generally complex) eigenfrequencies are found in analytical form and correspond to CPA. These frequencies acquire physical meaning when they become

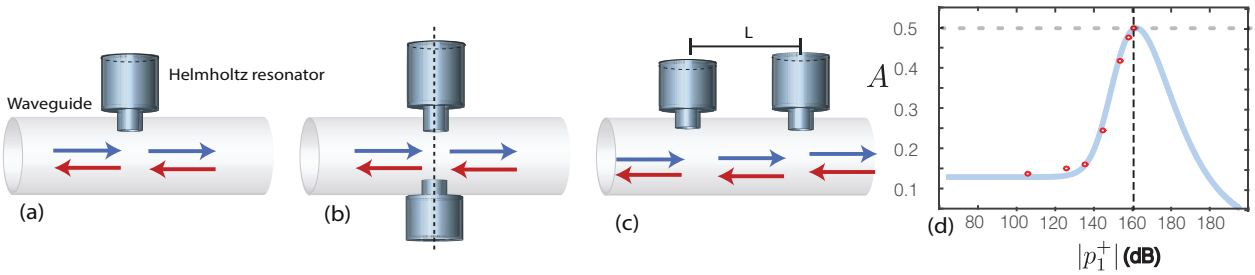



Figure 1: The three different configurations we study: (a) a single HR sideloaded to a cylindrical waveguide, (b) two resonators located at the same position with respect to the direction of propagation and (c) two HRs separated by a distance $L$. Experimental results for the configuration of (a), showing that critical coupling (and thus an absorption of $A = 0.5$) occurs at 160 dB.

real, and coincide with the zeros of the respective scattering matrix. In contrast to the complex plane analysis of the scattering matrix, the analytical expressions allow for a selective tuning of parameters, e.g. the resonance frequency of each resonator, the coupling with the waveguide, or the viscothermal losses, in order to have CPA in a specific setting. Experimental results for sufficiently small amplitude incident waves verify our findings. Considering high amplitude waves and using the nonlinear impedance model for each resonator, we find that nonlinear losses may break the critical coupling when a system is linearly critically coupled, or they can induce CPA in the opposite case. This result suggests that nonlinearity must be taken into account in potential applications of CPA devices with HRs. More importantly it illustrates how nonlinearity can be used as an additionally parameter to control acoustic wave propagation.

Control of absorption by the wave amplitude with sub-wavelength structures constitutes a topic of great theoretical interest and can find applications in noise reduction, and in the absorption of high amplitude pressure waves in aircraft engines or rocket launch pads. By means of a simplified nonlinear model of the HR we obtain the CPA conditions for different settings. We experimentally validate critical coupling, for an one-sided incidence configuration. The description of the system with two HRs by a non-Hermitian matrix, may allow for a direct connection with recently observed wave control phenomena, such as $\mathcal{PT}$-symmetry and non-reciprocal scattering. Extension of this study into more complex configurations could lead to the design of broadband high amplitude acoustic absorbers with applications into aeronautics.

## ACKNOWLEDGMENT

This work has been funded by the Metaudible project ANR-13-BS09-0003, co-funded by ANR and FRAE.

## REFERENCES

1. Hermann A. Haus, *Waves and Fields in Optoelectronics*, (Prentice Hall, New Jersey, 1984), pp. 197-216.
2. Y. Xu, Y. Li, R. K. Lee, and A. Yariv, "Scattering-theory analysis of waveguide-resonator coupling", Phys. Rev. E **62**, 7389 (2000).
3. V. Romero-Garcia, G. Theocharis, O. Richoux, A. Merkel, V. Tournat, V. Pagneux, "Perfect and broadband acoustic absorption by critically coupled sub-wavelength resonators", Sci. Rep. **5**, 19519; doi: 10.1038/srep19519 (2015).
4. V. Leroy, A. Strybulevych, M. Lanoy, F. Lemoult, A. Tourin, J. H. Page, "Superabsorption of acoustic waves with bubble metascreens", Phys. Rev. B **91**, 020301 (2015).
5. A. Merkel, G. Theocharis, O. Richoux, V. Romero-Garcia and V. Pagneux, "Control of acoustic absorption in one-dimensional scattering by resonant scatterers", Appl. Phys. Lett. **107**, 244102 (2015).
6. S.W. Rienstra, A. Hirschberg, *An Introduction to Acoustics*, Technical Report, Technische Universiteit Eindhoven, Revised and updated version of IWDE 92-06 (2012).
7. V. Achilleos, O. Richoux, G. Theocharis, "Coherent Perfect Absorption induced by the nonlinearity of a Helmholtz resonator", arXiv:1601.03912

# Tunable waveguide and cavity in a phononic crystal/acoustic metamaterial plate by controlling whispering-gallery modes

**Y. Jin[1,2*], Y. Pennec[1], Y. Pan[2], and B. Djafari-Rouhani[1]**

[1]Institut d'Electronique, de Microélectronique et de Nanotechnologie, UMR CNRS 8520, Université de Lille 1, 59655, Villeneuve d'Ascq, France

[2]School of Aerospace Engineering and Applied Mechanics, Tongji University, 100 Zhangwu Road, 200092, Shanghai, China

[*]corresponding author: yabin.jin@ed.univ-lille1.fr

**Abstract**- We investigate the properties of a phononic crystal plate with hollow pillars and introduce the existence of whispering-gallery modes (WGMs). We show that, when tuning the inner radius of the hollow pillar, these modes can merge inside both Bragg and low frequency band gaps, deserving phononic crystal and acoustic metamaterial applications. These modes can be used as narrow pass bands by increasing their quality factors. The confined WGMs are applied to wavelength division in multiplexer devices using heteroradii pillars introduced into waveguide and cavity structures.

We theoretically investigate the vibration properties of a phononic crystal (PC) plate with hollow pillars on top. The computed dispersion curves show the occurrence of two new branches of dispersion that do not appear in the native PC. These branches originate from the excitation of whispering gallery modes (WGM's) circulating around the upper boundary of the hollow pillar[1]. By changing the inner radius of the hollow cylinder, we have been able to tune the frequencies of the WGM's inside the Bragg band gap. Through the computation of the transmission coefficient of an antisymmetric Lamb wave, we have shown that one of the WGM gives rise to a transmitted pass band that can be used as a filter. The quality factor of the filter has been further improved by inserting a solid cylinder in between the plate and the hollow pillar. We then applied the high resolved filter to different kind of multiplexers, based on multichannel or monochannel waveguides or cavity, e.g. Figure 1. We also showed that the WGMs can reach the low frequency bang gap[2], allowing the utilization of the localized modes in the field of acoustic metamaterials, e.g. Figure 2. The demonstration of an efficient sub-wavelength waveguide with high quality factor has been done. We believe that this structure will pave the way to future new physical behaviors for phononic crystal and acoustic metamaterials by changing the nature of the constitutive elements or filling the hollow cylinders with liquids, rubber or other core-shells elements. The investigations and achievements of these PC resonator structures will show the possibility to build acoustic sensors, filter and acoustic resonators working with improved performances that makes them excellent candidates for wireless communication and sensing applications.

**Acknowledgements**, This work was supported by the "Agence Nationale de la Recherche (ANR)" and the "Délégation Générale de l'Armement (DGA)" under the project Metactif, Grant No. 443 ANR-11-ASTR-015, France. Yabin Jin acknowledges a scholarship provided by China Scholarship Council N0. 201406260170

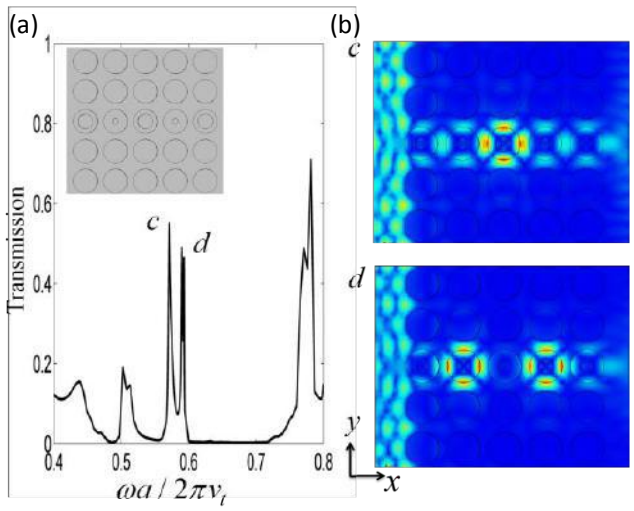



**Figure 1.** (a) (Inset) Schematic representation of the monochannel wavelength multiplexer. (Graph) Transmission spectrum of the antisymmetric Lamb wave when consecutive hollow pillars inside the waveguide have radii of $r_i^{(c)}/a$ = 0.145 and $r_i^{(d)}/a$ = 0.140 where *a* is the period of the square lattice phononic crystal. (b) Displacement field distributions at the frequency of the two narrow pass bands 'c' and 'd'.

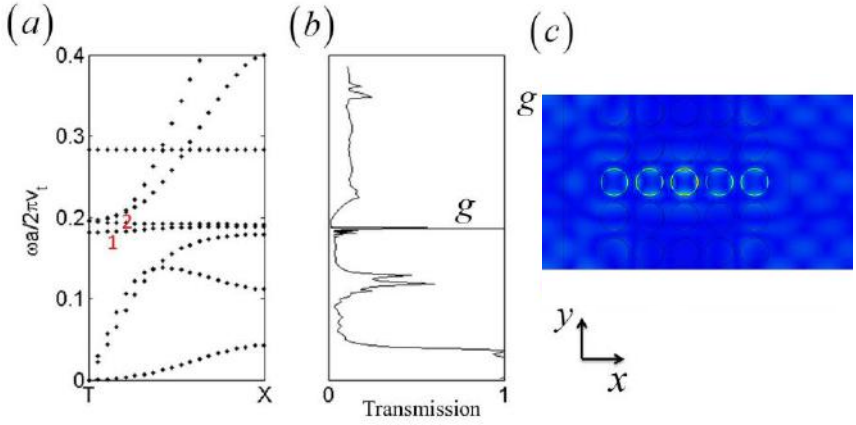



**Figure 2.** (a) Dispersion curve in the low frequency range [0; 0.4] corresponding to the perfect phononic crystal made of hollow pillars on plate with the set of geometrical parameters $r_i/a$ = 0.35, $l/h$ = 0.49, $h/a$ = 0.45, $r/a$ = 0.4, and $e/a$ = 0.1. Here *h, l and e* are respectively the height of the pillar, the height of the full part of the pillar and the thickness of the plate. (b) Transmission spectrum of the antisymmetric Lamb wave through the waveguide of hollow pillars inserted inside a full silicon pillar crystal. (b) Displacement field distributions at the reduced frequency 0.19 corresponding to the narrow pass bands 'g'.

## REFERENCES


1. Jin, Y, Fernez, N, Pennec, Y, Bonello, B, Moiseyenko, R. P, Hémon, S, Pan, Y and Djafari-Rouhani, B. "Tunable waveguide and cavity in a phononic crystal plate by controlling whispering-gallery modes in hollow pillars", *Phys. Rev. B*, Vol. 93, No. 5, 054109-1–054109-8, 2016
2. Pennec, Y, Djafari-Rouhani, B, Larabi, H, Vasseur J. O. and Hladky-Hennion A. C. "Low frequency gaps in a phononic crystal constituted of cylindrical dots deposited on a thin homogeneous plate", *Phys. Rev. B*, Vol.78, No. 10, 104105-1–104105-8, 2008.

# Simultaneous Full Control of Elastic Waves in Plates by Gradient Index Devices

**Y. Jin[1,2*], D. Torrent[3], Y. Pennec[1], Y. Pan[2], and B. Djafari-Rouhani[1]**

[1]Institut d'Electronique, de Microélectronique et de Nanotechnologie, UMR CNRS 8520, Université de Lille 1, 59655, Villeneuve d'Ascq, France

[2]School of Aerospace Engineering and Applied Mechanics, Tongji University, 100 Zhangwu Road, 200092, Shanghai, China

[3]Université de Bordeaux, Centre de Recherche Paul Pascal, UPR 8641, 115 Avenue Schweitzer, 33600 Pessac, France

[*]corresponding author: yabin.jin@ed.univ-lille1.fr

**Abstract**- We present a method for designing gradient index (GRIN) devices for elastic waves in plates based on Fourier homogenization of phononic crystals/ acoustic metamaterials. The method allows the design of devices to control the three fundamental Lamb modes, despite the fact that their dispersion relation is managed by different elastic constants. It is shown that by means of complex GRIN phononic crystals and thickness variations, it is possible to independently design the three refractive indexes of these Lamb modes, hence realizing their simultaneous control.

In this work, a homogenization theory[1] for phononic crystals/acoustic metamaterials is developed and applied to the homogenization of phononic crystal plate[2], which provides the solution of the refractive indexes of the three fundamental Lamb modes. It is shown that by means of a complex unit cell, consisting of a circular inclusion with a hole in its center, together with thickness variations of the plate, it is possible to design independently the refractive index of the three plate modes. The performance of the method is demonstrated by means of the design of a flat GRIN lens and a circle Luneburg and Maxwell lens working simultaneously for the three modes. In Figure 1, GRIN lens simulations are shown at the same frequency $\omega a / 2\pi c_t = 0.178$, whose wave numbers for the three Lamb modes are given by $k_S a = 0.65, k_{SH} a = 1.11$ and $k_A a = 1.5$. The corresponding field distributions are shown in left, center and right panels. Besides, a more advanced device is shown in Figure 2, which consists in a circle lens working as a Luneburg lens for the $S_0$ and $SH_0$ polarizations (left and middle panels where a plane incident wave is focused at the exit of the lens) and as a Maxwell lens for the $A_0$ one (right panel where the image of a point source is a point).

As the method is based on a homogenization theory in the quasi-static limit, the devices are shown to work in a broad frequency region. This method can be efficiently employed to the device design for the control or harvesting of mechanical energy since it allows the full control of vibrations excited in a finite elastic plate. Finally, it must be pointed out that the method can be applied to more complex waves in solids or fluids, being a general approach for the control of multi-model mechanical waves.

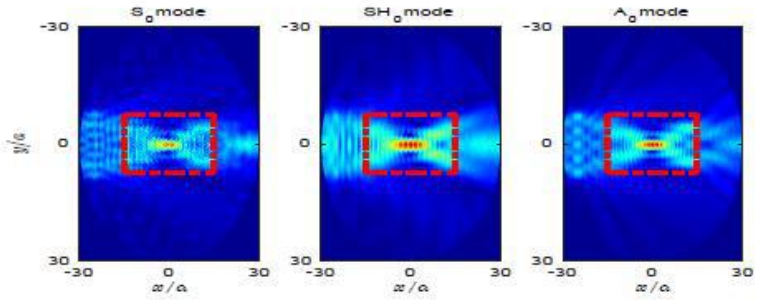



**Figure 1.** GRIN flat lens made with a slab of 15 rows and 34 columns of gold-hole inclusions in an Aluminum plate of thickness $h=a$.

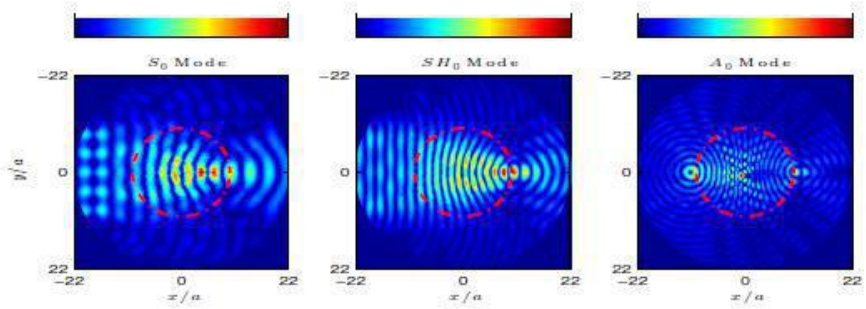



**Figure 2.** The three illustrations of an advanced omnidirectional lens are given for the same wave number $k_A a = 1.5$ which corresponds to the frequencies $\omega a / 2\pi c_t = 0.41, 0.24$ and 0.17 for the $S_0$, $SH_0$ and $A_0$ polarizations, respectively.

**Acknowledgements**, This work was supported by the "Agence Nationale de la Recherche (ANR)" and the "Délégation Générale de l'Armement (DGA)" under the project Metactif, Grant No. 443 ANR-11-ASTR-015 and by the LabEx AMADEus (ANR-10-444 LABX-42) in the framework of IdEx Bordeaux (ANR-10-445IDEX-03-02), France. Yabin Jin acknowledges a scholarship provided by China Scholarship Council N0. 201406260170

**REFERENCES**

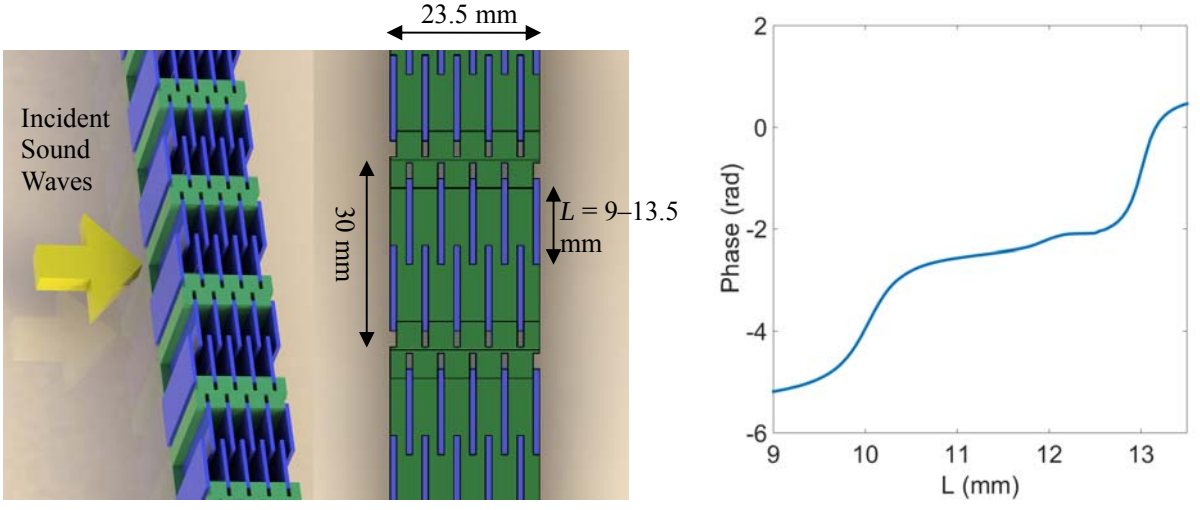
1. Torrent, D, Pennec, Y and Djafari-Rouhani, B. "Resonant and nonlocal properties of phononic metasolids", *Phys. Rev. B*, Vol.92, No. 17, 174110-1–174110-8, 2015.
2. Jin, Y, Torrent, D, Pennec, Y, Pan, Y and Djafari-Rouhani, B. "Simultaneous control of the $S_0$ and $A_0$ Lamb modes by graded phononic crystal plates", *J. Appl. Phys*, Vol. 117, No. 24, 244904-1–244904-8, 2015

# Reconfigurable Acoustic Metasurface for Dynamic Steering of Sound Waves

**Po-Han Fu, Tsung-Yu Chiang and Ding-Wei Huang***
National Taiwan University, Taiwan, R.O.C.
*corresponding author: dwhuang@ntu.edu.tw

**Abstract**- A reconfigurable acoustic metasurface was designed and constructed for manipulating the propagation of sound waves. The acoustic metasurface consists of an array of 3D-printed cells containing motor-driven interdigitated walls. By changing the positions of the interdigitated walls in each cell, the acoustic metasurface can change the phase distribution of the sound waves passing through it. In this way, dynamic steering of sound waves can be achieved.

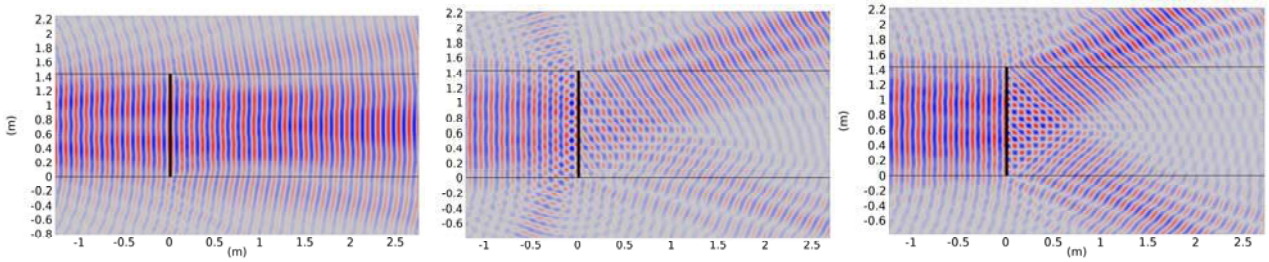
Static acoustic metasurfaces having resonant chambers have been demonstrated for effectively changing the phase distribution of the sound waves passing through the metasurfaces [1–3]. In this study, we designed and constructed a reconfigurable acoustic metasurface which can be controlled for changing the phase distribution of the sound waves and thus manipulating their propagation behavior dynamically. The acoustic metasurface is shown in Fig. 1(a), which consists of an array of plastic resonant chambers (cells) made of plastic by 3D printing technique. Each cell (30 mm wide and 23.5 mm deep) has movable interdigitated walls which are driven by servo motors. The sound waves pass through each cell in the winding paths defined by the walls. As the interdigitated walls move close to or apart from each other, *i.e.*, small or large opening, the phase of the transmitted sound waves can be varied. Figure 1(b) shows the relation between the phase of the transmitted sound waves (frequency = 3 kHz) and the protrusion of the interdigitated walls. The phase can be varied in the range of ~2π (rad) as the protrusion of the wall changes from 9 to 13.5 mm.




(a) (b)

Fig. 1 (a) Structure of the reconfigurable acoustic metasurface and (b) the phase of the transmitted sound waves as a function of the protrusion ($L$) of interdigitated walls

Based on the relation between the transmitted phase and the protrusion of the interdigitated walls, the required phase for each cell can be calculated and the corresponding positions of the interdigitated walls in each cell can be assigned by triggering each servo motor to a certain rotation angle to drive the walls. When there is no phase difference (0 rad) for all cells, the plane sound waves pass through the metasurface without any change of the propagation behavior as shown in Fig. 2(a). When the phase distribution is linear and the phase difference between any two consecutive cells is $\pi/4$ (rad), the sound wave changes its direction by 28.45° after passing through the metasurface as shown in Fig. 2(b). As the phase difference between any two consecutive cells becomes $\pi/3$ (rad), the propagation direction becomes 39.43° off the incident direction as shown in Fig. 2(c).




(a) (b) (c)

Fig. 2 Propagation behavior of sound waves with the phase difference of (a) 0, (b) $\pi/4$, and (c) $\pi/3$ radians between consecutive cells.

Because of the size limitation of the servo motors for driving the interdigitated walls, the width of each cell is 30 mm which is not small enough to minimize the higher-order diffraction of sound waves. All the servo motors are controlled by a fast microcontroller circuit, and thus the time required for changing the acoustic metasurface from one configuration to another is limited by the time required for each servo motor to rotate to a target angle, which is approximately 0.2–0.5 ms. Although only the steering of sound waves is demonstrated in this work, other possible configurations for focusing, branching, and frequency-division multiplexing of sound waves are also under investigations.

The authors are grateful for the financial support from the Ministry of Education and the Ministry of Science and Technology of Taiwan, R.O.C. with the grant number: MOST 103-2221-E-002-060.

**REFERENCES**

1. Y. Li. B. Liang, Zh. Gu, X. Zou, and J. Cheng, “Reflected wavefront manipulation based on ultrathin planar acoustic metasurfaces,” *Scientific Report* **3**:2546, 2013.
2. Y. Xie, W. Wang, H. Chen, A. Konneker, B.I. Popa, and S.A. Cummer, “Wavefront Modulation and Subwavelength Diffractive Acoustics with an Acoustic Metasurface,” *Nat Commun.***5**:5553, 2014.
3. Y. Li, X. Jiang, R. Li, B. Liang, X. Zou, L. Yin, and J. Cheng, “Experimental Realization of Full Control of Reflected Waves with Subwavelength Acoustic Metasurfaces, *Phys. Rev. Applied* **2**:064002, 2014.

# Hybridization of multi-mode waves in thin plates

**M. Rupin[1*], P. Roux[2], G. Lerosey[1], and F. Lemoult[1]**

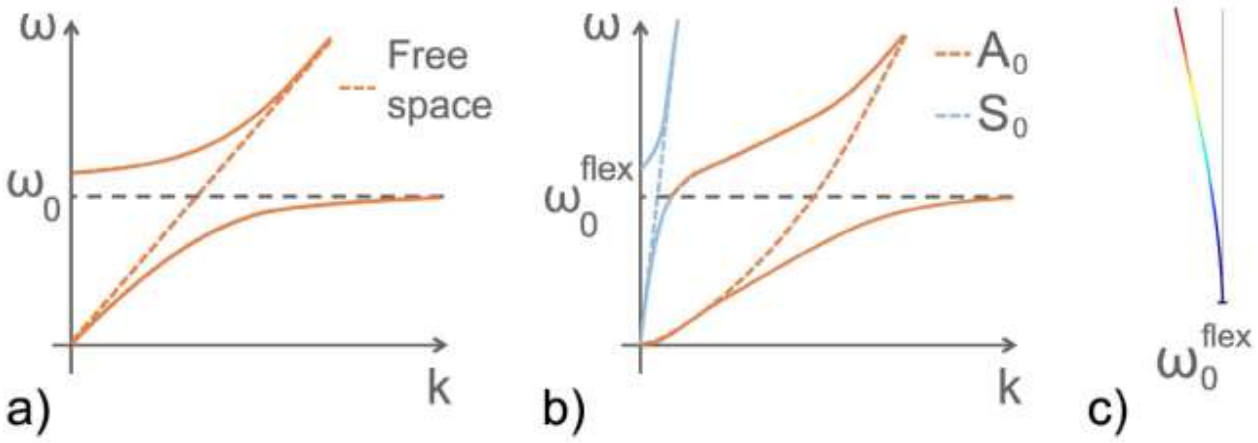
[1]Institut Langevin, ESPCI ParisTech and CNRS UMR 7587, PSL Research University, 1 rue Jussieu, 75005, Paris, France.

[2]Institut des Sciences de la Terre, UMR 5275, Université Grenoble Alpes, Grenoble, 38000, France.

[*]corresponding author: matthieu.rupin@espci.fr

**Abstract**-This work concerns the study of the effect of multiple localized resonances on multiple propagative modes. We demonstrate the possibility to break the natural orthogonality of elastic plate waves (A0 and S0 Lamb modes) using an assymetric metamaterial composed by an ensemble of long metallic rods closely packed and coupled to a one side of a thin metallic plate. We believe that our approach is valid for any medium that supports two propagating modes at the same frequency.

For a scalar wavefield, a locally resonant metamaterial has a dispersion that is induced by a local resonance that shows two hybrid modes when observed in the frequency-wavenumber space (see Figure 1(a)). This results from the anti-crossing effects between a continuum of frequency with a localized frequency, which are also known as polariton branches [1]. An interesting question then arises: what about a medium with multiple propagative modes that interacts with multiple localized resonances?




**Figures 1:** (a) Schematic representation of the hybridization effect for a polariton-like configuration: the interaction between a propagating wave (orange dashed line) and a local resonance $\omega_0$ leads to the appearance of two hybrid modes. Below the resonance, the sub-wavelength branch, and above the resonance, the supra-wavelength branch. Both are separated by a bandgap. (b) When two orthogonal modes are the solution of the wave equation, and considering a localized resonance where modal deformation induces a local motion of the plate that is compatible with both modes (see (c)), the hybridization effect causes the appearance of a third branch. This latter corresponds to a hybrid mode with an evolving symmetry with respect to the wavenumber. (c) Representation of the modal deformation of the asymmetric system of plate + resonator at the resonance $\omega_0^{flex}$

that induces a local longitudinal and transverse deformation on the plate. This modal deformation is responsible for the coupling between the A0 and S0 Lamb waves.

To answer this question we are interested in the study of elastic guided waves propagating in a thin aluminum plate (the host medium) coupled with an ensemble of long aluminum rods (the local resonators) glued on one face. This **asymmetric metamaterial** has already been studied in the past [2-5] but only for the scalar (or acoustic) hybridization of the antisymmetric Lamb mode with the compressional resonances in the rods. In the present work, we describe and interpret the vectorial (elastic) hybridization of both antisymmetric (A0) and symmetric (S0) Lamb modes with the flexural resonances of the rods.

This elastic hybridization presents an peculiar signature in the fk diagram (see Figure 1(b)). Indeed, a third branch appears in between the dispersion of the slow A0 Lamb mode and the fast S0 Lamb mode. It corresponds to a propagating mode with an evolving symmetry with respect to the wavenumber. This is a consequence of the breaking of the natural orthogonality of the A0 and S0 Lamb modes. We also demonstrate the possibility to retrieve this orthogonality using a **symmetric metamaterial**.

**Acknowledgements**, This work is supported by LABEX WIFI (Laboratory of Excellence within the French Program "Investments for the Future") under references ANR-10-LABX-24 and ANR-10-IDEX-0001-02 PSL* and by Agence Nationale de la Recherche under reference ANR-13-JS09-0001-01. ISTerre is part of Labex OSUG@2020.

**REFERENCES**

1. Lagendijk, A, *Ultrashort Processes in Condensed Matter*, Springer US, New York, 1993.
2. Rupin, M. and Catheline, S. and Roux, P., “Super-resolution experiments on Lamb waves using a single emitter,” *Appl. Phys. Lett.*, Vol. 106, 024103, 2015.
3. Colombi, A. and Roux, P. and Guenneau, S. and Rupin, M., “Directional cloaking of flexural waves in a plate with a locally resonant metamaterial,” *J. Acoust. Soc. Am.*, Vol. 137, No. 4, 1783-1789, 2015.
4. Williams, E.G. and Roux, P. and Rupin, M. and Kuperman, W.A., “Theory of multi-resonant metamaterials for A0 Lamb waves,” *Phys. Rev. B*, Vol. 91, 104307, 2015.
5. Rupin, M. and Lemoult, F. and Lerosey, G. and Roux, P., “Experimental demonstration of ordered and disordered multi-resonant metamaterials for Lamb waves,” *Phys. Rev. Lett.*, Vol. 112, 234301, 2014.

# Annular Hole Phononic Crystals for Surface Acoustic Waves

**B. J. Ash**[1], **S. R. Worsfold**[1], **P. Vukusic**[1] **and G. R. Nash**[1]
[1]College of Engineering, Mathematics and Physical Sciences, University of Exeter, United Kingdom

**Abstract**- Novel annular hole arrays are used as phononic crystals for surface acoustic waves. Simulations show dispersions with low frequency bandgaps that can be tuned by the geometry of the annular holes and experiments validate these simulations through expected attenuation of propagating waves. These annular holes improve upon cylindrical pillar phononic crystals that have been the focus of much recent interest.

Surface acoustic waves (SAW) devices are currently used in a broad range of applications including RF signal processing and gas sensing. As such the increased control and manipulation of SAWs could result in improved performance for these applications as well as lead to novel SAW device functions. One way of manipulating SAWs is through the use of phononic crystals (PnCs). PnCs are periodic elastic composites that can exhibit bandgaps in phonon dispersions which can be used to create transmission filters or achieve acoustic confinement within waveguides or cavities.[1] One of the most commonly used designs for SAW PnCs is that of an array of cylindrical pillars which can support local resonances to open low frequency bandgaps away from the soundline, avoiding leaky modes at functional frequencies.[2] In this work we introduce the novel concept of an array of annular etched holes as a SAW PnC which can also support local resonances but improve upon pillars with enhanced structural integrity, an additional geometrical degree of freedom and also allow for the deposition of planar materials on top of the propagating surface. Here we report simulated and experimental evidence for the validity of this type of PnC, demonstrating the tune-ability of the system for SAW bandgaps, and present a preliminary example of how such a PnC could potentially be used in gas sensing.

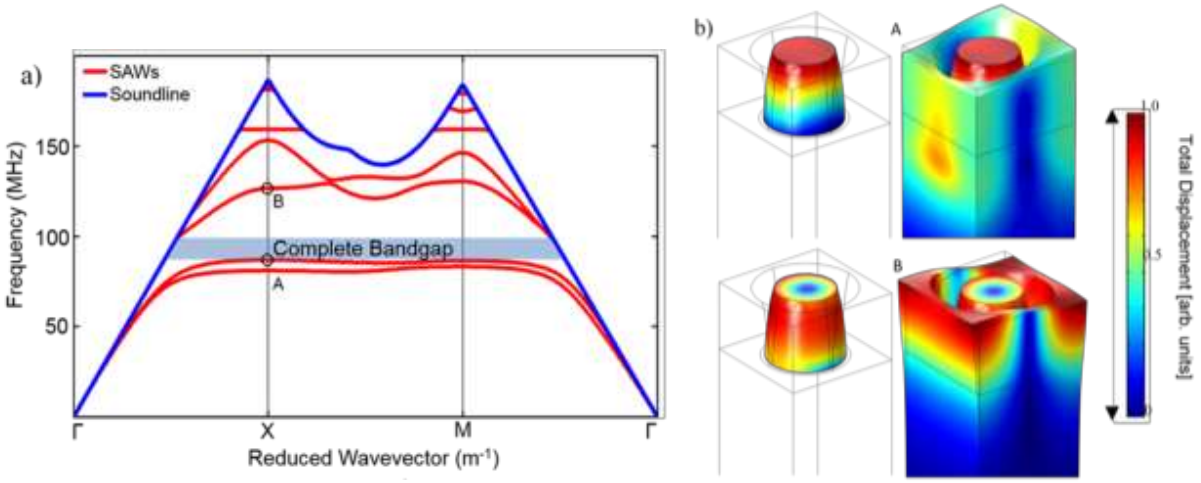



**Figure 1. (a)** Simulated annular hole SAW PnC dispersions showing a complete bandgaps within the soundline at a center frequency of 100MHz. **(b)** Displacement plots for two of these modes annotated on the dispersions, illustrating the depth and radial dependences of supported local resonances within the structures

**Acknowledgements** Funded by the EPSRC as part of the $XM^2$ Metamaterials CDT in Exeter.

**REFERENCES**

1. Benchabane, S., Gaiffe, O., Salut, R., Ulliac, G., Laude, V. and Kokkonen, K. "Guidance of surface waves in a micron-scale phononic crystal line-defect waveguide," *Appl. Phys. Lett.*, Vol. 106, 081903, 2015.
2. Addouche, M., Al-Lethawe, M. A., Choujaa, A., and Khelif, A. "Superlensing effect for surface acoustic waves in a pillar-based phononic crystal with negative refractive index," *Appl. Phys. Lett.*, Vol. 105, 023501, 2014.

# Zero-frequency and extremely slow edge states in mechanical granular graphene

**Li-Yang Zheng,* Vincent Tournat, Georgios Theocharis, and Vitalyi Gusev***

LAUM, UMR-CNRS 6613, Université du Maine, Av. O. Messiaen, 72085 Le Mans, France

*corresponding authors: liyang.zheng.etu@univ-lemans.fr, vitali.goussev@univ-lemans.fr

**Abstract**-The edge states in a semi-infinite mechanical granular graphene with the zigzag and armchair edge configurations are investigated. The dispersion curves of edge states are theoretically derived and numerically analyzed in detail. We also study the quasi-flat edge modes when the torsional or/and bending rigidities are weak. These quasi-flat dispersion curves, supporting the propagation of waves with extremely slow group velocity, tend to be perfect zero-frequency modes for zero torsional rigidity or vanish for zero bending rigidity.

Granular crystals are spatially periodic structures with particles (mostly spherical homogeneous elastic beads) arranged in crystal lattices.[1-8] Basically, the beads are linked through their contacting areas or by interconnects, both of much smaller dimensions than the dimensions of the beads, and the interactions between beads take place predominantly via normal and transverse rigidities of these links. In granular crystals, due to the non-central shear forces, rotation of individual beads can be initiated, thus the rotational degree of freedom (DOF) of the individual beads, the particle dimensions and the interactions through non-central forces can not be ignored.[1-4] It has been theoretically reported[5,6] and experimentally tested[7, 8] that thanks to the rotational DOFs of individual beads, additional coupled rotational/transverse[7] and pure rotational modes[8] can be observed in granular crystals. Here we theoretically study the existence of edge states on the free boundaries of a 2D semi-infinite mechanical granular graphene, where elastic beads are arranged in a monolayer honeycomb structure.

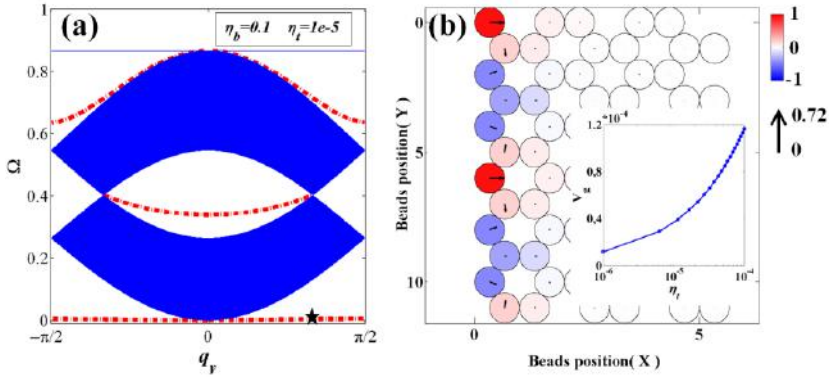



**Figure 1.** (a) Dispersion curves of zigzag edge states for the normalized torsional and bending rigidities of the contacts $\eta_b$=0.1 and $\eta_t$=$10^{-5}$, respectively, in a part of the spectrum neighboring with zero frequency. A quasi-flat band with near zero frequency is exhibited. (b) Movement of beads of the near zero frequency mode at point $q_y$=π/3 highlighted in (a) by a black star. The insert shows the relation between the normalized group velocity of near zero frequency modes for a fixed wave vector $q_y$=π/3 and normalized torsional rigidity $\eta_t$. The color marked on each bead represents the normalized amplitude of displacement which could be read from the color bar. The orientation of arrows represents the rotating directions of beads. The length of arrows represents the normalized amplitude of rotations of beads.

The out-of-plane motion is imposed to the considered granular graphene with the zigzag and armchair boundaries. Consequently, each individual bead possesses one out-of-plane translational and two in-plane rotational DOFs and the mechanical contacts among them are provided by linear shear, bending and torsional rigidities, respectively. The dispersion curves of edge modes for varying bending/torsional rigidities are studied.

Due to the rotational DOFs, the energy branches of edge state can be modified by tuning the bending and torsional rigidities. We also demonstrate that near zero-frequency modes may appear on both the zigzag and armchair edges when bending/torsional rigidities are weak (Fig. 1 and Fig. 2). We show that the existence of zero-frequency edge modes is intimately related to the weakness of bending/torsional intergrain couplings.

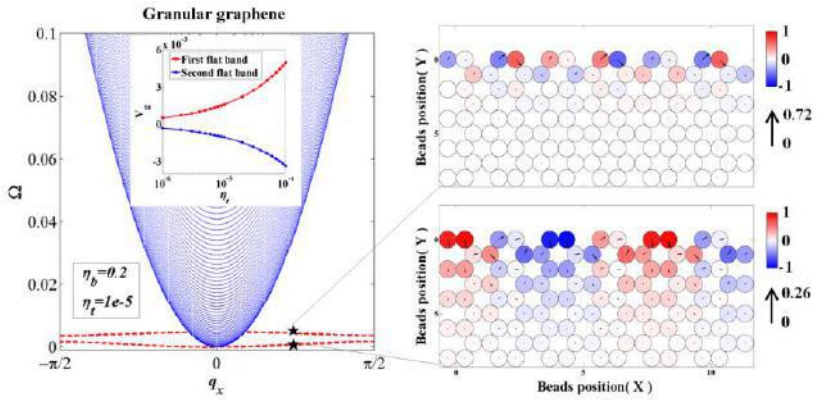



**Figure 2.** (a) The dispersion curves of armchair edge modes with slow velocity for the normalized torsional and bending rigidities of the contacts $\eta_b$=0.2 and $\eta_t$=$10^{-5}$, respectively, in a part of the spectrum neighboring with zero frequency. Two quasi-flat bands appear for weak torsional rigidity. The movements of beads for the wave vector $q_y \approx \pi/4$ noted by the black stars are studied. (b) The oscillation of beads on the edge for the second quasi-flat band. (c) The oscillation of edge state for the first quasi-flat band. The insert scheme in (a) illustrates the variations of normalized group velocity of the quasi-flat bands as a function of $\eta_t$.

The study of the near-zero-frequency modes caused by the existence of weak rotational interactions is useful for the potential realistic design of soft granular crystals supporting the controllable propagation of the extremely slow edge waves. In addition, it paves the way for the analysis of a variety of possible modifications of the granular graphene with a goal of proposing granular metamaterials supporting one-way propagating edge states.

## ACKNOWLEDGEMENTS

This work was supported by the fellowship of China Scholarship Council for L.-Y. Zheng and by the Région Pays-de-la-Loire through Grant “PROPASYM” (Pari Scientifique 2013).

## REFERENCES

1. L. M. Schwartz, D. L. Johnson, and S. Feng, “Vibrational Modes in Granular Materials,” *Phys. Rev. Lett.* 52, 831, 1984.
2. A. S. J. Suiker, A.V. Metrikine, and R. de Borst, “Comparison of wave propagation characteristics of the Cosserat continuum model and corresponding discrete lattice models,” *Int. J. Solids Struct*. 38, 1563–1583, 2001.
3. I. S. Pavlov, A. I. Potapov, and G. A. Maugin, “A 2D granular medium with rotating particles,” *Int. J. Solids Struct*. 43, 6194–6207, 2006.
4. H. Muhlaus, and F. Oka, “Dispersion and wave propagation in discrete and continuous models for granular materials,” *Int. J. Solids Struct*. 33, 2841, 1996.
5. V. Tournat, I. Perez-Arjona, A. Merkel, V. Sanchez-Morcillo, and V. Gusev, “Elastic waves in phononic monolayer granular membranes,” *New J. Phys.* 13, 073042, 2011.
6. L. -Y. Zheng, H. Pichard, V. Tournat, G. Theocharis, and V. Gusev, “Zero-frequency and slow elastic modes in phononic monolayer granular membranes,” *Ultrasonics*, DOI: 10.1016/j.ultras.2015. 11.005, 2015.
7. A. Merkel, V. Tournat, and V. Gusev, “Experimental Evidence of Rotational Elastic Waves in Granular Phononic Crystals,” *Phys. Rev. Lett.* 107, 225502, 2011.
8. J. Cabaret, P. Béquin, G. Theocharis, V. Andreev, V. E. Gusev, and V. Tournat, “Nonlinear Hysteretic Torsional Waves,” *Phys. Rev. Lett.* 115, 054301, 2015.

# Multi-particle trapping and patterning using phononic crystal plates

**Tian Wang[1*], Manzhu Ke[1*], and Zhengyou Liu[1,2*]**

1 School of Physics and Technology, Wuhan University, Wuhan 430072, China
2 Institute for Advanced Studies, Wuhan University, Wuhan 430072, China
[*]corresponding author, Electronic mail: wangtian12@whu.edu.cn, mzke@whu.edu.cn, zyliu@whu.edu.cn

**Abstract**- We experimentally demonstrated multi-particle trapping and patterning assisted by phononic crystal plates. Polystyrene particles with sub-millimeter size can self-pattern in, for example, the square, triangular or quasi-periodic arrays, depending on the structures of the phononic crystal plates with varying sub-wavelength holes array. The analysis shows that the resonant transmission field highly localized near the sub-wavelength apertures, yields a negative acoustic radiation force on the nearby particle. We expect this system may pave a new route for particle self-assembly.

It is well known that acoustic radiation force (ARF) is effective in contactless manipulation of microscale objects, which may have potential application in particle sorting, chemical sensing, micro/nano fabricating. To date, a variety of studies have been done by researchers to analyze acoustic manipulation of microscale objects both in theoretical analysis [1, 2] and experimental research [3-5].

In this letter, we report on the ARFs on particles above the phononic crystal slabs (PCs), which consists of metal plates with perforated holes in two dimensional (2D) array. Firstly, we consider the sample of a brass plate ($\rho$=8600 kg/m$^3$, $c_l$=4400 m/s and $c_t$=2160 m/s) with perforated holes in square array immersed in water. As illustrated in Figure 1a, the period (p) of the holes array is 1.5 mm, and the radius (R) of the holes and the thickness (t) of the plate are 0.25 mm and 0.5 mm respectively. When excited by acoustic plane waves, enhanced acoustic transmission as well as enhanced acoustic field confined in the aperture appear, as shown in Figure1a and b, the localized acoustic field is critical importance in near filed particle trapping.

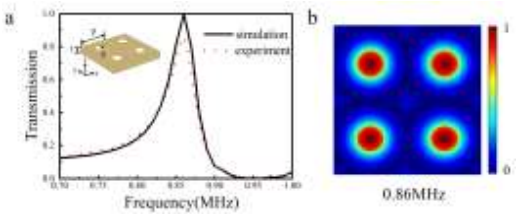



Fig.1. (a) Schematic of PCs and corresponding transmission spectrum, (b) calculated pressure field distribution in x-y plane.

As illustrated in Figure 2(a), a polystyrene (PS) particle ($\rho$=1050 kg/m$^3$, $c_l$=2170 m/s and $c_t$=1100 m/s) with radius ($r_1$) of 0.3 mm is placed above the PCs. When acoustic plane waves normally incident from the bottom of plate, we can get the ARF on the PS particle (as denoted by black solid line in Fig. 2(b)), it can be observed that the particle will experience a “negative” acoustic force within a wide frequency which attracts the particle toward the hole. We also plot the force map in one unit cell in Fig.2(c), where the direction and magnitude of the force are indicated by the orientation and length of the black arrow respectively, the result reveals that the particle will always experience stably attractive ARFs directed to the hole.

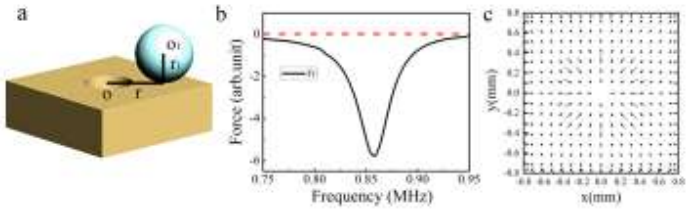



Fig.2. (a) Model schematic of numerical analysis for ARF on a PS particle in one unit cell, (b) calculated ARF on the particle versus frequency,(c)transversal force map in one unit cell.

We perform an experiment to demonstrate the phenomena of particles trapping and patterning, three groups of snapshots are shown in Figure 3. Initially, PS particles ($r_1$=0.3mm) are randomly distributed on the PCs, under the action of force field induced by the interaction of acoustic waves with PCs, the PS particles move quickly towards the adjacent holes and form stable patterns, for example, the square, triangular, or quasi-periodic arrays, depending on the structures of the phononic crystal plates.

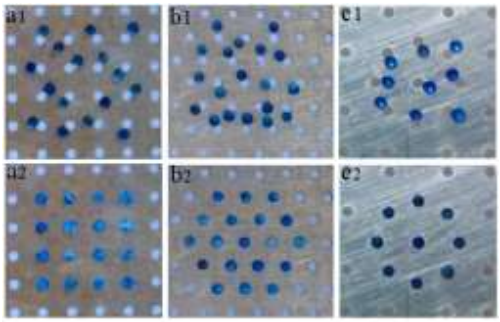



Fig.3.Snapshots of acoustic trapping and patterning of PS particles, figures (a1)-(c1) and (a2)-(c2) respectively denote the status of particles before patterning and after patterning.

**Acknowledgements**

This work was supported by 973 Research Program of China (Grant No. 2015CB755500), the National Natural Science Foundation of China (Grant Nos. 11574233 and 11374233).

**REFERENCES**

1. Xu, S., Qiu, C. & Liu, Z. Transversally stable acoustic pulling force produced by two crossed plane waves. Europhysics Letters, 99, 44003, (2012).
2. Li, Y., Qiu, C., Xu, S., Ke, M. & Liu, Z. Theoretical Study of Large-Angle Bending Transport of Microparticles by 2D Acoustic Half-Bessel Beams. Scientific reports 5, 13063(2015).
3. Wu, J. Acoustical tweezers. The Journal of the Acoustical Society of America 89, 2140-2143 (1991).
4. Li, F. *et al*. Phononic-Crystal-Based Acoustic Sieve for Tunable Manipulations of Particles by a Highly Localized Radiation Force. Physical Review Applied, 1.051001 (2014).
5. Wang, T. *et al*. Dexterous acoustic trapping and patterning of particles assisted by phononic crystal plate. Applied Physics Letters 106, 1.4918999 (2015).

# Effect of Material Parameters on Band Gap of Sonic Crystals (BaTiO3/Polar Liquids)

**Oral Oltulu[1], Amirullah M. Mamedov[2,3*], Ekmel Ozbay[2]**

[1] Department of Physics, Faculty of Science and Letters, Harran University, Sanliurfa, Turkey
[2] Nanotechnology Research Center (NANOTAM), Bilkent University, Ankara, Turkey
[3] International Scientific Center, Baku State University, Baku, Azerbaijan
*corresponding author, E-mail: mamedov46@gmail.com

## Abstract

The propagation of acoustic waves in two-dimensional sonic crystals (SC) is studied theoretically. Effects of elliptical rod orientations on the acoustic band gaps in periodic arrays of rigid solid rods embedded in a polar liquid are investigated. We have found that the pass bands and forbidden bands of the sonic crystals can be changed by utilizing the rotational anisotropy of the structure factor at different rotation angles of the scatterers. The plane wave expansion (PWE) method is used to calculate the band structure. The variation of the absolute band gap was also investigated as a function of any filling fraction at a fixed orientation of the elliptical columns. The gap-tuning effect can be controlled by the rotational asymmetry and eccentricity of the scatterers.

## 1. Introduction

The propagation of acoustic waves in a composite medium has been an interesting topic for the last decade mainly due to its technological applications in condensed matter physics, especially in phononics[1,2]. Since their invention, phononic crystals have triggered considerable interest because of their unusual acoustical properties. The unique properties of phononic crystals open up new and major fields in acoustics. Sonic crystals (SCs) are defined as structured materials formed by a periodic distributions of acoustic scatterers embedded in a host material, with strong periodic modulations in their density and elastic coefficients between the constituent materials. The periodicity of the scatterers in a surrounding material gives rise to the appearance of sonic band gaps, a range of frequencies for which sound propagation is forbidden inside the crystal. These stop bands were observed at frequencies depending on the lattice constant of the array in the band structures of crystals with various lattice geometries.[3-5]. The SCs have induced several application proposals and enabled development of many new technologies. Recent studies in this field have attracted a great interest due to the splendid application prospects, such as acoustic filters [6,7], shield devices[8-10], defect states for acoustic filters and wave guides [11], and so on. Recently, an increased attenuation at low frequencies has been achieved by the locally resonant sonic materials formed by soft and rigid elements [12]. Several theoretical methods have been used to study the elastic/acoustic band structures, such as, the plane-wave expansion (PWE) method [13,14], the finite difference time domain (FDTD) method [15], the extended plane wave expansion (EPWE) method [16,17], the multiple scattering theory (MST) [18], perturbative approach [19], and variational method [20]. Among them, the PWE is the most widely used method for calculating the band structures. In the literature, acoustic band gaps of various two-dimensional sonic crystal structures were investigated and these structures mostly consist of circular cross-section scatterers in square, triangular, rectangular lattices, the constituent being either both solids or fluids, or mixed solid-fluid [21]. Practically, band gaps properties of sonic crystal structures or the acoustic dispersion of the branches can be controlled by the lattice filling factor, the constituent material contrast between the rods and the surrounding, and the lattice symmetry, and as well as the scatter shape [22]. However, there are fewer studies that consider the shape of the inclusions despite the fact that shape factor is an important quantity for the propagation of acoustic waves in 2D phononic crystals [23-25]. Moreover, most of the work in this field focuses on the calculations of the band structure of 2D phononic crystals of circular rods.

In the present paper, the propagation of audible acoustic waves in two-dimensional periodic arrays of elliptic rigid solid rods embedded in polar liquids is considered. We have investigated the effects of orientations of elliptic rods on the acoustic band gaps. As a choice of material, we have considered polar liquids and perovskite-type materials. The speed of sound and the conductivity in most polar liquids increases with temperature [26]. On the other hand, the perovskite-type materials have been the subject of ongoing research for over 50 years. ABO3-type perovskite crystals are used extensively for technological applications. In this study, we have chosen water as a polar liquid and a well-known classic ferroelectric BaTiO3. BaTiO3 is a promising material that has a wide range of applications in dielectric capacitors, pyroelectric detectors, nonlinear optical devices, phononic crystals, and surface-acoustic wave devices [27-31].

## 2. Theory

In this study, we consider a two-dimensional periodic composite that composed of solid elliptic rods immersed in polar liquids. Since mixed fluid/solid model can be simplified by imposing elastic rigidity to the solid media, the solid can be reasonably approximated as fluid inclusions. Then, the model allows only the longitudinal wave to propagate through the fluid media. Therefore, the acoustic wave equation in a sonic crystal can be written as a second order inhomogeneous differential equation in the form of pressure waves:

$$\left(\rho c^2\right)^{-1}\frac{\partial^2 p}{\partial t^2}=\vec{\nabla}\cdot\left(\rho^{-1}\nabla p\right), \qquad (1)$$

where $p$ is the pressure, $\left(\rho c_l^2\right)^{-1}$ is the longitudinal elastic constant $C_{11}$ , and $\rho$ is the mass density, and $\nabla(x,y)$ is the two-dimensional Nabla. Solution of this equation gives the band-gap structure of sonic crystals by the plane-wave expansion (PWE) method. According to the PWE method, $\rho^{-1}$ and $(\rho c^2)^{-1}$ can be expanded as material parameters in two-dimensional Fourier series [32]. Hence, the Fourier series expansion for $C_{11}$ and $\rho$ can be expressed as

$$\left(\rho c_l^2\right)^{-1}(\vec{r})=\sum_{\vec{G}}\eta^{-1}\left(\vec{G}\right)e^{i\vec{G}.\vec{r}},\quad \rho^{-1}(\vec{r})=\sum_{\vec{G}}\sigma^{-1}\left(\vec{G}\right)e^{i\vec{G}.\vec{r}} \qquad (2)$$

The Fourier expansion coefficients for the inverse of mass density

$$\sigma^{-1}\left(\vec{G}\right)=\frac{1}{A_c}\int\rho^{-1}(\vec{r})\,d^2r\begin{cases}\rho_a f+\rho_b(1-f) & \text{for } \vec{G}=0\\ (\rho_a-\rho_b)S\left(\vec{G}\right) & \text{for } \vec{G}\neq 0\end{cases}, \qquad (3)$$

where $A_c$ is the area of the unit cell, $f$ is the filling fraction, describing the ratio of the surface area of the column to the area of the total unit cell, the subindex "*a*" and "*b*" stands for the scatterers and background material, respectively. S(**G**) term in the equation is the structure factor defined for the system of elliptic rods with rotation angle $\theta$ in two-dimensional system as [33]

$$S_{RC}\left(\vec{G}\right)=2f\frac{J_1\sqrt{r_x^2G_x'^2+r_x^2G_x'^2}}{\sqrt{r_x^2G_x'^2+r_x^2G_x'^2}}, \qquad (4)$$

where $G_x'$ and $G_y'$ are the vectors in the primed system while $G_x$ and $G_y$ are the G vector components in the original coordinate system, $J_1(x)$ is the Bessel function of the first kind of order one, $r_y$ and $r_x$ are the half length of the long and the short axis, respectively. The new G vector in primed coordinates can be expressed more compactly, in matrix form, as

$$\begin{pmatrix}G_x'\\ G_y'\end{pmatrix}=\begin{pmatrix}cos\theta & sin\theta\\ -sin\theta & cos\theta\end{pmatrix}\begin{pmatrix}G_x\\ G_y\end{pmatrix}, \qquad (5)$$

where the angle $\theta$ is defined as the angle between the long axis and $k_x$ direction.

## 3. Results and Discussion

The model discussed here is shown in Fig.1. Elliptical columns in water were arranged in a square lattice. In general, the band gap properties of phononic or sonic crystals are controlled by the lattice type, geometry, material density, speed of sound, and the filling ratio. In this study, we fix the material parameters for the elliptic rods in the sonic crystal and rotate the rods in the polar liquid media to extract the dependence of the sonic properties. BaTiO3 is chosen as the material for the elliptical inclusions. The mass density and sound speeds of BaTiO3 and polar liquid (water) are as follows: $\rho$=5550 kg/m$^3$, $c_l$=5640 m/s, for BaTiO3; $\rho$ =1000 kg/m$^3$, $c_l$ =1500 m/s for water, respectively. The lattice constant of the sonic crystal is $a_o$=*13 mm*, and the long axis of elliptic rods $r_x$=*0.3*$a_o$ mm and the short axis is $r_y$=*0.5*$a_o$ mm. Numerical calculations based on these equations were performed by the code written by Elford [34] after some modifications.

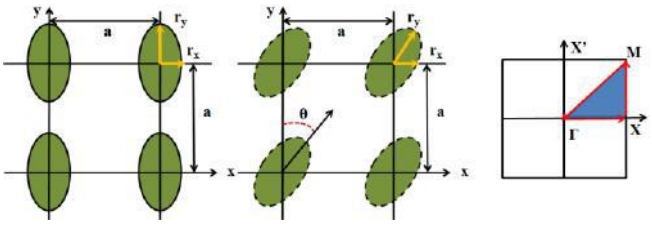



Figure 1: (a) Transverse cross section of the 2D square lattice consisting of elliptical BaTiO3 rods embedded in a polar liquid, (b) rotated rods by an angle θ, (c) and the related first Brillouin zone of the 2D square lattice.

Figure 2 shows the band structure for BatiO3 columns in water for the constant filling fraction angles.

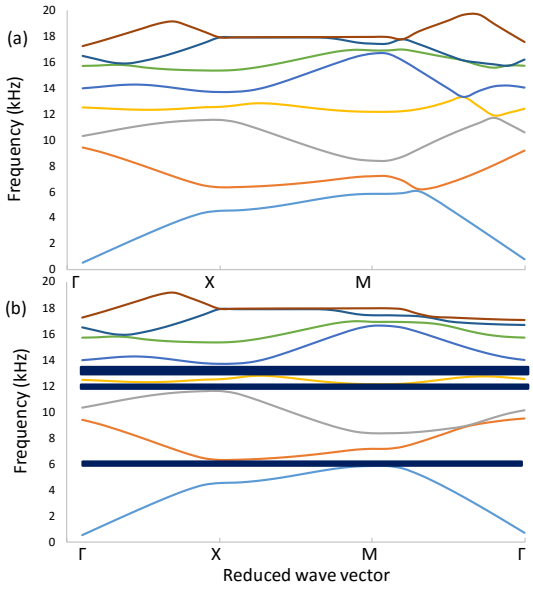



Figure 2: Band structure for elliptical rods in polar liquid water at filling fraction f=0.32 at (a) θ=-45$^o$, (b) θ=45$^o$. The absolute gaps are indicated by the shaded area.

For a square lattice with a lattice constant of $a_o$, the filling fraction $f$ is given by $f=r_x\, r_y\, \pi/A_c$, where $A_c$ is the area of the unit cell. The results shown in Fig. 2 are for constant filling fraction of $f_{BaTiO3}$ =0.32 for two different rotation angles of (a) θ=-45°, and (b) θ=45°. From figure 2(a), it is seen that the absolute sonic band gap does not exist at θ=-45°. The non-existent bands at θ=-45° start to open up at a positive angle of 45° . Therefore, it can be concluded that the gaps only appear at certain angles. This is simply due to rotational anisotropy of the structure factor at these angles.

When a band-gap has been found for a sonic crystal, the acoustic sound waves can be confined in a waveguide. In such systems, it is convenient and usually customary to express the absolute band gap widths in dimensionless units in order to make the gap scale independent of crystal size. The size of the photonic band gap can be characterized by expressing the quantity in terms of the mid-gap to band gap ratio. This ratio is defined as $\Delta\omega/\omega_g$[35], where Δω is the frequency width of the gap and $\omega_g$ is the frequency at the middle of the gap. In this way, the ratio becomes more meaningful compared to the gap width, Δω, itself. if the system is scaled up or down, the ratio remains invariant to size scaling.

The variation of the bandgap is investigated based on the rotational asymmetry of the elliptic cylinders. The band gap structure can be controlled by rotating the elliptic $BaTiO_3$ rods which modifies the geometric factor of a sonic crystal. Therefore, rotation of the rods will cause a geometric anisotropy on the sonic wave propagation through the structure. Figure 3 shows the results of the calculation for the normalized width of the lowest band gap as a function of the rotation angle $\theta$. The filling fraction for the calculation is fixed at approximately 0.47. It must be noted that the largest value of the first band gap was found to be almost equal at θ=0° and θ=90°.

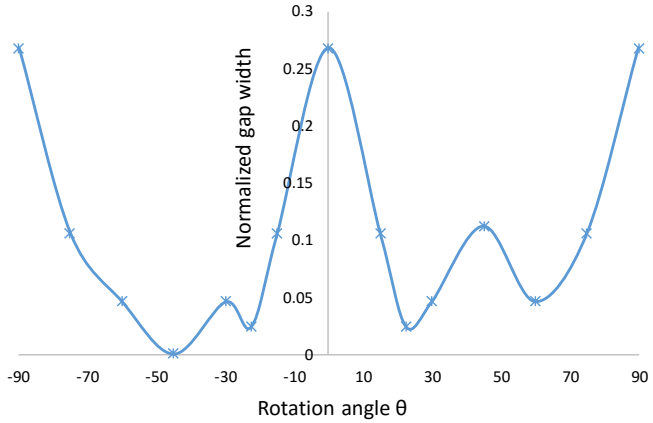



Figure 3: The normalized gap-width $\Delta\omega/\omega_g$ of the lowest band gap as the function of the rotation angle θ.

In order to see the variation of the normalized gap-width $\Delta\omega/\omega_g$ as a function of the filling factor f, the long axis of the elliptic rod is kept constant, and then the eccentricity is varied by changing the short axis. Figure 4 shows the $\Delta\omega/\omega_g$ variation of the lowest three bands as a function of different filling fractions. The length of the major axis $r_y$ is fixed at $0.5a_o$ while the minor axis increment is set to $0.05a_o$ in $\Delta r_x$.

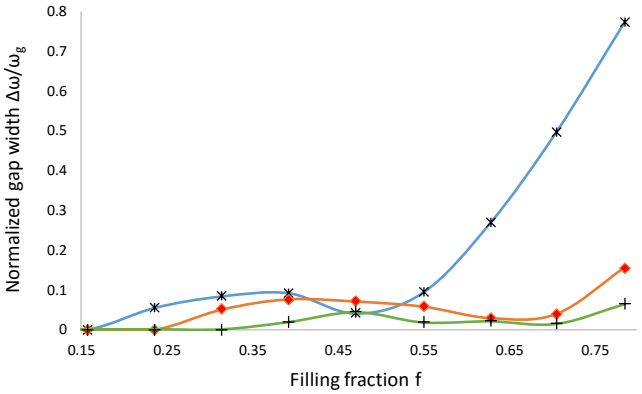



Figure 4: The normalized gap-width Δω/ωg of the lowest three band gaps as a function of different filling fractions.

The highest symmetry was obtained from setting $r_x$ and $r_y$ to $r=0.5a_o$ yielding the largest normalized band width. Obviously, the shape of the rods becomes circular and the circle has the highest symmetry of all.

## 4. Conclusions

In this article, the acoustic wave propagation of a square lattice sonic crystal is studied. A sonic crystal made of elliptic cross-section of $BaTiO_3$ rods in a polar liquid (water) was considered to investigate the existence of complete band gaps. The largest normalized gap-width $\Delta\omega/\omega_g$ of the lowest band gap as the function of the rotation angle was found to be the same at two different angles, θ=0° and θ=90°. The existence of tunable band gaps in the frequency regime are found. The appearance and disappearance of the band gaps imply rotational anisotropy for angles of ±45o. The influence of filling fraction on the sonic eigenfrequencies was also taken into consideration. The study showed that when the fill factor reaches its maximum the band gap widths was enlarged by opening up in the direction of lower and higher frequencies. Sonic crystal thus offers an alternative way towards the control and arbitrary manipulation of the sound waves. The findings may be useful for some of the applications of sonic crystal in acoustic devices, such as frequency filter, acoustic waveguides, metamaterials.

## Acknowledgements

The author (Ekmel Ozbay) acknowledges partial support from the Turkish Academy of Sciences.

## References

[1] M. Sigalas, M. S. Kushwaha, E. N. Economou, M. Kafesaki, I. E. Psarobas, W. Steurer, Classical vibrational modes in photonic lattices: theory and experiment, *Z. Kristallogr.* 220: 765-809, 2005.

[2] Y. Pennec, J. Vasseur, B. Djafari-Rouhani, L. Drobrzyski, P. Demier, Two-dimensional phononic crystals: Examples and applications, *Surface Science Reports* 65(8): 229-291, 2010.

[3] T. Miyashita, Sonic crystals and sonic wave-guides, *Meas. Sci. Technol.* 16: 47–63, 2005

[4] X.D. Zhanga, Z.Y. Liu, Negative refraction of acoustic waves in two-dimensional phononic crystals, *Appl. Phys. Lett.* 85: 341-343, 2004.

[5] M.S. Kushwaha, B. Djafari-Rouhani, Sonic-stop bands for periyodic arrays of metallics rods: honeycomb structure, *J. Sound Vib.* 218(4): 697-709, 1998.

[6] M. S. Kushwaha, P. Halevi, Stop bands for periodic metallic rods: sculpture that can filter the noise, *Appl. Phys. Lett. 7:* 3218-3220, 1997.

[7] J. V. Sánchez-Pérez, C. Rubio, R. Martínez-Sala, R. SánchezGrandía, and V. Gómez, *Appl. Phys. Lett.*81(27): 5240-5242, 2002.

[8] R. Martínez-Sala, J. Sancho, J. V. Sánchez-Pérez, J. Llinares, F. Meseguer, Sound attenuation by sculpture, *Nature* 378: 241-241, 1995.

[9] J. V. Sánchez-Pérez, C. Rubio, R. Martínez-Sala, R. Sánchez-Grandía, V. Gómez, Acoustic barriers based on periodic arrays of scatterers, *Appl. Phys. Lett.* 81: 5240–5242, 2002.

[10] A. Uris, C. Rubio, H. Estellés, J. V. Sánchez-Pérez, R. Martínez-Sala, and J. Llinares, Design of lightweight multilayer partitions based on sonic crystals, *Appl. Phys. Lett.* 79: 4453–4454, 2001.

[11] M. Kafesaki, M. M. Sigalas and N. Garcia, Frequency modulation in the transmitivity of wave guides in elastic band gap materials, *Phys. Rev. Lett.* 85: 4044-4047 2000.

[12] Z. Liu, X. Zhang, Y. Mao, Y. Y. Zhu, Z. Yang, C. T. Chan, and P.Sheng, Locally resonant sonic materials, *Science*: 289(5485):1734-1736, 2000.

[13] M.S. Kushwaha, P. Halevi, G. Martinez, L. Dobrzynski, B. Djafari-Rouhani, Theory of acoustic band structure of periodic elastic composites, *Phys. Rev. B* 49: 2313-2322, 1994.

[14] J.O. Vasseur, B. Djafari-Rouhani, L. Dobrzynski, P.A. Deymier, Acoustic band gaps in fibre composite materials of boron-nitride structure. *J. Phys.: Condens. Matter*. 9: 7327-7341, 1997.

[15] M.M. Sigalas, Theoretical study of three dimensional elastic band gaps with the finite difference time-domain method, J. Appl. Phys. 87: 3122-3125, 2000.

[16] V. Romero-García1, J. V. Sánchez-Pérez, L. M. Garcia-Raffi, Evanescent modes in sonic crystals:Complex dispersion relation and supercell approximation, *J. Appl. Phys.* 10: 044907, 2010.

[17] V. Laude, Y. Achaoui, S. Benchabane, and A. Khelif, Evanescent Bloch waves and the complex band structure of phononic crystals *Phys. Rev. B* 80: 092301, 2009.

[18] M. Kafesaki, E. N. Economou, Multiple scattering theory for 3D periodic acoustic composites, *Phys. Rev. B* 60: 11993-12001, 1999

[19] F.G. Wu, Z.L. Hou, Z.Y. Liu, Y.Y. Li, Point defect states in two-dimensional phononic crystals, *Phys. Lett.A* 292: 198-202, 2001.

[20] J. V. Sánchez-Perez, D. Caballero, R. Martínez-Sala, C. Rubio, J. Sánchez Dehesa, F. Meseguer, J. LLinares, F. Gálvez, Sound attenuation by a two-dimensional array of rigid cylinders, *Phys. Rev. Lett.* 80: 5325–5328, 1998.

[21] H. Pichard, O. Richoux, J.-P. Groby, Experimental demonstrations in audible frequency range of band gap tunability and negative refraction in two-dimensional sonic crystal, *J. Acoust. Soc. Am.* 132(4): 2816–2822, 2012.

[22] R. Wang, X. Wang, B. Gu, G. Yang, Effects of shapes and orientations of scatterers and lattice symmetries on the photonic band gap in two dimensional photonic crystals, *J. Appl. Phys.* 90:4307-4013, 2001.

[23] S.A. El-Naggar, S.I. Mostafa, N.H. Rafat, Complete band gaps of phononic crystal plates with square rods, *Ultrasonics* 52: 536–542, 2012.

[24] H. Salehi, M. Aryadoust, M. Z. Shoushtari, The generalization of structure factor for rods by polygon section in two-dimensional phononic crystals, *IJST* 37A4: 457-462, 2013.

[25] X. Li, F. Wu, H. Hu, S. Zhong, Y. Liu, Large acoustic band gaps created by rotating square rods in two-dimensional periodic composites, *J. Phys. D: Appl. Phys.* 36: L15–L17, 2003.

[26] R.F. Probstein, Physicochemical Hydrodynamics: An Introduction, Butterworth Publishers, MA, pp. 19-20, 1989.

[27] A.R. Johnston, Dispersion of electro-optic effect in BaTiO3, *J. Appl. Phys.* 42(9): 3501-3507 ,1971.

[28] Y.-Z. Wang, F.-M. Lia, W.-H. Huanga, X. Jiangc, Y.-S. Wangd, K. Kishimotob, Wave band gaps in two-dimensional piezoelectric/piezomagnetic phononic crystals, *Int. J. Solids Struct.*45:4203-4210, 2008.

[29] X.-K. He, L-B. Zeng, Q.-S. Wu, L.-Y. Zhang, K. Zhu, Y.-L. Liu, Determination of elastic, piezoelectric, and dielectric constants of an R : BaTiO3 single crystal by Brillouin scattering, *Chin. Phys. B* 21(6): 067801-067805, 2012.

[30] C. Renu, Structural, Elastic and Thermal Properties of BaTiO3, *Invertis Journal of Science and Technology* 7(2); 72-77, 014.

[31] S. Piskunov, E. Heifets, R.I. Eglitis, G. Borstel, Bulk properties and electronic structure of SrTiO3, BaTiO3, PbTiO3 perovskites: an ab initio HF/DFT study, *Comp. Mater. Sci.* 29: 165–178, 2004.

[32] T. Miyashita, Sonic crystals and sonic wave-guides, *Meas. Sci. Technol.* 16: R47–R63, 2005.

[33] L.-Y. Wu, L.-W. Chen, The dispersion characteristics of sonic crystals consisting of elliptic cylinders, *J. Phys. D*: Appl. Phys. 40: 7579–7583, 2007.

[34] D.P Elford, Band gap formation in acoustically resonant phononic crystals. PhD thesis. Loughborough University Institutional Repository, 2010.

[35] R. H. Lipson, C. Lu, Photonic cr ystals: a unique partnership between light and matter, *Eur. J. Phys.* 30: S33–S48, 2009.

# Wave Propagation and Acoustic Band Gaps of Two-Dimensional Liquid Crystal/Solid Phononic Crystals

**Oral Oltulu[1*], Amirullah M. Mamedov[2,3], Ekmel Ozbay[2]**

[1] Department of Physics, Faculty of Science and Letters, Harran University, Sanliurfa, Turkey
[2] Nanotechnology Research Center (NANOTAM), Bilkent University, Ankara, Turkey
[3] International Scientific Center, Baku State University, Baku, Azerbaijan
*corresponding author, E-mail: oltulu@harran.edu.tr

## Abstract

The vast majority of acoustic wave propagation in phononic band studies has been usually carried out by scattering inclusions embedded in a viscoelastic medium, such as air or water. In this study, we present calculated band structure results for the two dimensional (2D) square array geometry of a solid cylindrical scatterer surrounded by a liquid crystal (LC) matrix. Liquid crystals(LCs) provide a unique combination of liquid-like and crystal-like properties as well as anisotropic properties. The purpose of using liquid crystal material is to take advantage of longitudinal acoustic waves propagating parallel (||) and perpendicular (⊥) to the nematic liquid crystal (NLC) director *n*. The compound used in this study was a room temperature (NLC), called 5CB (4-pentyl-4'-cyanobiphenyl). The acoustic band structure of a two-dimensional phononic crystal containing a 5CB NLC and Lithium Tantalate ($LiTaO_3$) were investigated by the plane-wave-expansion (PWE) method. The theoretical results show that the solid/LC system can be tuned in a favorable configuration for adjusting or shifting acoustic band gaps.

## 1. Introduction

Phononic crystals (PnCs) [1, 2], also known as phononic band gap materials, are artificial structures designed for controlling and manipulating the propagation of mechanical waves. They have received a great deal of interdisciplinary research attention across condensed matter physics and materials science for both fundamental and applied research, and are expected to find commercial applications soon. The periodicity of the elastic moduli and mass densities of the constituents in space generates the phononic crystal effects [3]. They show interesting physical characteristics due to their ability to block the propagation of acoustic waves by forming energy band structures, called phononic bands. Phononic band gaps (PnBGs) can be adjusted to allow desired frequency to pass through as well as tune the PBG [4-5]. This can be done through the careful design of the geometry of the structure as well as adjusting the crystal lattice parameters, and selecting appropriate materials to find partial or complete band gaps. Therefore, phononic crystals are engineered acoustic band gap materials that belong to the group of metamaterials with designed properties that are usually unknown in nature. The periodic spatial modulation of elasticity and mass density with an appropriate choice of the geometrical and physical parameters have found several potential applications, such as acoustic shielding, acoustic mirrors, demultiplexers [6], and also in the field of wave guiding and filtering [7] (including the modes due to the linear and point defects) as well as in the field of sound isolation [8]. In addition, acoustic negative refraction and an imaging effect of acoustic waves were achieved in the phononic crystals [9]. In general, most of the investigations for solid–fluid periodic structures, known as mixed phononic crystals, focused on placing rigid or liquid materials in air background, water, glycerin, chloroform , or mercury by creating relative density difference between the component materials [10-11]. However, these are all fixed parameters and cannot be changed easily unless one of the materials is physically replaced by placing another material. On the other hand, the effect of other material parameter values such as the speed of sound in a fluid medium (gas or liquid) also has an effect on the band structure. The sound waves travel through each of these mediums as longitudinal waves and its propagation depends on the elasticity or bulk modulus and the mass density. Therefore, it appears that the sound velocity cannot be changed without changing the density or the bulk modulus. That leaves us with not many parameters to make adjustments for the structure under study. Therefore, we suggest a phononic structure that may allow us to change the acoustic velocity nonlinearly to observe the effects on the phononic band gaps.

Liquid crystals (LCs) are remarkable materials with strange properties[12-13]. They are more like liquids than they are like solids but their molecules are aligned like those in crystals. That leaves them with symmetries that are intermediate between those of isotropic liquids and crystalline solids. 4-n-pentyl-4-cyano-biphenyl (5CB) is one of the most interesting and well known liquid crystals and also the most widely studied one. 5CB is uniaxial and has a nematic phase between 297 and 308.3 K [14]. In a nematic phase, 5CB molecules have directional order rather than positional order by self-aligning themselves with their long axes almost parallel. This direction is referred to as the director of the liquid crystal and its orientation is

responsible for determining the unique optical properties of the material. The anisotropic nature and uniaxial symmetry of liquid crystals must give rise to acoustic anisotropy related to sound velocity, elastic properties, and the attenuation coefficient. The acoustics of liquid crystals are based on scientific progress in various fields, such as crystal physics, optics, and acoustical physics [15-17]. Hence, their acoustic properties, like acoustic attenuation, acoustic impedance, and absorption coefficients have not yet been completely reported. Therefore, it is also an open field to explore the acoustic properties of LCs and they can be promising materials for constructing tunable phononic crystals.

## 2. Model and the calculation method

Liquid crystals (LCs) are highly structured organic fluids that consist of rod-shaped molecules. The most commonly studied thermotropic liquid crystal 4-pentyl-4'-cyanobiphenyl (5CB) was used in this study since it is a relatively stable room temperature nematic liquid crystal (NLC). At temperatures above the nematic-isotropic phase transition temperature $T_{NI}$, the long axes of the liquid crystal molecules are randomly oriented, resulting in isotropic properties. At lower temperatures, below the nematic-isotropic transition temperature $T_{NI}$, the elongated molecules, on average, align themselves approximately parallel to one another along an arbitrarily chosen preferred direction in space (x,y,z). This long-range orientational order is called the nematic phase. The nematic phase exhibits a unique property that comes from the geometry and dynamics of that particular direction. The mean value of the direction of the molecular long axes is described by a vector as a function of space. This is known as the director vector $n(r)$. The magnitude of the director has no significance since it is taken as a unit vector.

Here, we focus on the acoustic wave propagation through a periodic array of cylindrical scatterers. We model the matrix as a fluid medium in order to make use of solid/fluid approximation. Such approximation is reasonable if we only consider that the waves propagate as longitudinal waves by means of adiabatic compression and decompression. Fortunately, the longitudinal waves propagating along the director $\boldsymbol{n}$ of 5CB will provide that opportunity. In order to do that, we will consider two possible orientations of the director vector. For simplicity, it will be assumed an axial alignment, in which the liquid crystal director is firstly parallel to the long axis of the cylindrical scatterers, and secondly perpendicular to that of the cylinders. The direction of the directors with respect to cylinder is shown in Figure 1. According to Figure 1(a), the sound velocity $c_{||}$ is in direction parallel to the direction vector $\boldsymbol{n}$ while $c_{\perp}$ is in direction perpendicular to the director $\boldsymbol{n}$.

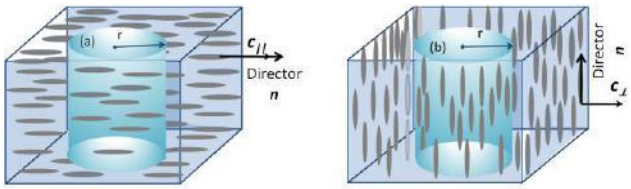



Figure 1: A 3-D representation of a unit cell of a square lattice composed of a solid cylinder and liquid crystal molecules. Director direction *n* is perpendicular to the long axis of the cylinder (a), director n is along the long axis of the cylinder (b).

For an arbitrary orientation, the wave velocity can be expressed as

$$V(\phi)=\frac{1}{\sqrt{2\rho}}\left[\begin{array}{l}\left(C_{11}sin^2\phi+C_{33}cos^2\phi\right)+\\ \sqrt{\left(C_{33}cos^2\phi-C_{11}sin^2\phi\right)^2+C_{13}^2sin^2 2\phi}\end{array}\right]^{1/2},(1)$$

where ρ is the LC density, $\phi$ shows the angular direction of the director [17,18]. It is noteworthy that the shear mode of the nematic phase is in general considered to be negligible. Therefore, the elastic components related to this mode are neglected and assumed to be zero, $C44 = C55 = C66 \approx 0$ [17].

Lithium Tantalate (LiTaO3 or LTA) is our material of choice, since it possesses unique properties, which as a material finds uses in Electro-Optical and Acousto-Optical applications. Some of the technological applications of this well-suited material include: bulk acoustic wave devices, acoustic transducers, piezo-electric transducers and piezoelectric sensors [19]. Its good mechanical and chemical stability make LTA already widely used as a substrate in surface acoustic wave (SAW) devices [20]. LiTaO3 has twelve independent acoustic physical constants. They are six elastic constants, four piezoelectric stress constants, and two dielectric constants. For the sake of simplicity, we will only consider the elastic constant component related to longitudinal velocity. All the piezoelectric, electro optical effects and medium viscosity will be neglected since piezoelectric phase mostly influences the z-mode [21].

Assuming a homogeneous and isotropic medium, we can separate the wave modes and use methods based on acoustic wave theory. To calculate the band gaps for phononic crystals, a Plane Wave Expansion (PWE) method in frequency domain [**22**] is used. due to its simplicity. The considered system is a 2D phononic crystal composed of $LiTaO_3$ inclusions in a 5CB LC host in a square lattice. A square lattice formed of cylindrical rods has a lattice constant of a=0.033 m and the scatterers' radius, $r_0$= 0.0165 m. The calculation model of the studied system and its unit cell is shown in Fig. 2.

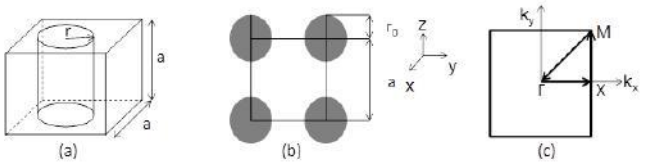



Figure 1: Unit cell of a square lattice two dimensional phononic crystal (a). Transverse cross-section of a representative 2-D phononic crystal (b) and Brillouin zone of 2-D square lattice PCs (c).

The material properties are $\rho_1$ = 1022 kg/m$^3$ at 297 K [23] and $c_\perp$=$c_{L1}$= 1784m/s and $c_\parallel$ = $c_{L1}$,= 1620m/s for the 5CB LC, and $\rho_2$ = 7450 kg/m$^3$ and $c_{L2}$=5592 m/s for $LiTaO_3$. The equation that describes the wave motion is given by the acoustic wave equation as

$$(C_{11})^{-1}\frac{\partial^2 p}{\partial t^2}=\vec{\nabla}\cdot\left(\rho^{-1}\nabla p\right), \qquad (2)$$

where p is the pressure wave, $C_{11}=\rho c_L^2$ is the longitudinal velocity and ρ is the mass density, and $\nabla=(\partial/\partial x,\partial/\partial y)$ is the two-dimensional Nabla. This equation is a scaler wave equation. The periodicity of the phononic system may be utilized to expand $C_{11}^{-1}(r)$ and $\rho^{-1}(r)$ in two-dimensional Fourier series. Hence, the Fourier coefficients for $C_{11}$ and ρ can be expressed as

$$F\left(\vec{G}\right)=\begin{cases}F_a^{-1}f+F_b^{-1}(1-f)=\overline{F^{-1}} & \text{for } \vec{G}=0\\ \left(F_a^{-1}-F_b^{-1}\right)S\left(\vec{G}\right)=\Delta\left(F^{-1}\right)S\left(\vec{G}\right) & \text{for } \vec{G}\neq 0\end{cases}, \qquad (3)$$

where *F* is the physical parameter used for $C_{11}$ and for ρ, the subindex "a" and "b" stands for the inclusions and the host material, respectively. S(**G**) term in the equation is the structure factor defined in two-dimensional system as

$$S\left(\vec{G}\right)=2fJ_1(Gr_0)/(Gr_0), \qquad (4)$$

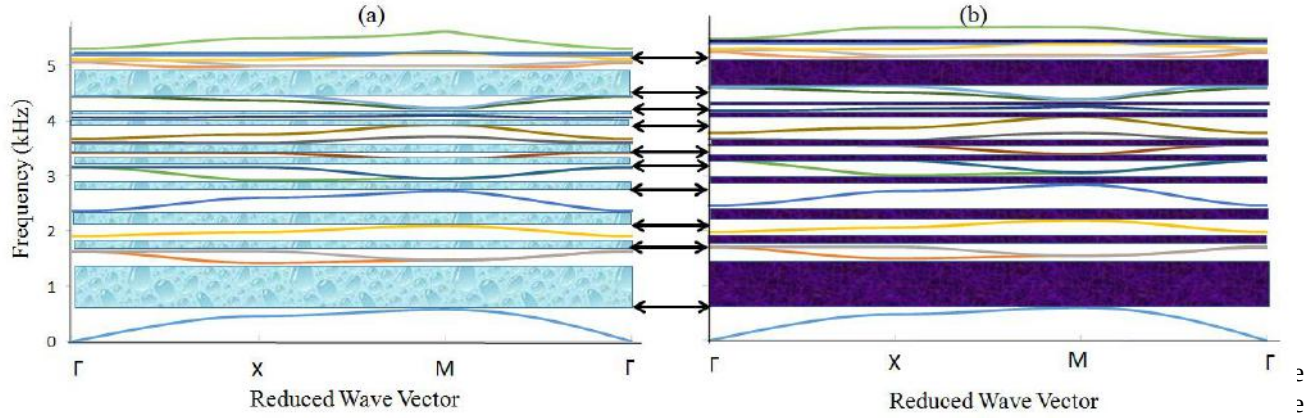
where f is the filling fraction of the cylindrical rods with lattice constant a, $J_1(x)$ is the Bessel function of the first kind of order one, **G** is the two-dimensional reciprocal lattice vector, and $r_0$ is the cylinder's radius. The acoustic wave equation then can be solved as an eigenvalue equation by applying the Bloch theorem. A software implementation and numerical calculation was carried out by the code written by Elford [24] with minor modifications.

## 3. Discussion

The computational model based on the PWE method and the physical parameters of the system have been given in the above section. Numerical results for the band structure are given in Fig. 3. Figures 3(a) and 3(b) show the acoustic band structure for the homogeneous and the homeotropic orientation of the LC directors, respectively. To obtain Figure 3(a), homogeneously aligned 5CB liquid crystals are assumed to be perfectly parallel to the surface of the circular cross section of the cylindrical rod. The wavevector is in the plane of the planar section and the longitudinal acoustic mode velocity $c_\parallel$ is used. It is clear that complete acoustic band gaps are formed due to the overlapping of frequency bands in different directions of periodicity. On the other hand, in a similar manner to the previous system, homeotropically aligned LC molecules are assumed to be perpendicular to the circular cross section of the cylinder. The longitudinal wave velocity in this case is $c_\perp$, and the band structure corresponding to this mode is shown in Figure 3(b). It is evident that a similar band structure is obtained and, therefore, the widths of the full gaps in both figures are insignificant. This is not an unexpected observation since the difference between the LA wave velocities $\Delta c$=($c_\parallel$ - $c_\perp$) is rather small. However, the frequency values of the gaps are shifted to the higher values of frequency when Figure 3(a) and (b) are compared. The shifting levels are shown by black arrows in Figure 3. From Figures 3(a) and 3(b), it can be deduced that a possible tunable phononic crystal structure can be obtained. This can be done by changing the acoustic wave velocity continuously with respect to the director vector. We may consider that as a quasilongitudinal mode and one needs to know the sound velocity for each director orientation.

Figure 4 shows the corresponding phononic density of states (DOS) of the 2D phononic crystal as a function of frequency for perpendicular and parallel alignment of the NLC molecules. DOS for homogeneous orientation is given by the solid line, and DOS calculated for the wave vector aligned perpendicular to the directors is shown by the dashed line.

Calculation of DOS was carried out by sampling k-points in




same rod in homogenously oriented 5CB LC host (b).

the two dimensional BZ. A sum of all bands over all frequencies yields the density of states as a function of frequency. DOS calculations are particularly important since some physical properties, such as thermal conductivity and specific heat, can be modified by changing the phonon density of states in a phononic crystal. Briefly, they provide insight into both microscopic and macroscopic properties. In figure 4, it is clear that there is a shift in the DOS states as a function of frequency, and the shift is more apparent at higher frequencies compared to lower frequencies

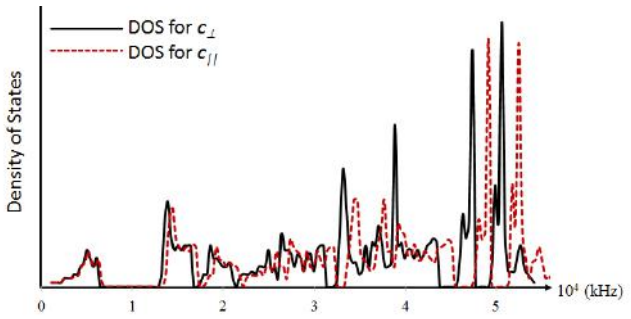



Figure 4: Density of states (DOS) calculated for perpendicular and parallel alignment of the NLC molecules for the 2D phononic crystal system. DOS for homogenous orientation is represented by the solid line, and DOS calculated for the wave vector aligned perpendicular to the directors is shown by the dashed line.

It is easier to understand the refraction and reflection phenomena of certain waves in k space since the law of conservation of momentum is met at reflection and refraction of waves. This can be best done by introducing the equi-frequency surface (EFS) of the acoustic wave. This surface is obtained directly from the calculated eigenmodes inside the unit cell to form the dispersion surfaces of acoustic waves. Figures 5(a) and 5(b) show the dispersion surfaces of the 2D PnC system for the first modes including homogeneous and homeotropic orientation of the host 5CB LC molecules. At first glance, there is almost no noticeable difference in both figures. The difference in dispersion curves in Figures 6(a) and 6(b) is more virtually noticeable compared to Figures 5(a) and 5(b). However, all of these dispersion surfaces hold vital information because each point on the surface gives the possible eigen solutions that consist of all the allowed wave vectors in the first Brillouin zone. It can be deduced that dispersion curves may be useful for quantitative information. Therefore, isotropic or anisotropic wave propagation of waves in PnC can be best analyzed by the equal frequency contour (EFC). Figures 5 (c), 5(d), 6(c) and 6(d) show the EFCs of the waves at some different frequencies in the Phononic crystal. The contours in Figures 5(c) and 5(d) are similar in shape and circular at first for points close to the center. However, the contours become non-circular at higher frequency values when the director vector is perpendicular to the cylinder axis. The deviation from circular shape is faster than homeotropic orientation. This deviation simply implies an anisotropic phase velocity of the longitudinal acoustic wave. Figures 5(c) and 5(d) show that the contours are also non-circular, which means phase velocity depends on wave propagation direction. Moreover, all of these can be understood much better by a known approach known as the conventional

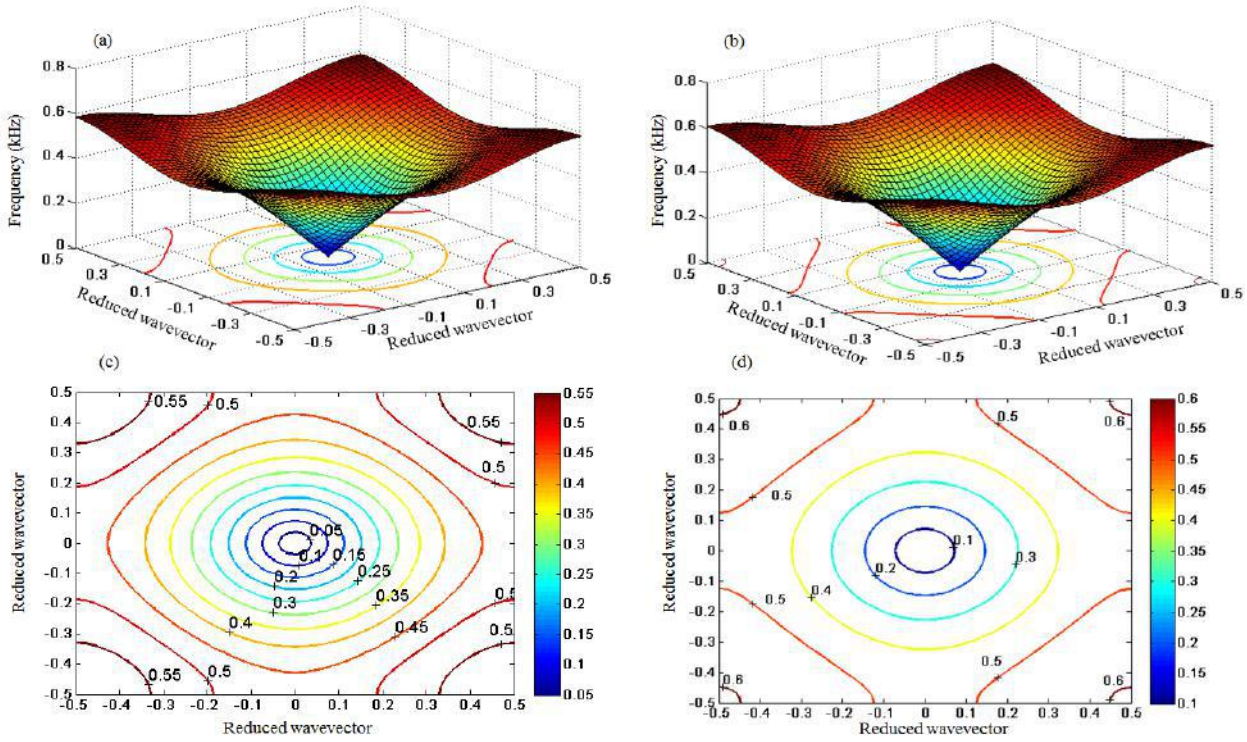



Figure 5: (a) The dispersion, ω(k), relation for the first mode of the square PC, calculated for all k-vectors in the first Brillouin zone and (b) the equifrequency contours for the first mode.

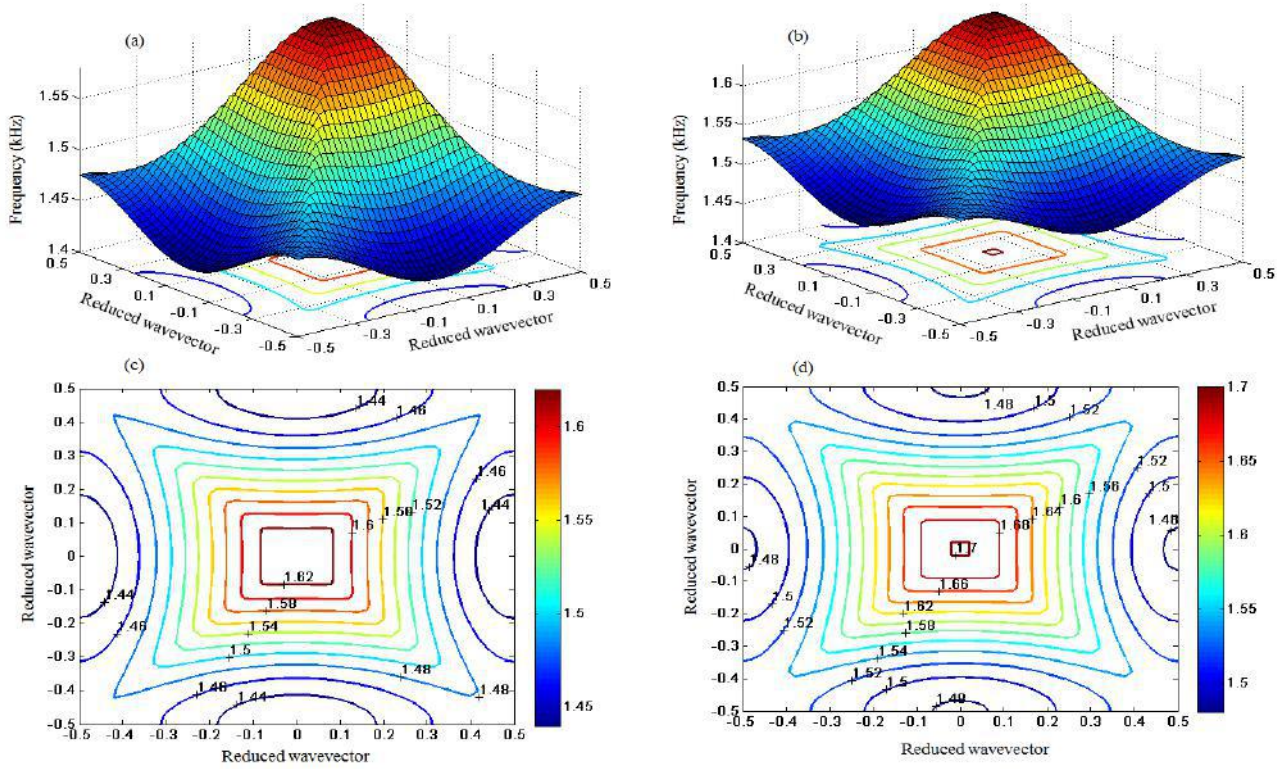



Figure 6: (a) The dispersion, ω(k), relation for the first mode of the square PC,calculated for all k-vectors in the first Brillouin zone and (b) the equifrequency contours for the first mode.

The conventional approach is that a straight line from the central point (Γ point) to another point on a contour gives the direction of the phase velocity while the direction of velocity of energy is presented by the normal direction on the contour. Therefore, deviation from circular contour accounts for the different directions of phase and energy velocities.

## 4. Conclusions

In conclusion, we have studied the propagation of longitudinal waves perpendicular to the infinite periodically aligned inclusions. The conventional PWE method applied to a two-component system consisting of solid cylinders in a liquid matrix with slightly different acoustic parameters was studied and compared. Summarizing, we demonstrated the existence of acoustic band gaps of a two-dimensional phononic crystal containing a 5CB NLC and Lithium Tantalate (LiTaO3). Also, we showed the existence of possible tunability of the acoustic band gaps based on the orientation of the LC molecules. Longitudinal acoustic waves propagating parallel (||) and perpendicular (⊥) to the nematic liquid crystal (NLC) director n gives two different band gap structure. These gaps are structural ones, but they have relative differences in the band gap widths. Furthermore, band gap features coexist in the same structure. These two examples show that introducing LC material into phononic crystal systems may be an effective approach for creating and tuning band structures.

## Acknowledgements

The author (Ekmel Ozbay) acknowledges partial support from the Turkish Academy of Sciences.

## References

[1] Y. Lai, X. Zhang, Z.-Q. Zhang, Engineering acoustic band gaps, *Appl. Phys. Lett.* 79(20): 3224-3226, 2001.

[2] Dowling, J. P, Sonic band structure in fluids with periodic density variations, *J. Acoust. Soc. Am.* 91: 2539-2543, 1992.

[3] Y. Pennec, J.O. Vasseur, B. Djafari-Rouhani, L. Dobrzyński , P.A. Deymier, Two-dimensional phononic crystals: examples and applications, *Surf. Sci. Rep*. 65: 229–291, 2010.

[4] J. Yeh, Control analysis of the tunable phononic crystal with electrorheological material, *Physica B* 400: 137–144, 2007.

[5] H. Larabi, Y. Pennec, B. Djafari-Rouhani, J. O. Vasseur, Multicoaxial cylindrical inclusions in locally resonant phononic crystals, *Phys. Rev. E* 75: 066601, 2007.

[6] R. Lucklum, J. Li, Phononic crystals for liquid sensor applications, *Meas. Sci. Technol.*, 20: 124014, 2009.

[7] Y. Pennec, B. Djafari-Rouhani, J. O. Vasseur, H. Larabi, A. Khelif, A. Choujaa, S. Benchabane, V. Laude, Acoustic channel drop tunnelling in a phononic crystal, *Appl. Phys. Lett.* 87: 261912, 2005.

[8] Z. Liu, X. Zhang, Y. Mao, Y. Y. Zhu, Z. Yang, C. T. Chan, and P. Sheng, Locally resonant sonic materials, *Science* 289(5485): 1734–1736, 2000.

[9] L. Feng X.-P. Liu, M.-H. Liu, Y.-B. Chen, Y.-F. Chen, Y.-W. Mao, J. Zi, Y.-Y. Zhu, S.-N. Zhu, N.-B. Ming, Refraction control of acoustic waves in a square-rod-constructed tunable sonic crystal, *Phys. Rev. B* 73(19): 193101-193104, 2006.

[10] T. Kurose, K. Tsuruta, C. Totsuji,H. Totsuji. Negative refraction of acoustic waves in a two-dimensional phononic crystal via FDTD simulation, *Mater. Trans.*, 50(5): 1004 – 1007, 2009.

[11] Y. Tanaka, Y. Tomoyasu,S.-I. Tamura. Band structure of acoustic waves in phononic lattices: Two-dimensional composites with large acoustic mismatch, *Phys. Rev. B* 62(11): 7387-7392, 2000.

[12] S.Singh, D. Dunmur, Liquid crystal fundamentals, World Scientific, New Jersey , pp. 92-94, 2002.

[13] P. Oswald, P. Pieranski, D. Constantin, Nematic and cholesteric liquid crystals : concepts and physical properties illustrated by experiments, Taylor & Francis, , Boca Raton, pp. 65-71,2005.

[14] J.W. Emsley,G.R.Luckhurst, G.N. Shilstone, The Orientational order of solutions of a dye molecule in liquid-crystalline solvents, *J. Chem. SOC.,Faraday Trans. 2* (83): 371-385, 1987.

[15] L. Benguigui, P. Ron, F. Hardouin, M. Mauzac. Acoustical properties of the polymer liquid crystal (P41)35 in the nematic, smectic A and glass phases. *Journal de Physique*, 50(5): 529-538, 1989.

[16] J.-H. Ko, Y.H. Hwang, J.-H.Kim, Sound propagation in 5CB liquid crystals homogeneously confined in a planar cell, *J. Inf. Disp*. 10( 2): 72-75, 2009.

[17] J.H. Kim, T.H. Kim, J.-H. Ko, Acoustic anisotropy in 5CB liquid crystal cells as determined by using br illouin light scatter ing, *J. Korean Phys. Soc.* 61: 862-866, 2012.

[18] J. K. Krüger, C. Grammes, R. Jiménez, J. Schreiber, K.-P. Bohn, J. Baller, C. Fischer, D. Rogez, C. Schorr, P. Alnot, Second-order elasticity of liquid crystals within their nematic state at high frequencies, *Phys. Rev. E* 51: 2115-2128, 1995.

[19] B. Drafts, Acoustic Wave Technology Sensors, *IEEE Trans. Microw. Theory Tech.*49: 795-802,2001.

[20] K. Länge, B.E. Rapp, M. Rapp, Surface acoustic wave biosensors: a review, *Anal. Bioanal. Chem*. 391:1509–1519, 2008.

[21] Y.-Z. Wanga, F.-M.Lia, W.H. Huanga, X. Jiangc, Y.-S. Wangd, K. Kishimotob, Wave band gaps in two-dimensional piezoelectric/piezomagnetic phononic crystals, *Int. J. Solids Struct.* 45: 4203–4210, 2008.

[22] M.S. Kushwaha, P. Halevi, L. Dobrzynsi, B. Diafari-Rouhani, Acoustic band structure of periodic elastic composites, *Phys. Rev. Lett.* 71: 2022-2025, 1993.

[23] S. Sen, P. Brahma, S. K. Roy, D. K. Mukherjee, S. B. Roy, Birefringence and order parameter of some alkyl and alkoxycyanobiphenyl liquid crystals , *Mol. Cryst. Liq. Cryst*. 100: 327-340, 1983.

[24] D.P Elford, Band gap formation in acoustically resonant phononic crystals. PhD thesis. Loughborough University Institutional Repository 2010.

**Materials for photonics (Graphene, MoS2, WS2, etc)**

# Correlative Microscopy for 2D Material Characterization

**U. Schmidt[1*], E. Bailo[2], D. Steinmetz[1], and T. Dieing[1]**
[1]WITec GmbH, Ulm, Germany
[2]WITec GmbH, Barcelona, Spain
[*]corresponding author: ute.schmidt@witec.de

**Abstract**- Raman imaging is a non-destructive and highly sensitive technique for the differentiation of number of layers, stacking, chirality, and defects in graphene and transition metal dichalogenides (TMDs). The information obtained from Raman imaging can be complemented by other techniques such as Photoluminescence (PL), Atomic Force Microscopy (AFM), Scanning Near-field Optical Microscopy (SNOM) or Scanning Electron Microscopy (SEM). In this contribution various examples of such correlative studies will be presented, all having been acquired using a single correlative microscopy platform.

The characterization of low-dimensional materials such as graphene or transition metal dichalogenides (TMDCs) often requires more than one technique to obtain a thorough understanding of their attributes for specific applications. Graphene and TMDCs both have layered structures and properties that vary significantly with thickness as compared to single layer conformations, making them very interesting for electronics design [1-3]. Their photonic and optoelectronic qualities have been shown to enable ultrafast carrier dynamics and ultra-sensitivity in the UV-VIS, IR and THz frequency ranges [2]. Electronic device performance optimization can benefit greatly from knowledge of their crystalline structure and exciton dynamics. The aim of the following analysis is to show how several spectroscopy (Raman/Photoluminescence) and microscopy techniques (AFM/SNOM/SEM) can, in correlation, provide a more richly detailed depiction of low-dimensional materials than the constituent measurements could offer in isolation.

Fig. 1 shows an example of a correlative AFM-PL-Raman-FLIM measurement of CVD-grown $WS_2$ crystal on a $Si/SiO_2$ substrate. For this group of low-dimensional materials the information obtained through correlation was revelatory as some show photoluminescence (PL) only in single layers, which can be measured with exceptionally high resolution using SNOM-PL.

Furthermore, using RISE microscopy (a combination of Raman imaging and SEM) allows the characterization of these sensitive materials inside the vacuum chamber without exposure to air. In Fig. 2 a RISE study of a CVD-grown $MoS_2$ crystal is shown. The high resolution SEM image reveals the edge defects of the $MoS_2$ crystal, which can be unequivocally correlated to changes in the Raman signal.

**REFERENCES**

1. Geim A. K., Grigorieva I. V. "Van der Waals heterostructures" *Nature* Vol. 499**,** 419-425, 2013.
2. Koppens F. H. L., Nueller T., Avouris P., Ferrari A.C., Vitiello M. S., Polini M. "Photodetectors based on graphene, other two-dimensional materials and hybrid systems" M. Nat. Nano 9**,** 780-793, 2014.

3. You Y., Ni Z., Yu T., Shen Z., "Edge chirality determination of graphene by Raman spectroscopy", Appl. Phys. Letters 93,13112_1-3, 2008.

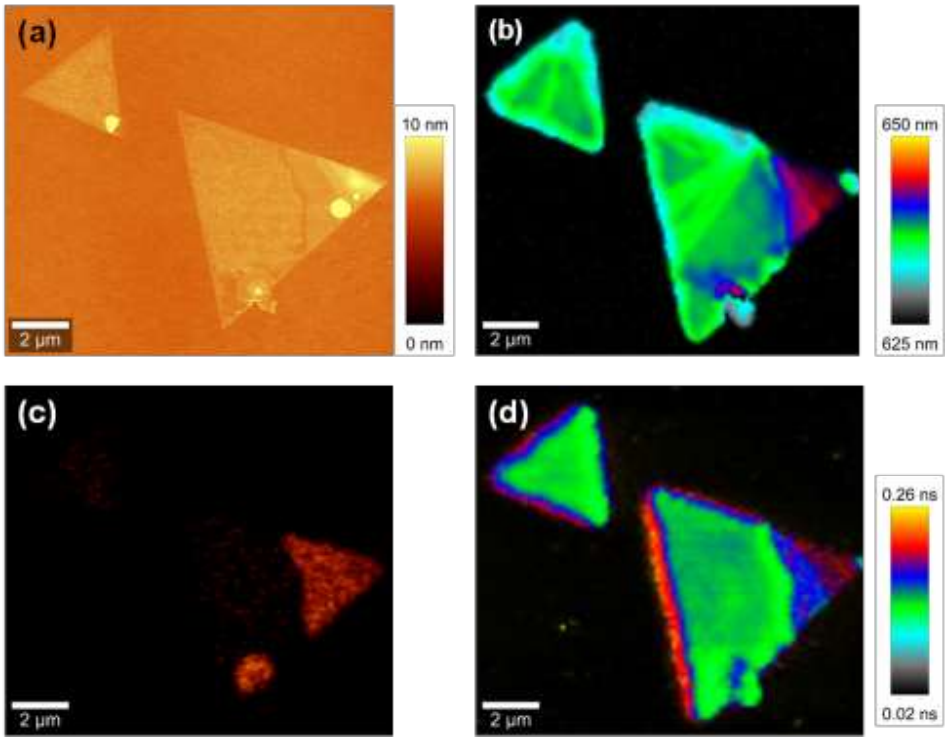



**Figure 1.** (a) AFM topography image of a 2D $WS_2$ crystal CVD grown on a $SiO_2$/Si substrate. (b) Correlated PL image displaying the position of the emission peak, clearly showing the layer-dependent band-gap. (c) Correlated Raman image showing the peak intensity at 27 $cm^{-1}$, revealing the weak phonon interaction between layers. (d) Correlated FLIM image based on the PL in (b), showing different exciton lifetimes at different layers and structural edges.

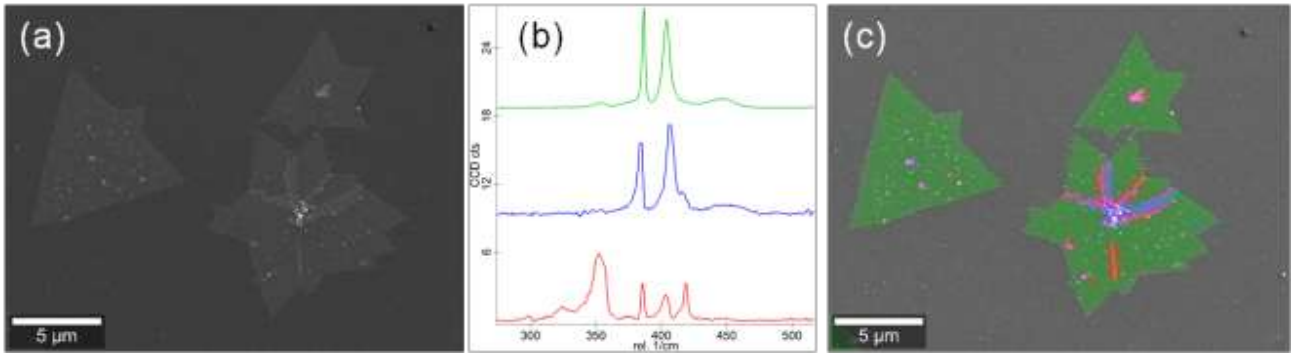



**Figure 2.** (a) SEM image (acquired with a Germini SEM from Zeiss equipped with RISE) of 2D $MoS_2$ crystals CVD grown on a $SiO_2$/Si substrate, (b) color coded Raman spectra evaluated from the 2D spectral array of 100x100 complete Raman spectra, and (c) RISE image of the 2D $MoS_2$ crystals.

# Resonance Raman scattering studies of tungsten diselenide ($WSe_2$)

**Hankyoul Moon, Ja-yeong Kim, and Seokhyun Yoon***
Department of Physics, Ewha Womans University, Seoul 120-750, Korea *
corresponding author: syoon@ewha.ac.kr

Large amount of research has been conducted over two-dimensional materials including transition metal dichalcogenide monolayers (TMDCs) such as $MoS_2$, $WS_2$, $MoSe_2$, $WSe_2$, and $MoTe_2$ since production of the single- and the multi-layered graphene. These materials exhibit interesting 2-dimensional physics and, in principle, can be utilized for electronic and optoelectronic devices. For example, a field-effect transistor (FET) made of $WSe_2$ shows the mobility near 500 $cm^2V^{-1}S^{-1}$ for p-type conductivity and is stable in both acidic and basic conditions, which make TMDCs even more attractive for applications. Also, monolayers of $WSe_2$ are transparent photovoltaic materials and show properties as tunable LED. In this study, we made $WSe_2$ samples by exfoliation method and deposited the $WSe_2$ flakes on Si substrates with a 300 nm $SiO_2$ layer. For measuring basic characteristics such as lattice properties and information regarding the electronic band structures of the samples, we performed Raman scattering spectroscopy by using five different excitation energies of 457.9 nm (2.71 eV), 488 nm (2.54 eV), 514.5 nm (2.41 eV), 532 nm (2.33 eV), and 632.8 nm (1.96 eV) and also measured temperature dependence of $WSe_2$. We report anomalous phonon behavior that depends on the number of layers and the resonant effect reflecting the underlying electronic band structure.

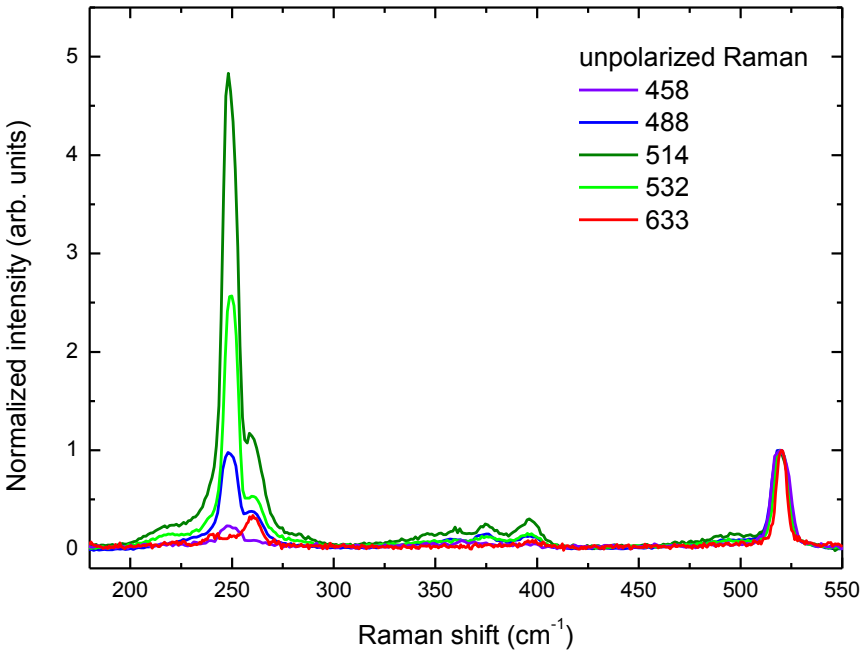



**Figure** Raman spectra of $WSe_2$ monolayer using different excitation energies

**REFERENCES**


1. Wang, Q. H., Kalantar-Zadeh, K., Kis, A., Coleman, J. N., Strano, M. S. "Electronics and optoelectronics of two-dimensional transition metal dichalcogenides". Nature Nanotechnology Vol.**7**, No.11, 699–712.
2. Johnson, D. "Tungsten Diselenide Is New 2-D Optoelectronic Wonder Material", IEEE Spectrum. Retrieved 19 March 2014
3. Zhang, X., Qiao, X.-F., Shi, W., Wu, J.-B., Jiang, D.-S., Tan, P.-H. "Phonon and Raman scattering of two-dimensional transition metal dichalcogenides from monolayer, multilayer to bulk material", Chemical Society Reviews 2015, volume 44, 2757-2785

# Electro-modulation spectroscopy of electronic band structure for $MoS_2$, $MoSe_2$, $WS_2$, and $WSe_2$ crystals and single layers

**R. Kudrawiec[1*], J. Kopaczek[1], M. Welna[1], M. Baranowski[1], M. Polak[1], P. Scharoch[1], K. Wu[2], B. Chen[2], and S. Tongay[2]**

[1]Faculty of Fundamental Problems of Technology, Wroclaw University of Technology, Wybrzeże Wyspiańskiego 27, 50-370 Wrocław, Poland

[2]School for Engineering of Matter, Transport and Energy, Arizona State University, Tempe, Arizona 85287, United States

[*]corresponding author: robert.kudrawiec@pwr.edu.pl

**Abstract**-Electro-modulated reflectance (contactless electroreflectance (CER) and photoreflectance (PR)) has been applied to study direct optical transitions in $MoS_2$, $MoSe_2$, $WS_2$, and $WSe_2$ crystals and single layers. For bulk crystals spectral features related to optical transitions at K and H point of Brillouin zone have been clearly observed in CER and PR spectra. Due to reduction of crystal size to a few layers spectral features related to optical transitions at H point disappear that is very consistent with theoretical predictions.

The electronic band structure of bulk transition metal dichalcogenides (mostly $MoS_2$) have been investigated both in the past and quite recently when researchers studied the evolution of the electronic band structure in these crystals with reduction of their sizes from a bulk regime through a few layers to a monolayer [1, 2]. However some issues for bulk materials are still unclear. One of them is the electronic band structure at H point of Brillouin zone and optical transitions at this point. Recently Saigal and Ghosh [3] studied bulk $MoS_2$ by photoreflectance (PR) and have proposed that excitonic transitions at H point of Brillouin zone are observed ~30 meV above excitonic transitions at K point of Brillouin zone. The authors have concluded about such interpretation of PR spectra on the basis of detailed lineshape analysis of PR resonances without theoretical calculations of the electronic band structure for this crystal. Very similar situation is expected for $MoSe_2$, $WS_2$, and $WSe_2$ crystals but optical transitions at H point of Brillouin zone were not studied yet for these crystals.

In this work the electronic band structure for $MoS_2$, $MoSe_2$, $WS_2$, and $WSe_2$ crystals is calculated from first principles within density functional theory for various points of Brillouin zone including H point. It is clearly shown that the electronic band structure at H point is very symmetric and hence a strong optical transitions at this point of Brillouin zone is expected in absorption-like spectra. This prediction is confirmed by experimental studies of the electronic band structure of $MoS_2$, $MoSe_2$, $WS_2$, and $WSe_2$ crystals by contactless electroreflectance (CER) and PR [4], i.e., modulation spectroscopy which is very sensitive to critical points of Brillouin zone [5]. It is clearly shown that the electronic band structure for bulk crystals at H point of Brillouin zone is very symmetric and similar to the electronic band structure at K point, see Fig. 1, and therefore direct optical transitions at H point are observed in CER and PR spectra besides the direct optical transitions at K point of Brillouin zone, see Fig. 2. With the reduction of crystal size to a few layers spectral features related to optical transitions at H point disappear that is very consistent with theoretical predictions.

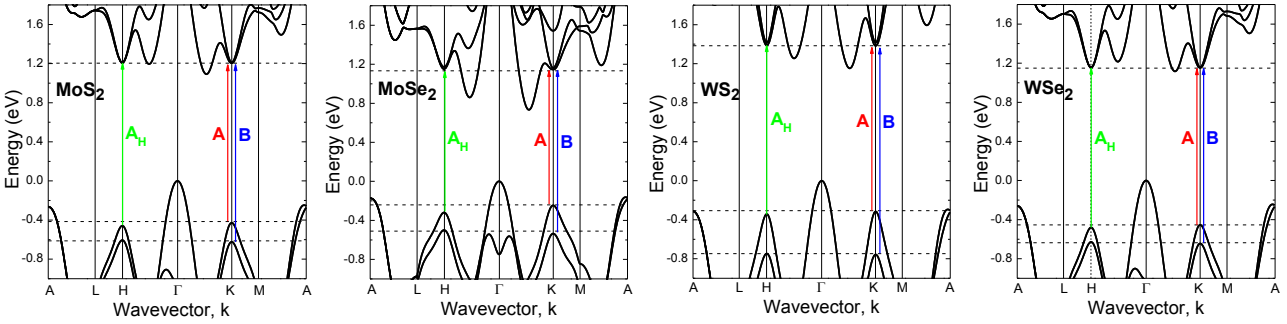



**Figure 1.** Electronic band structure of $MoS_2$, $MoSe_2$, $WS_2$, and $WSe_2$ crystals together with the marked optical transitions observed in PR and CER. The energy separation between A and $A_H$ transition equals ~30-50 meV.

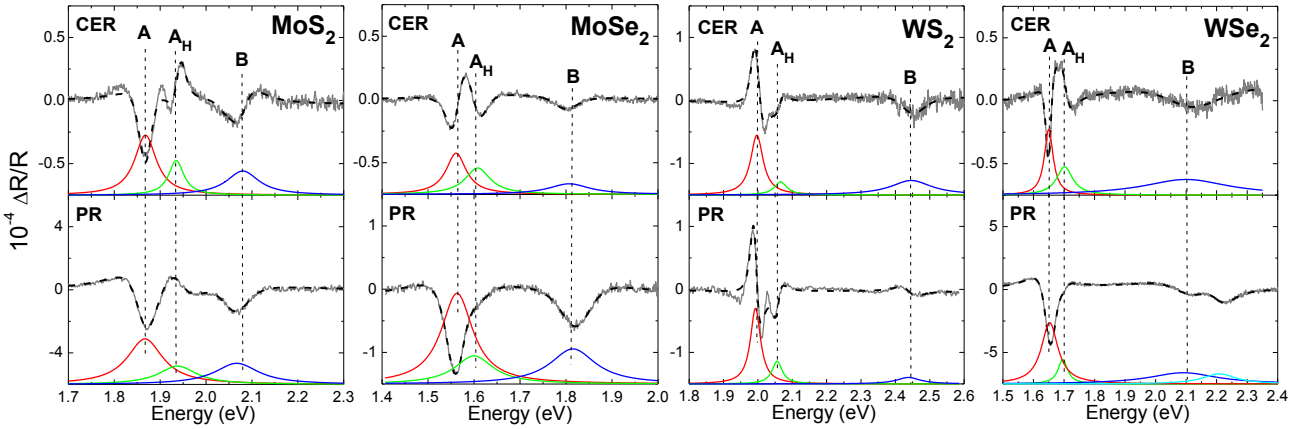



**Figure 1.** Room temperature contactless electroreflectance and photoreflectance spectra of $MoS_2$, $MoSe_2$, $WS_2$, and $WSe_2$ crystals.

**Acknowledgements** This work was performed within the grant of the National Science Centre (grant no. 2012/07/E/ST3/01742). Calculations have been carried out in Wroclaw Centre for Networking and Supercomputing (http://www.wcss.pl).

## REFERENCES

1. Cheiwchanchamnangij T., and Lambrecht, W.R.L., "Quasiparticle band structure calculation of monolayer, bilayer, and bulk $MoS_2$," *Phys. Rev. B* 85, 205302 (2012).
2. Roldán, R., Silva-Guillén, J.A., Pilar López-Sancho, M., Guinea, F., Cappelluti, E., and Ordejón, P., "Electronic properties of single-layer and multilayer transition metal dichalcogenides $MX_2$ (M = Mo, W and X = S, Se)," *Ann. Phys. (Berlin)* 526, 347 (2014).
3. Saigal, N. and Ghosh, S., "H-point exciton transitions in bulk $MoS_2$," *Appl. Phys. Lett.* 106, 182103 (2015).
4. Kopaczek, J., Polak, M., Scharoch, P., Wu, K., Chen, B., Tongay, S., and Kudrawiec, R., "Direct optical transitions at K- and H-point of Brillouin zone in bulk $MoS_2$, $MoSe_2$, $WS_2$, and $WSe_2$," *Phys. Rev. B* submitted 2016.
5. Kudrawiec, R. and Misiewicz, J., "Photoreflectance and contactless electroreflectance measurements of semiconductor structures by using bright and dark configurations", *Rev. Sci. Instrum.* 80, 096103 (2009).

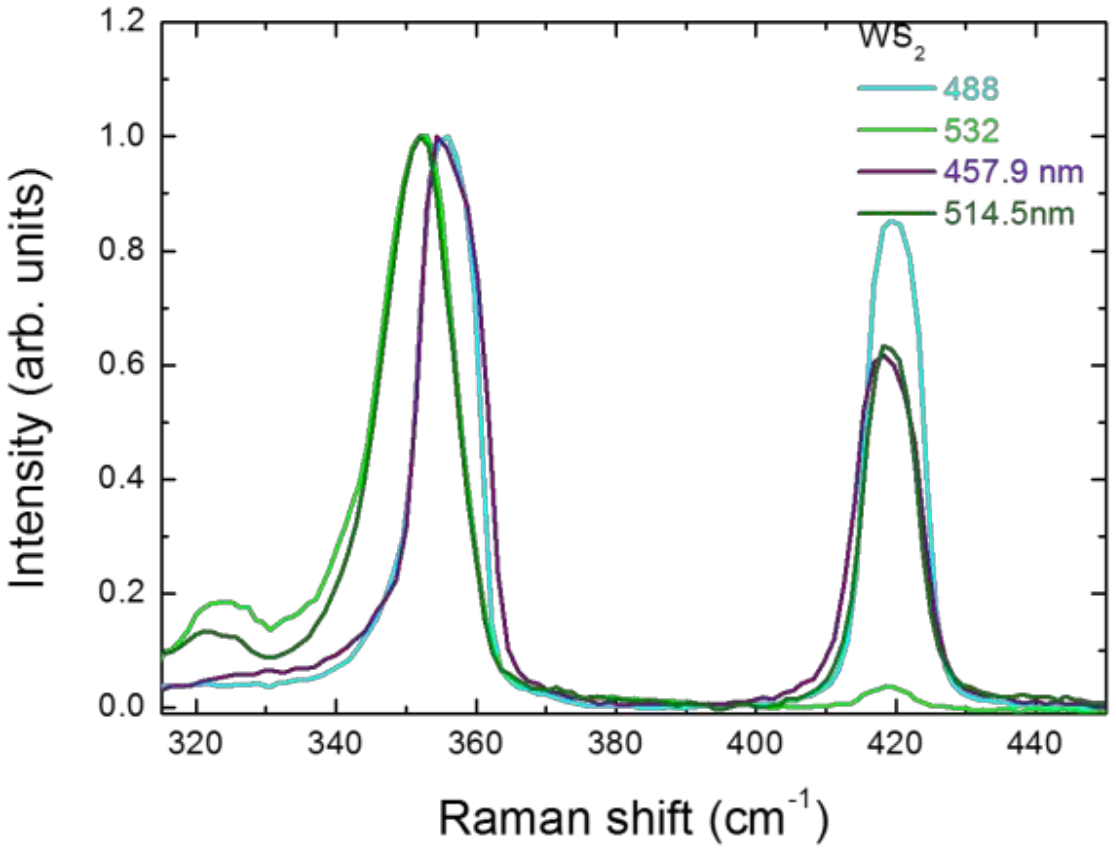
# Raman scattering studies of tungsten disulfide ($WS_2$)

**Ja-yeong Kim, Hankyoul Moon, and Seokhyun Yoon***

Department of Physics, Ewha Womans University, Seoul 120-750, Korea

*corresponding author: syoon@ewha.ac.kr

**Abstract**- The advent of new facile fabrication techniques of producing the single- and the multi-layered graphene, has led to large amount of research over other two-dimensional materials. We report anomalous phonon behavior that depends on the number of layers and the resonant effect reflecting the underlying electronic band structure by Raman scattering spectroscopy.




The emergence of new facile fabrication techniques of producing the single- and the multi-layered graphene has led to large amount of research over other two-dimensional materials such as MoS2, WS2, MoSe2, WSe2, and MoTe2. These materials can be applied to be electronic and photonic devices such as transistors, emitters, and detectors as well as have interesting two-dimensional physics. Especially, WS2 bilayer shows

mobility above 300 cm2V-1S-1 at low temperatures that implies possible low losses through the Joule effect. In this study, we made WS2 samples by exfoliation method. We deposited WS2 flakes on Si substrates with a 300 nm SiO2 layer, and the typical size of WS2 flakes were about few micrometers. We performed Raman scattering spectroscopy using four different excitation energies of 457 nm (2.71 eV), 488 nm (2.54 eV), 514.5 nm (2.41 eV), 532 nm (2.33 eV), and 632.8 nm (1.96 eV) in different temperatures to study basic characteristics such as lattice properties and information regarding the electronic band structures of the samples. We report the low energy breathing and shear modes and anomalous phonon behavior that depends on the number of layers, temperatures, and the resonant effect reflecting the underlying electronic band structure.

**REFERENCES**


1. Thripuranthaka M., and Dattatray J. Late, "Temperature Dependent Phonon Shifts in Single-Layer $WS_2$," *Applied materials & Interfaces(ACS)*, 6, 1158-1163, 2014.
2. Molina-Sanchez.A. and L. Wirtz, "Phonons in single-layer and few-layer $MoS_2$ and $WS_2$," *Physical review* , B 84, 155413, 2011.
3. Ayse Berkdemir, Humberto R. Gutiérrez, Andrés R. Botello-Méndez, Néstor Perea-López, Ana Laura Elías, Chen-Ing Chia, Bei Wang, Vincent H. Crespi, Florentino López-Urías, Jean-Christophe Charlier, Humberto Terrones & Mauricio Terrone., F. M. Lastname and F. M. Lastname, "Identification of individual and few layers of WS2 using Raman Spectroscopy," *Scientific Reports3*, 1755, 2013.

# Linear enhancement of the Kerr nonlinear index in the epsilon-near-zero regime

**L. Caspani[1], R. P. M. Kaipurath[1], M. Clerici[2], M. Ferrera[1], T. Roger[1], A. Di Falco[3], J. Kim[4], N. Kinsey[4], V. Shalaev[4], A. Boltasseva[4], D. Faccio[1,*]**

[1]Institute of Photonics and Quantum Sciences, SUPA, Heriot-Watt University, Edinburgh EH14 4AS, UK

[2]School of Engineering, University of Glasgow, Glasgow G12 8LT, UK

[3]SUPA, School of Physics and Astronomy, University of St. Andrews, St. Andrews KY16 9SS, UK

[4]School of Electrical and Computer Engineering and Birck Nanotechnology Center, Purdue University, 1205 West State Street, West Lafayette, Indiana, 47907-2057 USA

[*]d.faccio@hw.ac.uk

**Abstract–**We study the potential for enhanced nonlinear refractive index ($n_2$) that exploits the low complex permittivity attained in the epsilon-near-zero (ENZ) regime. Our approach does not resort to optical resonances nor to the enhancement of the longitudinal field component. Experiments performed on Al-doped ZnO (AZO) thin films show a six-fold increase of the nonlinear refractive index at the ENZ wavelength (~1300 nm). This enhancement, combined with the low losses in the film, may enable studies of non-perturbative nonlinear effects.

Epsilon-near-zero media, i.e. materials featured by a real part of the dielectric permittivity that is zero or close to zero, have received significant attention in recent years. Thanks to recent progress in material design and fabrication, different devices and linear propagation regimes exploiting the ENZ condition have been proposed [1]. Similarly, the nonlinear properties of ENZ have recently started to be investigated both theoretically (e.g. [2]), and experimentally [3-5]. It has been observed that at the ENZ condition the nonlinear response of a medium is increased at ~45˚ incident angle, as a consequence of the enhancement of the longitudinal electric field component [4]. This enhancement has been proposed as a possible alternative to strategies relying on e.g. the engineering of optical resonances [6], which inevitably exacerbates the detrimental role of linear and nonlinear losses.

Here we demonstrate that significant enhancement in the nonlinear response can be achieved without resorting to the use of optical resonances or angles of incidence which are far from normal. The origin of this enhancement is simply due to the small magnitude of the linear properties of the medium. To illustrate this, we consider the cross-phase modulation phenomenon, where the refractive index change induced by an intense pump on a weak probe can be written as $\delta n = n_2 I_p$, where $I_p$ is the pump intensity and $n_2$ is the nonlinear refractive index defined by:

$$n_{2r} = \frac{3}{2\epsilon_0 c}\frac{n_r\chi_r^{(3)}+n_i\chi_i^{(3)}}{n_r^{pump}[n_r^2+n_i^2]}; \qquad n_{2i} = \frac{3}{2\epsilon_0 c}\frac{n_r\chi_i^{(3)}-n_i\chi_r^{(3)}}{n_r^{pump}[n_r^2+n_i^2]} \ . \tag{1}$$

Here, the subscripts $r$ and $i$ indicate the real and imaginary part, respectively, $\epsilon_0$ is the vacuum permittivity, $c$ is the speed of light in vacuum, $n$ is the linear refractive index at the probe wavelength, and $n_r^{pump}$ is the real part of the refractive index at the pump wavelength. It is clear from Eqs. (1) that the linear properties of the medium (expressed by $n_r$ and $n_i$) have an effect on the nonlinear Kerr index $n_2$. In particular, under the assumption of a non-frequency dependent nonlinearity ($\chi^{(3)}$) and that $\chi^{(3)}{}_r \sim \chi^{(3)}{}_i$, a strong enhancement of the real part of the nonlinear refractive index is expected at the ENZ wavelength. Similarly, the nonlinear absorption coefficient, $\beta_2 \equiv 4\pi n_{2i}/\lambda$,

is found to approach zero at the ENZ wavelength (where $n_r \sim n_i$). In particular, the expected behaviour of $n_2$ and $\beta_2$ according to Eqs. (1) with the measured linear properties of the AZO film is shown in Fig. 1(a). We demonstrate the occurrence of this enhancement experimentally, employing a 900 nm thick film of oxygen-deprived aluminium-doped zinc oxide (AZO) [5].

We characterized the nonlinear response of the AZO film with a pump and probe experimental setting, by measuring the pump-induced change in reflectivity and transmissivity of a weak probe field for different pump intensities. From the reflectivity and transmissivity values we retrieve the permittivity in the pumped case ($\varepsilon_{nl}$) applying an inverse transfer matrix approach. If the dependence of $\varepsilon_{nl}$ from $I_p$ is linear, we determine the third order nonlinearity from the relation $\chi^{(3)} = n_r^{pump} \epsilon_0 c/3 \cdot \partial \varepsilon_{nl}/\partial I_p$ [7]. From the measured values of $\chi^{(3)}$, we retrieved the real part of the nonlinear refractive index, $n_{2r}$, and nonlinear absorption coefficient, $\beta_2$, respectively (Fig.1b-c). A clear six-fold enhancement of $n_{2r}$ is observed and $\beta_2$ is found to approach zero near the ENZ wavelength.

In conclusion, we show that the interplay between the real and imaginary parts of the linear refractive index and $\chi^{(3)}$ leads to an enhancement of the real part of the nonlinear index, which in turn is associated to a nonlinear phase shift in the probe beam. For the laser pulse intensities used in our experiments, this gives a refractive index change that is almost of the same order of the linear refractive index ($\delta n_r = 0.178$, i.e. 30% of the linear refractive index, for $I_p$=500 GW/cm$^2$ at the ENZ wavelength). This large modulation places the ENZ nonlinearity in AZO at the limit of the non-perturbative regime, where the actual approximation of expanding the material's polarization into a power series breaks down.

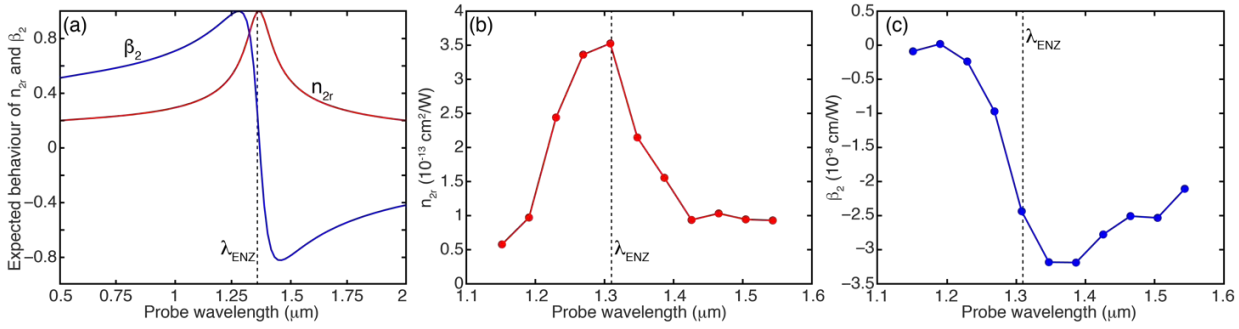



**Figure 1:** (a) Theoretical plots of the normalised values of $n_{2r}$ and $\beta_2$ following Eqs. (1) assuming no $\chi^{(3)}$ dispersion and $\chi^{(3)}_r \sim \chi^{(3)}_i$. (b) and (c) display the corresponding experimental results retrieved from the measured values of $\chi^{(3)}$ at different probe wavelengths.

## REFERENCES


1. R. Ziolkowski, "Propagation in and scattering from a matched metamaterial having a zero index of refraction," *Phys. Rev. E* **70**, 046608 (2004).
2. M. Kauranen et al., "Nonlinear plasmonics," *Nature Photon.* **6**, 737 (2012).
3. H. Suchowski et al., "Phase mismatch–free nonlinear propagation in optical zero-index materials," *Science* **342**, 1223 (2013).
4. A. Capretti et al., "Enhanced third-harmonic generation in Si-compatible epsilon-near-zero indium tin oxide nanolayers," *Opt. Lett.* **40**, 1500 (2015).
5. N. Kinsey et al., "Epsilon-near-zero Al-doped ZnO for ultrafast switching at telecom wavelengths," *Optica* **2**, 616 (2015).
6. N. Lepeshkin et al., "Enhanced nonlinear optical response of one-dimensional metal-dielectric photonic crystals," *Phys. Rev. Lett.* **93**, 123902 (2004).
7. R. Kaipurath et al., "Optically induced metal-to-dielectric transition in Epsilon-Near-Zero metamaterials," arXiv 1601.07088, (2016).

# Numerical simulations of nonlinear optical properties of carbon quantum dots embedded in a polymeric matrix

**Cristian Kusko**[1], **Roxana Tomescu**[1], **and Mihai Kusko**[1]
[1]National Institute for Research and Development in Microtechnologies (IMT-Bucharest)
[*]corresponding author: cristian.kusko@imt.ro

**Abstract**- We calculate using the finite difference time domain (FDTD) method the third order nonlinear response of a nanocomposite consisting in carbon quantum dots (CQD) embedded in a polymeric matrix. We show that due to the intrinsic high Kerr susceptibility presented by CQD, the composit exhibits significant nonlinear optical properties suggesting promising applications of these materials in photonics. We numerically investigate the optical response of the nanocomposite as a function of CQD's shape, size, and concentration.

Recently it was shown theoretically and experimentally that carbon quantum dots (QCD) present significant nonlinear optical properties rendering this class of nanomaterials interesting for possible applications in optoelectronics and photonics. For instance, ab-initio analyses proved that graphene nanoparticles present nonlinear third order susceptibility ( Kerr susceptibility) which is larger within magnitude orders than the susceptibility associated to the metallic nanoparticles [1,2]. Measurements show that carbon nanoparticles present Kerr defocusing nonlinearity with a negative Kerr susceptibility $\chi^{(3)=}10^{-13}$ e.s.u.. Since these results have been obtained using colloidal solutions, it is interesting to investigate the CQD nonlinear properties when they are immersed in a transparent polymer.

This work presents the results of FDTD simulations of the optical field propagation in a nanocomposite consisting in a transparent polymer with the refractive index $n$=1.5 embedding a cubic "closed packed" array of CQD with a diameter of 8 nm.

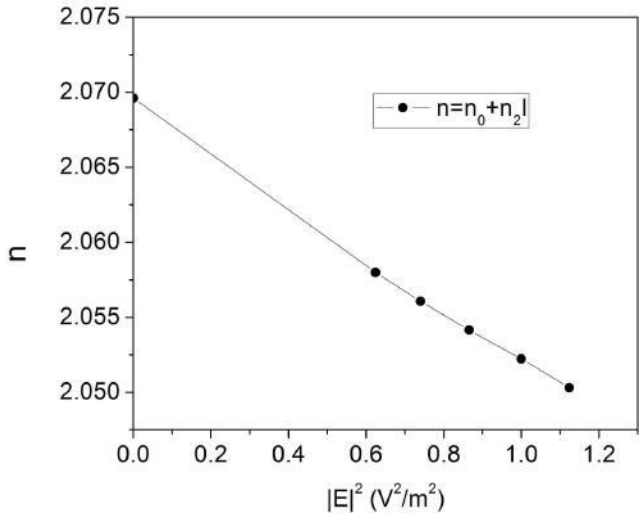



*Fig. 1 Numerical results showing the variation of the nanocomposite refractive with the square of the electrical field*

*represented in $10^{-18}V^2/m^2$ units.*

The material parameters of CQD were taken from the literature [4] such that the CQDs linear refractive index is considered to be n = 2.5 and the Kerr susceptibility is $\chi^{(3)}=-10^{-13}$ e.s.u.

The numerical simulations showed a linear decrease of the refractive index with the field intensity presented in Fig 1 show the presence of a strong nonlinear Kerr susceptibility. This suggests that those QCDs+ transparent polymer nanocomposites may be useful for photonic and optoelectronic applications

**Acknowledgements**, This work was supported by CNCS–UEFISCDI Romania, under the project number PNII-ID-PCCE-0069/2011.

**REFERENCES**

1. Joel D. Cox and F. Javier Garcıa de Abajo **5**, 5725 (2014).
2. Sharma S. R. K. C. Yamijala, Madhuri Mukhopadhyay, and Swapan K. Pati, *J. Phys. Chem. C*, ***119***, 12079, (2015).
3. Athanasios B. Bourlinos et al., Carbon **61**, 640 (2013).
4. Guoyan Zhang, et al., J. Mater. Chem**.**, **22**, 21218 (2012).

# Non-volatile Optoelectronic Phase-Change Meta-Displays

**S. García-Cuevas Carrillo[1*], C. D. Wright[1], P. Hosseini[3] and H. Bhaskaran[2]**
[1] Department of Engineering, University of Exeter, Exeter EX4 4QF, UK
[2] Department of Materials, University of Oxford, Parks Road, Oxford OX1 3PH UK
[3]Bodle Technologies Ltd., Begbroke Science Park, Woodstock Road, Oxford OX5 1PF, UK
[*]corresponding author: sg445@exeter.ac.uk

**Abstract**-Phase-change materials have a pronounced contrast between their electrical and optical properties when in the amorphous to crystalline phases, and can be switched between these phases quickly and repeatedly by electrical or optical means. These characteristics have very recently been exploited to produce a novel form of non-volatile optoelectronic display technology. In this paper we combine such phase-change display devices with metamaterial arrays, so as to gain additional control over their spectral properties.

Chalcogenide phase-change materials, such as the ternary alloy germanium antimony telluride ($Ge_2Sb_2Te_5$, GST) used here, are well known for exhibiting a fast reversible change in their structure (from amorphous to crystalline) over a great number of cycles and resulting in a very considerable change in their optical (refractive index) and electrical (resistivity) properties between phases. This has made phase-change materials very attractive use in non-volatile optical and electrical memory applications [1]. However, in very recent times there has been much interest in the development of new functionalities for these remarkable materials, such as the exploitation of ultra-thin phase-change layers to deliver an entirely new form of non-volatile optoelectronic display [2], along with the combination of phase-change materials with metamaterial structures to provide tuneable/adaptable meta-devices, such as perfect absorbers and reflectarrays [3].

In this paper we combine ideas from metamaterial array design with that for a phase-change based optoelectronic display, with a view to providing more control over the purity of the colour spectrum produced by phase-change pixels. The basic structure for a phase-change display is shown in Fig.1(a), along with an example (reflection) image produced by such an approach (for further details see [2]). The proposed modification to this basic structure is the inclusion of a metamaterial array in the form of split-ring resonators embedded in the bottom ITO layer, as shown in Fig. 1(b) or in the form of metal strips patterned on top of the upper ITO layer (not shown). The effect of introducing the metamaterial arrays can clearly be seen in the reflectance spectra shown in Figs. 1(c) and (d); the inclusion of the metamaterial resonator structures leads to ‘purer’ colour spectra. Such reflectance spectra were here simulated using COMSOL Multiphysics, and photometric and colorimetric calculations and optimisations of various phase-change meta-display configurations, which will also be reported, were carried out using Matlab and Livelink for Matlab [4].

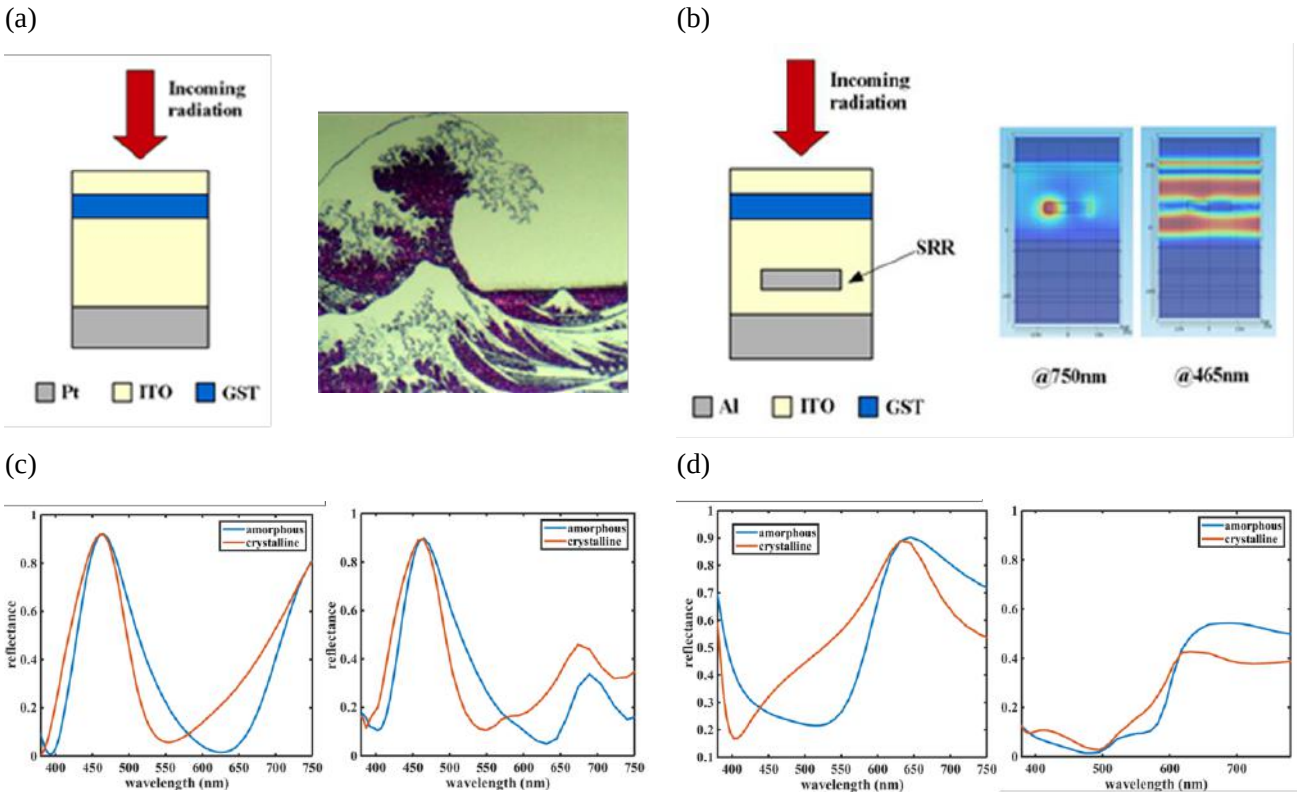



**Figure 1. a)** (left) Phase-change display device structure proposed in [2], formed by a platinum bottom mirror and a GST layer sandwiched between two ITO layers; (right) a high resolution (70x70 μm) image produced in such a structure. **b)** (left) Introduction of an embedded **s**plit ring resonator (SRR) array into the display structure and (right) electric field plot at the excitation wavelengths for maximum (750nm) and minimum (450nm) interaction of the resonance of the cavity with the SRR. **c)** Reflectance spectra with the GST layer in amorphous and crystalline phases for the photonic cavity without (left) and with (right) the SRR**.** A reinforcement in blue wavelengths in the reflectance spectra caused by the interaction of the plasmonic resonator with the standing wave can be observed. **d)** Reflectance spectra of the photonic cavity without (left) and with (right) an alternative metamaterial array structure consisting of patterned metal strips on top of the upper ITO layer; this structure attenuates blue wavelengths and preserve red wavelengths.

**REFERENCES**


1. Raoux, S., F. Xiong, M. Wuttig and E. Pop. "Phase-change materials and phase-change memory," *MRS Bulletin***,** Vol. 39, No. 08, 703–710, 2014.
2. Hosseini, P., C.D. Wright and H. Bhaskaran, "An optoelectronic framework enabled by low-dimensional phase-change films" *Nature*, Vol. 511, No. 7508, 206–211, 2014.
3. Zou, L., M. Cryan and M. Klemm, "Phase-change material based tunable reflectarray for free-space inter/intrachip interconects," *Opt. Express*, Vol. 22, No. 20, 24142–8, 2014.
4. Aldrich, M., "pspectro: Photometric and Colorimetric Calculations." *Matlab File Exchange*, 2010.

# Characterisation and Dynamic Control of Graphene-Liquid Crystal Composite Microfluidic Systems.

**Ben Hogan[1*], Salma Younesy[1,2], Lorcan Brennan[3], Tatiana Perova[4,5] , Yuri Gun'ko[3,5] , Sergey Dyakov[6] Monica Craciun[1] and Anna Baldycheva[1]**

1 University of Exeter, College of Engineering Mathematics and Physical Sciences, Exeter, EX4 4QF, UK

2 École Nationale Supérieure de Mécanique et des Microtechniques, Besançon, France

3 School of Chemistry, Trinity College, The University of Dublin, Dublin 2, Ireland

4 Department of Electronic and Electrical Engineering, Trinity College, The University of Dublin, Ireland

5 ITMO University, 49 Kronverskiy pr., St.-Petersburg, 197101, Russia

6 Skolkovo Institute of Science and Technology, Photonics and Quantum Material Center, Nobel street 3, Moscow, Russia

*Corresponding author: bh341@exeter.ac.uk

**Abstract**- *Fabry-Pérot micro-resonator design of microfluidic structures on silicon-on-insulator chips has been used to enhance the Raman signal from synthesised composites of graphene oxide nanoparticles dispersed in nematic liquid crystal fluid host. Enhancement has been quantified through simulations of the structures and then verified experimentally. Polarised microscopy has been utilised to show the dynamic reconfiguration of the nanocomposites under the influence of an applied electric field.*

Graphene-fluid composite materials with dynamically tuneable characteristics are highly desirable for the emerging field of metamaterials and for the realization of on-chip reconfigurable and tuneable metadevices [1,2]. Such metadevices have great potential in modern renewable energy, optical communications, and security and defence technologies [3].

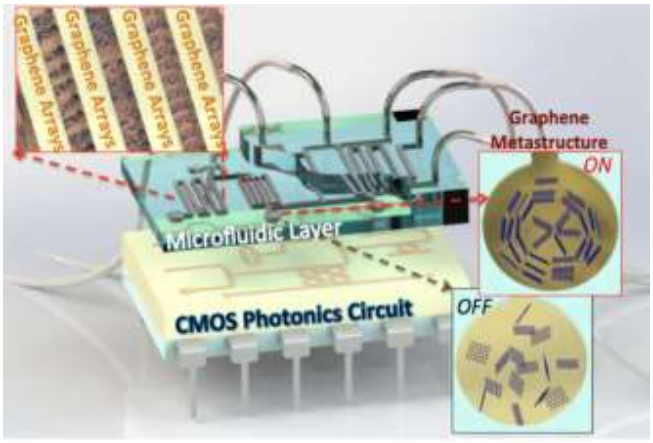



Figure 1. An example of a future device integrating graphene metastructures into a microfluidic layer and coupling to a CMOS photonic circuit to enhance functionality

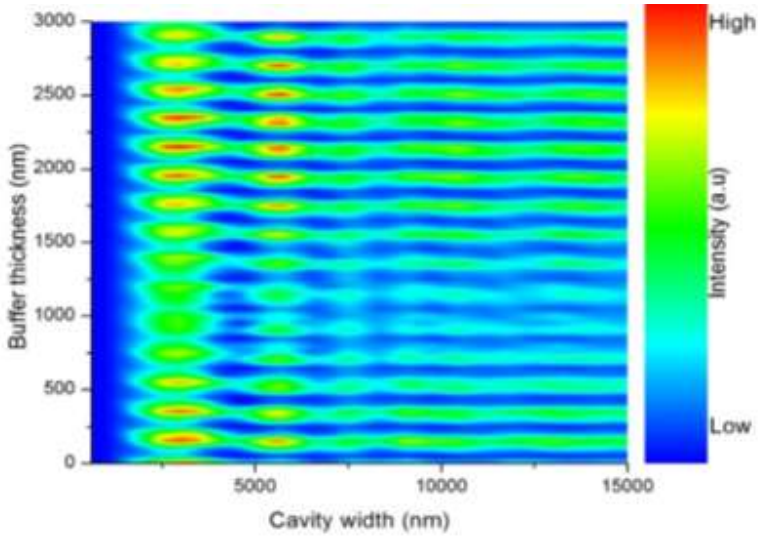



Figure 2. Simulated enhancement of Raman signal intensity at a wavelength of 574nm with the variation of microfluidic cavity width and insulator layer thickness. Specific combinations of parameters can be seen to optimise the enhancement.

In particular, composites of graphene (and related 2D materials) dispersed in a liquid crystal host fluid (GLCs) are of significant interest [4]. The unique electrical, optical and magnetic properties of GLC composite materials arise from the combination of the well-known, outstanding properties of graphene and the liquid crystal's unique combination of fluidic behaviour, large degree of intermolecular order and electro-optical characteristics. The molecular ordering capability inherent in LCs can be utilized for building up unique, dynamic spatial geometries based on nanoparticles incorporated in composites. GLC composite materials can be readily reconfigured by external stimuli and therefore possess a unique capability to controllably interact with light, with the ability to utilise a wide range of possibilities in plasmonics and quantum optics. At the same time, the nano-composite can be integrated on silicon chip- by means of microfluidic techniques- to create a spectrum of compact and low-power multi-functional devices (Fig. 1), for example light sources, tuneable optical filters and nano-antenna phased arrays.

However, *in-situ* characterisation of such fluid nano-composite materials under various applied external stimuli, e.g. electric field, remains challenging. In this work, we have developed theoretically, and experimentally demonstrated a practicable approach for on-chip detection of nanoparticles and the monitoring of their spatial alignment within the host fluid, using *in-situ* polarised micro-Raman spectroscopy and polarised microscopy techniques.

Spontaneous Raman scattering is a quantum mechanical process with a random spatial distribution of the photons involved. We have used a model of oscillating dipoles in which the ensemble of elementary scatterers is considered to be a system of chaotically oriented oscillating electrical dipoles, combined with a scattering matrix method to simulate the effect of microfluidic geometry on the Raman signal intensity (Fig. 2).

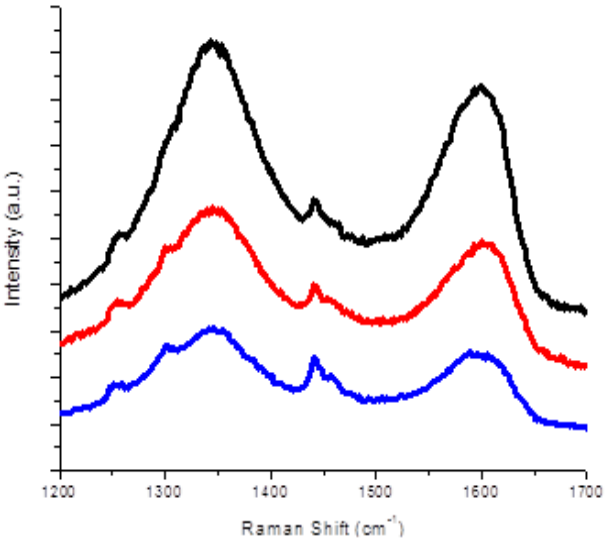



Figure 3. Significant enhancement of the Raman signal intensity for a graphene oxide- liquid crystal composite integrated in microfluidic cavities of different widths: in an infiltration reservoir of width 100μm (blue), in a cavity of width 11.6μm (red) and in a cavity of width 3.6μm (black).

GLC composites were synthesised using solvent induced methods and characterised by exploiting: (1) opto-fluidic technology for integration of nanocomposites on silicon chip and effective trapping of graphene oxide nanoparticles in microfluidic cavities, (2) Fabry-Pérot micro-resonator design of the microfluidic cavities to achieve a significant enhancement of Raman scattering intensity in back scattering geometry, for GLCs (Fig. 3) and (3) polarised microscopy to show dynamic configurability of GLC alignment under external stimuli. The obtained spectral characteristics for GLC nanocomposites validated the developed characterisation methodology and the practicability of dynamically reconfigurable fluidic metamaterials for use in a wide range of CMOS photonic devices.

## References:

[1] C. Zakri *et al*, "Liquid crystals of carbon nanotubes and graphene," *PTRSA*, Vol.371, No. 1988, 20120499, 2013.

[2] N. Behabtu *et al*, "Spontaneous high-concentration dispersions and liquid crystals of graphene," *Nat. Nano.*, Vol. 5, No. 6, 406-411, 2010.

[3] Zheludev, N.I. and Y.S.Kivshar, "From metamaterials to metadevices," *Nat. Mat.*, Vol. 11, No. 11, 917-924, 2012.

[4] A. Madani *et al*, "Tunable metamaterials made of graphene-liquid crystal multilayers," *Prog. Electromag. Res.*, Vol. 143, 545-558, 2013.

# Photoconductivity of Few-Layer $MoTe_2$

**T. J. Octon[1*], K. Nagareddy[1], M. F. Craciun[1] and C. D. Wright[1]**
[1]Department of Engineering, University of Exeter, Exeter, EX4 4QF, UK
[*]corresponding author: tjo201@ex.ac.uk

**Abstract** – A photoconductivity study of few-layer $MoTe_2$ in a field effect transistor (FET) configuration was performed to find the photoresponsivity and photocurrent response of the material. The mechanisms for $MoTe_2$ with no applied gate voltage were found to be dominated by the photovoltaic effect, showing its potential for use in solar cells. Due to the band gap of $MoTe_2$ being 1.1 eV, $MoTe_2$ is a suitable photodetector for optical wavelengths and potentially the near infrared.

Transition metal dichalcogenides (TMDCs) have been the subject of intense research due to their impressive optoelectronic properties, showing lower noise photodetection than silicon photodiodes,[1] and high photoresponsivities.[2-4] $MoTe_2$ has a band gap of ~1 – 1.2 eV from bulk to the monolayer thickness, transitioning to a direct gap at monolayer thickness.[5] In our work, we measure the optoelectronic properties of this overlooked TMDC as a transistor and photodetector. We fabricated the FETs using electron beam lithography and thermal evaporation of a Cr/Au layer. We characterized the layer thickness using three techniques, optical contrast, atomic force microscopy and Raman spectroscopy. Measurements were taken using a DC measurement setup and a 685 nm laser and 50x objective lens. So far our results show signs that $MoTe_2$ is suitable for both fast and responsive photodetection.

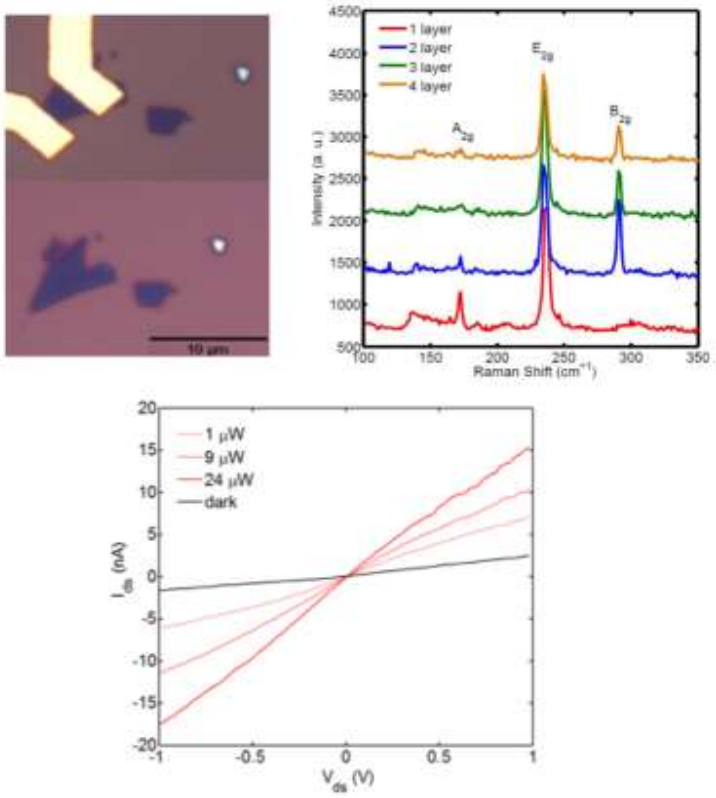



Fig. 1(a) we show an optical image of a 4 layer $MoTe_2$ flake before and after our fabrication. In Fig. 1(b) the Raman spectra of $MoTe_2$ is included up to four layers, the ratio of areas underneath the $E^1_{2g}$ and $B^1_{2g}$ peaks provide information for the layer thickness. Fig. 1(c) An output characteristic of few layer $MoTe_2$ with a 685 nm laser up to powers of 24 μW.

**REFERENCES**


1. Lopez-Sanchez, O., Lembke, D., Kayci, M., Radenovic, A. & Kis, A. Ultrasensitive photodetectors based on monolayer MoS2. *Nat. Nanotechnol.* **8,** 497–501 (2013).
2. Yin, L. *et al.* Ultrahigh sensitive MoTe2 phototransistors driven by carrier tunneling. *Appl. Phys. Lett.* **108,** 043503 (2016).
3. Zhang, W. *et al.* High-gain phototransistors based on a CVD $MoS_2$ monolayer. *Adv. Mater.* **25,** 3456–61 (2013).
4. Furchi, M. M., Polyushkin, D. K., Pospischil, A. & Mueller, T. Mechanisms of Photoconductivity in Atomically Thin MoS 2. *nano Lett.* (2014).
5. Lezama, I., Arora, A., Ubaldini, A., Giannini, E. & Morpurgo, A. F. Indirect-to-Direct Band Gap Crossover in Few-Layer MoTe 2. *Nano Lett.* (2015). doi:10.1021/nl5045007

# Sensitivity of Graphene-Nonlinear Waveguide Sensors

**H. J. El-Khozondar[1*], M. M. Shabat[2], and R. Khalefa[2]**
[1]Electrical Engineering Department, Islamic University of Gaza, Gaza, Palestine
[2]Physics Department, Islamic University of Gaza, Gaza, Palestine
[*]corresponding author: hkhozondar@iugaza.edu.ps

**Abstract**-Sensors are counted by their abilities to measure small changes in the measured quantities. Further, their size and weight are other important factors to consider while designing a sensor. In this work, we proposed a sensor consists of three layers: Dielectric film sandwiched between thin graphene layer topped with air and nonlinear substrate. The dispersion relation for the structure is derived for TE guided modes. The homogenous sensing is calculated using maple 17.

Waveguides sensors are essential elements in different industrial and medical applications. They are usually used to detect and respond to small variation of the desired measures such as temperature, pressure, stress and strains, and blood sugar [1]. We proposed a three layer sensor composed of a thin layer of graphene inserted between air and dielectric material (with thickness d) supported by nonlinear substrate. Nonlinear medium is an artificially constructed material that can exhibit properties not found in nature [2]. Its response to electromagnetic radiation can be characterized by the intensity of light during the propagation of light [3, 4]. In this work, we considered Kerr like nonlinear material. Kerr effect refers to the alteration of the refractive index of a system by the electric field [5]. Graphene is a single layer of carbon atoms packed in a hexagonal lattice (honeycomb), with a carbon-carbon distance of 0.142 nm. It is the first two-dimensional crystalline material and it is a characteristic of a whole class of 2D materials [6]. The concept of sensing in the waveguide structure depends on the interaction of electromagnetic waves and unidentified, undesirable substances coming from the outside waveguide structure.

Mathematical and theoretical works are done using the Maxwell's equation and the boundary conditions to solve for Transverse Electric (TE) modes. The homogenous sensitivity [7] is measured by the rate of change of the modal effective index with respect to cover index (in this case air). Maple 17 is used to get numerical solutions for the sensitivity. Figure 1 displays the proposed sensor structure. The simulation results are shown in figure 2. In the simulations, the conductivity of graphene (σ) is considered to be constant.

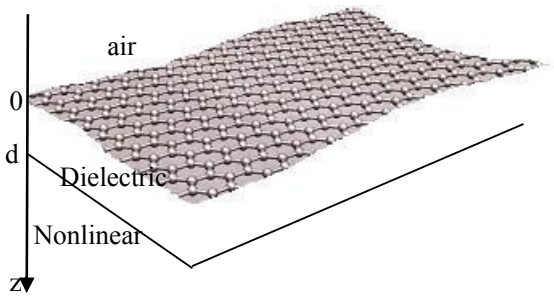



Figure 1. The proposed sensor structure

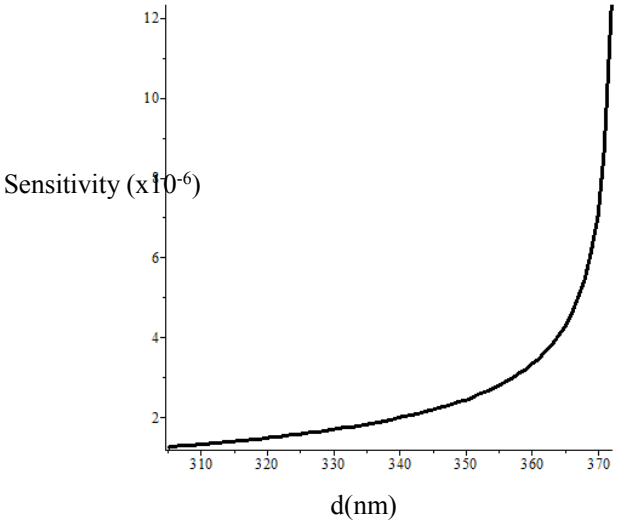



Figure 2. The calculated sensitivity as function of d.

It can be seen from figure 2 that the sensitivity increases as the thickness of the dielectric increases. Moreover, the values of measured sensitivity is in the order of $10^{-6}$. Thus we may recommend this sensor for small measures.

**REFERENCES**


1. Hayat, W. and J. Buck, *Engineering Electromagnetics*, McGraw- Hill, New York, 2012.
2. Krowne, C. M. and Y. Zhang, *Physics of Negative Refraction and Negative Index Materials: Optical and Electronic Aspects and Diversified Approaches*, Springer, Germany, 2007.
3. El-Khozondar, H., R. El-Khozondar and M. Shabat, "Temperature dependence of the optical nonlinear waveguide sensor on thermal stress effects," *Islamic university journal for natural science and Engineering*, Vol. 16, No. 2, 29-40, 2008.
4. El-Khozondar, H. J., "Hydrostatic Stress Effect on the Optical Performance and the Stress Sensitivity of Optical Nonlinear Waveguide", *An - Najah Univ. J. Res.* (*N. Sc.*), Vol. 34, 1-16, 2008.
5. Bludov, Y. V., D. A. Smirnova, Y. S. Kivshar, N. M. R. Peres and M. I. Vasilevskiy, "Extraordinary localization of TE-waves at the graphene layer," *arXiv preprint arXiv*, Vol. 1307, , 8288-8293, 2013.
6. Novoselov, K. S., D. Jiang, F. Schedin, T. J. Booth, V. V. Khotkevich, S. V. Morozov, and A. K. Geim, "Two-dimensional atomic crystals," *Natl. Acad. Sci USA*, Vol. 102, No. 30, 10451-10453, 2005.
7. El-Khozondar, H., R. El-Khozondar and M. Shabat, M. M., Koch, A. W., "Stress Effect on Optical Nonlinear Waveguide Sensor," *J. Opt. Commun.*, Vol. 28, No. 3, 175- 179, 2007.

# Plasmon Characteristics of Chemically-Doped Graphene Revealed by Near-Field Optical Nanoscopy

**Zebo Zheng, Huanjun Chen***

†State Key Laboratory of Optoelectronic Materials and Technologies, Guangdong Province Key Lab of Display Material and Technology, School of Electronics and Information Technology, Sun Yat-sen University, Guangzhou 510275, China

*Corresponding author: chenhj8@mail.sysu.edu.cn

**Abstract** In this study, we cultivated the near-field optical properties of chemically-doped graphene with improved surface plasmon characteristics. By using a scattering-type scanning near-field optical microscope (s-SNOM), we showed that the plasmons of the graphene can be improved by chemical doping. Furthermore, the plasmon-related characteristics, including the plasmon wavelengths and damping rates, can be obtained from the near-field plasmonic fringes observed in the graphene. The experimental findings were further corroborated by theoretical results from density functional theory (DFT).

In recent years, graphene has received enormous attention for its fascinating optical and optoelectronic properties. Many of these properties stem from the collective Dirac electron oscillation that is associated with the atomic thickness and unique electronic band structure of graphene[1-3]. The graphene plasmons has been demonstrated to exhibit unprecedented spatial confinement with broadband response up to mid-infrared region.[7,8] More importantly, plasmonic characteristics of graphene can be tailored by adjusting the charge carrier density via external doping with different strategies. These distinct characteristics have made graphene outstanding platform for light focusing and manipulation in two dimension. However, One obstacle for the real applications of graphene plasmon is the strong loss induced by defects, coupling with substrate phonons, as well as other adsorbates on the graphene surface[4]. A variety of studies have proposed strategies to tune the graphene plasmon and reduce its damping, such as electrostatic gating, substrate engineering, and optical doping[5,6].

Among the various strategies, chemical doping is of high interest as an efficient method for controlling and improving the graphene plasmons. On one hand, the carrier density of the graphene can be modulated in a broad range by the chemical doping, and as a result the graphene plasmon characteristics can be tailored and enhanced. On the other hand, in comparison with other counterparts, the chemical doping method is facile to be implemented. The doping of charge carriers can even be achieved by simply exposed the graphene to dilute molecule vapor. This is especially beneficial for large-area postprocessing and highthroughput occasions. During the past few years, chemical doping was widely utilized for

tuning graphene plasmon wavelengths, tailoring the plasmon response of stacked graphene nanostructures, and enhancing the plasmonic terahertz response of graphene films. However, most of these studies mainly paid attention to the macroscopic plasmon responses of the chemically-doped graphene. A study on the nanoscale behaviors, especially direct visualization of the plasmons of graphene after chemical doping is as of yet unreported, although similar study has been conducted on electric-gated graphene. Such a study can eliminate ensemble and inhomogeneous averaging, which can help for elucidating the intrinsic characteristics of plasmons in chemically-doped graphene.

In our study, we reported the near-field optical study on chemically-doped graphene with improved surface plasmon characteristics. $HNO_3$ vapor was used to dope the CVD-growth graphene. The s-SNOM was then employed to directly image the plasmon propagation in $HNO_3$-doped graphene, with a spatial resolution down to 25 nm. The plasmon fringes near the graphene edge can thereafter be extracted, which allowed for deriving the plasmon wavelengths, plasmon damping rates, and $E_F$. In comparison with the pristine graphene, the chemical doping can reduce the plasmon damping rate and therefore enhance the plasmon strength. In addition, the chemically-doped graphene exhibited a longer plasmon wavelength. The extracted $E_F$ agreed with the DFT results, which indicated that the improved plasmon characteristics were due to the injection of holes into the graphene from the $HNO_3$. Our study has provided a direct picture on the plasmons in graphene after chemical doping, which can help to understand the mechanisms governing the improvement of graphene plasmon characteristics *via* chemical doping procedures.

In summary, we study on the ameliorative plasmonic characteristics of chemically-doped graphene by utilizing infrared nano-imaging technique, which provides direct visualization of the optical near-field distribution on $HNO_3$-doped graphene with nanoscale spatial resolution. By comparing the plasmonic interferometry data near the intrinsic edge of graphene before and after $HNO_3$ treatment, we conclude that the raising of $|E_F|$ resulted from hole doping by $HNO_3$ would modify the scaling of graphene plasmon. More importantly, our results suggest that the reduction of plasmon damping can be obtained by $HNO_3$ doping.

**REFERENCES**


1. Castro Neto, A. H.; Guinea, F.; Peres, N. M. R.; Novoselov, K. S.; Geim, A. K. The electronic properties of graphene. Rev. Mod. Phys. 81, 109, 2009.
2. Mikhailov, S. A.; Ziegler, K. New Electromagnetic Mode in Graphene. Phys. Rev. Lett. 99, 016803, 2007.
3. Bordag, M.; Pirozhenko, I. G. Transverse-electric surface plasmon for graphene in the Dirac equation model. Phys. Rev. Lett. 89, 035421, 2014.
4. Yan, H.; Low, T.; Zhu, W.; Wu, Y.; Freitag, M.; Li, X.; Guinea, F.; Avouris, P.; Xia, F. Damping pathways of mid-infrared plasmons in graphene nanostructures. Nat. Photonics. 7, 394–399, 2013.
5. Woessner, A.; Lundeberg, M. B.; Gao, Y. D.; Principi, A.; Alonso-González, P.; Carrega, M.; Watanabe, K.; Taniguchi, T.; Vignale, G.; Polini, M.Highly confined low-loss plasmons in graphene–boron nitride heterostructures Nat. Mater. 14, 421–425, 2015.
6. Alexander, M. D.; Tao, J.; Yu, X. C.; Nikolay, I. Z.; Wang, Q. J. The reduction of surface plasmon losses in quasi-suspended graphene. Sci. Reports. 5, 09837, 2015.

# Dynamic Metamaterial based on the Graphene Split Ring High-Q Fano-resonnator for Terahertz Sensing Applications

**Weiwei Tang[a,b], Lin Wang[a,b], Xiaoshuang Chen[a,b], and Wei Lu[a,b]**

[a]National Laboratory for Infrared Physics, Shanghai Institute of Technical Physics, Chinese Academy of Sciences, 500 Yu Tian Road, Shanghai, Shanghai 200083, China

[b]Synergetic Innovation Center of Quantum Information & Quantum Physics, University of Science and Technology of China, Hefei, Anhui 230026, China

[*]corresponding author: xschen@mail.sitp.ac.cn

**Abstract**- Structured plasmonic mematerials offer a new way to design functionalized optical and electrical components. Here, we theoretically investigated the electrical active split ring resonators based on graphene metamaterials. Fano resonance and quadrupole resonance are excited at the crossed directions of electric polarization. Such metamaterials could facilitate the designing of active modulation, and slow light effect for terahertz wave. Potential outcomes such as higher sensing ability and higher-Q resonances at terahertz frequencies are demonstrated through numerical simulations with realistic parameters.

Graphene has the thickness of one atom layer and can be considered as a potential two-dimensional plasmonic material due to its high carrier mobility, electrically active and low-loss. The only material property of graphene needed for the active electromagnetic metamaterial is the conductivity spectrum over the terahertz frequency range. The intraband conductivity of graphene at terahertz frequency is modeled with a semiclassical Drude model with a finite temperature correction[1] as

$$\sigma(\omega) = \frac{2e^2}{\pi\hbar^2} k_B T \cdot ln\left[2 \times cosh\left(\frac{E_f}{2k_B T}\right)\right] \cdot \frac{i}{\omega + i\tau^{-1}} \quad (1)$$

where $\omega$ is the radiation frequency, $\hbar$ is the reduced Planck's constant, $k_B$ is the Boltzmann constant and $i$ is the imaginary unit, $T$ is the environmental temperature, $E_f = \hbar v_F \sqrt{\pi n}$ is the Fermi level[32], $n$ is the carrier density and $v_F = 10^6 m/s$ is the Fermi velocity in graphene. $\tau$ is the relaxation time which is derived from loss of the electronic impurities, flaws and the scattering of electron-phonon interaction, it determines the carrier mobility $\mu$ in graphene[2] as $\tau = \mu E_f / e v_F^2$.

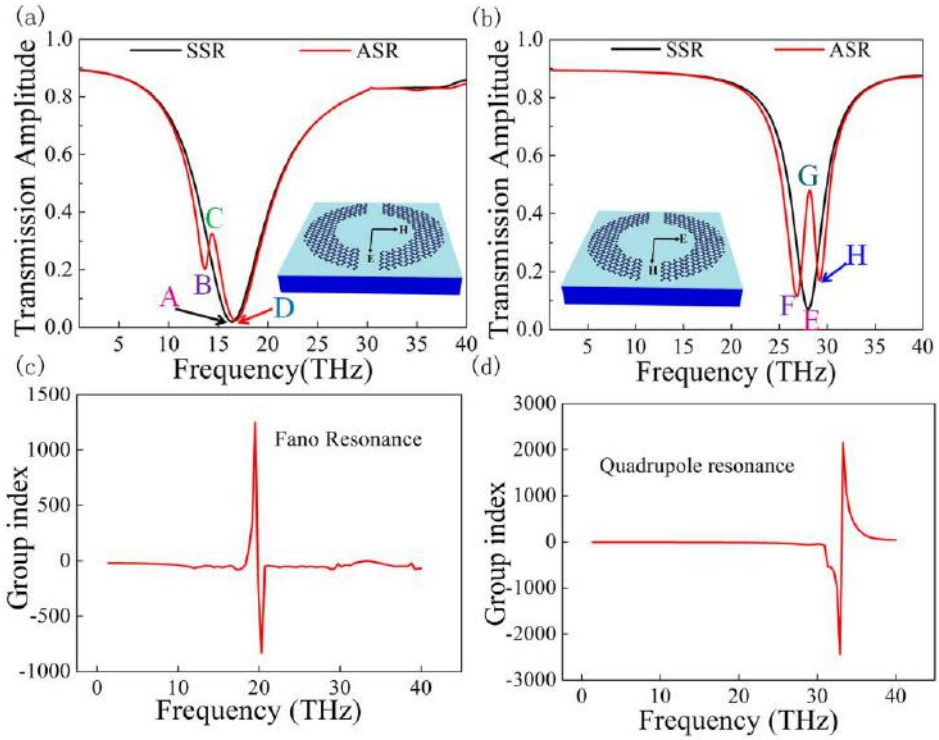



Fig. 1 (a)(b) Simulated transmission amplitude spectra for symmetrical (SSR, black line) and asymmetric split ring array (ASR) (red line) of graphene for E field orientation: (a) perpendicular to the gap; (b) parallel to the gap. The insets show the E and H field orientation. The Fermi level in graphene is 0.5eV. (c) (d) Effective group index $n_g$ versus frequency for (c) Fano resonance, (d) Quadrupole resonance excited by different electric polarizations.

In this work, the high-Q Fano and quadrupole resonances are realized when the structure is symmetry broken and at high Fermi levels or electrostatic doping in graphene. Theoretical analysis based on the coupled Lorentz oscillator model verifies that this phenomenon is due to the suppression of the dark plasmon mode. The sensitivities achieved via using graphene-based metamaterials are higher than metal-based plasmonics. We believe that the impact of our results would be helpful in the design of ultrasensitive sensing, such as real time on-chip chemical and biomolecular detection at the terahertz regime.

**REFERENCES**

1. Falkovsky L A., "Optical properties of graphene," *Journal of Physics: Conference Series,* Vol. 129, No. 1, 1–7, 2008.
2. Christensen, J., Manjavacas, A., Thongrattanasiri, S., Koppens, F. H., & García de Abajo, F. J., "Graphene plasmon waveguiding and hybridization in individual and paired nanoribbons," *ACS nano,*, Vol.6, No. 1, 431-440, 2011.

# Tungsten disulfide nanotubes decorated with gold nanoparticles as electrochemical electrodes with improved response

**F. Ligmajer[1,2*], L. Kejík[1,2], A. Daňhel[3], M. Kolíbal[1,2], M. Fojta[3,4] and T. Šikola[1,2]**

[1]Central European Institute of Technology, Brno University of Technology, Technická 10, 616 00 Brno, Czech Republic

[2]Institute of Physical Engineering, Brno University of Technology, Technická 2, 616 69 Brno, Czech Republic

[3]Institute of Biophysics, Academy of Sciences of the Czech Republic, v.v.i., Královopolská 135, 612 65 Brno, Czech Republic

[4]Central European Institute of Technology, Masaryk University, Kamenice 5, CZ-62500, Brno, Czech Republic

[*]corresponding author: filip.ligmajer@ceitec.vutbr.cz

**Abstract-** Combination of plasmonic and electrochemical pathways in both analytical and technological applications could provide many advantages arising from the interplay between electrons and photons. Here, we demonstrate how properties of transparent electrochemical electrodes improve with increasing coverage of tungsten disulfide nanotubes and how decoration of these nanotubes with plasmonic nanoparticles influences the main parameters of resulting electrodes. Our results are relevant to plasmon-enhanced electrochemistry of transition-metal dichalcogenides and also to other systems where light interacts with chemical currents.

Electrochemistry is a traditional branch of physical chemistry where charged carriers serve as a probe for study and control of chemical reactions on surfaces of electrodes.[1] The major benefit of electrochemistry is the fact that it does not require complicated and expensive instrumentation, while it still provides accurate and detailed information about presence of large amount of chemicals in a solution and/or about ongoing chemical reactions. Besides, it is capable to do so *in situ* requiring only very short measurement times.[2] Recently, in a way similar to other established fields, electrochemistry has also benefited from the advance of nanotechnology. Examples include utilization of metallic nanoparticles for electrochemical detection of single base mismatches of DNA or of carbon nanotubes as signal/current amplifying elements.[3] As electrochemical methods inherently involve movement of charges, it is natural to presume that electrochemical studies could gain some advantage from plasmonic materials and approaches. One example which demonstrates that this symbiosis could be fruitful has recently appeared: Electrochemical methods exploiting unique properties of nanostructured electrodes from $TiO_2$, which is not plasmonic in a traditional sense of the word, but as a well-known photocatalytic material merges two fundamental components of plasmonics – electrons and photons.[4]

Here we present a study devoted to inherent electrochemistry of tungsten disulfide ($WS_2$) nanotubes, and how it is influenced by presence of nearby plasmonic nanoparticles (Fig. 1a). We chose $WS_2$ as a representative of class of transition metal dichalcogenides[5], that have been proposed as potentially useful materials for electrochemical sensing[6,7] and photocatalysis[8]. We show how the properties of transparent conductive electrodes made of indium tin oxide (ITO) are modified by presence of different amounts of $WS_2$ nanotubes (Fig. 1b,c). We also demonstrate using standard redox probes, how the presence of gold nanoparticles modifies main characteristics of ITO+$WS_2$ electrodes, such as achievable current magnitudes and reversibility of redox reactions. Our results are relevant to

applications of transition metal dichalcogenides in plasmon-enhanced electrochemistry and to other similar systems which combine chemically- and plasmonically-active substances.

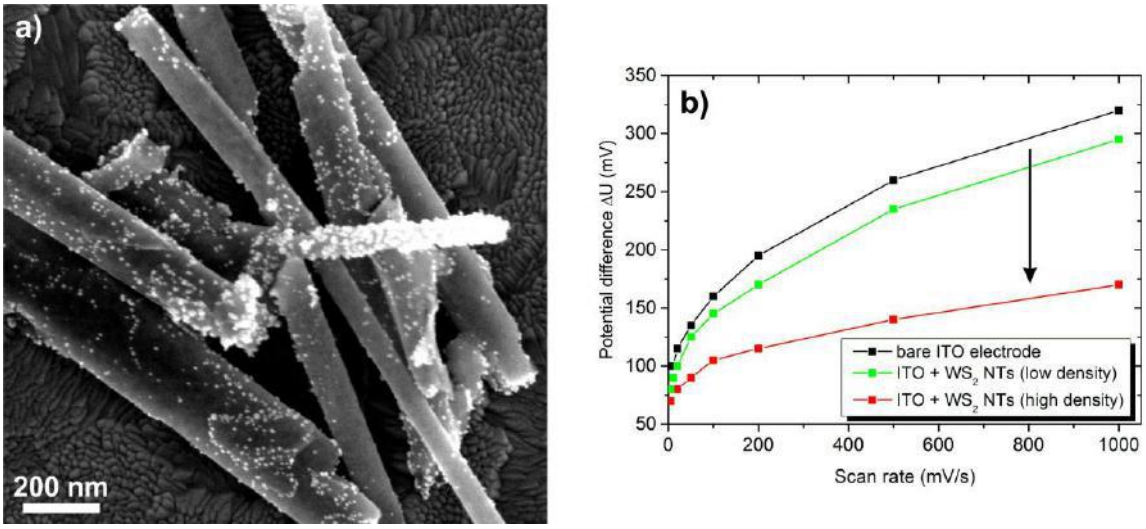



Figure 1. a) SEM image of WS2 nanotubes decorated with gold nanoparticles on an ITO substrate. b) Potential difference ($\Delta U=E_{p,a}-E_{p,c}$), related to reversibility degree of redox reactions, between oxidation and reduction peaks of 0.5mM potassium ferricyanide in 0.1M KCl. The presence of bare $WS_2$ nanotubes (without nanoparticles) increases reversibility of the reaction.

This research has been financially supported by the Grant Agency of the Czech Republic (grant No. 15-21581S), European Regional Development Fund (project No. CZ.1.05/1.1.00/02.0068), MEYS CR (project No. LQ1601 – CEITEC 2020), Technology Agency of the Czech Republic (grant No. TE01020233) and by the Czech Science Foundation (P206/12/G151).

**REFERENCES**

1. Wang, J., *Analytical Electrochemistry*. *Third Ed.*, John Wiley & Sons, 2006.
2. Batchelor-Mcauley, C., Dickinson, E. J. F., Rees, N. V., Toghill, K. E. and Compton, R. G., "New electrochemical methods," *Anal. Chem.*, 84, 669–684 (2012).
3. Mehrgardi, M. A. and Ahangar, L. E., "Silver nanoparticles as redox reporters for the amplified electrochemical detection of the single base mismatches," *Biosens. Bioelectron.* 26, 4308–4313 (2011).
4. Takahiro, K., Naya, S. and Tada, H., "Highly Active Supported Plasmonic Photocatalyst Consisting of Gold Nanoparticle-Loaded Mesoporous Titanium(IV) Oxide Overlayer and Conducting Substrate," *J. Phys. Chem. C* 118, 26887–26893 (2014).
5. Chhowalla, M. *et al.*, "The chemistry of two-dimensional layered transition metal dichalcogenide nanosheets," *Nat. Chem.* 5, 263–275 (2013).
6. Pumera, M. and Loo, A. H., "Layered transition-metal dichalcogenides (MoS2 and WS2) for sensing and biosensing." *TrAC Trends Anal. Chem.* 61, 49–53 (2014).
7. Sarkar, D. *et al.*, "Functionalization of Transition Metal Dichalcogenides with Metallic Nanoparticles: Implications for Doping and Gas-Sensing," *Nano Lett.* 15, 2852–2862 (2015).
8. Zhang, J., Liu, S., Liang, H., Dong, R. and Feng, X., "Hierarchical Transition-Metal Dichalcogenide Nanosheets for Enhanced Electrocatalytic Hydrogen Evolution." *Adv. Mater.* 27, 7426–7431 (2015).

# Improvement of Metal-Based THz Patch Antenna Parameters Using Monolayer Graphene

**M. T. Gatte[1 2 *], P. J. Soh[1], M. F. Jamlos[1], R. B. Ahmad[1], M. F. Malek[1,3], H. A. Rahim[1]**

[1] Advanced Communication Engineering (ACE) CoE, School of Computer and Communication Engineering, Universiti Malaysia Perlis, Malaysia

[2]Ministry of Science and Technology, Bagdad, Iraq

[3]Faculty of Engineering and Information Sciences, University of Wollongong in Dubai, Block 15, Dubai Knowledge Village, PO Box 20183, Dubai, United Arab Emirates

*corresponding author, E-mail: mohtaih@gmail.com

## Abstract

Terahertz antennas are highly suited to fulfill the demands of next generation wireless communication, detection, sensing, spectroscopy and imaging devices. The design and implementation of antennas in this frequency band, however, is challenging. To design an efficient THz antenna, a suitable solution is by using nanomaterials. In this paper, monolayer graphene is used to coat the metallic surface of a THz patch antennas. It showed a 10% improvement for, gain, radiated power and radiation efficiency, besides featuring lower loss.

## 1. Introduction

The band of frequencies that lies between infrared and millimeter wave in the electromagnetic (EM) spectrum represents Terahertz (THz) bands, typically between 0.1 to 10 THz [1]. Its antenna is one of the main devices in THz system. The design of an efficient THz antenna requires detailed characterization from the fields of material science and physics [2]. Recently the development of THz transceivers utilized graphene, which can be used in building of nanoantennas with efficient THz radiation [1].

Graphene generally can also be used in the coating of metals. The utilization of chemical vapor deposition graphene films demonstrates its ability to avoid air oxidation of the metallic surfaces. Besides that, its growth on Cu and Cu/Ni alloy has been reported for the first time in [3]. Monolayer graphene could be considered as the thinnest and most conductive surface [4]. This leads it to be a good alternative material for noble metals such as gold and platinum which are commonly used as conducting materials in the milimeterwave (mmwave) and THz frequency bands[5]. According to their 2D surface properties, graphene supports resonation in the THz band for graphene-based microstrip patch antenna [6]. Besides this, better radiation characteristics than conventional metal based antennas is also indicated [7]. Microstrip patch antenna is suitable for application in the THz frequency band due to its low profile, light weight, ease of fabrication, low cost, and compactness. In this work the effect of monolayer graphene coating on pure copper is investigated on a THz patch antenna. It demonstrated that such coating on the patch and feed line improved most antenna parameters: gain, radiated power and radiated efficiency. This improvement is doubled when both conducting layers (patch and ground) coated with graphene. The rest of paper is organized as follows. The next section explains the properties of graphene in the mmwave and THz spectrum. The design and parametric study of the patch antenna is then presented in Section 3, while the resulting improvement is discussed in Section 4 prior to the concluding remarks.

## 2. Graphene Surface Properties

To first understand the properties of the graphene coating, a single-atom thick graphene is first modelled, prior to its implementation on the metallic sections of the antenna. This two dimensional material can be modelled as an infinite sheet with a surface conductivity using the Kubo formula [8] [9]:

$$\sigma(\omega,\mu_c,\Gamma,T)=\frac{jq_e^2(\omega-j2T)}{\pi\hbar^2}\left[\frac{1}{(\omega-j2\Gamma)^2}\int_0^\infty \epsilon\left(\frac{\partial f_d(\epsilon)}{\partial\epsilon}-\frac{\partial f_d(-\epsilon)}{\partial\epsilon}\right)\partial\epsilon - \int_0^\infty \frac{f_d(-\epsilon)-f_d(\epsilon)}{(\omega-j2\Gamma)^2-4(\frac{\epsilon}{\hbar})^2}\partial\epsilon\right] \quad (1)$$

The two terms on the right represent the frequency dependent, inter and intra conductivity of graphene. Other variables do not significantly affect conductivity except for the chemical potential ($\mu_c$).

$$\sigma(\omega)=\sigma_{intra}(\omega)+\sigma_{inter}(\omega) \quad (2)$$

The first term represents an intraband contribution while the second is an interband contribution. Intraband effect dominates the value of total conductivity below 5 THz. It is given as:

$$\sigma_{intra}(\omega,\mu_c,\Gamma,T)=\frac{q_e^2K_BT}{\pi\hbar^2(\omega-j2\Gamma)}\left[\frac{\mu_c}{K_BT}+2\ln\left(e^{-\mu_c/K_BT}+1\right)\right] \quad (3)$$

where $j$ is the imaginary unit, $q_e$ the electron charge, $\hbar$ the reduced Plank constant, $K_B$ the Boltzmann's constant, $T$ the transport relaxation time, $T$ the temperature, $\mu_c$ the chemical potential, and $\omega$ the operating angular frequency. The scattering rate $\Gamma = 1/2\tau$ represents loss mechanism while $\tau$ is the relaxation time. Meanwhile, the second term in (1) has no significant effect on total conductivity value as shown in Figure 1.

$$\sigma_{inter}(\omega, \mu_c, \tau, T) = \frac{q_e^2}{4\pi\hbar}\left[\frac{2|\mu_c| - (\omega + j\tau^{-1})}{2|\mu_c| + (\omega + j\tau^{-1})}\right] \qquad (4)$$

The calculation of equations (3) and (4) represent the surface conductivity of graphene. The total value of surface conductivity is dominated by the value of first term (intraband term) in the frequency range below 5 THz, whereas the second (interband) term doesn't have a significant effect on the total surface conductivity in this band, as shown in Figure 1.

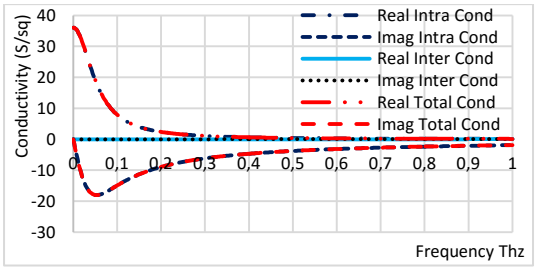



Figure 1: Conductivity of Graphene

Figure 2 shows the real and imaginary parts of the surface impedance in the mmwave to THz spectrum. It is modelled based on computed surface impedance from the Kubo formula and surface conductivity. These frequency-dependent values will then be inserted into a commercial electromagnetic solver, CST Microwave Studio to be evaluated in the form of a microstrip antenna design.

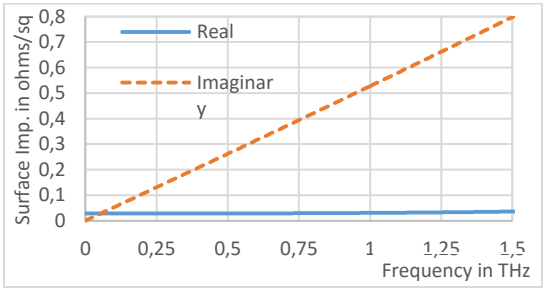



Figure 2 Surface Impedance of Graphene

### 3. Modeling of the Microstrip Antenna

The excellent surface properties and conductivity in the THz band makes graphene suitable as coating material to improve the performance of microstrip antennas. It is a dielectric substrate sandwiched between two conducting layers: typically the ground plane deposited on one side of substrate while the patch and feed line deposited on the other side of substrate. The dielectric permittivity and thickness of substrate must comply with the conventional limitations, generally the dielectric permittivity ($\epsilon_r$) of the substrate layer is ($2.2 \leq \epsilon_r \leq 12$), while its thickness (h) needs to be $h << \lambda_0$ and $0.003\lambda_0 \leq h \leq 0.05\lambda 0$). These limitation have to be take in consideration in the design of such antenna to prevent the surface wave generation in such classical metallic antennas [10]. The performance of the antenna depends on the geometric design of the conducting patch and feedline, which is then integrated with the mechanism of matching impedance. The dimensioning of the patch antenna is made based on the resonant frequency, impedance matching, substrate thickness and dielectric permittivity (in this case, $\epsilon_r$=3.6 for Plexiglass). The most preferred patch shapes are rectangular and square, due to their simple and ease of simulation, analysis and fabrication. Other patch shapes includes triangles, circles, etc. In this work, a rectangular patch is chosen to be modeled and its physical parameters are explained in Table 1. Figure 3 illustrates the inset-fed rectangular patch antenna. The proper design of the feed line and its inset gap is necessary for proper antenna impedance matching.

**Table 1**: Parameters of the proposed patch antenna.

| **Parameters** | **Symbol** | **Value** |
|---|---|---|
| Resonant Frequency | *fr* | 1.0 THz |
| Width of Patch | W | 100 μm |
| Length of Patch | L | W×3/4 |
| Substrate length and width | Ls × Ws | 2*L×2*W |
| Substrate thickness | h | W/20 |
| Substrate dielectric constant | $\epsilon_r$ | 3.6 |
| Microstrip Fed Line Length | Lf | (L/2+Lg) |
| Microstrip Fed Line Width | Wf | W/5 |
| Microstrip Fed Line Inset Gap Width | Wg | Wf/4 |
| Microstrip Fed Line Inset Gap Length | Lg | L/10 |

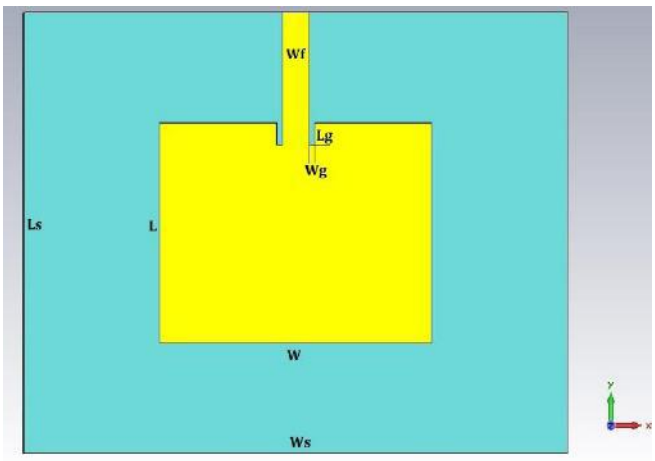



Figure 3 Two-dimensional diagram of the proposed rectangular patch antenna.

### 4. Results and Discussion

The contribution of the graphene coating is evaluated systematically by evaluating its performance using the three coating configurations:

a) Configuration 1 (C1): A copper-based microstrip patch antenna (noncoated)
b) Configuration 2 (C2): A copper-patch and feedline coated with monolayer graphene

c) Configuration 3 (C3): Both copper (patch and ground) layers are coated using monolayer graphene

The simulation result of the three configurations are then summarized in Table 2. The graphene coating for C2 mainly improved the antenna in terms of gain and radiation efficiency. This is despite the experienced small shift in resonance frequency. No change in directivity is seen. Simulations for coating configuration C3 showed about twice the improvements in gain and radiation efficiency compared to C2, see Table 2. These improvements are due to the improved radiated power and reduced metal losses, as will be studied in the next section. The coating of the all antenna conducting layers using graphene improved the C3 antenna parameters by approximately 10 % relative to C1. Figures 4, illustrates the far field antenna radiation pattern for the C3.

**Table 2**: Performance comparison of the patch antennas for the three above configurations C1, C2 and C3

| Patch material | C1 | C2 | C3 |
|---|---|---|---|
| *fr* in THz | 1.0 | 0.998 | 0.996 |
| $\eta_{rad}$ at *fr* (%) | 83 | 88.4 | 92.5 |
| Dir at *fr* in dB | 7.12 | 7.12 | 7.12 |
| Gain at *fr* in dB | 6.32 | 6.58 | 6.78 |

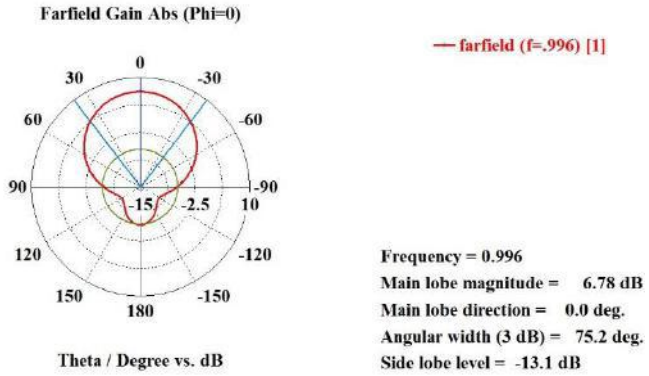



Figure 4 Far field radiation pattern for the graphene-coated patch and ground (C3)

A comparison of all simulated coating configurations is shown in Figure 5. It indicates that the coating of both conducting layers using monolayer graphene (C3) reduces the metal loss by more than half compared to that of the uncoated antenna (C1).

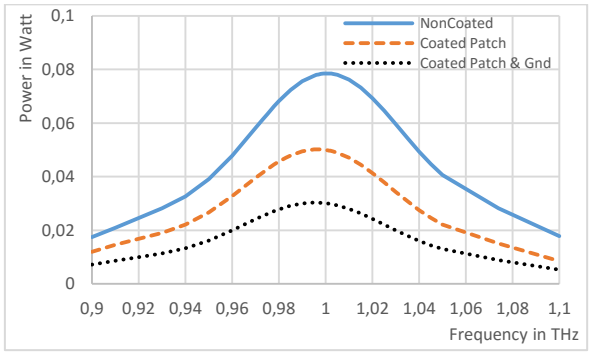



Figure 5 The power loss comparison for uncoated (C1), patch-coated (C2) and patch and ground-coated (C3) antennas

Besides the conducting elements, simulations were also performed to study the dielectric loss of the antenna when implemented on a common Plexiglas substrate. Results indicated that the dielectric loss behaves differently for different coating configurations, as shown in Figure 6. The coated antenna has a higher dielectric loss than the uncoated version. However, this dielectric loss is one order less than metal loss, making the latter the dominant factor in improving an antenna in this particular band.

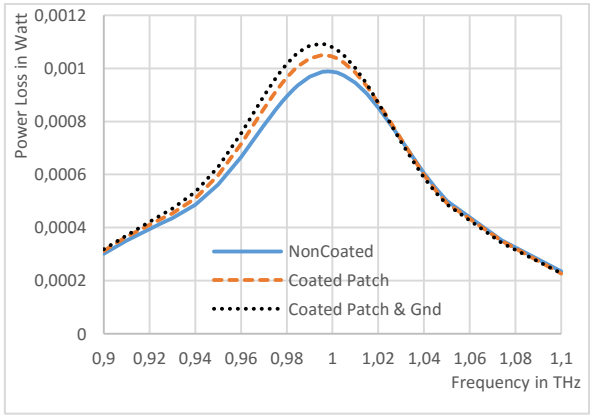



Figure 6 The dielectric loss comparison for uncoated (C1), patch-coated (C2) and patch and ground-coated (C3) antennas

The improvement in radiated power when the C1 antenna's conducting layers is coated using monolayer graphene is depicted in Figure 7.

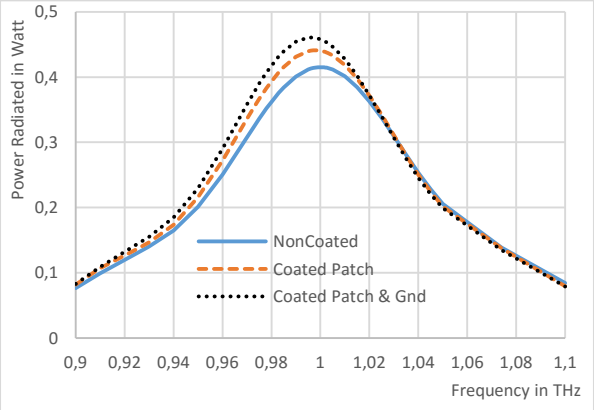



Figure 7 The radiated power comparison for uncoated (C1), patch-coated (C2) and patch and ground-coated (C3) antennas

Figure 8 compares the reflection coefficient (S11) and the 10dB-bandwidth of the uncoated antenna (C1), patch-coated (C2) and patch and ground-coated antenna (C3). It can be concluded that both parameters have shown some degradation due to the coating.

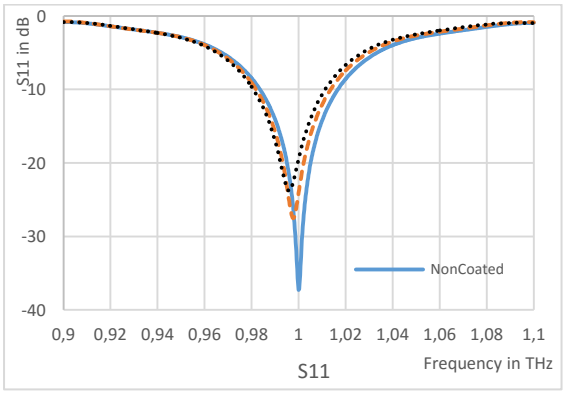



Figure 8 The reflection coefficient (S11) comparison for uncoated (C1), patch-coated (C2) and patch and ground-coated (C3) antennas

Nonetheless, the post-coating antenna reflection coeficient is still acceptable in the target frequency band, whereas bandwidth reduction after coating is small and insignificant. However, this antenna bandwidth is already much higher than those of antennas working in the microwave and millimeterwave frequencies.

## 5. Conclusions

This paper inspects the ability of the monolayer graphene to improve THz microstrip antenna parameters when it is used as coated material for the conductive parts of these antennas. Besides featuring anti oxidation and chemical degradation behavior, coating of the conducting layers using graphene improves the antenna performance by reducing metal loss to less than half of the noncoated antenna. In addition, about 10% increase in gain, radiation efficiency and radiated power is also observed. On the contrary, coating slightly degrades the antenna reflection coefficient and bandwidth. The simulation results also showed that graphene can potentially be used as coating material in the THz band due to its favorable properties.

## References


[1] I. F. Akyildiz, J. M. Jornet, and C. Han, "Terahertz band: Next frontier for wireless communications," *Physical Communication*, vol. 12, pp. 16-32, 2014.

[2] Y. Huang, N. Khiabani, Y. Shen, and D. Li, "Terahertz photoconductive antenna efficiency," pp. 152-156.

[3] S. Chen, L. Brown, M. Levendorf, W. Cai, S.-Y. Ju, J. Edgeworth, *et al.*, "Oxidation resistance of graphene-coated Cu and Cu/Ni alloy," *ACS nano*, vol. 5, pp. 1321-1327, 2011.

[4] P.-Y. Chen and A. Alù, "Atomic-scale mantle cloak using a graphene monolayer," presented at the The Fifth International Congress on Advanced Electromagnetic Materials in Microwaves and Optics, 2011.

[5] T. Niu, W. Withayachumnankul, B. S. Y. Ung, H. Menekse, M. Bhaskaran, S. Sriram, *et al.*, "Reflectarray antennas for terahertz communications," *arXiv preprint arXiv:1210.0653*, 2012.

[6] I. Llatser, C. Kremers, A. Cabellos-Aparicio, J. M. Jornet, E. Alarcón, and D. N. Chigrin, "Graphene-based nano-patch antenna for terahertz radiation," *Photonics and Nanostructures-Fundamentals and Applications*, vol. 10, pp. 353-358, 2012.

[7] S. Anand, D. S. Kumar, R. J. Wu, and M. Chavali, "Graphene nanoribbon based terahertz antenna on polyimide substrate," *Optik-International Journal for Light and Electron Optics*, vol. 125, pp. 5546-5549, 2014.

[8] V. P. Gusynin, S. G. Sharapov, and J. P. Carbotte, "Magneto-optical conductivity in graphene," *Journal of Physics: Condensed Matter*, vol. 19, p. 026222, 2006.

[9] G. W. Hanson, "Dyadic Green's functions for an anisotropic, non-local model of biased graphene," *Antennas and Propagation, IEEE Transactions on*, vol. 56, pp. 747-757, 2008.

[10] C. A. Balanis, *Antenna theory: analysis and design* vol. 1: John Wiley & Sons, 2005.

# Graphene three-port circulator

**Victor Dmitriev[1], Wagner Castro[1,2], Clerisson Nascimento[1]**

[1] Department of Electrical Engineering, Federal University of Para, Para, Brazil
[2] Federal Rural University of Amazonia, Para, Brazil
*corresponding author, E-mail: wagnerormanes@yahoo.com.br

## Abstract

A new type of THz graphene-based three port Y-circulator is suggested and analyzed. The cross-section of the component presents a three-layer structure that consists of a layer of graphene, of silica and of silicon. The in-plane figure contains a circular graphene resonator and three graphene waveguides symmetrically connected to it. The structure is magnetized normally to the substrate by a DC magnetic field. The input waveguide excites resonances of surface plasmon polaritons in the central element. The resonance of the resonator has a dipole standing wave configuration such that it can be oriented according to the direction and value of the external magnetic field with a node in the isolated port. The central frequency of the device can be controlled by Fermi energy of the graphene resonator. The circulator magnetized by a DC magnetic field 1.1 T has isolation of -15 dB and insertion loss less than -2 dB in the frequency band of 7% with the central frequency 8.23 THz.

## 1. Introduction

Circulators are important passive nonreciprocal components which are used both in microwave and optical frequency regions. These devices permit mitigate the harmful influence of reflections in circuits on the sources of electromagnetic waves. In microwaves, the most popular circulators are based on waveguide and microstrip technology with magnetized ferrite elements [1, 2]. Optical circulators have been also discussed in literature [3, 4, 5, 6].

Graphene is the first 2D material obtained experimentally. The fact that the charge carriers are confined in an atomic layer leads to a unique electronic structure. The graphene is a very promising material for electronic and photonic devices [7, 8, 9]. Due to anisotropic characteristic of its conductivity tensor under magnetization [10, 11], this material exhibits gyrotropic properties. This allowes one to project nonreciprocal devices based on graphene in THz region.

Recently, an interesting idea of an edge-guided graphene circulator was discussed in [12]. However, the device presents a multi-layer graphene-dielectric structure and this can complicate its production technology. In our work, we suggest and numerically analyze a new type of THz Y-circulator. It has a very simple structure that consists of graphene nanostrip waveguides connected to a graphene circular resonator placed on a dielectric substrate.

## 2. Problem description

The geometric configuration of the circulator is shown in Fig. 1. The structure consists of three graphene waveguides connected to a graphene circular resonant cavity placed on a dielectric substrate. The graphene is magnetized by a DC magnetic field $\mathbf{B}_0$ along the z-axis. The operation frequency of the circulator depends mostly on the radius of the resonator $R$. As an example, we present below the numerical simulations for a circulator with the resonator which has the radius $R$ =320 nm. The graphene waveguides have the width $w = 140$ nm and length $L = 600$ nm. The circulator is placed on a dielectric substrate composed by a layer of silicon with the thickness $h_1 = 200$ nm and silica with the thickness $h_2 = 600$ nm. The relative permittivities of them are $\varepsilon_1 = 11.9$ and $\varepsilon_2 = 2.09$, respectively. This two-layer dielectric structure permits diminish the insertion losses of the circulator.

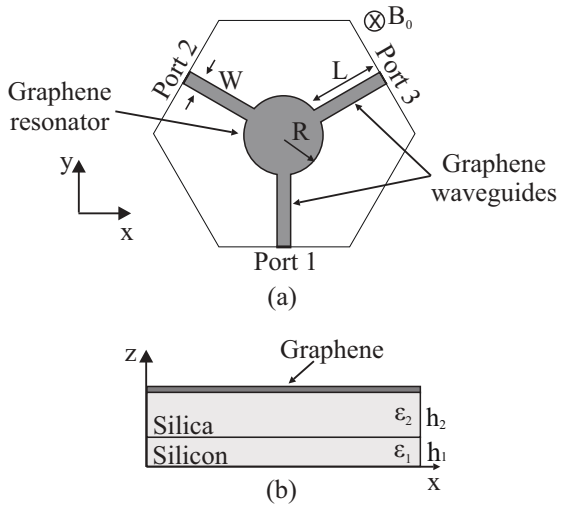



Figure 1: (Color online) Schematic representation of graphene circulator: a) top view, b) side view, $\mathbf{B}_0$ is bias DC magnetic field.

Numerical simulations were performed by using commercial software COMSOL [13]. We calculated the transmission coefficient $|S_{ij}| = |E_j|/|E_i|$, where $E_i$ and $E_j$ represents $E_z$ electric field component of the signal injected in port $j$ and received by port $i$. The bandwidth of the circulator is defined as $BW = (f_2 - f_1)/f_0 \times 100$, where $f_2$ and $f_1$ are the extreme frequencies which define the trans-

mission level better than -2 dB and the isolation level below -15 dB, $f_0$ is the central frequency of the circulator.

In the presence of the bias field $\mathbf{B}_0$, the charge carrier of graphene are deflected by Lorentz force and move in cyclotron orbits. As a result the tensor of optical conductivity acquires anti-symmetrical characteristics [14]. This 2D tensor can be written as

$$[\sigma_s] = \begin{bmatrix} \sigma_{xx} & -\sigma_{xy} \\ \sigma_{xy} & \sigma_{xx} \end{bmatrix}. \quad (1)$$

In the frequency region where interband transitions can be neglected, one can use the classical Drude form of the tensor [15]:

$$\sigma_{xx} = \frac{2D}{\pi} \frac{1/\tau - i\omega}{\omega_c^2 - (\omega + i/\tau)^2}, \quad (2)$$

$$\sigma_{xy} = -\frac{2D}{\pi} \frac{\omega_c}{\omega_c^2 - (\omega + i/\tau)^2}, \quad (3)$$

where $D = 2\sigma_0\epsilon_F/\hbar$ is the Drude weight, $\sigma_0$ is the miminum conductivity of graphene, $\epsilon_F$ is related with Fermi energy of graphene, $\omega_c = eB_0v_F^2/\epsilon_F$ is the cyclotron frequency, $\hbar$ is the reduced Planck's constant, $e$ is the electron charge, $\tau$ is the relaxation time, $\omega$ is the frequency of the incident wave, $v_F$ is the Fermi velocity, $B_0$ is the magnetic field and $i = \sqrt{-1}$. Frequency dependence of the real and imaginary parts of the tensor components are shown in 2a and 2b.

In numerical calculus, graphene is modeled as a bulk material with the conductivity tensor defined by $[\sigma_v] = [\sigma_s]/\Delta$ where $[\sigma_s]$ is the surface conductiviry tensor [16]. Its components are given by (2) and (3), and $\Delta = 1$ nm is the thickness of the graphene. This artificial parameter is used only for calculation purposes.

## 3. Numerical Result

It is well known that graphene strips can support two kinds of guided surface plasmon polaritons (SPP) modes, namelly guide modes and edge modes which are discussed in details in [17, 18]. In our case, we have chosen the former one, once the electromagnetic field in this mode is distributed along the width of the ribbon as shown in the insert of Fig 3. The dependence of effective refractive index for different values of frequency with respect to the width of the graphene ribbon is shown in Fig. 3 .

The working principle of the circulator is similar to that of the microstrip one [1]. The direction of circulation (input port $\rightarrow$ output port) is defined by the direction of the DC magnetic field $\mathbf{B}_0$: the clockwise direction (1$\rightarrow$3, 2$\rightarrow$1, 3$\rightarrow$2) and the counter-clockwise direction (1$\rightarrow$2, 2$\rightarrow$3, 3$\rightarrow$1).

In order to analyse the dependence of the frequencies of the two rotating dipole modes with respect to magnetic field $B_0$ (see Fig. 4), we calculated the structure with one waveguide coupled to the resonant cavity (insert in Fig. 4).

The guided SPP wave in the input waveguide excites in the circular resonator two degenerate clockwise with

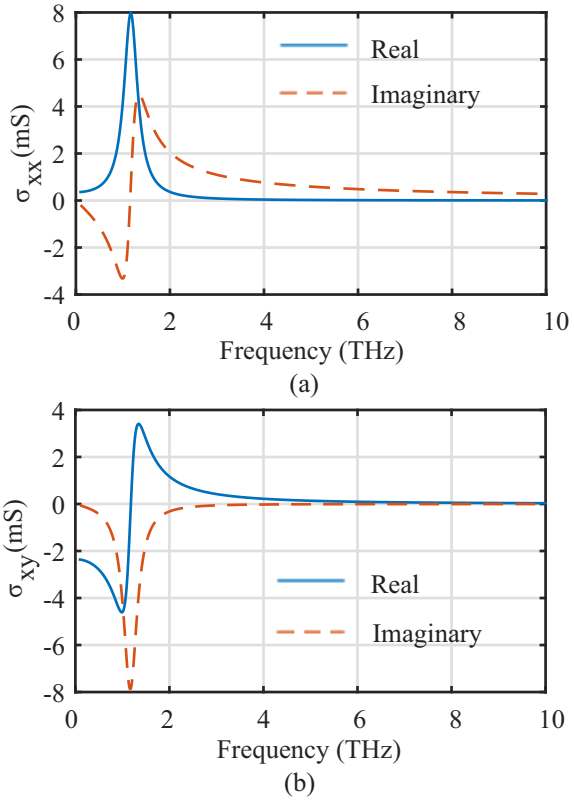



Figure 2: (Color online) Real and imaginary parts of components $\sigma_{xx}$ and $\sigma_{xy}$ of electric conductivity tensor of graphene, $\epsilon_F = 0.15$ eV, $\tau = 0.9$ ps, $B_0 = 1.1$ T.

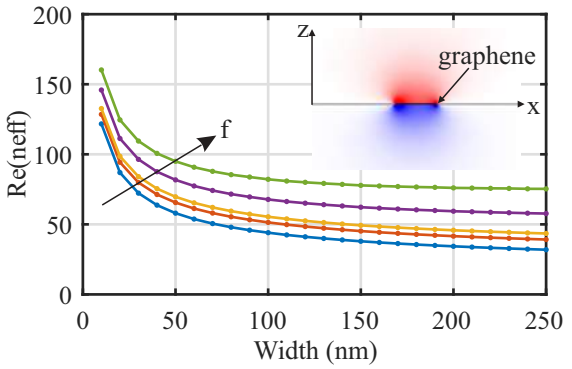



Figure 3: (Color online) Width dependence of effective mode index for (upwards) 5 THz, 8 THz, 10 THz, 15 THz, 20 THz. Insert is the $|E_z|$ profile of guided mode in graphene strip.

the frequency $\omega^+$ and counter-clockwise with $\omega^-$ rotating modes. These two modes produce a dipole aligned to the input waveguide, which leads to a transmission in both output ports (see Fig. 5a). The DC magnetic bias of $B_0 = 1.1$T brakes the degeneracy and makes the field pattern of the standing wave to rotate by 60° placing the node in port 3. Thus, if the signal is injected into the port 1 it will be transmitted to port 3 and port 2 is isolated. If the signal is injected in port 2, it is transmitted to port 1. Analogously in

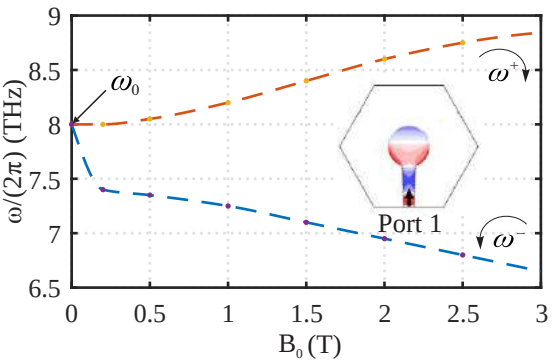



Figure 4: (Color online) Magnetic field dependence of rotating mode resonances. Insert: resonator feeding scheme for calculus of resonances.

the case of incidence in port 3: the signal is transmitted to port 2, as shown in Fig 4b, 4c, 4d, respectively.

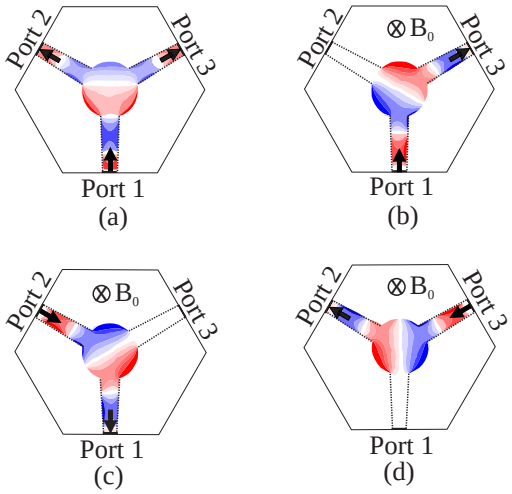



Figure 5: (Color online) $|E_z|$ field distribution in circulator, a) nonmagnetized case, and magnetized cases b) (1→3), c) (2→1) and d) (3→2).

Fig. 6 presents a spatial distribution of the magnetic field $|\mathbf{H}|$ with respect to $z$-axis. One can see the exponential decay behaviour of the field which is a characteristic of the plasmonic waves.

The calculated frequency characteristics of the circulator are shown in Fig. 7. At the central frequency of 8.23 THz, the device has the transmission coefficient of -1.2 dB, the isolation of -33 dB, DC magnetic field is $B_0 = 1.1$T. The bandwidth is 7% for the transmission level -2 dB and the isolation -15 dB.

### 3.1. Control by Fermi energy of graphene

Varying Fermi energy of graphene, one changes the carrier density on the graphene. This leads to different values of the components of the conductivity tensor and gives a possibility of dynamical control of responses of the circulator.

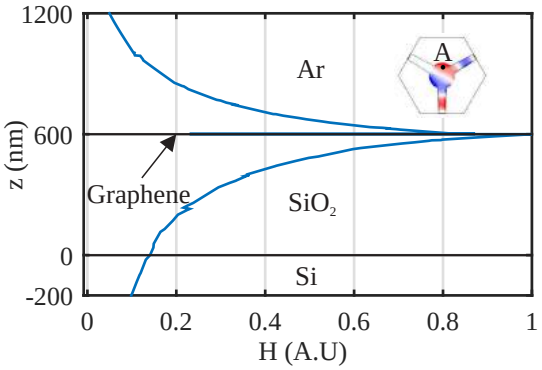



Figure 6: (Color online) z-dependence of magnetic field $|\mathbf{H}|$ in circulator calculated in point A.

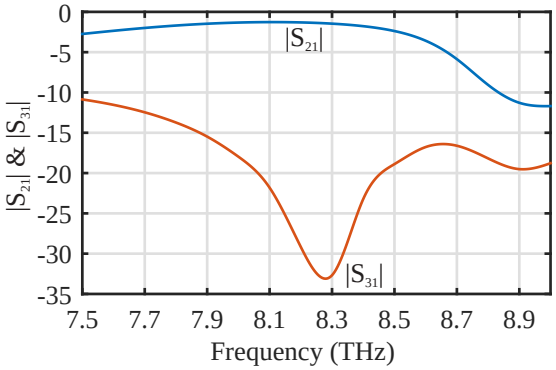



Figure 7: (Color online) Frequency responses of circulator.

An increase of $\epsilon_F$ shifts the central frequency of operation to higher frequencies (see Fig. 8). For the values of $\epsilon_F$ between 0.12 eV and 0.19 eV, the central frequency varies from 7.3 THz to 9.3 THz. However changing $\epsilon_F$ from its optimum value $\epsilon_F = 0.15$ eV deteriorates the insertion and isolation losses and narrows down the bandwidth of the device.

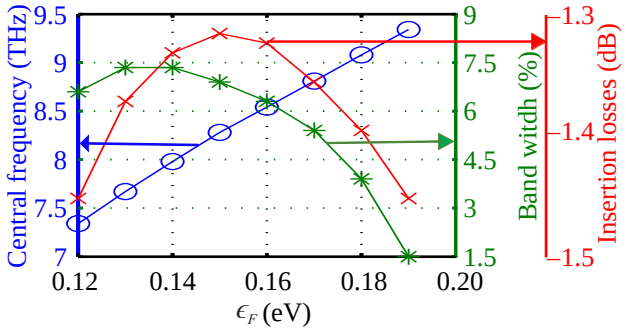



Figure 8: (Color online) Chemical potential dependence of central frequency (circle marks), bandwidth (asterisk marks) and of insertion losses (x marks).

## 4. Conclusions

In this work we have suggested and confirmed by numerical simulations a possibility of realization of a controllable three-port graphene-based Y-circulator operating in the THz region. This component has a very simple structure composed only by a graphene elements over a dielectric substrate. The frequency characteristics of the circulator excited from different ports are the same due to its three-fold rotational symmetry. The device simulations demonstrated that at the central frequency of 8.23 THz, the bandwidth is 7 % with respect to the level of isolation -15 dB and insertion loss better than -2 dB with bias DC magnetic field $B_0 = 1.1$T.

## Acknowledgement

This work was supported by Brazilian agency CNPq.

## References

[1] Helszaln, J., "The stripline circulators: Theory and Practice", *Wiley-IEEE Press*, New Jersey, 2008.

[2] Saib, A., Darques, M., Piraux, L., Vanhoenacker-Janvier, D., and Huynen, I., "An unbiased integrated microstrip circulator based on magnetic nanowired substrate", *IEEE Transactions on Microwave Theory and Techniques*, Vol. 53, No. 6, 2043 – 2049, 2005.

[3] Dmitriev, V., Kawakatsu, M. N. and de Souza, F. J. M., "Compact three-port optical two-dimensional photonic crystal-based circulator of W-format", *Optics Letters*, Vol. 37, No. 15, 3192 – 3194, 2012.

[4] Wang, Q., Ouyang, Z., Lin, M. and Liu, Q., "Compact photonic crystal circulator with flat-top transmission band created by cascading magneto-optical resonance cavities", *Applied Optics*, Vol. 54, No. 33, 9741 – 9746, 2015.

[5] Dmitriev, V., Portela, G. and Martins, L., "Three-port circulators with low symmetry based on photonic crystals and magneto-optical resonators", *Photonic Network Communications*, Vol. 31, No. 1, 56 – 64, 2015.

[6] Wang, Q., Ouyang, Z., Zheng, Y., Lin, M. and Zheng, G., "Broadband six-port circulator based on magneto-optical-rod ring in photonic crystal", *Applied Physics B*, Vol. 121, No. 3, 385 – 389, 2015.

[7] Dmitriev, V., Nascimento, C. M., "Planar THz electromagnetic graphene pass-band filter with low polarization and angle of incidence dependencies", *Applied Optics*, Vol. 54, No. 6, 1515 – 1520, 2015.

[8] Dmitriev, V., Nascimento, C. M., "Planar graphene multifunctional component ", *Microwave and Optical Technology Letters*, Vol. 57, No. 7, 1755 – 1760, 2015.

[9] Sheng, S., Li, K., Kong, F. and Zhuang, H., "Analysis of a tunable band-pass plasmonic filter based on graphene nanodisk resonator", *Optics Communications*, Vol. 336, No 1, 189 – 196, 2015.

[10] Fallahi, A., Carrier, J., P., "Manipulation of giant Faraday rotation in graphene metasurfaces", *Applied Physics Letters*, Vol. 101, No 23, 52 – 56, 2012.

[11] Hanson, G. W., "Dyadic Green's functions and guided surface waves fora surface conductivyti model of graphene", *Journal of Applied Physics*, Vol. 103, No 6, 64 – 73, 2008.

[12] Lin, X., Xu, Y., Zhang, B., Hao, R., Chen, H. and Li, E., "Unidirectional surface plasmons in nonreciprocal graphene", *New Journal of Physics*, Vol. 15, No. 11, 113 – 128, 2013.

[13] www.comsol.com

[14] Chamanara, N., Caloz, C., "Fundaments of graphene magnetoplasmons principles, structures and devices", *Forum electromagnetic research methods and application technologies (FERMAT)*, Vol. 10, No. 2, 01 – 15, 2011.

[15] Crassee, I., Levallois, J., Walter, A. L., Ostler, M., Bostwick, A., Rotenberg, E., Seyller, T., Van Der Marel, D. and Kuzmenko, A. B., "Giant Faraday rotation in single-and multilayer graphene", *Nature Physics.*, Vol. 7, No. 1, 48 – 51, 2011.

[16] Vakil, A., Engheta, N., "Transformation optics using graphene", *Science*, Vol. 332, No. 6035, 1291 – 1294, 2011.

[17] Nikitin, A. Yu., Guinea, F., Vidal, G. F. J. and Moreno, M. L., "Edge and waveguide terahertz surface plasmon modes in graphene microribbons", *Physical Review B*, Vol. 84, No. 16, 161 – 165, 2011.

[18] He, S., Zhang, X. and He, Y., "Graphene nano-ribbon waveguides of record-small mode are and ultra-high effective refractive indices for future VLSI", *Optics Express*, Vol. 21, No. 25, 30664 – 30673, 2013.

# Graphene-Based Multi-Resonant Metamaterial Absorber in the Terahertz Regime

**Reza Parvaz and Hamid Reza Karami***

Department of Electrical Engineering, Bu-Ali Sina University, Hamedan, Iran
*corresponding author, E-mail: Hamidr.karami@basu.ac.ir

## Abstract

Recent developments in metamaterial designs have opened up the possibility of the absorption in the terahertz frequency range. In this paper we present a multi-resonant perfect absorber that can be tuned to produce either single wideband or multi-band resonance in order to suit any special requirements. We demonstrate that the proposed structure leads to the absorption peaks in terahertz regime. This periodic metal-backed structure consists of a metallic ring positioned on a graphene nano-ribbon per unit cell. In addition, we derive the equivalent circuit and transmission line model based on the reflected fields to facilitate analysis of the proposed design and comprehension of full-wave simulation results.

## 1. Introduction

Since J.B. Pendry et al, explained that some periodically placed metallic wires and split ring resonators (SRRs) can yield negative effective permittivity and permeability, respectively, there have been a large number of research in the metamaterial applications [1, 2]. At the beginnings, Metamaterials were just supposed to be only left-handed materials (LHM), but now metamaterials own much broader definition than LHM. The concept of metamaterial has been blended with the ability to control electromagnetic waves.
This artificial material has been developed to bend electromagnetic waves for making a superlens due to its negative refractive index by D.R. Smith by the year 2005. In 2006, Pendry et al, accomplished in the realization of invisible cloaking by proposing transformation optics in microwave frequencies [3], [4].
Recently, graphene a two-dimensional material in which carbon atoms constitute a honey-comb lattice with one atomic thickness, fulfills numerous purposes in electronics, plasmonics and photonics [5]. This anisotropic material possesses a great strength, thermal and electrical conductivity in a wide frequency spectrum due to its large electron mobility [6], [7]. In the far-infrared detectors, graphene plays a significant role to achieve a broadband absorption and ultrafast response [8]. Furthermore, possession of particular plasmonic properties, graphene has attracted intense attention of research community in studying plasmonic waveguides.
graphene sheet also has a great conductivity amount due to its high electron mobility. The electron mobility of this platform can be adjusted either by chemical doping or gate voltage to produce desired conductivity. In addition to electron mobility, its function can be tuned by manipulating such parameters as temperature and frequency range, too.
Another advantage of using graphene in plasmonics is its compressed surface plasmon wavelength so that it smooths the path for designing ultra-compact electronic and plasmonic devices [9].
THz absorbers play an important role in photodetectors, photovoltaic and stealth applications [10]. In this paper, we first utilize the desirable graphene parameters to achieve the proposed absorber structure and results. We will then present the investigated equivalent circuit and examine the results for oblique incidence. It is demonstrated that this absorber is based on scattering cancellation caused by destructive interference

## 2. Graphene properties

The surface conductivity and permittivity of this platform is expressed as follows:

### 2.1. Graphene conductivity

The complex surface conductivity of graphene sheet can be derived by Kubo formula [11], [12]:

$$\sigma(\omega,\tau,\mu_c,T) = \frac{-ie^2(\omega+i\tau^{-1})}{\pi\hbar^2}\left[\frac{1}{(\omega+i\tau^{-1})}\int_0^{\infty}\left(\frac{\partial f_d(\varepsilon)}{\partial\varepsilon} - \frac{\partial f_d(-\varepsilon)}{\partial\varepsilon}\right)\varepsilon d\varepsilon - \int_0^{\infty}\frac{f_d(-\varepsilon)-f_d(\varepsilon)}{(\omega+i\tau^{-1})^2-4\left(\varepsilon/\hbar\right)^2}d\varepsilon\right] \quad (1)$$

where $-e$, $\omega$, $\hbar$ and $\varepsilon$ represent charge of electron, angular frequency, reduced Planck constant and the energy, respectively. And $f_d(\mathcal{E}) = -\left(e^{(\mathcal{E}-\mu_c)/K_BT}+1\right)^{-1}$ is Fermy-Dirac distribution, $\tau$ denotes the relaxation time and $T$=300 K is the temperature. Graphene conductivity includes both semi-classical, intraband $\boldsymbol{\sigma}_{intra}$ conductivity and quantum-dynamical, interband $\boldsymbol{\sigma}_{inter}$ conductivity. Therefore the complex conductivity can be expressed as the relations below:

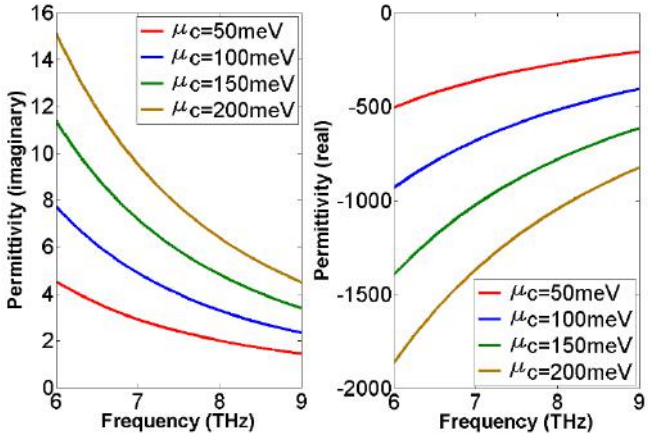



Figure 1: Permittivity of graphene sheet in the frequency range of interest for different values of chemical potential ($\mu_c$).

$$\sigma_{GR}(\omega) = \sigma_{intra}(\omega) + \sigma_{inter}(\omega) \quad (2)$$

$$\sigma_{intra}(\omega) = i\frac{e^2 K_B T}{\pi\hbar^2(\omega + i\tau^{-1})}\left[\frac{\mu_c}{K_B T} + 2\ln(e^{-\mu_c/K_B T} + 1)\right] \quad (3)$$

$$\sigma_{inter}(\omega) = \frac{ie^2}{4\pi\hbar}\ln\left(\frac{2|\mu_c| - (\omega + i\tau^{-1})\hbar}{2|\mu_c| + (\omega + i\tau^{-1})\hbar}\right) \quad (4)$$

Where $K_B$ is Boltzmann's constant, $\tau$=3.3 ps is the graphene relaxation time and $\mu_c$=100meV denotes chemical potential [13].

### 2.2. Graphene permittivity

We employed CST.MWS for full-wave simulation [14]. Since the material is two-dimensional, we can not apply its parameters directly into the software. Instead, we used a special technique to model graphene in 3D software environment, which was first introduced by Vakil and Engheta [15]. According to this work, by defining a certain thickness for graphene (e.g. Δ = 1nm), we can compute the bulk conductivity by the expression $\frac{\sigma(\omega)}{\Delta}$ to use it in permittivity formula. Therefore, permittivity of graphene can be expressed as follows:

$$\varepsilon(\omega) = \varepsilon_0 + \frac{i\sigma(\omega)}{\omega\Delta} \quad (5)$$

Now the permittivity values may be imported as material parameters in the CST.MWS. We found that the simulation resulted by the obtained values from the Eq. 5 are in accordance with the analytical formula. Fig. 1 shows the permittivity of graphene for different values of chemical potential.

## 3. Graphene-based perfect absorber

### 3.1. The structure layout and design

In the previous sections, we demonstrated the way graphene properties are formulated. Now in this section we intend to indicate the layout of our proposed structure by employing

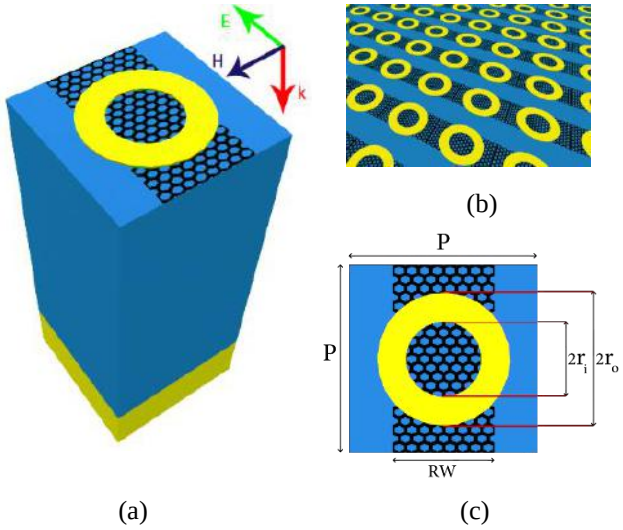



Figure 2: The layout of the interest. (a) Perspective of the unit cell which is composed of a backed metal slab, a dielectric substrate, a graphene sheet and a metallic ring. (b) The periodic integration of some unit cells. (c) The dimensions of the design.

the yielded parameters of graphene. Fig. 2 shows the schematic of the discussed perfect absorber layout and dimensions. It should be noted that the resonator consists of a graphene micro-ribbon and a metallic ring that had been separately offered in the papers [16, 17] and [18]. We utilized a ring and slab of gold with a conductivity of $4.561 \times 10^7$ and a SiO2 dielectric ( $\varepsilon_r = 4.41$ ). The geometrical parameters of the design are as follows: periodicity of $P = 2\mu$m, ring inner radius of $r_i = 0.4\,\mu m$, outer radius of $r_o = 0.7\mu m$, ring thickness of $T_R = 0.025\mu m$, ground plate thickness of $T_G = 0.8\mu m$ and dielectric thickness of $d = 3.9\mu m$. These are constant values. For ribbon width ($RW$) we have considered different values that are determined in the next sections.

### 3.2. The equivalent circuit and transmission line model

In this section, we present the investigated equivalent circuit and transmission line model of the proposed structure for facilitation purposes. In this structure, we employed a sufficiently thick PEC at the behind to ensure the transmission

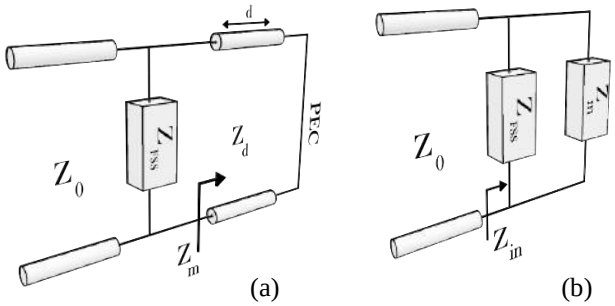



Figure 3: The transmission line model and input impedance of an absorber.

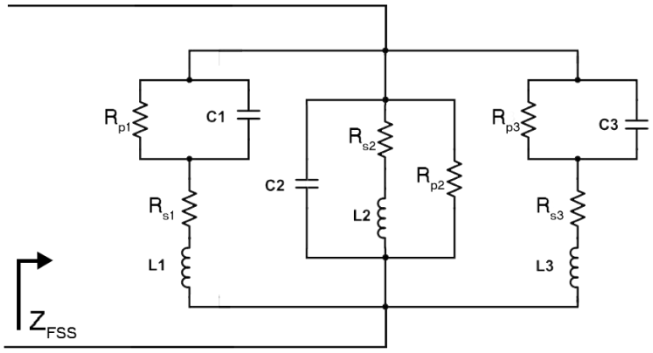



Figure 4: The schematic of $Z_{FFS}$ equivalent circuit.

is zero and considered it as a short circuit in transmission line model analysis due to its zero-characteristic-impedance.
Since, the dielectric is lossless, the relative permittivity only includes a real part and is obtained by the relation below:

$$Z_d = j\frac{\eta_0}{\sqrt{\varepsilon_r}}\tan\left(k_0 d\sqrt{\varepsilon_r}\right) \tag{6}$$

where $\eta_0$, $k_0$ denote the free space characteristic impedance and wavenumber, respectively, and $d$ is the dielectric thickness. The general transmission line model of the mentioned structure is depicted in Fig. 3.
Now first consider $Z_m$ as the input impedance of the short circuit terminated TL which is seen looking toward the PEC in the Fig. 3 (a). The general expression of the transmission line input impedance is expressed as follows:

$$Z_m = \eta_d \frac{Z_L + j\eta_d \tan(k_0 d\sqrt{\varepsilon_r})}{\eta_d + jZ_L \tan(k_0 d\sqrt{\varepsilon_r})} \tag{7}$$

where $\eta_d = \frac{\eta_0}{\sqrt{\varepsilon_r}}$ and $Z_L = 0$ are the dielectric and the PEC's characteristic impedance, respectively. Finally, $Z_m$ can be expressed as follows:

$$Z_m = j\eta_d \tan(k_0 d\sqrt{\varepsilon_r}) \tag{8}$$

According to the eq. 8, $Z_m$ is obviously equal to $Z_d$.
As it is illustrated in the Fig. 3 (b) $Z_{FSS} = R_{FSS} + jX_{FSS}$ and $Z_m = jX_m$ are in parallel arrangement. Now we have suggested the $Z_{FSS}$ equivalent circuit in the Fig. 4. This optimal circuit is in high accordance with the full-wave simulation results.
After $Z_{FSS}$ measurements, $Z_{in}$ and reflection coefficient (R) are yielded by the eq. 9, 10:

$$Z_{in} = \frac{Z_{FSS} Z_m}{Z_{FSS} + Z_m} \tag{9}$$

$$R = \frac{Z_{in} - Z_0}{Z_{in} + Z_0} \tag{10}$$

In order the reflectance to be zero, the input impedance has to be matched with the free space characteristic impedance.

## 4. The results

### 4.1. Absorption mechanism

The absorption is achieved by destructive interferences of reflected waves. According to Fig. 5 the total reflectance is expressed as follows [19]:

$$\begin{aligned} R_{tot} = {} & |r_{12}|e^{-\varphi_{r12}} + \\ & |t_{12}||r_{23}||t_{21}|e^{-(\varphi_{t12}+\varphi_{r23}+\varphi_{t21})} + \\ & |t_{12}||r_{23}||r_{21}||r_{23}||t_{21}|e^{-(\varphi_{t12}+2\varphi_{r23}+\varphi_{r21}+\varphi_{t21})} + \\ & \ldots \end{aligned} \tag{11}$$

It is obvious that the eq. 11 consists of geometric series and also $r_{23}e^{-\varphi_{r23}} = -1$ due to ground slab shielding. Thus the total reflectance is simplified to the following relation:

$$R_{tot} = |r_{12}|e^{-\varphi_{r12}} - |r_m|e^{-\varphi_{rm}} \tag{12}$$

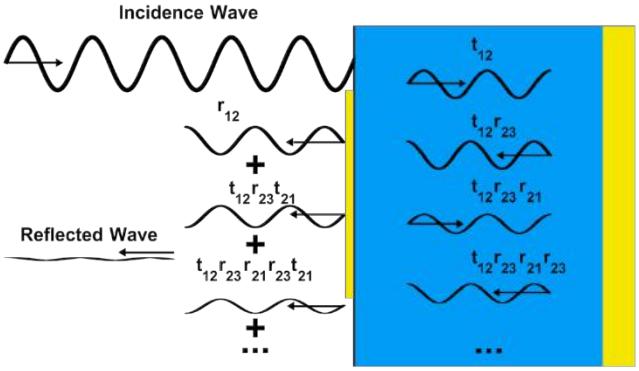



Figure 5: The overview of destructive-interferences-based perfect absorption.

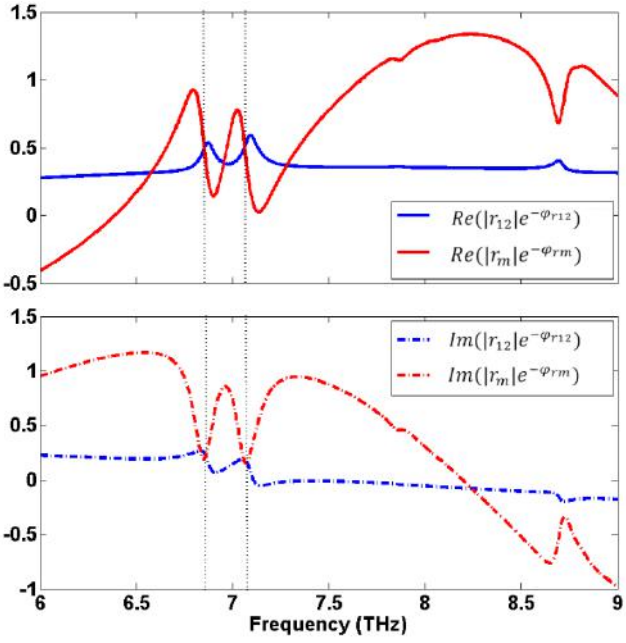


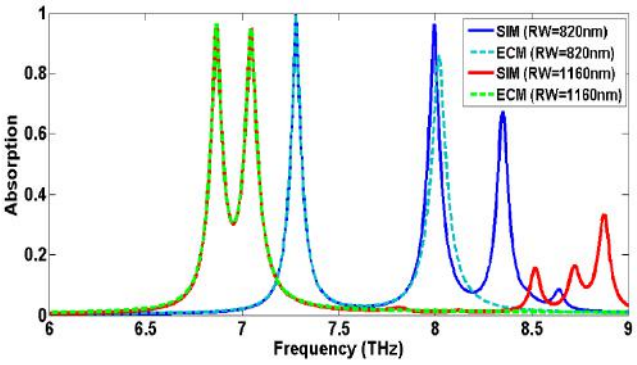

Figure 6: Real and imaginary parts of first-order and higher-orders-summation reflectance of the absorber.

$$|r_m|e^{-\varphi_{rm}} = \frac{|t_{12}||t_{21}|e^{-(\varphi_{t12}+\varphi_{t21})}}{1+|r_{21}|e^{-\varphi_{r21}}} \quad (13)$$

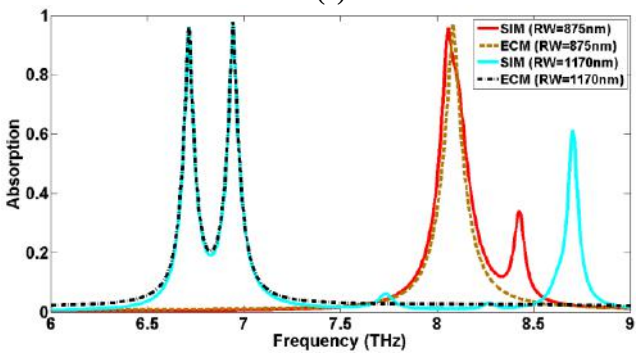
The values of real and imaginary parts of $|r_{12}|e^{-\varphi_{r12}}$ and $|r_m|e^{-\varphi_{rm}}$ have been depicted for the ribbon width ($RW$) of 1160 $nm$ in Fig. 6. It can be observed that the resonance frequency is the point where these two plots meet for both real and imaginary parts. On the other hand, the interaction between the first-order and the sum of higher orders of the reflected waves with $\pi$ phase difference causes destructive interferences. Therefore the reflected waves are suppressed for the sake of near unity absorption.

### 4.2. The absorption results

We have suggested a kind of metamaterial absorber which responses for numerous values of ribbon width ($RW$) and in order one to achieve arbitrary resonances it is highly recommended to manipulate $RW$. It simply causes the resonance frequencies to move in the range of 6 to 9 THz. By tuning $RW$, we can also have the resonance frequencies close enough to obtain a broadband perfect absorption.
It should be mentioned that our equivalent circuit model (ECM) possesses a high compliance with the results simulated by CST.MWS that is shown in Fig. 7 (a), (b).
Now we present the efficient equivalent circuit components values for the suggested responses in the tables 1, 2.




(a)




(b)

Figure 7: The absorption results derived by Simulating (SIM) structure in CST.MWS and the equivalent circuit model (ECM) for different values of RW.

Table 1: The equivalent circuit components values for difference RWs.

| $RW$ | $R_{p1}(M\Omega)$ | $R_{p2}(M\Omega)$ | $R_{p3}(M\Omega)$ | $R_{s1}(\Omega)$ | $R_{s2}(\Omega)$ | $R_{s3}(\Omega)$ |
|---|---|---|---|---|---|---|
| 820 nm | 32.1 | ∞ | 129.3 | 250.8 | 34.9 | 258.4 |
| 875 nm | 0 | ∞ | 2.9 | 2965 | 44.7 | 70.2 |
| 1160 nm | 13.3 | 1.5 | 61.5 | 186 | 27.2 | 183 |
| 1170 nm | 21.8 | 38.8 | 20.4 | 233 | 42.7 | 183 |

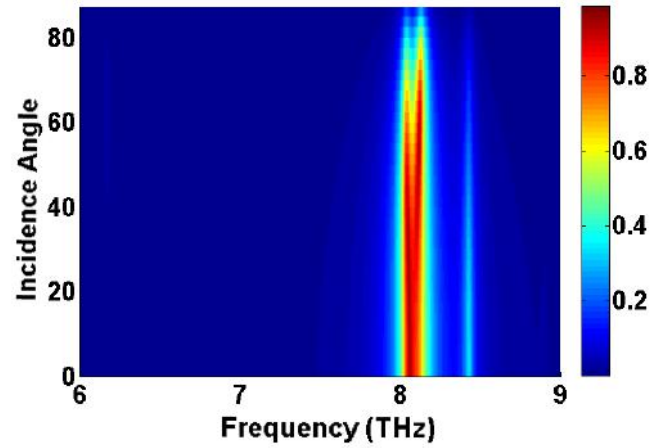
Table 2: The equivalent circuit components values for difference RWs.

| $RW$ | $C_1(aF^*)$ | $C_2(aF)$ | $C_3(aF)$ | $L_1(pH)$ | $L_2(pH)$ | $L_3(pH)$ |
|---|---|---|---|---|---|---|
| 820nm | 0.508 | 19.9 | 0.537 | 936 | 45 | 730 |
| 875nm | - | 4.4 | 0.732 | 1085 | 37.6 | 565 |
| 1160nm | 0.627 | 23.3 | 0.969 | 852 | 32 | 522 |
| 1170nm | 0.678 | 23 | 0.867 | 824 | 31.8 | 601 |

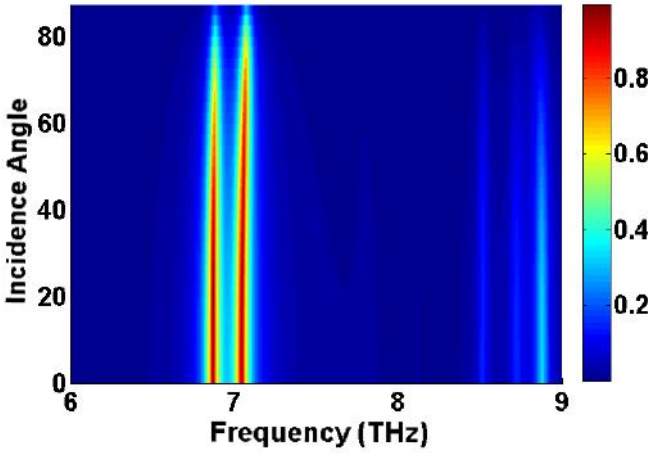
*denotes atto-farad or $10^{-18}$ farads.

### 4.3. Oblique incidence

In the previous section, absorptivity diagrams were plotted for different values of *RW* in the case of normal incidence. Now, we intend to discover whether the absorptivity is in high efficiency for the oblique angles as normal incidence wave. Fig. 8 (a) and (b) reveal sensitivity of the absorptivity to the angle of incidence wave for the *RW* value of 875nm and 1160nm, respectively.




(a)




(b)

Figure 8: Resonance frequency incidence angle sensitivity for *RW* of (a) 875nm and (b) 1160nm.

## 5. Conclusions

In this paper, a perfect absorber is suggested that works in far-infrared regime. We demonstrated that single or multi band is achieved by changing the ribbon width of this absorber. As a result, one can obtain the absorption peaks in every single frequency. Moreover, an equivalent circuit is investigated by full-wave simulation and the exact values are extracted by utilizing the scattering characteristics. Our perfect absorption is based on destructive interferences that is achieved by reflection and transmission suppressions and possesses high efficiency over the incidence angel of 75 degrees.

## References


[1] J.B. Pendry, A. J. Holden, D. J. Robbins, and W. J. Stewart, "Low frequency plasmons in thin-wire structures," *J. Phys. Cond. Mat.*10, 4785–4809, 1998.

[2] J.B. Pendry, A. J. Holden, D. J. Robbins, and W. J. Stewart, "Magnetism from conductors and enhanced nonlinear phenomena," *IEEE Trans. Microw. Theory Tech*., Vol. 47, No. 11, 2075– 2084, 1999.

[3] D.R. Smith, How to build a superlens, *Science*, 308, 502, 2005.

[4] D. Schurig, J.J. Mock, B.J. Justice, S.A. Cummer, J.B. Pendry, A.F. Starr, D.R. Smith, Metamaterial electromagnetic cloak at microwave frequencies, *SCIENCE*, 314, 977-980, 2006.

[5] A.K. Geim, K.S. Novoselov, The rise of graphene, *Nature materials* 6: 183-191, 2007.

[6] S.K. Pati, T. Enoki, C.N.R. Rao, Graphene and its fascinating attributes, *World Scientific*, 2011.

[7] A.K. Geim, P. Kim, Carbon Wonderland, *Scientific American*, 298, 90–97, 2008.

[8] Y. Yao, R. Shankart, P. Rauter, Y. Song, J. Kong, M. Loncar, F. Capasso, High-Responsivity mid-Infrared graphene detectors with antenna-enhanced photocarrier generation and collection, *Nano Lett. 14(7)*, 3749-3754, 2014.

[9] K.J.A. Ooi, H.S. Chu, L.K. Ang, P. Bai, Mid-infrared active graphene nanoribbon plasmonic Waveguide Devices, *Journal of the Optical Society of America B*, 30(12), 3111-3116, 2013.

[10] A. Rostami, H. Rasooli, H.Baghban, Terahertz technology, *Springer-Verlag Berlin Heidelberg*, 77, 2011.

[11] G.W. Hanson, "Dyadic Greens functions and guided surface waves on graphene, *J. Appl. Phys,*103, 064302, 2008.

[12] L.A. Falkovsky, S.S. Pershoguba, Optical far-Infrared properties of a graphene monolayer and multilayer, *Phys. Rev*. B 76, 153410, 2007.

[13] H.M. Bernety, A.B. Yakovlev, Cloaking of Dielectric and Metallic Elliptical Cylinders with a Nanostructured graphene Metasurface, *2014 IEEE Antennas and Propagation Society International Symposium (APSURSI)*, USA, 890-891, 2014.

[14] CST Microwave Studio 2006B, www.cst.com.

[15] A. Vakil, N. Engheta, Transformation optics using graphene, *Science* 332, 1291-1294, 2011.

[16] L. Ju, B. Geng, J. Horng, C. Girit, M. Martin, Z. Hao, H.A. Bechtel, X. Liang, A. Zettl, Y.R. Shen, F. Wang, graphene plasmonics for tunable terahertz metamaterials, *Nat. Nanotechnology* 6, 630–634, 2011.

[17] R. Alaee, M. Farhat, C. Rockstuhl, F. Lederer, A perfect absorber made of a graphene micro-ribbon metamaterial, *optics express*, 20 (27), 28017-28024 , 2012.

[18] Z.G. Dong, M.X. Xu, S.Y. Lei, H. Liu, T. Li, F.M. Wang, S.N. Zhu, Negative refraction with magnetic resonance

in a metallic double-ring metamaterial, *Appl. Phys. Lett*. 92(6), 064101, 2008.
[19] P. Yeh, Optical waves in layered media, Wiley, NewYork, 2005.

# Photonics based on 2D materials

# Mageto-transport study in GaAs/$Al_{0.3}Ga_{0.7}As$ nanostructure superlattice at very low temperature

**D. Barkissy, A. Nafidi*, A. Boutramine, A. Khalal, T. El Gouti and M. Massaq**

Laboratory of Condensed Matter Physics and Nanomaterials for Renewable Energy, Faculty of Sciences, University Ibn Zohr, Agadir, Morocco

*corresponding author: nafidi21@yahoo.fr

**Abstract**- We have investigated the band structures $E(d_1)$, $E(k_z, k_p)$ and the effective mass $m^*/m_0$ along the growth axis and in the plane of GaAs($d_1$=19 nm)/$Al_{0.3}Ga_{0.7}As$($d_2$=5 nm) nanostructure superlattice, based on the envelope function formalism. At 0.4 K, the band gap 1.53 eV situates this sample as near infrared detector. We have also interpreted the oscillations in the magneto-resistance observed by Smrčka et al. The position of Fermi level indicates n type conductivity in this sample.

The realization of type I nanostructures superlattices (SLs), consisting of alternating GaAs and $Al_xGa_{1-x}As$ compounds, was associated with different fundamental studies, since they are promising in different applications fields, like in optoelectronics [1] and in detectors [2,3].

We show in the Fig. 1.(a), the energy of the conduction ($E_i$), first light-hole ($h_1$) and the heavy-hole ($HH_1$) sub-bands at the center Γ ($k_z$= 0) and the limit ($k_z$= π/d) of the first Brillouin zone as a function of $d_1$ at T= 0.4 K. The case of the investigated sample ($d_1$=190 Å) is indicated by the vertical dashed line. The calculated band gap, from the bottom of the first conduction ($E_1$) to the top of the first valence ($HH_1$) sub-bands is $E_g(\Gamma)= E_1 - HH_1$= 1.53 eV and the corresponding cut-off wavelength λ= 811 nm, is located in the near infrared region. The dispersion curves of this sample are shown in Fig. 1.(b). The electronic states are quantized and discrete along $k_z$ direction because of the thick ($d_2$= 50 Å) barrier thickness, which separates two adjacent wells GaAs, leading to a weakly coupled system. In this case the electronic transport is dominated in the plane of this superlattice, in particular, in the GaAs layer with a large confinement of carriers charge.

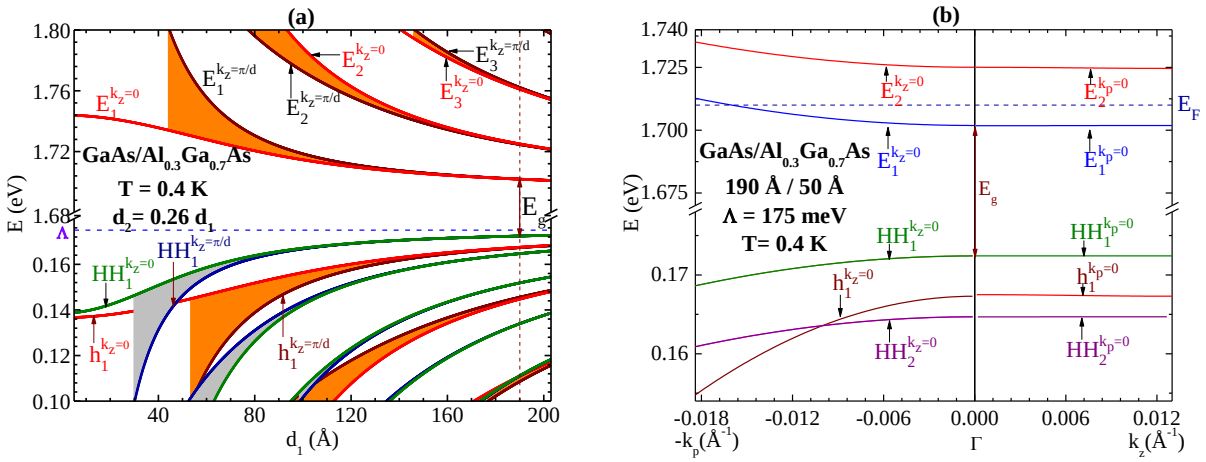



**Fig. 1**: **(a)** Energy of both conduction (upper part) and valence (lower part) sub-bands as function of well thickness at 0.4 K. The solid areas show the width of sub-bands. **(b)** Dispersion curves in the $k_z$ wave vector direction and in the plane $k_p$ of the superlattice, respectively.

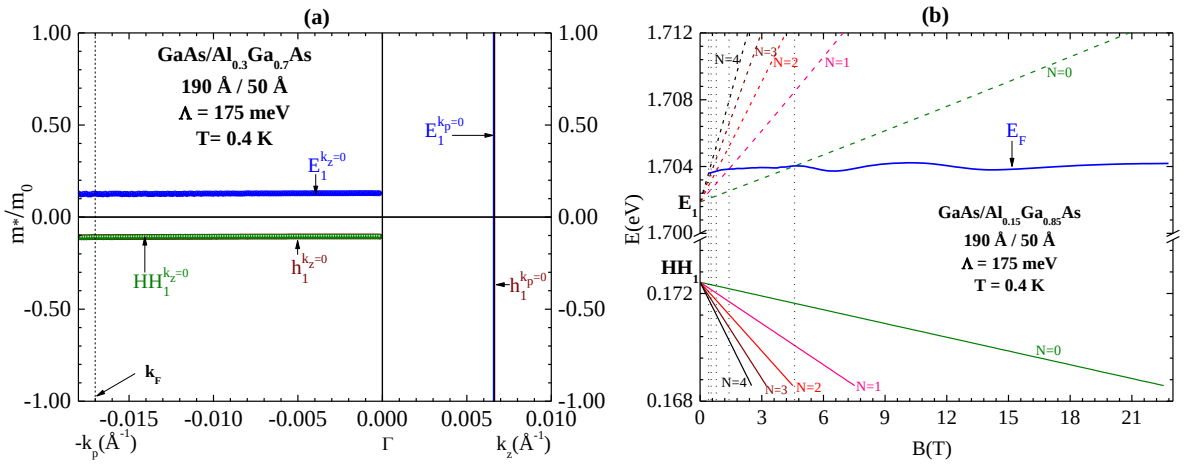



**Fig. 2**: **(a)** Carrier's effective masse calculated along the growth direction and in the plane of the investigated superlattice. **(b)** Energy position of the calculated Landau levels of the first conduction and valence sub-bands as a function of magnetic field. The position of the Fermi level is also shown as a function of the magnetic field.

The Fig. 2.(a), shows the carrier's effective mass of the first conduction and valence sub-bands, along the growth direction $k_z$ and in the plane $k_p$ of this superlattice. Along $k_p$, the effective masses of light and heavy holes are almost constant and equal to and $-0.11m_0$. For electrons $m^*_{E1}= 0.13m_0$. In order to estimate the Fermi level of the investigated sample we used the magneto-resistance data of Smrčka et al. [4]. The sheet carrier density obtained from Shubnikov de Haas data is: $n_{2D}= 4.4\ 10^{11}\ cm^{-2}$. The Fermi level of two dimensional electron gas (2DEG) is $E_F= 1.710$ eV. Therefore, this sample exhibits n type conductivity.

The application of an external magnetic field on such quantum Hall system, leads to a creation of landau levels and their calculated energies, for $E_1$ and $HH_1$ are shown in the Fig. 2.(b). When the magnetic field increases, the crossovers between the calculated Landau levels (for N= 0 to 4) and the Fermi level indicate the same minima of the transverse magneto resistance oscillations (Shubnikov-de Haas effect), observed in ref[4], at B= 4.6 T, 1.4 T, 0.8 T, 0.54 T and 0.4 T as shown in the Fig. 2.(b). We have also interpreted the observed quantum Hall effect in the GaAs quantum wells. .

## REFERENCES


1. Janiak, F., M. Dyksik, M. Motyka, K. Ryczko, J. Misiewicz, K. Kosiel and M. Bugajski "Advanced optical characterization of AlGaAs/GaAs superlattices for active regions in quantum cascade lasers," *Opt. Quantum Electron*, Vol. 47, 945–652, 2015.
2. Martyniuk, P., M. Kopytko and A. Rogalski "Barrier infrared detectors," *Opto-Electronics Rev*, Vol. 22, 2014.
3. Barkissy, D., A. Nafidi, A. Boutramine, H. Charifi, A. Elanique and M. Massaq "Electronic Properties of GaAs/AlAs Nanostructure Superlattice for Near Infrared Devices at Low Temperatures," *J. Low Temp. Phys*, Vol.182, 185–191, 2016.
4. Smrčka, L., N. A. Goncharuk, P. Svoboda, P. Vašek, Y. Krupko, and W. Wegscheider "Electron magnetotransport in GaAs/AlGaAs superlattices with weak and strong inter-well coupling," *Microelectronics J*, Vol. 39, No. 3–4, 411–413, 2008.

# Topological transition in anisotropic plasmonic metasurface

**A. A. Bogdanov**[1,2], **O. Y. Yermakov**[1], **A. I. Ovcharenko**[1], **M. Song**[1], **D. A. Baranov**[1], **I. S. Sinev**[1], **I. S. Mukhin**[1], **A. K. Samusev**[1], **I. V. Iorsh** [1], **A. V. Lavrinenko**[3], and **Yu. S. Kivshar**[1,4]

[1]ITMO University, St. Petersburg 197101, Russia
[2]Peter the Great St. Petersburg Polytechnic University, St. Petersburg 195251, Russia
[3]DTU Fotonik, Technical University of Denmark, Oersteds pl. 343, DK-2800 Kongens Lyngby, Denmark
[4]Nonlinear Physics Center, Australian National University, Canberra ACT 0200, Australia
a.bogdanov@metalab.ifmo.ru

**Abstract**— We study both theoretically and experimentally a new class of surface electromagnetic waves supported by resonant anisotropic metasurface. At certain frequency this type of metasurface demonstrates the topological transition from elliptical to hyperbolic regime.

Metasurfaces are known as a two-dimensional analog of metamaterials as they offer unprecedented control over light propagation, reflection, and refraction [1, 2]. One of the main advantages of metasurfaces is that these structures are fully compatible with modern planar fabrication technology and they can be readily integrated into on-chip optical devices, preserving most of the functionalities and unique properties of three-dimensional metamaterials.

In this work, we study both theoretically and experimentally the surface electromagnetic waves supported by a resonant anisotropic metasurface. We demonstrate the topological transition from elliptical to hyperbolic regime at the visible frequencies.

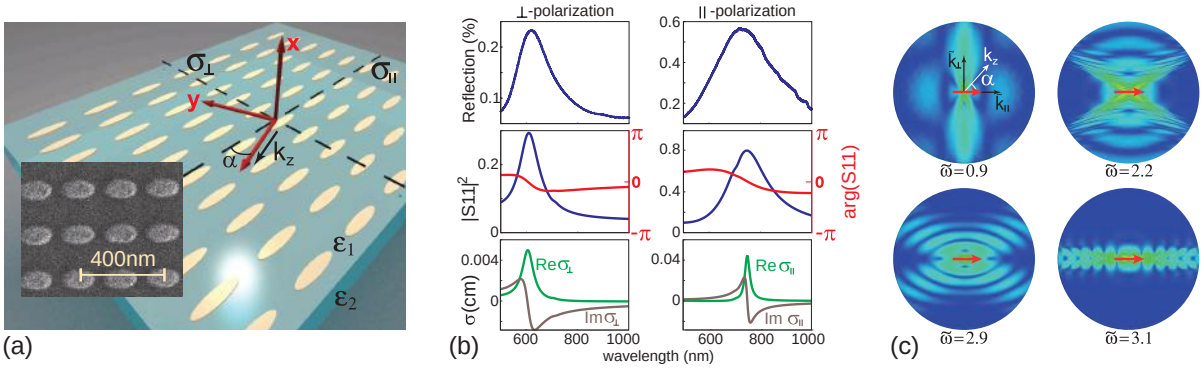



Figure 1: (a) Design of the anisotropic metasurface. Upper ($x > 0$) half space with $\varepsilon_1$ and lower ($x < 0$) half space with $\varepsilon_2$ are separated by an anisotropic conducting layer represented by an array of plasmonic nanoparticles. The principal axes of the conductivity tensor are shown by dashed lines. Surface wave propagates along z-direction. The inset shows scanning electron microscopy (SEM) image of the fabricated metasurface supporting surface waves in the optical range. (b) Reflectance spectra of the metasurface measured for two polarizations (top row), corresponding simulated $S_{11}$-parameters (middle row) and reconstructed components of anisotropic conductivity tensor $\sigma$ (bottom row). (c) Electric field amplitude map (logarithmic scale) of the surface waves excited by a point-like electric dipole in four different regimes determined by the magnitude of normalized frequency. The dipole orientation is denoted by a red arrow.

In the framework of the effective medium approximation, a metasurface can be described by a two-dimensional conductivity tensor $\hat{\sigma}$ (see Refs. [3, 4]). In the case of non-chiral anisotropic metasurface, the conductivity tensor has a diagonal structure $\hat{\sigma}(\omega) = \mathrm{diag}(\sigma_{\|}, \sigma_{\perp})$ with frequency-dependent components [5]. The dispersion equation of the surface waves supported by an anisotropic non-chiral metasurface can be derived from the Maxwell's equations straightforwardly[3]:

$$(c\kappa_1/\omega + c\kappa_1/\omega - 4\pi i\sigma_{yy}/c)\,(\omega\varepsilon_1/c\kappa_1 + \omega\varepsilon_2/c\kappa_2 + 4\pi i\sigma_{zz}/c) = 16\pi^2/c^2\sigma_{yz}^2. \qquad (1)$$

Here, $\sigma_{ij}$ are the tensor components in the rotated coordinate system [see Fig. 1(a)] and $\kappa_1$ and $\kappa_2$ are the inverse penetration depths of the wave in air and in substrate, respectively.

In this work, we consider a metasurface consisting of gold anisotropic nanoparticles placed on a fused silica substrate [see Fig. 1(a)]. The asymmetry of each particle splits its in-plane dipole plasmonic resonance with frequency $\Omega$ into two resonances with frequencies $\Omega_{\parallel}$ and $\Omega_{\perp}$. In the case of thin particles, the normal dipole response can be neglected. The resonance frequencies and the spectra of conductivity tensor components are retrieved from the reflectance spectra[6]. The phases of the reflectance coefficients [$\arg(S_{11})$, see Fig. 1(b)] were borrowed from the results of the corresponding numerical simulations. One can see that the imaginary parts of the conductivity tensor components change the signs in the vicinity of the resonance frequencies. This allows for realization of three dispersion regimes of the metasurface – capacitive, inductive, and hyperbolic[3].

Clear manifestation of both anisotropic and resonant properties of the metasurface can be seen in the experiment on the excitation of surface waves by a point dipole source placed in the vicinity of the metasurface. The role of the source can be played by a single defect introduced to the metasurface. The numerical simulations of the excitation of surface waves at different frequencies are shown in Fig. 1(c). One can see the strong dependence of the surface wave propagation behavior on the frequency of the source. Therefore, in the hyperbolic regime, simultaneous propagation of two hybridized modes is observed. In the $\sigma$-near-zero regime, quasi-one-dimensional propagation is possible.

In summary, we have studied both theoretically and experimentally the surface waves supported by a resonant anisotropic metasurface. We have shown that a metasurface consisting of anisotropic plasmonic nanoparticles exhibits three dispersion regimes and the topological transition from the elliptic to hyperbolic regime occurs at the visible frequencies. It provides ultimate control over the surface wave propagation required for the optical on-chip applications. The fabrication simplicity, rich functionality, and planar geometry make hyperbolic metasurfaces promising element for many optical and optoelectronic devices.

## ACKNOWLEDGMENT

The theoretical part of this work has been supported by Russian Foundation for Basic Research (project #16-37-60064, #15-32-20665). Numerical simulations, fabrication and optical experiments have been supported by the Russian Science Foundation (Grant #15-12-20028).

## REFERENCES

1. C. L. Holloway, E. F. Kuester, J. Gordon, J. O'Hara, J. Booth, D. R. Smith, "An overview of the theory and applications of metasurfaces: The two-dimensional equivalents of metamaterials," IEEE Trans. Antennas Propag. Mag., Vol **54**, 10–35, 2012.
2. N. Yu and F. Capasso, "Flat optics with designer metasurfaces," Nature Mater., Vol **13**, 139–150, 2014.
3. O. Y. Yermakov, A. I. Ovcharenko, M. Song, A. A. Bogdanov, I. V. Iorsh, and Y. S. Kivshar, "Hybrid waves localized at hyperbolic metasurfaces," Phys. Rev. B, Vol **91**, 235423, 2015.
4. J. S. Gomez-Diaz, M. Tymchenko, and A. Alù, "Hyperbolic plasmons and topological transitions over uniaxial metasurfaces," Phys. Rev. Lett., Vol **114**, 233901, 2015.
5. A. Nemilentsau, T. Low, G. Hanson, "Anisotropic 2D materials for tunable hyperbolic plasmonics," arXiv:1509.04383, 2015.
6. M. Danaeifar, N. Granpayeh, N. A. Mortensen, and S. Xiao, "Equivalent conductivity method: straightforward analytical solution for metasurface-based structures," J. Phys. D, Vol **48**, 385106, 2015.

# Terahertz Electron-Beam Radiation in Graphene

**K. Tantiwanichapan, X. Wang, A. Swan, and R. Paiella***
Department of Electrical and Computer Engineering, Boston University, Boston (MA) USA
*corresponding author: rpaiella@bu.edu

**Abstract**-Terahertz light emission based on electron-beam radiation mechanisms in graphene is investigated numerically. Specifically, we consider cyclotron-like emission in sinusoidally corrugated graphene, and the Smith-Purcell effect in a planar graphene sheet on a nanoscale dielectric hole array. Technologically significant power levels at geometrically tunable THz frequencies are computed for both device configurations even at room temperature.

The development of electrically driven solid-state sources of THz light is the subject of extensive research efforts, due to the lack of practical devices capable of room-temperature operation. While most activities to date have focused on quantum cascade lasers or microwave devices, the use of electron-beam radiation mechanisms has received little attention. These mechanisms involve charges traveling at constant speed in the presence of a periodic spatial modulation, in either their trajectory (e.g., cyclotron radiation) or the surrounding dielectric environment (the Smith Purcell effect). These ideas are commonly used in radiation sources based on high-energy electron beams in vacuum (e.g., free-electron lasers and microwave orotrons) – however, their demonstration in solid-state devices has remained a challenge. By virtue of its unique electrical properties (including linear energy dispersion, large Fermi velocity, and micron-scale electron mean free paths even at room temperature), graphene provides a natural candidate to overcome these limitations.

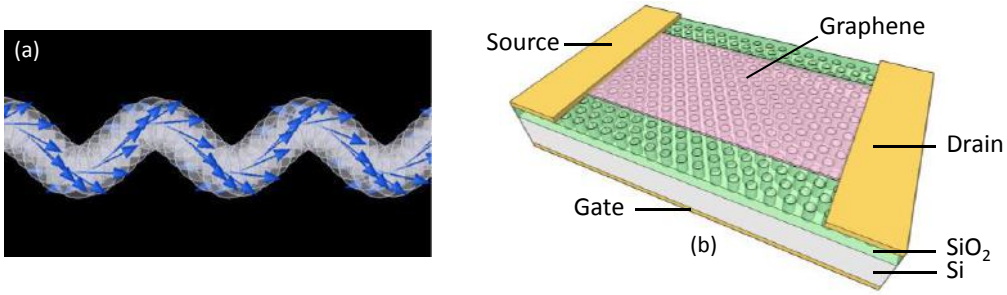



Figure 1. (a) Equivalent dipole distribution for the cyclotron-like radiation mechanism investigated in this work. (b) Schematic illustration of the Smith-Purcell device geometry.

In the present work, this basic idea is explored via rigorous full-wave simulations for two different device configurations. The first approach [1] is based on the conformal deposition of a sheet of graphene on a sinusoidal grating on the surface of a suitable substrate. In this geometry under dc bias, electrons (or holes) undergo periodic angular motion [Fig. 1(a)] by virtue of the graphene mechanical corrugation, combined with its 2D nature which ensures that the carrier trajectories perfectly conform to the corrugation. As a result, light is emitted based on a mechanism similar to cyclotron radiation, but without the need for any external magnetic field. In the second approach [2], a planar sheet of graphene is deposited over a 2D hole array in a solid substrate [Fig. 1(b)]. In this geometry, radiation is again expected from the graphene charge carriers (under uniform rectilinear motion) as they pass near the grating, via the Smith-Purcell effect [3].

The radiation output of both devices is evaluated by first computing the contribution from each electron in the graphene sheet via FDTD simulations. In these calculations, each electron is modeled with an equivalent dipole distribution **P**(**r**, t), whose time derivative is equal to the current density **J**(**r**, t) carried by the electron. With this approach, the important effect of electronic scattering can be directly included by setting the length of the equivalent dipole distribution equal to the electron mean free path between consecutive collisions. The overall emission spectrum is finally obtained by adding up the single-electron contributions over all values of the electronic wavevector **k**, properly weighted by the distribution function $f_{\mathbf{k}}$ (including Pauli blocking effects).

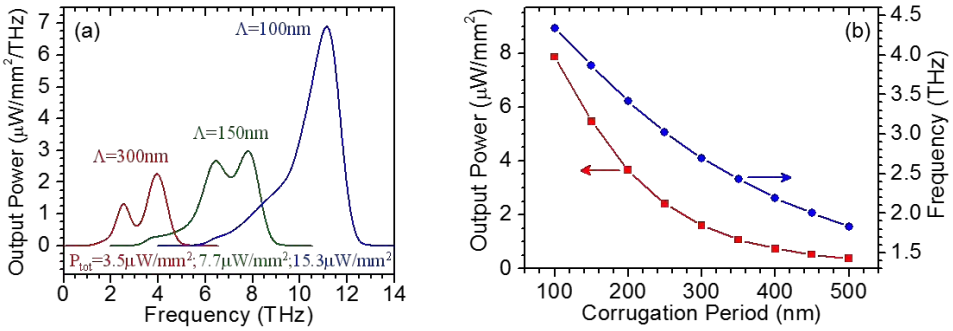



Figure 2. (a) Emission spectra of three graphene Smith-Purcell devices based on triangular hole arrays of different period Λ. The total output power per unit area of each structure, integrated over all frequencies, is also listed in the inset. (b) Peak emission frequency (circles) and total output power per unit area (squares) of corrugated graphene versus corrugation period, for a corrugation amplitude of 50 nm. The data shown in both panels were computed for graphene at room temperature.

Representative simulation results are shown in Fig. 2. Figure 2(a) shows the calculated radiation spectra of three Smith-Purcell devices of different grating period. In Fig. 2(b), we plot the peak emission frequency and total output power per unit area of a cyclotron-like device as a function of the corrugation period. These results show that technologically significant power levels of several μW/mm$^2$ can be obtained at room temperature, at geometrically tunable THz frequencies on the order of $v_F/\Lambda$ (where $v_F$ ~$1\times10^8$ cm/s is the graphene Fermi velocity and Λ is the period of either the sinusoidal trajectory or the nearby grating). Importantly, these power levels are obtained at frequencies of several THz, contrary to the case of traditional microwave oscillators which are generally limited to frequencies below ~1 THz. Combined with their inherent design simplicity and array scalability, the devices of Fig. 1 therefore represent an attractive candidate to extend the frequency range of existing room-temperature solid-state THz sources.

**Acknowledgements**. This work was supported by NSF under Grant #DMR-1308659.

**REFERENCES**

1. Tantiwanichapan K., J. DiMaria, S. N. Melo and R. Paiella, "Graphene electronics for terahertz electron-beam radiation," *Nanotechnology*, Vol. 24, Art. No. 375205, 2013.
2. Tantiwanichapan K., X. Wang, A. K. Swan and R. Paiella, "Graphene on nanoscale gratings for the generation of terahertz Smith-Purcell radiation," *Appl. Phys. Lett.*, Vol. 105, Art. No. 241102, 2014.
3. Smith S. J. and E. M. Purcell, "Visible light from localized surface charges moving across a grating," *Phys. Rev.*, Vol. 92, 1069 (1953).

# A subcell technique for numerical analysis of optical properties of graphene metamaterials with the finite-difference time-domain method.

**I. Valuev**[1,2], **S. Belousov**[1,3], **M. Bogdanova**[1], **O. Kotov**, **and Yu. Lozovik**[4]

[1]Kintech Lab Ltd., Russia
[2]Joint Institute for High Temperatures of the Russian Academy of Sciences, Russia
[3]National Research Centre "'Kurchatov Institute"', Russia
[4]Institute of Spectroscopy of the Russian Academy of Sciences, Russia
belousov@kintechlab.com

**Abstract**— A subcell technique for calculation of optical properties of graphene metamaterials with the finite-difference time-domain method is presented. The technique is applied for analysis of transmission, reflection and absorbtion spectra of various graphene metamaterials, and the results are compared to other theoretical approaches as well as experimental data. The method demonstrates a significantly better numerical efficiency and accuracy than a common approach, where graphene is represented by a thin film.

Graphene has emerged as a candidate for a large number of novel applications in the field of nanooptics. Unique optical properties of graphene are determined by a 2D nature of its conductivity, with one of the most notable consequences being the existence of ultra-subwavelength graphene surface plasmon polaritons on its surface in the THz frequency range [1]. Coupled with the fact that the conductivity of graphene is easily controlled by electrical gating, this effect can be utilized to create tunable graphene-based THz metamaterials [2].

The finite-difference time-domain method (FDTD) is used extensively for studying the properties of graphene metamaterials [3]. In a most common approach, 2D graphene sheet is represented by a thin film with its thickness of the order of a single mesh step. However, the mesh step should be superfine (tens of nanometers) compared to the wavelengths of interest in the THz range (100 microns) in order to provide a satisfactory approximation of a 2D sheet conducting properties, which makes the task computationally challenging. In this paper we present a new subcell technique for conducting 2D materials. This technique is based on our subcell technique for dispersive materials [4] and implemented in the framework of EMTL library [5]. At the heart of this technique is a tensor representation of the frequency-dependent dielectric permittivity at the graphene surface. The subcell technique supports generic non-planar graphene surfaces of arbitrary orientation. We show that the proposed technique does not require a superfine mesh and properly accounts for the interaction of TM plane waves with graphene sheets, unlike the thin film approach. We apply the subcell technique to calculating optical properties of selected graphene metamaterials and compare the results with available analytical predictions [6] and experimental data [2]. We also analyze the dependence of the accuracy on the spatial mesh step and compare it with the accuracy of the thin film approach.

In conclusion, we show that the subcell technique presents a flexible and efficient approach to the modeling of graphene metamaterials and can be applied to optimize their optical properties for various applications.

**REFERENCES**

1. Geim, A. K., "Graphene: Status and Prospects," *Science*, Vol. 324, 1530–1534, 2009.
2. Ju, L., Geng, B., Horng, J., Girit, C., Martin, M., Hao, Z., Bechtel, H. A., Liang, X., Zettl, A., Shen, Y. R., and Wang, F. "Graphene plasmonics for tunable terahertz metamaterials," *Nat. Nanotech.*, Vol. 6, 630–634, 2011.
3. Wang, X.-H., Yin, W.-Y., and Chen, -Z. "Broadband modeling surface plasmon polaritons in optically pumped and curved graphene structures with an improved leapfrog ADI-FDTD method," *Opt. Commun*, Vol. 334, 152–155, 2015.
4. Deinega, A., and Valuev, I. "Subpixel smoothing for conductive and dispersive media in the finite-difference time-domain method," *Opt. Lett.*, Vol. 32, 3429–3431, 2007.

5. http://fdtd.kintechlab.com.
6. Bludov, Yu. V., Ferreira, A., Peres, N. M. R., and Vasilevskiy, M. I. "A primer on surface plasmon-polaritons in graphene," *Int. J. Mod. Phys. B*, Vol. 27, 1341001, 2013.

# Resonant Visible Light Modulation with Graphene

**Renwen. Yu[1*], Valerio Pruneri[1,2], and F. Javier García de Abajo[1,2]**

[1] ICFO-Institut de Ciències Fotòniques, The Barcelona Institute of Science and Technology, 08860 Castelldefels (Barcelona), Spain

[2] ICREA-Institució Catalana de Recerca i Estudis Avançats, Passeig Lluís Companys 23, 08010 Barcelona, Spain

[*]corresponding author: renwen.yu@icfo.es

**Abstract**- No fundamental limit appears to prevent us from designing wavelength-sized devices capable of controlling the light phase and intensity at terahertz speeds in those spectral ranges. Here we have proposed a solution based upon graphene for fast modulation and switching of light at visible and near-infrared (vis-NIR) frequencies which is of utmost importance for optical signal processing and sensing technologies.

Here, we explore an alternative solution based upon the remarkable electro-optical properties of graphene. In particular, we predict unity-order changes in the transmission and absorption of vis-NIR light produced upon electrical doping of graphene sheets coupled to realistically engineered optical cavities. The light intensity is enhanced at the graphene plane, and so is its absorption, which can be switched and modulated via Pauli blocking through varying the level of doping. Specifically, we explore dielectric planar cavities operated under either tunneling or Fabry-Perot resonant transmission conditions, as well as Mie modes in silicon nanospheres and lattice resonances in metal particle arrays. Our simulations reveal absolute variations in transmission exceeding 90% using feasible material parameters, thus supporting the application of graphene in fast electro-optics at vis-NIR frequencies.

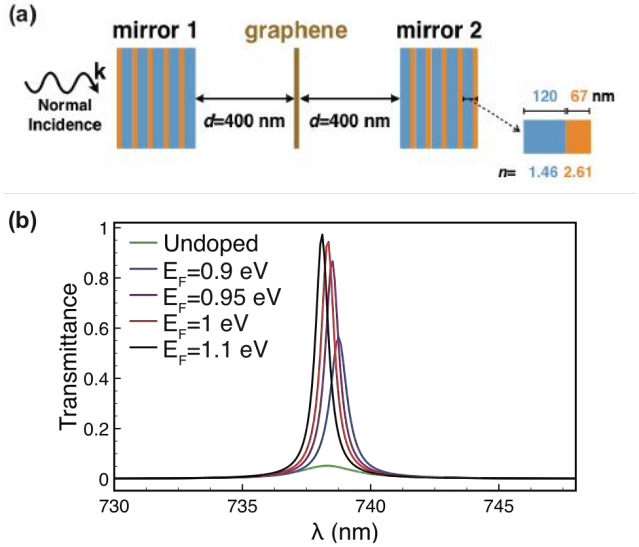



**Figure 1:** Graphene optical switch based on resonant Fabry-Perot transmission. (a) Fabry-Perot resonator

incorporating a tunable graphene layer inside the cavity flanked by two Bragg mirrors. (b) Normal-incidence transmittance for different levels of doping.

**REFERENCES**


1. R. Yu, *et al*., "Resonant visible light modulation with graphene," *ACS Photonics*, Vol. 2, 550, 2015.
2. R. Sainidou, *et al.*, "Extraordinary all-dielectric light enhancement over large volumes," *Nano Letters*, Vol. 10, 4450, 2010.
3. F. J. García de Abajo, "Graphene plasmonics: challenges and opportunities," *ACS Photonics*, Vol. 1, 135, 2014.

# Investigation in band structure and gap engineering of GaAs/$Al_xGa_{1-x}As$ nanostructures superlattices at high magnetic field and low temperature

**Driss Barkissy, Abdelhakim Nafidi*, Abderrazak Boutramine, Nassima Benchtaber, Ali Khalal, Thami El Gouti**

Laboratory of Condensed Matter Physics & Nano-Re, University Ibn Zohr, 80000 Agadir, Morocco
*corresponding author: nafidi21@yahoo.fr

## Abstract

We have investigated in the band structures $E(d_1)$, $E(k_z, k_p)$ and the effective mass $m^*/m_0$, respectively, along the growth axis and in the plane of GaAs ($d_1$= 19 nm)/$Al_{0.3}Ga_{0.7}As$ ($d_2$= 5 nm) superlattice, performed in the envelope function formalism. Our results show the effect of the well thickness $d_1$ and the temperature on the electronic structures of this superlattice. The latter has a direct band gap of 1.529 eV and the corresponding cut-off wavelength indicates that it can be used as a near infrared detector. The position of Fermi level, based on the magnetoresistance measurements of Smrčka et al. and Fermi-Dirac integral computation at 0.4 K, predict that this sample exhibits n type conductivity with a two dimensional electron gas.

## 1. Introduction

The successful development of molecular beam epitaxy (MBE) has allowed the elaboration of type I nanostructures superlattices (SLs), consisting of alternating GaAs (well) and $Al_xGa_{1-x}As$ (barrier) compound semiconductors (see figure 1a). Their bulk materials are well known as a relatively wide band gap with high electron mobility and a small lattice matching compounds [1, 2], allowing, these SLs, to reach good performances and high temperature operations.

Such artificial materials are expected to be useful in different applications fields. They can be applied in the Terahertz (THz) technologies as a source or even as a detector [3]. In their optimization of superlattices electronic devices (SLEDs), Paveliev et al. [4] have demonstrated a capability for high resolution spectrometer up to 3 THz, on a short period GaAs/AlAs superlattice multipliers, studied at 4 K, 77 K and room temperature. Therefore, such high frequencies make SLEDs good alternative to Schottky barrier diodes limited by different factors. Recently, Cárdenas et al. [5] present a promising alternative technique to produce THz waves based on the electron relaxations, between GaAs wells and AlAs barriers sub-bands, as well as Bloch–Landau oscillations in biased semiconductor superlattices (BSLs). They reported that an ideal Bloch oscillator can be realized at high magnetic field. As result, the THz emission could be more intense and coherent.

The GaAs/$Al_xGa_{1-x}As$ SLs could be used in infrared detection. Researches in this field show that, these SLs, can operate at very low bias voltage with an inter-sub-bands process, leading to an infrared spectral peak response at a chosen cutoff wavelengths. This could be extended out to 14.5 μm, in such nanostructures, with a doped GaAs wells and undoped $Al_{0.21}Ga_{0.79}As$ barriers as reported by Bandara et al. [6].

The concept of band structures is very important, since it provides a good understanding of many physical properties of these materials. Therefore, the energy difference between the conduction band minimum (CBM) and the valence band maximum (VBM) is well known as the band gap energy $E_g$ or forbidden band, which is useful in terms of explaining many electrical and optical properties. However, in the $Al_xGa_{1-x}As$ alloy, the CBM and VBM are not generally at the same electron momentum and their evolution depend on the aluminum concentration x. It's well known that GaAs (x=0) is a direct band gap compound semi-conductor and the lowest energy level is located at the center of the first Brillouin zone (Γ point) [7]. However, the photoluminescence (PL) studies of Lorenzo et al. [8] show that, the alloy $Al_xGa_{1-x}As$ becomes an indirect band gap as $x \geq 0.45$ at T= 300 K or $x \geq 0.38$ at low temperatures. Thus, $E_g$ becomes important at X point for a pure AlAs barrier (x= 1). In this case, the X minimum of AlAs is below that of GaAs. Those results were supported by the PL measurements of Fluegel et al. [9].

Several investigations on $(GaAs)_m/(AlAs)_n$ SLs, with m and n are the numbers of monolayers (ML) in one period, have predicted the existence of a transition from indirect to direct band gap for a certain range of layers thickness. Therefore, the PL observations of Litovchenko et al. [10], at 5 K on a number of asymmetric SLs, with a different well and barrier thicknesses ($m \neq n$), indicate that, when the ratio of the well to barrier thickness ($d_1/d_2$) is at least two, the superlattice exhibits a direct band gap. According to the combined photoacoustic spectroscopy, high excitation-intensity time-resolved luminescence and photoluminescence excitation measurements of Cingolani et

al. [11], at both T= 10 K and 300 K, such transition occurs on a symmetric SLs for m= n= 12 ML.

On the other hand, the study of magneto-transport properties is a powerful tool for characterizing low dimensional semiconductors systems. At sufficiently low temperatures and under high magnetic fields, different quantum phenomena have been observed. Among them, the Shubnikov de Haas effect (SDH) which consists of oscillations in the magnetoresistance and it can be used to deduce several transport parameters. For example, the periodicity of oscillations gives the carrier density and the Fermi level. Once the Fermi level and the density of donor impurities $N_d$ present in the sample are known, the donor level $E_d$ can be calculated. The latter show the effect of such impurities on the conductivity of the superlattice.

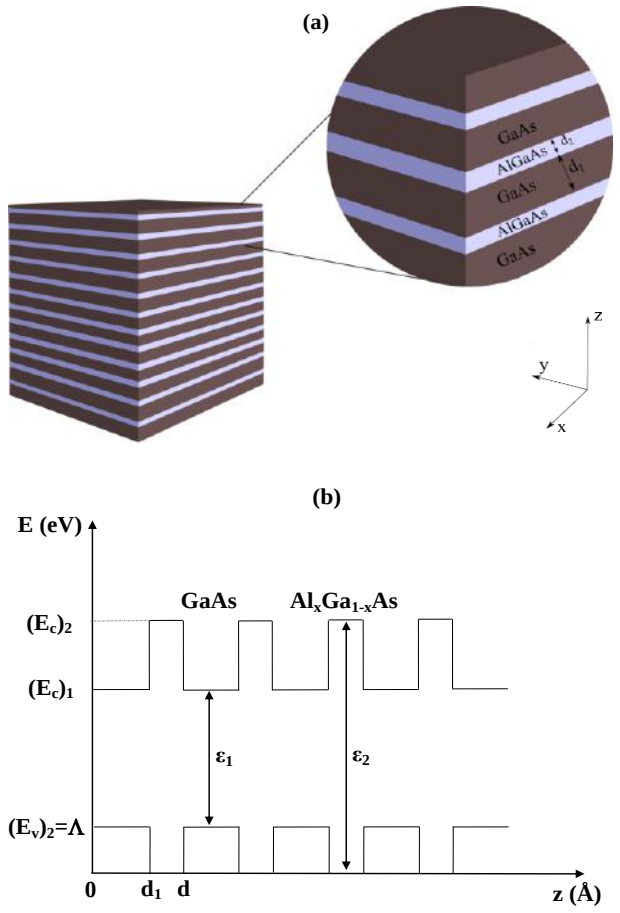



Fig. 1 (a) Illustration of periodic $GaAs/Al_xGa_{1-x}As$ superlattice. (b) Energy along the growth direction with different parameters related to the electronic band structures. $(E_c)_i$ and $(E_v)_i$ where i= 1, 2 are the bottom of conduction and the top of valence bands energies for GaAs and $Al_xGa_{1-x}As$ bulks, respectively.

## 2. Theoretical formulations and computational details

### 2.1. Dispersion relations of light particles and heavy holes sub-bands of superlattices

The calculations of GaAs/AlAs band structures have been performed in the envelope function formalism, in terms of some parameters denoted by 1 and 2 for GaAs and $Al_xGa_{1-x}As$ bulks materials, respectively, which will be discussed in more detail below.

The general expression of the dispersion relation for light particles (electrons and light holes) and heavy holes sub-bands is given by [12,13]:

$$\cos[k_z(d_1+d_2)] = \cos(k_1 d_1)\cos(k_2 d_2) - \frac{1}{2}[(\xi+\frac{1}{\xi}) + \frac{k_p^2}{4k_1k_2}(r+\frac{1}{r}-2)]\sin(k_1 d_1)\sin(k_2 d_2) \quad , (1)$$

With $k_z$ the wave vector in the direction of growth and $k_p(k_x,k_y)$ in the plane of the superlattice. The origin of the energy E was taken at the top of $Al_xGa_{1-x}As$ valence band as shown in the Fig. 1b. At given energy and in each host material, the two–band Kane model [14] gives the wave vector $(k_i^2+k_p^2)$. In this case, the energy E of light particles is given by:

$$\begin{cases} \frac{2}{3}P_1^2\hbar^2(k_1^2+k_p^2) = (E-\varepsilon_1-\Lambda)(E-\Lambda) & \text{for GaAs} \\ \frac{2}{3}P_2^2\hbar^2(k_2^2+k_p^2) = E(E-\varepsilon_2) & \text{for } Al_xGa_{1-x}As \end{cases} , \quad (2)$$

The expression of $\xi$ and r in the Eq.(1) are:

$$\xi = \frac{k_1}{k_2}r \text{ and } r = \frac{E-\varepsilon_2}{E-\varepsilon_1-\Lambda}, \quad (3)$$

We used here, the empirical expressions of GaAs and $Al_xGa_{1-x}As$ band gaps $\varepsilon_i$(i= 1, 2), at Γ point, for x≤ 0.69 as a function of temperature [15,16]:

$$\varepsilon_1(\Gamma) = 1.519 - \left(5.405\ 10^{-4}\ T^2\right)/(T+204), \quad (4)$$

$$\varepsilon_2(T,x) = (1.517+1.39x) - \frac{(5.5+3.35x)10^{-4}T^2}{T+(255+88x)}, \quad (5)$$

The Kane matrix element $P_i$ was calculated by using the Kane energy $E_{pi}$ formula [17,18]:

$$P_i^2 = \frac{E_{pi}}{2m_0}, \quad (6)$$

From the same equation (1), the superlattice heavy hole sub-bands can be calculated with the following relations:

$$\begin{cases} \frac{\hbar^2}{2m^*_{HH_1}}(k_1^2+k_p^2) = (E-\Lambda) & \text{for GaAs} \\ \frac{\hbar^2}{2m^*_{HH_2}}(k_2^2+k_p^2) = E & \text{for } Al_xGa_{1-x}As \end{cases} , \quad (7)$$

$$\text{With } \xi = \frac{k_1}{k_2}r \text{ and } r = \frac{m^*_{HH_2}}{m^*_{HH_1}}, \quad (8)$$

Where $m_{HH1}{}^* = 0.34m_0$ and $m_{HH2}{}^* = (0.33+0.18x)m_0$ are the heavy hole effective masses of GaAs and $Al_xGa_{1-x}As$ bulks, respectively [18,19].

In this work, we choose to use the valence band offset Λ, between heavy holes sub-bands edges of GaAs and $Al_xGa_{1-x}As$ at Γ point. The calculations of Yin Wang et al. [20] using atomistic first principles approach show that Λ(eV)= 0.587x.

The calculations of band structures consist of solving the general dispersion relation with the reported parameters. Thus, in the Eq. (1), the superlattice energy state exists if the right-hand side lies in the range -1 to 1. In other words, $-1 \leq \cos(k_z d) \leq 1$ implies $-\pi/d \leq k_z \leq \pi/d$ in the first Brillouin zone, with $d= d_1+d_2$ is the superlattice period. In the study of energy E as a function of wave vector in the direction of growth $k_z$ ($k_p$=0), the solving procedure consists of going with small steps of energy through the studied range. Then finding, for a given E, the value of $k_z$ which is root of the dispersion relations. The same procedure is used for studying E versus the wave vector in the plane of the superlattice $k_p$ ($k_z$=0 and $k_z= \pi/d$).

The sample studied here consists of alternating $d_1$(GaAs)= 190 Å and $d_2(Al_{0.3}Ga_{0.7}As)$= 50 Å. Consequently, $d_2/d_1$=0.26 and the superlattice period is $d= d_1+d_2$= 240 Å.

### 2.2. Fermi level calculations

In order to determine the Fermi level $E_F$ as a function of temperature T, one can use the Fermi-Dirac integral [21,22]. The general expression of such integral allows the calculation of carrier density n, in particular, the electron concentration, by the following formula:

$$n= N_c \; F_j(\eta_F)_i^2 , \qquad (9)$$

With $N_c$ the effective density of states at the edge of the conduction band and $F_j(\eta_F)$ is the Fermi integral of order j:

$$F_j(\eta_F)= \frac{1}{\Gamma(j+1)} \int_0^{+\infty} \frac{\eta^j}{1+e^{(\eta-\eta_F)}} \, d\eta ,$$

Where Γ(j+1) is the Gamma-function and $\eta=(E-E_c)/k_BT$ and $\eta_F=(E_F-E_c)/k_BT$ is the reduced Fermi energy, $E_c$ is the energy at the bottom of the conduction band and $k_B$ the Boltzmann constant.

In a three dimensional (3D) electron transport (j=+1/2), this integral becomes:

$$n_{3D}= \frac{2}{\sqrt{\pi}} N_c^{3D} \int_0^{\infty} \frac{\eta^{1/2}}{1+e^{(\eta-\eta_F)}} \, d\eta , \qquad (10)$$

$$\text{With } N_c^{3D} = 2\left( \frac{m^*_{E_1} k_B T}{\hbar^2} \right)^{3/2} ,$$

Where $m_{E1}$* is the electron effective mass and ħ is the reduced Planck's constant.

In the case of two dimensional (2D) systems, with only two degrees of spatial freedom (j= 0), the expression of Fermi–Dirac integral is given by:

$$n_{2D} = N_c^{2D} \int_0^{+\infty} \frac{1}{1+e^{(\eta-\eta_F)}} \, d\eta ,$$

(11)

$$\text{With } N_c^{2D} = \frac{m^*_{E_1} k_B T}{\pi \hbar^2} ,$$

The resolution of these integrals cannot be done analytically for non zero temperatures, but through numerical approaches with the calculated band structures parameters which will be discussed later. Therefore, the numerical evaluation consists of iterating the value of $E_F$ in the formulas (10) or (11) between $E_g$ and $E_c+100k_BT$ that gives a concentration of electrons in the conduction band near to the measured one.

## 3. Results and discussions

### 3.1. Band gap engineering

The Fig. 2a, shows the energy of conduction ($E_i$), first light-hole ($h_1$) and the heavy-hole ($HH_1$) sub-bands at the center Γ ($k_z$= 0) and the limit ($k_z= \pi/d$) of the first Brillouin zone as a function of $d_2$ at T= 0.4 K for $d_1$= 0.26 $d_2$. The well thickness of the studied sample is indicated by a vertical dashed line. The calculated band gap energy, from the bottom of the first conduction sub-band to the top of the first valence sub-band is $E_g= E_1-HH_1$= 1.529 eV.

We illustrate in the Fig. 2b, the band gap $E_g$ as a function of well thickness $d_1$ for various ratio $d_2/d_1$. For each $d_1$<105Å, the calculated $E_g$ increases as $d_2/d_1$ increases. For a given ratio, when the thickness $d_1$ increases

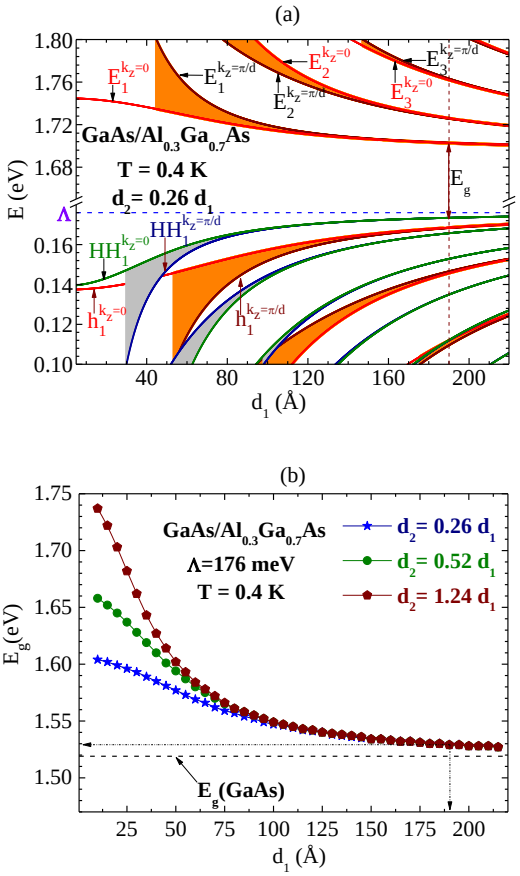



Fig. 2 (a) Energy of both conduction (upper part ) and valence (lower part) sub-bands as function of well thickness. The vertical dashed line show $E_g$ of the investigated SL and solid areas show the width of sub-bands. (b) Calculated band gap versus well thickness $d_1$ for various $d_2/d_1$ at 0.4 K.

the band gap decreases. This phenomenon can be attributed to the creation of more allowed states in the forbidden bands. The formation of such regions, available to be occupied by electrons, is due to the fact that the number of overlapping orbitals between nearest atoms grows with thickness. Consequently, the valence and conduction bands separation, starts to narrow, leading to a reduction of the band gap [23]. It is noteworthy that, this effect is more pronounced with GaAs thickness $d_1$ because of large confinement of the carriers charge in the well layer (GaAs). When $d_1$ is infinite, the band gap energy converges to that of GaAs and the superlattice, act like a set of isolated quantum wells.

In the investigated superlattice, the effect of temperature on the band gap, is presented in the Fig. 3. At low temperatures, the band gap varies hardly. Then, it decreases with temperature from 1.529 eV at 0.4 K to 1.431 eV at 300K. In order to explain such behavior in semi-conductors, Ünlü et al. [24] proposed a thermodynamic model and demonstrate that, the observed effect is due to the thermal energy and the expansion of the lattice constant with temperature, which cause an increase in the inter-atomic spacing and the potential seen by electrons decreases, leading to a smaller band gap.

In the Fig. 3, the calculated cut-off wavelength is given by:

$$\lambda_c\,(\mathrm{nm}) = \frac{1240}{E_g\,(\mathrm{eV})}\quad , \tag{12}$$

In the investigated temperature range of 0.4 K to 300 K, 811 nm ≤ $\lambda_c$ ≤ 867 nm, situates this sample in the near infrared region.

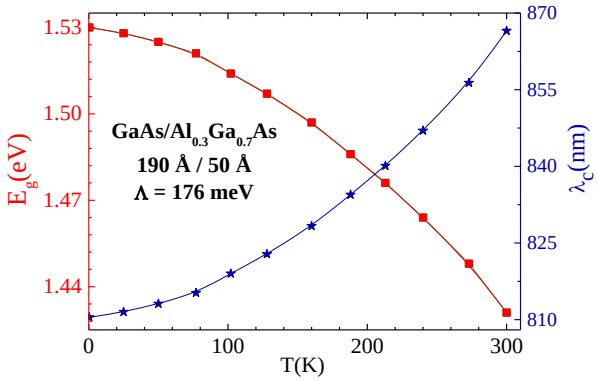



Fig. 3 Band gap Energy and cut-off wavelength $\lambda_c$ as a function of temperature.

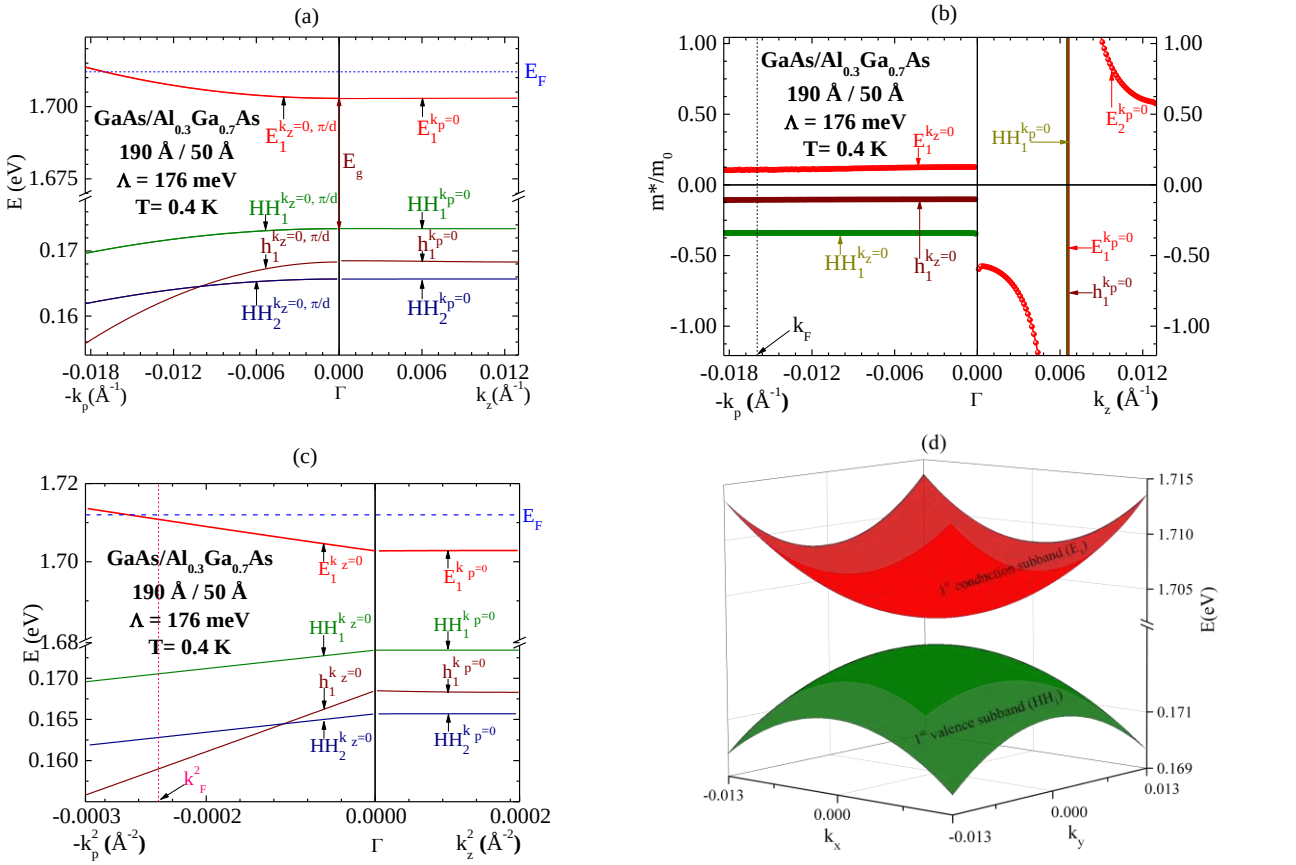



Fig. 4 (a) Band structures along $k_z$ and $k_p$, at 0.4 K. $E_F$ is the Fermi Level. (b) Carrier effective masses calculated along $k_z$ and $k_p$, in the growth direction and in the plane of the investigated superlattice, respectively. (c) Band structures along $k_p^2$ and $k_z^2$ of the investigated superlattice. (d) Energy dispersion relations $E(k_x,k_y)$ of the first conduction $E_1$ and valence $HH_1$ sub-bands in the first Brillouin zone (with $k_p^2 = k_x^2 + k_y^2$) at T=0.4 K.

In Fig. 4a, we show the conduction and valence sub-bands of $GaAs/Al_{0.3}Ga_{0.7}As$ superlattice at very low temperature. These calculations were performed from the centre to the limit of the first Brillouin zone, in the plane $k_p$ ($k_x$,$k_y$) and along $k_z$. In the $k_p$ wave vector direction, the first conduction sub-band $E_1$ increases with $k_p$ whereas $h_1$, $HH_1$ and $HH_2$ decrease. In addition, these dispersion curves show that, the electronic states are quantized and discrete in the $k_z$ direction and pseudo-continuous in the plane of the superlattice. Consequently, a weak coupled system can be distinguished. In this case, the electronic transport is dominated in the plane of the superlattice (parallel transport). The right side of energy spectra, in the Fig. 4a, can be used for interpreting the optical transitions, in the photoluminescence studies, between the conduction and valence sub-bands as well as in the electronic transport investigations of such sample. In addition, the Fig. 4c shows that $E_1$, $HH_1$ and $h_1$ are linear along $k_p^2$ and confirm the parabolicity of these sub-bands as shown in the Fig. 4d. The energy difference between the bottom of the conduction ($E_1$) and the top of the valence ($HH_1$) sub-bands is equal to the fundamental band gap reported above. Moreover, at low temperature, the Fermi level $E_F$, calculated below, is located in the conduction band, confirming that, this sample exhibits n type conductivity.

For $GaAs/Al_xGa_{1-x}As$ SLs, the carrier's effective mass is given by 3×3 tensor (anisotropic medium) and its elements along i and j directions, with the energy E, are defined by:

$$\left(\frac{1}{m^*}\right)_{ij} = \frac{1}{\hbar^2}\frac{\partial^2 E_{k_{ij}}}{\partial k_i \partial k_j}, \qquad (13)$$

In the Fig. 4b, we show the calculated effective mass of the first conduction and valence sub-bands, in the plane $k_p(k_x,k_y)$ and along the growth direction $k_z$ of the reciprocal space derived from Fig. 4a. Along $k_p$, the effective mass of heavy and light holes are almost constant $m^*_{HH1}$= -0.34$m_0$ $m^*_{h1}$= -0.11$m_0$ and that of electrons $m^*_{E1}$ decreases from 0.13$m_0$ at the center Γ to 0.11$m_0$ at the limit $k_p$= -0.0185Å$^{-1}$.

### 3.2. Interpretation of the quantum Hall Effect

In order to estimate the Fermi level as a function of magnetic field we used the magneto-resistance data of Smrčka et al.[25]. It's well known that the oscillations of the transverse magnetoresistance at very low temperatures are periodic with respect to 1/B, due to the Shubnikov de Haas effect. The electron concentration $n_{2D}$ is related to the period Δ(1/B) by:

$$n_{2D} = -\frac{e}{\pi\hbar\,\Delta(1/B)}, \qquad (14)$$

Thus, the inverse of the minima $1/B_{min}$ as a function of the entire N follow this expression:

$$\frac{1}{B_{min}} = \Delta(1/B)\left(N+\frac{1}{2}\right), \qquad (15)$$

The slope evaluated from the linear line is Δ(1/B)= -0.118 T$^{-1}$ and $n_{2D}$= 4.1 10$^{11}$ cm$^{-2}$. This result, is in good with the reported carrier density of $n_H$= 3.9 10$^{11}$ cm$^{-2}$ by Smrčka et al.[25].

Once the electron concentration $n_{2D}$ is known, the Fermi wave vector $k_F$ can be calculated with this formula:

$$k_F = (2\pi\, n_{2D})^{1/2}, \qquad (16)$$

$|k_F|$= 0.016 Å$^{-1}$ is indicated in the Fig. 4a by vertical dashed line. The corresponding electron $m^*_{E1}$, light hole $m^*_{h1}$ and heavy hole $m^*_{HH1}$ effective masses are 0.11 $m_0$, -0.11 $m_0$ and -0.35 $m_0$, respectively.

At low temperature, the Fermi level is given by:

$$\left|E_F - E_c\right| = -\frac{e\hbar}{m^*_{E_1}\,\Delta(1/B)} = \frac{n_{2D}\,\pi\hbar^2}{m^*_{E_1}}, \qquad (17)$$

With $E_c$=1.703 eV is the edge of the conduction band. As result, $E_F$= 1.712 eV. The same value was found with the Fermi-Dirac integral, formula (11), for which $E_F$=1.7115 eV. Therefore, this sample exhibits n type conductivity.

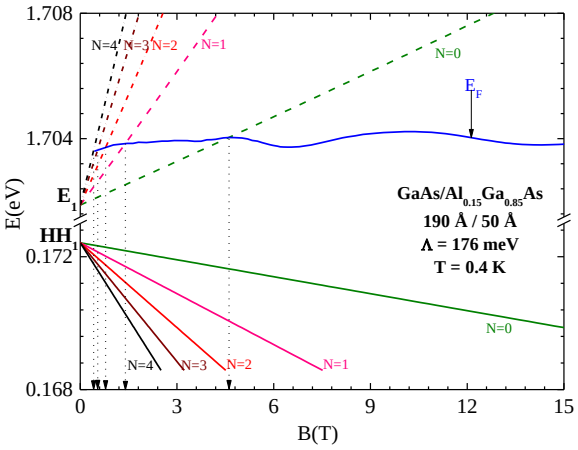



Fig. 5: Energy position of the calculated Landau levels of the first conduction $E_1$ and valence $HH_1$ sub-bands, and the Fermi level $E_F$, as a function of magnetic field.

The application of an external magnetic field on such quantum Hall system, leads to a creation of landau levels and their calculated energies, for $E_1$ and $HH_1$ are shown in the Fig. 5. When the magnetic field increases, the crossovers between the calculated Landau levels (for N= 0 to 4) and the Fermi level indicate the same minima of the transverse magneto resistance oscillations (Shubnikov-de Haas effect), observed in ref.[25], at B= 4.6 T, 1.4 T, 0.8 T, 0.54 T and 0.4 T as shown in the Fig. 5.

## 4. Conclusions

In this paper, we investigated the electronic properties of $GaAs/Al_{0.3}Ga_{0.7}As$ superlattice, based on the envelope function formalism at different temperatures, with a valence band offset of 176 meV. The effect of well thickness $d_1$, ratio $d_2/d_1$ and temperature on the band gap $E_g$ have been also studied. These calculations show that $E_g$ decreases with the well thickness and for each $d_1$, the band gap increases with the ratio $d_2/d_1$. The temperature dependence of the direct band gap indicates that $E_g$ decreases with temperature. In addition, the spectra of energy $E(k_z, k_p)$, $E(k_z^2, k_p^2)$ and effective mass $m^*/m_0$ in the direction of growth and in the plane of this superlattice, show that, the first conduction $E_1$ and valence $h_1$ sub-bands are parabolic and the two dimensional electron gas effective mass is 0.11 $m_0$ at 0.4 K.

The oscillations of transverse magnetoresistance (Shubnikov de Haas effect) measured by Smrčka et al. show a two dimensional electron gas with an effective mass of $0.245m_0$ at 4.2K. By using carrier density n and the calculated bands structure parameters, we have determined the Fermi level. As result, this sample exhibits n type conductivity with an electron concentration of $3.9\ 10^{11}$ $cm^{-2}$, $E_F$= 1.712 eV at T= 0.4 K.

## References


1. V. Andreev, in *Polym. Phosphors, Voltaics Radioisot. Microbatteries* (CRC Press, 2002), pp. 289–363.

2. M. Wilde, in *Magn. Meas. Low-Dimensional Electron Syst. High-Mobility GaAs SiGe Heterostruct.* (Cuvillier Verlag, 2005), pp. 34–40.

3. E. Bründermann, H.-W. Hübers, and M. F. Kimmitt, *Terahertz Techniques* (Springer Berlin Heidelberg, Berlin, Heidelberg, 2012).

4. D. G. Paveliev, Y. I. Koschurinov, V. M. Ustinov, and A. E. Zhukov, in *19th Int. Symp. Sp. Terahertz Technol. Groningen, 28-30 April 2008* (Groningen, The Netherlands, 2008), pp. 319–328.

5. J. R. Cárdenas, R. Ferreira, and G. Bastard, Superlattices Microstruct. (2015).

6. K. M. S. V. Bandara, J.-W. Choe, M. H. Francombe, A. G. U. Perera, and Y. F. Lin, Appl. Phys. Lett. **60**, 3022 (1992).

7. S. N. Data, U. III-V, and I.-V. Compounds, *New Data and Updates for III-V, II-VI and I-VII Compounds* (Springer Berlin Heidelberg, Berlin, Heidelberg, 2010).

8. L. Pavesi and M. Guzzi, J. Appl. Phys. **75**, 4779 (1994).

9. B. Fluegel, K. Alberi, J. Reno, and A. Mascarenhas, Jpn. J. Appl. Phys. **54**, 042402 (2015).

10. V. G. Litovchenko, D. V. Korbutyak, a. I. Bercha, Y. V. Kryuchenko, S. G. Krylyuk, H. T. Grahn, R. Hey, and K. H. Ploog, Appl. Phys. Lett. **78**, 4085 (2001).

11. R. Cingolani, M. Holtz, R. Muralidharan, K. Ploog, K. Reimann, and K. Syassen, Surf. Sci. **228**, 217 (1990).

12. G. Bastard, Phys. Rev. B **25**, 7584 (1982).

13. D. Barkissy, A. Nafidi, A. Boutramine, H. Charifi, A. Elanique, and M. Massaq, J. Low Temp. Phys. **182**, 185 (2016).

14. E. O. Kane, J. Phys. Chem. Solids **1**, 249 (1957).

15. M. A. Herman, W. Richter, and H. Sitter, in *Gr. IV Elem. IV-IV III-V Compd. Part B - Electron. Transp. Opt. Other Prop.* (Springer-Verlag, Berlin/Heidelberg, 2004), pp. 1–15.

16. I. Vurgaftman, J. R. Meyer, and L. R. Ram-Mohan, J. Appl. Phys. **89**, 5815 (2001).

17. G. Bastard, in *Wave Mech. Appl. to Semicond. Heterostruct.* (Les Editions de Physique, Paris, 1988), p. 49.

18. S. Z. Karazhanov, Semiconductors **39**, 161 (2005).

19. O. Madelung, U. Rössler, and M. Schulz, editors , in *Gr. IV Elem. IV-IV III-V Compd. Part B - Electron. Transp. Opt. Other Prop. SE - 553* (Springer Berlin Heidelberg, 2002), pp. 1–11.

20. Y. Wang, F. Zahid, Y. Zhu, L. Liu, J. Wang, and H. Guo, Appl. Phys. Lett. **102**, 132109 (2013).

21. R. Kim and M. Lundstrom, arXiv:0811.0116 (2008).

22. E. F. Schubert, *Doping in III–V Semiconductors* (Cambridge University Press, Cambridge, 1993).

23. S. V. Gaponenko, in *Opt. Prop. Semicond. Nanocrystals* (Cambridge University Press, Cambridge, 1998), pp. 27–54.

24. H. Ünlü, Solid. State. Electron. **35**, 1343 (1992).

25. L. Smrčka, N. A. Goncharuk, P. Svoboda, P. Vašek, Y. Krupko, and W. Wegscheider, Microelectronics J. **39**, 411 (2008).

# Chiral and bianisotropic materials

# The Electromagnetic Chirality of an Object

**I. Fernandez-Corbaton**[1] and **C. Rockstuhl**[1,2]

[1]Institute of Nanotechnology, Karlsruhe Institute of Technology, 76021 Karlsruhe, Germany
[2]Institut of Theoretical Solid State Physics, Karlsruhe Institute of Technology, 76131 Karlsruhe, Germany
ivan.fernandez-corbaton@kit.edu

**Abstract**— We introduce a definition of the electromagnetic chirality of an object. The definition allows the absolute ranking of objects according to their chirality and has an upper bound. The common definition of chirality lacks both these features. We then study the physical properties of the objects that achieve the upper bound and show that they have promising applications. We discuss two of them: A two-fold resonantly enhanced and background free circular dichroism measurement setup and angle independent helicity filtering glasses.

Chirality is studied in very diverse scientific disciplines. One of them is the interaction of chiral matter with electromagnetic fields. It started two centuries ago [1] and still attracts significant attention from both its theoretical (e.g. [2–9]) and practical sides (e.g. [10–17]).

An object is said to be chiral if it cannot be super-imposed onto its mirror image. This definition has significant problems that arise when attempting to measure chirality [18]. As discussed in [18–21], it is possible to establish whether an object is chiral or not, but it is impossible to rank objects according to their chirality in an absolute way. Moreover, it has been proven that the common definition of chirality do not have meaningful upper bounds. This implies that we cannot actually tell whether object A is more chiral than object B, or whether a given design has attained its maximum possible chirality. The lack of unambiguous ranking and upper bounds for the magnitude of chirality is a handicap for both theoretical and practical developments. In particular, in the design of chiral structures for interaction with the field, these ambiguities leave us unable to compare the chirality of different structures and without an extremal reference to design towards. Additionally, it leaves us with no other requirement besides chirality itself that could guide the design. With our definition of electromagnetic chirality, upper bounds exist and are attained when objects meet specific requirements.

In Ref. 22, we introduce the definition of the electromagnetic chirality of an object, which can be experimentally determined. The definition allows to rank all objects according to their electromagnetic chirality, which we show to be upper bounded by the square root of the object's scattering cross section. Using this definition, we study the properties of objects with maximum electromagnetic chirality. Notably, we discover that they shall not couple the states of definite polarization handedness, i.e. they must have duality symmetry. Dual symmetric objects, also said to have "balanced electric and magnetic responses", have been the recent object of much research attention, both theoretical, and experimental [17, 23, 24]. The fact that maximally electromagnetically chiral objects are dual-symmetric is in line with recent theoretical and experimental results, which establish a tight relationship between duality symmetry and optical activity [25–27].

Finally, we outline two applications for these extremal objects. The first application is a two-fold resonantly enhanced and background free circular dichroism measurement (CD) setup. This proposal solves two crucial problems in the use of nanostructures for sensitive CD: The fact that, even when the external field is circularly polarised, the near fields excited around the nanostructures contain both circular polarizations, and the fact that the resulting weak molecular field needs to be distinguished against a large background caused by the nanostructure itself. The second application shows how to overcome the main limitation of glasses for viewing 3D projections: The degradation of the 3D effect as the angle between the user and the normal of the projector grows. We present angle independent polarization filtering glasses.

## REFERENCES

1. J.-B. Biot. "Phénomènes de polarisation successive, observés dans les fluides homogènes". *Bull soc. philomath.*, **1**, 190 (1815).
2. Y. Tang and A. E. Cohen. "Optical chirality and its interaction with matter". *Phys. Rev. Lett.*, **104, 16**, 163901 (2010).

3. D. L. Andrews and M. M. Coles. "Optical superchirality and electromagnetic angular momentum". In *SPIE OPTO*, 827405–827405. International Society for Optics and Photonics (2012).
4. I. Sersic, M. A. van de Haar, F. B. Arango, and A. F. Koenderink. "Ubiquity of optical activity in planar metamaterial scatterers". *Phys. Rev. Lett.*, **108, 22**, 223903 (2012).
5. M. M. Coles, M. D. Williams, K. Saadi, D. S. Bradshaw, and D. L. Andrews. "Chiral nanoemitter array: A launchpad for optical vortices". *Laser & Photonics Reviews*, **7, 6**, 1088 (2013).
6. A. Canaguier-Durand, J. A. Hutchison, C. Genet, and T. W. Ebbesen. "Mechanical separation of chiral dipoles by chiral light". *New J. Phys.*, **15, 12**, 123037 (2013).
7. R. P. Cameron, S. M. Barnett, and A. M. Yao. "Discriminatory optical force for chiral molecules". *New J. Phys.*, **16, 1**, 013020 (2014).
8. K. Y. Bliokh, Y. S. Kivshar, and F. Nori. "Magnetoelectric effects in local light-matter interactions". *Phys. Rev. Lett.*, **113, 3**, 033601 (2014).
9. M. Nieto-Vesperinas. "Optical theorem for the conservation of electromagnetic helicity: Significance for molecular energy transfer and enantiomeric discrimination by circular dichroism". *Phys. Rev. A*, **92, 2**, 023813 (2015).
10. J. K. Gansel, M. Thiel, M. S. Rill, M. Decker, K. Bade, V. Saile, G. von Freymann, S. Linden, and M. Wegener. "Gold helix photonic metamaterial as broadband circular polarizer". *Science*, **325, 5947**, 1513 (2009).
11. M. Decker, R. Zhao, C. M. Soukoulis, S. Linden, and M. Wegener. "Twisted split-ring-resonator photonic metamaterial with huge optical activity". *Opt. Lett.*, **35, 10**, 1593 (2010).
12. J. Kaschke, J. K. Gansel, and M. Wegener. "On metamaterial circular polarizers based on metal n-helices". *Opt. Express*, **20, 23**, 26012 (2012).
13. R. Schreiber, N. Luong, Z. Fan, A. Kuzyk, P. C. Nickels, T. Zhang, D. M. Smith, B. Yurke, W. Kuang, A. O. Govorov, and T. Liedl. "Chiral plasmonic DNA nanostructures with switchable circular dichroism". *Nat Commun*, **4** (2013).
14. L. Chaix, S. De Brion, F. Lévy-Bertrand, V. Simonet, R. Ballou, B. Canals, P. Lejay, J.-B. Brubach, G. Creff, F. Willaert, *et al.* "Thz magnetoelectric atomic rotations in the chiral compound ba 3 nbfe 3 si 2 o 14". *Phys. Rev. Lett.*, **110, 15**, 157208 (2013).
15. M. Schäferling, X. Yin, N. Engheta, and H. Giessen. "Helical plasmonic nanostructures as prototypical chiral near-field sources". *ACS Photonics*, **1, 6**, 530 (2014).
16. J. H. Jung, S. H. Jung, J. Jeon, H. Kim, and J. Jaworski. "Chiral information in achiral solid state through helical rearrangement in self-assembled nanofibers". *Nanoscale.* (2015).
17. V. S. Asadchy, I. A. Faniayeu, Y. Ra'di, S. A. Khakhomov, I. V. Semchenko, and S. A. Tretyakov. "Broadband reflectionless metasheets: Frequency-selective transmission and perfect absorption". *Phys. Rev. X*, **5**, 031005 (2015).
18. P. W. Fowler. "Quantification of chirality: Attempting the impossible". *Symmetry: Culture and Science*, **16, 4**, 321 (2005).
19. A. B. Buda and K. Mislow. "A hausdorff chirality measure". *J. Am. Chem. Soc.*, **114, 15**, 6006 (1992).
20. M. Petitjean. "Chirality and symmetry measures: A transdisciplinary review". *Entropy*, **5, 3**, 271 (2003).
21. A. Rassat and P. W. Fowler. "Is there a most chiral tetrahedron?" *Chemistry A European Journal*, **10, 24**, 6575 (2004).
22. I. Fernandez-Corbaton and C. Rockstuhl. "Objects of maximum electromagnetic chirality". *arXiv preprint arXiv:1508.04049* (2015).
23. S. Person, M. Jain, Z. Lapin, J. J. Sáenz, G. Wicks, and L. Novotny. "Demonstration of zero optical backscattering from single nanoparticles". *Nano Lett.*, **13, 4**, 1806 (2013).
24. X. Zambrana-Puyalto, X. Vidal, M. L. Juan, and G. Molina-Terriza. "Dual and anti-dual modes in dielectric spheres". *Opt. Express*, **21, 15**, 17520 (2013).
25. I. Fernandez-Corbaton, X. Vidal, N. Tischler, and G. Molina-Terriza. "Necessary symmetry conditions for the rotation of light". *J. Chem. Phys*, **138, 21** (2013).
26. I. Fernandez-Corbaton, M. Fruhnert, and C. Rockstuhl. "Dual and Chiral Objects for Optical Activity in General Scattering Directions". *ACS Photonics*, **2, 3**, 376384 (2015).
27. X. Vidal, I. Fernandez-Corbaton, A. F. Barbara, and G. Molina-Terriza. "Polarization properties of light scattered off solutions of chiral molecules in non-forward direction". *Applied Physics Letters*, **107, 21**, 211107 (2015).

# Concentration and redirection of light in in metal nanoparticle/polymer nanocomposites waveguides

**M. Signoretto [1]*, I. Suárez[1], R. Abargues[2], P. Rodríguez-Cantó[2], V. Chirvony[1], and J. Martínez-Pastor[1]**

[1] C/Catedrático Jose Beltrán 2, ICMUV, University of Valencia, 46980 Paterna, Valencia (Spain)
[2] Intenanomat S.L, C/Catedrático José Beltrán 2, 46980 Paterna, Spain
*sigmatt@uv.es

**Abstract**-A nanocomposite made by in situ synthesis of metal nanoparticles (MNP) in the commercially available photoresist novolak (Nv) is proposed as a novel material for integrated optics. Size of MNP is controlled during the fabrication in order to provide a method to tune the absorption/scattering properties of the resulting nanocomposite and its effective refractive index. Practical applications of this nanocomposite, like coupling light into organic waveguide or enhancing the photoluminescence of an active material integrated in the structure are demonstrated.

Metal nanoparticles (MNPs) are potential candidates to provide novel functionalities in photonic devices [1]. Their exotic optical properties derived from the highly localized surface plasmon polariton (LR-SPP) can be applied to redirect photons or to concentrate the electromagnetic energy. For example MNPs have been used to increase efficiency of solar cells [2], to construct optical sensors [3] or to confine light in the nanometer scale [4]. Moreover, the development of layers or patterns of MNPs, creates not only a suitable technique to integrate these nanostructures in optoelectronic devices, but also a way to tune their optical properties.

In this way we propose a novel technology able to control in situ the size of Au MNPs embedded in the commercially available resist Novolak (NV). When the MNP-NV nanocomposite is embedded in a solution of the precursor metal salt, the MNPs can act as a seed for further MNPs growth [5]. In this way, the intensity and position of the MNP plasmonic resonance can be tuned with the size of the nanostructures, as it is presented in Figure 1. At the beginning of the process the radius of the MNPs was around 20 nm (inset in Figure 1a) and the corresponding plasmonic resonance peak was at 550 nm (Figure 1a). After 20 hours in the metal salt solution, the size of the MNP growth up to 50 nm (inset in Figure 1b) and the resonance peak was red-shifted to 650 nm (Figure 1b). In addition, since more and more Au is being incorporated in the NV layer, the effective refractive index of nanocomposite is increased in the plasmonic resonance region.

The host matrix is a commercially available resist suitable for e-beam or UV lithography so that the nanocomposite can be patterned (Fig. 2c) and hence can be easily integrated in different photonic structures. For example, we incorporated the nanocomposite in an optical waveguide by patterning a MNP-Nv film on a $SiO_2$/Si substrate and then capping with a PMMA layer [5], as it is illustrated in Fig. 2a. Since the effective refractive index of the nanocomposite layer is increased in the plasmonic resonance region, the MNP-Nv film can confine light at a range of wavelengths controlled by the fabrication conditions. In addition, the high scattering cross section of the MNP can be exploited to redirect light through the PMMA/$SiO_2$ waveguide. In this way, we demonstrate coupling of normally incident light to the PMMA waveguide in a broad wavelength range (400-780 nm) with the coupling efficiencies larger than 1 % measured at the output edge of the waveguide structure [5].

The photographs presented in fig. 2b show an example of blue, green a red light coupled into the structure. Finally, an active material was embedded into the PMMA film doped with an organic dye in order to study the interaction of the dye photoluminescence with the plasmonic resonance of the MNPs. In this way, a significant enhancement of the PL was detected for the cases when the PL spectrally overlaps with the plasmon resonance.

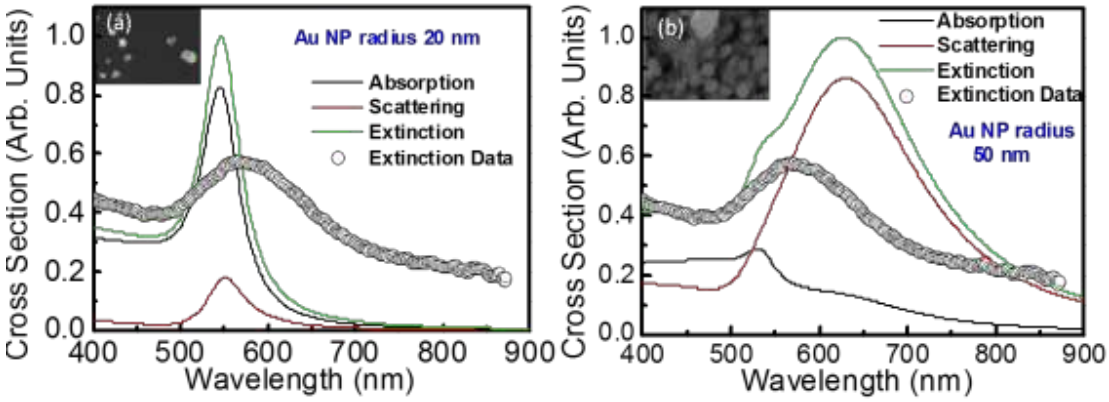



**Figure 1**. Extinction (green), absorption (black) and scattering (red) cross sections calculated from the Mie theory for spherical AuNPs with 20 (a) and 50 nm (b) radii and the measured extinction spectra (circules). SEM images of the MNPs insight the nanocomposite are shown in the inset.

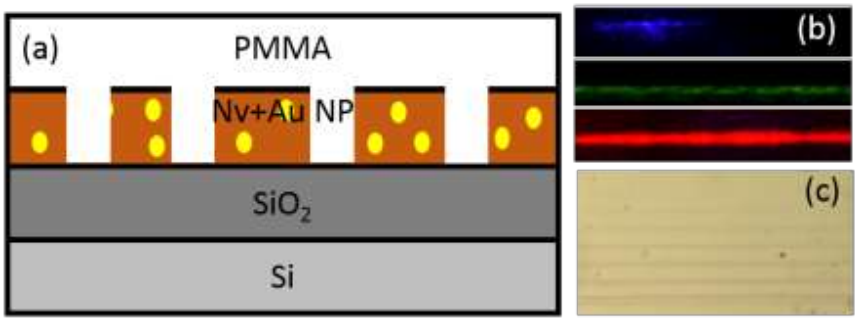



**Figure 2.** (a) The sample structure and (b) photographs of the light (λ=450, 533, 633 nm) coupled into the PMMA waveguide; (c) the image of the patterned sample.

## REFERENCES


1. P. Mulvaney, "Not all that's gold does glitter" *MRS Bull.*, 1009-1014, 2001.
2. Y.A. Akimov, Koh W. S. and Ostrikov K., "Enhancement of optical absorption in thin-film solar cells through the excitation of higher -order nanoparticle plasmon modes" *Opt. Express*, vol. 17, no. 12, 10195-10205, 2009.
3. R. Abargues, P. J. Rodríguez-Cantó, S. Albert, I. Suárez and J.P. Martínez-Pastor, " Plasmonic optical sensors printed from Ag-PVA nanoinks" Journal of Materials Chemistry C, vol. 2, 908-915, 2014.
4. Maier S. A., Kik P. G., Atwater H. A., Meltzer S., Harel E., Koel B. E. and Requicha A. A., "Local detection of electromagnetic energy transport below the diffraction limit in metal nanoparticle plasmon waveguides" *Nature*, vol. 2, 229-232, 2003.
5. Signoretto M., Suárez I., Chirvony V. S., Abargues R., Rodríguez-Cantó P. J., and Martínez-Pastor J., "Polymer waveguide couplers based on metal nanoparticle-polymer nanocomposites", *Nanotechnology*, vol. 26, no. 47, 475201-475210, 2015.

# Controllable Large Circular Dichroism of a Chiral Metasurface Induced by Coupling Localized and Propagating Modes

**Zeng Wang[1, 2], Yue Wang[1], Giorgio Adamo[2], Bing Hong Teh[1], Qing Yang Steve Wu[3], Jinghua Teng[3], and Handong Sun[*1, 2]**

[1]Division of Physics and Applied Physics, School of Physical and Mathematical Sciences, Nanyang Technological University, Singapore 637371, Singapore
[2]Centre for Disruptive Photonic Technologies, Nanyang Technological University Singapore 637371, Singapore
[3] Institute of Materials Research and Engineering, Agency for Science, Technology and Research (A*STAR), Singapore 138634, Singapore
[*]corresponding author: HDSun@ntu.edu.sg

**Abstract**-Herein, we introduce a novel chiral metasurface composed of a chiral arrangement of nanoslits carved in a continuous metal film, in which propagating surface plasmon modes are proved to be powerful tools to control the metasurface's chiral response. Numerical simulations help us devise a straightforward approach to the measurface's design and through which, by modifying the coupling between localized and propagating modes, we experimentally achieved controllable and remarkably strong chiral responses.

The ability of chiral metamaterials[1, 2] and metasurfaces is keeping surprising us and the on-going improvements are pushing this new class materials more approachable to practical photonic devices[3, 4]. However, as a key virtue, the tunability of the chiral metamaterials and metasurfaces is still a scarce property, especially in the visible range, which vastly limits the potential applications. Here, we demonstrate a chiral metasurface composed of a chiral arrangement of nanoslits, and through modifying the coupling between the localized mode and propagating mode, we theoretically raise a very straight-forward strategy and experimentally achieved the remarkable strong chiral response that can be also finely tuned in the visible range, which enables our design for various potential applications, such as chiral sensing. Besides, the conductive property of our continuous metasurface may open up the possibilities for optoelectronic using. What's more, the conductive property of our continuous metasurface may open up the possibilities for optoelectronic using.

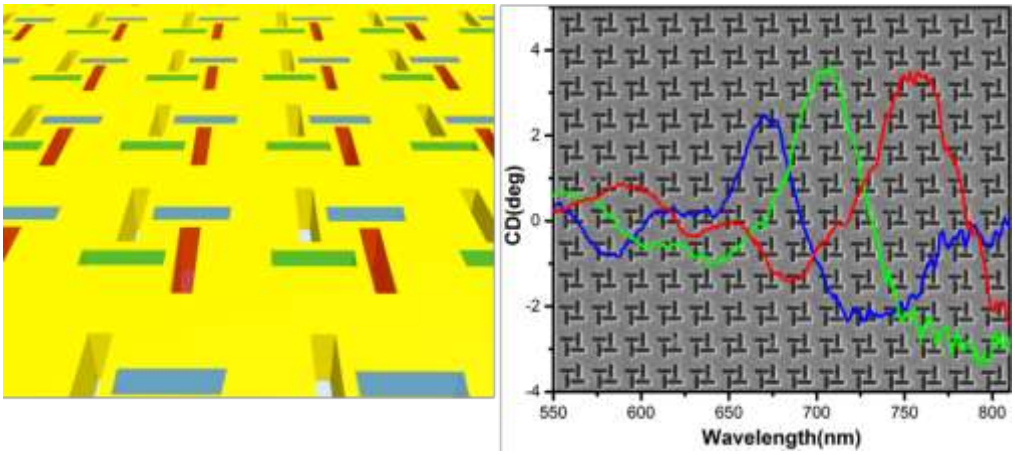



**Figure 1. (Left)** the chiral metasurface is formed by 4 groups of gratings labeled with different colors. **(Right)** the CD spectra of the chiral metasurface with various length of nanoslits, in which the obvious blue shift can be observed corresponding to the shortening of the nanoslit.

**Acknowledgements**: this research is supported by the Singapore Ministry of Education through the Academic Research Fund under Projects MOE 2011-T3-1-005 (Tier 3) and Tier 1- RG92/15.

**REFERENCES**

1. Papakostas, A.; Potts, A.; Bagnall, D.; Prosvirnin, S.; Coles, H.; Zheludev, N. *Physical review letters* **2003,** 90, (10), 107404.

2. Schwanecke, A.; Krasavin, A.; Bagnall, D.; Potts, A.; Zayats, A.; Zheludev, N. *Physical review letters* **2003,** 91, (24), 247404.

3. Gansel, J. K.; Thiel, M.; Rill, M. S.; Decker, M.; Bade, K.; Saile, V.; von Freymann, G.; Linden, S.; Wegener, M. *Science* **2009,** 325, (5947), 1513-1515.

4. Hendry, E.; Carpy, T.; Johnston, J.; Popland, M.; Mikhaylovskiy, R.; Lapthorn, A.; Kelly, S.; Barron, L.; Gadegaard, N.; Kadodwala, M. *Nature nanotechnology* **2010,** 5, (11), 783-787.

# Asymmetric Transmission with Chiral Photonic Crystals

**N. Parappurath**[1], **F. Alpeggiani**[1], **L. Kuipers**[1], **and E. Verhagen**[1*]

[1]FOM Institute AMOLF, Amsterdam, The Netherlands
*corresponding author: verhagen@amolf.nl

**Abstract**— Specifically tailored nanostructures that strongly affect the direction and polarization of light can enable extremely small optical devices. We investigate the magnitude and origin of asymmetric transmission (AT) in chiral photonic crystals. We show how AT is governed by the resonantly guided eigenmodes of the structure. Generalized coupled mode theory predicts the AT spectra from eigenmode properties. We derive the maximum AT offered by any chiral nanostructure and verify the theory with finite-element simulations for a bilayer dielectric photonic crystal.

New nanostructures that can manipulate light by controlling not only the direction but also the polarization of light waves are extremely important for realizing very small polarization rotators, half-wave plates etc. These components can add new functionalities for on-chip optical circuits. Asymmetric transmission (AT), the difference in transmission when polarized light is incident from opposite sides of the structure[1], is an important example of strongly chiral response, and relates directly to potential functionality such as spin-dependent light emission and enantioselective sensing.

So far, most of the efforts to realize strong chirality in thin structured media have employed plasmonic metamaterials. Several of these have been shown to offer AT[1, 2, 4], but as they rely on nanostructured metals they are of course intrinsically lossy. AT can in principle be achieved also with purely dielectric systems with the help of chiral photonic crystals. However, so far realizations have shown AT only for circularly polarized light[3]. To realize AT for linearly polarized light is significantly more challenging, as it strictly requires to have broken mirror symmetry in the propagation direction. In previous work, this symmetry was only weakly broken, relying on the asymmetric environment index due to the presence of a substrate[3]. In this work, we show that in thin dielectric bilayer photonic crystals, AT for linearly polarized light can be very strong. By comparing full-field simulations and analytical theory, we explore the origin of this AT in terms of the tailorable properties of the photonic crystal's eigenmodes.

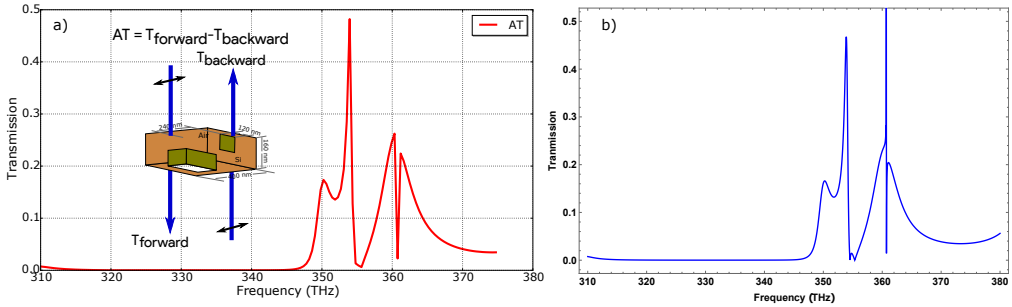



Figure 1: a) AT vs frequency of the incoming waves. (Inset: Unit cell of the proposed photonic crystal structure with AT definition.) b) Theoretical prediction of AT.

We simulated the polarization-dependent transmission of a chiral photonic crystal of high-index material with air holes built from rectangular sub-units (see unit cell depicted in inset of Fig. 1a). The periodicity was 400 nm and the complete thickness of the structure was 160 nm. The AT spectrum is pronouncedly structured, and already peaks at a value of 47% without any optimization (Fig. 1a).

We investigated the origin of AT in these structures by comparing transmission and eigenfrequency simulations. AT is seen to be strongly mediated by the resonantly guided eigenmodes of

the structure. To relate the eigenmode properties to the observed AT spectra, we developed a formalism based on coupled mode theory, which can describe the relationship between incoming and outgoing waves in terms of the eigenmode properties of the system[5]. We developed a theoretical formalism which can fully predict the scattering matrix for any structure with an arbitrary number of modes and arbitrary number of input-output channels without any assumption on the symmetry of the structure. So far, such descriptions have only considered a limited number of modes with specific symmetry properties[6]. We use our theory to derive an equation that predicts AT for our system (see Fig. 1b), considering a number of simulated quasinormal modes and the polarization properties of their far fields. We use the same formalism to predict the AT offered by any structure and with the help of this it is possible to tune the structural parameters to obtain maximum AT of 100%.

In conclusion, we propose the design of an all-dielectric chiral photonic crystal which can offer up to 47% AT for linearly polarized light. We investigated the origin of AT for linearly polarized light in chiral photonic crystals, and showed that it originates from the properties of the eigenmodes of the system. We developed a theoretical formalism which can fully predict the scattering matrix for any system having an arbitrary number of modes. This theory is helpful in designing new structures that can offer unity-efficiency asymmetric transmission.

**ACKNOWLEDGEMENT**

This work is part of the research programme of the Foundation for Fundamental Research on Matter (FOM), which is financially supported by The Netherlands Organization for Scientific Research (NWO). It is also funded by the European Research Council and an industrial partnership between Philips and FOM.

**REFERENCES**

1. Kenanakis, G., Xomalis, A., Selimis, A., Vamvakaki, M., Farsari, M., Kafesaki, M., Soukoulis, C.M. and Economou, E.N., "Three-dimensional infrared metamaterial with asymmetric transmission", *ACS Photonics*, 2(2), 287-294, 2015.
2. Li, Z., Gokkavas, M., and Ozbay, E., "Manipulation of asymmetric transmission in planar chiral nanostructures by anisotropic loss", *Advanced Optical Materials*, 1(7), 482-488, 2013.
3. Meng, X., Bai, B., Karvinen, P., Konishi, K., Turunen, J., Svirko, Y., and Kuwata-Gonokami, M., "Experimental realization of all-dielectric planar chiral metamaterials with large optical activity in direct transmission", *Thin Solid Films*, 516(23), 8745-8748, 2008.
4. Liu, D. J., Xiao, Z. Y., Ma, X. L., and Wang, Z. H., "Broadband asymmetric transmission and multi-band 90 polarization rotator of linearly polarized wave based on multi-layered metamaterial", *Optics Communications*, 354, 272-276, 2015.
5. Fan, S., Suh, W., and Joannopoulos, J. D., "Temporal coupled-mode theory for the Fano resonance in optical resonators", *JOSA A*, 20.3, 569-572, 2003.
6. Suh, W., Wang, Z. and Fan, S., "Temporal coupled-mode theory and the presence of non-orthogonal modes in lossless multimode cavities", *Quantum Electronics, IEEE Journal of*, 40(10), 1511-1518, 2004.

# Single-particle plasmonic structures reveal extrinsic chirality

**V.E.Bochenkov**[1,2], **D.S.Sutherland**[2]

[1]Chemistry department, Moscow State University, Russia
[2]Interdisciplinary Nanoscience Center (iNANO), Aarhus University, Denmark
boch@kinet.chem.msu.ru

**Abstract**— The concept of extrinsic chirality, i.e. optical activity of nonchiral media exhibited at oblique illumination, is generalized to include single-particle plasmonic nanostructures. We observe circular dichroism in irregular arrays of two different types of metallic nanostructures, non-concentric rings and asymmetrically stacked disks, in the visible and near-infrared regions. By using computer simulations, we show that extrinsic chirality in these systems is, importantly, due to individual nonchiral particles. We propose a mechanism for the chiroptical response of single-particle plasmonic structures.

Extrinsic chirality, implying an optical response of an achiral system arising at some particular mutual orientations with the direction of light propagation, requires simultaneous presence of co-aligned electric and magnetic dipole moments. This has previously been realized in a number of plasmonic structures, involving two or more interacting sub-units. However, to date, no evidence of extrinsic chirality observed in a single-particle plasmonic system has been reported.

Here, we show both experimentally and theoretically that the light-driven motion of charges in asymmetric particles, such as asymmetrically stacked metallic disks and non-concentric nanorings, under illumination with circularly polarized light induces an oscillating magnetic moment, oriented perpendicularly to the plane of the ring (see figure). Under oblique incidence, the projection of this magnetic moment on the plane normal to the wave propagation is non-zero, with its sign depending on the handedness of the light. This effect is responsible for the optical activity of these nanostructures, resulting in circular dichroism.

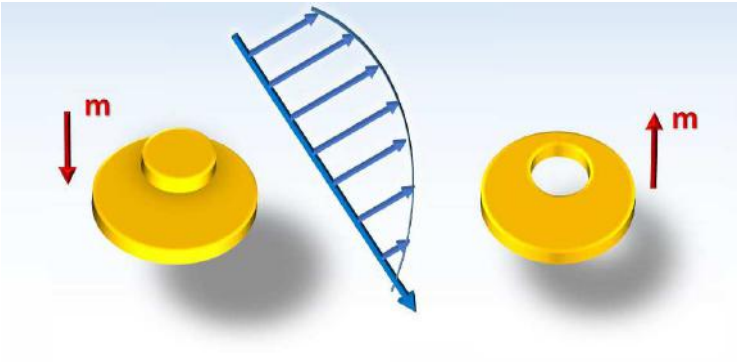



Figure 1: Magnetic dipole moments in asymmetric nanoring and asymmetrically stacked disks induced by light with polarization vector not contained in symmetry plane.

The effect has been demonstrated experimentally on gold nanoparticles, fabricated using colloidal lithography [1]. Our results open an avenue for new research of various single-particle nanostructures possessing extrinsic chirality. This may ultimately lead to the development of new tunable, highly active amorphous metamaterials and photonic devices.

## ACKNOWLEDGMENT

The work was supported by RFBR grant 15-03-99582.

## REFERENCES

1. Bochenkov, V. E., Todeschini, M., Chirumamilla, A., Sutherland, D. S. "Extrinsic chirality revealed in single-particle plasmonic nanostructures," *PRL,* submitted for publication.

# Chiral Metamaterial Structure With High Optical Activity Based On Conjugated Omega Particles

**Oscar Fernández[*1], Álvaro Gómez[1], Angel J. García-Collado[2], Gregorio J. Molina-Cuberos[3] and Angel Vegas[1]**

[1] Dpto. de Ingeniería de Comunicaciones, Universidad de Cantabria, Santander, Spain

[2] Dpto. de Ciencias Politécnicas, Universidad Católica San Antonio, Murcia, Spain

[3] Dpto. de Electromagnetismo y Electrónica, Universidad de Murcia, Murcia, Spain

[*]corresponding author: Oscar.fernandez@unican.es

**Abstract**- In this communication the authors present a novel chiral metamaterial structure formed by planar omega particles These omega particles, arranged in conjugated pairs, present high optical activity. Thanks to the high values of chirality, the structure provides negative refractive index with high figure of merit.

This communication presents a novel bilayered chiral metamaterial structure formed by planar omega particles. The pattern of one layer is the conjugated pattern of the other one. The structure is formed by combining alternately rows of horizontal conjugated omegas and vertical conjugated omegas (Fig 1a). In the proposed structure, the unit cell, with $C_4$ symmetry, (Fig. 1b), contains only half part of the conjugated omega structure. The full structure is completed with the neighbouring unit cells.

As chiral particles, the conjugated omega structures [1] insert cross-coupling between the electric and magnetic field. An incident $E_y$ electric field produces a magnetic moment on the horizontal omega pairs while an incident $H_x$ magnetic field induces an electric moment on the vertical conjugated omega structures.

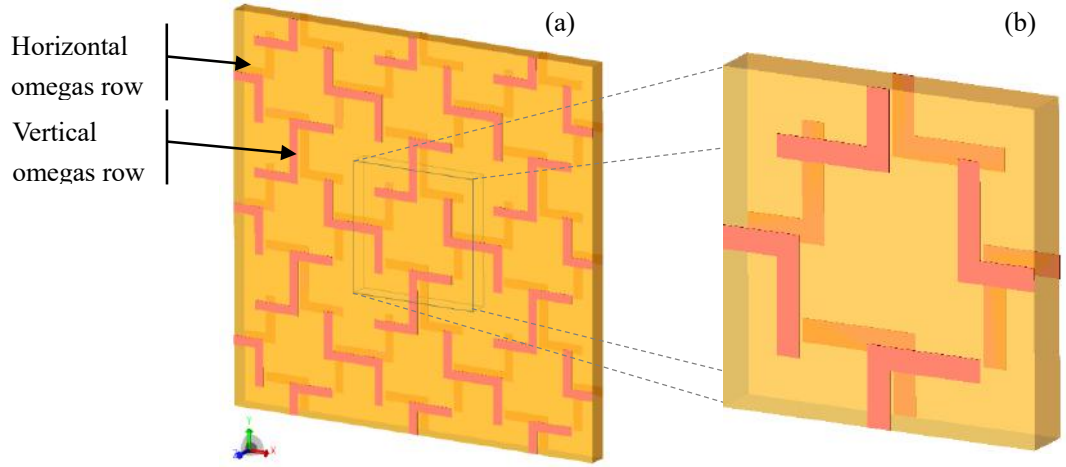



**Figure 1.** *(a) Conjugated omega structure, (b) unit cell*

The substrate, Rogers Duroid 3003, has a thickness of 60 mils, a dielectric constant $\varepsilon_r = 3$ a loss tangent *tan* $\delta = 0.0013$ and a copper cladding of 35 µm.The simulations were performed using the finite differences time domain engine of Keysight EMPro 3D electromagnetic simulation software. The characterization of the structure is done by means of the classical parameter retrieval algorithm proposed in [2] using the linear transmission and reflection coefficients.

The simulation results show high optical activity in the proposed chiral metamaterial structure. A linearly polarized incident field is transmitted through the structure with very low co-polar transmission coefficient but with a very high cross-polar transmission coefficient (Fig. 2a). As it is shown in Fig. 2b, the polarization plane rotates to about 90º (pure rotation).

The high optical activity is also reflected on the refractive index of the circularly polarized transmitted waves ($n_{\pm}$). Thanks to the high values of the chirality parameter, κ, (Fig. 1c) the real part of the refractive index $n_+$ or $n_-$ presents negative values (Fig. 1d).

As in others planar chiral metamaterials, the imaginary part of the refractive index ($n''_{\pm}$) is high at the resonance frequencies. In these frequency regions the negative refraction is not useful due to the high losses. This structure presents a frequency region, next to the resonance frequency, where $n'_-$ is still negative but $n''_-$ is nearly zero. In this region the figure of merit (FOM = $n'_-/n''_-$) present high values.

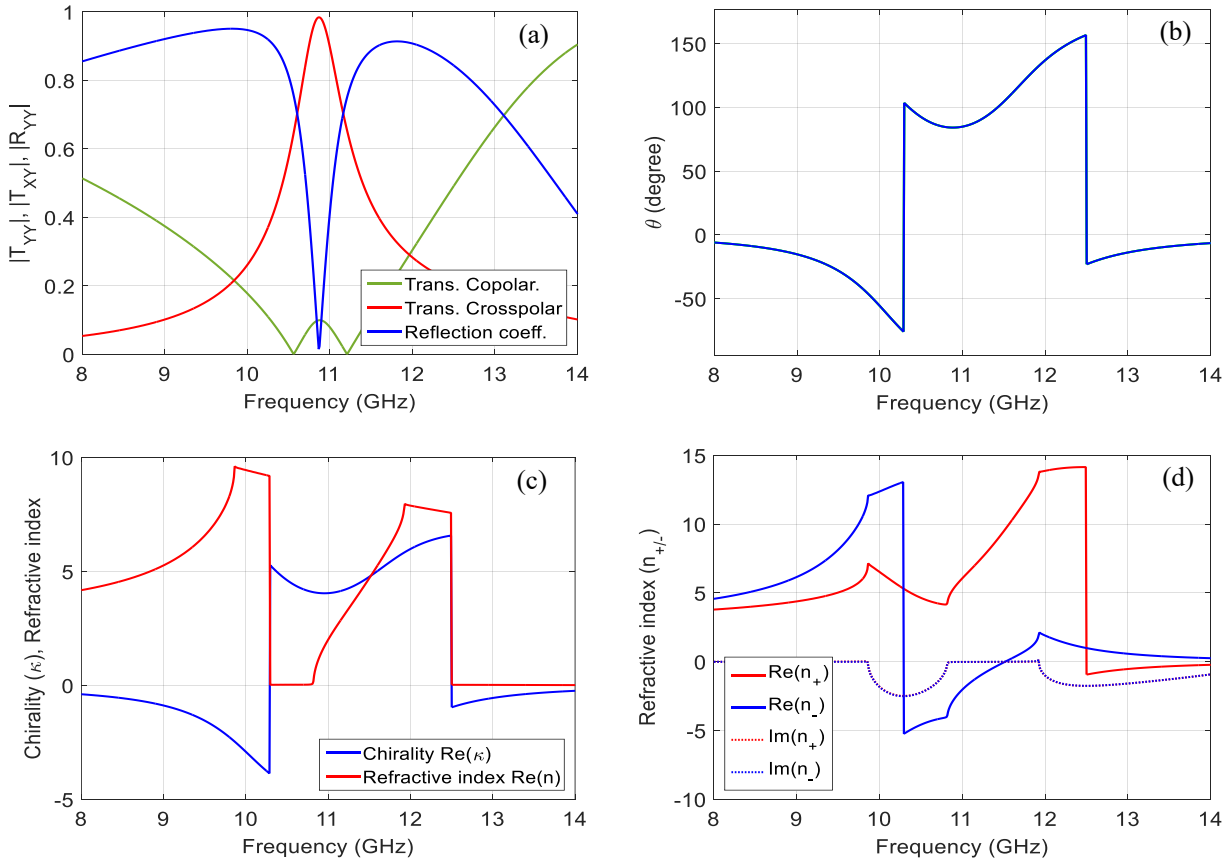



**Figure 2.** (a) Transmission and reflection coefficient, (b) Polarization plane rotation, (c) Chirality and refractive index ($n$), (d) Refractive index $n_+$ and $n_-$

**Acknowledgements**, this work has been supported by the Spanish Government MINECO through the Research Projects TEC2014-55463-C3-1-P, TEC2014-55463-C3-3-P and by the European Commission (ERDF).

**REFERENCES**

1. Zhao, R., Zhang, L., Zhou, J., Koschny, Th., and Soukoulis, C.M., "Conjugated gammadion chiral metamaterial with uniaxial optical activity and negative refractive index," *Phys. Rev. B*, Vol. 83, 035105, 2011.
2. Zhao, R., Koschny, T., and Soukoulis, C. M., "Chiral metamaterials: retrieval of the effective parameters with and without substrate," *Opt. Express*, vol. 18, no. 14, pp. 14553–14567. Jul 2010.

# Optical characterization of U-shaped resonators : from array to single scatterer.

**J. Proust [1], J. Grand [2], G. Guida [3], N. Bonod [1], B. Gallas [*4]**

[1] Aix-Marseille Université, CNRS, Centrale Marseille, Institut Fresnel, UMR 7249, 13013 Marseille, France

[2] Univ. Paris Diderot, Sorbonne Paris Cité, ITODYS, UMR CNRS 7086, 75013 Paris, France

[3] LEME, Univ. Paris Ouest, 92410 Ville d'Avray, France

[4] UPMC Univ Paris 06, CNRS UMR 7588, Institut des Nanosciences de Paris, 75005, Paris, France

[*]corresponding author: bruno.gallas@insp.jussieu.fr

**Abstract**- Transmission measurements have been performed on arrays and single U-shaped resonators. We show that optical activity can be evidenced in arrays of resonators and that this activity, associated with the magnetic modes, is already present in single resonators.

Metamaterials are made of arrays of subwavelength resonators exhibiting unprecedented optical properties. These properties can be reflected at the macroscopic level as effective permeability and permittivity tensors [1]. In this work we present measurements on arrays of U-shaped resonators and single resonators. One of their intriguing properties is the presence of optical activity which has already been described in arrays of resonators [2,3]. We show here that the activity in arrays originate partly in the presence of magneto-electric coupling at the level of each scatterer [4,5].

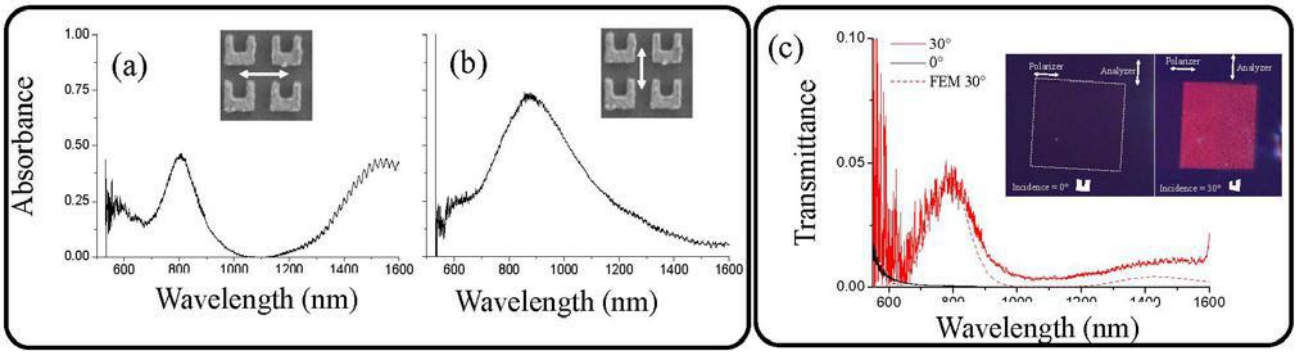



**Figure 1** : Absorbance measured on arrays of resonators for light polarized (a) parallel and (b) perpendicular to the bottom arm of the U-shaped resonators. (c) Transmittance measured between cross-polarizers at normal incidence (black line) and oblique incidence (red line). The inset shows the image of the array of resonators between crossed polarizers at normal and oblique incidence.

The measurements were performed on square arrays of U-shaped resonators and isolated U-shaped resonators realized using conventional e-beam lithography technique. The array consisted in a square lattice of constant of 320 nm (Fig.1(a)). The isolated resonators had a total footprint of 230x220 nm . The optical measurements in the 500 nm – 1600 nm range were performed in transmission in a home-made confocal microscope. The transmitted light was collected in a x100 microscope objective and the surface was either imaged on a camera to locate the region containing the resonators or on the core of a fiber, connected to a

spectrophotometer, hence realizing the spatial filtering of the surface. Two linear polarizers were placed before and after the lenses to select different polarization states of light. Fig. 1 presents the absorbance spectra obtained at normal incidence on the square array of resonators. For light polarized parallel to the bottom arm (Fig. 1(a)), the magnetic modes are observed near 1530 nm and 800 nm [2,3,6]. For light polarized along the lateral arms (Fig. 1(b)), the electric mode is observed near 875 nm [2,3,6]. The presence of magneto electric-coupling at the magnetic modes is evidenced by measuring the transmission between cross-polarizers for light propagating in the (y,z) plane (Fig. 1(c) [2,3].

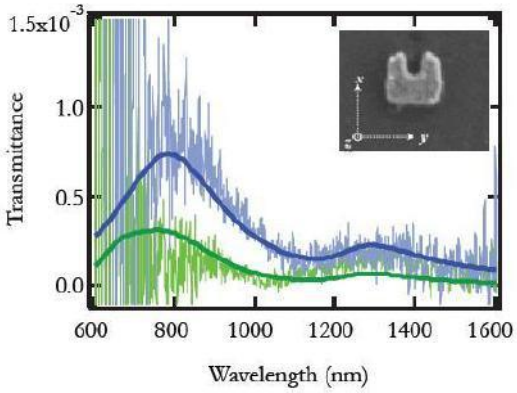



**Figure 2** : Transmission between crossed-polarizers for light propagating at oblique incidence in the (y,z) plane measured on one single resonator (inset : SEM image). The two measurements correspond to incident light polarized along *x* (blue line) and along *y* (green line).

Fig. 2 presents the measurements performed between cross-polarizers on an individual resonator. Transmission bands were observed only at oblique incidence and at the position of the magnetic modes. This observation is a clear experimental indication that optical activity exists at the level of the individual resonator at the magnetic mode.

**Acknowledgements**, Work at Institut Fresnel has been carried out thanks to the support of the A*MIDEX project (n ANR-11-IDEX-0001-02) funded by the Investissements d'Avenir French Government program managed by the French National Research Agency (ANR).

## REFERENCES

1. J.B. Pendry, D. Schurig, D. R. Smith, “Controlling Electromagnetic Fields,” Science, vol. 312, p. 1780, 2006.
2. I. Sersic, M. Frimmer, E. Verhagen, A.F. Koenderink, “Electric and Magnetic Dipole Coupling in Near-Infrared Split-Ring Metamaterial Arrays”, Phys. Rev. Lett., vol. 103, 213902, 2009.
3. N. Guth, B. Gallas, J. Rivory, J. Grand, A. Ourir, G. Guida, R. Abdeddaim, C. Jouvaud,J. de Rosny, “Optical properties of metamaterials: Influence of electric multipoles, magnetoelectric coupling, and spatial dispersion”, Phys. Rev. B, vol. 85, p. 115138, 2012.
4. F. B. Arango, T. Coenen, A. F. Koenderink “Underpinning Hybridization Intuition for Complex Nanoantennas by Magnetoelectric Quadrupolar Polarizability Retrieval” ACS Phot., vol. 1, 444-453, 2014
5. S. Varault, B. Rolly, G. Boudarham, G. Demesy, B. Stout, N. Bonod “Multipolar effects on the dipolar polarizability of magneto-electric antennas” Opt. Express, vol. 21, p. 16444, 20013
6. C. Rockstuhl, T. Zentgraf, E. Pshenay-Severin, J. Petschulat, A. Chipouline, J. Kuhl, T. Pertsch, H. Giessen, F. Lederer, “The origin of magnetic polarizability in metamaterials at optical frequencies - an electrodynamic approach” Opt. Express, vol. 18, p. 8871, 2007.

# Design of planar chiral metamaterials for near infrared regime

**Sabri Kaya[1,2,*], Mustafa Turkmen[1,2], and Omer Topaktas[1]**

[1] Department of Electrical and Electronics Engineering, Erciyes University, 38039, Kayseri, Turkey
[2] Department of Electrical and Computer Engineering, and Photonics Center of Boston University, Boston, MA 02215, USA
*corresponding author, E-mail: skaya@bu.edu

## Abstract

Planar chiral metamaterials (PCMs) comprising double-layer dielectric-metal-dielectric resonant structures in the shape of a windmill are presented for near-infrared regime. The circular dichroism is retrieved from transmission spectra. Effects of used materials on circular dichroism characteristics of PCM arrays are investigated for first time. The dependence of spectral characteristics on the geometrical parameters of the PCMs is analyzed by the finite-difference time-domain method. Due to the enhanced chiroptical near-field response and tunable spectral behavior, proposed PCM arrays may have potential for biosensing applications of chiral biomolecules.

## 1. Introduction

An object that cannot be superimposed onto its mirror image is called chiral. The optical response of planar chiral metamaterials (PCMs) is different for right-handed circularly polarized (RCP) and left-handed circularly polarized (LCP) incident light. Circular dichroism (CD), defined as the difference in absorption of LCP and RCP light excitations, is one of the most commonly used spectroscopic techniques for chirality applications [1-23].

In the literature, two- and three-dimensional chiral structures have been observed and analyzed [2-23]. Although the chiral optical response of three-dimensional plasmonic nano-structures is significantly enhanced, these nano-structures are difficult to fabricate comparing to planar structures [2-9]. On the other side, it has been demonstrated that even handed quasi-planar and planar plasmonic structures show profound chiral interaction with circularly polarized light despite the fact that they are not truly chiral [9-23]. Planar structures have been proposed to obtain the strong circular dichroism and optical chirality [9-23]. Whereas, to the best of our knowledge, effects of material type on circular dichroism characteristics of chiral structures is not studied yet.

In this study, planar chiral metamaterials comprising double-layer dielectric-metal-dielectric resonant structures in the shape of a windmill are presented for near-infrared regime. Effects of material type on circular dichroism characteristics of planar chiral metamaterial array are investigated for the first time. The circular dichroism, optical chirality, and electric field distributions of PCM array are determined by the finite difference time domain (FDTD) method [24]. The dependence of spectral characteristics on the geometrical parameters of the planar chiral metamaterials is also analyzed. Due to the enhanced chiroptical near-field response and tunable resonances, the proposed PCM arrays can be good candidates for biosensing applications of chiral biomolecules in near infrared regime.

## 2. Circular dichroism of PCM arrays

The structure of the proposed PCM is periodic, and one of the unit cells is shown in Figure 1. Proposed structure is composed of a dielectric spacer layer of thickness *h* between right-handed (RH) and left-handed (LH) windmill-shaped metal nanoparticles of thickness *d* as shown in Fig.1. In this figure, *L* illustrates the length of the triangular metal particles, *w* indicates the center gap width between metal particles. Dielectric constant of the metal is taken from ref. [25]. Periodic boundary conditions are used for *x*- and *y*-directions and perfectly matched layers are used along *z*-direction (propagation direction).

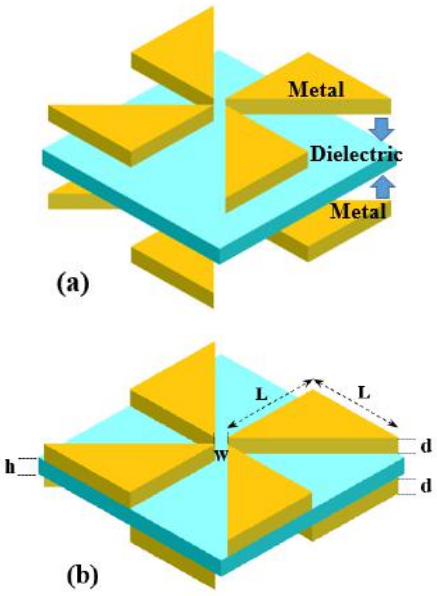



Figure 1: (a) Metal-dielectric-metal components (b) Schematic view of proposed PCM.

Figure 2(a) shows the simulated transmission spectra of the proposed PCM designed by using the Au - $SiO_2$ (glass) - Au materials with $L$ = 425 nm, $h$ = 50 nm, $d$ = 50 nm, and $w$ = 50 nm for the LCP ($T_{LCP}$) and RCP ($T_{RCP}$) waves. Figure 2(b) illustrates that PCM has a circular dichroism at the two resonances ($\lambda_1$ = 1167 nm and $\lambda_2$ = 1249 nm) which are calculated by using difference in transmission ($\Delta = T_{RCP} - T_{LCP}$) given in Figure 2(a).

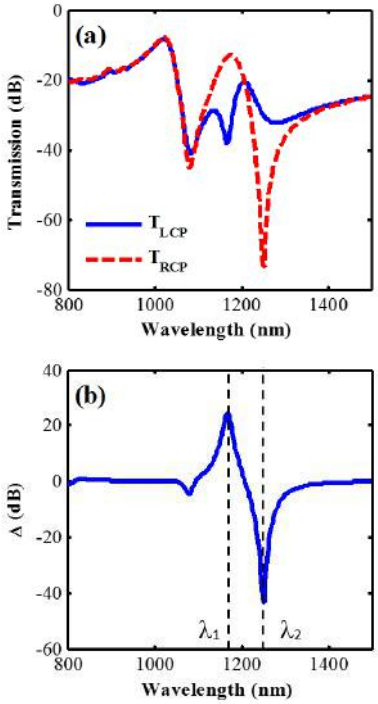



Figure 2: (a) Transmittance spectra of proposed PCM designed by using the Au - $SiO_2$ - Au materials for LCP and RCP excitation (b) Circular dichroism of PCM arrays ($L$ = 425 nm, $h$ = 50 nm, $d$ = 50 nm, and $w$ = 50 nm).

## 3. Chiroptical near-fields of PCM arrays

In order to understand the physical origin of the optical response of the proposed PCM arrays, the near-field distributions at the resonance peaks are analyzed under RCP and LCP excitations. Figures 3(a) and 3(b) show the electric field, |E|, distributions at the air-metal interface (top surface of the top gold layer) for RCP excitation at the $\lambda_1$ = 1167 nm and $\lambda_2$ = 1249 nm illustrated in Fig. 2(b), respectively. Similarly, Figs. 3(c) and 3(d) illustrate the electric field distributions for LCP excitation at $\lambda_1$ and $\lambda_2$, respectively. As can be seen from Fig. 3, the electric fields are mainly concentrated on the center and sharp corners of the structure. Molecules in these regions may undergo a much stronger interaction with the electromagnetic field than those that lie well away from metallic particles. This means that the dielectric environment of the near surface region of the PCM can strongly influence the resonant wavelengths. This phenomenon is the basis of the bio-sensing capabilities of chiral structures [16, 26].

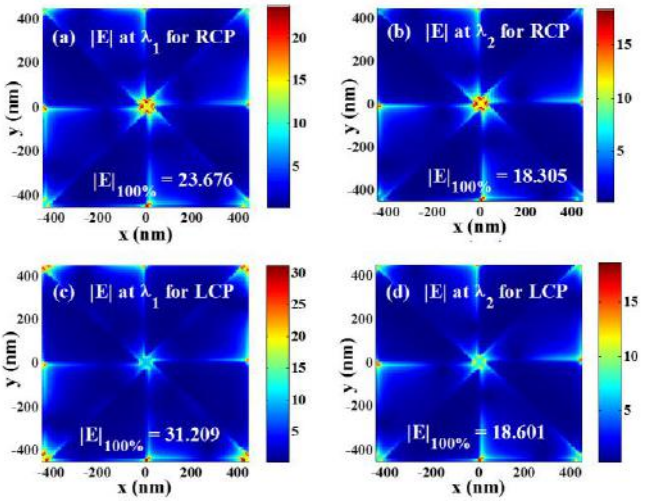



Figure 3: Electric field distributions by the PCM designed by using the Au - $SiO_2$ - Au materials illuminated with (a, b) RCP and (c, d) LCP at $\lambda_1$ and $\lambda_2$. The corresponding parameters are $L$ = 425 nm, $h$ = 50 nm, $d$ = 50 nm, and $w$ = 50 nm.

Local field enhancement (red points in Fig. 3) alone is not enough to account for the enhanced chiral response. The optical chirality ($C$), which is time-even pseudo scalar, can be used [27]:

$$C(\vec{r}) \equiv \frac{1}{2}\left[\varepsilon_0 \vec{E}(\vec{r}) \cdot \nabla \times \vec{E}(\vec{r}) + \frac{1}{\mu_0} \vec{B}(\vec{r}) \cdot \nabla \times \vec{B}(\vec{r})\right] \quad (1)$$

where $\varepsilon_0$ and $\mu_0$ are the permittivity and permeability of free space, and **E** and **B** are the local electric and magnetic fields. When considering only dipolar excitation of molecules, the chiral asymmetry in the rate of excitation is given by the product of optical chirality with the inherent chiral properties of the material [27]. The optical chirality measures the ability of a chiral molecule to absorb energy from the electromagnetic field.

Fig. 4 illustrates the calculated optical chirality ($C$) of the near fields generated by the present structure at $\lambda_1$ = 1167 nm and $\lambda_2$ = 1249 nm under RCP and LCP excitations for $L$ = 425 nm, $h$ = 50nm, $d$ = 50nm, and $w$ = 50nm. It can be seen from Fig. 4 that the PCM shows both positive and negative values of optical chirality with different absolute values at resonance points ($\lambda_1$ and $\lambda_2$) for RCP and LCP excitations. This asymmetric optical chirality behavior is similar with helix, spiral and oligomer chiral structures [20]. Locally enhanced optical chirality regions are located at the sharp corners and edge of structure and chirality values are not zero for both RCP and LCP excitations, which means proposed PCM array has ability to distinguish the left and right handed molecules.

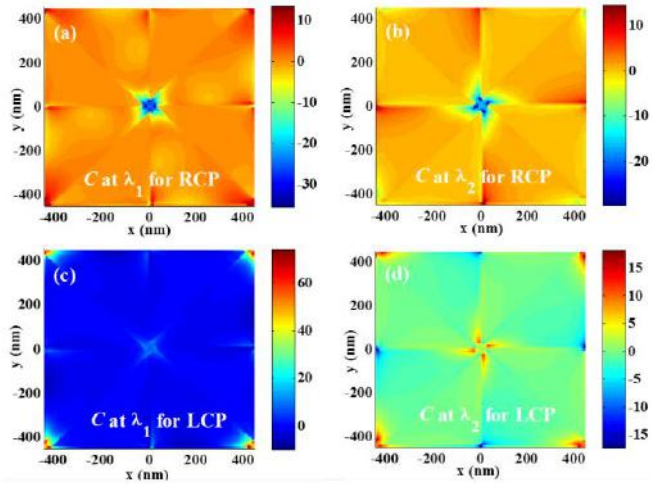



Figure 4: Optical chirality, *C*, enhancement by the PCM designed by using the Au - $SiO_2$ - Au materials illuminated with (a, b) RCP and (c, d) LCP at $\lambda_1$ and $\lambda_2$. ($L$ = 425 nm, $h$ = 50 nm, $d$ = 50 nm, and $w$ = 50 nm).

## 4. Tuning spectral response of the PCM arrays

To control the spectral response of the PCM arrays, dependence of the spectral response on length of metal (Au) nanoparticles, center gap width and thickness of dielectric spacer ($SiO_2$) is investigated. Figure 5 depicts the correlation between CD ($\Delta = T_{RCP} - T_{LCP}$) and geometrical parameters of PCM arrays. Figure 5(a) illustrates the effect of Au particle length ($L$) variation while other parameters kept constant. It has been observed that the resonance wavelengths of the CD increase with higher $L$ values. Third resonance wavelength of CD is also appeared with decreasing $L$. Figure 5(b) shows the CD results for center gap width ($w$) variation. As the center gap width of the structure increases, the resonance wavelengths of the structure decreases linearly. Figure 5(c) illustrates the dependence of the CD spectra on the thickness of $SiO_2$ (glass) layer. Resonance wavelengths decrease but amplitude of CD increase with increasing $SiO_2$ (glass) layer thickness.

Eventually, resonance frequencies of CD from PCM arrays are strongly dependent on the geometrical parameters ($L$, $w$ and $h$) of structure. Therefore, the resonance frequencies of CD from the proposed PCM arrays can easily be tuned by changing $L$, $w$, and $h$ values.

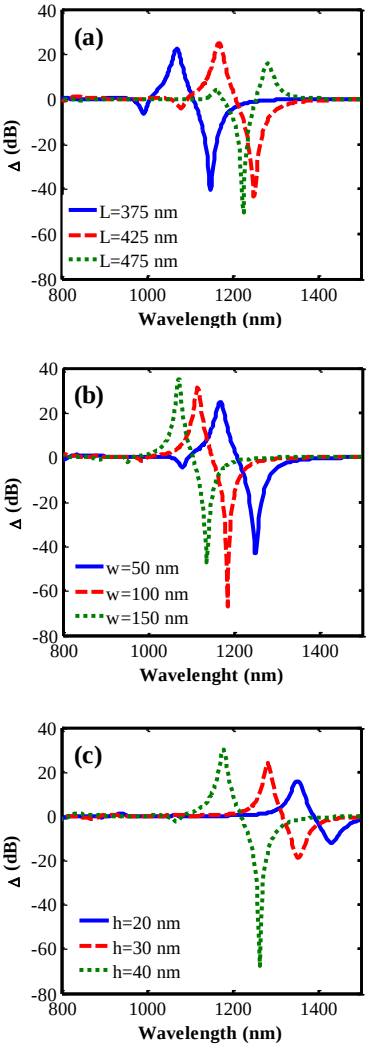



Figure 5: Circular dichroisms of PCM arrays designed by using the Au - $SiO_2$ - Au materials (a) $L$-variation at fixed $h$ = 50 nm, $d$ = 50 nm, $w$ = 50 nm (b) $w$-variation at fixed $L$ = 425 nm, $h$ = 50 nm, $d$ = 50 nm. (c) $h$-variation at fixed $L$ = 425 nm, $d$= 50nm, $w$= 50nm).

## 5. Effects of Material Type on Circular Dichroism

In this study, effects of material type on circular dichroism of PCM arrays are investigated. Figure 6(a) shows the CD spectrum of PCM array for Au nanoparticles and different dielectric spacer ($Al_2O_3$, $SiO_2$, and $MgF_2$). Highest resonance wavelengths and strongest CD is obtained from PCM array with $Al_2O_3$ while least resonance wavelengths and weakest CD obtained from PCM array of $MgF_2$ (Figure 6a). Figure 6(b) demonstrates the CD spectrum of PCM array for Ag nanoparticles and different dielectric spacer. Behavior of PCM array with Ag nanoparticles is same with Au nanoparticles but PCM array with Au nanoparticles has stronger CD values than Ag nanoparticles (Figure 6).

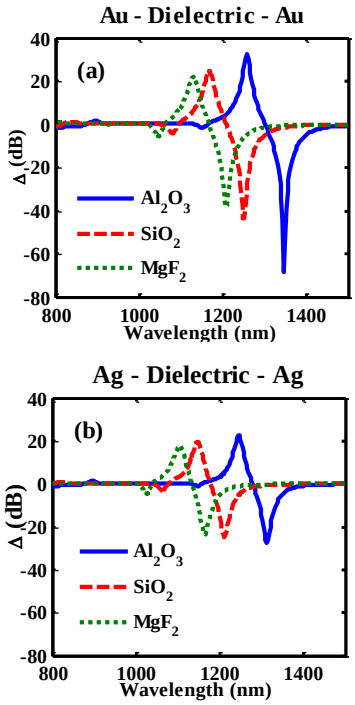



Figure 6: Comparison of CD spectrum of PCM arrays for different dielectric spacers (a) Au-Dielectric-Au design (b) Ag-Dielectric-Ag design.

In order to understand the effects of material type on electric field enhancements, the maximum electric field enhancement values of PCM array for Au nanoparticles with different dielectric spacer ($Al_2O_3$, $SiO_2$, and $MgF_2$) at corresponding resonance wavelengths (shown in Figure 6a) under RCP and LCP excitations are given in Table 1. Au-$MgF_2$-Au superior has the highest enhancement for both RCP and LCP excitations. Same comparison is given in Table 2 for PCM array with Ag nanoparticles (shown in Figure 6b) that Ag-$MgF_2$-Ag superior has the highest enhancement for both RCP and LCP excitations (Table 2). Table 1 and Table 2 show that PCM arrays with Ag nanoparticles have higher electric field enhancement than those with Au nanoparticles.

Table 1: Comparison of electric field enhancement for PCM array designed by using Au-dielectric-Au materials.

| Dielectric | FIRST MODE | | | SECOND MODE | | |
|---|---|---|---|---|---|---|
| | $\lambda_1$ (nm) | Max. \|E\| (RCP) | Max. \|E\| (LCP) | $\lambda_2$ (nm) | Max. \|E\| (RCP) | Max. \|E\| (LCP) |
| $SiO_2$ | 1167 | 23.676 | 31.209 | 1249 | 18.305 | 18.601 |
| $Al_2O_3$ | 1257 | 19.362 | 26.901 | 1346 | 16.483 | 16.728 |
| $MgF_2$ | 1130 | 25.831 | 33.140 | 1207 | 19.078 | 19.385 |

Table 2: Comparison of electric field enhancement for PCM array designed by using Ag-dielectric-Ag materials

| Dielectric | FIRST MODE | | | SECOND MODE | | |
|---|---|---|---|---|---|---|
| | $\lambda_1$ (nm) | Max. \|E\| (RCP) | Max. \|E\| (LCP) | $\lambda_2$ (nm) | Max. \|E\| (RCP) | Max. \|E\| (LCP) |
| $SiO_2$ | 1147 | 27.537 | 34.890 | 1212 | 22.116 | 22.238 |
| $Al_2O_3$ | 1244 | 22.447 | 30.470 | 1313 | 19.738 | 19.756 |
| $MgF_2$ | 1105 | 30.287 | 38.302 | 1165 | 23.404 | 23.583 |

## 6. Conclusions

In conclusion, a PCM array to obtain the circular dichroism and optical chirality for the near-IR regime is presented. CD from PCM array is determined. The effects of material type on CD and electric field enhancement of PCM array are investigated for the first time. The observations indicated that the circular dichroism characteristics of the proposed PCM arrays are strongly dependent on the type of metal and dielectric materials. PCM arrays designed with Au nanoparticles have stronger CD than those with Ag nanoparticles but PCM arrays with Ag nanoparticles have higher electric field enhancements. PCM arrays with $Al_2O_3$ have strongest CD while PCM arrays used $MgF_2$ have highest electric field enhancement. Due to tunable spectral behavior and the enhanced near-field chiroptical response, proposed PCM arrays can be used for biosensing applications such as detection of chiral biomolecules which have resonances in the near-IR regime.

## Acknowledgements

This work described in this paper is supported by The Scientific and Technological Research Council of Turkey, Project No: TUBITAK – 115E209.

## References

[1] D. L. Jaggard, A. R. Mickelson, C. H. Papas, On electromagnetic waves in chiral media, *Applied Physics* 18: 211, 1979.

[2] J. K. Gansel, M. Thiel, M. S. Rill, M. Decker, K. Bade, V. Saile, G. von Freymann, S. Linden, M. Wegener, Gold helix photonic metamaterial as broadband circular polarizer, *Science* 325: 1513-1515, 2009.

[3] A. Guerrero-Martínez, J. L. Alonso-Gómez, B. Auguié, M. M. Cid, L. M. Liz-Marzán, From individual to collective chirality in metal nanoparticles, *Nano Today* 6: 381-400, 2011.

[4] A. O. Govorov, Z. Fan, P. Hernandez, J. M. Slocik, R. R. Naik, Theory of circular dichroism of nanomaterials comprising chiral molecules and nanocrystals: Plasmon enhancement, dipole interactions, and dielectric effects, *Nano Letters* 10: 1374-1382, 2010.

[5] M. Hentschel, L. Wu, M. Schäferling, P. Bai, E. P. Li, H. Giessen, Optical properties of chiral three dimensional plasmonic oligomers at the onset of charge-transfer plasmons, *ACS Nano* 6: 10355-10365, 2012.

[6] Z. Zhou, H. Yang, Triple-band asymmetric transmission of linear polarization with deformed S-shape bilayer chiral metamaterial, *Appl. Phys. A* 119: 115-119, 2015.

[7] G. Armelles, A. Cebollada, H. Y. Feng, A. García-Martín, D. Meneses-Rodríguez, J. Zhao, H. Giessen, Interaction effects between magnetic and chiral building blocks: a new route for tunable magneto-chiral Plasmonic Structures, *ACS Photonics* 2: 1272-1277, 2015.

[8] V. Tasco, M. Esposito, F. Todisco, A. Benedetti, M. Cuscunà, D. Sanvitto, A. Passaseo, Three-dimensional

nanohelices for chiral photonics, *Appl. Phys. A* 122: 1-6, 2016.
[9] S. Oh, O. Hess, Chiral metamaterials: enhancement and control of optical activity and circular dichroism, *Nano Convergence* 2: 1-14, 2015.
[10] A. Papakostas, A. Potts, D. M. Bagnall, S. L. Prosvirnin, H. J. Coles, N. I. Zheludev, Optical manifestations of planar chirality, *Physical Review Letters* 90: 107404, 2003.
[11] M. Kuwata-Gonokami, N. Saito, Y. Ino, M. Kauranen, K. Jefimovs, T. Vallius, J. Turunen, Y. Svirko, Giant optical activity in quasi-two-dimensional planar nanostructures, *Physical Review Letters* 95: 227401, 2005.
[12] M. Decker, M. W. Klein, M. Wegener, S. Linden, Circular dichroism of planar chiral magnetic metamaterials, *Opt. Lett.* 32: 856-858, 2007.
[13] C. Menzel, C. Rockstuhl, T. Paul, F. Lederer, Retrieving effective parameters for quasiplanar chiral metamaterials, *Applied Physics Letters* 93: 233106, 2008.
[14] D.-H. Kwon, P. L. Werner, D. H. Werner, Optical planar chiral metamaterial designs for strong circular dichroism and polarization rotation, *Opt. Express* 16: 11802-11807, 2008.
[15] E. Plum, X. X. Liu, V. A. Fedotov, Y. Chen, D. P. Tsai, N. I. Zheludev, Metamaterials: Optical Activity without Chirality, *Physical Review Letters* 102: 113902, 2009.
[16] E. Hendry, T. Carpy, J. Johnston, M. Popland, R. V. Mikhaylovskiy, A. J. Lapthorn, S. M. Kelly, L. D. Barron, N. Gadegaard, M. Kadodwala, Ultrasensitive detection and characterization of biomolecules using superchiral fields, *Nat Nano* 5: 783-787, 2010.
[17] K. Konishi, M. Nomura, N. Kumagai, S. Iwamoto, Y. Arakawa, M. Kuwata-Gonokami, Circularly polarized light emission from semiconductor planar chiral nanostructures, *Physical Review Letters* 106: 057402, 2011.
[18] J. Li, F.-Q. Yang, J.-F. Dong, Design and simulation of L-shaped chiral negative refractive index structure, *Progress In Electromagnetics Research* 116: 395-408, 2011.
[19] F. Eftekhari, T. J. Davis, Strong chiral optical response from planar arrays of subwavelength metallic structures supporting surface plasmon resonances, *Physical Review B* 86: 075428, 2012.
[20] M. Schäferling, D. Dregely, M. Hentschel, H. Giessen, Tailoring enhanced optical chirality: Design principles for chiral plasmonic nanostructures, *Physical Review X* 2: 031010, 2012.
[21] S. Kaya, Circular dichroism from windmill-shaped planar structures operating in mid-infrared regime, *Opt. Mater. Express* 4: 2332-2339, 2014.
[22] T. Cao, C. Wei, L. Zhang, Modeling of multi-band circular dichroism using metal/dielectric/metal achiral metamaterials, *Opt. Mater. Express* 4: 1526-1534, 2014.
[23] W. Li, Z. J. Coppens, L. V. Besteiro, W. Wang, A. O. Govorov, J. Valentine, Circularly polarized light detection with hot electrons in chiral plasmonic metamaterials, *Nat Commun* 6: 8379, 2015.
[24] The numerical simulations are carried out using a finite-difference-time-domain package (Lumerical FDTD Solutions, 2015). www.lumerical.com
[25] P. B. Johnson, R. W. Christy, Optical constants of the noble metals, *Physical Review B* 6: 4370-4379, 1972.
[26] R. Tullius, A. S. Karimullah, M. Rodier, B. Fitzpatrick, N. Gadegaard, L. D. Barron, V. M. Rotello, G. Cooke, A. Lapthorn, M. Kadodwala, "Superchiral" Spectroscopy: Detection of protein higher order hierarchical structure with chiral plasmonic nanostructures, *Journal of the American Chemical Society* 137: 8380-8383, 2015.
[27] Y. Tang, A. E. Cohen, Enhanced enantioselectivity in excitation of chiral molecules by superchiral light, *Science* 332: 333-336, 2011.

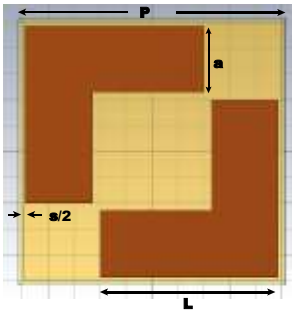
# Metamaterial-based devices and antennas

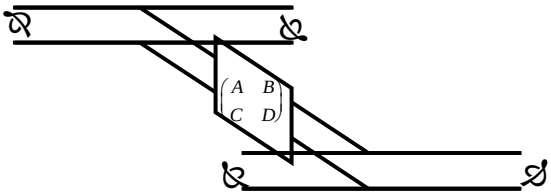
# Design by using equivalent circuits of reflective FSS's converting linear to circular polarization.

**Juan E. Page**
Grupo de Electromagnetismo Aplicado. Universidad Politécnica de Madrid
E.T.S.I. de Telecomunicación. Avda. Complutense 30 28040 Madrid (España)

**Abstract**- A dual mode equivalent circuit is used to design reflective FSS's converting the linear polarization of a normally incident wave to a circular polarization of the reflected one. The polarization sign can be selected during the design.

In a previous paper [1] we presented the dual mode equivalent circuit for the scatterer introduced by S. Bhattacharyya et al. [2] and used it to design a reflective FSS that rotates by 90º the linear polarization of a normally incident plane wave from vertical to horizontal (Fig. 1). The circuit is obtained by even-odd decomposition of the system and can be reduced to the connection shown in Fig. 2, with $Y_e$ and $Y_o$ two reactances (purely imaginary if losses are neglected).




$$\begin{pmatrix} A & B \\ C & D \end{pmatrix} = \begin{pmatrix} \dfrac{Y_o+Y_e}{Y_o-Y_e} & \dfrac{2}{Y_o-Y_e} \\ \dfrac{2Y_oY_e}{Y_o-Y_e} & \dfrac{Y_o+Y_e}{Y_o-Y_e} \end{pmatrix}$$

Fig. 1- Scatterer, dual-mode equivalent circuit and transmission matrix of the two-port.

In this paper we use the same circuit to obtain another kind of polarizer that transforms the linear vertical polarization of the incident wave in a circular polarized reflected wave with the possibility of selecting the sign of the polarization. To do it we terminate the FSS with a perfect conductor plate situated at an adequate distance, that can be calculated using directly the equivalent circuit proposed. The plate is then represented by a short-circuited transmission line loading the output ports 2 and 3 of the four-port with an admittance $Y_{L,}$ and the transmission and reflection coefficients of the resulting two-port are given by

$$\rho_1 = \frac{Y_0^2 - Y_eY_L - Y_oY_L - Y_eY_o}{[Y_0 + Y_e + Y_L][Y_0 + Y_o + Y_L]} \tag{1}$$

$$\tau_{41} = \frac{Y_o - Y_e}{[Y_0 + Y_e + Y_L][Y_0 + Y_o + Y_L]} \tag{2}$$

where $Y_0$ is the admittance of the free space.

It can be seen that reflection and transmission are 90º out of phase at all frequencies, so the circular polarization condition reduces to

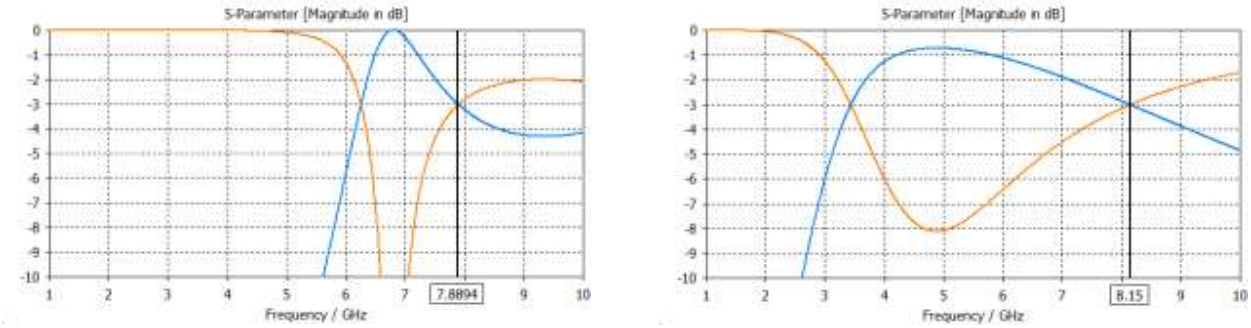
$$|\rho_1| = |\tau_{41}| \tag{3}$$

and consequently, for fixed values of $Y_e$ and $Y_o$ (fixed geometry of the scatterer), we have to take

$$Y_L = -\frac{Y_e + Y_o}{2} \pm \sqrt{\left(\frac{Y_e + Y_o}{2}\right)^2 + Y_0^2 - Y_e Y_o \pm j(Y_e - Y_o)Y_0} \tag{4}$$

a relation that gives the lengths of the required lines, that is the distances from the scatterers to the short circuit.

Let us consider an example. Using the same dimensions as in [1] for the patches, let us design a polarizer at 8.5 GHz. Equation (5) gives four different values for the distance, two of them providing right-handed polarization (1.74 mm and 2.06 mm) and the other two providing left handed polarization (0.93 mm and 10.31 mm).. The graphics of Fig. 2 give the values of the reflection and transmission coefficients obtained by CST simulations, without any optimization, for two of the solutions. It can be seen that the frequency error is less than 7% and can be corrected at equivalent circuit level, so the method proved to be enough accurate and very efficient.




Distance 2.06 mm (positive polarization) Distance 10.31 mm (negative polarization)

Fig. 2 Reflection and transmission of the FSS

**Acknowledgements**, This work has been supported by the project "Nuevos conceptos en reflectarrays y transmitarrays para antenas innovadoras y su validación experimental" financed by the "Programa Estatal de Fomento de la Investigación Científica y Técnica de Excelencia (TEC2013-43345-P)".

**REFERENCES**

1. Page, J. E. "Diseño mediante circuito equivalente de superficies reflectoras giradoras de polarización" XXX Symposium Nacional de la URSI, Pamplona (España) Sept. 2-4, 2015.
2. S. Bhattacharyya et al. "A Broadband Wide Angle Metamaterial Absorber for Defense Applications" IEEE International Microwave and RF Conference. Bangalore (India), Dec. 2014.

# Printed Monopole Single Notch UWB Antenna using Low loss Glass-Polytetrafluoroethylene Composite Material

M. Z. Mahmud[a, 1], M. T. Islam[b, 1], M. Samsuzzaman[c, 2]

[1]Dept. Of Electrical, Electronic and Systems Engineering

[1]Universiti Kebangsaan Malaysia

[2]Dept. of Computer and Computer Engineering

[2]Patuakhali Science and Technology University

Email: [a]zulfikerm@siswa.ukm.edu.my, [b]tariqul@ukm.edu.my, [c]sobuz@pstu.ac.bd

**Abstract:** A simple, low loss and compact printed planer monopole ultra-wideband (UWB) antenna with single band notch characteristics is proposed. The antenna consists a semi-circular radiating patch on one side and a modified ground plane on the other side of the substrate. The optimized design of the antenna has an overall dimension of 52.25 mm ×42 mm and is fabricated on 1.575 mm thick low dielectric substrate ($\varepsilon_r$= 2.33) of high frequency copper laminated glass microfiber reinforced composite substrate. The antenna design, simulation and parametric analysis have been performed on finite element method based full-wave 3D electromagnetic field simulation software. A circular slot has introduced in the semicircular patch for achieving the stop band at 4 GHz C band frequency range. The experimental results show that the fabricated antenna has achieved impedance bandwidths of 13.5 GHz (1.5 to 15 GHz) with a single frequency band-stop performance of 3.58 – 4.92 GHz. The proposed antenna shows almost consistent radiation patterns with adequate radiation efficiency over the operating frequency bands which make the antenna appropriate for providing services in L band, ISM, Wi-Fi, LTE 2600, Bluetooth and different UWB applications.

Keywords: Glass-Polytetrafluoroethylene, UWB, Printed antenna, Low loss

***References***

[1] F. C. Commission, "Revision of Part 15 of the Commission's Rules Regarding Ultra-Wideband Transmission Systems,"First Report and Order," FCC 02," *V48, April,* 2002)

[2] B. Allen, M. Dohler, E. Okon, W. Malik, A. Brown, and D. Edwards, *Ultra wideband antennas and propagation for communications, radar and imaging*: John Wiley & Sons,(2006).

[3] E. Fear and M. Stuchly, "Microwave detection of breast cancer," *Microwave Theory and Techniques, IEEE Transactions on,* 48(2000) 1854-1863.
[4] H. M. Jafari, M. J. Deen, S. Hranilovic, and N. K. Nikolova, "A Study of Ultrawideband Antennas for Near-Field Imaging," *IEEE Transactions on Antennas and Propagation,* 55(2007) 1184-1188.
[5] M. Klemm, I. Craddock, A. Preece, J. Leendertz, and R. Benjamin, "Evaluation of a hemi-spherical wideband antenna array for breast cancer imaging," *Radio Science,* 43(2008)
[6] R. Azim, M. T. Islam, and N. Misran, "Microstrip line-fed printed planar monopole antenna for UWB applications," *Arabian Journal for Science and Engineering,* 38(2013) 2415-2422.
[7] M. H. Ullah, M. T. Islam, and J. S. Mandeep, "A parametric study of high dielectric material substrate for small antenna design," *International Journal of Applied Electromagnetics and Mechanics,* 41(2013) 193-198.
[8] M. Ahsan, M. Islam, M. Habib Ullah, R. Aldhaheri, and M. Sheikh, "Design of high gain slotted patch antenna with defected ground for WLAN/WiMAX applications," *International Journal of Applied Electromagnetics and Mechanics,* 49(2015) 251-262.
[9] R. Azim, M. T. Islam, and A. T. Mobashsher, "Design of a dual band-notch UWB slot antenna by means of simple parasitic slits," *Antennas and Wireless Propagation Letters, IEEE,* 12(2013) 1412-1415.
[10] R. Azim, A. T. Mobashsher, and M. T. Islam, "UWB antenna with notched band at 5.5 GHz," *Electronics Letters,* 49(2013) 922-924.
[11] M. A. Dorostkar, M. T. Islam, and R. Azim, "Design of a novel super wide band circular-hexagonal fractal antenna," *Progress In Electromagnetics Research,* 139(2013) 229-245.
[12] D.-H. Lee, H.-Y. Yang, and Y.-K. Cho, "Tapered slot antenna with band-notched function for ultrawideband radios," *Antennas and Wireless Propagation Letters, IEEE,* 11(2012) 682-685.
[13] C. Wang, Z. H. Yan, B. Li, and P. Xu, "A dual band-notched UWB printed antenna with C-shaped and U-shaped slots," *Microwave and Optical Technology Letters,* 54(2012) 1450-1452.
[14] H.-W. Liu, C.-H. Ku, T.-S. Wang, and C.-F. Yang, "Compact monopole antenna with band-notched characteristic for UWB applications," *Antennas and Wireless Propagation Letters, IEEE,* 9(2010) 397-400.
[15] R. Azim, M. T. Islam, and N. Misran, "Design of a Planar UWB Antenna with New Band Enhancement Technique," *Applied Computational Electromagnetics Society Journal,* 26(2011)

# Design of plasmonic structures in CMOS technology for low-cost, enhanced infra-red gas sensors

**J. W. Gardner[1], Y. Xing[1], B. Urasinska-Wojcik[1], A. de Luca[2], and F. Udrea[2]**
[1]School of Engineering, University of Warwick, UK
[2]Department of Engineering, University of Cambridge, UK
[*]corresponding author: J.W.Gardner@warwick.ac.uk

**Abstract -** We have designed different plasmonic structures in CMOS technology that enhance infra-red emissivity at wavelengths useful for air quality applications. Plasmonic structures are presented comprising periodic arrays of holes in tungsten and aluminium for IR wavelengths associated with $CO_2$, CO and $H_2S$. These plasmonic structures are simulated using COMSOL and shown to provide enhanced IR emissivity at specific wavelengths. Our results enable fabrication of low-cost MEMS-based IR gas sensors with the ability to differentiate between different gases.

Non-dispersive infra-red (NDIR) spectroscopy is commonly used in gas sensing. It generally comprises an IR bulb, an optical filter, and IR detector; filters for $CO_2$, CO and $H_2S$ have centres at 4.3 µm, 4.6 µm and 7.3 µm, respectively. Initial work [1] on MEMS-based IR structures (without plasmonics) showed poor emission at lower wavelengths (< 8 µm). Now a MEMS based design has been patented [2] that employs a novel plasmonic structure to ameliorate the poor emissivity of current CMOS materials (e.g. oxide, Al). Here we report on the design and simulation of novel plasmonic structures for low-cost MEMS-based IR gas sensing at lower wavelengths. Figure 1 shows the design of a MEMS based IR emitter with heater made from metal layer M1. The top metal layer (M3) is periodically patterned for plasmon resonance; metal layer M2 is a heat sink for thermal uniformity. Tungsten and aluminium M3 metal layers have been designed with square lattice structure.

Based on the main absorption peak for the target gas, the diameter and the period of the pattern are adjusted accordingly. The models were simulated using COMSOL multi-physics soft-ware.

The designs will be manufactured using a CMOS process followed by a deep reactive-ion etch (DRIE) to form the membrane. In our model, the diameter and period were varied to simulate manufacturing tolerances of 5%, with the average value shown in Figure 2. The shaded area represents the IR filter with 180 nm bandwidth. The addition of the plasmonic structure into the emitter enhances the simulated emission to nearly 100% (from about 10%) for all three target gases, and all peaks are in the standard filter region. The ideal result is to have a distinct emission peak for the target gas and minimum cross correlation with the other gases. This is not only for detection sensitivity, but also for multi gas sensing purposes. For carbon monoxide and carbon dioxide, the tungsten plasmonic structure shows a better response with lower cross correlation while the hydrogen sulphide is more detectable with aluminium.

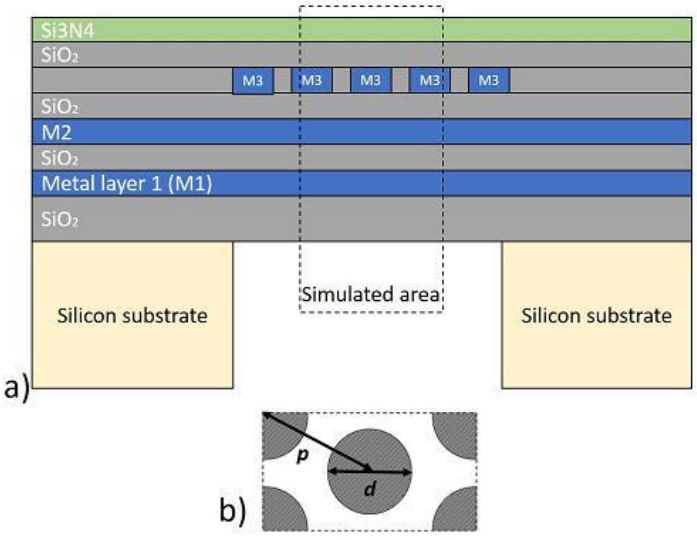



*Figure 1: a) CMOS MEMS emitter cross section (not to scale); b) circular holes pattern top view (p for period and d for diameter).*

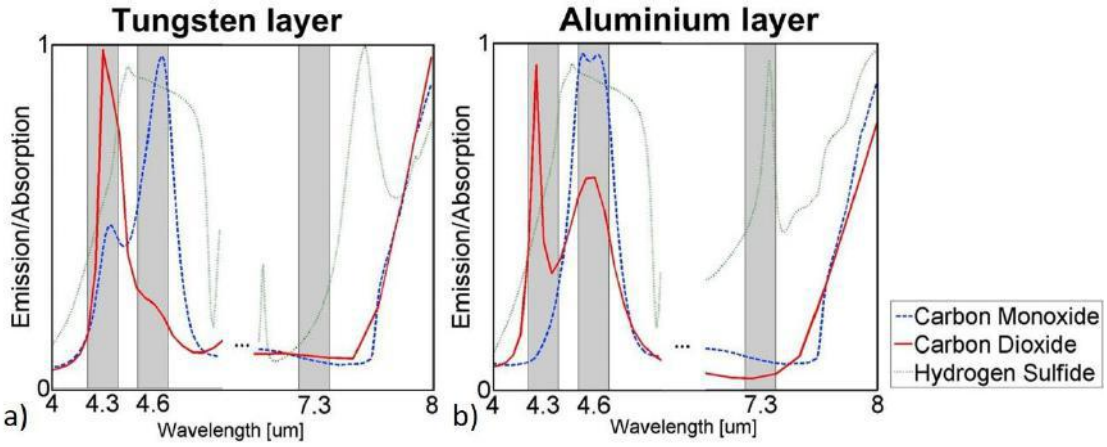



*Figure 2: COMSOL simulation results in a) tungsten metal layer (CO: d=3.1, p= 4.5; $CO_2$: d=3.6, p=4.2; $H_2S$: d= 3.1, p=7.4); b) aluminium metal layer (CO: d=3.1, p=4.5; $CO_2$: d=2, p=4.15; $H_2S$: d=5.4, p=7.6) (unit: µm).*

A model with similar plasmonic structure was manufactured [3], and due to the absence of a planarization step in the process, the plasmonic structure tends to be islands. The scanning electron microscope (SEM) graph shows in figure 3 is the manufactured structure. For this purpose, the models are also simulated with islands structure for comparison (see Figure 3). The islands structure has lower absorption than ideal holes, but it still have high response for all target gases. In summary, we have designed and simulated novel metal (W and Al) plasmonic structures for enhanced IR emissions at mid-IR wavelengths in CMOS technology. The structures were configured to detect polluting gases namely carbon dioxide, carbon monoxide and hydrogen sulphide. Simulations covered holes structures in tungsten and aluminium metal layers, for both planarized and non-planarized process. Our results suggest plasmonic structures not only greatly increase the IR performance of CMOS devices but also enable the discrimination of different gases at specific wavelengths. Perhaps even removing the need for a narrow band optical filter.

**References**


1. S. Z. Ali, A. De Luca, R. Hopper, S. Boual, J.W. Gardner, and F. Udrea, "A Low-Power, Low-Cost Infra-Red Emitter in CMOS Technology," *IEEE Sensors Journal*, Vol. 15, No. 12. 6775-6782, 2015.
2. S. Z. Ali, F. Udrea, J.W.Gardner, R. Hooper, A. De Luca, F. Chowdhury and I. Ponerau, "Plasmonic IR devices" *US Patent, Dec 15 2015*.

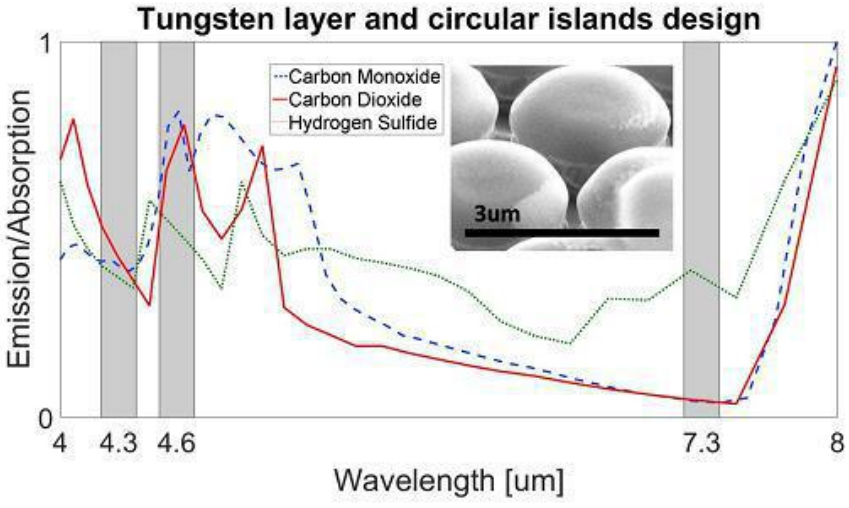




*Figure 3: Simulation results for different circular island designs.*


3. A. Pusch, A. De Luca, S. S. Oh, S. Wuestner, T. Roschuk, Y. Chen, S. Boual, Z. Ali, C. C. Phillips, M. Hong, S. A. Maier, F. Udrea, R. H. Hopper, and O. Hess, "A highly efficient CMOS nanoplasmonic crystal enhanced slow-wave thermal emitter improves infrared gas-sensing devices", *Scientific Reports*. 5, 17451, Dec. 7, 2015.

# Wood zone plate lens based on fishnet metamaterial

**B. Orazbayev[1*], M. Navarro-Cía[3], and M. Beruete[1,2]**

[1]Antennas Group – TERALAB, Universidad Pública de Navarra, Pamplona, Spain

[2]Institute of Smart Cities, Universidad Pública de Navarra, Campus Arrosadía, 31006 Pamplona, Spain

[3]School of Physics and Astronomy, University of Birmingham, Birmingham B15 2TT, UK

[*]corresponding author: b.orazbayev@unavarra.es

**Abstract**- A study of a low-profile hybrid Wood zone plate fishnet metamaterial lens working at $f$ = 99 GHz is presented. The use of fishnet metamaterial with effective refractive index close to zero ($n$ = 0.51) as a medium for Fresnel zones allows to reduce the reflections from the metalens and increase the overall efficiency, while maintaining low profile, low cost and ease of manufacturing. The performance of metalens was analyzed numerically and confirmed experimentally, demonstrating a good agreement.

The Fresnel zone plate lenses possess high reflections from the opaque rings (the even or odd zones), which deteriorate the focusing efficiency. In the Wood zone plate lens (WZPL) this disadvantage is overcome by replacing the opaque rings with dielectric rings that produce fields with a π phase difference with respect to the original transparent ring zones. When the refractive indices of the materials used for the even and odd zones are similar, the lens becomes thick and heavy. On the other hand, high index contrasts enable thinner lenses but at the expense of impedance mismatch with free-space, which causes a focusing efficiency reduction. [1], [2].

To tackle this problem, here we propose a hybrid half-wavelength WZPL based on a fishnet metamaterial. The fishnet metamaterial, which consists of closely-packed subwavelength hole arrays working under extraordinary optical transmission [3] [see Fig. 1(a)], can have a refractive index less than unity (for the design reported here, $n$ = 0.51) and therefore enable faster π phase difference between odd and even zones. Moreover, the fishnet metamaterial has the potential to minimize reflection, increasing the overall efficiency of the lens. In our metalens' design four periods of fishnet metamaterial (plus one dielectric layer as a protection cover) are used, which provide a good trade-off between total thickness and electromagnetic performance in terms of insertion loss. Therefore, the total thickness of the metalens is $w = 4d_z+t_d$ = 1.97 mm (~0.62$\lambda_0$) (where $d_z$ = 0.4 mm is the period of the fishnet metamaterial, $t_d$ = 0.38 mm is the thickness of dielectric layer). The required refractive index $n_f$ = 0.51 was derived from the equation of the thickness of the WZPL: $w = \lambda_0/(\sqrt{\varepsilon_r}-\sqrt{\varepsilon_f})$ (where $\varepsilon_r$, $\varepsilon_f$ is the permittivity of the dielectric and fishnet metamaterial respectively). The value of the refractive index of the fishnet metamaterial can be adjusted by varying the diameter of the holes $a$, which at the design frequency $f$ = 99 GHz ($\lambda_0$ ~ 3.03 mm) was found to be $a$ = 1.08 mm.

Figs. 2 (c, d) show the numerically-computed electric field distribution in the *xz*-plane (c) and the *yz*-plane (d). The focal length is $FL$ = 22.5 mm (7.4$\lambda_0$) and $FWHM_1 = FWHM_2$ = 2 mm (0.66$\lambda_0$) for *xz*- and *yz*-planes, respectively. The measurement can be seen in Fig. 2 (e, f) for the *xz*-plane and the *yz*-plane, respectively. The focal length is $FL$ = 23 mm (7.6$\lambda_0$) and $FWHM_1 = FWHM_2$ = 2.1 mm (0.69$\lambda_0$) for *xz*- and *yz*-plane respectively. Thus, the numerical and experimental results are in good agreement.

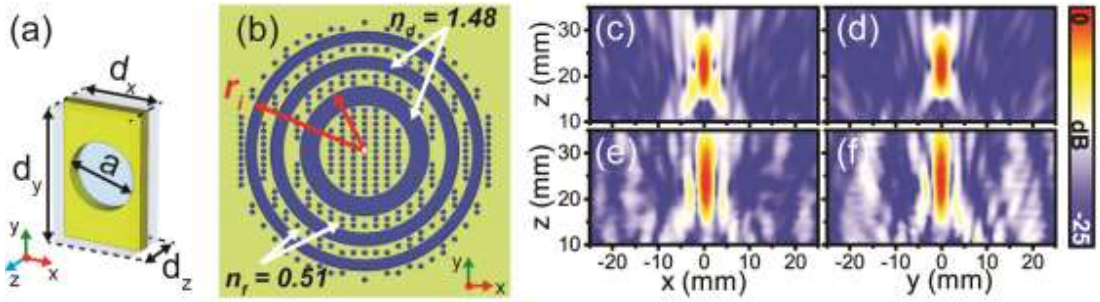



Fig.1. (a) Fishnet metamaterial unit cell. (b) Fabricated WZP fishnet metamaterial lens. Normalized electric field distribution in *xz*-plane (c,e) and *yz*-plane (d,f) for numerical (top) and experimental (below) results.

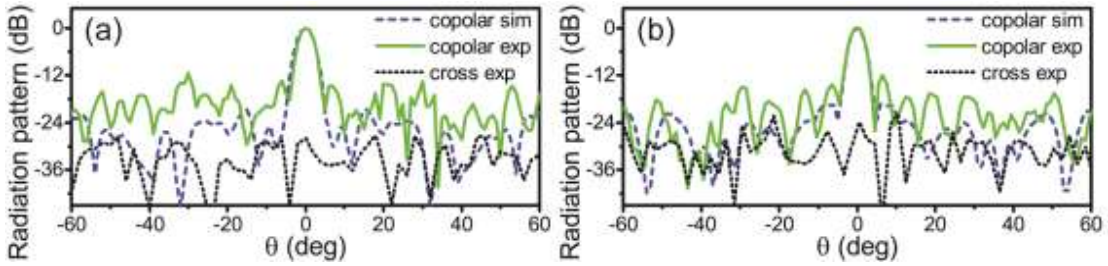



Fig. 2. Normalized radiation pattern for *E*-plane (a) and *H*-plane (b) (simulation and experimental).

The performance of the fishnet WZPL in lens-antenna configuration was also analyzed. The normalized numerical and experimental radiation patterns are shown in Fig. 2 (a, b) for *E*- (a) and *H*-plane (b) respectively. It is obvious that the radiation patterns for the main lobes are in good agreement, however the side lobes are higher in the experiment. This can be explained by the higher ratio main/sidelobe in numerical results, which results in lower lobes in the normalized radiation pattern.

Finally, a relatively high gain of 16.6 dB was measured at the design frequency $f$ = 99 GHz while the numerical gain is 24.3 dB. This disagreement may be explained by experimental errors (misalignment, accuracy of distance measurement) and by defects in the fabrication (non-perfect contact between dielectric and metallic plates, errors in the radius of the holes) and effective substrate losses higher than nominal values.

**Acknowledgment.** This work was sponsored by Spanish Government under contract TEC2014-51902-C2-2-R. B. O. is sponsored by Spanish Ministerio de Economía y Competitividad under grant FPI BES-2012-054909. M. N.-C. is supported by a Birmingham Fellowship. M. B. is sponsored by the Spanish Government via RYC-2011-08221.

**REFERENCES**

1. H. D. Hristov, *Fresnel Zones in Wireless Links, Zone Plate Lenses and Antennas*. Norwood, MA: Artech House, 2000.
2. I. V Minin and O. Minin, *Diffractional Optics of Millimetre Waves*. Bristol: CRC, 2004.
3. M. Beruete, M. Sorolla Ayza, I. Campillo, J. S. Dolado, L. Martín-Moreno, J. Bravo-Abad, and F. J. García-Vidal, "Enhanced millimeter-wave transmission through subwavelength hole arrays," *Opt. Lett.*, vol. 29, no. 21, pp. 2500–2, Nov. 2004.

# Bandwidth Enhancement of Multilayer Polymeric Comb Array Antenna for Millimeter Wave Applications

**W.A.W. Muhamad[1], R. Ngah[2], M. F. Jamlos[3] and P.J. Soh[4]**

[1,2]Wireless Communication Centre (WCC), Universiti Teknologi Malaysia, Skudai, Johor, Malaysia

[3,4]Advanced Communication Engineering Centre (ACE), School of Computer and Communication Engineering, Universiti Malaysia Perlis, Perlis, Malaysia.

[1]gongchan_89@yahoo.com

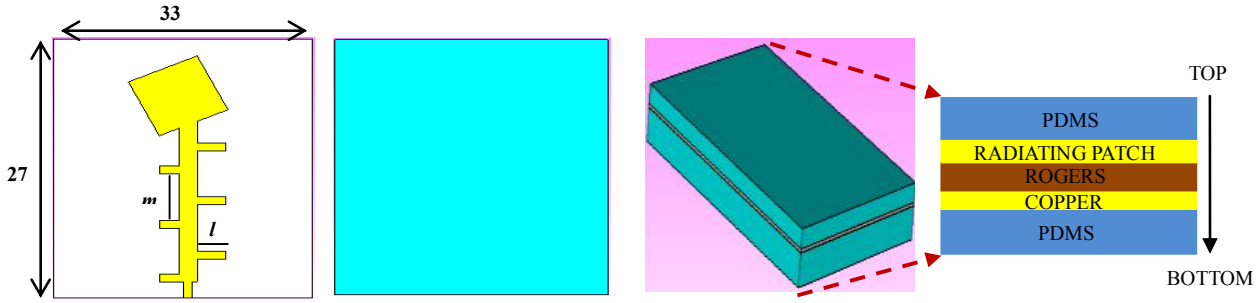
**Abstract-** ***A new multilayer polymeric comb array antenna is presented. The multilayer substrates of Polydimethylsiloxane (PDMS) and Rogers produced an increment bandwidth of 5.118 GHz compared to 0.608 GHz, which is non-polymeric antenna. Multilayer substrate, comb array structure and PDMS's epsilon of 2.7 contributing to such bandwidth ranging from 22.649 until 27.792 GHz and gain of 9.856 dB at 25 GHz resonance. Moreover, dimension of 33x27 mm$^2$ is considered compact in size.***

## SUMMARY

Nowadays, millimeter-wave communications have been greatly attention as a new technology in high frequency range with a demand of high data rate capacity [1]. Microstrip is one of good option as millimeter wave's antenna due to its interesting characteristics such as low profile and simple structure [2]. In order to enhance the data rate and broad bandwidth, material of dielectric substrate plays the significant role. For this concern, this paper presents a new combination of meta-material substrate; Polydimethylsiloxane (PDMS) with a compact microstrip comb array antenna.

PDMS is a new dielectric substrate which is consisted of silicone based elastomer and suitable for higher frequency up to terahertz [3]. The low epsilon of PDMS substrate which is 2.7 lead to bandwidth enhancement. This is due to the polarization effects theory. A low epsilon will gives more electric flux generated per unit charge and minor energy trapping inside the substrate. Therefore, it is ease to radiation move to free space and enhanced the performance of antenna.

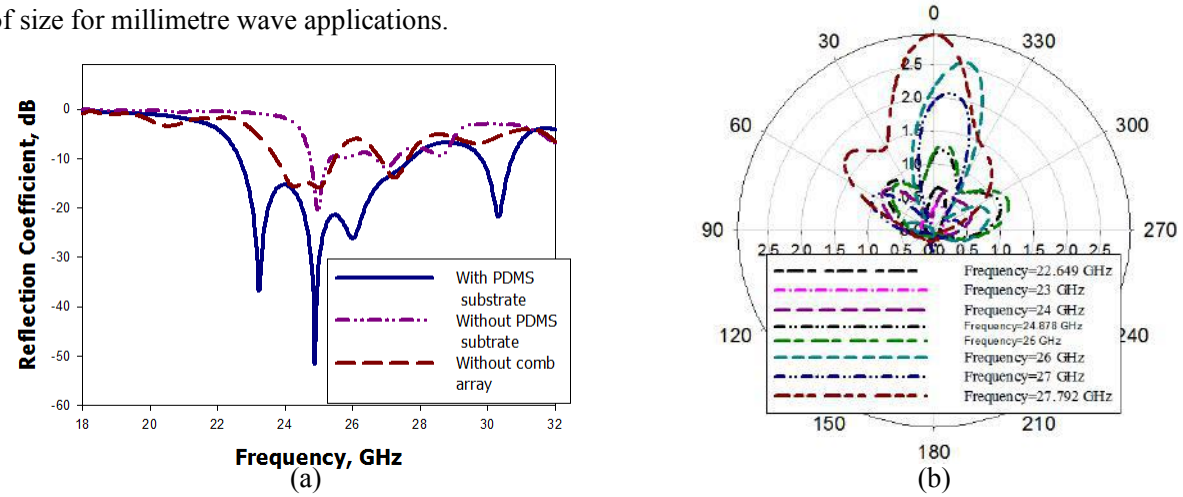
In this paper, the multilayer of PDMS with Rogers is designed with a compact size of 27x33 mm$^2$ for the width and length respectively as shown in Figure 1(a) while full ground plane depicted by Figure 1(b). The proposed multilayer antenna is consists of five layers as demonstrated in Figure 1 (c). An array structure of comb antenna is arranged in zig-zag with main radiating element inclined by -45 degrees. The length, $\boldsymbol{l}$ of each array is based on formula $\boldsymbol{l} = \lambda_g$ and the spacing between each array is m= $\lambda_g/2$ where $\lambda_g$ is the guided wavelength at the center frequency [4].




(a) (b) (c)

Figure 1. The multilayer polymeric comb array antenna (a) front view (b) back view and (c) perspective view.

Figure 2(a) shows the comparison of reflection coefficient, $S_{11}$ of Rogers substrate with (in blue line) and without (in purple line) PDMS. It is observed that the combination of PDMS with Rogers substrate produced more bandwidth which is up to 5.118 GHz compared to only 0.608 GHz (without PDMS). This is due to the low epsilon of 2.7. Comparison of multilayer polymeric antenna without comb array is analyzed as well. It is found out that the comb array antenna (in blue line) is better than without comb array (in red line) in term of bandwidth. The polar radiation pattern is illustrated in Figure 2(b) subject to the varieties of frequency ranging from 22.649 GHz until 27.792 GHz. The highest gain of 9.856 dB is recorded at 25 GHz. As conclusion, the new combination of polymeric comb array antenna generates good bandwidth and high gain as well as compactness of size for millimetre wave applications.




(a) (b)

Figure 2. (a) Reflection coefficient and (b) polar radiation pattern for multilayer polymeric comb array antenna.

## REFERENCES


1. Daniel Sanchez-Escuderos, Miguel Ferrando-Bataller, Jose I. Herranz, and Marta Cabedo-Fabres, "Periodic Leaky-Wave Antenna on Planar Goubau Line at Millimeter-Wave Frequencies, " *IEEE Antennas and Wireless Propagation Letters,*2013.
2. A. Pirhadi, G. A. Jafarabadi, " Design of Modified Microstrip Combline Design of Modified Microstrip Combline, " *Progress In Electromagnetics Research Letters*, Vol.14, 31-40, 2010.
3. Zheng Xu, Xiaodai Dong, and Jens Bornemann, "Design of a Reconfigurable MIMO System for THz Communications Based on Graphene Antennas," *IEEE Transaction on Terahertz Science and Technology,* Vol. 4, No. 5, September 2014.
4. Lin Zhang, Wenmei Zhang, and Y. P. Zhang, "Microstrip Grid and Comb Array Antennas," *IEEE Transactions on Antennas and Propagation,* VoL. 59, No. 11, November 2011.

# Tunable EIT-like effect in wire/ring structure metamaterial

**Q. Fu, F. Zhang*, and Y. Fan**

Key Laboratory of Space Applied Physics and Chemistry, Ministry of Education and Department of Applied Physics, School of Science, Northwestern Polytechnical University, Xi'an, 710072, People's Republic of China

*corresponding author: fuli.zhang@nwpu.edu.cn

**Abstract**-In this work, we integrate varactor diodes into wire/ring structure, and investigate the tunable EIT-like effect by simulation. Via interference between the electric dipole mode of wire and magnetic dipole mode of ring, EIT-like transmission spectrum with prominent slowing light behavior appears. The transmission peak of wire/ring structure exhibits a blueshift up to 0.97 GHz as the capacitance of varactor diodes ranges from 0.9 pF to 1.8 pF. The wire/ring structure demonstrates a transmission modulation with modulation depth of 97%.

Electromagnetically induced transparency (EIT) was originally observed in the context of quantum mechanics [1]. In 2007, Fedotov et al. first observed EIT-like effect in metamaterials [2]. The EIT-like characteristics in metamaterials and nanostructures have attracted great interest in recent years.

In this work, we introduce varactor diodes [3] into wire/ring structure, and investigate the tunable EIT-like effect inside a standard rectangular waveguide of BJ32 by simulation. Via interference between the electric dipole mode of wire and magnetic dipole mode of ring, EIT-like transmission spectrum with large dispersion appears. The transmission peak of wire/ring structure exhibits a blueshift up to 0.97 GHz as the capacitance of varactor diodes ranges from 0.9 pF to 1.8 pF. The wire/ring structure demonstrates a transmission modulation with modulation depth of 97%.

Figure 1 depicts the wire/ring structure for EIT-like effect. The scattering parameters are calculated by full wave simulation.

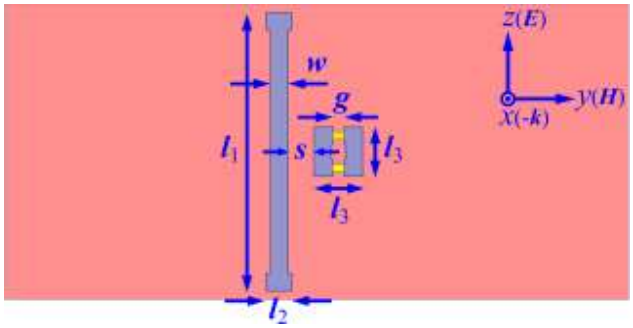



Figure 1. Schematic view of wire/ring structure. The metal layer is copper with a conductivity of 5.8e7 S/m, and the depth is 0.018 mm. The substrate is Teflon with a relative permittivity of 2.65 and a loss tangent of 4e-4, and the dimension is 72.14*34.04*1 $mm^3$. The dimensions of wire/ring structure are as follows: $l_1$=32 mm, $l_2$=3 mm, $l_3$=5.7 mm, $w$=2 mm, $g$=1.3 mm and $s$=5 mm. The two yellow rectangles represent varactor diodes.

Figure 2a shows that the EIT-like transmission spectrum of wire/ring structure appears due to the interference between the electric dipole mode of wire and magnetic dipole mode of ring, and the transmission peak reaches -2 dB. The steep phase variation leads to a large group delay of 14.2 ns at 3.27 GHz, corresponding

to a 3.29-m-long transmission line, see figure 2b. Figure 2c demonstrates the tunability of EIT-like effect by varactor diode. The transmission peak of wire/ring structure moves from 3.78 GHz to 2.81 GHz as the capacitance of varactor diodes ranges from 0.9 pF to 1.8 pF, exhibiting a blueshift of 0.97 GHz. Figure 2d demonstrates the transmission modulation of wire/ring, and the transmission can be modulated from -2 dB to -40 dB, realizing a modulation depth up to 97%.

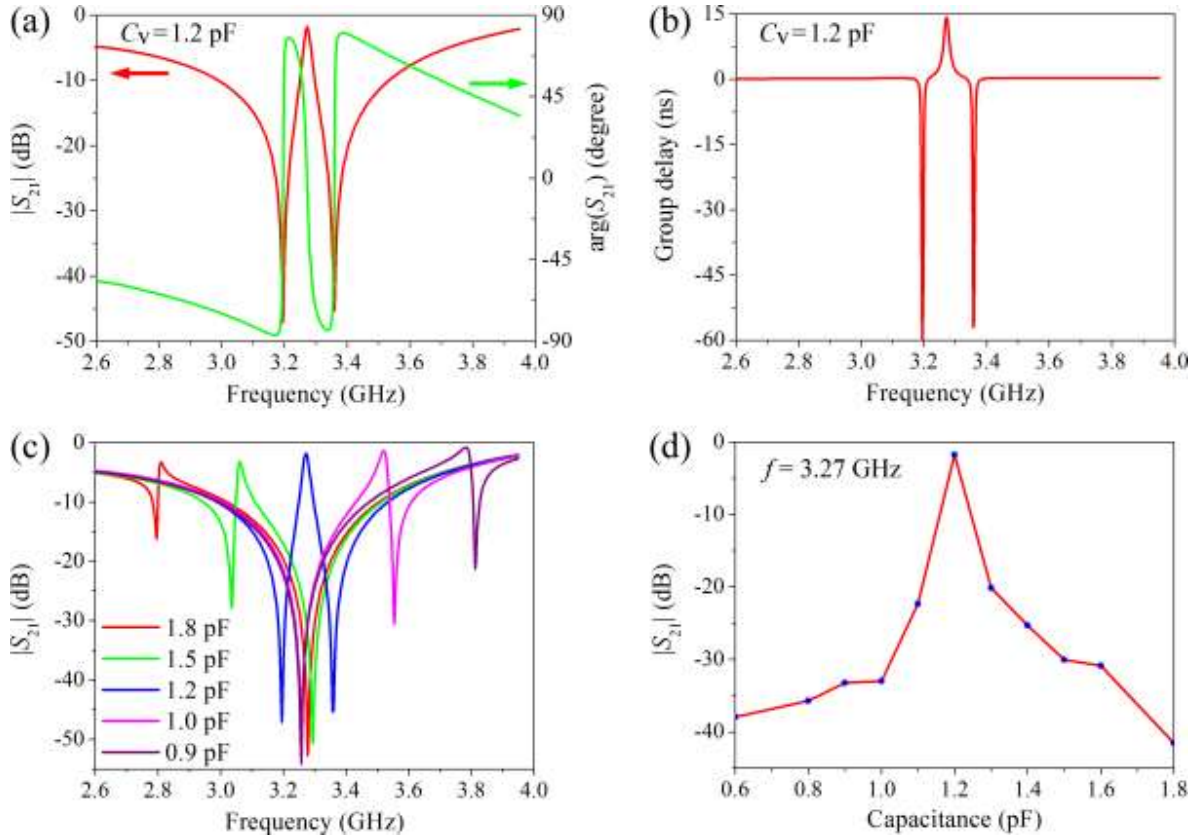



Figure 2. Transmission (a) and group delay (b) of wire/ring structure as the capacitance of varactor diodes is 1.2 pF. (c) Transmission spectra of wire/ring structure with the capacitance of varactor diodes ranging from 0.9 pF to 1.8 pF. (d) Transmission modulation of wire/ring structure at 3.27 GHz by varactor diode.

**Acknowledgements** We gratefully acknowledge the financial support from National Natural Science Foundation of China (Grant Nos. 61101044, 61505164 and 11372248), Fundamental Research Funds for the Central Universities (Grant Nos. 3102015ZY058 and 3102015ZY079), Shaanxi Project for Young New Star in Science and Technology (Grant No. 2015KJXX-11), and NPU Aoxiang Star Project.

**REFERENCES**

1. Fleischhauer, M., Imamoglu, A. and Marangos, J. P., "Electromagnetically induced transparency: Optics in coherent media," *Rev. Mod. Phys.*, Vol. 77, No. 2, 633–673, 2005.
2. Zhang, S., Genov, D. A., Wang, Y., Liu, M. and Zhang, X., "Plasmon-induced transparency in metamaterials," *Phys. Rev. Lett.*, Vol. 101, No. 4, 047401, 2008.
3. Chen, H. S., Wu, B. I., Ran, L. X., Grzegorczyk, T. M. and Kong, J. A., "Controllable left-handed metamaterial and its application to a steerable antenna," *Appl. Phys. Lett.*, Vol. 89, No. 5, 053509, 2006.

# Magnonic-crystal-based magnon transistor

**A. A. Serga**[1], **A. V. Chumak**[1], **and B. Hillebrands**[1]

[1]Fachbereich Physik and Forschungszentrum OPTIMAS, Technische Universität Kaiserslautern, 67663 Kaiserslautern, Germany
serga@physik.uni-kl.de

**Abstract**— Using a magnonic crystal—an artificial magnetic media with a periodic variation of its magnetic properties in space—to enhance nonlinear magnon-magnon interactions, we have succeeded in the realization of magnon-by-magnon control, and the development of a magnon transistor. We demonstrate that the density of magnons flowing from the transistors source to its drain can be decreased three orders of magnitude by the injection of magnons into the transistors gate.

With the fast growth in the volume of information being processed, researchers are charged with the primary task of finding new ways for fast and efficient processing and transfer of data. Spin waves and their quanta magnons are recognized to be perspective in the role of information carriers alternative to charged particles [1]. We have succeeded realization of magnon-by-magnon control and have developed the magnon transistor [2]. We present a proof of concept device that is made out of a magnetic insulator (single crystal film of yttrium iron garnet, YIG) in order to exclude any motion of free electrons. In this three-terminal device, the density of the magnon current flowing from the Source to the Drain (see the spheres with arrows in Fig. 1a) is controlled by the magnons injected into the Gate of the transistor (the spheres without arrows). The magnonic crystal in the form of an array of surface grooves [3] is used to increase the density of the gate magnons and, consequently, to enhance the efficiency of nonlinear four-magnon scattering. It was shown that the Gate-to-Drain magnon current can be decreased up to three orders of magnitude (see Fig. 1 1b). Moreover, the Source-to-Drain magnon current can be manipulated by the gate magnons having a density hundred times smaller, and thus an amplification of the magnon-carried signals is possible.

The magnon transistor constitutes a key component of magnon-based data processing and allows for the design of magnon computing units including XOR and NAND logic gates (see Fig. 1c). The potential for the miniaturization of this transistor will be discussed.

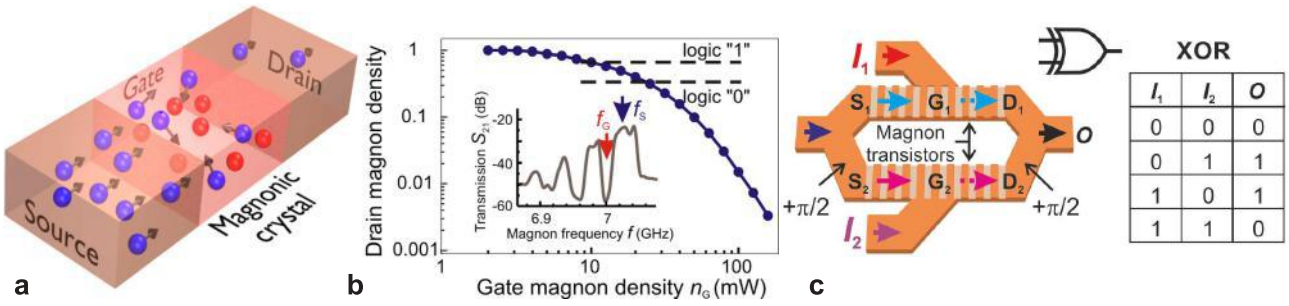



Figure 1: (a) Schematic of the operational principle of a magnon transistor. (b) The measured drain magnon density as a function of the gate magnon density. (c) All-magnon chip proposed for XOR logic operation.

## ACKNOWLEDGMENT

Financial support within EU-FET grant InSpin 612759 is gratefully acknowledged.

## REFERENCES

1. Chumak, A. V., V. I. Vasyuchka, A. A. Serga and B. Hillebrands, "Magnon spintronics," *Nature Physics*, Vol. 11, 453–461, 2015.
2. Chumak, A. V., A. A. Serga and B. Hillebrands, "Magnon transistor for all-magnon data processing," *Nature Comm.*, Vol. 5, 4700, 2014.
3. Chumak, A. V., A. A. Serga, S. Wolff, B. Hillebrands and M. P. Kostylev, "Scattering of surface and volume spin waves in a magnonic crystal," *Appl. Phys. Lett.*, Vol. 94, No. 17, 172511, 2009.

# Gold nanotube metamaterial for plasmonic cavity resonator

**J. X. Zhang[1, 2*], J. F. Wang[1], C. Zhang[3], H. J. Song[1], P. Wang[3], Y. H. Lu[3], G. T. Fei[1], L. D. Zhang[1], L. Zhang[2]**

[1]Key Laboratory of Materials Physics and Anhui Key Laboratory of Nanomaterials and Nanostructures, Institute of Solid State Physics, Chinese Academy of Sciences, Hefei 230031, P. R. China

[2]Aston Institute of Photonic Technologies (AIPT), School of Engineering & Applied Science, Aston University, Birmingham B4 7ET, UK

[3]Department of Optics and Optical Engineering, University of Science and Technology of China, Hefei 230026, P. R. China

[*]corresponding author: jxzhang@issp.ac.cn

**Abstract**- We present a plasmonic cavity resonator based on a gold nanotube array embedded in an anodic aluminum oxide membrane. The gold nanotube metamaterial performs multipolar resonance modes of surface plasmons. Furthermore, FDTD simulation demonstrates the electric fields of the longitudinal resonance modes are focused on the interfaces between the aluminum oxide and the gold nanotubes, which exhibit obvious standing-wave modes with high-order harmonics, thus the gold nanotube metamaterial can be worked as a plasmonic cavity resonator.

Plasmonic resonant cavities are capable of confining light at the nanometer scale, which exhibit promising applications in sources[1], sensing[2], enhanced nonlinear effects[3] etc. It has been noted that the conventional metal nanostrips as cavities have very large Ohmic losses due to the surface plasmons only existing at single metal-dielectric interfaces. Therefore enhancement of plasmonic mode coupling by designing two or multi metal-dielectric interfaces can decrease the Ohmic losses [4,5]. Here, we propose a plasmonic resonator by using periodic metal-dielectric interfaces in a gold nanotube metamaterial, which has the extraordinary optical transmission (EOT) due to the hollow geometry [6] and so performs much strong Fabry–Pérot (F-P) resonances [7].

The gold nanotube metamaterial, consisting of the gold nanotube array embedded into anodic aluminum oxide (AAO) membranes, was fabricated by using a galvanostatic electrodeposition in a three-electrode cell. Figure a and b show the typical SEM images of the hexagonal packed gold nanotube array, the outer and the inner diameters are about 65 nm and 30 nm, and the length is about 610 nm. The plasmonic property of the gold nanotube metamaterial was measured by a fixed-angle reflector (8°) and calibrated against a diffuse reflectance module, it is found that the gold nanotube array display multipolar resonance modes (Figure c). The transversal modes have two peaks corresponding to the resonances from the outer and inner surfaces of the nanotube walls (D), while the longitudinal resonances present multipolar modes (A, B and C). Figure d show the reflectance of the nanotube array by a FDTD simulation. Notes that the mode number of the longitudinal resonances from the theoretical result is basically accordance with that from the experiment, however, the bandwidth and the positions of the resonances display differences between the theoretical and experimental results, this may be attributed to an assumption that the nanotubes have perfectly smooth surfaces in the FDTD simulation. In fact, some scattering losses on the nanotube surfaces are inevitable because the nanotubes are not very smooth.

On the other hand, the electric fields of the transversal resonance mode concentrate on the incident end of the nanotubes, but those of the longitudinal resonance modes focus on the outer surfaces of the nanotube walls

(Figure e). Moreover, the electric fields on the nanotube surfaces have standing-wave modes for the longitudinal modes, therefore, the gold nanotube array can worked as a plasmonic cavity resonator, which originates from the F-P resonances between the nanotube terminations. In addition, both the standing-wave modes with the harmonics of odd orders are confined by a node at the incident end (i.e., at the bottom of the nanotubes) with the weakest fields and an antinode at the emergent ends (i.e., at the top of the nanotubes) with the strongest fields.

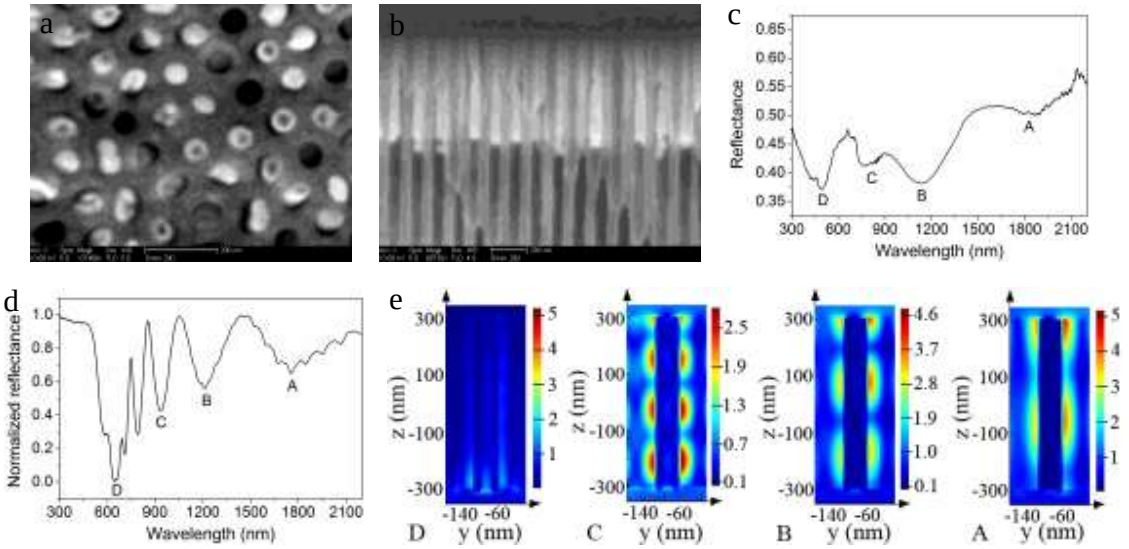



Figure (a), (b) Top and cross-sectional views of SEM images of the gold nanotube array embedded in AAO membrane, scale bar: 200 nm. (c) and (d) Experimental and theoretical reflectance spectra of the gold nanotube array. (e) Electric field distributions of the plasmonic resonance modes in the gold nanotube metamaterial.

**Acknowledgements**

This work was supported by the National Natural Science Foundation of China (No. 10804112) and the National Basic Research Program of China (No. 2012CB932303, 2012CB921900), The Seventh Framework Programme: Marie Curie International Incoming Fellowships (FP7-PEOPLE-2013-IIF, No. 623473).

**REFERENCES**

1. Zhou, W., M. Dridi, J.Y. Suh, C.H. Kim, D.T. Co, M.R. Wasielewski, G.C. Schatz and T.W. Odom, "Lasing action in strongly coupled plasmonic nanocavity arrays," *Nat. Nanotechnol.* Vol.8, No.7, 506–511, 2013.
2. Kabashin, A.V., P. Evans, S. Pastkovsky, W. Hendren, G.A. Wurtz, R. Atkinson, R. Pollard, V.A. Podolskiy and A.V. Zayats, "Plasmonic nanorod metamaterials for biosensing," *Nat. Mater.* Vol. 8, No. 11, 867–871, 2009.
3. Kauranen, M. and A.V. Zayats, "Nonlinear plasmonics," *Nat. Photon.* Vol. 6, No. 11, 737-748, 2012.
4. Zhang, J.X. and L.D. Zhang, "Nanostructures for surface plasmons," *Adv. Opt. Photon.* Vol. 4, No. 2, 157–321, 2012.
5. Lyvers, D.P., J.M. Moon, A.V. Kildishev, V.M. Shalaev and A. Wei, "Gold nanorod arrays as plasmonic cavity resonators," *ACS nano* Vol. 2, No. 12, 2569–2576, 2009.
6. Ebbesen, T.W., H.J. Lezec, H.F. Ghaemi, T. Thio and P.A. Wolff, "Extraordinary optical transmission through sub-wavelength hole arrays," Nature Vol. 391, No. 6668, 667–669, 1998.
7. Ditlbacher, H., A. Hohenau, D. Wagner, U. Kreibig, M. Rogers, F. Hofer, F.R. Aussenegg and J.R. Krenn, "Silver nanowires as surface plasmon resonators," *Phys. Rev. Lett.* Vol. 95, No. 25, 257403, 2005.

# Compensating wave packet distortion with active anomalously dispersive media or devices

**C. Wang[1], A. Zhu[1], S. Qiao[2], Y. Sun[3], D. Ye[1*], and L. Ran[1]**

[1]Laboratory of Applied Research on Electromagnetics (ARE), Zhejiang University, Hangzhou, China

[2]Zhejiang University City College, Hangzhou, China

[3] Nanjing Institute of Electronic Equipment, Nanjing, China

[*]corresponding author: desy@zju.edu.cn

**Abstract-** Recently, we have experimentally observed electromagnetic wave transmission with negative group velocity in the anomalous dispersion region of a simple structured metamaterial. This implies that the wave packet distortion due to the transmission with the subluminal group velocity in conventional media can be compensated by a properly designed anomalously dispersive property. Considering the considerable loss in the anomalous region of passive media, metamaterials or devices constructed with active elements, such as non-Foster elements, are good candidates. As the first step, we verified the compensation for severely distorted wave packets with a wideband floating non-Foster element, which has an inverted frequency dispersion. The preliminary result shows the potential to implement low-loss anomalously dispersive metamaterials or devices for wave packet compensation.

In electromagnetics, the classical Drude-Lorentz model offers an intuitive and accurate description of both normal and anomalous material dispersion in an extended spectrum from direct current to optical frequencies. As a direct consequence of the Kramers-Kronig relation, anomalous dispersion occurs as the wavelength approaches to the electric scale of the absorption resonance of the medium, exhibiting reversed spatial-temporal frequency dependence in the opposite of the normal dispersion case. Without violating the causality, anomalous dispersion in the absorption resonance region implies an electromagnetic (EM) wave packet propagating with a superluminal or negative group velocity, i.e., an EM pulse appears to exit the medium before it enters. This effect has been demonstrated in our recent simulation and experimental research.

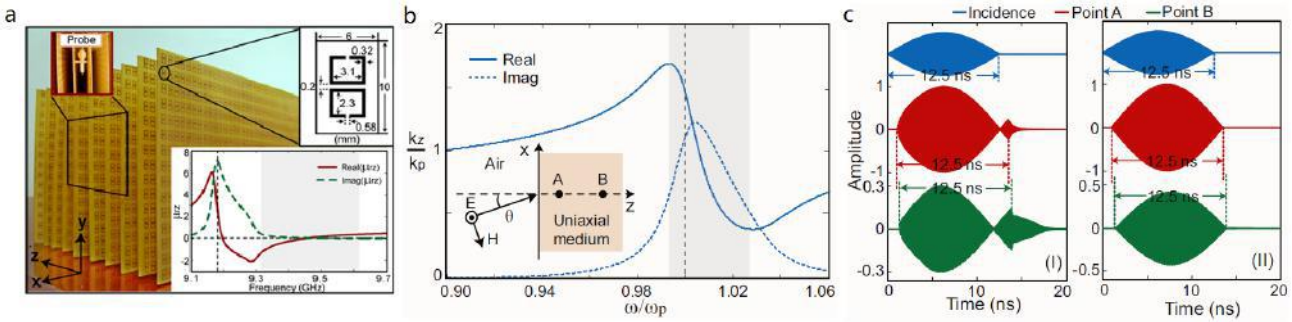



**Figure 1. The metamaterial sample, dispersion and simulated wave packet transmission with negative and positive group velocity.**

In simulation, two probes were placed at point ‘A’ and ‘B’, with a 120-mm increment. Figure 1 shows the uniaxial metamaterial sample used in our research, the simulation model and the simulated wave packet transmission with negative and positive group velocities, respectively. These simulated results are in agreement

with the experimental data (not shown here due to the page limit). We see that in the anomalous region, the wave packet distortion is "forward", while in the normal dispersion region, the distortion is "backward".

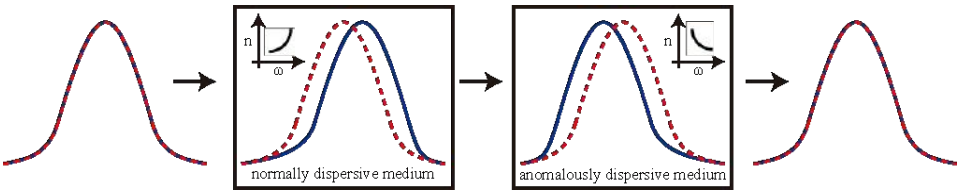



**Figure 2. Principle of the wave packet compensation with anomalously dispersive metamaterials or devices.**

This reminds us that if the anomalous dispersion can be properly engineered, the "backward" packet distortion can be compensated by letting such packets transmit through a metamaterial layer (or a device) with a specific anomalous dispersion, as shown in Figure 2. Considering the inherent loss of the anomalously dispersive medium, active elements can be introduced in the unit cells, obtaining a gain assisted metamaterial. In our research, the non-Foster element has been chosen to provide the negative dispersion.

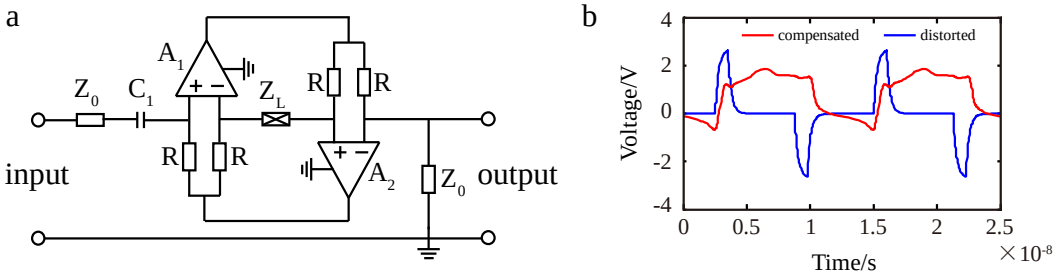



**Figure 3. The floating wideband non-Foster element and the simulated compensation for the distortion due to a differentiator.**

In our preliminary work, we have designed and implemented a floating wideband non-Foster element based on state of the art dual operational amplifiers, as shown in Figure 3. As an example, we used this element to compensate a severely distorted square wave signal due to a differentiating circuit. As seen in Figure 3, the simulated severe distortion of a square wave packet due to the differentiator can be mostly compensated.

In our further research, such elements will be embedded in circuit and metamaterial units. By obtaining controllable anomalous dispersion, the distortion of wave packages transmitted in both circuits and space can be compensated. We expect our method can be verified in the near future.

**Acknowledgements:** This work was supported by the NSFC under grants 61131002 and 61401393, ZJNSF under grant LY16F010009, and the Program for the Top Young Innovative Talents under grant Q1313-03

## REFERENCES

1. Dexin, Ye. & Lixin. Ran, "Negative Group Velocity in the Absence of Absorption Resonance," *Scientific Reports*, 3, 1628, 2013.
2. Dexin, Ye. & Lixin, Ran, "Observation of Wave Packet Distortion during a Negative-Group-Velocity Transmission," *Scientific Reports*, 2, 8100, 2015.
3. Antoniou, A. "Floating negative-impedance converters," *IEEE Trans. Circuit Theory*, Vol. 19, No. 3, 209-212, 1972.

# Active dispersion compensation for metamateirals and devices based on the wideband frequency response of non-Foster elements

**A. Zhu[1], C. Wang[1], S. Qiao[2], Y. Sun[3], D. Ye[1*], and L. Ran[1]**

[1]Laboratory of Applied Research on Electromagnetics (ARE), Zhejiang University, Hangzhou, China

[2]Zhejiang University City College, Hangzhou, China

[3] Nanjing Institute of Electronic Equipment, Nanjing, China

[*]corresponding author: desy@zju.edu.cn

**Abstract**-We experimentally investigated the full-range frequency response of non-Foster elements (NE) based on ultrahigh speed operational amplifiers. Our results indicate that the de-embedded impedance of an NE co-existing with a properly designed stabilization network has an inverted Lorentzian absorption resonance that satisfies the Kramers-Kronig relations. While the non-Foster response on the left side of the resonance is intrinsically accompanied by a negative, frequency dependent resistance, there also exists a non-Foster response on the right side of the resonance region. This characteristic can be used to achieve high-frequency non-Foster responses, and wideband compensation for the frequency dispersion of metamaterials and small-sized antennas.

Immittance that does not obey Foster's theorem exists in certain active networks, making it possible to obtain non-Foster element (NE) with imaginary immittance monotonically decreasing with frequency, creating a "negative" inductance or capacitance. This unique characteristic makes NEs be good candidates in the compensation of dispersion of metamaterials and microwave devices. However, a standalone NE is theoretically unstable due the "negative time constant" caused by the inverted frequency response, making it difficult to obtain wideband, high frequency non-Foster responses.

In this work, different from previous researches that mainly pay attention to the non-Foster response at the frequencies lower than the resonance region, we investigate the full-range frequency response of an RF NE. Analysis, simulation and experiments show that the complex-valued impedance of a physically realizable NE has an inverted Lorentzian resonance region, resulting in a wide-range frequency response that complies with the Kramers-Kronig relations. Our research indicates that while an NE can steadily co-exist with a properly designed stabilization network, its low-frequency non-Foster immittance is always accompanied by a negative, frequency-dependent resistance, which will affect the wide band impedance matching relying on the non-Foster immittance. Moreover, there exists another high-frequency non-Foster region on the right side of the resonance region, which can be used to overcome the difficulty inachieving high-frequency NEs in practical applications.

Figure 1 shows the schematic of an OP AMP based NE with stabilization network, the implemented circuit board and measurement setup, and the retrieved impedance of the de-embedded NE. It is seen that an inverted Lorentzian resonance is clearly seen at 0.53 GHz, which compiles well with previous simulations. A "negative" inductance can be clearly seen with a frequency-dependent resistance in the bottom-left inset, and a "negative" capacitance can also be seen in the bottom-right inset, both with negative slopes with frequency. Overall, the frequency-dependent resistance is negative from DC to 1 GHz, except for a narrow bandwidth on the right side of the resonance. The measured full-range frequency response of $Z_{NE}$ is consistent with the previous analysis and

simulations. In the frequency bands of DC-0.2 GHz, 0.2-0.4 GHz and 0.6-1 GHz, the reactance is around 0, 0~70 and 60 Ω, respectively, while the corresponding reactance is 0~-16, -16~-100 and 400~100 Ω, respectively. In the frequency bands of DC-0.2 GHz and 0.6-1 GHz, where the measured reactance of $Z_{NE}$ has negative slopes on the two sides of the resonance region, the frequency dependency of the reactance of the stabilization network determined by $Z_3$ and $Z_4$ are almost compensated, implying that $Z_{NE}$ exhibits non-Foster frequency response in the two bands.

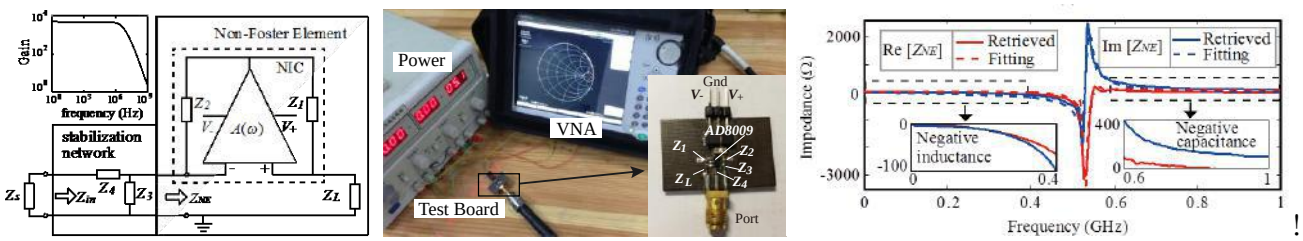



**Figure 1. The schematic of the stabilized NE, the measurement setup and the retrieved full range frequency response of the NE.**

Figure 2 shows the CPW fed electrically small antenna in parallel with a NE, and the comparison between the dispersion compensations using passive and non-Foster matching. It can be seen that compared with the conventional impedance matching using lumped capacitance and inductance, the wideband NE based method can indeed achieve wideband dispersion compensation. Further research will be conducted to compensate the inherent dispersion of metamaterials. We envision our method can be widely used in the future.

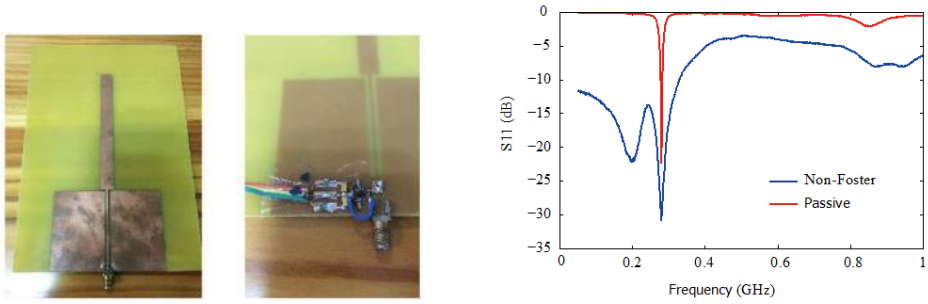



**Figure 2. CPW fed electrically small antenna and the comparison between the dispersion compensation using passive and non-Foster matching.**

**Acknowledgements:** This work was supported by the NSFC under grants 61131002 and 61401393, ZJNSF under grant LY16F010009, and the Program for the Top Young Innovative Talents under grant Q1313-03

## REFERENCES

1. R. M. Foster, "A reactance theorem," *Bell Systems Technical Journal*, vol.3, pp. 259-267, 1924.
2. N. Zhu, R. W. Ziolkowski, "Active metamaterial-inspired broad-bandwidth, efficient, electrically small antennas," *IEEE Antennas Wireless Propag. Lett.*, vol.10, pp.1582,1585, 2011.
3. S. E. Sussman-Fort and R. M. Rudish, "Non-Foster impedance matching of electrically-small antennas," *IEEE Trans. Antennas Propag.*, vol. 57, no. 8, pp. 22302241, 2009.
4. D. F. Sievenpiper, "Superluminal waveguides based on non-foster circuits for broadband leaky-wave antennas," *IEEE Antennas Wireless Propag. Lett.*, vol.10, pp.231,234, 2011.

# Tuning of the lattice mode in 2D array of split-ring resonators

**D. Seliuta[1,2*], G. Šlekas[1], R. Simniškis[1], I. Grigelionis[1], A. Vaitkūnas[1] and Ž. Kancleris[1]**

[1]Center for Physical Sciences and Technology, LT-01108 Vilnius, Lithuania

[2]Vilnius Gediminas Technical University, LT-03227 Vilnius, Lithuania

[*]corresponding author: dalius@pfi.lt

**Abstract**-Using continuous wave terahertz spectroscopy and numerical simulations we investigate fundamental eigenmodes and higher-order resonances in planar arrays split-ring resonators (SRRs). Special attention is paid to the interaction between SRRs in metamaterial arrays and properties of diffraction (lattice) mode in periodic arrays of SRRs. We observe tuning of resonant frequency of high-Q factor and high-frequency lattice mode by variation of parameters of individual resonators which may be advantageous for fabrication of tunable metamaterial filters and modulators.

Metamaterials (MM) have recently attracted considerable interest due to their potential applications in the "terahertz gap" in which lack of compact and effective passive components – filters, switches, modulators – still exists. The ability to control the strength, linewidth and spectral position of MM resonances is of particular importance in practical applications. For this purpose actively controllable metamaterials have been demonstrated at terahertz frequencies based on the implementation of photo- or electro-active elements [1, 2]. Also, tunability of the resonant frequency was achieved in array of varactor-loaded SRRs [3]. The latter approach is attractive from the practical point of view, however, scaling of such devices to higher frequencies is complicated. Here we study far-field transmission properties of planar arrays of SRRs paying special attention to the first and third order eigenmodes of SRRs as well as lattice modes related with the radiative coupling between SRRs in a periodic MM [4]. We demonstrate that lattice modes are characterized with high Q factor and possibility of relatively wide frequency tuning based on variation of effective capacitance of individual split rings. This could be implemented in narrow-band MM filters and modulators.

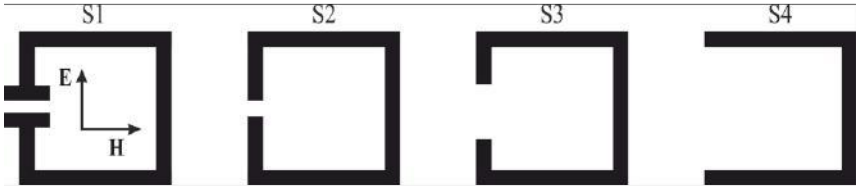



**Figure 1** Geometry of investigated SRRs: side length (outer dimension) 1000 μm, width of the conductive stripes 50 μm, width of the "capacitor" plates in S1 - 300 μm, gap width S1 – 50 μm, S2 – 50 μm, S3 – 300 μm and S4 – 900 μm

For fabrication of SRR arrays teflon film of thickness 50 μm with copper cladding of thickness 10 μm was used. SRRs were patterned using conventional photolithography and wet etching of the copper foil. In this study, four types of SRRs were investigated as shown in Fig. 1. Different effective capacitance of

the split gaps results in different resonant frequency of the structures. The four different structures were used to imitate the performance of a dynamically tunable MM capacitance of which is modulated optically [2] or electrically [3]. The experiments above 40 GHz were performed using frequency-domain terahertz spectrometer. For measurements in the range 20-40 GHz samples were placed in a rectangular waveguide using RF synthesizer as a signal source. In all experiments electromagnetic waves normally impinged on a surface of SRRs with electric field lying in parallel with the gap bearing sides of SRRs.

It was found that increase of the effective capacitance of the split gaps results in blue-shift of all resonances which were observed as transmission minima. This way, fundamental eigenmode $f_0$ ($LC$ resonance) of SRRs was tuned in the range 29-47 GHz, the third order (quadrupole) resonance $f_1$ – in the range 98-128 GHz following roughly the rule: $f_1 = 3\ f_0$.

In addition to the plasmonic eigenmodes, narrow transmission dips are observed at higher frequencies in the range 145-200 GHz. In this case transmission minima are related with radiative coupling between SRRs in the plane perpendicular to the propagation of the incident beam. Because radiative losses in direction of the propagating beam are small the energy of electromagnetic field gets "trapped" in the lattice plane and the lattice resonance is characterized with a relatively high Q factor.

When the period of SRRs in array is changed the lattice modes are spectrally shifted which makes them clearly distinguishable from almost stationary plasmonic modes. We found that the lattice resonance takes place when period of SRRs becomes equal to the radiation wavelength taking into account permittivity of the dielectric substrate.

Here we study in detail the lattice resonance by choosing appropriate geometries of SRRs as presented in Fig. 1. We found that decrease of the effective capacitance of the split gap results in diminishing of the resonant strength. In U-type resonators (S4), the lattice resonance is shallow similarly as in Ref. [4]. Moreover, we demonstrate for the first time that the spectral position of the lattice resonance may be effectively changed with the variation of the effective capacitance of the split gap. This approach might be interesting from the practical point of view since it allows for changing the resonant frequency of the lattice mode in high frequency domain by tuning the effective capacitance which is responsible for the plasmonic modes at lower frequencies.

**Acknowledgement.** This work was supported by the Research Council of Lithuania under grant MIP-059/2014.

**REFERENCES**

1. Chen, H. T., W. J. Padilla, J. M. O. Zide, A. C. Gossard, A. J. Taylor and R. D. Averitt. “Active terahertz metamaterial devices,” *Nature*, Vol. 444, No. 7119, 597–600, 2006.
2. Chen, H. T., J. F. O’Hara, A. K. Azad, A. J. Taylor, R. D. Averitt, D. B. Shrekenhamer and W. J. Padilla, “Experimental demonstration of frequency-agile terahertz metamaterials,” *Nat. Photonics*, Vol. 2, No. 5, 295–298, 2008.
3. Withayachumnankul, W., C. Fumeaux and D. Abbott, “Planar array of electric-*LC* resonators with broadband tunability,” *IEEE Antennas Wireless Propag. Lett.*, Vol. 10, 577–580, 2011.
4. Bitzer, A., J. Wallauer, H. Helm, H. Merbold, T. Feurer and M. Walther. “Lattice modes mediate radiative coupling in metamaterial arrays,” *Opt. Express*, Vol. 17, No. 24, 22108-22113, 2009.

# Conformal Dual Band Textile Antenna with Metasurface for WBAN Applications

**Fatin Nabilah Giman[1], Ping Jack Soh[1*], Mohd Faizal Jamlos[1,2], Herwanshah Lago[1], Azremi Abdullah Al-Hadi[1]**

[1,] Advanced Communication Enginerring Centre (ACE),
School of Computer and Communication Engineering,
Universiti Malaysia Perlis (UniMAP),
Pauh Putra, 02600, Arau, Perlis, Malaysia
[2]Falculty of Mechanical Engineering, Universiti Malaysia Pahang, Pekan, Malaysia
*corresponding author, E-mail: pjsoh@unimap.edu.my

## Abstract

This paper presents the design of a dual-band textile wearable planar slotted dipole integrated with an artificial magnetic conductor (AMC) plane. The overall structure operates in the 2.45 GHz and 5.8 GHz bands and is suited for wireless body area network (WBAN) applications. The AMC plane is formed using a diamond-shaped patch and is used as a reflector to reduce backward radiation towards the human body. Felt and ShieldIt is used as the antenna's substrate and radiating elements, respectively. The antenna operation is investigated under varying bending condition in the azimuth and elevation planes in the low (2.45 GHz) and high (5.8 GHz) frequency bands. The antenna operates with a good reflection coefficient, bandwidth, radiation pattern and realized gain, besides featuring physical characteristics suitable for wearable applications.

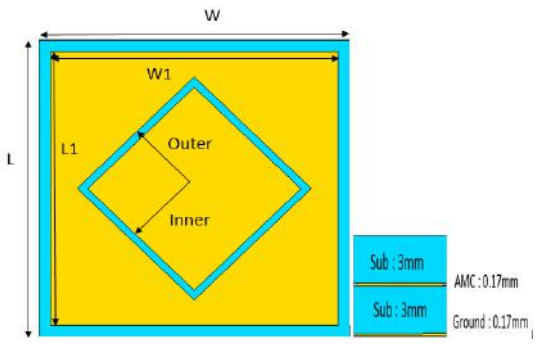
## 1. Introduction

Wearable devices are gaining popularity in various mobile communication applications in recent years [1]-[5]. Wireless body area network (WBAN) systems are promising to change the landscapes of body worn sensors, medicine, health monitoring and emergency rescue. Besides that, the wide usage of the Industrial, Scientific, and Medical (ISM) (2.45 GHz and 5 GHz) band implies the need for WBAN devices to be compatible to their frequencies. Moreover, one of the most important WBAN frequencies is the 2.4 GHz band. Properties of wearable antenna such as conformal, low profile, inexpensive, ease of fabrication are needed to ensure the antenna's suitability for wearable applications. Meanwhile, metasurface such as artificial magnetic conductor (AMC, high impedance surface (HIS), and electromagnetic bandgap (EBG) structure are widely used in the low profile antennas as they can be located close to the radiating elements and operates as the reflector [1]-[5]. One of the main advantages of AMC is its simple unit cell basic structure, either using square or rectangular patches. Besides that, the AMC is capable of operating across the 5 GHz Wireless Local Area Network (WLAN) band due to its wide bandwidth.

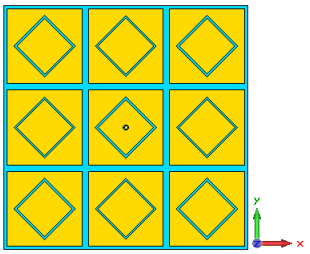
## 2. Antenna Specification and Material

### 2.1 Characterization of the Metasurface

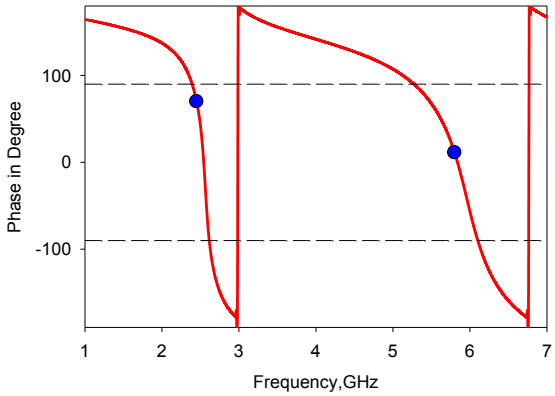
The AMC is designed on a felt substrate with a thickness of 3 mm, relative permittivity ($\varepsilon_r$) of 1.44, and loss tangent (tanδ) of 0.044. Its conductive elements are formed using the 0.17 mm thick ShieldIt Super, with an estimated conductivity of 1.18 x $10^5$ S/m. The AMC topology is illustrated in Figure 1. It consists of a rectangular patch and integrated with a diamond-shaped slot. The geometry of the inner and outer diamond-shaped slot determines the reflection phase points of the dual-band band AMC. The shorter current path provided by the diamond-shaped slot resulted in reflection phase bandwidth of 831 MHz (5.26-6.1GHz) in the upper band. Meanwhile, the rectangular patch with a longer electrical length created a reflection phase bandwidth of 227 MHz (2.38-2.61 GHz) in the lower band. The performance of the AMC in both bands is illustrated in Figure 1(c).




(a)



(b)

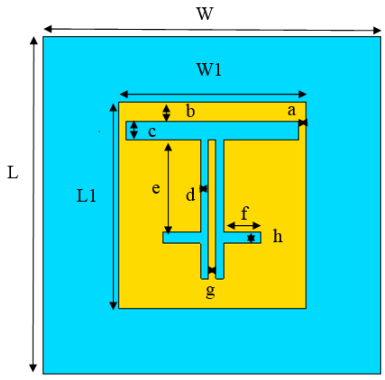



(c)

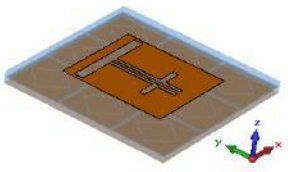
Figure 1: (a) Unit cell of the dual band AMC; (b) 3x3 AMC plane; (c) reflection phase of proposed AMC. The dimensions of AMC unit cell (in mm) with *L*=30, *W*=30, *L1*=27.75, *W1*=27.75, *inner*=10.3, *outer*=11.3.

### 2.2 Antenna design

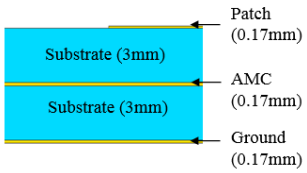
The proposed dual band antenna shown in Figure 2 operates in the lower band (2.45 GHz) and upper band (5.8 GHz). It is designed based on the conventional dipole antenna topology [1] which combines slot antenna (planar magnetic dipole) with an electric dipole. Next, four slots in the *x*-direction are introduced onto rectangular patch to enable its dual-band characteristic. Careful selection of their sizes will enable proper resonance at the desired lower and upper bands. The overall dimension of the proposed antenna is 90 mm x 90 mm. It is built using the same felt and ShieldIt textiles and is placed over the 3 x 3 AMC array.



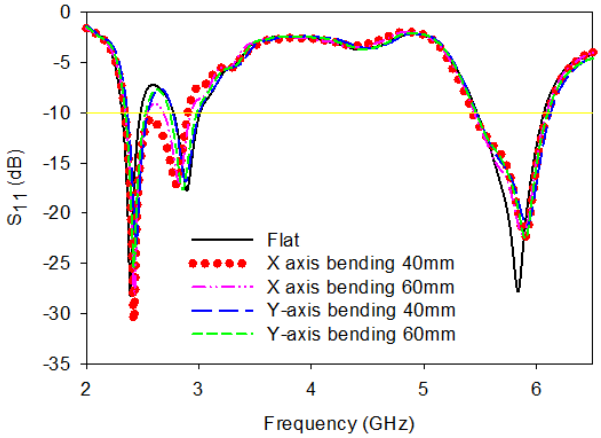

(a)



(b)




(c)




(d)

Figure 2: Details of the proposed antenna: (a) Topology (b) 3D view; (c) cross-section; and (d) reflection coefficients. The dimensions of the proposed antenna (in mm) are *L*=90, *W*=90, *L1*=55, *W1*=50, *a*=2, *b*=5, *c*=5, *d*=2, *e*=37, *f*=10, *g*=1, *h*=3.

## 3. Result and Discussion

Besides studying its performance in free space, the antenna performance is analyzed in bent conditions. It is expected that the on-body placement will result in some degree of deformation. In this work, the antenna is studied in the planar and two other bending conditions using CST MWS. The antenna is bent over cylindrical radii of $r$ = 40 mm and $r$ = 60 mm in the $x$-axis and $y$-axes, as illustrated in Figure 3. Their performance is compared in the following sub-sections.

### 3.1 Planar antenna

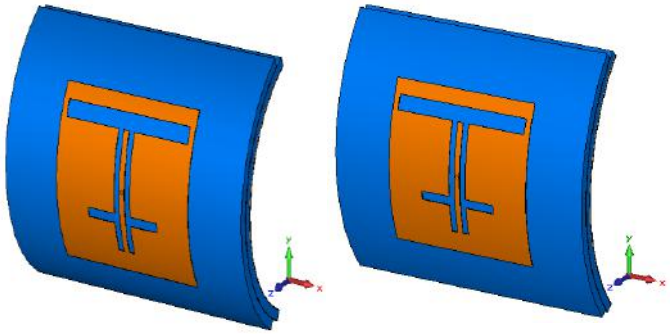
Antenna in the planar state provided an impedance bandwidth of 162 MHz and 592 MHz in the 2.45 GHz and 5.8 GHz bands, respectively, see Figure 2(d). The reflection coefficient is -12.97 dB at 2.45 GHz and -24.95 dB at 5.8 GHz. The planar antenna produced a directional radiation pattern and reduced back-lobe radiation. This is important as omnidirectional antenna usually results in a high SAR value in the human body, potentially affecting the health of body tissues [3]. The simulated front-to-back ratio (FBR) is higher than 20 dB in the lower band and 32 dB in the upper band. The realized gain of the antenna is about 3.01 dB at 2.45 GHz and 7.04 dB at 5.8 GHz. The performance comparison of the proposed antenna is summarized in Table 1.

Table 1: Comparison performance of proposed antenna

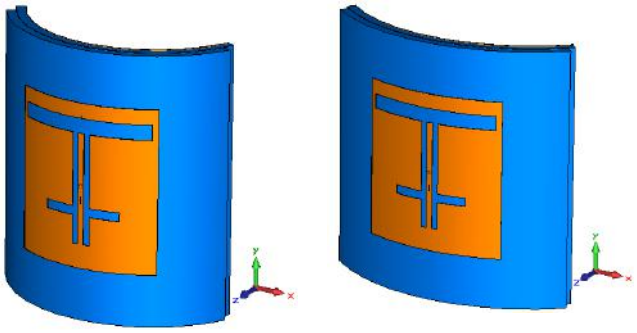
| Parameter | Condition of Antenna | Frequency (GHz) | |
|---|---|---|---|
| | | 2.45 | 5.8 |
| Reflection coefficient (dB) | Flat | -12.97 | -24.95 |
| | Bending x-axis 40mm | -16.24 | -19.08 |
| | Bending x-axis 60mm | -16.27 | -20.33 |
| | Bending y-axis 40mm | -12.73 | -19.73 |
| | Bending y-axis 60mm | -12.78 | -19.81 |
| Realized Gain (dB) | Flat | 3.01 | 7.04 |
| | Bending x-axis 40mm | 0.75 | 2.38 |
| | Bending x-axis 60mm | 1.7 | 3.34 |
| | Bending y-axis 40mm | 2.34 | 4.24 |
| | Bending y-axis 60mm | 2.66 | 4.25 |
| Directivity (dBi) | Flat | 7.72 | 11.4 |
| | Bending x-axis 40mm | 5.59 | 6.34 |
| | Bending x-axis 60mm | 6.28 | 7.38 |
| | Bending y-axis 40mm | 6.68 | 8.29 |
| | Bending y-axis 60mm | 7.07 | 8.52 |
| Bandwidth (MHz) | Flat | 164 | 592 |
| | Bending x-axis 40mm | 560 | 666 |
| | Bending x-axis 60mm | 198 | 641 |
| | Bending y-axis 40mm | 182 | 661 |
| | Bending y-axis 60mm | 181 | 637 |
| Front to Back Ratio, FBR (dB) | Flat | 20.32 | 32.69 |
| | Bending x-axis 40mm | 18.94 | 27.5 |
| | Bending x-axis 60mm | 19.81 | 29.78 |
| | Bending y-axis 40mm | 22.48 | 27.99 |
| | Bending y-axis 60mm | 21.44 | 31.77 |

### 3.2 Bending Evaluation

Figure 3 shows the comparison of the planar antenna and two bent conditions with $r$ = 40 mm and 60 mm at the $x$- and $y$-axes. The resulting $S_{11}$ is shown in Figure 2(d). It can be observed when bending radius is reduced; the lower bandwidth increases while upper bandwidth narrows for both $x$- and $y$-axes. The antenna improved by about 3 dB at 2.45 GHz in $x$-axis for $r$ = 40 mm. On the contrary, similar values with some small degradation are seen at both frequencies when bent in the $y$-axis. Nonetheless, the operation of the antenna in the desired bands are maintained with $S_{11}$ < -10 dB.



(a) (b)

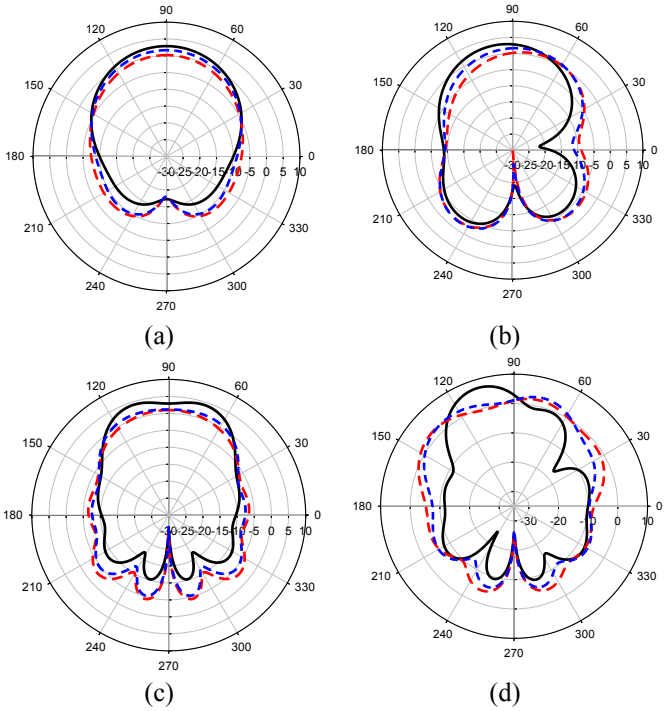


(c) (d)

Figure 3: Antenna bending over the cylindrical radius ($r$) at $x$-axis (a) 40 mm; (b) 60 mm; and at $y$-axis: (c) 40 mm; (d) 60 mm.

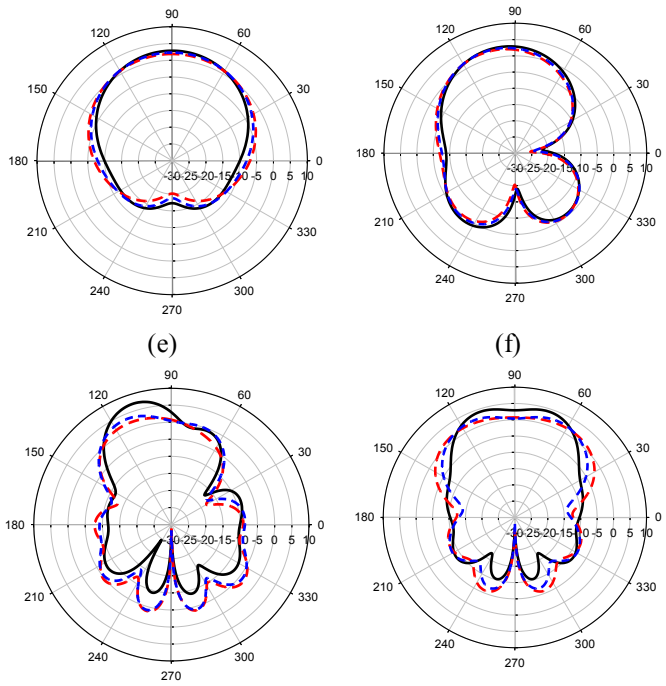
Figure 4 shows directional radiation pattern comparison of proposed antenna at 2.45 GHz and 5.8 GHz in the azimuth ($xz$) and elevation ($yz$) plane in planar and when bent at the $x$- and $y$-axes. It can be seen that the bending did not severely affect the antenna performance and therefore, can be efficiently used in wearable applications. Radiation pattern observation throughout the operating frequency indicated a directional pattern with high FBR, which implies reduced the backward radiation.

It is also seen that the bent antenna (for $r$ = 40 and 60 mm) at $x$-axis provided the most significant improvement in terms of impedance bandwidth, with 560 MHz (when bent with $r$ = 40 mm) and 198 MHz (with $r$ = 60 mm) compared to 164 MHz (in the planar condition) in the lower and upper bands, respectively. In general, the performance of the proposed antenna is satisfactory in terms of reflection coefficient, realized gain, directivity, bandwidth and FBR in the flat and both bent conditions for 2.45 GHz and 5.8 GHz.



(a) (b)

(c) (d)




(e) (f)

(g) (h)

Figure 4: Simulated radiation patterns for the planar and bent antennas: bent at the *x*-axis at (a) 2.45 GHz in the *xz*-plane (b) 2.45 GHz in the *yz*-plane (c) 5.8 GHz in the *xz*-plane (d) 5.8 GHz in the *yz*-plane; bent at the *y*-axis at (e) 2.45 GHz in the *xz*-plane (f) 2.45 GHz in the *yz*-plane (g) 5.8 GHz in the *xz*-plane (h) 5.8 GHz in the *yz*-plane. Note: solid (black) line: planar antenna, (red) long dash line: bent with $r$ = 40 mm, (blue) short dash line: bent with $r$ = 60 mm.

## 4. Conclusions

A wearable dual-band antenna with dual- and broadband AMC is proposed for operation in the 2.4 and 5.8 GHz frequency bands for WBAN applications. The antenna features a directional radiation and high FBR which potentially reduces SAR. The AMC plane is integrated with the antenna to reduce back radiation towards the human body. It consists of a 3 x 3 array of rectangular patches slotted with diamond-shaped slots to enable dual-band operation. This AMC structure is then combined with a patch antenna with a slotted-F dipole to enable its dual band property. The performance of proposed antenna is satisfactory in terms of reflection coefficient, realized gain, directivity, radiation pattern and bandwidth.

## References

[1] Yan, S., P. J. Soh, and G. A. E. Vandenbosch, "Wearable Dual-Band Magneto-Electric Dipole Antenna for WBAN/WLAN Applications," *IEEE Trans. Antennas Propag.,* Vol. 63, No. 9, pp. 4165-4169, 2015.

[2] Jiang, Z. H, D. E. Brocker, P. E. Sieber, and D. H. Werner, "A Compact, Low-Profile Metasurface-Enabled Antenna for Wearable Medical Body-Area Network Devices," *IEEE Trans. Antennas Propag.,* Vol. 62, No. 8, pp. 4021-4030, 2014.

[3] Afridi, A., S. Ullah, S. Khan, A. Ahmed, A. H. Khalil, M. A. Tarar, "Design of Dual Band Wearable Antenna Using Metamaterials," *Journal of Microwave Power and Electromagnetic Energy,* Vol. 47, No. 2, pp. 126-137, 2013.

[4] Yan, S., P. J. Soh, and G. A. E. Vandenbosch, "Low-Profile Dual-Band Textile Antenna With Artificial Magnetic Conductor Plane," *IEEE Trans. Antennas Propag.,* Vol. 62, No. 12, pp. 6487-6490, 2014.

[5] Di Y.-H., X.-Y. Liu, and M. M. Tentzeris, "A Conformable Dual-Band Antenna Equipped with AMC for WBAN Applications," in *3rd Asia-Pacific Conference on Antennas and Propag.*, pp. 388-391, Harbin, China, 2014.

# Effect of the material thicknesses on the transmission spectra of multi-resonant metamaterials

**S. Kaya*, M. Turkmen, and H. Karakaya**
Department of Electrical and Electronics Engineering, Erciyes University, 38039, Kayseri, Turkey
*corresponding author: skaya@bu.edu

**Abstract**- The effects of the material thicknesses on the spectral responses of multi-resonant metamaterials based UT-shaped nanoapertures are studied. Transmission spectra of the structure are determined different thicknesses of materials by using the finite-difference time-domain (FDTD) method. To obtain the refractive index sensing capability of UT-shaped multi-resonant metamaterials, the sensitivity and spectral tunability characteristics are investigated by loading different refractive indexed dielectric cladding media.

Metamaterials have received tremendous interest over the past few years due to their unusual electromagnetic properties [1-5]. Theoretical and experimental results have showed that the optical characteristics of the metamaterials based on nanoapertures are highly dependent on the shape and orientation of the apertures, aperture diameter, and lattice geometry [1-5]. In this study, we investigate the effects of material thicknesses on the spectral responses of UT-shaped multi-resonant metamaterial (MR-MM) nanoapertures which is given in Figure 1. In this figure, *L* indicates the length of the horizontal apertures, *H* indicates the heights, *w* indicates the gap width, and *s* indicates the distance between U- and T- shaped apertures. During the simulations based on FDTD method, the dielectric constants of metals are taken from Ref. [6]. In unit cell consist of the structure, periodic boundary conditions are used along *x* and *y* axes and perfectly matched layers are used along +*z* (the direction of the illumination source).

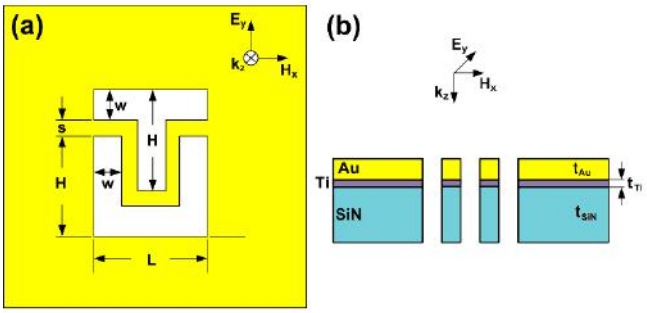



**Figure 1.** (a) Top view of UT-shaped MR-MM (b) Cross section of UT-shaped MR-MM

In this study, we determine the dependence of the spectra on the thicknesses of gold layer ($t_{Au}$) and silicon nitride dielectric layer ($t_{SiN}$) of UT-shaped MR-MM arrays. Figure 2(a) shows the effect of $t_{Au}$ variation while other parameters kept constant (L = 1200 nm, H = 720 nm, s = 200 nm, w = 120 nm, P = 1900 nm, $t_{ti}$ = 5 nm, and $t_{SiN}$ = 80 nm). The resonance frequencies shift and transmission increases with the increasing gold layer thickness for all three modes (Fig. 2a). Figure 2(b) illustrates that the resonance frequencies of structure slightly decrease with the increasing dielectric layer thickness for L = 1200 nm, H = 720 nm, s = 200 nm, w = 120 nm, P = 1900 nm, $t_{Ti}$ = 5 nm, and $t_{Au}$ = 50 nm).

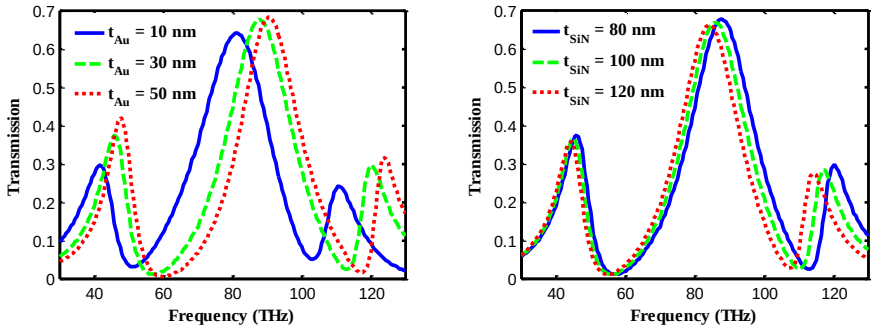
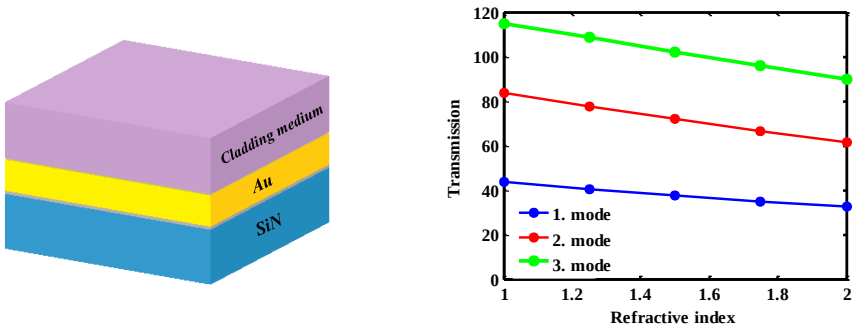



**Figure 2.** The transmission spectra UT-shaped MR-MM for **(a)** $t_{Au}$ variation and **(b)** $t_{SiN}$ variation.

To analyze the refractive index sensing capability of UT-shaped MR-MM, we determine the dependence of the resonance behavior of the UT-shaped metamaterials on the refractive index in Figure 3(a) (L = 1200 nm, H = 720 nm, s = 200 nm, w = 120 nm, P = 1900 nm, $t_{Ti}$ = 5 nm, $t_{Au}$ = 50 nm, and $t_{SiN}$ = 80 nm). We observe that the spectral responses of UT-shaped MR-MM are so sensitive to refractive index variations and the resonance frequencies of all three modes decrease with the refractive index of the dielectric loads with the thickness of 150 nm (Figure 3b). Due to tunable spectral behavior and high sensitivity to refractive index variations, UT-shaped MR-MM arrays may have potential for multiband sensing and high refractive index sensing applications.




**(a)** **(b)**

**Figure 3.** (a) Cross section view and (b) Transmission spectra of the UT-shaped MR-MM in different cladding medium.

**Acknowledgements** The work described in this paper is supported by The Scientific and Technological Research Council of Turkey, Project No: TUBITAK-115E209.

**REFERENCES**

1. Ebbesen, T. W., H. J. Lezec, H. Ghaemi, T. Thio and P. A. Wolf, "Extraordinary optical transmission through sub-wavelength hole arrays," *Nature*, Vol. 391, 667-669, 1998.
2. Thio, T., H. F. Ghaemi, H. J. Lezec, P. A. Wolff, T. W. Ebbesen, "Surface-plasmon-enhanced transmission through hole arrays in Cr films", *J. Opt. Soc. Am. B*, Vol. 16, 1743-1748, 1999.
3. Azad, A. K., Y. Zhao, and W. Zhang, "Transmission properties of terahertz pulses through an ultrathin subwavelength silicon hole array", *Appl. Phys. Lett.*, Vol. 86, 141102, 2005.
4. Turkmen, M., S. Aksu, A. E. Cetin, A. A. Yanik, and H. Altug, "Multi-resonant metamaterials based on UT-shaped nano-aperture antennas," *Opt. Exp.*, Vol. 19, 7921-7928, 2011.
5. Kaya, S. "Windmill-shaped subwavelength apertures operating in the Mid-IR regime", *IEEE Trans. on Nanotechnology*, vol.13, 1250-1256, 2014.
6. Palik, E. D., *Handbook of Optical Constants of Solids*, Academic, Orlando, FL, 1985.

# Optical Focusing via Epsilon-Near-Zero Plasmonic Metalens

**V. Pacheco-Peña[1], M. Navarro-Cía[2], M. Beruete[1,3*]**

[1] Antennas Group-TERALAB, Universidad Pública de Navarra, Campus Arrosadía, 31006 Pamplona, Spain

[2] School of Physics and Astronomy, University of Birmingham, Birmingham B15 2TT, UK

[3] Institute of Smart Cities, Public University of Navarra, 31006 Pamplona, Spain

[*]corresponding author: miguel.beruete@unavarra.es

**Abstract**-An ENZ metamaterial is engineered using a parallel plate plasmonic waveguide working near the cut-off of the transverse electric $TE_1$ mode. The ENZ region can be displaced to different wavelengths when the electrical width of the sandwiched dielectric is changed. Several converging lenses are designed at $\lambda_0$ = 474.9 nm with a focal length of $10.75\lambda_0$: a smooth concave, zoned and graded refractive index (GRIN) lens. It is demonstrated that the best performance in terms of the focal length and volume reduction is achieved with the GRIN design, achieving values of $10.23\lambda_0$ and ~52%, respectively.

Within the framework of metamaterials [1], media with low permittivity, so-called epsilon-near-zero (ENZ), have become a prominent subfield of research due to their unusual characteristics such tunneling, supercoupling and energy squeezing [2]. These features have been demonstrated at microwaves [3] and also at optical wavelengths using waveguides close to the cut-off of the $TE_{01}$ mode and also by metal-dielectric-metal multilayers, respectively [4], giving rise to different applications such as sensors[5] and lenses[6], [7].

In this work we use a plasmonic parallel plate waveguide in order to engineer an effective ENZ medium by working near the cut-off wavelength of the $TE_1$ mode under vertical polarization (electric field parallel to the waveguide) [8]. It is shown that the ENZ region can be tuned at different wavelengths within the optical spectrum when the width of the sandwiched dielectric of the plasmonic waveguide is changed. Several converging lenses are designed at $\lambda_0$ = 474.9 nm and evaluated numerically: a smooth profiled plano-concave lens, a zoned lens and a graded refractive index (GRIN) lens.

To begin with, the schematic representation of the waveguide is shown in Fig. 1(a) as an inset. Silica ($SiO_2$) is used as dielectric in between two silver plates (modeled as a Drude model). A vertically polarized planewave ($E_y$) is used to excite the structure in order to work with the transversal electric $TE_1$ mode. The propagation constant ($\beta$) of this structure is calculated by using the dispersion equation of a plasmonic waveguide (see [8]). This parameter has a clear dependence on the width of the dielectric slab ($h_x$) as can be corroborated in Fig. 1(a) where the complex value of $\beta$ is shown for the case of a plasmonic waveguide with $h_x$ = 95 nm and $h_x$ = 110 nm. It can be observed that the cut-off wavelength moves to longer wavelengths when $h_x$ increases, as expected. Around this inflection point $\beta$ is close to zero, which is one of the properties of an ENZ medium. Therefore, it is possible to work within this region and emulate an ENZ metamaterial.

Based on this structure, we design several lenses working at $\lambda_0$ = 474 nm with different profiles as shown in Fig. 1(b-d), in order to focus an incoming planewave at a focal length (FL) of $10.75\lambda_0$. The numerical results of the normalized power distribution along the *z*-axis are shown in Fig. 1(e) for all the designs. The best performance is achieved for the GRIN design with a FL = $10.23\lambda_0$, while it is at FL = $14.4\lambda_0$ and FL = $11.3\lambda_0$ for the lenses in Fig.1(b) and (c), respectively. Furthermore, a reduction of volume of ~52% is achieved with the

GRIN lens, which is attractive from a practical point of view.

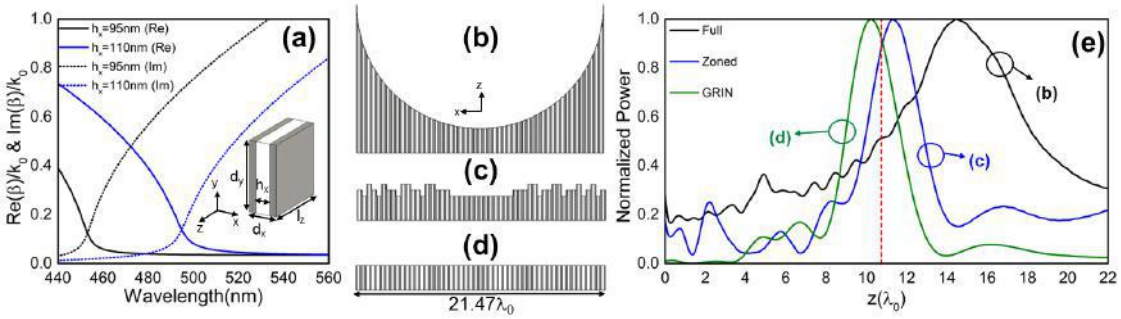



Figure 1. (a) Real (solid lines) and imaginary (dotted lines) parts of the propagation constant (β) normalized to the wavenumber in free-space($k_0$) for two plasmonic waveguides with $h_x$=95nm (black) and $h_x$=110nm (blue). Schematic representation of the metalenses with profiles: (b) plano-concave, (c) zoned and (d) GRIN. (e)Normalized power distribution along the *z*-axis for the three converging lenses under study along with the design FL (red dashed line).

**Acknowledgements**, this work was supported by the Spanish Ministerio de Economía y Competitividad under contract TEC2014-51902-C2-2-R. V.P.-P. is sponsored by Spanish Ministerio de Educación, Cultura y Deporte under grant FPU AP-2012-3796. M. N.-C. is supported by a Birmingham Fellowship. M.B. is sponsored by the Spanish Government via RYC-2011-08221.

**REFERENCES**

[1] R. Marqués, F. Martín, and M. Sorolla, *Metamaterials with Negative Parameters: Theory, Design and Microwave Applications*. Hoboken. NJ: Wiley, 2008.

[2] M. G. Silveirinha, "Theory of Supercoupling, Squeezing Wave Energy, and Field Confinement in Narrow Channels and Tight Bends Using ε-Near-Zero Metamaterials," *Phys. Rev. B*, vol. 76, 2007.

[3] B. Edwards, A. Alù, M. E. Young, M. Silveirinha, and N. Engheta, "Experimental verification of epsilon-near-zero metamaterial coupling and energy squeezing using a microwave waveguide," *Phys. Rev. Lett.*, vol. 100, no. 3, pp. 1–4, 2008.

[4] R. Maas, J. Parsons, N. Engheta, and A. Polman, "Experimental realization of an epsilon-near-zero metamaterial at visible wavelengths," *Nat. Photonics*, vol. 7, no. 11, pp. 907–912, Oct. 2013.

[5] A. Alù and N. Engheta, "Dielectric Sensing in ϵ-Near-Zero Narrow Waveguide Channels," *Phys. Rev. B*, vol. 78, no. 4, p. 15, 2008.

[6] M. Navarro-Cía, M. Beruete, M. Sorolla, and N. Engheta, "Lensing system and Fourier transformation using epsilon-near-zero metamaterials," *Phys. Rev. B*, vol. 86, no. 16, pp. 165130–1–6, Oct. 2012.

[7] V. Torres, B. Orazbayev, V. Pacheco-Peña, M. Beruete, M. Navarro-Cía, and N. Engheta, "Experimental demonstration of a millimeter-wave metalic ENZ lens based on the energy squeezing principle," *IEEE Trans. Antennas Propag.*, vol. 63, no. 1, pp. 231–239, 2015.

[8] V. Pacheco-Peña, M. Navarro-Cía, and M. Beruete, "Epsilon-near-zero metalenses operating in the visible," *Opt. Laser Technol.*, vol. 80, pp. 162–168, 2016.

# Perfect Absorbers for Microwave Energy Harvesting

**Thamer S. Almoneef**[1], **Omar M. Ramahi**[1]

[1]University of Waterloo, Waterloo, Canada
talmonee@uwaterloo.ca

**Abstract**— We introduce the design of a metamaterial collector inspired by the full absorption concept for electromagnetic energy harvesting. Different from previous metamaterial absorber designs, here the power absorbed is mostly dissipated across a resistive load rather than in the dielectric substrate. This is achieved by channeling the absorbed power to an optimal resistive load through a via hole.

Full absorption of an impinged electromagnetic wave can be realized by satisfying two conditions. First the metamaterial medium need to have an effective $\epsilon$ and $\mu$ such that the input impedance is matched to the free space impedance (e.g $\sqrt{\frac{\mu}{\epsilon}} \approx 1$), thus minimizing reflections from the metamaterial surface. In addition a sufficient loss is introduced in the medium so that all the incident power is dissipated within the cell. The fact that such medium is capable of absorbing all the incident power is indicative of its potential for energy harvesting. Different from metamaterial absorbers [1], metamaterial harvesters [2] require not only full absorption but also maximum power delivery to the load. However it has been shown in previous metamaterial absorber designs that the main contributor to the power dissipation of the absorbed power within the metamaterial medium is the dielectric substrate [1]. In fact, most metamaterial absorbers incorporate a lossy dielectric to ensure that all the power available at the metamaterial interface is dissipated within the unit cell.

In a recent work by Almoneef et al. [3], a 13 X 13 metamaerial ELC resonators were used to harvest electromagnetic energy with a conversion efficiency of 97% using the perfect absorption concept. In this paper, the perfect absorption concept is utilized to produce a metamaterial harvester.

A unit cell of the proposed energy collector is shown in Fig. 1. A via is placed at the top of the resonator to channel the absorbed power to a resistive load located between the via and the ground plane. With reference to Fig. 1, the cell was designed to operate at 3 $GHz$ having dimensions of $L = 13.25\ mm$, $d1 = 13\ mm$, $d2 = 1.5\ mm$, $w1 = 1.53\ mm$, and $w2 = 3\ mm$. The material parameters ( $\epsilon$ and $\mu$) were tailored by varying the 3-dipole resonator dimensions, the periodicity of the unit cell, the resistance of the load and the position of the via to achieve not only full absorption but also maximum power delivery to the load.

The absorption of the metamaterial medium obtained from $A(\omega)$=1-$|S_{11}|^2$-$|S_{21}|^2$ is shown in Fig. 2(a). The scattering parameters were calculated with reference to port 1 and 2 as indicated in Fig. 1. It is evident that the resonator experience full absorption at the operating frequency of 3 $GHz$. This can be attributed to two reasons: First, an impinged TEM wave seen from port 1 (see Fig. 1) experiences effectively an impedance equals to the free space impedance at the metamaterial interface as indicated by Fig. 2(b). Second, the resistive load dissipates the absorbed power within the unit cell. From the simulation, maximum power delivery to the load occurs with a load resistance of 185 Ω.

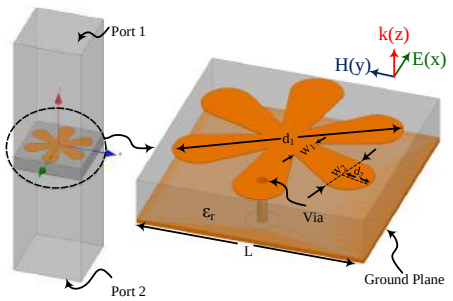
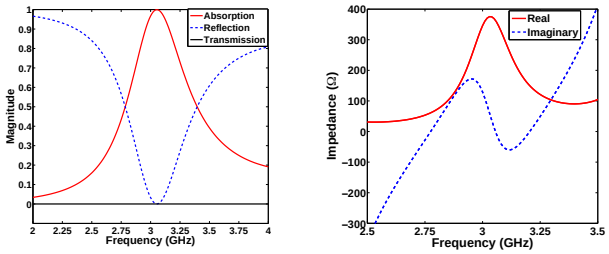


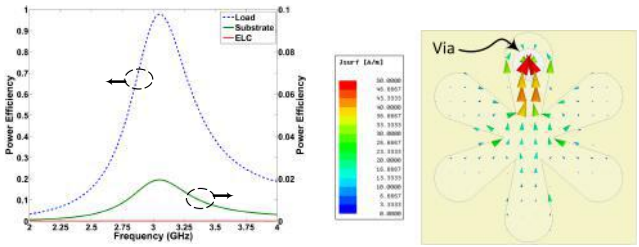

Figure 1: A unit cell of the proposed metamaterial collector.




(a) (b)

Figure 2: Simulation results showing (a) the absorption and, (b) the surface impedance of the proposed metamaterial.

The power loss across the load resistor, the 3-dipole resonator and the dielectric substrate were computed and shown in Fig. 3(a). We observe that 98% of the absorbed power is dissipated across the resistive load and only 2% is lost in both the dielectric and copper trace. These results show a significant difference from previous metamaterial absorber designs. In previous designs, the main contributor of dissipating the absorbed power within the metamaterial cell was the dielectric substrate. However, here we observe that almost all the absorbed power is channeled and dissipated across the load resistance. A number of factors led to diverting the dissipated power from the host




(a) (b)

Figure 3: Simulation results showing (a) the power absorbed in each component of the proposed metamaterial unit cell and, (b) the current distribution on the surface of the resonator at the resonance frequency.

material to the resistive load. First, a low loss dielectric substrate was selected to minimize the dielectric loss. In the design, the loss tangent of the selected substrate was $tan\delta = 0.002$ which is one order of magnitude less than FR4 substrate materials ($tan\delta = 0.02$) commonly used in previous microwave metamaterial absorber designs. Moreover, by placing the via at the top of the resonator as shown in Fig. 3(b), the current channels maximally to the resistive load. The via creates a path for the current to flow maximally from the 3-dipole resonator to the load resistance as indicated by the red color in Fig. 3(b).

In conclusion, we presented the design of an electromagnetic energy collector based on the full absorption concept. The simulation results show that the proposed collector can absorb almost all the power incident on the cell and deliver 98% of the absorbed power to a resistive load.

## ACKNOWLEDGMENT

We like to sincerely thank and acknowledge the support of Prince Sattam University, Saudi Arabia.

## REFERENCES

1. N. Landy, S. Sajuyigbe, J. Mock, D. Smith, and W. Padilla, "Perfect metamaterial absorber," *Physical review letters*, vol. 100, no. 20, p. 207402, 2008.
2. O. Ramahi, T. Almoneef, M. Alshareef, and M. Boybay, "Metamaterial particles for electromagnetic energy harvesting," *Applied Physics Letters*, vol. 101, no. 17, pp. 173 903–173 903, 2012.
3. T. S. Almoneef and O. M. Ramahi, "Metamaterial electromagnetic energy harvester with near unity efficiency," *Applied Physics Letters*, vol. 106, no. 15, p. 153902, 2015.

# Pattern Reconfigurable Antenna using Electromagnetic Band Gap Structure

**M. F. Ismail[1,2], M. K. A. Rahim[2], H. A. Majid[3] and M. R. Hamid[2]**
[1]Centre for Diploma Studies and [3]Faculty of Engineering Technology
Universiti Tun Hussein Onn Malaysia, Parit Raja 86400 Johor, Malaysia
[2]Faculty of Electrical Engineering, Universiti Teknologi Malaysia, Johor Bahru 81310 Johor, Malaysia
[*]corresponding author: ifaizal@uthm.edu.my

**Abstract**- A single patch antenna incorporated with an array of electromagnetic band gap (EBG) structures for the radiation pattern reconfigurability is proposed. The array of EBGs are positioned at both side of the antenna to produce three different main beam angles of radiation pattern which are -14, 0 and +14 degree.

## INTRODUCTION

Electromagnetic bandgap (EBG) structures have emerged as an effective antenna solution due to their wide stopband bandwidths, high stopband attenuation, and easily integrated with printed circuit board (PCB) [1]. EBG structure is normally realized by periodic arrangement of metallic conductors grounded with metal via on a dielectric material. Other than filter (band stop properties), EBG structure can be applied as reflector for antenna [1], mutual coupling reduction [2], and for reconfigurability purposes [3]. In this research, ten units of EBG structures are positioned at both right and left side of a single patch antenna as shown in Figure 1. Roger RF-35 substrate with a thickness of 1.52 mm and a dielectric constant of 3.5 is used as the substrate of the proposed antenna. The dimensions of the proposed antenna are: x=58mm, y=80mm, m=32mm, p=35.5mm, w=10.4mm and h=6.08mm. Since the surface wave of the patch antenna can be absorbed by the EBG, the EBG structure is positioned four times higher than the height of the antenna substrate for the pattern reconfigurability to occur. The copper strip is used as the diode in simulation studies while the actual PIN-diode is use for fabrication.

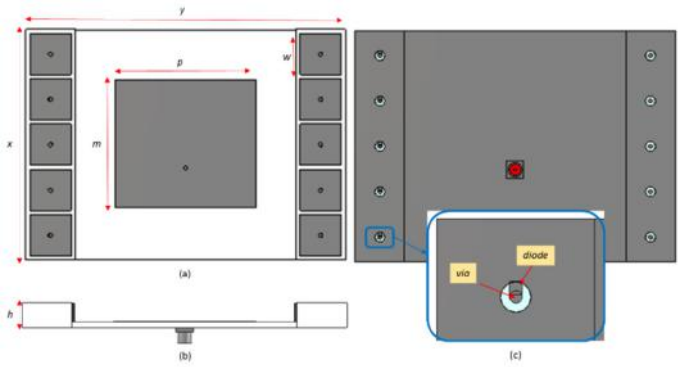



Figure 1 Proposed design with diode model in (a) front, (b) bottom, (c) back view.

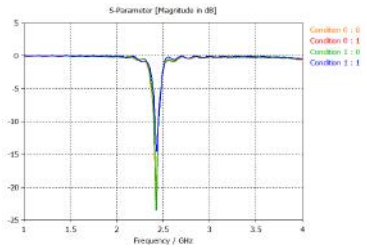
## ANTENNA DESIGN, RESULTS & DISCUSSION

Four EBG condition are tested by reconfiguring all the EBG structure at left and right side of the antenna. Figure 2(a) tabulates the EBG condition of the proposed antenna. Meanwhile, Figure 2(b) shows the return loss of the proposed antenna with the bandwidth from 2.4 GHz to 2.45 GHz for all condition. The radiation pattern is tilted approximately 14 degree for both condition 0:1 and 1:0, respectively. However, when both side of EBG are ON

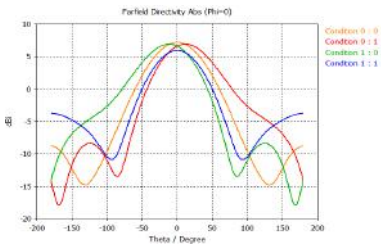
and OFF, the radiation pattern are returned to 0 degree. The radiation pattern is tilted when one side of EBG absorbs the surface wave from the patch antenna as shown in Figure 3. Figure 3 shows the current distribution and 3D radiation pattern of all EBG condition. An average gain of 7.2 dBi are recorded for all EBG condition. The gain of the antenna can be improved by increasing the unit of radiating path in array form. The size of EBG and the gap between the EBG and patch antenna give major contribution to return loss and radiation pattern results.

| Condition | EBG Left | EBG Right |
|---|---|---|
| 0 : 0 | OFF | OFF |
| 0 : 1 | OFF | ON |
| 1 : 0 | ON | OFF |
| 1 : 1 | ON | ON |

(a)




(b)




(c)

Figure 2 (a) Diode condition. (b) $S_{11}$ parameter for all condition. (c) Pattern in Cartesian for all condition

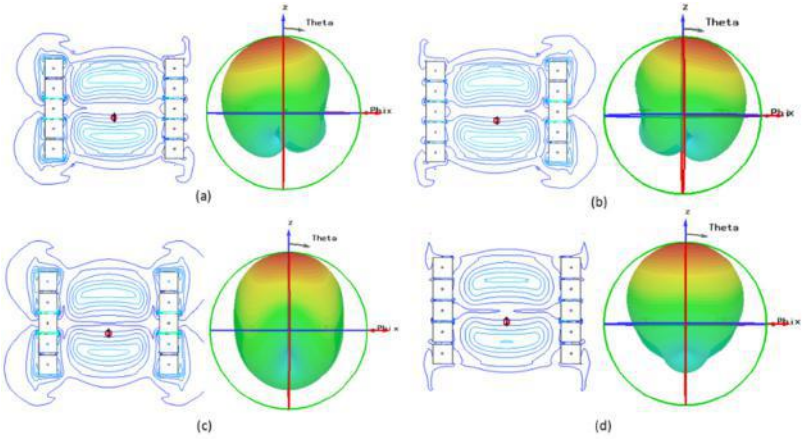



Figure 3 Current distribution and radiation pattern for condition (a) 1:0, (b) 0:1, (c) 1:1, (d) 0:0

## CONCLUSION

Pattern reconfigurable antenna is designed by using the EBG structure. The proposed antenna gives -14, 0 and +14 degree of pattern reconfigurability with an average gain of 7.2 dBi. The proposed antenna is suitable for MIMO, point-to-point and point-to-multipoint application.

## REFERENCES


1. M. Kim, D. G. Kam, "Wideband and Compact EBG structure with Balanced Slots", *IEEE Transaction on Components, Packaging and Manufacturing Technology*, Vol. 5, No. 6, 818-827, 2015.
2. Y. R. Samii, Mosallaei, "Electromagnetic Band Gap Structure: Classification, Characterization and Apllication", *Proceeding of IEEE-ICAP symposium*, pp. 560-4, 2001.
3. B. Liang, B. Sanz-Izquierdo, "A Frequency and Polarization Reconfigurable Circularly Polarized Antenna using Active EBG Structure for Satellite Navigation", *IEEE Trans. On Ant. and Prop.*, Vol. 63, No 1, 2015.

# A Microwave Planar Near-Field Sensor based on Metamaterial Unit Cells for Sensitivity Enhancement

**Ali M. Albishi**[1], *Student Member, IEEE*, **Mohamed K. El Badawe**[1], *Student Member, IEEE*, **and Omar M. Ramahi**[1], *Fellow, IEEE*[1]

[1]University of Waterloo, Canada
Omar.ramahi@uwaterloo.ca

**Abstract**—

This paper presents a microwave planar near-field sensor based on multi-complementary split-ring resonators (CSRRs) for sensitivity enhancement. CSRRs are electrically small resonators in which the largest dimensions are very small compared to the excitation wavelength. Thus, electromagnetic fields are localized and enhanced in small regions in the resonators' structures, which makes them strong candidates for designing selective and sensitive sensors. Many near-field sensors based on a single CSRR have been reported. However, near-field sensors based on multi-CSRRs for the sensitivity enhancement have not been proposed. This work shows numerically how the sensitivity can be enhanced using multi-CSRRs to detect dielectric variations in materials.

## 1. INTRODUCTION

Nowadays, selective, sensitive, and affordable sensors based technologies are critical to meet the needs for modern technologies from surface crack detection in materials, microfluidic applications to biomedical applications [1, 2, 3]. Microwave near-field based sensors can provide solutions to the modern technologies by providing high sensitivity, high penetration, and resolution. In fact, resolution as high as $\lambda/10^6$ has been experimentally proven [4]. Among microwave near-field sensing techniques, electrically-small resonators have been utilized to design near-field sensors. Electrically-small resonators, such complementary split-ring resonators (CSRRs), are fundamentally one of the constitutive building blocks of metamaterials [5]. The sensitivity of CSRRs based sensors is based on a single CSRR. However, the use of multi-CSRRs based sensors for the sensitivity enhancement have not been reported earlier.

In this paper, we present a novel sensor design based on multi-CSRRs for the sensitivity enhancement. The sensor design concept is based on exciting two identical CSRRs using two 100 Ω microstrip lines. The two CSRRs excited by the two microstrip lines will have an effective parallel resonator with a lower effective capacitance that leads to an increase in the sensitivity. The concept was proven numerically using a numerical tool (ANSYS HFSS [6]).

## 2. COMPLEMENTARY SPLIT-RING RESONATORS AS NEAR-FIELD SENSORS

In CSRRs, electromagnetic fields are concentrated in small regions of the CSRRs' structures, so the resonators are sensitive to changes in the nearby environment. The disturbance of the electromagnetic fields by changes in materials under test causes resonance frequencies to exhibit changes, which explains the underlying sensing mechanism of CSRRs based sensors.

## 3. SENSOR DESIGN AND SIMULATION RESULTS

The main objective of the design is to excite two identical CSRRs using two 100 Ω microstrip lines. The dimensions of the sensor design shown in Fig. 1 are g, a, and b= 0.5 mm; L= 7.5 mm; K= 7.626 mm; s(for a 100 Ω microstrip line) = 0.373 mm; W(for a 50 Ω microstrip line)=1.7 mm. To validate the sensitivity enhancement of the proposed sensor, we tested three types of sensors: a single 50 Ω microstrip line and CSRR, a single 50 Ω microstrip line and two cascade CSRRs, and two 100 Ω microstrip lines and two CSRRs (the proposed sensor). The sensors are utilized to resolve changes in a dielectric slab with a thickness of 3 mm. The dielectric constant of the slab was varied from 1 to 10, with a step size of 0.2. Figure 2 compares the three sensors by evaluating shifts in the resonance frequencies versus the changes in dielectric constant of the slab. The proposed sensor shows higher sensitivity than the single CSRR and cascade CSRRs based sensors.

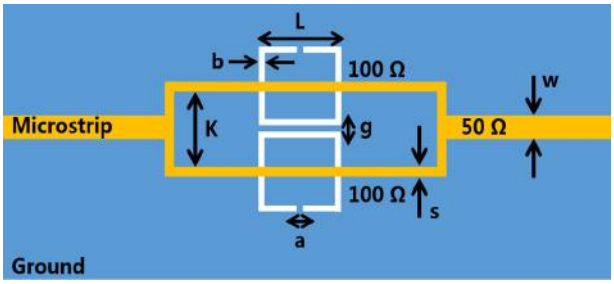



Figure 1: The proposed sensor utilizing two 100 Ω microstrip lines to excite two identical CSRRs (etched in the ground plane)

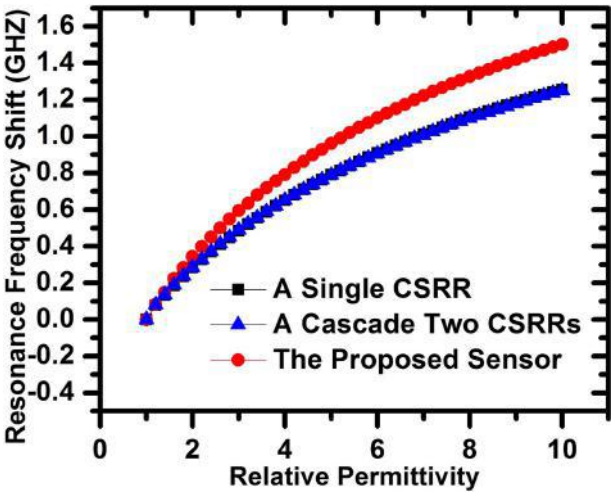



Figure 2: Resonance frequencies versus a dielectric constant that is varying from 1 to 10, with a step size of 0.2 for three types of resonators based sensors

.

## 4. CONCLUSION

We have shown a new way of exciting multi-CSRRs based sensors to increase their sensitivity. The sensor design is based on exciting two CSRRs with two 100 Ω microstrip lines. The sensitivity enhancement of the proposed sensor to detect variations in dielectric materials as small as 0.2 have been proven numerically compared to a single CSRR and cascade CSRRs based sensors. This finding is important since many modern sensing technologies especially in biomedical applications need high sensitive sensors.

## REFERENCES

1. A. Albishi, M. S. Boybay, and O. M. Ramahi, "Complementary split-ring resonator for crack detection in metallic surfaces," *Microwave and Wireless Components Letters, IEEE*, vol. 22, no. 6, pp. 330–332, June 2012.
2. A. Ebrahimi, W. Withayachumnankul, S. Al-Sarawi, and D. Abbott, "High-sensitivity metamaterial-inspired sensor for microfluidic dielectric characterization," *Sensors Journal, IEEE*, vol. 14, no. 5, pp. 1345–1351, 2014.
3. J. S. Daniels and N. Pourmand, "Label-free impedance biosensors: Opportunities and challenges," *Electroanalysis*, vol. 19, no. 12, pp. 1239–1257, 2007.
4. C. Gao and X.-D. Xiang, "Quantitative microwave near-field microscopy of dielectric properties," *Review of scientific instruments*, vol. 69, no. 11, pp. 3846–3851, 1998.
5. F. Falcone, T. Lopetegi, M. Laso, J. Baena, J. Bonache, M. Beruete, R. Marqués, F. Martin, and M. Sorolla, "Babinet principle applied to the design of metasurfaces and metamaterials," *Physical review letters*, vol. 93, no. 19, p. 197401, 2004.
6. "Ansys hfss version, 15.0.0, http://www.ansys.com."

# Flexible Ultra-Wideband Antenna with Incorporated Metamaterial Structures-Multiple Notches for Data Encoding of Chipless RFID Application.

**M. E Jalil [1], M.K.A Rahim[1], N A Samsuri[1], R. Dewan[1], and K Kamardin[2]**

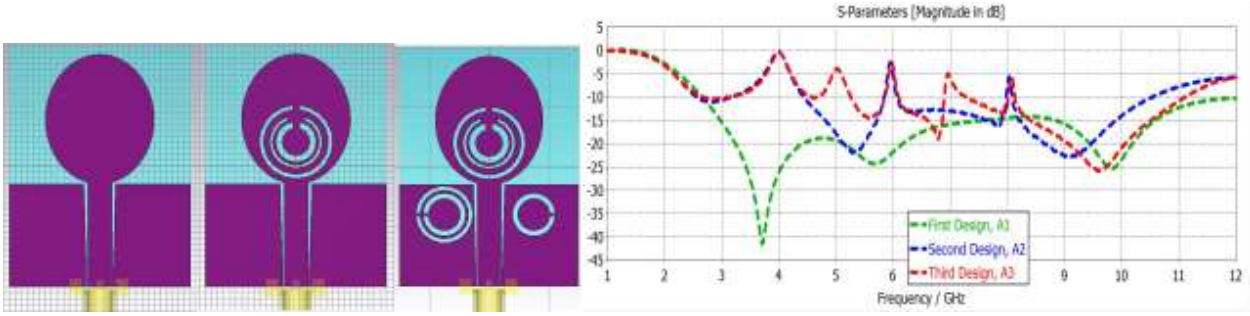
[1]Advanced RF and Microwave Research Group Communication Engineering Department,
Faculty of Electrical Engineering, University Technology Malaysia,
81310 Johor Bahru, Johor, Malaysia

[2]Computer Systems Engineering Group, Advanced Informatics School,
Universiti Teknologi Malaysia, 54100 UTM Kuala Lumpur, Malaysia.

[*]corresponding author: ezwanjalil@gmail.com

**Abstract**- A coplanar waveguide ultra-wideband antenna with incorporated metamaterial structure operating from 3.0-12.0 GHz is designed for data encoding for chipless RFID. A slotted modified complementary split ring resonator is introduced into the ultra-wideband antenna to produce multiple band-notches characteristics. To achieve encoding of 10-bits data, 5 MCSRRs are proposed with three slotted MCSRR in the radiator and three slotted MCSRR in the ground plane. This technique is suitable for creating a compact and a high capacity chipless RFID tag.

Barcode technology is an optical machine-readable data system. The data are represented by capturing the image code for identification activity such as purchasable products at the supermarket and asset tracking management commonly located at the store room. However, the limitations of barcode are the reading range, existence of image obstacle and orientation sensitivity. Therefore, Radio Frequency (RF) barcode is introduced to replace the conventional barcode which potentially can provide better performance. One of the challenges for designing RF barcode is high capacity but compact in size. To solve the aforementioned problem, metamaterial structure is proposed that can offers numerous potential benefits such as performance enhancement, minimizing structure size and provide multiple frequencies. Metamaterials have been widely used in designing filter, antenna and absorber design with miniaturization, multiple frequency and narrow bandwidth benefits. In microwave, the metamaterial structure has the ability to change the permittivity and permeability of the design, either positive or negative by altering the LC design circuit. From previous research, Predavovic et. Al (1) has started to design passive chip less with 35-bits capacity using two different polarizations of ultra-wideband (UWB) antenna with separation 35 number of spiral resonator from 3.1 -7 (UWB frequency range) with dimension of. 88 mm x 66 m. Cheung et. Al (2) has proposed possible 8-bits of chip less RFID combining between two CPW UWB antennas and coplanar waveguide resonator using only one side of the radiating element. Previously, an 8 bits passive chipless RFID has been designed using MCSRR structure and transmission line with the dimension of 25mm x 50 mm for near-field communication (3). In this paper, the CPW UWB antenna with integrated slotted modified complementary split ring resonator (MCSRR) which acts as the encoding element has been introduced to minimize the passive tag size by changing multiple resonators method to band-notches method. The antenna design has capability to produce 15 bits chip-less RFID dependent on the frequency range for each of the resonating bit and is suitable for far field communication application. Typically, band notch characteristic is widely used for the rejection of unwanted interference frequency band (4).




**(a1)** **(a2)** **(a3)**

**Figure 1; Antenna Design and S11 Result of Antenna Design; a) First Design A1 (left), Second design A2 (middle), Third Design A3 (right)**

**Design and Result:** Figure 1 shows the design evolution of the proposed antenna. The MCSRR has been introduced into the antenna structure to add multiple bands notch by properly adjusting the ring curvature and gap. The UWB antenna only, **(A1)** , the monopole with integrated 3 slotted MCSRR at the radiator **(A2)** and monopole with integrated 3 slotted MCSRR at the radiator and **(A3)** the double 2 slotted MCSRR at the backside are designed. All antennas have been designed on the fleece substrate with relative permittivity = 1.25, loss tangent 0.0025 (at 2 GHz) and thickness of 1 mm. A 50-ohm connector is connected on the upper of substrate to excite the antenna with feed width of 4 mm to obtain suitable impedance matching. To implement the three band notches characteristic for the antenna A2, the 3 ring slotted with curvature of 34.95 mm at 4.0 GHz, 23.10 mm at 6.0 GHz and 16.89 mm at 8.0 GHz are symmetrically arranged at the center of the radiator. The finalized antenna have frequency notch band at 4.0, 5.0, 6.0, 7.0 and 8.0 GHz with the addition of slotted rings with curvature of 27.44 mm and 19.28mm. For data encoding, each notch represents three bits with nine different frequency conditions. For example, the first notch will encode bits 000,001 and 0010 depending on the maximum notch frequency, (000=4 GHz, 001=4.1GHz and 010=4.2 GHz) by varying the gap between first outer ring at the patch. The combinations of the two final designs will be measured with two reference antenna for Radio Cross Section (RCS) measurement and S21, insertion loss for future work.

**Acknowledgements**, The authors thank the Ministry of Education (MOE), IETR Lab, University Rennes 1, Research Management Centre (RMC), School of Postgraduate Studies (SPS), Communication Engineering Department, Faculty of Electrical Engineering (FKE), and Universiti Teknologi Malaysia (UTM), Johor Bahru, for the support of the research under Grant Nos. 4F360, 05H35 and 4F277.The authors would also like to acknowledge all members of Advanced RF and Microwave Research Group (ARFMRG).

**REFERENCES**

1. S. Preradovic and N. C. Karmakar, "Design of fully printable planar chipless RFID transponder with 35-bit data capacity," *Microwave Conference, 2009. EuMC 2009. European*, Rome, 2009, pp. 013-016.
2. Y. F. Weng, S. W. Cheung, T. I. Yuk and L. Liu, "Design of Chipless UWB RFID System Using A CPW Multi-Resonator," in *IEEE Antennas and Propagation Magazine*, vol. 55, no. 1, pp. 13-31, Feb. 2013.
3. ME Jalil, MKA Rahim, NA Samsuri, R Dewan, Flexible printed chipless RFID tag using metamaterial–split ring resonator ,Applied Physics A, 2016
4. Q. X. Chu and Y. Y. Yang, "A Compact Ultrawideband Antenna With 3.4/5.5 GHz Dual Band-Notched Characteristics," in *IEEE Transactions on Antennas and Propagation*, vol. 56, no. 12, pp. 3637-3644, Dec. 2008.

# Positions of Dual-band Textile Diamond Dipole Antenna with Dual-band Textile Artificial Magnetic Conductor Waveguide Sheet for Body Centric Communication

**M. A. Abdullah, M. K. A. Rahim, N. A. Samsuri and H. A. Majid**
UTM -MIMOS CoE in Telecommunication
Communication Engineering Department, Faculty of Electrical Engineering, University Technology Malaysia,
81310 Johor Bahru, Johor, Malaysia
*azfar87@gmail.com, mkamal@fke.utm.my, asmawati@fke.utm.my, mhuda@uthm.edu.my*

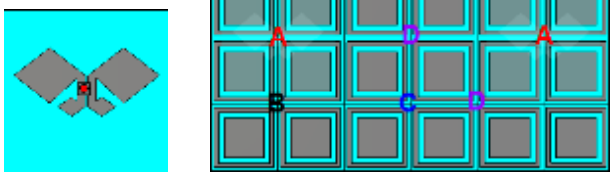
**Abstract-**
A dual-band textile Artificial Magnetic Conductor (AMC) sheet-like waveguide with dual-band textile diamond dipole antennas were designed to investigate the possibility of enhancing transmission between antennas. The AMC surface is designed to have in-phase reflection at 2.45GHz and 5.8GHz with the objective to enhance the transmission between antennas. Both structures made of fleece fabric with conductive patches made of SHIELDIT fabric. The performance of the two antennas with textile AMC sheet was investigated thoroughly in terms of transmission coefficient ($S_{21}$) parameters. The effect of different antennas' placement was also considered. Measurements were conducted rigorously to validate the simulated findings. Results show that the $S_{21}$ transmission between antennas improved significantly when having the AMC waveguide sheet beneath them.

## Introduction

Wireless Body Area Networks (WBANs) is one of body centric communication. This short-range communication has been getting attention from researchers all over the world due to the needed of a reliable communication within human body [1]. In recent years, wearable antennas have been investigated thoroughly for many applications such as healthcare, personal entertainment, military and smart home [2-3]. However the distinct properties of the human body cause the performance of the wearable antennas suffer degradation [4]. Therefore, by introducing the waveguide sheet beneath the wearable antennas, the performance of the antennas are enhanced [5].

## Design Considerations

Dual-band textile diamond dipole antenna which is operated at 2.4 GHz and 5.8 GHz is used to be incorporated with a dual-band textile AMC sheet. The dimension of the proposed antenna is 60mm x 60mmas shown in Figure 1. It has wideband bandwidth ranging from 2.3 GHz to 2.7 GHz and 5.2 GHz and 7.2 GHz with omni radiation pattern. In this paper, transmission of different position dual band antenna above the AMC is investigated. The positions are labeled as A, B, C, and D is shown in Figure 1.




a) b)

Figure 1a) Dual band Antenna structure b) Positions of dual band antenna

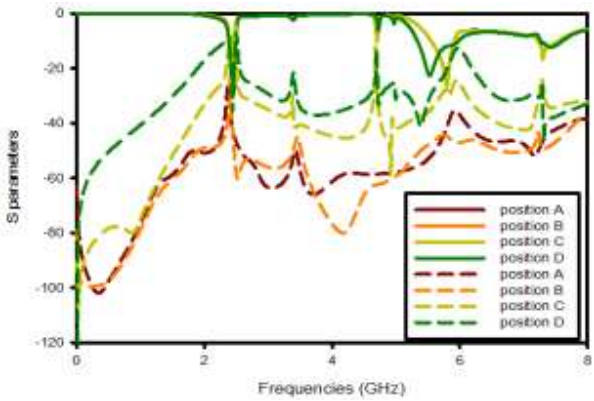



Figure 2: $S_{11}$ and $S_{12}$ parameters

**Results and Discussions**

From the S- parameters results (Figure 2), the S21 transmission which is indicated by dotted lines decreases as the distance increase, as predicted. The reflection coefficient (S11) of the antenna which are indicated by solid lines are following the AMC behavior. The transmission of the two dual-band antenna is improved with the presence of textile AMC waveguide. Highest S21 peak is observed at position D which is -19.3dB at 2.4 GHz while at -20dB at 5.8 GHz. Electromagnetic waves are being concentrated into the AMC surface, hence the low transmission loss between two antennas is observed.

**Conclusions**

For all positions, significant improvement transmission S21 are achieved when having AMC sheet compared to free space transmission. However, the S21 performance decreases as distance increases. The S11 results show that the bandwidth of the antenna above the AMC surface become narrower compare to the free space environment.

**REFERENCES**

1. P. S. Hall. 2007. Antennas and Propagation for Body-centric Communications. *Sem. on Ant. and Pro. for Body-Centric Wire. Com*. 1–4.
2. P. Salonen, et al. 1999. A Small Planar Inverted-F Antenna for Wearable Applications. *In The Third International Symposium Wearable Computers*. 95–100.
3. P. Salonen and L. Hurme. 2003. A Novel Fabric WLAN Antenna for Wearable Applications. In *IEEE Antennas and Propagation Society International Symposium*. 700–703., F. M. and F. M.
4. K. Eom and H. Arai. 2011. Smart Blanket: Flexible and Easy to Couple Waveguide. In *IEEE Topical Conference on Biomedical Wireless Technologies, Networks, and Sensing Systems*. 15–18.
5. A. Jafargholi. 2007. VHF-LB Vest Antenna Design. In I*nternational Workshop on Antenna Technology: Small and Smart Antennas Metamaterials and Applications*. 247–250.

# Improved Single Layer Microwave Absorber Performance of Rice Husk with CNT Composite

**Lee Yeng Seng[1], F.H. Wee[2], F. Malek[3], Y.K. You[4], Z. Liyana[1], H.A. Rahim[2], A.A.M Ezanuddin[1]**

[1]Fakulti Teknologi Kejuruteraan, Universiti Malaysia Perlis (UniMAP), Aras 1, Blok S2, Kampus UniCITI Alam, 02100 Sungai Chuchuh, Padang Besar, Perlis, Malaysia.
[2]School of Computer and Communication Engineering, Univerisiti Malaysia Perlis (UniMAP), Pauh Putra Campus, 02600 Arau, Perlis, Malaysia.
[3]Faculty of Engineering and Information Sciences, University of Wollongong in Dubai (UOW).
[4]Radio Communication Engineering Department (RaCED), Faculty of Electrical Engineering, UniversitiTeknologi Malaysia, Skudai, Johor 81310, Malaysia.

Corresponding author: leeyengseng@gmail.com

*Abstract*— This paper presents the enhanced microwave absorption of single layer microwave absorber based on rice husk (RH) with additional carbon nanotubes (CNTs) filler loading into the composites. The dielectric properties of RH and CNTs composites (RH/CNTs) were measured by using Agilent high temperature probe and 85070E software. The CST-MWS software is used to design and evaluate the microwave absorption of RH and RH/CNTs with metal backed plate. The microwave absorption of simulated and measured results is compared. The RH microwave absorber only absorbed maximum, -8 dB at 13.4 GHz of the incident electromagnetic radiation and the RH/CNTs absorbed less than -10 dB with wider bandwidth over 11.5-14.4 GHz compare with RH composites single layer microwave absorber. The results indicated that the RH/CNTs composites have enhanced the microwave absorption of RH composites.

Summary

Rapid growths of the telecommunication technology are caused the increases of electromagnetic interference (EMI). EMI are uncontrolled electromagnetic wave which are harmful human health and affect the performance of electronic device. Therefore, microwave absorbers are required to solve the EMI problem by reducing the EMI. Microwave absorber generally made by dielectric and/or magnetic materials which can absorb microwave energy and convert the microwave energy to heat []. Recent years, many researchers are interested to use investigated performance of agriculture wastes in microwave absorber applications []. This is due to the unique dielectric properties of some agriculture wastes which are able to absorb microwave energy with some specific designs and composites []. However, rice husk agriculture waste shows low microwave absorption performance ( > -10 dB) with thinner thickness of absorber. Iqbal has reported that the single layer microwave absorber based on rice husk composite with very good microwave absorption < -8 dB over 4-8 GHz.

In this study, carbon nanotubes material is used as additional filler composites with RH material to enhance the dielectric properties and microwave absorption performance of RH composite.

### *A. Measured and Simulated Single Layer Absorber*

In Figure 1, comparison between measured and simulated RH and RH/CNT are presented. It can be noticed that simulated curve shows similar behavior with respect to the measured. Very good agreement is observed between the simulated and measured results. In practical, it has been noticed that the RH/CNT composite materials are able to absorb the electromagnetic field much better than

the pure RH composite which had analyzed. The simulated and measured results also take into account of both impedance matching condition and dielectric losses of the composite material.

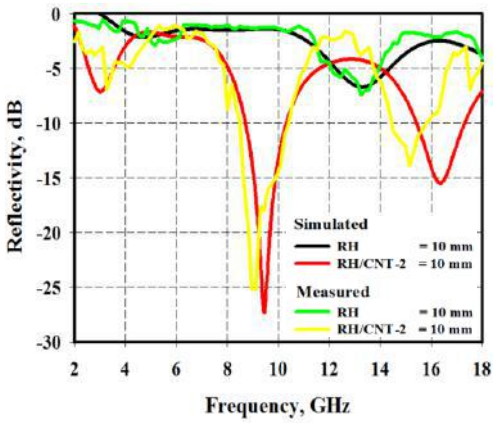



Figure 1: Comparison of reflectivity performance between measured and simulated of the RH and RH/CNT single layer absorber.

For the RH mixed 2 wt% CNTs (RH/CNT-2), the absorption curve illustrates that the simulated reflectivity of the corresponding composites is below -10 dB in the range of 8.8–10.4 GHz and 15.6-17.3 GHz, whereas the measured reflectivity is slightly shifted to a lower frequency for below -10 dB at 8.4-10.5 and 14.2-16 GHz. In additional, the minimum measured value is -25.19 dB and simulated value is -27.4 dB at 9.84 GHz. As analysed, the single layer absorber of RH/CNT composites can be used as tuning absorber, which means shifting the operate frequency range with modifying the thickness of the absorber. If thickness of the absorbing layer increases, the matching wavelength of the incident wave would increase. Therefore, the matching frequency will switch from a higher frequency to lower frequencies. This RH/CNT single layer absorber shows narrowband (resonant frequency) absorption with more than –10 dB (~90 %) reflectivity in specific frequency. The incident and reflected waves resulting in a quarter wavelength reflection which allows absorber to obtain the minimum reflected energy. For the single layer absorber, it is clearly shows that a small addition of CNT in the composite will produce efficient fillers in enhancing its dielectric properties and the thickness of the single layer absorber will be reduced for specific operate frequency. The frequency of single layer absorber can be tuned within the range of 2-18 GHz, by simply varying the dielectric properties and/or thickness of composite materials.

**REFERENCES**


[1] J.-B. B. Kim, S.-K. K. Lee, and C.-G. G. Kim, "Comparison study on the effect of carbon nano materials for single-layer microwave absorbers in X-band," *Compos. Sci. Technol.*, vol. 68, no. 14, pp. 2909–2916, Nov. 2008.

[2] K.-Y. Park, J.-H. Han, S.-B. Lee, J.-B. Kim, J.-W. Yi, and S.-K. Lee, "Fabrication and electromagnetic characteristics of microwave absorbers containing carbon nanofibers and NiFe particles," *Compos. Sci. Technol.*, vol. 69, no. 7–8, pp. 1271–1278, Jun. 2009.

[3] P. Saville, T. Huber, and D. Makeiff, "Fabrication of Organic Radar Absorbing Materials: A Report on the TIF Project," 2005.

[4] C. K. Das, P. Bhattacharya, and S. S. Kalra, "Graphene and MWCNT: Potential Candidate for Microwave Absorbing Materials," *J. Mater. Sci. Res.*, vol. 1, no. 2, p. p126, 2012.

[5] D. Micheli, C. Apollo, R. Pastore, R. B. Morles, M. Marchetti, and G. Gradoni, "Electromagnetic Characterization of Composite Materials and Microwave Absorbing Modeling," *Adv. Nanocomposites - Synth. Charact. Ind. Appl.*, pp. 360–384, 2011.

[6] T. Zhao, C. Hou, H. Zhang, R. Zhu, S. She, J. Wang, T. Li, Z. Liu, and B. Wei, "Electromagnetic wave absorbing properties of amorphous carbon nanotubes.," *Sci. Rep.*, vol. 4, p. 5619, 2014.

# Feed interactions in metamaterial diplexers and radomes

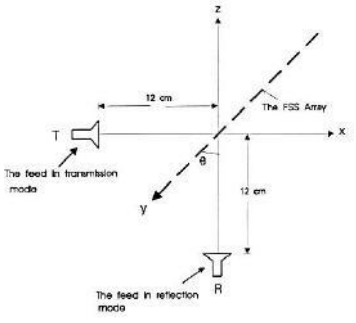
J(Yiannis) C. Vardaxoglou

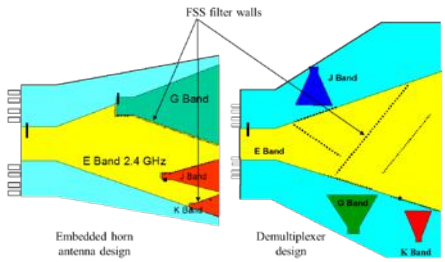
Wolfson School of Mechanical, Electrical and Manufacturing Engineering, Loughborough University, Loughborough, LE11 3TU, UK, j.c.vardaxoglou@lboro.ac.uk

Arrays forming structures of reflection/transmission selectivity (as customary called frequency selective surfaces, FSS) have been used as frequency filters (e.g. diplexers for a satcomms reflector antenna system, Fig.1) or as in Fig. 2. FSSs as flat subreflectors in a multiband feed system has been used widely on dual band systems where a design of a four frequency surface is required or in an aircraft sandwich radome where one of its skins is a periodic array, [1]. Looped elements, square and circular (rings), were used to provide the necessary reflection and transmission frequencies in S, X, Ku and Ka bands. In addition, the materials used need to be low loss and space qualified with good thermal and mechanical properties. The frequency responses need to be stable with regard the angle of incidence under a plane wave illumination. This is to achieve the correct frequencies and beamwidths when a diverging beam feed illuminates the surface. The situation becomes more dramatic where the feed is required to produce a shaped beam, Fig. 2, [2]. When the array is printed on a highly curved surface, as for example the FSS representing a radome, the coupling between the feed and the radome is exacerbated due to multiple internal interactions. The interactions of the FSS with their feed arrangement and to some extent the man reflector antenna cannot be ignored.

Ultra stable responses can be obtained by utilising two (or more) surfaces that are highly coupled or single layer arrays of convoluted elements. The objective is to remove, or at least reduce, the effects of grating lobes in the band of interest. Double layer arrays have been used in this context and produced good common bandwidths up to 10% for single polarisation. These are electrically thin FSS and have narrow passbands. One configuration used two closely spaced ring slot arrays with different diameters, providing dual polarised operation. Whether a reconfigurable or static structure has been used, the underlying factor has been the shift of the main resonance down in frequency from the grating lobe location. In effect, an electrically large element emerges as the result of layer coupling (or element convolution) and it would be possible to construct FSSs with radically reduced unit cell sizes, for use on curved surfaces.

This paper will review some of the complex antenna feed interactions with single and double arrays either in a diplexer environment. Simulations will be shown from an in house MoM/spectral composition FSS code and from EMPIRE XCcel Finite-Difference Time-Domain (FDTD) commercial software of IMST.



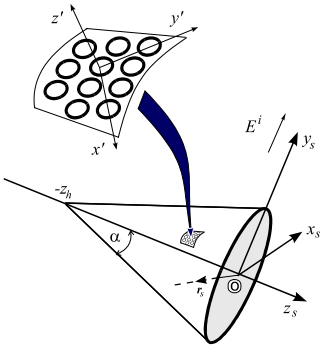




Fig 1 A planar array diplexer  Fig 2  Example of a multihorn feed  Fig 3 A curved metaradome

References:
1  Bin Liang; Ming Bai; Hui Ma; Haibo Zhao; Jungang Miao: 'Four-band frequency selective surface with circular ring patch elements', International Conference on Microwave and Millimeter Wave Technology (ICMMT), pages 1-4, 2012
2 Wyman L. Williams and James M. Howell; 'Communications Satellite Antennas with On-orbit Pattern Flexibility', Micowave Journal, pages 1-6, 2004

# Artificial Dielectrics Metamaterials for Antenna Applications

Shiyu Zhang [*1], Yiannis Vardaxoglou [1], Will Whittow [1], Raj Mittra[2]

[1] Wolfson School of Mechanical, Electrical and Manufacturing Engineering, Loughborough University, Loughborough, Leicestershire, LE11 3TU, United Kingdom

[2] EMC Laboratory, University of Central Florida, Florida, United States of America & EE Department, KAU, Saudi Arabia

j.c.vardaxoglouboro.ac.uk

The objective of this paper is to examine the problem of synthesizing non-resonant metamaterials (MTMs), in the context of several practical applications, e.g., flat GRIN lenses, and to propose a strategy of realizing the specified dielectric parameters that avoids the pitfalls in the previous design strategies based on the use of MTMs, which led to narrowband designs that were also lossy. We show a step-by-step procedure for designing a flat GRIN lens by systematically modifying COTS (commercially off-the-shelf) materials, by using inclusions in a background material that are either metallic or dielectric types. We then compare the performance of the lens, designed by using MTMS as described above, and show that the MTM-based lens typically exhibits a superior performance, not only over the conventional MTM/GRIN lenses, but also over those designed by using the recently introduced technique called TO (Transformation Optics).

Next, we present an example of a Metasurface, designed for a Reflectarray (RA) application. It is well known that the conventional reflectarrays are inherently narrowband, because they use resonant-type printed patches to realize the desired phase shit from the flat RA surface to achieve lens-like beam shaping properties. We show that the paradigm for synthesizing desired artificial dielectrics, described in this paper, enables us to achieve a relatively broadband performance, without compromising the gain. Historically, metamaterials were defined as “materials that don’t exist in nature.” This definition was introduced when everyone was looking for doubly-negative (DNG) materials to realize a perfect lens. Later, the scope as well as the definition of Metamaterials were generalized, and now it is not uncommon to find that almost any artificially synthesized material being referred to as MTMs. Although MTMs were promised to be the magic material for realizing superlenses and invisibility cloaks, difficulties in realizing DNG, MNG (m negative) and e or m materials with values less than unity severely hampered the practical realizations of superlenses and cloaks. This is due primarily to the fact that MTMS with the attributes mentioned above, and realized by embedding resonant inclusion--as they almost always were--turned out to be narrowband, dispersive and lossy, which severely limited their practical usage.

Fortunately, however, other electromagnetic devices were successfully designed later, and were found to be useful for enhancing the performance of antennas and rendering them low-profile --among others--for a number of applications, albeit in some niche areas. This has helped to kindled renewed interest in MTM synthesis in a way that circumvents the problems of narrow bandwidth, dispersion and losses.

# High efficient wireless power transfer system based on dielectric resonators

**P. V. Kapitanova*, M. Song, and P. A. Belov**
Department of Nanophotonics and Metamaterials
ITMO University
Saint Petersburg, Russia
*corresponding author: p.kapitanova@metalab.ifmo.ru

**Abstract**-We propose a high efficient magnetic near field resonance wireless power transfer system based on high permittivity dielectric resonators. Magnetic dipole and magnetic quadrupole modes of the resonator are investigated as the operating modes of the wireless power transfer system. The maximal efficiency of 60% at magnetic dipole mode and 83% at magnetic quadrupole mode can be experimentally obtained. Further, the system operating at magnetic quadrupole mode is proved to be more stable to the mutual orientation of the transmitter and receiver.

The recent need in wireless charging of portable devices such as cellphones, tablet, and laptop computers is driving the development of wireless powering and charging technologies [1-4]. The main targets to achieve are the increased efficiency, the extended operational distance, the WPT stability to the mutual orientation of transmitter and receiver in space, compact size and small weight.

Here we propose and experimentally verify a magnetic resonant wireless power transfer (WPT) system based on high permittivity dielectric spherical resonators (see Fig.1(a)). The operational principle of the proposed WPT system is based on the Mie theory, i.e. under a proper excitation a dielectric spherical resonator exhibits very strong magnetic resonances [5, 6]. The detailed analysis and numerical prediction of the WPT system efficiency have been reported in Ref. [7]. In this study we consider magnetic dipole (MD) and magnetic quadrupole (MQ) modes of the resonator as the operational frequencies for the WPT system and report the result of experimental investigations. As the resonator material the microwave ceramic characterized by high permittivity $\varepsilon$=80 and low tangent loss $\tan\delta=10^{-4}$ (measured at 3 GHz) have been chosen. The radius of the resonator has been optimized for ISM frequency band with the center frequency of 2.45 GHz corresponding to MQ mode of the resonator. Two identical ceramic resonators have been placed in a styrofoam material holder with permittivity close to 1. To excite the resonators, two identical non-resonant coaxial cable loops of radius 3 mm have been fabricated and connected to an Agilent PNA E8362C Vector Network Analyzer.

First, the S-parameters of the WPT system operating at MD and MQ modes as a function of the separation distance d have been measured. The WPT efficiency was extracted from the measured S-parameters using equation $\eta = \left|S_{21}{}^2\right| \Big/ \left(1-\left|S_{11}{}^2\right|\right)$, where $S_{21}$ and $S_{11}$ are the transmission and reflection coefficients, respectively.

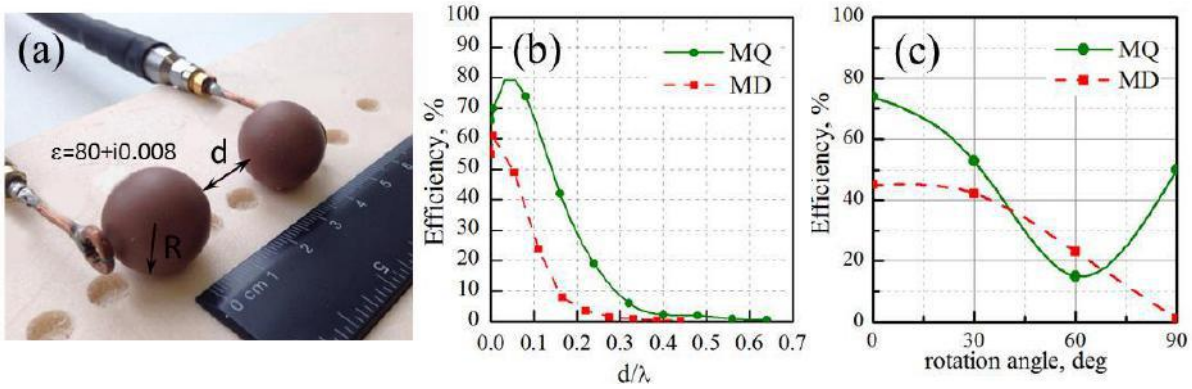



Figure 1. Design of the WPT system based on high permittivity dielectric resonators of radius R=1cm separated by the distance d. Metallic loops are used to excite the transmitting resonator and to receive the energy from the receiving resonator. (b) WPT efficiency of the system operating at MD and MQ modes as a function of normalized distance.

The extracted values of the WPT efficiency as a function of normalized distance (distance is normalized to the wavelength in the free space) are presented in Fig.1 (b). As one can see the WPT efficiency of the system operating at MD mode reaches up to 60%, whereas the efficiency over 80% is obtained at MQ mode.

The WPT efficiency stability to the mutual orientation of transmitter and receiver in space is very important. Thus we have experimentally studied the WPT efficiency of the proposed system when the receiver is rotates in accordingly to the transmitter. The measured WPT efficiencies for both MD and MQ modes for separation distance d=2cm are plotted in Fig. 1(c). For the MD mode the efficiency keeps dropping down to 0 with the increase of the rotation angle. When the systen operates at the MQ mode the efficiency first drops nearly down to 0 at $60^{o}$ rotation angle and then bounces back to a maximum.

This work was supported by Russian Scientific Foundation (project 14-12-00897). PK and PB acknowledge Scholarship and Grant of the President of Russian Federation.

**REFERENCES**

1. Brown, W. C., "The History of Power Transmission by Radio Waves," *IEEE Trans. Microwave Theory and Techniques*, vol.32, no.9, pp.1230,1242, Sep 1984
2. Karalis, A., J. D. Joannopoulos, M. Soljačić, “Efficient wireless non-radiative mid-range energy transfer,” *Annals of Physics*, vol.323, no.1, pp. 34-48 , Jan 2008
3. Kurs, A., A. Karalis, R. Moffatt, J. D. Joannopoulos, P. Fisher, M. Soljacich, “Wireless power transfer via strongly coupled magnetic resonances”, *Science*, vol.317, no.5834, pp.83-86, Jul 2007.
4. Hui, S.Y.R.; Wenxing Zhong; Lee, C.K., "A critical review of recent progress in mid-range wireless power transfer," *IEEE Trans. Power Electron.*, vol.29, no.9, pp.4500,4511, Sept. 2014
5. Stratton, J., “*Electromagnetic Theory*,” NY:McGraw-Hill, 1941.
6. Krasnok, A. E., A. E. Miroshnichenko, P. A. Belov and Yu. S. Kivshar, “Huygens optical elements and Yagi—Uda nanoantennas based on dielectric nanoparticles,” *JETP Letters*, vol.94, pp. 593-598, 2011.
7. Song, M., I. Iorsh, P. Kapitanova, E. Nenasheva, P. Belov, “Wireless power transfer based on magnetic quadrupole coupling in dielectric resonators” , Appl. Phys. Lett. vol.108, 023902, 2016

# Electrical control of circular dichroism and optical activity in graphene chiral metamaterials

**S. S. Oh[1], T.-T. Kim[2], H.-D. Kim[3], H.-S. Park[3], O. Hess[1], B. Min[3*], and S. Zhang[2*]**

[1]The Blackett Laboratory, Department of Physics, Imperial College London, SW7 2AZ, United Kingdom
[2]School of Astronomy and Physics, University of Birmingham, Birmingham B15 2TT, United Kingdom
[3]Department of Mechanical Engineering, Korea Advanced Institute of Science and Technology, Daejeon, 34141, Republic of Korea
corresponding author: bmin@kaist.ac.kr, s.zhang@bham.ac.uk

**Abstract**— Based on a chiral metamaterial combined with a gated single layer graphene we experimentally demonstrate the electrical tuning of the polarization state of terahertz waves. In particular, we show that transmission of a terahertz wave with one circular polarization can be electrically controlled without affecting that of the other circular polarization and the rotation angle of a linearly polarized terahertz wave can be controlled by the gate voltage.

Active control of polarization states by optical or electrical means enables various practical applications such as wireless and optical fiber telecommunications, and sensitive detection of biomolecule chirality. Optical tuning of the circular dichroism (CD) and optical activity (OA) of chiral metamaterials has been recently demonstrated [1, 2, 3, 4]. The optical approach, however, requires elaborate experimental setups such as pump lasers and appropriate optical components. Therefore, for the practical applications, an electrical approach is very important.

For this aim, graphene, a two-dimensional form of carbon, can be a good candidate because of its unique band structure with linear dispersion near the so-called Dirac point. Due to the low density of states compared to typical semiconductors, graphene can be used to achieve strong modulation of its terahertz (THz) property. For instance, a graphene integrated metamaterial has been proposed to enhance graphene absorption in the THz regime [5].

In this paper, we demonstrate gate-controlled active chiral metamaterials by integrating a single layer of graphene onto a chiral metamaterial called a conjugated double Z metamaterial (CDZM) [6]. As shown in Fig. 1(a), the transmission of a right-handed circular polarized (RCP) THz wave can be modulated by the gate voltage applied to the graphene layer leading to a change in circular dichroism. This modulation is possible because a variation of the gate voltage changes the optical conductivity of a graphene layer. Interestingly, in our graphene CDZM structure, the transmission for the left-handed circular polarization (LCP) remains very insensitive to the applied voltage. Moreover, it is shown that the rotation angle of an incident THz wave can be electrically controlled showing a controlled OA while the linear polarization state is maintained.

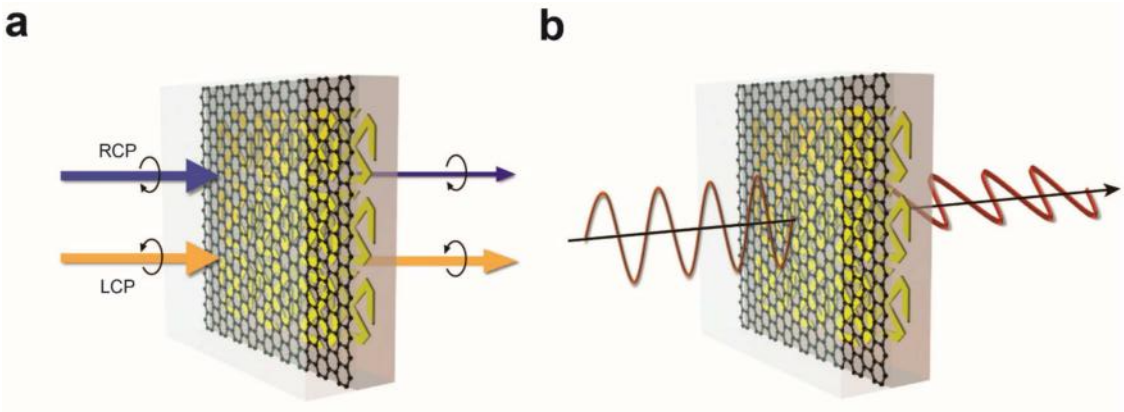



Figure 1: Circular dichroism and optical activity in graphene CDZM. (a) Circular dichroism: transmissions for RCP and LCP waves are different to each other due to the different absorption between RCP and LCP waves. (b) Optical activity: the electric field vector of linearly polarized light rotates around the axis parallel to its propagation direction while passing the graphene CDZM.

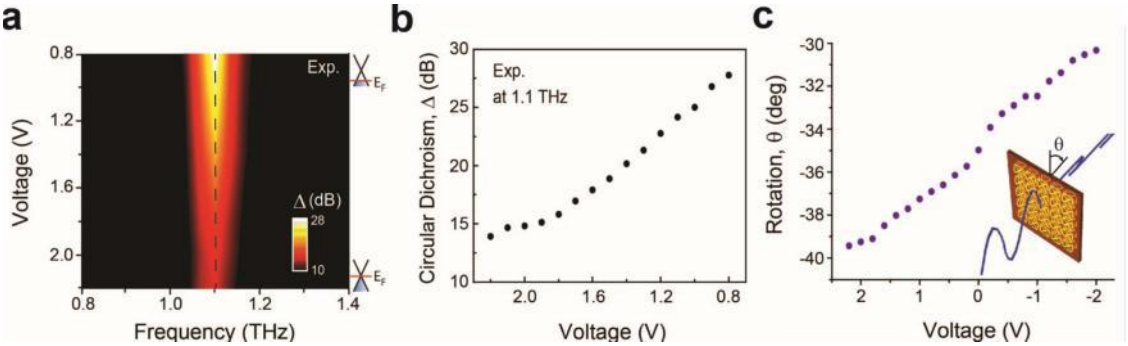



Figure 2: (a) Measured CD defined by the difference in transmission for RCP and LCP waves $\Delta = |T_{\mathrm{RCP}} - T_{\mathrm{LCP}}|$. (b) $\Delta$ at the resonance frequency 1.1 THz as a function of gate voltage. (c) Gate controllable OA: the rotation angle $\theta$ at the frequency for which $\eta \approx 0$ as a function of gate voltage

To confirm the gate-controlled CD and OA, we fabricated the graphene incorporated CDZMs with an ion-gel gate dielectric and characterized the fabricated graphene CDZM structures using the THz time-domain spectroscopy. As shown in Fig. 2 (a), the graphene CDZM shows a maximum CD at the resonance frequency of 1.1 THz (dashed line). Moreover, the CD at the resonance frequency increases as the gate voltage changes from 2.2 V to 0.8 V, which corresponds to a modulation depth up to 79% for the RCP wave at the gate voltage of 0.8 V while maintaining large transmission of the LCP wave up to 52% (Fig. 2 (b)). Figure 2 (c) shows that the graphene CDZM structure can achieve an active modulation of the polarization rotation angle up to 10° with the gate voltage change from 2.0 V to -2.0 V.

In conclusion, we have experimentally demonstrated a gate-controlled graphene chiral metamaterial in which the transmission of one selected circularly polarized light and the rotation angle of linearly polarized light can be strongly modified by variation of the applied voltage.

## ACKNOWLEDGMENT

S.S.O. and O.H. acknowledge financial support from the Leverhulme Trust.

## REFERENCES

1. Zhang, S., Zhou, J., Park, Y.-S., Rho, J., Singh, R., Nam, S., Azad, A. K., Chen, H.-T., Yin, X., Taylor, A. J., and Zhang, X., "Photoinduced handedness switching in terahertz chiral metamolecules.," *Nat. Commun.*, vol. 3, p. 942, 2012.
2. Zhou, J., Chowdhury, D. R., Zhao, R., Azad, A., Chen, H.-T., Soukoulis, C., Taylor, A., and O'Hara, J., "Terahertz chiral metamaterials with giant and dynamically tunable optical activity," *Phys. Rev. B*, vol. 86, no. 3, pp. 2–7, 2012.
3. Kanda, N., Konishi, K., and Kuwata-Gonokami, M., "All-photoinduced terahertz optical activity," *Opt. Lett.*, vol. 39, no. 19, pp. 3274–3276, 2014.
4. Oh, S. S. and Hess, O., "Chiral metamaterials : enhancement and control of optical activity and circular dichroism," *Nano Converg.*, pp. 1–29, 2015.
5. Lee, S. H., Choi, M., Kim, T.-T., Liu, M., Yin, X., Choi, H. K., Choi, C.-G., Choi, S.-Y., Zhang, X., and Min, B., "Switching terahertz waves with gate-controlled active graphene metamaterials.," *Nat. Mater.*, vol. 11, no. 10, pp. 1–6, 2012.
6. Kim, T.-T., Oh, S. S., Park, H.-S., Zhao, R., Kim, S.-H., Choi, W., Min, B., and Hess, O., "Optical activity enhanced by strong inter-molecular coupling in planar chiral metamaterials.," *Sci. Rep.*, vol. 4, p. 5864, 2014.

# Design, Fabrication and Testing of Negative Index Metamaterials for X, Ku, and K Microwave bands.

**David A. Lee[1], L. James Vedral[2,3], Randall L. Musselman,[3] and Anatoliy O. Pinchuk[2,*]**

[1]The MITRE Corporation
1155 Academy Park Loop, Colorado Springs, CO 80910, USA

[2]Physics and Energy Sciences Department
University of Colorado at Colorado Springs
1420 Austin Bluffs Parkway, Colorado Springs, CO 80918, USA

[3]Electrical and Computer Engineering Department, U.S. Air Force Academy
2354 Fairchild Dr., Suite 2F6, Colorado Springs, CO 80840, USA

[*]corresponding author: apinchuk@uccs.edu

**Abstract**-Metamaterials with negative index of refraction have potential to improve the efficiency and reliability of microwave systems, such as antennae and radomes. However, high losses and narrow frequency band of most negative index metamaterials hamper practical applications of these novel materials. In this work we present our recent theoretical and experimental results of the design, fabrication and testing of low-loss and wide band negative index metamaterials for X, Ku, and K microwave frequency bands. We use an S-shaped split ring resonator as a unit cell for metamaterials slabs. Experimental results match reasonably well the HFSS theoretical calculations.

The metamaterials designed for X, Ku, and K microwave frequency bands were fabricated by using RO4003C with uniformly-sized unit cells arranged in regular arrays on both sides of the board with 10 unit cells in the direction of propagation of the electromagnetic waves and 50 unit cells in the perpendicular direction, as shown in Fig. 1. The metamaterial boards were assembled into a slab by using a holder with equally-spaced slots.[1] The slabs of material were characterized for their transmission and reflection coefficients (S-parameters) in the near-field by holding all components stationary on a bench and using two microwave feeds and a network analyzer. After testing the S-parameters with the uniform slabs, the boards were cut into stair-step prisms to test the refraction of the electromagnetic waves. Fig. 2 shows the experimentally measured transmitted power of the electromagnetic wave refracted at the back surface of the prism at different angles relative to the normal to the surface. The measurements were performed at different frequencies in the X-Ku range. Negative angles of refraction correspond to negative indices of refraction according to the Snell's law. The measurement of power-angle transmission with the most pronounced negative refraction occurred between 12.5 and 15 GHz.

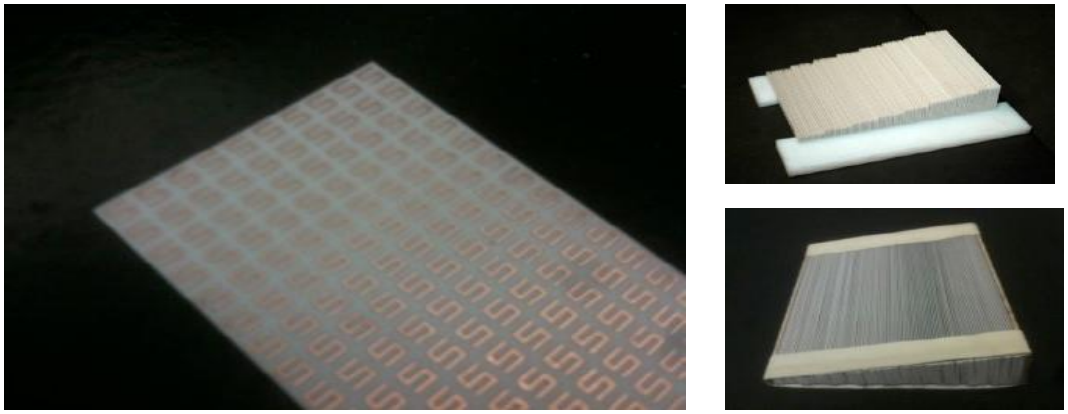


**Figure 1. Photographs of the metamaterials with S-shaped, split-ring resonators for K-band board and X-Ku prism 8.1 degrees and K-band prism 13.6 degrees.[1]**

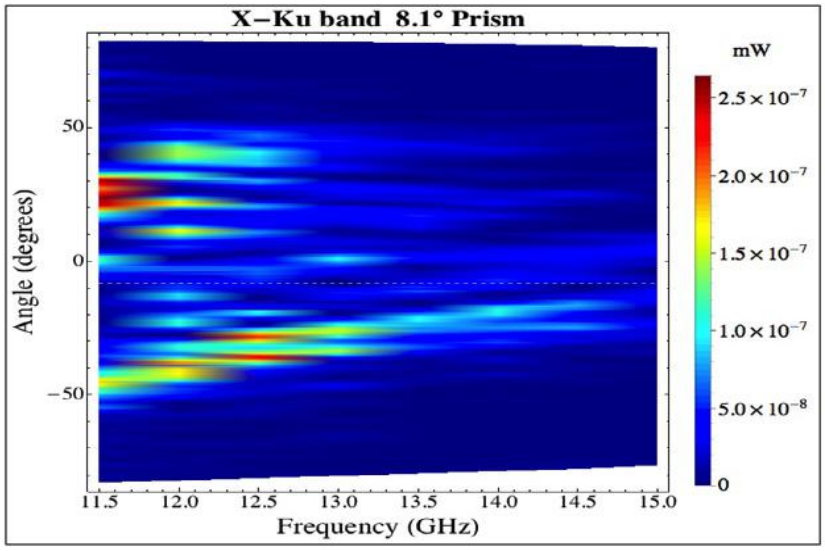



**Figure 2. Experimentally-measured intensity of the transmitted electromagnetic wave as a function of the frequency and angle relative to the normal to the prism.[1]**

**Acknowledgements**, D.L. gratefully acknowledges the support of this project by the U.S. Air Force Space Command. A.P. acknowledges the partial support from the U.S. Air Force Summer Faculty Fellowship Program.

## REFERENCES

1. Lee, D. A., Vedral, L. J., Smith, D. A., Musselman, R. L., Pinchuk, A. O. (2015). Low-loss negative index metamaterials for X, Ku, and K microwave bands. *AIP Advances*, *5*(4), 047119.

# Excitation, Verification and Exploitation of Prohibited Modes of Dielectric Resonators

**A. Kianinejad**[1,2], **Z. N. Chen**[1*], **and C.–W. Qiu**[1]

[1]*Department of Electrical and Computer Engineering, National University of Singapore, 4 Engineering Drive 3, Singapore 117583, Republic of Singapore*

[2]*Institute for Infocomm Research, Agency of Science, Technology and Research, Singapore, 1 Fusionopolis Way, Singapore 138632, Republic of Singapore*

[*]corresponding author: eleczn@nus.edu.sg

**Abstract**-We present a microwave plasmon-based method to enable the excitation of the prohibited modes of dielectric resonators (DRs). A meander transmission line is implemented to couple the microwave plasmon modes to a DR. Resonating at the prohibited modes, the DR acts like parallel magnetic dipoles and with benefiting from high efficient coupling, it make promises for application as antennas and filters in microwave communication systems.

Dielectric Resonators (DRs) have drawn many attention for many years and have been applied as filters and antennas (DRAs)[1–3]. Taking advantage of much lower loss in compare with the metal based antennas, DRAs are the ideal choices for application at millimeter-wave and terahertz bands. Various feeding methods have been proposed to excite DRs; however, the TE dominated modes have always been missed due to suppression of the horizontal electric field by the metallic ground plane in the feeding configuration. The excitation of the fundamental TE mode of cylindrical DRs is studied in[4]. This work implements microwave plasmon modes to excite the higher order TE dominant modes of dielectric resonators.

Recently, meander cells as spoof surface plasmon structures have become of interest in many works[5–8]. With a proper coupling to microwave energy sources, SSP cells can form slow wave transmission lines[4, 9]. Here we applied a meander transmission line to excite two higher order prohibited modes of a DR, $EH_{21\delta}$ and $EH_{31\delta}$ modes. The DR is a cylinder with the diameter of 25mm, height of 4mm and dielectric constant of 25.

$EH_{21\delta}$ and $EH_{31\delta}$ modes are hybrid modes with dominant magnetic fields in the axial direction. According to Figure 1($a_1$), the $EH_{21\delta}$ resonates in the azimuth direction while there is no resonance in the axial direction, which acts like four parallel magnetic dipoles with $\pi$ radian phase difference. The resonance frequency of this mode is 5.3GHz. The electric field vectors are plotted in Figure 1($b_1$) and aligned in the concentric circles around each dipole. This DR radiate with very high efficiency of higher than 90%. Figure 1($c_1$) depicts the radiation patterns in the azimuthal plane and presents four main lobes, corresponding to the direction of the magnetic dipoles in Figure 1($a_1$). The field distributions of $EH_{31\delta}$ mode are also presented in Figure 1($a_2$), and ($b_2$). This mode resonates at 6.3GHz. The $H_z$ component as shown in Figure 1($a_2$) forms six resonating dipoles along with the electric field vectors, plotted in Figure 1($b_2$), swirling around them. The far-field radiation pattern in the azimuthal plane, plotted in Figure 1($c_2$), also demonstrates six main lobes corresponding to the six magnetic dipoles. Operating as an efficient antenna and as well as a filter, the prohibited modes could find application in communication systems.

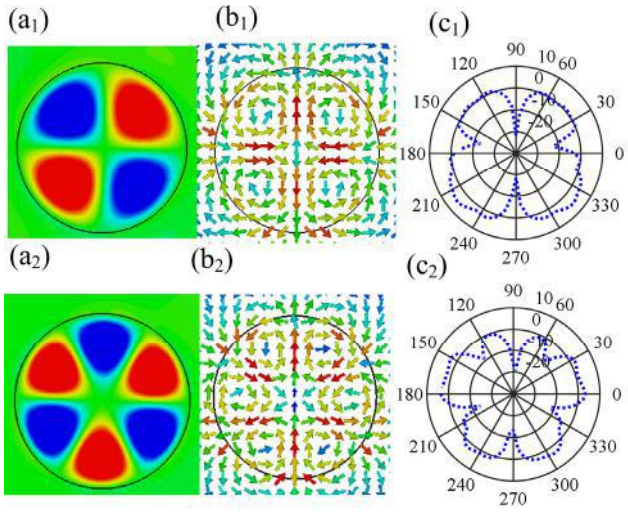



Figure 1 (color online) The field pattern of the lost higher order modes excited by the SW-TL. The axial component of the magnetic field for $EH_{21\delta}$ ($a_1$) and $EH_{31\delta}$ ($a_2$). The electric field vectors for $EH_{21\delta}$ ($a_1$) and $EH_{31\delta}$ ($a_2$). The far field radiation pattern of the co-polaraized component of the electic fields at three planes for $EH_{21\delta}$ ($a_1$) and $EH_{31\delta}$ ($a_2$).

**Acknowledgements:** A. Kianinejad would like to express his gratitude to Agency for Science, Technology and Research (ASTAR) for providing SINGA scholarship.

## REFERENCES

1. T. Nobis, E. M. Kaidashev, A. Rahm, M. Lorenz, and M. Grundmann, "Whispering Gallery Modes in Nanosized Dielectric Resonators with Hexagonal Cross Section," *Physical Review Letters*, vol. 93, no. 10, p. 103903, Sep. 2004.
2. S. Chang, A. G. Mann, A. N. Luiten, and D. G. Blair, "Measurements of radiation pressure effect in cryogenic sapphire dielectric resonators," *Physical review letters*, vol. 79, no. 11, p. 2141, 1997.
3. A. A. Savchenkov, V. S. Ilchenko, A. B. Matsko, and L. Maleki, "Kilohertz optical resonances in dielectric crystal cavities," *Physical Review A*, vol. 70, no. 5, p. 051804, Nov. 2004.
4. A. Kianinejad, Z. N. Chen, L. Zhang, W. Liu, and C. W. Qiu, "Spoof Plasmon-based Slow-wave Excitation of Dielectric Resonator Antennas," *IEEE Trans. Antennas Propagat.*, vol. PP, no. 99, pp. 1–1, 2016.
5. V. Torres, R. Ortuño, P. Rodríguez-Ulibarri, A. Griol, A. Martínez, M. Navarro-Cía, M. Beruete, and M. Sorolla, "Mid-infrared plasmonic inductors: Enhancing inductance with meandering lines," *Scientific Reports*, vol. 4, Jan. 2014.
6. P. A. Huidobro, X. Shen, J. Cuerda, E. Moreno, L. Martin-Moreno, F. J. Garcia-Vidal, T. J. Cui, and J. B. Pendry, "Magnetic Localized Surface Plasmons," *Physical Review X*, vol. 4, no. 2, p. 021003, Apr. 2014.
7. J.-Y. Ou, E. Plum, J. Zhang, and N. I. Zheludev, "An electromechanically reconfigurable plasmonic metamaterial operating in the near-infrared," *Nature Nanotechnology*, vol. 8, no. 4, pp. 252–255, Mar. 2013.
8. A. Berrier, B. Gompf, L. Fu, T. Weiss, and H. Schweizer, "Optical anisotropies of single-meander plasmonic metasurfaces analyzed by Mueller matrix spectroscopy," *Physical Review B*, vol. 89, no. 19, p. 195434, May 2014.
9. A. Kianinejad, Z. N. Chen, and C.-W. Qiu, "Design and Modeling of Spoof Surface Plasmon Modes-Based Microwave Slow-Wave Transmission Line," *IEEE Trans. Microw. Theory Techn.*, vol. 63, no. 6, pp. 1817–1825, Jun. 2015.

# Plasmon based three-layer antireflection coating for infrared photodetectors

**Jun Oh Kim[1], Jiyeon Jeon[1, 2], Khagendra Bhattarai[3], Jiangfeng Zhou[3], Augustine Urbas[4], Zahyun Ku[4] and Sang Jun Lee[1,*]**

[1]Division of Convergence Technology, Korea Research Institute of Standards and Science, Daejeon, 34113, Korea

[2]Department of Electrical Engineering, Sejong University, Seoul, 05006, Korea

[3]Department of Physics, University of South Florida, Tampa, FL 33620, USA

[4]Air Force Research Laboratory, Wright-Patterson Air Force Base, OH 45433, USA

[*]corresponding author: sjlee@kiriss.re.kr

At surface plasmon (SP) resonances, we experimentally and theoretically investigate the enhanced transmission by the metamaterial based antireflection coating that is composed of the metallic disk array (MDA) atop the dielectric film. The optimized condition (zero reflectance) is analyzed by using a three-layer model and calculated reflection using matrix method which is good correspondence with measured transmission results. It is possible to multifunctional infrared sensor as new mechanism to the enhanced transmission application.

We experimentally and theoretically investigate the phenomenon of enhanced extraordinary optical transmission [1] due to metamaterial (MM) based antireflection coating (ARC) atop the metal hole array in the mid-infrared region (Figure 1a) [2]. Our MM based ARC consists of a metal disk array (MDA) on top of a benzencyclobutene (BCB) layer. We are performed the experiment with 1.8 μm pitch of metal hole array and metal disk array depending on variable BCB thickness. As shown in Figure 1b, it shows that the simulated transmission agrees very well with the FTIR-measured transmission. The highest measured (simulated) enhancement ratio at the first SP resonance wavelength of metal hole array is ~88% (~82%) as compared with no MM-ARC layered MHA. To confirm the measured and simulated results, we analyze phenomenon by using a three-layer model and calculated reflection using matrix method. The simulated reflectance shows good match with calculated reflectance in the first plot of figure 1c. As shown in the second plot of Figure 1c, it shown that the amplitudes of $r_{12}$ and $\alpha \cdot r_{23}$ are same at the first SP resonance wavelength (~6.25 μm). Finally, the phase condition is also equal (red $\theta$ crosses gray $\pi$) in the third plot of figure 1c. Our work can lead to improved performance in multifunctional infrared sensors and infrared imaging applications.

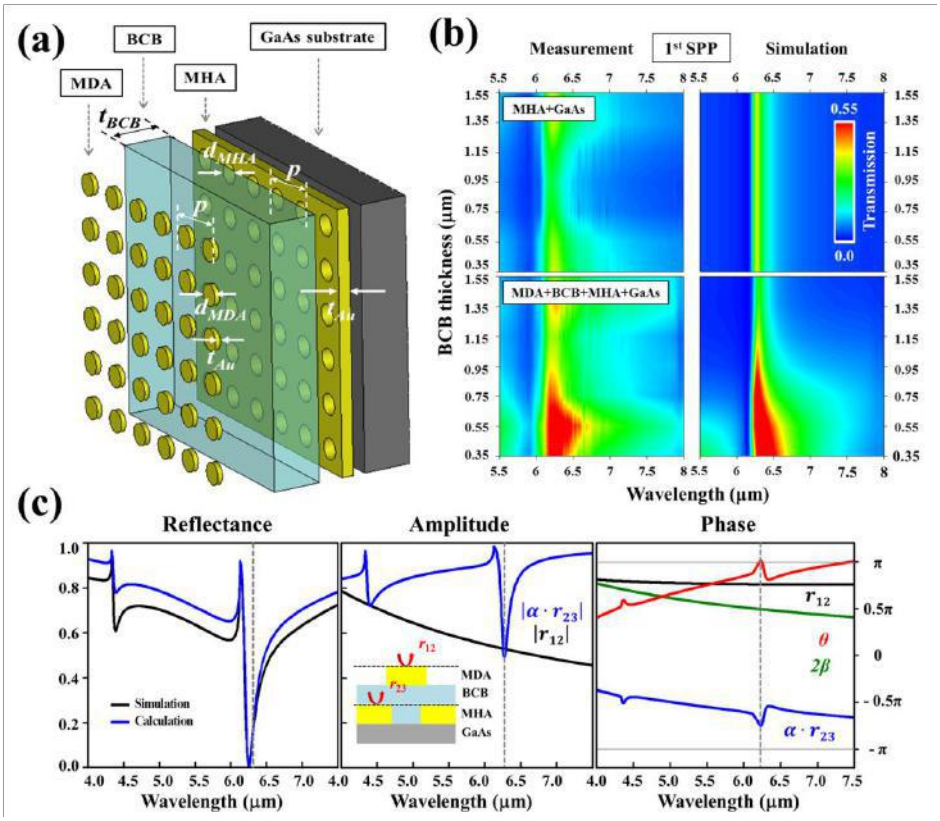



Figure 1. (a) Schematic view of metamaterial based antireflection coating layer on MHA structure. (b) Colormap of measured and simulated transmission with BCB thickness (from 0.35 μm to 1.55 μm with 0.2 μm step). (c) Reflectance, amplitude and phase condition for ARC.

**REFERENCES**

[1] Ghaemi, H. F. "Surface plasmons enhance optical transmission through subwavelength holes." *Physical review B* Vol.58, No.11, 6779, 1998.

[2] Park, Myung-Soo. "Enhanced transmission due to antireflection coating layer at surface plasmon resonance wavelengths." *Optics express* Vol.22, No.24, 30161-30169, 2014.

# Voltage Controlled Unidirectional Propagation of Microwaves in Metastructures Ferrite/Conductive Elements with Varactors

**Valery Butylkin*, Yuri Kazantsev, Galina Kraftmakher, Valeri Mal'tsev**

Kotelnikov Institute of Radioengineering & Electronics RAS, Moscow, Russia
*vasebut@ms.ire.rssi.ru

## Abstract

Voltage controlled nonreciprocal frequency bands and inversion of nonreciprocity sign have been observed at microwaves with metastructures 'ferrite plate/array of magnetically excited varactor-loaded twice split rings (TSR) as well double split rings (DSR)' placed along rectangular waveguide axis. The effects are due to the nonreciprocal absorbing under interaction between ferromagnetic resonance (FMR) in ferrite and magnetic resonance (MR) in rings (<< wavelength). It has been also used varactor-loaded single dipole in the form of butterfly as well twice split ring as twin half-wave dipoles under excitation of dipole resonance (DR) by microwave electric field *E*. Possibility of application for fast controlled nonreciprocal devices are discussed.

## 1. Introduction

Based on ferromagnetic resonance (FMR) nonreciprocal interactions of microwaves with magnetized ferrite continue to be the object of attention of the metamaterial community [1-4]. The suggested applications are thin unidirectional devices [1, 2] and scanned leaky-wave antennas [3,4]. We are interested in control of the nonreciprocity sign. Usually variable bias magnetic field is used for this aim. Authors of [1-4] considered combinations of ferrites with various conducting elements (linear and/or annular ones) hereinafter called 'ferrite/conductive elements' metastructures (FCEM). At first theoretical investigations of FCEM were devoted to infinitely long linear elements [5] (as well as in [1] and in [6, 7] where wires are embedded into a ferrite slab). However, in reality conducting elements have finite dimensions. It results in resonances of electrodynamic characteristics including transmission coefficients $T$ and the nonreciprocity $\delta T$ which is defined as difference between forward $T_f$(dB) and backward $T_b$(dB) transmission coefficients of a metastructure. Such resonances together with FMR have been observed by our measurements of $\delta T$ of FCEM with different conducting elements (planar double split rings, Γ–form, zigzag-form, butterfly-form and rectilinear dipoles, planar spirals, non-convex polygonal loops [8-15]). As it turns out, retuning connected with conducting elements resonances can be used for control of the FCEM nonreciprocity [16-18].

Voltage controlled nonreciprocal effects due to influence of the FMR and DR were investigated in [16-18] where metastructure contains ferrite plate and varactor-loaded single twice split ring as twin half-wave dipoles [16] as well varactor-loaded single dipole in the form of "Butterfly" [17, 18]. Electrically controlled frequency bands have been observed in metastructure with dipole twice split ring (TSR) [16] and reversal of nonreciprocity sign with dipole Butterfly [17, 18]. DR is due to dipole currents induced by microwave electric field *E*. It is of interest to study nonreciprocal effects under interaction between the FMR and resonance connected with closed ring currents induced by microwave magnetic field *h* in small TSR and DSR (magnetic resonance, MR).

In this paper we measure transmission coefficients $T$ of metastructures in rectangular waveguide and demonstrate a way for both voltage retuning of nonreciprocal frequency bands and switching sign of nonreciprocity at the same frequency band. Different planar metastructures containing ferrite plate and array of varactor-loaded *h*-excited TSR or DSR, as well *E*-excited dipole TSR and dipole "Butterfly" are examined. Mechanism of control, switching time and possibility of application for fast nonreciprocal devices are discussed.

## 2. Measurements methods, investigated metastructures, results

It is known that when required for the FMR excitation field $H$ is applied and senses of the spins precession around $H$ and rotating microwave magnetic field $h$ are the same, power of the wave is absorbed by a ferrite. In the case when senses of precession and *h*-field rotating are opposite, absorption is absent. Senses of the *h*-field rotating are opposite for forward and counter-propagating waves. Senses of the spins precession are opposite for opposite direction of magnetization. The nonreciprocity $\delta T$ (dB) of microwave propagation is characterized as a difference between transmission coefficients $T$(dB) for two situations. In the first situation senses of spin precession and rotating *h*-field are the same. In the second situation senses of spin precession and rotating *h*-field are opposite. We use single-channel measurements. In this case the nonreciprocity $\delta T$ can be defined not by reversal of the propagation direction as usually [19] but as the difference between $T$ corresponding to the opposite directions of magnetization,

when senses of *h*-field rotation are the same but senses of spin precession are opposite.

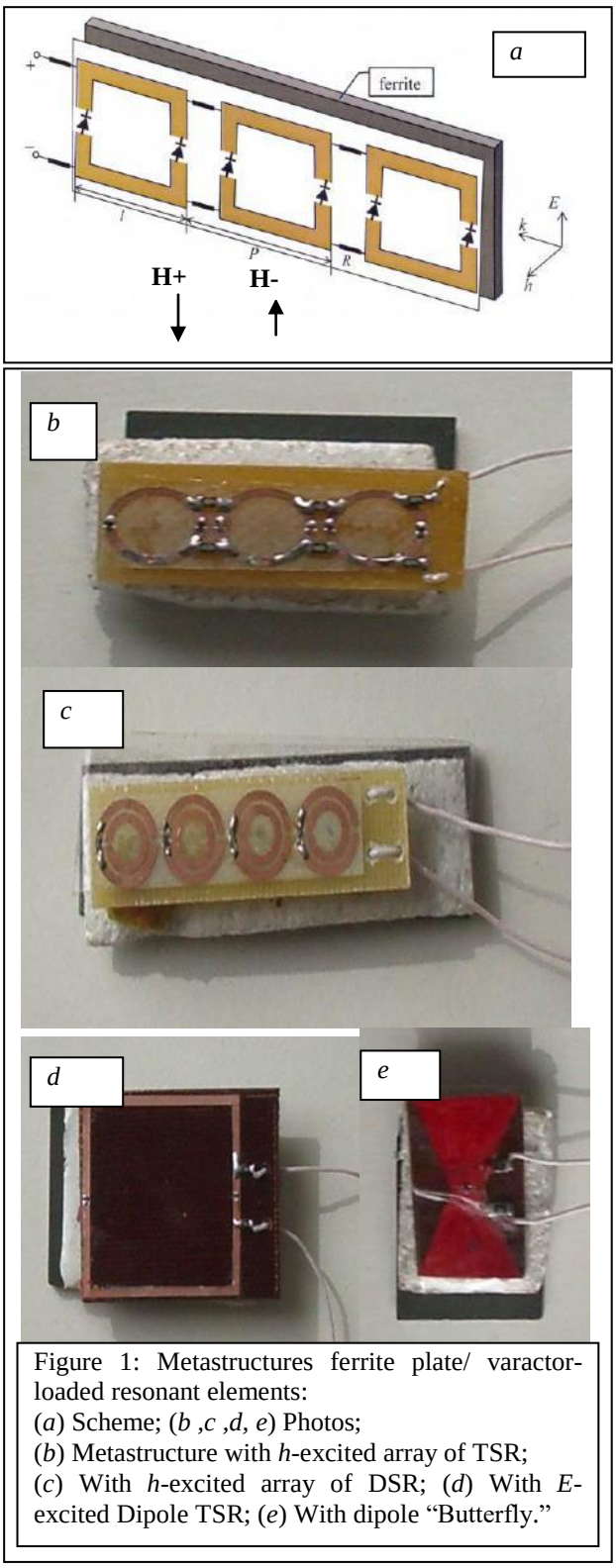



Figure 1: Metastructures ferrite plate/ varactor-loaded resonant elements:
(*a*) Scheme; (*b* ,*c* ,*d*, *e*) Photos;
(*b*) Metastructure with *h*-excited array of TSR;
(*c*) With *h*-excited array of DSR; (*d*) With *E*-excited Dipole TSR; (*e*) With dipole "Butterfly."

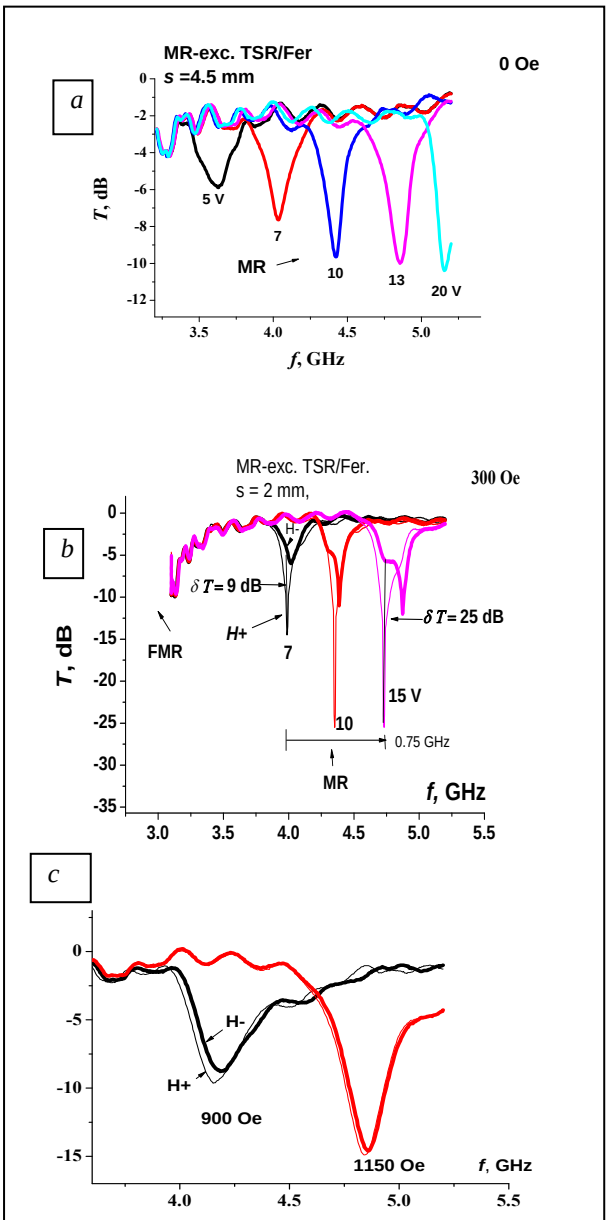



Figure 2: Measured frequency dependences of transmission coefficients *T* with metastructure ferrite plate /array of *h*-excited TSR:
(*a*) Voltage retuned MR at *H* =0 Oe;
(*b*) Retuned nonreciprocal frequency bands of MR at H = 300 Oe by $V_{DC}$ variation;
(*c*) FMR in free ferrite controlled by *H*-field;
(*d* ,*e*) Different positions ($\delta f$ sign) of the FMR relative to fixed MR by the *H*-field variation;
(*f*, *g*) Different positions ($\delta f$ sign) of the MR relative to fixed FMR by $V_{DC}$ variation;
(*h*) Inversion of sign of $\delta T$ (dB) under FMR at 900 Oe by variation of $V_{DC}$ from 9 to 15V.

$$\delta T(\text{dB}) = T(H_-) - T(H_+). \qquad (1)$$

$H_-$ and $H_+$ correspond to opposite directions of the external transverse field $H$ (magnitudes of $H$-field are the same). In this case senses of $h$-field rotation are the same but senses of spins precession are opposite.

The planar metastructures under study are shown in **Fig. 1**: *a* - scheme; *b,c,d,e* – photos. They involve a plate of polycrystalline iron-yttrium garnet near which array of resonant elements (or single element) made of polyamide film on copper foil are placed on a 0.5-mm-thick hardened paper substrate at distance *s*. **Fig. *1b*** shows metastructure with ferrite plate (21x14x2 mm) with array of *h*-excited copper TSR (diameter of 6.6 mm). **In Fig. 1*c*** metastructure contains the same ferrite plate and array of *h*-excited DSR, outer diameter 6.6 mm. **Fig. 1*d*** shows metastructure with ferrite plate (29x21x2 mm) and *E*-excited dipole TSR, l = 22mm. **In Fig. 1*e*** metastructure contains the same ferrite plate and *E*-excited dipole "Butterfly" (20x10 mm).

Varactors MA46H120 (MACOM), with a capacitance variable from 1 to 0.15pF by supplying back bias voltage $V_{DC}$ from 0 to 30V, is welded into the gaps of elements. The sizes of elements are chosen so that the resonance response will be observed in the given range 3 -6 GHz of the voltage standing wave ratio (VSWR) panoramic measurer.

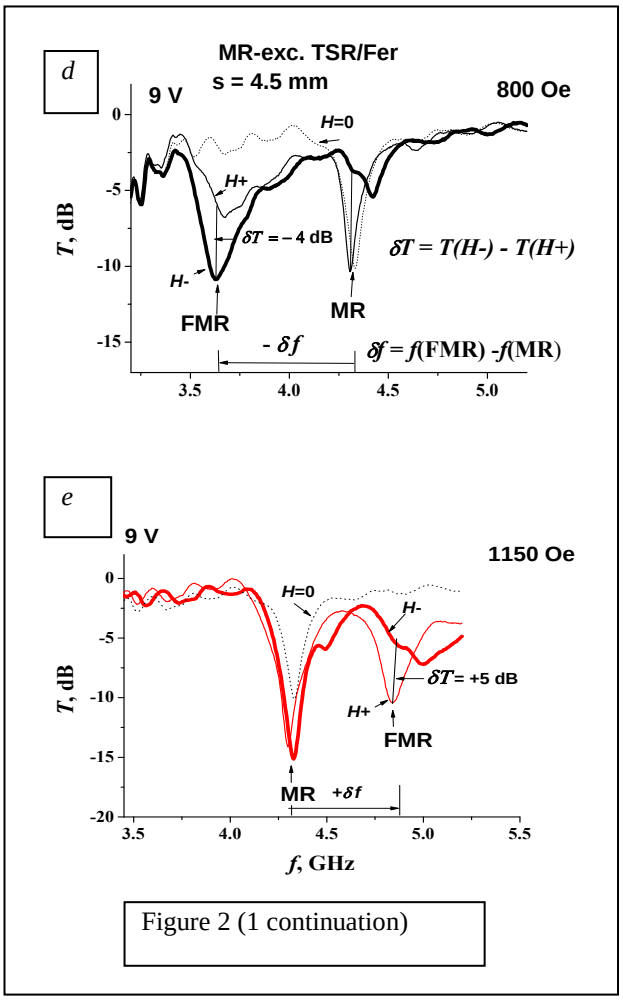



Figure 2 (1 continuation)

We measure transmission coefficients $T$ in rectangular waveguide with metastructures under different conditions. Metastructure is placed along waveguide axis.

**Fig. 2** shows properties of metastructure ferrite plate/array of *h* –excited split rings. We see two resonance effects.

The first resonance is magnetic resonance (MR) due to induced ring current; it is excited by microwave *h*-field without static magnetic field $H$ and can be retuned by the application of a bias voltage $V_{DC}$ to varactors **(Fig. 2*a*)**.

The second resonance effect is the FMR in ferrite; it is excited in the presence of $H$-field and shifts to higher frequencies with $H$-field magnitude increase.

In the case when the FMR approaches to the MR, regime of coupled resonances is achieved; the FMR and MR are getting nonreciprocal and the metastructure acquires capability of the simultaneous magnetic and voltage control of $\delta T$ in both FMR and MR-domains.

**Fig. 2*b*** shows nonreciprocal MR, its frequency and intensity can vary with the magnitude of $H$ in limited frequency band depending on distance *s* as well by voltage in $H$-field (300 Oe), which is substantially lower than the field exciting the FMR in free ferrite at this frequency. As $V_{DC}$ across the varactor varies from 0 to 20V, along with retuning of MR frequency nonreciprocal band is also retuned. **Fig. 2*c*** corresponds to free ferrite without TSR, it shows retuned FMR with $H$-field variation from 900 to 1150 Oe, nonreciprocity $\delta T$ is absent because of $T(H-) = T(H+)$. By reducing distance *s* between ferrite and TSR we can increase resonances coupling and expand tuning range of nonreciprocal MR.

One can also switch microwaves unidirectionality to the opposite one in the FMR-domain without shifting frequency band when coupling between FMR and MR is not strong because there is dependence of sign of $\delta T$ on the FMR-position relative to the MR frequency (by the sign of $\delta f$).

$$\delta f = f_{\text{FMR}} - f_{\text{MR}} \qquad (2)$$

**Fig. 2*d, e*** demonstrates transmission for different position of the FMR relative to fixed MR; (**Fig. 2*f, g***) corresponds to different position of the MR relative to fixed FMR In the case of fixed MR, position "FMR below MR" (**Fig. 2*d***) changes to "FMR above MR" (**Fig. 2 *e)*** by variation of $H$-field value. In the case of fixed FMR, position "FMR above MR" (**Fig. 2*f)*** changes to "FMR below MR" (**Fig. 2*g***) by variation of voltage $V_{DC}$. With positive $\delta f$, positive $\delta T$ is observed and vice-versa with negative $\delta f$, $\delta T$ is negative. Inversion of $\delta T$ sign by variation of voltage is demonstrates in **Fig. 2*h***. Here FMR frequency practically is not changed because of necessary resonances coupling. Voltage controlled inversion of $\delta T$ sign by use of array of *h*-excited DSR is demonstrates in **Fig. 3.** Inversion of $\delta T$ sign signifies inversion of nonreciprocal propagation direction.

Simulation of *h*-excited TSR or DSR by bianisotropic layer confirms dependence of sign of $\delta T$ on FMR-position relative to MR (sign of $\delta f$, **Fig. 4**).

**Fig. 5** demonstrates similar properties with metastructure ferrite plate/dipole"Butterfly". Under H= 0 the DR is

excited at 3.5 GHz and retuned by variation of bias voltage $V_{DC}$ from 0 to 20V (**Fig. 5*a***). In the presence of *H*-field = 100 Oe, for *s* =2 mm (strong coupling between ferrite and dipole), the DR shifts to 4.25 GHz and is getting nonreciprocal and retuned by variation of $V_{DC}$ (**Fig. 5*b***). FMR is excited in the presence of *H*-field and shifts to higher frequencies with its increase. If coupling between FMR and DR is not strong, FMR-frequency is not practically changed on voltage application but the sign of nonreciprocity $\delta T$ depends on position relative to DR.

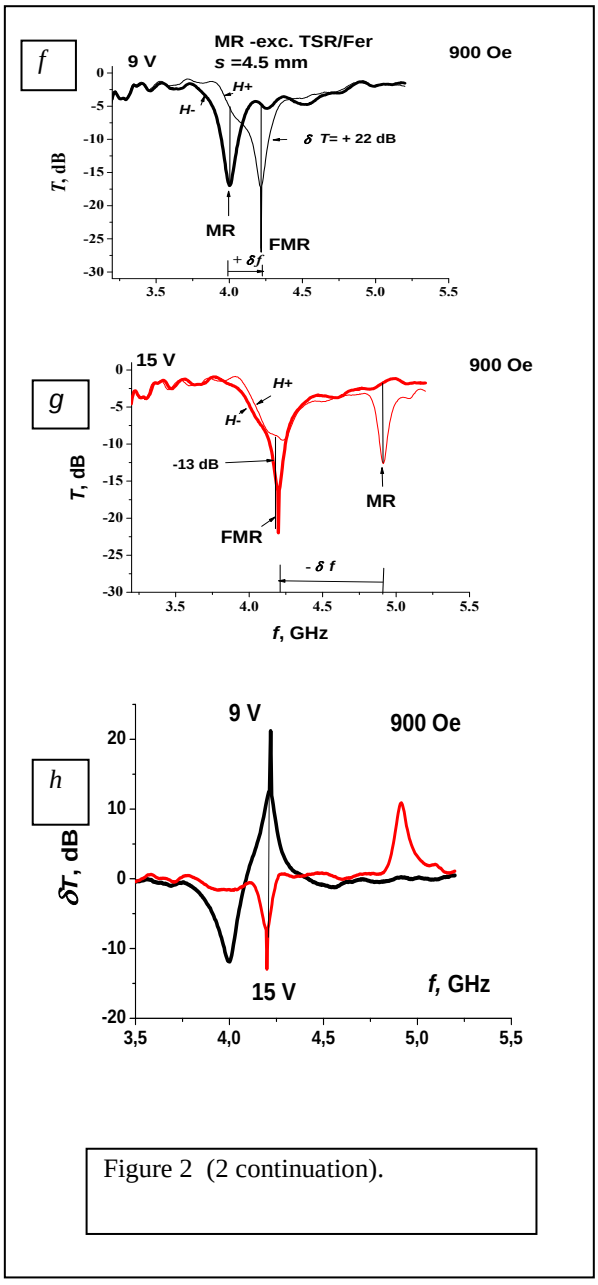



Figure 2 (2 continuation).

**Fig. 5*c d ,e*** demonstrates properties in the case of different position of fixed FMR (*H* = 800 Oe) relative to DR for *s* = 8.5 mm. Frequency of DR is changed by voltage variation. When DR passes through frequency of the FMR, position of the DR relative the FMR is changed and inversion of sign of $\delta T$ is observed. Similar properties are observed for metastructure ferrite/dipole twice split ring (22mm) where ring behaves as twin dipoles with properties due to induced counter currents (**Fig. 6**).

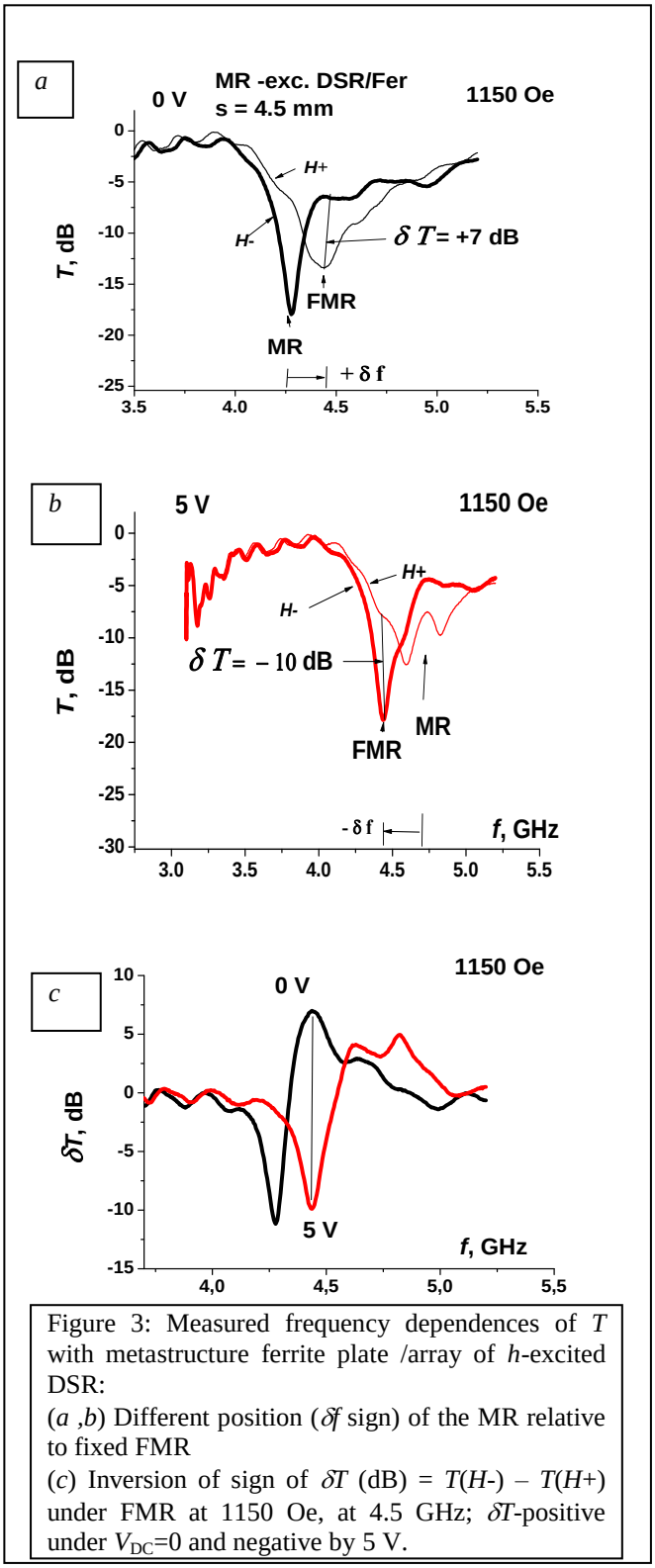



Figure 3: Measured frequency dependences of *T* with metastructure ferrite plate /array of *h*-excited DSR:
(*a* ,*b*) Different position ($\delta f$ sign) of the MR relative to fixed FMR
(*c*) Inversion of sign of $\delta T$ (dB) = $T(H-) - T(H+)$ under FMR at 1150 Oe, at 4.5 GHz; $\delta T$-positive under $V_{DC}$=0 and negative by 5 V.

In the case of free ferrite without TSR there is no $\delta T$ (**Fig. 6*a***). In metastructure nonreciprocal DR is observed in the presence of *H*-field 100 Oe, which is substantially lower than the field (900 Oe) exciting the FMR in free ferrite in this area (about 4 GHz). Nonreciprocal DR is retuned by $V_{DC}$ variation (**Fig. 6b).**

**Fig. 6*c, d*** shows properties in the case of different position ($+\delta f$) and ($-\delta f$) of fixed FMR ($H$ = 600 Oe) relative to voltage retuned DR. **Fig. 6*e*** shows voltage controlled inversion of $\delta T$ sign.

.

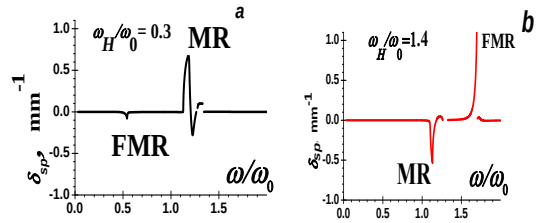



Figure 4: Calculated specific transmission nonreciprocity parameter $\delta_{sp}$ per unit length of a bianisotropic-ferrite metastructure in dependence on relative frequency $\omega/\omega_0$ ($\omega_0$ – intrinsic frequency of bianisotropic material with chiral elements, $\omega_H$ – **FMR** frequency): (*a*) $\omega_H/\omega_0$ =0.3 (**FMR** is excited lower then the magnetic resonance M**R,** $\delta_{sp}$ is negative); (*b*) $\omega_H/\omega_0$ =1.4 (**FMR** is excited higher then the **MR,** $\delta_{sp}$ is positive) [20].

## 3. Discussion

**3. 1.** Observed unusual nonreciprocal phenomena are due to interaction between FMR, and MR or DR, as well to features of microwave magnetic field in metastructure near conductive elements. This field is superposition of the incident and scattered waves' fields and possesses required for nonreciprocal absorbing elliptical polarization at frequencies around MR (DR). Its sense of rotation and ellipticity depend on phase of induced running which are by-turn defined by detuning between current and resonance frequency of conductive elements. So, total *h*-field rotates in one direction at frequencies above the MR (DR) and in the opposite direction below the MR (DR). **Fig. 7** presents calculated time-dependent rotating normalized total magnetic field using approach [17, 18]. **Fig. 7a** shows that left-handed *h*-field takes place at frequencies $\omega > \omega_0$ ($\omega_0$ is the dipole resonance frequency) while right-handed *h*-field corresponds to $\omega < \omega_0$ (**Fig. 7*b***). Therefore one can change the sense of the *h*-field rotating by retuning elements resonance frequency by voltage application to varactors embedded in gaps of rings or dipoles.

1. Reversing the sign of the nonreciprocity $\delta T$ occurs as follows:

Let field $H_-$ is applied and spin precession is left-handed and the FMR is excited above the MR (DR) ($\omega > \omega_0$) In this case there are left-handed precession of spins and left-handed *h*-field; ferrite absorbs power of direct wave and does not absorb power of counter-propagation wave, nonreciprocity is positive. By the application of a bias voltage to a varactor, frequency of the MR (DR) passes through the FMR frequency (FMR below the DR (MR), $\omega < \omega_0$) and left-handed *h*-field is transformed into right-handed but sense of spin precession is not changed because direction of *H*-field is not reversed.

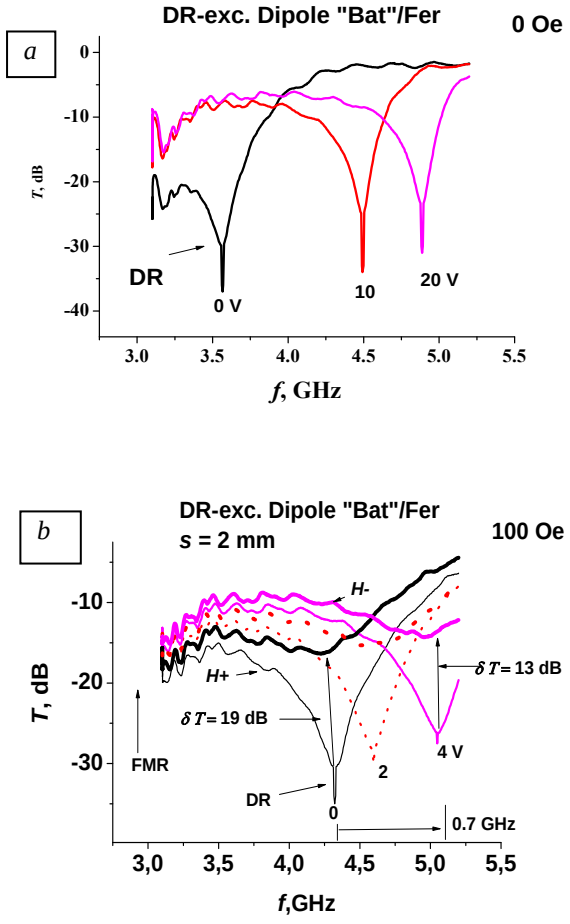



Figure 5: Measured frequency dependences of $T$ with metastructure ferrite plate /*E*-excited dipole "Butterfly":
(*a*) Voltage Retuned DR at $H$ = 0 Oe;
(*b*) Retuned nonreciprocal DR at $H$ = 100 Oe by $V_{DC}$ variation from 0 to 4V;
(*c, d*) Different position of the DR relative to fixed FMR at 800 Oe; (*e*) Inversion of $\delta T$ sign by $V_{DC}$ variation from 0 to 20V.

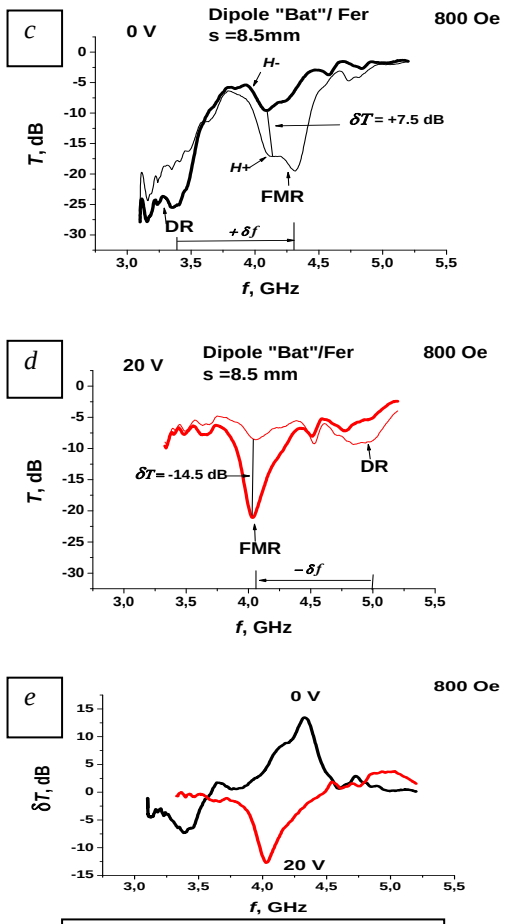



Figure 5 (continuation)

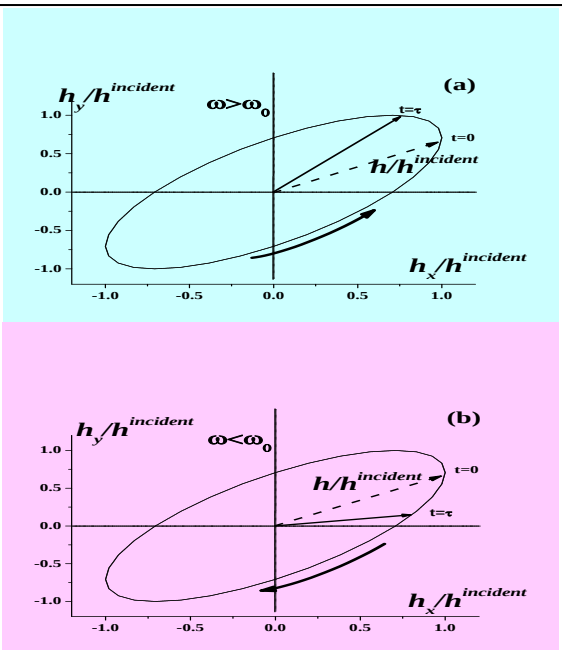



Figure 7: Calculated magnetic field near dipole [17].

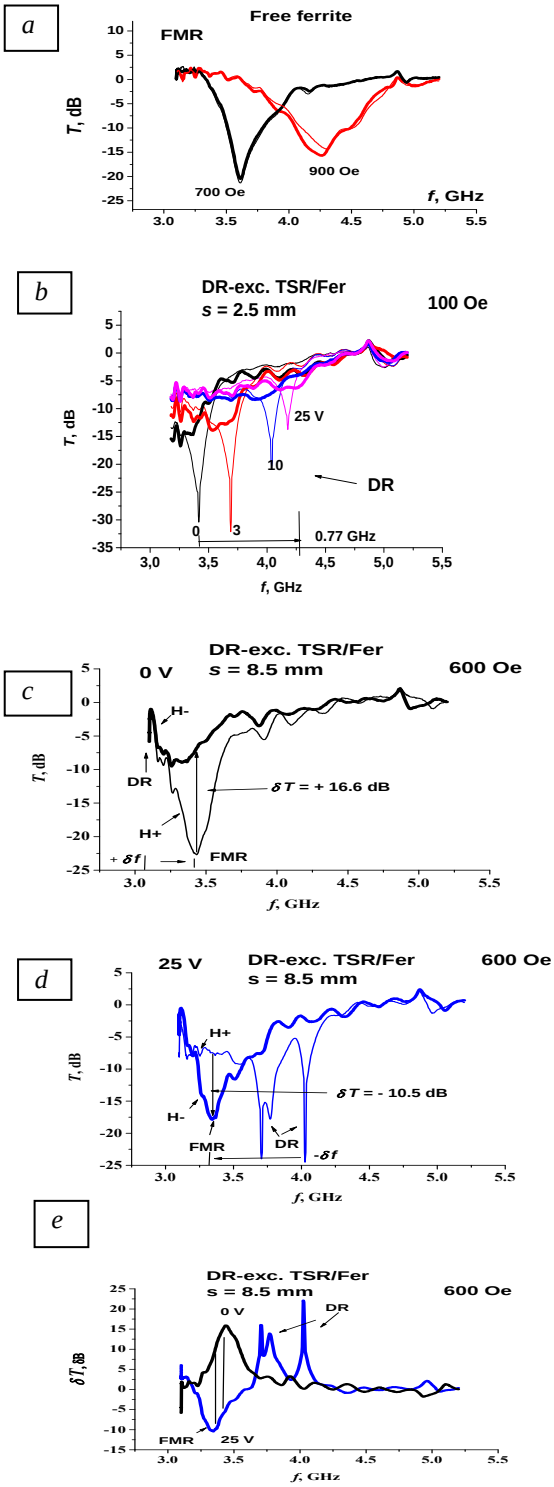



Figure 6: Measured frequency dependences of $T$ for metastructure ferrite plate/dipole TSR: (*a*) Free ferrite; (*b*) Voltage retuned nonreciprocal DR at 100 Oe; (*c*) $+\delta f$; (*d*) $-\delta f$; (*e*) Inversion of $\delta T$ sign by $V_{DC}$ variation.

In this case there are left-handed precession and right-handed *h*-field; ferrite does not absorb power of direct wave but absorbs power of counter-propagation wave.
Nonreciprocity is getting negative. Usually reversing the sign of $\delta T$ in ferrite is achieved by reversal of magnetization direction, as a result of which reversal of sense of spins precession occurs.

**3. 2.** Is voltage control faster than magnetic?

Let us discuss temporal progress of voltage nonreciprocity reversal on the example of nonreciprocal device consisted of a varactor-loaded split dipole of finite length and neighboring ferrite [18]. One can pick out four stages: ***i)*** change of varactor capacitance (or of oscillator which simulates dipole [18]) under alteration of a bias voltage; ***ii***) change of a current in oscillator because of tuning of dipole frequency; ***iii)*** delay of scattered wave arrival to ferrite and forming of rotating microwave magnetic field; ***iv)*** change of movement of ferrite magnetic moment. As [21] shows, ***i)***-stage duration is 1-5 ns. To estimate ***ii)***-stage duration let us use stepwise approximation of temporal dependency of the capacitance. Well-known solutions of the equation of linear oscillator show that current contains a forced oscillation on frequency ω of the incident wave and damped oscillations on frequency

$$\Omega = \sqrt{(1/LC) - (R/2L)^2} \qquad (3)$$

(*L*, *R* and *C* are the inductance, resistance and capacitance of the equivalent oscillator simulating dipole). Decay time is equal to *R*/2*L* and can be found from half-width of resonance response for scattered wave. In the case of dipole "Butterfly" the width is 1 GHz, which corresponds to decay time about 2 ns. Delay time in ***iii)***-stage is about nanoseconds at GHz-range because the distance between ferrite and resonant element does not appreciably exceed the wavelength. In ***iv)***-stage relaxation time of precession of ferrite magnetic moment can be found through the inverse value of ferromagnetic resonance line-width:

$$\tau_{relax} = 2 / \gamma \Delta H \qquad (4)$$

Here $\gamma$ is the gyromagnetic ratio. Whereas gyromagnetic resonance line-width is about 30-100 Oe, relaxation time is about 38-11 ns. Thereby, the time of nonreciprocity reversal by voltage control is of the order of some tens of nanoseconds what is much faster than by traditional magnetic control (about microseconds [22]).

## 4. Conclusions

Thereby, our investigations have shown that metastructures containing ferrite plate and varactor-loaded conductive elements can provide voltage controlled nonreciprocal transmission by use of both half-wavelength dipoles and small magnetically excited double split rings (DSR) or twice split rings (TSR). One can expect that such structures are perspective for development of fast-acting switching of channels "transmitting – receiving". At that for ferrite magnetization one can use permanent magnet and provide the FMR excitation in the absence of direct currents and related thermal losses. One can also use hexaferrites which are not needed in external magnetic field and, respectively, in magnet. Both small magnetically excited TSR and DSR and electrically excited half-wavelength dipoles provide ability of controlled nonreciprocity but small elements are of interest for decrease of reflectance and losses.

## References


[1] A. Degiron and D.R. Smith, One-way glass for microwaves using nonreciprocal metamaterials, *Phys. Rev. E*., Vol. 89, 053203-1-5, 2014.

[2] Y. Ra'di, V.S, Asadchy, and S.A. Tretyakov, One-way transparentsheets, *Phys. Rev. B*., Vol. 89, 075109. 2014.

[3] N. Apaydin, .K. Sertel, and J.L. Volakis, Nonreciprocal and Magnetically Scanned Leaky-Wave Antenna Using Coupled CRLH Lines, *IEEE Trans. Antennas & Propag.*, Vol. 62, No.6, 2954-2961, 2014.

[4] G. Cochet, P. Queffelec, A.G. Schuchinsky, V. Laur, and R. Cahill, Non-reciprocity in Doubley Periodic Strip Arrays on Ferrite-Dielectric Substrate, in *Proceedings of 7th International Congress on Advanced Electromagnetic Materials in Microwave and Optics-Metamaterials 2013, Bordeaux*, France, 16-21 September 2013.

[5] Charray Surawatpunya, Makoto Tsutsumi, and Nobuaki Kumagai, Bragg Interaction of Electromagnetic Waves in Ferrite Slab Periodically Loaded with Metal Strips, *IEEE Transactions on Microwave Theory and Techniques*, Vol. MTT-3, No. 7, 689-695, 1984.

[6] I.S. Nefedov, A.S. Soloviev, A.C. Tarot, and W. Abdouni, Surface waves in a magnetized ferrite slab filled with a wire medium, *Eur. Phys. J. Appl. Phys.* Vol. 45, Art. No. 32606, 32606-1-5, 2009.

[7] I.S. Nefedov, A.C. Tarot, and K. Mahdjoubi, Wire Media-Ferrite Substrate for Patch Antenna Miniaturization, *Proc.Antenna Technology: Small and Smart Antennas Metamaterials and Applications*, 2007, IWAT'07. International Workshop on, Cambridge, 101-104, 2007.

[8] V.S. Butylkin and G.A. Kraftmakher, Giant nonreciprocal effect under conditions of mutual influence of ferromagnetic and chiral resonance, *Tech. Phys. Letters*, Vol. 32. No. 9, 775-778, 2006.

[9] V.S. Butylkin and G.A. Kraftmakher, Nonreciprocal microwave transmission in metastructures with transversely magnetized ferrite plate and a grating of resonant elements, *Tech. Phys. Letters*, Vol. 33. No 10, 856-860, 2007.

[10] G.A. Kraftmakher and V.S. Butylkin, Nonreciprocal amplitude-frequency resonant response of metasandwiches "ferrite plate-grating of resonant elements", *Proc. of "Metamaterials'2008",* Spain, Pamplona, 1-3, 2008.

[11] V.S. Butylkin and G.A. Kraftmakher, Nonreciprocal transmission spectrum of a ferrite plate/resonant element grating metasandwich with split resonance, *Tech. Phys. Letters*, Vol. 3. No 5, 397-400, 2009.

[12] V.S. Butylkin and G.A. Kraftmakher, Nonreciprocal effects in propagation of microwaves along a waveguide structure formed from a ferrite plate and a lattice of resonant elements, *J.Commun. Technol. Electron*, Vol. 54. No 7, 775-782, 2009.

[13] V.S. Butylkin, G.A. Kraftmakher and V.P. Mal'tsev, Surface waves guided by a plane made from a bianisotropic resonance metamaterial, *J.Commun. Technol. Electron*, Vol. 54. No 10, 1124-1135, 2009.

[14] G.A. Kraftmakher and V.S. Butylkin, Nonreciprocal multiple splitting of giant ferromagnetic resonance in "ferrite plate-wire grating" planar metasandwiches, *Proc. of "Metamaterials'2009",* 611-612, London, 2009.

[15] G.A. Kraftmakher and V.S. Butylkin, Nonreciprocal amplitude-frequency resonant response of metasandwiches "ferrite plate-grating of resonant elements", *European Physical Journal, Applied Physics*, Vol. 49. No 3, 33004, 2010.

[16] G.A. Kraftmakher V.S. Butylkin and Yu.N. Kazantsev, Electrically controlled frequency bands of nonreciprocal passage of microwaves in metastrucrtures, *Tech. Phys. Letters*, Vol. 39. No 6, 505-508, 2013.

[17] G.A. Kraftmakher V.S. Butylkin and Yu.N. Kazantsev, Electrically controlled nonreciprocity inversion in a metastructure based on ferrite and a varactor-loaded dipole, *Tech. Phys. Letters*, Vol. 41. No 8, 723-726, 2015.

[18] Valery Butylkin, Galina Kraftmakher, and Yury Kazantsev, In Re Electric Switching Sense of Microwave Magnetic Field Rotation near Varactor-loaded Dipole Excited by a Plane Wave, *Final Proceedings of PIERS 2015*, July 6-9, Prague, CZESH REPUBLIC, 949-953, 2015.

[19] Dirk Jalas, Alexander Petrov, Manfred Eich et al., What is — and what is not — an optical isolator, *NaturePhotonics*, Vol. 7, 579-582, 2013.

[20] V.S. Butylkin, G.A. Kraftmakher, V.P. Mal'tsev, To the theory of nonreciprocal microwave transmission along a bianisotropic-dielectric-ferrite metasandwich, *Proc. AES 2012*, Telecom Paristech, France, pp. 649, 1-6, 2012.

[21] Future Electronics, URL: *http://www.futureelectronics.com/en/diodes/switching diodes.aspx*.

[22] Bodger Billings, Tony Edridge, Ferrite Circulator Switches and Their Applications, *Microwave J.*, November 1, 2003.

# EBG-based transmission lines with slow-wave characteristics and application to miniaturization of microwave components

*Jordi Selga, Paris Vélez, Jordi Bonache, and Ferran Martín

CIMITEC, Departament d'Enginyeria Electrònica, Universitat Autònoma de Barcelona, 08193 Bellaterra, Spain
*corresponding author, E-mail: Jordi.Selga@uab.cat

## Abstract

In this paper, artificial transmission lines implemented by means of electromagnetic bandgaps (EBGs) and consisting of a host line periodically loaded with reactive elements (either shunt capacitances or series inductances) are presented. The considered implementations are restricted to microstrip lines either loaded with patch capacitors or with inductive slots (etched in the ground plane). It is demonstrated that these structures are useful for device miniaturization due to the slow-wave effect associated to the presence of the reactive elements. A prototype device example, consisting of a microstrip power divider implemented by means of a 35.35Ω slow-wave impedance inverter with inductive slots is reported. It is shown that, by virtue of the slow wave effect, the length of the inverter is reduced by a factor of two. The performance of the resulting power divider is comparable to the one based on an ordinary inverter. The possibility to suppress spurious (harmonic) bands by means of the Bragg effect is also discussed.

## 1. Introduction

Size reduction and suppression of spurious or harmonic bands in distributed circuits have been two of the battle horses in microwave engineering for years. The suppression of spurious bands has been achieved by loading the devices with small resonant elements conveniently tuned (e.g. by using split rings [1],[2]), or by replacing the ordinary lines with artificial lines based on electromagnetic bandgaps (EBGs) [3]. Particularly, planar filters based on a periodic modulation of the width of the constitutive transmission lines have been reported in [4],[5]. In such filters, efficient spurious suppression was achieved thanks to the Bragg effect, derived from periodicity [6],[7] but size was not reduced. One strategy to reduce size and eventually suppress undesired spurious bands is to reactively load the line with shunt capacitors or series inductors [8]-[22]. By periodically loading the line with shunt capacitors, the effective line capacitance is enhanced, and thereby the phase velocity is reduced. This slow wave effect is also achievable with series inductances, in this case increasing the effective line inductance.

Many examples of slow wave transmission lines and applications based on capacitively-loaded lines can be found in the literature [11],[14],[23]-[26]. However, slow wave transmission lines based on inductive loading are less common [27]. In this paper a comparative analysis of capacitively- and inductively-loaded lines is carried out, and then the focus is on the implementation of inductively-loaded slow-wave transmission lines in microstrip technology, where the inductive effect is achieved by etching slots in the ground plane.

The work is organized as follows: in Section 2, the above mentioned analysis is carried out. Section 3 is focused on the design of a slow wave impedance inverter based on a slot-loaded microstrip line. In Section 4, such inverter is used for the implementation of a power splitter with reduced size. Finally, the main conclusions are highlighted in Section 5.

## 2. Analysis of capacitively and inductively loaded transmission lines

The schematics of the capacitively- and inductively-loaded lines under study are depicted in Figs. 1(a) and (b), respectively. The host line is described by the characteristic impedance, $Z_o$, and by the phase constant, $k$, and $l$ is the physical length of the unit cell. The shunt connected capacitances and series connected inductances are designated by $C_{ls}$ and $L_{sw}$, respectively. In these structures, the dispersion relation and the characteristic (or Bloch) impedance are different than the corresponding values in the host line, due to the presence of the reactive loads.

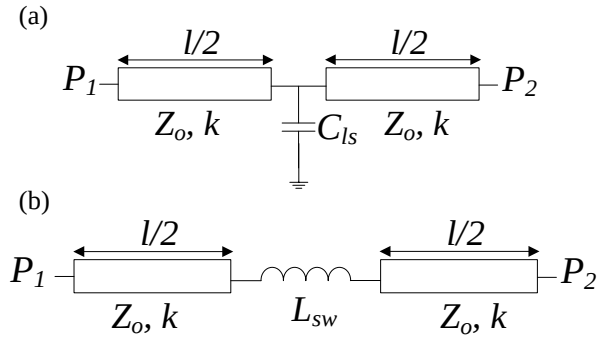



Figure 1: Schematic of the (a) capacitively- and (b) inductively-loaded line.

To obtain the dispersion relation and Bloch impedance, we consider the unit cell as composed of three cascaded sections, i.e., the reactive element cascaded between two transmission lines of length *l*/2. The transmission *ABCD* matrix of each section can be easily obtained [28], so that the transmission *ABCD* matrix of the whole unit cell is given by the product of the individual matrices. Once the transmission matrix is obtained, the dispersion relation and the Bloch impedance can be inferred from the *ABCD* matrix parameters by using well known formulas [3], that is:

$$\cos(\beta l) = A \tag{1}$$

$$Z_B = \frac{B}{\sqrt{A^2 - 1}} \tag{2}$$

where *A* and *B* are elements of the *ABCD* matrix, and the previous expressions correspond to a symmetric structure with *A* = *D*. Expression (1) is valid in the band pass regions and by considering that the structure is lossless (i.e., the attenuation constant $\alpha$ is zero in such regions). For the capacitively-loaded line, the dispersion and characteristic impedance are given by:

$$\cos(\beta l) = \cos(kl) - \frac{\omega C_{ls} Z_0}{2}\sin(kl) \tag{3}$$

$$Z_B = \frac{Z_o\left\{\sin(kl) - Z_o \omega C_{ls}\sin^2(kl/2)\right\}}{\sin(\beta l)} \tag{4}$$

whereas for the inductively-loaded lines the following results are derived:

$$\cos(\beta l) = \cos(kl) - \frac{\omega L_{sw}}{2Z_0}\sin(kl) \tag{5}$$

$$Z_B = \frac{Z_o \sin(kl) + \omega L_{sw}\cos^2(kl/2)}{\sin(\beta l)} \tag{6}$$

In the previous expressions, $\beta$ is the phase constant of the loaded line and $\omega$ is the angular frequency. An important parameter in these slow wave transmission lines is the slow-wave ratio, *swr*, defined as the ratio between the phase velocities of the loaded and unloaded lines. For both lines, it is given by

$$swr = \frac{v_p}{v_{po}} = \frac{\omega/\beta l}{\omega/kl} = \frac{kl}{\beta l} \tag{7}$$

and it determines the level of miniaturization of the considered artificial line.

Note that the equations providing the phase constant and the characteristic impedance are formally very similar for both types of reactively loaded lines. Inspection of equations (3)-(6) reveals that for finite values of $C_{ls}$ and $L_{sw}$, the phase constant of the unloaded line, *k*, is smaller than the phase constant of the loaded line, $\beta$, indicating that the phase velocity is smaller in the loaded line (slow-wave effect). The larger the values of $C_{ls}$ and $L_{sw}$ are, the smaller the slow wave ratio becomes. Hence, to achieve significant slow-wave effect and, as consequence, important size reduction (length) in these reactively-loaded artificial lines, the reactive element values must be large. To gain insight on this, let us calculate the *swr* for both types of lines in the low frequency limit (where $kl \to 0$ and $\beta l \to 0$). For the capacitively-loaded line, the dispersion relation in this limit can be expressed as:

$$1 - \frac{(\beta l)^2}{2} = 1 - \frac{(kl)^2}{2} - \frac{\omega C_{ls} Z_0}{2} kl \tag{8}$$

where the trigonometric functions have been approximated by their Taylor expansions. Since $kl = \omega Z_0 C$ (*C* being the line capacitance of the unit cell), expression (8) can be rewritten as

$$\beta l = kl\sqrt{1 + \frac{C_{ls}}{C}} \tag{9}$$

from which the slow wave ratio is found to be

$$swr = \frac{1}{\sqrt{1 + \frac{C_{ls}}{C}}} \tag{10}$$

and the necessary condition to achieve significant slow wave effect is $C_{ls} >> C$.

For the inductively-loaded line, *kl* can be expressed as $kl = \omega L/Z_0$, where *L* is the line inductance of the unit cell, and an analysis similar to the previous one gives

$$\beta l = kl\sqrt{1 + \frac{L_{sw}}{L}} \tag{11}$$

and

$$swr = \frac{1}{\sqrt{1 + \frac{L_{sw}}{L}}} \tag{12}$$

i.e., the condition $L_{sw} >> L$ suffices to achieve a significant reduction in the phase velocity of the inductively-loaded line.

The slow-wave capacitively-loaded lines can be implemented in microstrip technology by using square patches (Fig. 2a). These lines have been applied to the design of miniature components, such as power splitters [29] and filters [11],[26] including devices with spurious suppression. Inductively loaded lines have been implemented in coplanar waveguide (CPW) technology by symmetrically etching rectangular slots in the ground plane [30]. In this paper, we propose the implementation of slow-wave inductively-loaded lines in microstrip technology by etching inductive slots in the ground plane, as indicated in Fig. 2(b).

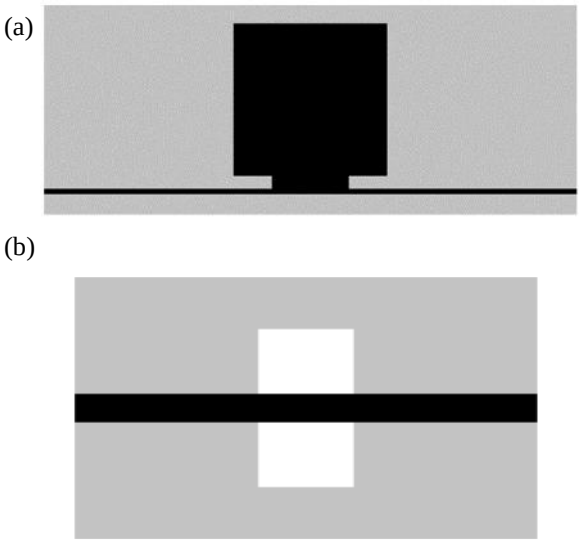



Figure 2: Typical topology (unit cell) of the capacitively (a) and inductively loaded microstip line (b). The upper metal level is indicated in black color, and the ground plane in grey color.

## 3. Design of a slow-wave impedance inverter

The design of an impedance inverter based on an inductively loaded microstrip line is reported in this section. The loading inductance is implemented by means of a radial slot etched in the ground plane. Since the inverter will be later used for the implementation of a power splitter, the impedance of the inverter is set to $K = 35.35\ \Omega$. The slow wave ratio is set to $swr = 0.5$, providing 50% length reduction, and the electrical length of the loaded line must be set to $\beta l = 90^o$, corresponding to the required phase of an inverter (the design frequency is set to $f_0 = 1$ GHz). In this particular application the focus is size reduction, rather than spurious suppression, and for this reason, the slow-wave impedance inverter is implemented by means of a single unit cell.

To achieve the previous line parameters and slow wave ratio, and by using equations (5)-(7), we have calculated the parameters of the host line and the value of the loading inductance. The inferred values are $kl = 45^o$, $Z_o = 14.64\ \Omega$ and $L_{sw} = 4.661$ nH. Then we have optimized the topology in order to obtain these line parameters at the layout level. The resulting layout of the inverter is depicted in Fig. 3(a), whereas the dispersion diagram and Bloch impedance are shown in Figs. 3(b) and (c), respectively (the *Rogers RO3010* substrate with thickness $h = 1.27$ mm and dielectric constant $\varepsilon_r = 10.2$ has been considered). It can be appreciated that the required values of phase ($90^o$) and Bloch impedance ($35.35\ \Omega$) at the design frequency (1 GHz), are obtained. Fig. 3(d) depicts de frequency response of the inverter by considering 35.35 Ω ports, where it can be appreciated that perfect matching occurs at 1GHz, indicative of the 35.35 Ω impedance at this frequency, as well.

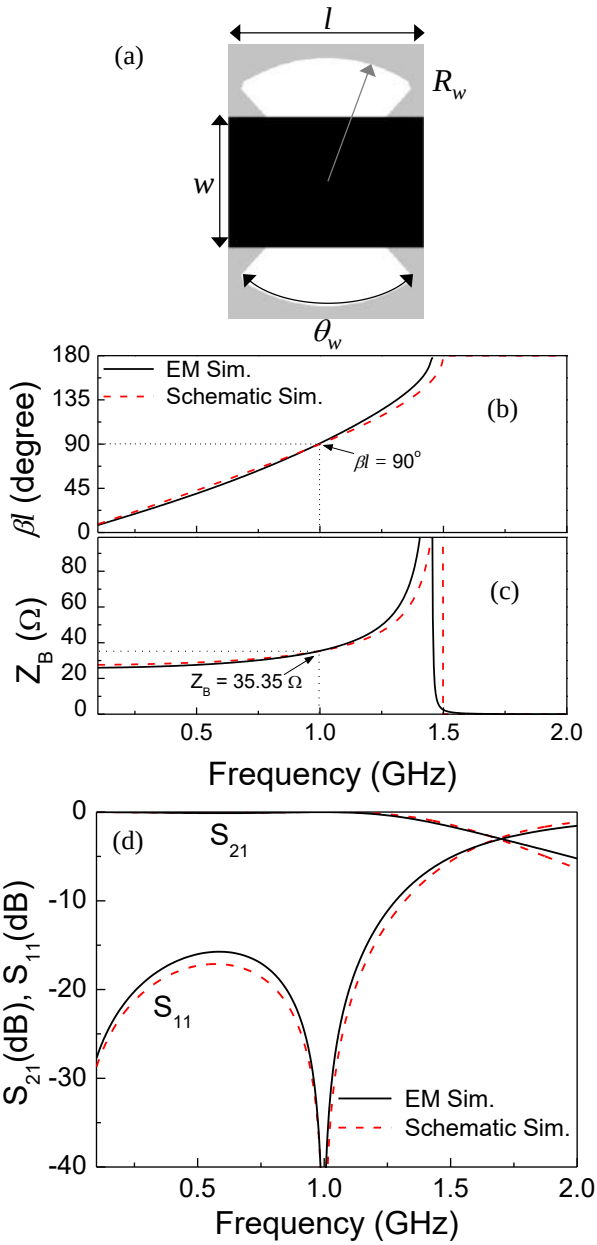



Figure 3: Topology of the designed impedance inverter (a), dispersion (b) Bloch impedance (c) and frequency response (d). Dimensions are: $l = 12.89$ mm, $w = 8.69$ mm, $R_w = 8.46$ mm, $\theta_w = 77^o$

## 4. Slow-wave power splitter

Once the topology has been optimized, the inverter has been fabricated by adding one 50 Ω access line to the input port and two 50 Ω access lines to the output port, resulting in a power splitter [28]. The photograph, compared to the one of the conventional splitter, and the responses of both devices are shown in Fig. 4. The functionality of the splitter is obtained, with good matching at the design frequency, and power splitting near 3dB (ideal value). However, the most important aspect is the fact that splitter length is roughly half the length of the conventional one, by virtue of the considered slow wave ratio.

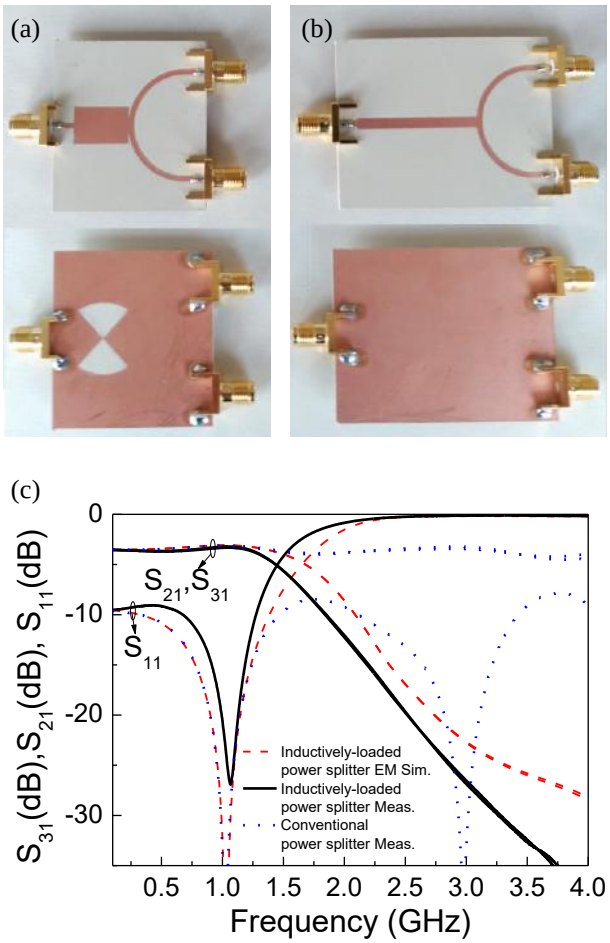



Figure 4: Photograph of the splitter based on inductive loading (a), conventional splitter (b) and frequency responses (c).

Additionally, due to the stop band effect of the loading inductance, the functionality at the first harmonic band of the splitter ($3f_0$ in the conventional implementation) is suppressed. The result is a power splitter with filtering capability, of interest in certain applications where size is a due. Even though the filtering functionality of the splitter was not the main focus of the paper, it is obvious that the stop band is intimately related to the response of the inverter [see Fig. 3(d)]. The dispersion relation (5) provides the pass band regions of the inverter (and hence the stop band regions). Nevertheless, it is possible to predict (estimate) the cutoff frequency by considering the simplified lumped element equivalent circuit model of the inductively loaded line, depicted in Fig. 5. In this model, $L$ and $C$ are the line inductance and capacitance, respectively. This model is valid as long as $L_{sw} >> L$. In our case, this condition is satisfied to a reasonable approximation, provided $L_{sw} = 3L$, as it follows from the considered *swr*. In the $\pi$-model of Fig. 5, the dispersion relation, derived from (1), can be expressed in terms of the series, $Z_s$, and shunt impedance, $Z_p$, as

$$\cos(\beta l) = 1 + \frac{Z_s}{Z_p} \tag{13}$$

This gives

$$\cos(\beta l) = 1 - \frac{(L + L_{sw})C\omega^2}{2} \tag{14}$$

and the cutoff frequency, given by the first frequency providing a purely imaginary value of $\beta$ is found to be

$$f_c = \frac{1}{\pi\sqrt{C(L + L_{sw})}} \tag{15}$$

From the considered *swr* (0.5), and characteristic impedance of the unloaded line (14.64Ω), and taking into account that $L_{sw}$ = 4.661 nH, the element values of the circuit of Fig. 5 are found to be $C$ = 7.23 pF, $L$ = 1.55 nH. Introducing these values in (15) provides a cutoff frequency of $f_c$ = 1.51GHz, in agreement to Fig. 3(d) and 4.

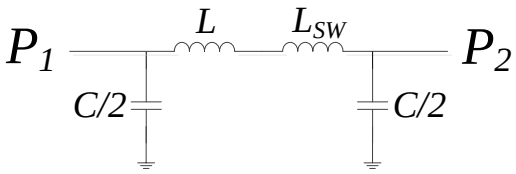



Figure 5: Lumped element equivalent circuit model of the inductively-loaded line unit cell.

## 5. Conclusions

In summary, slow-wave transmission lines based on inductive loading, and implemented by etching inductive slots in the ground plane of a microstrip line, are useful for the implementation of compact devices. In particular, a power splitter based on a slow-wave 35.35 Ω impedance inverter has been reported in this work. The performance is comparable to the one of the ordinary splitter, whereas reduction in length by a factor of two has been demonstrated. Moreover, the splitter provides filtering functionality, so that a compact multi-functional device (splitter/filter) is obtained.

## Acknowledgements

This work was supported by MINECO-Spain (projects TEC2013-40600-R and TEC2013-49221-EXP), Generalitat de Catalunya (project 2014SGR-157), Institució Catalana de Recerca i Estudis Avançats (who awarded Ferran Martín), and by FEDER funds.

## References

[1] J. García-García, F. Martín, F. Falcone, J. Bonache, I. Gil, T. Lopetegi, M.A.G. Laso, M. Sorolla, R. Marqués, "Spurious passband suppression in microstrip coupled line band pass filters by means of split ring resonators", *IEEE Microwave and Wireless Components Letters*, vol. 14, pp. 416-418, September 2004.

[2] J. García-García, F. Martín, F. Falcone, J. Bonache, J.D. Baena, I. Gil, E. Amat, T. Lopetegi, Miguel A.G. Laso, J. A. Marcotegui-Iturmendi, M. Sorolla, and R. Marqués, "Microwave Filters with Improved Stop Band

based on Sub-wavelength Resonators", *IEEE Transactions on Microwave Theory and Techniques*, vol. 53, pp. 1997-2006, June 2005.

[3] F. Martin, *Artificial Transmission Lines for RF and Microwave Applications*, John Wiley, Hoboken, NJ, 2015.

[4] T. Lopetegi, M.A.G. Laso, J. Hernández, M. Bacaicoa, D. Benito, M.J. Garde, M. Sorolla and M. Guglielmi, "New microstrip wiggly-line filters with spurious passband suppression", *IEEE Trans. Microw. Theory Tech.*, vol. 49, pp 1593-1598, 2001.

[5] T. Lopetegi, M.A.G. Laso, F. Falcone, F. Martín, J. Bonache, L. Pérez-Cuevas, M. Sorolla, "Microstrip wiggly line band pass filters with multispurious rejection", *IEEE Microw. Wireless Compon. Lett*., vol. 14, pp.531-533, 2004.

[6] E. Yablonovitch, "Photonic band gap structures", *J. Opt. Soc. Amer. B* 10, pp. 283-295, 1993.

[7] J. D. Joannopoulos, R. D. Meade, and J. N. Winn, *Photonic Crystals: Molding the Flow of Light*, Princeton University Press, Princeton, NJ, 1995.

[8] A. Görür, "A novel coplanar slow-wave structure," *IEEE Microw. Guided Wave Lett*., vol. 4, pp. 86–88, 1994.

[9] A. Görür, C. Karpuz and M. Alkan, "Characteristics of periodically loaded CPW structures", *IEEE Microw. Guided Wave Lett*., vol. 8, pp. 278-280, 1998.

[10] F. Martín, J. Bonache, I. Gil, F. Falcone, T. Lopetegi, M. A. G,. Laso and M. Sorolla, "Compact spurious free CPW band pass filters based on electromagnetic bandgap structures", *Microw. Opt. Techn. Lett*, vol. 40, pp. 146-148, 2004.

[11] J. García-García J. Bonache and F. Martín, "Application of electromagnetic bandgaps (EBGs) to the design of ultra wide band pass filters (UWBPFs) with good out-of-band performance", *IEEE Trans. Microw. Theory Tech*., vol. 54, pp. 4136-4140, 2006.

[12] F. Martín, F. Falcone, J. Bonache, T. Lopetegi, M.A.G. Laso, M. Sorolla, "New periodic-loaded electromagnetic bandgap coplanar waveguide with complete spurious passband suppression", *IEEE Microw. Wireless Compon. Lett*., vol. 12, pp. 435-437, 2002.

[13] F. Martín, F. Falcone, J. Bonache, T. Lopetegi, M. A. G. Laso, M. Sorolla, "Analysis of the reflection properties in electromagnetic bandgap coplanar waveguides loaded with reactive elements", *Prog. Electromag. Research, PIER*, vol. 42, pp. 27-48, 2003.

[14] F. Martín, F. Falcone, J. Bonache, M.A.G. Laso, T. Lopetegi, M. Sorolla, "New CPW low pass filter based on a slow wave structure", *Microw. Opt. Techn. Lett*., vol. 38, pp. 190-193, 2003.

[15] F. Martín, F. Falcone, J. Bonache, M. A. G. Laso, T. Lopetegi, M. Sorolla, "Dual electromagnetic bandgap CPW structures for filter applications", *IEEE Microw. Wireless Compon. Lett.*, vol. 13, pp. 393-395, 2003.

[16] K. W. Eccleston and S.H.M. Ong, "Compact planar microstripline branch-line and rat-race couplers", *IEEE Trans. Microw. Theory Tech*., vol. 51, pp 2119-2125, 2003.

[17] L. Zhu, "Guided-wave characteristics of periodic microstrip lines with inductive loading: slow-wave and bandstop behaviors", *Microw. Opt. Techn. Lett*., vol. 41, pp. 77-79, 2004.

[18] F.-R. Yang, K-P. Ma, Y. Qian, and T. Itoh, "A uniplanar compact photonic-bandgap (UC-PBG) structure and its applications for microwave circuits", *IEEE Trans. Microw. Theory Tech*., vol. 47, pp. 1509-1514, 1999.

[19] J. Sor, Y. Qian, and T. Itoh, "Miniature low-loss CPW periodic structures for filter applications", *IEEE Trans. Microw. Theory Tech.*, vol. 49, pp. 2336-2341, 2001.

[20] D. Nesic, "A new type of slow-wave 1-D PBG microstrip structure without etching in the ground plane for filter and other applications", *Microw. Opt. Techn. Lett.*, vol. 33, pp. 440-443, 2002.

[21] S-G. Mao, M-Y. Chen, "A novel periodic electromagnetic bandgap structure for finite-width conductor-backed coplanar waveguides", *IEEE Microw. Wireless Compon. Lett*., vol. 11, pp. 261-263, 2001.

[22] S-G. Mao, C-M. Chen, and D-C. Chang, "Modeling of slow-wave EBG structure for printed-bowtie antenna array", *IEEE Ant. Wireless Propag. Lett*., vol. 1, pp. 124-127, 2002.

[23] J. G. Lee, W. S. Lee, J. J. Ryu, Y. K. Moon, J. H. Jang, H. C. Kim, and H. C. Choi, "Compact semilumped bandstop resonators using the capacitively loaded parallel coupled microstrip line", *Microw. Opt. Techn. Lett.*, vol. 49, pp. 367-369, Feb. 2007.

[24] L. Li, F. Xu, K. Wu, S. Delprat, J. Ho, and M. Chaker, "Slow-wave line coupler with interdigital capacitor loading", *IEEE Trans. Microw. Theory Techn*., vol. 55, no. 11, pp. 2427-2433, Nov. 2007.

[25] C. I. Shie, J. C. Cheng, S. C. Chou, and Y. C. Chiang, "Transdirectional coupled-line couplers implemented by periodical shunt capacitors", *IEEE Trans. Microw. Theory Techn.*, vol. 57, no 12, pp. 2981-2988, Dec. 2009.

[26] J. Selga, P. Vélez, M. Orellana, A. Rodríguez, V. Boria, F. Martín, "Size reduction and spurious suppression in microstrip coupled line bandpass filters by means of capacitive electromagnetic bandgaps", *IEEE MTT-S Int. Microw. Symp.* (IMS'16), San Francisco, May 2016.

[27] H. M. Liu, S. J. Fang, Z. B. Wang, and Y. Zhou, "Miniaturization of trans-directional coupled line couplers using series inductors", *Prog. Electromagn. Res. C*, vol. 46, pp. 171-177, 2014.

[28] D. M. Pozar, *Microwave Engineering*, Addison Wesley, 1990.

[29] J. Selga, P. Vélez, F. Martín, "Reactively-Loaded EBG-Based Transmission Lines and Application to Power Splitters", *10th International Congress on Advanced*

*Electromagnetic Materials in Microwaves and Optics* (*Metamaterials* 2016), Creete, 17-22 September 2016.

[30] P. Vélez, J. Selga, J. Bonache and F. Martín, "Slow-wave inductively-loaded electromagnetic bandgap (EBG) coplanar waveguide (CPW) transmission lines and application to compact power dividers", *European Microw. Conf.* (EuMC'16), London (UK), 3-7 October 2016.

# Multi-Band CRLH Loaded Patch Antenna

**Sally I. El-Henawy[1], Ahmed A. Omar[2], Amr M. E. Safwat[1], and Hadia S. El-Hennawy[1]**

[1]Electronics and communication Eng. Department Faculty of Engineering,
Ain Shams University Cairo, Egypt
[2]School of Electrical & Electronic Engineering Nanyang Technological University
50 Nanyang Avenue, Singapore
*corresponding author, E-mail: sally.elhenawy@eng.asu.edu.eg

## Abstract

A multi-band patch antenna loaded with Composite Right/Left-Handed (CRLH) unit cell is presented in this paper. It operates at three bands, which are not harmonically related, covering several communication standards. The first and third bands have patch like radiation pattern, the second band has monopole like radiation pattern. These bands can be controlled by varying the patch size and unit cell elements values. The performance was analyzed using both electromagnetic and circuit simulations furthermore measurements were carried out and all were in good agreement.

## 1. Introduction

With the vast development in wireless communications, modern communication systems and devices are urged to support more than one communication scheme each having its own frequency band. Accordingly, the need for small size integrated antennas with low profile that can cover multi-band has arisen. To accomplish multi-band antenna design, several design methodologies are used among which are; beginning with a broadband antenna and notching some bands by introducing slots to create multi-band antenna [1]. Another method is to load antenna with metamaterial unit cells, this method can be used with dipole antenna [2], monopole antenna [3-4], slot antenna [5], loop antenna [6-8] and with patch antenna [9-11].

In this paper CRLH unit cell is used to load a patch antenna to provide multi-band operation. It has three operating bands that support WLAN, Wi-Fi and WiMax bands. The antenna design and circuit model are provided in section 2, the simulations results and the measurements are presented in section 3 and finally a conclusion is given in section 4.

## 2. Antenna Design

### 2.1. Antenna Design and Circuit Model

A coaxially fed square patch antenna is designed to resonate around 3.6 GHz [12] on Rogers 5870 with substrate thickness of 1.57mm, metal thickness of 35 μm and dielectric constant (εr) of 2.33. The patch is loaded with balanced CRLH unit cell as shown in Fig. 1, where the resonance of the series arm equals that of the shunt arm, with the balanced frequency equals to the patch resonance frequency. Moreover, the π-network for the unit cell is used rather that the T-network for enhancing the unit cell inductance. Also, the unit cell is set to be symmetric so that even if any radiation occurs from it then, the radiation from both the left and right sides will cancel out accordingly, the radiation pattern will controlled mainly the antenna and the effect of the unit cell is minimal. All dimensions and lumped elements values are given in Table 1.

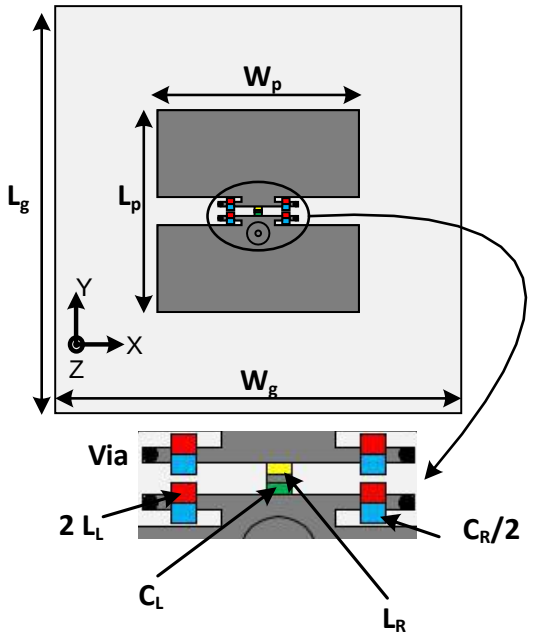



Figure 1: Proposed patch antenna loaded with CRLH unit cell.

The unit cell simple equivalent circuit is shown in Fig. 2 (a). However, there is a parasitic inductor introduced due to the step discontinuity between the patch and the unit cell input and output ports, so the unit cell equivalent circuit is modified to be as shown in Fig. 2(b).

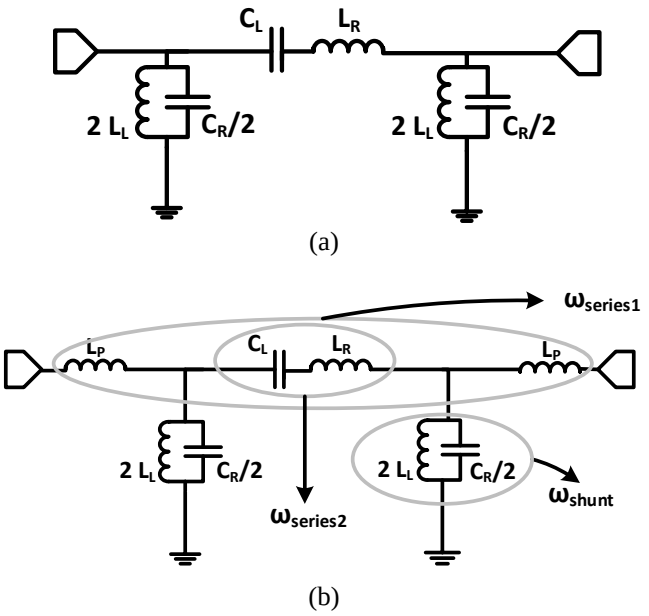



Figure 2: Circuit model for the CRLH unit cell (a) conventional model, (b) modified model.

Table 1: Dimensions of the proposed antenna and values of the lumped elements.

| symbol | Dimensions[mm] | Symbol | Value |
|---|---|---|---|
| $L_g$ | 55 | $C_L$ | 0.4 pF |
| $W_g$ | 55 | $L_L$ | 1.8 nH |
| $L_P$ | 26.75 | $C_R$ | 1.1 pF |
| $W_P$ | 26.75 | $L_R$ | 2.2 nH |

### 2.2. Theory of Operation

As shown in Fig. 3 the loaded patch generates three bands. The first band occurs when both the shunt arm and the total series arm are at resonance and it is equal to the resonance frequency of the microstrip patch antenna. The total series arm resonance $\omega_{series1}$ is defined in (1), where $L_{series}$ is the total series inductance and given in (3), whilst the shunt arm resonance $\omega_{shunt}$ is defined in (2). Being at resonance, the series and shunt arms act as short and open circuit respectively, accordingly the equivalent circuit become as shown in Fig. 4(a) with the current flow indicated by the red arrow. The whole structure, the antenna and the unit cell, will generate λ/ 2 resonance of the patch.

The second resonance band is above $\omega_{shunt}$, so the shunt arm will be capacitive more than inductive, furthermore the series arm consisting of $L_R$ and $C_L$ will be at resonance acting as a short circuit where $\omega_{series2}$ is defined in (4). The equivalent circuit will be as indicated in Fig. 4(b) where the current flow is indicated by the red arrow. In this band the patch is loaded with series parasitic inductor $L_P$ and a shunt capacitor to the ground $C_R$, this capacitor will behave as a series inductor loading the antenna as noted in [13]. So a λ resonance of the patch is generated.

Third band is above $\omega_{series2}$, so series arm will be open circuit and the shunt arm will be more capacitive so the equivalent circuit will be as shown is Fig. 4(c), such that the red arrows indicate the current flow. Here the patch is loaded with series capacitor, as the capacitor makes the patch look shorter so it generates λ/2 resonance of the patch.

$$\omega_{series1} = \frac{1}{\sqrt{L_{series} C_L}} \quad (1)$$

$$\omega_{shunt} = \frac{1}{\sqrt{L_L C_R}} \quad (2)$$

$$L_{series} = (2 \times L_P) + L_R \quad (3)$$

$$\omega_{series2} = \frac{1}{\sqrt{L_R C_L}} \quad (4)$$

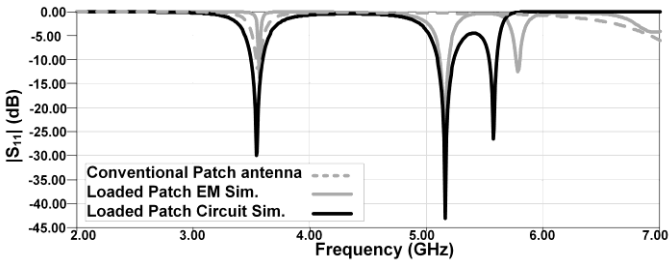



Figure 3: Simulated $|S_{11}|$ for the conventional patch and patch loaded with the balanced CRLH unit cell.

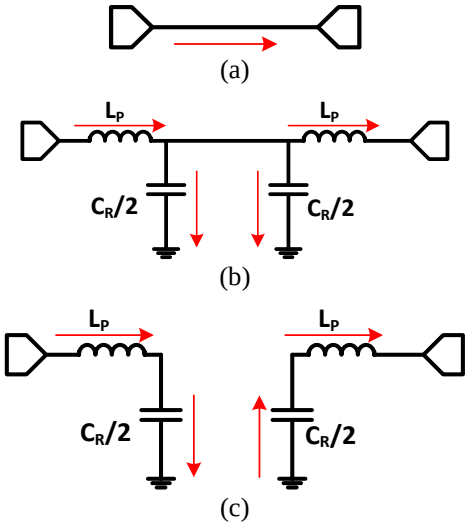



Figure 4: Equivalent Circuit model for (a) First band "3.57 GHz", (b) second band "5.17 GHz" and (c) third band "5.85 GHZ", red arrows indicate current flow path.

## 3. Simulations and Experimental Verifications

A prototype for the proposed antenna with the above stated dimensions and lumped elements values is fabricated, Fig. 5(a). Simulated reflection coefficient, circuit and EM simulations, is shown in Fig. 3. There is little difference between circuit and full wave simulations due to some

parasitic in full wave simulation which are not captured by equivalent circuit simulation. Moreover the measured reflection coefficient is shown in Fig. 5(b), $S_{11}$ was measured using Anritsu MS4647A vector network analyzer (70 GHz).

Figure 6 shows simulated vector current flow at the three bands, which proof our analysis for the way current flows in the previous section.

Simulated and measured radiation patterns for the three operating bands are shown in Fig. 7. All antenna simulations are carried out on ANSYS HFSS V.15 and Designer V.8. While radiation pattern measurements were carried out in the anechoic chamber at the Microwave and Antenna Research Lab. At Faculty of Engineering, Ain Shams University.

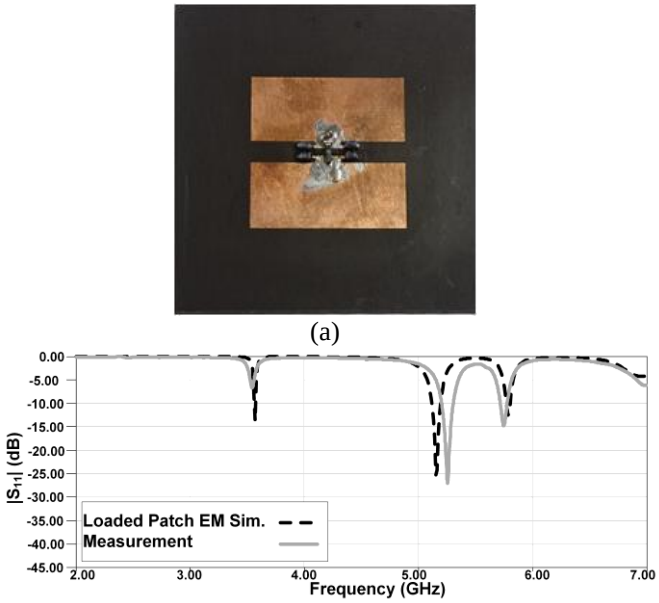



Figure 5: (a) Fabricated patch antenna, (b) simulated and measured $|S_{11}|$ for the proposed antenna.

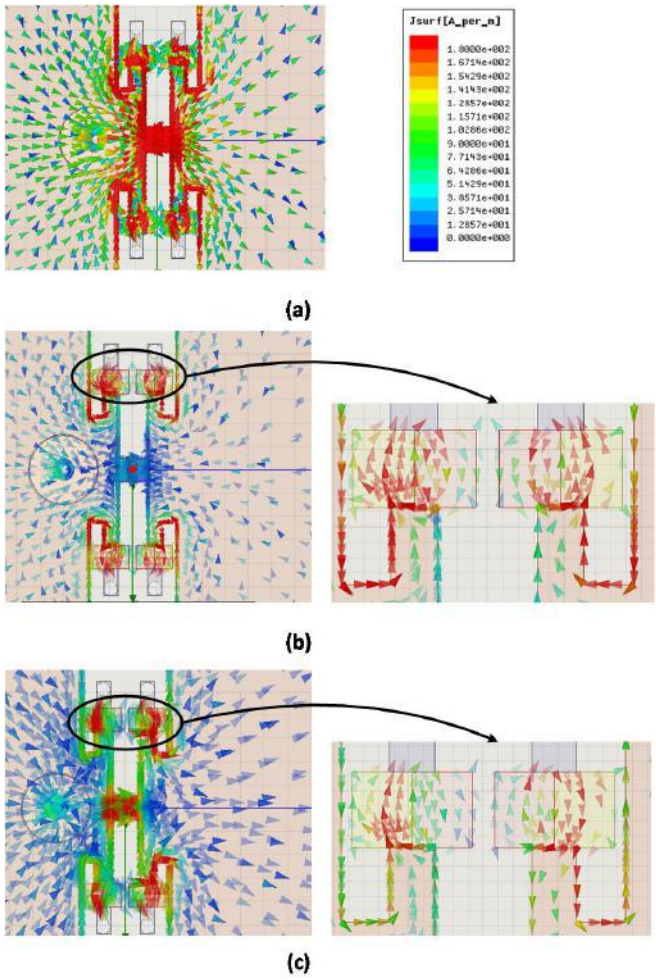


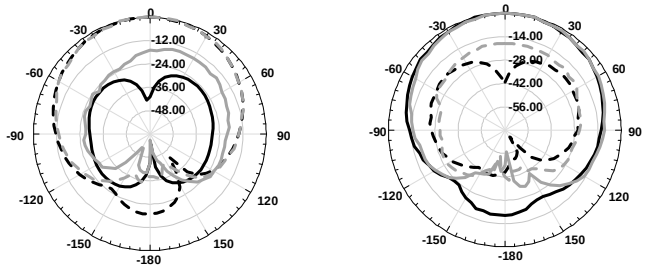

Figure 6: Current density plot on the unit cell for (a) 3.57 GHz, (b) 5.17 GHz and (c) 5.85GHz.

## 4. Conclusions

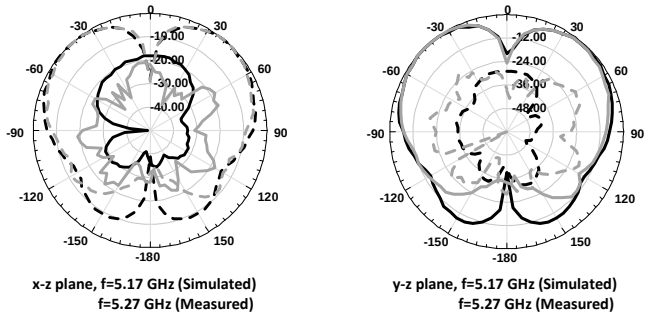
A multi-band patch antenna loaded with CRLH unit cell was proposed. A circuit model was provided that analyzed the antenna behavior. Circuit analysis, simulation results as well as measurements are in good agreement. The operating bands of the antennas can be determined by the values of the lumped elements as well as the antenna dimensions.


## Acknowledgements

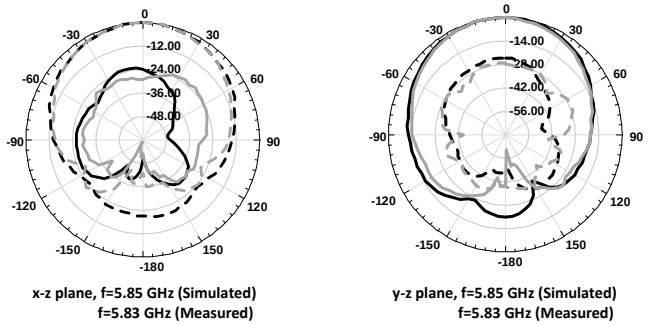
This project was supported financially by the Science and Technology Development Fund (STDF), Egypt, Grant No. 14933.




(a)




(b)




(c)

Figure 7: Simulated Radiation pattern for Y-Z plane at (a) 3.6 GHz, (b) 5.2 GHz and (c) 5.8GHz, with solid lines for $E_\theta$ and dashed lines for $E_\varphi$ (Simulation is plotted in black lines while measurements in gray lines).

## References


[1] W. S. Lee, D. Z. Kim, K. J. Kim and J. W. Yu, "Wideband planar monopole antennas with dual band-notched characteristics," IEEE Trans. Microwave Theory Tech., vol. 54, no. 6, pp. 2800-2806, June 2006.

[2] H. Iizuk and P. S. Hall, "Left-handed dipole antennas and their implementations," IEEE Trans. Antennas Propag., vol. 55, no. 5, pp. 1246–1253, May 2007.

[3] A. A. Ibrahim, A. M. E. Safwat and H. El-Hennawy, "Triple-band microstrip-fed monopole antenna loaded with CRLH unit cell," IEEE Antennas and Wireless Propag. Letters, vol.10, pp.1547-1550, 2011.

[4] Amr A. Ibrahim, and Amr M. E. Safwat, "Microstrip-fed monopole antennas loaded with CRLH unit cells," IEEE Trans. Antennas Propag., vol. 60, no. 9, pp. 4027–4036, Sept. 2012.

[5] P. B. Nesbitt and G. Mumcu, "A small slot dipole loaded with CRLH TL unit cells," IEEE AP-S Int. Symp. Dig., Jul. 2011, pp. 1032–1035.

[6] C. Caloz and T. Itoh, Electromagnetic Metamaterials: Transmission Line Theory and Microwave Applications. Hoboken, NJ: Wiley Interscience, 2006.

[7] Ahmed R. Raslan, Amr A. Ibrahim, and Amr M. E. Safwat, "Resonant type antennas loaded with CRLH unit cell," IEEE Antennas and Wireless Propag. Letters. vol.12, pp. 23 - 26, 2013.

[8] M. I. Ibrahim, S. I. El-Henawy, and A. M. E. Safwat, "Dual-band orthogonal-beam multi-standard CRLH loop antenna," in Proc 42nd EuMC, Nuremberg, Germany, Oct. 2013, pp. 1063–1066.

[9] C.-J. Lee,K.M.K.H. Leong, and T. Itoh, "Composite right/left-handed transmission line based compact resonant antennas for RF module integration," IEEE Trans. Antennas Propag., vol. 54, no. 8, pp. 2283–2291, Aug. 2006.

[10] F. J. Herraiz-Martínez, V. González-Posadas, L. García-Muñoz, and D. Segovia-Vargas, "Multi-frequency and dual-mode antennas partially filled with left-handed structures," IEEE Trans. Antennas Propag., vol. 56, no. 8, pp. 2527–2539, Aug. 2008.

[11] M. Schüßler, J. Freese, and R. Jakoby, "Design of compact planar antennas using LH transmission lines," inProc. IEEEMTT-S Int. Microw. Symp., Jun. 2004, vol. 1, pp. 209–212.

[12] C. A. Balanis, Antenna theory: Analysis and design, 3rd ed., NJ: Wiley, 2005.

[13] J. Oh, and K. Sarabandi. "Low profile vertically polarized omnidirectional wideband antenna with capacitively coupled parasitic elements," IEEE Trans. Antennas Propag., vol. 62, no. 2, pp977-982, Feb. 2014.

# Bandwidth Enhancement of Multilayer Polymeric Comb Array Antenna for Millimeter Wave Applications

**W.A.W. Muhamad[1], R. Ngah[2], M. F. Jamlos[3,4], P.J. Soh[5], M.T.Ali[6]**

[1,2]Wireless Communication Centre (WCC), Universiti Teknologi Malaysia, Skudai, Johor, Malaysia
[3,5]Advanced Communication Engineering Centre (ACE), School of Computer and Communication Engineering, Universiti Malaysia Perlis, Perlis, Malaysia.
[4]Faculty of Mechanical Engineering, Universiti Malaysia Pahang (UMP), Pekan, Malaysia.
[6]Antenna Research Centre (ARC), Microwave Technology Centre (MTC), Faculty of Electrical Eng. (FKE), UiTM Shah Alam.
[1]gongchan_89@yahoo.com

## Abstract

A new multilayer polymeric comb array antenna is presented. The multilayer substrates of Polydimethylsiloxane (PDMS) and Rogers produced an increment bandwidth of 5.118 GHz compared to 0.608 GHz, which is non-polymeric antenna. Multilayer substrate, comb array structure and PDMS's epsilon of 2.7 contributing to such bandwidth ranging from 22.649 until 27.792 GHz and gain of 9.856 dB at 25 GHz resonance. Moreover, dimension of 33x27 $mm^2$ is considered compact in size.

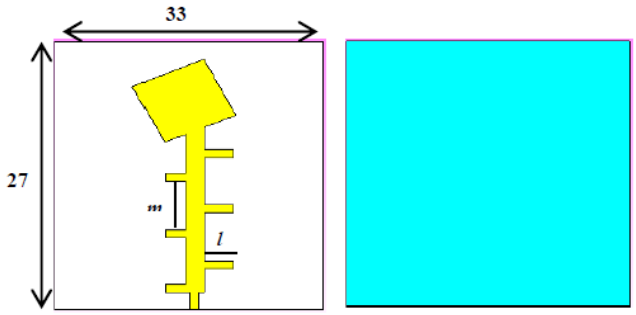
## 1. Introduction

Nowadays, millimeter-wave communications have been greatly attention as a new technology in high frequency range with a demand of high data rate capacity [1]. Microstrip is one of good option as millimeter wave's antenna due to its interesting characteristics such as low profile and simple structure [2]. In order to enhance the data rate and broad bandwidth, material of dielectric substrate plays the significant role. For this concern, this paper presents a new combination of meta-material substrate; Polydimethylsiloxane (PDMS) with a compact microstrip comb array antenna.

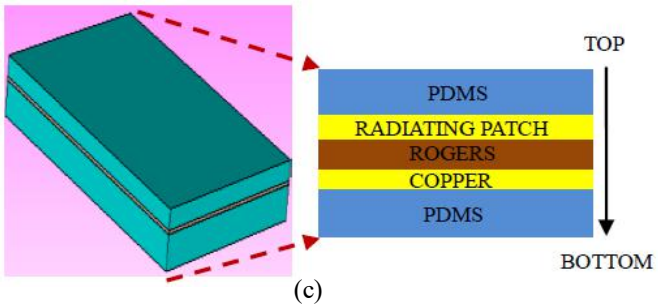
PDMS is a new dielectric substrate which is consisted of silicone based elastomer and suitable for higher frequency up to terahertz [3]. The low epsilon of PDMS substrate which is 2.7 lead to bandwidth enhancement. This is due to the polarization effects theory. A low epsilon will gives more electric flux generated per unit charge and minor energy trapping inside the substrate. Therefore, it is ease to radiation move to free space and enhanced the performance of antenna.

## 2. Antenna Design

In this paper, the multilayer of PDMS with Rogers is designed with a compact size of 27x33 $mm^2$ for the width and length respectively as shown in Figure 1(a) while full ground plane depicted by Figure 1(b). The proposed multilayer antenna is consists of five layers as demonstrated in Figure 1 (c). An array structure of comb antenna is arranged in zig-zag with main radiating element inclined by -45 degrees. The length, $\boldsymbol{l}$ of each array is based on formula $\boldsymbol{l} = \lambda_g$ and the spacing between each array is $m = \lambda_g/2$ where $\lambda_g$ is the guided wavelength at the center frequency [4].




(a) (b)

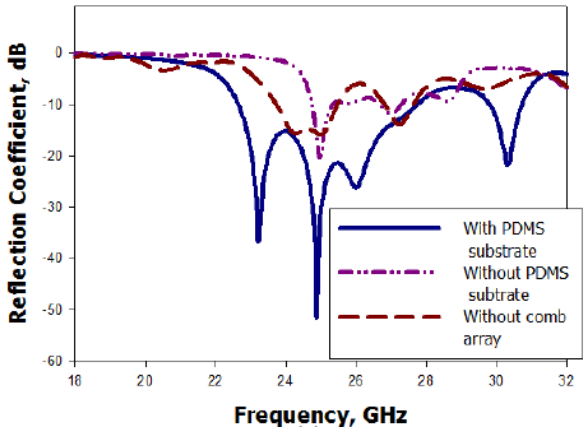



(c)

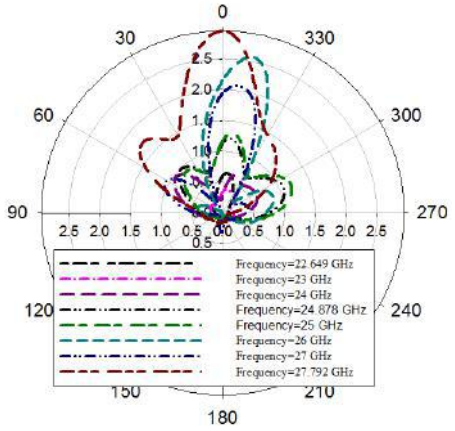
Figure 1. The multilayer polymeric comb array antenna (a) front view (b) back view and (c) perspective view.

## 3. Results and Discussion

Figure 2(a) shows the comparison of reflection coefficient, S11 of Rogers substrate with (in blue line) and without (in purple line) PDMS. It is observed that the combination of PDMS with Rogers substrate produced more bandwidth which is up to 5.118 GHz compared to only 0.608 GHz (without PDMS). This is due to the low epsilon of 2.7. Comparison of multilayer polymeric antenna without comb array is analyzed as well. It is found out that the comb array antenna (in blue line) is better than without comb array (in red line) in term of bandwidth. The polar radiation pattern is illustrated in Figure 2(b) subject to the varieties of frequency ranging from 22.649 GHz until 27.792 GHz. The highest gain of 9.856 dB is recorded at 25 GHz.




(a)




(b)

Figure 2. (a) Reflection coefficient and (b) polar radiation pattern for multilayer polymeric comb array antenna.

## 4. Conclusion

As conclusion, the new combination of polymeric comb array antenna generates good bandwidth and high gain as well as compactness of size for millimetre wave applications.

## Acknowledgements

The authors acknowledge the contribution of Universiti Teknologi Malaysia, Skudai, Johor (UTM) and Universiti Malaysia Perlis, Kangar, Perlis (UniMAP). Our gratitude also goes to grant of FRGS MOHE 9003-00522.

## References

[1] Daniel Sanchez-Escuderos, Miguel Ferrando-Bataller, Jose I. Herranz, and Marta Cabedo-Fabres, "Periodic Leaky-Wave Antenna on Planar Goubau Line at Millimeter-Wave Frequencies, " *IEEE Antennas and Wireless Propagation Letters,*2013.

[2] A. Pirhadi, G. A. Jafarabadi, " Design of Modified Microstrip Combline Design of Modified Microstrip Combline, " *Progress In Electromagnetics Research Letters*, Vol.14, 31-40, 2010.

[3] Zheng Xu, Xiaodai Dong, and Jens Bornemann, "Design of a Reconfigurable MIMO System for THz Communications Based on Graphene Antennas," *IEEE Transaction on Terahertz Science and Technology,* Vol. 4, No. 5, September 2014.

[4] Lin Zhang, Wenmei Zhang, and Y. P. Zhang, "Microstrip Grid and Comb Array Antennas," *IEEE Transactions on Antennas and Propagation,* VoL. 59, No. 11, November 2011.

# High Gain Polydimethylsiloxane-Glass Microsphere (PDMS-GM) Antenna for 5G Applications

**W.A.W. Muhamad[1], R. Ngah[2], M. F. Jamlos[3,4], P.J. Soh[5], , M.T.Ali[6]**
[1,2]Wireless Communication Centre (WCC), Universiti Teknologi Malaysia, Skudai, Johor, Malaysia
[3,5]Advanced Communication Engineering Centre (ACE), School of Computer and Communication Engineering, Universiti Malaysia Perlis, Perlis, Malaysia.
[4]Faculty of Mechanical Engineering, Universiti Malaysia Pahang (UMP), Pekan, Malaysia.
[6]Antenna Research Centre (ARC), Microwave Technology Centre (MTC), Faculty of Electrical Eng. (FKE), UiTM Shah Alam.
[1]gongchan_89@yahoo.com

## Abstract

A new synthesization meta-material of Polydimethylsiloxane (PDMS) and glass microsphere substrate is presented. The PDMS-glass microsphere (PDMS-GM) offered a lower permittivity of 1.85 than PDMS without glass microsphere, 2.7 of permittivity. The proposed PDMS-GM antenna contributed a broad bandwidth of more than 50 GHz and boosts the gain up to 13.3 dB compared to PDMS without glass microsphere which is only 5.5 dB. Therefore, the PDMS-GM antenna is highly recommended to be deployed for the fifth generation Wireless Systems.

## 1. Introduction

Wireless communication's era has become trendier in last few years due to revolution and evolution from the first generation (1G) up to fourth generation (4G). However, the currently trendy is more towards to fifth generation (5G). In designing 5G antenna, substrate's material is playing an important factors to get a good result. From the literature review on variety of substrate's material such as in [1] by Alina et. al. The author is presented a Composite Right/Left Handed (CRLH) antenna operating at 28 GHz using silicone dielectric substrate and its gain is only 2.99 dBi. Another work on LTCC substrate using a 2x2 stacked patch antenna array attained a realized gain of 10.35 dBi [2]. It is observed that those antenna structures are complex and complicated in fabrication process. Therefore, this paper proposes a new composite meta-material of Polydimethylsiloxane and glass microsphere (PDMS-GM) with a low epsilon of 1.85.

## 2. PDMS-GM Antenna Design

The PDMS-GM antenna is designed with a dimension of (50x40)mm2 for the width and length respectively as shown in Figure 1(a). Moreover, the proposed antenna has a low permittivity of 1.85 with loss tangent of 0.014 compared to the PDMS without glass microsphere which is 2.7 of permittivity with loss tangent of 0.022. The proposed antenna is contained of six layers where radiating patch and Rogers substrate is immersed in PDMS-GM substrate as illustrated in Figure 1(b). The thickness of dielectric substrate is 8.18 mm which is quite thick but the characteristic of PDMS-GM which is light weight give an advantage to prevent from having a weighty antenna.

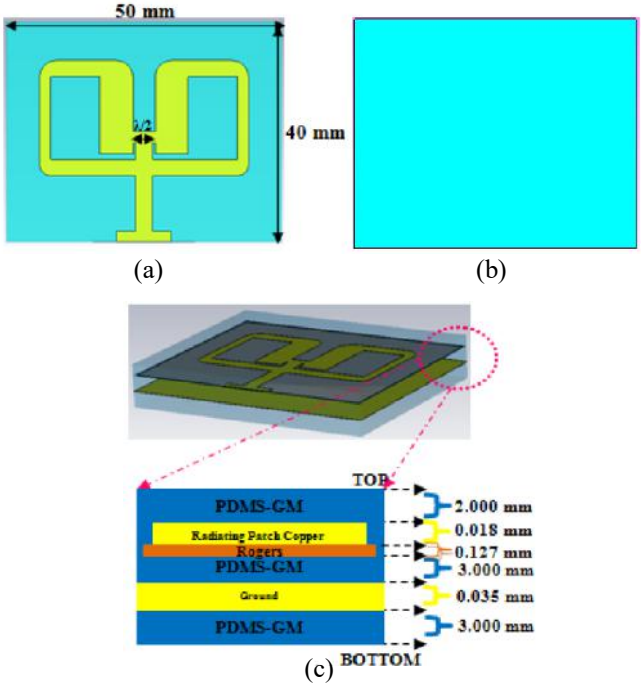



Figure 1. The Polydimethylsiloxane Glass microsphere (PDMS-GM) antenna (a) front view (b) back view and (c) perspective view.

## 3. Results and Discussion

Figure 2(a) shows the comparison reflection coefficient, S11 of with and without PDMS-GM substrate. From the observation, the bandwidth of with and without PDMS-GM is comparable due to the equivalent of homogeneous dielectrics [3] starting from the frequency 25.37 GHz up to

more than 75 GHz. The comparison of gain values between antenna with and without PDMS-GM is illustrated in Figure 2(b). The authors choose randomly several frequencies starting from 18 GHz, 28 GHz 38 GHz, 48 GHz and 58 GHz. From the observation, it shows that the gain of PDMS-GM substrate is higher than without PDMS-GM substrate. The highest gain recorded for PDMS-GM substrate is 13.3 dB at operating frequency of 28 GHz compared only 5.5 dB, gain without PDMS-GM substrate. Figure 2(c) is represented the simulation of polar radiation pattern for PDMS-GM antenna at chosen frequency which are 18 GHz, 28 GHz, 38 GHz, 48 GHz, and 58 GHz.

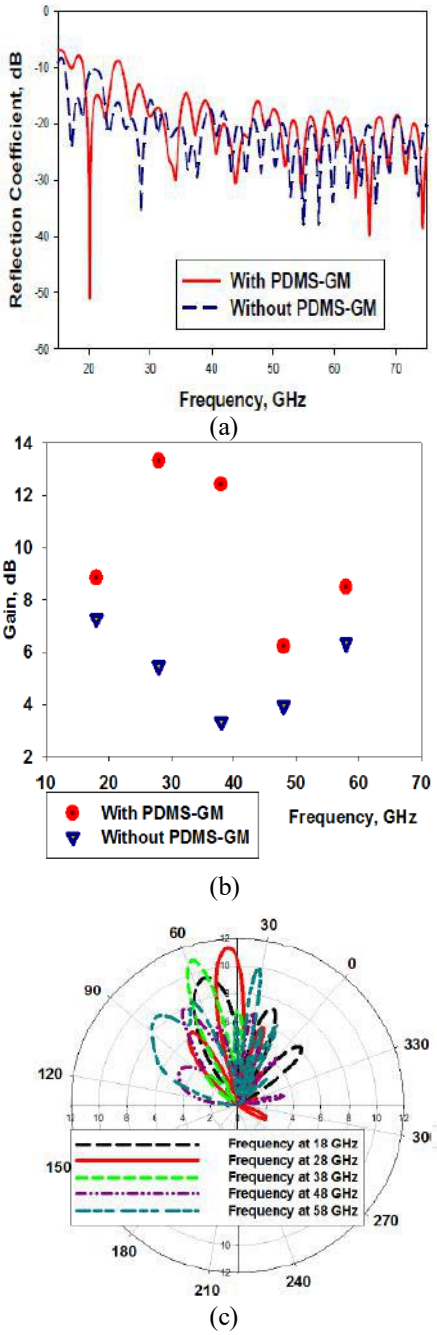



Figure 2. (a) The reflection coefficient with PDMS-GM (solid line) and without PDMS-GM (dotted line), (b) the parametric study on gain at chosen frequency which are 18 GHz, 28 GHz, 38 GHz, 48 GHz, and 58 GHz with PDMS-GM (circle symbol) and without PDMS-GM (triangle symbol) and (c) polar radiation pattern for PDMS-GM antenna.

## 4. Conclusions

Due to the enhanced performance, the proposed antenna potentially serves as a good option for 5th Generation Wireless Systems (5G) which requires a high realized gain and low profile topology.


## Acknowledgements

The authors acknowledge the contribution of Universiti Teknologi Malaysia, Skudai, Johor (UTM) and Universiti Malaysia Perlis, Kangar, Perlis (UniMAP). Our gratitude also goes to grant of FRGS MOHE 9003-00522.


## References


[1] Alina-Cristina Bunea, Florea Craciunoiu, Gheorghe Sajin, "28 GHz CRLH Antenna on Silicon Substrate," *Proceedings of the 41st European Microwave Conference,* 2011, pp. 579-582.

[2] Kuo-Sheng Chin, Ho-Ting Chang, Jia-An Liu, Hsien-Chin Chiu, Jeffrey S. Fu and Shuh-Han Chao, "28-GHz Patch Antenna Arrays with PCB and LTCC Substrates," *Cross Strait Quad-Regional Radio Science and Wireless Technology Conference*, July 26-30, 2011, pp. 355-358

[3] Jovanche Trajkovikj, Jean-François Zürcher, and Anja K. Skrivervik, "PDMS, A Robust Casing for Flexible W-BAN Antennas," *Laboratory of Electromagnetics and Acoustics, Lema Ecole Polytechnique Fédérale de Lausanne (EPFL) CH-1015 Lausanne*, Switzerland, 2013.

# Bandwidth Enhancement of Array Antenna using Double Positive Artificial Magnetic Conductor

**H. Lago[1], M. F. Jamlos[1,2], P. J. Soh[1], M. H. Muslim[3]**

[1] Advanced Communication Engineering Centre (ACE), School of Computer & Communication Engineering, Universiti Malaysia Perlis, 01000, Perlis, Malaysia.
[2] Faculty of Mechanical Engineering, Universiti Malaysia Pahang, Pekan, Malaysia.
[3]National Agency Space of Malaysia (ANGKASA), Ministry of Science, Technology & Innovation, Kuala Lumpur, Malaysia.
E-mail: herwansyahlago@gmail.com

## Abstract

The integration of an artificial magnetic conductor (AMC) into an array antenna at 9.41 GHz is proposed. The AMC plane with an array of 9 x 12 slotted elements. Each rectangular AMC unit cell is slotted using four circular slots. It is observed that the permittivity and high permeability of the proposed AMC plane rectangular circular-slotted unit cell significantly contributed to such results. The combined AMC and array antenna increased its efficiency from 95.91 % to 96.31 %. Ultimately, the bandwidth of the overall structure is increased from 4.61 % to 20.59 %.

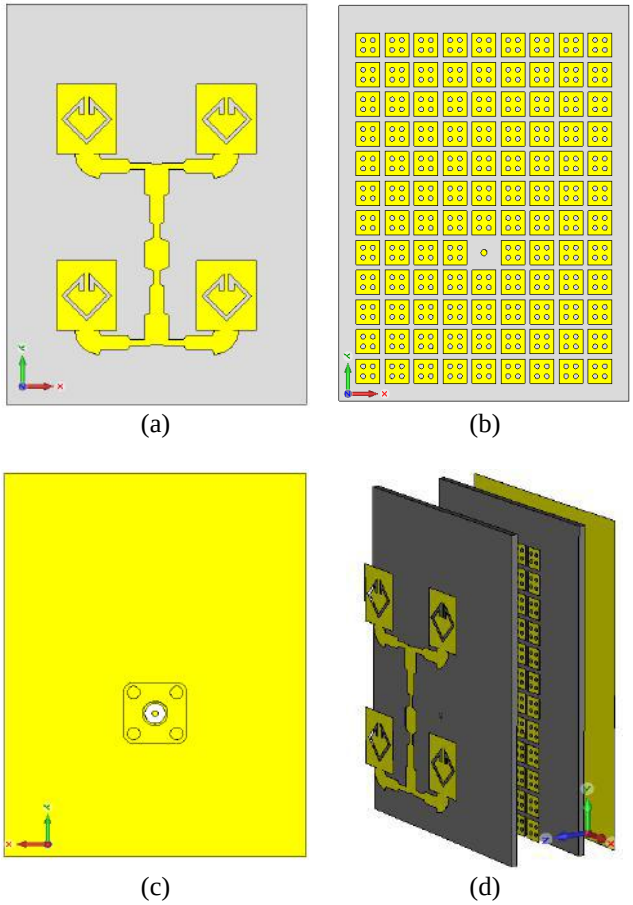
## 1. Introduction

An Artificial Magnetic Conductor (AMC) is classified as a metamaterial [1] which exhibits Perfect Magnetic Conductor (PMC) characteristic at a specific resonant frequency [2]. The main PMC's characteristic is that it exhibits zero degree of phase reflection. Since PMC is not available in nature [3], this research aims to propose an AMC ground layer which can be placed closer to the resonant structure. To evaluate it, a microstrip array antenna is designed as the radiating structure and placed on the top of AMC layer. The microstrip antenna topology is chosen due to its intrinsic narrowband property. This will then ease the quantification of its bandwidth broadening level when integrated with the AMC plane.

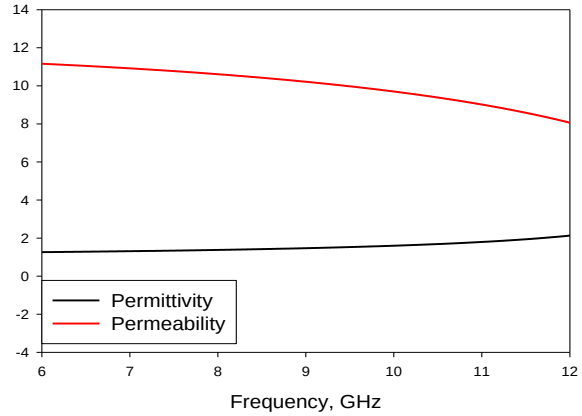
## 2. Results and discussion

The design of the array antenna and AMC plane is illustrated in Figure 1 (a)-(d). The overall dimension of the proposed patch array antenna is 80 x 60 $mm^2$. It is designed on a Taconic TLY-5 substrate. This substrate features a permittivity of 2.2, loss tangent of xxx, and thickness of 1.5748 mm.

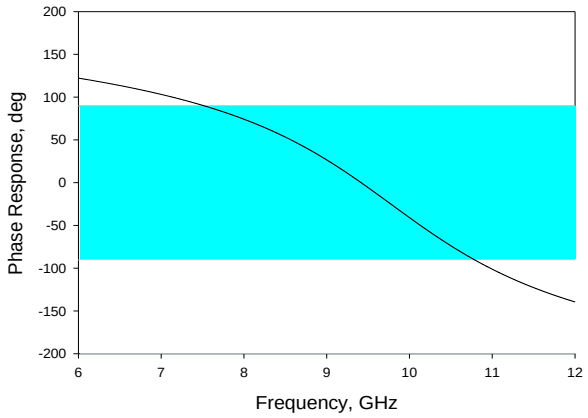
As depicted in Figure 1(e), the AMC features a positive permittivity and high permeability at the desired operating frequency. From Figure 1(f), the proposed AMC unit cell on Taconic TLY-5 indicated a 3.2 GHz bandwidth and behaves as a PMC at 9.41 GHz. The AMC was designed and analyzed using unit cell simulation which available in CST MSW.



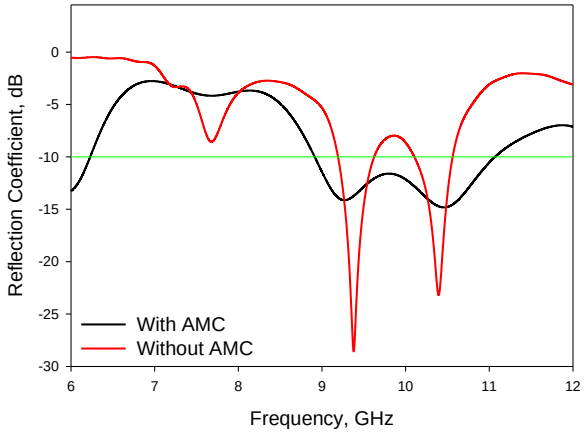
(a) (b) (c) (d)




(e)




(f)




(g)

Figure 1: (a) The proposed patch array antenna, (b) the proposed 9 x 12 AMC unit cell, (c) the rear ground, (d) the overall antenna structure, simulated AMC unit cell results of (e) simulated permittivity and permeability of the AMC cell, (f) phase response of the AMC, and (g) the improvement of antenna bandwidth with the incorporation of the AMC.

## 3. Conclusions

A slotted array antenna integrated with an AMC plane is proposed. Simulations indicated that the AMC plane can be placed near the radiating element. Besides that, the PMC-like behavior of the AMC with high permittivity and permeability enabled the enhancement of the typically narrowband microstrip array antenna in terms of impedance bandwidth, total efficiency, gain up to 2.15 GHz, 96.31 %, and 8 dB respectively.

## Acknowledgements

The authors acknowledge the contributions from the members of Advanced Communication Engineering (ACE) CoE for their valuable input and discussions. This work was supported by FRGS 9003-0522.

## Referencese

[1] Fiddy, M.A., and Tsu, R., Understanding metamaterials, *waves in Random and Complex Media*, vol. 20 pp. 202-222, 2010.

[2] Yan, S., Soh, P.J., and Vandenbosch, G.A.E., Low-profile dual-band textile antenna with artificial magnetic conductor plane, *IEEE Trans. Antennas Propag.*, vol. 62, no.12, pp. 6487-6490,2014.

[3] Abbasi, N.A., and Langley, R.J., Multiband-integrated antenna/artificial magnetic conductor, *IET Microwaves, Antenna and Propagation*, vol. 5, pp. 711-717, 2011.

# Metasurface for Low Profile X-Band Antenna Application with High Permeability and Low Permittivity Substrate

**H. Lago[1], M. F. Jamlos[1,2], P. J. Soh[1], M. H. Muslim[3]**

[1] Advanced Communication Engineering Centre (ACE), School of Computer & Communication Engineering, Universiti Malaysia Perlis, 01000, Perlis, Malaysia.
[2] Faculty of Mechanical Engineering, Universiti Malaysia Pahang, Pekan, Malaysia.
[3]National Agency Space of Malaysia (ANGKASA), Ministry of Science, Technology & Innovation, Kuala Lumpur, Malaysia.
E-mail: herwansyahlago@gmail.com

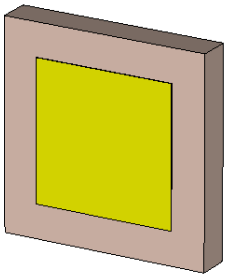
## Abstract

A comparison of a novel design with three basic shape designs of artificial magnetic conductor (AMC) is presented. The proposed AMC design successfully enhanced the operating bandwidth by about 12.02 % compared to the others designs while maintaining operation at 9.41 GHz. In addition, it is observed that the proposed AMC unit cell is capable of featuring higher permeability of 6.26 and lower permittivity of 1.06 at the target design frequency.

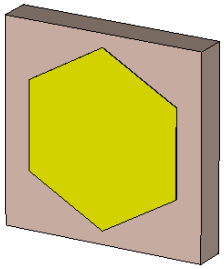
## 1. Introduction

Enhancing the performance of antennas while miniaturizing their sizes have been one of the main scientific activities of the antenna community in recent years. A metallic reflector and ground plane is typically used to redirect the radiation to particular direction and reduce the front-to-back ratio (FBR). To be effective, this reflector needs to be placed with a gap of a quarter wavelength of the center frequency from the radiating element [1]. This constraint can be reduced by implementing a metasurface plane in between the ground plane and the radiating element. However, an AMC exhibits a reflection phase of zero degree at resonance [2]. Thus, they suffer from narrow bandwidth as the AMC's bandwidth is defined as the band in which the reflection phase, $\phi$ is in the range of $-\pi/4 \leq \phi \leq \pi/4$.

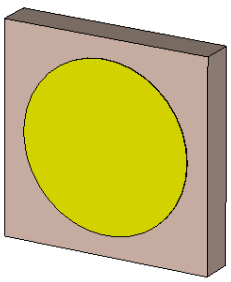
Besides that, microstrip patch antennas are also typically limited by their operating bandwidths. While their bandwidth can be broadened via the use of high permeability and permittivity material [3], such high permeability materials does not exist in nature.



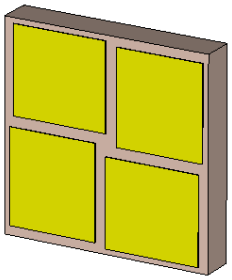
(a)



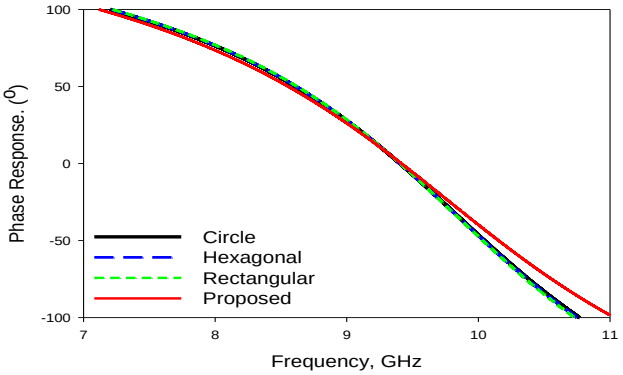
(b)



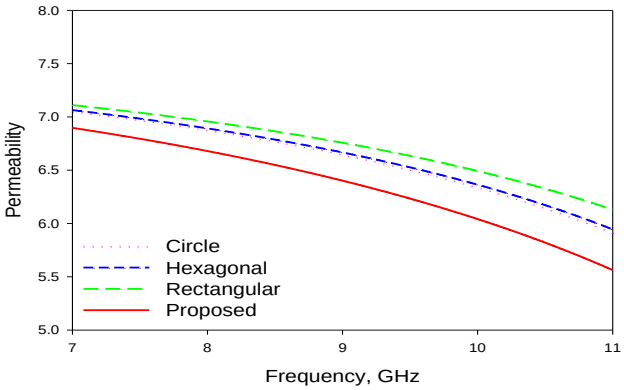
(c)



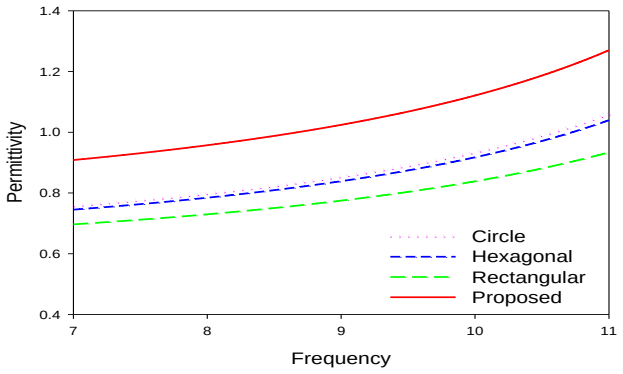
(d)




(e)




(f)




(g)

Figure 1: (a) Basic rectangular AMC, (b) basic hexagonal AMC, (c) basic circular AMC, (d) the proposed AMC design, the simulated AMC unit cell result of (e) phase response (f) permeability, and (g) permittivity.

## 2. Discussion

To validate the proposed model, three basic shapes of metasurface have been designed on the same materials and simulations setup. Taconic TLY-5 was used as the substrate and copper as the metallic elements. The performance of the AMC with different shapes was investigated using the CST Microwave Studio software, see Figure 1. Figure 1(e) shows the proposed model with a larger operating bandwidth compared to the basic shaped at 9.41 GHz. Besides that, the proposed shape featured a high permeability and low permittivity as illustrated in figure 1(f) and 1(g).

## 3. Conclusions

In this paper, an AMC design featuring a high permeability and low permittivity is proposed. To validate the effectiveness of the proposed AMC, the design was compared with another three basic AMC designs. All AMC are placed under a basic rectangular antenna and studied in terms of permittivity, permeability and reflected phase. Simulations indicated that the antenna integrated with the proposed AMC is performing better than antennas with the basic AMC designs in all three aspects. This antenna exhibited a 500 MHz 10 dB impedance bandwidth, with a resonant frequency of 9.41 GHz. Besides that, the presence of the proposed AMC on the antenna enabled the achievement of 6.16 dB of gain and 92 % of total efficiency at 9.41 GHz

## Acknowledgements

The authors acknowledge the contributions from the members of Advanced Communication Engineering Centre (ACE) for their valuable input and discussions. This work was supported by FRGS 9003-0522.

## References

[1] Gao, X., Qi, Y., and Jiao, Y.-C., Design of multiplate back-reflector for a wideband slot antenna, *IEEE Antennas Wireless Propag. Lett.*, vol. 12, pp. 773-776, 2013.

[2] Yan, S., Soh, P.J., and Vandenbosch, G.A.E., Low-profile dual-band textile antenna with artificial magnetic conductor plane, *IEEE Trans. Antennas Propag.*, vol. 62, no.12, pp. 6487-6490,2014.

[3] Cai, T., Wang, G.-M., Zhang, X.-F., Wang, Y.-W., Zong, B.-F., and Xu, H.-X., Compact microstrip antenna with enhanced bandwidth by loading magneto-electro-dielectric planar waveguide metamaterials, *IEEE Trans. Antennas Propag.*, vol. 63, no. 5 pp. 2306-2311, May 2015.

# Complex permittivity of Sugarcane Bagasse and Rubber Tire Dust Within 1 to 18 GHz Frequency Range

**L. Zahid[1*], M.Jusoh[1], M. R. Kamarudin[2], S.K.A.Rahim[2], Y.S.Lee[1], H. A. Rahim[1], M. K. A. Rahim[2], T.Sabapathy[1]**

[1]Bioelectromagnetics Research Group (BioEM), School of Computer and Communication Engineering, Universiti Malaysia Perlis (UniMAP), Kampus Pauh Putra, Perlis, Malaysia
[2]Wireless Communication Center (WCC), Universiti Teknologi Malaysia (UTM), 81300 Skudai, Johor, Malaysia*corresponding author, E-mail: liyanazahid@gmail.com

## Abstract

This paper presents complex permittivity measurements of sugarcane bagasse and rubber tire dust materials. These two materials are found to be useful as potential materials to be the absorbing material in microwave frequency to allow absorption of microwave EMI energy. The materials were combined and fabricated in the composite structure. A measurement system using open-ended coaxial probe method has been used for characterizing the dielectric properties of the materials in the 1 to 20 GHz microwave frequency range.

Keywords – open-ended coaxial probe, permittivity, microwave absorber

## 1. Introduction

Recently, with the rapid growth of microwave device fabrication technology, modern technologies and communication product, communication system can be operating in the higher and broader frequency. Some of the natural and man-made EMI sources can affect and degrade the performance of any unprotected nearby electronic circuit. The effects of EMI include the malfunction, or even the permanent damage to the electronic devices which can lead to the failure [1]–[3]. In this work, the results of dielectric characterization along with the wave propagation characteristics of the composite samples composed of lossy sugarcane bagasse and lossy rubber tire dust are presented. Sugarcane bagasse and rubber tire dust are dielectric materials with $\mu_r$ = 1+0j, therefore only relative complex permittivity was measured and the results are presented in this chapter. In dielectric materials, the dielectric constant and the dissipation factor of energy are the main properties that enable them to be applicable as microwave absorbers as Equation (1) below. In designing the absorber materials, the following equation can be used to determine the absorption capability of the material that relies on the conductivity, dielectric loss, or magnetic loss of the absorber material [4]. The dielectric properties were essential in determining the material performance used in microwave absorption. The permittivity is a function of frequency and can vary over even a small frequency range significantly [5].

$$A = ½ \sigma E2 + ½ \omega \varepsilon 0 \varepsilon_R E^2 + ½ \omega \mu_0 \mu_R H^2 \quad (1)$$

Where A (W/m3) is the electromagnetic energy absorbed per unit volume; E(V/m) is the electric field strength of the electromagnetic signal; H (A/m) is the magnetic field strength of the electromagnetic signal; σ (S/m) is the conductivity of the material; ω(sec-1) is the angular speed of the electromagnetic wave; $\varepsilon_0$ is the dielectric permittivity of vacuum; $\varepsilon_R$ is the complex permittivity of the material; $\mu_0$ is magnetic permeability of the vacuum and $\mu_R$ is the complex permeability of the material. The open-ended coaxial probe has been used for measurements on a number of agricultural products such as rice husk [6] and grain[7]. It requires calibration before starting the measurements by terminating it in a short circuit, an open and a broadband load [8].This method consists of a network analyzer and a coaxial probe. It includes a mechanical load for short circuit calibration, air for open calibration and water (at room temperature) as a broadband load. Figure 1 and 2 below shows the dielectric properties of the water and air after calibration.

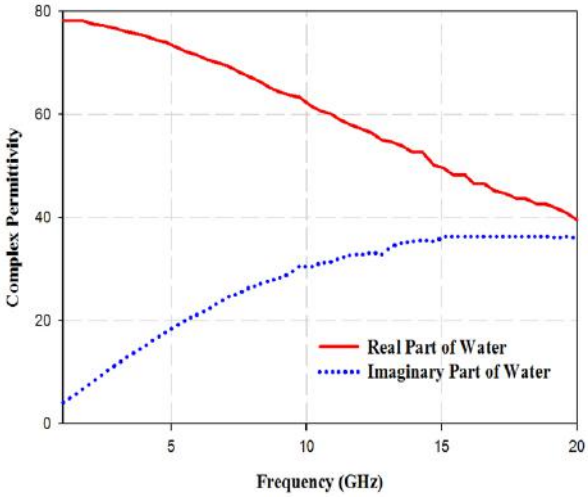



Figure 1: Complex Permittivity of Water

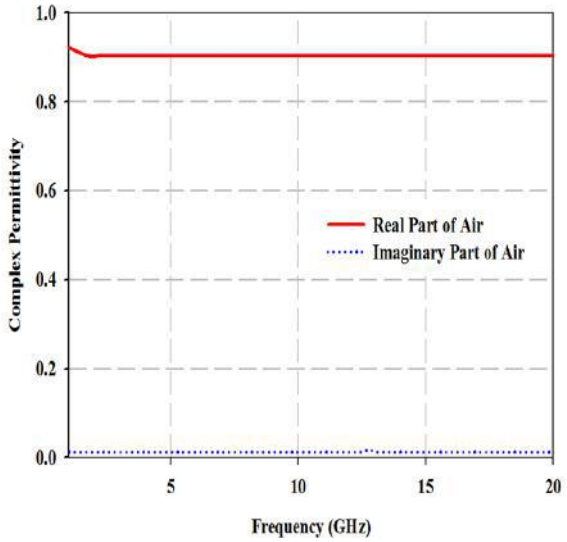



Figure 2: Complex Permittivity of Air

Instead of using water as a broadband load, any solid dielectric material with known values of the dielectric properties can also be used as broadband load. However, there is a problem in the unavailability of the data on the dielectric properties of the known materials in broad frequency ranges. Many researchers have used this calibration technique due to the unavoidable air gap at the probe-sample interface in determining the dielectric properties of the solid samples [9] [10].

At first, the samples are fabricated in three categories which are pure sugarcane bagasse, pure rubber tire dust and composite of lossy filler of sugarcane bagasse and rubber tire dust. By using the transmission line rectangular waveguide technique, the permittivity and permeability of the samples can be determined. Full 2 port calibration or TRL calibration is needed for accurate phase measurements, particularly of reflection[11]. Sample fit inside the coax or waveguide is very important as a poorly fit sample will not yield good results. As frequencies extend into millimeter waves, calibration and sample fit become even more critical due to the short wavelength. Magnetic constant and magnetic loss factor of the sugarcane bagasse (SCB), rubber tire dust (RTD) and sugarcane bagasse rubber tire dust (SCBRTD) composite samples were measured by using this technique. Based on the result, the relative magnetic properties are nearly equal to free space, μr=1-j0. So, from the result, these materials are non-magnetic materials. Figure 3 and Figure 4 below show the magnetic constant and magnetic loss factor of the material.

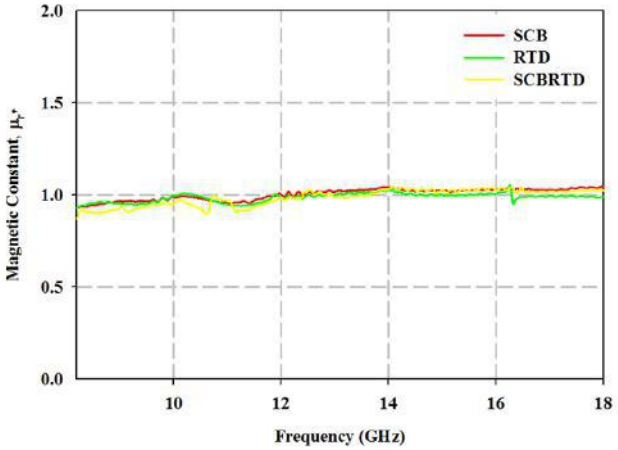



Figure 3: Magnetic Constant of the Material

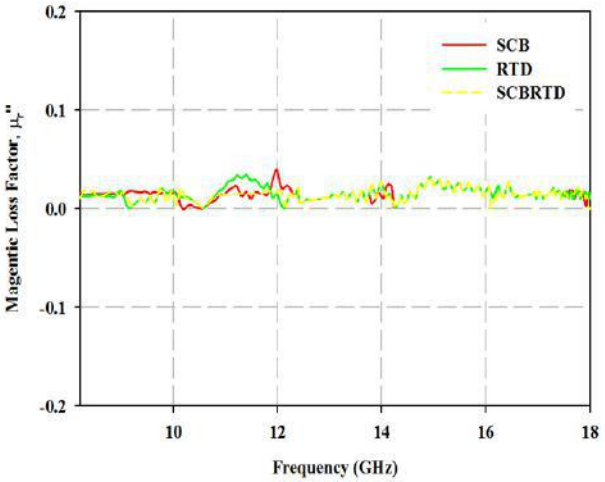



Figure 4: Magnetic Loss factor of the Material

## 2. Discussion and Results

Since the materials used in this work are dielectric materials, the loss mechanism is purely dielectric. The loss can arise from a variety of sources within the dielectric. The commercialize dielectric absorbers are usually made in a low cost foam form but can also be used with elastomers. The advantages are low cost and weight. Absorbers are characterized by their electric permittivity and magnetic permeability. The permittivity is a measure of the material's effect on the electric field in the electromagnetic wave. The permittivity arises from the dielectric polarization of the material. The quantity ε' is sometimes called the dielectric constant which is something of a misnomer when applied to absorbers as ε' can vary significantly with frequency. The quantity ε" is a measure of the attenuation of the electric field cause by the material. So, the dielectric constant of sugarcane bagasse, rubber tire dust and composite samples composed of SCB and lossy rubber tire dust (RTD) need to be defined first to know the material performance. The

complex dielectric properties of a medium can give impact to the propagation parameters of an electromagnetic (EM) plane wave to describe the wave behavior in that medium.Absorbers are usually composed of materials that have dissipation of loss and hence attenuate the propagating wave inside the material. The impedance of electromagnetic wave propagating in free space is;

$$\eta_o = \sqrt{\mu_o \varepsilon_o} \quad (2)$$

Where

$\mu_o = 4\pi \times 10^{-7}$ *Henry/m*
$\varepsilon_0 = 8.854 \times 10^{-12}$ *Farad/m*

When the same wave interacts with a lossy dielectric medium such as SCB and RTD, the characteristic impedance of the medium can be expressed as

$$\eta_m = \eta_o / \sqrt{\varepsilon'_r - j\varepsilon''_r}\,. \quad (3)$$

The impedance is discontinuity at the interface of the air-dielectric ($\eta_0 \neq \eta_m$), so the wave energy is reflected back into the incident medium. The remaining energy that keeps on propagating within the lossy material can be expressed with the complex wave propagation constant;

$$\gamma = (2\pi/\lambda)\sqrt{\varepsilon'_r - j\varepsilon''_r}\,. \quad (4)$$

(α) is the real part of the propagation constant and β is the imaginary part which resembles the phase shift per unit length in the medium and the speed at which the signal was propagated. These two equations below express theα and β of the material dielectric properties.

$$\alpha = \frac{2\pi}{\lambda}\sqrt{\frac{\varepsilon'_r}{2}\left(\sqrt{1+\tan^2\delta}-1\right)} \quad (5)$$

$$\beta = \frac{2\pi}{\lambda}\sqrt{\frac{\varepsilon'_r}{2}\left(\sqrt{1+\tan^2\delta}+1\right)} \quad (6)$$

The important parameters of an absorbing material are to attenuate the electromagnetic wave and prevent the EM wave from being reflected back or transmitted pass through the material. The characteristic impedance is important in determining the performance of the absorbing material. Reflection can happened at the air-absorber interface due to the impedance mismatch between free space and characteristic impedance of the material. The reduction of the reflected wave from the front layer or surface can occur when the impedance of the material is matching to the impedance of free space (377Ω). If the impedance by the wave at the surface of the material is equal to 377Ω, the wave will be totally and completely absorbed by the material. The impedance of a material is given by the following relation,

$$Z = 120\,\pi\sqrt{\mu_r/\varepsilon_r} \quad (7)$$

From this equation, this is clearly showed that the basic parameters for the absorption characteristics depend on permittivity and permeability. Therefore, in this work, the samples were fabricated and the complex permittivity was being measured by using Agilent Dielectric probe technique. Figure 5 below shows the dielectric constant of sugarcane bagasse and rubber tire dust.

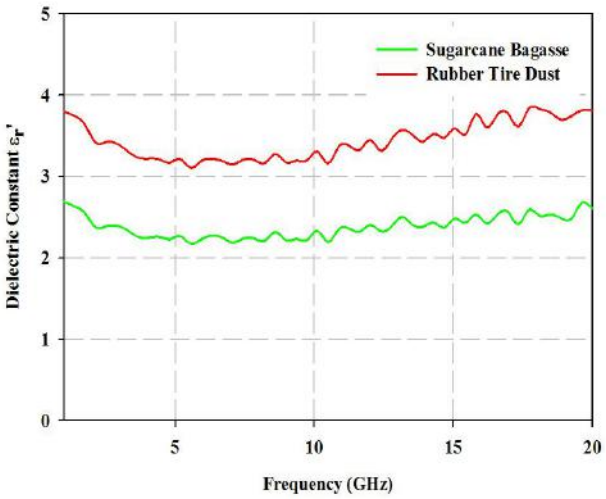



Figure 5: Dielectric Constant of Sugarcane Bagasse

Based on the graph in Figure 5, rubber tire dust has the highest dielectric constant compare to sugarcane bagasse which is in range between 3.2 to 3.8.This was related to mechanism of polarization .At microwave frequencies, when a dielectric material is exposed to a time varying electromagnetic field, the electric field component of the wave polarized the molecules [12]. The higher content of carbon in the rubber tire dust is another factor that contributes to the higher dielectric constant. For the sugarcane bagasse, the average value of the dielectric constant is between 2.2 to 2.7 in the frequency range 1 to 20 GHz.

The reflectivity of the sample was being measured to determine the S Parameter (reflectivity of the absorber). The reflectivity was being determined by using rectangular waveguide technique (2-port measurement) in the X Band frequency range. So, the adapter of the rectangular waveguide that has been used is WR- 90. The reflectivity was being measured in X-Band frequency (8.2 to 12.4 GHz) as this is the frequency that has been used in satellite communication, radar and amateur radio. Figure 6 below shows the reflectivity of the sample of sugarcane bagasse.

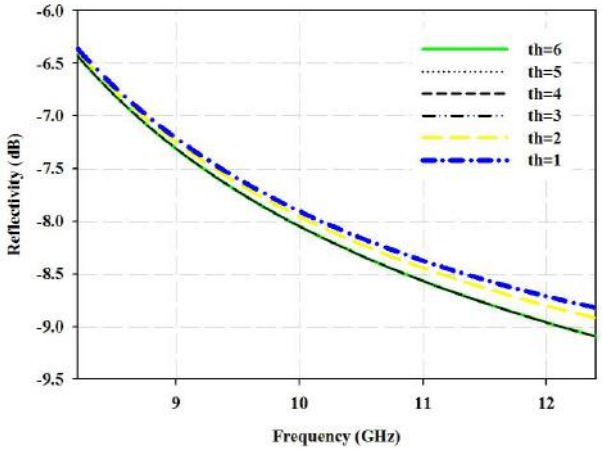



Figure 6 : Reflectivity of the Sample of Sugarcane Bagasse

Based on the result above, the thickness of the sample has been varied from 1mm to 5mm. The thickness from 3 mm to 6 mm did not give change in reflectivity from -6.5 to -9.0 dB from 8.2 to 12.4 GHz. Whereas the thickness from 1 to 2 mm have reflectivity from -6.4 to -8.8. The study continues by adding the filler of rubber tire dust to sugarcane bagasse and the result shows that the reflectivity can achieve until less than -10dB (~90 % absorption). Figure 7 below shows the reflectivity of sample of sugarcane bagasse composited with rubber tire dust.

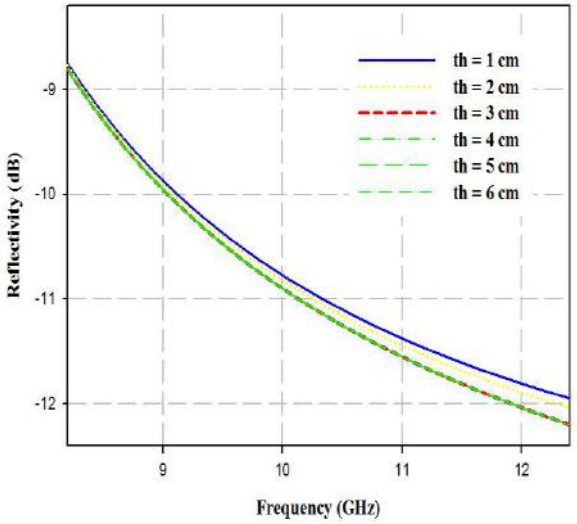



Figure 7: Reflectivity Of Sample Of Sugarcane Bagasse Composited With Rubber Tire Dust

In the range frequency between 9 to 12.4 GHz, the reflectivity of all the samples is from -10 to -12.5 dB for all the thickness. The reflectivity of the sample material shows better result with the higher value of dielectric constant for rubber tire dust filling.

Figure 8 below shows the dielectric constant of five samples with different percentages of fillers (sugarcane bagasse and rubber tire dust). Six samples with different percentages of fillers (sugarcane bagasse and rubber tire dust).

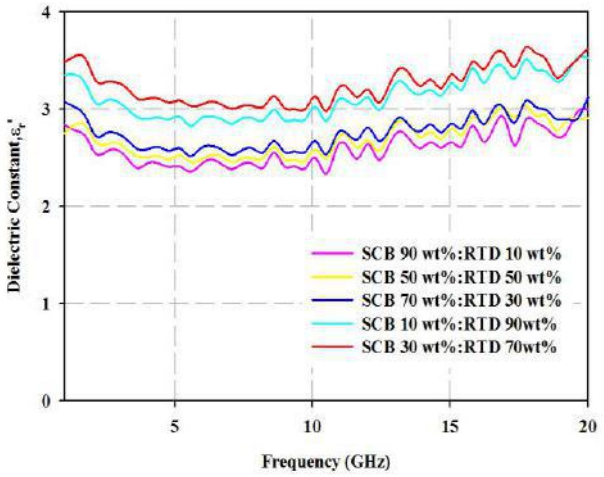



Figure 8: Dielectric Constant of Different Percentage of Fillers (Sugarcane bagasse mixed with Rubber Tire Dust)

The complex permittivity increases when there is increasing percentage of fillers in the composite samples. The addition of sugarcane bagasse and rubber tire dust increased the number of dipoles as they are the lossy dielectric fillers. The electrostatic dipole energy and capacitance of the medium is increased when the energy from the incident wave is stored in these dipoles. Therefore, the dielectric constant increases with the increasing of the filler loading. From this result, the attenuation constant can be determined to analyze the propagation wave into the material. Figure 9 below shows the attenuation constant of the material for different filler loadings.

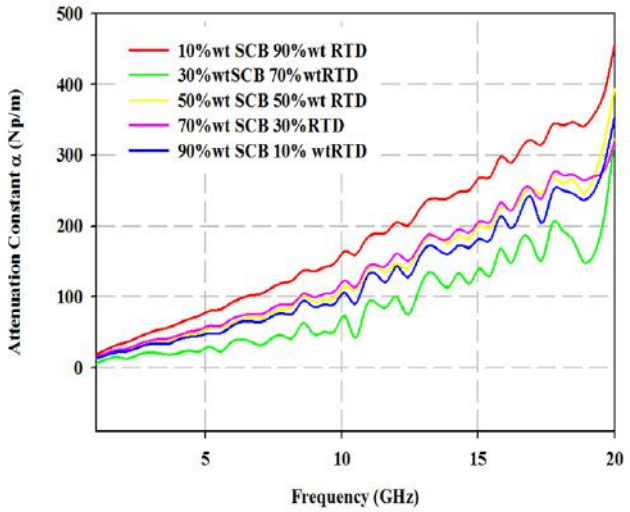



Figure 9: Attenuation Constant of the Material for Different Filler Loading

Attenuation constant increased with an increasing frequency. The values of the depth of penetration were smaller at high frequencies and become higher at lower frequencies. This is because, at high frequencies, the wavelength is shorter so the wave was not being able to be embedded and penetrate deep into the medium due to the large attenuation offered by the medium. Figure 10 below shows the depth of penetration of the material. The value of depth of penetration was calculated by using the formula.

$$d = \tfrac{1}{2}\alpha \qquad (8)$$

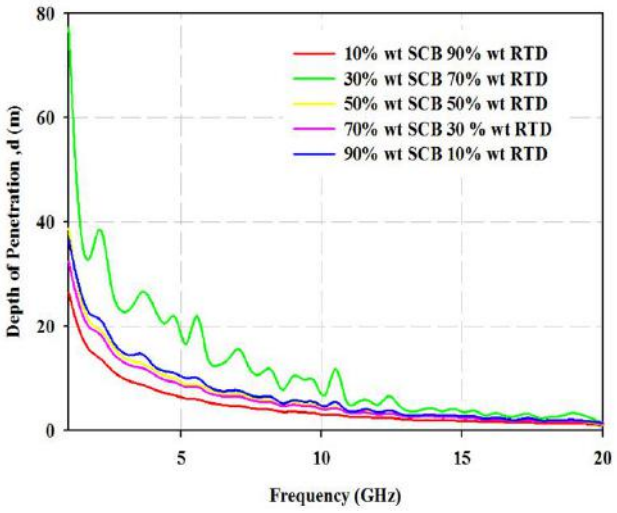



Figure 10: Depth of Penetration of the Material

Table 1 shows the measured relative values of the complex permittivity and magnitude of normalized characteristic impedance $|Z_a|$ for different SCB and RTD filler compositions.

Table 1: Values of Complex Permittivity and Magnitude of Normalized Impedance of the Composite of Sugarcane Bagasse and Rubber Tire Dust

| Samples | | Properties | Average |
|---|---|---|---|
| SCB (wt %) | RTD (wt %) | | |
| 10 | 90 | $\varepsilon_r$' | 3.121 |
| | | $\varepsilon_r$" | 0.236 |
| | | tan δ | 0.005 |
| | | \| Z \| | 207 |
| 30 | 70 | $\varepsilon_r$' | 3.253 |
| | | $\varepsilon_r$" | 0.123 |
| | | tan δ | 0.003 |
| | | \| Z \| | 250 |
| 50 | 50 | $\varepsilon_r$' | 2.686 |
| | | $\varepsilon_r$" | 0.218 |
| | | tan δ | 0.007 |
| | | \| Z \| | 230 |
| 70 | 30 | $\varepsilon_r$' | 2.762 |
| | | $\varepsilon_r$" | 0.176 |
| | | tan δ | 0.005 |
| | | \| Z \| | 227 |
| 90 | 10 | $\varepsilon_r$' | 2.598 |
| | | $\varepsilon_r$" | 0.153 |
| | | tan δ | 0.004 |
| | | \| Z \| | 234 |

Impedance discontinuity ($\Delta Z = 377 - Za$) is least for the case of 30 wt% of SCB loading, however in this case the value of the tangent loss is also minimum. This shows the maximum transmission of the signal with less attenuation and is not preferred in the case of absorbers. An absorber must be a lossy medium with least impedance discontinuities at the interfaces. The greatest value of tangent loss is (0.007) when 50 wt% of SCB and RTD filler was being used and the impedance is 230.

## 3. Conclusions

The materials that have been used in this study are sugarcane bagasse and rubber tire dust. Based on the result of permittivity, these materials can be considered as dielectric and lossy material. The real part of permittivity has been found to be strongly dependent on frequency. When the frequency increased, the value decreases. The imaginary part of the permittivity also showed variation with frequency but not as much as in the case of real permittivity. From the permittivity, the propagation constant including of attenuation constant and the depth of penetration were being investigated. The wave impedance of the material was also being calculated. From the result, the composition of 50 wt% of sugarcane bagasse and 50 wt% of rubber tire dust shows the highest lost tangent and less impedance discontinuities and it has the potential to be a good absorbent material. The reflectivity of the materials has been analyzed for varying thickness values of the samples. When the rubber tire dust filler was added to the sugarcane bagasse composite, the performance can achieve better than -10 dB. This means that the proposed absorber material can absorb more than 90 % of the incident wave. The usage of agricultural waste material such as sugarcane bagasse as a potential material to develop microwave absorber can help in reducing the abundant of the waste and the harmful of ecological as well.

## References


[1] T. Williams, *EMC for Product Designers*. 2001, p. 3rd Edition.

[2] R. Schmitt, *Electromagnetics explained: a handbook for wireless/RF, EMC, and high-speed electronics, Elsevier Science*. USA, 2002.

[3] X. C. Tong, *Advanced Materials and Design for Electromagnetic Interference Shielding*. CRC Press ,Taylor & Francis Group,Broken NW, Suite 300,Boca Raton, 2009.

[4] "Sony ' s Electromagnetic Wave Absorber Reduces EMC and SAR Problems."

[5] A. Sharma and M. N. Afsar, "Accurate Permittivity and Permeability Measurement of Composite

Broadband Absorbers at Microwave Frequencies," no. 1, 2011.
[6] H. N. F. Malek, E. M. Cheng, O. Nadiah, P. J. S. M. Ahmed, M. Z. A. Abd Aziz, A. R. Osman, and and M. N. T. A. A. H. Azremi, A. Hasnain, "RUBBER TIRE DUST-RICE HUSK PYRAMIDAL MICROWAVE ABSORBER," *Prog. Electromagn. Res.*, vol. 117, no. March, pp. 449–477, 2011.
[7] S. O. Nelson, "Fundamentals of Dielectric Properties Measurements and Agricultural Applications," vol. 44, no. 2, pp. 98–113, 2010.
[8] A. Note, "Agilent Basics of Measuring the Dielectric Properties of Materials."
[9] S. O. Nelson, W. Guo, S. Trabelsi, and S. J. Kays, "Dielectric spectroscopy of watermelons for quality sensing," *Meas. Sci. Technol.*, vol. 18, no. 7, pp. 1887–1892, Jul. 2007.
[10] P. Savi, M. Miscuglio, M. Giorcelli, and A. Tagliaferro, "Analysis of Microwave Absorbing Properties of Epoxy MWCNT Composites," vol. 44, no. October 2013, pp. 63–69, 2014.
[11] T. E. Ch, "Tech Theory and Application of RF/Microwave Absorbers."
[12] M. Hotta, M. Hayashi, M. T. Lanagan, and D. K. Agrawal, "Complex Permittivity of Graphite , Carbon Black and Coal Powders in the Ranges of X-band Frequencies ( 8 . 2 to 12 . 4 GHz ) and between 1 and 10 GHz," vol. 51, no. 11, pp. 1766–1772, 2011.

# BRANCH-LINE COUPLER USING PDMS AND SHIELDIT SUPER FABRIC CONDUCTOR

S. A. Babale[1], S.K.A.Rahim[1], M.Jusoh[2]

[1]Wireless Communication Centre (WCC) Faculty of Electrical Engineering,
Universiti Teknologi Malaysia, UTM Skudai, 81310, Johor, Malaysia.
[2]Bioelectromagnetics Research Group (BioEM), School of Computer and Communication Engineering,
Universiti Malaysia Perlis, 02600 Pauh Putra, Perlis, Malaysia
sababale.ele@buk.edu.ng, sharulkamal@fke.utm.my, muzammil@unimap.edu.my

## Abstract

In this paper, a new 3 dB branch line coupler using PDMS substrate and Shieldit Super fabric conductive material is presented. The Shieldit Super fabric has low resistance less than 0.1 /sq. and resulting in good conductivity. Both the simulated and fabricated coupler circuits demonstrated a 3±1dB Fractional Bandwidth (FBW) for the coupling as a result of the microstrip-slot created at the ground is in the range of 4.69GHz to 7.22GHz which stands for 42.2%; while the FBW for $90^0 \pm 5^0$ phase balance is in the range of 5.10GHz to 6.94GHz or 30.70%. Within this range, both the return loss and the isolation are kept below -10dB.

Keywords - PDMS substrate, Shieldit Super fabric, microstrip-slot, Fractional Bandwidth.

## 1. Introduction

Branch-Line Couplers (BLC) are widely used in many Radio Frequency (RF) circuits, such as power dividers and combiners, modulators, demodulators, balanced mixers, image rejection mixers, matched attenuators, filters, balanced amplifiers, and so on. They are also use to feed networks in antenna arrays. Conventional hybrid coupler utilizes λ/4 transmission lengths and provides narrow bandwidths of 10-20%. This is one of its major limitations. To overcome this limitation, a simple technique of cascading more sections had been suggested [1]. However, this result in large circuit area adds to cost of production.

The recently proposed 5G technology for wireless communication is expected to pave ways for wireless connection not only between base stations and mobile stations but from device-to-device. Due to the conformal nature of some devices, a flexible and conformal antenna/microwave device has to put in place to enable every type of gadget works properly. Most of the researches on flexible devices were carried out on antenna and very little or none have been reported on microwave devices like BLC. For example, in [2], a flexible broadband unbalanced dipole antenna with fan-shaped and trapezoidal elements was demonstrated using PDMS. In contrast, few among many that use non flexible substrates are reported in [3] and [4].

Various polymer materials like Polyethylene terephthalate (PET), Liquid Crystal Polymers (LCP) and Polyetherimide (PEI) were used to produce flexible antenna [5], but, PDMS is one of the most frequently used substrate material for flexible antenna. This is due to its exceptional electrical and mechanical properties and transparent nature. But its chemical property and shiny surface makes it very difficult to be metallize due to low adhesion [6].

When copper is used as the conducting element on PDMS, it makes the whole system not flexible as cupper suffered from poor durability, easy crashing after several bending cycle. In this research, a new 3dB coupler with simple and cost effective fabrication processes using PDMS substrate flexible fabric conductor is proposed and developed. The proposed structure makes use of λ/4 sections of transmission lines in both the series and the shunt branch lines. The ports were inclined at $45^0$ to reduce the effect of fabrication difficulties and minimize effects of coupling between adjacent arms. The proposed structure is conformal and hence could be suitable for applications in wearable antenna where beamforming network is required.

## 2. Design Theory

At the centre frequency the scattering parameters of a branch-line coupler are given by

$$S_{21} = -jZ_{0s}/Z_0 \quad \text{..... (1)}$$

$$S_{31} = -Z_{0s}/Z_{0p} \quad \text{..... (2)}$$

Where $Z_0$ denotes the impedance of various ports of t branch-line coupler. The scattering parameters of a branch-line coupler also satisfy the following condition, which follows from the principle of conservation of energy:

$$|S_{21}|^2 + |S_{31}|^2 = 1 \quad \text{..... (3)}$$

From equations (1), (2) and (3) $Z_{0s}$ and $Z_{0p}$ are related as follows:

$$(Z_{0s}/Z_0)^2 + (Z_{0s}/Z_{0p})^2 = 1 \text{……..} (4)$$

The characteristic impedances of the main-line and shunt branches of a branch-line can be computed from equations (1) to (4) as:

$$Z_{0s} = Z_0\sqrt{1-|S_{31}|^2} \text{……..……..} (5)$$

and

$$Z_{0p} = \frac{Z_{0s}}{\sqrt{1-|S_{21}|^2}} \text{……..……} (6)$$

Where $Z_{0s}$ and $Z_{0p}$ are the characteristic impedances of the main line and shunt branch line of any branch-line coupler.

If all the ports are matched to the characteristic impedance of the microstrip transmission line, $Z_0$=50Ω, then for 3dB branch line coupler, the coupling from Input port to the coupled port will be 3dB. Using these information together with equations (5) and (6), the characteristic impedances of the main line and shunt branch line can be computed to be 35.35Ω and 50Ω respectively.

## 3. Implementation of The PDMS 3dB Coupler

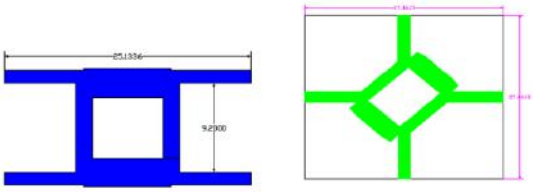
The objective of the research work is to design a low cost flexible 3dB coupler using PDMS with realizable impedances and a tight coupling of -3dB. It should also have high isolation and bandwidth over which both S11 and S14 are below -20 dB, at the same time maintaining a coupling level and the phase difference better than 3±1dB and $90^0$±$5^0$ respectively.

A fabric Shieldit Super was used as the conductor for both the patch and ground plane. Shieldit Super from Less EMF Inc. USA is a flexible conductive textile with measured conductivity of $10e^6$ S/m and a thickness of 0.14-mm. PDMS with a thickness of 0.7mm, εr = 2.9 and a loss tangent of 0.02 was moulded as the substrate. The Simulation was carried out in CST Microwave Studio 2004®. The simulated structure was then exported, processed and precisely cut with Silhouette CAMEO studio into an appropriate dimension.

After obtaining the desired structure from the Silhouette CAMEO cutting machine, the PDMS and the Hardener (curing agent) were mixed in a clear container at a ratio of 10:1 respectively. The mixture was vigorously stirred with a spatula for about 7-10mins. This was carefully done until when the curing agent is homogeneously distributed and the final mixture becomes uniformly cross linked and bubble free ready for curing.

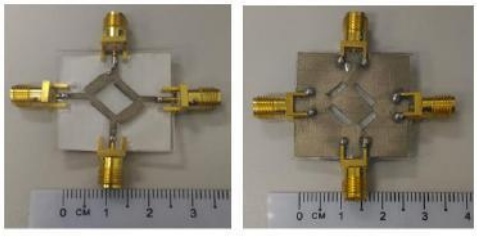
This clear and bubble free PDMS mixture is used to obtain the PDMS substrate. But, due to the fact that finally cured PDMS has a shiny surface and lead to difficulties in metallizing its surface, the curing was strategically made all together with the conductive structure. Finally, by placing the mixture of the PDMS together with the mould on a hotplate at temperature of about 150$^o$C for 6-8 mins yield a cured substrate. But in this research, the trick was to leave the mixture to cure naturally at room temperature. After about 10 hours, it became sticky and ready for pasting the conductive material. After about additional 10hours the PDMS together with all conductive materials became cooled and properly cured.

Figure 1(a) shows a conventional BLC operating at a centre frequency of 6GHz. The BLC result suffered from a very low bandwidth as shown in Figure 3. The fractional bandwidths defined by the fluctuation of the coupling level and the phase difference less than 3±0.1dB and $90^0$±$1^0$ is less than 1GHz. Another setback can be observed from Figure 1(a) is that, it will be difficult to fabricate the BLC due to its dimension constrain. The length of the branch arm as is only 0.92mm. With this structure, SMA connectors cannot be mounted without overlapping. As a result of these setbacks, another structure was proposed as shown in Figure 1(b), which alleviates the problem of fabrication and construction. Even though there is an improvement in the bandwidth of the proposed BLC as can be seen from Figure 4, there is need to further improve the bandwidth.



(a) (b)

**Figure 1:** Geometry of the Branch Line Coupler; (a) Conventional, (b) Proposed BLC.



(a) (b)

**Figure 2:** Prototype of the fabricated BLC; (a) Top view, (b) The Ground.

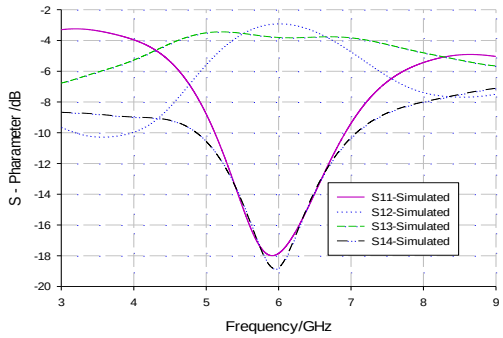



**Figure 3:** S- Parameter for the Conventional BLC showing the Bandwidth.

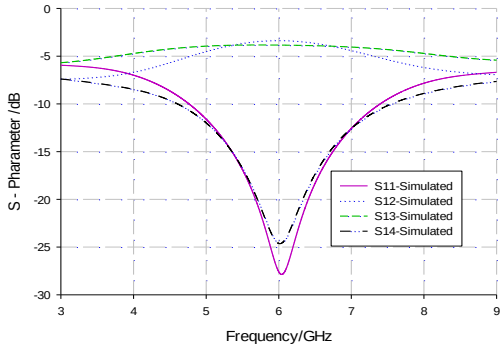



**Figure 4:** S- Parameter for the Modified BLC showing an improvement in the Bandwidth

To further improve the fractional bandwidth of the proposed coupler, a microstrip-slot was created in the ground for bandwidth improvement. Figure 2 shows the Prototype of the fabricated BLC; (a) Top view, (b) The Ground. The S- Parameter for the Modified BLC showing the improvement in Bandwidth for a coupling level and the phase diff erence less than 3±1dB and $90^0 \pm 3^0$ respectively is shown in figure 4 while Figure 5 and 6 respectively compared the S- parameter and the amplitude imbalance for the simulated and the measured coupler.

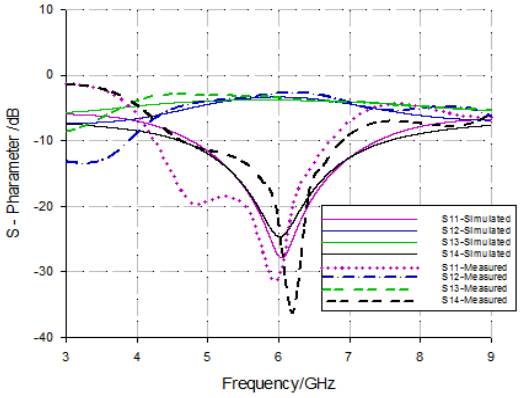



Figure 5: Measured and Simulated S- Parameter for the Modified BLC

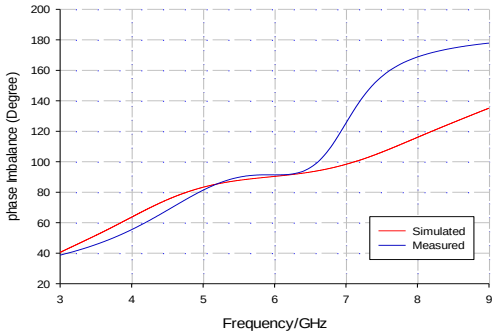



**Figure 6:** Measured and Simulated Phase Imbalance for the Modified BLC

## 4. Conclusion

From the results obtained in this research, it can be observed that the 3±1dB Fractional Bandwidth (FBW) for the coupling as a result of the microstrip-slot created at the ground is in the range of 4.69GHz to 7.22GHz which stands for 42.2%; while the FBW for $90^0 \pm 5^0$ phase balance is in the range of 5.10GHz to 6.94GHz or 30.7%. Within this range, both the return loss and the isolation are kept below -10dB. The slight difference observed in the simulated and measured FBWs is due the fabrication limitations.

Table 1.0

| Reference | Frequency (GHz) | 10dB FBW | ±1dB FBW | ±5° FBW |
|---|---|---|---|---|
| Conventional | 6 | 30.8% | 16.3% | 30.8% |
| [3] | 2.45 | 38.8% | 21% | NA |
| [4] | 5.2 | 31% | 31% | 47% |
| This work | 6 | 42.2% | 42.2% | 30.7% |

Table I compares the characteristics of the proposed branch line coupler, conventional and the one presented in [3] and [4]. It is clearly observed that both the two bandwidths of the proposed coupler are substantially larger than those in comparison with the exception of $\pm 5^o$ of that reported in [4].

## References

[1] Ghosh, D. and Kumar, G. "A four branch microstrip coupler with improved bandwidth and isolation." *Communications (NCC), 2015 Twenty First National Conference on*. IEEE, 2015.

[2] Hiraguri, K., Koshiji, F. and Koshiji, K. "A flexible broadband antenna with fan-shaped and trapezoidal elements formed on printed circuit board for ultra-wideband radio." *Electronics Packaging (ICEP), International Conference on*. IEEE, 2014.

[3] Sa'ad, B.M et al. "Transparent Branch-Line Coupler Using Micro-Metal Mesh Conductive Film." *Microwave and Wireless Components Letters, IEEE* 24.12 857-859, 2014.

[4] Chen, T. Y., & Chi, P. L. "Bandwidth-enhanced branch-line coupler using the center-loaded vertical line and distributed capacitors." *Microwave Conference Proceedings (APMC), Asia-Pacific*. IEEE, 2012.

[5] Trajkovikj, J., Zurcher, J. F., & Skrivervik, A. K. "Soft and flexible antennas on permittivity adjustable PDMS substrates." *Antennas and Propagation Conference (LAPC), Loughborough*. IEEE, 2012.

[6] Mata A, Fleischman AJ, Roy S. "Characterization of polydimethylsiloxane (PDMS) properties for biomedical micro/nanosystems." *Biomedical micro-devices* 7.4, 281-293, 2005.

# A wideband corner-notched artificial magnetic conductor (AMC) integrated with a rectangular ring antenna

**N. F. M. Aun[1*], P. J. Soh[1], M. F. Jamlos[1,2], H. Lago[1], A. A. Al-Hadi[1]**

[1]Advance Communication Engineering Centre (ACE),
School of Computer and Communication Engineering, Universiti Malaysia Perlis (UniMAP),
Pauh Putra Campus, 02600, Arau, Perlis
[2]Faculty of Mechanical Engineering, Universiti Malaysia Pahang, Pekan, Malaysia
*farahiyah86@gmail.com

## Abstract

This paper presents the design of a wideband Artificial Magnetic Conductor (AMC) for operation at 8 GHz with 2 GHz of bandwidth. This is to suit the Wireless Body Area Network (WBAN) Ultra Wideband (UWB) mandatory channel 6. The proposed AMC is subsequently incorporated on a rectangular-ring patch antenna to determine the contribution of the AMC in improving the antenna reflection coefficient and impedance bandwidth.

## 1. Introduction

Body-worn textile antennas have been presented for various frequency bands as they are more ergonomic and comfortable compared to the rigid structures. Besides that, the ability to ensure that the human body is protected from undesired electromagnetic radiation is the main additional requirement for a textile antenna compared to a conventional design.

Microstrip patch antennas are widely used for wearable applications however, these antennas are relatively narrow band. Moreover, the performances may be slightly degraded in terms of frequency and physical deformation when placed conformal to the human body. Consequently, the performance of an artificial magnetic conductor based antennas have been intensely investigated to resolve above mentioned issues with various design have been reported in the literature, [1] – [8]. AMC is a type of metamaterial which is unavailable in nature which exhibits zero degree reflection phase characteristics of Perfect Magnetic Conductor at resonance frequency.

The main idea for this antenna is to integrate the upper WLAN band at 5.5 GHz with UWB mandatory channel 6 at 8 GHz. Thus, in this paper an AMC plane consisting 3 x 3 corner-truncated rectangular elements is proposed to improve the impedance matching and bandwidth of a rectangular-ring patch antenna.

## 2. AMC and Antenna Design

In this work, a rectangular corner-notched unit cell is chosen then, duplicated and placed periodically to the complete AMC plane. Fig. 1 shows the simulated reflection phase for the AMC. It can be seen that the phase of the reflected wave is about 0° in the 8 GHz band, which exhibits a PMC-like characteristic with the operating bandwidth from 6.78 GHz to 8.77 GHz.

Fig. 2 (a) shows the diagram of rectangular ring patch antenna while Fig. 2 (b) shows the integrated structure of AMC-antenna. The full structure consists of the AMC plane which is placed underneath the same 1.5 mm thick felt substrate consisting of a radiating patch made from the *ShieldIt*. Fig. 3 shows the fabricated antenna prototype.

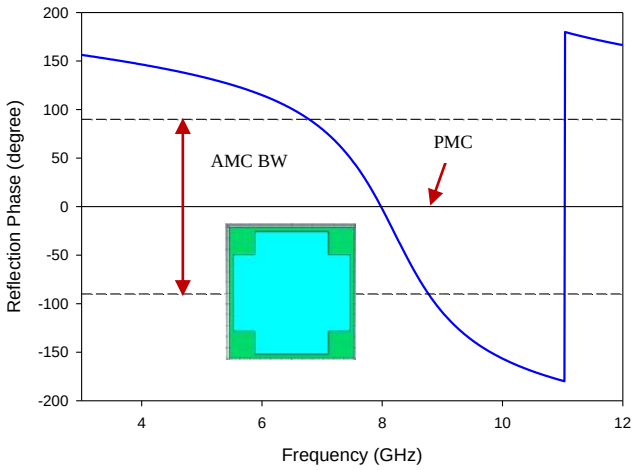



Figure 1: The reflection phase of the AMC unit cell

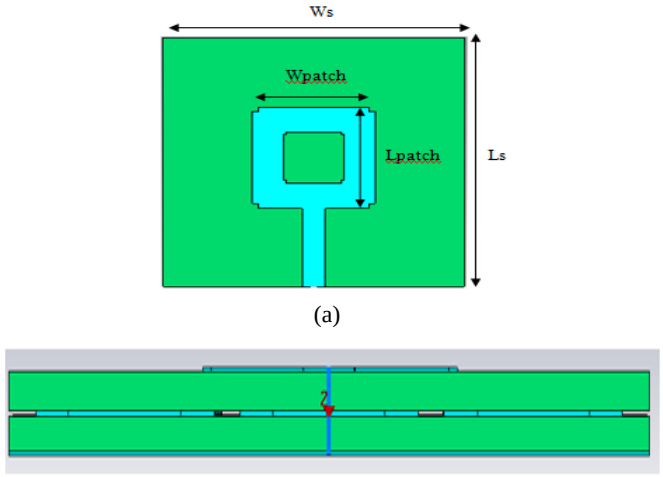



Figure 2: Topology of the proposed antenna (a) antenna patch (b) the cross-sectional view of the multilayered AMC-integrated antenna. Ws = Ls = Wg = Lg = 40 mm, Wpatch = 15.02 mm, Lpatch = 16.16 mm, Wcell = 11.2 mm, Lcell =7

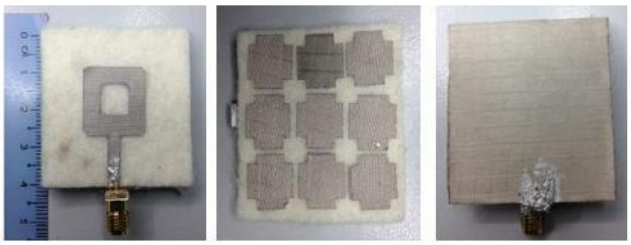


Figure 3: Fabricated prototype

## 3. Results and Discussion

Fig. 4 shows the simulated and measured reflection coefficient for antenna with AMC and without AMC structure. It has been observed that the incorporation of the AMC structure into the antenna improved the matching to achieve a minimum value of -24.03 dB compared to the reference antenna resonating at 8 GHz. Besides that, an additional band operating in the 5.5 GHz WLAN band is also noticed due to the rectangular-ring shaped design, which allows the excitation of two modes. The radiation pattern has been obtained at 5.5 GHz and 8 GHz as in Fig. 5.

To study the body's influence, a three layered rectangular biological tissue model consisting layers of skin, fat and muscle is placed in proximity of the proposed antenna. Fig. 6 shows the simulation results of $S_{11}$ with different antenna-body gaps. It has been observed that there is no significant frequency detuning due to the effect of the AMC plane. After that, the calculated results of SAR simulations are summarized in Table 1 to investigate the contribution of the metasurface placed between the antenna and the human body. The results clearly demonstrate that the AMC has decreased the power absorption resulting in a low SAR value and its further reduced when simulating using a larger area of human tissue at 10 mm distance from the antenna ground layer.

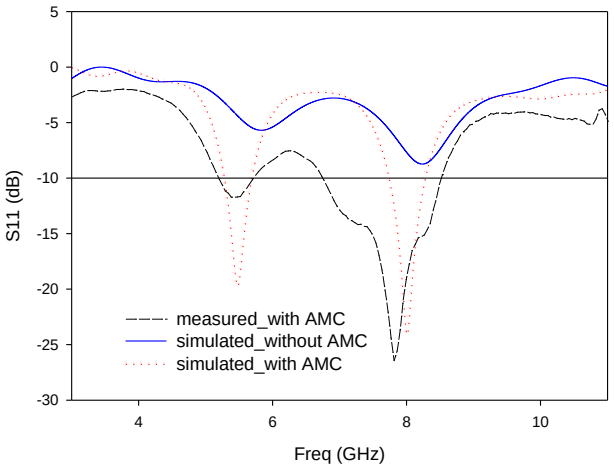



Figure 4: Simulated and measured reflection coefficients of the antenna

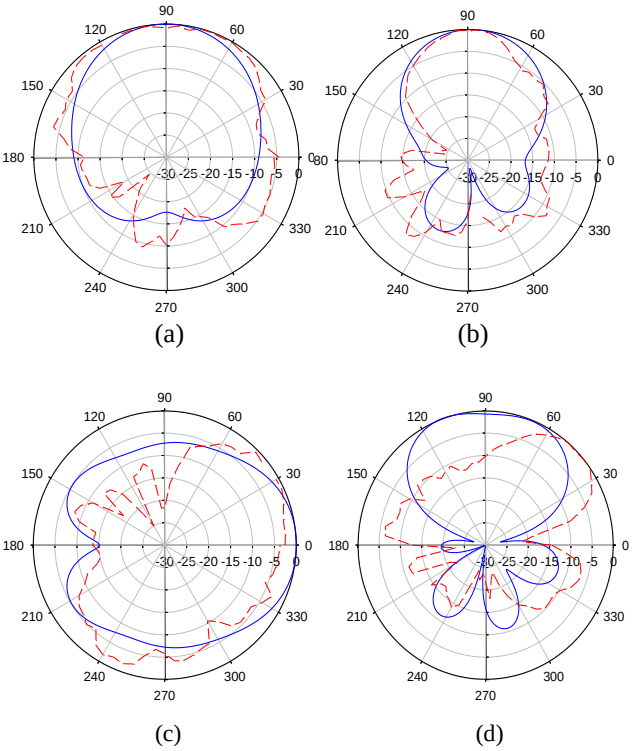



Figure 5: Radiation pattern of the proposed antenna at (a) 5.5 GHz (*xz*-plane); (b) 5.5 GHz (*yz*-plane), (c) 8 GHz (*xz*-plane); and (d) 8 GHz (*yz*-plane). Solid (blue) line: simulated, dashed (red) line: measured

SAR simulations were then performed using a Hugo human body model in the CST Microwave Studio. The antenna is positioned on a reasonably sized portion of the chest to reduce the simulation resources as shown in Fig. 7. It has been observed that the proposed antenna achieved a SAR value of 0.305 W/Kg and 0.624 W/Kg at 5.5 GHz and

8 GHz respectively. This SAR value is below the safety limit which is defined 2 W/Kg, indicating the antenna is safe for on-body usage.

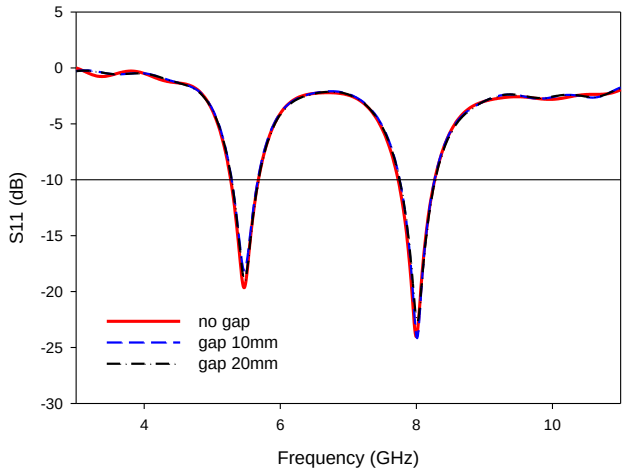



Figure 6: Influence of the gap between antenna and the human skin on antenna reflection coefficient

Table 1: Simulated SAR

| frequency | antenna with 40x40 $mm^2$ tissue (W/kg) | antenna with 120x120 $mm^2$ tissue (W/kg) |
|---|---|---|
| 5.5 GHz | 0.5517 | 0.3126 |
| 8 GHz | 1.247 | 0.797 |

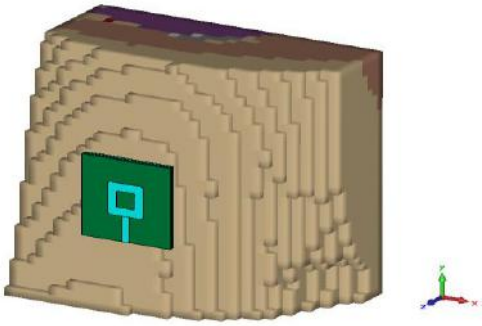


Figure 7: The placement of the antenna on the Hugo human model for SAR evaluation of the proposed antenna.

## 4. Conclusions

A rectangular-shaped, corner-notched AMC unit cell is proposed in this work. It features a center frequency of 8 GHz with an impedance bandwidth of 6.78 GHz to 8.77 GHz. The inclusion of the AMC structure onto a conventional microstrip-fed rectangular-ring patch antenna successfully improved impedance matching with $S_{11}$ = -16.43 dB and -14.2 dB at 5.5 GHz and 8 GHz, respectively. Their impedance bandwidth of 410 MHz and 540 MHz are exhibited for simulated while better impedance bandwidth are obtained for measured which is 490 MHz and 1710 MHz for lower and upper band accordingly.

## Acknowledgements

This project is supported by the Fundamental Research Grant Scheme provided by the Malaysian Ministry of Higher Education (MOHE) (grant no: 9003-00537). The authors would like to acknowledge the members of the Advance Communication Engineering, Universiti Malaysia Perlis for their help, guidance, and the use of the facilities.

## References

[1] S. Yan, P. J. Soh, and G. A. E. Vandenbosch, "Low-Profile Dual-Band Textile Antenna With Artificial Magnetic Conductor Plane," *IEEE Trans. Antennas Propag.*, vol. 62, no. 12, pp. 6487–6490, 2014.

[2] L.-R. Zhong, G.-M. Yang, and Y.-W. Zhong, "Gain enhancement of bow-tie antenna using fractal wideband artificial magnetic conductor ground," *Electron. Lett.*, vol. 51, no. 4, pp. 315–317, 2015.

[3] M. K. A. Rahim, N. A. Samsuri, K. Kamardin, and P. S. Hall, "Vertical and horizontal transmission enhancement between antennas using textile artificial magnetic conductor waveguide sheet," *Electron. Lett.*, vol. 51, no. 9, pp. 671–673, 2015.

[4] R. Dewan, S. K. A Rahim, S. F. Ausordin, M. Z. M. Nor, and B. M. Saad, "Crescent moon-shaped artificial magnetic conductor ground plane for patch antenna application," *2013 IEEE Symp. Wirel. Technol. Appl. ISWTA.*, Kuching, Malaysia, pp. 254–258, 2013.

[5] F. Rahmadani and A. Munir, "Microstrip patch antenna miniaturization using artificial magnetic conductor," *2011 6th Int. Conf. Telecommun. Syst. Serv. Appl.*, Bali, Indonesia, pp. 219–223, 2011.

[6] H. R. Raad, A. I. Abbosh, H. M. Al-Rizzo, and D. G. Rucker, "Flexible and compact AMC based antenna for telemedicine applications," *IEEE Trans. Antennas Propag.*, vol. 61, no. 2, pp. 524–531, 2013.

[7] P. Lu, "Combination of Bow-tie Shaped Meander Slot Antenna with Wideband AMC Structure," *2014 IEEE Antennas and Propagation Society International Symposium (APSURSI).*, Memphis, Tennessee, pp. 2066–2067, 2014.

[8] R. R. Ihsan and A. Munir, "Utilization of artificial magnetic conductor for bandwidth enhancement of square patch antenna," *2012 7th Int. Conf. Telecommun. Syst. Serv. Appl. TSSA 2012.*, Bali, Indonesia, no. 003, pp. 192–195, 2012.

# Circularly Split Ring Resonator Based Frequency Reconfigurable Antenna

**M. A. Rahman[1], M. R.I. Faruque[1*], and M. T. Islam[2]**

[1]Space Science Centre, Universiti Kebangsaan Malaysia, Malaysia
[2]Dept. of Electrical, Electronic and Systems Engineering, Universiti Kebangsaan Malaysia,
43600 UKM, Bangi, Selangor D.E., Malaysia
[*]corresponding author: rashedgen@yahoo.com

**Abstract**

In this paper, a frequency reconfigurable antenna based on a circularly split ring resonator (CSRR) is presented. The proposed reconfigurable monopole antenna consists of a microstrip-fed hook shaped structure and a CSRR having single reconfigurable split only. A new band of radiation unlike the band radiated from monopole only is observed due to magnetic coupling between the CSRR and the monopole antenna. The resonance frequency of the CSRR can be arbitrarily chosen by varying the dimension and relative position of its gap with the monopole, which leads the antenna to become reconfigurable one. By using a single switch with perfect electric conductor (PEC) at the gap of CSRR cell, the effect of CSRR can be deactivated and hence it is possible to suppress the corresponding resonance, resulting in a frequency reconfigurable antenna. Commercially available Computer Simulation Technology (CST) microwave studio based on finite integration technique (FIT) was adopted throughout the study.

## 1. Introduction

In response to the ever-increasing demand of multi-functional wireless devices, it is necessary for the communication terminals are compatible with multiple frequency bands. In order to fulfil the current user expectation, all communication devices need to be compact, low profile, lightweight and with multi-functional transceivers capabilities. As a wireless device, it is particularly true for cognitive radios (CRs) where the transceivers have the ability to change the operating frequency band when needed [1, 2]. Thus, modern radios are necessarily multi-standard, which results in a high hardware complexity that is usually dealt with at the front-end and at the digital part of the radios. Nevertheless, the complexity of the hardware is approaching saturation and systems designers have started thinking of moving some of the complexity towards the antenna. In this perspective, one of the important functionalities that can be integrated to the antenna is filtering. Instead of filtering unwanted signals at the front-end, by using a bank of filters, a lot of space can be saved if some of the filtering is performed at the antenna level. Examples of antennas with integrated filtering capabilities can be found in [3, 4]. In these examples, the antennas are wideband and the filtering consists in suppressing parts of the operating frequency band. Another approach that can be used is, using multi-band antennas with the capability of suppressing either of the bands[5, 6].

The proposed antenna is a multi-band one with frequency reconfiguration capability based on CSRR properties. To achieve multi-band behaviour, CSRR cell is used in conjunction with a monopole to create new resonance. To achieve frequency reconfiguration, a switch is integrated to the CSRR cell in order to activate or deactivate them. The on/off states of the switches are modelled by the presence or absence of a perfect conductor. The basic idea behind this approach is that the radiating element is sensitive to the presence of the resonator due to the magnetic coupling with monopole. The resonator alters the antenna's radiation characteristics effectively by acting as 'metamaterial' unit cell.

Metamaterial is an engineered electromagnetic material having exotic electromagnetic properties and is being utilized in almost all electromagnetic fields besides antenna applications [7-10]. SRR is a proven shape of metamaterial. By using a resonating element such as a split-ring resonator (SRR), with carefully selected geometric dimensions, one can obtain an electrically small antenna operating at wireless communication frequencies [9]. Previously, very few attempts were taken to design reconfigurable antenna using circular SRR. Like in [11], D. K. Ntaikos *et al.* presented a metamaterial-based monopole antenna but they adopted two SRR in their design. H. Cheribi *et al.* proposed a metamaterial-based reconfigurable antenna but they utilized two double square-shaped SRR in their work [12]. M. I. Hossain *et al.* designed a metamaterial-based reconfigurable antenna but the size of antenna was $100\times80$ mm$^2$ [13].

Therefore, the main purpose of this study is to provide a compact size antenna by combining an electrically small planar monopole antenna with a single SRR cell. The CSRR make resonant at

wavelengths much smaller than the dimensions of the ring due to the large capacitance in the gap within it. The combination of the monopole antenna and the CSRR results in multi-band operation, with the individual resonances. Its resonances can be controlled independently as either monopole or CSRR antenna. Hence, the design of the monopole and SRR can be considered quite separately, with only minimal modifications required to make the entire antenna operational.

## 2. Reconfigurable antenna geography

The proposed monopole antenna without a circularly split ring resonator (CSRR) is presented in Fig 1. It is composed of a microstrip-fed hook shaped line with a width of $W_f$ = 4 mm to form monopole on a Rogers 5880 substrate with $h$ = 1.575 mm thickness. The relative permittivity and loss tangent of substrate material is 2.2 and 0.0009 respectively with a dimension of $W_s \times L_s$ = 30 mm × 30 mm. As resonating part a CSRR is disposed at right side of the monopole. The CSRR is shown in the Fig.2. The inner and outer diameter of CSRR is chosen $d_r$ = 6 mm and $D_r$ = 7 mm respectively with a $g_s$ = 0.5 mm split gap. The minimum distance from the monopole to the CSRR is 0.5 mm. In addition, the ground having $W_g$ = 30 mm width and $L_g$ = 10 mm length placed at the backside. Copper annealed conductor with $t$ = 0.035 mm thick is chosen for monopole, ground and CSRR. The monopole antenna with CSRR is being displayed in Fig.3.

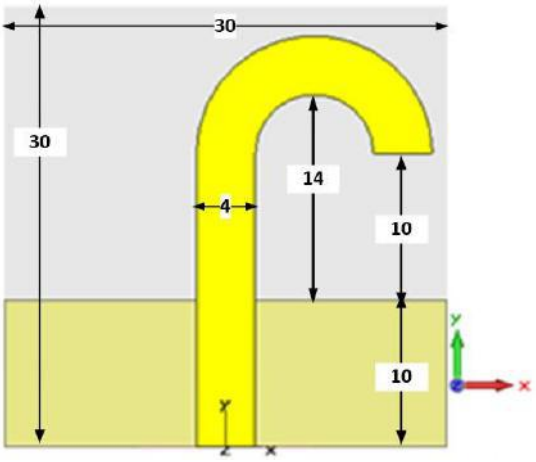



Figure-1: Geometry of proposed monopole antenna without CSRR

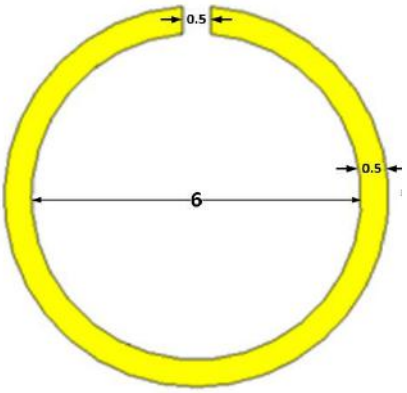



Figure-2: Geometry of CSRR

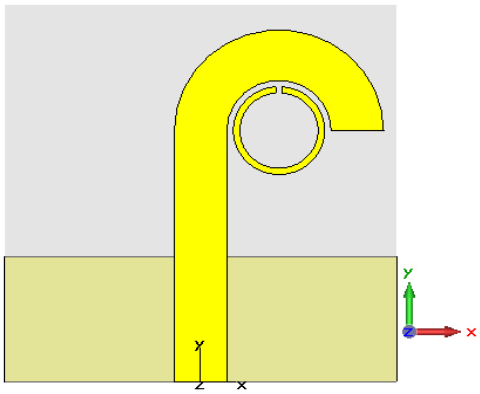



Figure-3: Geometry of the proposed monopole antenna with CSRR.

## 3. Result and Discussion:

The antenna monopole is investigated with and without the CSRR to compare the impact of the CSRR on the reflection coefficient using CST microwave studio. Initially, the proposed antenna monopole without CSRR simulated which gives resonance around 2.69 GHz with high return loss shown in Fig. 4.

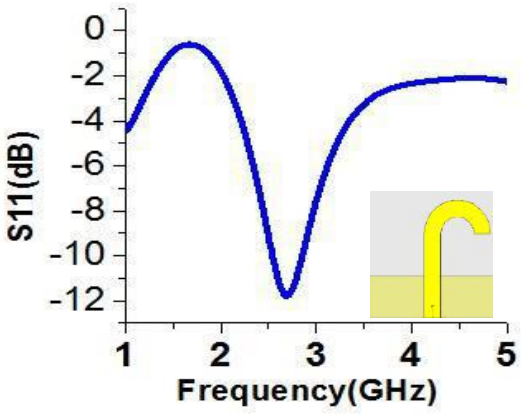



Figure-4: Simulated reflection coefficient ($S_{11}$) of antenna monopole without CSRR

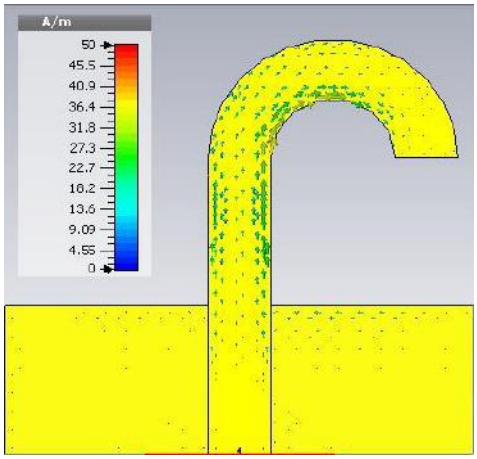



Figure-5: Current distribution of the monopole antenna without CSRR

In the Fig.5, the current distribution in the antenna at 2.69 GHz without CSRR is shown. Minor current is seen following in the antenna. The S-parameters of CSRR were also investigated with the CST microwave studio software. The transmission property is shown in the Fig.6. A sharp transmittance is visible in the Fig.6 at the frequency of 4.6 GHz.

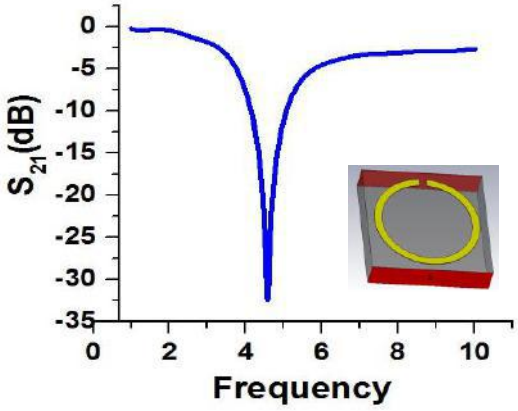



Figure-6: Transmission property ($S_{21}$) in dB of the CSRR

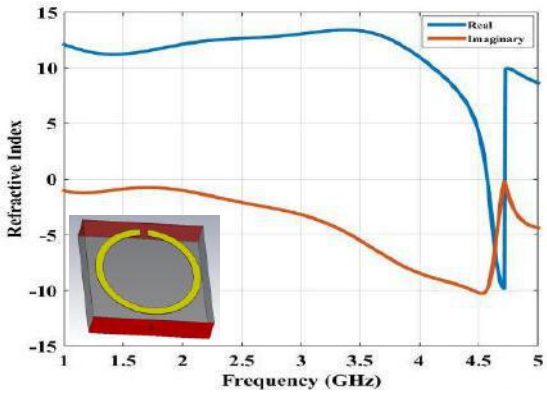



Figure-7: Refractive index property of the CSRR

The refractive index of the CSRR was determined directly from the S-parameters using the direct refractive index (DRI) method depicted in [14]. The refractive index curve is presented in the Fig. 7. Negative refractive index property is visible from the Fig.7 at the same frequency of transmittance for the CSRR.

Then the CSRR was incorporated at right side of the monopole as Fig. 3 and simulation gives an additional resonance at the same point of transmittance for the CSRR at 4.59 GHz with very low return loss as seen at Fig. 8.

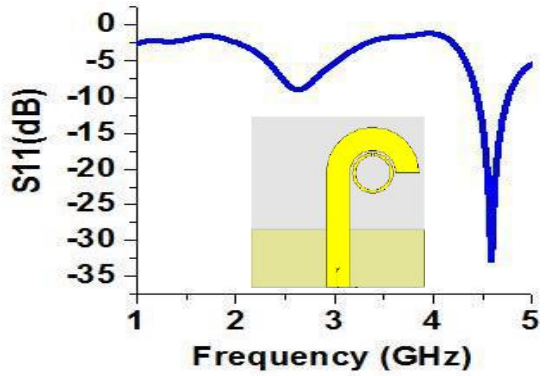



Figure-8: Simulated reflection coefficient ($S_{11}$) of antenna monopole with CSRR

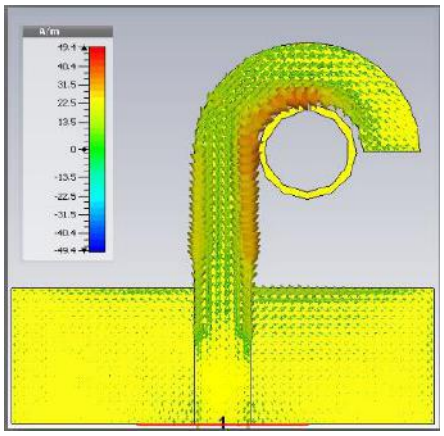



Figure-9: Current distribution of the monopole antenna without CSRR

It is clear from the Fig.8 that, the new resonance ~~is~~ has occurred due to primarily magnetic coupling of the CSRR to the monopoles near field. Moreover, capacitive coupling with the CSRR-monopole gap affecting both the resonant frequency and the CSRR quality factor and hence, the antenna bandwidth. The first one is a monopole resonance, i.e., at frequencies where its length is closer to quarter wavelength, since it is also present in the cases without the CSRR. The second resonance is a clear higher-order CSRR resonance, as this is not observed in the case of a simple monopole. Current

distribution of the antenna with CSRR is also depicted in the Fig.9 at the frequency of 4.59 GHz where increased current is seen following in the antenna at a frequency of 4.6GHz. This increment was gained due to magnetic coupling of CSRR with the antenna.

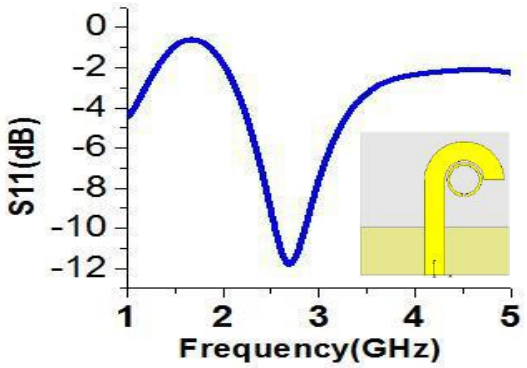



Figure-10: Simulated reflection coefficient ($S_{11}$) of antenna monopole with CSRR having split gap in opposite direction

The bandwidth of operation is quite narrow since the useful bandwidth is more or less controlled by the CSRR geometric features, although it is also significantly affected by its coupling to the monopole. This is more obviously demonstrated in the case of CSRR having split gap in opposite direction as shown in Fig. 10, where the CSRR is coupled very poorly to the monopole and resulting no resonance as before. The resonance is seen almost as same as the simple monopole antenna without CSRR. In this case the CSRR acts as a parasitic element only which cause a slight shift in resonance frequency as compared to the antenna monopole only.

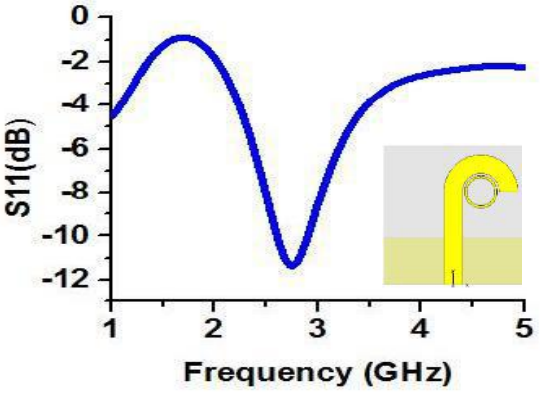



Figure-11: Simulated reflection coefficient ($S_{11}$) of antenna monopole by closing the gap of the CSRR.

For further realization about the effect of CSRR on monopole, simulation was done by closing the split gap of CSRR as shown in Fig. 11 and no additional resonance is seen accept near to the monopole resonance. Aslight shift in frequency comparing with simple monopole resonance is occurred since the additional closed CSRR acts as a parasitic element only instead of behaving as a resonator.

To achieve frequency reconfiguration, one can play on the CSRR geometry in order to activate or deactivate at the appropriate band. By closing the gap of CSRR, which can be done by means of a switch, the resonator behaviour of the cell disappears and their effect deactivated. Fig. 11 gives the $S_{11}$ corresponding to the closed gap CSRR configurations of the antenna. As can be seen from Fig. 11, the effect of the CSRR can be deactivated by closing the gap of CSRR with switch. Deactivating the CSRR, the corresponding higher resonance also disappears and the antenna regains the monopole resonance around 2.75 GHz.

The effect of CSRR also investigated by placing it at the ground plane as shown in Fig. 12. In this case, the CSRR provides resonance at a slightly shifted comparing with Fig. 3, because of different coupling level between CSRR and monopole. A small increase in return loss (-25 dB) also found in this case, which is very low (-56 dB) when the CSRR placed at monopole plan. However, the overall effect of CSRR on monopole antenna is being shown in the Table-1.

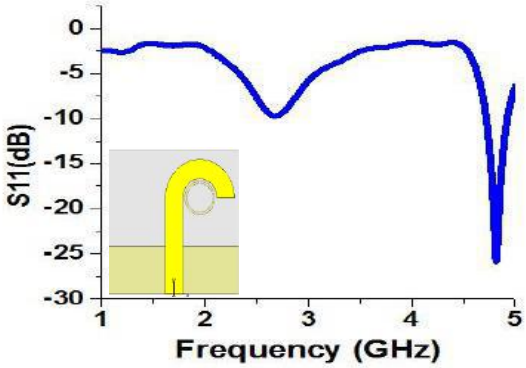
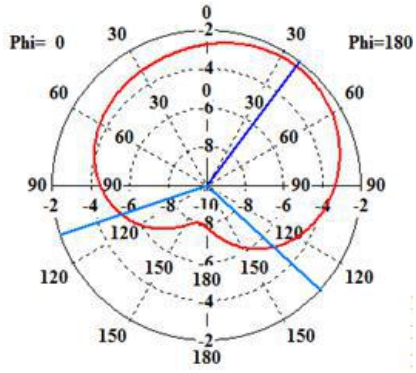


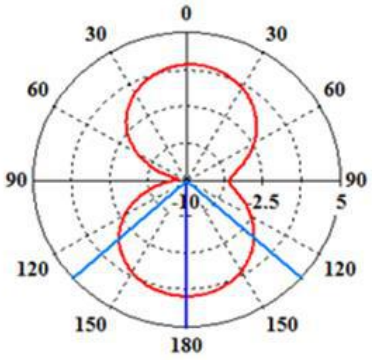

Figure-12: Simulated reflection coefficient ($S_{11}$) of the antenna monopole with the CSRR at ground.

**Table 1.** Antenna configuration versus resonance frequency

| Antenna configuration | Resonance frequency |
|---|---|
| Monopole antenna without CSRR | 2.69 GHz |
| Monopole antenna with CSRR | 2.69 GHz and 4.59 GHz |
| Monopole antenna with CSRR with gap at opposite side | 2.64 GHz |
| Monopole antenna with gap closed of CSRR | 2.75 GHz |
| Monopole antenna with CSRR at ground | 2.65 GHz and 5 GHz |




(a)



(b)

Figure-13: (a) E-plane Radiation pattern of antenna without CSRR at φ=0 and (b) E-plane Radiation pattern of antenna with CSRR at φ=0.

In the Fig.13, the numerical E-plane radiation pattern (φ=0) of the monopole antenna in the far field region at 2.69 GHz with and without CSRR is being displayed. It is evident that the incorporation of the CSRR in the antenna does not create major effect on the radiation pattern especially on its omni-directional nature.

## 4. Conclusion

A frequency reconfigurable antenna based on CSRR has been presented. It is composed of a hook shape monopole with a CSRR cell that are used to create new resonance. The CSRR produces a magnetic coupling with the monopole that starts to radiate at new frequencies. The antenna with the CSRR now exhibits two bands; the lower one corresponds to the monopole only and the higher one is the result of the coupling between the monopole and the SSSR. The resonance around 2.69 GHz corresponds to the monopole and at 4.59 GHz corresponds to the CSRR. The interest of this proposed approach is that the effect of the CSRR cell can be easily deactivated by closing the gap of the CSRR. So, by using a single switch at the CSRR, the antenna can be switched between two different frequency responses, giving afrequency reconfigurable antenna.

**Acknowledgments.** This work is supported by the Ministry of Education Malaysia (MOE) under Grant No. FRGSTOPDOWN/2014/ TK03/UKM/01/1 and the UKM research Grant Code No. GUP-2016-028.

## References

[1] P. Hall, Z. Hu, P. Song, M. Hamid, and Z. Wang, "Creating reconfigurable adaptive antennas for cognitive radio applications considering cost and portability," in *Cognitive Radio Communications: European Activities and Progress, IET Seminar on*, 2010, pp. 1-44.

[2] S. Haykin, "Cognitive radio: brain-empowered wireless communications," *Selected Areas in Communications, IEEE Journal on*, vol. 23, pp. 201-220, 2005.

[3] M. Hamid, P. Gardner, P. S. Hall, and F. Ghanem, "Vivaldi antenna with integrated switchable band pass resonator," *Antennas and Propagation, IEEE Transactions on*, vol. 59, pp. 4008-4015, 2011.

[4] F. Ghanem, P. Hall, and J. Kelly, "Two port frequency reconfigurable antenna for cognitive radios," *Electronics Letters*, vol. 45, pp. 534-536, 2009.

[5] A. P. Saghati, M. Azarmanesh, and R. Zaker, "A novel switchable single-and multifrequency triple-slot antenna for 2.4-GHz bluetooth, 3.5-GHz WiMax, and 5.8-GHz WLAN," *Antennas and Wireless Propagation Letters, IEEE*, vol. 9, pp. 534-537, 2010.

[6] M.-J. Chiang, S. Wang, and C.-C. Hsu, "Compact multifrequency slot antenna design incorporating embedded arc-strip," *Antennas and Wireless Propagation Letters, IEEE*, vol. 11, pp. 834-837, 2012.

[7] S. S. Islam, M. R. I. Faruque, and M. T. Islam, "A two-component NZRI metamaterial based rectangular cloak," *AIP Advances*, vol. 5, p. 107116, 2015.

[8] M. R. I. Faruque, M. T. Islam, and N. Misran, "Design analysis of new metamaterial for EM absorption reduction," *Progress In Electromagnetics Research*, vol. 124, pp. 119-135, 2012.

[9] A. Erentok and R. W. Ziolkowski, "Metamaterial-inspired efficient electrically small antennas," *Antennas and Propagation, IEEE Transactions on*, vol. 56, pp. 691-707, 2008.

[10] J. Carver, V. Reignault, and F. Gadot, "Engineering of the metamaterial-based cut-band filter," *Applied Physics A,* vol. 117, pp. 513-516, 2014.

[11] D. K. Ntaikos, N. K. Bourgis, and T. V. Yioultsis, "Metamaterial-based electrically small multiband planar monopole antennas," *IEEE Antennas and Wireless Propagation Letters,* pp. 963-966, 2011.

[12] H. Cheribi, F. Ghanem, and H. Kimouche, "Metamaterial-based frequency reconfigurable antenna," *Electronics Letters,* vol. 49, pp. 315-316, 2013.

[13] M. Hossain, M. R. I. Faruque, M. T. Islam, and M. Ali, "Design and analysis of coupled-resonator reconfigurable antenna," *Applied Physics A,* vol. 122, pp. 1-4, 2016.

[14] S. S. Islam, M. R. I. Faruque, and M. T. Islam, "A new direct retrieval method of refractive index for the metamaterial," *Current Science (00113891),* vol. 109, 2015.

# Wideband Textile Antenna with AMC Plane

**Ezzaty Faridah Nor Mohd Hussin[1], Ping Jack Soh[1*], Mohd Faizal Jamlos[1,2], and Herwansyah Lago[1]**

[1]Advance Communication Engineering (ACE), School of Computer and Communication Engineering, Universiti Malaysia Perlis, Pauh Putra Campus, 02600 Arau, Perlis, Malaysia
[2]Faculty of Mechanical Engineering, Universiti Malaysia Pahang, Pekan, Pahang, Malaysia
*Corresponding author: pjsoh@unimap.edu.my

## Abstract

A wideband miniaturized textile planar antenna with AMC plane is presented. The antenna is initially designed using the combination of two rectangular microstrip antennas operating at 1.5 GHz and 2.5 GHz before being further optimized for a wideband operation using various broadbanding techniques. This optimized radiator is then placed on over an array of unit elements forming an artificial magnetic conductor (AMC) plane. Each unit element is a square patch slotted using a circular ring, and is designed to operate at 2 GHz. To validate the contribution of the AMC plane in reducing backward radiation towards the human user, the performance of the proposed antenna is compared to a similar antenna without the AMC plane. This investigation indicated that the proposed antenna is capable of reducing backlobe while simultaneously increasing directivity and bandwidth.

## 1. Introduction

Metamaterial is an artificial structure that is designed to obtain specific characteristics which are not naturally available in nature [1]-[2]. The unique characteristics of metamaterial have been used extensively in antennas and microwave applications for performance improvement [3].

The Artificial Magnetic Conductor (AMC) has been validated to function as an effective reflector to improve the radiation characteristics of planar antennas [4]-[8]. Among the improvements of AMCs when integrated in wearable low-profile antennas is in terms of gain, bandwidth and directivity [5]. In this investigation, a wideband planar wearable antenna with an AMC plane is proposed. It operates between 2 and 3 GHz and is expected to increase the antenna bandwidth and reduce back radiation towards the human body.

This paper is organized as follows. Section 2 presents a description of the materials used in the proposed antenna. Section 3, discusses the detailed antenna design strategies. The results of the simulation and discussions are presented in Section 4 and finally concluded in Section 5.

## 2. Textile Materials

Two textiles materials were used in this design. First is a 3 mm-thick non-conductive textile used as substrate. It features a relative permittivity ($\varepsilon_r$) of 1.44 and loss tangent (tan-$\delta$) of 0.044. The other textile is Shieldit Super, which is used to form the antenna conductive elements (radiators and ground plane). It is a 0.17 mm-thick textile with a conductivity of 1.18 x $10^5$ S/m. It also features an adhesive reverse side and this enables ease of attachment onto the felt substrate. The proposed antenna is fed using a 50Ω SMA connector. CST Microwave Studio software is used for the numerical simulations.

## 3. Antenna Design

The proposed AMC unit cell is a square patch slotted with a circular ring, as shown in Figure 1. Its resulting reflection phase is plotted in Figure 2, indicating operation at 2 GHz with 370 MHz of bandwidth. This unit cell is then multiplied into a 3 x 5 array to form the AMC.

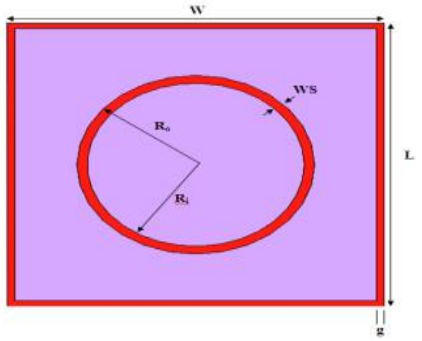



Figure 1: The unit cell of the 2 GHz AMC (patch size = 35 mm x 35 mm, outer radius = 11.5 mm, inner radius = 10.5 mm)

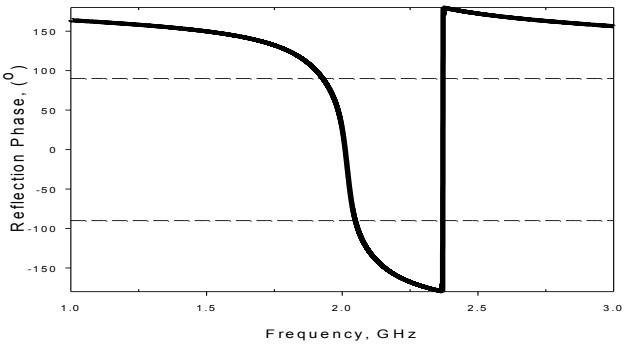



Figure 2: Reflection phase of the proposed AMC unit cell

The AMC plane is then integrated beneath the optimized antenna which is illustrated in Figure 3. To form the antenna, two rectangular patches are first designed to operate at 1.5 GHz and 2.5 GHz. Next, several broadbanding techniques such as additional slots, parasitic patches, etc. are employed on the radiator to overcome the inherent narrow band of the microstrip topology. The resonance overlapping techniques is applied by integrating both patches as a single radiator by interconnecting them using a feed line. In Figure 3, the top patch operates at 1.5 GHz and the bottom patch operates at 2.5 GHz.

Next, a double-E shaped slot is integrated onto the top patch, and F-slit is incorporated onto the bottom patch to enable multi-banding of these patches. It also enables an overall size reduction. A parasitic radiator is then placed in the proximity of the upper and lower patches. The coupling between the parasitic and the patches contributes to the bandwidth increase. Next, to alleviate the mismatches caused by the implemented broadbanding techniques, blend steps are introduced in the patches and parasitic element. The overall structure's impedance is tuned using these methods to obtain satisfactory reflection performance across the whole targeted band which is between 2 and 3 GHz.

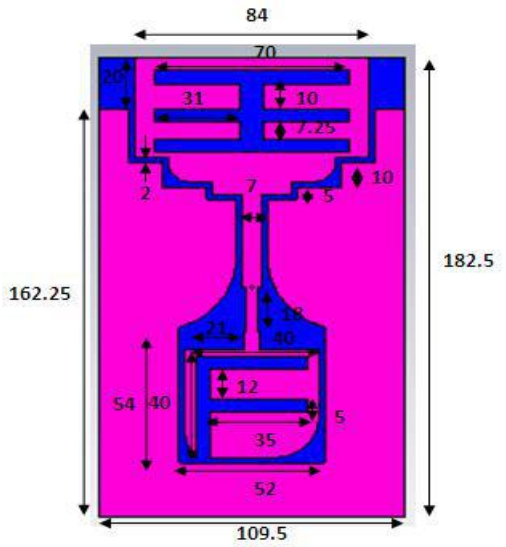



Figure 3: Wideband textile planar antenna (all dimensions in mm)

The contribution of the AMC plane is then evaluated by comparing the bandwidth increment and the radiation performance of the proposed antenna with a similar antenna without the AMC plane at 2 GHz.

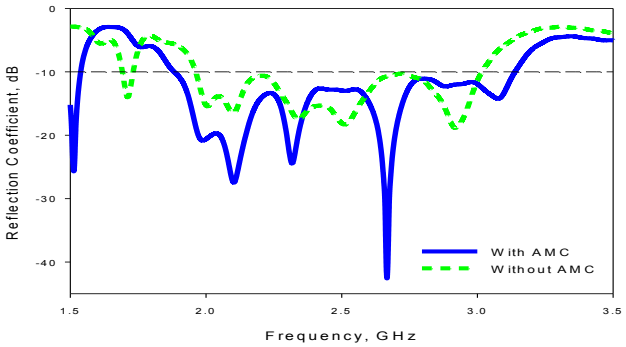
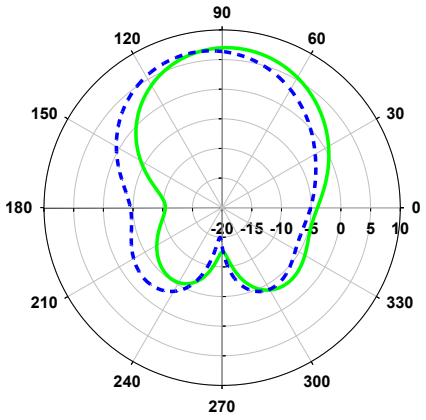
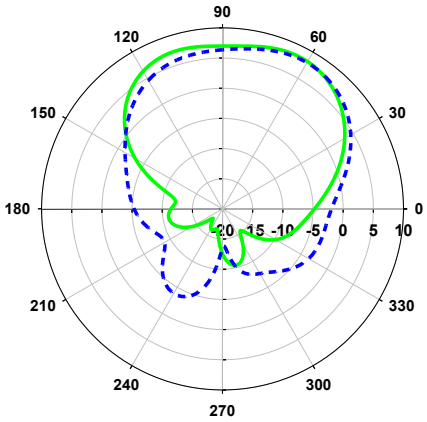



Figure 4: Comparison of reflection coefficient between the antenna with AMC and without AMC

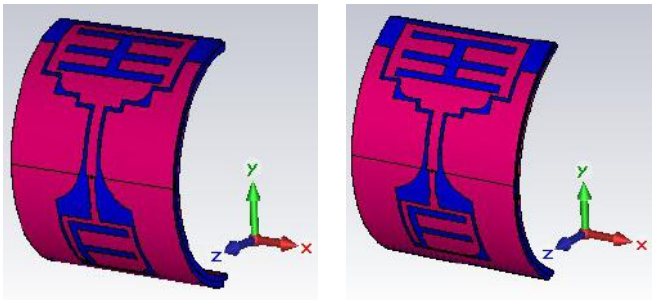



(a)

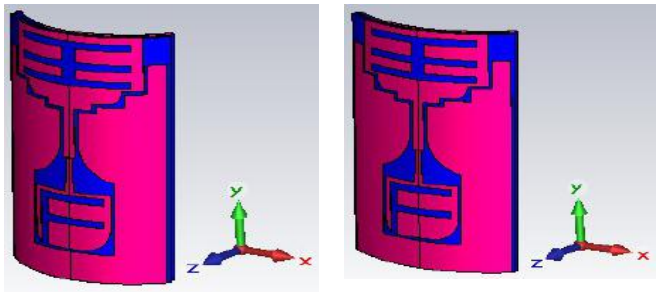



(b)

Figure 5: Comparison of the radiation performance of the proposed antenna with a similar antenna without the AMC plane : (a) $\varphi = 0$ and (b) $\varphi = 90$. Solid line (green): with AMC, dash line (blue): without AMC.

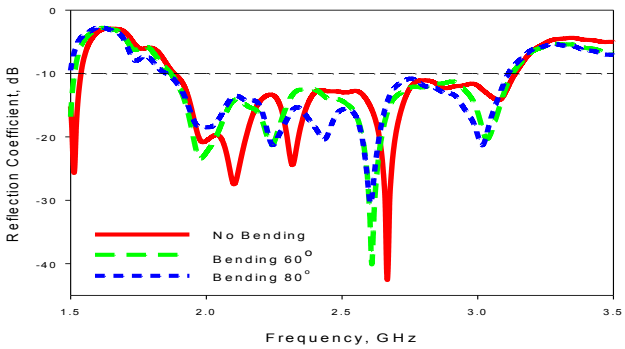



(a) (b)

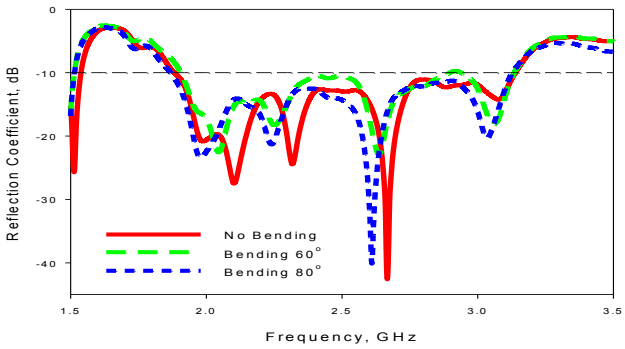


(c) (d)

Figure 6: Proposed antenna with two different bending radii ($r$) and at two different axes: (a) $r$ = 60 mm bent at $x$-axis, (b) $r$ = 80mm bent at $x$-axis, (c) $r$ = 60 mm bent at $y$-axis, (d) $r$ = 80mm bent at $y$-axis




(a)



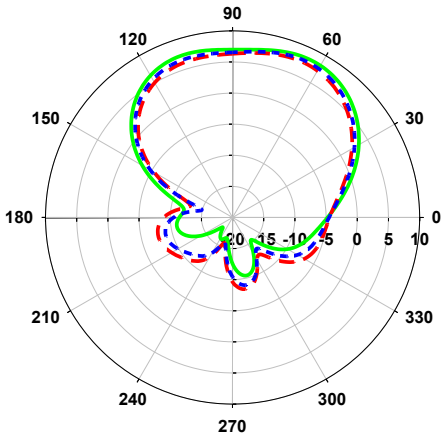

(b)

Figure 7: Bending performance of antenna at (a) $x$-axis and (b) $y$-axis

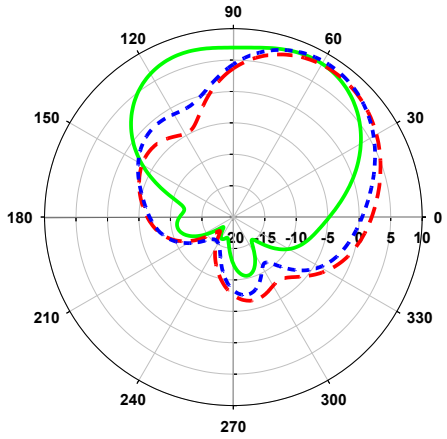
## 4. Results and Discussion

The proposed antenna is studied and compared to similar antenna without AMC plane in terms of reflection coefficient, bandwidth and radiation patterns. It can be observed from Figure 4 that the proposed antenna operates with a wide bandwidth from 1.8 GHz to 3.1 GHz, covering an equivalent fractional bandwidth of 50 %. Meanwhile, the antenna without AMC plane operates from 1.9 GHz to 3 GHz with an equivalent fractional bandwidth of 42 %. The comparison of both antennas in terms of radiation patterns indicate a significant backlobe reduction for the proposed antenna at $\varphi = 0$ and $\varphi = 90$, see Figure 5. It achieved a gain of 3.061 dB at 2 GHz.

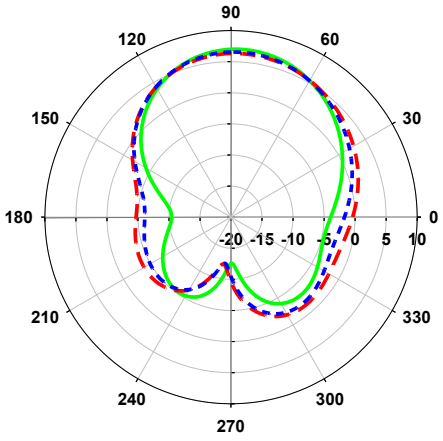
Next, the bending performance of the antenna is studied by wrapping it conformally around a cylinder with radii of $r$ = 60 mm and 80 mm, see Figure 6. Bending was performed at the $x$- and $y$-axes, and their performance is presented in Figure 7. Bending at the $x$-axis with $r$ = 80 mm indicated a total bandwidth increment to 1.26 GHz compared to a flat antenna (with a bandwidth of 1.25 GHz). On the contrary, bending at the $y$-axis with $r$ = 60 mm decreased the bandwidth to 1.22 GHz while bending at $x$-axis with $r$ = 60 mm and bending at $y$-axis with $r$ = 80 mm have the same bandwidth as flat antenna which is 1.25 GHz. Bending performance also applied to the similar antenna without AMC. Flat antenna has a bandwidth of 1.05 GHz. Bending at $x$-axis with $r$ = 60 mm and $r$ = 80 mm show 1.04 GHz and 1.02 GHz of bandwidth. Meanwhile for bending at $y$-axis with $r$ = 60 mm have 1.09 GHz bandwidth and 1.08 GHz bandwidth for bending at $y$-axis with $r$ = 80 mm. Other than that, the front-to-back ratio (FBR) is evaluated on both antennas at 2 GHz. Proposed antenna show 20.78 dB of FBR while bending at $x$-axis with radii 60 mm and 80 mm have 15.67 dB and 16.98 dB. For bending at $y$-axis, the FBR is evaluated to be 17.02 dB with radii 60 mm and 18.2 dB with radii 80 mm. A similar antenna without AMC show the value of FBR is 21.47 dB in flat condition. In bending condition, at $x$-axis with radii 60 mm and 80 mm, the FBR of the antenna is 13.422 dB and 14.67 dB while at $y$-axis, 20.19 dB is FBR for radii 60 mm and 21.99 dB is FBR for radii 80 mm. The summary of the antenna front-back-ratio and bandwidth for both antennas is presented in Table 1.



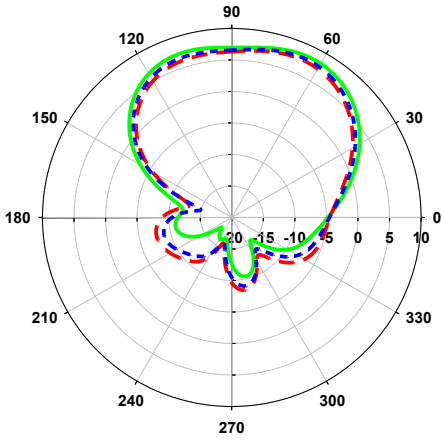

(a)




(b)




(c)




(d)

Figure 8: Simulated radiation pattern in bending performance of proposed antenna at *x*-axis, (a) $\varphi$=0, (b) $\varphi$=90 and *y*-axis, (c) $\varphi$=0, (d) $\varphi$=90. Solid line (green): no bending, long dash line (red): bending 60 mm, short dash line (blue): bending 80 mm

Table 1: Summary of the antenna front-back-ratio and bandwidth when bent at different axes and radii.

| Antenna | Condition | FBR (dB) | Bandwidth (GHz) |
|---|---|---|---|
| With AMC | Flat | 20.78 | 1.25 |
| | Bending at *x*-axis with *r* = 60mm | 15.67 | 1.25 |
| | Bending at *x* -axis with *r* = 80mm | 16.98 | 1.26 |
| | Bending at *y*-axis with *r* = 60mm | 17.02 | 1.22 |
| | Bending y-axis with *r* = 80mm | 18.2 | 1.25 |
| Without AMC | Flat | 21.47 | 1.05 |
| | Bending at *x* -axis with *r* = 60mm | 13.422 | 1.04 |
| | Bending at *x* -axis with *r* = 80mm | 14.67 | 1.02 |
| | Bending at *y*-axis with *r* = 60mm | 20.19 | 1.09 |
| | Bending at *y*-axis with *r* = 80mm | 21.99 | 1.08 |

The radiation patterns of the proposed antenna in flat and bent configurations are shown in Figures 5 and 8, respectively. The antenna radiated towards the forward direction with low backlobe.

## 5. Conclusions

A wideband planar wearable antenna with AMC plane and reduced back radiation is presented. The radiator is first designed using a combination of various broadbanding techniques to operate from 2 GHz to 3 GHz. The AMC plane consists of a 3 x 5 square patches which are slotted using circular rings. It is validated to be capable of increasing the bandwidth and reducing backward radiation at 2 GHz. Its performance indicated a wideband antenna with a fractional bandwidth of 50 % and a gain of 3.061 dB at 2 GHz.

## References

[1] R. Dewan, S. K. A. Rahim, S. F. Ausordin, D. N. A. Zaidel, B. M. Sa'ad and T. Purnamirza, "Bandwidth Widening, Gain Improvement and Efficiency Boost of an Antenna Using Artificial Magnetic Conductor (AMC) Ground Plane," *Jurnal Teknologi (Sciences & Engineering),* no. 70:1, pp. 35-41, 2014.

[2] A. Kumar, and D. Kumar V., "High-performance Metamaterial Patch Antenna," *Microwave Optical Tech. Lett.,* vol. 55, pp. 409-413, 2013.

[3] W. Cao, B. Zhang, A. Liu, T. Yu, D. Guo, and Y. Wei, "Gain Enhancement for Broadband Periodic Endfire Antenna by Using Split-Ring Resonator Structures," *IEEE Trans. Antennas Propag.,* vol. 60, no.7, pp. 3513-3516, 2012.

[4] D. Qu, L. Shafai, and A. Foroozesh, "Improving microstrip patch antenna performance using EBG substrates," *IEEE Proceedings on Microwaves, Antennas and Propag.,* vol. 153, pp. 558-563, 2006.

[5] P. B. Samal, P. J. Soh and G. A. E. Vandenbosch, "A Systematic Design Procedure For Micro-Strip-Based Unidirectional UWB Antennas," *Progress In Electromagnetics Research,* vol. 143, pp. 105-130, 2013.

[6] G.Gnanagurunathan and K. T. Selvan, "Artificial Magnetic Conductors on Wide-Band Patch Antenna," *Progress In Electromagnetics Research Letters,* vol. 36, pp. 9-19, 2013.

[7] D. A. Elsheakh, H. A. Elsadek, E. A. Abdallah, H. Elhenawy, and M. F. Iskander, "Enhancement of microstrip monopole antenna bandwidth by using EBG structures," *IEEE Antennas Wireless Propag. Lett.,* vol. 8, pp. 959-962, 2009.

[8] M. E. De Cos, Y. Alvarez-Lopez, and F. Las-Heras, "On the influence of coupling AMC resonances for RCS reduction in the SHF band," *Progress In Electromagnetics Research,* vol. 117, pp. 103-119, 2011.

# Design of Multiple Layer Microwave Absorbing Structure Based on Rice Husk and Carbon Nanotubes

**Lee Yeng Seng[1], F.H. Wee[2], H.A. Rahim[2], Y.K. You[4], Z. Liyana[1], F. Malek[3], and A.A.M Ezanuddin[1]**

[1]Department of Electronic Engineering Technology, Faculty of Engineering Technology, Universiti Malaysia Perlis (UniMAP), Perlis, Malaysia.
[2]School of Computer and Communication Engineering,Univerisiti Malaysia Perlis (UniMAP), Perlis, Malaysia.
[3]Faculty of Engineering and Information Sciences, University of Wollongong in Dubai (UOW).
[4]Radio Communication Engineering Department (RaCED), Faculty of Electrical Engineering, UniversitiTeknologi Malaysia, Skudai, Johor, Malaysia.
* Corresponding author: leeyengseng@gmail.com

## Abstract

This paper is present a multi-layered microwave absorber using rice husk and carbon nanotube composite. The dielectric properties of each layer composite are measured and analyzed. The different layer of microwave absorber enables to control the microwave absorption performance. The microwave absorption performances are demonstrated through measurements of reflectivity over the frequency range 2-18 GHz. An improvement of microwave absorption less than -20 dB is observed with respect to a high lossy composite placed at bottom layer of multiple layers. Reflectivity evaluations indicate that the composites display a great potential application as wideband electromagnetic wave absorbers.

## 1. Introduction

Microwave absorbing material (MAMs) are widely used in commercial applications. MAMs basically involve the specific dielectric and/or magnetic materials which enable MAMs to absorb the incident radiation in a frequency range and dissipate it into heat [1]. Recent years, RH, RHA and carbon nanotubes (CNTs) have attracted high attention for the composite of microwave absorber [1]–[3]. CNTs have been widely studied in microwave radiation absorbing materials due to their unique material properties such as conductivity, dielectric, physical, mechanical properties [4]–[6]. The operating bandwidth can be extended from narrowband condition to a broader bandwidth by applying two or more layers into the microwave absorber design. The Jaumann absorber was the well-known design for such upgrades, which implement multiple resistive layers of carbon-loaded sheets that contribute to multiband absorption [7], [8]. The layers were decreasing value of resistive sheets towards the metal back plate. There are several researches that contribute on layer type absorbers; hexagonal Salisbury screen absorbers [9], ferrite multilayer [10]–[12], hexagonal ferrite wide band [13], multi-layered wideband [14], and multilayer microwave [15].

In this paper we investigated the performance of RH, RHA and CNT composite operating as a stacking multiple layered microwave absorber. The composite is made of a stacking method multilayered with graded dielectric properties of CNTs, while its thickness and shape each layer is equal. The fabricated multilayered absorbers behaves like a multiple narrow narrow-bands microwave absorber, with a low reflectivity (< -15 dB) over 2-18 GHz was discussed.

## 2. Experimental

The sample under test (SUT) fabricated using RH, RHA, CNT mixed with resin (polyester) and harden agent (MEKP). Five different type of SUT was prepared; RH, RHA, RHA/CNT-1, RHA/CNT-2 and RHA/CNT-5 composite. The flat microwave absorbers were fabricated by using different type of mould with constant length and width (45 cm x 45 cm) but different thickness: 5 mm and 10 mm. In this fabrication, agriculture waste RH and RHA was mixed with various wt% of CNT. Then, the polyester and 10 wt% of the MEKP was added to the mixture manually. After stirring the mixture, the mixture poured into the steel mould. The mould was designed and consisted of four removable parts include a top plate, side plate, bottom plate and different high surrounding walls to fabricate the mixture into flat square shape as shown in Figure 1. Figure 2 shows the square mould and fabricated flat microwave absorber. The fabricated SUT must be flat and smooth face to avoid from inaccurate results in measurement.

The dielectric properties ($\varepsilon_r = \varepsilon'_r - j\varepsilon''_r$) of SUT was measured using Agilent High temperature probe support with 85070E software over 2-18 GHz. The probe are connect to a perfomance network analyzer model E8362B

using a coaxial cable. In order to measure the dielectric properties of the SUT, the probe are attached on smooth and flat surface of the SUT as shown in Figure 3. Then, the dielectric properties of the SUT are displayed in network analyzer with the support of 85070E software. Table 1 shows the Measured dielectric properties of RH, RHA and CNT over 2 - 18 GHz frequency range. The results show RH has the lowest dielectric properties $\varepsilon'_r$ =3 and $\varepsilon''_r$ = 0.29. The dielectric properties of RHA was increases when increasing the weight percentage of CNT in the composite. The RHA/CNT-5 with 5 wt% CNT shows the highest dielectric properties $\varepsilon'_r$ =10.89 and $\varepsilon''_r$ = 4.81.

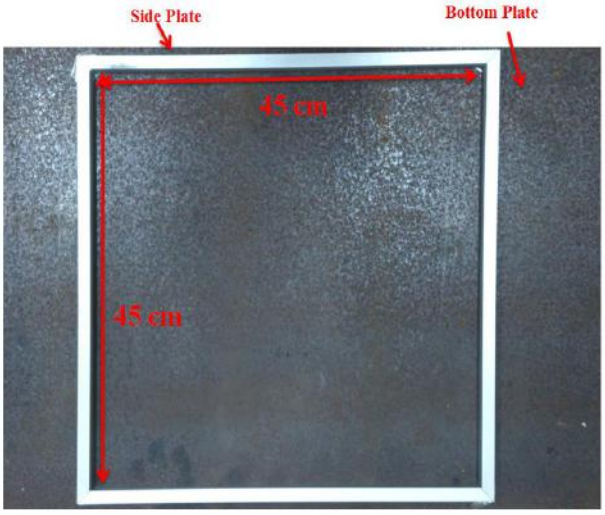



Figure 1: Square mould for fabricate flat microwave absorber.

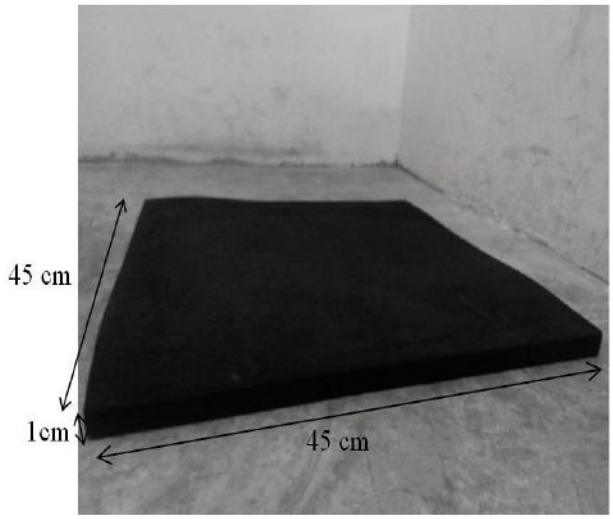



Figure 2: Fabricated flat microwave absorber with 45 cm x 45 cm x 1 cm..

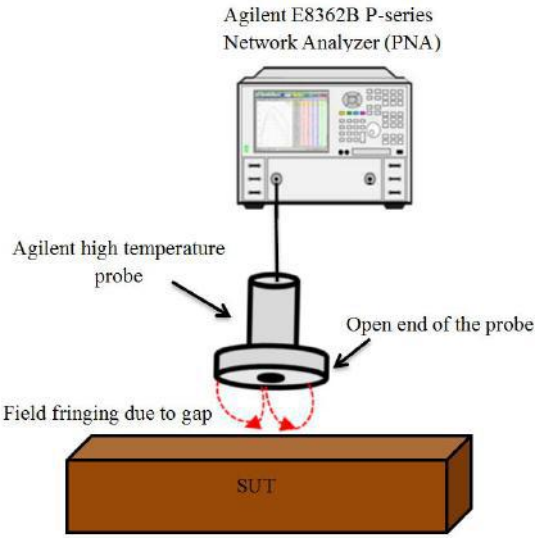



Figure 3: Multiple layers of MUT using an equivalent electric circuit explanation.

Table 1: Measured average dielectric properties of rice husk and carbon nanotubes over 2-18 GHz.

| SUT | $\varepsilon'_r$ | $\varepsilon''_r$ |
|---|---|---|
| RH | 3.00 | 0.29 |
| RHA | 4.45 | 0.41 |
| RHA/CNT-1 | 5.86 | 1.09 |
| RHA/CNT-2 | 7.08 | 2.07 |
| RHA/CNT-5 | 10.89 | 4.81 |

## 3. Multiple layer absorbers

Multiple layer absorbers can be classified as graded interfaces impedance matching. Electromagnetic wave that impinges upon an interface will experience some reflection that is proportional to the magnitude of the impedance step between incident and transmitting media. These features typically are a gradual transition in material properties for impedance matching layers, which means the front layer interface with air must be lowest lossy materials and the material for following layer must be lossier than the previous layer. In this multiple layer absorber design, the main requirements are that the front absorbers should minimize the front-face reflection and impedance matching from the air to absorber interface. This absorber places a transition absorbing layer between the incident and absorbing media. The transition layer has a thickness and impedance values that are between the two impedances to be matched between the first layer of the absorber and incident media. The multiple layer absorbers are the combination of the impedance from the first, second, and third layers to have an equal the impedance of the incident media. This matching occurs when the thickness of the

matching layer is one quarter of a wavelength of the radiation in the layer.

The microwave characteristic impedances were used to study a transmission line representing a condition where an incident electromagnetic field propagating in the free space encounters a multiple layer absorbers based on composite materials. The multiple layer absorbers can be designed by studying the transmission line reflection coefficient of such equivalent free space system shown in Figure 4. For reflectivity characteristics of each composite meant for aiding in the design of single layered MAMs were performed using the theory of reflection in a multiple layered MAMs. There are three conditions that can minimize the EMI reflection from a surface. When an electromagnetic wave, propagating through a free space with impedance of Z=0 $\Omega$, happens upon a semi-infinite dielectric material boundary of impedance $Z_{in}$, a partial reflection. Therefore, the second and third layer absorber must be lossy than the first layer absorber, so that the EM energy can be dissipated within the lossy material and impedance matched at the first layer absorber which cause the electromagnetic wave is not reflected back. Figure 5 shows the illustration of the incidence, reflecting and transmitting of the electromagnetic wave through the composite materials of multi-layered absorber.

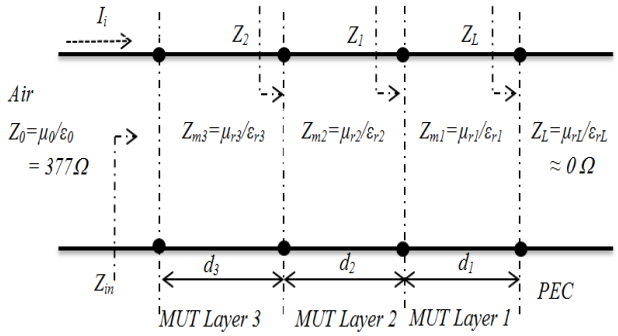



Figure 4: Multiple layers of MUT using an equivalent electric circuit explanation.

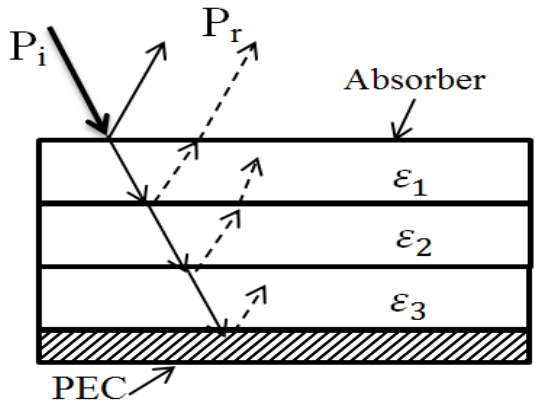



Figure 5: Illustration of the electromagnetic wave through the composite materials of multi-layered absorber.

Some of these structures are characterized by a surface impedance $Z_{in}$, close as possible to the free-space impedance (~377 Ω), and then changing their intrinsic impedance by gradually increasing their conductivity to keep the reflectivity at the boundary of each layer as low as possible, and allow the materials to convert the EM energy into heat for dissipating. Using Equation (1)-(4) iteratively, the corresponding input impedance at each layer interface can be calculated [16]–[18]

PEC wave impedance;

$$Z_L = 0\ \Omega \tag{1}$$

First layer wave impedance;

$$Z_1 = Z_{m1} tanh\left(\frac{2\pi\sqrt{\varepsilon_{r1}\mu_{r1}}}{\lambda} d_1\right) \tag{2}$$

Second layer wave impedance;

$$Z_2 = Z_{m2}\frac{Z_1 + Z_{m2} tanh\left(\frac{2\pi\sqrt{\varepsilon_{r2}\mu_{r2}}}{\lambda} d_2\right)}{Z_{m2} + Z_1 tanh\left(\frac{2\pi\sqrt{\varepsilon_{r2}\mu_{r2}}}{\lambda} d_2\right)} \tag{3}$$

Third layer (front layer) wave impedance;

$$Z_{in} = Z_{m3}\frac{Z_2 + Z_{m3} tanh\left(\frac{2\pi\sqrt{\varepsilon_{r3}\mu_{r3}}}{\lambda} d_3\right)}{Z_{m3} + Z_2 tanh\left(\frac{2\pi\sqrt{\varepsilon_{r3}\mu_{r3}}}{\lambda} d_3\right)} \tag{4}$$

And the resulting impedance matching condition between free space and the MUT structure can be optimized with the equation (5) [19], [20]:

$$RL\ (dB) = 20log\left|\frac{Z_{in}-1}{Z_{in}+1}\right| \tag{5}$$

## 4. Results and Discussion

The multiple narrow-bands occur based on a quarter-wavelength resonance and gradation in dielectric properties of each layer. The results obtained for the microwave characteristic impedances were used to design a multiple layer microwave absorber that capable to minimize the reflection of an incident

electromagnetic wave. The matching layer absorber attempts to reduce the thickness required for the gradual transition materials. As a consequence, the design of an absorber is a compromise between the front-face reflectivity and the energy loss. Multilayer absorber is one method to search for the best compromise within the wider frequency band. In order to distinguish the three layers more easily, the last layer of composite absorber is designated as L1 which are backed with metal plate. L2 is indicates the second layer of absorber, and L3 represents the front layer of the composite absorber which is the first layer to interact with the incident wave as depicted in Figure 6. These layers were fabricated in such a way that the impedance L3> L2>L1, where the L3, L2, and L1 represent the front, middle, last layer respectively. These multilayers were achieved by using stacking method of each layer with the various composite of RH, RHA and RHA/CNT.

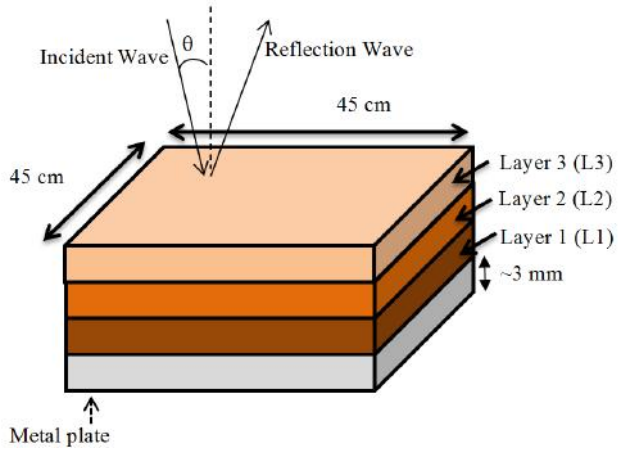



Figure 6: Illustration of absorbing multilayer structure with backed metal plate.

The three layers of absorber were designed and optimized by using the material properties of composite materials in each layer of absorber with well set up in CST-MWS software. In this study, the multilayer absorbers are design in two different thicknesses. The first design was composed of the three layer absorbers of equal thicknesses (0.5 cm) but consist of different dielectric properties of each layer. For another design, the L3 and L2 thickness are 1 cm and L1 is 0.5 cm with different arrangement of composite layer. In this multiple layered design, the RH composites as the top layer of the three layer absorbers which it were the lowest dielectric properties among the entire composites. Figure 7 and Figure 8 show the reflectivity of the three layer absorbers with an overall thickness of 1.5 cm and 2.5 cm respectively. The results can be noticed that the most of reflectivity signal is lower than 10 dB in multiple bands. Based on the three layer absorber with 1.5 cm thickness, the reflectivity results show that the L2 replace with lossier RHA/CNT-1 composites have better reflectivity less than -10 dB compare to the L3=RH, L2 = RHA, L1= RHA/CNT-2 shown in Figure 7.

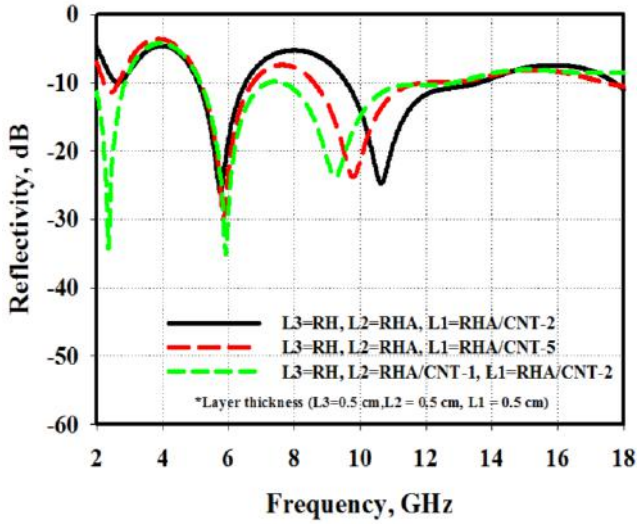



Figure 7: Reflectivity of three layer absorber with 1.5 cm thickness (L3 = 0.5 cm, L2 = 0.5 cm and L1 = 0.5 cm).

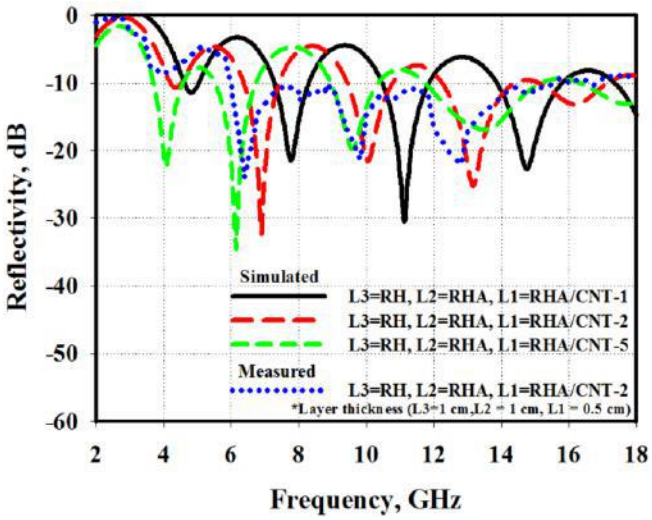



Figure 8: Reflectivity of three layer absorber with 2.5 cm thickness (L3=1 cm, L2 = 1 cm and L1 = 0.5 cm).

For second multiple layered designs with 2.5 cm thickness, the results show that more multiple reflectivity less than -10 dB compare to 1.5 cm thickness multiple layered absorbers. This is due to the multiple resonant frequencies matching due to the matching wave length. Therefore, by increasing the thickness of the L1 and L2 to 1 cm able to increase the multiple reflectivity that less than -10 dB over 2-18 GHz frequency. The microwave absorption of these multiple layer composite absorbers has been verified by free space bi-static method. The measured results were also shows very good agreement with the simulations in terms of the overall RL characteristics and absorbing bandwidth less than -10 dB as shown in Figure 8. This good agreement implies that the measurement and

simulation techniques using the dielectric properties of material in a multiple layered structure are well set up.

## Conclusions

As a conclusion, the RH, RHA and CNT composite have been investigated in dielectric properties and microwave absorption. The dielectric properties of RHA/CNT shows increased with increasing the CNT weight ratio in the composite. The Multiple layer absorbers performance sown to be dependent in each layer dielectric properties, thickness and the order in which the layers were organized. Multiple layered absorber designs presenting a graded impedance structure to the incident radiation resulted in the best performance. The reflectivity results indicate that the microwave absorber with multiple layers has the wider absorption bandwidth and lower reflectivity than the single-layer absorber. Reflectivity evaluations indicate that the composites display a great potential application as wideband electromagnetic wave absorbers.

## Acknowledgements

We appreciate the support and facilities provided by school computer and communication under universiti Malaysia Perlis.

## References

[1] Y. S. Y. Lee, M. M. F. B. A. Malek, E. M. E. E. M. Cheng, W. W. Liu, K. Y. You, M. N. Iqbal, F. H. Wee, S. F. Khor, L. Zahid, and M. F. bin Haji Abd Malek, "Experimental determination of the performance of rice husk-carbon nanotube composites for absorbing microwave signals in the frequency range of 12.4-18 GHz," *Prog. Electromagn. Res.*, vol. 140, no. April, pp. 795–812, 2013.

[2] M. N. Iqbal, M. F. Malek, Y. S. Lee, L. Zahid, and M. S. Mezan, "A Study of the Anechoic Performance of Rice Husk-Based, Geometrically Tapered, Hollow Absorbers," *Int. J. Antennas Propag.*, vol. 2014, pp. 1–9, 2014.

[3] Y. S. Lee, F. Malek, E. M. Cheng, W. W. Liu, F. H. Wee, M. N. Iqbal, L. Zahid, F. Abdullah, A. Z. Abdullah, N. S. Noorpi, and others, "Composites Based on Rice Husk Ash/Polyester for Use as Microwave Absorber," in *Theory and Applications of Applied Electromagnetics*, Springer, 2015, pp. 41–48.

[4] P. Saini, V. Choudhary, B. P. P. Singh, R. B. B. Mathur, and S. K. K. Dhawan, "Polyaniline–MWCNT nanocomposites for microwave absorption and EMI shielding," *Mater. Chem. Phys.*, vol. 113, no. 2–3, pp. 919–926, Feb. 2009.

[5] Z. Wang and G. Zhao, "Microwave Absorption Properties of Carbon Nanotubes-Epoxy Composites in a Frequency Range of 2 - 20 GHz," *Open J. Compos. Mater.*, vol. 3, no. April, pp. 17–23, 2013.

[6] W.-S. Jou, H.-Z. Cheng, and C.-F. Hsu, "The electromagnetic shielding effectiveness of carbon nanotubes polymer composites," *J. Alloys Compd.*, vol. 434–435, no. 0, pp. 641–645, May 2007.

[7] Y. Ye, L. X. Song, X. L. Song, and T. Zhang, "Analysis and Design of Transparent Microwave Absorbing Materials Based on the Destructive Interference at the Microwave Range," *Adv. Mater. Res.*, vol. 887–888, pp. 432–436, Feb. 2014.

[8] A. Tennant and B. Chambers, "Design of wideband Jaumann radar absorbers with optimum oblique incidence performance," *Electron. Lett.*, vol. 30, no. 18, pp. 1530–1532, Sep. 1994.

[9] Y. Luo, Y. Zhuang, and S. Zhu, "Thin and broadband Salisbury screen absorber using Minkowski fractal structure," *APMC 2009 - Asia Pacific Microw. Conf. 2009*, pp. 2573–2576, 2009.

[10] Y. K. Fetisov, K. E. Kamentsev, and a. Y. Ostashchenko, "Magnetoelectric effect in multilayer ferrite-piesoelectric structures," *J. Magn. Magn. Mater.*, vol. 272–276, no. III, pp. 2064–2066, 2004.

[11] K. E. Kamentsev, Y. K. Fetisov, and G. Srinivasan, "Ultralow-frequency magnetoelectric effect in a multilayer ferrite-piezoelectric structure," *Tech. Phys.*, vol. 52, no. 6, pp. 727–733, 2007.

[12] D. M. Wells, J. Cheng, D. E. Ellis, and B. W. Wessels, "Local electronic and magnetic structure of mixed ferrite multilayer materials," *Phys. Rev. B*, vol. 81, no. 17, pp. 1–12, 2010.

[13] M. R. Meshram, N. K. Agrawal, B. Sinha, and P. S. Misra, "Characterization of M-type barium hexagonal ferrite-based wide band microwave absorber," *J. Magn. Magn. Mater.*, vol. 271, pp. 207–214, 2004.

[14] A. Kazemzadeh and A. Karlsson, "Multilayered Wideband Absorbers for Oblique Angle of Incidence," *IEEE Trans. Antennas Propag.*, vol. 58, no. 11, pp. 3637–3646, 2010.

[15] M. Cao, J. Zhu, J. Yuan, T. Zhang, Z. Peng, Z. Gao, G. Xiao, and S. Qin, "Computation design and performance prediction towards a multi-layer microwave absorber," *Mater. & Des.*, vol. 23, no. 6, pp. 557–564, 2002.

[16] I. Kong, S. Hj Ahmad, M. Hj Abdullah, D. Hui, A. Nazlim Yusoff, and D. Puryanti, "Magnetic and microwave absorbing properties of magnetitethermoplastic natural rubber nanocomposites," *J. Magn. Magn. Mater.*, vol. 322, no. 21, pp. 3401–3409, 2010.

[17] M. S. Cao, W. L. Song, Z. L. Hou, B. Wen, and J. Yuan, "The effects of temperature and frequency on the dielectric properties, electromagnetic interference shielding and microwave-absorption of short carbon fiber/silica composites," *Carbon N. Y.*, vol. 48, no. 3, pp. 788–796, 2010.

[18] F. Xu, L. Ma, Q. Huo, M. Gan, and J. Tang, "Microwave absorbing properties and structural design of microwave absorbers based on polyaniline and polyaniline/magnetite nanocomposite," *J. Magn.*

*Magn. Mater.*, vol. 374, pp. 311–316, Jan. 2015.

[19] B. Belaabed, J. L. Wojkiewicz, S. Lamouri, N. El Kamchi, and T. Lasri, "Synthesis and characterization of hybrid conducting composites based on polyaniline/magnetite fillers with improved microwave absorption properties," *J. Alloys Compd.*, vol. 527, pp. 137–144, Jun. 2012.

[20] P. Bhattacharya, S. Dhibar, M. K. Kundu, G. Hatui, and C. K. Das, "Graphene and MWCNT based bi-functional polymer nanocomposites with enhanced microwave absorption and supercapacitor property," *Mater. Res. Bull.*, vol. 66, pp. 200–212, 2015.

# Multi resonance perfect absorber based on graphene micro ribbons

**Majid Roshanaei[1], Erfan Dezhband[1], Hamidreza Karami[1], Reza Parvaz[1]**

[1]Department of Electrical Engineering, Bu-Ali Sina University, Hamedan, Iran
*corresponding author, E-mail: hamidr.karami@basu.ac.ir

## Abstract

Metamaterial-based perfect absorbers are used in many applications like photo-detectors, sensors, special light modulators, wireless communications and photovoltaic. The mechanism of absorption is based on the complete suppression of reflection and transmission of incident wave. Here we present a multi resonances perfect absorber made of Graphene micro-ribbons that each ribbons have different values of chemical potential witch brought us tunability, which by changing the value of chemical potential for each ribbon we can change the frequency of resonances independently and we can achieve to a tunable bandwidth. In the following the results for reflection and absorption from simulation are presented. Finally an equivalent circuit model is proposed for our structure and shown to very accurately predict the element absorption.

## 1. Introduction

Graphene is a monatomic layer of carbon atoms arranged in a honeycomb structure, which has unique properties, such as optical transparency, flexibility, high electron mobility and conductivity. The electrical conductivity of Graphene can be controlled using electrochemical potential via, for example, magnetic field, electric field bias or optical excitation [1]–[3].

Graphene is an alternative material for plasmonic applications [4]. Graphene exhibits much higher confinement of surface plasmon polaritons and supports relatively longer propagation [5], [6]. Therefore, Graphene can be used in many plasmonic applications such as modulators, filters, hyperlenses, absorbers and polarizers [7]-[10].

In this paper, we present a multi-resonance perfect absorber made of graphene micro-ribbons in terahertz regime. The key to achieve multi-resonance absorption is applying different value of electrochemical potential or gate voltage to each ribbons of Graphene. We can almost tune the frequency of the absorption independently by changing the gate voltage of each ribbon or by tuning the width of ribbons. Finally, we have proposed physical equivalent circuit based on transmission line model for our structure by using vector fitting method [11]. The values of circuit elements can be easily extracted from the reflection scattering parameter of the Graphene micro-ribbons at boundary between air and substrate. The accuracy of the proposed equivalent circuit is validated by comparing the obtained results with the well-known frequency-domain CST-MWS solver.

## 2. Structure of the perfect absorber

The structure of the proposed multi-resonance prefect absorber is shown in Fig. 1, it consist of a patterned graphene micro-ribbon in front and a ground plate made of Gold with a conductivity $\sigma = 4\times10^7$ S/*m* on the back that perfectly reflecting wave in terahertz regime and a dielectric with refractive index (n = 2.1) placed between them.

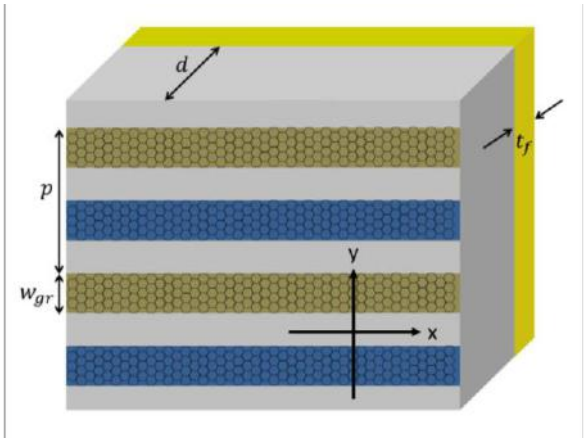
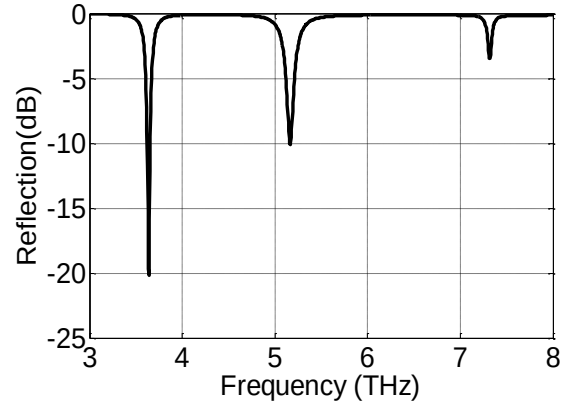



Figure 1: Schematic of the perfect absorber. The geometrical parameter of proposed absorber are $p$=2μ*m*, $w_{gr}$=2 μ*m*, $d$=4.7 μ*m*, and $t_f$= 1μ*m*. The blue micro ribbon made of graphene has $\mu_c$=100 *me*V and the yellow one has $\mu_C$=200 *me*V.

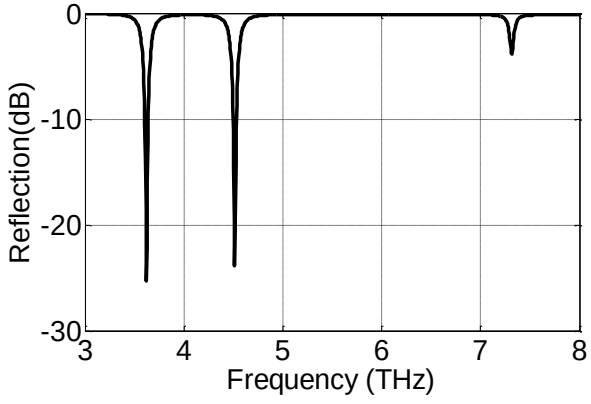
This proposed structure is periodic in (***y***) direction with periodicity $p$=2μ*m* and infinitely extended in (***x***) direction. The permittivity of graphene is calculated from $\varepsilon_{GR}=\varepsilon_0+j\sigma_{GR}/\omega\Delta$ which $\Delta$=1n*m* is the thickness of the graphene layer and $\sigma_{GR}$ is the surface conductivity of graphene sheet that can be derived from Kubo formula [12] and write as:

$$\sigma_{GR} = \frac{ie^2}{2\pi\hbar^2} Ln\left[\frac{2|\mu_c| - (\omega + i2\Gamma)\hbar}{2|\mu_c| + (\omega + i2\Gamma)\hbar}\right] \quad , \quad (1)$$
$$+ \frac{ie^2 K_B T}{\pi\hbar^2(\omega + i2\Gamma)}\left[\frac{\mu_c}{K_B T} + 2Ln(e^{-\mu_c/K_B T} + 1)\right]$$

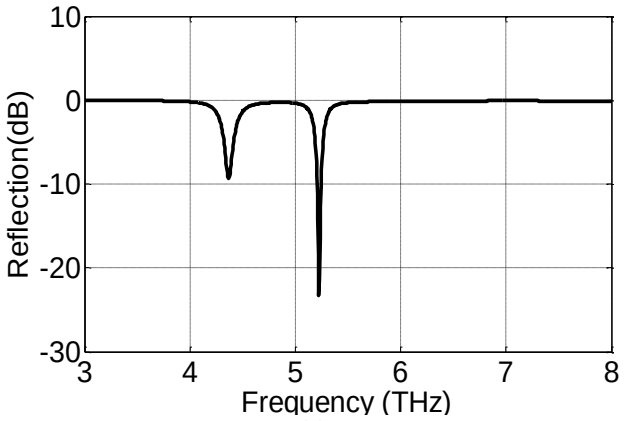
where $e$, $\hbar$ and $K_B$ are universal constant related to the electron charge, Plank's and Boltzmann's constant, respectively. T is the temperature and is fixed to 300K. $\mu_C$ and $2\Gamma$ ($2\Gamma=\hbar/\tau$, $\tau$ is the electron-phonon relaxation time) are physical parameters of the Graphene sheet and account for chemical potential (or Fermi energy) and intrinsic losses, respectively. According to (1) by changing the value of chemical potential ($\mu_C$) we can change the conductivity of graphene and use this fact for tune the frequency of absorption. The reflection of incident wave from simulation using CST-MWS [13] for the structure with two different chemical potential 100meV and 200*me*V are plotted in Fig. 2-(a). As it seems there is a first mode resonance in 3.64 THz related to ribbon with $\mu_C$ = 100meV and another one in 5.16 THz for $\mu_C$ = 200*me*V. By changing the value of chemical potential for each ribbon we can tune the frequency of absorption, for example we can reduce $\mu_C$ for the second ribbon and reduce the frequency of second absorption therefore as it decrease we can achieve to a bandwidth of absorption. The result for second ribbon with $\mu_C$ = 150meV and the first one without change are plotted in Fig. 2-(b), as it's obvious two peak of reflection are getting closer to each other and just the second resonance have been moved.




(a)



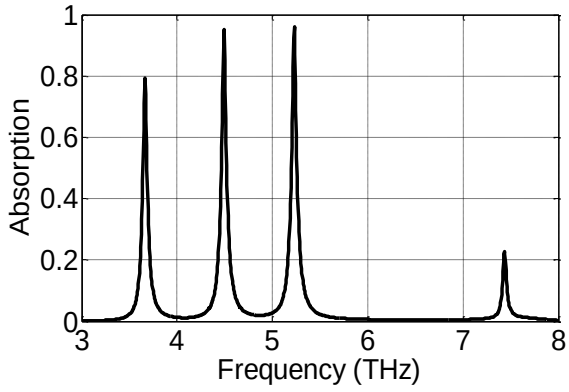

(b)



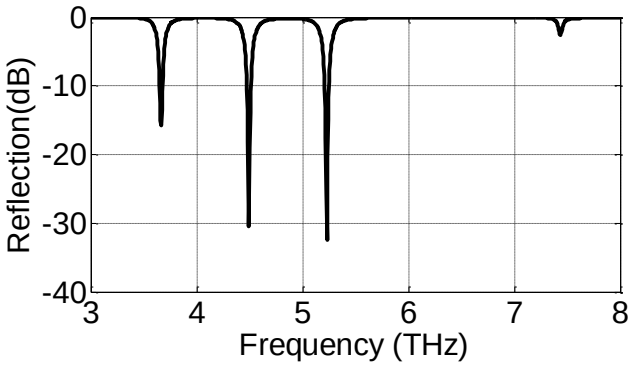

(c)

Figure 2: The reflection scattering parameter of the proposed structure shown in Fig. 1, (a) for $\mu_C$=100,200*me*V, (b) for $\mu_C$ = 100,150*me*V, and (c) for $\mu_C$=150, 200*me*V.

Now assume that we fixed $\mu_C$ for the second ribbon on 200 *me*V and change $\mu_C$ for the first ribbon from 100 *me*V to 150 *me*V and we see that the second resonance are fixed and the first resonance are getting closer to the second one Fig. 2-(c).




(a)




(b)

Figure 3: (a) Absorption of the proposed structure in Fig. 1, (b) Reflection scattering parameter.

Consequently we achieve to a dual frequency of absorption which are independently tunable, also by raising the number of ribbon with different value of chemical potential we can

have a multi resonance perfect absorber. Reflection and absorption for a three resonance absorber with $\mu_C$ = 100, 150, 200 *me*V respectively are plotted in Fig. 3-(a) and Fig. 3-(b).

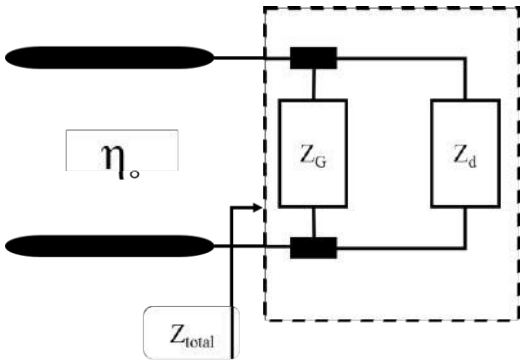



Figure 4: Transmission line model for the proposed structures shown in Fig. 1.

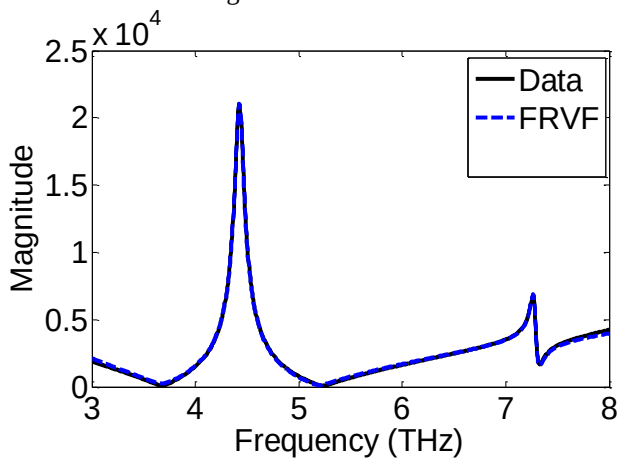



Figure 5: Magnitude of $Z_G$ obtained by CST-MWS (solid/black curve) and using vector fitting method (dashed/blue curve).

## 3. Purposed equivalent circuit model

One of the most important novelties of our work is calculating an equivalent circuit model for our purposed structure. We can replace a transmission line model instead of our structure shown in Fig. 4, which the impedance of Graphene array could be placed in parallel with impedance of dielectric that is shorted with a PEC. $Z_d$ is the impedance of dielectric that calculated from $Z_d = j\eta_d \tan(\beta_d l_d)$. Now we need to calculate $Z_G$ to model our structure with a transmission line model. To this end we can use reflection scattering parameter (S11) from result of simulation using CST-MWS to calculate $Z_{total}$ as follow:

$$\Gamma = S11 = \frac{Z_{total} - \eta_0}{Z_{total} + \eta_0}, \tag{2}$$

where,

$$Z_{total} = Z_G \,||\, Z_d, \tag{3}$$

and,

$$Z_G = \frac{Z_d Z_{total}}{Z_d - Z_{total}}, \tag{4}$$

Now we can fit a transfer function to this impedance $Z_G$ using vector fitting method [11] with residue and poles as listed in Table 1 for a dual resonance absorber that chemical potential for each ribbon are 100 *me*V and 200 *me*V respectively, and fitted curve are plotted in Fig. 5. we can write transfer function as:

$$H(s) = \sum_{i=1}^{5} \frac{res_i}{s - p_i}, \tag{5}$$

Which $res_i$ are residues and $p_i$ are poles. Now we should find an equivalent circuit for this transfer function, [14] we know for real pole we have a circuit which a resistor is placed in parallel with a capacitor shown in Fig. 6 and the element of the equivalent circuit are calculated as:

$$H_r(s) = \frac{\frac{1}{C_r}}{s + \frac{1}{R_r C_r}} = \frac{res_1}{s - p_1}, \tag{6}$$

where,

$$C_r = \frac{1}{res_1}, R_r = -\frac{1}{p_1 C_r}, \tag{7}$$

Table 1: value of residues and poles from vector fitting method.

| Poles($p_i$) [$\times 10^{13}$ ] | Residue ($res_i$) |
|---|---|
| -0.1039 + 0.0000j | 9.5324e+16 + 0j |
| -0.0280 + 2.7809j | 5.8815e+15 - 6.8056e+13i |
| -0.0280 - 2.7809j | 5.8815e+15 + 6.8056e+13j |
| -0.0164 + 4.5720j | 8.7541e+14 - 3.3407e+13j |
| -0.0164 - 4.5720j | 8.7541e+14 + 3.3407e+13j |

For complex pole pair the equivalent circuit would be like what in Fig. 7. and the element are calculated as:

$$C_{p1} = \frac{1}{res_2 + res_3}, C_{p2} = \frac{1}{res_4 + res_5}, \tag{8}$$

$$R_{p1} = -\left(\frac{res_2 + res_3}{p_2 + p_3}\right), R_{p2} = -\left(\frac{res_4 + res_5}{p_4 + p_5}\right), \tag{9}$$

$$L_{p1} = \left(\frac{res_2 + res_3}{p_2 p_3}\right), L_{p2} = -\left(\frac{res_4 + res_5}{p_4 p_5}\right), \tag{10}$$

$$b_1 = -(res_2 p_3 + res_3 p_2), b_2 = -(res_4 p_5 + res_5 p_3), \tag{11}$$

By replacing data from Table 1 in (6) to (11) we can listed the value of circuit elements as in Table 2. The final equivalent circuit for $Z_G$ is consist of three series circuit as shown in Fig. 8. This circuit is placed in parallel with $Z_d$ and could be used instead of proposed structure as shown in Fig. 1.

Table 2: The values of circuit elements.

| Circuit Elements | Values |
|---|---|
| **$C_r$[F]**, $R_r$[Ω] | **1.0491e-17**, 9.1759e+04 |
| **$C_{p1}$[F]**, $R_{p1}$[Ω], **$L_{p1}$[H]**, $b_1$ | **5.2453e-18**, 3.4004e+05, **2.4651e-10**, 5.3445e+28 |
| **$C_{p2}$[F]**, $R_{p2}$[Ω], **$L_{p2}$[H]**, $b_2$ | **5.2453e-18**, 5.8226e+05, **9.1205e-11**, 3.1211e+28 |

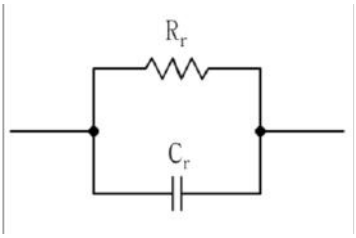


Figure 6: Equivalent circuit for real pole.

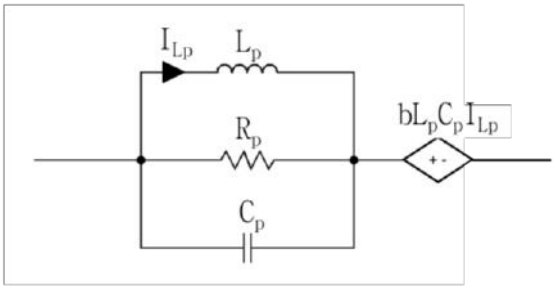


Figure 7: Equivalent circuit for complex poles pair.

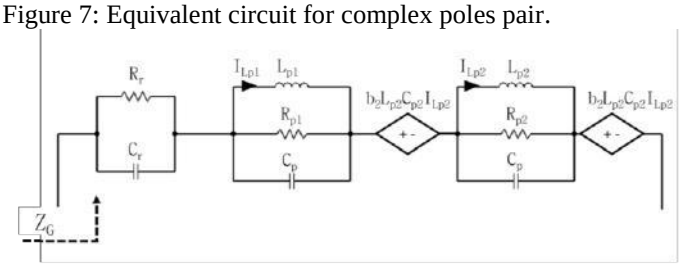


Figure 8: Equivalent circuit for $Z_G$

## 4. Conclusions

In this paper we present a multi-resonance perfect absorber that each resonance can be tuned independently by changing the value of chemical potential $\mu_C$ and also by tuning the width of graphene ribbon we can relocate the frequency of absorption. Therefore we can achieve a bandwidth of absorption. In the following for the first time we purposed an algorithm to find an equivalent circuit for our structure. To this end first we calculated impedance of patterned graphene by using the results of CST-MW and then by applying vector fitting method which brought us residues and poles we can obtain a transfer function, after that we used a method for synthesis of an equivalent circuit model of transfer function and simply calculate the value of circuit's element.

## References


[1] K. Bolotin, K. Sikes, Z. Jiang, M. Klima, G. Fudenberg, J. Hone, P. Kim, and H. Stormer, Ultrahigh electron mobility in suspended graphene, *Solid State Commun*. 146: 351–355, 2008.

[2] A. Geim, Graphene: status and prospects, *Science* 324: 1530–1534, 2009.

[3] K. S. Novoselov, V. I. Fal'ko, L. Colombo, P. R. Gellert, M. G. Schwab, and K. Kim, A roadmap for graphene, *Nature* (London) 490: 192–200, 2012.

[4] West, P. R. *et al.*, Searching for better plasmonic materials, *Laser Photonics Rev* **4**: 795–808, 2010.

[5] S. A. Mikhailov, K. Ziegler, New electromagnetic mode in graphene, *Phys. Rev. Lett.* 99, 016803, 2007.

[6] A. Vakil, N. Engheta, Transformation optics using graphene, *Science*, 332: 1291−1294, 2011.

[7] A. Andryieuski, A. V. Lavrinenko, Graphene metamaterials based tunable terahertz absorber: effective surface conductivity approach, *Optics express*, 21(7): 9144-9155, 2013.

[8] T. Otsuji, S. A. Boubanga Tombet, A. Satou, H. Fukidome, M. Suemitsu, E. Sano, V. Popov, M. Ryzhii, V. Ryzhii, Graphene-based devices in terahertz science and technology, *J. Phys. D* 45, 303001, 2012.

[9] A. Andryieuski, A. Lavrinenko, and D. Chigrin, Graphene hyperlens for terahertz radiation, *Phys. Rev. B* 86, 121108, 2012.

[10] R. Alaee, M. Farhat, C. Rockstuhl, and F. Lederer, A perfect absorber made of a graphene micro-ribbon metamaterial, *Opt. Express 20*, 28017–28024, 2012.

[11] B. Gustavsen and A. Semlyen, Rational approximation of frequency-domain responses by vector fitting, *IEEE Trans. Power Delivery*, 14: 1052–1061, 1999.

[12] G. W. Hanson, Dyadic Greens functions and guided surface waves on graphene, *J. Appl. Phys.* 103, 064302, 2006.

[13] www.cst.com, CST microwave studio 2011

[14] G. Antonini, SPICE equivalent circuits of frequency-domain responses, *IEEE Trans. Electromagnetic Compatibility*, 45(3), 502-512, 2003.

# Electronically tunable band-stop plasmonic filter based on spoof surface plasmon polaritons

**Qian Xun Xiao [1], Yong Jin Zhou [1,*] , Liu Yang [1], and Chong Tan [2]**

[1] Key Laboratory of Specialty Fiber Optics and Optical Access Networks, Shanghai University, Shanghai 200072, China
[2] Shanghai Institute of microsystem and information technology, CAS, Shanghai 200050, China
*corresponding author, E-mail: yjzhou@shu.edu.cn

## Abstract

We propose a band-stop filter based on spoof plasmonic waveguide loaded with C-shaped split ring resonator (SRR) on the back of the substrate. It has been shown that by introducing the varactor diode, the resonant frequency of the band-stop filter can be electronically tuned by varying the reverse voltage on the varactor diode. The numerical simulations verified that tunable resonant frequency of the band-stop filter varies from 5.90Hz to 6.15 GHz when the reverse bias voltage is changed from 5V to 20 V. Such plasmonic filter could find potential applications in plasmonic integrated circuits at the microwave and terahertz frequencies.

## 1. Introduction

Surface plasmon polaritons (SPPs) are surface electromagnetic (EM) waves confined at the interface of metal and dielectric, which propagate on the interface and decay exponentially in the transverse direction at optical frequencies.1 Since it can overcome the diffraction limit and strong local-field enhancement, they have been of interest for increasing applicationgs in the highly integrated optical circuits, super-resolution imaging and data storage [2, 3], etc. However, SPP cannot be supported on the surface of the metal at microwave or terahertz (THz) frequencies due to perfectly electric conductor (PEC) behavior of metals. In order to realize highly confined propagating surface waves at such frequencies, spoof (or designer) SPP based on the structured metal surfaces were proposed [4, 5], opening the way to design and realize SPPs waveguides and components operating at microwave and THz frequencies [6-11]. However, the aforementioned plasmonic waveguides and devices have a major limitation in applications in the planar circuits because of their inherent 3D geometries. Recently, it has been shown that ultrathin corrugated metallic strips can support conformal SPPs, which pave the way to the design of ultrathin microwave and THz plasmonic functional devices [12-16]. More recently, spoof SPP on ultrathin corrugated waveguides with symmetrically corrugated single grating have been investigated [17]. An ultra-wideband surface plasmonic filter based on double corrugated gratings has been proposed in the microwave frequency [18].The high-efficiency and broadband conversion between conventional guided wave to SPPs opens up a new avenue for advanced plasmonic integrated functional devices and circuits [19].

With the successful mode conversions between conventional guided wave to SPPs, plasmonic functional devices attract more and more attentions. The optical properties of plasmonic devices are determined by their structural parameters, such as size, shape, and arrangement. As these structures are firmly fixed on substrates, it is not easy to tune their optical properties once fabricated. To the best of our knowledge, previous works on plasmonic devices have almost exclusively focused on passive components with properties fixed by the structural parameters of structures. However, there is a strong demand for tunability in devices like some typical integrated optics technology. To realize tunable plasmonic devices, several innovative strategies have been proposed, during which the optical properties of the device can be controlled by optical excitation [20],temperature variation [21], mechanical control [22], application of voltage [23], and liquid crystal technology [24-27].

Plasmonic Filters are one of the most key components of plasmonic devices, which play an important role in the plasmonic circuits and systems. Recently a method to control the rejections of SPPs has been proposed using electrically resonant metamaterial particles, which can serve as good narrow and broadband filters for the spoof SPP waves in the microwave and terahertz frequencies [28]. By adding a simple wire-based metamaterial between the SSPP strip and the ground, it was shown that the SSPP wave can be greatly rejected, which shows good stop band performance [29]. It has been demonstrated that multiple rejections of spoof SPP modes can be easily realized by use of the localized SPP structures in an ultrathin spoof plasmonic combined system [30]. More recently, by introducing a defect unit or multiple defect units into an ultra-thin periodic corrugated metallic strip on the back of the coplanar waveguide, multiple narrow stop bands would be generated flexibly and conveniently [31]. However, the above SPP filters are either untunable or mechanically tunable with slow tuning speed. Compared to mechanically tunable filters, an electronically tunable filter promises greater functionality, high tuning speed, high-factor, and

broad tuning range. Based on our knowledge so far, there is no research on electronically tunable plasmonic filter based on spoof surface plasmon polaritons. Here, a novel tunable band-stop filter based on spoof plasmonic waveguide loaded with C-shaped SRR is presented. The unit cell of the band-stop filter is formed by printing a single SRR on the back of the substrate. By loading the varactor diodes at the split region of the C-shaped SRR, the resonant frequency of the band-stop filter can be electronically adjusted by tuning the reverse voltage of the varactor diodes. We believe it will be applied in plasmonic integrated circuits at the microwave and terahertz frequencies..

## 2. Dispersion relation of spoof plasmonic waveguides and designing principles

The proposed high-efficiency spoof SPP waveguide is shown in Fig. 1(a), which consists of three parts. Figs. 1(b)-(d) illustrate details of three parts, respectively, denoted as Part I, II and III. The whole structure is printed on a substrate (F4B) whose dielectric constant is 2.65 and thickness is 0.5mm. The thickness of the metal is 18 μm. Part 1 is plotted in Fig. 1 (b), where a slotline is used to couple EM energies from the bottom microstrip shown by the black dashed lines and the circular metal disk with radius $r_1$ =1.8mm at the end of microstrip is used to increase the coupling degree. The circular hole with radius $r_2$ = 1.8 mm at the end of slot line is also used to increase the coupling degree of EM energies and eliminate the reflected waves [32]. The length $l_1$ and width $w_1$ of the slot line are 10.2 mm and 0.5mm, respectively. As shown in Fig.1(c), Part II is momentum matching section, where a stepped slot line with length $l_2$ = 8mm is employed to improve impedance matching between the slot line and the proposed spoof SPP waveguide to decrease reflections as much as possible. To increase the matching condition of wave vectors between the slotline and plasmonic waveguide, we introduce seven gradient grooves with groove depth varying from $h_1$ to $h_7$, changing from 0.5 mm to 3.5 mm with equal step. Part III is a SPP transmission line illustrated in Fig. 1(d), which consists of double ultrathin metallic gratings corrugated with a periodic array of uniform grooves. The period and width of grooves are denoted as $p$ and $a$, and the groove depth is marked as $h$, where $p$ = 6mm, $a$ = 2mm, $h$ = 4mm. The width of the gap between double metallic gratings $w$ = 1.5mm, and the number of periodic grooves is set as $N$ = 5. To demonstrate momentum matching from slot line to plasmonic waveguide, we calculate the dispersion curves of spoof SPPs with different groove depths by the eigenmode solver of commercial software (CST Microwave Studio). As shown in Fig. 1(e), the smaller the groove height of the periodic array of rectangular grooves are, the higher the dispersion curves are, which nearly approaches to light line. Thus, momentum matching is realized between the slotline and spoof SPP waveguide.

.

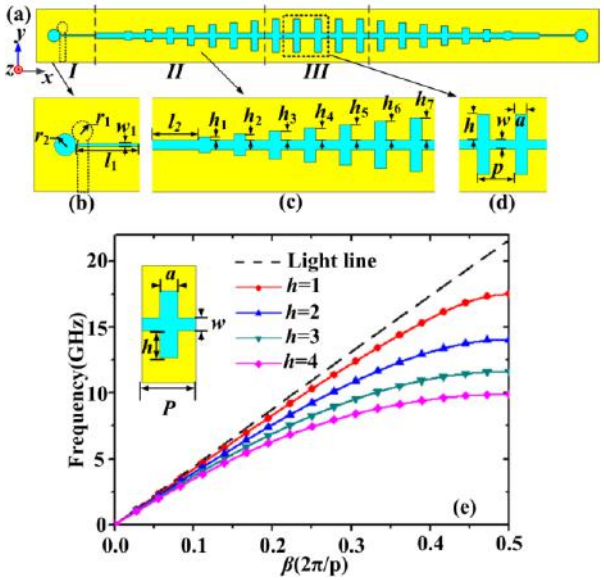



Figure 1:(a) Schematic picture of spoof SPP waveguide, which is divided into three regions (I, II and III). (b) The detailed structure to couple signals for the spoof SPP waveguide. (c) The detailed momentum matching transition with stepped slot line and gradient grooves. (d) The double ultrathin metallic gratings corrugated with double periodic of uniform rectangular grooves. (e)The dispersion curves of spoof SPPs waveguide with different groove depths, in which $p$ = 6 mm, $a$ = 2 mm, $h$ = 4 mm, $w$ =1.5mm.

## 3. Plasmonic stop-band filter based on C-shaped SRR

SRR is a planar magnetic resonator, which can be excited by an axial magnetic field [33]. The magnetic fields on the *xz*-plane of the C-shaped SRR at 5.63 GHz are demonstrated in Fig. 2(a). Figure 2(b) illustrates the magnetic fields on the *xz*-plane of the spoof SPP waveguide at 5.63 GHz. Good magnetic field matching between the C-shaped SRR and spoof SPP waveguide can be observed. Hence, it has the potential to excite strong responses when C-shaped SRR are introduced in the vicinity of the groove, which can be used to manipulate the propagations and rejections of spoof SPP wave in the propagating band. That's because the strong magnetic coupling between the C-shaped SRR and the spoof SPP strip will affect the transmission of spoof SPP wave. Here we design a C-shaped SRR particles printed on the back substrate of the spoof SPP waveguide, as shown in Fig. 2(c). Figure 2(d) illustrates the enlarged detailed arrangement of C-shaped SRR, where the contour black dashed lines help mark the location of SPP waveguide on the top surface. The outer width, line width, and outer height of C-shaped SRR are denoted as $l_s$ , $w_s$, and $d$, respectively, where $l_s$ = 7.5mm , $w_s$ = 0.2mm, and $d$ = 4mm. The spilt width $g$ of C-shaped SRR is fixed to 4.5 mm. The gap $g_1$ between spilt bottom edge of C-shaped SRR and bottom edge of metallic gratings groove

is 0.4 mm, and the gap $g_2$ between two sides of spilt and metallic gratings groove is set to 1.52mm.

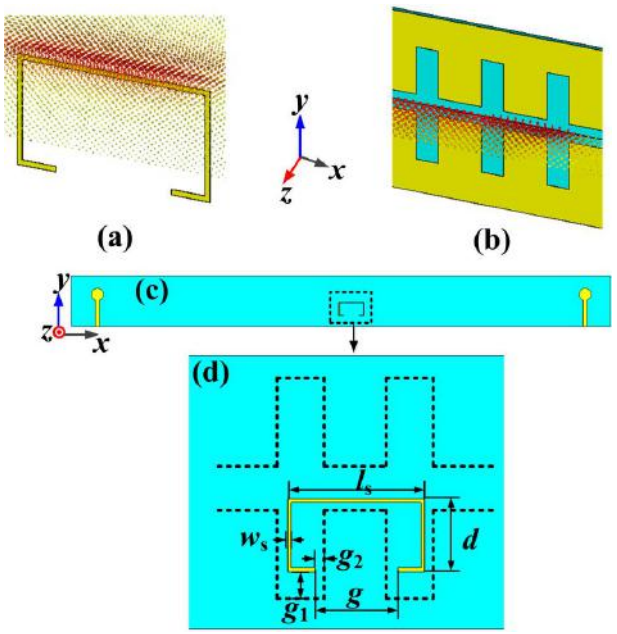



Figure 2: (a) The magnetic fields in the xz-plane for C-shaped SRR at 5.63 GHz of the spoof SPPs waveguide. (b) The magnetic fields in the *xz*-plane for spoof SPP waveguide at 5.63GHz. (c) The bottom view of spoof SPPs waveguide with C-shaped SRR. (d) The detailed arrangement of C-shaped SRR.

In order to evaluate the influence of SRR on the spoof SPP wave propagation quantitatively, we simulate the scattering parameters of the structure, as shown in Fig. 3(a). In details, the black solid line with square marks and the red solid line with circle marks correspond to $S_{11}$ and $S_{21}$, respectively. From the scattering parameters curves, we can clearly observe that the $S_{21}$ has a stopband from 5.47 GHz to 5.79 GHz with the transmission coefficients below -10dB. It is also obvious that a dip at 5.63GHz with the transmission coefficient below -15dB in the stopband can be observed. Figure 3(c) illustrates the simulated $E_z$ field distributions on the plane 1 mm above the structure at the rejection frequency 5.63GHz, where SPP fields are stopped off at the places. As expected, at non-resonant frequencies (5.05and 6.15 GHz), the SPP fields are propagating to the other end, as shown in Figs. 3(b) and 3(d).

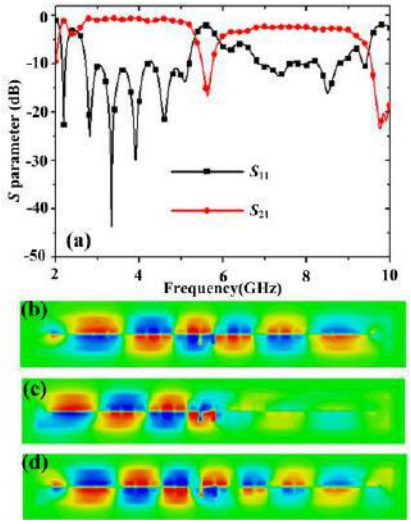



Figure3: (a) The simulated *S* parameters of spoof SPP waveguide with C-shaped SRR. (b)-(d) The simulated near electric-field distributions at frequencies 5.05GHz, 5.63GHz, 6.15GHz.

## 4. Electronically tunable plasmonic stop-band filter

Based on the proposed plasmonic stop-band filter, an electronically tunable plasmonic stop-band filter is proposed by placing the varactor diodes at the split region of the C-shaped SRR. Figure 4(a) shows the configuration of the C-shaped SRR loaded with varactor diodes. The LC resonance of the C-shaped SRR is driven by the magnetic field perpendicular to the structure's surface. The resonant frequency is mainly depended on the lumped parameter, which varies when the reverse bias voltage applied to the diode changes. Therefore, the reflection and transmission coefficients of the proposed band-stop filter can be adjusted by the applied bias voltage. In our design, an SMV1405 varactor diode from SKYWORKS in SC-79 package has been adopted as a tuning element, whose capacitance varies from 2.67pF to 0.63pF when the reverse bias voltage changes from 0 to 30V. To predict the tunable performance of the proposed plasmonic stop-band filter, we perform full-wave simulations using CST. Three cases of DC voltage are considered for simulation: 5v, 10v, and 20v, which corresponds to capacitance are 1.17pF, 0.95pF and 0.77pF, respectively. As expected, the frequency for the minimum $S_{21}$ shown in Fig. 4(b) shifts upwards from 5.8GHz to 6.18GHz. In details, the black solid line with square marks, the red solid line with circle marks, and the blue dotted line with triangle marks correspond to the case of DC voltage under 5V, 10V and 20V, respectively. To further visualize band-stop filtering effect, Figs. 4(c)-(e) depict the simulated electric-field distributions on the plane 1 mm above the structure at the rejection frequencies corresponding to the resonant dips. As expected, good band-stop filtering effects are achieved at the corresponding frequencies when the capacitance varies from 0.77 pF to 1.17 pF. The near-field distributions prove that the proposed plasmonic stop-band

filter has good performance within its tunable frequency range.

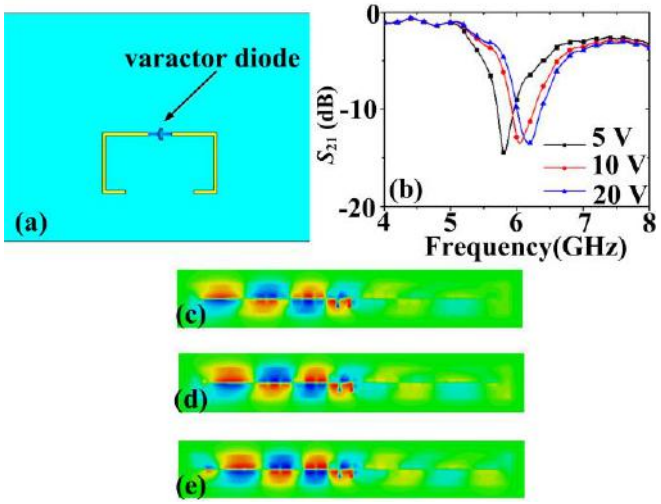



Figure 4: (a) The configuration of the C-shaped SRR loaded with varactor diodes. (b) The simulated $S_{21}$ for different bias voltages ranging from 5 to 20 V. (c)-(e) The simulated near-electric-field distributions of the stop-band filter at 5.80GHz, 6.04GHz,and 6.18GHz, respectively.

## 5. Conclusions

In summary, we have investigated a plasmonic stop-band filter theoretically based on C-shaped SRR. By loading the varactor diodes at the split region of the C-shaped SRR, the resonant frequency of the band-stop filter can be electronically adjusted by tuning the reverse voltage of the varactor diodes. We believe the plasmonic filter could find potential applications in plasmonic integrated circuits at the microwave and terahertz frequencies.

## Acknowledgements

This work was supported in part by National High Technology Research and Development Program 863 under Grant No. 2015AA016201, in part by Shanghai Municipal Science and Technology Commission under Grant No. 13ZR1454500, and in part by the Specialized Research Fund for the Doctoral Program of Higher Education under Grant No. 20133108120016..

## References

[1] E. Ozbay, Plasmonics: merging photonics and electronics at nanoscale dimensions, *Science* 311: 189-193, 2006.

[2] V. S. Volkov, S. I. Bozhevolnyi, E. Devaux, J. Y. Laluet, T. W. Ebbesen, Wavelength selective nanophotonic components utilizing channel plasmon polaritons, *Nano Letters* 7: 880-884, 2007.

[3] D. K. Gramotnev, S. I. Bozhevolnyi, Plasmonics beyond the diffraction limit, *Nature Photonics* 4: 83-91, 2010.

[4] J. B. Pendry, L. Martín-Moreno, and F. J. Garcia-Vidal, Mimicking surface plasmons with structured surfaces, *Science* 305: 847-848, 2004.

[5] A. P. Hibbins, B. R. Evans, J. R. Sambles, Experimental verification of designer surface plasmons, *Science* 308: 670-672, 2005.

[6] W. Q. Zhu, A. Agrawal, and A. Nahata, Planar plasmonic terahertz guided-wave devices, *Optics Express* 16: 6216-6226, 2008.

[7] Q. Gan, Z. Fu, Y. J. Ding, and F. J. Bartoli, Ultrawide-bandwidth slow-light system based on THz plasmonic graded metallic grating structures, *Physical Review Letters* 100: 256803, 2008.

[8] A. I. Fernandez-Dominguez, E. Moreno, L. Martín-Moreno, and F. J. García-Vidal, Terahertz wedge plasmon polaritons, *Optics Letters* 34: 2063-2065, 2009.

[9] D. Martín-Cano, M. L. Nesterov, A. I. Fernandez-Dominguez, F. J. Garcia-Vidal, L. Martin-Moreno, and Esteban Moreno, Plasmons for subwavelength terahertz circuitry, *Optics Express* 18: 754-764, 2010.

[10] W. Zhao, O. M. Eldaiki, R.Yang, and Z. Lu, Deep subwavelength waveguiding and focusing based on designer surface plasmons, *Optics Express* 18: 21498-21503, 2010.

[11] G. Kumar, S. Pandey, A. Cui, and A. Nahata, Planar plasmonic terahertz waveguides based on periodically corrugated metal films, *New Journal of Physics* 13: 033024, 2011.

[12] X. P. Shen and T. J. Cui, Planar plasmonic metamaterial on a thin film with nearly zero thickness, *Applied Physics Letters* 102: 211909, 2013.

[13] X. P. Shen, T. J. Cui, D. Martin-Cano, and F. J. García-Vidal, Proc. Natl. Acad, Conformal surface plasmons propagating on ultrathin and flexible films, *Proceedings of the National Academy of Sciences* 110: 40-45, 2013.

[14] J. J. Wu, D. J. Hou, K. X. Liu, L. F. Shen, C. A. Tsai, C. J. Wu, D. Tsai, and T. J. Yang, Differential microstrip lines with reduced crosstalk and common mode effect based on spoof surface plasmon polaritons, *Optics Express* 22: 26777-26787, 2014.

[15] X. Y. Liu, Y. J. Feng, B. Zhu, J. M. Zhao, and T. Jiang, High-order modes of spoof surface plasmonic wave transmission on thin metal film structure, *Optics Express* 21: 31155-31165, 2013.

[16] R. Quesada, D. Martín-Cano, F. J. García-Vidal, and J. Bravo-Abad, Deep-subwavelength negative-index waveguiding enabled by coupled conformal surface plasmons, *Optics Letters* 39: 2990-2993, 2014.

[17] X. Y. Liu, Y. J. Feng, K. Chen, B. Zhu, J. M. Zhao, and T. Jiang, Planar surface plasmonic waveguide devices based on symmetric corrugated thin film structures, *Optics Express* 22: 20107-20116, 2014.

[18] X. Gao, L. Zhou, Z. Liao, H. F. Ma, and T. J. Cui, An ultra-wideband surface plasmonic filter in microwave frequency, *Applied Physics Letters* 104: 191603, 2014.

[19] H. F. Ma, X. P. Shen, Q. Cheng, W. X. Jiang, and T. J. Cui, Broadband and high‐efficiency conversion from guided waves to spoof surface plasmon polaritons, *Laser & Photonics Reviews* 8: 146-151, 2014.

[20] M. A. Vincenti, A. D'Orazio, M. Buncick, N. Akozbek, M. J. Bloemer, and M. Scalora, Beam steering from resonant subwavelength slits filled with a nonlinear material, *JOSA B* 26: 301-307, 2009.

[21] M. K. Chen, Y. C. Chang, C. E. Yang, Y. H. Guo, J. Mazurowski, S. Yin, P.Ruffin, C. Brantley, E. Edwards, and C. Luo, Tunable terahertz plasmonic lenses based on semiconductor microslits, *Microwave and Optical Technology Letters* 52: 979-981, 2010.

[22] P. Li, T. Sasaki, L. F. Pan, and K. Hane, Open foundry platform for high-performance electronic-photonic integration, *Optics Express* 20: 12222-12232, 2012.

[23] C. Huang, R. J. Lamond, S. K. Pickus, Z. R. Li, and V. J. Sorger, A Sub--Size Modulator Beyond the Efficiency-Loss Limit, *Photonics Journal*, *IEEE*, 5: 2202411-2202411, 2013.

[24] W. Dickson, G. A. Wurtz, P. R. Evans, R. J. Pollard, and A. V. Zayats, Electronically controlled surface plasmon dispersion and optical transmission through metallic hole arrays using liquid crystal, *Nano Letters* 8: 281-286, 2008.

[25] Y. Zhao, Q. Z. Hao, Y. Ma, M. Q. Lu, B. X. Zhang, M. Lapsley, I. C. Khoo, and T. J.Huang, Triple-point-type morphotropic phase boundary based large piezoelectric Pb-free material-Ba (Ti0. 8Hf0. 2) O3-(Ba0. 7Ca0. 3) TiO3, *Applied Physics Letters* 100: 222910, 2012.

[26] A. C. Tasolamprou, D. C. Zografopoulos, and E. E. Kriezis, Liquid crystal-based dielectric loaded surface plasmon polariton optical switches, *Journal of Applied Physics* 110: 093102, 2011.

[27] M. Bahramipanah, S. A. Mirtaheri, and M. S. Abrishamian, Electrical beam steering with metal-anisotropic-metal structure, *Optics Letters* 37: 527-529, 2012.

[28] B. C. Pan, Z. Liao, J. Zhao, and T. J. Cui, Controlling rejections of spoof surface plasmon polaritons using metamaterial particles, *Optics Express* 22: 13940-13950, 2014.

[29] W. J. Zhang, G. Q. Zhu, L.G. Sun, and F. J. Lin, Trapping of surface plasmon wave through gradient corrugated strip with underlayer ground and manipulating its propagation, *Applied Physics Letters* 106: 021104, 2015.

[30] Z. Liao, X. Shen, B. C. Pan, J. Zhao, Y. Luo, and T. J. Cui, Combined system for efficient excitation and capture of LSP resonances and flexible control of SPP transmissions, *ACS Photonics* 2: 738-743,2015.

[31] B. Z. Xu, Z. Li, L. L. Liu, J. Xu, C. Chen, P. P. Ning, X. L. Chen, and C. Q. Gu, Tunable band-notched coplanar waveguide based on localized spoof surface plasmons, *Optics Letters* 40: 4683-4686, 2015.

[32] B. Schuppert, Microstrip/slotline transitions: Modeling and experimental investigation, *IEEE Transactions on Microwave Theory and Techniques* 36:1272-1282,1998.

[33] R. Marques, F. Mesa, J. Martel, and F. Medina, Comparative analysis of edge-and broadside-coupled split ring resonators for metamaterial design-theory and experiments,*IEEE Transactions on Antennas and Propagation* 51:2572-2581,2003.

# Absorption Modulation of FSS-Polymer nanocomposites through Incorporation of Graded Conductive nano-fillers

**Rajkumar Jaiswar*[1], Yann Danlée[1], Henok Mesfin[2], Arnaud Delcorte[2], Sophie Hermans[3], Christian Bailly[2], Isabelle Huynen[1]**

[1]Institute of Information and Communication Technologies, Electronics and Applied Mathematics (ICTEAM),
[2]Institute of Condensed Matter and Nanosciences (IMCN),Division of Bio and Soft Matter (BSMA),
[3]Institute of Condensed Matter and Catholique de Louvain, Belgium Nanosciences (IMCN), Division of Molecules, Solids and Reactivity(MOST), Université Catholique de Louvain, Belgium
*Corresponding author: rajkumar.jaiswar@uclouvain.be

## Abstract

The hybrid concept of utilizing Frequency selective surface (FSS) and polymer nanocomposite (PNC) for absorption modulation is presented in 8-18GHz frequency band. The extruded PNCs are fabricated incorporating different weight% fraction of conductive fillers, CNTs and GNPs, in high, low and mixed nano-filler concentration configuration in a polycarbonate matrix. The FSS metallic resonator is patterned over a dielectric substrate which then backed by grounded PNCs loaded with conductive fillers. Then absorption is depends on wt% fraction of conductive inclusions in polycarbonate matrix, i.e. variation in conductivity of grounded PNCs due to varying concentration of conductive fillers results in absorption modulation. Nearly 100% absorption magnitude peaks and modulated absorption band is observed at 8.2GHz and from 12 to 18GHz frequency band respectively, for varying conductivity of polymer-nanocomposite. The novel concept can also be extended to various other configuration or heterostructure having inclusions of conductive and magnetic properties which can be utilized for EM absorption modulation.

## 1. Introduction

In last decades, conductive polymer-nanocomposite (PNCs) emerges as a potential candidate for broadband electromagnetic shielding element in aircraft, stealth, and communication industries[1-5]. Conductive fillers such as carbon nanotubes (CNTs) and graphene nanoplatelets (GNPs) in polymer matrix makes PNCs an excellent choice for EM absorption application due to its multifunctional features: easy of fabrication, low-cost, ultralight weight, large scale production, thermal and mechanical stability and so on[6-9]. Generally, EMI shielding in composite material can be achieved through high reflection, destructive interference or dissipation of EM wave inside the material. Polymer loaded with low concentration of CNTs shows a higher EMI shielding than graphene nanoplatelets due to aspect ratio of nano-fillers as well as formation of percolating network inside polymer matrix. 1-D tubular geometry of CNTs allows the electron to flow in tube-axis direction while in the planar 2D-structure of GNPs electron flows in plane of their surface therefore tubular structure and low-density of CNT make it more attractive for EMI even at lower concentration than planar graphene nanoplatelets in the hosted polymer matrix[10-13].

The electromagnetic parameters i.e. conductivity, permeability, loss tangent can be tuned depending on the concentration of conductive and lossy nano-fillers in polymer matrix. The optimization of weight concentration, physicochemical properties of polymer, processing conditions for composite fabrication has significant impact on the homogenous distribution of nano-inclusions inside the polymer matrix which directly influences the EM properties of hybrid composite[14-15].

Apart from polymer nanocomposite, other kind of composites are also exits for electromagnetic absorption application based on sub-wavelength resonant FSS structure and grounded dielectric substrate such as Salisbury screen, multilayer structures, resistive-ink metamaterials [16-18]. Landy et.al. introduced a single-wavelength metamaterial structure for perfect unity absorber consisting of metallic SRR and wire with no ground plane. In these kind of composite structure absorption is based on electric and magnetic dipole coupling schemes[19-21].

In this paper, we propose to combine the two different concepts of FSS-dielectric and polymer nanocomposite loaded with conductive nanofillers to realize the modulated absorption at resonator resonances as shown in Fig.1.

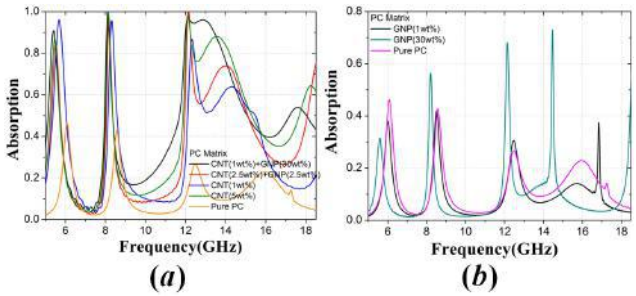



Figure 1. Absorption indexes for SRR/dielectric/PNCs composite in which PNCs consisting of, (a) CNTs and GNPs mixed with high wt% fraction, (b) GNPs in low and high wt% fraction.

*1.1 Component design approach*

The modulation of absorption band is realized through a metamaterial composite consisting of metallic square ring resonator (SRR) patterned on a Roger RO3010 substrate backed by a grounded polymer nanocomposites (PNCs). The polymer nanocomposite incorporates different weight ratio in high and low concentrations of carbon nanotube CNTs (1wt% and 5wt%), graphene nanoplatelets GNPs (1wt% and 30wt%) and mixed concentration of CNT+GNPs (1wt%+30wt%, and 2.5wt%+2.5wt%) in polycarbonate (PC) matrix[22, 23]. This novel approach opens up the idea to utilize the PNCs with Frequency Selective Surfaces for broadband absorption application. The simulation is performed using CST-Microwave Studio to explore the absorption mechanisms. It is understood that high absorption originates at FSS resonator resonance due to the dielectric and ohmic loss in the grounded PNCs having various weight stoichiometry of conductive inclusions. The fabricated PNCs with CNT and GNPs inclusions in various composition are measured through waveguide method in X and Ku-band regime [7]. TRL calibration technique is used to measure the S-parameter of PNCs EM parameters: permittivity and conductivity, are retrieved for all the PNCs[3].The retrieved EM parameters of PNCs is simulated and fitted to utilize it as grounded PNC in SRR/dielectric configuration.

## 2. Experimental

### 2.1. Materials and sample preparation

FSS-SRR (square ring resonator) is patterned over Rogers RO3010 substrate having a permittivity of 10.2, tanδ=0.0022 and thickness 1.28mm. The polycarbonate (PC) pellets Makrolon$^{TM}$ OD2015 resins were purchased from Bayer. Carbon nanotube NC7000 were provided by Nanocyl and graphene nanoplatelets TIMREX-BNB90 is provided by Timcal. Nanocomposites are prepared by polymer extrusion method. PC pallets are preheated at 80ºC for 24 hours in vacuum to remove any water content from polymer. The nano-fillers CNTs and GNPs are taken in various concentrations as mentioned in earlier section and melt-cmponded with polycarbonate resin at 250ºC for 10 minutes at 150rpm in DSM15 twin-screw micro-compounder. The extrudates were hot pressed further for 3 minutes at 250ºC at 10MPs pressure and molded in approximate 400μm thickness flat sheets for characterization.

### 2.2. Morphological characterization

TEM micrographs were obtained using a LEO 922 OMEGA Transmission Electron Microscope operating at 120kV. Fig.4 show the TEM images of the fabricated PNCs with different loading rate. Samples flakes were cut with ultra-microtome having less than 80nm thickness and deposited on carbon coated copper grid to avoid charging effects in TEM.

### 2.3. EM characterization

In first part, fabricated sample PNCs are measured in waveguide method in X and Ku-band with Agilent PNA-X vector network analyzer and scattering parameters $S_{11}$ and $S_{12}$ are used to retrieve the EM parameters of PNCs to evaluate the shielding effectives($SE_T$) and conductivity of polymer-nanocomposite. Then in second part, initially, FSS-grounded dielectric composite is measured to verify its resonances, after then PNCs are placed between the FSS-dielectric and ground plane for absorption modulation measurement at FSS resonance.

## 3. Results and discussion

### 3.1. TEM analysis

Fig.2 show the TEM images of the cross-sectional morphologies of PNC composites. It is observed that CNTs are distributed uniformly as well as entangled to form a connective network throughout the composite at 1wt% and 5wt% loading rate. In the mixed configuration of CNT and GNPs i.e. (1wt% CNT & 30wt% GNP) and (2.5wt% CNT & 2.5wt% GNP) the high aspect ratio of both nano-fillers makes homogenous connectivity of fillers in polymer matrix. Composites having only GNPs in 1wt% and 30wt% concentration also show the good spacious spreadness but connectivity between the nanoplatelets is very low due to smaller 2D planar structure than 1D tubular CNTs. It is also observed that higher filling of the conductive fillers makes composite more conductive but its flexibility gets compromised.

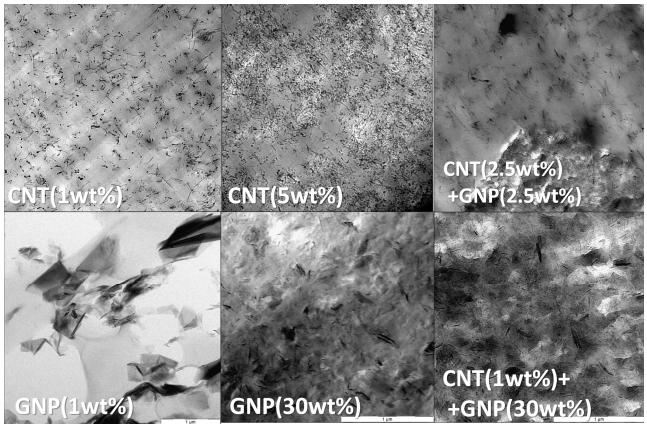



Figure 2. TEM images of polynanocomposite loaded with different wt% fraction of conductive nanofillers.

It is clear that CNT-GNP-PC PNCs composites consist of homogenously distributed multi-component network in sample. It's worth mentioning here that the distribution, orientation of fillers, connectivity and processing condition of composite greatly influences the conductivity of PNCs and hence the EMI shielding of polymer nanocomposite [14-15, 24].

### 3.2. Measurement and characterization

The EMI shielding effectiveness (SE) and EM parameters, conductivity and loss tangent, of PNCs are investigated in X and Ku band in waveguide method using Wiltron 360B VNA and TRL calibration is applied to measure the scattering parameters $S_{11}$ and $S_{21}$ through hybrid composites. EMI shielding can be understood by three mechanism i.e. reflection, absorption and multi-reflection through the nanocomposite. Since the sample thickness is around 400μm then contribution from multi-reflection can be ignored since its effect is dominant only when the sample thickness is comparable to the skin depth ($\delta=\sqrt{(\pi\mu f\sigma)^{-1}}$) of composite. The incident EM-wave is partially reflected (R), transmitted (T) and absorbed (A) while propagating through the material and absorption can be calculated as follows, A=1-R-T, where $R=|S_{11}|^2$ and $T=|S_{21}|^2$. Fig.3 shows the dominant mechanism of EMI shielding through the hybrid composite and waveguide measurement setup for PNCs [25-27].

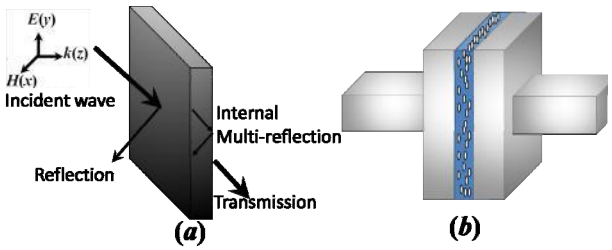



Figure 3. Schematic illustration of (*a*) EMI shielding mechanism , (*b*) Waveguide composite measurement setup.

As it is mentioned that EMI SE measures the ability of composite to attenuate the wave passing through its medium and in our case absorption and reflection are the dominant mechanism for wave attenuation. Therefore, total shielding effective($SE_T$) can be determined by sum of absorption($SE_A$) and reflection($SE_R$) which can be expressed as follows[28-31];

$$SE_T = SE_A + SE_R = 10log\left(1/|S_{21}|^2\right)$$

$$SE_R = 10log\left(1/1-|S_{11}|^2\right) \qquad \text{.....(1)}$$

$$SE_A = 10log\left(\frac{1-|S_{11}|^2}{|S_{21}|^2}\right)$$

Fig.4 shows the Shielding effectiveness for hybrid composites calculated from equation (1). It can be observed in Fig.4 that PNC having 5wt% CNT possesses higher shielding ability around 25dB to attenuate incident EM-wave than composite with 1wt% CNTs having 8dB. This is an obvious expectation since higher loading rate of CNTs forms a more connected conductive network of entangled CNTs distributed throughout the sample than the low wt% PNCs. Similarly, composite with high loading 30wt% of GNPs also have homogenous spreadness with wave attenuation capability around 20dB, indeed higher than the PNC with 1wt% GNPs having $SE_T$ around 3dB.

The connectivity between the GNPs segments is relatively lower than CNTs composite even with high filler concentration due to GNPs 2-D planner structure and can be seen in TEM images. Since, the aspect ratio of 1D CNTs and 2D GNPs has great impact not only on conductivity, shielding efficiency, flexibility of PNCs but also on required amount of material to achieve the highest shielding. Therefore, the concept of mixed concentration of CNTs and GNPs is tried to overcome these and other influencing factors mentioned factors in sec.3.1 in a way to achieve higher EM-wave shielding composites. As it can be seen in Fig.4 the two PCs composites with mixed concentration i.e. CNT+GNPs (1wt%+30wt%, labeled as sample PCG130, and 2.5wt%+2.5wt%, labeled as sample PCG25) show total EMI SE nearly independent of frequency with higher ability of wave attenuation.

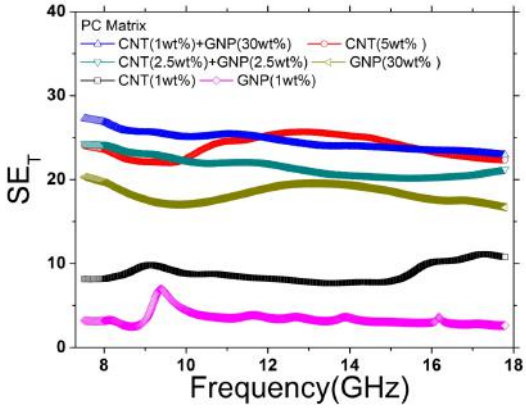



Figure 4. Measured total shielding effectiveness of PNCs having mixed, high &low concentration stoichiometry of CNT,GNPs in PC-matrix.

It is worth mentioning here that after polymer extrusion sample PCG25 shows much better flexibility than sample PCG130 having little brittleness similar to PNC composite with GNP 30wt% loading but absorption efficiency were much higher as predicted in fig.1.

The EM parameters are retrieved using transmission line theory where measured scattering parameters, $S_{11}$ & $S_{21}$, are converted into transfer-matrix, and conductivity(σ) and loss tangent factor (tanδ) are extracted from transfer matrix coefficients as follows [32].

$$T = \begin{pmatrix} \cos(nkd) & -\frac{z}{k}\sin(nkd) \\ \frac{k}{z}\sin(nkd) & \cos(nkd) \end{pmatrix};$$

$$n = \frac{1}{kd}\cos^{-1}\left[\frac{1}{2S_{21}}(1-S_{11}^2+S_{21}^2)\right];\ z = \sqrt{\frac{(1+S_{11})^2-S_{21}^2}{(1-S_{11})^2-S_{21}^2}};$$

$$\varepsilon = n/z,\ \mu = 1;\quad \varepsilon = \varepsilon' - j\frac{\sigma}{\omega\varepsilon_0};$$

$$\sigma = \omega\varepsilon_o\varepsilon^{"};\ \tan\delta = \frac{\varepsilon^{"}}{\varepsilon}; \qquad \text{.....(2)}$$

Where *n* is the refractive index and z is wave impedance of the non-magnetic composite slab of thickness *d*. *k* and $\varepsilon_o$ are free space wave number and permittivity. Fig.5 shows the loss tangent (tanδ) i.e. dissipation factor for all fabricated

PNC composites. The dissipation factor, tanδ, is related to the permittivity which is a measure of the energy loss due to dielectric response of the hybrid composite[33-34].

Fig.6 shows conductivity (σ) for hybrid non-magnetic ($\mu$ =1) composites extracted from equation (2). It is evident from Fig.4 that conductivity of composite increases with increase in wt% of conductive nano-fillers. When an EM wave is incident on the conductive composite the induced conduction current due to nano-fillers improves the imaginary part of permittivity and contributes to dielectric loss and dissipates the incoming electromagnetic energy into heat, which is consistent with conductivity and loss tangent analysis.

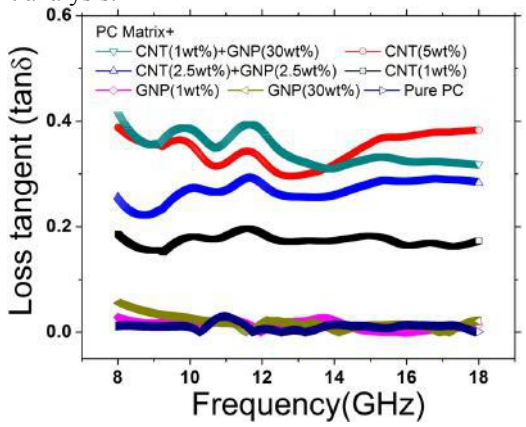



Figure 5. Measured loss tangent i.e. dissipation factor for all PNCs.

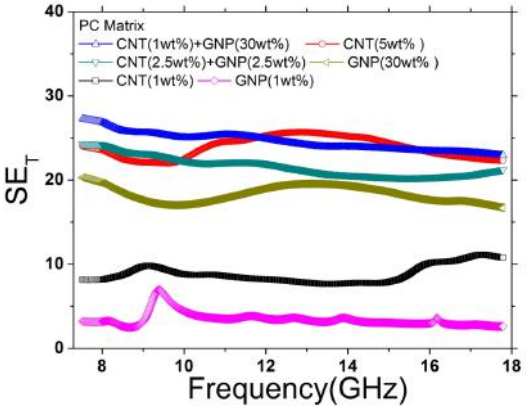



Figure 6. Measured conductivity (σ) for all fabricated PNCs.

Therefore, it can be concluded that composite with higher loading rate have the higher ability to attenuate the incident EM wave through the PNC materials. Though shielding efficiency increases with increase in composite conductivity, it remains difficult to establish a general relation between SE and wt% of nano-fillers in case of mixed ratio of CNT and GNPs. Our main objective focuses on to utilization of the conductive PNCs in combination with frequency selective surface (FSS) for absorption modulation at FSS-SRR resonator resonances. In next section, we discuss the experimental and simulation of SRR/dielectric/ground metal as well as SRR/dielectric/grounded PNCs heterostructure for absorption.

Fig.7 shows the FSS-SRR patterned over Rogers substrate and backed alternatively by ground metal and or grounded PNCs to test the proof of concept following the simulation results as shown in Fig.1. For simulation purpose, mean values of retrieved EM parameters are utilized to design artificial layers of the PNCs in CST-Microwave studio. Results are the compared with experimentally measured values and Fig.8 shows the experimental setup for measurement of scattering parameters for heterostructure. For the sake of clarity, measured parameters are fitted filtered to remove unwanted artifacts caused during measurement due to instrumental and human error.

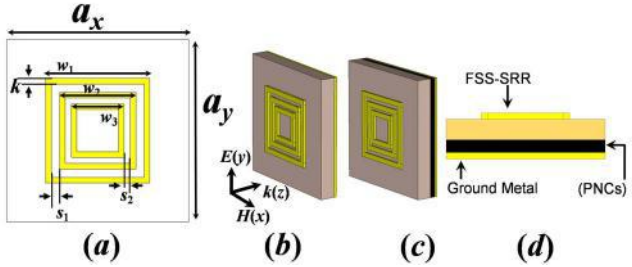



Figure 7. (a) Front side of FSS-SRR, (b) SRR-dielectric-ground metal (dielectric is Rogers RO3010, $\varepsilon_r$=10.2, tanδ =0.002, thickness $d$=1.28mm), (c) SRR-dielectric-grounded Polymer nanocomposite(PNCs) and, (d) Side view of individual layers. Dimensions of FSS-SRR are $a_x$=$a_y$=9.8, $k$=0.3,$w_1$=5.6, $w_2$=4.1, $w_3$=2.5, $s_1$=0.45,$s_2$=0.35, Units are in mm.

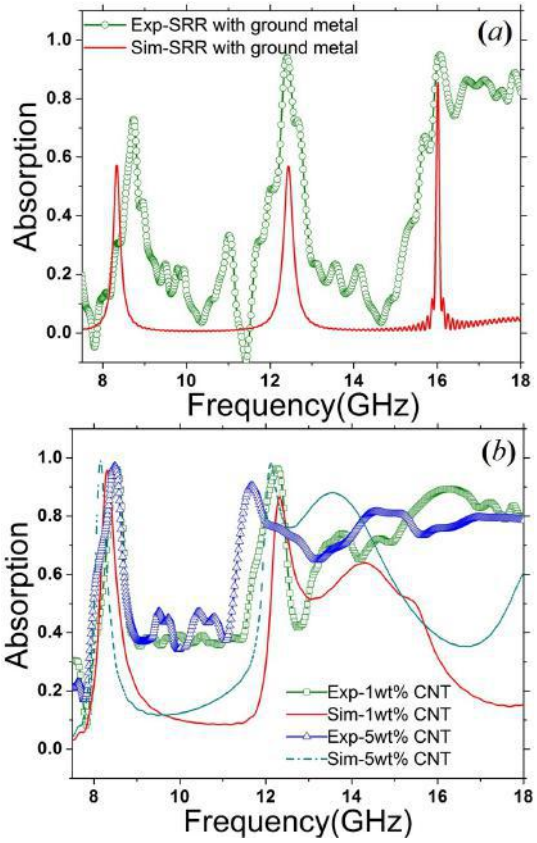



Figure 8. Measured and simulated absorption spectrum for (a) FSS-dielectric-ground metal and (b) FSS-dielectric-Grounded PNCs loaded with CNTs nano-fillers in 5wt% and 1wt% in PC-matrix.

The mismatch between the measured and simulation values are obvious due to many factors such impedance mismatch, assumption of mean fitting parameters, experimental setup, variation in surface roughness and thicknesses of PNCs and so on, which could be optimized for better performance of tunable absorption. Fig.8 (a)&(b) shows the measured and simulation results for absorption modulation at FSS-SRR resonance peaks for grounded metal and grounded PNCs loaded with 5wt% and 1wt% of CNT nano-fillers. It is observed that numerically evaluated SRR peaks occur at 8.2GHz, 12.3GHz, and 16GHz which has good match with measured values peaks for SRR with grounded metal. On other hand, when PNCs loaded CNTs placed between the SRR-dielectric and ground metal, absorption shows an excellent modulation in simulation.

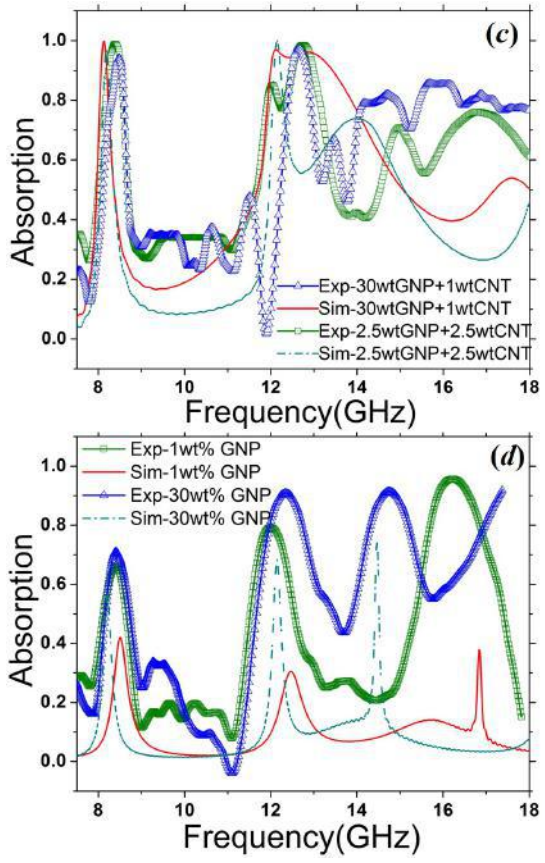



Figure 8. Measured and simulated absorption spectrum for (c) FSS-dielectric-Grounded PNCs loaded with CNTs & GNPs nano-fillers in (1wt%+30wt%,Sample-PCG130) and (2.5wt%+2.5wt%,Sample-PCG25) and, (d) FSS-dielectric-Grounded PNCs loaded with GNPs nano-fillers in 30wt% and 1wt% in PC-matrix.

As well measured values also show quite observable difference in absorption after 12GHz. It can be seen that around 8.2GHz the absorption is nearly 100% while at 12.3GHz absorption peaks varies from 100% to 80% between 12.3GHz to18GHz for PNCs having 5wt% and 1wt% CNTs. Similarly, Fig.8 (c)&(d) also shows 100% and 95% absorption magnitude at 8.2GHz for PNCs PCG25 and PCG130 respectively while after 12GHz absorption shows a roughly 20% magnitude difference between the two samples as can be seen in Fig.8 (d). At 12.5GHz absorption value is nearly 100% while between 13 to 17GHz PCG130 has roughly 80% and PCG25 varies around 60% absorption magnitude. In third configuration of PNCs loaded with 30wt% and 1wt% of GNPs in PC matrix, absorption occurs at resonance peaks with much improved magnitude than numerically estimated as shown in Fig.8 (d).

Since, measured absorptions magnitude varies in an unpredicted manner at some frequency points, which is attributed to experimental factors, it is difficult to set the definite values of magnitude but nevertheless the predicted behavior of absorption modulation shows excellent agreement with experiments. Fig.1 to Fig.8 show a systematic approach for significant modulation of resonant absorption peaks in proposed composite structure which demonstrates the proof of concept of utilizing hybrid structure of polymer nanocomposite with FSS-SRR metamaterials. Further analysis can also be performed with different SRR patterns on a variety of dielectric and nanocomposite materials.

## 4. Conclusions

In Summary, the concept of hybrid structure of SRR-dielectric-polymer nanocomposite is demonstrated for absorption modulation in X-and Ka-band experimentally and numerically. The PNCs are fabricated by incorporating different wt% fraction of CNTs and GNPs in high, low and mixed configuration in polycarbonate matrix. Then extracted electromagnetic parameters of nanocomposite are used to simulate PNCs as grounded plane in SRR metamaterial structure for absorption modulation at resonant peaks of FSS-SRR. The results are significant with narrow and broader absorption modulating at 8.2GHz and from 12.3 to 18GHz between 100% to 60% for various PNCs with varying material conductivity. The proposed concept can also be applied to any configuration of polymer matrix having inclusions of not only electric properties but also magnetic properties with even multilayer structure for improved performance.

## Acknowledgements

This work is supported by the Wallon Region, through the project ”Nano4waves” funded by its research program ”Actions de Recherche Concertées”..

## References

[1] M.F. L. De Volder, et.al.,"Carbon Nanotubes: Present and Future Commercial Applications," Science, 339(6119), pp 535-539, 2013.

[2] H. Kim, A. Abdala, C.W. Macosko," Graphene/Polymer Nanocomposites," Macromolecules ,43(16), pp 6515–6530, 2010.

[3] F. Qin and C. Brosseau," A review and analysis of microwave absorption in polymer composites filled with carbonaceous particles," J. Appl. Phys. 111, 061301 (2012)

[4] W. K. Chee, et.al., "Nanocomposites of graphene /polymers: a review," RSC Adv.,5, 68014-68051, 2015.

[5] J.R Potts, et.al ,"Graphene-based polymer nanocomposites." Polymer 52(1), 5–25, 2011.

[6] M. Moniruzzaman and K.I. Winey, "Polymer Nanocomposites Containing Carbon Nanotubes," Macromolecules, 39(16), pp 5194–5205, 2009.

[7] S.C.Tjong,"Polymer Composites with Graphene Nanofillers: Electrical Properties and Applications," J. Nanosci. and Nanotech., 14(2), pp1154-68, 2014.

[8] J.M. Thomassin, et.al, "Polymer/carbon based composites as electromagnetic interference (EMI) shielding materials," Materials Science and Engineering: R: Reports, 74( 7), pp 211–232, 2013.

[9] J-M Thomassin, et.al, "Foams of polycaprolactone /MWNT nanocomposites for efficient EMI reduction," J. Mater. Chem., 18, 792-796, 2008.

[10] T. Kuilla, et.al."Recent advances in graphene based polymer composites," Prog. Polym. Sci. 35(11),pp 1350–1375, 2010.

[11] P. mukhopadhyay, R.K. Gupta," Graphite, Graphene, and their polymer nanocomposites,"CRCPress, Taylor & Francis, 2013.

[12] C. K. Kum, et.al "Effects of morphology on the electrical and mechanical properties of the polycarbonate/multi-walled CNT composites," Macromolecular Research, 14(4), pp 456-460, 2006.

[13] P. B. Jana, A. K. Mallick, S. K. De,"Effects of sample thickness and fiber aspect ratio on EMI shielding effectiveness of carbon fiber filled polychloroprene composites in the X-band frequency range," IEEE Electromagnetic Compatibility,34(4),pp 478 -481, 1992.

[14] S. Pegel, P. Pötschke, G. Petzold, I. Alig, S.M. Dudkin, D. Lellinger, " Dispersion, agglomeration, and network formation of multiwalled carbon nanotubes in polycarbonate melts," Polymer, 49(4), 974-984, 2008.

[15] JY. Yi, G.M. Choi, "Percolation Behavior of Conductor-Insulator Composites with Varying Aspect Ratio of Conductive Fiber," Journal of Electroceramics, 3(4), 361-369, 1999.

[16] R. L. Fante M. T. McCormack, "Reflection properties of the Salisbury screen," IEEE Antennas and Propagation, 36(10), pp 1443 -1454, 1988.

[17] Y. Danlée, C. Bailly, I. Huynen, "Thin and flexible multilayer polymer composite structures for effective control of microwave electromagnetic absorption," Composites Sci. and Tech. , 100, 182–188, 2014.

[18] M.Olszewska-Placha, et.al, A Broadband Absorber With a Resistive Pattern Made of Ink With Graphene Nano-Platelets," Ieee Transactions On Antennas And Propagation, 63(2), 565-72, 2015.

[19] N. I. Landy, S. Sajuyigbe, J. J. Mock, D. R. Smith, and W. J. Padilla. "Perfect metamaterial absorber," Physical Review Letters., 100, 207402, 2008

[20] X. Shen, Y. Yang, Y. Zang, J. Gu, J. Han, W. Zhang, T.J. Cui,"Triple-band terahertz metamaterial absorber: Design, experiment, and physical interpretation," Applied Physics Letters, 101, 154102, 2012.

[21] F.Costa, A. Monorchio, "Electromagnetic Absorbers based on High-Impedance Surfaces: From ultra-narrowband to ultra-wideband absorption," Advanced Electromagnetics, 1(3), pp 7-12, 2012.

[22] B Yuan, et.al,"Comparison of electromagnetic interference shielding properties betwee single-wall carbon nanotube and graphene sheet/polyaniline composites," J.Phys D Appl Phys, 45(23),235108, 2012.

[23] Y. Yang, et.al "Comparative Study of EMI Shielding Properties of Carbon Nanofiber and Multi-Walled CarbonNanotube Filled Polymer Composites," J. Nanosci. and Nanotech., 5(6), pp 927–931, 2005.

[24] D. M. Bigg "The Effect of Compounding on the Conductive Properties of EMI Shielding Compounds," Advances in Polymer Tech., 4(3-4), 255-266, 1984.

[25] I. Molenberg, et.al,"Convenient and non-destructive electromagnetic characterisation technique for composite and multiscale hybrid samples at microwave frequencies", Microwave and Optical Technology Letters, 56(2), pp. 504-509, 2014

[26] J.M. Thomassin, et.al, "A convenient route for the dispersion of CNT in polymers: application to the preparation of electromagnetic interference (EMI) absorbers. Polymer,53(1), pp169–174, 2012

[27] Y. Danlée , I. Huynen and C. Bailly, "Frequency-selective multilayer electromagnetic bandgap structure combining carbon nanotubes with polymeric or ceramic substrates,"Applied Physics Letters, 105, 123118, 2014.

[28] D.D.L. Chung, "EMI shielding effectiveness of carbon materials," Carbon,39, 279–285, 2001.

[29] M.H. Al-Saleh, W.H. Saadeh, U.Sundararaj,"EMI shielding effectiveness of carbon based nanostructured polymeric materials: A comparative study," Carbon 60, 146-156, 2013.

[30] J.Liang, et.al., "EMI shielding of graphene/epoxy composite," Carbon, 47, pp 922-925, 2009.

[31] D-X Yan, P-G Ren, H.Pang, Q.Fu, M-B Yanga, Z-M L, "Efficient electromagnetic interference shielding of lightweight graphene/polystyrene composite," J. Mater. Chem., 22, 18772,2012.

[32] D. R. Smith, et.al, "Electromagnetic parameter retrieval from inhomogeneous metamaterials," Physical Review, E 71, 036617, 2005.

[33] F. Costa,et.al, "Waveguide Dielectric Permittivity Measurement Technique Based on Resonant FSS Filters," IEEE Microwave and Wireless Components Letters, 21(5), pp 273-275, 2011.

[34] F. Costa, et.al,"A Circuit-Based Model for the Interpretation of Perfect Metamaterial Absorbers," IEEE Microwave and Wireless Components Letters, 61(3), pp 1201-1209, 2013.

# Compact and Broadband Antenna using Double Negative Transmission line Metamaterial

**M. M. Islam[1, *], M. R. I. Faruque[2], M. T. Islam[3], and M. F. Mansor[3]**

[1]Department of Software Engineering, Daffodil International University, Dhaka 1207, Bangladesh
[2]Space Science Centre (ANGKASA), Universiti Kebangsaan Malaysia, 43600 UKM, Bangi, Malaysia
[3]Deparment of Electrical, Electronic & Systems Engineering, Universiti Kebangsaan Malaysia, 43600 UKM, Bangi, Malaysia
*corresponding author, E-mail: mmoiislam@yahoo.com

## Abstract

In this manuscript, double negative transmission line (TL) metamaterial inspired antenna has been proposed with compactness and improved bandwidth. This antenna is made of double negative meander lines, microstrip feed and partial ground. Double negative TL metamaterials show negative permittivity and permeability, simultaneously and play important role for antenna miniaturization and the impedance bandwidth improved. The antenna provides 600 MHz bandwidth (-10dB) with 23.81% fractional bandwidth. The antenna radiating element size is 0.07λ×0.07λ at 2.51 GHz frequency with 3.72 dBi maximum gain where the electrical dimension is 0.30λ×0.30λ.

## 1. Introduction

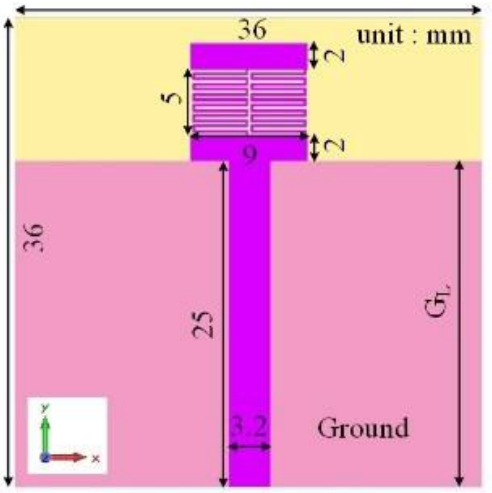
The prediction of negative index medium holding extraordinary electromagnetic properties were conducted by Russian Scientist Veselago in 1968 [1] The liability of the engineered negative index medium has been verified experimentally[2] and enormous feasibilities would be opened in optics and electromagnetics. However, many researchers are inspired with metamaterials which are used for improving multiple applications. Miniaturized antenna design and implementation is one of the challenges in today's mobile communication systems. The traditional antenna belongs to the typical difficulties such as narrow bandwidth, low gain and low profile. Itoh mentions transmission lines [3] that deliver a new way for designing and implementing compact metamaterial antennas[4-12]. A metamaterial antenna is explained with an epsilon-negative transmission line where 12.4% is the bandwidth [4]. Compact zeroth-order antenna is presented using metamaterials with 15 MHz bandwidth and 1.22 dBi gain [5].Resonant antennas are reviewed using CRLH TL metamaterial with 0.4% bandwidth and 0.07λ×0.07λ radiating element [6]. An epsilon negative resonator antenna is proposed with 1.30 dBi gain and 25 MHz bandwidth [7]. A planar antenna is presented using transmission line metamaterial structure [8] with narrow bandwidth (3%). A planar antenna is reviewed using CRLH TL with <1% fractional bandwidth in [9]. Couple electric field resonator is utilized to form metamaterial antenna in [10] and 20.7% bandwidth is attained. An interdigital capacitor is used for a CRLH resonant antenna with narrow bandwidth (6.8%) and large ground [11].

Double negative TL metamaterial inspired antenna having compact size, wide impedance and high gain has been mentioned in comparison with the antennas reported above in the letter. The metamaterial unit cell is made of meander lines which show both permittivity and permeability negative simultaneously. The fabrication and experiment of the prototype antenna have been performed. The measured radiations and reflection coefficient have been explained and the comparisons to metamaterial antennas are executed.

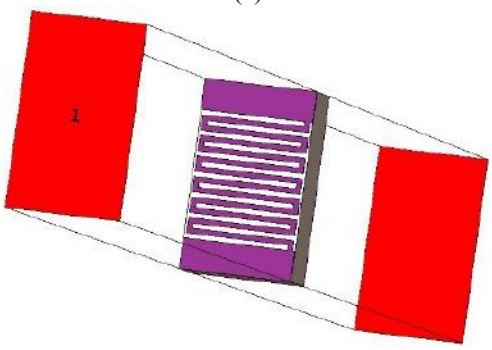
## 2. Unit Cell and Antenna Design Architecture

Double negative transmission metamaterials are used for attaining compact antenna with high gain and wide bandwidth. The proposed antenna configuration, unit cell simulation geometry, and unit cell equivalent circuit are illustrated in Fig.1. This antenna is made of double negative TL structure, microstrip feed and partial ground plane. The radiating patch and the conducting ground of side length 25mm ($G_L$) have been fabricated on the front side and the back side of 1.905 mm thick Roger's 6010 substrate material, respectively. The substrate's permittivity and loss tangent are 10.2 and 0.0023, respectively. 0.2 mm is the width of the meander lines. A 50Ω microstrip line of length and width of 25mm and 3.2mm, respectively has been applied for feeding the radiating element. The electrical dimension of the radiating element and the antenna are 0.07λ × 0.07λ and 0.30λ × 0.30λ respectively. FDTD based simulation software, CST microwave studio is applied for attaining the S-parameters. Perfect boundaries (magnetic and electric) are set after the unit cell is kept between two waveguide ports. An electromagnetic plane wave is propagated in the z direction whereas a perfect magnetic conductor (PMC) and a perfect electric conductor (PEC) boundary condition are defined in the y directions and x direction, respectively. One resonance is realized in the transmission characteristics, S21 at 2.51 GHz frequency according to the Fig.2 (a) and Fig. 2(b). The real values of the effective permittivity and permeability have been retrieved from the S-parameters exhibited in Fig.2 (c) and

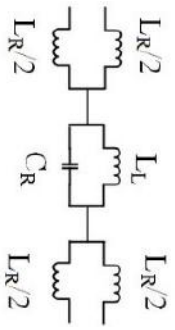
Fig 2(d) using the method explained in [13, 14]. It can be observed obviously from the Fig.2 (c) and Fig. 2 (d) that both the permittivity and permeability hold on negative values such as and -40.87 and -87.90, respectively at the 2.51 GHz resonant frequency. However, this TL structure can be said to be a left handed (LH) metamaterial.




(a)

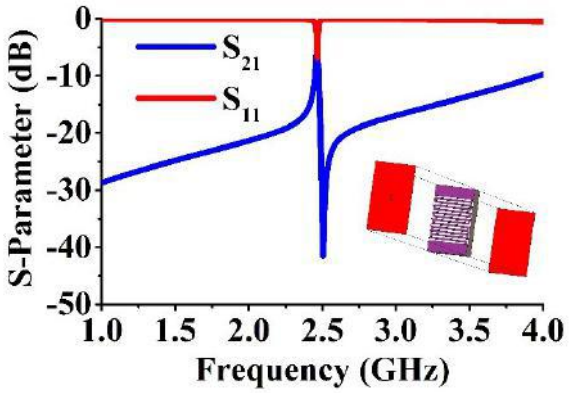


(b)

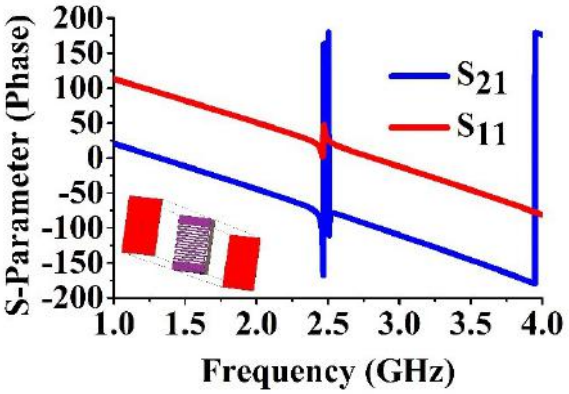



(c)

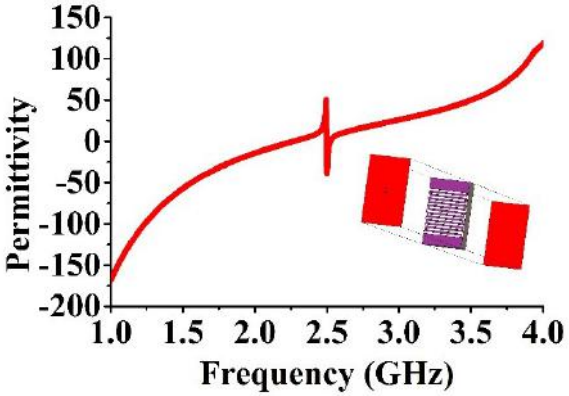
Figure 1: (a) The proposed antenna geometric layout (b) unit cell simulation geometry (c) unit cell equivalent circuit.



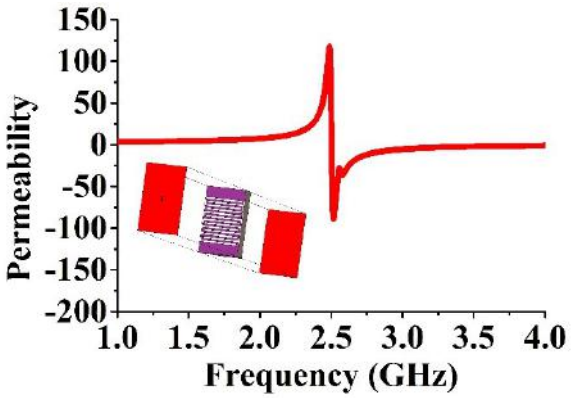

(a)




(b)




(c)

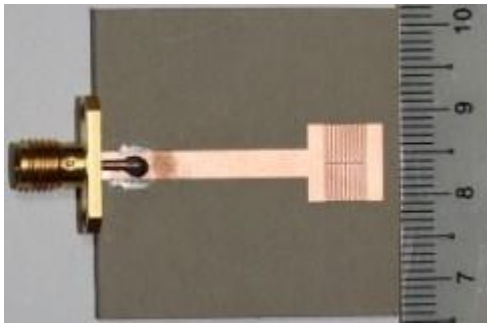



(d)

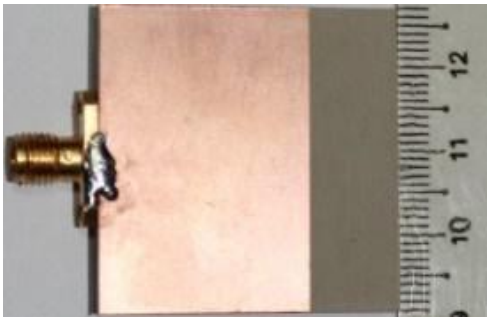
Figure 2: The proposed unit cell (a) S-parameters in dB (b) S-parameters in phase (c) permittivity (real value) (d) permeability (real value).

### 3. Results and Discussion

The fabricated antenna prototype has been illustrated in Fig. 3. The performance of the designed antenna with the proposed left handed TL metamaterial is explored and optimized by FDTD based simulation software, CST microwave studio. For experimental validation a pair of prototypes is fabricated on commercially available Rogers's 6010 PCB substrate. An Agilent E8362C PNA series vector network analyzer is used to measure the input impedance characteristics. The simulated and measured reflection coefficient curve of the proposed design is depicted in Fig. 4. From simulations, 520 MHz is the impedance bandwidth (-10 dB) covering 2.26-2.78 GHz frequency range with fractional bandwidth 20.63% at 2.51 GHz center frequency. On the other hand, from measurements, 600 MHz is the impedance bandwidth (-10dB) with fractional bandwidth 23.81% (2.22-2.82 GHz) at 2.51 GHz centre frequency. The measured result is fairly agreed with that of the simulation. Left handed TL metamaterials play an important role on the broadband of the antenna. The effects of ground plane are exhibited in Fig. 5. $G_L$=25 mm is the optimized value to attain the minimum centre frequency and the broad impedance bandwidth.



(a)



(b)

Figure 3: The fabricated antenna prototype (a) top view (b) bottom view.

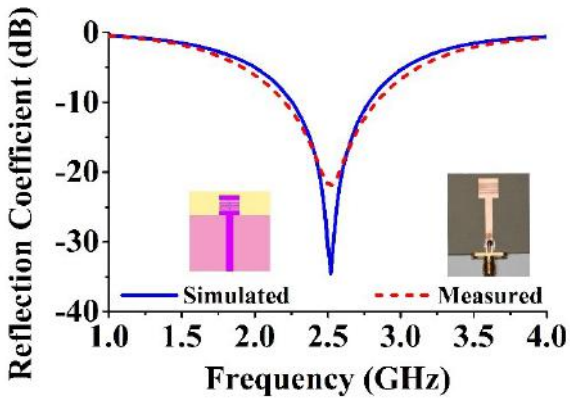



Figure 4: Measured and simulated reflection coefficient of the proposed ML metamaterial antenna.

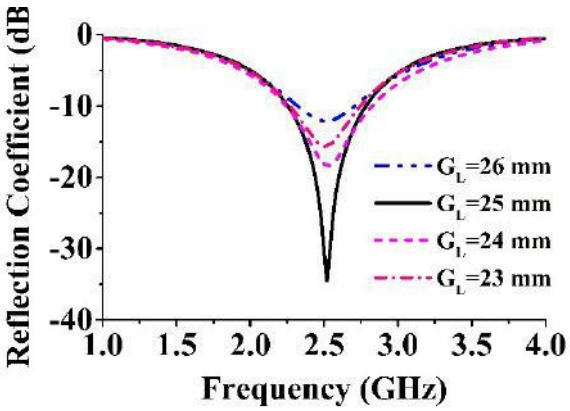
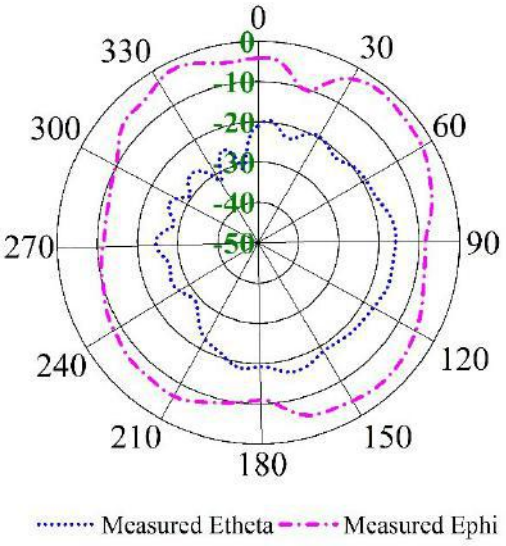


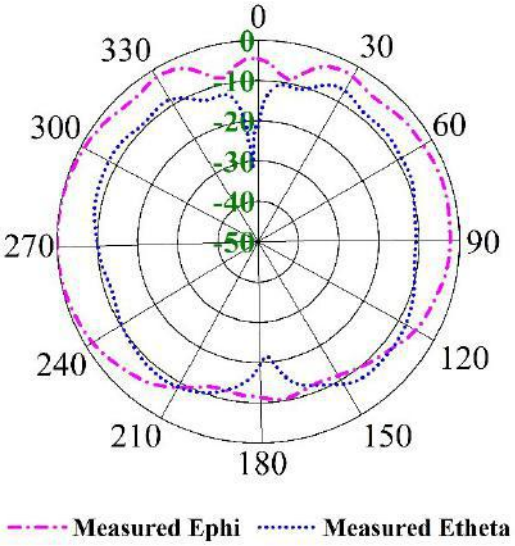

Figure 5: Comparisons of the effects of the ground length on the reflection coefficient.

The measured radiation patterns are illustrated in Fig. 6 at 2.41 GHz and 2.51 GHz frequency. It is found that dipole like and nearly omnidirectional radiation pattern have been attained in the E-plane and H-plane, respectively at both frequency (2.41 GHz & 2.51 GHz). The surface current distribution at 2.41 GHz and 2.51 GHz frequency is shown

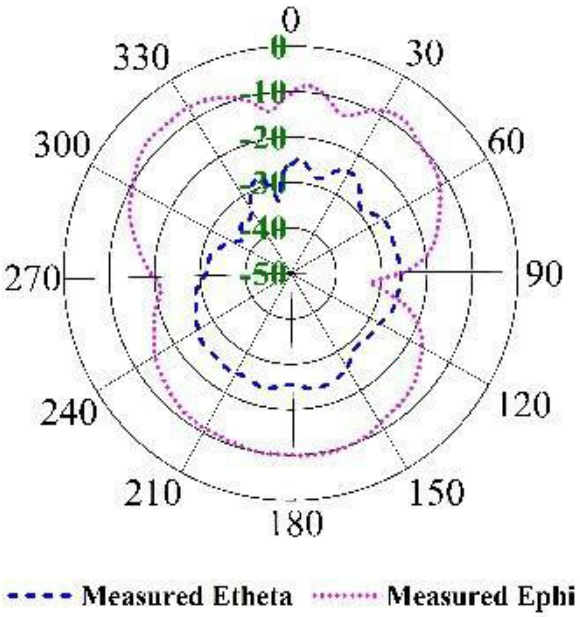
in Fig. 7. It is realized that a strong current exists on the meander lines owing to play as the main radiating element. Moreover, the currents flow over the entire operating frequency bands. The gain (simulated &measured) of the TL metamaterial antenna has been demonstrated in Fig. 8. The gain firmly rises and reduces with the frequencies and holds its maximum level 3.92 dBi (simulated) and 3.72 dBi (measured). In case of simulations, gain variation is .92 dBi (3-3.92 dBi), on the other hand, .69 dBi (3.03-3.72 dBi) is the gain changes for measurement.



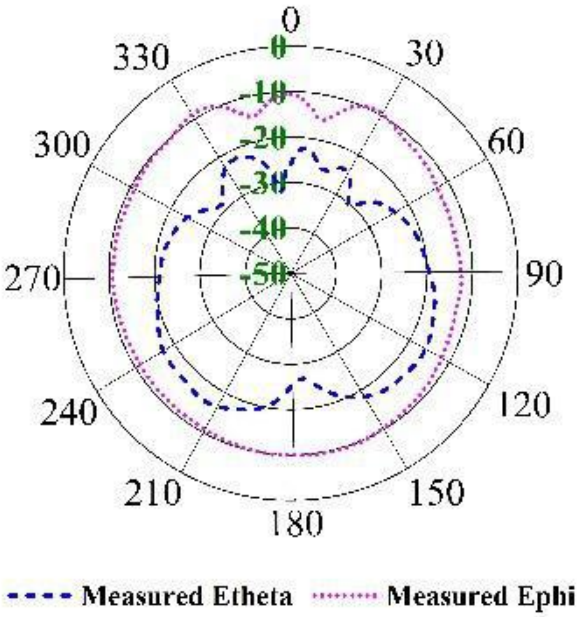

(a)




(b)

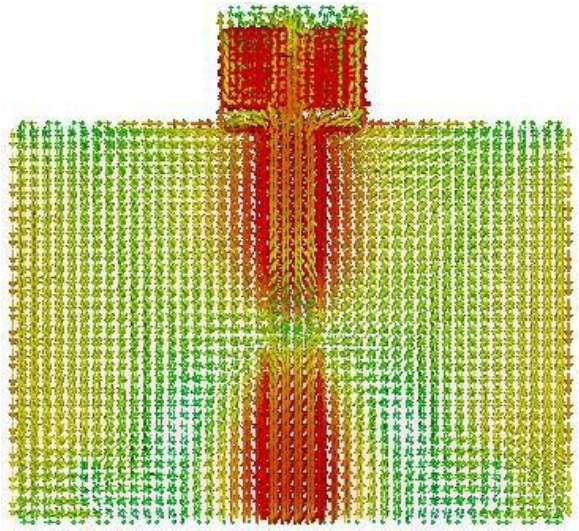



(c)

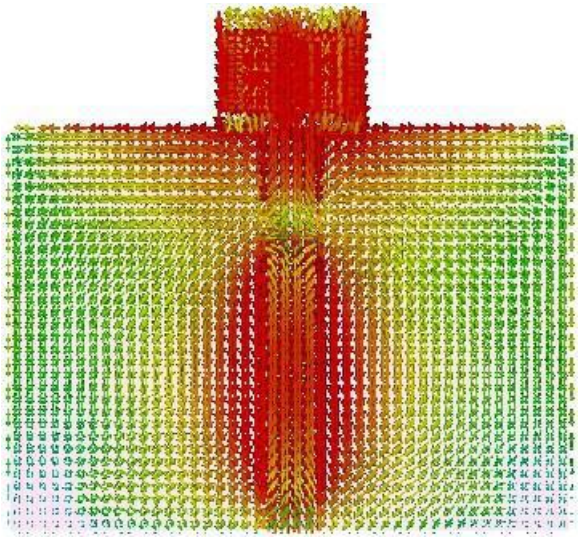



(d)

Figure 6: Measured radiation patterns (a) E- plane at 2.41 GHz. (b) H- plane at 2.41 GHz (c) E-plane at 2.51 GHz, (d) H-plane at 2.51 GHz.



(a)



(b)

Figure 7: The surface current distribution at (a) 2.41 GHz (b) 2.51 GHz.

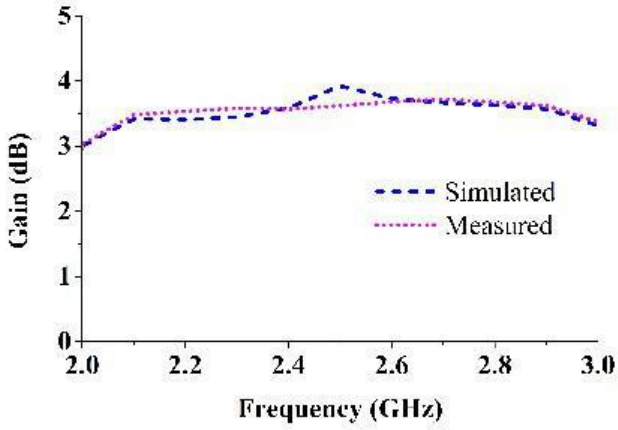



Figure 8: The measured and simulated gain of the TL metamaterial antenna.

Table 1: Comparisons between the proposed and existing antennas

| parameters | frequency[μm] | Overall size | Radiating element size | Bandwidth [-10 dB] |
|---|---|---|---|---|
| [4] | 2.66 | 0.35λ × 0.35λ | 0.10λ × 0.08λ | 12.4% |
| [5] | 2.70 | 0.23λ × 0.34λ | 0.05λ × 0.13λ | 0.6% |
| [6] | 1.17 | 0.31λ × 0.25λ | 0.07λ × 0.07λ | 0.4% |
| [7] | 1.78 | 0.13λ × 0.18λ | 0.06λ × 0.09λ | 1.4% |
| [8] | 3.30 | 0.55λ × 0.55λ | 0.25λ × 0.14λ | 3% |
| [9] | 3.38 | --- | 0.17λ × 0.17λ | <1% |
| [10] | 2.62 | 0.35λ × 0.39λ | 0.12λ × 0.09λ | 20.7% |
| [11] | 3.80 | 0.38λ × 0.33λ | 0.24λ × 0.24λ | 6.8% |
| [12] | 2.03 | 0.14λ × 0.17λ | 0.10λ × 0.11λ | 6.8% |
| This work | 2.51 | 0.30λ × 0.30λ | 0.07λ × 0.07λ | 23.81% |

The overall performance of the proposed double negative TL metamaterial antenna has been listed in Table 1 for comparing with the metamaterial antennas reported in the literature. It is observed that the proposed double negative ML metamaterial antenna delivers compactness with high gain and improved bandwidth.

## 4. Conclusions

In this manuscript, double negative TL metamaterial inspired compact antenna is proposed with bandwidth improved. The proposed TL metamaterial antenna (0.30λ × 0.30λ) is prototyped and it is found that the designed antenna can achieve a fractional bandwidth of 23.81% ranging from 2.22 - 2.82 GHz. The antenna also achieved a good gain (maximum gain 3.72 dBi) and exhibits stable dipole-like radiation and nearly omni-directional patterns. The attractive features of this proposed double negative TL metamaterial antenna such as simple structure, less expensive, low profile makes it very suitable for WLAN (2.40-2.48 GHz) and WiMAX (2.5-2.69 GHz) applications.

## Acknowledgements

This work was supported by the Research University (RU) grant, Malaysia under GUP-2016-028 and GUP-2016-029.

## References

[1] V. G. Veselago, "The electrodynamics of substances with simultaneously negative values of permittivity and permeability," *Physics-Uspekhi,* vol. 10, pp. 509-514, 1968.

[2] R. A. Shelby, D. R. Smith, and S. Schultz, "Experimental verification of a negative index of refraction," *Science,* vol. 292, pp. 77-79, 2001.

[3] S. Lim, C. Caloz, and T. Itoh, "Metamaterial-based electronically controlled transmission-line structure as a novel leaky-wave antenna with tunable radiation angle and beamwidth," *Microwave Theory and Techniques, IEEE Transactions on,* vol. 52, pp. 2678-2690, 2004.

[4] M. S. Majedi and A. R. Attari, "A compact and broadband metamaterial-inspired antenna," *IEEE Antennas and Wireless Propagation Letters,* vol. 12, pp. 345-348, 2013.

[5] T.-G. Kim and B. Lee, "Metamaterial-based compact zeroth-order resonant antenna," *Electronics letters,* vol. 45, pp. 12-13, 2009.

[6] C.-J. Lee, K. M. Leong, and T. Itoh, "Composite right/left-handed transmission line based compact resonant antennas for RF module integration," *Antennas and Propagation, IEEE Transactions on,* vol. 54, pp. 2283-2291, 2006.

[7] J. Q. Huang and Q. X. Chu, "Compact epsilon negative zeroth-order resonator antenna with higher radiation efficiency," *Microwave and Optical Technology Letters,* vol. 53, pp. 897-900, 2011.

[8] J. Zhu and G. V. Eleftheriades, "A compact transmission-line metamaterial antenna with extended bandwidth," *Antennas and Wireless Propagation Letters, IEEE,* vol. 8, pp. 295-298, 2009.

[9] A. Lai, K. M. Leong, and T. Itoh, "Infinite wavelength resonant antennas with monopolar radiation pattern based on periodic structures," *Antennas and Propagation, IEEE Transactions on,* vol. 55, pp. 868-876, 2007.

[10] B. Bala, M. Rahim, and N. Murad, "Small electrical metamaterial antenna based on coupled electric field resonator with enhanced bandwidth," *Electronics Letters,* vol. 50, pp. 138-139, 2014.

[11] J. Ha, K. Kwon, Y. Lee, and J. Choi, "Hybrid mode wideband patch antenna loaded with a planar metamaterial unit cell," *Antennas and Propagation, IEEE Transactions on,* vol. 60, pp. 1143-1147, 2012.

[12] T. Jang, J. Choi, and S. Lim, "Compact Coplanar Waveguide (CPW)-Fed Zeroth-Order Resonant Antennas With Extended Bandwidth and High Efficiency on Vialess Single Layer," *IEEE Transactions on Antennas and Propagation,* vol. 59, pp. 363-372, 2011.

[13] M. M. Islam, M. T. Islam, M. Samsuzzaman, and M. R. I. Faruque, "Compact metamaterial antenna for UWB applications," *Electronics Letters,* vol. 51, pp. 1222-1224, 2015.

[14] M. M. Islam, M. T. Islam, M. Samsuzzaman, and M. R. I. Faruque, "A negative index metamaterial antenna for UWB microwave imaging applications," *Microwave and Optical Technology Letters,* vol. 57, pp. 1352-1361, 2015.

# A Double-Layer Metamaterial-Based Technique for Interference Mitigation and Shielding of Planar Microwave Structures

**Athanasios Papadimopoulos[1], Theodosios Karamanos[1], Nikolaos Tsitsas[2], Constantinos Valagiannopoulos[3], Nikolaos Kantartzis[1*], and Theodoros Tsiboukis[1]**

[1]Department of Electrical and Computer Engineering, Aristotle University of Thessaloniki, 54124 Thessaloniki, Greece
[2]Department of Informatics, Aristotle University of Thessaloniki, 54124 Thessaloniki, Greece
[3]Department of Physics, Nazarbayev University, Astana 010000, Kazakhstan
*corresponding author, E-mail: kant@auth.gr

## Abstract

An efficient cloaking-shielding technique based on the use of a double superstrate-layer overlay is developed in this paper for planar microstrips. The metamaterial-inspired formulation reduces considerably the induced on the strip current and the reflected from the microstrip electric field, thus alleviating the electromagnetic susceptibility of microstrip transmission lines. For this purpose, the mathematical analysis and optimization procedure are founded on a semi-analytic integral equation algorithm, while a set of numerical results certifies its promising merits.

## 1. Introduction

The controllable confinement of electromagnetic interactions between devices and their environment, thus rendering them invisible and immune to potential interferences, has recently triggered a significant research interest in the microwave regime [1, 2]. Amid diverse devices, microstrip transmission lines, despite their compact and economical structure, are vulnerable to crosstalk and unintentional radiation. Toward this direction, various noteworthy designs have been presented, exploiting different implementation concepts [3, 4]. In this paper, a double superstrate-layer, metamaterial-oriented method is introduced and verified in order to concurrently attain low electromagnetic reflections as well as considerable levels of shielding of planar microwave configurations.

## 2. The cloaking-shielding method

Let us consider an external, distant noise-source as a $z$-polarized plane wave with an incidence angle $\varphi_i$ that impinges on the configuration of Fig. 1. The Green's function expressions for the homogeneous (without the perfect electric conducting (PEC) strip) structure are derived analytically [3], with the secondary part of Green's function in the substrate's layer (region 3) receiving the form of

$$G_3^{\rm sec}(x,y) = \frac{1}{4\pi}\int_{-\infty}^{\infty} A_1 \cosh\left[(y+w)\sqrt{l^2-k_3^2}\right] + A_2 \sinh\left[(y+w)\sqrt{l^2-k_3^2}\right] dl, \quad (1)$$

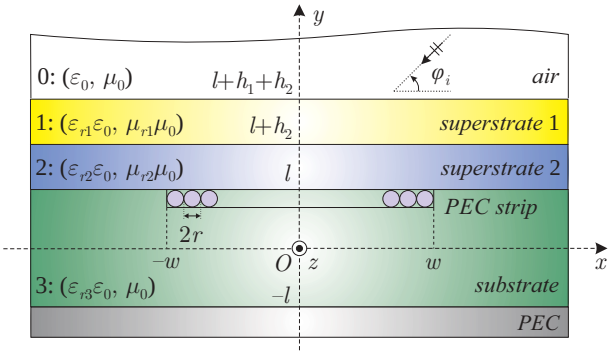



Figure 1: The cloaked microstrip transmission line.

with $A_1, A_2$ constant coefficients that depend on the relative position of every layer with regard to its source current, thickness, and constitutive parameters. Next, the PEC strip is decomposed into a properly selected large number $N$ of thin cylindrical wires of surface $C_n$, so that it can be safely assumed that the surface current $J_n$ on each wire is constant. Thus, the scattered electric field in region $i = 0, 1, 2, 3$ can be expressed as

$$E_i^{\rm scat}(x,y) = -j\omega\mu_0 \sum_{n=1}^{N} J_n \int_{C_n} G_i(x,y)dS. \quad (2)$$

Applying the boundary conditions on the surface of the thin wires, a $N \times N$ linear system results in the form of

$$j\omega\mu_0 \sum_{n=1}^{N} J_n \int_{C_n} [G_3^{\rm pr}(x,y) + G_3^{\rm sec}(x,y)]dS = E_3^{\rm ind}(x_k, w-r), \quad (3)$$

where $E_3^{\rm ind}$ is the induced electric field in region 3 of the strip-free structure, superscripts pr and sec indicate the primary and secondary parts of Green's function in region 3, and $(x_k, w-r)$ are the coordinates of the $k_{th}$ wire center. By solving this linear system, the induced current on the strip and the scattered electric field, through (2), are obtained.

For our analysis, two superstrate layers are overlaid atop the microstrip line. In essence, our objective is two-fold,

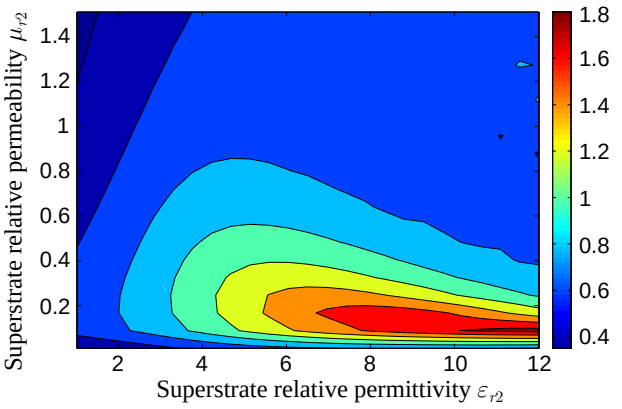



Figure 2: Contour plot of the ratio of the total current induced on the strip for the cloaked to the non-cloaked case, on the map of the superstrate $\varepsilon_{r2}$ and $\mu_{r2}$.

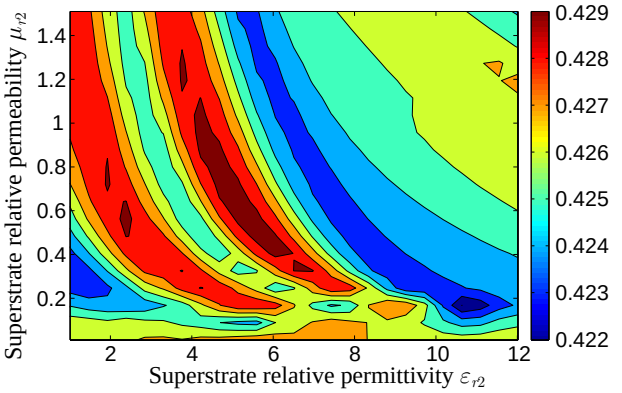



Figure 3: Contour plot of the ratio of the reflection coefficients for the cloaked to the non-cloaked case, on the map of the superstrate $\varepsilon_{r2}$ and $\mu_{r2}$.

namely the reduction of the reflected from the structure electric field and the mitigation of the induced current on the strip, so that the electromagnetic interference from external sources to a nearby microwave structure is decreased. To this goal and based on the above formulation, an extensive optimization process that involves the dimensions and electromagnetic parameters of the two layers is conducted. A key asset of the featured technique is its ability to provide fast and precise estimations of the induced on the strip current and the structure's reflected field. Therefore, for our optimization procedure, we can safely select the frequency spectrum of [6 GHz,10 GHz] and a range of incidence angles $\varphi_i \in [15°, 90°]$ for the external noise-source. Moreover, an FR-4 substrate is employed with a thickness of $2w = 1.5$ mm and a relative permittivity of $\varepsilon_{r3} = 4.3 - j0.0966$, while the dimensions of the conducting strip are $1.5\,\text{mm} \times 48.4\,\mu\text{m}$.

Initially, the dimensions and material parameters of the first layer (region 1) are determined. Our selections refer to values that correspond to typical dielectric boards, so that the final structure can be easily manufactured. In particular, thickness is chosen as $h_1 = 298$ mm, whereas

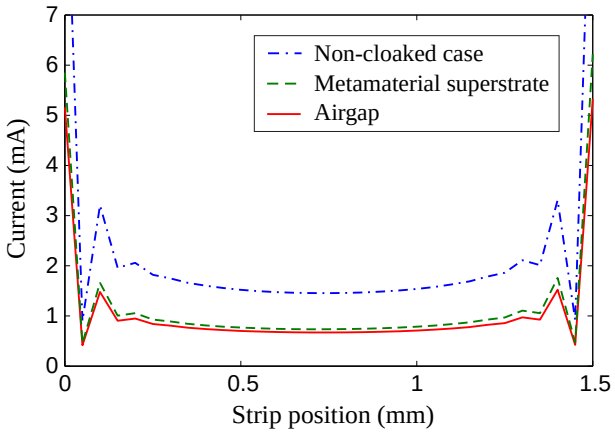



Figure 4: Current along the conducting strip.

$\varepsilon_{r1} = 2.8 - j0.042$ and $\mu_{r1} = 1$. Then, the characteristics of the second superstrate layer (region 2) are specified. A common board thickness of $h_2 = 5$ mm is selected, while extensive numerical simulations are conducted, as shown in Figs. 2 and 3, to define a pair of optimal and realizable media parameters. Two solutions are preferred: (i) $(\varepsilon_{r2}, \mu_{r2}) = (1.0, 1.0)$, corresponding to an air-gap or synthetic polymer and (ii) $(\varepsilon_{r2}, \mu_{r2}) = (11.48, 0.72)$, corresponding to a $\mu$-near-zero (MNZ) metamaterial. The significant reduction of the induced current is shown in Fig. 4 for both designs.

## 3. Conclusions

A novel method for the cloaking-shielding and interference mitigation of planar microstrips, that involves a double-layer overlay atop of the strip, is proposed in the current work. Its effectiveness and design is examined through meticulous numerical simulations of the featured algorithm.

## Acknowledgement

This research has been financed by the A. S. Onassis Public Benefit Foundation, under Grant GZL060-1/2015-2016.

## References

[1] A. Alù, N. Engheta, Cloaking a sensor, *Phys. Rev. Lett.* 102: 233901(1–4), 2009.

[2] P. Alitalo, S. Tretyakov, Broadband electromagnetic cloaking realized with transmission-line and waveguiding structures, *Proc. of IEEE* 99:1646–1659, 2011.

[3] C.A. Valagiannopoulos, N.L. Tsitsas, Integral equation analysis of a low-profile receiving planar microstrip antenna with a cloaking superstrate, *Radio Sci.* 47: RS2022(1–12), 2012.

[4] O. Paul, Y. Urzhumov, C. Elsen, D. Smith, M. Rahm, Construction of invisibility cloaks of arbitrary shape and size using planar layers of metamaterials, *J. Appl. Phys.* 111: 123106(1–7), 2012.

# Dual Band Wearable Fluidic Antenna with Metasurface Embedded in a PDMS Substrate

**Muhammad Nazrin Ramli[1], Ping Jack Soh[1*], Mohd Faizal Jamlos[1,2], Herwansyah Lago[1], and Norazizan Mohd Aziz[1]**

[1]Advance Communication Engineering Centre (ACE), School of Computer and Communication Engineering, Universiti Malaysia Perlis, Pauh Putra Campus, 02600 Arau, Perlis, Malaysia
[2]Faculty of Mechanical Engineering, Universiti Malaysia Pahang, Pekan, Pahang, Malaysia
*Corresponding author: pjsoh@unimap.edu.my

## Abstract

In this paper, a flexible fluidic antenna with an Artificial Magnetic Conductor (AMC) plane embedded in a polydimethylsiloxane (PDMS) structure is presented. The antenna is designed based on the combined operating principles of dipole and rectangular loop to cover dual band WLAN ISM (2.4 GHz and 5.8 GHz). The AMC plane which is placed behind the proposed antenna reduces backward radiation towards the human users. The evaluation of the antenna indicated satisfactory performance in terms of reflection coefficient, bandwidth and radiation patterns.

## 1. Introduction

Wearable systems with simultaneous computing and wireless communication functionalities have garnered a great amount of interest in both academia and industry. This is due to their promising potential applicability in a variety of fields ranging from health monitoring, patient tracking, smart houses, battlefield survival, etc. [1]. It is important that potentially harmful radiation towards human body is minimized in these applications, which is possible by implementing a metasurface on the reverse side of the antenna.

This work proposes a flexible and robust antenna with artificial magnetic conductor (AMC) metasurface implemented using polydimethylsiloxane (PDMS) as substrate and eutectic gallium indium alloy (EGaIn) as its conductor. EGaIn is composed of 75.5% of Gallium and 24.5% of Indium. [2], resulting in an electrical resistivity of about 29.4 x $10^{-6}$ Ω-cm. Meanwhile, the PDMS used as the substrate has a permittivity ($\varepsilon_r$) of 2.7 and a loss tangent ($tan\delta$) of 0.0134 [3]. The liquid EGaIn metal is proposed to be injected into microfluidic channels embedded in the multilayered elastomeric substrate, and is advantageous as it will provide extra robustness and flexibility for wearable applications [4].

## 2. Antenna Design

The overall structure is formed using six layers, and consists of two parts, the radiator and the AMC. A copper foil is used as the ground plane and forms the bottom-most layer. This is followed by a layer of 3 mm-thick PDMS substrate. The AMC array formed using EGaIn is placed 2 mm deep into this layer before another layer of 3 mm-thick PDMS covers it. Similarly, the radiator will then be placed 2 mm into this substrate before a final 3 mm-thick PDMS is used to cover it, see Figure 1. CST Microwave Studio software is used for simulations. The detailed descriptions of the two main antenna elements will be described in the following sections.

### 2.1. AMC Design

A simple square AMC unit cell is chosen in this work to ensure fabrication simplicity, see Figure 1. Its patch is sized at 34 x 34 $mm^2$, and other dimensions are summarized in Table 1. Its bandwidth, determined from the ±90° range of the reflection phase is 90 MHz (2.34 to 2.43) GHz in the lower band and 55 MHz (5.61 to 6.16 GHz) in the upper band, as illustrated in Figure 2. Next, this unit element is duplicated to form a 3 x 3 array consisting of nine elements, see Figure 3. This AMC plane placed behind the antenna is used to reduce backward radiation and potentially reduces electromagnetic absorption in human tissues.

Table 1: Values of the AMC parameters

| parameter | length[mm] |
|---|---|
| W | 49 |
| W1 | 34 |
| L | 49 |
| L1 | 34 |
| T1 | 1 |
| T2 | 2 |
| T3 | 3 |

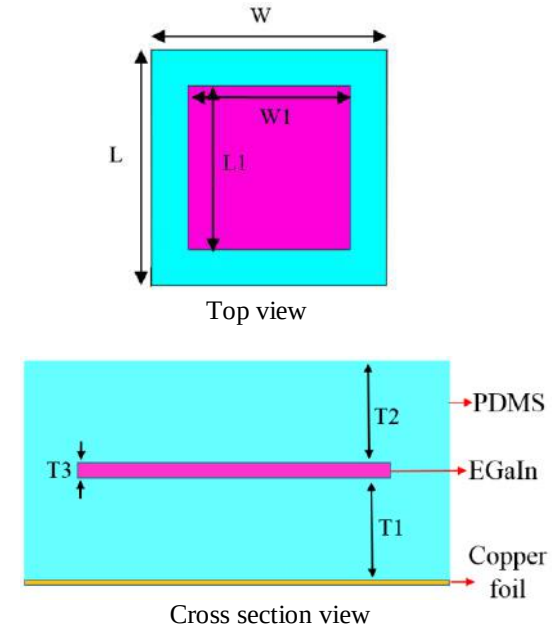



Figure 1: The unit cell of the 2.4 GHz and 5.8GHz AMC.

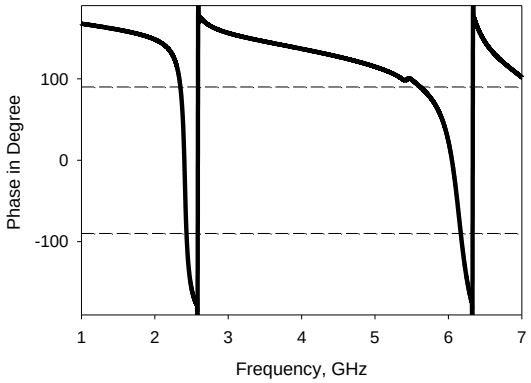



Figure 2: Reflection phase of the proposed AMC unit cell.

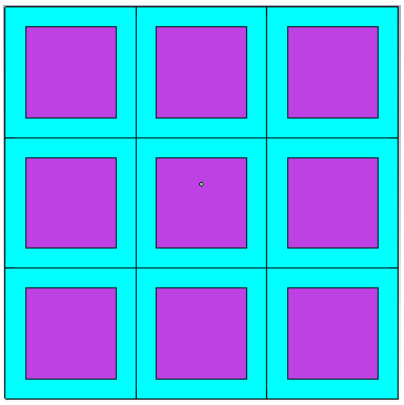


Figure 3: Topology of the proposed 3 x 3 AMC plane.

### 2.2. Radiator Topology

Next, the optimized AMC is then integrated with the a radiator to form the antenna with an overall PDMS area of 147 x 147 mm$^2$. The radiator is designed based on a rectangular patch topology sized at 40 x 30 mm$^2$, see Figure 4. It is integrated with two 10 x 10 mm$^2$ slits on its left and right position to enable dual-band operation. The tuning of its size facilitated the impedance matching improvements in both the lower (2.4 GHz) and upper (5.8 GHz) bands. A square slot sized at 8 x 8 mm$^2$ is then introduced onto the patch to ensure its size miniaturization. A summary of the antenna dimension is listed in Table 2. The overall structure is fed from the bottom-most layer using a coaxial probe. Its position on the patch also facillitates impedance matching.

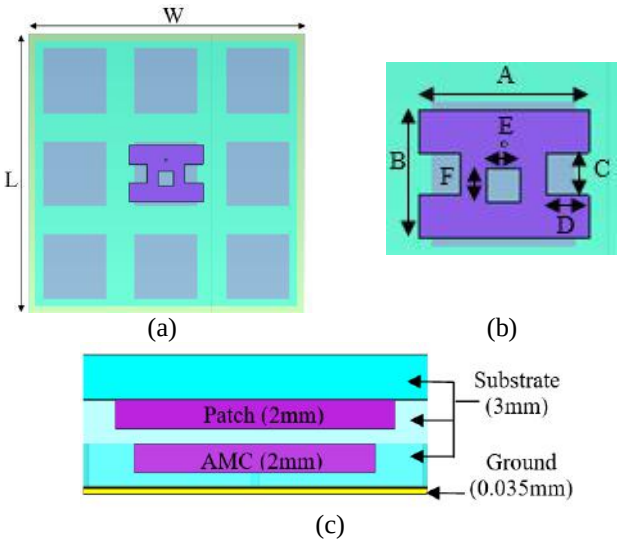



Figure 4: Proposed antenna: (a) Top view (b) Topology (c) Cross section view

Table 2: Values of the antenna's parameters

| parameter | length[mm] |
|---|---|
| W | 49 |
| L | 49 |
| A | 40 |
| B | 30 |
| C | 10 |
| D | 10 |
| E | 8 |
| F | 8 |

## 3. Results and Discussion

Integration of the AMC and the proposed antenna resulted in an operation from 2.37 to 2.41 GHz (in the lower band) and 5.71 to 5.85 GHz (in the upper band)., see Figure 5. This translates into a bandwidth of 39 MHz (1.64%) and 145 MHz (2.5%) in the lower and upper band, respectively. Meanwhile, the radiation pattern of the antenna is presented in Figure 6 in the *xz*-and *yz*-plane. It can be noticed that the radiation is directed towards the forward direction, with a gain of of 0.3353 dB for 2.4GHz and 4.114 dB at 5.8GHz. Moreover, the incorporation of the AMC plane resulted in the reduction of its back radiation, with a front-to-back

(FBR) ratio, 12.84 dB for 2.4GHz and 12.82 dB for 5.8GHz.

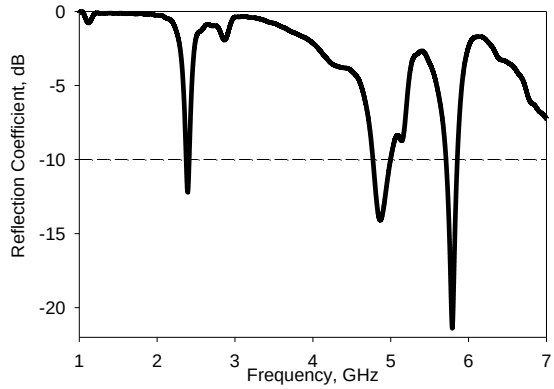
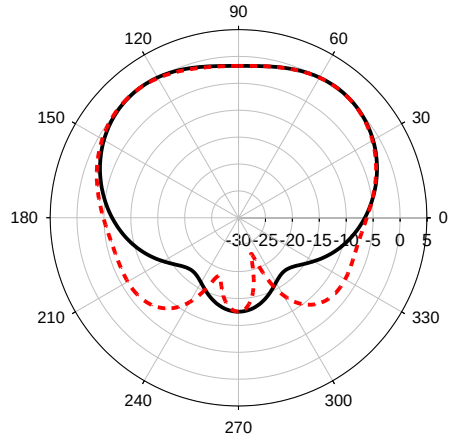
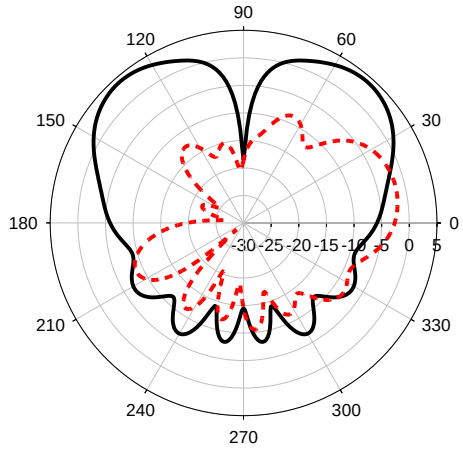



Figure 5: Reflection coefficient of the proposed antenna on AMC plane.




(a)




(b)

Figure 6: Simulated radiation pattern for (a) 2.4 GHz and (b) 5.8 GHz at xz-plane (black solid line) and yz-plane (red dash line).

## 4. Conclusions

The design of a new fluidic antenna integrated with AMC is investigated. This antenna is built using PDMS as its substrate and a metallic fluid, EGaIn, as its conductor. A square AMC unit cell is first designed and evaluated. It is capable of operating with a bandwidth of 90 MHz (2.34 to 2.43 GHz) in the lower band and 55 MHz (5.63 to 6.16 GHz) in the upper band. This AMC plane is then used as a reflector to reduce back radiation towards potential users when used in a wearable form. A rectangular-shaped radiator is chosen and formed on top of the AMC. The incorporation of the slot and slits in the rectangular radiator resulted in a compact size and dual-band antenna operation in the 2.4 and 5.8 GHz bands. It is validated to operate from 2.37 to 2.41 GHz (in the lower band) and 5.71 to 5.85GHz (in the upper band). A directional radiation and low back radiation is produced by the antenna, with a gain of 0.3353 dB for 2.4GHz and 4.114 dB at 5.8GHz. Meanwhile, front-to-back ratio is evaluated at 12.84 dB for 2.4GHz and 12.82 dB for 5.8GHz.

## Acknowledgements

This project is supported by the Fundamental Research Grant Scheme provided by the Malaysian Ministry of Higher Education (MOHE) (grant no: 9003-00537).

## References

[1] P. S. Hall and Y. Hao, “Antenna and propagation for body-centric wireless communications,” *in Proceedings of the First European Confrence on Antennas and Propag.* Artech House, Norwood, MA, United States, 2006.

[2] J.-H. So, J. Thelen, A. Qusba, G. J. Hayes, G. Lazzi, and M. D. Dickey,“Reversibly deformable and mechanically tunable fluidic antennas,” *Adv. Funct. Mater*, vol. 19, pp. 3632–3637, 2009.

[3] G. J. Hayes, J. H. So, A. Qusba, M. D. Dickey and G. Lazzi, "Flexible Liquid Metal Alloy (EGaIn) Microstrip Patch Antenna," *IEEE Transactions on Antennas and Propagation*, vol. 60, no. 5, pp. 2151-2156, 2012.

[4] Alqadami, A. S. M., Jamlos, M. F., Soh, P. J., & Vandenbosch, G.” Assessment of PDMS Technology in a MIMO Antenna Array,” *IEEE Antennas and Wireless Propag. Lett., 1225(c),* 1–1. http://doi.org/10.1109/LAWP.2015.2513960

[5] D. Zrnic, D. S. Swatik, “On the resistivity and surface tension of the eutectic alloy of gallium and indium,” *J. Less-Common Metal*, vol.18, pp. 67-68, 1969.

[6] P. B. Samal, P. J. Soh and G. A. E. Vandenbosch, "A Systematic Design Procedure For MicroStrip-Based Unidirectional UWB Antennas," *Progress In Electromagnetics Research*, vol. 143, pp. 105-130, 2013

# A triangular coupled-resonator antenna for ultra-wideband applications

**Md Zulfiker Mahmud[1], Touhidul Alam[1,2], Mohammad Tariqul Islam[1],**

[1]Dept. Of Electrical, Electronic and Systems Engineering, Universiti Kebangsaan Malaysia, Malaysia
[2]Dept. Of Computer Science & Engineering, Int'l Islamic University Chittagong, Bangladesh
*corresponding author, E-mail: triqul@ukm.edu.my

## Abstract

A triangle shaped coupled resonator microstrip patch antenna is presented for ultra-wideband wireless applications. The antenna achieves bandwidth of 116.5% with electrical dimension of 0.154 λ × 0.133 λ × 0.016λ at the lower frequency band. The antenna performances has been analyzed using the finite integration technique of computer simulation technology microwave studio and validated with another EM simulating software HFSS and in measurement.

## 1. Introduction

Nowadays, UWB communication is becoming a potential candidate in wireless communication system due to its some special features like extremely high data transmission rate, low interference and low spectral power density. Designing of a proficient compact UWB antenna is still a challenging issue to the antenna researchers.

In the last decades, various types of antennas have been developed for ultra wideband wireless applications, such as microstrip patch antenna, coplanar waveguide-fed antenna [1]. Besides this several new techniques have been exposed to enhancing antenna operating frequencies[2-7]. Liang *et al.* proposed circular disc monopole antenna for UWB application, which can operate within 2.78 to 9.78 GHz [2].

Azim et al. modified antenna radiating patch into tapered-shape to enhancing UWB frequency band with an overall dimension of 22 × 24 $mm^2$ [3]. Coplaner Coplanar waveguide (CPW) antennas have also drawn attention for achieving UWB bands with miniature antenna. Gautam *et al.* proposed a 25 × 25 × 1.6 $mm^3$ CPW antenna for achieving UWB bands [4]. Metamaterials have created a new milestone in antenna designing. Various types of metamaterial are using to miniature the antenna size as well as ensuring UWB bandwidth [6].

In this paper, a new triangular coupled-resonator antenna is proposed that attains a compact UWB profile with good antenna performances.

## 2. Antenna configuration and analysis

The geometric layout of the proposed UWB antenna is depicted in Figure 1. The proposed antenna is designed on commercially available inexpensive FR4 substrate material having a dielectric constant of 4.3 and loss tangent 0.0025. The proposed antenna consists of a triangle shape coupled resonator patch on the top side and the ground plane on the bottom side of the substrate. The orientation of the ground plane and shape of patch has a strong effect to the impedance matching. Therefore, by properly selecting ground orientation and patch shape, good impedance bandwidth and radiation characteristics have been achieved. The proposed antenna is fed by a 50 Ω microstrip line. The antenna parameters are optimized using CST microwave studio. Moreover, the ground plane is modified by cutting slots on the top edge to form a symmetrical sawtooth shape [8].

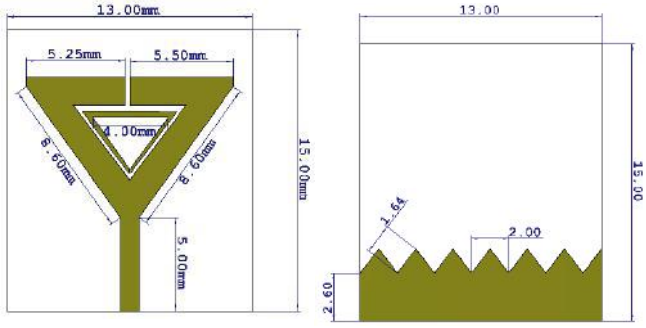



Figure 1: Geometric layout of the proposed UWB antenna-Top view (left) and bottom view (right).

The reflection coefficient of the proposed antenna has been analyzed CST simulator and verified using another electromagnetic simulator HFSS, shown in Figure 2. The antenna achieves -10dB impedance bandwidth of 8.57 GHz (3.07- 11.64 GHz), which covers the entire UWB frequency band. The results using both CST and HFSS software show that the antenna achieves good impedance matching. The surface current distribution of the proposed antenna has been investigated for better

understanding surface current and proper electromagnetic behavior. The surface current distribution of the proposed antenna at 3.7 GHz and 9.7 GHz is depicted in Figure 3 for observing EM behavior.

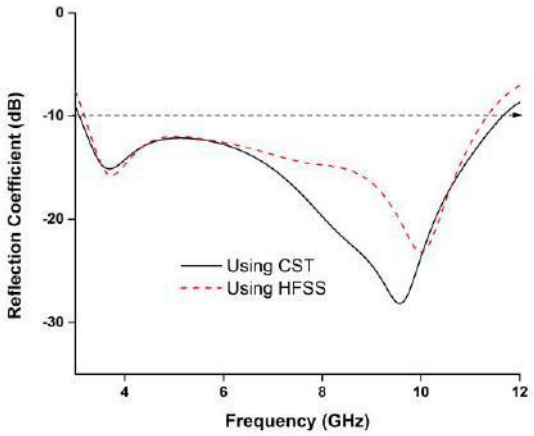
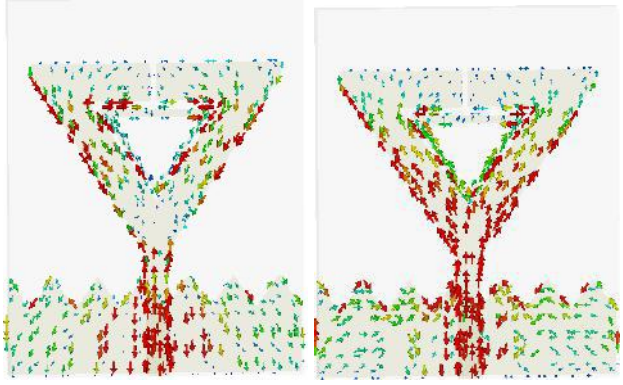



Figure 2: Reflection coefficient of the proposed antenna



(a) (b)

Figure 3: Surface current distribution of the antenna- (a) at 3.7 GHz and (b) at 9.7 GHz

## 3. Antenna experimental performance analysis

The optimized structural parameters have been found after lots of optimization and parameter sweeps on antenna performance. The optimized parameters are mentioned in Figure 1. A set of prototype of the proposed antenna has been fabricated for experimental validation, illustrated in Figure 4. The reflection coefficient of the fabricated antenna has been measured using Agilent PNA N5227A network Analyzer and the result is depicted in Figure 5. It is observed from Figure 5 that there is a little disagreement between measured and simulated results. This may happen due to fabrication tolerances.

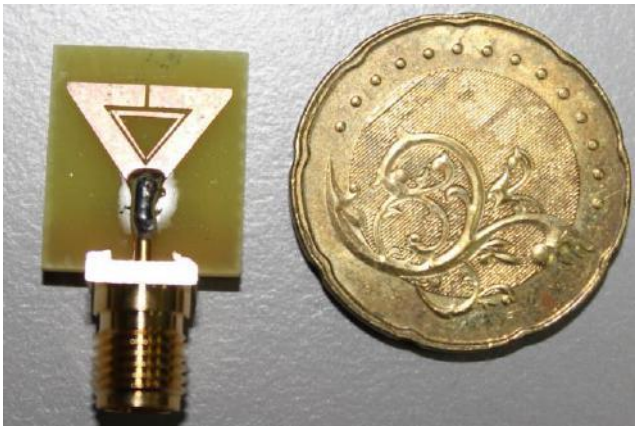


Figure 4: Fabricated prototype of the proposed antenna

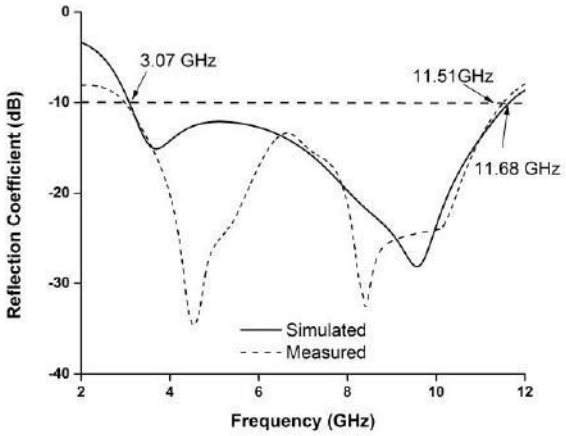



Figure 5: Measured and simulated reflection coefficient prototype of the proposed antenna

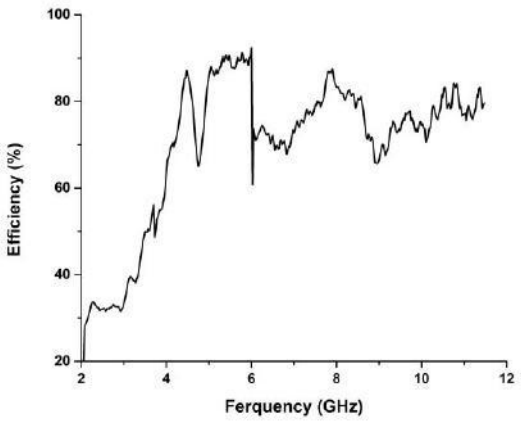



Figure 6: Measured radiation efficiency of the proposed antenna

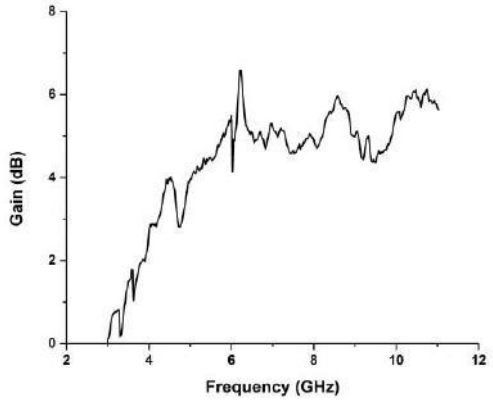
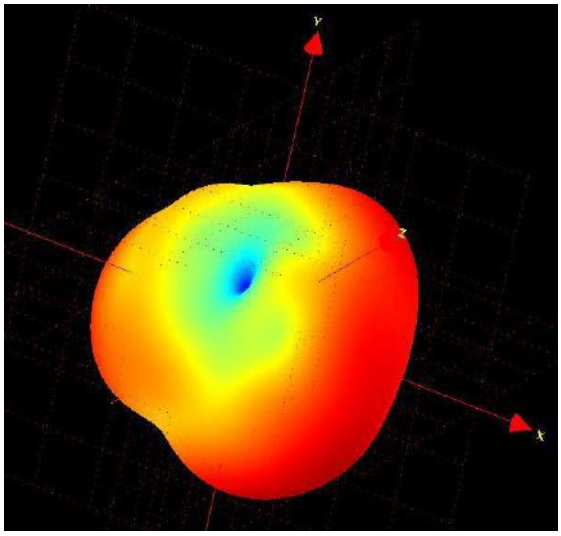


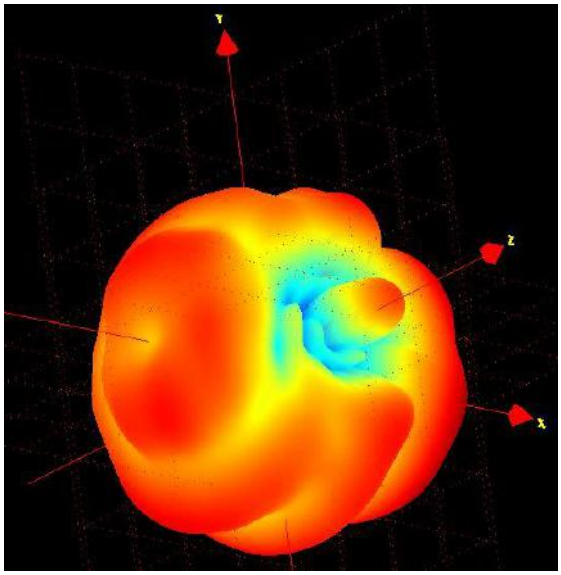

Figure 7: Measured peak gain of the proposed antenna

The farfield characteristics have been measured using SATIMO's StarLab. Figure 8(a)–(b) shows the 3-D measured radiation patterns of the proposed antennas at 3.7, and 9.7 GHz, respectively.

The measure radiation efficiency of the fabricated antenna is illustrated in Figure 6 and the average radiation efficiency is observed about 70%. Moreover, from Figure 7, it is shown that the minimum peat gain is 0.13094dB at 3.08 GHz and the maximum peak gain achieved at 6Hz is 5.49976 dB.




(a)




(b)

Figure 8: Measured radiation pattern of the proposed antenna- (a) at 3.7 GHz and (b) at 9.7 GHz

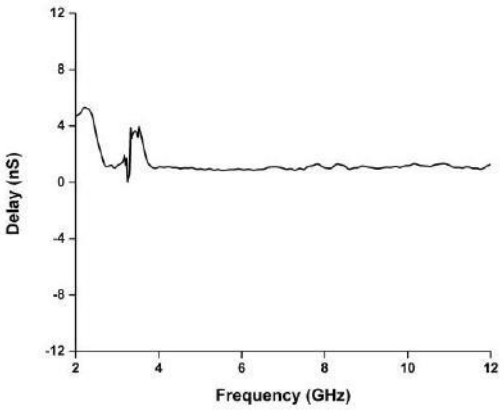



Figure 9: Measured group delay of the proposed antenna

The group delay of the proposed antenna has been measured by placing two fabricated antennas at a distance of 50 cm and is shown in Figure 9. It is observed from Figure 9 that the group delay of the proposed antenna is less than 2.5 ns, which ensure the good linear transmission performance within the operating regions.

The compactness of wideband antenna can be expressed in terms of the Bandwidth dimension ratio (BDR).This index term will show the achieved percentage operating bandwidth for per electrical area unit. The BDR equation is written as follows:

$$BDR = \frac{(BW\%)}{(\lambda_{lenght} \times \lambda_{width})}$$

Using the formula the proposed antenna has been achieved the BDR value of 5705.967. To ensure equitable

comparison between the proposed antenna and the reviewed antennas is shown in Table 1.

Table 1: Comparison of the proposed antenna with reported antennas

| Ref | Size [$mm^2$] | BDR | Operating Frequency (GHz) |
|---|---|---|---|
| [2] | 42× 50 | 530.78 | 2.78-9.78 |
| [3] | 22 × 24 | 2187.36 | 3-11.2 |
| [4] | 25× 25 | 2136.06 | 2.6-13.04 |
| [6] | 16 × 21 | 2652.28 | 3.40- 12.5 |
| [8] | 22 × 30 | 2046.81 | 3.08 -15.9 |
| [9] | 16 × 20 | 1227.03 | 4.8 - 14.5 |
| [10] | 20 × 25 | 2285.36 | 3.1 -12.08 |
| Proposed | 13 ×15 | 5705.967 | 3.07-11.64 |

## 4. Conclusions

A printed miniaturized antenna has been proposed having a dimension of 13 × 15 $mm^2$. The perceptible novelties of the proposed antenna are using triangular coupled-resonator for UWB antenna miniaturization. It is observed from simulation and measurement that the proposed antenna has attained -10dB impedance bandwidth of 8.57 GHz (3.07 to 11.64 GHz), which covers the entire UWB band. According to the measured gain, efficiency and radiation pattern, the proposed antenna can be a good candidate for UWB applications.


## Acknowledgements

Acknowledgements belong here.


## References


[1] Guha, Debatosh, and Yahia MM Antar, *Microstrip and printed antennas: new trends, techniques and applications*, John Wiley & Sons, 2011.

[2] Liang, J., et al. "Printed circular disc monopole antenna for ultra-wideband applications." Electronics letters 40.20 (2004): 1.

[3] Azim, Rezaul, Mohammad Tariqul Islam, and Norbahiah Misran. "Compact tapered-shape slot antenna for UWB applications." Antennas and Wireless Propagation Letters, IEEE 10 (2011): 1190-1193.

[4] Gautam, Anil Kr, Suneel Yadav, and Binod Kr Kanaujia. "A CPW-fed compact UWB microstrip antenna." Antennas and Wireless Propagation Letters, IEEE 12 (2013): 151-154.

[5] Alam, T., et al. "Dual elliptical patch antenna design on low cost epoxy resin polymer substrate material." International Journal of Applied Electromagnetics and Mechanics 49.1 (2015): 23-29.

[6] Islam, Md Moinul, et al. "A miniaturized antenna with negative index metamaterial based on modified SRR and CLS unit cell for UWB microwave imaging applications." Materials 8.2 (2015): 392-407.

[7] Saraswat, Ritesh Kumar, and Mithilesh Kumar. "Miniaturized slotted ground UWB antenna loaded with metamaterial for WLAN and WiMAX applications." Progress In Electromagnetics Research B 65 (2016): 65-80.

[8] Azim, Rezaul, Mohammad Tariqul Islam, and Norbahiah Misran. "Ground modified double-sided printed compact UWB antenna." Electronics Letters 47.1 (2011): 9-11.

[9] Shakib, M. N., M. Moghavvemi, and W. N. L. Mahadi. "Design of a Compact Planar Antenna for Ultra-wideband Operation." ACES. Vol. 30. No. 2. 2015.

[10] Jyoti Gogoi, Pragyan, Dhruba Jyoti Gogoi, and Nidhi S. Bhattacharyya. "Modified ground plane of patch antenna for broadband applications in C - band." Microwave and Optical Technology Letters 58.5 (2016): 1074-1078.

# Textile Antenna Integrated with an AMC Plane for WBAN

**H. Lago[1], P. J. Soh[1,2*], M. F. Jamlos[1,3], N. Shohaimi[1], S. Yan[2], and G. A. E. Vandenbosch[2]**
[1]Advanced Communication Engineering (ACE) CoE, School of Computer and Communication Engineering, Universiti Malaysia Perlis, 02600 Arau, Perlis, MALAYSIA.
[2]ESAT-TELEMIC Research Div., KU Leuven, Kasteelpark Arenberg 10 Box 2444, 3001 Leuven, BELGIUM.
[3]Faculty of Mechanical Engineering, Universiti Malaysia Pahang, Pekan, Malaysia.
*corresponding author, E-mail: pjsoh@unimap.edu.my

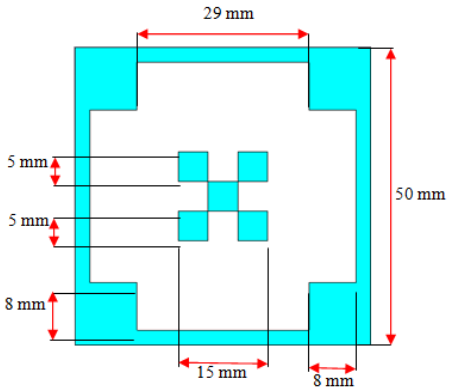
## Abstract

A novel wearable antenna with artificial magnetic conductor (AMC) fully fabricated using textile for Wireless Body Area Network (WBAN) is presented. The AMC unit element is designed based on a rectangular patch structure, which is then integrated using slots and slits for bandwidth broadening. Simulated and measured reflection and radiation performance indicate a satisfactory agreement, fulfilling the requirements for WLAN/WBAN applications both in free space and on body.

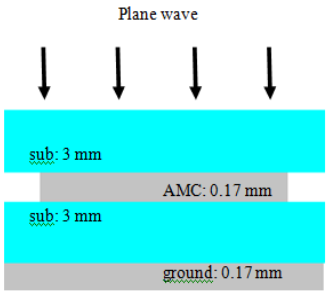
## 1. Introduction

Due to the lossy nature of the human body, electromagnetic interaction with the antenna must be minimized. A high front-to-back ratio (FBR) of the radiation is beneficiary to reduce this interaction. To enable a high FBR, artificial magnetic conductors (AMC) have been suggested as an effective solution [1-3]. In this work, a slotted microstrip antenna backed by an AMC plane is proposed for WLAN applications. The AMC plane is designed based on a slotted rectangular structure to ensure compactness. Compared to previous literature, this work features a relatively compact AMC unit cell sized at 50 x 50 mm2, which is about 0.4 x 0.4 λ, for operation at 2.4 GHz, see Figure 1. The AMC bandwidth is from 2.24 GHz to 2.51 GHz. The main radiator consists of a square patch with C-shaped notches in the middle of each of the edges, as illustrated in Figure 2. A rectangular ring slot is positioned centrally and fed using a 50 Ω SMA coaxial connector. The measured S11 is -12.4 dB and the simulated S11 is -15.65 dB at the desired frequency of 2.45 GHz.

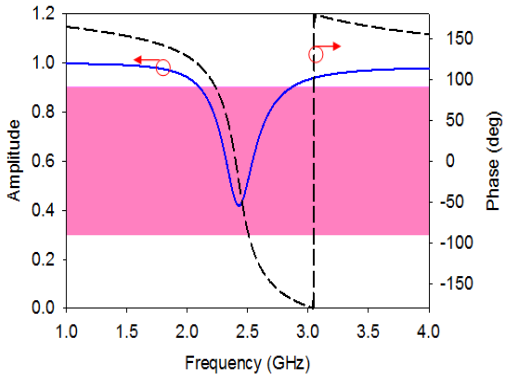
The maximum realized gain and bandwidth of the antenna is about 2.42 dB and 9.85 % at 2.45 GHz respectively, while its total efficiency is more than 40 % at 2.45 GHz, which is typical for textile antennas fabricated using these materials. It is also demonstrated that the AMC is effective in isolating the main radiator from the body. Besides that, the proposed AMC layer is also validated to be capable of reducing the antenna front-to-back ratio (FBR), gain improvement and bandwidth enhancement. When a normal ground is applied to the antenna without the AMC layer, a lower gain and bandwidth of 0.41 dB and 5.53 % is obtained at 2.45 GHz, while the total efficiency is also lower than 40 %. Suppressed backward radiation and reduced front-to-back ratioare ensured by the placement of an all-textile AMC plane. Effectively resulting in a reduced electromagnetic coupling with the body, it ensures a low SAR level of 0.0721 W/kg, which is far below the regulatory limit of 2 W/kg. Simulations and measurements performed in free space and on body are in good agreements, satisfactory fulfilling the requirements for WLAN / WBAN applications.




(a)

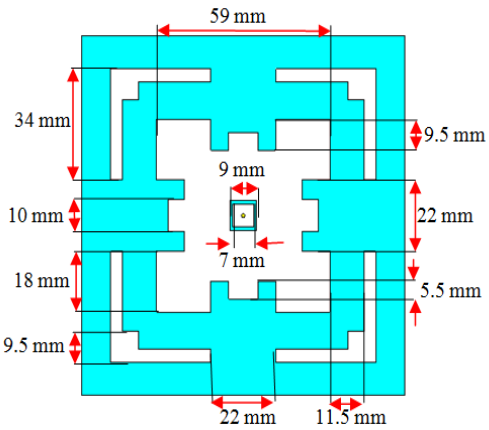



(b)

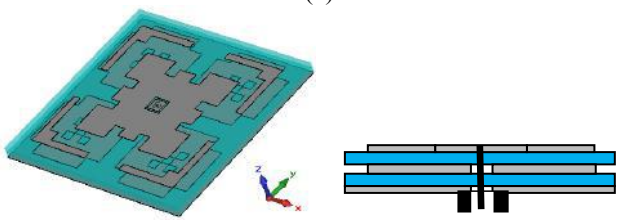



(c)

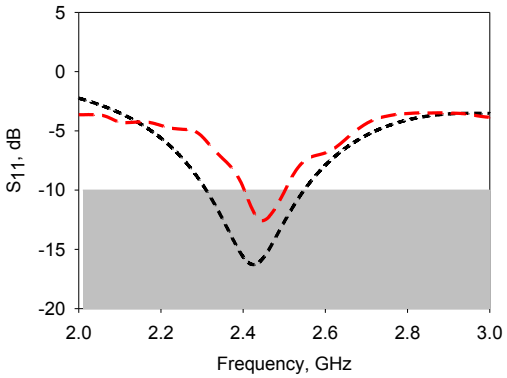
Figure 1: AMC unit cell topology. (a) AMC dimensions, (b) side view and (c) performance.




(a)



(b)




(c)

Figure 2: The proposed antenna (a) topology and dimensions, (b) perspective and side views; and (c) performance (black short dash line: simulated, long dash line: measured).


## Acknowledgements

This project is supported by the Fundamental Research Grant Scheme provided by the Malaysian Ministry of Higher Education (MOHE) (grant no: 9003-00537).


## References


[1] Rahim, M.K.A., N.A. Samsuri, K. Kamardin, and P. S. Hall, "Vertical and Horizontal Transmission Enhancement between Antennas Using Textile Artificial Magnetic Conductor Waveguide Sheet." Electronics Letters, vol. 51, no. 9, 671–673, 2014.

[2] Soh, P. J., G. A. E. Vandenbosch, S. L. Ooi, and M.R.N. Husna. "Wearable Dual-Band Sierpinski Fractal PIFA Using Conductive Fabric" Electronics Letters, vol. 47 no. 6, 365-366, 2010.

[3] Yan, Sen, Ping Jack Soh, and Guy A E Vandenbosch. 2014. "Low-Profile Dual-Band Textile Antenna With Artificial Magnetic Conductor Plane" IEEE Trans. Antenna and Propagat., vol. 62 no. 12, 2014.

[4] Best, S R, and D L Hanna. 2008. "Design of a Broadband Dipole in Close Proximity to an EBG Ground Plane." Antennas and Propagation Magazine, IEEE, vol. 50, no. 6, 52–64, 2008.

# Double Negative Metamaterial for Mobile Phone Application

**M. I. Hossain[1], M. R. I. Faruque[1], M. T. Islam[2]**

[1]Space Science Center, Universiti Kebangsaan Malaysia, Bangi, Malaysia
[3]Department of Electrical, Electronic, and System Engineering, Universiti Kebangssan Malaysia, Bangi, Malaysia
*E-mail: ipk_eee@yahoo.com

## Abstract

In this paper, a new design and analysis of metamaterial and its applications to modern handset is presented. The proposed metamaterial unit-cell design consists of two connected square spiral structures, which leads to increase the effective media ratio. The finite instigation technique (FIT) based on Computer Simulation Technology (CST) Microwave Studio is utilized in this investigation and the measurement is performed in an anechoic chamber. A good agreement is observed among simulated and measured results. The results indicate that the proposed metamaterial can successfully cover cellular phone frequency bands. Moreover, the uses of proposed metamaterial in modern handset antennas are also analyzed. The results reveal that the proposed metamaterial attachment significantly reduces SAR values without reducing the antenna performances.

## 1. Introduction

Due to many newborn applications, the research on metamaterials are increasing day by day. The metamaterials are artificial electromagnetic (EM) materials with some extraordinary EM properties [1]. However, the negative-index metamaterial is such material which exhibits negative value of the effective refractive index over a certain frequency range. Usually, the index of reflection of a medium can be negative when both the effective permittivity and effective permeability of the media show negative values [2]. Metamaterials are being used for lots of applications such as super lens [3], biomedical equipment [4], invisible cloaks [5] and so no. Moreover, the use of metamaterials is also increasing for electronic and communication devices [6, 7]. The antenna performances can be enhanced using metamaterials [8] or it can be used to degrade the EM absorption of human body tissue [9]. Moreover, metamaterial antennas are introduced as a new way of constructing small and compact antennas [10].

The metamaterial characteristics of the artificial structures are obtained only for a specific frequency band. In [11], an analysis of dielectric substrate effects on metamaterial characteristics was presented in terahertz frequency range. In [12], metamaterial superlens was proposed imaging in the optical frequency range. In [13], nanostructure cloak was proposed for optical frequencies. Although, the metamaterials are nano-structures for optical frequencies, those dimensions become to millimeters for microwave frequencies. In [14], design and analysis of double negative metamaterial was presented for X-band applications. A compact double negative metamaterial based on electric and magnetic resonator was introduced [15]. The results showed the negative refractive index from frequency 6.3 to 7.1 GHz. In [16], a metamaterial design was proposed for C-, and S-band applications. The presented results showed that the proposed design was applicable from 3 GHz to upper frequencies. However, the mobile phone applications use microwave frequency range from 0.5 GHz to 6 GHz. To date, metamaterials are being used in this frequency range, the main drawback is that the dimensions can become impractically large. In [17], a new design of metamaterial structure is demonstrated for UTMS band, where the size of presented metamaterial array is not compatible with a modern cell phone. In [18], a metamaterial structure is used successfully for the SAR reduction in the human head for 900 MHz and 1800 MHz. But, the size of those structures is too large for mobile phone applications.

In this paper, a new negative index metamaterial design is proposed for lower microwave frequencies. The applications of proposed metamaterial to the present mobile phone antenna are also analyzed to validate the proposed design. This includes the use of proposed metamaterial in the mobile phone and corresponding analysis of the effects of metamaterial on antenna performances and specific absorption rate (SAR) in the human head.

## 2. Design Analysis of Metamaterial

The metamaterial for modern portable devices should be slim and compact in size. It also should have the capability of covering lower microwave frequency bands as the cellular phones use a frequency range from 0.5 GHz to 6 GHz. To design such metamaterial, significant improvement in the ratio of its resonant wavelength $\lambda_0$ and its physical size ‘a’ to may create new opportunities for portable device application. This effective media ratio ($\lambda_0$/a) can be improved by increasing the inductance with multiple windings.

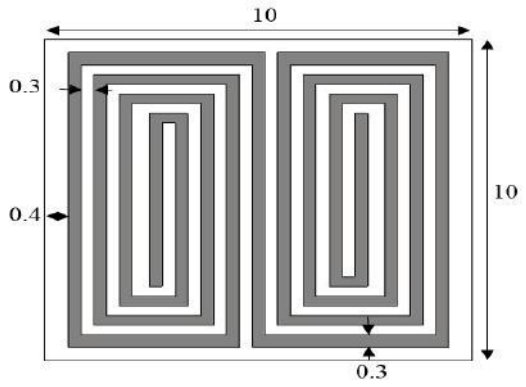



Figure 1: Geometry of proposed metamaterial (dimensions in millimeters).

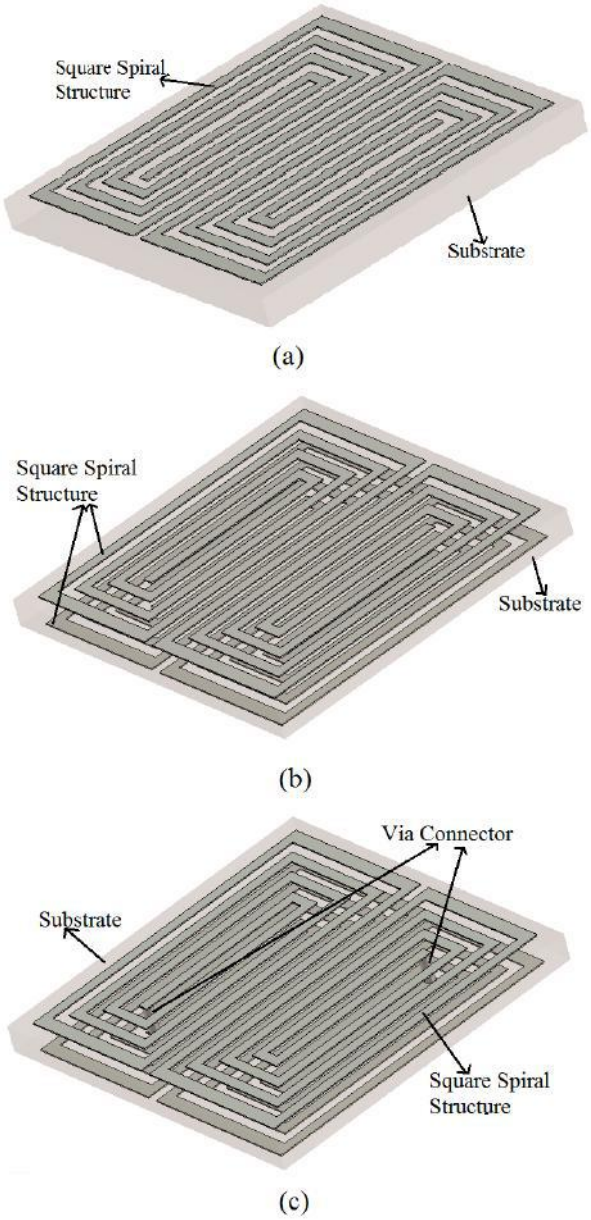



Figure 2: Unit-cell configurations: (a) unit-cell A, (b) unit-cell B, and (c) unit-cell C.

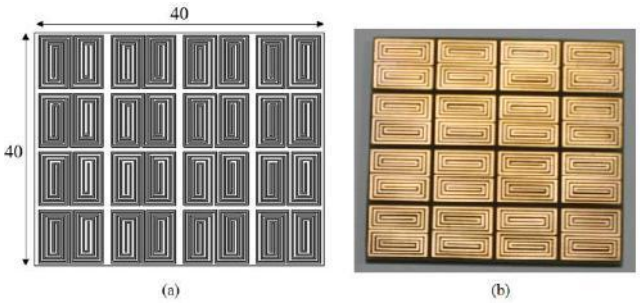



Figure 3: Array configuration: (a) array geometry of unit-cell A and (b) fabricated prototype.

In this paper, a new design of metamaterial is proposed using two connected spiral structures capable of increasing inductance as indicated in Figure 1. Basically, such structure operates as like as an LC resonant circuit. The printed metal strip length is mainly responsible for creating inductance and splits are responsible for originating capacitance. Those inductance and capacitance lead to determine resonance frequencies. Three different unit-cell configurations- spiral structure on one side of the substrate (unit-cell A), spiral structure on both sides of substrate (unit-cell B), and both spiral structures connected using via (unit-cell C) as indicated in Figure 2 are studied in this paper. A 0.8 mm thicken FR-4 substrate is used for all unit-cell configurations.

## 3. Numerical Method

The metamaterial for modern portable devices should be slim and compact in size. It also should The effective constitutive parameters of a metamaterial are extracted using an algorithm described in [19] from the effective thickness (d) and the complex S-parameters of slab. Equation (1) expresses the complex wave impedance in terms of S-parameters.

$$Z_{eff} = \pm\sqrt{\frac{(1+S_{11})^2 - S_{21}^2}{(1-S_{11})^2 - S_{21}^2}} \tag{1}$$

The complex effective refractive index, $N_{eff}(\omega) = n_{eff}(\omega) + ik_{eff}(\omega)$ can be expressed by following equations (2)-(4) following above mentioned method. Here, $n_{eff}$ denotes the refractive index and $k_{eff}$ is extinction coefficient.

$$N_{eff} = \frac{1}{k_0 d}\{\mathrm{Im}[\ln(e^{iN_{eff}k_0 d}) + 2m\pi - i\,\mathrm{Re}[\ln(e^{iN_{eff}k_0 d})]\} \tag{2}$$

$$n_{eff} = \frac{1}{k_0 d}\{\mathrm{Im}[\ln(e^{iN_{eff}k_0 d}) + 2m\pi\} \tag{3}$$

$$k_{eff} = -\frac{1}{k_0 d}\mathrm{Re}[\ln(e^{iN_{eff}k_0 d})] \tag{4}$$

where, $k_0$ is the free space wave number, $m$ is integer indicating branch index and $\omega$ is the angular frequency.

The effective permittivity ($\varepsilon_{ef}$) and effective permeability ($\mu_{eff}$) of medium can be determined by using equations (5) and (6) respectively.

$$\varepsilon_{eff} = \frac{N_{eff}}{Z_{eff}} \tag{5}$$

$$\mu_{eff} = N_{eff} Z_{eff} \tag{6}$$

In simulation setup, metamaterial unit cell and arrays are imposed both perfect electric and magnetic boundaries and tested placing between two waveguide ports. The frequency range 0.5 GHz to 6 GHz is considered in this investigation. The simulations are performed in the design environment of CST Microwave studio.

## 4. Effective Parameters of Metamaterial

The effective parameters of the proposed design are extracted from S parameters and plotted using the described method in section III. Figure 4(a)-(c) indicate the effective relative permittivity for three different unit-cell configurations. Both real and imaginary part of effective permittivity are plotted. The unit-cell configurations called unit-cell A, unit-cell B, and unit-cell C are considered as described in section II. The effective permittivity of unit-cell configurations show multiple resonances in the frequency range. The effective permittivity curves exhibit little bit variation for different unit-cell configurations. Strong resonance is found around 2 GHz. For Unit-cell A, the real part of effective permittivity exhibits negative values from 0.9 to 0.95 GHz, 2 to 2.5 GHz, from 2.8 to 3.75 GHz, from 4.08 to 4.7 GHz, and 5.5 to 6 GHz. For unit-cell B, the effective permittivity curves change significantly compared to unit-cell A because of the spiral copper structure on both sides of the substrate. In case of unit-cell C, the interconnection between spiral copper structures reduces the capacitance between them and increase the total inductance. Hence, the effective permittivity curves change and the strong resonances are found compared to unit-cell A and B.

Figure 5(a)-(c) show both real and imaginary parts of effective relative permeability for unit-cell A, B, and C, respectively. For three different unit-cell configurations, the real part of effective permittivity curves show nearly identical resonance but the amplitude range varies significantly. The unit-cell A exhibits negative permeability from 3.1 to 6 GHz frequency considering real part. Unit-cell B and C also exhibit negative permeability from around 3.1 GHz to the end of the frequency range. The effective refractive index also shows little bit variation for different unit-cell configurations as indicated in Figure 6(a)-(c). Although the effective refractive index show multiple resonances, the real part of effective refractive index starts negative value from 2.8 GHz to the end of the frequency range. For unit-cell A, effective refractive index exhibit negative characteristics from 2.79 to 6 GHz.

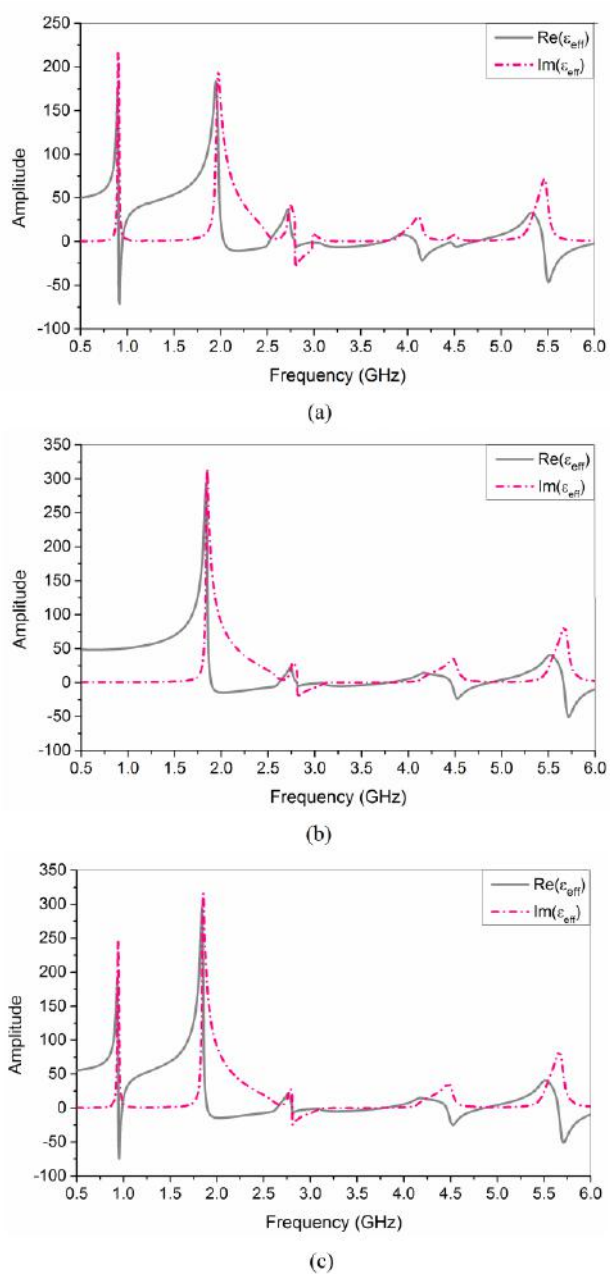



Figure 4: Effective relative permittivity of proposed metamaterial unit-cell: (a) unit-cell A, (b) unit-cell B, and (c) unit-cell C.

A planar one dimensional array of unit-cell A is used for measurement purpose. The array is formed using 4 × 4 unit-cell configurations (16 unit-cell). A comparison of the measured simulated data is plotted in Figure 7 in terms of a real part and imaginary part of the refractive index. In the measurement, only the array of unit-cell A is used to validate the simulated results. However, the S parameter (S11 and S21) is measured in an anechoic chamber and the post processing of the data is performed using identical

methods used in simulated data processing to extract effective parameters. The measured results show a similar tendency as simulated results with a slight shift in frequency.

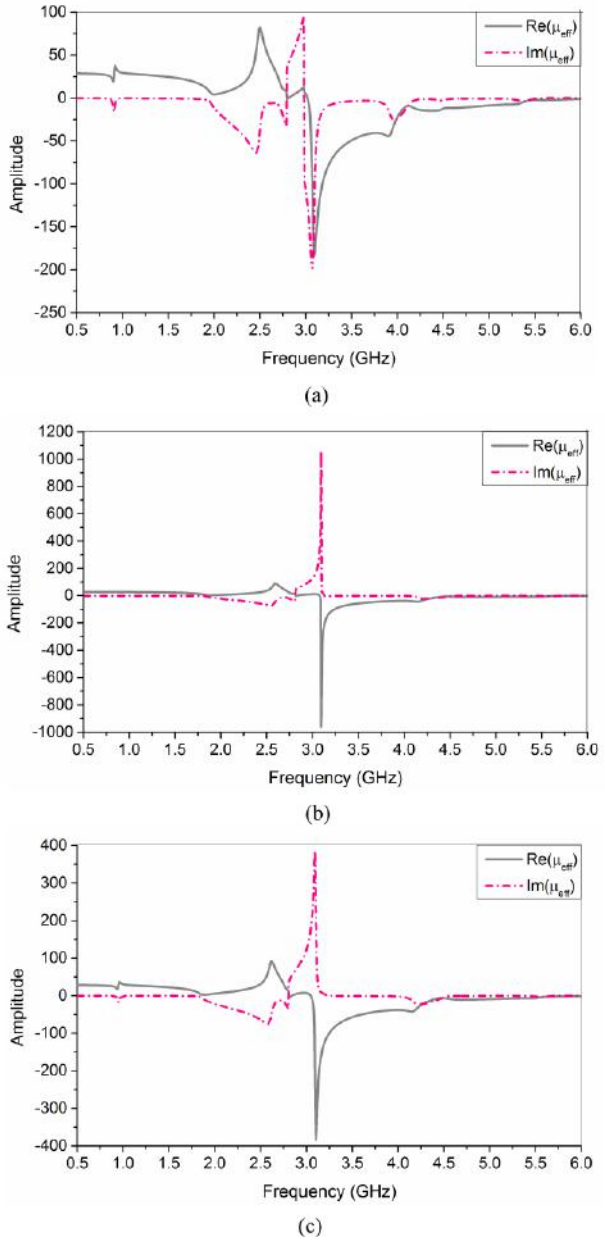



Figure 5: Effective relative permeability of proposed metamaterial unit-cell: (a) unit-cell A, (b) unit-cell B, and (c) unit-cell C.

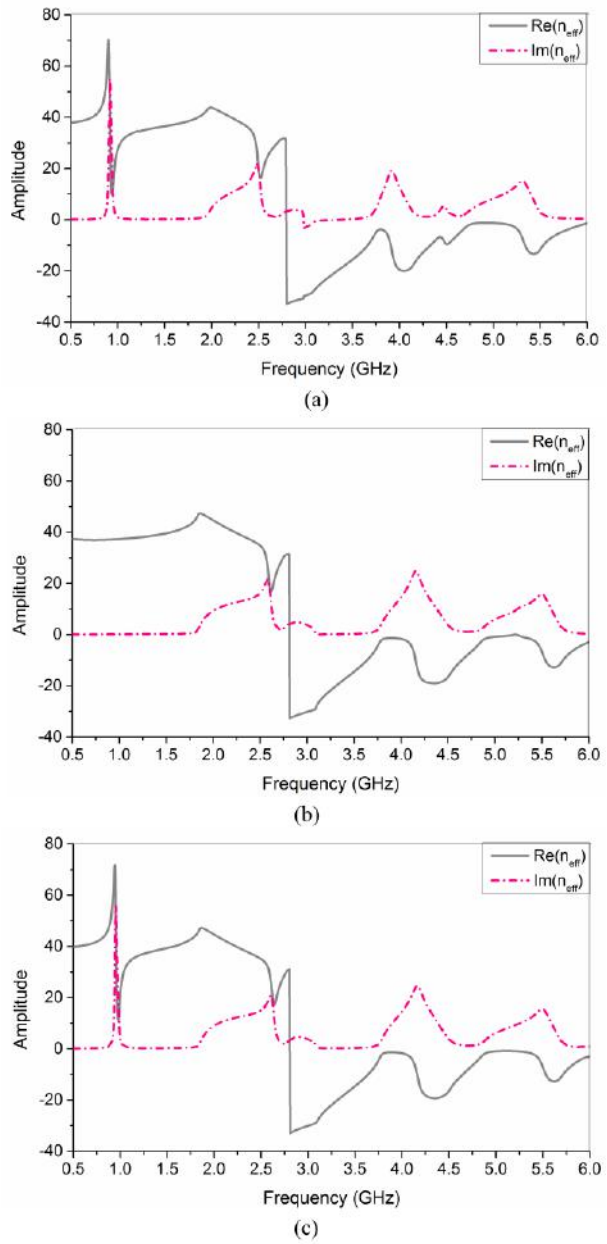



Figure 6: Effective refractive index of proposed metamaterial unit-cell: (a) unit-cell A, (b) unit-cell B, and (c) unit-cell C.

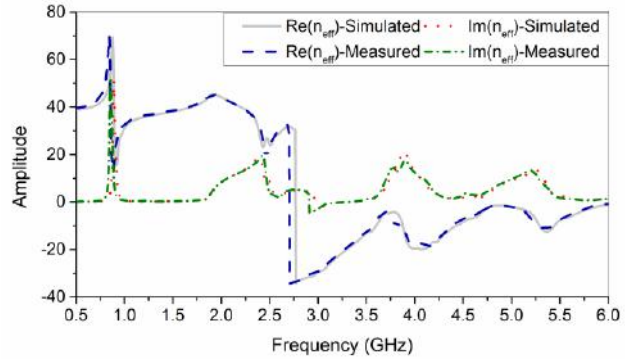



Figure 7: Measured and simulated effective refractive index of array of unit-cell A.

## 5. SAR Reduction Using Metamaterial

In this section, the effects of proposed metamaterial attachment in a mobile phone antenna are analyzed. The effects of metamaterial on antenna EM absorption characteristics are evaluated. A tri-band printed monopole antenna along with complete mobile phone model is used in this investigation. The geometry of the printed monopole antenna is collected from [20]. Although the used monopole antenna has three operating bands- GSM 900 MHz, GPS 1500 MHz, and DCS 1800 MHz, the present study focus only two operating bands comprising GSM 900 MHz and DCS 1800 MHz. Figure 8(a) and 8(b) indicate the antenna geometry and fabricated prototype of antenna respectively. A fabricated prototype of one dimensional planar array of proposed metamaterial is shown in Figure 8 (c). The metamaterial array consists of 32 unit-cell (8 × 4) with 80 mm × 40 mm × 0.8 mm total dimensions. The complete mobile phone model with monitor, casing, battery, RF component, PCB, speaker, camera, and buttons is used in this study. The mobile phone model with the relative position of the antenna and metamaterial is shown in Figure 9 (a). To evaluate the specific absorption rate (SAR) values and a homogeneous SAM head phantom is utilized [21]. The properties of the tissue are collected from [22, 23]. Figure 9(b) indicates the cheek position of talk mode configuration of mobile phone and human head. The metamaterial is attached inside the mobile phone just next to the LCD monitor and the antenna is placed near to the back side of the mobile phone case box to ensure maximum separation between the antenna and metamaterial. This is due to the fact that the metamaterial is a resonator structure and it may affect the antenna resonance points and bandwidth. On the other hand, the metamaterial is placed near to the front side of the mobile phone so that it can provide EM shielding towards human head. In this investigation, the 7.5 mm maximum possible distance between antenna and metamaterial structure is maintained as 10 mm thickness of mobile phone is used.

The SAR values of antenna with and without metamaterial are evaluated using the cheek position of talk mode configuration. The stimulated power 1 W (peak) is set for both antennas with and without metamaterial configurations. The equation (7) is used in calculating SAR values in the human head with the value of induced electric field strength (E), the conductivity (σ) and the density (ρ) of tissue [18].

$$SAR = \frac{\sigma E^2}{2\rho} \tag{7}$$

An IEEE standard algorithm [25] is utilized to determine the peak SAR in the human head averaged over standard 1 g and 10 g tissue.

Figure 10 illustrates the 3D surface distribution of SAR along with values at 900 MHz and 1800 MHz for both with and without metamaterial configurations. The results indicate a significant amount of reduction in SAR values towards the human head due to the effects of metamaterial. At 900 MHz metamaterial leads to reduce 17.4% 1 g SAR and 18.6% 10 g SAR. Likewise, 30.7% reduction is observed for 1 g SAR and 42.05% for 10 g SAR at 1800 MHz. Basically, the metamaterial can trap a part of EM energy by its extraordinary electromagnetic properties.

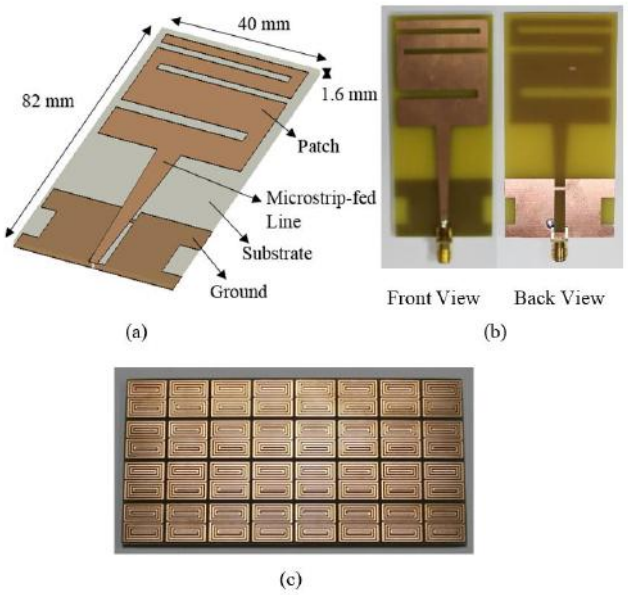



Figure 8: (a) Printed monopole antenna geometry, (b) fabricated prototype of antenna, and (c) fabricated prototype of metamaterial.

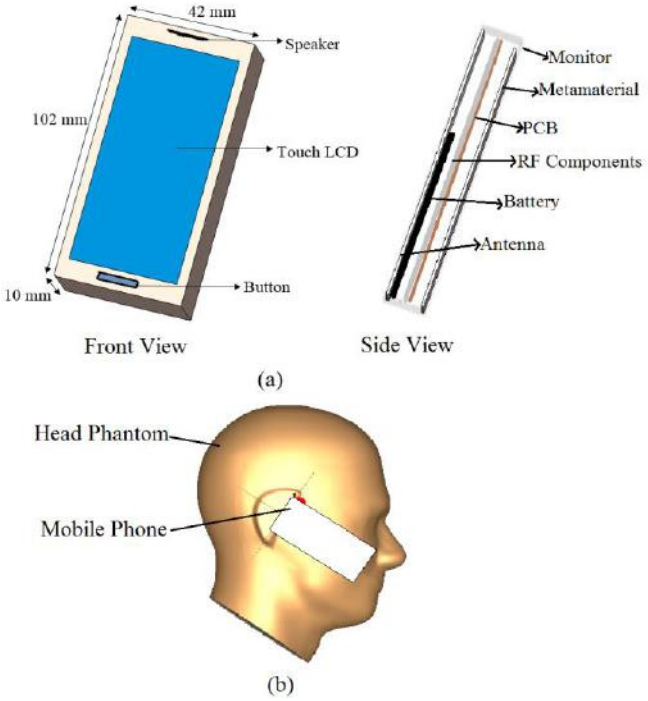



Figure 9: (a) Mobile phone model and (b) cheek position of talk mode configuration of mobile with SAM head.

The measurement of SAR values is performed using the COMOSAR measurement system as indicated in Figure

11. Only the mobile phone with metamaterial configuration is used in the measurement and measurement results are compared to simulated data to validate the results. Figure 12 shows the comparison of measured and simulated SAR values in case of antenna with proposed metamaterial attachment only. The results indicate almost identical SAR values for both simulation and measurement.

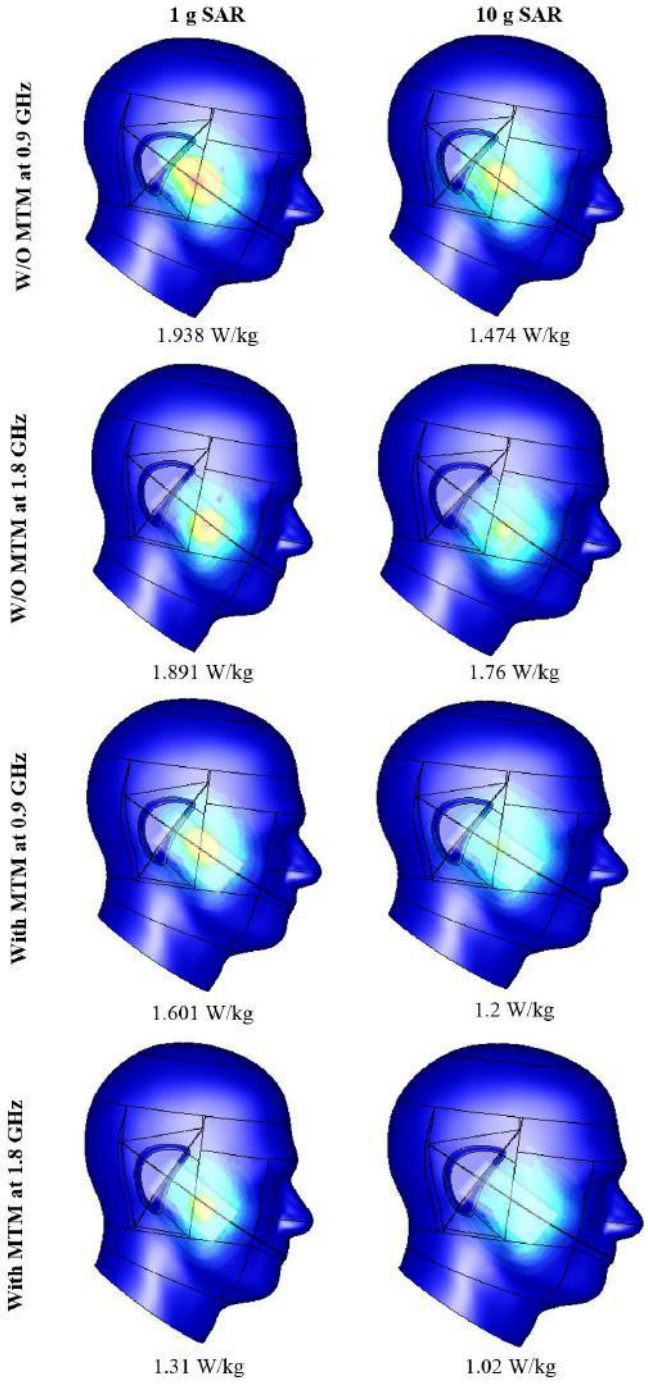



Figure 10: SAR values with and without metamaterial configurations.

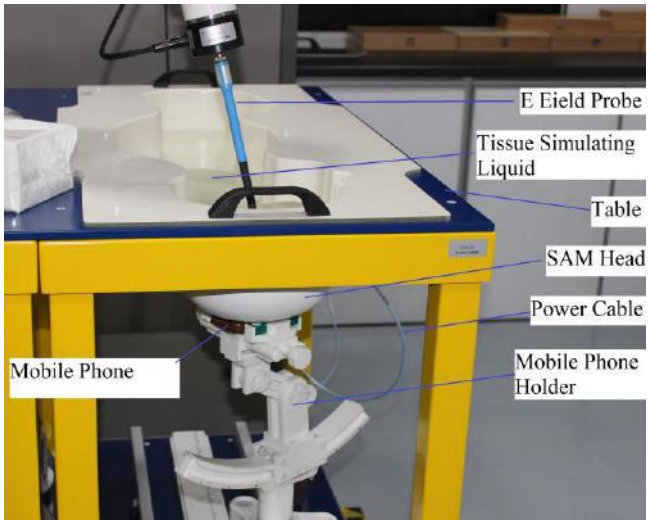



Figure 11: Experimental set-up for the measurement SAR.

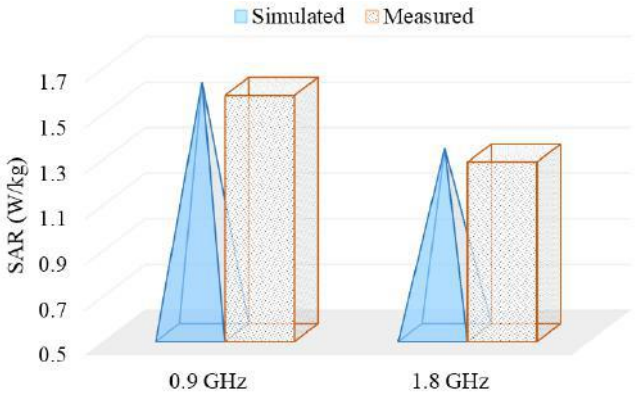



Figure 12: Measured and simulated SAR values for with metamaterial configuration.

## 6. Conclusions

This study presents design, analysis and application of a new negative index metamaterial for modern mobile phone. The proposed metamaterial unit-cell has successfully exhibited negative refractive index from 2.9 GHz to 6 GHz. In addition, the designed metamaterial shows negative permittivity at cellular phone frequencies (GSM 900 MHz, DCS 1800 MHz, and GSM 1900 MHz). A one dimensional planar array of proposed metamaterial unit-cell is used in mobile phone with printed monopole antenna. The results indicate significant reduction in SAR values in the human head with a little bit improvement of antenna performances.

## References

[1] D. R. Smith, J. B. Pendry, and M. C. Wiltshire, Metamaterials and negative refractive index, *Science* 305 (5685): 788–792, 2004.

[2] P. N. L. Viktor G Veselago, The electrodynamics of substances with simultaneously negative values of ε and μ, *Sov. Phys. Uspekhi* 10 (4): 509–514, 1968.

[3] B. D. F. Casse, W. T. Lu, Y. J. Huang, E. Gultepe, L. Menon, and S. Sridhar, Super-resolution imaging using a three-dimensional metamaterials nanolens, *Appl. Phys. Lett.* 96 (2): 023114, 2010.

[4] M. Puentes, M. Maasch, M. Schussler, and R. Jakoby, Frequency multiplexed 2-dimensional sensor array based on split-ring resonators for organic tissue analysis, *Microw. Theory Tech. IEEE Trans. On* 60 (6): 1720–1727, 2012.

[5] F. Bilotti, S. Tricarico, and L. Vegni, Plasmonic metamaterial cloaking at optical frequencies, *Nanotechnol. IEEE Trans. On* 9 (1): 55–61, 2010.

[6] R. W. Ziolkowski, Metamaterial-based antennas: Research and developments," *IEICE Trans. Electron.* 89 (9): 1267–1275, 2006.

[7] M. I. Hossain, M. R. I. Faruque, and M. T. Islam, Design and Analysis of Metamaterial inspired Low SAR PIFA for Mobile Phone, *International Journal of Applied Electromagnetics and Mechanics* 48 (4): 459-467, 2015.

[8] R. W. Ziolkowski and A. D. Kipple, Application of double negative materials to increase the power radiated by electrically small antennas, *Antennas Propag. IEEE Trans. On* 51 (10): 2626–2640, 2003.

[9] M. R. I. Faruque and M. T. Islam, Design of Miniaturized Double-Negative Material for Specific Absorption Rate Reduction in Human Head, *PloS One* 9 (10): e109947, 2014.

[10] M. Achour, A. Gummalla, M. Stoytchev, and B. Franz, *Antennas, devices and systems based on metamaterial structures*. Google Patents, 2014.

[11] D. J. Park, S. J. Park, I. Park, and Y. H. Ahn, Dielectric substrate effect on the metamaterial resonances in terahertz frequency range, *Curr. Appl. Phys.* 14 (4): 570–574, 2014.

[12] N. Fang, H. Lee, C. Sun, and X. Zhang, Sub–diffraction-limited optical imaging with a silver superlens, *Science* 308 (5721): 534–537, 2005.

[13] L. H. Gabrielli, J. Cardenas, C. B. Poitras, and M. Lipson, Silicon nanostructure cloak operating at optical frequencies, *Nat. Photonics* 3 (8): 461–463, 2009.

[14] R. W. Ziolkowski, Design, fabrication, and testing of double negative metamaterials, *Antennas Propag. IEEE Trans. On* 51 (7): 1516–1529, 2003.

[15] T. D. Karamanos, A. I. Dimitriadis, and N. V. Kantartzis, Compact double-negative metamaterials based on electric and magnetic resonators, *Antennas Wirel. Propag. Lett. IEEE* 11: 480–483, 2012.

[16] M. I. Hossain, M. R. I. Faruque, M. T. Islam, and M. H. Ullah, A New Wide-Band Double-Negative Metamaterial for C- and S-Band Applications, *Materials* 8 (1): 57–71, 2014.

[17] M. Latrach, H. Rmili, C. Sabatier, E. Seguenot, and S. Toutain, Design of a new type of metamaterial radome for low frequencies, *Microw. Opt. Technol. Lett.* 52 (5): 1119–1123, 2010.

[18] J.-N. Hwang and F.-C. Chen, Reduction of the peak SAR in the human head with metamaterials, *Antennas Propag. IEEE Trans. On* 54 (12): 3763–3770, 2006.

[19] Z. Szabo, G-H, Park, R. Hedge, E-P. Li, A unique extraction of metamaterial parameters based on Kramers–Kronig relationship, *Microw Theory Tech IEEE Trans On* 58: 2646–2653, 2010.

[20] M. I. Hossain, M. R. I. Faruque, and M. T. Islam, Low SAR Microstrip Patch Antenna for Mobile Phone, *Frequenz* 69 (9-10): 399-405, 2015.

[21] M. I. Hossain, M. R. I. Faruque, and M. T. Islam, A New Design of Cell Phone Body for the SAR Reduction in the Human Head, *Applied Computational Electromagnetics Society Journal* 30 (7): 792-798, 2015.

[22] C. Gabriel, Compilation of the dielectric properties of body tissues at RF and microwave frequencies, Books Air Force Technical Report AL/OE-TR-1996-0037, 1996.

[23] K. Fukunaga, S. Watanabe, Y. Yamanaka, H. Asou, Y. Ishii, K. Satou, Y. Miyota, Dielectric Properties of tissue equivalent liquids in practice, *Tech. Rep. IEICE*, No. EMCJ2002-44, pp. 13-17, 2002.

[24] "IEEE Standard for Safety Levels with Respect to Human Exposure to Radio Frequency Electromagnetic Fields, 3 kHz to 300 GHz - Amendment 1: Specifies Ceiling Limits for Induced and Contact Current, Clarifies Distinctions between Localized Exposure and Spatial Peak Power Density," *IEEE Std C95.1a-2010 (Amendment to IEEE Std C95.1-2005)*, pp. C1 –9, Mar. 2010.

# Low SAR Metamaterial Inspired Printed Monopole Antenna

**M. I. Hossain[1], M. R. I. Faruque[1], M. T. Islam[2], M. T. Ali[3]**

[1]Space Science Center, Universiti Kebangsaan Malaysia, Bangi, Malaysia
[3]Department of Electrical, Electronic, and System Engineering, Universiti Kebangssan Malaysia, Bangi, Malaysia
[3]Centre for Communication Eng. Studies, Universiti Teknologi Mara, Malaysia
*E-mail: ipk_eee@yahoo.com

## Abstract

In this paper, a low SAR metamaterial embedded planar monopole antenna is introduced for a wireless communication system. A printed monopole antenna is designed for modern mobile, which operates in GSM, UMTS, LTE, WLAN, and Bluetooth frequency bands. A metamaterial structure is designed to use in the mobile handset with a multi-band printed monopole antenna. The finite integration technique (FIT) of the CST microwave studio is used in this study. The measurement of antenna performances is performed in an anechoic chamber and the SAR values are measured using COMOSAR system. The results indicate that metamaterial structure leads to reduce SAR without affecting antenna performance significantly. According to the measured results, the metamaterial attachment leads to reduce 87.7% Peak SAR, 68.2% 1 g SAR, and 46.78% 10 g SAR compared to antenna without metamaterial.

## 1. Introduction

The portable terminal devices become the part and parcel of modern life and the uses of those are increasing day by day. The electromagnetic (EM) radiation from those devices is exposed on human for a long duration of the day. This may lead potential health hazard, because the radiation from the antenna can penetrate the human body tissue [1]. It is either caused short term effects or long term effects. In previous research, it was found out that the frequent use of mobile phone increased twofold risk of affected by brain cancer and fivefold of the similar risk increased among the youngsters [2]. According to the World Health Organization (WHO), EM radiation from portable devices may cause cancer [3]. This is in-line with the International Agency for Research Cancer (IARC) classification which claimed that the EM fields were possibly carcinogenic to humans under the Group 2B carcinogen [4]. The specific absorption rate (SAR) values are defined to evaluate EM absorption in the body tissue [5]. This SAR could be defined as power absorbed over a unit mass of body tissue and denoted in terms of watt per kilogram. International authoritative bodies regulated the limits of safe SAR absorbed upon human. The SAR safe limit of 1.6 W/kg over 1 g and 2 W/kg for 10 g of body tissue [6].

In the last decade, several methods have been proposed for the reduction of EM radiation towards human for different types of antenna. Antenna design is changing day by day due the meet the increasing demand of the market. The first generation of mobile phone antenna was external antenna such as monopole, dipole and helical antenna, which usually mounted on the top of cell phone body [7]. However, the recent trend is to use internal and planar antenna such as planar inverted-F antenna (PIFA), printed monopole antenna, and microstrip path antenna for handset devices to get low profile, high gain and multi-band characteristics. In previous research, the radio frequency (RF) shielding using ferrite sheet has been used for reduction of the SAR in the human head in case of PIFA, helical and monopole antenna [8]–[10]. The reduction of power absorption in the head was also investigated by increasing the antenna directivity which can be achieved by using director or reflectors coupled with monopole or dipole antenna [11], [12]. In addition, the reduction of SAR values have been also performed by using artificial magnetic conductor (AMC) or electromagnetic band gap (EBG) surfaces using the stop band of those periodic structures at designing frequency [13], [14]. Recently, metamaterials have been proposed for the SAR reduction of cell phone as they exhibit extraordinary physical properties over a frequency band [15], [16]. The Metamaterial technique of SAR reduction seems to be more suitable for modern compact multi-band mobile phone.

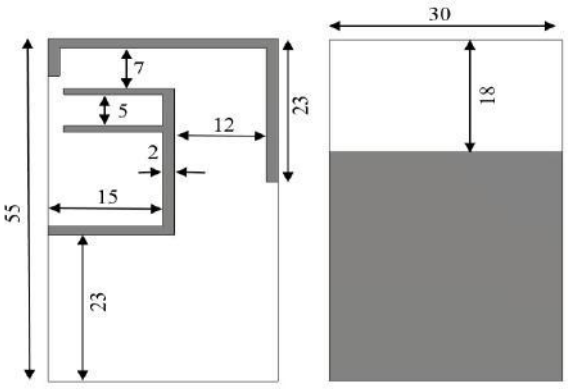
In [16], an investigation of the SAR reduction of dipole antenna using metamaterial was presented considering GSM 900 MHz and 1800 MHz frequency bands. The results reported that the metamaterial structure placed between antenna and human head can reduce the EM absorption in the human head tissue. Although the results showed an effective SAR reduction, the proposed SRR structure size is not compatible with handset antenna. In [17], a study on miniaturization of microstrip antenna with double negative metamaterial was presented. The results showed that the microstrip antenna size as well as SAR in the human head can be reduced by this technique. In [18], an analysis of SAR reduction using single negative metamaterial was presented for PIFA at 900 MHz. In [19], a split ring resonator (SSR) structure was proposed for the reduction of SAR for ultra wideband (UWB) vest antenna.

In [20], a metamaterial based handset PIFA antenna is presented as low SAR antenna at WiMAX (2.4 GHz) band by adding extra meta-surface in the ground plane of the antenna. A miniature triangular shaped metamaterial in [21] was used in between human head and a PIFA to reduce SAR at GSM 900 MHz. In [22], a low SAR PIFA was introduced with modified ground plane of the antenna using metamaterial arrays for dual band operation at GSM 900 MHz and 1800 MHz.

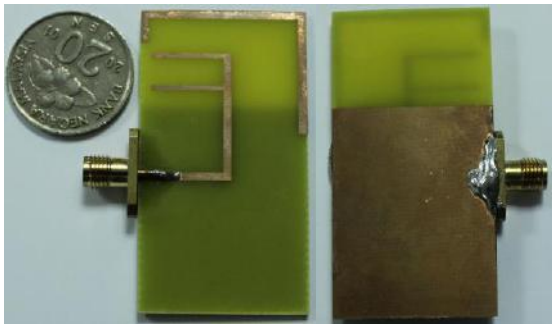
In this paper, the metamaterial structure is imposed in a handset with a printed monopole antenna. The printed monopole antenna is designed for wireless communication to operate over GSM, UMTS, LTE, WLAN, and Bluetooth frequency bands. The antenna performances comprising return loss, efficiency, gain, and radiation pattern are analyzed with and without metamaterial configurations. Moreover, the SAR in the human head and total absorbed power by the user are evaluated and the effectiveness of SAR reduction of metamaterial is analyzed in this study.

## 2. Antenna Design Analysis

Figure 1(a) indicates the geometry of proposed printed monopole antenna. Black color indicates the copper layer on the substrate. The antenna design consists of an F-shaped radiation coupled with a microstrip-fed line and a U-shaped parasitic element printed on the front side of the substrate. A 0.8 mm thicken FR-4 material is used as the substrate. A partial ground plane is used on the other side of the substrate.




(a)



(b)

Figure 1: Proposed printed monopole antenna: (a) antenna geometry (dimensions in millimeter) and (b) fabricated prototype.

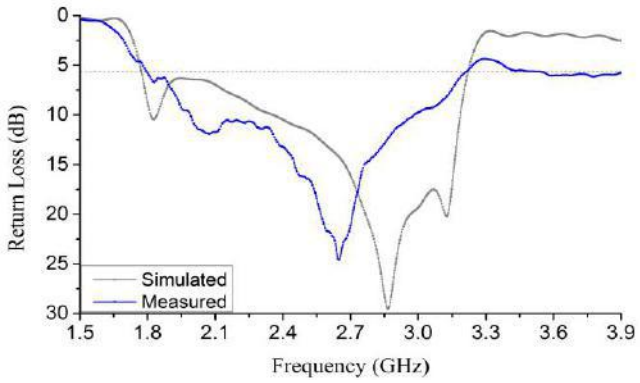
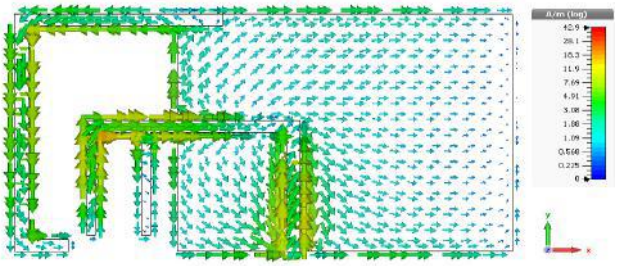
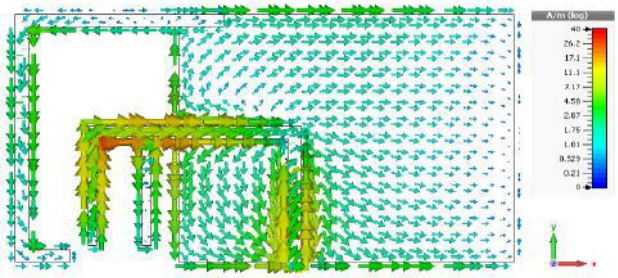


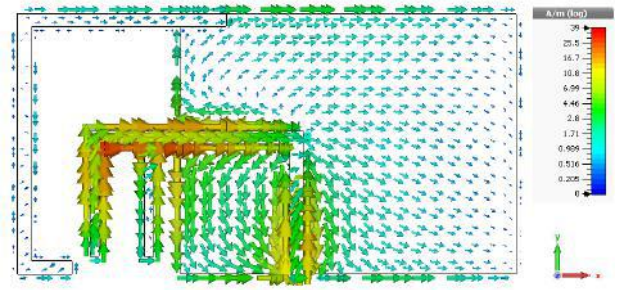

Figure 2: Simulated and measured return loss of proposed antenna.



(a)



(b)



(c)

Figure 3: Current distribution of proposed antenna: (a) at 2.1 GHz, (b) at 2.3 GHz, and (c) at 2.5 GHz.

A 50 Ω SMA connector is used as the feeding port between the end of microstrip-fed line and ground plane. The design simulation is performed in CST Microwave studio and the measurement is done in an anechoic chamber. Figure 2 indicates simulated and measured return loss characteristics of proposed antenna. An Agilent vector

network analyzer (VNA) is used to evaluate reflection coefficient of antenna and then it converted into return loss. The measured result exhibits very good agreement with simulated data indicating almost equal impedance bandwidth (from 1.8 GHz to 3.2 GHz). The simulated current distributions of proposed antenna are presented in Figure 3(a)-(c) at 2.1 GHz, 2.3 GHz, and 2.5 GHz respectively. The current distribution clearly shows that the parasitic element carries more current at the lower frequencies and less current at the upper frequencies.

## 3. Metamaterial Design Analysis

Figure 4(a) exhibits the structure of metamaterial unit-cell. The geometry of metamaterial unit-cell is collected from [23]. The dimensions of metamaterial unit-cell are 16 mm × 12 mm × 0.8 mm. A planer one layer metamaterial array is formed arranging 6 × 3 unit-cell (18 unit-cell). The array dimensions are 96 mm × 36 mm × 0.8 mm. The metamaterial array is fabricated on 0.8 mm thicken FR-4 substrate using printed copper strips. A fabricated prototype of metamaterial array is shown in Figure 4(b). The effective constitutive parameters of a metamaterial are extracted using an algorithm described in [24] from the effective thickness (d) and the complex S-parameters of slab. Equation (1) expresses the complex wave impedance in terms of S-parameters.

$$Z_{eff} = \pm\sqrt{\frac{(1+S_{11})^2 - S_{21}^2}{(1-S_{11})^2 - S_{21}^2}} \tag{1}$$

The complex effective refractive index, $N_{eff}(\omega) = n_{eff}(\omega) + ik_{eff}(\omega)$ can be expressed by following equations (2)-(4) following above mentioned method. Here, $n_{eff}$ denotes the refractive index and $k_{eff}$ is extinction coefficient.

$$N_{eff} = \frac{1}{k_0 d}\{\mathrm{Im}[\ln(e^{iN_{eff}k_0 d}) + 2m\pi - i\,\mathrm{Re}[\ln(e^{iN_{eff}k_0 d})]\} \tag{2}$$

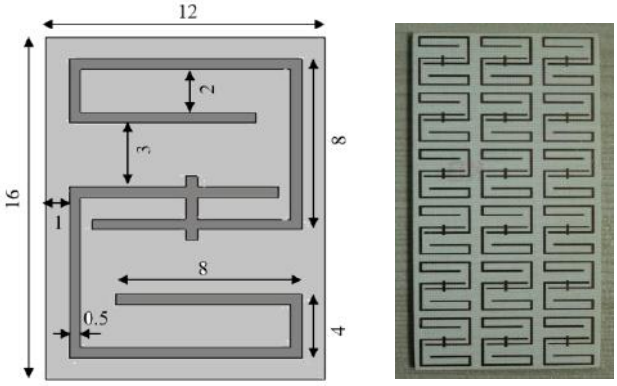
$$n_{eff} = \frac{1}{k_0 d}\{\mathrm{Im}[\ln(e^{iN_{eff}k_0 d}) + 2m\pi\} \tag{3}$$

$$k_{eff} = -\frac{1}{k_0 d}\mathrm{Re}[\ln(e^{iN_{eff}k_0 d})] \tag{4}$$

where, $k_0$ is the free space wave number, $m$ is integer indicating branch index and $\omega$ is the angular frequency.
The effective permittivity ($\varepsilon_{ef}$) and effective permeability ($\mu_{eff}$) of medium can be determined by using equations (5) and (6) respectively.

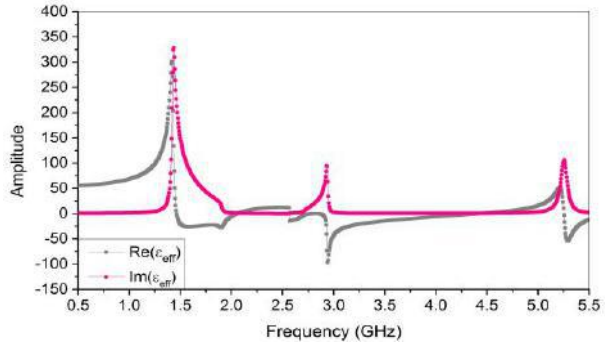
$$\varepsilon_{eff} = \frac{N_{eff}}{Z_{eff}} \tag{5}$$

$$\mu_{eff} = N_{eff} Z_{eff} \tag{6}$$

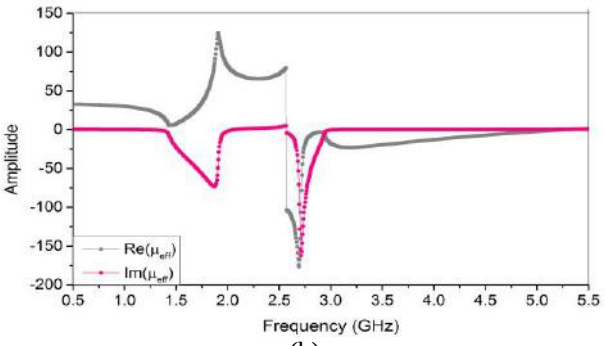



(a) (b)

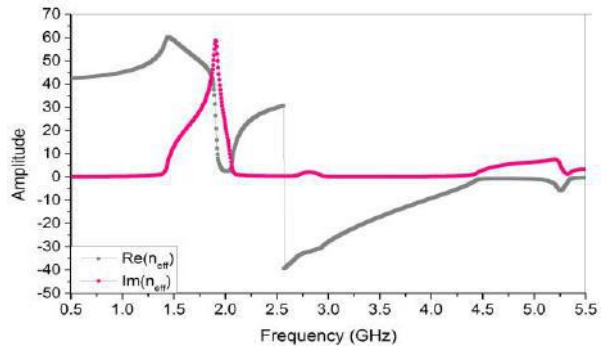
Figure 4: (a) Metamaterial unit-cell geometry (dimensions in millimeter) and (b) fabricated prototype of metamaterial array.




(a)




(b)




(c)

Figure 5: Effective parameters of metamaterial: (a) effective permittivity, (b) effective permeability, and (b) effective refractive index.

The dimension of the metamaterial unit - cell are chosen to get double-negative characteristics of the operating frequency bands of proposed antenna. The scattering parameters of the unit-cell are obtained from the CST design environment, imposing perfect electric conducting (PEC) and perfect magnetic conducting (PMC) boundaries [25]. Figure 5 exhibits the effective permittivity, effective permeability and effective refractive index of proposed metamaterial unit-cell. The results successfully show that the designed metamaterial unit-cell acts as a double-negative metamaterial from 2.9 GHz to 5 GHz. The presented metamaterial array configuration leads to shift resonance points slightly compared to unit-cell and the simultaneous negative values of effective permittivity and permeability are still observed from them at the operating frequency bands of the antenna.

## 4. Antenna Performances Analysis

In this study, a complete handset model (dimensions 102 mm × 42 mm × 10 mm) with battery, camera, speaker, circuits, LCD screen, and the plastic housing is used. The LCD dimensions are 94 mm × 40 mm × 2 mm, which is modeled using LCD film type material with 4.78 relative permittivity ($\varepsilon_r$). The plastic housing is made of polyvinyl chloride material (PVC) with 2.8 relative permittivity. Other components- battery, camera, and speaker are modeled using perfect electric conductor (PEC) material. A 3D view of handset model is indicated in Figure 6.

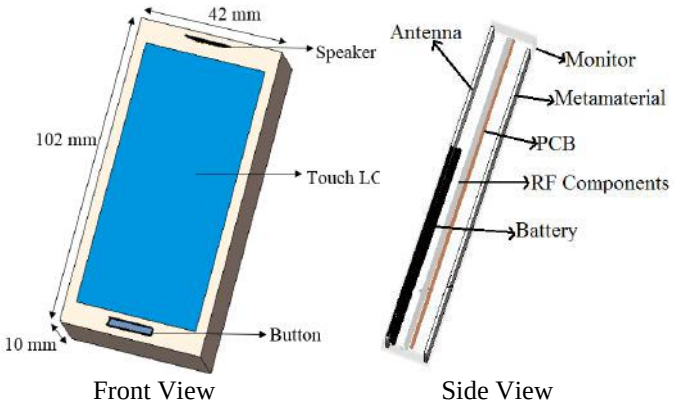



Figure 6: Handset model.

The antenna performances in terms of return loss, efficiency, gain, and radiation pattern are evaluated for both antennas with and without metamaterial configurations. Figure 7 shows the return loss characteristics of proposed antenna with and without metamaterial. The results reveal that the metamateial loading leads to two more resonance point, but does not change the operating bandwidth of antenna considerably. The antenna without metamaterial shows impedance bandwidth from 1.8 GHz to 3.2 GHz, which can cover DCS 1800 MHz, PCS 1900 MHz, GSM 1900 MHz, UMTS 2100 MHz, LTE (2300-2400) MHz, LTE (2500-2690) MHz, Bluetooth (2400-2800) MHz, WLAN (2400-2485) MHz, WiMAX (2500-2690) MHz. On the other hand, the antenna with metamaterial exhibits impedance bandwidth from 1.96 GHz to 3.15 GHz (about 1.2 GHz). Figure 8 shows the measured gain radiation pattern of proposed antenna at 2.5 GHz. The results show near omnidirectional radiation patterns in the Phi=90 degree plan. The radiation patterns of proposed antenna are quite similar to the planar quarter-wavelength mono-pole antenna. The measured values of gain of proposed antenna are 2.64 dB and 2.47 dB for without metamaterial and with metamaterial configurations respectively. Moreover, antenna total efficiencies for without metamaterial and with metamaterial are quite similar amounting 90% and 88.2% respectively.

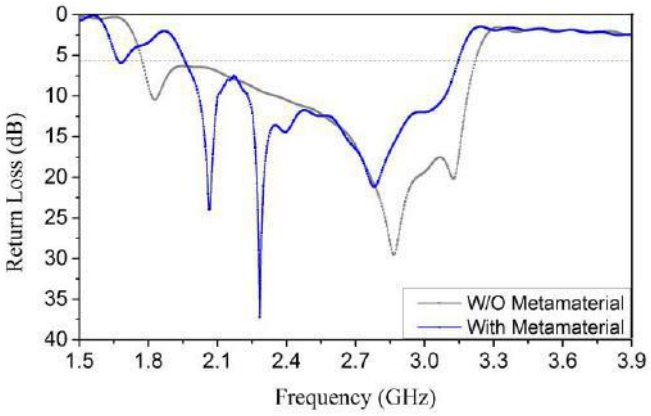



Figure 7: Return loss charcteristics of proposed antenna with and without metamaterial configurations.

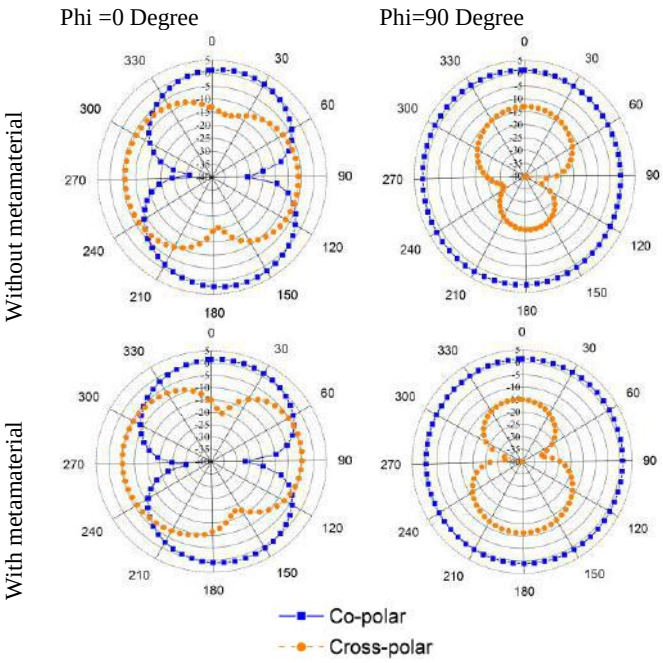



Figure 8: Measured gain radiation pattern of proposed antenna at 2.5 GHz.

## 5. Specific Absorption Rate Analysis

The interaction between the mobile phone antenna and human body tissue is evaluated using SAM flat phantom. The SAR values are measured using the COMOSAR measurement system in the SAR Measurement Laboratory of Universiti Teknology Malaysia (UTM). Figure 9 indicates the SAR measurement setup. The COMOSAR measurement system consists of 6 axis robot, E-field probe, SAM flat phantom, tissue simulating liquid, mobile phone holder, and data acquisition system. The frequency dependent parameters permittivity and conductivity of human tissues was considered. A standard algorithm (IEEE 1528) [26] is used to evaluate SAR averaged over 1 g and 10 g of head tissue. Table 1 shows the SAR values of proposed antenna at 2.1 GHz and 2.5 GHz frequencies considering cheek position of talk mode. The 1 g SAR, and 10 g SAR are calculated from 3D area scan (dx=14mm, dy=14mm, and h= 5.00 mm) around the hotspot. The obtained results indicate a significant amount of SAR reduction in the human head due to the metamaterial attachment compared to without metamaterial antenna. The metamaterial attachment leads to reduce 68.2% 1 g SAR, and 46.78% 10 g SAR at 2.1 GHz compared to antenna without metamaterial. As expected, results from 2.5 GHz also show a similar tendency.

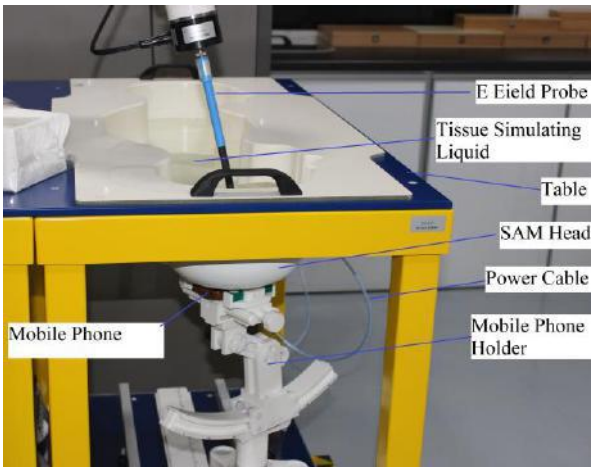



Figure 9: SAR measurement setup.

Table 1: SAR values in the human head for proposed antenna.

| | SAR at 2.1 GHz | | SAR at 2.5 GHz | |
|---|---|---|---|---|
| Averaging Mass | 1 g | 10 g | 1 g | 10 g |
| W/O Metamaterial | 2.546 | 1.211 | 2.946 | 1.412 |
| With Metamaterial | 1.456 | 0.782 | 1.756 | 0.962 |

Figure 10 indicate the surface distribution of SAR of antenna without metamaterial and with metamaterial attachment. In the surface distribution of SAR, X- and Y-directions are considered in horizontal and vertical planes. On the other hand, Z-direction is considered normal to the XY surface, which can indicates length inside human head tissue. In Figure 10, constant Z=0.3 is used and the intensity of SAR is plotted with the variations of X and Y. A color scale is added to the plot, which indicates the value of SAR at different points. The surface distribution of SAR also confirms that the antenna with metamaterial attachment produces lower power absorption in the human head compared to the without metamaterial configuration.

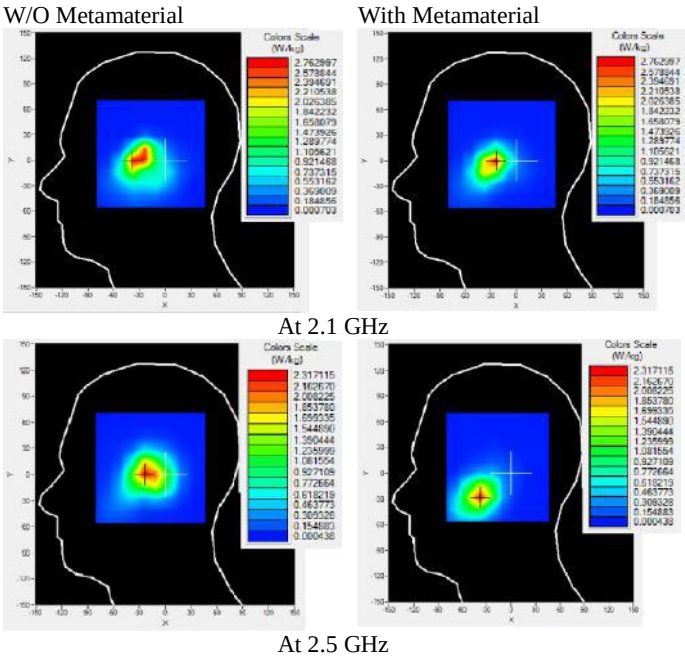



Figure 10: Surface distribution of SAR at 2.6 GHz: (a) antenna without metamaterial and (b) antenna with metamaterial.

## 6. Conclusions

In this paper, a metamaterial inspired low SAR printed-monopole antenna is proposed for wireless communication. The antenna shows impedance bandwidth from 1.8 GHz to 3.2 GHz. The results indicate that the metamaterial attachment reduces the SAR in the human head significantly without affecting antenna performances significantly. The measured results indicate that the metamaterial attachment leads to reduce 87.7% Peak SAR, 68.2% 1 g SAR, and 46.78% 10 g SAR compared to antenna without metamaterial.

## References

[1] L. Kheifets, Science, Uncertainty and Policy for Power and Mobile Frequency EMF, in *Bioelectromagnetics Current Concepts*, Springer: 323–330, 2006.

[2] L. Hardell and M. Carlberg, Mobile phones, cordless phones and the risk for brain tumours, *Int. J. Oncol.* 35 (1): 5–17, 2009.

[3] "WHO: Cell phone use can increase possible cancer risk." [Online]. Available: http://www.cnn.com/2011/HEALTH/05/31/who.cell.phones/index.html. [Accessed: 25-Oct-2014].

[4] I. W. G. on the E. of C. R. to Humans, W. H. Organization, and I. A. for R. on Cancer, *Non-ionizing Radiation: Static and extremely low-frequency (ELF)*

*electric and magnetic fields*. World Health Organization, 2002.

[5] M. I. Hossain, R. I. F. Mohammad, M. T. Islam, and N. H. M. Hanafi, Application of Auxiliary Antenna Elements for SAR Reduction in the Human Head, *Advanced Materials Research* 974: 288–292, 2014.

[6] F. C. Commission and others, "Evaluating compliance with FCC guidelines for human exposure to radiofrequency electromagnetic fields. Washington, DC: FCC," Tech. Rep. Suppl. C to OET Bulletin 65, 2001.

[7] Q. Guo, R. Mittra, F. Lei, Z. Li, J. Ju, and J. Byun, Interaction between internal antenna and external antenna of mobile phone and hand effect, *Antennas Propag. IEEE Trans. On* 61 (2): 862–870, 2013.

[8] L. K. Ragha and M. S. Bhatia, Evaluation of SAR Reduction for Mobile Phone Using RF Shield, *Int J Recent Trends Eng. Technol.* 2 (5), 2009.

[9] W. Jianqing and O. Fujiwara, Reduction of electromagnetic absorption in the human head for portable telephones by a ferrite sheet attachment, *IEICE Trans. Commun.* 80 (12): 1810–1815, 1997.

[10] M. I. Kitra, C. J. Panagamuwa, P. McEvoy, J. C. Vardaxoglou, and J. R. James, Low SAR ferrite handset antenna design, *Antennas Propag. IEEE Trans. On* 55 (4): 1155–1164, 2007.

[11] K. Noguchi, N. Goto, M. Hirose, U. N. O. Toru, and Y. Kamimura, Directional antennas for portable telephones, *IEICE Trans. Commun.* 79 (9): 1234–1241, 1996.

[12] M. Bank and B. Levin, The development of a cellular phone antenna with small irradiation of human-organism tissues, *IEEE Antennas Propag. Mag.* 49 (4): 65–73, 2007.

[13] S. I. Kwak, D. U. Sim, J. H. Kwon, and H. D. Choi, Experimental tests of SAR reduction on mobile phone using EBG structures, *Electron. Lett.* 44 (9): 568–570, 2008.

[14] R. Ikeuchi, K. H. Chan, and A. Hirata, SAR and radiation characteristics of a dipole antenna above differentfinite EBG substratesin the presence of a realistichead model in the 3.5 GHz band, *Prog. Electromagn. Res. B* 44: 53–70, 2012.

[15] M. R. I. Faruque, M. T. Islam, and M. A. M. Ali, A New Design of Metamaterials for SAR Reduction, *Meas. Sci. Rev.* 13 (2): 70–74, 2013.

[16] J.-N. Hwang and F.-C. Chen, Reduction of the peak SAR in the human head with metamaterials, *Antennas Propag. IEEE Trans. On* 54 (12): 3763–3770, 2006.

[17] G. Singh, Double negative left-handed metamaterials for miniaturization of rectangular microstrip antenna, *J. Electromagn. Anal. Appl.* 2010, 2010.

[18] M. B. Manapati and R. S. Kshetrimayum, SAR reduction in human head from mobile phone radiation using single negative metamaterials, *J. Electromagn. Waves Appl.* 23 (10): 1385–1395, 2009.

[19] M. Fallah, A. A. Heydari, A. R. Mallahzadeh, and F. H. Kashani, Design and SAR Reduction of the Vest Antenna using Metamaterial for Broadband Applications, in *ACES* 26 (2):, 2011.

[20] S. Kahng, K. Kahng, I. Yang, and T. Park, "A Metamaterial-Based Handset Antenna with the SAR Reduction," *J. Electr. Eng. Technol.*, vol. 9, no. 2, pp. 622–627, 2014.

[21] M. R. I. Faruque and M. T. Islam, Design of Miniaturized Double-Negative Material for Specific Absorption Rate Reduction in Human Head, *PloS One* 9 (10): e109947, 2014.

[22] M. I. Hossain, M. R. I. Faruque, and M. T. Islam, Design and analysis of metamaterial inspired low SAR PIFA for mobile phone, *Int. J. Appl. Electromagn. Mech.* 48 (4): 459-467, 2015.

[23] M. I. Hossain, M. R. I. Faruque, M. T. Islam, and M. H. Ullah, A New Wide-Band Double-Negative Metamaterial for C- and S-Band Applications, *Materials* 8 (1): 57–71, 2014.

[24] Z. Szabo, G.-H. Park, R. Hedge, and E.-P. Li, A unique extraction of metamaterial parameters based on Kramers–Kronig relationship, *Microw. Theory Tech. IEEE Trans. On* 58 (10): 2646–2653, 2010.

[25] M. Latrach, H. Rmili, C. Sabatier, E. Seguenot, and S. Toutain, Design of a new type of metamaterial radome for low frequencies, *Microw. Opt. Technol. Lett.* 52 (5): 1119–1123, 2010.

[26] IEEE 1528: Recommended Practice for determining the peak Spatial-Average Specific Absorption Rate (SAR) in the Human Head from Wireless Communications Devices: Measurement Techniques. Institute of Electrical and Electronics Engineers, INC., 2003.

# Response of $ZnAl_2O_4$ Ceramics to Ultra Wideband Antenna

**Ashiqur Rahman[1], Mohd. Termizi Ali[2], Mohammad Tariqul Islam[3], Mandeep Jit Singh[3], Norbahiah Misran[3]**

[1]Space Science Centre, Universiti Kebangsaan Malaysia, Bangi 43600, Selangor, Malaysia
[2]Antenna Research Group, Fakulti Kejuruteraan Elektrik, Universiti Teknologi MARA, 40450 Shah Alam, Selangor Darul Ehsan, Malaysia
[3]Department of Electrical, Electronic and Systems Engineering, Faculty of Engineering and Built Environment, Universiti Kebangsaan Malaysia, Bangi, 43600, Selangor, Malaysia

*corresponding author, E-mail: ashiqur@siswa.ukm.edu.my; mizi732002@salam.uitm.edu.my; tariqul@ukm.edu.my,

## Abstract

In this paper, we study the response of $ZnAl_2O_4$ (zinc aluminate) ceramics to an ultra-wideband (UWB) antenna. The $ZnAl_2O_4$ is prepared by the sol-gel technique. The X-ray diffraction (XRD) pattern and the Fourier transform infra-red (FTIR) reveal the characteristic peaks of $ZnAl_2O_4$ with the standard pattern of face centered cubic (fcc) spinel structure and indicate the formation of metal oxide along with the presence of $H_2O$ molecules. A dielectric constant ($\varepsilon_r$) of 8.50 and loss tangent ($tan\delta$) of 0.05 are obtained for $ZnAl_2O_4$ ceramics. The measurement results show a remarkable achievement of 127% bandwidth (return loss > 10 dB) with a bandwidth ratio of 4.5: 1. The impedance bandwidth, stable radiation pattern of the proposed antenna makes it appropriate for many wideband communication applications.

## 1. Introduction

The $ZnAl_2O_4$, is a rare mineral belonging to a spinel group [1] having a general formula of $AB_2O_4$. In general, A-site is the divalent cations and B-site is the trivalent cations in the face center cubic (fcc) oxygen lattice of the spinel structure [2]. According to various researchers, $ZnAl_2O_4$ has become very popular in its spinel groups due to their unique electrical and optical properties [3]. $ZnAl_2O_4$ has been used as ceramic, optical and electrical materials [6] and also catalyst support [4, 5]. The high mechanical resistance and thermal stability and low surface acidity of the aluminum spinel was confirmed by many researchers [7]. Microwave dielectric ceramics which were based on $ZnAl_2O_4$ were reported that, this material has good research potential in the future of microwave applications [8, 9].

The multi-frequency microstrip antenna has become one of the most important devices and attracted much interests. There are many commercial services such as WiMAX, WLAN, GPS, ISM (Industrial, Scientific and Medical) and mobile that use microstrip antenna due to their low profile. However, the dielectric substrate of microstrip antennas limit the size as well as affecting efficiency and bandwidth. To overcome such drawback of the microstrip antenna, a dielectric ceramics consist of high dielectric permittivity and low loss tangent could be one of the solutions. Several techniques such as co-precipitation method [12], solid state reaction [10, 11] and sol-gel method [13] were utilized to synthesize $ZnAl_2O_4$. Compare to all other techniques, sol-gel method draws most attention due to their unique characteristics of producing fine and pure powder at low temperature [14].

The current users of wireless communication are strongly searching for an ultra-wideband antenna to cover both the short range and high data rate transmission for numerous applications. Since Federal Communication Commission (FCC) releases unlicensed band (3.1 GHz-10.6 GHz) for UWB communication, several techniques have been introduced to design UWB antenna to support high data rate transmission in wireless communication. It is still quite challenging to design a wideband antenna which is compact in size, efficient and at the same time light in weight. Several researchers suggested to use coplanar waveguide fed and microstrip line-fed antennas for UWB applications. Many other techniques for bandwidth antenna such as- connecting numerous radiating elements to form an array antenna [15], log periodic array antenna [16], inserting a capacitive coupling between the patch and ground plane [17], introducing slots on the radiating patch [18, 19], using a tapered feed line [20], notching the ground plane and/or the patch [21,22], modifying the shape of the radiating element and adding a shorting pin [23] were also reported. However the antennas mentioned above are not planar structured as they were set above a big ground plane which resulted increased antenna size and cannot easily embedded into wireless devices or cannot be integrated with other RF circuits. In recent years several other techniques have been introduced for bandwidth enhancement, such as: modified trapezoid shaped hole in the patch [24], implanting notches both in patch and ground plane [26], feeding strip of trident shape

with impedance transformer [25], two bevel slots and two semicircle slots on upper and bottom edge respectively [27], rectangular slot on upper portion of the ground plane [28] and staircase structured bowtie radiating patch [29]. Several other methods like increased steps to the lower edge of the radiating patch [30], addition of circular round shape patch [31], adding extra stub at the edge of the circular patch [32] and inclusion of slit at any side of the patch [33] were also reported.

In this paper, a printed ultra-wideband antenna fabricated on a $ZnAl_2O_4$ ceramics substrate with dimensions of 28.5 × 20 $mm^2$ is proposed. The use of high dielectric permittivity helps to reduce the overall dimension. An ultra-bandwidth is achieved by executing an appropriate impedance-matching asymmetric feed line and a partial ground plane. Measured results demonstrate that the antenna has an extremely wide bandwidth ranging from 2.8–12.6 GHz with a ratio bandwidth of 4.5:1. In addition, the proposed antenna is compact, simple and easy to fabricate. The proposed antenna's design and measurement results obtained for this antenna is described in details in the following sections.

## 2. Materials and Methods

The starting raw materials were Zinc nitrate [Zn $(NO_3)_2.6H_2O$, M=297.49 $gmol^{-1}$], Aluminum nitrate [Al $(NO_3)_3.9H_2O$, M=375.13 $gmol^{-1}$], Citric acid [$C_6H_8O_7.H_2O$, M=210.14 $gmol^{-1}$] and polar solvent (e.g. distil water). The raw materials were weighed out in stoichiometric proportion and completely dissolved in distilled water with molar ratio 1:1. Citric acid was used as chelating agent. The solution was heated at 70° C for 5 to 6 hours with continuous stirring until the formation of gel. Yellow gel was obtained after evaporated the water completely by heating several more hours.

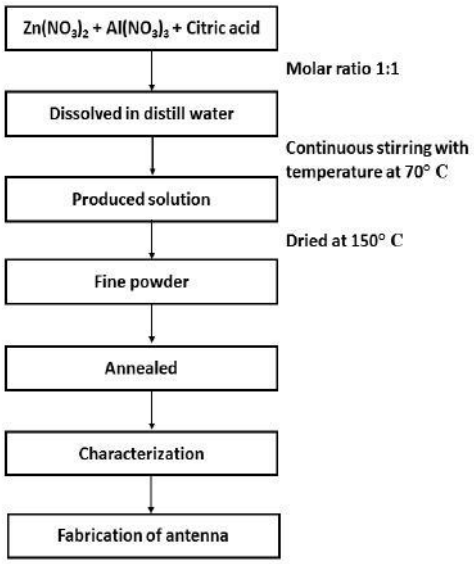



Fig.1 Flowchart for sample preparation of $ZnAl_2O_4$ compounds

The gel was then dried at 150°C for 2 to 4 hours in alumina crucible furnace till the powder became saggy and turned into greenish color. It was annealed at 450°C, 550°C and 650°C at crucible furnace for 1 hour after grinding the precursor. The synthesized powder was then added to a PVA solution and was heated at 60° C for 72 hours. Polymer substrate was obtained after evaporated the water completely. The film phase with CuKα radiation was analyzed by X-ray diffractometer (XRD) at wavelength 1.5406 Å at XRD (Siemens D-500). FTIR spectroscopy analysis was used to identify the chemical bonding states of the $ZnAL_2O_4$ compounds. The dielectric permittivity and loss tangent were measured by using dielectric measurement kit (DAK3.5) at 1-6 GHz frequency range. The brief procedure of the preparation is shown in the flowchart in Fig. 1.

## 3. Results and Discussion

Fig. 2 shows the XRD patterns of the $ZnAl_2O_4$ samples annealed at 450° C, 550° C and 650° C for 1 hour. The extend of samples' crystallization were analyzed using XRD. The annealed samples show the diffraction patterns of $ZnAl_2O_4$ phase which were indexed in JCPDS 01-070-8181. All the observed peaks of $ZnAl_2O_4$ appearing at $2\theta$ =31.16°, 36.76°, 44.76°, 55.66° and 59.48° can be indexed as (220), (311), (331), (422) and (511) crystal planes structure respectively. This pattern confirms the development of phase-centered cubic structure.

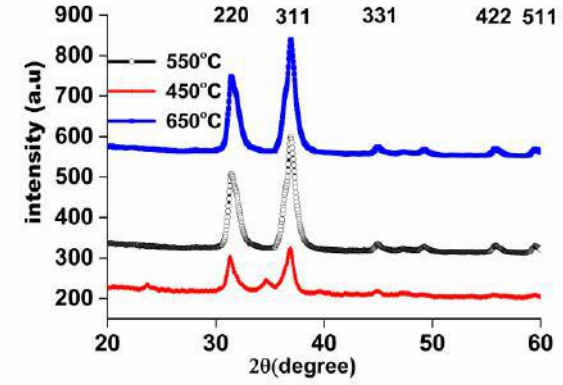



Fig.2 XRD patters of $ZnAl_2O_4$ nanostructure for different annealing temperatures

The diffraction peaks that we found are well match with those described by Khaledi [34] and Zulfakar [35]. The crystallite size, $D$ of prominent peak (311) can be calculated using Scherrer's equation formula [36]:

$$D = \frac{k\lambda}{\beta \cos\theta} \quad (1)$$

Where $\lambda$ refers to X-ray wavelength (1.54059 Å), $k$ denotes Scherrer constant (0.94), $\beta$ indicates the broadening of the diffraction line which was measured at the half of its maximum intensity in radians and $\theta$ represents the diffraction angle. The average crystallite

size of each samples were calculated within range of 20-80º (2$\theta$) from the broadening XRD diffraction lines have been listed in Table I. These variations can be attributed to change in the morphology of the nanostructure powders during thermal treatment. The experimental lattice parameter reduced from 8.085 Å to 8.084 Å due to XRD spectra that shifted to higher (right) angle. Normally, the decreases of lattice parameters are able to increase the density as well as dielectric constant.

TABLE I: Specific data for diffraction angle, crystallite size and plane for $ZnAl_2O_4$ samples with different annealing temperature

| Annealed Temperature | 2$\theta$ (Degree) | Crystallite size, *D* | hkl |
|---|---|---|---|
| 450 | 36.70 | 18.03 | 311 |
| 550 | 36.76 | 19.92 | 311 |
| 650 | 36.74 | 19.12 | 311 |

The FTIR spectrum of the $ZnAl_2O_4$ nanoparticles prepared by sol-gel method presented in Fig. 3. The analysis of the ceramics was performed in the wave number region from 400 to 4000 per cm. It was used to determine the vibrational stretch frequency of metal-oxygen bond. In Fig. 3, a broad absorption band centered at 3440.4 $cm^{-1}$ corresponds to the OH group. This band is attributed to the deformative vibration of water molecules [36]. In plot (b), the band at 1500 $cm^{-1}$ corresponds to the formation of metal hydroxides as an intermediate compound before the formation of zinc aluminate spinel. In plot for 450°C, the peak observed at 2339.2 $cm^{-1}$ indicates to the presence of oxygen-oxygen bonds in the fcc crystal lattice of oxygen

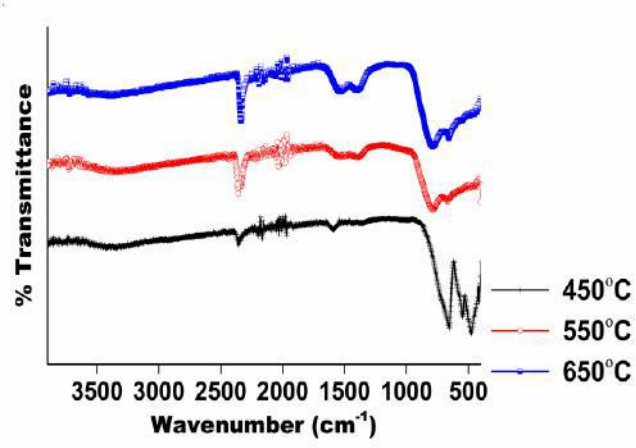



Fig.3 FTIR spectrum of $ZnAl_2O_4$ prepared by sol-gel method

atoms [37]. This peak can be treated as a characteristic feature of spinel structured crystallites. Three sharp absorption bands are visible within the range of 400-900 $cm^{-1}$ associated with the vibration of Zn-O, Al-O and Zn-O-Al bonds, indicating the formation of $ZnAl_2O_4$ [34]. A dielectric measurement kit (DAK 3.5) was employed to measure the dielectric properties of $ZnAl_2O_4$.

The measurement was plotted in frequency range from 1 GHz to 6 GHz. Fig 4 depicts a steady decrease in the dielectric constant with applied frequency for all the samples. Such decreases in dielectric constant is the subsequent of existing interfacial polarization which increase the relaxation time compared to the dipolar polarization. This phenomenon is known as Debye equation. The samples annealed at 550º C reported the highest dielectric value 8.70 which is in agreement with the previous report [38]. The measured dielectric

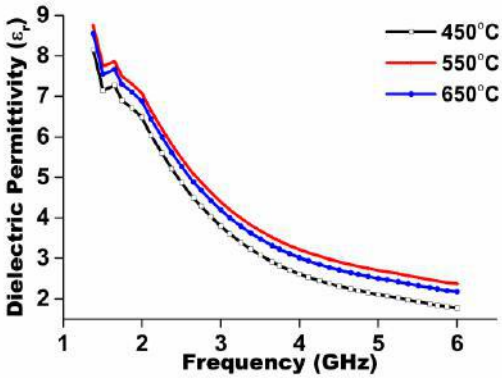



Fig.4 Variation of dielectric permittivity for $ZnAl_2O_4$ samples for different annealing temperatures

permittivity value varied from 8.10-8.70. This increased value of dielectric permittivity was caused by the increased crystallite size when annealed at higher temperatures.

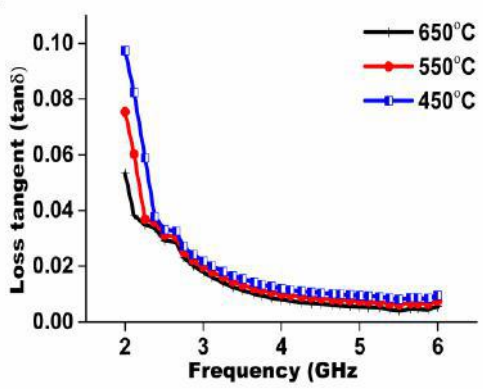



Fig.5 Variation of loss tangent for different annealing temperatures

There are two types of losses in dielectric materials. A conduction loss, due to the flow of electron charges and a dielectric loss caused by the atom movement in an alternating field. Among the total core loss, dielectric loss plays an important role in microwave dielectric materials. The loss tangent is defined as the ratio of the lossy reaction to the electric field E in the curl equation to the lossless reaction and is less than 90°. The dielectric loss is

measured from this loss tangent angle. Antenna efficiency increases with the decrease of dielectric loss. The values of loss tangent are tabulated in Table II.

TABLE II: Microwave dielectric properties of $ZnAl_2O_4$ samples at different annealing temperature

| Annealed Temperature | Dielectric Constant | Loss Tangent |
|---|---|---|
| 450 | 8.10 | 0.09 |
| 550 | 8.70 | 0.07 |
| 650 | 8.50 | 0.05 |

Fig. 6(a) depicts the geometries of realized planar monopole antenna. In this study, we selected the planar antenna due to their unique feature of miniature size, minimal cost, least power density, simple design, stable radiation characteristics, easy assembling and integrated with microwave circuitry. The square patch with dimension $Wp \times Lp$ is coated with copper target of 200 nm on a $ZnAl_2O_4$ substrate utilizing the magnetron sputtering. The radiation patch is 3.6 mm away from the left edge of the substrate. For the impedance matching that results in bandwidth enhancement, an asymmetric feed line technique is introduced. A microstrip feed line of width $W_f$, which is connected to the radiating patch is coated 6.3 mm away from the left edge of the substrate. The dimensions of the ground plane plays a significant role on reflection coefficient (S11) and bandwidth. The fractional ground plane of dimension $W \times L_G$, width of 5.5 mm, that is taken as optimized value is coated with copper target, using magnetron sputtering with 200nm of thickness on the opposite side of the substrate. A 50 Ω characteristic impedance is achieved with 6mm microstrip feed line. A 50 Ω SMA connector is connected to the microstrip feed line. The space between the microstrip line and the partial ground plane, (*h*) plays an important role in achieving ultra-wideband width. An optimized value of 0.5 mm is chosen to maintain the good impedance

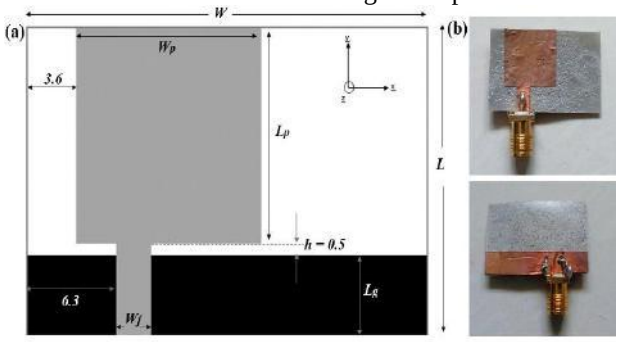



Fig.6 (a). Geometry of the proposed antenna (b). Prototype of the proposed antenna

bandwidth with better return loss values. The overall dimension of the proposed antenna is $W \times L$. The prototype of the antenna is shown in Fig. 6 (b).

The high frequency simulation software (HFSS) which is based on finite element method have been employed to analyze the performance of the proposed antenna. A vector network analyzer N5227A PNA (10 MHz-67 GHz) was deployed to measure the reflection coefficient of the realized antenna. Fig. 7 presents the reflection coefficient (S11) of the proposed antenna for both measured and simulation. Here, the proposed antenna achieved a bandwidth of 127% (from 2.8 to 12.6 GHz) and a ratio bandwidth of 4.5:1. The proposed antenna can cover the operating spectrum of ISM (2/5 GHz), WiMAX (3.5/5.5 GHz), WLAN (5.2/5.8 GHz), UWB (3.1-10.6 GHz) and upcoming 5G (above 6 GHz). A small deviation was observed due to the fabrication tolerance.

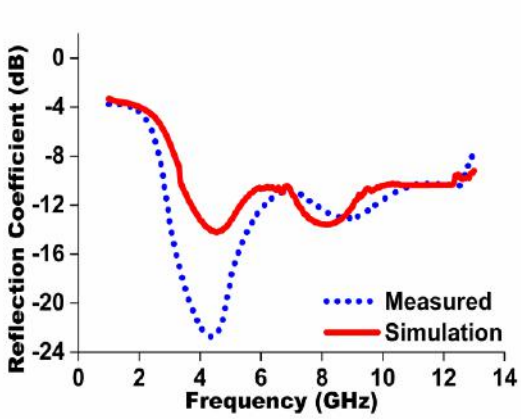



Fig.7 Measured and simulated reflection coefficient of the proposed antenna

Fig. 8 depicts the measured radiation patterns in two principal planes-namely, *E* (XZ) and *H* (XY) planes for two resonant frequencies at 4.38 and 8.96 GHz. Satimo hybrid StarLab in an anechoic chamber were deployed to measure the radiation patterns. It is observed that the radiation patterns in the *E* plane at the low frequency of 4.4 GHz has the typical figure-eight shape for co polarization and near omnidirectional radiation pattern for cross-polarization. As the frequency increases, higher order current modes get excited and the radiation patterns become directional with slight deformations. Ripples can be observed at higher frequencies in both *E* and *H*- planes owing to the generations of higher-order resonant modes. The cross polarization components increase at higher frequencies due to the increase in orthogonal surface currents.

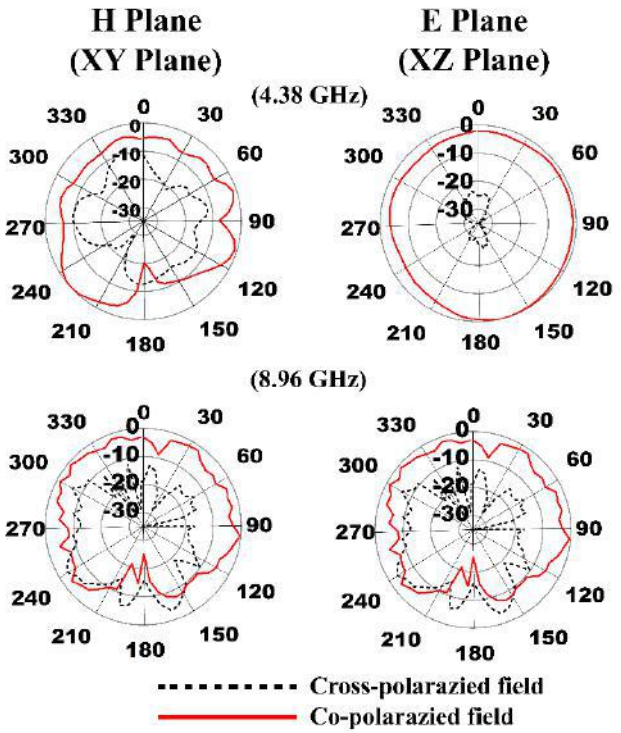



Fig.8 Measured radiation patterns of realized antenna at different frequencies

## 4. Conclusions

A microstrip line-fed printed planar antenna has been proposed and fabricated on $ZnAl_2O_4$ ceramics substrate. Experimental results confirm the formation of zinc aluminate of high dielectric constant with low loss tangent. The structure of the proposed antenna is simple and can easily be manufactured. The measurement shows that the proposed antenna achieves good impedance bandwidth and stable radiation pattern over an operating bandwidth of 2.8-12.6 GHz. The corresponding -10 dB $S_{11}$ bandwidth was 127% with 4.5: 1 ratio bandwidth. The stable radiation pattern with a linear phase variation and stable group delay makes the proposed antenna suitable for being used in UWB applications.

## Acknowledgements

The authors would like to thank the Faculty of Electrical Engineering (Antenna Research Centre), Universiti Teknologi MARA (UiTM), Malaysia and Ministry of Higher Education (MOHE) Malaysia for the financial support under Fundamental Research Grant Scheme (FRGS 600-RMI/FRGS 5/3).

## References

1 Xiulan Duan, Duorong Yuan, Zhihong Sun, Haiqing Sun, Dong Xu, and Mengkai Lv, Journal of crystal growth 252 (1), 4 (2003).

2 AR Phani, M Passacantando, and S Santucci, Materials chemistry and physics 68 (1), 66 (2001).

3 Prathaban Mookiah and Kapil R Dandekar, Antennas and Propagation, IEEE Transactions on 57 (10), 3283 (2009).

4 Xiuhua Wei and Donghua Chen, Materials Letters 60 (6), 823 (2006).

5 Ping Cheng, Changsheng Deng, Mingyuan Gu, and Wenfeng Shangguan, Journal of Materials Science 42 (22), 9239 (2007).

6 Suresh K Sampath and James F Cordaro, Journal of the American Ceramic Society 81 (3), 649 (1998).

7 M Zawadzki and J Wrzyszcz, Materials research bulletin 35 (1), 109 (2000).

8 Jia-Min Wu, Wen-Zhong Lu, Wen Lei, and Xiao-Chuan Wang, Materials Research Bulletin 46 (9), 1485 (2011).

9 Huda Abdullah, Mohd Syafiq Zulfakar, Wan Nasarudin Wan Jalal, Mohammad Tariqul Islam, and Sahbudin Shaari, Journal of Sol-Gel Science and Technology 69 (1), 183 (2014).

10 Wan-Shick Hong, Lutgard C Jonghe, Xi Yang, and Mohamed N Rahaman, Journal of the American Ceramic Society 78 (12), 3217 (1995).

11 NJ Van der Laag, MD Snel, PCMM Magusin, and G De With, Journal of the European Ceramic Society 24 (8), 2417 (2004).

12 MA Valenzuela, J-P Jacobs, P Bosch, S Reijne, B Zapata, and HH Brongersma, Applied Catalysis A: General 148 (2), 315 (1997).

13 Nolven Guilhaume and Michel Primet, Journal of the Chemical Society, Faraday Transactions 90 (11), 1541 (1994).

14 Fatemeh Davar and Masoud Salavati-Niasari, Journal of Alloys and Compounds 509 (5), 2487 (2011).

15 C. A. Balanis, Antenna Theory Analysis and Design, John Wiley & Sons, New York, 1997.

16 M. K. Rahim and P. Gardner, "The Design of Nine Element Quasi Microstrip Log Periodic Antenna," RF and Microwave conference, Malaysia, pp. 132 – 135, October 2004.

17 H. Rmili and J. M. Floc'h, "Design and Analysis of Wideband Double-Sided Printed Spiral Dipole Antenna with Capacitive Coupling," Microwave and Optical Technology Letters, vol. 50, no. 5, pp. 1312-1317, May 2008.

18 A. K. Shackelford, K. F. Lee, and K. M. Luk, "Design of Small Size Wide-Bandwidth Microstrip Patch Antennas," IEEE antennas and Propagation Magazine, vol. 45, no. 1, pp. 75-83, February 2003.

19 J. Y. Chiou, J. Y. Sze, and K. L. Wong, “A Broad- Band CPW Fed Strip Loaded Square Slot Antenna,” IEEE Transactions on Antennas and Propagation, vol. 51, no. 4, pp. 719 – 721, April 2003.

20 R. S. Kshetrimayum and R. Pillalamarri, “Novel UWB Printed Monopole Antenna with Triangular Tapered Feed Lines,” IEICE Electronics express, vol. 5, no. 8, pp. 242- 247, April 2008.

21 S. Tourette, N. Fortino, and G. Kossiavas, “Compact UWB Printed Antennas for Low Frequency Applications Matched to Different Transmission Lines,” Microwave and Optical Technology Letters, vol. 49, no. 6, pp. 1282-1287, June 2007.

22 X. Zhang, W. Wu, Z. H. Yan, J. B. Jiang, and Y. Song, “Design of CPW-Fed Monopole UWB Antenna with a Novel Notched Ground,” Microwave and Optical Technology Letters, vol. 51, no. 1, pp. 88-91, January 2009.

23 M. N. Shakib, M. T. Islam, and N. Misran, “Stacked Patch Antenna with Folded Patch Feed for Ultra-Wideband Application,” IET Microw. Antennas Propag. vol. 4, no. 10, pp. 1456–1461, October 2010.

24 M. Ojaroudi, G. Kohnehshahri, and J. Noory, “Small Modified Monopole Antenna for UWB Application,” IET Microwave Antennas and Propagation, vol. 3, no. 5, pp. 863-869, August 2009.

25 Q. Wu, R. Jin, J. Geng, and M. Ding, “Printed Omni-Directional UWB Monopole Antenna with Very Compact Size,” IEEE Transactions on Antennas and Propagation, vol. 56, no. 3, pp. 896–899, March 2008.

26 J. Jung, W. Choi, and J. Choi, “A Small Wideband Microstrip-Fed Monopole Antenna,” IEEE Microwave and Wireless Components Letters, vol. 15, no. 10, pp. 703–705, October 2005.

27 C. Y. Hong, C. W. Ling, I. Y. Tarn, and S. J. Chung, “Design of a Planar Ultrawideband Antenna with a New Band-Notch Structure,” IEEE Transactions on Antennas and Propagation,vol. 55, no. 12, pp. 3391–3396, December 2007.

28 R. Azim, M. T. Islam, and N. Misran, “Printed Planar Antenna for Wideband Applications,” Journal of Infrared Millimeter and Terahertz Waves, vol. 31, no. 8, pp. 969-978, August 2010.

29 Y. J. Cho, K. H. Kim, D. H. Choi, S. S. Lee, and S.-O. Park, “A Miniature UWB Planar Monopole Antenna with 5-GHz Band-Rejection Filter and the Time-Domain Characteristics,” IEEE Transactions on Antennas and Propagation, vol. 54, no. 5, pp. 1453–1460, May 2006.

30 R. Zaker, C. Ghobadi, and J. Nourinia, “Novel Modified UWB Planar Monopole Antenna with Variable Frequency Band-Notch Function,” IEEE Antennas and Wireless Propagation Letters, vol. 7, pp. 112–114, 2008.

31 L. Liu, S. W. Cheung, R. Azim, and M. T. Islam, “A Compact Circular-Ring Antenna for Ultra-Wideband Applications,” Microwave and Optical Technology Letters, vol. 53, no. 10, pp. 2283-2288, October 2011.

32 K. P. Ray and Y. Ranga, “Ultrawideband Printed Elliptical Monopole Antennas,” IEEE Transactions on Antennas and Propagation, vol. 55, no. 4, pp. 1189 1192, April 2007.

33 J. Choi, K. Chung, and Y. Roh, “Parametric Analysis of a Band-Rejected Antenna for UWB Applications,” Microwave and Optical Technology Letters, vol. 47, no. 3, pp. 287-290, November 2005.

34 AG Khaledi, S Afshar, and HS Jahromi, Materials Chemistry and Physics 135 (2), 855 (2012).

35 Mohd Syafiq Zulfakar, Huda Abdullah, Wan Nasarudin Wan Jalal, Zalita Zainuddin, and Sarada Idris, Journal of Sol-Gel Science and Technology 71, 1 (2014).

36 R Thinesh Kumar, N Selvam, C Ragupathi, L John Kennedy, and J Judith Vijaya, Powder Technology 224, 147 (2012).

37 E Muhammad Abdul Jamal, KUMAR D SAKTHI, and MR Anantharaman, Bulletin of Materials Science 34 (2), 251 (2011).

38 Youssef Mobarak, M Bassyouni, and M Almutawa, Advances in Materials Science and Engineering 2013 (2013).

# Microstrip Antenna Gain Enhancement by Metamaterial Radome for millimiter wave applications

**S. Attachi, C. Saleh, M. Bouzouad**

Telecommunications, Signal and Systems Laboratory,
BP 37G, Route de Ghardaïa, 03000, Laghouat, Algérie.
*corresponding author, E-mail: s.attachi@lagh-univ.dz

***Abstract***

*In this work, a high gain patch antenna using multilayer FSS radome is proposed for millimiter wave applications. The antenna operating frequency is operating at 43.5 GHz.*

*The antenna/radome system consists of one, two, three, or four layers of metasurfaces (FSS) placed in the near-field region of microstrip patch antenna (MPA). The antenna/radome system gain is improved by 9 dBi compared to patch antenna alone and the radiation pattern half-power beamwidth is reduces to 20) in both E- and H-planes.*

***Key words:*** *Antenna, Frequency selective surface (FSS), Metamaterial, Finite FSS radome.*

## 1. Introduction

Frequency Selective Surfaces (FSS) are planar infinite array of periodically arranged unit cell on dielectric substrate [1] [2]. The cells are constructed from metallic patch or aperture element that exhibits perfect reflection or transmission, respectively, in the neighborhood of the resonant element [3]. FSSs are widely and intensively investigated [4] and the progress in terms of manufacturing of micro- and nanostructures on one hand, and the promising properties of the artificial periodic structures on the other hand, made necessary the use of FSSs very attractive for many applications. Many design are proposed such as ultra-band or dual-band FSS using multilayer FSSs [5]-[6], compact FSS using the fractal configuration [7]-[8], and radomes for aeronautical applications [3]. These designs greatly improve the FSSs performances.

Radomes are electromagnetic pass-band filters. Ideally, they have to be electromagnetically transparent, in the operating frequency band. They are essential components that protect radars against physical environment and help to reduce the operational coast [9].

In practical applications, FSS radomes have usually curved shapes and are of finite extent. In addition, when the radome is located close to the antenna, mutual coupling between the antenna and FSS cannot be neglected. These factors will seriously modify the radiation performance of antenna [10][11]. Another adverse effect of radomes is the presence of water or ice which causes radio signals degradations.

Depending on the operating frequency and physical elements, radomes can significantly deteriorate radar signals especially for higher frequencies [*12]. In consequence, millimeter-wave systems introduce a set of particular severe requirements from the antenna point of view. Therefore, high directive antennas are required to overcome the aforementioned degradation. Finally, the antennas must be small, low-profile, lightweight, and low-cost in order to be successfully integrated in a commercial wireless system.

In this paper, an FSS radome is proposed to improve a patch antenna gain and make it more directive. The proposed FSS radome is then used as a superstrate. The FSS radome is placed in the near-field region of the MPA to form an antenna/radome system. The antenna and FSS unit are designed separately.

## 2. Frequency selective surface design

Up today, the most used FSS are constituted by cascading several sheets (metasurface), one behind the other and separated by spacer [13]. The addition of a superstrate layer over microstrip patch antenna (MPA) has been reported to enhance the antenna gain and radiation efficiency. Furthermore, superstrate layers can be used as radome to protect the MPA when placed on aircrafts and missiles. In this work, a microstrip patch antenna (MPA) and FSS metasurface are designed at millimeter-wave band to improve the patch antenna gain and directivity.

The radating element, of the antenna/radome system, is a microstrip patch antenna, shown in Fig. 1(a), operating at 43.5 GHz. The radome is conctituted by one, two, three, or four layers of metasurfaces (FSS). The FSS unit cell, depicted in Fig. 1-(b), is formed by a perfect cross type conductor, with metallization thickness $t = 0.017$mm, printed on a dielectric substrate of permittivity $\varepsilon_r = 2.17$ and a thickness $d = 0.914$ mm, where 20 holes are drilled to reduce the effective dielectric permittivity. The unit cell geometrical parameters, conducting strip width $w$, metallization thickness $t$, substrate permittivity $\varepsilon_r$ and thickness $d$ directly govern the FSS electromagnetic properties. Since we have fixed some of them ($t$, $\varepsilon_r$ and $d$), we use $w$ as design parameter to tune on-demand the FSS behavior. The desired FSS metasurface behavior is a flat refraction index profile and close to unity in the operating frequency band. The FSS metasurface must be transparent to electromagnetic wave at these frequencies. A parametric study is used to obtain the dimensions of the metamaterial unit cell.

The FSS constitutive parameters (ε and μ) and the refractive index $n$ of the FSS, shown in fig. 2 and 3 respectively, are obtained with the Fresnel inversion method using the S parameters [14], obtained by a finite difference method based commercial code.

The antenna/radome system operating frequency is 43GHz. consequently the corresponding wavelength in free space is 6.9 mm. Accordingly, the FSS periode $a$ and hence

the gretest dimension of the FSS unit cell must be much lower than the operating wavelength, to respect the homogenization criterion [15]. So it's fixed at $a = 1$ mm (lower than $\lambda/3 \approx 2.3$ mm).

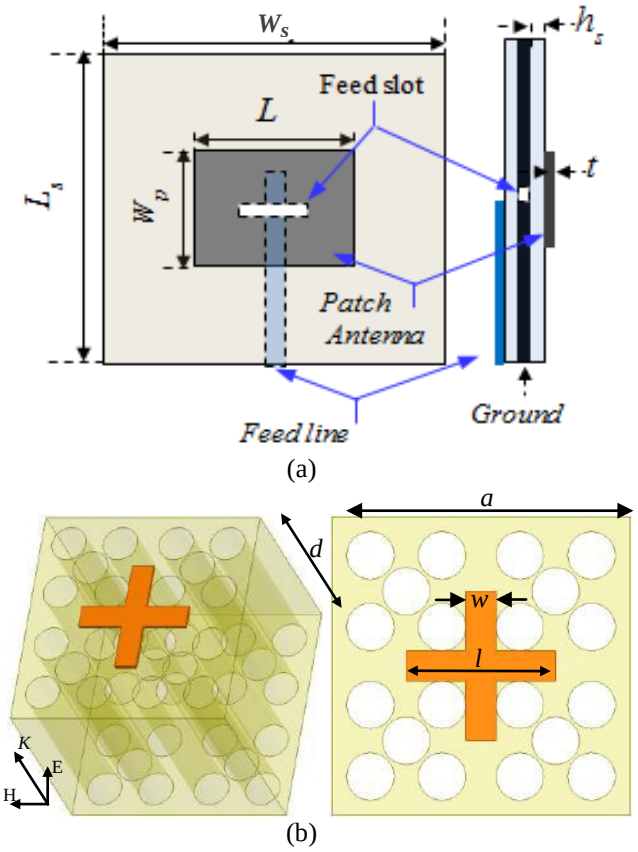



*Figure 1: (a) Antenna slot feeding details. (b) FSS unit-cell; $d = 0.914$ $W = 0.1$, $l = 0.5$, $t = 0.017$, $a = 1$, $L_s = 25$, $W_s = 20$, $h_s = 0.05$, $L_p = 0.257$, $W_p = 0.184$ [units = mm].*

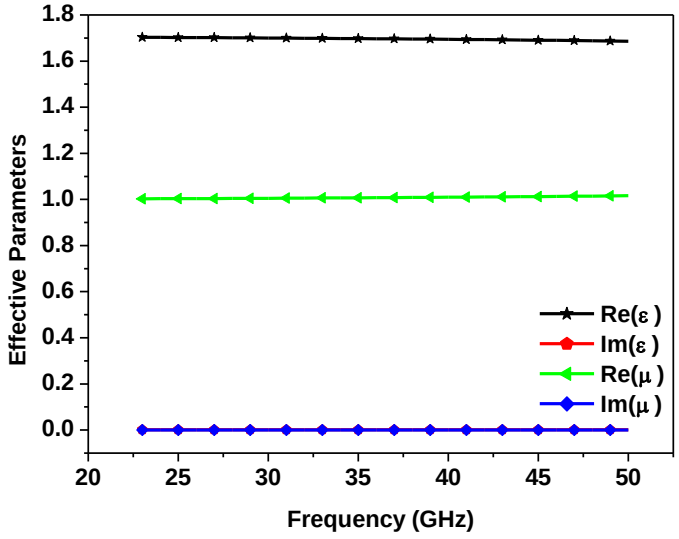



*Figure 2: The FSS effective permittivity and permeability.*

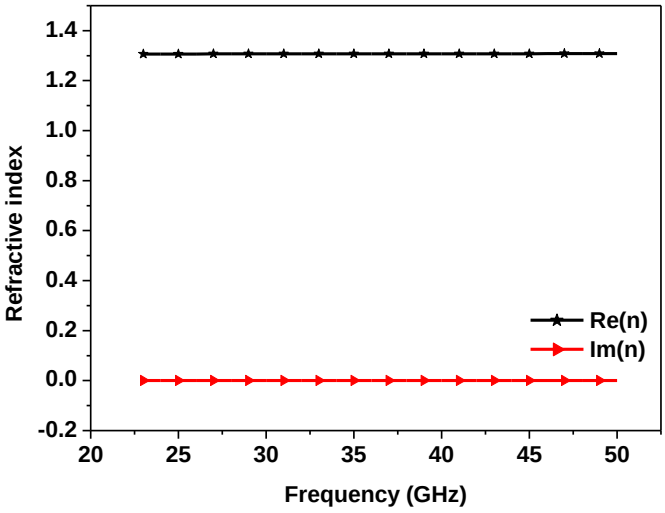



*Figure 3: The FSS refractive index*

## 3. Antenna/radome design

Figure 4 shows the configuration of the proposed antenna/radome system. The patch antenna is covered with the metamaterial radome. Each metasurfac is composed by 25×20 unit cells. The antenna/radome system consists of one, two, three, or four layers of metasurfaces (FSS) placed at heights $h_1$, $h_2$, $h_3$ and $h_4$ away from the antenna substrate respectively.

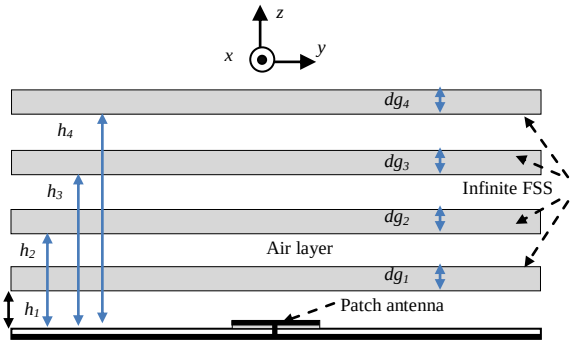



*Figure 4: Configuration of the proposed antenna covered with metamaterial radome.*

## 4. Simulation results

A parametric study is used to optimize the FSS radome parameters. The obtained results are: $d_{g1}$ =1.24 mm, $h_1$ = 3.2 mm; $d_{g2}$ = 1.6 mm, $h_2$ = 6.4 mm, $d_{g3}$ = 1.4 mm, $h_3$ = 9.6 mm $d_{g4}$ = 1.8 mm and $h_4$ = 12.5 mm.

Table 1 shows the gain of the antenna/radome system. It clerly observed that the antenna/radome gain (16.3 dBi) is much greater compared to that of the antenna alone. The antenna alone gain is 7.3 dBi and incresing the number of FSS radome layers, from 1 to 4, increases the antenna/radome system gain from 9.4 dBi to 16.3 dBi, repectively.

Figures 5 and 6 show the raddiation pattern for the antenna/radome system compared to that of the antenna alone, at the operating frequency of 43.5 GHz. It can be observed

that the FSS radome increases considerably the anteanna/radome system gain, narrows the main lobe half power beamwidth and anhences the directivity, in both E-and H-plnes. From table 2, it can be seen that the radiating system half power beamwidth decreases from 66° (antenna alone) to 20° (antenna/radome with 4 layers) in th E-plane and from 80°(antenna alone) to 20° (antenna/radome with 4 layers) in the H-plane. Unfortunately, increasing the number of FSS radome layers increases the antenna/radome system radiation pattern back lobes.

*Table 1 Antenna/radome system gain*

| Antenna type | Gain (dBi) |
|---|---|
| Antenna alone | 7.3 |
| Antenna/radome with 1 FSS layer | 9.4 |
| Antenna/radome with 2 FSS layers | 12.1 |
| Antenna/radome with 3 FSS layers | 14.7 |
| Antenna/radome with 4 FSS layers | 16.3 |

*Table 2 Antenna/radome radiation pattern characteristics*

| | *hi i* = 1,4 [mm] | E-plane $\theta_{-3dB}$ | H-plane $\theta_{-3dB}$ |
|---|---|---|---|
| Antenna alone | // | **66°** | **80°** |
| Antenna/Radome with 1 layer | **3.2** | **48°** | **52°** |
| Antenna/Radome with 2 layers | **6.4** | **32°** | **38°** |
| Antenna/Radome with 3 layers | **9.6** | **24°** | **26°** |
| Antenna/Radome with 4 layers | **12.8** | **20°** | **20°** |

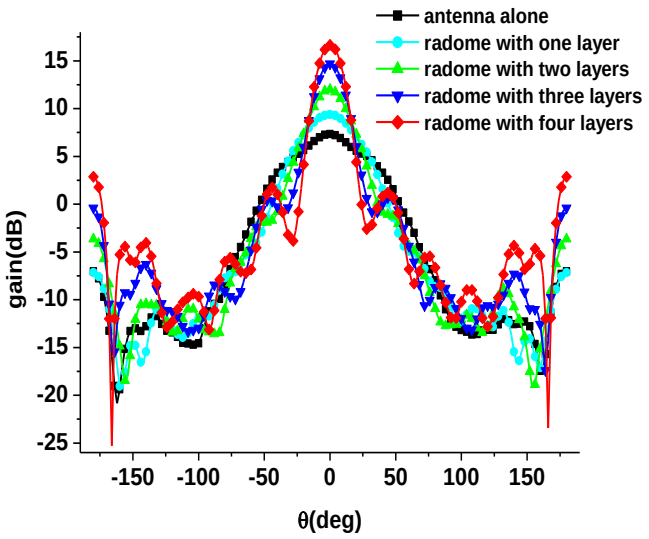



*Figure 5: Radiation pattern of proposed antenna and cover with metamaterial radome on E-plane.*

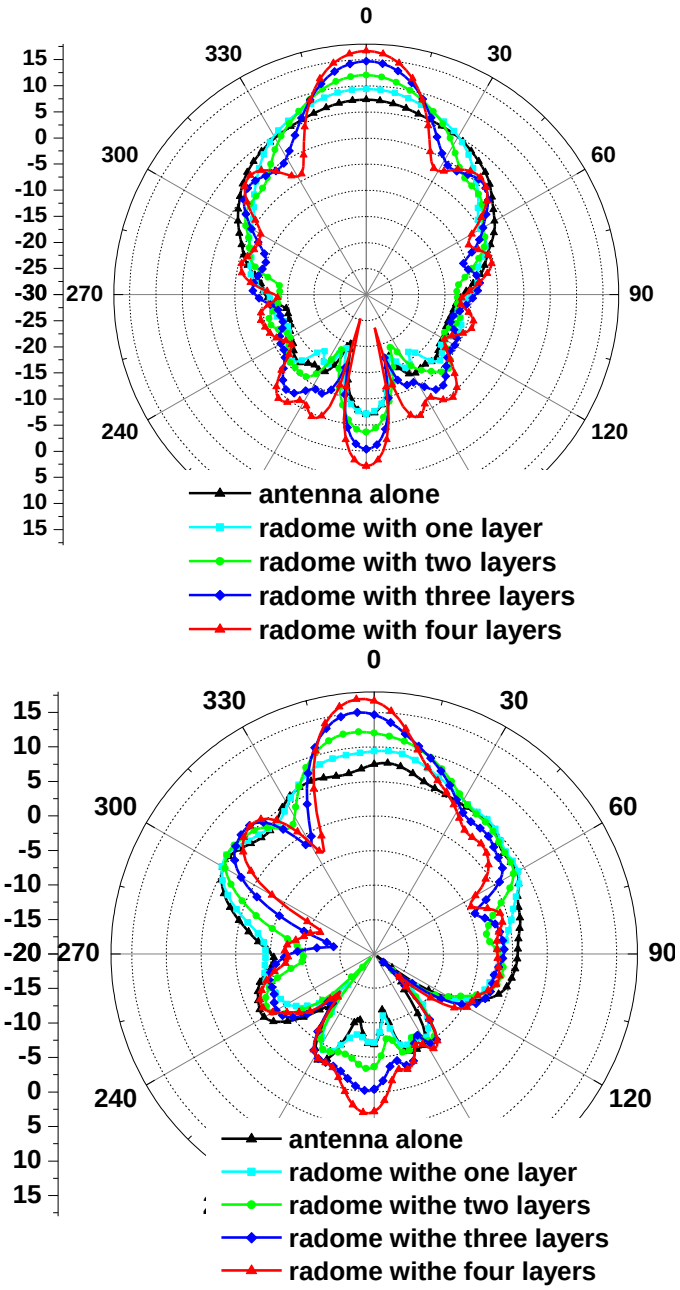



*Figure 6: Radiation pattern of proposed antenna and cover with metamaterial radome on E-plane (up) and H-plane (down).*

## 5. Conclusion

In this paper we propose a high gain patch antenna using multilayer FSS radome is proposed for millimeter wave applications. The proposed design consists of FSS radome placed in the near-filed zone of the radiating element. The antenna/radome system gain increases with the number of the FSS radome layers. The gain is increased, by about 9 dBi compared to that of the patch antenna alone. The FSS radome reduces also the radiation pattern half power beamwidth to 20° in both E- and H-planes. Unfortunately, It increses the radiation pattern back lobes.

## References


[1] B. A. Munk, Frequency Selective Surfaces: Theory and Design. New York: John Wiley & Sons Inc. 2000.

[2] Sakran, F. and Y. Neve-Oz, "Absorbing frequency-selective surface for the mm-wave range," IEEE Tran. Ant. Prop., Vol. 56, No. 8, 2649–2655, 2008

[3] Vardaxoglou, Frequency Selective Surfaces: Analysis and Design. New York:Wiley & Sons, Inc. 1997.

[4] R. J. Luebbers and B.A.Munk, "Mode matching analysis of bi-planar slot arrays", IEEE Trans Antennas Propagation, vol. AP-27, No. 3, pp. 441-443, May 1979.

[5] J. P. Gianvittorio, et al., "Self-similar prefractal frequency selective surfaces for multiband and dual-polarized applications". IEEE Transactions on Antennas and Propagation, vol. 51, No. 11, pp. 3088–3096, Nov. 2003.

[6] Hou Xinyu, Wan Wei, Tong Mingan and Wan guobin, "Analysis of Transmission properties of a symmetrical double-layer FSS", Journal of Electronics, vol. 21, No. 4, pp. 569-572, July 1999.

[7] Kamal Sarabandi and Nader Behdad, "A Frequency Selective Surfaces with Miniaturized Elements", IEEE Trans Antennas Propagation, vol. 55, pp. 1239-1245.may 2007.

[8] A. L. P. S.Campos, E. E. C. Oliveira,and P. H. F. Silva, "Miniaturization of frequency selective surfaces using fractal Koch curves". Microwave and Optical Technology Letters, vol. 51, No. 8, pp. 1983-1986, 2009.

[9] Walton, J. (1970). Radome Engineering Handbook: Design and Principles. Marcel Dekker, Inc.

[10] Guo Qing Luo, Wei Hong, Hong Jun Tang, Ji Xin Chen, "Filtenna Consisting of Horn Antenna and Substrate Integrated Waveguide Cavity FSS", IEEE transactions on antennas and propagation, vol.55. NO.1. January 2007.

[11] T. Koleck, H. Diez, J. C. Bolomey , "Techniques for analyzing finite Frequency Selective Surfaces", 10th International Conference on Antennas and Propagation, Conference Publication No. 436,IEE 1997.

[12] Hirsch, H. and Grove, Practical Simulation of Radar Antennas and Radomes. Artech House, 1988.

[13] A. A. Abdelaziz 'A Novel Technique for Improving the Performance of Salisbury Screen,' Progress In Electromagnetics Research Letters, Vol. 1, 1–8, 2008.

[14] C.R. Simovski et al., "Homogenization of Planar Bianisotropic Arrays on the dielectric interface", Electromagnetics, 22: p. 177-189, 2002.

[15] D. R. Smith "Electromagnetic parameter retrieval from inhomogeneous metamaterials", PHYSICAL REVIEW E 71, 036617 2005.

# Agile Radiation Pattern Control of Metamaterial Microstrip antenna

**D. Bensafieddine[1*], S. Attachi[1], S. M. Chaker[1], M. Laamari[1], and M. Bouzouad[1],**

[1,2,3,4,5]Telecommunications, Signal and Systems Laboratory, BP 37G, Route de Ghardaïa, 03000, Laghouat, Algeria
* corresponding author: d.bensafieddine@lagh-univ.dz

## Abstract

*We are interested in this work, with the antenna radiation pattern agility. The aim is to control the radiation pattern using an agile metamaterial lens. This latter is based on an agile metamaterial. For this purpose we design an agile metamaterial unit cell which can flips between two different behaviors. The first one corresponds to an effective medium with a refractive index close to zero and the second one corresponds to an effective medium having a refractive index greater than unity. This agile lens is used to enhance a microstrip antenna gain and control its radiation pattern. The maximum realized gain obtained is up to 12 dB. The radiation pattern main lobe can be rotated from -47° to 47° in the E-plane and from -33° to 33° in the H-plane. We obtain also a main lobe beamwidth of 32° in the E-plane and 46° in the H-plane.*

## 1. Introduction

Among the most important metamaterial applications in the antenna field we can cite the antenna performances enhancement and size reduction [1][2]. However, antenna characteristics control remains a major objective of metamaterial use in the antenna field. The goal of this work is to control and steer the radiation pattern of a microstrip patch antennas using an agile metamaterial lens. The agile metamaterial lens is by two grides, each constituted by two regions: the first one forms the lens body and the second one a focusing zone (FZ), the characteristics of which it is possible to change using an external control system. This metamaterial lens is,then, placed on the top of a microstrip antenna at a distance *h* from the patch. There are two key factors to be optimized to obtain a better antenna gain and more radiation pattern steering. These are the focusing zone size $a_z$, and the grids spacing in the z-axis direction (the heights $h_1$ and $h_2$).

## 2. Agile and programmable metamaterial

We design an agile planar metamaterial which can be controlled by an external command system. Our agile elementary unit cell, sketched in figure 1, is made of disconnected cross-like conducting strips of width *w* and metallization thickness *t* = 0.035 mm, printed on a dielectric substrate of permittivity $\varepsilon_r = 2.2$ and of thickness *d*. The ends of the disconnected cross type conductor are all interrupted with a small gap g as shown in figure 1-(b) and (c). The branches of a disconnected cross type conductor of each unit cell can be joined to its four neighbors by four switches (PIN diodes, MEMs, etc.). According to switch states (ON or OFF), the unit cell has two different commutable behaviors. The first one corresponds to the disconnected cross type metamaterial (switch OFF) and behaves like an effective medium with a refraction index $n_1$ higher than unity. The second one corresponds to the connected cross type metamaterial (switch ON) and has a positive and close to zero refraction index $n_2$. The actionable behavior of our unit cell allows us to introduce the metamaterial agility.

The agile metamaterial elementary motifs are periodicaly arranged with a period *a* in both *x*- and *y*-diretions. The antenna operating frequency is 40 GHz, hence the corresponding wavelength in free space is 7.5 mm. To respect the homogenization conditions, the greatest dimension of the unit cell must be much lower than the operating wavelength. So, we fixed the period metamaterial period to a = 1 mm.

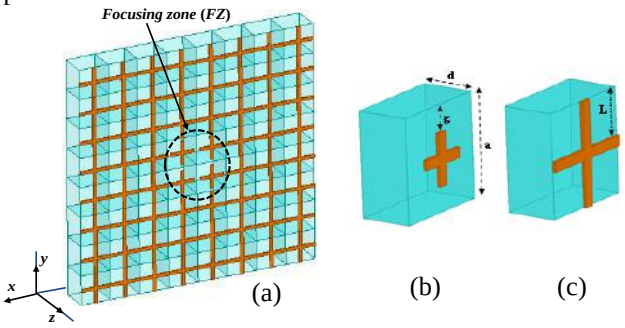



*Figure 1: Agile metamaterial elementary cell: (a) Agile lens grid, (b) disconnected cross, (c ) connected cross.*

We use the programmable metamaterial to design the grids of the agile lens as shown in figure 1-(a). These grids are made up of two regions; the first one forms a focusing zone (FZ) and the second one, the lens body (host medium). The refraction index ( $n_1$ or $n_2$ ), the size, shape and position of the FZ can be programmed by acting on the switching devices (state ON or OFF). Modifying the FZ parameters (size, shape, position, and refraction index), allows us to control the antenna radiation pattern properties, main lobe direction (pointing angle) and beam-width in both E- and H-planes.

The conducting strip width *w*, the gap size *g* and many other factors, such as the metallization thickness *t*, the substrate permittivity $\varepsilon_r$ and thickness *d*, directly govern the agile metamaterial electromagnetic properties.

## 3. Agile metamaterial characterization

We fixed the substrate thickness at $d$ = 0.914 mm to ensure a plasma frequency of 43 GHz, which is within our antenna operating frequency range.

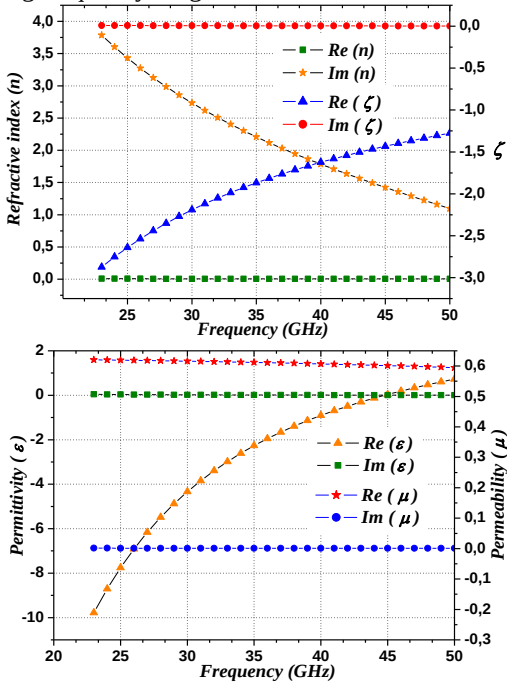



*Figure 2: Electromagnetic properties of connected cross type metamaterials.*

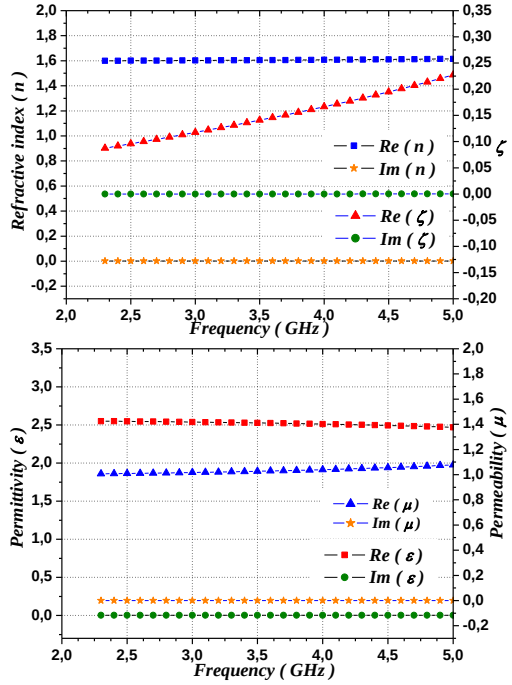



*Figure 3: Electromagnetic properties of disconnected cross type metamaterials.*

The simulation results of the magnetoelectric coupling coefficient $\zeta$ , permittivity $\varepsilon_{reff}$ , permeability $\mu_{reff}$ , and refractive index $n$, for the connected cross type metamaterial are shown in figure 2. It can be seen that the real part of the refractive index $n$ is positive and close to zero in the operating frequency range (40-45 GHz). Note that the metamaterials present a plasma frequency equal or a little less than 43 GHz. The imaginary parts of the constitutive parameters are positive in concordance with the Lorentz dispersion model and the uniqueness theorem for passive media [1], [3] and [4]. They account for losses in the effective medium.

The simulation results of the electromagnetic properties of the disconnected cross type metamaterials are shown in figure 3. It can be seen also that the imaginary part of the permittivity is rather small for the connected cross type metamaterial compared with that of the disconnected cross type.

The maximum value of the refractive index is about 1.69 over the operating frequency range (40-50 GHz).

## 4. Double Layer Superstrate (DLS) Metamaterial Lens.

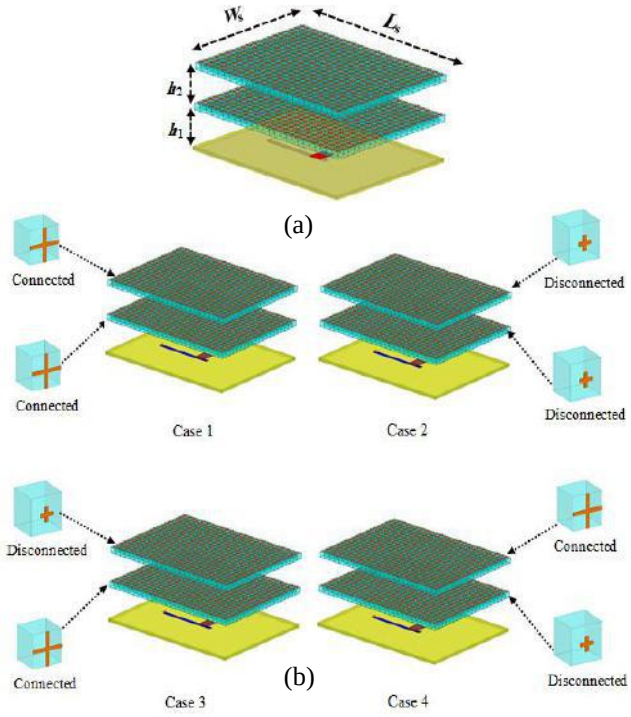



*Figure 4: (a)-Patch antenna with double layer metamaterial lens (Ls=2.5cm, Ws=2cm), (b)-Different possible combinations of the metamaterial lens.*

We have already use a metamaterial double layer superstrate (DLS) to enhance a microstrip antenna gain and directivity [5][6][7]. The metamaterial layer superstrate is composed of a periodic arrangement of cross type unit cells and behaves as a near zero refractive index medium (NZIM). The NZIM based superstrate focuses the radiated waves in the direction normal to the superstrate and thereby enhances the antenna gain and directivity. Based on these results we will design a double layer superstrate agile metamaterial lens using the agile cross type unit cell. The perspective view of the proposed antenna with the double

layer superstrate is shown in figure 4. The spacing from the patch to the bottom of the first layer of the superstrate is $h_1$ and from the top of the first layer to the bottom of the second layer is $h_2$. These two parameters ($h_1$ and $h_2$) have to be optimized to get the best antenna gain and directivity. In this study we seek after the better combinations of metamaterials type constituting lens body. Table 1 and figure 4, summarizes the different possible combinations of materials for forming the lens body.

The simulation results of all possible combinations for different values of $h_1$ and $h_2$ are shown in table 1. It can be seen that the best antenna gain is obtained using the lens with a first layer based on a connected cross type metamaterial and a second layer based on a disconnected cross type metamaterial, which correspond to the case 3. From a parametric study we obtain the the following spacing parameters $h_1$ = 2 mm and $h_2$ = 1.6 mm. The return loss $S_{11}$ of the antenna with and without metamaterial superstrate (the four cases cited in table 1) are shown in figure 5.

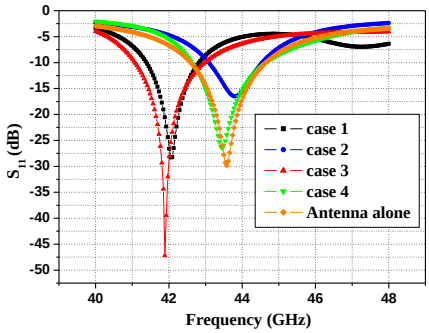



*Figure 5: Return loss (S11), for the conventional patch antenna and the metamaterial DLS patch antenna.*

*Table 1: Characteristics of the antenna with DLS lens for the four possible combinations and for different values of h1 and h2*

| $h_1$ (mm) | $h_2$ (mm) | Realized gain (dB) | $\theta_{-3dB}$ E-plane | $\varphi_{-3dB}$ H-plane | $B$ (%) | cases |
|---|---|---|---|---|---|---|
| 1.7 | 0.8 | 11.73 | 32.35 | 63.24 | 3.16 | Case 1 |
| 2.4 | 2.4 | 6.004 | 49.19 | 70.35 | 3.05 | Case 2 |
| 2 | 1.6 | 13.57 | 29.09 | 37.94 | 4.42 | Case 3 |
| 2.4 | 2.2 | 10.11 | 39.22 | 63.25 | 4.6 | Case 4 |

It is observed from figure 5, that the resonance frequency of the antenna is slightly shifted to lower frequencies (about 3 %) when it is loaded with the metamaterial DLS corresponding to the cases 1 and 3 (Table 1), in other words, when the superstrate first layer is mad of connected cross type metamaterial. Note that for case 2 and 4, when the superstrate first layer is mad of disconnected cross type metamaterial, there is no shift in the antenna resonance frequency. Indeed, in these cases the wave power reflected by the first layer is less than 20 % and the transmitted power is greater than 80 %. Almost all the incident EM waves are transmitted by the metamaterial layer. So, this later do not constitute with the antenna ground plane a Fabri-Peirrot resonant cavity, as does the first layer, mad of connected cross type metamaterial, in cases 1 and 3, where the reflected power is greater than 70 % and the transmitted power is less than 30 %. In these cases the first metamaterial layer constitutes with antenna ground plane a Fabry-Pierrot resonant cavity which influence the overall structure resonance frequency.

The radiation pattern, in the E and H plane, of the proposed antenna for the case 1 and case 3 are shown in figure 6. It is clear from the plots that the antenna is more directional with a DLS corresponding to case 3. The maximum realized gain obtained is 13.57 dB. The main lobe beam-width in both E and H plane are 29.09 º and 37.94º, respectively.

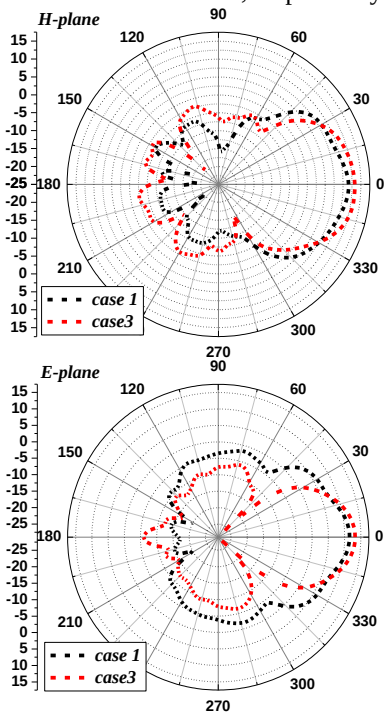



*Figure 6: Radiation pattern of MPA loaded with MDLS for cases 1 and 3(Table 1).*

## 5. Focusing zone influences for the Antenna with Metamaterial DLS

To investigate the control of the radiation pattern, we will in a first step, search for the optimal size of the focusing zone when it is placed on the middle position $P_0$ (see figure 7), for each case cited in table 1. The optimal dimension of the focusing zone $a_Z$, is that for which the antenna realized gain is maximum. In a second step, we explore how the positions of the focusing zone impact the radiation pattern. We have done many simulations to get the optimum focusing zone characteristics.

We have tried all possible metamaterial (connected cross type and disconnected cross type) combinations for the focusing zones and grids body constituting the agile metamaterial lens. The best obtained results correspond to the case 1 and are presented in table 2 and figure 8, where both focusing zones are based on disconnected cross type metamaterial. These results correspond to focusing zones placed in the center position $P_0$.

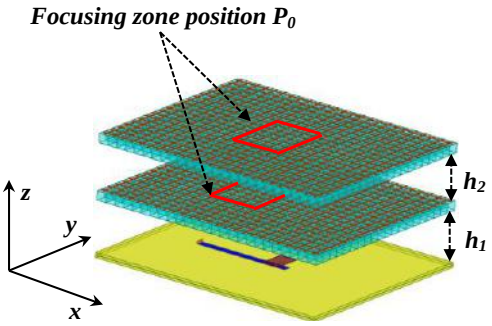



*Figure 7: Focusing zone in the position P0.*

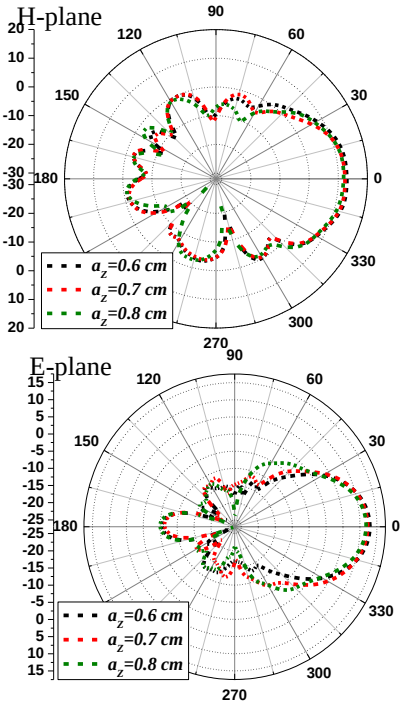



*Figure 8: Radiation patterns of metamaterial patch antenna for different values of FZ size $a_Z$.*

*Table 2: Focusing zone size optimization for the case 1 for h1 = 1.7 mm, h2 = 0.8 mm*

| $a_z$ (cm) | Realized gain (dB) | $\theta_{-3dB}$ | $\varphi_{-3dB}$ |
|---|---|---|---|
| 0.2 | 9.43 | 33.23 | 46.8 |
| 0.3 | 8.94 | 36.68 | 50.61 |
| 0.4 | 10.10 | 36.74 | 54.39 |
| 0.5 | 9.74 | 37.94 | 46.8 |
| 0.6 | 12.90 | 32.18 | 46.53 |
| 0.7 | 12.38 | 38 | 31.9 |
| 0.8 | 11.34 | 35.41 | 36.74 |

From table 2, it can be seen that the maximum realized gain is 12.90 dB obtained for $a_Z$ = 0.6 cm and grids spacing $h_1$ = 1.7 mm, and $h_2$ = 0.8 mm. The radiation pattern half-power beamwidth, at the operating frequency, in E and H-plane respectively, are observed to be 66.5º and 80.1º for the antenna alone, 32.35º and 63.24º for the antenna with a double layer superstrate, and 32.18º and 46.53º for the antenna with a double layer substrate in the presence of focusing zones, as shown in table 2. The half power beam width reduction is about 21.72 %, with DLS in the H-plan and 48.64 %, in the E-plane, while it is about 60 % in the case of a DLS loaded with FZs in both H-and E-plane.
The peak value of the realized gain is 12.90 dB for the DLS in presence of the FZs.

## 6. Radiation pattern control

Once the size of the focusing zone is determined, we will see the effect of the focusing zone positions on the radiation pattern. The extreme positions which confers the maximum control are: three positions (*P1*, *P5* and *P7*) in the right of the central position (*P0*), three positions (*P2*, *P6* and *P8*) in the left of *P0*, three positions (*P3*, *P5* and *P6*) in the direction of positive x (forward), and three positions (*P4*, *P7* and *P8*) in the in the direction of negative x (backward) as shown in Figure 9.
It is observed from table 3, that the main beam direction remains at 0° in the position *P0*, and is rotated from +46° to -46°, in the E-plane, if the focusing zones is moved from position *P1* to *P2*, as illustrated also in Figure 10.
Similarly, the beam direction is rotated from +30 and -30, in H-plane, if the focusing zones is moved from positions *P3* to *P4*. The main beam is rotated by +38° and -38° in E-plane and +32°, -32° in H plane for the positions *P5* and *P8*, respectively, and by +38° and -38° in E-plane and +32°, -32° in H plane for the positions *P6* and *P7*, respectively.
The focusing zone acts on the radiation pattern E-plane when it moved from *P1*, to *P2* passing by *P0* and on the H-plane when it moved from *P3*, to *P4* passing by P0. While it acts on both E- and H-planes when it moved from position *P6* to *P7*, and from *P5* to *P8*.

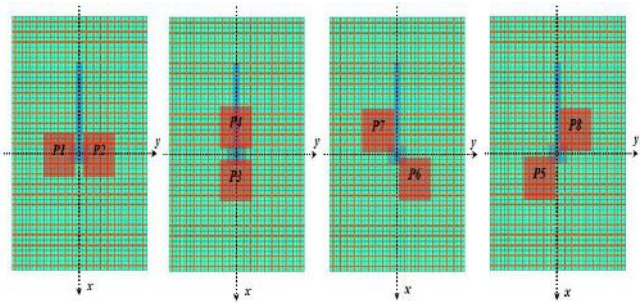



*Figure 9: Focusing zone positions (top View).*

We can also note that the FZ in *P5* rotates the main beam pattern by -38.54° in E-plane and by 32.25° in H-plane, while it rotates by 38.17° in E-plane and -32.11° in H-plane if it is positioned in P8. Note that the radiation pattern main-lobe, in the H-plane, is rotated toward the positive direction and have the same amplitude when FZ is in positions P5 and P6. On the contrary, always for H-plane, the main lobe is rotated toward the negative direction if the FZ is positioned in P7 and P8, as shown in Figure 9. Similarly, from the same figure we observe that the radiation pattern main-lobe, in the E-plane, are rotated toward the positive direction and have the same amplitude, when FZ is in positions P6 and P8, and it is rotated toward the negative direction if the FZ is positioned in P5 and P7.

*Table 3: Radiation Patter steering by focusing zone positioning.*

| | FZ Position | | E-plane | H-plane | |
|---|---|---|---|---|---|
| | $x_p$ (cm) | $y_p$ (cm) | $\theta_{max}$ | $\varphi_{max}$ | Realized gain (dB) |
| Position $P_0$ | 0 | 0 | 0 | 0 | 12.90 |
| Position $P_1$ | 0 | -0.3 | -46.71 | 0 | 9.42 |
| Position $P_2$ | 0 | 0.3 | 46.22 | 0 | 9.37 |
| Position $P_3$ | 0.3 | 0 | 0 | 30.75 | 11.79 |
| Position $P_4$ | -0.3 | 0 | 0 | -30.74 | 11.95 |
| Position $P_5$ | 0.3 | -0.3 | -38.54 | 32.25 | 9.19 |
| Position $P_6$ | 0.3 | 0.3 | 38.53 | 32.26 | 9.21 |
| Position $P_7$ | -0.3 | -0.3 | -38.53 | -32.03 | 9.11 |
| Position $P_8$ | -0.3 | 0.3 | 38.17 | -32.11 | 9.12 |

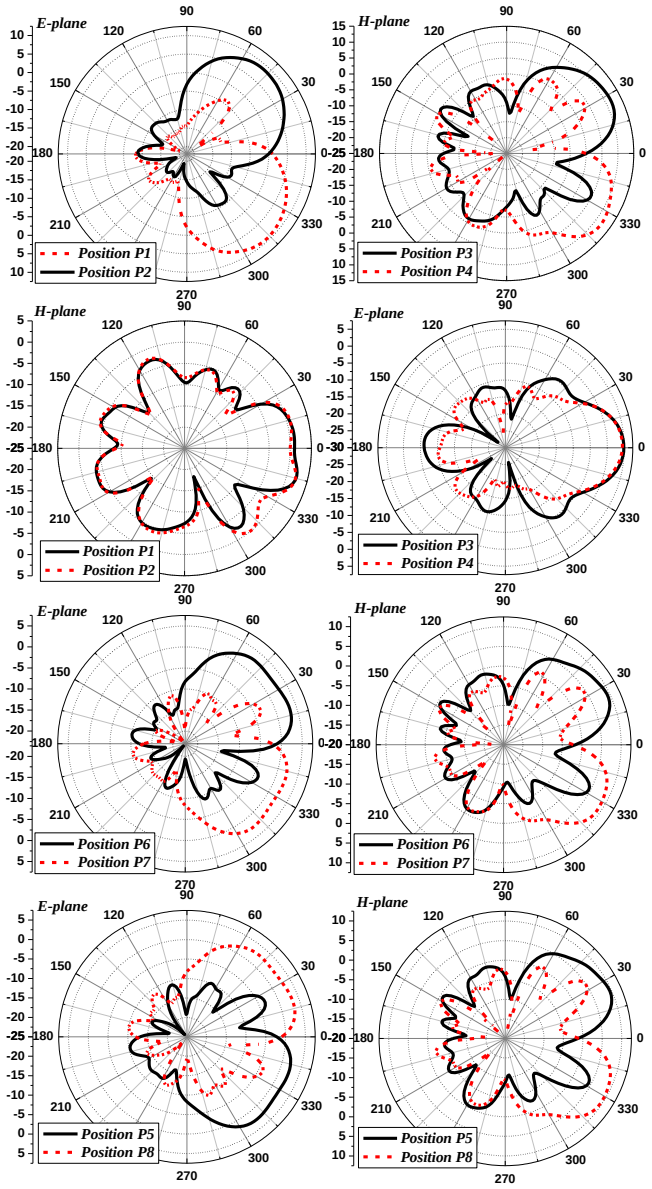



*Figure 10: Radiation pattern steering for different positions of FZ.*

## 7. Conclusions

We have demonstrated the possibility of steer and control the antenna radiation pattern by modifying the focusing zone parameters. The obtained results show that the maximum realized gain obtained is 12.9 dB. The half power beam width in E and H planes, respectively are about 47º and 32°.The main lobe can be rotated by about 47º, in both side of the central direction, in E-plane and 32º, in both side of the central direction, in H-plane.

## References


[1] F. Bilotti and L. Sevgi, "Metamaterials: definitions, properties, applications, and FDTD based modeling and simulation (invited paper)," Int. J. RF Microw. CAE 22, 422–438 (2012).

[2] C. A. Balanis, Advanced Engineering Electromagnetics second edition (Wiley,2012).

[3] G. Lubkowski, B. Bandlow, R. Schuhmann, and T. Weiland, "Effective modeling ofdouble negative metamaterial macrostructures," IEEE Trans. Microw. Theory Tech. 57,1136–1146 (2009).

[4] C. A. Balanis, "Advanced Engineering Electromagnetics," Wiley, 1989.

[5] S.M. Chaker M. Bouzouad "Metamaterial patch antenna radiation pattern agility"Appl Phys ADOI 10.1007/s00339-013-8037-0 (5 October 2013).

[6] M. Bouzouad, SM Chaker, D.Bensafielddine, E. M. Laamari , "Gain enhancement with near-zero-index metamaterial superstrate, " Applied Physics A Materials Science & Processing, 121 (3), 1075-1080 (2015).

[7] SM Chaker, D.Bensafielddine, E. M. Laamari, M. Bouzouad, "A Zero-Index Metamaterial Single Layer Superstrate for Patch Antenna Gain Enhancement," Acta Physica Polonica, A. 128 (2015).

# EM absorption reduction of wireless mobile antenna using printed paper based metamaterial

**Touhidul Alam[1], Mohammad Tariqul Islam[1], Salehin Kibria[1], and Mohammad Rashed Iqbal Faruque[2]**

[1]Dept. Of Electrical, Electronic and Systems Engineering, Universiti Kebangsaan Malaysia, Malaysia
[2]Space Science Centre (ANGKASA), Universiti Kebangsaan Malaysia, Malaysia
*corresponding author, E-mail: tuhid13@siswa.ukm.edu.my

## Abstract

This paper presents a negative index metamaterial printed for electromagnetic (EM) absorption reduction of portable wireless antenna. The perceptible novelty exhibited in this paper is that EM absorption reduction towards the human head with paper based metamaterial attachment. This research has been performed using human head phantom integrated in the commercially available CST Microwave Studio software package. The EM absorption has been reduced by13.2% and 6% at 900MHz and 1800MHz, respectively.

## 1. Introduction

In recent years, an extensive research on the human health risk caused by hazardous electromagnetic fields is in progress. The EM radiation exposed from wireless devices can be evaluated by measuring the SAR in a human-head phantom. The specific absorption rate (SAR) is a measure of the amount of EM power absorbed by the biological tissue whilst using wireless devices.

RF radiation exposure from mobile phones are expressed in terms of SAR, whether a mobile phone complies with the safety guidelines. At present, to international recognized institutions [1,2] have developed EM exposure guidelines for users and manufacturers. These guidelines are based on a detailed assessment of the available scientific evidence. One of them is ICNIRP and another one is IEEE. ICNIRP recommends the local SAR limit in the head is 2 W/kg averaged over any 10g mass of tissues in the head. Moreover, 4W/Kg of SAR value may raise the fraction of a degree Celsius temperature in the human head tissues. IEEE SAR guidelines published for wireless devices is 1.6 watts per kilogram (1.6 W/kg) over any 1g mass of human tissues.

Lots of work is going on to find out the different ways to reduce radiation toward human biological till today. Several techniques have been developed, some show effective results and some fail to achieve proper success. The easiest way to reduce SAR is increasing the distance between the head and antenna structures. But there is limitation of this method due to gigantic demands of ultra thin mobile technology.

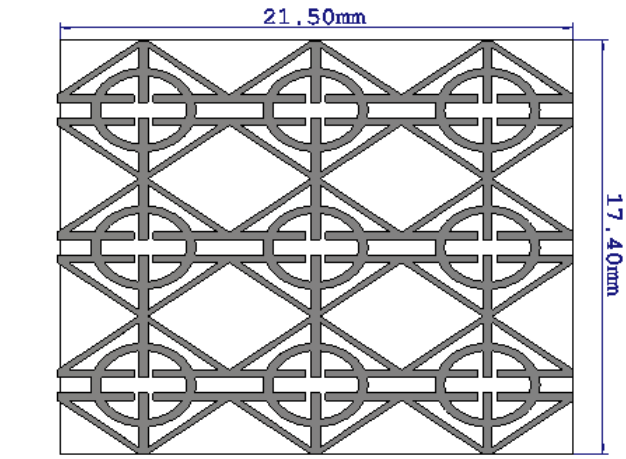
Following the recent advent of artificial metamaterials, there has been much interest in EM absorption reduction [3-6]. The metamaterial structure interacts with electromagnetic waves and shows some special properties, such as frequency pass bands, stop bands. In [3], the SRRs were used to reduce the SAR value in a lossy material. The metamaterials are designed on a circuit board so that it may be easily integrated with the cellular phone. Moreover, metamaterial groundplane has been ued to reduce SAR values of the antenna in [4], but it needs more space to itegratedin inside the mobile phone.

In this paper, a paper based metamaterial structure is proposed. The main attractive feature of this work is the used of thin paper based metamaterial for EM absorption without degrading antenna performances.

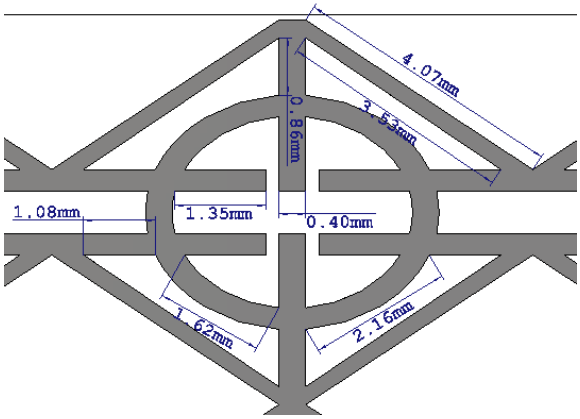
## 2. Metamaterial design and characterization

The proposed paper based metamaterial structure has been designed and analyzed using widely used electromagnetic simulator CST Microwave Studio based on Finite Integration Technique (FIT). The metamaterial structure is depicted in Figure 1. The metamaterial array is fabricated on oil impregnated paper having dielectric constant of 3.87 and thickness of 0.177mm. The dimension of the 3×3 array size of the proposed metamaterial is 21.5×17.40×0.177 $mm^3$.

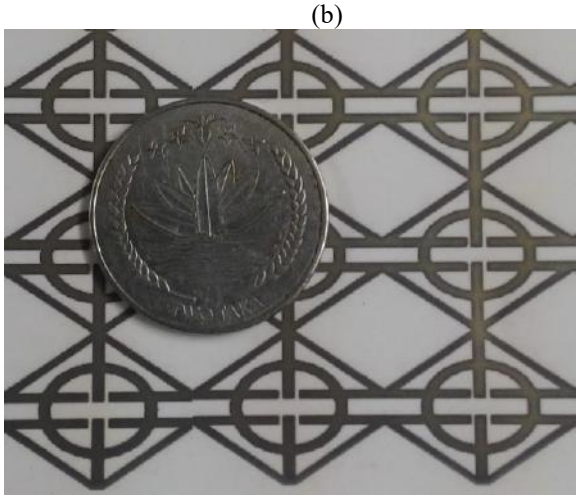
The metamaterial simulation has been performed according to [6] and the constitutive parameters of the metamaterial retrieved from scattering parameters equation in [7]. The permittivity and permeability of the metamaterial is illustrated in Figure 2. It is shown from Figure 2 that the retrieved negative permittivity regions of the structure are found 1.93–1.955 GHz and 3.89–6.72 GHz.




(a)

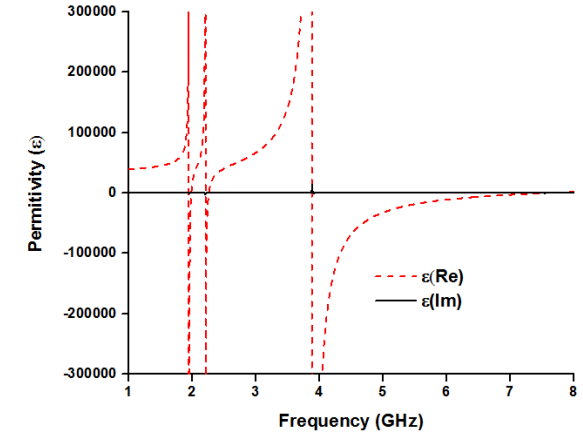



(b)

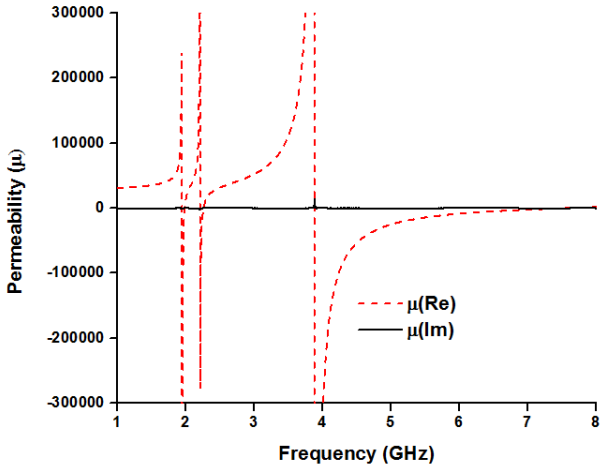


(c)

Figure 1: (a) proposed 3×3 metamaterial array- simulated design, (b) Unit cell configuration and (c) fabricated prototype




(a)




(b)

Figure 2: (a). Calculated permittivity of the proposed metamaterial and (b) calculated permeability of the proposed metamaterial structure

## 3. Specific absorption rate (SAR) analysis

In this work, the commercially available CST Microwave Studio software package including human head phantom has been adopted.The reference power of the wireless device is set to 500mW. The SAM head phantom consists of head equivalent liquid (εr = 40, σ =1.4) and shell (εr = 5, tangent delta = 0.05).

Moreover, a complete handset model, consists of a circuit board, keypad, LCD display, battery and housing has been used with SAM phantom. The relative conductivity and permittivity of the distinct components are set to comply with the industrial standards. The paper based metamaterial has been placed inside the mobile phone, shown in Figure 3. The complete SAR simulation setup is shown in Figure 4.

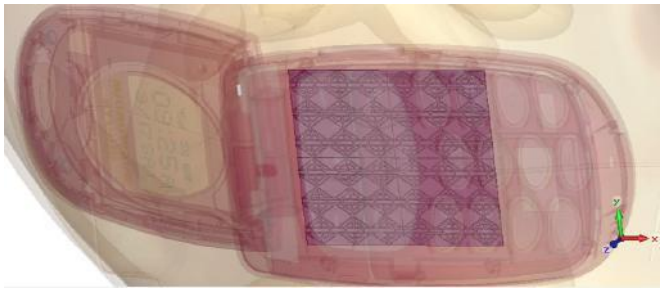


Figure 3: Metamaterial placement in the mobile phone

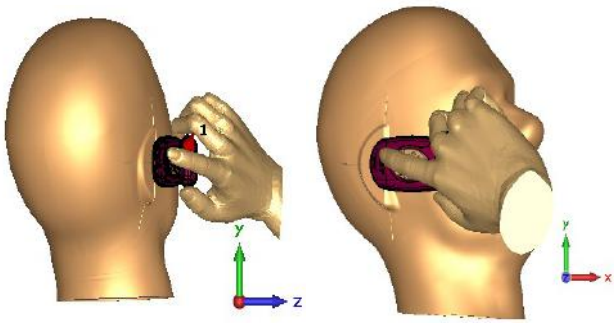


Figure 4: Complete model of SAR simulation head and hand - mobile phone model

The SAR value has been analyzed using CST built in head and hand - mobile phone model. Initially, the simulation was conducted without placing paper based metamaterial at 900 MHz and 1800 MHz, shown in Figure 5. It is observed from Figure 5 that peak SAR values shown 0.636W/Kg and 0.74 W/Kg at 900 MHz and 1800 MHz, respectively. After that, paper based metamaterial has been placed inside mobile handset and re-simulate the SAR values. The achieved SAR results with metamaterial is presented in Figure 6. Figure 6 illustrated that the SAR values at 900 MHz and 1800 MHz are found 0.552 W/Kg and 0.695W/kg, respectively. The SAR values of both with and without metamaterial attachment is listed in Table 1.

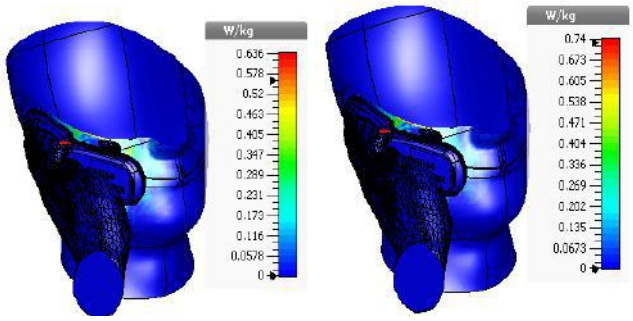



Figure 5: Simulated 1 g SAR values without metamaterial attachment (a) at 900 MHz and (b) at 1800 MHz

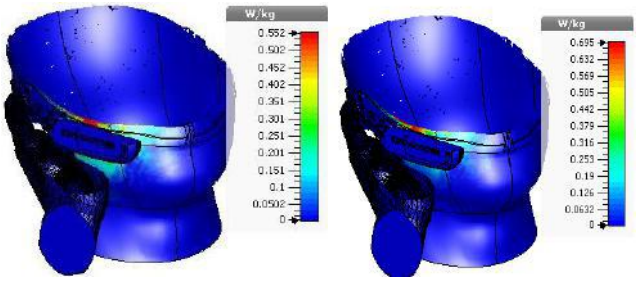



Figure 6: Simulated 1 g SAR values with metamaterial attachment (a) at 900 MHz and (b) at 1800 MHz

Table 1: comparison of SAR analysis

| Type | Frequency (MHz) | SAR values (W/Kg) | Rate |
|---|---|---|---|
| Without maetamaterial | 900 | 0.636 | 100 |
| | 1800 | 0.74 | 100 |
| With maetamaterial | 900 | 0.552 | 86.79245 |
| | 1800 | 0.695 | 93.91892 |

## 4. Conclusions

The proposed metamaterial structure exhibits an EM absorption reduction without degrading antenna performance. Therefore, by using proposed printed metamaterial the human body can be sheltered from the hazardous effects of the electromagnetic field.

## Acknowledgements

This work was supported by the Ministry of Education (MOE), Malaysia, under Grant No. FRGSTOPDOWN/2014/TK03/UKM/01/1.

## References

[1] ICNIRP guidelines for limiting exposure to time - varying electric, magnetic and electromagnetic fields (up to 300 GHZ) Health Physics 74(4): 494 - 522.

[2] IEEE standard for safety levels with respect to human exposure to radio frequency electromagnetic fields, 3 kHz to 300 GHz, IEEE Std C95.1 Ed.: Institute of Electrical and Electonics Engineers, Incorporated, 2005..

[3] Hwang, Jiunn-Nan, and Fu-Chiarng Chen. , “Reduction of the peak SAR in the human head with metamaterials,” Antennas and Propagation, IEEE Transactions on, Vol.54, No. 12, 3763-3770, 2006

[4] Alam, T., Mohammad Rashed Iqbal Faruque, and Mohammad Tariqul Islam. "Specific absorption rate reduction of multi-standard mobile antenna with double-negative metamaterial." Electronics Letters 51.13, 970-971, 2015.

[5] Faruque, M.R.I., Islam, M.T. and Misran, N., “Electromagnetic (EM) absorption reduction in a muscle cube with metamaterial attachment,” Medical engineering & physics, Vol. 33, No. 5, 646-652, 2011.

[6] Alam, Touhidul, Mohammad Rashed Iqbal Faruque, and Mohammad Tariqul Islam. "Specific absorption rate analysis of broadband mobile antenna with negative index metamaterial." Applied Physics A 122.3 , 1-6, 2016.
[7] Shi, Yan, et al. "An improved NRW method to extract electromagnetic parameters of metamaterials." Microwave and Optical Technology Letters 58.3, 647-652, 2016.

**Metasurfaces and optical antennas**

# Coherent control of the optical absorption and fluorescence enhancement in a plasmonic lattice coupled to a luminescent layer

**Giuseppe Pirruccio[1,2*], Mohammad Ramezani[2,3,4], Said Rahimzadeh-Kalaleh Rodriguez[2,5] and Jaime Gomez Rivas[2,3,4]**

*1- Instituto de Fisica, Universidad Nacional Autonoma de Mexico, Mexico D.F. 01000, Mexico.*
*2- Center for Nanophotonics, FOM Institute AMOLF, c/o Philips Research Laboratories, High Tech Campus 4, 5656 AE Eindhoven, The Netherlands*
*3- Dutch Institute for Fundamental Energy Research (DIFFER), De Zaale 20, 5612 AJ, Eindhoven, The Netherlands.*
*4- Department of Applied Physics, Eindhoven University of Technology, 5600 MB, Eindhoven, The Netherlands.*
*5- Laboratoire de Photonique et de Nanostructures, LPN/CNRS, France.*

*Corresponding author: pirruccio@fisica.unam.mx*

**Abstract:** We experimentally demonstrate the coherent control, i.e. the phase controlled enhancement and suppression, of the absorption, optical losses and fluorescence enhancement in an array of plasmonic particles covered by luminescent layer.

Optical loss and absorption associated with metallic structures have been one of the long-lasting drawbacks of plasmonic materials and is considered as a major obstacle for various applications spanning from solid state lighting to solar cells.

In this work, we have used an array of aluminium nanoparticles covered with 200 nm layer of polymer (polystyrene) doped with fluorescent organic molecules [1]. In Fig.1 (a), the schematic representation of the investigated sample is shown. Our array supports localized surface plasmon resonances (LSPRs) as well as a collective surface lattice resonance (SLR) that are weakly coupled to the molecules. We experimentally demonstrate the coherent control of the absorption and the modulation of the emission from the ensemble of molecules through phase-dependent enhancement or suppression of the electromagnetic field.

For the coherent control experiment, we have used a Mach-Zender interferometer comprising two coherent, collinear and counter-propagating laser beams illuminating the sample at normal incidence with equal intensities. The relative phase is controlled by changing the optical path length of one beam with respect to the other. A schematic drawing of the interferometer is shown in Fig. 1 (b). In order to probe the response of the system with respect to the relative phase of the incident beams, we have measured the modulation of the photoluminescence intensity emitted by the sample at 14 degrees from the surface normal, which reaches a value as high as 50%.

Using this set-up enables us to coherently control the symmetry of the excitation field at the position of the dye layer. This leads to efficient control of the resonant excitation based on the match between the symmetry of the incident field in the dye layer and the symmetry of the field scattered off the nanoparticles. Spatial redistribution of the electric field intensity in the near-field for different phases implies a change in the relative absorption in the polymer layer and the metallic particles. Spatial distribution of the electric field intensity is shown in Fig.1 (c-d) when the structure is illuminated with two counter propagating beams with relative phase difference of 0° and 180°.

We have calculated the absorption ratio $\frac{A_{dye}}{A_{tot}}$ for different relative phases, where $A_{dye}$ is the absorption in the polymer layer and $A_{tot}$ is the absorption in the polymer layer along with the absorption in the metal. The absorption ratio is increased to 90% for coherently controlled excitation while, in the case of single beam excitation, the absorption ratio is 63%. The significantly higher absorption ratio for the two-waves illumination is the result of reduced pump enhancement by the nanostructure. Creating a condition where the absorption in the plasmonic particles can be controlled and efficiently suppressed solves one of the major barriers in the field of plasmonics and opens up a new degree of freedom to control the unwanted dissipations in the metals.

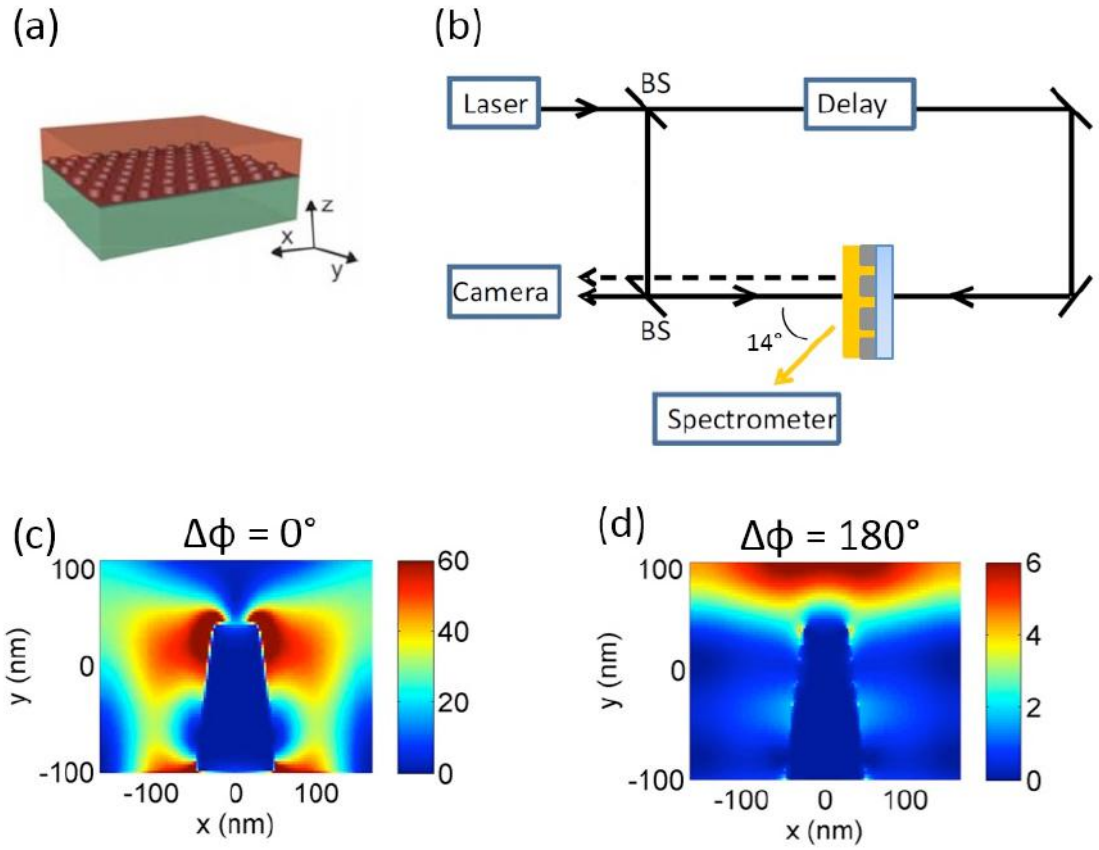



Figure 1. (a) Schematic representation of the investigated structure. The fluorescent molecules are embedded in the 200 nm layer of polystyrene. (b) Drawing of the Mach-Zender interferometer used for coherent excitation of the array. (c,d) Spatial distribution of the electric field intensity when the structure is illuminated with two counter propagating beams with relative phase of 0° and 180°.

**Acknowledgements.** This work was supported by the Netherlands Foundation Fundamenteel Onderzoek der Materie (FOM) and the Nederlandse Organisatie voor Wetenschappelijk Onderzoek (NWO), and is part of an industrial partnership program between Philips and FOM.

**Reference**

[1] G. Pirruccio, M. Ramezani, S. R. K. Rodriguez and J. Gomez Rivas “Coherent control of the optical absorption in a plasmonic lattice coupled to a luminescent layer”, accepted for publication in Phys. Rev. Lett.

Manuscript available at: arXiv:1601.04611.

# Single metasurface for hybrid function realization

**Dandan Wen[1], Shumei Chen[2], Fuyong Yue[1], Kinlong Chan[2], Ming Chen[1, 3], Marcus Ardron[4], King Fai Li[2], Polis Wing HanWong[5], KokWai Cheah[2], Edwin Yue Bun Pun[5, 6],Guixin Li[7], Shuang Zhang[7], Xianzhong Chen[1]***

1. SUPA, Institute of Photonics and Quantum Sciences, School of Engineering and Physical Sciences, Heriot-Watt University, Edinburgh, EH14 4AS, UK
2. Department of Physics, Hong Kong Baptist University, Hong Kong
3. Guangxi Experiment Center of Information Science, Guilin 541004, China
4. Renishaw PLC, Research Avenue North, Riccarton, Edinburgh EH14 4AP, UK
5. Department of Electronic Engineering, City University of Hong Kong, 83 Tat Chee Avenue, Hong Kong.
6. State Key Laboratory of Millimeter Waves, City University of Hong Kong, 83 Tat Chee Avenue, Hong Kong
7. School of Physics & Astronomy, University of Birmingham, Birmingham, B15 2TT, UK

*corresponding author: x.chen@hw.ac.uk

**Abstract**-Traditional polarization-selective optical elements are mainly based on birefringence, which is realized by using the well-designed structure of each phase pixel. However, further reduction of the pixel size and improvement of the phase levels are hindered by the complicated fabrication process. We present and demonstrate an approach to realize a metasurface device that possesses two distinct functionalities. The designed metasurface device has been experimentally demonstrated to function as either a lens or a hologram, depending on the helicity of the incident light.

As one of the important multifunction optical elements, polarization selective optical elements (PSOE) can achieve multiple functionalities according to the polarization status of the incident beam, which have been applied in optical encryption, image processing and so on. Benefiting from the easy fabrication and the flexible control of the light propagation, metasurfaces have provided new opportunities to realize virtually flat optics [1][2][3][4]. We experimentally proposed and demonstrated a novel method to realize a metasurface device that possesses two distinct functionalities [5]. The realization of each functionality depends on the helicity of the incident light. As shown in Fig. 1, the metasurface device acts as a hologram when the polarization state of the incident light is left circular polarization (LCP), while the same device will turn into a convex lens when the polarization state is changed to right circular polarization (RCP). To realize this novel inter-changeable functionality, a phase-only hologram for the target image of 'cat' is firstly generated. Then by encoding the phase function of $\Phi(x,y) = -\frac{2\pi}{\lambda}(\sqrt{x^2+y^2+f^2} - f)$ onto the metasurface, a convex lens with the focal length *f* is created for the incident/detected combination of RCP/LCP. Finally, the two sets of data are merged together with a displacement vector.

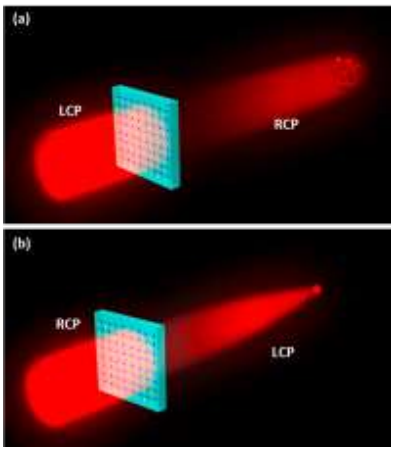



Figure 1 Schematic to show the polarization selectivity of the metasurface device. The metasurface functions as (a) a hologram to reconstruct an image of 'cat' or (b) a lens that converge the incident light into the focal point, depending on the incident/detected light combination.

Benefiting from arbitrary phase control and uniform scattering amplitude from different nanorods, the metasurface device may pave the way of creating more compact, broadband and versatile optical components for integrated optics. This type of metasurface device opens a new avenue to achieve a high density of functionality along the vertical direction, effectively scaling down the size of photonic systems.

**REFERENCES**

1. Yue, N.and Federico, C., "Flat optics with designer metasurfaces," *Nature materials*, Vol. 13, No. 2, 139–150, 2014.
2. Chen X, Huang L, Muhlenbernd H, and Zhang S, "Dual-polarity plasmonic metalens for visible light," *Nature communications*, Vol. 13, No.3,1198, 2012.
3. Lin, Dianmin, Fan, P., and Hasman, E., "Dielectric gradient metasurface optical elements," *Science*, Vol.345, No.6194, 298-302, 2014.
4. Huang, L., Chen, X., Mühlenbernd, H.,and Zhang, S.,. "Dispersionless phase discontinuities for controlling light propagation," *Nano letters*, Vol.12, No.11, 5750-5755, 2012.
5. Wen D, Chen S, Yue F, Chan K, Chen M, Ardron M, Li KF, Wong PW, Cheah KW, Pun EY, Li G., "Metasurface Device with Helicity‐Dependent Functionality," *Advanced Optical Materials*. 2015 Nov 1.

# Tunable Metasurfaces in Control of Beam Steering and Surface State Resonance with Liquid Crystals

**Kuo-Ping Chen[1*], Mong-Yin Lin[1], Shi-Cheng Ye[1], Mao-Guo Sun[1], and Chi-Yin Yang[1]**

[1]Institute of Imaging and Biomedical Photonic, National Chiao-Tung University, 301 Gaofa 3rd Rd., Tainan 711, Taiwan

[*]corresponding author: kpchen@nctu.edu.tw

**Abstract**- Metasurfaces got immense attention because of the ability controlling the flow of light. The tunability of metasurfaces system could be realized by combining with liquid crystals. In this work, several novel devices, including diffraction control of binary gratings metasurfaces, and tunable optical Tamm state resonance would be presented.

Planar photonics, like metasurfaces and nanoantennas, got immense attention because of the ability controlling the phase, polarization, and rotation of light. The tunability of metasurfaces system could be realized by combining with liquid crystals. In this work, several novel devices, like tunable nanoantennas arrays with color, diffraction control of binary gratings metasurfaces, and optical Tamm states would be presented. First, by changing different dimensions of nanoantennas, the anchoring energy of liquid crystal could be adjusted in nanoscale. The different shapes of nanoantennas show the difference in color or monotone change when applying different voltages. Second, the diffraction ratio of metasurface could be controlled by nematic liquid crystal by controlling the polarization direction by applying voltages. Third, optical Tamm states could be realized and adjustable by combining liquid photonic crystal with metasurface. All of those ideas are realized in both modeling and experimental, which could give a great impact to the field of future application in tunable metasurfaces.

Figure 1 shows the diagram of tunable metasurface system with liquid crystal. By controlling the voltage which applies to the liquid crystal, the intensity of anomalous diffraction could be control. In addition, by combining metasurfaces with photonic liquid crystal, optical tamm state could be excited at the boundary that the localized electric field is observed. The position of the resonance dip could be possibility controlled by temperature or voltages.

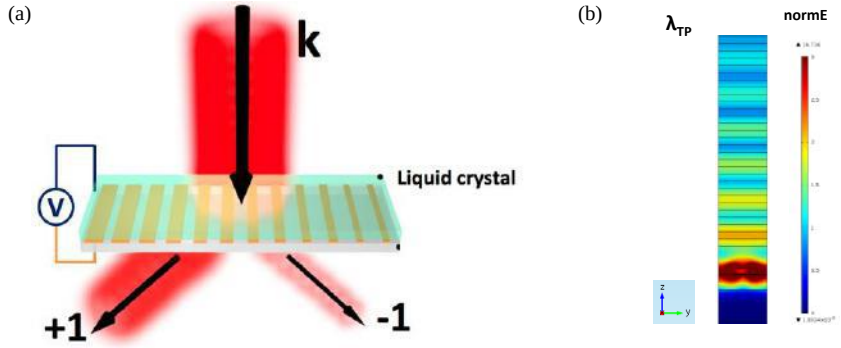



Fig. 1 (a) Metasurface with liquid crystals. (b) Strong localized electric fields distribution of tunable optical Tamm states of metasurface and liquid crystal.

**Acknowledgements**, This work is supported by MOST 104-2221-E-009-130-MY3. The authors would like to thank Dr. Shie-Chang Jeng's and Prof. Wei Lee's support of liquid crystals.

**REFERENCES**

1. Kildishev, Alexander V., Alexandra Boltasseva, and Vladimir M. Shalaev. "Planar photonics with metasurfaces." Science 339, no. 6125 (2013): 1232009.
2. Sasin, M. E., R. P. Seisyan, M. A. Kalitteevski, S. Brand, R. A. Abram, J. M. Chamberlain, A. Yu Egorov, A. P. Vasil'Ev, V. S. Mikhrin, and A. V. Kavokin. "Tamm plasmon polaritons: Slow and spatially compact light." Applied Physics Letters 92, no. 25 (2008): 251112.
3. Auguié, Baptiste, María Cecilia Fuertes, Paula C. Angelomé, Nicolás López Abdala, Galo JAA Soler Illia, and Alejandro Fainstein. "Tamm plasmon resonance in mesoporous multilayers: toward a sensing application." ACS Photonics 1, no. 9 (2014): 775-780.
4. Chang, Che-Yuan, Yi-Hsun Chen, Yu-Lin Tsai, Hao-Chung Kuo, and Kuo-Ping Chen. "Tunability and Optimization of Coupling Efficiency in Tamm Plasmon Modes." Selected Topics in Quantum Electronics, IEEE Journal of 21, no. 4 (2015): 262-267.

# Observation of magneto-optic terahertz effects in a hybrid graphene-embedding metasurface

**S. Zanotto**[1*] **, C. Lange**[2]**, T. Maag**[2]**, A. Pitanti**[3]**, V. Miseikis**[4]**, C. Coletti**[4]**, R. Degl'Innocenti**[5]**, L. Baldacci**[6]**, R. Huber**[2]**, and A. Tredicucci**[7]

[1]Istituto Nazionale di Ottica – CNR, and LENS, Via Nello Carrara 1, 50019 Sesto Fiorentino (FI), Italy

[2]Department of Physics, University of Regensburg, 93040 Regensburg, Germany

[3]NEST, Istituto Nanoscienze – CNR and Scuola Normale Superiore, Piazza San Silvestro 12, 56127 Pisa (Italy)

[4]CNI@NEST, Istituto Italiano di Tecnologia, P.za S. Silvestro 12, 56127 Pisa, Italy

[5]Cavendish Laboratory, University of Cambridge, J. J. Thomson Avenue, Cambridge CB3 0HE, United Kingdom

[6]Scuola Superiore Sant'Anna, Institute of Life Sciences, P.za Martiri della Libertà 33, 56127 Pisa, Italy

[6]NEST, Istituto Nanoscienze-CNR and Dipartimento di Fisica "E. Fermi", Università di Pisa, L.go Pontecorvo 3, 56127 Pisa, Italy

*corresponding author: simone.zanotto@ino.it

**Abstract**- By placing a material in close vicinity of a resonant optical element, its intrinsic optical response can be widely tuned. Here we show that a graphene monolayer in close vicinity to a split ring resonator metasurface, exhibits a magneto-optical response which is strongly influenced by the presence of the metasurface itself. This hybrid system holds promises in view of thin optical elements working in the terahertz spectral range; moreover, it could be chosen as the playground for investigating the cavity electrodynamics of Dirac fermions in the quantum regime.

Among the photonic resonant structures which find applications in the terahertz spectral range, split-ring resonators are one of the most widespread due to their flexibility and ease of fabrication [1-3]. They have proven to be a versatile tool for tailoring the far- and near-field response of surfaces; in addition, proper combinations of the inductive and capacitive elements used in split-ring resonators allow for extremely low mode volumes. Nevertheless, hybrid graphene-split ring resonator metasurfaces have not yet been studied in great detail for what concerns the magneto-optic response. Here we present experimental and numerical results on such a structure, where the magnetic-field induced modification of the Drude-like response of Dirac fermions gives rise to resonant transmission modulation of up to 10%. We believe our concept holds promises, thanks to the tunability of the split ring resonator metasurface, in view of magneto-optic applications like non-reciprocal terahertz photonic devices, and for implementing frontier experiments aimed at investigating the cavity quantum electrodynamics of graphene cyclotron transitions [4].

We investigated the structure sketched in Fig. 1 (a). It consists of a gallium arsenide substrate, patterned with an array of metallic split ring resonators (SRRs). On this surface we deposited a thin $SiO_2$ spacer, and, finally, a graphene film. The sample transmission is measured by time-domain spectroscopy, while the sample was mounted in a cryostat holding it at liquid helium temperature. By tuning the magnetic field acting on the sample, the transmittance is modulated, with a pronounced effect in correspondence to the resonance frequency of the

metasurface. This effect increases almost linearly with the applied field: as it can be observed from Fig. 1 (b), a transmittance modulation contrast of about 10% has been measured, at the frequency of 0.9 THz. Support to the experimental data is provided by a numerical simulation (performed through finite element modeling), where the sole element having a response to the magnetic field was the graphene layer.

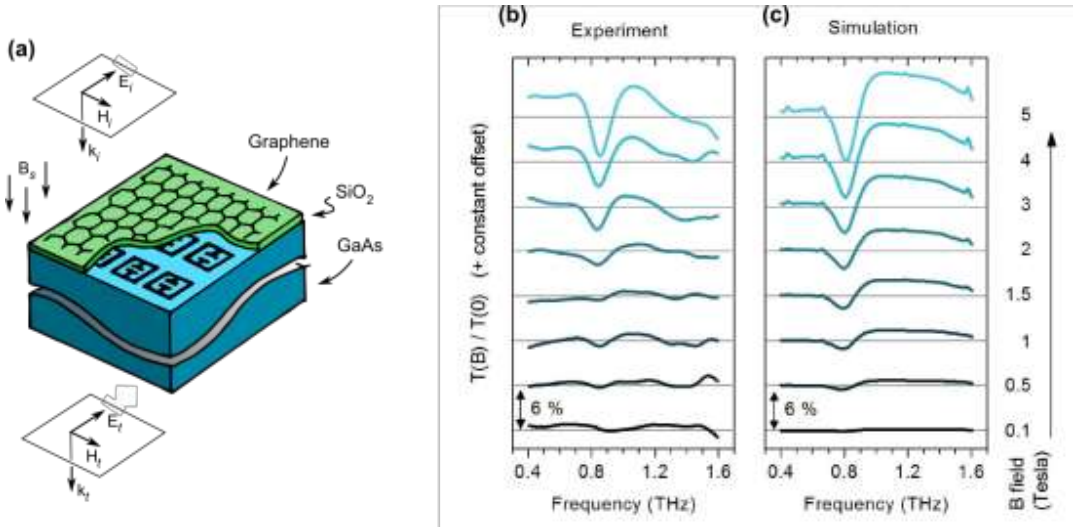



**Fig. 1.** Panel (a): schematic of the sample under investigation. Panels (b-c): experimental and simulated transmittance modulation driven by a magnetic field acting perpendicularly to the sample surface. A dip is observed at 0.9 THz, which is the resonance frequency of the hybrid graphene-split ring resonator metasurface.

It can be hence concluded that a transmittance modulation clearly induced by the presence of graphene, placed in close vicinity to a resonant metasurface, has been observed. The present device can be considered as a prototype which opens the way towards more complex and functional components, such as polarization rotators and nonreciprocal optical elements. Furthermore, the present concept could prove fruitful in view of frontiers experiments aiming at the observation of cavity quantum electrodynamics of magnetically biased graphene.

## REFERENCES


1. D. Shurig, J. J. Mock, and D. R. Smith, *"Electric-field coupled resonators for negative permittivity metamaterials"*, Appl. Phys. Lett. **88**, 041109 (2006).
2. H.-T. Chen, W. J. Padilla, J. M. O. Zide, A. C. Gossard, A. J. Taylor, and R. D. Averitt, *"Active terahertz metamaterial devices"*, Nature **444**, 597 (2006).
3. A. K. Azad, A. J. Taylor, E. Smirnova, and J. F. O'Hara, *"Characterization and analysis of terahertz metamaterials based on rectangular split-ring resonators"*, Appl. Phys. Lett. **92**, 011119 (2008).
4. D. Hagenmuller and C. Ciuti, Phys. Rev. Lett. **109**, 267403 (2012).

# Full cloaks based on metasurfaces

**Hongchen Chu[1], Jie Luo[1], Yun Lai[1]***

[1] College of Physics, Optoelectronics and Energy & Collaborative Innovation Center of Suzhou Nano Science and Technology, Soochow University, Suzhou 215006, China

*corresponding author: laiyun@suda.edu.cn

**Abstract**- We propose two full cloaking schemes by using an ultra-thin cloaking shell consisting of metasurfaces and other thin optical device, such as zero-index material and antireflection layer. The metasurface is designed to manipulate the incident waves and radiation waves, so as to avoid the total reflection and to restore the propagating wave front. Full-wave simulation shows good cloaking effects for cloaks of almost arbitrary shapes. Our design provides a feasible approach for the cloaking of large areas with ultra-thin shells.

Since the concept of cloaking was proposed under the guideline of transformation optics [1], tremendous efforts have been devoted to achieving this intriguing effect. Typical invisibility cloaks are made of cloaking shells composed of gradient media with anisotropic parameters, which can bend and guide the incident light around the cloaked area, rendering invisibility. Since seminal theoretical proposals, the cloaking effects have been experimentally demonstrated at frequencies from microwave to optical regime. However, despite the previous inspiring achievements, there are still some major obstacles in the practical application of the cloaking technology. One primary concern is the bandwidth limit, which was recently shown to be solvable by a design of ray optics cloaks. Another major obstacle is the large area/volume of the cloaking shells, usually comparable to the cloaked area/space. The original cloaking schemes fail to meet the requirement of making an ultra-thin cloaking shell for large cloaked space in practice. Very recently, metasurfaces have been applied to realize mantle cloaking based on scattering cancellation [2] and carpet cloaking [3] based on phase compensation. By applying metasurface to cloaking, the cloaking shell can be enormously reduced in size. However, mantle cloaking cannot cloak large objects (compared to wavelengths) neither and carpet cloaks work only in the reflection geometry. A full space ultra-thin cloak in transmission geometry with large-volume cloaked space is still lacking.

In this study, we propose another unidirectional cloaking scheme by using a combination of metasurface and zero-index medium (ZIM). In this design, the cloaking shell is a two-layered structure. The outer layer is a gradient metasurface and the inner layer is a thin layer of ZIM. Interestingly, this cloaking scheme does not require the cloaking shell to exhibit a complex spatial distribution of parameters. Therefore, the cloaking shell can go ultra-thin, even in the deep sub-wavelength scale. More importantly, when the size of the cloak increases while the shell thickness remains fixed, which also means an increased ratio, the constituents of the cloaking shell remain almost unchanged, free from turning singular as in the original scheme. This new cloaking scheme thus provides a feasible approach for the cloaking of a large area with an ultra-thin cloaking shell. Analogously, we also propose a new scheme of so-called ‘sensor cloak’ [2] by combining metasurfaces and an antireflection layer. The sensor cloak shell composed of two metasurfaces and an antireflection layer sandwiched between them. On the entry side, metasurfaces are utilized to manipulate the wavefront by phase compensation and hence to ensure that the impinging wave is normal incident on the antireflection layer and the transmitted wave from the

antireflection layer regain the initial incident angle. On the exiting side, metasurfaces work in almost the same way as that on the entry side. As shown in Fig1, full-wave simulation results show good cloaking effects for cloaks of almost arbitrary shapes.

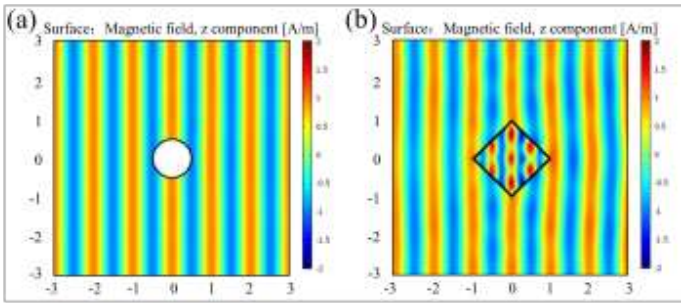



Figure1. Simulation results of the full cloaks based on metasurfaces. (a) Full cloak by combining metasurface and ZIM. (b) Sensor cloak by combining metasurface and antireflection layer.

**Acknowledgements**, This work is supported by the State Key Program for Basic Research of China (No. 2014CB360505, No. 2012CB921501), National Natural Science Foundation of China (No. 11374224, No. 11104169), and a Project Funded by the Priority Academic Program Development of Jiangsu Higher Education Institutions (PAPD).

## REFERENCES

1. Pendry, J. B., Schurig, D. and Smith, D. R., "Controlling electromagnetic fields, "*Science* , Vol. 312, No. 5781, 1780-1782, 2006.
2. Alù, A. and Engheta, N., "Cloaking a Sensor, " *Phys. Rev. Lett.* ,Vol. 102, No. 23, 233901, 2009.
3. Ni, X., Wong, Z. J., Mrejen, M., Wang, Y. and Zhang, X. "An ultrathin invisibility skin cloak for visible light, "*Science* ,Vol. 349 No. 6254, 1310-1314, 2015.

# Broadband polarization conversion in plasmonic metasurfaces with symmetry breaking

**Shengyan Yang[1], Zhe Liu[1], Xiaoxiang Xia[1], Junjie Li[1], and Changzhi Gu[1]***

[1]Beijing National Laboratory for Condensed Matter Physics, Institute of Physics, Chinese Academy of Sciences, Beijing 100190, China

*corresponding author: czgu@iphy.ac.cn

**Abstract**-We propose and demonstrate ultrathin, efficient and broadband single-layer metasurface-based polarization converters in transmission mode at telecommunication wavelengths. Combining with the broadband operation and improved linear polarization conversion efficiency, the metasurface has opened a new avenue for creating ultrathin, broadband, and high performance polarization converters.

Polarization is one of the intrinsic features of electromagnetic waves conveying valuable information in signal transmission and detection. Manipulation of the polarization state represents an important ability for controlling light and enables many practical applications such as photography, liquid crystal displays, fiber communication, optical imaging and sensing. Conventional approaches to control the light polarization states utilizing the birefringence or total internal reflection in crystals and polymers, which were applied in many wave-plates and Glan-Taylor prisms [1], are usually restricted to quite bulky configurations, limited available materials, high loss, specific device thickness and narrow band operation frequency. Obviously, those traditional methods are unsuitable for miniaturization and integration in optical system. Recently, polarization modulation utilizing metamaterials or metasurfaces has achieved considerable developments, and many artificial chiral metamaterials have been proposed to realize polarization manipulation such as three-dimensional chiral structures[2-5], and multilayer metamaterials[6-8].

In this work, we demonstrate ultrathin, broadband, and efficient single-layer metasurface-based polarization converter in transmission mode at telecommunication wavelengths. The metasurface composed of SRR with broken symmetry and rectangular metallic hole. The combination of rectangular metallic holes with extraordinary optical transmission and SRR with broken symmetry exhibits broadband polarization conversion. Figure 1(a) exhibits the schematic of the symmetric and asymmetric metasurface. The simulated cross-polarized transmission spectrum is shown in Fig 1(b). For the symmetric metasurface, extremely weak cross-polarized electric fields are induced. Intriguingly, it can be observed that a strong and broadband cross-polarized component with the highest transmission amplitude of 0.48 for the case of δ= 300 μm in asymmetric metasurface. What's more, the transmission amplitude of the cross-polarized light in the metasurface could be tuned by varying the δ parameter from 0 to 300 μm. The polarization conversion rate (*PCR*), which is defined as $PCR = t_{xy}^2 / (t_{yy}^2 + t_{xy}^2)$, was applied to characterize the optical activity, as shown in Fig.1(c). For the asymmetric metasurface with δ= 200 μm, the *PCR* exceed 60% has a bandwidth of about 101THz. More details will be reported in the paper.

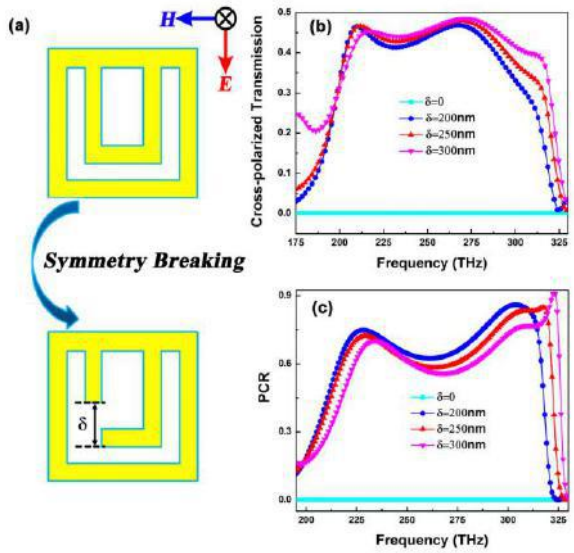



Fig. 1 (a) Symmetric and asymmetric metasurface; (b) the simulated cross-polarized transmission spectra and (c) corresponding polarization conversion rate (*PCR*) with different δ parameter.

**Acknowledgements** This work is supported by the National Natural Science Foundation of China under Grant Nos. 11174362, 91323304, 61390503, 11374358, 11434017 and 61475186; the Knowledge Innovation Project of CAS (Grant No. KJCX2-EW-W02).

**REFERENCES**

1. M. Born , E. Wolf , "Principles of Optics ," Cambridge University Press ,Cambridge, UK 1999 .
2. J. K. Gansel, M. Thiel, M. S. Rill, M. Decker, K. Bade, V. Saile, and M. Wegener, *Science* 325, 1513 (2009).
3. S. Zhang, J. Zhou, Y.- S. Park, J. Rho, R. Singh, S. Nam, A. K. Azad, H.-T. Chen, X. Yin, A. J. Taylor and X. Zhang, "Photoinduced handedness switching in terahertz chiral metamolecules," *Nat. Commun.* 3, 942 (2012)
4. H. S. Park, T.-T. Kim, H.-D. Kim, K. Kim, and B. Min, "Nondispersive optical activity of meshed helical metamaterials," *Nat. Commun.* 5, 5435 (2014).
5. C. Helgert, E. Pshenay-Severin, M. Falkner, C. Menzel, C. Rockstuhl, E.-B. Kley, A. Tunnermann, F. Lederer, and T. Pertsch, "Chiral Metamaterial Composed of Three-Dimensional Plasmonic Nanostructures," *Nano Lett.* 11, 4400-4404 (2011)
6. N. K. Grady, J. E. Heyes, D. R. Chowdhury, Y. Zeng, M. T. Reiten, A. K. Azad, and H.-T. Chen, *Science* 340, 1304 (2013).
7. C.Pfeiffer, C. Zhang, V. Ray, L. J. Guo, and A. Grbic, "High Performance Bianisotropic Metasurfaces: Asymmetric Transmission of Light," *Phys. Rev. Lett.* 113, 023902 (2014)
8. L. Cong, N. Xu, J. Gu, R. Singh, J. Han, and W. Zhang, "Highly flexible broadband terahertz metamaterial quarter-wave plate," *Laser Photonics Rev.* 8, 626-632 (2014)

# Extrinsic orbital Hall effect in cyclic group symmetric metamaterial

**Yeon Ui Lee[1], Igor Ozerov[2], Frederic Bedu[2], Ji Su Kim[1], Frederic Fages[2], and Jeong Weon Wu[1*]**

[1] Department of Physics, Quantum Metamaterial Research Center, Ewha Womans University, Korea

[2] Aix Marseille University, CNRS, CINaM, Campus de Luminy, France

[*]corresponding author: jwwu@ewha.ac.kr

**Abstract**- We designed and fabricated a cyclic group symmetric metamaterial possessing *n*-fold rotation symmetry, composed of plasmonic tapered arc antennas. We show how the far field intensity distribution of vortex beam with orbital angular momentum can be tailored through cyclic group symmetry designs. The extrinsic orbital Hall transverse shifts from metamaterials exhibit geometrical patterns associated with the order *n* of *n*-fold rotation symmetry. We found that the experimentally observed geometrical patterns agree well with those obtained from FDTD theoretical simulation.

Optical spin Hall effect originates from a spin-orbit coupling present in an optical beam following a curvilinear trajectory, and the transverse shift is described by a Lorentz equation of motion in the momentum space, where Berry curvature plays a role of magnetic field provided by a topological monopole. While the optical spin Hall effect is intrinsic in the sense that the trajectory of an optical beam has a spin-dependent shift, the spin being an intrinsic angular momentum, a spin-dependent shift can also be achieved in an optical beam passing through a Pancharatnman-Berry phase-variant optical element (PVOE), resulting from a spin-dependent optical phase acquired through the PB PVOE, which is called an extrinsic spin Hall effect.

Laguerre-Gaussian beam is a vortex beam possessing an orbital angular momentum (OAM), and an optical orbital Hall effect can be observed intrinsically or extrinsically. While an intrinsic orbital Hall effect is rather straightforward in connecting with an intrinsic spin Hall effect, the analogy of an extrinsic orbital Hall effect with an extrinsic spin Hall effect is not simple, since a spin-dependent vortex beam formation in a PB PVOE involves a transfer of spin angular momentum to orbital angular momentum. In other words, an extrinsic orbital Hall effect is described by a spin-rotation coupling where a spin-dependent geometric phase is acquired by an optical beam through a PB PVOE consisting of q-plate-like rotated subwavelength scatterers.[1,2] In fact, plasmonic structures consisting of concentric ring antennas periodically spaced from a center spot have shown extraordinary optical transmission, directionality effect [3], q-plate operation, and creation of OAM by utilizing the spin-orbit coupling in inhomogeneous anisotropic media [4, 5, 6].

In this work, we introduce cyclic group symmetric metamaterials (CGSMs), which leads to a spin-dependent spatial splitting of vortex beam with different signs of OAM in the far field, an example of an extrinsic orbital Hall effect of light. CGSMs possess *n*-fold rotation symmetry and they are composed of plasmonic tapered arc (TA) antennas. For a circularly polarized beam, TA antennas show a helicity-dependent scattering efficiency. Spin-dependent far-field intensity distribution of the vortex beam is attributed to the presence of a chirality of geometric phase and amplitude, which comes from an interaction of circularly polarized light with a chiral structure of CGSMs.

Because TA antennas are arranged in a metamaterial belonging to a cyclic group *n*-fold rotation symmetry, the extrinsic orbital Hall transverse shifts from CGSM exhibit a geometrical pattern with the same symmetry. However, CGSMs with odd and even symmetry orders show a strongly contrasting difference in the character of transverse shifts.

We used electron beam lithography to fabricate 30nm thick gold metamaterials patterned on borosilicate glass substrates. Six types of CGSMs with the symmetry order *n* from 1 to 6 were fabricated and measured. Each CSGM is composed of multiple TA antennas with the width varying from 45nm to 150nm organized in 8**n* azimuthal segments of concentric rings repeated with 600nm radial spacing.

As the light source, we used a single mode fiber pigtailed laser diode at a wavelength of 1300nm. The metasurfaces were illuminated by circularly polarized beams of right (+)/left (-) helicity, and transmitted far-field intensity distributions of left (-)/right (+) helicity were measured by CCD camera. Figure 1 shows such normalized far-field intensity images for CGSMs possessing *n*-fold rotational symmetry. The observed geometrical patterns agree well with those obtained from FDTD theoretical simulation.

In summary, we designed and fabricated cyclic group symmetric metamaterials, anisotropic media showing an extrinsic orbital Hall effect of light associated with the *n*-fold rotation symmetry. We found that the experimentally observations agree well with FDTD theoretical simulation. We believe that this study provides significant advantages for applications in quantum communications, chemical/bio-sensing and understating of spin symmetry breaking properties of metasurface.

**Acknowledgement** This work was supported by National Research Foundation and the Ministry of Science, ICT and Future Planning (2015037609, 2015001948, and 201000453).

**REFERENCES**

1. Li, G., Kang, M., Chen, S., Zhang, S., Pun, E. Y. B., Cheah, K. W., and Li, J., "Spin-enabled plasmonic metasurfaces for manipulating orbital angular momentum of light," *Nano Lett.*, Vol. 13, No. 9, 414, 2013.
2. Li, G., Chen, S., Pholchai, N., Reineke, B., Wong, P. W. H., Pun, E. Y. B., and Zhang, S., "Continuous control of the nonlinearity phase for harmonic generations," *Nat. Mater.*, Vol. 14, No. 6, 607, 2015.
3. Lezec et al., "Beaming light from a subwavelength aperture," *Science* Vol. 297, No. 5582, 820, 2002.
4. Marrucci et al., "Optical spin-to-orbital angular momentum conversion in inhomogeneous anisotropic media," *Phys. Rev. Lett.*, Vol. 96, No. 16, 163905, 2006.
5. Marrucci, L. et al., "Spin-to-orbital conversion of the angular momentum of light and its classical and quantum applications", *J. Opt.*, Vol. 13, No. 6, 064001, 2011.
6. Osorio, Clara I., Abbas Mohtashami, and A. Femius Koenderink., "K-space polarimetry of bullseye plasmon antennas", *Sci. Rep.*, Vol. 5, 9966, 2015.

# Angle-resolved far-field scattering/extinction characteristics of single Ag nanowire

**Jinhyung Kim[1], Ho-Seok Ee[1], Min-Soo Hwang[2], Kwang-Yong Jeong[2], Ju-Hyung Kang[2], Hong-Gyu Park[2], Min-Kyo Seo[1]**

[1]Department of Physics, Korea Advanced Institute of Science and Technology, Deajeon, South Korea

[2]Department of Physics, Korea University, Seoul, South Korea

[*]corresponding author: Jinhyung.kim@kaist.ac.kr

**Abstract**-We directly measured far-field extinction/scattering spectra of a single Ag nanowire over the entire semi-meridian with varying detection angle. The angle-resolved extinction/scattering spectra reveal that the far-field pattern of the nanowire carries two features of the near-field: Fabry-Perot resonances of SPPs propagating along the nanowire and phase-matching conditions between SPPs and free-propagating radiation depending on the emission angle and wavelength.

Scattering properties of a plasmonic nanowire have been investigated through dark-field microscopy[1], back-focal plane imaging[2] and so on. Surface plasmon polaritons (SPPs) supported by the metallic nanowire have a large wavevector and cause strong scattering radiations to the direction of a large angle even beyond the numerical aperture (N.A.) of the microscope objective employed in the conventional methods. To overcome this limitation and obtain the full information of scattering characteristics, we directly measured far-field extinction/scattering spectra of a single Ag nanowire over the entire semi-meridian. SPPs of the nanowire on a coverslip are excited by white-light illumination focused on one end of the nanowire by an objective. The detection part, 0.23 m distant from the nanowire, scans the entire northern semi-meridian with an angular resolution of 2 degrees and collects scattering radiations into an optical fiber attached to a spectrometer. Beyond the N.A. of the focusing objective, purely scattered signal is detected, while, within the N.A., the extinction by the nanowire is observed. The angle-resolved scattering spectra reveal that the far-field scattering pattern of the nanowire carries two features of the near-field: Fabry-Perot resonances of SPPs propagating along the nanowire and phase-matching conditions between SPPs and free-propagating radiation depending on the emission angle and wavelength[3,4]. We believe that the study on the angle-resolved far-field scattering spectra will be useful to understand scattering characteristics of a desired optical nanostructure.

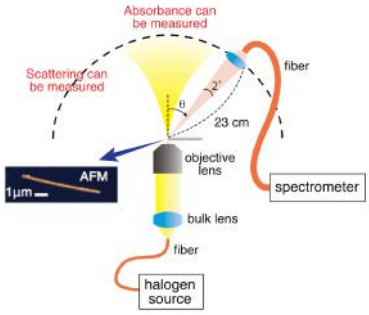



*Figure 1. Experimental setup to measure the angle-resolved far-field spectra.*

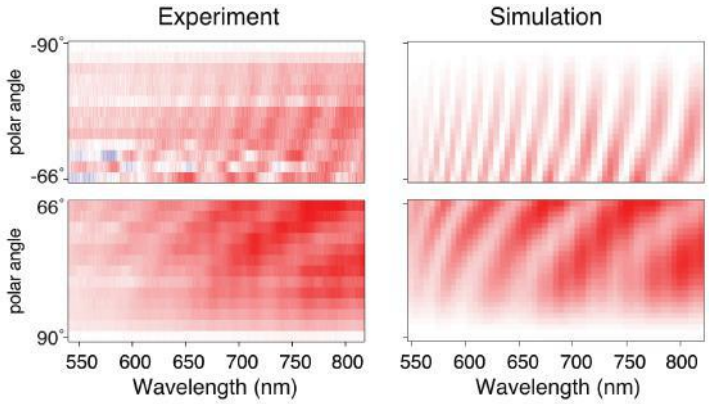



*Figure 2. The angle-resolved far-field scattering measurement and simulation results.*

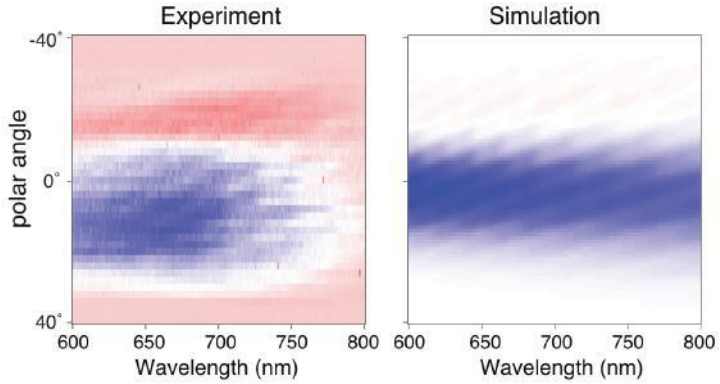



*Figure 3. The angle-resolved far-field extinction measurement and simulation results.*

**REFERENCES**


1. Kang, T. et al., "Rainbow radiating single-crystal Ag nanowire nanoantenna" *Nano Lett*, Vol. 12, 2331, 2012.
2. Curto, A. G. et al., "Multipolar radiation of quantum emitters with nanowire optical antennas," *Nature Commun*, Vol. 4, 1750, 2013.
3. Dorfmüller, J. et al., "Fabry-Pérot Resonances in One-Dimensional Plasmonic Nanostructures," *Nano Lett*, Vol. 9, 2372, 2009.
4. Taminiau, T. H. et al., "Optical nanorod antennas modeled as cavities for dipolar emitters: evolution of sub- and super-radiant modes" Vol. 11, 1020, (2011)

# Reshaping Electromagnetic Emissions with Meta-substrate based on Spoof Plasmons

Y. Gao, A. Maurel, A. Ourir
Institut Langevin,ESPCI ParisTech, CNRS UMR 7587, 1 rue Jussieu, 75005 Paris, France

***Abstract*—We investigate the efficiency of a metasurface supporting spoof plasmons to control the electromagnetic emission of a radiating element. The three dimensional metasurface is made of an array of metallic grounded rods and it is used as the substrate of a printed antenna. Such substrate provides a transmission band at low frequencies, corresponding to spoof plasmon propagation, and a total electromagnetic band gap above the cut-off frequency. We show how an efficient and directive emission with low side lobe levels and backward radiation can be obtained when the operating frequency of the antenna is considered in the band gap. The role of the spoof plasmons is further demonstrated by tuning the transmission band at the operating frequency. The proposed meta- substrate is an original and efficient alternative to reshape the emission of electromagnetic sources.**

***Index Terms*—antennas, metamaterial, electromagnetic band gap, spoof plasmons, reshaping the radiation.**

## I. Introduction

Electromagnetic radiating sources involve planar structures susceptible to support surface waves. These waves, bounded to the interface, propagate and when they reach edges or corners, they diffract in free space. This mechanism is used as the main radiating mechanism in the travelling-wave antennas (or leaky-wave antennas) based on the design of a guiding structure enable to efficiently couples the surface waves with free space. It is in contrast to resonant antennas which use resonances of radiating elements (as monopoles or dipoles). However, even in this case, surface waves are involved but in an undesirable way. Indeed, such antennas are mounted over a larger plane surface (the ground plane), which is susceptible to support surface waves, as surface plasmons for metallic ground plane in the optical frequencies. The antennas are designed considering an infinite ground plane, that is ignoring surface wave radiation. Because of the finite size of the ground plate in the practice, the surface waves are scattered, and thus, interact with the radiation field of the radiating elements. It results in the appearance of undesired ripples and high level side lobes in the radiation pattern, responsible for a decrease in the overall performances of the antenna. To avoid such perturbations, one has to forbid the wave propagation on the ground plane. This means that the surface waves have to be associated to a dispersion relation with frequency ranges where the propagation is forbidden, namely with band gaps.

In 1999, two designs of improved antennas have been proposed [1], [2], where the planar interface of the ground plane is replaced by a periodically structured interface. In the former reference, the structure consists in piercing a square array of air columns in a dielectric substrate. The array being at wavelength scale realizes a photonic crystal type substrate which present a forbidden band gap at the Bragg frequency. In the latter reference [2], the forbidden frequency band is realized using a mushroom-like array being design at a subwavelength scale. The concept of surface impedances is used to characterize the response of the structure, resulting in the so-called high impedance surfaces, associated with forbidden frequencies for the surface waves.

The present paper follows the idea of using the dispersion relation of surface waves to reshape the radiation pattern of printed antennas. In our case, the surface waves bounded at a corrugated metallic interface, usually called spoof plasmons, are considered. Spoof plasmons refer to the waves guided at the corrugated interface of a perfect conductor metal. In the simplest case, the corrugation consists in rectangular grooves, with height $L$ and volume fraction of air $\varphi$. In this case, the dispersion relation of the the spoof plasmons, derived in [3] for acoustic waves and in [4], [5] for electromagnetic waves with transverse magnetic polarization ($H(x,z)$ along $y$, inset of Fig. 1.a) reads

$$k_{\text{SP}} = k\sqrt{1+\varphi^2\tan^2 kL}, \quad \text{for} \quad \tan kL > 0, \qquad (1)$$

where $k_{\text{SP}}$ is the wavevector of the spoof plasmon along $x$ and $k$ the wavenumber in air (or say, the frequency). Note that the restriction to $\tan kL > 0$ is not mentioned in [3], [4], [5] although it is essential to define the band gaps, and it can be obtained by using classical homogenization technique [6], [7]. The wavefield in air is $H(x,z) = H_0 e^{ik_{\text{SP}}x - \alpha z}$, with $k^2 = k_{\text{SP}}^2 - \alpha^2$. The forbidden frequency ranges correspond to negative values of $\tan kL$, leading to the usual first total band gap is for $\pi/2L \leq k \leq \pi/L$ [7]. In the following, we refer to the forbidden frequency range, the corresponding range of frequency $f$ such that $c/4L \leq f \leq c/2L$, with $c = 3.10^8$ m.s$^{-1}$.

In the context of improved antenna, the existence of stop bands is interpreted in terms of high impedance surface (HIS) [2], with the surface impedance being $Z_s = E_x/H$ with our notations. Being the ratio of two conserved quantities, $Z_s$ is notably continuous at the interface $z = 0$ between the corrugated layer and air. Thus, if $Z_s(0^-)$ is known, one can solve the problem only in the air ($z \geq 0$) using the boundary condition at the equivalent surface $z = 0$ (obviously, the difficulty is precisely to find $Z_s$, which requires to solve the problem for $z < 0$). In our two dimensional configurations, $Z_s$

imposes a boundary condition of Robin type $\partial_z H(x=0,z) = i\omega Z_s H(x=0,z)$ (since $\partial_z H = i\omega E_x$ when considering a time dependence $e^{-i\omega t}$). When locking for a surface waves, $H(x,z>0) = H_0 e^{ik_{SP}x-\alpha z}$, we simply get $\alpha = -i\omega Z_s$. This means that surface waves (with $\alpha$ real positive) will be supported for $Z_s$ having a positive imaginary part (inductive impedance). Next if $Z_s$ tends to infinity, $\alpha$ and $k_{SP} = k^2 + \alpha^2$ also tends to infinity, which indeed coincides with the limits of the stop bands in our case, Eq. 1, at $\tan kL \to \pm\infty$.

In the following, we use the concept of plasmon band gap (given by the condition $\tan kL < 0$ in Eq. 1) to design our metamaterial substrate and we demonstrate experimentally and numerically its capability to improve the performances of patch antenna.

## II. Spoof plasmons band gap in a three dimensional metamaterial

Let us start by considering the simplest structure (one dimensional structuration) with rectangular grooves and parameters $\varphi a = 6$ mm and $a$ = 13 mm. Two different groove lengths, $L = 6$ and $L = 15$, mm are considered. The Fig. 1(a) shows the corresponding dispersion relations given by Eq. 1. A band gap is observed in each geometry and can be easily tuned by the groove length. However, for practical realization, it is tempting to go toward a two dimensional structuration, as shown in Fig. 1(b): instead of massive rectangular grooves invariant along $y$, we consider cylindrical rods periodically located along $x$ and $y$ with the same parameters $(a, L)$ and $2R = \varphi a$. Numerical calculations (CST Studio software) have been used to determine the dispersion relation of this structure, and the result is reported in Fig. 1(c). Two different cylinder lengths , $L = 6$ and $L = 15$, mm are considered. As expected, along $\Gamma - X$, the obtained dispersion relation resembles the dispersion relation given by Eq. 1 and presented in Fig 1(a). A full transmission band gap for surface waves is clearly observed for frequency in the range 3.8 - 9.5 GHz for $L = 15$ mm. The band gap for $L = 6$ mm starts at f=8.5 GHz, resulting in a possible tuning of the band structure by adjusting the length of the rods, according to the Eq. 1.

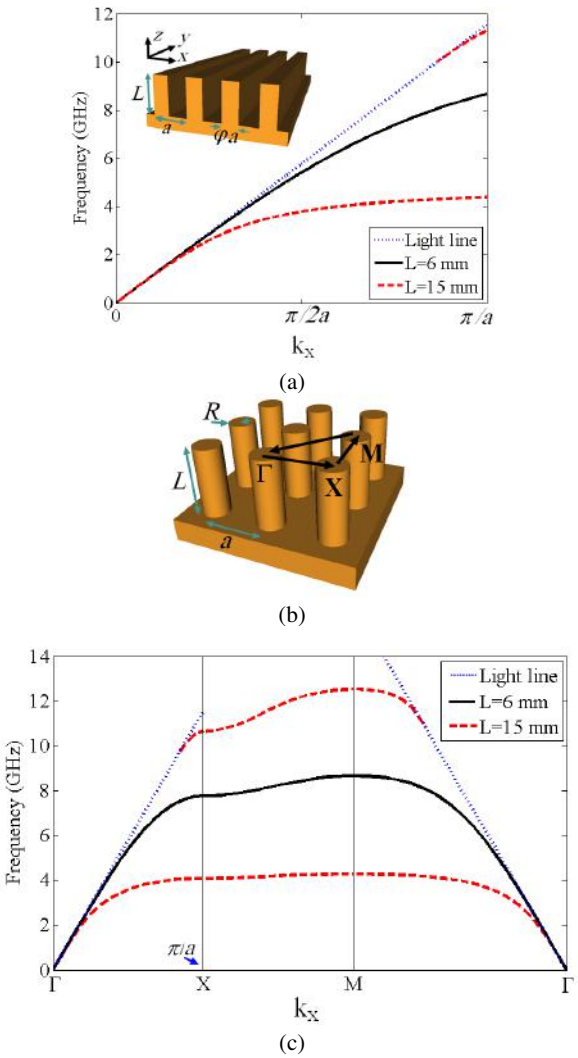



Fig. 1. (a) Schematic view and dispersion diagram of a corrugated surface (factor $\varphi = 0.46$ and $a = 13$ mm) for two different groove lengths. (b) Schematic view of the metamaterial made of an array of grounded rods. (c) Dispersion diagram of the proposed metamaterial calculated for two different cylinder lengths. The light line is plotted as well (dotted line).

## III. Reshaping the radiation pattern

At microwave frequencies, patch antennas are the most commonly radiating sources employed in integrated circuits that play the important role of emitting signals off the chip into free space. As previously said, these patch antennas are placed on a dielectric substrate over a metallic ground plane, which can support surface waves and couples power into substrate modes. The diffraction of these waves at the edges of the substrate affects the antenna efficiency and causes ripples and high level side lobes in the radiation pattern. We will now inspect the ability of our metamaterial substrate to avoid such unpleasant effects by forbidding the surface wave, or plasmon, propagation. We realize a patch antenna resonating around 10 GHz, with an antenna element being fed by a coax line via a hole near the center of the ground plane. The antenna element is then placed in the center of a 6 by 6 cylinder array with $L = 6$ mm, as shown in the Fig. 2(a) (and from Fig. 1(c), we know that this structure provides a band gap that surrounds the resonant frequency of the antenna even after adding the thin layer of the epoxy substrate).

Fig. 2(b) shows the reflection coefficient of the patch antenna for the antenna alone and for the antenna being surrounded by the cylinders; in both cases, a minima of the reflection is obtained around 10 GHz, corresponding to the operating frequency of the antenna (that is the frequency at which the antenna emits efficiently). Thus, the presence of the array does not affect significantly the operating frequency, although a slight red shift is observed. Note also in Fig. 2(b) the resonant frequencies $(f_1, f_2, f_3)$ which are very weak in the present case; additional results on these low frequency resonances are reported in the appendix, where we show that the structure can be optimized to work efficiently at these

frequencies [8], [9], [10].

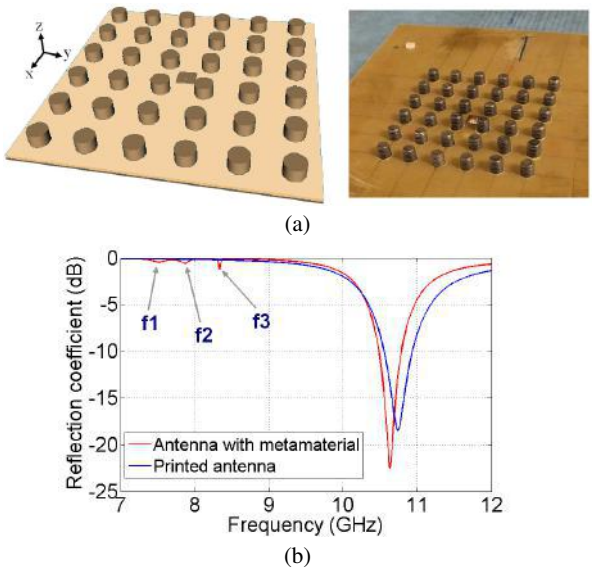



Fig. 2. (a) Schematic view and a photography of the printed antenna surrounded by the metamaterial structure. (b) Reflection coefficients calculated for the antenna with and without the metamaterial.

The radiating patterns have been measured in the E and H planes, and the results are reported in Figs. 3 and 4. A significant enhancement of the directivity of the antenna is achieved thanks to the metamaterial substrate. A reduction of the backward radiation and the side lobe levels, in particular for angles higher than 90 degree, are also obtained in the two planes. An average value of reduction of 10 dB is observed. Moreover, the gain of the antenna is increased of about 2 dB at the operating frequency. This improvement is higher (of about 1 dB) than the one obtained with photonic crystals (PCs) and high impedance surfaces (HISs) when considering similar lateral dimensions.

We end our study by inspecting further the role of the band gap structure in the reported results. This is done by considering now higher cylinders, with $L = 15$ mm, for which the spoof plasmon propagation is possible at the operating frequency of the printed antenna ($f_0 \simeq 10$ GHz, see Fig. 1(c)). The results are reported in Fig. 5. As previously, the operating frequency is not significantly affected by the presence of the array, with a slight red shift (Fig. 5(a)).

Next, the Figs. 5(b) and (c) report the radiation patterns in the E and H planes. These patterns have to be compared with the radiation patterns of the antenna in the absence of the metamaterial, Figs. 3(a) and 4(a). The appearance of high secondary lobes are noticeable in the E plane at $\pm 45$ deg, and this effect is accompanied by a decrease in the main lobe gain, which is found to be lower of about 2 dB when compared to the gain of the antenna alone. Clearly, the directivity of the antenna has not be improved, and this confirms that the efficiency of the antenna previously observed is due to the band structure of the meta- substrate.

In this work, we have realized a meta- substrate made of a finite array of grounded metallic rods realizing a transmission band for surface waves at low frequencies and a total electromagnetic band gap above a specific cut-off frequency. This meta- substrate has been shown to efficiently reshape the radiated field of a printed antenna, and the role of the band structure has been evidenced. Finally, for operating frequency being in the transmission band, one can think to reshape the

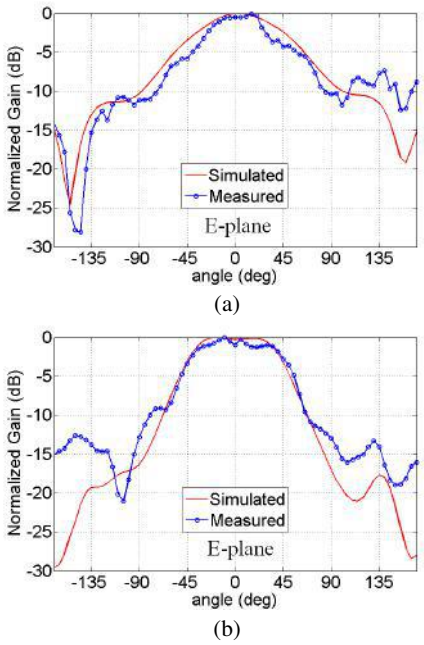



Fig. 3. Measured radiation patterns in the E plane for (a) the antenna alone and (b) the antenna surrounded by the metamaterial surface (numerical results are reported for comparison).

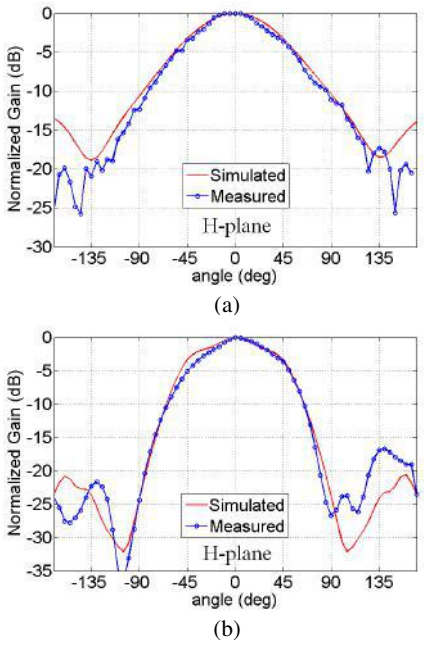



Fig. 4. Same representation than in Fig. 3 for the measurements in the H plane.

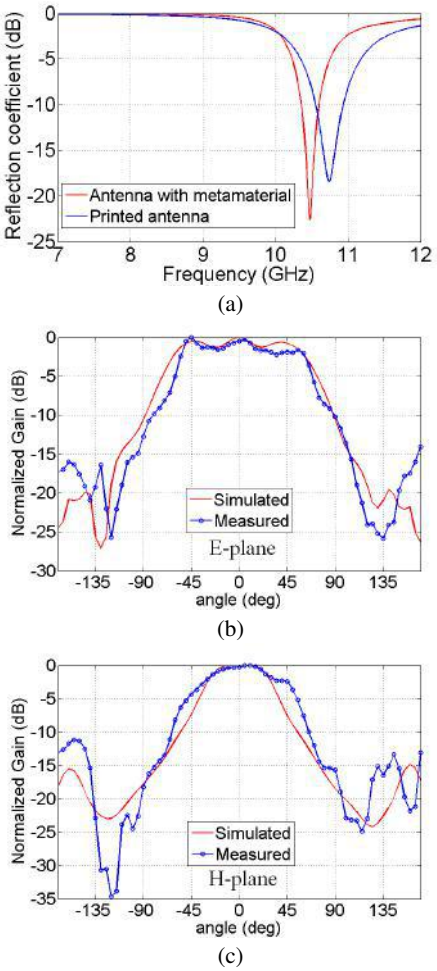



Fig. 5. (a) Reflection coefficients of the antenna in the absence and in the presence of the metamaterial surface. (b) and (c) Radiation patterns of the printed antenna surrounded by the metamaterial measured respectively in the E plane and in the H plane.

radiation pattern in a different way, for instance to realize additional lobes, as observed in our second experiments at -45, 0 and 45 deg.

**Acknowledgement :** This work is supported by LABEX WIFI (Laboratory of Excellence within the French Program "Investments for the Future") under references ANR-10-LABX-24 and ANR-10-IDEX-0001-02 PSL*.

## REFERENCES

[1] R. Gonzalo, P. de Maagt, and M. Sorolla, "Enhanced patch-antenna performance by suppressing surface waves using photonic-bandgap substrates," *Microwave Theory and Techniques, IEEE Transactions on*, vol. 47, pp. 2131–2138, Nov 1999.

[2] D. Sievenpiper, L. Zhang, R. Broas, N. Alexopolous, and E. Yablonovitch, "High-impedance electromagnetic surfaces with a forbidden frequency band," *Microwave Theory and Techniques, IEEE Transactions on*, vol. 47, pp. 2059–2074, Nov 1999.

[3] L. Kelders, J. F. Allard, and W. Lauriks, "Ultrasonic surface waves above rectangular-groove gratings," *Acoustical Society of America Journal*, vol. 103, pp. 2730–2733, May 1998.

[4] J. B. Pendry, L. Martn-Moreno, and F. J. Garcia-Vidal, "Mimicking surface plasmons with structured surfaces," *Science*, vol. 305, no. 5685, pp. 847–848, 2004.

[5] F. J. Garcia-Vidal, L. Martn-Moreno, and J. B. Pendry, "Surfaces with holes in them: new plasmonic metamaterials," *Journal of Optics A: Pure and Applied Optics*, vol. 7, no. 2, p. S97, 2005.

[6] A. Maurel, S. Flix, J.-F. Mercier, and A. Ourir, "Effective birefringence to analyze sound transmission through a layer with subwavelength slits," *Comptes Rendus Mcanique*, vol. 343, no. 12, pp. 612 – 621, 2015. Acoustic metamaterials and phononic crystals.

[7] J.-F. Mercier, M. L. Cordero, S. Félix, A. Ourir, and A. Maurel, "Classical homogenization to analyse the dispersion relations of spoof plasmons with geometrical and compositional effects," *Proceedings of the Royal Society of London A: Mathematical, Physical and Engineering Sciences*, vol. 471, no. 2182, 2015.

[8] F. Lemoult, G. Lerosey, J. de Rosny, and M. Fink, "Resonant metalenses for breaking the diffraction barrier," *Phys. Rev. Lett.*, vol. 104, p. 203901, May 2010.

[9] A. Ourir, G. Lerosey, F. Lemoult, M. Fink, and J. de Rosny, "Far field subwavelength imaging of magnetic patterns," *Applied Physics Letters*, vol. 101, no. 11, p. 111102, 2012.

[10] C. Jouveaud, A. Ourir, and J. Rosny, "Surface waves radiation by finite arrays of magnetoelectric resonators," *Progress In Electromagnetics Research*, vol. 132, pp. 177–198, 2012.

## IV. APPENDIX : ELECTROMAGNETIC RADIATION FROM THE FINITE SIZE METAMATERIAL

In the previous configurations, we have investigated the effect of the array on the radiation pattern at the operating frequency of the antenna. We have actually studied two configurations where this frequency is considered inside and outside the spoof plamsons band gap. Nevertheless, we have not discussed yet all the perceptible effects on the reflection spectrum of the antenna observed in the first configuration. These effects are illustrated in Fig. 2(b) of the main paper. While we have already studied the behavior of the structure at the main resonance, we have not investigated yet the collection of resonant pics observed at the lower frequencies of the reflection spectrum. Here, we propose to focus on this phenomenon.

It appears that such reflection coefficient response has been recently observed in a finite size structure called metalens [8], [9], [10]. This structure consists of a finite size periodic array of sub-wavelength resonators. The formalisms used to study this type of resonant media have shown that the coupling splits the single resonance of the atom, considered in each unit cell, to different modes that show at different frequencies. This hybridization process produces a number of modes that equals at best the number of atoms. However, due to mode overlapping and symmetries, it is not always possible to individually excite each of these modes.

While designed to mimic corrugated surfaces in order to support spoof SPs in three-dimensional configuration, our structure can be considered as a cluster of a resonant grounded rods disposed periodically according to a two-dimensional square lattice. This overview incites to consider this structure as a metalens and predicts the appearance of the collection of resonant modes presented in Fig. 2(b) in the main paper.

In our configuration, we observe that the first branch of the dispersion relation, calculated for the infinite array of the grounded rods, covers the collection of resonant frequencies. At this frequency band, the printed antenna alone is not resonating. The obtained resonances are obtained at low

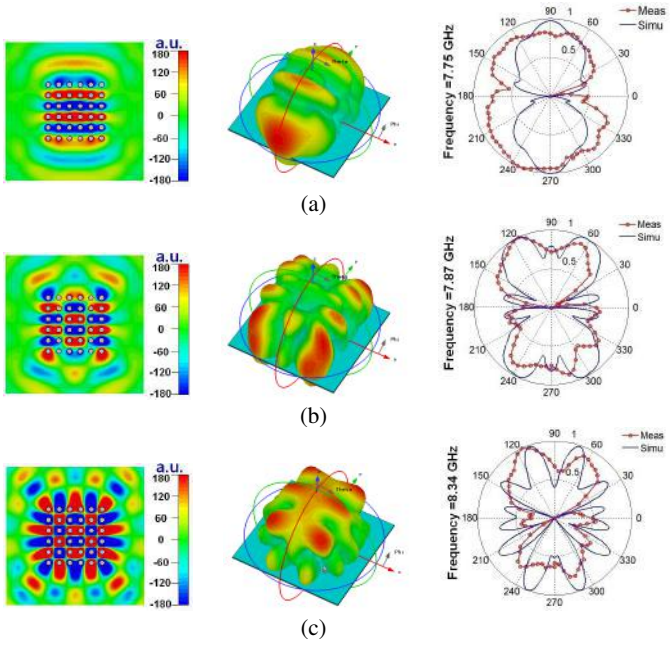



Fig. 6. Electric field distribution (left) and radiation patterns (center for 3D and right for 2D patterns) calculated at the resonant mode frequencies $f_1$ (a), $f_2$ (b) and $f_3$ (c). The frequencies are defined in fig. 2. Measurements are also given for the in-plane 2D patterns.

frequencies by coupling power from the near evanescent field of the (non radiating) antenna to the finite size metamaterial . In order to take a closer look in the near field variations at these resonant frequencies, we have performed numerical simulations. Fig. 6 shows the cartography of the electric field variation above the structure at the three main resonant frequencies. The spatial fluctuations on the near field patterns relates the Fabry-Perot resonant behavior of the structure. These modes can be expressed in terms of the in-plane wavenumber $k_{sp} = \frac{\pi}{a}(m\vec{x} + n\vec{y})$, where $m$ and $n$ are integers inferior or equal receptively to the number of the columns and lines of the considered array and where $a$ is the lattice constant of the array.

These results match the metalens behavior presented hereinabove [10]. Thereby, we expect a far field radiation in the plane of the structure with a specific pattern at each resonant frequency. We have performed calculations and measurements in order to characterize the radiation patterns. Fig. 6 shows the obtained results at the three main considered frequencies. We can notice that each pattern expresses the fluctuation observed in the corresponding near field resonant mode.

The resonant modes obtained here by hybridization do not present resonances with high magnitude because the coupling of the structure to the main source (patch antenna) has not been optimized here to that aim. In fig. 7, we present the spectrum obtained with a configuration where such coupling is amplified. In such configuration, efficient radiation at each resonance and a wide diversity of radiation patterns can be obtained. This structure can be used as an original and efficient solution to reshape the radiation pattern for specific configurations.

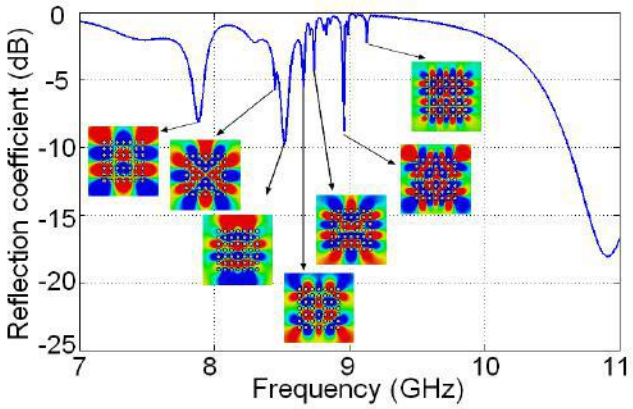



Fig. 7. Radiation Pattern and Magnetic Field Distribution on plane

# Orthogonally polarised modes sharing a single metasurface for dual-pol antennas

**A. Tellechea[1*], F. Caminita [2,3], E. Martini[2,3], I. Ederra[1], J.C. Iriarte[1], R. Gonzalo[1] and S. Maci[2]**

[1] Dept. of Electrical and Electronic Engineering, Public University of Navarra Campus Arrosadía, 31005 Pamplona, Spain

[2] Dept. of Information Engineering and Mathematics, University of Siena, 53100 Siena, Italy

[3] Wave Up Srl, 50126 Firenze, Italy

[*]amagoia.tellechea@unavarra.es

**Abstract**- This paper presents a new approach for the design of a metasurface antenna capable to provide dual circularly polarized broadside radiation. In the configuration, two decoupled surface waves of transverse electric and transverse magnetic types are excited balanced in amplitude, and propagate in the structure with the same phase velocity. Surface impedance characterization allows field radiation towards broadside direction. Two orthogonal modes in phase quadrature are employed to excite the structure, obtaining both right-hand or left-hand circular polarization.

Metasurface (MTS) antennas have been presented as a new alternative to conventional technologies designs, taking advantage of their low profile, easy fabrication process and versatility to achieve different radiation patterns with control over field polarization [1]-[2]. These structures can be characterized by means of an equivalent impenetrable surface impedance tensor when they are composed by a dense layer of anisotropic metallic sub-wavelength elements over a grounded dielectric. Proper modulation of the tensor components enables to control the structure radiation properties.

The proposed MTS solution is based on the excitation of two decoupled cylindrical surface waves (SWs) of transverse magnetic (TM) and transverse electric (TE) types balanced in amplitude. They propagate in the structure with the same phase velocity at the working frequency and therefore, the magnitudes of the radial propagation wavevectors are equal $k_{TM}=k_{TE}=k$. Under the resonance condition [3], $k_{TM,TE}$ can be related with the average normalized eigenvalues of the impenetrable anisotropic surface reactance tensor defined at the metasurface-air interface. When the impenetrable reactance tensor components are sinusoidally modulated in radial direction, fields are radiated outside the structure [4]. Control over the applied modulation parameters allows radiation towards the desired broadside direction at the working frequency. Furthermore, as reported in [5], exciting the rotationally symmetric MTS with two orthogonal modes in phase quadrature broadside radiation with right-hand (RH) or left-hand (LH) circular polarization (CP) can be obtained. Fig. 1 shows copolar and crosspolar simulated radiation patterns obtained with an ideal continuous MTS implemented following the theoretical basics:

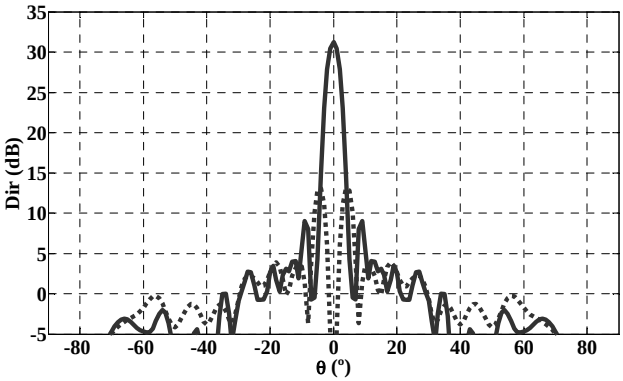
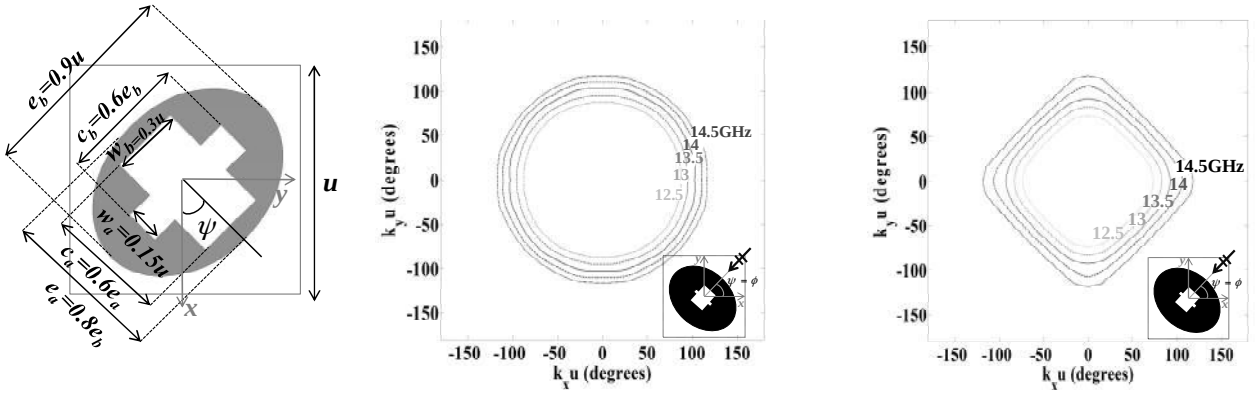



Fig. 1 Co-pol (continuous) and cross-pol (dashed) radiation patterns obtained with an ideal MTS at 13.5GHz.

Metallic elliptical shaped elements with cross-shaped aperture inside have been selected for the practical implementation of the MTS. Several geometric parameterizations of the unit cells have been studied. Dispersion diagrams for TM and TE modes show the required phase velocity at the working frequency (Fig. 2). The spatial dispersion shown by the pixel for the TE case has to be also taken into account to implement the structure.




a) b) c)

Fig. 2. a) Details of the unit cell characterized by $u$=3mm, $\varepsilon_r = 10.2$, $h = 1.27mm$ and $\psi$ (rotation inside the unit cell). Isofrequency dispersion curves of TM (b) and TE (c) modes for different propagation directions $\phi$, being $\phi = \psi$.

Further details about the theoretical operation principle, MTS implementation and required feeding system to obtain dual CP broadside radiation will be extended in the conference.

**Acknowledgements**, this work was supported by the NEWFOCUS, COST ACTION IC1102, Spanish Ministry of Science and Innovation (project TEC2013-47753-C3-1-R).

**REFERENCES**

1. B. H. Fong, J. S. Colburn, J. J. Ottusch, J. L. Visher, and D. F. Sievenpiper, "Scalar and tensor holographic artificial impedance surfaces", *IEEE Trans. Antennas Propag.*, vol. 58, no. 10, pp. 3212–3221, Oct. 2010.
2. G. Minatti, M. Faenzi, E. Martini, F. Caminita, P. De Vita, D. González-Ovejero, M. Sabbadini, and S. Maci, "Modulated Metasurface Antennas for Space: Synthesis, Analysis and Realizations", *IEEE Trans. Antennas Propag*., vol. 63, no. 4, pp. 1288–1300, Apr. 2015.
3. S. Maci, M. Caiazzo, A. Cucini, and M. Casaletti, "A pole-zero matching method for EBG surfaces composed of a dipole FSS printed on a grounded dielectric slab", *IEEE Trans. Antennas Propag*., vol.53, no. 1, pp. 70–81, Jan. 2005.
4. A. Oliner and A. Hessel, "Guided waves on sinusoidally-modulated reactance surfaces," *IRE Trans. Antennas Propag.*, vol. 7, no. 5, pp.201–208, Dec. 1959.
5. A. Tellechea, F. Caminita , E. Martini, I. Ederra, J.C. Iriarte, R. Gonzalo, and S. Maci, "Dual Circularly-Polarized Broadside Beam Metasurface Antenna", *IEEE Trans. Antennas Propag.* Submitted for Publication.

# Wideband Metasurface Energy Harvester

**M. K. El Badawe, A. M. Albishi, and O. M. Ramahi**

University of Waterloo, Canada
oramahi@uwaterloo.ca

**Abstract**— We present wideband metasurface for electromagnetic energy harvesting and wireless power transfer. The metasurface is composed of crescent shaped Split-Ring Resonators (CS-SRRs). Affecting the current path lead to an inductance that varies with frequency, thus yielding wideband frequency response. For validation, we designed an array of a $9 \times 9$ resonators, and showed through numerical simulation that appreciable power conversion efficiency and bandwidth enhancement compared with harvester arrays reported in the literature.

## 1. INTRODUCTION

The emergence of metamaterials and metasurfaces has expanded the boundary of electromagnetic research and lead to new and important applications. One critical application of metasurface is energy harvesting. The property of tuning $\epsilon$ and $\mu$ in metasurfaces have led to full absorption and harvesting by matching the material impedance to free space impedance. In recent years, extensive research has been carried out to design and fabricate metasurface energy harvesters. High harvester conversion efficiency has been achieved in both microwave [1] and infrared regimes [2]. Also, a wideband energy harvester has been reported recently using ground packed split-ring resonator [3].

Maximizing the conversion efficiency and minimizing the footprint are always primary goals for energy harvesting. In this work, a wideband metasurface energy harvester is proposed. The proposed energy harvester is based on a scalable CS-SRR, which makes the topology easy to be designed at any desired range of frequency and easy to be fabricated and measured.

## 2. DESIGN METHODOLOGY

Figure.1 shows the metasurface harvester composed of an ensemble of $9 \times 9$ split-ring resonators periodically arranged on a Rogers substrate with total dimensions of $4.35 \times 4.35cm$. The cell has a crescent shape with a small gap and was designed to operate at 5.25 GHz. The crescent shaped split-ring resonators (CS-SRRs) are designed by considering two cylinders with small thicknesses and different radii subtracted from each other and a small split where the small cylinder is not aligned in the center, thus creating a crescent shaped topology. The crescent resonator is hosted on a $t = 0.76mm$ thickness Rogers RO4350 substrate with a dielectric constant of 3.66 and a loss tangent of 0.004. The designed crescent resonator has geometrical dimensions of $outer - radius = 2.4mm$, $inner - radius = 2.2mm$, gap $g = 0.2mm$, copper thickness of $35\mu$m, and periodicity between the resonators of $S = 0.1mm$. The harvester array was designed using the commercial full wave simulator CST Microwave Studio [4].

## 3. SIMULATION RESULTS

The antenna was placed in the middle of a radiation box. The boundary conditions were chosen to force the incident magnetic fields to be normal to the surface while forcing the electric field to be parallel to the structure surface. By using such excitation mechanism, a relatively high electric field develops across the gap of the structure. To harvest this voltage, a resistive load was placed across the gap. The resistor value was swept over a wide range. A resistance of 1100 Ohm yielded the maximum power efficiency occurs. In this work, we calculate AC conversion efficiency using the formula below [1]:

$$\eta = \frac{P_{received}}{P_{incident}},$$

Where $P_{received}$ is the total time-average power received by the metasurface array (dissipated in the resistive load), and $P_{incident}$ is the total time average power incident on the array. Figure.2 depicts the conversion efficiency of the proposed harvester over a wide range of frequency. Wideband and high conversion efficiency were observed with the highest conversion efficiency reaching 93%.

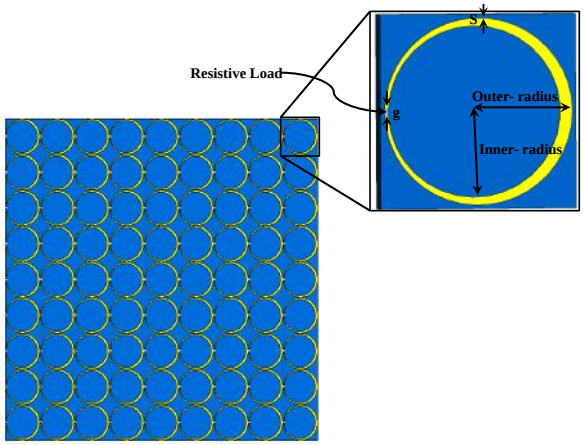



Figure 1: Schematic showing the harvester elements and the unit cell.

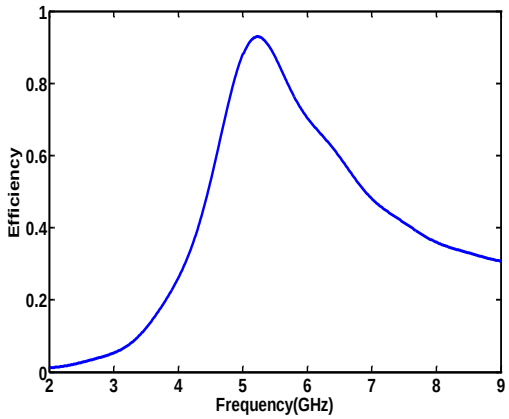



Figure 2: Calculated power conversion efficiency and the frequency bandwidth of the designed infinite array of CS-SRRs.

## 4. CONCLUSION

The feasibility of using a metasurface composed of an ensemble of 9×9 Crescent Split-ring resonators to harvest electromagnetic energy was studied. A resistive load with an optimal value was placed across the gap of the resonators to harvest the voltage developed at the gap. The power dissipated across the resistors was calculated. In this work we focused on microwave to Ac conversion efficiency. Wide-band and high AC conversion efficiency was achieved.

## REFERENCES

1. O. M. Ramahi, T. S. Almoneef, M. AlShareef, and M. S. Boybay, "Metamaterial particles for electromagnetic energy harvesting," *Applied Physics Letters*, vol. 101, no. 17, p. 173903, 2012.
2. M. R. AlShareef and O. M. Ramahi, "Electrically small resonators for energy harvesting in the infrared regime," *Journal of Applied Physics*, vol. 114, no. 22, p. 223101, 2013.
3. B. Alavikia, T. S. Almoneef, and O. M. Ramahi, "Wideband resonator arrays for electromagnetic energy harvesting and wireless power transfer," *Applied Physics Letters*, vol. 107, no. 24, p. 243902, 2015.
4. C. S. SUITE, "Computer simulation technology," *CST Computer Simulation Technology AG, www.cst.com.*

# High-performance planar holographic structures for complex focusing of terahertz beams

**S. A. Kuznetsov**[1,2,3*], **M. A. Astafev**[1], **A. N. Gentselev**[3],
**M. Navarro-Cía**[4], **M. Beruete**[5], **and A. V. Arzhannikov**[1,3]
[1]Novosibirsk State University, ATIC HT&NM, Russian Federation
[2]Institute of Semiconductor Physics SB RAS, Novosibirsk Branch"TDIAM", Russian Federation
[3]Budker Institute of Nuclear Physics, Russian Federation
[4]School of Physics and Astronomy, University of Birmingham, UK
[5]Public University of Navarra, Institute of Smart Cities, Spain
[*]corresponding author: SAKuznetsov@nsm.nsu.ru

**Abstract**-We overview the research results on electromagnetic optimization and experimental realization of low- and high-aspect plasmonic structures designed for simple and sophisticated focusing at the frequencies of 0.35 and 0.65 THz. The structures are considered both in the reflect- and transmit-array configurations whose surface phase distribution is synthesized with a computer holography technique. The overall diffraction efficiency reaching 80% is experimentally demonstrated. The methods of structure fabrication using UV and deep X-ray lithography are discussed.

Last years, searching for effective ways to a complex wavefront manipulation becomes a hot topic in physics of metamaterials [1-5]. This task is evaluated to be important for various applications where beam-shaping and beam-focusing structures are highly demanded, especially in the relatively young terahertz (THz) domain which occasionally faces the lack of high-performance devices of this kind. Using plasmonic structures with a properly designed spatial-dependent reflection/transmission phase, which is normally synthesized by methods of computer holography, such a problem can be elegantly solved [2-5]. As a result, the holographic meta-structures (HMSs) turn out to be purely flat and thin devices with striking functionalities and high efficiency typically unreachable in conventional optics.

In this work, we present the results of electromagnetic optimization and experimental implementation for high-performance THz HMSs of several types, which are tested in the experiments on radiation focusing into the focal areas of simple and complicated shapes including single and several spaced spots, as well as "Latin letters" (Fig.1). The HMSs of the first kind are the reflect-arrays optimized for operation at the frequency of 0.35 THz. In a basic design they are realized as a single-layer photolithographically-patterned metasurface laying upon a grounded polypropylene slab 190 um thick [5]. To cover the range of 360° phase variation, we employed the "patch-to-SRR" topological morphing to attain the polarization-sensitive focusing [5], while and the "patch-to-ring" transformation was utilized for the polarization-insensitive case. The HMSs of the second kind are represented by the transmit-arrays optimized for 0.65 THz, which are made as the single-layer high-aspect structures with a wavelength-comparable thickness. We proposed a relatively simple but effective method for their fabrication, which is based on deep X-ray lithographic patterning of a carrying PMMA layer followed by its entire surface metallization [6, 7].

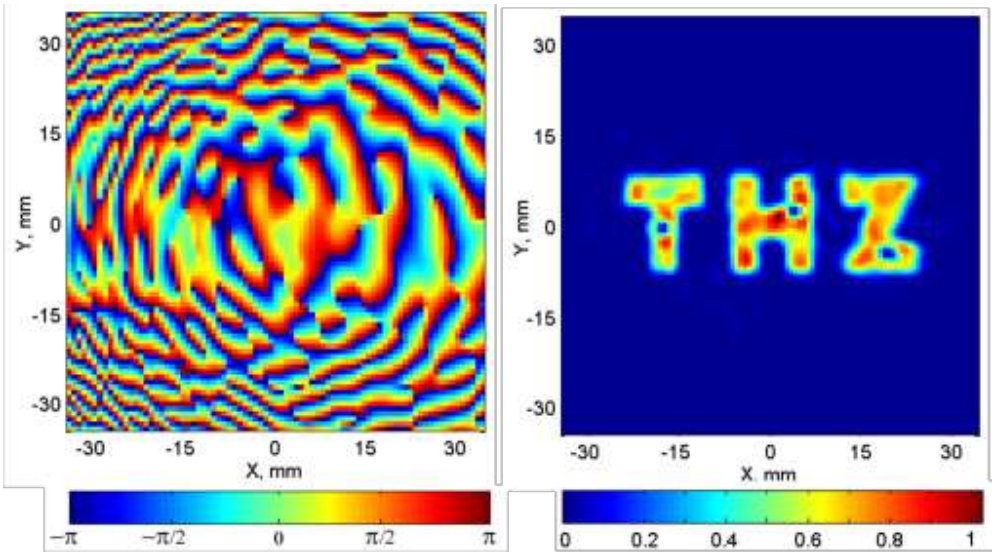



**Figure 1. Example of the optimized surface phase distribution (left) for the holographic reflectarray designed to focus a Gaussian beam into the letters "THZ" at 0.35 THz. The right graph shows the measured intensity distribution in the focal plane positioned at F=120 mm from the HMS center ($90^0$-reflection scheme, see [5]).**

To attain the required phase distribution over the HMSs surface, all the developed HMSs were designed via the Gerchberg-Saxton holographic algorithm [5] which was mastered to maximize the diffraction efficiency (DE) of the HMSs. This allowed us to reach ~80% for the experimentally measured DE values. Such a high efficiency outperforms similar characteristics of many analogues operating at THz frequencies and demonstrates the effectual way in creating relatively inexpensive, flat, light-weight, and high-performance focusing devices.

This work was supported by the Ministry of Education and Science of the Russian Federation under the State Assignment Contract #3002**.**

## REFERENCES

1. Luo, J., Yu., H., Song, M., Zhang, Z., "Highly efficient wavefront manipulation in terahertz based on plasmonic gradient metasurfaces," *Optics Letters*, Vol. 39, No. 8, 2229–31, 2014.
2. Yu, N. F., & Capasso, F., "Flat optics with designer metasurfaces," *Nat. Materials*, Vol. 13, 139–150, 2014.
3. Rui, G. and Zhan, Q., "Tailoring optical complex fields with nano-metallic surfaces," *Nanophotonics*, Vol. 4, No. 1, 2–25, 2015.
4. Huang, L., Mühlenbernd, H., Li X., Song, X., Bai, B., Wang, Y., Zentgraf, T., "Broadband Hybrid Holographic Multiplexing with Geometric Metasurfaces," *Adv. Mat.*, Vol. 27, No. 41, 6444–64491, 2015.
5. Kuznetsov, S. A., Astafev, M. A., Beruete, M. & Navarro-Cia, M., "Planar Holographic Metasurfaces for Terahertz Focusing," *Scientific Reports*, 5, 7738, Jan. 13, 2015.
6. Kuznetsov, S. A., Astafev, M. A., Gelfand, A. V., Gentselev, A. N., and Bessmeltsev, V. P., "Frequency Filters and Planar Lenses for the Terahertz Band: Configurations with Low- and High-Aspect Microstructures" // in *Proceedings of 40th Int. Conf. on Infrared, Millimeter and Terahertz Waves (IRMMW-THz 2015)*, Hong Kong, China, August 23 - 28, 2015, T2E5 – 3136553.
7. Kuznetsov, S. A. at al., "High-performance subterahertz high-pass filters and planar focusing devices produced with deep X-ray lithography," *To be submitted*, 2016.

# Novel Photonic Devices with Spatiotemporally Engineered Metasurfaces

**A. M. Shaltout[1], A. V. Kildishev, and V. M. Shalaev[1,*]**
[1]School of Electrical and Computer Engineering, Purdue University, West Lafayette, IN 47907, USA
[*]corresponding author: shalaev@purdue.edu

**Abstract-** Metasurfaces have expanded the ability of planar control over photonic momentum, angular-momentum and/or spin states, through locally controlled phase and/or polarization, enabling a novel family of ultrathin flat devices. Another class of time-varying metasurfaces opens up a new horizon of light control based on space-time duality of wave equations. Temporally-engineered metasurfaces break Lorentz-reciprocity paving the way for developing magnetic-free optical isolators. Furthermore, they induce a wavelength-shift that could compensate for Doppler-shift and render a velocity cloak for moving objects.

The emergence of photonic metamaterials has enabled a new paradigm of light control through *spatial engineering* of materials/structures, leading to unprecedented physical effects. In addition, the advent of photonic metasurfaces [1] introduced another degree of freedom over light control through surface discontinuities, overcoming the fabrication challenges associated with volumetric metamaterials. Space-gradient metasurfaces consist of planar arrays of nano-structured antennas with locally induced phase and/or polarization to propagating light. As a consequence, photons propagating through space-gradient metasurfaces can be engineered to undergo a change to their momentum, angular momentum and/or spin state. This has led to a relaxation of Snell's law, a pivotal relation in optical engineering, and has enabled a whole new family of flat optical devices. We have utilized the engineered control over photonic spin and momentum to implement a set of planar ultra-compact metasurface based devices including a chiroptical spectrometer [2] used in biochemical sensing (see fig 1a), a polarization rotator [2,3] used in secure quantum communications (see fig 1b), and nano-cavities [4] to enhance photonic spontaneous emission using the Purcell effect (see fig 1c).

The area of flat photonics can be further empowered if *temporal engineering* of materials is introduced along with *spatial engineering*. Since space and time play dual roles in wave equations, then temporal engineering of materials should obtain complementary properties to those obtained by their analog spatially engineered structures. The introduction of time-gradient metasurfaces [5] provided a new genus of optical devices and new physical effects can be realized provided one can overcome some fundamental limitations of metasurfaces with space-gradient alone. Photons experience inelastic interactions with time-varying metasurfaces resulting in a Doppler-like wavelength shift. Experimental verification of the artificial Doppler shift has been achieved (15nm shift) for telecommunication pulses using Aluminum-doped-ZnO with dynamic refractive index operating in the epsilon-near-zero regime [6]. Furthermore, Snell's relations are modified in dynamic metasurfaces to a more universal form not limited by Lorentz reciprocity (see fig 1d), hence meeting all the requirements to build magnetic-free optical isolators. Consequently, metasurfaces with both *space- and time-gradients* can have a strong impact on a plethora of photonic applications and provide versatile control over the physical properties of

light.

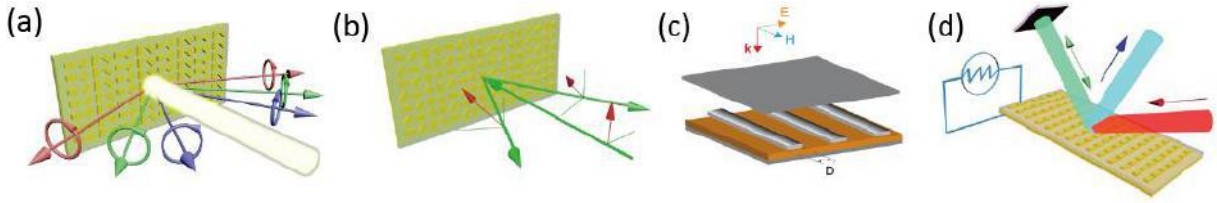



Figure 1: (a) Space-gradient metasurface working as a chiroptical spectrometer using photonic spin Hall effect. The metasurface spectrometer reflects light of opposite spins in different directions at a wavelength dependent angle. From [2]. (b) Space-gradient metasurface that rotates angle of polarization by $45^0$. From [2]. (c) Subwavelength nano-cavity of 140 nm thickness and support resonant wavelengths up to 900nm. (d) Time-gradient metasurface that changes wavelength (color) of reflected light and its angle of reflection deviates from Snell's law. Under time-reversal, neither incident color or direction is restored (non-reciprocal). From [5].

**Acknowledgements**, The authors acknowledge support from AFOSR FA9550-12-1-0389, ARO W911 NF-13-1-0226, and NSF DMR- 1120923.

**REFERENCES**

1. N. Yu, P. Genevet, M. A. Kats, F. Aieta, J.-P. Tetienne, F. Capasso, *et al.*, "Light propagation with phase discontinuities: generalized laws of reflection and refraction," *Science*, Vol. 334, No. 6054, 333-337, 2011.
2. Shaltout, A. M., Liu, J., Kildishev, A. V., and Shalaev, V. M., "Photonic spin Hall effect in gap–plasmon metasurfaces for on-chip chiroptical spectroscopy," *Optica*, vol. 2, No. 10, 860-863, 2015.
3. Shaltout, A. M., Liu, J., Shalaev, V. M., and Kildishev, A. V., "Optically Active Metasurface with Non-Chiral Plasmonic Nanoantennas," *Nano Letters*, Vol. 14, No. 8, 4426-4431, 2014.
4. Shaltout, A. M., Kildishev, A. V., and Shalaev, V. M., "Compact Subwavelength Cavities Using Reflecting Metasurfaces," in *2015 Conference on Lasers and Electro-Optics (CLEO) and Quantum Electronics and Laser Science Conference (QELS)*, San Jose, CA, USA, 2015.
5. Shaltout, A. M., Kildishev, A. V., and Shalaev, V. M., "Time-varying metasurfaces and Lorentz non-reciprocity," *Optical Materials Express*, vol. 5, No 11, 2459-2467, 2015.
6. Kinsey, N., DeVault, C., Kim, J., Ferrera, M., Shalaev, V. M., and Boltasseva, A., "Epsilon-near-zero Al-doped ZnO for ultrafast switching at telecom wavelengths," *Optica*, vol. 2, No 7, 616-622, 2015.

# Resonances in metasurfaces and their applications in SPR sensing

**I. Richter*, J. Lelek, P. Kwiecien, and J. Fiala**
Czech Technical University in Prague, Faculty of Nuclear Sciences and Physical Engineering,
Department of Physical Electronics, Břehová 7, 115 19 Prague 1, Czech Republic
*corresponding author: ivan.richter@fjfi.cvut.cz

**Abstract**- We study the resonant processes in nanostructured metasurfaces, mainly in arrayed configurations, and assess their potential for surface plasmon resonance effect applied in biosensor applications. Metasurface building blocks with various shapes and arrangements on suitable substrates and configurations have been analyzed, in terms of their resonances in reflection / transmission and figures of merit. The analysis has been performed with a combination of (quasi)analytical approaches and numerical studies, using a combination of our in-house rigorous coupled-wave analysis technique and finite difference time domain method.

Optical sensors based on surface plasmon resonance (SPR), as a well-developed technique, have recently attracted large attention in many sensing application of various chemical and biochemical species [1]. Additionally, there has been increasing interest in novel approaches to SPR sensing, based on designing novel types of plasmonic nanostructures [2] in either periodic or random spatial arrangements, allowing combination of propagating surface plasmons with localized SP (LSP). Bearing in mind various possibilities of nanostructures supporting LSP, only recently, it has been realized that a fruitful inspiration can be brought with metasurfaces [3]. Since the physics of resonances in metasurfaces is rich, combining Fano-type resonances of individual building blocks with lattice resonances due to periodic arrangements, metasurfaces can soon become a complementary platform to traditional SPR based plasmonic biosensors [4-5], providing proper understanding and exploitation of such combined resonant processes. Our analysis relays on both in-house two-dimensional rigorous coupled wave analysis (RCWA) technique [6] and finite difference time domain method (FDTD Lumerical and Crystal Wave of Photon Design), combined with suitable (quasi)analytical approaches [7-8]. By means of this approach, we study the complex resonant behavior of various metasurfaces, with respect to their geometrical and morphological properties, with the aim of understanding the resonant processes and selecting proper structures for SPR sensor applications (using relevant quantifying indicators as sensitivities to RI changes and figures of merit (FOMs). The first example of the spectral dependence of the reflectivity spectra of the fishnet metasurface is shown in Fig. 1 where the effects of two parameters are shown (width a of the fishnet arm, scaling). The second example in Fig. 2 shows the effect of morphologic transitions of metaatoms on the reflectivity resonant behavior, from a square metaatom through an U shape to a cut wire structures, for both polarizations of the incident light. Based on the analysis of the influence of geometrical parameters and structural morphology and transformations on the SP resonances, identifying promising resonances, we have proceeded with the analysis of both bulk and surface refractive index sensitivities and FOMs for the selected metasurface configurations, identifying optimum arrangements. Such an systematic approach allows for both direct comparison of considered arrangements and configurations, and identification of suitable parameters, leading to further structure optimization with respect to building block morphology. Finally, we have made efforts to interpret the origin of the resonances, with the help of the Fano approach.

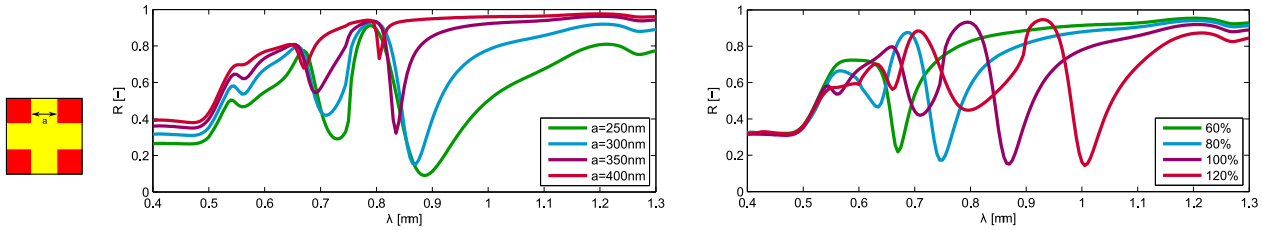



Fig. 1. Example of the dependence of the reflectivity spectra of the fishnet metasurface, with respect to: a) width a of the fishnet arm, b) structure scaling.

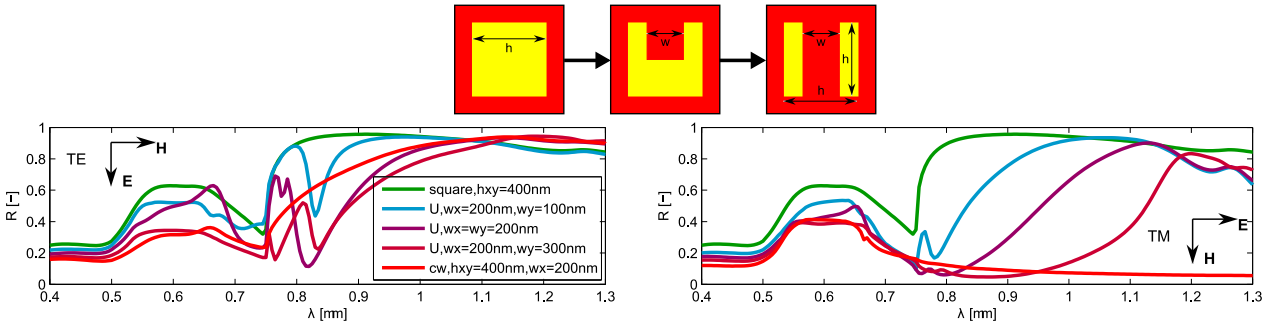



Fig. 2. Example of the morphologic transition of metaataoms: from square through U shape to cut wires: a) TE polarization, b) TM polarization.

**Acknowledgements.** The support from the following projects is greatly acknowledged: Czech Science Foundation (project No. P205/12/G118) and the Ministry of Education, Youth, and Sports of the Czech Republic (LD15075) with the action COST MP1403.

## REFERENCES

1. Homola, J. (Ed.), *Surface plasmon resonance based sensors (Vol. 4)*, Springer Science & Business Media, Berlin Heidelberg, 2006.
2. Špačková, B., P. Lebrušková, H. Šípová, P. Kwiecien, I. Richter, and J. Homola, "Ambiguous refractive index sensitivity of fano resonance on an array of gold nanoparticles," *Plasmonics*, Vol. 9, 729-735, 2014.
3. Meinzer, N., W.L. Barnes, and I.R. Hooper, "Plasmonic meta-atoms and metasurfaces," *Nature Photonics*, Vol. 8, 889-898, 2014.
4. Jakšić, Z., S. Vuković, J. Matovic, and D. Tanasković, "Negative refractive index metasurfaces for enhanced biosensing," *Materials*, Vol. 4, 1-36, 2010.
5. Cao, C., J. Zhang, X. Wen, S.L. Dodson, N.T. Dao, L.M. Wong, and Q. Xiong, "Metamaterials-based label-free nanosensor for conformation and affinity biosensing," *ACS Nano*, Vol. 7, 7583-7591, 2013.
6. Maes, B., J. Petráček, S. Burger, P. Kwiecien, J. Luksch, and I. Richter, "Simulations of high-Q optical nanocavities with a gradual 1D bandgap," *Optics Express*, Vol. 21, 6794-6806, 2013.
7. Lelek, J., P. Kwiecien, I. Richter, J. Homola, "Morphological studies of resonances in plasmonic metasurfaces for SPR sensing," *Proceedings of SPIE*, Vol. 9506, 95060O:1-14, 2015.
8. Lelek, J., P. Kwiecien, J. Fiala, I. Richter, "Study of resonant processes in plasmonic metasurfaces for SPR sensing," *Proceedings of Metamaterials 2015 Conference*, Oxford, IK, September 2015, 618-620.

# Far field dark modes excitation and electromagnetically induced transparency

**Elena Bochkova[1], Shah Nawaz Burokur[2], André de Lustrac[1,3], Anatole Lupu[1,4]**

[1]IEF, CNRS, UMR 8622, Univ Paris Sud, Université Paris-Saclay, 91405 Orsay cedex, France

[2]LEME, EA 4416, Université Paris Ouest, 92410 Ville d'Avray, France

[3]Université Paris Ouest, 92410 Ville d'Avray, France

[4]CNRS, Orsay, 91405, France

[*]corresponding author: anatole.lupu@u-psud.fr

**Abstract-**

We introduce new concepts of direct dark modes and electromagnetically induced transparency excitation based on a resonant element and incoming field symmetries matching and far field coupling of resonant elements using their antenna emission properties. This greatly relaxes fabrication constraints for the optical domain where such kind of resonances presenting sharp spectra are highly desirable for sensing applications.

## 1. Introduction

The achievement of high performance metasurfaces usually requires good resonance quality factors, which are difficult to achieve with metallic resonators. High quality factor are extremely desirable for planar metamaterial optics and also for other applications such as the detection of biological molecules or chemical species using plasmonic nano-resonators.

The low quality factor of metallic resonators is due to the losses related both to heat dissipation of the electrons in the metal (Joule effect), as well as to the radiative losses because the metallic resonator acts as a emitter antenna. Though there is no means to reduce Joule losses, it is nevertheless possible to decrease radiation damping by using the excitation of dark modes resonances that are only weakly coupled to the dipole radiation. In literature, the excitation of dark modes is most often described as the result of interaction between a superradiant element bearing an electric dipolar momentum and acting as a radiative or bright mode, with a subradiant element bearing an electric quadripolar or magnetic dipolar momentum and playing the role of the dark (or trapped) mode. The mode hybridization induced by a strong coupling between bright and dark elements leads to the opening of a narrow electromagnetically induced transparency (EIT) window inside the absorption band [1-3]. However the great sensitivity of mode hybridization to the variation of separation distance between elements yields reliable fabrication of such kind of structures highly challenging for sensing applications in the optical domain.

To circumvent the issues related to the modes hybridization, we recently considered a different dark mode excitation mechanism based only on symmetry matching conditions [4-6]. We bring evidence that dark mode excitation neither relies on hybridization mechanism nor on interference effects, and is thus distinctly different from EIT. In the present study we further extend this concept and provide theoretical and experimental results making evidence that in its turn EIT also can also be achieved by using mechanisms different from hybridization.

## 2. Direct dark mode excitation in Z-metasurface

For a free space configuration, we demonstrate the possibility of direct excitation of the dark mode via the magnetic component of the incident field. This mechanism of excitation is entirely determined by the structure's symmetry and does not rely on the coupling of near-field between the elements. We consider a single-layered metasurface composed solely of Z resonators of identical dimensions [Fig. 1(a)]. For all angles of incidence, a resonance is produced around 4.6 GHz, corresponding to the basic *LC* resonance of the structure. Under oblique

incidence, a second resonance is observed around 13.8 GHz whose origin is related to the excitation of a dark mode occurring at this frequency [Fig. 1(b)]. The Z resonator is considered to be an arrangement of two V antennas. The dipolar moments of the antisymmetric modes of these two V antennas are in opposite directions and cancel each other under normal incidence, and therefore the mode is trapped or forbidden. The excitation of this mode becomes possible under oblique incidence, where the current induced by the magnetic field flows in the same direction in the two V antennas, giving rise to a magnetic dipolar moment.

Using a bi-layered enantiomeric structure composed of two antisymmetric Z meta-atoms on the counterpart allows exciting the second order electric dark mode under normal incidence as shown in Fig. 1(c). Excitation of dipole and qudrupole magnetic poles is also allowed under oblique incidence.

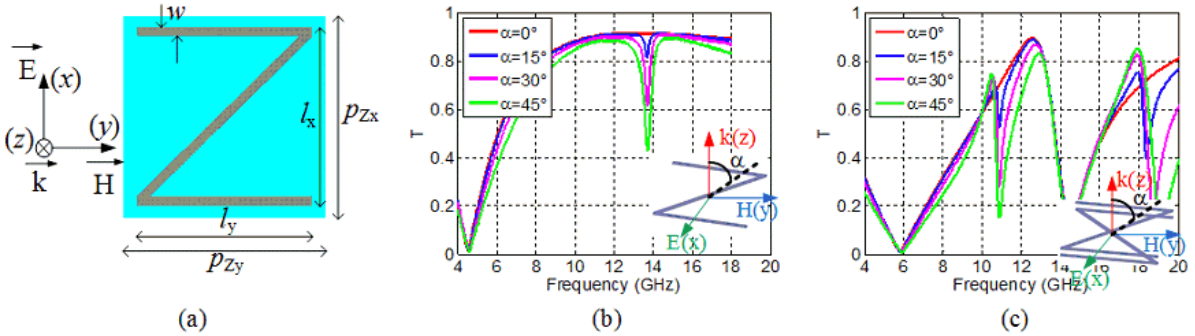



**Fig. 1. (a) Geometry of the Z meta-atom. (b) Transmission coefficient of a single-layered structure. (c) Transmission coefficient of a bi-layered enantiomeric structure.**

### 3. EIT not relying on hybridization

The basic message of the theories revisiting EIT [7, 8] is that sharp narrow band transmission is obtained when Fano interference effect occurs between two modes with essentially equal radiative strength. In the present work, based on the example of several metasurface structures operating in the microwave domain, we provide modeling and experimental demonstration of the EIT obtained with identical radiative strength. We discuss the physics of these mechanisms relying of far-field coupling antennas properties of resonant elements.

### REFERENCES


[1] B. Luk`yanchuk, et al, "The Fano resonance in plasmonic nanostructures and metamaterials," Nat. Mater. 9, 707 (2010).

[2] B. Gallinet and O. J. F. Martin, "Refractive index sensing with subradiant modes: a framework to reduce losses in plasmonic nanostructures," ACS Nano 7, 6978 (2013).

[3] B. Gallinet and O. J. F. Martin, "Influence of electromagnetic interactions on the line shape of plasmonic Fano resonances," ACS Nano 5, 8999 (2011).

[4] A. Dhouibi, et al, "Excitation of trapped modes in single element planar metamaterial composed of Z-shaped meta-atom," Appl. Phys. Lett., 103, 184103 (2013).

[5] S.N. Burokur, A. Lupu and A. de Lustrac, "Direct dark mode excitation by symmetry matching of a single-particle-based metasurface," Phys. Rev. B 91, 035104 (2015).

[6] E. Bochkova, S. N. Burokur, A. de Lustrac, A. Lupu, "Direct dark modes excitation in bi-layered enantiomeric atoms-based metasurface through symmetry matching," Opt. Letters 41, 412-415 (2016).

[7] C. Forestiere, L. Dal Negro, and G. Miano, "Theory of coupled plasmon modes and Fano-like resonances in subwavelength metal structures," Phys. Rev. B 88, 155411 (2013).

[8] B. Hopkins, A. N. Poddubny, A. E. Miroshnichenko, and Y. S. Kivshar, "Revisiting the physics of Fano resonances for nanoparticle oligomers," Phys. Rev. A 88, 053819 (2013).

# Periodic arrays of film-coupled nanoparticles as tunable all-dielectric metasurfaces

**E. Almpanis[1*], N. Papanikolaou[2], V. Yannopapas[1], and N. Stefanou[3]**

[1] Department of Physics, National Technical University of Athens, Athens GR-15780, Greece

[2] Institute of Nanoscience and Nanotechnology, NCSR "Demokritos," Ag. Paraskevi, Athens GR-15310, Greece

[3] Department of Solid State Physics, National and Kapodistrian University of Athens, Athens, GR-157 84, Greece

[*]corresponding author: almpanis@central.ntua.gr

**Abstract**-Electromagnetic coupling of nanoparticles with a thin film gives rise to various optical modes that enable the control of light in many different ways. Such ultrathin geometries with exotic optical behaviour, also known as metasurfaces, are advantageous for flat optics applications compared to three-dimensional metamaterials. In this work we demonstrate the performance of all-dielectric metasurfaces and propose architectures for plasmon-like field concentrations, total absorption, and enhanced magneto-optical effects.

Engineering ultrathin surfaces consisting of film-coupled nanoresonators has opened the way for tailoring the light-matter interaction in various brand-new ways. Essentially, a resonator, such as a metallic nanoantenna, confines strongly the electromagnetic (EM) field at its surface due to the excitation of the so-called surface plasmon polaritons. Metallic nanoparticles of various shapes acting as nanoantenas coupled with an appropriate substrate funnel the EM field in subwavelength dimensions and cause significant changes on the amplitude, the phase, or the polarization of an incident wave [1, 2]. Recently, a lot of effort has been devoted in replacing the metals with high-refractive-index dielectrics [3-6]. In this work we study, by means of full electrodynamic calculations, non-metallic surfaces consisting of dielectric substrate layers decorated with periodic nanoparticle arrays. More specifically, we show that a monolayer of weakly absorbing high-refractive-index nanoparticles on top of a Bragg stack, which acts as a mirror, is sufficient to obtain totally absorbing surfaces. As dictated by scattering theory, tuning the amount of losses in the nanoparticle, total absorption at specific resonances can be achieved [3]. In a similar manner, we demonstrate that nanoparticle arrays on top of reflecting substrates are ideal in exciting guided resonances that confine the EM field at the surface of the dielectric particles, giving rise to subwavelength plasmon-like field concentrations [4, 5]. On the other hand, we provide evidence for enhanced and tuneable magneto-optical effects, such as Faraday or Kerr rotation of light incident on a dielectric magnetic film coated with a periodic array of dielectric nanoparticles. All of these applications show that arrangements of nonmetallic particles and films provide a promising and versatile platform for engineering easily-integrated metasurfaces, which allow for strong field concentration and drastic modification of its wavefront, excitation of guided resonances of the substrate, and enhancement of magneto-optical effects. We review our work on all-dielectric metasurfaces and present in more detail our recent results on non-metallic magneto-photonic metasurfaces that can efficiently rotate the plane of polarization of an incident light beam in the presence of an external static magnetic field.

## REFERENCES


1. Estakhri N. M. and A. Alu, "Recent progress in gradient metasurfaces," *J. Opt. Soc. Am. B*, Vol. 33, No. 2, A21–30, 2015.
2. Yannopapas V. "Periodic arrays of film-coupled cubic nanoantennas as tunable plasmonic metasurfaces," *Photonics*, Vol. 2, No. 1, 2015.
3. Almpanis, E. and N. Papanikolaou, "Designing photonic structures of nanosphere arrays on reflectors for total absorption," *J. Appl. Phys*. Vol. 114, No. 8, 083106, 2013.
4. Almpanis E. and N. Papanikolaou, "Comparison of Ag and Si nanoparticle arrays: mimicking subwavelength plasmonic field concentrations with dielectric components," *J. Opt. Soc. Am. B*, Vol. 33, No. 1, 99–104, 2016.
5. Almpanis E. and N. Papanikolaou, "Dielectric nanopatterned surfaces for subwavelength light localization and sensing applications," *Microel. Eng.*, Vol. 159, No. 15, 60–63, 2016.
6. Jahani S. and Z. Jacob, "All-dielectric metamaterials," *Nature Nanotechnol.* Vol. 11, No. 1, 23–36, 2016.

# Nanoantennas for controlled enhancement and interference of higher-multipole molecular transitions

**K. Słowik**[1], **E. Rusak**[2], **M. Göddel**[2], **J. Straubel**[2], **M. Kühn**[2], **F. Weigend**[2], **and C. Rockstuhl**[2],

[1]Nicolaus Copernicus University, Toruń, Poland
[2]Karlsruhe Institute of Technology, Germany
karolina@fizyka.umk.pl

**Abstract**— The spontaneous emission of quantum emitters can be modified by engineering their optical environment. A resonant nanoantenna can significantly modify the radiative properties of a quantum emitter. In this contribution, we go beyond the common electric dipole approximation for the molecular electronic transition, and take higher-multipole channels into account. We theoretically investigate the impact of metallic and dielectric nanoantennas on the interference effects in the emission via different multipolar pathways of a specific molecular transition.

Nanoantennas are nanostructured optical devices, metallic, dielectric, or even made of more exotic materials such as graphene, able to dramatically enhance the light-matter interaction [1]. This is due to their extraordinary ability to concentrate light in subwavelength spatial domains. A molecule placed into such hot spots interacts with a field of extreme strength. However, a nanoantenna can do much more. It allows to overcome paradigms that have been prevalent for long time when considering the light-matter interaction in free-space or in traditional cavities. There, it is assumed that the spatial extent of the molecule is much smaller than the wavelength of light; being a length scale for the spatial variations of the electric field. In consequence, the electric field can be considered as constant across the molecule. This allows to use the dipole-approximation where quantum state transitions are considered as purely electric dipolar.

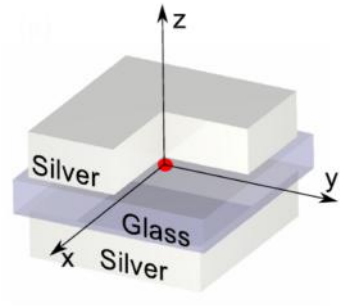



Figure 1: A scheme of the plasmonic patch nanoantenna considered in this work. The red dot represents a molecule positioned in the gap region, where field variations are most significant.

This assumption is lifted by plasmonic [2, 3] and even dielectric nanoantennas [4]. They provide not just huge electric fields but also huge electric field modulations, allowing to stimulate quantum state transitions that are usually considered as hardly accessible in free space: i.e. those characterized by a higher order multipolar moments. In our work, we explore the possibility to superimpose and to coherently control the different pathways of quantum emitters linked to different multipolar contributions of the same transition. We identify scenarios where the local density of states is largely enhanced but also fully suppressed. This is possible by exploiting the quantum mechanical interference of the different transition pathways. The full suppression due to destructive quantum interference corresponds to a specific and novel kind of a photonic band gap. A specific emitter brought in a specific position and orientation relative to the nanoantenna remains excited through lifetimes enhanced by many orders of magnitude, since there is no photonic mode into which this excitation can be damped. This largely enhanced lifetime of the emitter is the key for many applications in the context of quantum computing, quantum storage, and quantum communication. In

all such applications a short lifetime of the emitter constitutes a limitation; a limitation that can be overcome with optical nanoantennas.

In our contribution, we consider a plasmonic patch nanoantenna, consisting of two silver patches and a glass spacer in-between (Figure 1) [6]. Its spectral profiles and characteristics of scattered fields are calculated with a finite element method in the frequency domain. We investigate different multipolar contributions of a quantum transition between the ground and two excited states of an $OsO_3$ molecule, corresponding to the free-space wavelength of 553 nm. For this purpose, we exploit the Fermi golden rule:

$$\Gamma = \frac{2\pi}{\hbar} \sum_f |\langle \mathrm{f}|H|\mathrm{i}\rangle|^2 \rho(\omega_\mathrm{f} = \omega_\mathrm{i} \pm \omega), \tag{1}$$

where $\Gamma$ is the modified transition rate between the initial state $|\mathrm{i}\rangle$ and a set of final states $|\mathrm{f}\rangle$, $\rho(\omega)$ is the nanoantenna-modified density of states, and the $\pm$ sign corresponds to an absorption or an emission, respectively. The interaction Hamiltonian $H$ combines in general several multipolar contributions:

$$H = -\mathbf{d}.\mathbf{E}(\mathbf{r}_m) - \mathbf{m}.\mathbf{B}(\mathbf{r}_m) - [\mathbf{Q}.\nabla]\,.\mathbf{E}(\mathbf{r}_m), \tag{2}$$

where $\mathbf{E}(\mathbf{r}_m)$ and $\mathbf{B}(\mathbf{r}_m)$ are the electric and magnetic fields at the position $\mathbf{r}_m$ of the molecule, while $\mathbf{d}$, $\mathbf{m}$ and $\mathbf{Q}$ are the molecular transition electic dipole, magnetic dipole, and electric quadrupole moments, respectively. They have been provided for our calculations by means of the time-dependent density functional theory [5]. Due to the symmetry properties of the $OsO_3$ molecule, the transitions we consider are electric-dipole-forbidden. Therefore, two higher-multipole pathways: the magnetic dipole and the electric quadrupole, can be directly accessed and are strongly enhanced by the plasmonic nanoantenna. Depending on the position and orientation of the molecule relative to the nanoantenna, these channels can interfere, leading, e.g., to an enhancement of molecular lifetime by many orders of magnitude.

Finally, we will supplement our contribution with an analysis of a potential of dielectric nanoantennas in such higher-multipolar context [6]. According to our findings, even though metallic nanoantennas are capable of a drastic enhancement of higher-multipole transition probabilities, their magnetic-dipole and electric-quadrupole resonances overlap. This is not the case with dielectric nanoparticles. The latter, though typically weaker in performance, offer possibilities to tune the relative position of resonances, which may provide an additional and important knob to control the light-matter interactions. We demonstrate such capability by exploiting a silicon nanodisk to coherently control the magnetic dipole and electric quadrupole channels of a similar molecule.

Our results are an essential step on the road to the design of integrated, tunable platforms for precise control of molecular dynamics on the higher-multipolar level. Another direct application is related to photonic sciences, namely to a design and construction of new types of nanostructured materials and integrated devices. They may provide tunable, high-performance sources of exotic states of light obtained via a predefined emission channel or an interference thereof. Photons emitted in a higher-multipolar molecular transition would be characterized by unusual properties, such as larger values of angular momentum or even parity. Their applications include orientational manipulation of particles or particle aggregates in optical tweezers, higher-dimensional quantum information encoding for quantum cryptography, high-bandwidth information encoding in free-space quantum communication and computation applications, as well as sensitive optical detection.

**REFERENCES**


1. Biagioni, P., J.-S. Huang, and B. Hecht, "Nanoantennas for visible and infrared radiation", *Rep. Prog. Phys.*, Vol. 75, 024402, 2012.
2. Feng, T., Y. Zhou, D. Liu and J. Li, "Controlling magnetic dipole transition with magnetic plasmonic structures". *Opt. Lett.*, Vol. 36, 2369–2371, 2011.
3. Filter, R., S. Mühlig, T. Eichelkraut, C. Rockstuhl, and F. Lederer. "Controlling the dynamics of quantum mechanical systems sustaining dipole-forbidden transitions via optical nanoantennas", *Phys. Rev. B*, Vol. 86, No. 3, 035404, 2012.
4. Schmidt, M. K., R. Esteban, J. J. Sáenz, I. Suárez-Lacalle, S. Mackowski, and J. Aizpurua ,"Dielectric antennas - a suitable platform for controlling magnetic dipolar emission", *Opt. Express*, Vol. 20, 13636, 2012.
5. Furche, F., R. Ahlrichs, C. Hättig, W. Klopper, M. Sierka and F. Weigend, "Turbomole", *WIREs COMPUT. MOL. SCI.*, Vol. 4, 91–100, 2014.
6. E. Rusak, et al., in preparation; M. Göddel, et al., in preparation.

# Multimodal nanoantennas for engineering quantum light

**K. Słowik**[1], **J. Straubel**[2], **R. Sarniak**[1], **R. Filter**[3], **and C. Rockstuhl**[2]

[1]Nicolaus Copernicus University, Toruń, Poland
[2]Karlsruhe Institute of Technology, Germany
[3]Friedrich Schiller University, Jena, Germany
karolina@fizyka.umk.pl

**Abstract**— Integration of optical nanoantennas holds promise for a significant boost of performance of quantum emitters as nonclassical light sources. Moreover, nanoantennas can be exploited to engineer the emission characteristics, or even quantum properties of light, such as statistics or degree of entanglement. These applications are here proposed and discussed within the cavity quantum electrodynamics (cQED) framework. It allows to account for nanoantennas, whose spectra are characterized with multiple resonances, coupled to two- or multilevel quantum emitters.

Quantum emitters, such as atoms, molecules, nitrogen-vacancy centers in diamond, etc., can be exploited as sources of nonclassical light. Especially promising in this context are artificial structures such as quantum dots, whose spectral properties can potentially be tailored, so that the emitted light is characterized by desired quantum statistics, spectrum, polarization, or even high degree of entanglement [1].

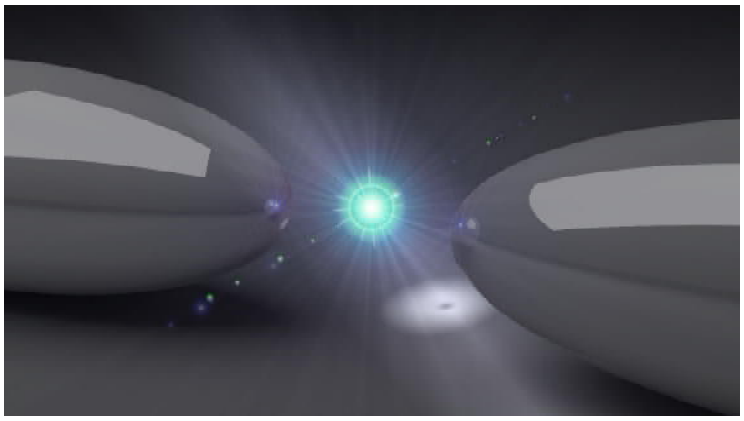


Figure 1: An artistic vision of a metallic nanoantenna coupled to a quantum emitter.

Harvesting light from bare quantum emitters is, however, extremely inefficient, since the radical mismatch between their size and the optical wavelength renders the corresponding coupling coefficients to be very weak. Commonly, they are enhanced with high-finesse cavities, whose performance is however restricted by the natural diffraction limit. This limitation can be waived if plasmonic nanoantennas are exploited instead of traditional cavities [2]. They are capable of light confinement into subwavelength spatial domains, leading to unprecedented coupling strengths between light and quantum matter. What is more, nanoantennas can convert between localized and propagating electromagnetic fields. In this way, they greatly enhance the brightness of quantum emitters as nonclassical light sources. Such impact is usually expressed in terms of the Purcell enhancement factor. So far, enhancement of emission rate by 3 orders of magnitude has been reported [3]. Moreover, nanoantennas, usually including dielectric components, significantly improve the directivity of the emission [4], promising much better collection efficiencies of the emitted photons.

In our work, we propose to exploit nanoantennas for engineering quantum light. We discuss several applications of nanoantennas, whose scattering and absorption spectra can be described by multiple resonances. This includes (1) controlling quantum statistics with a bright, triggered source of single photons, based on a lambda-configuration quantum dot or molecule [5]; (2) a conversion

between two nanoantenna modes at the single-photon level, whose efficiency is significantly boosted due to a presence of, e.g., a nitrogen-vacancy center in diamond [6]; or even (3) generation of light, with emission modes highly entangled in the degree of freedom related to the occupation number [7]. All these applications exploit multiple resonances in the nanoantenna spectra.

To account for the complicated scattering characteristics, we have developed a method based on the cQED framework. We obtain the spectral properties of nanoantennas by solving the Maxwell's equations in the frequency domain with the finite element method. In practice, such spectra can be well represented with a finite and small number of Lorentzian or Fano-shaped resonances, associated respectively with uncoupled or interacting quasi-normal modes. Their properties can be expressed in terms of a limited number of parameters, namely the central frequencies of the resonances, their spectral width, the coupling coefficients between the individual modes, as well as coupling strengths to adjacent quantum emitters of predefined dipole or even higher-multipole moments. This means that the standard tools known from the cQED can be applied [8]. The Lindblad equation accounts for the dynamics of the density matrix $\rho(t)$ of the hybrid system

$$\dot{\rho}(t) = -i\left[\mathcal{H}_0 + \mathcal{H}, \rho(t)\right] - i\mathcal{L}\left[\rho(t)\right], \tag{1}$$

where $\mathcal{L}\left[\rho(t)\right]$ describes all the incoherent processes, such as optical pumping or spontaneous emission. $\mathcal{H}_0$ is responsible for the free evolution, and the interaction Hamiltonian takes the Tavis-Cummings form

$$\mathcal{H} = \sum_{\mathrm{j}} \left( g_{\mathrm{j}} \sigma_{\mathrm{j}}^{\dagger} a_{\mathrm{j}} + g_{\mathrm{j}}^{\star} a_{\mathrm{j}}^{\dagger} \sigma_{\mathrm{j}} \right), \tag{2}$$

with the coupling constant $g_{\mathrm{j}}$ between the mode described by the annihilation operator $a_{\mathrm{j}}$ and the corresponding quantum transition in the emitter, associated with the flip operator $\sigma_{\mathrm{j}}$. This methodology directly provides tools to discuss the quantum poperties of light, e.g., in the context of the applications listed above.

The investigated examples indicate, that due to their unprecedented ability to enhance light interaction with quantum matter, nanoantennas may provide means to bring the cavity quantum electrodynamics down to the nanoscale. They can become an essential ingredient of compact on-chip devices, robust and tunable, able to improve the performance of exotic light sources: their brightness, directivity, and even nonclassical properties.


## ACKNOWLEDGMENT

The study was supported by a research fellowship within the project Enhancing Educational Potential of Nicolaus Copernicus University in the Disciplines of Mathematical and Natural Sciences (project no. POKL.04.01.01-00-081/10.) and the Karlsruhe School of Optics and Photonics (KSOP).


## REFERENCES


1. Michler, P., "Single Quantum Dots: Fundamentals, Applications and New Concepts", Springer Science & Business Media, New York, 2003.
2. Giannini, V., A. I. Fernández-Domínguez, S. C. Heck, and S. A. Maier, "Plasmonic nanoantennas: fundamentals and their use in controlling the radiative properties of nanoemitters". *Chem. Rev.*, Vol. 111, No. 6, 3888–3912, 2011.
3. Akselrod, G. M., C. Argyropoulos, T. B. Hoang, C. Cirací, C. Fang, J. Huang, D. R. Smith, and M. H. Mikkelsen, "Probing the mechanisms of large Purcell enhancement in plasmonic nanoantennas", *Nat. Phot.*, Vol. 8, No. 11, 835–840, 2014.
4. Devilez, A., B. Stout, and N. Bonod, "Compact metallo-dielectric optical antenna for ultra directional and enhanced radiative emission", *ACS Nano*, Vol. 4, No. 6, 3390–3396, 2010.
5. Straubel, J., R. Filter, C. Rockstuhl, and K. Słowik, "A plasmonic nanoantenna based triggered single photon source", arXiv:1510.07906, 2015.
6. Straubel, J., R. Filter, C. Rockstuhl, and K. Słowik, "Efficient mode conversion in an optical nanoantenna mediated by quantum emitters", arXiv:1602.00974, 2016.
7. Straubel, J., R. Sarniak, C. Rockstuhl, and K. Słowik, "Entangled light from bimodal optical nanoantennas", in preparation.
8. Waks, E., and D. Sridharan, "Cavity QED treatment of interactions between a metal nanoparticle and a dipole emitter", *Phys. Rev. A*, Vol. 82, No. 4, 043845, 2010.

# Band stop filters for THz waves based on dielectric metasurfaces

**J. F. Algorri*, R. Vergaz, V. Urruchi, J. M. Sánchez-Pena, and B. García-Cámara**
Group of Displays and Photonic Applications (GDAF-UC3M), Carlos III University of Madrid, Spain.
*corresponding author: jalgorri@ing.uc3m.es

**Abstract**- In this work, we propose and design a dielectric metasurface based on Silicon (Si) subwavelength pillars. A previous study of the directional conditions of the scattering is carried out in order to obtain the optimum sizes. The metasurface can operate as a band-stop filter to realize blocking back THz waves in the designed band range, while transparent transmission over the rest of the range.

Nowadays, most of the frequency spectrum has been exploited. Despite this, the gap between microwaves and infrared is still in a research stage. This range known as 'terahertz gap' corresponds to frequencies from 0.3 THz to 3 THz. Recent advances in THz sources and detectors have accelerated the THz application and techniques. Some of the most relevant applications are biosensors [1], security [2] and high speed communication [3]. However, in addition to efficient sources and detectors, these applications also require other optical devices to control and manipulate these kind of waves.

The research of dielectric metasurfaces has attract a lot of interest in recent years. Some applications are planar photonics [4], flat optics [5] and flat lenses [6]. These kind of structures have opened new venues of research in the control of THz frequencies. The use of dielectric materials produces low insertion losses in comparison with metallic counterparts but similar effects when an overlap of the electric and magnetic-dipole resonances are produced. Moreover, in some cases as Si, the CMOS compatibility makes an easy integration with other kind of optical devices. In this work, it is demonstrated how the use of Si subwavelength pillars can be used in order to create selective filters for THz waves. A previous study of the directional conditions of the scattering is carried out in order to obtain optimum sizes. By using this study it is possible to choose the stop-band of the filter. The Si pillars are placed on a substrate of a low-loss THz polymer.

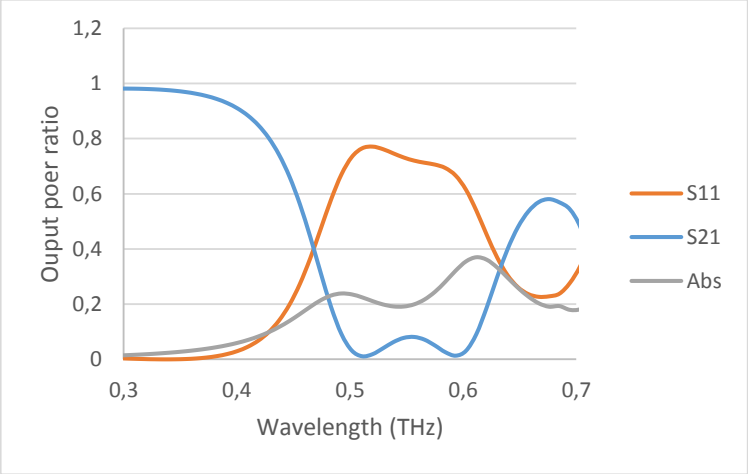



Figure 1. Band stop filter in the region between 0.5 to 0.6 THz.

As an example, Fig. 1 shows the result of a metasurface designed to have the band rejection around 0.5THz. The nanopillars are structured in a metasurface configuration with a periodic space between nanopillars of 100μm. The structure is based on Si nanopillars with height 180μm and radius 70μm. The metasurface can operate as a band-stop filter to realize blocking back THz waves in a band range of 0.5–0.6 THz, while transparent transmission over a range of 0.1–0.4 THz. As can be observed, for this specific design a range of 100GHz can be filtered. The transmission is almost zero in this range, indicating an optimum rejection band. The interesting THz band-stop filtering properties suggest a promising application in the modern THz communication systems, THz time-domain spectroscopic imaging and THz continuous wave imaging.

**Acknowledgements.** This work has been supported by Ministerio de Economía y Competitividad of Spain (grant no. TEC2013-50138-EXP & TEC2013-47342-C2-2-R) and the R&D Program SINFOTON S2013/MIT-2790 of the Comunidad de Madrid.

**REFERENCES**

1. H.-B. Liu, G. Plopper, S. Earley, Y. Chen, B. Ferguson, and X.-C. Zhang, "Sensing minute changes in biological cell monolayers with THz differential time-domain spectroscopy," Biosens. Bioelectron. 22, 1075–1080 (2007).
2. J. F. Federici, B. Schulkin, F. Huang, D. Gary, R. Barat, F. Oliveira, and D. Zimdars, "THz imaging and sensing for security applications-explosives, weapons and drugs," Semicond. Sci. Technol. 20, 266–280 (2005).
3. I. F. Akyildiz, J. Jornet, C. Han, "Terahertz band: Next frontier for wireless communications," Phys. Comm., 12, 16-3 (2014).
4. Kildishev, A. V., Boltasseva, A. & Shalaev, V. M. Planar photonics with metasurfaces. Science 339, 1232009 (2013).
5. Yu, N. & Capasso, F. Flat optics with designer metasurfaces. Nature Mater. 13, 139–150 (2014).
6. Quanlong Yang, Jianqiang Gu, Dongyang Wang, Xueqian Zhang, Zhen Tian, Chunmei Ouyang, Ranjan Singh, Jiaguang Han, and Weili Zhang, "Efficient flat metasurface lens for terahertz imaging," Opt. Express 22, 25931-25939 (2014)

# All-dielectric bianisotropic metasurface for microwave applications

**M. A. Odit**[1], **P. V. Kapitanova**[1], **Yu. S. Kivshar**[2], **and P. A. Belov**[1]

[1]Department of Nanophotonics and Metamaterials, ITMO University, St. Petersburg 197101, Russia
[2]Nonlinear Physics Centre, Australian National University, Canberra ACT 0200, Australia
odit@mail.ifmo.ru

**Abstract**— All-dielectric bianisotropic metasurface for microwave applications has been designed, fabricated and experimentally investigated in the frequency range 4-9 GHz. Radar cross-section of the metasurface unit cell posses different ratio for forward/backward scattering depending on plane wave excitation propagation direction. At the frequency 7 GHz the metasurface transmission characteristics exhibit a $2\pi$ phase change in the reflection spectrum while the measured amplitude of the reflection coefficient is close to 1. Thus the metasurface can be used as a reflect array with a $2\pi$ reflection phase while being excited from one side, whereas remains transparent outside this operational frequency range.

Metasurfaces are two-dimensional metamaterials allowing to control and manipulate the properties of electromagnetic waves by employing the concepts and designs of flat optics [1, 2]. In comparison with bulk structures, metasurfaces are compact and relatively more simple to manufacture.

Recently, high-index all-dielectric metasurfaces attracted a lot of attention since they are free from conducting loss [3]. It was also shown that metasurfaces with both electric and magnetic dipolar responses can suppress dramatically the wave reflection, increasing significantly overall metasurface efficiency [4]. A better control of electromagnetic radiation can be achieved by exploiting *magnetoelectric coupling* (or *bianisotropy*) of the metasurface elements in addition to their electric and magnetic dipolar response [5]. This allows in particularly to polarize incident waves or to make a metasuface transparent from one direction while being fully opaque from the opposite direction.

Here we demonstrate experimentally the all-dielectric bianisotropic metasurface operating in microwave frequency range 4-9 GHz. The metasurface under study is composed of bianisotropic high-index dielectric particles that are periodically arranged on a square lattice with a period $a = 2.7$ cm. The individual particle has a form of a cylinder with a finite hole inside [see inset to Fig. 1(a)]. The cylinder has a radius of $R = 1$ cm and a height of $H = 1$ cm. The radius of the hole inside the cylinder is $R_0 = 0.5$ cm and the height is $H_0 = 0.5$ cm. The dielectric particle material is a microwave ceramic with permittivity $\varepsilon = 10$ and loss tangent tan$\delta$=0.0007. The ambient material is air.

First we studied numerically and experimentally the radar cross section (RCS) of the single particle excited by a plane wave. Under the forward excitation direction, we assume that the wave vector $k$ is co-directional with the $z$ coordinate, and refer to this propagation direction as $k^+$. Under the backward excitation direction, we assume that the wavevector $k$ is counter directional with the $z$ coordinate, and refer to this propagation direction as $k^-$. From the simulated results and measured data one can conclude that the bianisotropic particle possesses an identical forward scattering $RCS^+$ for both $k^+$ and $k^-$ excitation directions. However, the backward scattering $RCS^-$ depends on the excitation direction. At the frequency 7.4 GHz, the bianisotropic particle has a minimum in the backward scattering $RCS^-$ for the forward excitation direction $k^+$ while for the backward excitation direction $k^-$ it is close to its maximum.

All-dielectric bianisotropic metasurface composed of the particles studied above have been fabricated and studied experimentally [see Fig. 1(a)]. An array of 9 x 9 inverse particle shapes was drilled in a custom holder made of a Styrofoam material ($\varepsilon \approx 1$) and filled with a ceramic powder Eccostock HiK with $\varepsilon = 10$ and loss tangent tan$\delta$=0.0007. The period was $a = 2.7$ cm, and the total size of the metasurface was 24 cm x 24 cm. The metasurface was placed in an anechoic chamber between two horn antennas at the distance of 2 meters from each antenna. The antennas were connected to the ports of the vector network analyzer. To avoid an additional reflection from the metasurface edges and also border effects, the metasurface perimeter was surrounded by microwave absorbers. Complex S-parameters of the system were measured for the forward and

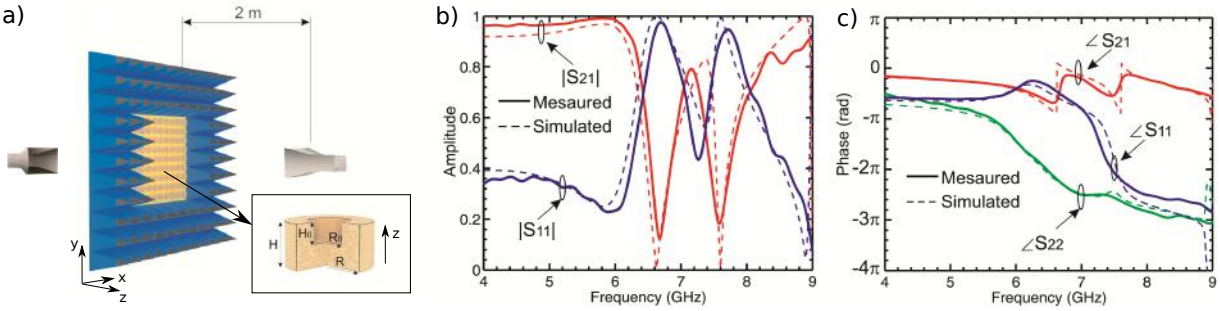



Figure 1: (a) Experimental setup for measurement of the metasurface scattering parameters. The inset demonstrates the metasurface unit cell. Measured (solid lines) and simulated (dashed lines) amplitude (b) and phase (c) of the metasurface scattering parameters.

backward plane wave excitations. To suppress the effects of multiple reflections between the metasurface sample and the antennas, the postprocessing of measured data by means of time-domain gating was employed.

The measured amplitude and phase of the transmission and reflection coefficients are shown in Fig. 1 (b) and (c) respectively. The measured phases of the transmission coefficient $S_{12}$ and $S_{21}$ are equally identical due to reciprocity of the system (thus we plot only $S_{21}$ parameter). In a contrast, since the particles have small dielectric losses, the reflection coefficient $S_{11}$ and $S_{22}$ amplitudes have to be different for opposite excitation directions due to the magnetoelectric coupling. At the frequency 7 GHz the measured phase difference amounts to $\arg(S_{22})$-$\arg(S_{11}) \approx 2\pi$, while the measured amplitude of the reflection coefficient is close to 1. At this frequency the metasurface behaves as a reflect array with a $2\pi$ reflection phase while being excited from one side, whereas remains transparent outside this operational frequency range.

In conclusion, we have designed, fabricated, and studied experimentally the all-dielectric metasurface composed of all-dielectric bianisotropic particles with different backward and forward scattering. We have demonstrated experimentally bianisotropic properties of the metasurface consisting of periodically arranged all-dielectric bianisotropic particles, that can behave as a reflect array with a $2\pi$ reflection phase while being excited from one side, whereas remains transparent outside this operational frequency range.

## ACKNOWLEDGMENT

This work was supported by the Russian Foundation for Basic Research (Project Nos. 140231761, 150708302, 15-32-20665 and 155745141), DAAD (PPP Australien), and the Australian Research Council. PK and PB acknowledge Scholarship and Grant of the President of Russian Federation.

## REFERENCES

1. A. V. Kildishev, A. Boltasseva, and V. M. Shalaev, "Planar photonics with metasurfaces," *Science*, vol. 339, no. 6125, 2013.
2. N. Yu and F. Capasso, "Flat optics with designer metasurfaces," *Nat Mater*, vol. 13, pp. 139–150, Feb. 2014.
3. A. E. Krasnok, A. E. Miroshnichenko, P. A. Belov, and Y. S. Kivshar, "All-dielectric optical nanoantennas," *Opt. Express*, vol. 20, pp. 20599–20604, Aug 2012.
4. F. Monticone, N. M. Estakhri, and A. Alù, "Full control of nanoscale optical transmission with a composite metascreen," *Phys. Rev. Lett.*, vol. 110, p. 203903, May 2013.
5. R. Alaee, M. Albooyeh, A. Rahimzadegan, M. S. Mirmoosa, Y. S. Kivshar, and C. Rockstuhl, "All-dielectric reciprocal bianisotropic nanoparticles," *Phys. Rev. B*, vol. 92, p. 245130, Dec 2015.

# Highly Sensitive Room Temperature Graphene-based Sub-terahertz Photoconductor via Electromagnetic Gating Effect

Lin Wang[a,b*], Xiaoshuang Chen[a,b*] , Changlong Liu[a,b], Weiwei Tang[a,b], Wei Lu[a,b]

[a]National Laboratory for Infrared Physics, Shanghai Institute of Technical Physics, Chinese Academy of Sciences, 500 Yu Tian Road, Shanghai, Shanghai 200083, China

[b]Synergetic Innovation Center of Quantum Information & Quantum Physics, University of Science and Technology of China, Hefei, Anhui 230026, China

[*]corresponding author: xschen@mail.sitp.ac.cn

**Abstract**：Generating electron-hole pair through photon absorption is routinely the photodetection process promoting widespread applications ranging from security to human life. Recently, exploiting terahertz (THz) photodetection technique receives unprecedented attention due to its great promising for noninvasive imaging, communication, *etc*[1,2]. However, it is still lacking of efficient way for sensitive room-temperature detection due to the low photon energy. Gapless graphene is highly sought-after as a potential candidate for active material in photodetection across whole spectrum. Even though considerable amount of THz photons can be absorbed by graphene, the efficient photo-to-electric conversions are not well-developed. Among them, photodetection dominated by the plasma wave nonlinear-rectifying and photothermoelectric effects by exploiting specific device structure, chemical doping or dissimilar contacts are proposed[3-5]. Beyond the conventional interband mechanism, we report biased photoconductive detector but otherwise homogeneous graphene-channel with sensitivity exceeding 400V/W ($4\times10^3$V/W) at room temperature and noise-equivalent power less than (0.5 nW/Hz$^{0.5}$), reference to the incident (absorbed) power. The performance is competitive with optimal coupled room-temperature terahertz detector and attributed to the fast carrier recombination driven by thermoelectric origin and high current gain, rather than the bolometric origin[6,7]. Our analysis appealingly opens the perspective to properly engineering preferred photodetection mechanism for addressing the targeted THz application requirements.

## I. Graphene-based terahertz detector design

The graphene detectors were fabricated on graphene grown by chemical vapor deposition. The large-area graphene on copper was transferred to insulating sapphire substrate by a wet transfer process followed by oxygen plasma etching. The antenna was subsequently patterned by Ultra-violet (UV) lithography after Raman characterization. The antenna is a log-periodic antenna with an outer diameter of 1 mm, consisting of a 80 nm thick Au layer on top of a 20 nm thick Cr layer as shown in Fig.1(a). Graphene outside the channel area was etched for device isolation. The dc resistance of the devices ranged approximately between 170 Ω to about 240 Ω, which is attributed to variation of the contact resistance and external environment. The carrier mobility was extracted from the $R_{DS}$ data, the electron and hole mobilities were found to be 2000cm$^2$/Vs. The relatively low mobility is due to interactions with the substrate as well as impurities introduced during processing.

## II. Experimental results

The averaged photovoltage $\Delta U$ is obtained by lock-in technique under terahertz radiation at 0.15THz and no discernable change of photoresponse is observed even with chopper frequency $f$ increased up to 50 kHz (Fig. 1a).

The terahertz transient response is characterized by square wave with a rise time of less than 2μs, and the fall time is about 2.2 μs as shown in Fig. 1c. It means that the detectors are suited to high-speed response. The Drude response of free electron gas leads to strong absorption of light at terahertz frequency, resulting in non-uniform heating of hot electron temperature along the channel. To this regard, the hot holes mostly heated in the middle of channel spread over to the side contacts following the heat flow (Fig. 1b), resulting in the formation of potential-well-like profile (from the Mott relation. The thermoelectric power $S=\pi^2 k_B^2 T dR/dE_F/3eR$ is between 150μV/K and 300μV/K with the $E_F$ around 0.1eV~0.2eV, and the electron temperature rise $\Delta T_e(x)$ is around~10K with only 0.1μW absorbed power $P_{abs}=\sigma_{abs}P_{in}$, $\sigma_{abs}$~0.1 is the absorption ratio). As driven by the potential disturbance, additional electrons $\Delta n/n$~0.5% (pertinent resistance change $\Delta R$~7Ω, $\Delta n/n=(E_F+S\Delta T/E_F)^{0.5}$-1~$eS\Delta T/2E_F$, a good agreement between experiment and theory can be obtained with $S$~200μV/K and $E_F$~0.2eV) injected from metal-graphene contact deplete the holes and enable the photoconduction indirectly. The responsivity $R_v$ defined by the ratio between voltage and the absorbed/incident power $P_{abs}$ and $P_{in}$ is shown simultaneously in Fig. 1d to present the ultimate potential of our photoconductor. The voltage change $\Delta U$ due to terahertz radiation is ~300μV ($I_{dc}$~0.4mA), yielding indeed an extremely high electrical responsivity $R_v$ of 4kV/W or 400V/W in relative to the absorbed power $P_{abs}$ ~0.2μW or incident power $P_{in}$ ~2μW. Our reported responsivity is at least orders of magnitude larger than earlier reported graphene-based device, which is benefited from the high current gain under electrical bias.

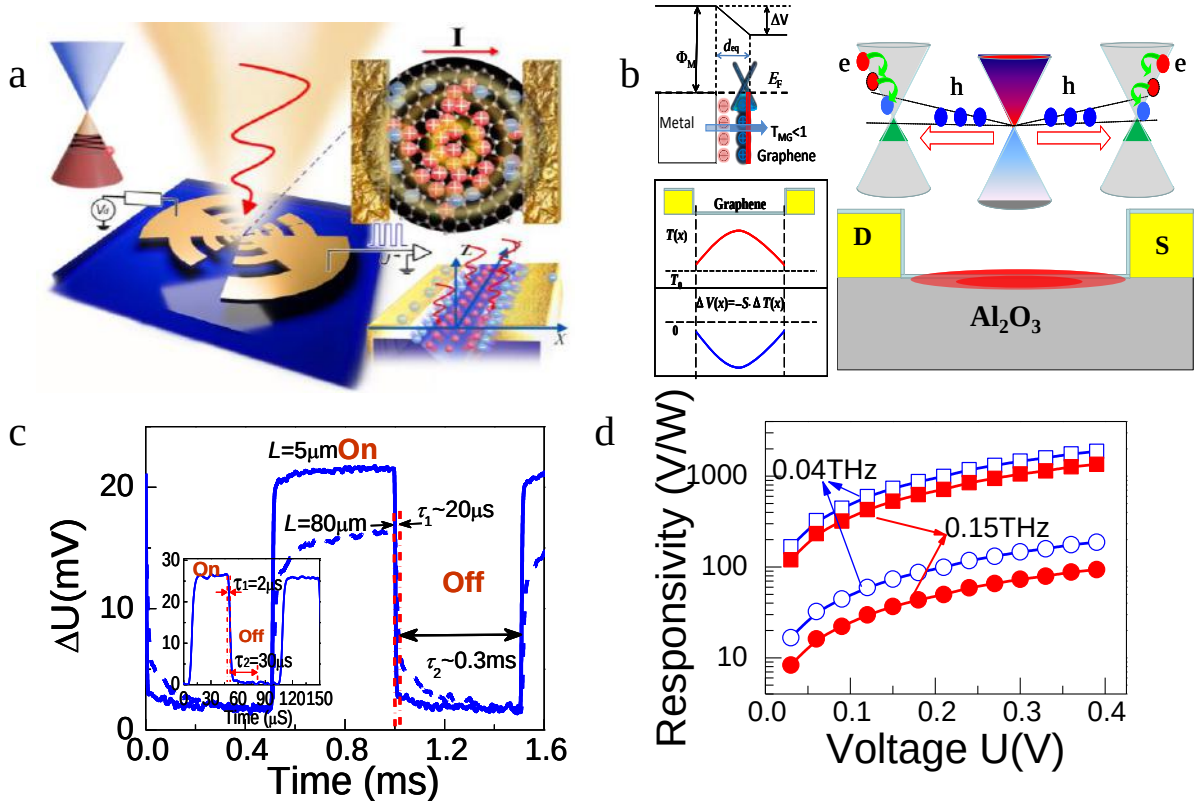



Fig. 1. (a) Schematic illustration of the terahertz photoconductor and its operation principle of electromagnetic gating effect (b): Drude response of free carrier absorption leads to nonuniform potential distribution along the channel driven by thermoelectric causing electrical injection from contacts and resistance change $\Delta R$ in the graphene channel, during the process the electromagnetic wave behaves as a gate tuning the conductivity of graphene. (c) The pulse response of graphene photoconductor with rise and fall times below 2μs. (d) is the

responsivity of the device calculated from response $\Delta U$ in relative to absorbed power $P_{abs}$ and incident power $P_{in}$.

## III. Conclusions

In this work, we have proposed and experimentally demonstrated high performance terahertz photoconductor based on electromagnetic-induced gating on homogeneous graphene. Due to both the high optical and electrical gains, we have observed experimentally that the proposed detectors with performance competitive with commercially available ones in respects of fast response time, sensitivity, low NEP, all of which play key roles in room temperature real-time imaging. The choice of photoconductive architecture, terahertz receiving antenna, and bias feed in our study are arbitrary, and the enhancement concept can be similarly applied to enhance the performance of detectors with variety of antennas with and without plasmonic contacts. In this regard, the sensitivity of our prototype detectors can be further improved through use of resonance cavity, antenna with higher bandwidth and radiation resistance.

## References

[1] Tonouchi, M. Cutting-edge terahertz technology, Nature Photonics, 1, 97-105 (2007).
[2] Horiuchi, N. Strength in diversity-view from IRMMW-THz, Nature Photonics, 9, 714-716 (2015).
[3] Cai, X.; Sushkov, A. B.; Suess, R. J.; Jadidi, M. M.; Jenkin, G. S.; Nyakiti, L. O.; Myers-Ward, R. L.; Li, S.; Yan, J.; Gaskill, D. K.; Murphy, T. E.; Drew, H. D.; Fuhrer, M. S. Sensitive room-temperature terahertz detection via the photothermoelectric effect in graphene, Nature Nanotechnology, 9, 814-819 (2014).
[4] Vicarelli, L.; Vitiello, M. S.; Coquillat, D.; Lombardo, A.; Ferrari, A. C.; Knap, W.; Polini, M.; Pellegrini, V.; Tredicucci, A. Graphene field-effect transistors as room-temperature terahertz detectors, Nature Materials, 11, 865-871 (2012).
[5] Li, J.; Niu, L.; Zheng, Z.; Yan, F. Photosensitive graphene transistors, Adv. Mater. 26, 5239-5273 (2014).
[6] Yan, J.; Kim, M.-H.; Elle, J. A.; Sushkov, A. B.; Jenkins, G. S.; Milchberg, H. M.; Fuhrer, M. S. and Drew, H. D. Dual-gated bilayer graphene hot-electron bolometer, Nature Nanotechnology, 7, 472-478 (2012).
[7] Spirito, D.; Coquillat, D.; De Bonis, S. L.; Lombardo, A.; Bruna, M.; Ferrari, A. C.; Pellegrini, V.; Tredicucci, A.; Knap, W.; Vitiello, M. S. High performance bilayer-graphene terahertz detector, Appl. Phys. Lett. 104, 061111 (2014).

# Quantitative characterization of a plasmonic zone plate using coherence-controlled holographic microscopy

**J. Babocký[1], F. Ligmajer[1,2], R. Kalousek[1,2], A. Křížová[1,2], L. Kejík[1], M. Hrtoň[1,2], P. Dvořák[1,2], M. Týč[1], V. Křápek[1,2], R. Chmelík[1,2] and T. Šikola[1,2]**

[1]Central European Institute of Technology, Brno University of Technology, Technická 10, 616 69 Brno, Czech Republic
[2]Intitute of Physical Engineering, Brno University of Technology, Technická 2, 616 69 Brno, Czech Republic
jiri.babocky@ceitec.vutbr.cz

**Abstract**— Here we present application of holographic quantitative phase imaging for plasmonic metamaterial analysis. As a demonstration we show the possibility to measure phase spectra from arrays of plasmonic antennas and quantitative phase imaging of a plasmonic zone plate.

Upon resonance plasmonic nanoantennas influence the phase of transmitted light significantly, which makes them ideal building blocks for metamaterials, but measurements of these effects are usually complicated and often require a complex data post-processing. In this work we present application of Coherence-Controlled Holographic Microscopy (CCHM)[1] for analysis of such phase effects. CCHM belongs to the family of interferometric methods providing quantitative phase contrast for each pixel of the observed image. In combination with the wavelength-tunable light source it is possible to perform wavelengthresolved quantitative phase imaging of metamaterial surface. Figure 1 shows the ability of the method to deliver a dependence of the transmitted light phase on illumination wavelength for a well-known system consisting of discshaped silver antennas on a glass substrate.

As an example of utilization of imaging capability of CCHM for metamaterial design and analysis we have investigated a zone plate made out of disc plasmonic nanoantennas. By changing the focus of CCHM we are able to obtain three-dimensional phase maps showing the behavior of the plasmonic zone plate. Figure 2 shows the cross section of the 3D map.

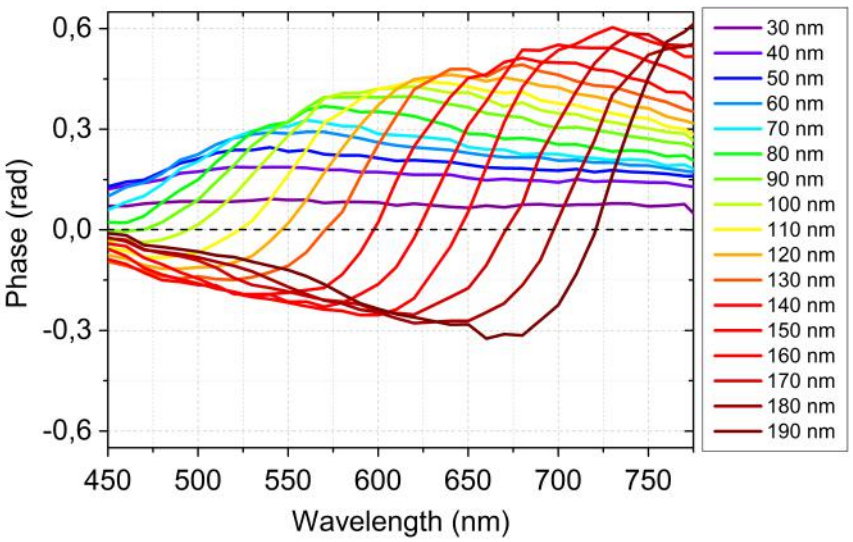



Figure 1. Phase spectra of silver disc antenna arrays with different antenna diameters measured by CCHM.

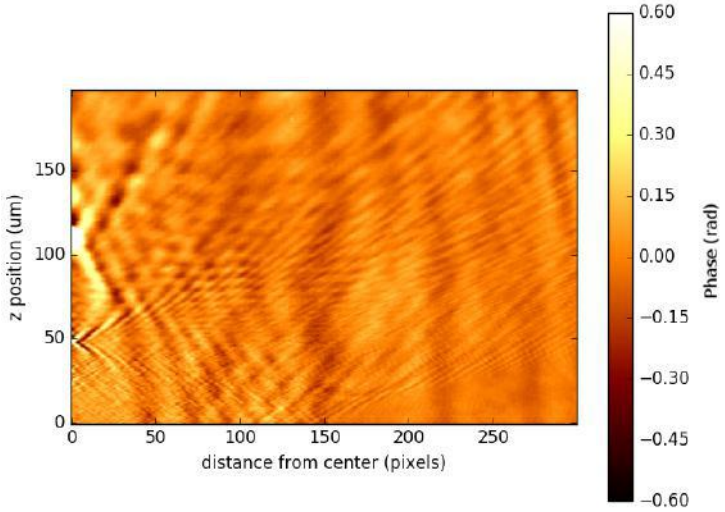



Figure 2. Cross section of a 3D phase map showing focusing of light by the plasmonic zone plate designed with the main focal point 100 μm above its plane.

We acknowledge the support by the Grant Agency of the Czech Republic (grant No. 15-21581S), European Regional Development Fund (project No. CZ.1.05/1.1.00/02.0068), MEYS CR (project No. LQ1601 – CEITEC 2020), Technology Agency of the Czech Republic (grant No. TE01020233), VaV MŠMT ČR (FSI/STI-J-15-2879).

**REFERENCES**

1. Kolman, P., Chmelík, R., "Coherence-controlled holographic microscope," *Opt. Express*, Vol. 18, No. 21, 21990–22004, 2010.

# Blackbody Metamaterial Composite film of Nanoparticle and Polymer

**K. Kajikawa**, **H. Karube**

Tokyo Institute of Technology, Japan
kajikawa@ep.titech.ac.jp

**Abstract**— We studied blackbody metamaterial composite-films of metallic nanoparticles and polymer. Reflectance, transmittance and absorption of the film are calculated on the basis of the Mie theory and Clausius Mossottii relation. We also fabricated the composite metamaterials in which gold nanoparticles are dispersed in a polyvinylpyrrolidone film. Although the experimental results are in agreement with the calculated spectra in the composite of binary gold nanoparticles with different sizes, the results are deviated from the calculated spectra of the composite of single-component nanoparticles. This may be due to aggregation of the gold nanoparticles at high volume fraction.

Light absorbers are important media for light-harvesting technology and light emitters. Since metamaterials allow us to form very thin light-absorbers, a few studies have been carried out[1-4]. Here we report a blackbody metamaterial composite film of nanoparticles and polymer. The broad-band absorption property stems from the interaction between the nanoparticles, whereas isolated nanoparticles have rather narrow absorption band at peak wavelengths. The film is formed by a simple fabrication procedure and has a high absorption over the visible wavelengths.

We fabricated a 750-nm thick composite film of gold nanoparticles and polyvinylpyrrolidone (PVP) polymer. The diameter of the nanosphere particles was $r = 100$ nm, and the volume fraction was $f = 0.4$. Experimental results of of $R$, $T$ and $A$ of the 750-nm thick composite film of gold nanoparticles in a polymer thin film matrix in Figure 1(a). The refractive index of the composite film calculated is shown in Figure 1(b). The calculation was made on the basis of the Mie theory and Clausius Mossottii relation[1, 5]. The $R$, $T$ and $A$ based on the calculated refractive index are shown in Figure 1(c). While the results of experimental and theoretical results were in good agreement at wavelengths 400−500 nm, they are deviated at the wavelengths longer than 500 nm. The possible reason is that aggregation occurs owing to the high concentration $f = 0.4$ and the optical absorption is changed from the assumption that the nanoparticles are isolated and dispersed in the polymer matrix.

We also fabricated a composite of binary particles with radii of $r_1 = 100$ and $r_2 = 37.5$ nm at volume fractions of $f_1 = 0.3$ and $f_2 = 0.1$ in a PVP film. The experimental results of $R$, $T$ and $A$ of the 260-nm thick composite film of binary gold nanoparticles with different sizes are shown in Figure 2(a). Experimental results of $R$, $T$ and $A$ of the 260-nm thick composite film in

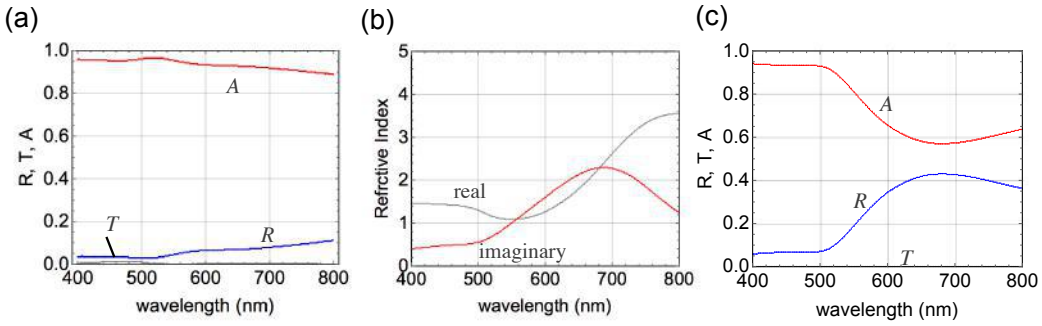



Figure 1: (a) Experimental results of $R$, $T$ and $A$ of the 750-nm thick composite film of gold nanoparticles in a thin film PVP matrix. The diameter of the nanoparticles was $r = 100$ nm, and the volume fraction was $f = 0.4$. (b) The refractive index of the composite film and (c) $R$, $T$ and $A$ calculated with the parameters $r = 100$ nm and $f = 0.4$

Figure 2(b). The absorption of the composite film over 0.8 in visible spectrum range with negligible transmittance and low reflection below 0.1. The refractive index of the composite film calculated with the parameters is shown in Figure 2(b) and the calculated $R$, $T$ and $A$ are shown in Figure 2(c). The results were almost in agreement, because of absence of aggregation in the binary particle composite.

In summary, theoretical and experimental results of blackbody metamaterial films of nanoparticles and polymer are presented. It is shown that this calculation can be used to interpret the optical properties of the blackbody metamaterial film.

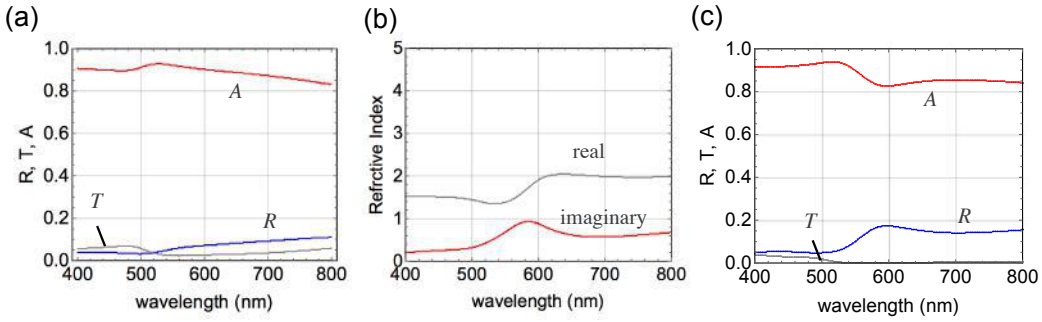



Figure 2: (a) Experimental results of of $R$, $T$ and $A$ of the 260-nm thick composite film of binary mixture of gold nanoparticles in a thin film PVP matrix. The nanoparticles were $r_1 = 100$ and $r_2 = 37.5$ nm with volume fractions of $f_1 = 0.3$ and $f_2 = 0.1$. (b) The refractive index of the composite film and (c) $R$, $T$ and $A$ calculated with the parameters $r_1 = 100, r_2 = 37.5, f_1 = 0.3$ nm and $f_2 = 0.1$.

## ACKNOWLEDGMENT

This work was partially supported by a Grant-in-Aid for Scientific Research (No. 25109707, 26600023, 26286058, 16K13696) and Bilateral Program from the Japan Society for the Promotion of Science.

## REFERENCES

1. Kravets, V. G., Neubeck, S. and Grigorenko, A. N, "Plasmonic blackbody: Strong absorption of light by metal nanoparticles enbedded in a dielectric matrix," *Phys. Rev. B*, Vol. 81, 165401, 2010.
2. Kravets, V. G., Schedin, F. and Grigorenko, A. N, "Plasmonic blackbody: Almost complete absorption of light in nanostructured metallic coatings," *Phys. Rev. B*, Vol. 78, 205405, 2008.
3. Ebihara, Y., Ota, R., Noriki, T., Shimojo, M. and Kajikawa, K.,"Biometamaterials: Black Ultrathin Gold Film Fabricated on Lotus Leaf," *Sci. Rep.*, Vol. 5, 15992, 2015.
4. Ebihara, Y., Sugimachi, Y., Noriki, T., Shimojo, M. and Kajikawa, K.,"Biometamaterial: dark ultrathin gold film fabricated on taro leaf," *Opt. Mat. Express*, Vol. 6, 1429–1435, 2015.
5. Doyle, W. T., "Optical Properties of a suspension of metal spheres," *Phys. Rev. B*, Vol. 39, 9852–9858, 1989.

# Gradient phase Metasurface lens to focus electromagnetic waves

**Akram BOUBAKRI[1*], Fethi CHOUBENI[1], Tan Hoa Vuong[2] and Jacques.David[2]**

[1]INNOVCOM Lab SUPCOM, Tunisia
[2]Plasma and energy conversion Lab INPT, France

[*]corresponding author, E-mail: akram.boubakri@supcom.tn

## Abstract

Metamaterials offer abilities to manipulate the electromagnetic wave by enabling the control of amplitude, polarization and phase of the light beam at subwavelength scale. Recent progress has shown that flat metasurfaces with reduced dimensions are capable to provide an abrupt phase change which is responsible for the modification of the wave front beam and enable the development of a novel ultrathin flat lens. Here, we present a flat metasurface lens consisting of a metal-dielectric-metal structure operating at 6GHz and enable the improvement of the antenna gain of about 12% with a shift of the main beam 4 degrees anticlockwise.

## 1. Introduction

The control of electromagnetic waves is a key aim of several researches over the past decade. Those researches have showed that Metamaterials have a strong abilities to manipulate the electromagnetic waves on a subwavelength scales thanks to its unconventional properties that are not available in natural materials. In addition metamaterials have provided fascinating effects such as negative refraction index, super imaging and invisibility cloaking…

Inspired by Pendry's super lens[1]that could focus a point source to a point image, many efforts were devoted utilizing metamaterial lenses to avoid some drawbacks presented by conventional lenses such as curved shape and bulky size. Metasurfaces have been used by several researchers for antenna performance improvement. The main mechanical advantages of those structures over three dimensional material structures are ease of fabrication and a smaller required volume. In this work we showed that a well designed metasurface lens can efficiently control the beam direction of an incident plane wave and enhances the gain of a patch antenna thanks to its near zero refractive index.

According to the Fermat's principle, the wave front beam can be modified by controlling its phase [2][3]. As well as, while the convergence of optical waves relies on a gradual phase accumulation during the propagation in conventional lenses, focusing mechanism resulting from abrupt phase change can be achieved using phased array metasurfaces.

## 2. Design of the proposed metalens

The proposed 40×32 mm$^2$ bi-layered metalens is comprised of periodically distributed 5×3 I shaped unit cell on the top layer and identical symmetrical slots on the bottom as depicted in figure 1. The two layers are built over a Roger substrate with a height of about 1.36 mm.

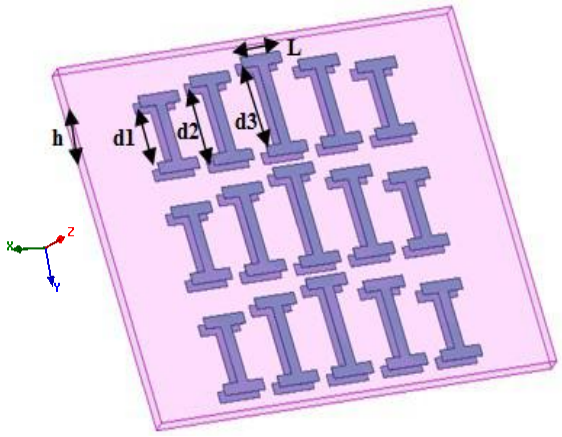



Figure 1: The metalens design with d1=5mm, d2=6mm, d3=7mm , L=4mm and h=1.36.

By varying the geometric parameters of each slot unit, a abrupt phase change is obtained at different positions that enable the gradient metasurfaces to focus electromagnetic wave. This phase shift is illustrated on the figure 2.

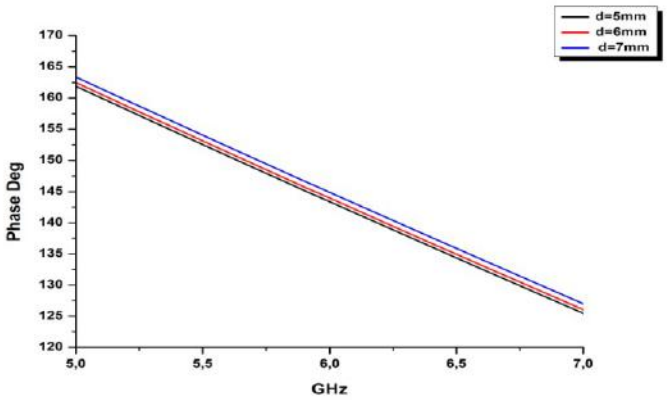



Figure 2: Phase change for the three different unit cells.

The transmitted wave through the metalens at different position should meet the phase relationship as described below:

$$\Delta\varphi = \left(\sqrt{f^2 + r^2} - f\right)\frac{2\pi}{\lambda} \quad , \qquad (1)$$

Where Δφ represent the phase change and f is the focal length. The above equation has three variables and if one of them is known, the relationship between the other two could be easily obtained. From equation 1, we found that f is directly related to the working wavelength while their relation is not simply being reciprocal since Δφ is also determined by the wavelength in a more complicated way[3].

For a better focusing effect and to engineer the required phase change, our proposed metalens was designed with three different metasurfaces unit cells and two spaced layers. Those unit cells are separated by a subwavelength distance and the interaction of the near field is relatively small. When an oscillating electric field is applied to the metasurfaces, free electrons in unit cells oscillate forced by the electric field and restoring force[4]. The strong interaction between incident wave and surface plasmons of unit cells is the key of the phase shift. Unit cells with spatially varying geometry work as resonators, giving rise to phase discontinuity through the subwavelength thickness.

The electromagnetic properties of the proposed metalens were numerically demonstrated by using HFSS. The incident wave is linearly polarized along the z axis. Figure 3 below shows the scattering parameters for a double layered and a single layered metalens.

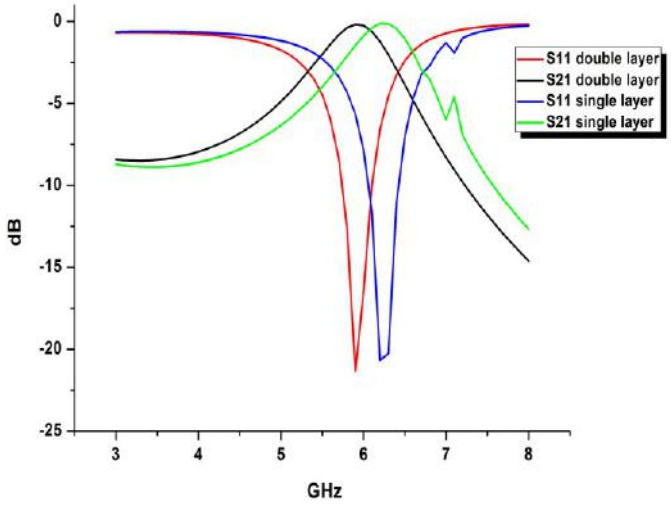



Figure3: Scattering parameters of the proposed metalens.

For both metalens structure, the operating frequency is around 6 GHz with a return loss of about -22 dB. The small frequency shift is due to mutual coupling between the two layers. From the simulation results it can be clearly observed that the operating bands of the proposed metalens are suitable for WLAN applications(IEEE 802.11 a).

Based on HFSS simulation results, and using smith retrieval method[5], we obtained the refractive index and the effective permittivity and permeability of the two proposed metalenses (Single layered and double layered). It's clear from the figure 4 that the two proposed metalens have both a near zero refractive index ( negative value equal to -0.04 for the single layered and positive value equal to 0.056 for the double layered ).The most attractive properties of near zero refractive index lens is that the electromagnetic field propagate with near zero phase variety inside the structure . According to snell's law of refraction, a Near Zero Refractive index structure causes the electromagnetic wave to emanate in any direction away from the primary source and to reflect nearly parallel to the normal of the surface structure. This characteristic offers an outstanding technique for beam control and gain enhancement.

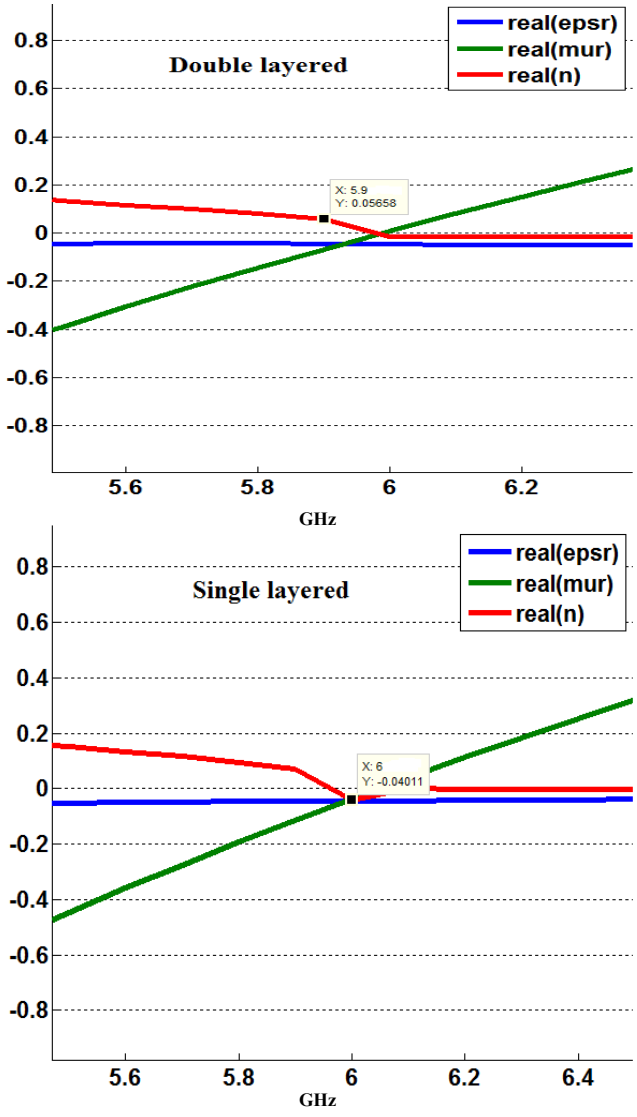



Figure 4: Near-zero refractive index of the two proposed metalens.

## 3. Metalens for Antenna gain enhancement and beam shifting

A patch antenna operating at 6GHz , suitable for WLAN applications, with known parameters is used as reference antenna. It gives a gain of about 7.9 dB with a return loss of about -20dB as illustrated in the figure 5 below.
The key feature of the proposed metalens are low profile, ease of integration with active microwave component and coupling reduction. Based on that, the studied metalens is used as a superstrate for antenna performance enhancement.

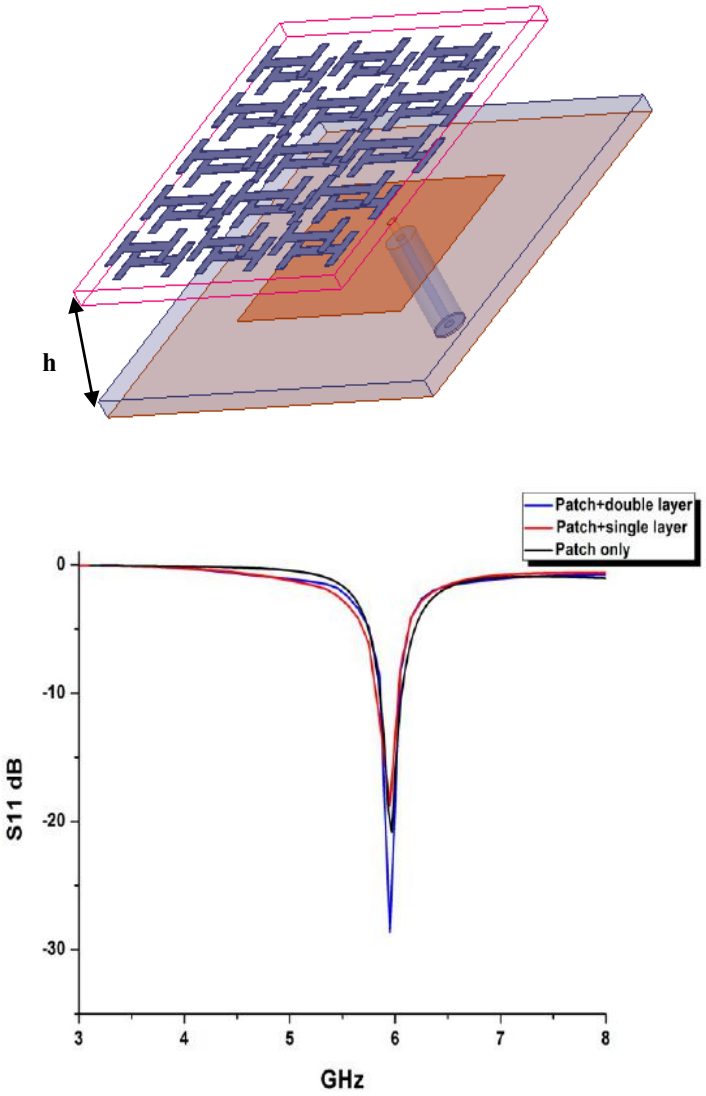



Figure 5:Enhancement of antenna characteristics with single and bi-layered metalens.

When the number of layers is further increased, the focusing effect is much more enhanced. To show that, we tried to study the behavior of the antenna with single layered or bi- layered metalens superstrate.

The optimal space width h between the antenna and the superstrate metalens was found to be 10 mm. With that value the single layered metalens gives a gain of about 8.3dB (5% enhancement) with a return loss of the whole structure of –18dB. Nevertheless the bi-layered metalens enhance the antenna gain of about 12% and gives a value of 8.9 dB with a return loss of -29 dB as depicted in figure 5.

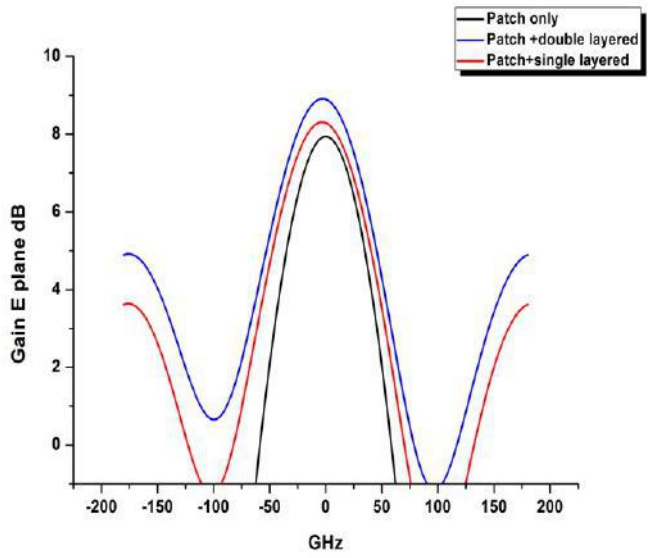



Figure 6:2D gain of different simulation structures.

In the light of the foregoing, we can say that however the value of the refractive index of the metasurfaces lens is close to zero and positive for the bilayered case. The radiated electromagnetic field of the metasurfaces produces an internal oscillation, which introduced an identical illumination that improves the overall radiation performance [6][7]. Nevertheless, inspite the enhancement of the reference antenna gain using the superstratre metalens, its clear in figure 6 that the backward radiation has been also increased which may be considered as a disadvantages for this flat metalens.

As we said before, a Near Zero Refractive index structure causes the electromagnetic wave to emanate in any direction away from the primary source and to reflect nearly parallel to the normal of the surface structure. This characteristic offers an outstanding technique especially for beam control.
In our case and in addition to the gain enhancement. The metalens superstrate gives a shift in the E plane main beam of about 4 degrees anticlockwise for the bi-layered metalens superstrate and of -2 degrees anticlockwise for the single case as it's illustrated in figure 7 below.

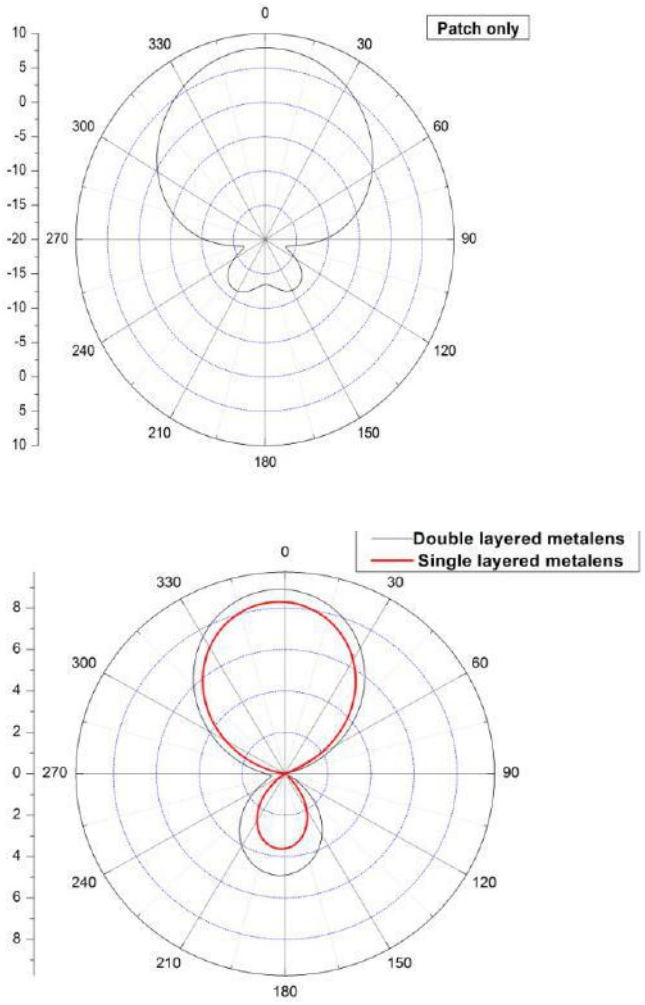



Figure 7:E palne Radiation pattern of the structure.

## 4. Conclusions

Here in this work, we have studied the behavior of two types of NZRI metalens based on I shaped slot metasurface. Thanks to the gradient phase of the structure, the single layered metalens exhibits an improvement of the antenna gain of 5% and a shift of the main beam of 2 degrees anticlockwise. However, for the two layered metalens case we obtained 12% of gain improvement and 4 degrees of beam shift anticlockwise. Finally, our proposed metalens can be used in WLAN applications.

## References

[1] J.B Pendry, Negative refractive index makes a perfect lens, Phy.Rev.Lett, 85(18),3966-3969, 2000.

[2] S.Sun and all, Gradient index metasurfaces as a bridge linking propagating waves and surface waves, Natural materials 11,426,2012.

[3] Quanlong and all, Efficient flat metasurfaces lens for terahertz imaging, Optic express, Vol 22, N 21,2014.

[4] Minkyung Kim and Junsuk Rho, Metamaterials and imaging, Nano convergence Springer, 2015.

[5] R.A.Shelby, DR.Smith, S.Schultz, Experimental verification of negative index of refraction, Science vol 292 p77-79 May 2001.

[6] Mohammad Habib Ullah and all, A near zero refractive index metasurfaces structure for antenna performance improvement, Materials 13, 6,5058,5068, 2013.

[7] Mohammad Habib Ullah and all, A new metasurfaces reflective structure for simultaneaous enhancement of antenna bandwidth and gain, smart material and structures,23,2014.

# Plasmon-enhanced photovoltaics, photocatalysis, and solar fuels

# Silver as Terbium-Yterbium sensitizer in glass and glass-ceramic thin films for photovoltaic efficiency enhancement

**S. Belmokhtar[1], A. Bouajaj[1*], M.R. Britel[1], J. Heminej[2], F. Enrichi[3,4], C. Armellini[4], G. Battaglin[5], F. Belluomo[6], E. Cattaruzza[5], M. Ferrari[4], F. Gonella[5], A. Łukowiak[7], M. Mardegan[5], S. Polizzi[5], C. Sada[8], E. Trave[4]**

[1] Laboratoire des Technologies Innovantes, LTI, Département de Génie industriel ENSA – Tanger, Université Abdelmalek Essaâdi. Tanger, Morocco.
[2]Université Hassan II Mohammedia-Casablanca, LPMC-FST , Mohammedia , Maroc.
[3] Veneto Nanotech, Laboratorio LANN, C.so Stati Uniti 4, 35127 Padova, Italy.
[4] CNR-IFN, Istituto di Fotonica e Nanotecnologie, CSMFO Lab. & FBK-CMM, Via alla Cascata 56/C, Povo, 38123 Trento, Italy
[5] Center for Nanosciences and Nanobiomaterials, Department of Molecular Sciences and Nanosystems, Università Ca' Foscari Venezia, via Torino 155/b, 30172 Venezia-Mestre, Italy
[6] Meridionale Impianti SpA, Via Senatore Simonetta 26/D, 20867 Caponago (MB), Italy
[7] Institute of Low Temperature and Structure Research, PAS, ul. Okolna 2, 50-422 Wroclaw, Poland
[8] Dipartimento di Fisica G. Galilei, Università di Padova, Via Marzolo 8, 35131 Padova, Italy
[*]Author for correspondence: dbouajaj@yahoo.fr

**Abstract**- One of the keys to improve the efficiency of photovoltaic solar cells is the match between solar spectrum and semiconductor band gap. This can be done by inserting in the front or rear of the solar cell an optically active layer doped with rare earth ions which acts as down-converter or up-converter. This is just one of the possibilities that involve several structures and geometries such as waveguide configuration and radiation trapping systems. Among these systems glass ceramics play a crucial role especially because they combine the optical properties of glasses with the spectroscopic properties of the crystals activated by luminescent species. However, one of the major issues of rare earths is that they suffer from a small absorption cross section. Therefore, the use of silver nanoparticle as antenna systems to enlarge the absorption spectral region and the efficiency of the process can improve significantly the optical performance of the down converting layer. In this work we will focus the attention on the cooperative energy transfer between $Tb^{3+}$ ion and two $Yb^{3+}$ ions in a $70SiO_2$-$30HfO_2$ glass-ceramic waveguide. These systems allow to cut one high energy photon at wavelength shorter than 488 nm into two low energy photons around 980 nm. On the other hand we will show how the presence of silver nanoaggregates and nanoparticles can enlarge the absorption spectral region and strongly enhance the absorption efficiency of rare earths.
Different rare-earth concentrations and silver ion exchange conditions were studied in order to obtain favorable conditions for improving the performance of photovoltaic solar cells.

**Acknowledgements**. The research activity was performed in the framework of the CNR-CNRST joint project (2014-2015).

# Plasmonic improvement of low cost anatase nanoparticles for dye sensitized solar cells

**M. M. Rashad[1*], M.S. Sanad[1], A. E. Shalan[1]**

Central Metallurgical Research and Development Institute (CMRDI)

P.O. Box: 87 Helwan, Cairo, Egypt

E-mail: rashad133@yahoo.com

## Abstract

A low cost mesoporous $TiO_2$ nanoparticles has been synthesized using hydrothermal route based on $TiOCl_2$ produced from Abu Ghalaga ilmenite ore, Egypt. The precious metallic nanoparticles; Ag, Pt and Pd have been nanoparticles from spent catalysts have been extracted and embedded between the anatase particles using in situ reduction step. XRD and TEM investigations revealed that the as-prepared powders crystallized as anatase $TiO_2$ phase with sphere-like structure of average particle size ~6.5–8.0 nm for un-doped titania sample, whereas the noble metals doped titania samples were appeared in an oval-like structure of average particle size ~10–12 nm. The $N_2$ adsorption–desorption measurements demonstrated the mesostructure nature of all samples, with a surface area range of 124.1–175.7 $m^2\ g^{-1}$ and pore volume range of 0.18–0.27 $cm^3\ g^{-1}$. The 0.5% precious metal doped samples NPs exhibit absorption enhancement over a broad wavelength range due to the excitation of localized surface plasmons (LSPs) at different wavelengths which also exhibited very good and enhanced photovoltaic performance as a result of the strong scattering light resulting of noticeable improvement of charge transfer rates. The as-prepared meso $TiO_2$ sample was showed the lowest overall conversion efficiency ($\eta$) ~ 3.0% and highest fill factor (*FF*) ~ 69.7%, respectively. As expected the as-prepared Ag@$TiO_2$ sample, superior photovoltaic performance was achieved with ~50% improvement in the overall solar device conversion efficiency has been achieved. Overall, from best of our knowledge, this work has sufficiently shed the light on examining the synergistic effects for combining the ore materials mesostructure titania form with surface plasmonic nanoparticles for the first time.

# Metamaterials for Solar Cell Applications

**N. Sharac[1], R. Flynn[2], H. Kim[2], H. Kim[2], A. Makinen[3], L. Hirst[2], C. Ellis[2], J. Tischler[2], P. Jenkins[2], P. Campbell[2], J. Owrutsky[2], J. Caldwell[2] and O. Glembocki[2]**

[1]NRC Postdoctoral Fellow (residing at NRL, Washington, DC)

[2] U.S. Naval Research Laboratory, 4555 Overlook Ave, S.W., Washington, D.C. USA

[3]Office of Naval Research, 875 N. Randolph Street, Arlington, VA. USA

**Abstract**- In this talk we present a light trapping metamaterial structure, consisting of metallic 1D and 2D gratings which couple light through a thin insulating dielectric layer and into a thin doped transparent conducting oxide (TCO) film, which forms a Schottky contact with Si. This configuration absorbs light in the visible through interband transitions (normal operation) and uses hot electrons in the IR. The gratings show broad plasmon resonances in the visible and near-IR range, where enhanced photocurrent is observed.

# Topological photonics

# A Photonic Analog of Chern Insulators Predicted

**Hsun-Chi Chan**[1], **Ta-Chun Lin**[1], **and Guang-Yu Guo** [1*]
[1]Department of Physics, National Taiwan University, Taipei 10617, Taiwan
[*]Corresponding author: gyguo@phys.ntu.edu.tw

**Abstract**-Based on electromagnetic simulations, we predict that a square lattice photonic crystal has a band gap with a nonzero Chern number due to time-reversal symmetry breaking. We also show that the system has topological nontrivial one-way edge state, complying with bulk-edge correspondence principle.

Optical analogs of topological insulators and Chern insulators have recently attracted much attention in the nanophotonic community [1]. Here by using electromagnetic numerical simulations, we investigate topological properties of square lattice photonic crystals, a class of zero-refractive-index materials which also have interesting properties in wave propagation [2]. We find that when the dielectric in the two-dimensional photonic crystal is replaced by a magneto-optical material which breaks time-reversal symmetry, a nontrivial band gap is opened at the Dirac point. The topological nature of the band gap is confirmed by our further calculations of the Chern number [3] due to nonzero Berry curvatures in the momentum space. We also study numerically the corresponding gapless edge states by putting a point source and a metal obstacle on the edge of the system. Our numerical simulations demonstrate that a running wave in the system can only propagate along the edge in one direction and can by-pass the metal obstacle, as shown in Fig. 1.

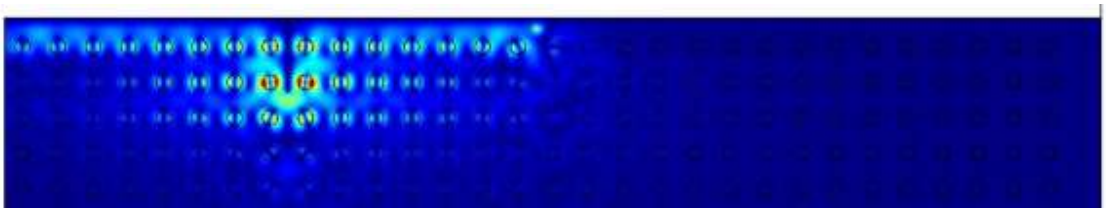


**Figure 1:** A numerical simulation showing the one-way property of the edge state on the system.

## REFERENCES

1. Lu, L., Joannopoulos, J. D. and Soljacic, M. "Topological photonics," Nat. Photon., Vol. 8, 821-829, 2014.
2. Huang, X., Lai, Y., Hang, Z. H., Zheng, H. and Chan, C. T. "Dirac cones induced by accidental degeneracy in photonic crystals and zero-refractive-index materials," Nat. Mater., Vol. 10, 582-586, 2011.
3. Fukui, T., Hatsugai, Y. and Suzuki, H. "Chern Numbers in Discretized Brillouin Zone: Efficient Method of Computing (Spin) Hall Conductances," J. Phys. Soc. Jpn., Vol. 74, 1674-1677, 2005.

# Topological properties of nearly flat bands in two-dimensional photonic crystals

**B. Yang[1, 2*], T. Wu[1], and X. D. Zhang[1]**

[1]School of Physics and Beijing Key Laboratory of Nanophotonics & Ultrafine Optoelectronic Systems, Beijing Institute of Technology, China

[2]School of Physical Science and Information Engineering and Shandong Provincial Key Laboratory of Optical Communication Science and Technology, Liaocheng University, China

[*]corresponding author: yangbingln2002@163.com

**Abstract**-Based on exact numerical calculations and physical analyses, we demonstrate that there are two types of nearly flat band in two-dimensional (2D) magnetic photonic crystals (PhCs). One has trivial topology with zero Chern number and the other has non-trivial topology with nonzero Chern number. Physical origins and topological properties of these two types of flat band are studied comparatively.

Recently the topological flat band states in electron systems have received a great deal of interest because of their importance in fractional quantum Hall effect [1, 2]. While in optical systems, the studies of flat band states are mainly focused on areas of slow light in PhCs [3] and diffraction-free transmission and localized states in photonic lattices waveguides without concerning with topological aspects [4, 5] up to now. In this work, we demonstrate there are two kinds of flat band states with different topological class in 2D magnetic PhCs, and theoretically study their physical origins and associated topological properties.

The 2D PhCs considered here are composed of magnetic material rods embedded in air. When an external dc magnetic field is applied along axis of the rods, the rods perform strong gyromagnetic anisotropy which breaks the time-reversal symmetry (TRS) of the system and may lead to topologically non-trivial states.

The topologically trivial flat band states originate from resonant scatterings of the single rod or the cavity modes encircled by rods in PhCs with complex lattices, while the topologically non-trivial flat band states come from strong gyromagnetic coupling interactions of fields at boundary between adjacent unit cells.

For topologically trivial flat band Berry curvatures are all almost zero in the whole BZ, and for topological flat band, they vary slowly in the entire wave vector space.

Energy transfers of two types of flat band states also perform different characteristics in PhCs [6]. In Fig. 1 we show the simulation results for them in 2D finite sized PhCs constructed by a $13\times13$ array of square complex lattice. Here the complex lattice is composed of a $3\times3$ simple square lattice with the central rod removed. When a point source with the frequency corresponding to the trivial flat band is placed inside the PhCs, its radiation is easily cloaked by metal obstacles as shown in Figures 1(a)-1(c). In contrast, non-trivial flat band states possess unidirectional propagation characteristics in 2D all space that are robust against obstacles as shown in Figures 1(d)-1(f), which corresponds to the case of backscattering-free one-way wave propagation for chiral edge states. We believe that our findings are useful for realizing physical phenomena of cloaking and transparency of waves.

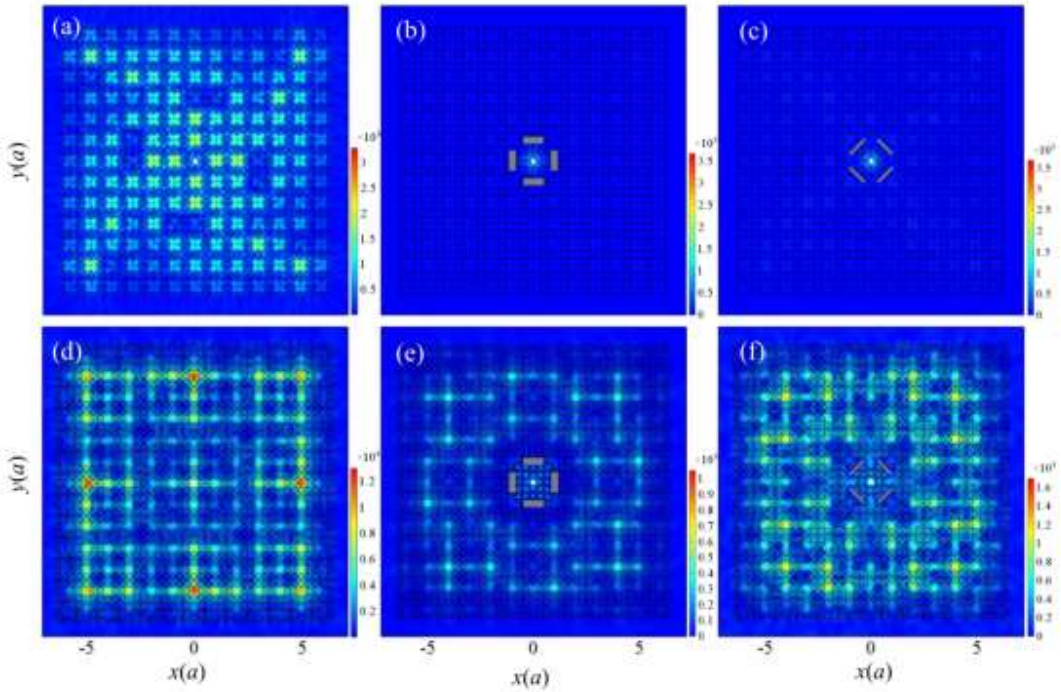



Figure. 1. Simulations of energy transfer in PhCs. (*a*)-(c) Results with frequency corresponding to topologically trivial flat band. (d)-(f) Results with frequency corresponding to topologically non-trivial flat band. (*a*), (d) Wihtout metal obstacles, (b), (c), (e), (f) Four rectangular metal obstacles (perfect electronic conducts) are inserted at different positions in PhCs. The point source is denoted by a white star at (0,0) and metal obstacles are denoted by gray rectangles.

**Acknowledgements**, This work is supported by the National Natural Science Foundation of China (11574031 and 61421001).

**REFERENCES**

1. Sun, K., Z. Gu, H. Katsura and S. Das Sarma, "Nearly Flatbands with Nontrivial Topology," *Phys. Rev. Lett.*, Vol. 106, 236803, 2011.
2. Regnaultand, N. and B. A. Bernevig, "Fractional Chern Insulator," *Phys. Rev. X*, Vol. 1, 021014, 2011.
3. Baba, T. "Slow light in photonic crystals," *Nat. Photonics*, Vol. 2, 465–473, 2008.
4. Vicencio, R. A., C. Cantillano, L. Morales-Inostroza, B. Real, C. Mejía-Cortés, S. Weimann, A. Szameit and M. I.Molina, "Observation of Localized States in Lieb Photonic Lattices," *Phys. Rev. Lett.*, Vol. 114, 245503, 2015.
5. Mukherjee, S., A. Spracklen, D. Choudhury, N. Goldman, P. Öhberg, E. Andersson and R. R. Thomson, "Observation of a Localized Flat-Band State in a Photonic Lieb Lattice," *Phys. Rev. Lett.*, Vol. 114, 245504, 2015.
6. Yang, B., T. Wu and X. D. Zhang, "Topological properties of nearly flat bands in two-dimensional photonic crystals," *preparing*.

# Quantum photonics

# Optimal Ultra-wide Spatial-Spectral Windows for Hyperentangled Two-photon Emission

**S. F. Hegazy**[1,2], **J. El-Azab** [1], **Y. A. Badr**[1], **and S. S. A. Obayya**[2*]

[1] National Institute of Laser Enhanced Sciences, Cairo University, 12613 Giza, Egypt

[2] Centre for Photonics and Smart Materials, Zewail City of Science and Technology, 12588 Giza, Egypt

[*]corresponding author: sobayya@zewailcity.edu.eg

**Abstract-** While being optimally compensated for spatial phase variations, the two-photon state produced by the two-crystal emission exhibits spatial and spectral decoherence off the central emission modes. In this paper, we present an experimentally convenient method to optimize the ultra-wide spatial and spectral windows; allowing the minimum spatial-spectral decoherence for a required two-photon flux.

The creation of hyperentangled photons entails two-photon emission over relatively wide extent in frequency and transverse space within which the photons are simultaneously entangled in energy, spatial mode and polarization [1-3]. Because the creation process runs in nonlinear domain(s) which is always dispersive and birefringent, the output two-photon state undergoes loss of relative-phase coherence over frequency and space. This offers the vital role of spatial-spectral phase compensation using birefringent element [2, 4] so as to restore partially the state coherence in the two degrees of freedom. After compensation, the two-photon state emerges with much better phase flatness allowing collection over wider spatial and spectral ranges. However, over ultra-wide windows, the spatial and spectral modes away from the central *truly* compensated modes suffer strong phase variations appears to dominate the scene. In this paper, we present an experimentally convenient approach to optimizing the ranges of the ultra-wide spatial and spectral filters so as to diminish decoherence of the two-photon state at fixed photon-pair flux. Consider a paraxial pump field linearly polarized on 45 deg. and described as a sum of monochromatic plane waves $E_p(r,t) = \iint dw_p\, dq_p\, A_p(w_p, q_p) \exp i(k_p.r - w_p t)$. As depicted in Fig. 1(a), this pump field illuminates two contiguous identical type-I crystals whose principal planes are orthogonal to each other, the two-photon state (excluding vacuum) can be expressed to first order as

$$|\psi\rangle = \int dw_s\, dw_i dq_s\, dq_i\ \chi^{(2)}(w_s, w_i; w_s + w_i)\, A_p(w_s + w_i, q_s + q_i)\, d\,\mathrm{sinc}\left(\frac{\Delta\kappa d}{2}\right) \times \left\{|H\rangle_{q_s,w_s}|H\rangle_{q_i,w_i} + \exp i[\Phi_o + \Phi_{DC}(q_s, q_i, w_s, w_i)]\,|V\rangle_{q_s,w_s}|V\rangle_{q_i,w_i}\right\} \quad (1)$$

where $\chi^{(2)}$ is the second-order effective susceptibility, $(q_s, q_i)$ and $(w_s, w_i)$ are the transverse wavevectors and angular frequencies of the signal and idler photons, respectively, $\Phi_o$ is the initial phase difference between the pump components, $\Phi_{DC}$ is the relative phase accumulated in the SPDC process, $d$ is the crystal length, and $\Delta\kappa$ is the longitudinal wavevector mismatch. and $A_p(w_p, q_p)$ is assumed to be a real function centered on $w_p = w_p^0$ and $q_p = 0$. Assuming that the effective susceptibility is slowly varying within that spectral window and the spatial-spectral function $A_p(w_s + w_i, q_s + q_i)$ is very narrow relative to the remainder of the integrand in (1), the probability of the photon pair to be detected along a mode in the momentum-frequency space $(q_s)\otimes(w_s)$ is then

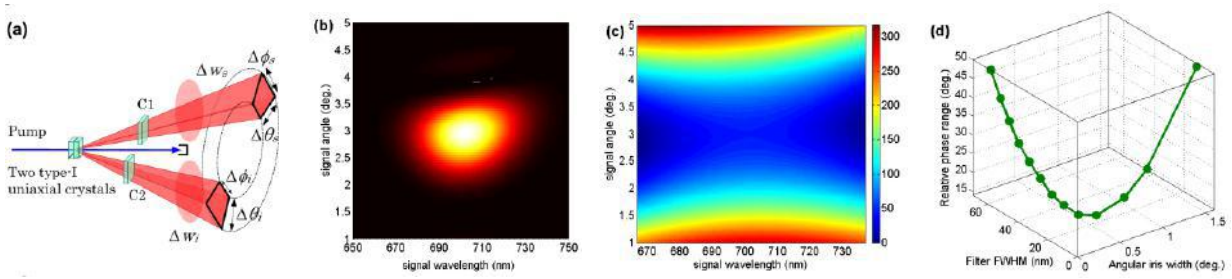



Fig. 1 (a) hyperentangled photon source equipped with optimal compensation crystals and ultra-wide iris and spectral filters. (b) spatial-spectral two-photon probability and (c) relative phase map calculated behind two compensation elements acting by the optimal compensation. The pump laser is taken at 351.1 nm and the SPDC and compensation crystals are BBO crystals with $d = 0.59$ mm and cut angle 33.9° producing degenerate emission centered at ~3° opening angle. The spectral filters are assumed to have a normalized Gaussian profile of 70-nm FWHM. (d) Optimization of residual relative-phase over different arrangements of ultra-wide spatial and spectral windows realizing the fixed two-photon flux.

$$P(q_s, w_s) \propto \left| \mathrm{G}(w_s - w_d^0)\ \mathrm{G}(w_p^0 - w_s - w_d^0)\ \mathrm{sinc}\left(\frac{\Delta\kappa(q_s, w_s)\ d}{2}\right)\right|^2 \tag{2}$$

behind two filters of spectral profile $\mathrm{G}(w)$ centered at the degenerate frequency $w_d^0$. One should notice that since the SPDC crystals are thin and the two-photon emission is at small angles, both the probability $P(q_s, w_s)$ and the phase map $\Phi_{\mathrm{DC}}(q_s, w_s)$ depend negligibly on the azimuthal angle [5].

A major request by an experimentalist is thereby to obtain the FWHM of the spectral filter as well as the width of the iris that allow a required rate of coincidence counts while optimally minimize the phase map difference. Given the spatial-spectral two-photon probability in (2) [see Fig. 1.(b)], one can determine an array of arrangements of ultra-wide spatial and spectral windows realizing fixed two-photon flux. Now, recalling the compensated relative-phase map obtained in ref. [4] [see Fig. 1.(c)], each of these fixed-flux arrangements leads to a particular range of phase map variations. The points in Fig 1.d therefore represent the phase-map range corresponding to the variant fixed-flux arrangements. For the optical setup parameters in Fig. 1, a 30-nm interference filter and ~0.5-deg acceptance iris are found offering the minimum phase map variations compared with the other arrangements of the same pair flux.

**Acknowledgements**, This work was supported by the Information Technology Industry Development Agency (ITIDA-ITAC), ministry of communication, Egypt.

## REFERENCES

1. Kwiat, P. G., Waks, E., White, A. G., Appelbaum, I., and Eberhard, P. H. (1999). Ultrabright source of polarization-entangled photons. Phys. Rev. A, 60(2), R773.
2. Altepeter, J., Jeffrey, E., and Kwiat, P. (2005). Phase-compensated ultra-bright source of entangled photons. Opt. Express, 13(22), 8951-8959.
3. Hegazy, S. F., Mansour, M. S., and El-Nadi, L. (2013). Enhanced type-I polarization-entangled photons using CW-diode laser. In Proceedings of the 4th International Conference on Modern Trends in Physics Research (Vol. 10, pp. 211-220).
4. Hegazy, S. F., and Obayya, S. S. A. (2015). Tunable spatial-spectral phase compensation of type-I (ooe) hyperentangled photons. J. Opt. Soc. Am. B, 32(3), 445-450.
5. Hegazy, S. F., El-Azab, J., A. Badr, Y., Obayya, S. S. A.. Accurate relative phase and time delay maps all over the emission cone of hyperentangled photon source. To be In Proc. of SPIE (2016).

# Modeling of optical gain in Ge-based two dimensional structures

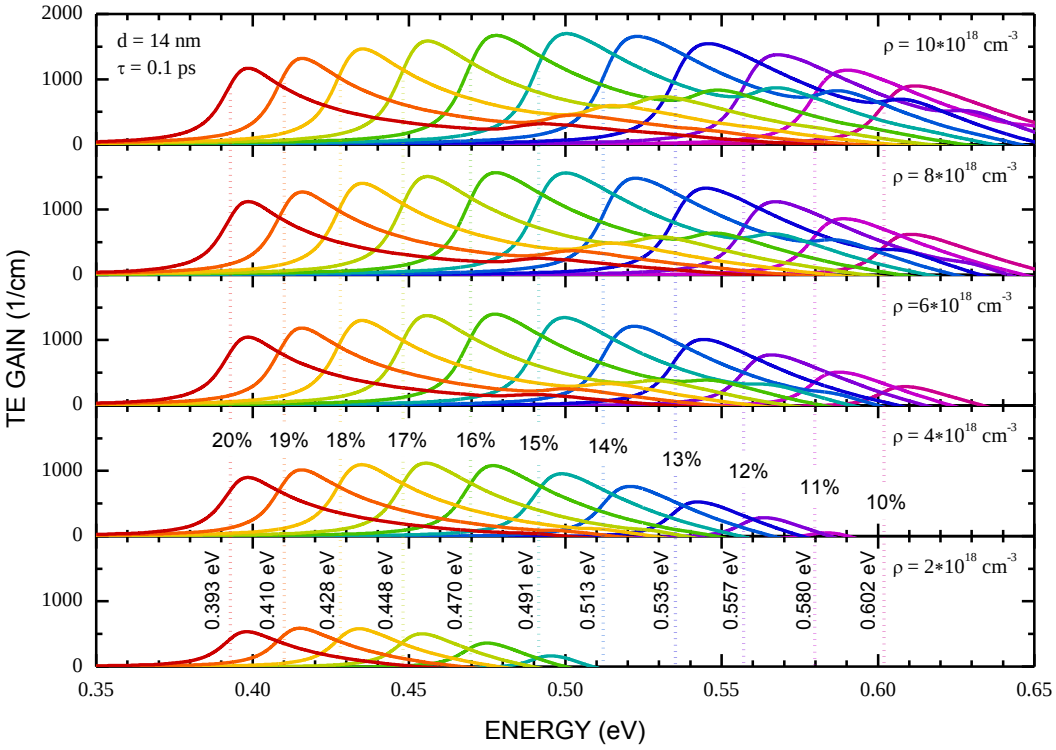
**M. Gladysiewicz*, H. Maczko, and R. Kudrawiec**
Faculty of Fundamental Problems of Technology, Wroclaw University of Technology,
Wybrzeże Wyspiańskiego 27, 50-370 Wrocław, Poland
*corresponding author: marta.gladysiewicz@pwr.edu.pl

**Abstract**-The 8-band *kp* Hamiltonian is applied to calculate the electronic band structure and the optical gain for $Ge_{1-x}Sn_x$/Ge quantum wells (QW) grown on Ge substrate. Sn-related changes in the electronic band structure of $Ge_{1-x}Sn_x$ alloy are modeled according to recent *ab-inito* calculations and the strain-related modification in the electronic band structure are included according Bir-Pikus theory. It is clearly shown that $Ge_{1-x}Sn_x$/Ge QWs with x~10-20% are type–I with a strong optical gain. It means that this material system is very promising for photonic applications and integration with Si platform.

In recent years $Ge_{1-x}Sn_x$ alloy has been very intensively investigated due to its potential application in optoelectronic devices including infrared optical detectors, light emitters, and high-speed integrated circuits [1]. This interest results from Sn-related changes in the electronic band structure of $Ge_{1-x}Sn_x$, i.e., the change of bandgap character from indirect to direct with the increase in Sn incorporation [2]. While outstanding progress on synthesis of $Ge_{1-x}Sn_x$ alloy has been done, the optical gain for Ge-based quantum wells (QWs) containing $Ge_{1-x}Sn_x$ alloy was not intensively explored so far. In this work the 8-band *kp* Hamiltonian is applied to calculate the electronic band structure and the optical gain for $Ge_{1-x}Sn_x$/Ge QWs grown on Ge substrate. Sn-related changes in the electronic band structure of $Ge_{1-x}Sn_x$ alloy are modeled according to recent *ab-inito* calculations and the strain-related modification in the electronic band structure are included according to Bir-Pikus theory [3]. In order to determine optical gain spectra, a conventional method is applied [4]. The method is based on the relaxation time approximation convoluted with Lorentzian function with a proper broadening time, which is assumed to be 0.1ps. In this approximation, the transverse electric (TE) and transverse magnetic (TM) gains are given by the following expression

$$g_{\beta}^{TE(TM)}(\hbar\omega) = C_0\beta^{-1}\sum_{n_c,n_v}\int dk\left(f_{n_c}(k)-f_{n_v}(k)\right)\sum_i M_{ci}^{TE(TM)}\left|I_{n_v i}^{n_c}(k)\right|^2 L(n_c,n_v,k),$$

where $C_0=q^2/(\omega m_0^2\tau c\varepsilon_0)$ (q – elementary charge; $m_0$ – electron mass; ω – angular frequency, τ – time constant; c – speed of light; $\varepsilon_0$ – dielectric constant), *i* represents heavy and light hole subbands, β is the propagation constant of the TE and TM mode, $M_{ci}^{TE(TM)}$ is the matrix element of TE (TM) mode, and $I_{nvi}^{nc}(k)$ is the overlap integral. More details regarding the Fermi Dirac distribution for electrons and holes can be found in Ref. [4]. In our calculation L-valley is taken into account in order to calculate the proper position of Fermi Levels for a given carrier concentration. In this work we have considered $Ge_{1-x}Sn_x$/Ge QWs of Sn concentration varying from 10% to 20%. An example of results of material gain calculations for such QWs are shown in Fig. 1.




**Figures 1.** The optical gain calculated for 14 nm wide $Ge_{1-x}Sn_x$/Ge QWs of various Sn concentrations. Carrier concentration in QW varies from $2*10^{18}$ $cm^{-3}$ to $10*10^{18}$ $cm^{-3}$.

**Acknowledgements** This work was performed within the grant of the National Science Centre, Poland (Grant No. 2013/10/E/ST3/00520).

## REFERENCES

1. Wirths, S., Geiger, R., Driesch, N., Musser, G., Stoica, T., Mantl, S., Ikonic, Z., Luysberg, M., Chiussi, S., Hartmann, J. M., Sigg, H., Faist., J., Buca, D. and Grutzmacher D., "Lasing in direct-bandgap GeSn alloy grown on Si," *Nature Photonics* 9, 88, 2015.
2. Gang, H. and Atwater, H. A., "Interband Transitions in $Sn_xGe_{1-x}$ Alloys," *Phys. Rev. Lett.* 79, 10, 1997.
3. Zelazna, K., Polak, M., Scharoch, P., Serafinczuk, J., Gladysiewicz, M., Misiewicz, J., Dekoster, J. and Kudrawiec, R., "Electronic band structure of compressively strained $Ge_{1-x}Sn_x$ with $x < 0.11$ studied by contactless electroreflectance," *Appl. Phys. Lett.* 106, 142102, 2015.
4. Gladysiewicz, M., Kudrawiec, R., Miloszewski, J. M., Weetman, F., Misiewicz, J. and Wartak, M. S., "Band structure and the optical gain of GaInNAs/GaAs quantum wells modeled within 10-band and 8-band *kp* model," *J. Appl. Phys*. 113, 063514, 2013.

# Integrated Photonics Platform for

# Single Quantum Dots at Telecom Wavelengths

K. Mnaymneh, D. Dalacu, S. Haffouz, J. Lapointe, P. J. Poole and R. L. Williams
National Research Council Canada
Ottawa, Canada
khaled.mnaymneh@nrc-cnrc.gc.ca

**Abstract**- We report on progress towards an integrated photonics architecture for single self-assembled quantum dots. Specifically, we use InAs dots in an InP matrix that act as our non-classical light sources for telecommunication wavelengths. The emission of these dots is collected and routed using our semiconductor-under-insulator platform technology.

Quantum optics promises both next-generation capability and disruptive technologies based upon the non-classical properties of light. However, transitioning from complicated fixed laboratory demonstrations to real-world mobile solutions is still very challenging. Large non-linear crystals, complex lens arrays and huge optical breadboards preclude any form of scalability. Enter single self-assembled quantum dots. Their well known confinement dynamics are very capable of generating single- and entangled photons reliably and deterministically[1]. A very promising path towards real-world solutions is our site-selected growth techniques[2] and its associated photonics integration platform. In this talk, we will discuss two ways of site-selecting single InAs quantum dots. The first method uses a self-directed template technology amenable for re-growth and higher levels of integration[3] while the second method uses a vapour-liquid-solid (VLS) epitaxial growth phase for generating wurtzite InP nanowires[4]. We then will discuss an associated photonics integration platform[5] capable of collecting and routing the non-classical light generated by such dots in a scalable fashion, placing quantum information-processing-on-a-chip capability within reach for the foreseeable future.

**REFERENCES**

1. Santori, C., M. Pelton, G. Solomon, Y. Dale and Y. Yamamoto, "Triggered Single Photons from a Quantum Dot," *Phys. Rev. Lett*, Vol. 86, No. 8, 1502–1505, 2001.
2. Williams, R. L., G. C. Aers, P. J. Poole, J. Lefebvre, D. Chithrani and B. Lamontagne, "Controlling the self-assembly of InAs/InP quantum dots," *J. Crystal Growth*, Vol. 223, 321–331, 2001.
3. Dalacu, D., K. Mnaymneh, V. Sazonova, P. J. Poole, G. C. Aers, J. Lapointe, R. Cheriton, A. J. Springthorpe and R. L. Williams, "Deterministic emitter-cavity coupling using a single-site controlled quantum dot," *Phys. Rev. B*, Vol. 82, 033301, 2010.
4. Dalacu, D., A. Kam, D. G. Austing, X. Wu, J. Lapointe, G. C. Aers and P. J. Poole, "Selective-area vapour-liquid-solid growth of InP nanowires," *Nanotechnology*, Vol. 20, 395602, 2019
5. K. Mnaymneh, D. Dalacu, S. Frederick, J. Lapointe, P. J. Poole and R. L. Williams, "A semiconductor under insulator technology in indium phosphide," *Appl. Phys. Lett*, Vol. 101, 151120, 2012

# Nanobiophotonics

# Single bacteria identification with an optical silicon microcavity

**M. Tardif [1,2,*], J-B Jager [2], C. Pin [1,2,3], E. Picard [2], E.Hadji[2], D. Peyrade [1]**

[1] Univ. Grenoble Alpes, CNRS, CEA-Leti Minatec, LTM - Micro & Nanotechnologies for Health, 38054 Grenoble Cedex, France

CEA & Univ. Grenoble Alpes, INAC-SP2M-SINAPS, 38000 Grenoble, France

[3] Groupe d'Optique de Champ Proche, Laboratoire ICB - Université de Bourgogne Franche-Comté, France

[*]manon.tardif@cea.fr

**Abstract** - SOI optical microcavities provide an extremely effective confinement of the electromagnetic field, spectrally and spatially. The evanescent field of these structures allows trapping, assembly, handling and sorting of colloidal objects in optofluidic devices. In this work, we show its efficiency to trap bacteria at the single level in order to identify their nature.

Optical forces are used to move or manipulate micro and nano objects. It is generally implemented in free space through a microscope, as optical tweezers **[1, 2]**. Recently, other optofluidic devices have emerged, using on-chip integrated optical components such as waveguides **[3, 4]** or microcavities **[5, 6, 7, 8, 9]**. It is now challenging to use these new systems to manipulate biological objects to understand their interaction with the electromagnetic field. Here we present the optical trapping of three kinds of bacteria and their identification/discrimination thanks to spatial and temporal characterization of their trapping.

**Optofluidic trapping device, set-up and bacteria phenotypes**

The optofluidic chip was obtained by combining electron beam lithography and RIE etching (Ar, $SF_6$, $CH_2F_2$) **(Fig.1a)**. We created 1D microcavity resonator ($\lambda_{res} \approx 1,55$ µm, $Q \approx 7000$) on SOI substrate (250 nm / 2µm / 700µm). A PDMS fluidic system **(Fig.1b)** placed above the optical structure leads the bacteria swimming above the optical component.

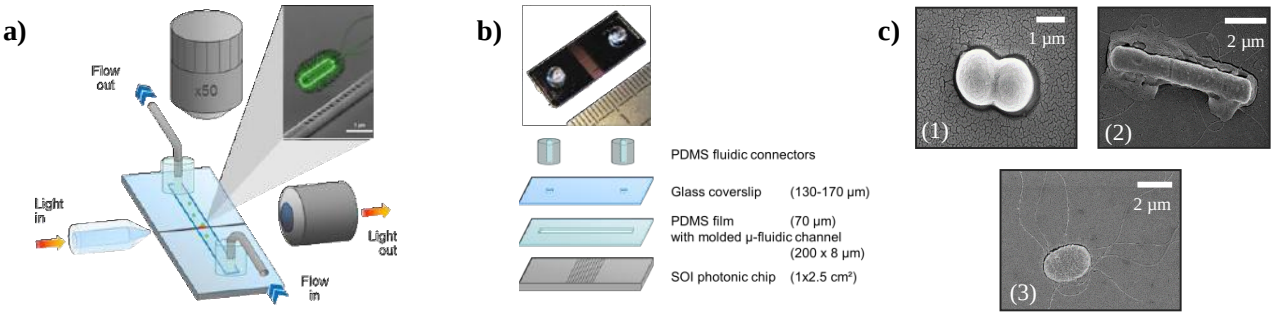



**Fig.1 a) Trapping Setup** **b) Optofluidic system** **c) SEM images of bacteria**

By injecting the resonance wavelength in the microcavity, we create an intense and confined electromagnetic field in the fluid located above the cavity. Two microscope objectives are placed on-line/on-top of the chip and connected to detection devices: we record simultaneously the position of the trapped object and the fluctuation of the transmitted signal.

The under study bacteria are listed on **Fig.1c: (1)** Staphylococcus epidermidis, **(2)** Bacillus subtilis and **(3)** Escherichia coli. We chose them because of their different sizes, shapes and properties (flagella, dimer) and their global equivalence in size to the polystyrene beads we have studied previously **[7, 8, 9]**.

**Spatial and temporal signature of bacteria trapping**

**Fig.2a (1)** presents the spatial signature of trapped E. Coli characterized by two preferential areas linked to the two maximums of the electromagnetic field of the cavity **[9]**. Extended to other bacteria types, **Fig.2a (2)** compares the spatial distribution of their position. We identify three signatures, characteristic of the nature of each bacterium. The flagella presence (E. Coli and B. Subtilis) seems to induce a larger displacement in the trap (same optical trap used for all bacteria).

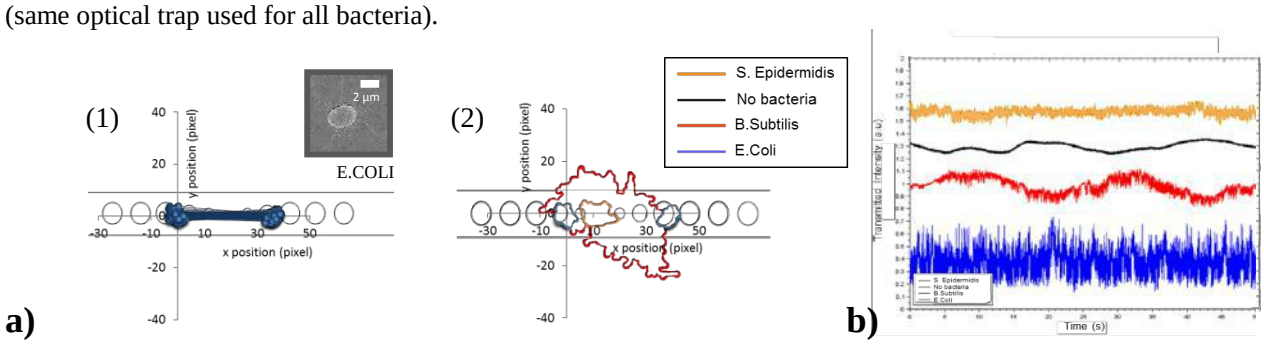



**Fig.2 a.1) Trapped E. Coli trajectory on microcavity (1 pixel = 60 nm); a.2) Global shape of trapped bacteria trajectories; b) Transmitted signal for three types of trapped bacteria (colored) and no bacteria trapped (black)**

**In Fig.2b** the fluctuation of the optical signal transmitted by the cavity during the trapping is represented. Depending on the amplitude and the characteristic frequencies of the signal, it allows to detect trapping (oscillations) and to identify the nature of the bacteria.

To conclude, we demonstrated here the trapping and the discrimination of three types of bacteria with SOI integrated optofluidic device dedicated to telecom wavelength. In the future, we will focus on the characterization of the behavior of a single trapped bacteria in response to external events (life and death situation, cell division).

**REFERENCES**


1. A. Ashkin, JM Dziedzic, "Optical trapping and manipulation of viruses and bacteria", *Science*, Vol. 235, No. 4795, 1517-1520, 1987.
2. D. G. Grier, "A revolution in optical manipulation", *Nature*, Vol. 424, 810–816, 2003.
3. S. Gaugiran et al., "Optical manipulation of microparticles and cells on silicon nitride waveguides," *Opt. Express*, Vol. 13, 6956–6963, 2005.
4. B. S. Schmidt et al., "Optofluidic trapping and transport on solid core waveguides within a microfluidic device", *Opt. Express*, Vol. 15, 14322–14334, 2007.
5. T. van Leest and J. Caro, "Cavity-enhanced optical trapping of bacteria using a silicon photonic crystal", *Lab on a Chip*, Vol. 13, 4358, 2013.
6. A. Rahmani and P. C. Chaumet, "Optical trapping near a photonic crystal ", *Opt. Express*, Vol. 14, 6353–6358, 2006.
7. C. Renaut et al., "On chip shapeable optical tweezers", *Scientific Reports 3*, No. 2290, 2013.
8. C. Pin et al., "Optofluidic taming of a colloidal dimer with a silicon nanocavity", *APL*, Vol. 105, 171108, 2014.
9. C. Pin et al., "Optofluidic Near-field Optical Microscopy: Near-field Mapping of a Silicon Nanocavity using Trapped Microbeads", *ACS Photonics*, 2015.

# Plasmonics enhanced ultrafast laser nanosurgery: Fundamentals and applications in nanomedecine

**M. Meunier**
Laser Processing and Plasmonics Laboratory, Department of Engineering Physics, Polytechnique Montreal, Montreal, Canada H3C 3A7
*corresponding author: michel.meunier@polymtl.ca

**Abstract**- Recent developments of the fundamentals and applications of nanoplasmonics enhanced ultrafast laser nanosurgery of living cells is presented. Modeling and experiments were developed to understand the basic phenomena occurring during ultrafast laser irradiation of plasmonics nanostructures. Applications of laser optoporation and transfection of cells in various field of nanomedecine is discussed. Then technique has been successfully used to locally stimulate neurons.

Irradiating metallic nanostructures with a femtosecond laser beam produces highly localised processes on the nanoscale in the surrounding medium. This particular process is mainly attributed to the surface plasmon resonance of the nanostructures. When these nanomaterials are imbedded in a biological media, their irradiation by a femtosecond laser could results in a highly localized plasma, heat production and mechanical effects yielding to the nanosurgery of cells (1-12).

A complete partial differential equation based model has been developed to describe the interaction of an ultrafast laser with a plasmonic nanostructure in water (2-3). Apart from heating the structure itself, it is shown that this interaction also leads to the generation of a plasma in the water medium and to the production of a strong pressure wave and a nanobubble in the vicinity of the structure. Plasma collision and relaxation are shown to be the main source of mechanical stress in the medium and the dominant factor for the pressure wave and bubble creation.

An all-optical technique able to detect plasmonic enhanced bubble formation and pressure wave generation is also presented (2, 6-7). Results show that for longer pulses, bubbles are independent of the polarization, in agreement with a linear thermally induced formation mechanism. In opposition, for shorter femtosecond pulses, bubble sizes are shown to depend on the polarization, a characteristic signature of nonlinear energy absorption in the near-field of the particle. This result thus offers a simple and intuitive demonstration that strongly supports plasma-mediated mechanism for off-resonance ultrafast laser nanocavitation.

We also demonstrated with a single-particle monitoring that 100 nm AuNPs irradiated by off-resonance femtosecond (fs) laser in the tissue therapeutic optical window ($\lambda$ = 800 nm), can act as a durable nanolenses in liquid and provoke nanocavitation while remaining intact (9, 11). We observed an effective laser processing window, ranging from 145 mJ/cm$^2$ to 240 mJ/cm$^2$, in which, the plasmonic AuNPs act as durable nanolenses, resulting in successive generation of multiple nanobubbles (radius : 550 nm - 700 nm, life time : 34 ns - 44 ns). The latter is of significant importance for future development of *in-vivo* AuNP-assisted laser nanosurgery and theranostic applications, where AuNP fragmentation should be avoided to prevent side effects, such as cytotoxicity and immune system's response.

These nanoparticles could be functionalized to target specific biological entities, thus performing multiple targeted surgeries on the nanoscale (10). As an example, the laser nanosurgery technique was employed to perform gene transfection in living cell with an optoporation efficiency as high as 80% (1). For human cancer melanoma cells, the treatment leads to a very high perforation rate of 70%, transfection efficiency three times higher than for conventional lipofection, and very low toxicity (< 1%) (1). Off- resonance laser excitation inhibited the fracture of the nanoparticles into possibly toxic DNA intercalating particles. This efficient and low toxicity method is a promising alternative to viral transfection for skin cancer treatment. Our laser technique shows promises as an innovative tool for fundamental research in biology and medicine as well as an efficient alternative nanosurgery technology that could be adapted to therapeutic tools in the clinic.

The technique is now being developed in close collaboration with researchers in hospital for applications in cancer treatment and neurology. Laser-induced stimulation of neurons and monitoring of the localized $Ca^{2+}$ signaling has been demonstrated using a standard confocal microscope (12). The proposed techniques provide a new complement to light-dependent methods in neuroscience.

**References**


1- J. Baumgart, L. Humbert, E. Boulais, R. Lachaine, JJ. Lebrun, M. Meunier, "Off-resonance plasmonic enhanced femtosecond laser optoporation and transfection of cancer cells", Biomaterials, 33, 2345-2350 (2012).

2- E. Boulais, R. Lachaine and M. Meunier "Plasma mediated off-resonance plasmonic enhanced ultrafast laser induced nanocavitation", Nanoletters, 12, 4763-4769 (2012).

3- E. Boulais, R. Lachaine, A. Hatef and M. Meunier **"**Plasmonics for pulsed-laser cell nanosurgery: fundamentals and applications**"**. Journal of Photochemistry and Photobiology C, 17, 26-49 (2013)

4- E. Boulais, R. Lachaine and M. Meunier, "Plasma-Mediated Nanocavitation and Photothermal Effects in Ultrafast Laser Irradiation of Gold Nanorods in Water", J. Physical Chemistry C, 117, 9386-9396 (2013)

5- B. St-Louis Lalonde, É. Boulais, JJ. Lebrun, and M. Meunier, "Visible and Near infrared resonance plasmonic enhanced nanosecond laser optoporation of cancer cells", Biomedical Optics Express, 4, 490-499 (2013)

6- R. Lachaine, E. Boulais, E. Bourbeau and M. Meunier, "Effect of pulse duration on plasmonic enhanced ultrafast laser-induced bubble generation in water", Applied Physics A 112 (1), 119-122 (2013).

7- R. Lachaine, E. Boulais and M. Meunier, "From Thermo- to Plasma-Mediated Ultrafast Laser Induced Plasmonic Nanobubbles", ACS Photonics, 1, 331-336 (2014)

8- A Hatef and M Meunier "Plasma-mediated photothermal effects in ultrafast laser irradiation of gold nanoparticle dimers in water" Optics express 23 (3), 1967-1980 (2015)

9- C. Boutopoulos, E. Bergeron and M. Meunier, "Cell perforation mediated by plasmonic bubbles generated by a single near infrared femtosecond laser pulse", Journal of Biophotonics, 1-6 (2015).

10- E. Bergeron, C. Boutopoulos, R. Martel, A. Torres, C. Rodriguez, J. Niskanen, J.-J. Lebrun, F. M. Winnik, P. Sapieha, and M. Meunier, "Cell-specific optoporation with near-infrared ultrafast laser and functionalized gold nanoparticles", Nanoscale, 7, 17836-17847 (2015)

11- C. Boutopoulos, A. Hatef, M. Fortin-Deschênes, and M. Meunier, "Dynamic imaging of single gold nanoparticle in liquid irradiated by off-resonance femtosecond laser", Nanoscale 7 (27), 11758-11765 (2015).

12- F. Lavoie-Cardinal, C. Salesse, E. Bergeron, M. Meunier, P. De Koninck "Gold nanoparticle-assisted all optical localized stimulation and monitoring of $Ca^{2+}$ signaling in neurons" Scientific Reports, 6, 20619 (2016)

# Octupolar Metastructures for a sensitive detection of bacteriophages by surfaced enhanced Raman spectroscopy

**M. Rippa[1], R. Castagna[1], M. Pannico[2], P. Musto[2], R. Paradiso[3], G. Borriello[3], J. Zhou[4], J. Zyss[5,1] and L. Petti [1*]**

[1] Institute of Applied Sciences and Intelligent Systems "E. Caianiello" of CNR, 80072 Pozzuoli, Italy

[2] Institute for Polymers, Composites and Biomaterials of CNR, 80072 Pozzuoli, Italy

[3] Istituto Zooprofilattico Sperimentale del Mezzogiorno, 80055 Portici, Italy

[4] Institute of Photonics, Faculty of Science, Ningbo University, Ningbo 315211, China

[5] Laboratoire de Photonique Quantique et Moléculaire (LPQM), ENS-Cachan, 94230 Cachan, France

corresponding author: L.petti@isasi.cnr.it

**Abstract**- Surface-Enhanced Raman Spectroscopy (SERS) on Au-octupolar metastructures with precisely controlled size and spacing fabricated via electron beam lithography is investigated. This SERS substrate shows high efficiency at 785 nm excitation in the detection of 4-Mercaptobenzoic acid (4-MBA). Our plasmonic functionalized nanostructures have been tested for sensing of bacteriophages. Here we show that coating Au-octupolar metastructures with 4MBA can provide label-free analysis of bacteriophages via surface-enhanced Raman spectroscopy (SERS) leading to a ~9-fold increase in SERS enhancement.

Plasmonics is a rapidly growing field with substantial broader impact in numerous directions, especially for bio-applications such as biosensing and biophotonics. In particular, for the emerging fields of plasmonics and nanophotonics, the ability to engineer metals down to the nanometric scale allows for the development of new devices and physical phenomena. With the use of plasmonic nanostructures, it is possible to synthesize novel nanobiosensors characterized by selective responses, which, in turn, undergo significant frequency shifts in presence of biological material. Recently, imaging techniques based on vibrational spectroscopy have emerged as powerful tools for the molecular characterization of biospecies. In particular, Surface Enhanced Raman Spectroscopy (SERS) has gained increasing attention in view of its applications to the detection of analytes at extremely low concentrations. In SERS, it is of crucial importance to develop metal nanostructures capable of producing high field enhancement with highly reproducible features.[1,2] By using electron beam lithography (EBL), one can rationally design and precisely control the size and shape of nanostructures and the distance between them.

In this work, we conceived reproducible SERS nanosensors based on tailored octupolar metasurfaces (Fig. 1a), which can combine high enhancement factor and remarkable molecular selectivity. The term "octupolar" refers to the 3-fold symmetry and the related rotational properties of the quadratic susceptibility tensor that behaves under rotations as an octupolar charge distribution tensor.[3]

The attachment of molecules to a support, for use in the immobilization of a target molecule, has found multiple applications in industrial chemistry and biosensing devices. Bacteriophages, a group of viruses specifically recognizing and lysing target bacteria, have recently gained much attention as recognition elements for biosensing purposes. The many advantages of bacteriophages make them an important component for the

detection and identification of bacterial pathogens as well as potentially excellent tools for diagnostics and therapeutics of bacterial diseases. Particular advantages include the specificity of the interaction of this type of viruses with their target host cell. This work has been directed toward investigating novel metastructures, based on a self-assembled monolayer (SAM) to chemically bind bacteriophages onto the metasurfaces, enabling, SERS response of the assembly before and after bacteriophages immobilization.

We characterized the fabricated nanopatterns obtained by varying the inter-metamolecules distances, using optical (dark field microscopy) and morphological (Scanning Electron Microscopy and Atomic Force Microscopy) imaging techniques. Comparison between numerical simulation from a FDTD approach and experimental results have been performed. Bacteriophages (Caudovirales, Podoviridae family) were immobilized on the nanosensors and monitored by the SERS response. Figure 1b shows such SERS response of bacteriophages attachment onto the Au-metasurfaces after their immobilization due to a 4MBA SAM. A giant enhancement of the 4-MBA spectra is observed due to the presence of the viruses. Our results based on designing well-controlled octupolar coupling platforms opens up interesting new opportunities to the use of bacteriophages as recognition elements for biosensing techniques.

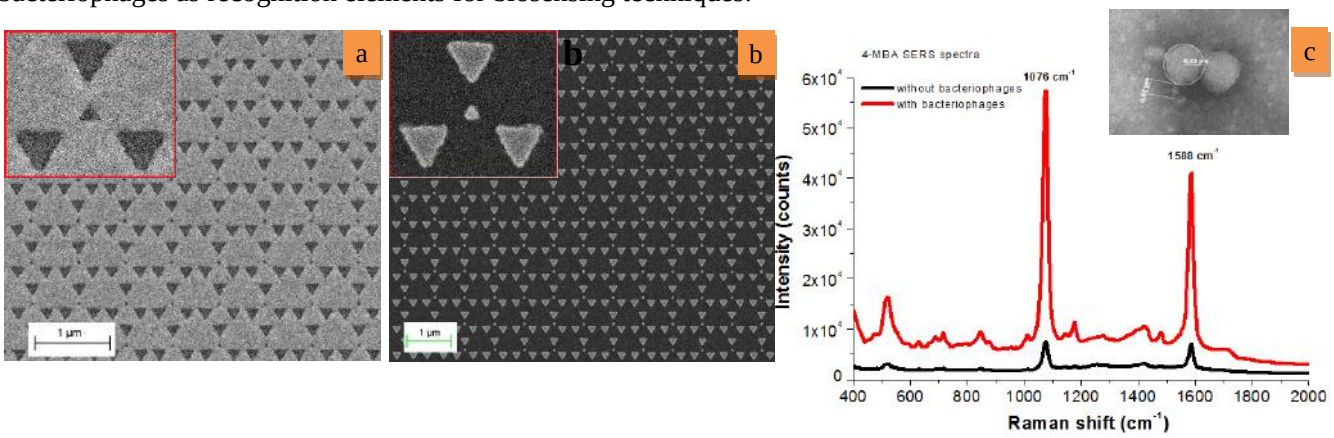



Figure 1: a) SEM images of the 3D holes-octupolar nanostructures (Au thickness 50nm on 90nm of ZEP polymer, 25nm-inter-molecule distance) and b) SEM images of Au-octupolar nanostructures of 25nm-inter-molecule distance on a quartz substrate, c) SERS spectra of 100µM 4-MBA SAM adsorbed on the 3D octupolar pattern (black) and with functionalized bacteriophages (red); in inset a TEM image of bacteriophages Podoviridae.


## Acknowledgements

This work was supported by the European Regional Development Fund-FESR of POR Campania 2007-2013 - Call Innovation Window (Project title ‘‘Kit for Brucella Abortus e B. Melitensis nano-BIosensing RApid detection–AMBRA’’).


## REFERENCES


1. Sonntag M. D., J. M. Klingsporn, A. B. Zrimsek, B. Sharma, L. K. Ruvuna and R. P. Van Duyne, “Molecular plasmonics for nanoscale spectroscopy,” *Chem. Soc. Rev*., Vol. 43, 1230-1247, 2014.
2. Harper M. M., K. S. McKeating and K. Faulds, “Recent developments and future directions in SERS for bioanalysis,” *Phys Chem Chem Phys*., Vol. 15, 5312-5328, 2013.
3. Kolkowski R., L. Petti, M. Rippa, C. Lafargue and Joseph Zyss, “Octupolar Plasmonic Meta-Molecules for Nonlinear Chiral Watermarking at Subwavelength Scale,” *ACS Photonics*, Vol. 2, No. 7, 899-906, 2015.

# Enhanced molecular overtone absorption by light-on-a-chip.

**A. Karabchevsky**[1] **and A. V. Kavokin**[2]

[1]Department of Electro-Optical Engineering and the Ilse Katz Institute for Nanoscale Sciences and Technology, Ben-Gurion University of the Negev, Beer Sheva 84105, Israel
[2]Department of Physics and Astronomy, University of Southampton, Southampton, SO17 1BJ, UK.
CNR-SPIN, Viale del Politecnico 1, I-00133 Rome, Italy
alinak@.bgu.ac.il

**Abstract**— The diffusion of light in materials by a stationary disorder is an established phenomenon. Here we show the giant enhancement of the absorption of light on a glass chip. Due to the elastic scattering, the pathway of light in the absorbing media is strongly enhanced that results in a giant absorption. Our results pave the road to the new disorder based optical sensors for detection of explosive materials and diagnostics of psychoactive stimulants based on amines.

'What do lotus flowers have in common with human bones, liquid crystals with colloidal suspensions, and white beetles with the beautiful stones of the Taj Mahal?' [1]. The answer is disorder which scatters the light. The diffusion of light by random materials is an established phenomenon. Neverthless, many intriguing physical effects can be discovered in disordered materials. Here, the disorder-enhanced absorption and a strong scattering in random molecular layers of primary and secondary amines is discussed. Due to the elastic scattering, the pathway of light in the waveguides containing N-Methylaniline and Aniline organic molecules adsorbed to their surfaces is strongly enhanced. This results in a remarkable increase of absorption, that would be impossible in the ballistic regime of light propagation.

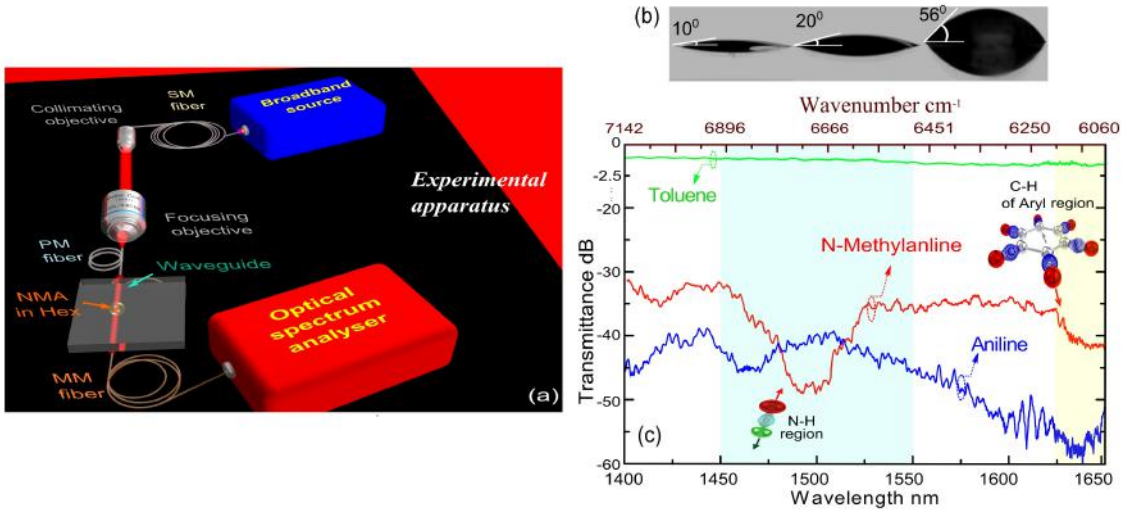



Figure 1: Experimental results. (a) - An artistic impression of the experimental setup.(b) surface modification measurement of planar waveguide with the contact angle $\angle$ of the water droplet on the clean glass as $\angle 10°$, $\angle 20°$ close to the immersion area strongly exposed to the solution vapour and a droplet of water on the immersed surface with a contact angle of $\angle 56°$. (c) NIR transmittance spectra of Toluene, aniline and NMA on our device [2].

**Fabrication**: The waveguides were fabricated by photolithographical patterning of 250nm thick hard mask on silicate glass. This results in the stripe openings of 6$\mu$m width. Then, the glass was immersed in a KNO3 molten for 11hr at 395°C. After ion-exchange the end facets of the glass were polished perpendicular to the waveguide resulting in formation of waveguides length ~35mm. Planar waveguides were characterized using Metricon prism coupler and found to be single mode

operating at 1.5m and having three modes at 632.8nm. Effective index at 632.8nm using transverse electric (TE) polarization of the fundamental mode (zero order mode) is 1.5191, 1.5170 for the first order mode and 1.5157 for the second order mode. At 1.5m effective index of the fundamental mode was measured as 1.5093 [4].

**Experiment**: Optical waveguide measurements of transmittance spectra were conducted using the apparatus shown in Fig. 1a. The measurements were realized using the infra-red light generated by a high power fibre continuum source (Fianium SC-600-FC) which is operating at the central wavelength of 1060nm with spectral bandwidth spanning from 450nm to beyond 1750nm and generating optical pulses with duration less than 10 ps. Broadband light was collimated and focused onto polarisation maintaining fibre (PMF) using Melles Grot objective NA 0.65 and magnification x40 to control polarization in the system. PMF was directly fibre-coupled into a channel waveguide (with coupling efficiency of 8dB/nm) and the power transmitted through the waveguide was fibre-coupled using graded index multimode fibre into an optical spectrum analyser (OSA, Yokogawa AQ6370). N-Methylaniline probe molecule, index of nNMA=1.57118, was diluted in hexane, index of nHex=1.37508, ratio 2:3 resulting in the mixture index of 1.46769. The indices of the liquids were measured using RA 510 refractometer. To conduct the measurements with Aniline, prior the measurement, the waveguides were cleaned and charged by oxygen anions in Tepla 300 Plasma Asher machine [2].

An enhanced absorption by molecular overtones of primary and secondary amines is presented. This evidence, paves the road to the new disorder based optical sensors for detection of explosive materials and diagnostics of psychoactive stimulants based on amines.

**REFERENCES**


1. Wiersma, D. S., "Disordered photonics," *Nature Photonics*, Vol. 7, No. 1038, 188–196, 2013.
2. Karabchevsky, A. and A. V. Kavokin, "Giant absorption of light by molecular vibrations on a chip," *Scientific Reports*, Vol. 6, No. 21201, 1–7, 2016.
3. Ash, E. A., C. W. Pitt, and M. G. F. Wilson, "Integrated optical circuits for telecommunications," *Journal Title Nature*, Vol. 261, No. 10, 377–381, 1976.
4. Karabchevsky, A. K., et al, "Broadband near-infrared spectroscopy of organic molecules on compact photonic devices," in *5th International Topical Meeting on Nanophotonics and Metamaterials (NANOMETA 15) Conference*, Seefield, Austria , January 2015.

# Electrical Detection of miRNA using Photoconductance in Plasmonic Nanowire

**Jihye Lee**[1,2]**, Jeong Hyeon Kim**[1,2]**, and Jong-Souk Yeo**[1,2*]
[1] School of Integrated Technology, Yonsei University, Incheon, Republic of Korea
[2] Yonsei Institute of Convergence Technology, Yonsei University, Incheon, Republic of Korea
[*]corresponding author: jongsoukyeo@yonsei.ac.kr

## Abstract

Here, we have demonstrated the electrical sensing platform of miRNA based on the plasmon coupling effect between nanowire and nanoparticle by measuring the change of photoconductance in plasmonic nanowire at the presence of hybridizing miRNA.

## Introduction

Nanoplasmonics is based on the interaction of light-matter to generate an oscillation of electrons on the surface of metals [1]. The movement of electrons provides unprecedented characteristics when merging with photonics, electronics, and biology. Especially on the biological applications, the surrounding environment around the target nanostructure is important for the sensitive and selective detection of bioanalyte. Conventionally, many researchers have paid much attention on the optical transduction with the nanoparticles to measure the shift in scattering spectra from the localized surface plasmon due to the change in refractive index around the nanostructure [2]. However, the optical read out alone can be limited by the scattering noise from the background substrate, so the subtle change in scattering intensity with the nanoparticle cannot be detected. Also, the single variant oligonucleotide is very hard to distinguish when only utilizing the optical scattering spectra. To overcome these limitations, we have demonstrated the nanowire plasmonic biosensing platform which takes advantage of optical-electrical transduction with the change in photocurrent [3, 4], thus enabling to detect the miRNA with highly sensitivity as shown in Figure 1.

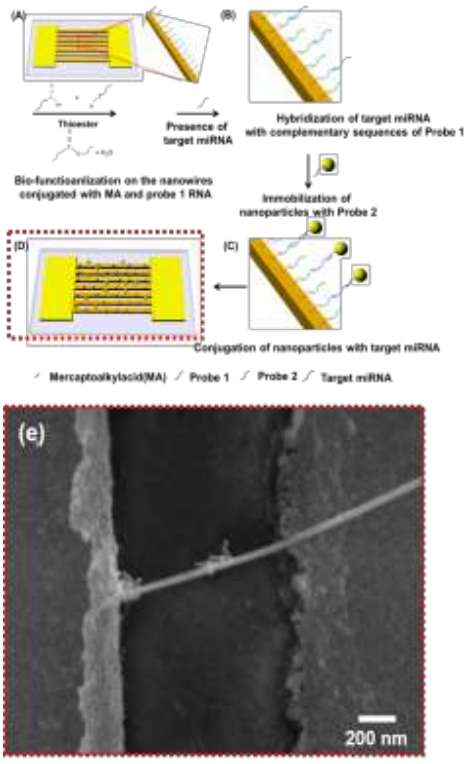



**Figure 1** Schematics of the nanowire-nanoparticle assemblies linked by two strands of miRNA probe oligonucleotides (a)-(d). (e) Scanning electron microscopy images of the nanowire-nanoparticle assemblies.

## Results and Discussion

The 40 nm nanowires linked on the electrical contact pad are functionalized by the carboxylic acid and its functionalization can attach the miRNA probe 1. The probe 2 is prepared by the functionalization on the 30 nm sized nanoparticles. When the miRNA is present, the nanowire-nanoparticle assembly can be formed by two complementary strands leading to a plasmon coupling effect [5, 6]. The strong coupling between the functionalized nanoparticles and the nanowire arrays changes the characteristics of plasmonic resonance at the presence of miRNA-21 to make a red shifted spectra (650 nm). This leads to the negative change in photocurrent on the electrical detection of the plasmonic nanowire. When the light is off, the photocurrent ($2.68\times10^{-12}$ pA) only depends on the biased voltage (3 V) and conductance of the nanowire. However, with the light on, the flow of the photocurrent is affected by the plasmons induced in the nanowire (resonance at 550 nm, $0.318\times10^{-12}$ pA). Figure 2 shows the shifted resonance spectra and corresponding change in negative photocurrent at the condition of miRNA attachment. The result in negative photocurrent correlates well with the spectral shift (resonance at 650 nm, $0.244\times10^{-12}$ pA).

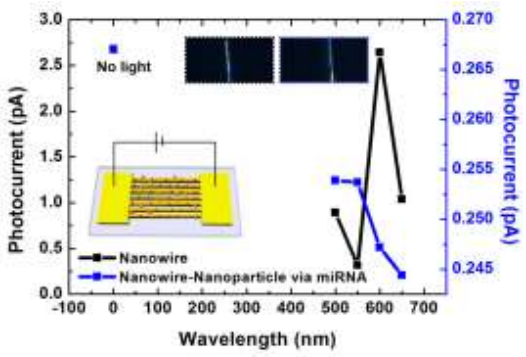



**Figure 2** The shift in the negative induced photocurrent shows the change in the resonance condition for the nanowire (550 nm) and the nanowire-particle assemblies via miRNA (650 nm).

## Conclusion

The miRNA detection from the changed photoconductance of nanowire has been demonstrated to show a sensitive detection of the single oligonucleotides.


## Acknowledgements

This research was supported by the MSIP (Ministry of Science, ICT and Future Planning), Korea, under the "IT Consilience Creative Program" (IITP-2015-R0346-15-1008) supervised by the IITP (Institute for Information & Communications Technology Promotion).


## References


1. Maier. S. A., *"Plasmonics: Fundamentals and Applications"*, Springer, New York, 2007
2. Anker. J. N., Hall. W. P., Lyandres. O., Shah. N. C., Zhao. J., and Van Duyne. R. P. "Biosensing with Plasmonic Nanosensors" *Nat. Mater*., Vol. 7, 442-453, 2008
3. Kim, J. H. and Yeo, J. S. "Enhanced Detection of Broadband Incoherent Light with Nanoridge Plasmonics" *Nano Lett*., Vol. 15, No. 4, 2291-2297, 2015
4. Zheng, G., Patolsky, F., Cui, Y., Wang, W. U. and Lieber, C. M. "Multiplexed electrical detection of cancer markers with nanowire sensor arrays." *Nat. Biotechnol*, vol. 23, No. 10, 1294-1301, 2005
5. Park, J. and Yeo, J. –S. "Colorimetric detection of microRNA miR-21 based on nanoplasmonic core–satellite assembly", *Chem. Commun*., Vol. 50, 1366-1368, 2014
6. Lee. J., Park. J., Lee. J. –Y, and Yeo. J. –S. "Contact Transfer Printing: Contact Transfer Printing of Side Edge Prefunctionalized Nanoplasmonic Arrays for Flexible microRNA Biosensor" *Adv. Sci*., Vol. 2, No. 9, 1500121, 2015

# Fabrication of random optical diffusers with prescribed scattering properties using three-dimensional printers

**Alma K. González-Alcalde**[1], and **Eugenio R. Méndez**[1]

[1]Centro de Investigación Científica y de Educación Superior de Ensenada, Baja California, Mexico.
emendez@cicese.mx

**Abstract**— We report the design and fabrication of random optical diffusers with special characteristics using three-dimensional (3D) printers. The designs are tested by computer simulations and the scattering properties of the fabricated samples are evaluated experimentally.

The interaction of electromagnetic waves with randomly rough surfaces has been a problem of long-standing interest. It is a subject of relevance in several fields of applied science, such as surface metrology, remote sensing, and illumination engineering. Due to the statistical assumptions made in most theoretical work (*i.e.* that the surface profile is a statistically stationary Gaussian random process and that the height correlation function is also Gaussian), it is often difficult to compare directly the results of theoretical and experimental work. Moreover, the assumption of Gaussian statistics is very restrictive for the design of diffusers with prescribed properties, like diffusers that scatter light uniformly within a specified range of angles [1, 2]. The photolithographic method proposed by Gray [3] has been useful for the validation of scattering theories, but does not have the flexibility required for the fabrication of multiscale surfaces or for the implementation of strategies to control the scattering pattern.

In this work, we explore the possibilities of using 3D printers for the fabrication of random surfaces with different kinds of statistical properties, and for the fabrication of surfaces with prescribed scattering properties. We have fabricated surfaces that scatter light uniformly within a specified range of angles, surfaces with different forms of the correlation function, Kolmogorov phase screens, and ocean-like surfaces. The fabricated surfaces have been characterized by measuring their profiles as well as their scattering properties.

In Fig. 1, we present photographs of Gaussian surfaces with one and two-dimensional roughness, for which the standard deviation of slopes $\delta$ is equal to the transverse height correlation length $a$. The standard deviation of slopes is then $\delta_s = \sqrt{2}$. The successful fabrication of these surfaces demonstrates that 3D printing techniques can be used for such purposes and that the fabricated surfaces can have surface slopes that are much higher than those achievable by traditional methods (*e.g.* surface grinding, sand-blasting or photolithography [3]). At present, the smallest scale that can be fabricated with our printers is of some dozens of microns, and this constitutes the main limitation of the technique. Still, the fabricated surfaces are useful in experimental studies of multiple scattering effects, and in laboratory simulations of atmospheric wave propagation and ocean wave scattering.

An example that illustrates the results obtained on the fabrication of achromatic uniform diffusers is presented in Fig. 2. We show photographs of the fabricated diffuser and of the scattering patterns it produces with laser and white light illumination. As can be appreciated in 2(a), the number of correlation lengths (statistically independent irregularities) within the sample is small; due to the limited resolution of the printer, it proved difficult to fabricate surfaces with smaller lateral scales. A consequence of this limitation is that the statistical fluctuations observed in the scattering pattern from sample to sample can be large and, thus, that the measured scattering pattern is not as uniform as expected. The relatively smooth transition from light to dark at the cutoff angle is also related to the limited resolution of the printer. Nevertheless, these results demonstrate that, with some limitations that are primarily associated to the resolution of current 3D printer technologies, it is possible to use such techniques for the fabrication of optical diffusers that can be useful in laboratory work and in applications that involve controlled diffuse illumination.

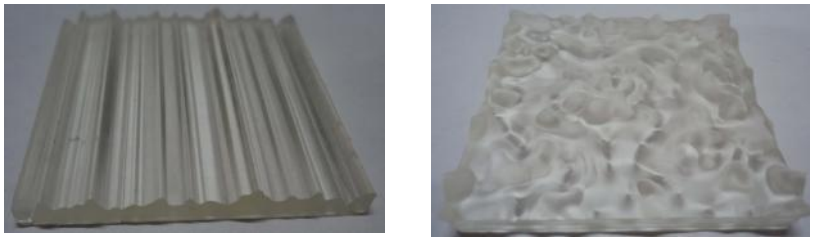


Figure 1: Photographs of surfaces with Gaussian statistics and a Gaussian height correlation function. In this case, the standard deviation of heights $\delta$ is equal to the transverse correlation length $a = 1\,\mathrm{mm}$. (a) One-dimensional surface and (b) two-dimensional surface.

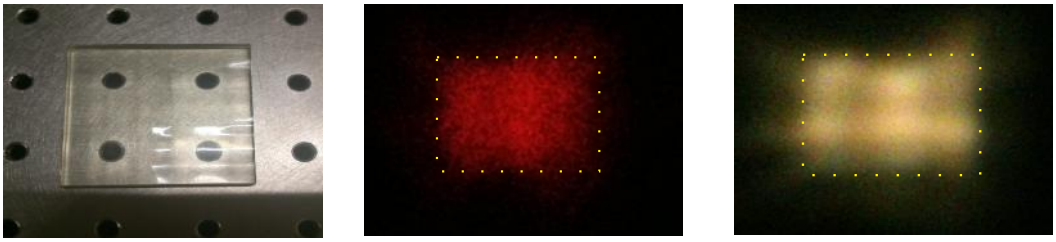


Figure 2: Photographs of (a) an achromatic band-limited uniform diffuser fabricated with a 3D printer, (b) the scattering pattern obtained in transmission with laser beam illumination, and (c) the scattering pattern obtained in transmission with directional white light illumination. The dotted rectangles denote the region over which uniform illumination was to be expected.

**REFERENCES**


1. Méndez, E. R., García-Guerrero, E. E., Escamilla, H. M., Maradudin, A. A., Leskova, T. A., and Shchegrov, A. V. "Photofabrication of random achromatic optical diffusers for uniform illumination," Appl. Opt. Vol. 40, 1098-1108, 2001.
2. Maradudin, A. A., Méndez, E. R., and Leskova, T. A., *Designer Surfaces*, Elsevier, 2008.
3. Gray P. F. "A method of forming optical diffusers of simple known statistical properties", *Optica Acta*, Vol. 25, 765-775, 1978.

# Near-field optics and nano-optics

# Near-field dichroism of azo-polymers for optical switching and image storage.

**S. S. Kharintsev[1,2*], A. V. Kharitonov[1,2], M. D. Dmitrieva[1], A. I. Fishman[1] and S. G. Kazarian[3]**
[1]Institute of Physics, Kazan Federal University, Russia
[2]Tatarstan Academy of Sciences, Russia
[3]Department of Chemical Engineering, Imperial College London, United Kingdom
[*]corresponding author: skharint@gmail.com

**Abstract**-This work aims at the study of antenna-driven near-field dichroism of a sub-10 nm epoxy-based azo-polymer thin film. Orientation mechanisms of azo-chromophores (DO3) covalently attached to a polymer backbone as a side-chain are spectroscopically and electrically explored with tip-enhanced Raman scattering and differential scanning capacity microscopy, respectively. Photo-induced heating of a substrate-free polymer film and its glassy temperature is investigated with scanning thermal microscopy. Nanoscale dichroism of the azopolymers opens the door to improved optical data storage performance.

Azobenzene polymers play a crucial role in optical storage due to their ability to be photo-oriented within amorphous and liquid crystal polymeric environments [1-3]. Azobenzenes are covalently attached to a polymer backbone as a side-chain (T-polymer) and function as both photo-sensitive chromophores and mesogens [1]. Underlying photo-isomerization allows one to handle the ordering of azo-chromophores exposed to polarized light. Alternatively, the same effect can be achieved with dc electrical field, for example, with corona poling of the azo-polymer at above glassy temperature. Due to a highly anisotropic nature of the azo-chromophores, they can be spectroscopically probed with tip-enhanced Raman scattering (TERS) at the nanoscale, avoiding photo-bleaching. Based on this clue, one can record and retrieve optical information unambiguously. .

Direct access to a single azo-molecule with the help of optical near-fields allows one to increase information recording density by two orders of magnitude (up to Pbit/cm$^2$) in a single layer, compared to diffraction-limited optical methods. Despite the fact that photo-isomerization is a fast process (a trans-cis cycle takes several ns'), the photo-orientation of the whole polymer goes too slowly, hundreds of μs'. This is related to a large number of azo-chromophres and their limited mobility in glassy environments. Thus, confined optical near-fields are able to increase recording speed up to hundreds of ns' and provide lesser energy consumption down to several mW/cm$^2$. Obviously, it provides new possibilities and perspectives for optical switching and image storage.

In the paper, we focus on the study of near-field dichroism of a sub 10-nm thick azo-polymer film, which is handled with a biased plasmonic nanoantenna, as shown in Fig. 1(a). The in-plane and out-plane arrangement of chromophores in the glassy polymer, assigned to transverse and longitudinal optical anisotropy, are mapped with the polarization-controlled TERS microscopy when a radially polarized and azimuthally polarized laser light are used [4]. Changing the near-field polarization allows us to optically align the azo-chromophores at arbitrary direction. Thus, the determination of a polarization state of the near-field is a task of high priority [4,5]. Fig. 2(b) shows a light illuminated bent gold tip with a point dipole at its apex. The dipole orientation can be found from polarization-dependent Rayleigh scattering patterns (Fig. 1(c)). Amorphous-to-liquid crystal (nematic phase)

transition effect on the sub-10 nm azo-polymer film is demonstrated with a biased plasmonic nanoantenna. Orientation polarization and birefringence of the azo-polymer is visualized with differential scanning capacity microscopy. We are confident that this study paves the way to apertureless optical technology for further increasing information recording density and electro-optical switching speed on amorphous and liquid crystal azo-polymers.

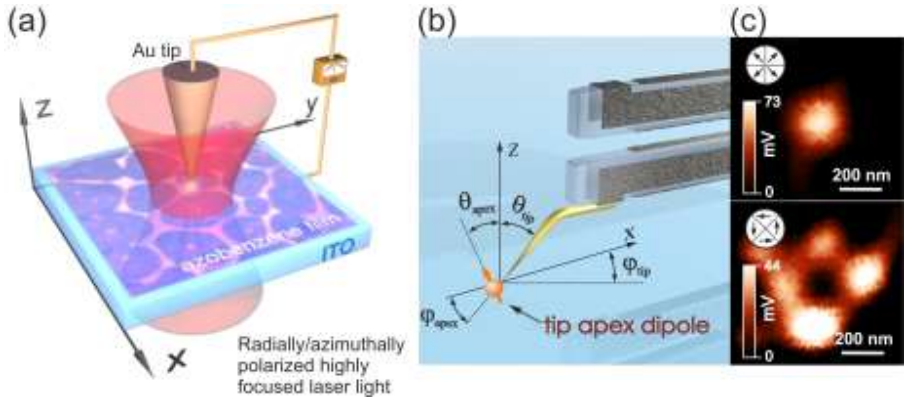



Figure 1. (a) Schematic view of the experimental setup for nanoscale electro-optical poling of the azo-polymer, (b) a bent gold antenna with a point dipole at the tip apex, (c) confocal images of the tip apex scanned over a focal spot of radially- and azimuthally laser light.

**Acknowledgements**, this work is financially supported by the Russian Foundation for Basic Research (Grant No. 15-42-02339).

**REFERENCES**

1. Ikeda T., Tsutsumi O., "Optical Switching and Image Storage by Means of Azobenzene Liquid-Crystal Films," *Science*, Vol. 268, 1873-1875, 1995.
2. Natansohn A., Rochon P., Pezolet M., Audet P., Brown D., To S., "Azo Polymers for Reversible Optical Storage. 4. Cooperative Motion of Rigid Groups in Semicrystalline Polymers," *Macromolecules*, Vol. 27, 2580-2585, 1994.
3. Mahimwalla Z., Yager K. G., Mamiya J., Shishido A., Priimagi A., Barrett C.J. "Azobenzene photomechanics: prospects and potential applications," *Polym. Bull.* Vol. 69, 967-1006, 2012.
4. Kharintsev S. S., Fishman A. I., Kazarian S. G., Gabitov I. R. and Salakhov M. Kh., "Experimental Evidence for Axial Anisotropy beyond the Diffraction Limit Induced with a Bias Voltage Plasmonic Nanoantenna and Longitudinal Optical Near-Fields in Photoreactive Polymer Thin Films," *ACS Photonics*, Vol. 1, No. 10, 1025, 2014.
5. Mino T., Saito Y., and Verma P., "Quantitative Analysis of Polarization-Controlled Tip-Enhanced Raman Imaging through the Evaluation of the Tip Dipole," *ACS Nano*, Vol. 8, No. 10, 10187, 2014.
6. Kharintsev S.S., Fishman A.I., Kazarian S.G., Salakhov M.Kh. "Polarization of near-field light induced with a plasmonic nanoantenna," *Phys. Rev. B*, Vol. 92, 115113-1, 2015.

# Study of Near and Far Fields of a Super-Gaussian Beam on a Step Discontinues Interface using FFT-BPM

**Adel Shaaban[1,2], L. R. Gomaa [3], Mohamed Farhat O. Hameed[1, 4], S. S. A. Obayya[1]***

[1]Centre for Photonics and Smart Materials, Zewail City of Science and Technology, Sheikh Zayed District, 6th of October City, Giza, Egypt sobayya@zewailcity.edu.eg*.

[2]*Radiation Eng. Dep., National Center for Radiation Research and Technology (NCRRT), Atomic Energy Auth., Nasr City, 11787 Cairo, Egypt.*

[3]*Faculty of engineering of Shoubra-Banha university, Cairo, Egypt.*

[4]Faculty of Engineering, Mansoura University, Mansoura 35516, Egypt.

**Abstract**- In this paper, accurate modeling analysis of super-Gaussian field on a step discontinues dielectric interface is investigated using fast Fourier transform based beam propagation method (FFT-BPM). The propagation of super-Gaussian field is very difficult to solve analytically [1]. However, in this analysis we present for the first time to the best of our knowledge the super-Gaussian field with oblique incident at critical angle on a planar dielectric interface using FFT-BPM. The lateral field shift is also investigated. The obtained results are in accordance with the theory of the non-specular phenomena of the electromagnetic field interaction at the same situation. Additionally, they are in a good agreement with theoretical predictions and significant improvement over the previously published results is achieved. The suggested work has profound implications for future studies of Super fields' interaction at dielectric interfaces.

The propagation of super-Gaussian field attracts a lot of interest in recent years. In some cases it called flat top beam; due its flat peak shape. The field can be expressed as:

$$E(x,z) = Ae^{(-(\frac{x}{w})^s)} \quad (1)$$

where A is the normalization factor, *w* is the field beam waist, and s is the Super-Gaussian power which is an even integer. In Gaussian case s is equal to 2. However, the super-Gaussian field is very difficult to evaluate its propagation in realm of analytical expression. In particular, numerical methods used to study the propagation features of super-Gaussian [1, 2]. However, the non-specular shifts for the beam weren't studied before. In this analysis we present the field interaction using FFT-BPM [3]. The FFT-BPM is a powerful method with angular spectrum representation of the electromagnetic field. The simplicity and powerfulness of the FFT-BPM are sought at the analytical and numerical levels [4]. The FFT-BPM reliable and efficient in order to study devices for which no analytical solutions exist. Additionally, suitable for testing the validity of approximate methods for studying different waveguiding structures with complicated shapes with nonlinear effects. Besides, a large number of modified algorithms such as: Fourier transform, finite difference, finite element, mode expansion, and Green's function approximations have been suggested in the literatures for optical applications [4-5]. These

methods might be superior, with respect to reliability and efficiency for a certain class of application problems and some desired accuracy.

Figure 1 shows the schematic diagram for a super-Gaussian field impinges on a dielectric surface. The plane $x$=0 is the step discontinues interface between two dielectric media having refractive indices $n_1$ and $n_2$ with $n_1 > n_2$. In this analysis the geometry of the problem is invariant with respect to the $y$-coordinate. At $x=x_d$, the field propagates towards the interface. The beam's axis makes an angle $\theta_i$ with respect to the $z$-axis which corresponds to the critical angle of incidence ($\theta_c = \sin^{-1}(n_1/n_2)$) measured with respect to the normal to the interface. In this regard, consider a Gaussian and super-Gaussian beams with the same properties: the wavelength in the denser medium $\lambda_1$ is equal to 1.55 μm, $w=20\lambda_1$, $x_d=5.2w$, $n_1$= 1.5152, and $n_2$=1. The beam's axis makes an angle $\theta_i = (\pi/2) - \theta_c = 48.7017°$. Figure 2 shows the total field propagation overview on a dielectric interface in case s=2 (Gaussian field). However, Figure 3 shows the total field propagation overview on a dielectric interface at s=4 (super-Gaussian). The incident field intersection with the interface at the point $Z_{go}$ point which represents the geometric optics point. However, the reflected and transmitted fields shifted from this point by some distances called lateral shift (Goos-Hanchen) [6]. This is due to the interference between the transverse wave vectors under the phase changes. In this analysis the Goos-Hanchen shift is equal to 5.0296 μm and 5.63μm in Gaussian and in super-Gaussian fields' cases respectively.

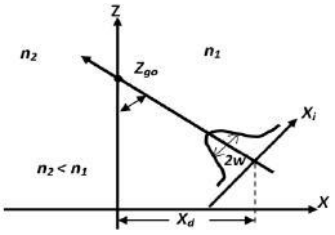



Figure 1 Schematic diagram of super-Gaussian field incident on a dielectric interface.

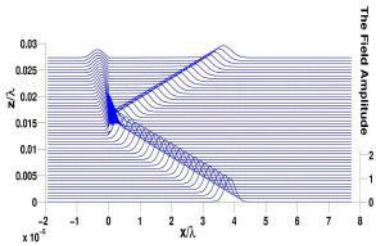



Figure 2 The total field propagation on a dielectric interface at s=2.

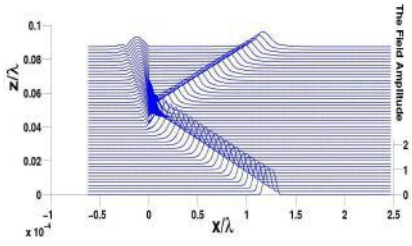



Figure 3 The total field propagation on a dielectric interface at s=4.

**REFERENCES**


1. Yajun Li, "Light beams with flat-topped profiles," *Optics Letter*, Vol. 27, 1007-1009, 2002.
2. C. Kamacıoglu and Y. Baykal, "Generalized Expression for Optical Source Fields," *Optics & LaserTechnology,* Vol. 4, 1706–1712, 2012.
3. Feit, M. D., and J. A. Fleck., "Light propagation in graded-index optical fibers," *Applied optics* Vol. 17, 3990-3998, 1978.
4. H. J. W. M. Hoekstra, "Theory and numerical strategies of BPMs On beam propagation methods for modeling in integrated optics," *Optical and Quantum Electronics,* VOL. 29, 157-171, 1997.
5. K. Okamoto, Fundamentals of Optical Waveguides, Elsevier Inc., 2006.
6. Wang X., Yin C., and Cao Z., In Progress in Planar Optical Waveguides, Springer Berlin Heidelberg, 2016.
7. A. Shaaban, M. B. El Mashade, L. R. Gomaa, M. Sayed, M. F. O. Hameed, S. S. A. Obayya, "Comparison Analysis of the Gaussian Beam On a Planer and Corrugated Dielectric Interfaces", International Conference on Renewable Energy (INCORE2016), Sharm El Sheikh, Egypt (2016).
8. Obayya, Salah. Computational photonics, John Wiley & Sons, 2011.

# Analysis of Lorentz Beam Propagation at Critical Angle Using Accelerated Beam Propagation Method

**A. shaaban[1], M. F. O. Hameed[1,2], M. sayed[1,3], H. I. Saleh[3], L. R. Gomaa[4],S. S. A. Obayya[1*]**

[1]Centre for Photonics and Smart Materials, Zewail City of Science and Technology, Sheikh Zayed District, 6th of October City, Giza 12588, Egypt.

[2]Mathematics and Engineering Physics Department, Faculty of Engineering, Mansoura University, Mansoura, Daqahlia 35516, Egypt.

[3]Radiation Eng. Dep., National Center for Radiation Research and Technology (NCRRT), Atomic Energy Auth., Nasr City, 11787 Cairo, Egypt.

[4]Faculty of engineering of Shoubra-Banha university, Cairo, Egypt.

*Corresponding author: sobayya@zewailcity.edu.eg

**Abstract**- In this paper, the characteristics of an incident monochromatic Lorentz light beam at sharp critical angle are investigated and analyzed. The numerical results are obtained using fast Fourier transform based beam propagation method (FFT-BPM). Further, the FFT-BPM is implemented on a graphical processing unit (GPU) platform using CUDA-C program to decrease the execution time significantly. In this study, the interference between the incident and reflected beams is reported. Additionally, the angular spread of the refracted beam in the rare medium and its direction of propagation are considered. The non-specular shifts are also calculated using the FFT-BPM at sharp critical angle which is very difficult to examined using analytical methods. The obtained results are in a good agreement with theoretical predictions and significant improvement over the previously published results is achieved.

The phenomenon of the total reflection of Lorentz beams has significant importance in the field of integrated optics and free space optics. Most of guidance phenomena rely on total reflection at a dielectric interface, with spatially–bounded guided fields. However, the analysis of guided-wave phenomena assumes guided plane waves rather than more realistic spatially-bounded fields. Therefore, simple, powerful and versatile method is needed for the analysis of the guidance phenomena of such fields. There are main features relevant to the process of total reflection at critical incidence such as: the lateral displacement of the reflected and transmitted beams from the position predicted by geometric optics (GO) point [1], the penetration of energy in the less dense medium where the field is basically evanescent and the lateral field which extends well beyond the reflected and transmitted fields. Pioneering research paper [2] was concerned with well collimated beams to study this phenomena.

The FFT-BPM is a most powerful method with angular spectrum representation of the electromagnetic field. The simplicity and powerfulness of the FFT-BPM are sought at the analytical and numerical levels. This is justified by the very wide class of problems which had been handled by the FFT-BPM [4-6] such as: the fundamental characteristics of optical fibers, waveguide modulators and couplers, bent waveguides, nonlinear effects in fibers, solitons and propagation in anisotropic media.

In this paper, we present the analysis of Lorentz light beam at sharp critical angle of oblique incidence on a dielectric interface using FFT-BPM. At critical angle of incidence, the main relevant features [3] of the

phenomenon of total reflection are strongly manifested as: the diffraction effects of the lateral field, the refraction of some energy in the rarer medium and the Goos-Hanchen (GH) shift. In order to verify the validity, the results are compared with analytical methods drawn from literature [2-3]. The FFT-BPM measures the refractive indices changes in phase correction function, consequently, it not faces any singularity problem during the calculations [1], and it gives the results at any incident angle. Figure 1 shows the schematic diagram for the incident Lorentz field on a dielectric interface. The incident beam wavelength "λ" is equal to 1.33μm, and the beam waist $w$=20λ. The FFT-BPM result for the Lorentz fields (incident, reflected, and transmitted fields) can be evaluated from Fig. 2. The numerical results show that the lateral shift for the beam is equal to 5.45μm.

The BPM error depends on the square of the used step size Δz [6]. In order to decrease the error, we need to increase the number of samples. However, software and hardware limitations are arised. Therefore, the reported BPM program is implemented using different programing languages: FORTRAN, MATLAB, and CUDA-C. Figure 3 depicts the execution time for the BPM running in modern central processing unit (CPU), where CPU specs is: 2.5 GHz, D processor, and 32 GB RAM, and the GPU device "Quadro-k2000". We choose the same field parameters, where, $\Delta x=0.35(\lambda/2)/n_1$, $\Delta z=0.01\lambda/(n_1-n_2)$ with the propagation distance of 82.5 μm. It is revealed from the figure that the execution time for the FORTRAN program is greater than that of the other programs. Additionally, the propagation step size Δz should be changed due to the allocated memory limitations of the FORTRAN language. However, the MTALAB based-BPM program can be run at different number of samples, without the need to change the steps size. Further, the execution of the CUDA-C program on the GPU platform is faster. For comparison, at a number of samples of $0.16384\text{x}10^5$, the MATLAB program is 30 times faster than the FORTRAN program on the same CPU. However, the GPU speeds the execution process up to 581 times faster than the MATLAB program and $17\text{x}10^3$ times faster than the FORTRAN program.

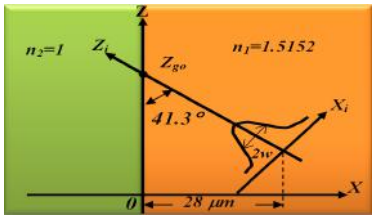



Figure 1 Schematic diagram of Lorentz field incident on a dielectric interface.

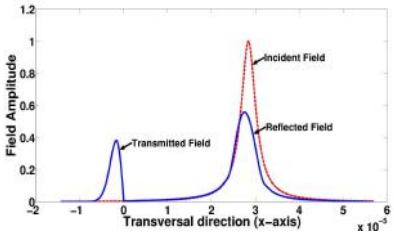



Figure 2 The incident reflected, and transmitted fields.

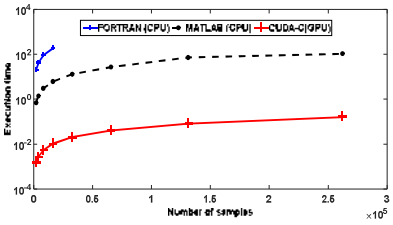



Figure 3 The execution running time for the BPM program at different programing language.

## REFERENCES


1. Wang X., Yin C., and Cao Z., In Progress in Planar Optical Waveguides, Springer Berlin Heidelberg, 2016.
2. Horowitz, B. R., "Total reflection of a light beam at a dielectric interface: A comparative study," *Applied physics,* Vol.3, 411-416, 1974.
3. Antar, Y. M. M., and W. M. Boerner. "A generalized approach to beam wave interaction with a dielectric interface," *Applied physics,* Vol. 7, 295-301, 1975.
4. Feit, M. and J. Fleck., "Light propagation in graded-index optical fibers," *Appl. Opt.* Vol. 17, 3990, 1978.
5. A. Shaaban, M. B. El Mashade, L. R. Gomaa, M. Sayed, M. F. O. Hameed, S. S. A. Obayya, "Interaction Analysis of the Gaussian Beam On a Planar Dielectric Interface," International Conference on Renewable Energy (INCORE2016), Sharm El Sheikh, Egypt (2016).
6. Obayya, Salah. Computational photonics, John Wiley & Sons, 2011.

# Enhancement of light emission from an optically pumped bias driven tunneling junction.

**Xiao Wang,* Kai Braun, Dai Zhang, Heiko Peisert, Hilmar Adler, Thomas Chasse´, and Alfred J. Meixner***

Institute of Physical and Theoretical Chemistry and LISAt, University of Tübingen,

Auf der Morgenstelle 18, 72076 Tübingen, Germany

*corresponding author: xiao.wang@uni-tuebingen.de; alfred.meixner@uni-tuebingen.de.

**Abstract**- We experimentally demonstrate enhancement of photoluminescence from an optically pumped bias driven pristine Au-substrate/Au-tip tunneling junction and a molecular tunneling junction (Au-substrate/self-assembled molecular monolayer/Au-tip) with molecules chemically bound to the Au substrate.

Due to the excitation of localized surface plasmons (LSP), noble metal nanostructures can concentrate light into nanometer scale volumes with strongly enhanced local optical fields. For two closely spaced metallic nano particles interacting with incident light, their LSP are coupled and confined in the gap. The resulting strong optical field leads to the enhanced surface-, tip-enhanced Raman scattering (SERS/TERS) and amplified molecular luminescence. LSP can also be excited by electrons, for instance by inelastic electron tunneling (IET) across a nano gap formed by a metal tip and a substrate in a scanning tunneling microscopy. Hence, the combination of optical pump and bias voltage variation in a tunneling junction provides a new approach for controlling light emission.

Experimentally, we implemented a tunneling current feedback function into a homebuilt parabolic mirror scanning near-field optical microscope. Tip illumination and optical signal collection are performed from the top of the sample under perfect diffraction and polarization conditions with a radially polarized laser beam.[1-3] Two type of samples, pristine Au-substrate/Au-tip tunneling junction and the molecular junction (Au-substrate/self-assembled molecular monolayer/Au-tip) with molecules chemically bound to the Au substrate, are investigated [4, 5]. For the Au-Au junction, emission spectra are recorded as a function of bias voltage with and without laser illumination. We conclude that the enhanced intensity induced by laser illumination originates from the radiative decay of hot electrons closely above the Fermi level via inelastic tunneling and photon emission into the plasmon modes formed by the tip-substrate gap. For the optically pumped molecular junction, it behaves as a bias-driven superluminescent point light-source, operating at ambient conditions and providing almost three orders of magnitude higher electron-to-photon conversion efficiency than electroluminescence induced by inelastic tunneling without optical pumping. The enhanced emission can be modelled by rate equations taking into account hole-injection from the tip (anode) into the highest occupied orbital of the closest substrate bound molecule (lower level) and radiative recombination with an electron from above the Fermi-level (upper level), hence feeding photons back by stimulated emission resonant with the gap mode. Our study will advance the fundamental understanding of quantum plasmonics and lead to new applications in actively controlled photonics devices.

**Acknowledgements**,

Financial support by the Projektförderung für Nachwuchswissenschaftler/Innen Uni-Tübingen and the DFG (Grant ME1600/5-3 and the priority program 1391) is gratefully acknowledged

**REFERENCES**

1. Wang, X.; Zhang, D.; Braun, K.; Egelhaaf, H. J.; Brabec, C. J.; Meixner, A. J. "High-Resolution Spectroscopic Mapping of the Chemical Contrast from Nanometer Domains in P3HT:PCBM Organic Blend Films for Solar-Cell Applications," Adv. Funct. Mater., 20, 492-499, 2010
2. Zhang, D.; Heinemeyer, U.; Stanciu, C.; Sackrow, M.; Braun, K.; Hennemann, L. E.; Wang, X.; Scholz, R.; Schreiber, F.; Meixner, A. J. "Nanoscale Spectroscopic Imaging of Organic Semiconductor Films by Plasmon-Polariton Coupling," Phys. Rev. Lett., 104, 056601, 2010
3. Sevinc, P. C.; Wang, X.; Wang, Y. M.; Zhang, D.; Meixner, A. J.; Lu, H. P. "Simultaneous Spectroscopic and Topographic Near-Field Imaging of TiO(2) Single Surface States and Interfacial Electronic Coupling," Nano Lett. 11, 1490-1494,2011
4. Wang, X.; Braun, K.; Zhang, D.; Peisert, H.; Adler, H.; Chassé, T.; Meixner, A. J. "Enhancement of Radiative Plasmon Decay by Hot Electron Tunneling," ACS Nano, 9, 8176-8183, 2015
5. Braun, K.; Wang, X.; Kern, A. M.; Adler, H.; Peisert, H.; Chasse, T.; Zhang, D.; Meixner, A. J. "Superluminescence from an optically pumped molecular tunneling junction by injection of plasmon induced hot electrons," Beilstein Journal of Nanotechnology, 6, 1100-1106, 2015

# Near-field optical response of gold gap nanoantennas

**Michele Celebrano[1], Milena Baselli[1], Giovanni Pellegrini[1], Xiaofei Wu[2], Bert Hecht[2], Lamberto Duò[1], and Marco Finazzi[1], Paolo Biagioni[1,*]**

[1]Physics Department – Politecnico di Milano, Piazza Leonardo Da Vinci 32, 20133 Milano, Italy.

[2]Nano-Optics & Biophotonics Group - Department of Physics - Experimental Physics 5, University of Würzburg, Am Hubland, 97074 Würzburg, Germany.

*corresponding author: paolo.biagioni@polimi.it

**Abstract** – The near-field optical response of highly pure single-crystal gold gap nanoantennas was analyzed by means of near-field aperture probes. Due to the interference phenomena occurring in the near field of the nanoantennas, both the complex response of the dipolar oscillator associated with the plasmon resonance could be observed. The near-field optical response of the gap antennas is found to diverge from that of single gold nanorods and a possible model to describe this behavior is proposed.

Scanning near-field optical microscopy (SNOM) is a powerful tool to analyze local field oscillations in plasmonic nanoantennas [1,2]. It has been shown that contrast in elastic-scattering near-field maps of gold nanoparticles is ruled by the interference between the direct field emitted by the tip and the one radiated by the plasmon oscillations in the nanoparticle. Therefore, both amplitude and phase of the particle polarizability contribute to the near-field optical map. Such interference generates a positive (negative) contrast for particles illuminated below (above) resonance. Using a suitable combination of far-field confocal extinction maps and SNOM imaging based on hollow-pyramid probes, together with a simple model for the analysis, we demonstrated that the real and imaginary part of the particle polarizability can be disentangled [3].

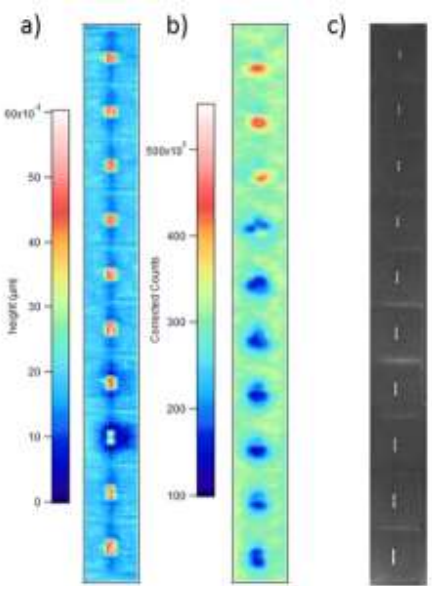



**Figure 1**. a) Topographical map of the gap antennas retrieved by the piezo feedback. b) Near-field maps of the gap antennas. c) Scanning Electron Microscope image of the gap antennas. Maps size is 1 x 10 μm.

Here we report on the results from recent experiments that extend the previous approach to the analysis of double-rod gap antennas produced by focused ion-beam milling starting from single-crystal gold plates [4]. We imaged an array of gap nanoantennas with arm lengths varying from 100 to 200 nm using the same combination of near-field and far-field techniques with an illumination wavelength centered at 980 nm.

Preliminary data analysis reveals that the interference process occurring in the near-field of gap antennas is sensibly different from that of single nanorods [3]. In particular the interference phenomena are weaker n the former case and phase shifts are more pronounced than in single nanorods. Using finite-difference time-domain simulations and analytical methods we discuss possible models that account for this observations.

**REFERENCES**


1. Biagioni, P., et al., "Nanoantennas for visible and infrared radiation" *Rep. Prog. Phys*., Vol. 75, 024402, 2012.
2. Duò, L., et al, "Recent developments in linear and nonlinear near-field microscopy on single plasmonic nanoparticles" *Phys. Status Solidi B*, Vol. 247, 2040, 2010.
3. Celebrano, M., et al., "Retrieving the complex polarizability of single plasmonic nanoresonators" *Phys. Rev. B*, Vol. 80, 153407, 2009.
4. Huang, J.-S., et al., "Atomically flat single-crystalline gold nanostructures for plamonic nanocircuitry" *Nat. Comm*., Vol. 1, 150, 2010.

**Anomalous spectral shift of near- and far-field plasmonic resonances in nano-gaps**

Dr Anna Lombardi[*1], Dr Angela Demetriadou[2,3], Dr Lee Weller[1], Patrick Andrae[1], Felix Benz[1], Rohit Chikkaraddy[1], Prof Javier Aizpurua[2], Prof Jeremy J. Baumberg[1]

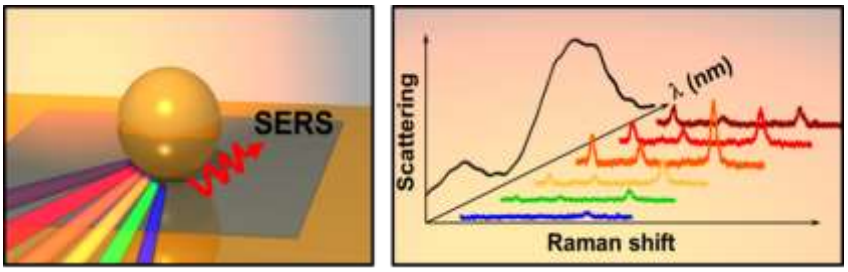
[1] NanoPhotonics Centre, Cavendish Laboratory, University of Cambridge, Cambridge, CB3 0HE, UK
[2] Centro de Física de Materiales, Centro Mixto CSIC-UPV/EHU and Donostia International Physics Center (DIPC), Paseo Manuel Lardizabal 4, 20018 Donostia-San Sebastián, Spain
[3] Blackett Laboratory, Department of Physics, Imperial College London, SW7 2AZ, United Kingdom

*corresponding author: al716@cam.ac.uk

The control and tuning of near-field and far-field responses in plasmonic nanostructures represents a crucial aspect in the design of optimized platforms for field-enhanced spectroscopy. Due to the lack of methods that can directly compare and correlate both responses under similar environmental conditions, near- and far-field spectral behaviors have been often assumed to be identical.

We develop a widely tuneable optical technique to probe the near-field resonances within individual plasmonic structures and to directly compare it to the corresponding far-field response.

We investigate individual gold nanoparticles spaced 1nm above a gold mirror by a molecular monolayer [1]. We measure the near-field spectral resonance by devising a widely-tunable optical technique to track the SERS signals across the dark-field spectrum simultaneously measured on the same nanoparticle. For every nanostructure, we find the extracted near-field enhancement has a narrow Gaussian profile, always blueshifted (>40meV) with respect to the dark field scattering coupled mode. We find this agrees with theoretical predictions in such strongly coupled plasmonic systems. Using a transformation optics approach, we show the observed spectral shifts can be clearly ascribed to the different way that interference of plasmon gap modes operates in the near- and far-field. An additional benefit of our approach is to show that the ever-present SERS background, highly debated in the literature, does not come from the same spatial locations as the near-field controlled SERS peaks [2].




[1] Felix Benz et al., "Nano-optics of molecular-shunted plasmonic nanojunctions", *Nano Lett.* **15**, 669 (2015)
[2] Anna Lombardi et al. "Anomalous spectral shift of near- and far-field plasmonic resonances in nano-gaps", *ACS Photonics* **3**, 471 (2016)

# The Spectral Phase and Temporal Shape of Femtosecond Laser Pulses in the Nearfield of Plasmonic Nanostructures

**R. Ciesielski[1*], T. Mancabelli[1], J. Kraus[2], A. Comin[1], S. Günther[2] and A. Hartschuh[1]**
[1]Department Chemie and CeNS, Ludwig-Maximilians-Universität München, Germany
[2]Chemie Department Technische Universität München, Germany
[*]corresponding author: richard.ciesielski@cup.lmu.de

**Abstract** We show that the spectral phase of the light field near a plasmonic nanostructure, induced by a laser pulse, is substantially different from the phase at its surface. We propose to use external materials as local probes instead of the second harmonic light generated at the surface of the structure to characterize the pulse length in the nearfields. In a proof-of-principle experiment, graphene's near-degenerate four-wave mixing is used to demonstrate the effect on resonant gold nanorods.

The ability to simultaneously control the spatial extend of light pulses on a nanometer length scale and their temporal duration on a femtosecond time scale is a key requirement to study the dynamics of individual nanostrutures [1]. Examples are coherent dynamics in molecules, new materials or plasmonics, in which cases both temporal and spatial resolution are needed to investigate the underlying mechanisms.

The general farfield limit of about half the wavelength for the optical resolution can partly be circumvented by nearfield optics, utilizing the strong field enhancement in the vicinity of plasmonic nanostructures [2]. Using an optical pulse shaper, also the temporal form of a laser pulse can be controlled to a very high degree of accuracy [3,4]. The task is to bring together the two techniques in order to benefit from the high spatial confinement and control in nearfield optics and from the temporal resolution of pulse shaping microscopy at the same time. Attempts in this direction have been made since at a number of years, including adiabatic plasmon compression at nanotips [5], scattering configurations [6] and localized nanoantennas [7].

The pulse length in the nearfield of a plasmonic nanostructure is spatially inhomogeneous, which manifests in different spectral phase profiles for different positions. We compare the spectral phase outside a nanoparticle with the phase at the surface and find significant differences. The model system we use consists of individual gold nanorods, placed on single layer graphene, which we resonantly excite with a 20 fs pulsed laser, centered at 1.55 eV. The phase at the structure's surface can be determined by measuring the second harmonic generation of the particle [7]. Additionally, we use the four-wave mixing signal of graphene [8] as a probe for the nearfield phase (see figure 1). We find that the measured phase profiles do not coincide (figure 1b), which implies that the pulse length at the particles surface is distinctly different from the pulse length in the nearfield. As shown in figure 1a, the difference is expected and can be retraced to the dielectric function of the material used.

Our conclusion is that in case of resonant plasmonic nanostructures, the task of pulse control in the nearfield has to take into account the spatial inhomogeneities of the field distribution. Once known and understood, this fact can also be exploited for better localization of nonlinear effects [1].

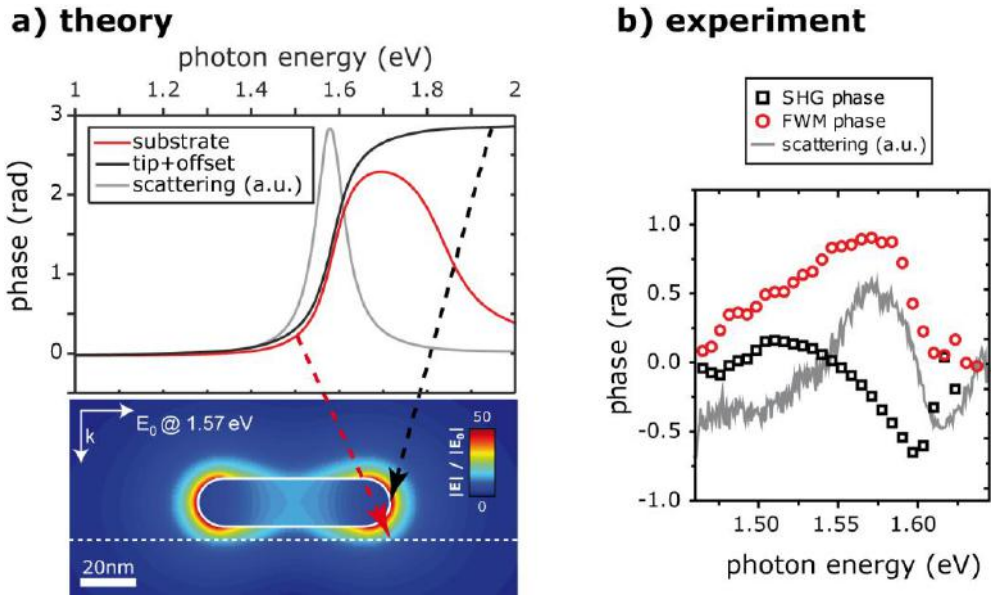



**Figure 1:** Spectral phase of a resonantly excited gold nanorod at the particle's surface and in its nearfield. **(a)** Numerical simulation, **(b)** measurements, using the second harmonic generation (SHG) of the particle and the four-wave mixing (FWM) of graphene, placed underneath the nanorod. In theory and experiment, the resulting phase profiles show large differences, indicating different pulse lengths at the two positions.

**Acknowledgements**: We acknowledge support by ERC starting grant NEWNANOSPEC (279494) and the Nanosystems Initiative Munich (NIM).

**REFERENCES**

1. Brixner, T., Garcia de Abajo, F. J., Schneider, J., Spindler, C. and Pfeiffer, W., "Ultrafast adaptive optical near-field control," *Phys. Rev. B*, 73, 125437, **2006**
2. Mauser, N. and Hartschuh, A., "Tip-enhanced nearfield optical microscopy," *Chem. Soc. Rev.*, 43, 1248-1262, **2014**
3. Lozovoy, V. V., Pastirk, I. and Dantus, M., "Multiphoton intrapulse interference. (IV). Ultrashort laserpulse spectral phase characterization and compensation," *Opt. Lett.*, 29, 775-777, **2004**
4. Comin, A., Ciesielski, R., Piredda, G., Donkers, K. and Hartschuh, A., "Compression of ultrashort laser pulses via gated multiphoton intrapulse interference phase scans," *JOSA B*, 31, 1118, **2014**
5. Berweger, S., Atkin, J. M., Xu, X. G., Olmon, R. L. and Raschke, M. B., "Femtosecond Nanofocusing with Full Optical Waveform Control," *Nano Lett.*, 11, 4309-4313, **2011**
6. Pawlowska, M., Goetz, S., Dreher, C., Wurdack, M., Krauss, E., Razinskas, G., Geisler, P., Hecht, B. and Brixner, T., "Shaping and spatiotemporal characterization of sub-10-fs pulses focused by a high-NA objective", *Opt. Express*, 22, 31496, **2014**
7. Accanto, N., Piatkowski, L., Renger, J. and van Hulst, N. F., "Capturing the Optical Phase Response of Nanoantennas by Coherent Second-Harmonic Microscopy," *Nano Lett.*, 14, 4078-4082, **2014**
8. Ciesielski, R., Comin, A., Handloser, M., Donkers, K., Piredda, G., Lombardo, A., Ferrari, A. C., Hartschuh, A., "Graphene Near-Degenerate Four-Wave Mixing for Phase Characterization of Broadband Pulses in Ultrafast Microscopy," *Nano Lett*. 15, 4968-4972, **2015**

# Plasmonic Pickup Head with Dual Wavelength Operations

**K. H. Chang[1*] and Po-Tsung Lee[1]**

[1]Department of Photonics and Institute of Electro-Optical Engineering, National Chiao Tung University, Taiwan

[*]corresponding author: openhowgood@gmail.com

**Abstract**-We propose and design plasmonic lens with circular nanoslits surrounded by circular grooves as plasmonic pickup head to achieve two focal lengths by dual wavelength operations. Two focal planes at 650nm and 780nm working wavelengths are measured at 375nm and 1020nm height above the plasmonic pickup head respectively.

The optical pickup head is the critical component for reading and writing in CD/DVD system. However, the resolution of traditional objective lens is usually limited at $\lambda/2$. Although the improved resolution of solid immersion lens is scaling down by the numerical aperture (*NA*) factor but the small gap control is difficult [1]. Recently, the plasmonic lens (*PL*) has been widely investigated due to the unique feature of extraordinary enhanced transmittance and subwavelength resolution by exciting the surface plasmon polaritons [2]. The plasmonic zone plate has been used as optical pickup head with high resolution and long focal length, which can avoid the collision between the pickup head and the recording disc [1].

In this work, we propose a novel *PL* designed with the combination of inner circular nanoslits and outer circular grooves as plasmonic pickup head. Different focusing mechanisms result in two focal lengths, which can read and write the two sides of the near field reading flexible optical disc (NFR-FOD).The focusing properties modulated by varying the outer groove depth are investigated by simulation. Finally, the proposed *PL* is fabricated and the focusing spots are measured by the near-field scanning optical microscopy (NSOM).

Figure 1(a) shows schematic illustration of the proposed *PL*. The working wavelengths of plasmonic pickup head are designed at 650 nm and 780 nm for CD/DVD system. As shown in Figure 1(b), light with short wavelength can be focused at closer distance by properly varying nanoslit widths to produce parabolic wavefront [3], while long focal length can be obtained by light with long wavelength by arranging outer grooves at suitable positions to generate total constructive interference. The focusing properties shown in Figure 1(c) are investigated using Comsol Multiphysics Software.

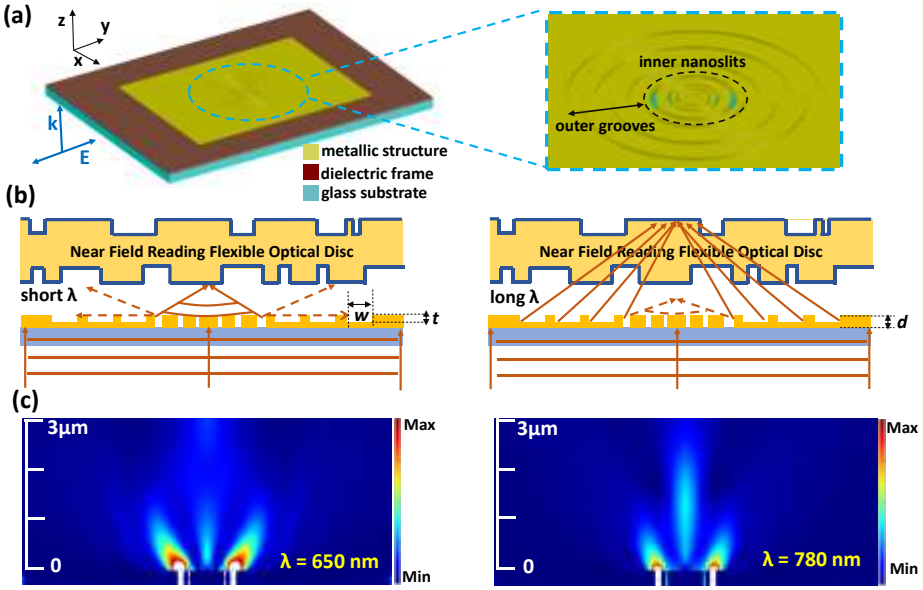



Fig. 1. (a) Schematic illustration of plasmonic pickup head with the combination of inner nanoslits and outer grooves. (b) Plasmonic pickup head operating at different wavelengths focuses light at different sides of NFR-FOD. (c) Plots of power flows at wavelengths of 650 nm and 780 nm with different focal lengths in the *y*-*z* plane.

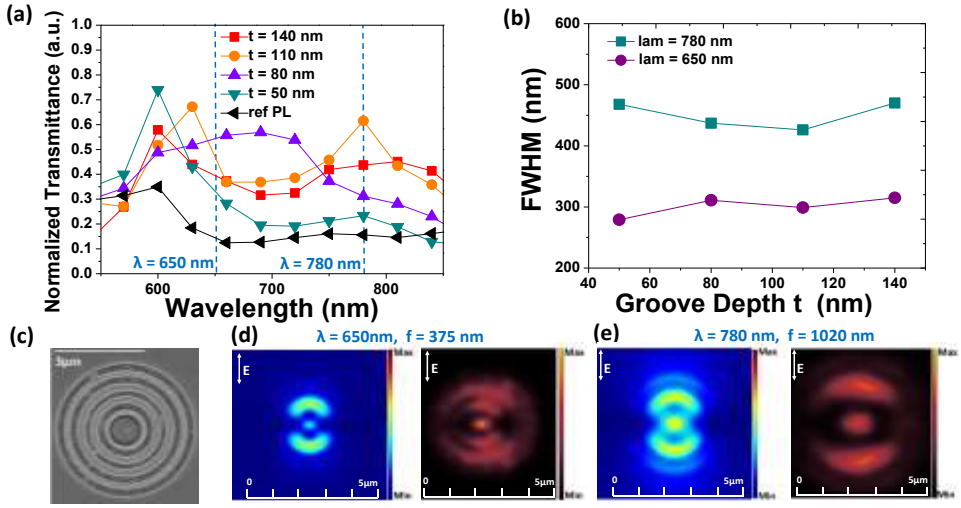



Fig. 2. (a) Simulated normalized transmittance spectra of plasmonic pickup head with varied groove depths *t* and the reference *PL* without outer grooves. (b) Simulated FWHM of focusing spots of plasmonic pickup head operating at two wavelengths when varying the groove depth *t*. (c) SEM image of fabricated plasmonic pickup head. Simulated and measured power intensity distributions of focusing spots with different focal lengths *f* in the *x*-*y* plane when the operating wavelengths are (d) 650 nm and (e) 780 nm.

From the simulated transmittance spectra shown in Figure 2(a), the transmittance of proposed *PL* is obviously enhanced compared with that of reference *PL* without outer grooves because outer grooves can transfer energy from surface to free space instead of dissipating on the metal surface. For focusing properties, Figure 2(b) shows that the simulated full width at half maximum (FWHM) of focusing spot varies for different groove depths because the varied focusing wavefronts are induced [4]. The optimized groove depth *t* is 110 nm for the high transmittance and small focusing spot.

To fabricate the plasmonic pickup head, we deposit a gold film on glass substrate, and then the pattern is made using focus ion beam (FIB). The SEM image is shown in Figure 2(c). In measurement, we use NSOM to obtain the focusing image of the plasmonic pickup head with $t$ = 125 nm, $w$ = 200 nm, and $d$ = 250 nm. Figure 2(d) shows the simulated and measured power intensity distributions of focusing spot at $z$ = 375 nm focal plane when operating at wavelength of 650 nm. Figure 2(e) shows the case at $z$ = 1020 nm focal plane when operating at wavelength of 780 nm. The measured FWHM of focusing spots are 408 nm and 474 nm respectively, which are smaller than that of traditional objective lens [1].

We develop the novel plasmonic pickup head designed with circular nanoslits surrounded by circular grooves. In simulation, the transmittance and focusing properties are investigated by changing groove depth and the optimized value is around 110 nm. In experiment, the near-field focusing at two focal planes using dual wavelengths is demonstrated with 408 nm and 474 nm FWHM, respectively. These excellent focusing properties can be applied to novel optical data storage with a NFR-FOD to achieve high-density recording.

We would like to acknowledge the help of NSOM measurements from Prof. Wen-Hau Chang and Yen-Chun Chen at National Chiao Tung University, Taiwan.

## REFERENCE

[1] Q. Wu, G. D. Feke, R. Grober, and L. P. Ghislain, "Realization of numerical aperture 2.0 using a gallium phosphide solid immersion lens," *Appl. Phys. Lett.*, Vol. **75**, No. 26,4064-4066, 1999.

[2] Y. Fu, Y. Liu, X. Zhou, Z. Xu, and F. Fan, "Experimental investigation of superfocusing of plasmonic lens with chirped circular nanoslits," *Opt. Express*, Vol. **18**, No. 4, 3438-3443, 2010.

[3] L. Verslegers, P. Catrysse, and S. Fan, "Planar lenses based on nanoscale slit array in a metal film," *Nano Lett.*, Vol. **9**, No. 1, 235-238, 2009.

[4] H. Shi, C. Du, and X. Luo, "Focal length modulation based on a metallic slit surrounded with grooves in curved depths," *Appl. Phys. Lett.*, Vol. **91**, No. 093111,1-3, 2007.

# Introducing nano-FTIR:

# Imaging and Spectroscopy at 10nm spatial resolution

**A. Cernescu**
Neaspec GmbH, Germany
adrian.cernescu@neaspec.com

**Abstract**- Scattering-type Scanning Near-field Optical Microscopy (s-SNOM) allows to overcome the diffraction limit of conventional light microscopy or spectroscopy enabling optical measurements at a spatial resolution of 10nm not only at visible frequencies but also in the infrared or terahertz spectral range.

s-SNOM [1] employs an externally-illuminated sharp metallic AFM tip to create a nanoscale hot-spot at its apex. The optical tip-sample near-field interaction is determined by the local dielectric properties (complex refractive index) of the sample and detection of the elastically tip-scattered light yields nanoscale resolved near-field images simultaneous to topography.

Development of a dedicated Fourier-transform near-field detection module for analyzing light scattered from the tip which is illuminated by a broadband laser source enables IR spectroscopy (nano-FTIR) of complex polymer nanostructures [2]. Applications presented further demonstrate characterization of embedded structural phases in biominerals (bone) [3], organic semiconductors [4] and direct visualization of field modes of nano-antennas and waveguide structures [5]. The patented modular system design enables straight forward integration of synchrotron-based broadband IR light sources [6] or to realize pump-probe near-field measurements [7].

**REFERENCES**

1. Keilmann F, H. Hillenbrand. “A Near-field microscopy by elastic light scattering from a tip,” *Phil. Trans. R. Soc. Lond. A*, Vol. 362, 787-805, 2004.
2. Huth F, et al., “NanoFTIR Absorption Spectrosopy of Molecular Fingerprints,” *Nano Lett.*, Vol. 12, 3973-3978, 2012.
3. Amarie S, et al., “Nano-FTIR chemical mapping of minerals,” *Beilstein J. of Nanotech.*, Vol. 3, 312-323, 2012.
4. Westermeier C, et al., “Sub-micron phase coexistence in small-molecule organic thin films revealed by infrared nano-imaging, “ *Nature Comm.*, Vol. 5, 4012, 2014.
5. Zenin V, et al., “Boosting Local Field Enhancement by on-Chip Nanofocusing and Impedance-Matched Plasmonic Antennas,” *Nano Lett.*, Vol. 15, 8148, 2015.
6. Barcelos I.D, et al., “Graphene/h-BN Plasmon-phonon coupling and plasmon delocalization observed by infrared nanospectroscopy,” *Nanoscale*, Vol. 7, 11620-11625, 2015.
7. Eisele M, et al., “Ultrafast multi-terahertz nano-spectroscopy with sub-cycle temporal resolution,” *Nature Phot.*, Vol. 8, 841, 2014.

# Numerical simulations of signal acquisition in aperture SNOM

**M. Hrtoň**[1,2], **P. Dvořák**[1,2], **T. Šamořil**[1,2], **F. Ligmajer**[1,2], **and T. Šikola**[1,2]

[1]Central European Institute of Technology, Brno University of Technology, Technická 10, 616 00 Brno, Czech Republic
[2]Institute of Physical Engineering, Brno University of Technology, Technická 2, 616 69 Brno, Czech Republic
[*]corresponding author: martin.hrton@ceitec.vutbr.cz

**Abstract:** Using FDTD simulations combined with analytical calculations, the signal acquisition process in aperture SNOM has been studied. The emphasis was placed on the role of individual electric field components in the image formation. The results show that although the transmission through the aperture can be tuned to selectively favor one of these components, the resulting sensitivity is eventually determined by the efficiency of their coupling to the loss-less guided modes of the tip.

Scanning near-field optical microscopy (SNOM) represents one of a few techniques allowing us to directly study and analyze evanescent optical fields formed in the vicinity of metallic structures and surfaces. In the aperture type SNOM, the evanescent fields are usually probed with a subwavelength aperture drilled into a metal-coated dielectric tip. Apparently, the question of how much the experimental a-SNOM images correspond to the actual distribution of electric field at the sample surface is of utmost importance. Previous studies have shown that the acquired signal largely comes from the out-of-plane component of the probed electric field and thus the detection of the in-plane component is quite challenging[1].

In this work, we address this issue of sensitivity of the a-SNOM tip towards the different electric field components by performing full numerical simulations of the signal acquisition, including the collection of evanescent fields by the aperture and propagation of the resulting electromagnetic waves through the tip towards the detector. Our results reveal that the poor sensitivity to the in-plane component is caused by its inefficient coupling to the loss-less guided modes of the metal-coated tip, and we discuss a possible solution to this problem. Furthermore, we show that by changing geometrical parameters of the tip, one can selectively enhance the transmission of a chosen electric field component through the aperture, an important feature necessary for full-vector mapping of optical-fields by a-SNOM.

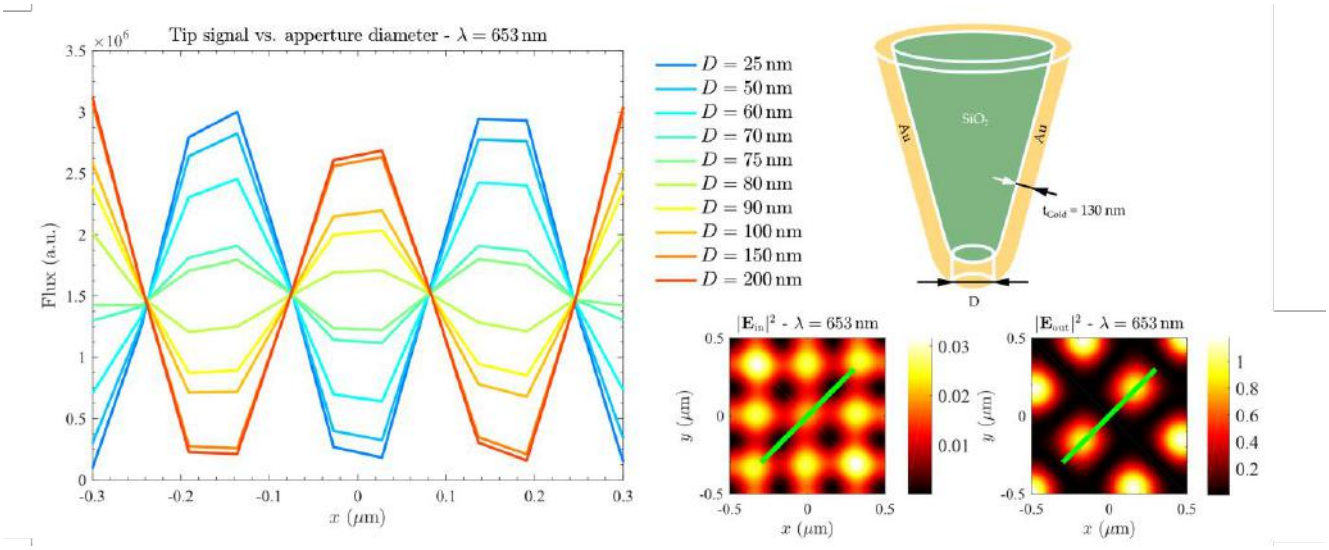



**Fig. 1**: Changes in the "sensitivity" of the a-SNOM aperture towards the in-plane and out-of-plane components with the aperture diameter D. Scanning of the tip along the diagonal of the SPP interference pattern (indicated by the green line) should reveal different electric field profiles, depending whether we detect preferentially the in-plane (maximum in the center) or the out-of-plane component (minimum in the center). For small apertures, the signal at the apex of the tip is dominated by the out-of-plane component, whereas larger apertures are more favorable towards the in-plane component.

**Acknowledgements:** We acknowledge the support by the Grant Agency of the Czech Republic (grant No. 15-21581S), European Regional Development Fund (project No. CZ.1.05/1.1.00/02.0068), MEYS CR (project No. LQ1601 – CEITEC 2020), Technology Agency of the Czech Republic (grant No. TE01020233) and BUT (project No. STI-J-15-2747).

## REFERENCES

1. Dvořák, P. et al., "Control and Near-Field Detection of Surface Plasmon Interference Patterns," *Nano Lett.*, **13,** 2558–2563, 2013.

# Spectroscopic measurements of near-field interference patterns by a-SNOM

**P. Dvořák[1,2], Z. Édes[1,2*], M. Kvapil[1,2], T. Šamořil[1,2], F. Ligmajer[1,2], M. Hrtoň[1,2], R. Kalousek[1,2], V. Křápek[1,2], P. Dub[1,2], P. Varga[2], and T. Šikola[1,2]**

[1]Institute of Physical Engineering, Brno University of Technology, Technická 2, 616 69 Brno, Czech Republic

[2]Central European Institute of Technology, Brno University of Technology, Technická 10, 616 00 Brno, Czech Republic

[*]corresponding author: zoltan.edes@ceitec.vutbr.cz

**Abstract**

Scanning near-field optical microscopy (SNOM) in combination with interference structures is a powerful tool for imaging and analysis of surface plasmon polaritons (SPPs). In this article we address how the wavelength and polarization state of illumination influence SPPs interference patterns measured by aperture-SNOM. Using the SNOM setup equipped with a supercontinuum laser and utilizing numerical simulations, we identified the role of individual near-field components in formation of SNOM images.

As SPPs are inherently connected to near-fields, they are a frequent object of study by SNOM – both in their localized (confined to metal nanoobjects) and propagating form (along metal-dielectric interfaces) [1,2]. Due to the fact that SNOM detects the time-averaged value of the fields, for experimental detection it is necessary to create a pattern of SPP standing waves. These can arise on plasmonic interference structures, formed e.g. by pairs of slits in a continuous metal film which act as linear sources of SPP when illuminated by light.

Our samples with interference structures consisting of four slits were prepared by carving out a 200 nm-thick gold film on a glass substrate using Ga focused-ion-beam (FIB) milling [3]. The spectroscopic measurements were performed on the fabricated sample by our a-SNOM setup equipped with a supercontinuum laser for both polarized and unpolarized light. Together with numerical finite-difference time-domain (FDTD) simulations, our results provide comprehensive description of principles behind SNOM image formation.

For linearly polarized illumination the measured patterns possessed a diamond-like character. It corresponds to the dominant out-of-plane component of the SPP electric field and is in good agreement with the simulations. For unpolarized illumination the experiments revealed more complex behavior, as we observed not only the theoretically predicted square-like pattern, but also a randomly distributed diamond-like pattern. This effect is attributed to the non-zero degree of polarization of illuminating light and demonstrates the sensitivity of the observed pattern to symmetry-breaking perturbations and anisotropies of the setup, which makes interference structures a useful tool for detection and elimination of such aberrations in SNOM experiments.

Our results revealed, that although the inherently larger out-of-plane component dominates the SNOM images regardless of the wavelength or polarization state, there is a major difference between the interference patterns formed under polarized and unpolarized illumination. Besides, we recognized another potentially interesting property of SPP interference patterns, namely that the patterns corresponding to the in-plane and out-of-plane components of SPP electric field are mutually shifted. This aspect of SPPs could find its use in

assessment of SNOM probe sensitivity to these two near-field components, which would be an important step towards full vector a-SNOM mapping.

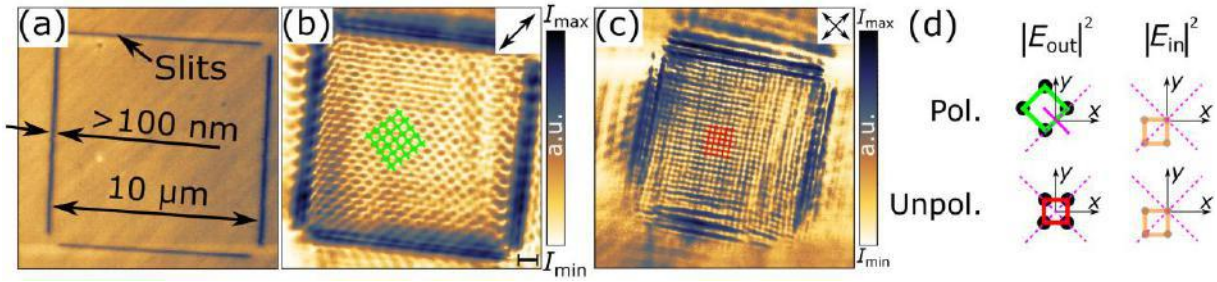



**Figure 1**: (a) Square-like interference structure. Measured interference pattern for the linearly polarized (b) and non-polarized (c) illumination (polarization direction is shown by the arrow in the inset). (d) The absolute position of various interference patterns (polarized vs. unpolarized illumination; $E_{in}$ vs. $E_{out}$ components) with respect to the center of the interference structure.

**Acknowledgements**

We acknowledge the support by the Grant Agency of the Czech Republic (grant No. 15-21581S), European Regional Development Fund (project No. CZ.1.05/1.1.00/02.0068), MEYS CR (project No. LQ1601 – CEITEC 2020), Technology Agency of the Czech Republic (grant No. TE01020233) and BUT (project No. STI-J-15-2747).

**REFERENCES**

1. Schnell, M. et al. ”Real-Space Mapping of the Chiral Near-Field Distributions in Spiral Antennas and Planar Metasurfaces” *Nano Lett.*, Vol. 16, No. 1, 663–670, 2016.
2. Lin, J. et al. ”Polarization-Controlled Tunable Directional Coupling of Surface Plasmon Polaritons” *Science* Vol. 340, 331–334, 2013.
3. Dvořák, P. et al. “Control and Near-Field Detection of Surface Plasmon Interference Patterns” *Nano Lett.* Vol. 13, No. 6, 2558–2563, 2013.

# Transformational electromagnetics, cloaking

# Ultrathin metasurface carpet cloak

**B. Orazbayev[1*], N. Mohammadi Estakhri[2], M. Beruete[1,3], and A. Alú[2]**
[1]Antennas Group-TERALAB, Universidad Pública de Navarra, Pamplona, Spain
[2]Dept. of Electrical and Computer Engineering, The University of Texas at Austin, Austin, TX 78701, USA
[3]Institute of Smart Cities, Public University of Navarra, 31006 Pamplona, Spain.
[*]corresponding author: b.orazbayev@unavarra.es

**Abstract**- We demonstrate the design of an ultrathin carpet cloak based on a metasurface with ring resonators. In order to obtain the cloaking performance, the phase of the scattered wave along the edge of the bump is manipulated by an array of closed ring resonators. This allows to hide a triangular surface bump placed on a flat ground plane. The designed cloak is numerically analyzed at the operation frequency and demonstrates a good performance in both near field and far field.

Recent advances in cloaking devices have become possible thanks to the advent of metamaterials, which allows us to tailor permittivity and permeability at will [1]. In this regard, many efforts have been focused either on transformation optics [2] or scattering cancellation [3]. The first approach requires materials with extreme electromagnetic parameters, which are difficult to obtain in a physical medium. The second method is simpler and more robust [4], however it is limited in the size of the hidden object [5]. In order to avoid extreme values and anisotropy of electromagnetic parameters, carpet cloaks based on quasi-conformal mapping have been proposed to conceal objects over a flat surface [6]. However, despite their relatively simple design and good cloaking abilities, these structures are bulky, which makes them difficult to apply for macroscopic objects.

In this work, we propose a carpet cloak based on an ultrathin cloaking metasurface with closed ring resonators. In our design, a metasurface is used to restore the scattered wavefront from the bump (with center height of 4.1 mm and base length of 22.5 mm) by recovering the phase distribution on its edge. The unit cell of such metasurface is shown in Fig. 1(a) and consists of two concentric metallic rings, placed on a thin silicon layer. The period of the unit cell is $l$ = 400 um ≈ $\lambda_0/10$ to provide a good resolution of the phase distribution of the reflected beam. Control of the phase response of the reflected beam from each block is realized by varying the radii of the rings, covering almost the entire 2π phase range. The obtained amplitude (red line) and phase (blue line) of the reflection coefficient as a function of the radius of the ring are shown in Fig. 1(b). The phase of the scattered wave at an arbitrary point on the boundary with height $h$ is reconstructed by compensating the phase difference δ, which can be calculated at each point of the bump's edge as: $\delta = \pi - 2k_0 h\cos\theta$, where $k_0$ is the free space wave vector at the operation frequency, $h$ is the height of the unit cell center from the ground plane, and θ is the angle of incidence of the incoming wave with respect to the back-plane normal.

The numerical results for the spatial distribution of electric field ($E_y$ component) at the operation frequency $f$ = 80 GHz are shown in Fig. 2(a-c) for three cases: (a) ground plane, (b) bare bump and (c) cloaked bump. As it can be seen, the bump introduced on the ground plane scatters the Gaussian beam in a wide range of the angles. After the cloaking metasurface is applied, the near-field distribution of the reflected wave is reconstructed to the original Gaussian beam. The beam recovery is also confirmed in Fig. 1(c), where the far-field radiation patterns for all three cases are plotted. When the bump is cloaked the far-field radiation pattern is similar to the case when the beam is reflected from a bare ground plane.

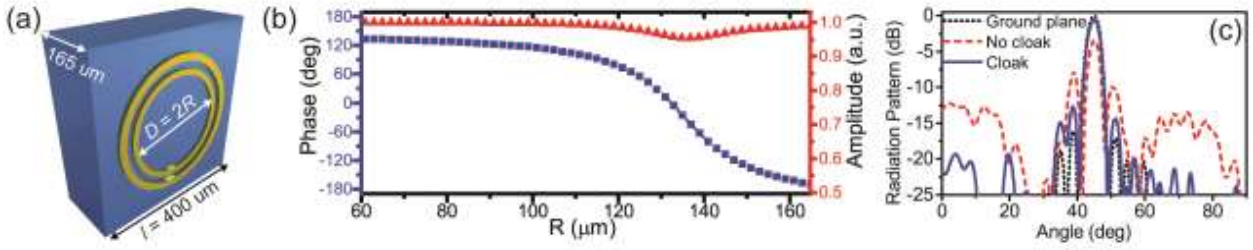



Fig. 1. (a) Unit cell geometry of the cloaking metasurface. (b) Amplitude (red line) and phase (blue line) of the reflection coefficient of the unit cell as a function of the radius of the ring. (c) Radiation pattern for the reflected Gaussian beam from the ground plane (dash-dotted black line), the bump without cloak (dashed red line) and from the cloaked bump (solid blue line).

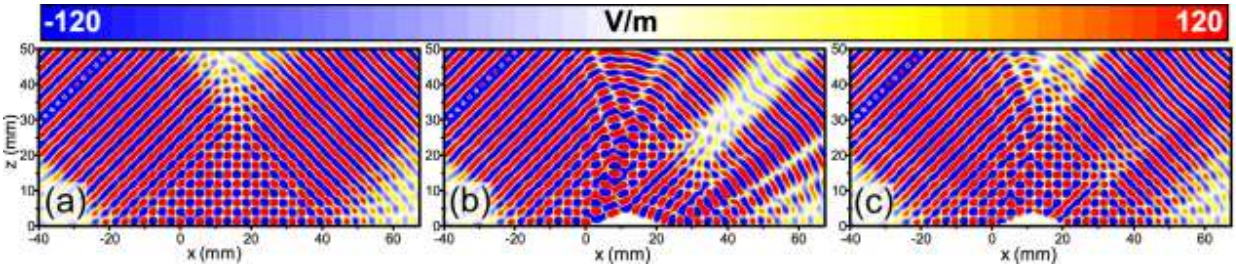



Fig. 2. Electric field distribution on *xz*-plane for (a) ground plane, (b) bare bump and (c) cloaked bump.

The proposed cloak is ultra-compact and has a simple geometry, which facilitates the fabrication and reduces cost. Beam reconstruction of the proposed cloak design has been numerically confirmed at the operation frequency $f$ = 80 GHz in the near-field as well as in the far-field. Such cloak design is potentially scalable for macroscopic objects and may find applications in radar and antenna systems.

**Acknowledgment.** This work was supported in part by the Spanish Government under Contract TEC2014-51902-C2-2-R. B. O. is sponsored by the Spanish Ministerio de Economía y Competitividad under grant FPI BES-2012-054909. M.B. is sponsored by the Spanish Government via RYC-2011-08221. N.M.E. and A.A. have been supported by the NSF CAREER award No. ECCS-0953311 and the AFOSR grant No. FA9550-13-1-0204.

**REFERENCES**

1. N. Engheta and R. W. Ziolkowski, *Metamaterials: Physics and Engineering Explorations*. Hoboken, NJ, USA: John Wiley & Sons, Inc., 2006.
2. U. Leonhardt, "Optical conformal mapping," *Science*, vol. 312, no. 5781, pp. 1777–80, Jun. 2006.
3. A. Alù and N. Engheta, "Achieving transparency with plasmonic and metamaterial coatings," *Phys. Rev. E*, vol. 72, no. 1, p. 016623, Jul. 2005.
4. A. Alù and N. Engheta, "Plasmonic materials in transparency and cloaking problems: mechanism, robustness, and physical insights.," *Opt. Express*, vol. 15, no. 6, pp. 3318–3332, 2007.
5. F. Monticone and A. Alù, "Do cloaked objects really scatter less?," *Phys. Rev. X*, vol. 3, no. 4, p. 041005, Oct. 2014.
6. J. Li and J. B. Pendry, "Hiding under the Carpet: A New Strategy for Cloaking," *Phys. Rev. Lett.*, vol. 101, no. 20, p. 203901, Nov. 2008.

# Wave Propagation in Complex Coordinates, Reflectionless Media and Localization

**C. G. King**[1], **S. A. R. Horsley**[1], **and T. G. Philbin**[1]

[1]University of Exeter, United Kingdom
cgk203@exeter.ac.uk

**Abstract**— We derive conditions for planar permittivity profiles to exhibit perfect transmission with zero reflection, for all angles of incidence. This is done through investigating the analytic continuation of the wave equation into complex coordinates using the phase integral method. We then consider a family of disordered media constructed using this method, showing that the real and imaginary parts of the permittivity can separately exhibit random fluctuations, but if they are connected via a spatial Hilbert transform, the transmission remains unity.

In applications it is often desirable to obtain spatially inhomogeneous media which do not scatter radiation and allow control of transmission and absorption through the material. Here we consider light propagating through a material inhomogeneous in one direction, as shown in figure 1. By

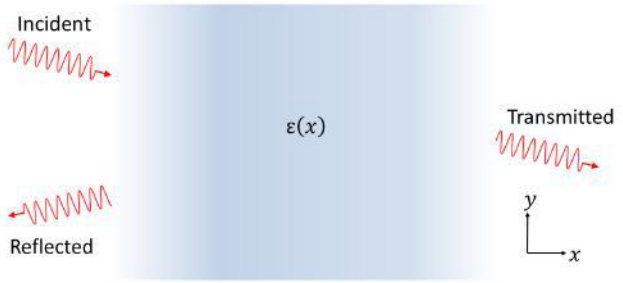



Figure 1: A wave of wave vector $\mathbf{k} = (k_x, k_y, 0)$ is incident on a material inhomogeneous along the $x$-axis. Insight into the reflection and transmission coefficients depend on the behaviour of the permittivity $\epsilon(x)$.

allowing the position variable $x$ to be complex valued $x \to z = x_1 + \mathrm{i}x_2$ and considering the analytic continuation of the wave equation into the complex *position* plane and, using the phase integral method, we derive a family of permittivity profiles $\epsilon(z)$ which are reflectionless for left incident waves for all angles of incidence and all frequencies of radiation [1, 2]. The conditions satisfied by this family are precisely those satisfied by the Kramers-Kronig relations for the permittivity; $\epsilon(z)$ should be an analytic function of position $z$ in the upper half complex plane and should approach vacuum permittivity as $x \to \pm\infty$. Furthermore, we use this method to obtain a formula for the transmission coefficient for such permittivity profiles built from poles in the lower half position plane. In particular, if the permittivity consists only of a finite number of poles of order two, or higher:

$$\epsilon(z) = 1 + \sum_{k=1}^{n} \frac{b_k}{(z - z_k)^{n_k}} \tag{1}$$

where $n_k \geq 2$, then the medium exhibits perfect transmission. This is a very large family of perfectly transmitting media, an example of which is shown in figure 2. A subset of this family is highly disordered. Anderson (strong) localization [3] predicts that the transmission through highly disordered media will be exponentially small with its length [4]. However, we have found a large set of media that don't exhibit it, as shown in figure 3.

In conlusion, we have found a family of non-reflecting disordered permittivity profiles exhibiting perfect transmission, and therefore we don't get the usually predicted localization for propagation through disordered media.

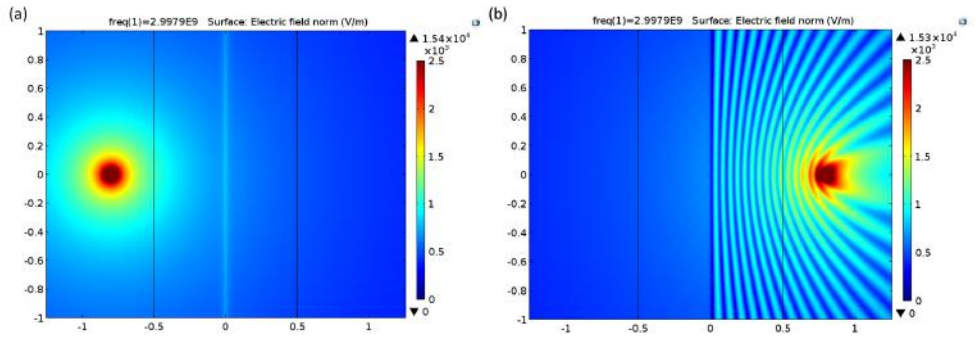



Figure 2: A simulation from COMSOL Multiphysics of the absolute value of the out of plane component of the electric field corresponding to propagation through a material with permittivity $\epsilon(z) = 1 - \frac{1}{(z/a+\mathrm{i})^2}$ where $a = \lambda/10$ and $\lambda = 0.1m$ is the wavelength. (a): A point source placed to the left of the material undergoes zero reflection from the material for all angles of incidence, as evident from the lack of ripples. (b): A point source is placed to the right of the material undergoes reflection, as evident by the ripples. In both cases the transmission coefficient through the material is unity.

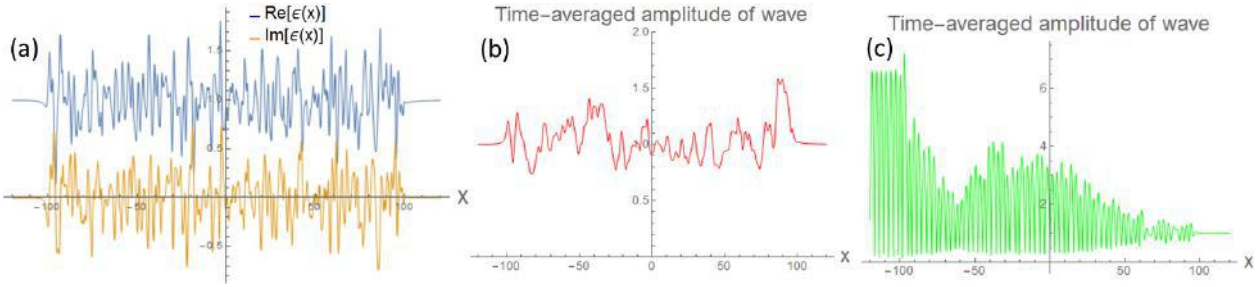



Figure 3: (a): The real and imaginary parts of a permittivity profile constructed by placing double poles randomly in a compact region of the lower half position plane. (b): The electric field plotted for a right travelling wave through this permittivity. As expected a right travelling wave isn't reflected at all and has perfect transmission. (c): The electric field plotted for a right travelling wave through the real part of permittivity. Transmission decreases approximately exponentially with length. The presence of the Kramers-Kronig related imaginary part removes this localization.


## ACKNOWLEDGMENT

C. G. King acknowledges financial support from the EPSRC Centre for Doctoral Training in Electromagnetic Metamaterials EP/L015331/1. S. A. R. Horsley and T. G. Philbin acknowledge financial support from EPSRC program grant EP/I034548/1.


## REFERENCES


1. Horsley, S. A. R., C. G. King and T. G. Philbin, "Wave propagation in complex coordinates," *arxiv*, No. 1508.04461, 2016.
2. Horsley, S. A. R., M. Artoni and G. C. La Rocca, "Spatial Kramers-Kronig relations and the reflection of waves," *Nature Photon.*, Vol. 9, 436–439, 2015.
3. Anderson, P. W., "Absence of Diffusion in Certain Random Lattices," *Phys. Rev.*, Vol. 109, No. 1492, 1958.
4. Berry, M. V. and S. Klein, "Transparent mirrors: rays, waves and localisation," *Eur. J. Phys.*, Vol. 18, No. 3, 222–228, 1996.

# Random Transformation Optics

**G. Favraud**[1], **J. S. Totero Gongora**[1], **and A. Fratalocchi**[1]

[1]PRIMALIGHT, Faculty of Electrical Engineering, Applied Mathematics and Computational Science, King Abdullah University of Science and Technology (KAUST), Thuwal 23955-6900, Saudi Arabia
gael.favraud@kaust.edu.sa, http://primalight.org

**Abstract**— Random metamaterials based on disordered structures provide promising features such as broadband energy harvesting. Through transformation optics, an equivalence can be established between geometric structures and materials with special electromagnetic properties. However, a major problem is the determination of appropriate transformations for complex geometries. We propose a method to determine such transformations and show that this approach gives rise to a new class of metastructures with unconventional properties, which can open a new manifold of nanoptics applications.

Metamaterials are traditionally composed of an ordered assembly of microstructures, each one of these having known properties. They provide a way to control and direct electromagnetic fields, allowing the creation of novel devices that could not be designed with material found in nature, the most popular of them being invisibility cloaks [1, 2]. To design these devices, transformation optics has been widely used. It provides a theoretical frame to establish an equivalence between a geometrical structure, and a new material with spatially varying effective permittivity $\varepsilon$ and permeability $\mu$ tensors. Typically, special geometries are considered, either because they correspond to an *a priori* known transformation, or because they are regular geometries for which a transformation could be found. Although these approaches have proved to be successful in the microwave and infrared wavelength scales, their realization in the nanoscale rose some challenges.

On another hand, metamaterials based on randomness and irregular geometrical structures have been given a growing interest recently since they also show promising features, like for instance broadband energy harvesting in the visible light [3]. Besides, their fabrication can be rather accessible and efficient by taking advantage of random processes like chemical reactions or deposition. Since the properties of these new random metamaterials mainly rely on their geometry, transformation optics also appears as a natural tool to study them. However, the modeling of completely irregular or random structures is a major issue when performing coordinate transforms that aim at preserving the orthogonality of the grid, as well as the boundary conditions of Maxwell equations. Even though methods exist for moderate irregular surfaces [4], they are bound to limitations, and finding the appropriate transformation able to describe an arbitrary geometry can still be a very challenging issue. The development of methods to apply transformation optics to irregular structures appears to be an important step to efficiently model these materials.

In this contribution, we develop a new transformation optics approach that allows to derive conformal maps for arbitrary irregular structures. Conformal maps are privileged transformations that allow to obtain transformed materials with diagonal $\varepsilon$ and $\mu$ tensors, which are easier to study and characterize in terms of effective media.

In our analysis, we consider a $z-$ invariant, irregular surface on $(x, y)$ that separates an isotropic medium with constitutive parameters $\varepsilon$ and $\mu$ (typically air) and a metal, as depicted on Fig. 1a. We seek to determine a coordinate transformation that maps this irregular surface in the physical coordinates $(x, y, z)$ to a flat metallic surface in the transformed coordinates $(\varphi, \psi, z)$. This particular choice is justified by the consideration that the light-matter interaction occurring at the metal-dielectric interface, generates surface plasmon polariton wave (SPP), which propagates by following the curvature of the metal [5] (Fig. 1a, inset). The motion of SPP in the geometry of Fig. 1a can be very complex, and it is a natural choice to describe it in a reference coordinate that is conformal to the metallic surface, where this motion appears simply described by straight line (Fig. 1b, inset). According to transformation optics formulas [1] the constitutive parameters $\varepsilon$ and $\mu$ are transformed into tensors

$$\varepsilon' = \varepsilon \frac{1}{\det \mathsf{J}} \mathsf{J}\mathsf{J}^T \text{ and } \mu' = \mu \frac{1}{\det \mathsf{J}} \mathsf{J}\mathsf{J}^T, \tag{1}$$

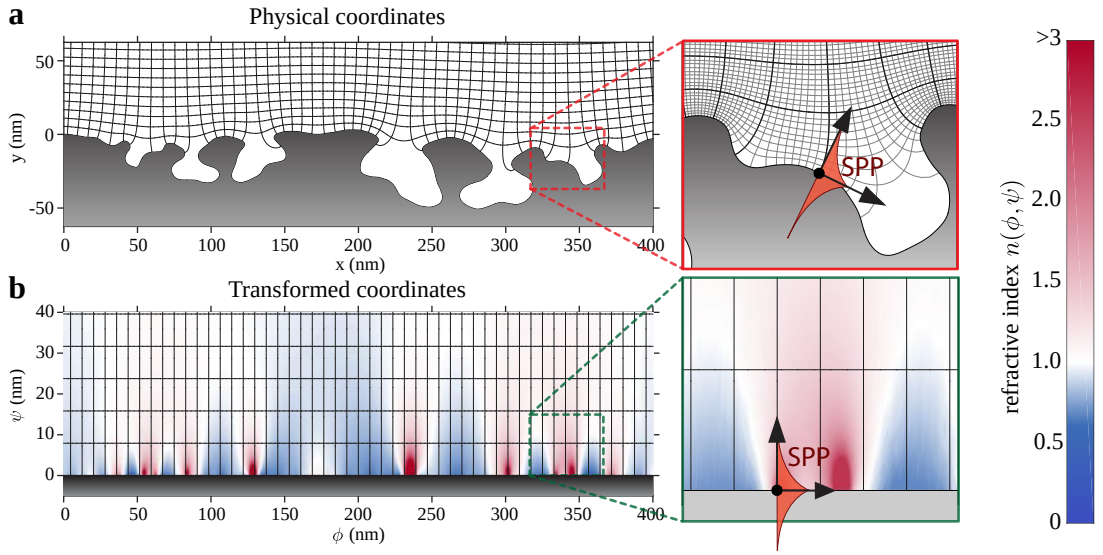



Figure 1: Conformal mapping of an irregular surface. The transformation maps (a) the physical coordinates $(x, y)$ to (b) the transformed coordinates $(\varphi, \psi)$. The mesh represents the orthogonal coordinate grid corresponding to constant values of $\varphi$ and $\psi$. This mesh is deformed in (a) to fit to the boundary and relax to the identity far from it. This results in a spatially varying refractive index in (b) represented by the color code. Note that the $\psi$ axis is dilated in (b).

where J is the Jacobian matrix of the transformation. There exist an infinite number of possible transformations, but most of them would result in complex $\varepsilon'$ and $\mu'$ tensors with important anisotropy. To obtain the simplest possible form for $\varepsilon'$ and $\mu'$, we focus on conformal mappings, for which the coordinates satisfy the so called Cauchy-Riemann equations

$$\frac{\partial \varphi}{\partial x} = \frac{\partial \psi}{\partial y}, \qquad \frac{\partial \varphi}{\partial y} = -\frac{\partial \psi}{\partial x}. \tag{2}$$

A direct consequence of this is that $\varepsilon'$ and $\mu'$ then takes a very simple form:

$$\varepsilon' = \varepsilon \begin{bmatrix} 1 & 0 & 0 \\ 0 & 1 & 0 \\ 0 & 0 & n^2(\varphi, \psi) \end{bmatrix}, \qquad \mu' = \mu \begin{bmatrix} 1 & 0 & 0 \\ 0 & 1 & 0 \\ 0 & 0 & n^2(\varphi, \psi) \end{bmatrix}, \tag{3}$$

where $n = 1/\sqrt{\det \mathsf{J}}$ acts as a refractive index. The mapping linking $x$ and $y$ to $\varphi$ and $\psi$ is computed by solving an equivalent hydrodynamic problem where physical coordinates are mapped into fluid flows and viceversa. This problem can be solved up to numerical precision for any arbitrary surface. Figure 1 shows an example of application of this method. The grid lines of constant $\varphi$ and $\psi$ is represented on the top figure. On the bottom is represented the variation of the refractive index. This transformation generated a new complex material with complex modulation of refractive index, which changes between high level values to epsilon-near-zero regions on the scale where the curvature of the metal varies. We discuss how such complex index generates unconventional properties in these metamaterials that can be used to mold the flow of light at the nanoscale.

**REFERENCES**


1. Pendry, J. B., D. Schurig. and D. R. Smith, "Controlling Electromagnetic Fields," *Science*, Vol. 312, No. 5781, 1780–1782, 2006.
2. Leonhardt, U., "Optical conformal mapping," *Science*, Vol. 312, No. 5781, pp. 1777–1780, 2006.
3. Huang, J., C. Liu, Y. Zhu, S. Masal, E. Alarousu, Y. Han and A. Fratalocchi, "Harnessing structural darkness in the visible and infrared wavelengths for a new source of light," *Nature Nanotech.*, Vol. 11, No. 1, 60–66, 2016.
4. Favraud, G. and V. Pagneux, "Multimodal method and conformal mapping for the scattering by a rough surface," *Proc. R. Soc. A*, Vol. 471, No. 2175, 20140782, 2015.
5. Maier, S. A., *Plasmonics: Fundamentals and Applications*, Springer, New-York, 2007.

# Implementation of Remote Mach-Zehnder Switch by Illusion Optics

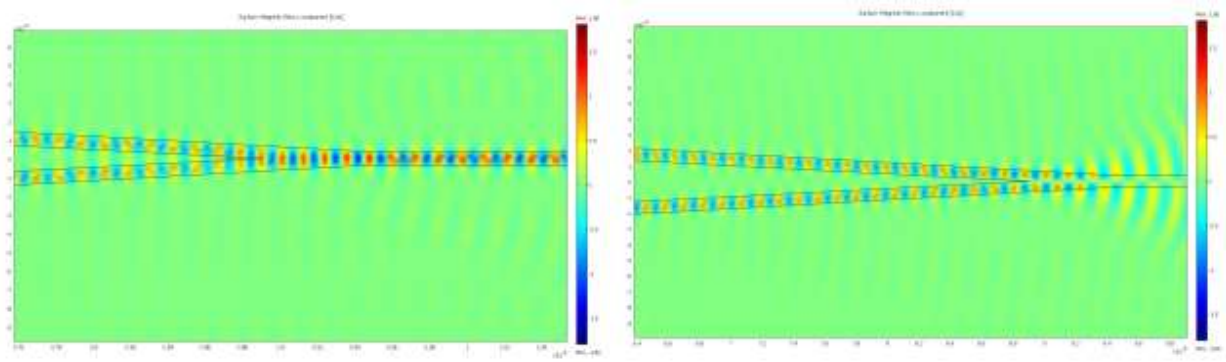
**H. R. Shoorian[1*], R. Rezapour, and D. Margusi[2]**
[1]University of Torbate-e-Heydarieh, Iran
[2]Author Azad University of Shahre-Rey, Tehran, Iran
[*]corresponding author: hamed.shoorian@gmail.com

**Abstract**- Based on illusion optics theory, in this paper a new method is introduced for remote beam manipulating and implementing a Mach-Zehnder switch. In the presence of an illusion device, the effective refractive index of a certain length of one of Mach-Zehnder arm is remotely changed to produce 180 degree phase differences to the other arm and results in destructive interference giving OFF state. When the illusion device is removed, constructive interference between both arms results in the ON state. In comparison with conventional methods, our proposed method avoids any physical changes or damages in the original structure. It is possible to realize the proposed illusion device by using effective medium theory and isotropic layered materials.

The field of transformation optics has inspired a fresh look at the designing of optical devices with novel properties. Transformation optics and Illusion optics which is a more generalized concept, give us the possibility of controlling the flow of light and manipulating electromagnetic waves which can result in the design of new optical devices with desired functionalities. In this work, we present a new technique to remotely change the effective refractive index of a certain length of an optical waveguide in one of Mach-Zehnder arm, by the aid of an external device at a distance which is called illusion device and designed based on illusion optics theory and transformation optics technique. Hence, any physical change or damage does not apply to the waveguide.

Mach-Zehnder interferometer (MZI) principle was developed in 1891/1892 by Ludwig Mach and Ludwig Zehnder. A Mach-Zehnder interferometer is one of most important components in integrated optical circuits and has been utilized for optical devices such as switches, modulators, and etc. It takes an input optical wave, splits it equally along two paths and then recombines the wave to create an interference effect. In order to control the optical output, extra phase shifts are added to one of its arms, by changing the refractive index, optical path length, thermo optic effect, and using liquid crystals. The simplest Mach-Zehnder which is used in this work has a single input waveguide that splits into two arms for a certain distance and recombines again to a single output waveguide. Introducing a phase difference between both MZ arms before the recombine results the on-off switching behavior of the MZ modulator. For the MZI configuration with Y-branches at the input and the output, 0° phase difference equals a constructive interference giving the ON state for amplitude modulation. In OFF state, a phase difference of 180 degree between both arms results in destructive interference with no light being sent to the output.

In the following full-wave two-dimensional finite element simulations are performed by the COMSOL MULTIPHYSICS commercial software package. For a MZ constructed of an optical waveguide with effective refractive index of 2.21, $z$ component of magnetic field at $\lambda$=1550nm is shown in Figure 1.a for ON state. For OFF state which is shown in Figure 2.b, effective refractive index of a certain length of optical waveguide at the upper arm should be changed to 1.5 to produce 180 degree phase differences to the other arm.



**Figures 1:** magnetic field for **a**) ON state. **b**) OFF state

In this work, based on illusion optics theory we demonstrate a new method to remotely change the effective refractive index of a certain length of an optical waveguide in one of Mach-Zehnder arm without any physical change on damage in the structural parameters. This can be achieved as shown in Figure 2 by the aid of an external device at a distance which is called illusion device and designed based on illusion optics theory and transformation optics technique [1,2].

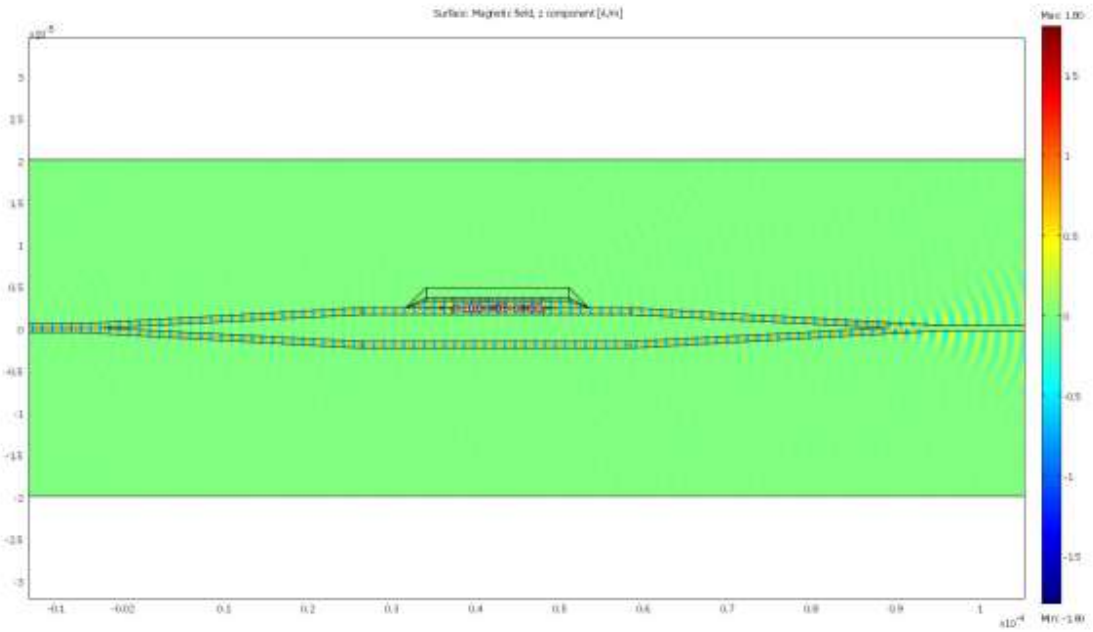


**Figure 2.** FE simulation of implementing remote MZ switch by illusion device

**REFERENCES**


1. Shoorian, H. R. and Abrishamian, M. S. "Design of optical switches by illusion optics," *Journal of Optics*, Vol. 15, No. 10, 055107(7pp), 2013.
2. Margusi, D. and Shoorian, H. R., "Remote nano-optical beam focusing lens by illusion optics," *Appl. Phys. A*, Vol. 117, No. 2, 505–511, 2014.

# Low Profile Superstrate using Transformation Optics to modify Radiation Pattern of Antenna

**C. Joshi*, A.C. Lepage, and X. Begaud**
LTCI, CNRS, Télécom ParisTech, Université Paris-Saclay, France
*corresponding author: chetan.joshi@telecom-paristech.fr

**Abstract**- A superstrate to modify the radiation pattern of a patch antenna designed using transformation optics method is presented. At first, the transformation relations between the physical and virtual space are described. Then, material parameters calculated from transformation optics method are used to design a three dimensional low profile superstrate that reorients the radiation pattern in azimuthal plane.

Transformation Optics is a powerful tool to control the electromagnetic wave behavior. The invariance of Maxwell's equation under coordinate transformation allows calculating new permittivity and permeability values to reinterpret a physical space with respect to a virtual space [1]. In [2], a TO superstrate was presented to achieve antipodal radiation pattern. In this paper, we propose an improved solution with lower thickness and reduced material complexity.

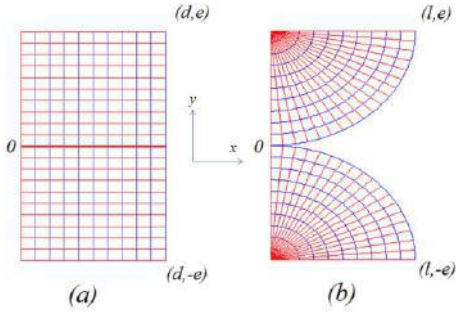



**Fig. 1 (a) Physical Space (b) Virtual Space**

$$x' = \sqrt{(a.x)^2 + (y \pm e)^2} \tag{1}$$

The simplified problem may be restricted to two dimensions i.e. x-y plane. The patch antenna is modeled in COMSOL by an idealized current sheet backed with a PEC plane. The electric field has z-component only. Fig. 1 (a) and (b) show physical and virtual spaces. Compression along x-axis is governed by a factor '*a*', such that *l* = *d*/*a*. When *a=1*, then *l* = *e*. In [2], compression factor is chosen as a = 2. The transformation relation to transform blue lines of Fig.1 is given in (1). The dimensions have been chosen so as to correspond to the frequency of operation, *f* = 1.25 GHz. On using TO method, material parameter (MP) distribution can be given by relations described next. As only $E_z$ is considered, the primary MP profile may be proposed using $\mu_{xx}$, $\mu_{yy}$ and $\varepsilon_{zz}$. Using TO concept, $\mu_{xx} = \pi.x'/e$, $\mu_{yy} = 1/\mu_{xx}$ and $\varepsilon_{zz} = a.\mu_{xx}$. In [2], a further simplification of MP profile was

necessary to limit variation to two MP's ($\mu_{yy}$ and $\varepsilon_{zz}$). This extra step resulted in extreme permittivity and permeability values in MP Profile. In the proposed solution, we do not undertake this simplification; instead a higher compression of the profile has been favored. The resulting values of permittivity and permeability vary in a smaller range. A full wave solution is obtained by simulating a three dimensional cylindrical superstrate based on profile obtained above, it is shown that the radiation pattern of antenna has been modified as expected. The antenna radiates in broadside (along x), as seen in Fig. 2(a). When the TO superstrate is placed over the patch antenna, the radiation is guided to the azimuthal (y-z) plane, as seen in Fig. 2(b). Addressing the anisotropy in material parameters remains a concern, which shall be discussed in the final paper.

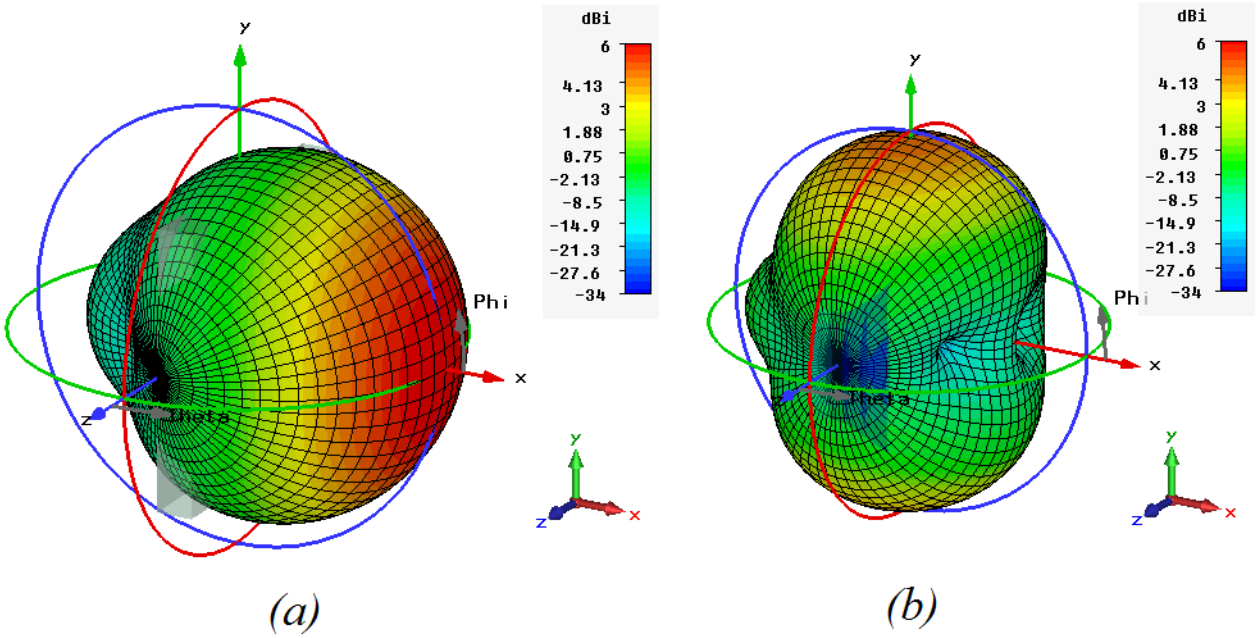



**Fig. 2 Radiation Patterns (Directivity) (a) Antenna alone, (b) Antenna with TO Superstrate**

To conclude, a TO superstrate has been presented where a thin profile has been achieved with reduced material parameter complexity. The profile is 23% thinner than reported in earlier works. In the final paper, the performance of the design shall be discussed in detail. More information shall be presented on different aspects i.e. analysis of anisotropy, discretization of continuous profile, fabrication strategy, etc.

This work is supported by the NanoDesign project funded by IDEX Paris-Saclay, ANR-11-IDEX-0003-02.

**REFERENCES**

1. Pendry, J.B., D. Schurig and D.R. Smith, "Controlling electromagnetic fields," *Science*, Vol. 312, 1780-1782, 2006.
2. Clemente Arenas, M., A.C. Lepage and X. Begaud, "Antipodal radiation pattern of a patch antenna combined with superstrate using transformation electromagnetics," *Appl. Phys. A*, Vol. 117, No. 2, 699–703, 2014.

# Numerical modeling of time-domain cloaking with metamaterials

**Yunqing Huang**[1], **Jichun Li**[2], **and Wei Yang**[1]

[1]Xiangtan University, China
[2]University of Nevada Las Vegas, USA
jichun.li@unlv.edu

**Abstract**— In this talk, we will present some of our recent works on mathematical analysis and finite element modeling of cloaking devices constructed by metamaterials. Our talk will focus on the cloaking simulation in time-domain.

In June 23, 2006's issue of Science magazine, Pendry et al and Leonhardt independently published their works on electromagnetic cloaking. In Nov.10, 2006's Science, Pendry et al demonstrated the first practical realization of such a cloak with the use of artificially structured metamaterials. Since then, there is a growing interest in using metamaterials to construct invisibility cloaks cf.[1, Ch.9]. In this talk, we first present an overview of our recent work on time-domain cloaking simuations, then focus on time-domain carpet cloak [2].

A triangular carpet cloak shown in Fig.1 (Left) can be achieved with spatially homogeneous anisotropic dielectric materials. The cloaked region is the bottom triangle with vertices $(0, H_1), (-d, 0)$ and $(d, 0)$. The cloaking region is the quadrilateral region formed by vertices $(-d, 0), (0, H_1), (d, 0)$ and $(0, H_2)$, where $H_1, d > 0$. In order to make the hiden objects inside the cloaked region invisible to outside observer, the permittivity and permeability in the cloaking region need to be specially designed:

$$\varepsilon = \begin{bmatrix} a & b \\ b & c \end{bmatrix} = \begin{bmatrix} \frac{H_2}{H_2-H_1} & -\frac{H_1H_2}{(H_2-H_1)d}\mathrm{sgn}(x) \\ -\frac{H_1H_2}{(H_2-H_1)d}\mathrm{sgn}(x) & \frac{H_2-H_1}{H_2} + \frac{H_2}{H_2-H_1}(\frac{H_1}{d})^2 \end{bmatrix}, \quad \mu = \frac{H_2}{H_2-H_1},$$

where $\mathrm{sgn}(x)$ is the standard sign function. By construction, it is assumed that $H_2 > H_1 > 0$.

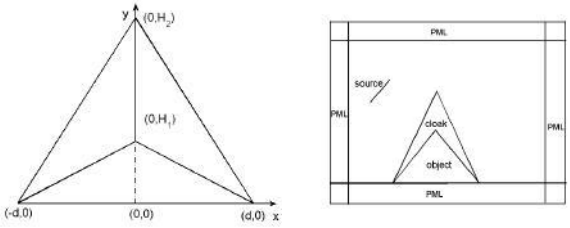



Figure 1: The physical space of the carpet cloak.

Denote

$$\lambda_1 = \frac{a+c-\sqrt{(a-c)^2+4b^2}}{2}, \quad \lambda_2 = \frac{a+c+\sqrt{(a-c)^2+4b^2}}{2},$$

$$p_1 = \sqrt{\frac{\lambda_2-a}{\lambda_2-\lambda_1}}, \quad p_2 = \sqrt{\frac{a-\lambda_1}{\lambda_2-\lambda_1}}\cdot\mathrm{sgn}(x), \quad p_3 = -\sqrt{\frac{\lambda_2-c}{\lambda_2-\lambda_1}}\cdot\mathrm{sgn}(x), \quad p_4 = \sqrt{\frac{c-\lambda_1}{\lambda_2-\lambda_1}},$$

and matrices $M_A = \begin{pmatrix} p_1^2\lambda_2+p_2^2 & p_2p_4+p_1p_3\lambda_2 \\ p_2p_4+p_1p_3\lambda_2 & p_3^2\lambda_2+p_4^2 \end{pmatrix}$, and $M_B = \begin{pmatrix} p_2^2 & p_2p_4 \\ p_2p_4 & p_4^2 \end{pmatrix}\omega_p^2$, where $\omega_p$ is the plasma frequency. We can obtain the governing equations for the carpet cloak:

$$\boldsymbol{D}_t = \nabla\times H, \quad \mu_0\mu H_t = -\nabla\times\boldsymbol{E}, \tag{1}$$

$$\varepsilon_0\lambda_2\left(\boldsymbol{E}_{t^2}+\omega_p^2\boldsymbol{E}\right) = M_A\boldsymbol{D}_{t^2}+M_B\boldsymbol{D}, \tag{2}$$

where $H$ denotes the magnetic field, and $\boldsymbol{D}$ and $\boldsymbol{E}$ represent 2D electric displacement and electric field. The curl operators are in 2D sense. To make the model complete, we assume that (1)-(2) satisfy the initial conditions

$$\boldsymbol{D}(\boldsymbol{x},0)=\boldsymbol{D}_0(\boldsymbol{x}),\quad \boldsymbol{E}(\boldsymbol{x},0)=\boldsymbol{E}_0(\boldsymbol{x}),\quad H(\boldsymbol{x},0)=H_0(\boldsymbol{x}),\quad \forall\ \boldsymbol{x}\in\ \Omega, \tag{3}$$

and the PEC boundary condition: $\boldsymbol{n}\times\boldsymbol{E}=\boldsymbol{0}$ on $\partial\Omega$, where $\boldsymbol{D}_0,\boldsymbol{E}_0$ and $H_0$ are some properly given functions, $\boldsymbol{n}$ is the unit outward normal vector to $\partial\Omega$, and $\Omega$ denotes the cloaking region.

The well-posedness of this model and the following stability is proved. A leap frog type scheme with edge elements is developed for our model and many simulations are carried out. Due to page limit, here we show one example by choosing $H_1=0.05m, H_2=0.2m, d=0.2m$, and $\Omega=[-0.3,0.3]\ m\times[0,0.3]\ m$, which is partitioned by a uniform triangular mesh with a mesh size $h=0.00625$. The PML region surrounding $\Omega$ is partitioned by a uniform rectangular mesh. Our final mesh yields 53330 total edges, 26960 total triangular elements, and 6258 total rectangular elements. In the test, we choose the time step size $\tau=2*10^{-13}$ s, and the total number of time steps 15000, i.e., the final simulation time $T=3.0$ nanosecond (ns).

The incident wave is generated by a plane wave source $H_z=0.1\sin(\omega t)$ imposed at line $x=-0.3$, where $\omega=2\pi f$ with frequency $f=3.0$ GHz. The numerical electric fields $E_y$ at different time steps are presented in Fig.2, which shows clearly that the plane wave pattern is recovered very well after passing through the cloaking region, which makes any objects hiden inside the cloaked region invisible to observers at the far end.

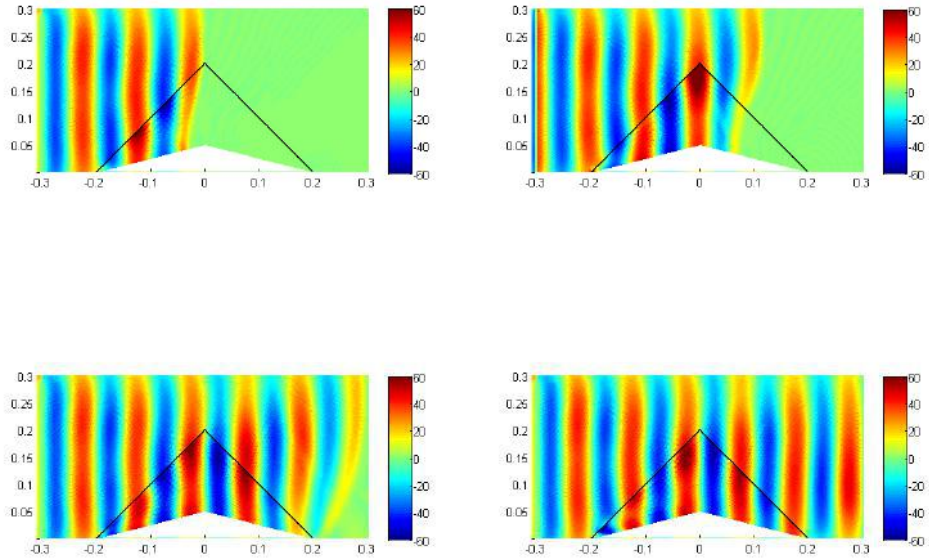


Figure 2: The $E_y$ fields at 5000, 7000, 10000, and 15000 time steps.

**REFERENCES**


1. J. Li and Y. Huang, *Time-Domain Finite Element Methods for Maxwell's Equations in Metamaterials*, Springer, 2013.
2. J. Li, Y. Huang, W. Yang and A. Wood, "Mathematical analysis and time-domain finite element simulation of carpet cloak," *SIAM J. Appl. Math.* Vol. 74, No. 4, 1136–1151, 2014.
3. Y. Huang and J. Li, "Total reflection and cloaking by triangular defects embedded in zero index metamaterials," *Advances in Applied Mathematics and Mechanics*, Vol. 7, No. 2, 1–10, 2015.

# A level-set based topology optimisation of cloaking devices with the boundary element method

**Kenta Nakamoto**[1], **Hiroshi Isakari**[1], **Toru Takahashi**[1], **and Toshiro Matsumoto**[1]

[1]Nagoya University, Japan
k_nakamoto@nuem.nagoya-u.ac.jp
isakari@nuem.nagoya-u.ac.jp
ttaka@nuem.nagoya-u.ac.jp
t.matsumoto@nuem.nagoya-u.ac.jp

**Abstract**— We investigate a topology optimisation, which is one of design methods based on computer simulation, for cloaking devices. In this study, we employ the level set method, in which the configuration of the cloaking material is expressed by a scalar function (level set function), and the distribution of the level set function is updated by the reaction-diffusion equation. As the source term of the reaction-diffusion equation, we use the topological derivative which characterises the sensitivity of the objective function to an appearance (or removal) of an infinitesimal cloaking material. In the updating process for the level set function, the topological derivative is evaluated by the boundary element method (BEM) since the topological derivative is associated with solutions of the Helmholtz equation defined in an infinite domain. We confirm the effectiveness of the proposed method by some numerical examples.

Many varieties of researches on new devices which are constructed by metamaterials have been conducted. A cloaking device is one of the most attractive example of such devices. Cloaking is a technology to hide an object. By putting a cloaking device around an object the light path is manipulated in a way to go around the object, which makes the object invisible. Smith experimentally showed that it is possible to construct a cloaking device by putting metamaterials periodically [1]. Manufacturing the cloaking device is, however, still based mostly on trial and error process.

In this study, we apply a topology optimisation to design problem of cloaking devices. A topology optimisation is one of simulation-based design methods. We can determine an optimal shape and topology which maximise efficiency of engineering devices with this method. In this study, we employ the level set method as a configuration expression method in the topology optimisation. In the level set method, configuration of a design object is expressed as distribution of a level set function $\phi(\boldsymbol{x})$ $(-1 \leq \phi(\boldsymbol{x}) \leq 1)$. Each domain is expressed by the value of the level set function as follows:

$$\Omega_1 = \{\boldsymbol{x} \mid -1 \leq \phi(\boldsymbol{x}) < 0 \}, \tag{1}$$
$$\Gamma = \{\boldsymbol{x} \mid \phi(\boldsymbol{x}) = 0 \}, \tag{2}$$
$$\Omega_2 = \{\boldsymbol{x} \mid 0 < \phi(\boldsymbol{x}) \leq 1 \}, \tag{3}$$

where $\Omega_1$ and $\Omega_2$ denote outside and inside domain of design objects, respectively. Also, $\Gamma$ denotes the boundary of $\Omega_2$. We update distribution of the level set function by solving the following reaction-diffusion equation:

$$\frac{\partial \phi}{\partial t} = C\mathcal{T}(\boldsymbol{x}) + \tau l^2 \nabla \phi(\boldsymbol{x}), \tag{4}$$

where, $t$ is a fictitious time corresponding to an optimisation step. The first term in right hand side (RHS) denotes the direction and scale of the update. $\mathcal{T}$ denotes a topological derivative; sensitivity of an objective function when an infinitesimal cloaking material is allocated. Also, $C$ is a constant which is used to arrange the scale of update. The second term in RHS is used to arrange the complexity of the configuration which is obtained after the update. $\tau$ is a constant and $l$ denotes characteristic length. In the optimisation problem of cloaking devices in 2D TE polarised field, an objective function is defined as follows:

$$J = \sum_{m=1}^{M} \|u(\boldsymbol{x}_m^{\mathrm{obs}}) - u^{\mathrm{inc}}(\boldsymbol{x}_m^{\mathrm{obs}})\|^2, \tag{5}$$

where $u$ and $u^{\mathrm{inc}}$ denote the magnetic field and incident field, respectively. $\boldsymbol{x}_m^{\mathrm{obs}}$ is coordinate of some fixed observation points. For the objective function (5), the topological derivative when we put an infinitesimal circle in domain $\Omega_j$ in a domain $\Omega_i$ is derived as follows:

$$\mathcal{T} = \Re\left[\frac{2(\varepsilon_j - \varepsilon_i)}{\varepsilon_i(\varepsilon_i + \varepsilon_j)}\nabla u \cdot \nabla \tilde{u}\right], \tag{6}$$

where $\varepsilon_i$ denote permittivity in the domain $\Omega_i$. Also, $u$ and $\tilde{u}$ denote the magnetic field and adjoint field, respectively. In the 2D TE polarised field, the $u$ and $\tilde{u}$ satisfies the Helmholtz equation. Hence, we firstly solve the Helmholtz equation and obtain $u$ and $\tilde{u}$. Then, we calculate the topological derivative and update the level set funciton by solving the equation (4). By repeating this procedure, we obtain an optimal configuration.

For the calculation of $u$ and $\tilde{u}$, the finite element method (FEM) is usually employed. The FEM, however, cannot analyze the problem in the infinite domain such as electro-magnetic field analysis. Hence, in the case that we apply the FEM to the topology optimisation of cloaking devices we need to approximate the infinite domain as a finite domain with an appropriate boundary condition. In order to avoid deterioration of accuracy due to this approximation, we employ the boundary element method (BEM) in this study since the BEM can treat the infinite domain exactly.

We confirm the effectiveness of proposed method by some numerical examples. We consider a configuration optimisation problem of dielectric element which make a circle shape PEC invisible for a TE polarised plane incidence which propagates in $x$ direction. Radius of the PEC is 375[nm] and wavelength of the incident wave is 750[nm]. The size of a design domain in which we determine configuration of dielectric elements is $3.75 \times 3.75[\mu\mathrm{m}]$. Also, permittivity of dielectric elements is set to be 2.0 which corresponds to that of a polypropylene. We determine the initial configuration as a domain in which the topological derivative without dielectric elements is less than 0. The result is shown in Figure 1. In the case that there are no dielectric elements and the case of initial shape, the magnetic field is scattered on the surface of PEC and dielectric elements. In the optimal configuration, magnetic field is almost same with plane wave, which indicates that the configuration works as a cloaking device.

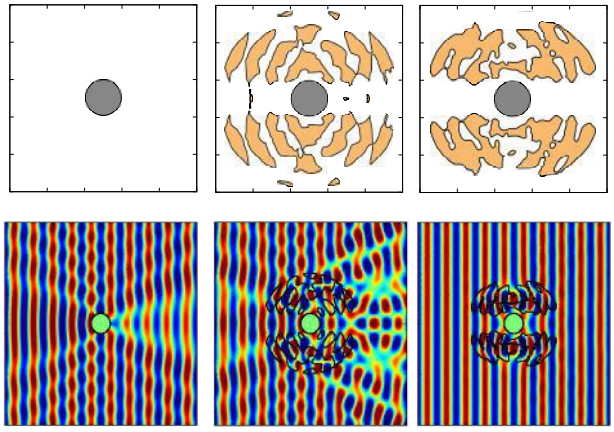


Figure 1: The magnetic response of circle shape PEC (left), initial configuration (center) and the optimal configuration at step 60 (right).

**REFERENCES**


1. Schurig, D., J. J. Mock, B. J. Justice, S. A. Cummer, J. B. Pendry, A. F. Starr and D. R. Smith, "Metamaterial electromagnetic cloak at microwave frequencies," *Science*, Vol. 314, No. 5801, 977–980, 2006.

# Multi-physics simulations for 3D isotropic transformation optics

**Dongheok Shin**[1] **and Kyoungsik Kim**[1*]
[1]Department of Mechanical Engineering, Yonsei University, Republic of Korea
[*]corresponding author: kks@yonsei.ac.kr

**Abstract**-We used multi-physics simulation to design and verify 3D isotropic transformation optical device. Previously we proposed design method for 3 dimensional transformation optical medium using structure-wave multi-physics simulation. For very small wavelength compare to the entire device, wave simulation is grossly inefficient. So we took another multi-physics simulation with structure and ray optics to verify its usefulness.

Transformation optical medium (TOM) is warped physical space with newly distributed optical properties mapped from virtual space. In the warped medium such as an optical cloak, transformed Maxwell's equations are always valid with transformed optical parameters which control the propagation of electromagnetic waves along the warped space [1]. Isotropic transformation optical medium is designed using quasi-conformal mapping (QCM) technique. By QCM, included angles (generally 90 degrees) between grid elements are maintained after transformation, so that the area of each grid element undergoes isotropic change. A mapped electric permittivity or refractive index of quasi-conformally transformed medium is also an isotropic one [2].

The design of 3D isotropic TOM is complicated to achieve but expected to easily fabricate using 3D printing technology. In 2014, García-Meca et al. reported the full 3d isotropic transformation media designed using Green coordinate transformation [3].

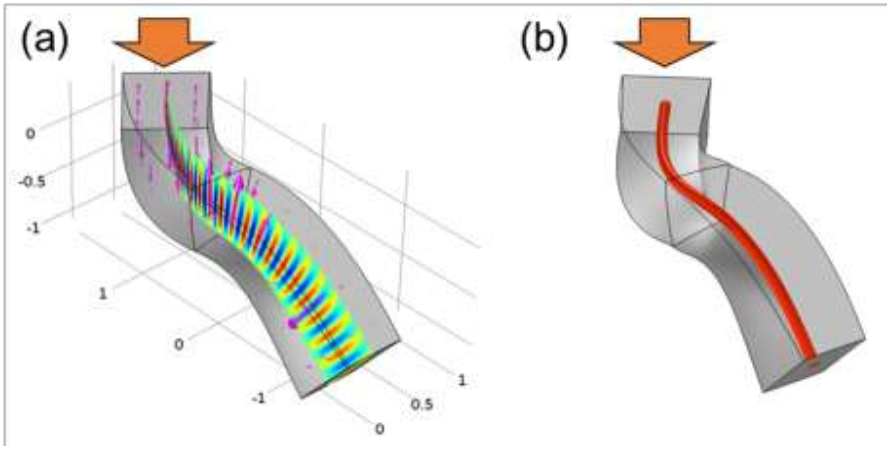



Figure 1. 3D isotropic bended TOM using structure-wave and structure-ray multi-physics.

We obtain 3D TOM using simple and intuitive design method of smart transformation optics. In smart transformation optics, space transformation is regarded as solid deformation and mapped optical properties are calculated by deformation gradient tensor of deformed solid. To get isotropic TOM, the solid must have the

critical property of Poisson's ratio close to -1 [4]. In the case of 3D TOM, we need another important condition of free boundary condition allowing additional boundary deformation induced by main deformation. This condition reduce anisotropy induced by deformation, therefore the deformed solid maintains its own isotropy [5].

Figure 1 shows comparison of 3 dimensionally bended TOM simulated with structure-wave and structure-ray multi-physics. In multi-physics simulations, the first step is applying 3D structural deformation to initially homogeneous solid. With proper condition, the calculated permittivity or index distribution apply to deformed solid. In the second step, we take two different optics simulations of wave and ray to verify the 3D TOM. The main difference between wave and ray optics simulation results is operating wavelength about the TOM. For the meter-scaled TOM, the wave in Fig. 1(a) and the ray in Fig. 1(b) have wavelengths of 15 cm (2 GHz) and 600nm respectively.

We verified the isotropic 3D TOM designed by smart transformation optics using two kinds of multi-physics simulations using wave and ray optics. Although the model in this paper has simply deformed geometry, the times taken on two kind of simulations are quite different. Multi-physics simulation with wave optics consumes much more computing power than the case of ray optics. To simulate a large scale 3D TOM in comparison with operating wavelength, the multi-physics with ray optics will be better choice.

**REFERENCES**


1. Pendry, J. B., D. Schurig, and D. R. Smith, "Controlling electromagnetic fields," *Science,* Vol. 312, No. 5781, 1780-1782, 2006.
2. Li, J., and J. B. Pendry, "Hiding under the carpet: a new strategy for cloaking," *Physical Review Letters,* Vol. 101, No. 20, 203901, 2008.
3. García-Meca, C., et al., "Full three-dimensional isotropic transformation media," *New Journal of Physics,* Vol. 16, No. 2, 023030, 2014.
4. Shin, D., et al., "A versatile smart transformation optics device with auxetic elasto-electromagnetic metamaterials," *Scientific reports,* Vol. 4, 4084, 2014.
5. Shin, D., et al., "Design of 3D isotropic metamaterial device using smart transformation optics," *OPTICS EXPRESS,* Vol. 23, No. 17, 21892, 2015.

# Identifying Microwave Magnetic Resonance in Chiral Elements for Creation of Controlled Matched Absorbing Metastructures

**G. A. Kraftmakher*, V. S. Butylkin, Yu. N. Kazantsev, V. P. Mal'tsev, and Yu. Sh. Temirov**

Kotelnikov Institute of Radioengineering & Electronics RAS, Moscow, Russia
*gkraft@ms.ire.rssi.ru

## Abstract

It has been suggested a method for identifying and separating magnetic and electric microwave resonance responses in conductive chiral elements by reflection of electromagnetic waves in the standing and traveling-wave modes. It has been observed experimentally (in waveguide) and confirmed numerically (in free space) that magnetic resonance, which is excited by microwave magnetic field *h*, and electric resonances, excited by electric field *E*, show drastically different resonance curves of reflection. These distinctions allow to identifying the magnetic resonance response and using magnetically excited elements for broadband matching of absorbers instead of traditional quarter-wavelength layer. We have fabricated and tested matched absorbing metastructures which are controlled by voltage as well by light of remote laser pointer.

## 1. Introduction

The interest in chiral media on bases of chiral elements, which are much less than wavelength, is mainly due to the unique effects caused by resonant ring (closed) currents. These currents can be induced in elements by the microwave magnetic field *h* (magnetic excitation, *h*-exc.) or by electric field *E* (electric excitation, *E*-exc) or simultaneously by *E*- and *h*-fields. The current induced by magnetic field *h* creates the ac magnetic and electric dipole moments; the magnetic moment contributes to permeability μ, while the electric moment contributes to the chirality parameter affecting the magnetic induction. When the ring current is induced by electric field *E*, the magnetic and electric dipole moments are formed. But in this case, the electric moment contributes to permittivity ε and magnetic moment contributes to chirality parameter affecting the electric induction. In addition, in chiral elements the electric field can induce resonant currents, which cause the resonance effects analogously to ordinary dipoles. The resonance effects caused by the ring currents will be called the "ring resonance" (RR); by "magnetic response" "magnetic resonance" (MR) we shall mean magnetic excitation (*h*-exc.) of RR; by "electric response" or "electric resonance" (ER) we shall mean electric excitation (*E*-exc.) of RR. The resonance effects excited by the dipole currents will be called the "dipole resonance" (DR).

Separating different resonance effects is important to identify MR which is used for creation of artificial magnetic materials and left-handed media. Whereas multitude of resonance effects in various conductive elements and difficulties in direct measurement of permeability and permittivity [1], it is necessary to develop methods for identifying the type of excitation.

The available identification methods are based on studying transmittance *T* spectra [2, 3]. These methods require additional special samples or evanescent waveguide structures.

This paper proposes to identify magnetic and electric excitation by reflection in free space or in waveguide in the standing-or traveling modes by the features observed in the dispersion characteristics. The disclosed features open a new aspect of the absorption problem, specifically, the possibility of broadband compensation of frequency-dependent reflections from traditional absorbing composites based on resistive threads or films. Array of *h*-excitated elements, placed closely to absorber, is used for broadband matching instead of traditional quarter-wavelength layer. In this case metastructures absorber/elements acquire new functional possibility as voltage (or light) fast control of matching through tuning MR if elements are loaded with varactor (or varactor in combination with photodiode).

## 2. Chiral elements and metastructures for waveguide measurements

Fig. 1*a* shows photos of investigated samples: *1* –double split ring (DSR), *1** -capacitance-loaded DSR, *1^* -varactor-loaded DSR; *2* –twice split one ring (TSR), *2** - two capacitance-loaded TSR, *2^* - two varactors-loaded TSR, *3* –1.5 turn planar spiral (Sp). Diameter of rings is the same and equal to 6.6 mm. To achieve voltage tuning MR we solder MA46H120 (MACOM) varactor in additional gap in the outer ring of DSR and being gaps of TSR. To achieve light controlled MR the voltage bias for the varactor is produced by a photodiode VD which operates in photoconductive mode as is shown in Fig.1*f*.

Photodiodes can be operated in two different modes:

*Photovoltaic mode*: the illuminated photodiode generates voltage for the varactor [4]. *Photoconductive mode*: a reverse voltage is applied to the diode (i.e., a voltage in the direction where the diode is not conducting without incident light) and measures the resulting photocurrent.

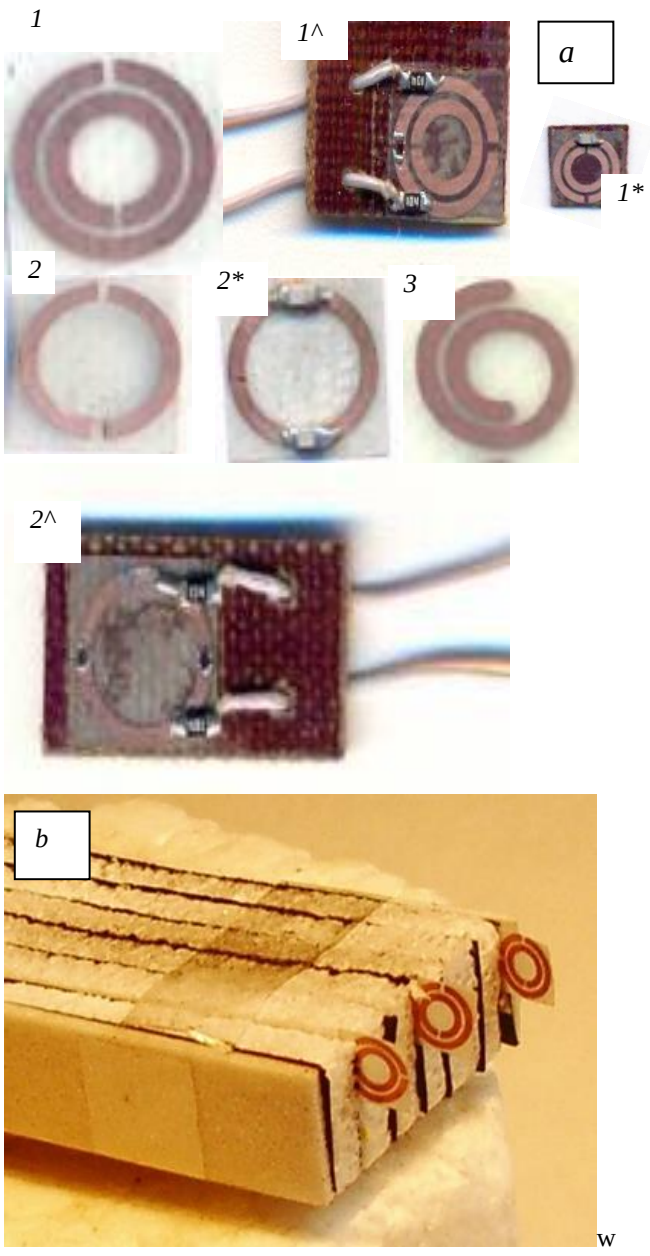



Figure 1: Samples for measurements in waveguide; (*a*) 1-DSR, 1^-varactor-loaded DSR, 1*-capacitance-loaded DSR; 2-TSR, 2*-capacitance-loaded TSR, 2^- varactor-loaded TSR; 3- Sp
(*b*) Metastructure absorber/DSR, (*c*) Metastructure absorber/TSR, (*d*) Metastructure absorber/array of Sp, (*e*) Voltage controlled metastructure absorber/varactor-loaded TSR; (*f*) Scheme of measurement of light controlled reflection for varactor-loaded TSR in combination with photodiode (photoconductive mode); resistanse $R_1$=100 kΩ. $R_2$ =10 kΩ

The photocurrent is linearly proportional to the illuminance. Photodiodes exhibit their fastest switching speeds when operated in the photoconductive mode.

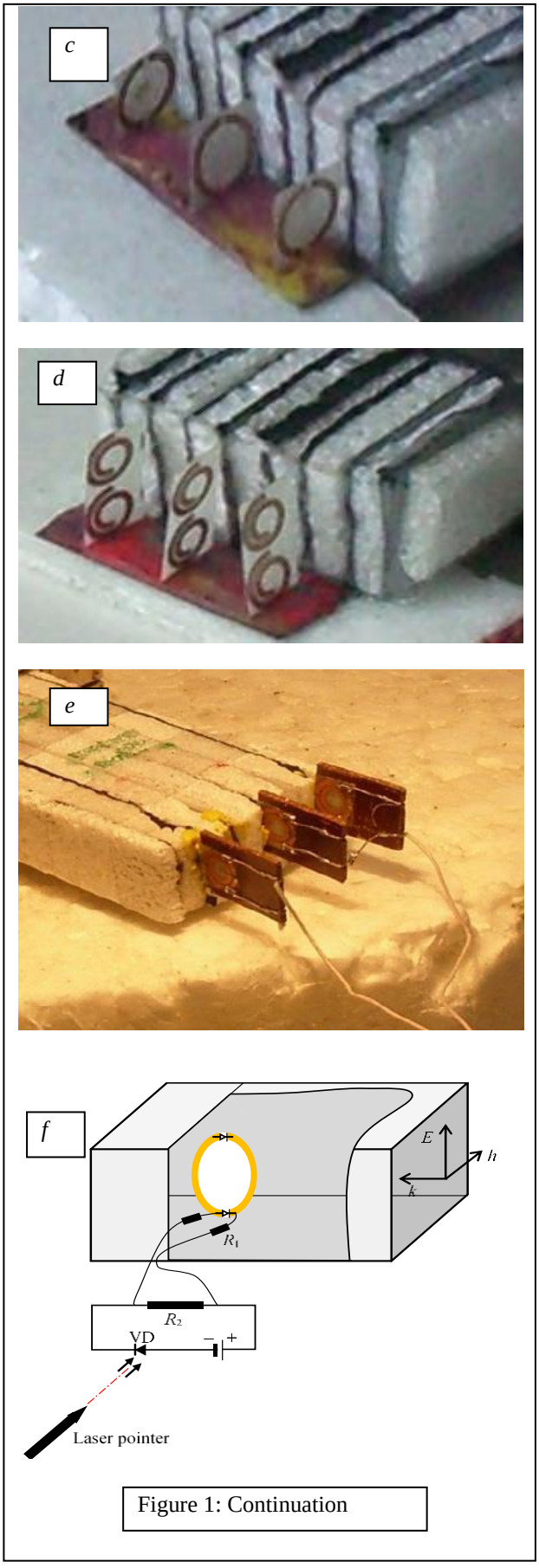
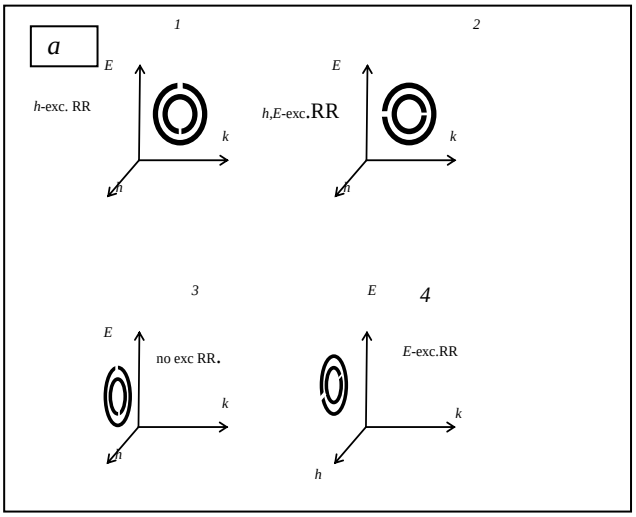



Figure 1: Continuation



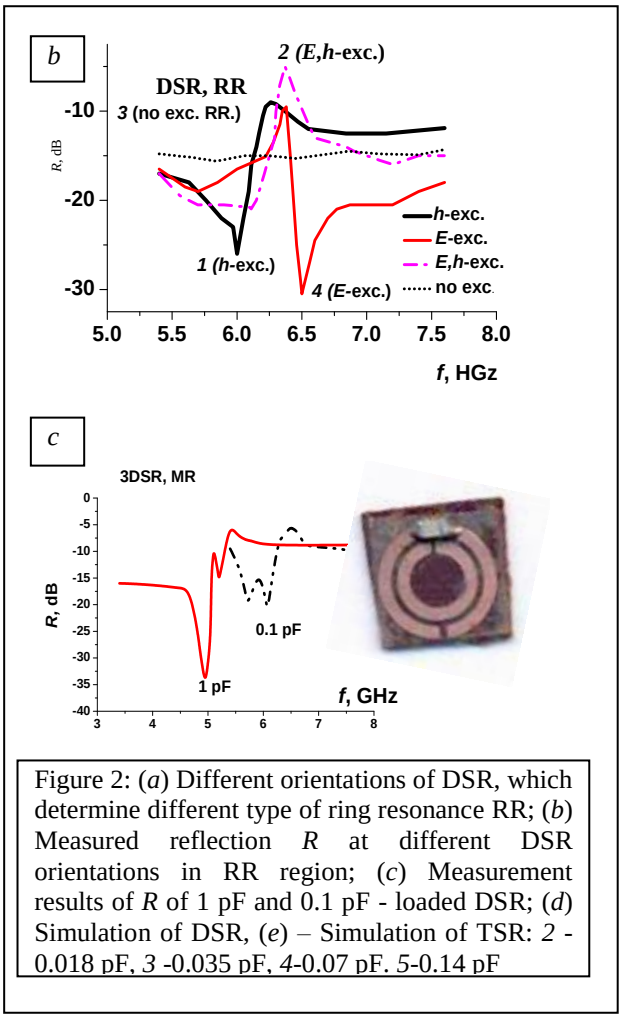
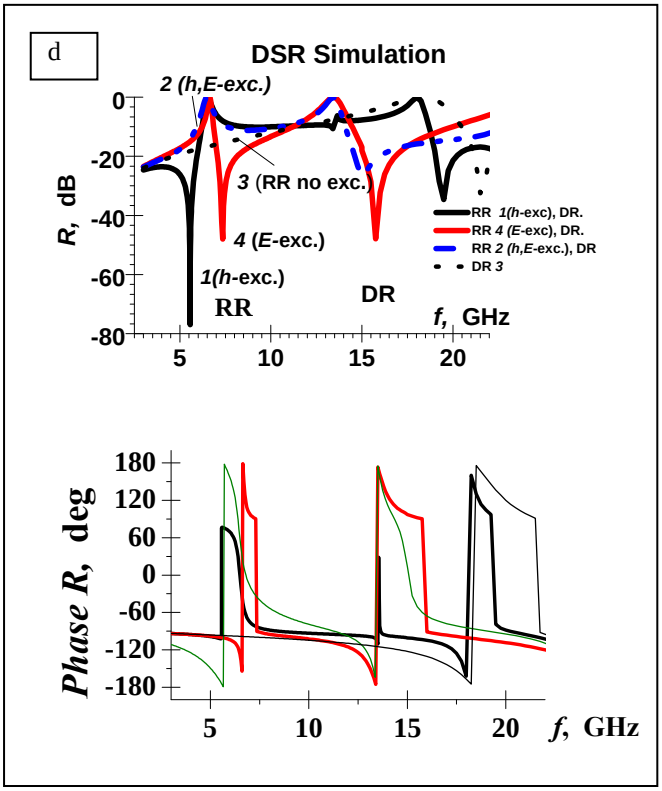




Figure 2: (*a*) Different orientations of DSR, which determine different type of ring resonance RR; (*b*) Measured reflection *R* at different DSR orientations in RR region; (*c*) Measurement results of *R* of 1 pF and 0.1 pF - loaded DSR; (*d*) Simulation of DSR, (*e*) – Simulation of TSR: *2* - 0.018 pF, *3* -0.035 pF, *4*-0.07 pF. *5*-0.14 pF

In the case of voltage control amplitude-frequency resonance response depends on bias voltage for varactor. In the case of light control amplitude-frequency response depends on bias voltage when light illuminates diode. Without light resonance effects in rings do not depend on reverse voltage which is applied to the diode.

Some photos of metastructures with broadband matching are presented in Fig. 1*b* (absorber/DSR), 1*c* (absorber/TSR), 1*d* (absorber/ array of Sp), 1e (absorber/varactor-loaded TSR).



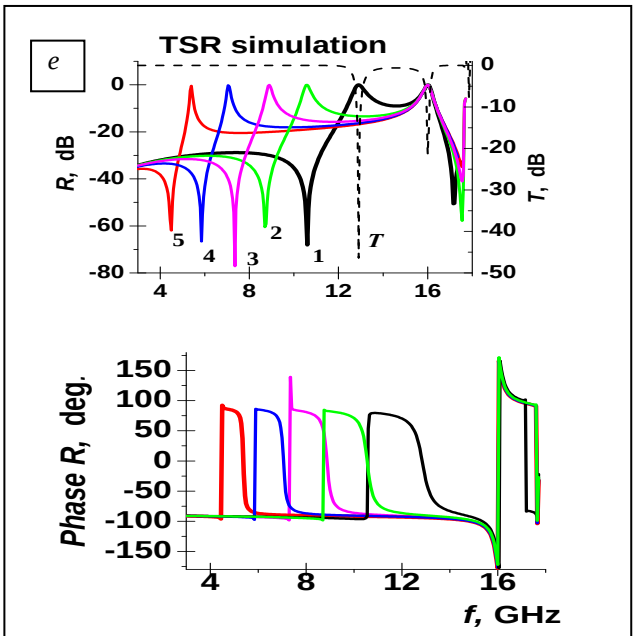




Figure 2: Continuation (*d*, *e*)

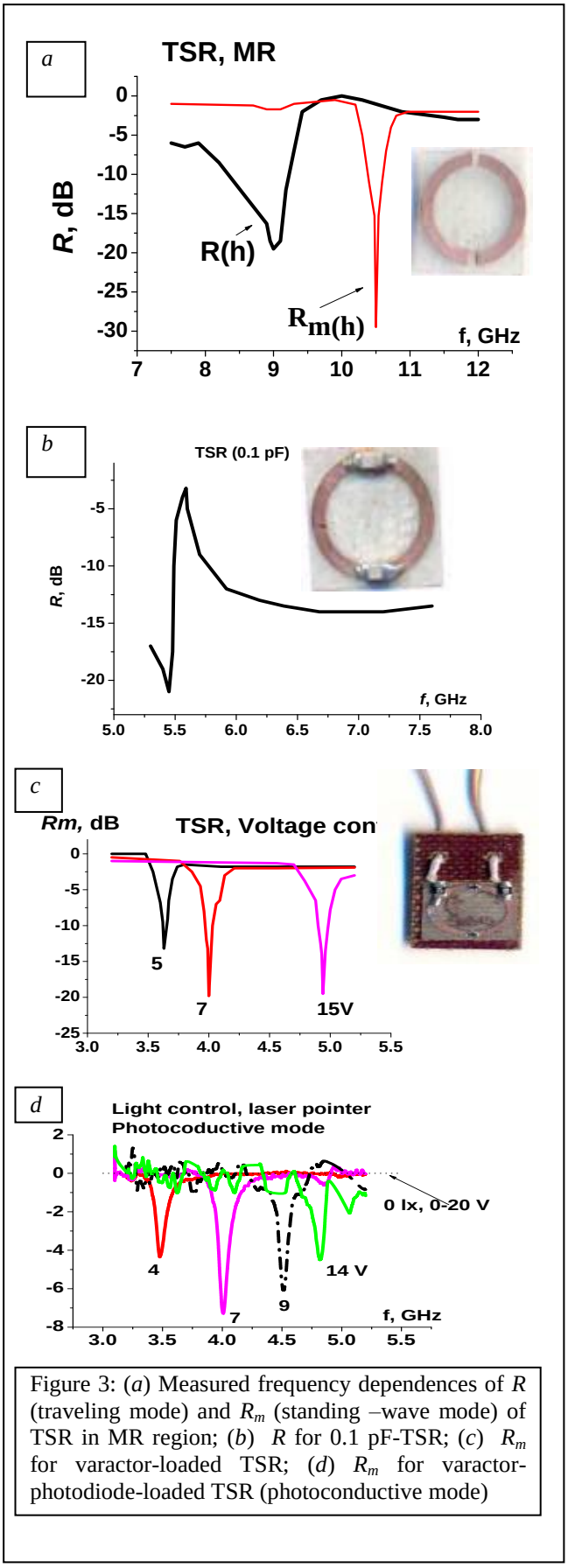



Figure 3: (*a*) Measured frequency dependences of *R* (traveling mode) and $R_m$ (standing –wave mode) of TSR in MR region; (*b*) *R* for 0.1 pF-TSR; (*c*) $R_m$ for varactor-loaded TSR; (*d*) $R_m$ for varactor-photodiode-loaded TSR (photoconductive mode)

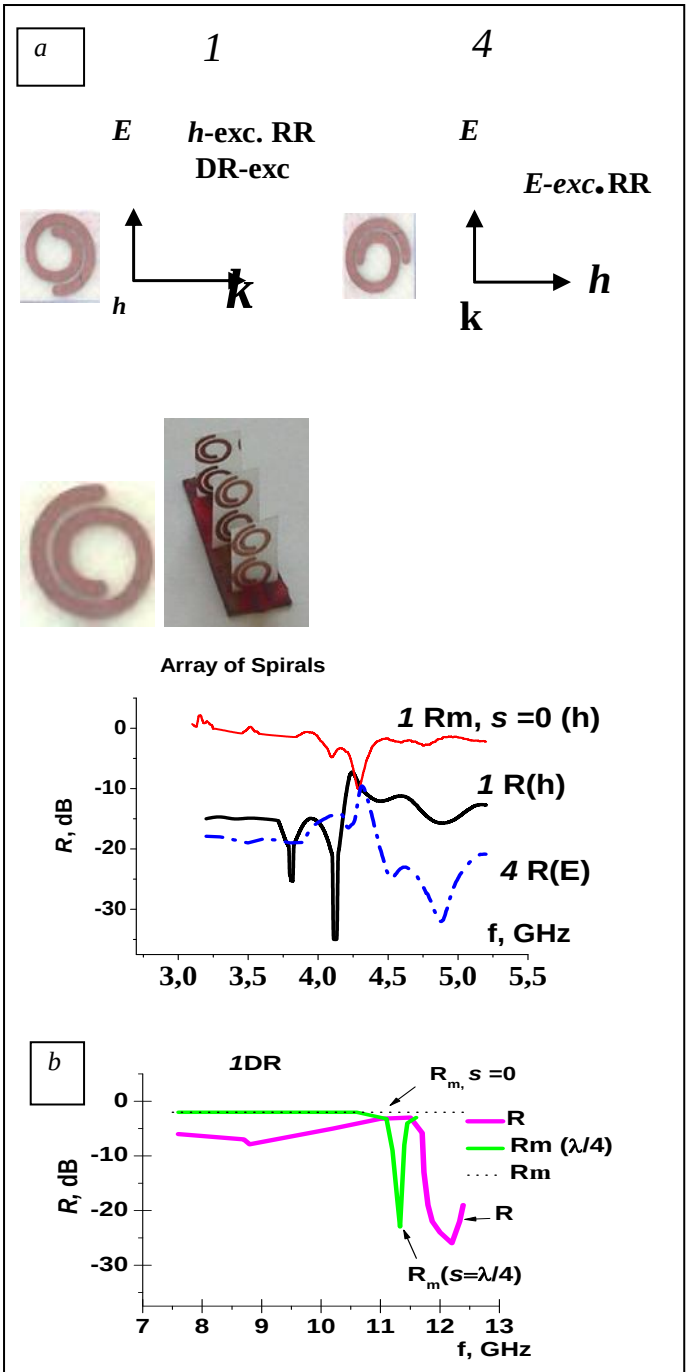



Figure 4: (*a*) Measured frequency dependences of *R* of Spirals array at orientations *1*, *4* in the traveling-wave mode (*R*) and standing-wave mode ($R_m$) in the RR region; (*b*) *R* and $R_m$ in the DR region

We used P2-58 (3-5.5 GHz), P2-59 (5.3-7.6 GHz) and P2-61 (7.5-12.5 GHz) voltage standing wave ratio meters and a one channel method for measuring reflection *R* in a rectangular waveguide: the standing-wave mode with a

metal plug and the traveling-wave mode with a matched load. Split ring is placed at the center of rectangular waveguide with a cross section of 48 x 24; 35 x 15; and 23 x 10 mm in different orientations relative to the components of the incident electromagnetic field (Fig. 1*f*, Fig. 2*a*).

## 3. Identifying magnetic resonance

We particularly analyze identifying MR and ER by DSR because the resonance excitation in the DSR was thoroughly investigated analytically and numerically, for example, in [5, 6].

Fig. 2 demonstrates results of measurement (in rectangular waveguide) and simulation (in free space) for DSR. In Fig. 2*a* the ring resonance (RR) excitation type is indicated for each investigated DSR orientation (*1 – 4*). In the standing-wave mode, for the DSR located on the metal plug, i.e., in the antinode of magnetic field *h*, in orientation *1 (h*-exc.*)*, the resonance minimum of the reflection $R_m$ is observed, which vanishes in the minimum of field *h* when the DSR is located at a distance of $s = \lambda/4$ from the plug. At $s = \lambda/4$ resonance is observed in orientation *4* (*E* –exc.) in the maximum of field *E* and vanishes at *s* =0 in the minimum of *E*. This simple method for separating the magnetic and electric excitations requires samples that are small relative to the wavelength, so that the sample will not be affected by an electric (magnetic) field in its antinode.

In the traveling-mode, resonance effects manifest themselves in the form of a resonance dip in the frequency dependences of transmission, which corresponds to resonance maximum in the reflection curve. Such curves are typical of composites consisting of randomly located resonance elements. However, in the case of oriented chiral elements, in the case of oriented chiral elements, including single ones, the resonance reflection curves are more complex: along with the resonance maximum, one can observe the related resonance minimum whose position depends on the type of excitation. At the electric excitation, the resonance minimum is observed at higher frequencies than the resonance maximum. Under magnetic excitation, the resonance minimum is observed at lower frequencies; in this case, from the side of higher frequencies relative to the maximum the reflection slowly decreases, remaining fairly large in a certain frequency range. In addition, during magnetic excitation, the reflection phase changes smoothly and passes through zero at the resonance frequency, in contrast to its stepwise change under electric excitation.

The measured frequency dependences of reflection *R* in the RR region in the traveling-wave mode are shown in Fig. 2*b*. We can see that the frequency dependences of *R* are drastically different at different orientations. Along with the resonance maxima at frequency $f_{max}$ = 6.3 GHz, there are resonance minima at frequencies that are lower at the magnetic excitation (*h*-exc.) and higher at the electric excitation (*E*-exc.): $f_{min,h\text{-}exc.}$ = 6 GHz, and $f_{min,E\text{-}exc.}$= 6.5 GHz. In orientation *2*, both *h*-exc. and *E*-exc. can take place; then, the *R* curve contains spread minima. Orientation *3* does not allow RR excitation, and the *R* curve does not demonstrate the resonance effect. Fig. 2*c* demonstrates that magnetic resonance (MR) excited by *h*-field remains features of *R* with tuning by use of capacitance –loaded DSR.

The curves obtained numerically for absolute value and phase of *R* also have distinguishing features (Fig. 2*d*). The shape of the resonance *R* curve significantly depends on the excitation, in contrast to the resonance dip of transmission.

Below we show that these features are confirmed for inclusions in the form of twice split one ring TSR (Fig. 2*e* – simulation, Fig. 3 – experiment) and 1.5 turn planar spiral (Fig. 4 – experiment).

*Twice split ring* (TSR)*:* Ring resonance RR can be excited in orientation *1* and *2* by *h*-field (MR *h*-exc) and tuned by use of capacitance-loaded TSR; by voltage in varactor-loaded TSR; and light in photoconductive mode with varactor/photodiode-loaded TSR. Fig. 2*e* shows calculated frequency dependences of *R* in orientation *1:* MR at frequency about 13 GHz with resonance minimum at lower frequency and DR at frequency about 16 GHz with resonance minimum at higher frequency. The MR is tuned with variation of capacitance and remains its features. Fig. 3 demonstrates measured frequency dependences of *R* (traveling-wave mode) and $R_m$ (standing-wave mode) in orientation *1* in the MR region for TSR (Fig. 3*a*), 1 pF-loaded TSR (*b*), and varactor-loaded TSR (*c*), as well varactor-photodiode-loaded TSR (*d*).

*Array of 1.5 turn planar spirals.*

Measured frequency dependences of reflection are presented in Fig. 4 in dependence of spirals orientation. We see resonance effects at about 4.2 GHz (Fig. 4*a*). In orientation *1* along with the resonance maximum one can see the resonance minimum at lower frequencies that corresponds to magnetic excitation of RR, while in orientation *4* resonance minimum is observed at higher frequencies that corresponds to electric excitation of RR. In the standing-wave mode, for the Sp located on the metal plug, in orientation *1* the resonance minimum of the reflection $R_m$ is observed, which vanishes in the minimum of field *h* when Sp. are located at a distance of $s = \lambda/4$ from the plug.

One more resonance effect is observed in orientation *1* at 11.5 GHz (Fig. 1*b*). This resonance possesses features of *E*-excitation: resonance minimum is observed at higher frequencies from maximum in traveling-wave mode and in standing-wave mode resonance minimum of the reflection $R_m$ is observed, when Sp. are located at a distance of $s = \lambda/4$ from the plug and vanishes at $s = 0$. That is dipole resonance which is excited by field *E*.

The difference between the frequency characteristics makes it possible to identify the type of excitation and separate the magnetic and electric resonance responses for inclusions of different shapes.

## 4. Controlled matching of absorbers

The disclosed features in the frequency characteristics of *R* under magnetic excitation (smooth phase variation at the large value kept above the resonance frequency) open a

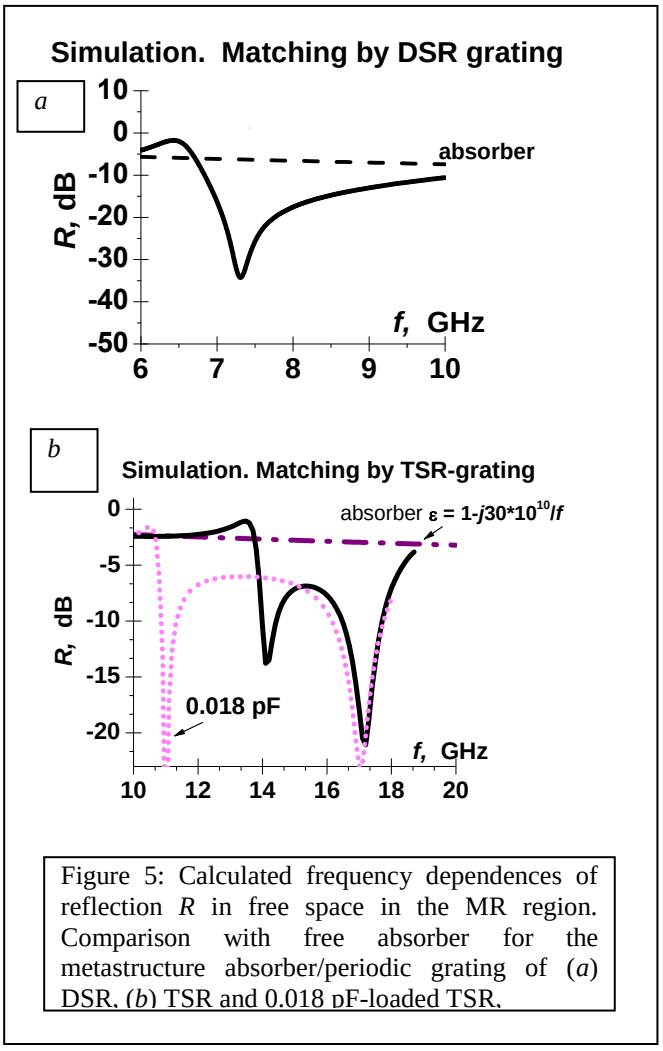



Figure 5: Calculated frequency dependences of reflection *R* in free space in the MR region. Comparison with free absorber for the metastructure absorber/periodic grating of (*a*) DSR, (*b*) TSR and 0.018 pF-loaded TSR.

possibility of broadband compensation of frequency-dependent reflections from traditional absorbing composites based on resistive threads or films with ensured equal values of antiphase reflections from the composite and the adjacent grating of resonance elements excited by the magnetic field of the wave above their resonance frequency.

Such metastructures were fabricated from absorbing composites, (length is 80 – 90 mm, transmission is more than 30 dB) containing layers of carbon paper with a thickness of 0.07 mm and $\varepsilon' = 15$and foamed polystyrene with thickness of 1, 2 and 4 mm and $\varepsilon' = 1.02$. The *R* values of metastructures were measured in a waveguide in comparison with free absorbers without resonance elements.

Fig. 5 shows simulation results of metastructures and a possibility of matching of absorber with reflection decrease by DSR-grating (Fig. 5*a*), by TSR-grating (Fig. 5b) in magnetic resonance (MR) region. Fig. 5*b* shows also that frequency dependence of *R* changes by use of capacitance of 0.018 pF in gaps of TSR. In this case MR tunes and conditions of matching are changed.

The results of the *R* –measurement are presented in Fig. 6*a*, *b*, *c*, *d* for metastructures absorber/DSR. In Fig. 6*a* we see frequency dependences of free absorbers *1*, *2*. *3* in comparison with relative metastructure *1^*, *2^* and *3^* which

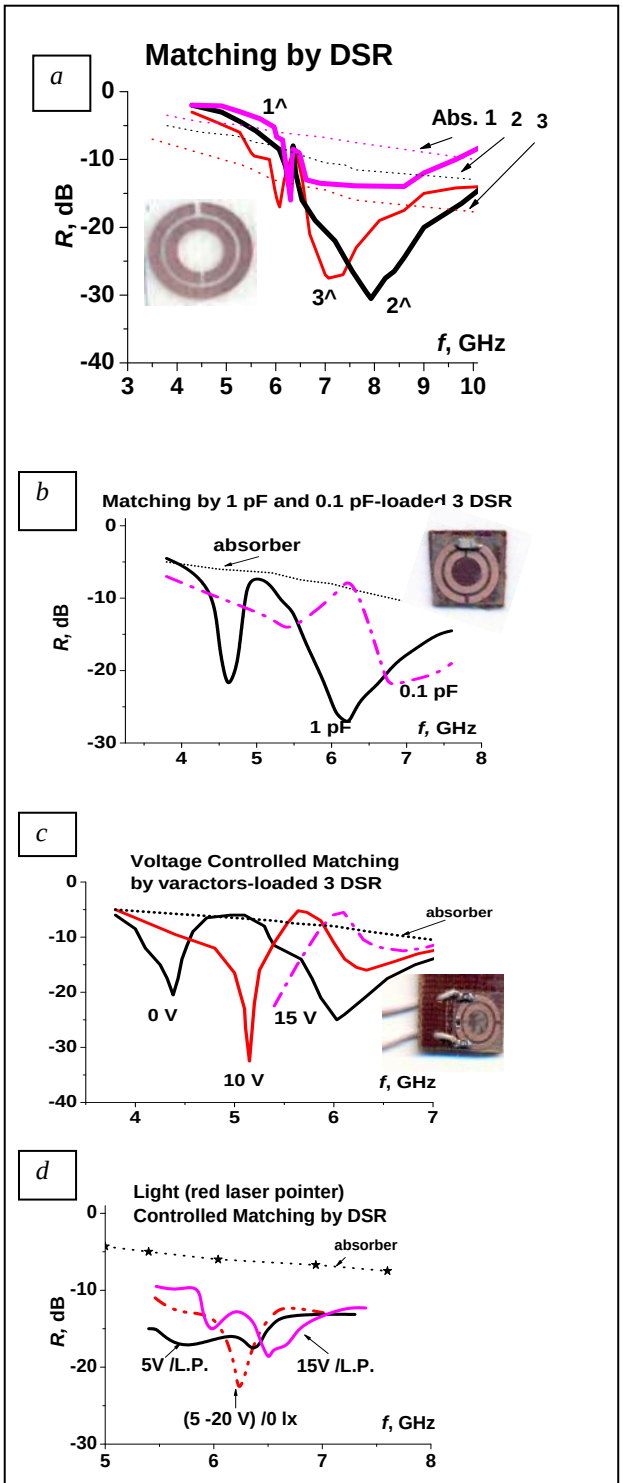



Figure 6: Measured frequency dependences of reflection *R*: (*a*) Metastructures absorber/DSR (*1^*, *2^*, *3^*) in comparison with free absorbers (*1*, *2*, *3*); (*b*) Metastructure with 0.1 and 1 pF-loaded DSR; (*c*) Metastrucrure with varactor-loaded DSR; (*d*) Metastructure with varactor-photodiode-loaded DSR. Comparison with free absorbers

show broadband matching of absorbers (decrease of *R* more than 15 dB) and perfect matching at certain frequency. One

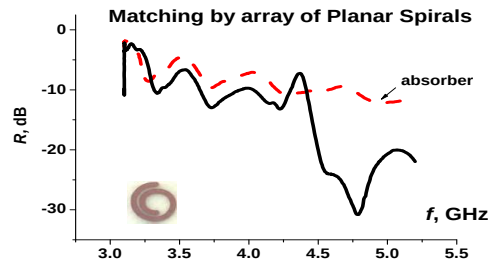



Figure 7: Measured frequency dependences of *R* for metastructure absorber/array of planar spirals. Comparison with free absorber

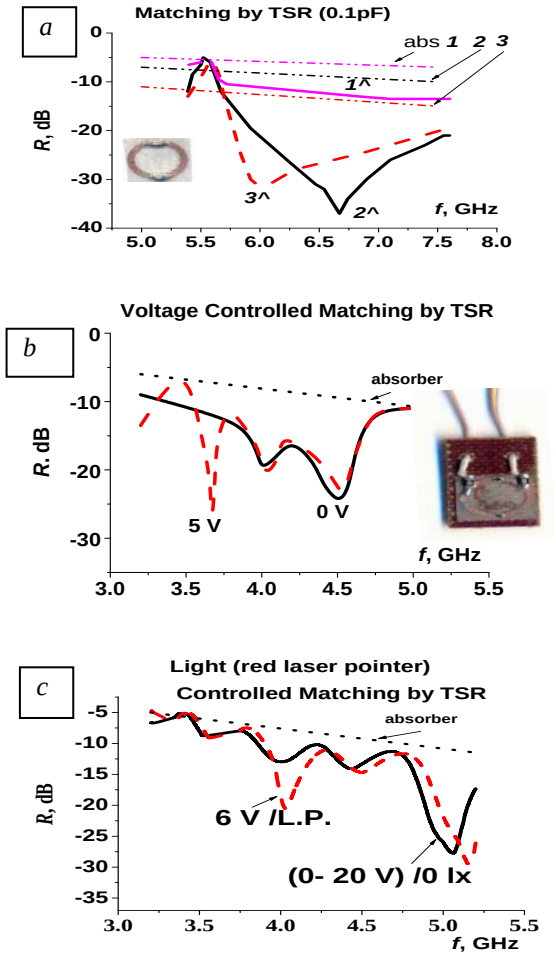



Figure 8: Measured frequency dependences of reflection *R*: (*a*) Metastructure absorber/0.1 pF-TSR (*1^*, *2^*, *3^*) with comparison of free absorber (*1*, *2*, *3*); (*b*) Metastrucrure with varactor-loaded TSR; (c) Metastructure with varactor-photodiode-loaded TSR. Comparison with free absorbers

can control matching by use of capacitance-loaded DSR (Fig. 6*b*). Fig. 6*c* shows voltage controlled matching by use of varactor-loaded DSR. Fig. 6*d* demonstrates light (red laser pointer, 7 klx) controlled matching by varactor/photodiode-loaded DSR in photoconductive mode. In Fig. 6*d* we see absorber matching without light around 6.2 GHz which does not depend on reverse voltage for diode. With light change of amplitude-frequency response appears with dependence of reverse voltage; there is difference between amplitude-frequency response under 5V and 15 V.

We observe effect of matching with metastructure absorber/ array of magnetically excited planar spirals too (Fig. 7).

Fig. 8*a,b,c* demonstrates the *R*–measurement for metastructures absorber/TSR. Fig. 8*a* corresponds to 0.1 pF-loaded TSR. One can see effect of matching for metastructure 2^ and 3^, containing absorbers 2 and 3 with magnetically excited TSR. Fig. 8*b, c* show voltage (by use of varactor-loaded TSR) and light controlled matching (by varactor/photodiode-loaded TSR) under reverse voltage of 6V for diode. Thus, suggested method of absorber matching has been verified numerically and confirmed by measurement with different absorbing metastructures.

## 5. Conclusion

The disclosed features in the frequency reflection characteristics of the magnetic and electric microwave responses make it possible to reveal the magnetic response for inclusions of different shapes, which is not only useful for the development and application of metamaterials with artificial magnetism and left media, but also opens a new aspect of application of the magnetic response for voltage and light fast controlled broadband compensation of reflections from absorbing composite materials.

## References

[1] D. R. Smith, S. Schultz, P. Markos, and C. M. Soukoulis, "Determination of effective permittivity and permeability of metamaterials from reflection and transmission coefficients", *Phys.Rev. B.*, Vol. 65, 195104-1 – 195104-5, 2002.

[2] N. Katsarakis, T. Koschny, M. Kafesaki, E. N. Economou, and C. M. Soukoulis, "Electric coupling to the magnetic resonance of split ring resonators", *Appl. Phys. Lett*., Vol. 84, No.15, 2943 – 2945, 2004.

[3] Galina Kraftmakher, "New realization and microwave properties of double negative material", *Int. J. of Applied Electromagnetics and Mechanics*, Vol. 19, No. 1-4, 57 - 61, 2004.

[4] I. V. Shadrivov., P. V. Kapitanova, S. I. Maslovski, and Yu. S. Kivshar, "Metamaterials controlled with Light", *Phys.Rev. Lett.*, Vol. 109, 083902, 2012.

[5] R. Marques, F. Medina, R. Rafii-El-Idrissi, "Role of bianisotropy in negative permeability and left-handed metamaterials", *Phys.Rev. B*, Vol. 65, 144440, 2002.

[6] B. Sauvias, S.R. Simovski, S.A. Tretyakov, "Double split-ring resonators: Analytical modeling and numerical simulations", *Electromagnetics*, Vol.24, 317 – 338, 2004.

# A New Metamaterial-based C-band Electromagnetic Cloak

**S. S. Islam[1], M. R.I. Faruque[1*], and M. T. Islam[2]**

[1]Space Science Centre, Universiti Kebangsaan Malaysia, Malaysia
[2]Dept. of Electrical, Electronic and Systems Engineering, Universiti Kebangsaan Malaysia, Malaysia
[*]corresponding author: sikder_islam@yahoo.co.uk

**Abstract** A new metamaterial-based wideband electromagnetic cloak is being introduced in this study. The metamaterial unit cell shows sharp resonance in the C-band where the effective permittivity and permeability curve exhibits negative and positive characteristics consecutively. The metamaterial unit cell was then applied in designing a square-shaped electromagnetic cloak. Scattering reduction technique was adopted for the cloaking operation. The cloak operates in the C-band and hides a metal cylinder electromagnetically. The experimental results were provided as well for the metamaterial and the cloak.

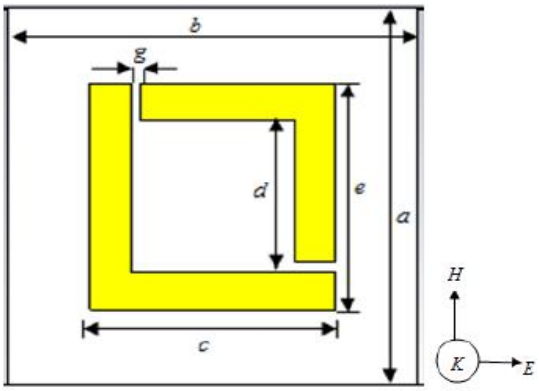
## 1. Introduction

Artificially constructed metamaterial is now contributing in almost all the fields of electromagnetism including invisibility cloak design. Metamaterial provides essential property to synthesize proper electromagnetic cloak. An electromagnetic cloak can hide an object electromagnetically. Cloaking is usually used in the defense sector for hiding aircraft, satellite or missile from the hostile radar system. An object can be hidden electromagnetically if it does not scatter wave in any direction. In other sense, it does not absorb any power. Utilization of metamaterial guides the applied electromagnetic waves around the object instead of scattering and restores the waves to its original path that results transparency to the observer. Since the first successful attempt was done in [1] based on transformation optics (TO) technique, several research groups adopted numerous approaches to build an invisibility cloak [2-5]. In TO-method, a volume of no-field region is formed making the volume electromagnetically undetectable. However, the property requirement for the material that is utilized in designing a TO-cloak is difficult. A material with value of effective permittivity or permeability is between zero and greater than one can be utilized for the construction of TO-based cloak. Moreover, multiple layers are needed for designing metamaterial-based TO-cloak [6]. Among the other cloaking methods, scattering reduction method is easier to obtain the cloaking operation. Usually a good cloak reduces the normalized total scattering width (NTSW) of an object close to zero [7]. Actually, a physical cloak diminishes the normalized total scattering width to some non-zero value, below one. A metamaterial with epsilon negative property is suitable for designing a cloak to suppress the scattering of an object [4]. Scattering reduction method was realized as well for the TO-cloak [6]. Previously few studies were performed on metamaterial-based cloak. However, most of the cloaks were cylindrical in shape and very few of them were found operating in C-band. Like, Xiaohui Wang et *al.* in [7], proposed a dielectric resonator based metamaterial X-band cloak but it was cylindrical in shape. They demonstrated that their cloak reduced the total scattering width below one in the X-band. A metamaterial-based 3D plasmonic cylindrical cloak was presented by D. Rainwater *et al.* in [8] and it was operating for S-band. A metasurface-based single layer cylindrical cloak was claimed by Matekovits *et al.* in [9] but it was operating in the K-band of microwave region.

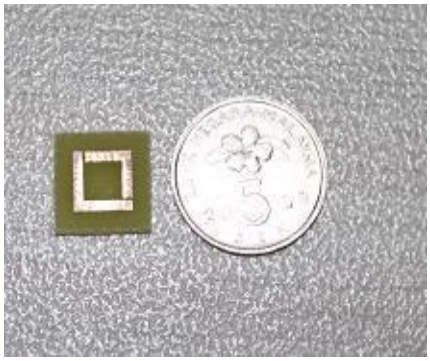
In this study, a new metamaterial is developed that shows epsilon negative property in the C-band. Later on, a new square-shaped cloak was built using the metamaterial that also operates in the C-band. For designing the cloak, only one layer of metamaterial shell has been utilized.

## 2. Design and characteristics investigations of the metamaterial unit cell

The design and the S-parameters investigation of the metamaterial unit cell was done by the finite integration technique based CST Microwave Studio software. Two orthogonal copper arms were etched on a FR-4 substrate material face to face keeping short gaps between them. The two orthogonally placed copper arms with two nominal splits at each end construct a square shaped structure. The dielectric constants and thickness of the substrate material was 4.2mm and 1.6mm respectively. Fig.1a and Fig.1b depicts the new square-shaped metamaterial unit cell and its fabricated sample consecutively. The structure and size of the proposed metamaterial unit cell was finalized to obey the proper effective medium ratio. The effective medium ratio for the metamaterial unit cell was $\lambda/a=7.5$, where $\lambda$ is the wavelength. At each side, 2 mm gaps were maintained from the resonator to the end of the substrate. The design parameters' were expressed in the table-1. Each arm of the square-shaped resonator is taking part to generate the inductive effect and the two gaps between the metal arms are responsible for generating the capacitive effect. The inductive and capacitive effects constitute the negative effective medium property for the metamaterial.




(a)



(b)

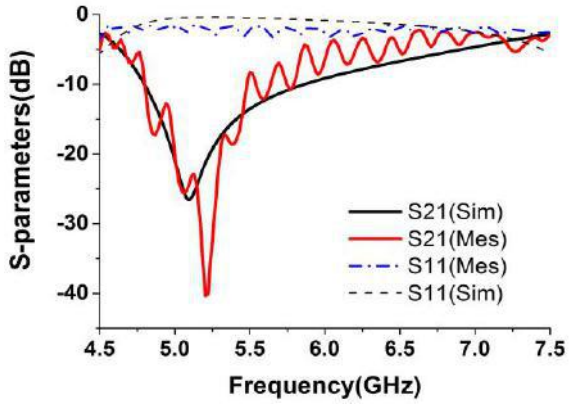
Figure-1. (a) Schematic diagram of the unit cell (b) Fabricated sample of the metamaterial unit cell

Table-1: Unit cell design parameters

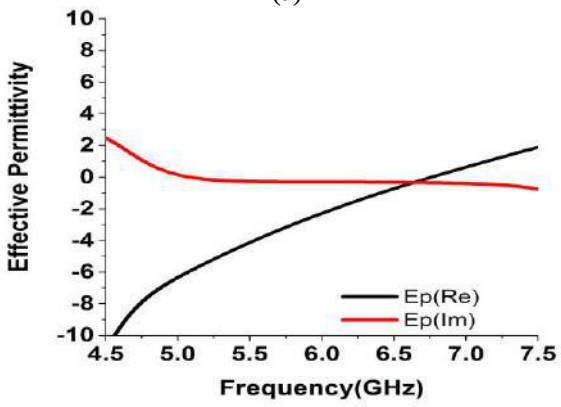
| Parameter name | Value (mm) |
|---|---|
| a | 10 |
| b | 10 |
| e | 6 |
| g | 0.2 |
| d | 3.8 |
| c | 6 |

To calculate the S-parameters of the metamaterial unit cell, electromagnetic wave was propagated through the unit cell using two waveguide ports. Perfect electric-magnetic boundary condition was applied for the simulation. The acquired S-parameters were adopted to evaluate the effective medium property of the material. For the calculation of the effective medium property of the material, Nicolson-Ross-Weir method [10] was utilized.

To perform the measurement of the unit cell, a sample unit cell metamaterial prototype was fabricated using LPKF laser based electronic machine. The fabricated sample was placed between two C-band waveguides WR137, acting as transmitter and receiver. The waveguides were linked to the vector network analyzer (VNA) N5227A. From the VNA the S-parameters were obtained.




(a)




(b)

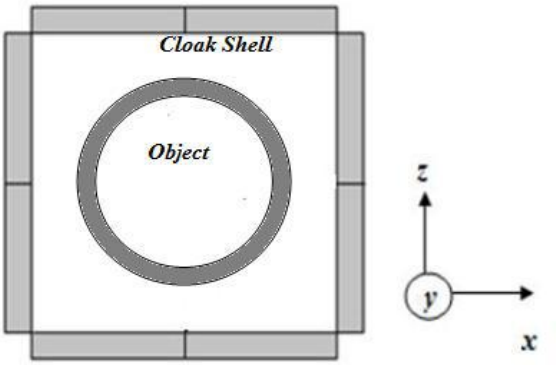
Figure-2. (a) Simulated and measured S-parameters for the unit cell (b) effective permittivity for the metamaterial unit cell

The simulated and measured results of S-parameters are shown in the Fig.2a for the metamaterial unit cell. Form the Fig.2a, the numerical curve shows one transmittance at the frequency of 5.10 GHz. The experimental transmittance also follows the numerical curve well. Similarly, the experimental reflection parameter agrees well with the numerical one. The effective permittivity curve is also presented in the Fig.2b where the curve displays negative peak from 4.5-6.71 GHz in the frequency range. The curve also reveals the epsilon-near-zero region from 6.40-7.13 GHz in the frequency range that has significant effect for creating cloaking zone. This type of near zero regions maintains slow phase variation for a long electromagnetic path that is useful for cloak operation. However, the imaginary part of the effective permittivity curve also shows the epsilon-near-zero region in the same region.

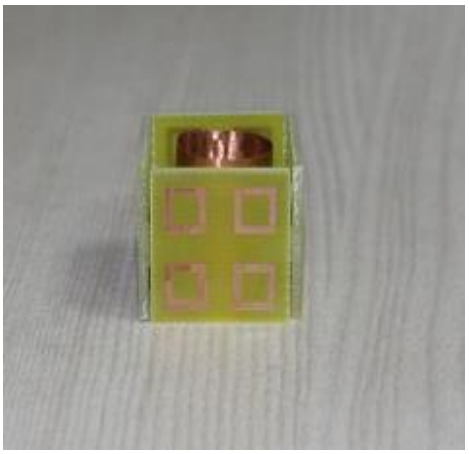
## 3. Development and performance investigations of the metamaterial-based cloak

The newly developed metamaterial was applied for the construction of an electromagnetic cloak. The same CST Microwave Studio tool was also adopted for the design and numerical investigation of the metamaterial-based cloak. Scattering suppression technique was chosen to perform the cloaking operation. In this technique, a kind of dielectric shell or coating is surrounded by the object to be cloaked.

The shell helps to reduce the scattering from the object and return the electromagnetic waves back to its usual path at a certain frequency. Therefore, the electromagnetic waves bend around the object and thereby make the object hidden to the observer or radar. To perform such operation, four walls were prepared each of the walls composed of four unit cells of the proposed metamaterial in this study. The dimension of each wall was 20×20mm$^2$. As an object, a copper made cylinder was chosen that has 8mm inner and 9mm outer radius with equal height of the cloak. The four metamaterial walls were arranged to form a square shape structure. The object was placed at the centre of the cloak. The top view of the square-shaped cloak structure is being displayed in the Fig.3a with the object inside it.



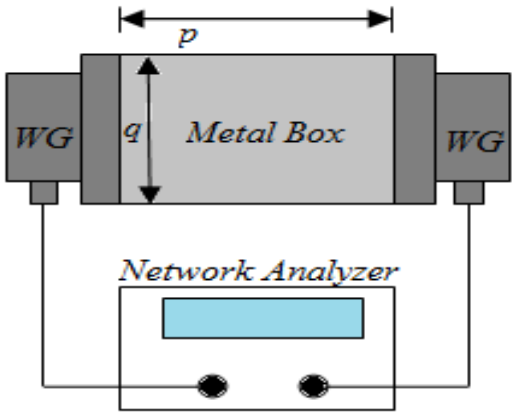

(a)Top view



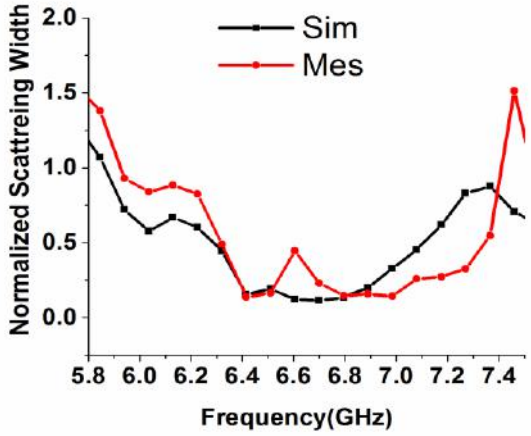
(b)

Figure-3. (a) The square-shaped cloak structure with an object (b) Fabricated cloak prototype with copper made cylider inside.

To perform the numerical investigations, the transverse electric ($TE_{10}$) wave was propagated through the *x*-axis of the cloak using the waveguide ports. For the performance evaluation of the cloak, the radar cross section per unit length i.e. normalized scattering width (NSCW) is determined. Total scattering width is the ratio of scattered and incident energy from the cloaked object. Normalized scattering width is the ratio of total scattering width (TSCW) of cloaked object normalized by the total scattering width of uncloaked object that can be calculated according to the equation mentioned in [7]. Similarly, for the measurement purpose, four 20×20 mm$^2$ walls were fabricated and each of the walls consists of 2×2 unit cells of the metamaterial. The WR137 waveguides as well as the VNA were also utilized for the measurement. The metamaterial walls were arranged in such a way that had produced a square-shaped cloak. A copper made metal cylinder with diameter 16mm in the inner surface was utilized as object having same height of the cloak so that the metal cylinder can be placed easily inside the cloak. Fig. 3b shows the fabricated cloak sample with a metal object inside.




(a)




(b)

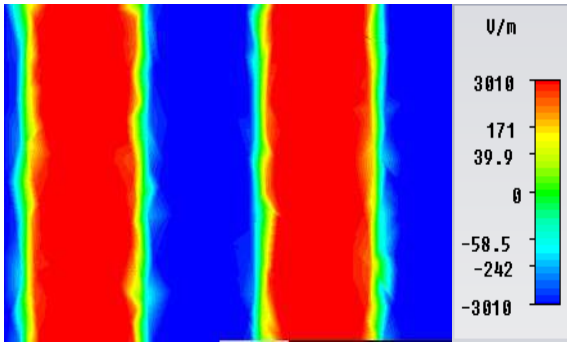
Figure-4. (a) The measurement setup for the cloak (b) simulated and measured results of TSCW of cloaked object normalized to the TSCW of bare object in the *xy*-plane

Moreover, a volumetric aluminium box was prepared for the measurement purpose having height, length and width were *q*=49.4 mm, *p*=44 mm and 68.5 mm respectively. The metal box had two sides open so that the face of the waveguides could be inserted in it facing them face to face. The waveguides were connected to VNA as well. The whole cloak measurement setup is seen in the Fig.4a.

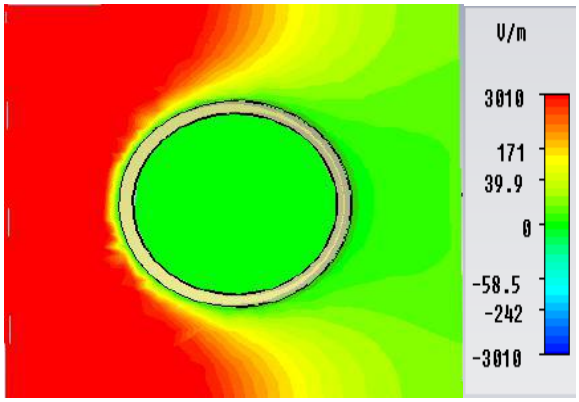
For the evaluation of NSCW, field status of incoming and scattering were measured. By placing the two waveguides

face to face into the metal box, the incoming (Ei) field was measured. Afterwards, the metal object was placed between the waveguides inside the metal box and field parameters were measured that actually integrates total filed (Et) including the incoming and scattering field (Es). Deducting the incoming field from the total filed, the scattering field can be obtained. In addition, field measurement was also performed after placing the cloaked object inside the metal box and the scattering field was measured following the same way as mentioned above.

In the Fig.4b, the simulated and measured result of normalized TSCW of cloaked object normalized by the TSCW of uncloaked object is being displayed. According to the numerical result of Fig.4b, it is evident that the simulated normalized scattering width curve shows less than one value from 5.9 GHz to 7.30 GHz in the frequency range. The lowest value is 0.11 and it was achieved at the frequency of 6.79 GHz. Moreover, the metamaterial unit cell exhibits epsilon-near-zero region at this lowest point with the complex value $\varepsilon$ =0.513-j0.331. However, the frequency range 5.9 GHz to 7.30 GHz can be considered as the zone where the cloaking operation is taking place. The measured normalized scattering width is found complying well with the numerical result although the lowest point was found at the frequency of 6.89 GHz instead of 6.79 GHz with the value 0.14. Moreover, at this frequency the metamaterial unit cell also exhibits epsilon near-zero value, $\varepsilon$= 0.36-j0.37. The measured curve shows less than zero value from 5.96 GHz to 7.38 GHz in the frequency range that covers more than 1 GHz bandwidth. Therefore, this region can be considered as the realistic cloak operating area.




(a)




(b)

Figure-5. (a) Free space E-field distribution in the *xy*-plane(b) E-field distribution for the uncloaked object at the lowest cloaked frequency (6.80 GHz) in the *xy*-plane.

In the Fig.5a, the numerical electric field distribution in the *xy*-plane for the open space condition is being shown. The red and blue field lines refer to the positive and negative polarization respectively. The Fig.5b shows the electric field distribution over the metal object in the *xy*-plane. From the Fig.5b it is evident that, electric field is being scattered in the forward direction by the bare metal object. Moreover, no wave front reconstruction is taking place in the forward direction and therefore zero field region is being created in the forward direction i.e. right side of the object.

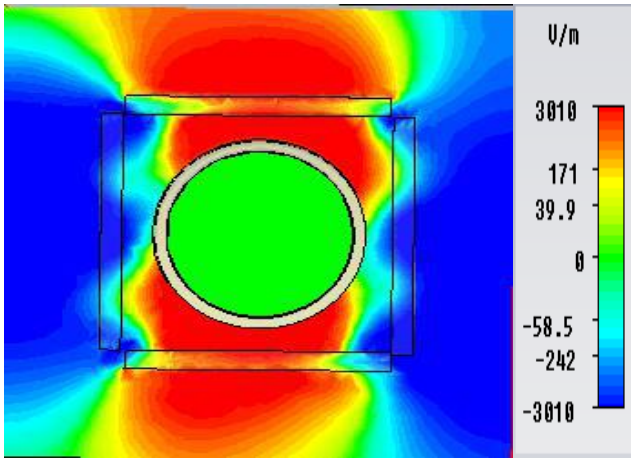



Figure-6. Distribution of E-field for the cloaked object at the cloaked frequency (6.80 GHz) in the *xy*-plane.

In the Fig.6, the electric field map in the *xy*-plane is revealed at cloaked frequency, where the metal object has been cloaked with the metamaterial-shell. It is seen from the Fig.6 that, no forward scattering was taking place there and reconstruction of wave front in the forward direction was achieved. This reconstruction of wave was gained due to the metamaterial-shell around the object and it points towards the competency of scattering diminution of the metamaterial walls. Therefore, any hostile observer or radar will not be able to track the object. This has happened due to the epsilon near zero property of the metamaterial as it maintains an environment of uniform phase distribution, which prevents the scattering from the object being cloaked.

## 4. Conclusion

In this paper, a new metamaterial unit cell was introduced and its characteristics were evaluated. The characteristics of the metamaterial reveal the epsilon-near-zero property in conjunction with the negative-permittivity at certain region of the microwave C-band. Moreover, a square-shaped cloak was designed using the metamaterial and a metal cylinder was cloaked perfectly in the wide region of C-band where the metamaterial contains the epsilon-near-zero property as well as the negative-permittivity properties. Experimental results for metamaterial and the cloak was provided to the validated the performance of the metamaterial and the cloak.

Therefore, the metamaterial and the cloak can be efficiently utilized for the C-band operation.

## Acknowledgements

This work is supported by the Ministry of Education Malaysia (MOE) under grant no. FRGS TOPDOWN/2014/TK03/UKM/01/1 and DIP-2014-03.

## References

[1] D. Schurig, J.J. Mock, B.J. Justice, S.A. Cummer, J.B. Pendry, A.F. Starr, D.R. Smith, 'Metamaterial electromagnetic cloak at microwave frequencies'. *Science*, 314, 977–980, 2006.

[2] J. Andkjær and O. Sigmund, 'Topology optimized low-contrast all-dielectric optical cloak'; *Appl. Phys. Lett.*, 98, 021112 ,2011.

[3] B. Kante, D. Germain, A.D. Lustrac, 'Experimental demonstration of a nonmagnetic metamaterial cloak at microwave frequencies', *Phys. Rev. B* , 80, 201104, 2009

[4] S. S. Islam, M.R.I Faruque, and M. T. Islam, 'a two-component NZRI metamaterial based rectangular cloak'. *AIP Advances*, 5, 107116:1-9, 2015

[5] S. Xu, R. Zhang, and H. Chen; 'TE-polarized microwave broadband carpet cloak', International Workshop on Metamaterials; Nanjing, Chaina, 2012; pp.1-3 ; Doi: 10.1109/META.2012.6464959

[6] N. Kundtz, D. Gaultney, D.R. Smith, 'Scattering cross-section of a transformation optics-based metamaterial cloak'. *New J. Phys.*, 12, 043039, 2010.

[7] X. Wang, F. Chen, E. Semouchkina, 'Implementation of low scattering microwave cloaking by all-dielectric metamaterials', *IEEE Microw. Wirel. Comp. Lett.*, 23, 63–65, 2013.

[8] D. Rainwater, A. Kerkhoff1, K Melin, J C Soric, G Moreno and A. Alu; 'Experimental verification of three-dimensional plasmonic cloaking in free-space', *New J. Phys.*, 14 013054:1-13, 2012

[9] L. Matekovits, T.S. Bird, 'Width-modulated microstrip-line based mantle cloak for thin single and multiple cylinders'. *IEEE Trans. Ant. Prop.*, 62, pp.2606–2615, 2014.

[10] O. Luukkonen, S.I. Maslovski, S.A. Tretyakov, A Stepwise Nicolson–Ross–Weir-Based Material Parameter Extraction Method. *IEEE Antennas Wirel. Propag. Lett.*, 10, 3588–3596 , 2011.

**FSS, HIS and Extraordinary transmission**

# Design of a THz-MEMS Frequency Selective Surface for Structural Health Monitoring

**J. P. Pavia[1,2], W. J. Otter[3,4], S. Lucyszyn[3,4] and M. A. Ribeiro[1,2]**

[1]University Institute of Lisbon - ISCTE-IUL, Av. das Forças Armadas, 1649-026 Lisbon, Portugal
[2]Instituto de Telecomunicações, Av. Rovisco Pais, 1049-001 Lisbon, Portugal
[3]Centre for Terahertz Science and Engineering, Imperial College London, UK
[4]Optical and Semiconductor Devices Group, Electrical and Electronic Engineering, Imperial College, UK
joao_pedro_pavia@iscte-iul.pt

**Abstract**— This paper characterizes the relationship between applied force and reflectance/ transmittance of a terahertz frequency selective surface for use as a sensor in structural health monitoring. Numerical modelling of both the mechanical and electromagnetics, solving the elasticity equation and Maxwell's equations, respectively, has been undertaken for a 3 layer device. The unit cell comprises of a metal cross wire embedded within a (hard) silicon substrate, interleaved with stacks of (soft) low density polyethylene.

Structural health monitoring (SHM) is an important multidisciplinary topic in engineering which can benefit from emerging terahertz (THz) and microelectromechanical systems (MEMS) [1]. Frequency selective surfaces (FSSs) can also be used with THz-MEMS, as demonstrated in a polarization modulator [2]. Here we combine THz-MEMS with a FSS architecture to create a passive sensor that can be discretely integrated into the (sub)surface of structures, without impeding its functionality. We present a study of both the electromagnetic [3] and mechanical design of a THz-MEMS FSS stress sensor, operating at 668.5 GHz.

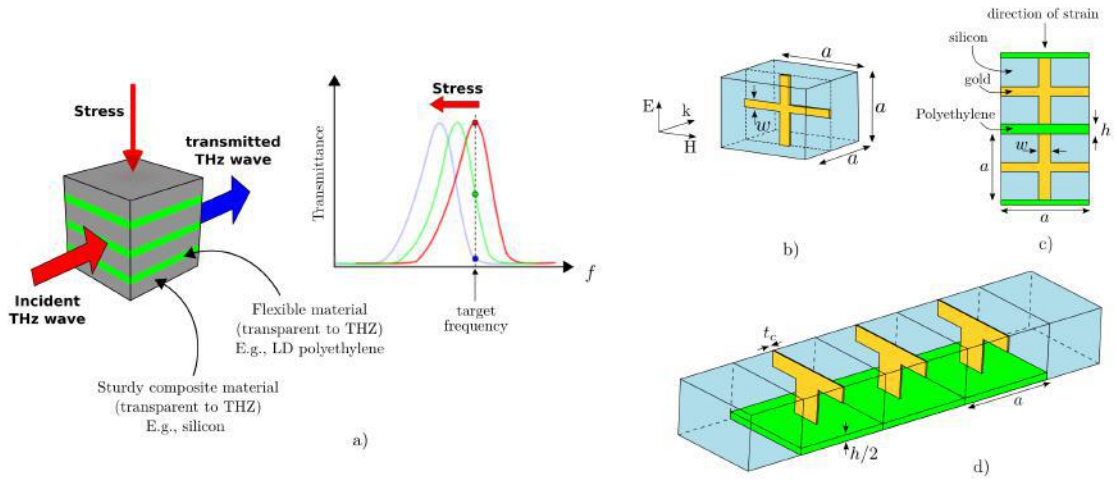



Figure 1: Illustrations of a) overview of working principle, b) a unit cell of the cross wire FSS structure, c) how cells are stacked between layers of LDPE to build the FSS structure, and d) the 3-layer reduced model used in the electromagnetic simulations.

Figure 1(a) represents a conceptual illustration of the device and overview of its operating principle. The device comprises of stacks of hard and soft materials that when compressed cause a shift in the frequency response. To achieve this, a FSS is embedded within the hard material. When compressed, the element spacing of the FSS is reduced, causing the required frequency shift, resulting in a decrease in transmittance at the operating frequency. Figure 1(b-d) shows the unit cell, geometry and materials of the THz-MEMS FSS structure. An operating frequency of 668.5 GHz was chosen as this is the absorption minimum in the window of interest of 500-700 GHz [4]. Through optimization, the following parameters were determined: lattice parameter $a = 47.45$ $\mu$m, wire width $w = 14.75$ $\mu$m, wire thickness $t_c = 500$ nm and the Low Density Polyethylene (LDPE) layers have a thickness $h = 12.7$ $\mu$m (0.50 mil) when no external force is applied.

Figure 2(a) and 2(b) show the numerical results for the reflectance and transmittance, respectively, of the 3-layer stack FSS as it is compressed. The optimization curve is a maximum at the optimum operating frequency, where the maximum dynamic range between compressed and uncompressed states is found.

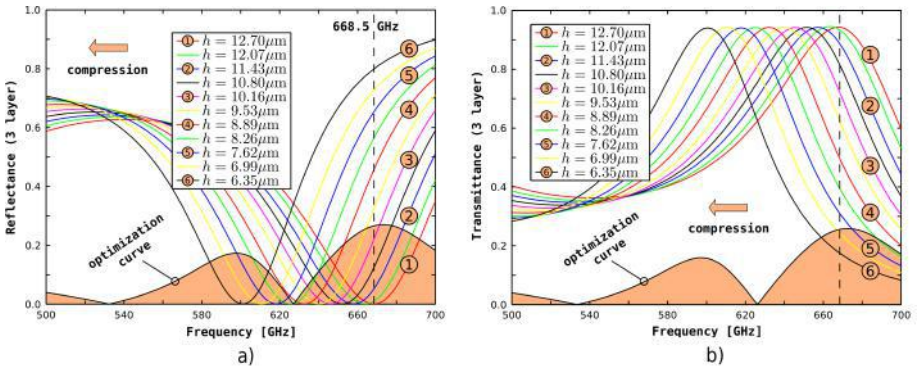



Figure 2: a) Reflectance, and b) transmittance of the 3-layer THz sensor.

Mechanical simulations of the device were undertaken to calculate the force required to displace the sensor. Figure 3a) shows the simulated mesh and mechanical displacement when a force of 100 $\mu$N is applied to the top and bottom of the structure. Figure 3(b) demonstrates the change in reflectance and transmittance for a 3-layer structure at 668.5 GHz, when different forces are applied. By changing the soft material, under compression, the range of applied forces at which the sensor operates can also be optimized.

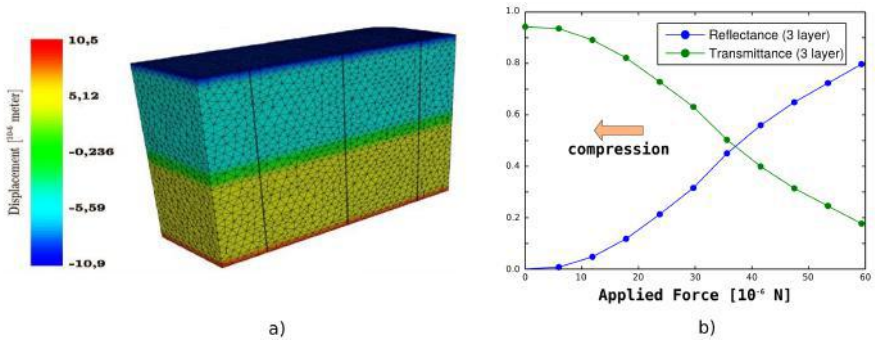



Figure 3: Mechanical analysis of the FSS: a) mesh and displacement data from a FEM simulation of the elasticity equation, and b) reflectance and transmittance as a function of applied force.

In conclusion, rigorous computational analysis has been presented of a THz-MEMS FSS for use as a stress sensor, having several applications in SHM. In particular we have described a method to determine the reflectance and transmittance as a function of applied force, which can be easily adapted to the design of other structures.

**REFERENCES**


1. S. Lucyszyn (Editor), "Advanced RF MEMS", Cambridge University Press, Cambridge, Aug. 2010.
2. T. Kan, A. Isozaki, N. Kanda, N. Nemoto, K. Konishi, H. Takahashi, M. Kuwata-Gonokami, K. Matsumoto and I. Shimoyama, "Enantiomeric switching of chiral metamaterial for terahertz polarization modulation employing vertically deformable MEMS spirals", *Nature Communications*, 8422, 1-7, Oct. 2015.
3. C. D. Duque and M. A. Ribeiro, "Effect of Uniaxial Compression in the Transmittance of a Novel Terahertz Sensor for Structural Health Monitoring", in *Proceedings of 2013 Loughborough Antennas Propagation Conference*, Loughborough, United Kingdom, November 2013, 122-126.
4. D. M. Slocum, E. J. Slingerland, R. H. Giles and T. M. Goyette, "Atmospheric absorption of terahertz radiation and water vapor continuum effects", *Journal of Quantitative Spectroscopy and Radiative Transfer*, vol. 127, 49-63, 2013.

# THz sensing with FSS at oblique incidence

**P. Rodríguez-Ulibarri**[1*], **S. A. Kuznetsov**[2], **and M. Beruete**[1, 3]

[1] Antennas Group-TERALAB, Public University of Navarra, Spain

[2] ATIC HT&NM, Novosibirsk State University, Russian Federation

[3] Institute of Smart Cities, Public University of Navarra, Spain

[*]corresponding author: pablo.rodriguez@unavarra.es

**Abstract**- In this work a cross dipole based frequency selective surface is proposed for sensing applications in the terahertz regime. Characterization under normal and oblique incidence is provided for both TM and TE polarization. For TM polarization, wide angle operation is possible in terms of sensing capabilities. While the sensitivity is maintained the width of the fundamental resonance becomes narrower, leading to more selective sensors. For TE polarization, the fundamental resonance experiences redshift with the angle of incidence.

Frequency selective surfaces (FSS) have been widely used in radar applications in the microwave regime. At THz and optical frequencies, they are very good candidates for sensing applications [1]. For instance, refractometers can be easily synthesizes by coating an FSS with different materials and measuring the shift of the fundamental resonance of the FSS.

In this work, a cross-dipole FSS is proposed as a sensor and its performance under normal and oblique incidence is characterized for TE and TM polarization [2]. Due to the symmetry of the element, under normal incidence the FSS is polarization independent. However, at oblique incidence operation a different behavior is obtained for TM and TE polarization. In terms of sensing, under TM polarization the performance is enhanced when the angle of incidence increases given that the fundamental resonance is narrowed due to hybridization with an asymmetrically excited bent mode. For TE polarization, the fundamental resonance becomes wider and shifts to lower frequencies. This is consequence of the dependence of the first diffraction order cut-off frequency with the angle of incidence [3].

Numerical and experimental results are presented for normal and oblique incidence ($\theta$ = 30 deg) in Figure 1. The FSS is patterned on a polypropylene substrate of 41 μm. Afterwards, it is spin-coated with a photo-resistive material of relative permittivity of $\varepsilon_a \approx 2.56$ that acts as analyte. The thickness of the photo-resistive layer is approximately 20 μm. For the experimental characterization an ABmm$^{TM}$ [4] VNA is used along with a quasi-optical bench. The experimental results are in good agreement with the full wave numerical simulations. Sensitivities of about 20% are achieved for a wide angle range for both polarizations [2]. The sensitivity in this context is defined as frequency/wavelength shift of the resonance with respect to a variation of the refractive index of the analyte material. As prospective work, the proposition of different FSS arrangement and elements in order to improve the sensing performance should be studied.

This work was supported by the Spanish Ministerio de Economía y Competitividad under contract TEC2014-51902-C2-2-R. P. R-U. is sponsored by Public University of Navarra via a predoctoral scholarship. SAK is supported by the Ministry of Education and Science of the Russian Federation under the State Assignment Contract #3002. M. B. acknowledges funding by the Spanish Government via RYC-2011-08221.

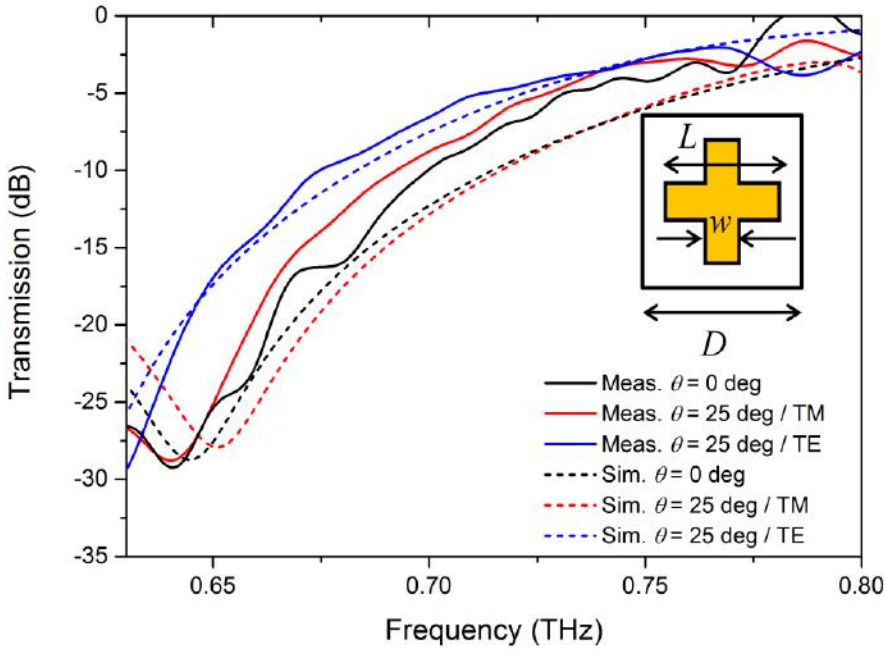



**Figure 1. Transmission results of an FSS under normal and oblique incidence. Solid and dashed lines correspond to measurements and simulations respectively. Inset: Unit cell schematic of the cross dipole FSS. Dimensions: *L* = 175 µm; *w* = 57 µm; *D* = 200 µm.**

## REFERENCES


1. Munk, B. A., *Frequency Selective Surfaces: Theory and Design*, Wiley-Interscience, USA, 2000.
2. Rodriguez-Ulibarri, P., Kuznetsov S. A. and Beruete M., "Wide angle terahertz sensing with a cross-dipole frequency selective surface", *Submitted to Appl. Phys. Lett.*, 2016
3. García-Viguera, M., Mesa F., Medina F., Rodriguez-Berral R., and Gómez-Tornero, J. L., "Simplified circuit model for arrays of metallic dipoles sandwiched between dielectric slabs under arbitrary incidence," *IEEE Trans. On Ant. Prop.* 60, 4637, 2012.
4. See http://www.abmillimetre.com for "AB Millimetre – Company Specialized in MVNA manufacturing, 2016

# Off-Axis Beaming 3D-Printed Bull's-Eye Antenna

**U. Beaskoetxea[1*], S. Maci[2], M. Navarro-Cía[3] and M. Beruete[1,4]**

[1] Antennas Group-TERALAB, Public University of Navarra, Spain

[2] Department of Information Engineering, University of Siena, Italy

[3] School of Physics and Astronomy, University of Birmingham, UK

[4] Institute of Smart Cities, Public University of Navarra, Spain

[*]corresponding author: unai.beaskoetxea@unavarra.es

**Abstract**- We present a theoretical analysis, along with numerical and experimental results of an off-axis beaming Bull's-Eye (BE) antenna working at 96 GHz. The antenna presents a 17 dB gain beam pointing at 16.5º, with −10dB side lobe level and 3.5º beamwidth. The prototype is fabricated by 3D printing stereolitography and then copper-coated, resulting in a 75% weight reduction compared to a fully metal fabricated design. Interesting applications in the fields of microsatellites, unmanned aerial vehicles or point-to-point communications are envisioned.

Leaky wave antennas (LWAs)[1] are low profile devices which present radiation characteristics even higher than those achieved by larger volume antennas, such as horn antennas. Among them, a special type of structure is that consisting of a flat metallic slab patterned with periodic grooves surrounding a central radiating slot. Several works have been published [2]–[5], showing different geometries and analyzing their leaky wave radiation mechanism both at microwaves and optics for solid metallic structures. For some applications, lightening the structure and engineering it for off-axis beaming [6] may be of interest.

In this work we present a Bull's-Eye antenna with off-axis radiation. A scheme of the antenna is shown in Fig. 1(a). The deduction of the equation which governs the elliptical grooves' distribution and shape was done by means of a thorough holography analysis and reported in [7]. The central slot width sets the transversal resonance (which fixes the operating frequency at which fed power is coupled to the output side) and its height governs the quality factor. Taking the theoretical values as a starting point, the structure was then optimized by launching numerical simulations with the commercial simulator CST Microwave Studio™. The final design was fabricated by stereolitography and metallized in a four step chemical process followed by an electroplating process, see Fig. 1 (b).

Ideal simulation and measurement [Fig. 1(c, d)] results show good agreement, except for a 4 GHz shift towards higher frequencies in the experimental measurements in both $S_{11}$ and maximum gain frequency, which takes place at $f$ = 92 GHz for the simulation. A decrease of about 3 dB appears in the experimental gain (peak gain of 17 dB), which is probably due to fabrication tolerances and possible extra losses introduced by the metal roughness, whereas a slight deviation of approximately 1.5º in the beaming angle ($\theta$ = 16.5°) might be due to additional experimental errors.

To unveil the origin of the disagreement, the final prototype was inspected under a microscope and the measured dimensions were included in the simulation model. Figure 1 (c) and (d) display the $S_{11}$ and E-plane radiation diagrams at the simulated design frequency $f$ = 92 GHz, (black curves) and experimental frequency $f$ = 96 GHz (red curves), respectively. It can be seen in Fig. 1(c, d) that the final simulation model (blue curves) provides a better agreement with the experimental results with only a reduction of 1dB in the peak gain.

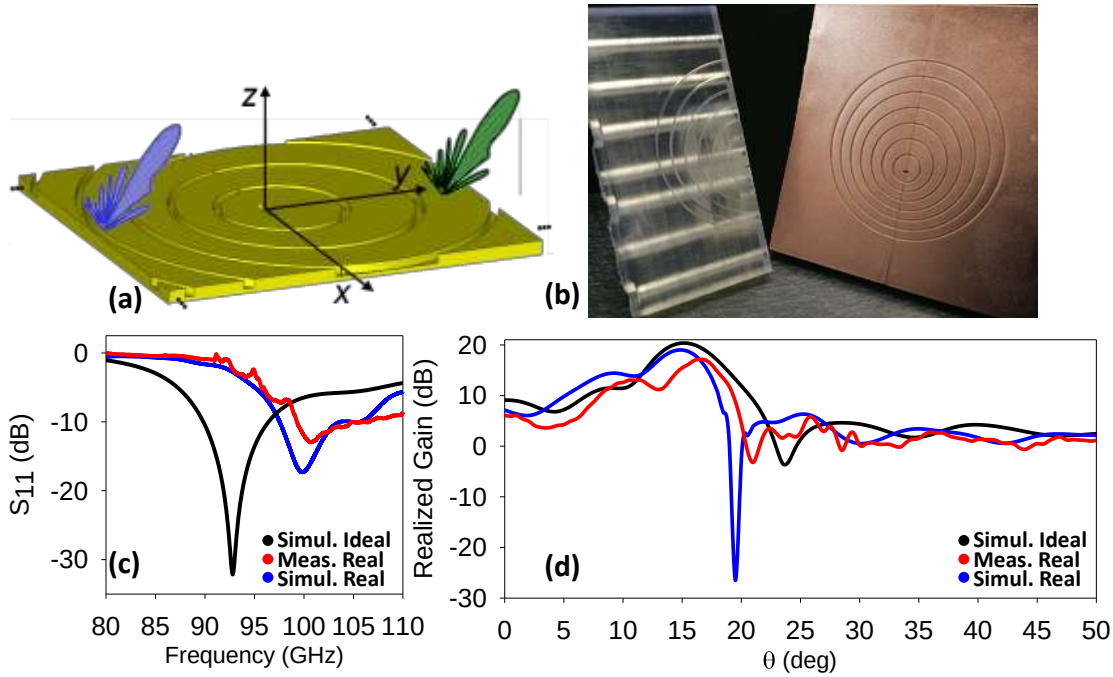



Figure 1. (a) Schematic of an off-axis Bull's-Eye. (b) Picture of printed non-coated half antenna and coated antenna. (c, d) $S_{11}$ and E-plane radiation diagram for simulated ideal (black curve), measured real (red) and simulated real (blue curve) antennas, respectively.

**Acknowledgments.** This work was supported by the Spanish Government under contract TEC2014-51902-C2-2-R. M. N.-C. is supported by University of Birmingham [Birmingham Fellowship]. M.B. acknowledges support by the Spanish Government under contract RYC-2011-08221.

**REFERENCES**

[1] A. A. Oliner and D. R. Jackson, "Leaky-Wave Antennas," in *Antenna Engineering Handbook*, McGraw-Hil., J. L. Volakis, Ed. New York: Mc Graw-Hill, 2007, pp. 11–1/11–56.

[2] M. Beruete, I. Campillo, J. S. Dolado, E. Perea, F. Falcone, and M. Sorolla, "Very Low-Profile 'Bull' s-Eye' Feeder Antenna," *IEEE Antennas Wirel. Propag. Lett.*, vol. 4, no. 2, pp. 365–368, 2005.

[3] U. Beaskoetxea, V. Pacheco-Peña, B. Orazbayev, T. Akalin, S. Maci, M. Navarro-Cía, and M. Beruete, "77 GHz High Gain Bull's-Eye Antenna With Sinusoidal Profile," *IEEE Antennas Wirel. Propag. Lett.*, vol. 14, pp. 205–208, 2015.

[4] T. Thio, K. M. Pellerin, R. A. Linke, H. J. Lezec, and T. W. Ebbesen, "Enhanced light transmission through a single subwavelength aperture.," *Opt. Lett.*, vol. 26, no. 24, pp. 1972–1974, 2001.

[5] L. Martín-Moreno, F. J. García-Vidal, H. J. Lezec, A. Degiron, and T. W. Ebbesen, "Theory of highly directional emission from a single subwavelength aperture surrounded by surface corrugations," *Phys. Rev. Lett.*, vol. 90, no. 16, p. 167401, Apr. 2003.

[6] M. Nannetti, F. Caminita, and S. Maci, "Leaky-wave based interpretation of the radiation from holographic surfaces," in *IEEE Antennas and Propagation Society, AP-S International Symposium (Digest)*, 2007, pp. 5813–5816.

[7] U. Beaskoetxea, S. Maci, M. Navarro-Cía, and M. Beruete, "3D-Printed 96 GHz Bull's-Eye Antenna with Off-Axis Beaming," *IEEE Trans. Antennas Propag.*, Submitted for Publication.

# New compact AMC structure for low profile antenna

**N. Kristou[1*], J-F. Pintos[1], K. Mahjoubi[2]**
[1] CEA-LETI, MINATEC Campus, 17 rue des martyrs, 38054 Grenoble Cedex 9, FRANCE
[2] IETR, Université de Rennes 1, 35042 Rennes, France
[*]corresponding author: Nebil.KRISTOU@cea.fr

**Abstract**- In this paper, an alternative technique for Artificial Magnetic Conductors (AMCs) unit cell miniaturization is proposed. A miniaturized novel planar AMC unit cell is designed; the reflection coefficient is simulated and then compared with a conventional equally thick mushroom-like unit cell in order to determine the achieved level of miniaturization. Subsequently, a 5×5 AMC unit cell finite structure for low profile antenna is designed to operate at 900 MHz and simulated to demonstrate the potential of the new proposed structure.

The aim of this paper is to propose a novel miniaturized AMC structure. The proposed unit cell, inspired by a previous work done in CEA-LETI [1], comprises two superposed substrates, a set of four metallic vias formed in the two substrates and crossing the entire thickness of the structure. Each of these metallic vias comprising an upper end in contact with the top square metallic patch and a lower end passing through one of the holes of the ground plane with no electrical contact and reaching a meandered line network at the bottom face of the bottom substrate. This results in creating a meandered network at the bottom side of the structure that connect every single unit cell to its near neighbors.

Low-cost FR4 substrates ($\varepsilon_r$ =4.4, Tan δe=0.02) of thickness 5.1mm for top substrate and 0.8 mm for the bottom one are selected for the design of each unit cell (See Figure 1).. In this case, the meandered lines introduce a phase shift around 150° The dimensions of the unit cell, shown in Figure 1, are 38×38 mm$^2$.

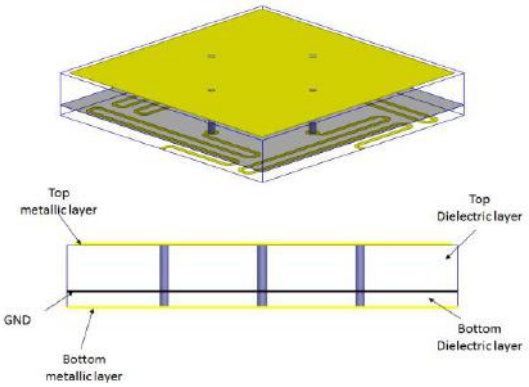



Figure 2. Perspective view and cross section of the proposed unit cell

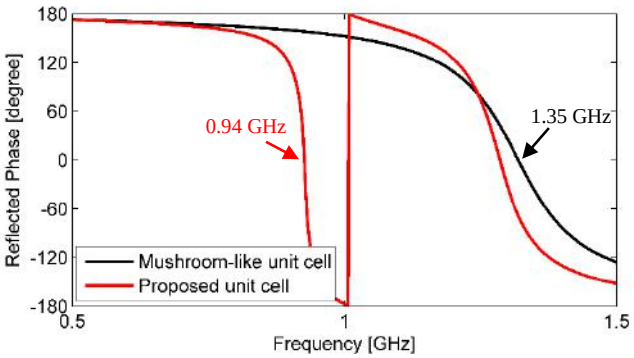



Figure 1. Phase of the reflection coefficient of the proposed AMC compared to with a conventional mushroom-like unit cell

According to the computed phase profile of the proposed AMC structure, frequency corresponding to the zero degree reflection phase is close to 0.94 GHz (red curve). For the same dimensions (size and thickness) and with

the same substrate properties, a conventional mushroom-like unit cell [2] presents a zero degree reflection phase close to 1.35 GHz (black curve). The novel unit cell achieve a 36% reduction in one dimension, compared a conventional mushroom-like unit cell.

The use of this new technique is illustrated through the design of novel compact AMC structure for low profile antenna. A rectangular dipole antenna of length 150 mm and width 3.5 mm has been placed at a height of $0.05\times\lambda_0$ above a 5 × 5 grid of the novel AMC surface. The total dimensions, including the extension of the ground plane are $0.57\lambda_0\times0.57\lambda_0\times0.069\lambda_0$.

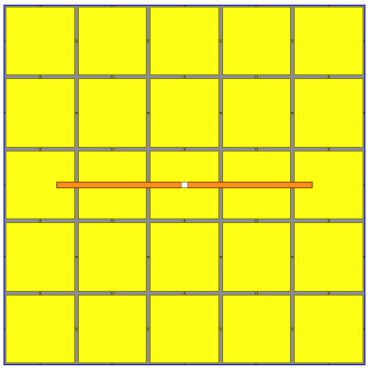


Figure 3. Top view of the proposed 5x5 AMC structure with a dipole antenna

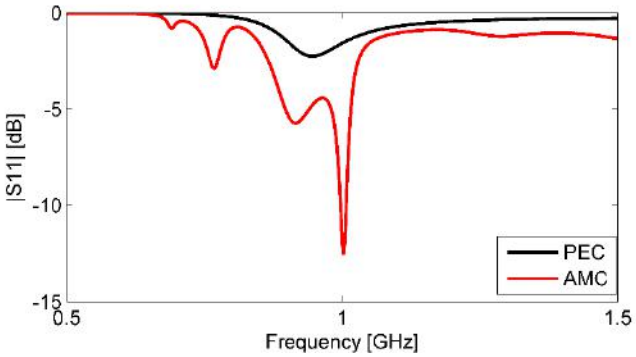



Figure 4. Return loss comparaison of the dipole antenna

Figure 4 compares the simulated return loss of dipole antenna placed at a distance $d=0.05\lambda_0$ above Perfect Electric Conductor (PEC) and AMC ground planes. The input impedance in each case is matched to a 50 Ω feeding port. With the PEC surface as the ground plane, the return loss of the dipole is only −1.4 dB at 900 MHz. A better return loss of −5.5dB is achieved by the dipole antenna over the AMC ground plane at the same frequency.

The resulting patterns show a maximum directivity of 7.7 dBi with 85% of radiation efficiency at 900 MHz. Such performance is comparable to that of a conventional metasurface-based mushroom-like unit cell but with 68% surface reduction at the same operating frequency and for the same number of cells.

**Conclusion:** A novel technique for AMC/EBG miniaturization was proposed; a new compact AMC structure for low profile antenna was designed and simulated at 900 MHz. Realization are under progress and measurement results will be presented in the final paper.

**REFERENCES**

1. J-F. Pintos, O. El Bouayadi, “Electromagnetic Wave Propagation Disruption Device And Method For Producing Same”, Patent, US2014354502 (A1).
2. D. Sievenpiper, “High-impedance electromagnetic surfaces,” Ph.D. dissertation, Dept. Elect. Eng., Univ. California at Los Angeles, Los Angeles, CA, 1999.

# Frequency Selective Surfaces to improve the performance of systems with dual-band antennas

**E. M. Fernandes**[1], **M. W. Silva**[1], **L. J. Matos**[1] **and A. P. L. Barbero**[1]
[1]Telecommunications Department, School of Engineering, Federal Fluminense University - UFF, Niterói, RJ, Brazil
elidianemirella@gmail.com, mauricio.weber@gmail.com, lenijm@id.uff.br, pablo@telecom.uff.br

**Abstract**- This paper proposes the design of a frequency selective surface formed by Jerusalem crossed grids to improve the performance of systems with dual-band antennas, operating in 2.4 GHz and 5.8 GHz. The analysis and the results of the calculated FSS structure are presented.

The development in wireless technology is growing increasingly, especially for applications in the unlicensed frequency band. Nowadays, the WLAN system has been widely used due to numerous advantages such as the absence of wires between users and access points, fast installation providing the most efficient use of the physical space and flexibility in the reception area allowing connection from different places. However, it is known that radio signals from wireless systems may spread beyond the desired location and can cause interference in co-existing systems. There are many studies about interference, which may improve the operation in environments with low signal-to-noise ratio or the quality of desired signals avoiding interference with other systems. One of them is the use of Frequency Selective Surfaces (FSS), which are planar periodic structures composed of both patch-type or aperture-type elements, usually printed on a dielectric substrate [1,2].

FSS have been applied in many areas such as microwave absorbers and radomes, in which bandpass FSS filters are used in conjunction with an antenna system to reduce the radar cross-section (RCS) [3]. In recent years dual band applications have been the subject of study. The authors demonstrated in [4] an improvement in the radiation pattern of a simple vertical monopole on high surface impedance with less power wasted in the backward direction. It must be highlighted the use of FSS with multi-band antennas. This type of antenna has been widely used to integrating services operating at different frequency bands. A common approach uses FSS as a subreflector in addition to the large reflecting dish in a reflector antenna. The subreflector, which is a FSS, is designed to be reflective at a frequency band and be simultaneously transparent at another desired band. For instance, in [5] the authors obtained performance improvement of an antenna array by using double-layer FSS. In this context, this paper aims to design a frequency selective surface to improve the performance of systems with dual-band antennas. In contrast to what has been described in [5], this work uses simple geometry and aims to improve the performance of a single antenna rather than an arrangement. The FSS works at two frequency bands, the frequencies are 2.4 GHz and 5.8 GHz, which belong to the ISM band (The Industrial, Scientific and Medical radio bands). In order to observe the transmission and reflection coefficients from a single unit cell with periodic boundary condition, it was utilized the CST Microwave Studio.

Figure 1 presents the FSS geometry and its geometrical parameters. The dimensions of the designed FSS unit cell are: $d$ = 20.5 mm, $h$ = 0.7 mm, $w$ = 2.25 mm, $p$ = 36 mm. The substrate material is FR-4, whose thickness $t$ = 1.6 mm and $\varepsilon_r$ = 4.3. Figure 2 shows the simulation results of the transmission $S_{21}$ and reflection $S_{11}$

characteristics of the Jerusalem Cross FSS under normal angle of incidence. It can be observed the absorbing of the signal at the frequencies 2.4 GHz and 5.8 GHz. It was achieved these frequencies accurately according to the requirements of the ISM band. At the first resonant frequency, the bandwidth measured was 150 MHz and at the second resonant frequency, it was obtained 800 MHz. Both are covering the bandwidth required by ISM band standard, which are 83.5 MHz and 125 MHz, respectively.

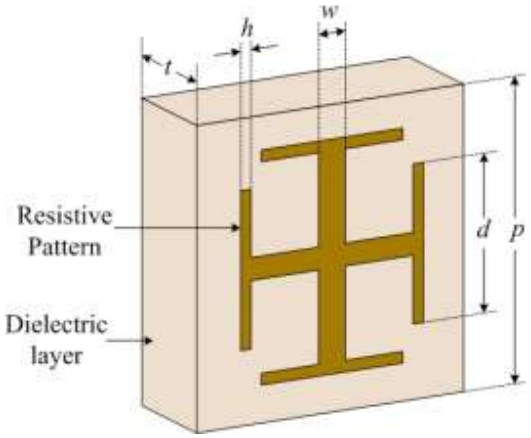



**Figure 1: Layout and parameters of a metallic FSS Jerusalem Cross pattern over a dielectric slab.**

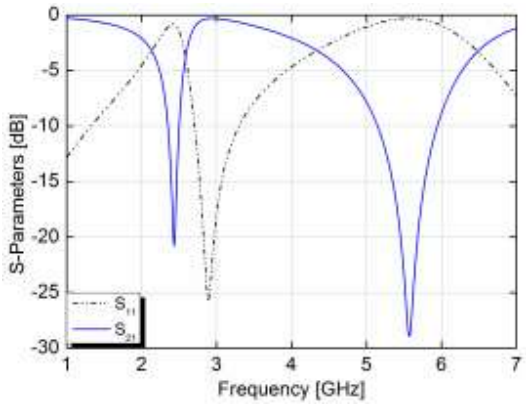



**Figure 1: Simulation results of the dual band FSS filter for the Jerusalem Cross.**

## REFERENCES


1. Munk, B. A., *Frequency-selective surfaces: Theory and Design*, John Wiley & Sons, 2000.
2. Campos, A. L. P. S., *Superfícies Seletivas em Frequência - Análise e Projeto*, IFRN, 2009.
3. M. Paquay, J.-C. Iriarte, I. Ederra, R. Gonzalo, and P. de Maagt, "Thin AMC Structure for Radar Cross Section Reduction," IEEE Transactions on Antennas and Propagation, vol. 55, no. 12, pp. 3630–3638, 2007.
4. Sievenpiper, D., R. Broas and E. Yablonovitch, "Antennas on High-Impedance Ground Planes," *IEEE MTT-S International Microwave Symposium Digest*, Vol. 3, 1245–1248, 1999.
5. Almeida, V. A. and A. L. Campos, "Performance Optimization of Microstrip Antenna Array Using Frequency Selective Surfaces", *Journal of Microwaves, Optoelectronics and Eletromagnetic Applications*, Vol. 13, No. 1, 31-46, 2014.

# Frequency Reconfigurable Antenna with Metamaterial Electromagnetic Band Gap (EBG) structures

**Raimi Dewan[1*], M.K.A. Rahim [1], M.R. Hamid[1], M.E. Jalil[1] and H.A. Majid[2]**
[1]Communication Engineering Department, Faculty of Electrical Engineering,
Universiti Teknologi Malaysia (UTM), 81310 Johor Bahru, Johor.
[2] Department of Electrical Engineering Technology, Faculty of Engineering Technology,
Universiti Tun Hussein Onn Malaysia, Parit Raja, Batu Pahat, Johor
[*]corresponding author: raimidewan@gmail.com

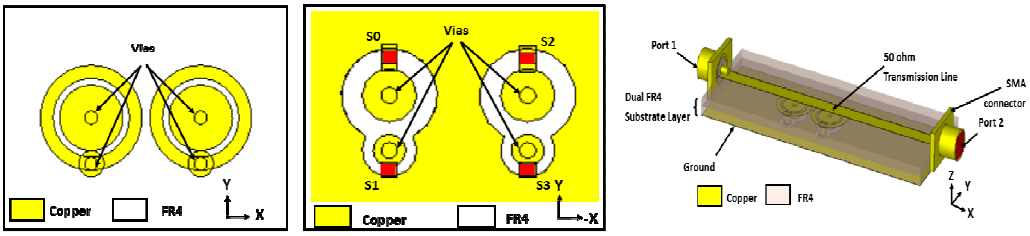
**Abstract**- A metamaterial of Electromagnetic Band Gap (EBG) incorporated to a wideband antenna for frequency reconfigurability is proposed. The EBG consists of two identical unit cells that provides multiple band gaps at 1.88-1.94 GHz, 2.25-2.44 GHz, 2.67-2.94 GHz, 3.52-3.54 GHz, and 5.04-5.70 GHz with different EBG configurations. The antenna is then incorporated with EBG. The corresponding incorporated structure successfully achieve various reconfigurable center frequencies at 1.60 GHz, 1.91 GHz, 2.41 GHz, 3.26 GHz, 2.87 GHz, 5.21 GHz, and 5.54 GHz.

## Introduction

EBG is a metamaterial that manipulate the propagation of electromagnetic waves within a structure [1, 2]. EBG can be implemented as a filter, where its bandgaps properties block particular frequency of the propagating waves within the microwave devices. In this research, EBG is incorporated to the antenna as the reconfigurable mechanism. By manipulating different EBG configurations (A, B, C or D), various band gaps can be achieved. Subsequently, the incorporation of EBG to the antenna successfully achieve multiple operating frequency. The reconfigurable frequency antenna is advantageous than single band antenna and is a potential candidate for reducing interference between various operating frequencies in wireless communication services (WCS).

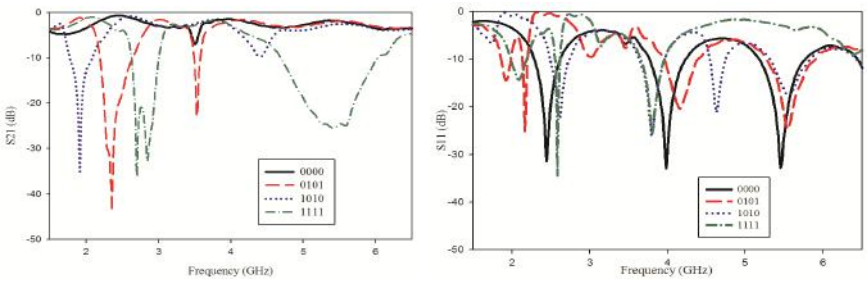
## Result and Discussion

Figure 1(a) and 1(b) shows the front and back view of two EBG unit cells. The EBG on the front side is connected to the ground using vias. Each of the connections of the EBG circular structure are connected or disconnected from the ground using four copper strips of S0, S2, S1 and S3. This mechanism correspond to "1" and "0". The EBG bandgap, S21 is validated using suspended transmission line method as in Figure 1(c). The corresponding bandgap and return loss of the EBG are shown in Figure 1(e)-(f). In Figure 2(a), the EBG is then incorporated to the antenna. The incorporated structure achieves multiples reconfigurable frequencies as shown in Figure 2(b).



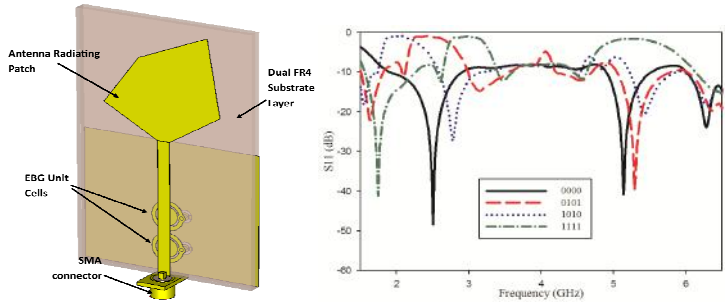

(a) (b) (c)

| State | S0 | S1 | S2 | S3 |
|---|---|---|---|---|
| A | 0 | 0 | 0 | 0 |
| B | 0 | 1 | 0 | 1 |
| C | 1 | 0 | 1 | 0 |
| D | 1 | 1 | 1 | 1 |




(d) (e) (f)

**Figure 1.** (a) Front and (b) back side of EBG unit cells. (c)Suspended transmission line method to evaluate band gap (S21) and return loss (S11). (d) A, B, C, D configuration with different diode state (S0S1S2S3). The corresponding (d) S21 and (f) S11 results.




(a) (b)

**Figure 2.** (a) Antenna incorporated with EBG unit cells in dual substrate layer. (b) The corresponding reconfigurable frequencies of the antenna with different EBB configurations.

**Conclusion:** Frequency Reconfigurable antenna using EBG is proposed. By utilizing band gap properties of the EBG-metamaterial, multiple reconfigurable frequencies have been achieved at 1.60 GHz, 1.91 GHz, 2.41 GHz, 3.26 GHz, 2.87 GHz, 5.21 GHz, and 5.54 GHz. The incorporation of EBG is successful as the antenna reconfigurable mechanism. The reconfigurable antenna is suitable for RFID (2.45GHz), WLAN (2.45 GHz/5.8 GHz), LTE (1.6 GHz/2.6 GHz), WiMAX (2.3 GHz/3.5GHz/5.2 GHz/5.5GHz) and other ISM applications.

**Acknowledgements** The authors thank the Ministry of Education (MOE) for supporting the research work; Research Management Centre (RMC), Faculty of Electrical Engineering (FKE) UTM. Special Thanks to Universiti Tun Hussein Onn Malaysia for the support of the research under grant number U435.

## REFERENCES

[1] A. Pirhadi, M. Hakkak, F. Keshmiri, and R. Karimzadeh Baee, "Design of compact dual band high directive electromagnetic bandgap (EBG) resonator antenna using artificial magnetic conductor," *IEEE Transactions on Antennas and Propagation,* vol. 55, pp. 1682-1690, 2007.

[2] Y. J. Lee, J. Yeo, R. Mittra, and W. S. Park, "Application of electromagnetic bandgap (EBG) superstrates with controllable defects for a class of patch antennas as spatial angular filters," *IEEE Transactions on Antennas and Propagation,* vol. 53, pp. 224-235, 2005.

# 10.7 GHz Switchable Metamaterial Absorber/ Reflector for X-band Applications

**M.M. Gajibo*, M. K. A. Rahim, N. A. Murad, O. Ayop, M. R. Hamid, H. A. Majid**
Department of Communication Engineering, Faculty of Electrical Engineering,
Universiti Teknologi Malaysia, 81310 Johor Bahru, Johor, Malaysia
*mmgajibo@yahoo.com, mkamal@fke.utm.my, asniza@fke.utm.my, osman@fke.utm.my,
rijal@fke.utm.my, huda_set@yahoo.com

**Abstract**- A double layer structure consisting of a Metamaterial (MTM) absorber and an artificial magnetic conductor (AMC) reflector is presented in this report. An FR4 substrate was used and the incidental wave angles were varied from $0^o$ to $85^o$. A peak absorption of 99.99% was achieved at 10.7GHz by the absorber for both TE and TM polarization incident waves. On the other side close to 80% peak reflection was achieved at same frequency (10.7GHz) by the AMC reflector.

***Keywords***- *Metamaterial, Absorber, Reflector, AMC.*

## I. INTRODUCTION

Electromagnetic waves (EMW) absorbers neither reflect nor transmit (EMW) but instead they minimize reflection by maximizing energy loss where as EMW reflectors are structures that reflects the remnants of EMW left after a minimum conduction loss from an incidental EMW. The theories and concept behind exotic properties of metamaterials (MTM) have long been established [1]. MTM, being unique structures purposely engineered to have properties not found in nature have in recent years drawn numerous attention. Researchers in the EM (electromagnetic) field are at their heels racing to exploit all benefits offered by MTM. Manipulating or tempering with the structural configuration of these substances yields unusual properties, which could be desirable for certain applications such as low profile ground plane, cloaking, EM filters, sensing, focus antenna beam, reflectors, phase shifting [2] etc. Furthermore, MTM is divided into subareas which includes artificial magnetic conductor, AMC, electromagnetic bandgap (EBG), frequency selective surface (FSS), left-handed metamaterial (LH-MTM).

## II. PROPOSED DESIGN AND SIMULATION

The proposed MTM structure comprises of a MTM absorber on one side with an AMC Reflector on the other side sandwiching a copper ground plane. The structure is shown in Figure 1, and was designed using an FR4 substrate with a dielectric constant of 4.6 with loss tangent of 0.019. The MTM absorber has a circular ring shape where as the AMC reflector has a shape combining both square and a circle.

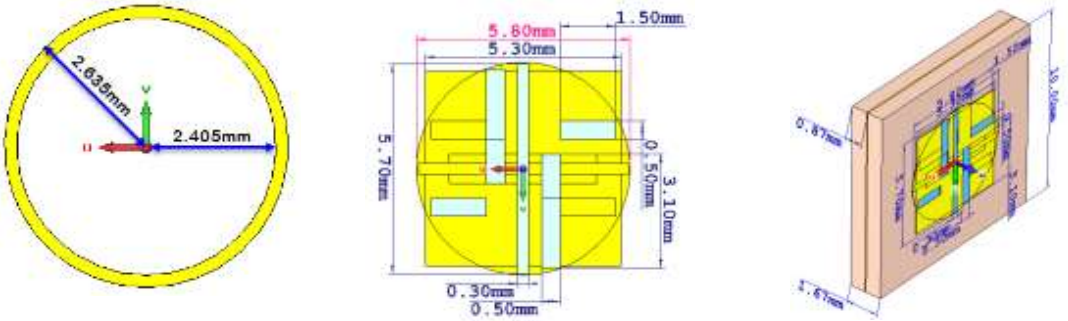



Figure 1. (a) MTM absorber (b) AMC reflector (c) Side view

## III. SIMULATION RESULT AND DISCUSSION

### a. *Absorbance Magnitude for Different Polarization*

The proposed absorber was simulated with different polarization angles ($0^o$, $15^o$, $25^o$, $45^o$ $55^o$, $70^o$ and $85^o$). The simulated results indicated above 99% absorption for angles $0^o$, $15^o$, $25^o$ at 10.7GHz which deteriorates as the angle increases with $85^o$ being the least (less than 30% absorption). Additionally, there is a little shift in resonance frequency as the angle increases. The results for both TM and TE mode seems same with negligible difference. Absorbance, A(ω) was calculated using A(ω)=1-R(ω)-T(ω) where reflectance, R(ω) is $|S_{11}|^2$ and transmittance, T(ω) is $|S_{21}|^2$ [4]. Figure 2a shows the comparisons.

### b. *AMC's Reflection Magnitude for Different Polarization state*

Similarly, the proposed AMC reflector was simulated with different polarization angles ($0^o$, $15^o$, $25^o$, $45^o$ $55^o$, $70^o$ and $85^o$). The simulated results demonstrated a maximum reflection close to 80% at resonance frequency of 10.7GHz which deteriorate and gains shift in frequency as the polarization angle increases. The least reflection (30%) was recorded at angle $70^0$ with the frequency shifted to 11GHz. Figure 2b shows the AMC's reflection.

### c. *AMC's Reflection Phase for Different Polarization state*

In AMC structure, reflection phase is crucial ($-180^o$ to $180^o$) and thus it is reported. In a similar fashion, the results of the reflection phase at resonance frequency of 10.7GHz show that at angles $0^o$, $15^o$ and $25^o$ there close to 1.5GHz bandwidth ($-90^o$ to $90^o$) which gradually falls with increase in the angles. Angle $85^o$ indicated virtually no bandwidth and significant shift in resonance frequency. In almost all the angles, a phase of $-180^o$ to $180^o$ was achieved despite angle $85^o$ having no bandwidth at resonance frequency. Figure 2c shows the AMC's reflection phase.

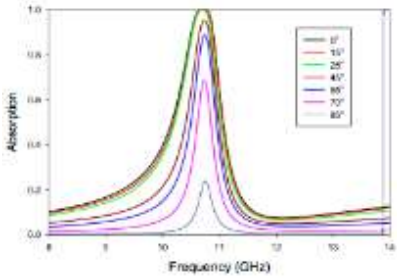
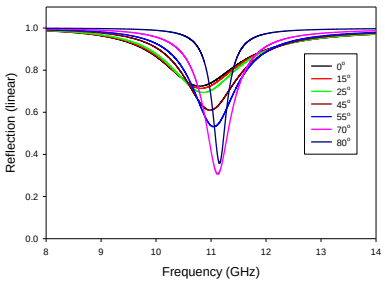
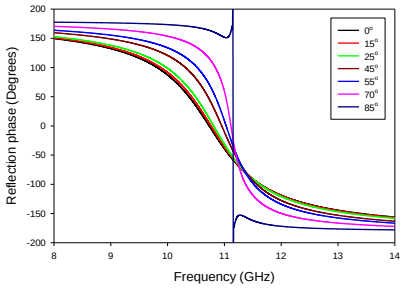



Figure 2. (a) Absorption




(b). AMC's Reflection




(c). AMC's Reflection phase

## IV. CONCLUSION

In this report a dual layer MTM absorber/ reflector was presented. The performance of both the absorber and the AMC reflector were observed. They both tend to perform excellently in polarization angles of $0^o$ to $30^o$ at resonance frequency of 10.7GHz. Furthermore, their performance drops with shift in resonance frequency for polarization angles of greater than $30^o$.

## REFERENCES


[1] Landy, N.I, S. Sajuyigbe, J.J Mock, D. R. Smith and W.J. Padilla, "Perfect metamaterial absorber," *Physical Review Letters*, Vol. 100, 207402, 2008

[2] Ayop O., M.K.A. Rahim, N.A. Murad and N.A. Samsuri, "Dual-resonant polarization-independent and wide-angle metamaterial absorber in X-band frequency", Journal of Applied Physics, Vol. 122, issue 4, p1-7, 2016

[3] Abu, M. and M.K.A. Rahim, "Single-band and dual-band artificial magnetic conductor ground planes for multi-band dipole antenna," *Radio Engineering Journal, issue 4, p999-1006, 2012*

[4] Ayop, O., M. K. A. Rahim and N. A. Murad "Double Layer Circular Ring Metamaterial Absorber for Dual-Directional Application at 10 GHz," *2013 IEEE International RF & Microwave Conference (RFM2013)*, Penang, Malaysia, Dec. 09-11, 2013

[5] Abu, M., E.E. Hussin, M.S.M. Isa, Z. Zakaria and Z.A. Baharudin, "Designing artificial magnetic conductor at 2.45 GHz for metallic detection in RFID tag Application," *2014 International journal and Engineering technology (IJET)* ISSN: 0975-4024

# Alternative Approach to Miniaturize an AMC Structure

**N. Kristou**[1*], **J-F. Pintos**[1], **K. Mahjoubi**[2]
[1] CEA-LETI, MINATEC Campus, 17 rue des martyrs, 38054 Grenoble Cedex 9, FRANCE
[2] IETR, Université de Rennes 1, 35042 Rennes, France
[*]corresponding author: Nebil.KRISTOU@cea.fr

**Abstract**- This paper proposes an alternative approach to modify the behavior of an Artificial Magnetic Conductor (AMC), through interconnected meandered lines located behind the ground plane using of offset metallized vias. The novel design allows to get high-level miniaturization factor for AMC unit cell.

A significant amount of research has been made recently on unit cell miniaturization and several works have been widely proposed in the literature with various miniaturization techniques [1]. The aim of this paper is to propose an alternative approach to miniaturize an AMC strcuture. A single layer unit-cell with off-center quadruple-via under each patch is firstly investigated, as shown in Figure 1. The effect of the distance between the vias and the patch edges is shown in Figure 2. The reflection phase results of the centered single-via is compared with the off-centered quadruple-via cases. As the vias are closer to the patch edges, the reflection phase of the wave increases to the high frequencies. That resonance frequency is mainly determined by the distance between the vias and patch edges. The off-centered vias do not seem to offer the best results for unit cell miniaturization [2] but it has been observed in [3] that interconnected cells may modify the behavior of the metasurface.

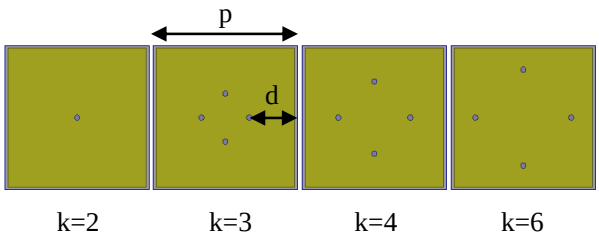



Figure 1. Bottom views of the square patch unit cell with offset vias for several offset parameter k.

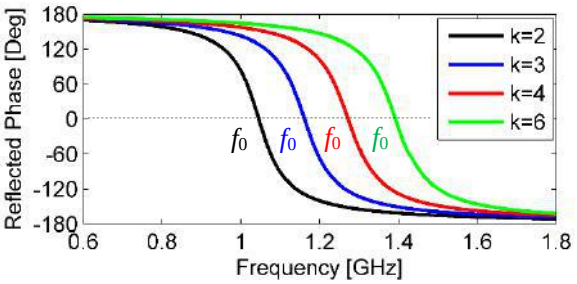



Figure 2. Simulated reflection coefficient phase versus frequency for different offset parameter k.

The proposed unit cell comprises two superposed substrates as explained in [3], a set of four metallic vias formed in the two substrates and crossing the entire thickness of the structure. Each of these metallic vias comprising an upper end in contact with the top square metallic patch and a lower end passing through one of the holes of the ground plane with no electrical contact and reaching a meandered line at the bottom face of the bottom substrate. This results in creating a meandered network at the bottom side of the structure that connect every single unit cell to its near neighbors. The position of the offset four-vias ($d$) and the phase shift ($\Delta\varphi$ : relative to the meander length for each unit cell) represent the main parameters of this new approach offering a novel way to modify the behavior of the unit cell. The parameter $k$ is defined by the following relationship:

$$k = \frac{p}{d} \tag{1}$$

Where: *d* represents the distance between the vias center and the patch edges and *p* the periodicity of the unit cell. The dimensions of the designed unit cell are 53×53 $mm^2$. Low-cost FR4 substrates ($\varepsilon_r$ =4.4, $\tan\delta_e$=0.02) of thickness 5 mm for top substrate and 1.6 mm for the bottom one are selected for the design of each unit cell (See Figure 3).

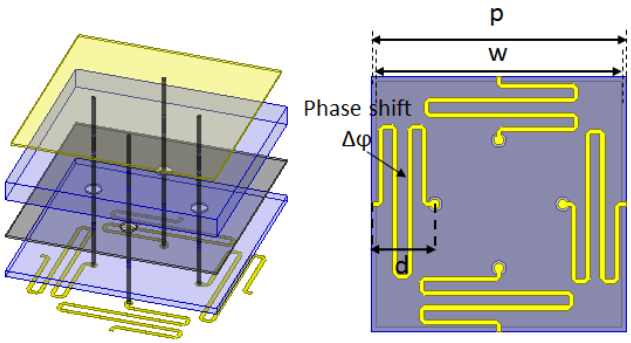



Figure 3. Unit-cell geometry of the proposed AMC.

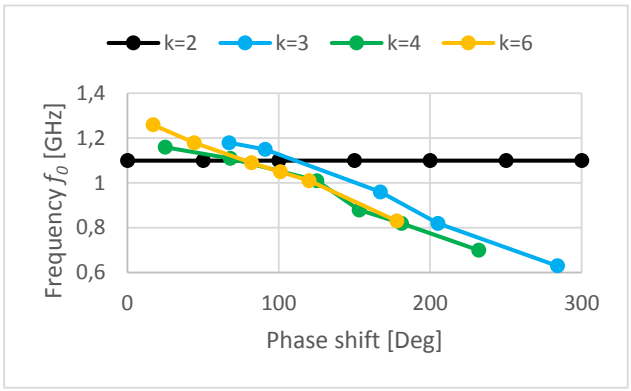



Figure 4. Zero phase frequency $f_0$ of the proposed unit-cell versus phase shift $\Delta\varphi$, for different values of *k*.

Figure 4 above resumes the effect of vias positions (through k parameter) and phase shift (Δφ) on the zero reflection-phase profile of the planar AMC structure. If *k* increases (or *d* decreases) the reflection-phase shifts to higher frequencies and if $\Delta\varphi$ increases the reflection-phase shifts to lower frequencies. Thus, for a given unit cell periodicity p, there will be a tradeoff between the distance of the vias from the patch edges and the implementable phase shift. For example, with k=3 (blue curve) and a phase shift $\Delta\varphi$ close to 280°, a frequency shift of 50% is reached. In contrast, when $k = 2$ (via at the center), the reflection phase of a normally incident plane wave remains the same and does not change according to the phase shift $\Delta\varphi$ (black curve).

An application of this approach is presented in [4], where 5×5 AMC unit cell finite structure for low profile antenna is designed to operate at 900 MHz and simulated to demonstrate the potential of the proposed structure. It achieves 68% surface reduction at the same operating frequency and for the same number of cells when compared to a conventional metasurface-based mushroom-like unit cell.

**Conclusion:** An alternative way to modify the behavior of a metamaterial is proposed by adding extrinsic setting to the metamaterial structure. This is done through the interconnection of the conductive elements at the top side of the metasurface to each other using meander lines at the bottom side and exploiting all available area behind the ground plane for maximum phase shift introduction. This type of phase shift setting by dimensioning the meandered lines allows to set the resonance frequency of the metamaterial and to reduce the cell size at a selected frequency.

## REFERENCES


1. M. Grau, R. Serra and J. Parrón, "Miniaturisation of artificial magnetic conductors: comparison methodology and realisation of compact unit cell," in *Electronics Letters*, vol. 50, no. 19, pp. 1340-1342, September 11 2014.
2. Yang, F. and Rahmat-Samii, Y., "Polarization-dependent electromagnetic band gap (PDEBG) structures: Designs and applications," *Microw. Opt. Technol. Lett.*, 41: 439–444, 2004.
3. J-F. Pintos, O. El Bouayadi ,"Electromagnetic wave propagation disruption device and method for producing same". Patent, US2014354502 (A1).
4. N. Kristou, J-F. Pintos, K. Mahjoubi, "New compact AMC structure for low profile antenna", *META'16, the 7th International Conference on Metamaterials, Photonic Crystals and Plasmonics*, Torremolinos, Spain, 2016.

# Two Equivalent Circuit Models for Double Concentric Squares AMC

**Mohamad Mantash and Anne-Claude Tarot**

Institute of Electronics and Telecommunications of Rennes1, University of Rennes 1, Rennes, France
tarot@univ-rennes1.fr

## Abstract

Two equivalent circuit models to estimate the resonant frequency and reflection coefficient phase of double concentric square Artificial Magnetic Conductor (AMC) are proposed. The AMC structure is composed of an array of square surrounded by a loop printed on grounded dielectric substrate without vias. This approach is based on the Transmission Line Model (TLM) for waves normally incident on the structure. The both proposed models have been validated via a comparison between measurements and simulations results for different samples and by a parametric study of the design parameters.

## 1. Introduction

In the recent years, Artificial Magnetic Conductor (AMC) structures [1] composed of Frequency Selective Surfaces (FSSs) arrays printed on grounded dielectric without vias were used in wearable applications in order to protect the human body from the antenna backward radiation [1-11]. Various geometries have already been used for the design of an AMC such as loop [10], square [9], Hexagon [10], Jerusalem cross [12], etc. As the shape of the FSS with the grounded dielectric slab determinates the resonance frequency, a very easy way to implement a dual band AMC is to double its shape e.g. double squares [4-5], double hexagons [6]. Equivalent circuit models have been proposed in [8, 12-20] for different types of FSS and AMC except for the double concentric square one.

There are several reasons to model the AMC through an equivalent circuit. The most common one is for better understanding the operation mechanism of the periodic structure. Another reason is for reducing the computational time compared to the one required by full-wave electromagnetic simulation methods.

In this work, we propose two analytical Equivalent Circuit Models (ECMs) based on the transmission line theory for a double concentric square AMC structure (see Fig. 1) illuminated by plane wave under normal incidence. Moreover, this structure is one of the most used in flexible [4] and wearable applications [5] as it has several advantages such as dual band, compact size, easy design, broad operation bandwidth and, above all, neither via holes, simplifying practical implementation and integration with planar antennas. In section II, two different methods to calculate the impedance of the FSS are presented in order to determine the final model of the AMC. Then the two models validation on different substrates and for different geometric parameters is presented in section III. Finally, some conclusions are provided in section IV.

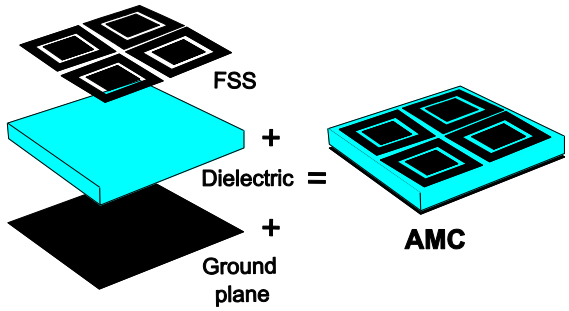



Figure 1: Artificial magnetic conductor (AMC) structure.

## 2. Equivalent circuit model

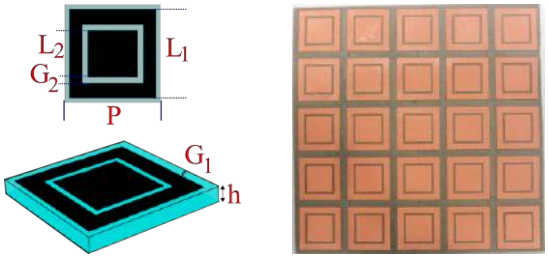
The parameters of the AMC structure are shown in Fig. 2(a). The FSS of the concentric square AMC structure is composed by: an inner square patch (width $L_2$) surrounded by an outer loop (width $L_1$); a gap width between patch-loop $G_2$; a gap between loop-loop $2G_1$; and a substrate of thickness h.

The analytical expression for calculating the reflection coefficient phase is as follows:

$$\phi = \mathrm{Im}\left[\frac{Z_{AMC}-\eta}{Z_{AMC}+\eta}\right] \quad (1)$$

where $Z_{AMC}$ is the AMC surface impedance and $\eta = 120\pi$ is the free space impedance.

Based on the transmission line theory, the AMC surface impedance ($Z_{AMC}$) can be decomposed into two parts: the FSS impedance ($Z_{FSS}$) and the Grounded Dielectric Slab impedance ($Z_{GDS}$) as in Fig. 3.




(a) (b)

Figure 2: Double concentric squares AMC: (a) Top view and side view of the unit cell geometry (b) planar AMC manufactured prototype.

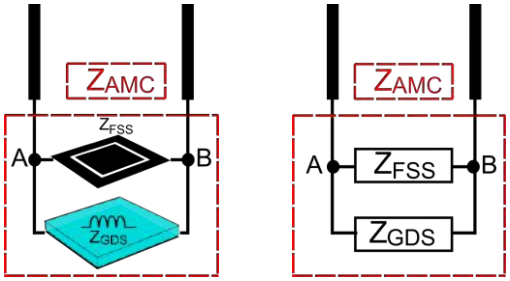



Figure 3: Equivalent transmission line model for normal wave incident.

The resulting surface impedance $Z_{AMC}$ is calculated from the parallel connection of $Z_{FSS}$ and $Z_{GDS}$ ($Z_{AMC}$ = $Z_{FSS}$ // $Z_{GDS}$).

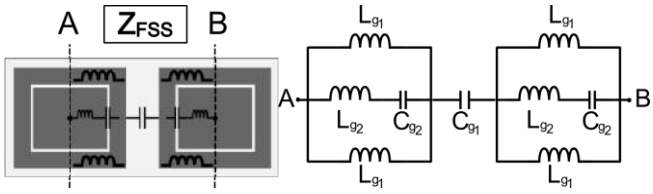



Figure 4: The first equivalent circuit model of FSS.

Using the well-known expression of the input impedance for a shorted transmission line [12-13], and as βh << 1, tan (βh) ≈ βh, where β is the phase constant and h the thickness of the substrate. The GDS impedance $Z_{GDS}$ of the thin dielectric for the two models is computed as in (2).

$$Z_{GDS} = j\omega L_{GDS} = j\omega\mu_0 h \qquad (2)$$

In order to calculate $Z_{FSS}$, the first equivalent circuit model may be obtained as follows: the coupling between two adjacent metallic lines can be modeled as a capacitor, whereas a thin conductor line can be modeled as an inductor. Thus, the equivalent circuit model for $Z_{FSS}$ (between A and B) can be modeled as in fig. 4.
The basic equations for the lumped components values have been proposed in [8] for capacitance by (3):

$$C_{gi} = \frac{L\varepsilon_\circ(1+\varepsilon_r)}{\pi}\cosh^{-1}\left(\frac{L+g_i}{g_i}\right) \quad i=1,2 \qquad (3)$$

where $\varepsilon_0 = 4\pi \times 10^{-12}$ F/m, L is the conductor length, $\varepsilon_r$ is the dielectric constant and gi is the gap between the two squares: $g_1 = 2G_1$ and $g_2 = G_2$.
The inductance is given [16] by (4):

$$l_{gi} = L\frac{\mu_\circ}{4\pi}\ln\left\{1+\frac{32h^2}{w_i^2}\left[1+\sqrt{1+\left(\frac{\pi w_i^2}{8h^2}\right)^2}\right]\right\} i=1,2 \qquad (4)$$

where $\mu_0 = 4\pi \times 10^{-7}$ H/m, w is the conductor width:
$w_1 = (L_1-(L_2+(2*G_2)))/2$ and $w_2=L_2$.
Finally, the inductances are as follows:

$$\begin{cases} L_{g1} = k\ l_{gi} \\ L_{g2} = k\ l_{gi} \end{cases} \qquad (5)$$

where k represents a correction term.

The **second** equivalent circuit model proposed by Langley et al. [20] for double square loops FSS is presented in fig. 5.

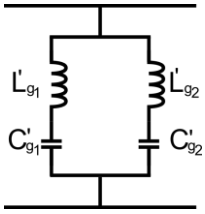



Figure 5: The second equivalent circuit model of FSS.

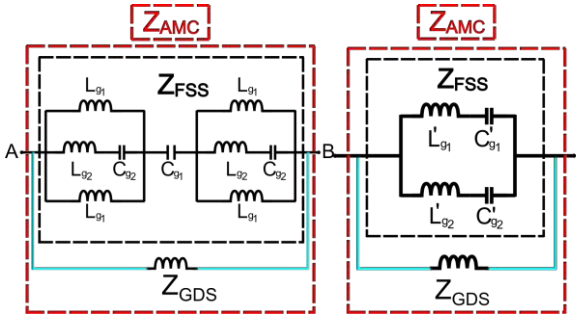
The equivalent circuit of the double loops FSS is modeled as a combination of capacitors and inductors in series and parallel as presented in fig. 5. The same combination is used in this work to calculate $Z_{FSS}$, but replacing the inner loop by a square.
$L'_{g1}$, $L'_{g2}$, are calculated applying (5) using the same width w used for the first model, without correction term (k = 1).
The capacitances $C'_{g1}$ and $C'_{g2}$ are calculated using (3) where:

$$\begin{cases} C'_{g1} = k'_1\ C_{g1} \\ C'_{g2} = k'_2\ C_{g2} \end{cases} \qquad (6)$$

With $k'_1$ and $k'_2$ representing the correction terms[20].

The correction terms used in the two models do not change when different substrates are used or when changing the dimensions of the FSS.

The ECM for the AMC is shown in Fig. 6(a) for the first model and in Fig. 6(b) for the second one.




(a) (b)

Figure 6: The final equivalent circuit model of AMC: (a) first (b) second.

## 3. Validation of the two models

### 3.1. Validation for Neltec substrate

In order to validate the accuracy of the analytical models proposed in the previous section, an AMC on Neltec substrate ($\varepsilon_r$ = 2.2, tanδ = 0.0009 and h = 3.15 mm) has been designed, manufactured and measured. The reflection coefficient phase of both models has been compared with the ones obtained using two full-wave numerical simulations (Ansoft HFSS [21] and CST Microwave studio [22]) and with measurements.

The simulation setup consists in drawing a unit cell of the structure with boundary conditions to assure an infinite periodic structure, excited by a source of an incident plane wave. The reflection coefficient phase cancels at the resonance frequencies of the AMC (denoted $F_L$ and $F_H$, for low and high frequencies). The structural parameters of the proposed FSS sample are selected as follows: $L_1$ = 24.5 mm, $L_2$ = 15.14 mm, $G_1$ = 2.05 mm, $G_2$ = 1 mm and P = 28.6 mm to achieve the 0° phase around 2.5 GHz and 5.5 GHz (Wi-Fi application).

For experimental validation, a 5 x 5 unit cells AMC on Neltec substrate with 143 mm x 143 mm dimensions was manufactured using a laser micromachining (Fig. 2(b)). The prototype has been measured in a RCS measuring chamber in quasi normal incidence from 2 GHz to 3 GHz and from 3.5 GHz to 6.5 GHz. After that, it has been compared with reference measurement (metallic plate) in a far field conditions using the same methodology presented in [6].

The reflection coefficient phases resulting from the equivalent circuit models, the simulations (HFSS and CST) and the measurements of the dual band structure on Neltec are shown in Fig. 7. As it can be observed, the two models are in good agreement with the simulations and measurement.

Table 1: ECMs, Simulations and Measurements $S_{11}$ Phase Results on Neltec

| Neltec | $F_L$ | $F_H$ |
|---|---|---|
| HFSS (GHz) | 2.56 | 5.53 |
| CST (GHz) | 2.55 | 5.51 |
| Measurement (GHz) | 2.55 | 5.46 |
| Model 1 (GHz) | 2.51 | 5.68 |
| Model 2 (GHz) | 2.60 | 5.59 |
| Error Model 1 Vs Meas (%) | 1.56% | 4.00% |
| Error Model 2 Vs Meas (%) | 1.96% | 2.38% |

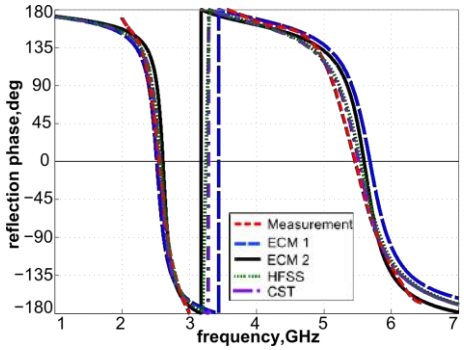



Figure 7: The comparison between ECM1, ECM2, simulations and measurements results of the AMC on Neltec substrate.

Accuracy between the two models and measurement is carried out by calculating the relative error:

$$error(\%) = \left| \frac{f_r^{ECM} - f_r^{Meas}}{f_r^{Meas}} \right| \times 100 \quad (7)$$

Low frequency, high frequency (HFSS, CST, measurement and models results) and accuracy comparison are gathered in Table 1.

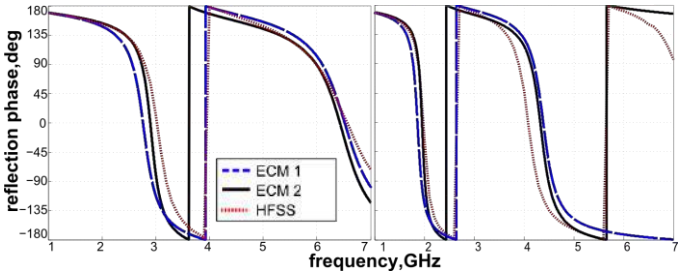
Using the first model, the resonant frequency is adequately predicted to within 1.56% at the lower bandwidth (2.55 GHz) and to within 4% at the upper bandwidth (5.5 GHz), while using the second model, the resonant frequency is adequately predicted to within 1.96% at the lower bandwidth and to within 2.38% at the upper bandwidth.

### 3.2. Validation for different substrates

In order to validate the model for different substrates, two AMCs on Felt ($\varepsilon_r$ = 1.22, tanδ = 0.016, h = 4 mm) and Getek (εr = 3.9, tanδ = 0.012, h = 4 mm), have been designed having the same dimensions on Neltec. For each substrate, the results of the reflection coefficient phase have been compared with HFSS and plotted respectively in Fig. 8(a) and Fig. 8(b). In addition, the resonance frequencies obtained by ECMs and HFSS have been summarized in table 2.

Table 2: ECMs and simulations $S_{11}$ phase on felt and getek

| Substrate | Felt | | Getek | |
|---|---|---|---|---|
| | $F_L$ | $F_H$ | $F_L$ | $F_H$ |
| HFSS (GHz) | 3.02 | 6.56 | 1.99 | 4.10 |
| Model 1 (GHz) | 2.76 | 6.51 | 1.86 | 4.38 |
| Model 2 (GHz) | 2.90 | 6.43 | 1.95 | 4.32 |




(a) (b)

Figure 8: The comparison between ECM 1, ECM 2 and HFSS for different substrate: (a) Felt and (b) Getek.

The accuracy comparison in terms of relative errors has been studied. For Felt, the resonance frequency is adequately predicted to within 8.91% for model 1 and 4.29% for model 2 at the lower bandwidth and to within 1.06% for model 1 and 2.27% for model 2 at the upper bandwidth.

For the Getek, the highest error is 7% for model 1 and 2.5% for model 2 at the lower bandwidth and to within 6.82% for model 1 and 5.36% for model 2 at the upper bandwidth.

One can note that the obtained results using the two proposed models are in good agreement with the simulated ones. However, the frequency shift in the case of Felt and Getek is slightly higher than the one in the case of a Neltec. This is mainly due to the correction terms were chosen based on the Neltec substrate.

### 3.3. Parametric study of the structure for Neltec Substrate

The resonance frequencies of the structure are mainly determined by four parameters $L_1$, $L_2$, $G_1$ and $G_2$. In order to validate the models for these parameters and to see the behavior of the structures, a parametric study has been carried out for different substrates and both models. Fig. 10 only shows the reflection coefficient phase simulated with model (ECM2) and HFSS, for Neltec substrate. The results show that $L_1$ and $L_2$ are respectively responsible for the lower and upper resonance frequencies while $G_2$ is responsible for both. Furthermore, the figure shows that as $G_1$ increases the bandwidth decreases.

Comparing model 2 with HFSS simulation, close agreement and same behavior are obtained at the two resonant frequencies (2.5 GHz and 5.5 GHz) for $L_1$, $L_2$ and $G_1$. At the upper resonance (5.5 GHz), the model is less satisfied for $G_2$. However, in order to control the upper resonant frequency when designing the double concentric square AMC structure using these models, $L_2$ can be used.

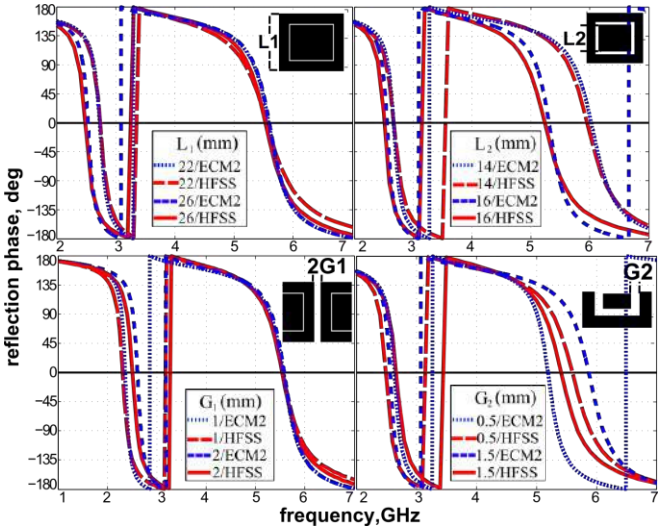



Figure 9: ECM2 and HFSS reflection coefficient phase on Neltec for different design parameters.

It should be noticed that both models are able to predict the resonance frequencies of the double square AMC. Nevertheless, the second model is closer to the measured results. This is due to the more precise correction terms used in this model. Moreover, from a physical point of view, the first model is more representative of the AMC geometry since it takes into account the metallization form in the AMC.

## 4. Conclusions

Two equivalent circuit models based on transmission line theory for normally incident waves have been proposed in order to estimate the resonance frequencies and reflection phase diagram of the double concentric square AMC. The validity of these proposed models has been verified by numerical and experimental comparisons for different substrates and checking their accuracy. A parametric study has been also discussed.

## References


[1] D. Sievenpiper, L. Zhang, R. F. J. Broas, N. G. Alexopolous, and E. Yablonovitch, "High-impedance electromagnetic surfaces with a forbidden frequency band," *IEEE Trans. Microw. Theory Tech.*, vol. 47, no. 11, pp. 2059–2074, Nov. 1999.

[2] W. Yang, H. Wang, W. Che, and J. Wang, 'A wideband and high-gain edge-fed patch antenna and array using artificial magnetic conductor structures', IEEE Antennas Wireless Propag. Lett, 2013, **12**, pp. 769–772.

[3] K. Kamardin, M. K. A. Rahim, P.S. Hall, N. A. Samsuri, M. E. Jalil and M. F. Abd. Malek, "Textile Diamond Dipole and Artificial Magnetic Conductor Performance under Bending, Wetness and Specific Absorption Rate Measurements", Radioengineering, Septembre 2015, **24**,(3), pp. 729-738.

[4] S. Zhu, R. Langley, "Dual-band wearable textile antenna on an EBG substrate," *IEEE Trans. Antennas Propagat.*, vol.57, no.4, pp. 926–935, 2009.

[5] M. Mantash, A. C. Tarot, S. Collardey, and K. Mahdjoubi, "Dual-band CPW-fed G-antenna using an EBG structure," *in Proc. LAPC*, 2010, pp. 453–456.

[6] M. Mantash, M.E. de Cos, A.C. Tarot, S. Collardey, K. Mahdjoubi and F. Las-Heras, "Dual-band textile hexagonal artificial magnetic conductor for WiFi wearable applications," *in Proc. 6th EuCAP*, Prague, Czech Republic, Apr. 2012, pp. 1395-1398.

[7] P. S. Hall and Y. Hao: 'Antennas and Propagation for Body Centric Communications Systems', 2nd ed. London (UK): Artech House, 2012, p. 63–64.

[8] F. Yang and Y. Rahmat-Samii, "*Electromagnetic Band Gap Structures in Antenna Engineering*," Cambridge University Press, 2009.

[9] A. P. Feresidis, S. Wang, and J. C. Vardaxoglou, "Artificial magnetic conductor surfaces and their application to low profiles high-gain planar antennas," *IEEE Trans. Antennas Propag.*, vol. 53, no. 1, pp. 209–215, Jan. 2005.

[10] M. E. de Cos, F. Las-Heras , "On the advantages of loop-based unit-cell's metallization regarding the angular stability of artificial magnetic conductors,". *Appl. Phys. A*, 118, pp. 699–708, 2015.

[11] G. Goussetis, A. P. Feresidis, and J. C. Vardaxoglou, "Tailoring the AMC and EBG characteristics of periodic metallic arrays printed on grounded dielectric substrate," *IEEE Trans. Antennas Propag.*, vol. 54, no. 1, pp. 82–89, Jan. 2006.

[12] M. Hosseinipanah and Q. Wu, "Equivalent Circuit Model for Designing of Jerusalem Cross-Based Artificial Magnetic Conductors," *Radioengineering*, Vol. 18, no. 4, pp. 544–550, 2009.

[13] C. R. Simovski, P. D. Maagt, I. V. Melchakova, ' High impedance surfaces having stable resonance with respect to polarization and incidence angle', IEEE Transaction on Antennas Propagation, 2005, **53**, (3), pp. 908-914.

[14] I. Anderson, "On the theory of self-resonant grids," *Bell Syst. Tech. J.*, vol. 54, no. 4, pp. 1725–1731, 1975.

[15] M. Grelier, F. Linot, A.C. Lepage, X. Begaud, J.M. Le Mener and M. Soiron, "Analytical methods for AMC and EBG characterisations," *Appl. Phys. A*, 103(3), pp. 805–808, 2011.

[16] F. Costa, S. Genovesi, and A. Monorchio, "On the bandwidth of printed frequency selective surfaces for designing high impedance surfaces," *in Proc. Antennas and Propagation Society International Symposium*, Charleston, South Carolina, 2009, pp. 1–4.

[17] F. Costa, S. Genovesi, and A. Monorchio, "On the bandwidth of high-impedance frequency selective surfaces," *IEEE Antennas Wireless Propag. Lett.*, vol. 8, pp. 1341–1344, 2009.

[18] F. Costa, A. Monorchio, and G. Manara, "An equivalent circuit model of frequency selective surfaces embedded within dielectric layers," in Proc. IEEE Antennas Propag. Soc. Int. Symp., Charleston, SC, Jun. 2009, pp. 1–4.

[19] R. J. Langley and E. A. Parker, "Equivalent-circuit models for arrays of square loops," *Electronics Letters*, vol. 18, no. 7, pp. 294–296, 1982.

[20] R. J. Langley and E. A. Parker, "Double-square frequency-selective surfaces and their equivalent circuit," *Electronics Letters*, vol. 19, no. 17, pp. 675–677, 1983.

[21] Ansys HFSS, From Ansoft Corporation, http://www.ansys.com.

[22] CST Microwave Studio, http://www.cst.com.

# Modeling, Computational Techniques and Verification of Theory

# Discontinuous Galerkin Time Domain Methods for Nonlocal Dispersion Models and Electron Beam Modeling in the Context of Nanoplasmonics

**S. Lanteri**[1], **C. Scheid**[1,2], **N. Schmitt**[1,2,†], **and J. Viquerat**[1]

[1]INRIA Sophia Antipolis-Méditerranée Research Center, France
[2]Universtity of Nice-Sophia Antipolis, France
[†]nikolai.schmitt@inria.fr

**Abstract**— We present recent advancements of the development of our DGTD solvers for computational nanophotonics, particularly for metallic nanostructures irradiated by laser pulses or electron beams. By this means, we firstly discuss the numerical treatment of a nonlocal dispersion model for the electron gas which is necessary for structures in the regime of 2 nm to 25 nm. Subsequently, we deal with the modeling of electron beams in 3D simulations for e.g. electron energy loss spectroscopy or cathodoluminescence.

## 1. INTRODUCTION

The relatively new field of nanophotonics has gained significant importance in the last twenty years. Mainly due to technological advancements on the fabrication side that do now allow the controlled manufacturing of detailed nanostructures for photonic experiments and applications.

Computational nanophotonics is mainly concerned with the accurate modeling of the appearing physical effects in the frequency range of interest and the subsequent solution of the modeling equations. This allows access to detailed understanding of microscopic effects which are fairly often extremely hard to obtain via measurements. Hence, appropriate physical and mathematical models allow systematic optimization, uncertainty quantification, and many other kinds of studies that can be performed at relatively low costs compared to experiments.

Our here presented contribution is the continuation of the presented work in [1]. For the considered geometry and frequency regime, we model electromagnetics by macroscopic Maxwell's equations with additional material equations for the electron gas of the metal structure. Depending on the geometrical size different models have to be considered. We present recent results of time domain simulations of a nonlocal dispersion (also known as nonlocal Drude) model for structures in the regime of approx. 2 nm to 25 nm. The second part of this work deals with the modeling of electron beams for structures in the regime of approx. 20 nm to 500 nm where local dispersion (e.g. Drude, Drude-Lorentz) models are appropriate. In order to efficiently and precisely solve the above-mentioned equations we use a special time domain Finite Element (FE) method. This method is referred to as Discontinous Galerkin (DG) method. The DG method is easily parallelizable, allows local mesh refinement, conforming meshes, curvilinear elements, etc. and can thus precisely handle large structures in reasonable computational times on modern cluster computers.

## 2. DISCONTINOUS GALERKIN TIME DOMAIN METHOD

The DG Time Domain (DGTD) method is based on a local FE formulation with particular basis functions [2]. This leads to discontinuous solutions in contrast to classical FE methods. Due to the local formulation of DGTD methods only local mass matrices are inverted which yields a significant advantage by means of computational efficiency in comparison to continuous FE methods. Hence, DGTD methods can combine high order basis functions with explicit time stepping and unstructured meshes where the latter is particularly important for complex geometries.

## 3. NONLOCAL DISPERSION MODEL

Nonlocal dispersion models model the nonlocal nature, i.e. mutual electron interaction in the electron gas for metallic nanostructures. In contrast to local models (Drude, Drude-Lorentz,...), nonlocal models take the microscopic electron interaction directly into account and allow additional solutions by means of electron density waves that can travel inside the bulk. [4, 3] The underlying equa-

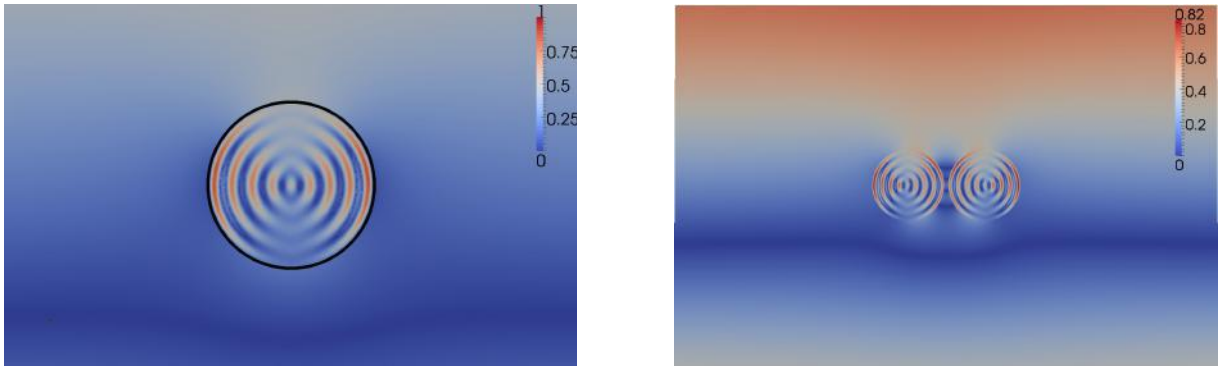



Figure 1: Fourier transformed field plot of $|\mathbf{E}|$ at $\omega = 1.1963\ \omega_\mathrm{p}$. The left plot shows the bulk plasmon mode for an single infinitely long nanowire and the right plot two coupled wires. The coupling of the two wires in terms of the mode pattern is obvious.

tions are:

$$\begin{aligned} \nabla \times \mathbf{H} &= \partial_t \mathbf{D}, \\ \nabla \times \mathbf{E} &= -\mu_0 \partial_t \mathbf{H}, \end{aligned} \tag{1}$$

$$\begin{aligned} \partial_t \mathbf{D} &= \varepsilon_0 \varepsilon_\infty \partial_t \mathbf{E} + \mathbf{J}, \\ \omega_\mathrm{p}^2 \varepsilon_0 \partial_t \mathbf{E} &= \partial_{tt} \mathbf{J} + \gamma \partial_t \mathbf{J} - \beta^2 \nabla(\nabla \cdot \mathbf{J}), \end{aligned} \tag{2}$$

where (2) is a linearized nonlocal Drude model. Here, $\mathbf{H}$, $\mathbf{D}$, $\mathbf{E}$, $\mathbf{J}$, $\mu_0$, $\varepsilon_0$, $\varepsilon_\infty$, $\omega_\mathrm{p}$, $\gamma$, and $\beta$ respectively are the magnetic field, electric displacement, electric field, polarization current, vacuum permeability, vacuum permittivity, relative permittivity at infinite frequencies, plasma frequency, damping constant, and the quantum parameter.

We have successfully implemented equations (1) and (2) in our DG time domain framework. Figure 1 shows the electric field distribution for a single and coupled infinitely long nanowire.

## 4. ELECTRON BEAM MODELING

The second part of our contribution addresses the modeling of electron beams in the context of nanoplasmonics. Electron beams traveling in the vicinity or even penetrating plasmonic structure excite plasmons. Microscopy techniques like Electron Energy Loss Spectroscopy (EELS) and Cathodoluminescence (CL) exploit this effect in order to measure/map plasmonic mode patterns [5]. We have recently implemented electron beams and the modeling of EELS as well as CL into our DG time domain framework. First simulation results will be presented.

## ACKNOWLEDGMENT

The authors gratefully acknowledge support from the University of Nice-Antipolis which funds N. Schmitt.

## REFERENCES

1. Lanteri, S., Scheid C., Viquerat J., "Numerical Modeling of Light/Matter Interaction at the Nanoscale with a High Order Finite Element Type Time-domain Solver," *PIERS Proceedings*, Prague, Czech Republic, July 2015, 2235-2241.
2. Fezoui, L., S. Lanteri, S. Lohrengel, and S. Piperno, "Convergence and stability of a discontinuous Galerkin time-domain method for the 3D heterogeneous Maxwell equations on unstructured meshes," *ESAIM: Math. Model. Numer. Anal.*, Vol. 39, No. 6, 11491176, 2005.
3. Schmitt, N., Scheid C., Lanteri, S., Viquerat, J., and Moreau, A., "A DGTD method for the numerical modeling of the interaction of light with nanometer scale metallic structures taking into account non-local dispersion effects," *Research Report*, INRIA Sophia Antipolis, Project-team NACHOS, 2015.
4. Jauho A.-P., Wubs M. Mortensen N. A., Raza S., Toscano G., "Unusual resonances in nanoplasmonic structures due to nonlocal response," *arXiv:1106.2175v2 [cond-mat.mes-hall]*, 2011.
5. Garcia de Abajo, F. J., "Optical excitations in electron microscopy," *Review of Modern Physics*, Vol. 82, No. 1, 209-275, 2010.

# Modeling of periodically-structured fiber-reinforced laminates with multiple fibers absent

**Z.C. Liu**[1], **C.Y. Li**[2], **D. Lesselier**[1], **and Y. Zhong**[3]

[1]Laboratoire des Signaux et Systèmes, UMR8506 CNRS-CentraleSupélec-Université Paris Sud, Université Paris Saclay, 3 rue Joliot-Curie, 91192 Gif-sur-Yvette, France

[2]BioMedical-Electromagnetics Group, Engineering Product Department, Singapore University of Technology and Design, 8 Somapah Road, 487372 Singapore

[3]A*STAR, Institute of High Performance Computing, 138632 Singapore

zicheng.liu@l2s.centralesupelec.fr

**Abstract**— Electromagnetic modeling of periodically-structured, fiber-reinforced laminates with some fibers missing is investigated, this applying as well to similarly disorganized photonic crystals. Parallel fibers are periodically positioned in a layer between two half-spaces. Absent fibers destroy the periodicity. The supercell concept involving an auxiliary periodic structure and first-order approximations calling for the Green function of the sound structure provide complementary solutions, as it will be illustrated by comprehensive numerical simulations.

Fiber-reinforced laminate composites are widely used due their stiffness and strength. For reliable usage, electromagnetic modeling and imaging of defects in them are necessary yet remain a challenge (going from MHz to THz frequency ranges as a function of the composites tested). Also, due to similarities in terms of organization, methods developed for such composites apply to man-made photonic crystals and optical regimes, e.g., [1][2], and their behavior in case of disorganization is of interest as well. Accurate forward analysis and stable inversion algorithms with pertinently high resolution (upon availability of near-field data) are then needed. Focus here is put on the former, yet the latter is kept in mind especially since we aim at situations of potential practical interest.

The laminated structure which one is concerned with is made of finitely-thick planar layers sandwiched between air half-spaces as terminations. Within each layer (matrix), longitudinally-orientated circular cylindrical fibers of same cross-section are periodically embedded along the transverse direction. Fiber orientation and radius may differ from one layer to another, which adds to the complexity of the analysis. The present work is on the single-layer case as a first step, the aim being to analyze the electromagnetic behavior of the disorganized one when a finite number of fibers is absent (one at least, possibly a few near one another or well apart), refer to the left sketch in Figure 1, the modeling of the sound structure (no missing fibers) being analyzed in [3].

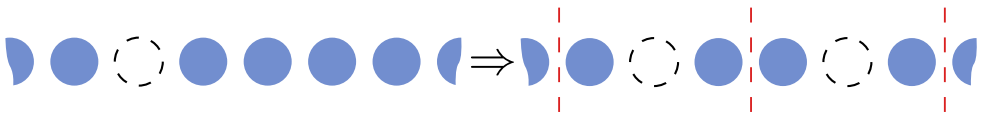


Figure 1: Sketch for the composition of super-cell periodic structure, $L = 3$.

For most methods that are dealing with periodic structures as discussed in aforementioned contributions and references therein including, e.g., [4], the Floquet theorem is applied from the field pseudo-periodicity so that the field analysis can be focused onto the primary unit. However, since the periodicity is destroyed from absent fibers, this favorable prior knowledge becomes irrelevant.

Upon introduction of the concept of supercell, defined as a cell including multiple fibers and defects within the central area, denoted by the area bounded by dashed lines in the right sketch of Figure 1, this can be overcome. Repeating the supercell along the transverse direction, a new periodic structure is obtained. Enlarging the number of fibers in a given supercell (including absent ones), $L$, the field within the central region of the supercell, and above or below it (at least close enough to the interfaces) is expected to converge to the true field, for planar, beam and line sources, for TM polarization (electric field with longitudinal component only) and dual TE one.

Yet proper conditions of convergence should be met, depending upon operation frequencies, illuminations, materials and geometry. The approach in [1] is similar with the one to be followed in the field analysis of the supercell periodic structure. The key difference is that, despite mutual scattering from other periodic cells, the coupling among fibers inside the supercell has to be taken into account. This generates an infinite series of specific form, or relative lattice sum [5], with known slow convergence, and a fast computational approach is then put forth. The total electric field inside and outside the supercell follows.

In parallel, the Green function as the response of the non-damaged laminate to a line source set anywhere in space (with the help of reciprocity) can be computed. The source is an integration of elementary plane waves with different weights and propagation constants, and the total scattered field follows as a Fourier-type spatial wavenumber integration of elementary scattered fields.

No closed form expression is available in the above situation, while singularities of the integrand, e.g., [4][6], associated to more or less peculiar wavefield behaviors emerge within a properly cut wavenumber complex plane, those possibly associated to sharp peaks along the real line of integration —and slow decrease along it when interested into very near fields—, and the easier to deal with, the lossier the matrix (for composites, e.g., with epoxy, the loss tangent is small yet is not negligible). An adaptive numerical integration can thus be run, while detouring like along the revised original path (ROP) [7] or according to fancier techniques [8] to manage the Fourier integral in computationally efficient way can be employed.

Then, since the missing fibers are of small cross-sectional areas, a first-order approach can be developed, now involving only primary fields at the centers of the missing fibers and Green's functions with sources at these centers and observations at assumed locations set outside the laminate —data are usually collected along a line parallel with the upper interface, in multi-static multi-frequency reflection mode, the sources with spatial and frequency diversity being set in the upper half-space.

A detailed theoretical and numerical analysis of the two proposed models will be found within the extended contribution.

**REFERENCES**


1. Li, C.Y., D. Lesselier, and Y. Zhong, "Recursive matrix schemes for composite laminates under plane-wave and Gaussian beam illumination," *J. Opt. Soc. Amer. B.*, Vol. 32, No. 8, 1539-1549, 2015.
2. Li, C.Y., D. Lesselier, and Y. Zhong, "Full-wave computational model of electromagnetic scattering by arbitrarily-rotated 1-D periodic multilayer structure," *IEEE Trans. Antennas Propagat.*, IEEE Early Access Articles, 2016.
3. Li, C.Y., D. Lesselier, and Y. Zhong, "Electromagnetic small-scale modeling of composite panels involving periodic arrays of circular fibers," *Appl. Phys. A*, Vol. 117, No. 2, 567-572, 2014.
4. Groby, J-P., A. Wirgin, L. De Ryck, W. Lauriks, R. P. Gilbert, and Y. S. Xu, "Acoustic response of a rigid-frame porous medium plate with a periodic set of inclusions," *J. Acoust. Soc. Amer.*, Vol. 126, No. 2, 685-693, 2009.
5. Botten, L. C., N.-A. P. Nicorovici, A. A. Asatryan, R. C. McPhedran, C. Martijn de Sterke, and P. A. Robinson, "Formulation for electromagnetic scattering and propagation through grating stacks of metallic and dielectric cylinders for photonic crystal calculations. Part I. Method," *J. Opt. Soc. Am. A*, Vol. 126, No. 2, 2165-2176, 2000.
6. Watanabe, K., and K. Yasumoto, "Two-dimensional electromagnetic scattering of non-plane incident waves by periodic structures," *PIER*, Vol. 74, 241-271, 2007.
7. Cui, T. J., and W. C. Chew, "Fast evaluation of Sommerfeld integrals for EM scattering and radiation by three-dimensional buried objects," *IEEE Trans. Geoscie. Remote Sensing*, Vol. 37, No. 2, 887-900, 1999.
8. Zhong, Y., P.-P. Ding, M. Lambert, D. Lesselier, and X. Chen, "Fast calculation of scattering by 3-D inhomogeneities in uniaxial anisotropic multilayers," *IEEE Trans. Antennas Propagat.*, Vol. 62, No. 12, 2415-2428, 2014.

# Disordered metamaterials achieve broadband enhancement of quantum efficiency of photoelectrochemical devices for water splitting

**M. Bonifazi**[1], **H.C. Fu**[2], **J.H. He**[2†], **A. Fratalocchi**[1‡]

[1]PRIMALIGHT, Faculty of Electrical Engineering; Applied Mathematics and Computational Science, King Abdullah University of Science and Technology (KAUST), Thuwal, Saudi Arabia
[2]Computer, Electrical, and Mathematical Science and Engineering (CEMSE), King Abdullah University of Science and Technology (KAUST), Thuwal, Saudi Arabia
[†] jrhau.he@kaust.edu.sa
[‡]andrea.fratalocchi@kaust.edu.sa

**Abstract**— By Finite-Difference Time-Domain (FDTD) simulations and experiments, we study a new surface nanostructuring process for photoelectrochemical devices for the production of hydrogen from water splitting. Our material is based on suitably disordered micro-structures that achieve a broadband reflectivity reduction across the visible and near infrared, leading to broadband optical quantum efficiencies (QEs) up to 95%.

### Introduction

In past years the global demand for energy has been increasing steeply, and the interest in photoelectrochemical (PEC) devices for water splitting has been growing fast [1]. One of the main challenge in optimizing the quantum efficiency (QE) of these devices lies in minimizing the optical losses occurring at the PEC interfaces in contact with water[2]. These are composed by layers of silicon and photocatalyst, with the photocatalyst usually made by platinum (Pt).
In this study we present a novel strategy for minimizing the reflectivity from these surfaces. Our approach employs suitably disordered micro-structures. Finite Difference Time Domain (FDTD) simulations and experiments shows that this strategy reduces reflectivity up to 40% in a broad optical window between 400 nm and 900 nm wavelengths, leading to QEs up to 95%.

### Results and Conclusion

Parallel FDTD simulations are carried out by our dispersive FDTD code NANOCPP [4]. To guarantee realistic results, we modeled point by point the dispersion curves of the materials employed in the simulations by using existing measurements available in the literature [3]. We considered two different types of interfaces: water/Pt/Si interface and water/$SiN_x$/$Al_2O_3$/Si. These different interfaces typically characterize the top or bottom structure of realistic PEC devices, where the water/Pt/Si is where the reduction of hydrogen occurs, while the water/$SiN_x$/$Al_2O_3$/Si is the interface typically exposed to sunlight. The high reflectivity of the Pt hampers the possibility to achieve high quantum efficiency in a back illuminated architecture, where light is directly injected on the photocatalysts side.
Figures 1a-b illustrate FDTD models of nanostructured surfaces used in our study to minimize light reflections at these interfaces. In our simulations, we investigated a realistic scenario by considering nanostructuring processes that can be experimentally realized. In Si/Pt surface of the device (Fig. 1a), we used a random, gaussian-correlated disorder with correlation length of 1$\mu$m and average surface height of 800 nm. On the water/$SiN_x$/$Al_2O_3$/Si surface (Fig. 1b), conversely, we consider random aggregates of micropyramids made by $SiN_x$, with average height of 500 nm and width of 600 nm. All parameters (correlation length, average height, pyramid width and heigh) are taken from SEM images of fabricated structures.
Figures 1c-d reports the reflectivity spectra of the two surfaces (solid lines), which have been averaged over many disorder configurations. Average spectra are then compared with experimental results on fabricated samples (circle markers). Theory and experiments agree quite well, showing the possibility to achieve a broadband reduction of the reflectivity to very low values if compared to a planar structure constituted by the same materials, as it is shown in Figures 1e-f. In both cases reflectivity is highly diminuted, reaching a 40% average decrease in Si/Pt case, and it is a

broadband effect (Fig. 1e, solid red line). In the interface with water/$SiN_x$/$Al_2O_3$/Si, we observe a flattening of the reflectivity over the whole visible spectrum to values as low as 3% (Fig. 1f, solid red line). This improves considerably the performances of a planar layer made by the same materials, which show a low reflectivity only between 600 nm and 700 nm (Fig. 1f, blue solid line). The surface plot of the distribution of energy inside the device is presented in Figures 1g-h. (Si/Pt and $SiN_x$/$Al_2O_3$/Si respectively). As we observe in these figures, a considerable amount of energy is transmitted inside the device thus increasing the optical generation rate and the quantum efficiency of the system. These result open the development of a new generation of high performances, eco-friendly and cost-effective water splitting PEC devices.

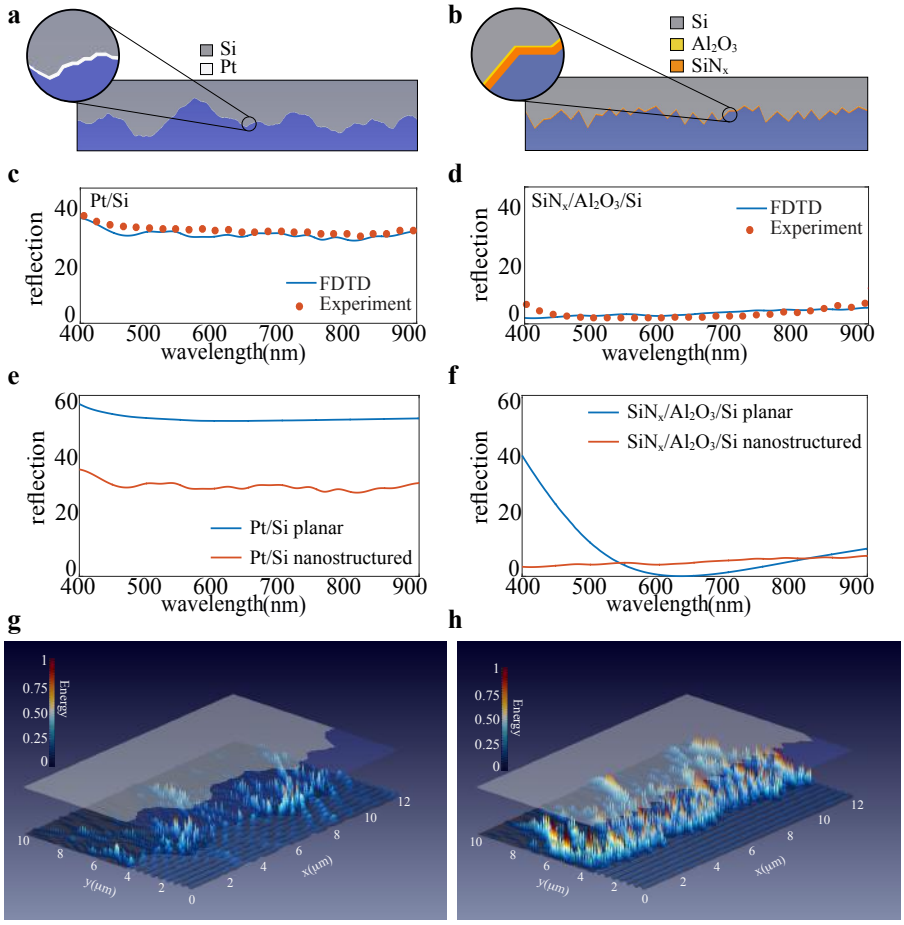



Figure 1: Simulation results for a fabricated water splitting device. a - b: Examples of the complex surfaces used in the simulations. c - d: Reflectivity comparison between experimental data and FDTD results. e - f: Reflectivity spectra from planar and micro-structured surfaces made up by the same materials, solid blue lines and solid red lines respectively. g - h: Distribution of energy inside the device once illuminating it one side at a time. All the left side figures refer to Si/Pt surface while right side figure refer to $SiN_x$/$Al_2O_3$/Si.

**REFERENCES**


1. Caban-Avacedo, M., et al,"Efficient hydrogen evolution catalysis using ternary pyrite-type cobalt phosphosulphide", *Nat. Mat.*, Vol. 27, 6511-6518, 2015.
2. Ding, Q., et al, "Designing efficient solar-driven hydrogen evolution photocathodes using semi-transparent $MoQ_xCl_y$ (Q=S,Se) catalysts on Si micropyramids", *Adv. Mat.*, Vol. 14, 1245-1251, 2015.
3. Palik, E. D., "Handbook of Optical Constants of Solids", Academic Press, Boston, 1985
4. Liu, C., et al. "Enhanced energy storage in chaotic optical resonators", *Nat. Photonics*, Vol. 7, 473-478, 2013.
5. Liu, C., et al. "Harnessing structural darkness in the visible and infrared wavelengths for a new source of light", *Nat. Nanotech.*, Vol. 11, 60-66, 2016.

# Symmetry Analysis for Metamaterials with Periodic Microstructure

**Pu Zhang**[*]
School of Mathematics, The University of Manchester, Manchester M13 9PL, UK
[*]corresponding author: pu.zhang@manchester.ac.uk

**Abstract**-Lattice materials with periodic microstructures are the most popular metamaterials such as phononic/photonic crystals and auxetic materials. A fundamental property of these periodic metamaterials is their symmetry, which will inevitably affect their physical behaviors. This work aims at establishing a mathematical framework to analyze the point group symmetry of such kind of metamaterials. In addition, the symmetry breaking is also studied for reconfigurable metamaterials, which has potential application in designing tunable metamaterials.

Lattice materials are widely used in the field of metamaterials to design phononic/photonic crystals, auxetic materials, and among others. The microstructure of these periodic metamaterials can be tailored in favor of the desired properties, which provide enormous space for their application in engineering. A fundamental problem of these periodic metamaterials is their symmetry [1], which affects their overall physical behaviors including mechanical, electrical, and optical aspects. However, the symmetry property of lattice materials is more complex than crystals, which depends not only on the designed geometry but also on the material composing the metamaterials. Hence, it is quite necessary to develop a point group symmetry theory for lattice materials to analyze the symmetry properties of metamaterials with periodic microstructure. However, the lattice materials require both topology symmetry and material symmetry in one unit cell. To address this issue, a unified theoretical framework [2] is established to describe and determine the overall point group of lattice materials [3]. Current work reveals that the point group symmetry of lattice materials can be described by the invariant (or form-invariant) of a material type field and a material point group field. This is significantly different from the symmetry of single crystals, which only requires the invariant of the material type field. The proposed theory is applied to several examples to show the symmetry characteristics of lattice materials. In addition, the symmetry evolution and symmetry breaking of reconfigurable lattice materials is also investigated with an emphasis on the deformation-induced symmetry breaking for small strain cases [2]. The proposed theory will provide theoretical foundation for characterizing the physical properties of lattice materials and offer some guidance in designing tunable metamaterials by employing symmetry breaking.

**REFERENCES**

1. Newnham, R. E., *Properties of Materials: Anisotropy, Symmetry, Structure*, Oxford University Press, Oxford, 2005.
2. Zhang, P. and A. C. To, "Point group symmetry and deformation-induced symmetry breaking of superlattice materials," *Proc. Roy. Soc. A*, Vol. 471, No. 2182, 20150125, 2015.
3. Bradley, C. J. and A. P. Cracknell, *The Mathematical Theory of Symmetry in Solids*, Clarendon Press, Oxford, 1972

# First-order perturbation theory with analytical mode normalization for plasmonic nanoantenna arrays applied to refractive index sensing

**T. Weiss**[1], **M. Mesch**[1], **M. Schäferling**[1], **H. Giessen**[1], **W. Langbein**[2], **and E. A. Muljarov**[2]

[1]4th Physics Institute and Research Center SCoPE, University of Stuttgart, Pfaffenwaldring 57, D-70550 Stuttgart, Germany

[2]Cardiff University, School of Physics and Astronomy, The Parade, CF24 3AA, Cardiff, United Kingdom

t.weiss@pi4.uni-stuttgart.de

**Abstract**— We present a first-order perturbation theory to calculate the frequency shift and linewidth change of photonic resonances under modifications of the surrounding refractive index. Our method is based on the resonant state expansion and includes a simple analytical expression for the mode normalization. We apply our theory to calculate the sensitivity of plasmonic resonances in periodic arrays of nanoantennas for resonantly enhanced refractive index sensing.

Small changes in the concentration of molecules in a solution result in modifications of the refractive index, which can be detected optically. The changes in the optical spectra can be significantly enhanced by using resonant systems [1], in which a certain resonant feature is spectrally shifted due to the modifications of the dielectric surrounding, see figure 1a. As these changes of the dielectric surrounding are usually small, first-order perturbation theory is a quite natural approach for gaining deeper insight into the underlying physical mechanisms as well as for optimizing the designs for resonantly enhanced refractive index sensing. In particular, resolving the influence of tiny changes in the dielectric surrounding requires high numerical accuracy in solving Maxwell's equations. This is clearly detrimental in standard numerical calculations, where Maxwell's equations have to be solved subsequently for different refractive indices. In first-order perturbation theory, Maxwell's equations have to be solved only once in order to estimate the resonance shift and linewidth change as a function of analyte refractive index, thus significantly lowering the computational effort.

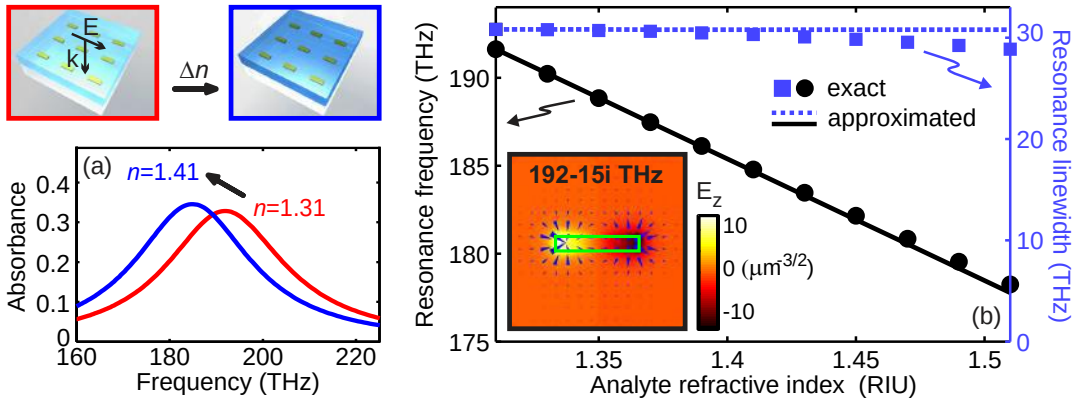



Figure 1: (a) Principle of resonantly enhanced refractive index sensing: A resonance shifts spectrally due to changes of the environment. For this example, the refractive index in a cover layer above a periodic array of gold rod antennas (see schematics on top) has been changed from $n = 1.31$ to $n = 1.41$. (b) Resonance frequency (black) and resonance linewidth (blue) as a function of the refractive index changes in the cover layer derived by first-order perturbation theory (lines) and full numerical calculations (symbols).

However, any perturbation theory requires an appropriate normalization of the modes in the unperturbed system. In standard quantum mechanics, the normalization of bound states is carried out such that integrating the absolute square value of the wavefunction over the whole space equals one. In optics, however, any mode that can radiate to the far-field possesses exponentially growing contributions towards the far-field region, so that a volume integral over the whole space diverges.

In contrast to existing approximate or numerical normalization schemes [2, 3], we present here an analytical normalization of radiating modes, in which the diverging contributions from the occurring volume integral are compensated by an appropriate surface term. Defining $\mathbf{E}_m$ as the resonant field distribution and $\omega_m$ as the corresponding complex resonance frequency, where $-2\mathrm{Im}(\omega_m)$ is the resonance linewidth, the normalization yields

$$1 = \int_{\mathcal{V}} \mathrm{d}V\, \mathbf{E}_m \cdot \left.\frac{\partial(\omega^2\varepsilon)}{\partial(\omega^2)}\right|_{\omega_m} \mathbf{E}_m + \frac{c^2}{2\omega_m} \oint_{\partial\mathcal{V}} \mathrm{d}S \left( \mathbf{E}_m \cdot \left.\frac{\partial^2 \mathbf{E}_m^{\mathrm{reg}}}{\partial s \partial \omega}\right|_{\omega_m} - \left.\frac{\partial \mathbf{E}_m^{\mathrm{reg}}}{\partial \omega}\right|_{\omega_m} \cdot \frac{\partial \mathbf{E}_m}{\partial s} \right) . \tag{1}$$

Here, $\mathbf{E}_m^{\mathrm{reg}}(\mathbf{r};\omega)$ denotes solutions of Maxwell's equations in the homogeneous and isotropic exterior regions such that $\mathbf{E}_m^{\mathrm{reg}}(\mathbf{r};\omega_m) = \mathbf{E}_m(\mathbf{r})$. Equation (1) can be further simplified for specific geometries such as single nanoantennas [4]. In the case of infinitely extended periodic systems, e.g., one- and two-dimensional periodic arrays of nanoantennas, the normalization condition can be formulated in terms of a plane wave decomposition of the resonant field distribution $\mathbf{E}_m$ in the homogeneous top and bottom half spaces.

Using the correct analytical normalization in a first-order approximation of the so-called resonant state expansion [4], the change of resonance frequency with the refractive index $n$ in a certain volume $\mathcal{T}$ becomes:

$$\frac{\partial \omega_m}{\partial n} = -\omega_m n \int_{\mathcal{T}} \mathrm{d}V \mathbf{E}_m^2 \, . \tag{2}$$

In figure 1b, we show a comparison between full numerical calculations for a periodic array of gold rod antennas carried out by the Fourier modal method [5] and the first-order perturbation theory. We find that the latter, given by equation (2) correctly approximates the dependence of the resonance frequency and resonant linewidth on the refractive index.

Our approach provides closed expressions for the sensitivity of resonances with respect to changes in the dielectric surrounding, so that we can efficiently design and optimize resonant systems for refractive index sensing applications. We will present different examples of nanoantennas and analyze the differences between dipolar and quadrupolar resonances with respect to mode sensitivity and optimal sensing volume. The correct analytical mode normalization has impact beyond refractive index sensing, as the derivation of the Purcell factor in open resonators requires the correct normalization of the modes [2, 6].

**ACKNOWLEDGMENT**

We would like to acknowledge support from ERC Advanced Grant COMPLEXPLAS as well as DFG, BMBF, Zeiss foundation, AvH foundation, MWK Baden-Württemberg, and the Baden-Württemberg Stiftung. W. L. acknowledges support by his Leverhulme Royal Society Research Fellowship (grant LT20085). E. A. M. and W. L. acknowledge support from EPSRC Impact Acceleration Account and Ser Cymru National Research Network.

**REFERENCES**

1. A. Unger and M. Kreiter, "Analyzing the performance of plasmonic resonators for dielectric sensing," *J. Phys. Chem. C,* vol. 113, pp. 12243-12251, 2009.
2. C. Sauvan, J. P. Hugonin, I. S. Maksymov, and P. Lalanne, "Theory of the spontaneous optical emission of nanosize photonic and plasmon resonators," *Phys. Rev. Lett.,* vol. 110, p. 237401, 2013.
3. Q. Bai, M. Perrin, C. Sauvan, J. P. Hugonin, and P. Lalanne, "Efficient and intuitive method for the analysis of light scattering by a resonant nanostructure", *Opt. Express,* vol. 21, pp. 27371-27382, 2013.
4. M. B. Doost, W. Langbein, and E. A. Muljarov, "Resonant-state expansion applied to three-dimensional open optical systems," *Phys. Rev. A,* vol. 90, p. 013834, 2014.
5. T. Weiss, N. A. Gippius, S. G. Tikhodeev, G. Granet, and H. Giessen, "Derivation of plasmonic resonances in the Fourier modal method with adaptive spatial resolution and matched coordinates," *J. Opt. Soc. Am. A,* vol. 28, pp. 238-244, 2011.
6. E. A. Muljarov and W. Langbein, "Exact mode volume and Purcell factor of open optical systems," *arXiv:1409.6877v3 [cond-mat.mes-hall],* 2014.

# The structural, elastic, electronic and dynamical properties of chalcopyrite semiconductor $BeGeAs_2$ from first principles calculations

**Yasemin Ö. Çiftci[1], Meryem Evecen[2]*, Emine Aldırmaz[2]**

[1]Department of Physics, Faculty of Sciences, Gazi University Teknikokullar, 06500, Ankara, TURKEY
[2]Department of Physics, Faculty of Arts and Sciences, Amasya University, 05100 Amasya, TURKEY
yasemin@gazi.edu.tr
*corresponding author: meryem.evecen@amasya.edu.tr

**Abstract**-The structural, elastic,electronic and vibrational properties of $BeGeAs_2$ with chalcopyrite structure are studied by *ab initio* calculations in the frame work of the density functional theory. The calculated ground state properties are in good agreement with the available experimental data. Pressure dependences of elastic constants and band gap are reported.

The chalcopyrite compounds of the form I-III-$IV_2$ and II-IV-$V_2$ have received significant attention in recent decades due to their high potential for applications in then on linear optics, electrooptics, and opto-electronics fields. These compounds possess several prominent features that make them interesting candidates for light-emitting diodes, solar cells, photovoltaic detectors, optical-light eliminators, lasers and modulators [1-3]. The structural, elastic, electronic and vibrational properties of $BeGeAs_2$ with chalcopyrite structure are studied by *ab initio* calculations in the frame work of the density functional theory. The calculated ground state properties are compared with the available experimental data. Pressure dependences of elastic constants and band gap are reported. The evolution of the elastic constants and the major elastic properties, Young and shear modulus, Poisson's ratios, and Zener anisotropy ratio, are described. The mechanical stability is analyzed, on the light of "Born generalized stability criteria," showing that $BeGeAs_2$ is mechanically unstable up to 50 GPa. For $BeGeAs_2$, the valance band maximum and conduction band minimum situated on different symmetry-points of the Brillouinzone, therefore indicating an indirect bandgap. The obtained phonon spectra for $BeGeAs_2$ does not exhibit any significant imaginary branches of the phonon spectrum.

**Acknowledgment,** this study was supported financially by the Research Centre of Amasya University (Project No: FMB-BAP 16-0174).

**REFERENCES**

[1] Kazmerski, L.L., NuovoCimento D. 2 2013 1983.
[2] Shay, J.L., Schiavone, L.M., Buehier, E., Wernick, J.H., J. Appl. Phys. 43 2805,1972.
[3] Horinaka, H., Mononobe, S., Yamamoto, N., Jpn. J. Appl. Phys. 32 (1993) 109.
[4] Krivosheeva, A. V., Shaposhnikov, V. L., d'Avitaya, F. A., Borisenko, V. E., & Lazzari, J. L. "Electronic and magnetic properties of Mn-doped BeSiAs2 and BeGeAs2 compounds", *Journal of Physics: Condensed Matter*, *21*(4), 045507, 2009.

# Density functional modeling studies of (E)-4-Bromo-N-(2-chlorobenzylidene)-aniline

**Hasan Tanak[1]*, Meryem Evecen[1], Emine Aldırmaz[1]**
[1]Department of Physics, Faculty of Arts and Sciences, Amasya University, 05100 Amasya, TURKEY
*corresponding author: hasantanak@gmail.com

**Abstract**- Density functional calculations of the molecular structure, atomic charges, molecular electrostatic potential, frontier orbitals and nonlinear optical properties have been performed at B3LYP/6-31G(d) level of theory for the title compound. The results of the optimized molecular structure are presented and compared with the experimental X-ray diffraction data.

Schiff-bases, having imine groups (CH=N) and benzene rings in the main chain alternately, and being π-conjugated, exhibit interest as materials for wide spectrum applications, particularly as corrosion inhibitors, catalyst carriers, thermo-stable materials, a metal ion complexing agents and in biological systems. The Schiff base compounds have been also under investigation during last years because of their potential applicability in optical communications and many of them have NLO behavior [1,2]. To investigate the reactive sites of the title compound the molecular electrostatic potential were evaluated using B3LYP/6-31G(d) method. The linear polarizability and first hyperpolarizability properties of the title compound were obtained by molecular polarizabilities basing on theoretical calculations. In addition, the atomic charges and frontier molecular of the title compound were carried out using the DFT calculations. These calculations are valuable for providing insight into molecular properties of the Schiff Base compounds.

**Acknowledgment,** this study was supported financially by the Research Centre of Amasya University (Project No: FMB-BAP 16-0175).

**REFERENCES**

1. Tanak, H. " Quantum chemical computational studies on 2-methyl-6-[2-(trifluoromethyl)phenyliminomethyl] phenol", *J. Mol. Struct. THEOCHEM*, Vol. 950, 5-12, 2010.
2. Tanak, H., Ağar, A.A., Büyükgüngör, O. " Combined experimental and DFT computational studies on (E)-1-(5-nitrothiophen-2-yl)-N-[4-(trifluoromethyl)phenyl]methanimine", *J. Mol. Struct.*, Vol. 1080, 41-50, 2013.

# Quantum chemical computational studies of (E)-N-(1-Benzothiophen-3-ylmethylidene)-2,6-dimethylaniline

**Hasan Tanak[1]***

[1]Department of Physics, Faculty of Arts and Sciences, Amasya University, 05100 Amasya, TURKEY

*corresponding author: hasantanak@gmail.com

**Abstract**- The molecular geometry of (E)-N-(1-Benzothiophen-3-ylmethylidene)-2,6-dimethylaniline in the ground state were calculated using the density functional method (B3LYP) with 6-31G(d) basis set. The calculated results show that the optimized geometry can well reproduce the crystal structure. Besides, molecular electrostatic potential nonlinear optical properties and frontier molecular orbital analysis of the title compound were investigated by theoretical calculations.

Schiff bases are an important class of organic compounds. Schiff bases have been playing an important role in the development of coordination chemistry related to catalysis and enzymatic reactions, magnetism and molecular architectures [1]. Moreover, Schiff bases have biological activities such as antimicrobial, antifungal, antitumor activities and herbicidal properties [2].

The title Schiff base compound has been synthesized and characterized by X-ray single-crystal determination [3]. The molecular geometry from X-ray experiment in the ground state has been compared using the density functional theory (B3LYP) method using the 6-31G(d) basis set. The chemical reactivity behavior of the title compound in solvent media has been examined using B3LYP method with the 6-31G(d) basis set by applying the PCM model. The nonlinear optical properties are also addressed theoretically. The molecular electrostatic potential at the B3LYP/6-311++G(d,p) basis optimized geometry has also been calculated to predict reactive sites for electrophilic or nucleophilic attack for the title compound.

**Acknowledgment,** this study was supported financially by the Research Centre of Amasya University (Project No: FMB-BAP 16-091).

**REFERENCES**

1. Miyasaka, H., Matsumoto, N., Okawa, H., Re, N., Gallo, E., and Floriani, C. " Complexes Derived from the Reaction of Manganese(III) Schiff Base Complexes and Hexacyanoferrate(III): Syntheses, Multidimensional Network Structures, and Magnetic Properties*", J. Am. Chem. Soc.,* 118, 981-994, 1996.

2. Holla, B. S., Rao, Sooryanarayana B., Shridhara, K. and Akberali, P. M. "Studies on arylfuran derivatives: part XI. Synthesis, characterisation and biological studies on some Mannich bases carrying 2,4-dichlorophenylfurfural moiety," *Farmaco,* 55, 338–344, 2000.

3. Yağcı, N.K., Dege, N., Gümüş, S., Ağar, E., Soylu, M.S. " (E)-N-(1-Benzothiophen-3-ylmethylidene)-2,6-dimethylaniline", *Acta Cryst. E*, 68, o623–o624, 2012.

# Accelerating Performances of a Waveguide Mode Solver Based on Boundary Integral Equations.

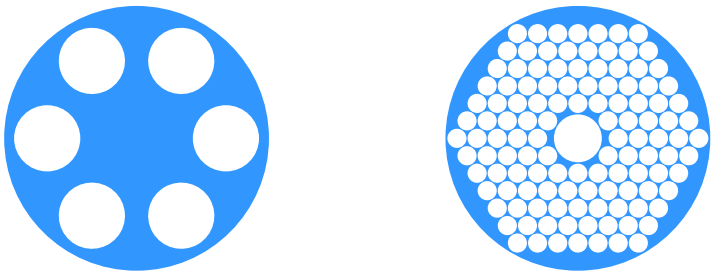
**J. Vincent**[1,2,3,4], **P. Daquin**[1,2], **R. Perrussel**[1,2], **J. R. Poirier**[1,2] **and H. C. Seat**[3,4]

[1]CNRS, LAPLACE, F-31071 Toulouse, France
[2]Univ. de Toulouse ; INP, UPS ; LAPLACE; ENSEEIHT, F-31071 Toulouse, France
[3]CNRS, LAAS, F-31400 Toulouse, France
[4]Univ. de Toulouse ; INP ; LAAS, F-31400 Toulouse, France
vincent@laplace.univ-tlse.fr

**Abstract**— Computations of Photonic Crystal Fibers with a waveguide mode solver based on boundary integral equations give rise to a nonlinear eigenvalue problem. In this paper, data-sparse approximations of matrices are investigated to optimize the computations without loss of accuracy.

**Introduction**: The propagation of light in Photonic Crystal Fibers (PCF) depends on several geometrical parameters and material characteristics [1], therefore numerical methods are needed to accurately treat various PCF geometries. In recent works [2, 3], a waveguide mode solver based on Boundary Integral Equations (BIE) was developed. This method showed high accuracy compared to other methods [4], such as the multipole method [5] or the finite-element method [6]. The main aim of this paper is to improve the efficiency of the computations by using numerical techniques on block matrices given by BIE method.

**Formulation of the problem and compression techniques**: As shown in Fig. 1, PCF cross section consists of homogeneous inclusions with refractive index $n_i$ surrounded by a medium with refractive index $n_e$. The total effective index $n_{eff}$ depends on these refractive indexes and the geometry of the PCF.



Figures 1: Schematic of two PCF cross sections. The medium surrounding the circular inclusions is considered as infinite.

Following [2, 3, 7], the problem can be written as a nonlinear eigenvalue problem.

$$F(n_{eff})x = 0, \tag{1}$$

where $x$ gathers the unknown values of the electromagnetic field, which are discretized at the boundary of the circular inclusions. $F$ is a sparse matrix, function of the effective refractive index $n_{eff}$. This matrix problem can be solved as a root finding process [8] for the function

$$f(n_{eff}) = \frac{1}{\phi^T F^{-1} \psi} = 0, \tag{2}$$

with two fixed random vectors $\phi$ and $\psi$. $F^{-1}\psi$ is computed by solving the system $F\chi = \psi$, with the low-rank matrix $F$ which can be written as a block matrix

$$F = \begin{bmatrix} A & B & C & 0 \\ D & E & 0 & 0 \\ \alpha C & 0 & A & \beta B \\ 0 & 0 & D & E \end{bmatrix} \tag{3}$$

where $\alpha = -n_e^2$ and $\beta = n_e^2/n_i^2$. $A$, $B$, $C$, $D$ and $E$ are block matrices deduced from Maxwell equations, the interface conditions on the hole boundaries and the use of the BIE method [2, 3, 5]. $D$, $E$ are diagonal block matrices and $A$, $B$, $C$ are data-sparse matrices.

The use of numerical techniques such as direct or iterative solver, preconditionning, or the Adaptive Cross Approximation (ACA) and the Hierarchical Matrices ($H$-Matrix) on blocks $A$, $B$, $C$ would allow to reduce the computation time and the memory space needed, thus to increase the number of degrees of freedom [9]. Therefore the $n_{\text{eff}}$ computations of the two previous PCFs would give a better accuracy with a good approximation error. Furthermore, the computation speed of the presented BIE formulation will be compared with other formulations [2, 4].

**Conclusion**: This study uses numerical techniques to treat the dense block matrices in a waveguide mode solver based on BIE method. The results on two different PCF examples will be presented and compared with other methods (FEM, ...).

**REFERENCES**


1. Russel, W., "Photonic-Crystal Fibers," *Journal of Lightwave Technology*, Vol. 24, n. 12, 4729–4749, December 2006.
2. Lu, W. and Y. Y. Lu, "Efficient Boundary Integral Equation Method for Photonic Crystal Fibers," *Journal of Lightwave Technology*, Vol. 30, n. 11, 1610–1616, June 2012.
3. Lu, W. and Y. Y. Lu, "Efficient High Order Waveguide Mode Solvers Based on Boundary Integral Equations," *Journal of Computational Physics*, Vol. 272, 507–525, September 2014.
4. Vincent, J., Calvez, A., Perrussel, R. and J. R. Poirier, "Accuracy of Waveguide Mode Solver Based on Boundary Integral Equations," in *Progress In Electromagnetics Research Symposium Abstracts*, Prague, Czech Republic, July 2015.
5. White, T. P., Kuhlmey, B. T., McPhedran, R.C., Maystre, D., Renversez, G., De Sterke, C. M. and L. C. Botten, "Multipole method for microstructured optical fibers. I. Formulation," *Journal of Optical Society of America B* , Vol. 19, 2322–2330, October 2010.
6. Hayata, K., Miura, K. and M. Koshiba, "Finite Element Formulation for Lossy Waveguides," *Microwave Theory and Techniques, IEEE Transactions on*, Vol. 36, 268–276, February 1988.
7. Kress, R.,"On the numerical solution of a hypersingular integral equation in scattering theory," in *Journal of Computational and Applied Mathematics*, Vol. 61, 345–360, August 1995.
8. Cheng, H., Crutchfield, W. Y., Doery, M. and L. Greengard, "Fast Accurate Integral Equation Methods for the Analysis of Photonic Crystal Fiber I: Theory," *Optic Express*, Vol. 12, n. 16, 3791–3805, July 2004.
9. Daquin, P., Poirier, J. R. and R. Perrussel, "Hierarchical Matrices for Scattering Problems," in *NUMELEC 2015*, Saint-Nazaire, France, June 2015.

# Microwave Permeability of Hollow Iron Spheres

**Conor McKeever, Dr. Mustafa Aziz, and Dr. Feodor Ogrin**
University of Exeter, XM2 EPSRC Centre for Doctoral Training in Metamaterials
School of Physics, Prince of Wales Road, EX4 4SB, Exeter, United Kingdom
cm537@exeter.ac.uk

**Abstract**- It is well documented in the literature that carbonyl iron composites comprised of particles which possess an alternating concentric geometry of iron and insulating iron carbide exhibit large permeability in the microwave region. However, predicting the microwave behavior of such composites has proved challenging due to a limited understanding of the underlying physics governing the particles. Here we report on micromagnetic computations showing several intensive peaks as high as 25 GHz in the permeability spectrum of hollow iron spheres when excited from their minimum energy state.

Microwave properties of carbonyl iron have long been applied in electronic devices such as plastic encapsulated inductor cores and electromagnetic wave absorbers. However, the permeability of carbonyl iron composites show significant differences in the high frequency range despite possessing comparable chemical composition and particle size distributions[1]. It has been found that processed carbonyl iron powders exhibit two regions of magnetic dispersion and higher absolute values of permeability and permittivity in the radio-frequency band. These large differences have been attributed to an onion-like multi-layered microstructure of the particles, where the multi-layers are comprised of concentric shells of conducting iron and insulating iron carbide. These "onion-ring" particles have diameters ranging from hundreds of nanometers to several microns and have garnered significant interest in radio-engineering due to their potential application as electromagnetic wave-absorbers.

Recently, two previously unknown intensive high-frequency peaks of magnetic absorption within 15 to 25 GHz have been observed for such composites[2]. This high-frequency absorption has been attributed to the Aharoni exchange modes, which are predicted to occur in small ferromagnetic spheres possessing a non-magnetic core[3]. Here we show that exchange modes as high as 25 GHz can be excited within hollow ferromagnetic spheres which have been relaxed into their minimum energy state. The real permeability is found to be negative above 20 GHz for these high frequency modes.

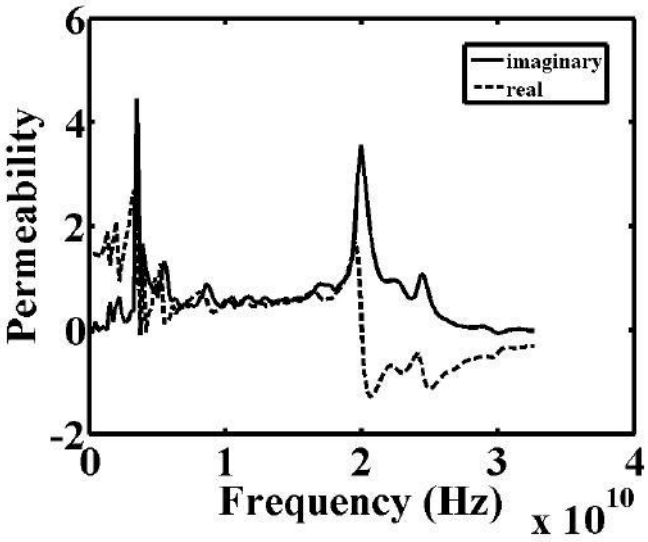



**Figure. 1**: Micromagnetic simulation of the permeability of a hollow iron sphere of outer diameter 750nm and shell thickness 190nm.

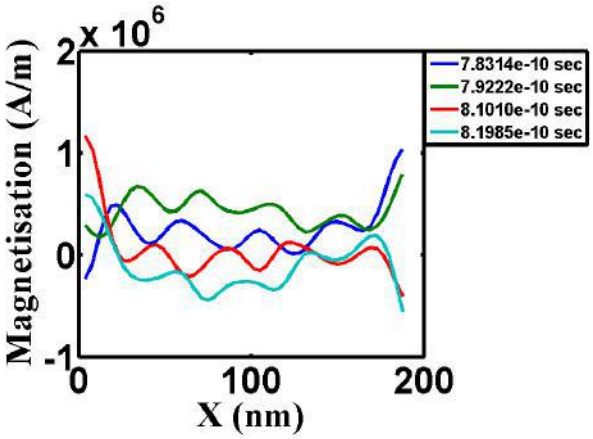



**Figure. 2:** Spatial distribution of the y-component of the magnetisation taken at the cross-section for a hollow sphere of outer diameter 750nm and shell thickness 190nm.

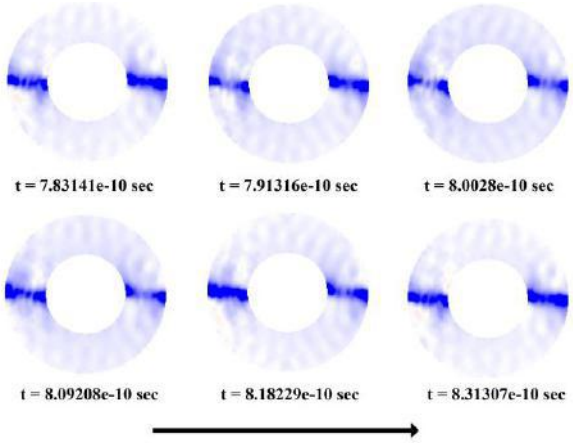



**Figure. 3:** Spatial distribution of the y-component of the magnetisation (blue) at the cross-section for a hollow sphere of outer diameter 750nm and thickness 190nm within one 20 GHz cycle.

Intensive peaks in the imaginary component of the permeability can be observed near 20 GHz (see Figure. 1), and a negative real permeability is found above 20 GHz. The spatial distribution of the magnetisation of these high frequency modes exhibits wave-like behaviour when excited (see Figure 2, 3), with large spatial variation occurring within one cycle. This behaviour is consistent with the Aharoni theory for exchange modes in hollow ferromagnetic spheres. Understanding how the permeability of such particles is influenced by dimensions (diameter, thickness, etc) as well as the domain structure is of key importance for the design and optimisation of electromagnetic wave absorbers utilizing shells of conducting iron.

## REFERENCES


1. Abshinova, Madina A., "Correlation between the microstructure and the electromagnetic properties of carbonyl iron filled polymer composites," *Com. A: App. Sc. Man.*, Vol. 38, No. 12, 2471-2485, 2007.
2. Lagarkov, Andrey N., "High-frequency modes in magnetic spectra of carbonyl iron," *J. Mag Mag. Mat.*, Vol. 324, 3402-3405, 2012.
3. Aharoni, A., "Exchange resonance modes in a hollow sphere," *Phy. Stat. Sol. (b)*, Vol. 231, No. 2, 547-552, 2002.

# Vortices and orbital angular momentum of naturally occurring patterns

**M. Babiker[1], Jun Yuan[1], Yuanjie Yang[2] and G. Thirunavukkarasu[1]**
[1]Department of Physics, University of York, York, YO10 5DD, UK
[2]School of Astronautics & Aeronautics, University of Electronic Science and Technology of China, Chengdu 611731, China

**Abstract-** In this talk we describe the design, analysis and experimental realisation of diffractive elements containing ordered sets of multi-pinhole spirals capable of the generation and selection of vortex beams. The elements are inspired by naturally occurring designs found in the plant and animal kingdoms much of which are rooted on mathematical principles associated with the Fibonacci numerology and involves spirals and helices such as those of Fermat and Archimedes. For example the arrangement of successive leaves on the shoot of a growing plant follows a helix. Mathematically the family of spirals forming a sunflower pattern is such that the nth spiral is placed at an angle an integer multiple of the golden angle and its distance from the centre is proportional to the square root of n. The physics is concerned with optical and matter vortex beams carrying orbital angular momentum (OAM) an area of much current interest. In general these are all de Broglie waves with a phase singularity, but they differ in scales and parameters. The main point is to explore what the broad range and variety of the natural designs can tell us about vortex beams. We also explore what kinds of vortex beams exist in nature and what roles they play in the system evolution.

# Scattering Calculation of Bianisotropic Particle Slabs for Normal Incidence via Retrieved Polarizabilities

**Theodosios Karamanos, Athanasios Papadimopoulos, Nikolaos Kantartzis*, and Theodoros Tsiboukis**

Department of Electrical and Computer Engineering, Aristotle University of Thessaloniki, GR-54124 Thessaloniki, Greece
*corresponding author, E-mail: kant@auth.gr

## Abstract

In this work, a methodology for the calculation of the reflection/transmission coefficients from bianisotropic metamaterial slabs is presented. Initially, simple bianisotropic particles that compose finite slabs are approximated as electric and magnetic dipoles. After the polarizabilities of the single particle and the wavenumber for a TEM wave, propagating in an infinite 3D array of such particles, are acquired, the dipole moments of the slab are evaluated for a TEM incidence. Finally, the reflection/transmission coefficient is obtained via the summation of the scattering fields from equivalent surfaces that comprise the slab. The proposed technique is applied to a bianisotropic particle and results are compared to those from numerical simulations.

## 1. Introduction

Over the past years, there has been a serious effort to model the artificial media structures, also known as metamaterials, in terms of periodically-arranged dipole moments [1, 2]. This class of techniques considers the scatterers that compose the periodic 2D/3D structures as electrically-small and then substitutes them with the respective electric and magnetic dipole moments. Then, the electromagnetic response of the original system is calculated as a summation of the response of all dipoles. Hence, the polarizability matrix of each scatterer is crucial for such methods, and, if periodicity occurs along the propagation axis, the respective wavenumber is also necessary to account for spatial dispersion effects. In this paper, we further expand this concept to the calculation of the scattering parameters for a slab of bianisotropic particles in the case of normal incidence.

## 2. Development of the technique

Let us consider the Cartesian coordinate system at a cubic-array, finite slab of identical bianisotropic particles, with vacuum as the background medium (Fig. 1). The slab can be studied as a summation of $N$ infinite 2D free-standing arrays. Thus, for a normally incident plane wave, following the analysis of [3], it holds that for each 2D array at $(x, y, z) = (0, 0, nd)$, one arrives at (1) (top of the next page), where $\alpha_{ee}^{xx}$, $\alpha_{ee}^{zz}$, $\alpha_{em}^{xy}$, and $\alpha_{mm}^{yy}$ are the electric-electric, electric-magnetic, and magnetic-magnetic polarizabilities of the particle, respectively. Moreover, $p_{x,n}^{\pm}$ and

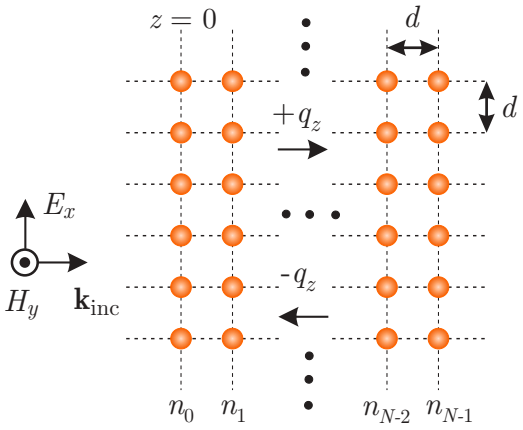



Figure 1: A transverse cut of a 3D metamaterial slab, whose periodicity is set to $d = 10$ mm toward all axes.

$m_{y,n}^{\pm}$ are the electric and magnetic dipole moments induced from a wave propagating inside the slab for the corresponding directions. Similarly, complying with the notation of [1], $C_{\text{3D},n}^{\pm}$ and $D_{\text{3D},n}^{\pm}$ are the co- and cross-polarization interaction coefficients from all other dipoles outside the surface, under study, while, $C_{\text{2D,n}}$ is the co-polarization interaction coefficient from the dipoles on the $n$-th 2D array. All interaction coefficients are obtained in terms of converging sums of Green's functions [1].

In this context, assuming a thick slab with a sufficient number of $N$ 2D arrays, we may apply the Bloch theorem and consider $p_{x,n}^{\pm} = p_{x,0}^{\pm}\, e^{\mp jq_z nd}$ and $m_{y,n}^{\pm} = m_{y,0}^{\pm}\, e^{\mp jq_z nd}$, with $q_z$ the wavenumber for the propagating TEM mode inside the slab. Wavenumber $q_z$ is also necessary for the calculation of $C_{\text{3D},n}^{\pm}$ and $D_{\text{3D},n}^{\pm}$, so, in this work we will presume it equal to that of a wave propagating through the infinite 3D array, retrieved through various techniques [4]. Finally, if we apply the Bloch theorem, the unknown dipole moments of the problem reduce to four, which can be acquired from the solution of a system of (1) for two different 2D arrays. Herein, we choose the first and the last array, i.e. $n = 0$ and $n = N - 1$, that provide an easier evaluation of all interaction coefficients. After the desired dipole moments are derived, the reflection, $R$, and transmission, $T$, coefficients of the finite slab are retrieved as a summation of the scattering fields from each 2D array. Hence, following the analysis of [3] and viewing each 2D

$$\left(\begin{bmatrix} \alpha_{ee}^{xx} & \alpha_{em}^{xy} \\ -\alpha_{em}^{xy} & \alpha_{mm}^{yy} \end{bmatrix}^{-1} - \begin{bmatrix} C_{2\mathrm{D},n} & 0 \\ 0 & C_{2\mathrm{D},n} \end{bmatrix} - \begin{bmatrix} C_{3\mathrm{D},n}^{+} & D_{3\mathrm{D},n}^{+} \\ D_{3\mathrm{D},n}^{+} & C_{3\mathrm{D},n}^{+} \end{bmatrix}\right)\begin{bmatrix} p_{x,n}^{+} \\ c_0^{-1}m_{y,n}^{+} \end{bmatrix}$$

$$+\left(\begin{bmatrix} \alpha_{ee}^{xx} & \alpha_{em}^{xy} \\ -\alpha_{em}^{xy} & \alpha_{mm}^{yy} \end{bmatrix}^{-1} - \begin{bmatrix} C_{2\mathrm{D},n} & 0 \\ 0 & C_{2\mathrm{D},n} \end{bmatrix} - \begin{bmatrix} C_{3\mathrm{D},n}^{-} & D_{3\mathrm{D},n}^{-} \\ D_{3\mathrm{D},n}^{-} & C_{3\mathrm{D},n}^{-} \end{bmatrix}\right)\begin{bmatrix} p_{x,n}^{-} \\ c_0^{-1}m_{y,n}^{-} \end{bmatrix} = \begin{bmatrix} \varepsilon_0 E_0 \\ c_0^{-1}E_0/\eta_0 \end{bmatrix} e^{-jk_0nd} \quad (1)$$

$$R_{z=0} = -\frac{j\omega\eta_0}{2d^2E_0}\sum_{n=0}^{N-1}\{(p_{x,n}^{+} - c_0^{-1}m_{y,n}^{+}) + (p_{x,n}^{-} - c_0^{-1}m_{y,n}^{-})\}e^{-jk_0nd} \quad (2)$$

$$T_{z=(N-1)d} = \left[1 - \frac{j\omega\eta_0}{2d^2E_0}\sum_{n=0}^{N-1}\{(p_{x,n}^{+} + c_0^{-1}m_{y,n}^{+}) + (p_{x,n}^{-} + c_0^{-1}m_{y,n}^{-})\}e^{-jk_0nd}\right]e^{-jk_0(N-1)d} \quad (3)$$

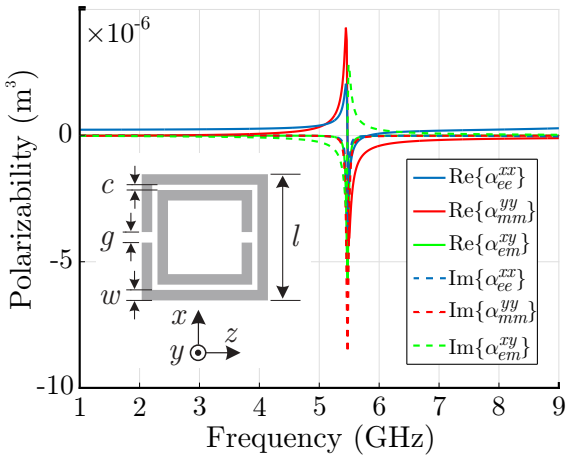



Figure 2: A square EC-SRR with $g = w = c = 0.5\,\mathrm{mm}$, $l = 6\,\mathrm{mm}$.

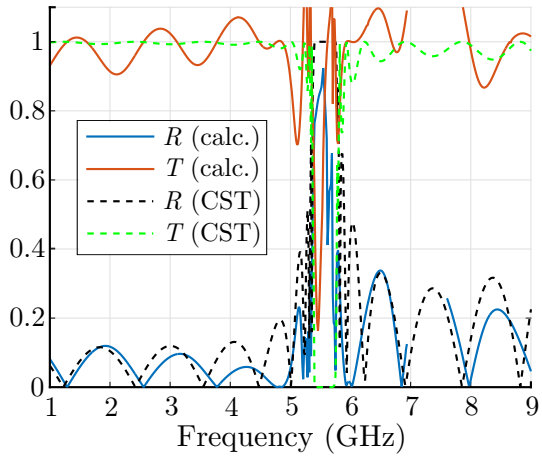



Figure 3: Comparison between calculated and numerically derived $R$ and $T$ coefficients.

array as an equivalent surface, the scattering parameters of the slab are extracted from (2) and (3) (top of the page).

## 3. Verification

In order to validate the featured algorithm, we examine the popular bianisotropic scatterer EC-SRR of Fig. 2 along with its extracted polarizabilities. Consequently, for a slab comprising $N = 11$ 2D arrays, the computed $R$ and $T$ are given in Fig. 3 and compared with those obtained from numerical simulations [5]. The proposed technique shows a promising performance, as it succeeds in providing the main resonance of the structure as well as the general behavior of the slab. However, some discrepancies occur, like the oscillation of $T$ around 1 and a narrower bandqap area. These can be mainly attributed to the oscillatory nature of the interaction coefficient convergence for the finite Green's function sums and the small deviations of infinite case $q_z$ from the finite one. Overall, the developed methodology offers very satisfactory solutions to the finite 3D array bianisotropic scatterer problem and significantly improved results.

## 4. Conclusions

In this paper, a consistent algorithm for the normally-illuminated, finite 3D array bianisotropic scatterer problem, has been proposed. The presented technique demonstrates encouraging conduct, and, as a future work, the algorithm should be further applied on popular metameterial setups.

## Acknowledgement

This research has been financed by the A. S. Onassis Public Benefit Foundation, under Grant GZL060-1/2015-2016.

## References

[1] A.D. Scher, E.F. Kuester, The electromagnetic response of a metamaterial slab in the case of normal incidence, *PIER B* 30: 1–26, 2011.

[2] A.I. Dimitriadis, N.V. Kantartzis, T.D. Tsiboukis, C. Hafner, Generalized non-local surface susceptibility model and Fresnel coefficients for the characterization of periodic metafilms with bianisotropic scatterers, *J. Comp. Phys.* 281: 251–268, 2015.

[3] T.D. Karamanos, A.I. Dimitriadis, N.V. Kantartzis, Robust technique for the polarisability matrix retrieval of bianisotropic scatterers via their reflection and transmission coefficients, *IET Microw. Antennas Propag.* 8: 1398–1407, 2014.

[4] A. Alù, N. Engheta, Three-dimensional nanotransmission lines at optical frequencies: A recipe for broadband negative-refraction optical metamaterials, *Phys. Rev. B* 75: 024304(1–20), 2007.

[5] CST MWS$^{TM}$: *Computer Simulation Technology: Microwave Studio*, Computer Simulation Technology Std., 2015.

# Emerging applications

# Energy Tunneling Behavior in Geometrically Separated Wave Guides

Muhammad Omar
United Arab Emirates University
Al-Ain-15551, UAE
muhammadomar@uaeu.ac.ae

Rashad Ramzan
United Arab Emirates University
Al-Ain-15551, UAE
rashad.ramzan@uaeu.ac.ae

Omar Farooq Siddiqui
Taibah University, Madinah
Saudi Arabia
omarsiddiqui2@gmail.com

***Abstract*— In this paper, characteristics of energy tunneling channel between the waveguides geometrically separated by a coaxial cable are studied. The novel aspect of design is use of coaxial channel to connect the waveguides while maintaining the energy tunneling phenomena. As anticipated the tunneling frequency depends upon the length of wire inside the waveguide and the length of the coaxial cable. The tunneling frequency also depends upon the dielectric constant of the material inside the waveguide and coaxial cable. At tunneling frequency the field strength (E and H) in the channel is extremely high, making the channel extremely sensitive to small change in permittivity of dielectric occupying the channel. The advantage of the proposed design is its ability to tune to desired tunneling frequency just by changing the length of the coaxial cable without the need to redesign the waveguide height to accommodate the long tunneling wires. This structure can be used as dielectric sensor both for solid or liquid dielectrics just by placing the sample in coaxial cable cavity, contrary to previously report work where the sample has to be placed inside the waveguide.**

## I. INTRODUCTION

The electromagnetic energy tunneling which takes place in narrow channels and bends loaded with epsilon-near-zero (ENZ) materials or resonant wires is accompanied by very intensive electric fields [1]-[2]. An intense electric field is created at the surface of this metallic wire, which is extremely sensitive to the dielectric material around it. This effect is exploited to design very sensitive dielectric sensor [3]. In order to design the robust and accurate dielectric sensors of different kinds, the detail and in depth study of tunneling channel and its characteristics is mandatory. The second equally important factor is the shape and physical size of the energy tunneling channel when used as a sensor. This is important in order to convenient placement and removal of sample in the channel. In this work, we have proposed the use of coaxial channel to connect the two waveguides with each other while maintaining the energy tunneling. Now, in this case, the coaxial cable segment has a potential to be used a sample holder both for solid and liquid dielectric samples. Moreover, the tunneling frequency can be programed at desired value just by changing the length of the coaxial cable, without changing the design of the waveguide. Thus alleviating the geometrical constraint that the tunneling frequency is determined by the length of wire and that wire cannot be longer than the height of the waveguide. The geometry of the proposed design is shown in Fig. 1 (a)-(d).

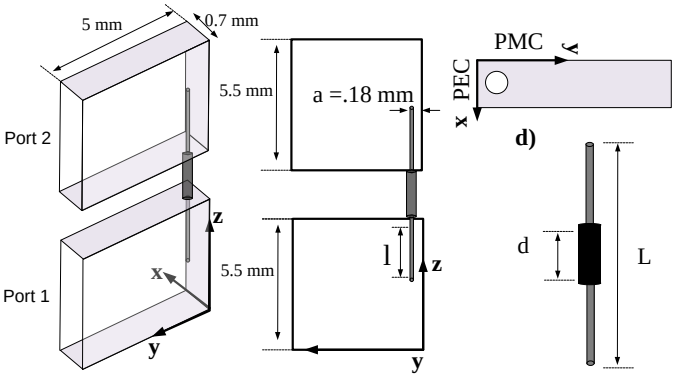



Fig.1 (a) Waveguides couples through cylindrical channel, shaded area represents PEC boundaries and unshaded area represents PMC boundaries (b) side view; (c ) metallic wire and channel between waveguides; (d) top View, location of aperture.

Both waveguides are geometrically separated through coaxial channel. In this present situation, the tunneling frequency of metallic wire embedded inside the waveguide is L=2l+d, where l is the length of wire protruding inside waveguide and d is the length of coaxial cable.

Moreover, in this proposed design, we can rotate, bend, and twist the channel without redesigning the whole system of waveguide as shown in Fig. 2. Hence, different arrangements of the channel connections reported in [4] can be achieved without redesigning the whole system. This will also allow the flexibility in the shape and size of the dielectric sample when this structure is used as a sensor.

The paper is divided as follows. In section II, The proposed structure is simulated using ANSOFT'S® HFSS™, and simulation results are presented along with comparison with recent LNAs and the paper is finally concluded in Section III.

## II. SIMULATION RESULTS

The design mentioned in Fig.1, is simulated and results are reported. The channel dimension is selected such that there is no energy tunneling in the absence of wire. The magnitude plot when channel is loaded with different dielectric materials is shown in Fig.3. Different dielectric materials are used with permittivity range from 1 to 3. Two magnitude peaks are noticed for each dielectric sample. The lower frequency peak is due to the metallic wire embedded inside the waveguide and

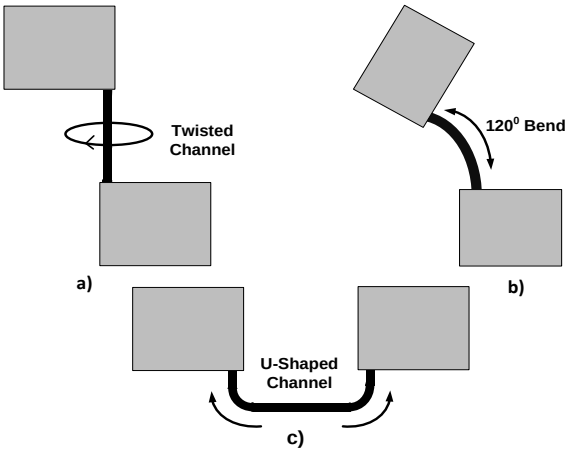



Fig.2.a) Twisted channel; (b) Channel bend at 120 degree ; (c) U-shaped bend

its tunneling frequency depends upon the wire length and channel length i.e., L, whereas the second frequency is because of Fabry-Perot resonance and depends upon the dimensions of the channel connecting them. It can be seen from figure that only higher frequency peak shifts and lower frequency peak is almost constant. As Fabry-Perot resonance only depends on the channel dimensions. If this approach is use then, we can tune the higher frequency peak too and even channel can be used for sensing. A large frequency shift of 3GHz is noticed for dielectric change from 1 to 2. If we increase the permittivity then after a certain range behavior of both peaks starts to change and for permittivity above 5, the shift in higher frequency peak slowly drop down and lower frequency peak starts to move with change in the permittivity of material filling the channel, as shown in Fig. 4.

As it discussed before that lower frequency peak depends on channel length too. If we increase the channel length d to a level that it becomes comparable with length 2l, then first resonance peak will also shift with higher frequency resonance peak. This property is very important and makes the sensor practically more flexible as operating frequency of the sensor can be adjust just by using large length of coaxial cable. The shift in tunneling frequencies with change in effective channel length is shown in Fig. 5. And due to this property we can tune the sensor at any desired lower frequency. It is also possible to inject liquid dielectric samples like, Toluene, Bromine, and Chlorine i.e., into the coaxial cable channel especially designed to hold the liquid samples. The Energy through primary

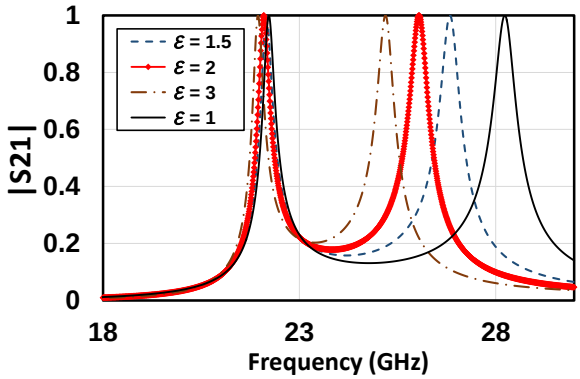



Fig.3. Effect of permittivity change from 1-3, on magnitude of transmission coefficient

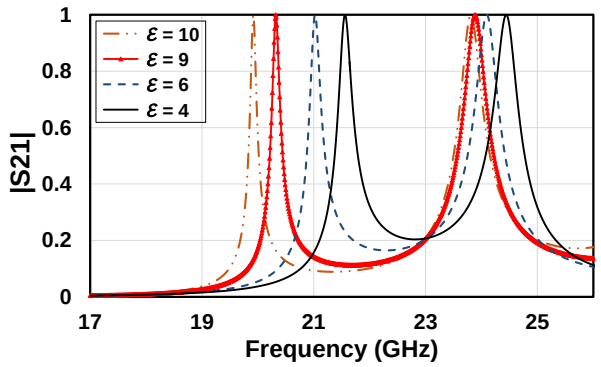



Fig.4. Effect of permittivity change from 4-10, on magnitude of transmission coefficient

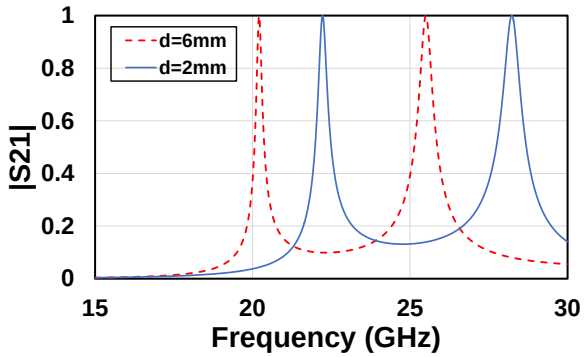



Fig.5. Effect of change in length coaxial cable on magnitude of transmission coefficient

waveguide can be further divide into N-number. This means that the either multiple sensors can be operate at same time at same frequency using the same waveguide.

## III. Conclusion and Future Directions

The effect of permittivity of the dielectric sample placed inside the coaxial cable and length of cable on the characteristic channel is studied and reported. It is shown that such configurations has a potential to be used an extremely sensitive sensor for solid, liquid and gas dielectrics. The use of power divide in coaxial cable channel open the new possibilities for sensor to work at different frequencies using the same waveguide structure, which is our future direction of work.

## References

[1] A. Alu and N. Engheta, “Light squeezing through arbitrarily shaped plasmonic channels and sharp bends,” Phys. Rev. B, vol. 78, p. 035440, Jul. 2008.

[2] A. Alu, M. Silveirinha, and N. Engheta, “Transmission-line analysis of epsilon-near-zero (ENZ)-filled narrow channels,” Phys. Rev. E, vol. 78, p. 016604, Jul. 23, 2008.

[3] R. Ramzan, O. Siddiqui, A. Nauroze, and O. Ramahi," Microstrip Probe Based on Electromagnetic Energy Tunneling for Extremely Small and Arbitrarily Shaped Dielectric Samples" IEEE antennas and wireless propagation letters, vol. 14, 2015.

[4] M. Kashanianfard, "Electromagnetic Wave Transmission through Sub-wavelength Channels and Bends Using Metallic Wires, M.S. thesis, Dept. Elect. And Comp. Eng., Univ. of Waterloo, Waterloo, Ontario, Canada, 2009.

# Plasmonic Color Filters for Industrial Applications

**L. Duempelmann[1,2], A. Luu-Dinh[1], D. Casari[1], B. Gallinet[1*], and L. Novonty[2]**
[1]CSEM, Thin Film Optics, Muttenz, 4132, Switzerland
[2] ETHZ Zürich, D-ITET, Zürich, 8092, Switzerland
[*]corresponding author: benjamin.gallinet@csem.ch

**Abstract** We present color filters based on plasmonic nanostructures showing an angle- or rotation-dependent color output. Such a tune-ability of color can be beneficial and key element for several applications such as anti-counterfeiting, sensing, solar cell or display. The structures and materials can be adapted to cover a wide spectral range; the fabrication method is in-line with industrial fabrication standards.

Structural color substrates based on plasmonics have strongly increased attention due to high "printing" resolution[1], non-bleaching properties and in particular tune-ability, enabling a direct change of the optical properties. In particular the plasmon resonance can be designed in such a way to be sensitive to the incident angle or polarization. In the following the concept of two novel types of tunable plasmonic color filters will be reported. They are fabricated using UV replication and metal evaporation, compatible with roll-to-roll manufacturing, which is an industrial standard due to its cost efficiency and large-scalability.

The first color filter is based on tilted periodic aluminum nanolamellas[2] (see Figure 1a). Incident light leads to the excitation of a plasmon resonance, for which the incident angle only defines the excitation efficiency and not the spectral position. Additionally, the periodic arrangement of the structures give rise to a secondary resonance effect (*c.f.* Wood-Rayleigh anomaly), which is strongly angle-dependent. Overall a strong coupling between these two resonances leads to an angle-dependent resonant system acting in the visible range. Because of the geometrical asymmetry of the nanolamellas this resonance effect only appears in one of the four possible directions of the substrate plane. This unique optical appearance makes it highly attractive for optical security. The color filter itself shows a high transmittance of ~80% with a FWHM ~50nm at the resonance (see Figure 1b). Due to the strong sensitivity of the plasmon resonance to the refractive index of the surrounding, this proposed system could be ideal for sensing applications. Moreover, the strong absorbance between the nanolamellas (~90%) could be utilized for solar cell applications.

Secondly, we present a compact plasmonic color filter based on silver nanowires[3] (see Figure 1c). Diagonal polarized light excites the two polarization axes of the periodic structure. The polarization perpendicular to the nanowires excites a plasmon resonance, causing a wavelength-dependent phase shift of this polarization axis around the resonance. A subsequent polarizer leads to a four-fold output, whereas a crossing of two states is observed at the plasmon resonance (see Figure 1d). This effect can be achieved with diverse plasmonic structures or materials, covering the complete visible range and beyond. Here the plasmonic structure is optimized to act nearly completely angle-independent. This paves the way for applications with diffuse light or where a large aperture is required. Tune-ability of the color output can be essential for display or optical security applications.

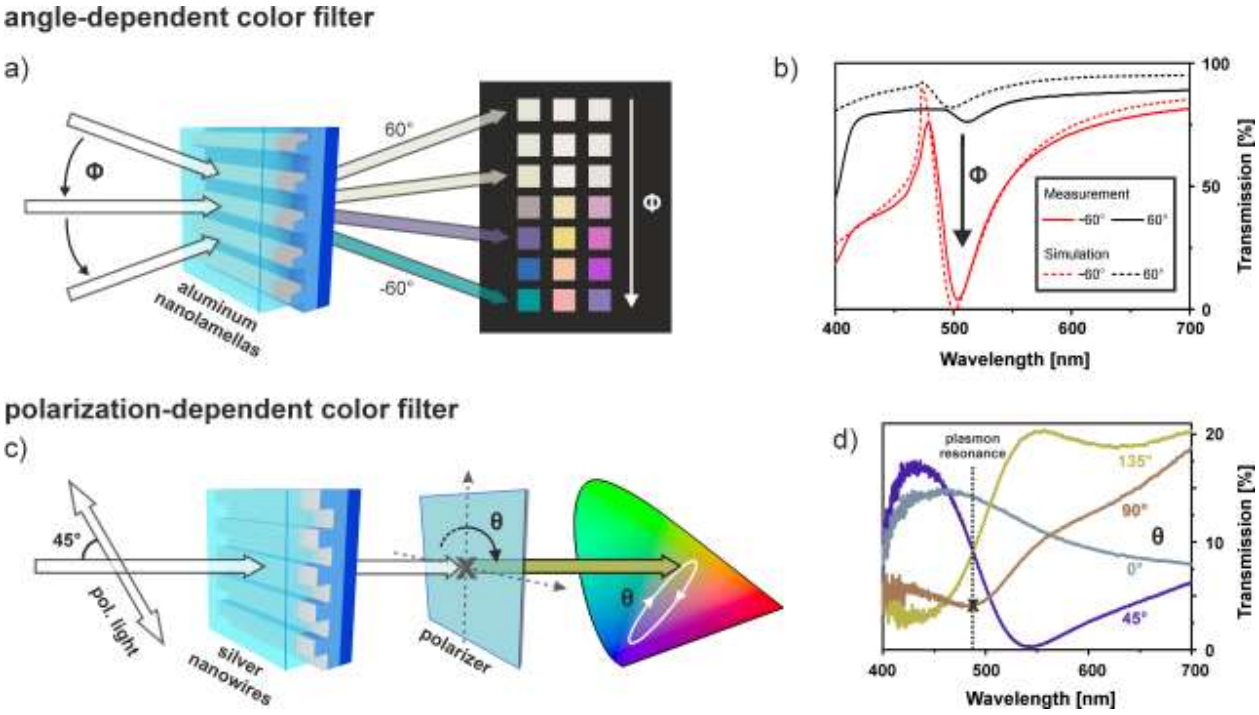



**Figure 1:** a) angle-dependent and c) polarization-dependent color filters. a) Different tilt angle of the incident light leads to different color appearances (the column of the colored patches indicated different samples), b) demonstrated by the strong angle-dependent excitation of the resonance. c) Rotation of a polarizer leads to a wide range of different colors, d) for which the measured states are spectrally crossing at the plasmon resonance.

Overall we present two kinds of plasmonic color filters capable of changing the filtering properties, angle- or orientation-wise. Replication of these filters can be done in a roll-to-roll compatible process and with a single evaporation step using inexpensive material. Finally, the structures are protected for use in ambient conditions. This enables integration of plasmonics into industrial applications such as optical security, solar cells or displays.

**REFERENCES**

1. Kumar, K., H. Duan, R. S. Hegde, S. C. W. Koh, J. N. Wei, J. K. W. Yang "Printing colour at the optical diffraction limit," *Nat. Nanotech.*, Vol. 7, No. 9, 557-561, 2012.
2. Duempelmann, L., D. Casari, A. Luu-Dinh, B. Gallinet and L. Novotny, "Color Rendering Plasmonic Aluminum Substrates with Angular Symmetry Breaking," *ACS Nano*, Vol. 9, No. 12, 12383–12391, 2015.
3. Duempelmann, L., A. Luu-Dinh, B. Gallinet and L. Novotny, "Four-Fold Color Filter Based on Plasmonic Phase Retarder," *ACS Photonics*, ASAP, 2015.

# An electromechanically tunable photonic crystal nanocavity with integrated photodetector for wavelength and displacement sensing.

**Ž. Zobenica[1], R.W. van der Heijden[1*], M. Petruzzella[1], F. Pagliano[1], R. Leijssen[2], T. Xia[1], L. Midolo[1], M. Cotrufo[1], Y.-J. Cho[1], F.W.M. van Otten[1], E. Verhagen[2], and A. Fiore[1]**

[1]COBRA Research Institute and Department of Applied Physics, Eindhoven University of Technology, PO Box 513, 5600 MB Eindhoven, The Netherlands

[2]Center for Nanophotonics, FOM Institute AMOLF, Science Park 104, 1098 XG Amsterdam, The Netherlands

[*]corresponding author: r.w.v.d.heijden@tue.nl

**Abstract**-A double-membrane, electromechanically tunable photonic crystal cavity is presented, with an internal photodetector integrated in one of the membranes. With the cavity resonance sensitively dependent on the membrane separation, the device can be operated as an integrated spectrometer for external radiation, or as a displacement sensor with sub-pm resolution and direct photocurrent output.

With the recent advancement of nanomechanical devices, the field of optomechanics has emerged, dealing with the intimate coupling of optical fields and forces with mechanical displacements [1]. Photonic crystals (PhCs) have a prominent role because of their small size, small mass and high quality factor ($Q$) optical resonances. However, the input/output coupling to PhC modes and the control of their resonant wavelength are difficult, preventing their application into compact sensing systems. In this contribution, we present an integrated nano-opto-electromechanical system (NOEMS) where the key functionalities of sensing, read-out and actuation are combined in a single device. It consists of an electromechanically tuneable double-membrane PhC cavity, with an integrated photodetector. The device can thus be employed as a spectrometer, wavemeter or displacement sensor, with a sensitivity for wavelength or displacement on a sub-pm scale.

The device, schematically shown in Fig. 1 a), is based on GaAs membranes, realised from an epitaxially grown layer stack with AlGaAs sacrifical etch layers. A photonic crystal with a cavity is etched in both layers simultaneously. The upper part is suspended through flexible arms to make it mechanically compliant. The adjacent parts of the two membranes are configured as an n-i-p diode, so that an electrostatic attractive force can be applied by reverse biasing the diode. The upper part is configured as another p-i-n diode, with a layer of Quantum Dots (QDs) in the center that absorb radiation in the resonant wavelength range of the cavity. The absorption of the QDs is strongly enhanced for incident radiation resonant with the cavity. A Scanning Electron Microscope image of a typical device is shown in Fig. 1 b).

The close proximity of the membranes (< 200 nm) couples their optical modes and produces a splitting [2]. Fig. 1 c) shows a photocurrent spectrum as a function of incident laser wavelength at fixed tuning voltage. From the linewidth it follows that the $Q$ is in the $> 10^4$ range, not significantly affected by the QD absorption loss. The mode is blue detuned with increasing absolute bias voltage, or decreasing membrane separation, see inset, as a result of the antisymmetric origin of the selected mode.

The large mechanical resonant frequency of the device (> 1 MHz) enables the electrostatically driven cavity resonance modulation, shown in Fig. 1 d). The modulation removes the nonresonant background absorption by

more than three orders of magnitude. It also yields a derivative dispersive lineshape, that can be used to lock the cavity to a fixed reference wavelength or the reverse. Finally, the wavelength or displacement resolution is improved to become orders of magnitude smaller than the linewidth, analogous to a Pound-Drever-Hall frequency modulation method [3].

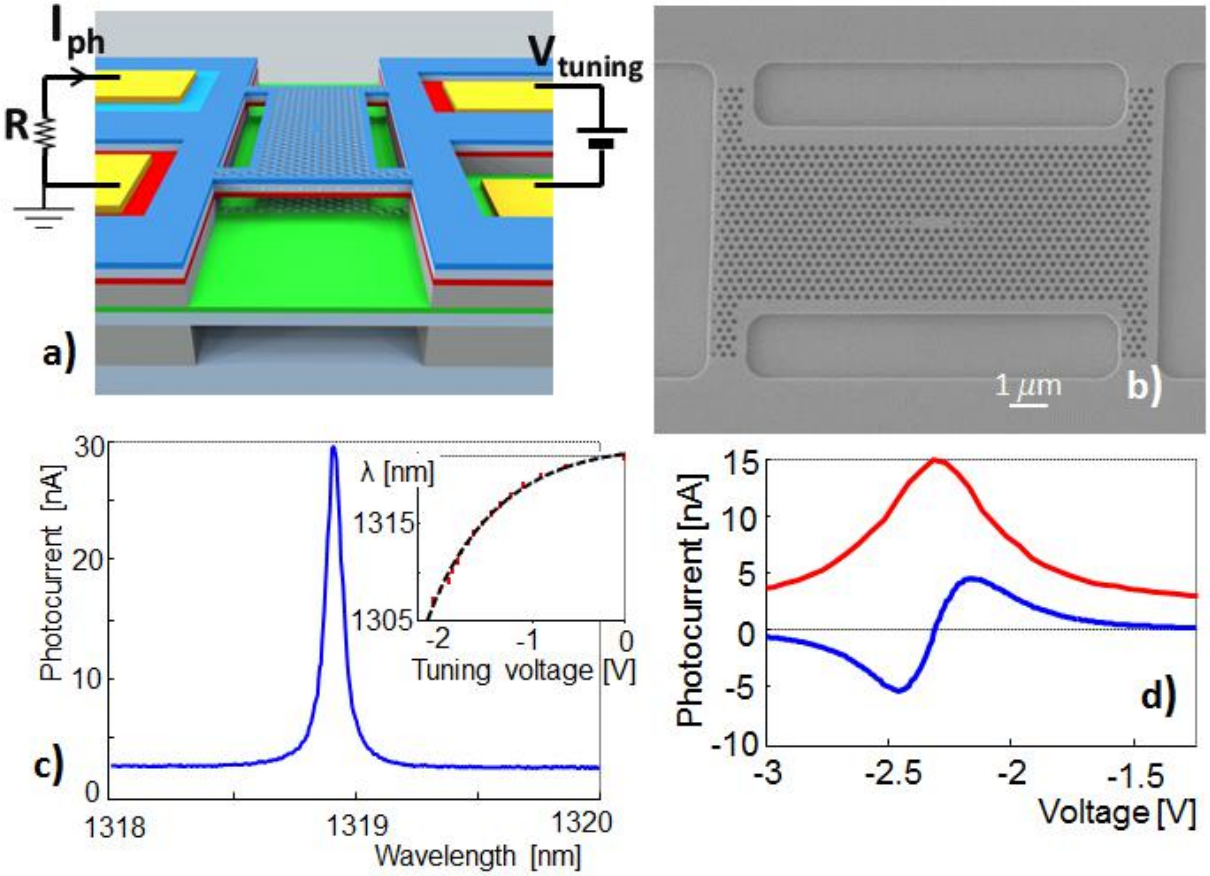



Figure 1. a) Schematic of the double membrane photonic crystal cavity, with the upper membrane suspended through tethers to increase its compliance. b) Scanning Electron Microscope image of a suspended double membrane device. c) Main figure: photocurrent spectrum at fixed tuning voltage as a function of wavelength with a *Q*-factor of ~ 17,000. Inset: tuning curve as a function of applied voltage, showing a blueshift with decreasing membrane separation. d) Upper: photocurrent as a function of applied tuning voltage for fixed incident laser wavelength. Lower: Phase sensitively detected photocurrent at the tuning voltage modulation frequency of ~ 300 Hz.

**REFERENCES**


1. Aspelmeijer, M., T.J. Kippenberg, and F. Marquardt, "Cavity Optomechanics," *Rev. Mod. Phys.*, Vol. 86, No. 4, 1391–1452, 2014.
2. Midolo, L., P. J. van Veldhoven, M. A. Dündar, R. Nötzel, and A. Fiore, "Electromechanical wavelength tuning of double-membrane photonic crystal cavities," *Appl. Phys. Lett.*, Vol. 98, 211120 1-3, 2011.
3. Black, E.D., "An introduction to Pound–Drever–Hall laser frequency stabilization," *Am. J. Phys.* Vol. 69, No. 1, 79-87, 2001.

# Tuning the Propagation of Spoof Surface-Plasmon Polaritons

**M. F. Pantoja[1*], Z. H. Jiang[2], P. L. Werner[2], and D. H. Werner[2]**

[1] Department of Electromagnetics, University of Granada, Granada 18071 Spain

[2] Electrical Engineering Department, The Pennsylvania State University, University Park, PA 16802 USA

[*]corresponding author: mario@ugr.es

**Abstract**- Spoof surface-plasmon polaritons (SSPPs) mimic the metal-dielectric confinement that occurs naturally at near-infrared and optical frequencies by including grooves in the metallic material. If the dispersion relation is known, then the SSPP properties can be manipulated by the groove geometry. This contribution presents a theoretical procedure linking waveguide theory with the interfacial boundary conditions. As an example, we apply this method to SSPPs based on radial grooves, which show a higher degree of tunability than those based on rectangular geometries.

In spite of the potential advantages derived from the high confinement of electromagnetic fields, the development and application of devices based on SSPPs remains limited. One of the reasons for this is because of the restricted tunability that can be achieved with conventional rectangular grooves such as those first introduced in [1]. This approach allows a designer to mimic optical surface-plasmon polaritons by employing a hollow grating along the metal-dielectric interface. Alternative geometries to a rectangular grating have been successfully demonstrated in the literature (*e.g.*, graded rectangular [2], thin rectangular [3], and trapezoidal grooves [4] [5]), but most of them have been either simulated numerically or manufactured for very specific problems. In this sense, the lack of analytical equations for most of the groove geometries restricts the examples to simple cases, and thus impedes the development of electromagnetic devices based on this phenomenon.

In this communication we contribute to the state of the art by: a) presenting a theoretical procedure to derive the dispersion relation by relating the input impedance of waveguides with the boundary conditions of the tangential and normal components of the electromagnetic fields, which enables the use of well-known expressions from the waveguide theory [6], and b) applying this analysis to spoof based on radial grooves (Fig. 1), which have been found to provide higher tunability in terms of resonance frequency and group velocity in comparison to the rectangular case. Validation of the presented dispersion relations for radial grooves has been carried out by using electromagnetic full-wave simulations [7].

In this way, the key point of the procedure is to combine the boundary conditions for the electromagnetic fields at the metal-dielectric interface such that:

$$\frac{\int_{L_a} E_y^I dy}{\hat{x}\times\left(H_z^I(a_i)-H_z^I(a_f)\right)} = \frac{\int_{L_a} E_y^{II} dy}{\hat{x}\times\left(H_z^{II}(a_i)+j_{sz}(a_i)-H_z^{II}(a_f)-j_{sz}(a_f)\right)} = Z_{in,waveguide} \tag{1}$$

and then follow the classical procedure based on the locations of the divergence in the reflection coefficient. For instance, the input impedance of radial waveguides can be considered in order to analyze SSPPs based on radial grooves. Figure 2a depicts the high confinement of the fundamental mode of propagation, a characteristic feature of SSPPs. The tunability of this structures is summarized in Fig. 2b, where the resonance frequency and the velocity of propagation are controlled by simply changing the inner angle of the radial grooves. The presentation will also address the use of a series arrangement of waveguides as another degree of freedom to tune the SSPPs.

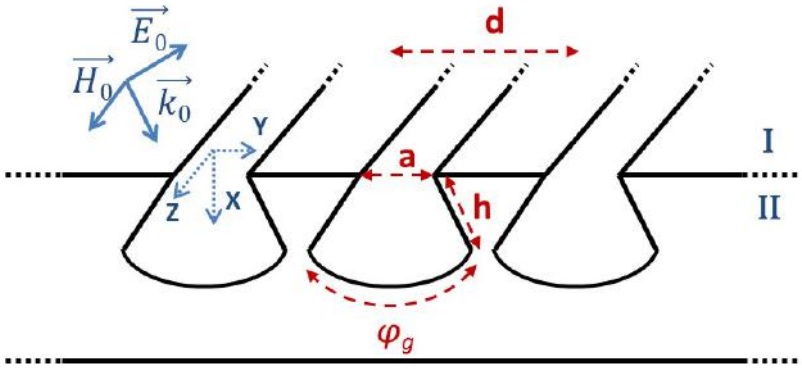
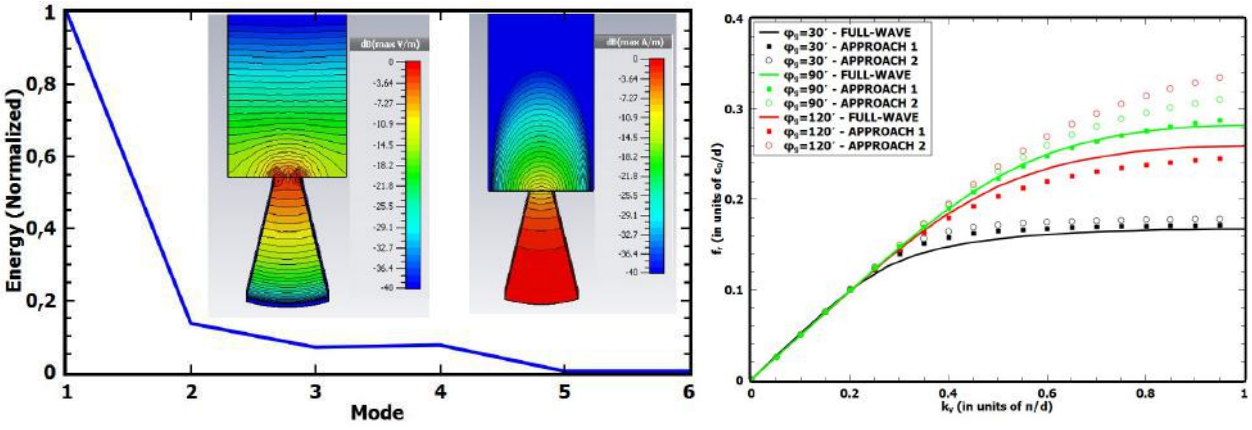



**Figure 1:** 1D array of radial waveguides, with a unit cell dimension of $d_u$. The degrees of freedom in the design are provided by the aperture $a$, height $h$, and inner angle $\varphi_g$.




**(a)** **(b)**

**Figure 2:** (a) Spatial confinement of the fundamental propagation mode in radial grooves. (b) Validation of the theoretical procedure with full-wave simulations.

## REFERENCES


1. Garcia-Vidal, F. J., L. Martin-Moreno, and J. B. Pendry, "Surface with holes in them: New plasmonic metamaterials," *J. Opt A: Pure Appl. Opt.*, Vol. 7, S97-S101, 2005.
2. Gan, Q., and F. J. Bartoli, "Graded metallic gratings for ultrawideband surface wave trapping at THz frequencies," *IEEE Journal of Selected Topics in Quantum Electronics*, Vol. 17, No. 1, 102-109, 2011.
3. Wan, X., and T. J. Cui, "Guiding spoof surface plasmon polaritons by infinitely thin grooved metal strip," *AIP Advances*, Vol. 4, No. 4, 047137/1-8, 2014.
4. Zhu, F., Y. Zhang, L. Shen and Z. Gao, "Subwavelength guiding of terahertz radiation by shallowly corrugated metal surfaces," *Journal of Electromagnetic Waves and Applications*, Vol. 26, No. 1, 120-129, 2012.
5. Liu, X., L. Zhu, Q. Wu and Y. Feng, "Highly-confined and low-loss spoof surface plasmon polariton structure with periodic loading of trapezoidal grooves," *AIP Advances*, Vol. 5, No. 7, 077123/1-7, 2015.
6. Mahmoud, S. F., *Electromagnetic Waveguides: Theory and Applications*, IET, England, 1991.
7. CST STUDIO SUITE®, CST – Computer Simulation Technology AG (www.cst.com).

# Hybrid Graphene-Copper UWB Array Sensor for Brain Tumor Detection via Scattering Parameters in Microwave Detection System

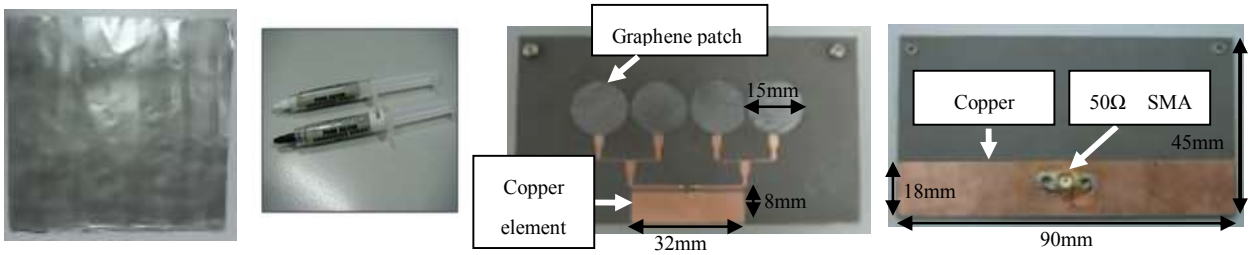
**M. A. Jamlos[1*], and A. H. Ismail[2]**

[1,2]Faculty of Technology Engineering (F-Tech), UniCITI Alam Campus, Universiti Malaysia Perlis (UNIMAP), Malaysia

[*]mohdaminudin86@gmail.com

**Abstract**-Hybrid graphene-copper UWB array sensor is successfully detecting brain tumor using scattering parameter (S-Parameter). The sensor made of graphene sheet as radiating element and copper for the rest conducting parts. The sheet has 97% carbon content, thichkness of 25µm and conductivity of $35\times10^8$ s/m. Hybrid sensor recorded bandwidth of 2.0GHz-10.6GHz with gain of 4.5dB-15.1dB. MATLAB software utilized to analyze S-parameter signals obtained from measurement. Tumor presence indicated by lower S-parameter values compared to higher values recorded by tumor absence.

Recently, graphene performed as the radiating material has obtained great interested within the communication device community. Conventional patch material such as copper has the great potential to be replaced by graphene since details analysis completed by [1] found that graphene patch antennas overall performance is completely better than Single Wall CNT, Multi Wall CNT and Copper patch antenna due to several advantages such as nanoscale size (0.33nm), great conductor (10ˆ8, electron travel 1/100 speed of light), lightest material (0.77 mg/1m) and strongest material (150,000,000 psi; 300 x stronger than steel) due to the single layer of carbon atoms packed in a two-dimensional honeycomb lattice structure. These features lead to higher gain and energy production for better penetration capability that is extremely essential for microwave imaging application [2]. Figure 1(a) show the graphene sheet and attached to the substrate using conductive epoxy glue as shown in figure 1(b) while figure 1(c) and (d) illustrate the sensor view for front and back respectively.

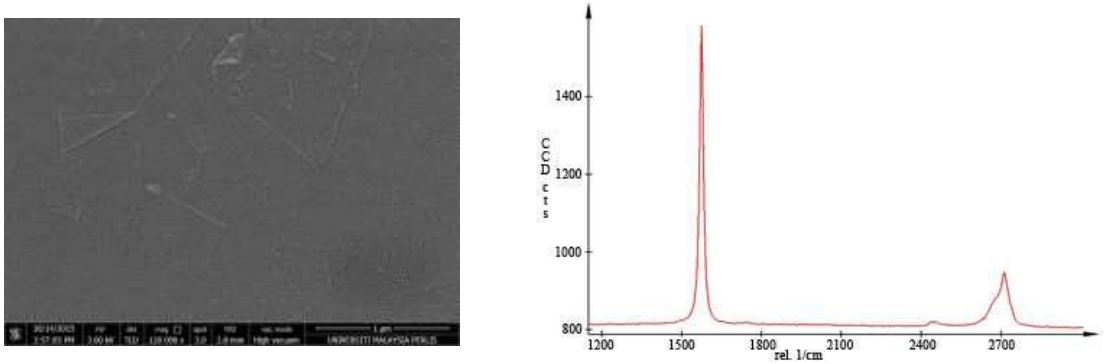



(a) (b) (c) (d)

Figure 1: (a) Graphene sheet, (b) epoxy glue, (c) sensor front view, (d) sensor back view

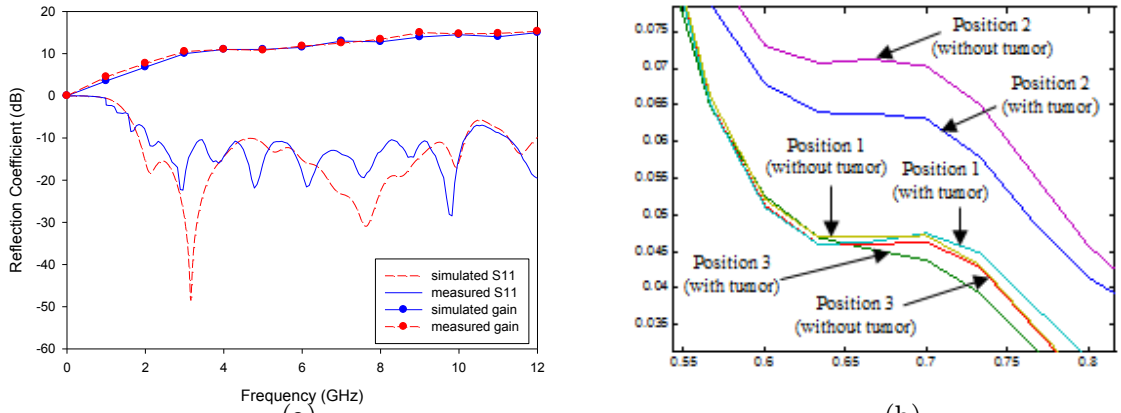
The micrometre scale image by FESEM display smooth, uniform and continuous layered surface indicated good structure and ideal as the patch for the sensor [3]. In Raman Spectrum, since the main spectral feature of graphene is derived from in-plane motion of the carbon atoms, the peaks would appear

at G band (1580 cm-1) as shown in figure 2(b) that is extremely sensitive to strain effects and is also a good indicator of the number of graphene layers [4]. Since tumor is present at position 2, S-parameter for with and without tumor condition at position 2 recorded the biggest gap compared with position 1 and 3 as shown in figure 3(b).




(a) (b)

Figure 2: (a) FESEM image of Graphene sheet, (b) Raman data of Graphene sheet




(a) (b)

Figure 3: (a) Sensor's measured and simulated S11 and gain, (b) S-parameter plot at position 1, 2 and 3

## REFERENCES


1. Moon, J. S. and Gaskill, D. K. "*Graphene: Its Fundamentals to Future Applications*", IEEE Transactions on Microwave Theory And Techniques, Vol. 59, No. 10, 2011.
2. Xuyang, L, Sit, Y. L., Zwirello, L., and Zwick, T., "*A Miniaturized UWB Stepped-Slot Antenna for Medical Diagnostic Imaging*", Microwave and Optical Technology Letters, Vol. 55, No. 1, 2013.
3. Bykkam, S., Venkateswara, R. K., Chakra, CH S., and Thunugunta, T., "Synthesis and Characterization of Graphene Oxide and Its Antimicrobial Activity Against Klebseilla and Staphylococus", International Journal of Advanced Biotechnology and Research, Vol 4, Issue 1, pp 142-146, 2013.
4. Isaac, C., Luis, A. J., Wonjun, P., Helin, C., and Yong P. C., "*Raman Spectroscopy of Graphene and Related Materials*", Chapter 19, Department of Physics, Purdue University, West Lafayette, IN, US.

# Plasmonic waveguide based mid-infrared lab-on-a-chip

**B. Schwarz**[1], **D. Ristanic**[1], **P. Reininger**[1], **H. Detz**[2], **A.M. Andrews**[1], **W. Schrenk**[1], **and G. Strasser**[1]

[1]Institute for Solid State Electronics and Center of Micro- and Nanostructures, TU Wien, Vienna, Austria
[2]Austrian Academy of Sciences, Vienna, Austria
benedikt.schwarz@tuwien.ac.at

**Abstract**— Dielectric-loaded plasmonic waveguides are perfectly suitable for on-chip sensing of fluids. They allow long propagation length and large mode overlaps above 96% with a the analyte. Dielectric-loading is a alternative approach to increase the confinement of mid-infrared surface plasmons without the need for sub-wavelength patterning. Direct excitation and detection is realized using chip integrated quantum cascade lasers and detectors, enabling the realization of a monolithically integrated mid-infrared lab-on-a-chip.

Mid-infrared spectroscopy is an extremely powerful and versatile technique. Sensors based on plasmonic resonances have been shown to strongly enhance the interaction with the analytes. Different to plasmonic resonance spectroscopy, here, the analyte is probed through the change of the absorption through the evanescent field that penetrates into the analyte. In dielectric waveguides, this evanescent tail is only a fraction of the mode, while in surface plasmon waveguides the major part (98-99%) can interact with the analyte. Different to the visible and near-infrared, SPPs at mid-infrared frequencies have very long propagation length of several ten millimeter due to the larger conductivity. However, this also goes with larger penetration into the dielectric such that the SPPs are only very weakly bound. In order to overcome this issue, we use the concept of dielectric-loading. Dielectric-loading is already known from visible and near-infrared plasmonics [1], where the additional layer is mainly used to achieve lateral guiding. In the mid-infrared, there is another much more important feature: The dielectric layer produces an increase of the effective modal index, enabling the support of well confined SPPs on noble metals [2]. Propagation properties similar to spoof plasmons can be achieved without the need for sub-wavelength patterning. In contrast to the visible and near-infrared, the dielectric layer thickness (100-300nm) is only a fraction of the mode width and the mode overlap with the surrounding fluid remains more than 96%. The strong surface sensitivity due to the evanescent nature of SPPs is interesting for surface sensitive biochemical sensing applications. The used materials are bio-compatible and might be functionalized with bio-receptors.

The excitation and detector of the SPPs is realized with quantum cascade technology. A special bi-functional design allows both emission and detection such that different parts on the chip can be used for laser and others for detectors [3]. Direct coupling between the active devices and the dielectric-loaded SPP waveguide is possible due to the same polarization and the optimized mode overlap with the etch depth and the thickness of the dielectric layer. The entire system serves as a flexible platform to realize plasmonic waveguide based single chip sensors [2]. The prototype sensor device is capable to detect water in isopropanol over a large range of concentrations in real-time with 50ppm resolution. Multiple units of such laser/waveguide/detector units can be used to probe different wavelength to address multiple chemicals.

This work was supported by the Austrian Science Funds (FWF) through project NextLite F4909-N23, as well as by the FP7 EU-project ICARUS (FP7-SEC-2011-285417). H.D. acknowledges funding through an APART Fellowship of the Austrian Academy of Sciences.

**REFERENCES**

1. Steinberger, B. et al., "Dielectric stripes on gold as surface plasmon waveguides," *Appl. Phys. Lett.*, Vol. 88, 094104, 2006.
2. Schwarz, B. et al., "Monolithically integrated mid-infrared lab-on-a-chip using plasmonics and quantum cascade structures," *Nat Commun.*, Vol. 5, 4085, 2014.
3. Schwarz, B. et al., "High performance bi-functional quantum cascade laser and detector," *Appl. Phys. Lett.*, Vol. 107, 071104, 2015.

# Design of Monopole Graphene Antenna for 5G Applications

**S. N. H. Sa'don[1], M. R. Kamarudin [1*] and F. Ahmad[2]**

[1]Wireless Communication Centre, Universiti Teknologi Malaysia, Johor, Malaysia

[2]Malaysia-Japan International Institute of Technology, Universiti Teknologi Malaysia, Malaysia

[*]corresponding author: mramlee@utm.my

**Abstract**- Fifth Generation (5G) is the next evolution of communication technology service which provides better features. The technology in 5G is precipitated since the frequency spectrum used for cellular communication have been used heavily and crowded. In this paper, a graphene antenna is proposed and designed at 15 GHz. The impedance bandwidth obtained is about 4.2 GHz (12.6 GHz to 16.8 GHz) and gain of 2 dBi that are considerably sufficient for 5G antenna user terminal.

**Introduction-** The desirable features for 5G technology are known to be very high in speed in the internet access and ultra-HD/3-D video streaming (downloading or uploading) and with ultra-low latency is believed to deliver uninterrupted communication flow between car drivers to reduce congestion and improve vehicle safety. In comparing to the average speed of 4G connections, 5G is expected to provide more than 1000 times faster than 4G. The 5G frequency spectrums still have not yet be finalized however some potential bands are discussed and proposed by Ofcom, UK [1]. With the effort of material engineering, it has been found a new substantial material could offer unique electrical, thermal and mechanical properties namely graphene. As reported in [2, 3], graphene's high electron mobily and field effect among others are extremely interesting for developing high frequency nanoelectronics. Therefore since the antenna can be made smaller with graphene, this research tends to design antenna in small size such as a millimeter size.

**Antenna design-** The antenna size is 9.8 mm x 6.8 mm width and length and designed with coplanar waveguide feeding. It has graphene as the radiator patch element with surface conductivity is $2.09 \times 10^6$ S/m calculated by using Kubo's formula [4] and substrate is A4 paper with dielectric constant of 3.2317 and tan $\delta$ is 0.0021. Figure 1 shows the antenna design and its parameters. The thickness of graphene and A4 paper is 2 nm and 0.05 mm, respectively. The stripline width is 1.2 mm. The patch size is 8 mm width and 4 mm length. The coplanar design is located side by side with stripline and has arm around patch. The gap between stripline and each coplanar is at 0.04 mm and coplanar width is 4.26 mm.

**Result and Analysis**- Figure 2 shows the reflection coefficient magnitude. The reflection coefficient magnitude obtained is about -31dB at 15GHz. While the bandwidth obtained (at -10dB level) is 4.2 GHz (12.6 GHz to 16.8 GHz). Figure 3 and Figure 4 show the radiation pattern at phi, $\theta = 0°$ and $\theta = 90°$. At phi, $\theta = 0°$, the radiation pattern is nearly omnidirectional and at phi, $\theta = 90°$ is bidirectional. The gain obtained is 2 dBi.

**Conclusion**-The graphene antenna is successfully designed. Wider bandwidth is achieved (more than 1GHz) so it will definitely provide high data rate and faster speed in 5G applications.

**Acknowledgements**- The authors would like to thank Ministry of Education (MOE) Malaysia and UTM for

sponsoring this work under HiCOE and GUP grants (Vot 11H59).

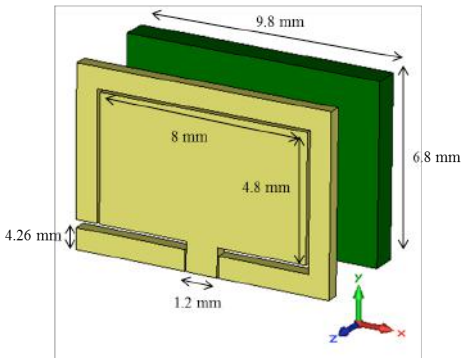



**Figure 1:** Antenna has two layers, graphene (front side) and A4 paper (back side).

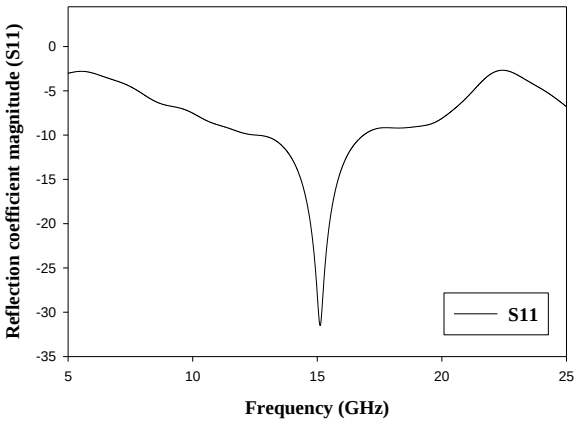



**Figure 2:** Reflection coefficient magnitude (S11)

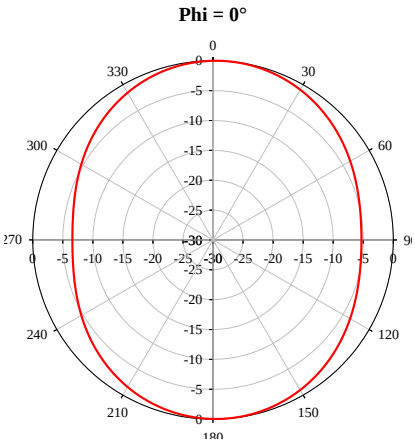



**Figure 3:** Radiation pattern at phi, θ = 0° is nearly omnidirectional.

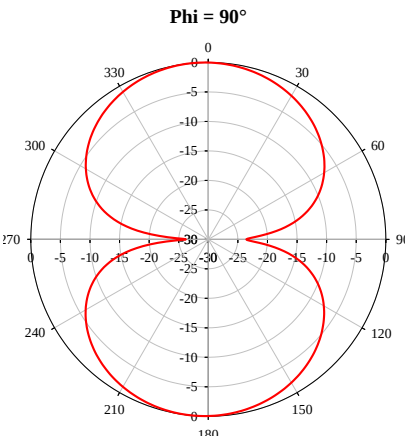



**Figure 4:** Radiation pattern at phi, θ = 90° is bidirectional.

## REFERENCES

1. Ofcom, “Spectrum above 6 GHz for future mobile communications,” in *[Online]. Avail- able: http://stakeholders.ofcom.org.uk/binaries/consultations/above- 6ghz/summary/spectrum above 6 GHz CFI.pdf*, 2015, February
2. P. Avouris, “Graphene: Electronic and photonic properties and devices,” *Nano Lett.*, vol. 10, no. 11, pp. 4285–4294, 2010
3. E. Carrasco and J. Perruisseau-Carrier, “Reflectarray Antenna at Terahertz Using Graphene,” *IEEE Antennas Wirel. Propag. Lett.*, vol. 12, pp. 253–256, 2013
4. M. Tamagnone, J. S. Gómez-Díaz, J. R. Mosig, and J. Perruisseau-Carrier, “Analysis and design of terahertz antennas based on plasmonic resonant graphene sheets,” *J. Appl. Phys.*, vol. 112, no. 11, 2012

# Electric field induced visually observable change in light scattering and absorption in doped ZnO nanowire colloidal suspensions

**M. Timusk[1,2*], A. Šutka[3], and M. Knite[1]**

[1] Institute of Technical Physics, Riga Technical University, Paula Valdena 3/7, Riga LV-1048, Latvia

[2] Institute of Physics, University of Tartu, Ravila 14c, 50411 Tartu, Estonia

[3] Institute of Silicate Materials, Riga Technical University, Paula Valdena 3/7, Riga LV-1048, Latvia

[*]corresponding author: martin.timusk@ut.ee

**Abstract**-We describe a novel electro-optical behavior of colloidal suspensions of doped ZnO nanowires (NWs). We show that suspension of doped, visible light absorbing ZnO NWs in optically transparent and low dielectric permittivity medium responds to electrostatic charges on the outer walls of the dispersion-containing glass vial and transition from chaotic to partially ordered state occurs. As a consequence of this negentropic transition strong visually perceptible variation of optical properties occurs in the form of color brightness change.

The apparent color change in materials induced by structural changes has potential for applications in sensors with power free detection or naked-eye readout [1]. Most commonly the visually perceptible color change of the material is observed in well-ordered structures consisting of building blocks or cavities having uniform size and spacing. It is possible to change or modulate this structural color by changing inter-particle distance by means of external physical or chemical stimulus. Well known example of these materials are opals and inverse opals where the observable color results from periodic variation of the refractive index in three dimensions (3D photonic crystal) [2]. In the present study we demonstrate that visible light absorbing and multiple scattering medium consisting of transition metal cation doped ZnO NW suspensions in polydimethylsiloxane (PDMS) exhibit color brightness change with some similarity to tunable structural color phenomena, resulting from NW negentropic orientational transition in electric field.

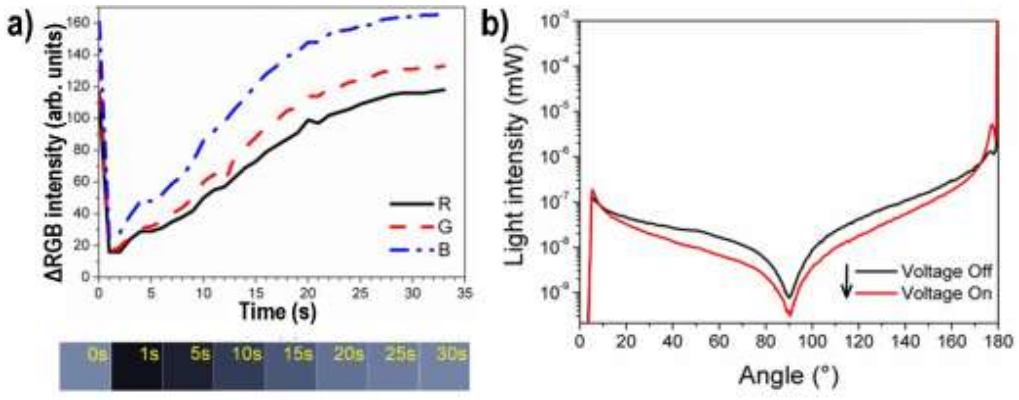



Figure 1. Graph (a) presents real time RGB color change profile for $Zn_{0.95}Ni_{0.05}O$ NW suspensions exposed to charged ions generated from a hand-held Zerostat antistatic gun and (b) Angular distribution of the scattered light intensity of 150 μm thick colloid layer with and without the applied voltage. The angle 0° corresponds to back-scattering and 180° to forward-scattering direction.

Depending on the dopant (Ni, Co or Mn), reversible gradual color transitions blue-black, green-black or yellow-black can be observed as NWs are electrokinetically aligned from disordered (chaotic) to partially ordered state. The observed color brightness change is different from structural colors since even in an aligned state the NWs only exhibit orientational ordering inside the medium and NWs exhibit wide diameter- and length distribution.

To investigate the origin of the observed optical behavior the angular scattering measurements were performed at a single wavelength using a diode laser (wavelength 532 nm) on the 150 μm thick colloid layers sandwiched between two ITO coated glass plates (Figure 1 b). Based on the measurement, it can be concluded that the light is scattered in both chaotic and aligned states of nanowires. However, both forward- and backscattering decreases (5.52 and 5.07% respectively) at the transition from chaotic to aligned state while the light transmittance (measured for the light beam that directly traverses the sample without scattering or absorption) increases from 40.0 to 45.75%. At the same time the light absorption increases from 2.92% in chaotic state to 9.13% in aligned state. The reduced back-scattering and increased absorption results in darker appearance of the sample and visually perceptible color brightness change when viewed from the back-scattering direction.

The observed optical behavior provides a basis for a power-free naked eye optical detection of triboelectric charges. Triboelectric charge detecting colloid can be filled in transparent test tubes from any material depending on electron affinity of material which should be compatible with other materials. Although the present work has been mainly focused on ZnO nanowires, the effect reported here is not brought about by any specific ZnO related properties, but is rather quite general in character.

The authors kindly acknowledge the financial support of the Estonian Research Council for the post-doctoral research grant of personal research funding in project PUTJD108 ‘‘Degenerate semiconductor nanowire-based transparent stretchable electrodes’’ and PUT1096 "Photonic hybrids with tunable optical properties".

**REFERENCES**

1. Burgess, I. B., Lončar, M. and Aizenberg, J. “Structural color in colorimetric sensors and indicators”, *J. Mater. Chem. C*, Vol 1, 6075–6086, 2013.
2. Hong, W., Li, H., Hu, X., Zhao, B., Zhang, F. and Zhang, D. “Independent multifunctional detection by wettability controlled inverse opal hydrogels,” *Chem. Commun.* Vol 48, 4609–4611, 2012.

# Enhancement of an Ultra-Wide Band Antenna System for Breast Cancer Detection using Metamaterials

**Asma Boudellioua, and Mohammed M. Bait-Suwailam**
Dept. of ECE, Sultan Qaboos University, Muscat, Oman
E-mails: asma.boudell@gmail.com; msuwailem@squ.edu.om

**Abstract**- Recently, microwave imaging brought attention as a promising method used for early breast cancer detection. The working principle of microwave imaging is based on the dielectric contrast between the malignant tumor tissues and the healthy ones. This paper presents a numerical study of a system based on ultra-wide band antennas that detect the existence of cancerous tissues. In order to further enhance the detection of such cancerous tissues, the proper use of metamaterial inclusions with the antenna system is investigated.

According to the World Health Organization (WHO), 14.1 million people were diagnosed with cancer in 2012 leading to 8.2 million cancer related deaths [1]. Breast cancer is one of the most common types of cancer and a major cause of death among women worldwide. Early diagnosis is the most important parameter to improve the survival rate of the patients.

Couple of standard methods are widely used nowadays in order to detect cancer tumors. For instance, Ultrasound, X-Ray mammography and Magnetic Resonance Imaging (MRI) are common practices in clinics for breast cancer detection and diagnosis [2]. However, these techniques suffer from flaws and limitations such as high rates of missed detections, ionizing radiation and painful breast compression in X-Ray mammography. MRI on the other hand is time consuming and expensive and ultrasound is considered to be too operator-dependent and of low specificity.

The newer approach using microwave imaging has the advantage of non-ionizing property. In addition, its test instrumentation is mature, compact, and relatively cheap. Microwave imaging is expected to become the best replacement of traditional clinical methods. Extensive researches focusing in microwave imaging are progressing to overcome the challenges in the antenna system design and image reconstruction algorithms using different techniques in which metamaterials are one of them.

This research project aims to develop metamaterial inclusions in a system based on UWB antennas in order to reduce the mutual coupling between the antenna array and improve the detection of cancerous tissues in women's breast. Multiple ultra-wide band antennas are modeled along with 3D structure mimicking properties of breast and the cancerous tissue. The time domain outputs of the simulated model using CST Microwave Studio are used to reconstruct the image using delay and sum beamforming algorithm [3]. This study will compare the system with and without incorporating suitable metamaterial structures specifically electromagnetic bandgap structures [4]. Several performance merits will be assessed to quantify the strength of the developed system.

**Acknowledgements** The authors would like to acknowledge Sultan Qaboos University for the continuous support and for funding provided for this project.

## REFERENCES

1. World Health Organization, Cancer, Available online at: http://www.who.int/mediacentre/factsheets/fs297/en/, accessed on 21.September.2015.
2. Nass, S. L., et al., " Mammography and Beyond: Developing Technologies for the Early Detection of Breast Cancer," *National Academy Press*, 2001.
3. Xu Li and and Susan C. Hagnes," A Confocal Microwave Imaging Algorithm for Breast Cancer Detection," Ieee Microwave and Wireless Components Letters, VOL. 11, NO. 3, MARCH 2001.
4. H. R. Cheng and Q. Y. Song, " Design Of A Novel EBG Structure And Its Application In Fractal Microstrip Antenna," *Progress In Electromagnetics Research,* C, Vol. 11, 81-90, 2009.

# Plasmonic Sensing Below the Quantum Noise Limit with Intensity Squeezed Light

**B.J. Lawrie[1*] and R.C. Pooser[1]**

[1] Quantum Information Science Group, Oak Ridge National Laboratory, Oak Ridge, TN, USA

[*]corresponding author: lawriebj@ornl.gov

**Abstract**-Surface plasmon resonance sensors have found widespread application for biochemical sensing, but they are increasingly limited by the quantum statistics of light. Replacing the classical laser readout with intensity squeezed states allows for either a 2.5 dB reduction of the noise floor or a 5 dB increase in signal amplitude, enabling detection of trace signatures previously buried in quantum noise.

Surface plasmon resonance (SPR) sensors are increasingly important for trace bio-chemical sensing. Recently, such devices have become extremely sensitive, pushing up against the quantum noise limits of the device, known as the shot noise limit (SNL) [1]. SPR sensors utilizing the Kretschmann geometry are capable of resolving changes in refractive index units of $10^{-7}$ by monitoring the critical angle at which surface plasmon polaritons are excited, but the SNL limits these classical sensors from producing further sensitivity enhancements. Here, we demonstrate that two mode intensity difference quantum noise reduction (also known as "squeezed" states) reduces the noise floor in Kretschmann geometry sensors below the SNL [2]. Figure 1 below illustrates the experimental setup associated with such a quantum sensor.

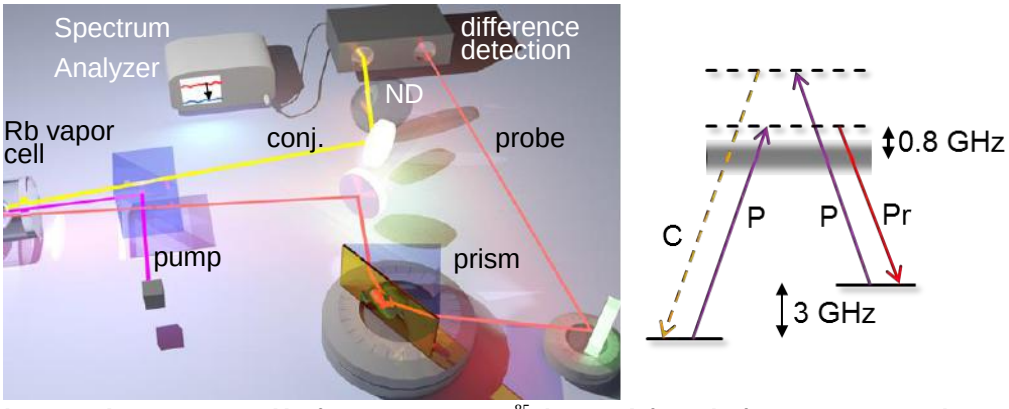



**Figure 1.** A two mode squeezed state is generated by four-wave-mixing in $^{85}$Rb vapor (left). The four-wave-mixing is the result of a weak probe (Pr) stimulating the coherent emission of a conjugate (C) photon for every emitted probe photon in a double lambda system (right). Large nonlinear gains result in bright optical fields for both probe and conjugate channels. The noise reduction observed on difference detection between the two fields allows the subtraction of classical and quantum noise so that the noise floor extends below the SNL. The probe field is modulated at 2 MHz by an acousto-optic modulator prior to being used as the readout field for the Kretschmann sensor comprised of a 43.5 nm Au film on an anti-reflection coated equilateral prism. A variable neutral density (ND) filter is used to proportionately attenuate the conjugate field so that quantum noise reduction is observed at all incident angles as the sensor is swept across the plasmon polariton absorption angle.

A four-wave-mixing process in $^{85}$Rb vapor was used to generate an intensity squeezed state exhibiting 5.5 dB of quantum noise reduction below the SNL. After modulating the probe at 2 MHz with an acousto-optic modulator and using it as the optical readout for a Kretschmann sensor designed to offer maximal sensitivity at a

wavelength of 795 nm, a variable neutral density filter was used to proportionately attenuate the conjugate field. Measuring the SPR response at an RF sideband effectively eliminates classical noise, while demodulating the RF peak is functionally equivalent to a dc measurement, so that the sensitivity can be compared directly to that of classical SPR sensors. The sensitivity of this quantum plasmonic sensor was characterized by varying the index at the Au film surface with index matching oils. At the inflection point, we witness 2.5 dB of quantum noise reduction, meaning the sensitivity is increased by 2.5 dB compared to the best classical SPR sensor relying on intensity modulation. Figure 2 shows the transmission and quantum noise reduction as a function of angle.

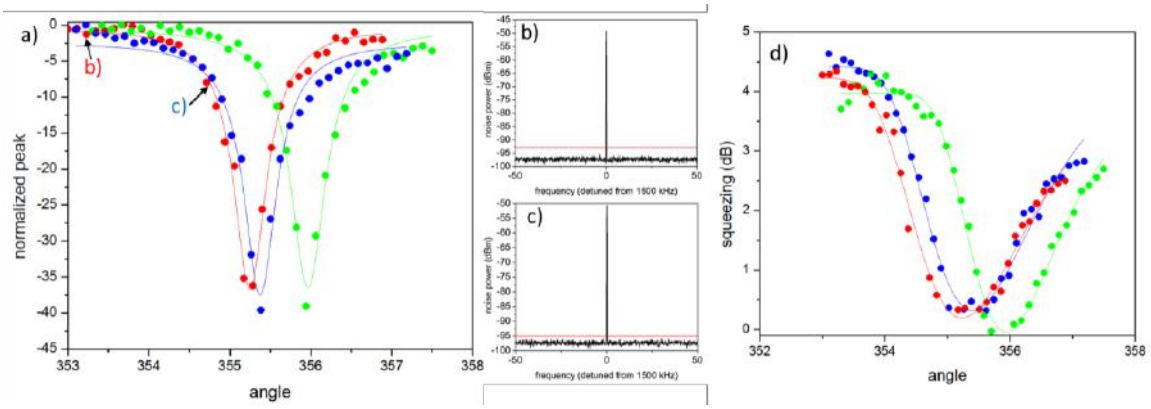



**Figure 2** (a) SPR 2 MHz sideband signal strength as a function of (uncorrected) incident angle for n=1.3, 1.301, 1.305 (red, blue, green). The noise floor for each data point in (a) is below the SNL, with representative data points illustrated in b) and c). The recorded quantum noise reduction, or squeezing, is plotted for all data points in d).

Interestingly, in the absence of a modulation signal on the probe, the quantum noise produced by the four wave mixing process itself can serve as a signal at dc. Figure 3 illustrates this property. The ND filter in the conjugate path along with the modulation of the probe field were removed, and the quantum noise reduction was used to probe the plasmon resonance.

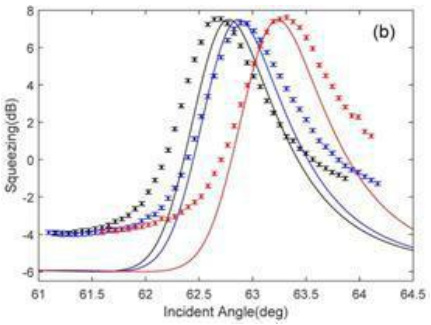



**Figure 3**. Quantum noise reduction plotted as a function of angle. As the probe is attenuated, the conjugate field is allowed to pass through to the detector without attenuation. The resulting excess quantum noise measured serves as a quantum signal which reveals the plasmon resonance. The index oils used are the same as those in Fig. 2. The solid lines are theoretical predictions based on a model for a pure quantum state followed by loss and detection.

This work was performed at Oak Ridge National Laboratory, operated by UT-Battelle for the U.S. Department of Energy under contract no. DE-AC05-00OR22725. The authors B.L. and R.P. recognize support from the Laboratory Directed Research and Development program. The gold films were grown at the Center for Nanophase Materials Sciences, which is a DOE Office of Science User Facility.

## REFERENCES

1. Piliarik, M., and Homola, J., "Surface plasmon resonance (SPR) sensors: approaching their limits?" *Optics express*, Vol. 17, No. 19, 16505-16517, 2009.
2. Pooser, R. C. and Lawrie, B. "Plasmonic trace sensing below the photon shot noise limit." *ACS Photonics*. Vol. 3, No. 1, 8-13, 2016.

# Nano-optomechanics with subwavelength light fields

**J. Muhonen, R. Leijssen, F. Ruesink, L. Freisem, G. La Gala, R. Meijer, R. Thijssen, and E. Verhagen***
Center for Nanophotonics, FOM Institute AMOLF, Amsterdam, The Netherlands
*corresponding author: verhagen@amolf.nl

**Abstract**-Optomechanical interactions provide a wealth of opportunities to control optical and mechanical fields. We exploit the extreme optomechanical interaction strengths offered by subwavelength field confinement to create large optical forces and sensitive readout of mechanical motion. We show that in this large coupling regime, the optomechanical transduction becomes highly nonlinear, even for thermal motion. This provides a path to the creation of quantum states of motion. Moreover, these systems can be used to establish nonreciprocal acoustic transport in optomechanical metamaterials.

The coupling between light and motion in nano-optomechanical systems enables extremely sensitive displacement measurements as well as nanomechanical actuation through radiation pressure. This provides a powerful way to interface nanomechanical sensors used to detect small force or mass. Moreover, the ability to perform displacement measurements of a nanomechanical resonator with sensitivity at the quantum level provides a path to controlling its quantum state of motion. We exploit subwavelength confinement in suitably engineered plasmonic or photonic crystal systems to achieving extreme optomechanical coupling strengths. We show how these can be used to perform extremely sensitive displacement measurements, in conjunction with record per-photon optical forces. Finally, we will discuss the potential for constructing effective metamaterials by coupling many of these optomechanical systems. Such materials would gain unique optical or acoustic response, due to the optomechanical interactions in each unit cell. These interactions can be used to create effective gauge fields for phonons, resulting in acoustic nonreciprocity and unidirectional topological edge states.

The interaction strength between optical fields and a mechanical resonator, as evidenced by mechanically-induced optical frequency shifts and the radiation pressure force, scales inversely with the size to which light is confined[1,2]. We explore two approaches to leveraging nanoscale confinement. Firstly, in a proof-of-principle experiment, we demonstrate how the Brownian motion of a metallic nanomechanical drum resonator can be sensitively read out using surface plasmons confined in the nanoscale gap between the drum and a metallic ground plane. Moreover, we show that plasmonic forces can be used to actuate the resonator. Secondly, in a specially designed silicon photonic crystal nanobeam, we exploit the subwavelength character of a guided optical mode to establish record photon-phonon coupling rates[3]. We use these to perform mechanical displacement measurements with an imprecision at the standard quantum limit, even for a device that has an optical linewidth of ~1 THz. For smaller linewidths, these systems enter a regime of strongly nonlinear optomechanical transduction – even for the pm amplitudes of Brownian motion. We analyze this regime for the first time, and demonstrate that in combination with feedback it provides a path to create non-Gaussian states of motion.

The large optomechanical coupling strength allows these systems to achieve strong effects already at large (THz) optical linewidths. This makes it possible to chain together multiple resonators in effective arrays, by

letting each optical mode couple to two mechanical modes and vice versa. Such chains support transport of photonic and phononic excitations with unusual properties. In particular, we discuss the possibility to establish nonreciprocal transmission of acoustic signals through such an array, and the appearance of effective gauge fields[4]. This opens the possibility to construct effective optomechanical metamaterials that are highly nonlinear and nonreciprocal.

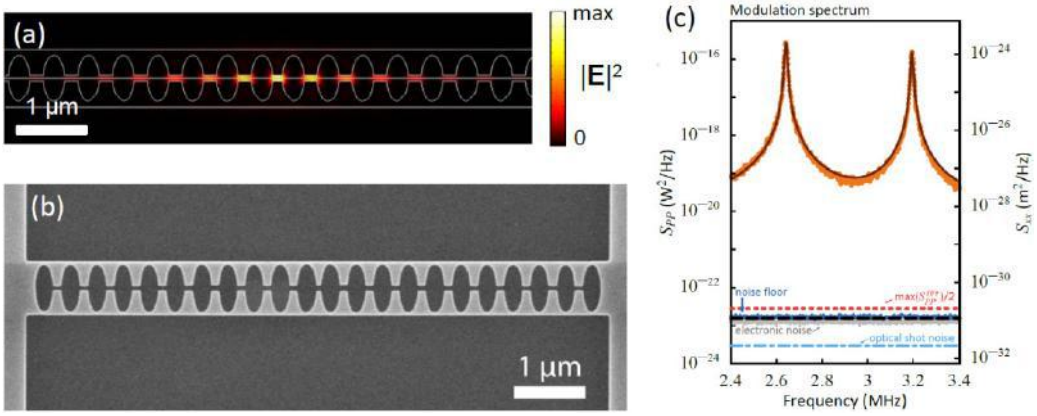



**Figure 1:** Nano-optomechanical system exhibiting extreme photon-phonon interaction strengths. (a) The subwavelength confinement of an optical cavity mode in a sliced photonic crystal nanobeam offers strong coupling to the MHz-frequency flexural mechanical motion of the beam halves. (b) Experimental realization. (c) The large optomechanical coupling results in efficient optical readout of thermal motion, with a noise imprecision equal to that at the standard quantum limit, even for optical cavities with bandwidths of several hundreds of GHz.

**Acknowledgements**, This work is part of the research programme of the Foundation for Fundamental Research on Matter (FOM), which is part of the Netherlands Organization for Scientific Research (NWO). E.V. gratefully acknowledges an NWO-Vidi grant for financial support.

**REFERENCES**

1. Aspelmeyer, M., T. J. Kippenberg, and F. Marquardt, "Cavity optomechanics," *Rev. Mod. Phys.*, Vol. 86, 1391, 2014.
2. Thijssen, R., T. J. Kippenberg, A. Polman, and E. Vehagen, "Plasmomechanical resonators based on dimer nanoantennas," *Nano Lett.*, Vol. 15, 3971, 2015.
3. Leijssen, R. and E. Verhagen, "Strong optomechanical interactions in a sliced photonic crystal nanobeam," *Sci. Rep.*, Vol. 5, 15794, 2015.
4. Peano, V., C. Brendel, M. Schmidt, and F. Marquardt, "Topological phases of sound and light," *Phys. Rev. X,* Vol. 5, 031011, 2015.

# Graphene Array Antenna for 5G Applications

**S. N. H. Sa'don[1], M. R. Kamarudin [1*], F. Ahmad[2] and M. Jusoh[3]**

[1]Wireless Communication Centre, Universiti Teknologi Malaysia, Johor, Malaysia

[2] Malaysia-Japan International Institute Technology, Universiti Teknologi Malaysia, Malaysia

[3]School of Computer and Communication Engineering, Universiti Malaysia Perlis, Malaysia

[*]corresponding author: mramlee@utm.my

**Abstract**- Fifth generation (5G) needs to provide better coverage than the previous generation. However, high frequency and millimeter wave experience penetration loss, propagation loss and even more loss in energy for long distance. Hence, a graphene array antenna is proposed for high gain to cover the long distance communications since array antenna enables in providing more directive beams. The proposed graphene antenna achieves 12 dBi with eight array elements with the separation of 0.84λ. The gain and impedance bandwidth obtained are sufficient for 5G applications.

**Introduction-** Fifth generation (5G) is defined as the next major phase of mobile telecommunications standards beyond the current 4G [1]. It is not limited to smart phone, laptop and computer but another devices or system around us will be connected without the intervention of human. With the rapid of material engineering research in electronic field, graphene has been found as a new material which offers the unique and excellent of electrical, thermal and mechanical properties [2]. Moreover, this material can be another choice for replacing copper because it has been proved to have reconfigurable capability. Most engineer and researcher propose high frequency and millimetre waves for 5G but these signals experience much kind of losses such as high penetration loss [3], the increasing of propagation loss if the range of a cell is more than 200 meters [4] and tend to loose more energy over long distance. Thus, to prevent the losses, this paper aims is to model high gain graphene antenna at least 12 dBi by increasing the elements in order to provide directive beam thus achieving long distance communication.

**Antenna design-** The array antenna is designed with size of 127.4 mm x 6.8 mm, width and length, respectively. It consists of eight elements with element of separation of 0.84λ. The graphene is patched as the radiator patch element with surface conductivity of 2.09 x $10^6$ S/m and supported by A4 paper substrate with dielectric constant of 3.2317 and tan δ of 0.0021. Each of element is fed by a coplanar waveguide (CPW) for simplicity [5]. Figure 1 shows the proposed antenna design. The thickness of graphene and A4 paper is 2 nm and 0.05 mm, respectively.

**Result and Analysis**-The antenna parameters that have been investigated were reflection coefficient magnitude (S11), bandwidth, radiation pattern, gain and antenna efficiency. Figure 2 shows the reflection coefficient magnitude. The reflection coefficient magnitude of -27.15 dB is obtained at 15 GHz. From this figure, the impedance bandwidth obtained is about 4 GHz (from 12.5 GHz to 16.5 GHz) at -10 dB level. Figure 3 and Figure 4 show the radiation pattern at phi, θ = 0° and θ = 90°, respectively. At phi, θ = 0°, the radiation pattern is bidirectional and consists of minor side lobes and at phi, θ = 90° is bidirectional. The gain obtained is 12 dBi and about 74% of the antenna efficiency s recorded.

**Conclusion**-The graphene array antenna is successfully designed. The results have met the minimum requirement for 5G and therefore this antenna is suitable for 5G communication system.

**Acknowledgements**-The authors would like to thank MoE and UTM for sponsoring this work under HiCOE and GUP grants (Vot 11H59, Vot 03G33).

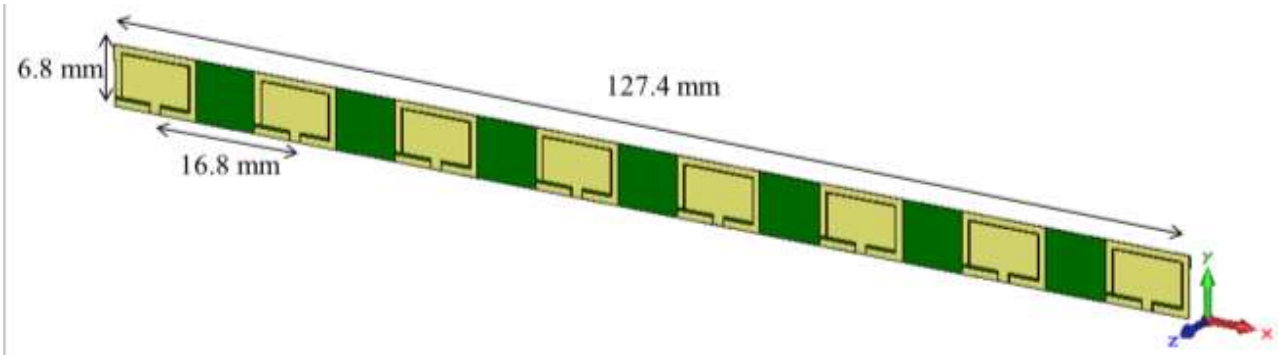



**Figure 1**: The array antenna consists of eight elements.

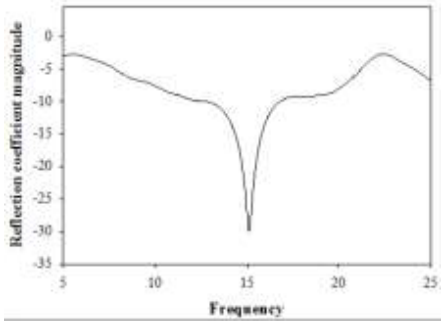



**Figure 2:** Reflection coefficient at 15GHz.

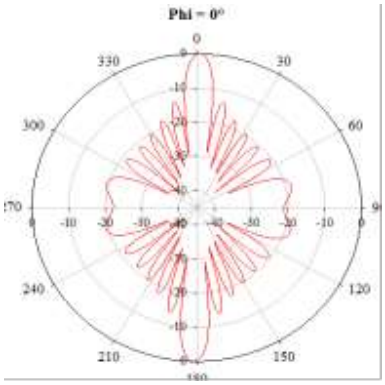



**Figure 3:** Radiation pattern at phi, θ = 0° consist of main lobes and minor lobes

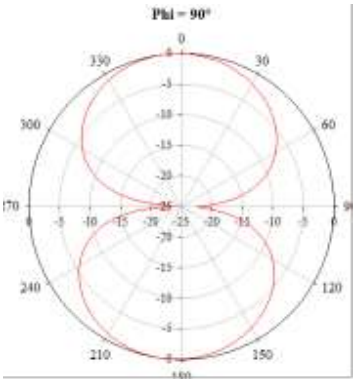



**Figure 4:** Radiation pattern at phi, θ = 90° is bidirectional.

## REFERENCES

[1] "5G," *Wikipedia*, 2016. [Online]. Available: https://en.wikipedia.org/wiki/5G. [Accessed: 13-Feb-2016].

[2] Y. Huang, L. S. Wu, M. Tang, and J. Mao, "Design of a beam reconfigurable thz antenna with graphene-based switchable high-impedance surface," *IEEE Trans. Nanotechnol.*, vol. 11, no. 4, pp. 836–842, 2012.

[3] C. X. Wang, F. Haider, X. Gao, X. H. You, Y. Yang, D. Yuan, H. M. Aggoune, H. Haas, S. Fletcher, and E. Hepsaydir, "Cellular architecture and key technologies for 5G wireless communication networks," *IEEE Commun. Mag.*, vol. 52, no. 2, pp. 122–130, 2014.

[4] X. Pang, W. Hong, T. Yang, and L. Li, "Design and implementation of an active multibeam antenna system with 64 RF channels and 256 antenna elements for massive MIMO application in 5G wireless communications," *China Commun.*, vol. 11, no. 11, pp. 16–23, 2014.

[5] H. Lee, E. Kim, J. Yook, J. Jung, H. Lee, E. Kim, J. Yook, and J. Jung, "Intrinsic characteristics of transmission line of graphenes at microwave frequencies Intrinsic characteristics of transmission line of graphenes at microwave frequencies," *Appl. Phys. Lett.*, vol. 100, no. 223102, p. 223102, 2012.

# Tunable assembly of plasmonic nanoparticles for use as reversible mirrors and sensors

**Leonora Velleman[1], Debabrata Sikdar[1], Yunuen Montelongo[1], Ye Ma[1], Yi Huang[1], James Million[1], William Pitchford[1], Vladimir A. Turek[1], Steve J. Roser[2], Anthony Kucernak[1], Alexei A. Kornyshev[1], and Joshua B. Edel[1]**

[1]Department of Chemistry, Chemical Physics Section, Imperial College London, Exhibition Road, South Kensington, London, SW7 2AZ, United Kingdom.
[2]Department of Chemistry, University of Bath, Claverton Down, Bath, BA2 7AY, United Kingdom.
Keywords. liquid−liquid interface; plasmonic ruler; nanoparticles; self-assembly; X-ray diffraction, reflectivity

[*]corresponding author: joshua.edel@imperial.ac.uk, a.kornyshev@imperial.ac.uk

**Abstract**-An (electro)chemical self-assembling, self-healing and renewable nano-plasmonic system is presented for use as ultrasensitive Raman spectroscopic sensors and reversible optical mirrors. The platform is based on the (electro)tuneable assembly of nanoparticles at a liquid|liquid, solid|liquid and mirror on mirror interfaces. By combining optical theory and simulation along with experimental data using optical reflectivity, x-ray diffraction, and Raman spectroscopy we show that we are able to build a complete picture which enables a better understanding of how and where nanoparticles assemble at such interfaces. Specifically X-ray reflectivity and X-ray diffraction studies revealed that by increasing electrolyte concentrations the nanoparticle inter-particle spacing could be controllably decreased. This study is the first method to directly elucidate this dependence. Optical reflectively can also be used, albeit indirectly, to correlate a red-shift in the reflectance spectra to a decrease in the inter-particle spacing. This effect is predominantly due to an increase in the plasmonic coupling between NPs as the spacing decreases. Combining these methods enables a clear and accurate structural understanding of such interfaces. We show that it becomes possible to generate novel two-dimensional metamaterials with unique optical properties, resulting in added functionality including enhanced sensitivity in the context of Raman spectroscopy, and controlled optical properties.

# Evaluation of Broadband Textile Monopole Antenna Performance for Subject-Specific On-body Applications

H. A. Rahim[1*], M. AbdulMalek[2], P. J. Soh[3], and G. A. E. Vandenbosch[4]
[1*] Bioelectromagnetics Research Group, School of Computer and Communication Engineering, Universiti Malaysia Perlis (UniMAP), Pauh Putra, Arau, Perlis 02600, Malaysia;
[2]Department of Engineering and Information Science, University of Wollongong in Dubai, Block 15, Dubai Knowledge Village, Dubai, UAE;
[3]Advanced Communication Engineering (ACE), Centre of Excellence, School of Computer and Communication Engineering, Universiti Malaysia Perlis (UniMAP), Pauh Putra, Arau, Perlis 02600, Malaysia;
[4]ESAT-TELEMIC, Katholieke Universiteit Leuven, Kasteelpark Arenberg 10, Leuven 3001, Belgium;
[*]corresponding author: haslizarahim@unimap.edu.my

**Abstract**- Human body characteristics with different dimensions and tissue properties, is one of the major factors in influencing the on-body radio propagation channel characteristics. A broadband textile monopole antenna operating at 2.45 GHz is evaluated to validate its performance on different subjects' characteristics. The results show that the textile monopole antenna is sufficiently robust against the variations introduced by the body up to 0.9% and 0.2% changes in the antenna's matching level and resonant frequency shift.

## Introduction

The body-centric wireless communication (BCWC) in the past few years revolved to aim for "anytime-anywhere personalized telecommunications." The miniaturization of wearable hardware, embedded software, and digital signal processing has made it possible to integrate onto the human body. BCWC has been expanding in a wide range of fields, e.g., medical monitoring and sensing, emergency response, military, sports and in the multimedia field [1-5].

One of the most important features for BCWC is the design of the antenna. Since the BCWC use the human body as a supporting environment, this necessitates the integration of many features onto the conformal radiating systems. Thus, it very critical to consider several main criteria of the designed body-worn antenna, such as low-profile, small size, its lightweight, the comfort offered to users, and the robustness in reducing the on-body detuning so a reliable communication network can be provided. The human body is a hostile environment in which to operate the antenna, because the body has a strong influence on the characteristics of both the channel and antenna [6]. This has resulted in significant changes in the antenna's characteristics due to the lossy medium of human body tissues. Hence, the wavelength values deviate from free space values when the antenna is positioned on a lossy medium (human body).

Several important characteristics of the antenna, such as resonant frequency, bandwidth, gain, radiation efficiency, and radiation pattern, are affected greatly by the lossy dielectric body tissues. The antenna suffers from the detuning effect when mounted on the body, depending on the types of antennas and body tissues. However, the rear-ground plane that exists on the antenna's topology is capable of reducing absorption of electromagnetic (EM) power by the human body tissues. In the case of antennas with no ground plane or a small

one, the EM field is radiated in both the forward and backward directions, thereby resulting a strong coupling to the human body. Thus, to overcome this detuning effect, the antenna should be mounted away from the human body. Furthermore, the textile-based antennas have gained in popularity recently because they provide flexibility, conformality, and ergonomicity to the users. Several textile-based antennas have been proposed both for narrowband and wideband WBAN. [7] proposed an innovative broadband textile PIFA that was well-suited to be integrated with clothing for WBAN applications in the frequency band of 1.8 to 3.0 GHz. In [8], the authors proposed a textile patch slotted antenna with circular polarization operating at 2.45 GHz for WBAN applications.

Thus, in this work, a broadband textile monopole antenna operating at 2.45 GHz is designed and evaluated to validate its performance on different subjects' characteristics.

**Antenna Design**

The antenna type that was used in the measurements is a quarter-wave planar Textile Monopole (TM), designed with CST Microwave Studio. This antenna topology was suited for many on-body links as it had an omnidirectional pattern [4]. However, the designed monopole was very big for realistic applications; hence, the TM was designed in a smaller size, comparable to [5]. It consists of a ground plane and a patch on a single layer of dielectric substrate (felt fabric) with $\varepsilon_r$ = 1.43, $tan\delta$ = 0.025 at 2.58 GHz, and with thickness 1.7 mm. The material characteristics were measured using the open-ended coaxial probe technique, and are consistent with the values given in [9]. The antenna is excited by a microstrip line with length $L_m$= 20 mm. The total dimension of TM is 40 x 60 mm$^2$, with a monopole patch length of, $L_M$ = 0.25$\lambda$ = 30.6 mm. ShieldIt Super electrotextile, manufactured by LessEMF Inc, is utilized for the conducting antenna parts. ShieldIt Super is a ripstop, woven polyester textile plated with copper and nickel with a thickness $t$ of 0.17 mm and an estimated weight of 230 g/m$^2$. Its surface resistance Rs is smaller than 0.05 Ω/sq. For simplicity, in CST, it was defined as a lossy metal with calculated conductivity, $\sigma$ = 1.18 x 10$^5$ Sm$^{-1}$. All dimensions of the designed structure and photos of the fabricated prototype are shown in Figure 1 (a) and (b). Table 1 presents the key parameters of TM when placed in free space and on body.

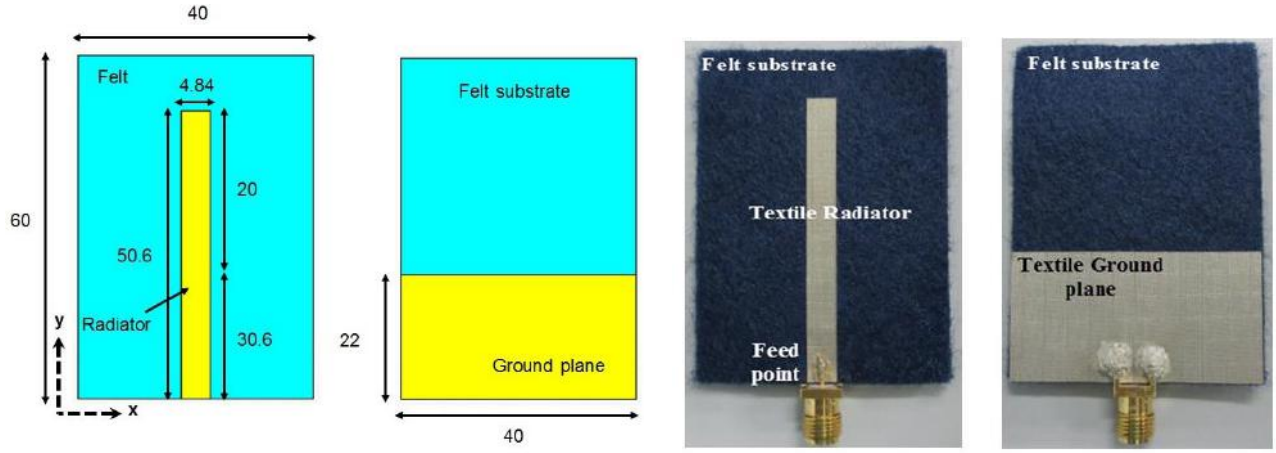


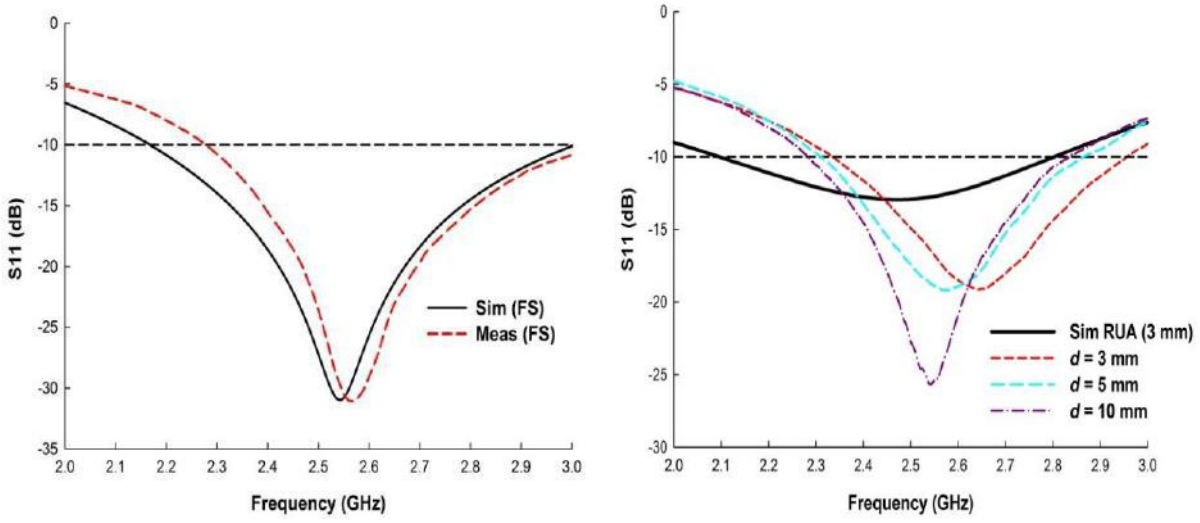

Figure 1: Structure and dimensions of (a) planar TM in millimeters and its (b) fabrication prototype in front and back views.

Table 1: Parameters of the textile monopole placed in free space and on the body.

| Parameter | | Textile Monopole (TM) | | |
|---|---|---|---|---|
| | | Free Space | On-Body | |
| | | | Upper Right Arm | Left Chest |
| **$S_{11}$** | Sim | -22.1 dB | -22.4 dB | -20.5 dB |
| | Meas | -18.6 dB | -18.0 dB | -19.0 dB |
| **Resonance** | Sim | 2.59 GHz | 2.54 GHz | 2.55 GHz |
| | Meas | 2.64 GHz | 2.56 GHz | 2.57 GHz |
| **Bandwidth** | Sim | 830 MHz | 790 MHz | 770 MHz |
| | Meas | 720 MHz | 550 MHz | 620 MHz |
| **Realized gain** | Sim | 2.41 dB | 2.10 dB | 2.94 dB |
| | Meas | 2.32 dB | -NA- | -NA- |
| **Radiation effciency** | Sim | 92% | 42% | 40% |
| **Total radiation efficiency** | Sim | 92% | 42% | 40% |
| **3 dB Beamwidth** | Sim | 85º | 74º | 76º |

**Results and Discussion**

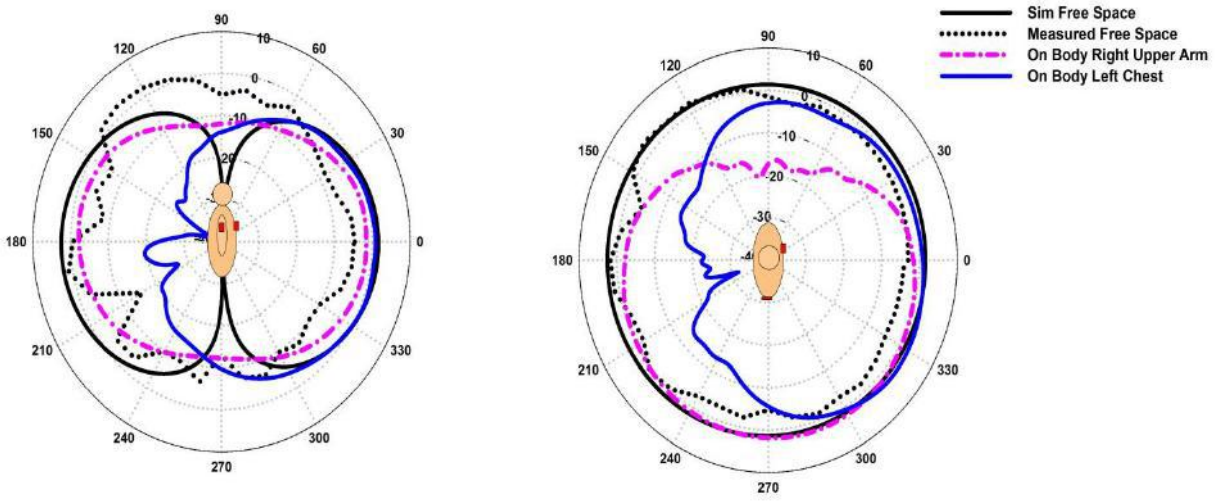
The simulated reflection coefficients ($S_{11}$) showed a good agreement with the measurement in free space, as illustrated in Figure 2 (a). Due to the high dielectric permittivity and conductivity of human body tissue, especially skin and muscles, it is well known that characteristics of an antenna can be seriously affected when placed on body. Thus, the effect of the distance to the body on the impedance matching of TM is investigated. The antenna-body separation was set at 3, 5, and 10 mm by placing foam, acting as an air gap (AG) between TM's ground plane and the subject's body. For on-body simulation, a Hugo body model is used. When the




(a) (b)

Figure 2: Simulated and measured $S_{11}$ of TM for (a) free space and (b) on right upper arm when placed at various distances from the body (3, 5, and 10 mm).

antenna is placed directly on the subject's skin of a male subject (defined as subject N and his dimension is shown in Table 2) with distance, $d$ = 3 mm on the right upper arm position, the impedance matching was severely affected due to the strong body-coupling. However, as the distance between TM and body increased, the impedance matching improved and less affected by the presence of human body. Since the TM is less influenced by the human body at $d$ = 10 mm, the antenna was placed at such distance using a thick foam with $\varepsilon_r \approx 1$, emulating realistic placement of antenna on the human body with clothing. Simulated and measured radiation patterns in free space, and simulated on-body patterns are shown in Figure 3 (a) and (b), respectively. Simulated and measured radiation patterns were in good agreement. The simulated on-body radiation pattern indicated that the TM backward radiation was absorbed by the human body tissues.




(a) (b)

Figure 3: Simulated and measured radiation pattern of TM antenna in free space and simulated radiation patterns on the body. (a) $\varphi$=90º (left) and (b) $\theta$=90º (right).

**On-Body Subject Specific Measurement**

Experimental on-body evaluations were also performed by placing TM on the chest. Figure 4 shows that measured $S_{11}$ when the TM was placed on subject N were found to be consistent with simulation on a Hugo body for both locations, i.e., right upper arm and left chest.

It was observed that the measured $S_{11}$ was less than -10 dB over the entire 2.3-2.9 GHz for both positions. Analyzing $S_{11}$ variation between different subjects from Figure 5, placing the TM on different subjects (UW, N, and OW, see Table 2) resulted in maximum of up to 0.9% and 0.2% changes in the antenna's matching level and resonant frequency shift, respectively, relative to the subjects' mean. The simulated result agrees well with the measured results, indicating that the transmitter antenna is able to preserve good impedance when placed in proximity of human body. This clearly shows that the antenna is less affected by the presence of human body

and human body characteristics. It is thus expected that the radiation pattern is not affected; only the efficiency will be different between different subjects.

Table 2: Characteristics of the six subjects.

| | **UW** | **N** | **OW** |
|---|---|---|---|
| **Height (cm)** | 157 | 167 | 176 |
| **Weight (kg)** | 44 | 60 | 110 |
| **BMI** | 17.9 | 21.5 | 35.5 |
| **Age** | 22 | 26 | 25 |
| **Chest (cm)** | 79 | 83 | 110 |
| **Waist (cm)** | 70 | 80 | 118 |

(UW - underweight, N - normal, OW - overweight)

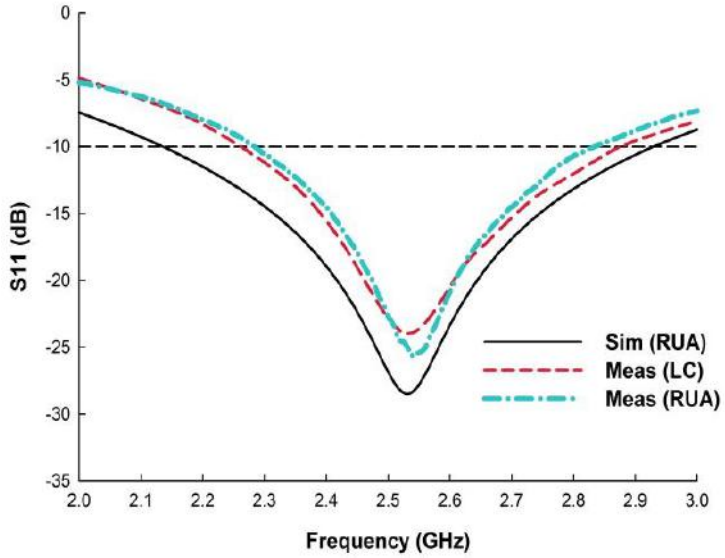
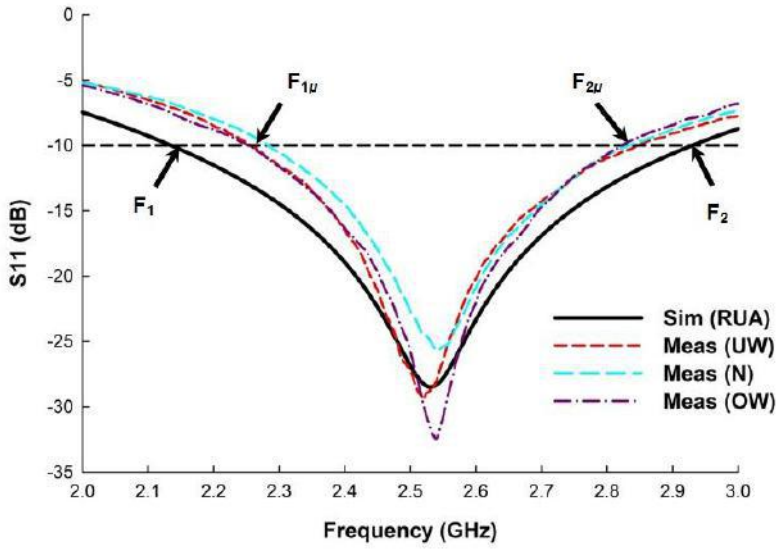



Figure 4: Simulated and measured $S_{11}$ of TM for on body (right upper arm and left chest).




(b)

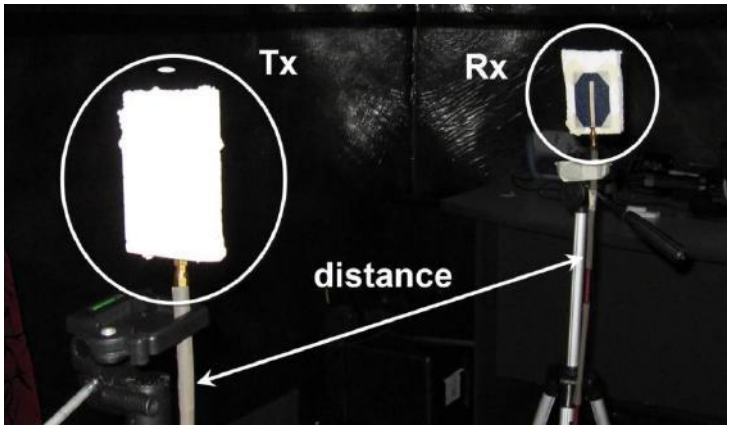
Figure 5: Simulated and measured $S_{11}$ for all subjects at upper right arm location ($F_1$ = 2.1 GHz, $F_{1\mu}$ = 2.3 GHz, $F_2$ = 2.9 GHz, and $F_{2\mu}$ = 2.8 GHz).

Simulated and measured radiation patterns in free space, and simulated radiation pattern on-body are shown in Figure 4. Simulated and measured radiation patterns showed good agreement. The simulated radiation pattern on-body indicates that the TM backward radiation was absorbed by the presence of the human body.

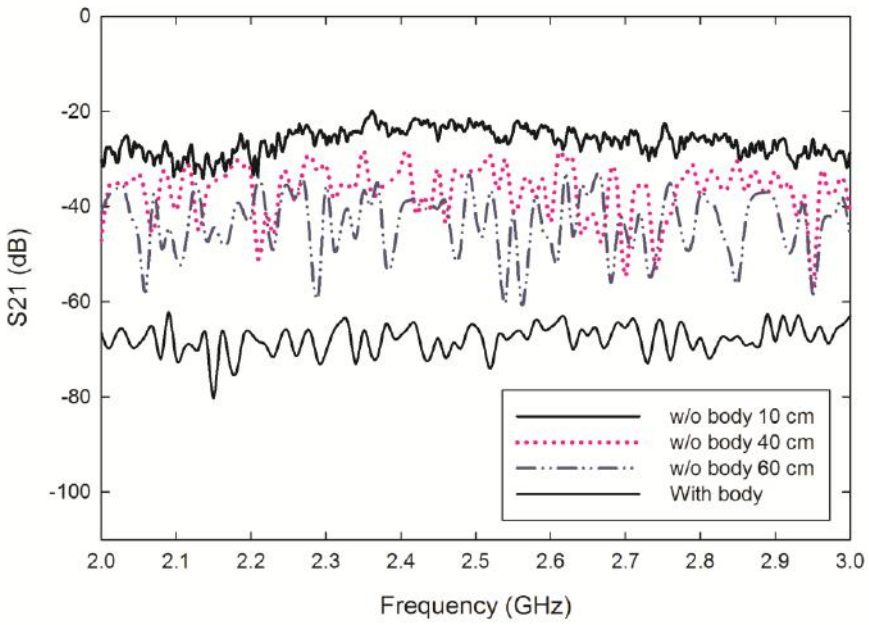
**On-Body Path Loss Measurement**

**Reference Measurement**

As a reference, measurements were done in the absence of a human body, as shown in Figure 6 (a). This measurement was conducted in an radiofrequency (RF)-shielded room at Electromagnetics Hypersensitivity (EHS) Laboratory, Politeknik Syed Sirajuddin, Perlis, Malaysia. The RF-shielded room was lined using microwave absorbing sheet. The Tx and Rxs were mounted on non-metallic tripods at a height of one meter above the floor, with vertical alignment. The distance between Tx and Rx varied from 10 to 80 cm. Figure 6 (b) shows that, as expected, the minimum path loss occurred at the minimum separation of 10 cm. The path loss increased as the distance increased. There was a significant difference between the values of path loss without a body (about -25 dB at 10 cm) and with a body (about -70 dB at the upper right arm-to-upper left arm, $d$ = 62 cm, of male subject) are obvious. The higher path loss value in the presence of the body was caused by the power absorption of lossy human body tissues.




(a)




(b)

Figure 6: Reference measurements: (a) without the presence of a human body; (b) measured $S_{21}$ for without body and with body cases.

Furthermore, in order to investigate the effect of the distance to the body, the antenna-body separation was set at 0, 5, and 10 mm by placing foam as AG between TM's ground plane and the subject's skin. The antenna locations were as follows: the Tx antenna was mounted on the right side of the subject's upper arm, while the Rx antenna was worn on the left upper arm, with the arms stretched alongside the body of the N2 subject). The results showed that the $S_{21}$ of TM reduced up to 22 dB as the AG distance increases from 0 mm to 10 mm (Figure 7).

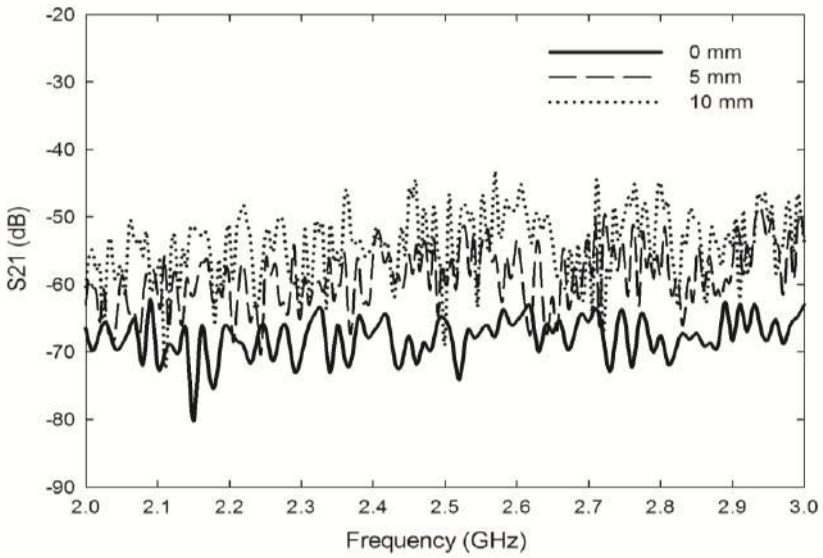


Figure 7: AG antenna-body separation of $S_{21}$

**Conclusion**

A broadband textile monopole antenna operating at 2.45 GHz designed in this work is evaluated on different subjects' characteristics. The results demonstrated that the textile monopole antenna is satisfactorily robust against the variations introduced by the body up to 0.9% and 0.2% changes in terms of antenna matching and resonant frequency when the antenna was mounted a distance away from the body.

**Acknowledgements**, The authors thank all volunteers for participating in the experiment. We also thank Surentiren Padmanathan and Nadeem Iqbal for their suggestions on the design of the experiment design and technical assistance in conducting the experiment. We also appreciate the financial support provided by grants from UniMAP and SKMM (9002-00028).

**REFERENCES**

1. Smith, D. B., Miniutti, D., Lamahewa, T. A. and Hanlen, L. W., "Propagation Models for Body-Area Networks," *Ant. and Prop. Magaz.*, Vol. 55, 97-117, 2013.
2. Movassaghi, S., Abolhasan, M., Lipman, J., Smith, D. and Jamalipour, A., "Wireless Body Area Networks: A Survey," *IEEE Communications Surveys & Tutorials*, 16, 1658–1686, 2014.
3. Alomainy, A. et al., "Statistical analysis and performance evaluation for on-body radio propagation with microstrip patch antennas," *IEEE Trans. Antennas Propag.*, 55, 245-248, 2007.
4. Hall, P. S. and Hao, Y., Antennas and Propagation for Body-Centric Wireless Communications, 2nd Edition, Artech House , 2012.
5. Alomainy, A., Hao, Y. and Davenport, D. M., "Parametric study of wearable antennas with varying distances from the body and different on-body positions," *IET Seminar on Antennas and Propag. for BCWC, IET Seminar Digest*, 11803 ed., 84-89, 2007.
6. Conway, G. A., & Scanlon, W. G., "Low-profile microstrip patch antenna for over-body surface communication at 2.45 GHz," *In International Workshop on ANtenna Technology: Small and Smart Antennas Metamaterials and Applications (IWAT '07)*, 416–419, 2007.

7. Soh, P. J., Van Den Bergh, B., Xu, H., Aliakbarian, H., Farsi, S., Samal, P., … Nauwelaers, B. K. J. C., "A smart wearable textile array system for biomedical telemetry applications," *IEEE Transactions on Microwave Theory and Techniques*, Vol. 61, No. 5, 2253–2261, 2013.
8. Soh, P. J., Vandenbosch, G. a E., Ooi, S. L., and Rais, N. H. M. "Design of a broadband all-textile slotted PIFA," *IEEE Transactions on Antennas and Propagation*, Vol. 60, No. 1, 379–384, 2012.
9. Locher, I., Klemm, M., Kirstein, T. and Roster, G. "Design and characterization of purely textile patch antennas," *IEEE Trans. on Adv. Packag*., 29, 777-788, 2006.

# Nanofabrication Technology

# High-Precision Fabrication Technology for Gold Nanoparticle Assemblies with Sub-10 nm Nanogaps

**Y. Niimura, N. Oonishi, K. Okubo, and E. T. Carlen***
Graduate School of Pure and Applied Sciences, University of Tsukuba, Japan
*corresponding author: ecarlen@ims.tsukuba.ac.jp

**Abstract**- A new top-down fabrication technology will be presented to realize gold nanoparticle assemblies with precise size and position for nanoplasmonics applications. The fabrication technology is based on conventional high-precision micromachining to form nanotemplate surfaces, and new deterministic template-guided thermal dewetting to form crystalline nanoparticle assemblies with high precision. High-precision deterministic thermal dewetting is accomplished with isolated nanotemplates to realize precise volumes of gold with nanometer-scale separations. Following thermal dewetting, nanoparticle assemblies are formed with precise position and sub-10 nm nanogaps.

One of the main challenges of nanoplasmonics is a reliable manufacturing technology for the realization of large area substrates of spatially uniform metal nanoparticles in arbitrary configurations with sub-10 nm nanogaps [1]. Many top-down and bottom-up fabrication technologies have been developed to realize nanoplasmonic substrates over the last three decades. However, none of the current technologies can precisely realize uniform nanoparticle assemblies with arbitrary arrangement and sub-10 nm nanogaps over large areas. Thermal dewetting of thin metal films offers a simple and low-cost method of producing single crystal nanoparticles [2]. Dewetting occurs when thin metal films on a solid substrate are heated, which induces clustering of the film and formation of voids (Figures 1(a)-(b)) that partition the film into isolated nanoparticles (Figure 1(c)). However, the void formation process produces random arrangements of nanoparticles with a large range of sizes and position, as shown Figures 1(d)-(e).

We have developed a deterministic template-guided thermal dewetting process to precisely form nanoparticle assemblies with precise size and position (Figure 1(f)). The fabrication technology does not require direct metal patterning or etching. The template is realized by patterning a thin silicon nitride (SiN) layer using electron-beam lithography and reactive ion etching (Figure 2(a)). Isolated SiN templates are formed by selectively removing the silicon (Si) between the templates using anisotropic wet etching to form the undercut regions (Figure 2(b)). Gold is then sputtered on the sample, where the undercut regions prevent the metal from forming a continuous layer, thus forming precise Au volumes and deterministic voids (Figure 2(c)). Thermal annealing induces metal dewetting and the formation of crystalline nanoparticle assemblies (Figure 2(d)).

Figure 3 shows scanning electron microscopy (SEM) images of gold nanoparticle assemblies made by the deterministic template-guided thermal dewetting technology. These images show that the new fabrication technology can precisely realize gold nanoparticle assemblies with arbitrary arrangement (Figure 3 (a)-(d)) and sub-10 nm nanogaps (Figure 3 (e)). In conclusion, we have developed a new simple fabrication technology capable realizing gold nanoparticle assemblies with high precision in arbitrary configurations. We will present our latest results with improved precision, reduced nanoparticle dimensions, and increased areal uniformity.

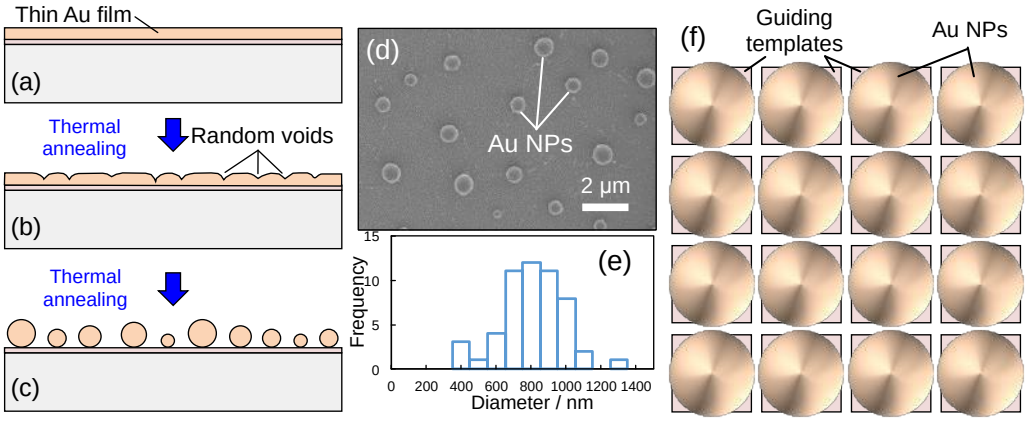



**Figure 1.** (a)-(c) Gold nanoparticles realized with conventional thermal dewetting demonstrating random size and position. (d) SEM of gold nanoparticles. (e) Particle diameter histogram. (c) Deterministic template-guided thermal dewetting for high-precision fabrication of nanoparticle assemblies.

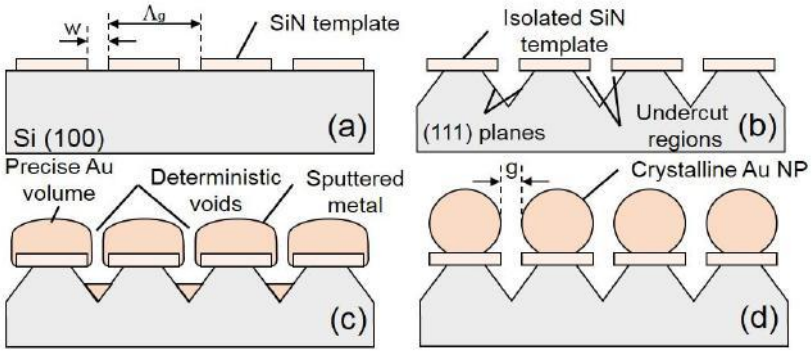



**Figure 2.** Fabrication of crystalline gold nanoparticle assemblies using template-guided thermal dewetting. (a) SiN template. (b) Isolated SiN templates using anisotropic Si etching. (c) Sputter metal. (d) Thermal annealing.

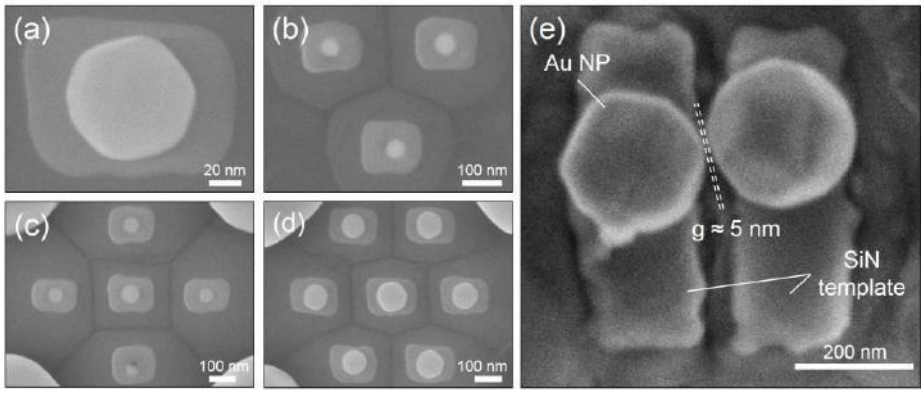



**Figure 3.** SEM images of gold nanoparticle assemblies fabricated with deterministic template-guided thermal dewetting showing precise nanoparticle size and position. (a) Monomer, (b) Trimer, (c) Pentamer, (d) Heptamer, (e) Dimer with g ≈ 5 nm gap.

**Acknowledgements** The authors than I. Kato for assistance with SEM imaging and M. Nagai for cleanroom assistance.

## REFERENCES

1. Le Thi Ngoc, L., M. Jin, J. Wiedemair, A. van den Berg, E. T. Carlen, "Large area metal nanowire arrays with tunable sub-20 nm nanogaps," *ACS Nano*, Vol. 7, No. 6, 5223-5234, 2013.
2. Giermann, A. L., C. V. Thompson, "Solid-state dewetting for ordered arrays of crystallographically oriented metal particles," *Appl. Phys. Lett.*, Vol. 86, 121903, 2005.

# Q-factor Tuning of Gold Nanoresonators by Thermal Annealing

**N. Oonishi, Y. Niimura, K. Okubo, and E. T. Carlen***
Graduate School of Pure and Applied Sciences, University of Tsukuba, Japan
*corresponding author: ecarlen@ims.tsukuba.ac.jp

**Abstract**- Nanoplasmonic resonators generate large electric fields by concentrating optical energy on metal nanostructures; however, the field enhancement is limited due to energy losses at optical frequencies, which is quantified by the resonance quality-factor. The quality-factor of gold nanoplasmonic resonators is limited to $Q \sim 20$ due to intrinsic material and extrinsic nanostructure properties. We use post-deposition annealing at low temperatures to activate grain growth and to reduce surface roughness. The quality-factor can be increased and resonance energy fine-tuned.

Nanoplasmonic resonators concentrate incident optical energy into nanoscale dimensions as localized surface plasmon resonance (LSPR) modes on metal nanostructures. The excitation of the LSPR modes depends on the characteristics of the metal dielectric function $\varepsilon(\lambda) = \varepsilon_1(\lambda) + i\varepsilon_2(\lambda)$, where $\varepsilon_1(\lambda_0) < 0$ satisfies the resonance condition for a surrounding medium with dielectric constant $\varepsilon_d > 0$ at resonance wavelength $\lambda_0$. Large negative values of $\varepsilon_1$ result in LSPR modes with an enhanced electric field in the near-field region of the nanostructure, which is an important property of nanoplasmonic resonators. However, $\varepsilon_2$ represents losses related to electron interactions and intraband transitions within the conduction band that limits the electric field enhancement and resonance quality-factor as $Q \approx (\omega\partial\varepsilon_1/\partial\omega)/2\varepsilon_2$. For gold, $\varepsilon_2$ is relatively large and the experimental quality-factor is limited to $Q \sim 20$. The quality-factor is important for many nanoplasmonics applications, such as surface-enhanced Raman scattering (SERS) where enhancements are $G \propto Q^4$. Therefore, it is important to maximize the quality-factor of gold in order to benefit from the large electric field enhancement.

The LSPR quality-factor of practical nanostructures is limited by the intrinsic properties of polycrystalline gold, and extrinsic properties such as radiation damping and structural inhomogeneities. For single-crystal gold, $\varepsilon_2$ is smaller compared to polycrystalline gold [1]. We present a simple method to improve the quality-factor of nanostructured gold surfaces using controlled low-temperature annealing. Figure 1 shows the top-down fabrication process and scanning electron microscopy (SEM) images of the nanostructured gold surfaces. The fabrication technology is based on template-guided formation of gold nanostructures during the deposition of the gold layer [2]. The silicon nitride (SiN) template is patterned with electron-beam lithography and reactive ion etching (Figures 1(a)-(b)). Isolated SiN templates are realized by removal of silicon (Si) using anisotropic etching (Figure 1(c)). Finally, a gold layer is sputtered on the templates, which results in well-controlled nanostructured gold surfaces (Figure 1(d)). Figure 1(e) is the SiN template surface. Figures 1 (f)-(h) show SEM images of the nanostructured gold surfaces with different pitch $\Lambda_g$.

Figure 2 shows SEM images and corresponding reflectance spectra of nanostructured gold surfaces following different annealing temperatures $T_a$ (1 hour annealing time). The quality-factor can be improved due to increased grain sizes and reduced surface roughness of the nanogap edges. Furthermore, the resonance energy can be precisely tuned. In conclusion, we show that a simple low-temperature annealing procedure can be used to increase the quality-factor and to fine-tune the LSPR energy. We will present our latest results with more annealing conditions and more complete analysis of the quality-factor improvement.

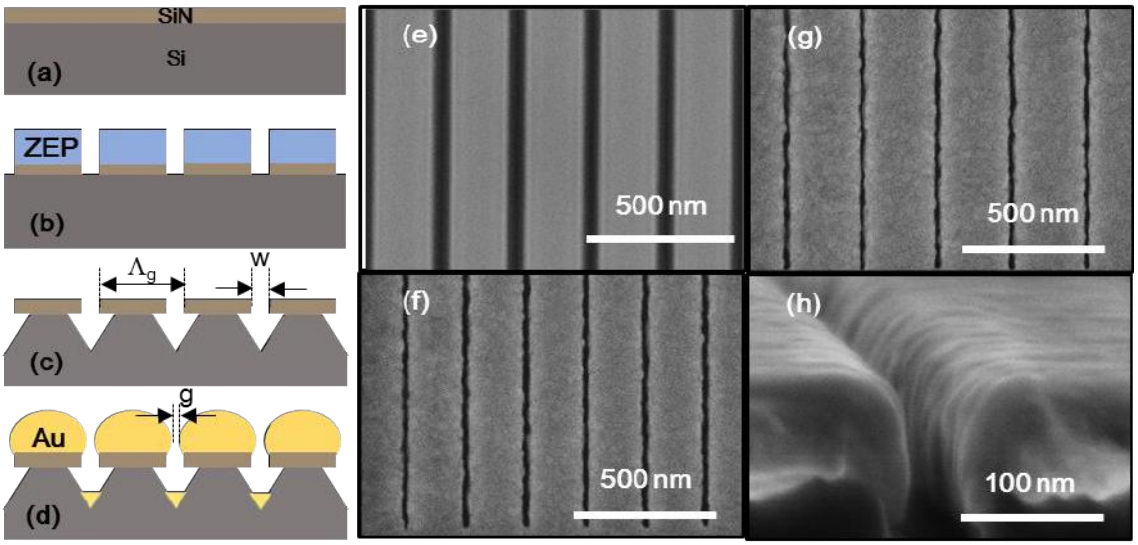



**Figure 1.** Fabrication sequence. (a) SiN on Si substrate. (b) Electron-beam lithography and reactive ion etching of SiN. (c) Anisotropic etching of Si. (d) Sputtering of gold (e)-(h) SEM images. (e) SiN template. (f)-(g) Substrate following gold deposition. ($\Lambda_g$ =200 nm and 250 nm). (h) Cross section.

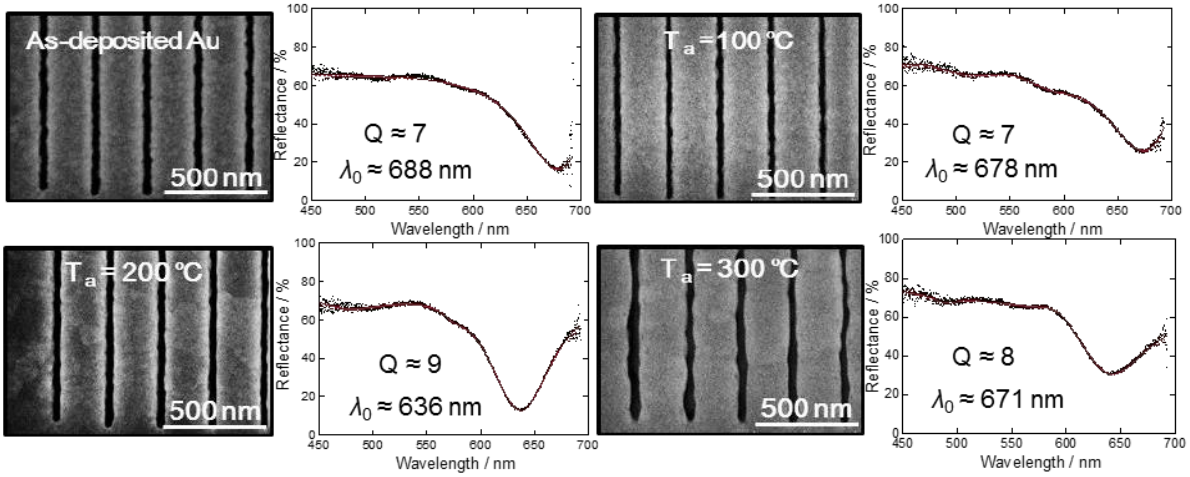



**Figure 2.** Reflectance spectra and accompanying SEM images of nanostructured gold surfaces before and after annealing at temperature $T_a$ (each for 1 hour).

**Acknowledgements** The authors thank I. Kato for assistance with SEM imaging and M. Nagai for clean room assistance.

## REFERENCES

1. Olmon, R. L., B. Slovick, T. W. Johnson, D. Shelton, S.-H. Oh, G. D. Boreman, M. B. Raschke, "Optical dielectric function of gold," *Phys. Rev. B*, Vol. 86, No. 23, 235147, 2012.
2. Le Thi Ngoc, L., M. Jin, J. Wiedemair, A. van den Berg, E. T. Carlen, "Large area metal nanowire arrays with tunable sub-20 nm nanogaps," *ACS Nano*, Vol. 7, No. 6, 5223-5234, 2013.

# Plasmonic nanorod array: novel fabrication methods and applications

**Z. K. Zhou[1,2*], J. Xue[1,2], J. Li[1,2], and X. H. Wang[1,2]**

[1] School of Physics, Sun Yat-sen University, China

[2] State Key Laboratory of Optoelectronic Materials and Technologies, Sun Yat-sen University, China

[*]corresponding author: zhouzhk@mail.sysu.edu.cn (Z.K.Z.)

**Abstract**- Due to its wide applications from fundamental physics to optoelectronic devices, plasmonic nanorod array (PNA) has long been cultivated as an important functional nanostructure. Herein, we propose two novel and facile methods for fabricating PNA, and with one of them, we are even able to easily obtain nanorod array with gaps between adjacent nanorods below 10 nm. Additionally, corresponding applications such as flexible light emission manipulating and photo-detection devices based on our obtained PNAs are also discussed.

Inheriting the ability of manipulating electronic fields and optical processes at nanoscale, as well as the advantages of working area, the plasmonic nanorod array (PNA) has made important contributions to the fabrication of various functional devices[1-2]. Despite of the great achievements, there are still some obstacles which hinder the development of device exploration based on PNA. Firstly, normal physical fabrication methods always involve expensive equipment of electron-beam lithography or focus ion beam,which is not favor for device application because of high cost and small sample area. Secondly, few efforts have been devoted into the device integration of PNA.

In this paper, we present two facile methods for PNA fabrication, both of which need the participation of the anodic aluminum oxide (AAO) template[3-5]. One is the combination of AAO growth and sputtering technique, by which we can easily obtain PNA with gaps between adjacent nanorods below 10 nm and the sample area can be up to centimeter-scale (Figure 1a and b). The other method is nanorod array deposition in the AAO template using pulse-alternating current (Figure 1c). This method can help us cut off some inevitable complicated processes in AAO direct current deposition and easily fabricate metallic nanorod array as uniform as those by direct current deposition. Additionally, we demonstrate the PNA made by our methods can be applied in constructing useful devices, from flexible plasmonic active emission source to hot-electron induced photodetection chip.

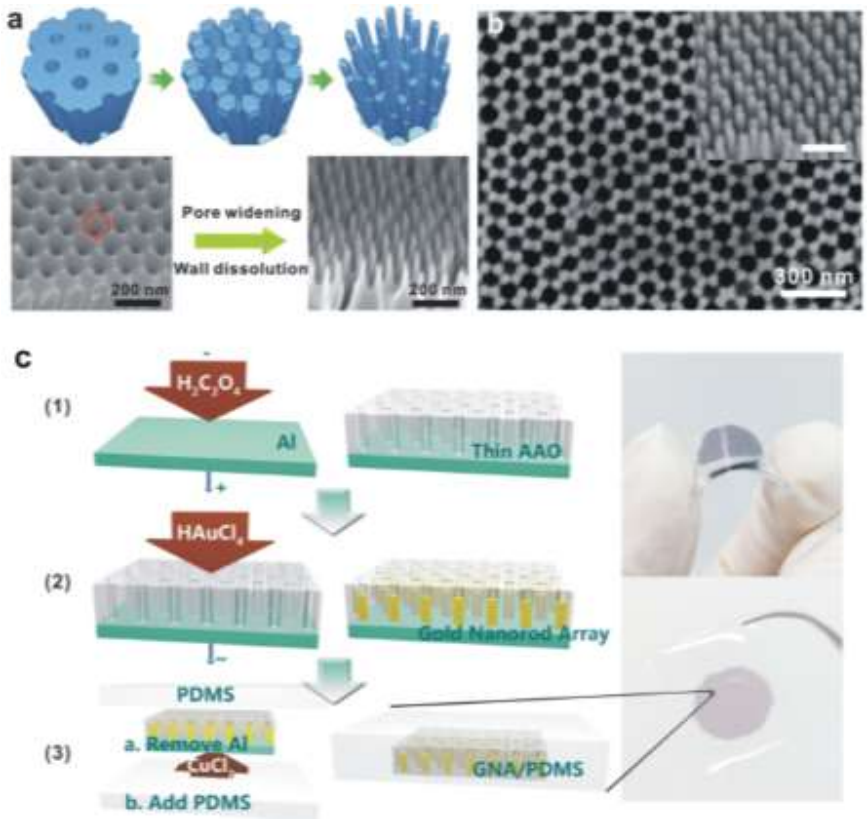



**Figure 1** (a) and (b) The growth of nanorod array with sub-10 nm gaps (c) The deposition of gold nanorod array with pulse-alternating current and making the obtained nanorod array film into flexible device.

**Acknowledgements:** This work was supported financially by National Natural Science Foundation of China (Grants 11204385 and 11511130056) and the Guangdong Natural Science Foundation (Grant 2014A030313140).

**REFERENCES**

1. Knight, M. W. *et al.* "Photodetection with active optical antennas," *Science*, Vol. 332, No. 6030, 702–704, 2011.
2. Zhou, W.*et al.* "Lasing action in strongly coupled plasmonic nanocavity arrays," *Nat. Nanotech.*, Vol. 8, No. 7, 506–511, 2013.
3. Zhou, Z.K. *et al.* "Shaping the emission spectral profile of quantum dots with periodic dielectric and metallic nanostructures," *Adv. Opt. Mater*. Vol. 2, No. 1, 56-64, 2014.
4. Li, J.*et al.* "A large-scale flexible plasmonic nanorod array with multifunction of strong photoluminescence emission and radiation enhancement," *Adv. Opt. Mater*. Vol. 3, No. 10, 1355-1361, 2015.
5. Zhou, Z. K. *et al.* "A centimeter-scale sub-10 nm gap plasmonic nanorod array film as a versatile platform for enhancing light-matter interactions," *Nanoscale* Vol. 7, No. 37, 15392-15403, 2015.

# Fine tuning of submicron pattern dimensions in Displacement Talbot Lithography

**E.D. Le Boulbar and P. A. Shields**

[1] Department of Electrical and Electronic Engineering, Claverton Down, University of Bath, Bath, BA2 7AY

[*]corresponding author: E.Le.Boulbar@bath.ac.uk

**Abstract**- We report the lithography of submicron hexagonal and linear grating patterns using the new lithography technique of Displacement Talbot Lithography. The filling factor was accurately controlled, from 8% to 17%, by varying the exposure dose. For a 600 nm pitch hexagonal pattern, we report a standard deviation of 3 nm on the average 208 nm hole diameter for an exposure dose of 35 mJ/cm$^2$. High-aspect ratio resist patterns (>3.5) were achieved for a linear grating with a period of 400nm.

Periodic patterns such as linear gratings or two-dimensional arrays are essential building blocks for many emerging technologies that use plasmonic and photonic crystal effects. The fabrication of fine, submicron patterns, and ultimately their related devices, can be achieved with several existing techniques. However, these techniques can be expensive (optical lithography), limited in resolution ~0.5-1 μm (proximity lithography), very accurate and flexible but slow (electron-beam lithography) or sensitive to particulates (nanoimprint lithography).

Displacement Talbot Lithography offers a way to produce periodic patterns across a large area with high-throughput, combined with the unique ability to control the feature size of the pattern by controlling the exposure dose. By integrating the diffraction field transmitted by a grating mask over a distance of one Talbot period, one can obtain an effective image that is independent of the absolute distance from the mask. In this way a high-resolution periodic structure can be printed without the depth-of-field limitation of Talbot self-images [1].

Photonic crystal devices are highly dependent on the characteristics of individual features (size and height, size dispersion etc.). From a research perspective, being able to control the filling factor whilst simultaneously fabricating high-aspect-ratio resist structures in order to tune the characteristics (feature size and height) would enable the fabrication of high aspect-ratio structures via a top-down approach. From an industrial and development point of view, a reliable process with a low run-to-run dispersion is a key feature for the mass production of photonic crystal based devices.

In this work we provide an in-depth analysis of the impact of process parameters on the resist feature characteristics. First, we will provide an insight of the run-to-run process reliability, focusing on the mean size of the features and its dispersion (Fig.1), for both a linear grating with a 400 nm period and a two-dimensional hexagonal pattern with a 600 nm pitch. We will demonstrate that high-aspect-ratio resist features >3.5 can be achieved using this equipment (Fig.2). We will report that a fine tuning of the filling factor can be achieved by varying the exposure dose (Fig.3).

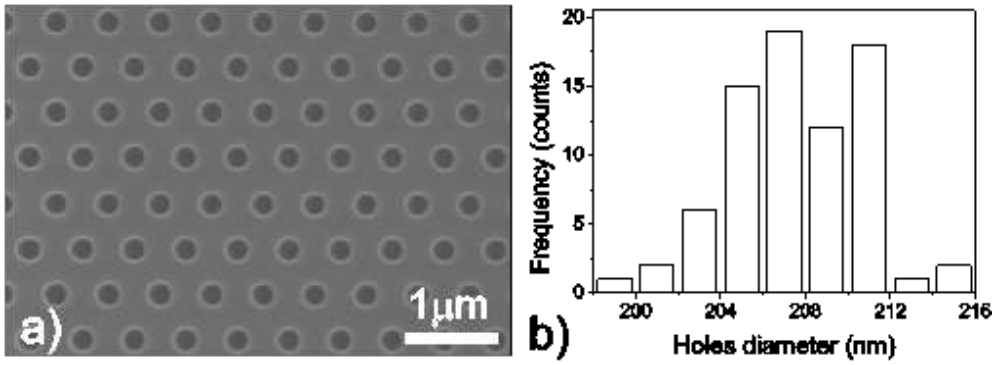



Figure 1: a) SEM image of a 600-nm-pitch hexagonal array pattern of holes obtained for a 35 mJ/cm$^2$ dose, and b) the dispersion of the hole diameter extracted through analysis of the SEM image.

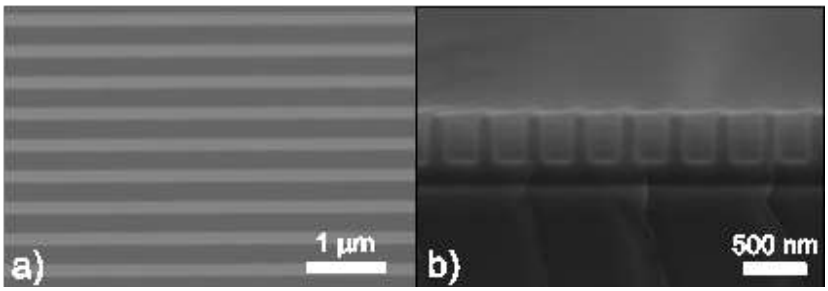



Figure 2: a) Planar and b) cross-section of 400nm linear grating obtained for a 35 mJ/cm$^2$ exposure dose.

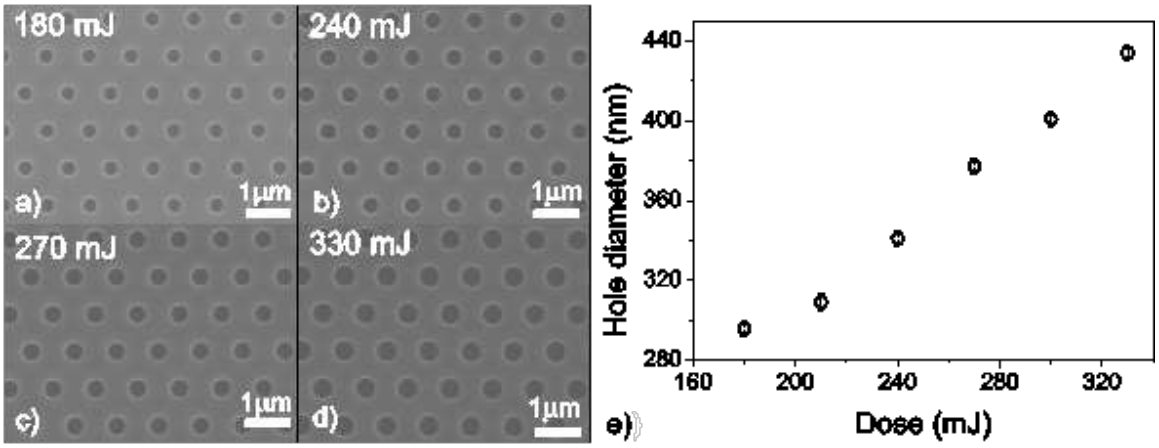



Figure 3: 1 μm pitch hexagonal array pattern of holes obtained for a) 180 mJ/cm$^2$, b) 240 mJ/cm$^2$, c) 270 mJ/cm$^2$, d) 330 mJ/cm$^2$ exposure dose, and e) the effect of the exposure dose on the hole diameter.

**Acknowledgements**: Financial support is acknowledged from the EPSRC, UK via Grant No. EP/M015181/1, "Manufacturing nano-GaN"

**REFERENCES**

1. Solak, H. H., C. Dais and F. Clube, "Displacement Talbot lithography: a new method for high-resolution patterning of large areas," *Opt. Exp.*, Vol. 19, No. 11, 2530-2535, 2011.

# 3D chiral plasmonic metamaterials fabricated by direct laser writing: The twisted omega particle.

**I. Sakellari[1*], X. Yin[1], M. Nesterov[1], K. Terzaki[2], A. Xomalis[2], and M. Farsari[2]**
[1]4th Physics Institute and Research Center Scope, University of Stuttgart, Germany
[2]Institute of Electronic Structure and Laser – Foundation for Research and Technology, Greece
[*]corresponding author: i.sakellari@pi4.uni-stuttgart.de

In this work, we combine direct laser writing and subsequent electroless silver plating to experimentally and theoretically study the plasmonic version of a 3D chiral meta-atom, which consists of a loop-wire structure, or the so-called "twisted omega particle". The metallic wire acts as a small electric dipole antenna, whereas the loop act as a split ring resonator which exhibits a magnetic dipole resonance, leading to the separation of right handed circularly polarized light and the left-handed one.

In chiral media, optical activity is a result of the coupling between electric and magnetic fields. Two classical approaches have been proposed to model the mechanisms of optical activity; a) the coupled oscillator model system, where optical activity arises from the coupling of two separate, non-collinear oscillators, and b) the one-electron model system, where an electron is bound on a helix giving electric and magnetic character to the optical transitions.

Recently, the plasmonic analog of the coupled oscillator model system, which consists of a system of two corner-stacked gold nanorods, was experimentally demonstrated [1]. This system resembles two coupled, vertically displaced electrons that carry out orthogonal harmonic oscillation driven by an external light field. In this work, we experimentally and theoretically study the plasmonic version of the one-electron model system, which comprises a loop-wire structure, namely the so-called "twisted omega particle". In this case, the metallic wire of finite length supports an electric dipole, whereas the loop acts as a split ring resonator which exhibits a magnetic dipole resonance, leading to the separation of right handed circularly polarized light (RCP) and the left-handed one (LCP) [2].

The twisted omegas are fabricated employing 3D Direct Laser Writing (DLW) by two photon absorption in combination with selective electroless silver plating. DLW by two photon polymerization is a versatile technique for the creation of solid 3D polymer nanostructures for photonics, biomedical, and microfluidic applications. By employing laser intensities that are only slightly above the nonlinear polymerization threshold, structures with submicron resolution can be fabricated. However, the realization of 3D chiral metamaterials with response at optical frequencies requires the fabrication of sufficiently small 3D chiral structures, which is limited by diffraction.

Recently, a novel route for resolution improvement in direct laser written structures has been proposed by exploiting the diffusion of a mobile quenching molecule in the scanned area [3]. The material employed is an inorganic-organic zirconium-silicon sol-gel composite, while the quencher used is also a photo-polymerizable monomer that becomes part of the polymer backbone upon fabrication. Furthermore, the quencher proposed is an amine-based monomer, where the amine moieties serve as metal binding sites allowing for the subsequent

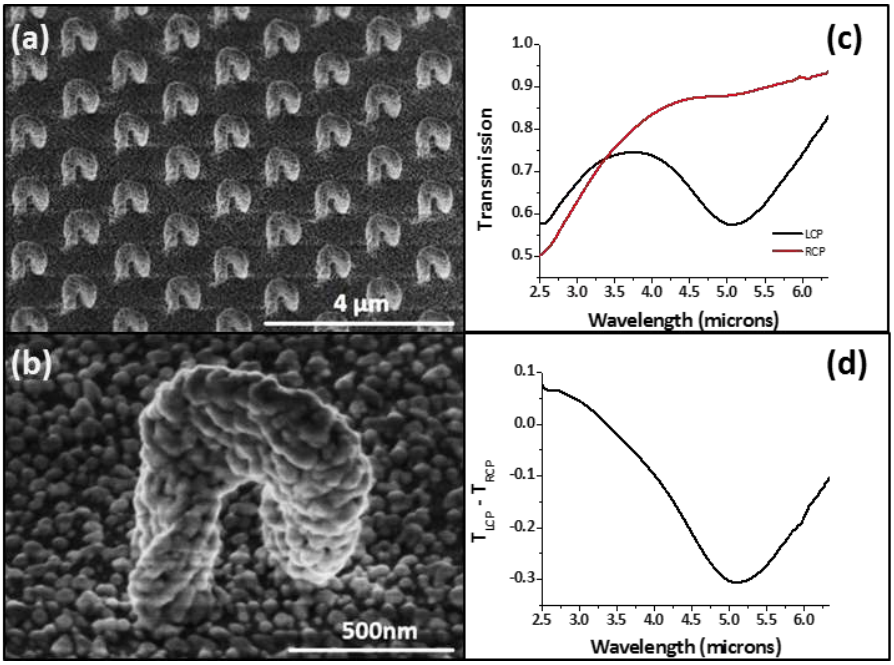



**Figure 1:** Silver electroless plated twisted omega particles with loop radius = 325nm = wire length made by DLW: a) overview of a 1.5microns x 1.5microns array of twisted omega particles, b) single twisted omega particle, c) transmission spectra of LCP and RCP incident light, and d) differential circular polarization response.

metallization of the pre-fabricated dielectric templates [4]. Employing the above mentioned approach based on on quencher diffusion in combination with subsequent electroless silver plating, we are able to fabricate high resolution 3D twisted omega meta-atoms with response in the IR wavelength region. FTIR spectroscopy is employed to electromagnetically characterize the fabricated structures for both circularly and linearly polarized waves demonstrating strong differential circular polarization response in the IR region in accordance with theoretical predictions.

**Acknowledgements:** This project has received funding from the European Union's Horizon 2020 research and innovation programme under the Marie Skłodowska-Curie grant agreement No 655249. X.Y. thanks Zeiss foundation, and M.N. thanks Alexander von Humboldt foundation. The work has been supported also by BW Stiftung and by the ERC Advanced Grant COMPLEXPLAS.

**REFERENCES**

1. Yin, X., Schäferling, M., B. Metzger and H. Giessen, "Interpreting Chiral Nanophotonic Spectra: The Plasmonic Born – Kuhn Model," *Nano Letters*, Vol. 13, 6238–6243, 2013.
2. Rockstuhl, C., Menzel, C., T. Paul and F. Lederer, "Optical activity in chiral media composed of three-dimensional metallic meta-atoms," *Phys. Rev. B*, Vol. 79, 035321, 2009
3. Sakellari, I., Kabouraki, E., Gray, D., Purlys, V., Fotakis, C., Pikulin, A., Bityurin, N., M. Vamvakaki and M. Farsari, "Diffusion –Assisted High Resolution Direct Femtosecond Laser Writing," *ACS Nano*, Vol. 6, 2302-2311, 2012.
4. Vasilantonakis, N., Terzaki, K., Sakellari, I., Purlys, V., Gray, D., Soukoulis, M. C., Vamvakaki, M., M. Kafesaki and M. Farsari, "Three-dimensional Metallic Photonic Crystals with Optical Bandgaps," *Advanced Materials*, Vol. 24, 1101–1105, 2012

# Tunable optical properties of some rare earth elements doped mayenite $Ca_{12}Al_{14}O_{33}$ nanopowders elaborated by oxalate precursor route

**M. M. Rashad[1], A.G. Mostafa[2], D. A. Rayan[1]**

[1]*Central Metallurgical Research and Development Institute (CMRDI), P.O.Box:87 Helwan (11421), Cairo, Egypt*

[2]*ME Laboratory, Physics Department, Faculty of Science, Al-Azhar University, Egypt*

## Abstract

Rare earth (RE) ions doped mayenite $Ca_{12}Al_{14-x}RE_xO_{33}$, nanopowders (where RE=La,Y and Gd, and $x$ = 0 to 1.0) were synthesized using the oxalate precursor technique. The as-prepared precursors were calcined at 800$^{o}$C for 2h. Obviously, All RE-doped $Ca_{12}Al_{14-x}RE_xO_{33}$ possessed a well crystalline cubic mayenite phase till RE content of 0.80. The crystallo-chemical aspects including crystallite size, lattice parameters, theoretical X-ray density and bulk density were robustly on RE nature and ratio. The microstructure and the average grain size were significantly influenced by the RE kind and content. The high transparency of $Ca_{12}Al_{14-x}RE_xO_{33}$ over 80% was found to be evinced in the visible wavelength range of 400-800 nm transmittance be above 80% in the visible region. Besides, the incorporation of RE cation was minimized the direct band gap energy from 4.42 eV for pure **mayenite to** 3.85 and 3.59 eV with $x$value 1.0 of $La^{3+}$ and $Gd^{3+}$ ions. The photoluminescence spectra of pure mayenite nanoparticles showed that the band edge emission ($\lambda_{exc}$ = 248 nm) with an intense visible emission band at 360 *nm* was detected. Otherwise, the band edge emission showed a slight shift towards short wavelength due to the substitution $Al^{3+}$ by $RE^{3+}$ ions. Such results open new avenue for application of mayenite as a good candidate for transparent lowtemperature electron conductor for optoelectronics applications.

* Corresponding author: rashad133@yahoo.com

# Optical Properties of Metal-Dielectric Nanocomposite Coatings Obtained by Gas Phase Condensation (GPC) and PECVD processes

**H. Nizard[1*], M.Maicu[1], D. Hecker[1,2], D. Gloess[1], P.Frach[1], G. Gerlach[2]**

[1] Fraunhofer Inst. for Organic Electronics, Electron Beam and Plasma Technology (FEP), Winterbergstr. 28, 01277 Dresden, Germany

[2] Dresden Technical University, Solid-State Electronics Laboratory, (IFE), Mommsenstraße 15, 01062 Dresden, Germany

[*]corresponding author: harry_nizard@yahoo.com

**Abstract**- We present the optical responses of nanocomposite coatings consisting of metallic nanoparticles embedded into a thin film matrix material. Coatings are obtained using a combination of gas phase condensation (GPC) and standard PECVD processes described in [1-3]: Metal nanoparticles (Ti, Ag, Au, Pt) are synthesized by means of the inert gas phase condensation (GPC) of sputtered atomic vapor, transferred into the gas flow by Gas Flow Sputtering (GFS). Organic (Plasma Polymer) or Inorganic Dielectric Matrix coatings are obtained by Low-Pressure Plasma-Enhanced CVD of organic or metal-organic precursors, respectively.

Optical analysis are carried out using UV/VIS Spectrophotometer and VASE Variable Angle Spectroscopic Ellipsometry. Nanocomposite coating optical properties are investigated for various GPC process parameters (power, sputtering time, gas flow). Observed absorption peaks are interpreted as Surface Plasmon Resonance (SPR). Results are discussed in perspective with nanoparticle size, shape and distribution as measured by other methods. Ag nanoparticles present a known 5-faceted structure, and a lattice parameter a=237pm, corresponding to that of 99.999% pure silver and comparable to similar results found in literature [4, 5].

UV/VIS spectra show typical plasmonic absorption peaks of Ag nanoparticles embedded in a plasma-polymer matrix. A redshift is observed with increasing particle sizes. A broadening of absorption peak is observed with increasing Ag content. SPR peak also depends on dielectric matrix material. An increase in the refraction index *n* results in a shift of absorption peak toward higher wavelength.

**Acknowledgements**: This work has been supported by the European Commission under the H2020 Marie Skłodowska-Curie Individual Fellowship Action. Project: Nano-LAPS

**REFERENCES**

1. R. Schmittgens, M. Wolf, E. Schultheiss, *A Versatile System for Large Area Coating of Nanocomposite Thin Films*, Plasma Process. Polym, 6 (2009) 912.
2. M. Maicu et al., *Photocatalytic Properties of $TiO_2$ Thin Films Modified with Ag and Pt Nanoparticles Deposited by Gas Flow Sputtering*, J. Nanosci. Nanotech. 15 (2015) 6478–6486
3. M. Maicu et al., *Synthesis and deposition of metal nanoparticles by gas condensation process*, J. Vac. Sci.

Technol. A 32 (2014) 02B113
4. W. P. Davey, *Precision Measurements of the Lattice Constants of Twelve Common Metals*, Phys. Rev. 25 (1925) 753
5. J. L. Elechiguerra, J. Reyes-Gasga, M. J. Yacaman, *The role of twinning in shape evolution of anisotropic noble metal nanostructures*, J. Mater. Chem. 16 (2006) 3906-3919

# Soft-glass scalable metamaterials: fiber drawn split ring resonators.

**A. Stefani*, J. Grigoleto Hayashi, X. L. Tang, and A. Argyros**
Institute of Photonics and Optical Science (IPOS), School of Physics,
The University of Sydney, NSW 2006, Australia
*corresponding author: alessio.stefani@sydney.edu.au

**Abstract**-We report on the fabrication by fiber drawing of split ring resonators (SRRs) made of soft-glass. We demonstrate how the structure can be, with this technique, easily scaled at least 2 orders of magnitude, tuning the magnetic response from the THz regime to the Infrared. We also investigate experimentally and numerically how the resonant frequency is affected by the SRRs orientation, distance and positioning within a SRRs array.

In the attempt of simplify fabrication and mass produce metamaterials, fiber drawing has shown, in the last years, a growing potential [1-5]. The advantages of this technique are both correlated to the scalability of the produced structures, but also to the realization of some types of metamaterial structures which are longitudinally invariant or slowly varying. Examples of such structures include waveguides [6] and hyperlenses [3]. However, the structures produced with this technique up to now have been limited to the THz frequency regime. In order to move towards the infrared, a change in materials is necessary. This is related to both the optical and mechanical properties of the materials. Soft-glasses represent the natural choice for this task. Metallic wire structures in a soft-glass host realized by fiber drawing have been recently theoretically investigated [4] and the fabrication of sub-micron wire structures was reported [5]. Here, we will go a step further and demonstrate that more complex structures, as split ring resonators, can be fabricated and scaled by fiber drawing.

We fabricated the SRRs by using the standard stack and draw technique and by choosing Soda-Lime glass as host material. The SRRs were filled with Tin. Figure 1 shows some of the fabricated SRRs. As it is possible to see from the figure, the drawing technique allows scaling the structure without compromising the structural integrity. We realized resonators spanning 2 orders of magnitude in size and having magnetic resonances from 3 mm to about 30 μm in wavelength. We expect to be able to scale the structure at least one more order of magnitude and reach the near-IR.

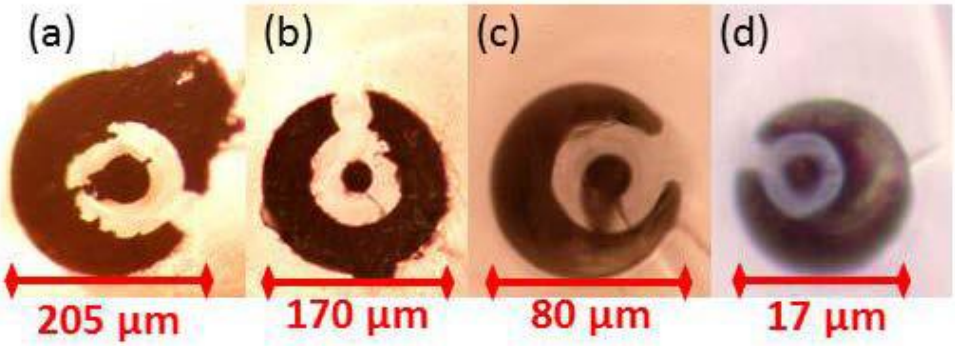



**Figure 1**: Microscope images of some of the fabricated split ring resonators. The SRRs in a, b and c are the ones used for the measurements. The dark area in the figures is metal, while the light one is glass.

We used the drawn SRRs to realize a magnetically resonant metamaterial by making arrays of resonators. The characterization of the magnetic response of some of the metamaterials, i.e. those made with the three larger SRRs of Fig. 1, was performed with a THz time domain system, as their resonant frequency is within the range of the system. The experimental results are shown in Fig. 2(a) together with the corresponding simulated spectra.

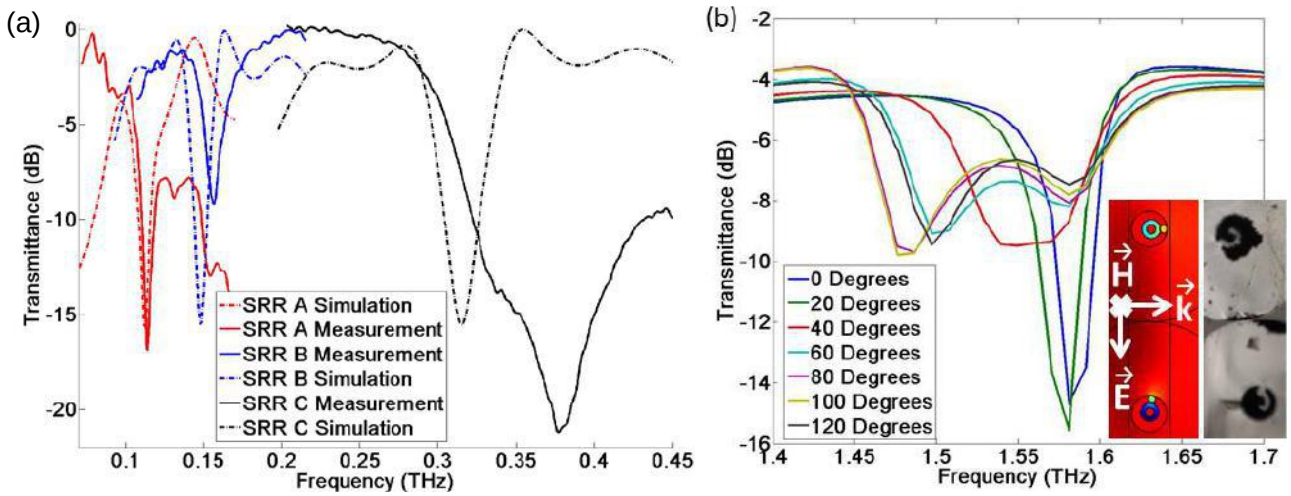



**Figure 2**: (a) Measured and simulated magnetic response of the metamaterials made with the SRRs of Fig. 1(a-c). (b) Numerical results of the dependence of the resonance on consecutive SRRs' reciprocal orientation. Inset: simulated and realized array structure of alternating orientation SRRs.

The magnetic response of a metamaterial constituted by SRRs, can be affected by the coupling of the various resonances. Therefore, we also investigated the dependence of the magnetic response on various parameters, such as the SRRs orientation, both of the entire array and of every second resonator, the alignment along the propagation direction, and the separation between SRRs. As an example, Fig. 2(b) shows, numerically, the effect on the resonance arising from changing the orientation of every second resonator in an array of SRRs.

**Acknowledgements**: This work was supported by the Eugen Lommel Stipend.

**REFERENCES**

1. N. Singh, A. Tuniz, R. Lwin, S. Atakaramians, A. Argyros, S.C. Fleming, B.T. Kuhlmey, "Fiber-drawn double split ring resonators in the terahertz range", *Opt. Mater. Express* 2, 1254-1259, 2012.
2. A. Tuniz, R. Lwin, A. Argyros, S.C. Fleming, E.M. Pogson, E. Constable, R. A. Lewis, B.T. Kuhlmey, "Stacked-and-drawn metamaterials with magnetic resonances in the terahertz range", *Opt. Express* 19, 16480-16490, 2011.
3. A. Tuniz, K.J. Kaltenecker, B.M. Fischer, M. Walther, S.C. Fleming, A. Argyros, B.T. Kuhlmey, "Metamaterial fibres for subdiffraction imaging and focusing at terahertz frequencies over optically long distances", *Nat. Commun*. 4, 2706. 2014.
4. J.G. Hayashi, S. Fleming, B.T. Kuhlmey, A. Argyros, "Metal selection for wire array metamaterials for infrared frequencies", *Opt. Express* 23, 29867-29881, 2015.
5. J.G. Hayashi, R. Lwin, S. Fleming, B.T. Kuhlmey, and A. Argyros, "Wire array metamaterial fibers based on soft-glass," in *2015 European Conference on Lasers and Electro-Optics - European Quantum Electronics Conference*, Munich, Germany (Optical Society of America, 2015), paper EH_P_1 3.
6. M. Yan, N.A. Mortensen, "Hollow-Core infrared fiber incorporating metal-wire metamaterial", *Opt. Express* 17 (17), 14851-14864, 2009.

# Template transfer for fabrication of freestanding gold nanohole membrane

**P. Jia[1*] and H. Ebendorff-Heidepriem[1]**

[1]ARC Centre of Excellence for Nanoscale BioPhotonics and Institute for Photonics and Advanced Sensing, School of Physical Sciences, The University of Adelaide, Adelaide, SA 5005 Australia

[*]Corresponding author: peipei.jia@adelaide.edu.au

**Abstract**- We developed a template transfer technique for fabrication of large-area freestanding gold nanomembrane with an array of holes with nanoscale diameter and periodicity. The freestanding membrane shows enhanced transmission compared to a membrane with the same features on a substrate. It is able to be attached on arbitrary curved surfaces and used for patterning nanoparticles. This membrane can also be cut and folded to 3D structures with dynamically and precisely controlled attitude.

Large-area freestanding metal membranes with nanoscale features are highly desirable plasmonic sensors since they can be attached to unconventional substrates that are incompatible to conventional fabrication methods. To date, several techniques have been achieved for the fabrication of freestanding nanomembranes, including spin-coating, layer-by-layer assembly, and monolayer self-assembled. However, these approaches are not applicable to metal. Therefore, fabrication of freestanding metal nanomembranes with submicron features is still a challenge and remains to be explored. In particular, fabrication of freestanding metal membranes with regular hole arrays over a large area and at relative low cost is difficult.

We have invented a new protocol to manufacture large-area freestanding gold nanomembranes (Fig.1). This method is based on the previous technique of template transfer, which uses a pre-patterned mold with nanostructures as the template to repeatedly produce exactly the same gold membranes [1, 2]. Our technique is particularly suitable to batch production because the template can be re-used in a time-efficient way. Thus it can be quickly transferred into large-scale manufacturing.

A Si template that is patterned with the desired nanohole array using projection deep UV photolithography and reactive ion etching is first deposited with 100 nm Au using e-beam deposition to form the metal nanomembrane. Thereafter a polymer polyvinylpyrrolidone (PVP) water solution (40% in weight) is dropped on top of the template with the Au nanostructured membrane. The dried polymer along with the Au membrane is then levered from the template using a razor. The Au membrane is attached to the PDMS of an annular holder such that the membrane completely covers the annulus. The holder is then placed above a beaker to keep the PVA adhesive in contact with water. After PVA is gradually dissolved, the holder with the metal nanomembrane is carefully pulled out of water. The metal membrane covering the hole of the holder becomes freestanding after water evaporation. The diameter of the circular membrane is 5 mm.

The freestanding Au nanomembrane with a hexagonal nanohole array (periodicity of 700 nm and hole diameter of 200 nm) has the same well-ordered pattern as that of the template and a smooth surface, as shown in the SEM imaging (Fig. 2a). We cut off a piece from the membrane using FIB milling to inspect the in-hole morphology. The SEM image of the membrane cross-section shows that the holes are open on both surfaces.

The transmission spectra at normal incidence of the same Au nanohole array membrane were measured in freestanding form and when placed on a transparent substrate (refractive index 1.52), respectively. We normalized both spectra according to the peak at 500 nm for comparison. The transmission efficiency of SPR significantly increases in the freestanding metal membrane compared to the nanohole array on the substrate (Fig. 2b). The dielectric materials with different dielectric constants on either side of the nanohole array film on the substrate make the SPR occurring at different wavelengths. By contrast, in the freestanding case, the uniform dielectric environment matches the SP energy on both surfaces, resulting in the coincidence of the SPR on both

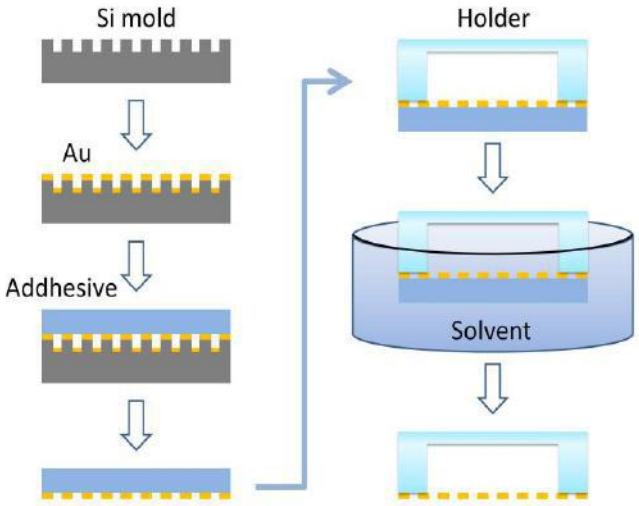



Fig. 1. Fabrication procedure of freestanding metal nanomembranes.

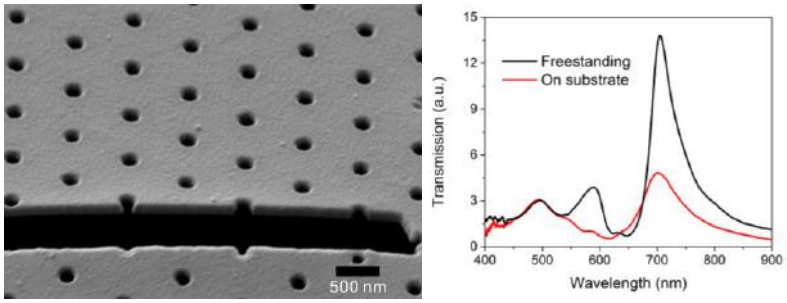



Fig. 2. a) SEM image of nanomembrane, b) transmission spectrum of freestanding and on-substrate surfaces and remarkable enhancement of the transmission intensity.

**Acknowledgements:** This work has been supported by the Centre for Nanoscale Biophotonics, through Australian Research Council (ARC) CE140100003.

**REFERENCES**

1. P. P. Jia and J. Yang, "A plasmonic optical fiber patterned by template transfer as a high-performance flexible nanoprobe for real-time biosensing," Nanoscale, vol. 6, pp. 8836-8843, Aug 2014.
2. P. P. Jia and J. Yang, "Integration of large-area metallic nanohole arrays with multimode optical fibers for surface plasmon resonance sensing," Appl. Phys. Lett., vol. 102, Jun 2013.

# Active, Nonlinear and Reconfigurable Plasmonics and Metamaterials

# Nanophotonics with Plasmonic Ceramics

N. Kinsey,[1] C. DeVault,[2] M. Ferrera,[3] U. Guler,[4] J. Kim,[1] A. Shaltout,[1] A. Dutta,[1] S. Saha,[1] A. Boltasseva,[1] and V. M. Shalaev[1,*]

[1] *Dept. of Electrical and Computer Engineering, Purdue University, West Lafayette, IN, 47907, USA*

[2] *Dept. of Physics & Astronomy, Purdue University, West Lafayette, IN, 47907, USA*

[3] *Institute of Photonics and Quantum Sciences, Heriot-Watt University, SUPA, Edinburgh, EH14 4AS, UK*

[4] *Nano-Meta Technologies, West Lafayette, IN, 47096, USA*

[*] *corresponding author: shalaev@purdue.edu*

**Abstract**- Alternative plasmonic materials are taking nanophotonics to new heights, enabling numerous applications across integrated optics, metasurfaces, dynamic systems, high temperature devices, and much more. Here we describe the roles that transition metal nitrides and the transparent conducting oxides play in developing practical nanophotonic systems for real-life applications such as thermal photovoltaics, waveguiding, and data manipulation.

For many years the plasmonic materials used in applications were limited to the noble metals [1]. Although excellent materials for many applications, several limitations such as lack of tunability, low melting point, and lack of CMOS-compatibility have restricted the development of nanophotonics applications [2]. To provide additional freedom in the design and optimization of various structures, research to find alternatives to the noble metals has exploded over the last decade [3]. Among the many potential candidates, the transition metal nitrides and the transparent conducting oxides are exceptionally promising materials for applications in the visible and near infrared spectral ranges.

The transition metal nitrides, such as titanium nitride and zirconium nitride, are dilute metal ceramics which exhibit optical properties that are similar to gold [4]. However, they also exhibit several important technological advantages such as a tunable stoichiometry (i.e. permittivity), epitaxial film quality on MgO, c-sapphire, and silicon, a high melting point (> 2900°C), and CMOS-compatibility. Together, these properties have made TiN and ZrN key materials for many applications. One such example is high temperature thermophotovoltaics whereby heat is converted to electrical energy [2]. Such systems can be significantly more efficient than typical photovoltaics since the emission of the material is controlled and designed to efficiently match the bandgap of a photovoltaic cell for optimal conversion efficiency. However, to achieve spectrally selective emission matching the semiconductor bandgaps, temperatures in excess of 800°C are required where many plasmonic materials simply melt and fail. TiN and ZrN provide suitable alternatives with sufficiently high quality plasmonic responses to facilitate numerous broad band perfect absorbing structures [5] and narrow band emitters to enable more efficient energy conversion systems.

In addition, the epitaxial quality of TiN and ZrN is critical for certain thin-film applications such as low loss plasmonic waveguiding [6]. However, for systems made of gold and silver there are two problems which face such waveguides: the lack of CMOS-compatibility and the increased surface roughness of thin films. TiN and ZrN can overcome both of these limitations enabling high quality epitaxial films with less than 0.5 nm surface roughness and semiconductor compatible materials. Using standard fabrication techniques, low-loss plasmonic waveguides using TiN and ZrN were fabricated on sapphire and are shown to have propagation lengths in excess of 5 mm with performance that exceeds that of similarly structured gold waveguides [7].

Another class of materials, transparent conducting oxides (TCOs), is particularly interesting in large part due to their ability to support extremely large doping densities, enabling them to achieve plasmonic properties in the near infrared range while maintaining low optical losses in the visible region [8]. Furthermore, they have shown the potential to be dynamically controlled either through optical or electrical means [9, 10]. Aluminum doped zinc oxide (AZO), one such TCO, was recently studied under interband excitation and shown to achieve more than 40%(30%) modulation of the transmission(reflection) with recovery times on the order of 300 fs mediated by defect enhanced recombination [10]. Consequently, AZO which can also be statically tuned during either pre- or post-deposition, is an extremely versatile plasmonic material with the ability to serve as a dynamic layer and a dielectric, metal, or epsilon-near-zero material depending upon the deposition conditions [11]. In addition to material dynamics, the integration of this material with nanophotonic waveguides was studied to facilitate a CMOS-compatible all-optical modulator. The resulting device was capable of 0.4 dB/μm of extinction for less than 0.1 dB of insertion loss while enabling the potential for operational speeds in excess of 1 THz [10].

The growth of nanophotonics is largely being fueled by the development of alternative plasmonic materials for various applications and the extreme versatility they provide. Some of the most promising of these alternative materials are the transition metal nitrides and the transparent conducting oxides. These materials have been shown to facilitate competitive devices/systems for several nanophotonic applications such as thermophotovoltaics, low loss waveguiding, and high speed modulation. As new plasmonic materials are continually developed, we look for the development of practical nanophotonic systems which can solve real world problems in the near future.

**Acknowledgements**: NSF Grant DMR-112923, AFOSR Grant FA9550-14-1-0138DEF, NSF Grant DMR-125457, ONR Grant N00014-10-1-0942, and ARO Grant 29017320-51640-D.

**REFERENCES**

1. A. Boltasseva, and H. A. Atwater, "Low-loss plasmonic metamaterials," Science **331** 290-291 (2011).
2. U. Guler, A. Boltasseva, and V. M. Shalaev, "Refractory Plasmonics," Science **344** 263-264 (2014).
3. G. V. Naik, V. M. Shalaev, and A. Boltasseva, "Alternative plasmonic materials: beyond gold and silver," Adv. Mater. **25**(24), 3264-3294 (2013).
4. G. V. Naik, J. L. Schroeder, X. Ni, A. V. Kildishev, T. D. Sands, and A. Boltasseva, "Titanium nitride as a plasmonic material for visible and near-infrared wavelengths," Opt. Mater. Express **2**(4), 478-489 (2012).
5. W. Li, U. Guler, N. Kinsey, G. V. Naik, A. Boltasseva, J. Guan, and V. M. Shalaev, "Refractory plasmonics with titanium nitride: broadband metamaterial absorber," Adv. Mater. **26**(47), 7959-7965 (2014).
6. P. Berini, "Long-range surface plasmon polaritons," Adv. Opt. Photon. **1**(3), 484-588 (2009).
7. N. Kinsey, M. Ferrera, G. V. Naik, V. E. Babicheva, V. M. Shalaev, and A. Boltasseva, "Experimental demonstration of titanium nitride plasmonic interconnects," Opt. Express **22**(10), 12238-12247 (2014).
8. G. Naik, J. Kim, and A. Boltasseva, "Oxides and nitrides as alternative plasmonic materials in the optical range," Opt. Mater. Express **1**(6), 1090-1099 (2011).
9. H. W. Lee, G. Papadakis, S. P. Burgos, K. Chander, A. Kriesch, R. Pala, U. Peschel, and H. A. Atwater, "Nanoscale Conducting Oxide PlasMOStor," Nano Lett. **14**(11), 6463-6468 (2014).
10. N. Kinsey, C. DeVault, J. Kim, M. Ferrera, V. M. Shalaev, and A. Boltasseva, "Epsilon-Near-Zero Al-Doped ZnO for Ultrafast Switching at Telecom Wavelengths," Optica **2**(7), 616-622 (2015).
11. J. Kim, G. Naik, N. Emani, U. Guler, and A. Boltasseva, "Plasmonic resonances in nanostructured transparent conducting oxide films," IEEE J. Sel. Topics Quantum Electron. **19** 46019071-46019077 (2013).

# Wavelength dependence of longitudinal photo-induced voltage in nano-porous gold thin film in visible frequencies

**M. Akbari, K. Iwata, and T. Ishihara***
Department of physics, Tohoku University, Sendai, Japan
*corresponding author: t-ishihara@m.tohoku.ac.jp

**Abstract**- We report wavelength dependence of photo-induced voltage in nanoporous gold (NPG) thin films induced by obliquely incident laser beam radiation in visible frequencies on the film for longitudinal configuration. The results show that for 450 -500 nm p- polarized incedent light, voltage is negative and for 500 -600 nm its sign changes to positive. The origin of this sign change maybe due to change in dielectric constant of the film and surface plasmon polariton excitation by p- polarized light.

When a laser beam is obliquely incident on a thin conductive film, voltage proportional to the light intensity is observed along and/or perpendicular to the incident plane, depending on the polarization states. We refer the phenomena to longitudinal photo-induced voltage (LPIV) or transverse photo-induced voltage (TPIV) effects, respectively. Photo-induced voltage (PIV) for obliquely incident light has been reported for various materials including carbon nanotubes [1] and graphene [2] and explained in terms of photon-drag effect. Mechanisms responsible for the observed photovoltage of conducting thin film structures are of interest because of their applications in the development of high speed photo detectors and angle sensors [3] as well as new physics in metamaterials with sub-wavelength structure. In previous studies this response has been interpreted in several mechanisms such as optical rectification and photon drag effect [4,5].

Recently we reported wavelength dependence of LPIV and TPIV in nanoporous gold (NPG) thin films induced by obliquely polarized laser radiation on the film for transverse for 450-600 nm laser light. As we can see in Fig.1 results showed that there is a sign change around 500nm for p- polarized light in LPIV. Angle dependence voltage for LPIV with 550 nm p- polarized light at +50° incident light showed opposite behavior for s- and p- polarization [6].

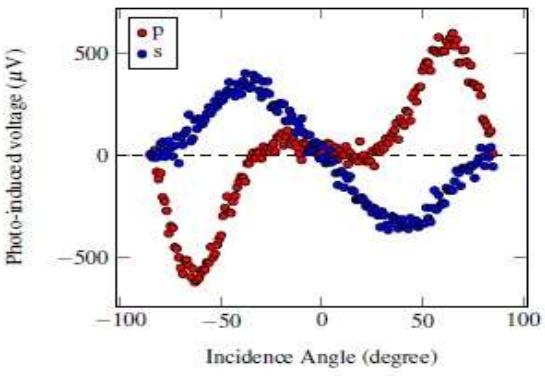



Fig.1 : Angle dependence LPIV for s- and p- polarization.

NPG film is prepared from 100 nm thick 50%-50% gold-silver alloy foil by etching Ag with nitric acid [3] and it looks more like copper rather than gold. Typical size of our sample was 7 mm x 7 mm. The excitation light source was 7 ns light pulses from optical parametric oscillator with repetition rate of 10 Hz. The polarization is controlled with achromatic half wave and quarter wave plates and Glan-laser prisms. Intensity of laser is about 4 MW/cm$^2$.

To investigate the origin of sign change for wavelength dependence LPIV with p- polarization, we measured angle dependence LPIV with 450 nm. Comparison of angle dependence voltage of film for 450 nm and 550nm incident light show that while for 450 nm generated voltage with p- polarization can be explained in terms of momentum transfer from photon to free electrons, for 550 nm voltage is generated due to excitation of surface plasmons in the film.

**REFERENCES**


1. Mikheev G. M, A. G. Nasibulin, R. G. Zonov, A. Kaskela, and E. I. Kauppinen, "Photon-Drag Effect in Single-Walled Carbon Nanotube Films," *Nano Letters* Vol.12, 77-83, 2011.
2. Glazov M.M., and S.D. Ganichev, "High frequency electric field induced nonlinear effects in graphene (review)," *Physics Report* Vol.535, 101-138, 2014.
3. Wittstock A., J. Biener, J. Erlebacher, and M. Baumer, eds. *Nanoporous Gold: From an Ancient Technology to a High-Tech Material*, RSC Publishing, Cambridge, 2012.
4. Noginova N. , V. Rono, F. J. Bezares and J. D. Caldwell, *New Journal of Physics* Vol.15, 1-11, 2013.
5. Hatano T., B. Nishikawa, M. Iwanaga, and T. Ishihara, "Optical rectification effect in 1D metallic photonic crystal slabs with asymmetric unit cell," *Optics Express*, Vol. 16, No. 11, 2008.
6. Akbari M., M. Onoda, T. Ishihara, "Photo-induced voltage in nano-porous gold thin film," *Optics Express*, Vol. 23, Issue 2, 823-832, 2015.

# Hyperbolic-Metamaterial Integrated Devices for Efficient Infrared Rectification

**Pai-Yen Chen**
[1]Department of Electrical and Computer Engineering,
Wayne State University, Detroit, Michigan 48202, USA
[*]corresponding author: userid@institution.edu

**Abstract**-We discuss possibility of rectifying infrared radiation using metal-insulator-metal tunneling nanodiodes, engineered as hyperbolic-metamaterials (HMMs). We demonstrate that responsivity of HMM-based devices can reach tens of mA/W in mid-infrared region, which may find interesting applications in photodetection and energy harvesting.

At radio frequency (RF), direct rectification of electromagnetic radiation using antennas loaded with nonlinear devices is a well-established method for wireless power conversion. It has been demonstrated that the RF-to-dc conversion efficiency can be greater than 90 % [1]. Scaling the metallic antennas to the infrared spectrum, the ultrafast rectification has been reported using MIM tunneling nanodiodes. To date, several research groups have investigated nano-antennas loaded with MIM nanodiodes, aiming to harvest solar and infrared emissive energy [2]. Moreover, plasmonic resonance and local field enhancement in nanostructured metals may further boost nonlinearity induced by tunneling plasmons in MIM junctions. However, so far the reported responsivity (or external quantum efficiency) is low, far from the mA/W level, which gives conversion efficiency less than 1 % [3].

In this work, we will investigate a MIM nanodiode tailored to the resonant dipole antenna (RDA) and the broadband log-period tooth antenna (LPDA), as shown in Fig. 1a, using realistic diode characteristics extracted from experiments. Further, we propose a nanostructured HMM that can perfectly absorb a broad range of incident infrared radiation, as shown in Fig. 1b. The slow-light modes excited in this HMM nanostructure may efficiently couple the infrared energy into the massively parallel MIM plasmonic junctions and nonlinearly rectify it into dc currents. Here we present optimized designs and venues for the experimental realization of infrared rectifiers based on MIM nano-diodes, integrated with nanoantenna and/or metamaterial geometries.

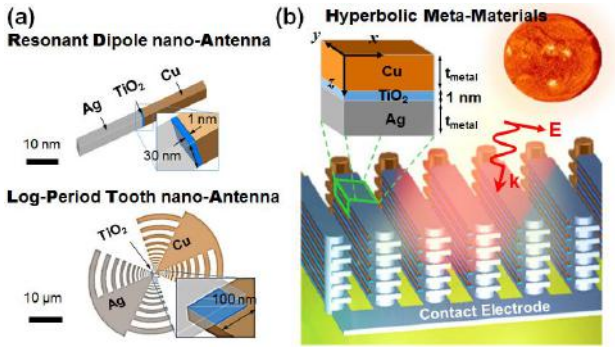


Figure1: Schematics of the infrared rectification devices based on (a) a resonant dipole antenna (RDA) and a broadband log period tooth antenna (LPTA), and (b) a nanostructured hyperbolic metamaterials (HMM).

Infrared rectification using nano-rectennas and HMMs. Here we assume the nano-rectennas and HMMs are made of silver (Ag)-titanium dioxide (TiO2)-copper (Cu) junctions, with the oxide thickness of 1 nm. The periodically trenched HMM substrate, shown in Fig. 1b, is somehow similar to an air/HMM/air waveguide array with period of 300 nm and air gap of 150 nm. The effective permittivity of such anisotropic medium can be calculated by the effective medium theory. Here realistic material properties for Ag, TiO2, and Cu were used [4]. We study conventional dipole and spiral nano-rectennas loaded with the MIM nanodiodes [Fig. 1a]. The responsivity, as the ratio of rectified static (dc) current to the incident flux, for single (i.e., rectenna) or multiple (i.e., HMM) MIM junctions is given by , where N is the number of MIM junctions, is the quantum-correlated second-order nonlinear conductivity [4], the is the electric field of incident light, is the local electric field inside the MIM gap, is free space impedance, and is the total area of HMMs or the aperture size of nano-rectennas. Figure 2a shows the spectral responsivity for different infrared rectifying devices using the same MIM nanodiodes. It is clearly seen that HMM-based devices can exhibit higher responsivity and broader bandwidth, when compared to conventional nano-rectennas that require a careful balance between the parasitics, impedance matching, and cut-off [3]. Figure 2b presents the corresponding angular responses, showing that the HMM structure is rather insensitive to variations of incident angle, when compared to a nano-dipole-based rectenna.

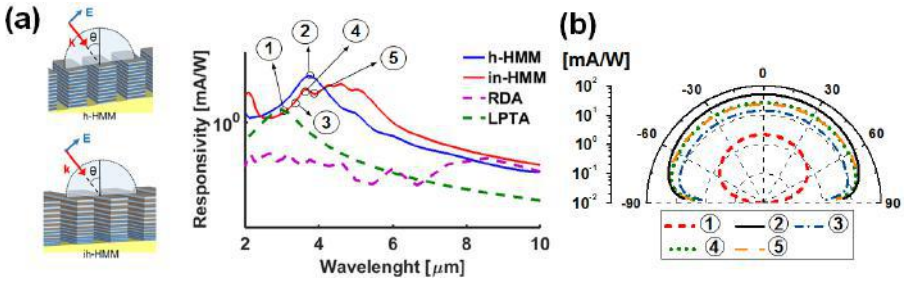



Figure 2: (a) Responsivity spectrum for different infrared rectifying devices. (b) Angular responses of the different rectifying devices in the polar plot; labels in (a) and (b) indicate the wavelengths of interest.

We have proposed and investigated a metamaterial-based quantum-tunneling device, which offers ultrafast rectification of infrared radiation. These devices will be particularly suitable for infrared photodetection and energy harvesting, with unique advantages of energy-efficient operation and no cryogenic cooling.

**REFERENCES**


1. J. O. McSpadden, L. Fan, and K. Chang, “Design and experiments of a high-conversion-efficiency 5.8-GHz rectenna,” IEEE Trans. Microwave Theory Techniq., vol. 46, 1998, pp. 2053-2060.
2. S. J. Byrnes, R. Blanchard, and F. Capasso, “Harvesting renewable energy from Earth’s mid-infrared emissions," Proc. Nat. Acad. Sci., vol. 111, 2014, pp. 3927-3932.
3. E. Briones, J. Alda, and F. J. González, “Conversion efficiency of broad-band rectennas for solar energy harvesting applications,” Opt. Express, vol. 21, 2013, pp. 412-418.
4. P. Y. Chen, K. Q. Le, and A. Alù. "Nonlinear nanocircuitry based on quantum tunneling effects." MRS Communicat., vol. 5, 2015, pp. 565-571.

# Anomalous spectral shifts in plasmonic nano-cavities

**A. Demetriadou**[1,2], **A. Lombardi**[3], **J. Mertens**[3], **O. Hess**[1], **J. Baumberg**[3], **and J. Aizpurua**[2]

[1]Blackett Laboratory, Imperial College London, London, UK
[2]Centro de Fisica de Materiales, Donostia-San Sebastian, Spain
[3]NanoPhotonics Centre, Cavendish Laboratory, University of Cambridge, Cambridge, UK
a.demetriadou06@imperial.ac.uk

**Abstract**— Nanoplasmonics have the ability to confine light in extremely small nano-cavities. We show using a theoretical model, numerical calculations and measurements that for these tightly-coupled nanoplasmonic structures, the correlation between the field enhancement (near-field) resonance and the radiative (far-field) resonance breaks down. This dissociation is determined by the nanocavity's geometry. The anomalous behaviour of plasmonic nanocavities is of significant importance for active and quantum plasmonics, where extreme nano-cavities are essential to observe strong coupling.

Plasmonic nanostructures have the ability to confine light in extremely small, sub-wavelength volumes, which leads to unprecedented field enhancements. Recently, it was shown that nano-cavities of just few nano-meters [1, 2] and even sub-nanometer [3] dimensions can be realized, by assembling a nanoparticle on a metallic surface (i.e. nanoparticle on mirror - NPoM) as shown in figure 1(a). This set-up has paved the route towards observing strong coupling [4] and intense surface-enhanced Raman scattering (SERS) [5] from just few molecules.

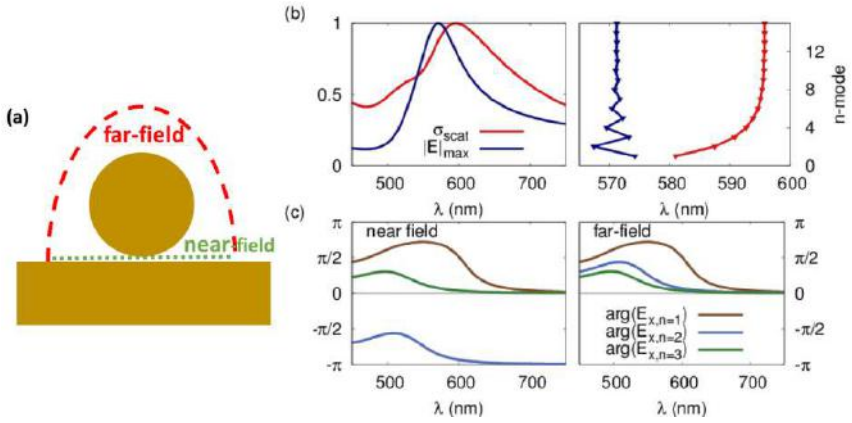



Figure 1: (a) The nanoparticle on mirror (NPoM) set-up. (b) The normalized scattering cross-section (far-field spectra) and the field-enhancement spectra ($|E|_{max}$) for the NPoM set-up (left figure). The higher order mode contribution to the resonance wavelength for the scattering cross-section and field enhancement. (c) The $E$-field phase of the three first modes of the NPoM system in the middle of the cavity (near-field) and on top of the nanoparticle (far-field).

So far, it has been assumed that the localized field enhancement of a plasmonic structure and its radiative far-field spectra are resonant at similar wavelengths, with the near-field resonance slightly red-shifted from the far-field resonance, and is a plasmonic property assumed to be universal [6]. However, we show that for tightly-coupled nanoplasmonics forming nano-cavities, this correlation between the near- and far-field spectra breaks down, with the near-field resonance always blue-shifted from the far-field spectra (see figure 1(b)) [5]. Using a theoretical model, we find that this spectra shift is due to the strong confinement and enhancement of the higher order modes in the nano-cavities. Although higher-order modes may not radiate in the far-field, they interference with and spectrally shift the bright modes of the plasmonic system [5]. This anomalous behaviour is due to the fact that within the cavity consecutive modes interfere destructively, but radiate in the far-field in-phase (figure 1(c)). These anomalous spectra shifts are also observed experimentally, where we used a widely-tuneable SERS technique to obtain the near-field resonances within individual NPoM and directly compare them to the corresponding far-field response from dark-field

measurements. As the nanoparticle is moved away from the mirror, higher-order modes become less prominent and the system reverts back to the universal state, where the near- and far-field spectra are resonant at close wavelengths.

Since nanoparticles are always faceted, the NPoM set-up produces geometrically varying nano-cavities. Through UV-laser irradiation, we grow and control the size of the facet, and observe that the plasmonic mode dominating the field enhancement in the nano-cavity, is not necessarily always the mode that radiates strongly to the far-field. This is also supported by numerical calculations shown in figure 2(a) [3]. In fact, we commonly observe that the far-field is resonant at a higher-order mode than the near-field. This anomalous behaviour is dependent on the size and geometry of the nanoparticle's facet, which forms the nano-cavity. It leads to sharp discontinuities in the far-field spectra as the NPoM is irradiated with the UV-laser [3]. Furthermore, by steadily bridging the nano-cavity, the dominant radiative mode gradually transitions to a lower order, and the plasmonic system reverts to the universal state with the near- and far-field closely correlated.

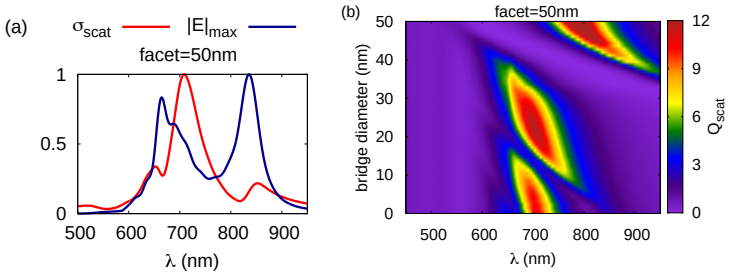



Figure 2: (a) The scattering cross-section and field enhancement spectra for a faceted NPoM, with facet=50nm. (b) The scattering efficiency of a faceted NPoM as bridge is formed within the nano-cavity.

The anomalous spectral shifts in extreme nano-plasmonic cavities have a profound impact on optimizing and tuning SERS devices and plasmonic sensors. Most importantly though, the distinct differences between the field-enhancement in nano-cavities and radiative spectra have strong implications in active and quantum plasmonics, and in particular for observing and understanding strong coupling processes.

## ACKNOWLEDGMENT

We acknowledge financial support from EPSRC grants EP/G060649/1, EP/L027151/1, EP/G037221/1, EPSRC NanoDTC, and ERC grant LINASS 320503. J.A. acknowledges support from project FIS2013-41184-P from Spanish MINECO and project NANOGUNE'14 from the Dept. of Industry of the Basque Country.

## REFERENCES

1. Taylor, R. W., F. Benz, D. O. Sigle, R. W. Bowman, P. Bao, J. S. Roth, G. R. Heath, S. D. Evans and J. J. Baumberg "Watching individual molecules flex within lipid membranes using SERS," *Scientific Reports*, Vol. 15, 669-674, 2015.
2. Benz, F., C. Tserkezis, L. O. Herrmann, B. de Nijs, A. Sanders, D. O. Sigle, L. Pukenas, S. D. Evans, J. Aizpurua and J. J. Baumberg "Nanooptics of Molecular-Shunted Plasmonic Nanojunctions," *Nano Letters*, Vol. 4, 5940, 2014.
3. Mertens, J., A. Demetriadou, F. Benz, R. W. Bowman, M. E. Kleemann, C. Tserkezis, Y. Shi, H. Y. Yang, O. Hess, J. Aizpurua and J. J. Baumberg, 2016, submitted.
4. Chikkaraddy, R., B. de Nijs, F. Benz, S. J. Barrow, O. A. Scherman, A. Demetriadou, P. Fox, O. Hess, E. Rosta, and J. J. Baumberg, "Single-molecule strong coupling at room temperature in plasmonic nanocavities," 2016, submitted.
5. Lombardi, A., A. Demetriadou, L. Weller, P. Andrae, F. Benz, R. Chikkaraddy, J. Aizpurua and J. J. Baumberg, "Anomalous Spectral Shift of Near- and Far-Field Plasmonic 2 Resonances in Nanogaps," *ACS Photonics*,2016, DOI: 10.1021/acsphotonics.5b00707.
6. Alonso-Gonzalez P., P. Albella, F. Neubrech, C. Huck, J. Chen, F. Golmar, F. Casanova, L. E. Hueso, A. Pucci, J. Aizpurua, and R. Hillenbrand, "Experimental Verification of the Spectral Shift between Near- and Far-Field Peak Intensities of Plasmonic Infrared Nanoantennas, "*Physical Review Letters*, Vol. 110, 203902, 2013.

# Nonlocal phenomena in metastructures with near-zero parameters

**I. Liberal**[1], **Y. Li**[1,2], **and N. Engheta**[1*]

[1] Department of Electrical and Systems Engineering, University of Pennsylvania, Philadelphia, Pennsylvania, USA

[2]Department of Electrical Engineering, Tsinghua University, Beijing, China

[*]corresponding author: engheta@ee.upenn.edu

**Abstract**-Metastructures with near-zero parameters provide alternative pathways to engineer light-matter interactions. Here, we emphasize the nonlocal properties of epsilon-near-zero (ENZ) media by demonstrating that the characteristics of a large scattering body can be manipulated with a single and small actuator. These and other examples of the nonlocal features of ENZ media will be discussed in our presentation.

Macroscopic media impact the propagation, concentration, emission and intrinsic properties of electromagnetic fields [1]. Thus, media with extreme features such as near-zero constitutive parameters provide unique opportunities in engineering light-matter-interactions, potentially leading to scenarios with qualitatively different physics [2-3]. For instance, one particularly striking property of epsilon-near-zero (ENZ, i.e., $\varepsilon \approx 0$) media is the possibility to suppress the spatial variations of the fields. Specifically, a spatially constant magnetic field (while being temporally dynamic) is required for TM modes in 2D ENZ in order to maintain a finite electric field: $\boldsymbol{E} = (j\omega\varepsilon_0\varepsilon)^{-1}\nabla \mathrm{H_z} \times \hat{\mathbf{z}}$ [2]. Although it might appear conceptually simple, a constant field over a potentially large body is the generator of a variety of nonlocal phenomena that will be reviewed in our presentation.

As a specific example aimed to illustrate the nonlocal features of ENZ media, we investigate here the scattering of a TM polarized plane wave by a nonmagnetic ($\mu = 1$) 2D cylindrical ENZ body with rectangular cross-section of area $A = 2\lambda \times 1\lambda$, containing a dielectric inclusion consisting of a cylinder of circular cross-section with radius $r_p$ and relative permittivity $\varepsilon_p = 10$ (see Fig. 1A). Generalizing the theoretical analyses presented in [4-6] to open systems, it can be demonstrated that the fields excited outside the body are identical to those of a homogeneous body of effective permeability $\mu_{\text{eff}} = \left(A_h + A_{\text{eff},p}\right)/A$, while maintaining a near-zero permittivity. Here, $A_h = A - \pi r_p^2$ is the area of the ENZ host, and $A_{\text{eff},p} = \int_{A_p} \psi^p(\boldsymbol{r}) dA$ is the effective area of the dielectric inclusion. $\psi^p(\boldsymbol{r})$ is the solution to the scalar Helmholtz equation subject to the boundary condition $\psi^p(\boldsymbol{r}) = 1$ on the inclusion boundary. For the canonical inclusion considered in Fig. 1A, the effective area can be simply written as $A_{\text{eff},p} = 2\pi r_p k_p^{-1} J_1\left(k_p r_p\right)/J_0\left(k_p r_p\right)$. Fig. 1B depicts the effective permeability as a function of the rod radius, though a similar tuning behavior would be attainable by changing the permittivity of the dielectric rod.

We remark that both the near and far electric and magnetic field distributions external to the scattering body are identical to those of the associated homogeneous body with effective permeability $\mu_{\text{eff}}$ and effective permittivity near zero. Note that this implies that a single, possibly distant, actuator is able to manipulate the boundary effects on the large scattering body, such that it locally reacts in the same way than a homogeneous medium. Among others, this extremely nonlocal feature may find applications in the design of flexible and reconfigurable metasurfaces. In order to illustrate this effect, Fig. C represents the magnetic field magnitude

distributions for the two extreme cases in which the composite (ENZ + dielectric inclusion) bodies emulates perfect magnetic conducting (PMC, i.e., $\mu \to \infty$, $\varepsilon \to 0$) and epsilon-and-mu-near-zero (EMNZ, i.e., $\mu \to 0$, $\varepsilon \to 0$) bodies. The numerical simulations were carried out with COMSOL Multiphysics® 5.0. It is evident from the figure that modifying the internal inclusion has a significant impact on the shadow generated by the scattering body. For the sake of comparison, Fig. 3 also includes the magnetic field magnitude distribution for actual PMC and EMNZ bodies.

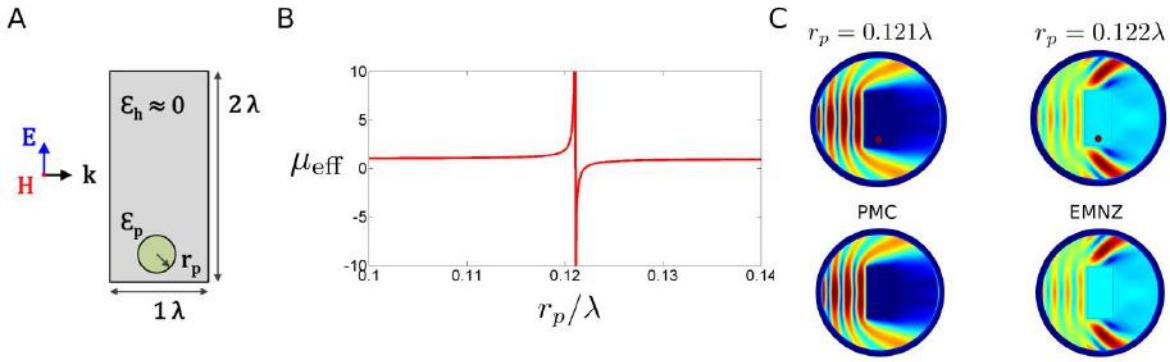



***Fig. 1. A.*** *Sketch of the geometry.* ***B.*** *Effective permeability as a function of the inclusion radius.* ***C.*** *Magnetic field magnitude distribution for inclusion radii of* $r_p = 0.121\lambda$ *and* $r_p = 0.122\lambda$*, mimicking the external fields of PMC and EMNZ bodies, respectively. The outer circular boundary corresponds to the PML layer employed in the numerical simulations.*

In conclusion, we numerically demonstrate that a single actuator is able to control and manipulate the scattering response of a large scattering ENZ body. Remarkably, this configuration enables reconstructing not only the far but also the near field distributions of PMC and EMNZ bodies. In this manner, the same approach could be adopted to modify the emission by and interaction between sources in the vicinity of these structures. In our presentation we will review these and other nonlocal effects triggered by metamaterials with near-zero parameters.

**Acknowledgements**, This work was supported in part by the US Air Force Office of Scientific Research (AFOSR) Multidisciplinary University Research Initiative (MURI) grant number FA9550-14-1-0389, and in part by the NSSEFF award number N00014-16-1-2029

**REFERENCES**

1. L. Landau and E.M. Lifshitz, *Electrodynamics of Continuous Media*, Pergamon Press, Oxford, 1960.
2. M. Silveirinha and N. Engheta, "Tunneling of electromagnetic energy through subwavelength channels and bends using ε-near-zero materials," *Phys. Rev. Lett.*, Vol. 97, p. 157403, 2006.
3. R.W. Ziolkowski, "Propagation in and scattering from a matched metamaterial having a zero index of refraction," *Phys. Rev. E*, Vol. 70, p. 046608, 2004.
4. M. Silveirinha, and N. Engheta, "Design of matched zero-index metamaterials using nonmagnetic inclusions in epsilon-near-zero media," *Phys. Rev. B*, Vol. 75, p. 075119, 2007.
5. V. C. Nguyen, L. Chen, and K. Halterman, "Total transmission and total reflection by zero index metamaterials with defects, " *Phys. Rev. Lett.*, Vol. 105. p. 233908 (2010).
6. A.M. Mahmoud and N. Engheta, "Wave-matter interactions in epsilon-and-mu-near-zero structures.," *Nat. Commun.*, vol. 5, p. 5638 (2014).

# Nonlinear Reconfigurable All-Dielectric and Hybrid Nanoantennae

**S.V. Makarov[1], A.E. Krasnok[1], D.A. Zuev[1], V.A. Milichko[1], I.S. Mukhin[1] and P.A. Belov[1]**
[1]ITMO University, St. Petersburg 197101, Russia
[*]corresponding author: belov@phoi.ifmo.ru

**Abstract**- We present our recent results on femtosecond laser-assisted reconfiguration of all-dielectric and hybrid nanoantennae and metasurfaces. In particular, we propose a novel concept for ultrafast manipulation by scattering properties of an individual silicon nanoantenna with a magnetic dipole resonance by means of generation of electron-hole plasma. In turn, all-optical precise reconfiguration of a hybrid Au/Si nanoantenna was achieved via selective laser-induced reshaping of a golden part, matching its electric resonance with magnetic and electric resonances of a silicon part.

In recent time nonlinear optics of resonant nanoparticles attracts much of attention because of both the fundamental and practical importance. The resonant metallic nanoparticles are proven to be efficient systems for the electromagnetic field control at nanoscale, owing to the ability to localize and enhance the optical field via excitation of strong plasmon resonances. In turn, high refractive index dielectric nanoparticles with low dissipative losses in the visible range, possessing magnetic and electric Mie-type resonances, offer great opportunity for light control via designing of scattering properties. The combination of these two paradigms in the form of metal-dielectric (hybrid) nanostructures (nanoantennas and metasurfaces) has allowed utilizing the advantages of both plasmonics and all-dielectric nanophotonics.

For all-dielectric nanoantennae with a magnetic Mie-type resonance, we propose a novel approach for efficient tuning of their optical properties by means of femtosecond laser irradiation. This concept is based on ultrafast photoinjection of dense (>1020 cm−3) electron−hole plasma within such nanoparticle, drastically changing its transient dielectric permittivity. This allows manipulation by both electric and magnetic nanoparticle responses, resulting in dramatic changes of its scattering diagram and scattering cross section (Fig. 1). Such a single-particle nanodevice enables designing of fast and ultracompact optical switchers and modulators.

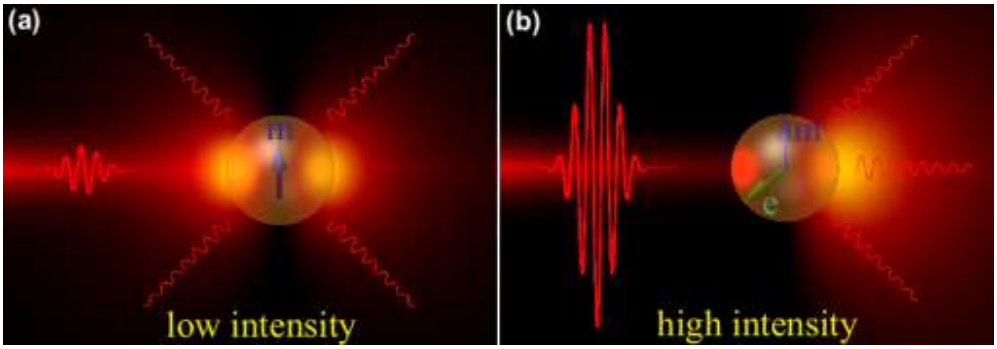



**Figure 1** Schematic illustration of scattering manipulation by a single weak (a) and intense (b) femtosecond laser pulse. Intense femtosecond laser pulse switch-on a Huygens source regime, when incident light is scattered in the forward direction.

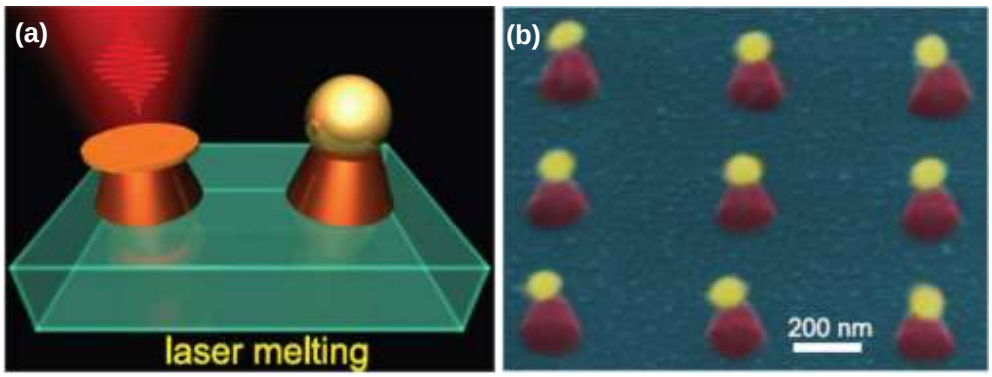



**Figure 2** (a) Schematic illustration of femtosecond laser-induced reshaping of a hybrid nanoantenna. (b) An electron image of a resulting array of reconfigured hybrid Au/Si nanoantennae.

On the other hand, femtosecond laser pulses allow permanent precise reconfiguration of a nanoantenna, when it consists of the parts with different melting thresholds causing their selective local reshaping (Fig. 2). Basing on this concept, we demonstrate a novel approach for the fabrication of hybrid nanostructures with magnetic optical response via femtosecond laser melting of asymmetrical metal–dielectric (Au/Si) nanoparticles created by lithographical methods. The approach of the highly precise femtosecond laser melting at the nanoscale offers unique opportunities for the fabrication of nanoantennae and metasurfaces consisting of asymmetrical hybrid nanostructures and manipulation of their optical properties. We believe that the represented results lay the groundwork of the fs-laser application for the large-scale fabrication of hybrid nanostructures and can be applied for effective light manipulation.

**Acknowledgements:** This work was financially supported by Russian Science Foundation (Grant 15-19-30023).

**References**

[1] Makarov, S., Kudryashov, S., Mukhin, I., Mozharov, A., Milichko, V., Krasnok, A., and Belov, P. Tuning of Magnetic Optical Response in a Dielectric Nanoparticle by Ultrafast Photoexcitation of Dense Electron–Hole Plasma. **Nano letters**, 15(9), 6187-6192 (2015).

[2] Zuev, D. A., Makarov, S. V., Milichko, V. A., Starikov, S. V., Mukhin, I. S., Morozov, I. A., and Belov, P. A. Fabrication of Hybrid Nanostructures via Nanoscale Laser-Induced Reshaping for Advanced Light Manipulation. **Advanced Materials** (2016). DOI: 10.1002/adma.201505346

# Experimental Time-Varying Light Reflection in an Epsilon-Near-Zero Active Medium

**A. M. Shaltout[1], M. Clerici[2], N. Kinsey[1], R. Kaipurath[3], J. Kim[1], E. G. Carnemolla[3], D. Faccio[3], A. Boltasseva[1], V. M. Shalaev[1], and M. Ferrera[3,*]**

[1]School of Electrical and Computer Engineering, Purdue University, West Lafayette, IN 47907, USA

[2]School of Engineering, University of Glasgow, Glasgow, G12 8LT, UK

[3]Institute of Photonics and Quantum Sciences, Heriot-Watt University, SUPA, David Brewster Building, Edinburgh EH14 4AS, UK

[*]corresponding author: m.ferrera@hw.ac.uk

**Abstract-** We experimentally demonstrate photonic time reflection from an Aluminum-doped-ZnO layer with epsilon-near-zero (ENZ) operation at telecom wavelengths. The refractive index of the layer is temporally engineered by an intense, <100 fs pulse at 785 nm. ENZ enhanced change in the material properties has driven a wavelength shift up to 10 nm for near-infrared (1250 nm) pulses.

The phenomena of time reflection and refraction that occur when light passes through a dynamic medium (i.e. with a time-varying refractive index), has been extensively studied in both bulk geometries [1, 2] and in thin films [3]. The temporal variation of the media optical properties brings forth another degree of freedom for molding the flow of light that is complementary with the spatial structural variations utilized in metamaterials [4]. Since space and time play dual roles in wave equations, temporal analogues of metamaterial based devices are expected to achieve a new horizon of light control, and possibly will enable a new genus of active optical devices. Accordingly, we previously studied the propagation of light through a surface with time-varying optical properties, foreseeing the incidence of a wavelength shift that emulates Doppler shift from a moving medium [5]. However, the realization of large frequency shifts requires a considerable contrast with regards to induced variation of the refractive index. Therefore, epsilon-near-zero (ENZ) [6] materials are very promising candidates to construct optical devices based on temporal surface engineering, with their potential to afford epsilon changes as high as their genuine values. In particular, Aluminum-doped-ZnO (AZO) [7] has recently demonstrated ENZ operation at telecom wavelengths, in addition to its ability to undergo a remarkable variation in optical response over a sub-picosecond time frame. In this work, we utilize an AZO layer with engineered time-varying optical properties to experimentally verify the artificial Doppler shift induced by a time-varying phase-gradient [5].

An AZO layer is utilized whose refractive index is modulated via a pump at 785 nm while probed by a second beam at 1250 nm which is controllably delayed from the pump by $\tau$ as shown in the inset of figure 1. At the probe wavelength, the AZO is in the ENZ regime, and upon excitation with the pump, $n$ undergoes a change in value comparable to its initial value. The probe pulse reflecting from the AZO layer will acquire a time-dependent phase shift $\psi$ that will dynamically change following the changes in $n$. Accordingly, the frequency shift induced to the wave-front is calculated by [5]:

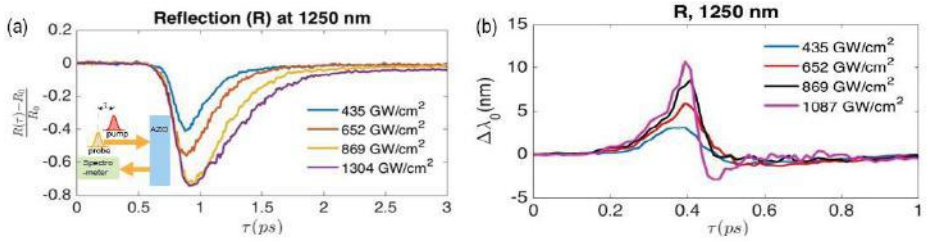



Figure 1: (a) Normalized variations in reflected power of probe signal as a function of pump-probe delay for different pump intensities. (Inset) Simplified sketch for the pump- probe measurement performed on the AZO layer, where τ is the pump-probe delay, and the probe signal is analyzed through a spectrometer. (b) Transient wavelength shift of the probe signal carrier obtained from the spectrograms of the reflected probe signal (for different pump intensities).

$$\Delta\omega = -\frac{\partial\psi}{\partial t} \tag{1}$$

Figure 1(a) presents the differential and normalized transient reflectivity as recorded by our pump and probe system for different pump intensities where $\tau$ is the pump-to-probe delay. According to Equation (1), the slope of $n$ (i.e. change in $R$) should correspond to a shift in the reflected probe wavelength. This is displayed in figure 1(b), where an induced wavelength shift up to 10 nm is detected from the spectral measurement of the reflected probe, which resembles the derivative of figure 1(a) in accordance with Equation (1).

In conclusion, the potentials of AZO as a dynamic ENZ material provide a suitable platform for the temporal engineering of optical materials, opening a new paradigm of light control, and possible integration towards developing dynamic meta-devices. The capabilities of these devices surpass those of static metamaterials enabling novel types of applications. For example, the demonstrated effect of an artificial Doppler-shift can be used to modify or compensate for the actual Doppler effect from a moving medium, enabling the realization of velocity cloaking.

**Acknowledgements**, The authors acknowledge support from AFOSR FA9550-12-1-0389, ARO W911 NF-13-1-0226, NSF DMR- 1120923, and the Marie Curie Actions IOF program - project n° [329346].

**REFERENCES**

1. F. M. Mendonca, J.T., Theory of Photon Acceleration, IoP publishing, 2001.
2. Biancalana , F., Amann, A., Uskov, A. V., and O'reilly, E. P., "Dynamics of light propagation in spatiotemporal dielectric structures," *Physical Review E,* Vol. 75, No. 046607, 2007.
3. Westerberg, N., and Faccio, D., "Experimental quantum cosmology in time-dependent optical media*," New J. Phys.*, Vol. 16, No. 075003, 2014.
4. Shelby, R. A., Smith, D.R., and Schultz, S., "Experimental verification of a negative index of refraction," *Science,* Vol. 292, No. 5514, 77-79, 2001.
5. Shaltout, A. M., Kildishev, A. V., and Shalaev, V. M., "Time-varying metasurfaces and Lorentz non-reciprocity," *Optical Materials Express*, Vol. 5, No. 11, 2459-2467, 2015.
6. Alù, A, Silveirinha, M. G., Salandrino, A., and Engheta, N., "Epsilon-near-zero metamaterials and electromagnetic sources: Tailoring the radiation phase pattern", *Physical review B*, Vol. 75, No. 155410, 2007.
7. Kinsey, N., DeVault, C., Kim, J., Ferrera, M., Shalaev, V. M., and Boltasseva, A., "Epsilon-near-zero Al-doped ZnO for ultrafast switching at telecom wavelengths," *Optica,* Vol. 2, No. 7 616-622, 2015.

# Quantum Hydrodynamic Theory of Second-Harmonic Generation

**C. Ciracì**

Istituto Italiano di Tecnologia (IIT), Center for Biomolecular Nanotechnologies, Italy
cristian.ciraci@iit.it

**Abstract**— We introduce a method based on the quantum hydrodynamic theory (QHT) for the study of second-harmonic generation (SHG), which includes nonlocal and nonlinear contributions of the kinetic energy and a quantum-like description of the electron density at the surface. This method is suitable for studying nonlinear optical process in nanometer-gap plasmonic structures.

Metallic structures supporting gap-plasmon modes have the ability to squeeze the light (with no cut-off) in nanometer size volumes producing incredibly strong local fields. Advances in nanofabrication techniques[1, 2] have made possible to achieve distances between to metallic elements (i.e. between two nanoparticles, or between nanoparticles and a metal film) of only few nanometers. At such distances nonlocal or quantum effects become non-negligible, producing modifications of the macroscopic optical response of the system, which have been experimentally observed[3, 4]. On the other hand, metals are compelling candidates for nonlinear optics, as they possess nonlinear susceptibilities that are orders of magnitude larger than dielectric materials. The origin of nonlinearity in metals arises from both volume and surface contributions. Nonlinear surface contributions are strictly related to the response of the electrons within few angstroms from the metal boundaries. In this sub-nanometer realm, electron-electron interactions become non-negligible, and quantum and nonlocal effects must be taken into account. While the nonlinear hydrodynamic model (within the limit of the Tomas-Fermi theory) has been successfully used to describe second-harmonic generation in metallic systems[5, 6], its basic assumption of a constant equilibrium electron density, prevents its applicability to more extreme condition in which a precise description of the electron density profile is required.

Here, we present a generalization of the nonlinear hydrodynamic theory that takes into account a more accurate description of the free-electron gas internal energy by adding to the Thomas-Fermi energy functional, the nonlocal (i.e. depending on the gradient of the charge density) von Weizsäcker energy functional[7, 8]. In particular we present the equations for the study of the SHG process.

Assuming undepleted pump approximation and a $e^{i\omega t}$ time dependence, it is possible to obtain the following set of equations for the fundamental ($\mathbf{P}_1$) and second-harmonic ($\mathbf{P}_2$) polarization vectors:

$$\begin{aligned} -\tfrac{en_0}{m_e}\nabla\Big(\tfrac{\delta G[n]}{\delta n}\Big)_1 - \left(\omega_1^2 + i\omega_1\gamma\right)\mathbf{P}_1 &= \tfrac{e^2 n_0}{m_e}\mathbf{E}_1, \\ -\tfrac{en_0}{m_e}\nabla\Big(\tfrac{\delta G[n]}{\delta n}\Big)_2 - \left(\omega_2^2 + i\omega_2\gamma\right)\mathbf{P}_2 &= \tfrac{e^2 n_0}{m_e}\mathbf{E}_2 + \mathbf{S}_{NL}, \end{aligned} \tag{1}$$

where:

$$\begin{aligned} \mathbf{S}_{NL} = -\tfrac{\omega_1^2}{en_0}\Big[\Big(2 + i\tfrac{\gamma}{\omega_1}\Big)\mathbf{P}_1\nabla\cdot\mathbf{P}_1 + (\mathbf{P}_1\cdot\nabla)\mathbf{P}_1 + \\ -\tfrac{\mathbf{P}_1\cdot\nabla n_0}{n_0}\mathbf{P}_1\Big] + i\omega_1\tfrac{e\mu_0}{m_e}\mathbf{P}_1\times\mathbf{H}_1 + \tfrac{en_0}{m_e}\nabla\Big(\tfrac{\delta G[n]}{\delta n}\Big)_2^{\mathrm{NL}}. \end{aligned} \tag{2}$$

$G[n]$ is the total internal energy functional, approximated as $G[n] \simeq T_{\mathrm{TF}}[n] + \frac{1}{\eta}T_{\mathrm{vW}}[n] + E_{\mathrm{XC}}[n]$, where $T_{\mathrm{TF}}[n]$ is kinetic energy functional in the Thomas-Fermi approximation, $T_{\mathrm{vW}}[n]$ is the von Weizsäcker kinetic energy functional and $E_{\mathrm{XC}}[n]$ is the local density approximation for the exchange-correlation energy functional. The term $\left(\frac{\delta G[n]}{\delta n}\right)_2^{\mathrm{NL}}$ contains elements that depends not only on $n$ but also its gradient. Here we report only the second-order nonlinear terms for the kinetic energy:

$$\begin{aligned} \left(\tfrac{\delta T_{TF}}{\delta n}\right)_2^{\mathrm{NL}} &= -\tfrac{5}{27}c_{TF}{n_0}^{-4/3}{n_1}^2 \\ \left(\tfrac{\delta T_{\mathrm{vW}}}{\delta n}\right)_2^{\mathrm{NL}} &= \tfrac{|\nabla n_1|^2}{n_0^2} - 4\tfrac{\nabla n_0\cdot\nabla n_1}{n_0^3}n_1 + 2\tfrac{\nabla^2 n_1}{n_0^2}n_1 + 3\tfrac{|\nabla n_0|^2}{n_0^4}n_1^2 - 2\tfrac{\nabla^2 n_0}{n_0^3}n_1^2 \end{aligned} \tag{3}$$

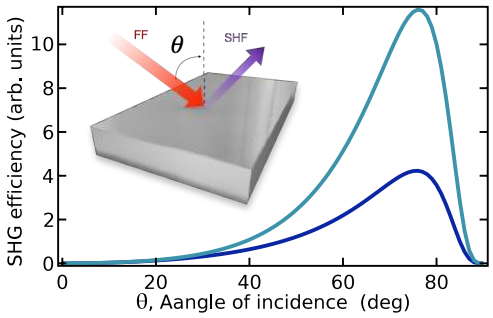



Figure 1: SHG efficiency as a function of the incident angle on a metal surface for two different density profiles.

Equations (1) are coupled with Maxwell's equations and are valid for any geometry. In Fig. 1 we show the amount of SHG produced at a simple metal film as a function for two values of the work function differing of about 20%. The amount of nonlinear currents strongly depends on how the equilibrium density $n_0$ varies across the jellium edge. This is not the case for the standard hydrodynamic model where a direct link with local calculations can be established[9]. It can be showed in fact that for a flat surface the amount of second-harmonic currents does not depend on how $\mathbf{P}$ varies across the surface (going from its bulk value to its surface value). This does not hold for the nonlinear QHT. In the configuration presented, nearly 3% of the incident light actually couples into the metal. Nano-gap plasmon structures not only can increase the local fields at the surface but can also bring the coupling of far-field radiation and surface very close to 100%[2]. The nonlinear QHT is a well-suited tool to take advantage of quantum interactions in deeply confined light modes in order to efficiently generate a nonlinear optical response.

**REFERENCES**


1. A. Rose, T. B. Hoang, F. McGuire, J. J. Mock, C. Ciracì, D. R. Smith, and M. H. Mikkelsen, "Control of radiative processes using tunable plasmonic nanopatch antennas," *Nano Lett.*, Vol. 14, 4797–4802, 2014.
2. J. B. Lassiter, X. Chen, X. Liu, C. Ciracì, T. B. Hoang, S. Larouche, S.-H. Oh, M. H. Mikkelsen, and D. R. Smith, "Third-Harmonic Generation Enhancement by Film-Coupled Plasmonic Stripe Resonators," *ACS Photonics*, Vol. 1, 1212–1217, 2014.
3. C. Ciracì, R. Hill, J. J. Mock, and Y. A. Urzhumov, "Probing the ultimate limits of plasmonic enhancement," *Science*, Vol. 337, no. 6098, 1072–1074, 2012.
4. K. J. Savage, M. M. Hawkeye, R. Esteban, and A. G. Borisov, "Revealing the quantum regime in tunnelling plasmonics," *Nature*, Vol. 491, 574–577, 2012.
5. J. E. Sipe, V. So, M. Fukui, and G. Stegeman, "Analysis of second-harmonic generation at metal surfaces," *Phys. Rev. B*, Vol. 21, 4389–4402, 1980.
6. M. Scalora, M. A. Vincenti, D. de Ceglia, V. Roppo, M. Centini, N. Akozbek, and M. J. Bloemer, "Second- and third-harmonic generation in metal-based structures," *Phys. Rev. A*, Vol. 82, 043828, 2010.
7. G. Toscano, J. Straubel, A. Kwiatkowski, C. Rockstuhl, F. Evers, H. Xu, N. A. Mortensen, and M. Wubs, "Resonance shifts and spill-out effects in self-consistent hydrodynamic nanoplasmonics," *Nat. Comm.*, Vol. 6, 7132, 2015.
8. W. Yan, "Hydrodynamic theory for quantum plasmonics: Linear-response dynamics of the inhomogeneous electron gas," *Phys. Rev. B*, Vol. 91, 115416, 2015.
9. C. Ciracì, E. Poutrina, M. Scalora, and D. R. Smith, "Origin of second-harmonic generation enhancement in optical split-ring resonators," *Phys. Rev. B*, Vol. 85, 201403(R), 2012.

# Silver grain nonlinear metamaterial

**T. Stefaniuk[1*], N. Olivier[1], A. Belardini[2], C. Sibilia[2], A. A. Wronkowska[3], A. Wronkowski[3], T. Szoplik[4], A. Zayats[1]**

[1]King's College London, UK

[2]Sapienza Università di Roma, Italy

[3]UTP University of Science and Technology, Poland

[4]University of Warsaw, Poland

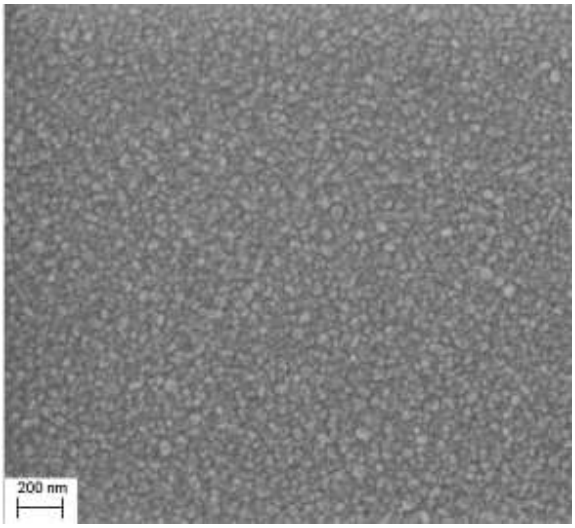
[*]corresponding author: tomasz.stefaniuk@kcl.ac.uk

**Abstract**- Silver is one of the most commonly used metals for constructing metamaterials working in the visible wavelength range. This is because it has low ohmic losses, associated with small values of imaginary part of permittivity. In this talk we will demonstrate that due to segregation of germanium atoms to silver grain boundaries, a smooth silver layer might become a metamaterial itself. This system exhibits such effects as localised plasmon resonances on encapsulated grains and extraordinary second harmonic generation.

Plasmonic metamaterials revolutionarily altered the way that people think about functional optical devices. Thanks to arrangement of two or more conventional materials with known bulk properties one can obtain a composite structure with quite exotic behaviour, very different from all of its constituents. For example, when the design incorporates metals in the unit structure, such a metamaterial can exhibit a hyperbolic dispersion relation and as a consequence sustain and enhance waves of infinitely high wavenumber [1]. Also the nonlinear effects in metamaterials such as nonlinear refraction and absorption [2] or second-harmonic generation (SHG) [3] have become a subject of intensive study.

Optical properties of silver makes it a perfect candidate for a metamaterial compound. Unfortunately, evaporation of thin films has been a continuing challenge because of their tendency to form clusters rather than smooth layers. Several methods were proposed in the literature to deal with this problem [4]. While the uniformity and smoothness of e beam evaporated metal films can be optimized through the use of a Ge wetting interlayer and proper choice of deposition temperature and rate [5], this approach in the long term leads to segregation of Ge atoms and increase of Ohmic losses [6]. Segregation appears as a result of inhomogeneities in the evaporated film, such as free surfaces, grain boundaries, interfaces between different phases or dislocations. All of these regions provide sites on which germanium atoms have lower Gibs free energy [7].

Although the penetration of Ge atoms along high-diffusivity paths in silver significantly limits the range of SPP wave propagation on the dielectric/metal interface, this metamaterial exhibits some other very unique properties. In particular, localized surface plasmon (LSP) resonances on encapsulated silver grains can be identified from the linear optical measurements, allowing to treat the thin Au/Ge film as a metamaterial. These LSPs have significant impact on second-harmonic generation from the metamaterial.




**Figures 1:** SEM image of the 100nm thick silver-germanium metamaterial.

**Acknowledgements.** This work was supported, in part, by EPSRC (UK) and the ERC iPLASMM project (321268). A.Z. acknowledges support from the Royal Society and the Wolfson Foundation.

**REFERENCES**

1. Dickson, W., Beckett, S., McClatchey, C., Murphy, A., O'Connor, D., Wurtz, G.A., Pollard, R., Zayats, A.V. "Hyperbolic Polaritonic Crystals Based on Nanostructured Nanorod Metamaterials," *Adv. Mater*., Vol. 27, 5974-5980, 2015.
2. Neira, A.D., Olivier, N., Nasir, M.E., Dickson, W., Wurtz, G.A., Zayats, A.V., "Eliminating material constraints for nonlinearity with plasmonic metamaterials," *Nat. Commun.*, Vol. 6, No. 7757, 2015.
3. M. Kauranen and A. V. Zayats, "Nonlinear plasmonics," *Nature Photon.*, Vol. 6, 737–748, 2012.
4. Stefaniuk, T., Wróbel, P., Górecka, E., Szoplik, T., "Optimum deposition conditions of ultrasmooth silver nanolayers," *Nanoscale Res. Lett*, Vol. 9, 2014.
5. Stefaniuk, T., Wróbel, P., Trautman, P., Szoplik, T., "Ultrasmooth metal nanolayers for plasmonic applications: Surface roughness and specific resistivity," *Appl. Opt.*, Vol. 10, B237-B241, 2014.
6. Wróbel, P., Stefaniuk, T., Trzcinski, M., Wronkowska, A.A., Wronkowski, A., Szoplik, T., "Ge wetting layer increases ohmic plasmon losses in ag film due to segregation," *ACS Appl. Mater. Interfaces*, Vol. 7, 8999-9005, 2015.
7. Mehrer, H., *Diffusion in Solids: Fundamentals, Methods, Materials, Diffusion-Controlled Processes*, Springer Science & Business Media, Berlin, 2007.

# Reconfigurable THz metamaterials based on nematic liquid crystals

**D. C. Zografopoulos**[1], **G. Isić**[2], **B. Vasić**[2], **R. Gajić**[2], **and R. Beccherelli**[1]

[1] Consiglio Nazionale delle Ricerche, Istituto per la Microelettronica e Microsistemi (CNR-IMM), Via del fosso del cavaliere 100, 00133, Roma, Italy

[2] Center for Solid State Physics and New Materials, Institute of Physics, University of Belgrade, Belgrade 11080, Serbia

**Abstract**— Novel liquid-crystal tunable metamaterial devices for terahertz wave manipulation are designed and investigated. Deeply subwavelength layers of nematic materials are introduced in metal-insulator-metal cavities, leading to strong interaction of the THz wave with the liquid crystal anisotropy. The enhanced response in the liquid-crystal layer yields extensive tunability of the electromagnetic resonances with fast response times in the millisecond range. Three specific components are targeted: a fishnet metamaterial with tunable effective refractive index, a tunable absorber, and a polarization controller.

Terahertz science is a rapidly advancing research field in view of numerous applications in security, material science, bio-imaging, and short-range wireless communications. Reconfigurable devices with broad tuning ranges can be envisaged by combining the electromagnetic resonances in subwavelength metamaterial structures with the electrical control of nematic liquid crystals (LC) [1]. Here, we discuss three particular designs that target tunable negative index metamaterials [2], efficient modulation on perfect absorbers [3], and tunable polarization control in resonant metal-liquid-crystal-metal cavities.

The design of the proposed LC-tunable THz metamaterials is based on the infiltration of the nematic material in µm-thick layers formed between metallic parts, as in the schematic of the perfect absorber presented in Fig. 1(a,b). By tuning the dimensions of the metallic network, the resonances of the device, as e.g. in Fig. 1(c), can be shifted at the target frequency of operation.

Subsequently, the application of a control voltage across the cell formed between the two opposing metallic electrodes switches the LC molecules and provides for large tunability of the structure's electromagnetic response. Figure 1(d) shows a higher than 15% spectral tuning range for the perfect

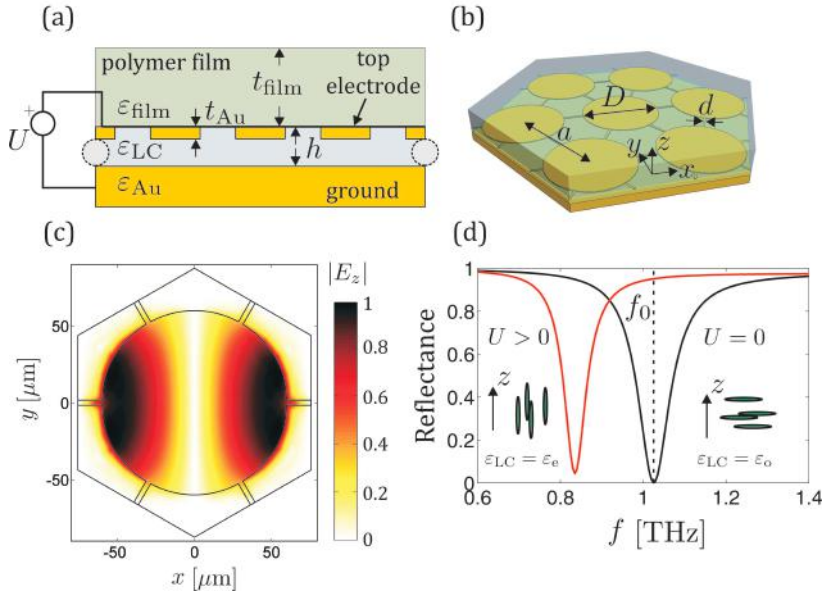



Figure 1: (a) Cross-section of the LC-tunable THz absorber, (b) bird's-eye view of the structure, (c) $z$-component of the resonant electric field calculated in the middle of the LC cell, (d) voltage-controlled modulation of the reflectance spectra.

absorber, which translates in modulation depths above 20 dB at the design frequency. The device responds in a few ms and a few tens of ms in the case of ON and OFF switching, respectively.

In conclusion, the introduction of µm-thick layers of nematic liquid crystals in metamaterial cavities enables the design of tunable components for the efficient control of terahertz wave propagation. The proposed reconfigurable devices feature extensive tunability, fast response times, and offer a low-cost solution for terahertz applications.

## ACKNOWLEDGMENT

This work was supported by the Italian Ministry of Foreign Affairs and International Cooperation, Directorate General for the Country Promotion (LC-NANOPLASM), and the Serbian Ministry of Education, Science and Technological Development under Project No. OI171005. The authors also acknowledge the contribution of the COST Action IC1208.

## REFERENCES

1. S. Savo, S. Shrekenhamer, and W. J. Padilla, "Liquid crystal metamaterial absorber spatial light modulator for THz applications," *Adv. Opt. Mater.*, Vol. 2, 275–279, 2014.
2. D. C. Zografopoulos and R. Beccherelli, "Tunable terahertz fishnet metamaterials based on thin nematic liquid crystal layers for fast switching," *Sci. Rep.*, Vol. 5, 13137, 2015.
3. G. Isić, B. Vasić, D. C. Zografopoulos, R. Beccherelli, and R. Gajić, "Electrically tunable critically coupled terahertz metamaterial absorber based on nematic liquid crystals," *Phys. Rev. Applied*, Vol. 3, 064007, 2015.

# Tunable Generation of Graphene Surface Plasmon Polaritons

*Mohamed Farhat and Hakan Bagci, Division of Computer, Electrical, and Mathematical Sciences and Engineering, King Abdullah University of Science and Technology (KAUST), Thuwal 23955-6900, Saudi Arabia*
*+966 12 808 4522, mohamed.farhat@kaust.edu.sa*

*Pai-Yen Chen, Department of Electrical and Computer Engineering, Wayne State University, Detroit, MI 48202, U. S. A.*
*+1 313 577 3758, pychen@wayne.edu*

*Sébastien Guenneau, Aix-Marseille Université, CNRS, Centrale Marseille, Institut Fresnel, Campus universitaire de Saint-Jérôme, 13013 Marseille, France,*
*+33 04 91 28 88 84, sebastien.guenneau@fresnel.fr*

**Abstract:** This work focuses on two recently proposed concepts in graphene plasmonics. (i) Generation and dynamic steering of Terahertz (THz) beams using graphene antennas. The surface reactance of the graphene is dynamically modulated using a bias circuit. The modulated reactance allows for steering of the beam over wide range of scan-angles. (ii) Efficient and tunable generation of graphene surface plasmon polaritons (GSSPs). The graphene sheet is converted into a grating using an acoustic wave. The grating allows for efficient coupling of the incident light to the GSSPs. Its period can be tuned by varying the frequency of the acoustic wave.

Plasmonics, one of the most active research fields in photonics and electromagnetics, focuses on the generation of surface plasmon polaritons on noble metal surfaces (e.g. gold) under excitation by light and manipulation/tunability of their characteristics such as resonance frequency, propagation distance, field localization and strength, etc. However, high levels of ohmic loss present in metals have hindered the development of real engineering applications of plasmonics. This has motivated researchers to look for/design novel materials that support surface plasmon polaritons but also are tunable and have lower levels of ohmic loss. Graphene, the one-atom-thick honeycomb carbon lattice, discovered in 2004, fulfils these requirements: It has low levels of ohmic loss thanks to its high electron mobility, its response to electromagnetic excitation can be tuned by applying an external gate voltage or modifying the level of chemical doping, and it supports surface plasmon polaritons at THz frequencies [1]. This work addresses on two different aspects of graphene plasmonics.

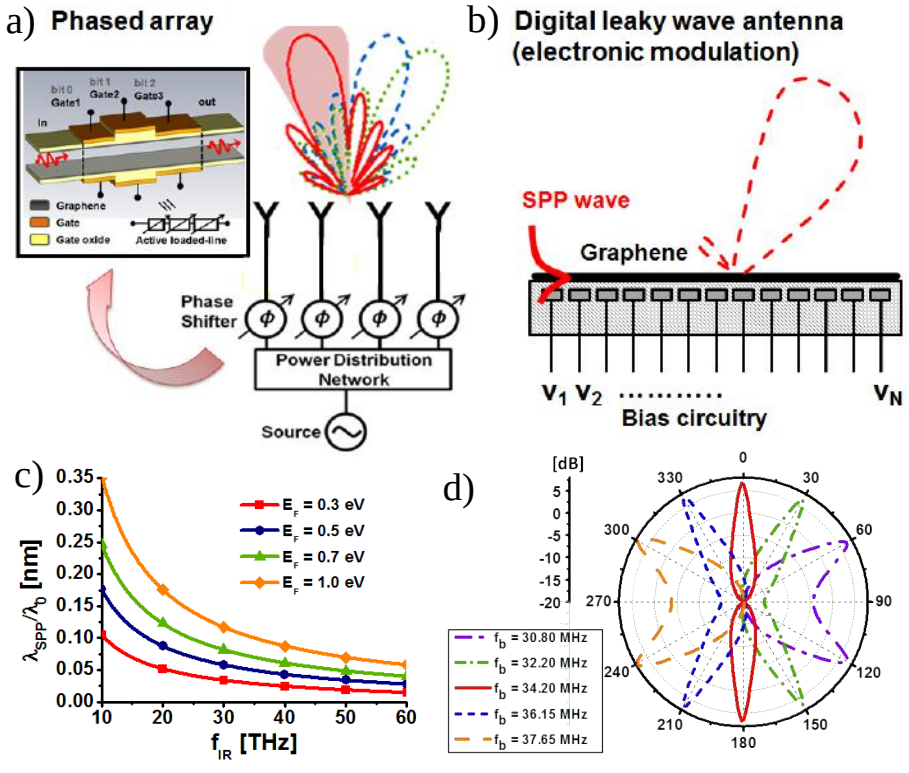


Figure 1. (a) and (b) Schematics of two different antennas used for THz beam steering. (c) The effective GSPP wavelength on a flat graphene sheet for different Fermi energies. The plot shows that the GSPPs are confined to the graphene surface and can be hardly excited. This problem is overcome by generating a dynamic grating on the graphene surface, which is molded using flexural elastic waves [2] to allow for efficient coupling of incident light to GSPPs. (d) The plot shows that the directivity of the antenna can be greatly enhanced by increasing the mobility of graphene (i.e., lowering the level of loss) [3]. This antenna can be used for fast switching of infrared or THz beams to various space channels, and represents an example of graphene-based plasmonic devices that can be used in practical applications such as switching, spatial multiplexing, or holography.

- Tunability of GSSPs suggests that graphene can be used to build antennas that can generate and dynamically steer THz radiation beams. Indeed, in this work a THz antenna made of a graphene sheet biased with a high-density circuit is designed for this purpose. The tunability of graphene's conductivity [1] permits the use of multiple-cascaded gates to modulate the surface reactance by biasing each gate with a different voltage [Fig. 1(a)]. Under no-bias condition, the graphene sheet supports a slow GSPP wave. When the gate-electrodes are biased, the surface reactance of graphene is modulated with "digitized" sinusoidal signal, which permits generation of high-order spatial harmonics on the surface of graphene and consequently the antenna supports a fast-leaky-wave-mode. Varying the period of the modulation periods using different bias-setups leads to the steering of the THz beam over a wide range of angles [Fig. 1(b)].

- One of the open-ended problems of the graphene plasmonics is the realization of efficient coupling of incident light to the GSSPs. This is a challenging task because of the large mismatch between the wavenumbers of the GSSPs and the free space. In this work, this problem is overcome by generating a dynamic two-dimensional grating on the graphene surface using an acoustic (flexural) wave [Fig. 2(a)]. The grating "forces" the wavenumbers to match permitting efficient coupling of energy from the incident field to the GSSPs. Additionally, the period of the grating can be tuned by varying the frequency of acoustic wave (i.e., mechanical vibration of the graphene sheet). This suggests that fast on/off switching of GSSPs might be possible with potential applications in bio-chemical sensing and detection [2].

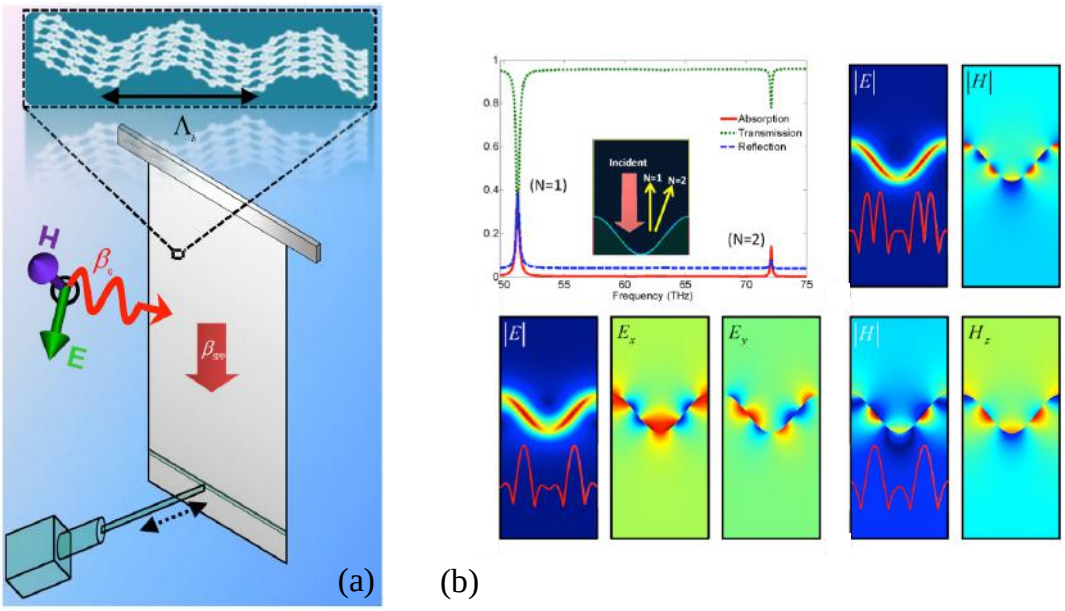



Figure 2. Efficient generation of GSSPs. (a) Schematics of the setup showing how the graphene grating is generated using an acoustic wave (i.e., mechanical vibration of the sheet). (b) Characterization of the GSSPs generated on the graphene grating.


[1] K. S. Novoselov, A. K. Geim, S. V. Morozov, D. Jiang, Y. Zhang, S. A. Dubonos, I. V. Grigorieva, and A. A. Firsov, Science **306**, 666–669 (2004).
[2] M. Farhat, S. Guenneau, and H. Bagci, Physical Review Letters **111**, 237404 (2013).
[3] P.-Y. Chen, M. Farhat, A. N. Askarpour, M. Tymchenko, and A. Alù, Journal of Optics **16**, 094008 (2014).

# Plasmonic Launchers for Quantitative Nonlinear and Quantum Plasmonics

**Alexandre Baron**[1,2,3]**, David R. Smith**[3]**, and Philippe Lalanne**[4]
[1]CNRS, CRPP, UPR8641, F-33600 Pessac, France
[2]University of Bordeaux, CRPP, UPR8641, F-33600 Pessac, France
[3]Center for Metamaterials and Integrated Plasmonics, Department of Electrical and Computer Engineering, Duke
[4]LP2N, Institut d'Optique, CNRS, Université de Bordeaux, 33400 Talence,France
[*]corresponding author: alexandre.baron@u-bordeaux.fr

**Abstract**- Coupled electromagnetic fields and charge densities oscillating at optical frequencies along a metal interface are surface modes called surface plasmon polaritons (SPPs). SPPs are quasi-particles that confine light to subwavelength dimensions. We review our design and characterization philosophy to produce efficient plasmonic launchers that are used for quantitative nonlinear and quantum plasmonics. These launchers can be used to measure the nonlinearity of metals and to evidence the particle nature of SPPs.

Surface Plasmon Polaritons (SPPs) are an important carrier of optical energy because: i) the electromagnetic field can be confined to subwavelength dimensions, which locally enhances the intensity of light and ii) SPPs are quasi-particles, namely that they consist of free electrons oscillating jointly with the electromagnetic field at optical (or near optical) frequencies. These two observations have led physicists and engineers to take advantage of SPPs for many applications including metamaterials [1], nonlinear optics [2], quatum optics [3], sensing [4] and metasurfaces [5].

In this context, a large number of devices have been fabricated with the aim of efficiently generating SPPs and controlling the direction in which they are launched from free-space photons. In 2011, we showed that it was possible to be quantitative in the determination of the power coupled to SPPs using a compact optimized antenna [6]. Using this antenna and our characterization procedure, we can apply it to optical experiments where it is crucial to be quantitative. In nonlinear optics for instance, quantitatively measuring the degenerate effective third-order susceptibility of a metal which induces intensity-dependent effects requires knowing the amount of energy transported by the propagating SPP [7]. Another example is in quantum optics, evidencing experimentally wave-particle duality of an SPP requires controlling the path information (namely the launching directions), the photon-plasmon conversion probability (quantitative efficiency) and path recombination (SPP beam splitter) in order to show anti-correlation.

We propose to review the design and characterization philosophy behind compact SPP launchers for quantitative optical measurements with plasmons. Furthermore, we shall describe how these concepts are useful for quantitative nonlinear and quatum plasmonics by highlighting two recent experiments. The first experiment uses a single compact antenna as a coupler and a decoupler to measure ultrafast self-action of SPPs on a gold surface, which enables us to measure the third-order nonlinear susceptibility [8]. The second experiment uses these antennas to launch single SPPs on separate paths which are recombined on an SPP splitter and evidence the particle nature of plasmons [9].

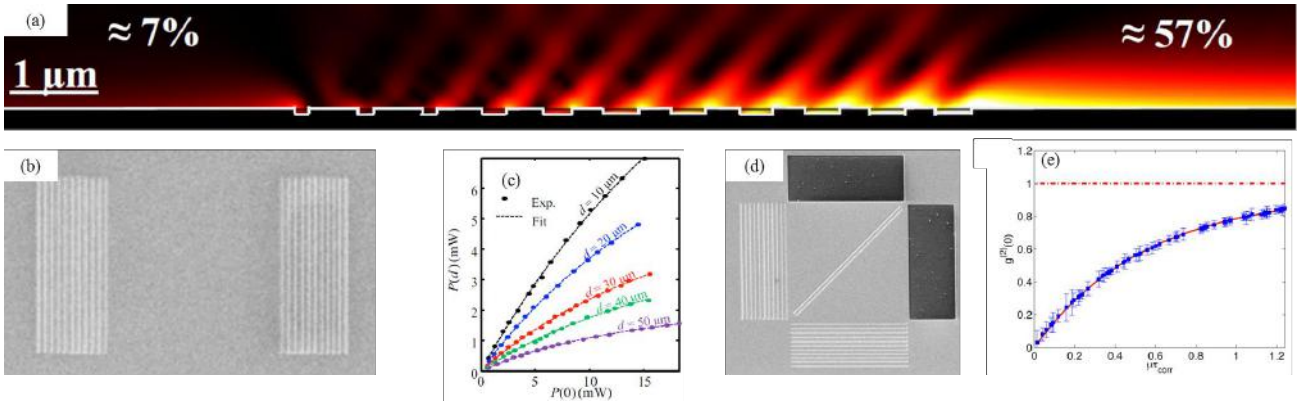



**Fig. 1 – Design and application of surface plasmon polariton (SPP) launchers for quantitative nonlinear and quantum measurements**. (a) Norm of the scattered Poynting vector near an optimized unidirectional SPP laucher. (b) SEM image of a single interface SPP waveguide with a unidirectional SPP launcher and decoupler at the waveguide input and output enabling a nonlinear characterization of a gold film. (c) Ouput power of the SPP waveguide as a function of the input power evidencing self-induced absortion. The fits enable a measurement of the third-order nonlinear susceptibility of gold. (d) SEM image of a sample containing two of the designed SPP launchers (bottom and left) and an SPP beam splitter. This setup is used to make a which-path quantum experiment the reveals the particle nature of the SPP. (e) Intensity correlation function at zero delay as a function of the mean photon number.

**Acknowledgements**, A. B. and D.R.S acknowledge support from the Air Force Office of Scientific Research (AFOSR Grant No. FA9550-12-1-0491).

## REFERENCES

1. T. Xu, *et al.*, "All-angle negative refraction and active flat lensing of ultraviolet light," *Nature*, Vol. 497, 470–474, 2013.
2. I.-Y. Park, S. Kim, J. Choi, D.-H. Lee, Y.-J. Kim, M. F. Kling, M. I. Stockman, and S.-W. Kim, "Plasmonic generation of ultrashort extreme-ultraviolet light pulses," *Nature Photonics*, Vol. 5, 677-681, 2011.
3. A. V. Akimov, *et al.*, "Generation of single optical plasmons in metallic nanowires coupled to quantum dots," *Nature*, Vol. 450, 402-406, 2007.
4. J. Toudert, *et al.*, "Plasmonic Optical Interferences for Phase-Monitored Nanoscale Sensing in Low-Loss Three-Dimensional Metamaterials," *ACS Photonics*, Vol. 2, 1443-1450, 2015.
5. A. V. Kildishev, *et al.*, "Planar Photonics with Metasurfaces," *Science*, Vol. 339, 1232009, 2013.
6. A. Baron, E. Devaux, J.-C. Rodier, J.-P. Hugonin, E. Rousseau, C. Genet, T. W. Ebbesen, and P. Lalanne, "Compact antenna for efficient and unidirectional launching and decoupling of surface plasmons," *Science*, Vol. 339, 1232009, 2013.
7. A. Baron, S. Larouche, D. J. Gauthier, and D. R. Smith, "Scaling of the nonlinear response of the surface plasmon polariton at a metal/dielectric interface," *J. Opt. Soc. Am. B*, Vol. 32, 9-14, 2015.
8. A. Baron, T. B. Hoang, C. Fang, M. H. Mikkelsen, and D. R. Smith, "Ultrafast self-action of surface-plasmon polaritons at an air/metal interface," *Phys. Rev. B*, Vol. 91, 195412-(1-7), 2015.
9. M.-C. Dheur, E. Devaux, T. W. Ebbesen, A. Baron, J.-C. Rodier, J.-P. Hugonin, P. Lalanne, J.-J. Greffet, G. Messin, and F. Marquier, "Single-plasmon interferences," *Sci. Adv.*, Vol. 2, e1501574, 2016.

# Inherently Nonreciprocal: Nonlinear Metamaterials.

**E. Poutrina[1,2] and A. Urbas[1]**

[1]Air Force Research Laboratories, USA
[2]UES, Inc., USA
ekaterina.poutrina.ctr.ru@us.af.mil; augutine.urbas@us.af.mil

**Abstract**— We demonstrate that non-reciprocity of nonlinear generation is inherent and realistically observable in the effective nonlinear multipolar response of nanostructures. A careful design of effective hyperpolarizability terms allows both a non-reciprocal and unidirectional nonlinear generation where the generation direction is preserved with respect to a fixed laboratory coordinate system when reversing the direction of the fundamental field. Alternatively, it can ensure a directionally selective inhibition of the nonlinear response for certain respective directions of the fundamental beams.

Light manipulation at the nanoscale, while providing a possible path for controlling interactions near an atomic-scale level, faces challenges unique to the microscopic nature of the processes involved. Not only scattering response is subject to usual limitations due to the reciprocity theorem [1], but the directionality control is overall considerably reduced due to the decrease in the degree of coherence occurring on interaction of even a highly coherent light beam with a nanoscale object: while focusing and re-routing of light are routine macroscopic operations, diffraction dominates on a nanoscale. As a result, the interference between the multipolar modes produced on scattering by the nanoelement [2]–the process inherent to nanoscale interactions–is at the heart of the directionality control. The interference between partial waves of the opposite parities (such as those of electric and magnetic dipolar modes) and of a comparable strength can strongly suppress linear scattering in either forward or backward direction, while near-doubling it in the opposite one. Subject to the reciprocity theorem, however, the suppression and doubling sides switch when reversing the direction of the excitation beam.

Similar to linear scattering, the nanoscale nature of the interaction prevents regular mechanisms such as phase matching from having an impact on the directionality of the nonlinear response. As a result, nonlinear generation from a nanoelement occurs nearly isotropically in all directions, for all nonlinear processes involved. Multipolar interference can, however, equally take place between the partial waves in the nonlinearly generated field, helping restoring the directionality control. Indeed, similar to the linear response, the interference between the nonlinearly produced electric and magnetic partial waves had been shown to induce some asymmetry between the "transmission" and "reflection" sides in the far field pattern of the second harmonic generated from plasmonic nanostructures [3, 4]. Further, the possibility of a complete suppression of the nonlinearly generated field in one of the hemispheres has been suggested theoretically [5] and demonstrated experimentally [6] to produce a unidirectional nonlinear generation in the microwave regime from deeply sub-wavelength metamaterial layers.The reported asymmetry in the far field pattern of the nonlinearly generated field was, however, entirely analogous to a similar phenomena in linear scattering where the suppression and doubling sides switch when reversing the direction of the excitation.

As we show here, nonlinear multipole interference offers capabilities fundamentally different from those provided by its linear counterpart. In particular, it allows *both* a non-reciprocal and unidirectional nonlinear generation where the direction of nonlinear generation is preserved with respect to a fixed laboratory coordinate system when reversing the direction of the fundamental field. Alternatively, it can ensure a directionally selective inhibition of the nonlinear response for certain respective directions of the fundamental beams. We show that the presented phenomena can be attributed to the existence of the common (electric or magnetic) pathways inducing the electric and magnetic Mie resonances via a nonlinear interaction, such that switching the phase of one (electric or magnetic) of the vectors of the fundamental field can change simultaneously the phase of all (electric and magnetic) nonlinearly generated multipoles. Furthermore, the interference can occur between various terms *within* the electric and magnetic (nonlinearly produced) dipolar modes themselves. We discuss that, as a result, non-reciprocity in terms of ensuring just a change

in the efficiency of nonlinear generation when reversing the direction of any subset of the fundamental beams is inherent to and expected in the nonlinear response of most nanoelements, even the symmetric ones, and for most of the nonlinear processes.

We develop the procedure for the retrieval of nonlinear magneto-electric polarizabilities [7, 8] and demonstrate numerically that the described phenomena can be achieved in the optical frequency range using purely symmetric dimer structures with realistic materials parameters. A metasurface formed by a planar arrangement of such nonlinear optical antennas can allow a series of phenomena not available with regular nonlinear materials, with an example of a non-reciprocal nonlinear imaging achieved with the process of difference frequency generation presented in Fig. 1. Combined with strong enhancements of the nonlinear response offered by plasmonic metasurfaces, the suggested approach can allow engineering artificial nonlinear nanomaterials with an enhanced and inherently non-reciprocal response that can serve as a keystone in a variety of applications in integrated optics and photonics.

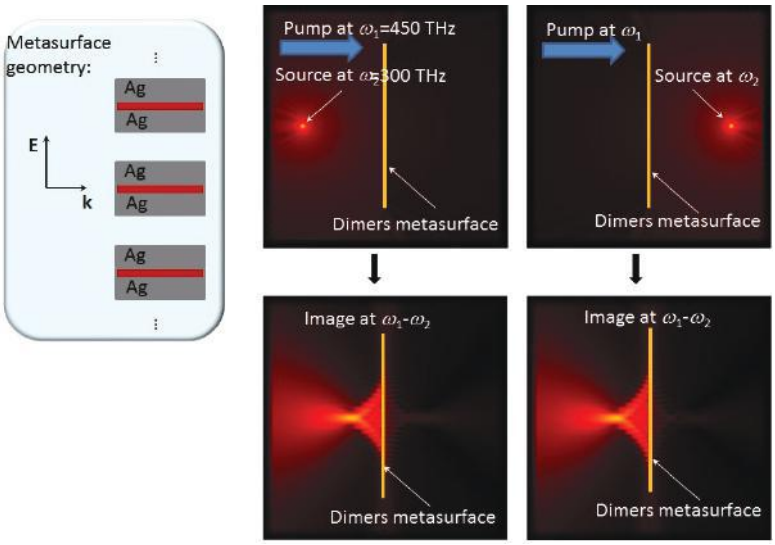



Figure 1: An example of a non-reciprocal nonlinear imaging produced via difference frequency generation, with the image of the point source ($\lambda_2 = 1$ $\mu$m) produced on the left side of the metasurface at $\lambda_3 = 2$ $\mu$m, independently of the source location. The yellow line shows schematically the metasurface location. The metasurface is made of the periodic arrangement of dimers formed by two silver strips (120 nm×35 nm) separated by a thin (15 nm, n = 1.58) layer of a dielectric, as shown in the inset.

**REFERENCES**


1. Landay, L. D., Lifshits, E. M., and Pitaevskii, L. P., *Electrodynamics of continuous media (2nd Edition), pp. 308-309*, Cambridge University Press, 1995.
2. Kerker, M., Wang, D. S., and Giles, C. L., "Electromagnetic scattering by magnetic spheres," *J. Opt. Soc. Amer.*, Vol. 73, 765–767, 1983.
3. Kujala, S., Canfield, B. K., Kauranen, M., Svirko, Y., and Turunen, J., "Multipole interference in the second-harmonic optical radiation from gold nanoparticles," *Phys. Rev. Lett.*, Vol. 98, 167403, 2007.
4. Kujala, S., Canfield, B. K., Kauranen, M., Svirko, Y., and Turunen, J., "Multipolar analysis of second-harmonic radiation from gold nanoparticles," *Opt. Express*, Vol. 16, 1719617208, 2008.
5. Rose, A., Larouche, S., Poutrina, E., and Smith, D. R., "Nonlinear magnetoelectric metamaterials: Analysis and homogenization via a microscopic coupled-mode theory," *Phys. Rev. A*, Vol. 86, 033816, 2012.
6. Rose, A., Huang, D., and Smith, D. R., "Nonlinear interference and unidirectionalwave mixing in metamaterials," *Phys. Rev. Lett.*, Vol. 110, 063901, 2013.
7. Poutrina, E. and Urbas, A., "Multipole analysis of unidirectional light scattering from plasmonic dimers," *J. Opt.*, Vol. 16, 114005, 2014.
8. Poutrina, E. and Urbas, A., "Multipole interference for non-reciprocal nonlinear generation," in review.

# Laser light generation in plasmonic crystals and metallic nanoparticles

**J. Cuerda[1], F. Ruting[1], F.J. García-Vidal[1], and J. Bravo-Abad[1*]**

[1]Departamento de Física Teórica de la Materia Condensada and Condensed Matter Physics Center (IFIMAC), Universidad Autónoma de Madrid, E-28049 Madrid, Spain

[*]corresponding author: jorge.bravo@uam.es

**Abstract**. We present our recent advances in the study of lasing action in plasmonic structures incorporating optically-pumped four-level gain media. We discuss two different classes of systems: plasmonic crystals supporting extended surface resonances and core-shell metallic nanoparticles supporting localized surface plasmons modes. The dynamics of the underlying gain-plasmon nonlinear interaction, as well as general strategies to access optimal lasing characteristics, are addressed in each case.

Plasmonic structures and metallic metamaterials have emerged as versatile platforms for achieving lasing action at length scales well below the diffraction limit. In this talk, first we discuss lasing action in active structures supporting extended plasmonic resonances. We particularly focus on periodic arrays of metallic nanowires and periodic arrays of subwavelength apertures milled in a metallic film and embedded in a optically-pumped four-level system gain medium [1]. Using a time-domain generalization of the finite-element method, we show that the excitation of dark plasmonic modes (via the gain medium) enables accessing the optimal lasing of the considered structures (Fig. 1). In addition, we find that, due to the larger temporal confinement of their plasmonic modes, arrays of nanowires feature improved laser characteristics with respect to periodic arrays of subwavelength apertures.

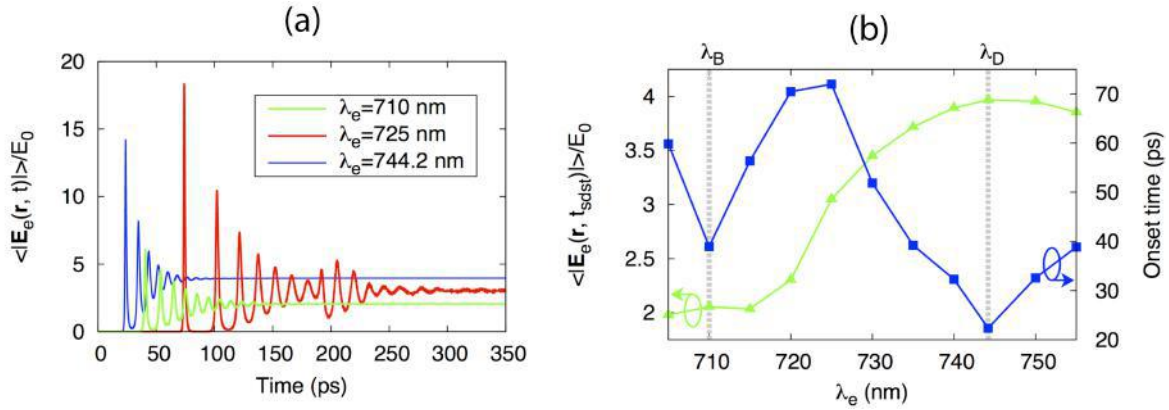



**Figure 1. (a)** Time evolution of the lasing *E*-field amplitude computed for a periodic array of gold nanowires (of periodicity 430 nm) embedded in an optically-pumped four-level organic dye, as obtained for three different values of the dye emission wavelength $\lambda_e$. **(b)** Computed steady-state values of lasing *E*-field amplitude (green triangles, left *y*-axis) and corresponding lasing onset times (blue squares, right *y*-axis) as a function of the emission wavelength. Dashed vertical lines mark the location of the bright ($\lambda_B$) and dark ($\lambda_D$) plasmonic modes supported by the structure.

In the second part of this talk, we analyze laser light generation in optically-pumped active core-shell metallic nanoparticles [2]. We start by discussing detailed finite-element time-domain simulations of the lasing dynamics and steady-state characteristics of a spherical metallic nanoparticle surrounded by a gain medium shell based on four-level system emitters. Then, we generalize our analysis and consider non-spherical geometries, focusing in the particular case of elongated nanorod geometries. We study the evolution with the nanorod geometry of the nonlinear interaction between the gain medium and the localized surface plasmons of the system. We find that there exists an optimal nanorod geometry that exhibits significantly improved lasing characteristics with respect to the conventional spherical configuration (Fig 2). These results could be of importance for further development of novel nanoscale light sources based on metallic nanoparticles.

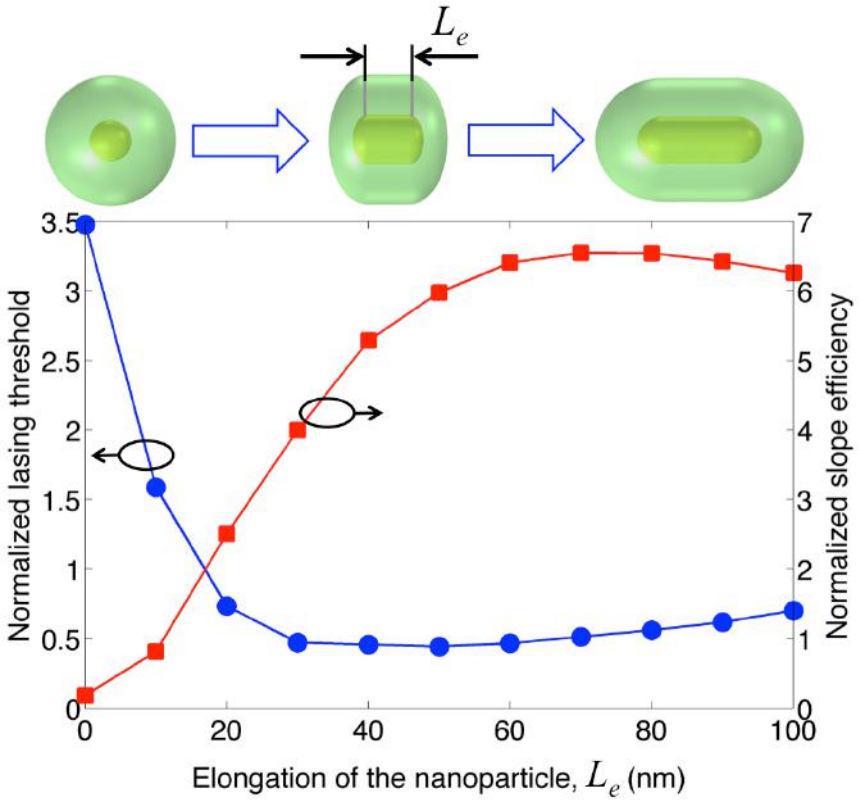



**Figure 2.** Computed steady-state values of the lasing thresholds (left *y*-axis, blue circles) and slope efficiencies (right *y*-axis, red squares) of plasmonic lasers based on single gold core-shell nanoparticles as a function of the elongation of the nanoparticles, $L_e$. Results for a broad range of values for $L_e$, ranging from $L_e$=0 (spherical case) to $L_e$=100 nm (elongated nanorod) are displayed.

## REFERENCES


1. J. Cuerda, F. Ruting, F.J. Garcia-Vidal, and J. Bravo-Abad, "Theory of lasing action in plasmonic crystals," *Phys. Rev. B Rapid Comm.*, Vol. 91, 041118(R), 2015.
2. J. Cuerda, F.J. Garcia-Vidal, and J. Bravo-Abad, "Laser light generation in active core-shell metallic nanoparticles," *submitted*, 2016.

# Antenna-enhanced third-order nonlinear response of an epsilon-near-zero medium

**M. Z. Alam[1*], S. A. Schulz[1], J. Upham[1], I. De Leon[1,2], and R. W. Boyd[1,3]**

[1]Department of Physics, Max-Planck Centre for Extreme and Quantum Photonics, University of Ottawa, Canada

[2]School of Engineering and Sciences, Tecnológico de Monterrey, Mexico

[3]Institute of Optics, University of Rochester, USA

[*]corresponding author: zahir@uottawa.ca

**Abstract**-We demonstrate experimentally that the linear optical response of a plasmonic dipole antenna array is significantly modified when placed on a thin epsilon-near-zero (ENZ) material. Moreover, the strong interaction between the dipole antenna array and the ENZ material results in a broadband (>500 nm) nonlinear metamaterial with $|n_2|$ values up to eight orders of magnitude larger than that of silica glass. Our results show a new way of designing ultra-broadband nonlinear metasurfaces with tailored third-order nonlinear strength and sign.

Materials with near-zero permittivity, commonly known as epsilon-near-zero (ENZ) materials, have interesting linear and nonlinear optical properties [1-3]. It has been recently reported that the emission pattern of a plasmonic antenna is significantly modified when it is placed on a micrometer-thick ENZ substrate [4].

In this work, we investigate the impact of a thin ENZ substrate on the linear and the nonlinear optical responses of a plasmonic nanoantenna array that is designed for operation near the ENZ wavelength of the substrate. We find that the linear optical response of our structure is significantly different from that of a recently reported case [4]. Our ENZ substrate is a thin film (23 nm) of indium tin oxide (ITO) with a bulk plasmon wavelength in the near-infrared region of the spectrum. We show that the strong coupling between the plasmonic mode of the antenna and the modes supported by the ITO film results in resonance splitting (Fig. 1) similar to the resonance splitting in a pair of strongly coupled oscillators and Rabi-splitting in an atom-cavity system.

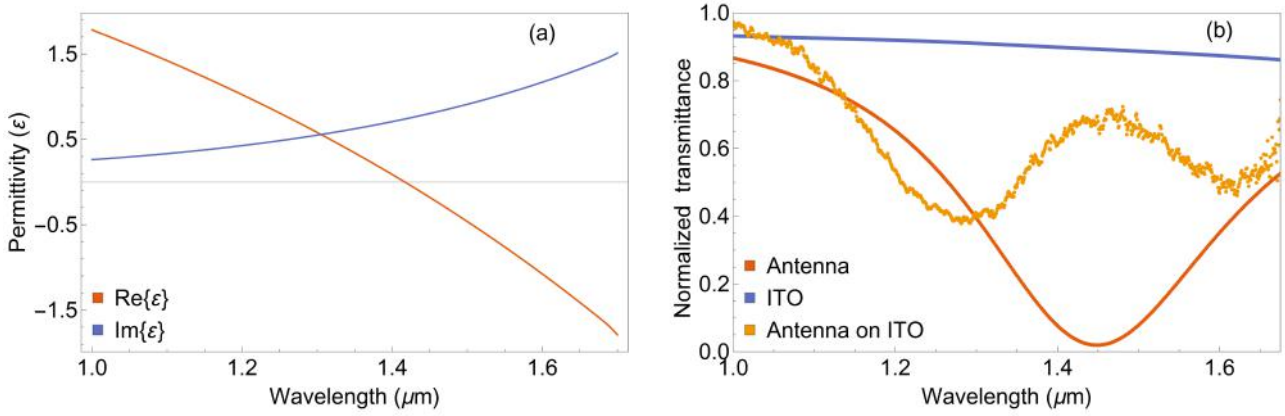



**Figure 1** The real part of the permittivity of a 23-nm-thin ITO film crosses zero at 1420 nm wavelength (a). Due to the strong coupling between the ENZ and the antenna modes, the antenna-ENZ structure exhibits resonance splitting (b).

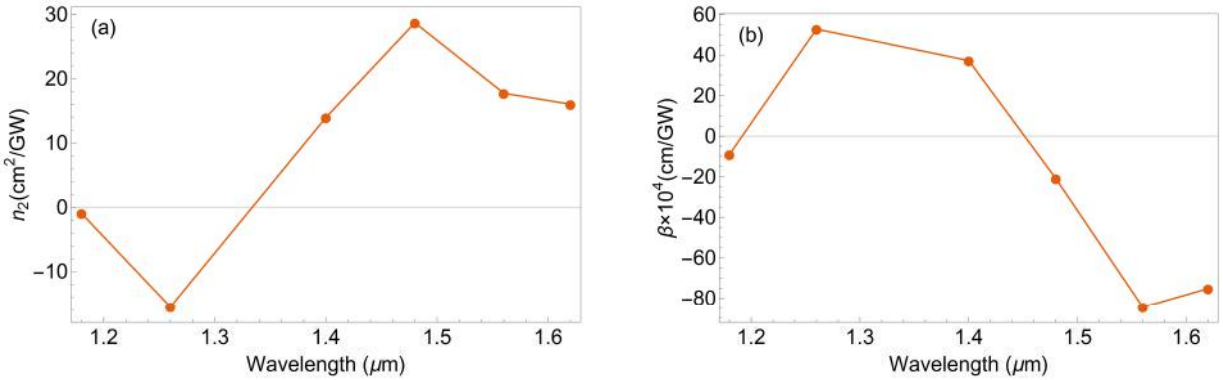



**Figure 2** The third-order nonlinear responses of the antenna-ENZ structure as measured by a z-scan setup. (a) Intensity dependent refractive index. (b) Intensity dependent absorption.

We use a z-scan setup to measure the intensity-dependent nonlinear response of our ENZ-antenna structure at normal incidence [5]. Through a series of such measurements using a ~100 fs laser source, we measure the nonlinear response of the structure over a broad spectral range. We find that the structure exhibits dispersive nonlinear response. Moreover, the material exhibits both positive and negative nonlinear responses: self-focusing and defocusing nonlinearity, as well as saturable and reverse saturable absorption (Fig. 2). We find that the nonlinear response of the structure is strongly enhanced over this entire spectral region. In particular, the absolute magnitude of the real part of the nonlinear refractive index coefficient ($|n_2|$) of this structure can be over a hundred million times stronger than that of silica glass, and over six orders of magnitude larger than that of a chalcogenide glass [5]. We also measure the time dependent nonlinear response of the structure (data not shown here) to understand the ultrafast nature of the response.

Our results introduce a new paradigm in enhancing nonlinearity in a nanostructured thin film [6], and offer a new way of designing highly nonlinear broadband metasurfaces.

## REFERENCES


1. Alù, A., M. G. Silveirinha, A. Salandrino, and N. Engheta, "Epsilon-near-zero metamaterials and electromagnetic sources: Tailoring the radiation phase pattern," *Phys. Rev. B*, Vol. 75, No. 15, 155410, 2007.
2. Christos, A., P. Chen, G. D'Aguanno, N. Engheta, and A. Alù, "Boosting optical nonlinearities in ε-near-zero plasmonic channels," *Phys. Rev. B*, Vol. 85, No. 4, 045129, 2012.
3. Alam, M. Z., I. D. Leon, and R. W. Boyd, "Nonlinear refractive index larger than linear index: towards all-optical switching with terahertz bandwidth using epsilon-near-zero thin film," *FiO, OSA Tech. Dig.*, paper FM3D.7, 2015.
4. Kim, J., A. Dutta, G. V. Naik, A. J. Giles, F. J. Bezares, C. T. Ellis, J. G. Tischler, A. M. Mahmoud, H. Caglayan, O. J. Glembocki, A. V. Kildishev, J. D. Caldwell, A. Boltasseva, and N. Engheta, "Role of epsilon-near-zero substrates in the optical response of plasmonic antennas," *Optica*, Vol. 3, 339-346, 2016.
5. Boyd, R. W., *Nonlinear Optics*, Academic Press, New York, 2008.
6. Sipe, J. E., and R. W. Boyd, "Nonlinear susceptibility of composite optical materials in the Maxwell Garnett model," *Phys. Rev. A*, Vol. 46, No. 3, 1614, 1992.

# Switchable and reconfigurable nanophotonics: from single antennas to complex systems

**Otto L. Muskens[1], Roman Bruck[1], Yudong Wang[1], Kees de Groot[1], Kevin Vynck[2], Philippe Lalanne[2], Goran Mashanovic[3], Graham Reed[3]**

[1] Physics and Astronomy, Zepler Institute, University of Southampton, UK

[2] LP2N, CNRS – IOGS - University Bordeaux, France

[3] Optoelectronics Research Centre, Zepler Institute, University of Southampton

[*]corresponding author: O.Muskens@soton.ac.uk

**Abstract**- I present a number of results aimed at achieving nanoscale switchable and reconfigurable devices. A single nanoantenna can concentrate intensity and produce an enhanced excitation and readout of a nonlinear Kerr medium. Next to single-antenna building blocks, we look at highly multimode, complex environments where the light field is the result of interference of many possible light paths. New types of all-optical control are achieved through reconfiguring the light field and the medium itself, including ultrafast wave shaping and reciprocity effects.

Photonic technologies are playing a tremendously important role in our society, through revolutionizing applications in telecommunication, broadband internet, data storage, and laser manufacturing. Currently, light is increasingly being manipulated at length scales comparable or even smaller than its wavelength, the field of research naturally being referred to as nanophotonics. In future systems, nanophotonics is expected to increasingly converge with electronics in essential functionalities, such as on-chip optical interconnects, optical data manipulation and storage, and quantum information devices.

The active control of nanoscale photonic devices is of interest as it allows dynamic routing of light, control of optical near fields and spontaneous emission. Efforts to develop switchable and reconfigurable nanophotonic devices are focusing on different routes, and can be roughly distinguished into two classes. One strategy uses a single resonator where energy is concentrated in space and time to achieve strong local fields and high sensitivity for perturbations. Another strategy uses a distributed system where electromagnetic waves propagate over a certain distance through a medium.

In recent studies, we have developed hybrid devices consisting of plasmonic nanoantenna and a nonlinear medium [1,2,3]. By selectively pumping the antenna resonance, it was demonstrated that strong local switching could be achieved in a range of actively tunable materials including metal oxides such as indium-tin oxide and vanadium dioxide. This strategy requires materials with a very large optical switching contrast.

As a second strategy, the use of distributed scattering potentials in controlling the flow of light is explored [4,5,6]. The basic idea is that the presence of a scattering potential landscape results in many paths leading from two points in a medium. By constructively shaping either the incident wavefront or the scattering potential, it is possible to achieve any transfer function for the medium, for example using inverse design [7]. For our new concept, referred to as ultrafast wave shaping, we induce a new

scattering potential which strongly varies in space and/or time, by using a femtosecond pulsed laser and a material with a sufficient nonlinear response. The ultrafast perturbation cannot only collapse the transfer function due to nonlinear dephasing and time reversal breaking [4,5], but also result in a new transfer function of the device. We have demonstrated efficient routing of light between the output ports of a multimode interference device with up to 97% efficiency and less than -27dB cross talk between channels [6]. Figure 1 shows the principle of the experiment, where a nonlinear pattern of perturbations is projected on the top of the device, where the individual perturbations effectively act in concert to reroute the light between the two output ports.

**Acknowledgements**, This work was supported by EPSRC through research grant EP/J016918.

## REFERENCES

1. M. Abb, P. Albella, J. Aizpurua, O. L. Muskens, “All-optical control of a single plasmonic nanoantenna-ITO hybrid,” *Nano Lett.* Vol. 11, 2457-2463, 2011.
2. M. Abb, Y. Wang, C. H. de Groot, O. L. Muskens, “Hotspot-mediated ultrafast nonlinear control of multifrequency plasmonic nanoantennas,” *Nature Communications* Vol. 5, 4869, 2014.
3. O. L. Muskens, L. Bergamini, Y. Wang, J. M. Gaskell, N. Zabala, C. H. de Groot, D. W. Sheel, J. Aizpurua, “Antenna-assisted picosecond control of nanoscale phase transition in $VO_2$,” submitted, 2016.
4. T. Strudley, R. Bruck, B. Mills, O. L. Muskens, “An ultrafast reconfigurable nanophotonic switch using wavefront shaping of light in a nonlinear nanomaterial,” *Light: Science & Applications* Vol. 3, e207, 2014.
5. O. L. Muskens, P. Venn, T. van der Beek, and T. Wellens, “Partial nonlinear reciprocity breaking through ultrafast dynamics in a random photonic medium,” *Phys. Rev. Lett.* Vol. 108, 223906, 2012.
6. R. Bruck, K. Vynck, P. Lalanne, B. Mills, D. J. Thomson, G. Z. Mashanovich, G. T. Reed, O. L. Muskens, “An all-optical spatial light modulator for reprogrammable silicon photonic circuits,” *Optica* Vol. 3, 2016.
7. A.Y. Piggott, J. Lu, K. G. Lagoudakis, J. Petykiewicz, T. M. Babinec, J. Vučković, “Inverse design and demonstration of a compact and broadband on-chip wavelength demultiplexer,” *Nature Photon.* Vol. 9, 374-378, 2015.

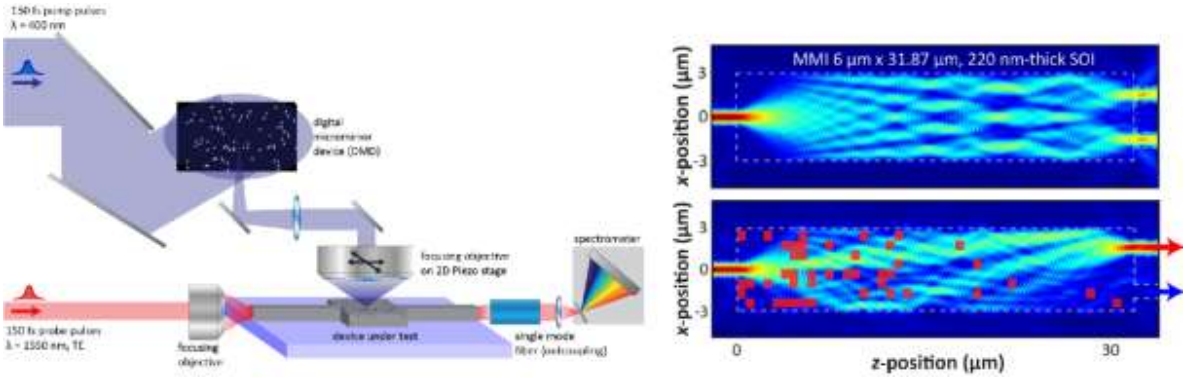



Figure 1 (left) Experimental setup used for wave shaping on a silicon chip, with (right) calculated intensity in MMI without and with perturbation pattern (red dots) [6].

# Second Harmonic Generation from sub-wavelength Triangular Hole Array in Au Thin Film

**M. Saikawa, Y. Hachiya, K. Iwata,**
**M. Matsubara, and T. Ishihara**

Department of Physics, Tohoku University, Sendai, Japan
*corresponding author, E-mail: t-ishihara@m.tohokuj.ac.jp

## Abstract

Transmitted second harmonic generation (SHG) is investigated for isosceles triangular hole array in 25 nm thick Au film on a quartz substrate. Even at normal incidence, due to lack of inversion symmetry in one direction for the triangular shape, SHG generated at the surface of the hole wall is not cancelled and thus observed. Numerical calculation based on the effective susceptibility formalism is compared to the experimentally observed resonance in SHG excitation spectra.

## 1. Introduction

Second-order optical nonlinearity exists at the surface where dielectric environment changes abruptly. In the oblique incident configuration, surface polarization is excited which generates SHG. For normal incidence it does not give SHG unless the surface has a structure which breaks the symmetry in the plane. The structure can be endowed by artificially carving the surface by using e-beam lithography for example. This structure can be considered as a new type of metamaterial where second order optical nonlinearity is designed. We have already shown that by breaking the symmetry, it is possible to observe SHG in semiconductor embedded structure [1]. Recently sub-wavelength shape dependent SHG was investigated and analyzed in terms of effective susceptibility concept [2,3,4]. By appropriately design the subwavelength structure, it may be possible to produce extremely nonlinear metamaterial, which can be an essential ingredient for integrated optical circuits. This time we employ simple triangle hole array geometry in Au thin film in order to confirm the validity of the approach.

## 2. Design and Fabrication

In order to investigate SHG from metamaterials experimentally, we designed the structure so that it has a structural resonance at the convenient wavelength around 1300 nm, for which SHG is below the absorptive wavelength. We employ a unit cell with a simple equilateral triangular hole arranged in a square array. Numerical calculation is carried out with commercial software (CST Microwave Studio). In order to avoid any diffraction, the period is set to be 400nm. Height and base of a triangle is 360nm.

Square array of triangles are fabricated on 25nm-thick Au sputtered on a quartz substrate.. Figure 1 shows Atomic Force Microscopy (AFM) image of our structure. Sample size is 0.6 mm x 0.6 mm.

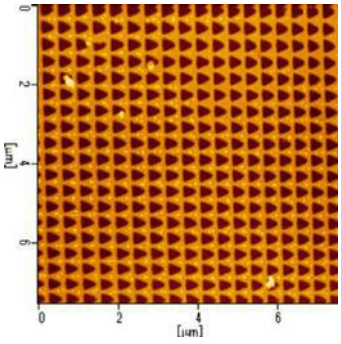



Figure 1: (a) AFM image of square array of triangular holes in Au film.

## 3. Experiment and Simulation

Square array of triangles with 360 nm-long height and base was patterned with e-beam lithography. Period of array is 400nm. Figure 1 shows atomic force microscope (AFM) image of our sample. Symmetry is broken for holizontal (x) direction.

Transmission spectra for x- and y-polarized light are shown in Fig. 2. Transmission peak at around 500nm is characteristic to Au, which can be seen in plain Au film as well. Transmission dip at 670nm is due to the triangular hole. According to the numerical calculation, the dip position is dependent on the structural parameter and is generally polarization dependent. In order to reproduce the experimental result, we had to use base and height to be 200 nm and blend radius to be 30nm. In this case, the resonant position is found to be similar for x- and y- polarization. The

dip at 570nm is deeper for y-polarized light. On the other hand transmission is higher for y-polarized light at around 900nm.

As a tunable excitation source for SHG measurement , we employed an optical parametric amplifier with 180 fs pulse width excited by 1kHz Ti:sapphire regenerative amplifier. In Fig.3, polar plot of SHG intensity for excitation at 1226 nm is shown. The laser peak intensity in front of the sample was estimated to be 1 GW/cm$^2$. The SHG intensity was proportional to the square of excitation intensity. We found that the SHG light is polarized to x-direction where inversion symmetry is broken.

Figure 3 shows SHG polarization for x- and y-polarized excitation at 1226 nm. It was found that the SHG is polarized along x-direction for both x- and y-polarized light. SHG intensity was about twice larger for y-polarized excitation at this wavelength.

Transmitted SHG intensity was measured as a function of laser wavelength as is plotted in Fig. 4. The SHG was polarized in x-direction for both x- and y-polarized excitation. A prominent resonance was observed at 1330 nm for y-polarized light, when its SHG corresponds to the resonant dip in linear transmission spectrum. The maximum SHG count was about 500 counts/sec in our experimental condition.

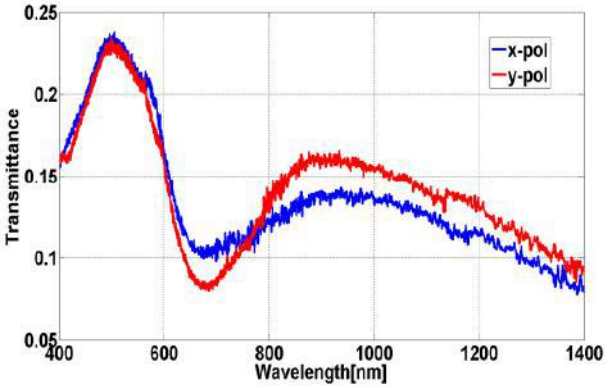



Figure 2: Transmission specta for x- and y-excitation.

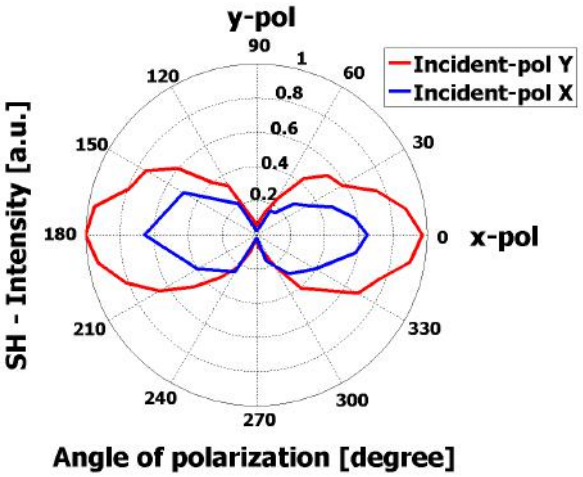



Figure 3: Polar plot of SHG intensity excited at 1226 nm.

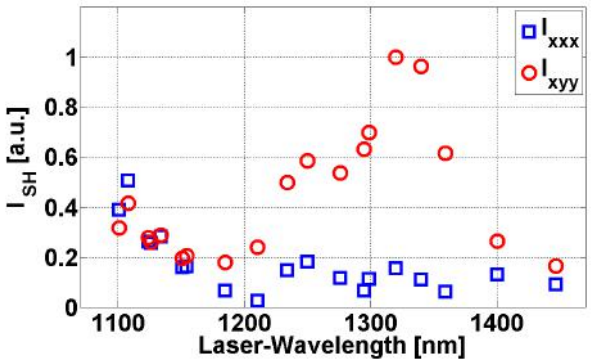



Figure 4: Exciation wavelength dependence of SHG intensity for x-polarized (red circle) and y-polarized light (blue square).

In order to understand the experimental observation, we have calculated SHG field following the effective susceptibility concept [2]. This concept was recently applied to SHG in metamaterials [3,4]:

$$E_{\mathrm{SH}}(2\omega) \propto \iint \chi_{nnn} E_n^2(\mathbf{r},\omega) E_n(\mathbf{r},2\omega) dS$$

Here, $E_n(\mathbf{r},\omega)$ is the normal component of an microscopic electric field excited by the incident laser at the nanostructure, while $E_n(\mathbf{r},2\omega)$ is the SHG field sent from the observation point. $\chi_{nnn}$ is all normal component of the nonlinear susceptibility at the surface. Unlike [3,4], where only structure parameter dependence is discussed for a fixed excitation wavelength, we measured wavelength dependence of SHG. The electric field distribution for fundamental and SHG wavelengths were numerically calculated. Effective susceptibility was estimated by using these electric fields just outside of the gold. For the calculation we assumed that normal component of nonlinear surface susceptibility is dominant and wavelength independent. We found in the calculation that at the resonance, which corresponds to the dip in the transmission spectrum, SHG is enhanced and y-excitation is a few times larger than x-excitation, which is consistent with our experiment. The calculation predicts that there is another resonance at shorter wabelength, where SHG intensity is by far larger.

## 4. Discussion

According to the effective susceptibility formalism, large second order optical nonlinearity in nanostructure does not necessarily mean that the SHG emission is strong. In order to estimate electric field of SHG at the farfield region, we calculate the overlapping integral with internal field distribution excited by the light sent from the observation point. Assuming that the normal component of second order optical nonlinear susceptibility at the metal

surface is dominant, we can reproduce experimental observation farily well.

The observed selection rule for SHG is obvious from this integral. As the structure is asymmetric upon x-inversion, $\chi^{(2)}_{xxx}$ and $\chi^{(2)}_{xyy}$ components are finite. On the other hand $\chi^{(2)}_{yyy} = 0$, because the system is invariant upon y-inversion. Whether $\chi^{(2)}_{xyy}$ is larger or smaller than $\chi^{(2)}_{xxx}$, can not be determined from symmetry. But with effective susceptibility calculation it can be predicted. As the electric field distribution at $\omega$ and $2\omega$ can be calculated with numerical simulation, it paves the way to explore artificial material with large optical nonlinearity.

## 5. Conclusions

SHG due to isosceles triangular holes sub-wavelength scale in Au thin film is observed at normal incidence. SHG enhancement is observed when SHG excites the lowest resonance of the triangular hole structure. Effective susceptibility explains SHG selection rules and wavelength dependence reasonably well. Symmetry of electric field distribution at SHG frequency determines SHG selection rules. Even larger enhancement is expected when the laser directly excites the lowest resonance.

## Acknowledgements

This work was partly supported by Grant-in-Aid for Scientific Research on Innovative Areas “Electromagnetic Metamaterials” No.22109005 from The Ministry of Education, Culture, Sports, Science and Technology (MEXT), Japan..

## References

[1] Ishihara, T., Koshino, K. and Nakashima, H., “Second Harmonic Generation due to Quadrupole Interaction in a Photonic Crystal Interaction: Angle Dependence and the Symmetry of the Unit Cell,” *Phys. Rev. Lett.* Vol. 91, 2003, 203901:1-4.

[2] Roke, S., Bonn, M. and Petukhov, A.B., “Nonlinear optical scattering: The concept of effective susceptibility,” *Phys. Rev.* B Vol.70, 2004, 1150106:1-10.

[3] O’Brien, K., Suchowski, H., Rho, J., Salandrino, A., Kante, B., Yin, X., and Zhang, X., “Predicting nonlinear properties of metamaterials from the linear response,” *Nature Materials* Vol.14, 2014, 379-383.

[4] Jeremy Butet and Olivier J. F. Martin, “Evaluation of the nonlinear response of plasmonic metasurfaces: Miller’s rule, nonlinear effective susceptibility method, and full-wave computation,” Journal of the Optical Society of America B, 33 (2016) A8-15.

# Acoustic, Mechanical and Thermal Metamaterials

# Theory and experimental realization of the emergence, coalescence and topological properties of multiple exceptional points

**Kun Ding[†], Guancong Ma, Meng Xiao, Z. Q. Zhang, and C. T. Chan[*]**
Department of Physics and Institute for Advanced Study,
The Hong Kong University of Science and Technology, Hong Kong
[†]presenting author: kun@ust.hk
[*]corresponding author: phchan@ust.hk

**Abstract**-We consider the emergence and interaction of multiple exceptional points in a four-state system theoretically and realize the system experimentally using four coupled acoustic cavities with asymmetric losses. We find the system exhibit multiple EPs that can collide and merge, leading to higher order singularities and topological characteristics not found in two-state systems. The new physics obtained here in acoustic systems can be extended to other kinds of waves.

Non-Hermitian systems, such as open systems and systems with asymmetric losses, are common in nature and have drawn a lot of attentions for a long time. Exceptional points (EPs) can exist in such systems when two eigenstates coalesce. This is the origin of a wide range of novel phenomena in different branches of physics such as level repulsion, superradiance, coherent perfect absorption, rings of EPs and loss-induced revival of lasing. Most of these phenomena can be understood by considering a simple 2x2 non-Hermitian matrix. At a higher dimension, more complex EP physics not found in two-state systems arises [1,2].

In this work, we investigate a four-state system both theoretically and experimentally. The emergence of multiple EPs, their topological properties, and their coalescence can be best summarized in a phase diagram featuring an exceptional point formation pattern (EPFP). The coalescence of two EPs and that of three EPs form two trajectories in the parameter space, partitioning the phase space into different regions each with a unique EPFP. Together with a two-state inversion line, the phase space is further divided into five regions, each with distinct topological properties. By using coupled acoustic resonant cavities with tunable eigenfrequencies, coupling strengths, and dissipative loss, these formation patterns were observed and characterized experimentally. The coalescence of three EPs produces a higher order singularity and the coalescence of a pair of EPs with the same chirality produces a linear crossing that is qualitatively different from the linear crossing at a diabolic point of Hermitian Hamiltonians.

**Acknowledgements**, This work was supported by Research Grants Council Hong Kong (Grant No. AoE/P-02/12).

**REFERENCES**

1. Kun Ding, Guancong Ma, Meng Xiao, Z. Q. Zhang, and C. T. Chan, "The emergence, coalescence and topological properties of multiple exceptional points and their experimental realization," arXiv:1509.06886 (2015).
2. Kun Ding, Z. Q. Zhang, and C. T. Chan, "Coalescence of exceptional points and phase diagrams for one-dimensional PT-symmetric photonic crystals," *Phys. Rev. B* **92**, 235310 (2015).

# Parity-time synthetic phononic media

**Johan Christensen**[1*]
[1]DTU, Denmark
[*]corresponding author: johan.christensne@gmail.com

**Abstract** In this presentation we show how active acoustic media can be engineered and tuned to work as a Parity-time (PT) synthetic phononic system. We demonstrate a feasible approach for the case of sound where the most important ingredients within synthetic materials, loss and gain, are achieved through electrically biased piezoelectric semiconductors. With colorful examples we demonstrate the rich physics involved and the broad landscape for applications associated with the PT properties.

.

# Total transmission super-resolution imaging with a hyperbolic elastic metamaterial

**Hyuk Lee[1], Joo Hwan Oh[2], Hong Min Seung[1], Seung Hyun Cho[3], and Yoon Young Kim[1, 2*]**

[1]School of Mechanical and Aerospace Engineering, Seoul National University, Korea

[2]Institute of Advanced Machines and Design, Seoul National University, Korea

[3]Korea Research Institute of Standards and Science, Korea

[*]corresponding author: yykim@snu.ac.kr

**Abstract**-Here we realize total transmission subwavelength imaging with a hyperbolic elastic metamaterial lens. The elastic parameters (mass density and stiffness) are delicately tuned and realized with our explicit analytical method by a mass-spring model. The essential conditions for super-resolution (by hyperbolic dispersion relation with negative effective mass density) and total transmission (by extremely large effective stiffness) are successfully realized. The fabricated metamaterial lens is capable of resolving subwavelength symmetric Lamb waves (up to 0.09λ).

Fine quality super-resolution (deep subwavelength scale) imaging of high transmission and low loss is crucially demanded for the broad range of ultrasonic imaging applications including non-destructive evaluation and biomedical screening. Although researches on the vast regime of subwavelength imaging with hyperbolic metamaterial lenses [1, 2] for electromagnetic waves and acoustic waves has been successfully carried out recently, elastic counterpart has been severely limited due to its complexity of higher-order tensor based material quantities. Even more, elastic metamaterial lenses inherit severely low transmission owing to the highly mismatched impedance with respect to the background medium, hence disturbing the ideal imaging.

Thus, in this work, we propose a hyperbolic elastic metamaterial lens which is capable of subwavelength imaging with total transmission. Our analytical mass-spring model for the unit cell structure and its realization in a continuum medium is shown in Fig. 1(a). The key idea is to implement the following two essential conditions for total transmission subwavelength imaging with our properly designed unit cell structure:

1. Total transmission realized by using extreme stiffness to compensate for the decreased impedance in the perforated metamaterial structure in the wave propagating direction (y direction).

2. Subwavelength resolution ability by utilizing hyperbolic dispersion (shown in Fig. 1(b)) induced from negative effective mass density in the perpendicular direction (x direction).

Such anomalous properties are caused by translational motion of the local resonators denoted as m that are connected to the main body mass M by the two-dimensional stiffness terms α, β, and γ.

The performance of the subwavelength imaging and total transmission is confirmed both by numerical simulation and experiment with a laser scanning vibrometer. As for incident subwavelength wave generation, a 20 mm wide line source (corresponding to 0.13λ) is considered. Two 2 mm-wide line sources with separation of 36 mm (corresponding to 0.23λ) and center-to-center separation of 56 mm (corresponding to 0.365λ), are installed 5mm in front of the lens. From Fig. 2(c), it is apparent that in contrast to the case without the metamaterial, the subwavelength details are preserved in the imaging domain when the metamaterial lens is installed as though the source is directly transferred through the lens.

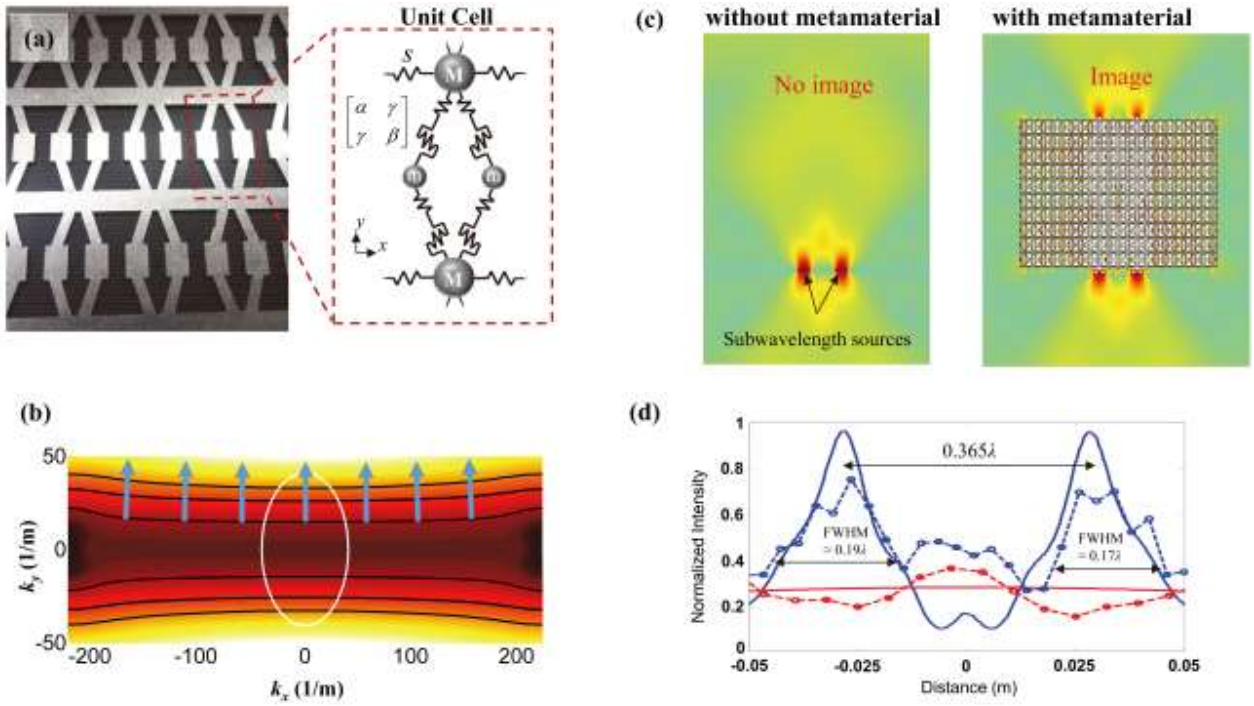



**Figure 1** (a) The fabricated elastic metamaterial and the corresponding mass-spring model for its unit cell structure. (b) Equi-frequency contours (metamaterial for black and isotropic aluminum for white) showing hyperbolic dispersion curve. (c) Numerical time-harmonic simulation. (d) Obtained intensity profiles confirming the subwavelength resolution ability. The dotted lines are from the experiment and the solid lines are from simulation. The red line is without the lens and the blue line is with the metamaterial lens.

As for experimental verification, the lens is fabricated in a base aluminum plate. For subwavelength sources, we utilized two magnetostrictive transducers [3] that are proven to have good wave mode tunability. The resolution (shown in Fig. 1(d)), under the definition of full-width at half maximum (FWHM) of the peak, for two-source experiment is 29.79 mm or 0.19λ and 27.42 mm or 0.17λ, respectively. Also, subwavelength distance of 56 mm or 0.365λ apart can be clearly resolved with the metamaterial lens. In fact, not shown here though, two sources as close as 1 lattice constant (14 mm or 0.09λ) was resolved by the definition of FWHM.

**Acknowledgements**

This work was supported by the National Research Foundation of Korea (NRF) Grant [no. 2015-021967, 2014M3A6B3063711 (Global Frontier R&D Program on Metamaterials)] funded by the Korean Ministry of Science, ICT and Future Planning (MSIP) contracted through IAMD at Seoul National University.

**REFERENCES**

1. Lu, D. and Liu, Z, "Hyperlenses and metalenses for far-field super-resolution imaging," *Nat. Commun*, Vol. 3, No. 1205, 2012.
2. Poddubny, A., Iorsh, I., Belov, P. and Kivshar, Y, "Hyperbolic metamaterials," *Nat. Photonics* Vol. 7, No. 948-957, 2013.
3. Kim, Y. Y. and Kwon, Y. E, "Review of magnetostrictive patch transducers and applications in ultrasonic nondestructive testing of waveguides," *Ultrasonics*, Vol. 62, No. 3-29, 2015.

# Rainbow trapping in mechanical vibrations

**R. A. Méndez-Sánchez[1*], A. Arreola-Lucas[2], G. Báez[3], F. Cervera[4]. A. Climente[4], and J. Sánchez-Dehesa[4]**

[1]Instituto de Ciencias Físicas, Universidad Nacional Autónoma de México, Cuernavaca, Mor., Mexico

[2]Posgrado en Ciencias e Ingeniería, Universidad Autónoma MetropolitanaAzcapotzalco, Mexico.

[3]Departamento de Ciencias Básicas e Ingeniería, Universidad Autónoma Metropolitana-Azcapotzalco, Mexico

[4]Wave Phenomena Group, Dept. of Electronics Engineering, Universitat Politècnica de Valencia, Valencia, Spain

[*]corresponding author: mendez@icf.unam.mx

**Abstract**-The emergence of the rainbow trapping effect is shown experimentally. We started with a beam in which a chirped structure was machined at one side. At the other side a passive vibration isolation system was used. In the middle wave packets were generated using an electromagnetic-acoustic transducer. For different values of the chirp intensity the analog the rainbow trapping effect, was found. The predicted effect was measured in the structured beam.

**Introduction:** The rainbow trapping, discovered few years ago in optics [1], is an effect in which a wave is slowed down. This effect has potential applications since it separates spatially different frequency components of a wave packet; it can be used to multiplex waves and to design buffers, filters and sorters, etc. Due to its importance several groups in the world have found its emergence in other frequency ranges. Inclusive, it has also been observed in acoustic waves [2,3]. Nevertheless, for mechanical waves, due to the complexity involved, this phenomenon has not been observed. Here we report the measurement of the rainbow trapping effect in mechanical waves.

**Numerics:** The transfer matrix method was used to calculate the dynamical behavior of the wave packet in the structured beam. In the rectangular beam 20 cells were designed using notches. The length $a_j$ of the cell $j$ is given by the distance between two consecutive notches, and depends on the chirp intensity $\lambda = (a_j - a_{j-1})/a_j$. An initial wave packet is expanded in 200 normal modes of the structured beam and the dynamics is calculated. When the chirp vanishes, the normal mode frequencies group together forming bands and gaps; for different values of the chirp intensity the band structure is modified slightly. When the central frequency $f_C$ of the initial packet lies inside the gap the packet is completely reflected by the structure; when the $f_C$ is inside the band the packet crosses the structure. When the chirp is different of zero, the wave packet arrives to different positions depending on the value of $f_C$. An example of the numerical behavior of the wave packets is plotted in the left part of the Figure 1.

**Experiment:** A structured beam was machined from a single aluminum piece with the chirped structure at one side. At the other side a passive vibration isolation system was built; in the middle, a uniform part remains. Using a PXI, a high fidelity audio amplifier and electromagnetic-acoustic transducers, torsional Gaussian wave packets of 1 ms of width and different central frequencies were generated. The response of the beam was measured with a Doppler Vibrometer and filtered and analyzed with LabView. The experimental results, show excellent agreement with the numerical predictions; they are plotted at the right part of the Figure 1.

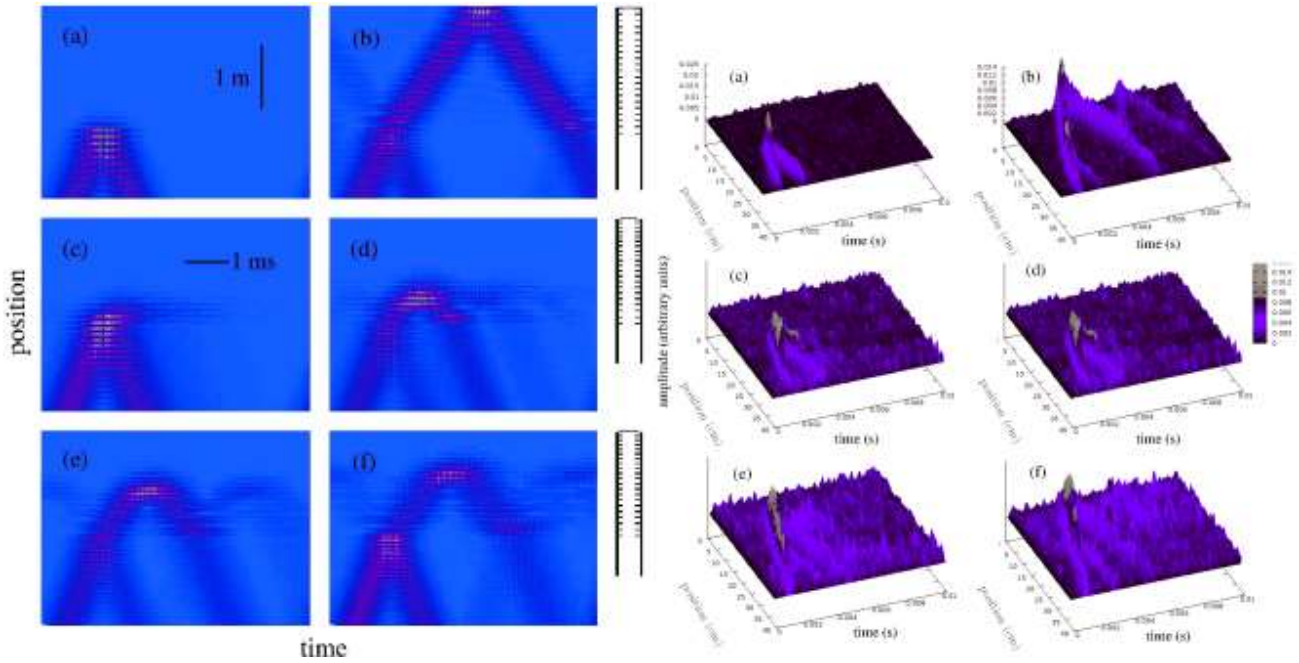



**Figure 1.** Dynamical behavior of a wave packet in a chirped structure, experiment right, numerics left. Cases a) and b) correspond to the periodic structure with $f_C$=8 and 11.5 kHz, respectively. Cases c), d), e) and f) to the chirped structure and $f_C$=9, 10, 11, 12 and 10, 12, 13, 14 kHz for the right and left parts, respectively.

**Conclusions:** We have shown that the rainbow trapping effect appears in torsional waves in beams. This result can be considered as a cornerstone since not only opens the possibility of controlling mechanical waves but also yields a guide in the design of new mechanical metamaterials.

**Acknowledgements**, This work was supported by DGAPA-UNAM under project PAPIIT IN103115 and by CONACYT. RAMS received support from DGAPA-UNAM under program PASPA. F.C, A.C. and J. S-D. acknowledge the support of the Spanish MINECO under the contract with Ref. TEC2014-53088-C3-1-R.

**REFERENCES**

1. Tsakmakidis, K. L., Boardman, A. D., and Hess, O. "'Trapped rainbow' storage of light in metamaterials." *Nature*, Vol. 450, 397–401, 2007.
2. Chen, Y. Y. et al. "Enhanced acoustic sensing through wave compression and pressure amplification in anisotropic metamaterials" *Nat. Comm*. 5, 5247 (2014).
3. V. Romero-García et al. "Enhancement of sound in chirped sonic crystals", App. Phys. Lett. 102, 091906 (2013).

# Three-dimensional Resonant Elastic Metamaterials with Fluid-like Property

**Guancong Ma**[1, 2*], **Caixing Fu**[1], **Guanghao Wang**[3], **Philipp del-Hougne**[1], **Johan Christensen**[4], **Yun Lai**[3], **Ping Sheng**[1, 2]

[1] Department of Physics, Hong Kong University of Science and Technology, Clear Water Bay, Kowloon, Hong Kong.

[2] Institute for Advanced Study, Hong Kong University of Science and Technology, Clear Water Bay, Kowloon, Hong Kong.

[3] College of Physics, Optoelectronics and Energy, Soochow University, Suzhou 215006, China.

[4] Department of Photonics Engineering, Technical University of Denmark, DK-2800 Kongens Lyngby, Denmark

[*]corresponding author: phmgc@ust.hk

**Abstract**- We present a three-dimensional anisotropic resonant elastic metamaterial. Due to the anisotropy, translation eigenmodes are not degenerate along all spatial directions. Repeating the subwavelength unit cells can lead to objects that are essentially elastic rods, which can withstand both longitudinal and flexural vibrations. Band structure analysis shows that within a finite frequency regime, only longitudinal wave can propagate, whereas waves transverse in their nature are forbidden – a hallmark property conventionally found only in fluids. This finding is realized with vibrational experiments.

Due to their ubiquity, elastic waves have been a study of pivotal importance in many areas. Recently, the study of elastic waves experienced an acceleration in pace, thanks to the emergence of man-made composites known as metamaterials[1]. Local resonances of subwavelength units[2] have been utilized to achieve many novel and exotic functionality in acoustic metamaterials[3]. Here, we link the concept of local resonance with elastic waves, and demonstrate with experiments that within a finite frequency regime, only longitudinal elastic waves can propagate, whereas the waves transverse in their nature meet a bandgap and therefore are not sustained – a property that is conventionally considered as the hallmark of fluid[4].

The unit cell has a simple design, as shown in Fig. 1a. A steel cylinder that is r=15.8mm in radius and h=37.6 mm in height is coated with silicone rubber. The silicone layers covering the top and bottom end surfaces are 1 mm in thickness, whereas the silicone around the curvilinear side surface is 5 mm thick. The silicone coated cylinder is then embedded in an epoxy cube with side a=60 mm. The thickness difference in silicone rubber introduces anisotropy into the unit cell, and breaks the spatial symmetry. This will have profound consequence.

Eigenmode analysis shows that the unit cell has three translational modes, in which the steel cylinder and the epoxy vibrate in an anti-phase manner. Due to the thinner silicone layer on the top and bottom surfaces, the eigenmode with vibration dominantly along the cylinder's axis (defined as z-axis) has a higher eigenfrequency than the two modes with vibrations in xy-plane.

By repeating the unit cells in z-direction, we obtain a one-dimensional periodic array, which is essentially a three-dimensional elastic object known as *rod*. A rod can withstand both longitudinal and flexural waves (with the latter being dominantly transverse.) In our system, we find that an excitation force transverse to the rod can trigger bending vibration (flexural wave), as well as a translation mode in xy-plane. Their coupling yields a polariton-like dispersion, together with a flexural wave bandgap. On the other hand, a force along the rod can excite the longitudinal branch, together with the translational z-mode. Owing to the higher eigenfrequency of the z-mode, the passband of longitudinal wave overlaps with the flexural wave bandgap (~1.1–1.7 kHz as shown in Fig. 1b). Therefore, in this frequency regime, only longitudinal waves can be sustained, whereas transverse wave's propagation is forbidden. Conventionally, such elastic property is only found in fluid. This finding is realized in vibrational experiment (Fig. 1b).

More results and detailed analyses are to be shown with an oral presentation. Our findings can see applications in many scenarios such as civil engineering and seismic wave control.

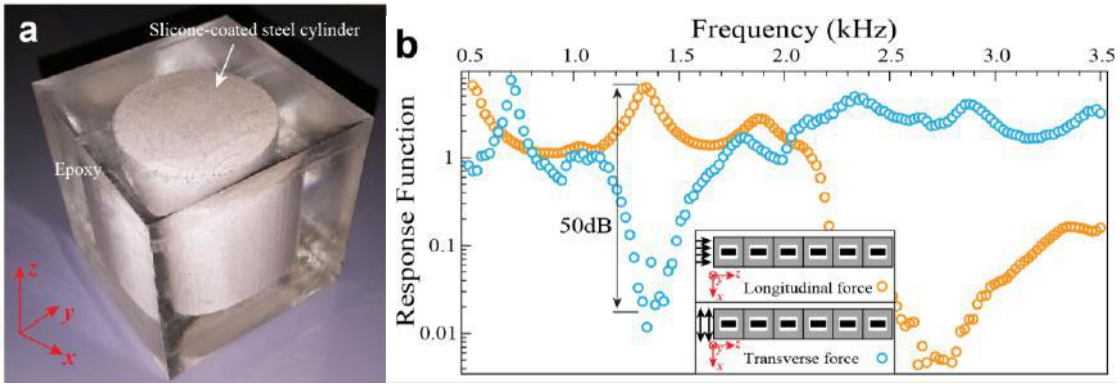



**Figure 1** A photographic image of a unit cell is shown in **a**. The measured response functions are shown in **b**. Orange markers represent the longitudinal response; blue markers represent flexural responses. Spectrally mismatched bandgaps are clearly observed. In particular, a bandgap for flexural waves is seen in ~1.1–1.7 kHz, which overlaps with longitudinal waves passband. The response difference is up to 50dB (around 1350 Hz). This means only longitudinal waves can be sustained in this frequency regime, an intriguing elastic property traditionally found only in fluids.

**Acknowledgements**: G. M. and P. S. thank the support of the Hong Kong Research Grants Council (Grant No. AoE/P-02/12).

## REFERENCES

1. Christensen, J., M. Kadic, O. Kraft, and M. Wegener, "Vibrant times for mechanical metamaterials," *MRS Commun.* Vol. 5, 453-462, 2015.
2. Liu, Z. *et al.*, "Locally resonant sonic materials," *Science* Vol. 289, 1734-1736, 2000.
3. Cummer, S. A., J. Christensen, and A. Alù, "Controlling sound with acoustic metamaterials," *Nat. Rev. Mater.* Vol. 1, 16001, 2016.
4. Lai, Y., Y. Wu, P. Sheng, and Z.-Q. Zhang, "Hybrid elastic solids," *Nat. Mater.* Vol. 10, 620-624, 2011.

# Dynamic elastic anisotropy and homogenisation

**R. V. Craster**[1], **D. Colquitt**[2] **and T. Antonakakis**[3]

[1]Imperial College London, UK
[2] Liverpool University, UK
[3]Multiwave AG, Switzerland
r.craster@imperial.ac.uk

**Abstract**—

The full elasticity equations are a vector system that connect stresses and displacements. For structured media, composites or materials that have resonators or inclusions embedded within them or upon them, it is natural to try and obtain effective media equations. Unfortunately in several applications one is not in a regime where quasi-static homogenisations is valid and so we consider dynamic homogenisation. A range of different problems are discussed and treated and analogies drawn, where possible, with electromagnetism. There are, for instance, analogous waves to spoof surface plasmons, that is, wave created purely by periodic geometric variation and these are discussed and used to illustrate the methodology of dynamic homogenisation.

The equations of elasticity, like the Maxwell equations of electromagnetism, are vector equations with the added complication that the simplest case of isotropy supports bulk waves that have two different wavespeeds. This complication leads to mode coupling at non-trivial interfaces and the emergence of surface (Rayleigh) waves at stress-free surfaces.

In electromagnetism there has been considerable interest in waves guided along surfaces by periodic corrugations [4] and it turns out that similar waves exist, and are of interest, in elasticity [1, 2]. The more typical situation, in elasticity, is of periodic arrays of inclusions within a material and of waves guided along the array. This is not in a low-frequency or quasi-static regime and so we investigate this using the dynamic homogenisation theory of [3]. A surprisingly simple, yet quantitatively accurate, effective representation of the field is found in terms of a short-scale and long-scale asymptotic method. The numerical results are shown in the figure.

**ACKNOWLEDGMENT**

The authors are grateful to S. Guenneau, P. Sebbah, G. Lefebvre, Y. Achaoui, amongst others for their input to this and results from joint work with them may well feature in the talk itself. The work was funded by the EPSRC.

**REFERENCES**

1. Every A. G. "Guided elastic waves at a periodic array of thin coplanar cavities in a solid" *Phys. Rev. B* Vol. 78, 174104, 200

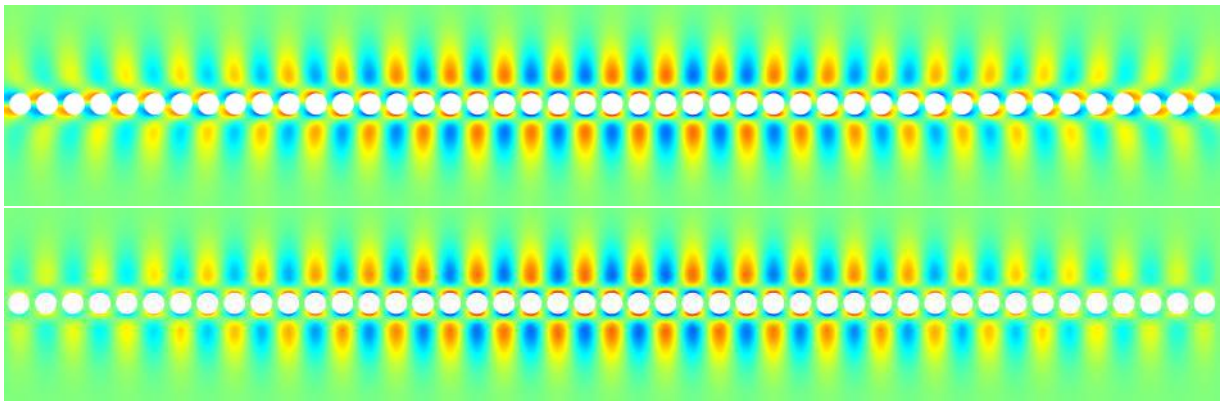


Figure 1: Top Numerics, bottom Asymptotics: $U_1^{(0)}$ (Mode two). Figure taken from [2].

2. Colquitt D. J., Craster R. V., Antonakakis T. and Guenneau S., "Rayleigh-Bloch waves along elastic diffraction gratings" *Proc. R. Soc. Lond. A*, Vol. 471:20140465, 2014
3. Antonakakis T., Craster R. V. and Guenneau S. "Homogenisation for elastic phononic crystals and metamaterials" *J. Mech. Phys. Solids* Vol. 71, 84–96, 2014
4. Pendry J. B. and Martin-Moreno L. and Garcia-Vidal F. J., "Mimicking surface plasmons with structured surfaces", *Science*, Vol. 305, 847-848, 2004,

# Locally resonant acoustic metamaterials beyond homogenization: subwavelength control of waves, slow waves, negative index and other exotic phenomena

***Nadège Kaina, Fabrice Lemoult, Mathias Fink, and Geoffroy Lerosey***

*Institut Langevin, ESPCI ParisTech and CNRS, 1 rue Jussieu, 75005 Paris, France*

In this talk we will show how going beyond the homogenization paradigm usually introduced in the context of locally resonant metamaterials permits to enrich the physics associated with them in a drastic way. Starting from the very simple example of a soda can metamaterial, that is, a very simple Helmholtz resonator based composite medium, we will first underline that its physics can be entirely understood at the light of polaritons in solid state physics. We will show, using a microscopic approach based on the transfer matrix that the metamaterials properties are strictly governed by interferences and propagation effects [1]. Namely, the physics of the system solely depend on a Fano interference between the scattered and the unscattered, and multiple scattering of waves between the unit cells of the metamaterial.

We will then demonstrate how this observation allows one to tailor this kind of composite media at the scale of the unit cell, hence going much further than in the homogenization approximation. Specifically, we will show how this allows to design various components such as cavities, waveguides, filters, that present deep subwavelength dimensions, much smaller than that of their phononic crystal counterparts [1]. We will discuss the possibility to slow down waves drastically using this kind of components, through a comparison with recent microwave experiments [2].

Starting again from our microscopic approach of locally resonant metamaterials, we will show how it can underline new effects that are totally hidden by other ones. In particular, we will explain briefly how a single negative metamaterial can turn double negative simply thanks to multiple scattering, provided that it is rightly structured [3]. Finally, to conclude, we will present a few exotic ideas that are direct consequences of the previous results and of a relatively new understanding of the physics of locally resonant metamaterials. For instance, we will show how a 2D soda can metamaterials can be turned into a sheet of "acoustic graphene" whose Dirac cone can be positioned at will within a given frequency range.

[1] F. Lemoult, N. Kaina, M. Fink and G. Lerosey. *Nature Physics* **9**, 55–60 (2013).
[2] N. Kaina, A. Causier, M. Fink, T. Berthelot and G. Lerosey. *submitted* (2015).
[3] N. Kaina, F. Lemoult, M. Fink and G. Lerosey. *Nature* **525** (2015).

# Total hyperelastic invariance - stretching the truth?

**William J. Parnell**[1], **Pu Zhang**[1] and **Vincent Pagneux**[2]

[1] School of Mathematics, University of Manchester, Oxford Road, Manchester, M13 9PL, UK
[2] Laboratoire d'Acoustique de l'Université du Maine, UMR CNRS 6613, Avenue Olivier Messiaen, 72085 Le Mans Cedex 9, France
William.Parnell@manchester.ac.uk

**Abstract**— The concept of hyperelastic invariance has been employed recently in various contexts associated with metamaterials and in particular in association with elastodynamic cloaking and elastic wave disentanglement. Here the concept of *total* hyperelastic invariance is investigated and it is shown that strain energy functions can be theoretically devised that leave certain linear elastic waves unaffected by the presence of nonlinear pre-stress.

## 1. INTRODUCTION

It is widely acknowledged that pre-stress of a hyperelastic, nonlinear material affects the propagation of subsequent linear elastic waves in the medium [1]. Nonlinear pre-stress has been employed to tune elastodynamic band-gaps [2, 3, 4] enabling them to be switched on and off and thus allowing for tunable phononic media. It was shown in [5, 6] that an incompressible neo-Hookean medium can be employed to enable antiplane elastic wave cloaking. The general hyperelastic transformation theory for elastodynamic cloaking was developed in [7], where it was shown that a semi-linear strain energy function could be used for cloaking coupled compressional/shear waves in two dimensions. An analogous concept was used in [8] to introduce the concept of *phononic cloaks*, media that geometrically would normally possess band-gaps but the presence of pre-stress precludes this possibility. The concept of hyperelastic transformation theory has been utilized to show that compressional and shear waves can theoretically be disentangled via simple shear [9, 10] so that a soft neo-Hookean device could be used as an elastodynamic demultiplexer.

Here we introduce a stronger concept of hyperelastic invariance, where elastodynamic waves are *not* affected by a finite deformation and propose strain energy functions that give rise to this possibility. We term this concept *total hyperelastic invariance*.

## 2. TOTAL INVARIANT ELASTODYNAMICS

For the purposes of this abstract let us study a simple body wave problem. Take an isotropic, homogeneous material that is capable of finite deformation; its constitutive behaviour is accounted for by a strain energy function (SEF) $\mathcal{W}=\mathcal{W}(\lambda_1,\lambda_2,\lambda_3)$, where $\lambda_j$ are the principal stretches, and it has infinitesimal shear modulus $\mu_0$. Assume an isochoric homogeneous deformation of the form $x=\lambda X, y=\lambda Y, z=Z/\lambda^2$ for some positive real constant $\lambda$ so that $\lambda_1=\lambda_2=\lambda$ and $\lambda_3=1/\lambda^2$.

Now consider the propagation of incremental shear waves, polarized in the $z$-direction and propagating in the $x,y$ plane with amplitude $w(x,y)$ and with time-harmonic form $e^{-i\omega t}$. It is straightforward to show that $w(x,y)$ satisfies the equation

$$\mathcal{A}\nabla^2 w(x,y)+\rho_0\omega^2 w(x,y)=0 \tag{1}$$

where $\mathcal{A}=\lambda_1^2(\lambda_1\mathcal{W}_1-\lambda_3\mathcal{W}_3)/(\lambda_1^2-\lambda_3^2)$ evaluated at $\lambda_1=\lambda_2=\lambda,\lambda_3=1/\lambda^2$, with $\mathcal{W}_j=\partial\mathcal{W}/\partial\lambda_j$. Although isotropic, this wave equation will generally have deformation-dependent wave speed. We ask *is there a SEF $\mathcal{W}$ such that the wave speed remains invariant under this deformation, i.e.,*

$$\text{Does there exist a } \mathcal{W} \text{ such that} \quad \lambda_1^2\left(\frac{\lambda_1\mathcal{W}_1-\lambda_3\mathcal{W}_3}{\lambda_1^2-\lambda_3^2}\right)=\mu_0 \quad ? \tag{2}$$

If such a SEF exists, we call this *total hyperelastic invariance* to deformation.

Restrict attention to $\lambda\geq 1$ and in order to investigate further, introduce the function $\overline{\mathcal{W}}(\lambda)=\mathcal{W}(\lambda,\lambda,1/\lambda^2)$. It is then straightforward to show that

$$\overline{\mathcal{W}}(\lambda)=\mu_0\left(\ln\lambda^2+\frac{1}{3\lambda^6}-\frac{1}{3}\right). \tag{3}$$

Writing this in terms of invariants gives the general form

$$\mathcal{W}(I_1, I_2) = \mu_0 \left( \ln\left(\frac{I_1}{3}\right) + \ln g(I_2/I_1^2) + \frac{9}{I_1^3 g^3(I_2/I_1^2)} - \frac{1}{3} \right) \tag{4}$$

where $g\left(I_2/I_1^2\right) = 1 + \sqrt{1 - 3\frac{I_2}{I_1^2}}$. With this form $T_{33} = 0$ and the in-plane stress-stretch behaviour is ilustrated in Fig. 1, noting that the required medium is a stress-softening material.

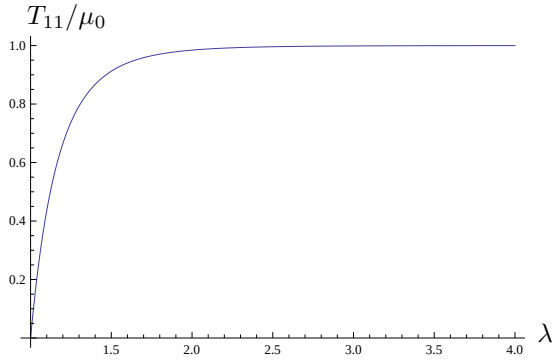



Figure 1: The predicted Cauchy stress $T_{11}/\mu_0$ as a function of $\lambda$.

## 3. CONCLUSIONS

Total hyperelastic invariance has been illustrated for shear waves, with a strain energy function of the form (4). It remains to fully understand the physical implications of the proposed medium and whether it can be devised and fabricated and one must also consider how this theory generalizes to other wave types, both of which shall be described in the talk.


## ACKNOWLEDGMENT

The author is grateful to the EPSRC, for his research fellowship EP/L018039/1.


## REFERENCES


1. Ogden, R. W., "Incremental statics and dynamics of pre-stressed elastic materials", In *Waves in nonlinear pre-stressed materials* (eds. Destrade, M. & Saccomandi, G.). CISM course and lectures No. 495. Springer Wien, New York, 1-26, 2007.
2. Parnell, W. J., "Effective wave propagation in a pre-stressed nonlinear elastic composite bar", *IMA J. Applied Math.*, Vol. 72, No. 2, 223–244, 2007.
3. Bertoldi, K. and Boyce, M. C., "Wave propagation and instabilities in monolithic and periodically structured elastomeric materials undergoing large deformations", *Physical Review B: Condensed Matter and Materials Physics*, Vol. 78, No. 18, 4107–4122, 2008.
4. Gei, M., Movchan, A. B. and Bigoni, D. "Band-gap shift and defect induced annihilation in prestressed elastic structures", *Journal of Applied Physics*, Vol. 105, No. 6, 3507–3513, 2009.
5. Parnell, W. J, "Nonlinear pre-stress for cloaking from antiplane elastic waves", *Proc. Roy. Soc. A*, Vol. 468, No. 2138, 563–580, 2012.
6. Parnell, W. J., Norris, A. and Shearer, T. "Employing pre-stress to generate finite cloaks for antiplane elastic waves", *Applied Physics Letters*, Vol. 100, No. 17, 171907, 2012.
7. Norris, A. N, Parnell, W. J., "Hyperelastic cloaking theory: Transformation elasticity with prestressed solids", *Proc. Roy. Soc. A*, Vol. 468, No. 2146, 2881-2903, 2012.
8. Barnwell, E. G, Parnell, W, J and Abrahams, I. D. "Antiplane elastic wave propagation in pre-stressed periodic structures; tuning, band gap switching and invariance", *Wave Motion*, In press.
9. Chang, Z., Guo, H. Y., Li, B. and Feng, X. Q. "Disentangling longitudinal and shear elastic waves by neo-Hookean soft devices", *Applied Physics Letters*, Vol. 106, No. 16, 161903, 2015.
10. Galich, P. and Rudykh, S., "Comment on Disentangling longitudinal and shear elastic waves by neo-Hookean soft devices [Appl. Phys. Lett. 106, 161903 (2015)]", *Applied Physics Letters*, Vol. 107, No. 5, 056101, 2015.

# Homogenisation of acoustic and elastic metamaterials

**M. Makwana**[1], **B. Maling**[2] , **S. Guenneau**[3], **R.V Craster**[2]

[1]Multiwave Technologies AG, Switzerland
[2]Imperial College London, UK
[3]Aix-Marseille Université, France
mehul@multiwave.ch

**Abstract**— The propagation of waves through microstructured media with periodically arranged inclusions has applications in many areas of physics and engineering, stretching from photonic crystals through to seismic metamaterials. In the high-frequency regime, modeling such behavior is complicated by multiple scattering of the resulting short waves between the inclusions. Our aim is to develop an asymptotic theory for modeling systems with arbitrarily shaped inclusions located on general Bravais lattices. Solutions of the effective medium equations are compared with the exact solutions, shedding further light on the underlying physics. We focus on examples that exhibit dynamic anisotropy as these demonstrate the capability of the asymptotic theory to pick up detailed qualitative and quantitative features (see figures).

As stated above our primary aim here is to generate homogenised, effective medium equations that capture the essential physics in a long-scale governing equation that encapsulates the short-scale structure in geometry-dependent coefficients. This is achieved using the multiple-scales methodology of high-frequency homogenisation (HFH) developed for square lattice structures in [1], and here generalised for Bravais lattices for which there are significant technical issues to overcome.

Our approach is to consider two distinct systems; physically the Helmholtz equation

$$\nabla_{\mathbf{x}} \cdot \left[\hat{a}\left(\mathbf{x}\right) \nabla_{\mathbf{x}} u(\mathbf{x})\right] + \hat{\rho}\left(\mathbf{x}\right) \omega^2 u(\mathbf{x}) = 0 \tag{1}$$

can be used to model transverse electric (TE) or transverse magnetic (TM) polarised electromagnetic waves, shear horizontal (SH) polarised elastic waves and pressure waves in the frequency domain.

A system closely related to the one described above is that of a structured elastic plate governed by the Kirchhoff-Love equation, for which vertical displacements satisfy

$$\nabla_{\mathbf{x}}^2 \left[\beta\left(\mathbf{x}\right) \nabla_{\mathbf{x}}^2 u\left(\mathbf{x}\right)\right] - \mu\left(\mathbf{x}\right) \Omega^2 u\left(\mathbf{x}\right) / l^4 = 0. \tag{2}$$

There has been considerable interest in such systems as platonic crystals, in which ideas from photonic crystals are transplanted into this setting [2, 3, 4, 5, 6, 7, 8, 9]. The additional derivatives in (2) compared to (1) lead to differences in the corresponding physical systems, but since the mathematics is closely related we choose to develop the theory for both equations in parallel.

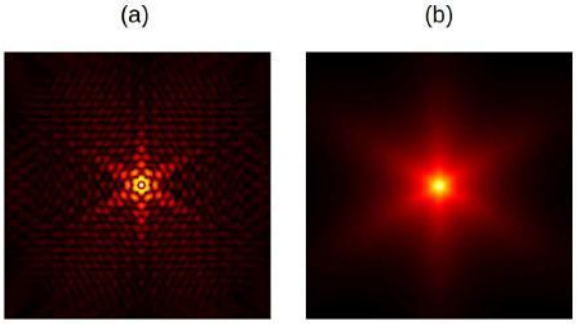



Figure 1: The Helmholtz case: A star shape is obtained by exciting the center of a hexagonal array of clamped points at a fixed frequency. Panel (a) is the full finite element simulation, where the source is approximated by a narrow Gaussian, and panel (b) is the HFH counterpart. In both cases, PML is used to avoid reflections at the boundary of the domain.

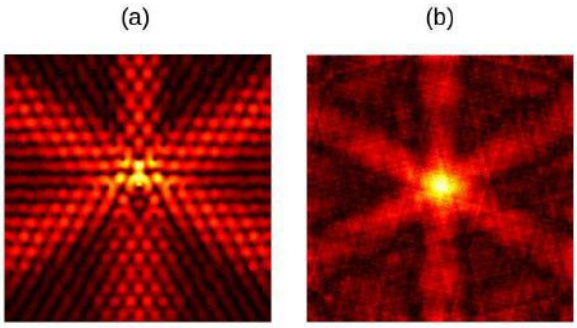



Figure 2: The Kirchhoff-Love case: A star shape is obtained by exciting the centre of a hexagon array of clamped points at a fixed frequency. Panel (a) shows the plate simulation, whilst panel (b) is the HFH effective medium simulation, both are for the finite radius. Similar to the Helmholtz case the three characteristics are obtained due to the inherent three-fold symmetry of the structure.

**REFERENCES**


1. R. V. CRASTER, J. KAPLUNOV, AND A. V. PICHUGIN, *High frequency homogenization for periodic media*, Proc R Soc Lond A, 466 (2010), pp. 2341–2362.
2. ——, *High-frequency homogenization of zero frequency stop band photonic and phononic crystals*, New J. Phys, 15 (2013), p. 103014.
3. S. BRULE, E. JAVELAUD, S. ENOCH, AND S. GUENNEAU, *Experiments on seismic metamaterials moulding surface waves*, Phys. Rev. Lett., 112 (2014).
4. M. DUBOIS, M. FARHAT, E.BOSSY, S.ENOCH, S.GUENNEAU, AND P.SEBBAH, *Flat lens for pulse focusing of elastic waves in thin plates*, Appl. Phys. Lett., 103 (2013).
5. M. FARHAT, S. GUENNEAU, AND S. ENOCH, *High-directivity and confinement of flexural waves through ultrarefraction in thin perforated plates*, European Physics Letters, 91 (2010), p. 54003.
6. M. FARHAT, S. GUENNEAU, S. ENOCH, A.B. MOVCHAN, AND G. PETURSSON, *Focussing bending waves via negative refraction in perforated thin plates*, Appl. Phys. Lett., 96 (2010), p. 081909.
7. R.C. MCPHEDRAN, A. B. MOVCHAN, N. V. MOVCHAN, M. BRUN, AND M. J. A SMITH, *Trapped modes and steered Dirac cones in platonic crystals*. arXiv:1410.0393, 2015.
8. M. J. A. SMITH, M. H. MEYLAN, AND R. C. MCPHEDRAN, *Flexural wave filtering and platonic polarisers in thin elastic plates*, Q. Jl. Mech. Appl. Math., 66 (2013), pp. 437–463.
9. D. TORRENT, D. MAYOU, AND J. SANCHEZ-DEHESA, *Elastic analog of graphene: Dirac cones and edge states for flexural waves in thin plates*, Phys. Rev. B, 87 (2013), p. 115143.

# Bio-inspired seismic metamaterials

**Ronald Aznavourian**[1*], **Tania Puvirajesinghe**[2], **Stéphane Brûlé**[3], **Stefan Enoch**[1] **and Sébastien Guenneau**[1]
[1]Aix Marseille Université, CNRS, Centrale Marseille, Institut Fresnel UMR 7249, 13013 Marseille, France
[2]CRCM, Inserm, CNRS, Institut Paoli-Calmettes, Marseille, F-13009, France
[3]Dynamic soil laboratory, Ménard, Nazay, France
[*]corresponding author: ronald.aznavourian@fresnel.fr

**Abstract:** We consider geometric transforms underpinning the design of cloaks in graphene in the context of elastodynamics. We generate a whole class of bio-inspired cloaks that are deduced from mappings of the plane with morphing techniques. Interestingly, morphing techniques allow us to straightforwardly deduce elastic wave patterns in bio-inspired cloaks from the rigorous computations performed with FDTD simulations. Analogies drawn between thermal waves in (nano-scale) graphene and seismic waves in structured soils conclude our survey of transformation biophysics for civil engineering.

The discovery of graphene [1], a one atom thick layer of graphite, has led to numerous applications in physics, chemistry and engineering. Applications can also be sought in control of drug diffusion for medical applications in cancer therapy [2]. At a very different scale, that of civil engineering, one can design structured soils to control the propagation of surface seismic waves [3]. We would like here to bridge concepts of transformation optics [4, 5] with designs of bio-inspired seismic metamaterials like in Figure 1: living cells display continuously changing shapes and we discovered that we can mimic this change in time with a morphing algorithm [6], so we use morphing to generate various designs of bio-inspired cloaks. A numerical tool of choice for numerical simulations is the finite difference time domain software simsonic [7], which is devoted to solving the full elasticity equations in heterogeneous media. We used simsonic to analyse the wave elastic waves propagates in bio-inspired cloaks. We shall discuss this in more detail in the talk. Finally, we complement the numerical analysis of coupled shear and pressure waves propagating in graphene-like bio-inspired seismic metamaterials with a morphing algorithm [6] that considerably speedup computations.

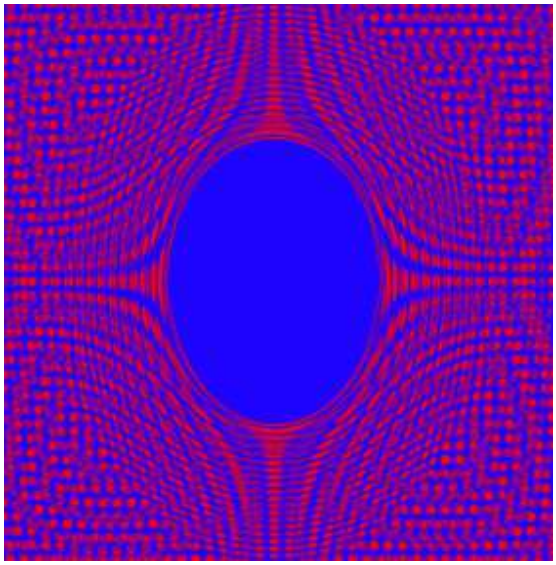


Figure 1: Bio-inspired cloak. Blue and red stand for the two phases of the structured medium.

**REFERENCES**


1. Novoselov, K. S., A. K. Geim, S. V. Morozov, D. Jiang, Y. Zhang, S. V. Dubonos, I. V. Grigorieva and A. A. Firsov, "Electric Field Effect in Atomically Thin Carbon Films," *Science*, 306, 5696, 666-669, 2004.
2. Puvirajesinghe, T. M., Z-L. Zhi, R. V. Craster and S. Guenneau, "Modulation of diffusion rate of therapeutic peptide drugs using graphene oxide membranes," arXiv preprint arXiv: 1512.08506.
3. Brûlé, S., E. H. Javelaud, S. Enoch and S. Guenneau, "Experiments on seismic metamaterials: Molding surface waves," *Phys. Rev. Let.*, 112, 13, 133901, 2014.
4. Pendry, J. B., D. Schurig and D. R. Smith, "Controlling electromagnetic fields," *Science*, 312, 1780-1782, 2006.
5. Leonhardt, U. "Optical Conformal Mapping," *Science*, 312, 1777-1780, 2006.
6. http://www.xiberpix.net/SqirlzMorph.html
7. http://www.simsonic.fr/



R. Aznavourian, T. Puvirajesinghe and S. Guenneau are thankful for an AMIDEX funding (BIOCLOAK project). S. Guenneau acknowledges European funding through ERC Starting Grant ANAMORPHISM.

# Applications of Local Resonances in Civil Engineering

# Seismic Protection

**B. Ungureanu**[1*], **Y. Achaoui**[1], **S. Brûlé**[2], **S. Enoch**[1], **and S. Guenneau**[1]

[1]Aix Marseille Université, CNRS, Centrale Marseille, Institut Fresnel UMR 7249, 13013 Marseille, France

[2]Dynamic Soil Laboratory, Ménard, 91 620 Nozay, France

[*]corresponding author: bogdan.ungureanu@fresnel.fr

**Abstract**- A cubic array of 3D inertial resonators, numerically investigated because of its potential to block bulk waves, gives new applications of metamaterials, using local resonances for seismic protection and seismic waves damping. We analyze rotational and bending resonance modes with 3 different variations on ligament number and size. Inertial resonators induce low frequency band gaps, which are relevant for seismic protection in sedimentary basins. Another aspect of this work is that by varying the number and the thickness of ligaments, we achieve wider low-frequency band gaps, which is of interest for the whole metamaterial's community.

Applying local resonances in civil engineering to seismic protection is a new idea coming from the spectral analysis of 3D dispersion diagrams such as in figure 1, with low frequency stop bands tuned thanks to inertial resonators behaving in accordance to the asymptotic formula (1) [1]. One can imagine that these resonators are dedicated structures or have a mixed role with the foundations.

$$f = \frac{1}{4\pi}\sqrt{\frac{\mu}{4\rho}\frac{\lambda+\mu}{\lambda+2\mu}\sum_{i=1}^{N}\frac{h_i^{\,2}}{R^{3}l_i}} \tag{1}$$

Moreover, damping of elastodynamic waves is further supported by transmission curves shown in figure 2. Furthermore, we put forward a new counter-intuitive feature that might be observed when considering different widths of ligaments. This trick permits us to exploit the eigenvibrations of three-dimensional inertial resonators to achieve ultra wide band gaps:

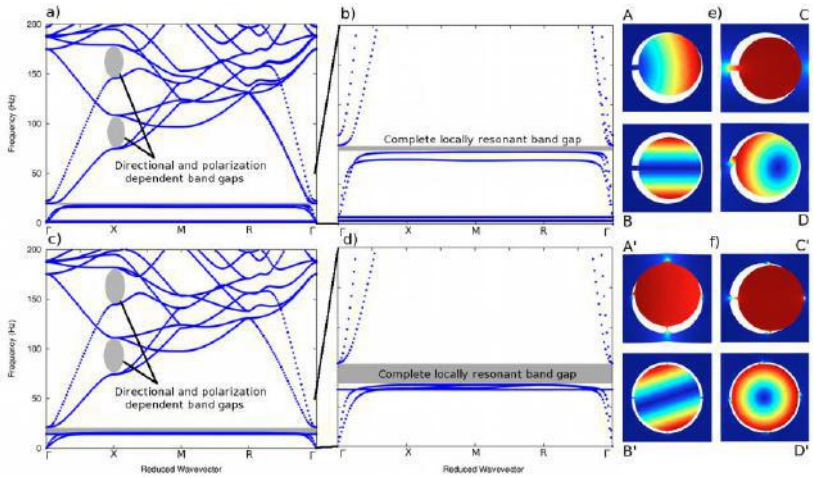



**Figure 1:** Band diagrams for elastic wave propagation with a periodic structure [1]

Recent work published on seismic metamaterials [2-7] based on Bragg and auxetic behaviors at high frequencies lies above the range of frequencies of interest for seismic wave protection (i.e. <20 Hertz). Here, we utilize 3D arrays of 3D inertial resonators composed of iron spheres connected to a bulk of concrete via iron. Each sphere can move freely within a surrounding air cavity but ligaments couple it to the bulk and further facilitate bending and rotational motions. We find complete stop bands (for all wave-polarizations) in the frequency range [16,21] Hertz for 7.4-meter diameter iron spheres with a 10-meter center-to-center spacing, when they are connected to concrete via steel ligaments. The scattering problem show that only bending modes are responsible for damping and that rotational modes are totally overwritten by bending modes. We consider concrete as a bulk medium, in which case the relative bandwidth of the low frequency stop band can be enlarged through ligaments of different sizes that allow for well separated bending and rotational modes. We finally achieve some damping of elastodynamic waves from 8 to 49 Hertz (relative stop band of 53 percent according to an energy loss of at least 10dB).

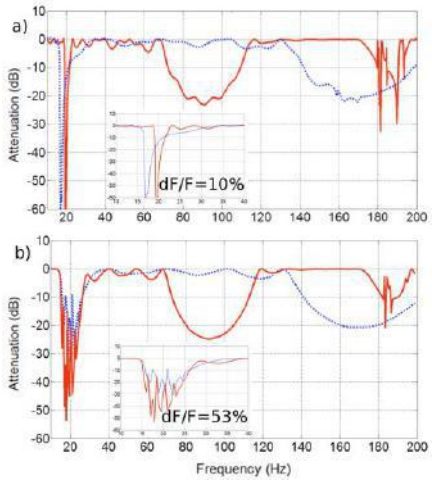



**Figure 2:** Transmission curves of shear polarized (red curves) and compressional waves (blue curves) in the case of (a) one ligament and (b) six chirped ligaments

The targeted application stated here is the field of seismic metamaterials but the concept can be implemented in phononic crystals or elastodynamic metamaterials with proper rescaling of geometric parameters.

**Acknowledgements**, B. Ungureanu and S. Guenneau are thankful for an AMIDEX funding (BIOCLOAK project). Y. Achaoui and S. Guenneau acknowledge European funding through ERC Starting Grant ANAMORPHISM.

**REFERENCES**

1. Achaoui, Y., B. Ungureanu, S. Enoch, S. Brûlé and S. Guenneau, "Seismic waves damping with arrays of inertial resonators," *Ex. Mech. Let.*, 2015.
2. Ungureanu, B., Y. Achaoui, S. Enoch, S. Brûlé and S. Guenneau, "Auxetic-like metamaterials as novel earthquake protections," *EPJ Appl. Metamat.*, 2016.
3. Brûlé, S., E. Javelaud, S. Enoch, and S. Guenneau, "Experiments on Seismic Metamaterials: Molding Surface Waves", *Phys. Rev. Lett.* **112**, 133901, 2014.
4. Finocchio, G., O. Casablanca, G. Ricciardi, U. Alibrandi, F. Garescì, M. Chiappini and B. Azzerboni, "Seismic metamaterials based on isochronous mechanical oscillators," *Appl. Phys. Lett.* 104, 191903, 2014.
5. Krödel, S., N. Thomé and C. Daraio, "Wideband-gap seismic metastructures", *Ex. Mech. Let.*, 2015.
6. Kim, H. and M. P. Das, "Seismic waveguide of metamaterials", *Mod. Phys. Lett. B* **26**, 1250105, 2012.
7. Sheng, P., *"*Viewpoint: A Step Towards a Seismic Cloak*", Physics* **7**, 34, 2014.

# Acoustic resonator systems with topological semimetal phases

Zhaoju Yang[1] and Baile Zhang[1,2*]

[1]*Division of Physics and Applied Physics, School of Physical and Mathematical Sciences, Nanyang Technological University, Singapore 637371, Singapore.*

[2]*Centre for Disruptive Photonic Technologies, Nanyang Technological University, Singapore 637371, Singapore.*

**To whom correspondence should be addressed:*

*E-mail: blzhang@ntu.edu.sg*

**Abstract**- We propose an approach of constructing acoustic topological semimetal phases in two-dimensional (2D) and three-dimensional (3D) systems by stacking one-dimensional dimerized chains as building blocks. The 2D acoustic system exhibits Dirac points with nonzero winding number. The 3D acoustic system exhibits Weyl nodes with by nonzero Chern number. For stacked 3D slab structures, topologically protected chiral surface states localize at the boundaries, which, can trace out the trajectories of "Fermi Arcs", similar to previous observations in condensed-matter Weyl semimetals.

Recently, the discovery of Weyl fermions [1-2] has opened a new chapter of topological physics in condensed matter physics as well as in photonics [3]. In acoustics, three-dimensional (3D) Weyl nodes [4] were theoretically proposed by applying on-site coupling difference and chiral coupling on a 3D graphite structure. Inspired by the proposal of constructing Weyl semimetals by stacking one-dimensional (1D) topological phases in ultra-cold systems, we resort to 1D acoustic dimerized chains to construct acoustic 2D topological gapless phase and Weyl semimetal phase, exhibiting 3D Weyl nodes characterized by nonzero Chern number.

The numerical calculation demonstrates the nearly flat edge states for 2D finite structure. For 3D cases, the topologically protected chiral surface states can trace out the "Fermi Arcs" (as red dotted lines in the following figure) at the surface Brillouin zone between two Weyl nodes (green and black dots in the figure) with opposite chirality, similar to the recent observations in condensed-matter Weyl semimetals. Furthermore, the method of stacking 1D dimerized chains here can apply to ultracold atom and photonic systems, and will be of interest to scientists from diverse backgrounds.

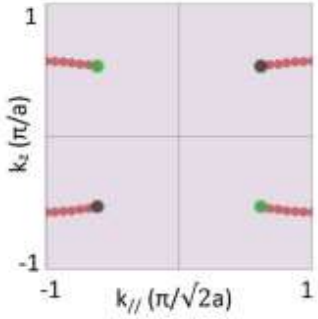



Figure legend: "Fermi arcs" traced out from topologically protected chiral surface states.

**REFERENCES**


1. S.-Y. Xu, et al. Science 349, 613–617 (2015).
2. B. Q. Lv, et al. Phys. Rev. X 5, 031013 (2015).
3. L. Lu, et al. Science 349, 622–624 (2015).
4. M. Xiao, W. Chen, W. He and C. T. Chan. Nature Phys. 11, 920-924 (2015).

# Heat mimicking of given objects

**A. Alwakil[1], M. Zerrad[2], M. Bellieud[3] and C. Amra[1]**

[1]CNRS, France

[2]Aix-Marseille Université, France

[3]Université de Montpellier 2, France

[*]corresponding author: ahmed.alwakil@fresnel.fr

**Abstract:** We address an inverse thermal engineering problem devoted to heat mimicking. The objects to cloak and mimic are predefined in shape and conductivity, which leads to emphasize a specific set of transformations.

Transformation optics have been extensively used these last years in various fields ranging from optics and microwaves, acoustics and mechanics, hydrodynamics and seismic [1-11]. Within this framework a great number of papers can be found which describe new phenomena related to invisibility and mimicking, together with prototypes involving cloaks, concentrators and rotators, absorber. Following these works devoted to waves, analogies were emphasized between optical propagation and thermal diffusion and promoted the extension of these transformations techniques to the field of heat conduction [12-24]. Additional results were given that concerned the isotherms correction and their quantification at the cloak exit of different devices for invisibility, concentration and rotation [13].

However in most problems devoted to space transformation, the objects to cloak or mimic emphasize arbitrary matrix gradients of their physical parameters, which makes them difficult to produce and also reduce the field of practical applications. Actually one would be interested in working with *predefined objects* of given shape and conductivity, and these objects would be over-coated in order to mimic other predefined objects beyond the cloak. Such inverse engineering problem introduces constraints which reduce the range of space transformations, and so classify the set of objects that can be mimicked with another one which is beforehand chosen. The talk will be focused on this specific inverse mimicking problem. It can be summarized as follows:

- An arbitrary given object $\Omega$ is overcoated to mimic the heat flux scattered from another object $\omega$
- Since $\Omega$ is given in shape ($\partial\Omega$) and conductivity ($k_\Omega$), the tensor $T_\Omega = (1/\det M)\,(M\, k_\Omega\, {}^tM)$ is given and forces the set of transformations $\{H_\alpha\}$required for mimicking, with the condition: $H(\omega) = \Omega$
- This constraint reduces the class of objects $\omega$ which can be mimicked as: $\{\partial\omega\}_\alpha = \{H_\alpha^{-1}(\partial\Omega)\}$
- For each transformation $H_\alpha$ a coat with an arbitrary shape $\partial E$ is designed with another $L_\alpha$ transformation with the conditions: $L(\partial\omega) = H(\partial\omega) = \partial\Omega$ and $L(E\backslash\omega) = E\backslash\Omega$ and $L(E) = E$
- Complementary conditions are fullfilled which concern continuity and derivative of the transformations

Analytic solutions are given in the case of diagonal conductivity matrix $k_\Omega$ and isotropic objects $\omega$. The general case is validated with numerical calculation. All results provide practical tools for an easier engineering of applications with thermal metamaterials.

**Acknowledgements**

This work was supported by 3 French agencies: Agence Nationale de la Recherche (ANR), Délégation Générale de l'Armement (DGA) and Centre National de la Recherche Scientifique (CNRS).

## REFERENCES


1. J.B. Pendry, D. Schurig and D.R. Smith, "Controlling Electromagnetic Fields," Science**312** (5781): 1780-1782, 2006.
2. U. Leonhardt, Optical conformal mapping. Science **312**, 1777-1780 (2006).
3. Guenneau S., Amra C., and Veynante D., "Transformation thermodynamics: cloaking and concentrating heat flux," Opt. Express 20 (7), 8207–8218 (2012).
4. A. Greenleaf, Y. Kurylev, M. Lassas, and G. Uhlmann, "Isotropic transformation optics: approximate acoustic and quantum cloaking," New J. Phys. 10, 115024 (2008).
5. S. Zhang, D. A. Genov, C. Sun, and X. Zhang, "Cloaking of matter waves," Phys. Rev. Lett. 100, 123002 (2008).
6. S. A. Cummer and D. Schurig, "One path to acoustic cloaking," New J. Phys. 9, 45–45 (2007).
7. H. Chen and C. T. Chan, "Acoustic cloaking in three dimensions using acoustic metamaterials," Appl. Phys. Lett. 91, 183518 (2007).
8. A. Norris, "Acoustic cloaking theory," Proc. R. Soc. London 464, 2411–2434 (2008).
9. G. W. Milton, M. Briane, and J. R. Willis, "On cloaking for elasticity and physical equations with a transformation invariant form," New J. Phys. 8, 248–268 (2006).
10. M. Brun, S. Guenneau, and A.,B. Movchan, "Achieving control of in-plane elastic waves," Appl. Phys. Lett. 94, 061903 (2009).
11. Diatta A. and Guenneau S., "Non singular cloaks allow mimesis," J. Opt., Vol. 13, no.2, 024012-024022, 2011.
12. Guan J., Li W., Wang W. and Fu Z., "General boundary mapping method and its application in designing an arbitrarily shaped perfect electric conductor reshaper," Opt. Express Vol. 19, Issue 20,
13. Petiteau D., Guenneau S., Bellieud M., Zerrad M. and Amra C., "Spectral effectiveness of engineered thermal cloaks in the frequency regime," Scientific Rep. 4, 7486, 2014
14. Leonhardt U., "Cloaking of heat," Applied Physics Nature 498, 440–441
15. Alu A., "Thermal cloaks get hot," Physics **7**, 12 (2014)
16. Han, T., Yuan, T., Li, and B. Qiu, C.-W., "Homogeneous thermal cloaks with constant conductivity and tunable heat localization," Sci. Rep. **3**, 1593 (2013).
17. Schittny S., Kadic M., Bückmann T. and Wegener M., "Invisibility cloaking in a diffusive light scattering medium," Science 345, 427–429 (2014).
18. Han, T. *et al.*, "Full control and manipulation of heat signatures: Cloaking, camouflage and thermal metamaterials," Adv. Mater. 26, 1731–1734 (2014).
19. Xu H., Shi X., Gao F., Sun H. and Zhang B., "Experimental demonstration of an ultra-thin three-dimensional thermal cloak," Phys. Rev. Lett. 112, 054301 (2014).
20. Han, T. *et al.* Experimental demonstration of a bilayer thermal cloak. Phys. Rev. Lett. 112, 054302 (2014).
21. Narayana S. and Sato V., "Heat flux manipulation with engineered thermal materials," Phys. Rev. Lett. 108, 214303 (2012)
22. Dede E. M., Nomura T., Schmalenberg P. and Lee J. S., "Heat flux cloaking, focusing, and reversal in ultra-thin composites considering conduction-convection effects," Appl.Phys. Lett. 103, 063501 (2013)
23. Narayana S., Savo S., and Sato Y., "Transient heat flux shielding using thermal metamaterials," Appl. Phys. Lett. **102**, 201904 (2013)
24. Han T., Yuan T., Li B., Qiu B. and Qiu C.-W., "Homogeneous thermal cloaks with constant conductivity and tunable heat localization," Scientific Rep. **3**, 1593 (2013)

# Double Zero Index Acoustic Metamaterial

**M. Dubois[1*], C. Shi[1], Y. Wang[1] and X. Zhang[1, 2]**

[1] NSF Nano-scale Science and Engineering Center (NSEC), University of California, Berkeley, 3112 Etcheverry Hall, Berkeley, CA 94720, USA

[2] Materials Science Division, Lawrence Berkeley National Laboratory, 1 Cyclotron Road, Berkeley, CA 94720, USA

[*]corresponding author: mdubois2014@berkeley.edu

**Abstract**- Acoustic plane waves, critical to imaging, sensing, detecting, etc., are usually difficult to generate because acoustic sources are small compared to the wavelength. Recently developed zero refractive index materials for electromagnetic waves [1, 2] provide a solution to plane wave generation because of the infinite phase velocity of waves travelling through them. We experimentally demonstrate that double zero index acoustic metamaterial has the ability to convert efficiently the cylindrical wavefront emitted by an embedded point source into a collimated planar wavefront.

This work focuses on the development of an acoustic metamaterial with simultaneous zero effective mass density and inverse bulk modulus, namely double zero index acoustic materials (DZIM). Zero index property is of great interest in terms of wave applications as the wavelength inside a zero index medium becomes infinite. This feature can be used to reduce the undesired scattering from rigid or soft structure and also to realize the collimation of acoustic radiation emitted from a point source (ultra-refraction). Although single zero index metamaterials have been explored recently, their performances are extremely limited by usual a large impedance mismatch [3]. Indeed, if only one of the effective parameters goes to zero, the impedance of the medium (proportional to the ratio of the parameters) has to be null or infinite. We propose to develop the first acoustic DZIM, in which both effective mass density and inverse bulk modulus are approaching very small values while maintaining a matching impedance of the metamaterial to the surrounding media. In this work, we experimentally demonstrate the collimation of an acoustic point source embedded inside a square slab of DZIM. Our experimental setup also allows the measurement of the pressure field distribution inside the metamaterial, thus we are able to directly map the equifrequency contours of the DZIM and confirm the existence of a Dirac cone degeneracy at the center of the Brillouin zone [4].

**Acknowledgements**, This research was supported by the Office of Naval Research (ONR) MURI program under grant no. N00014-13-1-0631.

**REFERENCES**

1. Huang, X., Lai, Y., Hang, Z. H., Zheng, H., and Chan, C. T., "Dirac cones induced by accidental degeneracy in photonic crystals and zero-refractive-index materials", *Nature Materials*, 10, 582 - 586 (2011).

2. Li, Y., Kita, S., Munoz, P., Reshef, O., Vulis, D. I., Yin, M., Loncar, M., and Mazur, E., "On-chip zero-index metamaterials", *Nature Photonics*, 9, 738 - 742 (2015).

3. Zheng, L.-Y., Wu, Y., Ni, X., Chen, Z.-G., Lu, M.-H., and Chen, Y.-F., "Acoustic cloaking by a near-zero-index phononic crystal", *Appl. Phys. Lett.*, 104, 161904 (2014).

4. Dubois, M., Shi, C., Wang, Y. and Zhang, X. "Double zero index acoustic metamaterial", *in preparation*

# Low frequency sound screening using an acoustic metamaterial made of space-coiled resonant cavities

**A. Elayouch**[1], **M. Addouche**[1], **Y. Tejda**[1] **and A. Khelif**[1*]

[1] Institut FEMTO-ST, Université de Franche-Comté, CNRS, 15B avenue des Montboucons, 25030 BESANCON Cedex, France

[*]corresponding author: abdelkrim.khelif@femto-st.fr

**Abstract**- In this work, we report on designs of locally resonant acoustic metamaterials that enable us to generate low frequency sound screening. We investigate both experimentally and theoretically how to generate asymmetric lineshapes of the transmission that lead to acoustic opacity. For this, we study the transmission properties of an acoustic metamaterial involving the coupling of space coiled Fabry-Perot cavities. Measurements reveal an attenuation up to 30 dB, with a relative bandwidth of 21% and a center frequency of 1400 Hz.

For more than twenty years now, Acoustic Metamaterials are experiencing a growing success, partly due to exotic phenomena and their wide variety of extremely promising applications: “Invisibility Cloak” is the most vivid example of this. Recently, various studies involving resonators have shown how to create acoustic transparency [1], or even acoustic opacity [2, 3], with resonators taking different shapes depending on the context. That is the case of Fabry-Perot resonators which, under certain conditions of periodicity and coupling, can generate an acoustic screening at the resonance frequencies. In the ultrasonic frequency range, such resonators can take the shape of an array of slits in a plate [4]. Applied to the sound, such structuration would involve cumbersome dimensions, because of long wavelengths at the operating frequency range. Recently, studies have highlighted some properties arising from using space-coiling in acoustic metamaterials. Among them, the possibility of generating extreme effective parameters [5], which offer promising applications such as negative refraction. Furthermore, subsequent studies have brought to light both non-resonant [6], and resonant [7] acoustic metamaterials involving space-coiling, even going so far as to achieve the Extraordinary Acoustic Transmission for wavelength 15 times bigger than the periodicity [8].

The aim of this work is to study how the coupling between two resonators, with different quality factors, can lead to the opaque counter-part of the low frequency Extraordinary Acoustic Transmission (EAT). For this purpose, we present experimental results obtained using a Kundt’s Tube. The transmission measurements of a wave impinging our structure are compared to transmission calculations realized using the Finite Elements Method FEM. In this study, we consider a structure having a thickness of $t=50\ mm$, and constituted of a 1D array having a period of $a=30mm$. Each unit cell is composed of two Fabry-Perot cavities, one of which is space-coiled in order to generate a low frequency resonance with a high quality factor. Indeed, taken separately, both cavity are acoustic resonators exhibiting a near-total transmission at their resonance frequencies, with a quality factor that can be tuned through geometrical parameters, and particularly inter-wall spaces.

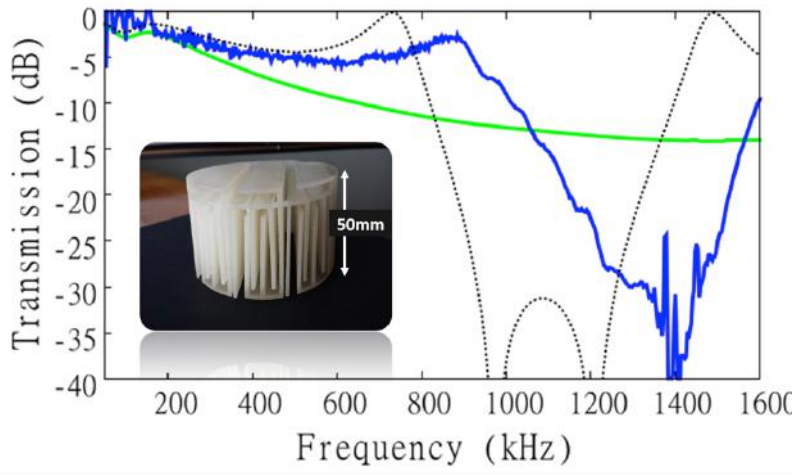



**Figure 1** Transmission spectra obtained experimentally (blue), by using FE method calculation (black dotted), and for a structure made of non-space-coiled Fabry-Perot cavities (green curve).

By combining these two resonators, a coupling is created when excited by an incident wave, which leads to a serie of asymmetric shape peaks in the transmission spectra. This leads to an enhanced transmission at the resonance frequencies as well as to improve the attenuation significantly at the antiresonance frequencies. Therefore, the composition between these antiresonance frequencies, through the geometrical features, permit to reach an attenuation of 30 dB, with a relative bandwidth of 21%, with a center frequency of 1400 Hz. At this operating frequency, the thickness of this acoustic metamaterials is seven times smaller than the wavelength. In doing so, we avoid one of the main limitation of omnidirectional capabilities involving locally resonant perforated plates, which is namely diffraction.

**REFERENCES**

1. Christensen, J., Martin-Moreno, L., and Garcia-Vidal, F. J., “Theory of resonant acoustic transmission through subwavelength apertures”, *Physical Review Letters*, 101, 014301, 2008.
2. Mei, J., Ma, G., Yang, M., Yang, Z., Wen, W., and Sheng, P., “Dark acoustic metamaterials as super absorbers for low-frequency sound”, *Nat. Commun.* 3, 756, 2012.
3. Estrada, H., Bravo, J. M., and Meseguer, F., “High sound screening in low impedance slit arrays”, *New J. Phys.* 13, 043009, 2011.
4. Elayouch, A., Addouche, M., Herth, E., and Khelif, A., “Experimental evidence of ultrasonic opacity using the coupling of resonant cavities in a phononic membrane”, *Appl. Phys. Lett.* 103, 083504, 2013.
5. Liang, Z. and Li, J., “Extreme acoustic metamaterial by coiling up space”, *Physical Review Letters*, 108, 114301, 2012.
6. Xie, Y., Popa, B.-I., Zigoneanu, L., and Cummer, S. A., “Measurement of a broadband negative index with space-coiling acoustic metamaterials”, *Physical Review Letters* 110, 175501, 2013.
7. Song, K., Lee, S.-H., Kim, K., Hur, S., and Kim, J., “Emission enhancement of sound emitters using an acoustic metamaterial cavity”, *Scientific Reports*, 4, 2014.
8. Li, Y., Liang, B., Zou, X.-Y., and Cheng. J.-C., “Extraordinary acoustic transmission through ultrathin acoustic metamaterials by coiling up space”, *Applied Physics Letters*, 103, 2013.

# Wave propagation in periodic structures and focusing of the ultrasound waves

**Piotr Fiborek[1*], Paweł Kudela[1], Maciej Radzieński[1], Wiesław M. Ostachowicz[1,2]**

[1] Institute of Fluid–Flow Machinery Polish Academy of Sciences, Poland
[2] Warsaw University of Technology, Poland
*corresponding author, E-mail: pfiborek@imp.gda.pl

## Abstract

Analytical studies and numerical simulations are performed in order to show capability of focusing of ultrasound waves in air by an acoustic lens. Wave focusing is realized by beamforming resulting from appropriate time delays of excited waves. Proposed type of acoustic lens is able to generate sound bullet in desired location. The feasibility of control of sound bullet is confirmed by series of experimental investigation on wave propagation in periodic structures.

## 1. Introduction

Focused ultrasound waves are utilized in many applications. They are used in medicine for biomedical imaging for many years and recently they give new possibilities in treatment of cancer [1, 2] or movement disorders like Parkinson's disease [3]. Acoustic lens can be also used for underwater sonar sensing [4] or non–destructive material testing [5].

Ultrasound waves usually are excited by the electromechanical transducers and they are focused in desired location by methods such as geometric focusing, time-reversal focusing, lenses based on refraction or beamforming via time delay. In geometric focusing all transducer are arrayed in equal distance from focal while time-reversal and time delay focusing methods required to set appropriate phase delay to maximize pressure in desired region. Clement *et al.* demonstrated the feasibility of non-invasive surgery through the human skull using the transducer elements arranged on hemisphere [6].

Ultrasonic focusing in inhomogeneous media by means of a time–reversal mirror made from array of piezoelectric transducers was presented by Fink [7]. Focusing process was realized in three steps. First a wavefront is generated by the transducer array and transmitted through the medium to a target *e.g.* gallstone, which generates a scattered pressured field. Next pressure field is recorded by the same transducer array and retransmitted in a reversed temporal chronology (last in first out) focusing on the target.

An example of acoustic lens based on refraction was presented by Håkansson *et al.* [8]. They designed a lenses made of sonic crystals consisting of periodic arrays of cylindrical rigid scatterers. Another example of that type of lens was presented by Welter *et al.* [9].

Spadoni and Daraio [10] designed a non–linear acoustic lens composed of one–dimensional array of granular chains. In contrast to linear lenses their device generates compact sound bullet with higher energy density that previously possible. Subsequently as a development of previous idea Donahue *et al.* realized two–dimensional non-linear lens [11]. The idea of acoustic lens given in [11] is followed here. In this case the excitation force is applied by piezoelectric transducer.

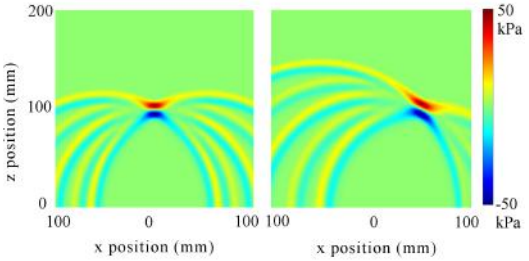



Figure 1: Analytical solution for pressure field at the time when acoustic energy accumulate in the focal point: A) x=0, y=0, z=0.1 [m], B) x=0.05, y=0, z=0.1 [m].

## 2. Acoustic lens with beamforming via time delay

### 2.1. Acoustic pressure field.

Focusing of acoustics waves generated by different sources is possible when all signals arrive at a desired location at the same time. If these sources are not arrayed in the equal distance from focal point the time of signal excitation has to be set regarding to differences of the wave paths. The possibility of formation of sound bullet in desired location was shown by using computer simulation and analytic solutions. Considering spherical propagating waves emitted from $N$ sources pressure field is expressed by (1) [10].

$$p(x,y,z,t) = \rho c \sum_{n=1}^{N} \frac{f(r_n/c - t + \Delta t_n)}{r_n}, \qquad (1)$$

where $N$–number of sources $\rho$–density of the fluid medium, $c$–the speed of sound, $f(t)$–the arbitrary function of particle velocity, $\Delta t_n$–the time delay and $r_n^2 = (x - x_n)^2 + (y - y_n)^2 + (z - z_n)^2$ is a distance of particular point

of host medium $(x, y, z)$ from the source $n$ at coordinates $(x_n, y_n, z_n)$. Figure 1 shows the pressure maps for two locations of focal point, a) along the axis of the lens and b) 5 cm off-axis, both 10 cm away from the lens. One can see that value of the pressure in focused area is about 4 times greater than in the others regions.

### 2.2. Parametric study

Acoustic lens should generate "sound bullet" with amplitude of the pressure around the focal point as high as possible. Therefore the parametric study was conducted by the analytical simulation in order to choose the most optimal geometric parameters for the acoustic lens. There are four sets of ultrasound sources under consideration in configuration as it is shown in Figure 2. They differ in shape of arrangement, number of sources and the size of the lens but average distance (Eq. 2) between sources and the mid point of the lens remains the same for all configurations. First configuration is composed of 13 sources and the rest of configurations has 36 sources each. Simulation was conducted four times for each configuration with average distance equal 25, 50, 100 and 150 mm. Focal length was set 100 mm away from mid point of the lens (the same for all simulations).

$$S = \sum_{i=1}^{N} \frac{\sqrt{(x_i - x_0)^2 + (y_i - y_0)^2}}{N} \qquad (2)$$

Obviously the configuration with the fewest number of sources generate "sound bullet" with the lowest pressure amplitude as it is shown in Figure 3. The pressure amplitude is only slightly different for configuration with the same number of sources. The pressure amplitude in focus depends on the size of the lens and the shorter average distance to mid point causes the higher amplitude. However, reducing of the distance increases the area of higher pressure around the focal. The pressure profile is much wider generated by the smaller lens than the bigger (Figure 4).

### 2.3. Non–linear acoustic lens

The time delay of excitation varies from 10 to 100 $\mu$s and in order to gain the highest amplitude of "sound bullet" the trigger should be pulled at the designated time. The time of waves excitation can be controlled through the mechanical means like in the non–linear acoustic lens designed by Spadoni *et al.* [10]. It was composed of several spherical particle chains compressed by the static forces. The waves were generated in the same time by they arrived to the end of each chain in time depending on the value of the forces [12].

## 3. Wave propagation in periodic structure

### 3.1. Wave velocity in the one-dimensional spherical particles chain

Spherical particles chain like other granular material is highly non-linear structure. Mathematical models provided

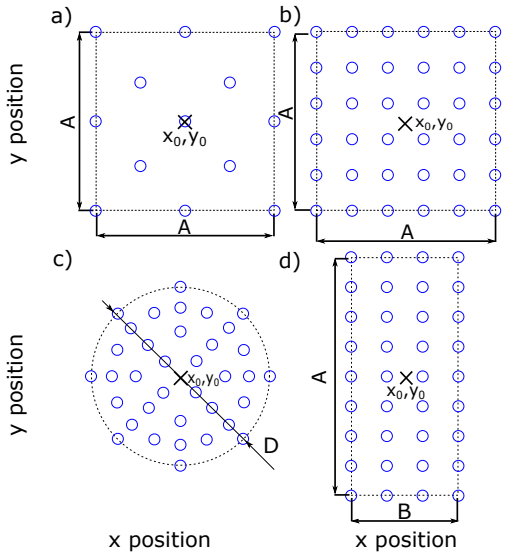



Figure 2: Arragements of acoustic lens

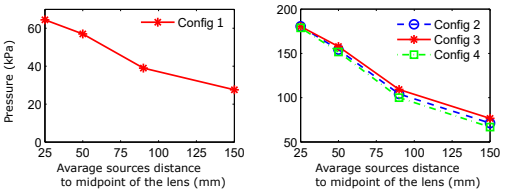



Figure 3: Maximum acoustic pressure at focal point

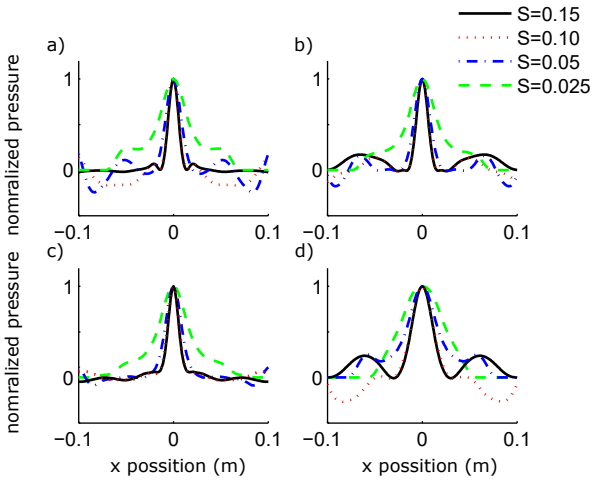



Figure 4: Normalized pressure on a line that intersects the focus normal to the incident wave a) Config 1, b) Config 2, c) Config 3, d) Config 4,

by Nesterenko [13] describe velocity of waves propagating through the one-dimensional chain of spherical particles as a function of maximal dynamic force between particles $F_m$ and initial pre–compression force $F_0$. According to the Hertz law particle equation of motion becomes

$$\ddot{u}_i = A(\delta_0 - u_i + u_{i-1})^{3/2} - A(\delta_0 - u_{i+1} + u_i)^{3/2}, \quad (3)$$
$$N - 1 \geq i \geq 2,$$
$$A = \frac{E(2R)^{1/2}}{3(1-\nu^2)m}, m = \frac{4}{3}\pi R^3 \rho_p$$

where $u_i$ is the displacement of given particle, $\delta_0$ is the initial displacement between particle centers, $N$ is the number of particles in chain, $R$, $E$, $\nu$ and $\rho_p$ is the radius, the Young modulus, the Poisson's ratio and mass density of particles, respectively. Equation (3) can be solved in two ways depending on the value of the ratio $F_r = F_m/F_0$.

In case of *"strong pre-compression"* chain where initial displacement $\delta_0$ is much larger than the change of the neighboring particle displacements in a wave *i.e.*

$$\frac{|u_{i-1} - u_i|}{\delta_0} \ll 1 \quad (4)$$

equation (3) can be transform into the Korteweg–de Vries equation with the exact solution:

$$V_s = c_0 + \frac{\sigma}{6c_0}\Delta\xi_m, \quad (5)$$
$$c_0^2 = A\delta_0^{1/2}6R^2, \sigma = \frac{c_0^2 R}{\delta_0},$$
$$\Delta\xi_m = \xi_m - \xi_0$$

where $V_s$ is the soliton phase velocity and $\xi_m, \xi_0$ is maximal and initial strain, respectively.

While in case of *"weak pre-compression"* chain i.e

$$\frac{|u_{i-1} - u_i|}{\delta_0} \gtrsim 1 \quad (6)$$

wave field is highly nonlinear and velocity is equal to (7).

$$V_S = \frac{c_0}{(F_r^{2/3} - 1)}\left\{\frac{4}{15}\left[3 + 2F_r^{5/3} - 5F_r^{2/3}\right]\right\}^{1/2} \quad (7)$$
$$c_0 = \sqrt{\frac{E}{\rho_p}}\left[\sqrt{\frac{81F_0}{\pi E}}\frac{1}{\pi 2R(1-\nu^2)}\right]^{1/3}$$

### 3.2. Experimental investigation

Elastic waves propagation in one–dimensional periodic chain was a subject of experimental investigation. The chain was composed of 30 stainless steel balls placed in tube as shown in Figure 9 and the tube was made of PCV–U in order to attenuate waves in transverse direction. PCV–U tube was inserted into a steel pipe to prevent the chain from deflection. Geometric and material properties are summarized in Table 1.

Acoustic waves were excited by a piezoelectric transducer made of two layers of plate actuator Noliac NAC2024

**Table 1: Geometric and material properties of the ball**

| | |
|---|---|
| Diameter | $D = 9.525\ mm$ |
| Young's Modul | $E = 195.5\ GPa$ |
| Density | $\rho = 8100\ kg/m^3$ |
| Poisson's ratio | $\nu = 0.33$ |

**Table 2: Properties of the piezoelectric actuator**

| | |
|---|---|
| Length | 3 mm |
| Width | 3 mm |
| Height | 2 mm |
| Max voltage | 200 V |
| Free stroke | 1.9 $\mu$m |
| Blocking force | 290 N |
| Stiffness $C_T$ | 161 $[N/\mu m]$ |
| Material | NCE46 |

(Table 2). As an excitation signal was chosen 10-cycle tone burst with the carrier frequency equal to 18 kHz (Fig. 5).

The particles velocity on the end of the structure were measured by means of Scanning Doppler Laser Vibrometer in function of two parameters, *i.e.* initial compression force $F_0$ and operating voltage $\Phi$ of the piezoelectric transducer. Amplitudes of the measured signals are shown in Figure 6.

### 3.3. Time of flight determination

Double-peak terchnique [14] was used to estimate the time of flight of propagated waves. The time difference between onset–time of the signal of actuator and sensor is just the time-delay estimation. While onset–time was assumed as a temporal means between the appropriate maxima and minima of the signals (Fig. 7). As the length of chains in the equilibrium state is well known it is easy to calculate the phase velocity of propagated wave.

## 4. Conclusions

Recent investigations confirm that sound focusing is possible and sound bullet can be achieved in desired location

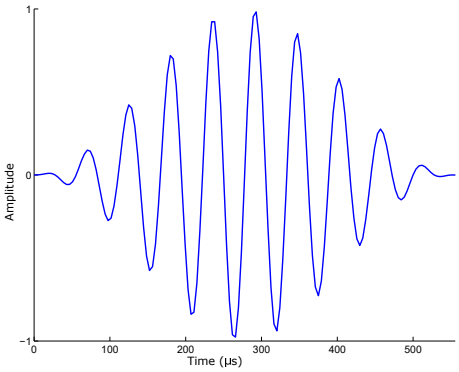



Figure 5: Excitation signal

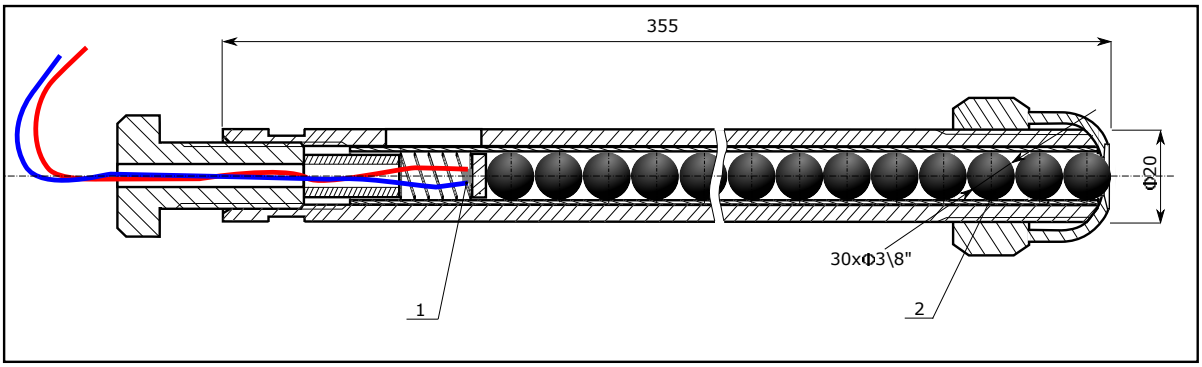



Figure 9: Chain of periodic balls: 1) piezoelectric transducer, 2) balls

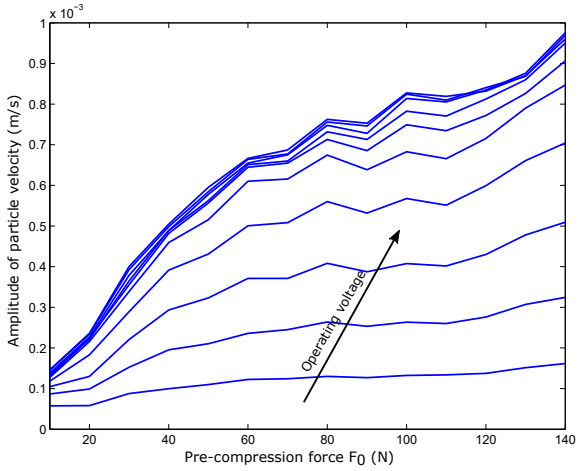



Figure 6: Amplitude of particle velocity of the last ball

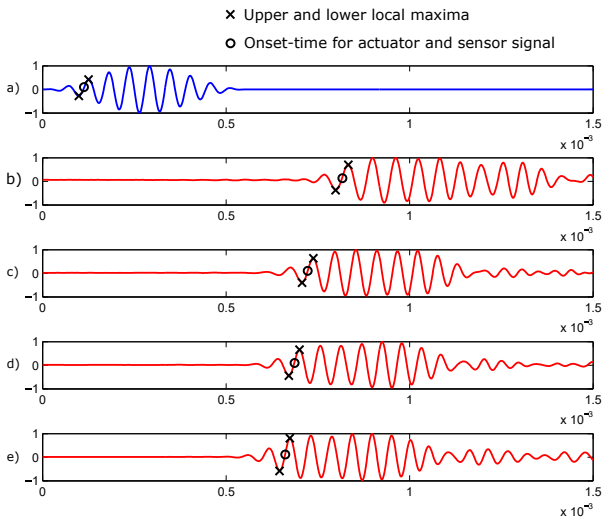



Figure 7: Time delay, a) actuator signal, b), c), d) and e) sensor signal for different value of pre–compression force $F_0$: 20, 60, 100, 140 [N], respectively

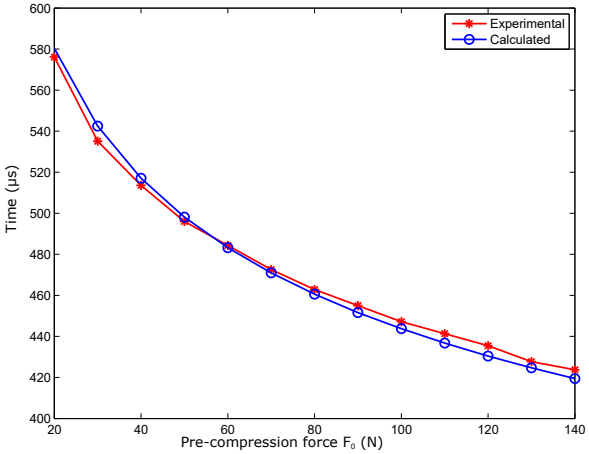



Figure 8: Time of flight

by controlling the time delay of wave excitation. Application of non-linear acoustic lens in the proposed form provides certain abilities to control sound speed by application of pre-compression force. However, better focusing control can be achieved by hardware-based manipulation of time delay in piezoelectric transducers used for wave excitation. Hence, new waveform generator with separate signal amplification capabilities at each channel will be developed and used in further investigations.

## Acknowledgement

The research was funded by the Polish National Science Center under grant agreement no DEC–2013/10/A/ST8/00071 in the frame of MAESTRO project entitled: Excitation and control of mechanical waves in nonlinear media.

## References

[1] Y–H. Hsiao, S–J. Kuo, H–D. Tsai, M–C. Chou, G–P. Yeh, Clinical application of High–intensity Focused Ultrasound in cancer therapy, *Journal of cancer* 7(3): 225-231, 2016

[2] F. Aoun, M. Zanaty, A. Peltier and R. van. Velthoven *Focal High Intensity Focused Ultrasound for Prostate*

*Cancer, Updates on Cancer Treatment*, Edited by L.B.A. Rangel and I.V. Silva, InTech, 2015

[3] A. Magara, R. Bühler , D. Moser, M. Kowalski, P. Pourtehrani, D. Jeanmonod First experiment with MR–guided focused ultrasound in the treatment of Parkinson's disease, *Journal of Therapeutic Ultrasound 2:11, 2014*

[4] M.J. Buckingham, B.V. Berkhout, S.A.L. Glegg, Imaging the ocean with ambient noise *Nature*, 356: 327-329, 1992

[5] J. Kushibiki, N. Chubachi Material Characterization by line–focus–beam acoustic microscope, *IEEE Transaction on Sonics and Ultrasonics* 32(2): 189-212, 1985

[6] G.T. Clement, J. Sun, T. Giesecke, K. Hynynen, A hemisphere array for non-invasive ultrasound brain therapy and surgery, *Physics in Medicine and Biology* 45, 3707–3719. 2000

[7] M. Fink Time reversal of ultrasonic fields—Part I: Basic principles, *IEEE Transactions on Ultrasonic, Ferroelectrics and Frequency Control* 39(5): 555–565, 1992

[8] A. Håkansson, J. Sánchez–Dehesa, L. Sanchis Acoustic lens design by genetic algorithms, *Physical Review B* 70. 214302, 2004,

[9] J.T. Welter, S. Sathish, D.E. Christensen, P.G. Brodrick, J.D. Heebl, M.R. Cherry, Focusing of longitudinal ultrasonic waves in air with an aperiodic flat lens, *Journal of the Acoustical Society of America* 130(5): 2789–2796, 2011

[10] A. Spadoni, C. Daraio, Generation and control of sound bullets with a nonlinear acoustic lens, *Proc. Natl. Acad. Sci. U.S.A.*, 107(16): 7230–7234, 2010.

[11] C.M. Donahue, P.W.J. Anzel, L. Bonanomi, T.A. Keller, C. Daraio, Experimental realization of a nonlinear acoustic lens with a tunable focus, *Applied Physics*, 104(1), 2014.

[12] C. Daraio, V.F. Nesterenko, E.B. Herbold, S. Jin, Tunability of solitary wave properties in one dimensional strongly nonlinear phononic crystals, *Physical Review E*, 73(2):26610, 2006.

[13] V.F. Nesterenko, *Dynamics of Heterogeneous Materials*, Springer–Verlag, New York, 2001.

[14] J. Moll, C. Heftrich, C–P. Fritzen Time–varying inverse filtering of narrowband ultrasonic signals, *Structural Heal Monitoring* 10(4): 403–415, 2010